ICCM24

24TH INTERNATIONAL CONFERENCE ON COMPOSITE MATERIALS

AUGUST 4-8, 2025

BALTIMORE CONVENTION CENTER

BALTIMORE, MARYLAND, USA

CONFERENCE
PROGRAM



Bristol UK: A world-leading hub for composites research and innovation

Partner

The Bristol Composites Institute (BCI) and NCC work in tandem to deliver cutting-edge research and innovation with demonstrable industrial impact.

Collaborate

Academic research at the Bristol Composites Institute benefits from industry partnerships, and generates new science and technology around novel material concepts, structural design and manufacturing of composites.

Innovate

NCC bridges the gap between academia and industry, helping companies of all sizes to capitalise on cutting-edge innovations to deliver more - at every stage of their journey and across the entire product lifecycle.



Visit stand 208

Email composites-institute@bristol.ac.uk

www.nccuk.com/ncc-and-bci

Welcome to ICCM24

The University of Delaware Center for Composite Materials (CCM) is pleased to host ICCM 24 as part of our 50th anniversary celebrations. This exciting conference is being held at the Baltimore Convention Center next to the Inner Harbor with its stunning waterfront views and is rimmed with spectacular museums. The conference features a dedicated industry track, international networking opportunities and cutting-edge research and insights.

CCM, based in nearby Newark, Delaware, has been a global leader in composites research for five decades. From our inception, we've pushed the boundaries and set the standard for advanced capabilities that have shaped the composites landscape.

We welcome you to Baltimore — a city renowned for its rich cultural and historical heritage and a strong manufacturing base. In the latter half of the 20th century, the defense industry began to expand its presence in and around Baltimore. New opportunities for advanced manufacturing and information technology have emerged here in the 21st century.

Today, Baltimore is known to be a diverse community with a lively arts and culture scene, historical landmarks, museums and attractions. Known for its skilled workforce, Baltimore leverages its strengths in advanced manufacturing and biotechnology to build a better future.

In addition to the conference, welcome reception, and banquet, we hope that you'll have time to celebrate our 50th anniversary at a social event on Wednesday, August 6 at the Power Plant Live! Baltimore Inner Harbor.

Along with my co-chair, Professor Erik Thostenson, I look forward to greeting you in Baltimore to participate in ICCM 24.



CONFERENCE CHAIR

Suresh Advani

Unidel Pierre S. du Pont Chair of Engineering
Professor, Mechanical Engineering and
Center for Composite Materials
University of Delaware



CONFERENCE CO-CHAIR

Erik Thostenson

Professor, Mechanical Engineering and
Center for Composite Materials
Joint Faculty, Materials Science and Engineering
University of Delaware

Table of Contents

Venue Overview 5
General Information 6
Social Events 8
Sponsor Recognition 10
Exhibition 11
Committees 12-13
Scientific Program
- Monday 16-21
- Tuesday 22-27
- Wednesday 28-33
- Thursday 34-39
- Friday 40-43

Poster Session 44-47
Mini-Oral Schedule 48-49

STAY CONNECTED

WITH THE ICCM24 APP

GET THE MOST OUT OF YOUR CONFERENCE EXPERIENCE

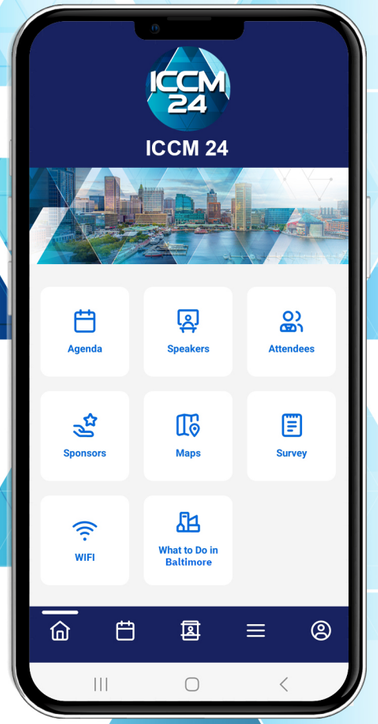

ARCTOS EVENTS – CONFERENCE APP

DOWNLOAD

Available on the App Store

GET IT ON Google Play

To access the conference app, search for **ARCTOS EVENTS - CONFERENCE APP** in the App Store or Play Store and download to your smartphone. After Install, you will be prompted to create an account. **ATTENDEES MUST USE THE EMAIL ADDRESS THEY REGISTERED WITH TO CREATE THE ACCOUNT IN ORDER TO RECEIVE VERIFICATION CODE AND GAIN ACCESS INTO THE APP AND ITS CONTENTS.**

Search for **ICCM 24** and you'll have access to all the app has to offer.

The entire conference is in the palm of your hand. Set-up your unique profile, build your own personalized agenda, connect with your colleagues, visit conference exhibitors, view speaker bios, and find your next session with venue maps.

DOWNLOAD THE CONFERENCE APP FOR THE COMPLETE CONFERENCE EXPERIENCE.

Venue Overview

Baltimore Convention Center

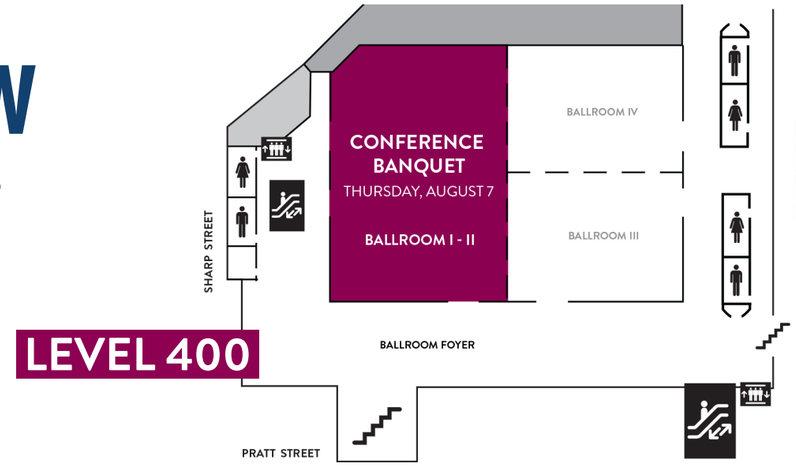

PARALLEL SESSION ROOMS

KEYNOTE, TECHNICAL, MINI ORALS

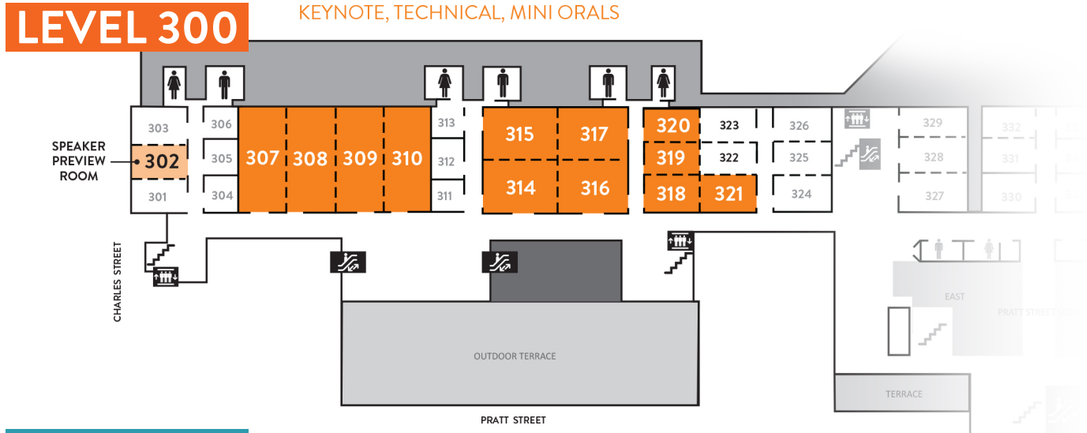

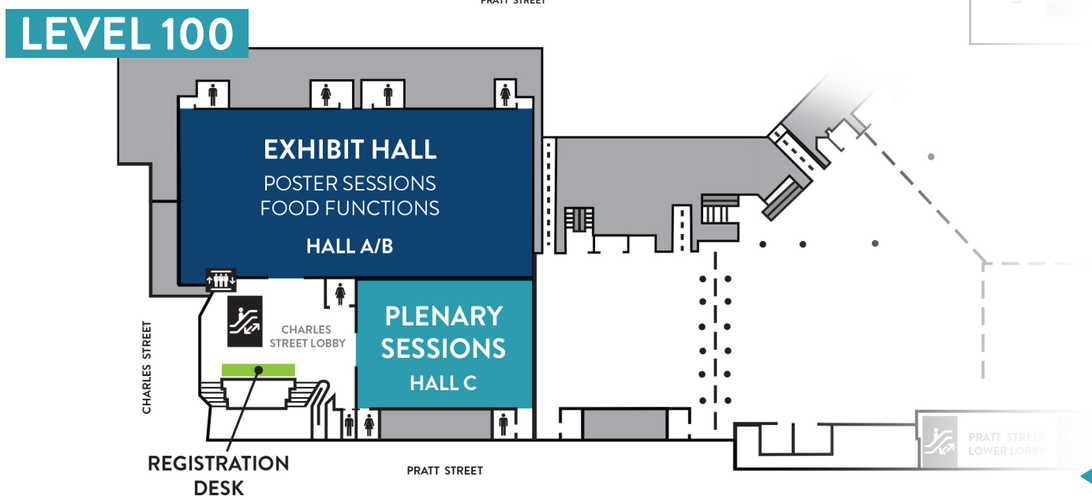

General Information

REGISTRATION

Please ensure you collect your Conference Badge from the Registration Desk located in the Charles Street Lobby, Level 100 of the Baltimore Convention Center.

You are required to wear your Conference Badge at all times. The registration desk will be open during the following times:

Sunday, August 3:	2:00 PM - 6:00 PM
Monday, August 4:	7:30 AM - 6:00 PM
Tuesday, August 5:	7:00 AM - 5:30 PM
Wednesday, August 6:	7:00 AM - 6:00 PM
Thursday, August 7:	7:00 AM - 5:30 PM
Friday, August 8:	7:00 AM - 12:30 PM

EXHIBIT HALL HOURS

The ICCM24 Exhibit Hall is located on Level 100 in Hall A/B. Food functions and Poster Sessions will be held inside the Exhibit Hall.

The Exhibit Hall will be open during the following times:

Monday, August 4:	7:30 AM - 4:30 PM
Tuesday, August 5:	7:00 AM - 5:30 PM
Wednesday, August 6:	7:00 AM - 4:30 PM
Thursday, August 7:	7:00 AM - 5:30 PM
Friday, August 8:	7:00 AM - 11:00 AM

SPEAKER PREVIEW ROOM

For the program to run efficiently presentations will be preloaded on each session's laptop daily. Due to time constraints and to respect your fellow speakers, the use of individual laptops is prohibited.

The speaker preview room will provide you with a means of uploading the most up-to-date version of your presentation. You must stop by the Speaker Preview room at least one (1) day prior of your speaking session to make any necessary changes. The Speaker Preview Room will be located on Level 300 in room 302, staffed by AV technicians, and open during the following times:

Sunday, August 3:	2:00 PM – 6:00 PM
Monday, August 4:	7:30 AM – 4:30 PM
Tuesday, August 5:	7:30 AM – 4:30 PM
Wednesday, August 6:	7:30 AM – 4:30 PM
Thursday, August 7:	7:30 AM – 4:30 PM

WIFI

WIFI access is complimentary through the Baltimore Convention Center with no password required.

EMERGENCY / FIRST AID

In an emergency, dial 911 for fire, police, and ambulance. The nearest local Hospitals with After Hour care are:

University of Maryland Medical Center
Address: 22 S Greene St, Baltimore, MD 21201
Phone: (410) 328-8667

Mercy Medical Center Emergency Department
Address: 301 Saint Paul St, Baltimore, MD 21202
Phone: (410) 332-9477

University of Maryland Medical Center Midtown Campus
Address: 827 Linden Ave, Baltimore, MD 21201
Phone: (410) 225-8000

The Johns Hopkins Hospital Emergency Room
Address: 1800 Orleans St, Baltimore, MD 21287
Phone: (410) 955-5000

LANGUAGE

The official language of the 24th International Conference on Composite Materials is English.

PROCEEDINGS

All accepted presentations will be included in the official ICCM proceedings. The proceedings will be available to registered ICCM24 attendees via the official website.

INSURANCE

The 24th International Conference on Composite Materials is unable to accept responsibility for accidents or damage to the private property of participants. Please ensure that you do not leave portable and valuable pieces of equipment unattended anywhere, and that you make your own arrangements for health, travel, general and other insurance.

ACM | Australian Composites Manufacturing CRC

ENABLING COMPOSITES MANUFACTURING R&D TO MEET AUSTRALIA'S NATIONAL SELF-SUFFICIENCY PRIORITIES

10 YEARS CRC Funding Term

30+ PARTNERS Industry, Research and Government

4 PROGRAMS Composite material design to product realisation

acmcrc.com

Meet Scientia Professor Ganga Prusty at ICCM24 to learn more about ACM CRC!



Scientia Professor Gangadhara Prusty

Director, ARC Training Centre for Automated Manufacture of Advanced Composites (AMAC)
The University of New South Wales (UNSW)
Mechanical & Manufacturing Engineering

Scan the code to meet up with Scientia Professor Prusty at ICCM24

Australian Government
Department of Industry, Science and Resources

Cooperative Research Centres Program

Social Events

A ticket is required to attend each event.

WELCOME RECEPTION

Monday, August 4 - 7:00 PM - 9:00 PM

National Aquarium
501 E. Pratt St. Baltimore, MD 21202



GRAD STUDENT EVENT

Tuesday, August 5 - 7:00 PM

Luckie's Tavern at Power Plant Live!
34 Market Place, Baltimore, MD 21202



CCM 50TH ANNIVERSARY CELEBRATION

Wednesday, August 6 - 7:00 PM - 10:00 PM

Angels Rock Bar at Power Plant Live!
10 Market Pl, Baltimore, MD 21202

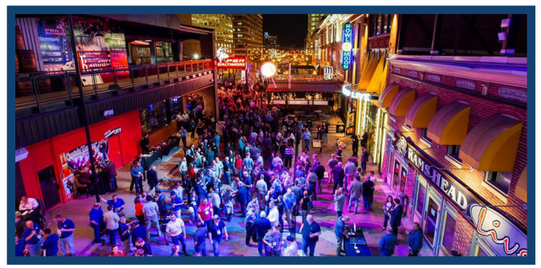

CONFERENCE BANQUET

Thursday, August 7 - 7:00 PM - 10:00 PM

Ballroom 1 - Level 400
Baltimore Convention Center



TOUR OF UD-CCM

Friday, August 8 - 2:15 PM - 4:15 PM

Center for Composite Materials
University of Delaware
Bus departs at 12:45 PM
Bus departs UD-CCM for return at 4:15 PM

LEADERS IN ADVANCED COMPOSITE MATERIALS

High-Performance Materials Institute
Department of Industrial & Manufacturing Engineering

Innovation + research for:

- Aerospace composites & high-performance nanomaterials
- Advanced manufacturing and sensors
- Artificial intelligence/machine learning for engineering, transportation & health care applications
- Data science-driven materials research & manufacturing

Learn more about HPMI and the joint college for research + advanced degrees at:

famufsu.engineer

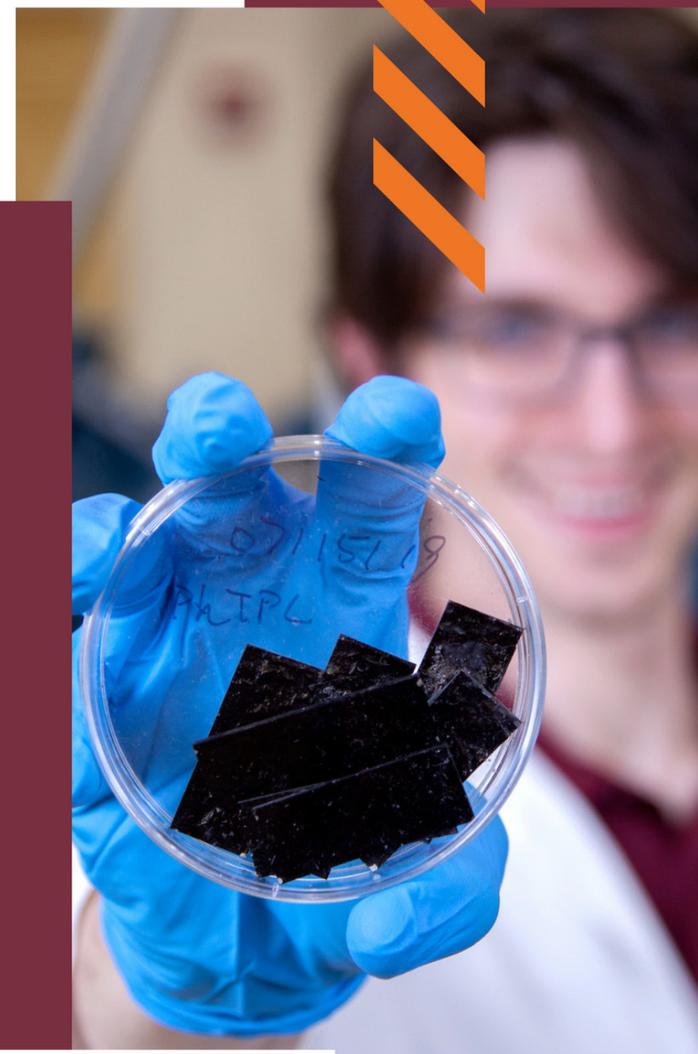

FAMU-FSU College of Engineering

The Joint College of Engineering for Florida A&M University and Florida State University

FAMU FSU

Sponsor Recognition

GOLD SPONSORS

University of BRISTOL

Bristol Composites Institute

NCC

Visit Booth 208

LANYARD SPONSOR

Anton Paar

Visit Booth 606

ADVERTISEMENT SPONSORS

ACM Australian Composites Manufacturing CRC

FAMU-FSU College of Engineering

Visit Booth 104

INSTRON®

Exhibition

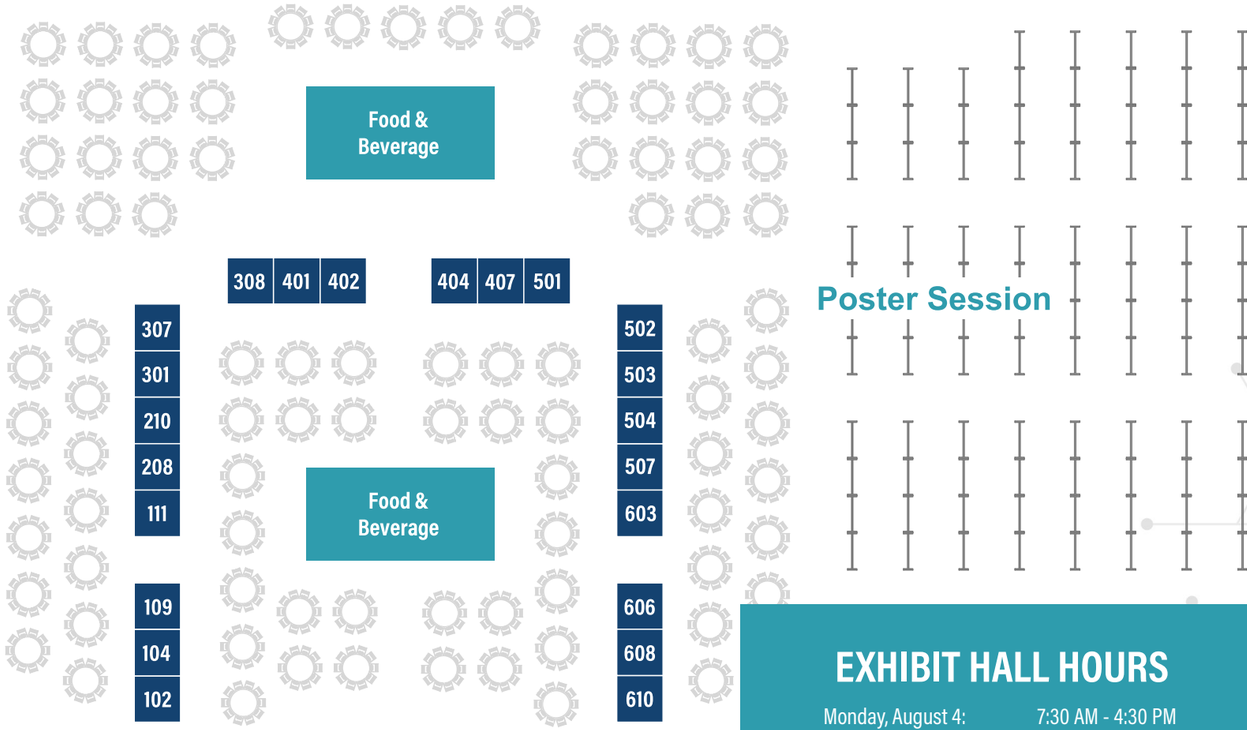

EXHIBIT HALL HOURS

Monday, August 4:	7:30 AM - 4:30 PM
Tuesday, August 5:	7:00 AM - 5:30 PM
Wednesday, August 6:	7:00 AM - 4:30 PM
Thursday, August 7:	7:00 AM - 5:30 PM
Friday, August 8:	7:00 AM - 11:00 AM

LIST OF EXHIBITORS

Accudyne Systems Inc	404
Anton Paar	606
CarbonForm Inc	308
Composites Knowledge Network	210
CTherm Technologies Ltd	608
ENERCOMP	402
Evonik Corporation	307
FAMU-FSU College of Engineering	104
IACMI The Composites Institute	109
ICCM26 - France Candidacy	504
Kai Scissors	501
MatchID US Inc	503
Math2Market	507
MDPI AG	603
Nexx Technologies	401
Shimadzu Scientific Instruments Inc	301
Specialty Materials	102
STEP Lab	407
TA Instruments	502
UD Center for Composite Materials	610
University of Bristol-Bristol Composites Institute	208
X-Sight	111

Committees

ICCM EXECUTIVE COUNCIL

- Pascal Hubert, Canada **President**
- Sayata Ghose, USA **Senior Vice President**
- Ole Thomsen, UK **Vice President, Region 1**
- Jinsong Leng, China **Vice President, Region 2**
- Martine Dubé, Canada **Vice President, Region 3**
- Woo-Il Lee, Korea **Immediate Past President**

Members

- Tomonaga Okabe, Japan
- Nancy Sottos, USA
- Bronwyn Fox, Australia
- Isabelle Paris, Canada
- Chiara Bisagni, Italy
- Matthew Jevons, Germany
- Stefanie Feih, Australia
- Hua-Xin Peng, China
- Carlos Cimini, Brazil
- Yentl Swolfs, Belgium
- Silvestre Pinho, UK
- Brian Falzon, Australia
- Conor McCarthy, Ireland

Honorary Members

- Anoush Poursartip, Canada
- Murray Scott, Australia
- Michael Wisnom, UK
- Paul Smith, UK
- Ozden Ochoa, USA
- Stephen Tsai, USA

INTERNATIONAL ORGANIZING COMMITTEE

- Ana Yong, UK
- Baris Caglar, Netherlands
- Brian G. Falzon, Australia
- Chady Ghnatios, USA
- Christian Breite, Belgium
- Christophe Binetruy, France
- Claire Steggall-Murphy, USA
- David Anthony, UK
- Debes Bhattacharyya, New Zealand
- Emiliano Bilotti, UK
- Erik Thostenson, USA
- Francisco Chinesta, France
- Han Zhang, UK
- Maedeh Amirpour, New Zealand
- Mahoor Mehdikhani, Belgium
- Marino Quaresimin, Italy
- Nam Kyeun Kim, New Zealand
- Nilmini Dissanayake, UK
- Nuno Correia, UK
- Odila Coffi, Brazil
- Philippe Geubelle, USA
- Ramesh Talreja, USA
- Samit Roy, USA
- Shanmugam Kumar, UK
- Suresh Advani, USA
- Veronica Ambrogi, Italy
- Veronica Calado, Brazil

LOCAL COMMITTEE

- Suresh Advani, USA
- Erik Thostenson, USA
- Corinne Hamed, USA
- Joe Deitzel, USA
- John Gillespie, USA
- Navid Kermani, USA
- Sagar Doshi, USA
- Srikanth Pilla, USA
- Tom Cender, USA
- Sai Aditya Pradeep, USA
- Dae Han Sung, USA
- Alasahin, Seyda Naz, USA



UNIVERSITY OF DELAWARE

CENTER FOR COMPOSITE MATERIALS

Celebrating 50 Years

Honoring the Legacy of the University of Delaware Center for Composite Materials

Since its establishment in 1974, the University of Delaware's Center for Composite Materials (UD-CCM) has consistently positioned itself at the forefront of research, education, and technology transfer in the field of composite materials. As we commemorate our 50th anniversary, we take this opportunity to reflect upon a legacy characterized by pioneering innovation, interdisciplinary collaboration, and significant global impact.

UD-CCM is internationally recognized as a Center of Excellence and has been instrumental in advancing the science and engineering of composite materials. Through over five decades of groundbreaking research encompassing materials synthesis, multifunctional systems, processing science, mechanics and design, sensing and control, and software development, we have fundamentally shaped the future of composites across diverse industries.

Our mission is defined by three core objectives:

1. To conduct transformative research that bridges fundamental discovery and real-world application.
2. To educate and inspire the next generation of scientists and engineers through immersive, hands-on learning experiences.
3. To facilitate the transition of technology to industry, empowering over 350 companies with innovative solutions and skilled talent.

With more than 53,600 square feet of advanced facilities and an investment of over $30 million in equipment, UD-CCM continues to lead in AI-enabled composites, smart materials, and sustainable composite solutions. Our efforts are supported by a robust network of federal agencies, including the U.S. Army Research Laboratory, U.S. Air Force, Office of Naval Research, DARPA, NASA, the National Science Foundation, the United States Department of Agriculture, and the Department of Energy, as well as a diverse array of industrial partners.

As we celebrate this significant milestone during ICCM24, we extend our gratitude to the visionary faculty, students, researchers, staff, and partners who have contributed to this journey. From our foundational breakthroughs to contemporary technological advancements, UD-CCM remains steadfastly committed to "Pioneering Innovation Excellence," a guiding principle that will propel us into the next fifty years.

Enjoy an evening of celebration, networking, and reflection on five decades of innovation in composites. We look forward to celebrating with you!

Join us in Celebration

We invite all ICCM24 attendees to commemorate this historic occasion at the CCM 50th Anniversary Celebration Dinner.

Wednesday, August 6, 2025

7:00 PM

Power Plant Live!
Baltimore Inner Harbor

Scan QR code for tickets.
Attendee: $50
Student: $25 *(Student ID Required)*

INSTRON®

Proud sponsors of ICCM24



DYNAMIC & FATIGUE TESTING SYSTEMS

1 kN ⟷ 5 MN

Instron is a pioneer in the field of testing composite materials, and have been working closely with our customers and participating in ASTM and ISO standards committees to develop new testing methods since the beginning of this industry.

Scan the QR code to find out more!

Scientific Program

Time	Ex Hall C - Plenary	Room 307	Room 308	Room 309	Room 310	Room 314	Room 315
7:30 AM	**Registration Desk Open** *(closes at 6:00 PM - located in Charles Street Lobby, Level 100)*						
7:30 AM	**Continental Breakfast** *(until 8:30 AM - located in Exhibit Hall A/B Level 100)*						
7:30 AM	**Exhibit Hall Open** *(closes at 4:30 PM - located in Exhibit Hall A/B, Level 100)*						
8:30 AM	**Opening Ceremony**						
8:50 AM	**SCALA Lecture: Composite Manufacturing Comes Full Circle** Prof Nancy Sottos, *Swanlund Endowed Chair, Head of the Department of Materials Science and Engineering, University of Illinois Urbana-Champaign*						
9:35 AM	**Plenary Speaker: Sustainability Driven Composite Development** Prof Véronique Michaud, *École Polytechnique Fédérale de Lausanne (EPFL)*						
10:20 AM	**Refreshment Break** *(located in Exhibit Hall A/B, Level 100)*						
	Move to Level 300 for Parallel Keynotes and Technical Sessions						
10:50 AM - 11:20 AM		**Keynote Speakers** **What 3D Printing Can't Achieve: Rethinking Composites in Additive Manufacturing** Prof Kelvin Fu - University of Delaware	**Permeability of Porous Media - A Mathematical Complexity Spanning Multiple Length-Scales** Prof Krishna Pillai - University of Wisconsin-Milwaukee	**A Review of Frontal Polymerization with Consideration of Future Directions** Prof John Pojman - Louisiana State University	**Fatigue Damage Evolution in Glass-Epoxy Laminates with Stress Concentrations Experiments and Modelling** Prof Marino Quaresimin - University of Padova Management & Engineering		
		Manufacturing: Resin Transfer Molding 1	**Materials and Precursors**	**Physical and Structural Behavior**	**Multifunctional Composites**	**Additive Manufacturing**	**Fatigue and Damage Mechanics of Composites**
11:25 AM - 11:45 AM		**Simulating the Resin Transfer Molding Process with Graph Neural Networks** Mr Jimmy Jean - Delft University of Technology	**Prepreg Surface Morphology: A Key Factor in Minimizing Interfacial Air and Interlaminar Voids** Mr Jaewoong Kim - Korea Advanced Institute of Science Technology	**Determination of Mechanical Properties of Polyimide Silica Nanocomposite using Micromechanical Modeling** Dr Nithin Kaliyath Parambil - University of Delaware	**Multifunctional Thermally Responsive Hydrogels Integrating Silver Nanoparticles and Herbal Medicines for Enhanced Diabetic Wounds** Ms Phuong Le - Institute of Applied Materials Science	**Effect of Compaction Force on Fiber Volume Fraction and Voids in Additively Manufactured Continuous Carbon Fiber Thermoset Composites** Mr Shaharear Md Emtiaz - University of Delaware	**Characterization of Mixed-mode Fracture Toughness and Traction Separation Laws for Woven S2 Glass/ Epoxy Composites** Ms Ankita Bisht - University of Delaware
11:45 AM - 12:05 PM		**Numerical Analysis of Macrovoid Formation Process in a Single-layered Woven Fibre Bundle Confined Between Parallel Plates** Mr Masaki Inagawa - Tokyo University of Science	**Behaviour of High Fibre Volume Ratio Polymer Composites in Response to Laser Exposure** Mr George Holiday - National Composites Centre	**Microscale Simulation for Nonlinear Stress-Strain Behavior of Unidirectional Carbon Fiber Phenyl-Ethynyl Terminated Polyimide Triax Composites** Mr Tatsuya Kobayashi - Tokyo University of Agriculture Technology	**Simultaneous Electromechanical Testing of a Structural Battery** Prof Tong-Earn Tay - National University of Singapore	**Analysis of Void Size and Void Distribution in Continuously Fiber Reinforced Filaments for Additive Manufacturing** Mr Jan-Uwe Schmidt - German Aerospace Center	**Characterisation and Prediction of Failure in Injection Moulded Short Fibre Composites, From Coupons to Components** Dr Soraia Pimenta - Imperial College London
12:05 PM - 12:25 PM		**Qualitative and Quantitative Benchmarking Comparison of Resin Infusion Simulation Software** Mr Kieran Guoite - National Composites Centre	**Validation Method for Film-based Sensor for In-situ Monitoring of the Curing of Fibre-Reinforced Plastics Based on Raman Spectroscopy and DSC Analysis** Mr Christian Lauter - PHWT	**Prediction and Validation of Crush Behaviors in Advanced Glass Mat Thermoplastic Tubes Using Innovative Simulation Technology** Dr Geunsu Joo - Korea Institute of Materials Science		**In-situ Foaming in the Material Extrusion Process: Development of a Nozzle Concept** Mr Wilfried Liebig - Karlsruhe Institute of Technology	**Direct Approach for Experimental Determination of Mixed-Mode Cohesive Tractions of Composites with Large-Scale Fiber Bridging** Mr Ruben Erives Anchondo - Technical University of Denmark
12:25 PM - 1:20 PM	**Group Lunch** *(located in Exhibit Hall A/B, Level 100)*						

Room 316	Room 317	Room 318	Room 319	Room 320	Room 321	Time
Registration Desk Open *(closes at 6:00pm - located in Charles Street Lobby, Level 100)*						7:30 AM
Continental Breakfast *(until 8:30am - located in Exhibit Hall A/B, Level 100)*						7:30 AM
Exhibit Hall Open *(closes at 4:30pm - located in Exhibit Hall A/B, Level 100)*						7:30 AM
						8:30 AM
						8:50 AM
						9:35 AM
Refreshment Break *(located in Exhibit Hall A/B, Level 100)*						10:20 AM
Move to Level 300 for Parallel Keynotes and Technical Sessions						
						10:50 AM - 11:20 AM
Aerospace Structures		**Frontal Polymerization**	**Computed Tomography**	**Permeability Measurement of Textiles**		
A Vibration Based SHM Model for Damage Detection and Monitoring in Curved Beam Aerostructures Dr Sindhu Bushpalli - Collins Aerospace Ireland		**A Mechanism-Based Reaction-Diffusion Model for Frontal Polymerization (FP) of Thermoset Polymers Towards Rapid Screening of New FP-Chemistries** Mr Donald Bistri - University of Illinois Urbana-Champaign	**Differences in Interfacial Damage Between Single, Double, and Multi-Fibre Composites Unravelled via In-situ Synchrotron Holo-Tomography** Mr Thanasis Chatziathanasiou - KU Leuven	**A Comparison of Various Methods for the Permeability Prediction of Textile-based Fiber Structures** Mr Patrick Nowakowski - Faserinstitut Bremen eV		11:25 AM - 11:45 AM
Efficient Failure Prediction Methodology for High Aspect Ratio Composite Wings with High Bend-Twist Coupling Mr Mario Miranda - Imperial College London		**Influence of Kinetic Models on the Simulation of Frontal Polymerization** Mr Ke Wang - Vrije Universiteit Brussel	**Unravelling Links Between Fibre Misalignment Resin-rich Pockets and the Fibre Break Development via In-Situ Holotomography** Miss Yeajin Lee - University of Southampton	**Characterisation of Heterogeneous Permeability in Liquid Composite Moulding Processes Using Stochastic Inversion and Neural Surrogates** Mr Andreas Endruweit - University of Nottingham		11:45 AM - 12:05 PM
		Controlled Frontal Polymerization and Direct Writing of Cyclooctadiene-Based Inks Dr Brandon Clarke - Harvard University	**Damage Evolution in Multilayer Braided Composite Tubes Under Torsion Studied by Time-Lapse X-ray Computed Tomography** Mr Dongze He - The University of Manchester	**In-plane Permeability of VARI Consumables: A Comparison of Experimental and Virtual Estimation Methods** Mr Ewald Fauster - Montanuniversitat Leoben		12:05 PM - 12:25 PM
Group Lunch *(located in Exhibit Hall A/B, Level 100)*						12:25 PM - 1:20 PM

Time	Ex Hall C - Plenary	Room 307	Room 308	Room 309	Room 310	Room 314	Room 315
1:20 PM	**Plenary Speaker: Toward Simpler Design and Manufacturing of Composite Laminates** Prof Daniel Melo, *Federal University of Rio Grande do Norte (UFRN)*						
Move to Level 300 for Parallel Keynotes and Technical Sessions							
2:10 PM - 2:40 PM		**Keynote Speakers**					
		Additive Manufacturing - Enabled Architected Cellular Composites Prof S. Kumar - University of Glasgow	**Toward Predictive Process Modeling of Polymer and Polymer-Derived Composites: Challenges and Emerging Approaches** Dr Marianna Maiaru - Columbia University	**Investigation of Particle Size Effect on the Fracture Behavior of Polymer-Graphene Nanocomposites via Crack Tip Shielding** Prof Samit Roy - University of Alabama	**Incorporating Nanostructures into Next Generation (sustainable) Fibres** Prof Milo Shaffer - Imperial College	**Energy Absorption Strategies for Occupant Protection Systems Using Cellular Materials and Smart Composites** Prof Norman Wereley - University of Maryland	
		Manufacturing: Forming 1	**Materials and Precursors**	**Physical and Structural Behavior**	**Multifunctional Composites**	**Additive Manufacturing**	**Fatigue and Damage Mechanics of Composites**
2:45 PM - 3:05 PM		**Induction Heating of Thermosetting CFRP Molds for Commingled PPGF Composite Forming** Ms Eunjung Kim - Korea Institute of Science & Technology	**Dual-surface Engineering of Carbon Fibers by Grafting Carbon Nanotubes and Chemical Functionalization** Mr Hassan Almousa - Imperial College London	**Model Fracture in Plainweave Glass Epoxy Composites Fracture Toughness Resistance Curve and Traction Separation Relationships** Mr Paul Dason Samuel - University of Delaware	**Self-healing of Structural Damage in Thermoplastic Composite Laminates via Incorporated Nano-engineered Heating Architecture** Mr Hyungmin Kim - KAIST	**A Magnetic Field Assisted Accelerated Composites Volumetric Manufacturing** Dr Hamed Yazdani Nezhad - University of Leeds	**Fatigue Limit of Unidirectional Fibre Composites - Comparison of Experimental Data from the Literature with Model Predictions** Mr Ashish Kumar Bangaru - DTU Wind & Energy Systems
3:05 PM - 3:25 PM		**Characterising the Interply Behaviour During Multi-ply Single Diaphragm Forming Process for Noncrimp Fabric Materials** Mr Yilong Li - University of Cambridge	**Electrospun Nanofibrous Interleaves for Improving the Permeability Resistance of Cryo-cycled Composite Laminates** Dr Othman Laban - The University of New South Wales	**Curvilinear Anisotropy for Notch Insensitive and Damage Tolerant Structures: An Analytical and Numerical Study** Dr Marco Salviato - University of Washington	**Externally Activated Self-healing in Structural Composites via Embedded Conductive Networks** Mr William Martin - North Carolina State University	**Microstructure Fiber Orientation Fiber Length and Porosity Control via Nozzle Design in Large-format Extrusion Process** Ms Brittany Rodriguez - Oak Ridge National Lab	**On and Off-axis Tension-compression and Self-heating Behavior of a Woven Carbon-fiber Reinforced Polymer Composite up to the Very High Cycle Fatigue** Mr Aravind Premanand - Albert Ludwigs University Freiburg
3:25 PM - 3:45 PM		**Thermoforming of Load-path-optimised Recycled Thermoplastic Composites Development of an AI-supported Emitter Technology and Process Evaluation** Mr Matthias Froning - Institut für Textiltechnik Augsburg gGmbH	**Graphene Coated Natural Fiber Composites for Marine Applications** Dr Marie Jonsson - Linköping University	**Influence of Consolidation Pressure on Tensile Strength of UHMWPE Composites** Mr Molla Ali - University of Delaware	**Autonomous Self-healing and Self-sensing in an Optovascular Structural Thermoset** Mr Zachary Phillips - NC State University		**Investigation of Thermomechanical Behaviour of Composites Under Vibration Fatigue Testing** Mr Friso Oude Tanke - University of Twente
3:45 PM - 4:10 PM	**Refreshment Break** *(located in Exhibit Hall A/B, Level 100)*						

MONDAY, AUGUST 4

Room 316	Room 317	Room 318	Room 319	Room 320	Room 321	Time
						1:20 PM
Move to Level 300 for Parallel Keynotes and Technical Sessions						
						2:10 PM - 2:40 PM
Aerospace Structures		**Frontal Polymerization**	**Computed Tomography**	**Permeability Measurement of Textiles**		
Structural Integrity of Loadcarrying H2 Pressure Tanks for Small Aircraft Ms Nicole Motsch-Eichmann - Leibniz Institut für Verbundwerkstoffe		**Out-of-autoclave Manufacturing of Thermoset Composites using Frontal Polymerization: An Overview** Prof Philippe Geubelle - University of Illinois Urbana-Champaign	**3D Observation of Delamination in Carbon Fibre-reinforced Composites Under Remote Mode II Loading Through In-situ Computed Tomography** Ms Panayiotis Tsokanas - KU Leuven	**Permeability Modeling for BD Fabric** Mr Mayur Godbole - Auburn University		2:45 PM - 3:05 PM
A Doublewall CFPR Hydrogen Storage and Distribution System as a Structural Component in Aircraft Applications Ms Nithya Sindhe Narayana Rao - Leibniz Institut für Verbundwerkstoffe GmbH IVW		**Internal Stresses in Vacuum-Infused Composite Plates Manufactured by Frontal Polymerization** Mr Clement Broggi - TU Delft	**High-speed X-ray Multi-Projection and Ultra High-Speed Radiography Imaging to Capture Transverse Cracking in Glass Fibre-Reinforced Composites** Dr Christian Breite - KU Leuven	**A Practical Approach to Uncertainty and Validation of Process Simulation for LCM Manufacture** Dr Ana Yong - NPL		3:05 PM - 3:25 PM
Pi-Preform Joint Revolutionary Improvement for Bonded Composite Structures Dr Felix Nguyen - Lockheed Martin Co		**Curing Time-Energy Optimization of Frontal Polymerization of Fiber-Reinforced Polymer Composites** Mr Sanghun Shin - University of Illinois Urbana-Champaign	**In-situ Synchrotron X-ray Microtomography of Void Evolutions During Nanoporous Network-Enabled Out-of-Autoclave Manufacturing of Aerospace-Grade Woven** Dr Jingyao Dai - University of Oklahoma			3:25 PM - 3:45 PM
Refreshment Break *(located in Exhibit Hall A/B, Level 100)*						3:45 PM - 4:10 PM

Time	Ex Hall C - Plenary	Room 307	Room 308	Room 309	Room 310	Room 314	Room 315
	Tsai Award Symposium	Manufacturing: Modeling and Applications	Materials and Precursors	Physical and Structural Behavior	Multifunctional Composites	Additive Manufacturing	Fatigue and Damage Mechanics of Composites
4:10 PM - 4:30 PM	**Experimental and Numerical Compression Analysis of 3D X-ray CT Scanned Uni-Directional Pultruded Carbon Fiber Composites** Ms Pinelopi Mageira - Technical University of Denmark	**Modeling the Impact of Void Distribution on Mechanical Properties of Short Fiber Recycled CFRTP Integration of Experimental Analysis and Finite Element Analysis** Mr Takumi Morishima - The University of Tokyo	**Electron-Beam and Gamma-Ray Radiation Treatments to Achieve High Strength in Carbon Nanotube Laminates** Mr Cecil Evers - Florida State University HPMI	**Orthotropic Impact Response of Unidirectional Glass/Epoxy Composites: A Yarn-Level Finite Element Analysis** Dr Shubham Shubham - Indian Institute of Technology Bombay	**Multifunctional Graphene-based Nanocomposites with Synergistic Effects of Chemical and Physical Interactions** Dr Seira Morimune-Moriya - Chubu University	**Additive Manufacturing Process for Fabricating Complex and Dynamic Poss-based 4D Structures** Ms Nicole Gorohovsky - Tel Aviv University	**The Discrete Model for Composites DM4C Mesoscale Modeling of Composites Via Physics-Based Discrete Mathematical Models of Fibers and Matrix** Dr Marco Salviato - University of Washington
4:30 PM - 4:50 PM	**Partially Carbonised Carbon Fibres as an Improved Multifunctional Structural Battery Electrode** Mr Ruben Tavano - Chalmers University of Technology	**High Resolution Induction Sensing for Feature Detection in Thin-Ply Carbon Fiber Reinforced Polymer** Mr Ehshan ul-Haq - Delft University of Technology	**Plasma-Treated PET Nanofibers Veils a Novel Interface Enhancement for Cryogenic Composite Applications** Mr Jeho Jin - Korea Advanced Institute of Science & Technology	**Testing and Progressive Failure Modelling of a Wind Turbine Blade Spar Capweb Joint Substructure** Dr Tobias Laux - University of Bristol	**Soft Composites for Charge Transport and Storage to Synergistically Enhance Energy Harvesting Performance of Triboelectric Generators** Miss Ziyan Gao - University of New South Wales	**Predicting and Optimizing FDM Print Performances: An AI Approach to Mechanical Property Optimization** Mr Marcello Laurenti - Sapienza	**Fatigue Simulation of Laminated Composites Under Mixed Mode Cyclic Loading Using a Damage-Mechanics-Based Fatigue Accumulation Model** Mr Rong-Can Hong - The University of Tokyo
4:50 PM - 5:10 PM	**Moisture Effects on Impact Strength and Recovery in Carbon Fiber Reinforced Vitrimers** Mr Jun Young Choi - Seoul National University	**Viscoelastic Biscale Modeling of Process-Induced Deformation in Noncrimp Fabric Composite** Ms Sera Koo - Tohoku University	**Multifunctional Carbon Nanotube-Based Composite Carbon Fibers for Enhanced Mechanical Properties** Dr Bon-Cheol Ku - Korea Institute of Science & Technology KIST	**Improving the Computational Efficiency of Impact Simulations on Woven FRP Composite Plates** Mr Jakov Ratkovic - University of Zagreb FAMENA	**Designing Novel Composite Structural Supercapacitors with Discrete Carbon Nanotube Electrodes and Polymer Electrolyte Separator Membranes** Dr Alex Harman - Defence Science & Technology Group	**Model Order Reduction Methods for Real-Time Prediction of Thermomechanical Properties of Additively Manufactured Composite Structures** Mr Pablo Castello Pedrero - Universitat Politicnica de Valencia	**Progressive Damage Behavior of Plain-Woven CFRP under Tensile-tensile Cyclic Loading** Mr Chihaya Hoshikawa - Nagoya University
5:10 PM - 5:30 PM	**A Structure-Integrated Nanocomposite Sensor System Capable of Simultaneous Measurement of Omnidirectional Strain and Temperature** Mr Sumin Lee - Korea Advanced Institute of Science & Technology	**Damage Tolerant Graphene-Metal Nanocomposite Thin Films by Chemical Vapor Deposition Synthesis** Dr Kaihao Zhang - The Hong Kong University of Science & Technology	**Unravelling the Effect of the Addition of a New Carbon Allotrope in Polymeric Composites: Investigation of Electrical Properties** Miss Silvia Zecchi - Politecnico di Torino	**Towards an Accelerated Nonlinear Solution Method Inspired by Multiscale and Multigrid Methods** Dr Ryan Whitehead - Bluehalo	**Polymer Nanocomposite Triboelectric Nanogenerators for Antimicrobial and Electrical Stimulation Platforms** Prof Yong Tae Park - Myongji University	**One Go Approach on Developing Topologically Interlocked Materials TIMs Via Fused Filament Fabrication Process** Dr Sabarinatham Palaniyappan - King Fahd University of Petroleum Minerals	**Strength Evaluation of Twill Woven CFRP Laminated Structure, Considering Knee Point** Dr Masataka Kawaguchi - Doshisha University
5:30 PM - 5:50 PM	**Prepreg Development for Rapid On-Orbit Composites Manufacturing via Frontal Curing** Mr Tyler Price - University of Illinois Urbana Champaign	**Insights from a Manufacturer Dedicated to Expanding the Role of Structural Composites in Commercial and Residential Construction** Dr Richard Rydin - Building Composites LLC	**Optimizing Hierarchical Carbon Nanotube-Grafted Carbon Fiber Production** Dr David Anthony - Imperial College London	**Strip Buckling Analysis to Predict Skin-Stiffener Debonding in Postbuckled Panels** Prof Richard Butler - University of Bath	**Wearable Body Temperature Sensing with Autonomous Self-Regulated Joule Heating and Passive Cooling for Healthcare Applications** Mr Hongxu Guo - Loughborough University	**Feasibility Study of a 3D-printed Honeycomb Core Structure as Thermal Vacuum Insulation for Liquid Hydrogen Composite Pressure Vessels** Mr Andreas Scherer - University of the Bundeswehr Munich	**High Temperature Fatigue Performance Evaluation of Fibre-Reinforced Polymer (FRP) Composites Utilizing Monotonic and Dynamic Mechanical Analysis** Dr Shoab Ahmed Chowdhury - TA Instruments
5:50 PM - 6:10 PM	**Surrogate Model-driven Automation for RVE Design and Validation of Long Discontinuous Carbon Fiber Composite Structures** Mr Akshay Zaveri - University of Connecticut	**Optimization of Processing Conditions for UHMWPE Composites in Body Armor Applications** Mr Alex Vanarelli - University of Delaware		**Influence of the Fiber Curvature on the Mechanical Properties of Long Fiber Reinforced Composites** Ms Celine Lauff - Karlsruhe Institute of Technology		**Effects of 3D Printing Orientation and Infill Patterns on the Impact Strength and Fracture Behavior of PLA-CFRP Hybrid Structures for Robotics** Mr Cheonghwa Lee - University of Connecticut	**Mechanical Characterization of MWCNT Based BFRP Composite by using the Mode I and Mode II** Dr Kalyan Singh - Indian Institute of Technology ISM Dhanbad
7:00 PM - 9:00 PM	**Welcome Reception** - *National Aquarium*						

Room 316	Room 317	Room 318	Room 319	Room 320	Room 321	Time
Aerospace Structures	AI Empowered Paradigm	Frontal Polymerization	Computed Tomography	Permeability Measurement of Textiles	Self Healing	
Analysis of the Mechanical Behaviour of CFRP Bosses in Composite Pressure Vessels Considering Different Stiffness Distributions Mr Gerrit Rehs - University of the Bundeswehr Munich	**Semantic Interoperable Data Model and Stochastic Multiscale Analysis of Short Fibre Composites** Dr Joerg Hohe - Fraunhofer-Institut fuer Werkstoffmechanik	**Multiphysics Modeling of Frontal Polymerization-Based Manufacturing of Woven Composites** Mr Michael Zakoworotny - University of Illinois Urbana-Champaign	**Deep Learning-Driven Segmentation of Resin-rich Areas in 3D CT Imaging of CFRTP-SMC** Mr Cheng Jin - The University of Tokyo	**Material Characterization for Particle-filled RTM in 3D Fibrous Preforms** Ms Leonie Marchand - GeM Lab	**Sustained Self-Sensing and Autonomous Self-healing via Electrothermal Coupling in Fiber-composites** Mr Jack Turicek - NCSU	4:10 PM - 4:30 PM
Improving Aeroelastic Performance of Hale Geometrically Nonlinear Flexible Wings Ms Najwa Zaqirah Binti Taufik - King Fahd University of Petroleum & Minerals	**A Data-Driven AI-Enabled Approach to Predict Crystal Morphology Evolution in Heterogeneous Semicrystalline Thermoplastic Composites** Mr Amit Makarand Deshpande - University of Delaware	**Energy-Efficient UV Curing of Non-Transparent Fibers in the VARI and RTM Process** Mr Jens Take - Universitut Stuttgart	**Prior Shape Analysis for Yarn Segmentation in XCT Images** Ms Hafsa El Herichi - Safran Group	**Can We Reliably Predict In-Plane and Out-of-Plane Permeability of a Reference Permeable Medium** Mr Andreas Endruweit - University of Nottingham	**Influence of the Addition of Thermoplastic Healing Agent to Epoxy Resin** Mrs Ana Paula Cysne Barbosa - Federal University of Rio Grande do Norte	4:30 PM - 4:50 PM
Ultrasonic Reconsolidation at 20 KHz: A Potential Repair Approach for Aerospace Composites Mr Balaji Ragupathi - University of Freiburg	**Graph Neural Networks for Effective Prediction of Mechanical Response in Composite Structures with Models using Unstructured Meshes** Mr Luca Patrignani - Imperial College London	**Buoyancy-Driven Convection in Adiabatic Horizontal Frontal Polymerization** Ms Laurence Rongy - Universite libre de Bruxelles ULB	**Robust Image Registration for Periodic Materials Application to 3D Woven Textiles** Mr Arturo Mendoza Quispe - Safran		**Self Healing Composites Influence of Self Healing Agent Fraction** Prof Maria Cioffi - UNESP	4:50 PM - 5:10 PM
Manufacturing Process for Large Space Structures and Supporting Long-Duration Human Space Mission Prof Susanna Laurenzi - Sapienza Universita di Roma	**AI-Based Generation of Simulation Models for Material Development from CT Data** Dr Oliver Rimmel - Math2Market GmbH	**Scaling Up the Efficient Manufacturing of Carbon Fiber Epoxy Composites Using Frontal Polymerization** Dr Yeqing Wang - Syracuse University	**Local and Global Strain and Defect Analysis of Discontinuous Glass Fiber Reinforced Polymers** Ms Julia Maurer - FHOOE Forschungs und Entwicklungs GmbH			5:10 PM - 5:30 PM
In-Situ Resource Utilization for Sustainable Space Exploration: 3D Printing PEKK-Space Regolith Composites Prof Mehdi Hojjati - Concordia University	**Hybrid 1D Convolutional Neural Network and Fuzzy Clustering for Damage Detection in Composite Plates Using Laser Ultrasonic Guided Waves** Mr Shain Azadi - Politecnico di Milano		**Mechanical Characterisation of Carbon Fibre-Reinforced Sheet Moulding Compounds and Introduction to X-ray In-situ Biaxial Testing of Composite Materials** Mr Salaheddine Madi - KU Leuven			5:30 PM - 5:50 PM
	A Bayesian Inference Approach for Estimating Heat Transfer Coefficients for Thermal Management in Composites Manufacturing Processes Prof Reza Vaziri - The University of British Columbia		**Fibre-Simulator: An Open-source Python Tool for Generating Fiber Phantoms** Ms Mary Chris Go - Universiteit Leiden			5:50 PM - 6:10 PM
Welcome Reception - *National Aquarium*						7:00 PM - 9:00 PM

Scientific Program

Time	Ex Hall C - Plenary	Room 307	Room 308	Room 309	Room 310	Room 314	Room 315
7:00 AM	**Registration Desk Open** *(closes at 5:30 PM - located in Charles Street Lobby, Level 100)*						
7:00 AM	**Continental Breakfast** *(until 8:00 AM - located in Exhibit Hall A/B, Level 100)*						
7:00 AM	**Exhibit Hall Open** *(closes at 5:30 PM - located in Exhibit Hall A/B, Level 100)*						
8:00 AM	**Welcome Remarks**						
8:05 AM	**Plenary Speaker: Composites Science and Technology Empowered by Physics Informed and Augmented Learning** Prof Francisco Chinesta, *Arts et Métiers Institute of Technology*						
Move to Level 300 for Parallel Keynotes and Technical Sessions							
9:00 AM - 9:30 AM		**Keynote Speakers** **Understanding Pore Formation in Reactive Acrylic Thermoplastic Resin Upon Polymerization** Dr Olivier De Almeida - Institute Clement Ader IMT Mines Albi	**Multiscale and Multiphysics Modelling and Characterisation of Structural Batteries** Prof Leif Asp - Chalmers University of Technology	**Thermoplastic Composites for Demanding Energy Environments: Solutions in Design and Challenges in Monitoring** Prof Gilles Lubineau - KAUST	**Shift the Paradigm of Composites Modeling Using Artificial Intelligence** Prof Wenbin Yu - Purdue University		
	Certification for Analysis Workshop	**Manufacturing: AFP/ATP 1**	**Materials and Precursors**	**Physical and Structural Behavior**	**Multifunctional Composites**	**AI Empowered Paradigm**	**Fatigue and Damage Mechanics of Composites**
9:35 AM - 9:55 AM	**9:35 AM - Welcome Remarks and Introductions** Prof Ole Thomsen - University of Bristol **9:45 AM - Integration of Multi-Scale Modeling, High-fidelity Experimentation and Bayesian Learning - Towards Certification by Analysis** Prof Richard Butler Dr Andrew Rhead - University of Bath **10:10 AM - Imaging Based Sub-Structure Testing and Data Fusion Methodologies for Integration of Virtual and Physical Data** Prof Janice Barton Prof Ole Thomsen - University of Bristol	**Investigation of the Mechanisms of Fuzzball Formation and Growth in Automated Fiber Placement AFP of Thermoset Composites** Mr Genki Matsubara - University of Washington	**Optimizing Oxidation Resistance of CC Composites with Multilayer SiC-Based Coatings for High Temperature Application** Mr Mosiur Rahaman - The University of Tulsa	**Simulation and Validation of Delamination Propagation and Migration in Composite Panels Subjected to Out-of-plane Bending** Miss Alice Pagnanini - KU Leuven	**Shape Memory Behaviour of Re-entrant Unit Cell Structure Based on 3D Printed Polyurethane Nanocomposites** Dr Yu Dong - Curtin University	**A Fast Uncertainty Quantification Method for Failure Prediction of Large Composite Structural Elements** Mr Mario Miranda - Imperial College London	**Effect of Cooling Rate on Mode II Fatigue Crack Growth Behavior in Carbon Fiber Reinforced Polyphenylene Sulfide** Dr Yu Zusho - The University of Tokyo
9:55 AM - 10:15 AM		**Enhancing Quality and Productivity in Automated Fiber Placement: Strategies for AFP Programming, In-process Inspection, and Process Optimization** Dr Jihua Chen - National Research Council Canada	**Biobased Composite Fibers and Films with Keratin from Chicken Feathers as Matrix and Calcium Carbonate as Nanoreinforcement Materials** Dr Yiqi Yang - University of Nebraska-Lincoln	**Effect of Clamping Force and Environmental Conditioning on the Mechanical Performance of Bolted Composite Laminates** Dr Neha Chandarana - University of Bristol	**Direct Ink Writing EM Radiator for Conformal Load Bearing Antenna Structure** Mr Jeaan Jeon - Inha University	**AI-Driven Method for Predicting Fibre Orientation in Composites** Mr Cesar Garcia-Gascon - Universitat Politecnica de Valencia	**Modified Curing Cycles and Accompanying Polymer and Adhesion Changes in Fiber Metal Laminates** Mr Andreas Baumann - Leibniz Institut für Verbundwerkstoffe GmbH
10:15 AM - 10:35 AM		**Smart Roller: An Essential Tool for Automated Fiber Placement** Mr Charles Picciotto - University of British Columbia	**Protein Based Bio-Composites from Cottonseed Meals Reinforced with Chitin-Nanoparticles** Miss Yuanyi Shao - University of Nebraska-Lincoln	**Numerical Simulation for Frequency Dependence of Fatigue Failure for Polymer and Polymer Composite** Dr Jun Koyanagi - Tokyo University of Science	**4D-printed Composite Structures for Space Applications Towards Multi-Axis Structural Shape-changing** Mr Julien Deschamps - Research Institute Dupuy De Lume	**Digital Twin Using Nested Machine Learning for Sintering Deformation of Ceramic Matrix Composites** Prof Jingzhe Pan - School Of Engineering University Of Leicester	**Conductive Superhydrophobic Coating on Gas Diffusion Layer for Enhanced Proton Exchange Membrane Fuel Cell Performance** Mr Myungjin Hong - Inha University
10:35 AM - 11:00 AM	**Refreshment Break** *(located in Exhibit Hall A/B, Level 100)*						

Room 316	Room 317	Room 318	Room 319	Room 320	Room 321	Time
Registration Desk Open *(closes at 5:30pm - located in Charles Street Lobby, Level 100)*						7:00 AM
Continental Breakfast *(until 8:00am - located in Exhibit Hall A/B, Level 100)*						7:00 AM
Exhibit Hall Open *(closes at 5:30pm - located in Exhibit Hall A/B, Level 100)*						7:00 AM
						8:00 AM
						8:05 AM
Move to Level 300 for Parallel Keynotes and Technical Sessions						
						9:00 AM - 9:30 AM
Thermoplastic Composites	**Frontal Polymerization**		**Computed Tomography**	**Design, Repair and Life Cycle**		
Modeling and Control of Exothermic Polymerization of an Acrylic Thermoplastic Resin in the Pultrusion Process Mr Farouk ZREIKA - IMT Mines Albi	**Optimization of Cationic Frontal Polymerization Experiments: An Analysis of Compositions Reproducibility and Materials** Mr Brecklyn Groce - Vrije Universiteit Brussel		**Alternative Reconstruction and Acquisition Techniques for Imaging Large CFRP Samples** Mr Ford Collins - University of Warwick	**Manufacturing Fiber Reinforced Recycled Pet Tapes: A Capillarity-Based Approach** Ms Elise Mathouillot - IMT Mines Ales		9:35 AM - 9:55 AM
Polymerization Induced Defects in Type IV Hydrogen Storage Tank Produced from Recyclable Liquid Thermoplastic Polymer and Carbon Fiber Dr Biltu Mahato - Luxembourg Institute of Science & Technology	**Photothermal Initiation of Frontal Polymerization for Additive Manufacturing of Discontinuous Fiber-Reinforced Thermoset Composites** Prof Mostafa Yourdkhani - Arizona State University		**Modeling the Folding and Stowing Behavior of Origami-Inspired Structures Based on the Real Composite Microstructure** Mr Israr Uddin - Khalifa University	**Reprocessing Thermoplastic Composite Trim Waste with High Temperature Compression Moulding** Dr Andi Haris - Singapore Institute of Mfg Technology		9:55 AM - 10:15 AM
Modelling Residual Stresses in Thick Section Thermoplastic Composites for Wind and Tidal Blades Ms Anastasia Tsavea - University of Sheffield			**Helical µCT Insights into Compaction Effects on Resin Distribution and Porosity in Thermo-Compressed Non-Crimp Polypropylene-glass Fiber Composites** Dr Abderrahmane AYADI - IMT Nord Europe	**Transforming Thermoplastic Waste through Manufacturing into Engineering Products** Mrs Shristi Ghosh - Georgia Institute of Technology		10:15 AM - 10:35 AM
Refreshment Break *(located in Exhibit Hall A/B, Level 100)*						10:35 AM - 11:00 AM

Time	Ex Hall C - Plenary	Room 307	Room 308	Room 309	Room 310	Room 314	Room 315
	Certification for Analysis Workshop	**Manufacturing: Process Physics**	**Materials and Precursors**	**Physical and Structural Behavior**	**Multifunctional Composites**	**AI Empowered Paradigm**	**Fatigue and Damage Mechanics of Composites**
11:00 AM - 11:20 AM	**11:00 AM - Aero Industry Building Block Certification Logic** Dr Carl Rousseau - Lockheed Martin Co	**The First European Benchmark Exercise on Squeeze Flow Testing of High-Performance Carbon Fibre Sheet Moulding Compounds** Prof Thomas Neumeyer - Leibniz Insitut für Verbundwerkstoffe GmbH	**Synthesis of Bio-Based Foams Derived from Birch Bark Extract** Ms Heather LaFrance - Rowan University	**Adhesion Mechanism Between Epoxy Resin and Thermoplastic Interlayers Modifying VARTM Processing Conditions to Improve Fracture Toughness** Dr Sagar Doshi - University of Delaware	**PEEK-Based Polymer Electrolyte with Tailored Morphology for Structural Battery Composites** Ms Mia Carrola - USAF AFRL	**A Simulation-Based Machine Learning Approach for Optimizing Preform Charges in Sheet Molding Compound Manufacturing** Dr Mikhael Tannous - Arts et Metiers Institute of Technology	**Development of a Height-tapered Double Cantilever Beam for Mode I Interlaminar Fatigue Testing** Mr Shagata Das - University of Delaware
11:20 AM - 11:40 AM	**11:25 AM - Smarter Testing Application to Composite Structures** Mr Adam Sawicki - The Boeing Co	**Rapid Curing of Composites by Filament Winding Technique** Mr Soroush Dashtizad - Arizona State University	**Rheology as a Rapid Method for Simple and Precise Determination of the Percolation Threshold in Shortfiber Polymeric Bio-composites Insights into Sus** Prof Giovanni Filippone - University di Napoli Federico II	**Influence of Laminate Surface Resin Depth on the Interface Strength of Overmoulded Composites** Dr Ruaraidh MacLennan - Queen's University Belfast	**Examination of a Novel Structural Supercapacitor Subjected to Compressive Loading** Dr Alex Harman - Defence Science & Technology Group	**Advanced Machine Learning Techniques for RTM Injection Surrogate Modeling** Ms Sofia Fernandez Leon - IMDEA Materials	**Influence of Fabric Architecture and Sizing on ILFT and LVI Property for Improving Durability and Damage Tolerance of GFRP Composites** Mr Munetaka Kubota - University of Delaware
11:40 AM - 12:00 PM	**11:50 AM - The Role of Analysis and Testing in the Engineering of Wind Turbine Rotor Blades** Mr Kyle Wetzel - Wetzel Wind	**Fabrication of SiC Fiber-Reinforced 3D Woven Composites Using Tow Sizing and Optimized Preform Structures** Mr Yoon-Min OH - Seoul National University	**Bone-inspired Self-adaptive Composites with Reprogrammable Self-folding Behaviors** Prof Sung Kang - Korea Advanced Institute of Science & Technology	**Experimental and Numerical Investigation on Lap Shear Fracture of Additively Manufactured Thermoplastic CFRP64 Titanium** Dr Keiichi Shirasu - Tohoku University	**Ultralow-Voltage High-Performance Soft Actuators using Polysulfonated Covalent-Organic Frameworks as Common Electrolyte-Electrode Hosts** Dr Manmatha Mahato - Korea Advanced Institute of Science & Technology	**A Neural Network Based Bayesian Method for Estimating and Predicting Resin Flow in Resin Transfer Moulding** Mr Nicholas Wright - University of Auckland	**Accelerated Fatigue Characterization of Advanced Composites Using Infrared Thermography** Dr Suhasini Gururaja - Auburn University
12:00 PM - 12:20 PM			**Sustainable Polymer Materials Effect of Agricultural Waste Reinforcement on the Performance of PBS and PBAT Composites** Dr Irene Bavasso - Sapienza University of Rome	**Uncertainty Quantification of a Ductile Damage Evolution Model in an Adhesively Bonded Single Lap Shear Joint** Dr Marcus Stanfield - SwRI	**Tailoring the Chemistry and Morphology of Vertically Aligned Carbon Nanotube Sponges Implications for Smart Electrodes** Mr Lev Rovinsky - Tel Aviv University	**Modeling Crack Propagation in Composites using Constitutively Informed Particle Dynamics** Dr Venkatesh Ananchaperumal - Clemson University	**Mechanical Properties and Damage Analysis of Braided CFRP Composite Rods** Dr Mazhar Peerzada - The University of Southern Queensland
12:20 PM - 1:15 PM	**Group Lunch** *(located in Exhibit Hall A/B, Level 100)*						
1:15 PM	**Plenary Speaker: Industrial-Scale Nano-Integration Strategies for Aerospace-Grade Fiber-Reinforced Polymer Composites: from Functional Coatings and Interface to Prepreg Manufacturing and Composite Repair** Prof Mehmet Yildiz, *Sabanci University*						
Move to Level 300 for Parallel Keynotes and Technical Sessions							
2:10 PM - 2:40 PM		**Keynote Speakers** **Kelly Prize: Challenges and Opportunities in Synchrotron Computed Tomography Imaging of Composites** Prof Yentl Swolfs - KU Leuven	**Crystallization Hybrid Modeling and Simulation of Robotic 3D Printing of Continuous Carbon Fiber Reinforced Thermoplastic Composites** Prof Chady Ghnatios - University of North Florida	**Process Monitoring for Defect Control – from RTM to Sandwich Panel Co-cure** Prof Steven Nutt - University of Southern California	**Manufacturing of Cellulose Composites Where the Reinforcing Fibers are Aligned in Multiple Scales** Mrs Kristiina Oksman - Lulea University of Technology	**Toward Autonomous Qualification of Aerospace Composites: From AI-Driven Calibration to Digital Estimation of Allowables** Dr Navid Zobeiry - University of Washington	

Room 316	Room 317	Room 318	Room 319	Room 320	Room 321	Time
Thermoplastic Composites		**Computational Modeling**	**Invariants and Double-Double Laminate**	**Design, Repair and Life Cycle**		
Effects of Activator and Catalyst Concentration on Reaction Kinetics and Polymer Properties in Reactive Thermoplastic Pultrusion of Nylon 6 Ms Hannah Decker - Fraunhofer Institute for Chemical Technology		**Numerical Simulation for Prediction of Residual Strength for CFRP After Cyclic Loading Considering Entropy Damage Criterion** Mr Takumi Sekino - Graduate School of Tokyo University of Science	**A Double Angle-Ply Laminate Approach to Designing for Controlled Near Zero Coefficient of Thermal Expansion** Dr Christopher York - Singapore Institute of Technology	**Artificial Neural Network-Based Sequential Approximate Optimization for Free Fiber Path Design in Variable-axial Composites** Mr Xin Wang - Hokkaido University Japan		11:00 AM - 11:20 AM
Leveraging In-situ Anionic Polymerization of Polyamide 6 for High Performance Basalt- and Flax-Fiber Thermoplastic Laminates Dr Giulia Fredi - University of Trento		**Experimental and Numerical Study on the Bending Behavior of Glass Fabric Rubber Composites** Mr Oguz Genc - Airbus Operations SAS Ecole des Mines d'Albi	**Double-Double (DD) Laminates: Homogenisation Mechanical Performance and Compression After Impact** Mr Aidan Hawkins - Queen's University Belfast	**Optimal Design of Seamless CSiC Composite with Multicooling Channels using a Data-Driven Model** Mr Kyeongmo Kang - Seoul National University		11:20 AM - 11:40 AM
High-Speed Reactive Processing of Thermoplastic Carbon Fiber-Reinforced Polyamide-6 Composites Mr Sang-Woo Kim - Korea Institute of Material Science		**Modeling High Temperature Cross-Linking Between Graphitic Surfaces and Glassy Carbon** Prof Jacob Gissinger - Stevens Institute of Technology	**Study of the Impact and Compression After Impact Behaviour of Double-Double Laminate** Mr Geoffrey Gisclon - Institut Clement Ader	**Deep Learning Guided Particle Filter for Remaining Useful Life Estimation of Composite Materials** Ms So Young Oh - UNIST		11:40 AM - 12:00 PM
Thermoplastic Infusion In-situ Polymerisation TPIIP and Double Diaphragm Forming DDF for Complex Parts at Scale Dr Gabrielis Cerniauskas - University Of Edinburgh		**Mesostructure-Informed Numerical Modelling of Post-Consolidation Architecture in Advanced Placed Ply Laminates** Mr Saral Mittal - University of New South Wales	**Probabilistic Approach to Evaluate Design Allowables for a Tailored Aircraft Composite Wing using Quad and Double-Double DD Laminates** Prof Carlos Cimini - UFMG Federal University of Minas Gerais	**Generative Model-Driven Design of Long Discontinuous Carbon Fiber Composites for Targeted Mechanical Properties** Dr Hyunsu Lee - University of Connecticut		12:00 PM - 12:20 PM
Group Lunch *(located in Exhibit Hall A/B, Level 100)*						12:20 PM - 1:15 PM
						1:15 PM
Move to Level 300 for Parallel Keynotes and Technical Sessions						
						2:10 PM - 2:40 PM

Time	Ex Hall C - Plenary	Room 307	Room 308	Room 309	Room 310	Room 314	Room 315
	Certification by Analysis Workshop	**Manufacturing: Machine Learning**	**Materials and Precursors**	**Physical and Structural Behavior**	**Multifunctional Composites**	**AI Empowered Paradigm**	
2:45 PM - 3:05 PM	**2:45 PM - Composite Structural Testing and Analysis, an FAA Perspective** Ms Cindy Ashforth - FAA	**High-Fidelity Digital Twin Autoclave Tool for Quality Informed Composite Fabrication** Dr Yuanjie Lua - Global Engineering & Materials Inc	**Enhancing Mechanical Properties and Moisture Durability of Flax Fibre Composites by Plasma Treatments** Mr Jianqun Hao - KU Leuven	**Precise Mode II Fracture Toughness Control in High-Performance Composites by Perforated Release Film Interleaves** Dr Gergely Czel - Budapest University of Technology & Economics	**Quasi-Distributed Pressure Sensors Embedded Into Surface Materials on Composite Laminates** Dr Per Hallander - Saab AB	**Inverse Design of Manufacturing Process using Physics-Informed Neural Operator Learning** Dr Zhen Li - Clemson University	
3:05 PM - 3:25 PM	**3:10 PM - Towards Certification by Analysis - Some Pragmatic Considerations** Mr Mike Hinton - High Value Manufacturing Catapult	**Smart Composite Production Line Planning using AI Based Digital Twin to Optimize the Production Planning under Uncertainty** Ms Shiva Abdoli - University of New South Wales	**Machine Learning-Based Pyrolysis Characterization in Ceramic-Matrix Composites** Ms Paulina Portales Picazo - University of Washington	**Assessment of Numerical Approaches for Quasistatic Fatigue and Dynamic Delamination Propagation in Curved Laminates** Mr Maikel Khella - Politecnico di Milano	**Comparative Study of Graphene Coated Glass Fibres and Vertically Aligned Carbon Nanotube Forests as Embedded Structural Health Monitoring Systems** Mr Tobias Karlsson - KTH Royal Institute of Technology	**Multiscale Modeling of Additively Manufactured Short Fiber Reinforced Thermoplastic Polymer Composites** Dr Taejoon Park - The Ohio State University	
3:25 PM - 3:45 PM		**Enhancing Cure Kinetics Estimation for Thermosetting Carbon Fiber-Epoxy Prepregs Through Chemistry-Informed Machine Learning** Mr Geun Young Kim - Georgia Institute of Technology	**The Effect of Functionalized Cellulose Nanocrystals on Glass Fibers Glass Fiber-Epoxy Composite Performance** Ms Kim Anh Pham - Georgia Institute of Technology		**Real Time Monitoring of Composite Laminated Structures with Embeddable Sensing Layers** Mr Joao Correia - Universidade do Minho	**Multifidelity Neural Network Approach for Warpage Prediction and Optimization in Injection Molding** Ms Elham Kianiharchegani - Brown University	
3:45 PM - 4:10 PM	**Refreshment Break** *(located in Exhibit Hall A/B, Level 100)*						
4:10 PM - 4:40 PM	**4:10 PM - Panel Discussion with Q&A** Dr Sayata Ghose - The Boeing Co Ms Isabelle Paris - Bombardier Aviation **4:55 PM - Wrap Up/Closing Comments** Prof Ole Thomsen - University of Bristol	**Mini-Orals** *See page 48 for detailed presentation schedule*					
4:10 PM - 5:30 PM	**Poster Session** *(located in Exhibit Hall A/B, Level 100)*						
7:00 PM	**Student Only Event** - *Luckie's Tavern at Power Plant Live!*						

Room 316	Room 317	Room 318	Room 319	Room 320	Room 321	Time
Thermoplastic Composites		**Computational Modeling**	**Bio Mass**	**Design, Repair and Life Cycle**		
Importance of Shearing Deformation in Dynamical Mechanical Tests for Viscoelastic Properties of Continuous Fiber Thermoplastic Composites Dr R Byron Pipes - Purdue University		**Simulating Additively-Manufactured Composite Structural Joints using FastDM4C** Dr Antonio Alessandro Deleo - ES3	**White-Rot Fungi Oxidative Cocktail as a Tool for Modifying Kraft Lignin into Sustainable Carbon Fiber Precursors** Prof Veronica Calado - Federal University of Rio de Janeiro	**Deployable Fiber-Reinforced Polymer for Robotics Application** Mr Seung Mo Son - Pusan National University		2:45 PM - 3:05 PM
A Mesoscale Model of Woven Fabric Thermoplastic Composites for Large Deformation Prof Vincent Tan - National University of Singapore		**Characterization of Additive Manufacturing Caused Defects and Their Impacts on Mechanical Properties of Polymeric Lattice Structures Fabricated by SLS** Mr Amirali Amirian - The University of Auckland	**Lignin as a Candidate for Flame-Retardant Composite Applications** Prof Veronica Calado - Federal University of Rio de Janeiro	**Framework for Optimization of AFP Composite Structures** Dr August Noevere - Collier Aerospace		3:05 PM - 3:25 PM
Tracking Ply Deformation during Thermoplastic Stamp Forming using Embedded Shape Sensor Mr Shu Minakuchi - The University of Tokyo		**Attack Angle Influence on Growth Efficiency of Vertically Aligned Carbon Nanotubes** Mr Lev Rovinsky - Tel Aviv University	**Development of High-Performance Biomass Composites using a PA11-Glycol Lignin Matrix** Dr Jonathon Tanks - National Institute for Materials Science	**Next Generation Wind Turbine Blade Repair Residual Stress and Void Analysis in UV-Cured Scarf Patches** Prof Puneet Mahajan - Indian Institute of Technology		3:25 PM - 3:45 PM
Refreshment Break *(located in Exhibit Hall A/B, Level 100)*						3:45 PM - 4:10 PM
						4:10 PM - 4:40 PM
Poster Session *(located in Exhibit Hall A/B, Level 100)*						4:10 PM - 5:30 PM
Student Only Event - *Luckie's Tavern at Power Plant Live!*						7:00 PM

Scientific Program

Time	Ex Hall C - Plenary	Room 307	Room 308	Room 309	Room 310	Room 314	Room 315
7:00 AM	**Registration Desk Open** *(closes at 6:00 PM - located in Charles Street Lobby, Level 100)*						
7:00 AM	**Continental Breakfast** *(until 8:00 AM - located in Exhibit Hall A/B, Level 100)*						
7:00 AM	**Exhibit Hall Open** *(closes at 4:30 PM - located in Exhibit Hall A/B, Level 100)*						
8:00 AM	**Welcome Remarks**						
8:05 AM	**Plenary Speaker: A Ride with Automotive Composites** Prof Srikanth Pilla, *University of Delaware*						
Move to Level 300 for Parallel Keynotes and Technical Sessions							
9:00 AM - 9:30 AM		**Keynote Speakers** **New Research Avenues, Metrologies, and Ideas for Optimizing Glass & Carbon Fiber Epoxy/Amine Composites** Dr Gale Holmes - National Institute of Standards & Technology	**Study of the Longitudinal Compressive Strength of Laminated Composites Using Various Classical and Innovative Tests at Different Temperatures** Mr Frederic Laurin - ONERA Paris-Saclay University	**Monitoring The Structural Condition of Composite Industrial Parts Through Embedded Optical Sensorization** Ms Helena Rocha - PIEP Centre for Innovation in Polymer Engineering	**Progress in Highly Aligned Discontinuous Fiber Composites** Dr Shridhar Yarlagadda - University of Delaware		
		Manufacturing: Resin Transfer Molding 2	**Materials and Precursors**	**Physical and Structural Behavior**	**Multifunctional Composites**	**AI Empowered Paradigm**	**Thermoplastic Composites**
9:35 AM - 9:55 AM		**Analysis of the Image-Based Evaluation of the Permeability of Carbon/Carbon Composites** Ms Tania Lavaggi - University of Delaware	**Studies on Cut-Protective Performance of Composites Yarn Based Knitted UHMWPE Textiles in Real-World Industrial Applications** Mr Shubham Singh - Indian Institute of Technology Delhi IIT Delhi	**Consideration of the Influencing Variables of Peel Plies on the Reaction Process of CFRP Samples Under Liquid Oxygen Environment at Impact Load** Mr Philipp Marin - University of the Bundeswehr Munich	**Nature Materials: Enhanced Functional Composites** Prof Jonghwan Suhr - Sung-Kyun-Kwan University	**Development of a Noniterative Artificial Neural Network Model for Enhanced Finite Element Analysis of Short Fiber-Reinforced Plastics** Mr Minjun Kwak - Seoul National University	**Inline Plasma Modified Carbon Fibre for Enhanced Thermoplastic Tape Manufacturing - Repurposing PA6PP Waste in New Zealand** Mr Maximilian Pitto - The University of Auckland
9:55 AM - 10:15 AM		**Monitoring RTM Infiltration Behavior of TFP Preforms Using Near-Net-Shaped Transparent Cavities** Mr Cameron Welker - Liebniz-Institut für Polymerforschung Dresden e.V.	**Single Carbon and Glass Fibre Tensile Properties and the Correlation with Their Geometry** Ms Elise Van Vlierberghe - KU Leuven	**Multidirectional Laminates with Ultrathin Plies for Cryogenic Environments Mechanical Testing and Permeability** Mr Serafn Sanchez-Carmona - University of Seville	**Self-sensing Technology for Dynamic Behavior Analysis and Damage Classification in Rotating Rotor Blades** Ms Juhyeong Jang - Ulsan National Institute of Science Technology	**Deep Learning-Based Geometrical Analysis and Tension Strain Mapping of Bamboo Fibre Microstructure** Mr Carlos Ivan Cardona Garcia - Luxembourg Institute of Science & Technology	**Mechanical Behavior of 3D Printed Carbon Fiber Reinforced Nylon Composite** Dr Siavash Sattar - Randolph College
10:15 AM - 10:35 AM		**Modelling the Polymer Resin Flow Through Fibres During Resin Transfer Moulding** Mr Rajinth Shanthar - The University of Manchester	**Tailoring Surface Chemistry and Interfacial Interactions of Carbon Fibrepolymer Composites** Prof Luke Henderson - Deakin University		**Enhanced Flow Monitoring in Resin Transfer Molding using Electrical Impedance Tomography with Embedded Carbon Nanotube Sensors** Ms Seyda Naz Alasahin - University of Delaware	**Bayesian Calibration of Finite Element C-spar Models using Digital Image Correlation** Dr Carl Scarth - University of Bath	**Influence of Specimen Geometry and UD Ply Layup on Thermoplastic Welded Double Notched Tension Test Specimen by use of Mechanical and Virtual Testing** Mr Sebastian Hamedinger - University of Applied Sciences Upper Austria
10:35 AM - 11:00 AM	**Refreshment Break** *(located in Exhibit Hall A/B, Level 100)*						

Room 316	Room 317	Room 318	Room 319	Room 320	Room 321	Time
Registration Desk Open *(closes at 6:00pm - located in Charles Street Lobby, Level 100)*						7:00 AM
Continental Breakfast *(until 8:00am - located in Exhibit Hall A/B, Level 100)*						7:00 AM
Exhibit Hall Open *(closes at 4:30pm - located in Exhibit Hall A/B, Level 100)*						7:00 AM
						8:00 AM
						8:05 AM
Move to Level 300 for Parallel Keynotes and Technical Sessions						
						9:00 AM - 9:30 AM
Aligned Discontinuous Fiber Composites	**Compressive Failure**	**Computational Modeling**	**Experimental Techniques**	**Design, Repair and Life Cycle**	**Industrial Applications**	
Characterization and Modeling of Toolply and Plyply Friction of Aligned Discontinuous Fiber Prepreg During Forming Ms Lauren Thomas - University of Delaware	**Is There a Hybrid Effect in Tensile and Compressive Failure of Carbon Fibre Composites** Prof Michael Wisnom - University of Bristol	**Lunar: A Tool for Setting Up Process Modeling Based on Molecular Dynamics Simulations** Dr Joshua Kemppainen - Michigan Technological University	**Uncertainty Quantification of X-ray CT Segmentation of Multiclass Microdamage in Advanced Composites via Deep Learning** Dr Reed Kopp - ATA Engineering Inc	**Virtual Testing of Recycled Glass Fiber Reinforced Polymer Sandwich Cores** Mr Michael Paulitsch - University of Applied Sciences Upper Austria	**Development and Manufacturing of a Conformable CFRP Tank Demonstrator with Tension-Strut-Reinforcement** Ms Elisabeth Gleis - Technical University of Munich	9:35 AM - 9:55 AM
Characterization and Modeling of Deformation Mechanisms of Aligned Discontinuous Fiber Prepreg During Thermoforming Mr Aidan Ford - University of Delaware	**FE Simulations of Large UDFRP Microstructures Under Longitudinal Compression** Dr Dimitrios Bikos - Imperial College London	**Incorporation of High-Fidelity Experimental Data into Finite Element Models for Enhanced Comparison and Analysis** Dr Meng Yi Song - University of Bristol	**A New Approach for Quantifying the Transverse Coefficient of Thermal Expansion in PAN-based Carbon Fibres at Low Temperatures via X-ray Diffraction** Mr Jiraphant Srisuriyachot - University of Bath	**Fatigue Life Prediction of Dissimilar Material Joints Using Neural Networks** Mr Young Bin Kim - Yonsei University	**Advanced Graphene-Enhanced Polyethylene Liners for Type IV Hydrogen Storage Tanks Enhancing Mechanical Properties and Gas Containment** Dr Jefferson Andrew Jeyakumar - Khalifa University	9:55 AM - 10:15 AM
Modeling Transvers Shearing Viscosity and Material Tool Friction Interaction with Rectangular Squeeze Flow Mr Rafe Garcia-Hidalgo - University of Delaware		**Simulating Particle-Based Interface Toughening Mechanisms of Laminated Composites** Dr Shiyao Lin - The University Of Texas At Arlington		**Predicting Material Properties of Shredded Recycled Carbon Composite using a Detailed Simulation Approach** Mr John Finder - TU Braunschweig Institut für Flugzeugbau und Lei	**Composite Materials Handbook CMH17: An Introduction and Overview** Mrs Teresa Vohsen - Wichita State University NIAR	10:15 AM - 10:35 AM
Refreshment Break *(located in Exhibit Hall A/B, Level 100)*						10:35 AM - 11:00 AM

Time	Ex Hall C - Plenary	Room 307	Room 308	Room 309	Room 310	Room 314	Room 315
		Manufacturing: AFP/ATP 2	Materials and Precursors	Physical and Structural Behavior	Multifunctional Composites	Industrial Applications	Thermoplastic Composites
11:00 AM - 11:20 AM		**Development and Control of Residual Stresses and Warpage During the ATP Process** Dr John Tierney - University of Delaware	**Dynamic Crush of Hollow Glass Microsphere Reinforced Polyurethane Foams** Dr Colleen Murray - University of Maryland	**Effect of Simulated Hygrothermal Ageing on the Interfacial Shear Strength of Carbon/Epoxy Composites** Mr Abdullah Iftikhar - University of Southern Queensland	**Sensing of Resin Flow and Cure in Continuous Fiber Additive Manufacturing** Mr Mohammad Tofayel Ahmed - University of Delaware	**A Novel Sleeve Assembly Method for SPM Motors using CFRP with Atypical Layup** Dr Kazunori Takagaki - Mitsubishi Electric Corp	**Effects of Fiber Type and Cooling Rate on the Crystallization Behavior of Low-Melt PAEK Thermoplastic Composites** Prof Anoush Poursartip - The University of British Columnia
11:20 AM - 11:40 AM		**Material Behavior of Prepregs in Automated Robotic Sheet Layup: A Comparative Study** Mr Moritz Lennartz - Institut for Textiltechnik of RWTH Aachen Uni	**Wearable Electronic Textiles for the Detection of Loneliness in Older Individuals** Dr Jingqi Liu - University of Leeds	**Degradation in Bio-epoxy Composites Under Hygrothermal Ageing** Ms Zaneta Senselova - University of Southern Queensland	**Featherweight Wearable Electronics Based on a PAN Electrospun Substrate** Professor Yu Shi - University of Leeds	**Feasibility of Developing Fiber-reinforced Thermoplastic Composite Couplers for Hydrogen Transmission Pipelines** Dr Chen Wang Dr Andi Haris - Singapore Institute of Mfg Technology	**Improved Thermal Conductivity and Structural Integrity in Thermoplastic Composites Using h-BN/PEEK Films and Resized Carbon Fibers** Ms Burcu Saner Okan - Sabanci University
11:40 AM - 12:00 PM		**An Investigation of Thermoplastic Tape-to-Tape Bonding Using Xenon Flash Lamp Heating** Prof David Williams - University of Bath	**Evaluation on Recession Behaviors of B4C Containing Porous Carbon Material as an Advanced Thermal Protection System** Mr Tatsuki Koshikawa - Japan	**Systematically Adapting Processing, Flame Retardancy, and Flexural Properties of Epoxy Glass Fiber Reinforced Composites for Railway Applications** Ms Sruthi Sunder - University of Bayreuth	**Electrical Impedance Tomography for Self-Sensing 3D Printed Cellular Composites** Mr Akash Deep - University of Glasgow	**In-Space Manufacturing of High-Performance Fiber Reinforced Composites Tubes** Dr Jeff Baur - University of Illinois	**Influence of Transient Radiative Heat Flux on Degree of Crystallinity in Thermoplastic Composites** Dr Paul Davidson - The University Of Texas At Arlington
12:00 PM - 12:20 PM		**A Comprehensive Approach to a Digital Twin Based on Asset Administration Shells for a Process Chain of Automated Tape Laying and Thermoforming** Prof Thomas Neumeyer - Leibniz Insitut für Verbundwerkstoffe GmbH	**Interlaminar Fracture Toughness Enhancement in Carbon Fiber Composites Via Asymmetric Flax Fiber Hybridization** Prof Jungil Song - Changwon National University	**Effect of Hygroscopic Aging on the Transverse Damage Behavior of Fiber-Reinforced Composites: A Computational Micromechanics Study** Dr Vaishakh Kottila Veedu - Brown University	**Embedding of Fiber Optic Sensors Under Industrial Conditions and Distributed Strain Sensing in Type 4 Composite Pressure Vessels** Mr Bartosz Popiela - Bundesanstalt für Materialforschung und -prüfung		
12:20 PM - 1:15 PM	**Group Lunch** *(located in Exhibit Hall A, Level 100)*						
1:15 PM	**Plenary Speaker: Assuring Safety of Composite Structures in Aviation** Ms Cindy Ashforth, *Federal Aviation Administration*						
	Move to Level 300 for Parallel Keynotes and Technical Sessions						
2:10 PM - 2:40 PM		**Keynote Speakers** **Overcoming Processing Hurdles in Multifunctional Polymers and Polymer (Nano) Composites** Prof Emiliano Bilotti - Imperial College London	**Liquid Composite Moulding Research as a Nucleus for Interdisciplinary Innovation in Composites** Prof Nuno Curado Correia - INEGI	**Generative Design of Additively Manufactured Composites with AI/ML Models** Prof Kishore Pochiraju - Stevens Institute of Technology	**Sustainable Composites Start with LCA: Seeing the Whole Picture** Prof Martina Salzano de Luna - University of Naples Federico II		

Room 316	Room 317	Room 318	Room 319	Room 320	Room 321	Time
Aligned Discontinuous Fiber Composites	Compressive Failure	Computational Modeling	Experimental Techniques	Design, Repair and Life Cycle		
Stamp Forming of Highly Aligned Discontinuous Fiber Composite Blanks via Epoxy Matrix Staging Mr Matthew Abraham - University of Delaware	**Unusual Effect of the Degree of Cure of Some Epoxy Resins on the Compressive Strength of Continuous Fibre Composites** Mr Vincent Keryvin - University Bretagne Sud	**Prediction of Microcrack Networks in Cryogenic Carbon Fibre Composite Hydrogen Tanks** Dr Wenkai Chang - University of New South Wales	**Detection of Progressing Material Defects with FMCW Radar Signals** Mr Florian Puch - Technische Universitat Ilmenau	**Composite 3D Printed Plate-Based Mechanical Metamaterials** Ms Aya Hosoi - Imperial College London		11:00 AM - 11:20 AM
Efficient Microstructural Models to Homogenize Anisotropic Viscoelastic Parameters of Highly Aligned Discontinuous Fiber Composites Mr Miguel de Carvalho Dr Nuno Curado Correia - INEGI	**Improving Fibre Reinforced Polymer Compressive Performance Through Intermittent Matrix Property Modification** Ms Hwei Linn Khoo - Imperial College London	**Compaction and Mechanical Performance of AFP Composites with Fiber Tow Gaps Experimental Investigation and Multiphysics Modeling** Mr Ahmadreza Ravangard - Old Dominion University	**Optimisation of 3D Woven Composite Structures for Bearing Performance in Single and Double Lap Joints Using Acoustic Emission Monitoring** Mr Callum Montgomery - Ulster University	**From Waste to Value Creating Composite Blends Out of Waste Low-density Polyethylene and Polystyrene for Fused Deposition Modeling Printing** Mr Ahmed Afzal - Texas A&M		11:20 AM - 11:40 AM
Tensile Behavior and Stress Relaxation of Uncured Prepreg of Aligned Discontinuous Fiber Materials Constitutive Model Development for Stretch Forming Dr Navid Niknafs Kermani - University of Delaware	**Polymer Composites Reinforced by Continuous Irregular Networks from Bioinspired Design to Fracture** Prof Tommaso Magrini - Eindhoven University of Technology	**Accelerating Progressive Damage and Failure Analysis of Composites using a Hybrid Implicit-Explicit Approach** Dr Shiyao Lin - The University Of Texas At Arlington	**Combined In-Situ Microscopy and Acoustic Emission Monitoring of Transverse Cracking in CFRP Cross-ply Laminates** Mr Spyridon Spyridonidis - University of Bristol	**Mechanical Recycling of Glass Fiber Reinforced Wind Turbine Blade Components into Reinforced Filaments for use in Additive Manufacturing** Mr Dimitrij Seibert - Leipzig University of Applied Sciences		11:40 AM - 12:00 PM
Impact of Fiber Aspect Ratio on Mechanical Performance of Short Fiber Composites Mr Uday Kiran Balaga - University of Delaware	**Bicontinuous Silica-Epoxy Interfaces** Dr Charles Shaw - Imperial College London	**Molecular Dynamics Simulation on the Failure Behavior of Carbon-Polycarbonate-carbon Structure-sensitivity Analyses of Interfacial Potential Parameter** Ms Bowen Cao - Clemson University	**Assessing the Effects of Edge-Reflections on Propagating Acoustic Waves in CFRP Panels** Ms Andrea Martinez - Delta Engineering Corp	**Enabling All-Composite Pressure Vessels Through Integrated Electrospun Nanofiber Architectures** Mr Jaejun Bae - Korea Advanced Institute of Science & Technology		12:00 PM - 12:20 PM
Group Lunch *(located in Exhibit Hall A, Level 100)*						12:20 PM - 1:15 PM
						1:15 PM
Move to Level 300 for Parallel Keynotes and Technical Sessions						
						2:10 PM - 2:40 PM

Time	Ex Hall C - Plenary	Room 307	Room 308	Room 309	Room 310	Room 314	Room 315
		Manufacturing: Process Monitoring	Materials and Precursors	Physical and Structural Behavior	Multifunctional Composites	Industrial Applications	Thermoplastic Composites
2:45 PM - 3:05 PM		**On Line Optimisation and Active Control of the Cure Process of Thick Composite Laminates** Dr Konstantinos Tifkitsis - Kalero Ltd	**Bio-Inspired Micropatterned Fibre Surfaces Alternating Adhesion Zones for Tougher Composites** Dr Carlos Fuentes - Luxembourg Institute of Science & Technology	**Study on Construction of Short Carbon Fiber Secondary Dispersion System and Its Strengthening Cement-Based Composites** Mr Dazhi Jiang - Sun Yat-Sen University	**GNP-Based Pyro-Resistive Eskin Integrated With Temperature Sensing and Self-Controlled Joule Heating Function** Mr Yansong Li - Queen Mary University of London	**PLA Reinforced with Tungsten Disulfide Nanotubes for 3D-Printed Bone Scaffold: In Vitro Assessment of Biocompatibility and Degradation** Mr Ofek Golan - Tel Aviv University	**Cooling-Rate Independent PEEK Composites via Oatmeal for High-Rate Processing** Mr Joseph Kirchhoff - University of Texas at Austin
3:05 PM - 3:25 PM		**Localised Convection Heat Transfer Coefficients in Curing Environments: A Heat Flux Approach** Mr Andrew Che - Swinburne University of Technology	**Evaluation of the Effect of Z-threaded Carbon Nanofibers on the Improvement of Flexural Properties of Carbon Fiber-Reinforced Polymer Laminates** Prof KuangTing Hsiao - University of South Alabama	**Characterization of Fiber Reinforced Thermoplastic Composites Fabricated by Composites-Based Additive Manufacturing CBAM Technology** Mr Gavin Stoker - Utah State University	**Characterisation of Embedded Channel Networks in CFRPs for Active Cooling** Mr Toby Wilcox - University of Bristol	**Friction and Wear Characteristics of 3D-Printed Carbon Fiber-Reinforced Polyamide Under Dry and Seawater Lubrication Conditions** Dr Amir Hamza Nazir Ahmed Siddiqui - Technical University of Denmark DTU	**Benchmarking of AM-CM System Capabilities: To Make Parts with Amorphous and Semi-Crystalline Composites** Dr Ahmed Hassen - Oak Ridge National Lab
3:25 PM - 3:45 PM		**Flow Analysis of the Capillary-Driven Underfill Process for the Use of Thermally Conductive Epoxy Composites in Semiconductor Packaging** Ms Jeeeun Lee - Korea Advanced Institute of Science & Technology	**Prevention of Dispersion in Flexural Strengths of Unidirectional Carbon Fiber Reinforced Composites by Applying Prepregs Containing Cellulose Nanofibe** Mr Shoutaro Shimora - Doshisha University	**Effect of Fiber Volume Fraction and Material Homogeneity on the Mechanical Performance of Recycled Woven Thermoplastic Composites** Mr Fausto Visser - TPRC	**Manufacturing Patterned Carbon Fiber Cathodes by Supercritical CO2 Spray Simultaneous Enhancement of Electrochemical and Mechanical Properties of Str** Prof Amir Asadi - Texas AM University	**Demonstration of a Novel High Pressure Vessel Structure Consisting of CFRP Overwrapped Cylinder and Belt Shaped Load Members for Fuel Cell Vehicles** Mr Ikumi Matsumoto - Tokyo University of Agriculture Technology	
3:45 PM - 4:30 PM	**Refreshment Break** *(located in Exhibit Hall A, Level 100)*						
4:30 PM - 6:30 PM	**ICCM General Assembly**						
7:00 PM - 9:00 PM	**CCM 50th Anniversary Celebration** - *Angels Rock Bar at Power Plant Live!*						

Room 316	Room 317	Room 318	Room 319	Room 320	Room 321	Time
Aligned Discontinuous Composites	Compressive Failure	Computational Modeling	Experimental Techniques	Design, Repair and Life Cycle		
Volumetric Quantification of Bridging and Wrinkling Defects in Composite Laminates Mr Cooper Williams - Montana State University	**Cure-induced Wrinkles and Compression Strength Knockdown in Unidirectional Composites** Dr Lars Mikkelsen - DTU Wind & Energy Systems	**Role of Modeling and Simulation in the Development and Application of Digital Twin for Liquid Composites Molding Processes** Dr Pavel Simacek - University of Delaware	**Application of Infrared Imaging to Reveal Hidden Defects in CFRP Laminates** Prof Janice Barton - University of Bristol	**Comparing the Local Predictions of the Strain Energy Release Rate by CZM and VCCT in Large and Curved Delaminations** Dr Luca Michele Martulli - Politecnico di Milano		2:45 PM - 3:05 PM
Interply Friction Characterization of Stretch Broken Carbon Fiber SBCF Composites During Forming Ms Tasnia Javin Nur - Montana State University	**Mechanics of Kinking in Fiber Reinforced Composites Under Compressive Loading** Dr Paul Davidson - The University Of Texas At Arlington	**Numerical Modeling of Fiber Bundle Architecture in the Robotic Coreless Filament Winding Process** Mr Sebastian Huegle - University of Stuttgart	**Combining Thermographic and Lamb Waves Investigation Data for the Characterisation of CFRP Delaminations** Dr Lea Lecointre Isaka - The University of Tokyo	**CFRP Recycling Method Compatible with a Wide Range of Epoxy Matrices** Mr Naoki Mori - Institute of Science Tokyo		3:05 PM - 3:25 PM
Sustainable Aligned Short Carbon Fibre Reinforced Composites with Electrospun Polymer Matrix Dr Shivdarshan Sherugar - University of Bath	**Fiber Waviness in Thermoplastic CFRP Mechanisms of Formation and Mechanical Influence** Mr Takayu Nishioka - The University of Tokyo	**Numerical Simulation for Thermal Cycle Fatigue Failure for Composite Materials Based on Entropy Damage Criterion** Mr Takumu Sugiyama - Graduate school of Tokyo University of Science	**Probability of Detection Analysis of Simulated Defects in Long Discontinuous Fiber Composites Via Transient Thermography** Mr Marco Didone - University of British Columbia			3:25 PM - 3:45 PM
Refreshment Break *(located in Exhibit Hall A, Level 100)*						3:45 PM - 4:30 PM
						4:30 PM - 6:30 PM
CCM 50th Anniversary Celebration - *Angels Rock Bar at Power Plant Live!*						7:00 PM - 9:00 PM

Scientific Program

Time	Ex Hall C - Plenary	Room 307	Room 308	Room 309	Room 310	Room 314	Room 315
7:00 AM	**Registration Desk Open** *(closes at 5:30 PM - located in Charles Street Lobby, Level 100)*						
7:00 AM	**Continental Breakfast** *(until 8:00 AM - located in Exhibit Hall A/B, Level 100)*						
7:00 AM	**Exhibit Hall Open** *(closes at 5:30 PM - located in Exhibit Hall A/B, Level 100)*						
8:00 AM	**Welcome Remarks**						
8:05 AM	**Plenary Speaker: Perspectives on the Application of Composite Failure Theories Since the World Wide Failure Exercise** Mr Adam Sawicki, *The Boeing Company*						
Move to Level 300 for Parallel Keynotes and Technical Sessions							
9:00 AM - 9:30 AM	**Societal and Industrial Impact Workshop** **9:00 AM - Keynote: IACMI-The Composites Institute - Enabling US Competitiveness in Advanced Composites Manufacturing - Convene, Connect & Catalyze** Dr Uday Vaidya - IACMI The Composites Institute	**Keynote Speakers** **Structural Fire Response of Polymer Composites** Prof Scott Case - Virginia Polytechnic Institute	**Next Generation Composites: Pushing the Boundaries of Performance and Sustainability** Prof Kyriaki Kalaitzidou - Georgia Institute of Technology	**Accelerating Airframe Development Tasks** Mr Carl Rousseau - Lockheed Martin	**Rapid Manufacturing Pathways for High-Performance Thermoplastic Composites** Prof Mehran Tehrani - University of California San Diego		
		Manufacturing: Forming 2	**Materials and Precursors**	**Physical and Structural Behavior**	**Multifunctional Composites**	**Industrial Applications**	**Additive Manufacturing**
9:35 AM - 9:55 AM	**9:30 AM - Fraunhofer- Applied Research for Lightweight Innovation** Dr Frank Henning - Fraunhofer Institute for Chemical Technology	**Forming Wrinkle-Free Curved C Channel with Unidirectional Fiber Reinforced Composites** Mr Suk Young Chey - Seoul National University	**Time-Dependency Phenomena in BOPP and SRPP Laminates** Miss Anna Kandinskaia - KU Leuven	**Effects of Cooling Rate on the Mechanical and Thermal Properties of Self-Reinforced Polyethylene Composites** Dr Yelin Ni - Pacific Northwest National Lab	**Evaluation of Multifunctional Properties of 2D-Materials Films Embedded Glass Fiber Reinforced Composites** Mr Muhammad Yasir Khalid - Khalifa University of Science Technology	**Design and Prototyping of Composite Deployable Booms for Solar Sails** Prof Susanna Laurenzi - Sapienza Universita di Roma	**Durability of Conventional vs 3D-printed Carbon Fiber in Harsh Saline Environments** Mr Omar El Arwadi - Texas AM University
9:55 AM - 10:15 AM	**9:50 AM - Carbon Nexus 10 years on – Lessons Learnt and Current Research Highlights** Prof Luke Henderson - Deakin University	**Draping Tool Generation for Image-Based Surrogate Draping Models using Free Form Deformation and Topography Modification** Ms Sophia Keller - University of Applied Sciences Upper Austria	**Understanding Towpreg Manufacturing — Combining Advanced Resin Formulation and Improved Processing Techniques for the Next Generation of Pressure Vess** Mr Marius Luik - University of Bayreuth	**Thermomechanical Property Evolution and Virtual Curing of an Aerospace Bismaleimide Resin via Experimentally Validated Molecular Dynamics Simulation** Mr Trevor Wavrunek - Michigan Technological University	**Fabrication of Aramid-Fiber Reinforced Composite for Improving the Shock-Wave Protection by Incorporating Polydimethylsiloxane** Mr Tae Kyeom Kim - Pusan National University	**Characterization and Mitigation of Droplet-Induced Impact Damage in Wind Blade Leading-edge Coatings** Mr PoWen Wang - University of Illinois Urbana-Champaign	**Additive Preform Molding of 3D High-Performance Continuous Carbon Fiber Thermoset Composites** Dr Kaiyue Deng - University of Delaware
10:15 AM - 10:35 AM	**10:10 AM - Fraunhofer Innovation Platform for Composites Research at Western University - High Performance Composites: Trends and Impact** Dr Frank Henning - Fraunhofer Institute for Chemical Technology *"on behalf of Prof Andrew Hrymak, University of Western Ontario"*	**Compaction and Fluid-structure Interaction Leading to Fiber Displacement in Resin Infusion of Composite Manufacturing** Dr Debabrata Adhikari - DTU Lyngby	**Modeling the Property Evolution of Cyanate Ester with Crosslinking, Strain-Rate, and Temperature** Dr Sagar Patil - Michigan Technological University	**Thermomechanical Properties Of Polybenzoxazine Resin in a Molecular Dynamics Model as a Function of Degree of Cure and Temperature** Mr Tristan Muzzy - Michigan Technological University	**Novel Recoverable Fiber Metal Laminates Based on NiTi/CFRP Thermoplastic Composites Subjected to Flexural Loading at Different Temperature Conditions** Mr Muzafar Hussain - Khalifa University	**Numerical and Experimental Analysis of Residual Deformations in Composite Plates Integration of Part/Mold Interaction and Compensated Mold Design** Prof Philippe Olivier - Clement Ader Institute	**Topology Optimization and Manufacturing of 3D Architected Composites using Additive Fiber Tethering** Mr Md Habib Ullah Khan - University of Delaware
10:35 AM - 11:00 AM	**Refreshment Break** *(located in Exhibit Hall A/B, Level 100)*						

THURSDAY, AUGUST 7

Room 316	Room 317	Room 318	Room 319	Room 320	Room 321	Time
Registration Desk Open *(closes at 5:30pm - located in Charles Street Lobby, Level 100)*						7:00 AM
Continental Breakfast *(until 8:00am - located in Exhibit Hall A/B, Level 100)*						7:00 AM
Exhibit Hall Open *(closes at 5:30pm - located in Exhibit Hall A/B, Level 100)*						7:00 AM
						8:00 AM
						8:05 AM
Move to Level 300 for Parallel Keynotes and Technical Sessions						
						9:00 AM - 9:30 AM
	Compressive Failure		**Experimental Techniques**	**Design, Repair and Life Cycle**		
	Arrest and Compartmentalisation of Unstable Compressive Failure in Carbon-Fibre Reinforced Polymer Laminates using a Ply-Discontinuity Feature Mr Bruno Santos - Imperial College London		**Experimental Characterization of Interface Failure Between Flexible and Rigid Additively Manufactured Materials** Prof Behrad Koohbor - Rowan University	**Vacuum-Assisted Techniques for Improved Repair Performance in Legacy Fibre-Reinforced Composites** Dr James Quinn - The University of Edinburgh		9:35 AM - 9:55 AM
	Effect of Heat Treatment on Compressive Strength of 3D Printed Onyx Mr Ertugrul Sari - Queen's University Belfast		**Comparative Evaluation of Size and Stacking Sequence Effects on the Performance of Thin Ply Laminates** Mr Joseph McDonald - Toray CMA	**SF6 Plasma Surface Engineered Spent Coffee Ground Derived Carbon Reinforced Waste HDPE Composites** Dr Sushrisangita Sahoo - Tuskegee University		9:55 AM - 10:15 AM
	Integration of Fuzzy Carbon Overbraids into Structural Members for Improved Compressive Performance Dr Laura Rhian Pickard - University of Bristol		**Quantitative Evaluation and Comparison of Terahertz and Ultrasonic Testing of Glass-fiber Reinforced Plastics** Mr Jens Schuster - University of Applied Sciences Kaiserslautern	**Enhancing the Mechanical and Thermal Properties of Recycled EVOH Films with Nano-Silica Incorporation** Ms Kowsar Rezvanian - Tuskegee University		10:15 AM - 10:35 AM
Refreshment Break *(located in Exhibit Hall A/B, Level 100)*						10:35 AM - 11:00 AM

Time	Ex Hall C - Plenary	Room 307	Room 308	Room 309	Room 310	Room 314	Room 315
	Societal and Industrial Impact Workshop	Manufacturing: Resin Transfer Molding 3	Materials and Precursors	Physical and Structural Behavior	Multifunctional Composites	Industrial Applications	Additive Manufacturing
11:00 AM - 11:20 AM	**Panel Discussion with Audience Q&A** Moderator: Prof Mike Hinton - High Value Mfg Catapult Panelist: Dr Uday Vaidya - IACMI The Composites Institute Dr Frank Henning - Fraunhofer Institute for Chemical Technology Prof Luke Henderson - Deakin University	**Assessing the Influence of Flax Fibers Humidity on the Properties and Processing of Composites with Infusion at Controlled Capillary Number** Dr Jean Baptiste Jouenne - ABTE	**Exfoliation and Dispersion of MXene in Epoxy Resin Using Dispersing Agents and Three-Roll Milling** Ms Kristina Zukiene - Kaunas University of Technology	**Tensile Cyclic Behaviour of Open-hole CFRP Laminates with Ultra-Thin Plies** Mr Carlos Sandino - Universidad de Sevilla	**Programmable Shape Transformation in Multilayer Fiber Composites Through 4D Printing** Mr Erdem Yildiz - University of Bristol	**Manufacturing and Experimental Testing of Carbon Fiber/Epoxy Composites using Advanced Induction Heating System** Mr Andrejs Pupurs - Riga Technical University	**Enhanced Structural Performance of Additively Manufactured 2D-Lattice Sandwich with Tailored Fiber Orientation using Hot Powder Bed Compaction** Mr Jimesh Bhagatji - Old Dominion University
11:20 AM - 11:40 AM		**Effect of Anisotropy in Fibre Bundle Spacing on Macrovoid Formation in Viscous-Fluid Impregnation to Woven Glass Fibre Bundles** Mr Tomoki Ito - Tokyo University of Science	**Identification of Cure Kinetic Parameters to Model Multiphysic Behavior of Thermoset Laminate Composite** Mr Quentin Marechal - LTDS Ecole Centrale Lyon	**Effect of Weave Architecture and Stuffer to Binder Ratio on Mechanical Performance of 3D-Woven Composite Core-Based Sandwich Panels** Mr Prabhjot Singh - Indian Institute of Technology Delhi	**Sustainable Phase Changing Fiber-Reinforced Composites** Mr Aidan Holihan - University of Tennessee	**Development of Multicell Bipolar Plate Composite Structures via Electrode Integration for Vanadium Redox Flow Batteries** Prof Jun Woo Lim - Jeonbuk National University	**Effect of Heat Treatment on the Tensile Performance of 3D-Printed Continuous Fiber-reinforced Composites** Mr Zizhao Peng - Swinburne University of Technology
11:40 AM - 12:00 PM		**RTMWorx Twins for Racetracking Classification** Mr Arjen Koorevaar - Polyworx BV	**Molecular Dynamics-Derived Mode I Traction Laws for Crystalline UHMWPE Fibrils** Dr Nuwan Dewapriya - University of Delaware	**Advanced Thermoplastic Honeycomb Cores: Efficiency Gains Through Coextruded Foamed Cell Walls in Sandwich Structures** Mr Gregor Jesse - Leipzig University of Applied Sciences	**Mechanical and Electrical Performance of Conformal Load-bearing Antenna Structures under Mechanical Loading** Dr Mitchell Dunn - The University of Queensland	**Sustainable Oxide/Oxide Ceramic Composites with Atomic Oxygen Protection for VLEO Satellite Applications** Mr Chaehwan Lim - Korea Aerospace University	**Effect of Process Parameters on Mechanical Performance of Additively Manufactured PCCF with Integrated Fiber Reinforcement using ATLAM** Mr Benjamin Steva - University of Maine
12:00 PM - 12:20 PM		**Real-Time Predictive Monitoring and Adaptive Control in Vacuum Infusion Development of a Physics-Based Digital Twin** Mr João Machado - INEGI	**Effect of Consolidation Pressure on the Deformation and Void Content Reduction within a Uniform Array of UHMWPE Fibrils** Dr Abdalsalam Fadeel - University of Delaware	**Impact and Damage Resistance of Sandwich Beams Made from Sustainable Materials at Low Temperatures** Mr Gabriel Sanchez Escudero - Universidad Carlos III de Madrid		**Electrical Insulation for Nb3Sn Superconducting Cables: Fibre Selection, Braiding Process, and Epoxy System Performance** Mr Roland Piccin - CERN	**Effect of Overlap Distance on Bead Geometry and Thermal Conductivity in Extrusion-Deposition Additive Manufacturing** Mr Eonyeon Jo - University of Tennessee Knoxville
12:20 PM - 1:15 PM	**Group Lunch** *(located in Exhibit Hall A/B, Level 100)*						
1:15 PM	**Plenary Speaker: Composites are for Bonding** Ms Michelle Johnson, *Lockheed Martin*						
Move to Level 300 for Parallel Keynotes and Technical Sessions							
2:10 PM - 2:40 PM	**Societal and Industrial Impact Workshop** **2:10 PM - Challenges and Opportunities of Translational Research** Mr Mark Summers - NCC **2:30 PM - From PhD Thesis to Industry Standard: The Power of Collaboration** Dr Sayata Ghose - The Boeing Co	**Keynote Speakers** **From Waste to Circularity: Vitrimerization in Thermoset Composites** Prof Veronica Ambrogi - University of Naples Federico II	**Integrating Machine Learning and Physics-Based Models for Probabilistic Design and Certification of Composite Laminates** Dr Roger Ghanem - University of Southern California	**Innovative Sustainable Composites for Lighter and Flame Retardant Electric Vehicle Parts to Boost Climate Benefits** Prof Manjusri Misra - University of Guelph	**Weaving Resilience: Engineering Damage-Tolerant Textile Composites** Prof Pavana Prabhakar - University of Wisconsin Madison		

Room 316	Room 317	Room 318	Room 319	Room 320	Room 321	Time
Sustainability	Compressive Failure	Computational Modeling	Experimental Techniques	Design, Repair and Life Cycle	Fire Performance	
Structural Integrity Assessment of Reused Wind Turbine Blade Composite Components using Acoustic Emission Testing and Ib-value Analysis Mr Philipp Johst - HTWK Leipzig	**Compression Behavior of Unidirectional Carbon Fiberfiller Reinforced Plastics** Dr Masahito Ueda - Nihon University	**Perforation and Penetration Mechanics of Composites: Theory, Experiment, and Finite Element Analysis** Dr Bazle Gama Haque - McLaurin Aerospace	**Mechanical and Shearographic Inspections of Stacking Sequences in Plydrop Composite Layups** Dr Hatice Sas - University of Sheffield	**Circular Economy Opportunities for Waste Glass Fibre Reinforced Sucker Rod Guides** Ms Chundu Tamang - University of Southern Queensland	**Development of Flame-Retardant Medium Density Wood Fibreboards Using Phosphorylated Casein and Polyamidoamine-epichlorohydrin Resin** Dr Nam Kyeun Kim - University of Auckland	11:00 AM - 11:20 AM
Validation of Possible Applications of Flake Laminates for Recycling of PA6-CF Production Scrap Ms Johanna Beckmann - University Paderborn	**Raman Spectroscopic and FIB-SEM Insights into Compressive Fragmentation of High Modulus Carbon Fibres Model Composites** Mr Cameron Woodgate - Imperial College London	**Finite Element Modeling of the Thermo-Oxidation Gradients in Organic Matrix Composites** Mr Juan Pablo Marquez Costa - PIMM ENSAM	**The Effect of Optical Fibre Cross-Sectional Shape and Microstructure on Out of Plane Strain Sensitivity in Flexible Photonic Sensors** Dr Robin Hartley - University of Bristol	**Life Cycle Assessment of PLA-based Green Composites Reinforced with Natural Fibers** Dr Martina Salzano de Luna - University of Naples Federico II	**Development and Synthesis of Novel DOPO-modified Epoxy Resin and its Glass and Sisal-Based 3D Woven Fiber-Reinforced Composite** Mr Shubham Agnihotri - Indian Institute of Technology Delhi	11:20 AM - 11:40 AM
Recycling of End-of-Life Wind Turbine Blades into Polymer Composites Effect of Reprocessing on Secondary Composites Mr Shashank Tumkur Karnick - Eindhoven University of Technology	**Methodology for Validating and Generating Micromodels to Predict Fiber-direction Compressive Failure in CFRPs** Dr Guillaume Seon - The University Of Texas At Arlington	**Numerical Analysis of Viscoelastic Creep and Transverse Cracking in Fiber-Reinforced Composites** Dr Yamato Hoshikawa - Tohoku University	**3D-Printed Core Reinforced with Unidirectional Tailored Fiber Placement and Braided Structures for use in Custom-Made Composite Knee Orthoses** Mr Marcin Barburski - Lodz University of Technology	**Comparison and Recycling of Uniquely Manufactured Flax Composites** Dr Monis Kazmi - University of Auckland	**Enhancing Fire Resistance of Carbon Fibre Composites Using Functionalised Ammonium Polyphosphate Nanoparticles** Prof Chun Wang - University of New South Wales	11:40 AM - 12:00 PM
Tin-catalyzed Epoxy Vitrimer Matrix: An Approach to Waste Reduction in Epoxy Composites Ms Emeline Waechter - Monash University	**Computational Investigation of Microstructural Instabilities using Discrete Model for Composites DM4C** Dr Mark Flores - ES3	**Characterization of Highly Filled Thermosetting Composite for the Numerical Prediction of Residual Stresses Development During the Production Process** Ms Joana Malheiro - PIEP Centre for Innovation in Polymer Engineering			**Effect of Halloysite Nanotubes and Waste Chicken Feathers as Fire Retardants in Green Composites** Dr Anil Netravali - Cornell University	12:00 PM - 12:20 PM
Group Lunch *(located in Exhibit Hall A/B, Level 100)*						12:20 PM - 1:15 PM
						1:15 PM
Move to Level 300 for Parallel Keynotes and Technical Sessions						
						2:10 PM - 2:40 PM

Time	Ex Hall C - Plenary	Room 307	Room 308	Room 309	Room 310	Room 314	Room 315
	Societal and Industrial Impact Workshop	Manufacturing: Urban Air Mobility	Smart Composite Materials	Physical and Structural Behavior	Multifunctional Composites	Industrial Applications	Additive Manufacturing
2:45 PM - 3:05 PM	**2:45 PM - Building a Global Extended Research Ecosystem** Mr Peter Wilkins - Baker Hughes UK **3:00 PM - The Innovation Pipeline: Collaborative Research Frameworks for the Future of Flight** Mr Tim Gaur - Airbus **3:15 PM - Stronger Together: Victrex's Collaborative Journey in Advanced Materials** Dr Claire Steggall-Murphy - Victrex **3:30 PM - From Fundamental Research to Implementation: How Public-private Participation Drives Thermoplastic Composite Innovation in the Netherlands** Ms Vanessa Marinosci - TPRC ThermoPlastic Composites Research Center	**Flexible and Efficient Manufacturing of Tailored Cabin Interior Panels for Urban Air Mobility Applications** Mr Johannes Baur - Institute of Aircraft Design Stuttgart	**Multifunctional Flexible and Biodegradable Phase Change Composites for Dual-mode Thermal Management of Lithium-ion Batteries** Mr Lichang Lu - Loughborough University	**Design and Optimization of Functionally Graded Honeycomb Structures for Out-of-Plane Stiffness and Energy Absorption** Dr Kaan Yildiz - Istanbul Technical University	**Evaluating the Impact of Carbon-Based Nanomaterials on the Thermomechanical Properties of High Performance Polymer Fibers** Prof Stergios Goutianos - Norwegian University of Science & Technology	**Optimum Boundaries for Maximum Load-Carrying Capacity of Misaligned Water-Lubricated Composite Journal Bearings Based on Elastohydrodynamics** Mr Wonvin Kim - KAIST	**Vertical Axis Wind Turbine Blade Made by 4D Printing of Composites** Dr Suong Hoa - Concordia University
3:05 PM - 3:25 PM		**Hollow Ball Core HBC Technology: A Novel Manufacturing Approach for Thermoplastic Sandwich Honeycomb Core with Design Flexibility** Mr Won Gyo Seo - Utah State University	**Detection of Delamination in CFRP Laminates by Integrated Fiberoptic Strain Distribution Sensors** Mr Tatsuro Kosaka - Kochi University of Technology	**Applicability of Gamma Irradiation for the Production of UHMWPE Composites for Joint Implant Inserts** Mr Istvan Nemes-Karoly - Budapest University of Technology & Economics	**Electrophoretic Deposition of Carbon Nanotube on Highly Aligned Short Carbon Fibers and Influence of Carbon Nanotube Coating on Piezoresistivity** Dr Amit Chaudhari - University of Delaware	**Lightweight Composite Materials for Radiation Shielding via Electrospinning Fabrication** Prof Maria Gabriella Santonicola - Sapienza University of Rome	**Toolpath Optimization of Polymer Composite Additive Manufacturing AM Printed Mold to Improve Performance for Compression Molding Applications** Dr Madhura Limaye - Oak Ridge National Lab
3:25 PM - 3:45 PM		**Hyperconnected Simulation Ecosystem Supporting Probabilistic Design and Predictive Manufacturing of Next Generation Aircraft Structures – CAELESTIS Pr** Dr Elena RodríguezSenín - AIMEN Tecnology Ctr	**Out-of-oven Manufacturing for Natural Fiber Composites with Integrated Sensing Capabilities and Water Barrier** Ms Yushen Wang - Queen Mary University of London	**Stochastic Modelling of the Spatially Distributed Viscoelasticity of Short Fibre-reinforced Composites by using Random Fields** Mr Eduard Klatt - Helmut Schmidt Univesity Hamburg	**Processing and Characterization of 3D Vascular CF/CM Composites** Mr Henry Holman - The University of Tulsa	**Innovating for a Sustainable Future: A New Class of Bare Overhead Aluminum Conductors Reinforced with Carbon Composite Strength Members** Mr Clement Hiel - CSSI New Composite Products Development	**3D-printed Stealth-Honeycomb Conductive-Nanoparticles-Filled PEEK Thermoplastic Resin Curve-Patch Composite for Enhanced RCS Reduction** Mr Jaewon Shim - Korea Aerospace University
3:45 PM - 4:10 PM	**Refreshment Break** *(located in Exhibit Hall A/B, Level 100)*						
4:10 PM - 4:40 PM	**4:10 PM - Sustainable Materials Driven Composites at Royce, 2D Materials to Textile Composites** Prof Prasad Potluri - University of Manchester **4:30 PM - How Translational Research Shapes the Future of Dental Composites from Innovation to Commercialisation** Prof Gangadhara Prusty - Australian Composites Manufacturing CRC **4:45 PM - Harnessing the Basic Research, Technical Innovation and Industrial Implementation: The Role of Chinese Society for Composites Materials** Mr Huaxin Peng - Zhejiang University **5:00 PM - Fraunhofer Innovation Platform for Composites Research at UNIST – Harnessing Global Partnership in Bridging Academia and Composites Industry in Korea** Prof YoungBin Park - Ulsan National Institute of Science Technology **5:15 PM - Beyond Academia, How ICC is Transforming Innovation into Commercial Impact** Mr Kiyoshi Uzawa - Knazawa Institute of Technology	**Mini-Orals** *See page 49 for detailed presentation schedule*					
4:10 PM - 5:30 PM		**Poster Session** *(located in Exhibit Hall A/B, Level 100)*					
7:00 PM - 10:00 PM	**ICCM 24 Conference Banquet** - *Ballroom 1, Level 400*						

Room 316	Room 317	Room 318	Room 319	Room 320	Room 321	Time
Sustainability	Compressive Failure	Vitrimer Matrix Composites	Experimental Techniques	Design, Repair and Life Cycle	Fire Performance	
Sustainable Alternatives to Thermoset Polymers for Aerospace Composites: A Comparison using LCA Mr Andrea Bologna - Politecnico di Milano	**A New Test for the Mechanical Characterisation of Composite Pultruded Rods Under Compression** Dr Gustavo Quino - Imperial College London	**Effect of Epoxy Amine Stoichiometry on the Structure Property and Reprocessing Relationships in Imine Based Vitrimer Polymer Networks and Their Compos** Prof Russell Varley - Deakin University	**Challenges and Recommendations for Longitudinal Tensile Testing of Unidirectional Composites Based on a Round-robin Programme** Prof Yentl Swolfs - KU Leuven	**Cost-Effectiveness of Structural Health Monitoring on the Lifecycle of Composite Aerospace Elements** Dr Pietro Ballarin - Politecnico di Milano	**Effect of Thermal Modification on the Fire Performance of Strand-based Mass Timber Composite Panels** Dr Avishek Chanda - Washington State University	2:45 PM - 3:05 PM
Mapping the Global Material and Energy Flows of Fiber Reinforced Polymer Composites Ms Zhuoer Li - University of Michigan	**The Experimental Investigation of the Compressive Performance of Pultruded Rod Composite Struts** Dr Bohao Zhang - University of Bristol	**Substitution Effects on Reprocessable Highly Aromatic Imine-Containing Epoxy Vitrimers** Ms Sharine Noelle Bendulo - Deakin University	**Advanced Characterization of Polymers and Composite Materials using Axial-Torsional Dynamic Mechanical Analysis** Mr Gunther Arnold - Anton Paar Germany GmbH	**Performance Improvement of Type-4 Hydrogen Pressure Vessel using Progressive Ply Failure Mechanism** Mr Akash Burolia - Indian Institute of Technology Kharagpur	**Burning Behaviour of Thermoplastic Glass Fibre Composites for a Bumper Beam Application** Ms Joana Malheiro - PIEP Innovation in Polymer Engineering	3:05 PM - 3:25 PM
Multistep Recycling of ElumT700 Composites via TuFF Technology Dr Joseph Deitzel - University of Delaware		**Cure Kinetics of a Transesterification-Type Vitrimer Derived from a Commercial Epoxy-Anhydride Thermoset** Mr Joshua Ilse - McGill University	**Identification of the Through-Thickness Orthotropic Stiffness Components of Thick Filament-Wounded Composite Tubes in an Industrial Context** Dr Isabella Jacobsen - MatchID US Inc	**Determination of Recycled Carbon Fiber Strength Distribution using Bundle Fiber Tensile Test** Mr Yoshiki Sugimoto - National Institute of Advanced Industrial Science	**Hydrochar-Based Flame Retardants from Brewers' Spent Grain for High-Performance NFRCs** Ms Alessia Pantaleoni - Sapienza University of Rome	3:25 PM - 3:45 PM
Refreshment Break *(located in Exhibit Hall A/B, Level 100)*						3:45 PM - 4:10 PM
						4:10 PM - 4:40 PM
Poster Session *(located in Exhibit Hall A/B, Level 100)*						4:10 PM - 5:30 PM
ICCM 24 Conference Banquet - *Ballroom 1, Level 400*						7:00 PM - 10:00 PM

Scientific Program

FRIDAY, AUGUST 8

Time	Ex Hall C - Plenary	Room 307	Room 308	Room 309	Room 310	Room 314	Room 315
7:00 AM	**Registration Desk Open** *(closes at 12:30 PM - located in Charles Street Lobby, Level 100)*						
7:00 AM	**Continental Breakfast** *(until 8:00 AM - located in Exhibit Hall A/B, Level 100)*						
7:00 AM	**Exhibit Hall Open** *(closes at 11:00 AM - located in Exhibit Hall A/B, Level 100)*						
8:00 AM	**Welcome Remarks**						
8:05 AM	**Plenary Speaker: Quality Measurement and Control in High Volume Composites Manufacturing: A Combined Academic and Industrial Perspective** Prof Simon Bickerton, *University of Auckland*						
9:00 AM	**Lagace Lecture: New Concepts and Products of Double-Double Laminate** Prof Stephen Tsai, *Stanford University*						
Move to Level 300 for Technical Sessions							
		Manufacturing: Welding	**Smart Composite Materials**	**Physical and Structural Behavior**		**Multiscale Behavior**	**Sustainability**
9:35 AM - 9:55 AM		**Sequential Resistance Welding of a Thermoplastic Composite Leading Edge Demonstrator from Laboratory Testing to Full-scale Welding** Mr Massimiliano Russello - AIMEN	**Effect of Atomic Oxygen Exposure on the Thermomechanical Properties and Shape Memory Behaviour of ±45° Glass Fibre Reinforced Cyanate Ester Based Shape Memory Polymer Composites** Prof Jayantha Epaarachchi - University of Southern Queensland	**Experimental Study on the Fatigue Performance of CFRP Beams with Structured Surface Load Introduction Under Cyclic Loading** Mr Torben Deutschmann - TUHH		**Multiscale Analysis for Woven Composite with Incomplete Periodicity** Mr Koki Tsuda - Nagoya University	**Composite Material Sustainability: Where are We Today and Where Do We Need to Go** Dr Edward Patton - Patton Engineering
9:55 AM - 10:15 AM		**Ultrasonic Welding of Metal and Fibre Reinforced Thermoplastics — Bond Formation and Joint Strength** Mr Moritz Liesegang - RPTU Kaiserslautern-Landau	**Performance Evaluation of Structural Behavior Monitoring using Smart Sensors** Dr Sung-Hwan Jang - Hanyang University ERICA	**Impact of Stacking Sequence on Tensile and Fatigue Performance of Quasi-isotropic Carbon/Epoxy Laminates** Mr Marc Gadinger - Friedrich Alexander Universitut Erlangen Nurnberg		**Multiscale Modeling for Bottom-up Prediction of Failure Parameters of Unidirectional Carbon-fiber-reinforced Composite Lamina from Atoms to Laminasc** Prof Yoshiaki Kawagoe - Tohoku University	**Untangling Decarbonization Strategies for Net Zero Carbon Fiber** Dr Kyle Pender - National Composites Centre
10:15 AM - 10:35 AM		**Development of Metal-carbon Composites from Poly(ether-ketone-ketone) for Ablative Thermal Protection Coatings** Ms Casey Barrett - Rowan University	**Rectifying Efficiency Measures for Vascular-based Thermal Regulation** Mr Sandeep Rajendra Kumar - North Carolina State University				**Production of Olefin-based Composite Materials by Recycling Discarded Carbon Fibres** Mr Corrado Sciancalepore - University of Parma
10:35 AM - 11:00 AM	**Refreshment Break** *(located in Exhibit Hall A/B, Level 100)*						

Room 316	Room 317	Room 318	Room 319	Room 320	Room 321	Time
Registration Desk Open *(closes at 12:30 PM - located in Charles Street Lobby, Level 100))*						7:00 AM
Continental Breakfast *(until 8:00am - located in Exhibit Hall A/B, Level 100)*						7:00 AM
Exhibit Hall Open *(closes at 11:00 AM - located in Exhibit Hall A/B, Level 100)*						7:00 AM
						8:00 AM
						8:05 AM
						9:00 AM
Move to Level 300 for Parallel Keynotes and Technical Sessions						
Experimental Techniques	**Compressive Failure**	**Vitrimer Matrix Composites**	**Fire Performance**			
Residual Strain Development in Carbon Fiber Reinforced Metal Hybrid Laminates: An Experimental Investigation using FBG Strain Sensors Mr Maximilian Pollak - Die FH OÖ Forschungs & Entwicklungs GmbH	**Laminate Hybridization using High Modulus Carbon Thin Plies for Enhanced Compressive Performance** Mr Yousef Rifai - University of Bristol	**Vitrimer Matrix Composites Manufactured by Filament Winding for Space Applications** Ms Josephine de Calbiac - Centre National d'Etudes Spatiales CNES	**Modeling and Prediction of Residual Strength of Polymer Composites Exposed to Heat** Mr Jianhua Huang - Luna Labs USA LLC			9:35 AM - 9:55 AM
Characterisation of Binder Powders in Glass Fibre Fabrics using Laser Microscopy and Deep Learning Segmentation Methods Mr Jesper Lisegaard - Technical University of Denmark	**Localized Hybridization using Boron Fibers: A Route to Improve Open Hole Compressive Performance** Dr Gursahib Singh Bhatia - Imperial College London	**Flexible and Recyclable Vitrimers for Sustainable Electronic Composites** Prof Aniruddh Vashisth - University of Washington Seattle	**Fire Modelling of Multifuel Composites with Varying Material Layers using Complex Stoichiometry** Prof Debes Bhattacharyya - University of Auckland			9:55 AM - 10:15 AM
Automated Construction of Viscoelastic Master Curves and Prony Series Models for Advanced Material Characterization Using DMA Data Mr Mahdi Tayyebati - Technical University of Denmark		**Rejuvenating Out-of-Date Carbon Fiber Prepregs with Imine-Epoxy Vitrimers** Ms Sharine Noelle Bendulo - Deakin University	**Experimental Evaluation of Interlaminar Shear Strength of Carbon Nanomaterial Z-threaded Carbon Fiber-Reinforced Polymer Laminates After Exposure to E** Prof Kuang-Ting Hsiao - University of South Alabama			10:15 AM - 10:35 AM
Refreshment Break *(located in Exhibit Hall A/B, Level 100)*						10:35 AM - 11:00 AM

FRIDAY, AUGUST 8

Time	Ex Hall C - Plenary	Room 307	Room 308	Room 309	Room 310	Room 314	Room 315
		Manufacturing: AFP/ATP 3	Smart Composite Materials	Physical and Structural Behavior		Multiscale Behavior	Sustainability
11:00 AM - 11:20 AM		**Differential Eddy Current Sensing Probe and It's Implementation in Automated Composite Manufacturing Applications** Mr Ege Arabul - University of Bristol	**Energy Efficient and Tailored Out-of-Oven Composites Manufacturing Towards Sustainable and Smart Composites** Dr Han Zhang - University of Warwick	**Fastblade: A Fatigue Testing Facility for Full Scale Blades** Dr Sergio Lopez Dubon - The University of Edinburgh		**A Novel Multiscale Digital Image Correlation Approach for Monitoring Stable Skin-Stringer Delamination Growth in Post-Buckled Composite Panels** Mr Andres Pereira - Delft University of Technology	**Sustainable Biodegradable Composites for a Circular Economy** Dr Amar Mohanty - University of Guelph
11:20 AM - 11:40 AM		**Pass Frequency as a Means for Increased LATP Productivity** Ms Emma Tobin - University of Limerick	**rCF-based Pyro-Resistive E-Skin Integrated with Temperature Sensing and Self-Controlled Joule Heating Function** Mr Yansong Li - Queen Mary University of London	**Compression-Compression Fatigue of Glass-Fibre Non-Crimp Fabric Composites by Four-Point Flexure** Ms Nicola Shepherd - The University of Auckland		**Multiscale Modelling of Cryogenic Hydrogen Permeability in Polymer-Matrix Composites** Mr Mustafa Okumus - University of Warwick	**Self-Contained Cost-Effective Plastic Recycling Facilities** Dr Ranji Vaidyanathaan - Oklahoma State University
11:40 AM - 12:00 PM			**Inspired by Ice Skates: Smart Aqueous Self-lubricating Coatings for Icephobic Applications** Ms Gelareh Momen - University of Quebec at Chicoutimi	**The Role of Pore Distribution and Hierarchical Structure of Marine Mussel Plaque Cores** Dr Tao Liu - Queen Mary University of London			**Manufacturing and Characterisation of Continuous Recycled Carbon Fibre Unidirectional Composites** Dr Monali Dahale - National Composite Centre
Move to Level 100 for Closing Ceremony							
12:10 PM - 12:30 PM	**Closing Ceremony** *(Exhibit Hall C, Level 100)*						
12:30 PM	**Box Lunch Pick-up** *(located in Exhibit Hall A/B, Level 100)*						
12:45 PM	**Bus Departs for UD-CCM Tour**						
2:15 PM - 4:15 PM	**Tour of UD-CCM**						
4:15 PM	**Depart UD-CCM and return to Baltimore Convention Center**						

Room 316	Room 317	Room 318	Room 319	Room 320	Room 321	Time
						11:00 AM - 11:20 AM
						11:20 AM - 11:40 AM
						11:40 AM - 12:00 PM
Move to Level 100 for Closing Ceremony						
Closing Ceremony *(Exhibit Hall C, Level 100)*						12:10 PM - 12:30 PM
Box Lunch Pick-up *(located in Exhibit Hall A/B, Level 100)*						12:30 PM
Bus Departs for UD-CCM Tour						12:45 PM
Tour of UD-CCM						2:15 PM - 4:15 PM
Depart UD-CCM and return to Baltimore Convention Center						4:15 PM

Poster Session

Posters will be on display in Exhibit Hall A/B, Level 100

Poster Title	Poster Presenter	Poster No.
Aerostructure Composites		
Filament Wound Carbon Fiber Reinforced Polymers Support Structures for Spacecraft Applications	Dr Abrar Ul Haq Khan Baluch	1
Aligned Discontinuous Fiber Composites		
Quantification of Alignment Quality of Discontinuous Fiber Composites Using 2D Fast Fourier Transform FFT	Dr John Tierney	2
Artificial Intelligence Empowering Composite S&T		
Specialized LLMs for Supporting Composite Material Processing and Equipment Operation	Dr Seokpum Kim	3
Composites AI: An AI-Powered Expert System for Composites Engineering	Prof Wenbin Yu	4
Biomass-Based Composite Materials		
Development and Characterisation of Bamboo and Natural Fibre Composite Wrapped Tow Reinforced Trusses	Mr Matthew Lillywhite	5
Biochar as an Alternative Filler for Composites	Prof Veronica Calado	6
Design, Repair and Life Cycle		
Machine Learning Based Residual Distortion Prediction for Extrusion-based Additive Manufacturing of Biocomposite	Ms Bhagyashree Prabhune Dr Madhura Limaye	7
AI Driven Methodologies for Advancing Composite Material Analysis and Applications	Mr Cesar Garcia Gascon	8
Designing Layered Composites for Improved Buckling Strength Using Auxetic Behavior	Dr Yeqing Wang	9
Observation of Bending Fractural Behavior of CFRTP Laminates with Fiber Discontinuity using DIC	Mr Kento Onozuka	10
Manufacturing and Mechanical Properties of Recycled Carbon Fiber Composites by Spinning Process	Mr Shinichi Tatsuta	11
A Non-Local Cohesive Zone Model for Delamination in Fiber-Reinforced Polymers Incorporating Extrinsic Energy Dissipation	Mr Xiaole Li	12
Determining Feasibility Bounds of Lamination Parameters using Neural Networks	Mr Swapan Madabhushi Venkata	13
Extension and Layup Optimization of Double-Double Laminates Based on Lamination Parameters	Mr Chen Du	14
Experimental Techniques		
Using Multiaxial Fatigue to Investigate the Anisotropic Performance in Additively Manufactured Material	Dr Peter Bailey	15
Nondestructive Assessment of Stiffness Degradation Owing to Mechanical Fatigue and Temperature-Accelerated Fatigue of GFRP by using NIR-spectroscopy	Mr Daniel Esse	16
Fire Performance of Composite Materials		
Development of Bench Scale Instrument for Testing Thermal Protective Performance in Different Orientations	Mr Sudhanshu Maurya	17
Thermal and Mechanical Analysis for Li-ion Battery Fire Containment	Dr Sindhu Bushpalli	18
Industrial Applications		
Glass Reinforced Epoxy GRE as an Alternative Pipeline for Onsite Surface Installations a Structural Integrity and Economic Feasibility Study	Mr Muhammad Tahir Waqas	19
Performance of Graphene Nanoplatelet Enhanced CFRP Composites under Post Cryogenic Thermal Cycling for Hydrogen Storage Applications	Dr Jabir Ubaid Parakkal	20
Development of Lightweight Sandwich Composites with Improved Reaction to Fire and UV Resistance	Ms Helena Rocha	21
Manufacturing		
Improving Interlayer Adhesion in Large Format Additive Manufacturing for Composite Tooling	Mr Nicolas Courion, Dr Pascal Hubert	22
Printing of Molten Metal Droplets Toward High Throughput Metal Matrix Composites Manufacturing	Dr Kaihao Zhang	23
An Anisotropic Constitutive Model for Carbon Fabric-Reinforced Shape Memory Polymer Composites Based on Phase Transition Concept	Mr Chen Jiajun	24
Manufacturing *(continued)*		
Design Optimization and Fabrication of Non-Conformal Thermal Cloak Using Continuous Embedded Metal Polymer Composites	Mr Muhammad Jawad Ahmad	25
Advanced Composite Bonding using Energy Efficient Localised Curing Based on Nanomodified Epoxy	Prof Daiva Zeleniakiene	26
Performance Evaluation of Natural Fibre Reinforced Polymer Matrix Composites Manufactured via Liquid Resin Infusion	Dr Chamil Abeykoon	27
Structural and Thermal Properties of 3D Printed Polylactic Acid Composites Filled with Bamboo Powder	Dr Chamil Abeykoon	28
Friction Behaviors of Carbon Fiber Tows and their Effect on the Manufacturability and Mechanical Properties of Composite Pressure Vessels	Ms Su Hyun Lim	29
Effect of Corner Curvature on Press Forming of Metalthermoplastic CFRP Laminates	Ms Naito Miumi	30
Multifunctional Natural Fibre Composites with Integrated Process Monitoring Damage Sensing Capabilities	Mr Yansong Li	31
Development of a Robotic Enabled Composite Part High-Resolution Inspection and Reverse Digital Twin Tool	Mr George Willis	32
Development of a 700 Bar Thermoplastic Type IV Pressure Tank for Compressed Hydrogen Storage in the Field of Mobility	Mr Pedro Abreu	33
Design and Analysis of Fiber-Reinforced Composite Hydrogen Storage Vessels for Transportation Vehicles Type IV and V	Mr Hyunchul Ahn	34
Effect of Incorporating Additional Thermoplastic into Carbon Fiber Epoxy Composites Prepared by Electrodeposition Resin Molding Method	Mr Md Tansirul Islam	35
Research on Longitudinal Torsional Ultrasonic Vibration Assisted Grinding of CFRP	Ms Yan Chen	36
Multi-Scale Modeling for the Curing-Induced Deformations of the Toughened Resin-Based Composite	Ms Meiyu Liu	37
Realtime Flowfront Prediction in Resin Transfer Molding Using Electromechanical Behavior and Generative Adversarial Network	Mr Dahun Lee	38
Development of Multifunctional Coaxial Fiber Sensor for Simultaneous Strain and Temperature Monitoring for Composite Manufacturing Process	Mr Seungyoon On	39
Materials and Precursors		
Helicobacter Pylori Detection via SERS Enhancement Using Synergistic Effects of Gold Nanorods Nano Mica Platelets ZnO Quantum Dots	Mr Ming Chang Lu	40
Effects of Dry Heat and Ultraviolet on the Tensile and Fatigue Strengths of Glass Fiber Reinforced Vinyl Ester	Mr Abdul Rahman Aravind	41
Construction of 3D Networked Epoxy Composite Using RGO and BPEI Coated Epoxy Microspheres for High Thermal Conductivity Applications	Miss Dayoung Kim	42
Enhanced Charge Transfer in Thermogalvanic Cells via Nitrogen Doping of Oxidized CNT Electrodes	Dr Seung Yeol Jeon	43
Evaluation of Cryo TMADMA for Determining the Stiffness Properties of Adhesives at Cryogenic Temperatures	Mr Patrick Nowakowski	44
Experimental Investigation of Mechanical Fiber Bundle Spreading	Miss Hannah Rabe	45
Evaluating Wool Fiber's Viability as a Sustainable Reinforcement in Composite Applications	Mr Tsegaye Lemmi	46
Valorization of Postconsumer Biodegradable Polymer Blend to Create Composites with Agroindustrial Byproducts as Reinforcing Fillers	Miss Erika Palazzi	47
Gas Diffusion Nanocomposite Layer with Enhanced Mass Transport with Surface Functionalization by Laser Irradiation	Dr Taesik Eom Prof Sang-Eui Lee	48
Novel Electrospinning PVDFBi2O3CeO2 Composite Yarns A Versatile Approach Towards Functional Xray Shielding Textiles	Miss Siyuan Zhao	49
Tribological Investigation of the Interface Between Steel Pin and CFRP Tube	Mr Floyd Daniel Bischop	50
Enhancing Mechanical and Thermal Properties of Recycled EVOH Films Using NanoSilica Additives	Ms Kowsar Rezvanian	51

Poster Session

Posters will be on display in Exhibit Hall A/B, Level 100

Poster Title	Poster Presenter	Poster No.
Materials and Precursors *(continued)*		
Interface Structure and Characterization Analysis of Carbon Fiberpolypropylene with -Crystals	Mr Dazhi Jiang	52
Microwave Assisted Synthesis and Characterization of GadoliniumDoped Nickel Ferrite Nanoparticles	Mr Ignatius Eboquansah	53
Polydopamine-Coated Hexagonal Boron Nitride for Heat Dissipation Application	Ms Yeon Hwa Jeong	54
Evaluation of the Effect of Z-Threaded Carbon Nanofibers on the Improvement of Flexural Properties of Carbon Fiber Reinforced Polymer Laminates	Prof Kuang Ting Hsiao	55
Enhancing the Properties of Laminated Composites with Vertically Aligned Carbon Nanotubes Interleaves	Mr Blagoj Karakashov	56
The Low Density and High Strength Epoxy Resin Based Solid Buoyancy Material was Prepared by a New Technology	Mr Xu Chengxin Xu	57
Development and Application of Low Smoke Epoxy Resin Based Carbon Fiber Prepreg	Mr Jiahui Tan	58
Dielectric and Electrical Properties of Polyetherketone–Silica Nanocomposites for High Performance Electronic Applications	Dr Mandar Joshi	59
Development and Characterization of a Novel FeCrAlAlumina Composite for Enhanced Corrosion Resistance and Biocompatibility	Ms Olga Tsurtsumia	60
Evaluation of the Plasticizing Effect of Polythylene Glycol 400 in a Polylactic Acid Polymer Matrix for Food Packaging Applications	Mr Daniel Alvarez Gomez	61
Multifunctional and Smart Composites		
Development of Nanomaterials-Based Antiicing-Deicing Devices for Aviation Sector	Dr Muhammad Zahid	62
Development of Phenolic Resin Nanocomposites Reinforced with Nanodiamond	Ms Yasuda Momoka	63
In-situ Synthesis of Polyamide Composites with Recycle Carbon Fiber	Mr Hasegawa Dai	64
Injectable Enzyme-free Catecholic Alginatepluronic Nanocomposite Hydrogel via the Peroxidase Mimicking Bioglass for Bone Regeneration	Mr Quyen Tran	65
Frequency-Selective Surface-Based Composite Radar Absorbing Structures Using Transferred Laser-Induced Graphene on Glass Fiber Fabric	Mr Kinal Kim, Prof SangEui Lee	66
Development of Composites Manufacturing Assisted Artificial Intelligence and Machine Learning based Automated 3D Defect Detection System	Miss Yagna Jadeja	67
Energy Storage Performance of DFO Incorporated PVDF Composite Thin Film	Mr Abhinav Yadav	68
Optimizing Conductivity and Performance of Conductive Graphene-Acetylene Black Reinforced Nitrile Rubber NBR Composites	Dr Zaheer ul Haq	69
Enhancing Ablative Resistance of Carbon-Epoxy Laminates via Interlayer of Silicone Elastomer Microparticles	Mr Se Jun Wang	70
Physical and Structural Behavior		
Insights into the Mechanical Degradation of Matrix and Fibre-Matrix Interface in Carbon Fibre-Reinforced Polymers (CFRPs) Under Hydrothermal Conditions	Dr Weizhao Zhang	71
Impact Characteristics of Sheet Molding Compound with Different Tape Morphology and Effect of Continuous CFRTP Overmolding	Mr Sang Won Lim	72
Computational Prediction of Fatigue-Induced Debonding in Multilayer Wind Turbine Blade Protective Coatings under Stochastic Raindrop Impacts	Dr Puneet Mahajan	73
Integrated Mesoscopic Modeling Scheme for 2D Woven Prepregs During Compression Molding	Mr Deyong Sun	74
Structural Integrity of Composite Manipulator Applied to the Automated Ropeway Inspection Using Flexible Multibody Dynamics Analysis	Mr ChiHyun Song	75
Multifunctional Stealthy Flexible Honeycomb Core and Lightning Protection Metamaterial Surface Composites for Lightning Strike Damage	Mr SeongHaeng Heo	76
Physical and Structural Behavior *(continued)*		
Assessing the Impact of Salt-Fog Exposure on the Performance and Recyclability of Biobased Epoxy Composites Eeinforced with Natural Fibres	Mr Vincenzo Fiore	77
Development and Modeling of Interfacially Engineered Composites with Designed Failure	Mr Gergo Zsolt Marton	78
Multiscale Analysis of Hybrid Hemp-Glass Composites for Sustainable Lightweight Automotive Torsion Beams	Mr Napat Nawawithan	79
A Novel Method for Evaluating the Biodegradability of Polymers by Tracking Changes in Tensile Properties During Degradation	Ms Lovisa Rova	80
Finite Element Model of Progressive Damage of Composite Grille Cylinder and Predication of Its Compressive Load Bearing Performance	Mr Dazhi Jiang	81
3D Printing Biosourced PLA-flax Composite Sandwich with Different Core Geometries and their Bending Behaviours	Ms Zhenyi Wang	82
Shear Thickening Fluid Thermoplastic Matrix Composite Bulletproof Vests	Mr Mauricio Jose Aires Malheiro	83
Nonlinear Behavior of Polymers and Structures Produced using Additive Manufacturing	Mr Elvijs Bojars	84
Characterization of Mechanical Properties of Induction-cured Carbon-glass-epoxy Hybrid Composites	Mr Andrejs Pupurs	85
Environmental Durability of Composites: Characterization of Temperature and Strain Rate Dependent Properties of Toughened Epoxy Resins	Dr Sagar Doshi	86
Self-Healing Composites		
Self-Healing In-situ Delamination Thermoplastic	Dr Samit Roy	87
Smart Composite Materials		
Fabrication and Characterization of Manganese Doped Cobalt Ferrite Reinforced with PVDF-TrFE for Electrical Applications	Mr Faruk Soso	88
Sustainability and Circular Economy		
Wind Blade Spar Cap Manufacture and Recycling with Discontinuous Carbon Composites	Dr John Tierney	89
Sustainability and Environmental Assessment of Composites		
Effective Decomposition Rate of Epoxy Resin using a Modified Shrinkingcore Model: Synergistic Hydrolysis and Glycolysis Reactions	Mr Jinsu Kim	90
Thermoplastic Composites		
Enhancing Mechanical Performance of Recycled CFPEKK Composites: The Role of Strand Optimization and Plasma-Activated Adhesive Bonding in Sandwich Structures	Dr Hatice Sas	91
Development and Characterization of Munja Grass Fiber-Reinforced HDPE Composites for Structural Applications	Mr Nitin Arya	92
Reconsolidation of CFPEKK Composites: Repair of Drilling-induced Damage and Hydrothermal-Aging Effects	Dr Hatice Sas	93
Effect of Needle Punching on the Dynamic Properties of Recycled Non-Woven Carbon Fiber-Reinforced Thermoplastics	Mr Zhang Fan	94

TUESDAY, AUGUST 5

Mini-Oral Schedule

Each Mini-Oral presentation will be 3 minutes.

Time	Room 307	Room 308	Room 309
4:10 PM	**Effect of Incorporating Additional Thermoplastic into Carbon Fiber Epoxy Composites Prepared by Electrodeposition Resin Molding Method** Mr Md Tansirul Islam	**Development of Nanomaterials-Based Antiicing-Deicing Devices for Aviation Sector** Dr Muhammad Zahid	**Evaulation of Cryo TMADMA for Determingin the Stiffness Properties of Adhesives at Cryogenic Temperatures** Mr Patrick Nowakowski
4:15 PM	**Advanced Composite Bonding using Energy Efficient Localised Curing Based on Nanomodified Epoxy** Prof Daiva Zeleniakiene	**Novel Electrospinning PVDFBi2O3CeO2 Composite Yarns A Versatile Approach towards Functional X-ray Shielding Textiles** Miss Siyuan Zhao	**Construction of 3D Networked Epoxy Composite Using RGO and BPEI Coated Epoxy Microspheres for High Thermal Conductivity Applications** Miss Dayoung Kim
4:20 PM	**Friction Behaviors of Carbon Fiber Tows and their Effect on the Manufacturability and Mechanical Properties of Composite Pressure Vessels** Ms Su Hyun Lim	**Environmental Durability of Composites Characterization of Temperature and Strain Rate Dependent Properties of Toughened Epoxy Resins** Dr Sagar Doshi	**Helicobacter Pylori Detection via SERS Enhancement Using Synergistic Effects of Gold NanorodsNano Mica PlateletsZnO Quantum Dots** Mr MingChang Lu
4:25 PM	**Structural and Thermal Properties of 3D Printed Polylactic Acid Composites Filled with Bamboo Powder** Dr Chamil Abeykoon	**Multifunctional Stealthy Flexible Honeycomb Core and Lightning Protection Metamaterial Surface Composites for Lightning Strike Damage** Mr SeongHaeng Heo	**Effects of Dry Heat and Ultraviolet on the Tensile and Fatigue Strengths of Glass Fiber Reinforced Vinyl Ester** Mr Abdul Rahman Aravind
4:30 PM	**Realtime Flowfront Prediction in Resin Transfer Molding Using Electromechanical Behavior and Generative Adversarial Network** Mr Dahun Lee	**Insights into the Mechanical Degradation of Matrix and Fibre-Matrix Interface in Carbon Fibre-Reinforced Polymers (CFRPs) Under Hydrothermal Conditions** Dr Weizhao Zhang	**Tribological Investigation of the Interface Between Steel Pin and CFRP Tube** Mr Floyd Daniel Bischop
4:35 PM	**Designing Layered Composites for Improved Buckling Strength Using Auxetic Behavior** Dr Yeqing Wang	**Development and Modeling of Interfacially Engineered Composites with Designed Failure** Mr Gergo Zsolt Marton	**Effective Decomposition Rate of Epoxy Resin using a Modified Shrinkingcore Model Synergistic Hydrolysis and Glycolysis Reactions** Mr Jinsu Kim
4:40 PM	**Mini-Orals Conclude**		

THURSDAY, AUGUST 7

Mini-Oral Schedule

Each Mini-Oral presentation will be 3 minutes.

Time	Room 307	Room 308	Room 309
4:10 PM	**Determining Feasibility Bounds of Lamination Parameters using Neural Networks** Mr Swapan Madabhushi Venkata	**Frequency-Selective Surface-Based Composite Radar Absorbing Structures Using Transferred Laser-Induced Graphene on Glass Fiber Fabric** Prof SangEui Lee	**Composites AI: An AI-Powered Expert System for Composites Engineering** Prof Wenbin Yu
4:15 PM	**Extension and Layup Optimization of Double-Double Laminates Based on Lamination Parameters** Mr Chen Du	**Enhancing Ablative Resistance of Carbon-Epoxy Laminates via Interlayer of Silicone Elastomer Microparticles** Mr Se Jun Wang	**Specialized LLMs for Supporting Composite Material Processing and Equipment Operation** Dr Seokpum Kim
4:20 PM	**Development of Bench Scale Instrument for Testing Thermal Protective Performance in Different Orientations** Mr Sudhanshu Maurya		**Development and Characterisation of Bamboo and Natural Fibre Composite Wrapped Tow Reinforced Trusses** Mr Matthew Lillywhite
4:25 PM	**Multi-Scale Modeling for the Curing-Induced Deformations of the Toughened Resin-Based Composite** Ms Meiyu Liu		
4:30 PM	**An Anisotropic Constitutive Model for Carbon Fabric-Reinforced Shape Memory Polymer Composites Based on Phase Transition Concept** Mr Chen Jiajun		
4:35 PM			
4:40 PM	**Mini-Orals Conclude**		

NOTES

NOTES

CONFERENCE HOST:



UNIVERSITY OF DELAWARE

CENTER FOR COMPOSITE MATERIALS

Celebrating 50 Years

VISIT THE CONFERENCE WEBSITE:

ICCM24.com

ICCM24
AUGUST 4-8, 2025
BALTIMORE CONVENTION CENTER
BALTIMORE, MARYLAND, USA

No Technical Paper Submission for:

Nancy Sottos

ICCM24
AUGUST 4-8, 2025
BALTIMORE CONVENTION CENTER
BALTIMORE, MARYLAND, USA

No Technical Paper Submission for:

Véronique Michaud

ICCM24
AUGUST 4-8, 2025
BALTIMORE CONVENTION CENTER
BALTIMORE, MARYLAND, USA

No Technical Paper Submission for:

Daniel Melo

ICCM24
AUGUST 4-8, 2025
BALTIMORE CONVENTION CENTER
BALTIMORE, MARYLAND, USA

No Technical Paper Submission for:

Kelvin Fu

ICCM24
AUGUST 4-8, 2025
BALTIMORE CONVENTION CENTER
BALTIMORE, MARYLAND, USA

No Technical Paper Submission for:

Krishna Pillai

Frontal Polymerization: Quo Vademus?

A Review with Consideration of Future Directions

John A. Pojman

Ad Maiorem Poimanorum Gloriam



go to pojman.com

http://www.pojman.com/home/frontal-polymerization-bibliography/

Objectives

- review origins and major advances
- shamelessly promote my own work
- consider future directions for research

What is Frontal Polymerization?

Thermal frontal polymerization is the coupling of the heat release of polymerization with the Arrhenius dependence of the reaction rate in an unstirred system, i.e., “liquid flame”.

Frontal Polymerization Scheme

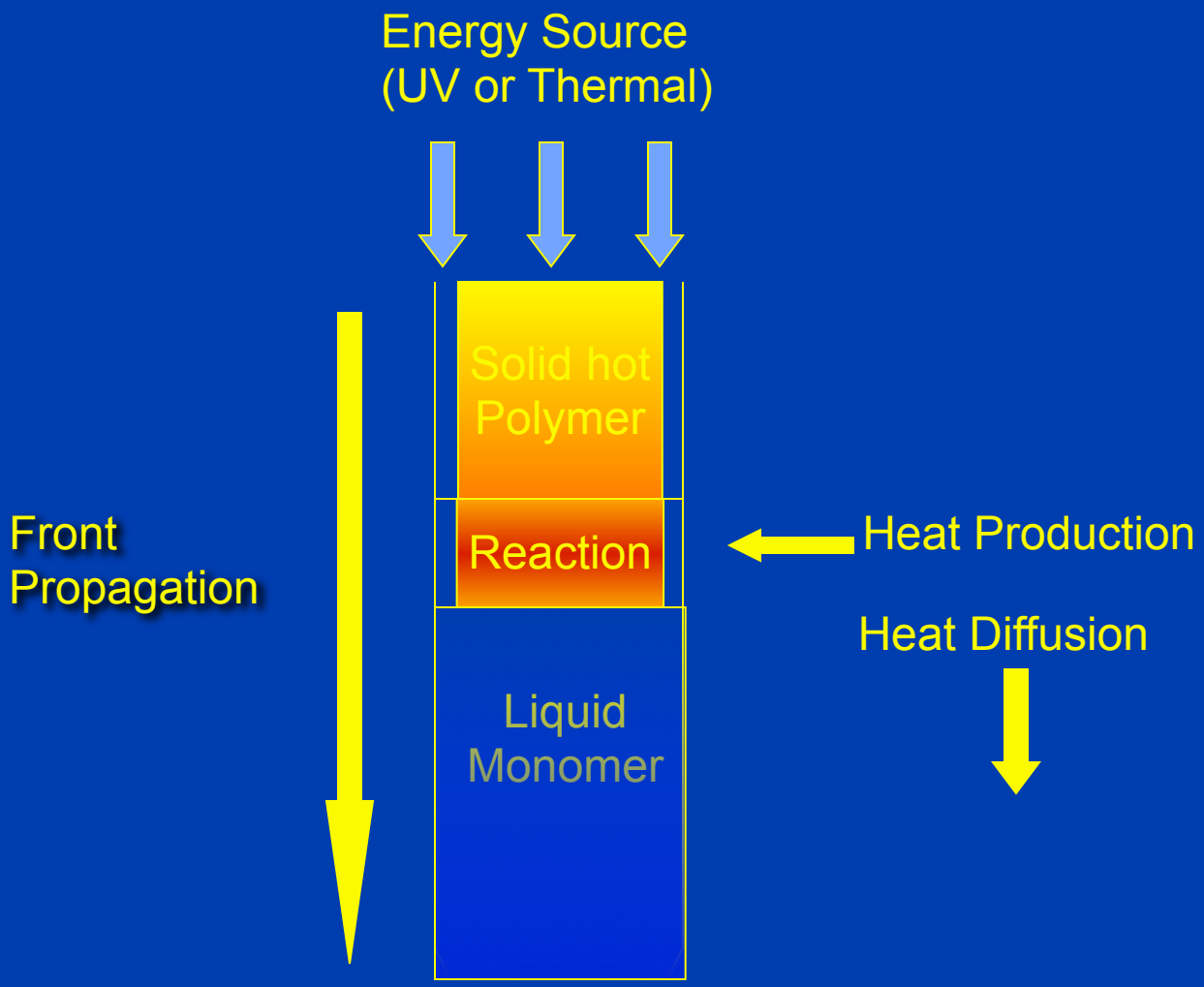

Large Temperature Gradient

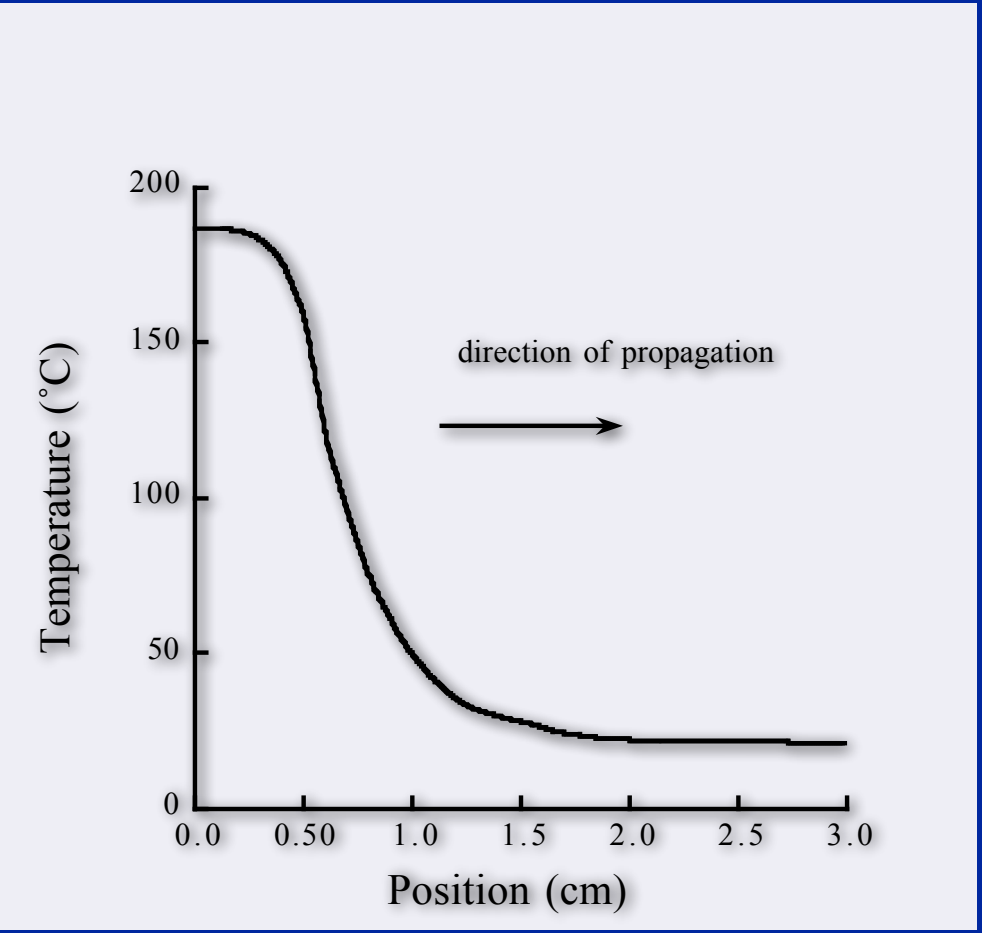

Early History

- inspired by SHS, FP discovered in Chernogolovka, Russia

Chechilo, N. M.; Khvilivitskii, R. J.; Enikolopyan, N. S. "On the Phenomenon of Polymerization Reaction Spreading," *Dokl. Akad. Nauk SSSR* **1972**, *204,* 1180-1181.

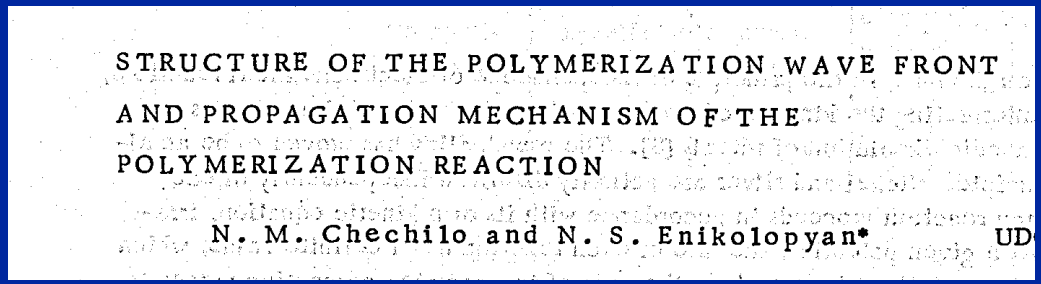

STRUCTURE OF THE POLYMERIZATION WAVE FRONT AND PROPAGATION MECHANISM OF THE POLYMERIZATION REACTION

N. M. Chechilo and N. S. Enikolopyan*

EFFECT OF THE CONCENTRATION AND NATURE OF INITIATORS ON THE PROPAGATION PROCESS IN POLYMERIZATION

N. M. Chechilo and N. S. Enikolopyan *

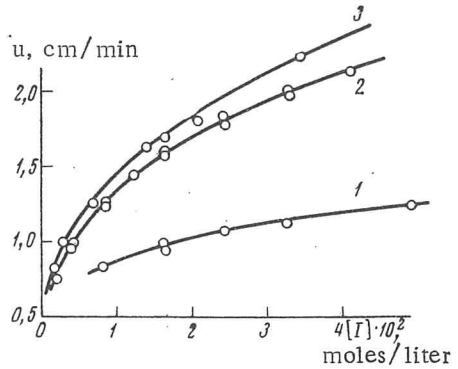

Fig. 1. Dependence of the propagation rate in MMA at P = 3500 kg/cm² and T_0 = 22°C on initiator concentration: 1) DTBP; 2) BP; 3) CPC.

SOME RULES GOVERNING THE EXTENSION OF THE FRONT OF RADICAL POLYMERIZATION OF VINYL MONOMERS*

G. G. Aleksanyan, Kh. A. Arutyunyan, V. L. Bodneva, S. P. Davtyan, E. V. Prut, B. A. Rozenberg, K. G. Shkadinskii and N. S. Yenikolopyan

Institute of Chemical Physics, U.S.S.R. Academy of Sciences

(*Received* 7 *January* 1974)

“rediscovered” in 1991

Traveling Fronts of Methacrylic Acid Polymerization

John A. Pojman

Department of Chemistry and Biochemistry
University of Southern Mississippi
Hattiesburg, Mississippi 39406-5043

Received April 29, 1991

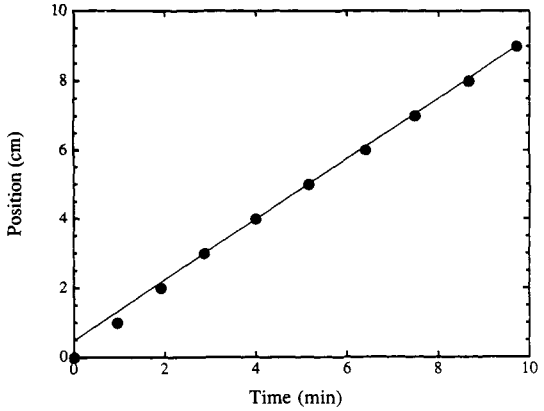

Figure 1. The position versus time of a traveling front of methacrylic acid polymerization. The position was determined visually by the presence of a sharp change from the monomer/initiator solution to solid polymer. Benzoyl peroxide concentration = 0.10 *m*.

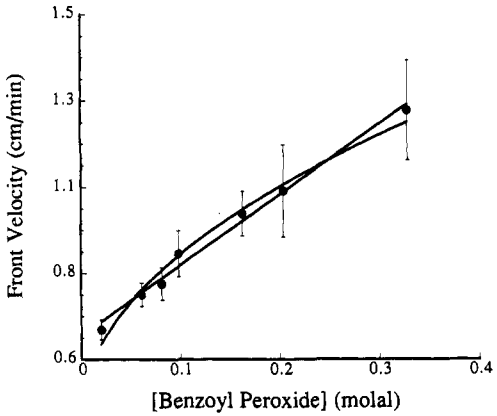

Figure 3. The front velocity as a function of the initiator concentration without promoter. The data were fit with a least-squares program to both a first-order (velocity = k_1[BPO] + constant) and a half-order dependence (velocity = k_2[BPO]$^{1/2}$ + constant). Higher concentrations of benzoyl peroxide were not possible because of limited solubility.

Traveling Fronts of Addition Polymerization with a Solid Monomer

John A. Pojman,*,† Istvan P. Nagy,†,‡ and Carl Salter†,§

Department of Chemistry and Biochemistry
University of Southern Mississippi
Hattiesburg, Mississippi 39406-5043
Department of Physical Chemistry
Kossuth Lajos University
Debrecen, Hungary H-4010
Department of Chemistry, Moravian College
Bethlehem, Pennsylvania 18018

Received August 27, 1993

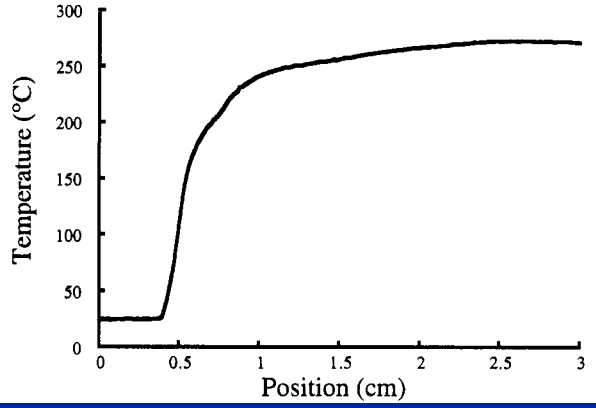

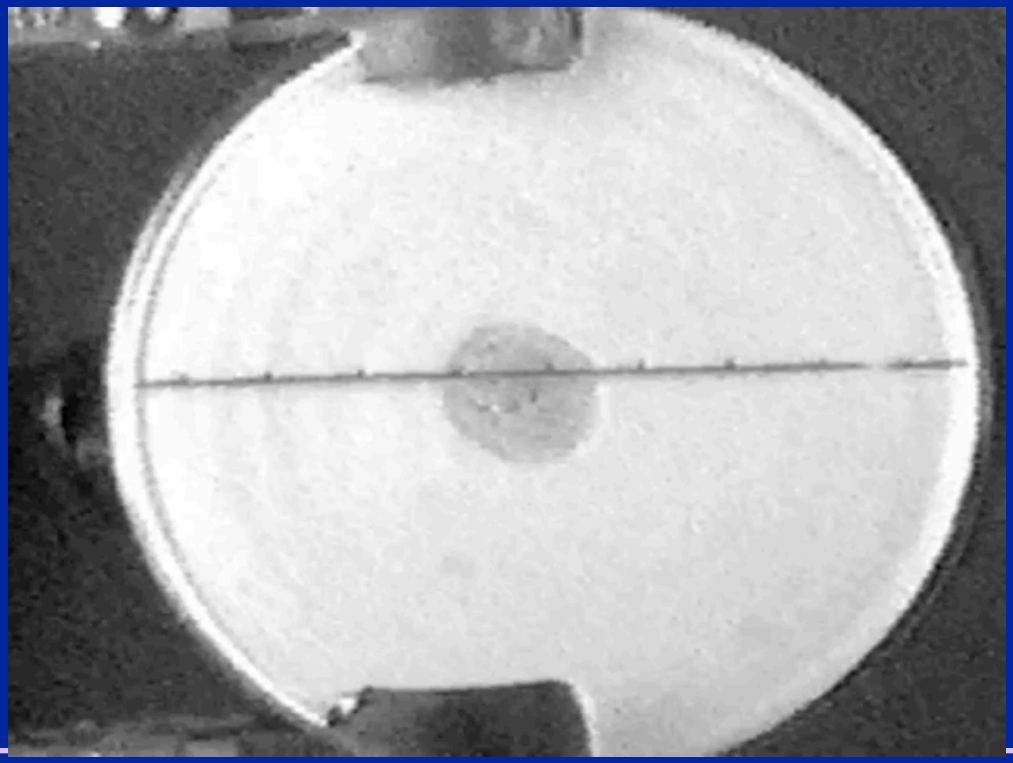

Transition Metal Nitrate complexes

Savostyanov, V. S.; Kritskaya, D. A.; Ponomarev, A. N.; Pomogailo, A. D. "Thermally Initiated Frontal Polymerization of Transition Metal Nitrate Acrylamide Complexes," *J. Poly. Sci. Part A: Poly. Chem.* **1994**, *32,* 1201-1212.

•

No initiator added.

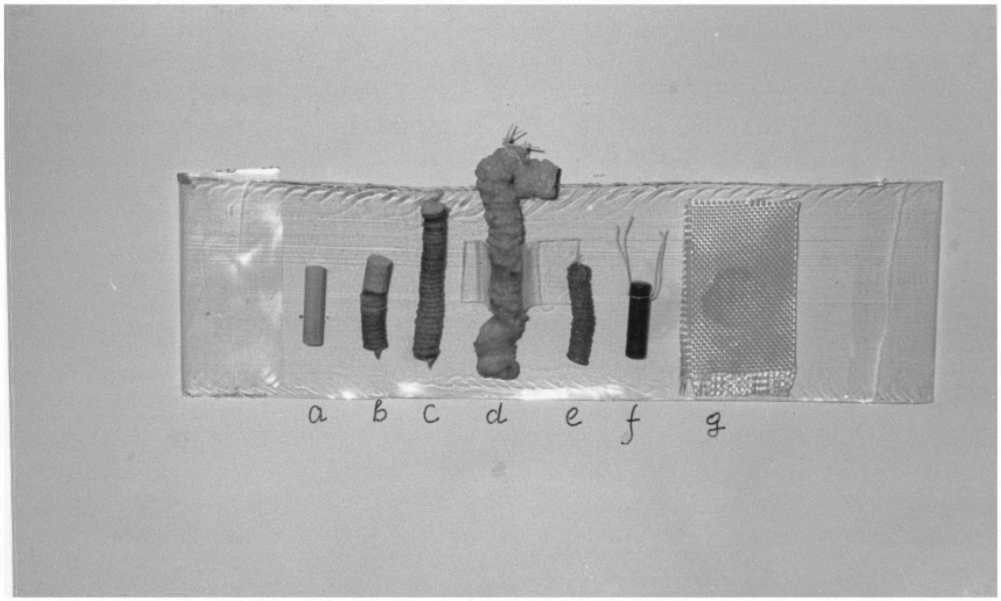

FIG. 2. (a) The view of the cylindrical tablet of the starting CoAAm complex; (b) *d*—the dynamic of the autowave regime at the front polymerization of CoAAm during (b) and at the end of the reaction (c), (d); (e)–(f) views of the samples of CoAAm composites with fiberglass fillers of 5(e) and 10 wt.% (f) contents after front polymerization; (g) the illustration of the front polymerization in the two-dimensional glass fabric system appreted by a 10% solution of CoAAm in methanol. [The tablets were pressed at $P = 1$ (c) and 6 MPa].

Barelko, V. V.; Pomogailo, A. D.; Dzhardimalieva, G. I.; Evstratova, S. I.; Rozenberg, A. S.; Uflyand, I. E. "The Autowave Modes of Solid Phase Polymerization of Metal-Containing Monomers in Two- and Three-Dimensional Fiberglass-Filled Matrices," *Chaos* **1999**, *9,* 342-347.

J. Am. Chem. Soc. **1996,** *118,* 3783−3784

Frontal Polymerization in Solution

John A. Pojman,* Ginger Curtis, and Victor M. Ilyashenko

Department of Chemistry and Biochemistry
University of Southern Mississippi
Hattiesburg, Mississippi 39406-5043

Received January 9, 1996

Frontal polymerization is a mode of converting monomer into polymer via a localized reaction zone that propagates, most often through the coupling of thermal diffusion and Arrhenius reaction kinetics. Frontal polymerization reactions were first discovered in Russia by Chechilo and Enikolopyan in 1972.[1] They studied methyl methacrylate polymerization to determine the effect of initiator type and concentration on front velocity[2] and the effect

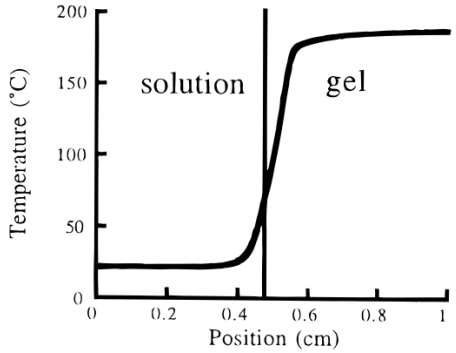

Figure 1. The temperature profile of a front with 1 g of acrylamide/1 mL of DMSO with potassium persulfate (0.02 M). The line indicates the transition from solution to gel, which occurs at 80 °C.

Free-Radical Polymerization

JOURNAL OF POLYMER SCIENCE Polymer Chemistry WWW.POLYMERCHEMISTRY.ORG ORIGINAL ARTICLE

The Effect of Acrylate Functionality on Frontal Polymerization Velocity and Temperature

Samuel Bynum, Michael Tullier, Catherine Morejon-Garcia, Jesse Guidry, Emma Runnoe, John A. Pojman

Department of Chemistry and the Macromolecular Studies Group, Louisiana State University, Baton Rouge, Louisiana 70803
Correspondence to: J. A. Pojman (E-mail: john@pojman.com)

Received 23 November 2018; accepted 17 February 2019
DOI: 10.1002/pola.29352

Other chemistries

a) amine-cured epoxies
b) urethanes
c) FROMP
c) cationic epoxy curing
d) Radical-Induced Cationic Frontal Polymerization (RICFP)

Amine-cured Epoxy

- **bulk curing starting from ambient temperature could avoid the charring of thick samples that can occur when cured in autoclaves**
- demonstrated in Russia in 1975
- Arutiunian, K. A.; Davtyan, S. P.; Rozenberg, B. A.; Enikolopyan, N. S. "Curing of epoxy resins of bis-phenol A by amines under conditions of reaction front propagation," *Dokl. Akad. Nauk SSSR* 1975, 223, 657-660.
- White, S. R.; Kim, C. "A Simultaneous Lay-Up and in situ Cure Process for Thick Composites,"*J. Reinforced Plastics and Comp*. 1993, 12, 520-535.
- For typical epoxy-amine systems, there is a relatively short pot life at room temperature.

Future Directions

- autoclaveless curing
- spontaneous patterning of materials
- foams
- additive manufacturing
- cure-on-demand polymerization
  - coatings
  - repair
  - adhesives

3D Printing

Self-Regulative Direct Ink Writing of Frontally Polymerizing Thermoset Polymers

Jia En Aw, Xiang Zhang, Arif Z. Nelson, Leon M. Dean, Mostafa Yourdkhani, Randy H. Ewoldt, Philippe H. Geubelle, and Nancy R. Sottos**

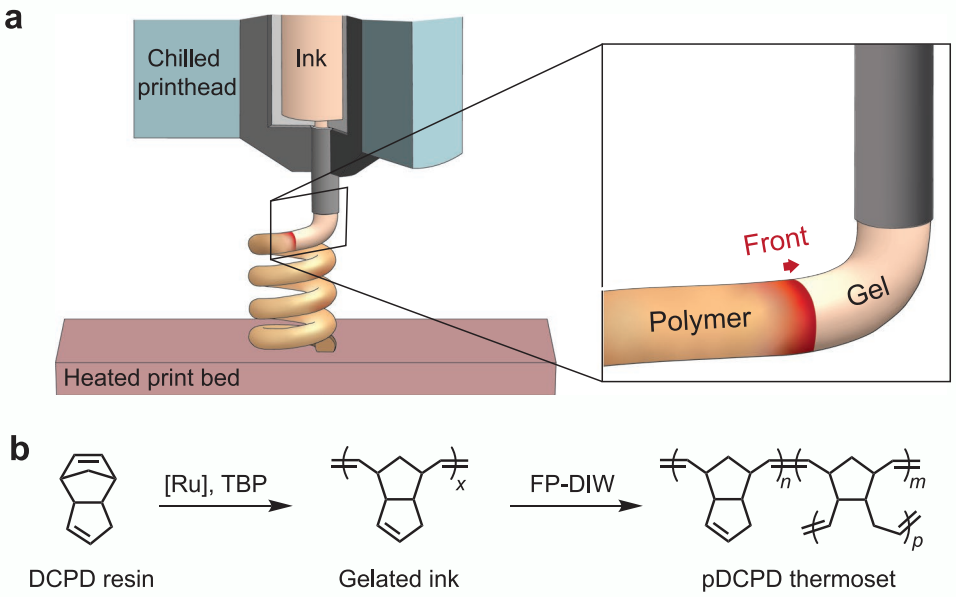

What is “cure-on demand”?

- A polymerization that reacts only when you want it to react.

JOURNAL OF Applied Polymer SCIENCE

Cure-on-demand wood adhesive based on the frontal polymerization of acrylates

TreyVon Holt,[1] Kylee Fazende,[1] Elizabeth Jee,[1] Qinglin Wu,[2] John A. Pojman[1]

[1]Department of Chemistry, Louisiana State University, 232 Choppin Hall, Baton Rouge, Louisiana 70803

[2]School of Renewable Natural Resources, Louisiana State University, Room 227 Renewable Natural Resources Bldg, Baton Rouge, Louisiana 70803

Correspondence to: J.A. Pojman (E-mail: john@pojman.com)

Challenges

- Create frontally-cured adhesive that will work on high thermal conductivity surfaces.
- Create frontally-cure adhesive that will work with very thin layer.

Coatings



Current technology requires evaporation of solvent, mixing or reaction with oxygen



$93 billion/year (2008)

Photocured coatings must be on simple surfaces because of shadows.

propagation in thin layer

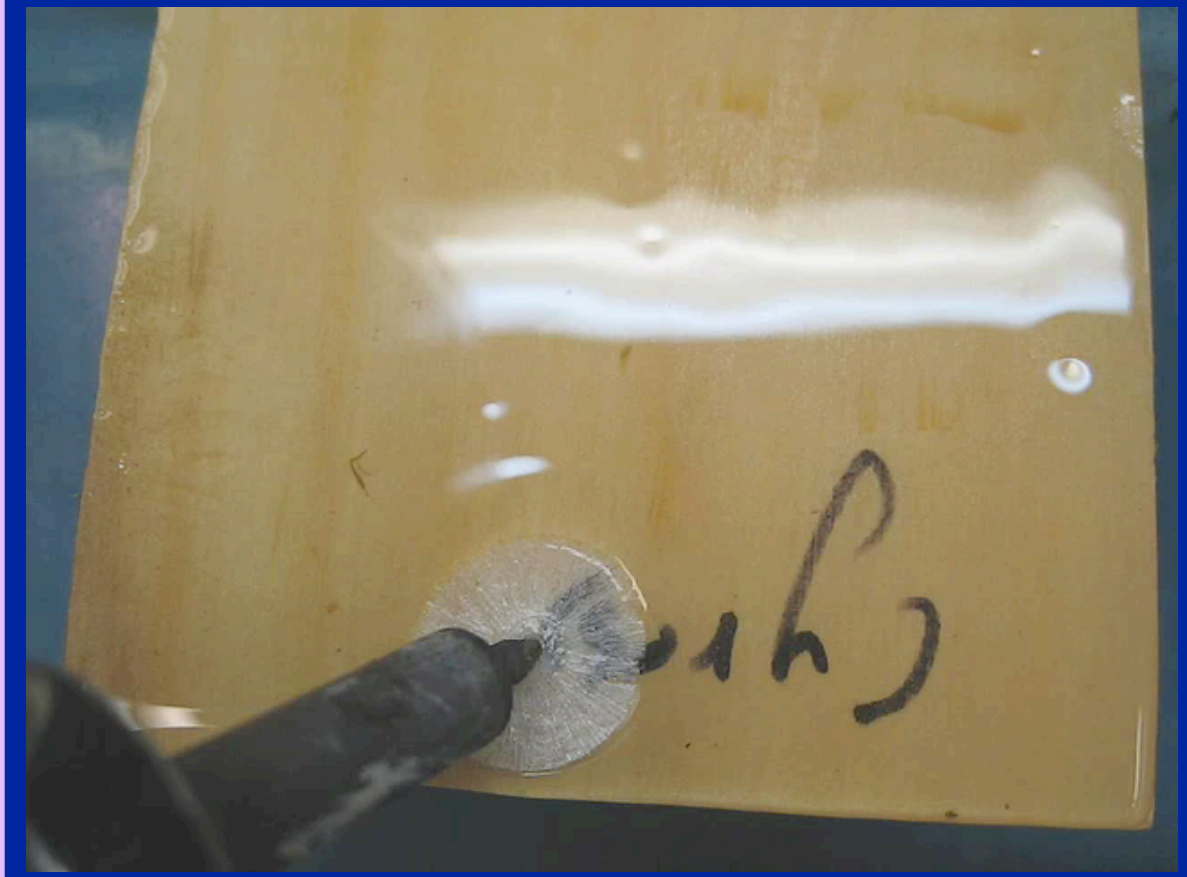

Bansal, K.; Pojman, J. A.; Webster, D.; Quadir, M. "Frontal Polymerization of a Thin Film on a Wood Substrate," *ACS Macro Lett.* **2020**, *9,* 169-173.

Future Challenges

- find new chemistries
- design systems that can work at lower temperatures but still have long pot lives
- demonstrate that materials are at least as good as current ones, e.g. composites
- explore how to use the “spin modes” to create unique materials

FATIGUE DAMAGE EVOLUTION IN GLASS/EPOXY LAMINATES WITH STRESS CONCENTRATIONS: EXPERIMENTS AND MODELLING

Marino Quaresimin, Paolo Andrea Carraro and Lucio Maragoni

University of Padova, Department of Management and Engineering, Stradella San Nicola, 3, 36100 Vicenza (Italy)

Email: marino.quaresimin@unipd.it, web page: http://www.gest.unipd.it

Keywords: Fatigue, Stress concentration, Damage mechanics, Modelling.

ABSTRACT

The work illustrates a fatigue design strategy, based on the physics of the damage evolution, developed by the Composite Group at the University of Padova over the last few years. After a brief introduction, where the motivations of the work are analyzed, examples of damage mechanisms at the macro- and micro-scale are discussed. Then the models for the quantitative description of these mechanisms are illustrated, together with experimental validation. Eventually, the application of the modelling framework to the prediction of the damage evolution in composite plate with central hole is presented.

1 INTRODUCTION

Most structural components made from composite materials are subjected to cyclic loading during their service life. This can result in the progressive evolution of damage, a corresponding loss of stiffness, and, ultimately, catastrophic failure. Designing against fatigue is therefore essential to enhance the reliability of composite structural components across a wide range of applications.

To address the growing need for fatigue-resistant composite design tools, the authors have spent several years developing a comprehensive design framework. This framework aims to predict the initiation of damage, its progression, and the final failure of composite laminates under cyclic loading conditions.

In the context of composite materials, characterized by a multitude of progressive damage mechanisms, "design against fatigue" can take on different meanings, depending on the requirements of the component. These include:

i) Design to prevent crack initiation;
ii) Design to prevent excessive stiffness degradation (damage-tolerant design);
iii) Design to prevent final failure.

As will be discussed in more detail later, damage development in composite laminates involves multiscale and hierarchical processes. These range from micro-scale damage initiation to the growth of macro-cracks and delamination, ultimately resulting in failure. The nature of these mechanisms depends on several factors, including the constituent materials, laminate lay-up, loading type, and multiaxial stress conditions [1].

To effectively tackle such a complex problem and deliver reliable design methods for each of the aforementioned objectives, it is necessary to develop models based on the physical damage mechanisms occurring at various length scales [1]. These models must then be integrated into a multiscale, multi-mechanism design strategy that must be also efficient and flexible to comply with real component design and industrial workflows.

The following sections present representative examples of the key mechanisms that drive laminate degradation and failure under cyclic loading. Subsequently, the proposed modelling strategy is introduced and an application on notched laminates is presented.

2 FATIGUE DAMAGE MECHANICS

The damage evolution in composite materials is a multiscale and hierarchical process, involving several mechanisms at different length scales. In this work, the macro-scale is related to the ply and laminate level, whereas the micro-scale is relevant to the fiber diameter and the inter-fiber spacing.

As widely proved in the literature (see Refs. [2-6] among the others), the first macro-scale damage event in a multidirectional laminate is represented by the initiation of off-axis cracks that involve the entire thickness of a ply and propagate along the fiber direction. The crack density increases during the lifetime and a saturation condition in reached after a certain number of cycles. The second observable mechanism, in chronological order, is represented by delamination. A delamination initiates from the tips of the off-axis cracks at the interface with confining layers and propagates in a direction normal to the off-axis cracks. These two mechanisms are not directly responsible for the laminate failure but cause a significant loss of stiffness that must be correctly predicted if a damage tolerant design approach is adopted. An example of the damage evolution, highlighting the initiation and propagation of multiple off-axis cracks, is shown in Figure 1.

The final failure is eventually typically controlled by the main load bearing plies, which means that it is caused by the failure of the 0°-oriented fibers.

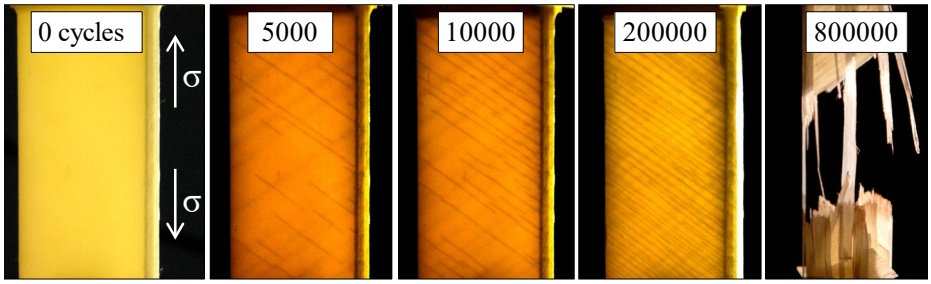

Fig. 1. Example of fatigue damage evolution and failure in a $[0/60_2/0/-60_2]_s$ laminate [6]

The mentioned macro-scale damage events have their precursors and interaction at the microscale, in the form of microcracks, fiber-matrix debonds and fiber breaks. In a damage-based approach, criteria for predicting the onset and evolution of the macroscopic damage modes should be, thus, based on the micro-scale damage mechanisms.

For instance, the micro-scale damage process leading to an off-axis crack formation consists in the initiation and growth of matrix micro-cracks, which eventually coalesce forming the off-axis crack (Figure 2). This is relevant to local stress states characterized by a sufficiently high $\lambda_{12}=\sigma_6/\sigma_2$ (shear to transverse stress ratio). For instance, Figures 2 shows such micro-cracks, in the external 45° ply of a $[45/-45/0]_s$ glass/epoxy laminate under tension/tension fatigue [7]. These micro cracks were shown to be normal to the Local Maximum Principal Stress (LMPS) in the matrix, that was then considered as the effective stress to be used for predicting crack formation in such conditions [8].

If the stress state in a ply is such that the in-plane stress component σ_6 is zero, it was proved [9] that the local stress state in the matrix, close to the fiber-matrix interface, is nearly hydrostatic. This induces a micro-scale failure mode consisting in a matrix cavitation-induced debonding, driven by the Local Hydrostatic Stress (LHS) in the matrix. This was proposed as

the effective stress to be used for predicting crack initiation under a nearly transverse stress state [8].

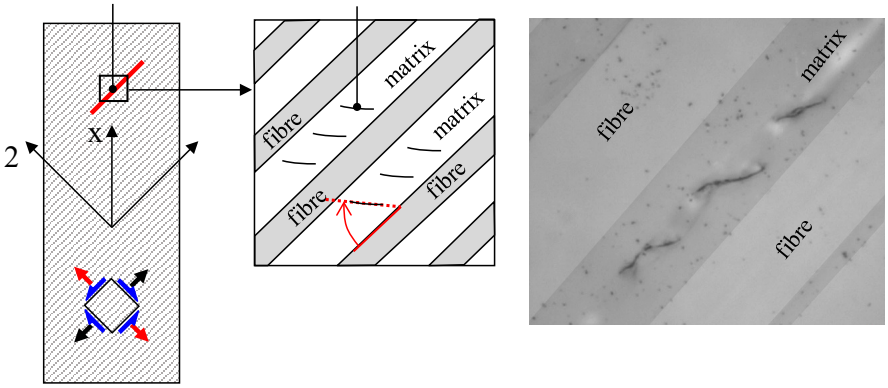

Fig. 2. Schematic and example of off-axis crack formation by initiation of inclined micro-cracks in the matrix of a 45° ply

Also the delamination and fiber failure phenomena were analyzed from the microscopic point of view, revealing their interaction with off-axis cracks. Fatigue tests were carried out on glass/epoxy cross-ply laminates. Edge micrographs of the specimens were taken, revealing the typical scenario shown in Figure 3. Delamination was triggered by the presence of the off-axis cracks. A micro-scale delamination was indeed seen to form exactly at the moment of the off-axis crack formation and then to propagate at the interface [10].

The role that transverse cracks and delamination play on the failure of the fibers is clear from Figure 3. 0° fiber breaks are concentrated in the vicinity of the transverse crack tip and above the delamination, the growth of which leads to more and more fiber breaks, until a critical condition is reached.

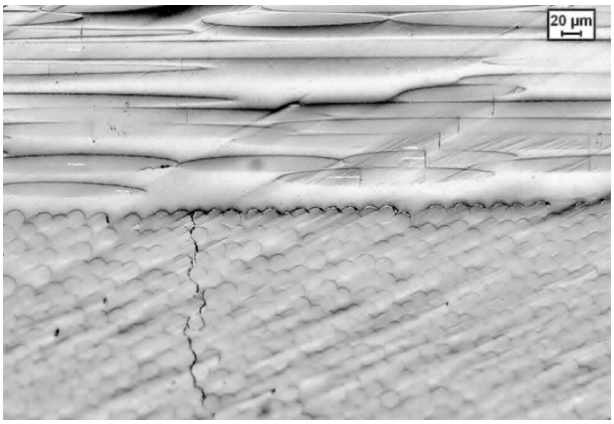

Fig. 3. Example of delamination from a transverse crack tip with broken fibers

3 PREDICTION METHODOLOGY

According to the experimental observations, the fatigue life of a composite laminate has to be divided in different phases, each characterized by a dominating damage mode. Therefore, for predicting the fatigue behavior of a composite laminate, the initiation and evolution of each mechanism has to be predicted, together with its effect on the stress re-distribution and the

stiffness degradation. In particular, within a discrete damage mechanics framework, it is necessary to:

i. Predict the cycles spent for crack initiation;
ii. Describe the crack propagation and the crack density evolution until the saturation condition;
iii. Predicting the cycles spent for the delamination initiation and propagation;
iv. Predicting the cycles spent for the failure of the fibers and the final laminate failure.

For each mechanism (mainly off-axis cracks and delamination), the associated stiffness reduction must be predicted as well.

According to this strategy, a procedure for predicting the damage evolution in composite laminates has been developed by the authors, integrating the following predictive models and criteria:

1) A criterion for predicting the off-axis fatigue crack initiation under multiaxial stress states [8];
2) A mixed mode crack propagation criterion [11];
3) A model for predicting the crack density evolution under a generic multiaxial loading, also under variable amplitude conditions [12];
4) A fracture mechanics-based model for predicting the delamination growth, in combination with multiple crack initiation and propagation [13];
5) An analytical model for describing the stress re-distributions and the stiffness degradation in the presence of off-axis cracks and delamination [14];
6) A model for predicting the load bearing fiber failure, accounting for the stress concentrations caused by off-axis cracks and delamination [15].

The entire framework was validated by means of experimental data, revealing a very good agreement both in terms of damage evolution and stiffness loss. Some examples are reported in Figures 4 -6.

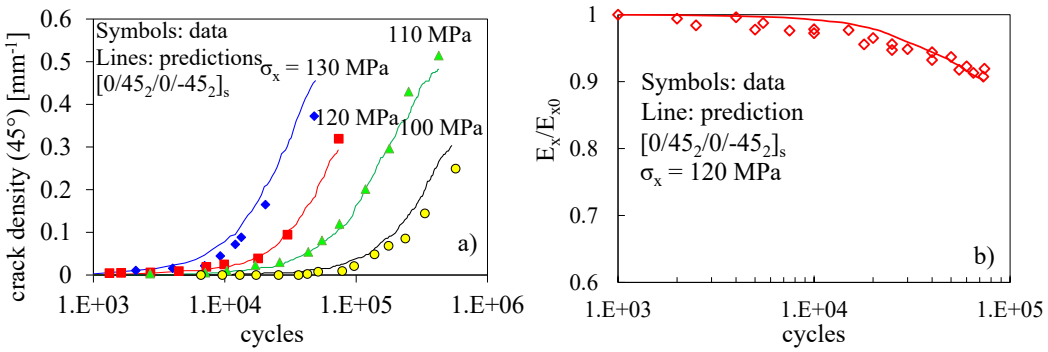

Fig 4. Validation of the procedure in terms of a) crack density and b) stiffness loss for a $[0/45_2/0/-45_2]_s$ plain laminate

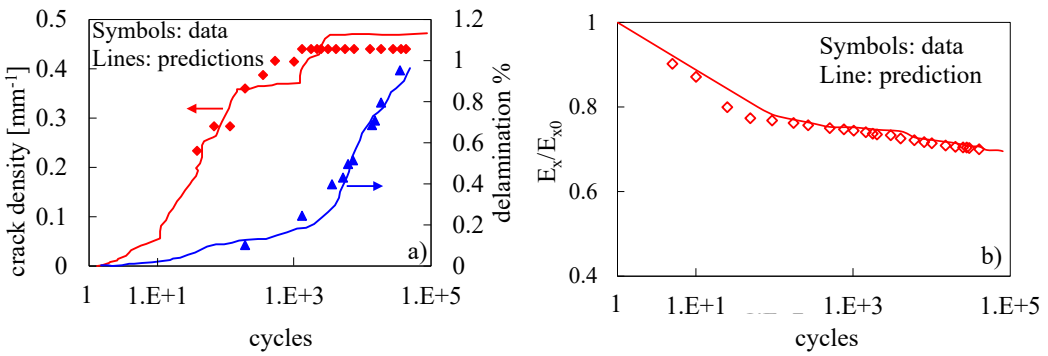

Fig. 5. Validation of the procedure in terms of a) crack density and delaminated area ratio and b) stiffness loss for a $[0/90_2]_s$ laminate

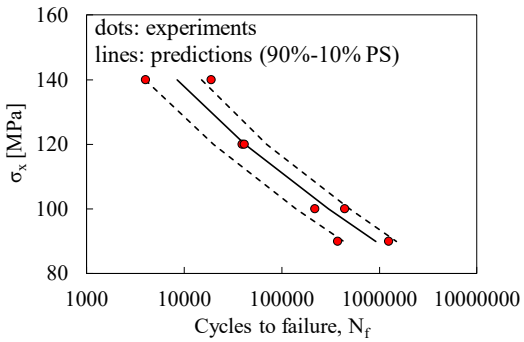

Fig. 6. Prediction of the fatigue life of $[0_2/90_4]_s$ laminates through the complete modelling framework

4 APPLICATION TO NOTCHED LAMINATES

The normal text should be written single-spaced, justified, using 11pt Times in one column. The first line of each paragraph must be indented 0.5cm..

The results shown so far were related to plain laminates, subjected to a uniform stress state. With the aim of using this strategy in the case of components with complicated geometry and loading conditions, all the developed models were implemented into a software tool (named RESCOMP – FLA) to be coupled with commercial Finite Element (FE) codes. The fatigue life can be simulated through a cycle jump approach. At each step, a linear-elastic FE analysis is carried out using layered shell elements. The results, in terms of element loads, are exported into the tool that analytically predicts the initiation and growth of damage events, as well as the element apparent elastic properties. These are then returned to the FE code as a starting point for the next cycle step. In this way it is possible to predict the damage evolution in components of any shape, that require the use of FE analyses for the assessment of the macro-scale stress distribution. At the same time the simulation is kept efficient as the discrete damage events are not physically present in the FE model, but only in a parallel database where the position of each damage mechanism is stored. As an example of applica-tion, the case of an open-hole cyclic test was is considered. Tension-tension fatigue tests were conducted on $[0/90]_s$ and $[0/45_2/0/-45_2]_s$ glass/epoxy specimens in plain and notched configurations. The notched specimens were 40 mm wide, with a 8 mm and 16 mm diameter circular central hole. For both specimen types, the progression of damage throughout the fatigue life was monitored through periodic imaging and quantified based on crack initiation and crack density evolution. As expected, cracks predominantly originated along the notch flanks, with stress concentrations playing a crucial role in the damage process. Through the tests on plain specimens, fatigue crack initiation and propagation parameters were obtained and later used to predict the damage evolution in the notched laminates, through the analytical discrete dam-age approach. As an example, the damage evolution in a cross-ply laminate with a 8 mm central hole, as predicted by the tool and obtained from tests, is shown in Figure 7, showing a good agreement.

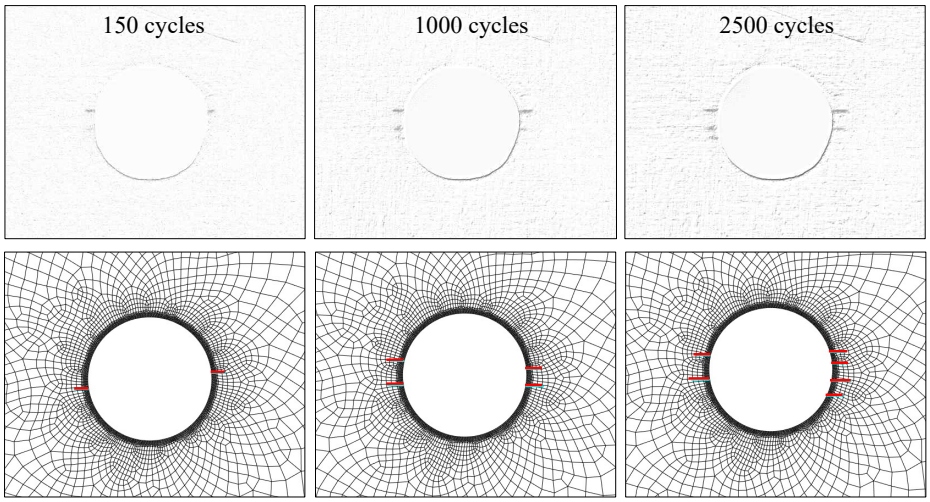

Fig. 7. Prediction of the fatigue life of $[0_2/90_4]_s$ laminates through the complete modelling framework

5 CONCLUSIONS

For an advanced and optimized design against fatigue of composite structures, tools to predict the onset and evolution of damage are required. In this work, a damage-based multiscale strategy was presented to predict the crack density evolution, the delamination growth and the associated stiffness loss in multidirectional laminates under cyclic loadings. To complete the framework and estimating the cycles to failure, a model to predict the failure of the load bearing plies has been also included.

The approach accounts for the interaction between different mechanisms. Criteria for the formation and growth of damage events were defined based on experimental observations at different length scales. The entire discrete damage approach was implemented into a software tool that the authors hope could be of help for improving the safety, the performance and the cost-efficiency of composite structures under cyclic loadings.

ACKNOWLEDGEMENTS

Financed by the European Union - NextGenerationEU (National Sustainable Mobility Center CN00000023, Italian Ministry of University and Research Decree n. 1033 - 17/06/2022, Spoke 11 - Innovative Materials & Lightweighting). The opinions expressed are those of the authors only, and should not be considered as representative of the European Union or the European Commission's official position. Neither the European Union nor the European Commission can be held responsible for them.

REFERENCES

[1] M. Quaresimin, L. Susmel, R. Talreja. Fatigue behaviour and life assessment of composite laminates under multiaxial loadings. International Journal of Fatigue, 32: 2-16, 2010.

[2] K. L. Reifsnider, E. G. Henneke, W. W. Stinchcomb and J. C. Duke. Damage mechanics and NDE of composite laminates, Editor(s): Zvi Hashin, Carl T. Herakovich, Mechanics of Composite Materials, Pergamon, 1983, Pages 399-420.

[3] J. Tong, F. J. Guild, S. L. Ogin, P. A. Smith, On matrix crack growth in quasi isotropic laminates-I. Experimental investigation. Composites Science and Technology, 57: 1527-1535, 1997.

[4] A.W. Wharmby, F. Ellyin, Damage growth in constrained angle-ply laminates under cyclic loading. Composites Science and Technology, 62: 1239-1247, 2002.

[5] S. Adden, P. Horst, Stiffness degradation under fatigue in multiaxially loaded non-crimped-fabrics. International Journal of Fatigue, 32: 108-122, 2010.

[6] M. Quaresimin , P.A. Carraro, L. Pilgaard Mikkelsen, N. Lucato, L. Vivian, P. Brøndsted, B. F. Sørensen, J. Varna, R. Talreja Damage evolution under internal and external multi-axial cyclic stress state: a comparative analysis. Composites Part B, 61: 282-290, 2014.

[7] M. Quaresimin, P.A. Carraro, L. Maragoni, Early stage damage in off-axis plies under fatigue loading, Composites Science and Technology. 128: 147-154, 2016.

[8] P.A. Carraro, M. Quaresimin, A damage based model for crack initiation in unidirectional composites under multiaxial cyclic loading. Composites Science and Technology, 99:154–163, 2014.
[9] L.E. Asp, L.A.Berglund, R. Talreja. Prediction of matrix initiated transverse failure in polymer composites. Composites Science and Technology, 56: 1089-97, 1996.
[10] P.A. Carraro, L. Maragoni, M. Quaresimin. Characterisation and analysis of transverse crack-induced delamination in cross-ply composite laminates under fatigue loadings. Int. J. Fatigue, 129: 105217, 2019
[11] J.A., Glud, P.A. Carraro, M. Quaresimin, J.M. Dulieu-Barton, O.T. Thomsen, L.C.T. Overgaard. A damage-based model for mixed-mode crack propagation in composite laminates. Compos. Part A-Appl. S., 107: 421-31, 2018.
[12] P.A. Carraro, L. Maragoni, M. Quaresimin. Prediction of crack density evolution in multi-directional laminates under fatigue loading. Composites Science and Technology, 145: 24-39, 2017.
[13] L. Maragoni, P. A. Carraro, M. Simonetto, M. Quaresimin, A novel method to include crack-induced delamination in a fatigue damage predictive procedure for composite lami-nates. Composites Science and Technology, 238: 110011, 2023.
[14] P.A. Carraro, L. Maragoni, M. Quaresimin. Stiffness degradation of symmetric laminates with off-axis cracks and delamination: an analytical model. International Journal of Solids and Structures, 213: 50–62, 2021
[15] M. Quaresimin, P.A. Carraro. Damage-based modelling of fatigue response of composites. In Fatigue in Composites, Science, Damage Mechanics, and Design Applications 2nd Edition - June 16, 2025, Woodhead Publishing, Editor: Marino Quaresimin.

ICCM24
AUGUST 4-8, 2025
BALTIMORE CONVENTION CENTER
BALTIMORE, MARYLAND, USA

No Technical Paper Submission for:

S. Kumar

ICCM24
AUGUST 4-8, 2025
BALTIMORE CONVENTION CENTER
BALTIMORE, MARYLAND, USA

No Technical Paper Submission for:

Marianna Maiaru

INVESTIGATION OF PARTICLE SIZE EFFECT ON THE FRACTURE TOUGHNESS OF POLYMER/GRAPHENE NANOCOMPOSITES AND CFRP DUE TO CRACK TIP SHIELDING

Sara Amirahmadi, Sankha Aditya, and Samit Roy

Department of Aerospace Engineering and Engineering Mechanics
University of Alabama, Tuscaloosa , USA

Keynote Talk Presented at the ICCM-24
Baltimore, Maryland
August 4, 2025

Motivation and Outline

Question: Why does the addition of stiff nanoparticles improve fracture toughness in brittle polymers with less than 1 wt% of nanofillers? Why is there a strong particle size effect ?

Research Objective: To develop an experimental/analytical approach to answer these fundamental questions to enhance optimal toughness and fatigue life of composite structures

Outline of Presentation:

- Macroscale Mode I fracture toughness test data for EPON 862 epoxy to investigate toughening effect and size effect due to graphene nanoplatelets (GNP/GOs)
- Development of a fundamental physics-based model to explain the toughening mechanism and GNP size effects at the microscale to predict macroscale toughness increase in polymers

Macro-scale Fracture Experiments to Investigate Crack Shielding Effect

Macro Scale Fracture Experiments

- Compact tension (CT) specimens were manufactured with three different graphene nanoplatelet sizes (median size 0.2, 2, and 5 microns) for 0.1,0.3, 0.5 and 0.7 wt% in epoxy, respectively
- High shear mixing and sonication were used to ensure good dispersion of GNP in EPON 862 epoxy
- At least five replicate 3 × 3 ×0.635 cm CT specimens were molded according to ASTM D5045-99 standard procedure*

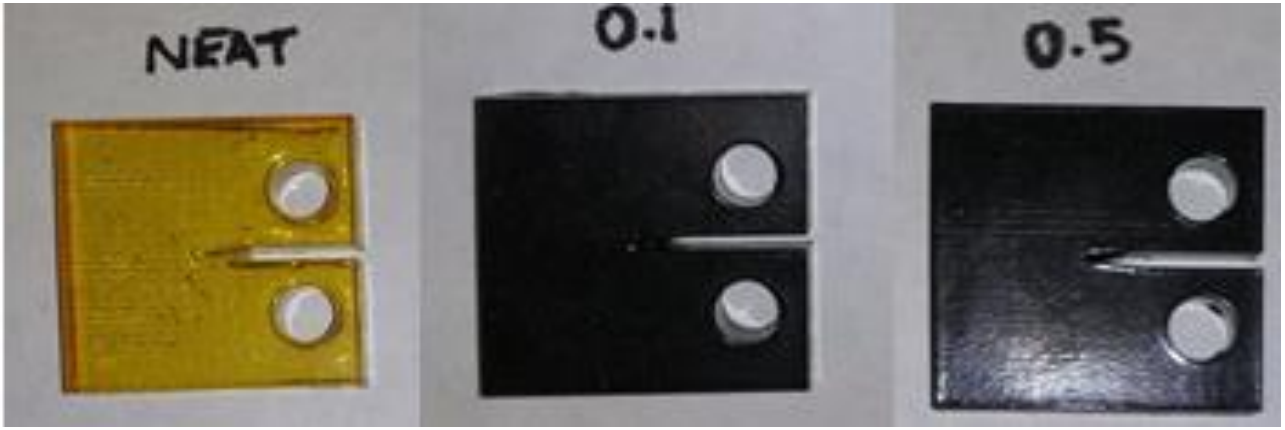

*Ref: Amirahmadi et al., *Composite Structures* 347 (2024) 118420.

Initiation Fracture Toughness and CSERR for EPON862/GNP

Cases	Mean K_{Ic} (MPa-$m^{1/2}$)	STD K_{Ic}	% Increase in K_{Ic} compared to baseline	Mean G_{Ic} (J/m^2)	STD G_{Ic}	% Increase in G_{Ic} compared to baseline
Baseline Epoxy	0.83	±0.03	-	264.9	±28	-
0.1 wt.% 5µ GnP	0.98	±0.026	18	328.8	±19	24
0.3 wt.% 5µ GnP	1.15	±0.03	38	444.8	±39	70
0.5 wt.% 5µ GnP	1.74	±0.1	110	1005.0	±74	279
0.7 wt.% 5µ GnP	1.46	±0.05	76	691.1	±29	161
0.1 wt.% 2µ GnP	1.06	±0.09	27	336.8	±43	27
0.3 wt.% 2µ GnP	1.27	±0.1	53	500.9	±42	89
0.5 wt.% 2µ GnP	1.86	±0.08	124	1150.9	±69	335
0.7 wt.% 2µ GnP	1.6	±0.05	93	910.8	±103	244
0.1 wt.% 0.2µ GO	2.1	±0.26	153	952.0	±164	260
0.2 wt.% 0.2µ GO	2.34	±0.2	182	1347.2	±262	408
0.25 wt.% 0.2µ GO	2.62	±0.14	216	1556.8	±82	488
0.3 wt.% 0.2µ GO	2.71	±0.12	227	1820.8	±142	587
0.35 wt.% 0.2µ GO	2.26	±0.17	172	1340.8	±87	406
0.4 wt.% 0.2µ GO	1.56	±0.08	88	838.1	±75	216
0. 5 wt.% 0.2µ GO	1.52	±0.09	83	843.5	±127	218

GNP Size effect in Mode I Fracture Behavior

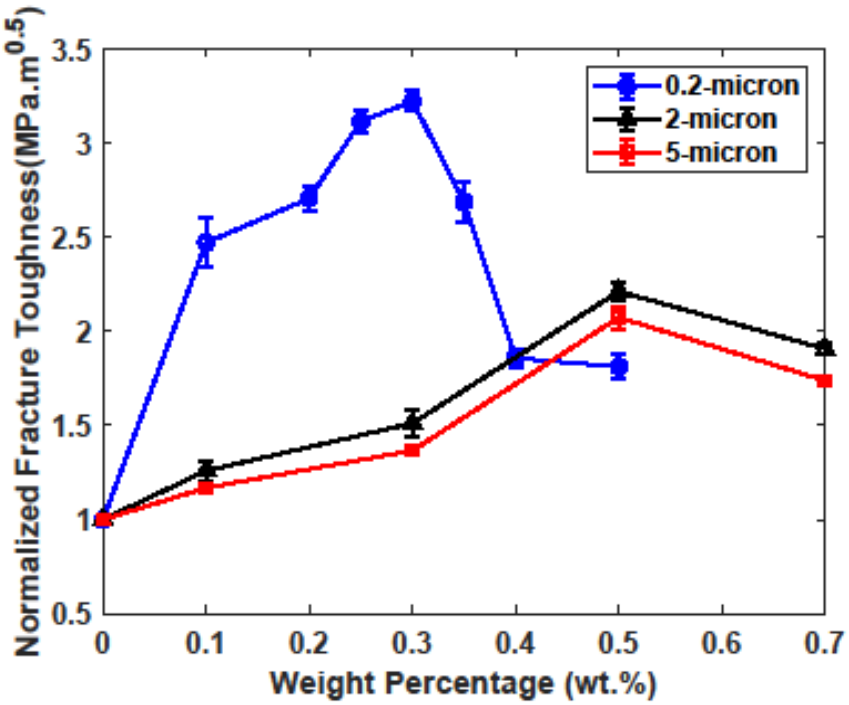

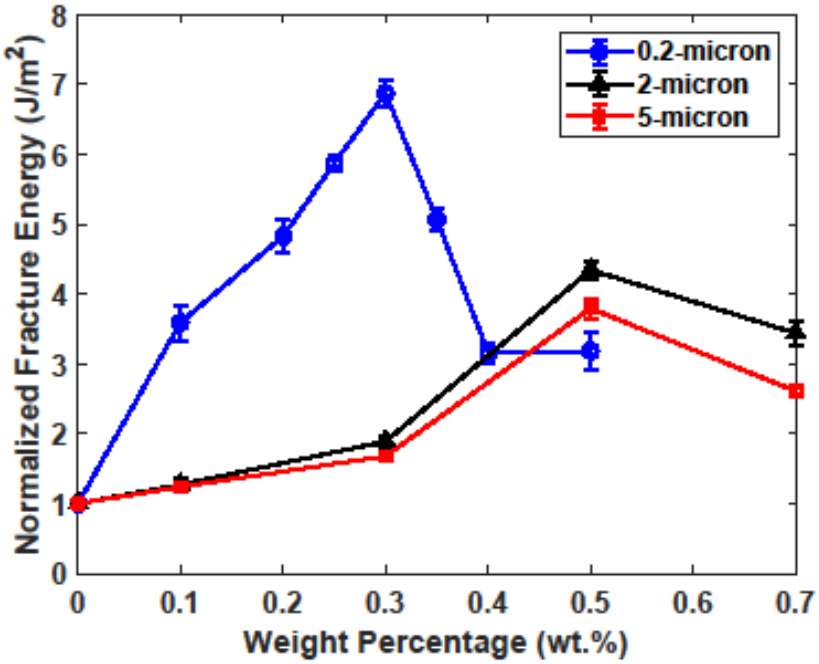

Comparison of GNP size effect on Fracture Toughness Comparison of GNP size effect on Fracture Energy

- 227 % increase in peak toughness, and 600 % increase in peak fracture energy for 0.2 micron GO @ 0.3 wt% , in comparison with baseline epoxy (0 wt%) is observed*
- Degradation in toughness enhancement due to particle agglomeration occurs earlier for 0.2 micron GO than for 2 and 5 micron GNP cases.

*Ref: Amirahmadi et al., *Composite Structures* 347 (2024) 118420.

SEM of Fracture Surface Morphology

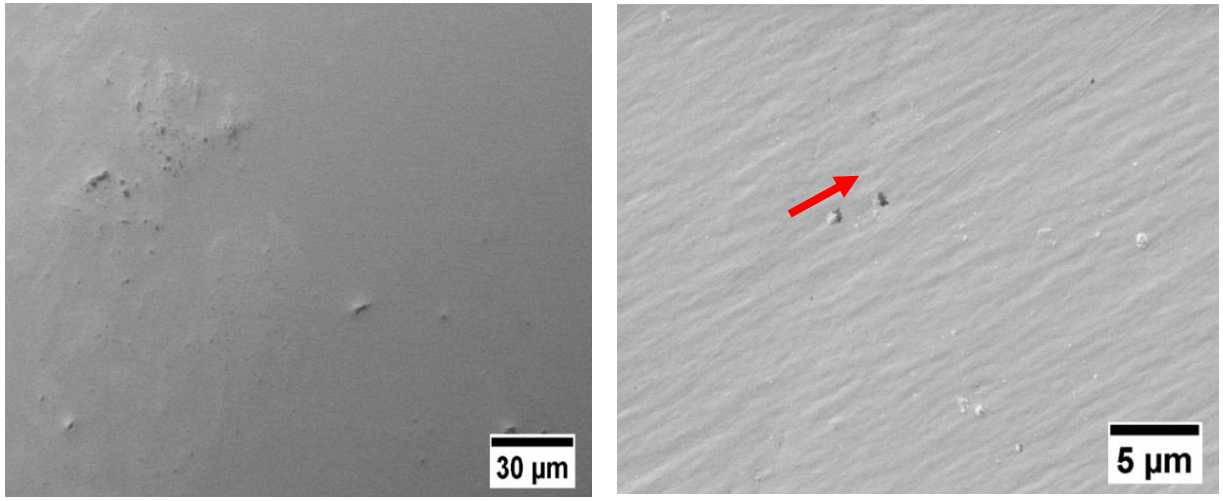

Fracture surface of baseline specimen (only epoxy resin) at (a) 500x and (b) 5000x magnification

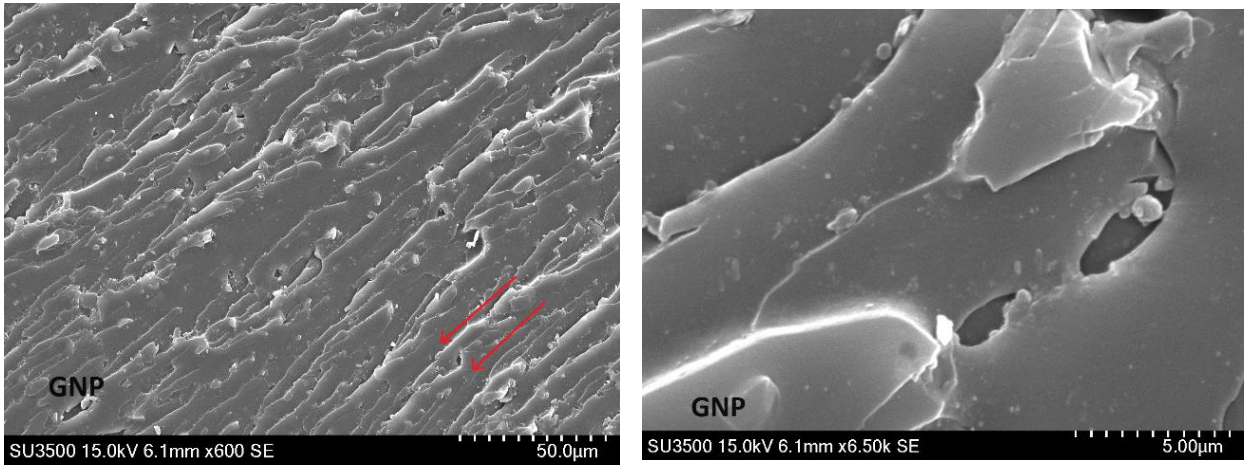

Fracture surface of 0.3 wt.% 5 µm size graphene reinforced epoxy composites

SEM of Fracture Surface Morphology

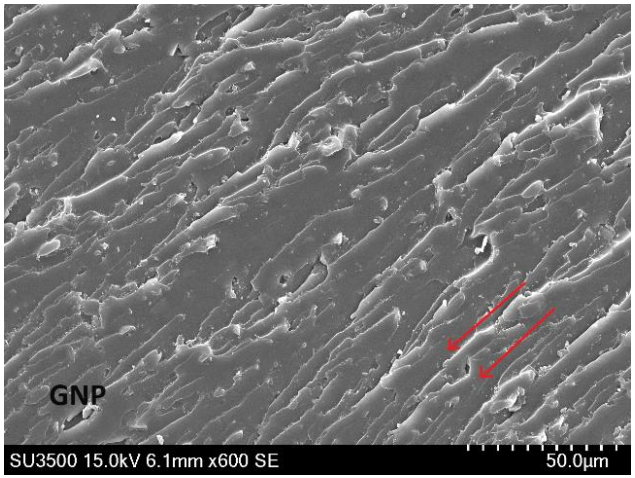

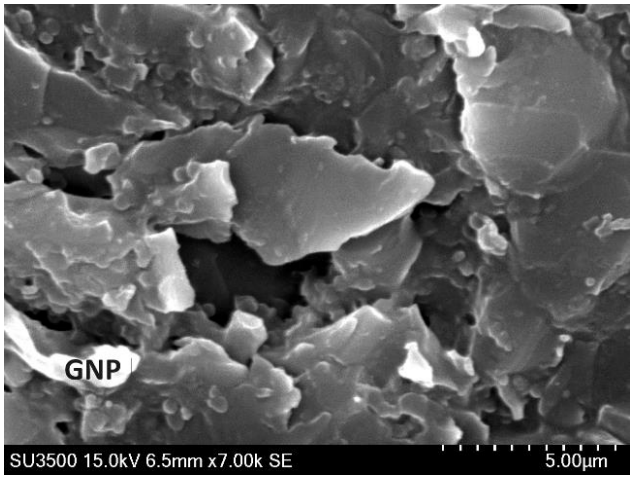

Fracture surface of 0.3 wt.% 2 µm size graphene reinforced epoxy composites

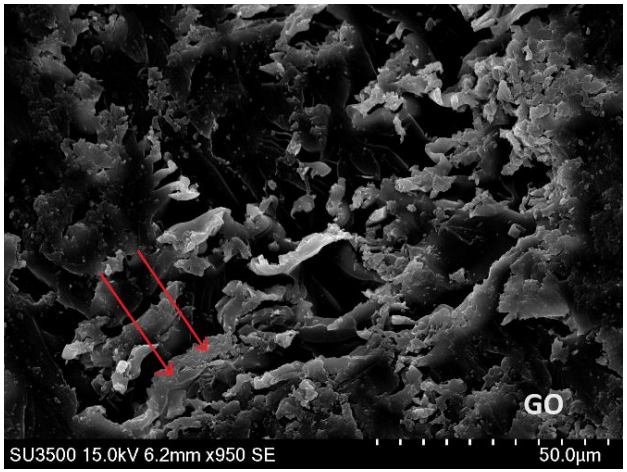

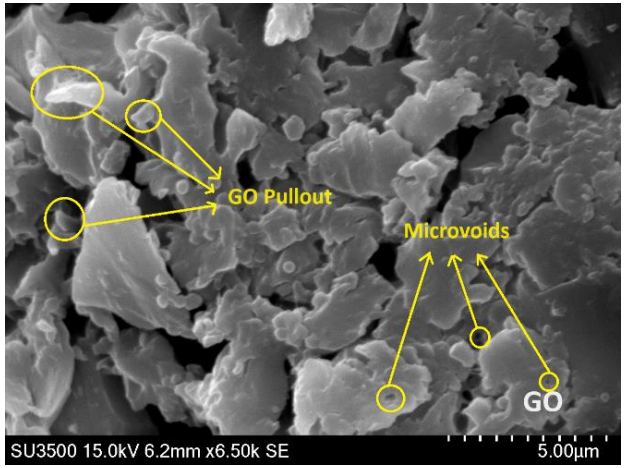

Fracture surface of 0.3 wt.% 0.2 µm size graphene reinforced epoxy composites

The 0.2 µm GO reinforced samples has a rougher morphology as compared with the baseline samples indicating **extensive damage** in FPZ at **crack initiation**, and crack deflection during **crack propagation**

TEM Imaging for GNP Dispersion

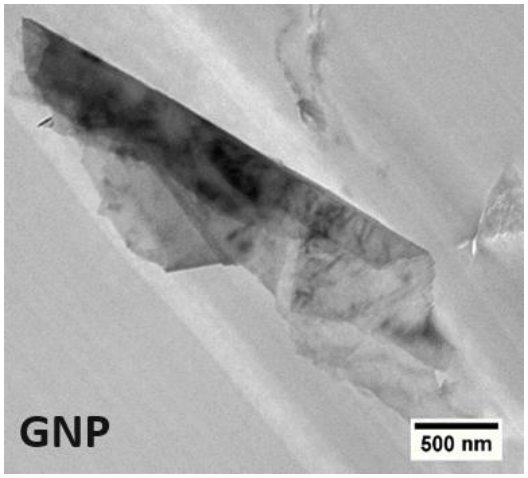

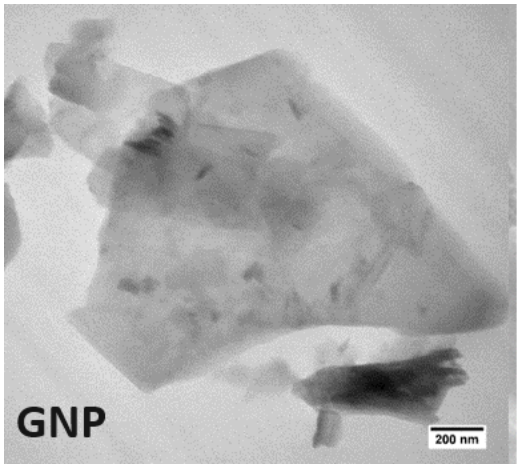

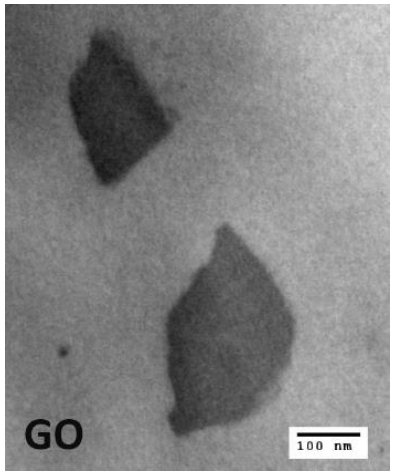

TEM images of dispersed nanographene platelets and graphene oxide in epoxy:
(a) 5 µm GNP at 0.3 wt%, (b) 2 µm GNP at 0.3 wt% , and (c) 0.2 µm GO at 0.3 wt%

Good level of exfoliation and dispersion are observed

Modeling of Particle Size Effect on Crack Initiation Toughness using Mechanism Based Approach

Conventional Modeling of Toughening Mechanism Polymer Nanocomposite with Dispersed Graphene Nanoplatelets (GNP)*

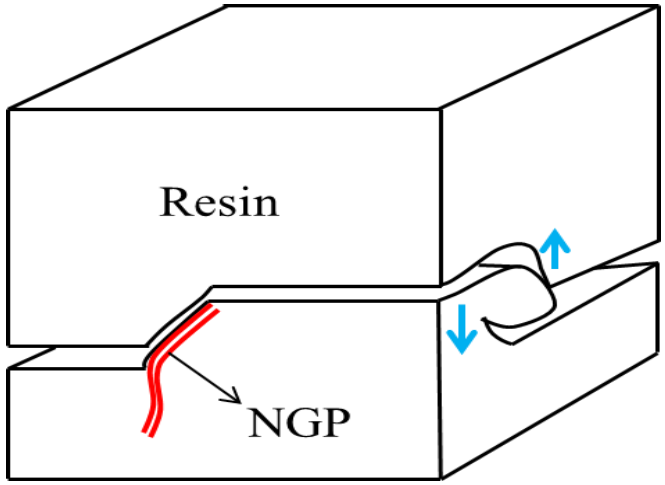

1. The macroscale crack impinges on nanographene platelet and deflects
2. After deflection, the fracture process zone (FPZ) consists of cracks at two levels
3. The two cracks coalesce through a shear failure mechanism in the process zone

- This explanation may be applicable during crack growth but not during crack initiation as it assumes a running crack, because deflection/coalescence can occur only after crack growth.
- The effect of platelet size is not included in this explanation, as larger GNP size should give rise to higher toughness

*Chandrasekaran, S., Sato, N., Tölle, F., Mülhaupt, R., Fiedler, B., and Schulte, K. "Fracture toughness and failure mechanism of graphene based epoxy composites," Composites Science and Technology, Vol. 97, 2014, pp. 90-99.

A New Approach to Initiation Toughness Modeling in Nanocomposites

- **Addition of nanoparticles transforms a brittle epoxy into a quasi-brittle material by inducing damage in the Fracture Process Zone (FPZ) near the crack-tip[1]. This results in two mechanisms:**

(a) Crack-tip shielding due to the reduction in local modulus caused by debonding (+ve effect)

(b) Micro-damage could decrease local initiation toughness near the crack tip (-ve effect)

- **These two competing effects determine overall initiation fracture toughness of the nanocomposite in this model [2]**

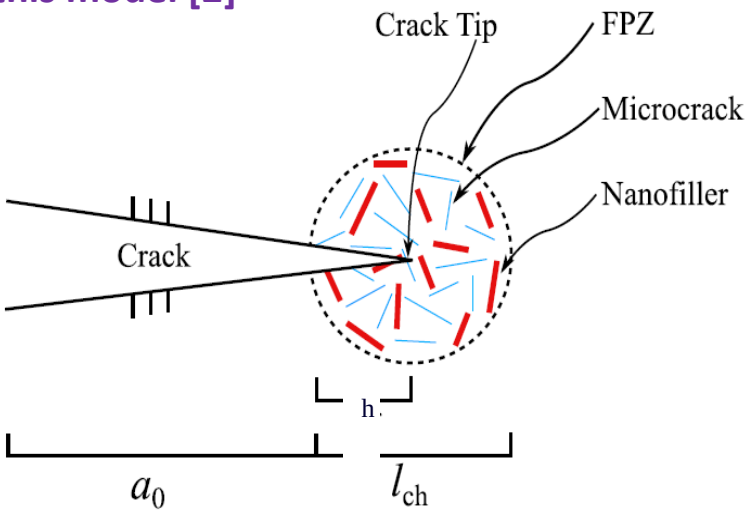

Fracture Process Zone (FPZ) with micro-damage for thermoset polymer with randomly dispersed graphene nanoplatelets (GNP)[1].

[1] Failure behavior and scaling of graphene nanocomposites, Cory Mefford, Yao Qiao, Marco Salviato, Composite Structures 176 (2017) 961–972

[2] G. Ravichandran et al. Crack Tip Shielding in Elastic Particulate Composites undergoing Damage, Eng. Fract. Mech. Vol. 59, No. 6, pp. 713-723,

Three zones in a nanocomposite that give rise to crack-tip shielding under far-field loading*

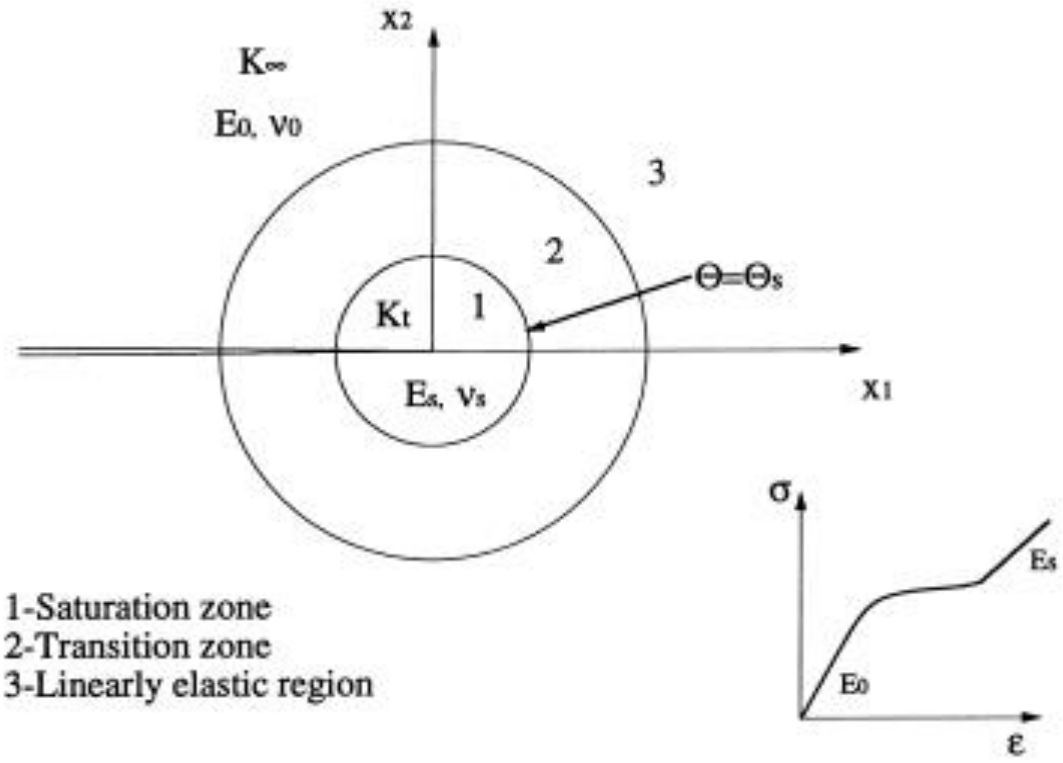

*[1] A.G. Evans, S. Williams, and P.W.R. Beaumont, On the Toughness of Particulate Filled Polymers, Journal of Material Science 20 (1985), 3668-3674.

[2] G. Ravichandran, and C.T. Liu, Crack Tip Shielding in Elastic Particulate Composites undergoing Damage, Engineering Fracture Mechanics Vol. 59, No. 6, pp. 713-723, 1998.

Partitioning of Far-field Stress Intensity as a Product of Crack-tip Shielding and Local Toughness Change Near the Crack tip in Epoxy

From path independence of $J-$ integral [*], $J_{NCtip} = J_{N.C_{FF}}$

*J.R. Rice, Journal of Applied Mechanics1968

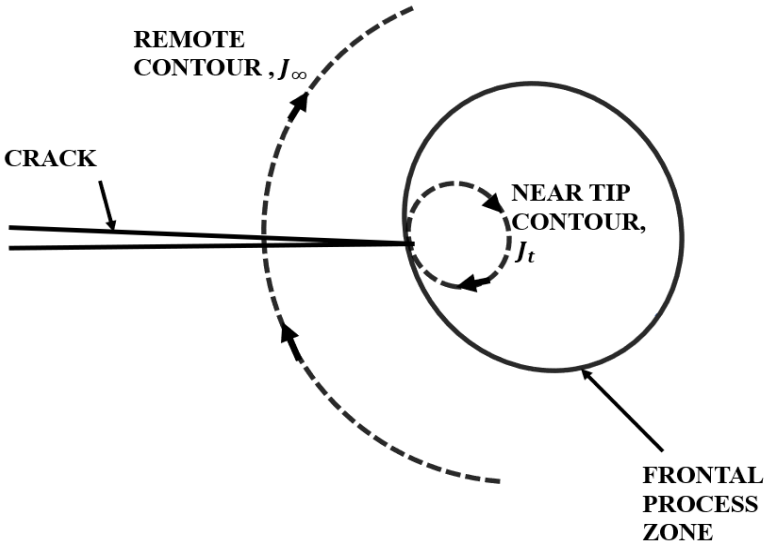

But for plane stress, $J = \frac{K^2}{E}$

$$\frac{K_{NCtip}^2}{E_{NCtip}} = \frac{K_{N.C.FF.}^2}{E_{N.C.FF}}$$

In general , $K_{N.C.FF} = K_{NCtip}\sqrt{\frac{E_{N.C.FF}}{E_{NCtip}}}$

At fracture, $K_{IC,N.C.FF} = K_{IC,NCtip}\sqrt{\frac{E_{N.C.FF}}{E_{NCtip}}}$

- The second factor on the R.H.S., $\sqrt{\frac{E_{NCFF}}{E_{NCtip}}}$, denotes the crack-tip shielding contribution
- The first factor on the R.H.S., $K_{IC,NCtip}$, is the actual local toughness at the tip of the macroscale crack in the presence of microcracks induced by nanofillers in the FPZ, and is a measure of the local toughness change due to micro-damage caused by the nanofillers
- These two competing effects determine overall far-field toughness of nanocomposite!

Model Development for Crack-tip Shielding and Local Toughness Change in Epoxy

$$K_{IC,N.C.FF} = K_{IC,NCtip}\sqrt{\frac{E_{N.C.FF}}{E_{NCtip}}}$$

$$E_{NCtip} = E_{epoxy}(K_{ICM}^2/K_{ICN.C.FF}^2) = E_{epoxy}(1-\beta n^q)$$

Where, K_{ICM} is the epoxy toughness, E_{epoxy} =1.68 GPa is the elastic modulus of the undamaged epoxy matrix without GNP, β (VfGNP) and *q* are power-law parameters, and *n* is the number density of GNP particles

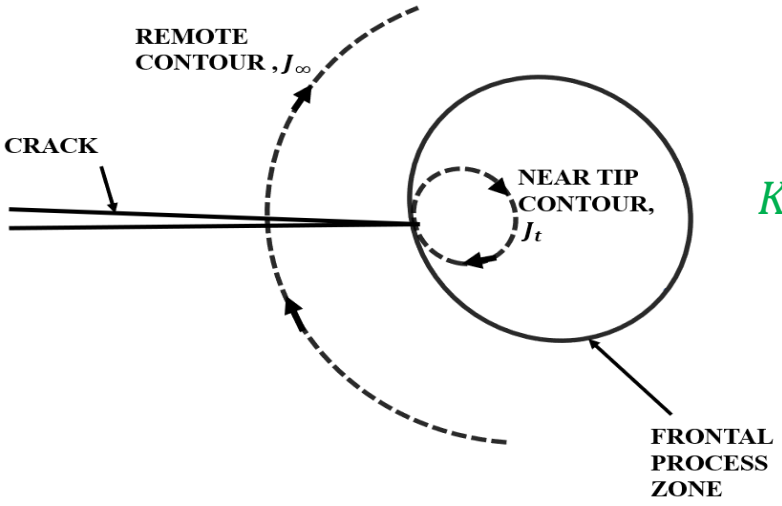

Assuming, $K_{IC,NCtip} = K_{IC_M}(1\text{-}V_{fGNP})$

$$K_{IC_{N.C.FF}} = K_{IC_M}(1\text{-}V_{fGNP})\sqrt{\frac{E_{N.C.FF}}{E_{poxy}(1-\beta n^q)}}$$

$$= K_{IC_M}(1\text{-}V_{fGNP})\frac{1}{\sqrt{\frac{E_{epoxy}}{E_{N.C.FF}}\left[1-\beta\left(\frac{V_{fGNP}}{{l_p}^2 t_p}\right)^q\right]}}$$

Where, l_p is the median particle size, and t_p is the median particle thickness.

MODEL PREDICTIONS

Comparison of Model Toughness Prediction for CT Specimens at RT

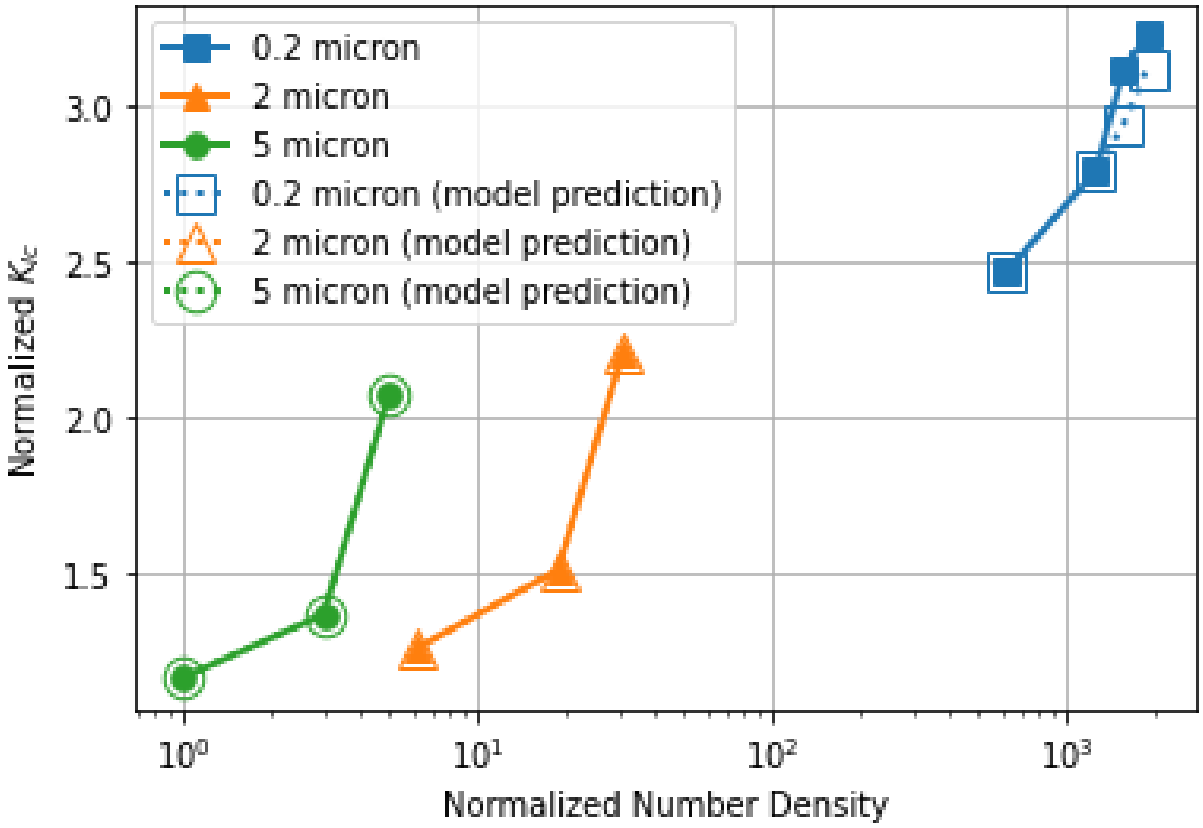

- Good agreement is observed between model prediction and actual CT test data
- The smaller the particle size greater is the toughness increase due to shielding effect
- Predicts 227 % **maximum** toughness increase with 0.2 micron GNP at 0.3 wt%
- The model is able to capture the peak increase in toughness before degradation due to agglomeration can set in. This enables unique prediction of optimum toughness!

Comparison of Model Toughness Prediction for CT Specimens at RT

Comparison with Test Data from Shirodkar et al.* for GNP/Epon862 Nanocomposite

Specimen	K_{Ic} (MPa.m$^{0.5}$)	Normalized K_{IC}	Model Prediction	Percentage Difference
Baseline epoxy	0.75	1.0	1.0	0
0.1 wt % 5 µm GNP in epoxy	1.1	1.4667	1.1667	-20.5
0.5 wt % 5 µm GNP in epoxy	1.58	2.1067	2.0714	-1.7

*Ref: Shirodkar N, Cheng S, Seidel GD. Enhancement of Mode I fracture toughness properties of epoxy reinforced with graphene nanoplatelets and carbon nanotubes. Composites B Eng 2021;224. https://doi.org/10.1016/j.compositesb.2021.109177.

Optimum Model Predictions Including Cut-Off Due to Agglomeration

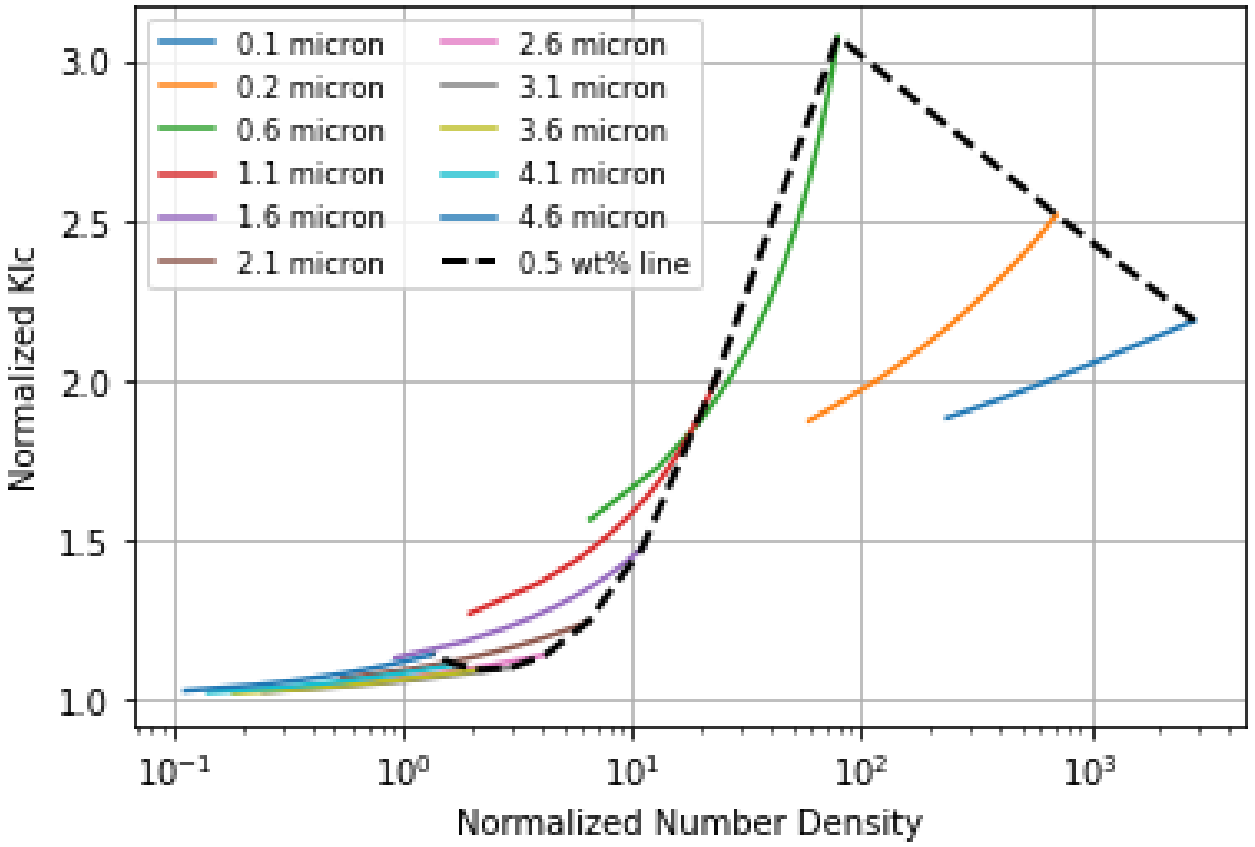

- **Using only 10 data points for model calibration, the model can predict optimum GNP size and number density required for maximum toughness enhancement**

- **Predicts** 310 % **maximum** toughness increase with 0.6 micron GNP size at 0.32 wt%

GNP SIZE EFFECT IN DELAMINATION TOUGHNESS ENHANCEMENT FOR CARBON COMPOSITE

Double Cantilever Beam (DCB) Test for Measuring Mode I Delamination Toughness *



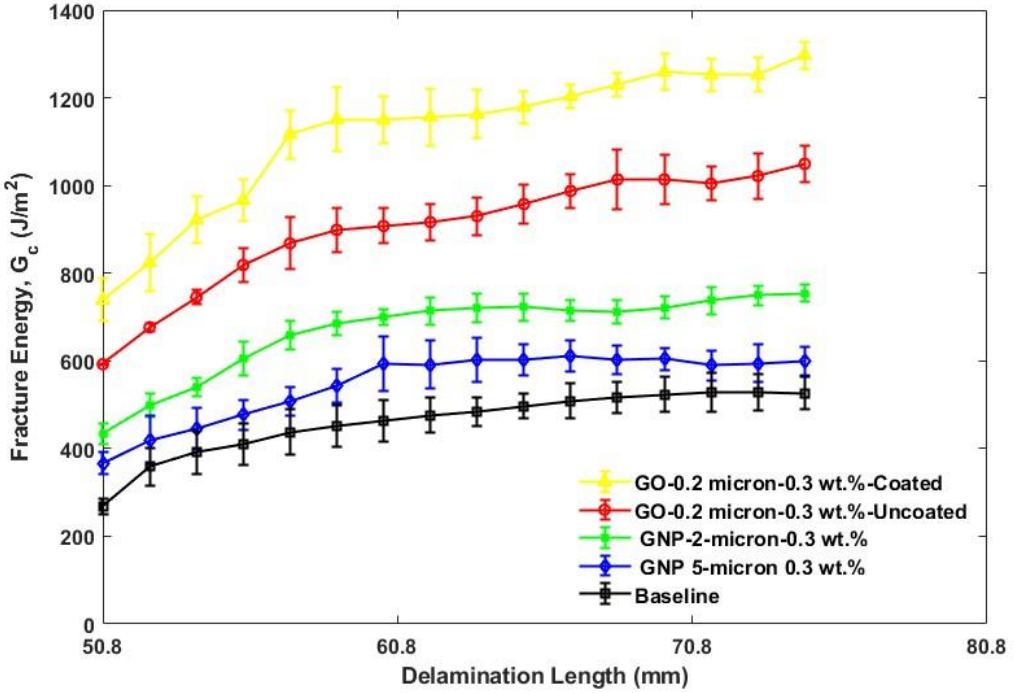

- Unidirectional IM7/EPON-862 laminates tested as per ASTM D5528 clearly indicate particle size effect as shown in the chart ; coating carbon fabric enhances toughness
- The enhancement in fracture energy is lower for the carbon composite as the toughened matrix causes the crack to partly propagate along the fiber-matrix interface

Double Cantilever Beam (DCB) Results for Mode I Delamination Toughness



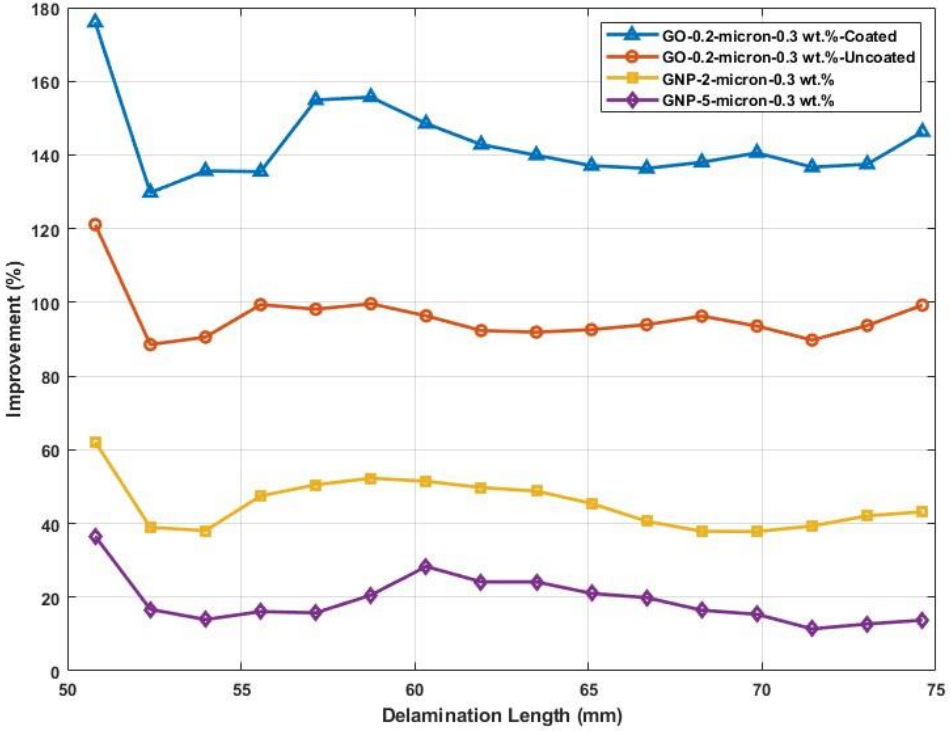

- Unidirectional IM7/EPON-862 laminates tested indicate particle size effect as shown in the chart with up to 180 % improvement over baseline case at initiation
- The enhancement in fracture energy is slightly lower for the carbon composite as the toughened matrix causes the crack to propagate along the fiber-matrix interface

SEM IMAGES OF DCB FRACTURE SURFACE FOR BASELINE CASE AND 0.2 Micron GO AT 0.3 wt%

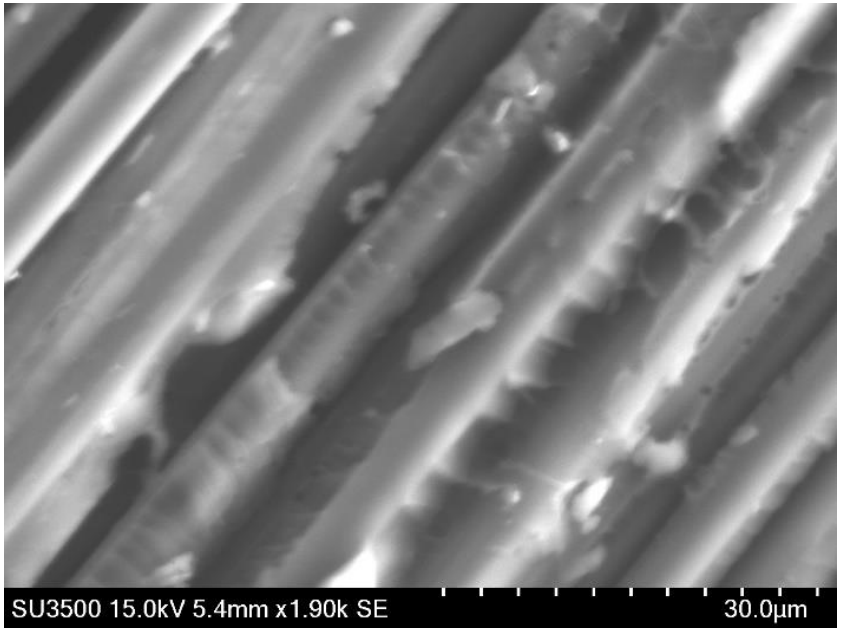

Baseline Laminate

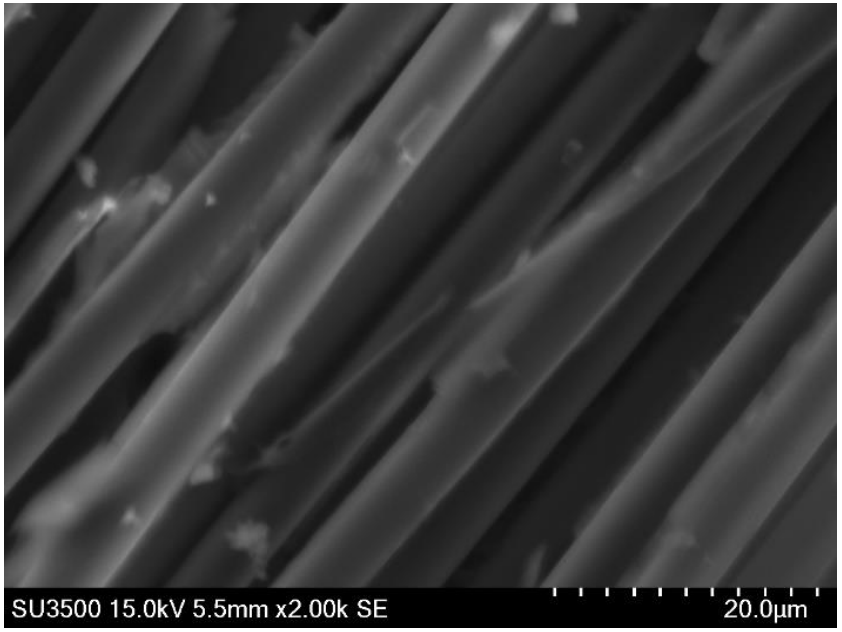

Laminate with 0.2 micron GO at 0.3 wt%

SEM images show evidence of cohesive fracture in the polymer in the case of baseline laminate (without GNP) but crack propagates along the fiber-matrix interface for GO case

- Toughening of fiber-matrix interface in addition to matrix toughening will therefore improve overall composite delamination toughness

Summary and Conclusions

- This paper presents clear evidence of the influence of GNP size on fracture toughness and CSERR in GNP/EPON862 as well as IM7/EPON862/GNP composite

- Our test data reveals a 227% peak enhancement (that is, 3.23 times improvement from the baseline value) in mode I fracture toughness (K_{IC}) and 587% peak enhancement in Gic over the baseline epoxy for specimens with 0.2 µm GO at 0.3 wt.% , likely due to crack tip shielding.

- The enhancement in Gic for the DCB specimens show similar size effect, although the degree of toughness enhancement was lower (~180%) due to debond failure

- Fracture toughness enhancement is observed to decrease with higher wt % of GNP

- An analytical model based on crack-tip shielding due to number density of GNP particles was developed and verified with test data (A patent was filed in 2023).

- Our future work will attempt to study these mechanisms in detail using in-situ AFM and/or SEM which will be used in conjunction with 2-D digital image correlation (DIC) to obtain local in-plane strain maps to provide a clearer understanding of crack shielding mechanisms in the fracture process zone, and crack propagation

Acknowledgement

Support for this research by NASA Glenn Research Center and by the AFOSR LDM Program is gratefully acknowledged

INCORPORATING NANOSTRUCTURES INTO NEXT GENERATION (SUSTAINABLE) FIBRES

Milo S.P. Shaffer[1,2]

[1]Department of Materials, Imperial College London, London, UK
South Kensington Campus, London, SW7 2AZ, United Kingdom

[2]Chemistry Department and Materials Department, Imperial College London
White City Campus, London, WC12 0BZ, United Kingdom
m.shaffer@imperial.ac.uk, https://profiles.imperial.ac.uk/m.shaffer

Keywords: Carbon fiber; Carbon nanotubes; Interface/interphase; Chemical Vapor Deposition (CVD); sustainable materials, lignin-derived carbon

Nanostructured materials offer the possibility to improve the performance and functionality of existing structural fibres. There are broadly two strategies (Figure 1): One involves the incorporation of the nanomaterial into existing state of the art fibres, in order to address critical weaknesses and/or introduce new functions. Examples of this first approach include the development of nanostructured interphases on existing carbon and glass fibres. Here, the nanomaterial improves load transfer between the fibre and the matrix and reduce stress concentration. Surface grafting of carbon nanotubes (CNTs) by direct CVD provides a hierarchical fibre with two differing reinforcement length scales. The advantages of this approach are well known, but typically limited by damage to the substrate fibres, and difficulties with scale-up. Informed by flow modelling and "dynamic snapshots", we have developed a continuous spool-to-spool process that produces controlled, uniform grafting throughout the tow. The products show excellent single fibre and small composite performance in thermosets[1] and thermoplastics[2], and are relevant to multifunctional applications such as structural heath monitoring[3].

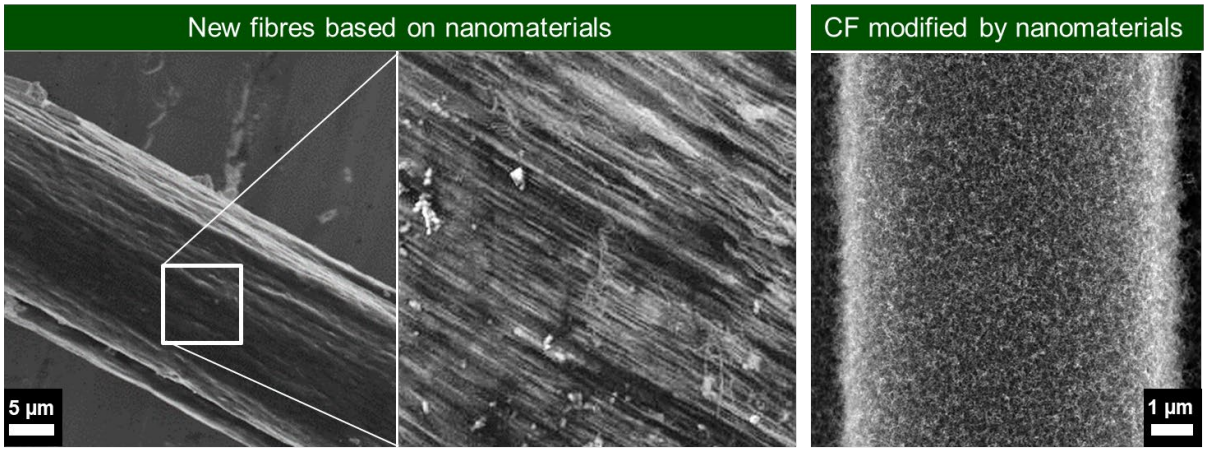

Figure 1: Schematic showing two alternative strategies for exploiting nanostructures in fibres : a) spinning new fibre systems based on 1D nanomaterial precursors (left, showing a single-wall carbon nanotube based fibre)[4] or b) modifying of an existing state of the art structural fibre with a nanomaterial enhancement (right, showing a PAN-based carbon fibre grafted with carbon nanotubes to reinforce its interphase.[2]

The second approach, which is more challenging but potentially more transformative, relies on the development of entirely new fibre systems from the nanostructured or nanocomposite constituents; however, new processes to assemble and orient the constituent nanostructures. One dimensional nanomaterials are particularly well suitable to unidirectional alignment in fibre formats. A wide range

of building blocks are possible, including nanotubes, nanorods, and nanowires, based on carbons, inorganic compounds, synthetic proteins, and biologically derived constituents; a variety of these options are explored here (Figure 2). In particular, individual perfect nanocarbon structures have exceptional properties; the challenge is often how to exploit their potential in real macroscopic systems. Whilst dry spinning approaches may be attractive, wet spinning is more obviously scalable and applicable. However, the formation of individualized solutions of functionalised single wall nanotubes (SWNTs) and graphenes is challenging. We exploit reductive charging to form pure nanotubides (nanotube anions) which can be redissolved, purified, or optionally functionalised, whist avoiding the damage typically associated with sonication and oxidation-based processing.[5] Nanotubide solutions form nematic phases which can be spun directly into coagulant baths in order to prepare functionalised SWCNT fibres in situ. Grafting of suitable polymer constituents can increase dispersibility of both nanotubes and graphenes and hence help to produce nanocomposite fibres with higher strength and strain to failure, [4] as well as multifunctional performance as supercapacitors. Non-carbon-based analogues of nanotubes offer different functions. For example, composite fibres containing inorganic (imogolite) nanotubes can generate healable structural fibres, with exceptionally high performance. [6] Imogolite nanotube dispersions also form liquid crystalline mesophases and it is possible to spin pure imogolite fibres, analogously to the carbon nanotube examples.[7] The imogolite system has the advantage of water compatibility and the opportunity for in situ process monitoring through optical birefringence and x-ray studies.[8]

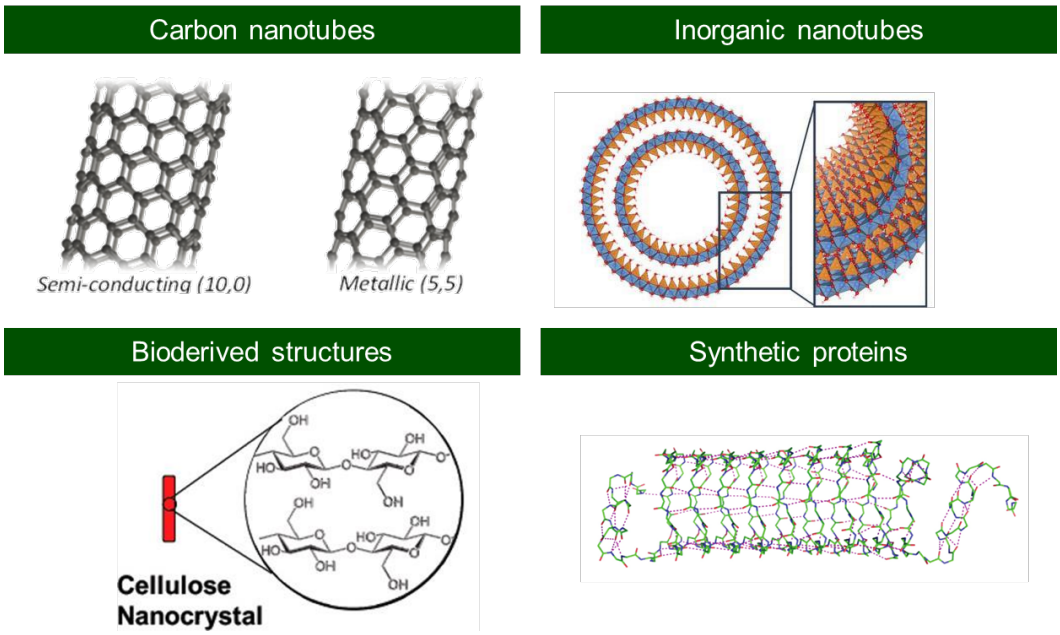

Figure 2: Schematic showing possible one dimensional nanomaterial building blocks for fibres

More sustainable fibre systems can be pursued by spinning bioderived nanomaterials, or by using nanomaterials to allow the spinning of lignin-based materials, for conversion into carbon fibre. Lignin-derived carbon fibers (CFs) are an attractive target for low-cost sustainable composite applications. Our lignin-based fibers are wet-spun using a low-cost (<$1/kg) ionic liquid, N,N – dimethylbutylammonium hydrogen sulfate ([DMBA][HSO_4]) as the dope solvent and water as the coagulation bath.[9] If the lignin is extracted from the biomass using an ionosolv approach based on the same low cost ionic liquid, it can be used directly as the feedstock for the wet-spinning process. This latter approach removes several process steps, including the need to dry the lignin powder during its isolation. An initial life cycle analysis (LCA) indicates that this new ionosolv approach offers significant scope to reduce the cost and global warming potential of lignin fibre production.[10] Very low loadings of CNTs can be used as the spinning aid for this ionosolv process, yielding fibers containing up to 96% lignin solid fraction. The presence of CNTs increases the estimated carbon fiber yield from ~40% to 54%, a critical factor for

technoeconomic outlook of lignin-based carbon fibers. In addition to enabling fiber spinning and increasing carbon yield, the CNTs may also act as graphitization templates and provide direct reinforcement of the lignin-derived carbon matrix, improving mechanical performance. Although the fibres do not yet match the strength or stiffness of state-of-the-art PAN-based carbon fibres, they may nevertheless be optimized to offer useful performance across a wide range of sectors from automotive to construction. In principle, CNTs can be bioderived, offering a fossil free route to low cost carbon fibers using only renewable carbon sources.

CONCLUSIONS

One dimensional nanomaterials are well suited to incorporation in fibre systems, both forming new types of pure fibre or in composite form. The aspect ratio and dimensionality are compatible with a high degree of alignment and efficient packing in the spun fibres, but also often generate lyotropic liquid crystal phases that play an important role in processing. Wet-coagulation spinning can exploit these phases and is readily scalable via established routes, from lab scale batches, through lab scale continuous monofilament, multifilament, and upwards towards pilot scale. Nanomaterials often offer excellent mechanical properties due to their high perfect and confined defect sizes but can also introduce a wide variety of functional benefits, including electrochemical energy storage and self-healing.

As specific examples, pure and composite carbon and imogolite nanotube fibres show promise as ductile and multifunctional reinforcements. Carbon nanotube fibres are conductive, loading-bearing, and with high electrochemical capacitance, relevant to structural supercapacitors Imogolite provides an analogous structure to CNTs that is easier to manipulate and study by POM & XRD, providing in situ insight into processing steps and other phenomenology that can be applied across the nanomaterial fibre domain.

Biomaterials provide routes to “green” carbon fibres and consumer textiles New types of lignin-derived carbon fibres, processed using water & IL only, are particularly promising for their potential low cost and reduced environmental impact. The introduction of carbon nanotubes, combined with new lignins, can improve graphitisability, yield, and performance.

While these new nanomaterials-based fibres offer great promise for the future, their commercial implementation will require time and investment. Meanwhile, nanomaterials can already be used to improve the performance existing state of the art structure fibres. For example, CNT-grafted fibres offer improved structural properties, improving interfacial strength and composite compression performance, whilst offering multifunctional opportunities for enhanced conductivity and self-sensing. A new process allows continuous uniform growth throughout a 12k fibre tow, allowing potential integration directly into existing carbon fibre production.[11]

ACKNOWLEDGEMENTS

This paper summarises work with many group members, colleagues, and collaborators including at Imperial: Adam Clancy, Joe Moore, Kalpana Balaskandan, Shirley Yang, Zoyia Kamora, Enny Tran, Hassan Almousa, Yanhao Sun, Hugo De Luca, Dr David Anthony, Dr Wonjun Lee, Dr Noelia Rubio, Dr James Serginson, Dr Hannah Leese, Dr Joane Ng, Prof Emile Greenhalgh, Dr Agi Brandt-Talbot, Dr James MacDonald, Prof Paul Freemont, Prof Nilay Shah, Dr Rukayya Muazu, and at the University of Paris Sud: Lucie Dieval, Dr Erwan Paineau, Dr Pascale Launois. We kindly acknowledge the funding for this research provided by UK Engineering and Physical Sciences Research Council (EPSRC), including via the programme Grant EP/T011653/1, Next Generation Fibre-Reinforced Composites (NextCOMP): a Full Scale Redesign for Compression, a collaboration between Imperial College London and the University of Bristol, as well as the Imperial-CNRS collaboration.

REFERENCES

[1] Anthony, D. B., Qian, H., Clancy, A. J., Greenhalgh, E. S., Bismarck, A., & Shaffer, M. S. P. (2017). Applying a potential difference to minimise damage to carbon fibres during carbon nanotube grafting by chemical vapour deposition. *Nanotechnology, 28*(30). doi:10.1088/1361-6528/aa783f

[2] Wang, J., Anthony, D. B., Fuentes, C. A., De Luca, H. G., Zhang, D. X., Bismarck, A., . . . Seveno, D. (2022). Wettability of carbon nanotube-grafted carbon fibers and their interfacial properties in polypropylene thermoplastic composite. *Composites Part A, 159*. doi:10.1016/j.compositesa.2022.106993

[3] De Luca, H. G., Anthony, D. B., Greenhalgh, E. S., Bismarck, A., & Shaffer, M. S. P. (2020). Piezoresistive structural composites reinforced by carbon nanotube-grafted quartz fibres. *Composites Science & Technology, 198*. doi:10.1016/j.compscitech.2020.108275

[4] Lee, W. J., Clancy, A. J., Fernandez-Toribio, J. C., Anthony, D. B., White, E. R., Solano, E., . . . Shaffer, M. S. P. (2019). Interfacially-grafted single-walled carbon nanotube / poly (vinyl alcohol) composite fibers. *Carbon, 146*, 162-171. doi:10.1016/j.carbon.2019.01.075

[5] Clancy, A. J., Bayazit, M. K., Hodge, S. A., Skipper, N. T., Howard, C. A., & Shaffer, M. S. P. (2018). Charged carbon nanomaterials: Redox chemistries of fullerenes, carbon nanotubes, and graphenes. *Chemical Reviews, 118*(16), 7363-7408. doi:10.1021/acs.chemrev.8b00128

[6] Lee, W. J., Paineau, E., Anthony, D. B., Gao, Y. L., Leese, H. S., Rouziere, S., . . . Shaffer, M. S. P. (2020). Inorganic nanotube mesophases enable strong self-healing fibers. *ACS Nano, 14*(5), 5570-5580. doi:10.1021/acsnano.9b09873

[7] Moore, J. F., Paineau, E., Launois, P., & Shaffer, M. S. P. (2021). Continuous binder-free fibers of pure imogolite nanotubes. *ACS Applied Materials & Interfaces, 13*(15), 17940-17947. doi:10.1021/acsami.1c00971

[8] Moore, J. F., Paineau, E., Launois, P., & Shaffer, M. S. P. (2023). Wet spinning imogolite nanotube fibres: An in situ process study. *Nanoscale Advances, 5*(12), 3376-3385. doi:10.1039/d3na00013c

[9] Yang, S. R. Y., Shaffer, M. S. P., & Brandt-Talbot, A. (2023). High lignin content carbon fiber precursors wet-spun from low-cost ionic liquid water mixtures. *ACS Sustainable Chemistry & Engineering, 11*(24), 8800-8811. doi:10.1021/acssuschemeng.3c00234

[10] Yang, S. R. Y., Tran, E., Ibrahim Muazu, R., Talbot, C. B, Shah, N., Shaffer, M., & Brandt-Talbot, A. (2025). Sustainable low-cost carbon fibres produced by integrating wood fractionation with lignin fibre spinning. *RSC Sustainability, In Press*.

[11] Almousa, H. A., Jiang, Y., De Luca, H. G., Anthony, D. B., Greenhalgh, E. S., Bismarck, A., & Shaffer, M. (2025). Dual-surface engineering of carbon fibers by grafting carbon nanotubes and chemical functionalisation. *ICCM24 Proceedings*.

INCORPORATING NANOSTRUCTURES INTO NEXT GENERATION (SUSTAINABLE) FIBRES

Milo S.P. Shaffer[1,2]

[1]Department of Materials, Imperial College London, London, UK
South Kensington Campus, London, SW7 2AZ, United Kingdom

[2]Chemistry Department and Materials Department, Imperial College London
White City Campus, London, WC12 0BZ, United Kingdom
m.shaffer@imperial.ac.uk, https://profiles.imperial.ac.uk/m.shaffer

Keywords: Carbon fiber; Carbon nanotubes; Interface/interphase; Chemical Vapor Deposition (CVD); sustainable materials, lignin-derived carbon

Nanostructured materials offer the possibility to improve the performance and functionality of existing structural fibres. There are broadly two strategies (Figure 1): One involves the incorporation of the nanomaterial into existing state of the art fibres, in order to address critical weaknesses and/or introduce new functions. Examples of this first approach include the development of nanostructured interphases on existing carbon and glass fibres. Here, the nanomaterial improves load transfer between the fibre and the matrix and reduce stress concentration. Surface grafting of carbon nanotubes (CNTs) by direct CVD provides a hierarchical fibre with two differing reinforcement length scales. The advantages of this approach are well known, but typically limited by damage to the substrate fibres, and difficulties with scale-up. Informed by flow modelling and "dynamic snapshots", we have developed a continuous spool-to-spool process that produces controlled, uniform grafting throughout the tow. The products show excellent single fibre and small composite performance in thermosets[1] and thermoplastics[2], and are relevant to multifunctional applications such as structural heath monitoring[3].

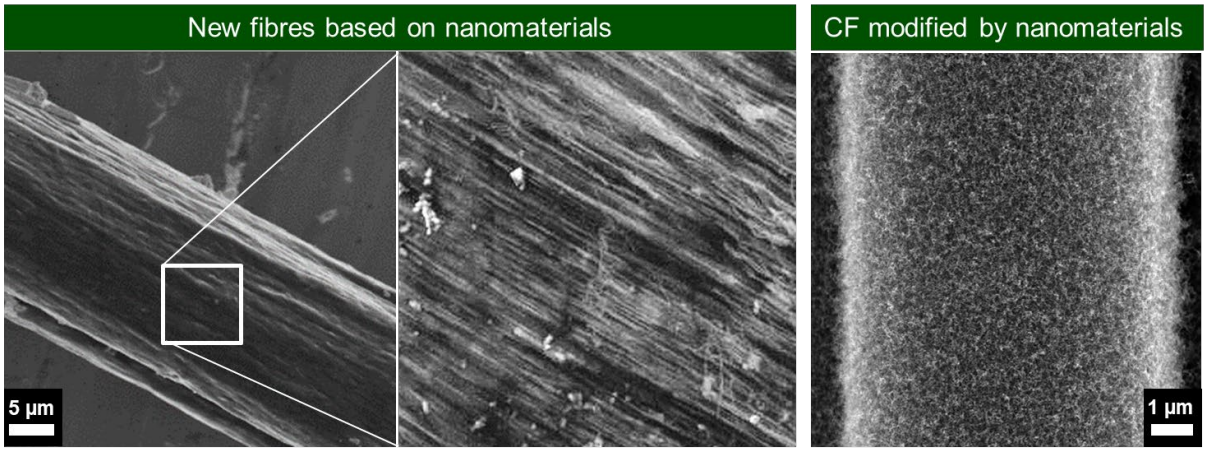

Figure 1: Schematic showing two alternative strategies for exploiting nanostructures in fibres : a) spinning new fibre systems based on 1D nanomaterial precursors (left, showing a single-wall carbon nanotube based fibre)[4] or b) modifying of an existing state of the art structural fibre with a nanomaterial enhancement (right, showing a PAN-based carbon fibre grafted with carbon nanotubes to reinforce its interphase.[2]

The second approach, which is more challenging but potentially more transformative, relies on the development of entirely new fibre systems from the nanostructured or nanocomposite constituents; however, new processes to assemble and orient the constituent nanostructures. One dimensional nanomaterials are particularly well suitable to unidirectional alignment in fibre formats. A wide range

of building blocks are possible, including nanotubes, nanorods, and nanowires, based on carbons, inorganic compounds, synthetic proteins, and biologically derived constituents; a variety of these options are explored here (Figure 2). In particular, individual perfect nanocarbon structures have exceptional properties; the challenge is often how to exploit their potential in real macroscopic systems. Whilst dry spinning approaches may be attractive, wet spinning is more obviously scalable and applicable. However, the formation of individualized solutions of functionalised single wall nanotubes (SWNTs) and graphenes is challenging. We exploit reductive charging to form pure nanotubides (nanotube anions) which can be redissolved, purified, or optionally functionalised, whist avoiding the damage typically associated with sonication and oxidation-based processing.[5] Nanotubide solutions form nematic phases which can be spun directly into coagulant baths in order to prepare functionalised SWCNT fibres in situ. Grafting of suitable polymer constituents can increase dispersibility of both nanotubes and graphenes and hence help to produce nanocomposite fibres with higher strength and strain to failure, [4] as well as multifunctional performance as supercapacitors. Non-carbon-based analogues of nanotubes offer different functions. For example, composite fibres containing inorganic (imogolite) nanotubes can generate healable structural fibres, with exceptionally high performance. [6] Imogolite nanotube dispersions also form liquid crystalline mesophases and it is possible to spin pure imogolite fibres, analogously to the carbon nanotube examples.[7] The imogolite system has the advantage of water compatibility and the opportunity for in situ process monitoring through optical birefringence and x-ray studies.[8]

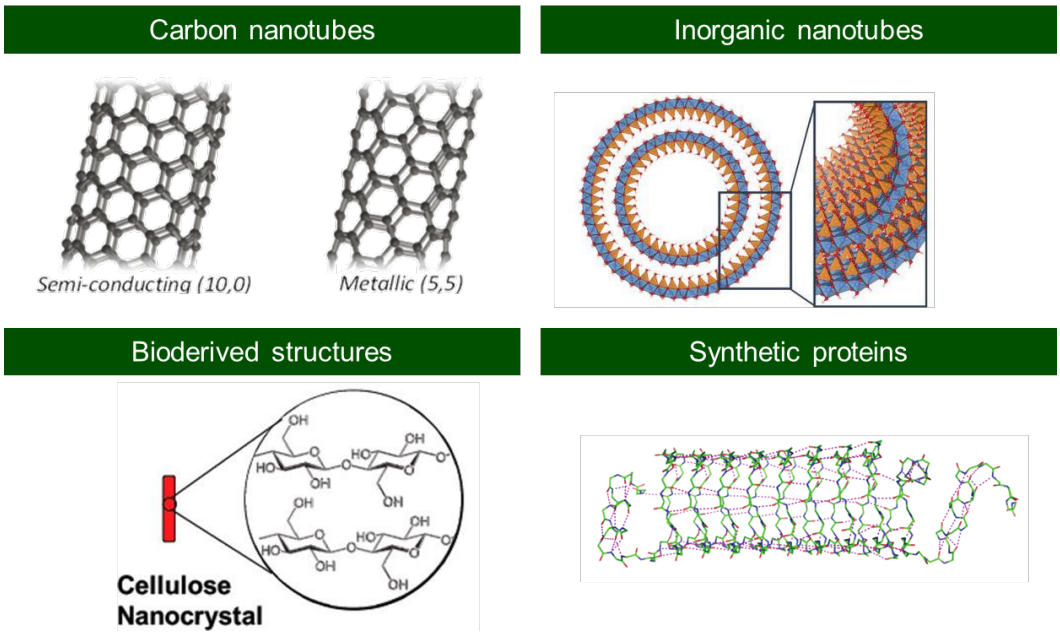

Figure 2: Schematic showing possible one dimensional nanomaterial building blocks for fibres

More sustainable fibre systems can be pursued by spinning bioderived nanomaterials, or by using nanomaterials to allow the spinning of lignin-based materials, for conversion into carbon fibre. Lignin-derived carbon fibers (CFs) are an attractive target for low-cost sustainable composite applications. Our lignin-based fibers are wet-spun using a low-cost (<$1/kg) ionic liquid, N,N – dimethylbutylammonium hydrogen sulfate ([DMBA][HSO_4]) as the dope solvent and water as the coagulation bath.[9] If the lignin is extracted from the biomass using an ionosolv approach based on the same low cost ionic liquid, it can be used directly as the feedstock for the wet-spinning process. This latter approach removes several process steps, including the need to dry the lignin powder during its isolation. An initial life cycle analysis (LCA) indicates that this new ionosolv approach offers significant scope to reduce the cost and global warming potential of lignin fibre production.[10] Very low loadings of CNTs can be used as the spinning aid for this ionosolv process, yielding fibers containing up to 96% lignin solid fraction. The presence of CNTs increases the estimated carbon fiber yield from ~40% to 54%, a critical factor for

technoeconomic outlook of lignin-based carbon fibers. In addition to enabling fiber spinning and increasing carbon yield, the CNTs may also act as graphitization templates and provide direct reinforcement of the lignin-derived carbon matrix, improving mechanical performance. Although the fibres do not yet match the strength or stiffness of state-of-the-art PAN-based carbon fibres, they may nevertheless be optimized to offer useful performance across a wide range of sectors from automotive to construction. In principle, CNTs can be bioderived, offering a fossil free route to low cost carbon fibers using only renewable carbon sources.

CONCLUSIONS

One dimensional nanomaterials are well suited to incorporation in fibre systems, both forming new types of pure fibre or in composite form. The aspect ratio and dimensionality are compatible with a high degree of alignment and efficient packing in the spun fibres, but also often generate lyotropic liquid crystal phases that play an important role in processing. Wet-coagulation spinning can exploit these phases and is readily scalable via established routes, from lab scale batches, through lab scale continuous monofilament, multifilament, and upwards towards pilot scale. Nanomaterials often offer excellent mechanical properties due to their high perfect and confined defect sizes but can also introduce a wide variety of functional benefits, including electrochemical energy storage and self-healing.

As specific examples, pure and composite carbon and imogolite nanotube fibres show promise as ductile and multifunctional reinforcements. Carbon nanotube fibres are conductive, loading-bearing, and with high electrochemical capacitance, relevant to structural supercapacitors Imogolite provides an analogous structure to CNTs that is easier to manipulate and study by POM & XRD, providing in situ insight into processing steps and other phenomenology that can be applied across the nanomaterial fibre domain.

Biomaterials provide routes to “green” carbon fibres and consumer textiles New types of lignin-derived carbon fibres, processed using water & IL only, are particularly promising for their potential low cost and reduced environmental impact. The introduction of carbon nanotubes, combined with new lignins, can improve graphitisability, yield, and performance.

While these new nanomaterials-based fibres offer great promise for the future, their commercial implementation will require time and investment. Meanwhile, nanomaterials can already be used to improve the performance existing state of the art structure fibres. For example, CNT-grafted fibres offer improved structural properties, improving interfacial strength and composite compression performance, whilst offering multifunctional opportunities for enhanced conductivity and self-sensing. A new process allows continuous uniform growth throughout a 12k fibre tow, allowing potential integration directly into existing carbon fibre production.[11]

ACKNOWLEDGEMENTS

This paper summarises work with many group members, colleagues, and collaborators including at Imperial: Adam Clancy, Joe Moore, Kalpana Balaskandan, Shirley Yang, Zoyia Kamora, Enny Tran, Hassan Almousa, Yanhao Sun, Hugo De Luca, Dr David Anthony, Dr Wonjun Lee, Dr Noelia Rubio, Dr James Serginson, Dr Hannah Leese, Dr Joane Ng, Prof Emile Greenhalgh, Dr Agi Brandt-Talbot, Dr James MacDonald, Prof Paul Freemont, Prof Nilay Shah, Dr Rukayya Muazu, and at the University of Paris Sud: Lucie Dieval, Dr Erwan Paineau, Dr Pascale Launois. We kindly acknowledge the funding for this research provided by UK Engineering and Physical Sciences Research Council (EPSRC), including via the programme Grant EP/T011653/1, Next Generation Fibre-Reinforced Composites (NextCOMP): a Full Scale Redesign for Compression, a collaboration between Imperial College London and the University of Bristol, as well as the Imperial-CNRS collaboration.

REFERENCES

[1] Anthony, D. B., Qian, H., Clancy, A. J., Greenhalgh, E. S., Bismarck, A., & Shaffer, M. S. P. (2017). Applying a potential difference to minimise damage to carbon fibres during carbon nanotube grafting by chemical vapour deposition. *Nanotechnology, 28*(30). doi:10.1088/1361-6528/aa783f

[2] Wang, J., Anthony, D. B., Fuentes, C. A., De Luca, H. G., Zhang, D. X., Bismarck, A., . . . Seveno, D. (2022). Wettability of carbon nanotube-grafted carbon fibers and their interfacial properties in polypropylene thermoplastic composite. *Composites Part A, 159*. doi:10.1016/j.compositesa.2022.106993

[3] De Luca, H. G., Anthony, D. B., Greenhalgh, E. S., Bismarck, A., & Shaffer, M. S. P. (2020). Piezoresistive structural composites reinforced by carbon nanotube-grafted quartz fibres. *Composites Science & Technology, 198*. doi:10.1016/j.compscitech.2020.108275

[4] Lee, W. J., Clancy, A. J., Fernandez-Toribio, J. C., Anthony, D. B., White, E. R., Solano, E., . . . Shaffer, M. S. P. (2019). Interfacially-grafted single-walled carbon nanotube / poly (vinyl alcohol) composite fibers. *Carbon, 146*, 162-171. doi:10.1016/j.carbon.2019.01.075

[5] Clancy, A. J., Bayazit, M. K., Hodge, S. A., Skipper, N. T., Howard, C. A., & Shaffer, M. S. P. (2018). Charged carbon nanomaterials: Redox chemistries of fullerenes, carbon nanotubes, and graphenes. *Chemical Reviews, 118*(16), 7363-7408. doi:10.1021/acs.chemrev.8b00128

[6] Lee, W. J., Paineau, E., Anthony, D. B., Gao, Y. L., Leese, H. S., Rouziere, S., . . . Shaffer, M. S. P. (2020). Inorganic nanotube mesophases enable strong self-healing fibers. *ACS Nano, 14*(5), 5570-5580. doi:10.1021/acsnano.9b09873

[7] Moore, J. F., Paineau, E., Launois, P., & Shaffer, M. S. P. (2021). Continuous binder-free fibers of pure imogolite nanotubes. *ACS Applied Materials & Interfaces, 13*(15), 17940-17947. doi:10.1021/acsami.1c00971

[8] Moore, J. F., Paineau, E., Launois, P., & Shaffer, M. S. P. (2023). Wet spinning imogolite nanotube fibres: An in situ process study. *Nanoscale Advances, 5*(12), 3376-3385. doi:10.1039/d3na00013c

[9] Yang, S. R. Y., Shaffer, M. S. P., & Brandt-Talbot, A. (2023). High lignin content carbon fiber precursors wet-spun from low-cost ionic liquid water mixtures. *ACS Sustainable Chemistry & Engineering, 11*(24), 8800-8811. doi:10.1021/acssuschemeng.3c00234

[10] Yang, S. R. Y., Tran, E., Ibrahim Muazu, R., Talbot, C. B, Shah, N., Shaffer, M., & Brandt-Talbot, A. (2025). Sustainable low-cost carbon fibres produced by integrating wood fractionation with lignin fibre spinning. *RSC Sustainability, In Press*.

[11] Almousa, H. A., Jiang, Y., De Luca, H. G., Anthony, D. B., Greenhalgh, E. S., Bismarck, A., & Shaffer, M. (2025). Dual-surface engineering of carbon fibers by grafting carbon nanotubes and chemical functionalisation. *ICCM24 Proceedings*.

ICCM24
AUGUST 4-8, 2025
BALTIMORE CONVENTION CENTER
BALTIMORE, MARYLAND, USA

No Technical Paper Submission for:

Norman Wereley

Investigating Interlayer Bonding and Defect Analysis in Roller-Compaction-Assisted Core–Shell Structured Additively Manufactured Composites

Shaharear Md Emtiaz[1,3], Nicola Shepherd[2,3] and Suresh G. Advani[1,3]

[1] University of Delaware, Newark DE 19711, USA
[2] University of Auckland, Auckland 1023, New Zealand
[3] Center for Composite Materials, University of Delaware



UNIVERSITY OF DELAWARE
CENTER FOR
COMPOSITE MATERIALS
Celebrating 50 Years

Outline

- Additive manufacturing process
- Research gaps
- Experimental setup
- Methodology
- Experimental analysis
- Conclusions

Introduction

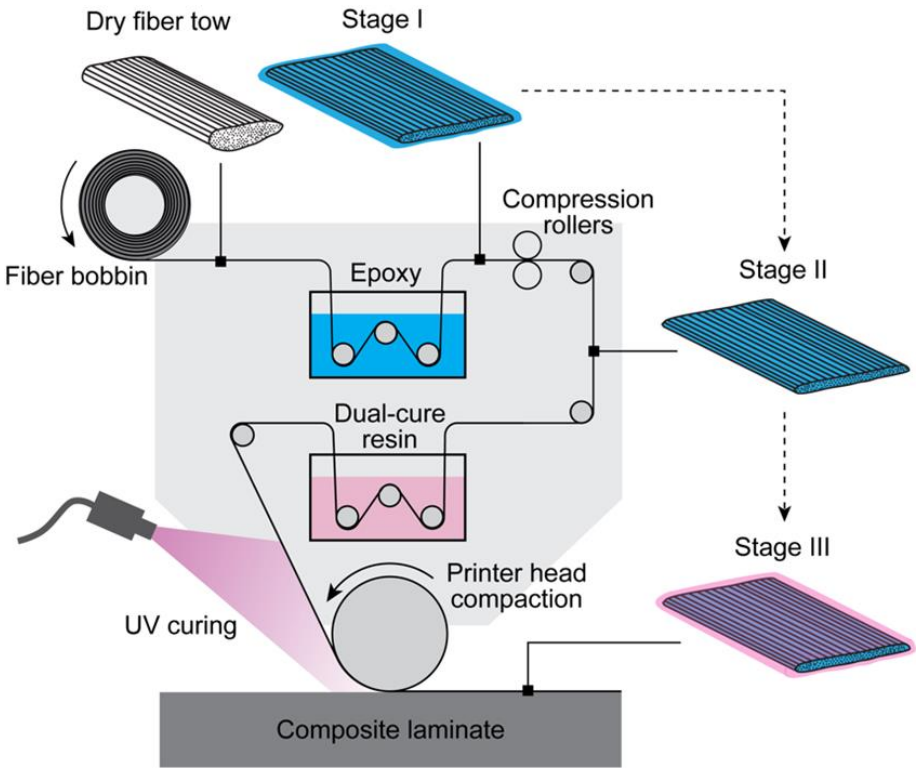

Current challenges:

- Low fiber volume fraction
- High void content
- Weak interlayer bonding

Approach

- Replicate the printing process for controlled impregnation & core shell formation.
- Quantitively apply roller assisted compaction pressure.
- Investigate the void fraction, FVF and SBS.

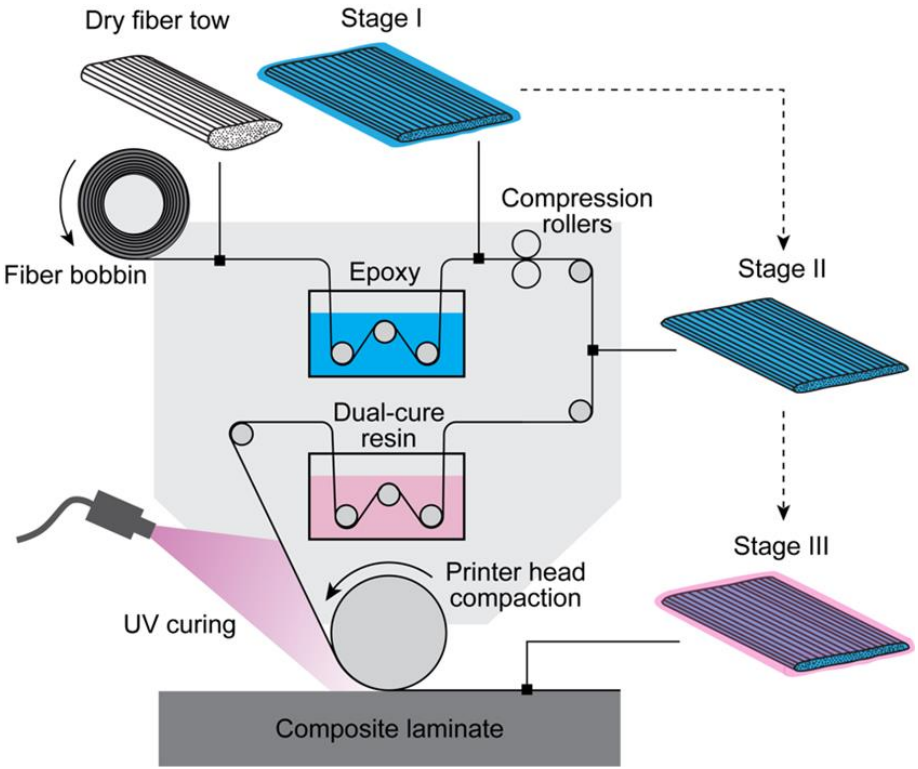

Introduction- Experimental Setup

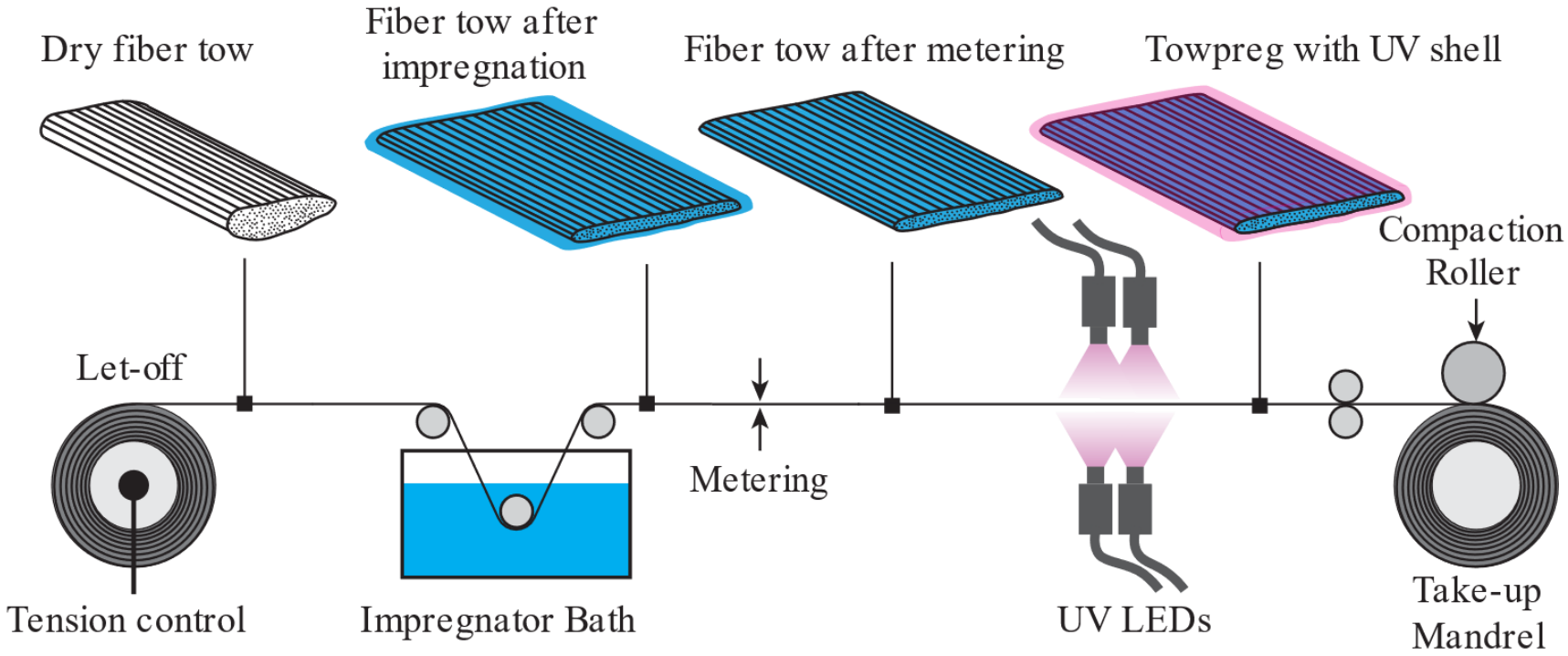

[1] Shaharear Md Emtiaz, Maximilian Pitto, Pavel Šimáček, Suresh G Advani, Role of fiber clustering and resin bleeding on voids and evolution of fiber volume fraction for additively manufactured continuous carbon fiber thermoset composites with dual-cure resins, Composites Part A: Applied Science and Manufacturing, Volume 189, 2025, 108601, ISSN 1359-835X, https://doi.org/10.1016/j.compositesa.2024.108601.

Introduction- Experimental Setup

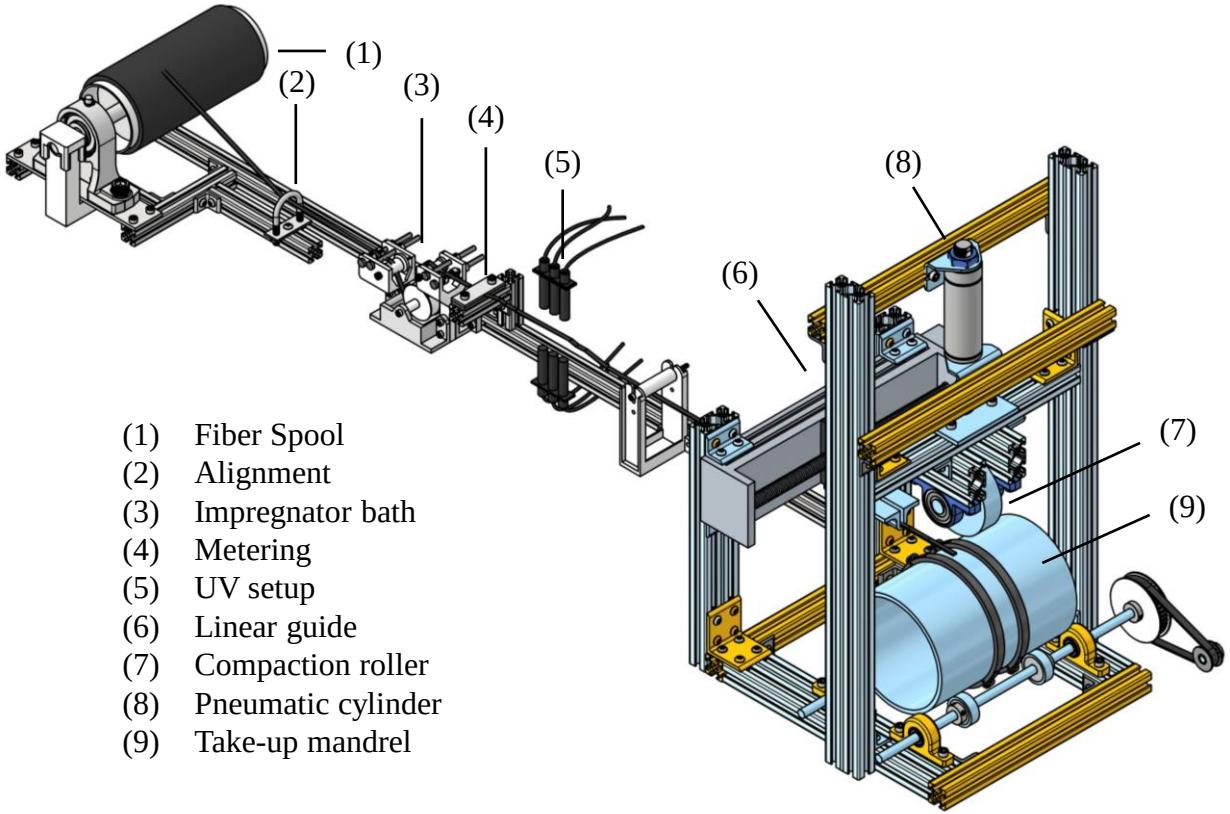

(1) Fiber Spool
(2) Alignment
(3) Impregnator bath
(4) Metering
(5) UV setup
(6) Linear guide
(7) Compaction roller
(8) Pneumatic cylinder
(9) Take-up mandrel

[1] Shaharear Md Emtiaz, Maximilian Pitto, Pavel Šimáček, Suresh G Advani, Role of fiber clustering and resin bleeding on voids and evolution of fiber volume fraction for additively manufactured continuous carbon fiber thermoset composites with dual-cure resins, Composites Part A: Applied Science and Manufacturing, Volume 189, 2025, 108601, ISSN 1359-835X, https://doi.org/10.1016/j.compositesa.2024.108601.

Sample Collection & Specimen Extraction

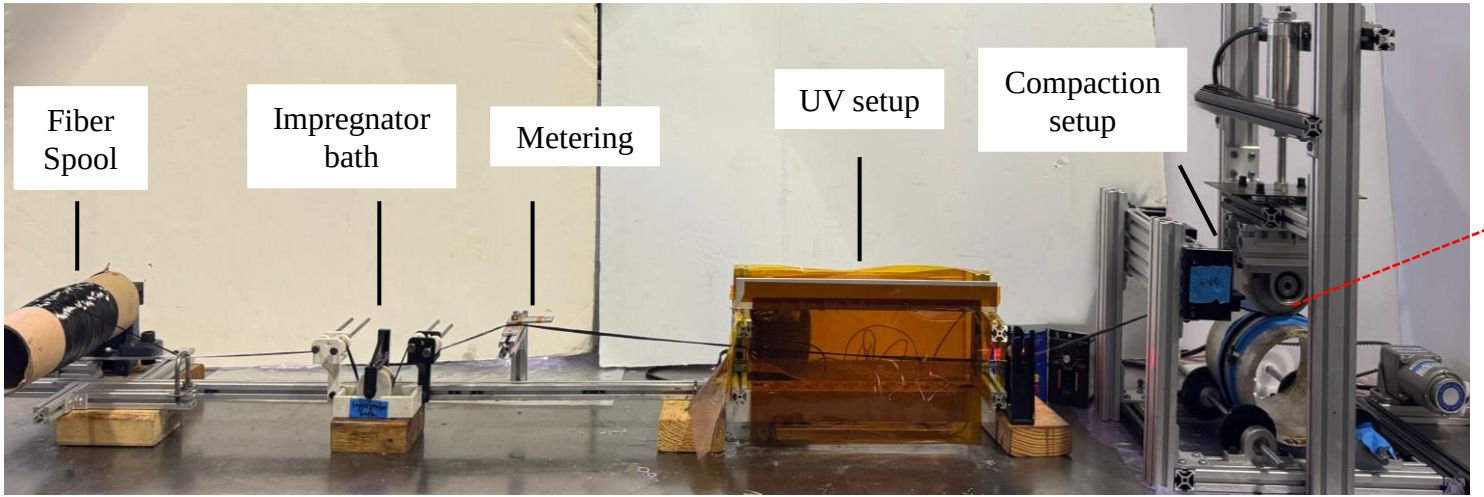



Dry Fiber: Hexcel IM7 unsized 12K tow
Resin: FibreGlast 4600 epoxy + FibreGlast 4690 hardener + Liqcreate Tough-x photopolymeric

Sample Collection & Specimen Extraction



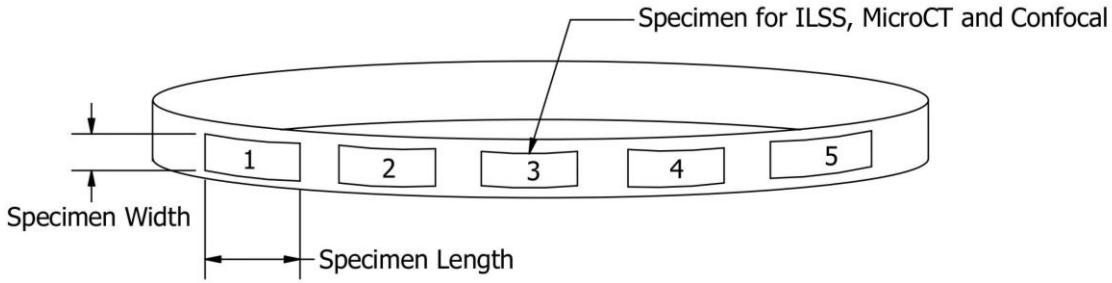

ILSS

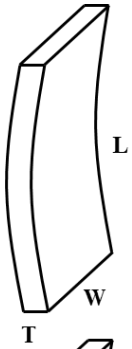

L = 6T
W = 2T
T = 3 to 4 mm

MicroCT

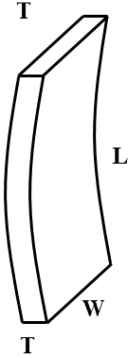

L = ~5 mm
W = ~15mm
T = 3 to 4 mm

Confocal

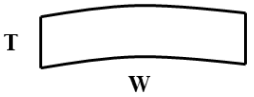

W = 11 mm
T = 2.5 mm

Methodology: Void Content Quantification

- CT Scanner: Bruker 1172 scanner (USA).
- Voltage ~40 kV, current 250 µA, frame averaging: 4 images per projection at a field of view of 4000 × 2664 pixels with a pixel size of 6 µm.
- Reconstruction: NRecon (Micro Photonics Inc., USA) and
- Image analysis: Dragonfly (Comet Yxlon, Germany).

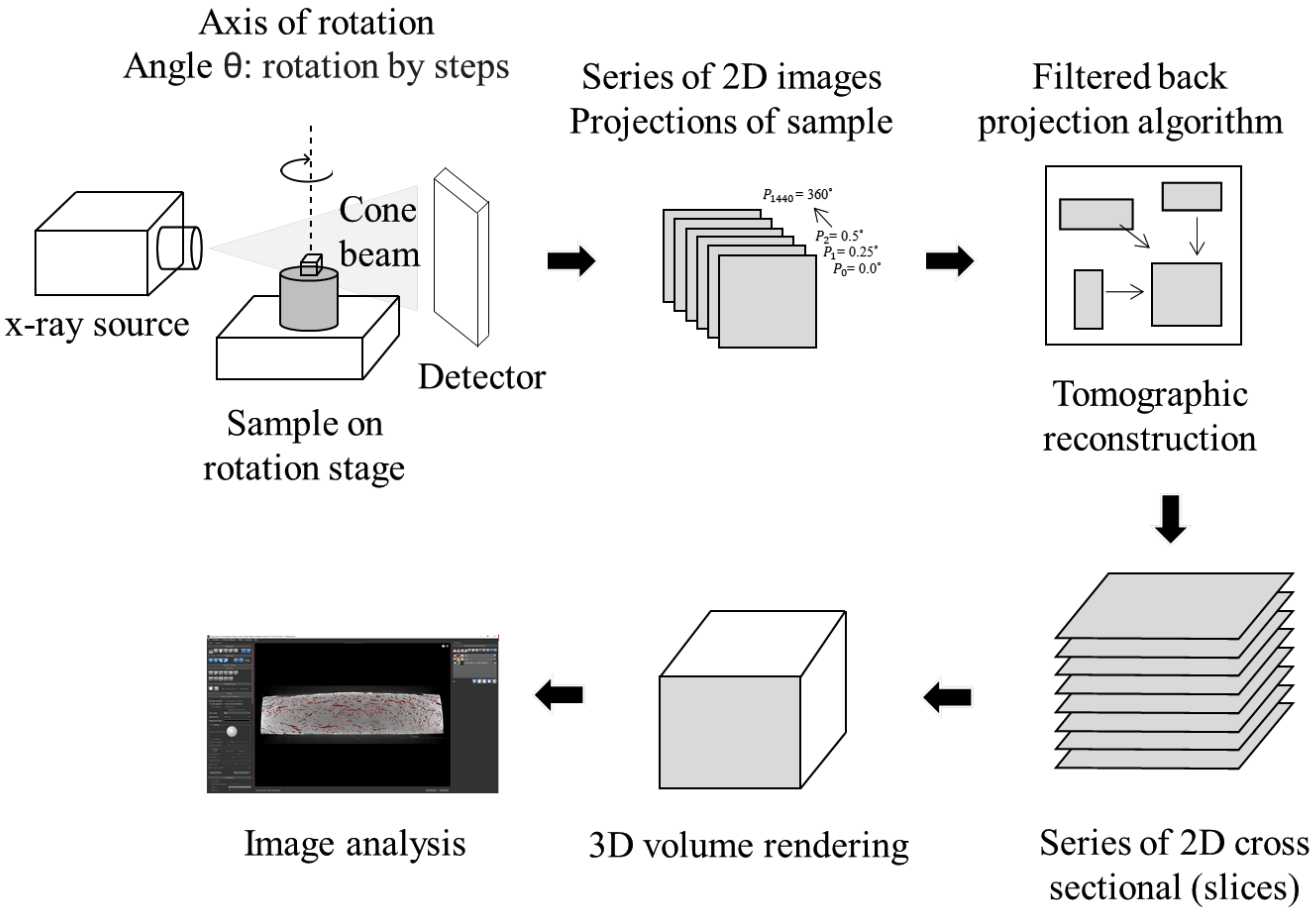

Methodology: FVF Calculation

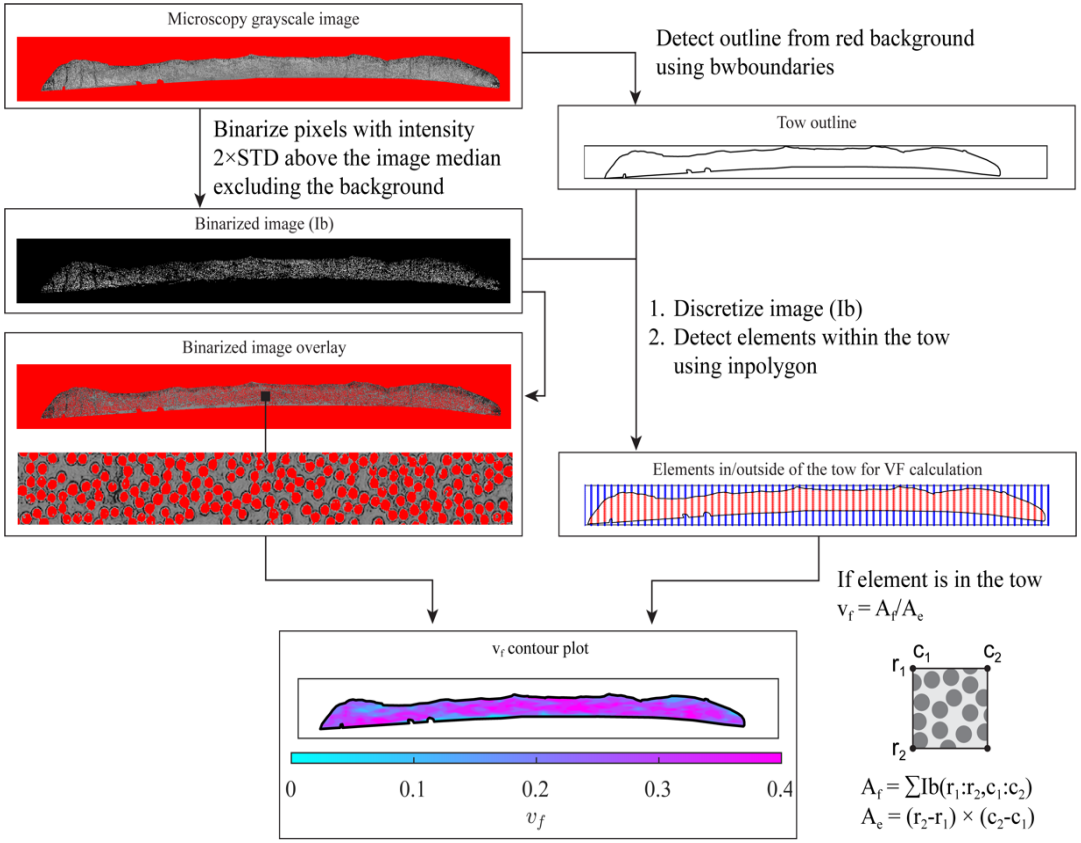

Discretization sensitivity

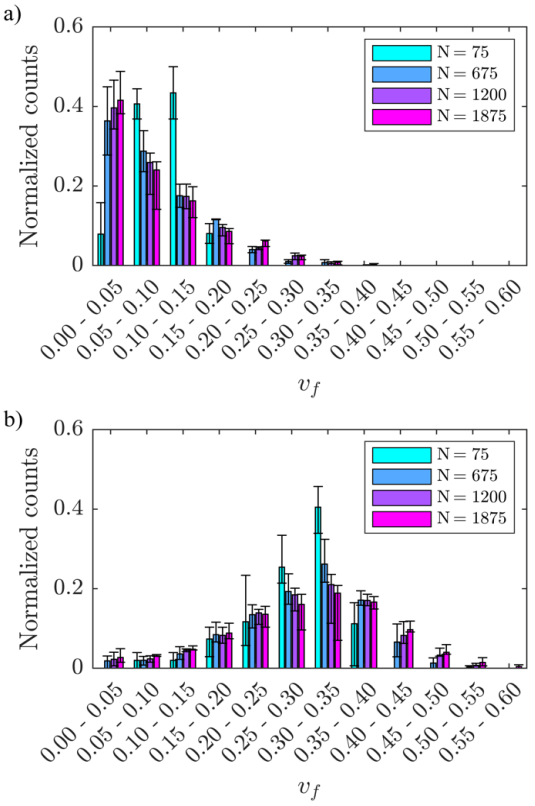

[1] Shaharear Md Emtiaz, Maximilian Pitto, Pavel Šimáček, Suresh G Advani, Role of fiber clustering and resin bleeding on voids and evolution of fiber volume fraction for additively manufactured continuous carbon fiber thermoset composites with dual-cure resins, Composites Part A: Applied Science and Manufacturing, Volume 189, 2025, 108601, ISSN 1359-835X, https://doi.org/10.1016/j.compositesa.2024.108601.

Void Fraction Analysis

$$\text{Void fraction} = \frac{Void\ area\ (Color\ Coded)}{Total\ Area}$$

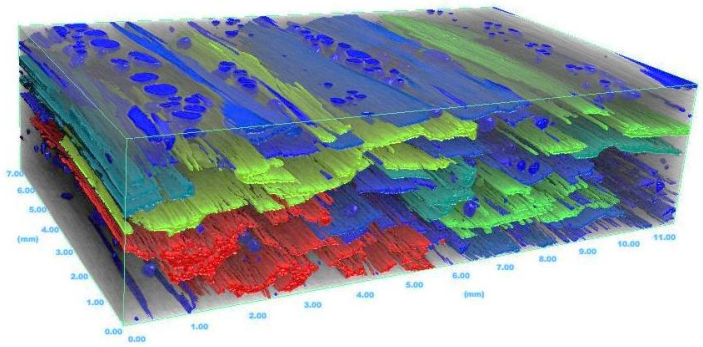

From MicroCT analysis

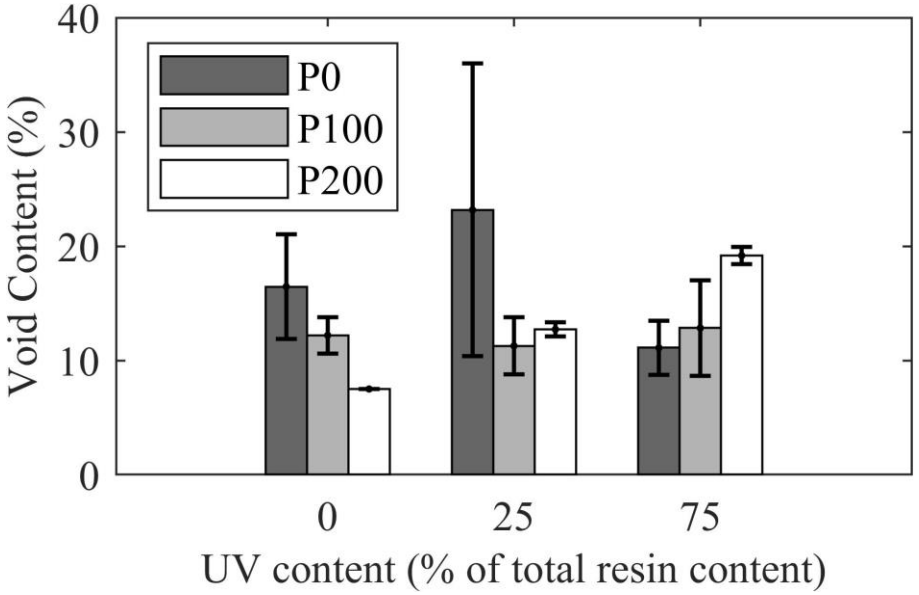

3D Rendering of Voids-Volume

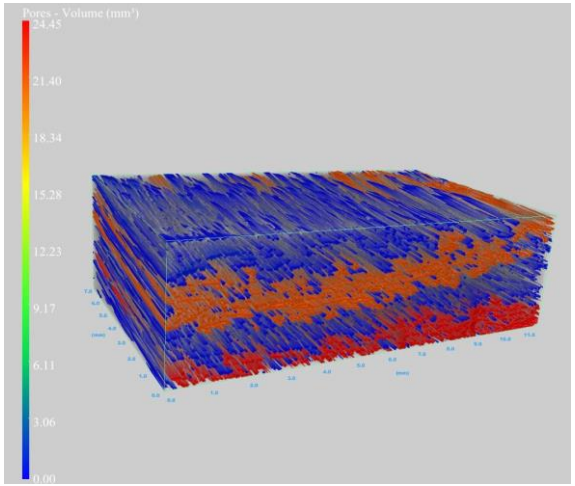

UV0_P0

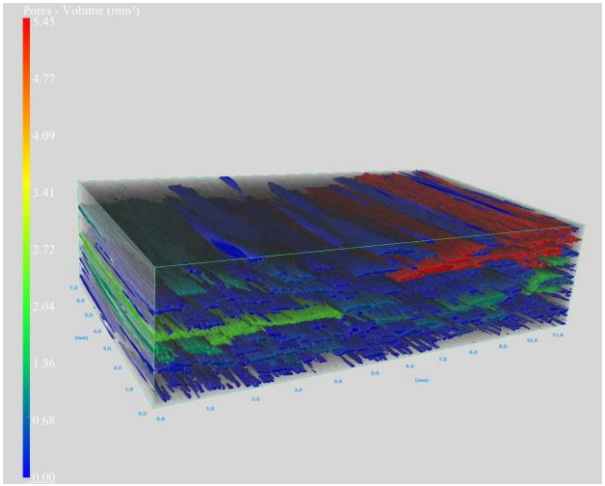

UV0_P100

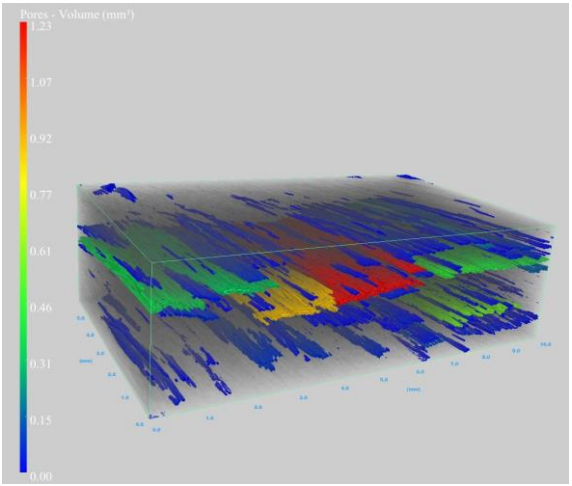

UV0_P200

FVF Analysis

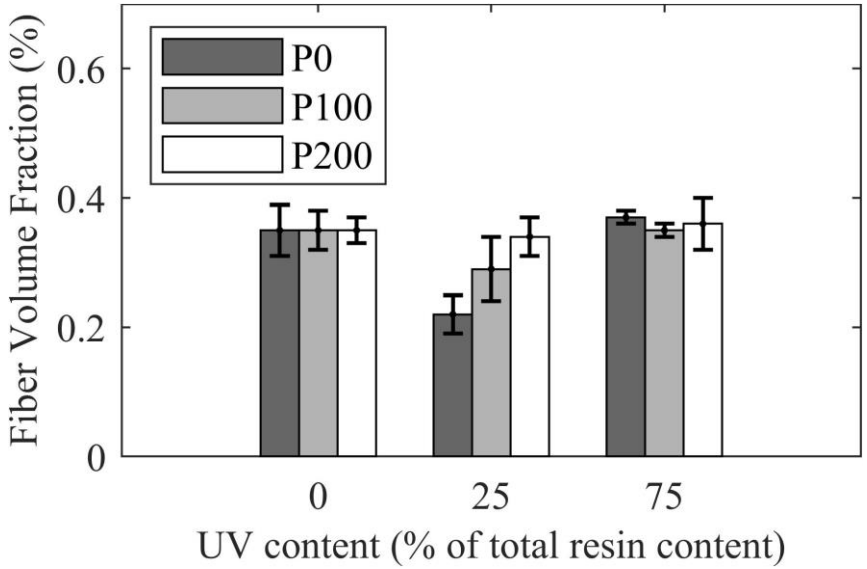

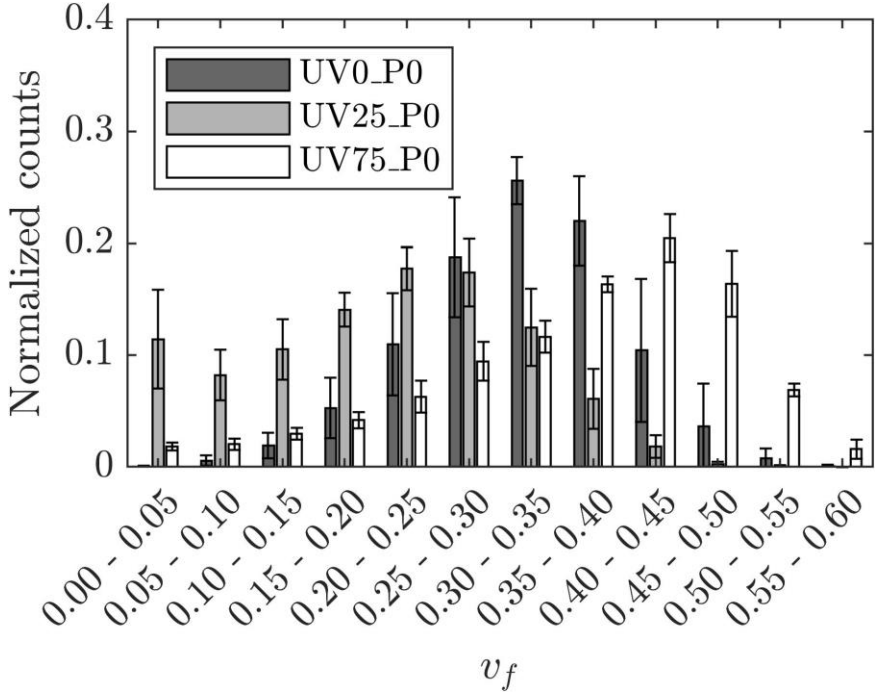

Force-Displacement Curves

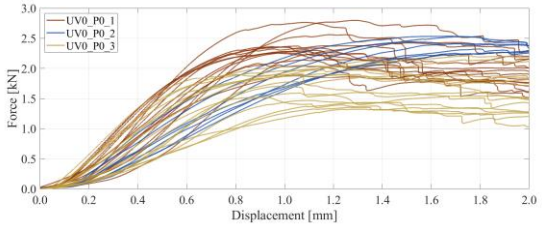

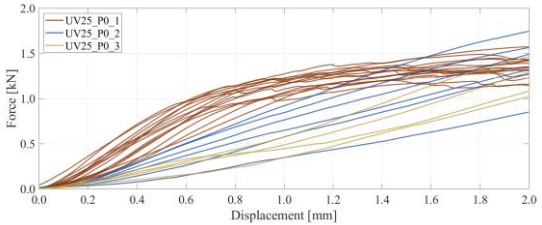

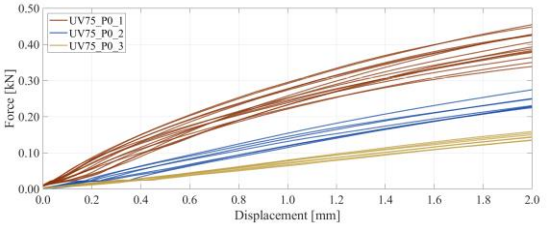

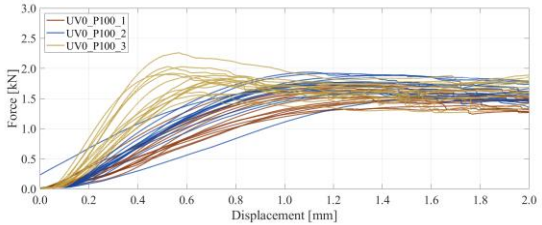

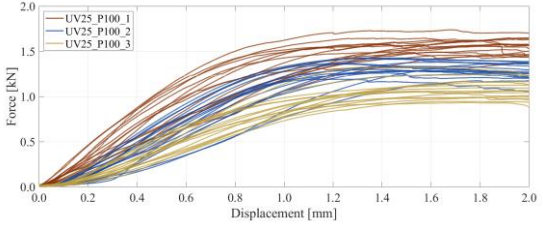

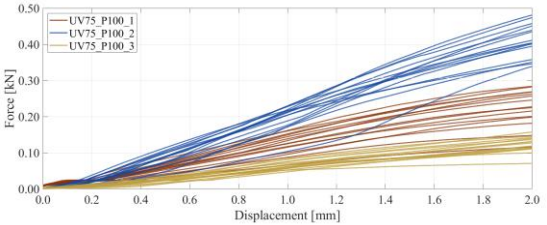

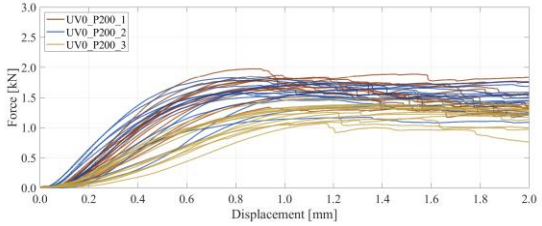

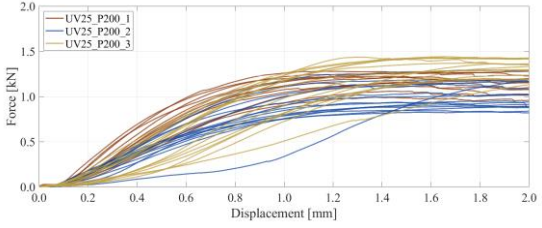

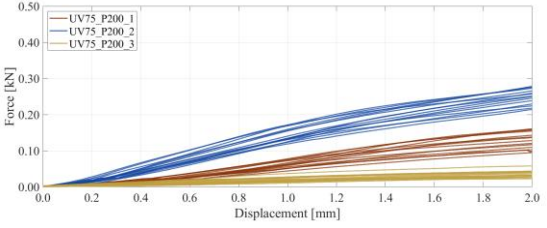

Short Beam Strength: ASTM D2344

$$SBS = \frac{0.75Pmax}{bh}$$

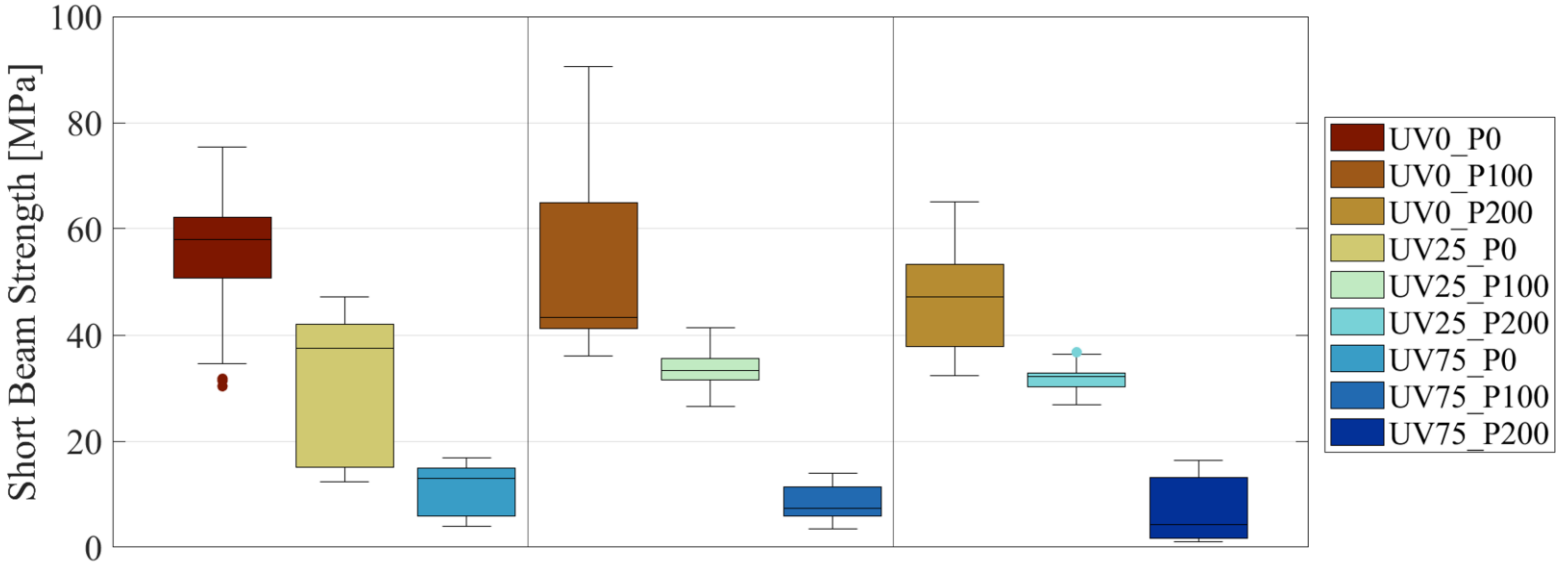

ICCM24 24TH INTERNATIONAL CONFERENCE ON COMPOSITE MATERIALS
AUG 4-8, 2025 · BALTIMORE CONVENTION CENTER · BALTIMORE, MARYLAND

ANALYSIS OF VOID-SIZE AND VOID-DISTRIBUTION IN CONTINOUSLY FIBER REINFORCED FILAMENTS FOR ADDITIVE MANUFACTURING

Jan-Uwe R. Schmidt[1], Maik Titze[1] and Hans Peter Monner[1]

[1] German Aerospace Center (DLR), Institute of Lightweight Systems, 38108 Braunschweig, Germany
Email: jan-uwe.schmidt@dlr.de, web page: http://www.dlr.de/

Keywords: Composite Additive Manufacturing, Voids, CFRP

ABSTRACT

Voids are well understood in traditional composite manufacturing processes. However, the evolving technology of fiber-reinforced additive manufacturing, with its unique constraints, requires adapting this knowledge to the specific materials and processes involved.

This paper evaluates the presence of different void types in continuously fiber-reinforced filaments used for composite additive manufacturing. It presents a study in which the void volume content of a filament, as well as the distribution of void sizes, is correlated with mechanical properties. Due to significant data scattering that complicates a clear evaluation, the study also investigates void mitigation strategies, focusing on the most detrimental void types in the printed parts—since the final printed component's quality is more relevant than the raw filament alone.

A distinct influence of certain void sizes is identified, indicating that these voids should be prioritized for reduction over others.

1 INTRODUCTION

Fiber-reinforced additive manufacturing, whether using short or continuous fibers, improves the properties of the base polymer depending on the type and volumetric content of the fibers. While short fibers often provide sufficient stiffness for a structure, continuous fibers are necessary to increase strength in specific sections [1].

There are different manufacturing technologies to produce such filaments. One versatile method is co-extrusion. For this technology, the German Aerospace Center (DLR), Institute of Lightweight Systems (SY), developed a patented process that uses ultrasound to improve filament quality.

Aeronautical applications require volumetric void contents below 2%. Since this applies to the final part, it is necessary to evaluate not only the void content of the filament after production but also to consider how the printing process affects voids within the filament [2].

Voids in the filaments occur at various scales. As filament diameters are about 1.1 mm (800 tex, 12K, 50% fiber volume content), the usual void classification cannot be directly applied. However, the typical classification into micro-, meso-, and macro-voids can be adapted for this purpose.

High-performance polymers such as Polyetherimide (PEI), Polypropylensulfide (PPS), and Polyetheretherketone (PEEK) are used because the material must meet high-performance requirements to justify its cost. These polymers tend to have relatively high viscosity, which challenges the co-extrusion process.

2 MATERIALS AND METHODS

Materials and production process:

The produced, printed, and evaluated filaments consist of carbon fibers from the AS7 fiber by Hexcel, which is a 12K fiber with 800 tex and no sizing. The polymer matrix is a commercially available PPS . The impregnation temperature is 330 °C, resulting in a measured dynamic viscosity of 155 Pa·s without applied shear forces.

The filament is manufactured on a co-extrusion line with a miniaturized extruder capable of processing about 2 kg of polymer per hour. The fiber insertion tool is designed to allow dry fibers to

enter while sealing the polymer-fiber contact area to up to 60 bar. An ultrasound impregnation cell is used to improve impregnation by reducing the polymer viscosity.

A hydraulically decoupled two-nozzle concept shapes the filament into a round semi-finished product according to the specimen requirements. Tempered tubes at the interface and after the last nozzle enable a gentle cooling ramp. The filament is then spooled and used on the printing end effector, where it is heated in a thermally decoupled nozzle. The nozzle diameter is only slightly larger than the filament diameter to reduce fiber buckling in the molten polymer, which can cause nozzle clogging.

Producing fiber-reinforced thermoplastic products is challenging in terms of quality assurance because the matrix material has higher viscosity and exhibits both elastic and viscous behavior [3]. Multiple production technologies exist, but most are not easily transferable between material systems. The classical fiber impregnation approach using e.g. thermoset matrix systems results in different void types—macro, meso, and micro voids—classified according to their location relative to the fiber tow [4]. Since this process uses only one tow, the classification must be adapted.

Methods:

The analysis of the filament after production and after printing single strands consists of multiple evaluation steps. First, the filaments are cut into specimens for 3-point bending tests. The specimens are marked with rotation angles to repeat measurements in six directions. Additionally, specimens are sputtered, cut, and polished to enable optical analysis of the voids present.

The bending tests are conducted according to ISO 178/141425. The bending results of each specimen are compared based on the loading direction (in 60° increments). The optical analysis results are benchmarked against overall void content measured by thermogravimetric analysis.

The optical analysis uses an automated algorithm to distinguish voids from fibers and polymer based on grey-scale thresholds. However, voids vary widely in symmetry, location, size, and shape. While the classical classification into micro-, meso-, and macro-voids could be applied to the cross-sectional Figure 1, the distinction is not always clear in literature. Therefore, voids are categorized in this paper by size into following classes: '< 0.0001 mm²', '< 0.001 mm²', '< 0.01 mm²', '< 0.05 mm²', and '> 0.05 mm²'.

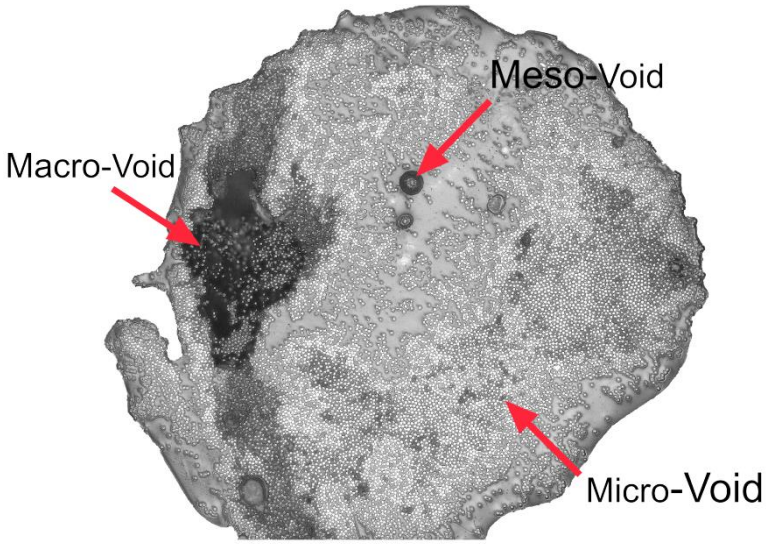

Figure 1 Modification of classical void classification

A main evaluation experiment is using three-point bending test. The experiment is designed using the norm DIN EN ISO 14125 [5]. However, since the filament is round, the pins were modified to position the filament according to the desired rotational positioning. The bending is set force driven (1N) newton to not provoke destructive testing as each specimen is needed for 6 measurements.

For the shear test, the filament is clamped into a rotational test device in which an oscillating, rotational movement is applied. Using the amplitude and the frequency, the shear modulus can be calculated [6].

3 EXPERIMENTS

To assign mechanical behavior to the voids, the described methodology was applied. Numerous filaments made from the same material combination—PPS and AS-7 fiber—were produced. However, manufacturing parameters such as production speed, impregnation pressure, and ultrasound impregnation amplitude were varied. The impregnation line speed ranged between 10 and 50 mm/s, while the impregnation pressure was set between 20 and 30 bar.

Figure 2 shows the calculated bending modulus of single filaments plotted against the global void volume content determined from cross-sectional images. For each filament, results from different angles of attack (0°, 60°, 120°, 180°, 240°, 300°) are indicated. It is important to compare opposite angles to reveal asymmetries in mechanical performance and the overall scattering of results. Average values are also presented. However, across more than 30 specimens with void volume content between 20–40%, no clear trend emerges from the data. Manufacturing pressure and speed were varied in order to produce different void volume contents.

The graph also includes information on the content of individual void size classes relative to overall void content. It appears that when a certain total void content is present, large voids dominate the void population, whereas smaller voids show less correlation with overall void content.

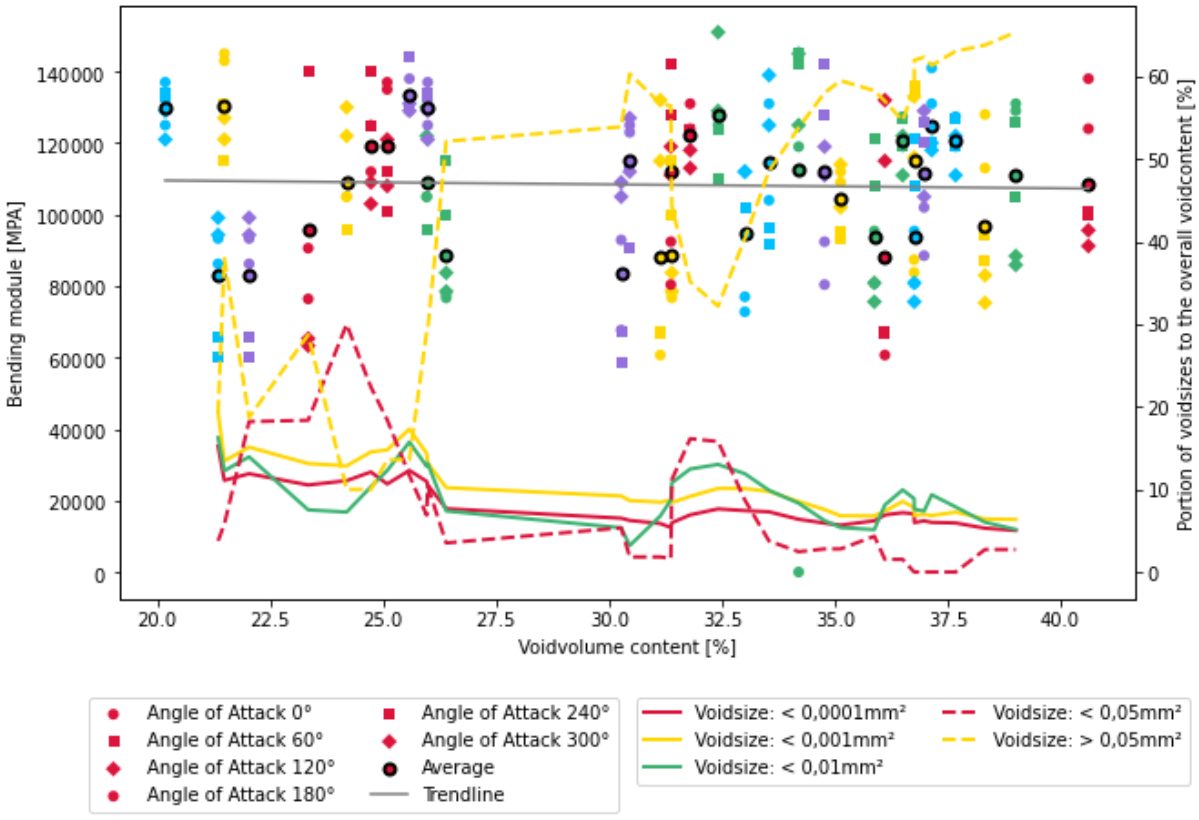

Figure 2 Bending to void volume content

Since bending tests did not reveal a significant correlation between voids and mechanical properties, the shear modulus was also tested and calculated (Figure 3). Again, results do not show a clear influence of increasing void content; interestingly, the expected loss in mechanical performance is not observed.

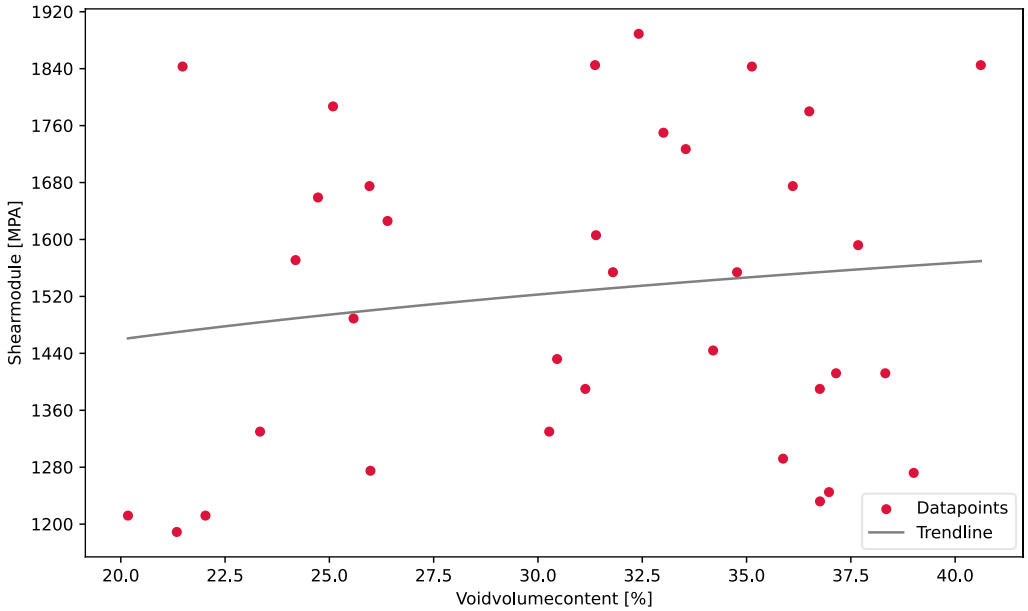

Figure 3 Shear modulus compared to the void volume content

Because void volume content does not correlate well with filament mechanical properties, a new approach is needed to analyze the influence of voids and their types. It is evident that data scattering is significant and that mechanical properties depend on additional factors which may mask the void effect. Major influencing parameters include fiber distribution and filament geometry as well as overall quality of impregnation. While the filament shape can be controlled relatively well with the machine setup, fiber distribution is less controllable and causes asymmetrical voids expected to have greater impact on bending and shear modulus than overall void content.

Since void restrictions mainly apply to the final additively manufactured part, not the filament material itself, the mitigation of voids during filament printing was evaluated.

Therefore, each filament batch was used in a classical FDM (Fused Deposition Moulding) where only a single filament was deposited, eliminating side effects like polymer oozing or acceleration/deceleration of the print head positioning system (Figure 4).

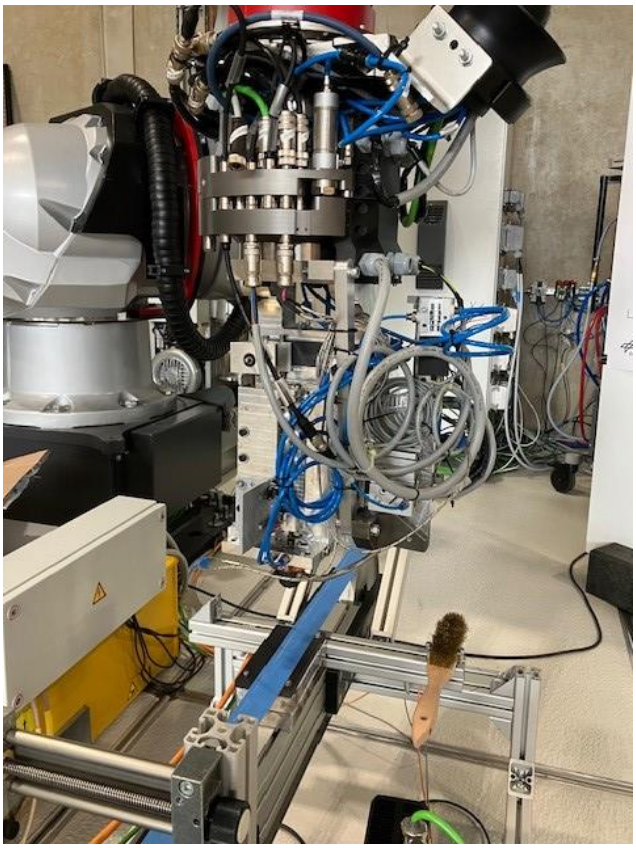

Figure 4 Filament printing

Subsequently, 3-point bending tests on printed filaments were conducted (Figure 5). Data shows a tendency of the printing influencing the bending modulus and void content, but no clear impact of printing speed is discernible.

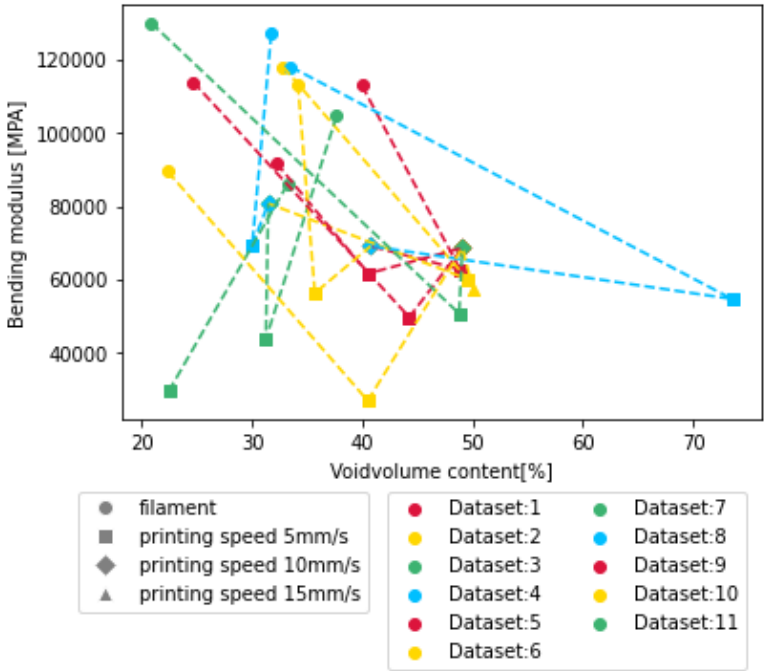

Figure 5 Bending of printed filaments

Optical evaluation of filaments before and after printing reveals a significant increase in voids due to printing.

	Filament	After printing
1	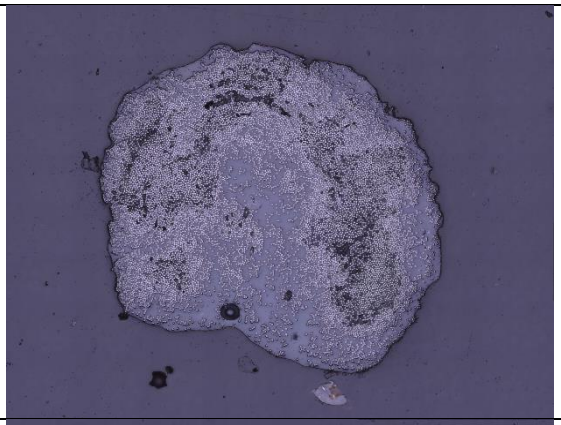	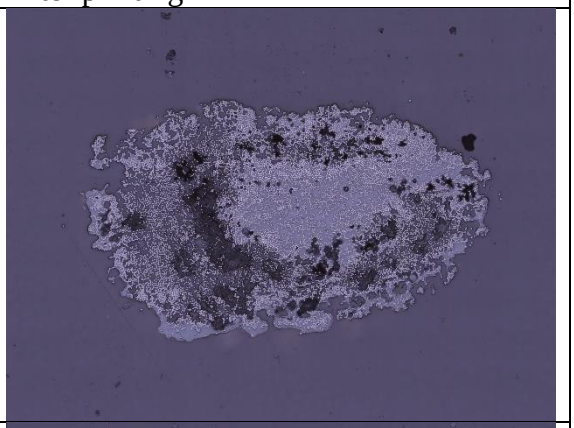
2	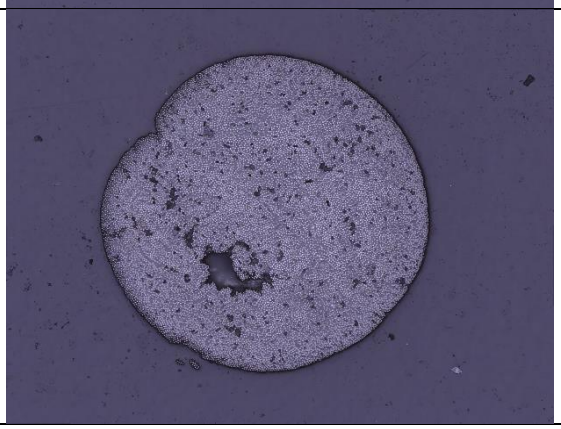	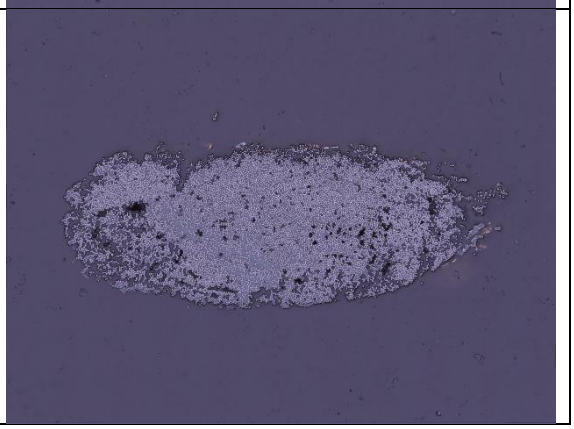

Table 1 Filament comparison to printed version

Table 1 presents four microscopic images showing large voids in filament 1 and only medium-sized voids in filament 2. Notably, printed filament 1 shows a significant increase in voids, while filament 2 only has a slight increase. Figure 6 quantifies this effect across evaluated specimens.

Voids smaller than 0.05 mm² do not tend to accumulate or grow significantly, whereas voids larger than '> 0.05 mm²' tend to increase, initiating cracks and raising overall void content during the process of printing the filament. The printing speed shows only minor influence, likely within data scattering.

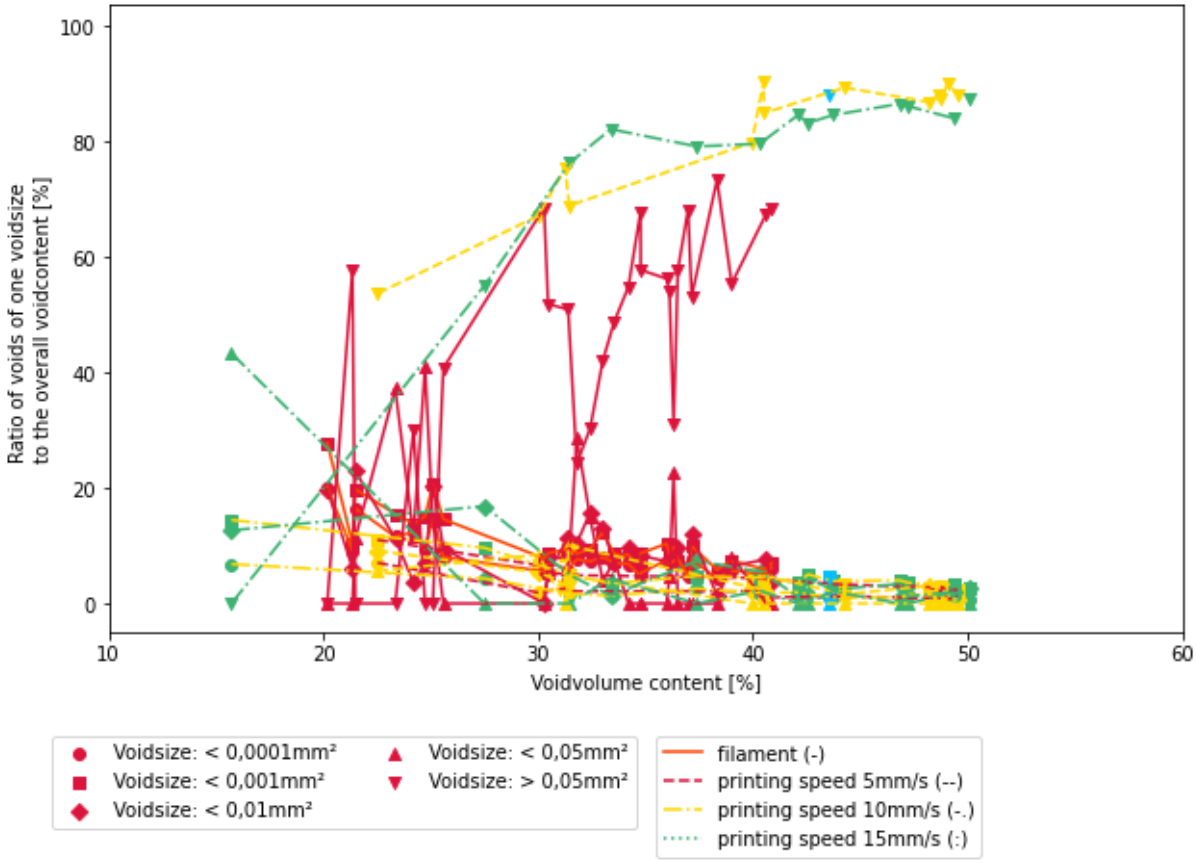

Figure 6 Void content comparison filament to printed specimen

4 CONCLUSION AND OUTLOOK

This study analyzing filaments produced by the co-extrusion process shows that the influence of voids on mechanical properties—such as bending modulus and shear modulus—is largely within the scattering caused by inhomogeneous fiber distribution as well as impregnation quality and imperfect filament geometry.

Nevertheless, certain types of voids have a notably harmful impact, especially when their mitigation is considered. While small individual voids appear largely unaffected by the printing process, larger voids significantly affect the printed parts by increasing the overall void content, which can lead to part rejection due to insufficient quality.

Given the manufacturing challenges of continuous fiber reinforced filaments, based on the utilized production process using ultrasound induced impregnation it seems to be not feasible to eliminate all voids immediately. However, this study identifies which void types should be prioritized for reduction.

Future work should investigate additional mechanical properties influenced by voids in the final parts. Moreover, improvements in fiber distribution are necessary to reduce the variability in material performance. Both theoretical considerations and engineering experience suggest that increased void content generally leads to reduced mechanical performance. By isolating other influencing factors, it may become possible to quantitatively assess the effects of void size, geometry, location, and type on mechanical behavior.

ACKNOWLEDGEMENTS

The funding body of the project Schall-FTP KA-TVP-06 within its transfer campaign (Helmholz-Gesellschaft, as well DLR Technology Transfer) is acknowledged for providing the funding of this work as part of a greater project around continuous fiber reinforced additive manufacturing.

REFERENCES

[1] Norbert Stötzner. Skalierbare, einstufge fertigung von hybridbauteilen. Lightweight Design, 12(1):56-59, 2019. ISSN 2192-8738. doi: 10.1007/s35725-018-0077- 0.

[2] Johann Kastner, Bernhard Plank, Dietmar Salaberger, and Jakov Sekelja. Defect and porosity determination offibre reinforced polymers by x-ray computed tomography. 2010

[3] Youbing Li, Kaizhi Shen, Jie Zhan. Improving rheological property of polymer melt via low frequency melt vibration. 2006.

[4] Mahoor Mehdikhani, Larissa Gorbatikh, Ignaas Verpoest, and and Stepan V Lomov. Voids in fiber-reinforced polymer composites: A review on their formation, characteristics, and effects on mechanical performance.

[5] Beate Bender Dietmar Göhlich. Dubbel Taschenbuch für den Maschinenbau-Band 1: Grundlagen und Tabellen. Springer Vieweg, Heidelberg, 2020

[6] Gottfried W. Ehrenstein. Thermische Analyse: Brandprüfung, Wärme- und Temperaturleitfähigkeit, DSC, DMA, TMA. Erlanger Kunststoff-Schadensanalyse. München: Hanser, 2020. ISBN: 978-3-446-46258-8

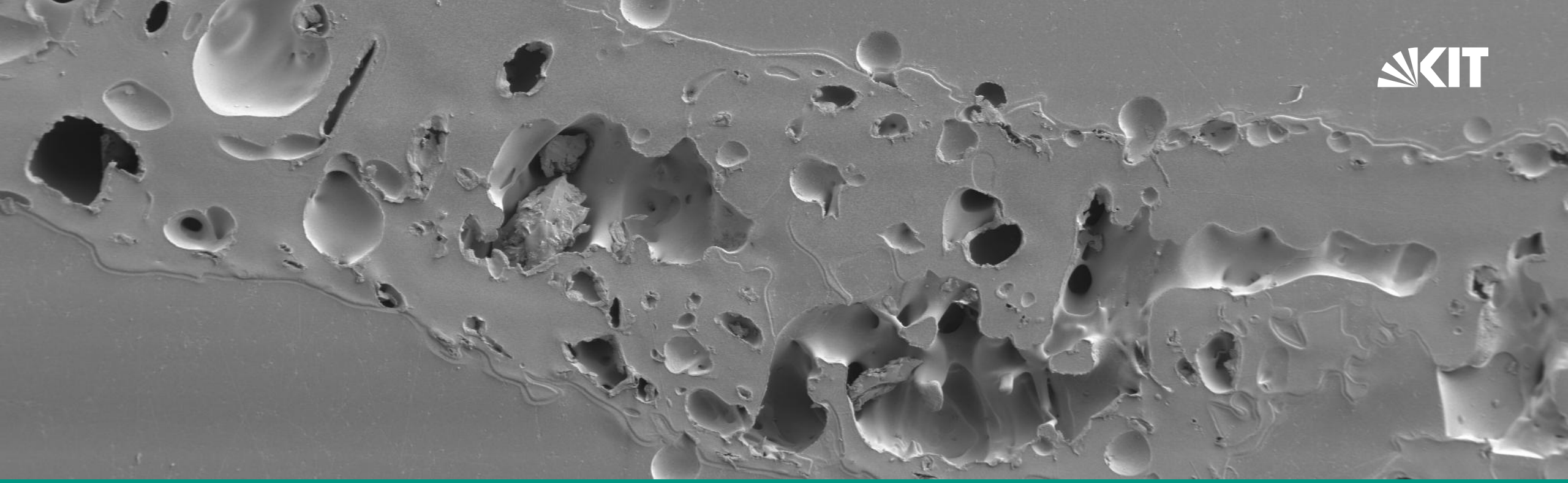

Development of a Nozzle Concept for In Situ Foaming in the Material Extrusion Process

Lars Eisele, Anselm Heuer, Wilfried Liebig

Motivation

Ex situ foaming

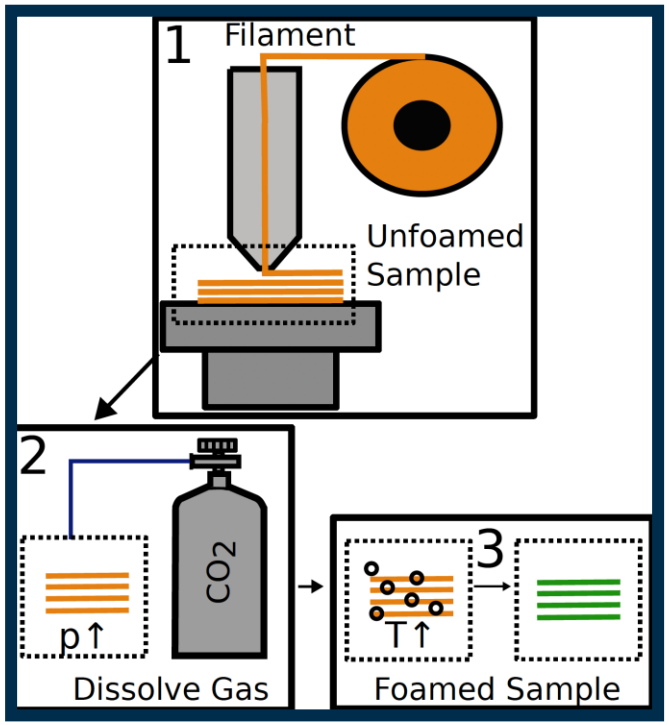

Figure modified from [1]

- Time consuming downstream process steps required
- Foaming degree within component cannot be varied

In situ foaming

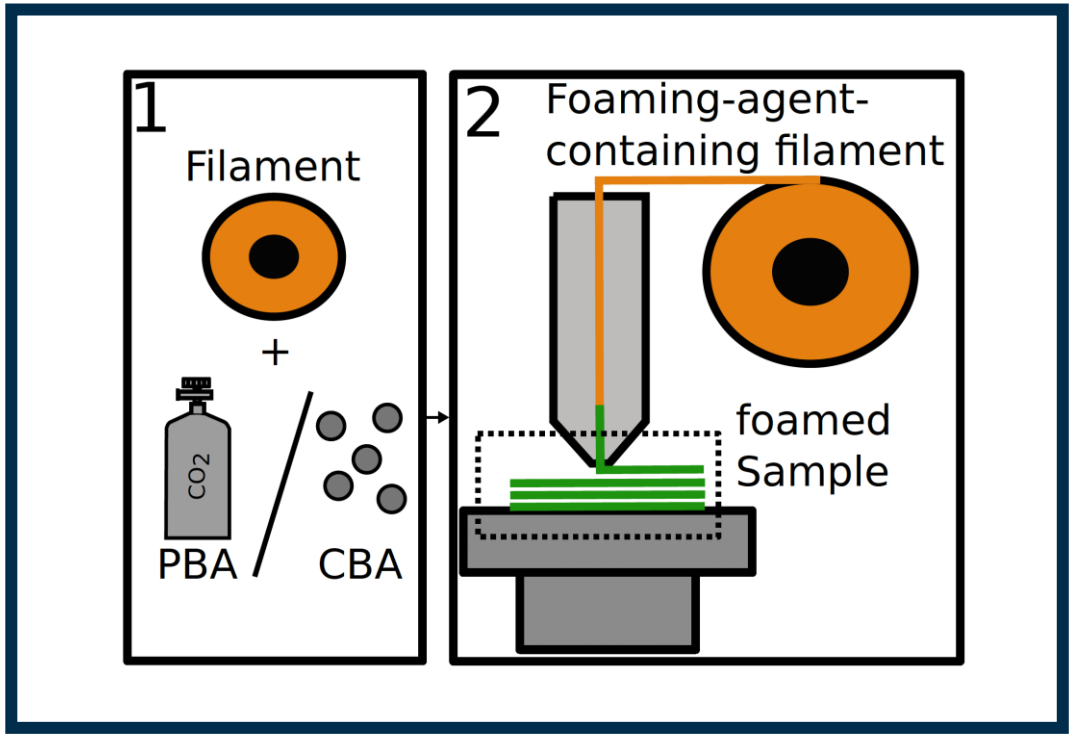

Figure modified from [1]

- Time consuming upstream process steps required
- In case of PBA: Degree of foaming depends on time

[1] Sun B and Wu L (2022), Research progress of 3D printing combined with thermoplastic foaming.

Motivation

Developing a nozzle concept iteratively

↓

Seal optimisation and process stabilisation

↓

Investigate parameter effects on foam structure

Novel foaming process

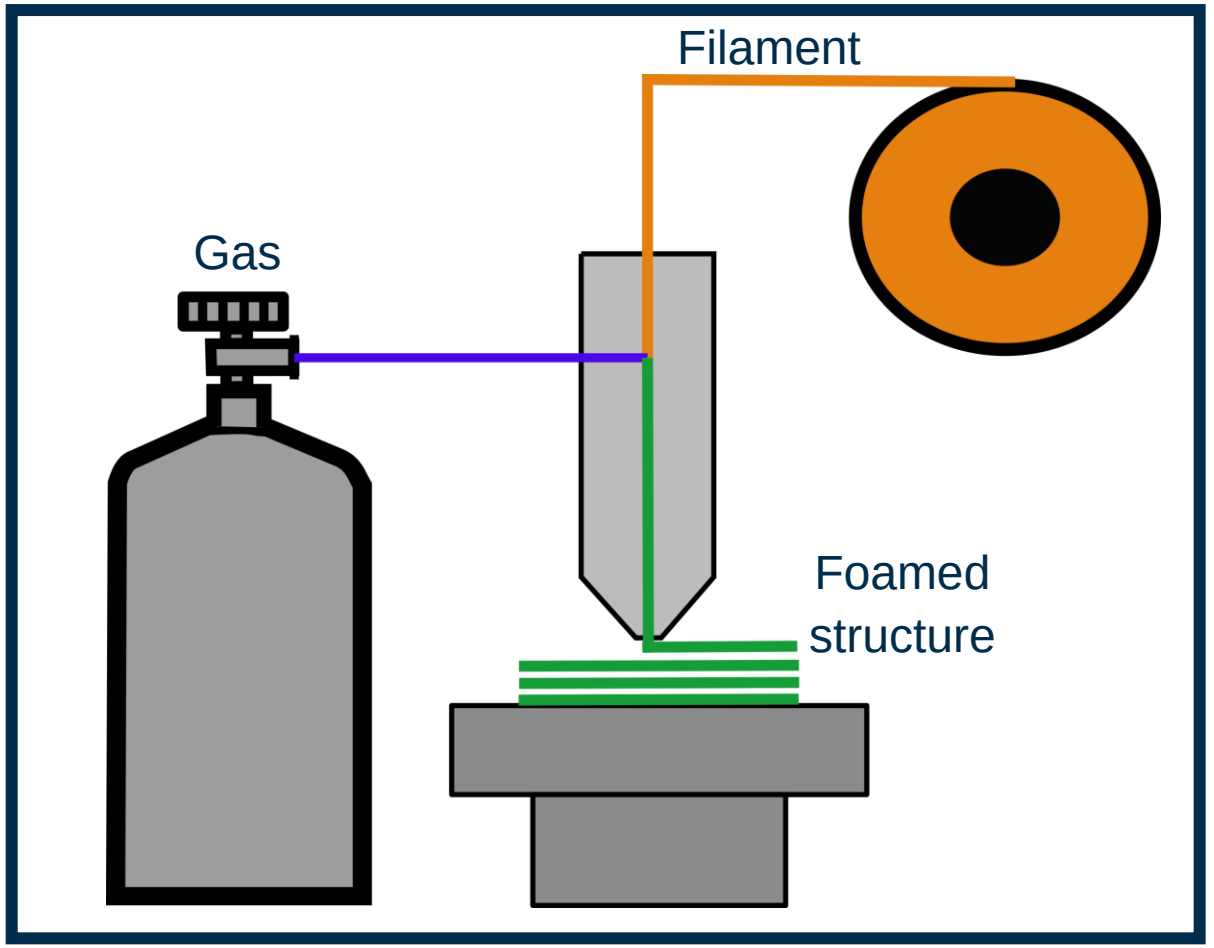

Final nozzle concept



[2]

Base nozzle

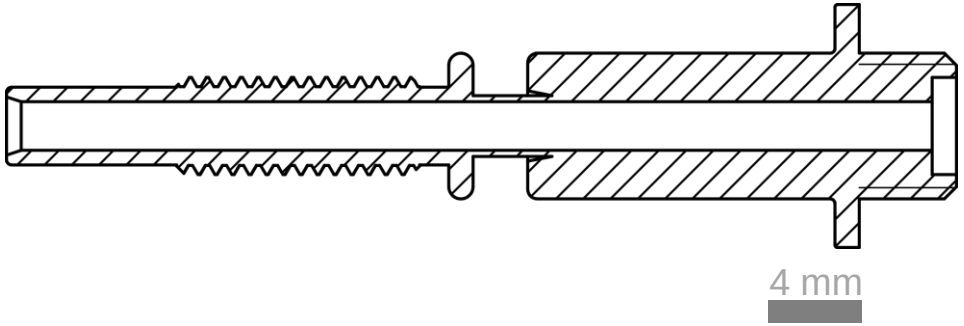

Porous material (PM)

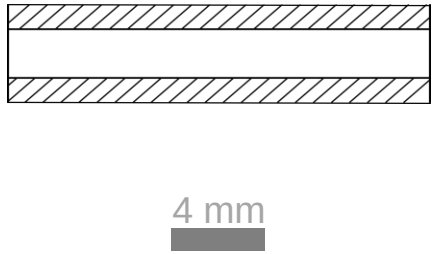

Modular nozzle

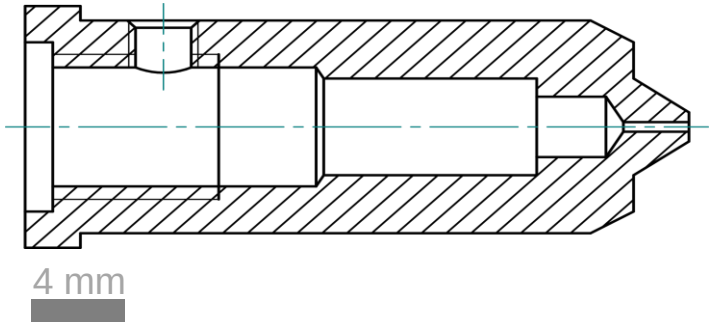

[2] https://amespore.com/de/product/amespore-b-scheibenfilter-aus-bronze/

Final nozzle concept



[2]

Base nozzle

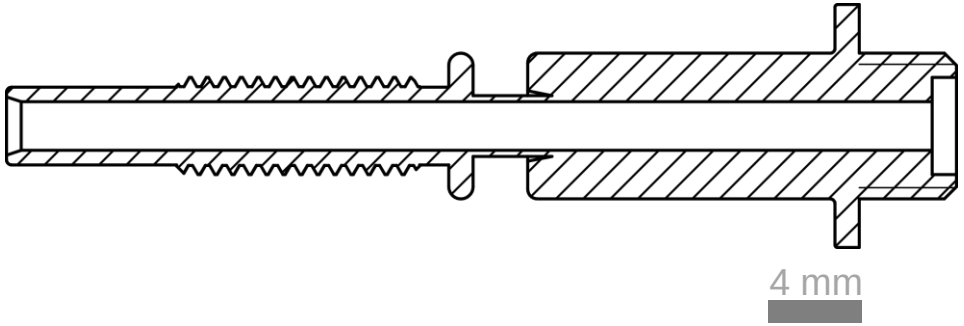

Porous material (PM)

4 mm

Modular nozzle

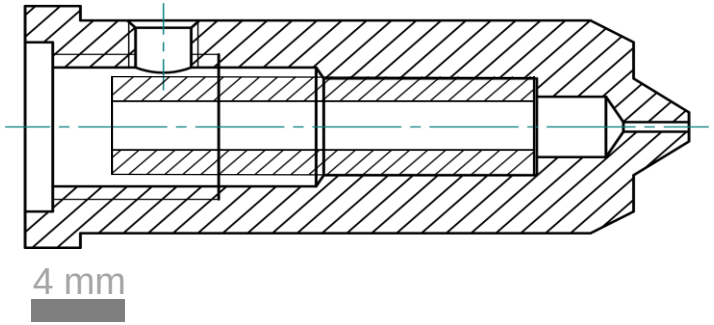

[2] https://amespore.com/de/product/amespore-b-scheibenfilter-aus-bronze/

Final nozzle concept

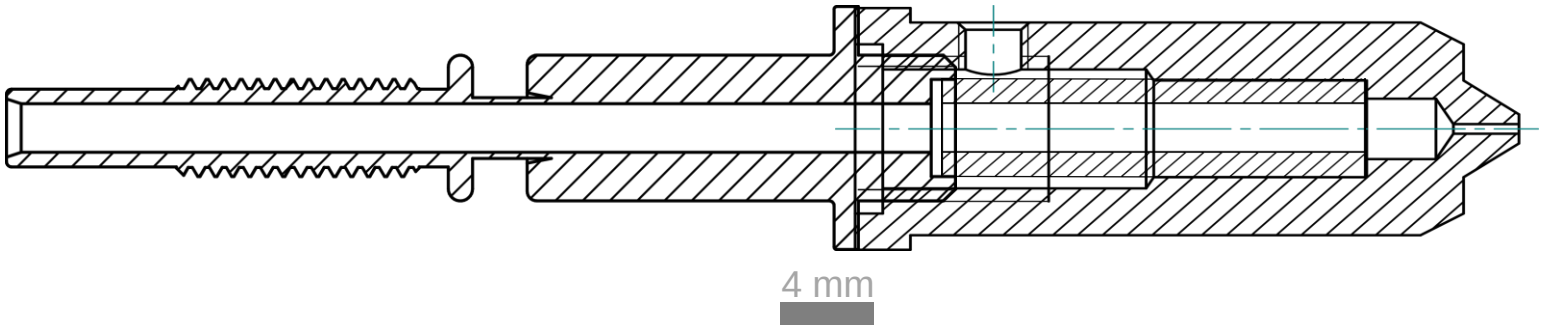

Final nozzle concept

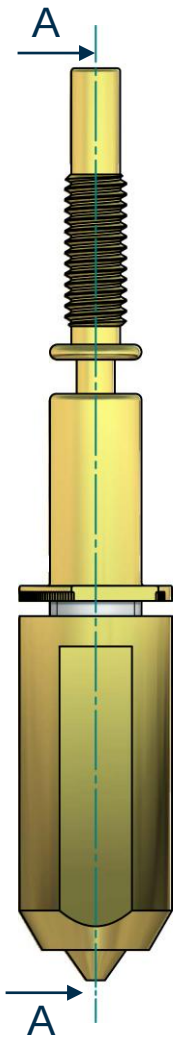

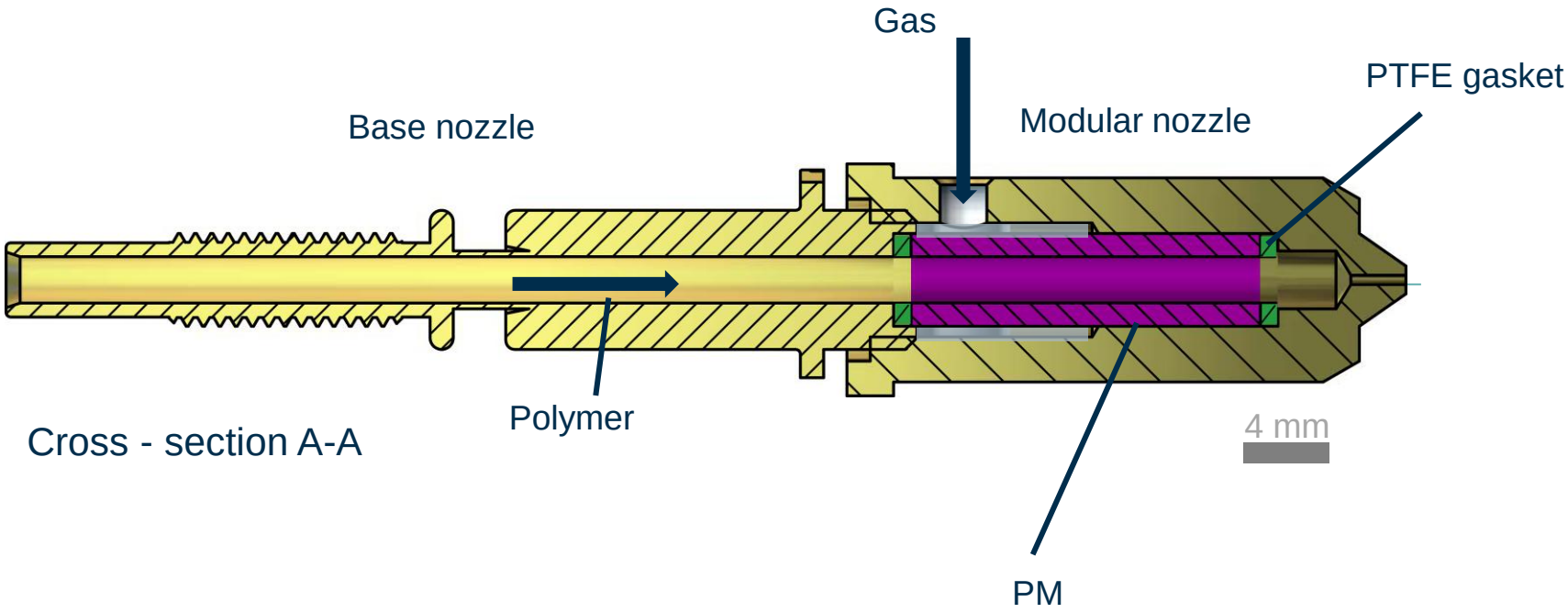

Cross - section A-A

Polymer Infiltration into Porous Materials

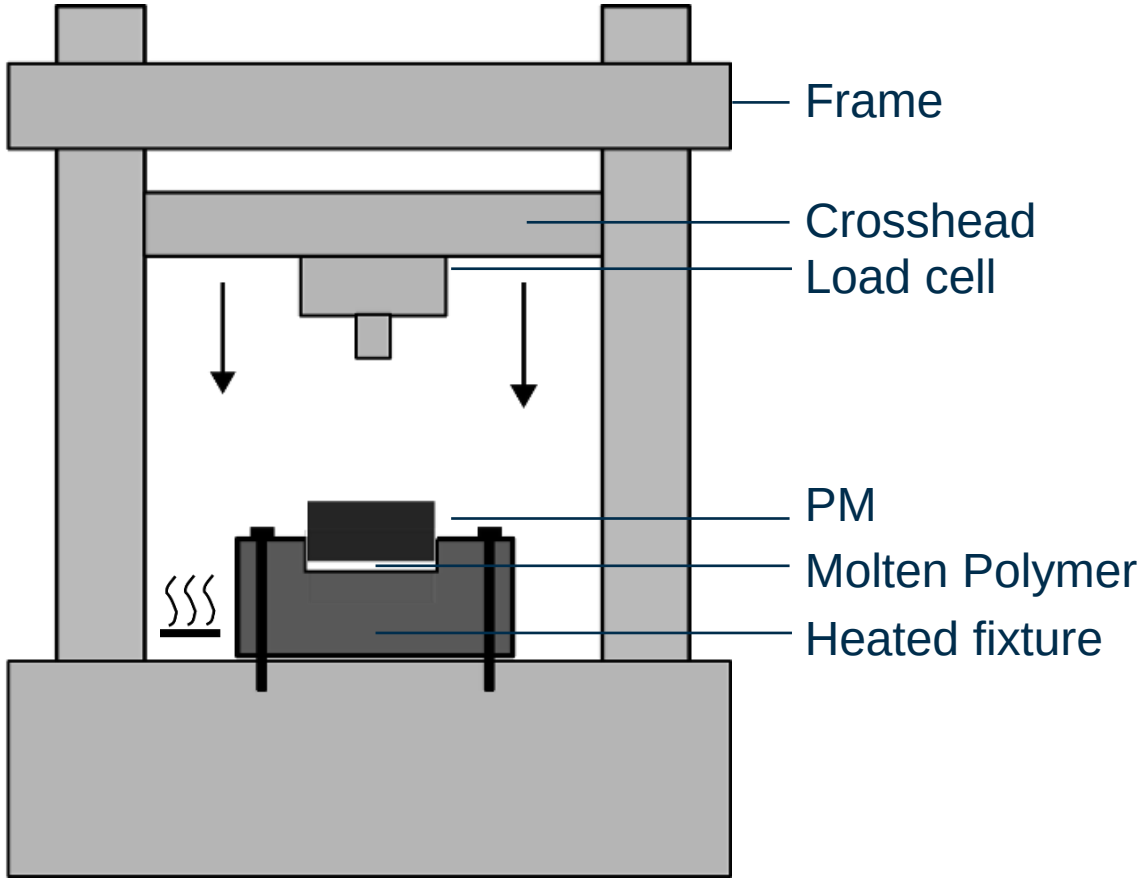

Schematic test setup for infiltration testing

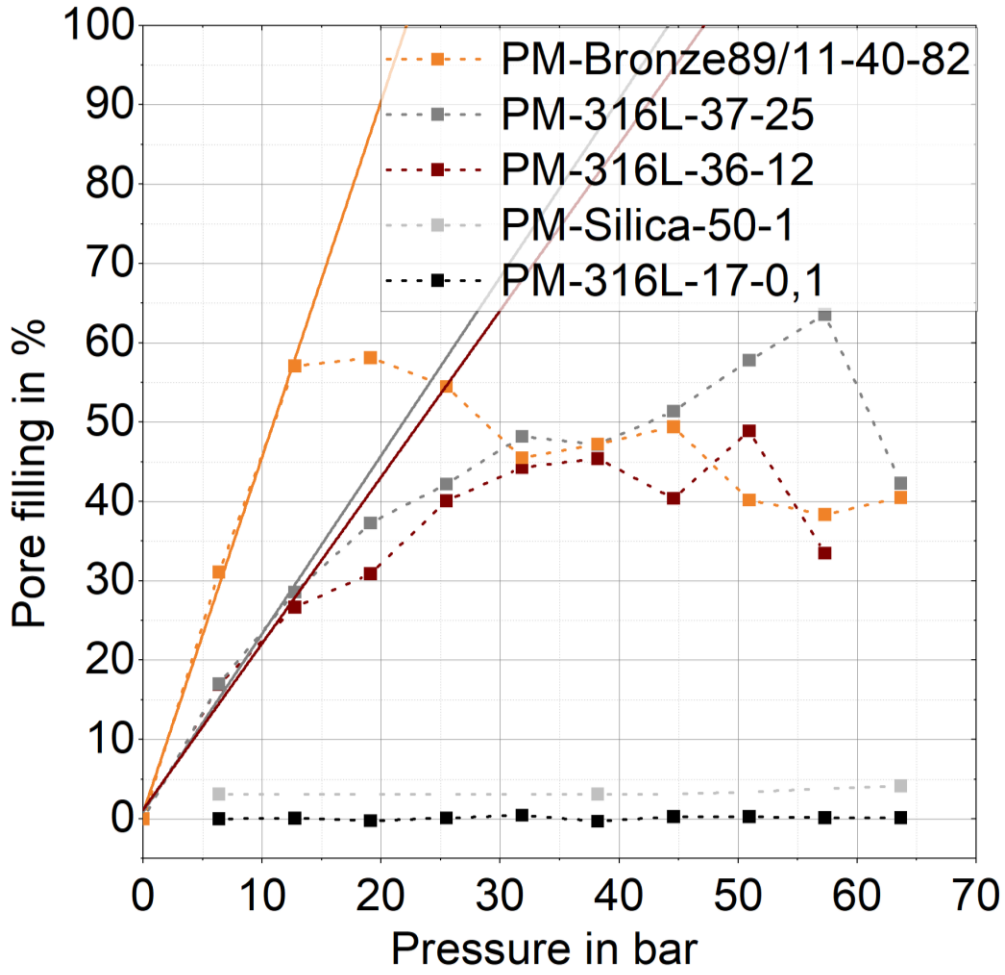

Effect of process parameters on foam structure

Study Setup:

- Hollow cylinder inside nozzle: PM-316L-17-0,1
- Varied:
  - Gas pressure p_G
  - Nozzle temperature T_N
  - Feed rate v

Conditions:

- $T_N \times p_G$ grid
- Each tested at
  - $v = 0{,}5\,\frac{mm}{s}$
  - $v = 2{,}0\,\frac{mm}{s}$
  - $v = 3{,}5\,\frac{mm}{s}$

→ 27 parameter combinations

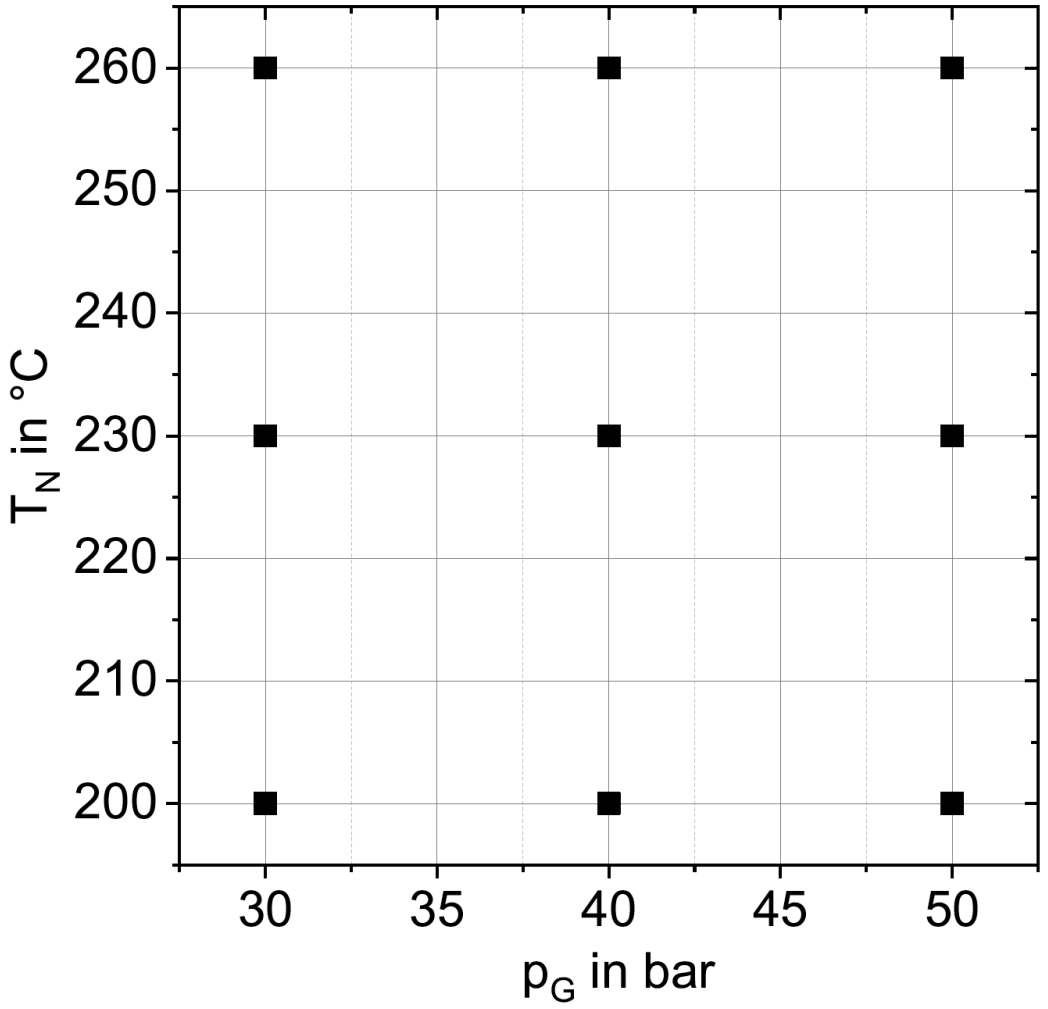

Effect of process parameters on foam structure

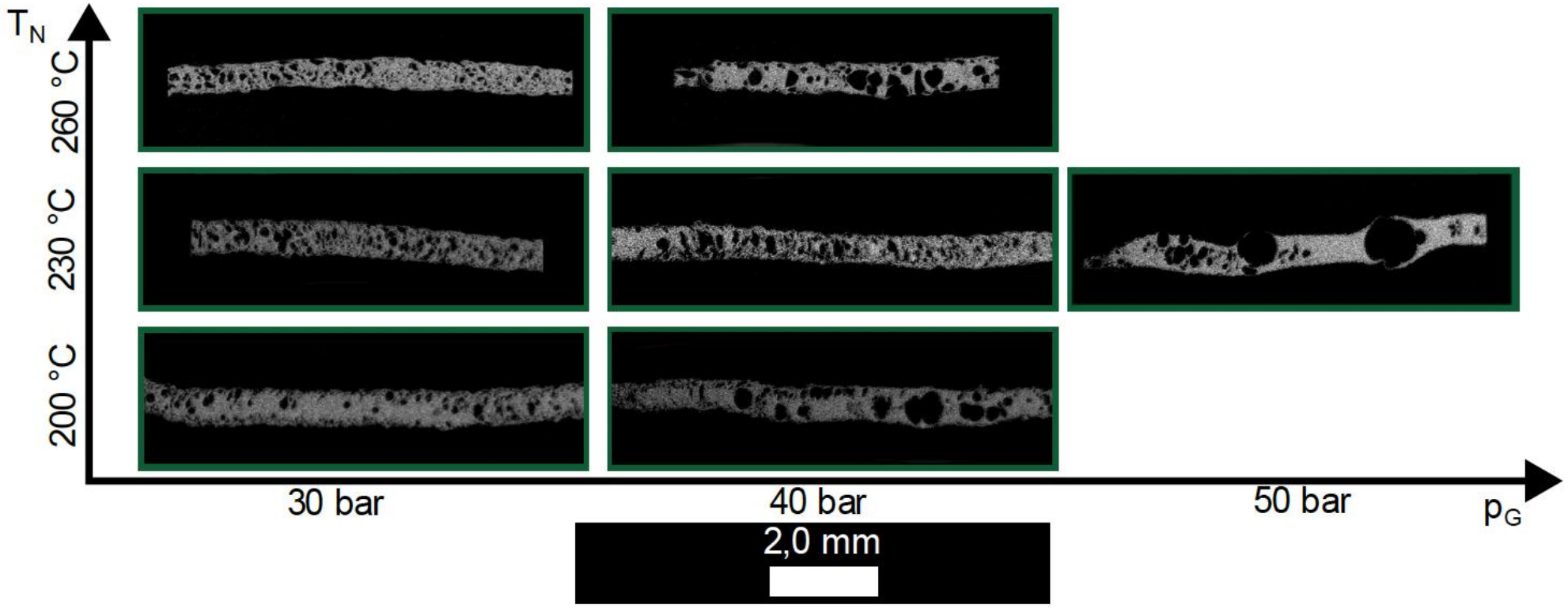

$$\mathbf{v = 0,5\ mm/s}$$

Effect of process parameters on foam structure

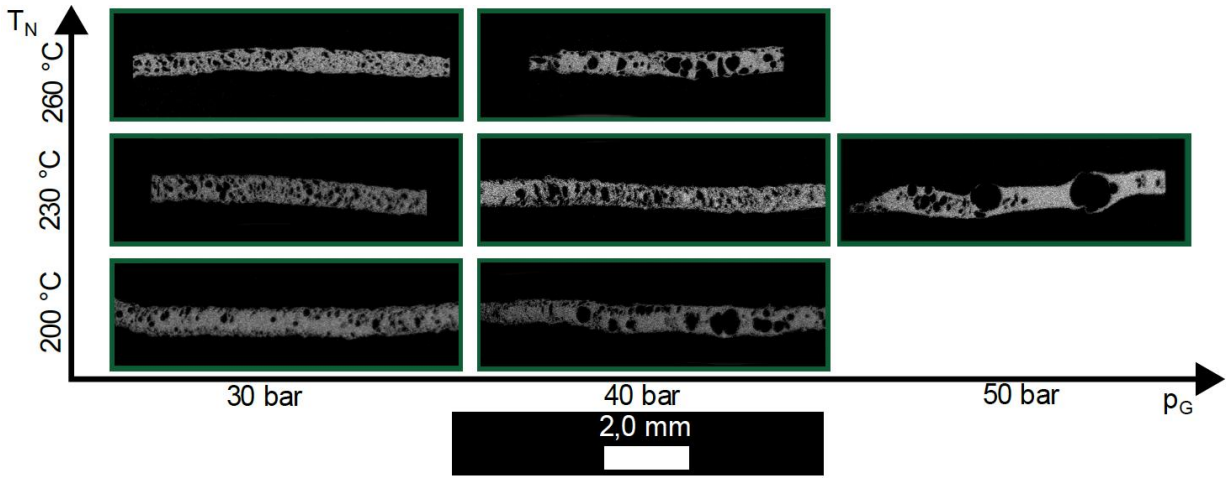

Porosity

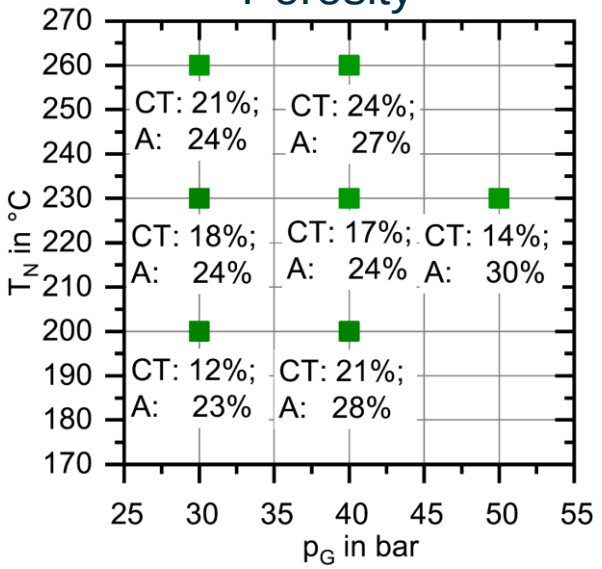

Mean pore diameter

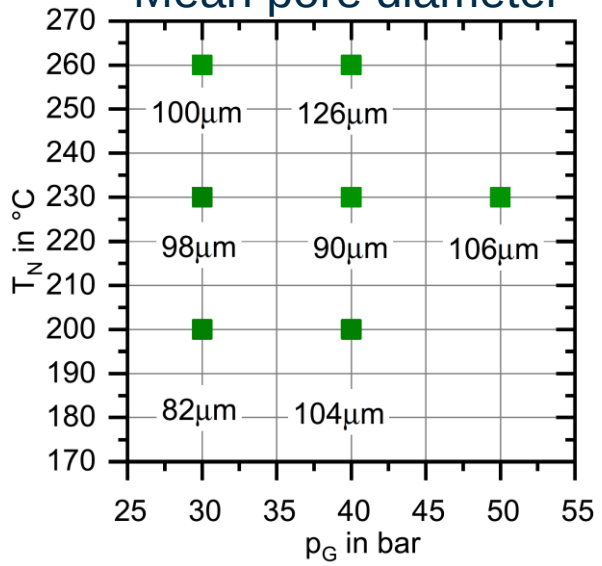

Effect of process parameters on foam structure

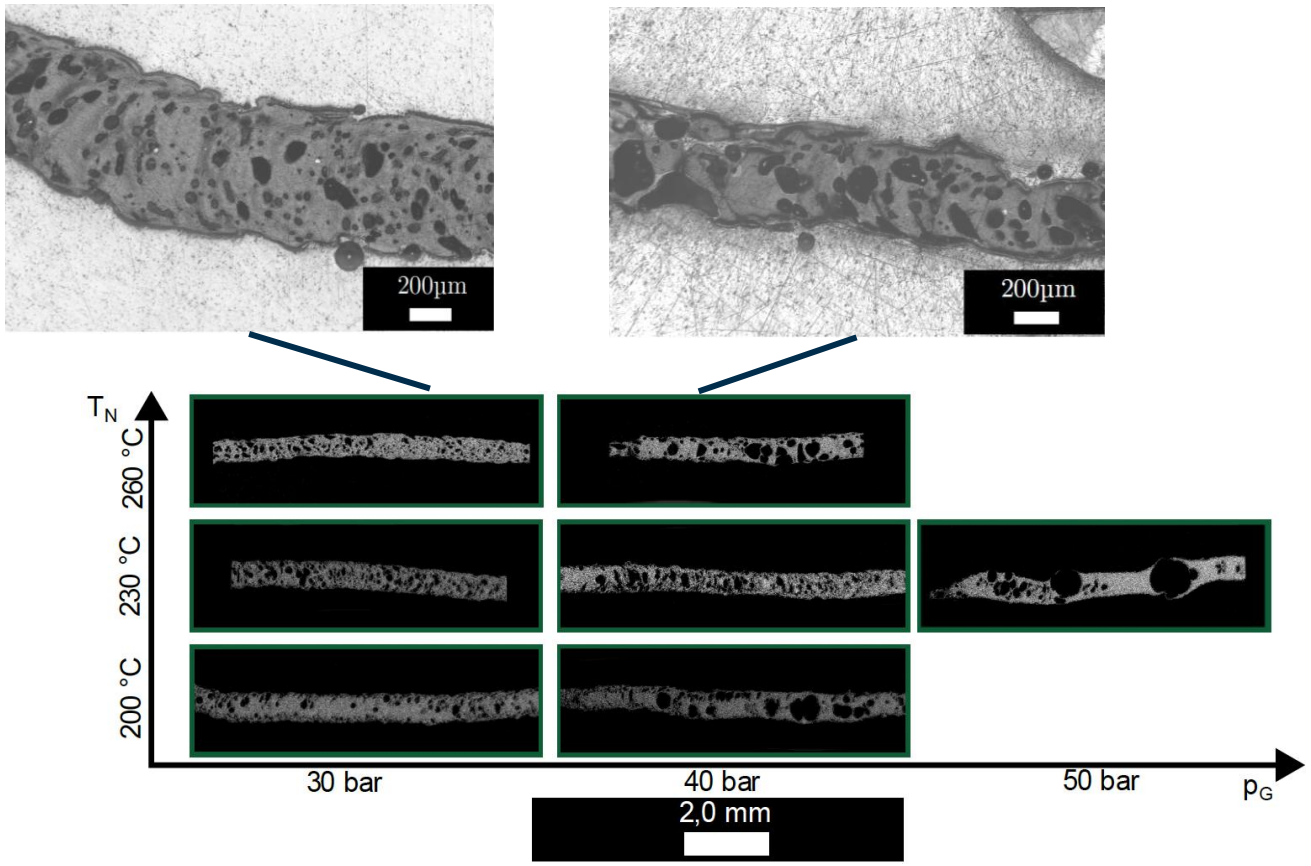

Porosity

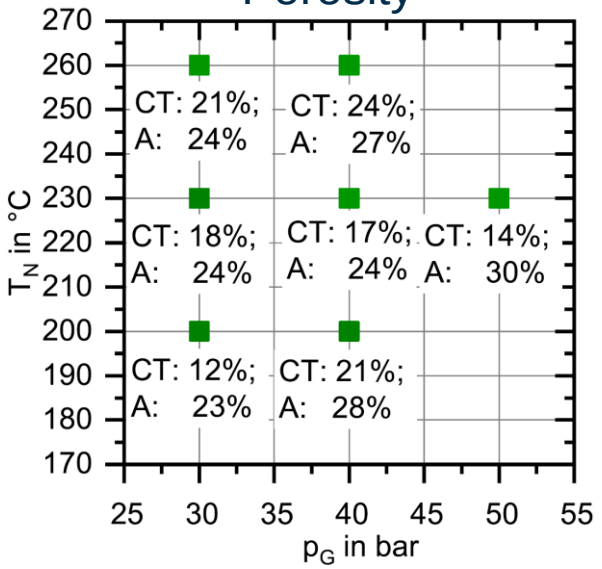

Mean pore diameter

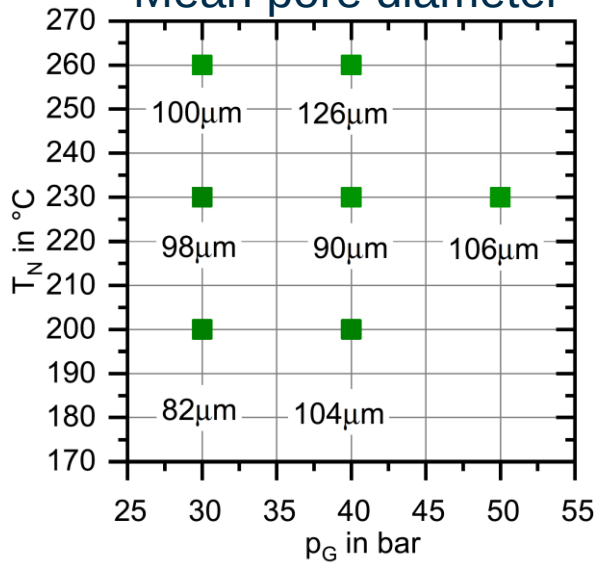

Effect of process parameters on foam structure

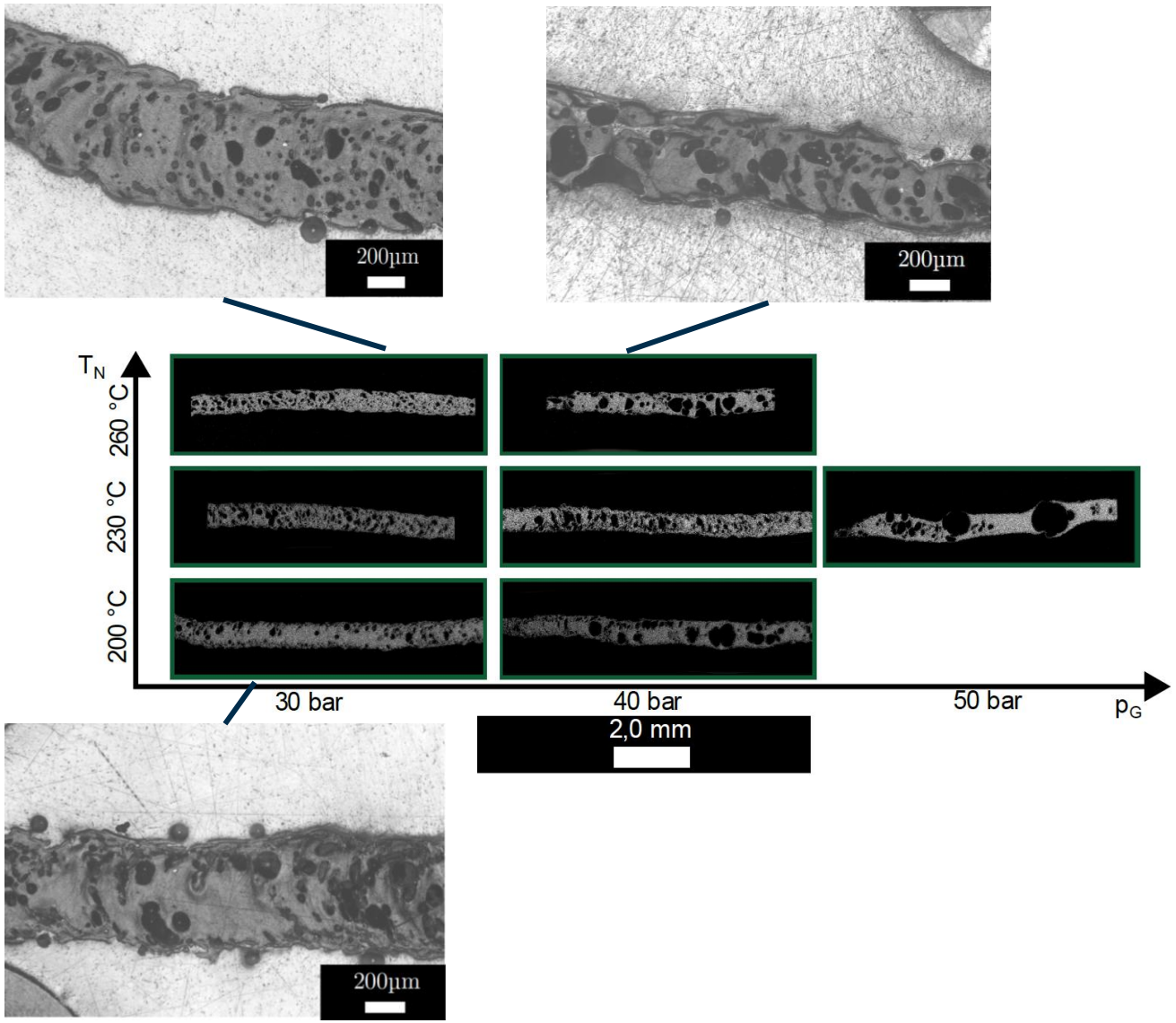

Porosity

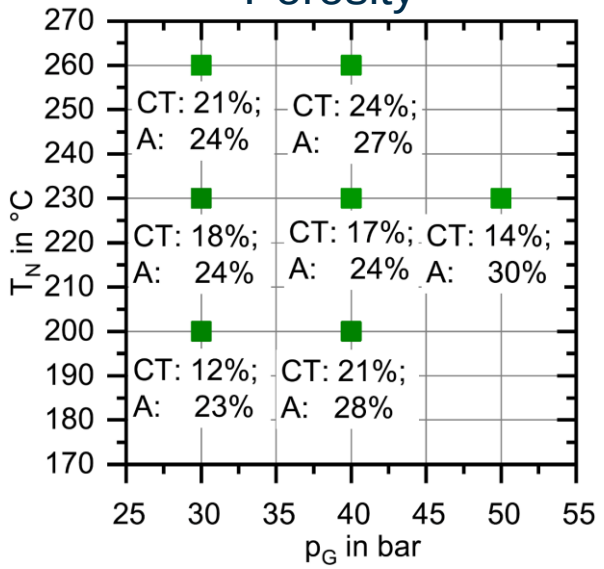

Mean pore diameter

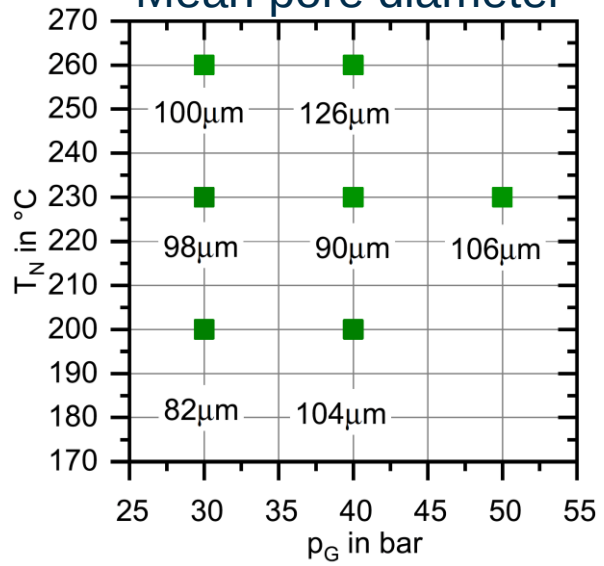

Effect of process parameters on foam structure

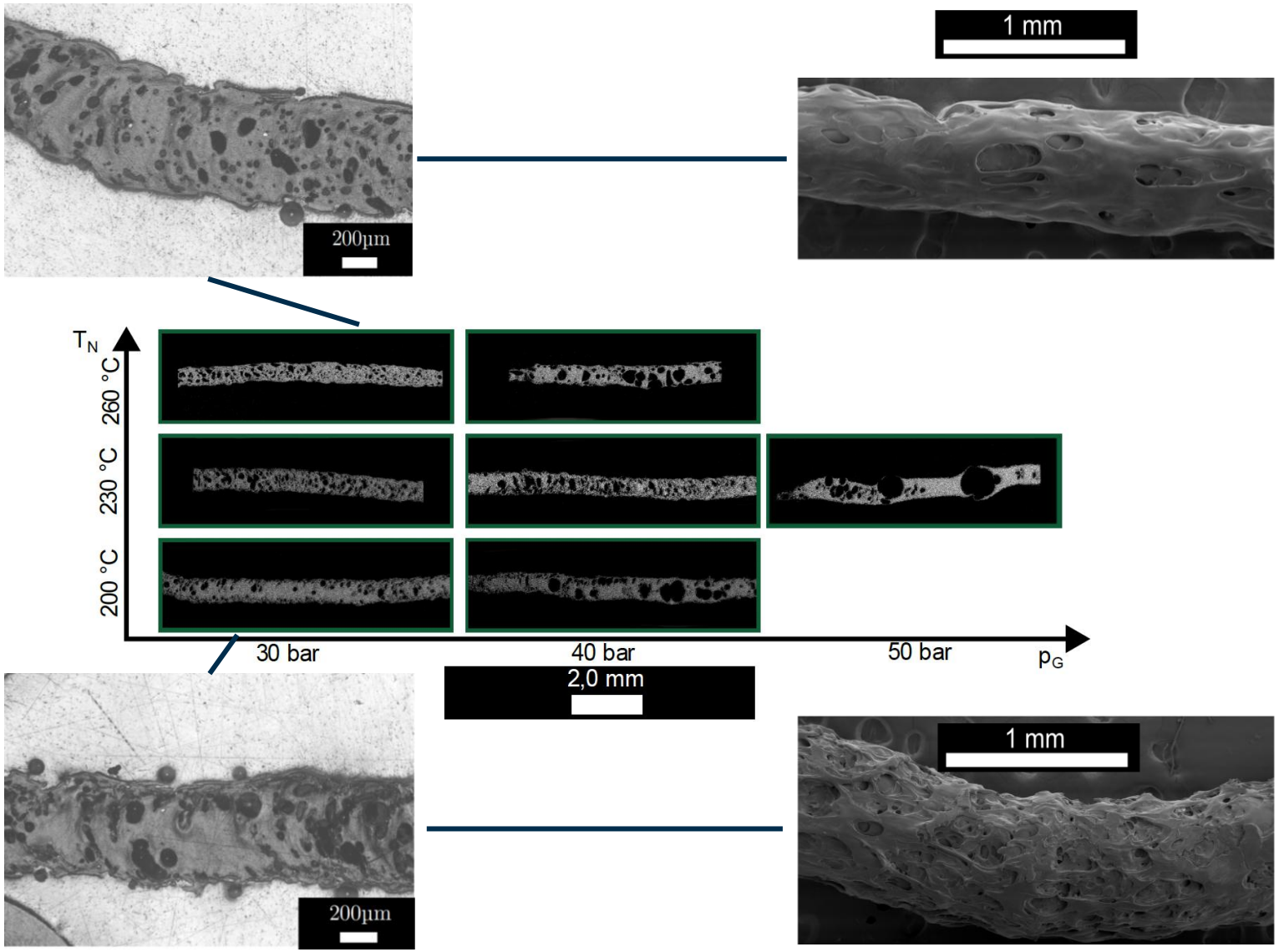

Porosity

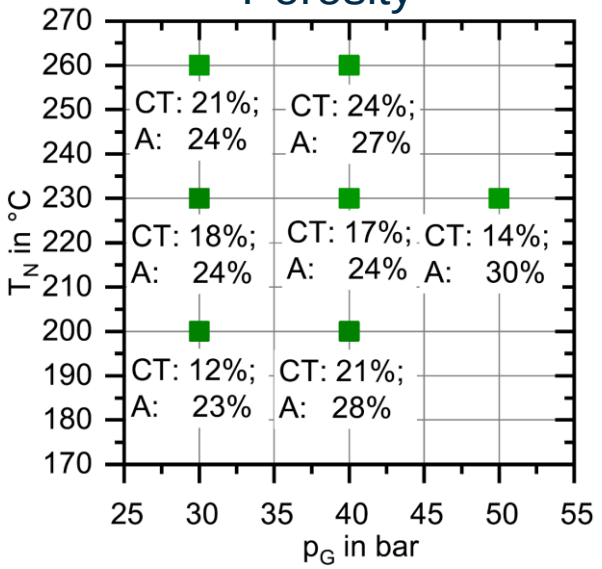

Mean pore diameter

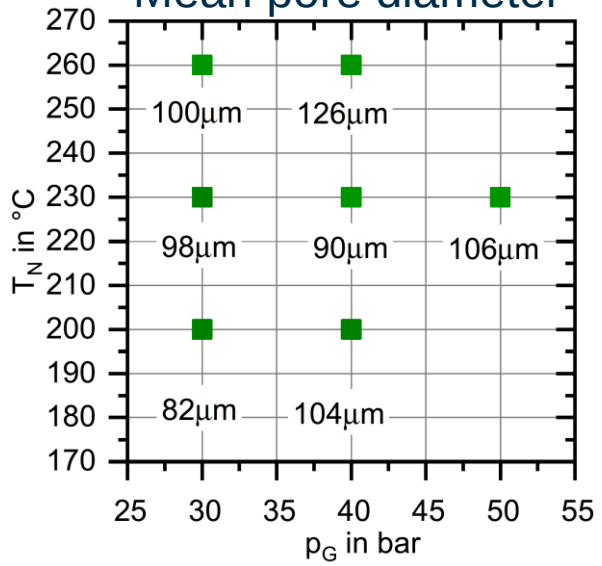

Effect of process parameters on foam structure

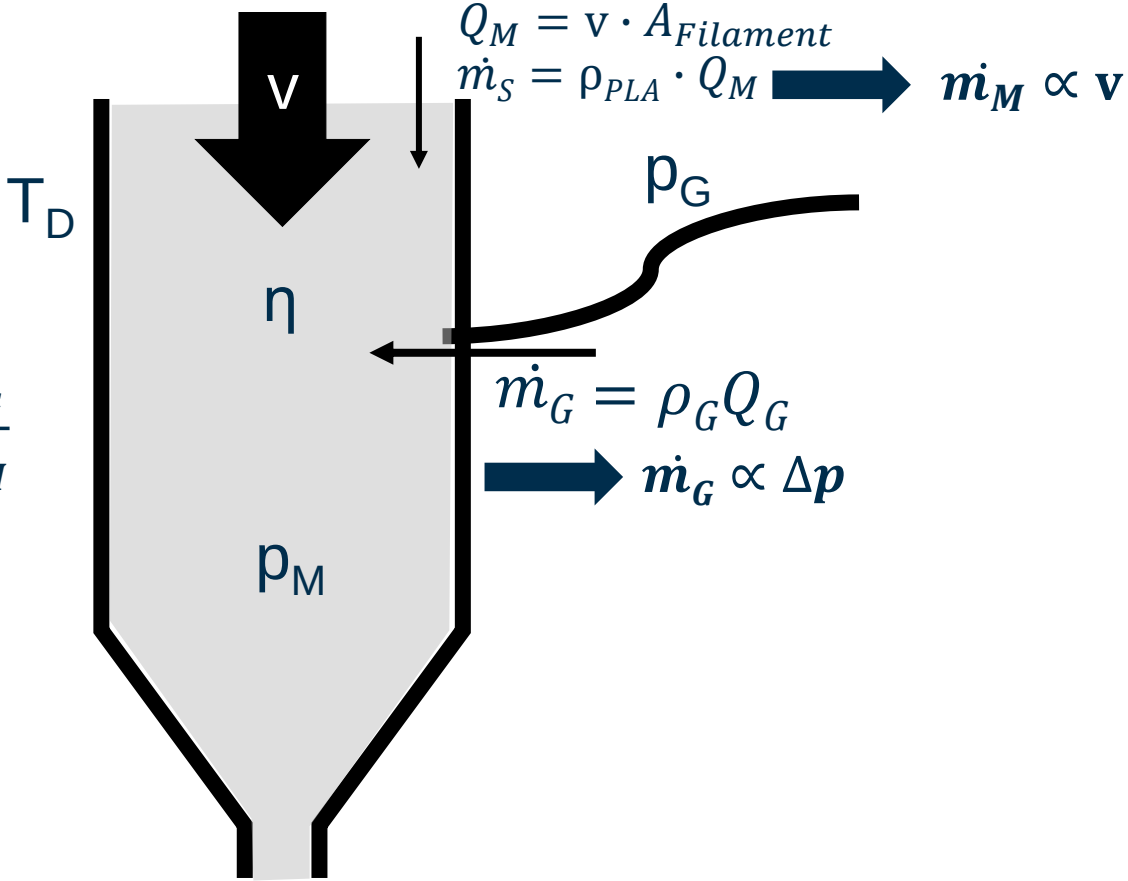

$$Q_M = \mathrm{v} \cdot A_{Filament}$$

$$\dot{m}_S = \rho_{PLA} \cdot Q_M \rightarrow \boldsymbol{\dot{m}_M \propto \mathrm{v}}$$

$$\boldsymbol{MR = \frac{\dot{m}_G}{\dot{m}_M}}$$

$$\dot{m}_G = \rho_G Q_G \rightarrow \boldsymbol{\dot{m}_G \propto \Delta p}$$

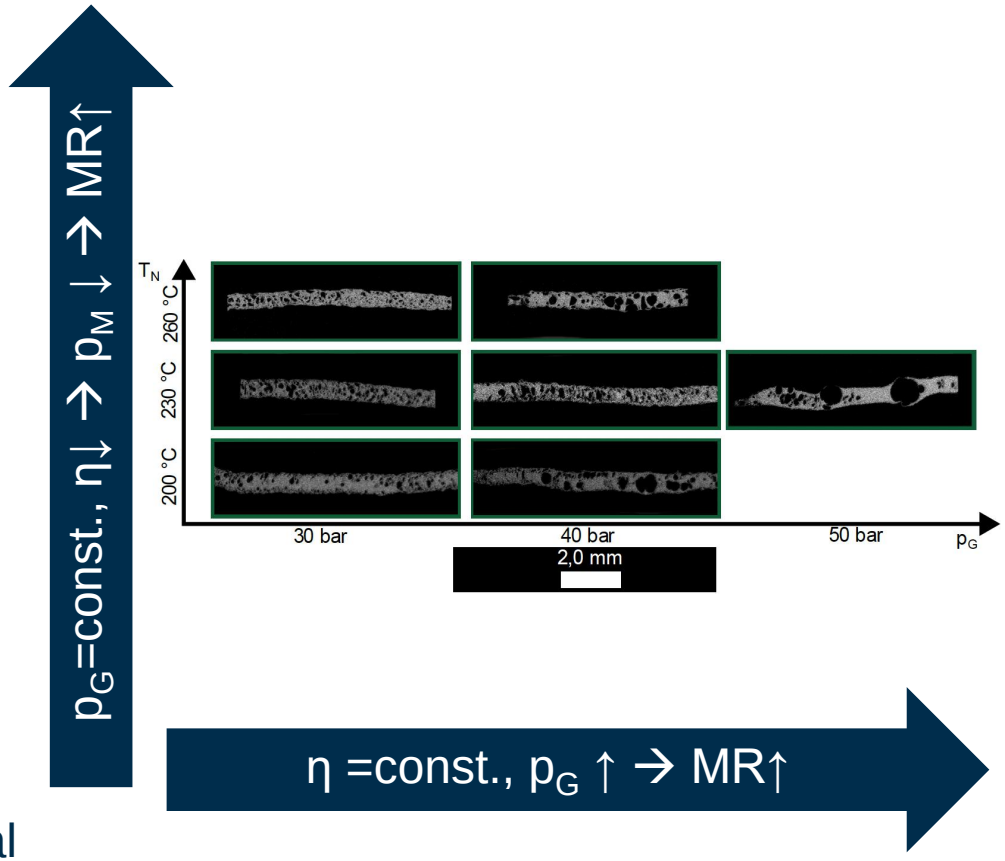

p_M can be idealized as steady, laminar flow through a cylindrical pipe:

$$p_M = \frac{128L}{\pi d^4} Q_M \cdot \eta \rightarrow \boldsymbol{\mathrm{p_M} \propto Q_M \cdot \eta}$$

Effect of process parameters on foam structure

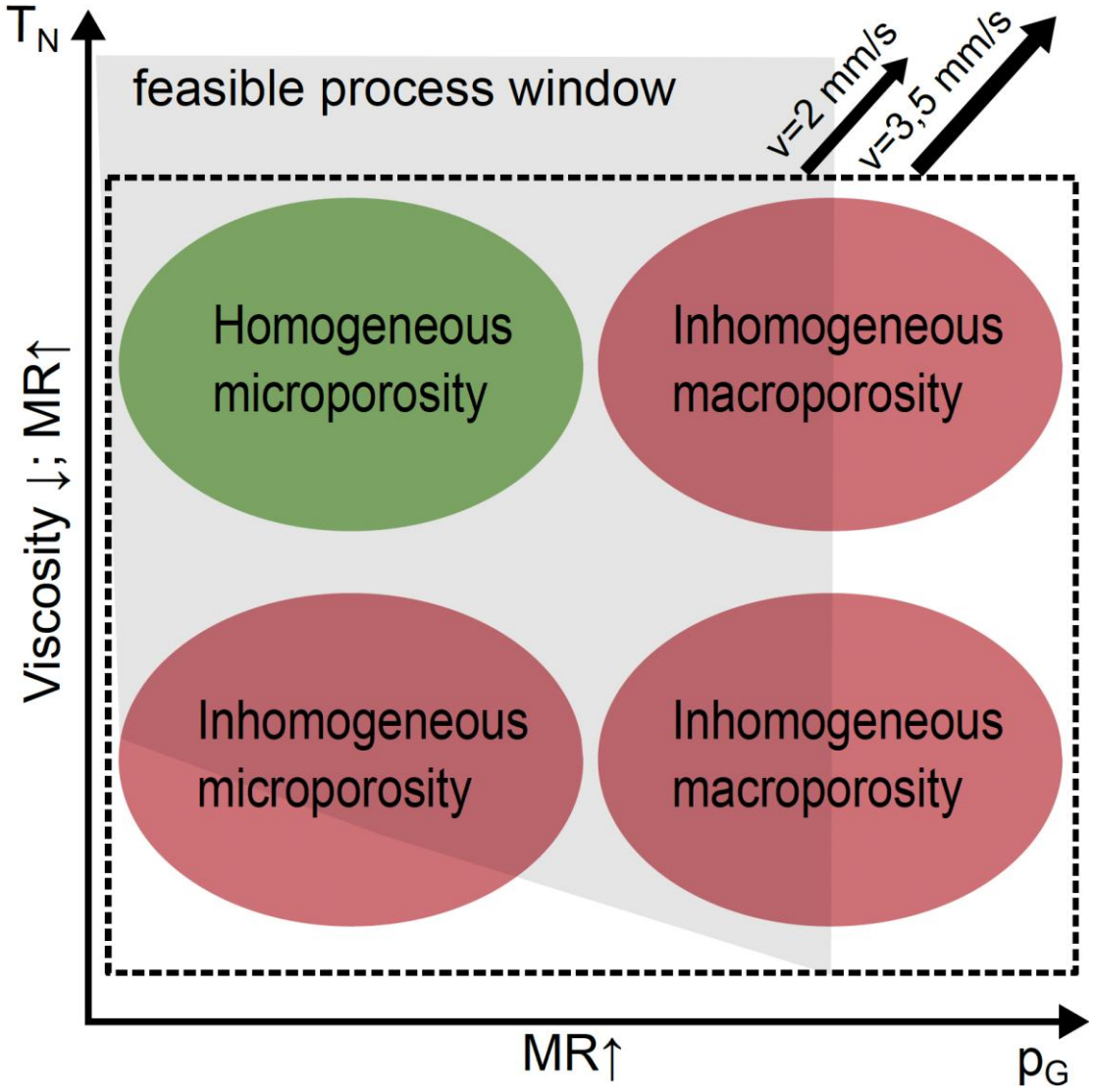

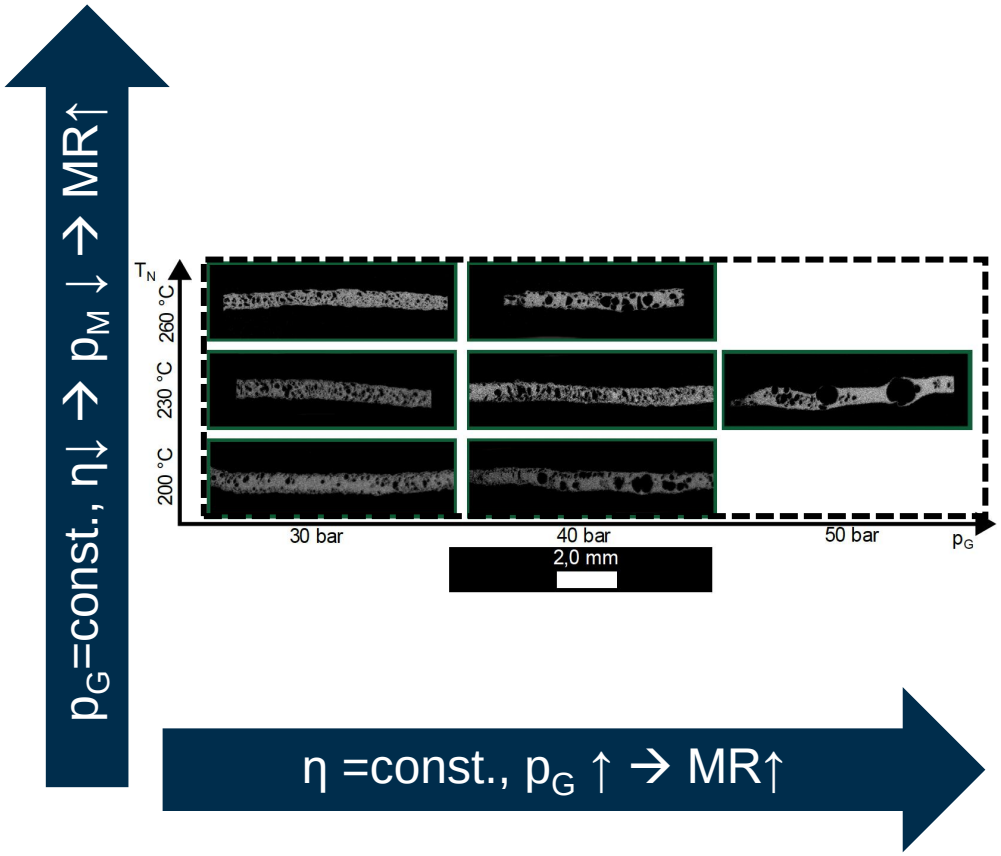

Summary and Outlook

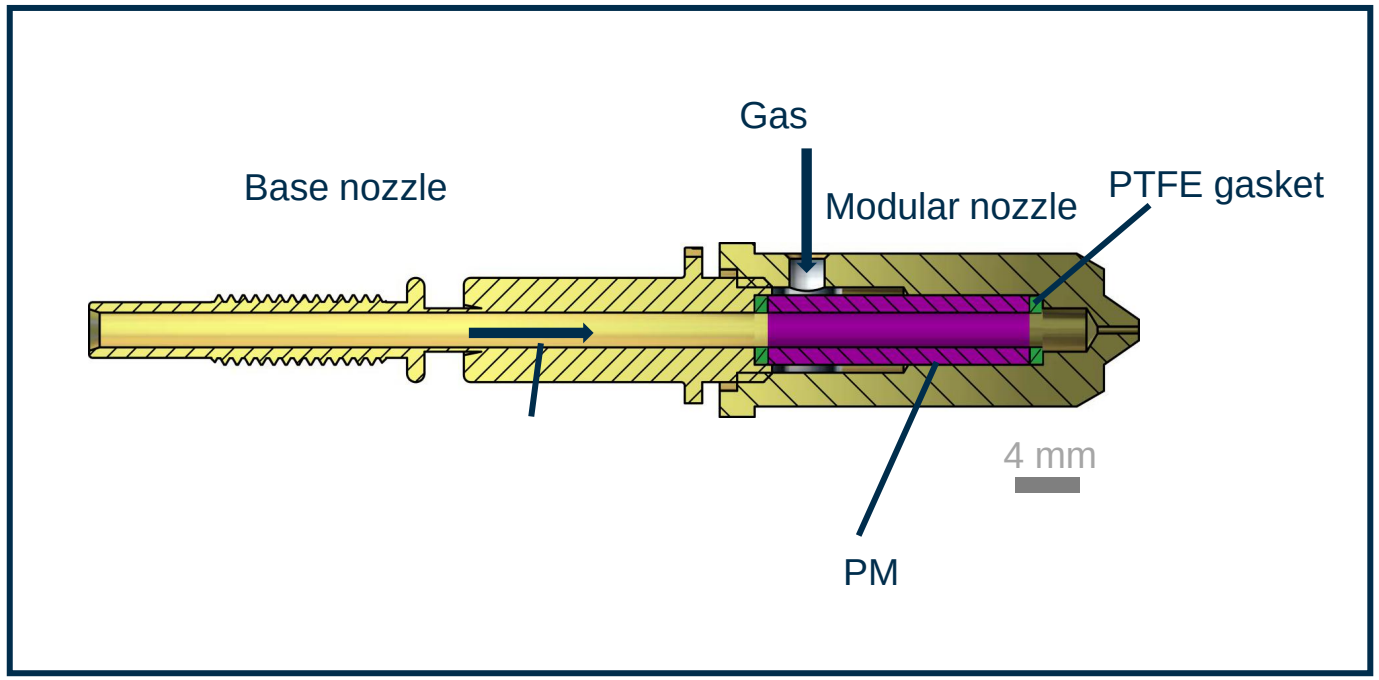

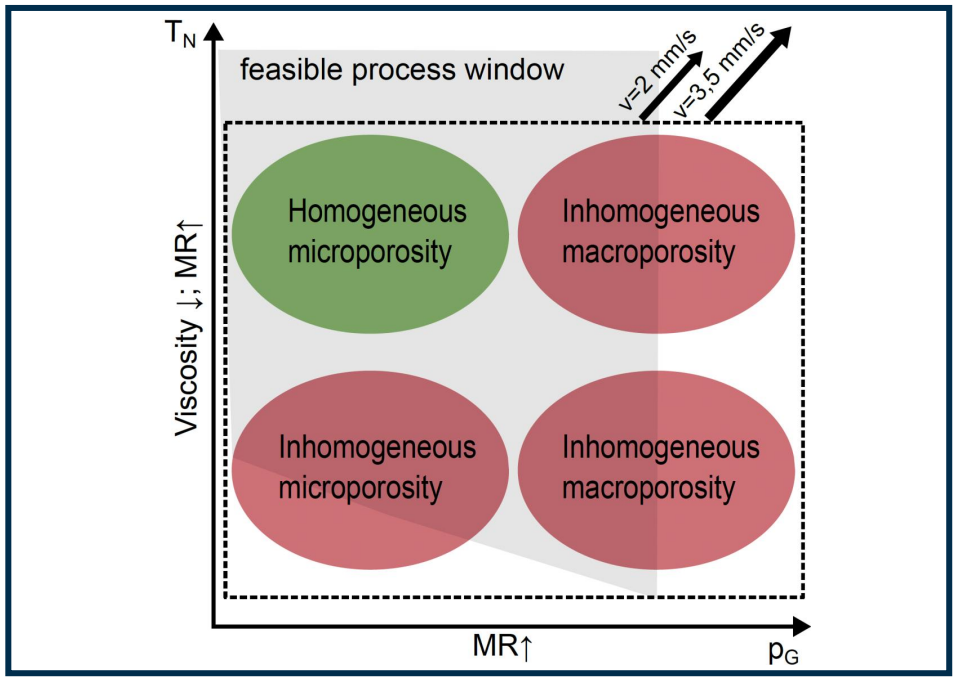

+ Adjustable porosity

+ Foaming degree not time-dependent

+ Nozzle can be integrated into existing MEX systems

Thank you for listening!

ICCM24
AUGUST 4-8, 2025
BALTIMORE CONVENTION CENTER
BALTIMORE, MARYLAND, USA

No Technical Paper Submission for:

Hamed Yazdani Nezhad

ICCM24
AUGUST 4-8, 2025
BALTIMORE CONVENTION CENTER
BALTIMORE, MARYLAND, USA

No Technical Paper Submission for:

Brittany Rodriguez



Additive Manufacturing of Complex & Oscillating POSS-based 4D Structures

Nicole Gorohovsky, Ronen Verker, Noa Lachman

Composite Structures & Interfaces (SCI) Lab

Tel Aviv University

What are Bilayer Actuators?

Shape change due to external stimuli (temperature, humidity, etc.).

Bilayers: two polymeric layers with different CTEs.

Applications: actuators, sensors, soft robotics, & more.

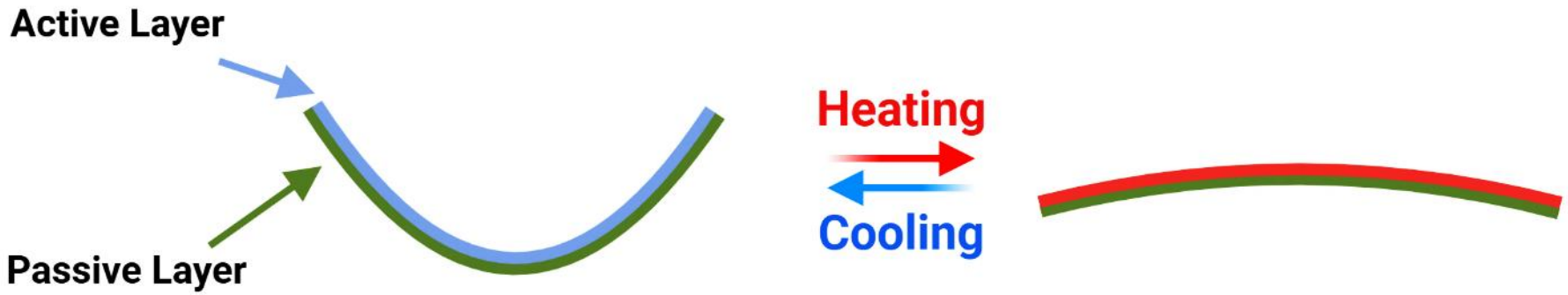

Motivation

Traditional manufacturing limits design complexity & efficiency.

3D printing allows precise & complex shapes.



https://lightandladder.com/

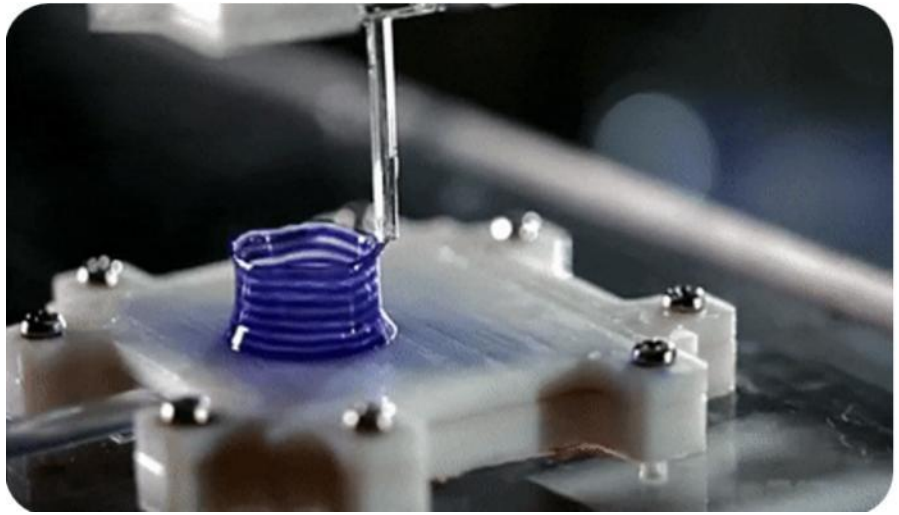

https://aspectbiosystems.com/

Research Objectives

01

Develop a Direct Ink Writing (DIW) process for high-performance bilayer actuators.

02

Key focus: material adhesion, rheological control, & layer uniformity.

03

Improve scalability, precision, & reproducibility.

Gorohovsky et al. 10.1080/17452759.2025.2527387

System Set Up

3D Printer





Syringe pump



Gorohovsky et al. 10.1080/17452759.2025.2527387

Materials

PolyPOSS – active layer

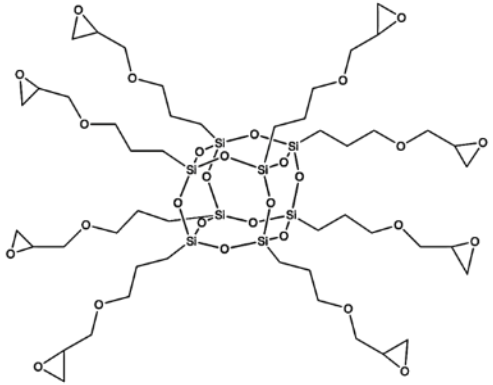

Polyhedral oligomeric silsesquioxanes (POSS)

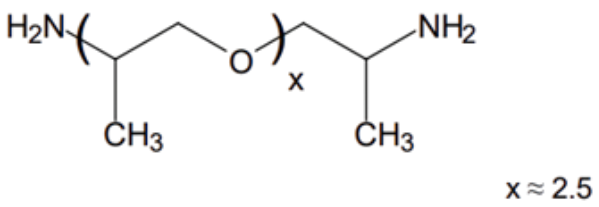

Jeffamine D-230

Kapton film – passive layer

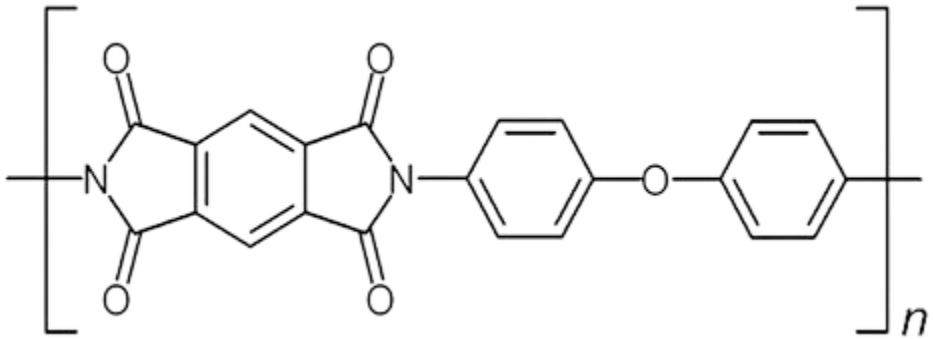

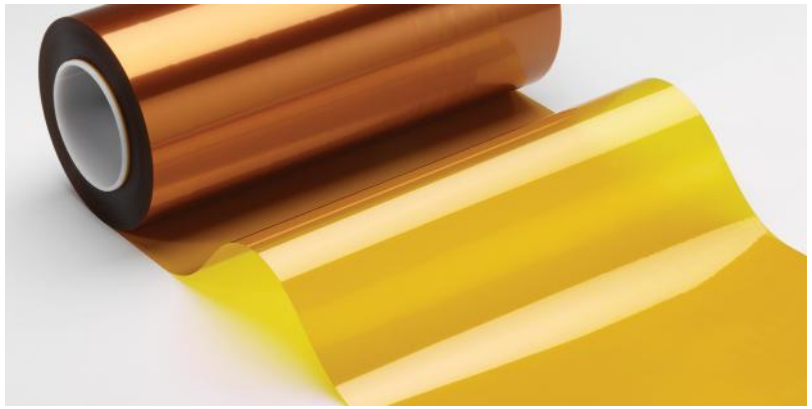

Carmiel et al. *Adv. Intell. Syst.* **2022** & Bram et al. *Nanomaterials*. **2022**

Gelation Time & Rheology

Rheometer



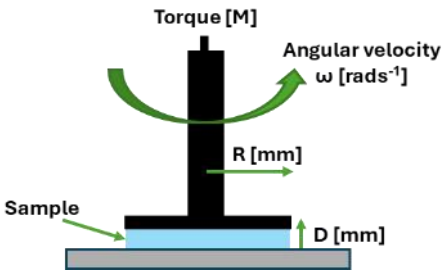

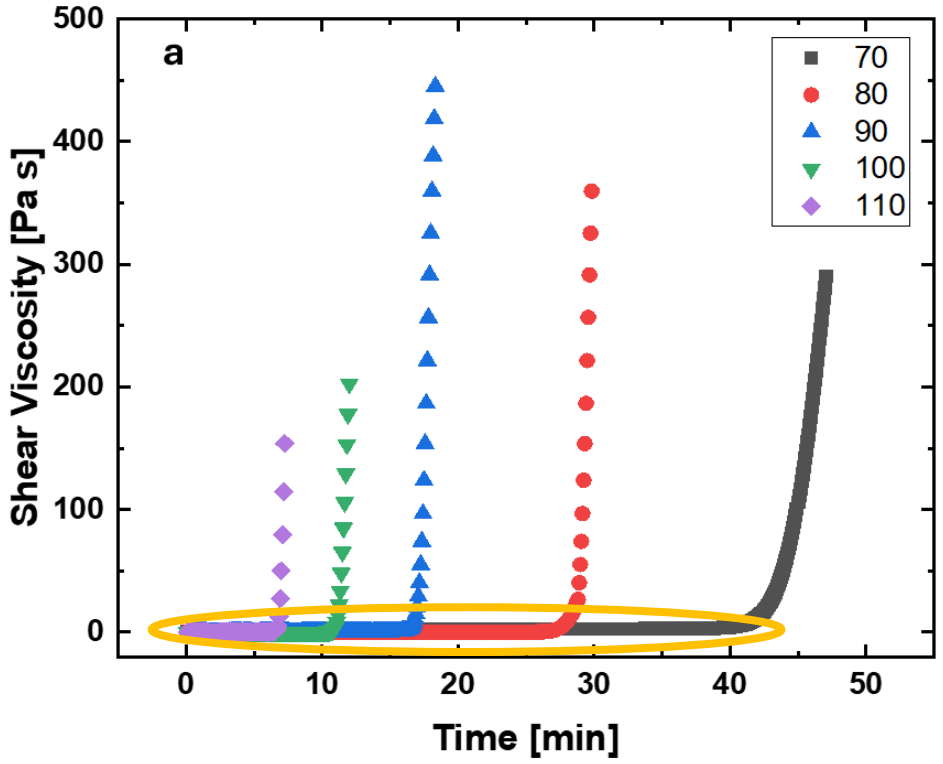

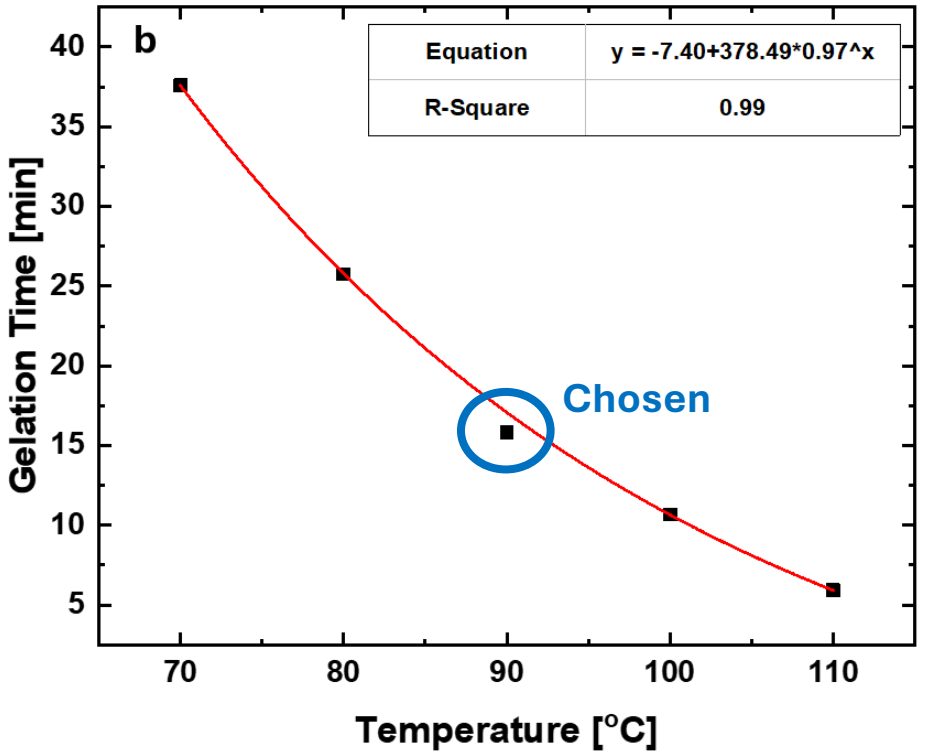

- **Inflection point = gelation time**

Gorohovsky et al. 10.1080/17452759.2025.2527387

Preliminary Print

Single line printing

- Result: - poor polyPOSS/Kapton wettability
  - many de-wetting points → polyPOSS is absent.

- Solution: increase vol. flow rate & surfactant addition.



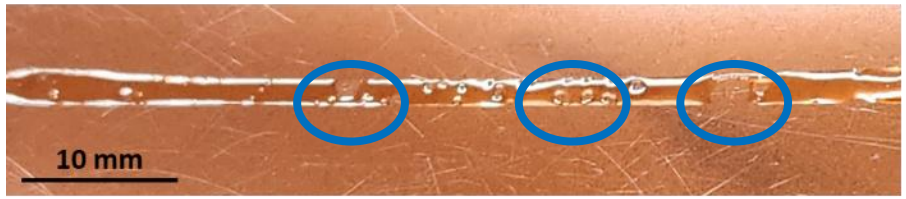

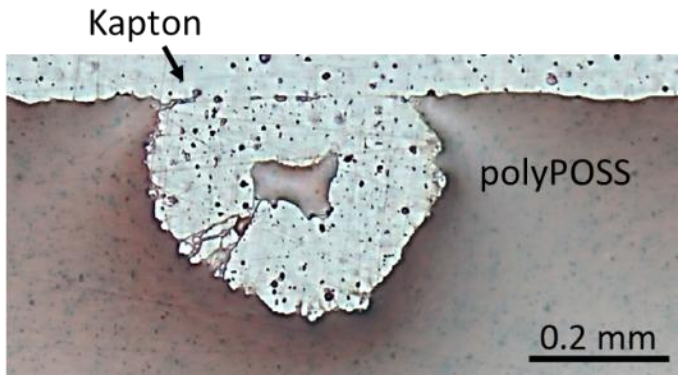

Gorohovsky et al. 10.1080/17452759.2025.2527387

Printing Quality Optimization: 1D

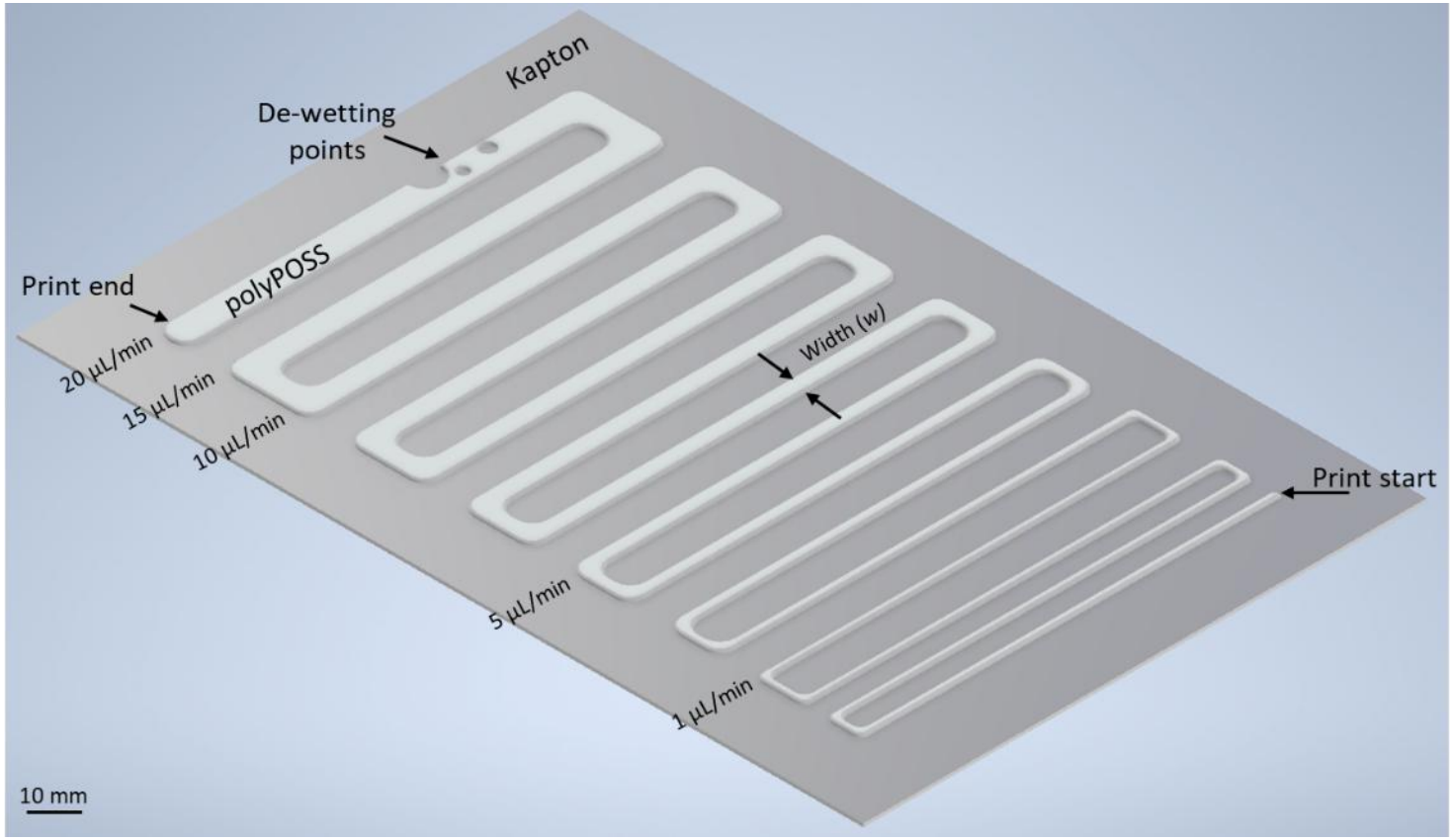

A printing index (*Pi*) was developed → optimization of printing parameters:

$$Pi = \frac{stdv}{avg}(w) \cdot \frac{stdv}{avg}(t) \cdot \left(\#_{dwp} + 1\right)$$

Gorohovsky et al. 10.1080/17452759.2025.2527387

Printing Quality Optimization: 1D (Cont.)

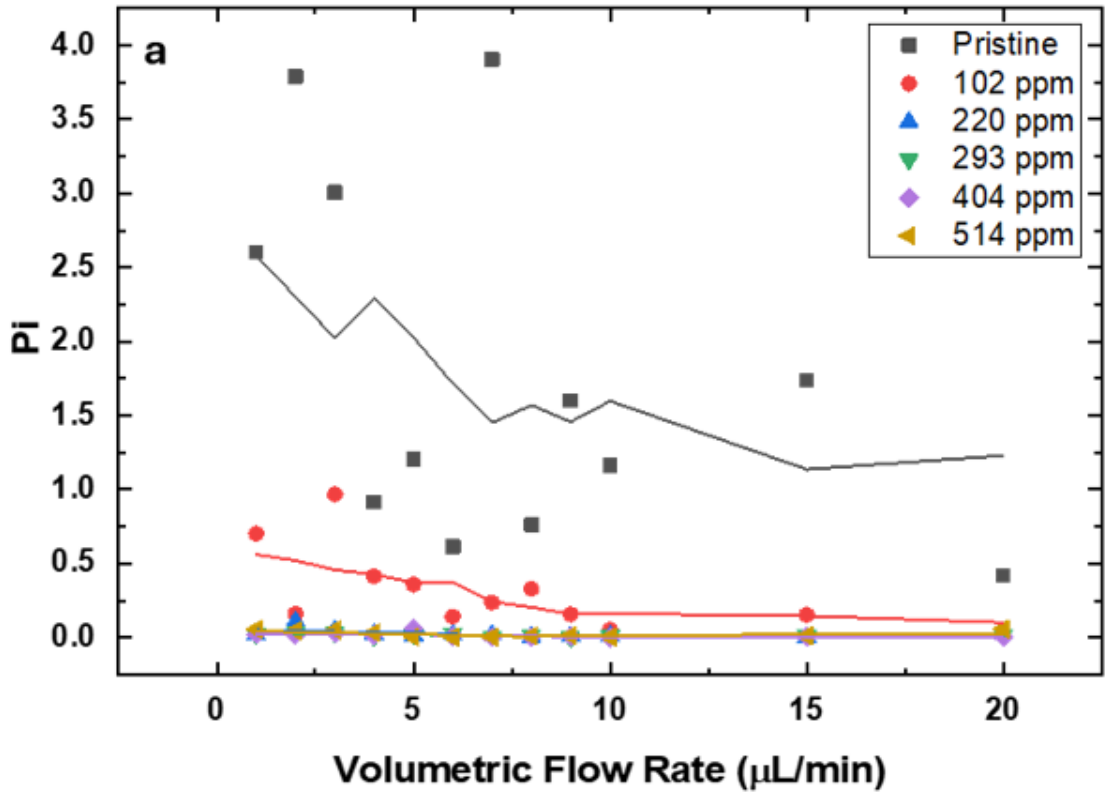

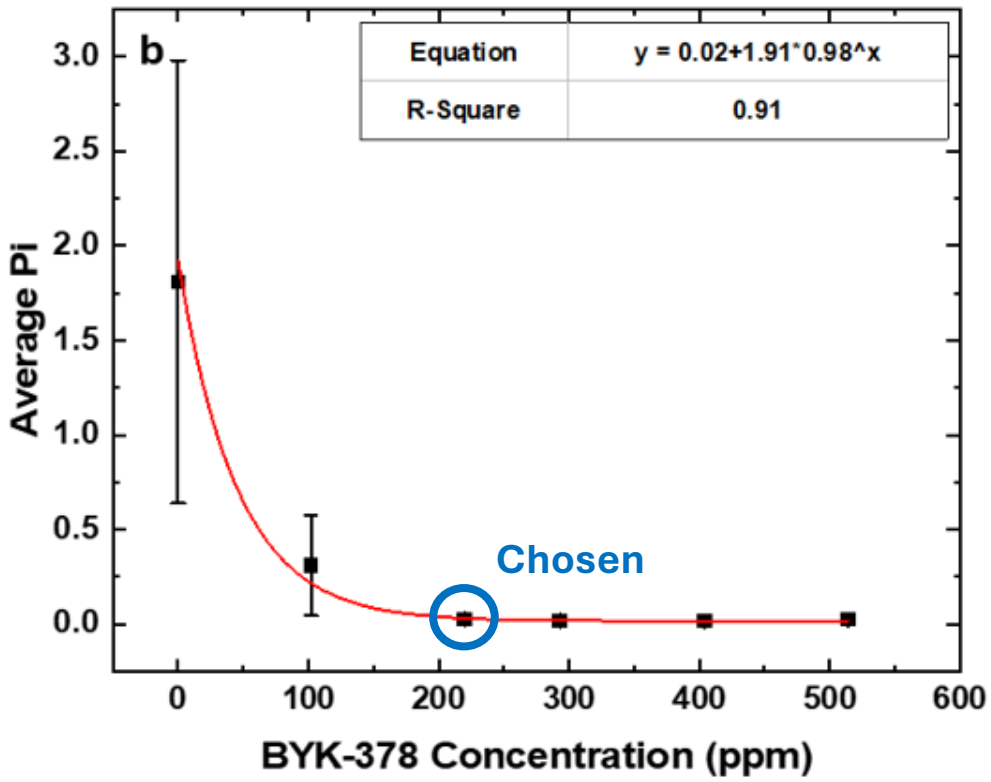

Gorohovsky et al. 10.1080/17452759.2025.2527387

Printing Quality Optimization: 2D

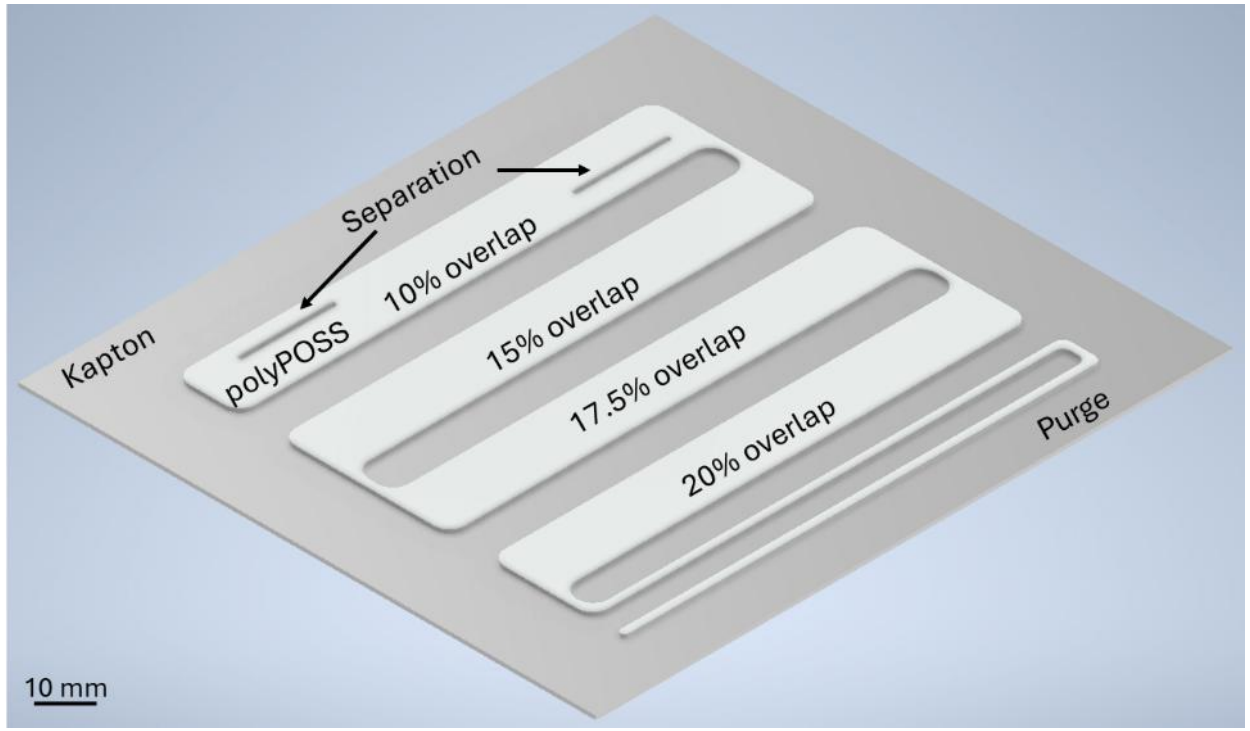

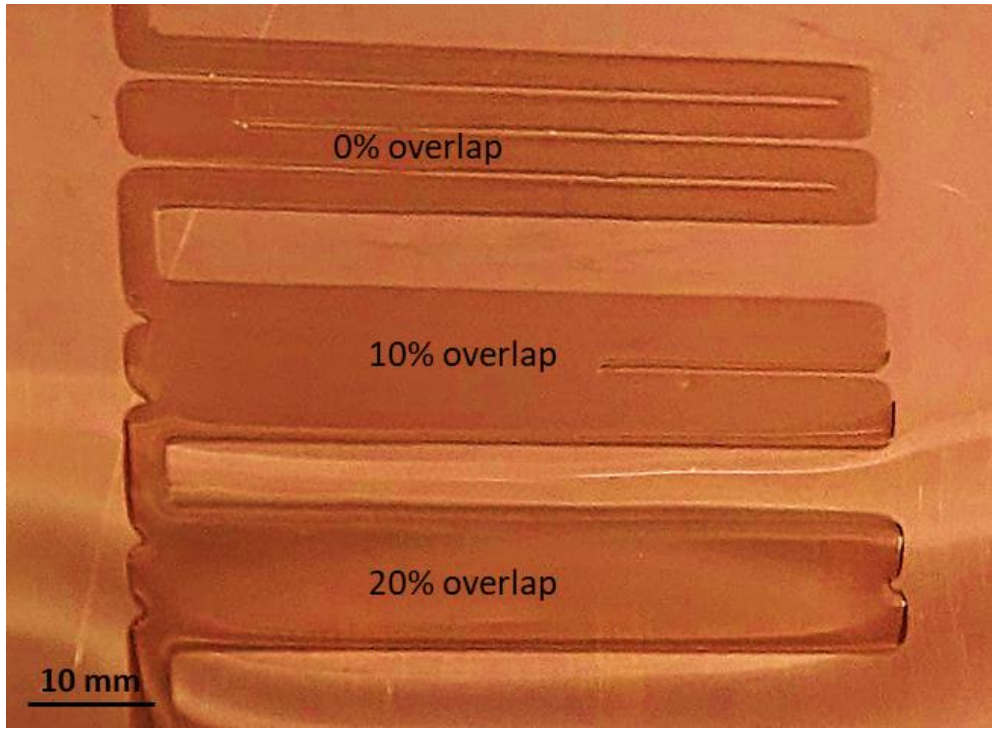

2D optimization: effect of line-overlap %

Gorohovsky et al. 10.1080/17452759.2025.2527387

Printing Quality Optimization: 3D

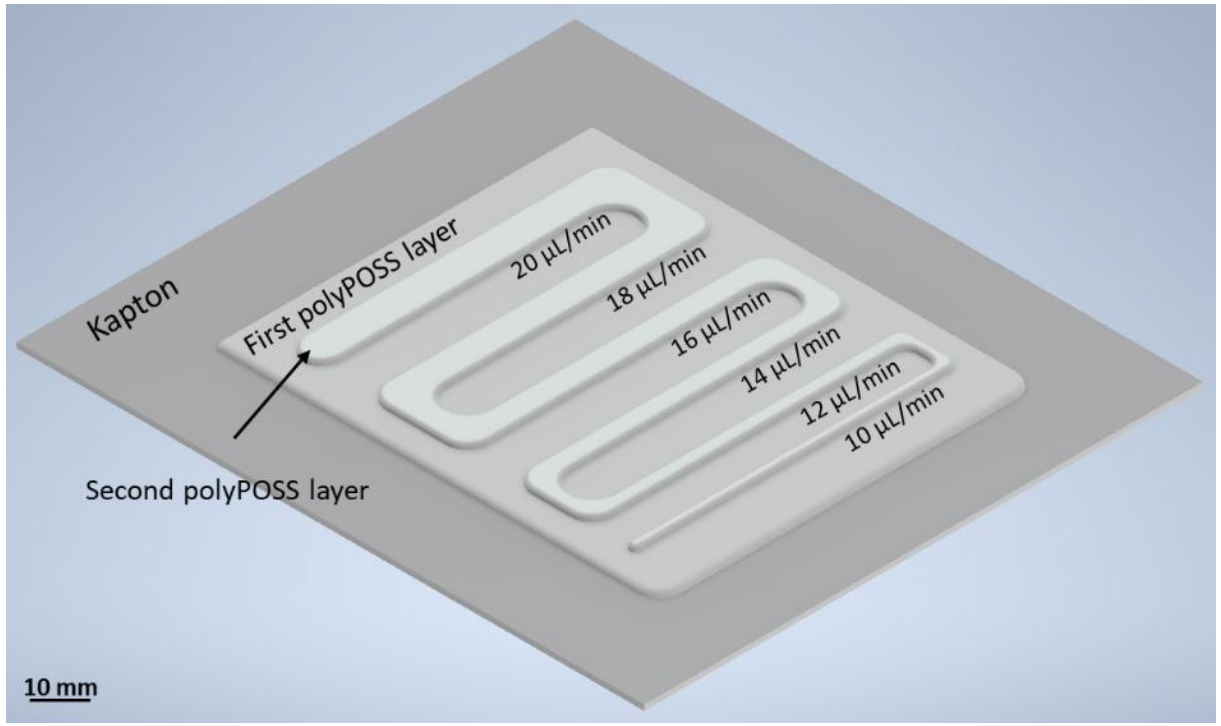

3D optimization: effect of
2nd layer vol. flow rate

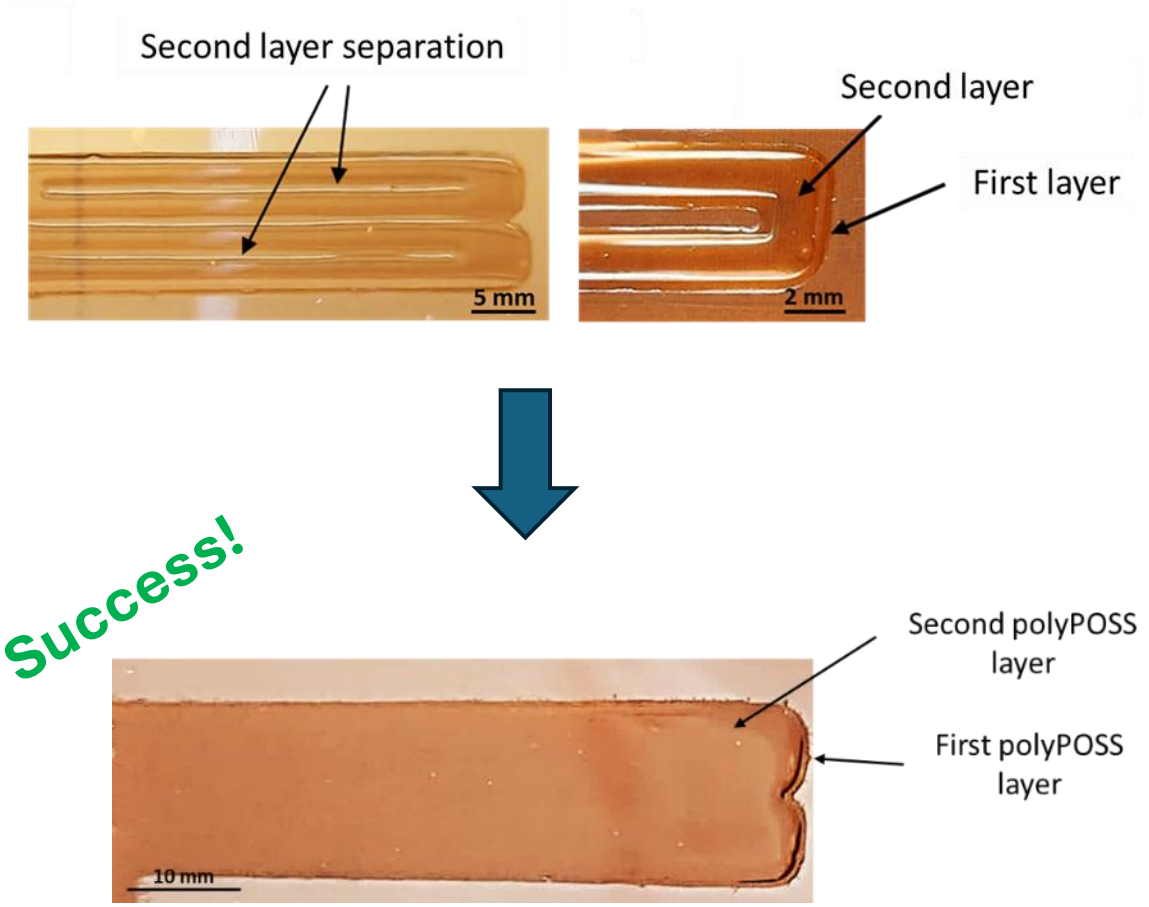

Gorohovsky et al. 10.1080/17452759.2025.2527387

Final Printing Achievements

- Material-substrate adhesion successfully controlled.
- Optimized DIW parameters → AMed reproducible, high-quality X-finger griping bilayer actuators.

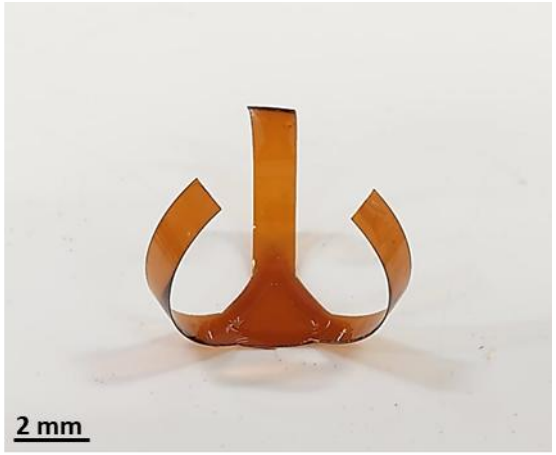

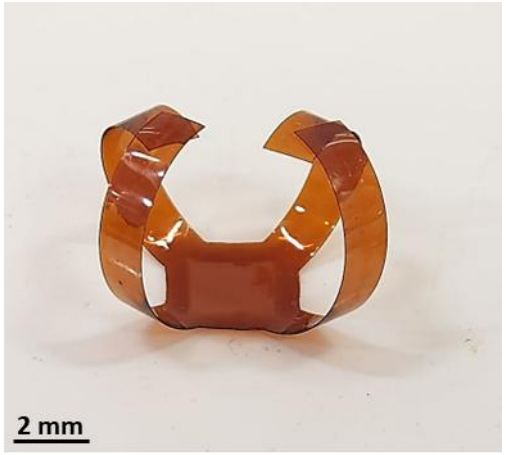



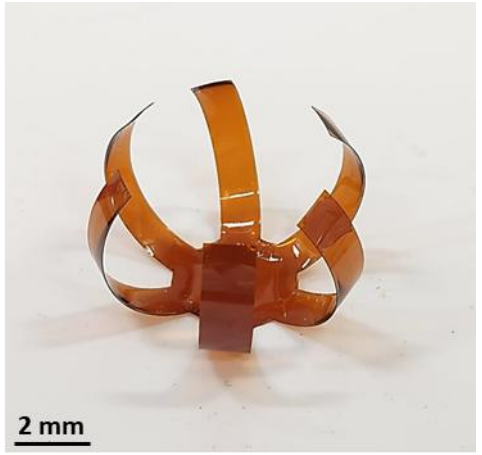

Gorohovsky et al. 10.1080/17452759.2025.2527387

X-Finger Actuators



Gorohovsky et al. 10.1080/17452759.2025.2527387

‘’Spider’’ Actuator

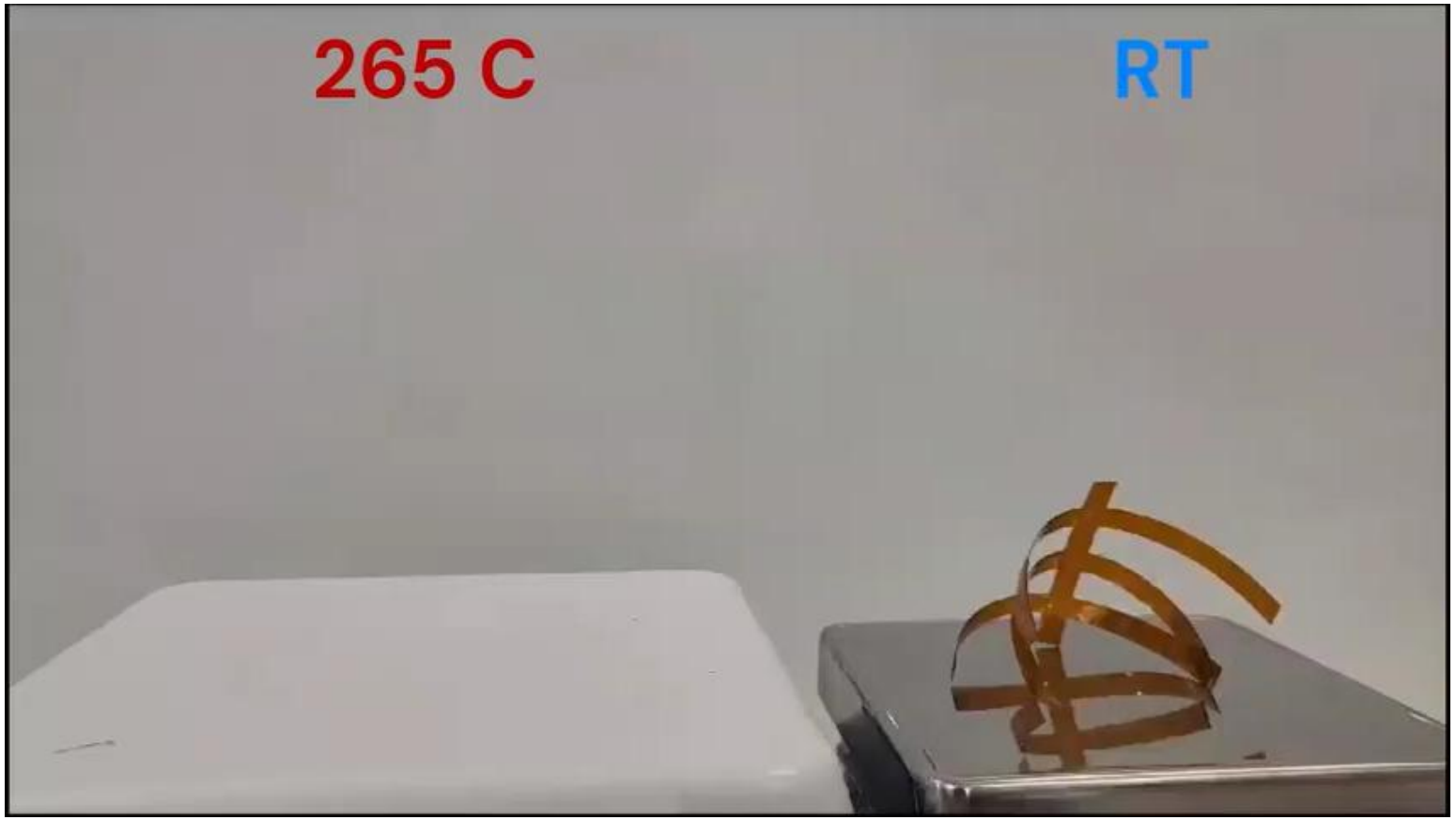

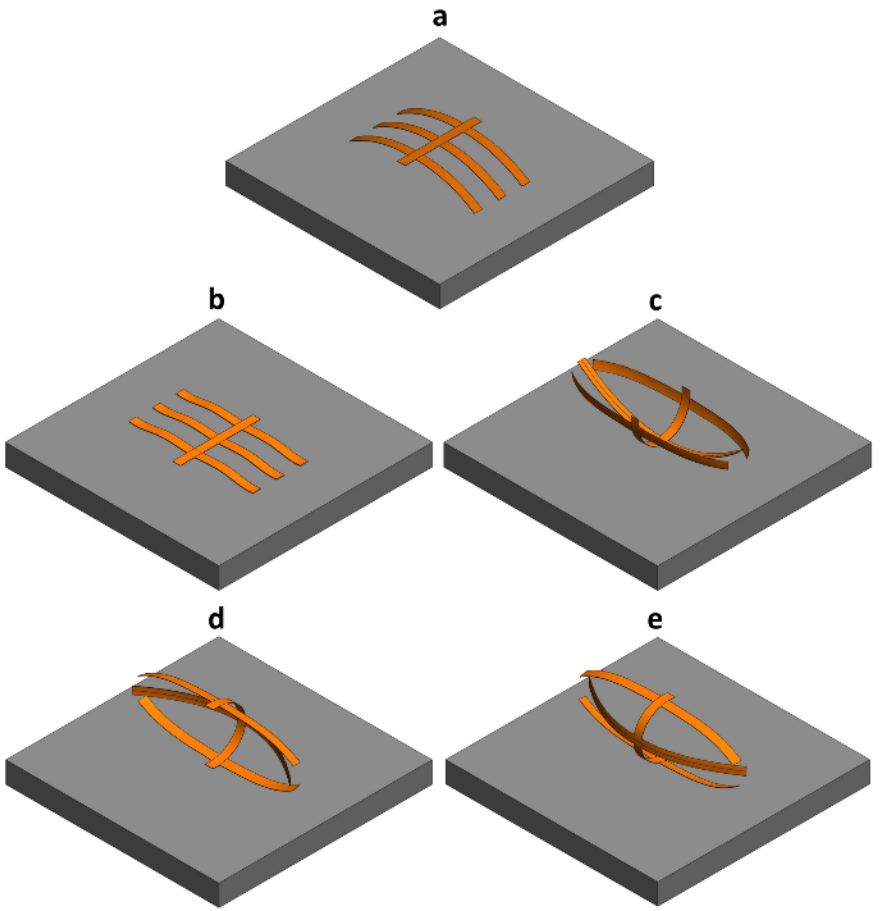

Gorohovsky et al. 10.1080/17452759.2025.2527387

Conclusions & Future Aspirations

Key achievements:

- Printing optimization process.
- DIW-based high performance bilayer actuators.

Future work:

- Mechanical properties.
- New material formulations.
- Downscaling.

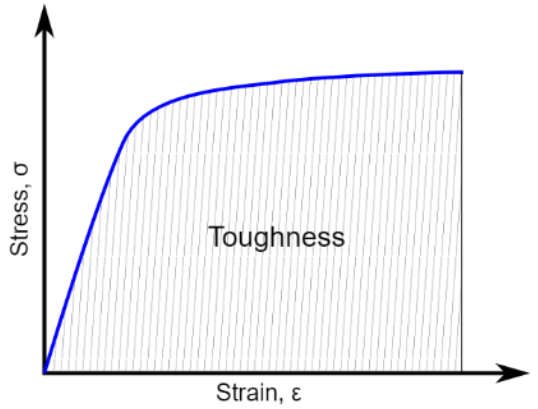

Mechanical properties

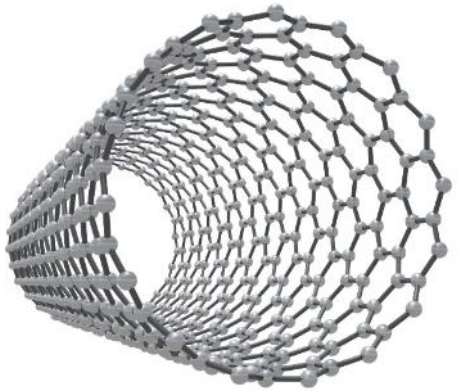

Effect of CNT addition on shape memory properties



Nozzle diameter effects

The Team



Special thanks to:

- Dr. Noa Lachman
- Dr. Ronen Verker
- Mr. Baruch Meirovich
- Mr. Arkadi Refalovich
- ADAMA center at Tel Aviv University
- CSI Lab members


ICCM24
24TH INTERNATIONAL CONFERENCE ON COMPOSITE MATERIALS
August 4-8, 2025 Baltimore Convention
Center - Baltimore, MD

QUESTIONS?

PREDICTING AND OPTIMIZING FDM PRINT PERFORMANCES AN AI APPROACH TO MECHANICAL PROPERTY OPTIMIZATION

M. Laurenti [1*], I. Bavasso[1], E. Palazzi[1], J. Tirillò[1], F. Sarasini[1], F. Berto[1]
[1] Department of Chemical Engineering Materials Environment, Sapienza University of Rome, Via Eudossiana 18, 00184 Roma, Italy

Email : marcello.laurenti@uniroma1.it

Keywords: Boosting Statistic Neural Network; Fused Deposition Modelling; Data Driven; Mechanical Properties; Genetic Optimization

ABSTRACT

Additive Manufacturing (AM), particularly Fused Deposition Modelling (FDM), enables the creation of intricate geometries with remarkable design freedom. Despite these advantages, the mechanical properties of FDM-fabricated parts are highly sensitive to variations in printing parameters and testing conditions. This work introduces an advanced machine learning framework aimed at accurately predicting the mechanical performance of polylactic acid (PLA) specimens, both in their pure form and when reinforced with natural fibers such as flax and wood flour. The methodology centers on Artificial Neural Networks (ANNs), specifically employing a Multi-Layer Perceptron (MLP) architecture that incorporates Gaussian and Gumbel-Gaussian activation functions. To address the challenge of high-dimensional process data, an encoder module based on a Variational Autoencoder (VAE) is integrated, enabling efficient data compression and feature extraction. The predictive capability of the model is further enhanced through a boosting neural network strategy and the application of a kernel-based truncated Taylor expansion, which together improve the model's ability to capture complex, nonlinear relationships between process parameters and mechanical outcomes. Experimental validation demonstrates the effectiveness of the proposed approach. The model achieves a low Continuous Ranked Probability Score Normalized (CRPSN) of 0.072, indicating high predictive accuracy. Additionally, the framework delivers a substantial improvement over a mean baseline, with a Skill score increase of 67%. Multi-Objective optimization carried using Non-Dominated Sorting Genetic Algorithm (NSGA-III) while inferring the trained neural network led to fast and accurate process' parameter optimization toward user defined desired mechanical properties. Experimental analysis performed by DSC confirmed the numerical relationships extracted by the two-step framework. Furthermore, results showed the proposed approach as a robust tool for guiding process optimization and material selection in additive manufacturing applications, paving the way for more reliable and tailored component performance within the constraints of AM technologies.

1 INTRODUCTION

Fused Deposition Modeling (FDM) stands as a cornerstone of Additive Manufacturing (AM) due to its accessibility, cost-effectiveness, and capacity for fabricating complex geometries. Its adoption has rapidly expanded from prototyping to end-use parts in sectors such as aerospace, automotive, and biomedical engineering, where the demand for customized, lightweight, and high-performance components is ever-increasing.

The intricate interplay between FDM process parameters affects microstructure, interlayer adhesion, and, ultimately, the mechanical behavior of printed specimens. This complexity poses significant challenges for accurate prediction and optimization of mechanical properties, necessitating advanced modeling approaches. In recent years, Machine Learning (ML) has emerged as a powerful tool for capturing the nonlinear and high-dimensional relationships inherent in AM processes. ML techniques have been successfully applied to predict both material and physical properties of FDM-fabricated parts. For example, Veeman et al. [1] developed a model to predict Rockwell hardness of ABS using process parameters and micrographs, while Castro et al. [2] utilized a Long Short-Term Memory (LSTM) neural network to forecast compressive strength from time-series sensor data, achieving high predictive accuracy. Wei et al. [3] integrated Takagi–Sugeno fuzzy inference with multilayer neural networks to optimize FDM parameters for PLA, resulting in significant strength improvements. Charalampous et al.

[4] and Shi et al. [5] further demonstrated the utility of supervised learning and feedforward neural networks for optimizing mechanical behavior and predicting properties of FDM-printed polymers. Surface quality, another critical aspect, has been modeled using artificial neural networks (ANNs) by Chinchanikar et al. [6] and Vahabli and Rahmati [7], the latter employing genetic algorithm (GA) optimization for parameter selection in medical applications.
Beyond property prediction, ML-driven approaches have been leveraged for geometric and process optimization in AM. Vaissier et al. [8] introduced a GA-based framework for optimizing lattice support structures, iteratively evolving parameters to minimize weight while maintaining mechanical integrity. The integration of ML and GA has also been explored for material discovery and multi-material design, as demonstrated by Borg et al. and Goh et al., respectively. Sondagar et al. [9] and Kosarac et al. [10] highlighted the effectiveness of ANNs in optimizing process parameters and machining conditions, even with limited datasets.

Artificial Neural Networks (ANNs), in particular, have demonstrated significant potential in modeling nonlinear dependencies within both large and small datasets. Sondagar et al. utilized ANNs to predict optimal process parameters in additive manufacturing, focusing on improving mechanical properties and dimensional accuracy. The ANN was trained on experimental datasets with inputs including temperature, speed, and layer thickness and enabled nonlinear mapping between parameters and quality metrics. Kosarac et al. optimized machining parameter using ANN trained on small datasets.
Recent studies highlighted as promising innovation direction the integration of Genetic Algorithms (GAs) for multi-objective optimization of FDM process parameters. GAs, inspired by natural selection, are adept at navigating complex, multi-dimensional search spaces to identify optimal or near-optimal solutions. In AM, GAs have been applied to optimize build orientation, packing, scheduling, and process parameters, often in conjunction with ML models to enhance both prediction and optimization capabilities. For example, hybrid ML-GA frameworks have been developed for sustainability optimization, surface roughness minimization, and mechanical property enhancement in FDM [11] , with the Non-Dominated Sorting Genetic Algorithm [12] (NSGA-II/III) frequently employed for multi-objective tasks. These approaches have demonstrated superior performance in balancing competing objectives such as strength, surface quality, and production efficiency, and have been validated through experimental studies and case analyses.

Recent studies have also explored the combination of GAs with neural networks for precision prediction and inverse design in FDM. Yang and Zhang [13] established a GA-optimized Backpropagation (BP) neural network model to improve dimensional accuracy predictions, showing that GA optimization significantly enhances model performance by avoiding local minima and improving convergence. Similarly, integrated frameworks combining LSTM networks with GAs have enabled efficient inverse design of 3D printed parts to meet target mechanical properties, further underscoring the synergy between ML and evolutionary algorithms in AM optimization.

Traditional Artificial Neural Network (ANN) architectures frequently encounter difficulties when dealing with high-dimensional process data and the intrinsic variability associated with Fused Deposition Modeling (FDM) printing [14], [15] . These challenges become particularly pronounced when numerous printing parameters are varied simultaneously, especially across wide ranges or near the mechanical limits of the 3D printer. To mitigate these issues, prior studies have typically limited their focus to a small subset of key parameters [16], [17] such as Extruder Temperature, Infill Type, and Infill Density, while holding other variables constant to improve model accuracy. However, this approach falls short of capturing the full complexity of the printing process, as it neglects intricate parameter interactions, thereby restricting the model's applicability in real-world scenarios that demand higher precision and process control.

To overcome these limitations, a novel machine learning framework has been developed, centered on a Multi-Layer Perceptron (MLP) [18] architecture augmented with a Variational Autoencoder (VAE) [19]. This design facilitates effective dimensionality reduction and feature extraction from complex input data. The framework is further enhanced by incorporating a boosting neural network strategy alongside a truncated Taylor series kernel applied to the model outputs, collectively boosting generalization performance and predictive accuracy for both physical and mechanical properties.
This study aims to comprehensively map the entire spectrum of FDM process parameters to the mechanical behavior of polylactic acid (PLA) and its natural fiber-reinforced composites (including flax

and wood flour), even under data-scarce conditions and while pushing printing and testing parameters close to the machine's operational limits. The result is a robust modeling solution capable of learning the nuanced dynamics of the process across its full domain, making it suitable for complex, real-world applications. By leveraging the statistical boosting-enhanced architecture, the framework accounts for the stochastic nature of FDM manufacturing, providing not only point predictions but also the associated statistical distributions. Treating the FDM process as stochastic rather than deterministic allows for more reliable engineering estimations, such as confidence intervals for lower and upper bounds, as well as analyses of distribution characteristics like kurtosis and skewness. Furthermore, the application of SHAP value analysis and GA parameter optimization on the virtual model environment enabled both a deeper understanding of the observed manufacturing processes and an automatic, tailormade, fast and accurate control on the specimen mechanical properties.

Extensive experimental validation on previously unseen data, including extreme conditions near the printer's mechanical constraints and across different polymer suppliers, confirmed the model's high accuracy and strong generalization capability. This positions the framework as a valuable tool for optimizing printing parameters and improving the mechanical reliability of components produced via FDM.

2 METHODS

2.1 Materials

The polymer filaments utilized in this study were commercially sourced from multiple suppliers. Neat PLA filaments were obtained from BambuLab, R3D, Sunlu, and Nanovia, while PLA filaments containing flax fibers and wood flour were acquired from Nanovia. All filament spools were kept in vacuum-sealed containers with silica gel desiccant packs and underwent additional drying at 55 °C for a minimum of 48 hours before the printing process.

2.2 Manufacturing process

During the 3D printing process, a variety of parameters play a crucial role in determining the final characteristics of the printed specimens. These parameters can notably impact heat transfer and mass flow within the extruder chamber and on the surface of the specimen, as well as influence the vibration frequency of the printer's frame.

To thoroughly assess how these printing variables affect the mechanical performance of the materials, all major process parameters were systematically varied across the full range permitted by both the equipment and the materials themselves. The specific ranges for each parameter are detailed in Table 1; except for the categorical Infill Type, these ranges represent the minimum and maximum values selected for each parameter.

Specimens were manufactured by using a BambuLab X1E, a commercial desktop 3D printer. The tensile specimen adhered to the ISO-527-2 (type 1BA, L0 = 30 mm) standard, with a nominal thickness of 2 mm and a nominal width of 5 mm. To capture the intrinsic statistical variation in the properties exhibited by the printing process, five specimens were realized for each set of parameters. In the presented analysis, the parameters intervals were maintained continuous, aside from the categorical or strictly discrete ones, and the tuples of values were chosen randomly using an uniform random distribution, within the interval boundaries, for each batch of specimens.

For each material, a total of 20 batches were realized with such criteria for a total of 100 specimens for material. Each one of them was composed by 5 specimens manufactured with the same parameters, accounting for the inner stochastic nature of the manufacturing process and thus allowing a more robust modelling. Each of those specimens were treated as single data entries to both allow a stronger modelling of the associated statistical distribution and to capture the influence of X and Y location on the build plate on the resulting mechanical properties. With those criteria, a total of 600 specimens have been manufactured and a total of 120 different parameters combinations have been explored.

Despite the relatively limited number of independent parameter combinations, typically a challenge for artificial neural network (ANN) modeling, especially in high-dimensional feature spaces, the proposed framework demonstrated strong predictive accuracy for all measured outputs. This highlights its effectiveness even under conditions of limited and unstructured data.

Table 1. Printing parameters intervals

Parameter	Intervals
Layer Height	*0.1 mm – 0.28 mm*
Line Width	*0.4 mm – 0.8 mm*
Number of Shells	*1 – 4*
Base Layers	*1 – 4*
Infill Type	*Cubic, Rectilinear, Honeycomb, Gyroid*
Infill Density	*5 % – 100 %*
Speed of Base Layers	*10 mm/s – 500 mm/s*
Speed of Infill	*10 mm/s – 500 mm/s*
Acceleration	*50 mm/s^2 – 13000 mm/s^2*
Jerk	*1 mm/s^3 – 9 mm/s^3*
Extruder Temperature	*190 °C – 240°C*
Heated Bed Temperature	*25 °C – 60 °C*
Chamber Temperature	*25°C – 60 °C*
Filament Dryer Temperature	*25 °C – 55 °C*
XY Position	*0 mm – 257 mm*

2.3 Specimen characterization

2.3.1 Mechanical properties

The uniaxial tensile tests of all manufactured specimens were carried out on a Zwick/Roell Z2.5 universal testing machine, equipped with digiClip extensometer (by Zwick/Roell) to accurately measure the strain (Fig. 1b). Tests were conducted in displacement control, varying the crosshead speed in an interval of 1 mm/min - 50 mm/min. The same strategy used in the manufacturing process was used here, so the test speed was chosen randomly in the interval boundaries for each batch of specimens. Such an approach allowed us to capture different strain-dependent mechanical behaviours, thus increasing the ANN's generalization capabilities.

2.3.2 Thermal properties

Differential scanning calorimetry (DSC) analysis of the materials was performed under a nitrogen flow of 60 mL/min (DSC 214 Polyma by Netzsch). Samples (around 10 mg) were placed in a aluminium concave crucible with a pierced lid and analysed according to the following thermal program: heating from 0 °C to 220 °C (5 min hold interval), cooling to 0 °C (5 min hold) and second heating to 220 °C, all steps performed with a rate of 10 °C/min. The thermal information gathered from this analysis have been used to enrich the input data for the modelling, leveraging the correlation between melting temperature and mechanical properties [20], thus enabling more accurate predictions.

2.4 Learning task

This study focused on examining how printing and testing parameters translate into the mechanical and physical properties observed in the specimens. This challenge can be framed as a multi-input-multi-output (MIMO) regression problem, where both the printing and testing conditions serve as inputs, and the resulting material properties are the outputs of interest. In the realm of computer science and artificial intelligence, the quality of the dataset is just as critical as the neural network's ability to generalize. To enhance the informational value of each data point, the input set was enriched by incorporating not only the thermal properties of the printed polymer but also its mechanical properties measured under standardized printing and testing conditions, including fixed strain rates.

The thermal information about the polymer and how it influences the printing process was introduced by defining four different relative temperatures defined as:

- ΔText-melt := Extruder temperature - Melting temperature
- ΔTbed-cryst := Heated bed temperature - Crystallization temperature
- ΔTbed-glass := Heated bed temperature - Glass transition temperature

- ΔTbed-ch := Heated bed temperature - Chamber temperature

Including the polymer's thermal properties in the model allowed it to distinguish between different polymers without relying on additional one-hot encoding schemes. This approach reduced the input dimensionality while establishing a meaningful correlation between the polymers' thermal and mechanical characteristics. Moreover, the temperature-dependent value shifts helped normalize the 3D printer's operating temperatures across different polymers, effectively creating a nearly uniform reference framework. This normalization eased the computational complexity of the modelling task.

Mechanical information was incorporated by producing six specimens per polymer using a fixed set of printing parameters consistent across all materials. These parameters were carefully selected to yield reliable and representative samples. For each polymer, half of the specimens were printed with a 0° raster angle and the other half with a 90° raster angle, allowing separate evaluation of the filament's intrinsic strength and the inter-layer bonding strength of parallel deposited filaments. Additionally, each polymer and raster angle combination were tested at three different strain rates, 5 mm/min, 20 mm/min, and 40 mm/min, to capture how mechanical behaviour varies with strain rate.

As a result of these enhancements, the input feature space expanded threefold, increasing from 25 to 75 features. However, the enriched data significantly offset the challenges of higher dimensionality, leading to a consistent improvement in the model's overall predictive accuracy.

2.5 Framework structure

The model architecture employed in this study is a multi-headed multilayer perceptron (MLP) featuring a Variational MLP Encoder (VE) as a shared backbone. In this design, the common backbone functions as an effective compressor that encodes and transforms the input features into a meaningful latent representation, while each individual head is dedicated to predicting a specific output feature.

Additive manufacturing (AM), particularly fused deposition modeling (FDM), operates in a partially observed environment where not all variables are known or controllable during production. To address this uncertainty, both the VE backbone and the MLP heads map their outputs onto Gaussian-shaped distributions, following approaches used in prior research dealing with uncertainty-driven scenarios. By producing statistical predictions rather than deterministic outputs, the model can more effectively navigate the loss landscape, reducing the risk of becoming trapped in local minimum.

This capability is achieved by duplicating each head and employing a Negative Gaussian Log Likelihood (NLL) loss function during training, which encourages the outputs to conform to Gaussian distributions. Consequently, the neural network can predict mechanical properties more accurately by providing both the expected mean and variance of each parameter, thereby capturing the uncertainty inherent in certain regions of the printing parameter space. For clarity, this type of neural network will be referred to as iBNN in the following sections.

To further explore the enhanced modelling capabilities offered by a more accurate statistical representation of the output, a similar NN (iBNNG) that maps the output features into a Gaussian-Gumbel [21] space has been realized.

The aforementioned statistical distribution can be defined as:

- $Y_{pdf}(x) = \frac{1}{\sqrt{2\pi\sigma^2}} e^{-\frac{(x-\mu)^2}{\sigma^2}}$ (1)
- $\mu_{pdf}(x) = \frac{1}{\beta} e^{-\left[\left(\frac{x-\mu^*}{\beta}\right)+e^{-\frac{x-\mu^*}{\beta}}\right]}$ (2)

Using this definition only three parameters – μ*, σ, β – are needed to actually represent the distribution, and they can be modelled by three different neural networks. As with the previous approach, each neural network within the triplet is a replica of the original head, which effectively reduces the hyperparameter search space during optimization. These networks were trained using a Gaussian-Gumbel Negative Log Likelihood (GGNLL) loss function combined with the Gumbel-Max reparameterization trick, enabling gradient backpropagation throughout training. The use of different statistical representations in this study allowed the model to capture both the inherent stochasticity of

the process, by mapping outputs into a Gaussian distribution, and the occurrence of catastrophic defects within specimens, by mapping into a Gaussian-Gumbel distribution, thereby providing a more precise characterization of the process dynamics.

To prevent the hyperparameter space from becoming excessively large, the MLP architecture employed here features a sequential and consistent reduction in the width of hidden layers. This layer size reduction is governed by a user-defined decay parameter, which simplifies the architectural design to just four key parameters: the number of layers, the decay rate, the initial hidden layer size, and the type of activation function. The calculation of input and output layer sizes is straightforward and summarized as follows:

- Input size of ith layer := $round\left(max\left(\frac{initial\ hidden\ size}{decay^{i-1}}, 1\right)\right)$
- Output size of ith layer := $round\left(max\left(\frac{initial\ hidden\ size}{decay^{i}}, 1\right)\right)$

In the proposed framework to further improve the predictions, the increase in accuracy offered by the boosting architectures has been leveraged; thus, similarly to the famous XGboost [22], the proposed models have been built and trained subsequentially to refine the prediction of the previous models, until no further meaningful increase of accuracy was reached.

2.6 SHAP Analysis

Following the training of the iBNN and iBNNG frameworks, a statistical analysis was conducted to assess the impact of input parameters on the models' outputs using Shapley Values. Typically, Shapley values are applied in scenarios where individual contributors have unequal but cooperative roles in achieving a collective outcome or payoff. Within the application of machine learning and AI interpretability, this mathematical tool provides quantitative estimates of each input feature's influence on the model's predictions. In the context of this study, assuming the models are accurate, these values serve as proxies to reveal the true effect of process parameters on the resulting mechanical properties.

After calculating both SHAP values and SHAP interaction values for the iBNN and iBNNG models, the insights gained were used to develop a novel kernel-based AI approach that accounts for the lack of interaction between input parameters. This kernel was designed as a truncated Taylor series expansion, where the model's output approximates the k-th order derivatives and truncation error, and can be represented as follows:

$$Y(x) = \sum_{i=1}^{N} \sum_{j=0}^{K} \frac{f_i^{(j)}}{j!}\left(x_i^j\right) \tag{3}$$

where:

- $f_i(j)$ is the j-th derivative of a generic function, relative to the i-th input variable. In this context $f_i(j)$ is approximated by the NN.
- x_i is the i-th input variable used in the i-th generic function, truncated at the K-order. Using this kernel, it was possible to force lower levels of interaction between input features, lowering the complexity of the optimization process.

The realized pseudo-physics informed NN (iPBNN) has been trained with the same methodology of iBNN and iBNNG, as shown in the next sections, truncation's degree was set as hyperparameter.

2.7 Dataset preprocess and training pipeline

The data preprocessing in this study involved a three-step procedure: one-hot encoding (OHE) , scaling, and partitioning. Following scaling, the dataset was split into training-test and validation sets with a ratio of 95:5. Because selecting optimal test points for an accurate performance metric was challenging, a 10-fold cross-validation [23] approach was employed to more reliably assess the models' predictive capabilities.

Model architecture optimization was performed using a Bayesian algorithm aimed at minimizing the test loss averaged over the cross-validation folds. The training process consisted of two main stages. First, a Variational Autoencoder (VAE) was trained on the input data. Next, a multi-headed MLP was constructed using the best-performing encoder from the VAE (the Variational Encoder, VE) as the

shared backbone. During the initial stage, a sweep evaluated 10,000 VAE models, selecting the one with the lowest average cross-validation loss. In the second stage, each MLP head underwent 10 boosting rounds, with 500 models assessed per round. After each boosting round, the top-performing model was chosen to serve as the booster for the subsequent round. This procedure was repeated for all 10 output heads, resulting in a total of 60,000 models being trained and evaluated to complete the entire training process.

2.8 Genetic Optimization

Genetic based algorithms were used on the converged AI framework to optimize process parameters on user defined mechanical and process constraints. Process parameters have been clustered into different genes using as discrimination criteria the effect exerted on the process; thus, allowing a more stable phenotypic expression and a smoother optimization. Each gene, structural, cinematic and thermic, was characterized by their own mutations, crossover and inversion coefficients to allow independent mutation dynamics and efficient hyperparameter search. Furthermore, mutation, inversion and inversion coefficients were also subjected to mutation and crossover rates to allow a smoother transition from the exploration to the exploitation stage. Finally, to allow a multi-objective optimization avoiding hierarchical objective function definition, NSGA-III [24] algorithm was used, with a population of 2048 individuals and with 100 generations per optimization.

AI fine-tuning was also performed to stabilize the NN prediction, avoiding numerical instabilities that could have occurred in interpolation or extrapolation regions. A Physic-Informed NN (PINN) criteria was then used, forcing a hierarchical relationship between the output parameters, for example Force UTS always greater than Force Yield. Since the defined soft-constrained PINN was characterized by multiple loss functions, a self-adaptive loss balanced algorithm was used to allow a faster and smoother convergence [25].

3 RESULTS AND DISCUSSION

The results are presented in the following sections. To avoid the bias associated with training and test datasets, which tend to favor overfitting, only predictions on the validation set are reported. Since conventional accuracy metrics like Mean Absolute Error (MAE) or Mean Absolute Percentage Error (MAPE) are not directly suitable for evaluating probabilistic forecasts, the Continuous Ranked Probability Score (CRPS) was employed as a generalized version of MAE for probabilistic predictions. By generating an empirical distribution (F) through N samples drawn from the probability density function, the CRPS is defined as follows:

$$CRPS(F,x) = \sum_{k=0}^{x} F(y_k)^2 + \sum_{k=x+1}^{n} (F(y_k) - 1)^2 \quad (4)$$

where n is the last element of the right tail of the PDF. To allow comparisons and a common metric through the output features, a pseudo Mean Absolute Percentage Error (MAPE) has been also introduced, based on CRPS values, called CRPS Normalized (CRPSN). Formally it has been defined as:

$$CRPSN(F,x) = \frac{CRPS(F,x)}{\frac{1}{N}\sum_{x \epsilon D}^{N} x_i} \quad (5)$$

where the denominator is the mean value of the real observed output feature.
Additionally, to facilitate a more straightforward comparison of accuracy across different models, an extra metric called Skill was introduced. This metric quantifies the improvement in accuracy relative to a naïve prediction, which is simply the mean of the observed values. Formally, the Skill metric is defined as:

$$Skill(F,x) = \frac{CRPS(x_{mean},x) - CRPS(F,x)}{CRPS\left(\frac{1}{N}\sum_{x \epsilon D}^{N} x_i, x\right)} * 100 \quad (6)$$

Lastly, to provide a more practical assessment of the models' reliability, an additional metric called the Confidence Region Score (CR score) was introduced. This metric is calculated using the 2.5th and 97.25th percentiles (Q(0.025) and Q(0.9725)), which together capture approximately 95% of the distribution's statistical significance. The CR score represents the average frequency with which the

actual observations fall within this ±2σ interval, meaning a higher score indicates a stronger alignment between the observed data and the predicted statistical distribution. Although this metric is unconventional, it enabled effective comparisons between the different statistical outputs of the model. Meanwhile, the CRPS metric provided a quantitative measure of error analogous to the Mean Absolute Error (MAE), facilitating more precise evaluations of the models' accuracy.

3.1 Framework predictions and Ablation Study

Table 2 presents CRPSN values on prediction for mechanical properties and physical properties relative to iBNN framework and its variants.

The iBNN predictions show increased variance under certain printing conditions, particularly at high Toughness values, highlighted by a high value in CRPSN for iBNN, iBNNG and iPBNN. This elevated variance is attributed to the significant statistical variability caused by unpredictable internal defects such as inclusions, under-extrusions from inconsistent filament diameter, and thermal degradation. These defects serve as nucleation points for voids and cracks, substantially reducing the specimen's maximum energy absorption and strain capacity.

Table 2. CRPSN values for every output feature, calculated on the validation partition for the proposed models, the baseline models, and the ablation study models.

Model	Rigidity	Force UTS	Strain UTS	Force Yield	Strain Yield	Strain Break	Toughness	b	h	P Tot	Mean
SVM	0.069	0.126	0.108	0.108	0.109	0.253	0.320	0.008	0.016	0.041	0.116
XGB	0.100	0.160	0.117	0.154	0.107	0.372	0.379	0.014	0.016	0.054	0.147
iBNNH	0.054	0.106	0.098	0.098	0.085	0.150	0.212	0.006	0.014	**0.031**	0.085
iBNN	0.045	0.073	0.065	**0.062**	**0.068**	0.172	**0.182**	0.005	**0.011**	0.040	**0.072**
iBNNG	0.049	0.114	0.073	0.103	0.083	0.175	0.189	0.005	0.014	0.058	0.086
iPBNN	**0.035**	**0.062**	**0.041**	**0.062**	0.084	0.176	0.292	**0.004**	0.012	0.034	0.080
BMLP	0.062	0.066	0.079	0.044	0.071	0.178	0.183	0.006	0.014	0.036	0.074
BNNH	0.067	0.091	0.067	0.078	0.102	**0.147**	0.183	0.006	0.016	0.048	0.080

Notably, the rise in confidence region values occurs consistently across all output features for the same input conditions, indicating that each model head has effectively and independently captured the process dynamics. This ability to learn variances linked to printing and testing parameters enables the model not only to predict mechanical properties in advance but also to identify and avoid parameter regions prone to unpredictable defects. Despite these high-variance regions, the models reliably capture the specimens' mechanical and physical behavior, as evidenced by consistently low CRPSN scores across all output features.

An ablation study was conducted on the proposed framework by systematically removing key components: first the Gaussian head, then the Variational Encoder, and finally the engineered input features. For clarity, models trained without engineered features are referred to as BNN and BNNG. Models without the Gaussian head are labeled BNNH and iBNNH, following the previously established naming convention. When both the head and backbone were removed, the resulting architecture became a standard Boosted MLP, referred to as BMLP. For baseline comparison, XGBoost (XGB) and Support Vector Machine (SVM) models were also included and optimized using the same Bayesian Optimization process as the main study.

Across nearly all output features, these simplified and comparative models showed higher CRPSN values than the full models. Traditional approaches like XGB and SVM also exhibited higher CRPSN values compared to both the complete and ablated neural network models. These results highlight that the proposed framework offers superior prediction accuracy in complex, highly stochastic scenarios such as FDM, outperforming conventional modeling techniques.

3.2 SHAP Analysis

AI modelling is frequently regarded as a black-box technique, effective at delivering accurate predictions but often lacking transparent and straightforward explanations of the underlying mathematical processes driving those predictions. To address this limitation, a statistical SHAP analysis was performed to uncover the physical relationships between the input variables and the model's output predictions.

The results reveal key insights into the process dynamics from a materials science perspective. For rigidity, the relative density of the specimen was the most influential factor, with lower density reducing stiffness. Additionally, a larger temperature difference between the heated bed and printer chamber negatively affected rigidity, likely due to uneven internal stresses. A similar negative correlation was observed between rigidity and the difference between extruder temperature and polymer melting point, suggesting thermal degradation of PLA, flax fibers, and wood powder. High jerk values also reduced rigidity, indicating that strong vibrations during deposition harm mechanical properties.

For toughness, the X position on the build plate had the strongest negative impact, implying that vibrations and thermal gradients near chamber walls cause defects that reduce energy absorption. Unlike rigidity, toughness was more sensitive to abrupt changes in acceleration rather than the speed of those changes. Structural parameters like shell and base layer count positively influenced toughness, highlighting the role of filament orientation. A strong negative correlation with layer height suggested the formation of meso-crystalline phases during printing, which enhance energy absorption during testing.

This hypothesis was supported by DSC analysis (Fig. 3), showing significant enthalpy release around 90–98 °C in printed specimens before and after testing, attributed to residual stress release and fusion of process-induced meso-crystals [26]. The increase in crystallinity from 6.08% to 11.35% during tensile testing confirmed these meso-crystals contribute to improved toughness.

Table 3. DSC analysis on high plastic PLA specimen in the deformed region, the undeformed region, and the reference second heating as baseline.

Specimen	$T_{cold\text{-}cryst}$ (°C)	T_{melt} (°C)	$\Delta H_{cold\text{-}crist}$ (J/g)	ΔH_{melt} (J/g)	χ (%)
As Printed	67.6	160.06	-26.25	31.91	6.08
Tested	70.01	159.06	-23.04	33.36	11.35
Reference	107.3	159.9	-27.65	35.53	8.47

3.3 Genetic Optimization

Genetic optimization was carried out on the converged and fine-tuned iBNN AI framework. To prove its effectiveness a run was performed with the objective of maximizing the Force Yield, while minimizing the theoretical density of the manufactured specimen. The results of the optimization process are shown in Figure 1, where the algorithm successfully identified the Pareto optimality frontier associated with the proposed task. Furthermore, analysing the proposed optimality frontier, it was found a significant high frequency in solutions of PLA-Flax reinforced respect to PLA-Wood reinforced, suggesting a lower fiber-matrix interface in the latter composite composition. SEM analysis on the fracture surface of PLA-Wood reinforce specimen was conducted and it was confirmed indeed the absence of an interface between PLA polymer and the wood particles reinforcement; thus, confirming the purely data-driven relationship discovered by the combined application of both NSGA-III and iBNN frameworks.

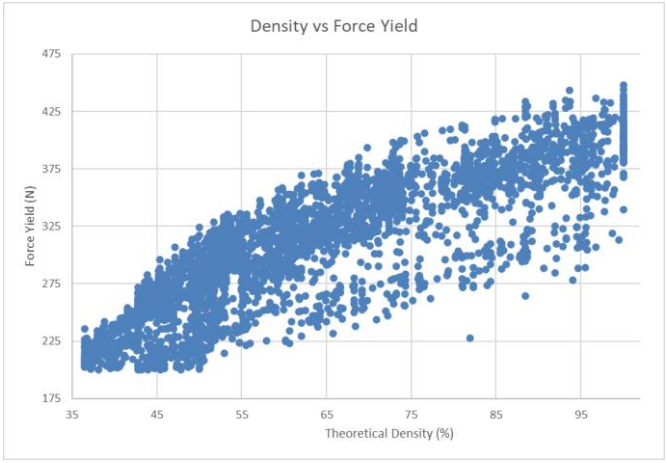

Figure 1. NSGA-III optimization using iBNN as virtual environment, maximizing Force Yield and minimizing the theoretical density of the specimen.

4 SUMMARY

This study aimed to develop an AI framework that efficiently maps printing parameters and testing conditions to the mechanical and physical properties of 3D-printed specimens, covering a wide range of process variations. The proposed model, a Boosting multi-headed Variational Encoder MLP combined with a kernel-based truncated Taylor expansion, successfully predicts outputs in both Gaussian and Gaussian-Gumbel spaces. Validated on unseen data, the models achieved low CRPS values (0.080, 0.072, and 0.086 for iPBNN, iBNN, and iBNNG respectively), outperforming traditional methods like XGB and SVM by effectively capturing variance in highly uncertain FDM processes.

SHAP analysis revealed meaningful correlations between process parameters and mechanical properties, which were experimentally confirmed, demonstrating the model's ability to learn complex relationships in additive manufacturing. Leveraging the minimal interaction between inputs identified by SHAP, a Pseudo-Informed Neural Network was created using a kernel-based truncated Taylor expansion, further enhancing performance where standard PINN approaches are not feasible.

Overall, this methodology offers a robust solution for FDM and other AM techniques, maintaining accuracy despite high-dimensional, sparse data, common in real-world scenarios with limited data availability. The coherent insights from SHAP and NSGA-III also suggest its potential as a tool not only for prediction but for understanding process dynamics.

ACKNOWLEDGEMENTS

Funded by the European Union (ERC, 101093897 Butterfly). Views and opinions expressed are however those of the author(s) only and do not necessarily reflect those of the European Union or the European Research Council Executive Agency.

REFERENCES

[1] D. Veeman, S. Sudharsan, G. J. Surendhar, R. Shanmugam, and L. Guo, "Machine learning model for predicting the hardness of additively manufactured acrylonitrile butadiene styrene," *Mater Today Commun*, vol. 35, Jun. 2023, doi: 10.1016/j.mtcomm.2023.106147.

[2] P. Castro, G. Pathinettampadian, C. S. D. Ravi, and M. K. Subramaniyan, "Prediction of compressive strength in additively fabricated part using long short term memory based neural network," *Mater Today Commun*, vol. 37, Dec. 2023, doi: 10.1016/j.mtcomm.2023.107139.

[3] H. Wei *et al.*, "Optimizing FDM 3D printing parameters for improved tensile strength using the Takagi–Sugeno fuzzy neural network," *Mater Today Commun*, vol. 38, p. 108268, Mar. 2024, doi: 10.1016/J.MTCOMM.2024.108268.

[4] P. Charalampous, N. Kladovasilakis, I. Kostavelis, K. Tsongas, D. Tzetzis, and D. Tzovaras, "Machine Learning-Based Mechanical Behavior Optimization of 3D Print Constructs Manufactured Via the FFF Process," *J Mater Eng Perform*, vol. 31, no. 6, pp. 4697–4706, Jun. 2022, doi: 10.1007/S11665-021-06535-0.

[5] B. Shi *et al.*, "Development of ANN model for predicting mechanical properties of 3D printed PEEK polymer using FDM and optimization of process parameters for better mechanical properties," *Phys Scr*, vol. 99, no. 11, p. 116005, Oct. 2024, doi: 10.1088/1402-4896/AD7F0F.

[6] S. Chinchanikar, S. Shinde, V. Gaikwad, A. Shaikh, M. Rondhe, and M. Naik, "ANN modelling of surface roughness of FDM parts considering the effect of hidden layers, neurons, and process parameters," *Advances in Materials and Processing Technologies*, vol. 10, no. 1, pp. 22–32, Jan. 2024, doi: 10.1080/2374068X.2022.2091085.

[7] E. Vahabli and S. Rahmati, "Improvement of FDM parts' surface quality using optimized neural networks - Medical case studies," *Rapid Prototyp J*, vol. 23, no. 4, pp. 825–842, 2017, doi: 10.1108/RPJ-06-2015-0075/FULL/PDF.

[8] B. Vaissier, J.-P. Pernot, L. Chougrani, and P. Véron, "Genetic-algorithm based framework for lattice support structure optimization in additive manufacturing," *Computer-Aided Design*, vol. 110, pp. 11–23, 2019, doi: https://doi.org/10.1016/j.cad.2018.12.007.

[9] H. Sondagar, S. S. Bhadauria, and V. S. Sharma, "Artificial neural network (ANN) based prediction of process parameters in additive manufacturing," *IOP Conf Ser Mater Sci Eng*, vol. 1136, no. 1, p. 012026, 2021, doi: 10.1088/1757-899X/1136/1/012026.

[10] A. Kosarac, C. Mladjenovic, M. Zeljkovic, S. Tabakovic, and M. Knezev, "Neural-Network-Based Approaches for Optimization of Machining Parameters Using Small Dataset," *Materials*, vol. 15, no. 3, Feb. 2022, doi: 10.3390/MA15030700.

[11] A. Sohail, "Genetic Algorithms in the Fields of Artificial Intelligence and Data Sciences," *Annals of Data Science*, vol. 10, no. 4, pp. 1007–1018, Aug. 2023, doi: 10.1007/S40745-021-00354-9/FIGURES/3.

[12] K. Deb, A. Pratap, S. Agarwal, and T. Meyarivan, "A fast and elitist multiobjective genetic algorithm: NSGA-II," *IEEE Transactions on Evolutionary Computation*, vol. 6, no. 2, pp. 182–197, Apr. 2002, doi: 10.1109/4235.996017.

[13] Y. Juan, Y. Dai, Y. Yang, and J. Zhang, "Accelerating materials discovery using machine learning," *J Mater Sci Technol*, vol. 79, pp. 178–190, Jul. 2021, doi: 10.1016/j.jmst.2020.12.010.

[14] Z. Hu and S. Mahadevan, "Uncertainty quantification and management in additive manufacturing: current status, needs, and opportunities," *International Journal of Advanced Manufacturing Technology*, vol. 93, no. 5–8, pp. 2855–2874, Nov. 2017, doi: 10.1007/S00170-017-0703-5.

[15] O. Ulkir, G. Akgun, and A. Karadag, "Mechanical Behavior Prediction of 3D-Printed PLA/Wood Composites Using Artificial Neural Network and Fuzzy Logic," *Polym Adv Technol*, vol. 36, no. 2, Feb. 2025, doi: 10.1002/pat.70103.

[16] M. Hassan, M. Misra, G. W. Taylor, and A. K. Mohanty, "A review of AI for optimization of 3D printing of sustainable polymers and composites," Oct. 01, 2024, *Elsevier B.V.* doi: 10.1016/j.jcomc.2024.100513.

[17] N. Contuzzi, A. Morvayová, L. Fabbiano, and G. Casalino, "Comparison of the performances of Statistical and Artificial Neural Network models in the prediction of geometry and density of PLA/wood biocomposite cubes manufactured by FDM," *International Journal of Advanced Manufacturing Technology*, vol. 133, no. 11–12, pp. 5849–5870, Aug. 2024, doi: 10.1007/s00170-024-14092-8.

[18] M.-C. Popescu, V. Balas, L. Perescu-Popescu, and N. Mastorakis, "Multilayer perceptron and neural networks," *WSEAS Transactions on Circuits and Systems*, vol. 8, Feb. 2009.

[19] D. P. Kingma and M. Welling, "An Introduction to Variational Autoencoders," Jun. 2019, doi: 10.1561/2200000056.

[20] R. W. Nunes, J. R. Martin, and J. F. Johnson, "Influence of molecular weight and molecular weight distribution on mechanical properties of polymers," *Polym Eng Sci*, vol. 22, no. 4, pp. 205–228, Mar. 1982, doi: 10.1002/PEN.760220402.

[21] A. Tridello, A. Ciampaglia, F. Berto, and D. S. Paolino, "Assessment of the Critical Defect in Additive Manufacturing Components through Machine Learning Algorithms," *Applied Sciences 2023, Vol. 13, Page 4294*, vol. 13, no. 7, p. 4294, Mar. 2023, doi: 10.3390/APP13074294.

[22] T. Chen and C. Guestrin, "XGBoost: A Scalable Tree Boosting System," Mar. 2016, doi: 10.1145/2939672.2939785.

[23] T.-T. Wong, "Performance evaluation of classification algorithms by k-fold and leave-one-out cross validation," *Pattern Recognit*, vol. 48, no. 9, pp. 2839–2846, Sep. 2015, doi: 10.1016/j.patcog.2015.03.009.

[24] K. Deb and H. Jain, "An evolutionary many-objective optimization algorithm using reference-point-based nondominated sorting approach, Part I: Solving problems with box constraints," *IEEE Transactions on Evolutionary Computation*, vol. 18, no. 4, pp. 577–601, 2014, doi: 10.1109/TEVC.2013.2281535.

[25] Z. Xiang, W. Peng, X. Liu, and W. Yao, "Self-adaptive loss balanced Physics-informed neural networks," *Neurocomputing*, vol. 496, pp. 11–34, Jul. 2022, doi: 10.1016/J.NEUCOM.2022.05.015.

[26] C. Zhou *et al.*, "Deformation and structure evolution of glassy poly(lactic acid) below the glass transition temperature," *CrystEngComm*, vol. 17, no. 30, pp. 5651–5663, Jul. 2015, doi: 10.1039/C5CE00669D.

ICCM24
24TH INTERNATIONAL CONFERENCE ON COMPOSITE MATERIALS
AUG 4-8, 2025 • BALTIMORE CONVENTION CENTER • BALTIMORE, MARYLAND

Model Order Reduction Methods for Real-Time Prediction of Thermomechanical Properties of Additively Manufactured Composite Materials

***P. Castelló-Pedrero*[12]**, *C. García-Gascón*[12], *J. Bas-Bolufer*[1], *J.A. García-Manrique*[1], *F. Chinesta*[2]

1. Instituto de Diseño y Fabricación (IDF), Universidad Politécnica de Valencia (UPV), Valencia, Spain
2. Processes and Engineering in Mechanics and Materials (PIMM), École Nationale Supérieure d'Arts et Métiers (ENSAM), Paris, France

UNIVERSITAT POLITÈCNICA DE VALÈNCIA
INSTITUTO DE DISEÑO Y FABRICACIÓN
Arts et Métiers Sciences et Technologies
Financiado por la Unión Europea NextGenerationEU
Plan de Recuperación, Transformación y Resiliencia

LFAM: Large Format Additive Manufacturing

LFAM machine: 1300 x 2500 x 1000 mm



CNCbárcenas DISCOVERY 3Dprinter

Composite materials



ABS + 20% **CF**



ABS + 20% **GF**

45º nozzle

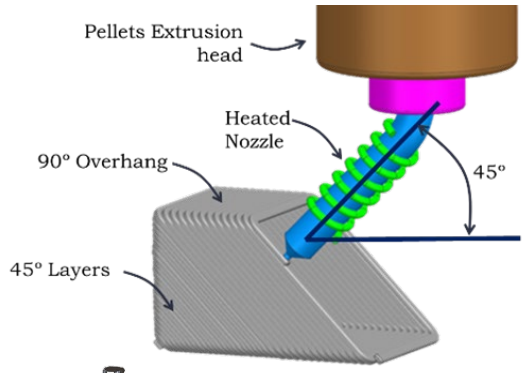

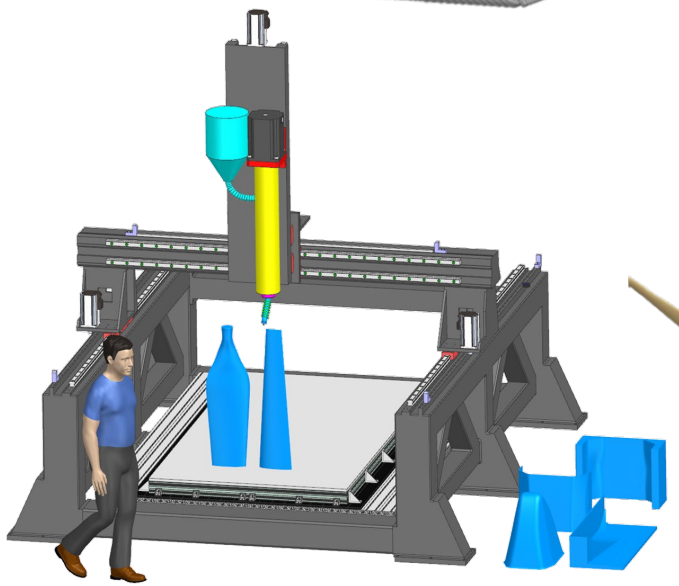

Applications

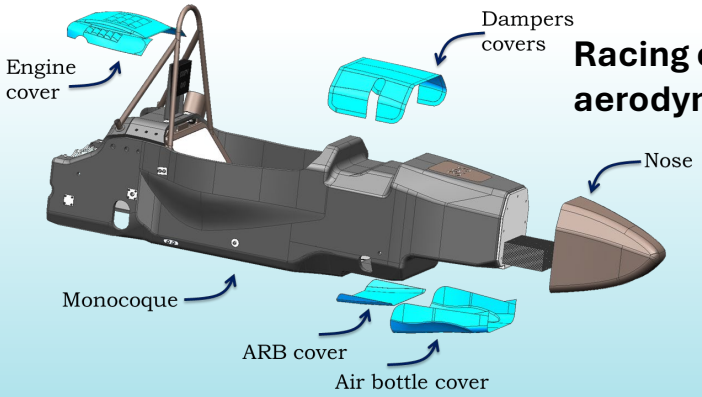

Racing car aerodynamics

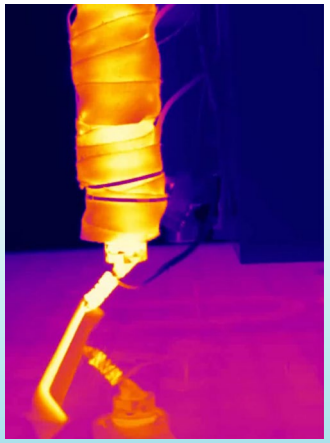

Wind turbine blade

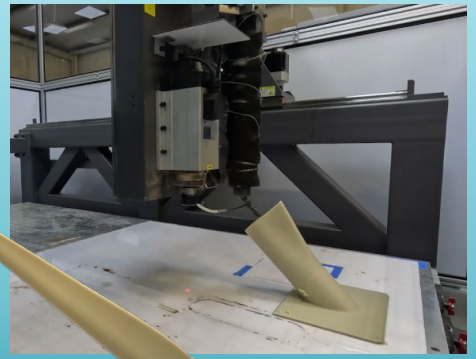



Aircraft spars

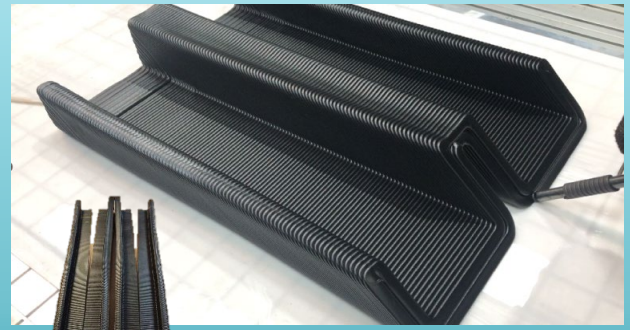



Warpage!!!

Interlayer adhesion study: Set-up

Parametric study: Set-up

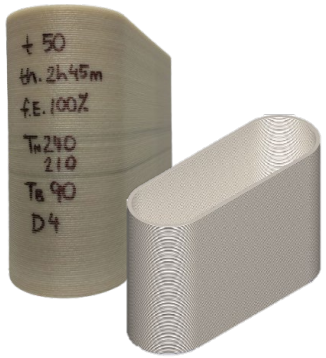

- Time per layer
- Nozzle temperature
- Extrusion factor

3 parameters ^3 variables
= 27 cases

➢ LFAM process: FGF

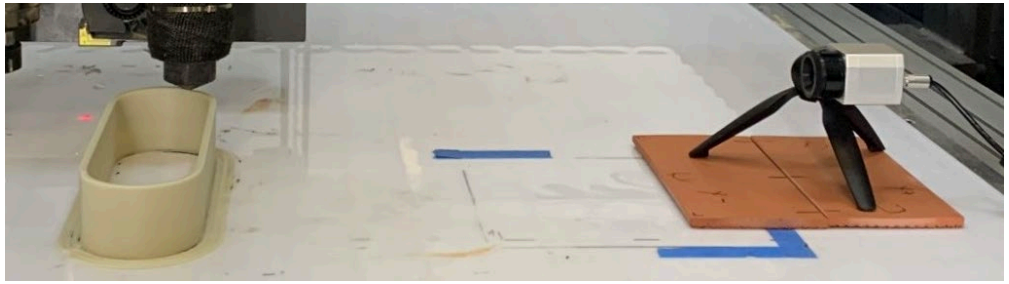

1 Thermal monitoring

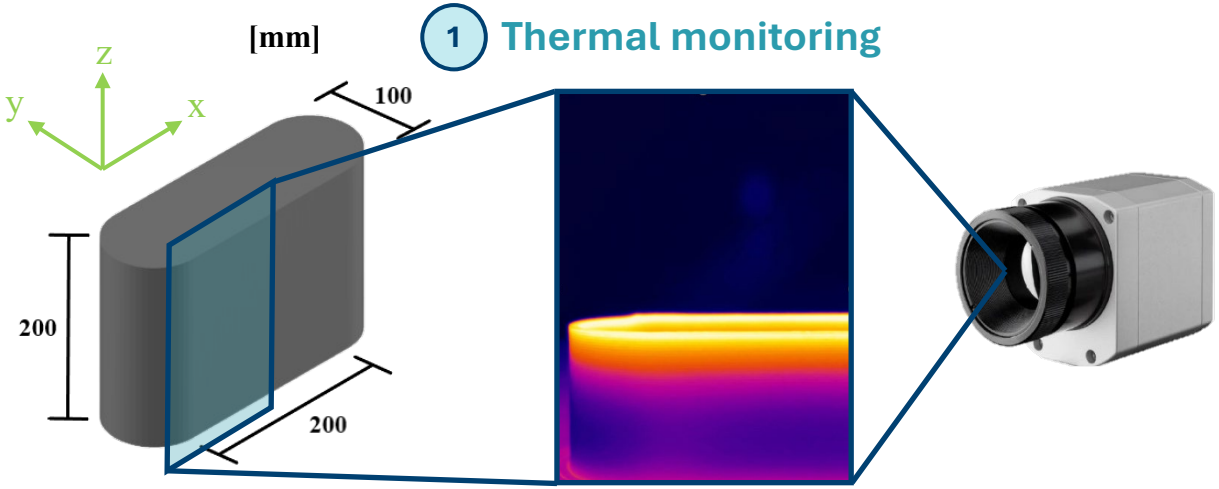

2 Tensile testing

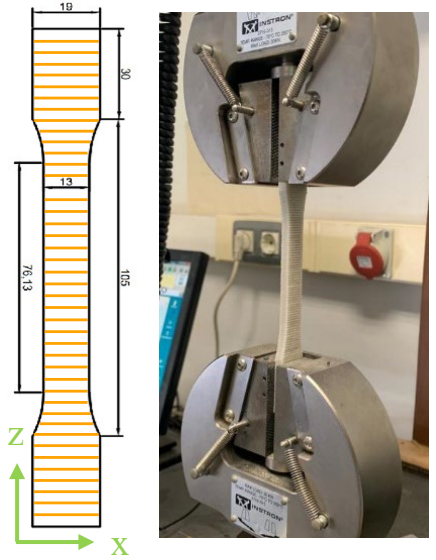

3 Microstructure observation

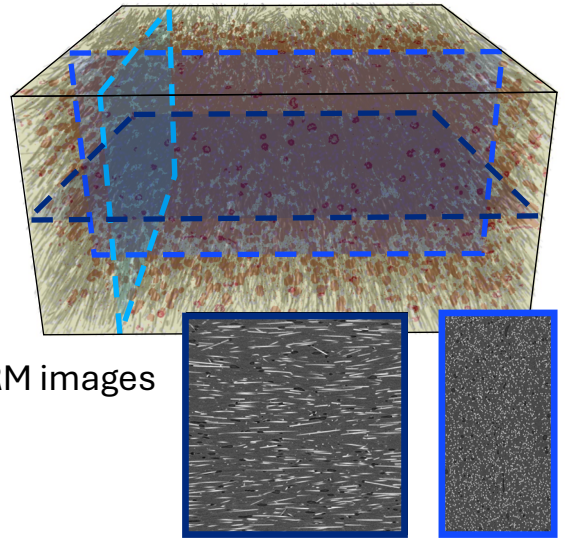

XRM images

Interlayer adhesion study: Results

Mechanical results

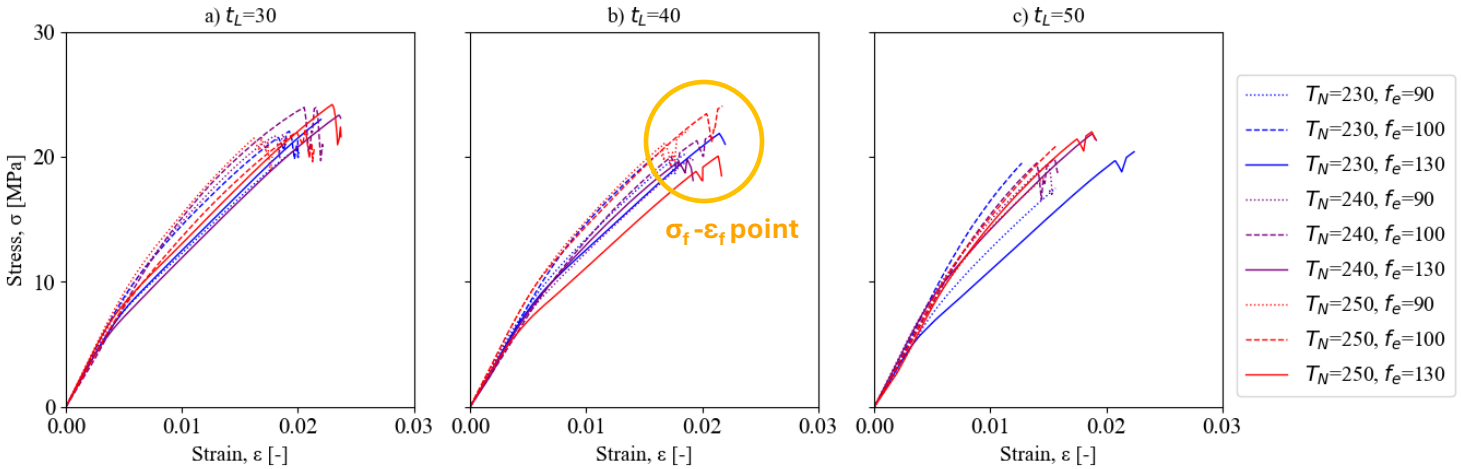

σ_f -ε_f fracture point

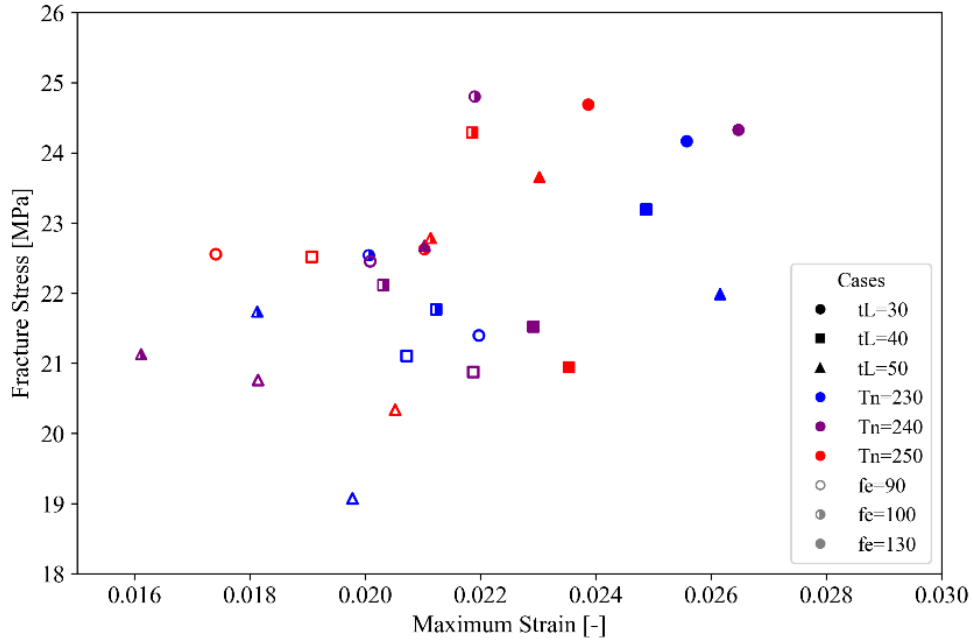

- **ANOVA** results: p-value per studied parameter

Parameter	t_L	T_N	f_e
σ_f (p-value)	**0.0193**	0.2872	**0.0140**
ε_f (p-value)	**0.0327**	0.3800	**0.0000**

➢ **t_L and f_e significatly influential**

Interlayer adhesion study: Results

Thermal results

Temperature evolution per layer along printing time

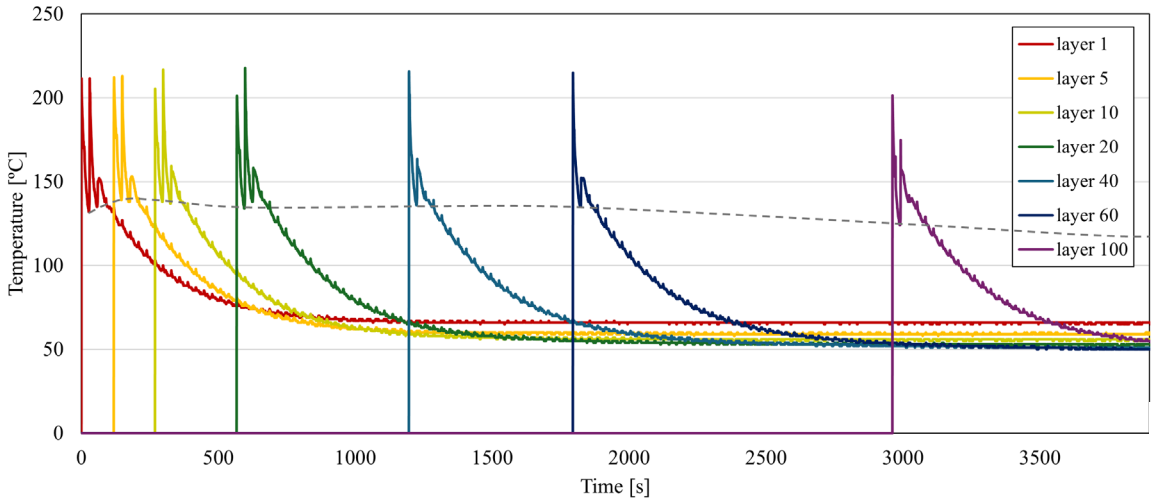

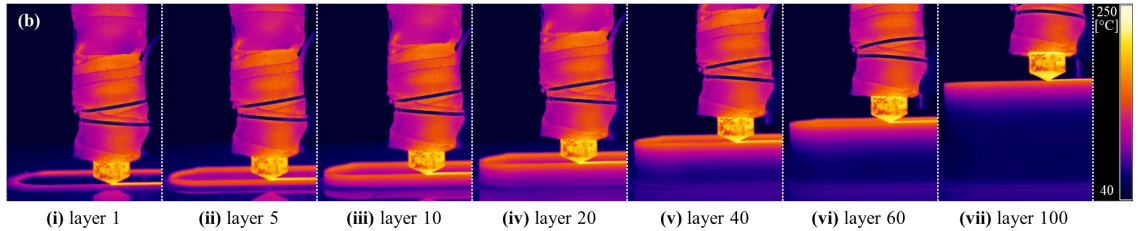

Top layer T evolution along the height of the structure

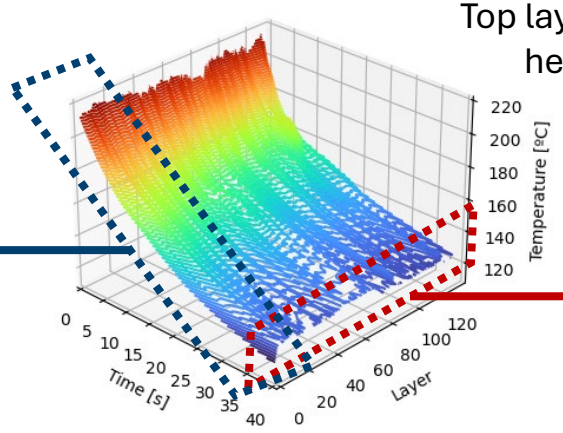

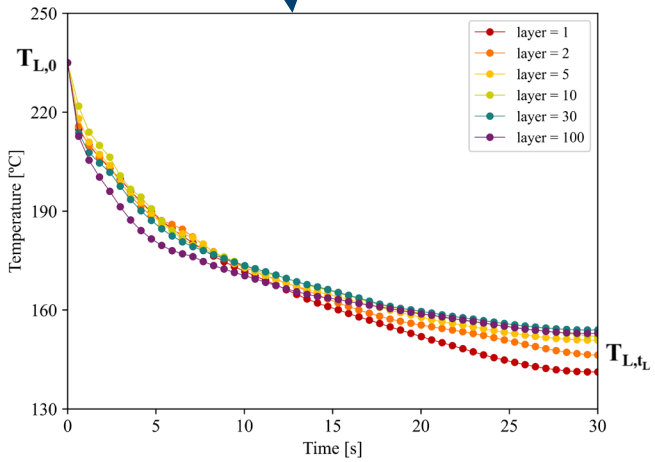

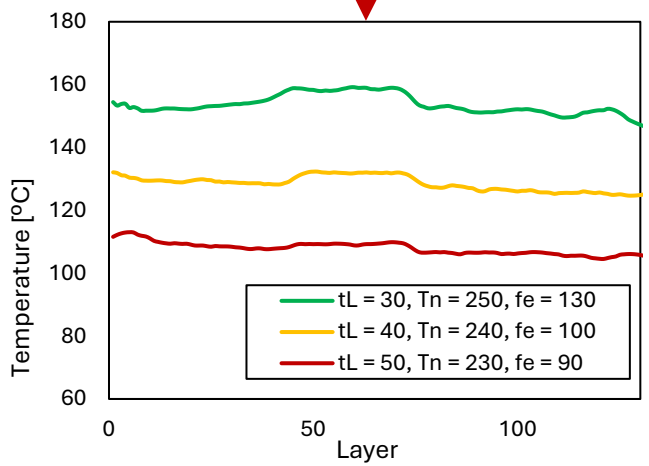

Objective

Real-time prediction with Reduced Order Models

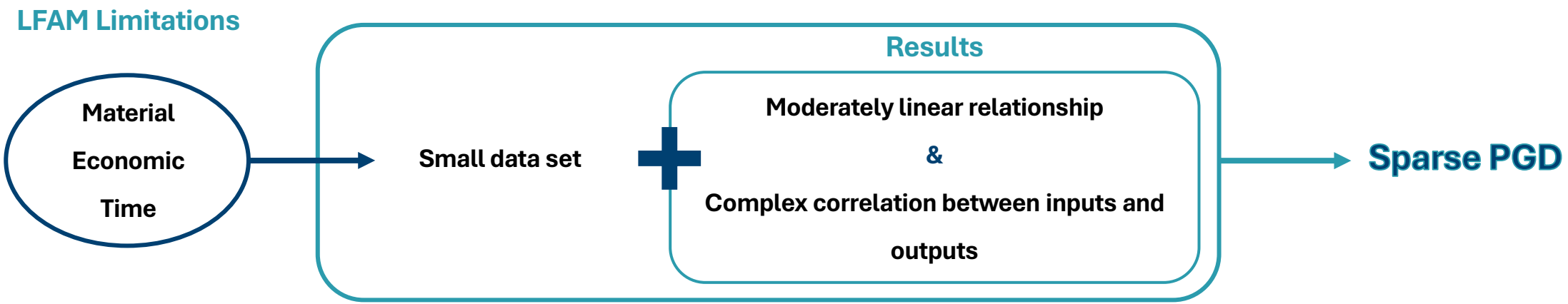

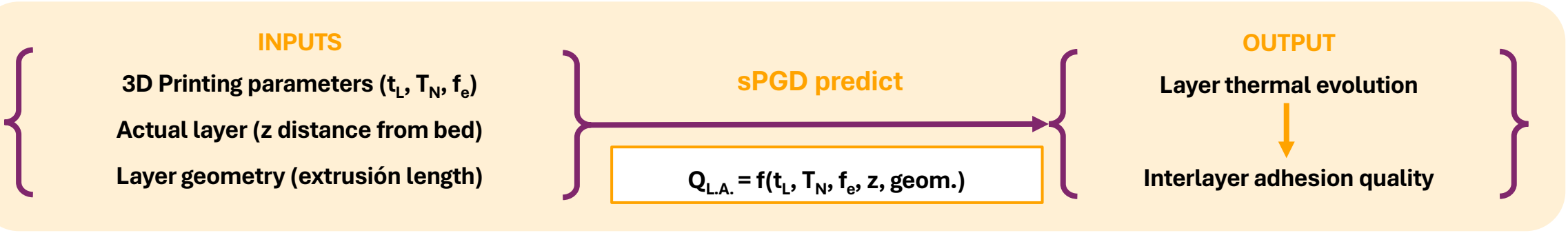

sPGD: Sparse Proper Generalized Decomposition

The Proper Generalized Decomposition (PGD) Method

$$f(v_1, v_2, \dots, v_n) \approx \sum_{k=1}^{m} X_1^k(v_1) X_2^k(v_2) \dots X_n^k(v_n)$$

Separated representation: $u(\vec{x}) \approx \sum_{k=1}^{m} \prod_{i=1}^{n} F_i^{(m)}(x_i)$

Solution in Space-Time: $u(x,t) \approx \sum_{k=1}^{m} X^{(m)}(x) \cdot T^{(m)}(t)$

Parametric PGD: $u(x,t,\mu) \approx \sum_{k=1}^{m} X^{(k)}(x) \cdot T^{(k)}(t) \cdot P^{(k)}(\mu)$

The Sparse (s)PGD for a 2D case

Minimization problem solved: $min \|u_m(v_1, v_2) - f(v_1, v_2)\|_2^2$

Known function: $f(v_1, v_2)$

PGD approximation: $u_m(v_1, v_2) = \sum_{k=1}^{m} X_1^k(v_1) X_2^k(v_2)$

PGD function construction for n-dimensions case:

$$X_n^k(v_n) = \sum_{j=1}^{n_{cp}} N_j^k(v_n) a_{v_n,j}^k = (N_{v_n}^k)^T a_{v_n}^k$$

PGD mode: *k*

Shape functions: $N_j^k(v_n)$ $a_{v_n,j}^k$

sPGD Application: Mechanical

Double sPGD: Stress – Strain curve prediction

Matrices required:

- 3 parameters: $\{t_L \ T_N \ f_e\}$
- 50 cases:

30	230	90
30	230	100
40	240	100
50	250	100
50	250	130

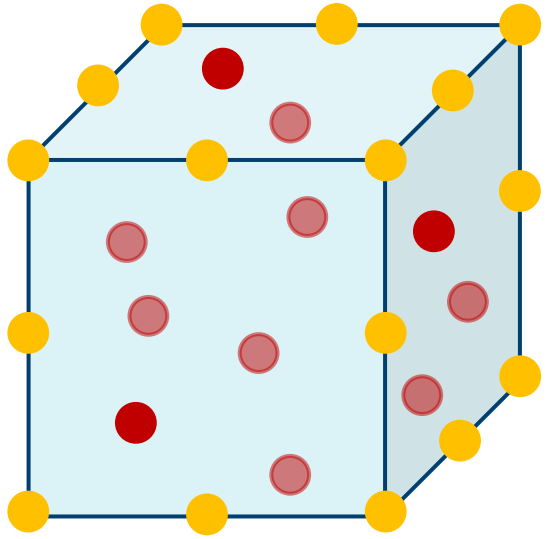

- Results: 50 x (~)300 stress-strain points

→ **Double sPGD needed**

Construction approach

1. **sPGD to predict stress**
   - Strain is normalized
   - Stress points interpolated
2. **sPGD to predict max. Strain**
   - Interpolate from the max. strain
3. **Combine predicted stress and strain**

DOE: structured data cases

Sparse: randomly distributed data

sPGD Application: Thermal

Single sPGD: Thermal evolution per layer prediction

Matrices required:

- 4 parameters: **{t_L T_N f_e} + {layer}**
- 50 cases:

30	**230**	**90**
30	**230**	**100**
40	**240**	**100**
50	**250**	**100**
50	**250**	**130**

× **133 layers**

- Results: T vs t_L → **Single sPGD needed**

Construction approach

sPGD to predict the termal evolution per layer

- Temperature vs time where t Є [0, tL]

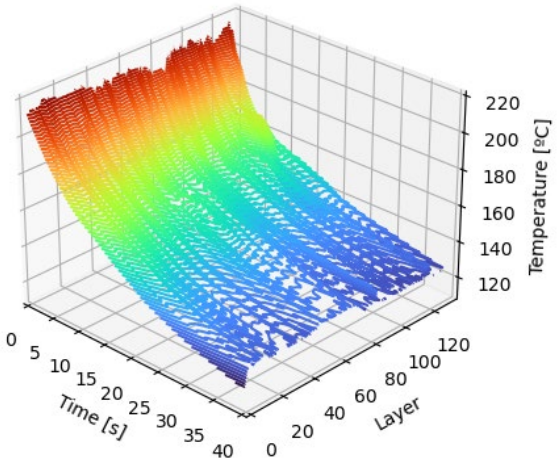

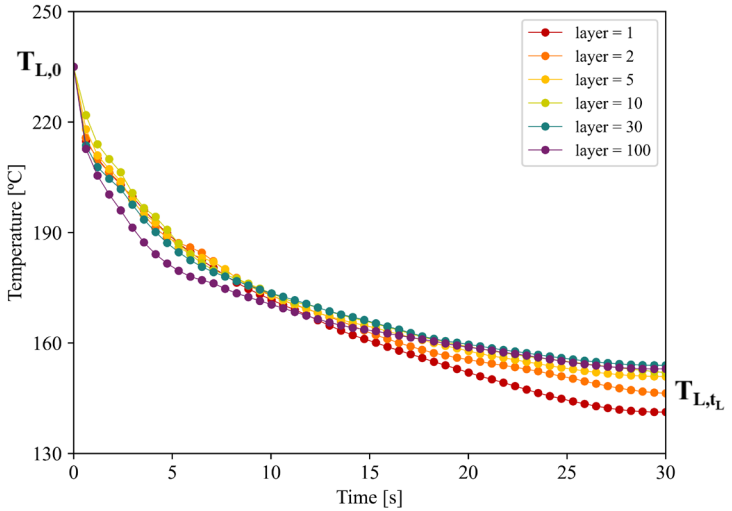

sPGD Results: Mechanical

Stress – strain curves prediction

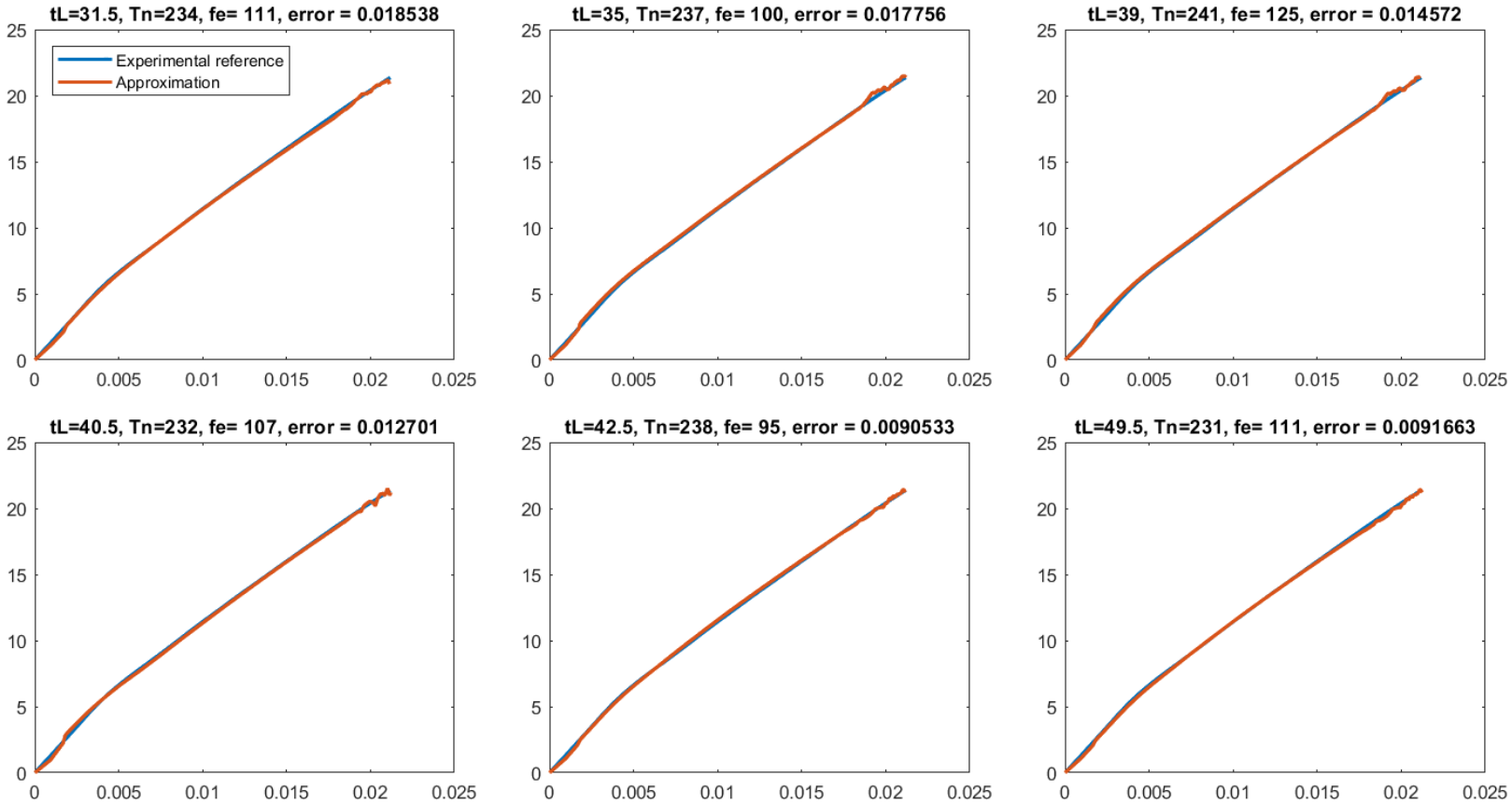

Note: Prior to sPGD application, noise removed by extrapolation of results from the lowest fracture point to the average.

- Shape functions: **Radial basis**
- Number of control points = **6**

Average error = 1.36%

sPGD Results: Thermal

Thermal evolution per layer curves prediction

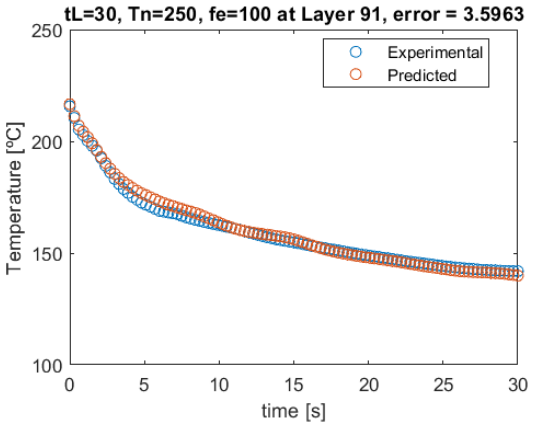

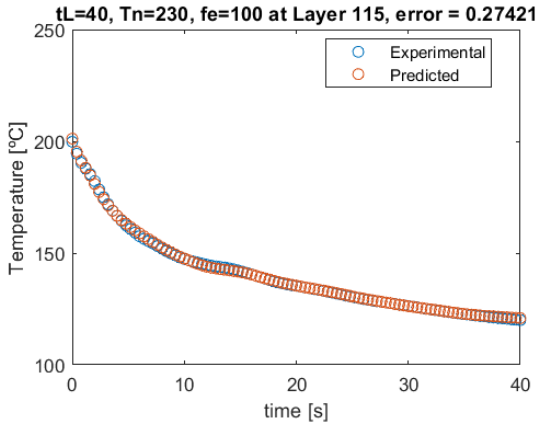

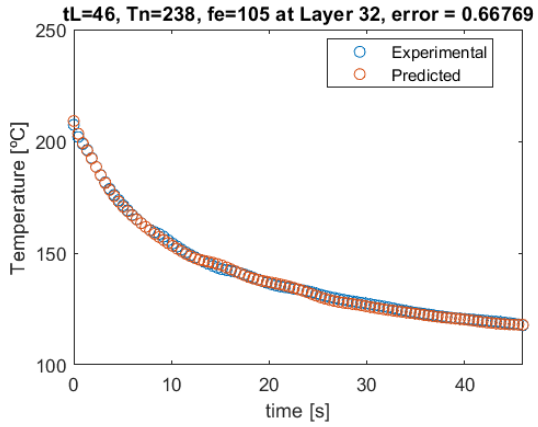

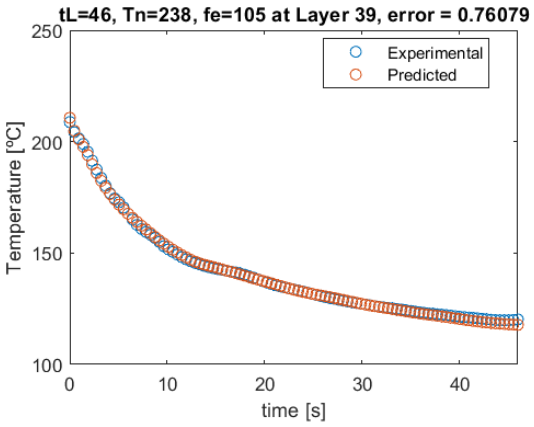

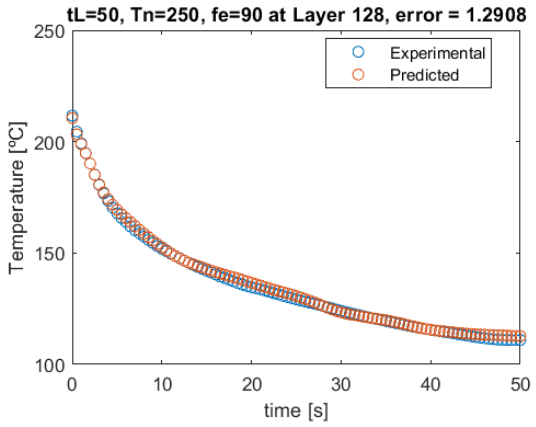

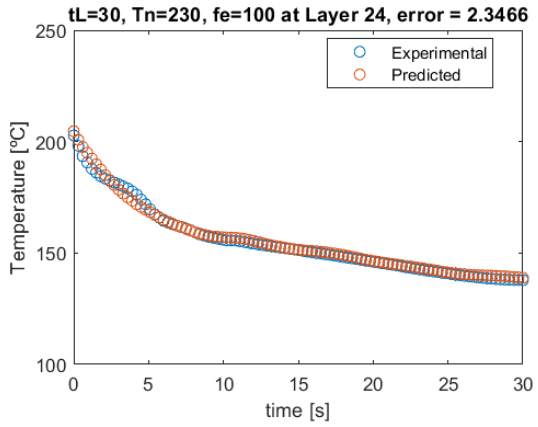

Note: Prior to sPGD application, termal data from the infrared data has been smoothened and cleaned to remove noise.

- Shape functions: **Radial basis**
- Number of control points = **12**

Average error = 4.96%

Conclusions

- Effective bonding between deposited layers in LFAM is achieved when the thermal gradient between adjacent layers is minimized.
- Adhesive strength is proven to be strongly correlated to termal evolution of layers.
- Interlayer adhesion quality is greatly influenced by the distance from the bed (layer number) and 3 printing parameters:
  - Time per layer
  - Nozzle temperature
  - Extrusion factor
- The reduced order model built using the Sparse PGD method predicts in real-time:
  - Stress-strain curves with an accuracy of 98.64%
  - Thermal evolution of layers with an accuracy of 95.04%
- Feeding the ROM with sparse data increases the prediction accuracy

Future work

- Feed the ROM with real-time data to optimise the interlayer adhesion at every single layer in LFAM
- Compare solution with other MOR and machine learning techniques

Model Order Reduction Methods for Real-Time Prediction of Thermomechanical Properties of Additively Manufactured Composite Materials



Thanks for listening!

Questions?

Contact: pabcaspe@idf.upv.es

UNIVERSITAT POLITÈCNICA DE VALÈNCIA
INSTITUTO DE DISEÑO Y FABRICACIÓN
Arts et Métiers Sciences et Technologies
Financiado por la Unión Europea NextGenerationEU
Plan de Recuperación, Transformación y Resiliencia

ICCM24
AUGUST 4-8, 2025
BALTIMORE CONVENTION CENTER
BALTIMORE, MARYLAND, USA

No Technical Paper Submission for:

Sabarinatham Palaniyappan

FEASIBILITY STUDY OF A 3D-PRINTED HONEYCOMB CORE STRUCTURE AS THERMAL VACUUM INSULATION FOR LIQUID HYDROGEN COMPOSITE PRESSURE VESSELS

A. Scherer [1], P. Heinke [2], M. Gross [3] and T. Dickhut [4]

[1]Institute Aeronautical Engineering, University of the Bundeswehr Munich
Werner-Heisenberg-Weg 39, 85579 Neubiberg
Email: andreas.scherer@unibw.de, web page: https://www.unibw.de/home-en

[2]Institute Aeronautical Engineering, University of the Bundeswehr Munich
Werner-Heisenberg-Weg 39, 85579 Neubiberg
Email: patrick.heinke@unibw.de, web page: https://www.unibw.de/home-en

[3]Institute Aeronautical Engineering, University of the Bundeswehr Munich
Werner-Heisenberg-Weg 39, 85579 Neubiberg
Email: markus.gross@unibw.de, web page: https://www.unibw.de/home-en

[4]Institute Aeronautical Engineering, University of the Bundeswehr Munich
Werner-Heisenberg-Weg 39, 85579 Neubiberg
Email: tobias.dickhut@unibw.de, web page: https://www.unibw.de/home-en

Keywords: CFRP Sandwich Structure, 3D Printed Honeycomb Core, Thermal Vacuum Insulation, Liquid Hydrogen Storage, Composite Pressure Vessel

ABSTRACT

Due to its approximately three times higher energy density by mass compared to conventional kerosene, hydrogen is one of the most promising technologies for reducing CO2 emissions in aviation. However, the energy density by volume is significantly lower than that of kerosene. For example, three thousand liters of gaseous hydrogen correspond only to the energy content of one liter of kerosene at ambient conditions (pressure, temperature). In the automotive sector, this problem is often solved by storing the gaseous hydrogen at a high pressure of 700 bar. Although this approach has already led to a significant improvement, it is still not sufficient for aircrafts, as weight and volume are particularly critical factors here. A further increase in energy density can only be achieved by cooling the hydrogen to 20 K (-253°C), where gaseous hydrogen turns into liquid hydrogen. At 20 K, four liters of liquid hydrogen correspond approximately to the energy density of one liter of kerosene. In order to maintain these cryogenic temperatures and minimize evaporation losses (boil-off), special requirements are placed on the cryogenic storage tanks and in particular on their insulation. Some of these cryogenic storage tanks consist of load-bearing double-wall concepts in which a vacuum ensures thermal insulation, which served as baseline for this study. The authors examined CFRP sandwich structures with 3D-printed honeycomb cores in terms of their manufacturability and their thermal insulation properties at cryogenic temperatures. 3D printing of the cores was chosen due to its advantages with respect to design freedom especially for curved structures such as tank domes but also due to its possibility of local reinforcement in areas of load introduction by means of adjustable cell density and cell wall thicknesses, anti-telegraphing design elements etc. [1]. A further advantage is the possibility to use materials with low outgassing behavior e.g. PEEK [2].

1 INTRODUCTION

The shift toward zero-emission aviation demanded innovative solutions for onboard energy storage and structural integration. Liquid hydrogen (LH_2) offered high energy density but required cryogenic

containment, which posed significant challenges for lightweight aircraft structures. This study was conducted within the framework of the CryoFuselage project, which focused on the development of insulated LH_2 tanks made from CFRP. A key objective was the integration of such tanks into load-bearing fuselage structures to enable multifunctionality and weight savings.

As a representative application case, a regional turboprop aircraft was used as an example in which a cylindrical LH_2 tank was integrated into the aft fuselage (see **Fig. 1**). Therefore, a load-bearing evacuated core concept with 3D-printed cores was chosen for the thermal insulation layer.

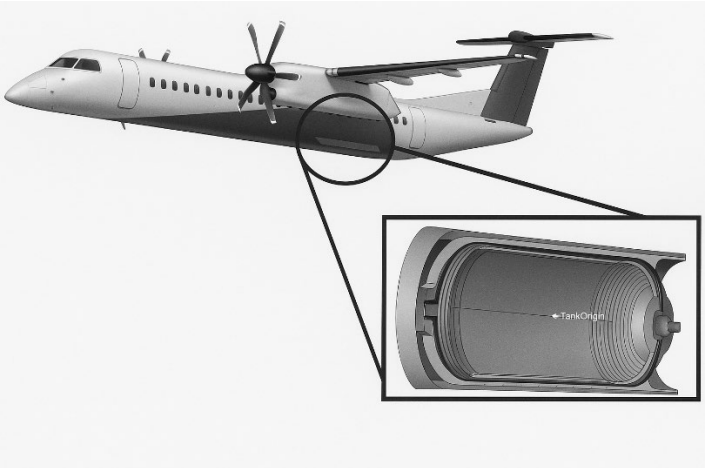

Figure 1: Schematic view of LH_2 tank in fuselage aft section

2 STATE OF THE ART: THERMAL INSULATION FOR CRYOGENIC HYDROGEN TANKS

2.1 Foam Insulation

Closed-cell foams (e.g., PU, PIR) are widely used due to ease of application and low cost. However, performance deteriorates under cryogenic conditions, and long-term dimensional stability is limited. Polyurethane (PU), polyisocyanurate (PIR), or PMI foams (e.g., ROHACELL) are established as closed-cell insulators. Their typical thermal conductivity is between 20–100 K [3-5]. They have been used, for example, in the Lockheed CL-400 [3] and in Space Shuttle tanks as spray-on foam insulation [4-5]. Oehlke [6] validates them for smaller aircraft tanks for an ATR 72, while Swanger and Fesmire [10] document mechanical and thermal aging under cryogenic cycling.

- Advantages: inexpensive, low density, simple application, load-bearing for small tank [6]
- Disadvantages: shrinkage, cracking, delamination under cycling [5-7]

2.2 Multilayer Insulation (MLI)

MLI uses alternating reflective and spacer layers and performs best under vacuum. It is highly effective against radiative heat transfer but fragile. MLI performance relies on maintaining a high vacuum and preserving separation between its reflective layers. Compression, crimping, or misalignment can collapse the insulating gaps, drastically increasing thermal conductivity. MLI cannot carry mechanical loads and must be decoupled from structural stress paths. This limits its integration in tank systems exposed to fuselage loads or direct mounting via Y-joints. Handling damage, installation variability, and lack of load-sharing capacity are key constraints. MLI systems consisting of reflective films and spacers can achieve <1 mW/m·K under high vacuum ($<10^{-3}$ Pa) [4], [6], [8]. Widely used in space applications [3], [8], they are not structurally load-bearing. Johnson [8] describes performance variability depending on the number of layers, compression, and penetrations. Swanger [4] points out outgassing and compression issues. Oehlke [6] documents a drastic increase in thermal conductivity in case of vacuum loss (×100–2000).

- Advantages: lowest thermal conductivity, very lightweight
- Disadvantages: sensitive to compression/folding, not load-bearing, high vacuum requirement [4], [6], [8]

Extensions: VDMLI and VCS
To address the limitations of classical MLI, advancements such as Variable Density MLI (VDMLI) and Vapor Cooled Shields (VCS) have been developed. Zheng et al. compare four insulation systems (MLI, MLI+VCS, VDMLI, VDMLI+VCS) and show that the combination VDMLI+VCS is thermally the most effective [9]. Wang et al. model hybrid concepts with HGM and MLI [10].

- Advantages: reduced thermal conductivity, targeted thermal optimization
- Disadvantages: not load-bearing, complex integration, vacuum still required [9], [10]

2.3 Perlite, Aerogels, HGM, Fiber-Based Insulators

Powder, granular, and fiber-based fillers (perlite, aerogel, hollow glass microspheres, glass wool) combine moderate insulation performance (10–50 mW/m·K) with more robust structure [4-5], [10-11]. Swanger [4] and Wilken [11] demonstrate stability under vacuum loss, though with higher weight. Modeling studies by Wang et al. [10] show advantages through variable density combinations.

- Advantages: robust, moderate performance, partially reusable
- Disadvantages: heavier than MLI, less geometric flexibility [4], [10-11]

2.4 Double-Wall Vacuum Insulation

Vacuum insulation uses a sealed, evacuated gap between tank walls to minimize convective and conductive heat transfer. It offers high insulation performance and can be combined with reflective coatings. A proven space architecture with an evacuated interspace. Applications include Space Shuttle ET, Delta IV, and X-33 [3], [7], [12]. Thermally efficient (<1 mW/m·K) but heavy and complex to assemble. Brewer [3] and Adler [7] describe the advantages; Johnson [12] emphasizes integration complexity.

- Advantages: high efficiency, optionally combinable with MLI [3], [7], [12]
- Disadvantages: double-wall structure, weight, complex around dome geometries [7], [12]

2.5 Evacuated Structural Sandwich Core

Sandwich structures with an evacuable cell core (e.g., perforated honeycomb) combine structural and insulation functions. The concept was introduced by Northrop Grumman in the NASA CCTD [12]; further developments in European studies (PHOEBUS, ICARUS) [13], Brewer [3] mentions early structural honeycomb approaches.

- Advantages: insulation & structure, low thermal conductivity, integrative
- Disadvantages: vacuum tightness, manufacturing complexity [3], [12-13]

3 DESIGN AND MANUFACTURING

3.1 Concept Rationale

As a thermal insulation solution, this work adopts the concept of vacuum insulation based on the Evacuated Core principle [12-13]. This approach is characterized by good thermal performance at cryogenic temperatures and the ability to structurally integrate the insulation into load-bearing components. As described in Section 2.5, this involves e.g. embedding perforated honeycomb cores into a sandwich structure and subsequently evacuating the internal cavity. Standard methods use pointwise needle-perforated or slotted Nomex honeycomb cores to ensure uniform pressure distribution and enable

outgassing. However, conventional approaches are associated with several drawbacks:

- Perforation displaces cell wall material locally, which can lead to unstable membrane regions during evacuation. These areas may deform under vacuum, a phenomenon which can be described informally as “flap effect.”
- Slotted cores exhibit reduced mechanical integrity, particularly at the interface with the face sheets, as both the continuous bonding surface and the cellular structure are interrupted.
- Traditional honeycomb structures are optimized for planar or single curved surfaces. When applied to double curved geometries (e.g., spherical domes), they suffer from the so-called saddle effect: the hexagonal cells twist or collapse due to forced adaptation, leading to geometric distortion and a significant reduction in mechanical properties [1]

3.2 Core Design

As part of the concept validation for a vacuum-insulated sandwich insulation system, an innovative approach using a 3D-printed, perforated honeycomb core was selected. This core architecture combines load-bearing capacity and thermal insulation within a single functional element. The required venting perforations are directly integrated during the additive manufacturing process, as illustrated in **Fig.2**.

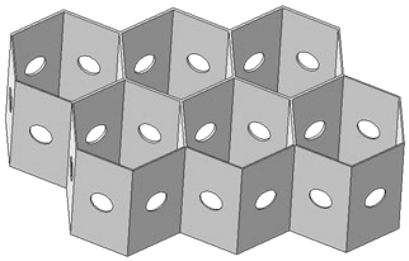

Figure 2: Perforated honeycomb

Key advantages of the 3D-printed design include design flexibility, the use of materials with low thermal conductivity and minimal outgassing (e.g., PEEK/GF), and the potential for functional integration, such as localized reinforcements or anti-telegraphing and snap-in coupling features, as shown in Fig. 3.

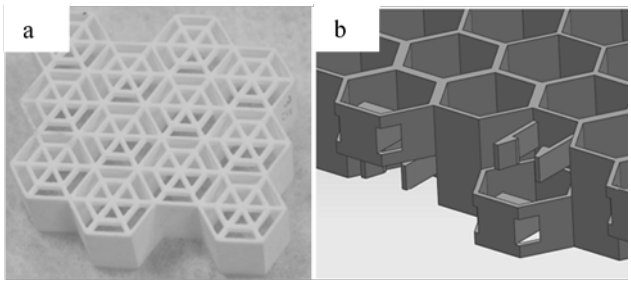

Figure 3: (a) anti-telegraphing solution; (b) honeycomb with snap-in connections [1]

However, challenges remain regarding the limited industrial maturity of the materials and processes involved, as well as the process-dependent variability in mechanical properties. One key challenge is to ensure that the materials withstand the temperature and pressure conditions of the autoclave process. The HT-PLA used in initial trials, with a heat deflection temperature (HDT) of 180 °C, proved unsuitable for autoclave curing at 130°C and an autoclave pressure of 2 bar. In contrast, the fabrication of a small sandwich panel using a 3D-printed PEEK/GF honeycomb with anti-telegraphing solution (spider-web) structure was successful. The printing was carried out on a high-performance polymer printer (INTAMSYS 410 Pro) acquired in 2024. **Fig. 4** shows both small sandwich panels, the collapsed HT-

PLA and the PEEK/GF.

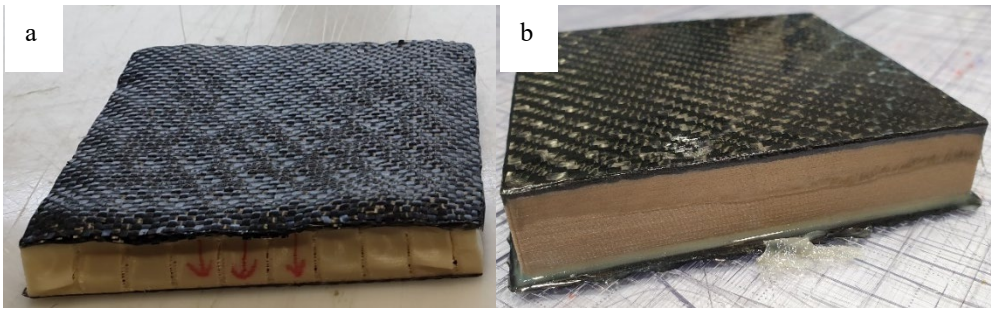

Figure 4: Autoclave process 130°C/2 bar: (a) collapsed honeycomb core with HT-PLA (HDT = 180 °C) - 2022; (b) intact honeycomb core with PEEK/GF (HDT = 300 °C) - 2024

3.3 Vacuum Panel Manufacturing

Due to printer limitations with respect to material and building space, four honeycomb core segments (each 187.6 mm × 144.3 mm × 20 mm) were printed and subsequently bonded together with a paste adhesive to form the full-size core tested in the vacuum insulation test. Future designs will consider the use of snap-in connectors, as illustrated in **Fig. 5**. Both CFRP face sheets for the sandwich panel were manufactured from four layers, each with a thickness of 0.25 mm, of a 2x2 twill weave fabric with 0/90 orientation and cured separately and bonded to the full-size core in a second step, since the originally used thermoplastic (HT-PLA) for early stages proved to be inadequate under the thermal and pressure conditions of the autoclave process, as described above. The four core segments during the bonding process, as well as the completed vacuum sandwich panel with a final format of approximately 292 mm × 378 mm, are shown in **Fig. 5**. The thickness from the top to bottom facesheet of the panel is 22 mm.

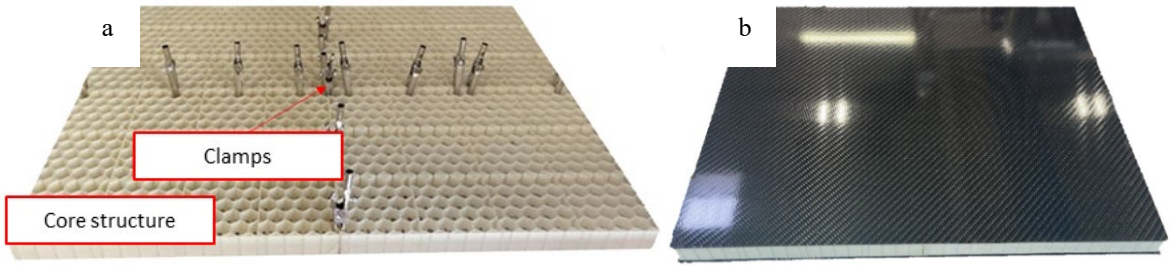

Figure 5: (a) Bonding process of four core segments; (b) final vacuum sandwich panel

4 TESTING METHODOLOGY AND EXPERIMENTAL SETUP

4.1 Test Methodology

The objective of this experiment was to qualitatively assess the thermal insulation performance of a vacuum sandwich panel incorporating a 3D-printed evacuable honeycomb core under cryogenic boundary conditions, and to investigate the impact of vacuum loss on thermal behavior. To achieve this, the test was structured into four consecutive load cases, each representing a distinct system state. The load cases are summarized in **Table 1**, along with relevant remarks regarding the temperature measurement approach:

Load Case	LC Description	Remarks on temperature measurement
LC 0	Calibration of thermocouples	with ice water / not displayed
LC 1	Evacuation of sandwich core at RT	with vacuum insulation
LC 2	Filling LN_2 / Thermal Equilibrium	with vacuum insulation
LC 3	Active venting of sandwich core / simulation of vacuum failure	without vacuum insulation

Table 1: Thermal Vacuum Insulation Test – Load Cases

4.2 Experimental Setup

Test Sample Configuration

To perform the vacuum insulation test, a dedicated test setup was constructed. For this purpose, a container was built made of four structural foam plates and afterwards bonded to the top CFRP facesheet of the composite sandwich panel with a paste adhesive to form a basin to hold LN_2 to expose the top CFRP facesheet to cryogenic temperatures. Vacuum and pressure ports were integrated in the bottom CFRP facesheet. which can be seen in **Fig. 6.**

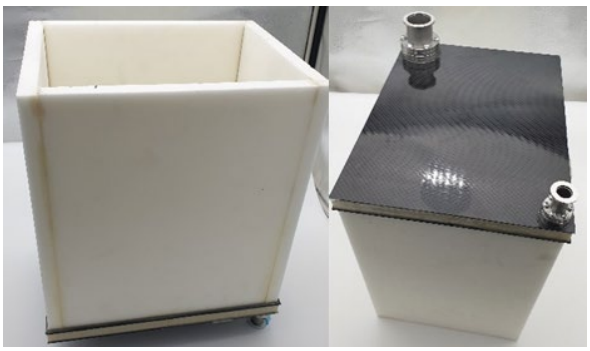

Figure 6: LN_2 foam basin and sandwich plate with ports

The principle test scheme, the temperature couples and placement of ports is given in Fig. 7.

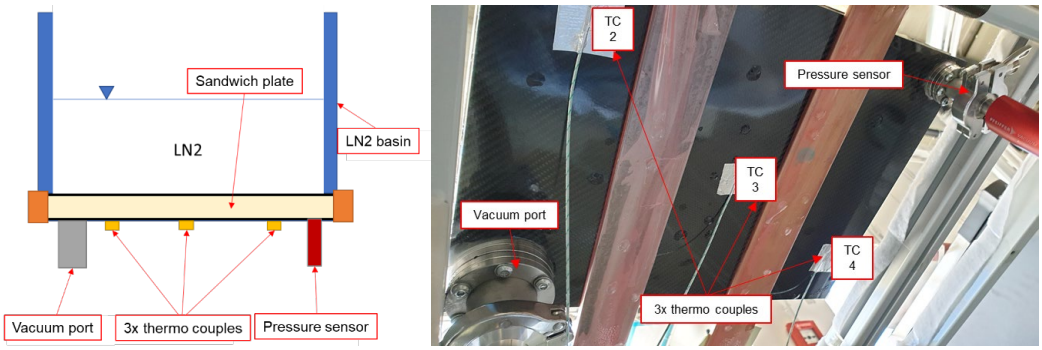

Figure 7: Thermal Vacuum Insulation Test – Test Setup

Temperature Measurement System

Temperature measurement was carried out using in total four thermocouples:

- TC1: ambient reference temperature, in 2m distance to test sample
- TC2 and TC4: located at the left and right edges of the bottom CFRP facesheet,
- TC3: located at the geometric center of the bottom CFRP facesheet.

with the following configuration:

- Sensor type: Thermocouple DT/G-TypK-2.0, Ø 2.0 mm
  - Nominal temperature range: −200 °C to +1100 °C
  - Calibration: Performed in an ice–water bath prior to testing (LC0)
  - Measurement limitation: Signal range limited to –55 °C due to DAQ configuration
- Data Acquisition System
  - Manufacturer: Gantner Instruments
  - Module type: Q.Brixx
  - Sampling & logging: via Gantner Q.station controller/Mlab software; post-processing MATLAB

Vacuum System

Evacuation of the sandwich core was performed using the following configuration:

- Pump type: Pfeiffer Duo 20M rotary vane pump
  - Nominal pumping speed: 21 m^3/h
  - Ultimate pressure (w/ gas ballast): ~1×10^{-2} mbar

In the present test setup, the pump was connected to a CF40 port located at the bottom CFRP facesheet of the sandwich panel while the pressure sensor was connected to a CF16 port.

5 RESULTS AND DISCUSSION

Before the start of the experiment, all thermocouples were calibrated using ice water, and accurate temperature readings were confirmed by comparison with the ambient hall thermometer. During the measurement, a fourth thermocouple (TC1) served as a reference for monitoring the ambient hall temperature. The temperature–time evolution recorded during the vacuum insulation experiment is shown in Figure 3. Temperature areas above 0°C are shown in light red, while temperature areas below 0°C are shown in light blue. The duration of the different load cases is separated by black vertical lines.

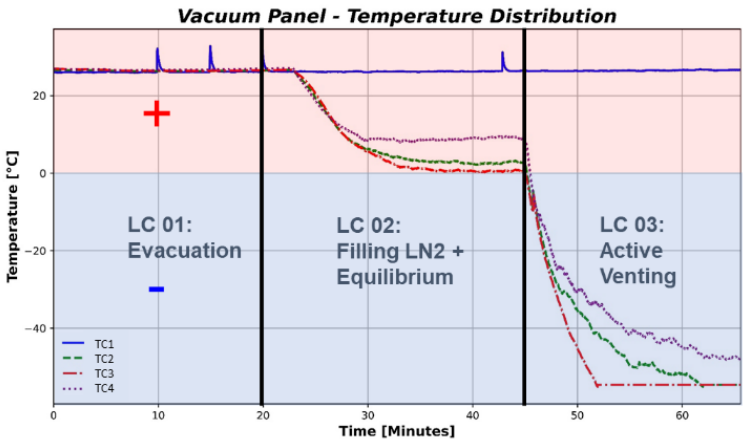

Figure 8: Thermal Vacuum Insulation Test – Temperature Measurement Results

Within the first 20 minutes of the test, during LC1, the sandwich panel was evacuated at room temperature condition and a steady pressure level of 1.7 mbar was reached in the panel. No significant

change in panel temperature was observed during this phase, confirming that no relevant thermal flux occurred prior to LN_2 filling and that all sensors operated correctly. Afterwards the vacuum pump was shut off.

During load case LC2, liquid nitrogen (LN_2) was filled in the LN_2 basin, leading to a rapid decrease in temperature at the bottom CFRP facesheet, as heat was conducted through the panel toward the fluid-sided top CFRP facesheet (−196 °C). After approximately 20 minutes, a quasi-steady thermal gradient was reached, characterized by the horizontal lines of temperature measurements of TC2-TC4. and approximately 0 °C, as recorded by TC3 at the bottom facesheet. For the single thermocouples the following temperatures were measured

- TC3 (center): 0.5 °C
- TC2 (left edge): 2.4 °C
- TC4 (right edge): 9.3 °C

This clear temperature difference between the fluid-sided top CFRP facesheet and the ambient-facing bottom CFRP facesheet indicates the panel's effective thermal insulation under vacuum condition. Slight asymmetries between TC2 and TC4 are attributed to edge effects. The pressure in the core dropped further to 0.86 mbar.

In load case LC3, active ventilation of the honeycomb core was initiated to ambient pressure condition. As a result, all three thermocouples (TC2–TV4) on the bottom face sheet exhibited an immediate and pronounced further decrease in temperature. Due to the signal range limitation in the DAQ setting (−55 °C), the lower threshold of measurement was quickly exceeded, leading to a loss of valid data below that limit.

- TC3 (center): –55.0 °C, within 9 minutes after loss of vacuum
- TC2 (left edge): –55.0 °C within 17 minutes after loss of vacuum
- TC4 (right edge): –48.2 °C by the end of LC3

In addition to the thermal measurements, visual observations revealed significant frost formation on the lower surface of the specimen, as shown in **Fig. 9** during LC3. This frost accumulation is attributed to the condensation and subsequent freezing of atmospheric moisture, driven by the steep thermal gradient across the face sheet during actively induced vacuum loss

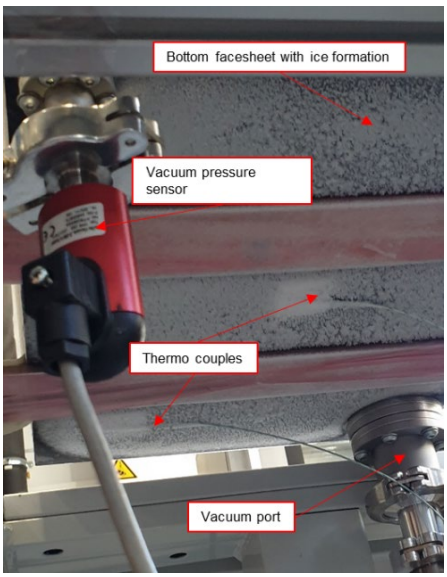

Figure 9: Thermal Vacuum Insulation Test – LC3: Frosting of bottom face sheet

The experiment confirms the proof-of-concept for a 3D-printed, evacuated honeycomb core as an integrated thermal insulation layer for cryogenic applications. Under vacuum conditions, the sandwich structure maintained a thermal gradient of nearly 200 K across a panel thickness of just 22 mm, with only minimal heat flux through the core. These results highlight the effectiveness of vacuum sandwich panels with 3D-printed evacuable cores in suppressing thermal conduction and enabling stable cryogenic temperature separation, although the sample configuration with HT-PLA as early test was not ideal. The steady-state pressure inside the core during Load Case 1 reached 1.7 mbar, which was higher than the nominal ultimate pressure of the vacuum pump. This deviation is attributed to internal outgassing from the polymer structure, in particular moisture and volatile components in the HT-PLA material, as well as anticipated minor line losses due to reduction in cross-section of the vacuum piping. The sandwich core was not pre-conditioned (e.g. by thermal bakeout), which further explains the elevated residual pressure despite continuous evacuation. In contrast, the rapid temperature decrease observed in Load Case 3, following intentional, active venting of the sandwich core, revealed the concept's sensitivity to vacuum integrity. Once the vacuum was lost, the insulation effect deteriorated within minutes, leading to a nearly uniform cryogenic transition on the ambient-facing side of the panel. This clearly illustrates the binary behavior of vacuum-based insulation systems and their dependence on stable pressure containment. Overall, the findings demonstrate that 3D-printed vacuum sandwich systems offer substantial insulation potential for use in cryogenic composite pressure vessels, as long as long-term vacuum sealing, structural robustness, and environmental durability can be ensured. While the insulation performance under vacuum was excellent, the observed failure mode highlights a key design constraint for aerospace implementation

6 CONCLUSIONS AND FUTURE WORK

The proposed vacuum-insulated CFRP sandwich panel with 3D-printed, evacuable honeycomb core was successfully tested. Results show that such structures can offer both high insulation performance and structural function, making them interesting for aerospace hydrogen tanks. Compared to foam or MLI, this concept offers superior integration potential, especially where tanks must carry load and interface with airframe structures, such as in fuselage integrated LH_2 tanks. The feasibility study successfully demonstrated the potential of a 3D-printed evacuable honeycomb vacuum core in a CFRP sandwich structure as cryogenic thermal insulation. The panel exhibited promising thermal resistance under vacuum and cryogenic temperatures. Compared to foam or MLI, the proposed system offers the unique ability to integrate insulation and mechanical function. This multifunctionality has high potential for aerospace LH_2 tanks subjected to both internal pressure and structural mounting in the airframe. Notable advantages include the design freedom for single and double-curved structures, the ability for local cell size refinement in areas with high structural demands, and the low outgassing behavior when using PEEK honeycombs. Main drawbacks are linked to loss of vacuum for such structures as intentionally induced in the LC3 load case, which is, however, a known challenge also for double-walled tanks with MLI. Additionally, the wall thickness is currently higher than that of conventional NOMEX honeycombs, negatively impacting mass efficiency. Furthermore, the component size is limited by the 3D printing hardware, necessitating segmentation for medium and large-scale structures. The material cost, especially when using PEEK, is also considerable. Nevertheless, the results provide a solid foundation for further investigations.

Therefore, the next steps will involve several focused investigations and development activities on flat samples for the 3D printed core and composite sandwich structure such as additional mechanical tests to evaluate flatwise tensile, compression and shear properties at room and cryogenic temperatures and under thermal cycling conditions. The work will also include investigations on wall thickness reduction methods and hence weight reduction and the manufacturing of single and double curved samples as well as small-scale CFRP technology demonstrator tanks. These will be used to simulate operational conditions and to verify both structural integrity and thermal behavior under realistic scenarios. In parallel, full thermal analyses will be performed.

ACKNOWLEDGEMENTS

The authors gratefully acknowledge the support and technical guidance provided by the German Aerospace Center (DLR) during the CRYOFUSELAGE project. Project funding was provided by the Bavarian Ministry of Economic Affairs, Regional Development and Energy (StMWi) under project number LABAY108B.

REFERENCES

[1] F. Riß, J. Schilp und G. Reinhart, Load-dependent optimization of honeycombs for sandwich components – New possibilities by using additive layer manufacturing, Phys. Procedia, Bd. 56, 2014, S. 327–335 (doi: 10.1016/j.phpro.2014.08.178).

[2] P. Chiggiato, Outgassing properties of vacuum materials for particle accelerators, in: *Proceedings of the CERN Accelerator School: Vacuum for Particle Accelerators*, Glumslöv, Schweden, 6.–16. Juni 2017, CERN Yellow Reports: School Proceedings, CERN-2021-001 (doi: 10.23730/CYRSP-2021-001), S. 1–47.

[3] G. D. Brewer, *Hydrogen Aircraft Technology*, CRC Press, Boca Raton, FL, USA, 1991.

[4] A. Swanger und J. E. Fesmire, Advanced Cryogenic Insulation Systems, in: *Proceedings of the 25th IIR International Congress of Refrigeration*, Montreal, Kanada, 24.–30. August 2019, Paper 1732 (DOI: 10.18462/iir.icr.2019.1732).

[5] T. F. Johnson, E. S. Weiser und P. G. Duong, Cryogenic insulation bondline studies for reusable launch vehicles, in: *Proceedings of the Space Technologies and Applications International Forum (STAIF)*, Albuquerque, NM, USA, 1999, NASA Langley Research Center, Bericht Nr. NASA/TM-1999-209560

[6] M. Oehlke, *Masseabschätzung eines Wasserstoff-Außentanks für ein Turboprop-Verkehrsflugzeug*, HAW Hamburg, 2009.

[7] E. Adler und J. R. R. A. Martins, Hydrogen-powered aircraft: Key technologies and environmental impacts, Progress in Aerospace Sciences, Bd. 141, 2023 (doi:10.1016/j.paerosci.2023.100922).

[8] W. L. Johnson, *Multilayer Insulation for In-Space Cryogenic Applications*, NASA Glenn Research Center, 2015.

[9] Y. Zheng, D. Zhang, H. Zhang und H. Chen, Thermodynamic analysis and comparison of four insulation schemes for LH_2 tanks, International Journal of Hydrogen Energy, Bd. 44, 2019, S. 15332–15341 (doi:10.1016/j.enconman.2019.02.073).

[10] P. Wang, L. Ji, J. Yuan, Z. An, K. Yan und J. Zhang, Modeling and optimization of composite thermal insulation system with HGMs and VDMLI for liquid hydrogen on-orbit storage, International Journal of Hydrogen Energy, Bd. 45, 2020, S. 7088–7097 (doi: 10.1016/j.ijhydene.2019.12.110).

[11] J. Wilken, S. Callsen, D. Daub, A. Fischer, M. Liebisch, C. Rauh, T. Reimer, H. Scheufler und M. Sippel, Combined cryogenic insulation and thermal protection systems for reusable stages, in: *Proceedings of the 9th European Conference for Aerospace Sciences (EUCASS)*, Lille, Frankreich, 3.–7. Juli 2022 (doi: 10.13009/EUCASS2022-4729).

[12] T. F. Johnson, D. W. Sleight und R. A. Martin, Structures and Design Phase I Summary for the NASA Composite Cryotank Technology Demonstration Project, in: *Proceedings of SAMPE 2012 Conference*, Baltimore, MD, USA, 21.–24. Mai 2012.

[13] M. Wolff, B. Höck und M. Quadt, Multi-scale development of CFRP pressure vessels for liquid hydrogen applications, in: *Proceedings of the 23rd International Conference on Composite Materials (ICCM23)*, Belfast, UK, 30. Juli – 4. August 2023.

EFFECTS OF 3D PRINTING ORIENTATION AND INFILL PATTERNS ON THE IMPACT STRENGTH AND FRACTURE BEHAVIOR OF PLA-CFRP HYBRID STRUCTURES FOR ROBOTICS

Cheonghwa Lee[1,3], Jun Young Choi[2], Sung-Hoon Ahn[2], Changwoo Park[4] and Ji Ho Jeon[1*]

[1]School of Mechanical, Aerospace, and Manufacturing Engineering, University of Connecticut, Storrs, Connecticut, USA
[2]Department of Mechanical Engineering, Seoul National University, Seoul, 08826, South Korea
[3]Department of Electrical and Computer Engineering, Seoul National University, Seoul, 08826, South Korea
[4]Graduate School of Engineering Practice, Seoul National University, Seoul, 08826, South Korea

**Corresponding author (jiho.jeon@uconn.edu)*

Keywords: Additive Manufacturing, Composite Material, Impact Strength, Fracture Behavior, Robot Structure

ABSTRACT

This study investigates the effects of additive manufacturing parameters such as printing orientation and infill pattern on the impact resistance of polylactic acid (PLA) and carbon fiber reinforced plastics (CFRPs) hybrid structures. PLA was used as the filament for fused filament fabrication (FFF) to produce geometrically complex base structures, while CFRP layers were wet-layed on top of the printed PLA to reinforce the structure and enhance mechanical properties. This hybrid approach was motivated by the need to fabricate complex geometries for robotic systems using additive manufacturing, while avoiding the cost and complexity associated with large-scale composite 3D printers or tooling. Impact testing, conducted according to ASTM D4812 standards, was used to assess energy absorption. Specimens were fabricated with four distinct printing orientations (upright, on-edge, flat, and tilt) and 11 infill patterns (concentric, honeycomb, triangle, and more). Among the tested parameters, printing orientation was the dominant factor affecting impact resistance. Specimens printed in the on-edge orientation exhibited the highest impact strength, while upright specimens showed the lowest due to poor interlayer adhesion along the build direction. Infill pattern also influenced mechanical performance, with concentric and honeycomb patterns demonstrating enhanced energy dissipation and improved load distribution under impact loading. Fractographic analysis revealed brittle failure in upright specimens and interfacial delamination in on edge and flat configurations. Microscopic examination confirmed that the PLA and CFRP layers were joined primarily through mechanical interlocking. Applications of the hybrid structure to a modular mobile robotic spine component validated its effectiveness in achieving both reduced weight and impact resistant by integrating the geometric versatility of fused filament fabrication with the high strength-to-weight ratio of CFRP.

1 INTRODUCTION

In robotics, the choice of materials for robot structures is critical, as it significantly influences both the mechanical performance (e.g., strength, stiffness, density, etc.) and the efficiency of the manufacturing process (e.g., time, cost, etc.). Materials used in robot structures are broadly classified into two categories: soft materials and rigid materials [1]. Soft materials, such as polydimethylsiloxane (PDMS) and rubbers, offer advantages due to their flexibility and impact-absorbing properties, making them ideal for applications that require compliance or safe human-robot interaction [2]. However, their low stiffness and limited durability restrict their use in systems requiring high load-bearing capacity, structural rigidity, or repeated performance. In contrast, rigid materials, such as aluminum, carbon fiber reinforced plastic (CFRP), and stainless steel, are preferred for applications requiring strength, stiffness, and durability. These materials are particularly well-suited for large-scale and load-bearing systems. Aluminum is widely used in robotics compared to other metals such as stainless steel and steel, primarily

due to its cost-effectiveness, lightweight nature, and satisfactory mechanical properties. However, aluminum is still heavier than non-metallic materials (e.g., plastics, composites, etc.) and requires expensive CNC machining for manufacturing [3]. Polylactic acid (PLA) is well-known for its cost-effective and time-efficient prototyping capabilities, as well as its design flexibility. However, its applications are typically limited to small-scale systems due to its limited mechanical strength [4]. As the size of the system increases, challenges such as structural deflection, which reduces control accuracy, and a higher risk of structural failure become significant concerns. CFRP is highly effective in robot structures, particularly for applications requiring lightweight designs, suitability for large-scale systems, and high-temperature resistance. Nevertheless, their fabrication is often labor-intensive, reliant on expensive molds, and requires specialized expertise, particularly for creating structures with complex geometries [5].

Hybrid material structures with mechanical interlocking offer a promising solution by addressing the limitations of individual materials and manufacturing constraints. For mechanical material hybridization, two main categories are commonly studied: soft-rigid and rigid-rigid material hybrids. Soft-rigid material hybrids are designed to leverage the strengths of each material by utilizing rigid materials for structural support, ensuring strength and stiffness, while incorporating soft materials at connection points or contact surfaces to provide flexibility and compliance [6]. Rigid-rigid material hybrids focus on optimizing mechanical properties by combining materials with complementary characteristics. For instance, in robotic arms, CFRP is utilized to minimize weight toward the extremity (i.e., the end-effector), while metals are employed between the motor and the CFRP to ensure effective power transmission. These materials are seamlessly integrated through mechanical interlocking, enabling them to function as a unified structure and maximize the strengths of each material [7].

This study focuses on rigid-rigid material hybrid for PLA-CFRP hybrid structures, combining 3D-printed PLA with CFRP. PLA is prized for its ductility, design flexibility, and ability to form complex geometries using cost-effective 3D printing, but it lacks sufficient strength for demanding applications. In contrast, CFRP provides superior strength and an excellent strength-to-weight ratio, though its brittleness and reliance on expensive molding processes present challenges. By hybridizing these materials, the study leverages the strengths of each: PLA serves as a versatile base structure that enhances manufacturing flexibility, and its compatibility with inexpensive molds reduces overall costs for CFRP fabrication. Meanwhile, CFRP selectively reinforces areas requiring enhanced mechanical performance.

To validate the mechanical properties of PLA-CFRP hybrid materials, this research examines the impact strength and fracture behavior of PLA-CFRP composites fabricated with 11 infill patterns (aligned line; AL, adaptive cubic; AD, Archimedean chords; AR, concentric; CO, gyroid; GY, Hilbert curve; HI, honeycomb; HO, lightening; LT, Octagram spiral; OC, rectilinear; RE, triangle; TR) and four printing orientations (upright, on-edge, flat, tilt), as shown in Fig. 1(a) and 1(b) [8]. Hybrid specimens were produced by 3D-printing PLA and bonding it with CFRP layers using an epoxy-based wet layup process. Impact strength was evaluated using a Digital Izod Impact Tester (QM700A) under ASTM D4812 standards [9], and fracture behavior was analyzed [10], [11].

2 METHOD

This section outlines the key additive manufacturing parameters, including print orientation and infill pattern, as well as the method used for CFRP hybridization. Additionally, it details the fabrication procedures, specimen configurations, and testing standard employed for impact testing.

2.1 Printing Orientation

Printing orientation defines the positioning of a part relative to the Z-axis during the layer-by-layer additive manufacturing process [12]. Because bonding strength between layers along the Z-axis is generally weaker than within layers, printing orientation affects the bonding area and geometry between layers, which in turn significantly influences the mechanical performance and structural reliability of the printed components. Figure 1 presents the four printing configurations investigated in this study: upright, on edge, flat, and tilt. The Tilt orientation, ranging from 0° to 90°, was represented by a 45° angle in this work.

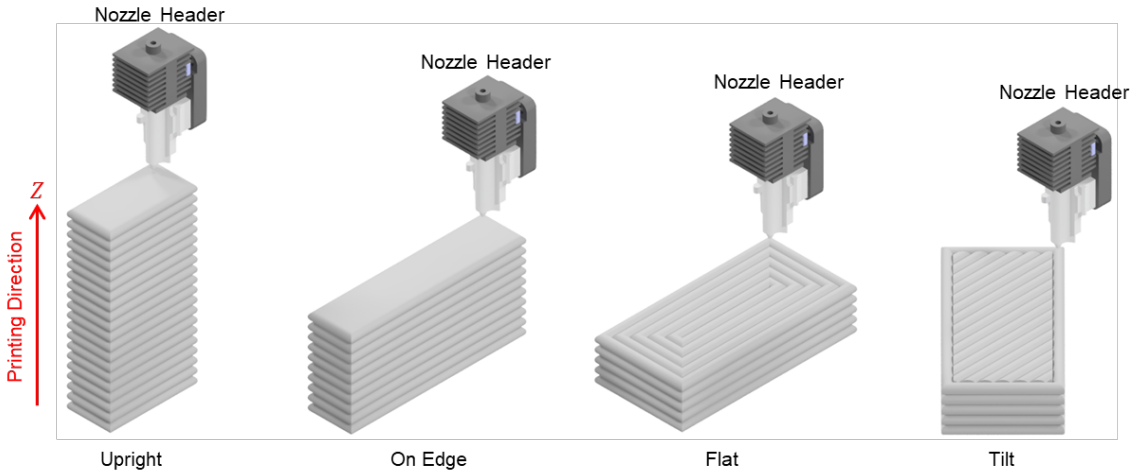

Figure 1: Schematic Illustration of Printing Orientations.

2.2 Infill Pattern

Infill pattern defines the internal geometry of a printed structure and is one of the most critical parameters in additive manufacturing [13]. It significantly influences not only mechanical performance but also weight, thermal behavior, and production time. As shown in Figure 2, this study investigates eleven infill patterns provided by the Bambu printer and Bambu Studio: Aligned Line (AL), Adaptive Cubic (AD), Archimedean Chords (AR), Concentric (CO), Gyroid (GY), Hilbert Curve (HI), Honeycomb (HO), Lightning (LI), Octagram Spiral (OC), Rectilinear (RE), and Triangle (TR). Some infill patterns, including AL, AD, GY, HI, RE, and TR, are influenced by printing orientation, resulting in slight variations in their internal geometry. In contrast, other patterns such as AR, CO, HO, LI, and OC remain largely unaffected by changes in printing orientation.

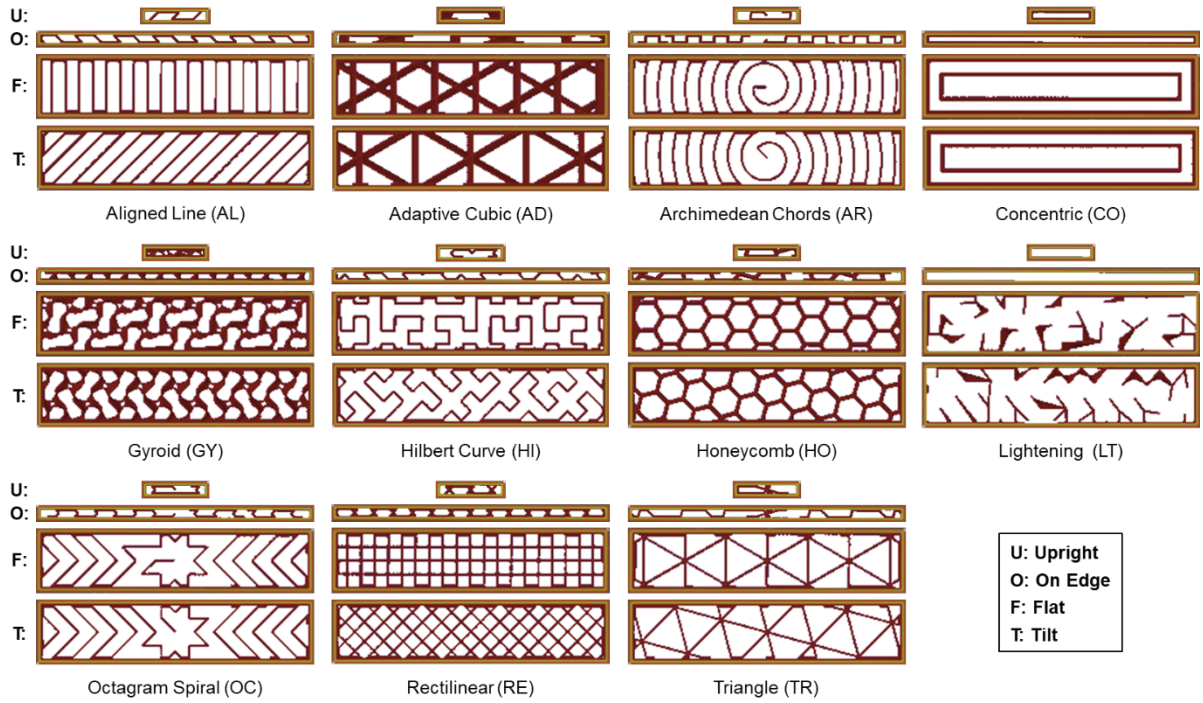

Figure 2: Infill Patterns by Printing Orientation.

2.3 PLA-CFRP Hybrid

The PLA-CFRP hybrid fabrication process involves two primary steps. In the first step, a PLA specimen is fabricated using additive manufacturing with a 3D printer [14]. In the second step, carbon

fiber reinforced polymer (CFRP) is laid up onto the PLA substrate. The CFRP fabrication requires both a fiber reinforcement and a resin matrix, with their compositions and properties detailed in Tables 1 and 2. The fiber reinforcement used in this study is a high-density 3K plain-woven carbon fabric (240 g/m², 1040 mm width, 0.30 mm thickness), making it ideal for manual lay-up processes [15]. The resin consists of RESOLTECH Epoxy System 1050 with 1056S hardener (100:35 weight ratio), exhibiting low viscosity, good deaeration, and high mechanical performance through ambient and post-curing, with a TG of up to 66.7°C and Shore D hardness above 90 [16].

Table 1: Fiber Specification.

Category	Specification
Fiber Type	Carbon Fiber
Tow Size	3K (3,000 filaments per tow)
Weave Type	Plain Weave
Areal Weight	240 g/m²
Thickness	0.30 mm

Table 2: Resin Specification.

Category	Specification
Epoxy	RESOLTECH Epoxy System 1050
Hardener	1056S
Mixing Ratio (by weight)	100 : 35 (Resin : Hardener)
Mixed Viscosity (23°C)	462 mPa·s
Gel Time (70 g at 23°C)	Approximately 37 minutes
Full Cure (Room Temperature)	14 days (TG: 49.1°C, Shore D Hardness: 89)

3 RESULTS

This section presents and validates the experimental results on impact strength, fracture behavior, and microstructural characterization of the interfacial region in the PLA-CFRP hybrid structure.

3.1 Impact Testing

Figure 3 presents the impact strength results as a function of printing orientation and infill pattern. Subfigures 3(a) to 3(d) correspond to PLA specimens fabricated in upright, on-edge, flat, and tilt orientations, respectively. The results indicate that printing orientation has a more pronounced effect on impact strength than infill pattern. Specimens printed in the upright orientation exhibited the lowest strength due to weak interlayer bonding, while the on-edge orientation showed the highest strength, as the layers were aligned perpendicular to the impact direction, thereby requiring more energy to initiate fracture. Flat and tilt orientations demonstrated intermediate performance, with the tilt orientation slightly outperforming the flat configuration. Among infill patterns, concentric and honeycomb designs provided relatively higher impact resistance, particularly in the on-edge orientation. However, their overall influence remained secondary to that of the printing orientation.

Figure 3(e) and 3(f) show the impact strength results for PLA-CFRP hybrid specimens fabricated in flat and tilt orientations. The results indicate that the overall trend related to printing parameters remains consistent with those observed in PLA-only specimens. Specifically, there is minimal difference in impact strength between flat and tilt orientations, and the effect of infill pattern is relatively insignificant in both cases. However, the application of CFRP reinforcement results in a substantial enhancement in impact resistance, with hybrid specimens exhibiting improvements of at least fivefold and up to tenfold compared to their PLA-only counterparts.

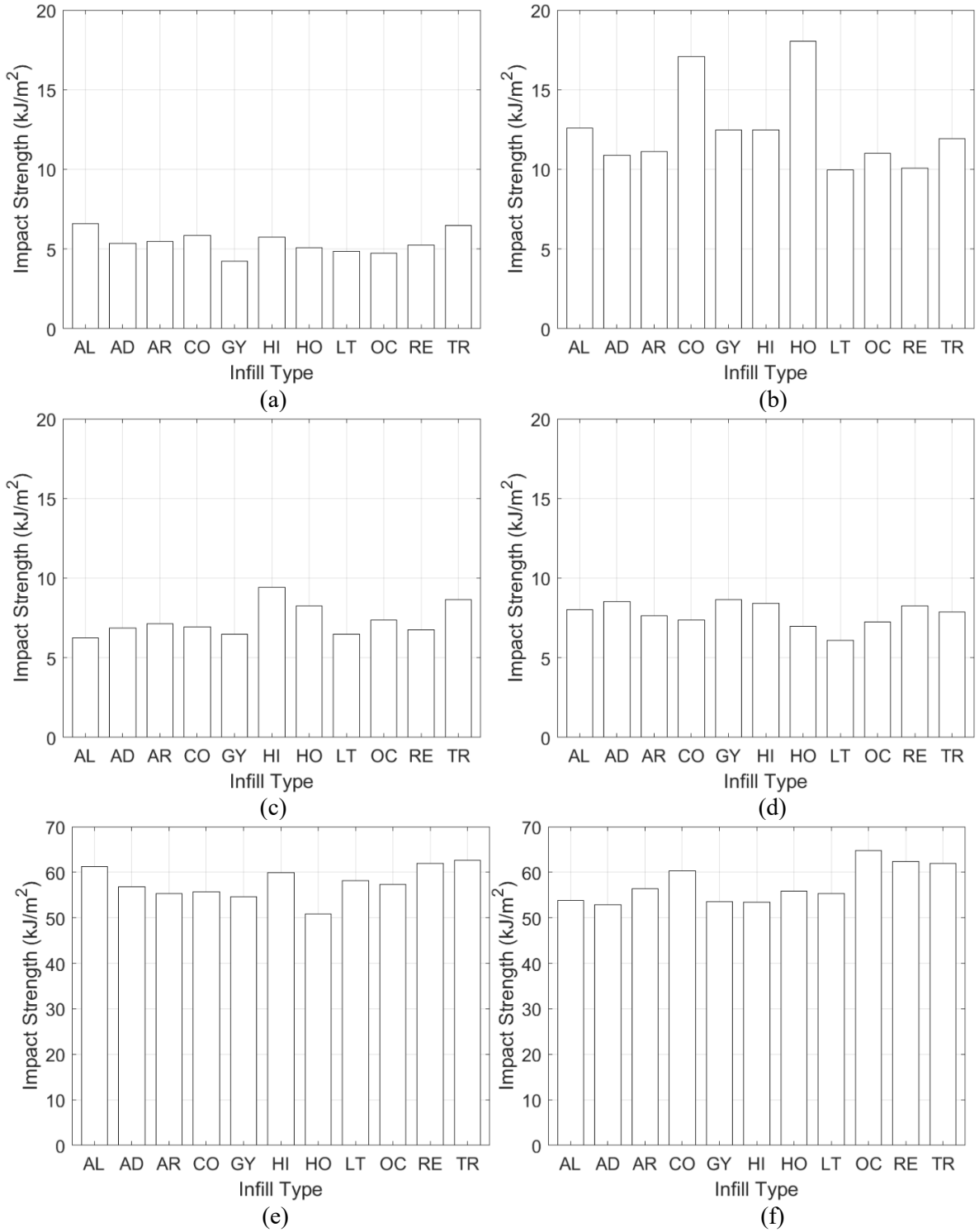

Figure 3: Impact Strength by Printing Orientation and Infill Pattern. (a) PLA upright. (b) PLA on edge. (c) PLA flat. (d) PLA tilt. (e) PLA-CFRP hybrid flat. (f) PLA-CFRP hybrid tilt.

3.2 Fracture Behavior

Figure 4 illustrates the fracture behavior of specimens with the rectilinear (RE) infill pattern across various printing orientations. In PLA-only samples, the upright, on edge, and flat orientations exhibited relatively brittle fractures with straight, vertically aligned cracks, primarily due to stress concentration along interlayer planes. In contrast, the tilt orientation showed more complex fracture surfaces with irregular crack paths following the rectilinear infill, indicating increased energy absorption and crack

deflection. Although the PLA-CFRP hybrid composites demonstrated significantly higher impact strength than the PLA-only specimens, their fracture behavior followed similar trends across printing orientations and infill configurations.

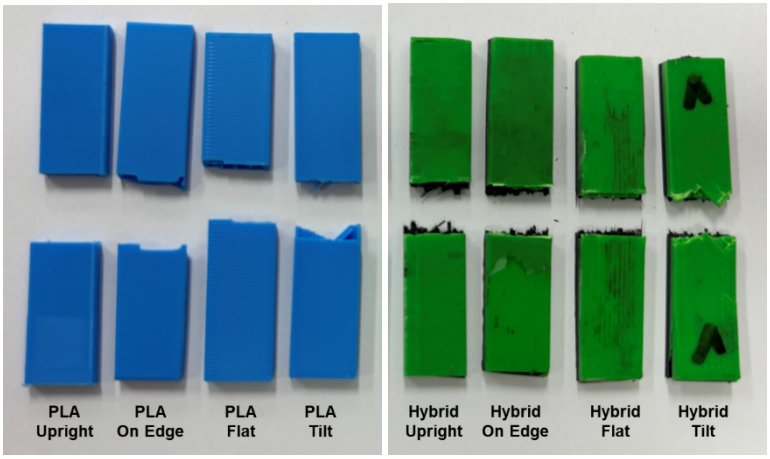

Figure 4: Fracture Behavior with Rectilinear (RE) Infill Pattern.

3.3 Microscopic Image

Figure 5 presents microscopic images of the interlocking surfaces formed at the interface between the PLA and CFRP in hybrid materials. In each image, the upper dark region corresponds to the CFRP layer, while the lower greenish region represents the 3D-printed PLA structure. All images were captured at the same magnification (scale bar = 500 μm) to facilitate direct comparison of the microstructural morphology and deposition patterns. Across all infill patterns, well-developed mechanical interlocking was observed, with minor micro voids confined to the CFRP bulk and no visible cracks. As these voids were away from the interface, bonding remained strong, contributing to improved interfacial adhesion and structural integrity.

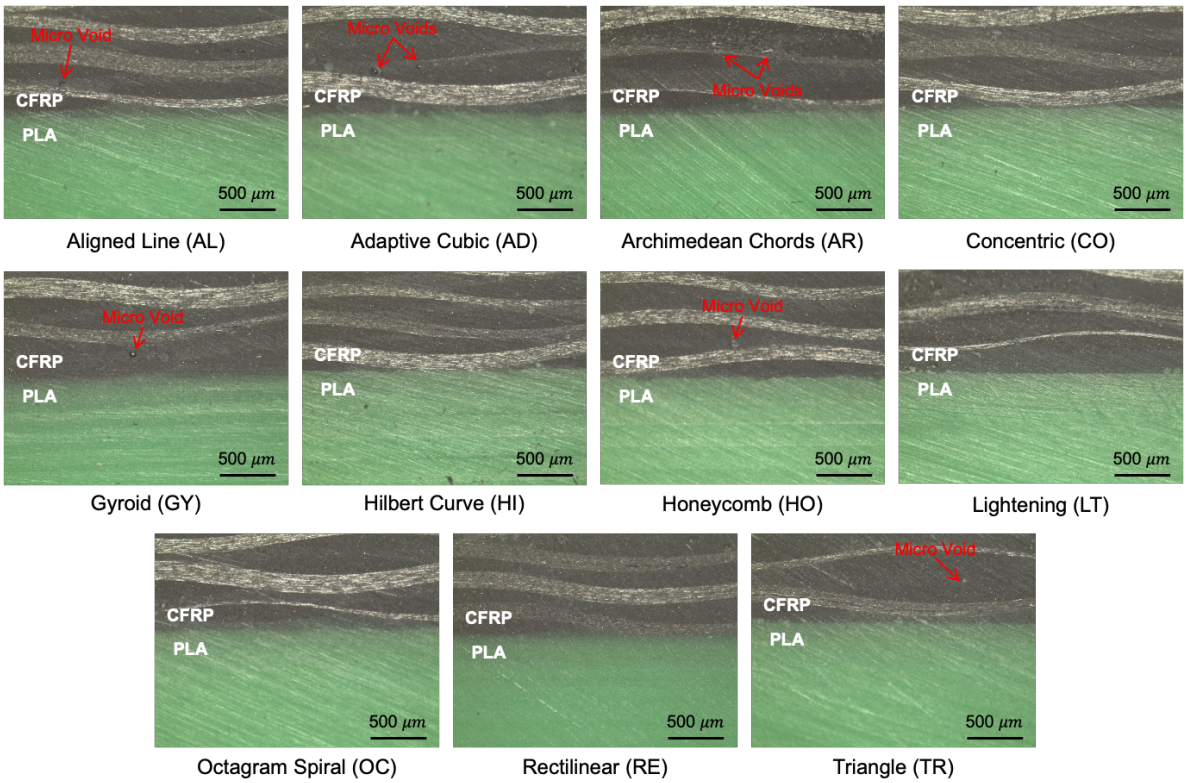

Figure 5: Microscopic Image of Interlocking Surfaces in PLA-CFRP Hybrids.

4 ROBOTICS APPLICATIONS

Figure 6 illustrates the overall fabrication process and final implementation of the proposed PLA-CFRP hybrid structure for robotic frame applications. The entire process consists of three main stages: (1) fabrication of a PLA core frame via 3D printing, (2) manual lamination of fiber and resin to form the CFRP shell frame, and (3) integration of the hybrid structure into a mobile robotic platform. This hybrid design approach, combining additive manufacturing and composite lamination, enables design flexibility, manufacturing efficiency, and improved mechanical performance, making it a promising strategy for developing next-generation robotic frames with complex functions and robust structural integrity.

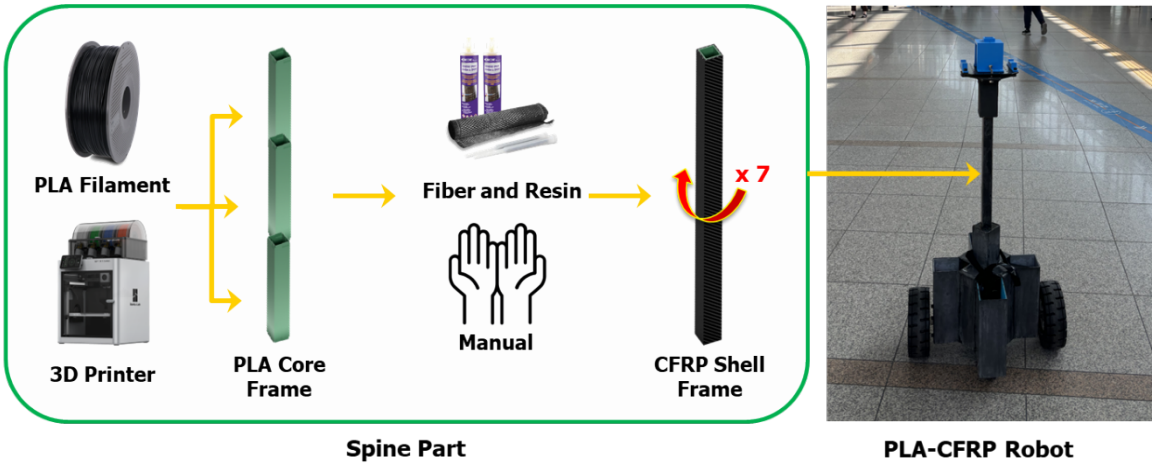

Figure 6: Fabrication Process and Robotic Integration of the PLA-CFRP Hybrid Spine Structure.

5 CONCLUSIONS

This study comprehensively evaluated the influence of 3D printing orientation and infill pattern on the mechanical behavior of PLA-CFRP hybrid structures. Impact tests identified printing orientation as the most critical factor affecting toughness and fracture characteristics, with the on-edge orientation delivering the highest impact resistance due to improved interlayer bonding, while the upright orientation exhibited the lowest performance. Among various infill patterns, concentric, honeycomb, and triangle patterns consistently showed enhanced impact strength, particularly in on-edge and flat orientations. Microscopic analysis demonstrated that mechanical interlocking at the interface, strengthened interfacial bonding and mitigated delamination. The observed fracture modes varied significantly with printing orientations, underscoring the crucial role of structural configuration in optimizing hybrid performance. The developed PLA-CFRP hybrid was successfully implemented as the central spine in a modular mobile robot, validating its applicability for lightweight, high-strength robotic components. Future work will extend to dynamic loading assessments, fatigue behavior analysis, and further optimization of multi-material interfaces to enhance the durability and functionality of hybrid structures.

ACKNOWLEDGEMENTS

This research was supported by a Korea Institute for Advancement of Technology (KIAT) grant funded by the Korean government (MOTIE) (RS-2024-00436124, Human Resource Development Program for Industrial Innovation (Global)).

REFERENCES

[1] [1] L. Wang, Y. Yang, Y. Chen, C. Majidi, F. Iida, E. Askounis, Q. Pei, Controllable and reversible tuning of material rigidity for robot applications, *Materials Today*, 21(5), 2018, pp. 563-576.

[2] S. Coyle, C. Majidi, P. LeDuc, K.J. Hsia, Bio-inspired soft robotics: Material selection, actuation, and design, *Extreme Mechanics Letters*, 22, 2018, pp. 51-59.

[3] P. Sutyasadi, Control improvement of low-cost cast aluminium robotic arm using arduino based computed torque control, *Jurnal Ilmiah Teknik Elektro Komputer dan Informatika*, 8(4), 2022, pp. 650-659.

[4] H. Demir, A.E. Coşgun, Comparison of PLA and ABS on Robot Arm Model and 3D Technology, *Eur. J. Adv. Eng. Technol.*, 6, 2019, pp. 38-44.

[5] H. Yin, J. Liu, F. Yang, Hybrid structure design of lightweight robotic arms based on carbon fiber reinforced plastic and aluminum alloy, *IEEE Access*, 7, 2019, pp. 64932-64945.

[6] W. Park, S. Seo, J. Bae, A hybrid gripper with soft material and rigid structures, *IEEE Robotics and Automation Letters*, 4(1), 2018, pp. 65-72.

[7] J.H. Jeon, J.Y. Choi, G.Y. Kim, S. Hong, J. Callanga, C. Lee, T. Gries, S.H. Ahn, Effect of laser texturing and thermomechanical joining parameters on bond strength of steel-flax fiber reinforced vitrimer composites, *Journal of Manufacturing Processes*, 124, 2024, pp. 212-225.

[8] S.H. Ahn, M. Montero, D. Odell, S. Roundy, P.K. Wright, Anisotropic material properties of fused deposition modeling ABS, *Rapid Prototyping Journal*, 8(4), 2002, pp. 248-257.

[9] K. Sravanthi, V. Mahesh, B.N. Rao, Influence of micro and nano carbon fillers on impact behavior of GFRP composite materials, *Materials Today: Proceedings*, 37, 2021, pp. 1075-1078.

[10] T. Tezel, M. Ozenc, V. Kovan, Impact properties of 3D-printed engineering polymers, *Materials Today Communications*, 26, 2021, 102161.

[11] B.A. Moreno-Núñez, M.A. Guerrero-Alvarado, A. Salgado-Castillo, C.D. Treviño-Quintanilla, E. Cuan-Urquizo, U. Sánchez-Santana, G. Pincheira-Orellana, Build and raster orientation effects on CFRP Onyx/Aramid impact absorption, *Composites Part C: Open Access*, 14, 2024, 100485.

[12] A. Farzadi, M. Solati-Hashjin, M. Asadi-Eydivand, N.A. Abu Osman, Effect of layer thickness and printing orientation on mechanical properties and dimensional accuracy of 3D printed porous samples for bone tissue engineering, *PLoS One*, 9(9), 2014, e108252.

[13] M.Q. Tanveer, G. Mishra, S. Mishra, R. Sharma, Effect of infill pattern and infill density on mechanical behaviour of FDM 3D printed parts – a current review, *Materials Today: Proceedings*, 62, 2022, pp. 100–108.

[14] Z. Du, Z. Liu, C. Chen, X. Wang, Stab resistance mechanism of lightweight PLA/CFRP hybrid composite structures, *Engineering Failure Analysis*, 156, 2024, 107795.

[15] Fiberman, Carbon fiber product page, https://www.fiberman.co.kr/goods/view?no=351 (accessed July 5, 2025).

[16] Resoltech, Epoxy System 1050 technical information, https://www.resoltech.com/en/markets/1050-detail.html (accessed July 5, 2025).



Sindhu Bushpalli, Saheed Ojo,

Vassilios Tsachouridis (PI), Alan Iziquel

El Hassan Ridouane

ICCM24

AUG 4-8, 2025 · BALTIMORE, MARYLAND

Collins Aerospace

A Vibration based SHM model for damage detection and monitoring in curved beam aerostructures

© 2025 Collins Aerospace | Collins Aerospace Proprietary | This slide contains technical data: UNCTD(EU)

Outline

- Introduction
- SHM algorithm
- Application
- Advantages
- Summary and next steps

© 2025 Collins Aerospace. | Collins Aerospace Proprietary | This slide contains technical data: UNCTD(EU)

Introduction

© 2025 Collins Aerospace. | Collins Aerospace Proprietary | This slide contains technical data: UNCTD(EU)

Research gaps, motivation and objectives

Research gaps

- ✓ Simulation of composite damage requiring more time due to higher than anticipated complexity.
- ✓ Limited or No methodical SHM study cases for composites in Collins.
- ✓ Advancements in SHM and reliability analysis have not yet been adequately leveraged by Collins to applications.



Fan cowl

1. Products | Collins Aerospace

Motivation

- ✓ Advanced application of composite materials in aerospace products including fan cowl stiffeners, struts and brackets.
- ✓ Simplicity and efficiency of analytical models (which can facilitate structural analysis and SHM of aerospace components).
- ✓ Higher-order accuracy and enhanced physics representation of strong form solutions.

Objectives

- ✓ Formulate analytical methodology for structural analysis and prediction of damage propagation and failure in composite structures (thermosets and thermoplastics).
- ✓ Develop an efficient structural health monitoring (SHM) tool for quality check during manufacturing
- ✓ Vibration-based SHM approach based on analytical tool integrated with UBOA optimization.

© 2025 Collins Aerospace. | Collins Aerospace Proprietary | This slide contains technical data: UNCTD(EU)

Capability development framework

Develop 1D analytical curved beam formulation for composite nacelle structures

- Free vibration analysis.
- Buckling and nonlinear postbuckling analysis.
- Dynamic analysis.

Develop deterministic constitutive damage model for laminated composites

- Develop constitutive responses considering progressive damage including delamination.

Validation of the curved beam models with available test data and 3D FEM model

- Tune buckling and free vibration model with test measurements using geometric and laminate parameters.

Develop damage detection routine for composite with fan cowl and thrust reversers as a use case

- Evaluate damage index of structural model, evaluate probability of detection.

© 2025 Collins Aerospace. | Collins Aerospace Proprietary | This slide contains technical data: UNCTD(EU)

1D model capability demonstration

1D analytical model capabilities

BUCKLING ANALYSIS

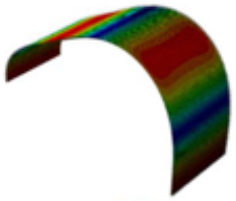

Critical buckling load

2.092×10^5N

FREE VIBRATION ANALYSIS



Fundamental frequency

3.72

FREQUENCY RESPONSE ANALYSIS

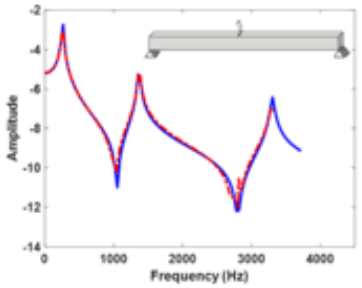

POST BUCKLING ANALYSIS

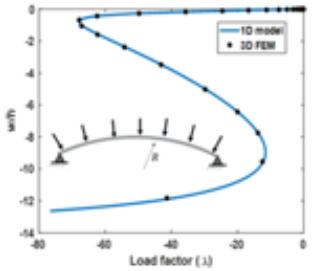

TRANSIENT ANALYSIS

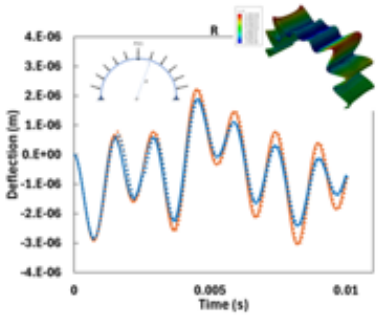

Degrees of freedom

1D Beam 63 < 3D FE 8.4 million

SHM DAMAGE DETECTION



UBOA prediction: x=0.78333

© 2025 Collins Aerospace. | Collins Aerospace Proprietary | This slide contains technical data: UNCTD(EU)

SHM algorithm

© 2025 Collins Aerospace. | Collins Aerospace Proprietary | This slide contains technical data: UNCTD(EU)

Unified butterfly optimization algorithm

- Local search

$$x_i^{t+1} = \mu[x_i^t + (r^2 \times x_j^t - x_k^t) \times f_i]$$

- Global search

$$x_i^{t+1} = (1-\mu)[x_i^t + (r^2 \times g_{best} - x_i^t) \times f_i]$$

$$\mu(t) = \exp\left(\frac{t \log 2}{t_{max}}\right) - 1$$

- Fitness function

$$F = \sqrt{\frac{1}{n}\sum_{i=1}^{n}(\omega_i^m - \omega_i^c)^2}$$

Position update

- Each particle/butterfly updates position using
  - Velocity-based mechanism for exploitation
  - Fragrance-based mechanism for exploration

Switching mechanism

- Algorithm alternates b/w UPSO & BOA position updates depending on fitness of the current population

Fitness evaluation

- Fitness is based on the objective function, and updates solution to move closer to g_{best}

© 2025 Collins Aerospace. | Collins Aerospace Proprietary | This slide contains technical data: UNCTD(EU)

SHM algorithm

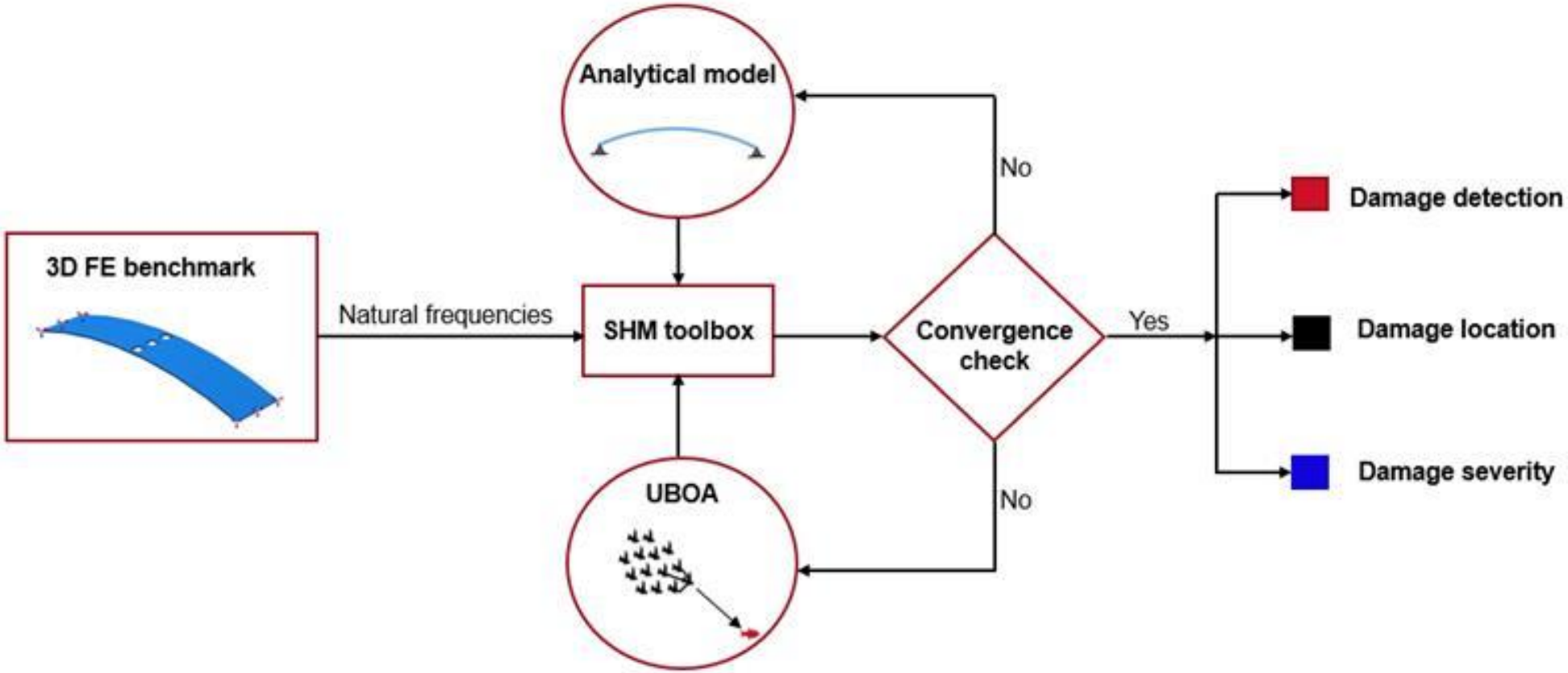

© 2025 Collins Aerospace. | Collins Aerospace Proprietary | This slide contains technical data: UNCTD(EU)

Application

© 2025 Collins Aerospace. | Collins Aerospace Proprietary | This slide contains technical data: UNCTD(EU)

Application: Straight beam composites

Free vibration of straight beams with bulk damage

- Compute natural frequencies of a healthy structure and compare it with damaged structure
- Predict damage location using frequency data: compute fitness function and iterate until stopping criteria is satisfied

Beam definitions

Geometry	Damage parameters
$L = 1$ m,	$\theta_c = 0.2L$ from the free end.
$R = 10^3 L$	$\gamma = 6.67\%$ of L centred at θ_c
$h = L/15$	
$b = 0.25$ m	

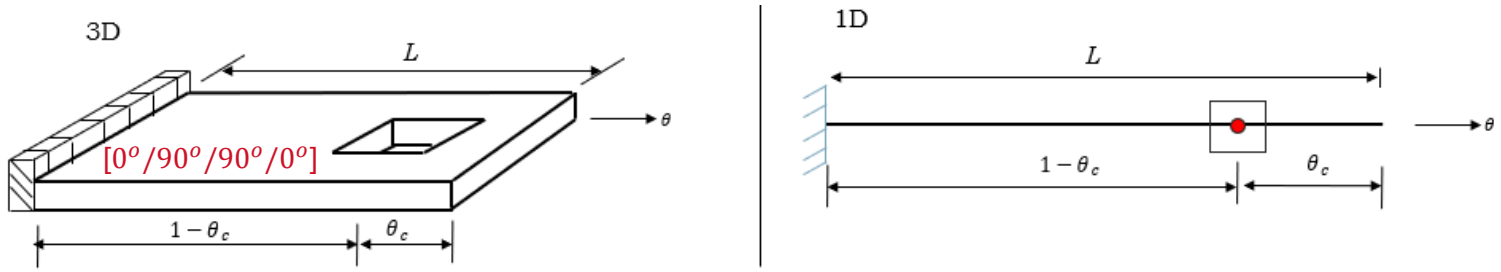

Fig: 3D and 1D illustration of a beam with clamped free boundary condition

1D analytical model results

Damage scenarios	Modes			
	1	2	3	4
2D FE (healthy)	0.92	4.87	11.38	18.60
1D Beam (healthy)	0.92	4.88	11.43	18.68
2D FE	0.91	4.68	11.07	18.12
1D Beam	0.91	4.68	10.48	17.23

Normalised natural frequencies of the beam

Damage detection using optimization algorithms

Total no. of modes	$\bar{\omega}$	PSO (% Error)	UPSO (% Error)	BOA (% Error)	UBOA (% Error)
1	0.91	0.64 (20%)	0.64 (20%)	0.64 (20%)	0.64 (20%)
2	4.68	0.80 (0%)	0.80 (0%)	0.80 (0%)	0.80 (0%)

Collins Aerospace
An RTX Business

© 2025 Collins Aerospace. | Collins Aerospace Proprietary | This slide contains technical data: UNCTD(EU)

Application: Curved beam composites

Free vibration of curved beams with bulk damage

- Compute natural frequencies of a healthy structure and compare it with damaged structure
- Predict damage location using frequency data: compute fitness function and iterate until stopping criteria is satisfied

Beam definitions

Geometry	Damage parameters
$L = 5.8$ m, $R = 5L/\pi$ m $h = 0.025$ m $b = 1.2$ m	• 3 equidistant squared notches of size 0.2 m centred at $\theta_c = 0.5L$

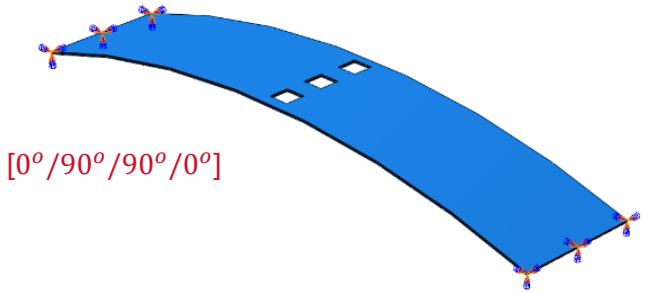

Fig: 3D illustration of a curved beam with clamped boundary condition

1D analytical model results

Damage scenarios	Modes (Hz)			
	1	2	3	4
1D model [Healthy]	19.80	35.57	64.51	89.76
3D FE model [Healthy]	19.74	35.45	64.28	89.46
1D model [with hole damage]	19.59	34.51	63.03	87.59
3D FE model [with hole damage]	19.35	34.07	63.90	87.67

Natural frequencies of Beam

Bulk damage detection using optimization algorithms

Total no. of modes	ω (Hz)	PSO (% Error)	UPSO (% Error)	BOA (% Error)	UBOA (% Error)
1	19.35	0.38 (24%)	0.37 (26%)	0.61 (22%)	0.38 (24%)
2	34.07	0.50 (0%)	0.50 (0%)	0.50 (0%)	0.50 (0%)

Detection of centre of damage

© 2025 Collins Aerospace. | Collins Aerospace Proprietary | This slide contains technical data: UNCTD(EU)

Application: Straight beam composites

Free vibration of straight beam with delamination damage

- Detect natural frequencies for various delamination lengths
- As the size of delamination increases from 20% of L→ 60% of L, the composite beam's strength gradually weakens due to delamination-induced stiffness reduction which in turn causes a reduction in the natural frequency

Beam definitions

Geometry	Damage parameters
$L = 5$ m, $R = 10^3$ m $h = 0.04$ m $b = 0.5$ m	20% delamination 40% delamination 60% delamination

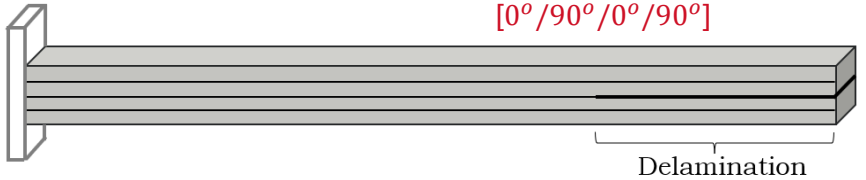

Fig: Illustration of delamination in a beam with clamped free boundary condition

1D analytical model results

Delamination	Fundamental frequency (Hz)		
	Analytical [bib]	Experimental	1D Model
0%	82.042	79.750	81.237
20%	80.183	77.001	80.567
40%	75.285	76.751	76.885
60%	66.936	66.375	67.207

Natural frequencies of Beam

© 2025 Collins Aerospace. | Collins Aerospace Proprietary | This slide contains technical data: UNCTD(EU)

Application: Highly curved composite panels

Damage detection analysis of curved composite panels

- Compute natural frequencies of a healthy structure and compare it with damaged structure
- Predict damage location using frequency data: compute fitness function and iterate until stopping criteria is satisfied

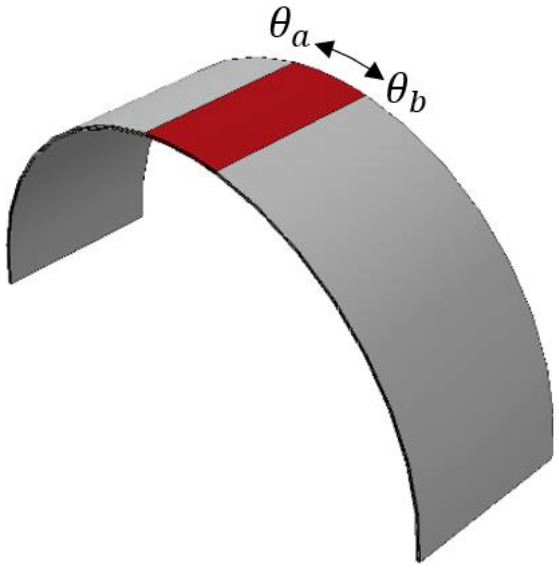

Beam	Material	Stacking sequence	Geometry
Beam-1	CFRP	$[0^o/90^o/90^o/0^o]$	$L = 5.8$ m, $R = 5L/\pi$ m $h = 0.025$ m $b = 1.2$ m Damage centre, $\theta_c = 0.5L$, Damage centre, $\gamma = 10\%$

Total no. of input modes	ω (Hz) (3D-FE simulated for $\Gamma = 0.2$)	PSO (% Error)	UPSO (% Error)	BOA (% Error)
1	13.94	0.30 (50%)	0.31 (55%)	0.31 (55%)
2	29.47	0.22 (10%)	0.20 (0%)	0.20 (0%)
3	56.32	0.20 (0%)	0.21 (5%)	0.21 (5%)
4	83.88	0.20 (0%)	0.20 (0%)	0.22 (10%)

Clamped-clamped BC

1st mode 2nd mode 3rd mode 4th mode

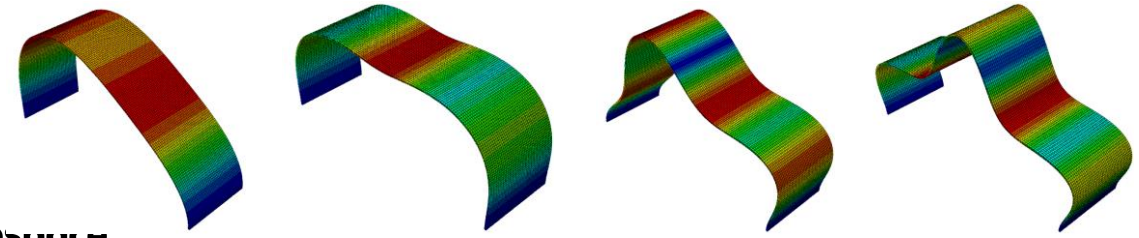

Total no. of input modes	ω (Hz) (3D-FE simulated for $\Gamma = 0.2$)	PSO (% Error)	UPSO (% Error)	BOA (% Error)
1	1.37	0.12 (40%)	0.12 (40%)	0.12 (40%)
2	4.19	0.11 (45%)	0.11 (45%)	0.11 (45%)
3	14.95	0.13 (35%)	0.13 (35%)	0.13 (35%)
4	32.22	0.20 (0%)	0.20 (0%)	0.20 (0%)

Clamped-free BC

© 2025 Collins Aerospace. | Collins Aerospace Proprietary | This slide contains technical data: UNCTD(EU)

Application: Highly curved composite panels

Damage detection analysis of curved composite panels

- Compute natural frequencies of a healthy structure and compare it with damaged structure
- Predict damage location using frequency data: compute fitness function and iterate until stopping criteria is satisfied

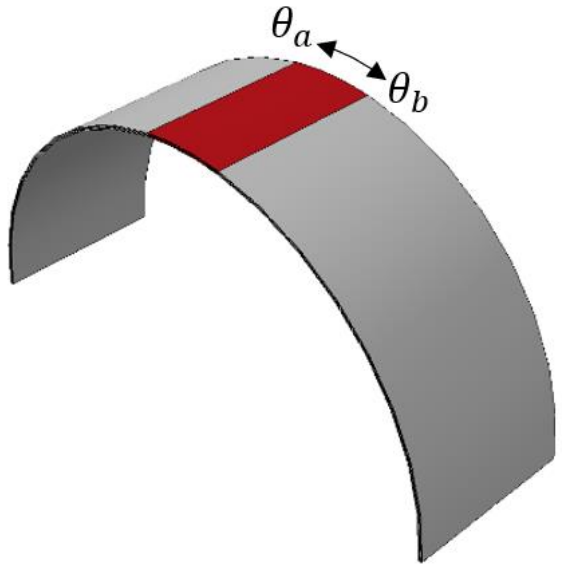

Beam	Material	Stacking sequence	Geometry
Beam-1	CFRP	$[0^o/90^o/90^o/0^o]$	$L = 5.8$ m, $R = 5L/\pi$ m $h = 0.025$ m $b = 1.2$ m Damage centre, $\theta_c = 0.5L$, Damage centre, $\gamma = 10\%$

Butterfly swarm movements

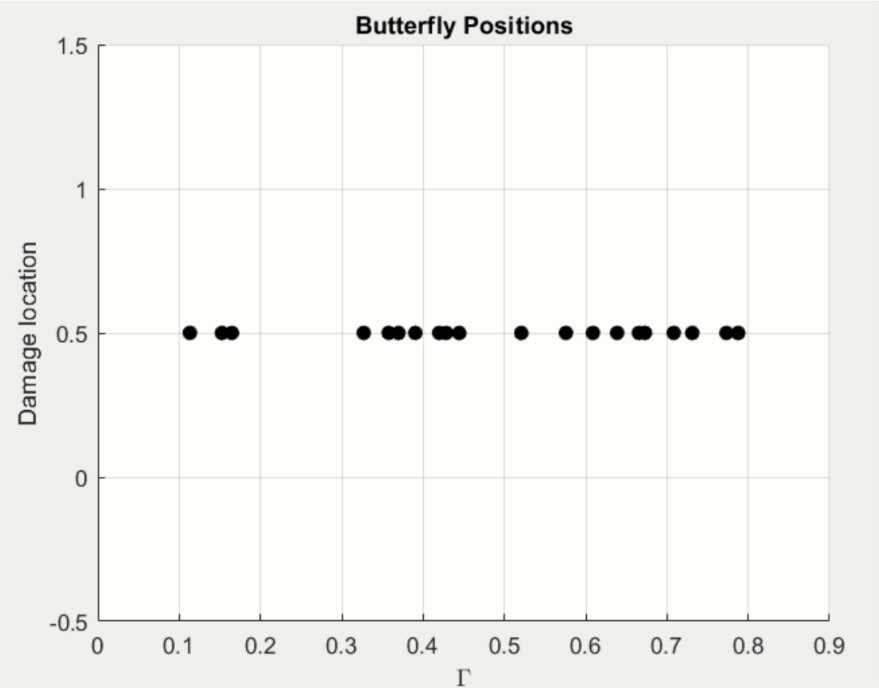

© 2025 Collins Aerospace. | Collins Aerospace Proprietary | This slide contains technical data: UNCTD(EU)

Advantages

© 2025 Collins Aerospace. | Collins Aerospace Proprietary | This slide contains technical data: UNCTD(EU)

Advantages

1D nonlinear analytical tool

- Simple computational tool for structural design as well as for SHM
- Free vibration, frequency response, buckling, post buckling, transient solutions
- Performance and efficiency of 1D model compared to 3D FEM

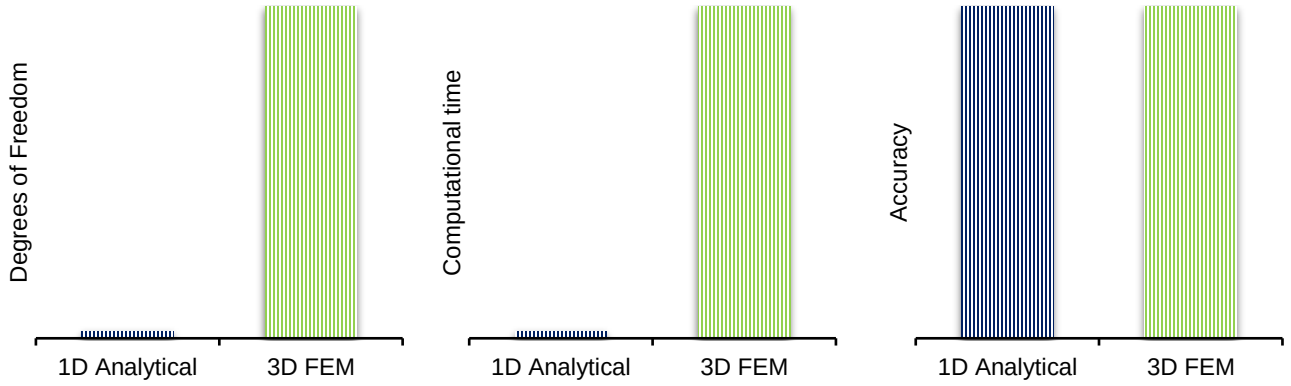

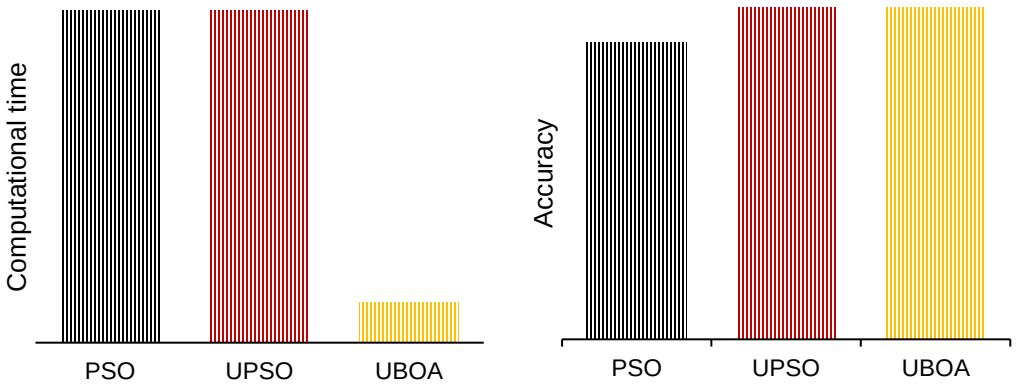

UBOA algorithm

- Superior convergence rates in terms of number of iterations and time
- UBOA: 75-80% increase in speed, 80-88% lower number of iterations
- Random switch b/w local and global search is supressed, minimising the randomisation of local search on global convergence, leading to better efficiency.

© 2025 Collins Aerospace. | Collins Aerospace Proprietary | This slide contains technical data: UNCTD(EU)

Summary and next steps

© 2025 Collins Aerospace. | Collins Aerospace Proprietary | This slide contains technical data: UNCTD(EU)

Summary and next steps

Summary

- Predictive SHM ability based on analytic formulae which allows easy certification and real system online implementation
- Adaptive framework for failure prediction of composite laminates
- Optimize airborne SHM systems accuracy to mitigate unplanned maintenance
- Low computational burden to enable nearly real-time SHM in contrast to CFD-based and FEM methods that are impractical for real-time applications

Next steps

- Expansion to higher order kinematics
- Explore more applications
- Implementation of analytical electromechanical model for sensing applications

© 2025 Collins Aerospace. | Collins Aerospace Proprietary | This slide contains technical data: UNCTD(EU)

Collins Aerospace
An RTX Business

Thank you

Sindhu Bushpalli

Sindhu.Bushpalli@collins.com

Collins Aerospace
An RTX Business

© 2025 Collins Aerospace. | Collins Aerospace Proprietary | This slide contains technical data: UNCTD(EU)

EFFICIENT FAILURE PREDICTION METHODOLOGY FOR HIGH ASPECT RATIO COMPOSITE WINGS WITH HIGH BEND-TWIST COUPLING

Mario Miranda[1], Alvaro Cea[1], Runze Li[1], Rafael Palacios[1] and Silvestre T. Pinho[1]

[1]Department of Aeronautics, Imperial College London, Exhibition Rd, South Kensington, London SW7 2AZ, UK

Email: m.miranda23@imperial.ac.uk

Keywords: Computational modelling, Finite element analysis FEA, Laminate mechanics, Strength, Aeroelasticity

ABSTRACT

As efficiency gains in traditional aircraft designs become more incremental, high aspect ratio wings offer vastly improved aerodynamic performance but introduce complex aeroelastic and structural challenges. Innovative structural concepts for this type of wings lack corresponding sizing methods for early-stage design. This work presents a novel methodology to predict composite failure in such wings, using as a proof of concept a wing featuring a novel Z-beam wingbox structure. Our approach combines a machine learning-based surrogate model for failure prediction with a non-linear aeroelastic solver. We use superelements to represent structural configurations within a global aircraft model, enabling efficient aeroelastic response analysis. Global aircraft-level strain data is then used to compute composite ply-level failure indices of critical components using an evolved LaRC05 criterion. This enables early-stage design evaluation of innovative composite wing structures.

1 INTRODUCTION

In order to get closer to the established net-zero goals, the aeronautics industry is making changes on their aircraft for these to be more efficient. Composite materials, especially Carbon Fibre Reinforced Polymers (CFRP), have played a major role in enabling the development of lighter and more efficient aircraft, such as the Airbus A350. Other important contributors (at the aircraft level) for the increase of efficiency are better engines, and wing geometry. As the gains in efficiency in aircraft have been asymptotically stagnating with the current, well established, design philosophies, other solutions are being investigated by the industry and the scientific community. One of the most promising solutions are very high aspect ratio wings, which are known to provide higher aerodynamic efficiency. However, the increased span introduces important changes that need to be carefully addressed at the structural sizing stage. Composite failure due to non-linearities, increased aeroelastic effects and increased-bending moments, is one of the main problems that arises when considering larger spans.

Bend-twist coupling (BTC) is a feature that allows to reduce the undesirable effects of high aspect ratio wings. This effect can be either induced by using specific material properties and/or orientations, such as tow-steered composites or by wing structures which inherently present this type of behaviour. One example of the latter is Airbus's patented Z-beam wingbox [1] (Fig. 1), which can provide different levels of coupling for aeroelastic tailoring.

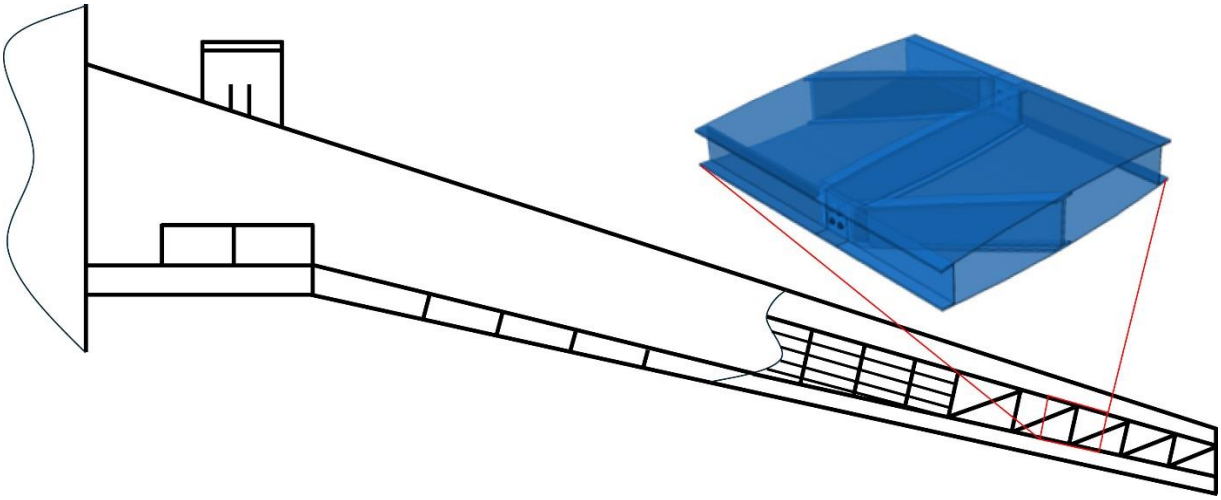

Figure 1: Z-beam concept in a high aspect ratio wing [2].

However, these novel architectures exhibit a complex composite failure response, especially due to their geometric complexity. This requires high-fidelity ply-level finite element modelling to achieve accurate structural sizing, leading to an unsurmountable computational expense at the sizing stage. This challenge is further exacerbated by the necessity of accounting for non-linear geometric effects in simulations, so that the estimated loads are not overly conservative. Consequently, there is a pressing need for efficient predictive frameworks capable of evaluating ply-level composite failure during the early design stages, where numerous structural configurations must be assessed efficiently.

In this work, we highlight a novel methodology to efficiently predict failure of composite components in high aspect ratio wings. It uses a machine learning based surrogate model [2] with an evolved [3,4] version of LaRC05 [5] for ply-level failure prediction (Fig. 2), which is coupled to a non-linear aeroelastic solver. We then developed a bespoke superelement to insert the novel wingbox concept in the outer part of the wing in a full aircraft model. Knowing the aeroelastic response, we are then able to obtain the failure indices of critical parts of the wingbox from macroscale loads.

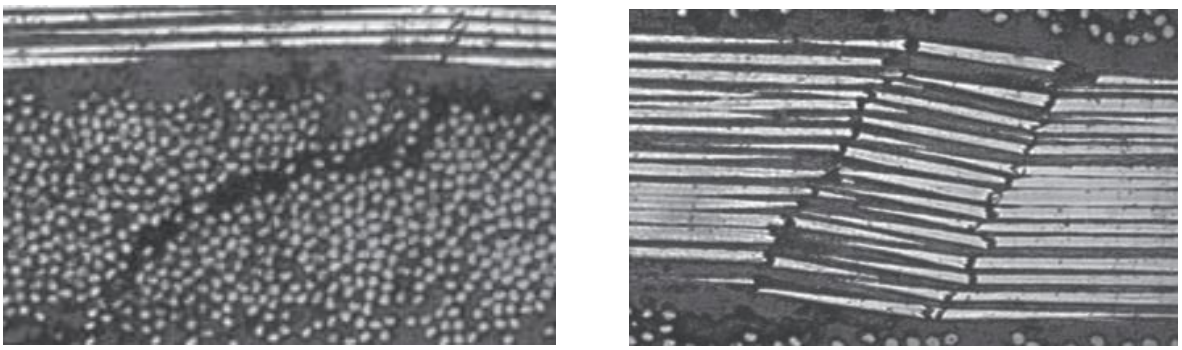

(a) Matrix cracking (b) Fibre kinking

Figure 2: Examples of failure mechanisms that can be predicted by the failure model [5].

In conclusion, this study presents an innovative framework that solves the problem of efficient prediction of failure indices in critical regions of high-aspect-ratio composite wings during sizing. Its adaptability makes it particularly valuable for early-stage analysis of any unconventional structures, offering flexibility for researchers and industry engineers to implement custom modifications.

2 METHODOLOGY

The methodology has two separate main parts, at two very different scales. One is a surrogate model to predict ply-level damage and the other is a non-linear aeroelastic solver to simulate the full aircraft behaviour. The physics guided machine learning based surrogate model, takes as input the homogenised strains in the wingbox and its design variables, and returns the failure index of a critical detail, in this case, bolted joints [2]. Additionally, the homogenised stiffness matrix of the wingbox is obtained, which will allow its inclusion in the aircraft model. An overview schematic of the surrogate model is shown in Fig. 3.

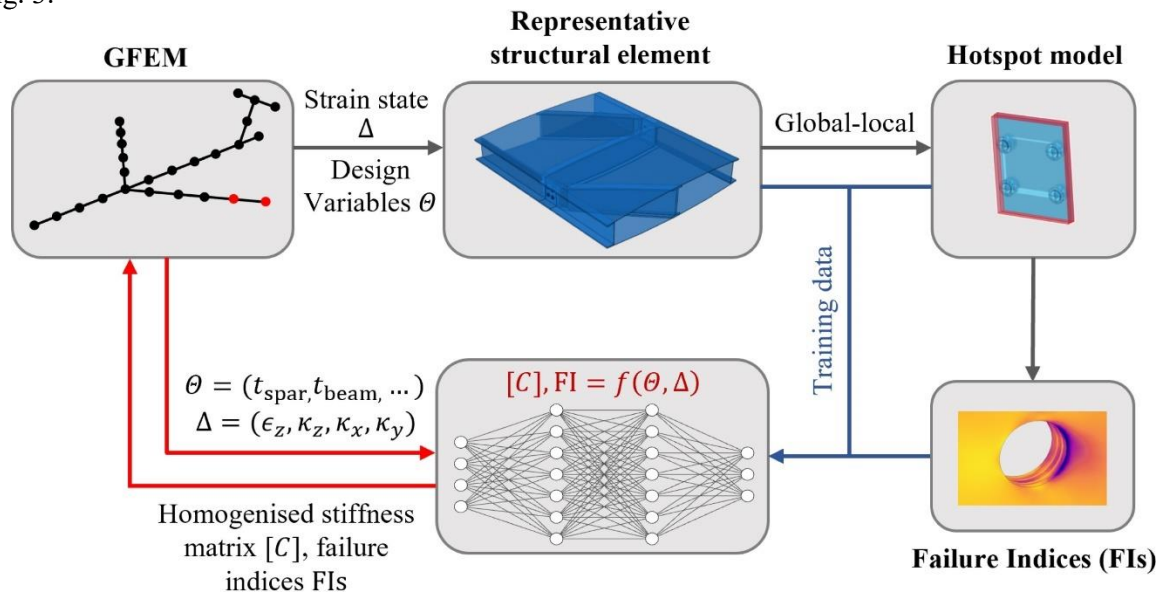

Figure 3: Multiscale analysis sequence for the prediction of ply-level failure indices [2].

The failure indices used for the surrogate model come from a detailed finite element model of the bolted connection, and are calculated using an evolved [3,4] LaRC05 [5] failure criterion. To simulate the aircraft response, a non-linear aeroelastic solver, FENIAX [6], is used. It uses the vibration modes of the condensed aircraft model to calculate the non-linear response (Fig.4).

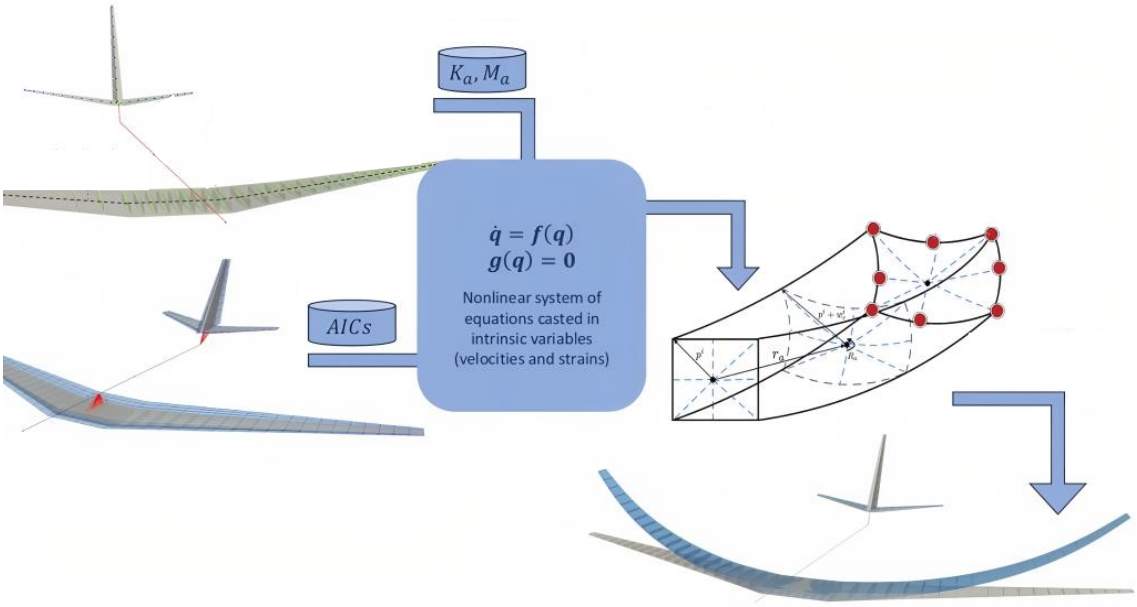

Figure 4: Workflow to obtain aeroelastic solution using FENIAX. After [6].

Superelements are then used to provide the required stiffness properties to the Global Finite Element Model (GFEM) of the aircraft. This approach is specifically useful since it allows to directly change only the outer part of the wing, not having to generate a full aircraft model for each design iteration. Additionally, since only the internal structure of the wing is being changed, i.e. there is no change in chord or airfoil shape, the aerodynamic characteristics are preserved for the entire procedure. A schematic of the overall methodology is shown in Fig. 5.

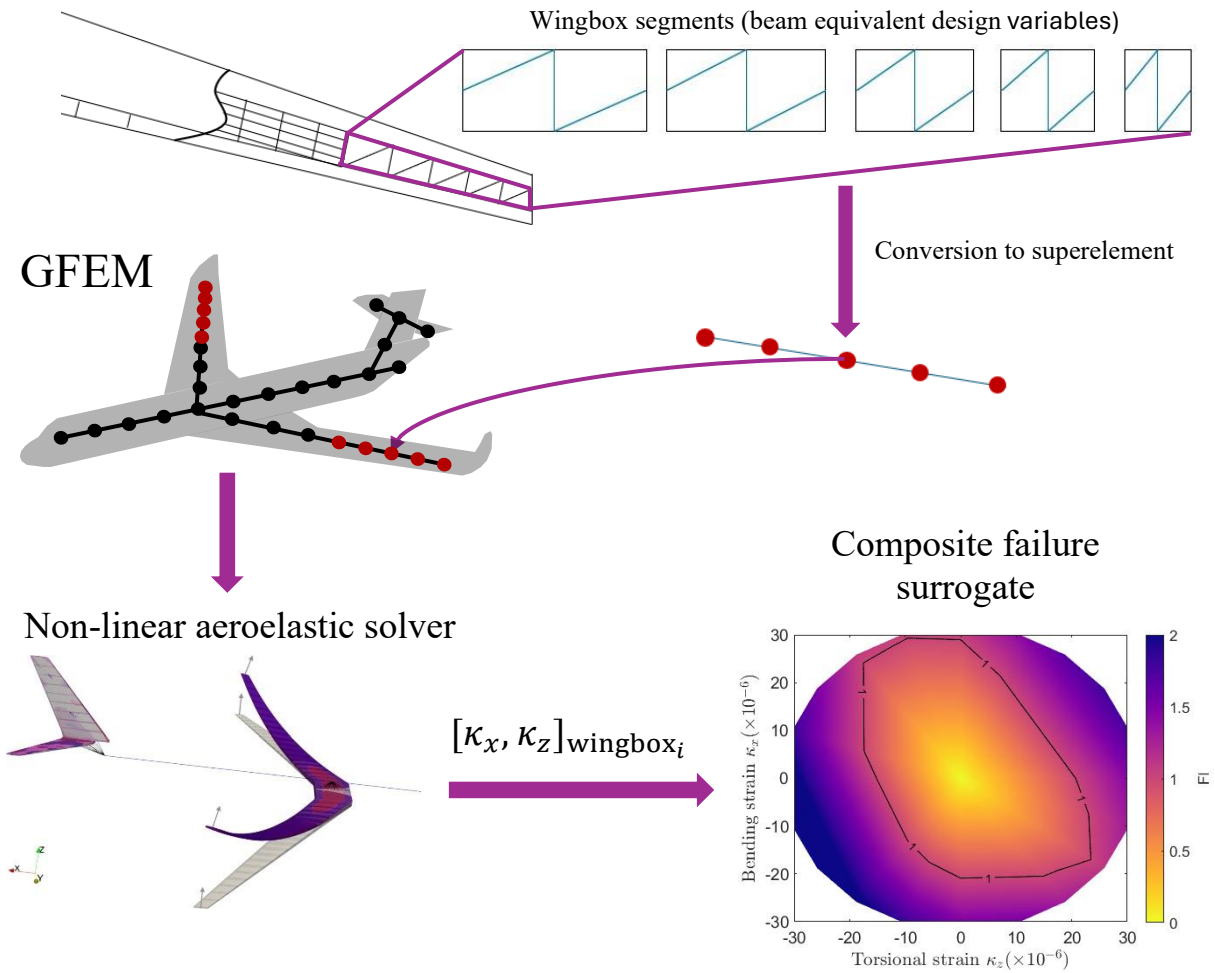

Figure 4: Overview of the methodology for composite failure prediction. After [2,6].

3 RESULTS

As a proof of concept of the multiscale structural analysis described in this work, a static follower vertical load of 21500 N is applied to both wingtips of the Bristol Ultra Green (BUG) model [7]. In this paper, a sequence of 10 Z-Beam wingboxes (as presented in Ref. [2]) is used to cover the last 11.28 m of each wing (section 3 of the wing in Ref. [7]). The homogenised strains of the first Z-beam wingbox, counted from the fuselage toward the wingtip, under the applied load (14 time steps), are presented in the failure index map shown in Fig. 6. As bending strain increases, a corresponding increase in torsional strain magnitude is observed, attributed to the bend-twist coupling characteristics inherent in the wingbox design.

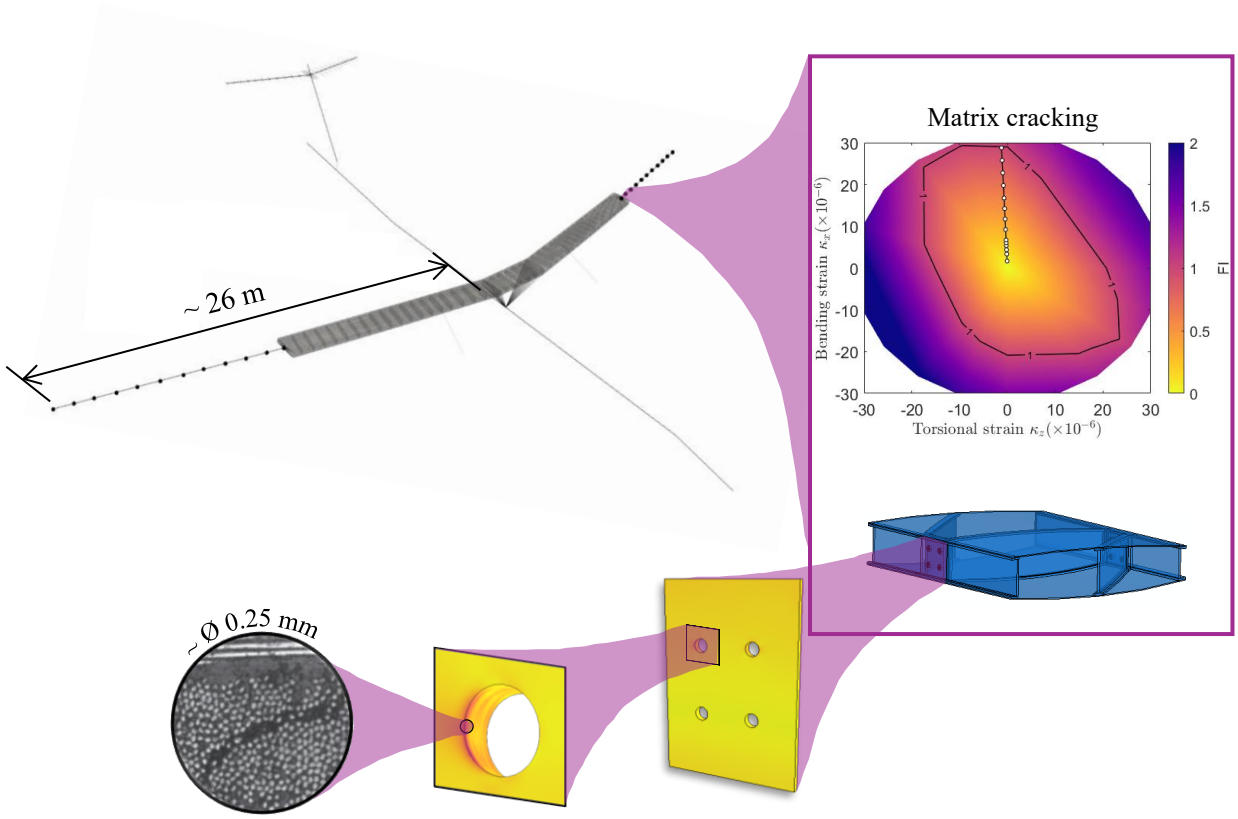

Figure 6: Prediction of matrix cracking failure mode in the outer part of a high aspect ratio aircraft [5].

The analysis reveals that matrix cracking failure occurs at the bolted joint under this loading condition. This failure mode demonstrates the effective integration of disparate length scales within the structural model, as illustrated in the figure. The coupling between local joint-level failure mechanisms and global structural response highlights the multi-scale nature of this work.

4 CONCLUSIONS

In this work, we present a multidisciplinary methodology for the efficient prediction of ply level failure in high aspect ratio composite wings. By leveraging a previously developed machine learning-based surrogate model, we accurately capture the failure behaviour of a novel composite component designed to induce bend–twist coupling. Applied to the outer wing region of a full-scale aircraft, this approach enables effective structural sizing by bridging vastly different scales, spanning at least five orders of magnitude. This methodology offers a modular and computationally efficient solution, making it adaptable to existing industrial and research workflows and thereby supporting early-stage design exploration and optimisation.

ACKNOWLEDGEMENTS

The authors would like to gratefully acknowledge the funding from Innovate UK under the Next Wing project, grant No. 10002372. The authors also thank Dr. Nicolae Lucian Iorga from Airbus UK for the support and helpful discussions.

REFERENCES

[1] L. Iorga, Aerofoil structures with stiffness properties adjustment component, United States Patent and Trademark Office (2023), U.S. Patent No. 11,772,780 B2

[2] M. Miranda, R. Li, L. Iorga, S. T. Pinho, Multiscale modelling strategy for a novel wingbox structure with increased bend-twist coupling, Composite Structures, Volume 370, 2025

[3] S. T. Pinho, M. Matos, R.O.S.S. Costa, A. Ibbotson, M. Ostergaard. Enabling multiscale analysis of very large composite structures. COMPOSITES 2021, 22-24, 2021

[4] S. T. Pinho, R.O.S.S. Costa, M. Matos, A. Ibbotson, M. Ostergaard. Multiscale analysis of an aircraft wingbox. ECCM20. 26-30, 2022

[5] S. T. Pinho, R. Darvizeh, P. Robinson, C. Schuecker, P. Camanho, Material and structural response of polymer-matrix fibre-reinforced composites. Journal of Composite Materials, Volume 46, 2012

[6] A. Cea, R. Palacios, JAX-based aeroelastic simulation engine for differentiable aircraft dynamics, Computer Physics Communications, Volume 311, 2025

[7] O. Stodieck, J. E. Cooper, S. A. Neild, M. H. Lowenberg, L. Iorga, Slender-Wing Beam Reduction Method for Gradient-Based Aeroelastic Design Optimization, AIAA Journal, Volume 56, 2018

Structural Integrity of Load Carrying H_2 Pressure Tanks for Small Aircraft

24th International Conference on Composite Materials (ICCM24)

Baltimore Convention Center, Baltimore Maryland

August 4-8, 2025

Dr.-Ing. Nicole Motsch-Eichmann

Leibniz-Institut für Verbundwerkstoffe

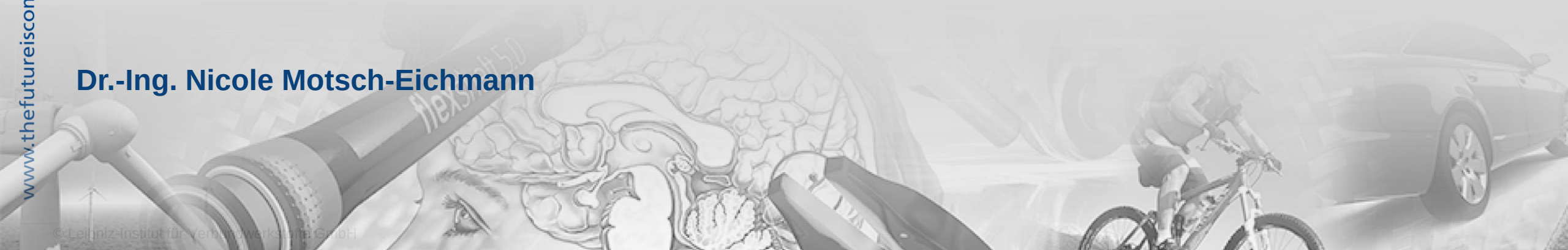

www.thefutureiscomposite.com

© Leibniz-Institut für Verbundwerkstoffe GmbH

Agenda

- Introduction
- Background and Motivation
- Design
- Manufacturing
- Testing
- Outlook and Summary

www.thefutureiscomposite.com

© Leibniz-Institut für Verbundwerkstoffe GmbH

Types of Hydrogen Storage Systems

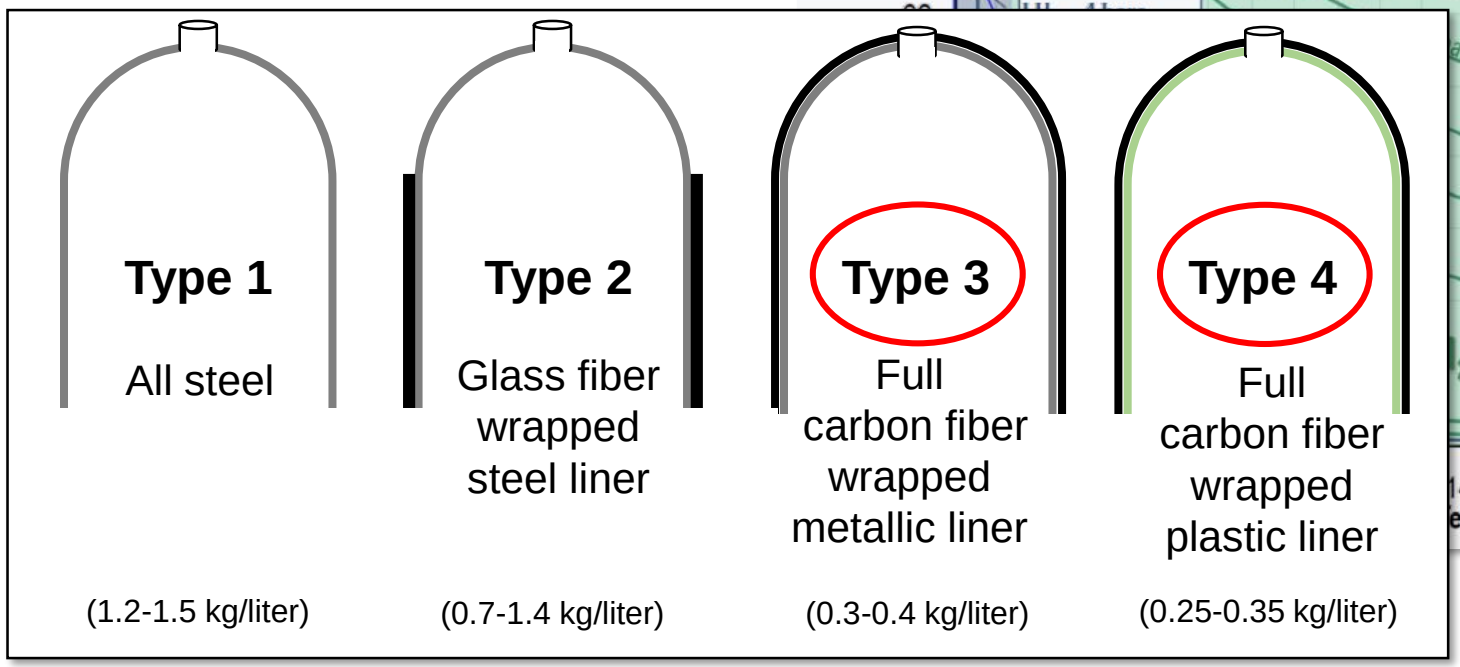

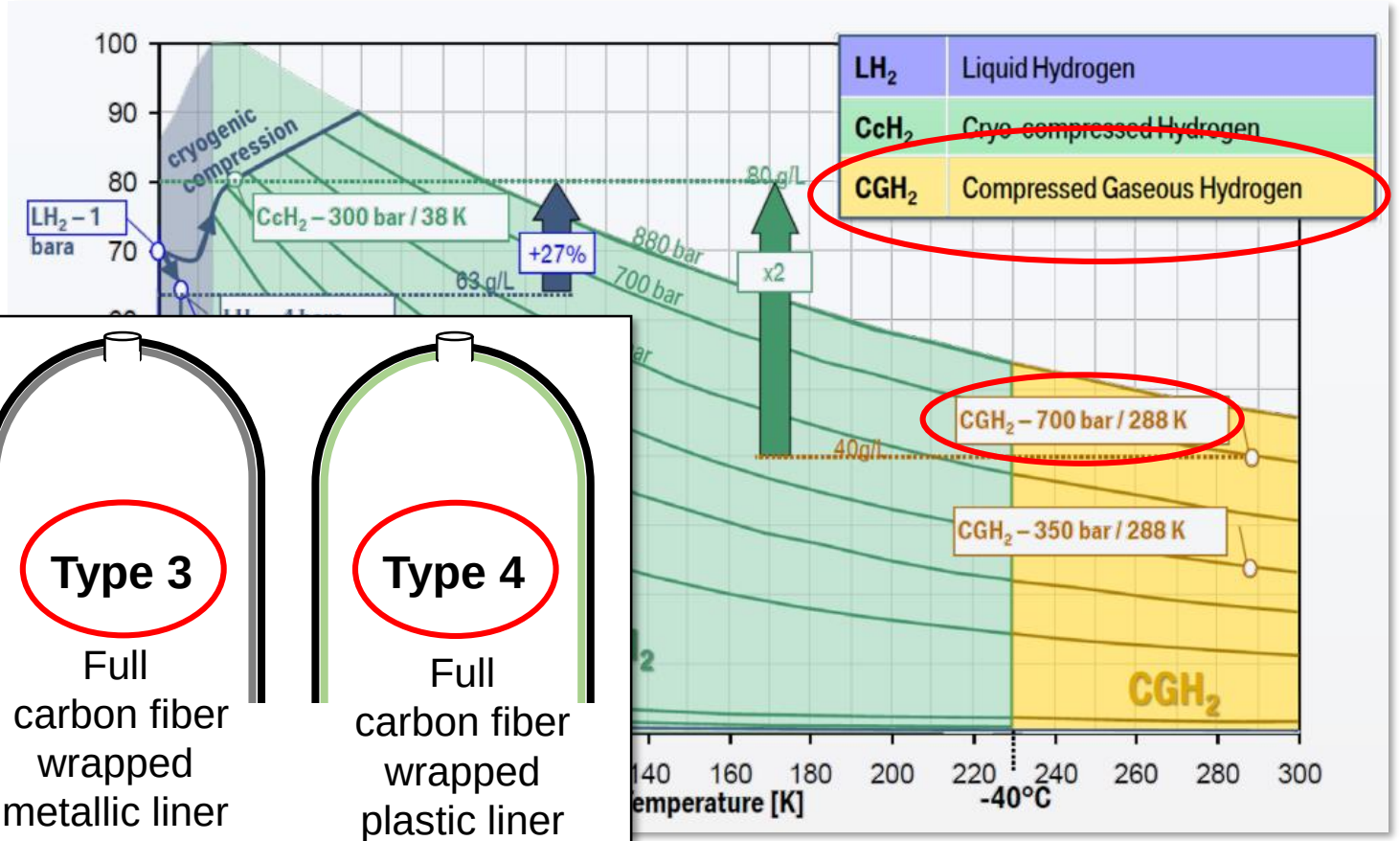

Source: Composites World, „Composites in Hydrogen Storage“, 2022.

www.thefutureiscomposite.com

© Leibniz-Institut für Verbundwerkstoffe GmbH

Design Spaces for Hydrogen Storage Systems

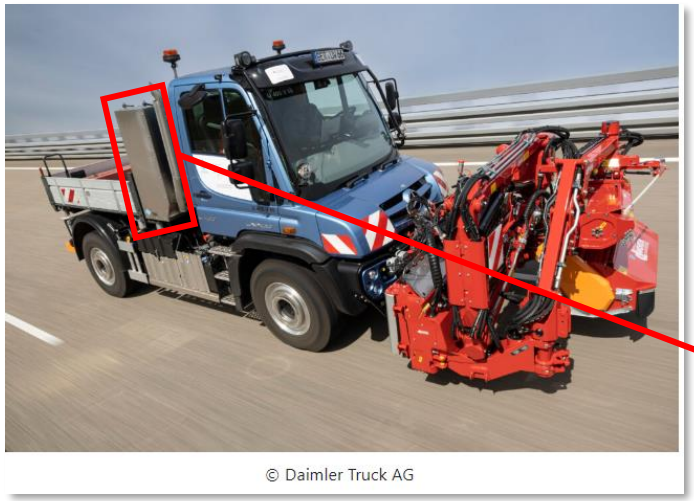

Source: https://wave.cvc-suedwest.com/

Possible design space for hydrogen tanks on a commercial vehicle

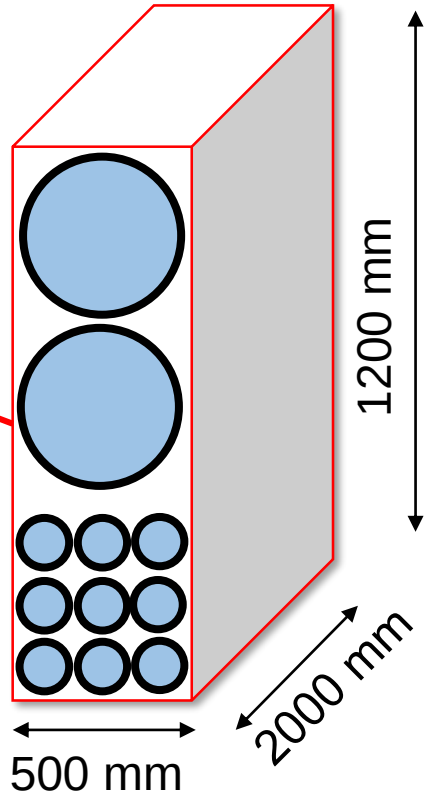

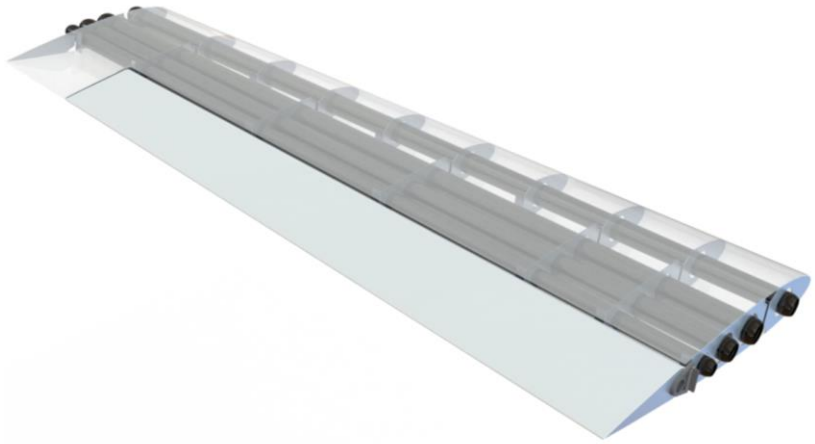

Possible design space for hydrogen tanks in the wing (e.g. CS-23)

⇒ **Flat** or **complex shaped** design spaces for hydrogen storage available
⇒ Better **design space utilization** by combination with „thin“ pressure vessels
⇒ Target operating pressure (gaseous hydrogen) = 700 bar (**Design pressure = 1,575 bar**)

www.thefutureiscomposite.com

© Leibniz-Institut für Verbundwerkstoffe GmbH

Conventional Type IV Pressure Vessels

Modern pressure vessels with CFRP (Type IV – state of the art)

Limitations due to manufacturing in a standard winding process:

No arbitrarily small diameters
⇒ Poor utilization of design space

Only small opening in the dome area
⇒ Difficult inspection and maintenance

Need for pre-manufactured liners
⇒ Costly
⇒ Difficulties in design changes (diameter, length)

No axial fibers
⇒ No additional load bearing capacities
⇒ No usage as structural part

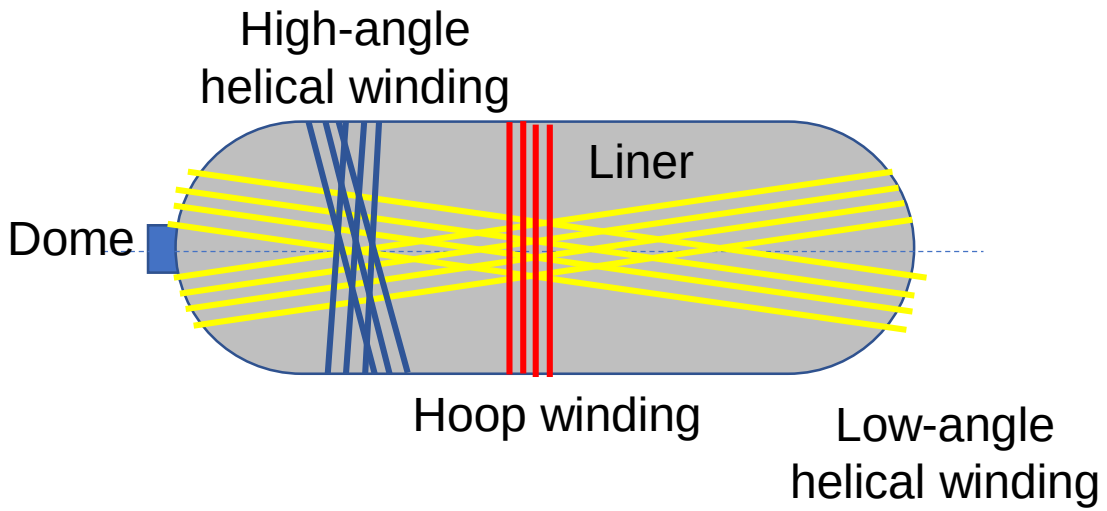

Source: Composites World, „Composites in Hydrogen Storage“, 2022.

www.thefutureiscomposite.com

© Leibniz-Institut für Verbundwerkstoffe GmbH

Patented IVW Load Introduction for Aviation Struts

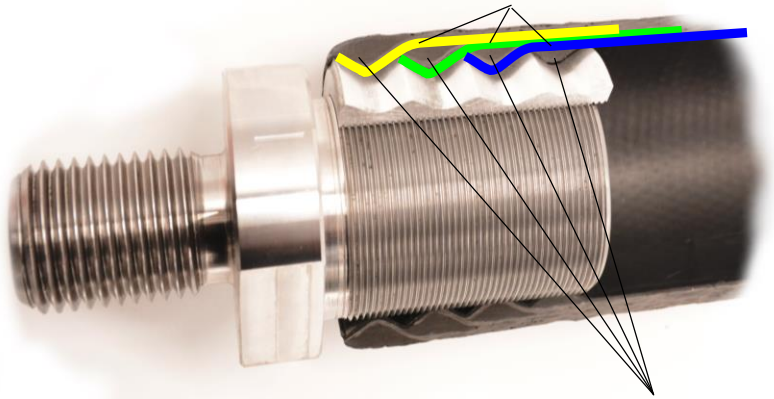

Circumferential cfrp layers

Weight:	910 g incl. metallic inserts
Laminate thickness:	2.5 mm
Length:	540 mm
Diameter:	66 mm
Load bearing:	ca. 250 kN

⇒ “Layer wise press fit”
⇒ Homogeneous load distribution with low stress peaks
⇒ Suitable for tension and compression rods

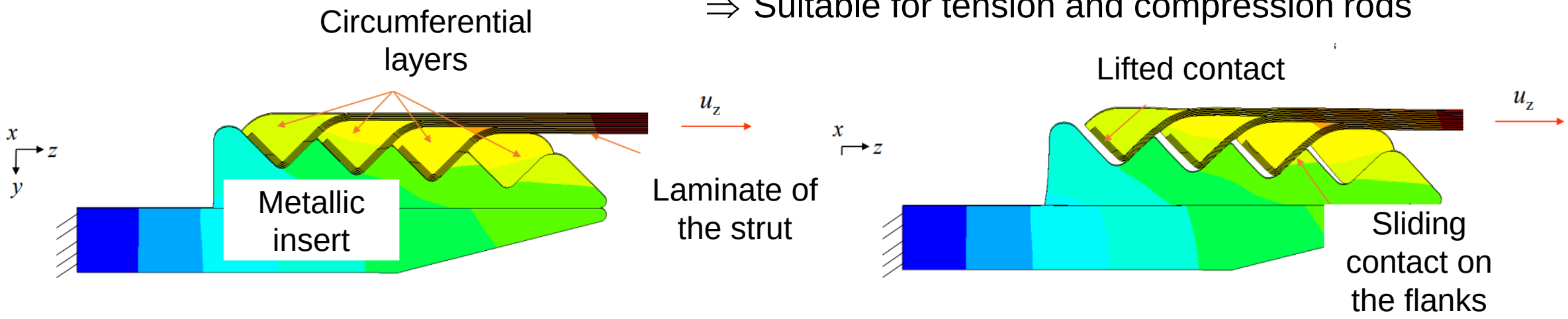

www.thefutureiscomposite.com

© Leibniz-Institut für Verbundwerkstoffe GmbH

Adaption to Hydrogen Pressure Vessel Design

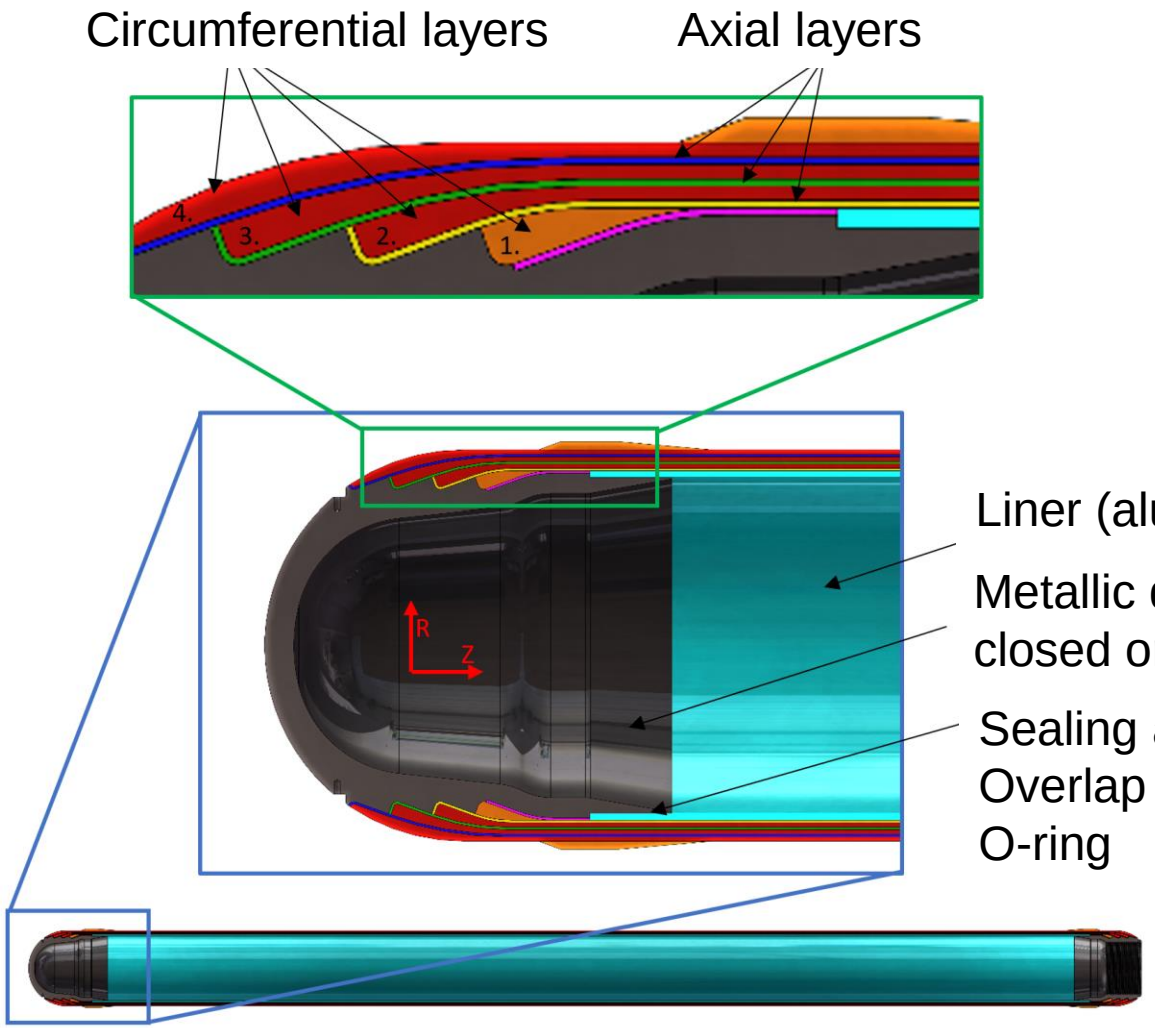

Small diameters
⇒ Good utilization of design space

Big opening in the dome area possible
⇒ Inspection and maintenance

No pre-manufactured liner necessary
⇒ Cheap
⇒ Easier design changes (diameter, length)

Axial fibers
⇒ Additional load bearing capacities
⇒ Usage as structural part

© Leibniz-Institut für Verbundwerkstoffe GmbH

Manufacturing of Demonstrators

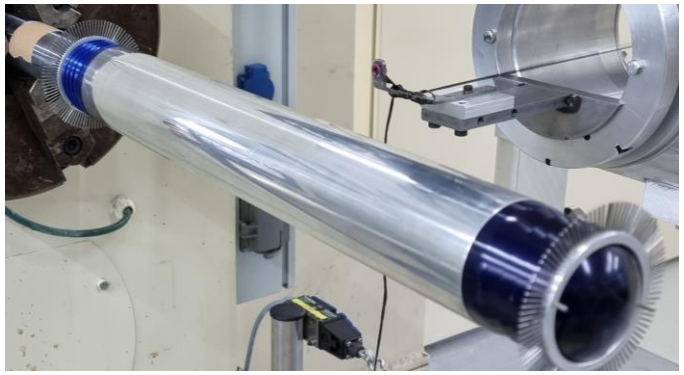

Assembly of inserts, liner and winding star at the IVW winding machine

Thermoset composite

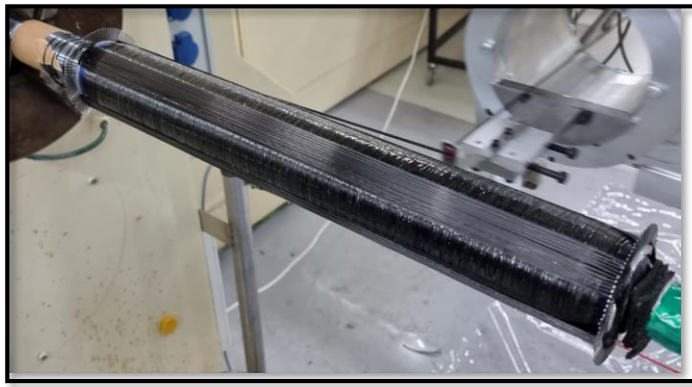

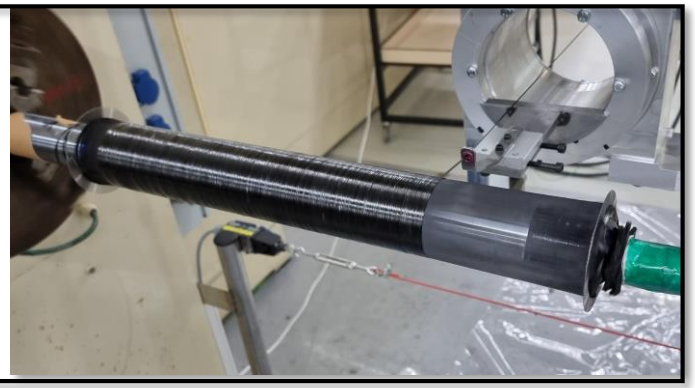

Axial Layers
Thermoset: Winding
Thermoplastic: Tape laying + hot forming

Circumferential layers
Winding

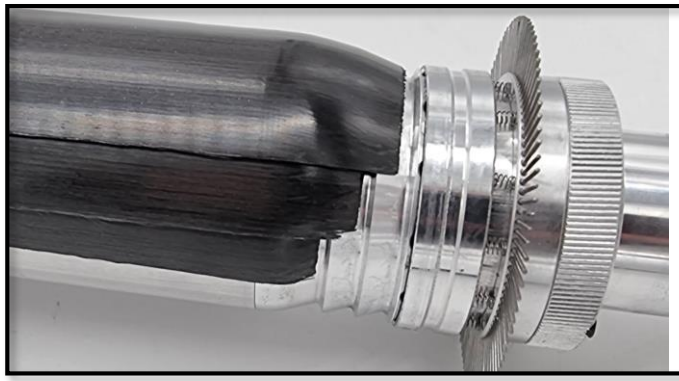

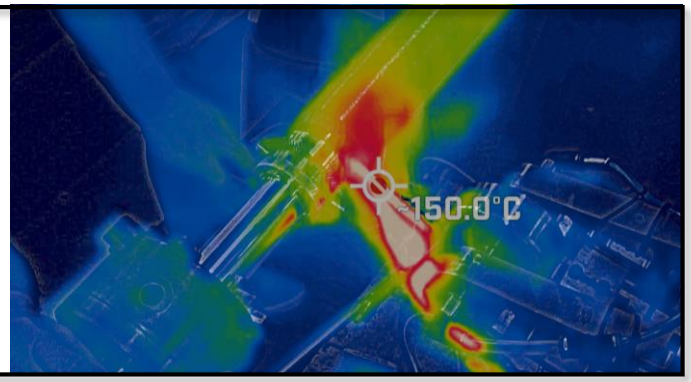

Thermoplastic composite

www.thefutureiscomposite.com

© Leibniz-Institut für Verbundwerkstoffe GmbH

Demonstrator Ready for Burst Pressure Test





www.thefutureiscomposite.com

© Leibniz-Institut für Verbundwerkstoffe GmbH

Burst Pressure Testing

Introduction | Motivation | Design | Manufacturing | Testing | Outlook

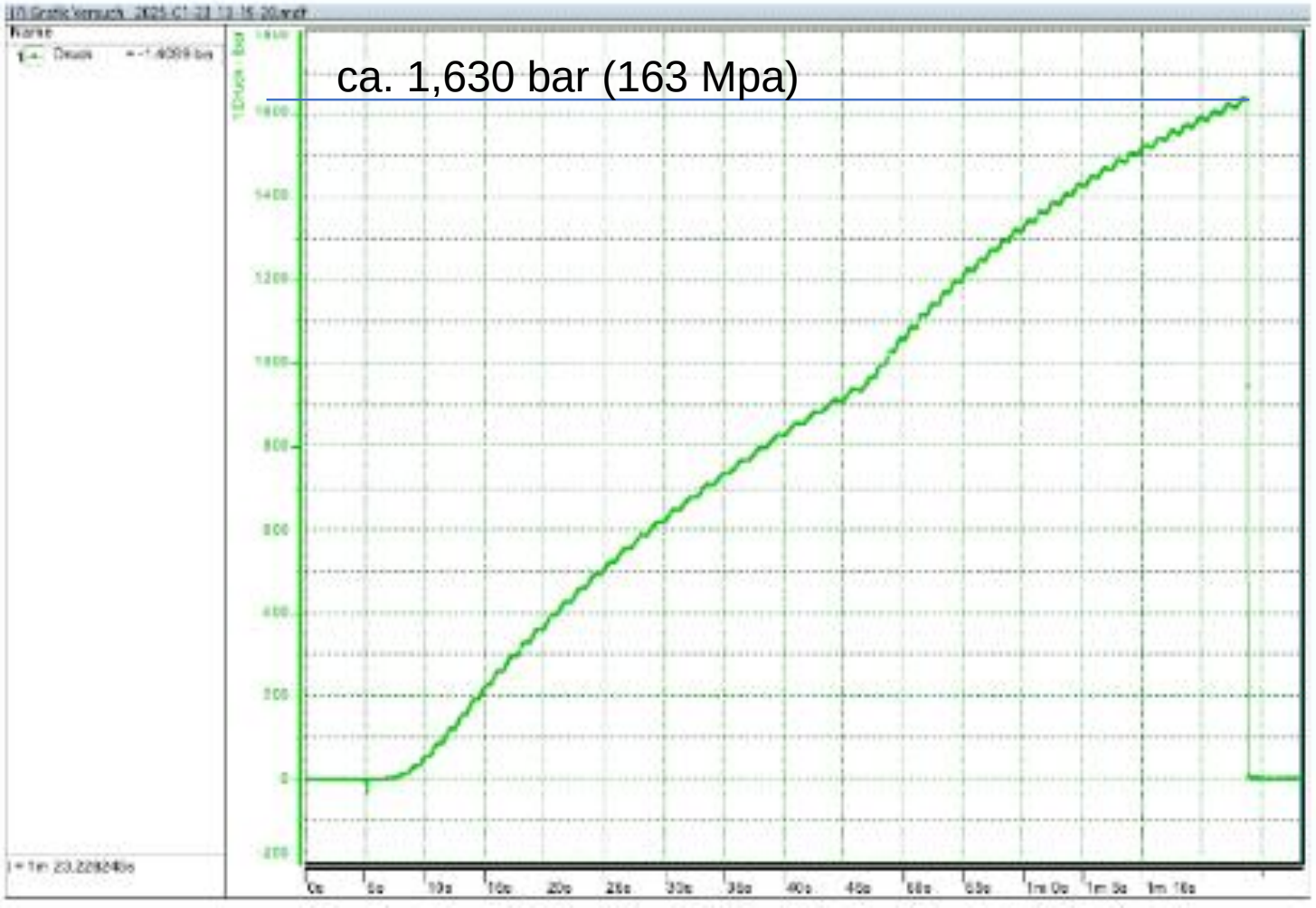



- Inner cone designed as massive part
- Circumferential layers reinforced
- Ca. 1,630 bar achieved
  (target 1,575 bar)

www.thefutureiscomposite.com

© Leibniz-Institut für Verbundwerkstoffe GmbH

R&D-project BMFTR ConnectH2Australia (2024-2026)

Introduction | Motivation | Design | Manufacturing | Testing | Outlook

Building Connecting Bridges for Lightweight Hydrogen Storage Solutions in Australia

Partner: AIR Hub - Swinburne University of Technology (Melbourne)

Conventional H_2-Pressure vessel

- Mass 4,250 g
- Hydrogen: 240 g
- **Weight efficiency** 5.34 %

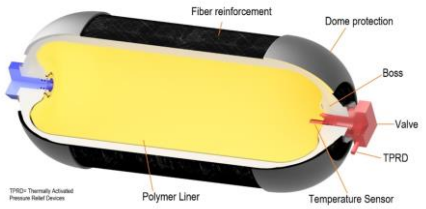

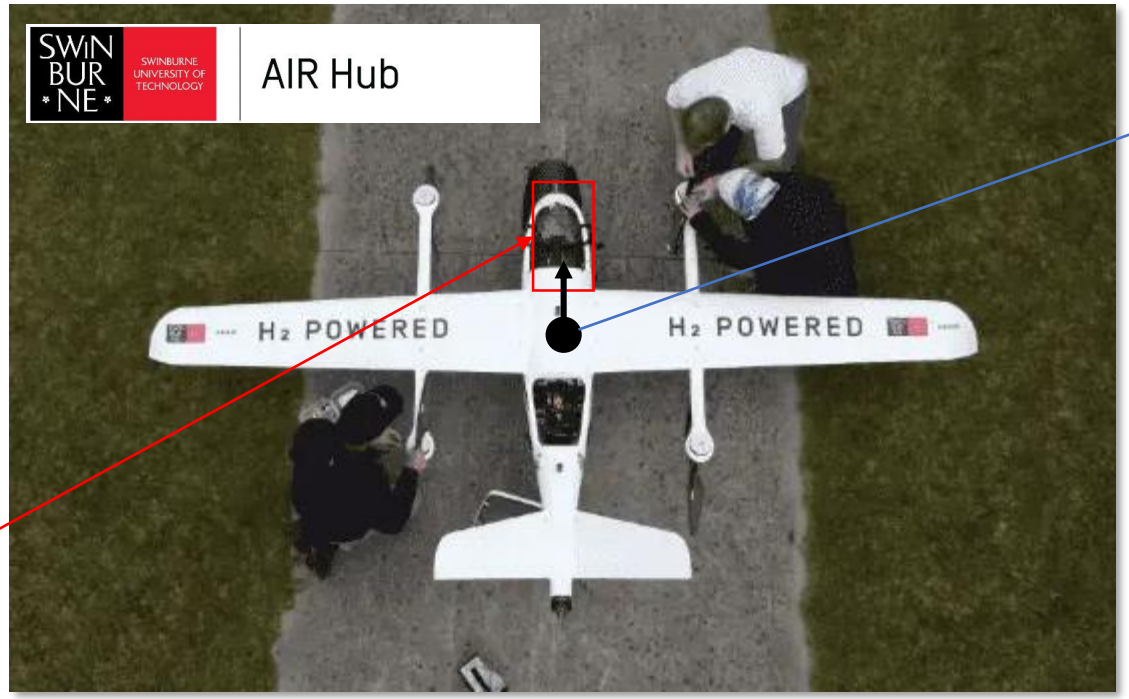

Shift in the center of gravity

⇒ Increased drag

⇒ Poorer maneuvarability

⇒ Increased forces on horizontal tail plane

Bundesministerium für Forschung, Technologie und Raumfahrt

www.thefutureiscomposite.com

© Leibniz-Institut für Verbundwerkstoffe GmbH

R&D-project BMFTR ConnectH2Australia (2024-2026)

Introduction | Motivation | Design | Manufacturing | Testing | Outlook

Bundesministerium für Forschung, Technologie und Raumfahrt

Three pressure vessels in the wing:

- 3500 mm length, diameter ca. 66 mm
- Mass per tank (w/o H_2): 4480 g
- H_2 per tank: **348 g**
- **Mass total (3 tanks):**
  13.440 kg (w/o H_2)
  14.486 kg (with H_2)
- **Weight efficiency: 7.2 %**

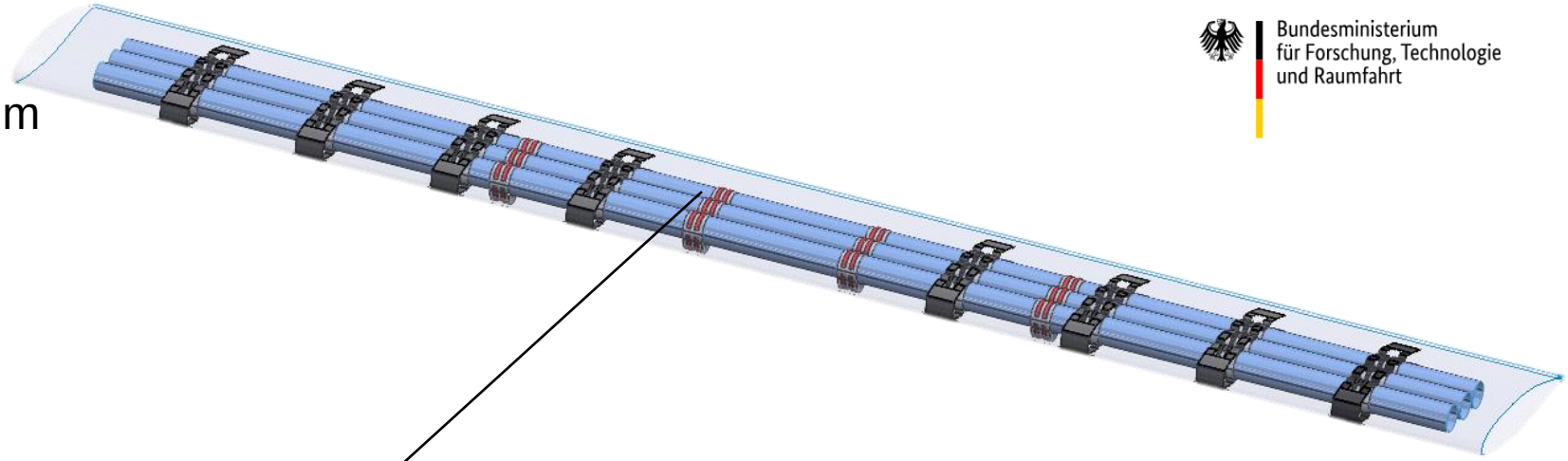

Advantages:

+ Payload space is not reduced
+ No additional drag
+ Less shift of the centre of gravity
+ Higher weight efficiency (substitution of spar)

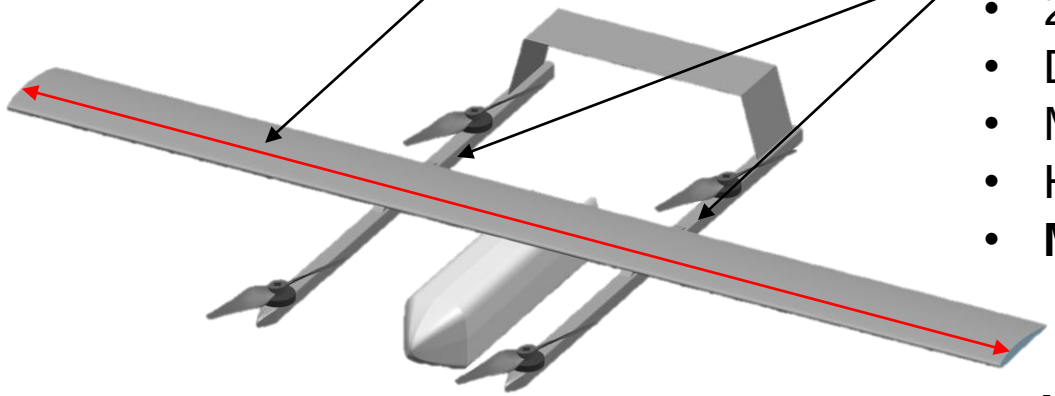

Wingspan 3.5 - 3.8 m

Two pressure vessel in the booms:

- 2000 mm length
- Diameter ca. 66mm
- Mass per tank (w/o H_2): 2876 g
- H_2 per tank: **196 g**
- **Mass total (2 tanks):**
  5752 g (w/o H_2)
  6143.34 g (with H_2)
- **Weight efficiency: 6.8 %**

www.thefutureiscomposite.com

© Leibniz-Institut für Verbundwerkstoffe GmbH

Summary

Opportunities

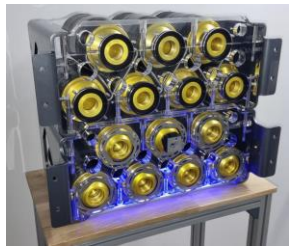

- **Optimized design space utilization** through small-diameter pressure vessels (usage as conformable tank)
- Patented IVW-design enables **lightweight pressure vessel** construction
- Integration of **tanks as structural components**

Challenges



- Metallic and composite parts under **high cyclic loading**
- **Relative displacement** between insert and CFRP layers
- Ensuring **sufficient coefficient of friction** between the two cones

Way forward

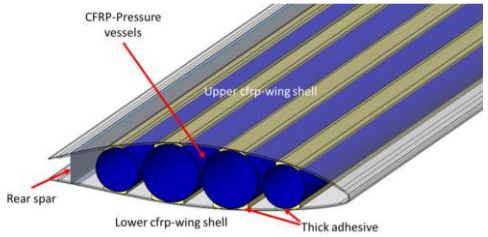

- **Optimizing insert geometry** to reduce weight (ongoing)
- **Validation for cyclic loading, impact, and H_2 filling** planned for 2025
- A manufacturing concept suitable for **large-scale production** *(ongoing)*
- **Proof of structural integrity** via cyclic bending tests on scaled demonstrators *(2025)*

www.thefutureiscomposite.com

© Leibniz-Institut für Verbundwerkstoffe GmbH

Acknowledgement

The project „H2Flex: Prozess- und Anlagenentwicklung zur Herstellung einer neuartigen, kostengünstigen, geometrisch hochflexiblen Leichtbau-Wasserstoff-Tank-Bauweise unter Verwendung von Kohlenstofffasern und einem biobasierten Harzsystem“ is funded by the Federal Ministry for Economics and Enregy on the basis of a decision by the German Bundestag (funding reference: 03LB3100A).

Bundesministerium für Wirtschaft und Energie

www.thefutureiscomposite.com

© Leibniz-Institut für Verbundwerkstoffe GmbH

Thank you for your attention!

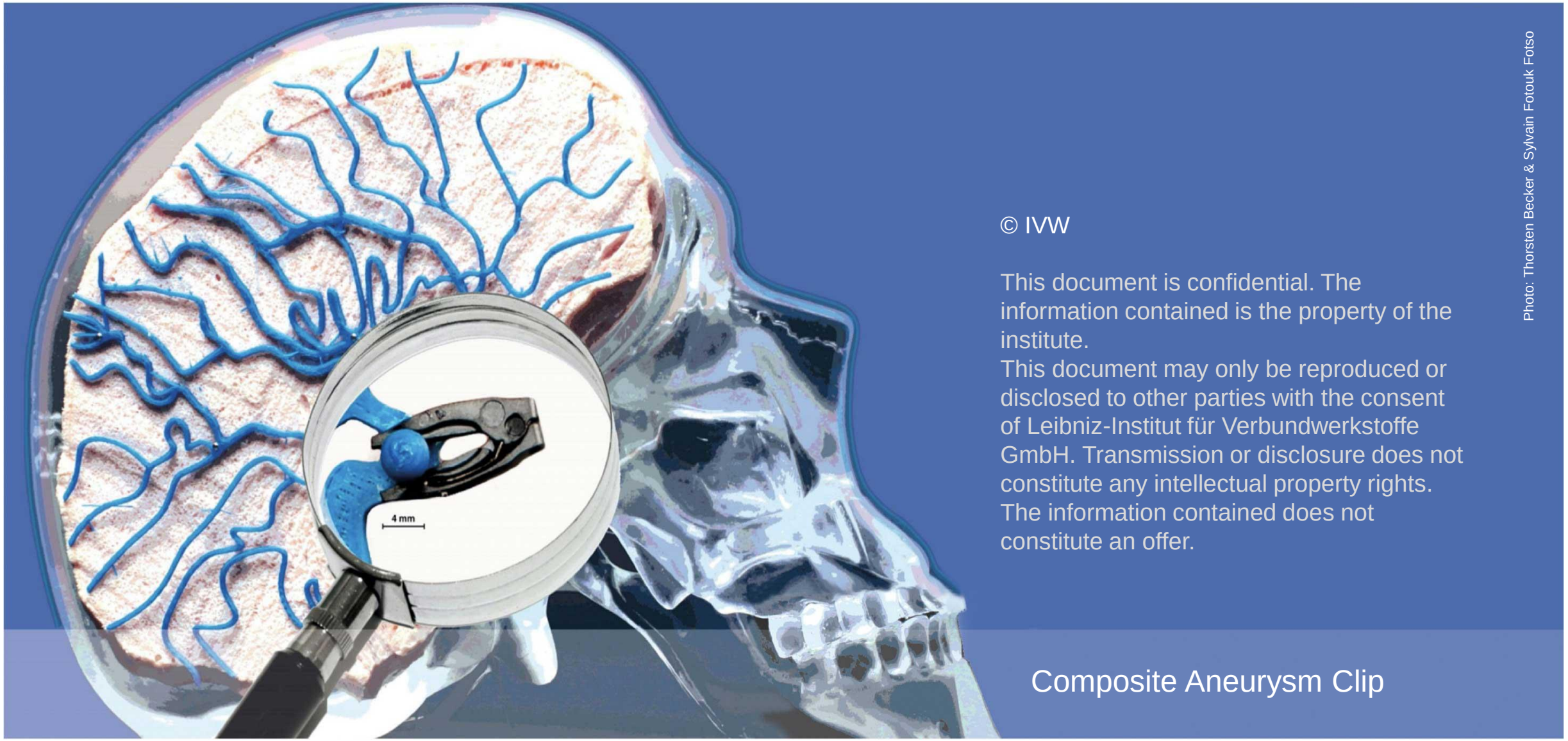

© IVW

This document is confidential. The information contained is the property of the institute.
This document may only be reproduced or disclosed to other parties with the consent of Leibniz-Institut für Verbundwerkstoffe GmbH. Transmission or disclosure does not constitute any intellectual property rights. The information contained does not constitute an offer.

Photo: Thorsten Becker & Sylvain Fotouk Fotso

Composite Aneurysm Clip

www.thefutureiscomposite.com

A double-wall CFPR hydrogen storage and distribution system as a structural component in aircraft applications- **CF-Hydro**

ICCM24

04.08.2025



Leibniz-Institut für Verbundwerkstoffe

Nithya Sindhe
Nicole-Motsch Eichmann
Thomas Pfaff
Blass Ulrich
Uwe Schmitt
Joachim Hausmann

www.thefutureiscomposite.com

© Leibniz-Institut für Verbundwerkstoffe GmbH

Agenda

- Introduction to CF-Hydro
- Challenges in H_2 storage
- Hydrogen storage types
- Overview of LH_2 distribution system
- LH_2 inner pipe production
- Suspension system concept
- Overview of CcH_2 distribution system
- Outer shell demonstrator test

www.thefutureiscomposite.com

© Leibniz-Institut für Verbundwerkstoffe GmbH

Introduction: CF-Hydro

<u>Overall Scientific Objectives:</u> Develop (TRL3) lightweight construction methods and processes for the manufacturing of CFRP pipelines for **hydrogen distribution** in aircrafts.

- Further investigate the possibilities of the developed designs and processes for the manufacturing of a **hydrogen storage** system.

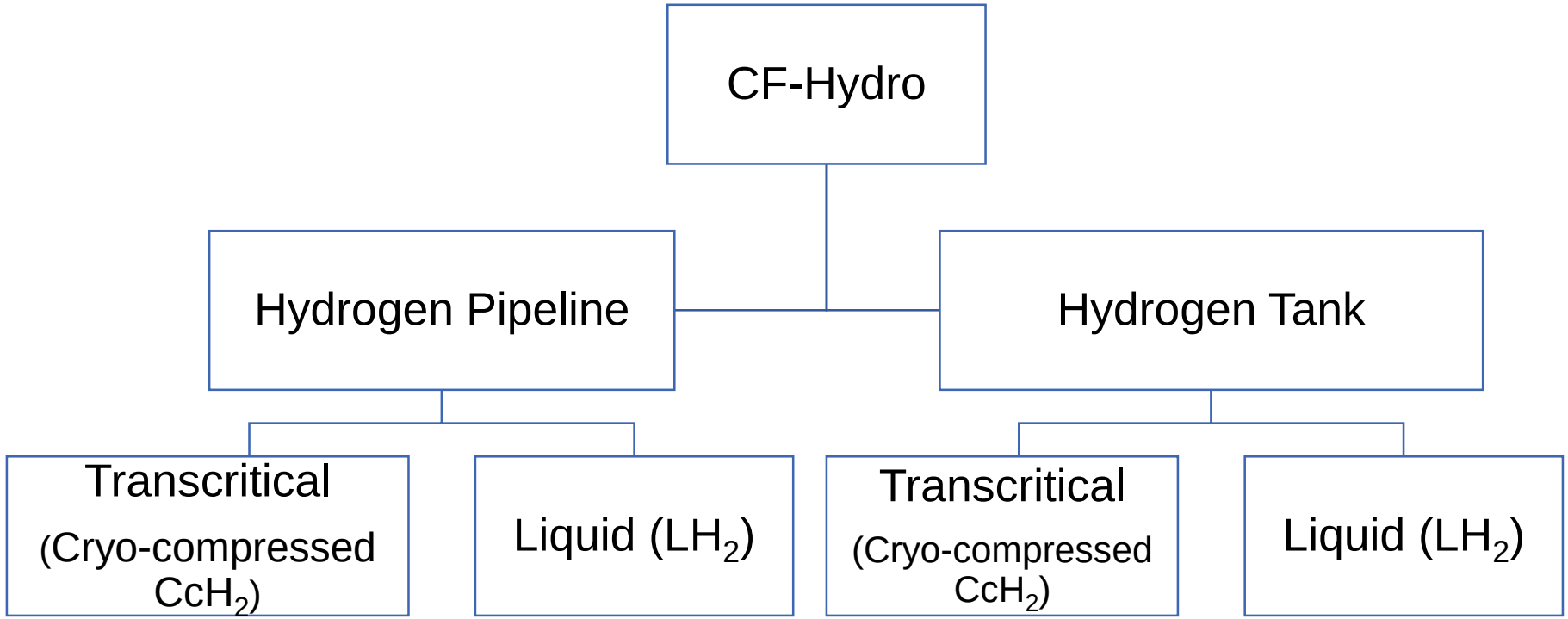

www.thefutureiscomposite.com

© Leibniz-Institut für Verbundwerkstoffe GmbH

Hydrogen storage types

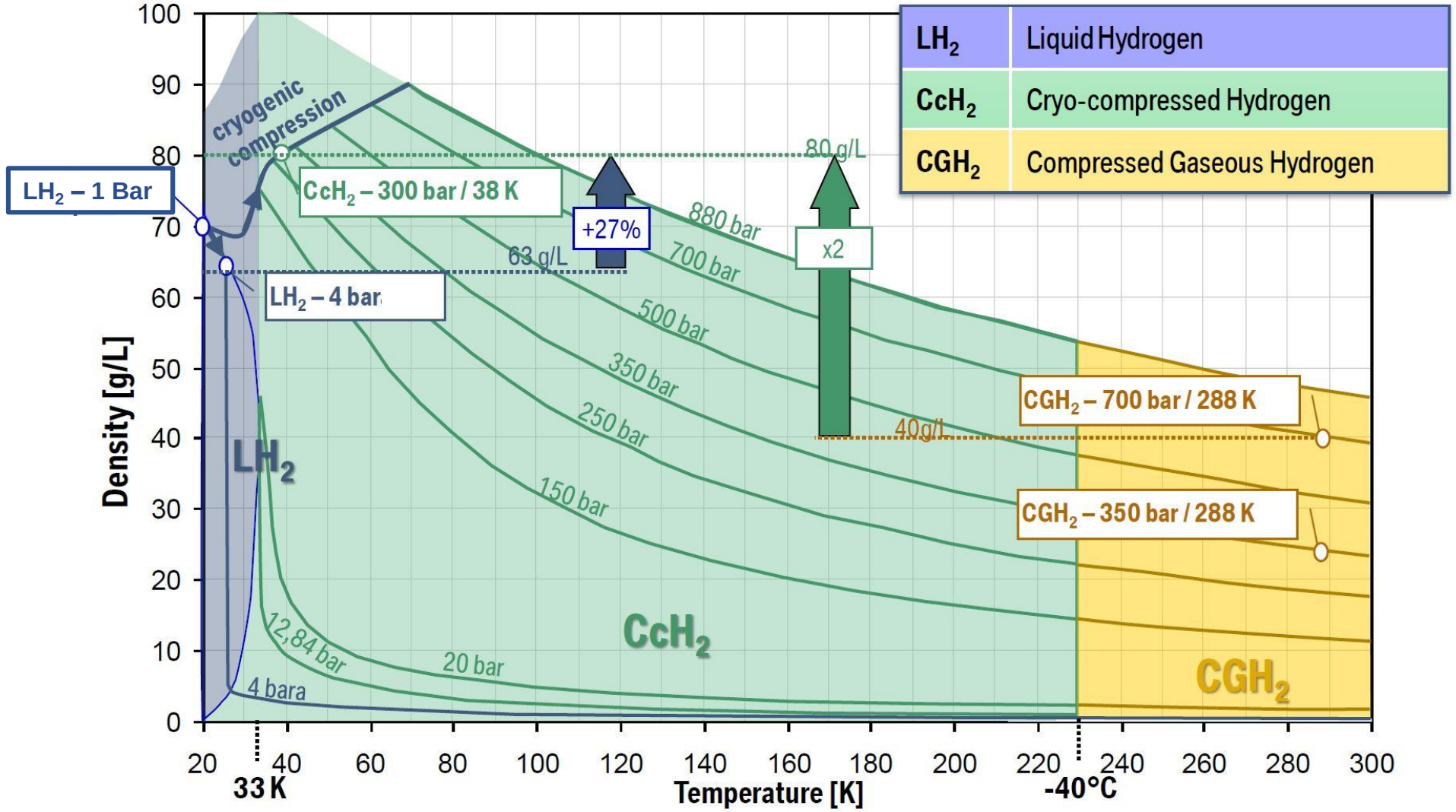

Source: BMW

www.thefutureiscomposite.com

© Leibniz-Institut für Verbundwerkstoffe GmbH

Challenges

Heat Transfer through
- Conduction
- Convection
- Radiation

Outer shell

-55 °C to +85 °C
Aircraft temp. range

Multi layer
vacuum insulation

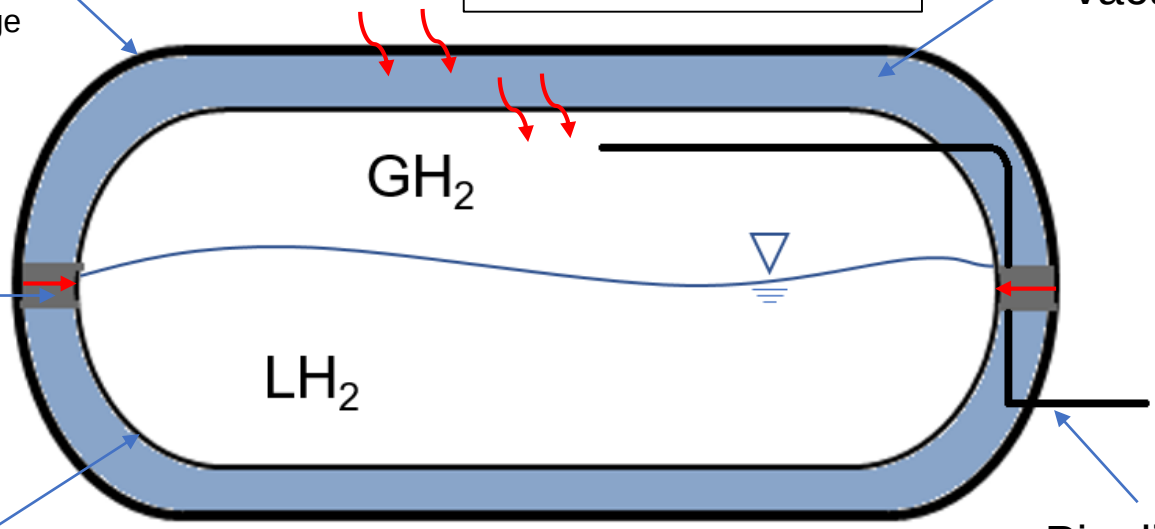

Suspension

Inner tank

-252 °C
LH_2 temp.

Pipeline

Filling line
Gas extraction
Liquid extraction

Things to account for:

- Thermal cycling
- Boil-off losses

→ Effective insulation system

- Thermal expansion/ Contraction
  - Relative displacements between parts

www.thefutureiscomposite.com

© Leibniz-Institut für Verbundwerkstoffe GmbH

Challenges

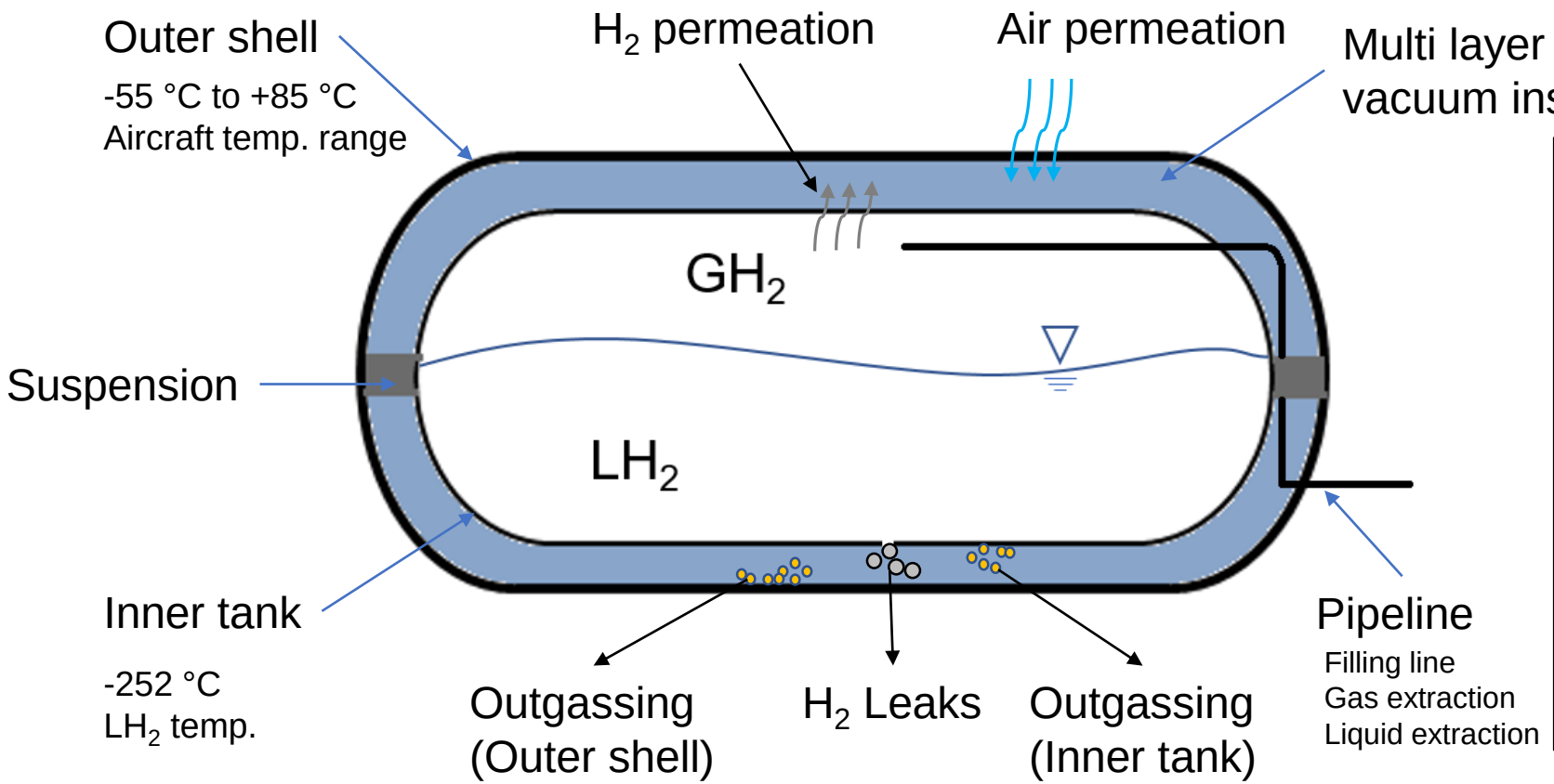

Things to account for:

- Diffusion
- Permeation
- Leakage

→ Ensure high vacuum tightness

- Sloshing of the liquid in cylindrical tanks

www.thefutureiscomposite.com

© Leibniz-Institut für Verbundwerkstoffe GmbH

Overview: LH_2 distribution system

- Cylindrical, double-walled, mechanically decoupled CFRP hydrogen pipeline

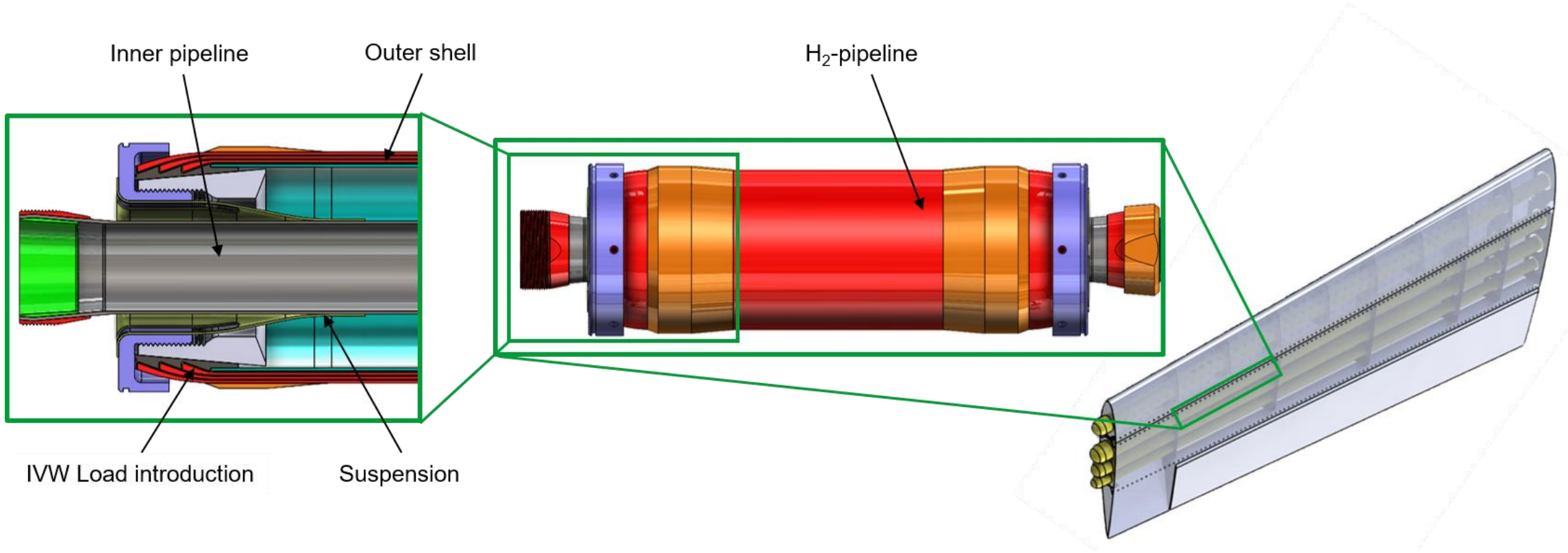

www.thefutureiscomposite.com

© Leibniz-Institut für Verbundwerkstoffe GmbH

Overview: Load transfer principle

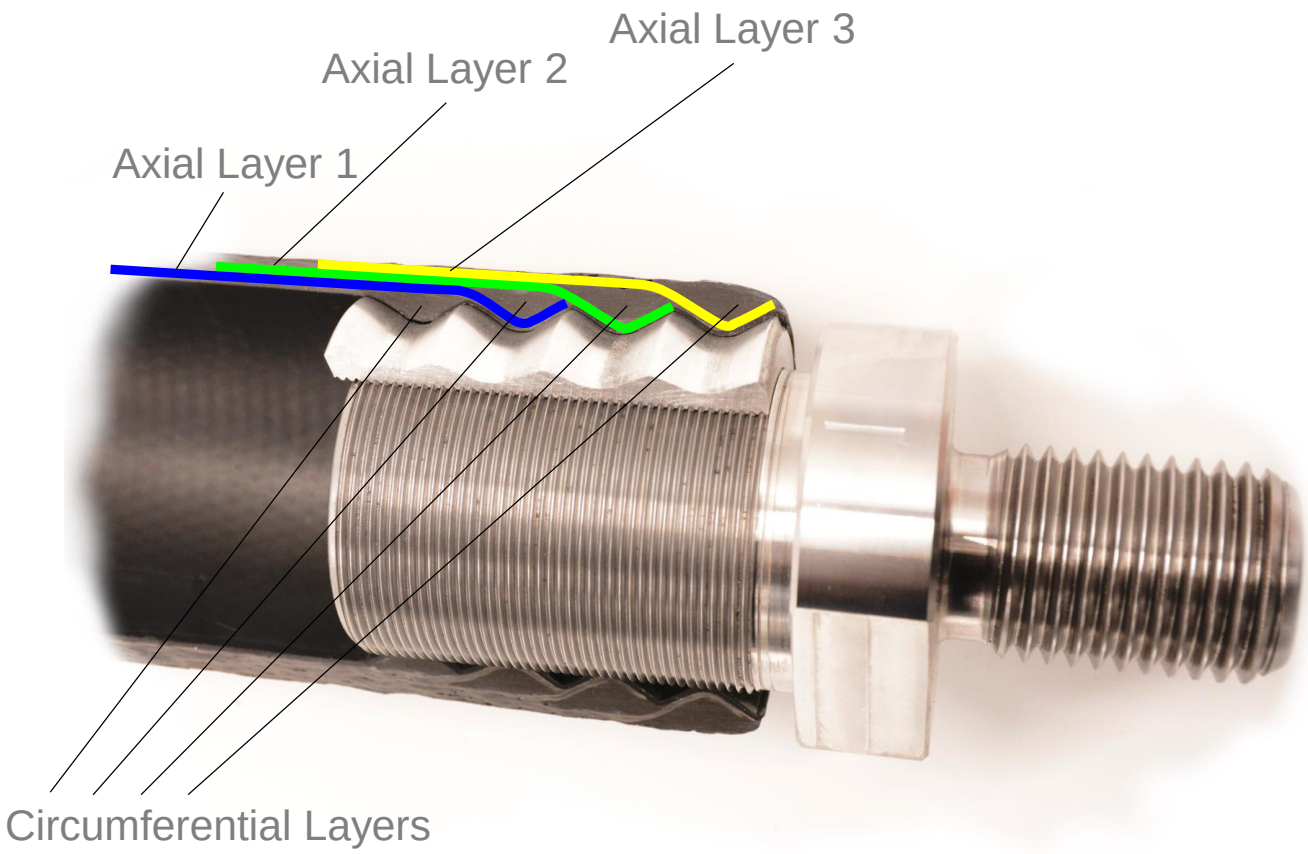

CF-Hydro Innovation

- Layer-by-layer transfer of the force from the CFRP into the metallic load introduction
  → High light weight potential
- Axial (0°) fiber direction without ondulation
  → High light weight potential
- No bonding between CFRP and Metal
  → no delta-alpha problem
- Open CFRP construction
  → access for maintenance and repair
- Mechanically decoupled inner pipe/outer shell
  → structural load bearing component

www.thefutureiscomposite.com

© Leibniz-Institut für Verbundwerkstoffe GmbH

LH_2 distribution pipeline

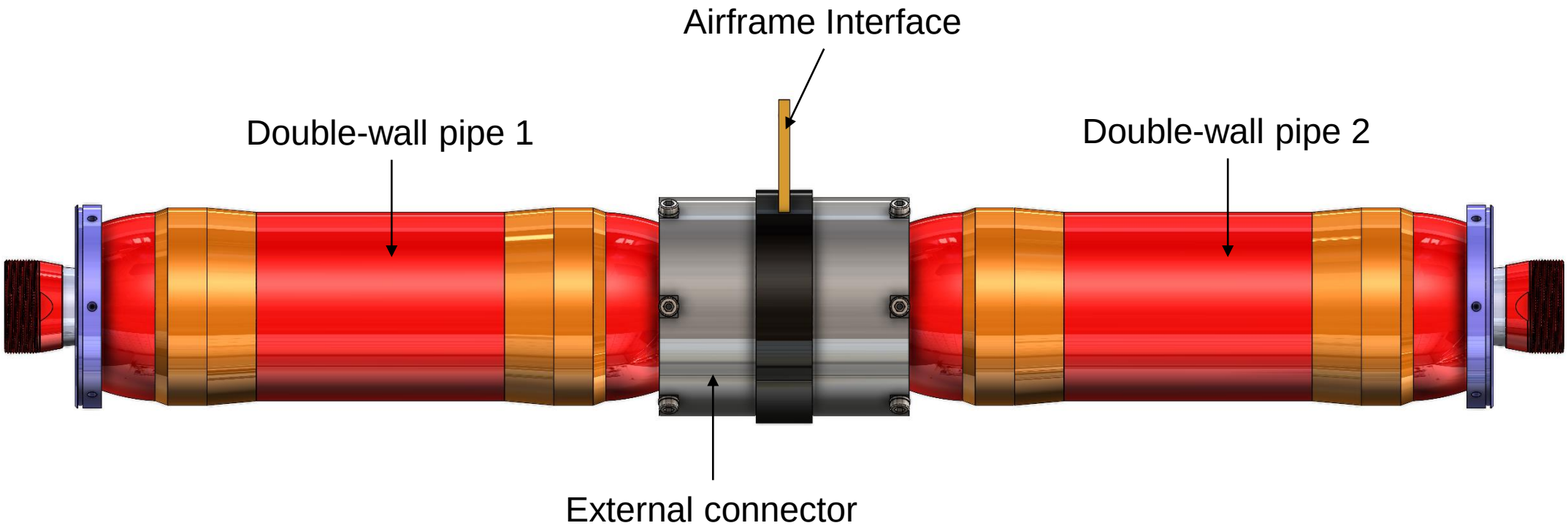

www.thefutureiscomposite.com

© Leibniz-Institut für Verbundwerkstoffe GmbH

LH_2 distribution pipeline

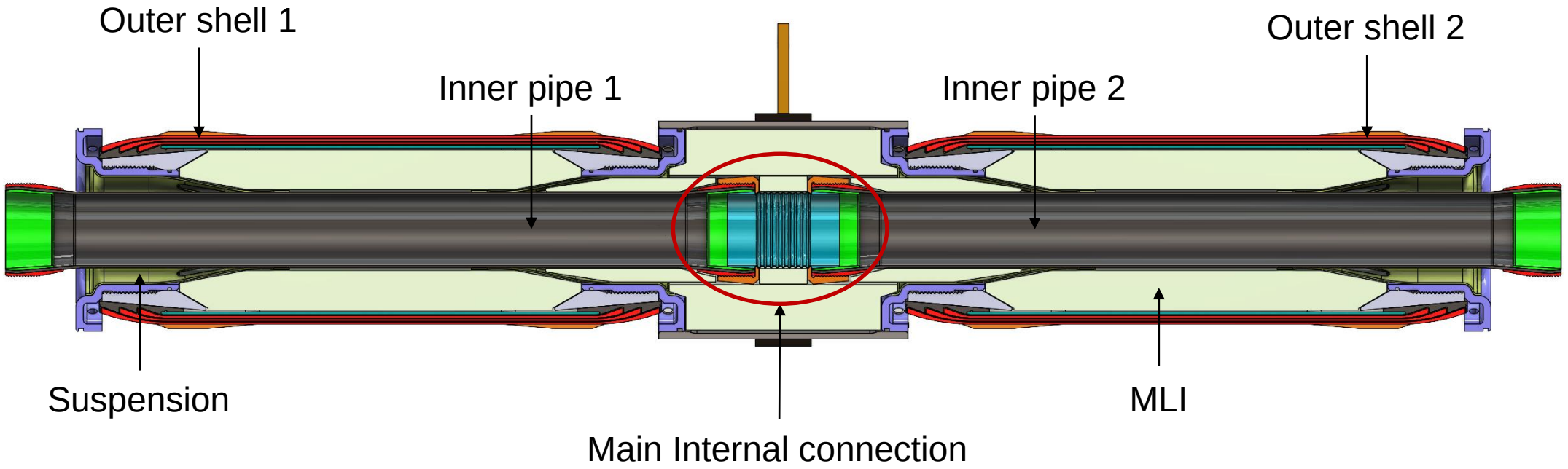

www.thefutureiscomposite.com

© Leibniz-Institut für Verbundwerkstoffe GmbH

LH_2 distribution pipeline

Pipeline cross-section without MLI

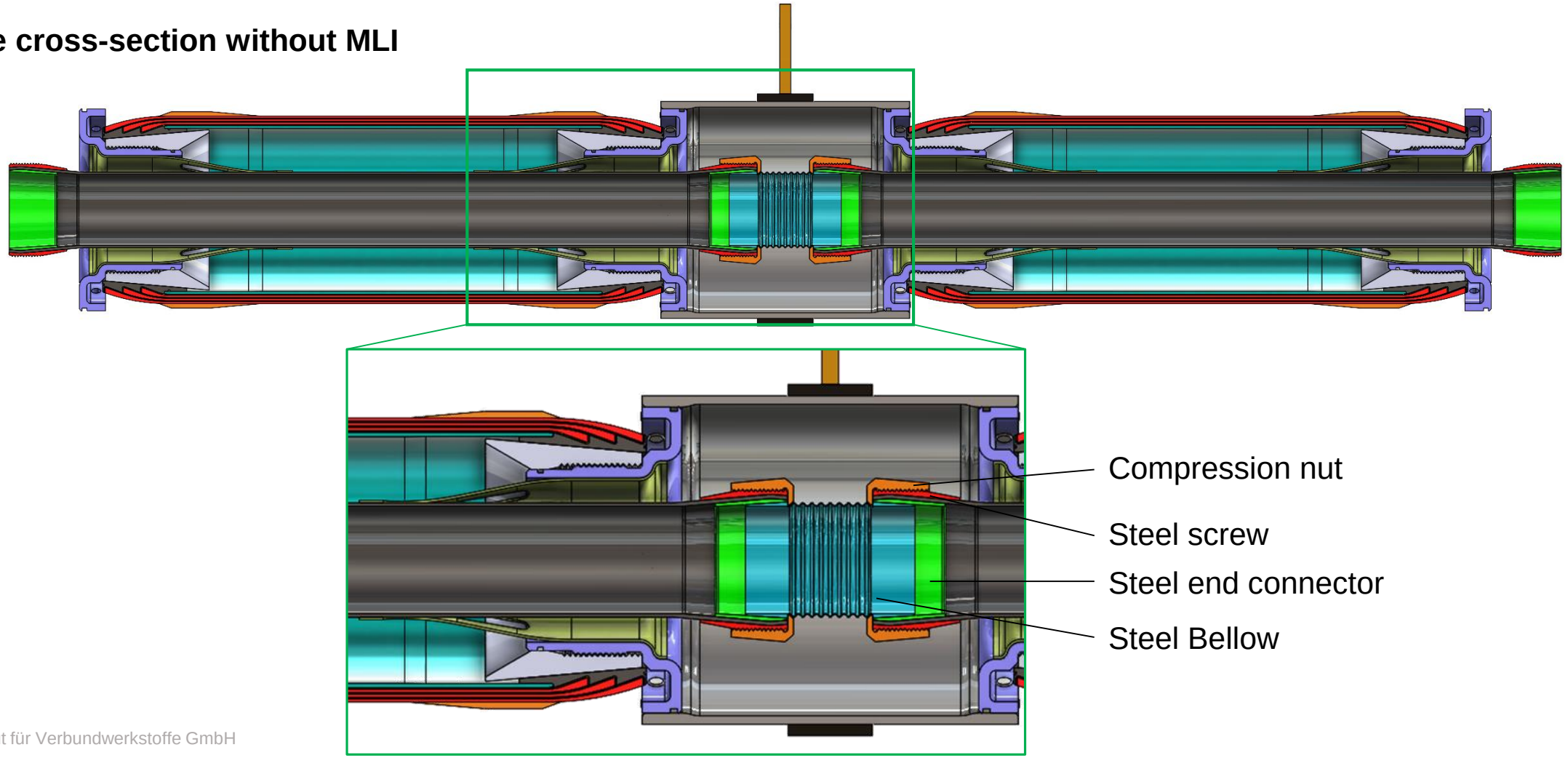

www.thefutureiscomposite.com

© Leibniz-Institut für Verbundwerkstoffe GmbH

LH_2 Inner Pipeline

Input parameters:

Design pressure	**4,8** MPa (48 Bar)
Inner diameter	38- 40 mm
Matrix	Epoxy
Fiber	T300 J carbon fiber
Strength (R_{11})	1860 MPa
Min Wall thickness (Boiler's formula)	< **0,3** mm

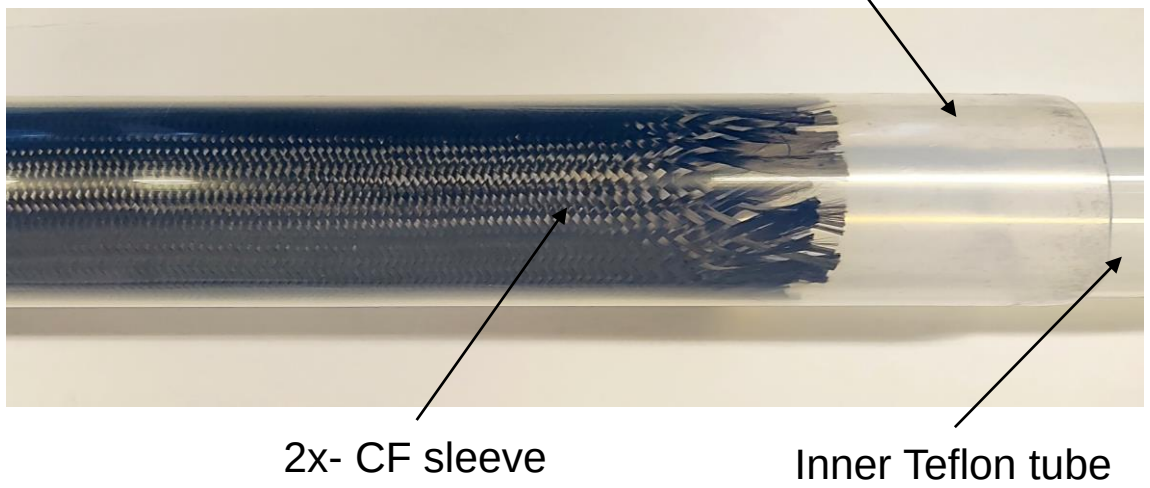

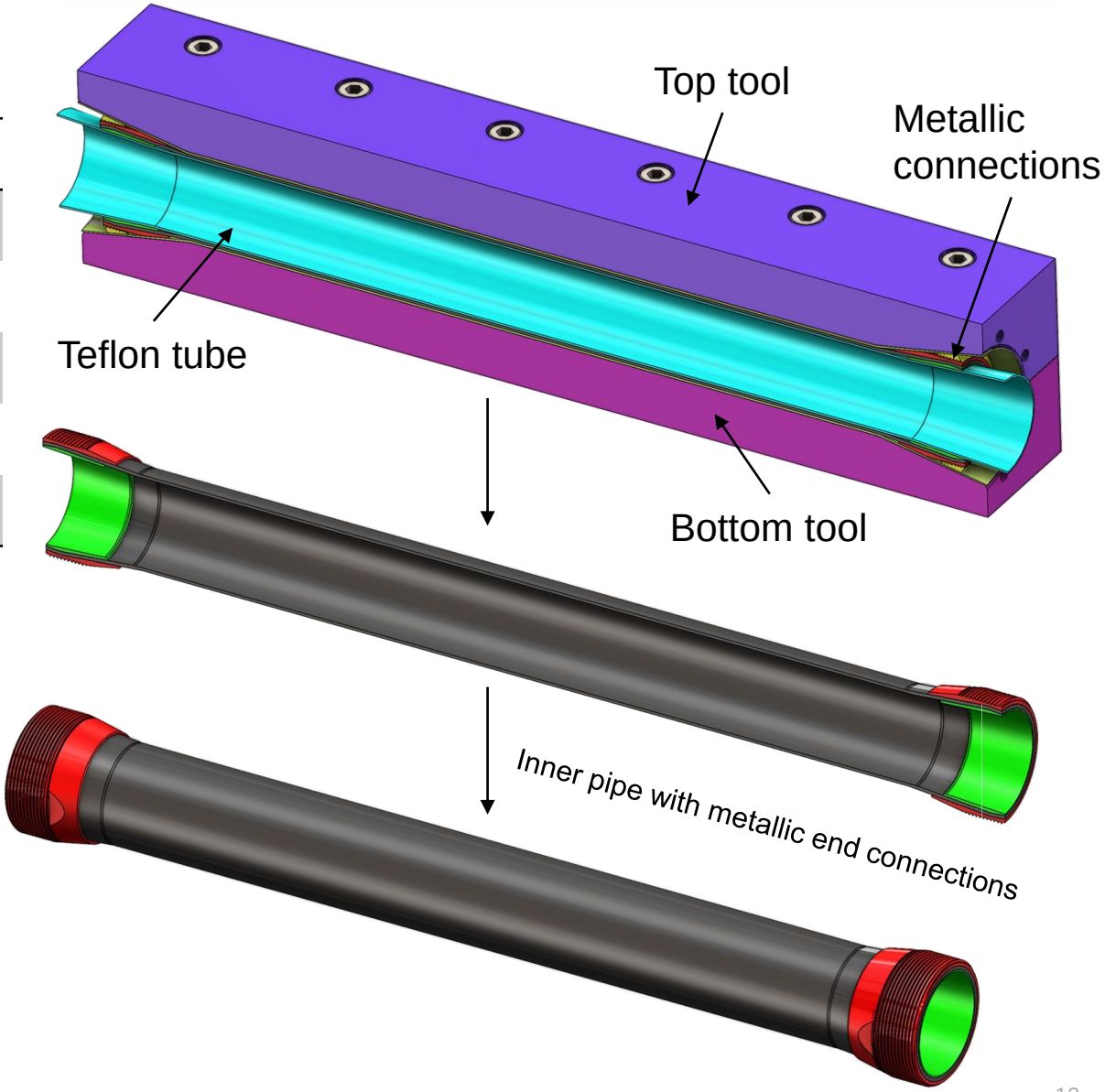

www.thefutureiscomposite.com

© Leibniz-Institut für Verbundwerkstoffe GmbH

Suspension system concept

Composite Z-profile suspension

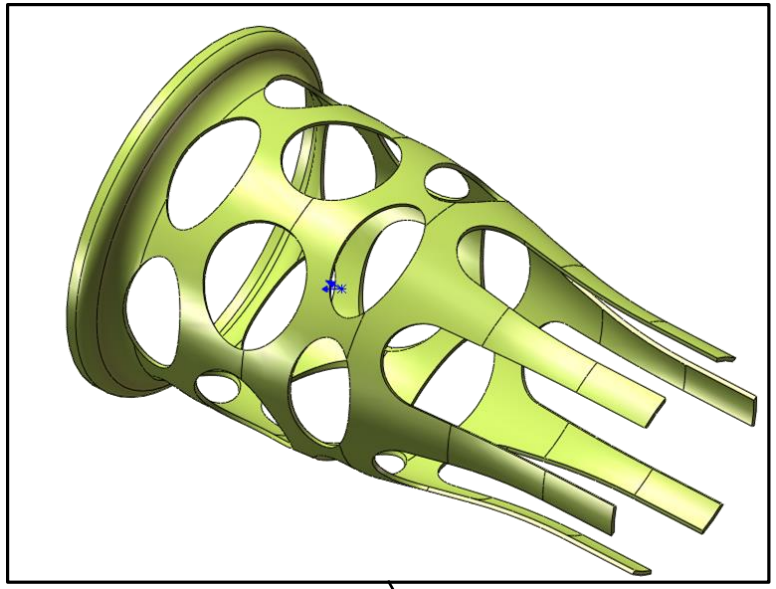

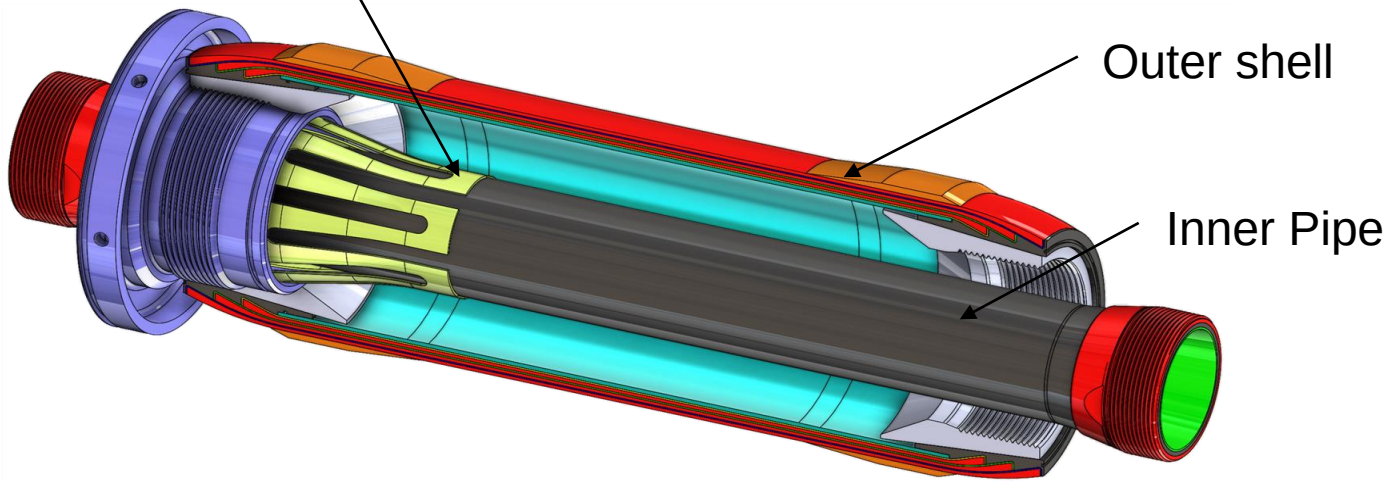

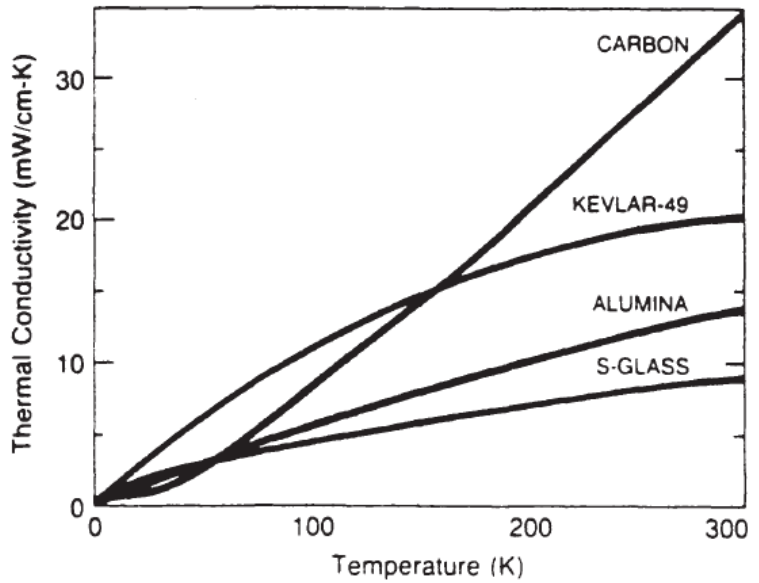

Source: Giesy, R.K. (1996). https://doi.org/10.1007/978-1-4757-9059-7_34

www.thefutureiscomposite.com

© Leibniz-Institut für Verbundwerkstoffe GmbH

CcH2 Inner Pipeline: Stress-free (1)

T = 293 K
p = 0 bar

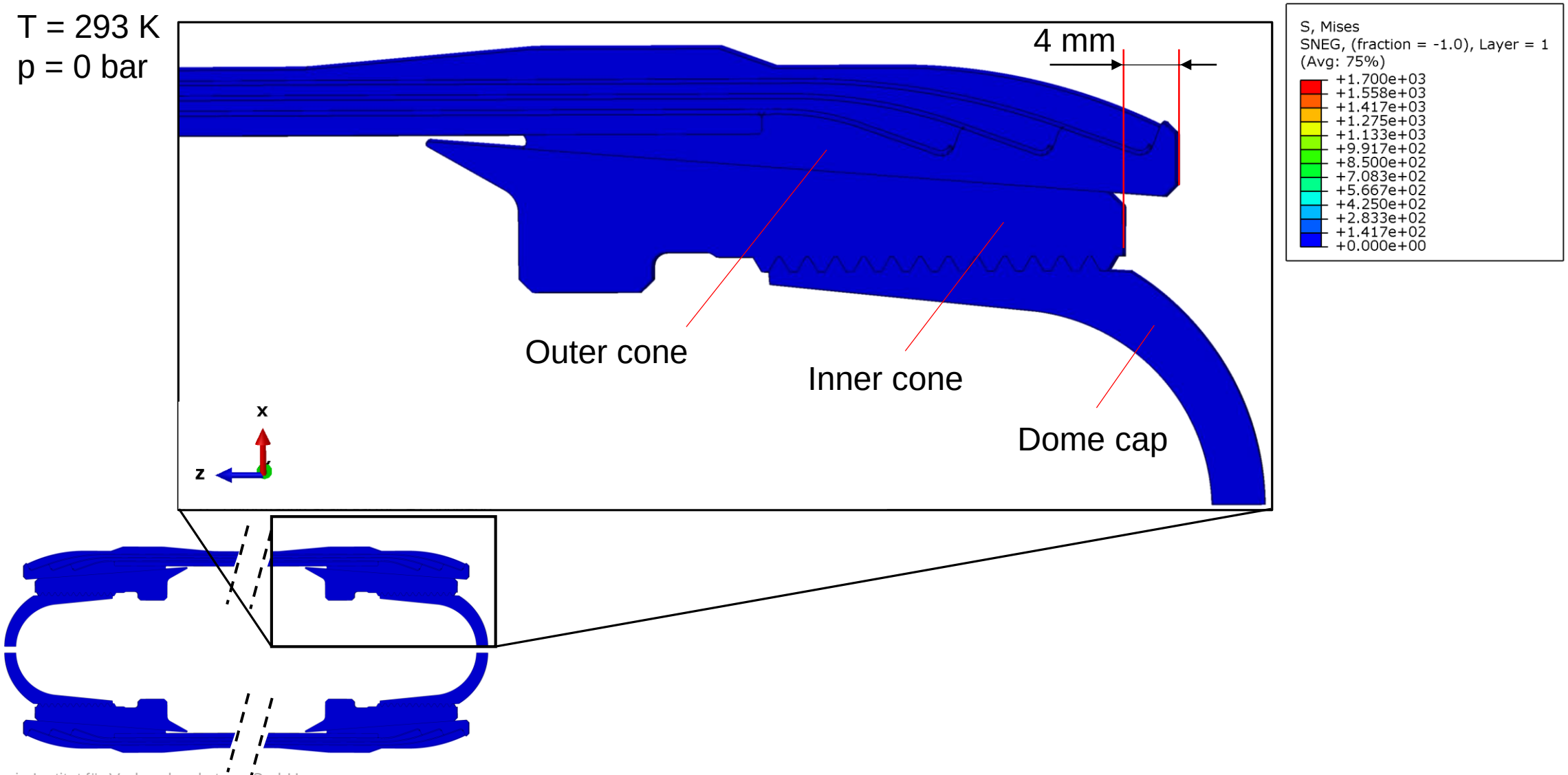

www.thefutureiscomposite.com

© Leibniz-Institut für Verbundwerkst[illegible] GmbH

CcH2 Inner Pipeline: Pre-tension (2)

T = **293** K
p = **0** bar

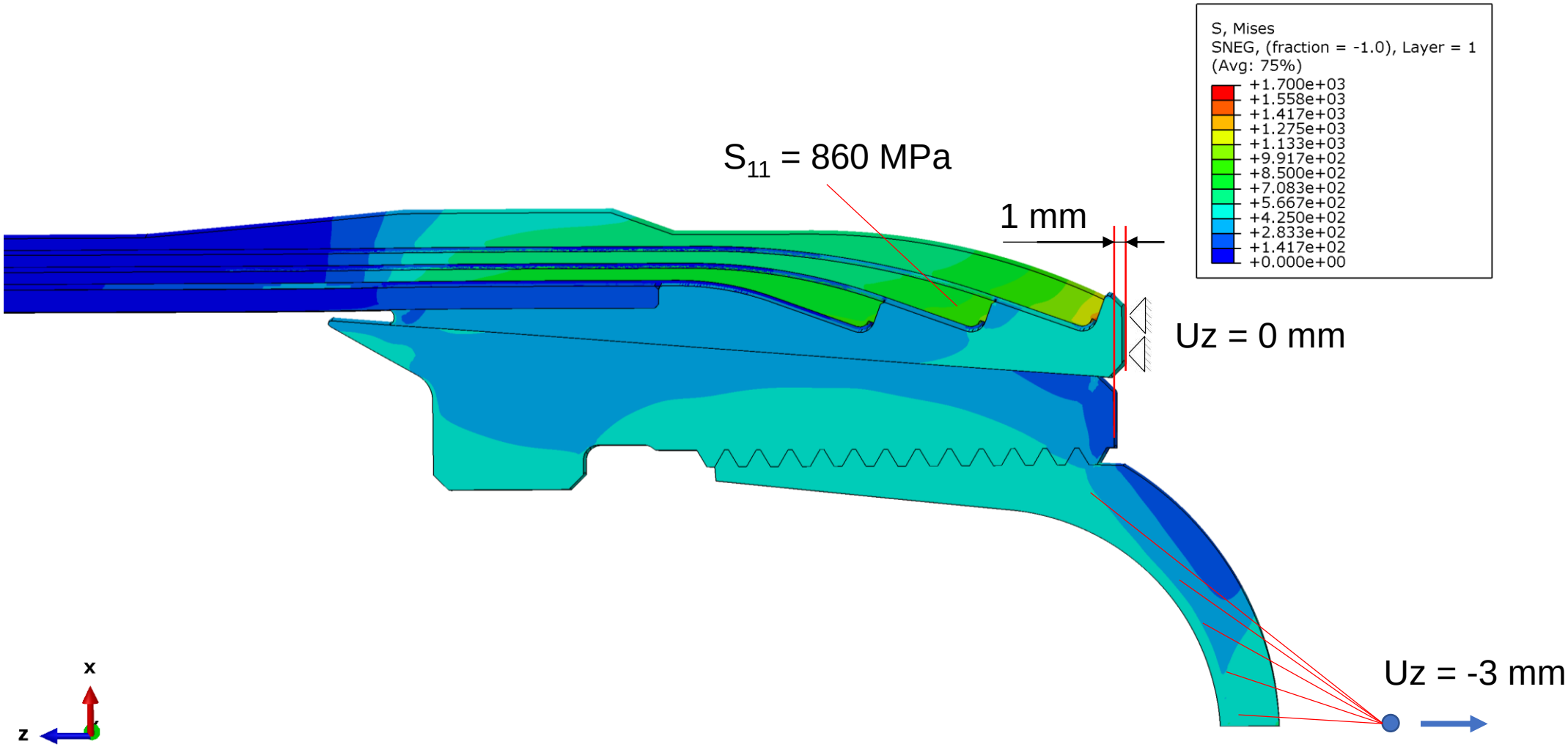

www.thefutureiscomposite.com

© Leibniz-Institut für Verbundwerkstoffe GmbH

CcH2 Inner Pipeline: cooling (3)

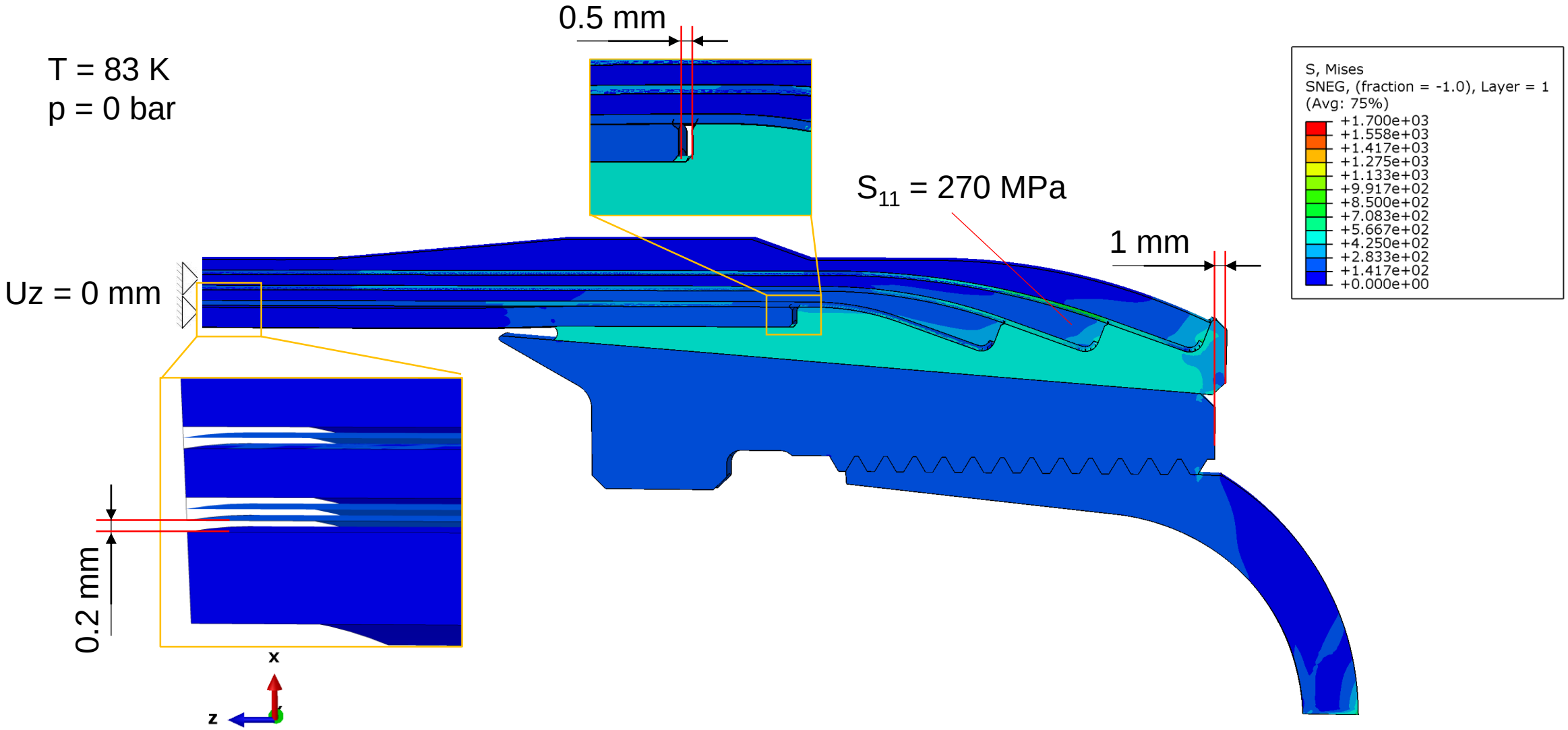

www.thefutureiscomposite.com

© Leibniz-Institut für Verbundwerkstoffe GmbH

CcH2 Inner Pipeline: cooled and pressurized (4)

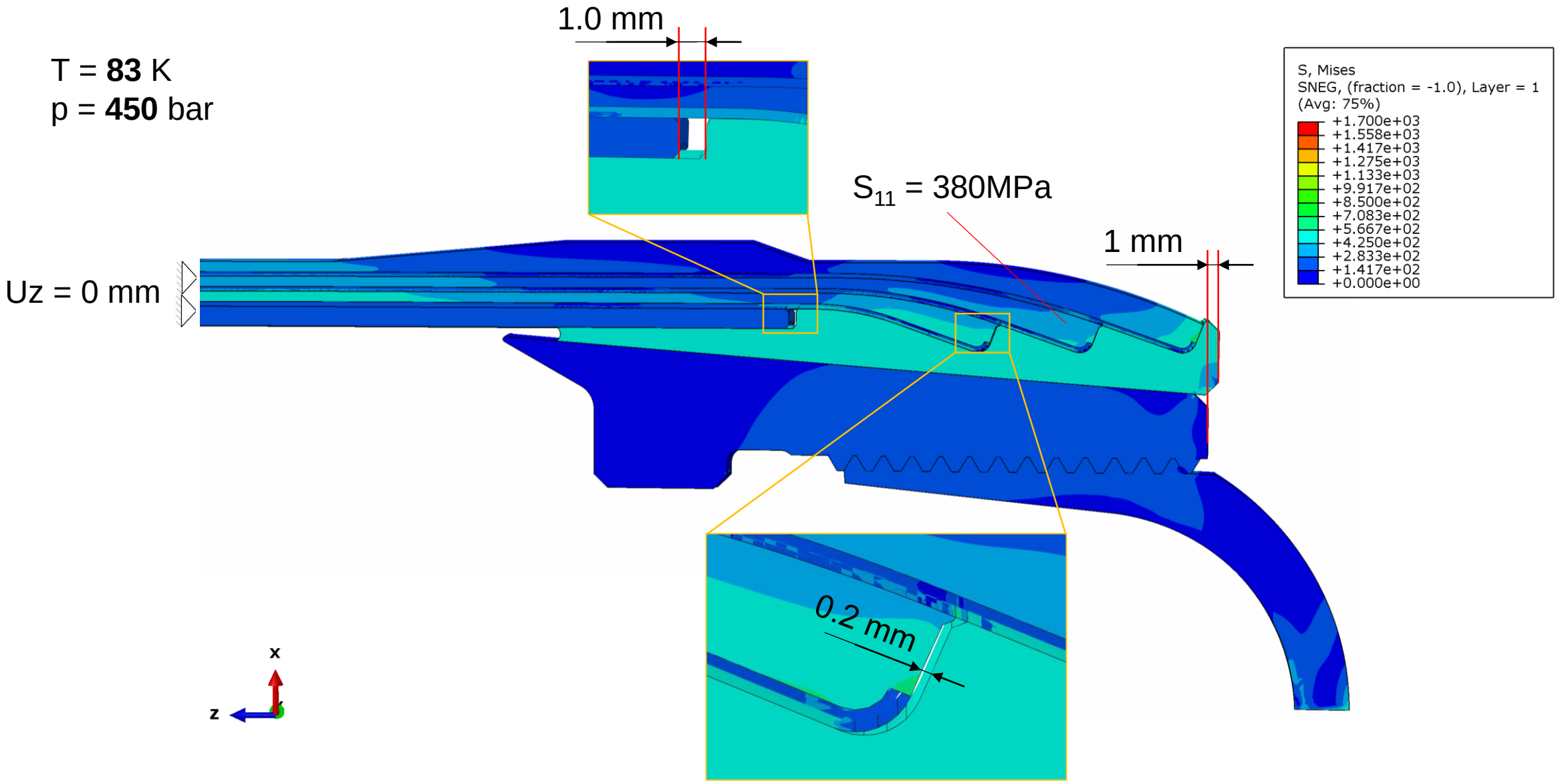

www.thefutureiscomposite.com

© Leibniz-Institut für Verbundwerkstoffe GmbH

Outer Shell: Demonstrator test

Demonstrator:

Weight:	910 g
(incl. Metallic Inserts)	
Laminate thickness:	2,5 mm
Length:	540 mm
Diameter:	66 mm

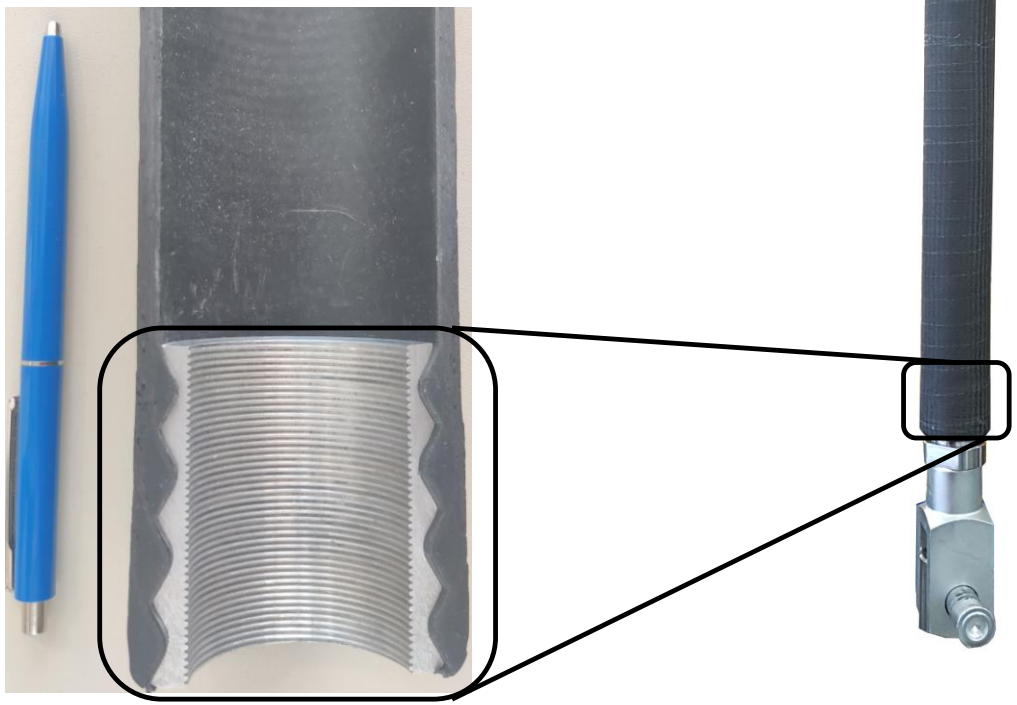



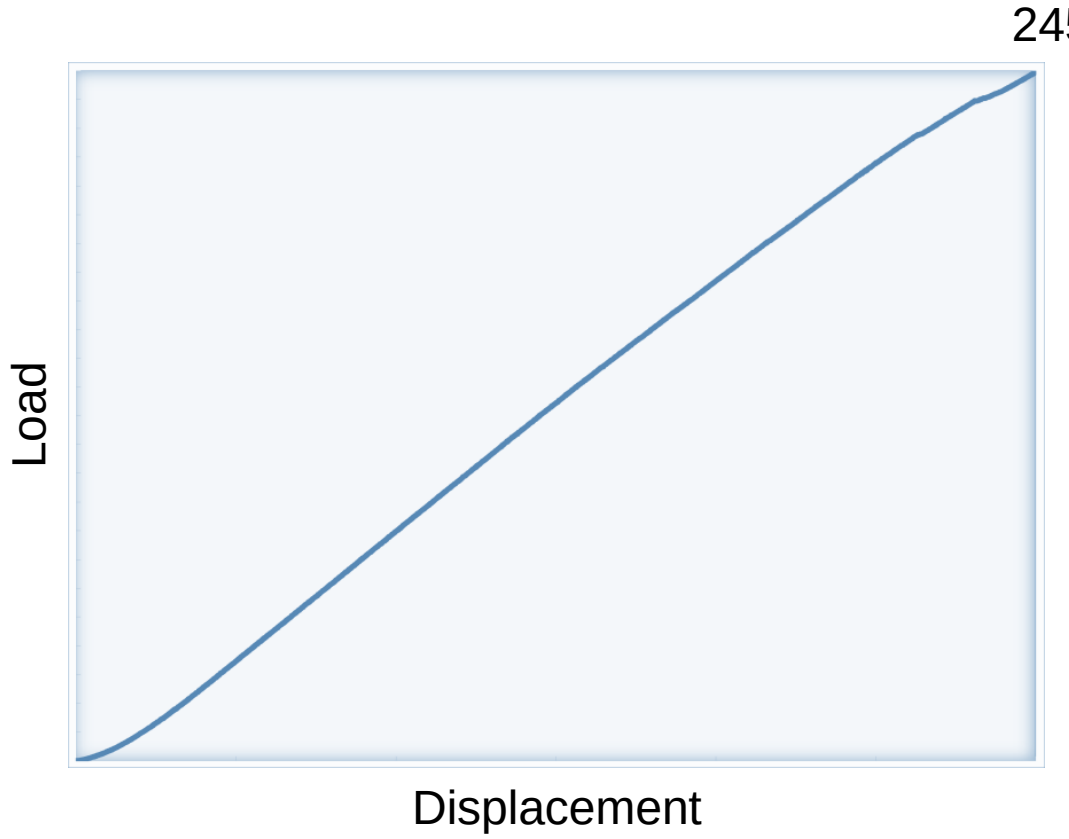

www.thefutureiscomposite.com

© Leibniz-Institut für Verbundwerkstoffe GmbH

Acknowledgements

Project: CFRP Hydrogen Leitung und Speicherung - **CF-Hydro**

Funding Source:

Federal Ministry for Economic Affairs and Climate Action within the framework of the Luftfahrtforschungsprogramme (LuFoVI-2)

Supported by:

Federal Ministry
for Economic Affairs
and Climate Action

on the basis of a decision
by the German Bundestag

www.thefutureiscomposite.com

© Leibniz-Institut für Verbundwerkstoffe GmbH

Thank you for your attention!



Contact details:
Nithya.sindhe@ivw.uni-kl.de
Tel: +49 (0)631 2017 273
www.ivw.uni-kl.de

© IVW

This document is confidential. The information contained is the property of the institute.
This document may only be reproduced or disclosed to other parties with the consent of Leibniz-Institut für Verbundwerkstoffe GmbH. Transmission or disclosure does not constitute any intellectual property rights. The information contained does not constitute an offer.

Photo: Thorsten Becker & Sylvain Fotouk Fotso

SpeedPreg Composite Tanks

www.thefutureiscomposite.com



Dream Chaser DC-101

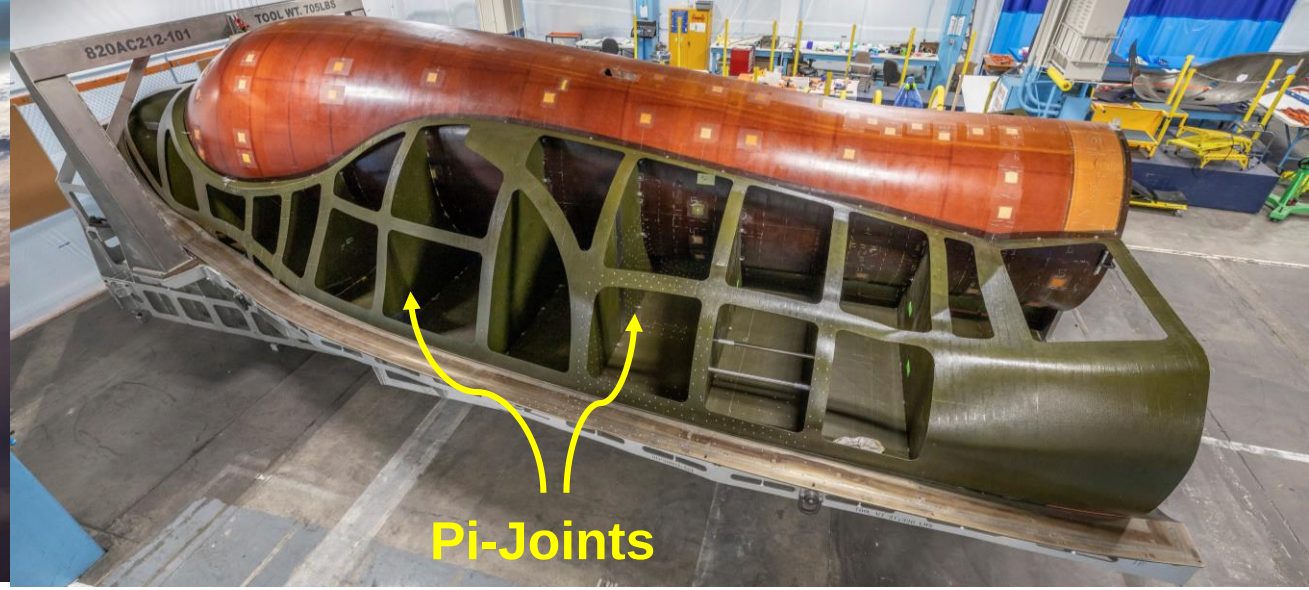

Pi-Joints

Photo credit: Sierra Nevada Corporation

Pi-Preform & Joint Revolutionary Improvement for Fastener-less Composite Structures

PIRA # CET2025060255

ICCM-24, Baltimore, MD, USA

Felix Nguyen, Ph.D., Associate Fellow, LM Corporate EOT
Bob Koon, Dan Hecht, Carl Rousseau, LM Aeronautics
Tim Carlson, Alec Olson, Hexcel
Greg Schmidt, Hirokazu Ohnishi, Damon Call, Toray

August 4, 2025

LOCKHEED MARTIN

HEXCEL

'TORAY'

Toray Composite Materials America, Inc.

© Lockheed Martin Corporation. All Rights Reserved.

Agenda

1. Lockheed Martin Corporate Overview
2. Background: Bonded Assemblies and Pi-joints
3. New Pi-Preform Design
4. New Pi-Preform Manufacturing Options
5. Summary

© 2025 Lockheed Martin Corporation. All Rights Reserved.



Lockheed Martin Corporate Overview

LOCKHEED MARTIN

As of March 2025

©2025 Lockheed Martin. All Rights Reserved

Lockheed Martin

Lockheed Martin is a global defense technology company driving innovation and advancing scientific discovery. Our all-domain mission solutions and 21st Century Security® vision deliver transformative technologies that deter potential adversaries and ensure America and its allies can achieve peace through strength.

121K Employees worldwide	**93%** Employees located in the U.S.	**20%** Employees who are veterans
70K Engineers, scientists and technologists	**350+** Facilities worldwide	**100+** Years of innovation

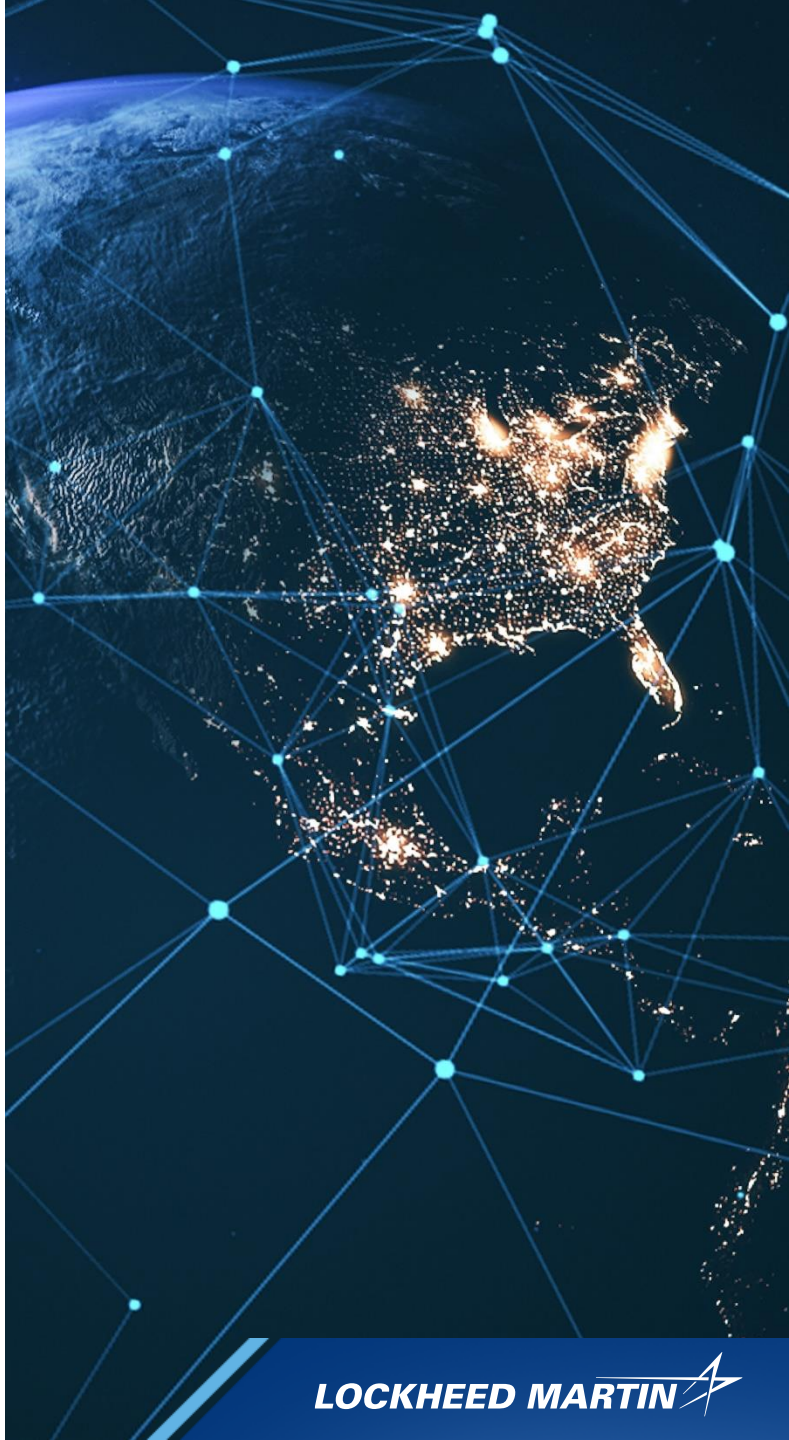

©2025 Lockheed Martin. All Rights Reserved

Values

Do What's Right

Respect Others

Perform With Excellence



©2025 Lockheed Martin. All Rights Reserved

Businesses

Our corporation, headquartered in Bethesda, Maryland, is organized around our core business areas specializing in defense tech.



Aeronautics, with approximately $28.6 billion in 2024 sales, which includes tactical aircraft, airlift, sustainment and aeronautical research and development lines of business.



Missiles and Fire Control, with approximately $12.6 billion in 2024 sales, which includes the High Mobility Artillery Rocket System (HIMARS) and PAC-3 Missiles as some of its high-profile programs.



Rotary and Mission Systems, with approximately $17.2 billion in 2024 sales, which includes Sikorsky helicopters, maritime systems, sensors, radar systems, command and control, combat simulation and training, undersea systems and full-spectrum cyber capabilities.



Space, with approximately $12.4 billion in 2024 sales, which includes development of national security, civil, commercial and weather spacecraft, strategic and missile defense solutions and hypersonics missions.

©2025 Lockheed Martin. All Rights Reserved

Customers






- Departments of
  - Defense
  - Homeland Security
  - Commerce
  - Energy
  - State
  - Transportation
- NASA
- Intelligence Community
- More than 100 nations globally


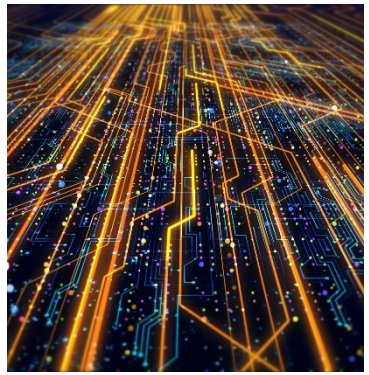
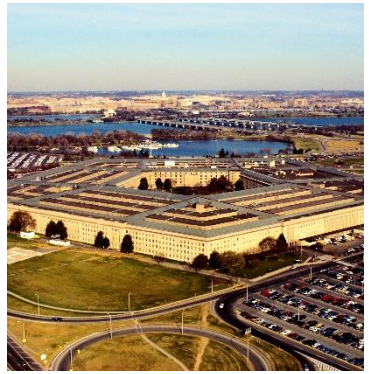


©2025 Lockheed Martin. All Rights Reserved

21st Century Security®

Lockheed Martin aims to build a more advanced, resilient and interoperable defense industry – working with industry and commercial partners to deliver cutting-edge capabilities faster and more affordably to customers.

The three lines of effort are:

- Aggressively adopting and inserting digital technologies into the defense enterprise with a standards-based, open architecture approach.
- Applying anti-fragility measures to ensure operations withstand shocks and disruptions on a large scale and at a faster speed.
- Fostering a more collaborative ecosystem that harnesses the advanced infrastructure of the U.S. and its allies to support America's strategic alliances.



©2025 Lockheed Martin. All Rights Reserved

Major U.S. Facilities

Number of sites per state with 250 or more employees and/or 500K SF or greater and the Business Areas in those locations

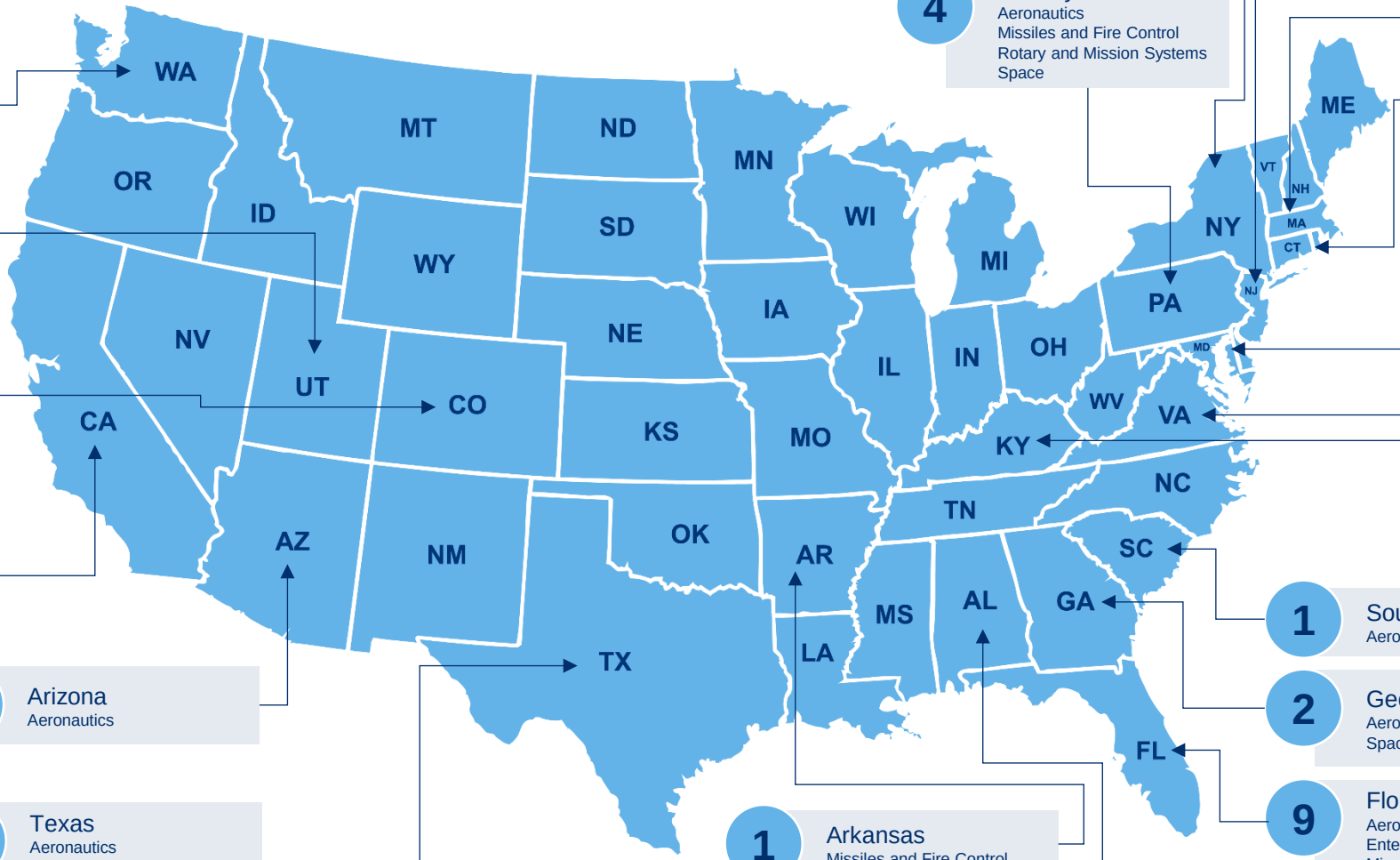

1 Washington
Space

1 Utah
Aeronautics

3 Colorado
Enterprise Operations
Rotary and Mission Systems
Space

4 California
Aeronautics
Missiles and Fire Control
Space

1 Arizona
Aeronautics

3 Texas
Aeronautics
Enterprise Operations
Missiles and Fire Control
Rotary and Mission Systems

2 New York
Rotary and Mission Systems

4 Pennsylvania
Aeronautics
Missiles and Fire Control
Rotary and Mission Systems
Space

1 Arkansas
Missiles and Fire Control

3 Alabama
Missiles and Fire Control
Rotary and Mission Systems
Space

2 New Jersey
Enterprise Operations
Rotary and Mission Systems

1 Massachusetts
Missiles and Fire Control

2 Connecticut
Rotary and Mission Systems

2 Maryland
Aeronautics
Enterprise Operations

4 Virginia
Enterprise Operations
Rotary and Mission Systems
Space

2 Kentucky
Missiles and Fire Control

1 South Carolina
Aeronautics

2 Georgia
Aeronautics
Space

9 Florida
Aeronautics
Enterprise Operations
Missiles and Fire Control
Rotary and Mission Systems
Space

©2025 Lockheed Martin. All Rights Reserved

LOCKHEED MARTIN

International Locations

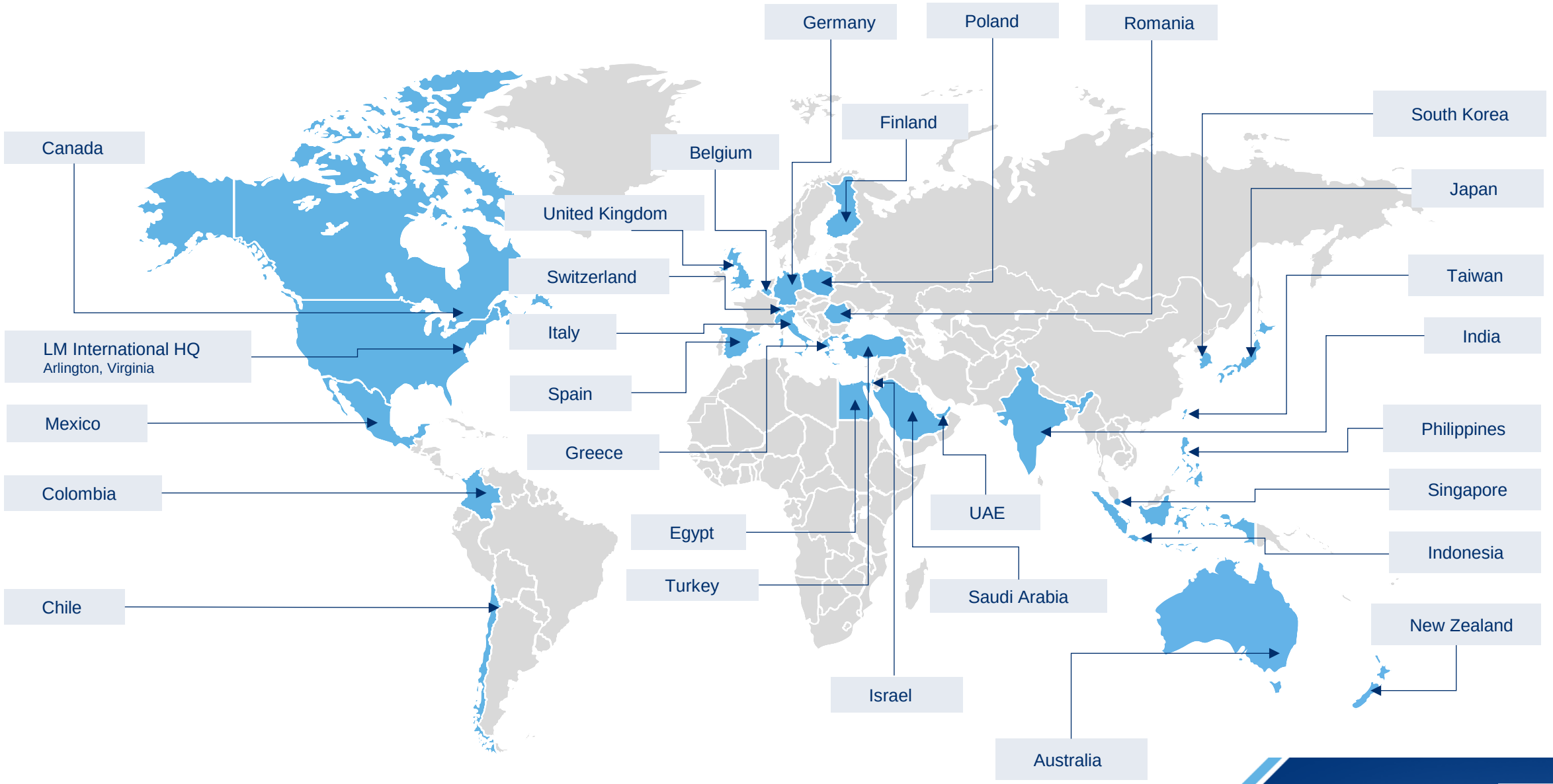

©2025 Lockheed Martin. All Rights Reserved

Success Story: Composite Bonded Assembly

X-55A Advanced Composite Cargo Aircraft

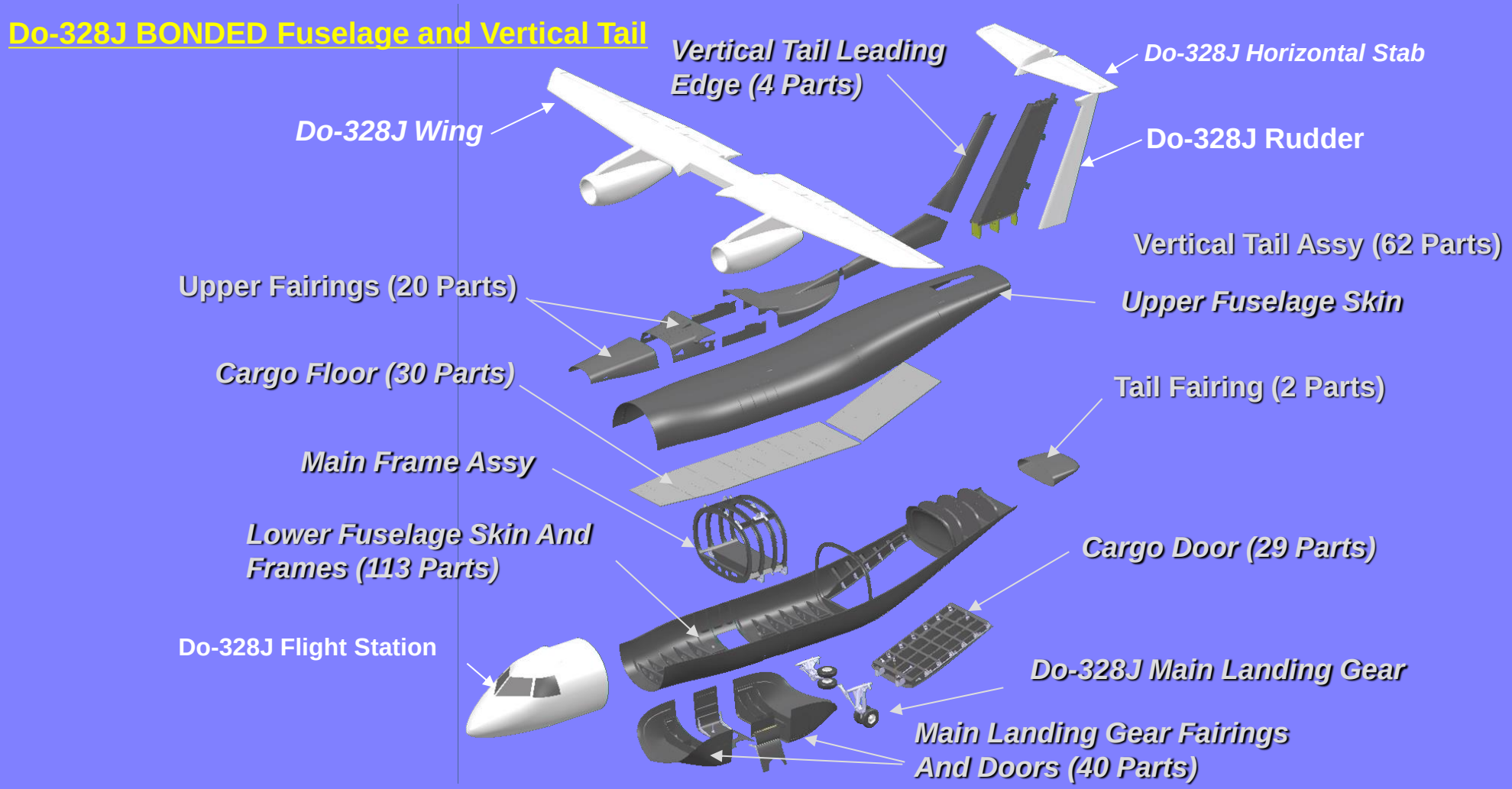

Reduce Structural Parts by 90% & Elimination of 15,000+ Fasteners

© 2025 Lockheed Martin Corporation. All Rights Reserved.

Background: Composite Bonded Assemblies

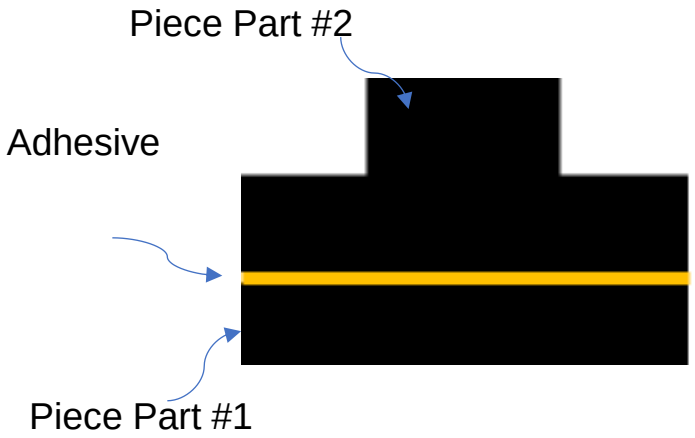

2D Joint

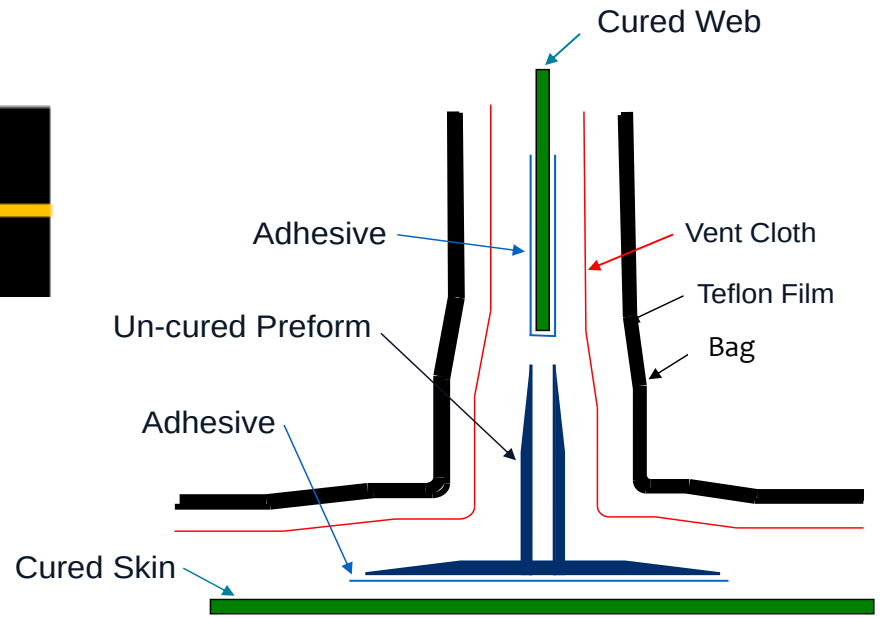

3D Joint (Pi)

Solid-Solid Joint

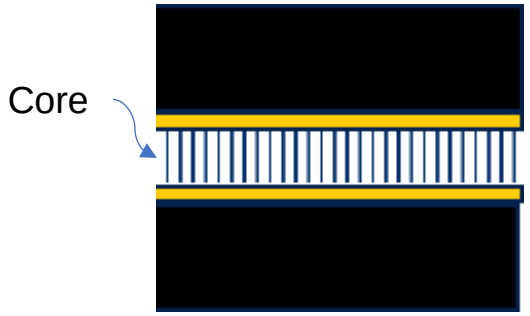

Solid-Core Joint

© 2025 Lockheed Martin Corporation. All Rights Reserved.

Background/Issue: Composite Bonding Process

1. First cure: >90% degree of cure

2. Assembly/Second cure: >>90% degree of cure

Secondary bonding

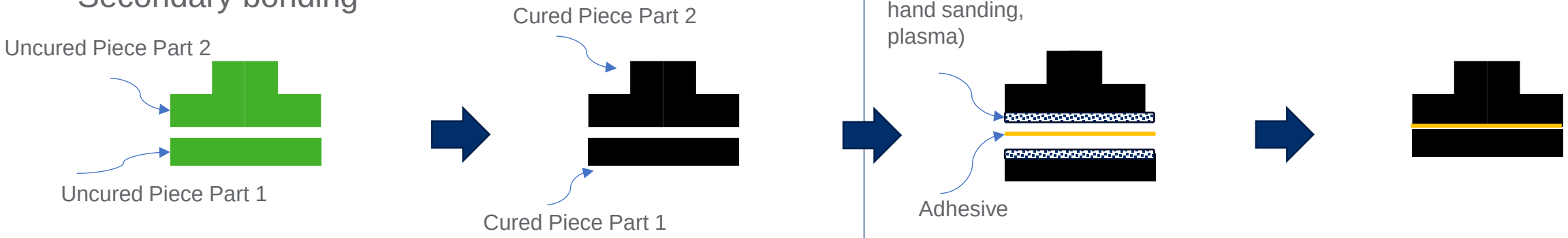

Co-bonding

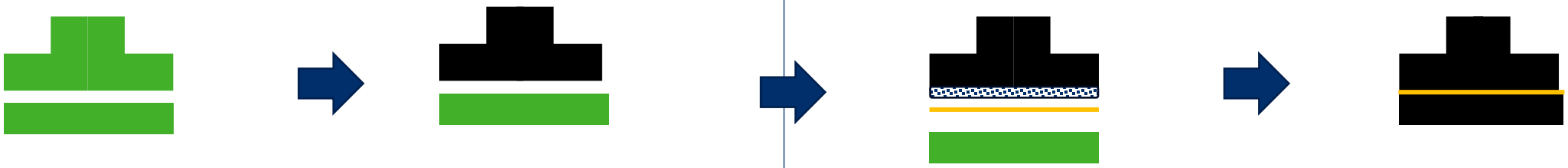

Issue/Challenge

- Piece parts manufacturing: material, tool, cure cycle/time
- Surface preparation: roughening, plasma
- Assembly: tool, bonding cycle/time
- Inspection/Qual

© 2025 Lockheed Martin Corporation. All Rights Reserved.

Baseline Developmental Bulkhead Sub-Component



BASELINE: Woven Pi-Preforms

- Expensive design and weaving parameters
- Many configurations
- BMI and epoxy resins

BULKHEAD Subcomponent Demo

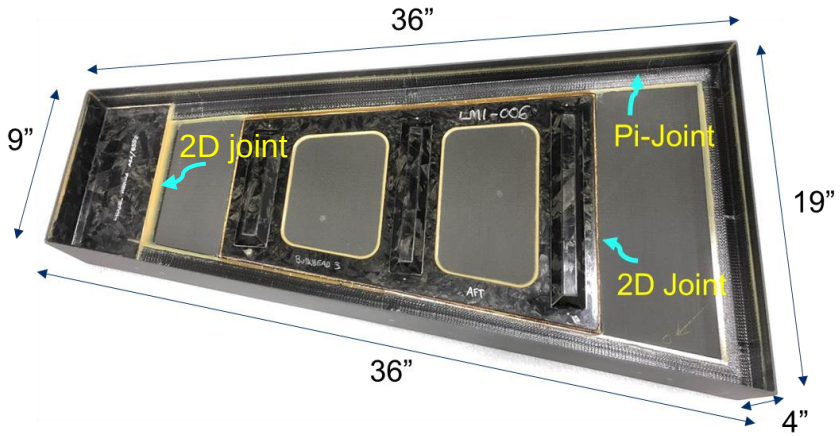

- 2D joint: bathtub fitting to web & stiffening array to web
- PI-joint: cap to web, all around

- Goal: investigate composite solutions vs machined aluminum bulkheads for cost and weight improvements

- Achievements
  - Subscale: Completed demos using continuous and discontinuous fiber composites and pi-preforms. Established correct stress method. Achieved 1.65 DLL.
  - Full-scale: Completed initial design. Projected ~20% weight saving at competitive cost

- Next step: refine design and build demo

© 2025 Lockheed Martin Corporation. All Rights Reserved.

New Pi-Preform Design and M&P

1. Base x 1
2. L-shape x 2
3. U-shape x 1
4. Noodle x 2
5. Adhesive (optional)

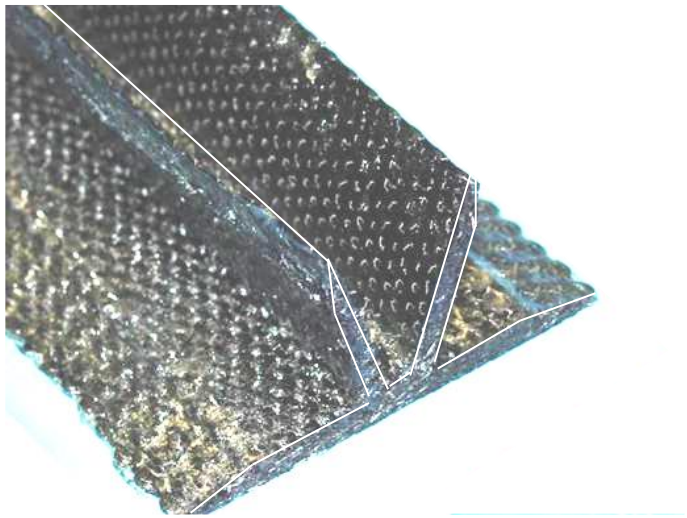

3D Woven Pi-Preform

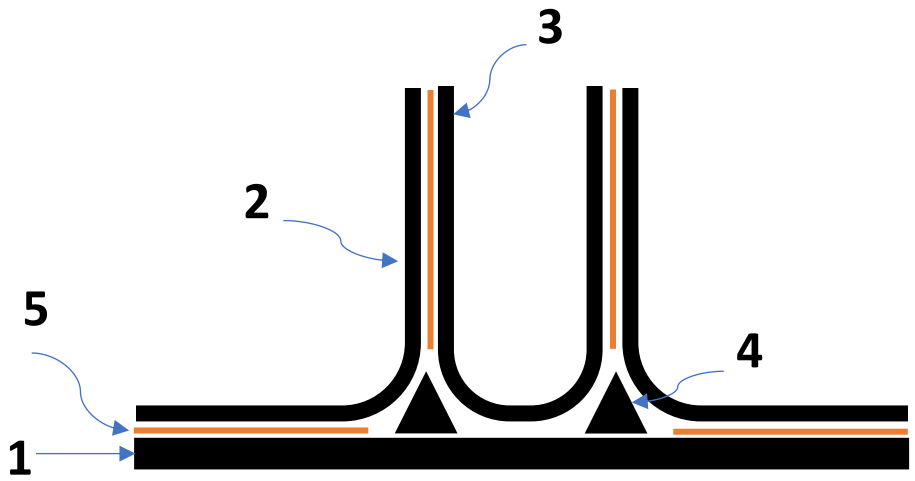

Oriented Ply-stack Pi-Preform

Design Parameter (selected)

1. **Material form**
   - Prepreg (discont. fiber)
   - Non-crimp fabric (cont. fiber)
2. **Configuration**
   - Ply stack up
   - Thickness
3. **Manufacturing method**
   - Forming/no wrinkles
   - Noodle
   - Assembly
     - B-stage
     - One-shot infusion

Resin infused pi-shaped preform and joints thereof, US20250001647A1 (2024)
Pi-shaped preform and bonded joints thereof, US20240198625A1 (2022), EP4385699B1 (2025)

© 2025 Lockheed Martin Corporation. All Rights Reserved.

New Pi-Preform with Prepreg: Accomplishments

Toray Composite Materials America, Inc.

Toray Torayca® ET-40 Material

https://www.cf-composites.toray/products/thermoset/others/extensible.html

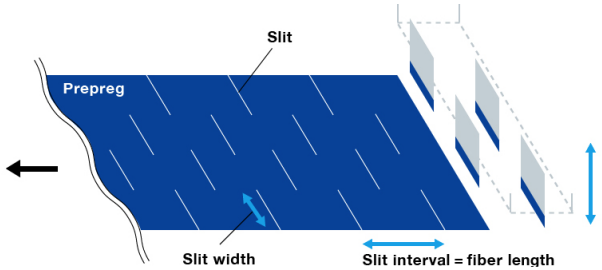



- Slits introduced to into UD
- Handle-ability similar to parent UD
- Excellent formability
- High mechanical (same mod, 80% strength)
- Press-molded complex shapes

Resulting Joint

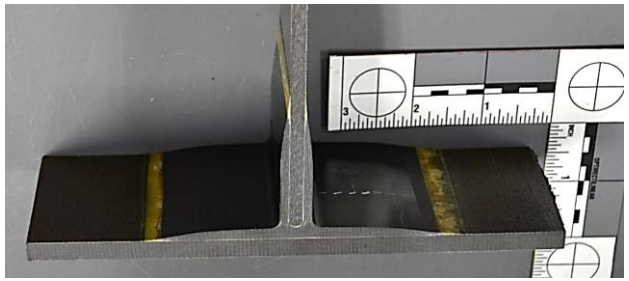

Pull off coupon

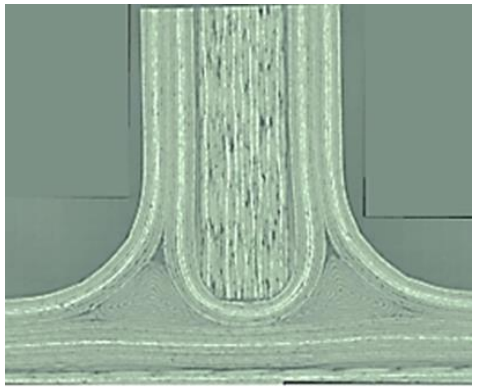

Joint Cross-section

- Robust processing into T panel config.
- Epoxy, BMI resins (4); T800, T1100 fibers; 3 noodles; 3 prepreg thicknesses fabricated
- Pull-off 132% and shear 225% higher
- Cost
  - Un-enhanced (manual process): cost similar
  - Fully tooled manual cost: <½ cost
- Next steps
  - Partial cured piece parts/bulkhead subcomponent demo
  - Automated forming cost <1/4cost

© 2025 Lockheed Martin Corporation. All Rights Reserved.

US20240198625A1 (2022, pending), EP4385699B1 (2025, granted)

LOCKHEED MARTIN

New Pi-Preform with Prepreg: Forming method

Toray Composite Materials America, Inc.

Charge Layup

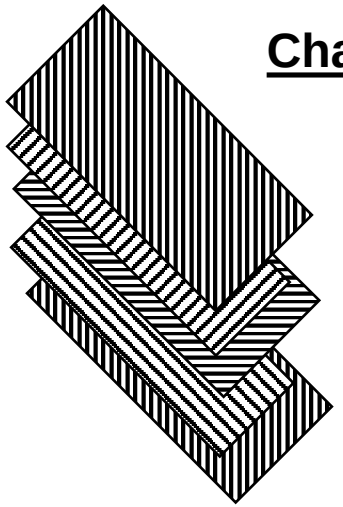

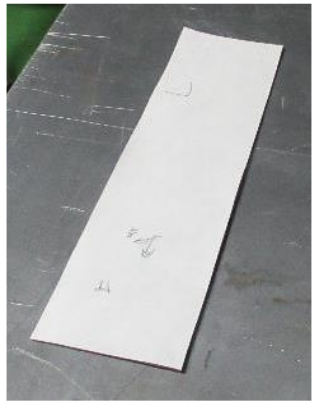

Layup ET-40 plies into flat charge

Forming

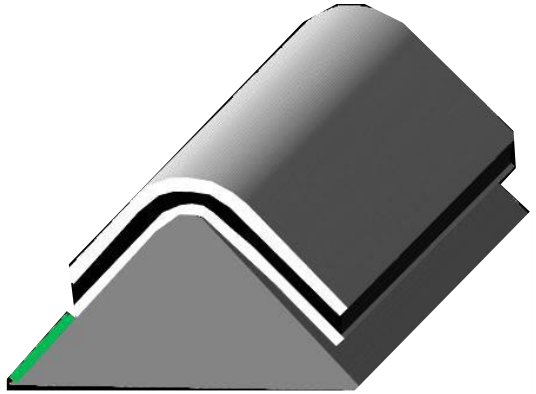

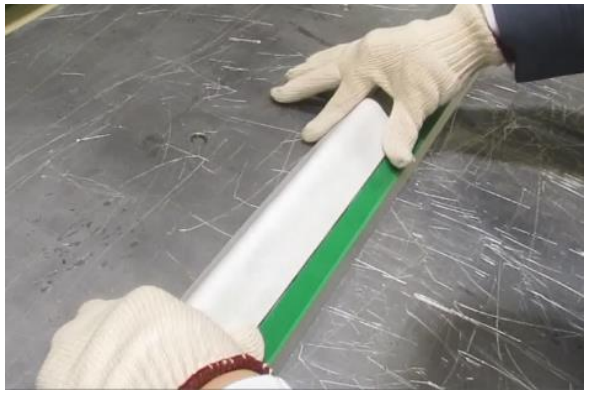

Form stack over heated mandrel

Inspection

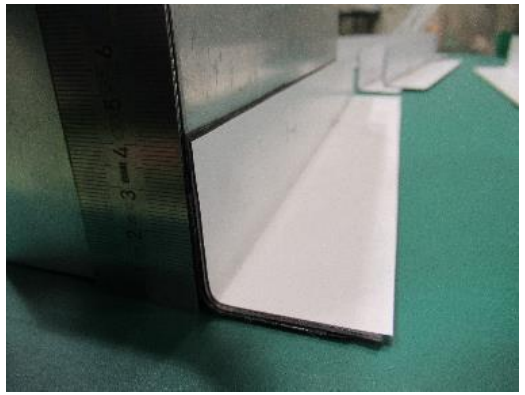

Verify geometry conformity

Assembly



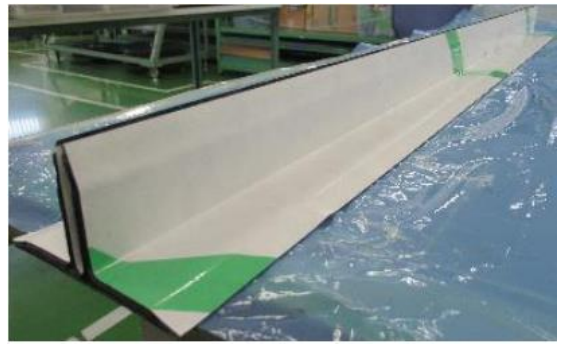

Pi-Preform assembly

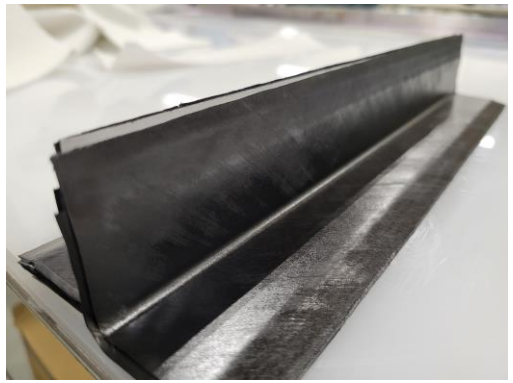

Pi-Preform ready
to co-bond

© 2025 Lockheed Martin Corporation. All Rights Reserved.

LOCKHEED MARTIN

New Pi-Preform with Dry Material: Accomplishments

Hexcel HiMax®

https://www.hexcel.com/Products/Fabrics-Reinforcements/HiMax-Carbon-Multiaxials

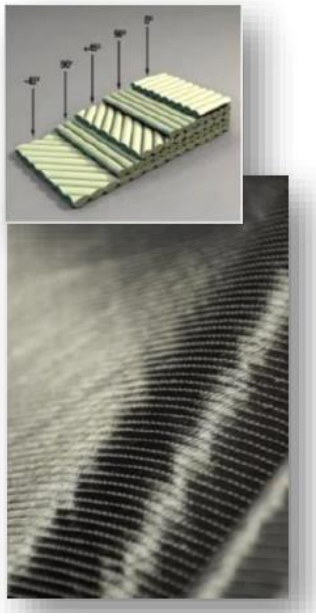

- NCF : Multilayer UD blanket
- Proprietary 20 dTex fine stitch
- High Drapability

HiMax® untoughened

- HiMax® + Powder binder

HiMax® toughened

- HiMax® + TP veil at each interleaf
- Veil acting as binder
- Breakthrough in damage tolerance

Resulting Joint

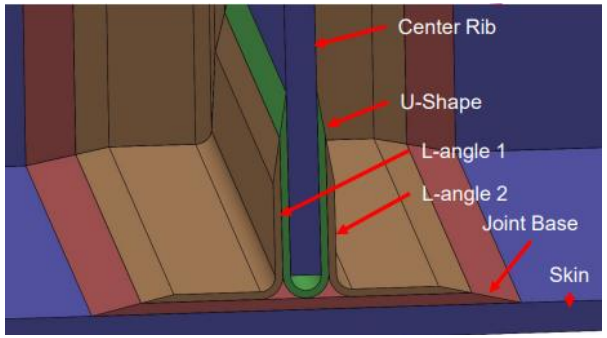

NCF Stackup



Joint Cross-section

- HiMax® IM8/1078-1 system @ 300gsm; knitted bi-axial textile with binder veil
- 2 trials for T panel test article
  - Porosity reduced for 2nd panel
  - First panel tested: highest & lowest pull-offs
- 2nd panel performance:
  - 91% pull-off, 180% shear
- Ultimate performance? Optimize stacking, material, stitching?

© 2025 Lockheed Martin Corporation. All Rights Reserved.

US20250001647A1 (2024, pending)

New Pi-Preform with Dry Material: HiMax® Preforming & Consolidation

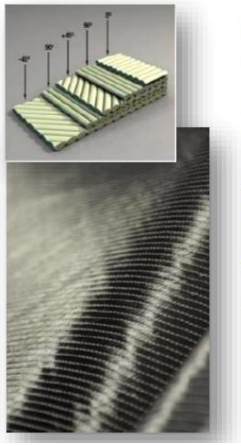

- NCF : Multilayer UD blanket
- Proprietary 20 dTex fine stitch
- High Drapability

HiMax® untoughened

- HiMax® + Powder binder

HiMax® toughened

- HiMax® + TP veil at each interleaf
- Veil acting as binder
- Breakthrough in damage tolerance

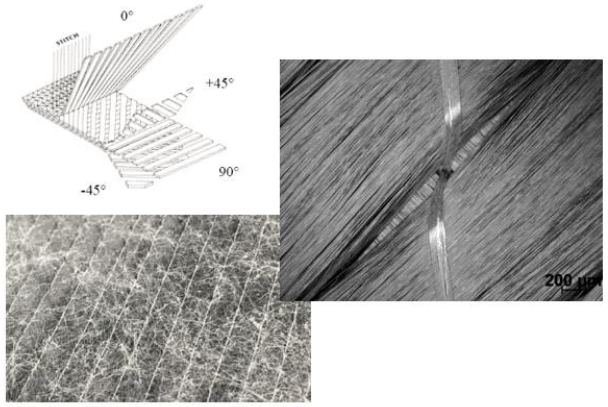

- High FVC after vacuum infusion (58%+)
- Low bulk after forming (<5% @60%FVC)
- High mechanical properties including CAI / G1C with RTM6
- Fully compatible with HiTape® (same veil)

Vacuum forming
Cold forming

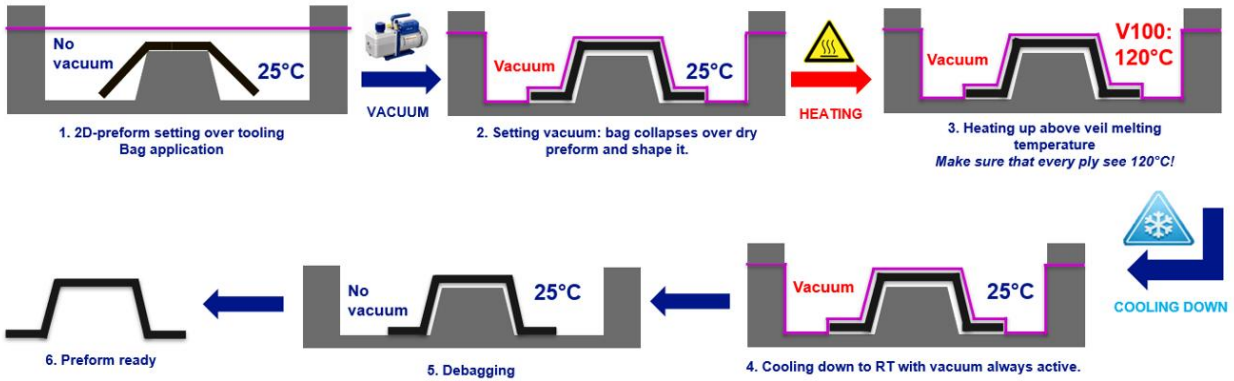

Example U-Shape preforming process

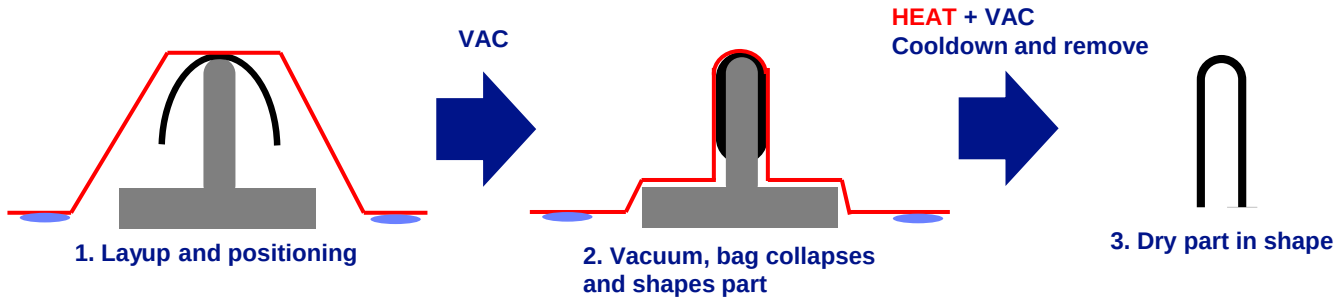

© 2025 Lockheed Martin Corporation. All Rights Reserved.

New Pi-Preform with Dry Material: Demo

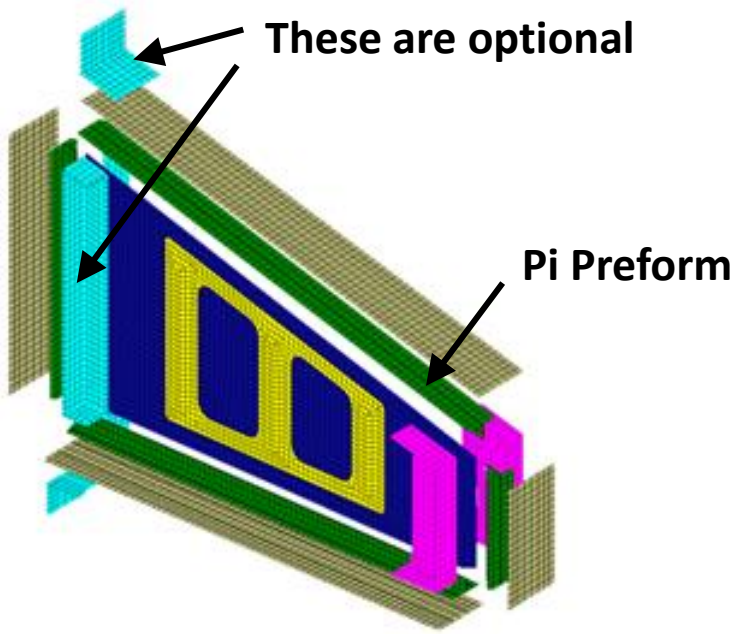

- Stiffening components on both sides

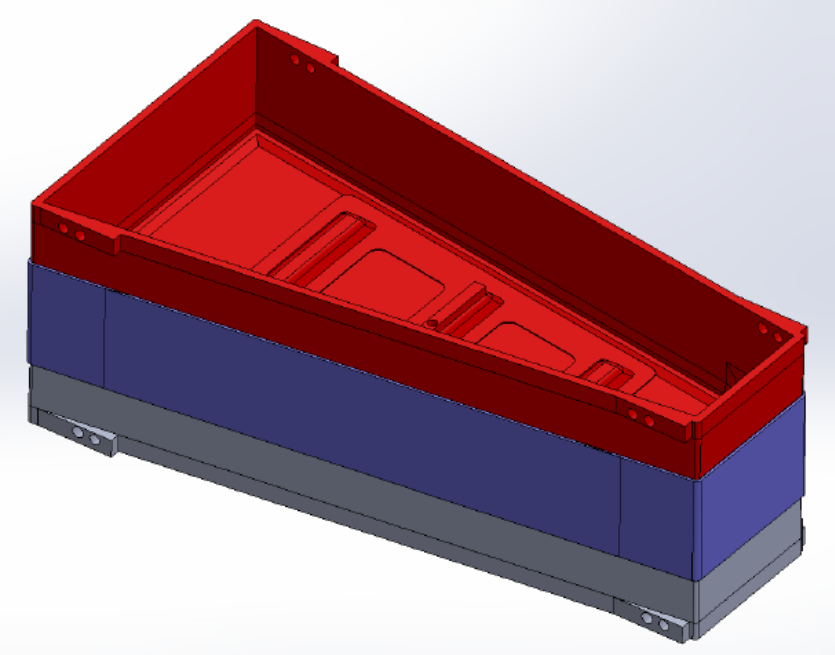

- Hard tooling concept completed
- Infusion strategy in work
- Demo completion in 2025-26

© 2025 Lockheed Martin Corporation. All Rights Reserved.

Summary

- New Pi-preform design with oriented ply stacks has anticipated lower cost vs. 3D woven baselines
- Manufacturing feasibility successfully demonstrated with Toray Torayca® ET-40 prepregs and Hexcel HiMax®
- Currently, achieved up to 2X higher in shear and marginal changes in pull off. Potentially higher performance with stitches for dry preform/infusion option
- One-shot resin infused bulkhead subcomponent with dry pi-preforms is in work

© Lockheed Martin Corporation. All Rights Reserved.


LOCKHEED MARTIN

ANALYSIS OF THE MECHANICAL BEHAVIOUR OF CFRP BOSSES IN COMPOSITE PRESSURE VESSELS CONSIDERING DIFFERENT STIFFNESS DISTRIBUTIONS

Gerrit Rehs[1], Janis Mörk[2] and Tobias Dickhut[3]

[1]Chair of Composite Materials and Engineering Mechanics,
University of the Bundeswehr Munich, Neubiberg, Germany
Email: gerrit.rehs@unibw.de, web page: https://www.unibw.de/aero

[2]Blackwave GmbH,
Rotwandweg 8, 82024 Taufkirchen
Email: moerk@blackwave.de, web page: https://blackwave.de/

[3]Chair of Composite Materials and Engineering Mechanics,
University of the Bundeswehr Munich, Neubiberg, Germany
Email: tobias.dickhut@unibw.de, web page: https://www.unibw.de/aero

Keywords: Finite element analysis, Composite Pressure Vessel, Layered structures

ABSTRACT

Reducing the weight of pressure vessels is a key objective in different sectors like automotive or aerospace. This can be achieved by replacing Type III and IV pressure vessels through Type V design. Nonetheless, Type V pressure vessels still use metallic bosses as an interface to surrounding structures. These metallic bosses lower the performance of the Type V design due to its mass and mechanical and thermal properties. This study investigates the feasibility of CFRP bosses using different stiffness distributions by means of finite element analysis. Different materials are investigated to demonstrate the potential of these structures. The weight benefit as well as the mechanical performance is compared to metallic bosses.

1 INTRODUCTION

The increasing demand for launch capabilities results in a high number of new players in the aerospace sector. Besides topics like reusability of launcher architectures, one aspect for being successful is to reduce the mass of the launcher architectures. [1]

In this research field, when it comes to the pressure vessel (PV) design, various studies focus on improving the performance of the PV by changing from a Type III to Type V design. By this, the metallic liner is replaced by the exclusive use of carbon fiber reinforced plastics (CFRP). This results in an estimated mass benefit of composite PVs (CPV) of up to approximately 55 % [2]. While this is an advantageous step towards lower structural mass, it also imposes design challenges, especially for the storage of cryogenic fluids. In the space sector, media such as liquid oxygen (LOx) or liquid hydrogen (LH2) are stored at cryogenic temperatures such as 77K for LOx and 20K for LH2. During the filling process of the PVs, the structure is cooled down starting from room temperature (RT) to the cryogenic service temperature. From a design perspective, this results in high thermal induced residual stresses in joining areas between different materials because of their differing coefficients of thermal expansion (CTE). State of art, type III as well as Type V designs still rely on metallic bosses as interface to surrounding structures and pipings. To reduce these thermal stresses, it is beneficial to replace the metallic bosses by CFRP material design concepts. In addition to the reduced thermal mismatch between the design materials, CFRP structures are also capable of providing higher specific strengths compared to special alloys such as Invar36. Invar36 is frequently used as a design solution to minimise the CTE difference between the metallic component and the CFRP overwrap of the PV because of its low CTE [3]. While the CTE mismatch is reduced, Invar36 has a high density of 8.1 g/cm^2 which lowers the structural performance [4]. Another disadvantage is the low strength at room temperature [5].

Concluding, the introduction of CFRP bosses leads to the following advantages:

- reduced mismatch of CTE between boss and laminate of the CPV
- increased specific strength of the CFRP boss based on the used CFRP material
- reduced density of the CFRP boss

These advantages make the development of CFRP bosses interesting for the future use in the aerospace sector. There are some studies, which highlight the potential described above of the CFRP bosses. *Whitehead et al.* integrated a CFRP boss manufactured by hand layup into a CPV to achieve weight reduction of the pressure vessel. A CFRP boss concept manufactured by resin infusion is shown by *Scherer et al.* [6]. Here, CFRP preforms are used to increase the performance of the boss structure. Another study showed that recycled material can be implemented into CFRP boss parts as core material, related to a sandwich structure design by *Korff et al.* [7]. The use of SMC bosses in an integrated Type V CPV design was demonstrated in a previous study by *Rehs et al.* [8]. Here, the performance of an SMC boss was compared to the Aluminum design in a Type V concept. Similar results for burst pressure performance as well as helium leak behaviour was demonstrated on part level. Furthermore, the manufacturing and integration of prepreg bosses on a 20L CPV was demonstrated. A weight saving of up to 57% in comparison to a steel boss is demonstrated by changing the boss material without considering the geometry. [8]

In this study, the performance increase of the CFRP bosses is assessed by the use of finite element (FE) analysis. Different materials and stiffness distributions of the CFRP boss structures are analysed based on the CFRP preform.

2 MATERIAL DEFINITION AND ANALYSIS MODEL

In this section, the material and analysis model are described. Five different materials are compared to highlight the potential of CFRP boss parts. The analysis focuses on the advantages which come with the material parameters as well as the manufacturing induced advantages.

2.1 Material Definition

Different materials can be used for the manufacturing of boss structures. Currently, state of the art boss structures are manufactured by metals such as Aluminum or Invar36. Replacing these structures by CFRP can be done using different CFRP preforms like fabrics, Sheet Moulding Compound (SMC), unidirectional (UD) prepregs or spiral ribbon.

This study focuses on the analysis of SMC and twill and UD prepregs, compared to the metal design of Aluminum 6082 and Invar36 to highlight the benefits of the CFRP structure.

Therefore, the design parameters such as strength, stiffness, density and CTE for the different materials are summarized in Table 1.

Table 1: Material data for metal and CFRP materials [4, 9-13]

Metal Materials			
Parameter		Al	Invar36
E	[MPa]	70714	143000
R_{yield}	[MPa]	298.3	270
CTE	[10^{-6}/°C]	23.5	1.3
ρ	[g/cm^3]	2.7	8.1

CFRP Materials				
Parameter		SMC	Twill Prepreg	UD Prepreg
E_f	[MPa]	25000	68000	164000
R_f	[MPa]	300	1050	2724
CTE	[10^{-6}/°C]	10	3.62	-0.5 – 12.5
ρ	[g/cm^3]	1.9	1.47	1.57

For the design of light structures different parameters are of interest, shown in Figure 1.

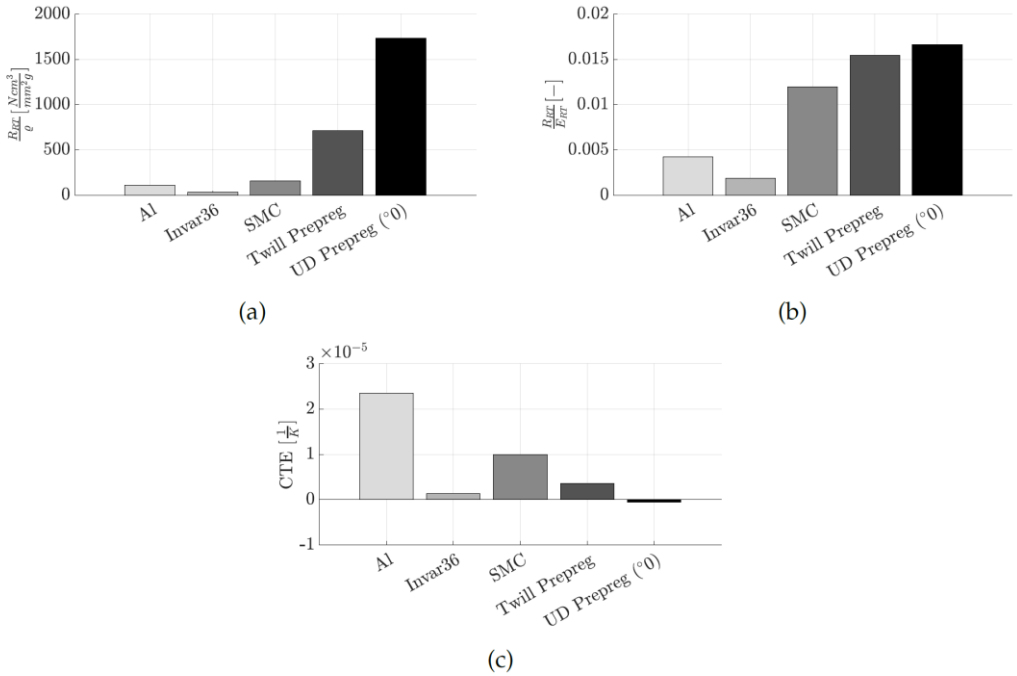

Figure 1: Material comparisons. (a) Strength to Density Ratio at RT, (b) Strength to Stiffness Ratio at RT, (c) CTE at RT

First, the strength to stiffness ratio is shown in Figure 1 (a), which is important for the lightweight potential. It can be seen, that Invar36 shows the lowest strength to density ratio and Prepreg material shows the highest strength. For the metal materials, the yield strength was chosen as strength value as typical design approaches follow a no yield design under service conditions. For the CFRP materials, the strength describes the stress at fiber failure.

Second, the design of boss structures is driven by a bending load in the boss runout. This is why a high strength to stiffness ratio is beneficial, shown in Figure 1 (b). Due to the inner pressure loading the CPV undergoes a deformation which is mainly driven by the CFRP laminate stiffness distribution. As the boss is attached to the overwrap, it undergoes this deformation as well. This deformation yields to bending in the runout. Therefore, a high strength to stiffness value of the design material is beneficial for the lightweight potential. It can be seen in Figure 1 (b) that CFRP materials offer higher values compared to the metal materials. This is also in accordance with experimental results observed in [8] on part level.

Third, for the use in cryogenic temperatures, the CTE is of interest, shown in Figure 1 (c). Here, a low CTE is proven to be beneficial. An optimal boss design would show the same CTE compared to the CFRP overwrap in the joining area. Due to the winding process and changing fiber angles in the boss region, the prediction of the CTE of the overwrap remains difficult and should be addressed in future studies. Based on the state of the art, where Invar36 proves to be a design solution it can be concluded that Invar36 and Prepreg Materials are of high interest, while SMC offers way better characteristics compared to Aluminum.

Concluding, the use of CFRP Materials for boss design proves to be a promising approach within Type V CPV design for further increasing the CPV performance index due to the following advantages:

- CFRP shows high *R/ρ* values especially compared to Invar36
- CFRP shows high *R/E* values especially compared to Invar36
- CFRP shows lower CTE values especially compared to Aluminum

2.2 Finite Element Model

A finite element (FE) model is used to predict the mechanical responses for the loading situation of the CPV including different boss designs and materials based on section 2.1.

The *Abaqus* FE-model is generated on basis of a winding simulation performed with the winding software *uChain* by *MeFeX GmbH*. The model consists of two parts, the boss part and the CFRP laminate. The CPV laminate is composed of 22 layers, containing helical and hoop layers. The design of the boss was chosen to withstand an inner pressure loading of 400 bar using Invar36 as design material. The loading is applied as inner pressure loading on the boss and the CFRP laminate inner surface as well as an axial force on a Reference Point (RP) to account for the cover loading. The load of the RP is transferred using a coupling to the boss structure. The analysis uses an axisymmetric approach using CAX3/4 element formulation with an element size of 0.75 mm. A symmetric boundary condition is used in the center of the CPV constraining the axial deformation. Second, a boundary condition is used at the RP.

Figure 2 shows boss part as well as the CFRP laminate of the CPV. The loading can be seen on the inner surface as well as the reference point.

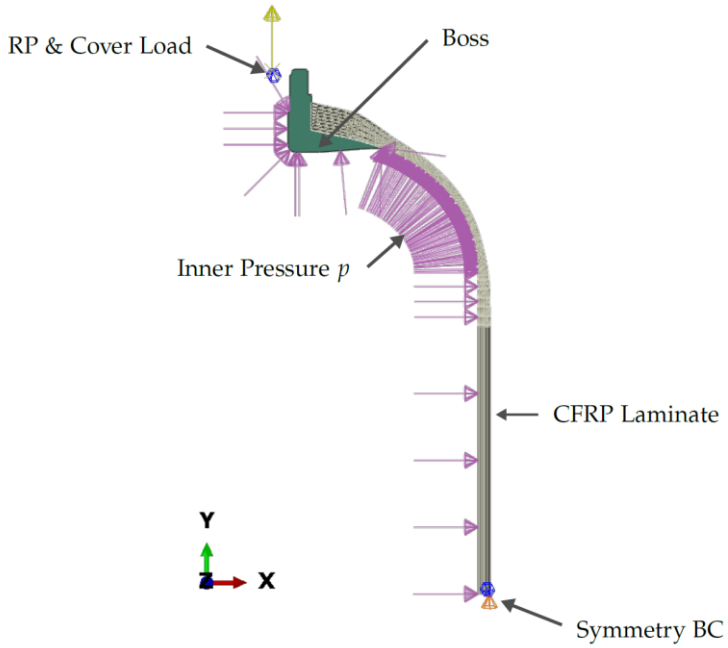

Figure 2: FE-model showing the two parts (boss and CPV laminate) as well as the loading and boundary conditions of the axisymmetric model.

Based on the shown design and FE model, different analyses are performed including geometric variations of the boss design as well as the analyses of different boss materials.

2.3 Boss manufacturing

As described before, different materials for CFRP are considered in this study: SMC and Prepreg. Based on this, the manufacturing process differs between these two materials.

In general, the CFRP boss consists of two parts. The CFRP main body and a metallic insert, which allows for connection of the CPV to pipes via standard pressure fitting [8]. The metallic insert is designed to be as small as possible to reduce weight and also have less absolute difference of thermal expansion between the parts. It is bonded to the CFRP main body in an extra step after the CFRP part is manufactured.

To use the advantages of a CFRP boss mentioned before, the manufacturing process has to be considered during the design of the boss. The two manufacturing methods are SMC compression molding and prepreg autoclave manufacturing.

In the SMC process, a preform that contains long fiber and resin is inserted in a two part heated mold. The mold is closed with a defined force to apply pressure. The viscosity of the resin decreases and can flow through the mold to fill the whole cavity and moving the fibers with it. In this process, relatively complex parts can be manufactured with short cycle times and minimal rework needed. Therefore, the process is well suited for high scale manufacturing. Another advantage of using this process for CFRP bosses is the freedom in the part geometry. The outer edge of the boss can be made thin to reduce stiffness gradients in the CPV. As the fibers in the preform have a random orientation the mechanical properties of the part will be quasi isotropic in in-plane direction.

The second manufacturing process considered for the CFRP boss is prepreg autoclave manufacturing. A positive mold which represents the underside of the boss is machined and CFRP prepreg is laid on it in multiple layers. Unidirectional and fabric material is used. The CFRP is cured inside an autoclave to apply pressure for compaction and good laminate quality. After curing the topside of the boss is milled to the exact contour as this cannot be achieved with the layup process alone. Advantages of this process are tailoring of the fiber directions to the loads in the boss and the use of endless fibers compared to isotropic materials resulting in high-strength parts. As a result, the boss can be made thinner and lighter with this manufacturing method.



Figure 3: CFRP Boss demonstrator manufactured from twill and UD prepreg. [8]

3 RESULTS AND DISCUSSION

This section presents the results of the loading and stress analysis based on Invar36 material design. Following this analysis results, different boss adaptations including geometric variations and material variations are presented.

3.1 Loading and stress analysis of the Invar36 boss design and its limitations

The detailed design procedure of the boss, which undergoes the deformation behaviour of the CFRP laminate is not focus of this study. Rather, on the basis of the shown design, different variations are analysed to highlight the mentioned potential of replacing metal bosses through CFRP design. The design is chosen for an operating CPV inner pressure of 400 bar.

For experimental validation of the shown design, the Invar36 boss with the CPV laminate was pressurized up to 500 bar using a hydrostatic pressure test bench. The design showed no failure of the boss structure.

All following results are derived at the operating pressure of 400 bar.

Figure 4 (a) shows the von Mises stress distribution of the Invar36 boss. The boss undergoes an axial displacement due to the CFRP overwrap deformation behaviour. For simplicity, the CFRP laminate is not shown in Figure 4. The volume towards the interface to the CFRP laminate is in a high tensile stress state. This is because of the bending loading situation triggered by the axial displacement of the CPV. As a result, the material towards the interface is loaded under tensile stresses, while the lower material is not highly loaded due to the presence of compressive stresses due to the bending. Reducing this area of the part is not advisable, due to the failure mode of shear out and further increasing the yielding tendency. If the part thickness becomes too low, the boss part can fail in the area which is highlighted in
Figure 4 (a). Due to the inner pressure loading, there are also stress components in the circumferential direction shown by the stress vectors of the maximum principal stresses in Figure 4 (b). Concluding, the boss stress state is complex due to the different aspects of the loading and there are different aspects to be considered in the optimization of the boss using layered structures.

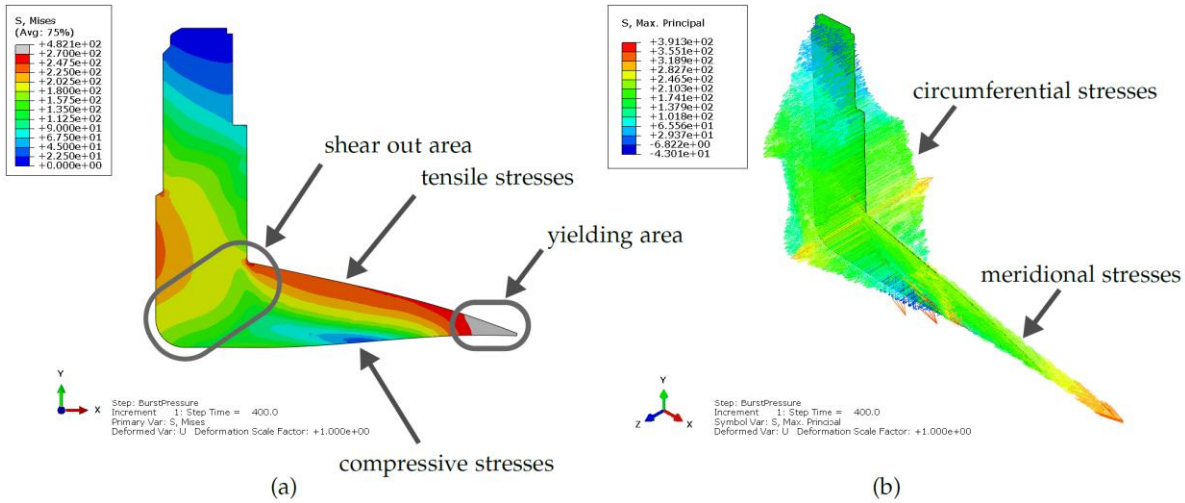

Figure 4: (a) Von Mises stress distribution of the Invar36 boss at 400 bar inner pressure loading. Stresses depicted in grey are above the $R_{p0,2}$ limit for Invar36. (b) Maximum principal stress distribution shown in vectors.

The high loading in the ending section of the boss (yielding area) can be reduced by increasing the thickness of this runout. While this accounts true for the boss, the CFRP laminate has to be also considered. This poses a design challenge. On the one side, the runout should be as thick as possible due to possible yielding failure in the boss runout. On the other side, the runout should be as thin as possible due to the presence of the stiffness jump in the interface between the boss and the CFRP laminate.

This design challenge is analysed in Figure 5. For this study, the overall boss geometry is kept similar, only the runout thickness of the boss is changed from 0.25 mm to 1.00 mm. By this, the global stiffness change of the runout variation for the CPV system is kept to a minimum. For analysis, the mean yield von Mises stress in the runout was extracted. Therefore, the von Mises stress was evaluated on the integration points in the runout volume, shown in red in Figure 5. The fiber stresses of layer 1 was derived directly in the interface boss to CFRP laminate (Layer 1 bottom) and the interface between Layer 1 and Layer 2 (Layer 1 top).

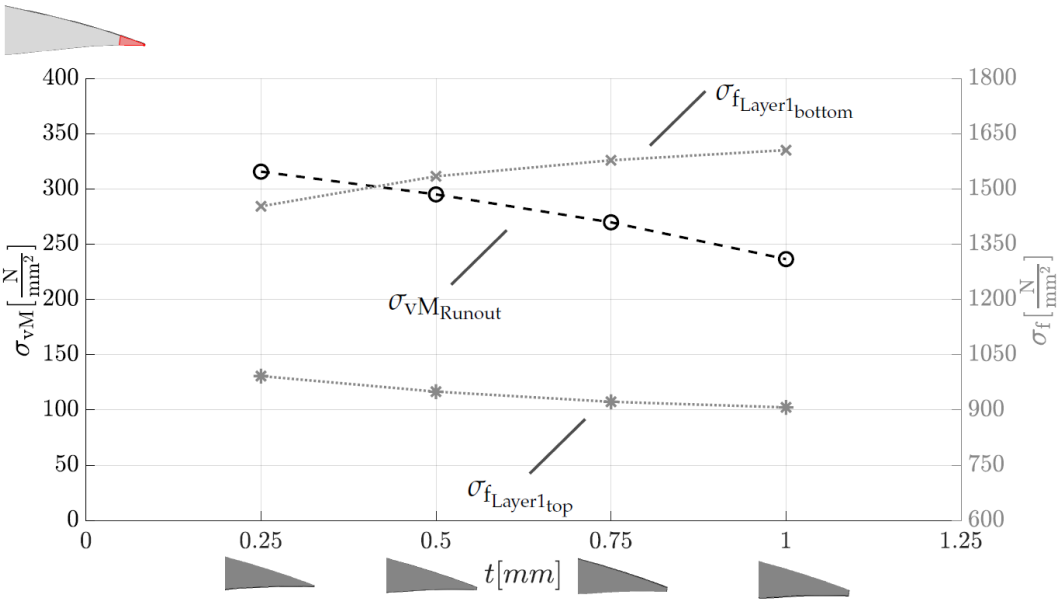

Figure 5 Fiber stress in the top and bottom of layer 1 at the location of the runout end of the boss as well as the yield stress in the runout end (shown in red) of the metal boss for an inner pressure loading of 400 bar in variation of the runout thickness end.

It must be noted, that the results shown in Figure 5 represent general design trends. The quantitative values may be affected by numerical singularities in the joining area of the boss and the CFPR overwrap. This is also a challenge of the boss interface and needs to be addressed in future research.

Figure 5 shows that the overall yield stress in the runout reduces with increasing runout thickness. Increasing the runout thickness therefore reduces the risk of yield induced failure as the runout area shows lower overall loading. The stresses for the fiber direction in Layer 1 of the CPV laminate show that the increase in runout thickness causes an increase in loading especially in the bottom of Layer 1. This joining area between boss and CPV laminate is a very important interface for functional requirements such as leakage, especially in Type V designs. This is why these trends shown in Figure 5 are critical.

The effect of increasing fiber stresses with increasing runout thickness is not present towards the upper layers of the laminate. The fiber stresses slightly decrease in the interface of Layer 1 and 2 which is due to the different deformation behaviour caused by the stiffness change of the boss runout.

A result of Figure 5 is that the engineer always has to choose between a low loading with regard to yielding of the boss or a lower loading of the CFRP layers in the laminate. The decrease in runout thickness is limited by the need to prevent the metallic bosses from yield failure. This is why the change of material to CFPR can be promising due to the material properties discussed in section 2.1.

Therefore, the next section discusses the change of boss material and highlights the possible benefits.

3.2 Analysis of different boss materials

Based on the results of the Invar36 boss, the use of Aluminum, SMC and prepreg materials is discussed. The design comparison between Invar36, Aluminum and SMC is shown in Figure 6.

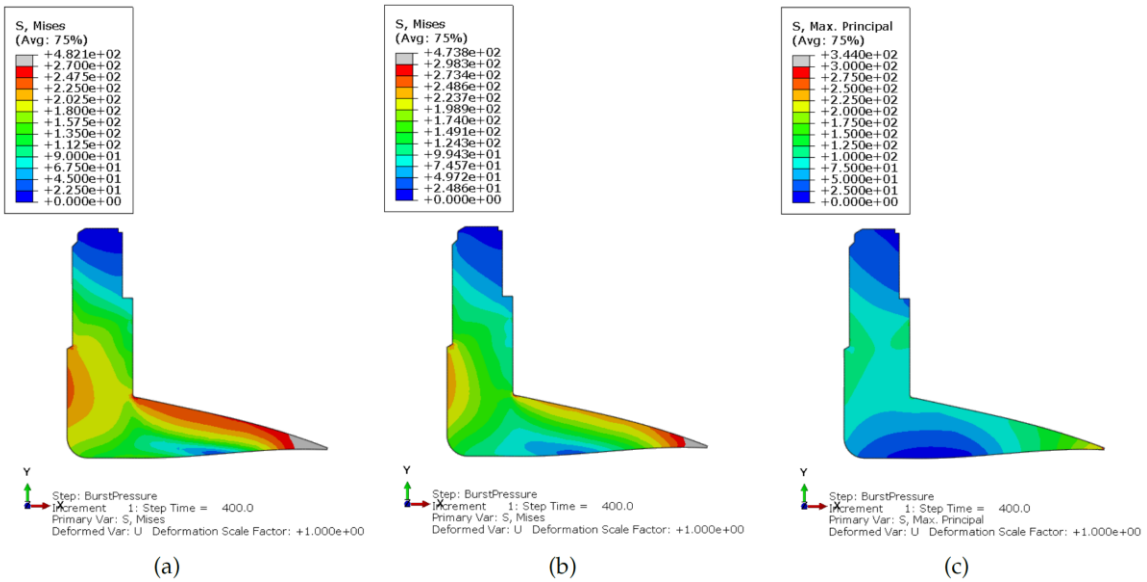

(a) (b) (c)

Figure 6: Boss Design Material Comparison: (a) Invar36 design, (b) Aluminum design, (c) SMC design. Shown is the von Mises stresses for (a) and (b) with $R_{p0,2}$ as limit, for (c) the maximum principal stresses are displayed with the failure stress of SMC as limit.

For Aluminum, the strength to density and strength to stiffness ratio is better compared to Invar36. Consequently, the yield behaviour at the same inner pressure is reduced compared to the Invar36 design, which can be seen in the von Mises stresses in Figure 6. Also, the overall stiffness is reduced, resulting in a less pronounced stiffness jump at the boss end. Both favours the Aluminum design. As a design adaptation, the thickness could be reduced resulting in lower mass not only due to the lower density but also due to the reduced need of metal material.

These benefits are limited to room temperature applications, as the CTE mismatch to the CFRP laminate is too high for the use in cryogenic conditions.

Similar results are observed for the SMC boss design. SMC offers even better strength to stiffness and strength to density values compared to Aluminum. The advantages of the Aluminum design are therefore also applicable to the SMC design. Lower density and higher strength can further decrease the weight of a SMC boss compared to Aluminum. In addition, the CTE is reduced compared to Aluminum. Further research needs to investigate until which temperatures SMC can be used in low temperature applications. Both, SMC and Aluminum also offer a significant weight decrease compared to the Invar36 design.

Based on the results discussed, a prepreg boss offers the unique chance to tailor the laminate more to the loading situation compared to isotropic materials. Above, SMC was treated as isotropic, as a simplification. Future research could also investigate the in- and out-of-plane stiffness distribution of SMC with regard to the mechanical and thermal behaviour of the CPV.

Reviewing Figure 4, the runout area should be reinforced with prepreg in fiber direction located towards the bending stresses. Like a sandwich design, fibers can be applied to the inner and outer contour and the middle section can be filled with twill prepreg, or even lower density materials as discussed in [7]. Towards the fluid adapters a high circumferential loading is observed in Figure 4. This loading can be taken up best by fibers located in circumferential direction (here called 90°).

A demonstration of this design procedure is shown in Figure 7. The layup of the prepreg boss is shown in Figure 7 (a). The SMC section in the upper part is a simplification for the analysis and not of relevance for the loading situation and offers no major influence on the deformation behavior and is therefore not further discussed.

Compared to the Invar36 design, the overall thickness is reduced, as prepreg offers higher strength compared to SMC. The results in Figure 6 (c) show that SMC already provides stresses below the strength of SMC. As a consequence, the loading of a boss with identical geometry will be even lower. That is why for this analysis, the overall thickness of the boss was lowered.

Figure 7 (b) shows the result of this analysis. Here, the maximum principal stresses are shown at 400 bar inner pressure. As a strength limit, the twill strength of 1050 MPa is chosen. As the UD strength is higher, see Table 1, this approach is conservative.

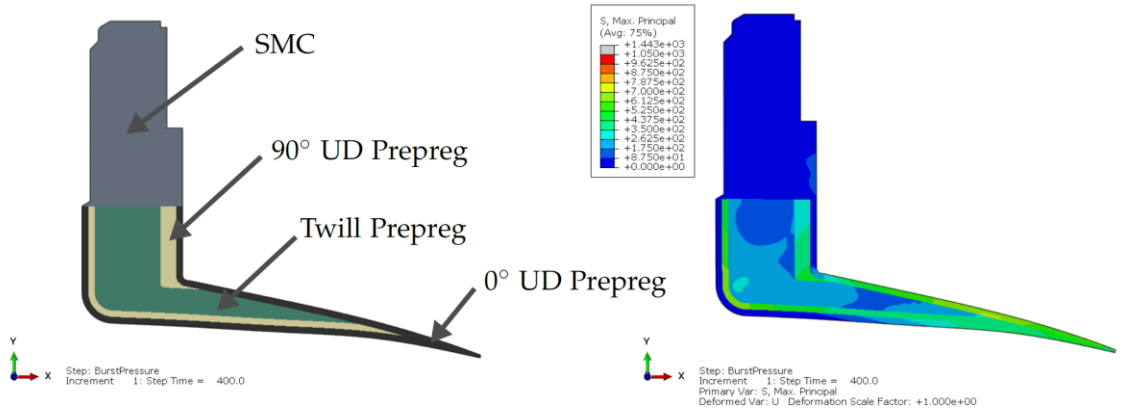

(a) (b)

Figure 7: CFRP Prepreg Boss: (a) Fiber distribution (0° following the boss contour, 90° in Z direction), (b) Maximum principal stresses with Twill Prepreg Strength as limit.

It can be concluded that the loading situation is lower compared to Invar36 design even with the lower part thickness regarding the twill strength. Also, the peak stress within the CPV laminate is reduced. Because of the use of CFRP material, the design challenge is shown in Figure 5 resolved. Low runout thicknesses are possible to the use of CFRP material with a suitable fiber orientation. This also causes the lower peak stress of the laminate at the bottom of layer 1. Additionally, the shear out failure mode can be resolved by the correct use of fiber orientation.

Comparing the volume of the two boss configurations, a volume reduction of 33% is observed for the CFRP boss. Taking the density into account, this adds up to a weight reduction of 87%. This lowers the mass from 2,29 kg per boss for the Invar36 boss to only 295 g for the CFRP bosses. Considering the neglected adapter for fluid adaption, which will lower the mass benefit, this still is a remarkable result, especially as the design can be further optimized considering the stress distribution in Figure 7 (b). Related to the overall tank mass, this would be a mass decrease of 28% for the whole CPV.

This emphasizes the structural benefit which is present in the concept of replacing Invar36 bosses through CFRP bosses. As the CTE of Twill and UD prepreg is also low, cryogenic temperatures are also in scope of the design solution. The CFRP boss offers lower mass and higher strengths compared to Invar36 and also a low CTE.

4 CONCLUSIONS

4.1 Summary

In conclusion, this study analyses and discusses the benefits of CFRP boss materials based on a tested CPV with Invar36 bosses.

First, a material comparison highlights a material selection to replace Invar36 as design material. The benefits of these materials are discussed and summarized in this study. Consequently, a FE-model is set up to investigate and evaluate the loading situation of the baseline boss material Invar36. A variation of the runout geometry is performed to show the design challenge using Invar36 as design material. Based on this, different materials for boss manufacturing are analysed. The results show that Aluminum and SMC show advantages over the Invar36 boss at room temperature. The use of prepreg materials such as UD and twill further increase these advantages. Due to the low CTE of prepreg CFRP bosses they can be also interesting in cryogenic temperatures.

Based on the results it can be concluded that the use of CFRP bosses offer a high potential for decreasing the weight of CPVs. Compared to the weight saving of changing from Type III or IV designs to Type V designs, this change of boss material should also be considered.

In addition to the weight savings of the boss itself, there is also a positive impact on the CPV laminate. The stiffness jump in the joining area of the boss to the CPV laminate can be tailored. Especially with the use of layered structures such as Twill and UD prepreg, the stiffness distribution can be adjusted to the predicted deformation behaviour of the tank system containing the boss and the CPV laminate. This has a direct impact on the design process of the CPV laminate which is expected to further decrease the system mass as helical layers, which are needed to control yielding in the boss region for metallic designs are less likely to be needed in case of a CFRP boss. Both, the lower CFRP boss weight and the lower CPV laminate weight are positive for the performance of the CPV system.

4.2 Future research

Future studies can investigate the detailed tailoring of the layered CFRP boss structure to the deformation behaviour of the CPV coupled to the CPV laminate deformation. This interaction of both parts will result in a lower overall CPV mass which can then be evaluated in an experimental campaign. A more detailed analysis of the SMC boss stiffness distribution increases the accuracy of the analysis.

Another aspect of future research is to evaluate the use of SMC in low temperature applications. It needs to be evaluated if the CTE mismatch between the CPV laminate and the SMC boss is sufficiently low enough for the use of SMC bosses at low temperatures. Detailed analysis of the deformation behaviour of the CPV laminate and the boss in a joined state are needed to evaluate this.

ACKNOWLEDGEMENTS

This work was supported by the German Federal Ministry for Economic Affairs and Climate Action through project *CHiLL* - Cryogenic Helium-Tanks in Low-Cost Linerless-Technology under Grant FKZ 50RK2142

REFERENCES

[1] Air and Space Academy, Small launchers: a European perspective. *Deutsche Gesellschaft für Luft- und Raumfahrt*, 2021, Bonn, Germany. ISBN 978-2-913331-91-4.

[2] Azeem M; Ya HH; Alam MA et al. Application of filament winding technology in composite pressure vessels and challenges: a review. *Journal of Energy Storage*, 2022, 49:103468. (https://doi.org/10.1016/j.est.2021.103468)

[3] Akgul B; Kul M; Erden F. The puzzling thermal expansion behavior of Invar36 alloys: a review on process-structure-property relationship. *Critical Reviews in Solid State and Materials Sciences*, 2023, 49(2):254–307. (https://doi.org/10.1080/10408436.2023.2170975)

[4] Datasheet: VDM Alloy 36, Werkstoffdatenblatt Nr. 7101 Revision 03, (https://www.vdm-metals.com/fileadmin/user_upload/Downloads/Data_Sheets/Datenblatt_VDM_Alloy_36.pdf)

[5] McCain WS; Maringer RE, Mechanical and physical properties of Invar36 and Invar36-type alloys. *Battelle Memorial Institute*, 1965, Defense Metals Information Center. Defense Technical Information Center, Accession No. ADS-474-255.

[6] Scherer A; Romeiks C; Gross M; Hübner F; Dickhut T., Feasibility study of a CFRP boss for application in linerless composite Type V tanks, *International Conference on Composite Materials*, Belfast, Northern Ireland, Jul 30-Aug 4, ICCM23_Poster_864, 2023, (https://zenodo.org/records/15317908)

[7] Maximilian Korff, Eduardo Szpoganicz, Georg Stegschuster, Fabian Hübner, Holger Ruckdäschel and Tobias Dickhut, Integration Concept for Recycled Carbon Fiber Nonwovens within CFRP Boss Structures for Pressure Vessels, *Proceedings of the 21st European Conference on Composite Materials ECCM 21*, 2024, Nantes France, (https://sdrive.cnrs.fr/s/Hsy686dM2S6fYGw?dir=undefined&openfile=4078179)

[8] Rehs, Gerrit, Janis Mörk, and Tobias Dickhut, Type V Pressure Vessel Design with Integrated Sheet Moulding Compound and Prepreg Bosses, *SAMPE Journal 61.2*, 2025. (https://doi.org/10.33599/SJ.v61no2.05)

[9] Schürmann, Helmut. *Konstruieren mit Faser-Kunststoff-Verbunden*. Vol. 2. Berlin: Springer, 2005.

[10] Guo, Xiaonong, et al. "Constitutive model of structural aluminum alloy under cyclic loading." *Construction and Building Materials* 180, 2018: 643-654. (https://doi.org/10.1016/j.conbuildmat.2018.05.291)

[11] Ahmed, Ashraf, et al. "Study of thermal expansion in carbon fiber-reinforced polymer composites." *SAMPE international symposium proceedings*. Charleston (SC), USA: SAMPE, 2012.

[12] Datasheet: HexPly® M49 120°C curing epoxy matrix (https://www.hexcel.com/user_area/content_media/raw/HexPly_M49_eu_DataSheet.pdf)

[13] Datasheet: HexPly® 8552 Epoxy matrix (https://www.hexcel.com/user_area/content_media/raw/HexPly_8552_eu_DataSheet(1).pdf)

ICCM24
AUGUST 4-8, 2025
BALTIMORE CONVENTION CENTER
BALTIMORE, MARYLAND, USA

No Technical Paper Submission for:

Najwa Zaqirah Binti Taufik

ULTRASONIC RECONSOLIDATION AT 20 KHZ - A POTENTIAL REPAIR APPROACH FOR AEROSPACE COMPOSITES

Balaji Ragupathi[1], Kay A. Weidenmann[4] and Frank Balle[1,2,3]

[1]Walter-and-Ingeborg-Herrmann-Chair for Power Ultrasonics and Engineering of Functional Materials (EFM), Department of Sustainable Systems Engineering (INATECH), Faculty of Engineering, University of Freiburg, 79110 Freiburg i. Br., Germany.
E-Mail : balaji.ragupathi@inatech.uni-freiburg.de

[2]Fraunhofer-Institute for High-Speed Dynamics, Ernst Mach Institute (EMI), 79104 Freiburg i. Br. Germany.

[3]Freiburg Materials Research Center (FMF), 79104 Freiburg i. Br., Germany.
E-Mail : frank.balle@inatech.uni-freiburg.de, Web page : www.inatech.de/frank-balle

[4]Institute for Materials Resource Management, University of Augsburg, 86159 Augsburg

Keywords: Repair, Power Ultrasonics, Carbon fiber, Mechanical properties

ABSTRACT

Recycling of end-of-use (EoU) aerospace composites and manufacturing waste has gained traction over the past decade. Conventional methods such as shredding, pyrolysis, and solvolysis are widely used, with recovery rates of 10–75% of the original mechanical performance. However, these methods often compromise value-retention factors such as fiber length, orientation, and component geometry, limiting their reuse in high-performance applications. A circular approach is therefore necessary—one that emphasizes the damage-free separation and reuse of continuous fiber-reinforced layers. Effective reuse requires either rebonding the separated layers to restore the original laminate structure or employing them as reinforcing patches in structural repairs. Recent research has demonstrated the viability of ultrasonic-assisted separation and reconsolidation to recover and reprocess carbon and glass fiber composites. In carbon fiber-reinforced PEEK systems, optimizing ultrasonic reconsolidation through Design of Experiments (DoE) has shown improvements in mechanical performance. Reconsolidation time and force—primarily governed by the temperature profile—define the process window. Hold time and holding force influence thermal characteristics and laminate integrity. Exceeding optimal holding force by 25% leads to fiber-matrix debonding and cohesive failure. When carefully controlled, ultrasonic reconsolidation provides a viable pathway for structural reuse and material circularity in thermoplastic composites.

1 INTRODUCTION

Fiber-reinforced composites are favored in aerospace and aeronautical applications due to their high strength-to-weight ratio. Carbon fiber composites, in particular, offer several advantages over traditional materials, including excellent fatigue resistance, enhanced fire and corrosion resistance, the ability to integrate functions, and flexibility in producing complex geometries [1]. These materials can be up to four times lighter than steel while maintaining comparable performance [2]. Additionally, they contribute to sustainable mobility by lowering CO_2 emissions by up to 20% during their operational life due to lightweightning [3]. However, a growing concern in the aerospace sector is the increasing volume of composite waste generated during production and at end-of-use (EoU). In line with the European Waste Directive, such waste must be managed through a hierarchy that prioritizes reduction, reuse, recycling, recovery, and finally, landfill [4]. Recycling composites remains challenging due to their complex mix of fibers, resins, and fillers, especially with thermoset matrices [5-7]. Common industrial

recycling methods like pyrolysis and solvolysis often degrade material quality [8, 9]. Therefore, recovery methods enabling reuse in high-performance applications are essential [4].

Thermoplastic composites (TPCs) offer significant advantages over thermoset composites, particularly in repairability, due to their ability to be reheated above their glass-transition (amorphous) or melting temperature (semi-crystalline). This thermal reversibility enables efficient joining and repair processes such as ultrasonic welding (USW), which has been increasingly recognized as a promising method for TPC repair. Compared to conventional fusion-based techniques like arc or resistance welding, USW offers several benefits including short cycle time, localized heating, reduced energy consumption, and high automation potential [10, 11]. USW relies on mechanical vibrations to generate heat through friction and viscoelastic dissipation at the interface, often facilitated by energy directors (EDs) in the form of thin films or meshes [12, 13]. Furthermore, successful spot welding without EDs has also been demonstrated [14, 15]. Recent advances demonstrate the growing potential of USW as a viable repair technique for TPCs. Li and Palardy reported high recovery rates (86–94.5%) in mechanical performance using USW with nanocomposite ED films across multiple repair cycles, outperforming resistance heating methods in terms of consistency and bond strength [16]. The thermoplastic matrix not only ensures strong mechanical integrity and chemical resistance but also allows repeated processing, making it ideal for sustainable repair strategies. Despite requiring more complex repair methods compared to thermosets, techniques like USW, induction, and resistance heating have shown proven effectiveness for restoring delaminated and damaged TPC structures in aerospace applications [17-19].

While ultrasonic welding (USW) is well-established for joining aerospace-grade thermoplastic composites, its application in repair remains underexplored. This study introduces our novel ultrasonic reconsolidation approach for repairing separated, multi-directional CF-PEEK laminates without energy directors. Using statistical design of experiments, optimal USW parameters were identified based on lap-shear strength. Repair quality was further assessed via 3D X-ray microscopy and temperature analysis during the post-reconsolidation phase. The influence of holding force and time on thermal behavior was analyzed in-depth. Additionally, successive repairs were evaluated through mechanical testing and microstructural analysis, highlighting ultrasonic reconsolidation as a promising alternative to conventional aerospace repair techniques.

.

2 MATERIALS AND METHODS

2.1 Thermoplastic composite laminate

Figure 1a illustrates the cross-ply thermoplastic carbon fiber (CF)-PEEK (poly-ether-ether-ketone) composite laminate examined in this study. The laminate, commercially known as CETEX-TC1200, was supplied by Toray Advanced Composites (Nijverdal, Netherlands). PEEK, a high-performance semi-crystalline thermoplastic from the polyaryletherketone (PAEK) family, exhibits exceptional mechanical strength and chemical resistance. With a glass transition temperature of 143 °C and a high melting point of 343 °C, it is well-suited for demanding aerospace and advanced medical applications. Ultrasonic C-scan inspections confirmed the laminate was free from critical manufacturing defects such as voids or delaminations. Table 1 presents the material properties of the CF-PEEK laminate as specified by the manufacturer. The laminate was fabricated with a cross-ply layup of alternating 0° and 90° fiber orientations, resulting in a final consolidated thickness of 2.48 ± 0.03 mm. Test specimens, each measuring 110 mm in length and 30 mm in width, were precision-cut from the laminate using micro water-jet cutting at Fraunhofer IWM (Freiburg, Germany), as shown in Figure 1a. The corresponding cross-sectional micrograph is presented in Figure 1c. Layer separation was achieved using a hybrid process that combined ultrasonic-assisted pre-cracking at 20 kHz [20] with mechanical delamination via a custom-built peel-off apparatus [21–23], as depicted in Figure 1b. The resulting top and bottom layer thicknesses were measured at 1.03 ± 0.05 mm and 1.74 ± 0.04 mm, respectively. The thickness of the top layer reflects the minimum achievable limit of the ultrasonic pre-cracking technique.

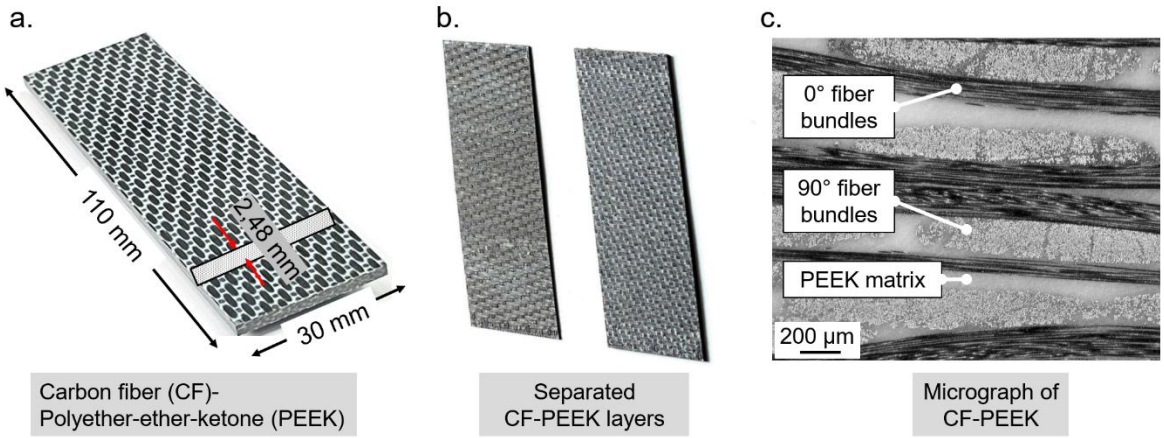

Figure 1: (a) CF-PEEK specimen with dimensions used for the investigation (b) Separated CF-PEEK layers and (c) Cross-sectional view of CF-PEEK specimen with 0° and 90° fiber orientation [24].

Material properties	Units	Values
Fabric type	–	5-Harness satin weave
Laminate layup	–	$[0/90/0/90]_s$
Number of plies	–	8
Cured ply thickness	[mm]	0.31
Area weight	[g/m^2]	0.0051
Glass transition temperature (T_G)	[°C]	140
Melting point (T_M)	[°C]	337
Decomposition temperature (T_D)	[°C]	>550
Ultimate tensile strength 1-direction	[MPa]	776
Young's Modulus E_{11} direction	[GPa]	56.1

Table 1: Material properties of CF-PEEK laminate. The table has been already published in [24].

2.2 Ultrasonic reconsolidation of CF-PEEK at 20 kHz

Ultrasonic repair experiments were conducted using a HiQ 20-6200 ultrasonic plastic welding system from Herrmann Ultraschalltechnik GmbH (Karlsbad, Germany), equipped with a 6.2 kW generator. A schematic of the setup is shown in Figure 2a. The resonance unit included a piezoelectric converter, quick-change adapter, a 1:2 booster, and a rectangular sonotrode (75 mm × 35 mm) capable of delivering a maximum amplitude of 49 µm. The converter transformed electrical energy into mechanical vibrations at a resonance frequency of 20 ± 0.5 kHz. These vibrations were transmitted through the booster to the sonotrode and applied to the joining interface under ambient conditions. Temperature monitoring at the repair interface was performed using thermocouples. Three independent experiments were conducted to record interface temperatures during reconsolidation and post-reconsolidation. A control PC triggered data acquisition via the generator, with temperature data collected through a LabVIEW interface. The separated CF-PEEK layers were joined in a single lap-joint configuration with a 35 mm overlap length and 30 mm width, as shown in Figure 3b. The thicker layers served as the bottom adherend, while thinner layers were placed on top. Prior to welding, the bonding surfaces were cleaned with ethanol to remove contaminants, and the samples were securely clamped using toggle clamps (Figure 3c). The ultrasonic reconsolidation process window was determined using a statistical design of experiment using a non-linear statistical "Central Composite Circumscribed" (CCC) model from the software MODDE [25].

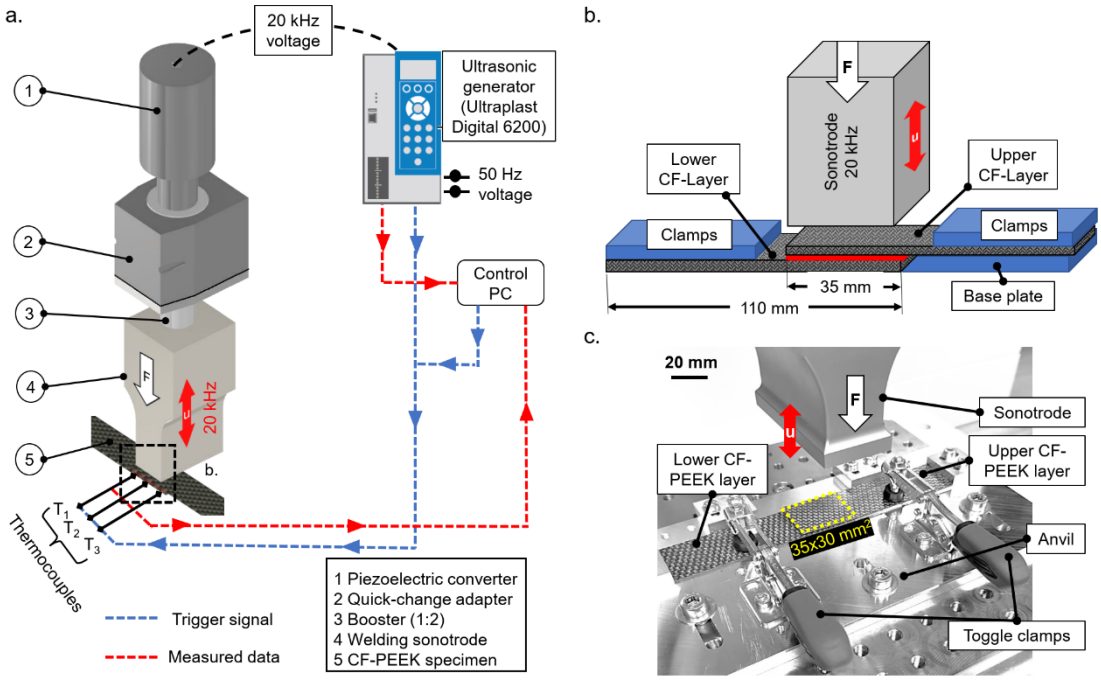

Figure 2: (a) Schematic representation of the ultrasonic repair setup with the oscillation unit. (b) Enlarged view of the clamping system at the reconsolidation zone and (c) actual setup of ultrasonic repair. Figure taken from [26].

2.3 Mechanical and microstructural characterization

The reconsolidated CF-PEEK lap-joint specimens were mechanically tested to determine their ultimate lap-shear strength using a universal testing system of type Z020 from Zwick/Roell (Ulm, Germany) with a 20 kN load cell. Tests were conducted under monotonic loading at a constant displacement rate of 2 mm/min, with the thin layer positioned on top and the thick layer at the bottom, aligned along the loading axis. Surface observations after post-failure were carried out using a Smart Zoom-5 light microscope (Zeiss, Oberkochen, Germany). Additionally, fracture surface analysis was performed using SEM (Zeiss EVO-15) to examine fiber and matrix behavior after repeated reconsolidation trials. Cross-sectional analysis on the repaired zone was not feasible as the repaired joints failed during the specimen preparation. Hence, a Zeiss Xradia Versa 520 system from Fraunhofer IAF (Freiburg, Germany) was used for the 3D X-ray microscopy (XRM) analysis on the repaired CF-PEEK samples.

2.3 Mechanical and microstructural characterization

The reconsolidated CF-PEEK lap-joint specimens were mechanically tested to determine their ultimate lap-shear strength using a universal testing system of type Z020 from Zwick/Roell (Ulm, Germany) with a 20 kN load cell. Tests were conducted under monotonic loading at a constant displacement rate of 2 mm/min, with the thin layer positioned on top and the thick layer at the bottom, aligned along the loading axis. Surface observations after post-failure were carried out using a Smart Zoom-5 light microscope (Zeiss, Oberkochen, Germany). Additionally, fracture surface analysis was performed using SEM (Zeiss EVO-15) to examine fiber and matrix behavior after repeated reconsolidation trials. Cross-sectional analysis on the repaired zone was not feasible as the repaired joints failed during the specimen preparation. Hence, a Zeiss Xradia Versa 520 system from Fraunhofer IAF (Freiburg, Germany) was used for the 3D X-ray microscopy (XRM) analysis on the repaired CF-PEEK samples.

3 RESULTS AND DISCUSSION

3.1 Identification of suitable ultrasonic reconsolidation process window

Ultrasonic repair experiments were conducted on CF-PEEK laminates to optimize process parameters and evaluate tensile lap-shear strength (F_{UTS}) performance. Surface plots were generated by varying two ultrasonic welding parameters while holding one constant: weld time t_{US} (750 ms), weld force F_{US} (601 N), and oscillation amplitude u (37.9 µm) as illustrated in Figure 3a-c. The resulting F_{UTS} values were approximately 15.65 ± 1.31 kN, 15.48 ± 1.78 kN, and 15.78 ± 1.45 kN, respectively. These results were validated through six additional trials, yielding an average lap-shear force of 15.61 ± 1.73 kN. In all cases, the tensile lap-shear force increased initially with weld time and force before decreasing, likely due to fiber bundle damage from excessive polymer squeeze-out. To prevent thermal degradation of the PEEK matrix, weld parameters were capped to ensure peak temperatures remained near 550 °C, below the decomposition threshold. The optimal process condition was identified at F_{US} = 600 N, t_{US} = 750 ms, and u = 37 µm, yielding a consistent F_{UTS} of 15.6 kN.

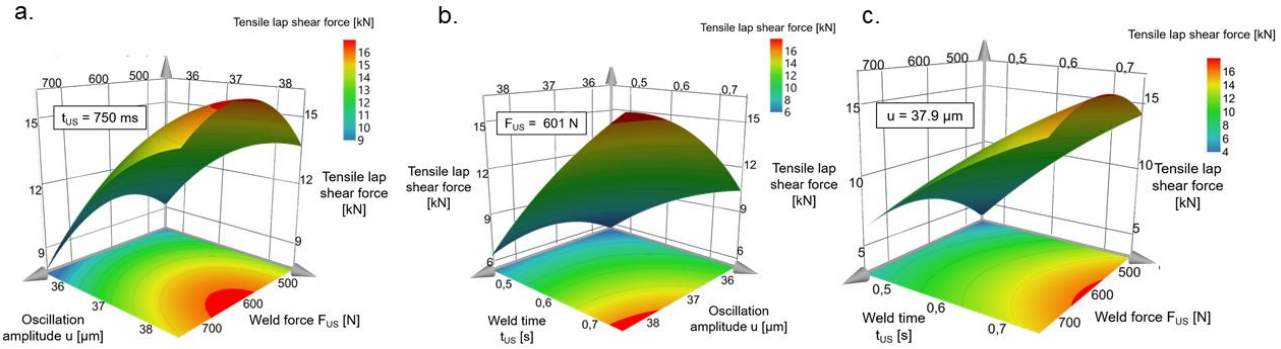

Figure 3: 3D surface plots of CCC model plotted for (a) constant reconsolidation time t_{US} = 750 ms, (b) constant reconsolidation force F_{US} = 601 N, (c) constant oscillation amplitude u = 37.9 µm. Figure adapted from [26].

Figure 4a shows the temperature measurements during ultrasonic repair revealed that oscillation amplitude significantly influences thermal behavior, whereas weld force has minimal impact. The highest temperatures recorded were 547.4 °C and 559.1 °C for the recommended parameter triple and the optimizer function, respectively. A marginal increase in amplitude by 0.9 µm resulted in a 12 °C rise in temperature, highlighting its critical role in thermal input. In contrast, variations in weld force showed negligible influence on peak temperature. When oscillation amplitude increased, temperatures exceeded the decomposition threshold, emphasizing the need for careful amplitude control. Differential scanning calorimetry revealed localized changes in crystallinity, although no significant impact on macroscopic properties was detected. Figure 4b shows the representative load-displacement curves during the tensile lap-shear test. Six repetitions have been performed for the determined suitable ultrasonic reconsolidation parameter and the average lap-shear force was found to be 15.6 ± 1.3 kN.

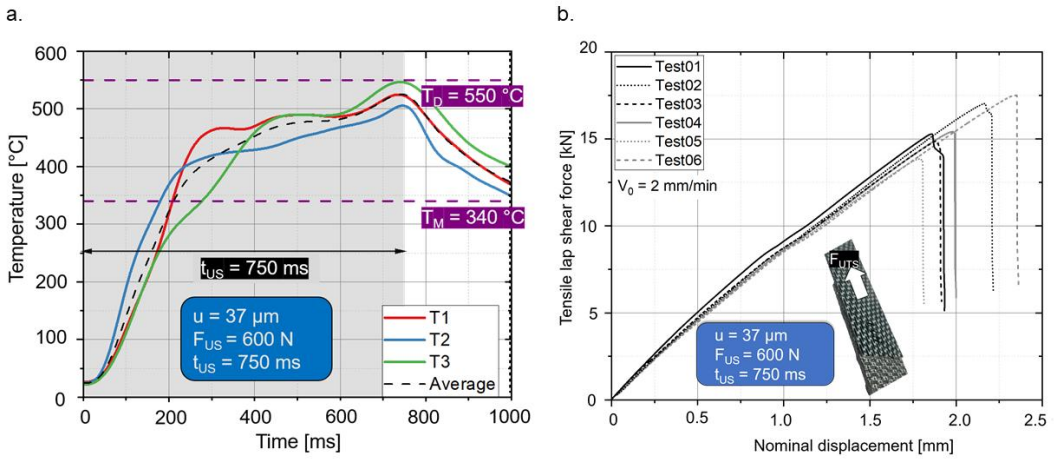

Figure 4: (a) Representative time-temperature curve for the determined suitable ultrasonic reconsolidation process parameter and (b) shows the representative load-displacement curve from the tensile lap shear test of the reconsolidated CF-PEEK laminates. Figure adapted from [26].

3.2 Temperature behavior and failure analysis during post-reconsolidation of CF-PEEK under varying holding forces and hold times

Temperature being a characteristic variable during USW influences the quality of joint performance based on ultrasonic process parameters. This section investigates the influence of holding force and hold time on the temperature distribution and microstructural behavior during the post-reconsolidation phase of ultrasonic welding in thermoplastic composites. Temperature measurements at four distinct locations (T1–T4) across the weld zone revealed spatial variation in thermal behavior, which directly influenced matrix diffusion and defect formation. The parameters used for the characterization of post-reconsolidation phase is listed in Table 2.

Oscillation Amplitude u [µm]	Reconsildation force F_{US} [N]	Reconsolidation time t_{US} [ms]	Holding force F_H [N]	Hold time t_H [s]
37	600	750	0	0
			700	2
			750	4
			800	5
			900	6

Table 2: Parameters used for ultrasonic reconsolidation experiments. The table has been already published in [24].

At a holding force of 700 N and a hold time of 2 s, temperature gradients were evident, with T1 and T2 showing 28% higher temperatures than T3 and T4. This non-uniformity suggested inconsistent residual polymer distribution, resulting in localized decomposition and pore formation (50–200 µm) due to incomplete matrix diffusion. Increasing the hold time to 4 s improved thermal uniformity and matrix diffusion, as reflected by fewer defects and better adhesion (see Figure 5a (i and ii)). At 6 s, the temperature disparity between sensors further decreased to 8%, and failure analysis showed hardened matrix improved consolidation. For a higher holding force of 800 N at 2 s, temperatures were 6% lower than those recorded at 700 N due to enhanced heat dissipation. However, despite higher pressure, insufficient hold time still led to poor matrix diffusion, though the pore size reduced to 5–50 µm. Extending the hold time to 4 s reduced temperature variation and enhanced polymer diffusion (see Figure 5b (i and ii)). At 6 s, thermal distribution became more uniform and matrix diffusion improved, with minor fiber dislocations likely caused by processing or mechanical testing. At 900 N, temperature measurements followed similar trends, though T1 data were unavailable. T2 consistently recorded higher

values than T3 and T4, but the overall temperature was 5–10% lower compared to lower forces. At 2 s, minimal porosity was observed, but significant fiber-matrix squeeze-out occurred, attributed to high compressive forces acting on the laminate before full diffusion. With increased hold time (4 s and 6 s), uniform cooling was achieved (see Figure 5a (i), but excessive pressure led to cohesive failures within the fiber bundles and even fiber breakage, indicating over-consolidation and shear-induced damage (see Figure 5a (ii) [24].

Experiments without applying holding force or hold time demonstrated a slower cooling rate. After 8 s, the temperatures at T1 and T2 remained near the glass transition temperature (T_G) of PEEK, while T3 and T4 were below T_G. Although the matrix had melted during ultrasonic reconsolidation, diffusion between fiber bundles was insufficient, leading to ductile failure of the residual matrix during mechanical testing due to inadequate solidification [24]. These results emphasize the critical role of optimized holding force and duration in achieving uniform thermal distribution, effective matrix diffusion, and defect-free welds. Short hold times, regardless of applied pressure, are insufficient for complete diffusion and defect mitigation. Conversely, excessive holding force applied for extended durations can lead to matrix squeeze-out and fiber damage. A balanced combination of force and time is therefore essential to ensure effective reconsolidation and mechanical integrity of the joint.

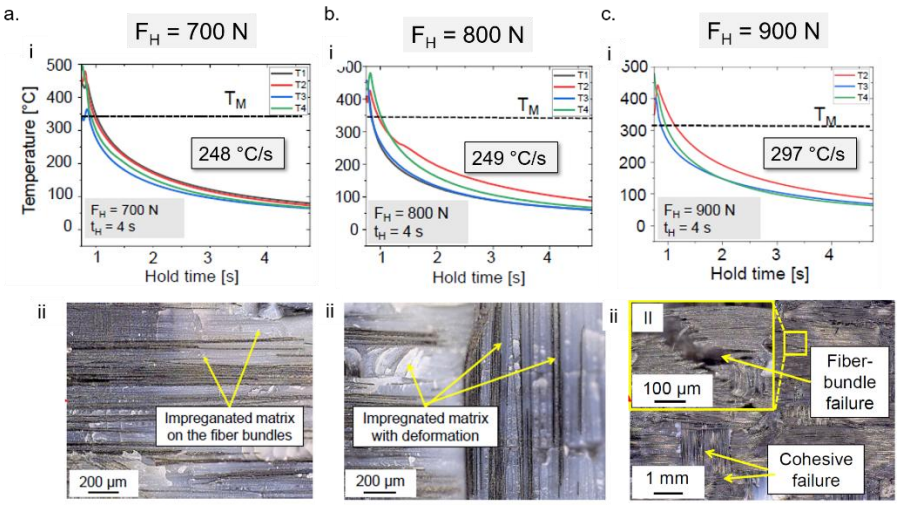

Figure 5: Temperature response during the post-reconsolidation phase, and the micrograph of the welded zone after tensile lap-shear test for (a) F_H = 700 N; t_H = 4 s, (b) F_H = 800 N; t_H = 4 s and (c) F_H = 900 N; t_H = 4 s. Figure adapted from [24].

3.3 Quality of ultrasonic reconsolidation of CF-PEEK after successive reconsolidation cycles

The mechanical performance of ultrasonically reconsolidated CF-PEEK joints was evaluated over three successive repair cycles using optimized process parameters: a holding force of 750 N and a hold time of 5 seconds. The first cycle corresponded to the initial reconsolidation following layer separation, with two additional repair cycles subsequently applied. A progressive reduction in lap-shear strength was observed with each cycle. The initial reconsolidation yielded an average lap-shear load of 15.65 ± 1.02 kN, whereas the third cycle showed a significant decline to 10.3 ± 1.5 kN, representing an approximate 35% reduction in joint strength. A representative load-displacement response revealed a drop in both load capacity and nominal displacement, with the displacement decreasing from 2.4 mm in the first cycle to 1.18 mm in later cycles [24]. The decrease in mechanical performance is attributed to surface degradation of the PEEK matrix. Repeated exposure to high temperatures during ultrasonic processing can induce thermo-oxidative degradation, forming a surface layer that inhibits effective reconsolidation, similar to observation in [27]. Although the core remains intact, the damaged surface layer likely limits matrix flow and interfacial bonding. Consequently, residual polymer accumulation with increasingly amorphous character was observed on the failure surfaces, leading to brittle failure

behavior in the later repair cycles.

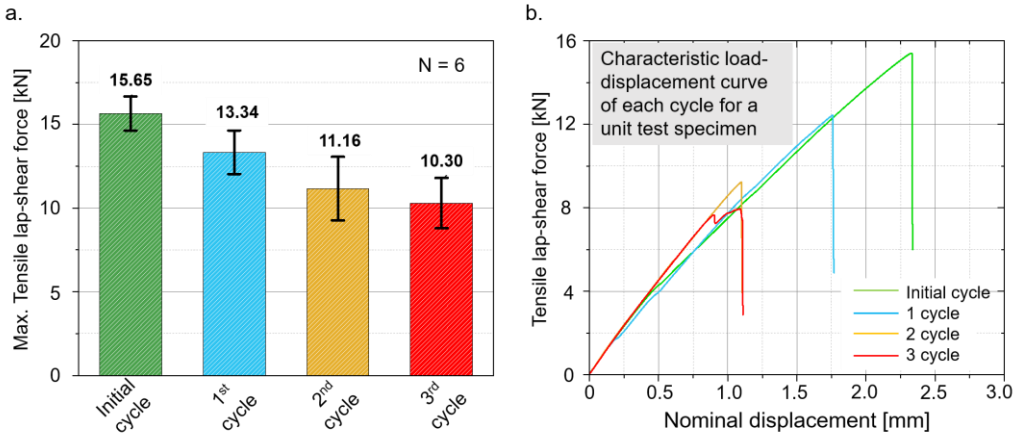

Figure 6: (a) Maximum tensile lap-shear force for 3-cycle repair of separated CF-PEEK layers by ultrasonic reconsolidation. (b) Representative load curve of a single specimen at each repair cycle tested with a displacement velocity of 2 mm/min. Figure taken from [24].

3.4 Ex-situ characterization of CF-PEEK by 3D X-Ray Microscopy (XRM)

3D-XRM scans were conducted on the repaired region within a volume of 5 mm × 5 mm, highlighted by the blue box. In a two-dimensional perspective, the scans encompass the reconsolidated interface (represented by the purple-shaded area) along with the top and bottom neighboring CF-PEEK layers (refer Figure 7a). Figure 7b shows the XRM scan in yz plane for the pre-determined ultrasonic reconsolidation process parameter which revealed void content upto 0.99% and poor interfacial contact near the weld line, attributed to uneven residual polymer distribution caused by material ejection during layer separation. This led to fiber-matrix debonding and cohesive failures above the weld interface. Additionally, fiber layer decohesion was observed near the weld zone. In contrast, specimens repaired using optimized reconsolidation and post-reconsolidation parameters exhibited significantly reduced voids (0.71%) and debonding, with no cohesive failures detected (see Figure 7c). These results confirm the effectiveness of optimized holding force and hold time time in enhancing interfacial bonding and maintaining structural integrity in the repaired CF-PEEK laminates [24].

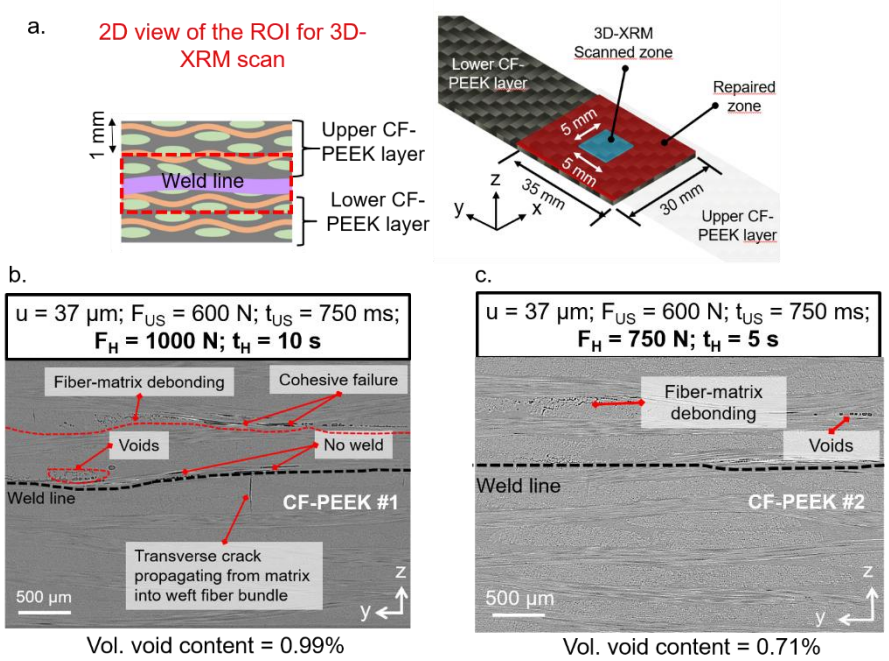

Figure 7: (a) Schematic of the CF-PEEK specimen with the identified optimal parameter scanned using 3D XRM. (b) 3D-XRM scan in yz plane for the (b) determined suitable reconsolidation parameter and for the (c) determined reconsolidation and post-reconsolidation parameter. Figure adapted from [26].

4 SUMMARY AND CONCLUSIONS

Ultrasonic repair of CF-PEEK laminates demonstrated that process parameters—particularly oscillation amplitude, weld force, and weld time significantly influence joint performance and thermal behavior. Optimal ultrasonic reconsolidation conditions (F_{US} = 600 N, t_{US} = 750 ms, u = 37 µm) consistently yielded high lap-shear strengths (approx.15.6 ± 1.3 kN) without exceeding the thermal degradation threshold of the PEEK matrix. Oscillation amplitude had the most pronounced effect on peak temperature, underscoring its critical role in thermal control during welding.

Post-reconsolidation analysis revealed that both holding force and hold time are essential for ensuring uniform thermal distribution and effective matrix diffusion. Inadequate hold time led to poor diffusion and porosity, while excessive holding force induced fiber damage and cohesive failure. A balanced condition (e.g., 750 N, 5 s) achieved optimal consolidation, minimizing voids and defects. Spatial temperature gradients across the weld zone further emphasized the need for controlled thermal management to avoid localized degradation.

Repeated ultrasonic repair cycles under optimized parameters showed a gradual decline in mechanical strength (approximately 35% after three cycles), primarily due to surface degradation and thermo-oxidative damage of the PEEK matrix. This led to reduced interfacial bonding and a shift toward brittle failure modes.

3D-XRM scans confirmed that poor reconsolidation parameters resulted in interfacial voids and fiber-matrix debonding, while optimized conditions improved bonding quality and reduced internal defects. Overall, the study demonstrates that precise control of ultrasonic and post-weld parameters is critical to ensure high-quality, repeatable repairs in CF-PEEK laminates, while repeated thermal exposure imposes limitations on long-term repairability.

5 OUTLOOK

To close the loop, alternative ways for the reconsolidation include bulk processing methods such as hot pressing are available. Therefore, a feasibility study has been carried out to assess this as an alternative to ultrasound-based reconsolidation. Hence, laminates consisting of polypropylene (PP) as a matrix and glass fibers (GF) as reinforcing fibers were cut in strips with the same process as described above and arranged in two layers in a shear edge mold. This dual layer was then reconsolidated into a single laminate in a Vogt Labopress P200S type hydraulic press at a consolidation temperature of 180°C and a pressure of 5 bar for 20 minutes. The consolidated composite laminates were then investigated by means of X-ray analysis on a Baker & Hughes Phoenix nanotom M X-ray Computed Tomography (CT) system and observation of a plastographic specimen with a Keyence 7000 optical microscope respectively.The plastographic specimen is prepared by sequentially grinding a 50 mm specimen with a cylindrical geometry (which contains a small section of the laminate embedded in an epoxy) with grit papers from coarse (320 grit for 4 minutes) to fine grain size (500, 800 and 1200 grit for 2 minutes each) on Silicon Carbide foils, followed by polishing with diamond pastes (9 micron for 3.5 minutes and 3 micron for 2.5 minutes) on a felt pad. The grinding and polishing are completed on a Streurs Tegramin-25 machine, with a continuous flow of water to clean the debris.

The laminate was segmented in a total of 720 slices in the due process of a scan that was conducted at an X-ray tube voltage of 100 kV and power of 12 W, which ran for 1500 ms. The 3D reconstruction of the laminate from CT-scan (Figure 8a) shows a consolidated PP-GF laminate, with minimal misalignments in the fiber bundle orientations and consistent bundle volumes. Furthermore, a highly regular mesostructure can be observed across major part of the Y-Z cross section (Figure 8b) of the laminate. The tows, or fiber bundles, are evenly sized and regularly spaced relative to each other. The exact cause for a section with spatially distorted fiber bundles (observed towards right hand end in Figure

8b, enclosed within the white dotted square) is likely a gap between the strips. The plastographic inspection of the X-Z plane (Figure 8c) further confirms the mesostructural observations from the CT-scan. Additionally, a homogenous distribution of fibers within the bundles can be clearly observed. Furthermore, lack of any noticeable of voids or defects confirms adequate consolidation of the laminate.

The evident regularity in the fiber distribution and a high degree of accuracy in the bundle characteristics at meso- and micro-levels, as well as a seemingly uniform quality of consolidation attest to the potential of hot pressing as an alternate reconsolidation route. Nevertheless, gaps during stacking have to be prevented as they may lead to fiber misorientation. Finally, the single strips recovered via ultrasound might not only be used for repair of existing laminates but might also serve as a basis for reuse of recycled bulk materials without significant loss of material integrity.

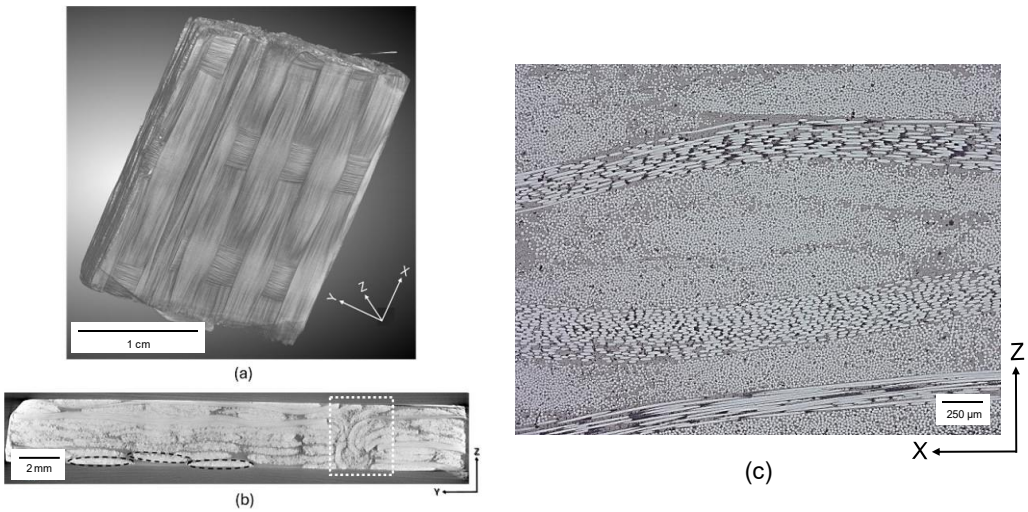

Figure 8: (a) 3D reconstruction of a PP/GF laminate consolidated with a hot press at 180°C, 5 bar for 20 minutes (b) Section of the consolidated PP/GF laminate in Y-Z plane showing mostly uniform fiber bundle (or tow) characteristics – except at gaps in between the single strips (enclosed within dotted white square). Some of the transverse fiber bundles are marked with the dotted black line (c) Plastograph of a representative section of the PP/GF laminate demonstrating regular intra-bundle fiber distribution as also nearly no defects and minimal resin-rich areas.

The evident regularity in the fiber distribution and a high degree of accuracy in the bundle orientation at a meso-level, as well as a seemingly uniform quality of consolidation attest to the potential of hot pressing as an alternate reconsolidation route. Nevertheless, gaps during stacking have to be prevented as they may lead to fiber misorientation. Finally, the single strips recovered via ultrasound might not only be used for repair of existing laminates but might also serve as a basis for reuse of recycled bulk materials without significant loss of material integrity.

ACKNOWLEDGEMENTS

The authors would like to thank the Carl-Zeiss Foundation and the Walter-and-Ingeborg-Herrmann Foundation for their financial support in the frame work of the project "Cross-scale Characterization of Robust Functional Material Systems (SCHARF)" and for all the ongoing power ultrasonic related research works at INATECH respectively. Additionally, the authors also thank Dr. Lutz Kirste and Dipl.-Ing. Mario Prescher from Fraunhofer IAF for their assistance in 3D X-Ray Microscopy measurements.

REFERENCES

[1] G. Giuvelzan, B. Carberry, P. Rempes, Composite recycling and disposal - an environmental issue, Boeing Environmental Technotes 861 8 (2003)

[2] R. Laessig, M. Eisenhut, A. Mathias, R. Schulte, F. Peters, T. Kühmann, T. Waldmann, W. Begemann, Series production of high-strength composites, Roland Berger and VDMA (2012)

[3] A. J. Timmis, A. Hodzic, L. Koh, M. Bonner, C. Soutis, A. W. Schäfer, L. Dray, Environmental impact assessment of aviation emission reduction through the implementation of composite materials, The International Journal of Life Cycle Assessment 20 (2015) 233–243.

[4] European-Parliment, Waste Framework Directive – European Commission-Council Directive, Official Journal of European Union 312 (2008) 99–126.

[5] Y. Yang, R. Boom, B. Irion, D. J. van Heerden, P. Kuiper, H. de Wit, Recycling of composite materials, Chemical Engineering and Processing: Process Intensification 51 (2012) 53-68 (doi: 10.1016/j.cep.2011.09.007).

[6] S. J. Pickering, T. A. Turner, F. Meng, C. N. Morris, J. P. Heil, K. H.Wong, S. Melendi, Developments in the fluidised bed process for fibre recovery from thermoset composites, *Proceedings of the 2nd Annual Composites and Advanced Materials Expo, CAMX 2015, Dallas, Texas USA.*

[7] S. Pimenta, S. T. Pinho, Recycling carbon fibre reinforced polymers for structural applications: Technology review and market outlook, Waste Management 31 (2011) 378–392 (doi: 10.1016/j.wasman.2010.09.019).

[8] S. K. Gopalraj, T. Kärki, Review on the recycling of waste carbon fibre/glass fibre-reinforced composites: fibre recovery, properties and life-cycle analysis, SN Applied Sciences (2020) (doi: 10.1007/s42452-020-2195-4).

[9] N. Niessner, Recycling of Plastics, Hanser Publishers (ISBN 978-1-56990-856-3), 2022.

[10] F. Lionetto, C. Mele, P. Leo, S. D'Ostuni, F. Balle, A. Maffezzoli, Ultrasonic spot welding of carbon fiber reinforced epoxy composites to aluminum: mechanical and electrochemical characterization, Composites Part B: Engineering 144 (2018) 134–142 (doi: 10.1016/j.compositesb.2018.02.026).

[11] I. F. Villegas, L. Moser, A. Yousefpour, P. Mitschang, H. E. Bersee, Process and performance evaluation of ultrasonic, induction and resistance welding of advanced thermoplastic composites, Journal of Thermoplastic Composite Materials 26 (2013) 1007–1024 (doi: 10.1177/0892705712456031).

[12] C. B. G. Brito, J. Teuwen, C. Dransfeld, I. F. Villegas, The effects of misaligned adherends on static ultrasonic welding of thermoplastic composites, Composites Part A: Applied Science and Manufacturing 155 (2022) 106810 (doi: 10.1016/j.compositesa.2022.106810).

[13] T. Zhao, Q. Zhao, W. Wu, L. Xi, Y. Li, Z. Wan, I. F. Villegas, R. Benedictus, Enhancing weld attributes in ultrasonic spot welding of carbon fibre-reinforced thermoplastic composites: Effect of sonotrode configurations and process control, Composites Part B: Engineering 211 (2021) 108648 (doi: 10.1016/j.compositesb.2021.108648).

[14] T. H. Lee, H.-T. Fan, Y. Li, D. Shriver, J. Arinez, G. Xiao, M. Banu, Enhanced performance of ultrasonic welding of short carbon fiber polymer composites through control of morphological parameters, Journal of Manufacturing Science and Engineering 142 (2020) (doi: 10.1115/1.4045444).

[15] Y. Li, B. Yu, B. Wang, T. H. Lee, M. Banu, Online quality inspection of ultrasonic composite welding by combining artificial intelligence technologies with welding process signatures, Materials & Design 194 (2020) 108912 (doi: 10.1016/j.matdes.2020.108912).

[16] W. Li, G. Palardy, Investigation of welding repair methods for thermoplastic composite joints, Composites Part B: Engineering 264 (2023) 110924 (doi: 10.1016/j.compositesb.2023.110924).

[17] X. Xiao, S. V. Hoa, K. N. Street, Repair of thermoplastic resin composite by fusion bonding, Thermoplastic Resin Composite (1994).

[18] J. B. Robles, M. Dubé, P. Hubert, A. Yousefpour, Repair of thermoplastic composites: an overview, Advanced Manufacturing: Polymer Composites Science 8 (2022) 68–96 (doi: 10.1080/20550340.2022.2057137).

[19] J. P. Reis, M. de Moura, S. Samborski, Thermoplastic composites and their promising applications in joining and repair composites structures: A review, Materials 13 (2020) 5832 (doi: 10.3390/ma13245832).

[20] B. Ragupathi, P. Jakkula, M. Rienks, F. Balle, Online monitoring of pre-crack initiation in carbon fiber-reinforced thermoplastic composites by an ultrasonic cutting tool using high-speed optical imaging and infrared thermography, Ultrasonics 143 (2024) 107411 (doi: 10.1016/j.ultras.2024.107411).

[21] B. Ragupathi, M. F. Bacher, F. Balle, First efforts on recovery of thermoplastic composites at low temperatures by power ultrasonics, Cleaner Materials 8 (2023) 100186 (doi: 10.1016/j.clema.2023.100186).

[22] B. Ragupathi, M. F. Bacher, F. Balle, Separation and reconsolidation of thermoplastic glass fiber composites by power ultrasonics, Resources, Conservation and Recycling 198 (2023) 107122 (doi: 10.1016/j.resconrec.2023.107122).

[23] B. Ragupathi, F. Balle, Characterization of glass-fiber reinforced thermoplastic composite after ultrasonic reconsolidation, European Journal of Materials 4 Volume:1 (2024) 2313316 (doi: 10.1080/26889277.2024.2313316).

[24] B. Ragupathi, L. Burger, F. Balle, Post-joining thermal characteristics and repair integrity of carbon fiber-reinforced thermoplastic composites during ultrasonic reconsolidation at 20 kHz, Composites Part C: Open Access 16 (2025) 100565 (doi: 10.1016/j.jcomc.2025.100565).

[25] Balle F, Eifler D. Statistical test planning for ultrasonic welding of dissimilar materials using the example of aluminum-carbon fiber reinforced polymers (CFRP) joints. Material Science and Engineering Technology 43(4) (2012) 381-358 (doi: 10.1002/mawe.201200943).

[26] B. Ragupathi, L. Rotzinger, M. Prescher, M. Rienks, L. Kirste, F. Balle, Ultrasonic reconsolidation of separated CF-PEEK composite layers at 20 kHz – An experimental study on parameter optimization and Ex-situ characterization, Composite Structures 353 (2025) 118722 (doi: 10.1016/j.compstruct.2024.118722).

[27] A. Pascual, M. Toma, P. Tsotra, M. C. Grob, On the stability of PEEK for short processing cycles at high temperatures and oxygen-containing atmosphere, Polymer Degradation and Stability 165 (2019) 161–169 (doi: 10.1016/j.polymdegradstab.2019.04.025).

ICCM24 24TH INTERNATIONAL CONFERENCE ON COMPOSITE MATERIALS
AUG 4-8, 2025 • BALTIMORE CONVENTION CENTER • BALTIMORE, MARYLAND

MANUFACTURING PROCESSES FOR LARGE SPACE STRUCTURES AND FOR SUPPORTING LONG-DURATION HUMAN SPACE MISSIONS

Susanna Laurenzi[1], Flavia Palmeri[1‡], Federica De Rosa[1], Lorenzo Martinazzoli[1], Maria Gabriella Santonicola[2]

[1]Department of Astronautical Electrical and Energy Engineering, Sapienza University of Rome, Via Salaria 851-881, Rome, 00138, Italy Email: susanna.laurenzi@uniroma1.it.

[2]Department of Chemical Engineering Materials Environment, Sapienza University of Rome, Via del Castro Laurenziano 7, Rome, 00161, Italy

[‡]Current address: California Institute of Technology, 1200 E. California Boulevard, MC 105-50, Pasadena, CA 91125-4600, U.S.A.

Keywords: Ultrathin composites, Deployable structures, Out-of-autoclave processes, dynamic behaviour

ABSTRACT

The ambition to expand human presence deeper into the solar system necessitates the development of technologies capable of fabricating, deploying, and maintaining large-scale space structures with minimal Earth-based support. Traditional logistics, reliant on frequent cargo resupply, incur exponentially increasing mass and volume penalties with distance from Earth. For long-duration lunar outposts, orbital missions, and Martian habitats, structures must be compact during launch, mechanically robust when deployed, and manufactured via scalable and adaptable in-situ processes. Composite materials are critical due to their superior strength-to-weight ratios and resistance to fatigue and corrosion. Out-of-autoclave (OoA) manufacturing techniques have emerged as key enablers, reducing production costs and increasing efficiency for large, complex components such as deployable composite booms, which facilitate compact storage and reliable deployment of membrane-supported systems (e.g., solar sails, antennas, reflectors). The integration of OoA methods with advanced materials promises transformative advances in space structure manufacturing. Concurrently, in-space manufacturing (ISM), including fused filament fabrication (FFF) 3D printing, enables on-demand production and customization of mission-critical components, decreasing dependency on Earth resupply. This study further shows the use of local material (regolith) into composite filaments suitable for FFF printing, enabling a closed-loop material lifecycle aboard space habitats. By combining ultra-thin composite booms with in-situ recycling and additive manufacturing, a sustainable, modular approach to structural maintenance and fabrication for long-duration missions on the Moon and Mars can be realized. This work presents ongoing research on OoA and ISM process development using novel materials to advance sustainable space exploration architectures.

1 INTRODUCTION

Ambitions to extend human presence deeper into the solar system are driving exceptional interest in technologies that can produce, deploy, and maintain large-scale structures in space using only minimal support from Earth. Conventional logistics chains, heavily reliant on cargo resupply, impose steep mass and volume penalties which grow exponentially with distance from Earth. For future lunar outposts, long-duration orbital missions, and Martian bases, the solution must involve structures that are compact during launch, robust when deployed, and manufactured using processes that are scalable and flexible enough to be adapted on site.

Composite materials are essential in the development of advanced space structures due to their excellent strength-to-weight ratios and resistance to fatigue and corrosion. These properties enable the

creation of lightweight yet robust components for aerospace applications, driving the need for cost-effective and scalable manufacturing methods. Out-of-autoclave (OoA) processes have emerged as a key solution, offering reduced production costs, improved efficiency, and flexibility, particularly for large, complex components [1,2]. A key application is the production of deployable composite booms, which help solve storage issues in launch vehicles and enable the deployment of large-scale structures in space. Boom structures are slender, elongated components that play a critical role in aerospace applications, particularly in the deployment and stabilization of membrane-based systems such as solar sails, antennas, and reflectors [3-5]. These structures are responsible for maintaining the desired geometry of the membrane throughout its operation, ensuring both precision and reliability.

Given the harsh conditions of the space environment, there is a pressing need for novel materials that offer enhanced durability and resilience. For instance, polymeric nanocomposites, enhanced by nanoparticles like carbon nanotubes and graphene, offer superior properties, including thermal and radiation protection, impact resistance, and enhanced mechanical performance [6-8]. These materials are adaptable to meet the specific demands of space missions, providing lightweight, multifunctional solutions. By integrating OoA manufacturing techniques with these advanced materials, the aerospace industry stands to achieve significant breakthroughs in the design and deployment of next-generation space structures.

In parallel, additive manufacturing, including 3D printing, is revolutionizing space manufacturing. This technique allows for precise customization of components and has already demonstrated its utility aboard the International Space Station (ISS) for in-situ production of tools and parts [9-11]. It allows precise customization of components and can enable the construction of habitats and infrastructure on lunar or Martian missions using local materials or recycled hardware [12-18]. Crewed missions generate streams of single-use packaging, especially in the form of food and drink containers [16-18]. These multilayer laminates, often combining LDPE, PET, and aluminium foil, present a recycling challenge on Earth, but in space, they become both a burden and an opportunity. Every gram of waste that can be repurposed into new functional feedstock eases the mass budget for resupply launches.

Both OoA and in-space manufacturing (ISM) share principles of reducing material waste and optimizing resource utilization, which are crucial for space-based operations with limited resources. OoA allows for large components without autoclave size constraints, while ISM eliminates payload limitations for constructing massive space structures. Together, advancements in composite material fabrication, OoA processes and 3D printing represent a paradigm shift in space structure manufacturing, fostering more efficient, sustainable, and scalable solutions for space exploration.

This study contributes to the expanding body of research aimed at advancing out-of-autoclave (OoA) manufacturing techniques for large-scale structures, while also exploring in-situ process technologies based on fused filament fabrication (FFF). Structural components, such as those used to deploy sensors or reflect sunlight for propulsion, can be produced in modular sections via OoA methods. When damage occurs, for example when a hinge fails or a clip snaps, discarded materials from daily operations may be shredded, reprocessed, and reprinted into functional replacements.

In this closed-loop framework, material science, structural engineering, and mission logistics intersect to create a model of sustainable space exploration. The work presented aims to highlight current research on the development of OoA and in-situ manufacturing techniques, emphasizing the use of novel materials for the construction of space structures and components intended for extended human missions on the Moon and Mars.

2 DEPLOYABLE STRUCTURES

Deployable boom structures are predominantly manufactured using carbon fiber/epoxy prepreg systems, commonly processed via autoclave curing or vacuum bag molding techniques [19–22]. While prepregs offer the advantage of precise resin control, ensuring consistent fiber wet-out and enhanced quality assurance, they inherently limit the diversity of fabric architectures that can be utilized. This limitation reduces design flexibility, particularly when optimizing mechanical properties or conformability for specific structural demands. In contrast, dry fiber reinforcements do not require refrigeration and possess a longer shelf life, thereby simplifying storage and handling logistics. Their cross-sectional geometry varies depending on specific functional requirements. Among the most

prevalent configurations, are storable tubular extendible members (STEM), collapsible tubular masts (CTM), and triangular rollable and collapsible (TRAC) booms. In the present work, the focus is directed specifically toward the fabrication of the A STEM configuration.

This study employs spread tow carbon fabrics combined with CYCOM® 823 epoxy resin. The resin was selected for its favourable viscosity at processing temperatures and its robust mechanical performance once cured.

Spread tow fabrics exemplify how incremental advancements in material architecture can unlock performance gains unattainable with conventional woven textiles. By unbundling standard fiber tows into flat tapes with highly aligned filaments, these reinforcements minimize void content and matrix-rich zones, enabling lighter and stiffer laminates at equivalent fiber volume fractions. When integrated into boom structures, spread tow tapes enhance bending stiffness and foldability, two properties often in competition in traditional woven laminates. During folding and subsequent re-extension, the laminate must endure repeated strain cycles without initiating cracks or causing fiber misalignment, a challenge that intensifies as the laminate thickness decreases to sub-millimeter scales.

The fabrication of ultrathin booms using spread tow composite technology necessitates meticulous control throughout the manufacturing process. This investigation utilizes TeXtreme® HS40 carbon fiber fabrics, featuring 12K filaments and an exceptionally low areal weight of approximately 42 g/m². Such reinforcements facilitate the production of extremely thin laminates while preserving high in-plane stiffness and excellent drapability. The lay-up procedure begins with precision cutting of fabric plies, employing custom-designed jigs to maintain strict ±45° fiber alignment. This orientation promotes optimal shear resistance during deployment and retraction cycles, which is critical for boom structures that transition from a coiled stowed configuration to a fully deployed state without suffering permanent deformation or fiber misalignment.

2.1 Fabrication of tubular extensible members

The hand lay-up technique is performed on a stainless-steel cylindrical mandrel, which acts both as a support and as a form to replicate the final tubular mast geometry. Special care is given to the manual impregnation of the carbon fabric with CYCOM® 823 epoxy resin. The resin is degassed in a Thinky ARE-250 planetary mixer prior to use, ensuring that no entrapped air pockets compromise the laminate's structural integrity. A thin film of PTFE, such as Teflease MG2, lines the mould to facilitate clean demoulding and preserve the surface finish, which is especially important in the context of structures that must withstand dynamic deployment loads. To achieve a fiber volume fraction V_f of approximately 60% in the final boom structures, an experimental investigation was carried out on various stacking sequences of auxiliary materials. Many boom samples were produced and analyzed to determine their resin content. To this end, different combinations of release films, both perforated and non-perforated, and varying numbers of peel ply layers were considered to regulate the amount of resin expelled from the composite part and thereby attain the desired V_f. The final process lay-up sequence identified as optimal for this specific laminate consists of the following: an initial layer of polytetrafluoroethylene (PTFE) tape serving as a release layer from the mold surface, followed by the composite laminate itself, then a wrap of Hi-Shrink Tape, a peel ply layer, a perforated Teflon film, a breather layer, and finally the vacuum bag. This optimized stacking arrangement is illustrated schematically in Fig. 1.

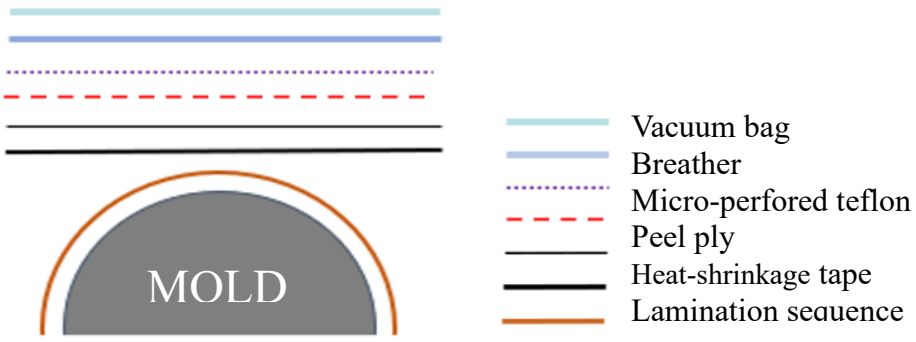

Figure 1. Consumable layer stacking sequence.

The mold used in this study (Figure 2) was specifically designed for the present application and

manufactured in stainless steel. It features a central through-hole along its longitudinal axis, allowing for the integration of thermal control actuators. One of the main challenges in the fabrication of composite booms, as opposed to flat laminate specimens, is the demolding process, i.e., the separation of the cured part from the mold surface. Typically, a release agent is applied to the mold to facilitate this operation. For the present application, the most suitable release material was identified as Teflease MG2, a polytetrafluoroethylene (PTFE) tape coated with a silicone-based adhesive. The use of this release system avoids potential chemical contamination of the resin caused by volatile compounds that may be generated during curing because of residual chemicals from conventional liquid release agents. Such volatile substances, if trapped within the laminate, could outgas once in orbit, posing a risk to both structural integrity and spacecraft subsystems. Moreover, this tape is easy to apply and does not require special safety precautions for operator health. In addition to ensuring reliable release of the cured composite from the mold, the Teflon tape also protects the mold surface from potential damage that may occur during demolding. Its use contributes to preserving the integrity of the mold and allows for an excellent surface finish of the final prototype. The lay-up of both the composite material and the consumable layers can be carried out directly on the cylindrical mold. The process begins with the placement of the first layer of dry fabric onto the mold surface. At this stage, difficulties were encountered due to the limited dimensional stability of the dry fabric, which tends to shift or deform when un-impregnated. To address this issue, a thin layer of resin was applied to the mold prior to laying down the fabric. This pre-coating promotes better adhesion between the fabric and the mold, stabilizing the positioning of the first ply.

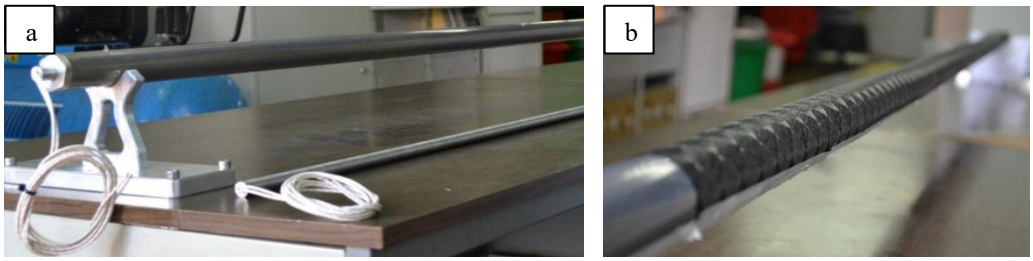

Figure 2. a) Detail of the mold surface covered with Teflease MG2 and the heating element; b) close-up of the fabric lay-up phase.

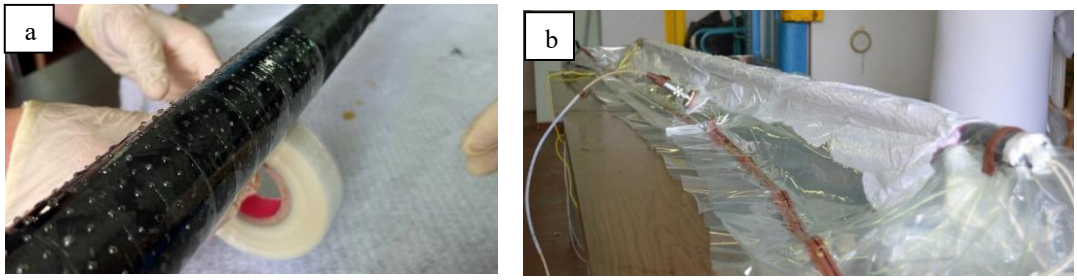

Figure 3. Application of the heat-shrink Hi-Shrink Tape; process configuration during the curing stage

Once laid up, the laminate stack is consolidated under vacuum. Breathers and perforated release films ensure that excess resin is evenly distributed and vented, minimising localised resin-rich zones which could otherwise act as failure points. After bagging, the assemblies undergo an OoA curing cycle, ramping from ambient to approximately 125–130 °C, maintaining a hold sufficient to complete the cross-linking reaction throughout the entire thickness (Figure 3). The final cured booms demonstrate minimal residual stress and excellent geometric fidelity. Despite the apparent simplicity of this process, each step embodies critical decisions that reflect the lessons learned from recent experimental campaigns on deployable structures for solar sails and high-area-to-mass-ratio devices [23-24]. To investigate the influence of key process variables, a series of prototypes was manufactured. The study focused on different laminate ply lay-up techniques, variations in consumable stacking sequences, and the selection

of cutting and sanding tools. The results of this experimental campaign, combined with detailed inspections of the fabricated components, informed the development of the processing procedure described earlier. Several representative prototypes were selected for analysis, as their post-process inspection provided critical insights that guided the refinement of the manufacturing methodology. Among the factors examined, particular emphasis was placed on the application of Hi-Shrink Tape, due to its significant impact on part quality and dimensional stability. Figure 4 illustrates two exemplar cases: on the top, a prototype produced without Hi-Shrink Tape; on the bottom, a counterpart fabricated with its use.



Figure 4. Top: 4-m prototype manufactured without heat-shrink tape. Bottom: 4-m prototype manufactured with heat-shrink tape.

Initially, a non-perforated Hi-Shrink tape was employed. While this version provided excellent compaction during curing, the resulting composite structure exhibited a degree of brittleness. Although the component retained its intended shape in the unrolled (production) configuration, it could no longer be rolled without fracturing due to an excessive accumulation of surface resin. To address this issue, a perforated Hi-Shrink tape was subsequently adopted. This alternative not only compacted the boom structure effectively but also facilitated the evacuation of excess resin during curing. The combined effect of improved compaction and controlled resin bleed led to a significant reduction in both thickness and weight of the prototype component. Specifically, the thickness decreased from 0.24 mm to 0.14 mm, as shown in Fig. 5, while the weight was reduced from approximately 20 g/m to 15 g/m.

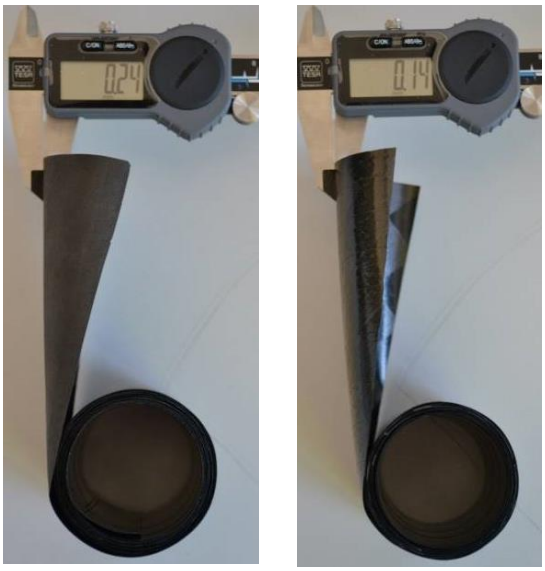

Figure 5. Thickness of the prototype manufactured without hi-shrink tape and with hi-shrink tape (right).

The reduction in laminate thickness corresponds to an increase in the fiber volume fraction Vf. This increase not only enhances the mechanical performance of the composite due to the greater contribution of the reinforcing fibers but also reduces the tendency of the structure to exhibit brittle behavior. In fact,

a resin-rich laminate would be more prone to matrix cracking during rolling and unrolling operations, eventually leading to composite failure. Furthermore, the reduced laminate thickness results in a more compact rolled configuration of the prototype (Fig. 6), thereby decreasing the overall volume and mass of the associated storage and deployment systems.



Figure 6. Prototype volume in rolled configuration: without Hi-Shrink Tape (left) and with Hi-Shrink Tape (right).

3 IN SITU MANUFACTURING

In-space manufacturing (ISM) refers to the production of components and structures directly in the space environment, rather than on Earth. It enables on-demand fabrication using local or recycled materials, reducing launch mass and mission costs. ISM supports adaptability and self-sufficiency in long-duration missions. It is a key enabler for sustainable space exploration and habitation.

In our studies, the material selected as the basis for studying in-situ manufacturing processes was low-density polyethylene (LDPE). Its hydrogen-rich composition offers inherent radiation shielding properties, particularly effective for neutron attenuation. This characteristic makes LDPE a suitable matrix for combination with high atomic number (Z) elements, enabling the fabrication of structural materials with enhanced shielding capabilities [12, 25-26]. In addition, the polyethylene is present in many elements presented on-board and it is one of the material of the astronaut food packaging [14,18]. The polymer matrix employed in this study was low-density polyethylene (LDPE) powder, supplied by Thermo Scientific Chemicals. The LDPE powder exhibited an average particle size of approximately 500 microns. The Martian regolith simulant (RE) was Biolit powder.

3.1 Fused filament fabrication for in-situ regolith/polyethylene composites

The process begins with the fabrication of composite pellets, which serve as the primary feedstock for the extrusion phase. These pellets were formulated by combining low-density polyethylene (LDPE) with varying weight percentages (5, 10, 15, 20, and 30 wt%) of Martian regolith simulant, acting as the reinforcing filler. Once prepared, the composite pellets were fed into a filament extruder (Felfil Evo), where they were melted, homogenized, and extruded into continuous filaments with controlled diameter and mechanical properties. The extrusion was carried out using a 1.75 mm nozzle at approximately 160 °C, with a screw rotational speed of 7 RPM. These parameters were carefully controlled to ensure consistent mixing and uniform filament quality—critical factors in maintaining dimensional stability and mechanical performance in the final printed parts.

To further enhance the dispersion of filler particles within the polymer matrix, the initially extruded filaments were shredded into smaller fragments and re-extruded. This additional processing step facilitated a more uniform distribution of the regolith simulant, minimized the formation of agglomerates, and consequently improved the structural and functional properties of the composite material.

Achieving the right balance between flexibility and rigidity in LDPE/regolith composite filaments is critical to ensuring both printability and mechanical reliability in fused filament fabrication (FFF) processes. While LDPE inherently offers low melting temperatures and good flexibility, favorable characteristics for extrusion, the addition of regolith simulant at high concentrations, such as 30 wt%,

tends to increase brittleness and reduce ductility. These changes can result in filament breakage, feeding instability, or inconsistent extrusion during the printing process.

Following extrusion and refinement, the filaments were spooled and prepared as feedstock for FFF-based 3D printing, enabling the in-situ fabrication of functional components in space environments. As illustrated in Figure 7a, a 20-meter-long filament containing 30 wt% filler content was successfully wound onto the spool, exhibiting adequate flexibility for handling and processing. Figure 7b highlights the tension applied to the filament during the spooling phase in the cooling stage, which is crucial for maintaining a consistent diameter and preventing deformation.

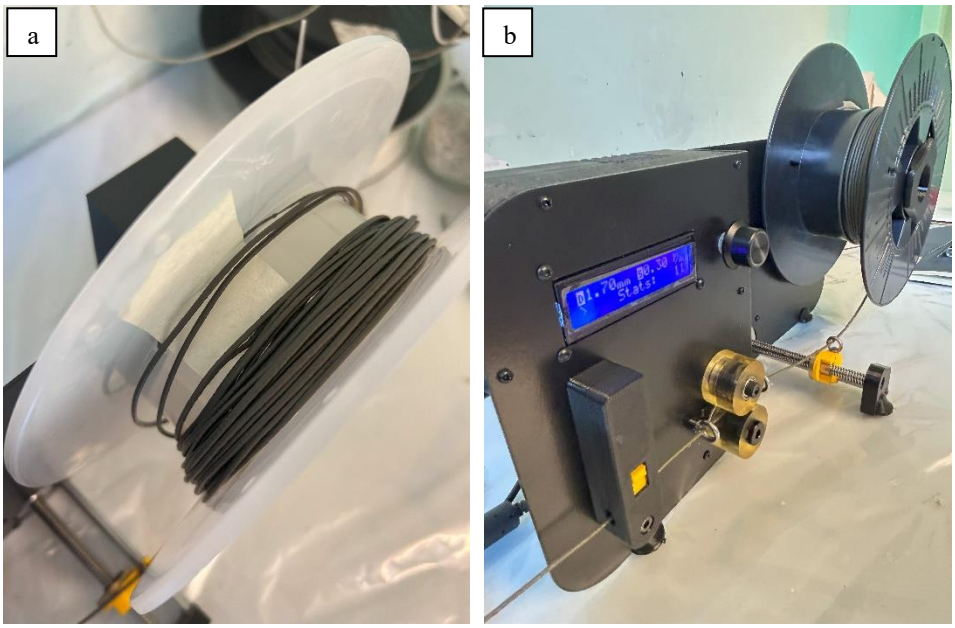

Figure 7. a) 20-meter-long LDPE/regolith composite filament with 30 wt% filler content wound onto the spool at the end of the extrusion process; b) view highlighting the filament tension during the spooling process in the cooling phase.

After the extrusion process, the LDPE/regolith composite filaments were used to fabricate test elements via fused filament fabrication (FFF), with process parameters carefully optimized to ensure print quality and dimensional accuracy. Figure 8 shows the 3D-printed specimens prepared for dynamic mechanical analysis.

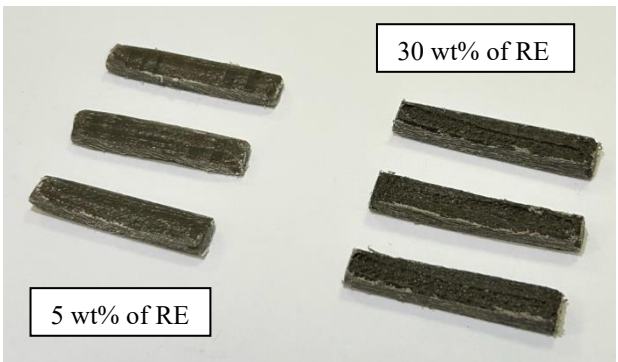

Figure 8. 3D-printed specimens of LDPE/RE composites at 5 wt% (left) and 30 wt% (right) of filler.

CONCLUSIONS

This study demonstrates the feasibility of fabricating deployable ultrathin composite boom structures and radiation-shielding materials using both traditional out-of-autoclave (OoA) and in-situ manufacturing (ISM) processes. For structural applications, the integration of spread tow carbon fiber

fabrics with a carefully optimized OoA lay-up and curing cycle enabled the production of high-performance, sub-millimeter-thick tubular booms with excellent stiffness-to-weight ratios, geometric fidelity, and foldability. The use of perforated Hi-Shrink Tape proved particularly effective in improving laminate compaction, reducing resin-rich zones, and enhancing both mechanical robustness and stowability of the final components.

Parallel efforts in the field of in-situ resource utilization focused on the development of LDPE/regolith composite filaments for additive manufacturing. The results highlight the importance of controlling filler dispersion, filament homogeneity, and mechanical flexibility to ensure reliable extrusion and printing performance in the context of fused filament fabrication (FFF). Filaments containing up to 30 wt% regolith simulant were successfully extruded, reprocessed for improved dispersion, and used to fabricate 3D-printed specimens with promising structural integrity. These findings support the viability of in-situ manufacturing strategies based on locally sourced or recycled polymers and regolith, offering a scalable pathway toward self-sustaining construction and maintenance capabilities in extraterrestrial habitats.

Together, these two experimental directions underscore the critical role of advanced material processing, both terrestrial and space-based, in enabling lightweight, deployable structures and functional components for future space exploration missions.

ACKNOWLEDGEMENTS

This work is performed under the Agreement between the Italian Space Agency and DIAEE – Sapienza University of Rome n. 2019-28-HH.0 - CUP n. F84I19001070005 related to R&D activities on solar photonic propulsion.

REFERENCES

[1] Razali, N., Mansor, M. R., Omar, G., Kamarulzaman, S. A. F. S., Zin, M. H., & Razali, N. (2021). Out-of-autoclave as a sustainable composites manufacturing process for aerospace applications. In *Design for Sustainability* (pp. 395-413).

[2] Chen, Y.; Zhang, J.; Li, Z.; Zhang, H.; Chen, J.; Yang, W.; Yu, T.; Liu, W.; Li, Y. (2023) Manufacturing Technology of Lightweight Fiber-Reinforced Composite Structures in Aerospace: Current Situation and toward Intellectualization. *Aerospace*, *10*, 206.

[3] Wilkie, K., & Fernandez, J. (2023, June). Advanced composite solar sail system (as3) mission update. In The 6th International Symposium on Space Sailing.

[4] De Zanet, G., Viquerat, A., & Aglietti, G. (2023). Predicted thermal response of a deployable high-strain composite telescope in low-Earth orbit. *Acta astronautica*, *205*, 127-143.

[5] Chao Xie, Zhiyi Wang, Yu Liu, Feng Gao, Li Qin, Jinping Yang, Fujun Peng, Wujun Chen. Design and demonstration of a roll-out membrane antenna based on thin-walled deployable composite booms. Thin-Walled Structures, 205, Part A, 2024, 112486.

[6] Laurenzi, S.; Zaccardi, F.; Toto, E.; Santonicola, M.G.; Botti, S.; Scalia, T. Fused Filament Fabrication of Polyethylene/Graphene Composites for In-Space Manufacturing. Materials 2024, 17, 1888.

[7] Peker, M. Y., Erbay, O., Çetin, M. E., Reyhancan, İ. A., & Avci, A. (2025). Gamma-ray and neutron attenuation of carbon fiber/epoxy composites with carbon nanotubes and boron nitride nanoparticles for passive shielding applications in space. *Polymer Composites*, *46*(8), 6983-6997.

[8] Clausi, M., Santonicola, M. G., Schirone, L., & Laurenzi, S. (2017). Analysis of ultraviolet exposure effects on the surface properties of epoxy/graphene nanocomposite films on Mylar substrate. *Acta Astronautica*, *134*, 307-313.

[9] Prater, T.J.; Werkheiser, M.J.; Jehle, A.; Ledbetter, F.; Bean, Q.; Wilkerson, M.; Soohoo, H.; Hipp, B. NASA's in-space manufacturing project: Development of a multimaterial fabrication laboratory for the international space station. In Proceedings of the AIAA SPACE and Astronautics Forum and Exposition, Orlando, FL, USA, 12–14 September 2017.

[10] Clinton, R.G., Jr. In Space Manufacturing and Extraterrestrial Construction: How Did We Get Here? Where Are We? Where Should We Be Going? The Challenge: Establish the Foundation

for Mission Readiness. In Proceedings of the DARPA NOM4D Phase 3 Kick-off Meeting, Huntsville, AL, USA, 29 January 2025.

[11] Risdon, D. In-Space Manufacturing (ISM) ISS Refabricator Technology Demonstration. In Proceedings of the Recycling and Sustainable Acquisition (RSA) Workshop, Huntsville, AL, USA, 2 May 2019. No. MSFC-E-DAA-TN68285.

[12] Zaccardi, F.; Toto, E.; Santonicola, M.G.; Laurenzi, S. 3D printing of radiation shielding polyethylene composites filled with Martian regolith simulant using fused filament fabrication. *Acta Astronaut.* **2022**, *190*, 1–13.

[13] Chengqing Wu, Zizheng Yu, Ruizhe Shao, Jun Li. A comprehensive review of extraterrestrial construction, from space concrete materials to habitat structures, Engineering Structures, 318, 2024, 11872.

[14] De Rosa, F.; Laurenzi, S. Printability Optimization of LDPE-Based Composites for Tool Production in Crewed Space Missions: From Numerical Simulation to Additive Manufacturing. *Aerospace* **2025**, *12*, 530.

[15] Jones, H.W. Take Material to Space or Make It There? *ASCEND* **2023**, *2023*, 4618.

[16] Anih, S. Crewed Space Mission Waste-Streams and Impact on Human Exploration of Mars. In *Assessing a Mars Agreement Including Human Settlements*; Springer International Publishing: Cham, Switzerland, 2021; pp. 129–146.

[17] Pitts, R. P., Kelley, M. D., & Smith, J. L. (2024, July). Extraction of Aluminum from Astronaut Waste Food Packaging for In-Space Manufacturing. In *Proceedings of the 53rd International Conference on Environmental Systems, Louisville, KY, USA* (pp. 21-25).

[18] De Rosa, F.; Palmeri, F.; Laurenzi, S. Recycling Space Beverage Packaging into LDPE-Based Composite Materials. *Aerospace* **2024**, *11*, 957.

[19] Bai, J.B., Chen, D., Xiong, J.J. and Shenoi, R.A., 2019. Folding analysis for thin-walled deployable composite boom. Acta Astronautica, 159, pp.622-636.

[20] C. Sickinger, L. Herbeck, T. Ströhlein and J. Torrez-Torres. Lightweight Deployable Booms: Design, Manufacture, Verification, and Smart Materials Application, AIAA 2004-I.4.10. 55th International Astronautical Congress of the International Astronautical Federation, the International Academy of Astronautics, and the International Institute of Space Law. October 2004.

[21] Zhang, Z., Guo, X., Pan, B., Sun, M., Zhang, G., Chai, H., ... & Jiang, S. (2023). Experimental study and numerical simulation of load-bearing/coiling characteristics of thin-walled lenticular composite booms. Composite Structures, 324, 117515.

[22] Ma, X., An, N., Cong, Q. et al. Design, modeling, and manufacturing of high strain composites for space deployable structures. Commun Eng 3, 78 (2024).

[23] Palmeri, F., Tortorici, D., Laurenzi, S., Santonicola, M., Circi, C., Pizzarelli, M, Pizzurro, S., Pellegrini, R. C., Cavallini, E. (2022). Structural design of booms for the solar sail of Helianthus sailcraft. In *International astronautical congress: IAC proceedings* (pp. 1-11). International Astronautical Federation, IAF.

[24] Tortorici, D., Sabatini, M., & Laurenzi, S. (2024). Numerical simulations and experimental results of the deployment of thin-walled bistable composite booms. *Composite Structures*, *327*, 117669.

[25] Zhang, X., Yang, M., Zhang, X., Wu, H., Guo, S., & Wang, Y. (2017). Enhancing the neutron shielding ability of polyethylene composites with an alternating multi-layered structure. *Composites Science and Technology*, *150*, 16-23.

[26] Laurenzi, S., De Zanet, G., & Santonicola, M. G. (2020). Numerical investigation of radiation shielding properties of polyethylene-based nanocomposite materials in different space environments. *Acta Astronautica*, *170*, 530-538.

ICCM24
AUGUST 4-8, 2025
BALTIMORE CONVENTION CENTER
BALTIMORE, MARYLAND, USA

No Technical Paper Submission for:

Mehdi Hojjati

Semantic interoperable data model and stochastic multiscale analysis of short fibre composites

Jörg Hohe, Benedikt Rohrmüller, Patrick Schneider, Niklas Toffert, Martin Koerdel, Nicolas Christ, Carla Beckmann

- Introduction
- Experimental observation
- Numerical homogenisation and stochastic enhancement
- Semantic interoperable data model
- Example
- Conclusions

Interoperable data model and stochastic analysis of short fibre composites

Introduction

- microstructural uncertainties in composite and other microheterogeneous materials

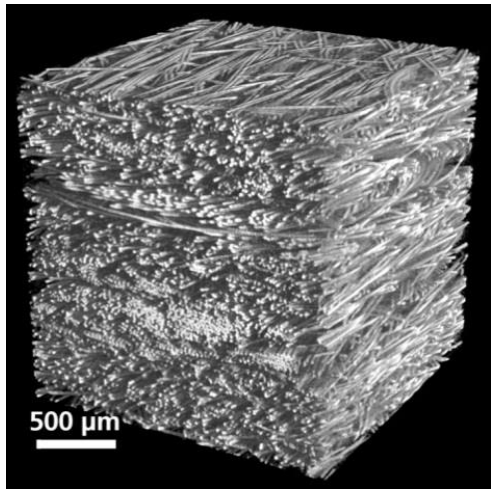

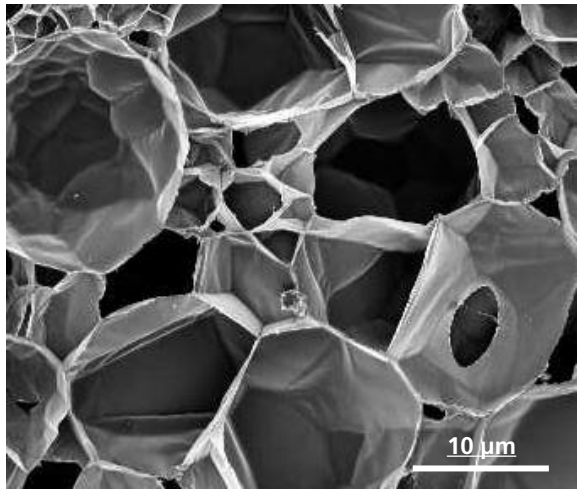

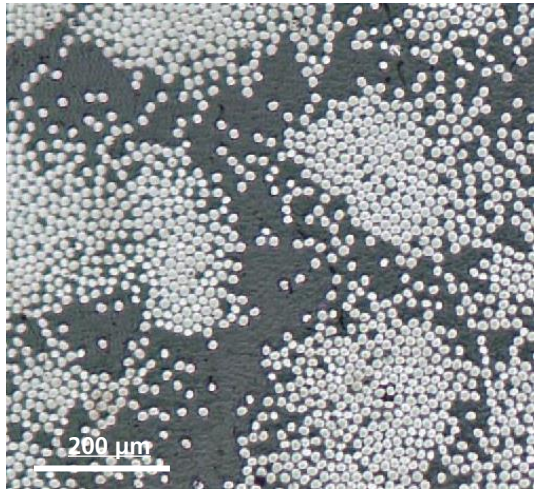

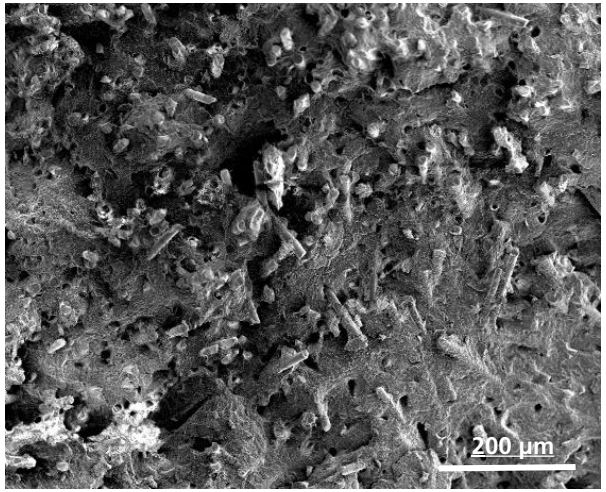

- uncertain fibre orientation, length, density, bundle formation, ...
- uncertain particle / void size, shape, density, ...
- uncertain constituent material properties
- uncertain distribution of defects, delaminations, interface properties, crack formation, ...

© Fraunhofer IWM unrestricted

Interoperable data model and stochastic analysis of short fibre composites

Experimental observation

- example: PA66 GF40
- stress-strain response
- overall
  - tensile tests within and perpendicular to flow direction
  - section 10 mm x 3 mm
  - overall scatter
- local
  - grey scale correlation system (ARAMIS)
  - distinct scatter on length scales below 10 mm

overall stress-strain response

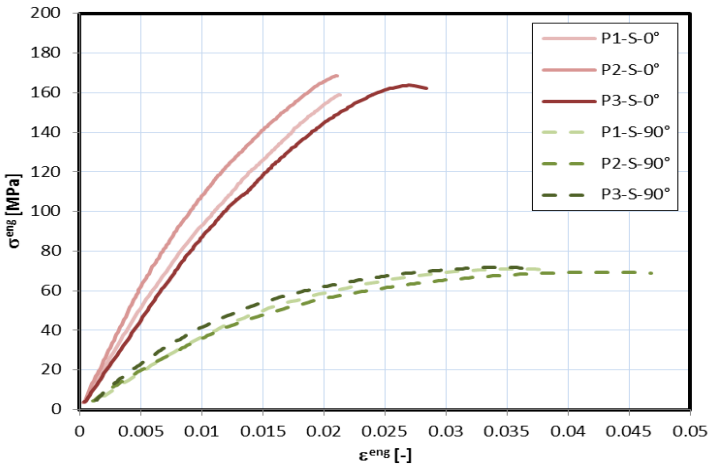

longitudinal and transverse Young's moduli

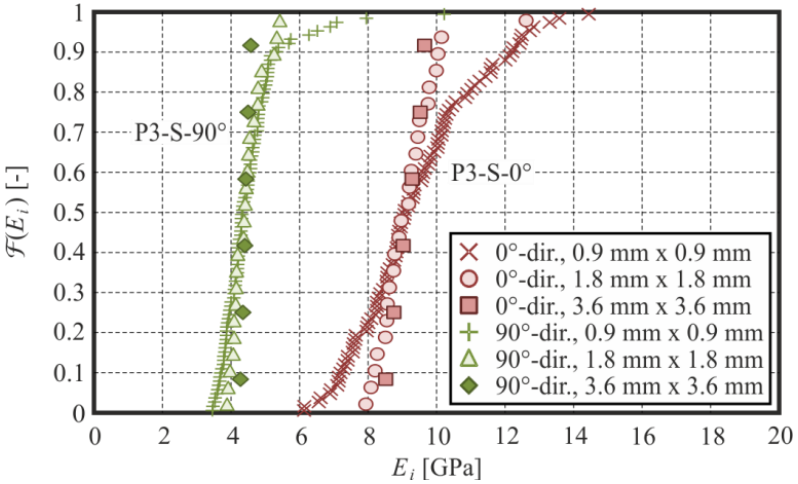

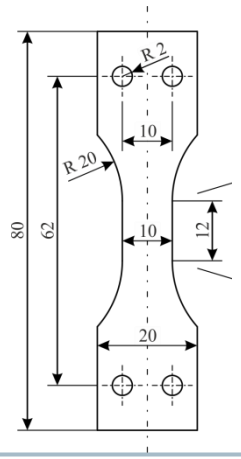

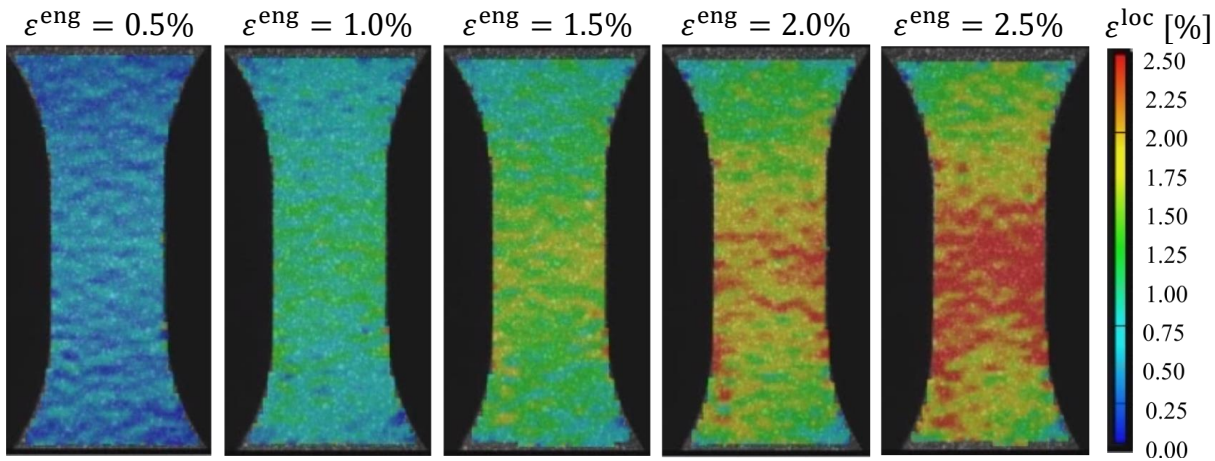

 © Fraunhofer IWM unrestricted

Interoperable data model and stochastic analysis of short fibre composites

Numerical homogenisation

- concept of the representative volume element

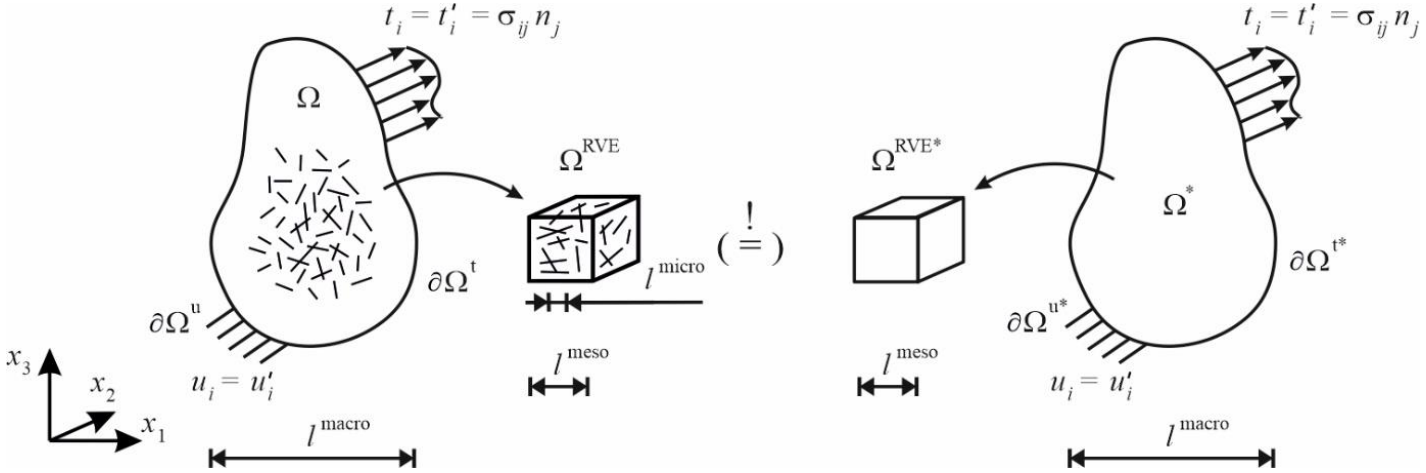

- energy based equivalence conditions

$$\bar{w} = \frac{1}{V^{\mathrm{RVE}}} \int_{\Omega^{\mathrm{RVE}}} w \, \mathrm{d}V = \frac{1}{V^{\mathrm{RVE}}} \int_{\Omega^{\mathrm{RVE}*}} w^* \, \mathrm{d}V^*$$

$$\bar{F}_{ij} = \frac{1}{V^{\mathrm{RVE}}} \int_{\Omega^{\mathrm{RVE}}} F_{ij} \, \mathrm{d}V = \frac{1}{V^{\mathrm{RVE}}} \int_{\Omega^{\mathrm{RVE}*}} F_{ij}^* \, \mathrm{d}V^*$$

© Fraunhofer IWM unrestricted

Interoperable data model and stochastic analysis of short fibre composites

Numerical homogenisation

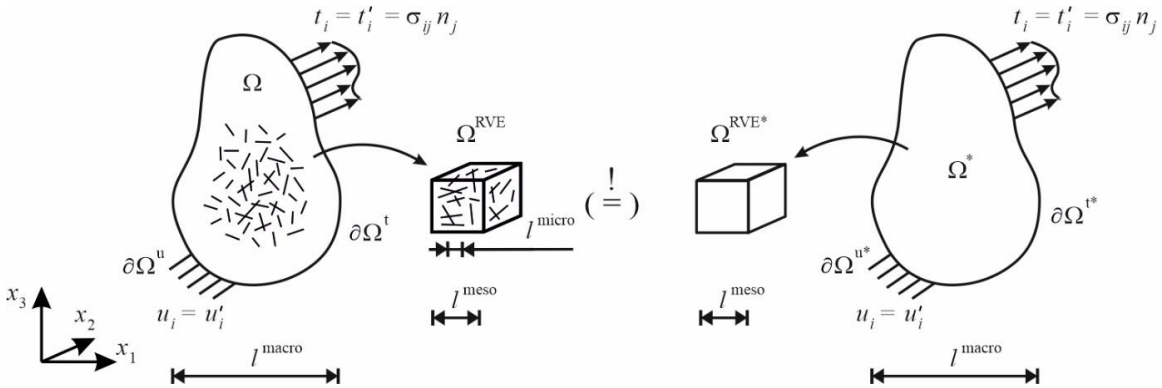

- discussion
  - requirements for the representative volume element
    - $L \gg l \gg \mathrm{d}l$
    - l sufficiently large to account for all possible microstructural effects
    - l sufficiently small for RVE representing a macroscopic material point
  - typical characteristic length scales for short fibre composites
    - $l_{\mathrm{micro}} = 100\ \mu\mathrm{m}, \ldots, 500\ \mu\mathrm{m} \quad \Rightarrow \quad l = 1\ \mathrm{mm}, \ldots, 5\ \mathrm{mm}$
    - $L \geq 2\ \mathrm{mm}, \ldots, 25\ \mathrm{mm}$
      - ➢ requirements might be contradictory
      - ➢ statistically representative volume element might not exist
      - ➢ probabilistic assessment required

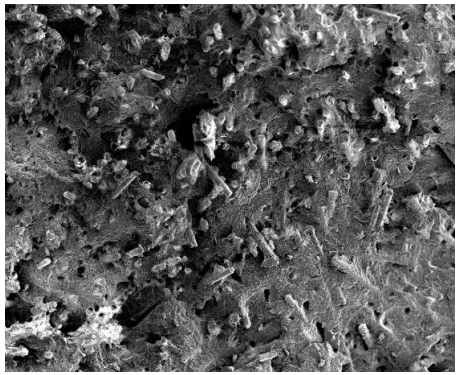



© Fraunhofer IWM unrestricted

Interoperable data model and stochastic analysis of short fibre composites

Numerical homogenisation

- alternative
  - approaches for assessment of the material uncertainty caused by the geometric uncertainty on the micro level
  - prediction of probability distributions for effective properties
  - probabilistic enhancement of the deterministic homogenization approach

- two different routes
  - multiple analysis of small scale testing volume elements with random microstructure
  - local homogenisation of small scale subsets in large-scale representative volume element
  - microstructure and volume related testing volume elements

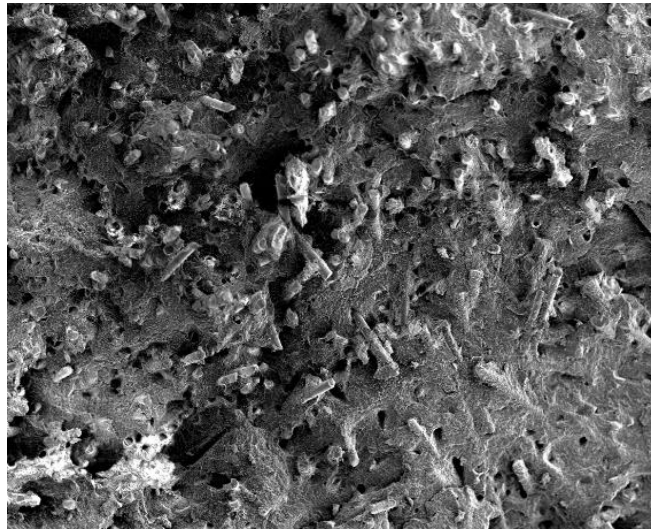



© Fraunhofer IWM unrestricted

Interoperable data model and stochastic analysis of short fibre composites

Semantic interoperable data model

- stochastic multiscale analysis requires extensive data handling
  - automated procedure required
  - holistic semantic interoperable data model
- knowledge graphs and ontologies
  - data model as directed graph
    - set of nodes, e.g., 1, 2, 3, and 4
    - set of edges, e.g., (1,2), (1,3), (3,2), (3,4), 3,4)
  - what makes a directed graph “knowledgable”?
    - everything has unique IDs called URI (except data properties)
    - knowledge graph as a set of triples including the ontology
    - syntax: triple (subject-predicate-object),
      where (subject, object) induces an edge and predicate is its label
    - ontologies are the scheme of a knowledge graph (giving structure to it)

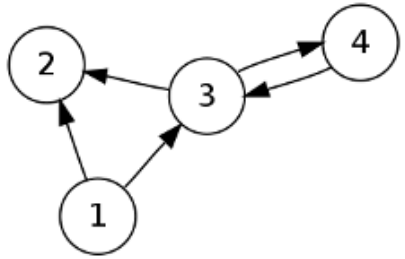

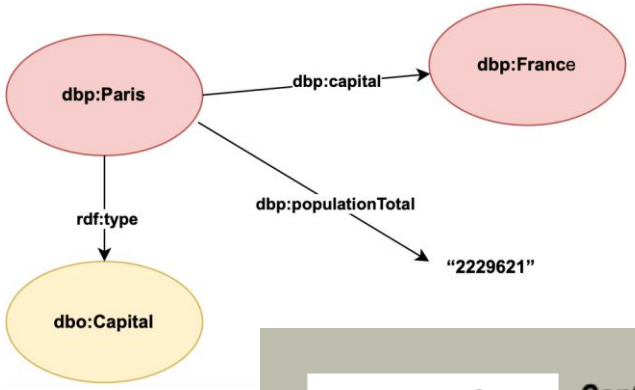

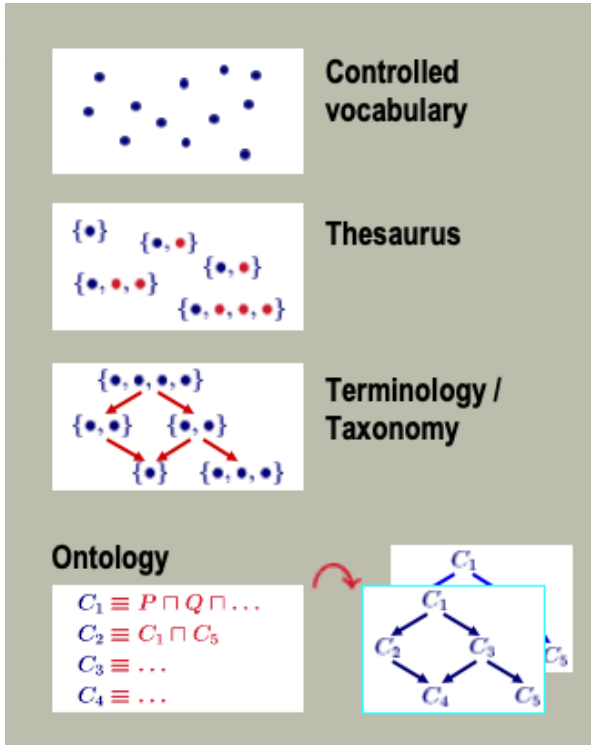

© Fraunhofer IWM unrestricted

Interoperable data model and stochastic analysis of short fibre composites

Semantic interoperable data model

- physical product and material

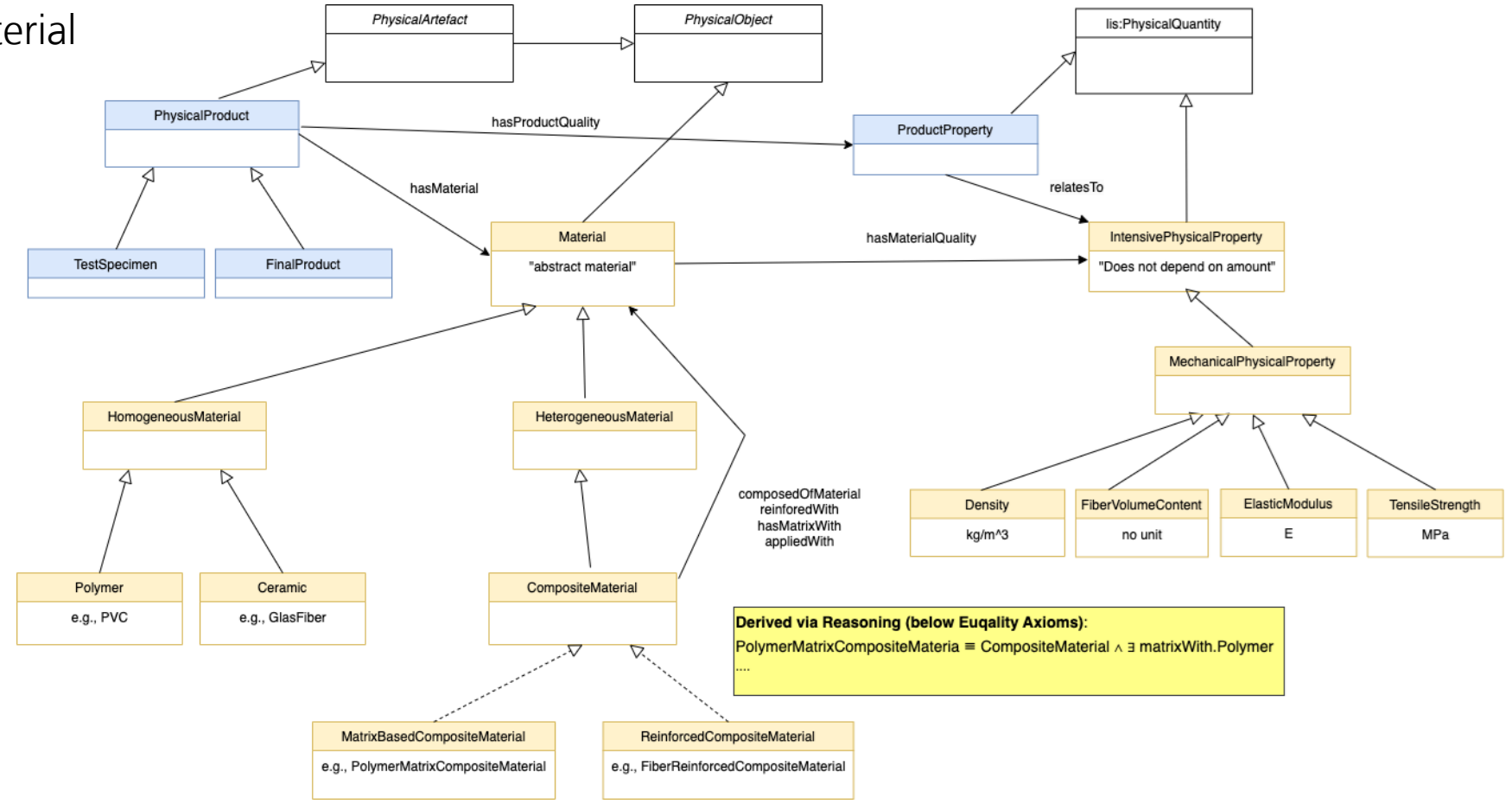

 © Fraunhofer IWM unrestricted

Interoperable data model and stochastic analysis of short fibre composites

Semantic interoperable data model

- modular set-up to account for uncertainties

deterministic multiscale analysis

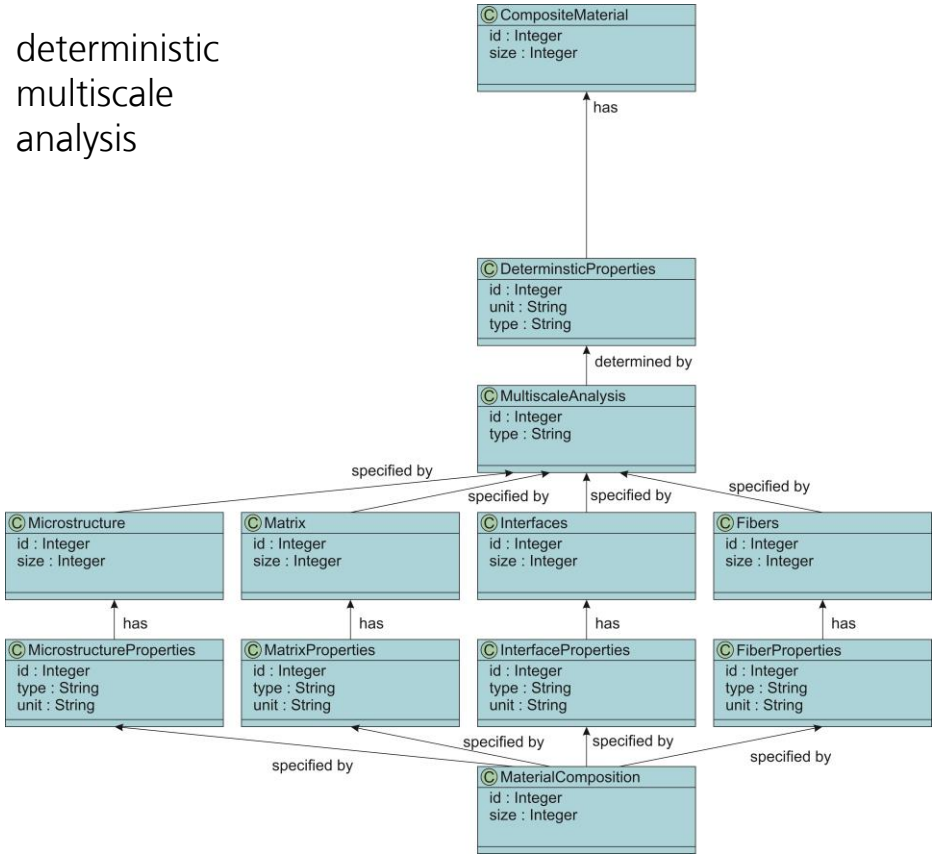

modular stochastic enhancement

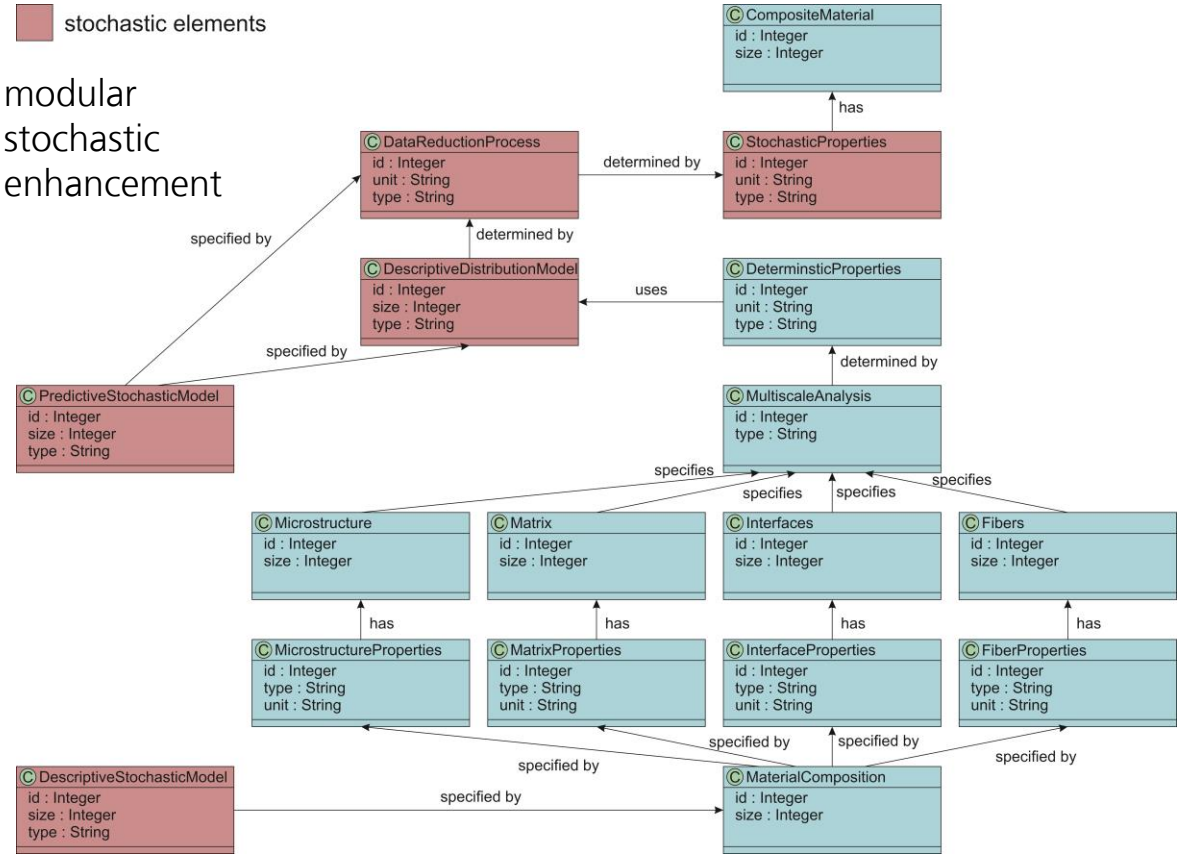

© Fraunhofer IWM unrestricted

Interoperable data model and stochastic analysis of short fibre composites

Example

- reference material
  - injection moulded material
  - phenolic resin matrix
  - short glass fibre reinforcement

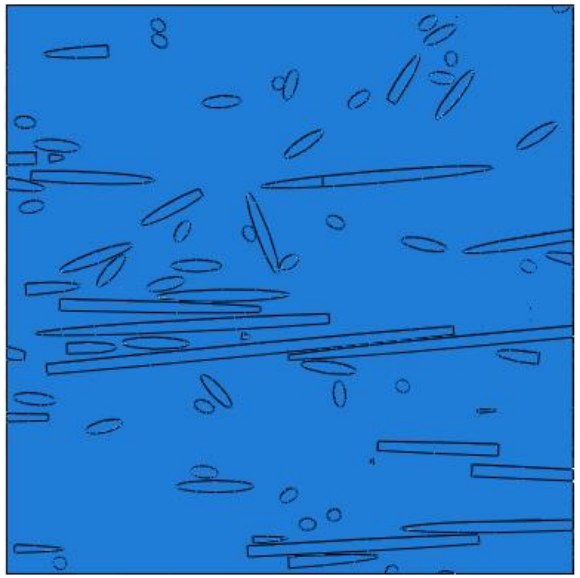

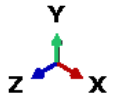

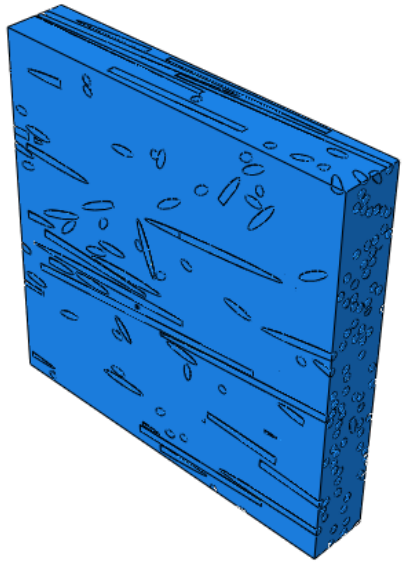

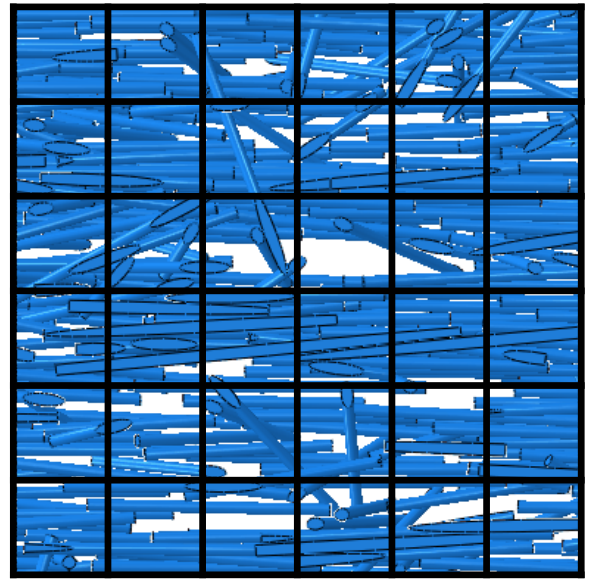

© Fraunhofer IWM unrestricted

Interoperable data model and stochastic analysis of short fibre composites

Example

- five different macroscopic fibre orientation states
- covering typical range for injection moulded plates
- definition in terms of second order fibre orientation tensor

$$a_{ij} = \frac{1}{n^{\mathrm{f}}} \frac{1}{\sum_{q=1}^{n^{\mathrm{f}}} l^{(q)}} \sum_{q=1}^{n^{\mathrm{f}}} l^{(q)}\, r_i^{(q)}\, r_j^{(q)}$$

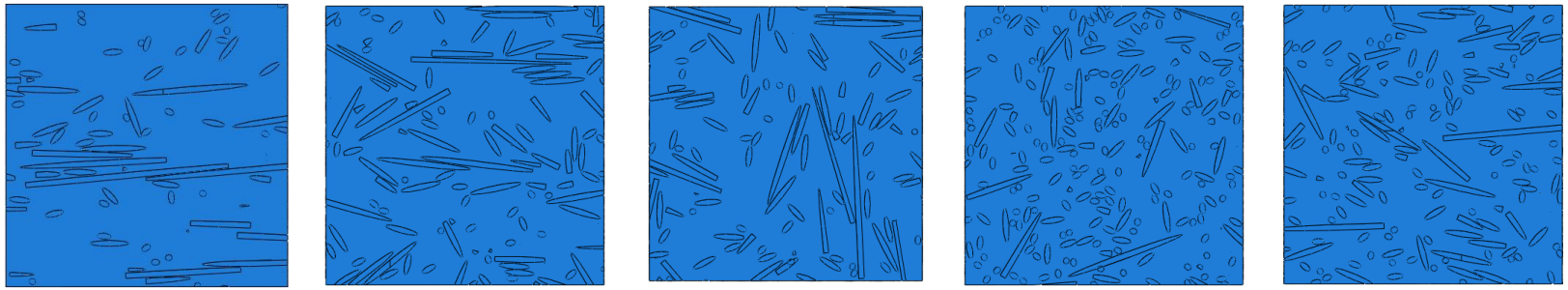

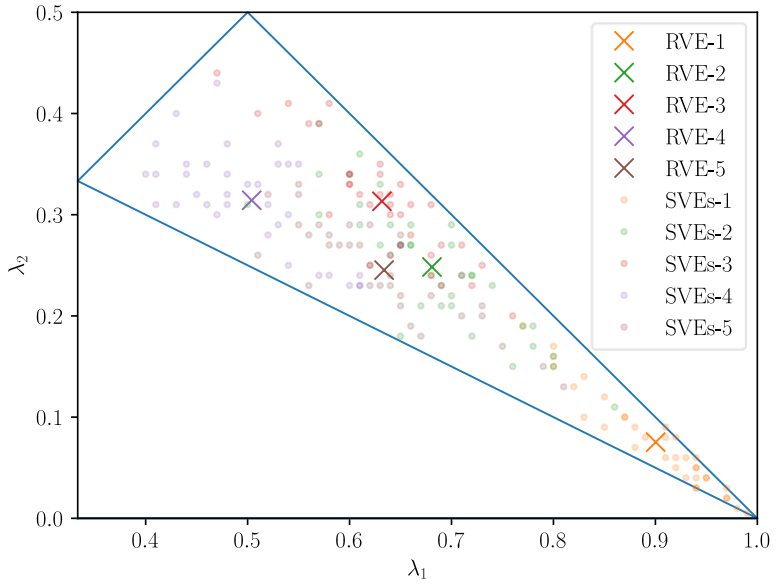

- subdivision into 6 x 6 stochastic volume elements
  - pronounced uncertainty in microstructural morphology
  - subsets with rather different microscopic orientations

© Fraunhofer IWM unrestricted

Interoperable data model and stochastic analysis of short fibre composites

Example

- deformation and failure
  - in-plane modes

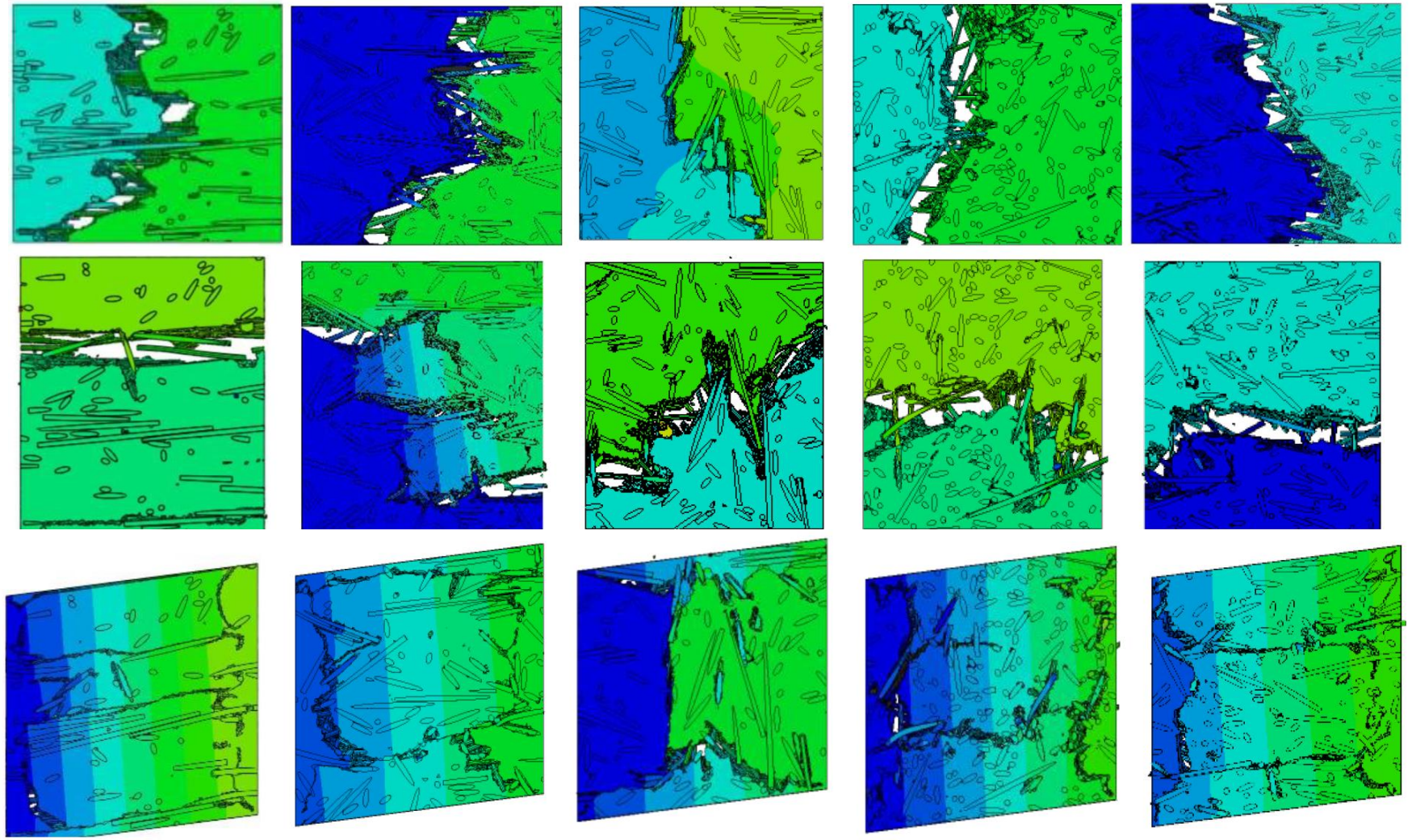

© Fraunhofer IWM unrestricted

Interoperable data model and stochastic analysis of short fibre composites

Example

- stress-strain response

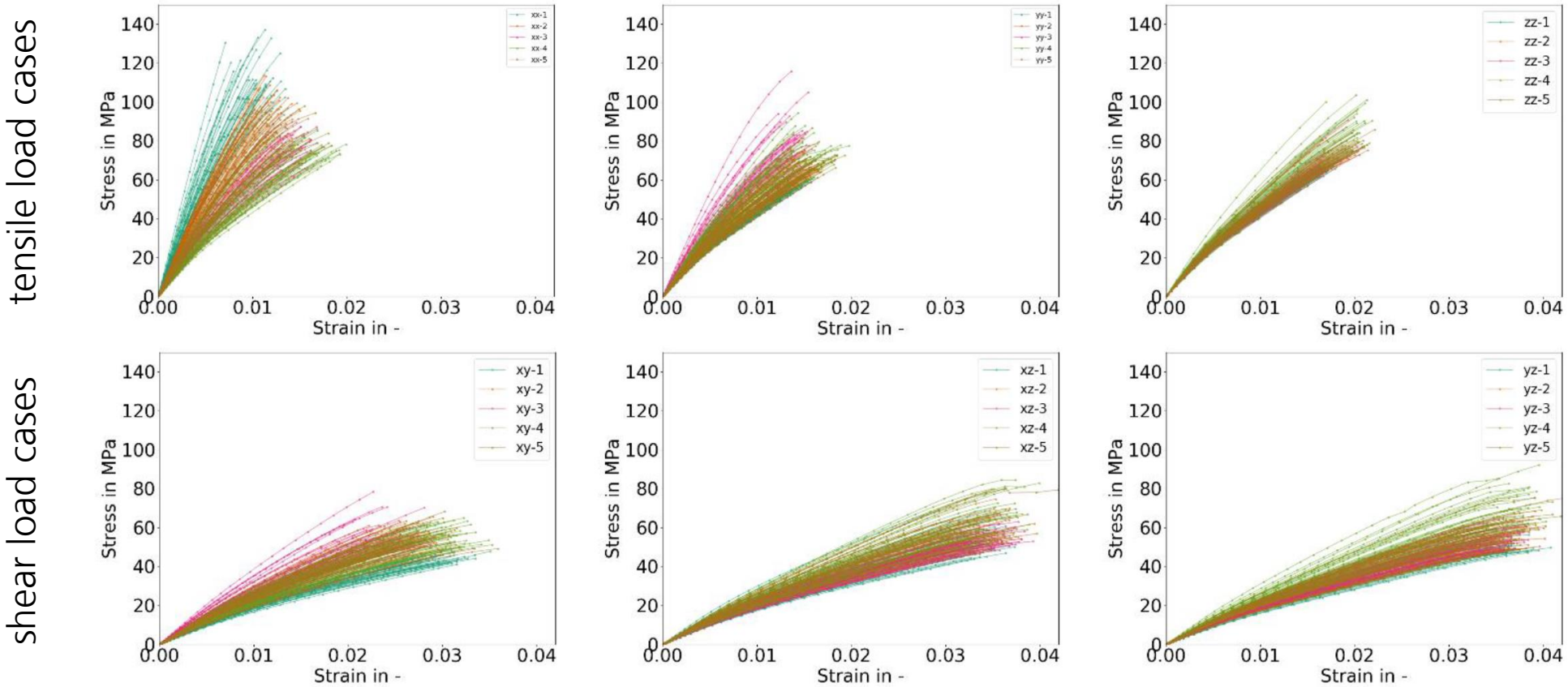

© Fraunhofer IWM unrestricted

Interoperable data model and stochastic analysis of short fibre composites

Example

- correlation matrix

$$\mathcal{C}(p_1, p_2) = \frac{\mathcal{E}\left((p_1 - \mathcal{E}(p_1))\,(p_2 - \mathcal{E}(p_2))\right)}{\left(\mathcal{E}\left((p_1 - \mathcal{E}(p_1))^2\right)\mathcal{E}\left((p_2 - \mathcal{E}(p_2))^2\right)\right)^{1/2}}$$

	a_I	a_{II}	a_{III}	f_V	E_1	E_2	E_3	G_{12}	G_{13}	G_{23}	H_{11}	H_{22}	H_{33}	H_{12}	H_{13}	H_{23}
a_I	1.000	-0.917	-0.561	0.088	0.703	-0.365	0.022	-0.317	-0.328	-0.219	-0.038	-0.406	-0.233	0.292	-0.055	-0.313
a_{II}	-0.917	1.000	0.186	-0.055	-0.589	0.438	-0.070	0.343	0.193	0.078	-0.059	0.218	-0.035	-0.316	0.182	0.436
a_{III}	-0.561	0.186	1.000	-0.100	-0.507	-0.011	0.091	0.070	0.408	0.379	0.206	0.545	0.644	-0.055	-0.234	-0.136
f_V	0.088	-0.055	-0.100	1.000	0.505	0.325	0.559	0.555	0.329	0.398	0.245	0.131	-0.100	-0.053	0.096	-0.168
E_1	0.703	-0.589	-0.507	0.505	1.000	-0.315	0.188	-0.058	-0.040	-0.103	0.229	-0.279	-0.240	0.126	-0.071	-0.410
E_2	-0.365	0.438	-0.011	0.325	-0.315	1.000	-0.001	0.251	0.080	0.311	-0.161	0.195	-0.117	-0.080	0.175	0.205
E_3	0.022	-0.070	0.091	0.559	0.188	-0.001	1.000	0.416	0.096	0.384	0.280	0.119	0.188	-0.127	-0.134	-0.072
G_{12}	-0.317	0.343	0.070	0.555	-0.058	0.251	0.416	1.000	0.183	0.275	0.150	0.307	-0.088	-0.164	0.207	0.139
G_{13}	-0.328	0.193	0.408	0.329	-0.040	0.080	0.096	0.183	1.000	0.063	0.279	0.427	0.243	-0.230	0.099	-0.183
G_{23}	-0.219	0.078	0.379	0.398	-0.103	0.311	0.384	0.275	0.063	1.000	0.163	0.306	0.387	-0.002	0.003	0.010
H_{11}	-0.038	-0.059	0.206	0.245	0.229	-0.161	0.280	0.150	0.279	0.163	1.000	0.356	0.165	-0.456	-0.479	-0.145
H_{22}	-0.406	0.218	0.545	0.131	-0.279	0.195	0.119	0.307	0.427	0.306	0.356	1.000	0.572	-0.368	-0.223	-0.352
H_{33}	-0.233	-0.035	0.644	-0.100	-0.240	-0.117	0.188	-0.088	0.243	0.387	0.165	0.572	1.000	-0.046	-0.361	-0.445
H_{12}	0.292	-0.316	-0.055	-0.053	0.126	-0.080	-0.127	-0.164	-0.230	-0.002	-0.456	-0.368	-0.046	1.000	0.179	-0.114
H_{13}	-0.055	0.182	-0.234	0.096	-0.071	0.175	-0.134	0.207	0.099	0.003	-0.479	-0.223	-0.361	0.179	1.000	0.270
H_{23}	-0.313	0.436	-0.136	-0.168	-0.410	0.205	-0.072	0.139	-0.183	0.010	-0.145	-0.352	-0.445	-0.114	0.270	1.000

© Fraunhofer IWM unrestricted

Interoperable data model and stochastic analysis of short fibre composites

Example

- dependence on orientation state (elastic moduli)
  - planar approximation of dependence on principal values of fibre orientation tensor
  - stochastic evaluation in terms of standard deviation of distance to approximation plane

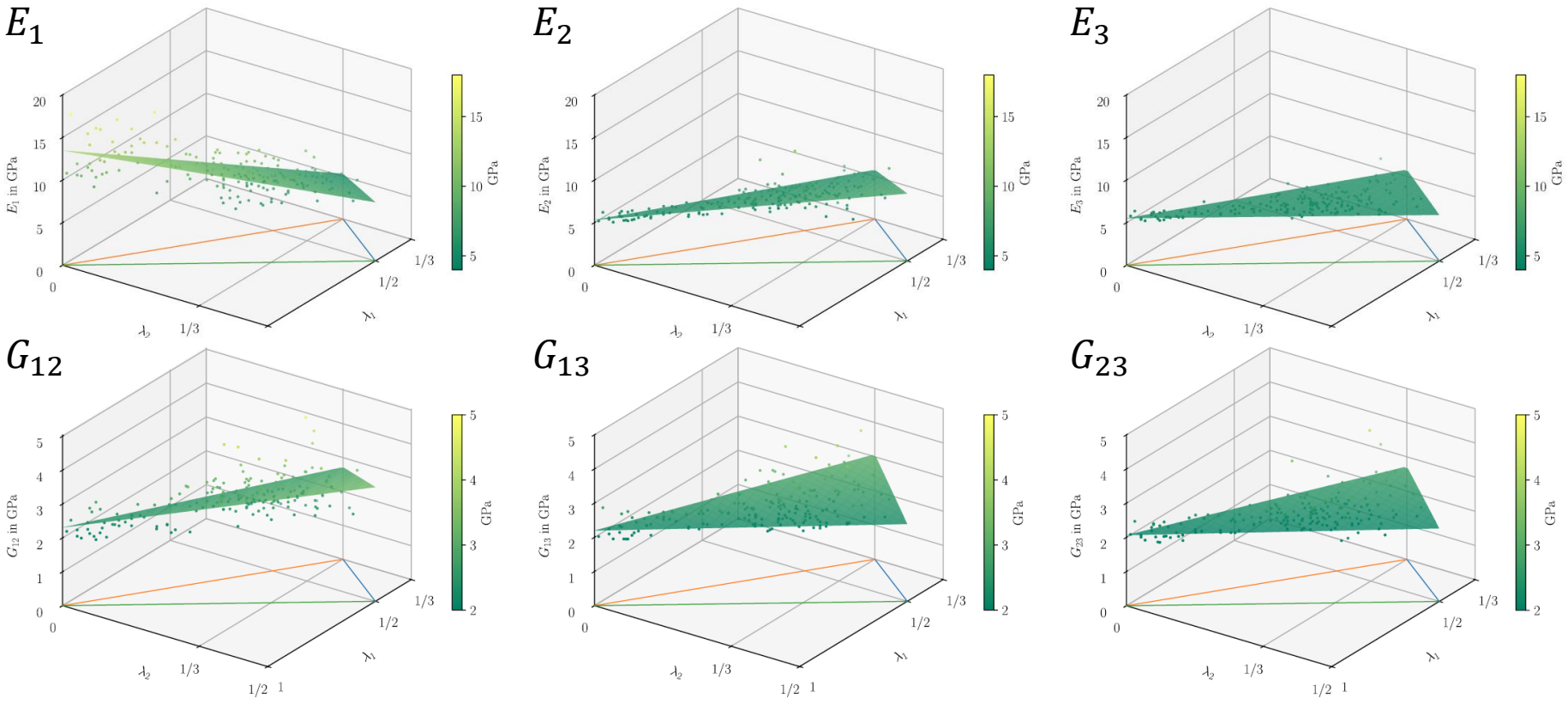

© Fraunhofer IWM unrestricted

Interoperable data model and stochastic analysis of short fibre composites

Conclusions

- stochastic analysis of macroscopic material response of short fibre composites
  - interoperable data model
  - stochastic multiscale homogenization analysis
- stochastic assessment necessary due to violation of RVE size requirements
- semantic interoperable data model
  - holistic ontology for short fibre composites including entire life cycle from processing to recycling
  - modular definition enables simple integration of stochastic pre- and postprocesses
- stochastic homogenization
  - based on stochastic volume elements defined as subsets of large-scale statistically representative volume element
  - results
    - correlation of mechanical properties with fibre orientation
    - distinct local (basic) uncertainty

contribution based on two projects funded by

Bundesministerium für Forschung, Technologie und Raumfahrt

DFG

 © Fraunhofer IWM unrestricted

SIEMENS Fraunhofer IWM

Interoperable data model and stochastic analysis of short fibre composites

References

(1) Christ, N., Wittemann, F., Rohrmüller, B., Hohe, J., Kärger, L., Beckmann, C.: *Numerical Analysis of uncertainty propagation in short fiber-reinforced composites: from injection molding to material testing*, Compos. Sci. Tech. (submitted).

(2) Koerdel, M., Milicic Brandt, M., Seidel, C., Toffert, N.A., Hohe, J.: Parametrierung und Automatisierung von Multiskalensimulationsketten für faserverstärkte Verbundwerkstoffe auf Grundlage strukturierter Materialcharakterisierungsdaten, 24th Symp. Verbundwerkstoffe und Werkstoffverbunde (Freiburg, May 22-24, 2024), electronic publication.

(3) Rohrmüller, B., Kneisel, F., Christ, N., Hohe, J., Beckmann, C.: *Experimental investigation into the uncertainty of the mechanical properties of short fibre-reinforced polymers*, J. Compos. Sci.\ (submitted).

(4) Rohrmüller, B., Christ, N., Hohe, J., Beckmann, C.: *Numerical study of the microstructure induced uncertainty in the mechanical properties of short fibre reinforced polymers*, Prob. Eng. Mech. (submitted).

 © Fraunhofer IWM unrestricted



Contact

PD Dr.-Ing. Jörg Hohe
Head of Composite Materials Group
Fraunhofer IWM
Wöhlerstr. 11 | 79108 Freiburg | Germany
Tel. +49 761 5142 340
joerg.hohe@iwm.fraunhofer.de

Foto © Oliver Kern, Freiburg

UNIVERSITY OF DELAWARE
CENTER FOR COMPOSITE MATERIALS
Celebrating 50 Years

A Data-driven, AI –Enabled Approach to Predict Crystal Morphology Evolution in Semi-crystalline Thermoplastic Composites

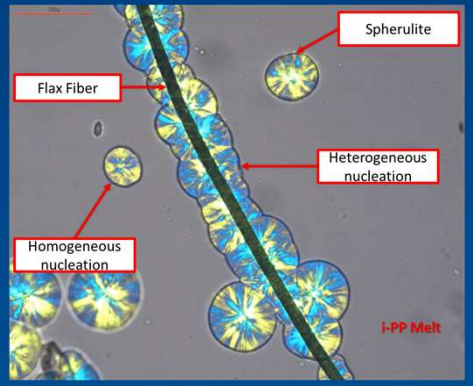

Presented By:

Amit M. Deshpande

Graduate Research Assistant, Center for Composite Materials

PhD Candidate, Department of Mechanical Engineering, University of Delaware

UNIVERSITY OF DELAWARE

About the Authors

UNIVERSITY OF DELAWARE
CENTER FOR COMPOSITE MATERIALS
Celebrating 50 Years

"to build an AI-enabled inverse design approach for fundamental understanding and integrated material-manufacturing design of advanced polymer composites."



https://www.energyfrontier.us/node/6537

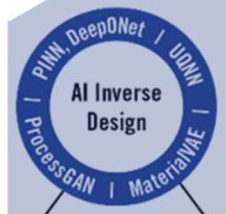



Dr. Elham Kiyani

Division of Applied Mathematics and School of Engineering, Brown University



Nikhil Kadivar

Division of Applied Mathematics and School of Engineering, Brown University



Dr. George Em Karniadakis

Division of Applied Mathematics and School of Engineering, Brown University

Simulation Data
Validation
Fast Prediction

Fast Prediction
Design
Validation



Material Data
Validation
Prediction



Dr. Gang Li

Department of Mechanical Engineering, Clemson University







Amit M. Deshpande
University of Delaware



Pierre-Yves Lavertu
University of Delaware



Dr. Srikanth Pilla

Director, Center for Composite Materials

Department of Mechanical Engineering, Material Science and Engineering, Chemical and Biomedical Engineering, University of Delaware

spilla@udel.edu



Dr. Sai Aditya Pradeep
University of Delaware

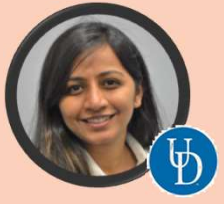

Dhanashree Shinde
University of Delaware

Introduction – Thermoplastic Composites

- Thermoplastics have been extensively used for non-structural and semi-structural purposes in electronics, automotive[1], [2], [3] and marine [4] applications.
- Additionally, there is noticeable interest in adopting continuous fiber reinforcements in thermoplastic composites in:
  - structural applications [4]
  - hydrogen storage (Type IV and Type V pressure vessels) [5],
  - medical prosthetics [6]
  - conformal electronics [7], [8]
  - sports equipment
- Globally, 7 to 9 million tons of thermoplastics were used as part of FRP composite systems [4].

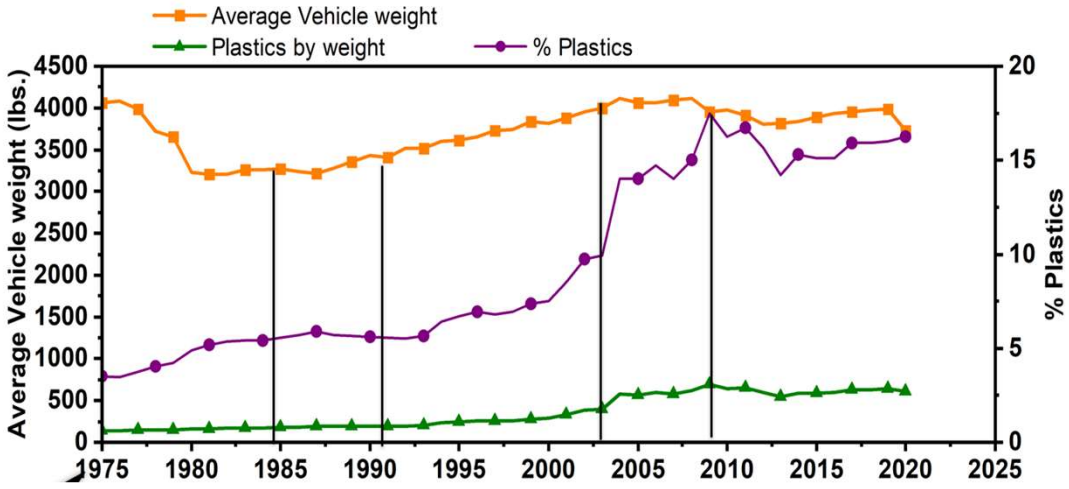

Figure 1: Growth in use of plastics and composites in passenger vehicles [1]

[1] S. A. Pradeep, S. Shukla, N. Brown, and S. Pilla, "Thermoplastics Foams : An Automotive Perspective," in Lightweight and Sustainable Materials for Automotive Applications, CRC Press, 2017, pp. 369–400. doi: 10.1201/9781315152967-11.
[2] S. A. Pradeep et al., "A Perspective on the Evolution of Plastics and Composites in the Automotive Industry," Applied Plastics Engineering Handbook, pp. 705–748, Jan. 2024, doi: 10.1016/B978-0-323-88667-3.00016-3.
[3] P. Davies, L. Riou, F. Mazeas, and P. Warnier, "Thermoplastic Composite Cylinders for Underwater Applications," http://dx.doi.org/10.1177/0892705705054397, vol. 18, no. 5, pp. 417–443, Sep. 2005, doi: 10.1177/0892705705054397.
[4] J. Zhang, G. Lin, U. Vaidya, and H. Wang, "Past, present and future prospective of global carbon fibre composite developments and applications," Compos B Eng, vol. 250, Feb. 2023, doi: 10.1016/j.compositesb.2022.110463.
[5] "CARBON FIBER: THE MATERIAL OF FUTURE." Accessed: Jun. 03, 2024. [Online]. Available: https://www.lucintel.com/lucintelBriefFile/market-research-brief-20220210120837.pdf
[6] M. S. Scholz et al., "The use of composite materials in modern orthopaedic medicine and prosthetic devices: A review," Compos Sci Technol, vol. 71, no. 16, pp. 1791–1803, Nov. 2011, doi: 10.1016/J.COMPSCITECH.2011.08.017.
[7] P. Lu, J. Liang, B. Huang, S. Yang, and W. W. Lee, "Thermoformed electronic skins for conformal tactile sensor arrays," Proc IEEE Int Conf Robot Autom, pp. 13898–13903, 2024, doi: 10.1109/ICRA57147.2024.10610733.
[8] K. Wu, Q. Zhou, H. Zou, K. Leng, Y. Zeng, and Z. Wu, "High Precision Thermoforming 3D-Conformable Electronics with a Phase-Changing Adhesion Interlayer," Micromachines 2019, Vol. 10, Page 160, vol. 10, no. 3, p. 160, Feb. 2019, doi: 10.3390/MI10030160.

Introduction – Manufacturing with Thermoplastic Composites

- Filler and fibers introduced in various forms to enhance mechanical properties.
- Trade-off in terms of added manufacturing complexity, and limitations in manufacturable geometries.
- General physics of manufacturing remains consistent across various thermoplastic composite manufacturing processes.
  - Heating:
    - pellets/filament/sheet heating above melt temperature (T_m)
  - Material Flow:
    - Suspension flow
    - Extrusion of melt
    - Draping of sheet
  - Cooling to near room temperature (T_{RT})

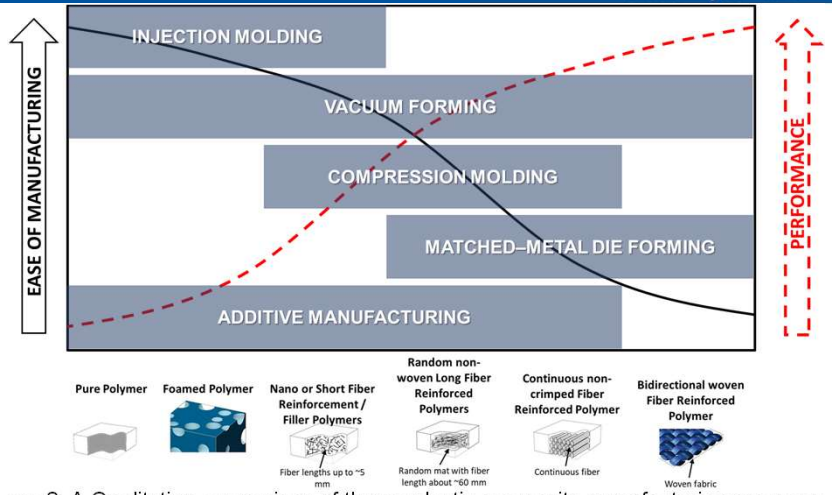

Figure 2: A Qualitative comparison of thermoplastic composite manufacturing processes

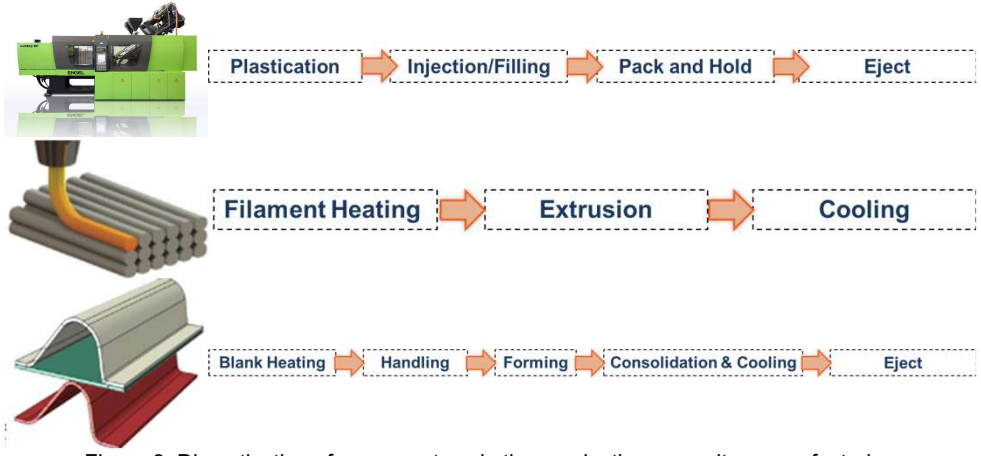

Figure 3: Discretization of process steps in thermoplastic composites manufacturing

Introduction – Semi-crystalline Thermoplastics and Crystallization

- Thermoplastics are divided into two broad categories:
  - semi-crystalline thermoplastics
  - amorphous thermoplastics
- Semi-crystalline thermoplastics form ordered structures or crystals in certain locations as polymer chains align as the thermoplastic cools.
- The cooling step, that crosses the recrystallization temperature (T_{RC}) influences the microstructure of the manufactured thermoplastic composite part.
- Microstructure influences mechanical properties.

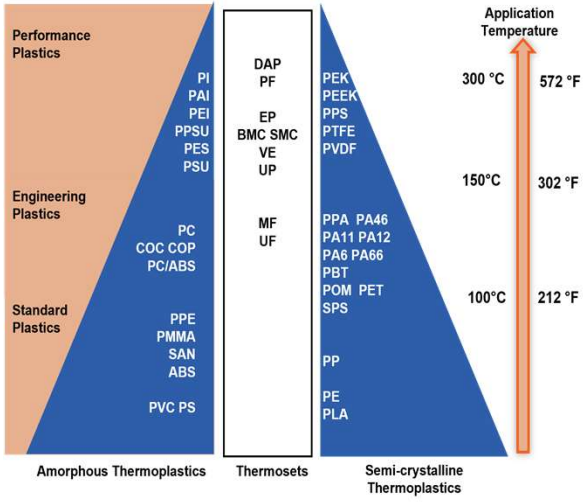

Figure 5: Thermoplastic Materials Pyramid

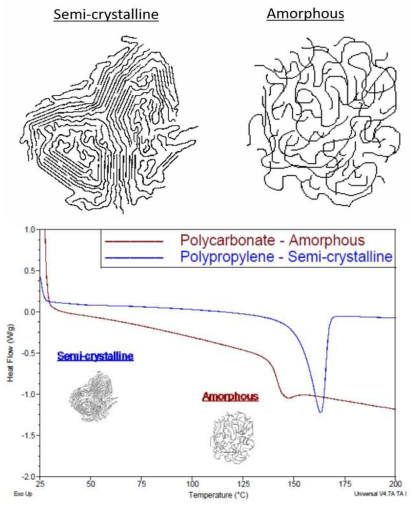

Figure 6: Behavior of Semi-crystalline and Amorphous Thermoplastics [9]

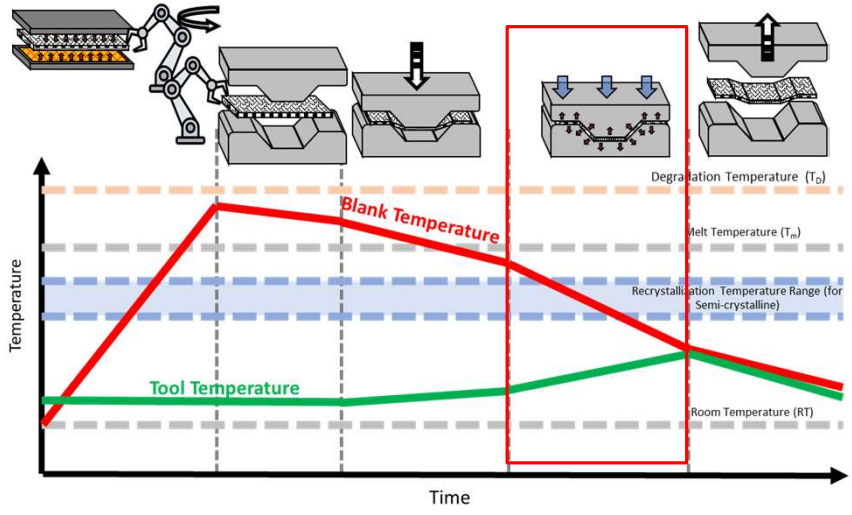

Figure 7: Cooling dynamics for a forming process for semi-crystalline thermoplastics composites

[9] https://madisongroup.com/the-importance-of-crystallinity-in-plastics-performance/

Motivation

Why is crystal morphology and its evolution important?

- Different crystalline phase distributions within homogeneous polymer results in different mechanical properties.

Table 1: Effect of different crystalline phases of i-PP on mechanical behavior

Monoclinic α-PP	• Higher strength • Higher stiffness	Typical cooling
Trigonal β-PP [10]	• Higher toughness • lower stiffness	• Supercooling • Varying temperature gradients • Shear • **Nucleating agents**

- Smaller spherulites result in improved impact strength, tensile strength and lower water absorption rate. [11]
- Addition of fillers change the oriented crystalline phase distributions. [12]

Table 2: Effect of different processes and presence of filler on crystalline phase distributions for PA6

Compression Molding	• Pure PA6: α-PA6 + γ – PA6	• PA6 + clay: γ – PA6
Cast Extrusion Process	• Pure PA6: γ – PA6	• PA6 + clay: higher γ – PA6

- **How do we identify the right processing parameters, polymer attributes and fiber/filler to achieve desired mechanical or chemical properties?**

⇨ THROUGH EXPERIENCE … OR WE UTILIZE **PREDICTIVE MODELS**

[10] Varga, J. (2002). β-MODIFICATION OF ISOTACTIC POLYPROPYLENE: PREPARATION, STRUCTURE, PROCESSING, PROPERTIES, AND APPLICATION. Journal of Macromolecular Science, Part B, 41(4–6), 1121–1171. https://doi.org/10.1081/MB-120013089
[11] Lin, Y., Zhong, W., Shen, L., Xu, P., & Du, Q. (2005). Study on the Relationship Between Crystalline Structures and Physical Properties of Polyamide-6. Journal of Macromolecular Science, Part B, 44(2), 161–175. https://doi.org/10.1081/MB-200049762
[12] https://doi.org/10.1002/pen.23813

Motivation – Need for Data-driven, AI-enabled models

- Most existing models are semi-analytical i.e. they depend on:
  - Experimental data to calibrate model constants
  - Empirically derived relationships

Hoffman-Lauritzen Growth Model [13]

$$G = G_0 \exp\left(-\frac{U^*}{R(T-T_\infty)}\right) \exp\left(-\frac{K_g}{fT\Delta T}\right)$$

G = Growth speed
G0 = pre-exponential factor determined experimentally
U* = Activation Energy
Kg = kinetic parameter for nucleation
F = correction factor
T∞ = Tg – 30 K

Table 3: Nucleation and Growth Models

	Nucleation Models [14]	Intrinsic Material Parameters		Process Parameters				
		Molecular weight	Presence of fiber	Thermal History	Isothermal	Non-isothermal (Cooling Rate)	Pressure	Shear Rate
Extended Volume Approach	Avrami (1939)	No	No	No	Yes	No	No	No
	Nakamura (1972)	No	No	No	Yes	Yes (considering successive isothermal stages)	No	No
Probabilistic Approach	Kolomogoroff (1937)	No	No	No	Yes	No	No	No
	Evans (1945)	No	No	No	Yes	No	No	No
	Ozawa (1971)	No	No	No	Yes	Yes	No	No
ODE	Haudin and Chenote	No	No	Yes	Yes	Yes	No	No
Geometrical	Schneider's Formalism (1988)	No	Yes	Yes	Yes	Yes	Possible	Possible

[13] Lauritzen JI, Hoffman JD. Theory of formation of polymer crystals with folded chains in dilute solution. J Res Natl Bureau Standards Sect A Phys Chem. 1960;64A(1):73. doi:10.6028/jres.064A.007
[14] https://onlinelibrary.wiley.com/doi/full/10.1002/pat.5918

Approach

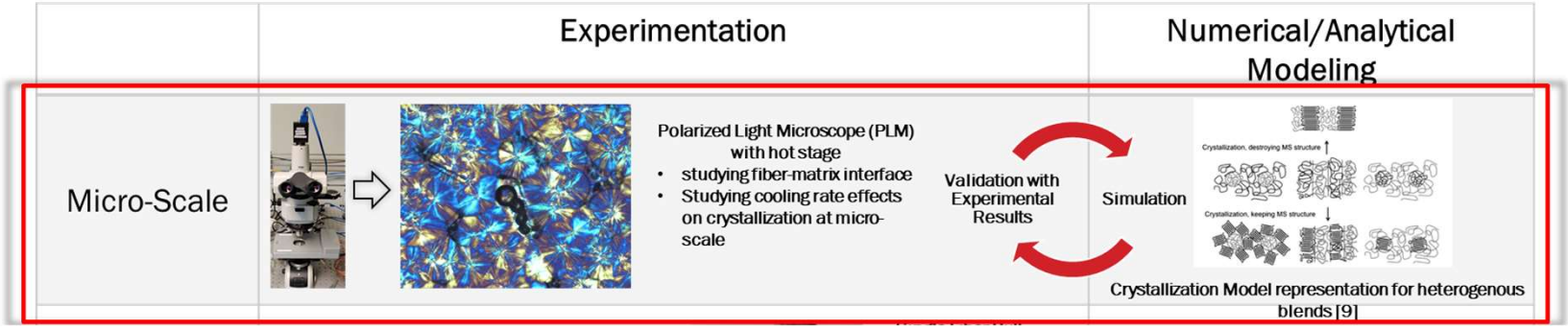

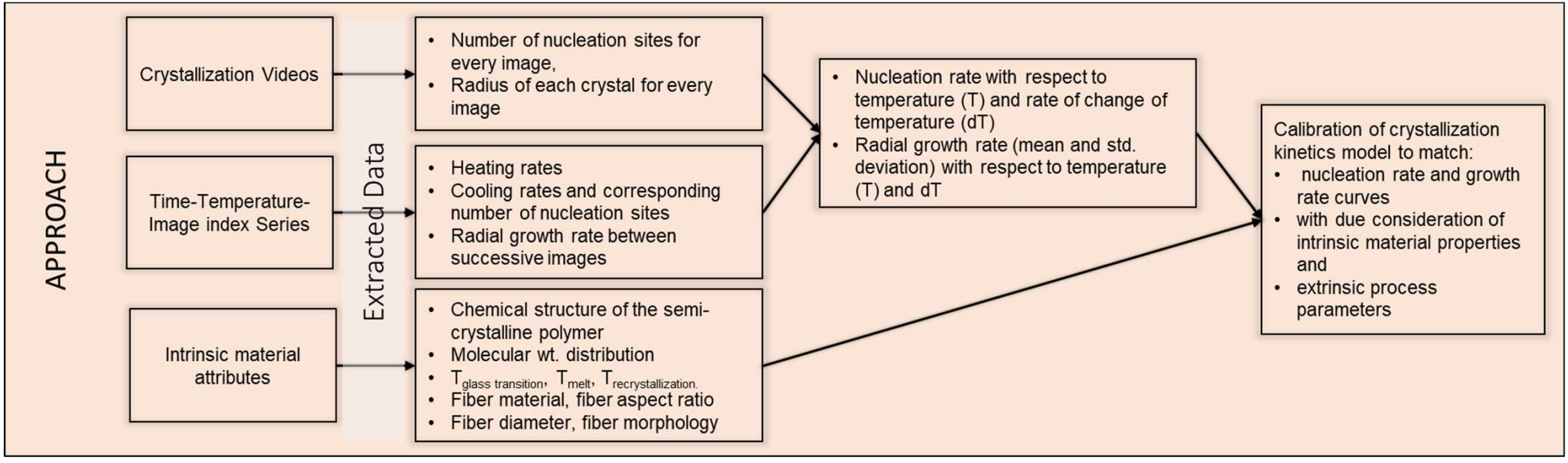

Figure 8: Approach for experimental data generation, post-processing and representative model development

Materials Selected for the Study

Fiber 1 : PAN-based Carbon Fiber [15]

T300, 12K Tow, Toray

Sizing burnt off at 600 °C

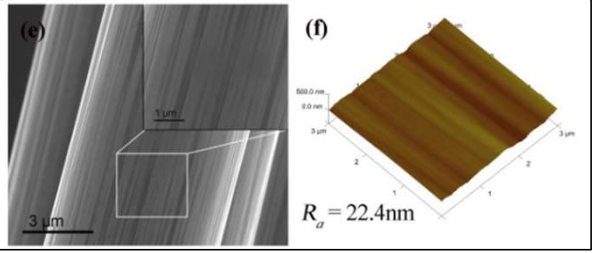

Fiber 2 : Glass Fiber [16]

A) S-Glass (from literature)

SiO_2 (65%), Al_2O_3 (25%) and MgO (10%)

B) E-Glass (Hexcel Hexforce 7781)

Spec'd out for additional trials.

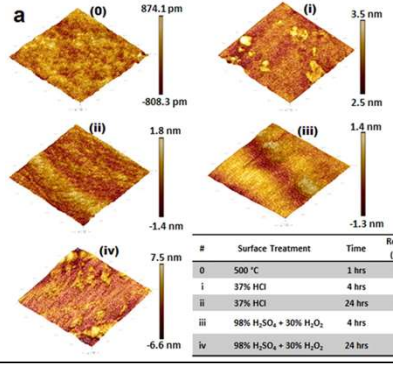

#	Surface Treatment	Time	Roughness (Ra, nm)
0	500 °C	1 hrs	0.17
i	37% HCl	4 hrs	0.50
ii	37% HCl	24 hrs	0.35
iii	98% H_2SO_4 + 30% H_2O_2	4 hrs	0.30
iv	98% H_2SO_4 + 30% H_2O_2	24 hrs	2.85

Fiber 3: Flax Fiber [17][18]

Fiber name	Mass content in %				
	Cellulose	Hemicelluloses	Lignin	Pectin	Waxes
Abaca	62.5	21	12	0.8	3
Alfa	45.4	38.5	14.9	-	2
Bamboo	34.5	20.5	26	-	-
Cotton	89	4	0.75	6	0.6
Flax	70.5	16.5	2.5	0.9	-
Hemp	81	20	4	0.9	0.8
Jute	67	16	9	0.2	0.5
Kenaf	53.5	21	17	2	-
Sisal	60	11.5	8	1.2	-

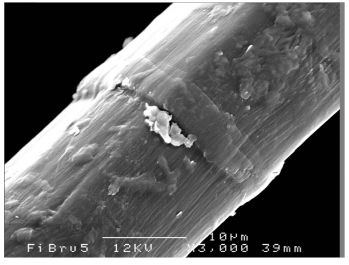

- High purity and controlled MW distribution polymer samples procured from Scientific Polymer Products, USA.

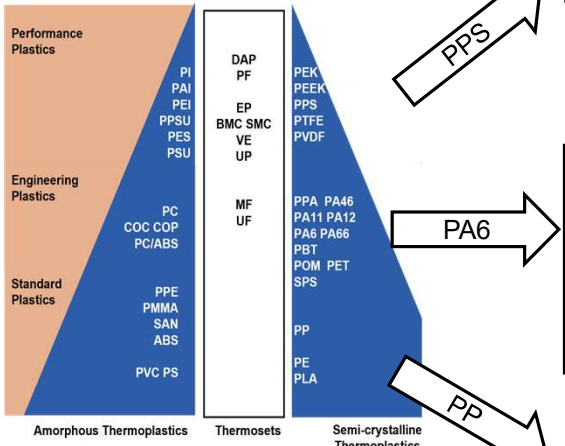

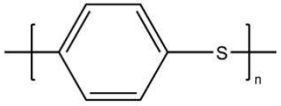

PPS

Approx Mn	10,000
Density	1.36 g/cc
Tg	150 C
Tm	285 C

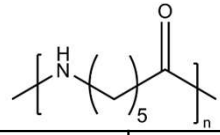

PA6

Approx Mw	25,000
Density	1.14 g/cc (@23 C)
Tg	62.5 C
Tm	220 C

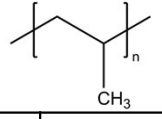

PP

Approx Mw	25,000
Density	0.9 g/cc (@23 C)
Tg	-26 C
Tm	160 C

[15] https://doi.org/10.1016/j.compositesa.2016.08.023
[16] https://www.nature.com/articles/s41598-019-40524-7
[17] http://dx.doi.org/10.3390/ma9020093
[18] Thesis. (2021). Quan Nguyen CHEMICAL MODIFICATION OF NATURAL FIBERS AND OPTIMIZING THE PROCESSING OF THERMOPLASTIC COMPOSITES BY COMPRESSING MOLDING METHOD.

Experimental Methodology

- Parallel Plate Rheometer (TA Instruments RH2) used.
- 0.5N axial force, $T_{max} = T_{melt} + 20C$

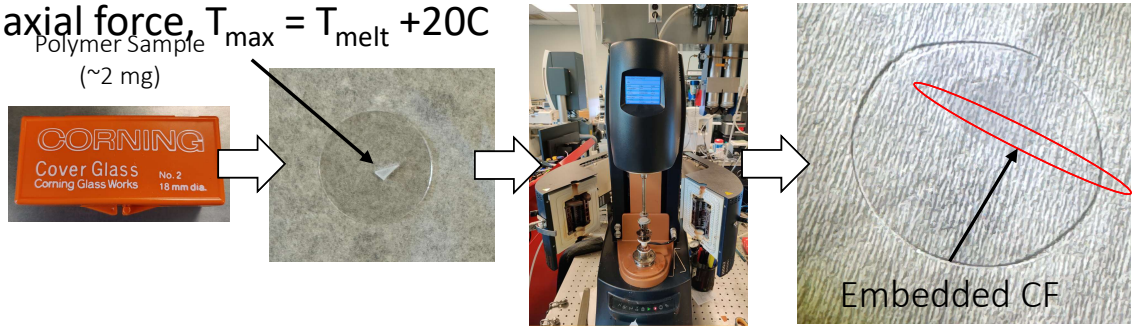

Figure 9: Sample preparation method for transmission-Polarized Light Microscopy (t-PLM)

- Nikon Eclipse LV100N with a 20x objective, 5 MP camera and a Linkam Hotstage for varying cooling rates was utilized.

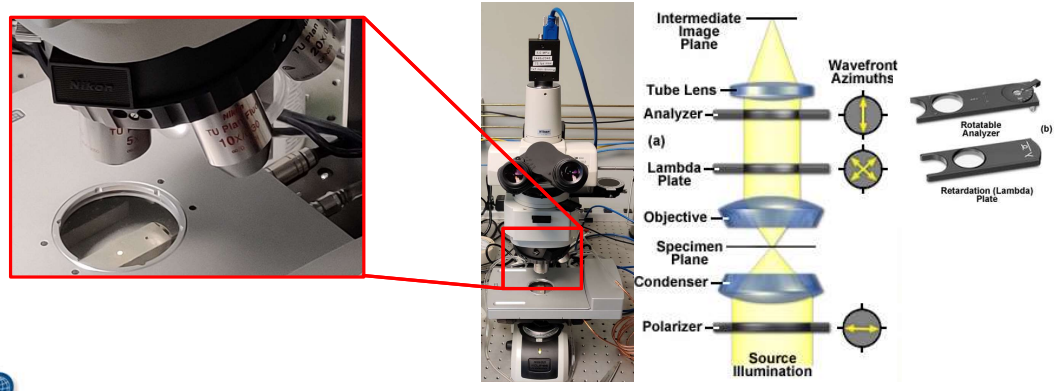

Figure 10: transmission-Polarized Light Microscopy (t-PLM) Setup

Table 4: Experimental Matrix for Cooling rate effects investigation

Matrix	CF	GF	Flax	Neat
i-PP	1C/min	1C/min	1C/min	1C/min
	5C/min	5C/min	5C/min	5C/min
	10C/min	10C/min	10C/min	10C/min
	20C/min	20C/min	20C/min	20C/min
PA6	1C/min	1C/min	Fiber Degrades for Processing Temperature of Thermoplastic Matrix	1C/min
	5C/min	5C/min		5C/min
	10C/min	10C/min		10C/min
	20C/min	20C/min		20C/min
PPS	1C/min	1C/min		1C/min
	5C/min	5C/min		5C/min
	10C/min	10C/min		10C/min
	20C/min	20C/min		20C/min

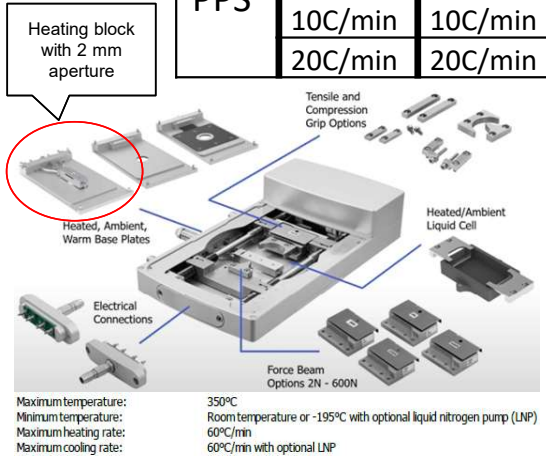

Experimental Results

Neat iso-PP crystallization

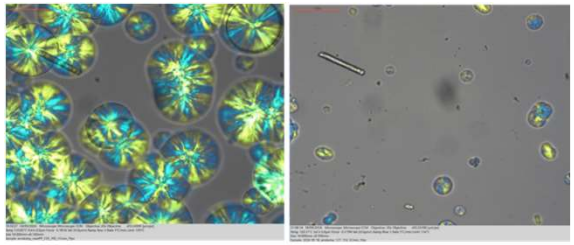

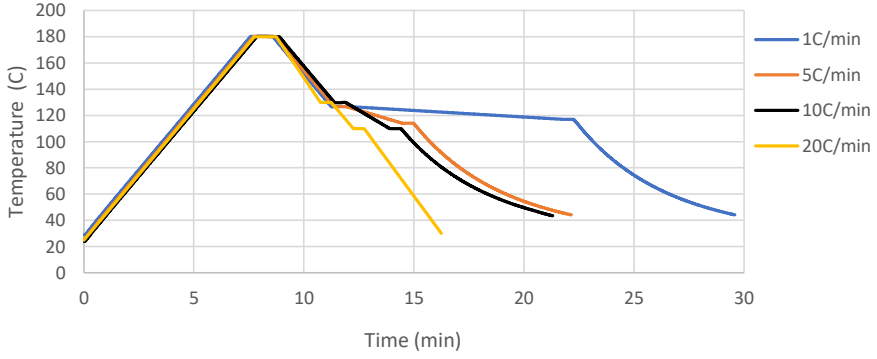

Flax-PP crystallization

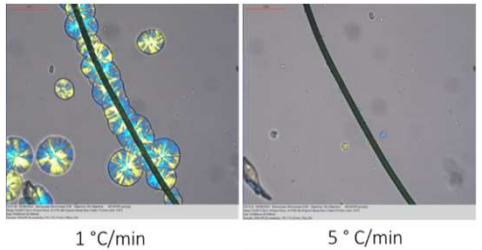

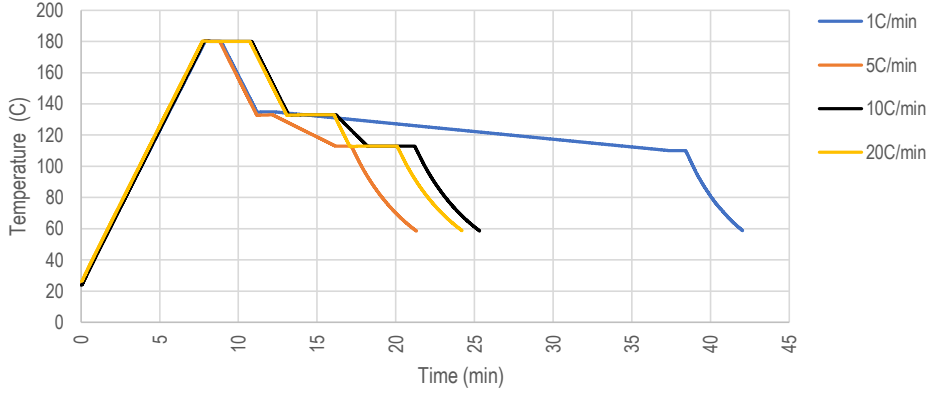

Results – CF-PPS

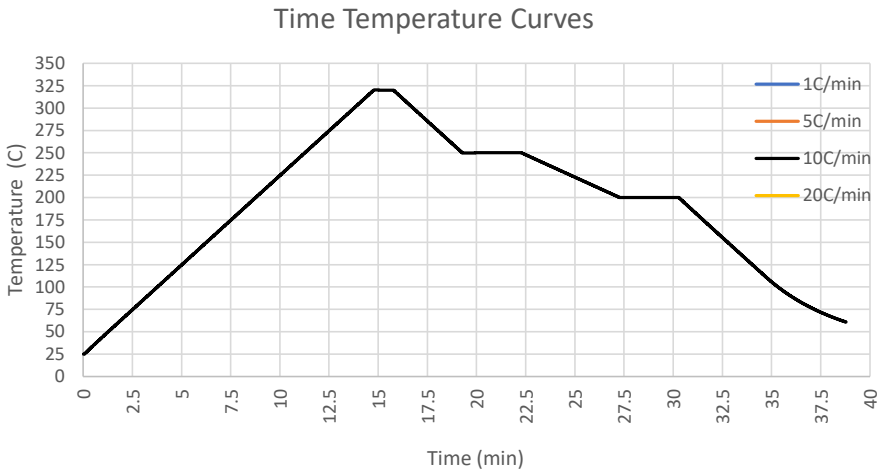

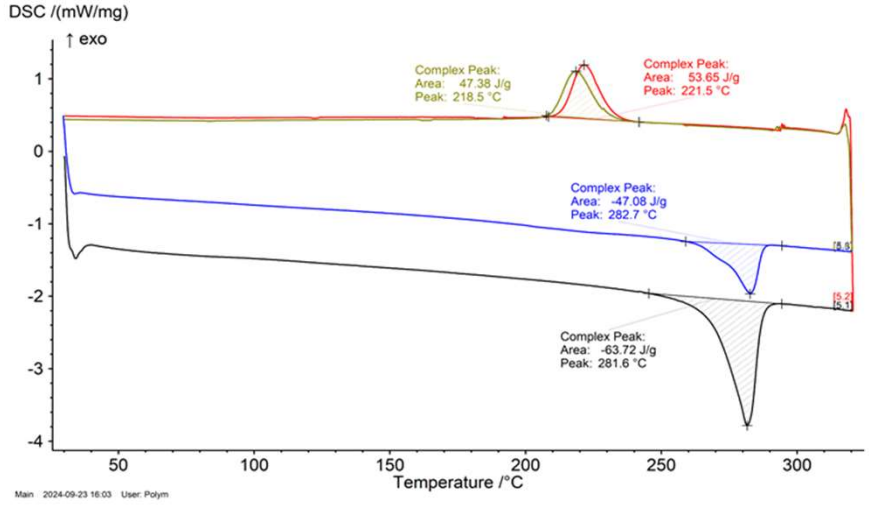



AI Model Development Approach

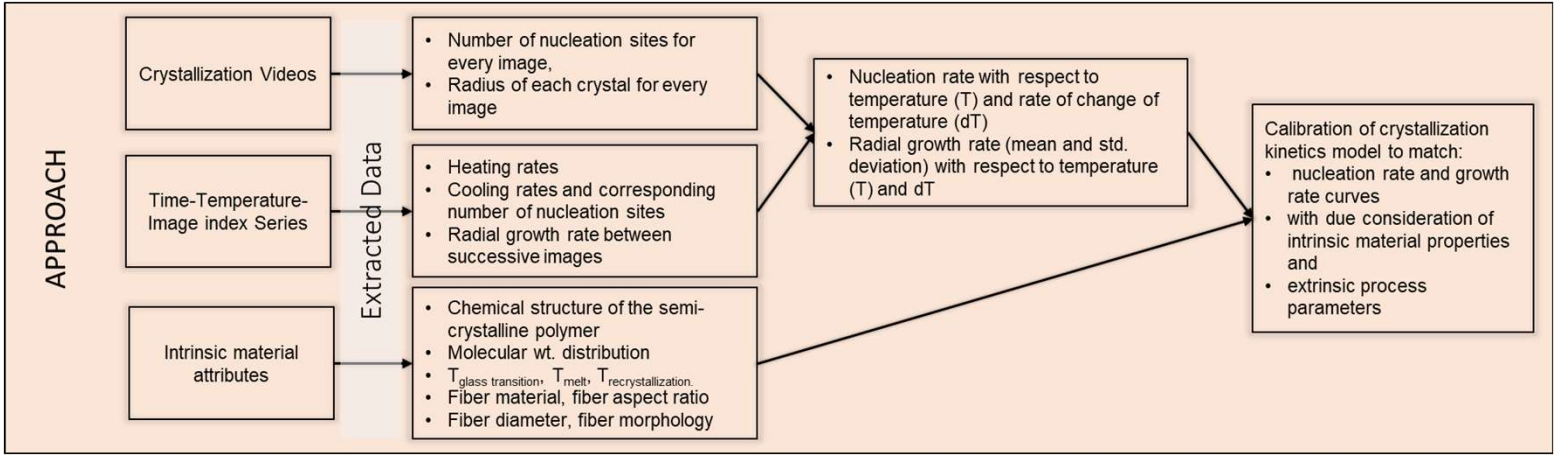

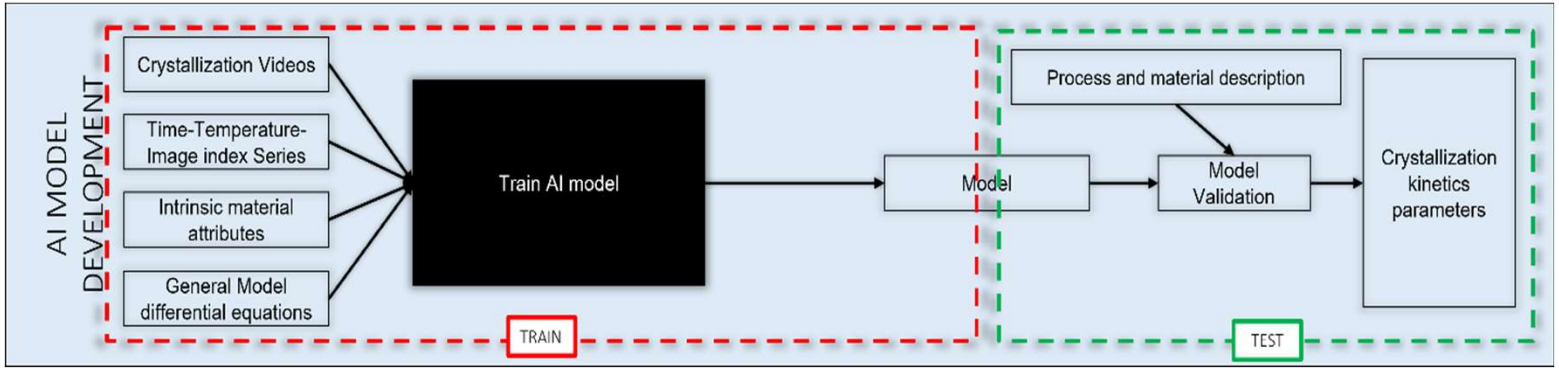

AI Model Development

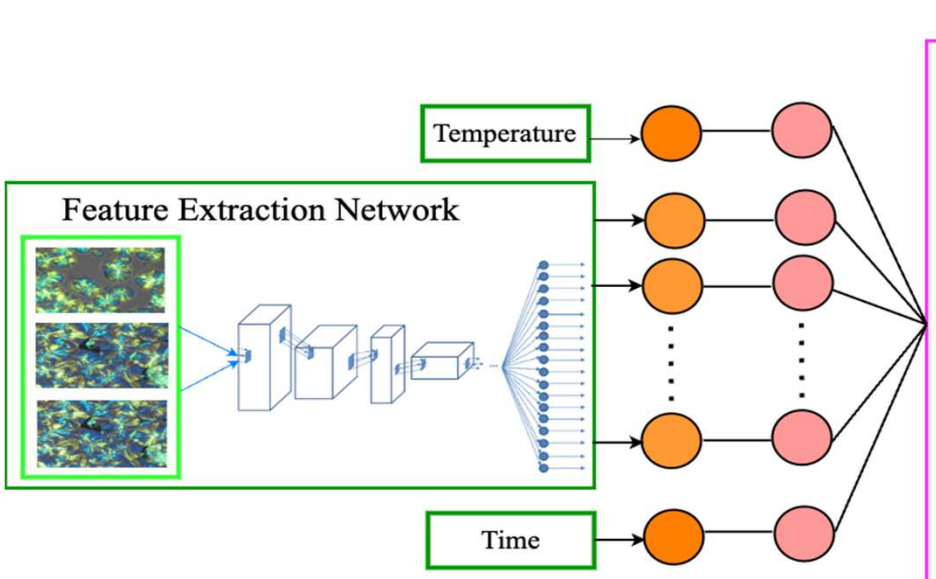

Physics-Informed Network

$$G = G_0 \exp\left(\frac{-U^*}{R(T - T_\infty)}\right) \exp\left(\frac{-K_g}{fT\Delta T}\right)$$

$$\phi_0 = \sum_i \frac{4}{3}\pi R_i^3$$

$$\frac{d\phi_0}{dt} = G\phi_1$$

$$\frac{d\phi_1}{dt} = G\phi_2$$

$$\frac{d\phi_2}{dt} = G\phi_3$$

$$\frac{d\phi_3}{dt} = 8\pi\dot{N}$$

- G = Crystal growth rate (m/s)
- G_0 = Pre-exponential factor
- U^* = Activation energy for chain motion
- R = Gas constant
- K_g = Kinetic growth parameter
- $\Delta T = T_0 - T$ = Supercooling
- $f = 2T/\Delta T$ = Correction factor
- $\dot{N}$ is the nucleation rate
- ϕ_0 = Extended crystalline volume fraction
- R_i = Radius of individual crystalline structures

Feature Extraction

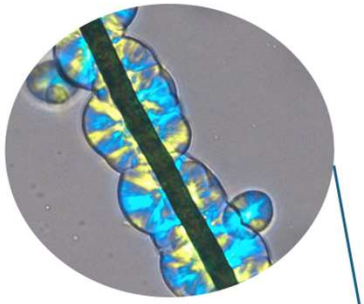

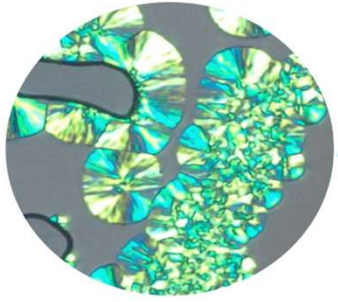

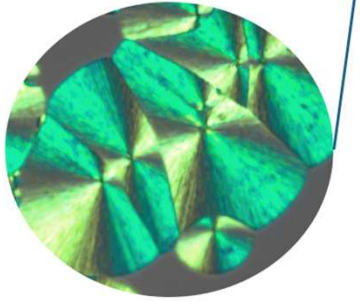

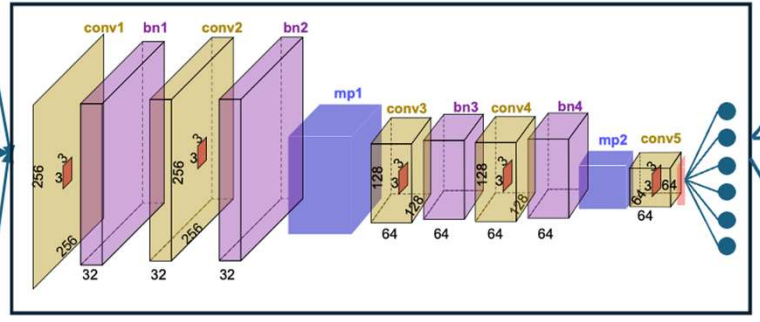

- Convolution layer
- Batch normalization
- Max-pooling
- Flatten

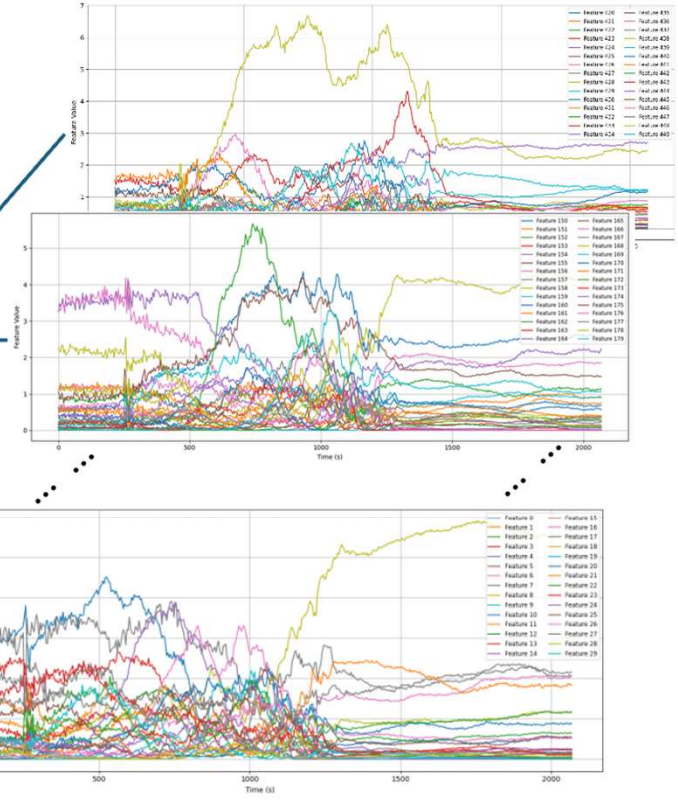

Features along with temperature and time were fed into the network

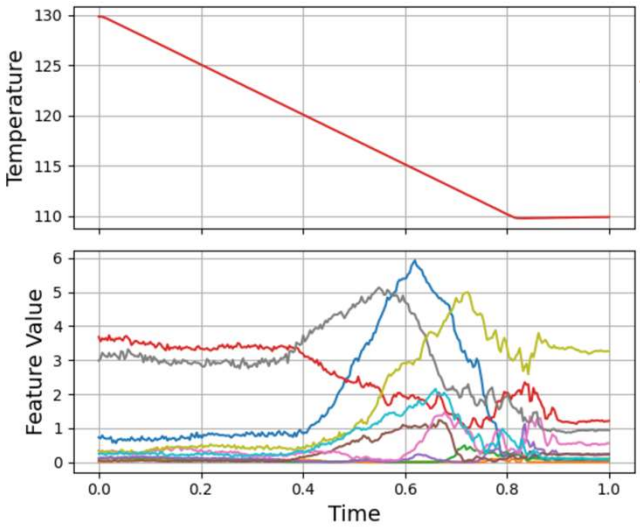

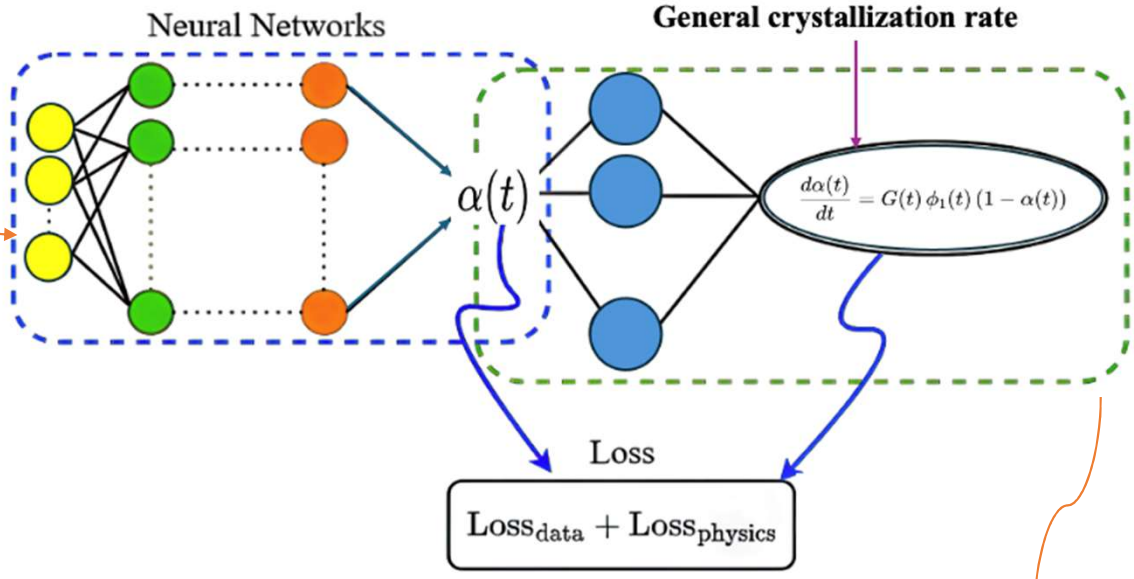

$$\phi_{tr}^{0}(t) = \frac{X_f}{1 - X_f} \cdot \frac{1}{R_f^2} \left[(R_f + e(t))^2 - R_f^2 \right]$$

X_f: fiber volume fraction

R_f: fiber radius

$e(t)$: transcrystalline layer thickness

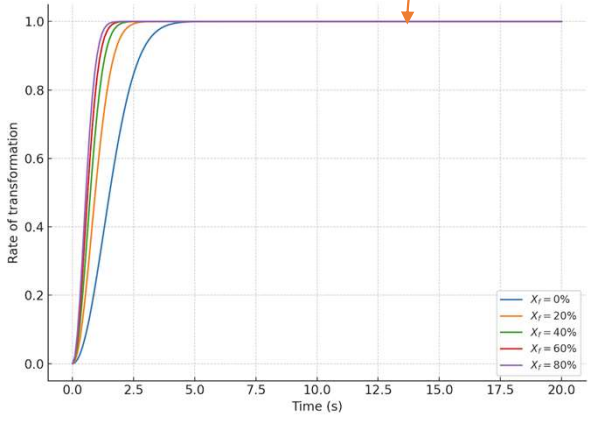

Next Steps

- Experimentation
  - Incorporation of additional physical conditions such as :
    - Shear: For GF/iPP composites, transcrystalline zone appeared only when the fiber is pulled out from the melt or when shear stress is applied at given crystallization temperature [19], [20].
    - Investigation of polymer blends such as TPOs (PP + EPDM + carbon black)
  - Incorporation of XRD to provide associated crystal orientation distribution information.
- Extraction of Nucleation rate, Radial growth rate, Crystalline volume fraction change through image segmentation
  - Dragonfly © software enables image segmentation for time successive images.
- Validation of extracted feature information from CNN against data extracted through image segmentation.
- Utilize trained Physics-informed CNN to predict microstructure morphology evolution.

[19] Varga, J., Karger-Kocsis, J. Direct evidence of row-nucleated cylindritic crystallization in glass fiber-reinforced polypropylene composites. Polymer Bulletin 30, 105–110 (1993). https://doi.org/10.1007/BF00296241
[20] Campbell, D. and Qayyum, M.M. (1980), Melt crystallization of polypropylene: Effect of contact with fiber substrates. J. Polym. Sci. Polym. Phys. Ed., 18: 83-93. https://doi.org/10.1002/pol.1980.180180107

Acknowledgements

› This work was supported as part of the AIM for Composites, an Energy Frontier Research Center funded by the U.S. Department of Energy, Office of Science, Basic Energy Sciences at the University of Delaware under award #DE-SC0023389.

› The authors would like to acknowledge Dr. Steve Sauerbrunn for sharing his insights that contributed towards experimental work.





BACK UP SLIDES

Image Preprocessing and Segmentation

UNIVERSITY OF DELAWARE
CENTER FOR COMPOSITE MATERIALS
Celebrating 50 Years

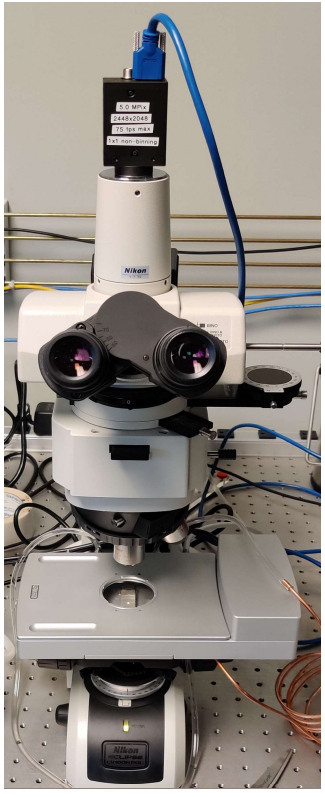

Extract images at specific sampling rate

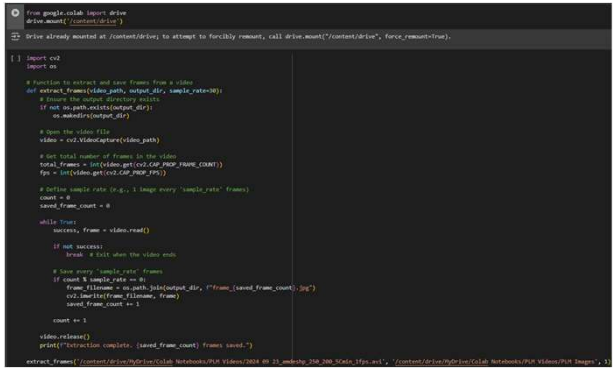

```
from google.colab import drive
drive.mount('/content/drive')
```

```
Drive already mounted at /content/drive; to attempt to forcibly remount, call drive.mount("/content/drive", force_remount=True).
```

```
[ ] import cv2
    import os

    # Function to extract and save frames from a video
    def extract_frames(video_path, output_dir, sample_rate=30):
        # Ensure the output directory exists
        if not os.path.exists(output_dir):
            os.makedirs(output_dir)

        # Open the video file
        video = cv2.VideoCapture(video_path)

        # Get total number of frames in the video
        total_frames = int(video.get(cv2.CAP_PROP_FRAME_COUNT))
        fps = int(video.get(cv2.CAP_PROP_FPS))

        # Define sample rate (e.g., 1 image every 'sample_rate' frames)
        count = 0
        saved_frame_count = 0

        while True:
            success, frame = video.read()

            if not success:
                break  # Exit when the video ends

            # Save every 'sample_rate' frames
            if count % sample_rate == 0:
                frame_filename = os.path.join(output_dir, f"frame_{saved_frame_count}.jpg")
                cv2.imwrite(frame_filename, frame)
                saved_frame_count += 1

            count += 1

        video.release()
        print(f"Extraction complete. {saved_frame_count} frames saved.")

    extract_frames('/content/drive/MyDrive/Colab Notebooks/PLM Videos/2024 09 23_amdeshp_250_200_5Cmin_1fps.avi', '/content/drive/MyDrive/Colab Notebooks/PLM Videos/PLM Images', 1)
```

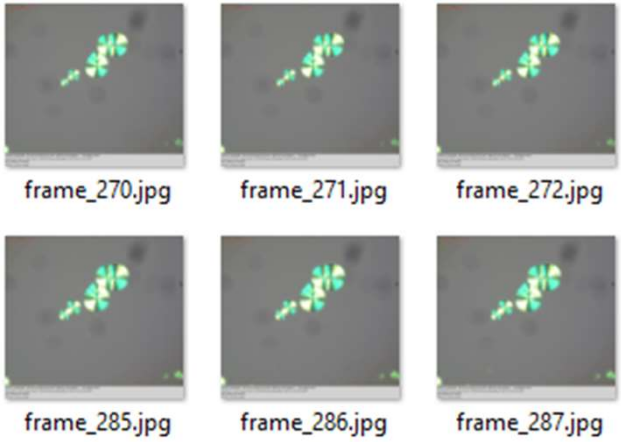

Normalized Intensity Histogram based Segmentation

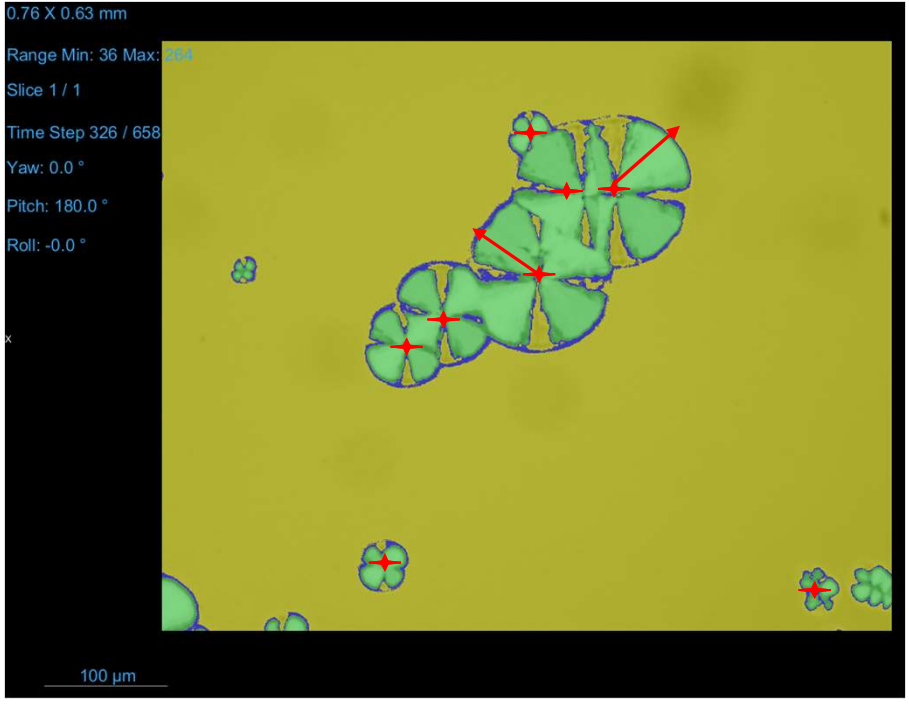

Extracting Nucleation rate, radial Growth rate from segmented Images **(In-Progress)**

ICCM24 24TH INTERNATIONAL CONFERENCE ON COMPOSITE MATERIALS
AUG 4-8, 2025 • BALTIMORE CONVENTION CENTER • BALTIMORE, MARYLAND

Graph Neural Networks for Effective Prediction of Mechanical Response in Composite Structures with Models using Unstructured Meshes

Luca Patrignani[1], Silvestre T. Pinho[2]

[1] Department of Aeronautics, Imperial College London, Exhibition Rd, South Kensington, London SW7 2AZ, UK
Email: l.patrignani@imperial.ac.uk, web page: https://www.pinholab.com

[2] Department of Aeronautics, Imperial College London, Exhibition Rd, South Kensington, London SW7 2AZ, UK
Email: silvestre.pinho@imperial.ac.uk, web page: https://www.pinholab.com

Keywords: Graph Neural Networks; Finite Element Analysis; Numerical analysis; Mechanical properties; Laminates

ABSTRACT

Graph Neural Networks (GNNs) are emerging as a transformative approach for predicting mechanical response in composite structures by naturally encoding unstructured finite element meshes as graphs. While traditional finite element analysis provides trusted solutions for structural mechanics problems, it encounters significant computational and scalability bottlenecks. We present a methodology that extends the MeshGraphNets framework with frequency-controlled hybrid local-global attention mechanisms that addresses the challenge of capturing both local behaviour around geometric discontinuities and global strain field patterns in composite laminates. Our approach integrates with industrial FEA workflows through an automated Abaqus-to-GNN pipeline that converts FEM simulations to graph representations. We validate our approach on Carbon Fiber Reinforced Polymer (CFRP) laminate plates with open holes. The results demonstrate exceptional predictive accuracy ($R^2 = 0.9775$) while achieving a 200× computational speedup over traditional finite element analysis. This represents a fundamental shift from computation-intensive iterative solving to near-instantaneous prediction for composite structure design applications.

1. Introduction

The aviation industry faces critical sustainability challenges as a major contributor to CO2 emissions [1]. This drive for sustainability is spurring novel aircraft configurations, particularly those incorporating alternative fuels, which requires a fundamental shift in design methodologies demanding high-performance predictive models of full-scale aircraft structures [2]. Finite Element Analysis offers trusted mesh-based solutions for structural mechanics problems involving partial differential equations [3]. However, FEA faces scalability and computational issues in large-scale applications, especially when various configurations need separate simulations, resulting in high computational costs [4]. Graph Neural Networks emerge as a natural solution by effectively representing and processing data on graphs [5, 6]. Pfaff et al. (2021) [7] developed a framework for learning mesh-based simulations using graph neural networks, demonstrating that GNNs can capture complex physical interactions through graph adjacencies while remaining resolution-independent [8]. While GNNs have been successfully applied to predict mechanical responses in structural components [9, 10], significant challenges remain. Current methodologies exhibit limited accuracy when addressing severe stress concentrations, particularly in complex geometries

with geometric discontinuities [11]. Additionally, they encounter difficulties with long-range information propagation during message passing, which can lead to over-smoothing issues [9]. In this work, we address these limitations by developing a novel GNN architecture that extends the MeshGraphNets model [7] with enhanced frequency-controlled hybrid local-global attention mechanisms. We validate our approach on Carbon Fiber Reinforced Polymer (CFRP) laminate plates with open holes, demonstrating excellent performance with 200× computational speedup while maintaining high accuracy for strain concentration prediction.

2. Graph Neural Networks for Mesh-Based Physics

Graph Neural Networks extend the concept of convolution to irregular topologies using message-passing mechanisms [5]. Unlike Convolutional Neural Networks which function on fixed neighborhood structures, GNNs can process unstructured mesh data directly. The process consists of three sequential operations: encoding, processing, and decoding. The **encoding** transforms raw node and edge features into latent representations through learnable transformations. The **processing** propagates information through the graph via iterative message exchange between connected nodes. The **decoding** maps the refined embeddings to target predictions. Full details will be given at the conference. For comprehensive information, please refer to the forthcoming journal paper to be submitted for publication (Patrignani, L., & Pinho, S. T., 2025).

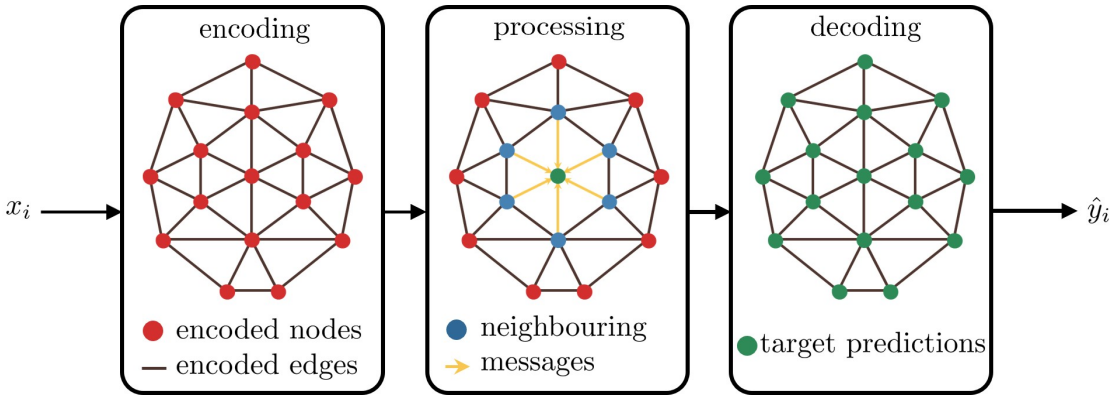

Figure 1: Graph Neural Network for Mesh-Based Physics architecture overview showing the three-stage encoder-processor-decoder framework.

3. Automated FEA-to-GNN Pipeline

We developed an automated pipeline that transforms FEA simulations into GNN training data, mapping the traditional *input-solver-output* workflow directly to supervised learning's *problem-solution* pairs. The pipeline encompasses sample generation, mesh-to-graph conversion, solver execution, and solution extraction as shown in Figure 2. This framework generates three tensor structures: node tensor encoding spatial coordinates and boundary conditions, edge tensor representing connectivity and geometric relationships, and target tensor containing solution field variables from FEA outputs. The automated framework transforms weeks of manual preprocessing into hours of computation, enabling rapid exploration across diverse structural mechanics problems.

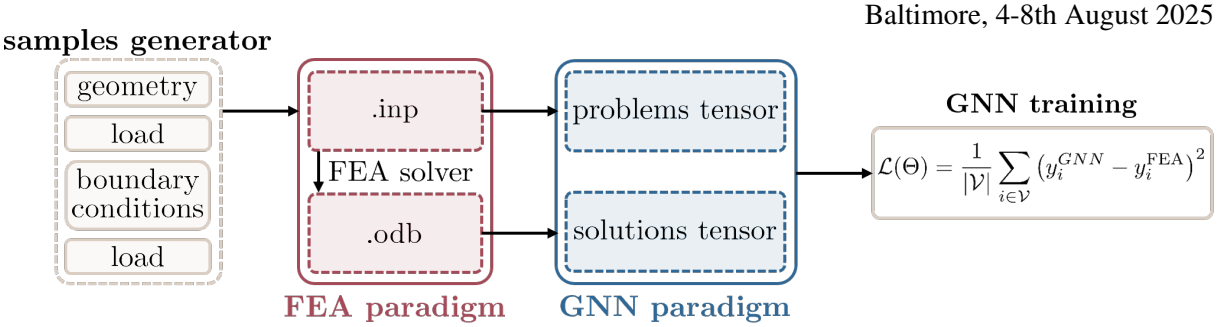

Figure 2: Automated FEA-to-GNN pipeline architecture transforming FEA workflow to GNN paradigm.

4. GNN Model for Composite Structures

This work develops a specialized GNN architecture for predicting longitudinal strain fields in CFRP open-hole tension plates. We extend the MeshGraphNets framework with frequency-controlled hybrid local-global attention mechanisms to capture both local behavior around geometric discontinuities and global strain field patterns.

4.1. Problem Setup

As shown in Figure 3, plate dimensions are randomly sampled with length and height ranging from 100 to 200 mm. Hole radius varies between 10 and 20 mm, with position factors ranging from *0.3* to *0.7* of plate dimensions. Applied displacement magnitude varies from 1 to 2 mm, generating 500 distinct samples with symmetric [0°/45°/90°/-45°]s layup configuration.

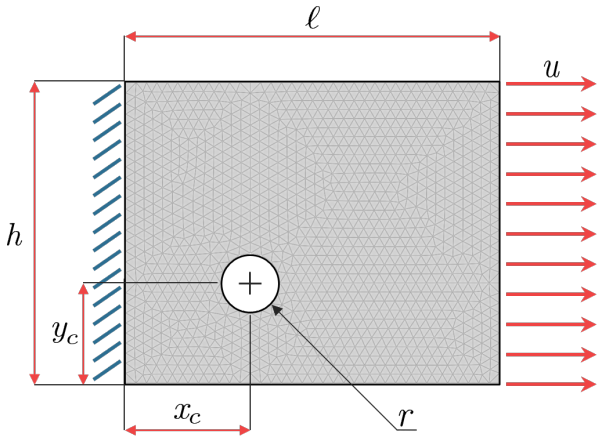

Figure 3: CFRP open-hole tension plate configuration showing variable features.

4.2. Data Representation

Node features incorporate geometric and physical information:

$$\mathbf{x}_i = [x_i, y_i, \mathbb{I}_{\text{fixed}}, \mathbb{I}_{\text{hole}}, \mathbb{I}_{\text{displaced}}, u_{\text{applied}}]^T \tag{1}$$

Edge features capture local geometric relationships:

$$\mathbf{e}_{ij} = [x_i - x_j, y_i - y_j, \|\mathbf{r}_{ij}\|_2]^T \tag{2}$$

Target variables represent longitudinal strain: $y_i = \varepsilon_{xx,i}$

4.3. Model Architecture

As illustrated in Figure 4, the model implements a three-stage encoder-processor-decoder framework with hybrid attention mechanisms.

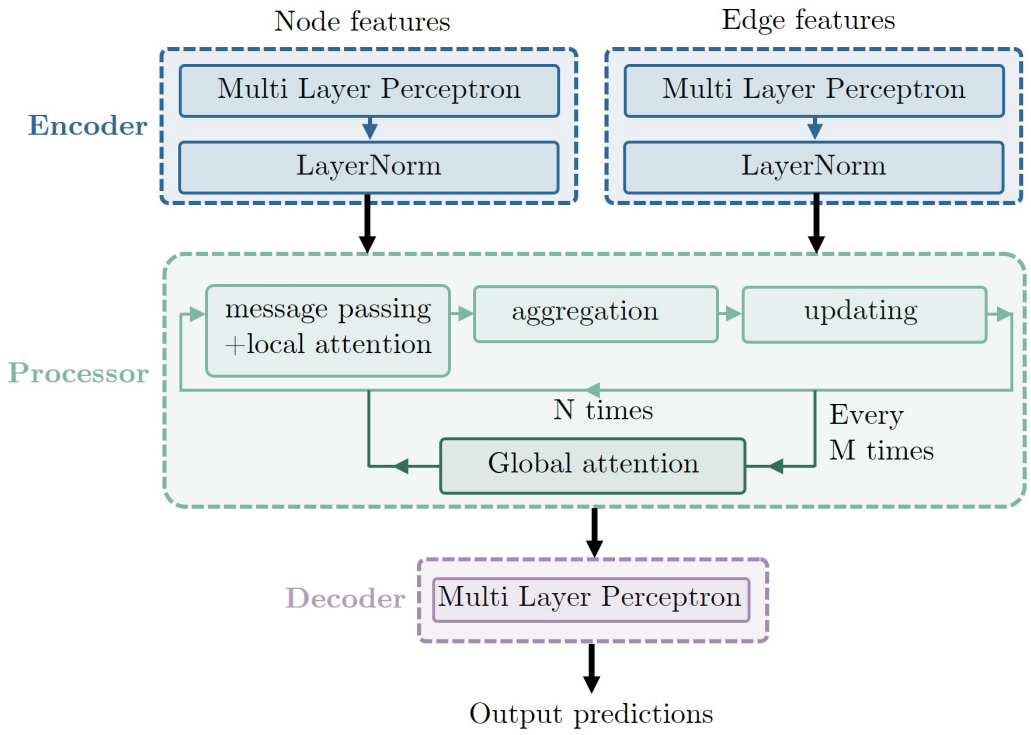

Figure 4: Complete GNN architecture with encoder-processor-decoder framework and attention mechanisms.

The processor implements message-passing with local attention at each step and global attention applied every M layers. Local attention coefficients weight neighboring information, while global attention enables direct long-range interactions following transformer architecture principles. The full details of the mathematical formulations and extended analyses of the GNN framework will be presented in the forthcoming journal paper to be submitted for publication (Patrignani, L., & Pinho, S. T., 2025).

4.4. Hyperparameter Optimization

Systematic hyperparameter tuning was performed using Optuna with Tree-structured Parzen Estimator sampling. Key findings identified learning rate and batch size as primary performance drivers. The optimal configuration achieved validation loss of 0.2621.

4.5. Results

Figure 5 demonstrates exceptional model accuracy with $R^2 = 0.9775$ and RMSE of 0.00022. The regression line closely follows the ideal diagonal, indicating minimal systematic bias across the full strain range. Training convergence analysis demonstrates substantial performance improvement with our hybrid attention architecture compared to standard message-passing, achieving approximately 64% improvement in training performance and 73% improvement in validation performance. The computa-

tional performance analysis reveals 200× speedup compared to traditional FEA, requiring only 0.5% of the original simulation time while maintaining high accuracy.

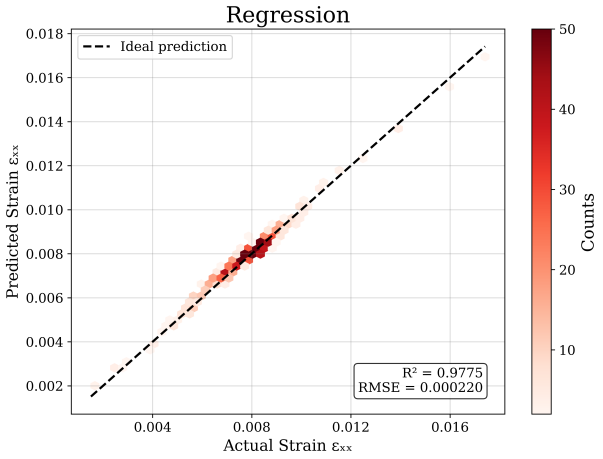

Figure 5: Predicted vs. actual strain correlation demonstrating excellent accuracy ($R^2 = 0.9775$).

5. Conclusions

This work presents a novel Graph Neural Network architecture that successfully addresses critical limitations in traditional finite element analysis for composite structural mechanics. By extending the MeshGraphNets framework with hybrid local-global attention mechanisms, we demonstrate significant computational acceleration while maintaining high predictive accuracy for strain field prediction in CFRP open-hole tension plates. Our key contributions include: (1) a hybrid attention mechanism that effectively captures local and global mechanical behaviour, achieving $R^2 = 0.9775$ accuracy while avoiding over-smoothing issues; (2) a 200× speedup compared to traditional finite element analysis; (3) an automated Abaqus-to-GNN pipeline that transforms weeks of manual preprocessing into hours of computation, facilitating seamless integration with existing commercial workflows. The demonstrated capability to predict mechanical response with minimal feature engineering requirements, combined with seamless FEA integration, positions this approach as an enabling tool for accelerating composite structure design and analysis in aerospace applications. The framework's extensibility to diverse structural mechanics problems using identical architectures represents a significant step toward practical surrogate modeling capabilities for engineering simulation.
Future research directions include extending the framework to progressive damage modeling and exploring multi-scale GNN architectures. For comprehensive details on computational complexity analysis, extended mathematical formulations, and hyperparameter optimization studies, please refer to the forthcoming journal paper to be submitted for publication (Patrignani, L., & Pinho, S. T., 2025).

References

[1] David S Lee, David W Fahey, Agnieszka Skowron, Myles R Allen, Ulrike Burkhardt, Qi Chen, Sarah J Doherty, Sarah Freeman, Piers M Forster, Jan Fuglestvedt, et al. The contribution of global aviation to anthropogenic climate forcing for 2000 to 2018. *Atmospheric environment*, 244:117834, 2021.

[2] Vittorio Cipolla, K Abu Salem, G Palaia, V Binante, and Davide Zanetti. A doe-based approach

for the implementation of structural surrogate models in the early stage design of box-wing aircraft. *Aerospace science and technology*, 117:106968, 2021.

[3] Olgierd Cecil Zienkiewicz, Robert Leroy Taylor, and Jian Z Zhu. *The finite element method: its basis and fundamentals*. Elsevier, 2005.

[4] S. T. Pinho, M. Matos, R. O. S. S. Costa, A. Ibbotson, and M. Ostergaard. Enabling multiscale analysis of very large composite structures. In *8th ECCOMAS Thematic Conference on the Mechanical Response of Composites*, 2021. doi: 10.23967/composites.2021.123.

[5] Franco Scarselli, Marco Gori, Ah Chung Tsoi, Markus Hagenbuchner, and Gabriele Monfardini. The graph neural network model. *IEEE Transactions on Neural Networks*, 20(1):61–80, 2008.

[6] Will Hamilton, Zhitao Ying, and Jure Leskovec. Inductive representation learning on large graphs. *Advances in neural information processing systems*, 30, 2017.

[7] Tobias Pfaff, Marc Fortunato, Alvaro Sanchez-Gonzalez, and Peter W Battaglia. Learning mesh-based simulation with graph networks. In *International Conference on Machine Learning*, pages 8459–8468. PMLR, 2020.

[8] Chunhao Jiang and Nian-Zhong Chen. Graph neural networks (gnns) based accelerated numerical simulation. *Engineering Applications of Artificial Intelligence*, 123:106370, 2023.

[9] Rutwik Gulakala, Vaishnav Bhaskaran, and Marcus Stoffel. A generative learning and graph-based framework for computing field variables in finite element simulations. *Computer Methods in Applied Mechanics and Engineering*, 428:117111, 2024.

[10] Marco Maurizi, Chao Gao, and Filippo Berto. Predicting stress, strain and deformation fields in materials and structures with graph neural networks. *Scientific reports*, 12(1):21834, 2022.

[11] Jiaqian Wu, Chaoyu Du, Benjamin Dillenburger, and Michael Anton Kraus. Fast prediction of stress distribution: A gnn-based surrogate model for unstructured mesh fea. In *Proceedings of the IASS 2024 Symposium: Redefining the Art of Structural Design*, volume 2024. International Association for Shell and Spatial Structures, 2024.



AI-BASED GENERATION OF SIMULATION MODELS FOR MATERIAL DEVELOPMENT FROM CT DATA

ICCM24, Baltimore
2025-08-04

Oliver Rimmel[1], Mike Marsh[2], Nelly Nunheim[1], Dominik Michel[1], Andreas Grießer[1], Rolf Westerteiger[1], Lilli Burger[1], Dennis Mosbach[1], Mevlud Kurpejovic[1]

[1] Math2Market GmbH
[2] M2M North America Inc.

© Math2Market GmbH

Short Speaker Biography

GeoDict

2022 - now	**Head of Digital Material Business, Math2Market GmbH, Kaiserslautern** Responsible for Foams, Composites, Ceramics, Metals, Additive Manufacturing, Nonwovens, Technical Textiles
2020-2022	**Process Developer, PFW Aerospace GmbH, Speyer** Responsible for process development in the area of laser metal deposition additive manufacturing
2015-2019	**PhD, Mechanical Engineering, TU Kaiserslautern** At the **Leibniz Institute for Composite Materials**, department of Manufacturing Science Topic: Experimental and simulative analysis of composite impregnation processes
2008 - 2014	**Diploma, Mechanical Engineering, TU Kaiserslautern** Focus on material science and composites



Dr.-Ing. Oliver Rimmel

© Math2Market GmbH

MATH 2 MARKET

Material Design

GeoDict

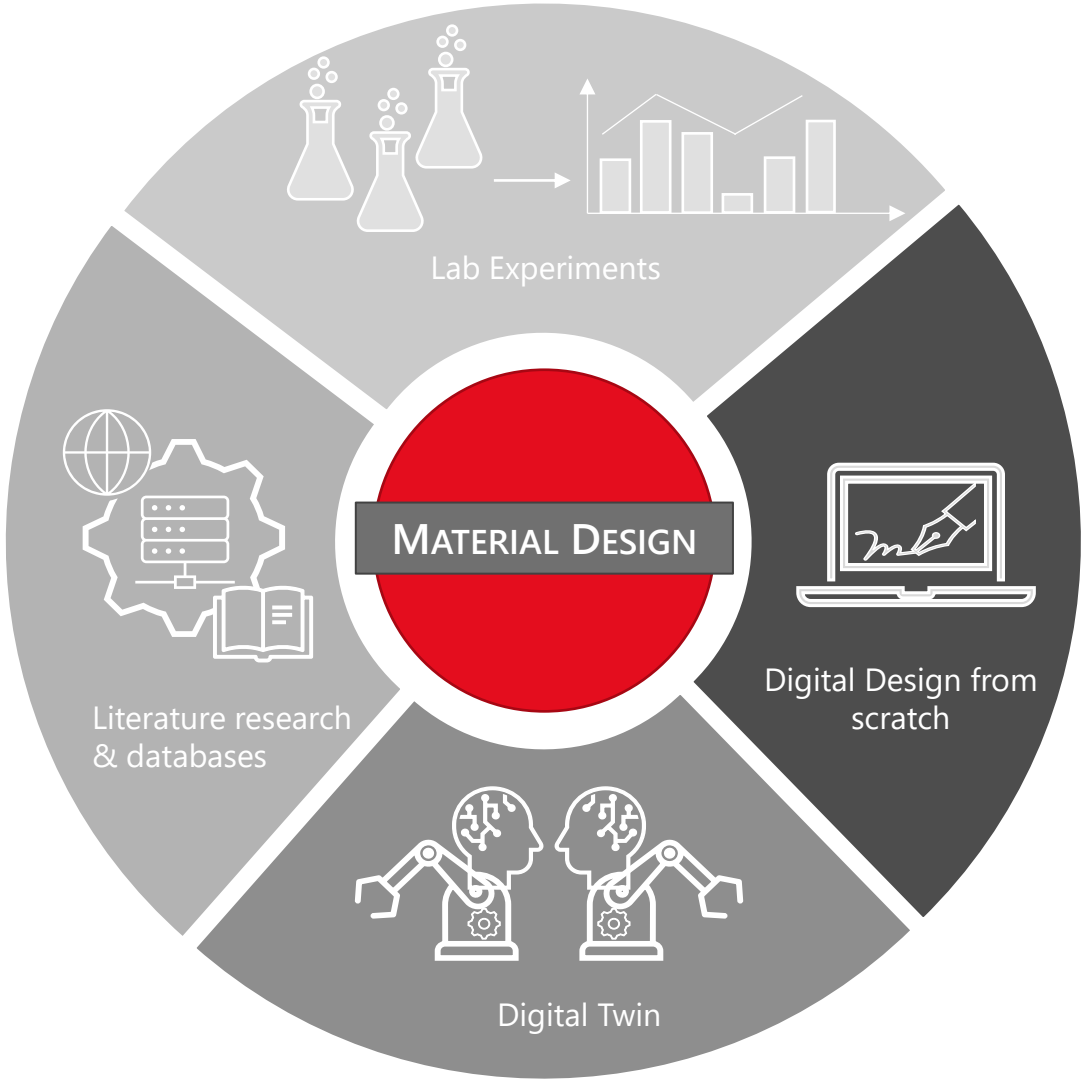

What are the options to improve a material and design a new and better one that suits your specific application ?

© Math2Market GmbH

MATH 2 MARKET

Introduction: Using µCT scans for composites development

Challenges

Start

Segmentation and analysis of the CT-Scans of fiber-reinforced polymer composites

Fibers cannot be fully distinguished by the software

Approach

Human eye can distinguish individual fibers and tows

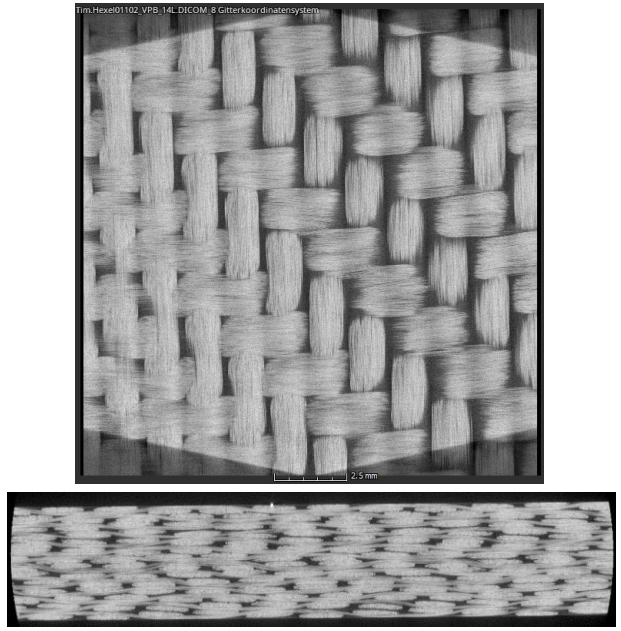

Solution

Goal

Discovering unknown material properties

Training a neural network

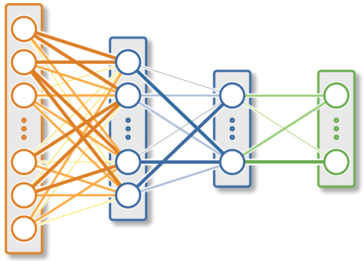

© Math2Market GmbH

Goal in Scan Processing

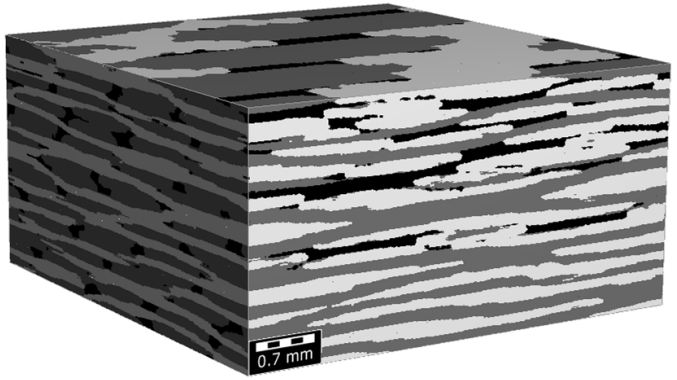

Identification and separate segmentation of groups of objects (here 0° and 90° fiber bundles)

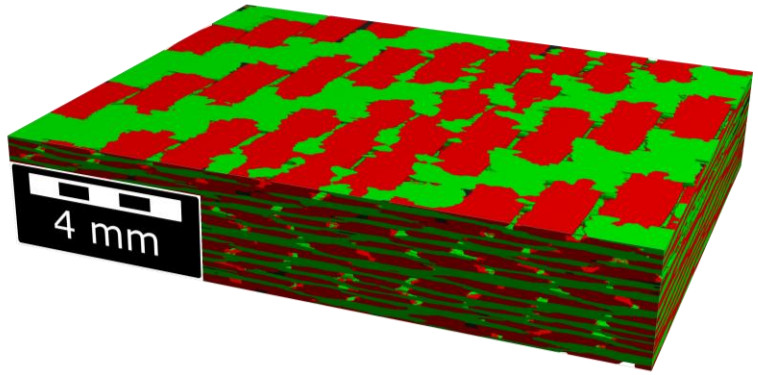

Identification of individual tows in the scan

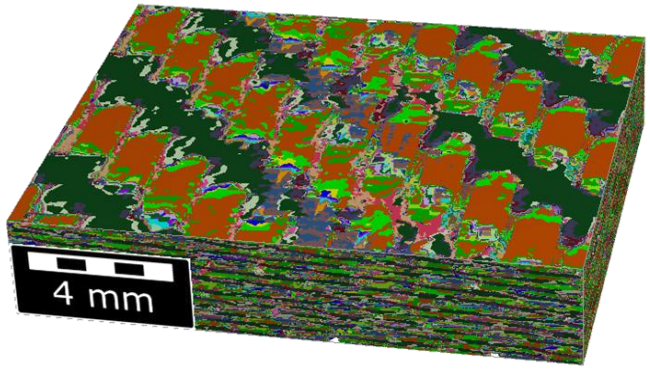

Identification of individual tows & additional information, e.g., local fiber orientation in tows

What is the goal?

Extracting detailed and quantitative information from the scans for the simulation models

© Math2Market GmbH

GeoDict

AI-based simulation models from CT data

Development of an AI-based workflow using the example of fiber-polymer composites which closes the gap between 3D imaging techniques and synthetically generated geometry models based on statistical data from real structures to improve material development.

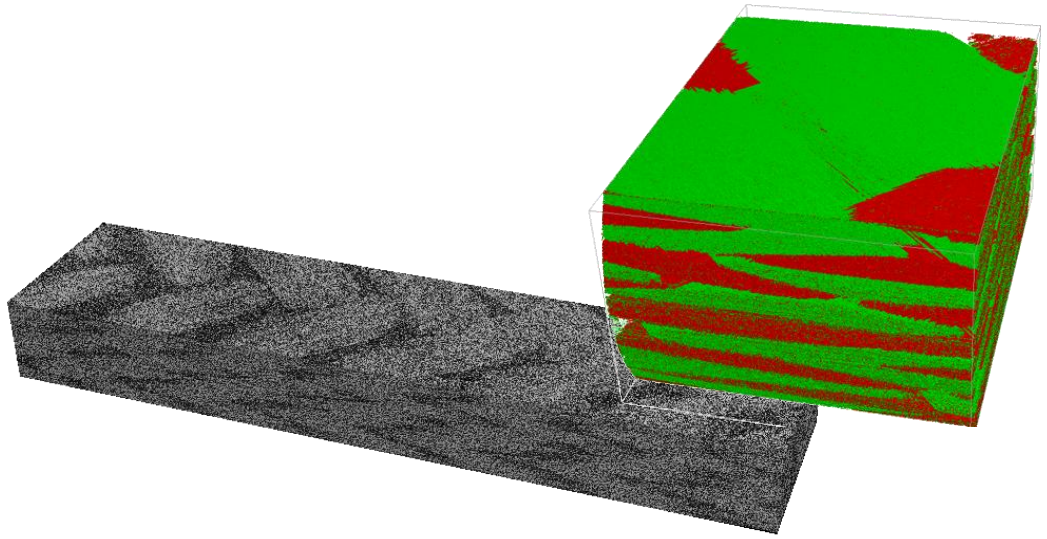

Funding Code
01IS23054 A

Duration
October 2023 – March 2026

Our partners

Supported by:
Federal Ministry for Economic Affairs and Climate Action
on the basis of a decision by the German Bundestag

Leibniz-Institut für Verbundwerkstoffe

Leibniz Gemeinschaft

© Math2Market GmbH

Approach of Project KI4Material Modeling

GeoDict

Real world µCT data

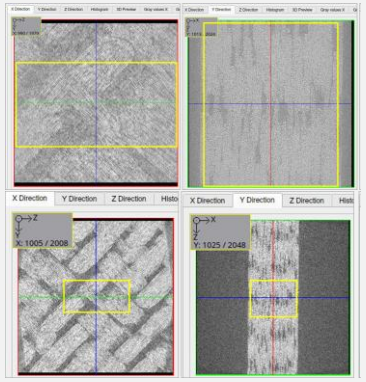

- ⊕ Real world data
- ⊖ Resolution limits
  Imaging artifacts
  Missing data

Statistically Generated Models

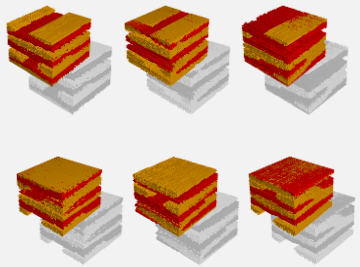

- ⊕ Parameter variation
  all details known
- ⊖ Less real variation

AI methods for object classification

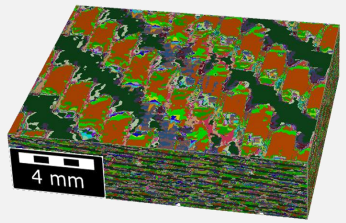

- Easy training of AI networks for new materials
- Improved detection of geometrical features with reduced manual labeling

AI methods for image enhancement

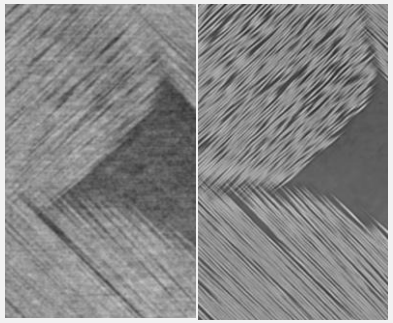

- Trained with real world data and artificial data
- Largely improved workflow efficiency

© Math2Market GmbH

MATH 2 MARKET

What is the use of artificial µCT images?

GeoDict

Why is it „fast“?

- No sinogram reconstruction
- No raytracing / beam simulation

This enables usage in fast parameter studies:

- Create a CT scan of a 1000^3 model in 5 minutes
- Vary image artifacts and noise
- Use artificial CTs to train neural networks

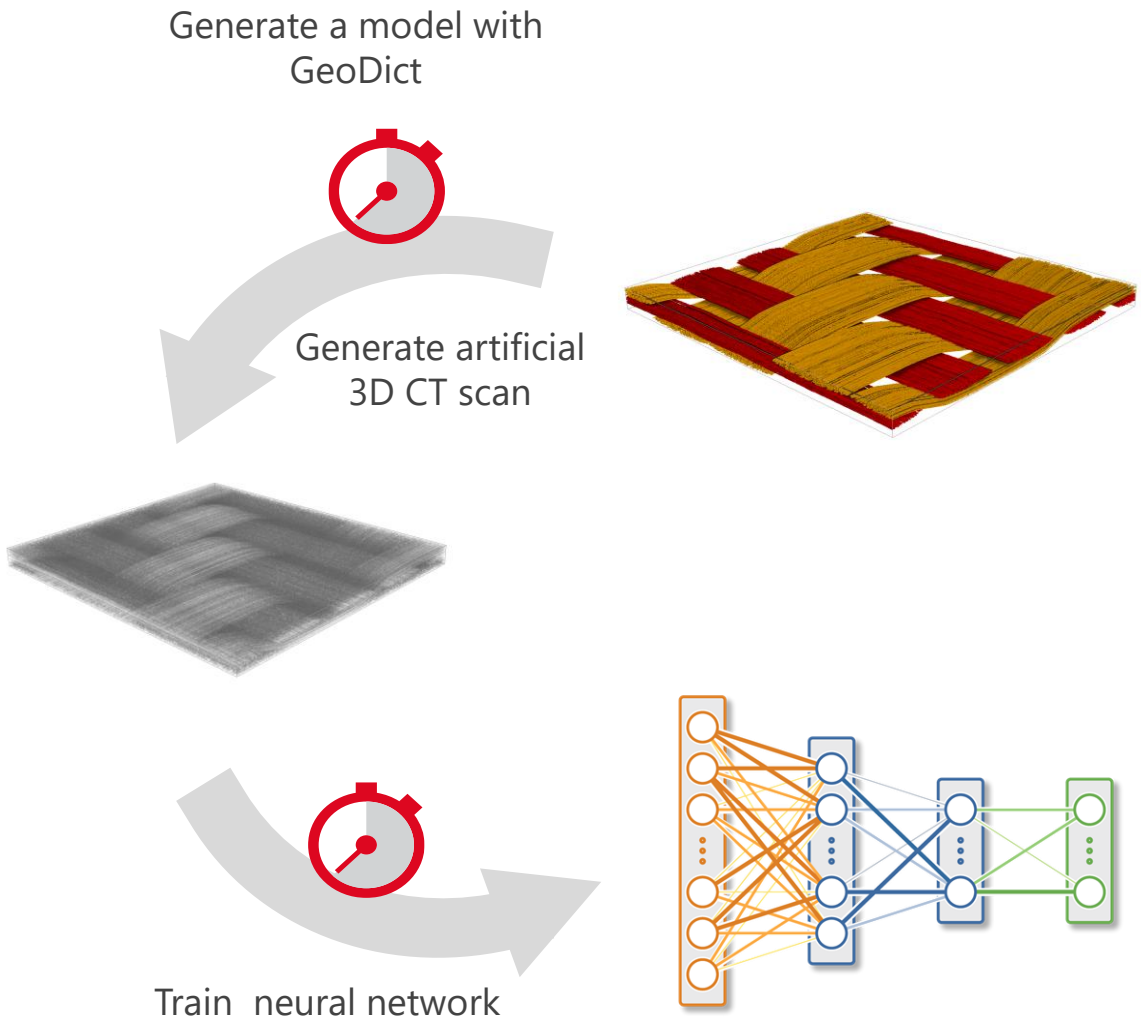

© Math2Market GmbH

MATH 2 MARKET

Creating Artificial CT Scans: Starting with Unit Cell Generation

GeoDict

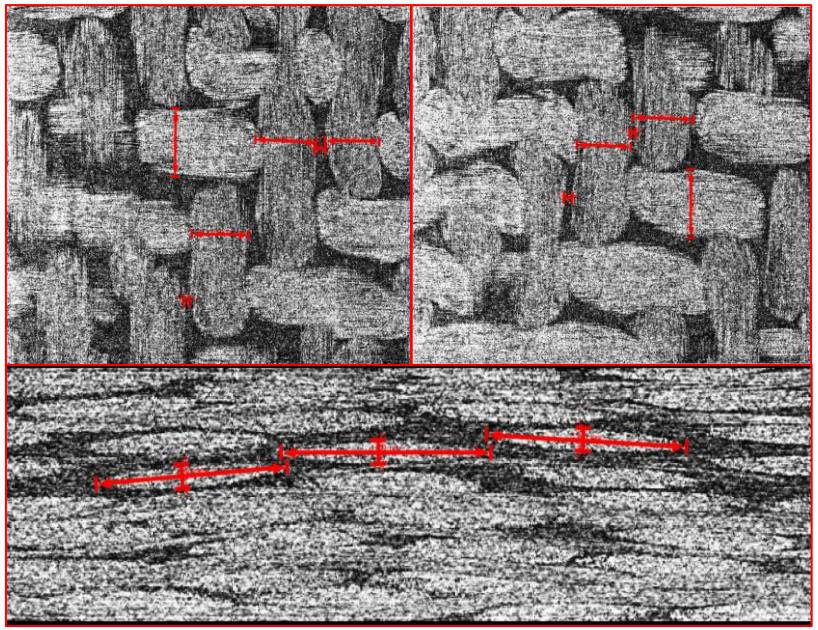

- Weft & Warp tows
- Width, Height, Gaps

GeoDict

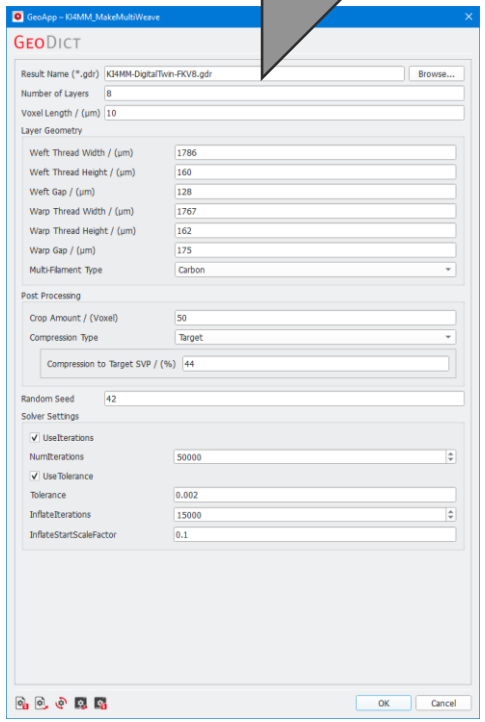

Parameters for unit cell generation

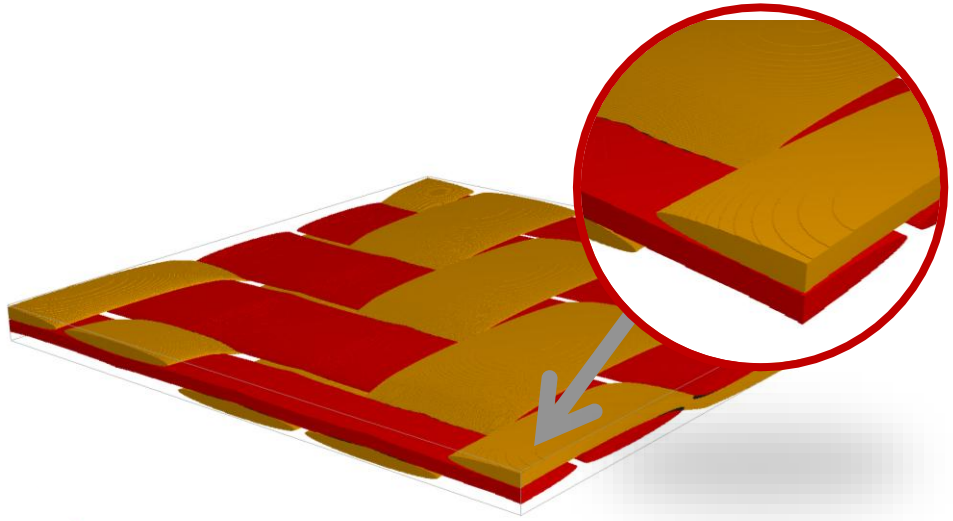

Fiber bundles



Single fibers within fiber bundles

© Math2Market GmbH

MATH 2 MARKET

Super Resolution of Carbon Fibers – Low Quality Scan

GeoDict

Low Resolution scan at 3.5µm voxel length

- High field of view
- Fiber details not visible

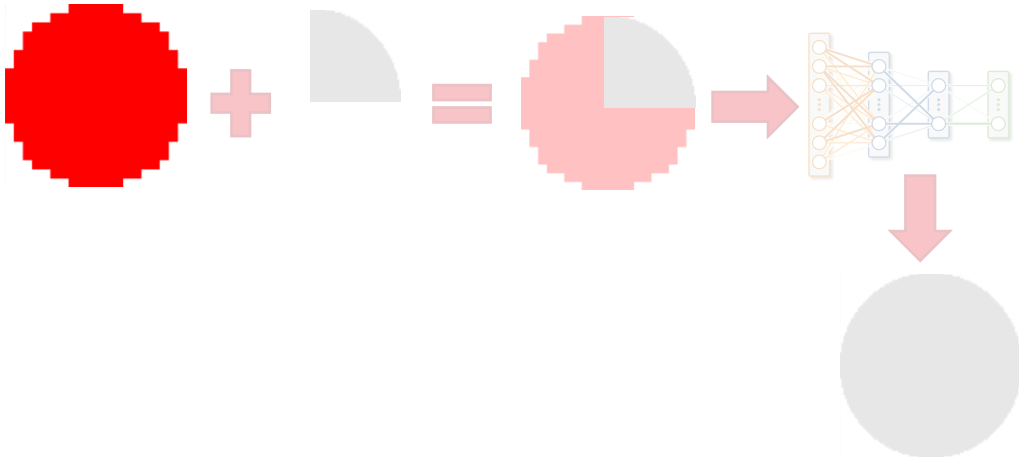

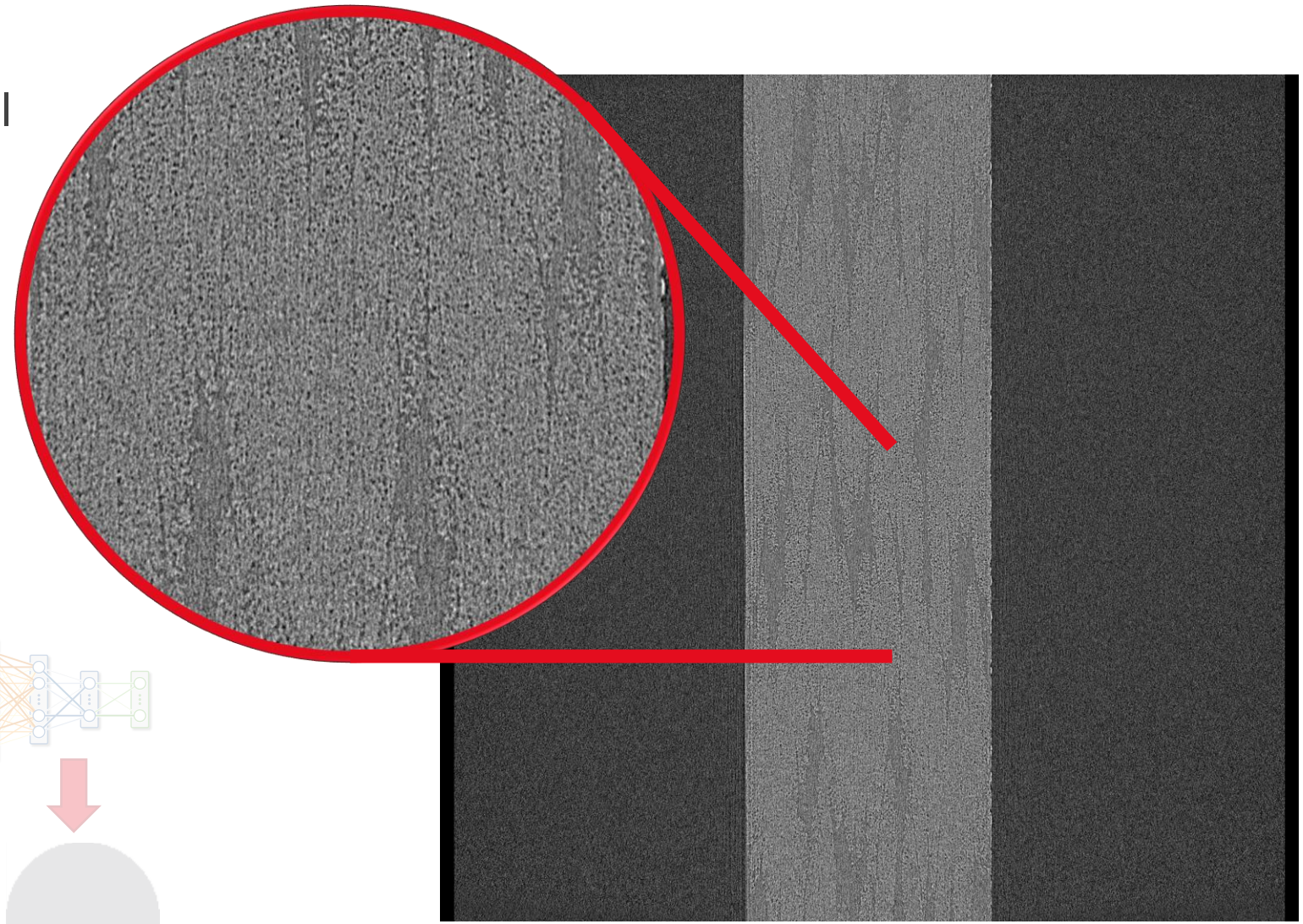

© Math2Market GmbH

MATH 2 MARKET

Super Resolution of Carbon Fibers – High Quality Scan

GeoDict

High Resolution scan at 1.75µm voxel length

- low field of view
- Fiber details visible



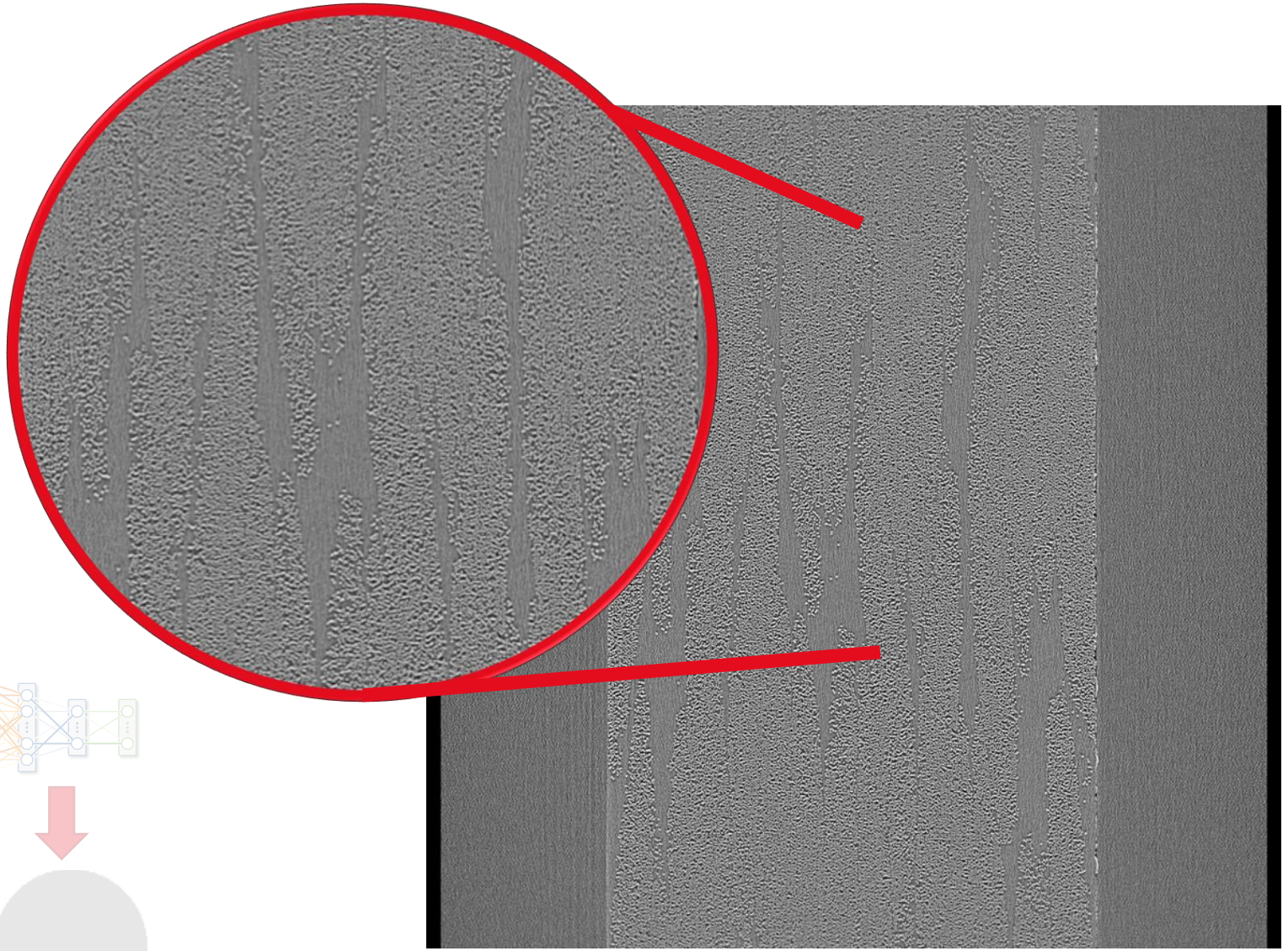

© Math2Market GmbH

MATH 2 MARKET

Super Resolution of Carbon Fibers – Combine Scans and Train Neural Network

GeoDict

- High Resolution scan is located at the center of the low-resolution scan
- Overlapping Area can be used to obtain training data for super resolution
- Trained convolution neural network (modified U-Net)

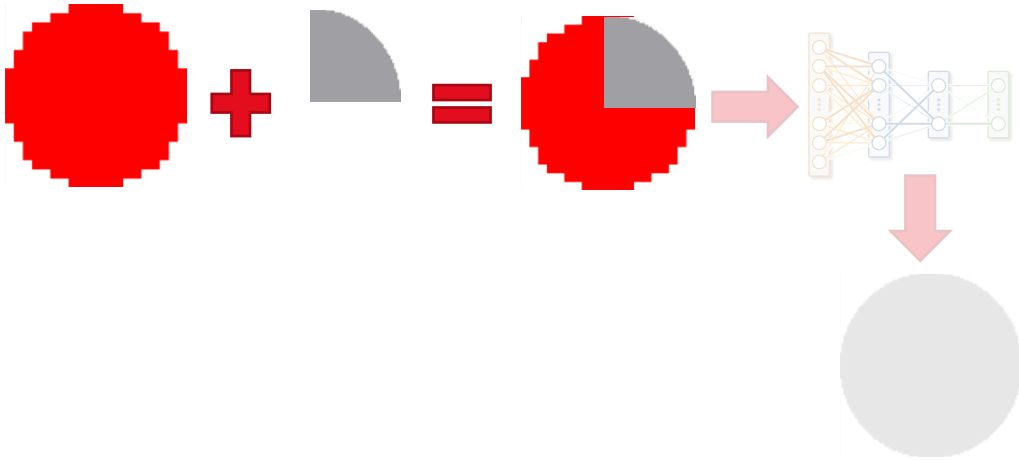

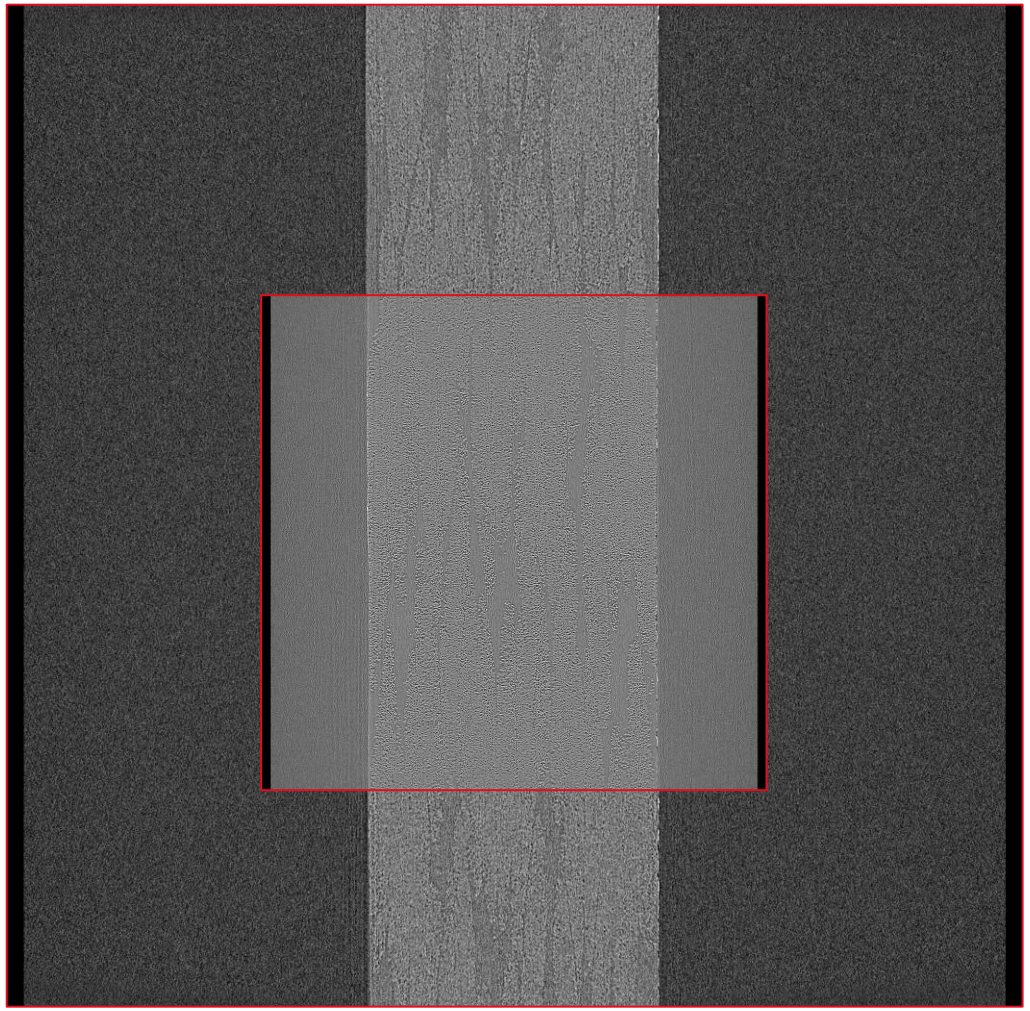

© Math2Market GmbH

MATH 2 MARKET

Super Resolution of Carbon Fiber – Apply AI Network

GeoDict

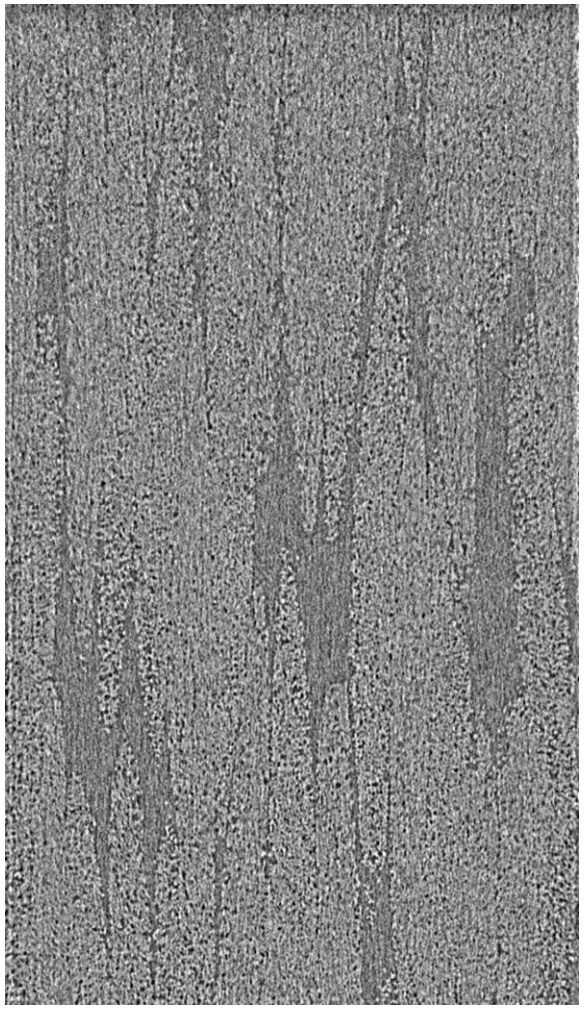

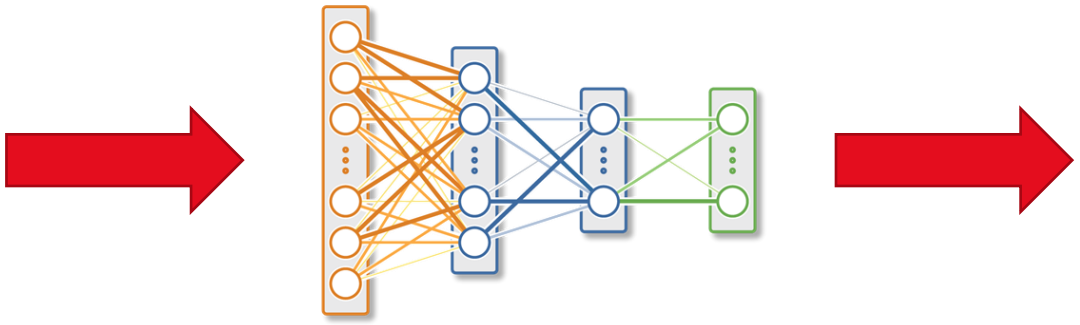

Train neural network and apply sample area that was not part of the training data

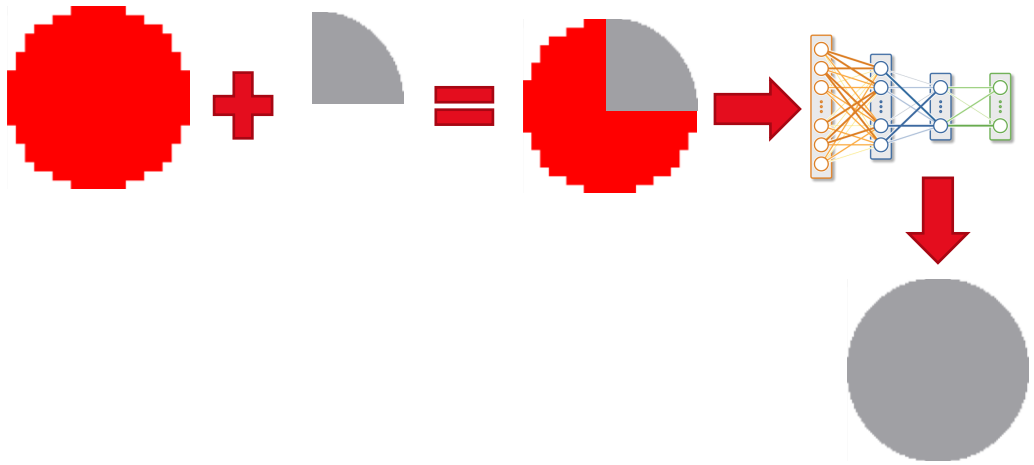

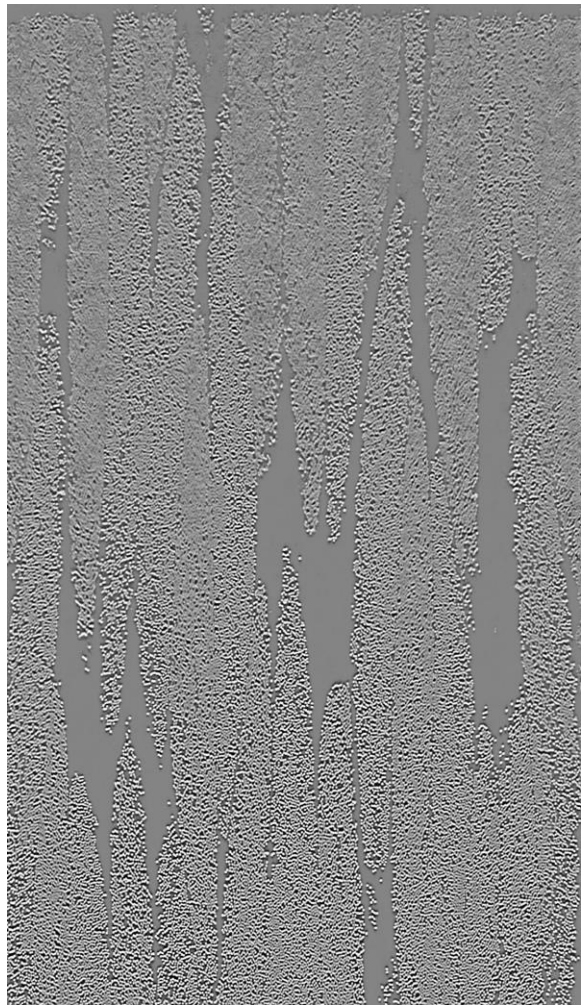

Original low-quality scan

Enhanced Scan

© Math2Market GmbH

MATH 2 MARKET

Apply Super Resolution to Glass Fibers

GeoDict

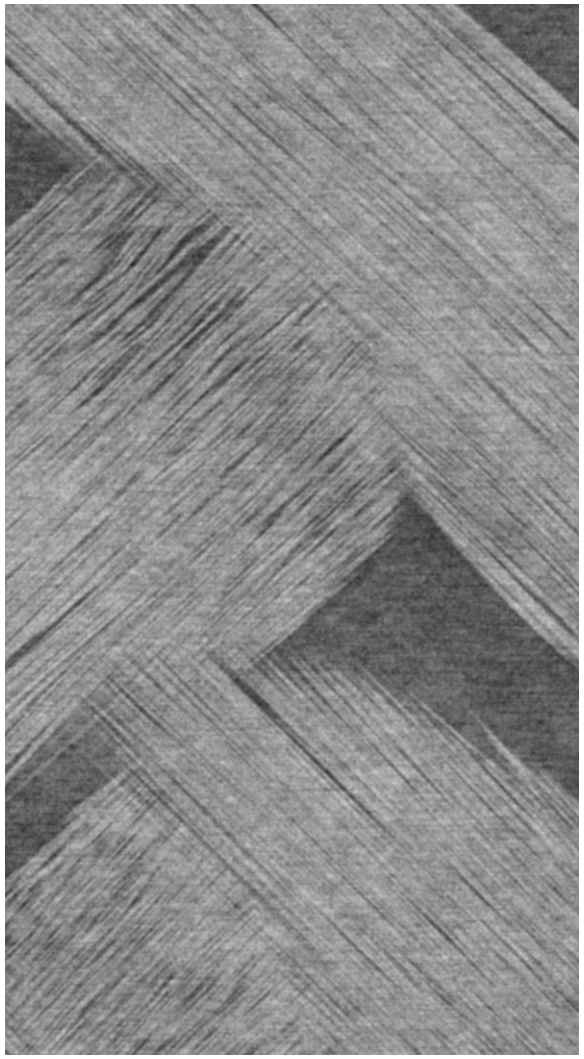

4.5µm

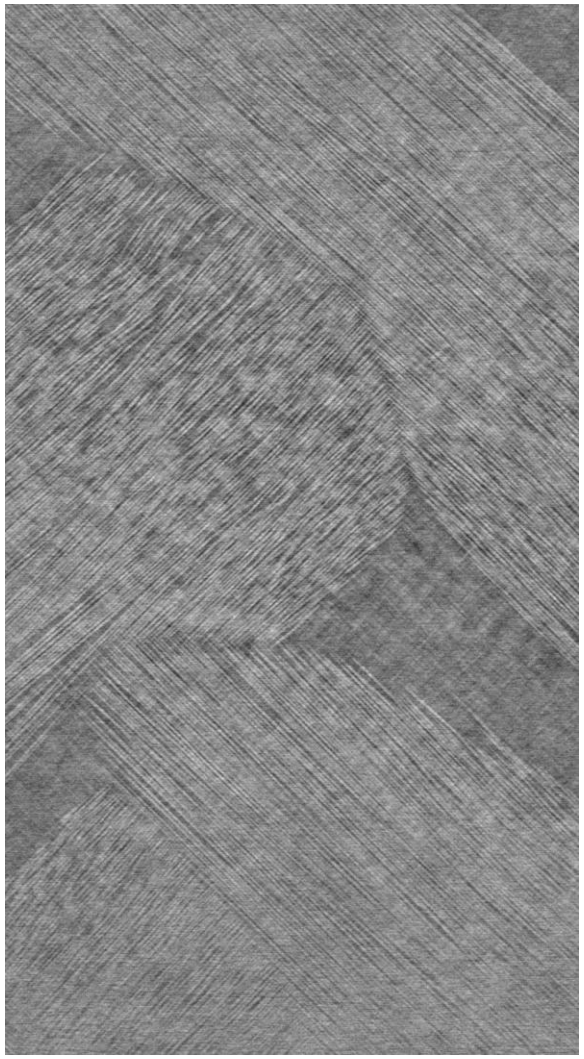

1.75µm

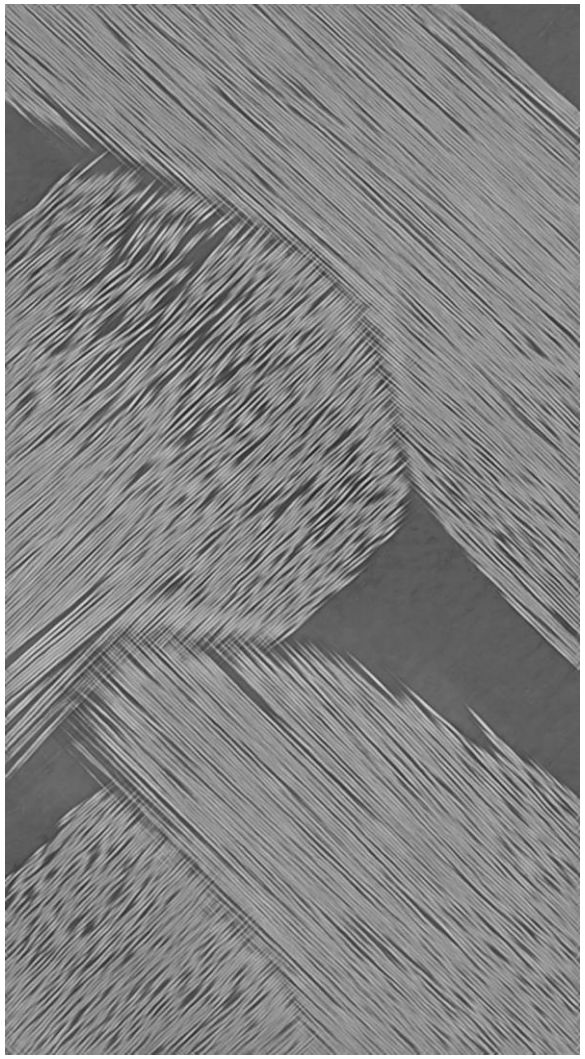

1.75µm
super resolution

© Math2Market GmbH

MATH 2 MARKET

Apply Super Resolution to Glass Fibers

GeoDict



This has been demonstrated with real scans, but in the next step, we will do the training with artificial CT scan data created with GeoDict!

4.5µm

1.75µm

1.75µm
super resolution

© Math2Market GmbH

MATH 2 MARKET

Digital Material: What is a Statistical Digital Twin

GeoDict

Statistical digital twin in GeoDict:

Parameters to generate microstructures with similar physical & geometrical properties as the real material





➢ Understand, improve and develop new materials

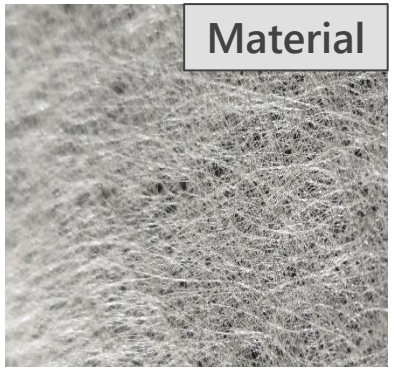

Determine properties
Create statistical digital twin

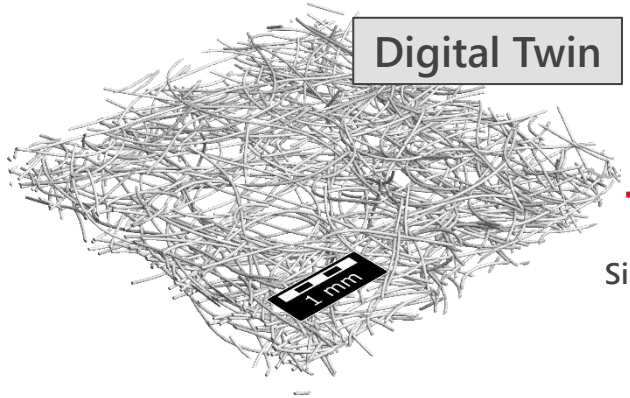

Change geometric parameters
Simulate effect on physical properties



© Math2Market GmbH

MATH 2 MARKET

Creating a Digital Twin of a Composite Material

GeoDict

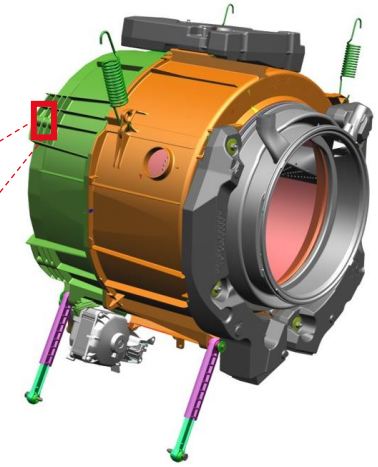

CAD model of a lye container with oscillating system and drum.
Source: BSH Hausgeräte GmbH

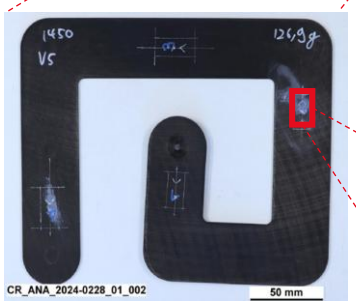



Image acquisition via µCT

Analysis in GeoDict:

- Fiber volume content
- Fiber alignment
- Void content
- Thickness of layers
- Fiber length distribution
- Void distribution

Creation of a statistical digital twin

Variation of parameters GeoDict:

- Fiber volume content
- Pore volume content

Determine the influence of fiber and volume content on the effective stiffness of this composite material

Funding
We thank the Federal Ministry of Economic Affairs and Climate Action (BMWK) for the ongoing funding under the funding code FKZ 03LB3044C

© Math2Market GmbH

MATH 2 MARKET

Creating Statistical Digital Twins of all Three Layers

GeoDict

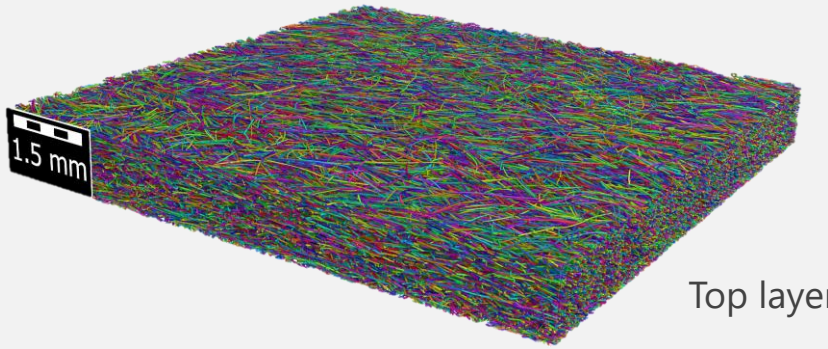

Top layer

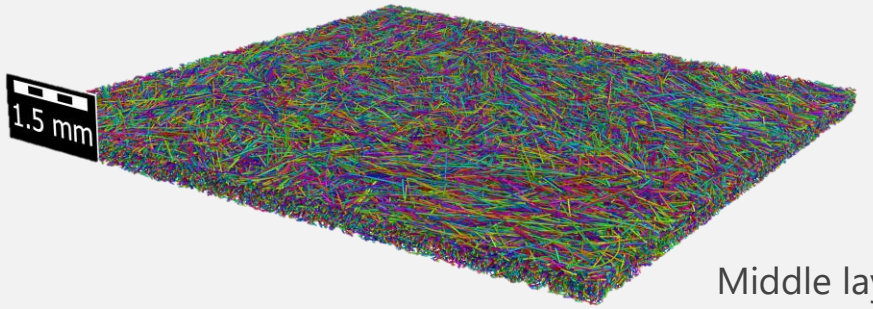

Middle layer

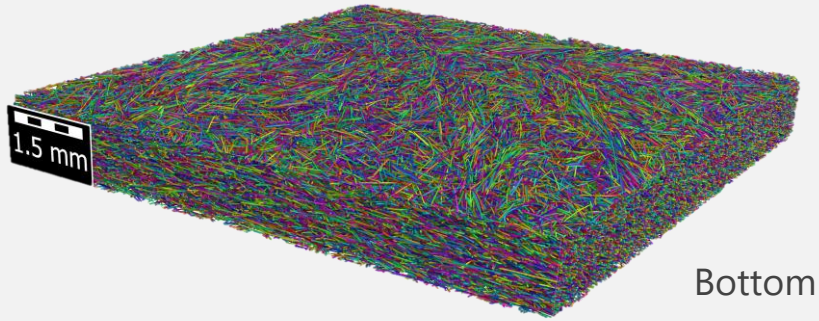

Bottom layer

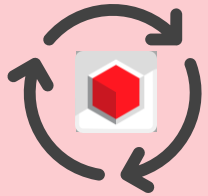

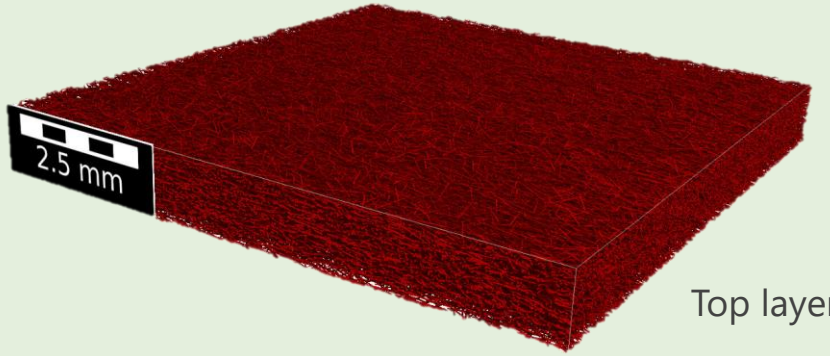

Top layer



Middle layer

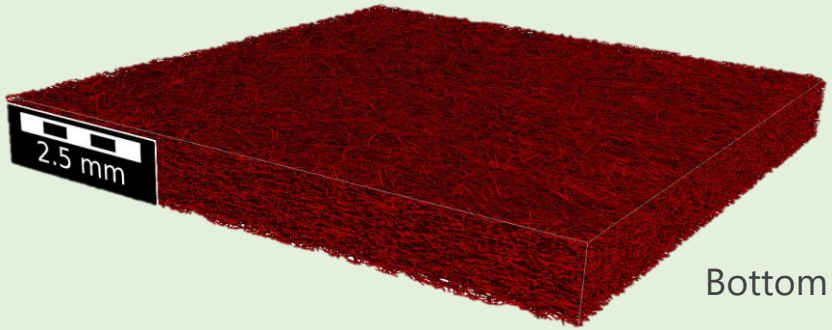

Bottom layer

© Math2Market GmbH

MATH 2 MARKET

Influence of Solid Volume Percentage on the Stiffness

GeoDict

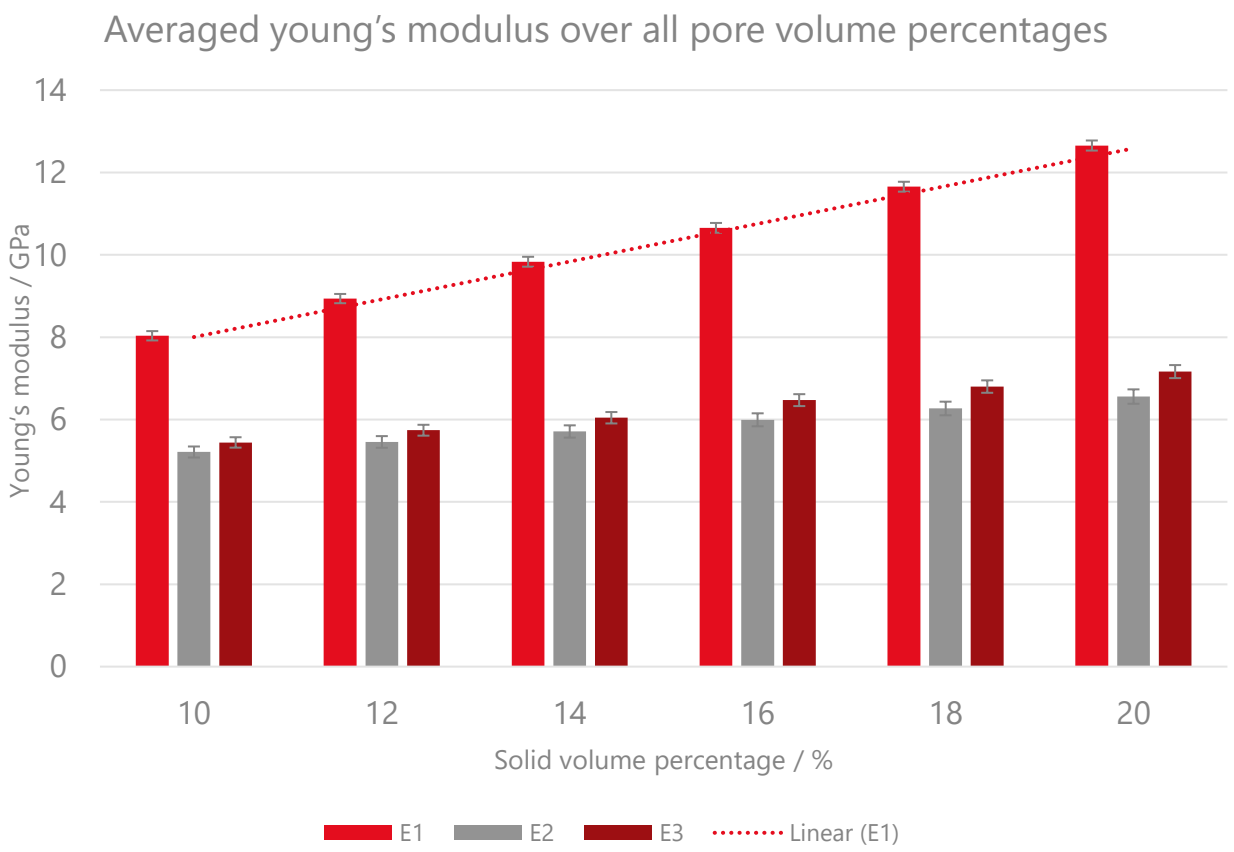

- Solid volume percentage influences E1 (stiffness along the fiber direction) heavily and the stiffness increases with higher solid volume percentages
- Lesser influence of the solid volume percentage on the stiffness in the transverse directions (E2 and E3)

© Math2Market GmbH

MATH 2 MARKET

Influence of Solid Volume Percentage on the Stiffness

GeoDict

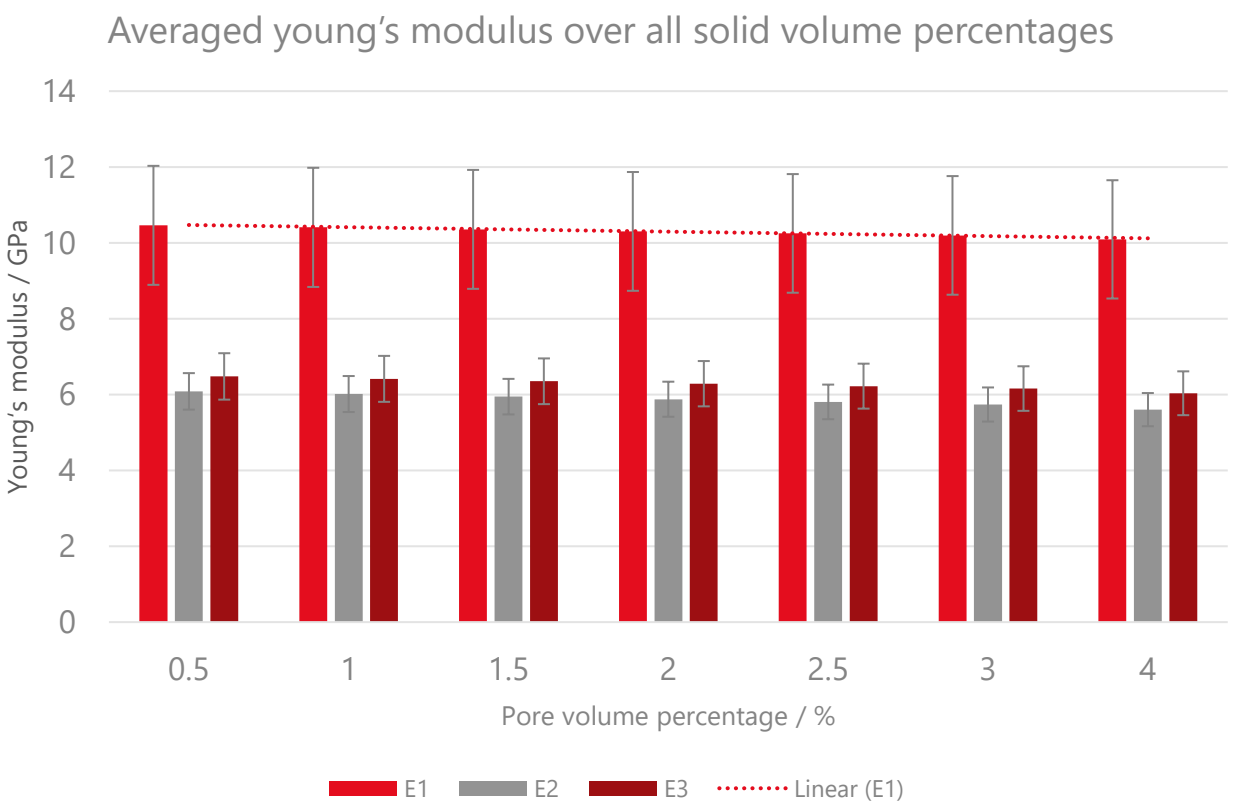

- Increasing pore volume percentage leads to an overall decrease of the stiffness
- Effect of increasing pore volume percentage is more pronounced for E2 and E3 than for E1

© Math2Market GmbH

MATH 2 MARKET

SUMMARY

GeoDict

Real world µCT data

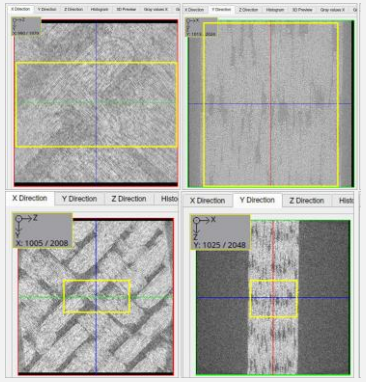

- Real world data
- Resolution limits
  Imaging artifacts
  Missing data

Statistically Generated Models

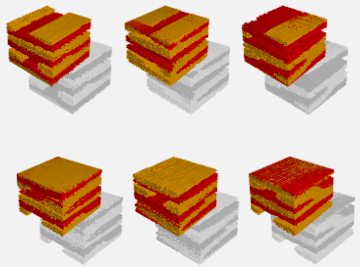

- Parameter variation
  all details known
- Less real variation

AI methods for object classification

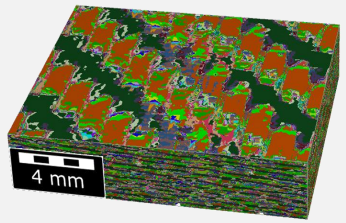

- Easy training of AI networks for new materials
- Improved detection of geometrical features with reduced manual labeling

AI methods for image enhancement

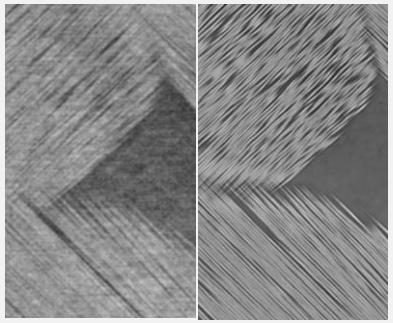

- Trained with real world data and artificial data
- Largely improved workflow efficiency

© Math2Market GmbH

MATH 2 MARKET

What is GeoDict?

GeoDict is

Data-Driven Digital Material Design
in an Easy-to-Use Software Solution

The innovative and easy-to-use material simulator GeoDict is the most complete solution for multi-scale 3D image processing, modeling of materials, visualization, material property characterization, simulation-based material development, and optimization of processes.



© Math2Market GmbH

Thank you for your attention

Visit us at our booth 507



Mike Marsh, Ph.D.



Dr. Oliver Rimmel

Dr.-Ing. Oliver Rimmel

Head of Digital Material Business

oliver.rimmel@math2market.de

+ 49 631 / 205 605 49

www.math2market.de

© Math2Market GmbH

ICCM24 24TH INTERNATIONAL CONFERENCE ON COMPOSITE MATERIALS
AUG 4-8, 2025 • BALTIMORE CONVENTION CENTER • BALTIMORE, MARYLAND

HYBRID 1D CONVOLUTIONAL NEURAL NETWORK AND FUZZY CLUSTERING FOR DAMAGE DETECTION IN COMPOSITE PLATES USING LASER ULTRASONIC GUIDED WAVES

Shain Azadi[1,2], Yoji Okabe[2] and Valter Carvelli[1]

[1]Department A.B.C., Politecnico di Milano
Piazza Leonardo da Vinci 32, 20133, Milano, Italy
Email: shain.azadi@polimi.it, valter.carvelli@polimi.it,

[2]Institute of Industrial Science, The University of Tokyo
4-6-1 Komaba Meguro-ku, 153-8505, Tokyo, Japan
Email: okabey@iis.u-tokyo.ac.jp,

Keywords: CFRP, Guided Waves, 1D-CNN, Clustering, Delamination

ABSTRACT

This paper introduces a hybrid learning framework for structural health monitoring (SHM) of composite laminates using laser ultrasonic guided waves (LUGWs) with limited labelled data. A lightweight one-dimensional convolutional neural network (1D-CNN) is trained on a small, spatially labelled subset to extract low-dimensional latent features from raw waveforms. These features are clustered using five classical algorithms (K-Means, GMM, BGMM, DBSCAN, and HDBSCAN) and a novel method, namely Probabilistic CNN–Fuzzy Clustering (PCFC). PCFC integrates CNN-derived class probabilities with fuzzy membership values from the Fuzzy C-Means algorithm, thereby enabling soft, uncertainty-aware clustering in the latent space. The quality of the clustering is evaluated through spatial cluster map reconstructions, with PCFC consistently producing coherent and physically meaningful clusters that are aligned with known delamination regions. In the latent feature space, Principal Component Analysis reveals a consistent separation between damaged and undamaged waveforms along the first principal component, thus offering an interpretable indicator of damage severity. The proposed approach has the potential to reduces annotation requirements by an order of magnitude and mitigate the limitations of fully supervised learning. It offers a scalable and interpretable solution for reliable damage detection in composite structures, particularly in scenarios where comprehensive labelling is impractical.

1 INTRODUCTION

Carbon-fibre-reinforced polymer (CFRP) laminates are widely employed in aerospace, aviation, automotive, constructions, and wind energy applications due to their high specific stiffness, strength, and resistance to corrosion [1]. However, their layered architecture renders them inherently susceptible to inter-ply delamination, an internal defect that reduces load-bearing capacity, degrades stiffness, and introduces stress concentrations [2]. Because delaminations are not externally visible, inspection relies on non-destructive evaluation (NDE) techniques.

Ultrasonic guided waves (UGWs) offer high sensitivity to subsurface damage and enable large-area inspection from a single excitation point, making them well-suited for volumetric structural health monitoring (SHM) [3]. When generated by pulsed lasers, UGWs can propagate into the structure without contact and maintain performance on curved or thermally challenging surfaces, enabling inspection in environments where conventional methods may fail [4]. However, the interpretation of UGW signals typically requires expert domain knowledge, a process that is both time-consuming and costly.

To reduce reliance on manual interpretation, deep learning has been increasingly applied to UGW data [5]. Convolutional neural networks (CNNs), trained on two-dimensional (2D) wavefield images or time–frequency representations, can achieve high classification accuracy. Nevertheless, these approaches often require substantial preliminary processing (e.g., windowing, padding, or wavelet

transforms) and comprise numerous f parameters, which hinders implementation on hardware platforms with limited resource [6].

One-dimensional CNNs (1D-CNNs) provide a more lightweight alternative, particularly suited to sequential data such as raw UGW signals. Convolving along the temporal axis enables 1D-CNNs to perform joint feature extraction and classification in a single, low-complexity pipeline. In comparison to their 2D counterparts, 1D-CNNs reduce the number of parameters by approximately an order of magnitude, thereby lowering computational overhead, reducing the risk of overfitting, and enabling real-time inference on consumer-grade hardware [7]. These characteristics render 1D-CNNs especially well-suited to onboard anomaly detection, a process characterised by the constraints of rapid inference and the scarcity of labelled data [8].

Despite their efficiency, even compact supervised models require fully labelled datasets that capture variation in sensor placement, laminate geometry, and damage morphology. These conditions are often impractical to reproduce comprehensively. The labelling of laser-ultrasonic datasets may involve destructive sectioning, micro-CT imaging, or artificial defect insertion. These processes are often labour-intensive and lack scalability, particularly in the context of rare or interacting damage modes. Consequently, the utilisation of supervised models that have been trained on limited labels renders them susceptible to overfitting and may impede their capacity to generalize to unseen conditions [9].

Unsupervised learning provides a complementary strategy by means of the identification of latent structure in unlabelled UGW data. Clustering and anomaly detection techniques, including K-Means, Density-Based Spatial Clustering of Applications with Noise (DBSCAN), Hierarchical DBSCAN (HDBSCAN), Gaussian Mixture Models (GMM), and Bayesian GMM (BGMM) [10], have been employed to extract damage-related patterns without requiring prior annotation. These approaches are especially valuable when damage signatures are poorly defined, heterogeneous, or too numerous to label manually. Nevertheless, a persistent limitation remains: the resulting clusters often lack direct physical meaning and require post hoc interpretation to map to damage mechanisms. This interpretation step is subjective and prone to error, especially when defects are subtle or interact in complex ways.

To address these challenges, this paper proposes a hybrid learning framework that combines supervised and unsupervised learning. A compact 1D-CNN (~93,000 parameters) [11] is first trained on approximately 10% of the dataset using spatially defined labels. Subsequent to the training phase, the SoftMax classification head is eliminated, and the network is repurposed as an encoder that maps each input waveform to a 128-dimensional latent embedding. This embedding enhances class separability while suppressing nuisance variability.

Clustering algorithms, including K-Means, GMM, DBSCAN, HDBSCAN, and a novel Probabilistic CNN–Fuzzy Clustering (PCFC) method, are then applied in the latent space. These algorithms result in the generation of spatially coherent clusters that exhibit a high degree of alignment with delamination regions, without requiring additional supervision. The anchoring of the latent space with a small, labelled subset, is a key aspect of the framework, as it preserves physical interpretability, enables probabilistic associations with known damage states, and leverages the diversity of unlabelled data to improve generalization.

The objective of this work is to demonstrate that incorporating a limited amount of labelled data can significantly enhance the physical interpretability of clustering outcomes, and that the proposed PCFC method outperforms five state-of-the-art clustering algorithms when evaluated under a consistent neural architecture. The resulting workflow reduces annotation requirements by an order of magnitude, remains computationally efficient for embedded implementation, and addresses the supervision bottleneck that has hindered the adoption of deep learning in operational SHM systems.

The remainder of this paper is organized as follows. Section 2 details specimen fabrication, laser–ultrasonic data acquisition, and the hybrid learning pipeline. Section 3 presents clustering results, spatial reconstructions, and an encoder ablation study. Section 4 concludes with key findings and directions for future work.

2 HYBRID LEARNING METHODOLOGY

2.1. Specimen Preparation and Laser Ultrasonic Data Acquisition

Eight-ply cross-ply CFRP laminates with a $[90_2/0_2]$s stacking sequence were fabricated using Toray T700SC/2500 prepreg [12]. Each plate measured 200 × 200 mm² with a nominal thickness of 1.12 mm (0.14 mm per ply). Nine plates contained centrally embedded square Teflon inserts to simulate delaminations of 5 × 5, 10 × 10, or 20 × 20 mm², located at three interlaminar depths (0.28, 0.56, and 0.84 mm), while one plate served as an undamaged control. Laminates were cured in a vacuum hot-press at 0.08 MPa and consolidated at a pressure of 8.6 MPa and a temperature of 130 °C for 2 hours, ensuring consistent fibre wet-out and minimal void content. The central insert placement suppressed edge effects and enabled a controlled matrix of size–depth combinations for waveform-to-damage analysis.

Laser-induced UGWs (LUGWs) were generated using a non-contact Laser Ultrasonic Visualization Inspector (LUVI-CP1, Tsukuba Technology), employing a 1064 nm, 10 ns Nd:YAG laser pulse focused to a 0.25 mm radius spot. The absorbed energy (~0.1 μJ) corresponded to a fluence of 0.27 J/cm², well below the CFRP's ablation threshold, ensuring purely thermoelastic excitation [13]. A 20 × 20 mm² region centred on each delamination was raster-scanned on a 195 × 195 grid with 0.103 mm pitch, yielding 38,025 excitation points (100 points/mm²) per scan. The laser incidence angle was maintained below 2°, which is well within the ~30° tolerance for amplitude stability [14].

Out-of-plane displacements were measured using a broadband piezoelectric sensor (AE-900S-WB, frequency range 0.3–1.5 MHz, sensitivity 50 dB ± 6 dB at 500 kHz). This sensor was mounted outside the laser scan region to prevent direct optical excitation. To characterize anisotropic wave propagation, the sensor was sequentially oriented along three directions relative to the 0° surface ply: PA (0°), PB (45°), and PC (90°). Each grid point was probed using four consecutive laser pulses, and the resulting signals were averaged to improve the signal-to-noise ratio while preserving bandwidth. Waveforms were sampled at 10 MS/s over a 100 μs acquisition window, resulting in 1000 discrete amplitude measurements per waveform. This window was truncated ~20 μs before the expected A_0-mode edge reflection, estimated using a 1.5 mm/μs group velocity and 90 mm edge distance, to isolate the primary A_0 and S_0 wave packets from boundary reflections.

The dataset under consideration is comprised of 1,140,750 raw waveforms, distributed across ten plates, three sensor orientations, and 38,025 scan points per measurement. All signals were standardized using global Z-score normalization [15], defined as $x' = (x - \mu)/\sigma$, where μ and σ are the global mean and standard deviation across the dataset, respectively. This step equalized amplitude scales across signals, accelerated model convergence, and preserved waveform phase information.

2.2. CNN-Guided Hybrid Learning Framework

A hybrid learning framework has been developed that integrates a pre-trained lightweight 1D-CNN (~93,000 parameters) with unsupervised clustering to identify latent delamination patterns in UGW data.

As illustrated in , the framework leverages physics-informed features learned from a limited labelled dataset to guide the discovery of physically meaningful structures within the high-dimensional feature space. Figure 1a illustrates the spatial region-based labelling strategy used to partition the 1D waveforms into a binary classification scheme, where signals originating from within the delaminated region are labelled as "damaged," while those from outside this region are labelled as "undamaged". Figure 1b shows a 1D-CNN pre-trained using a limited labelled dataset (~10%).

The SoftMax classification layer is removed from the 1D-CNN (Figure 1c), and the high-dimensional feature representations are extracted directly from the final dense layer. These features are then visualized in latent space, as shown in Figure 1d.

As illustrated in Figure 1e, several unsupervised clustering algorithms, including the proposed PCFC, are employed within the latent feature space to discern the underlying structure in the data. Finally, the clustering results are visualized both in the latent space and remapped onto the 2D wavefield (see Figure 1f), thereby providing a spatially interpretable representation of the detected patterns.

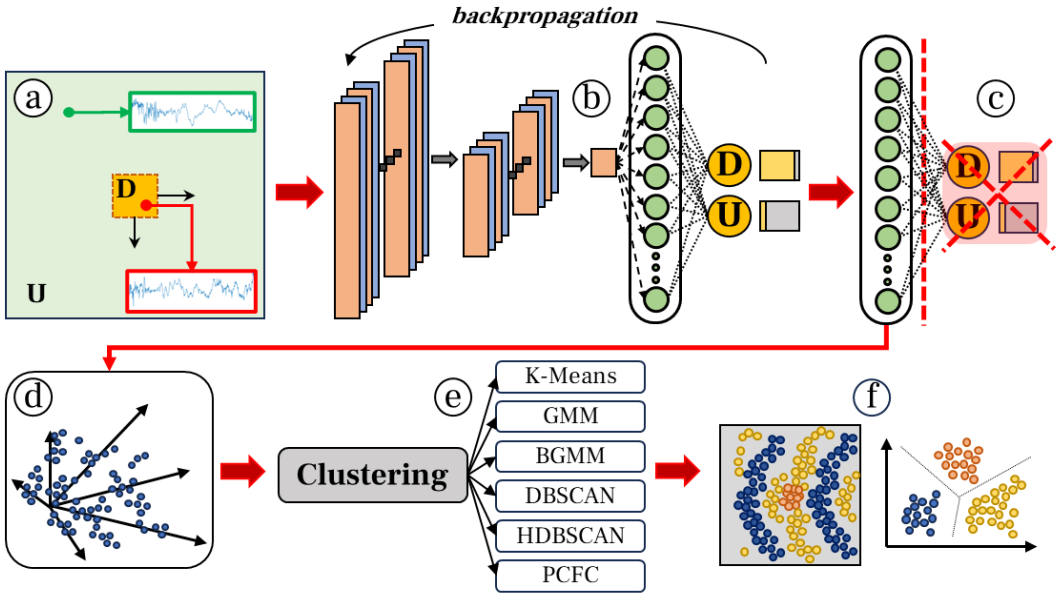

Figure 1: Overview of the hybrid learning framework. (a) region-based labelling separating undamaged and damaged waveforms; (b) 1D-CNN pre-trained on labelled data; (c) extracted high-level features; (d) visualization in latent space; (e) clustering using various algorithms; (f) analysis of clustering results.

2.3. Data Partitioning, Labelling, and Signal Preprocessing

A spatial region-based labelling strategy was adopted to pre-train the 1D-CNN using supervised learning. One damaged plate, representing approximately 10% of the total dataset, was selected as the reference for training. This plate contained a 5 × 5 mm² artificial delamination embedded at the laminate midplane.

The corresponding wavefield, acquired using the LUVI-CP1 system, was represented as a three-dimensional matrix indexed by (x, y, t). Let $\boldsymbol{r} = (x, y)$ denote a spatial location on the plate surface and let $w(\boldsymbol{r}, t)$ be the wave amplitude at position $\boldsymbol{r}$ and time step t. At each scan point, the root mean square (RMS) amplitude, defined in Equation (1), was computed to highlight regions of elevated acoustic energy. To enhance contrast and delineate potential damage boundaries, the spatial gradient of the RMS amplitude map was then calculated, as shown in Equation (2). The resulting maps are illustrated in Figure 2a.

$$RMS(\boldsymbol{r}) = \sqrt{\frac{1}{T}\sum_{t=1}^{T} w(\boldsymbol{r}, t)^2} \tag{1}$$

$$\nabla RMS(\boldsymbol{r}) = \left(\frac{\partial RMS}{\partial r_1}, \frac{\partial RMS}{\partial r_2}\right) \tag{2}$$

Based on this processed representation, spatial masks were applied to assign coarse binary labels. Waveforms originating within the delaminated region were labelled “D” (delamination), and those outside were labelled “N” (non-delamination), as illustrated in Figure 2b. Following this region-based labelling, approximately 7,200 waveforms were identified as originating from delaminated regions, representing 6.25% of the labelled dataset. This class imbalance reflects the small physical extent of the delamination relative to the full scan area. To preserve the natural distribution of the data and prevent overfitting to plate-specific characteristics, no data augmentation was applied.

In total, this labelling procedure yielded 114,075 waveforms for supervised training. The remaining 1,026,675 waveforms, acquired from the other nine plates, formed the unlabelled pool used for unsupervised learning. All signals were standardized using global Z-score normalization and stored

alongside with categorical metadata indicating their source plate and spatial coordinates within the scan grid.

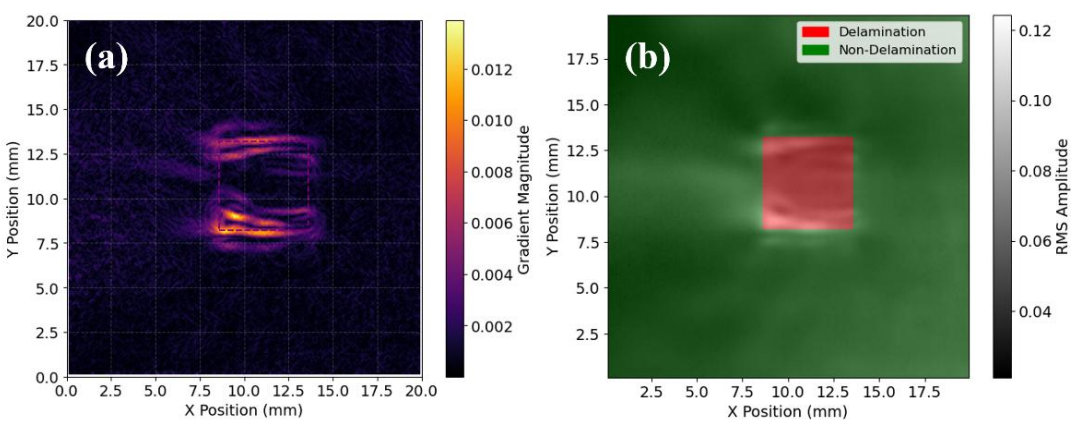

Figure 2: Two dimensional wavefield analyzed through RMS gradient (a) and with subsequent spatial-labelling mask applied (b).

2.4. Supervised Training of Lightweight 1D-CNN

A previously optimized shallow 1D-CNN architecture [11] was employed to perform supervised classification on the reduced, labelled dataset comprising 10% of the original data. The network begins with a single convolutional layer comprising 64 filters, each with a kernel size of 256. This is followed by batch normalization, a Parametric ReLU (PReLU) activation function, max pooling with a pooling size of 4, and a dropout layer with a rate of 20%. A global average pooling layer reduces the output to a 1 × 64 feature vector.

This vector is passed to a fully connected layer with 128 units. This is followed by a second dropout layer and a final dense layer with 2 output units, ending in a Softmax activation for classification. Weights were initialized using the Glorot normal scheme, and regularization techniques, including L1/L2 penalties and early stopping, were applied to improve generalization. The model was trained using the Adam optimizer with by a reduce-on-plateau scheduler handling learning rate adjustments.

The complete architecture contains approximately 93,000 trainable parameters, an order of magnitude fewer than typical 2D-CNN models, making it well suited to lightweight, real-time deployment. Training results, shown in Figure 3, demonstrate near-perfect classification accuracy with no observable signs of overfitting.

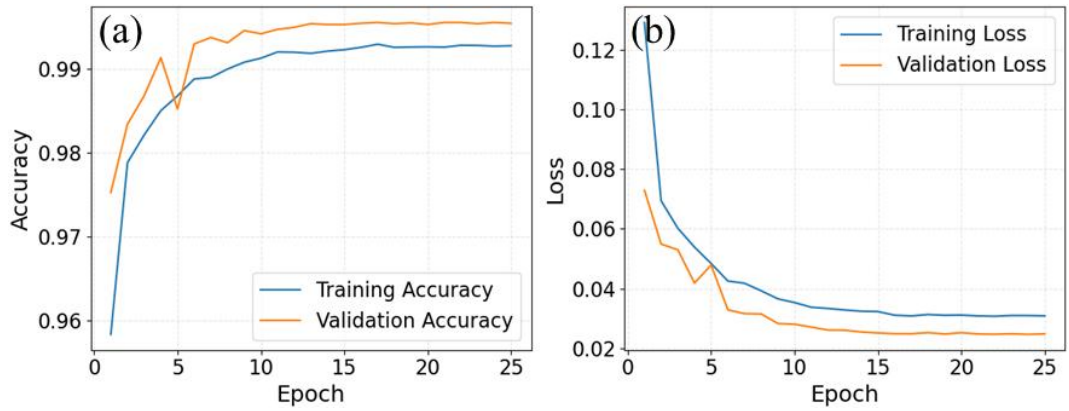

Figure 3: Supervised training results: (a) Training and Validation Accuracy, (b) Training and Validation Loss

2.5. Latent Feature Embedding and Cluster Number Estimation

To determine the optimal number of clusters k, a required parameter for many clustering algorithms, feature vectors were extracted from the penultimate dense layer of the pre-trained 1D-CNN when it was applied to the unseen dataset. This process yielded a 128-dimensional latent representation, thereby defining an encoder function $\varepsilon: \mathbb{R}^{1000} \rightarrow \mathbb{R}^{128}$. This function maps each input waveform $\boldsymbol{x}$ to a latent vector $\boldsymbol{z} = \varepsilon(\boldsymbol{x}) \in \mathbb{R}^{128}$. In this latent space, intraclass variability is attenuated, while features relevant to delamination are accentuated, thereby facilitating more effective clustering.

In the context of unsupervised learning, the evaluation of clustering quality is of critical importance in ensuring that the discovered structures represent meaningful patterns rather than artifacts arising from noise or random variation. In contrast to the supervised learning, in which the performance of the model is evaluated against a known ground truth, the unsupervised clustering relies on internal validation metrics to assess the compactness, separation, and cohesion of the clusters. These metrics enable the evaluation of clustering effectiveness in the absence of labelled data, thereby providing a framework for guiding model selection and parameter tuning.

In scenarios where no prior knowledge of the underlying class structure is available, internal validation indices assume particular importance. These indices assess cluster quality based solely on the intrinsic geometric and statistical characteristics of the data. Nevertheless, they are not without limitations. A significant number of internal metrics implicitly assume isotropic, spherical cluster shapes and are based on Euclidean distance and centroid-based formulations. Consequently, the efficacy of such methods may be diminished when applied to data characterised by elongated, overlapping, or non-convex clusters, potentially resulting in erroneous assessments of clustering performance.

To address the limitations inherent in individual internal validation indices, it is common practice to employ multiple such metrics in parallel. This enables a more robust and comprehensive evaluation of clustering quality. Each index captures a distinct facet of the cluster structure, such as compactness, separation, or cohesion, thus offering complementary perspectives on the organization of the data. The following internal validation metrics were utilized in this study: Dunn Index, Calinski–Harabasz Index, Silhouette Score, Davies–Bouldin Index, and Xie–Beni Index. The optimal number of clusters was determined by applying a majority voting scheme, with consensus across the indices indicating that $k = 2$ provided the most appropriate partitioning. A summary of the computed metric values and comparative results is presented in Table 1.

Internal Validation Metric	Optimal k	Score
Dunn Index	2	0.65
Calinski-Harabasz index	4	165000
Silhouette Score	2	0.51
Davies-Bouldin index	4	0.71
Xie-Beni Index	2	0.18

Table 1: Optimal number of clusters calculated using different internal metrics.

2.6. Unsupervised Clustering Algorithms and Proposed PCFC Method

Five classical clustering algorithms were benchmarked on the extracted latent feature space:

i. K-Means is a widely used partitioning algorithm that assigns data points to k clusters by minimizing within-cluster variance. It assumes spherical clusters of equal size and density.
ii. GMM is an extension of K-Means that models the data as a mixture of Gaussian distributions. GMMs perform soft clustering by estimating the probability that each data point belongs to each cluster.
iii. BGMM is a probabilistic generalization of GMMs that incorporates Bayesian inference. BGMMs treat the number of clusters and model parameters as random variables with prior distributions, allowing for automatic regularization and principled model selection.

iv. DBSCAN is a non-parametric algorithm that identifies clusters as dense regions in the data space, separated by lower-density areas. It is effective to identify arbitrarily shaped clusters and identifying noise points, without the necessity of inputting the number of clusters.
v. HDBSCAN is an extension of DBSCAN that builds a cluster hierarchy based on variable density thresholds. It removes the need to specify a global neighbourhood radius, making it more robust to datasets with varying local density.

In addition to these classical methods, a novel clustering approach, Probabilistic CNN-Fuzzy Clustering (PCFC), is proposed. PCFC integrates the discriminative feature extraction capabilities of a pre-trained 1D-CNN with the uncertainty modelling properties of the Fuzzy C-Means (FCM) algorithm. The 1D-CNN is employed to extract semantically meaningful representations from input signals, which are then passed through a SoftMax activation layer to generate probabilistic class assignments that reflect the underlying class structure learned during supervised training. Concurrently, FCM provides an unsupervised soft clustering mechanism, assigning each data point fractional membership across multiple clusters to capture uncertainty and gradual transitions between classes. The integration of the structured latent space generated by the CNN with the soft-partitioning behaviour of FCM facilitates effective clustering of PCFC in scenarios characterized by overlapping class boundaries and ambiguous data distributions.

Given an input sample x_i, the CNN generates class probability estimates via a SoftMax activation function, denoted as $p_{ij} = f_{CNN}^{Softmax}(x_i)$, where p_{ij} represents the predicted probability of sample i belonging to class j. To integrate these supervised predictions with fuzzy clustering, the PCFC framework introduces a hybrid membership function that combines the SoftMax output with fuzzy membership degrees computed in the CNN derived feature space. The hybrid membership degree $\hat{u}_{ij}$ of sample i in cluster j is defined as:

$$\hat{u}_{ij} = \alpha \cdot u_{ij}(z_i) + (1 - \alpha) \cdot p_{ij}, \quad with\ 0 \leq \alpha \leq 1 \tag{3}$$

In Equation (3), $u_{ij}(z_i)$ denotes the fuzzy membership degree assigned by the FCM algorithm based on the CNN-extracted feature vector z_i, and p_{ij} is the previously defined SoftMax probability. The parameter α controls the trade-off between the unsupervised fuzzy clustering and the supervised probabilistic classification, thereby facilitating the integration of data-driven uncertainty with learned discriminative structure. This formulation enables PCFC to capitalize on both the representational power of CNNs and the uncertainty-aware nature of fuzzy clustering, thus resulting in a more robust and adaptable clustering framework.

To improve the physical interpretability and visual reliability of the PCFC results when projected onto the two-dimensional wavefield domain, the continuous hybrid membership values $\hat{u}_{ij} \in [0,1]$, interpreted here as degrees of delamination, are discretized into four semantically meaningful categories:

- Non-Delamination (N): $0 \leq \hat{u}_{ij} < 0.25$. Represents signals that closely match baseline (healthy) responses.
- Quasi-Non-Delamination (Q-N): $0.25 \leq \hat{u}_{ij} < 0.50$. Indicates largely intact regions exhibiting minor variations due to benign phenomena.
- Quasi-Delamination (Q-D): $0.50 \leq \hat{u}_{ij} < 0.75$. Captures partial or ambiguous indications of damage, which are frequently linked to scattering or boundary effects.
- Delamination (D): $0.75 \leq \hat{u}_{ij} \leq 1.00$. This is indicative of significant deviations from the baseline, which is consistent with the presence of structural damage.

This categorisation of continuous fuzzy outputs translates nuanced membership values into diagnostically meaningful labels, enhancing both the interpretability and practical utility of PCFC in SHM applications.

3 RESULTS AND DISCUSSION

3.1. Spatial Analysis of Clustering Results

After clustering, the waveforms are mapped back onto the spatial grid to generate spatially resolved cluster maps, thereby enhancing visual interpretability of the results. In instances where clustering methods require a predefined number of clusters, the optimal value $k = 2$, as determined in Section 2.5., was employed.

Figure 4 presents a comparative evaluation of clustering performance on the training plate, with wave propagation along the PA direction. As illustrated in Figure 4a, K-Means provides a coarse distinction between delaminated and intact regions but lacks spatial precision. Figure 4b shows that GMM improves localization of damaged areas, however, the delineation of boundary regions remains ambiguous. BGMM offers enhanced isolation of the delaminated region and its boundaries However, it introduces excessive clusters that do not correspond to physically meaningful structures (see Figure 4c). Figure 4d reveals that DBSCAN is unable to differentiate between damaged and undamaged regions, with the majority of data points being assigned to a dominant cluster. Figure 4e demonstrates that HDBSCAN partially mitigates this limitation by identifying three principal regions, undamaged, delaminated, and transitional. However, it should be noted that the resulting clusters lack clear physical interpretability in the absence of the full 2D wavefield context.

In contrast, Figure 4f demonstrates that PCFC yields a coherent and physically meaningful clustering outcome. Hybrid membership values in the range $0.75 \leq \hat{u}_{ij} < 1.00$ reliably indicate delamination, while values in the range $0.50 \leq \hat{u}_{ij} < 0.75$ capture transitional zones influenced by wave scattering and boundary effects. The lower ranges correspond to intact regions and propagation artefacts. The integration of CNN-derived features with fuzzy logic by PCFC has been demonstrated to achieve two objectives: Firstly, it facilitates accurate damage identification. Secondly, it establishes interpretable spatial representation. This combination of features establishes the PCFC framework as a robust solution for SHM.

The results of the clustering process for an unseen, undamaged laminate are shown in Figure 5, with wave propagation along the PC direction. These examples are intended to appraise the efficacy of each algorithm in generalising and accurately identifying the absence of damage in conditions that have not been previously observed. K-Means (Figure 5a) identifies two clusters that correspond visually to the wavefront and the remaining plate area. GMM (Figure 5b) produces a similar segmentation with only minor discrepancies in point allocation. BGMM (Figure 5c) exhibits similar tendencies to earlier observations, over-segmenting the data into multiple physically implausible clusters. DBSCAN and HDBSCAN (see Figure 5d-e) both identify a dominant single cluster, accurately reflecting the uniform, undamaged condition of the plate. This outcome supports their reliability in damage-free scenarios.

As illustrated in Figure 5f, PCFC yields a result resembling K-Means. However, a salient feature of PCFC is that it assigns all waveforms membership values in the range $0 \leq \hat{u}_{ij} < 0.50$, indicating absence of delamination. The plate's status as undamaged is confirmed by the hybrid metric, which enables effective differentiation between benign wavefront structures and damage-related features.

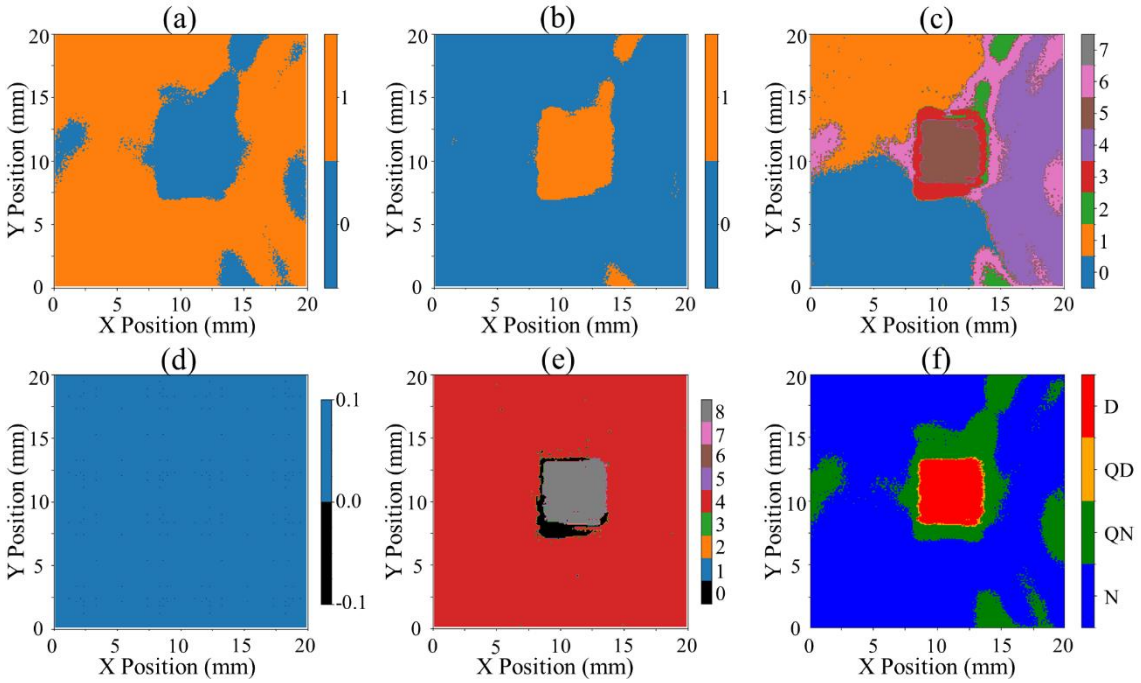

Figure 4: Clustering map analysis of the training plate with wave propagation PA, using: (a) K-Means, (b) GMM, (c) BGMM, (d) DBSCAN, (e) HDBSCAN, and (f) PCFC.

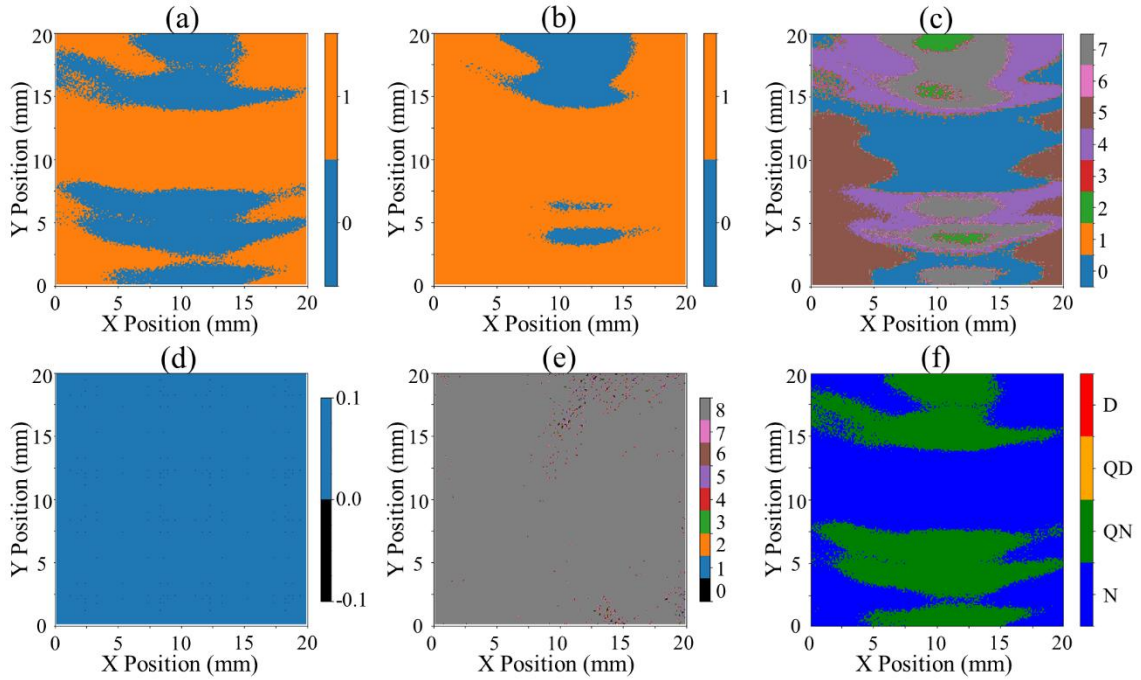

Figure 5 Clustering map analysis of an undamaged plate with wave propagation PC, using: (a) K-Means, (b) GMM, (c) BGMM, (d) DBSCAN, (e) HDBSCAN, and (f) PCFC.

3.2. Latent Feature Space Analysis via Principal Component Analysis

In addition to analysing clusters in remapped 2D wavefields, the latent feature space extracted by the 1D-CNN can be examined directly, independent of spatial context. The optimized network comprises a fully connected layer with 128 neurons, resulting in a high-dimensional representation that is not readily interpretable. In order to address this issue, Principal Component Analysis (PCA) [16] is employed to

project the feature space onto a two-dimensional plane whilst preserving the most significant variance in the data.

As illustrated in Figure 6, PCA projections of the latent space for the test plate measured along the propagation direction PA are presented. This visualization facilitates a comparative assessment of clustering behaviour across algorithms. It is evident that both K-Means and GMM yield analogous cluster distributions, with K-Means separating clusters near zero and GMM shifting the boundary closer to –1 along the first principal component. The results of the BGMM are sparse, unstructured clusters that lack geometric coherence. DBSCAN and HDBSCAN fail to generate meaningful partitions, often resulting in the data being collapsed into a single dominant cluster or the production of irregular groupings.

In contrast, PCFC consistently yields well-separated and physically interpretable clusters. Waveforms with low hybrid membership values $(0 \leq \hat{u}_{ij} < 0.25)$ are located on the positive side of the first principal component, whereas those with high membership values $(0.75 \leq \hat{u}_{ij} \leq 1.00)$ are concentrated around –2.5 to –3. This consistent pattern across datasets suggests a robust correspondence between the first principal component and damage severity. Specifically, waveforms from undamaged regions have a tendency to cluster in the positive domain, while those from delaminated regions map to the negative extreme, thereby providing a distinctive signature of structural integrity in composite laminates.

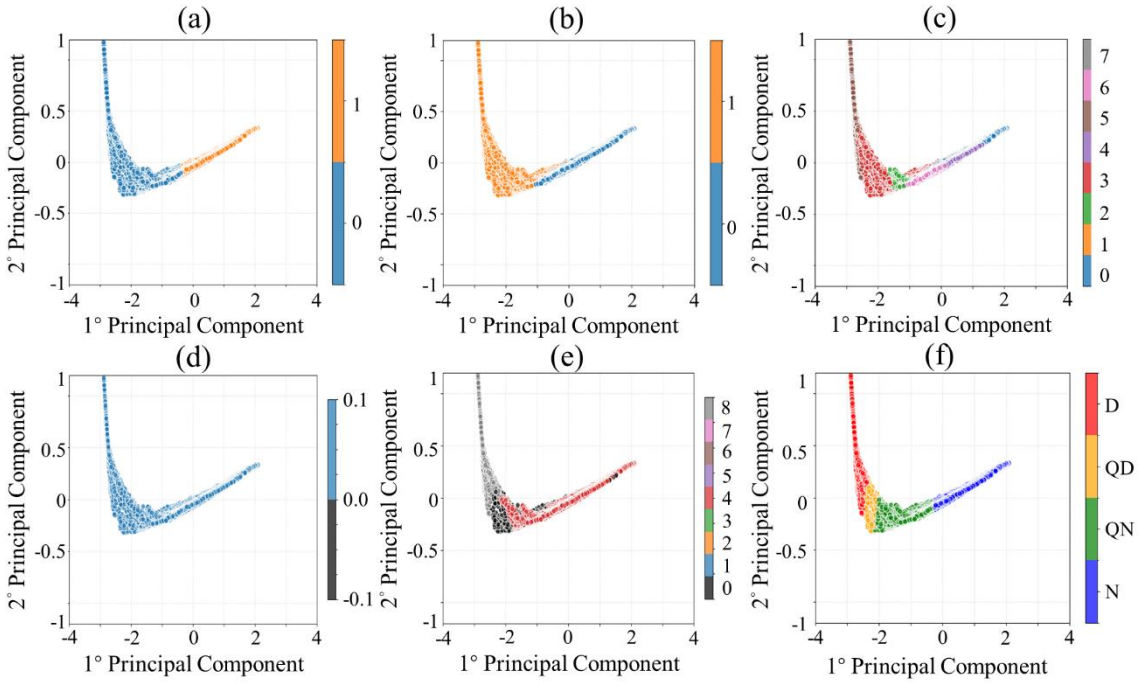

Figure 6: Feature space clustering analysis of the training plate with wave propagation PA, using: (a) K-Means, (b) GMM, (c) BGMM, (d) DBSCAN, (e) HDBSCAN, and (f) PCFC.

3.3. Effect of CNN Pre-training on Clustering Performance

To demonstrate the benefits of pre-training the 1D-CNN feature extractor, particularly in scenarios with limited labelled data, the clustering results of 2D remapped wavefields using K-Means are presented here. Figure 7 compares outputs for two laminates containing a 10 × 10 mm² delamination at different depths (0.84 mm and 0.56 mm) with wave propagation direction PA. Figure 7a–b show cluster maps from an untrained model, while Figure 7c–d illustrate the enhanced performance achieved with the pre-trained feature extractor.

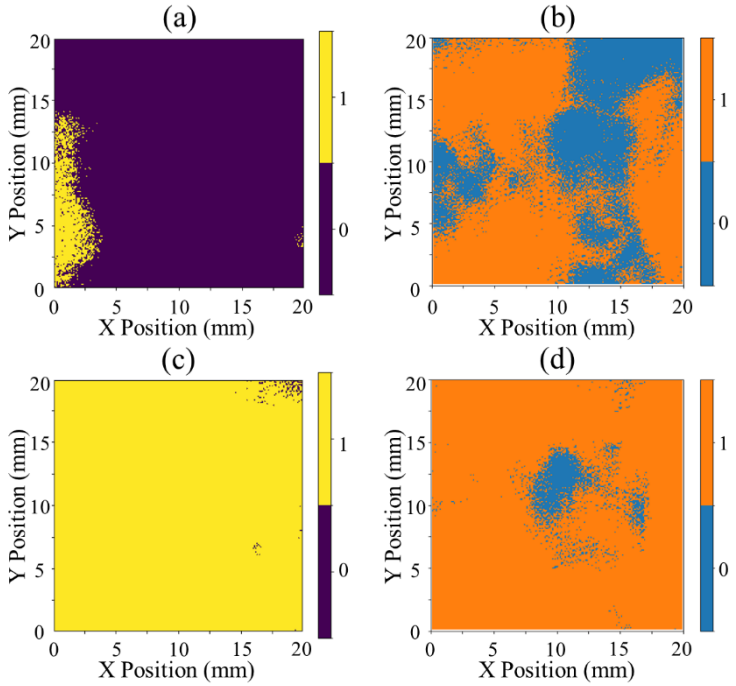

Figure 7: K-Means clustering comparison between an untrained (a, c) and pre-trained (b, d) 1D-CNN model with the same architecture, applied to plate two plates with 10 × 10 mm² delaminations located at 0.56 mm depth (a, b) and 0.84 mm depth (c, d), respectively.

4 CONCLUSIONS

This paper introduced a hybrid supervised–unsupervised learning framework designed to enable physically meaningful cluster analysis on unseen data, using only limited labelled input. Whilst the clustering itself lacks explicit physical interpretability, this limitation was addressed by incorporating a pre-trained 1D-CNN as an optimized feature extractor.

The 1D-CNN was trained on waveforms acquired from a single CFRP plate using the LUVI system. The reciprocity theorem was utilised to map these 1D measurements into 2D wavefields and to label them as “delamination” or “non-delamination” for supervised training. Following the completion of the training process, the CNN was able to extract low-dimensional feature representations from new, unlabelled datasets. This enabled clustering in a compact, discriminative space.

A comparative analysis of clustering algorithms(K-Means, GMM, BGMM, DBSCAN, HDBSCAN, and the proposed PCFC) was conducted on this embedded feature space. The proposed PCFC, which combines CNN-derived probabilities with fuzzy membership values from FCM, demonstrated consistent superiority in terms of accuracy and physical interpretability when compared to alternative methods. The visual representation of the damage was clear, and there was a strong alignment with the actual structural conditions. In contrast, DBSCAN failed to identify damaged regions, while BGMM, despite demonstrating effective segmentation performance, suffered from excessive granularity and high computational cost.

An important observation emerged from the feature space distribution: clusters associated with delamination consistently mapped to the negative axis of the first principal component (PC1), starting near −2.5, while undamaged regions aligned with the positive PC1 axis. This trend suggests a potentially generalizable indicator of delamination in unseen waveforms.

In summary, the proposed approach provides a robust, data-efficient solution for the detection of delamination, especially valuable when fully supervised datasets are not available.

REFERENCES

[1] D.D.L. Chung, Introduction to Carbon Composites, in: Carbon Composites, Elsevier, 2017: pp. 88–160. https://doi.org/10.1016/B978-0-12-804459-9.00002-6.

[2] I.S. Raju, T.K. O'Brien, Fracture mechanics concepts, stress fields, strain energy release rates, delamination initiation and growth criteria, in: Delamination Behaviour of Composites, Elsevier, 2008: pp. 3–27. https://doi.org/10.1533/9781845694821.1.3.

[3] W. Ostachowicz, P. Kudela, M. Krawczuk, A. Zak, Guided Waves in Structures for SHM, Wiley, 2012. https://doi.org/10.1002/9781119965855.

[4] A. Zarei, S. Pilla, Laser ultrasonics for nondestructive testing of composite materials and structures: A review, Ultrasonics 136 (2024) 107163. https://doi.org/10.1016/j.ultras.2023.107163.

[5] J. Jia, Y. Li, Deep Learning for Structural Health Monitoring: Data, Algorithms, Applications, Challenges, and Trends, Sensors 23 (2023) 8824. https://doi.org/10.3390/s23218824.

[6] M. Rautela, S. Gopalakrishnan, Ultrasonic guided wave based structural damage detection and localization using model assisted convolutional and recurrent neural networks, Expert Syst Appl 167 (2021). https://doi.org/10.1016/j.eswa.2020.114189.

[7] S. Kiranyaz, O. Avci, O. Abdeljaber, T. Ince, M. Gabbouj, D.J. Inman, 1D convolutional neural networks and applications: A survey, Mech Syst Signal Process 151 (2021) 107398. https://doi.org/10.1016/j.ymssp.2020.107398.

[8] O. Avci, O. Abdeljaber, S. Kiranyaz, M. Hussein, D.J. Inman, Wireless and real-time structural damage detection: A novel decentralized method for wireless sensor networks, J Sound Vib 424 (2018) 158–172. https://doi.org/10.1016/j.jsv.2018.03.008.

[9] Y. LeCun, Y. Bengio, G.E. Hinton, Deep learning, Nature 521 (2015) 436–444. https://doi.org/10.1038/nature14539.

[10] R. Xu, D. WunschII, Survey of Clustering Algorithms, IEEE Trans Neural Netw 16 (2005) 645–678. https://doi.org/10.1109/TNN.2005.845141.

[11] S. Azadi, Y. Okabe, V. Carvelli, Bayesian-optimized 1D-CNN for delamination classification in CFRP laminates using raw ultrasonic guided waves, Compos Sci Technol 264 (2025) 111101. https://doi.org/10.1016/j.compscitech.2025.111101.

[12] Inc. Toray Industries, Toray T700SC/2500 Technical Data Sheet, (2021). https://www.cf-composites.toray/resources/data_sheets/pdf/datasheets_2500.pdf (accessed October 30, 2023).

[13] J.-C. Cheng, Y.H. Berthelot, Theory of laser-generated transient Lamb waves in orthotropic plates, J Phys D Appl Phys 29 (1996) 1857–1867. https://doi.org/10.1088/0022-3727/29/7/020.

[14] Z. Zhang, O. Saito, Y. Okabe, Analysis on ultrasonic waves generated in anisotropic carbon fiber reinforced plastic laminate by laser incidence from various directions, Results Phys 31 (2021) 104927. https://doi.org/10.1016/j.rinp.2021.104927.

[15] S. Elfwing, E. Uchibe, K. Doya, Sigmoid-weighted linear units for neural network function approximation in reinforcement learning, Neural Networks 107 (2018) 3–11. https://doi.org/10.1016/j.neunet.2017.12.012.

[16] P. Baldi, K. Hornik, Neural networks and principal component analysis: Learning from examples without local minima, Neural Networks 2 (1989) 53–58. https://doi.org/10.1016/0893-6080(89)90014-2.

A Bayesian Inference Approach for Estimating Heat Transfer Coefficients for Thermal Management in Composites Manufacturing Processes

Presented by: Dr. Reza Vaziri[1]

Arghyanil Bhattacharjee[1], Kamyar Gordnian[2], Trevor Campbell[3], Anoush Poursartip[1,2]

[1]Composites Research Network, Department of Materials Engineering and Civil Engineering, The University of British Columbia
Vancouver, Canada

[2]Convergent Manufacturing Technologies
Vancouver, Canada

[3]Department of Statistics, The University of British Columbia
Vancouver, Canada

Process Simulation for Composites Manufacturing

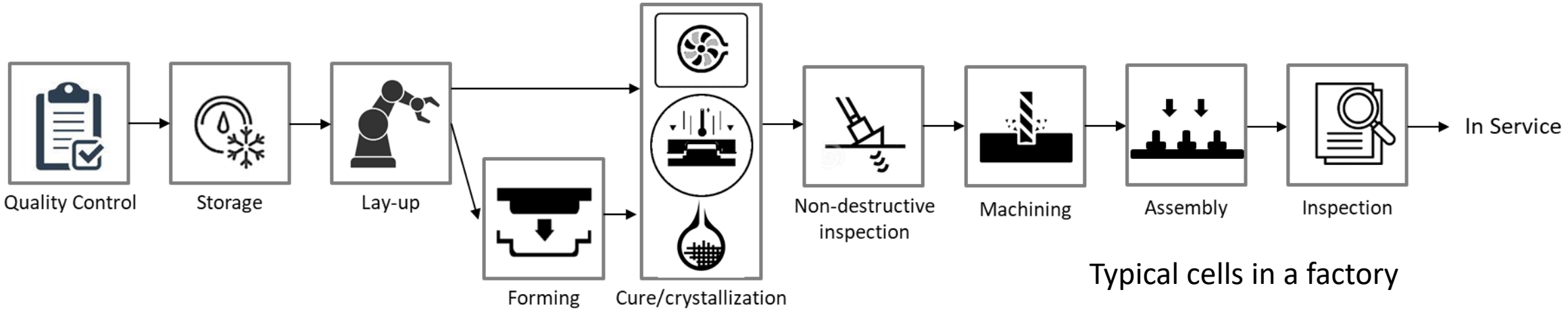

Typical cells in a factory

For high confidence process simulation, we need (a) appropriate mathematical model(s) of the underlying physics, and (b) sufficient knowledge of initial and boundary conditions during the process

Low confidence → *High confidence*

Using process simulation as job aids to explore the process design space – *test supported by simulation*

Using process simulation for detail process design, documentation and certification – *simulation supported by test*

CRN
Composites Research Network

© CRN UBC (2025) -- DO NOT REPRODUCE WITHOUT WRITTEN PERMISSION

Process Simulation for Composites Manufacturing

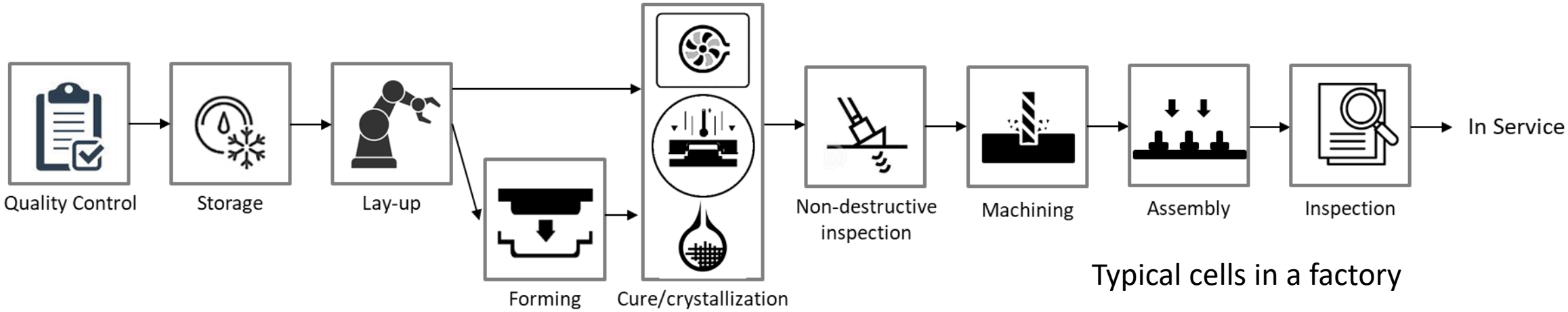

Typical cells in a factory

The amount of test data available is limited for composites manufacturing, particularly if it is a new material, process, tooling, equipment, or product.
By definition, test data will be expensive and take time to generate

Therefore, merging simulation and test data in the most efficient manner is a critical step in maximizing the value of composites process simulation

The key questions thus becomes: how confident are we in our process simulations, can we quantify our confidence, and how can we improve it?

CRN
Composites Research Network

© CRN UBC (2025) -- DO NOT REPRODUCE WITHOUT WRITTEN PERMISSION

Process Simulation for Composites Manufacturing

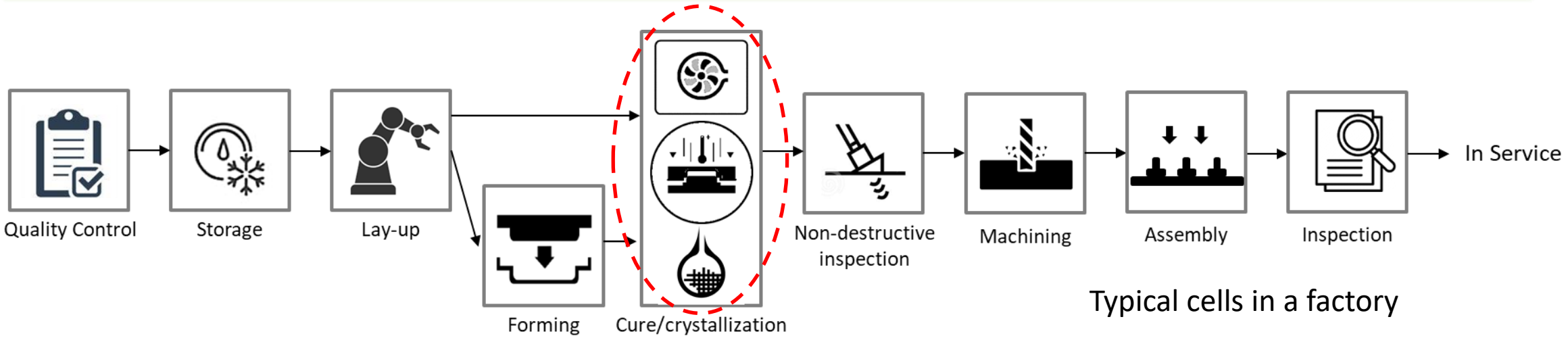

Typical cells in a factory

Thermal management simulation is a relatively mature area in process simulation

1980s

- Simple single material model
- 1D governing equations
- Effects of tool-equipment interaction were not modelled
- Minimal test data

2020s

- Effects of tool-equipment interaction
- 3D governing equations
- Wide range of material constitutive models, with extensive characterized material libraries
- Commercially available and increasingly used

Next gen

- Formal addition of uncertainty
- Virtual sensors
- Optimized physical sensor installation
- Better design and manufacturing practices
- ……

CRN
Composites Research Network

© CRN UBC (2025) -- DO NOT REPRODUCE WITHOUT WRITTEN PERMISSION

Process Simulation for Composites Manufacturing

$$Governing\ equation: \quad \frac{\partial(\boldsymbol{\rho C_p T})}{\partial t} = \frac{\partial}{\partial z}\left(\boldsymbol{k}\frac{\partial \boldsymbol{T}}{\partial z}\right) + \dot{Q}$$

$$\dot{Q_R} = (1 - \boldsymbol{v_f})\boldsymbol{\rho_R H_R}\frac{\partial \alpha}{\partial t}$$

$$Boundary\ condition: \quad -\boldsymbol{k}\frac{\partial T}{\partial n} = -\boldsymbol{h}(\boldsymbol{T} - \boldsymbol{T_{air}})$$

$$Cure\ Kinetics\ model: \quad \frac{\partial \alpha}{\partial t} = \boldsymbol{f}(\alpha, t)$$

Heat transfer. Accessed: Nov. 25, 2024. [Online]. Available: *https://compositeskn.org/KPC/A132*

The uncertainties in a process simulation model can stem from a number of sources including but not limited to:

- **Sensor data (Temperature measurements,…)**
- **Material properties and models (Thermal conductivity, heat of reaction, density, cure-kinetics models,…)**
- **Boundary conditions (Heat transfer coefficients, …)**
- …….

In this work, we present a Bayesian inference approach in quantifying uncertainty in boundary conditions and demonstrate an example of how to propagate it in a process simulation framework

Composites Research Network

© CRN UBC (2025) -- DO NOT REPRODUCE WITHOUT WRITTEN PERMISSION

HTCs in Thermal Process Simulation – What and why?

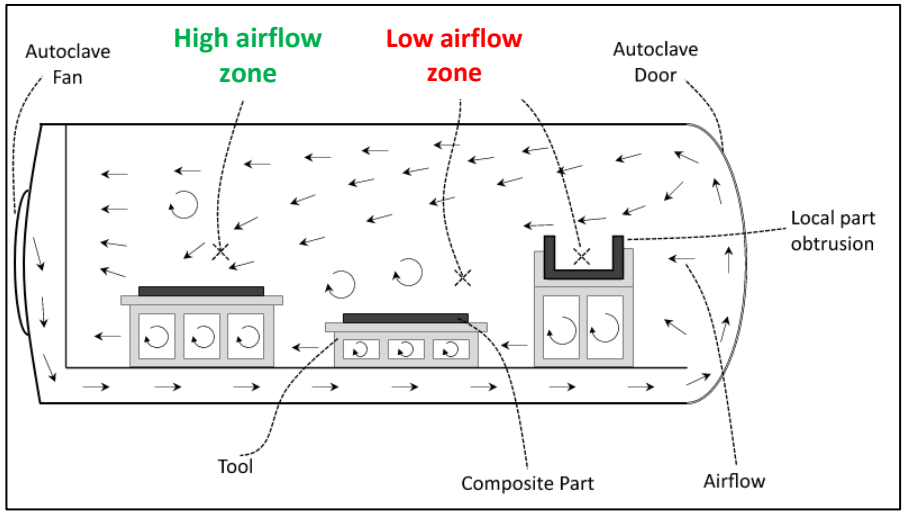

https://compositeskn.org/KPC/A106

Airflow in a typical autoclave can be very complex

The resultant HTCs are hence critical in determining system response

In thermal simulations, the heat transfer coefficients (HTC) play a critical role in predicting the tool-part thermal response.

The HTCs can vary significantly depending on the equipment:

1. Ovens – 20-50 W/m^2/K
2. Autoclaves – 40-200 W/m^2/K (depending on pressure inside)

In current state of the art process simulation, the **uncertainty around HTCs remain the Achilles' heel**.

Heat flow schematic

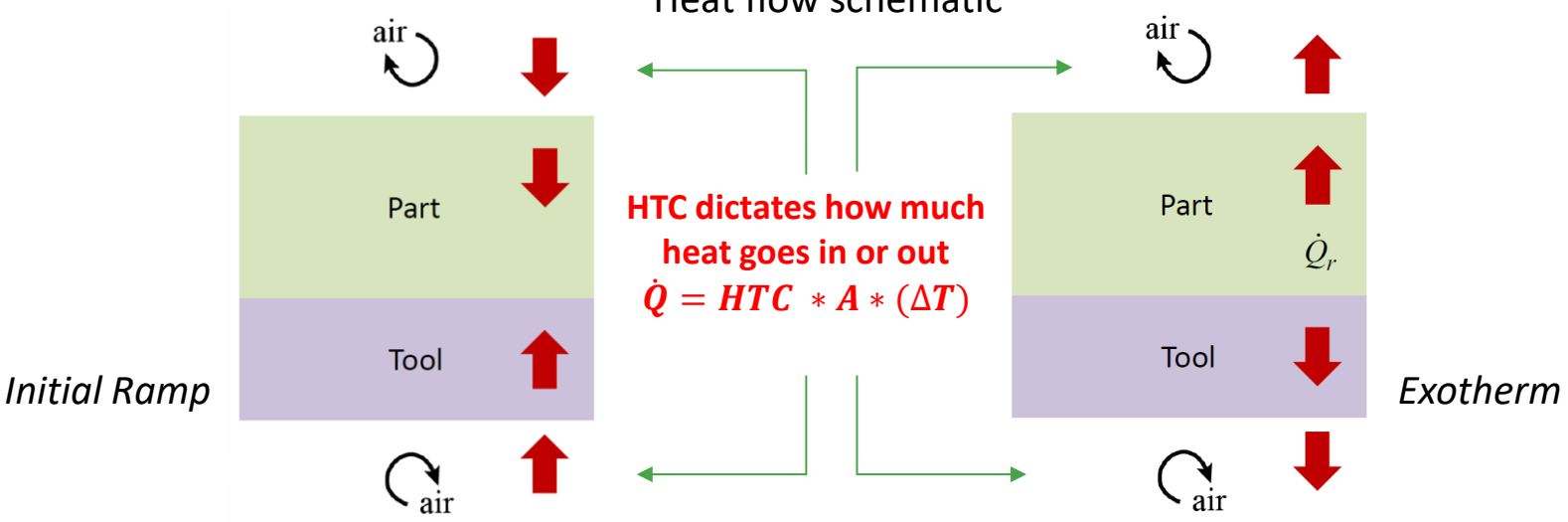

Heat transfer. Accessed: Nov. 25, 2024. [Online]. Available: https://compositeskn. org/KPC/A132

© CRN UBC (2025) -- DO NOT REPRODUCE WITHOUT WRITTEN PERMISSION

HTCs in Thermal Process Simulation – how?

Does not quantify uncertainty | **Quantifies uncertainty**

Methods	CFD	Lumped Mass Analysis	1D or 3D Conductive Heat Transfer FE Solution	Bayesian Inference (Using 3D Conductive Heat Transfer FE Solution)
	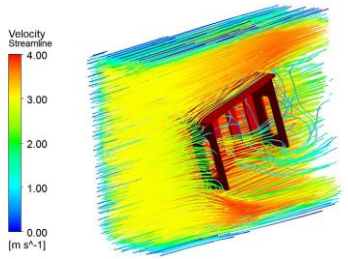		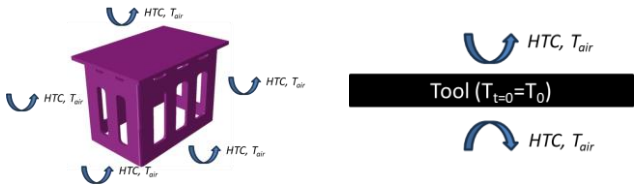	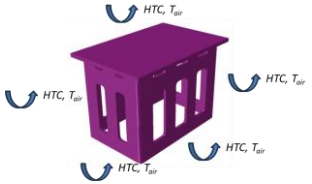
	$h = f(T, P, v)$	$hA\left(T_p(t) - T_{air}(t)\right) = \rho C_p V \frac{\partial T}{\partial t}$	$\frac{\partial}{\partial t}(\rho C_p T) = \nabla(k\nabla T) + \dot{Q}$ *Boundary condition* $-k\frac{\partial T}{\partial \eta} = h(T_\infty - T)$	$\frac{\partial}{\partial t}(\rho C_p T) = \nabla(k\nabla T) + \dot{Q}$ *Boundary condition* $-k\frac{\partial T}{\partial \eta} = h(T_\infty - T)$ $p(\theta\|T_E) = \frac{p(T_E\|\theta)p(\theta)}{p(T_E)}$ *Bayes Theorem*

© CRN UBC (2025) -- DO NOT REPRODUCE WITHOUT WRITTEN PERMISSION

Bayesian Inference

Bayesian inference can be used to infer HTCs from thermal data

$$p(\theta|T_E) = \frac{p(T_E|\theta)p(\theta)}{p(T_E)}$$

Bayes Theorem (quantifies how the belief in a hypothesis changes on observing new data)

HTC $(\boldsymbol{\theta})$

Thermal Data $(\boldsymbol{T_E})$

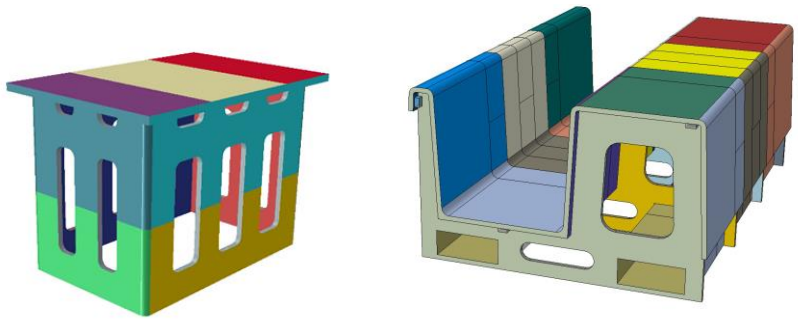

The surfaces of tools are divided into smaller zones with each zone having its own HTC

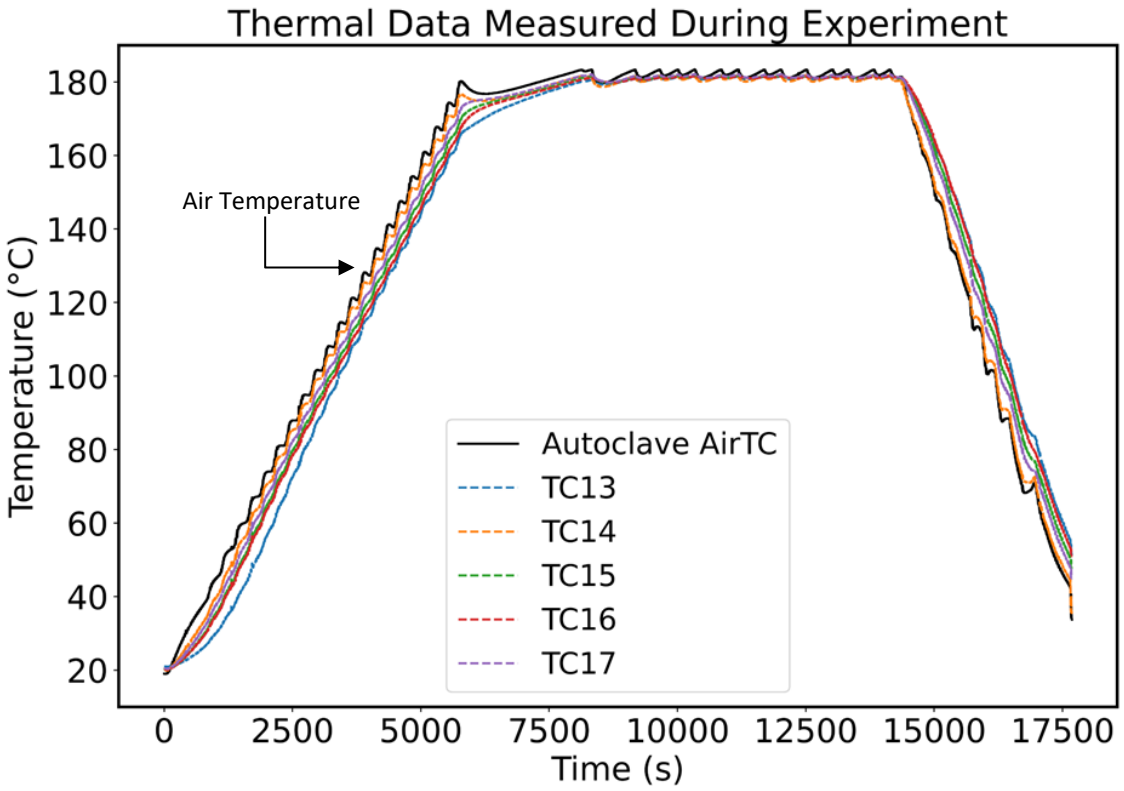

TC# denotes thermocouple position

Composites Research Network

© CRN UBC (2025) -- DO NOT REPRODUCE WITHOUT WRITTEN PERMISSION

Case study 1: Cooling of a preheated tool under forced convection

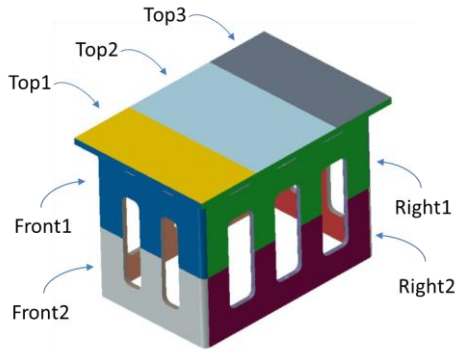

Tool preheated to 130°C in an oven

Cooled down in a custom wind tunnel and the thermal history was measured

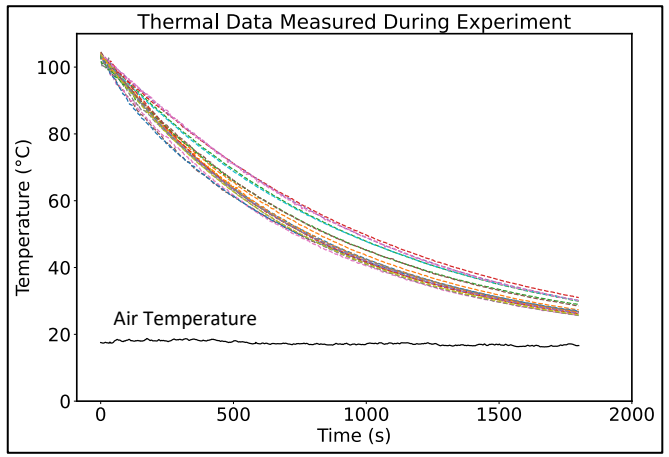

(Working TCs shown here only)
TCs installed: 28
TCs failed: 9

Prior

Likelihood

$$p(\theta|T_E) = \frac{p(T_E|\theta)p(\theta)}{p(T_E)}$$

Posterior (Final inferred HTCs)

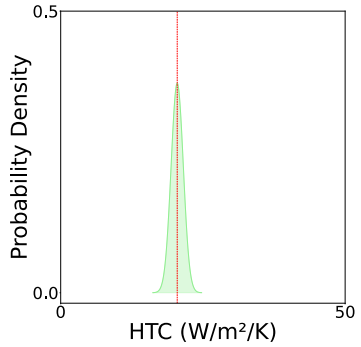

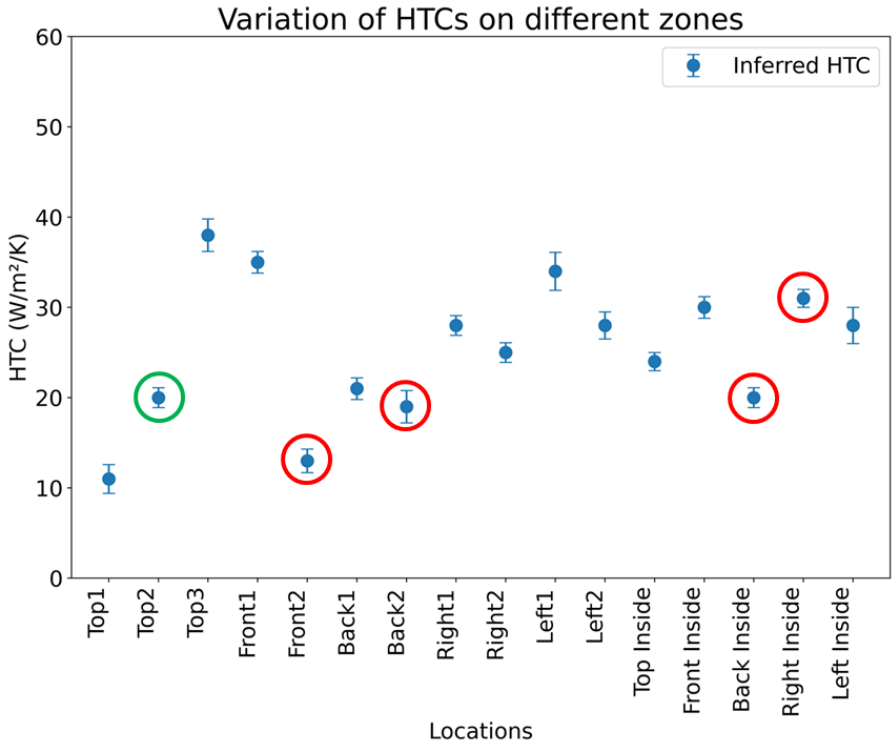

Denotes a zone where the installed TC malfunctioned

Denotes a zone where the installed TC data was available but not used in the inference process

Possible to estimate boundary conditions at locations without TC data

© CRN UBC (2025) -- DO NOT REPRODUCE WITHOUT WRITTEN PERMISSION

Uncertainty Propagation in Thermal History Predictions

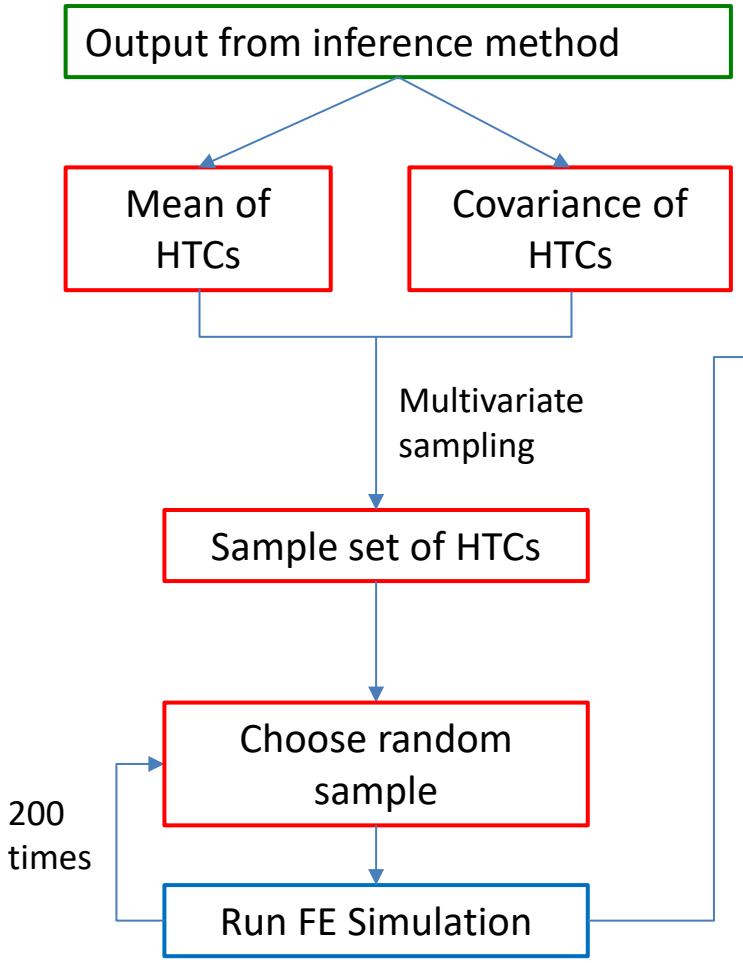

We get a credible interval for the temperature at a TC location from the predictions

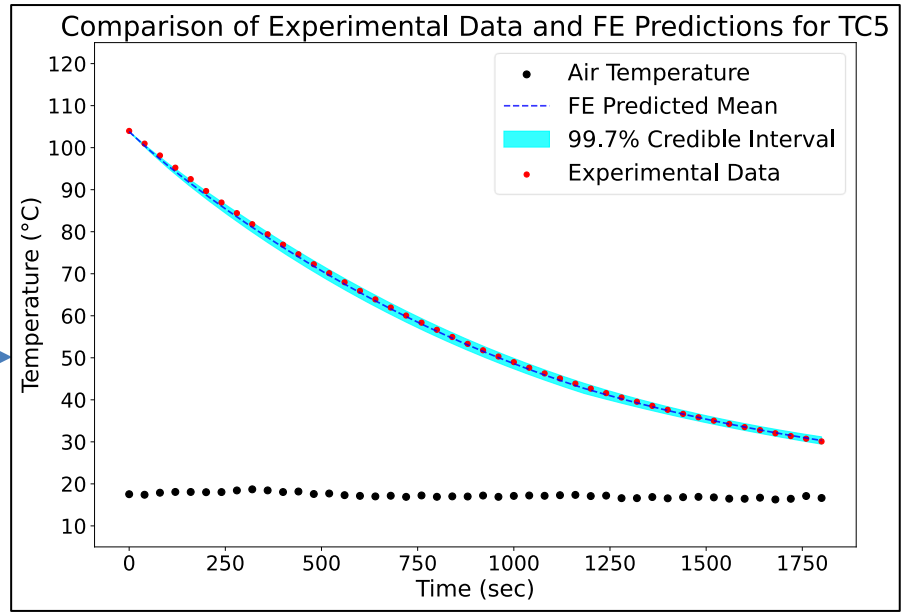

*We observe a **really good match** for a TC whose **data was not used while inferring** the HTCs.

High accuracy (match with mean)
High precision (narrow credible interval)

Composites Research Network

© CRN UBC (2025) -- DO NOT REPRODUCE WITHOUT WRITTEN PERMISSION

Uncertainty Propagation in Thermal History Predictions

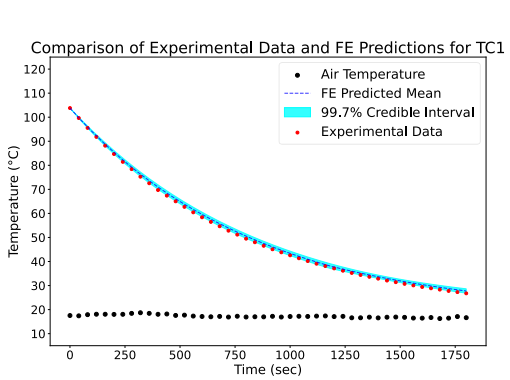

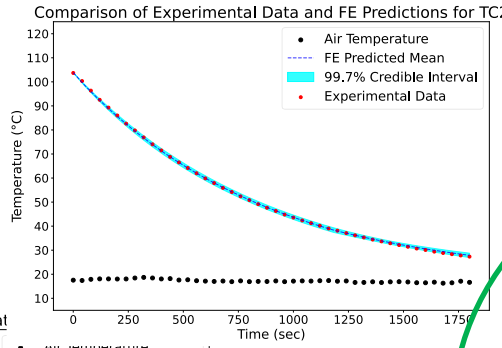

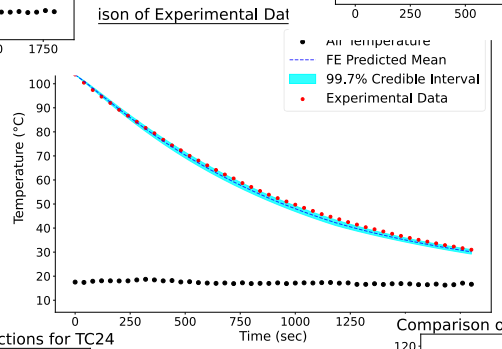

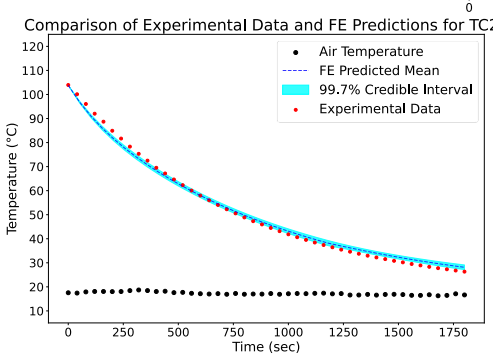

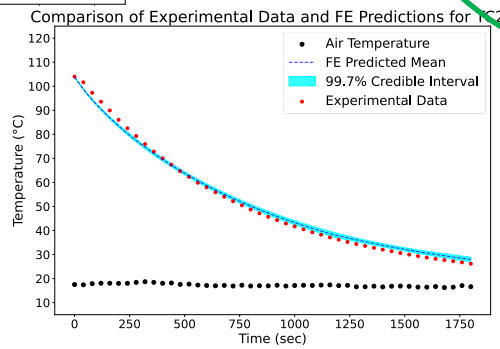

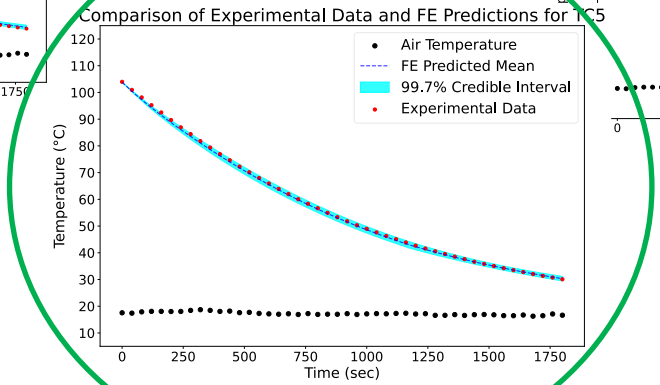

Data from this TC was not used for inferring HTCs

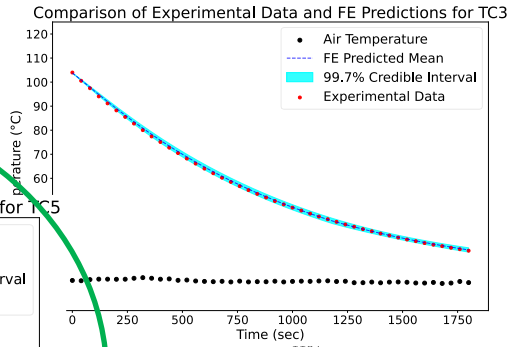

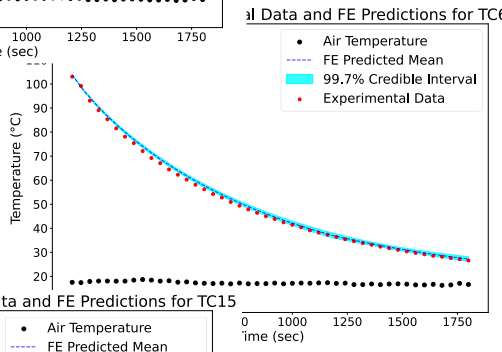

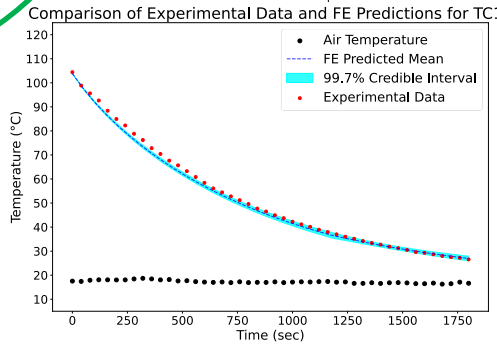

The forward model is able to accurately and precisely predict the experimental data using inferred HTCs

© CRN UBC (2025) -- DO NOT REPRODUCE WITHOUT WRITTEN PERMISSION

Uncertainty Propagation in Thermal History Predictions

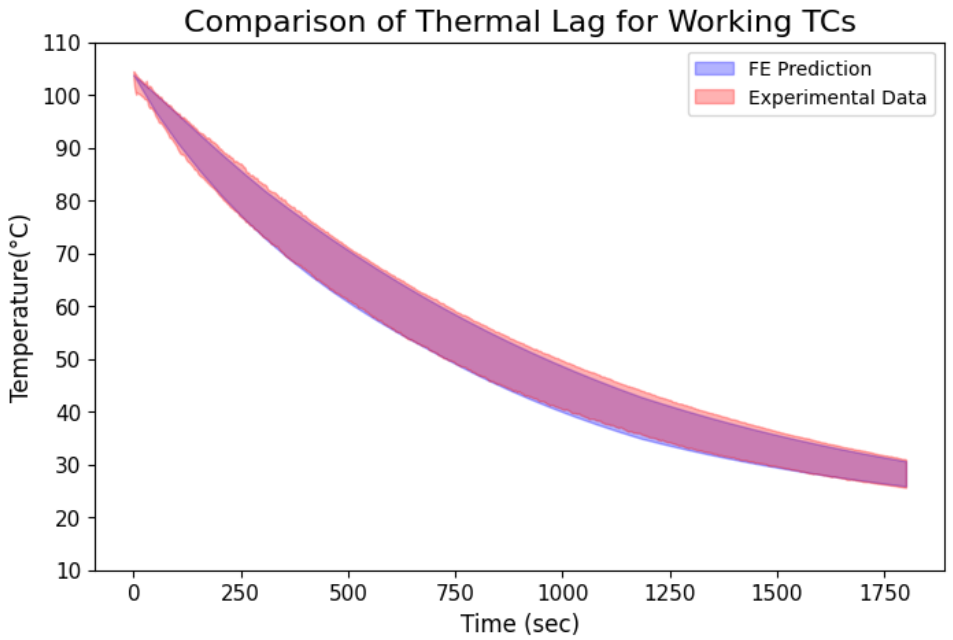

- We can correctly identify the lead and lag TCs based on the 19 working TCs.
- However, there are 9 TCs that failed during the experiments
- The actual lead and lag positions could be one of the TCs that failed.

Hence, we now also include the predictions at those TCs, to compare with the experimental data

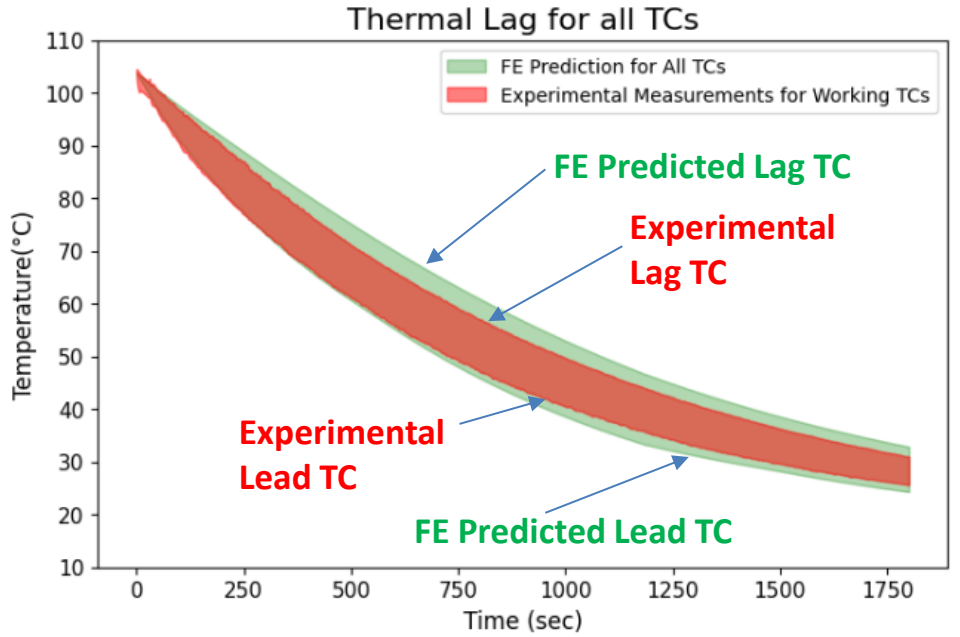

We plot the predictions for all the TCs (working + failed)

- **Actual lead and lag locations may be different from what our experiments tell us**
- This can occur if any of the critical TCs fail during the run, or if TCs are not placed at appropriate locations!

Composites Research Network

© CRN UBC (2025) -- DO NOT REPRODUCE WITHOUT WRITTEN PERMISSION

Case study 2: An invar tool undergoing an autoclave cycle

Material	BMS8-276
Shape	C90, 8ply quasi, 1.5mm thick
Tool	Invar CCMRD
Equipment	CRN Autoclave
Process	1.7°Cpm to 180°C, Isothermal 120 min, 2.8°Cpm to 20°C Pressure: 90psi

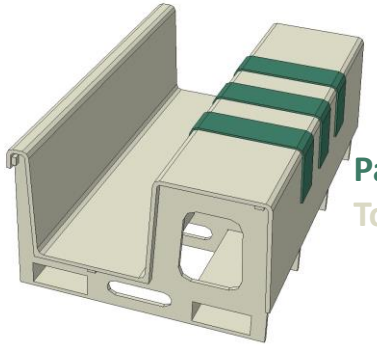

Total 41 zones were defined across the tool surface

The zoning was based on insights from CFD studies of the tool in the autoclave

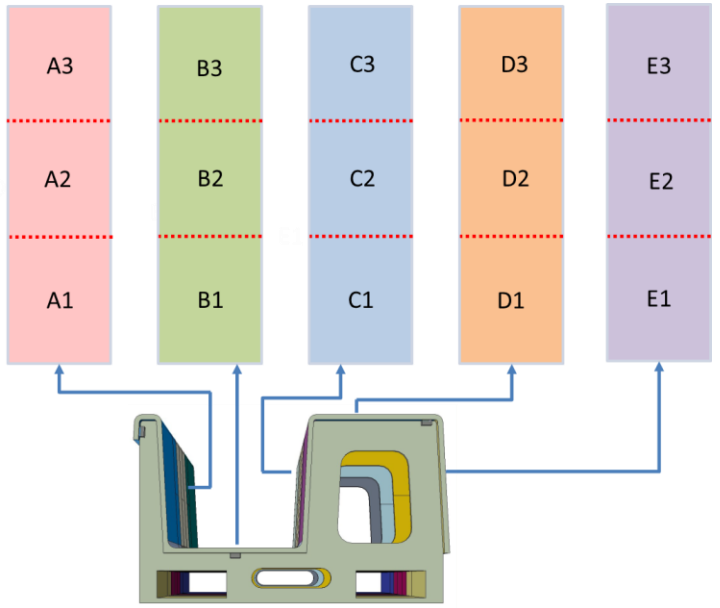

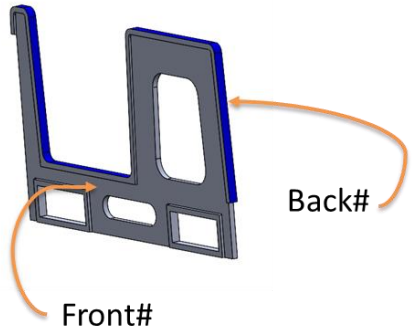

TC data on **tool locations only** were used from a curing run

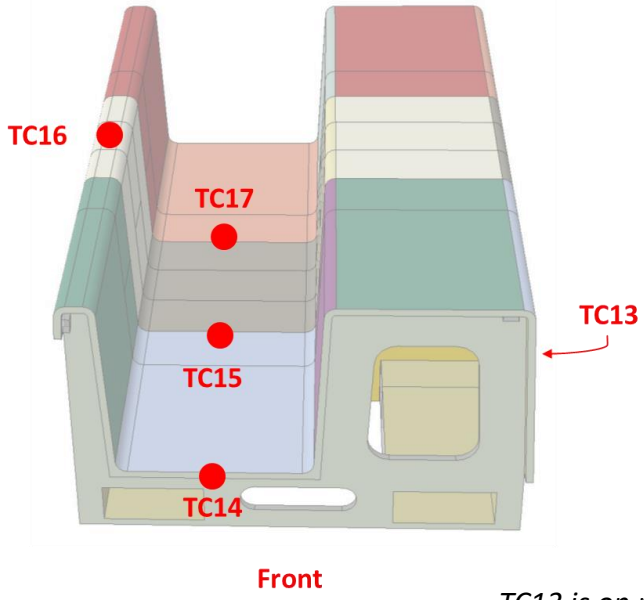

- Zone CI1 corresponds to inner face of zone C1
- Front and Back denote the front and back faces of the substructure elements
- Bottom denotes the floor of the tool

TC13 is on middle of the floor of the substructure

Composites Research Network

© CRN UBC (2025) -- DO NOT REPRODUCE WITHOUT WRITTEN PERMISSION

Case study 2: An invar tool undergoing an autoclave cycle

Material	BMS8-276
Shape	C90, 8ply quasi, 1.5mm thick
Tool	Invar CCMRD
Equipment	CRN Autoclave
Process	1.7°Cpm to 180°C, Isothermal 120 min, 2.8°Cpm to 20°C Pressure: 90psi

TC data on **tool locations only** were used from a curing run

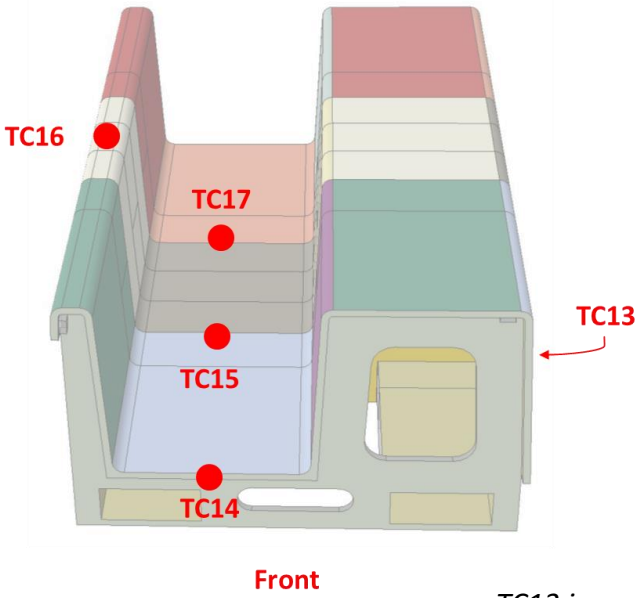

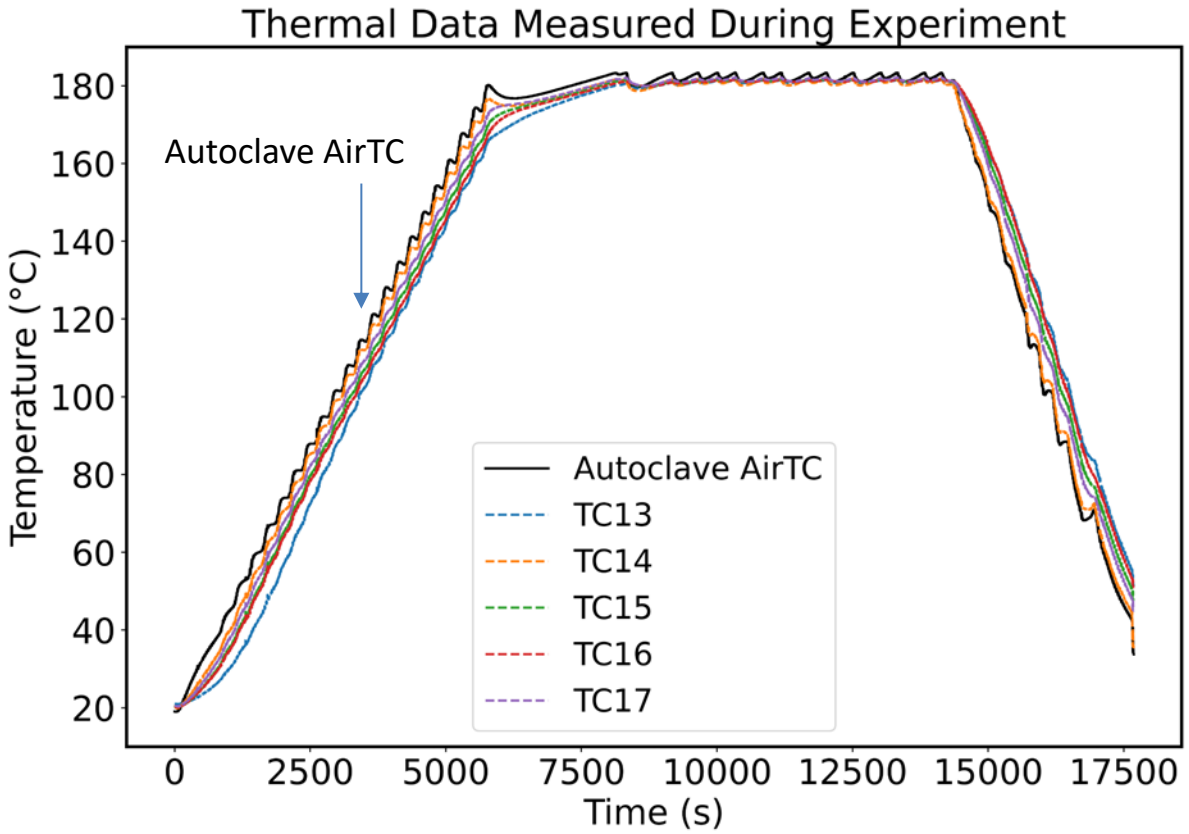

TC13 is on middle of the floor of the substructure

Composites Research Network

© CRN UBC (2025) -- DO NOT REPRODUCE WITHOUT WRITTEN PERMISSION

Case study 2: An invar tool undergoing an autoclave cycle

Material	BMS8-276
Shape	C90, 8ply quasi, 1.5mm thick
Tool	Invar CCMRD
Equipment	CRN Autoclave
Process	1.7°Cpm to 180°C, Isothermal 120 min, 2.8°Cpm to 20°C Pressure: 90psi

TC data on **tool locations only** were used from a curing run

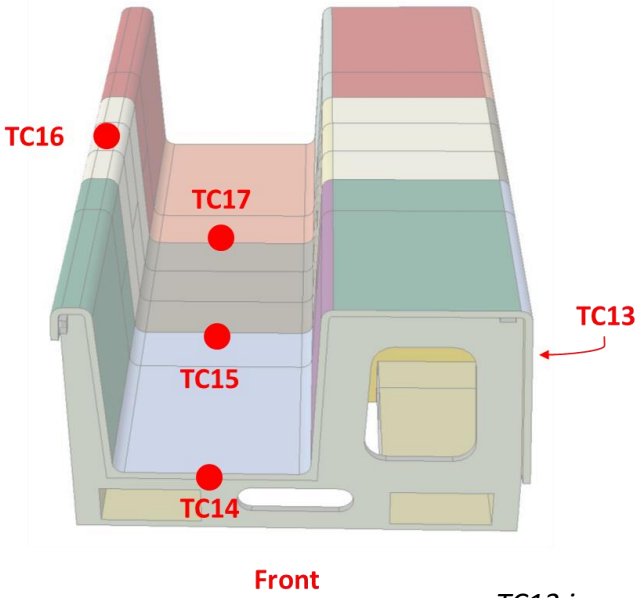

TC13 is on middle of the floor of the substructure

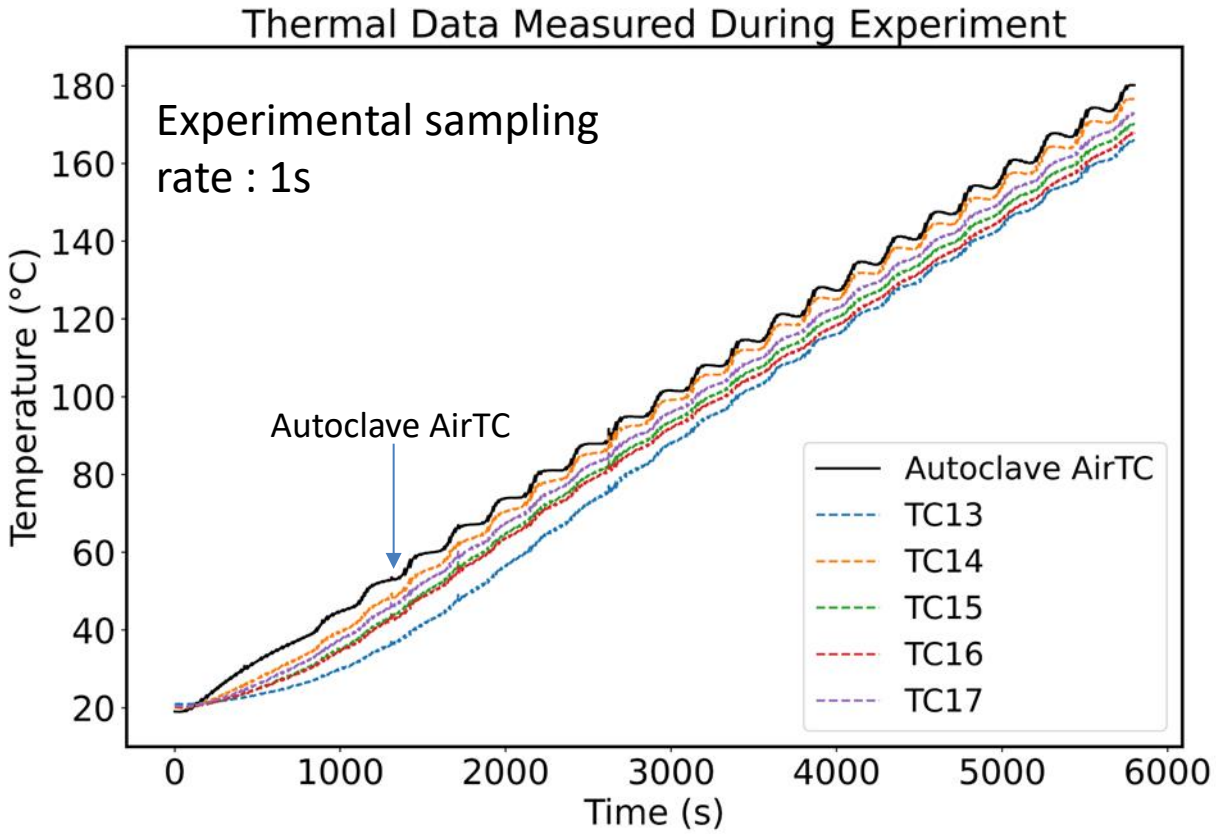

Currently we are using the ramp up stage of the cycle only to infer HTCs

Composites Research Network

© CRN UBC (2025) -- DO NOT REPRODUCE WITHOUT WRITTEN PERMISSION

Case study 2: An invar tool undergoing an autoclave cycle

Material	BMS8-276
Shape	C90, 8ply quasi, 1.5mm thick
Tool	Invar CCMRD
Equipment	CRN Autoclave
Process	1.7°Cpm to 180°C, Isothermal 120 min, 2.8°Cpm to 20°C Pressure: 90psi

TC data on **tool locations only** were used from a curing run

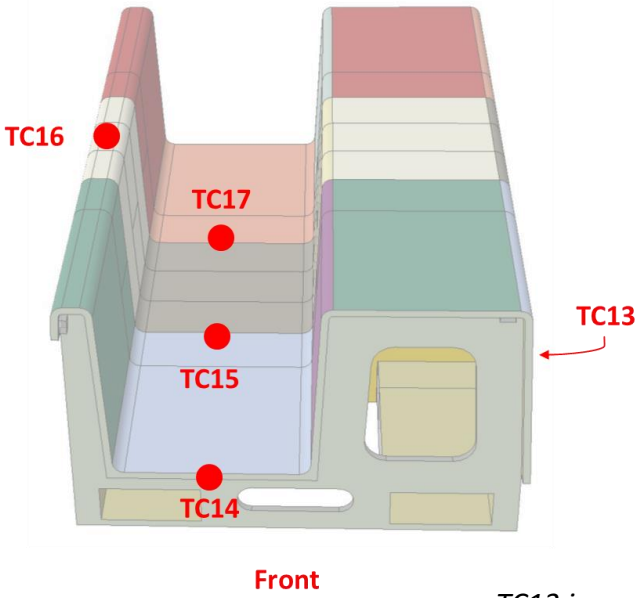

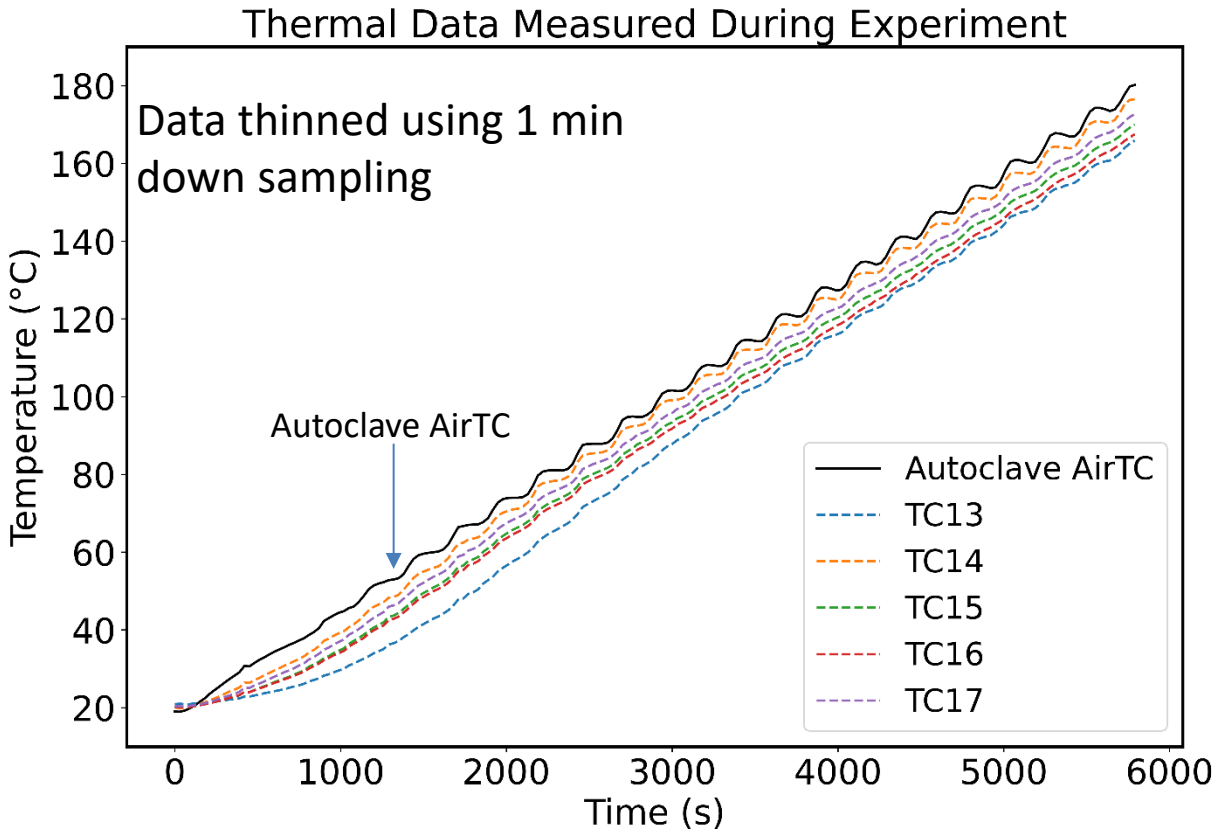

TC13 is on middle of the floor of the substructure

© CRN UBC (2025) -- DO NOT REPRODUCE WITHOUT WRITTEN PERMISSION

Case study 2: An invar tool undergoing an autoclave cycle

Material	BMS8-276
Shape	C90, 8ply quasi, 1.5mm thick
Tool	Invar CCMRD
Equipment	CRN Autoclave
Process	1.7°Cpm to 180°C, Isothermal 120 min, 2.8°Cpm to 20°C Pressure: 90psi

TC data on **tool locations only** were used from a curing run

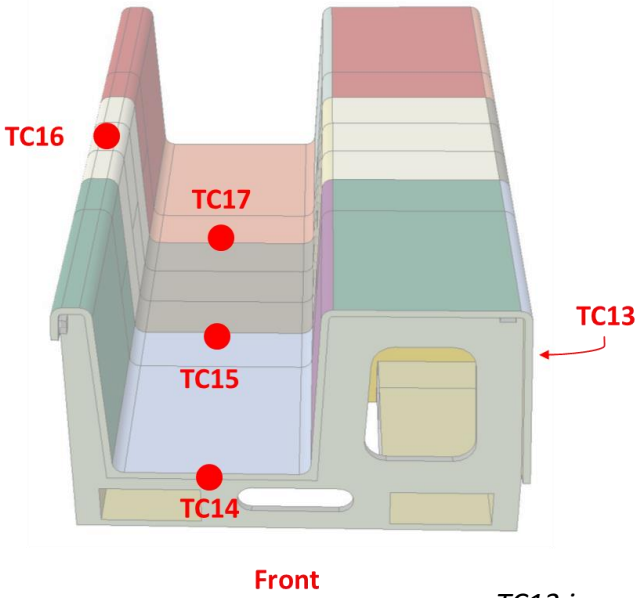

TC13 is on middle of the floor of the substructure

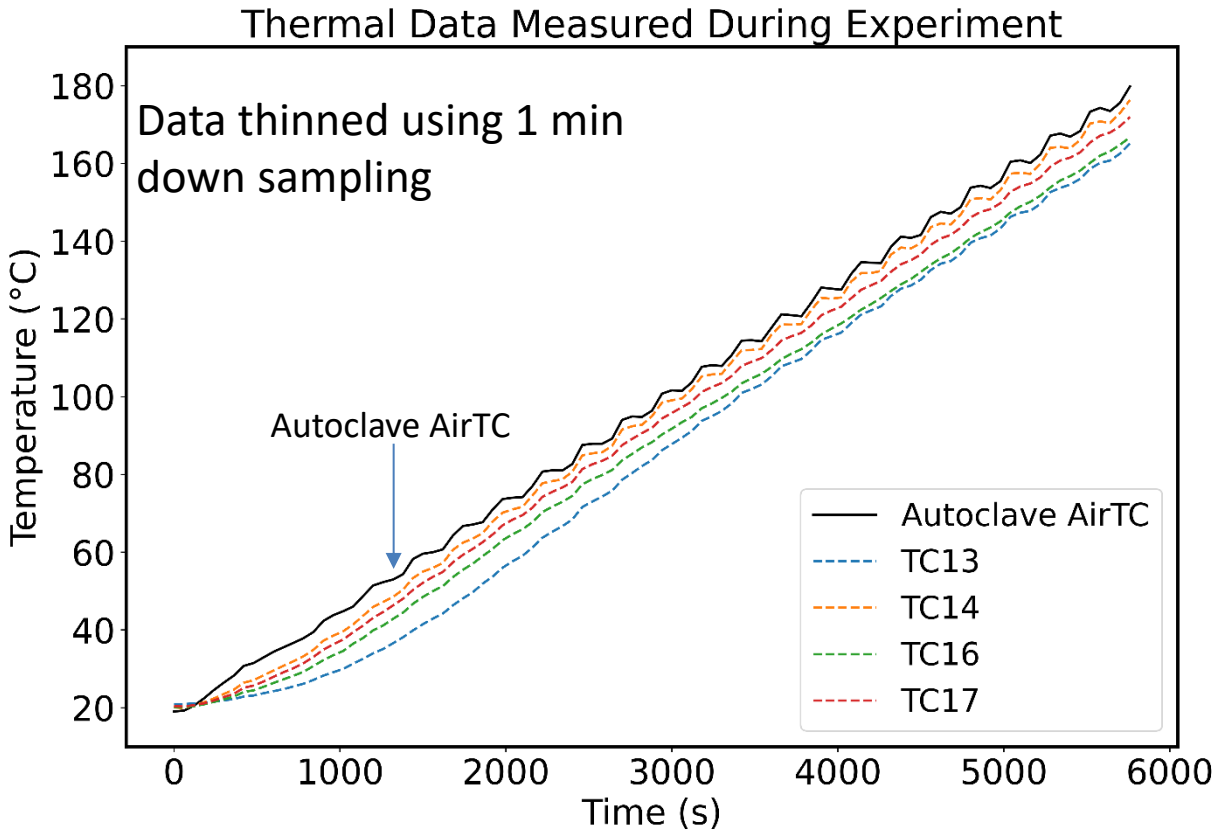

We remove TC15 from our inference in order to validate the HTCs in a later step

Composites Research Network

© CRN UBC (2025) -- DO NOT REPRODUCE WITHOUT WRITTEN PERMISSION

Case study 2: An invar tool undergoing an autoclave cycle

Material	BMS8-276
Shape	C90, 8ply quasi, 1.5mm thick
Tool	Invar CCMRD
Equipment	CRN Autoclave
Process	1.7°Cpm to 180°C, Isothermal 120 min, 2.8°Cpm to 20°C Pressure: 90psi

Inferred HTCs (W/m^{2}K)

Max	Min	Mean	SD
160	42	84	23

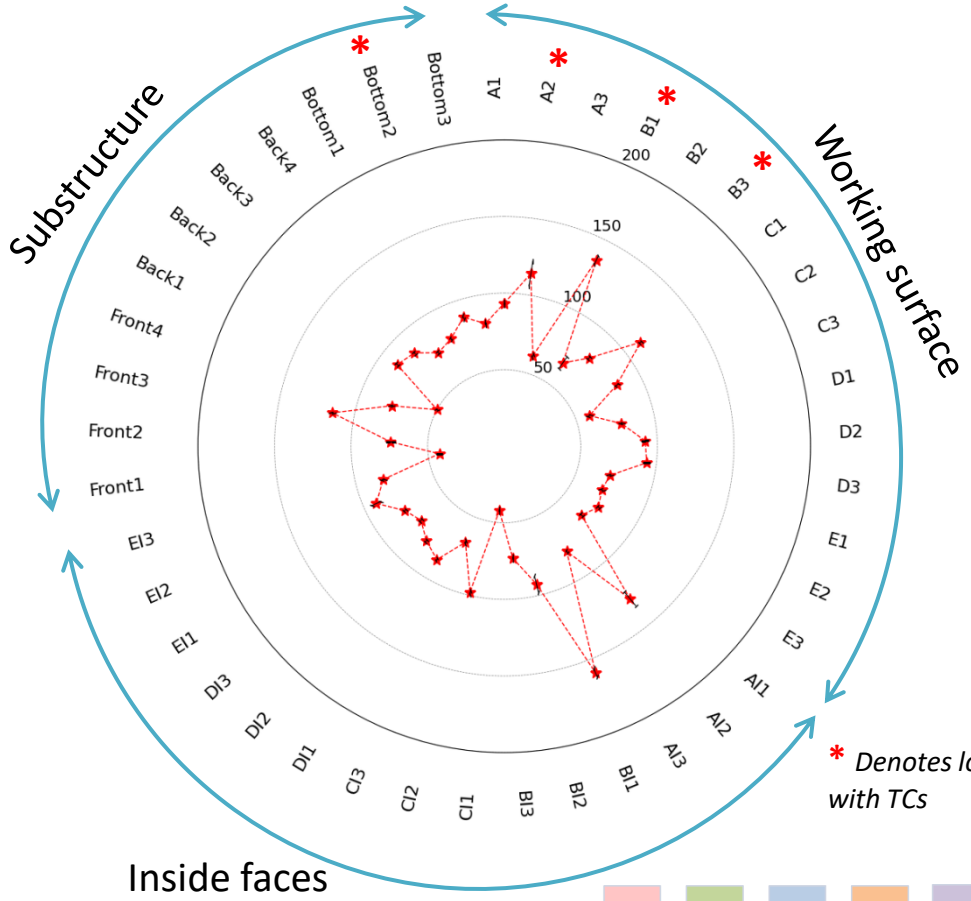

TC data on **tool locations only** were used from a curing run

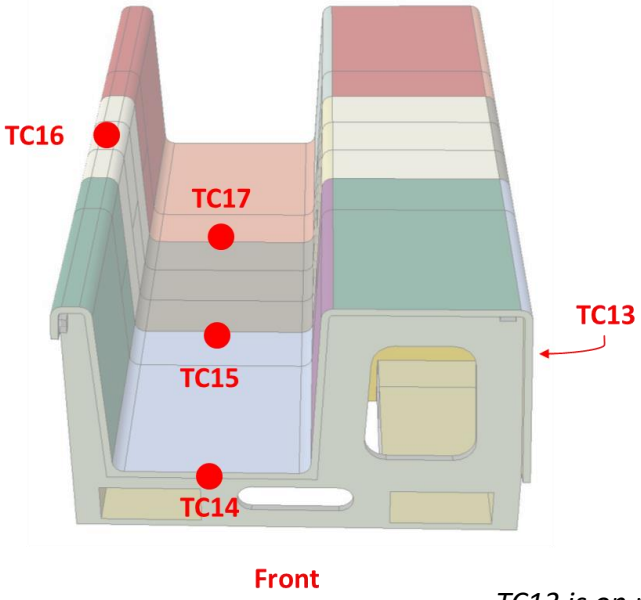

TC13 is on middle of the floor of the substructure

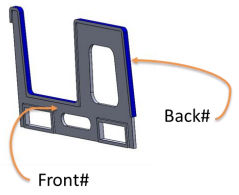

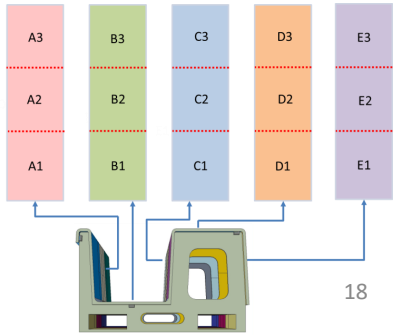

Composites Research Network

© CRN UBC (2025) -- DO NOT REPRODUCE WITHOUT WRITTEN PERMISSION

Uncertainty Propagation in Predicting Temperatures Using Inferred HTCs

Inference method

Output from inference method

Mean of HTCs

Covariance of HTCs

Multivariate sampling

Sample set of HTCs

Choose random sample

200 times

Run FE Simulation

We get a credible interval for the temperature at a TC location from the predictions

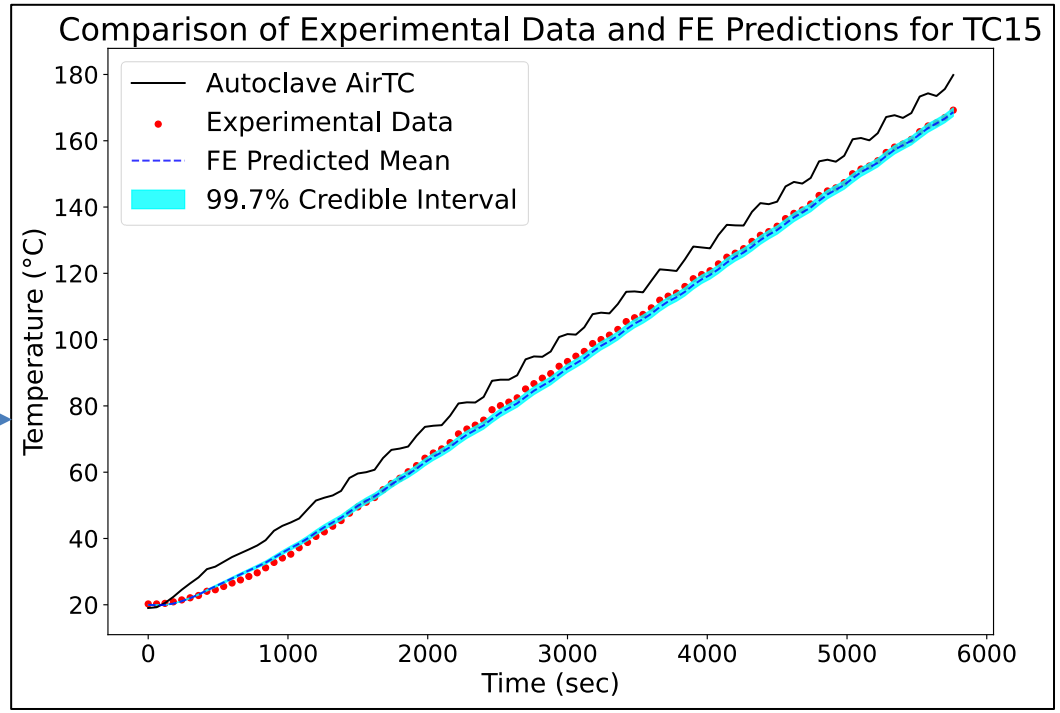

We again observe a **good match** for one of the TC locations on the tool

TC15 was not used to infer HTCs

High accuracy (match with mean)

High precision (narrow credible interval)

Composites Research Network

© CRN UBC (2025) -- DO NOT REPRODUCE WITHOUT WRITTEN PERMISSION

Uncertainty Propagation in Predicting Temperatures Using Inferred HTCs

Material	BMS8-276
Shape	C90, 8ply quasi, 1.5mm thick
Tool	Invar CCMRD
Equipment	CRN Autoclave
Process	1.7°Cpm to 180°C, Isothermal 120 min, 2.8°Cpm to 20°C Pressure: 90psi

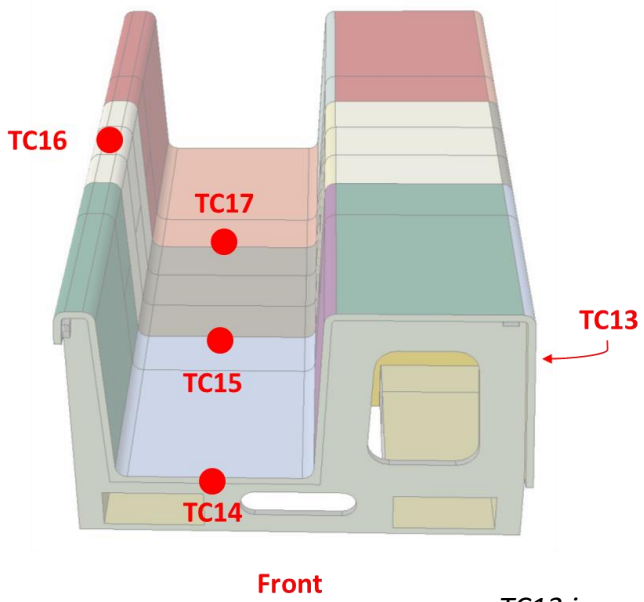

TC13 is on middle of the floor of the substructure

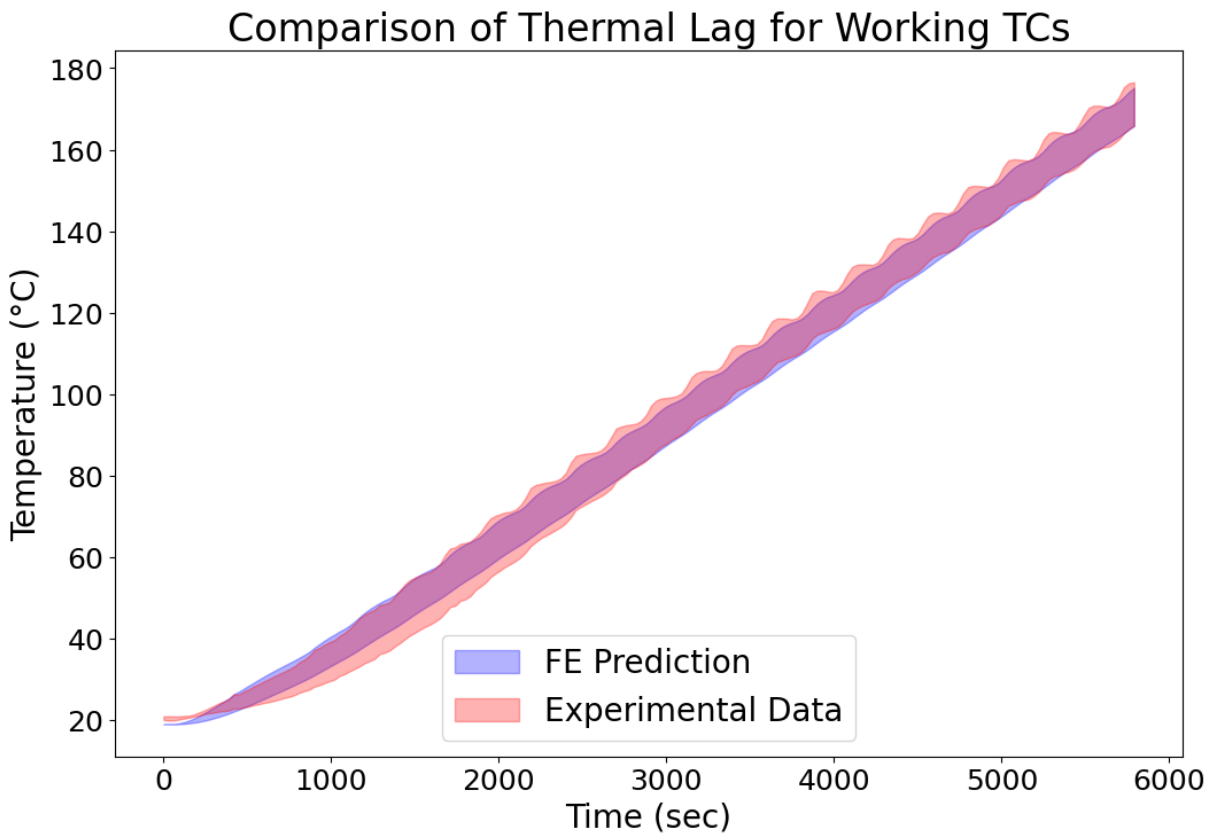

The **FE predicted thermal lag** is comparable to the **experimentally measured thermal lag**

Composites Research Network

© CRN UBC (2025) -- DO NOT REPRODUCE WITHOUT WRITTEN PERMISSION

Summary

- Quantification of uncertainty and its formal addition to process simulation models is critical in moving from a deterministic to a stochastic framework

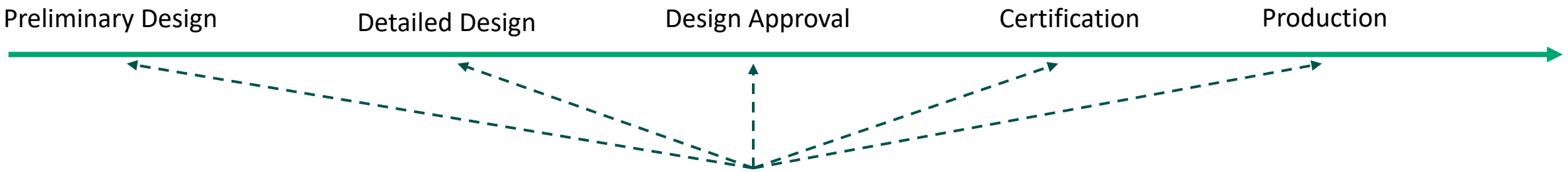

- A stochastic process simulation framework will enable efficient yet rigorous and traceable approach to:
  - Exploration of the range of potential outcomes in a processing window
  - Evaluation of current tool-equipment configurations
  - Determination of optimum bus-stop configurations of tools in an autoclave
  - Thermal profiling of part-tool-equipment combinations
  - Identification of locations of lead and lag temperatures in a part
  - Development of virtual/proxy TC approaches for low-cost, high reliability production

© CRN UBC (2025) -- DO NOT REPRODUCE WITHOUT WRITTEN PERMISSION

Acknowledgement

- Funding and support from
  - Composites Research Network industrial members (The Boeing Company, Toray, Convergent)
  - Canadian Federal Government (Western Economic Diversification)
  - Canadian Natural Sciences and Engineering Research Council (NSERC)
- All UBC, CRN and CMT colleagues

Composites Research Network

© CRN UBC (2025) -- DO NOT REPRODUCE WITHOUT WRITTEN PERMISSION

Thank You

© CRN UBC (2025) -- DO NOT REPRODUCE WITHOUT WRITTEN PERMISSION

Differences in interfacial damage between single-, double-, and multi-fibre composites, unravelled via *in situ* holotomography

T. Chatziathanasiou, Y. Lee, C. Breite, M. Diehl, I. Sinclair, M.N. Mavrogordato, S.M. Spearing, M. Mehdikhani, Y. Swolfs

Composite Materials Group
Department of Materials Engineering, KU Leuven

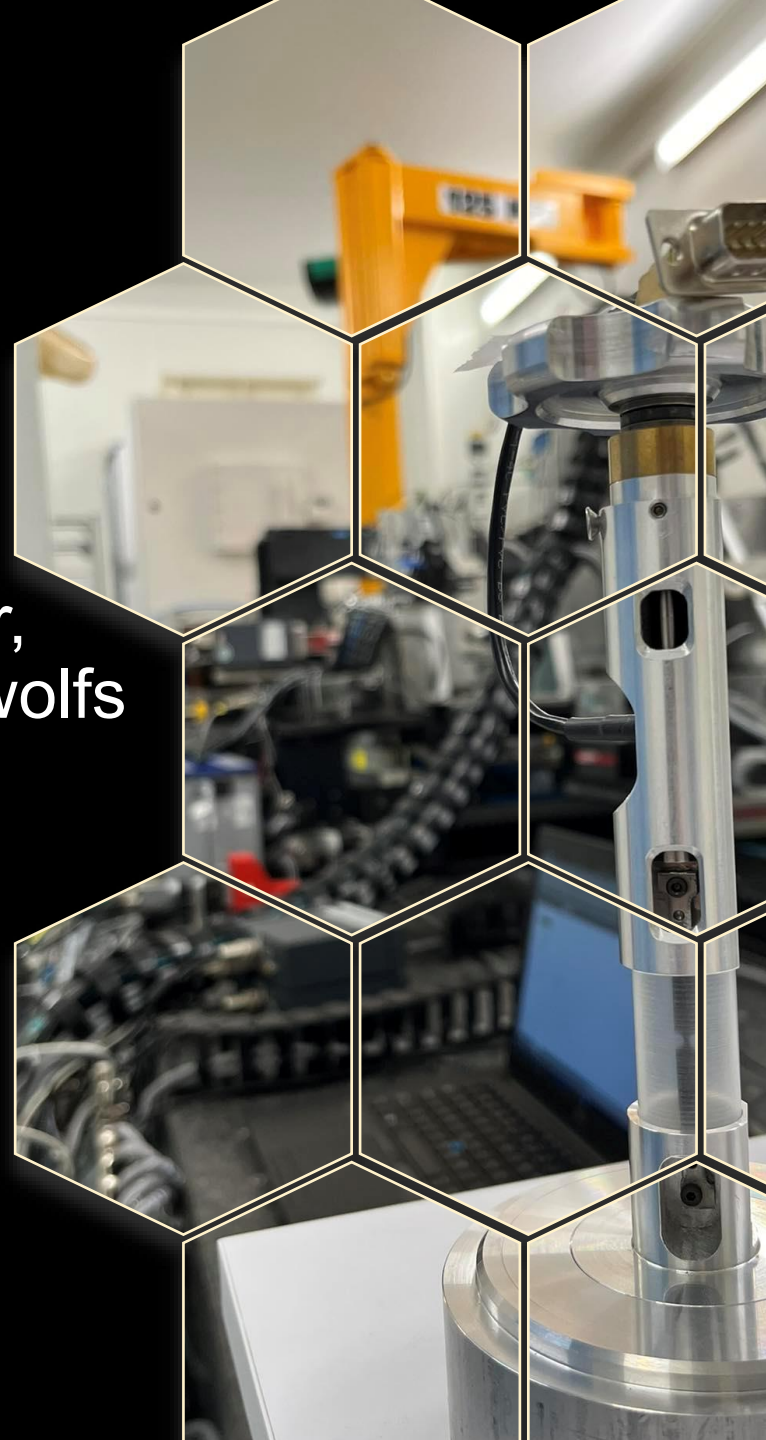

ICCM24
24TH INTERNATIONAL CONFERENCE ON COMPOSITE MATERIALS

The interface as the third constituent

Interface

Controls load transfer efficiency

Challenging to characterise reliably

Very small characteristic length

Interface properties

Needed for failure models

Single-fibre test methods

Sensitivity to geometry, absence of neighbouring fibres

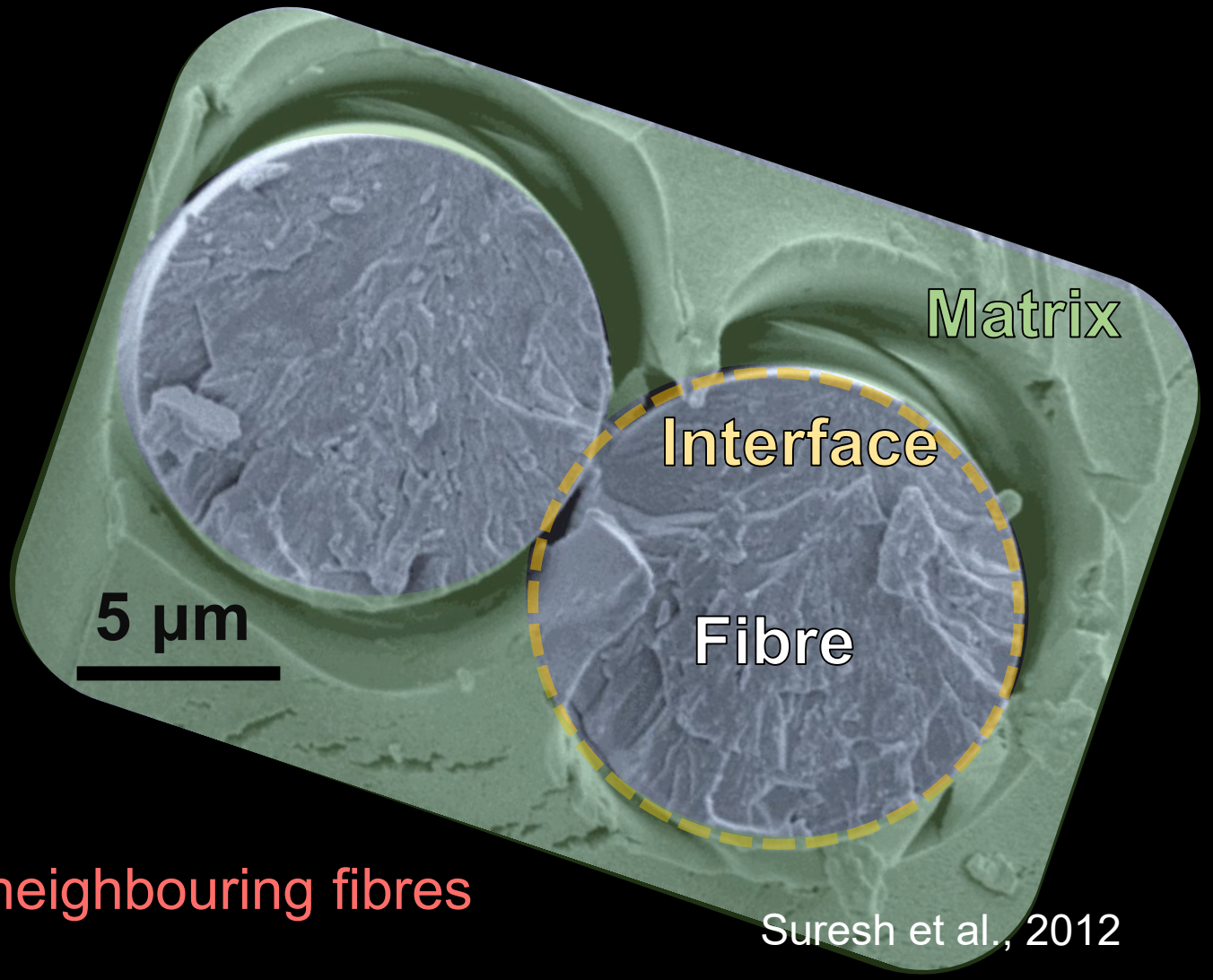

Suresh et al., 2012

The lack of consensus

Values for interfacial properties - Input for numerical models

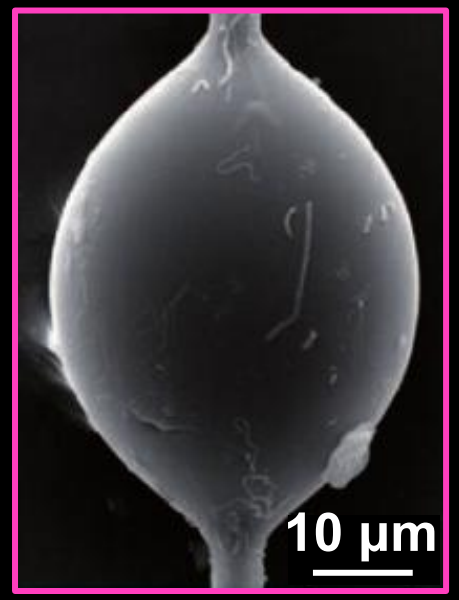

Pandey et al., 2012

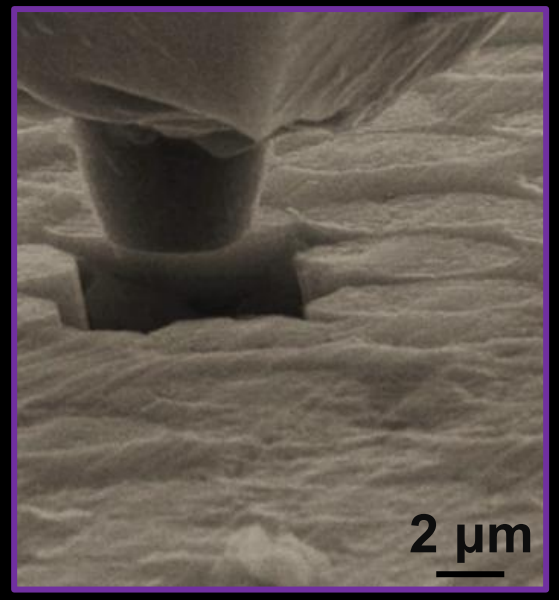

Bruker



Kim et al., 2002

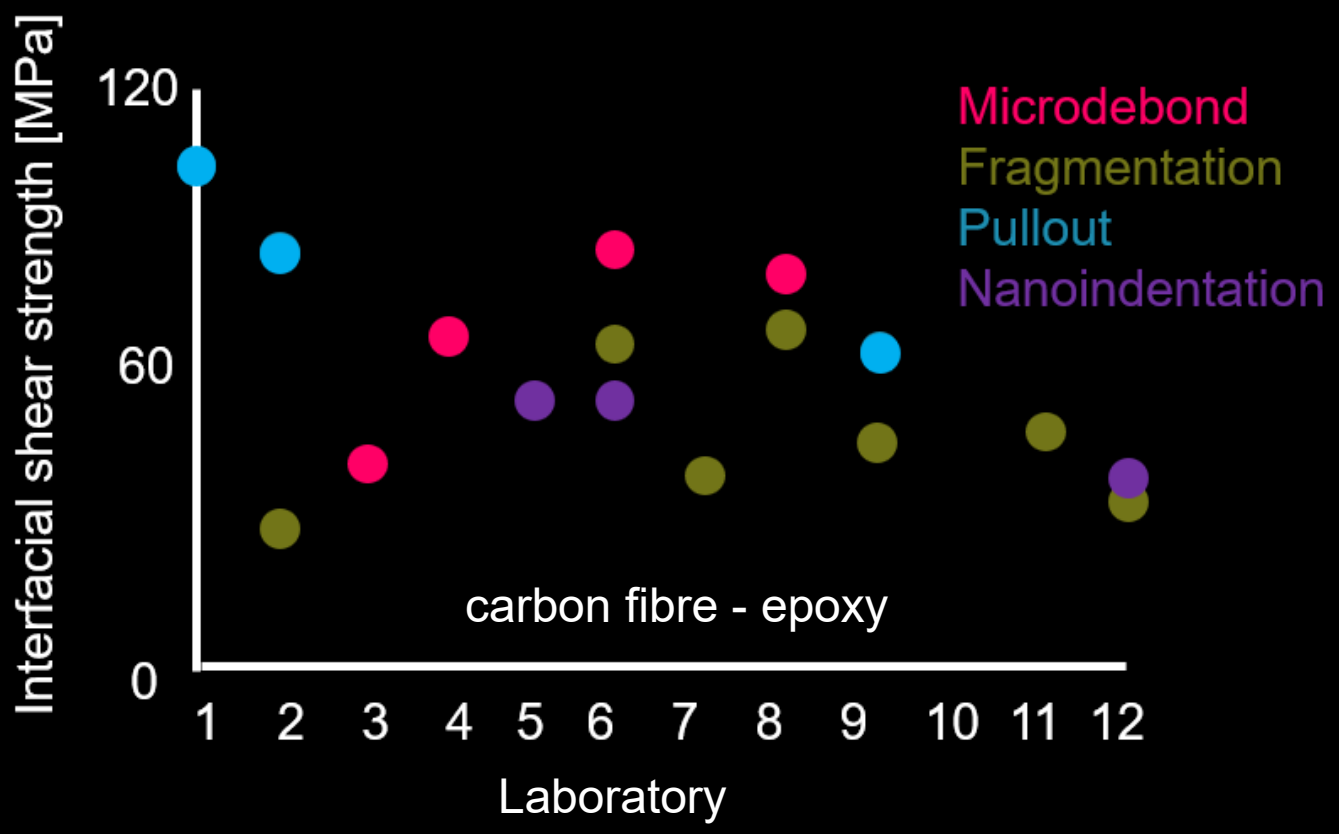

Pitkethly et al., 1993

Methodology

1

Synchrotron Computed Tomography

Tomography
Microscale
Qualitative

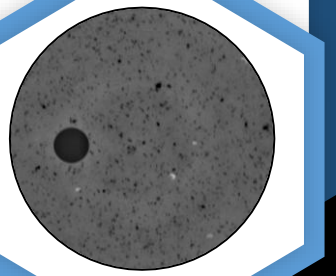

2

Digital Volume Correlation

Strain mapping
Microscale
Quantitative

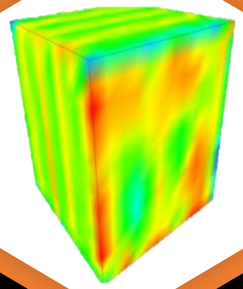

3

Experimental Validation

Conventional testing



4

Property Extraction

Reverse identification

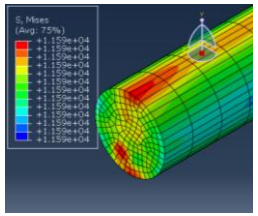

Beamline prerequisites

Material prerequisites

Setup prerequisites

Model prerequisites

Fundamental understanding of key constituent properties

Synchrotron tomography

ID16B, ESRF

- *In situ* capabilities
- Scans at different load steps
- Voxel size: 150 nm
- Acquisition time: < 20 sec



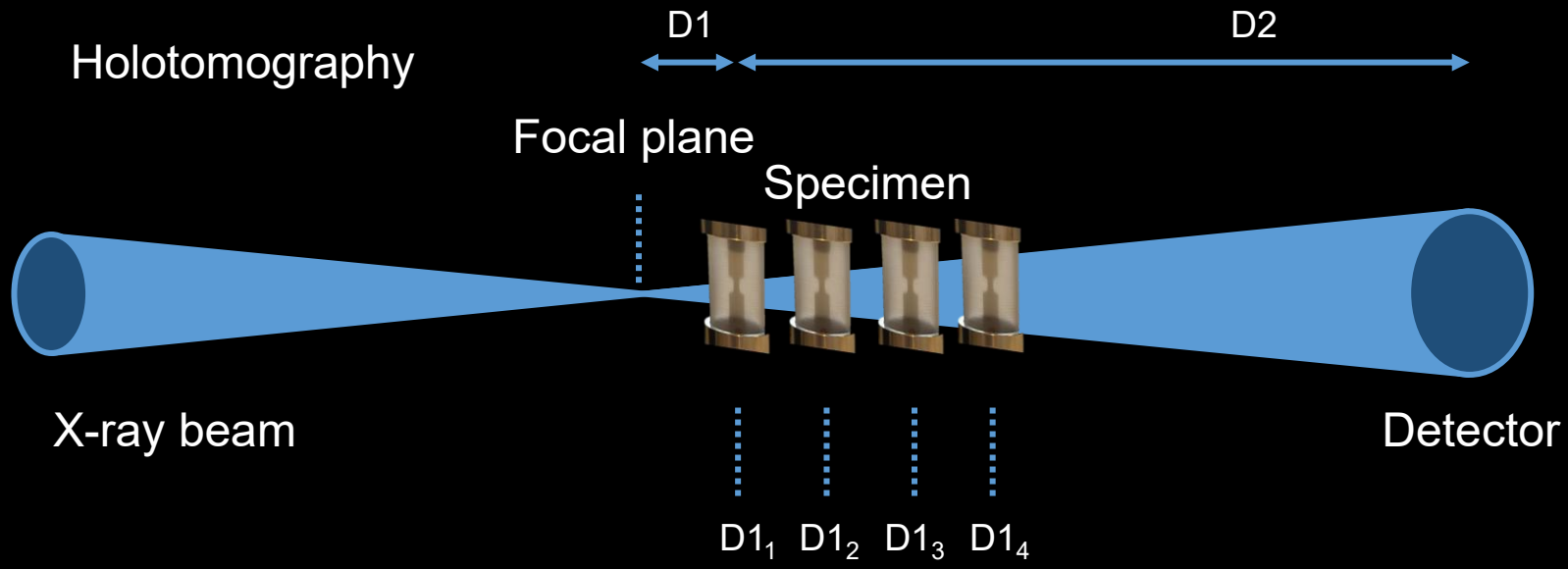

Digital Volume Correlation (DVC)

Digital Image Correlation – Surface

Digital Volume Correlation – Volume

- Intercorrelation of gray levels
- Spatial resolution ⇜ Strain resolution

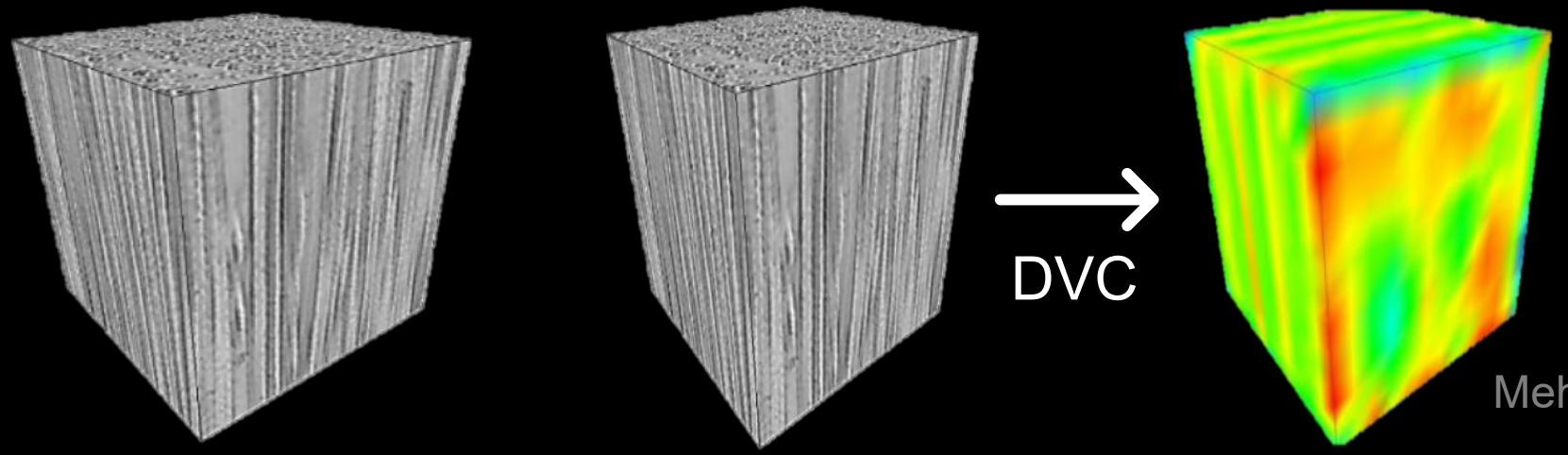

Undeformed Deformed Strain Field

Mehdikhani et al., 2021

DVC prerequisites

The need for heterogeneity

Intrinsic, stable, random speckle pattern

- Absent in conventional polymers
- Insufficient in typical composites

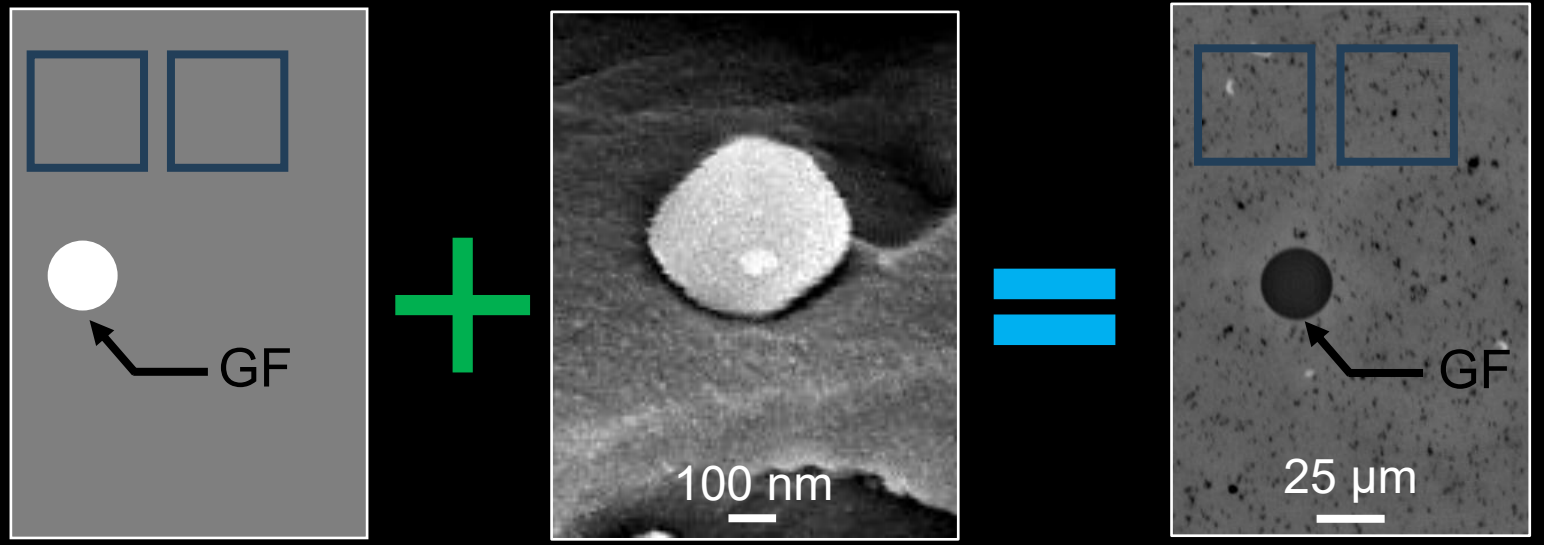

Neat
Simplified

$BaTiO_3$
nanoparticles

1.5 vol.% $BaTiO_3$
Real

Composites Part B: Engineering
Volume 276, 1 May 2024, 111381

Material representativeness of a polymer matrix doped with nanoparticles as the random speckle pattern for digital volume correlation of fibre-reinforced composites

Thanasis Chatziathanasiou [a], Okan Demir [a b], Jeroen Soete [a], Christian Breite [a], Mahoor Mehdikhani [a], Martin Diehl [a c], Yentl Swolfs [a]

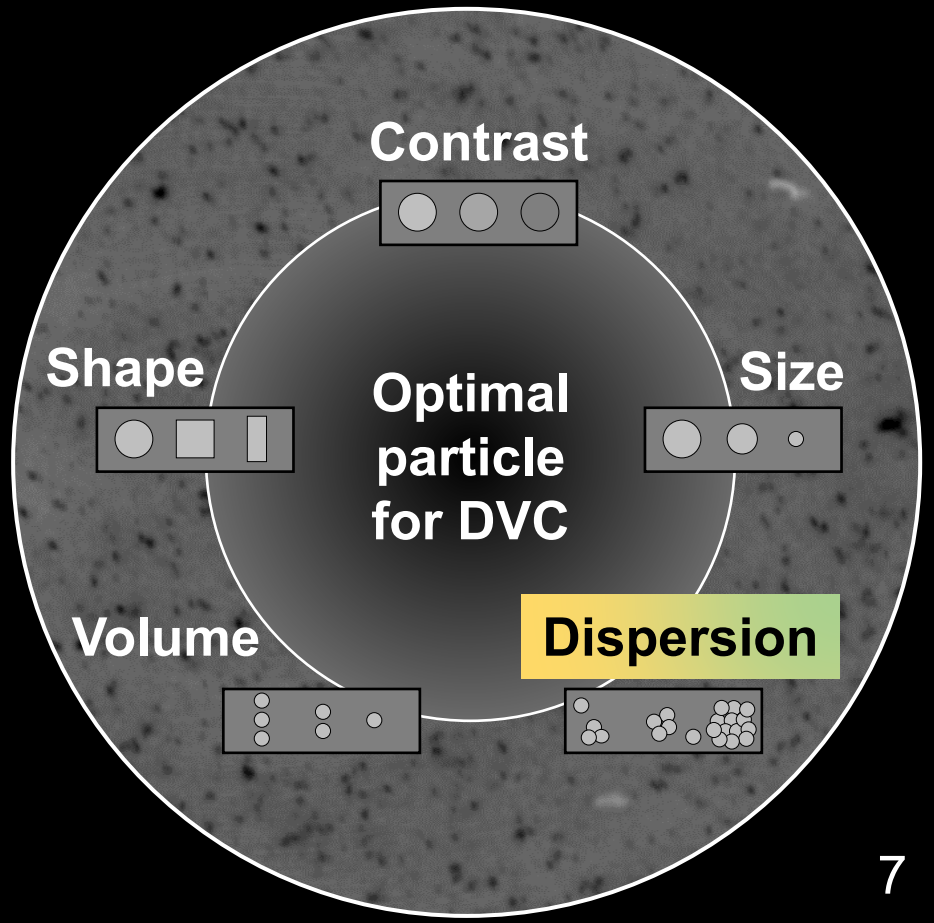

Ensuring representativeness

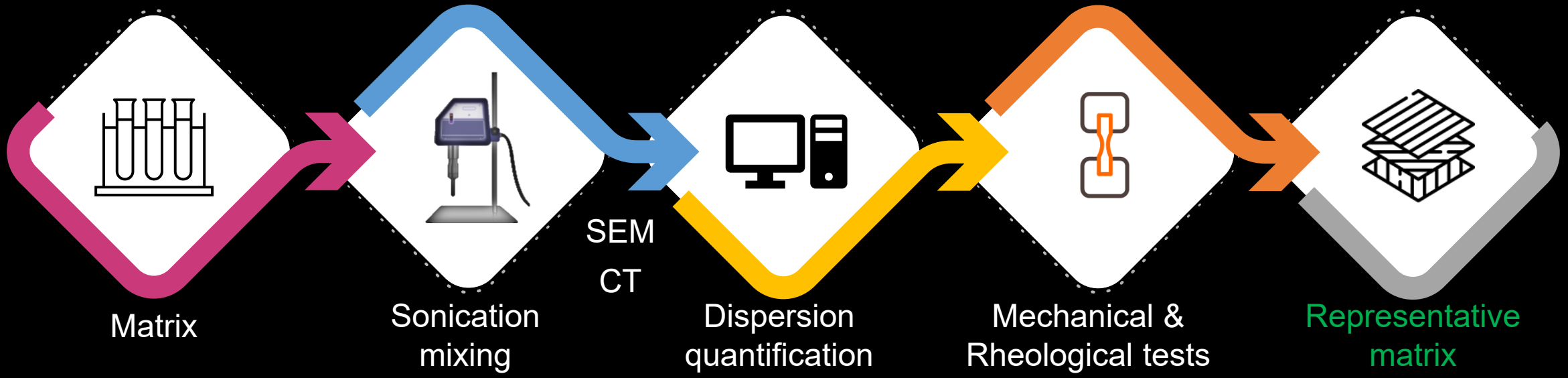

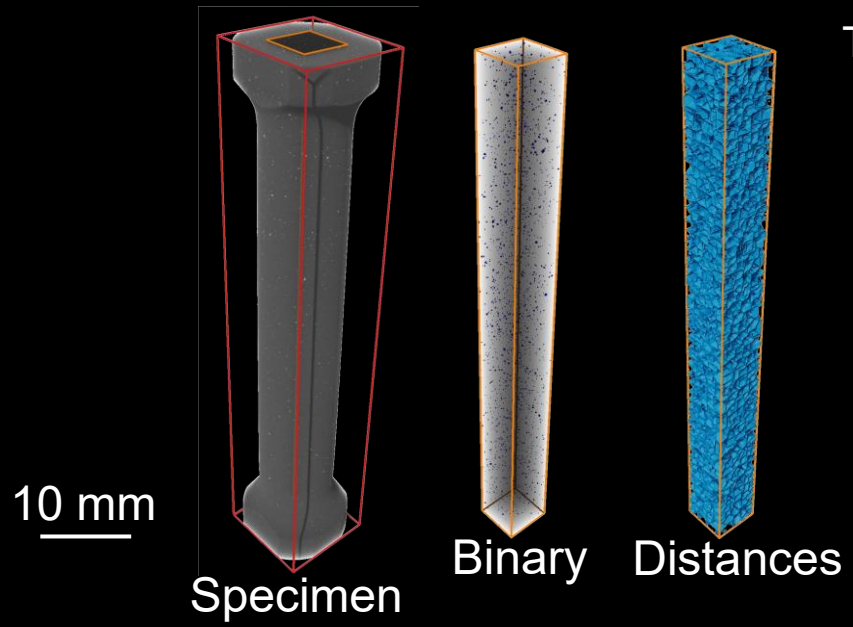

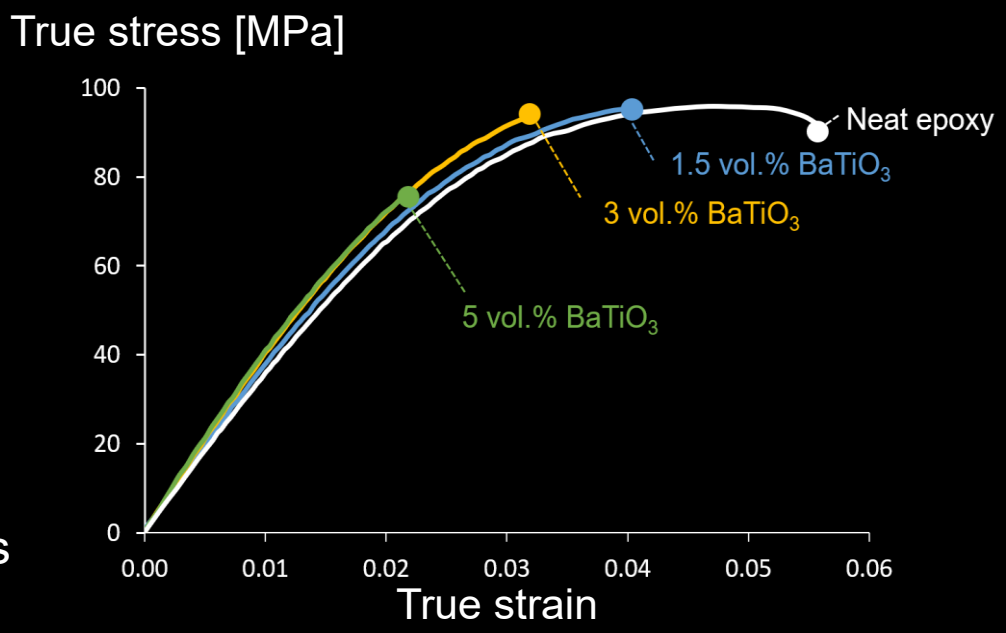

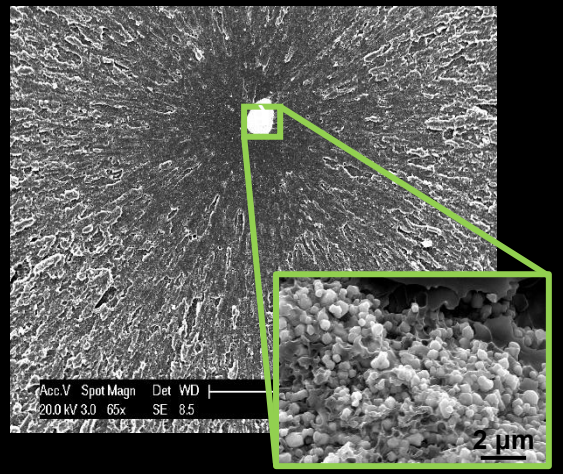

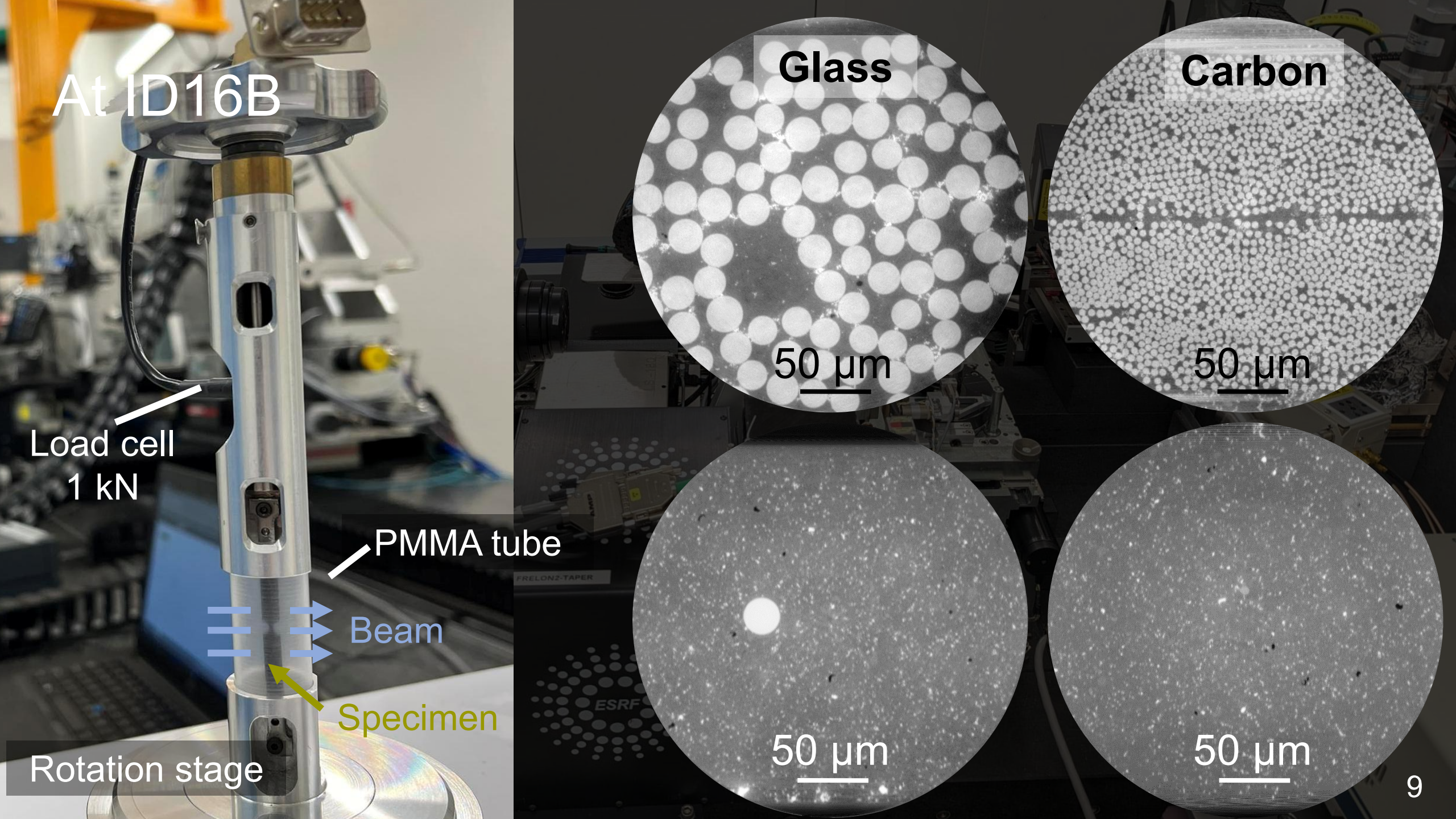
At ID16B
Load cell
1 kN
PMMA tube
Beam
Specimen
Rotation stage
Glass
50 µm
Carbon
50 µm
50 µm
50 µm

Fibre breakage

Fibre breaks visible in both fibres

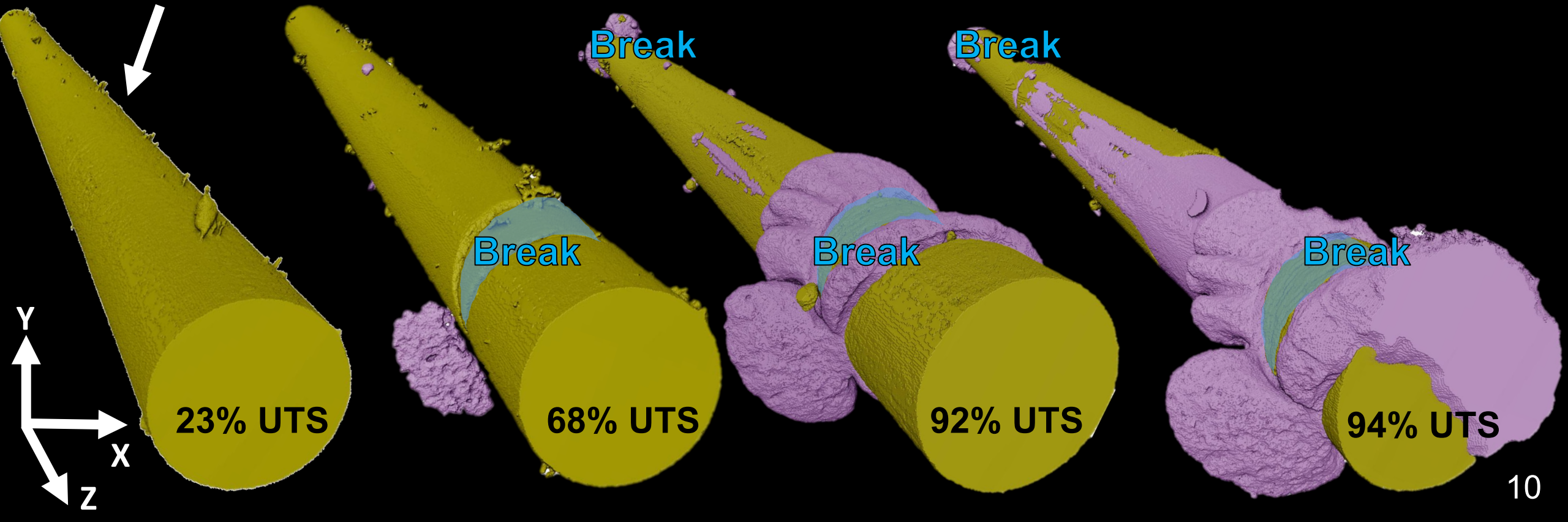

Interfacial debonding

First observation of longitudinal debonding in 3D

Visible in both fibres

Asymmetric along the fibre cross-section

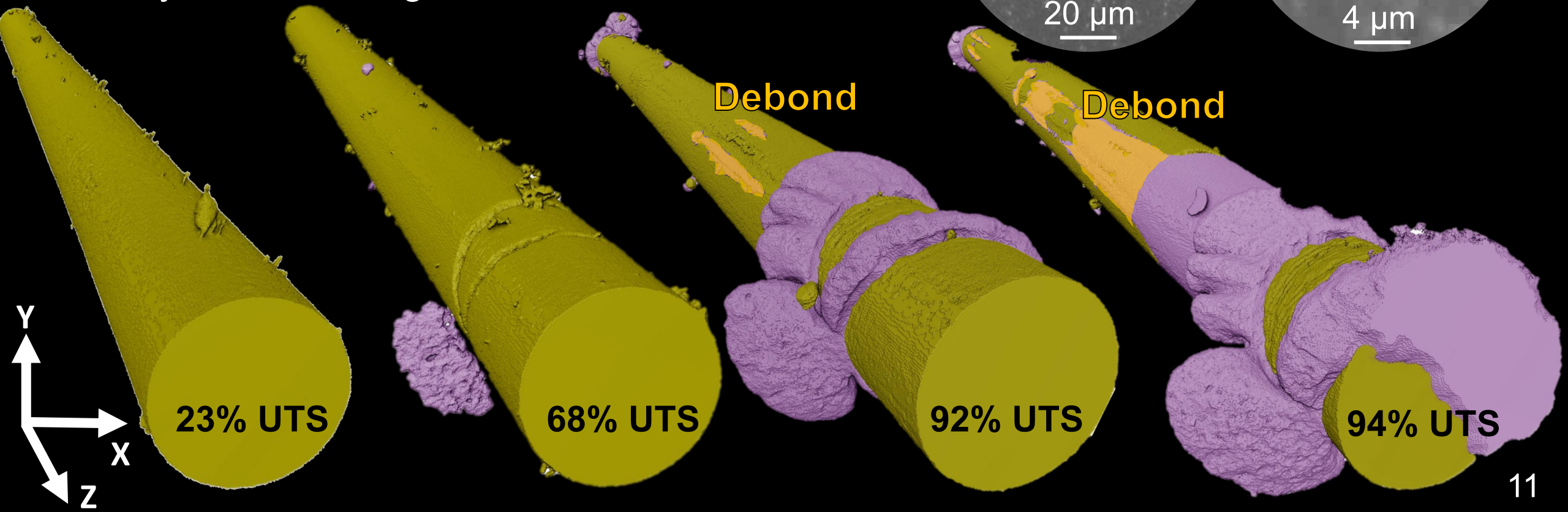

Matrix cracking

Extensive for glass fibre

Absent for carbon fibre

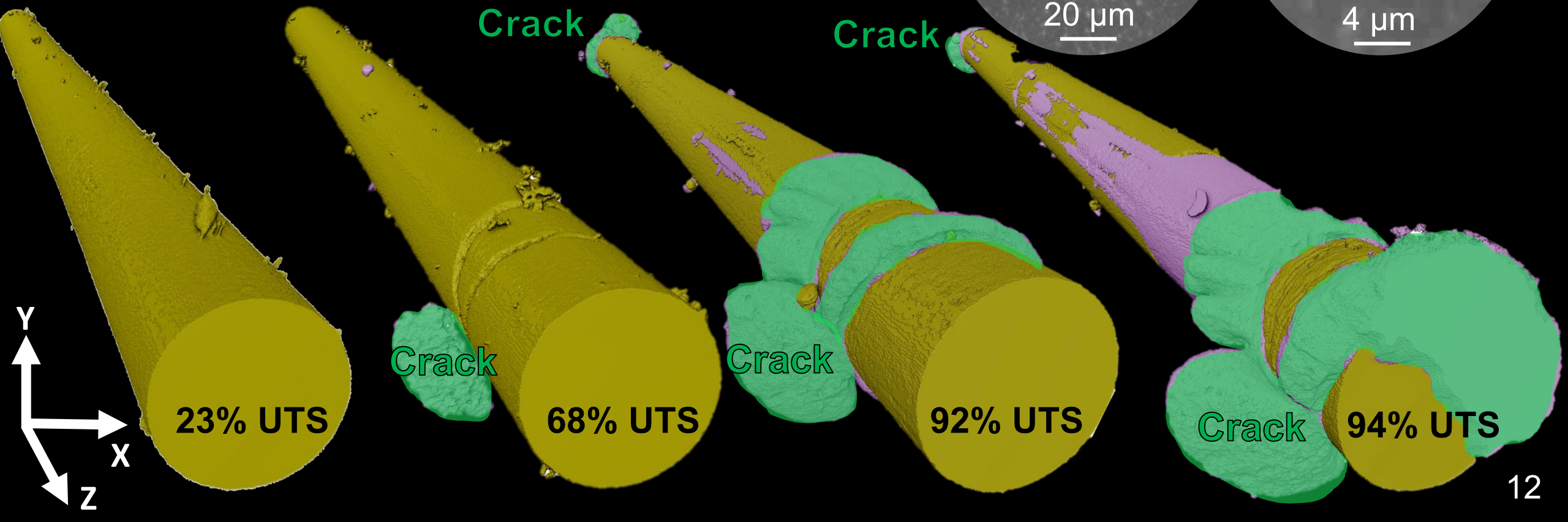

Double-fibre composites

Two embedded carbon fibres

Similar response as for the carbon single-fibre case

Extensive interfacial debonding

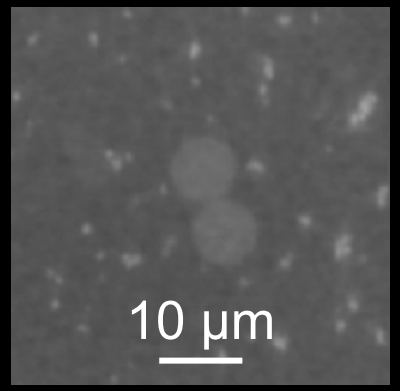

27% UTS

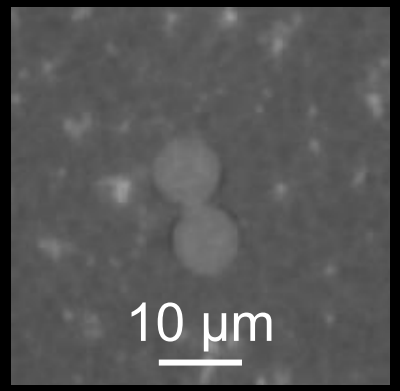

69% UTS

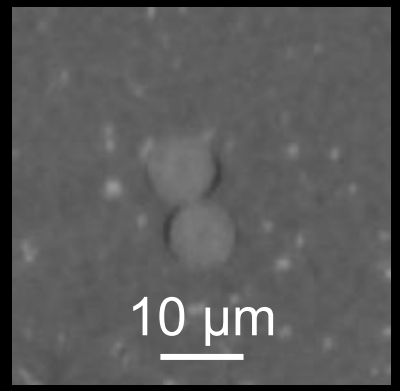

90% UTS

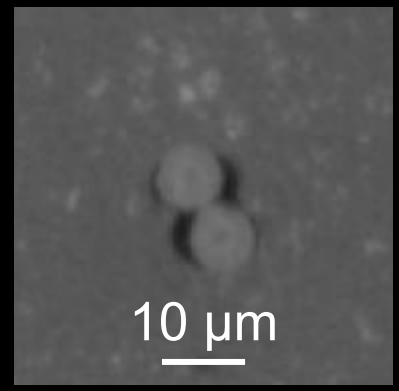

99% UTS

Multi-fibre composites

Absence of debonding

Negligible matrix cracking around fibre breaks

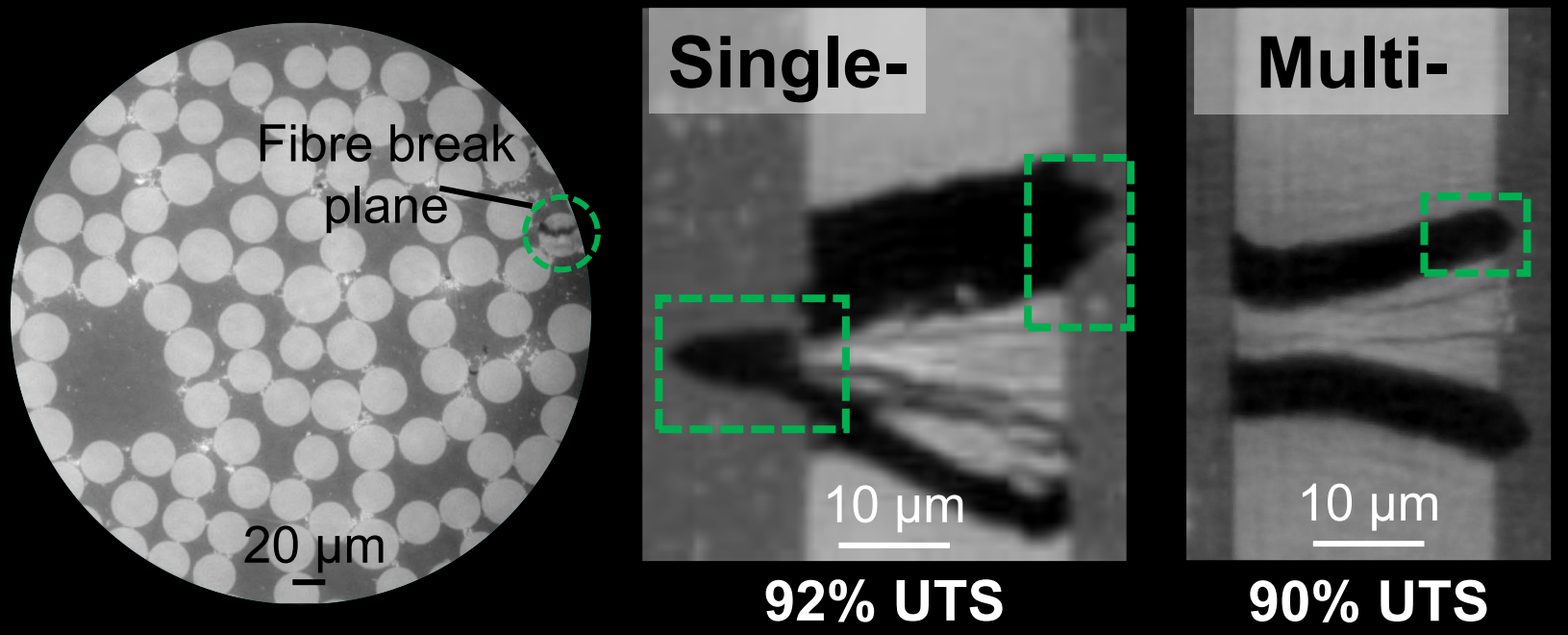

Possible reasons for the discrepancy

1. Matrix size effect
2. Interphase or matrix in situ effect
3. Strain energy release

RESEARCH ARTICLE

NANO · MICRO small
www.small-journal.com

Questioning the Representativeness of Damage Mechanisms in Single-Fiber Composites via In Situ Synchrotron X-Ray Holo-Tomography

Thanasis Chatziathanasiou, Yeajin Lee, Julie Villanova, Olga Stamati, Sina AhmadvashAghbash, Babak Fazlali, Christian Breite, Ian Sinclair, Mark N. Mavrogordato, S. Mark Spearing, Mahoor Mehdikhani, and Yentl Swolfs*

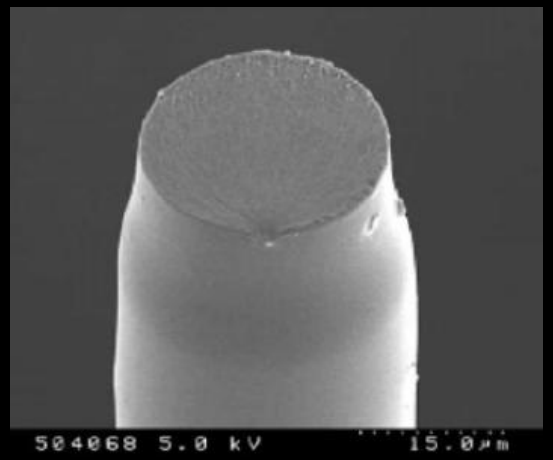

Hobbiebrunken et al., 2007

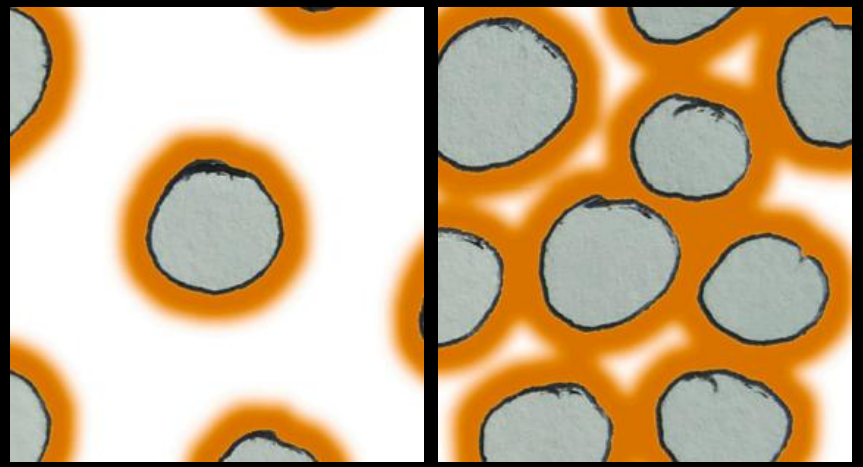

Herrmann et al., 2022

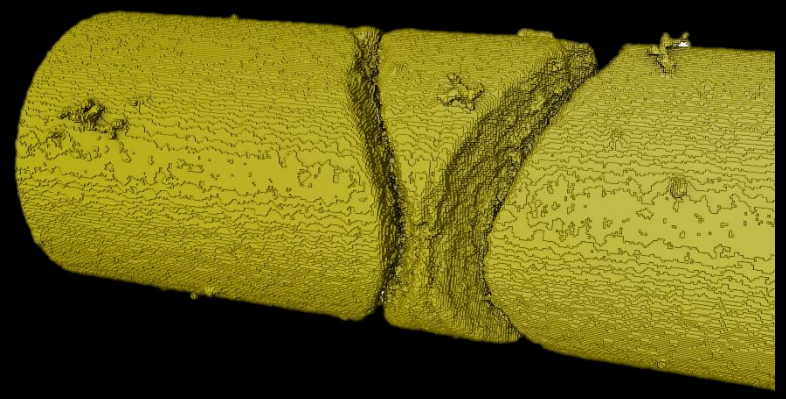

Conclusions

- The representativeness of single-fibre composites warrants further investigation.
- Advanced 3D nano-imaging techniques, such as synchrotron holo-tomography can effectively scrutinise interfacial damage response.

Ongoing research and future work

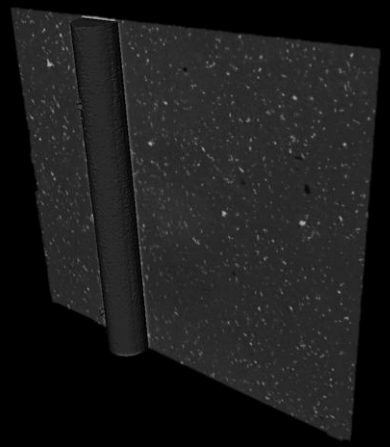

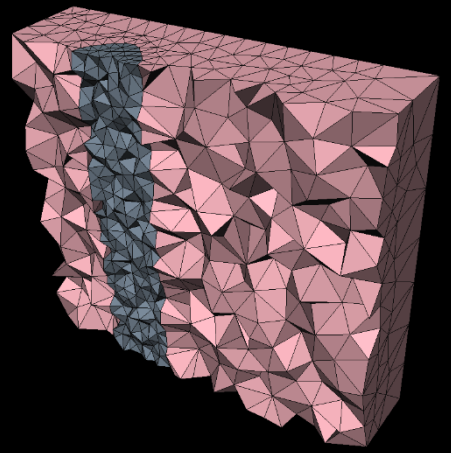

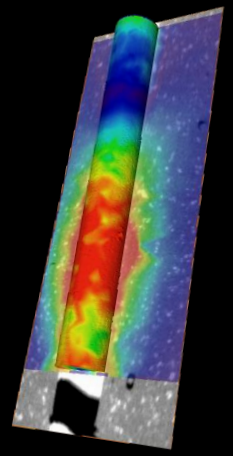

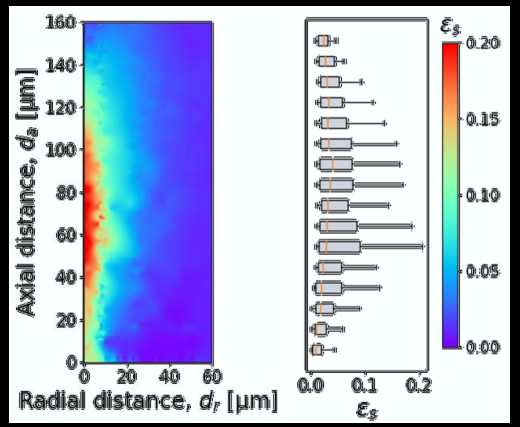



AIST

fwo

Thank you for your attention

T. Chatziathanasiou, Y. Lee, C. Breite, M. Diehl, I. Sinclair, M.N. Mavrogordato, S.M. Spearing, M. Mehdikhani, Y. Swolfs

Composite Materials Group
Department of Materials Engineering, KU Leuven

KU LEUVEN

University of Southampton

ESRF

ICCM24
24TH INTERNATIONAL CONFERENCE ON COMPOSITE MATERIALS

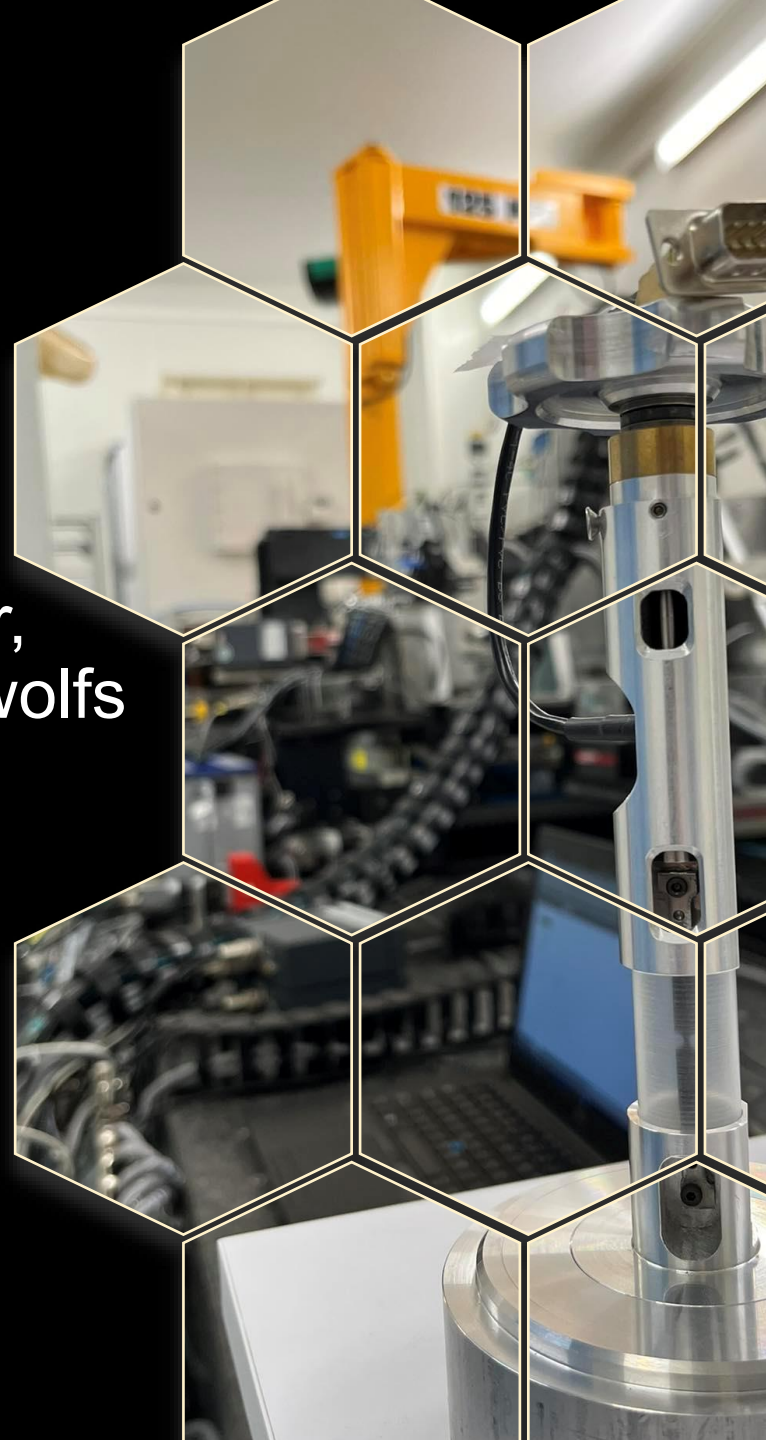

International Committee on Composite Materials

Student Status Confirmation Form for the ICCM Tsai Award

3rd June 2025

I, Simon Mark Spearing, hereby confirm that Yeajin Lee, who applied for the ICCM Tsai Award, was, at the date of the abstract submission 15th November 2024, a Ph.D student under my supervision at the University of Southampton.



_____

Simon Mark Spearing

Professor of Engineering Materials
Vice-President for Research and Enterprise
University of Southampton
Highfield
Southampton
SO17 1BJ
United Kingdom
spearing@soton.ac.uk
+44 79 1916 4783

UNRAVELLING LINKS BETWEEN FIBRE MISALIGNMENT, RESIN-RICH POCKETS, AND THE FIBRE BREAK DEVELOPMENT VIA *IN SITU* HOLOTOMOGRAPHY

Yeajin. Lee[1*], Thanasis. Chatziathanasiou[2], Christian. Breite[2], Mahoor. Mehdikhani[2], Yentl. Swolfs[2], Mark. N. Mavrogordato[1], S. Mark. Spearing[1], Ian. Sinclair[1]

[1] μ-VIS X-ray Imaging Centre, University of Southampton, United Kingdom
[2] Department of Materials Engineering, KU Leuven, Belgium
Email: yeajin.lee@soton.ac.uk

Keywords: CFRP, Synchrotron holo-tomography, Microstructural variations, Fibre breaks

ABSTRACT

Understanding the mechanical influence of microstructural variations on fibre break development is crucial for reducing uncertainties in predicting the longitudinal tensile failure of unidirectional composites. In this study, the interaction between local microstructural variations and fibre breaks is monitored using *in situ* X-ray holotomography at 150 nm resolution. Three distinctive microstructures are identified to drive the initiation and clustering of breaks. First, misplaced fibres within the 0°/0° interply region, which exhibit significant misorientation and cross multiple adjacent fibres, progressively trigger multiple single breaks and a co-planar cluster at their intersections. Second, resin-rich pockets within the 0°/0° interply region promote clustering of breaks, progressively forming a non-coplanar cluster of five breaks. This clustering is accompanied by non-uniform matrix microcracks and short interfacial debonds around the break sites. Third, larger resin-rich pockets, locally formed in regions with groups of misoriented fibres, play a critical role in driving pronounced break clustering. Their interactions exhibit severe matrix nonlinearity, as evidenced by matrix microcracks, short interfacial debonds, and damage features, including microvoids or the onset of matrix microcracks. The identified fibre break patterns, clustering behaviour, and damage associated with three microstructural cases provide new insights into how these microstructures serve as precursors to fibre break development, highlighting the importance of accounting for them in predicting longitudinal tensile failure to improve reliability.

1. Introduction

Carbon fibre-reinforced composites are now widely used in structural applications in the automotive, aerospace, and renewable energy sectors. Despite their widespread use, their relatively brittle structural response remains a key challenge in material design and failure prediction. Longitudinal tensile failure is arguably regarded as the most fundamental and crucial among all failure modes. It is widely recognised that the tensile final failure of multidirectional composites is determined by the failure of fibres oriented in the principal loading direction [1]. This failure scheme begins with the weakest fibres failing and culminates in the development of critical clusters that eventually trigger a self-sustaining cascade of fibre failures [2]. Each break diminishes load-carrying capacity, thereby redistributing the load to neighbouring fibres within a certain distance from the break. This redistribution is accompanied by shear-dominated deformation of both the matrix and the interface, involving various damage mechanisms such as matrix cracking and interfacial debonding.

To predict the size and severity of the region surrounding breaks, many studies have investigated stress redistribution around fibre breaks using finite element models [3-6]. However, uncertainties persist in these predictions, particularly because most models do not account for manufacturing-induced microstructural variations, such as severe local fibre misalignment and resin-rich pockets. In recent years, Synchrotron Radiation Computed Tomography (SRCT), pinnacle of computed tomography, has enabled 3D, *in situ*, imaging of composites at a resolution sufficient to distinguish individual fibre breaks [7, 8] and to correlate with microstructural features [9-11]. This has catalysed the opportunity for a deeper

understanding of how variations in microstructural features influence fibre breaks and, more broadly, composite strength in both experimental and numerical studies.

From an experimental perspective, Rosini *et al*. [11] examined the differences in local fibre misorientation between break and intact sites. Their statistical results demonstrated that fibres at single break sites have a higher standard deviation in their orientation distribution compared to intact fibre sites. Breite *et al*. [2] observed similar break behaviour through *in situ* SRCT, linking clustered breaks to fibre regions with significant in-plane misalignment. Findings from both studies remain limited to the initiation of single and clustered breaks, without elucidating the damage mechanisms that drive their formation and subsequent progression, or how clusters interact with local microstructural variations under increasing loads. In this context, Fritz *et al*. [12] used micro-CT to identify microstructural features in UD carbon fibre composites, but without performing *in situ* monitoring with applied loads. In particular, the study reported on the presence of *misplaced* fibres at ply interfaces, which deviate markedly from the main UD ply orientation and intersect multiple neighbouring fibres (as opposed to *misaligned* fibres, which may deviate from the nominal ply direction but are entirely constrained to their local tow).

FE models incorporating microstructural variations have also addressed their effects on stress localisation and composite strength. Malgioglio *et al*. [13] reported that increased variability in fibre misalignment reduced strength and increased the scatter in predicted strength values. Models in the study, however, are limited to the ply level. The replicated misorientation angles (-2° to 2°) remained insufficient to fully capture the range observed in commercially manufactured composites. Recently, Jafarypouria *et al*. [14] implemented microscale FE models to examine stress redistribution around a single fibre break in both misaligned and perfectly aligned fibres. This reported an increase of ~33% in the maximum stress concentration factors in neighbouring fibres for the misaligned case. However, the applicability of model is still limited by the studied range of misorientation angles (1.4° to 5°).

Although the studies discussed above have advanced the understanding of how local microstructural variations relate to tensile failure, two important questions remain open for further investigation:

- If fibres exhibit local misalignment exceeding the small angles typically studied (<5°), similar to the misplaced fibres reported by Fritz *et al*. [12], how do severely misaligned fibres interact with adjacent aligned fibres, and how does this influence break behaviour under tensile loading?
- When fibres break at sites with local microstructural variations, how do the localised stresses interact with the surrounding matrix and fibre-matrix interfaces, and how might the resulting damage cause clustering of fibre breaks?

Whilst SRCT has been shown to be a valuable tool for understanding fibre failure, imaging at resolutions better than ~500 nm is rarely conducted due to constraints in image acquisition. Given this resolution level and scale of carbon fibres, isolated matrix microcracks and interfacial debonds may not be reliably detected, because their openings may be smaller than 30% of the voxel resolution. Even if such damage features exist, they can be obscured by bright fringes originating from discontinuities (i.e. fibre breaks), which are typically observed in propagation-based SRCT. To address these imaging limitations, Chatziathanasiou *et al*. [15] conducted the first *in situ* X-ray holo-tomography of composites at a 150 nm resolution. This technique, based on phase contrast nano-imaging, enabled the detection of matrix cracks and interfacial debonds initiated from breaks in glass and carbon fibre composites.

In this work, we extend the use of 150 nm *in situ* holo-tomography to elucidate interactions between local microstructural variations and fibre breaks under longitudinal tensile loading. Our primary objective was to link microstructural variations to the initiation and progression of breaks into clusters, along with associated microscale damage, such as matrix microcracks and interfacial debonds. In particular, we focus on three distinctive microstructures influencing fibre break development: (i) misplaced fibres, *i.e.* fibres crossing several other fibres, (ii) resin-rich pockets, and (iii) larger resin-rich pockets locally formed along groups of misoriented fibres. By addressing two key research questions outlined above, this study bridges a gap in understanding the influence of microstructural variations on longitudinal tensile failure.

2. Materials and methods

2.1. Materials

$[90/0]_s$ cross-ply laminates of aerospace-grade carbon fibre/epoxy prepreg were provided by Mitsubishi Chemical Corporation, with a total thickness of ≈ 0.5 mm. MRZ65-18000 carbon fibre (Mitsubishi Chemical Corporation) was used, with a nominal fibre diameter of 5.4 μm and a tensile modulus of 287 GPa. A #350 series, amine curing epoxy (Mitsubishi Chemical Corporation) was used as the matrix and cured via a standard aerospace autoclave cycle in accordance with the manufacturer's specifications.

The epoxy matrix was doped with 2.3 vol.% of silicon dioxide particles (SiO_2, 500 nm, near-spherical) to facilitate digital volume correlation on the tomograms. The selected particle properties were intended to minimise impact on the mechanical behaviour of the polymer matrix system, as suggested in [15, 16]. While digital volume correlation analysis was performed on these material/tests, the results are not a focus of this work and will not be discussed further.

2.2. Specimen design

Double-notched specimens, with a notch section width of 0.8 mm between the notch roots, were prepared for *in situ* tensile testing. The sample geometry is described in further detail in [15]. The volume fraction of 0° fibres in the notch region, as measured from the 3D reconstructed volume, was 48.5%. The specimens were machined using waterjet cutting, a method used previously for machining similar specimens without causing significant damage. Straight aluminium tabs, 1.5 mm thick, were attached to both faces and both ends of specimens using aerospace adhesive, Scotch-Weld™ EC-9323 B/A (3M Company, Maplewood, MN, USA), to aid loading and mitigate stress concentrations at the specimen ends.

Prior to the *in situ* experiments at ID16B beamline, *ex situ* tensile tests were performed on five specimens to determine the ultimate tensile strength (UTS) specific to the notch region. Given that the 0° plies were expected to primarily determine the longitudinal tensile failure of the specimens, only their cross-sectional area prior to the onset of 0° fibre splitting was used to calculate the UTS. The average of the measured UTS values was 2545 ± 168 MPa, serving as a reference for determining the stepwise loads applied during *in situ* testing.

2.3. *In situ* synchrotron holotomography

In situ holotomography scans were undertaken at 150 nm nominal (voxel) resolution on the ID16B beamline of the European Synchrotron Radiation Facility (ESRF), Grenoble, France. Holotomography, based on phase contrast nano-imaging, delivers images with spatial resolutions down to 25 nm (voxel) and is particularly well suited to materials with low attenuation. For each scan at a given load level, four distinct holograms are acquired at different sample-to-detector distances, enabling the retrieval of detailed phase information. A single tomogram is therefore reconstructed with enhanced signal-to-noise ratio and improved image quality.

In situ tensile tests were performed using a screw-driven loading rig equipped with a 1 kN load cell, custom-designed at KU Leuven for integration with the beamline. A detailed description of the rig is provided in [15]. A tensile specimen was loaded to five incremental levels (5%, 67%, 86%, 91%, 96%) of the measured UTS, with scans taken at each level. A 2048 × 2048 $pixel^2$ detector (PCO Edge 4.2 CLHS sCMOS) was used, with geometrical magnification resulting in an effective voxel size of 150 nm. A "pink" beam with an energy of 29.6 keV was used [17]. Each scan acquired 2505 projections, with an exposure time of 10 ms per projection. Tomograms were reconstructed using in-house software at the ESRF [18].

3. Results and discussion

Fibre breaks formed in association with microstructural variations were identified in three regions (**Fig. 1**): misplaced fibres (Region 1), resin-rich pockets (Region 2), and larger resin-rich pockets locally formed along groups of misoriented fibres (Region 3). The causality of the breaks and their clustering was elucidated through hypothesised mechanisms contributing to the observed break behaviour, alongside microscale damage patterns developed near breaks.

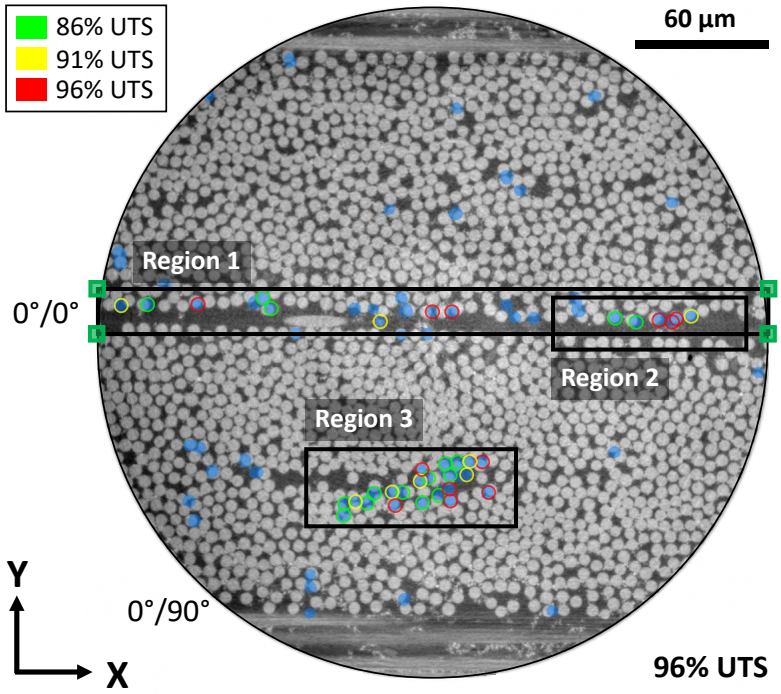

Fig. 1. A 150 nm SRCT image of the tested specimen containing two 0° plies, acquired at 96% UTS, showing all fibre breaks within the scan volume projected as blue dots. The black rectangles at the 0°/0° interply ('Region 1' and 'Region 2') and 0° intraply ('Region 3') mark the cropping regions for the stacks containing break sites identified as interacting with microstructural variations. Each region shows the projection of identified breaks, with outlines colour-coded in green, yellow, and red, to indicate their formation at 86%, 91%, and 96%, respectively.

3.1. Misplaced fibres within the 0°/0° interply region

3.1.1 Fibre breaks linked to misplaced fibres

This is the first report of fibre break behaviour occurring in regions where misplaced fibres are present, as monitored by *in situ* scans. **Fig. 2a** illustrates the XZ plane view of the stack in Region 1 at 96% UTS, revealing three misplaced fibres (labelled as fibres 1, 2, and 3) in the interply region, with misorientation angles of -26°, 79°, and -35°, respectively. These angles represent the deviation of fibre orientations within the XZ plane relative to the Z-axis loading direction, with the positive direction defined as clockwise from the Z-axis.

The three misplaced fibres appear to cross and come into close contact with adjacent fibres. To investigate how these misplaced fibres relate to break occurrence, the stack was first projected along the Y-axis using the *average intensity* Z-projection in ImageJ. **Fig. 2b** presents the resulting XZ slice, highlighting the projections of nine break sites (1 to 9) spatially aligned with the misplaced fibres. In parallel, the XY cross-sectional views of the nine breaks were visually examined. As illustrated in **Fig. 3**, crossings between misplaced and adjacent fibres appear to progressively trigger seven single breaks and one co-planar break pair ('duplet') at load levels up to 96% UTS, either within the misplaced fibres or in the adjacent aligned fibres at their intersections.

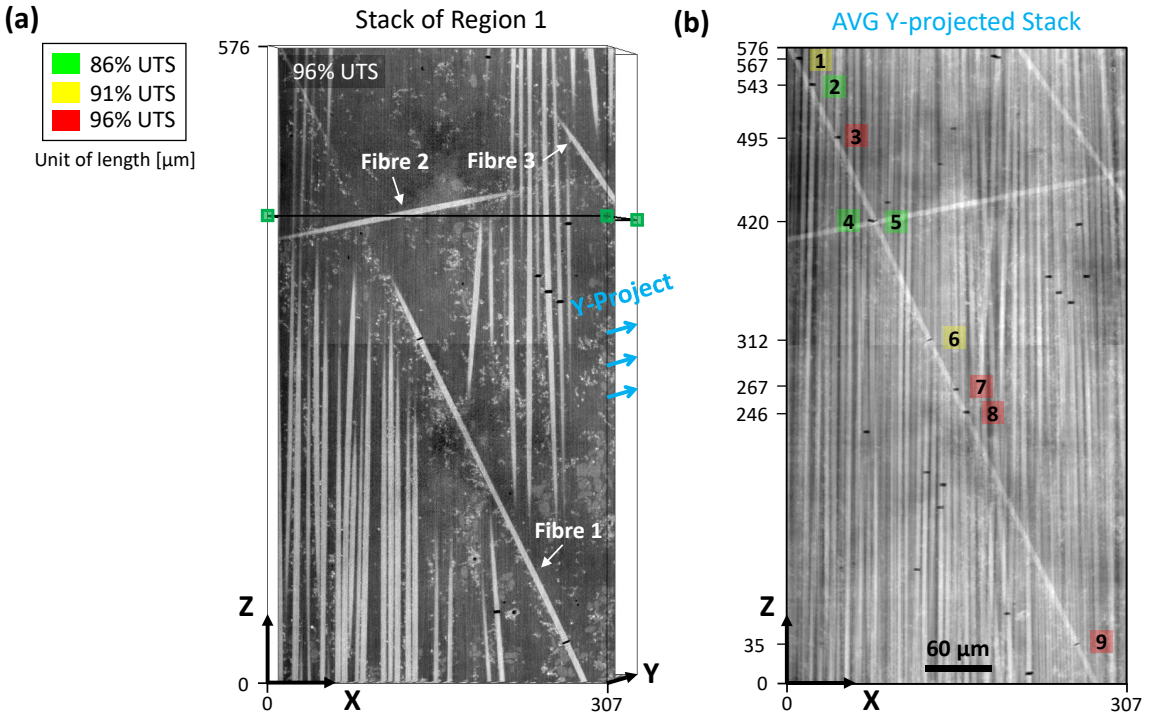

Fig. 2. (a) XZ plane view of the stack cropped from Region 1 at 96% UTS, showing three misplaced fibres (labelled 1, 2, and 3) crossing adjacent fibres. (b) XZ slice obtained by average intensity projection of the Region 1 stack along the Y-axis, revealing nine break sites at intersections between misplaced and adjacent fibres.

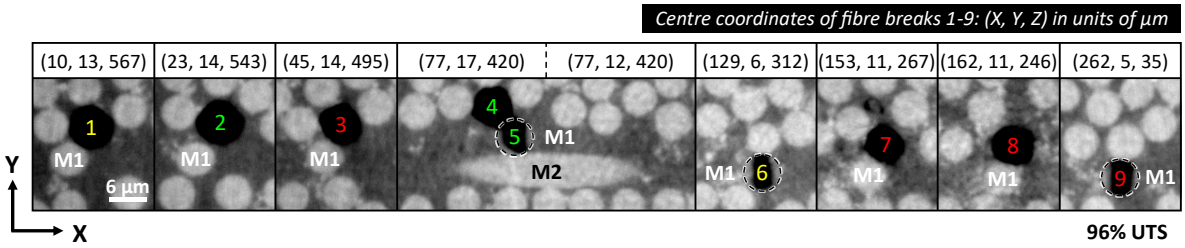

Fig. 3. XY fibre cross-sectional views of nine breaks formed within the Region 1 stack (**Fig. 2b**), with all break sites located either within misplaced or adjacent fibres at intersections. Misplaced fibres 1 and 2 are labelled as M1 and M2, respectively. Each break number is colour-coded by formation load level, with centre coordinates defined relative to the XYZ axes of the Region 1 stack.

3.1.2 Role of misplaced fibres in break initiation

We propose two hypotheses to explain the mechanisms underlying the observed behaviour. First, the formation of multiple breaks at the intersections might be related to the tow spreading and resin impregnation process during prepreg manufacturing. These two processes, when carried out using the direct contact (mechanical) method, employ spreading or impregnation rollers to flatten the fibre tows into a uniform prepreg sheet, bringing the surface fibres on each ply into contact with the rollers during processing. This contact can build up shear and frictional stresses on the fibre tows, as indicated by Moradi *et al*. [19]. It is plausible that these stresses could concentrate on misplaced and misaligned fibre tows crossing over aligned fibres on the ply surface, potentially causing damage to the filaments within the fibre tows. This, in turn, could introduce strength controlling defects at the crossing points. Consequently, we hypothesise that such defects could explain the increased prevalence of fibre breaks within the interply region. Mesquita *et al*. [20] similarly reported a higher occurrence of fibre breaks

near the ply interface in thin plies, despite the absence of strongly misaligned fibres. This was suggested to result from the fibre weakening introduced during the tow spreading, which is consistent with the hypothesis we propose.

Another possible explanation for the observed breaks (1 to 9) involves micro-mechanical influences arising from local fibre misalignments, particularly local stress concentrations at intersections between misplaced and adjacent fibres. When fibre bundles were subjected to tension, misplaced fibres themselves may have experienced bending stresses in addition to axial stresses, placing them in a multiaxial stress state. This, in turn, may induce higher shear stresses in the matrix surrounding the misplaced fibres, leading to the formation of inhomogeneous stress states in nearby fibres. Crossing over adjacent fibres, misplaced fibres are likely to have intensified local stress concentrations at their intersections. Consequently, this could impart elevated stresses to misplaced or aligned fibres, or both, increasing their susceptibility to failure. Notably, **Fig. 3** illustrates co-planar breaks (4 and 5) formed at 86% UTS, when two misplaced fibres 1 and 2 crossed and contacted adjacent fibres. This phenomenon could be attributed to intensified local stress concentrations at intersections, exemplifying the micro-mechanical influences we proposed.

3.2. Resin-rich pockets within the 0°/0° interply region

3.2.1 Fibre break clustering and microscale damage linked to resin-rich pockets

A cluster in this study was defined as fibre breaks separated by less than 10 fibre diameters longitudinally (Z-axis) and two fibre diameters radially (X and Y-axis), consistent with the definition used in [8]. **Fig. 4** illustrates the primary findings of break clustering and associated microscale damage that progressively occurred along resin-rich pockets in Region 2 up to 96% UTS.

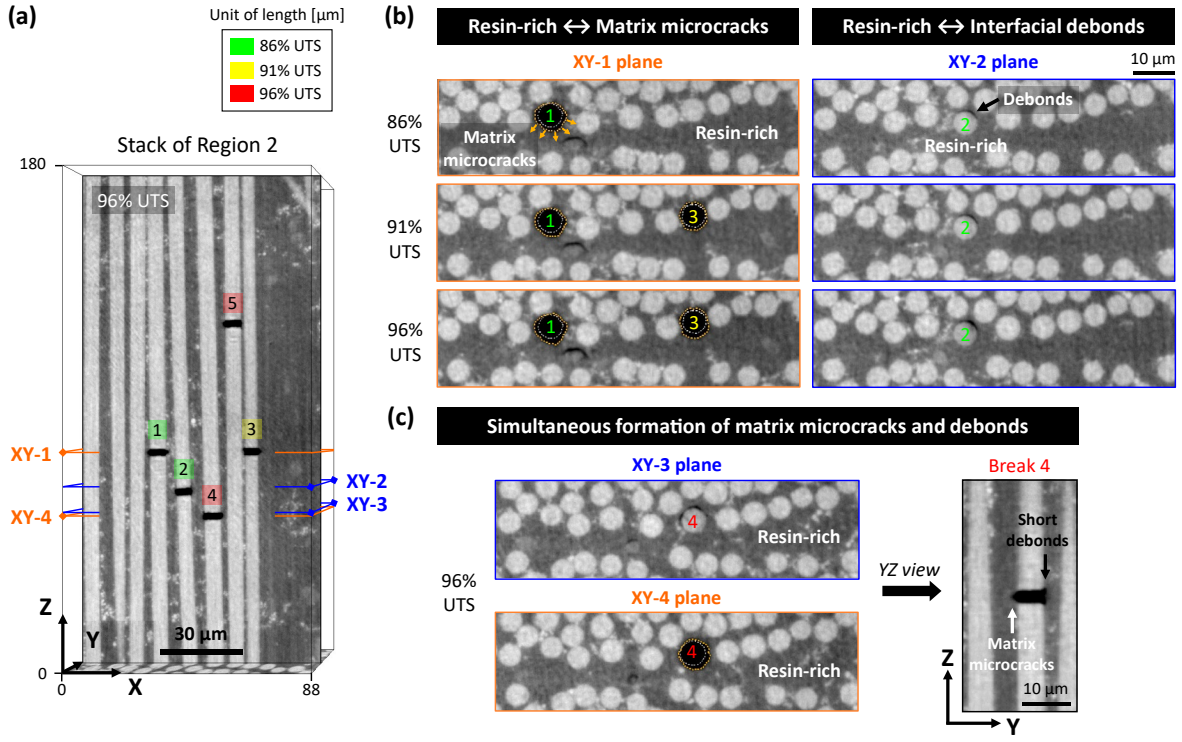

Fig. 4. (a) XZ plane view of the stack cropped from Region 2 at 96% UTS, showing non-coplanar breaks (1 to 5) near resin-rich pockets. Four marked positions (XY-1 to 4) indicate the locations used to extract XY cross-sectional planes at each break. (b) XY-1 and XY-2 planes of clustered breaks (1 to 3), revealing two distinct microscale damage patterns near resin-rich pockets, observed at 86%, 91%, and 96% UTS. The edges of matrix microcracks and fibres are delineated by orange and white dashed lines. (c) XY-3 and XY-4 planes at break 4, showing simultaneous formation of two microscale damage patterns.

No damage was observed in this region at 67% UTS. However, breaks 1 and 2 appeared as non-coplanar breaks at 86% UTS (**Fig. 4a**). The use of high-resolution phase contrast imaging facilitated a detailed examination of damage surrounding the breaks. The XY cross-sectional planes of each break reveal microscale damage in the form of matrix microcracks and short interfacial debonds (**Fig. 4b**). These two features contrast with their apparent absence around fibre breaks where no resin-rich pockets are present, as reported in [15]. Adjacent to break 1, a matrix microcrack of ~1.1 μm in extent formed at break edges facing resin-rich pockets and extended into these regions, creating a non-uniform crack pattern around the fibre circumference (see XY-1 plane). The crack tips also appear distinctly wide/blunted as they extend into resin-rich pockets, resembling those observed near break 4 at 96% UTS (see YZ plane in **Fig. 4c**). In contrast, break 2 exhibited short interfacial debonds measuring ~1.2 μm in axial length along the fibre direction (see XY-2 plane). These debonds were confined to the side opposite the resin-rich pockets, where the inter-fibre distance surrounding break 2 is small, leading to their asymmetric formation.

At 91% UTS, break 3 emerged in the vicinity of clustered breaks 1 and 2. While showing no visible debonds, the XY-1 break plane also reveals non-uniform matrix microcracks similar to those previously seen near break 1. With further loading to 96% UTS, additional breaks 4 and 5 formed in regions of fibres that were likely overloaded by neighbouring breaks 2 and 3. This consequently formed a non-coplanar cluster of five breaks (1 to 5) within approximately the same XZ plane located near resin-rich pockets. As shown in **Fig. 4c**, break 4 initiated matrix microcracking and short debonds simultaneously, consistent with the damage patterns seen near resin-rich pockets at lower loads (see XY-3 and XY-4 planes).

3.2.2 Role of resin-rich pockets in break clustering and microscale damage development

The observed patterns of matrix microcracks, characterised by non-uniform propagation towards resin-rich pockets with blunted crack tips, may be attributed to low local stiffness in resin-rich regions adjacent to broken fibre. These regions contain fewer surrounding fibres to suppress crack growth, permitting greater crack opening [5]. Despite their wide crack openings, the maximum extent of crack propagation remained relatively short (~1.6 μm). This cracking behaviour could be indicative of shear nonlinearity locally occurring in the resin-rich regions. Yang *et al.* [21] suggest that shear nonlinearity in carbon epoxy composites may originate from microscale processes such as matrix microcracking. Molecular-level plasticity in the resin is also reported as a potential source of shear nonlinearity.

In contrast, the clustered breaks exhibited asymmetric debonding that was highly localised near break edges farther from resin-rich pockets, with debond lengths reaching no more than ~1.5 μm. This debonding can be explained by the localisation of shear stresses induced by breaks, which tend to concentrate more in regions with smaller inter-fibre distances rather than near resin-rich pockets. From an energy standpoint, the short extent of the debonds suggests that the strain energy released from a fibre break was not favourably absorbed through debonding. Rather, a greater portion of the energy was likely absorbed by matrix cracking and matrix plasticity, as discussed above.

In light of these findings, the continuous formation of matrix microcracks and short debonds from 86% UTS onwards indicates that resin-rich pockets may have played a significant role in promoting break clustering. This suggests that breaks near resin-rich pockets may induce more localised stress concentrations in the matrix and interface, thereby reducing effective matrix stiffness and introducing shear nonlinearity. As a result, neighbouring intact fibres near both newly formed and pre-existing breaks may become overloaded at each load level. This could increase the likelihood of cascading effects that promote the clustering of breaks under increasing loads, which may explain the formation of non-coplanar clusters within the interply region. Furthermore, another factor contributing to the clustering could be linked to the increased prevalence of breaks at or near the ply interface (see section **3.1.2**).

3.3. Larger resin-rich pockets along misoriented fibre groups within the 0° intraply region

3.3.1 Fibre breaks linked to groups of misoriented fibres

Fig. 5 illustrates the primary findings on break initiation and clustering associated with groups of misoriented fibres and the resulting larger resin-rich pockets. The XY plane view of stack in Region 3

at 96% UTS is presented in **Fig. 5a**, showing projections of all breaks (1 to 22) formed at each load level within the stack. Groups of misoriented fibres are distributed across slices from XZ-1 to XZ-4 planes within the stack.

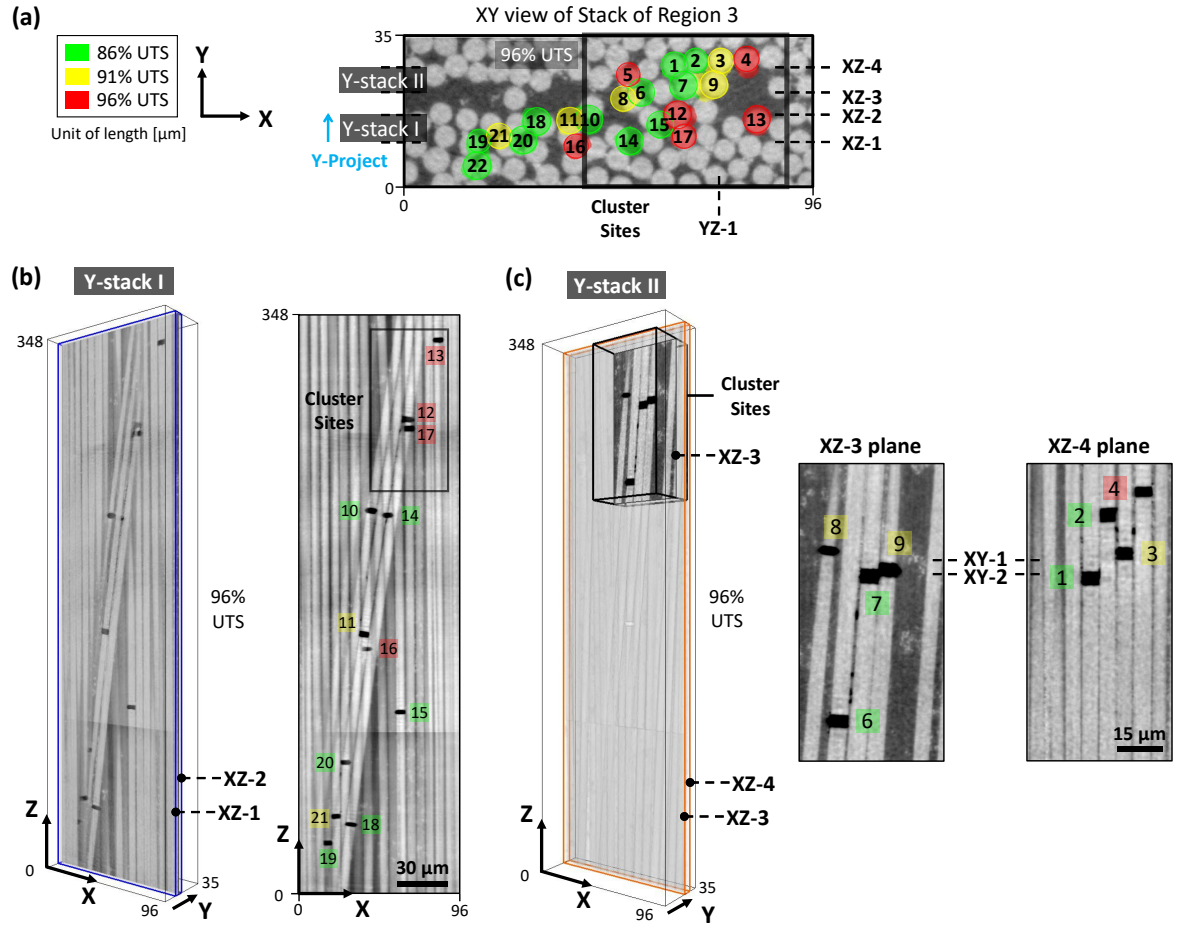

Fig. 5. (a) XY plane view of the stack cropped from Region 3, showing the projection of all detected breaks (1 to 22) within the stack, colour-coded by their formation load level. The black rectangle marks the cropping region containing the cluster sites. Five marked positions (XZ-1 to 4 and YZ-1) indicate locations used to extract XZ and YZ plane views at the cluster sites. (b) XZ plane view of 'Y-stack I' and an XZ slice obtained by average projection. (c) XZ plane view of 'Y-stack II' with magnified views of cluster sites at the XZ-3 and XZ-4 planes. Two marked positions (XY-1 to 2) indicate locations used to extract XY plane views at the cluster sites.

As shown in **Fig. 5b**, 'Y-stack I', sliced from XZ-1 to XZ-2 planes, is found to contain the most severely misoriented group of fibres, which collectively cross over adjacent aligned fibres with misorientation angles of 8°. Accordingly, larger resin-rich pockets were formed along the regions occupied by these misoriented fibres. The breaks accumulated up to 96% UTS in the Y-stack I are effectively visualised in 2D using the average projection along the Y-direction, consistent with the method used in section **3.1.1**. Breaks consistently occurred at intersections between misoriented fibre groups and adjacent fibres, closely resembling the break behaviour observed near misplaced fibres (see section **3.1.1**). As such, we propose that micro-mechanical effects, i.e. local stress concentrations arising at the intersections, could be linked to this break behaviour, consistent with the hypothesis proposed on breaks linked to misplaced fibres. In addition, Jafarypouria *et al.* [14] demonstrated that peak stress concentration factors in the neighbouring intact fibres near a break were ~33% higher in misaligned fibre bundles than in perfectly aligned ones, which further supports our hypothesis.

3.3.2 Fibre break clustering and microscale damage linked to larger resin-rich pockets

Fig. 5c presents 'Y-stack II', sliced from XZ-3 to XZ-4 planes within the Region 3 stack. A labelled region, referred to as cluster sites, contains non-coplanar breaks that developed near larger resin-rich pockets locally formed along misoriented fibre groups. Most of these breaks predominantly developed within the same XZ break planes up to 96% UTS, as revealed by 2D slices taken at XZ-3 and XZ-4 planes.

At 86% UTS, two pairs of non-coplanar breaks emerged: breaks 6 and 7 in the XZ-3 plane, and breaks 1 and 2 in the XZ-4 plane. In the XZ-3 plane, larger resin-rich pockets are clearly visible around the site of breaks 6 and 7, resulting from misoriented fibre groups. These misoriented fibres were also in contact with those identified in Y-stack I. As part of the clusters, breaks 7 and 1 lay within the same XY-2 fibre cross-sectional break plane and were located immediately adjacent to each other, forming a co-planar duplet. This co-planar duplet initiated both matrix microcracks and short interfacial debonds, showing damage patterns consistent with those observed around breaks located near resin-rich pockets (see section **3.2.1**).

At 91% UTS, three additional breaks were detected in close proximity to the non-coplanar breaks formed in the XZ-3 and XZ-4 planes: a single break 8 and non-coplanar duplet (9 and 3). The focus of observation was on breaks 9 and 3 because their break sites were immediately adjacent to the pre-existing co-planar duplet (7 and 1) and non-coplanar breaks (1 and 2). **Fig. 6a** additionally shows the breaks (9 and 3) in the YZ-1 plane view of the cluster sites. The lower left side of break 3 in the YZ-1 plane shows damage features, appearing as microvoids or the onset of matrix microcracks, within the inter-fibre matrix region between breaks 9 and 3, facing the larger resin-rich pockets. Similarly, damage features resembling microvoids were observed on the upper left side of break 3 in the XZ-4 plane (**Fig. 6a**), particularly within inter-fibre matrix region between break 2 and 3. These features were absent in the scans at lower loads, indicating that their formation is related to the surrounding break behaviour.

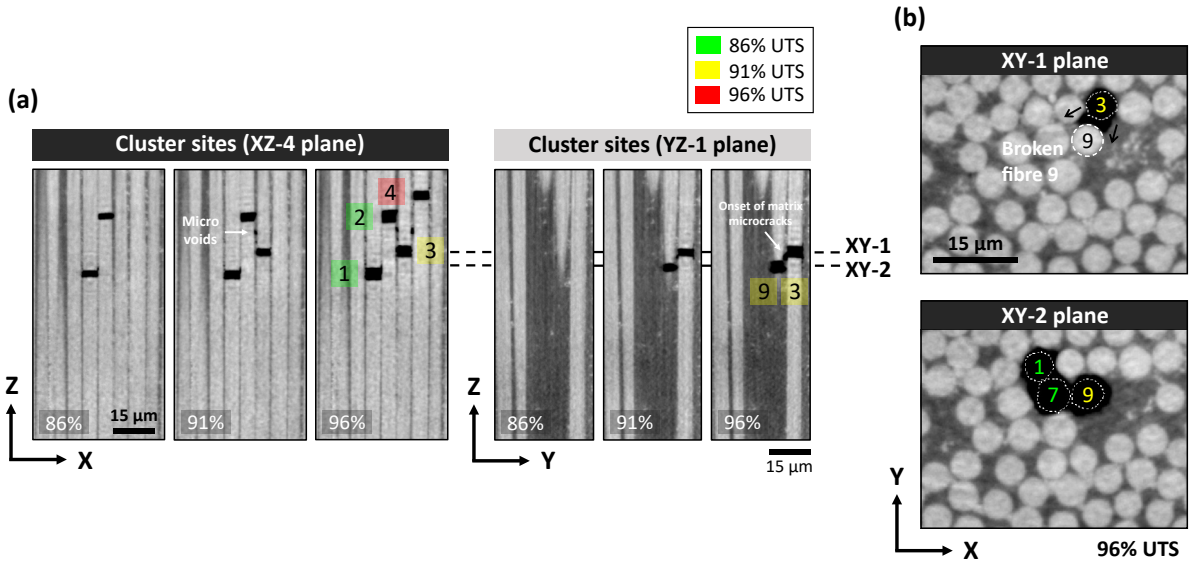

Fig. 6. (a) XZ and YZ plane views of the cluster sites (**Fig. 5c**) in 'Y-stack II' at XZ-4 and YZ-1 planes, showing non-coplanar breaks with associated microscale damage at 86%, 91%, and 96% UTS. Break numbers are colour-coded by their formation load level. (b) XY fibre cross-sectional views of non-coplanar breaks at 96% UTS, taken from cluster sites at XY-1 and XY-2 planes. Matrix microcracks near break 3 propagate extensively (black arrows), linking breaks 1, 3, 7, and 9, which formed earlier at 86% and 91% UTS.

At 96% UTS, two single breaks 4 and 13 were newly detected in fibres facing larger resin-rich pockets, with break 4 forming immediately next to the pre-existing non-coplanar cluster (1 to 3) in the XZ-4 plane. This progressive clustering also formed new microvoids within the inter-fibre matrix region between breaks 4 and 3, as observed at 91% UTS. As the pre-existing non-coplanar breaks (1 to 4) and (3 and 9) opened further with increasing load, the surrounding earlier-formed damage features (i.e. onset

of matrix microcracks) increased in size. As seen in YZ-1 plane (**Fig. 6a**), the damage features within the inter-fibre region of breaks 3 and 9 eventually coalesced, linking these two breaks that were previously unlinked at earlier loads. This damage progression, evident as significant propagation of matrix microcracks, was similarly observed along the inter-fibre regions of the pre-existing clustered breaks (7 and 9) and (7 and 1). **Fig. 6b** illustrates the XY-1 and XY-2 planes of these breaks at 96% UTS, revealing matrix microcracks at their maximum propagation in the fibre cross-sectional view. In the XY-1 plane, matrix microcracks initiated at break 3 prominently propagate across the inter-fibre matrix region toward the fibre where break 9 occurred, located near the larger resin-rich pockets. Consequently, the propagating matrix microcracks appear to connect with those surrounding clustered breaks 9, 7, and 1, forming a continuous damage zone.

Together with the micro-mechanical effects discussed earlier, we tentatively propose a hypothesis that could explain the pronounced increase in clusters near larger resin-rich pockets in Y-stack II. Following the formation of initial breaks near resin-rich pockets, stress redistribution between broken and neighbouring intact fibres may have been hindered by the combined effects of fibre misalignment, larger resin-rich pockets, and matrix nonlinearity. Moreover, the observed clustering was consistently accompanied by the formation of by matrix microcracks, short interfacial debonds, and microvoids. These damage features provide evidence of severe matrix nonlinearity in these break sites. Notably, with increasing loads, the propagation of matrix microcracks extended across the inter-fibre region, progressively linking pre-existing clustered breaks. This exemplifies the severity of matrix nonlinearity, particularly when break sites are influenced by both fibre misalignment and the resulting resin-rich pockets. Furthermore, Swolfs *et al.* [4] reported that the tips of matrix cracks may induce very high stress gradients across fibres. If so, these gradients could play an additional role in intensifying matrix nonlinearity, further supporting our hypothesis.

4. Conclusions

This study investigates the interaction between local microstructural variations and fibre breaks in 0° carbon fibre plies, elucidating how these interactions contribute to the initiation and clustering of breaks. We performed *in situ* tensile tests, combined with 150 nm-based X-ray synchrotron holo-tomography, to monitor the accumulation of breaks in regions with microstructural variations under increasing stress levels. The scans revealed three distinctive microstructural features that promote a pronounced increase in the occurrence of single and clustered breaks: misplaced fibres and resin-rich pockets within the 0°/0° interply region, and larger resin-rich pockets surrounding misoriented fibre groups within the 0° intraply region. Notably, the clustering of breaks near resin-rich pockets was consistently accompanied by non-uniform matrix microcracks, short interfacial debonds, and damage features resembling microvoids or onset of matrix microcracks. Such microscale damage strongly suggests the occurrence of severe matrix nonlinearity at these break sites, reinforcing the role of resin-rich pockets in promoting break clustering. The identified break patterns and associated microscale damage shed new light on the importance of considering their critical role in fibre break development for more reliable predictions of longitudinal tensile failure. Future work could focus on developing fibre break models that incorporate the microstructural variations identified in this study. This would help determine the extent to which these microstructural variations influence stress redistribution around breaks.

Acknowledgements

The authors acknowledge the contributions from the Mitsubishi Chemical Corporation (Advanced Molding and Composites Laboratory, Aichi R&D centre, Japan) and the dedicated MCC scientists – Fukuhara Yasuhiro, Takano Tsuneo, Sugiura Naoki – for their sponsorship, material supplies, and technical support. We also acknowledge the European Synchrotron Radiation Facility (ESRF) for the provision of synchrotron radiation facilities at the ID16B beamline under proposal number MA5729, and we greatly appreciate the technical support of Julie Villanova and Olga Stamati. We extend deepest gratitude to our colleagues – Babak Fazlali and Sina AhmadvashAghbash – for their invaluable assistance and insightful advice during the synchrotron experiments. The μ-VIS X-Ray Imaging Centre at the University of Southampton is acknowledged for providing image post-processing tools. Lastly, we acknowledge the KU Leuven Research Council for project C14/21/076 and the Research Foundation

Flanders for the postdoctoral fellowships ToughImage (126342IN), BIOPTOUGH (12B0624N), and COCOMI (1231322N).

References

[1] Y. Swolfs, I. Verpoest, L. Gorbatikh, A review of input data and modelling assumptions in longitudinal strength models for unidirectional fibre-reinforced composites, Compos Struct 150 (2016) 153-172.
[2] C. Breite, Aligning fibre break models for composites with the observable micro-scale material behaviour, (2021).
[3] M.R. Nedele, M.R. Wisnom, Three-dimensional finite element analysis of the stress concentration at a single fibre break, Composites science and technology 51(4) (1994) 517-524.
[4] Y. Swolfs, H. Morton, A.E. Scott, L. Gorbatikh, P.A.S. Reed, I. Sinclair, S.M. Spearing, I. Verpoest, Synchrotron radiation computed tomography for experimental validation of a tensile strength model for unidirectional fibre-reinforced composites, Compos Part a-Appl S 77 (2015) 106-113.
[5] Y. Swolfs, L. Gorbatikh, V. Romanov, S. Orlova, S.V. Lomov, I. Verpoest, Stress concentrations in an impregnated fibre bundle with random fibre packing, Composites Science and Technology 74 (2013) 113-120.
[6] S. AhmadvashAghbash, B. Fazlali, M. Mehdikhani, Y. Swolfs, Finite element analysis of the effect of longitudinal debonding on stress redistributions around fibre breaks in randomly packed fibres, Composites Science and Technology 227 (2022).
[7] A. Scott, M. Mavrogordato, P. Wright, I. Sinclair, S. Spearing, In situ fibre fracture measurement in carbon–epoxy laminates using high resolution computed tomography, Composites Science and Technology 71(12) (2011) 1471-1477.
[8] E. Schöberl, C. Breite, A. Melnikov, Y. Swolfs, M.N. Mavrogordato, I. Sinclair, S.M. Spearing, Fibre-direction strain measurement in a composite ply under quasi-static tensile loading using Digital Volume Correlation and Synchrotron Radiation Computed Tomography, Compos Part a-Appl S 137 (2020).
[9] M.J. Emerson, K.M. Jespersen, A.B. Dahl, K. Conradsen, L.P. Mikkelsen, Individual fibre segmentation from 3D X-ray computed tomography for characterising the fibre orientation in unidirectional composite materials, Compos Part a-Appl S 97 (2017) 83-92.
[10] T. Fast, A.E. Scott, H.A. Bale, B.N. Cox, Topological and Euclidean metrics reveal spatially nonuniform structure in the entanglement of stochastic fiber bundles, J Mater Sci 50(6) (2015) 2370-2398.
[11] S. Rosini, M.N. Mavrogordato, O. Egorova, E.S. Matthews, S.E. Jackson, S.M. Spearing, I. Sinclair, In situ statistical measurement of local morphology in carbon-epoxy composites using synchrotron X-ray computed tomography, Composites Part A: Applied Science and Manufacturing 125 (2019) 105543.
[12] N.K. Fritz, R. Kopp, A.K. Nason, X.C. Ni, J. Lee, I.Y. Stein, E. Kalfon-Cohen, I. Sinclair, S.M. Spearing, P.P. Camanho, B.L. Wardle, New interlaminar features and void distributions in advanced aerospace-grade composites revealed via automated algorithms using micro-computed tomography, Composites Science and Technology 193 (2020).
[13] F. Malgioglio, S. Pimenta, A. Matveeva, L. Farkas, W. Desmet, S.V. Lomov, Y. Swolfs, Microscale material variability and its effect on longitudinal tensile failure of unidirectional carbon fibre composites, Compos Struct 261 (2021).
[14] M. Jafarypouria, S.V. Lomov, B. Mahato, S.G. Abaimov, The effect of fibre misalignment in an impregnated fibre bundle on stress concentrations, Compos Part a-Appl S 178 (2024).
[15] T. Chatziathanasiou, Y. Lee, J. Villanova, O. Stamati, S. Ahmadvashaghbash, B. Fazlali, C. Breite, I. Sinclair, M.N. Mavrogordato, S.M. Spearing, M. Mehdikhani, Y. Swolfs, Questioning the Representativeness of Damage Mechanisms in Single-Fiber Composites via In Situ Synchrotron X-Ray Holo-Tomography, Small 20(52) (2024).
[16] E. Schöberl, C. Breite, S. Rosini, Y. Swolfs, M.N. Mavrogordato, I. Sinclair, S.M. Spearing, A novel particle-filled carbon-fibre reinforced polymer model composite tailored for the application of digital volume correlation and computed tomography, J Compos Mater 55(14) (2021) 1907-1934.
[17] G. Martínez-Criado, J. Villanova, R. Tucoulou, D. Salomon, J.-P. Suuronen, S. Labouré, C. Guilloud, V. Valls, R. Barrett, E. Gagliardini, ID16B: a hard X-ray nanoprobe beamline at the ESRF for nano-analysis, Synchrotron Radiation 23(1) (2016) 344-352.
[18] A. Mirone, E. Brun, E. Gouillart, P. Tafforeau, J. Kieffer, The PyHST2 hybrid distributed code for high speed tomographic reconstruction with iterative reconstruction and a priori knowledge capabilities, Nuclear Instruments and Methods in Physics Research Section B: Beam Interactions with Materials and Atoms 324 (2014) 41-48.
[19] A. Moradi, C.Z. Sun, Z.W. Guan, S. Rastegarzadeh, Technology for lateral spreading of fibre bundles for applications in manufacturing thermoplastic composites, Compos Part a-Appl S 167 (2023).
[20] F. Mesquita, Y. Swolfs, S.V. Lomov, L. Gorbatikh, In-situ synchrotron computed tomography tensile testing observations of the hybrid effect: A comparison with theory, Compos Part B-Eng 235 (2022).
[21] Q.D. Yang, D. Schesser, M. Niess, P. Wright, M.N. Mavrogordato, I. Sinclair, S.M. Spearing, B.N. Cox, On crack initiation in notched, cross-plied polymer matrix composites, J Mech Phys Solids 78 (2015) 314-332.

ICCM *International Committee on Composite Materials*

Authors Contributions

Manuscript title: Unravelling links between fibre misalignment, resin-rich pockets, and the fibre break development via *in situ* holotomography

Authors: Yeajin Lee, Thanasis Chatziathanasiou, Christian Breite, Mahoor Mehdikhani, Yentl Swolfs, Mark. N. Mavrogordato, S. Mark. Spearing, and Ian Sinclair

Author 1 (Tsai Award Applicant): Yeajin Lee (University of Southampton)

- ☒ Conception
  Established the experimental objectives and prepared the experiment accordingly
- ☐ Data curation
  Specify contribution in more detail (optional; no more than one sentence)
- ☒ Formal Analysis
  Performed analysis of the micro-mechanical behaviour based on synchrotron scan data
- ☒ Investigation
  Conducted synchrotron experiment at ESRF ID16B beamline
- ☒ Methodology
  Developed methodologies required for the in situ experiment and image post-processing
- ☐ Software
  Specify contribution in more detail (optional; no more than one sentence)
- ☐ Validation
  Specify contribution in more detail (optional; no more than one sentence)
- ☒ Visualization
  Processed synchrotron scan images using FIJI/ImageJ and Avizo software and created figures
- ☒ Wrote the paper (original draft)
  Wrote the full draft of the paper from beginning to end
- ☒ Wrote the paper (review and editing)
  Addressed feedback from all co-authors and revised the draft
- ☐ Other contribution
  Specify contribution in more detail (required; no more than one sentence)

Author 2: Thanasis Chatziathanasiou (KU Leuven)

- ☒ Conception
  Established the experimental objectives and prepared the experiment accordingly
- ☐ Data curation
  Specify contribution in more detail (optional; no more than one sentence)
- ☐ Formal Analysis
  Specify contribution in more detail (optional; no more than one sentence)
- ☒ Investigation
  Conducted synchrotron experiment at ESRF ID16B beamline
- ☒ Methodology
  Developed methodologies required for the in situ experiment and image reconstruction
- ☐ Software
  Specify contribution in more detail (optional; no more than one sentence)
- ☐ Validation
  Specify contribution in more detail (optional; no more than one sentence)
- ☐ Visualization
  Specify contribution in more detail (optional; no more than one sentence)
- ☐ Wrote the paper (original draft)
  Specify contribution in more detail (optional; no more than one sentence)
- ☒ Wrote the paper (review and editing)
  Read the original draft and provided constructive and growth-oriented feedback
- ☒ Interpersonal and Emotional support
  Provided constant encouragement and emotional support to the team during the beamtime

Author 3: Christian Breite (KU Leuven)

- ☒ Conception
  Established the experimental objectives and prepared the experiment accordingly
- ☐ Data curation
  Specify contribution in more detail (optional; no more than one sentence)
- ☐ Formal Analysis
  Specify contribution in more detail (optional; no more than one sentence)
- ☒ Investigation
  Conducted synchrotron experiment at ESRF ID16B beamline
- ☒ Methodology
  Designed in situ loading rig and developed methodologies required for the in situ experiment
- ☐ Software
  Specify contribution in more detail (optional; no more than one sentence)

☐ Validation
Specify contribution in more detail (optional; no more than one sentence)

☐ Visualization
Specify contribution in more detail (optional; no more than one sentence)

☐ Wrote the paper (original draft)
Specify contribution in more detail (optional; no more than one sentence)

☒ Wrote the paper (review and editing)
Read the original draft and provided constructive feedback

☒ Intellectual and Analytical support
Provided intellectual support in shaping the discussion of findings through idea sharing

Author 4: Mahoor Mehdikhani (KU Leuven)

☒ Conception
Established the experimental objectives and prepared the experiment accordingly

☐ Data curation
Specify contribution in more detail (optional; no more than one sentence)

☐ Formal Analysis
Specify contribution in more detail (optional; no more than one sentence)

☒ Investigation
Conducted synchrotron experiment at ESRF ID16B beamline

☒ Methodology
Designed in situ experimental studies and addressed unexpected issues during beamtime

☐ Software
Specify contribution in more detail (optional; no more than one sentence)

☐ Validation
Specify contribution in more detail (optional; no more than one sentence)

☐ Visualization
Specify contribution in more detail (optional; no more than one sentence)

☐ Wrote the paper (original draft)
Specify contribution in more detail (optional; no more than one sentence)

☒ Wrote the paper (review and editing)
Read the original draft and provided constructive and empathetic feedback

☒ Interpersonal and Intellectual support
Fostered a positive, collaborative environment during beamtime, actively suggesting new ideas

Author 5: Yentl Swolfs (KU Leuven)

☒ Conception
Submitted ID16B beamtime proposal and established the experimental objectives

☐ Data curation
Specify contribution in more detail (optional; no more than one sentence)

☒ Formal Analysis
Contributed in-depth micro-mechanical insights that enhanced the analysis of results

☒ Investigation
Conducted synchrotron experiment at ESRF ID16B beamline and lead the team

☒ Methodology
Proactively addressed unexpected challenges and adapted the methodology accordingly

☐ Software
Specify contribution in more detail (optional; no more than one sentence)

☐ Validation
Specify contribution in more detail (optional; no more than one sentence)

☐ Visualization
Specify contribution in more detail (optional; no more than one sentence)

☐ Wrote the paper (original draft)
Specify contribution in more detail (optional; no more than one sentence)

☒ Wrote the paper (review and editing)
Provided constructive, thoughtful, and detailed feedback offering valuable learning insights

☒ Motivational and inspirational support, and communicative leadership
Demonstrated authentic leadership that reminded team of the joy of research during this work

Author 6: Mark Noel Mavrogordato (University of Southampton)

☒ Conception
Advised on the experimental design in alignment with the ID16B experiment objectives

☐ Data curation
Specify contribution in more detail (optional; no more than one sentence)

☒ Formal Analysis
Contributed in-depth micro-mechanical insights that enhanced the analysis of results

☐ Investigation
Specify contribution in more detail (optional; no more than one sentence)

☒ Methodology
Provided support in sample preparation and valuable insights into image processing approach

☐ Software
Specify contribution in more detail (optional; no more than one sentence)

☐ Validation
Specify contribution in more detail (optional; no more than one sentence)

☐ Visualization
Specify contribution in more detail (optional; no more than one sentence)

☐ Wrote the paper (original draft)
Specify contribution in more detail (optional; no more than one sentence)

☒ Wrote the paper (review and editing)
Read the original draft and provided constructive feedback

☒ Analytical and Motivational support (supervision)
Provided continuous idea generation during data interpretation with an encouraging mindset

Author 7: Simon Mark Spearing (University of Southampton)

☒ Conception
Provided strategic advice on experimental planning to meet the ID16B experiment objectives

☐ Data curation
Specify contribution in more detail (optional; no more than one sentence)

☒ Formal Analysis
Contributed in-depth micro-mechanical insights that enhanced the analysis of results

☐ Investigation
Specify contribution in more detail (optional; no more than one sentence)

☒ Methodology
Provided valuable input on the ID16B experimental planning, offering strategic guidance

☐ Software
Specify contribution in more detail (optional; no more than one sentence)

☐ Validation
Specify contribution in more detail (optional; no more than one sentence)

☐ Visualization
Specify contribution in more detail (optional; no more than one sentence)

☐ Wrote the paper (original draft)
Specify contribution in more detail (optional; no more than one sentence)

☒ Wrote the paper (review and editing)
Provided constructive and detailed feedback, helping identify areas for deeper understanding

☒ Motivational and Inspirational support (supervision)
Provided insightful supervision that strengthened analysis, and mentored YL to stay motivated

YL refers to Yeajin Lee (TSAI applicant)

Author 8: Ian Sinclair (University of Southampton)

☒ Conception
Provided guidance on the experimental design to meet the ID16B experiment objectives

☐ Data curation
Specify contribution in more detail (optional; no more than one sentence)

☒ Formal Analysis
Contributed in-depth micro-mechanical insights that enhanced the analysis of results

☐ Investigation
Specify contribution in more detail (optional; no more than one sentence)

☒ Methodology
Provided guidance on experimental planning to ensure methodological clarity and feasibility

☐ Software
Specify contribution in more detail (optional; no more than one sentence)

☐ Validation
Specify contribution in more detail (optional; no more than one sentence)

☐ Visualization
Specify contribution in more detail (optional; no more than one sentence)

☐ Wrote the paper (original draft)
Specify contribution in more detail (optional; no more than one sentence)

☒ Wrote the paper (review and editing)
Provided constructive, actionable, and growth-oriented feedback with encouragement

☒ Intellectual and Inspirational support (supervision) and Funding acquisition
Acquired funding, Supported logical data interpretation and Offered consistent motivation

Conceptualization
Ideas; formulation or evolution of overarching research goals and aims.

Data Curation
Management activities to annotate (produce metadata), scrub data and maintain research data (including software code, where it is necessary for interpreting the data itself) for initial use and later reuse.

Formal Analysis
Application of statistical, mathematical, computational, or other formal techniques to analyze or synthesize study data.

Investigation
Conducting a research and investigation process, specifically performing the experiments, or data/evidence collection.

Methodology
Development or design of methodology; creation of models.

Software
Programming, software development; designing computer programs; implementation of the computer code and supporting algorithms; testing of existing code components.

Validation
Verification, whether as a part of the activity or separate, of the overall replication/reproducibility of results/experiments and other research outputs.

Visualization
Preparation, creation and/or presentation of the published work, specifically visualization/data presentation.

Writing – Original Draft Preparation
Creation and/or presentation of the published work, specifically writing the initial draft (including substantive translation).

Writing – Review & Editing
Preparation, creation and/or presentation of the published work by those from the original research group, specifically critical review, commentary or revision – including pre- or post-publication stages.

ICCM24
AUGUST 4-8, 2025
BALTIMORE CONVENTION CENTER
BALTIMORE, MARYLAND, USA

No Technical Paper Submission for:

Dongze He

3D OBSERVATION OF DELAMINATION IN CARBON FIBRE-REINFORCED COMPOSITES UNDER REMOTE MODE II LOADING THROUGH IN SITU COMPUTED TOMOGRAPHY

Panayiotis Tsokanas[1], Daelynn Ramanna[1], Thanasis Chatziathanasiou[1], Mahoor Mehdikhani[1] and Yentl Swolfs[1]

[1]Department of Materials Engineering, KU Leuven
Kasteelpark Arenberg 44 box 2450, 3001 Leuven, Belgium
Email: panayiotis.tsokanas@kuleuven.be, web page: http://www.composites-kuleuven.be

Keywords: Multidirectional composite, Remote mode II fracture loading, X-ray computed tomography, In situ observation

ABSTRACT

Delamination is a prevalent and life-limiting failure mode in laminated composites, with mode II delamination, driven by in-plane shear, being particularly difficult to characterise. Conventional edge-monitoring techniques are inherently limited, as they cannot capture the three-dimensional (3D) evolution of the delamination front and the associated damage mechanisms. Building on our group's recent work demonstrating the first in situ X-ray computed tomography (CT) experiment for visualising mode II delamination, this paper presents preliminary results from an ongoing study focused on capturing successive delamination migration events in multidirectional laminates. The investigated specimens feature a +45°//−45° delamination interface and ±45° angled plies. A custom-designed in situ four-point bending rig is employed for the experiments. The proposed in situ CT technique enables mesoscale visualisation of delamination migration within the bulk of the specimen—a capability beyond the reach of conventional edge-monitoring techniques. These results underscore the potential of in situ CT to advance the understanding of mode II fracture evolution in composite laminates.

1 INTRODUCTION

Fibre-reinforced composites are widely valued for their high stiffness-to-weight ratio, superior strength, and excellent design flexibility, making them ideal for lightweight structural applications. However, their susceptibility to delamination remains a major limitation, significantly hindering their broader industrial adoption. Delamination, also known as interlaminar fracture, is one of the most prevalent and critical failure modes in laminated composites. It leads to notable reductions in structural stiffness, strength, and compression-after-impact resistance. Mode II (shearing) delaminations, driven by in-plane shear loads, pose particular challenges. These often originate from off-axis cracking under tensile loads or from interlaminar shear stresses under flexural and impact loading. Unlike mode I (opening) delaminations, mode II failures are more difficult to mitigate. Therefore, accurate observation and characterisation of mode II delaminations are essential.

Conventional assessment techniques for mode II delaminations—such as visual inspection, edge microscopy, and digital image correlation—typically rely on monitoring one of the two lateral edges of the specimen to detect crack initiation and growth [1]. However, these edge-monitoring methods provide only two-dimensional insights, overlooking the full 3D morphology of the delamination front and the underlying damage mechanisms. For instance, it is well established that mode II delaminations frequently exhibit a curved front, with the crack advancing faster at the edges than in the centre. Furthermore, the fibre orientations at the delamination interface significantly affect the shape and evolution of the delamination front [2–5].

CT provides a non-destructive, volumetric imaging technique capable of capturing internal damage mechanisms in composite specimens [6]. Unlike traditional edge-monitoring approaches, CT enables full 3D visualisation of delamination propagation throughout the entire loading process. It also facilitates analysis of the interplay between delamination progression and factors such as ply

orientation at the delamination interface. The heterogeneous microstructure of fibre-reinforced composites is particularly well-suited to CT imaging, as the different material phases (i.e. fibres and matrix) can be differentiated by their X-ray attenuation properties, which depend on their chemical composition. The delamination front itself is readily identifiable as an air-filled region propagating inside the bulk. However, conventional absorption-based CT is most effective when cracks are sufficiently open and large relative to the resolution of the imaging system.

To date, most CT-based investigations of delamination in fibre-reinforced composites have been conducted ex situ. Gong et al. [2] used ex situ CT to study the effect of ply orientation on mode I delamination under both quasi-static and fatigue loading, revealing mechanisms such as delamination migration via ply splitting. Later, the same group extended their work to mode II loading using the end-loaded split test, again observing delamination migration through ex situ CT scans after each load step [7]. Similarly, Blondeau et al. [3] employed ex situ CT to analyse mode I delamination resistance in relation to ply orientation, identifying fibre bridging and delamination migration. Herráez et al. [4] extended this to mode II loading, while Pichler et al. [5] explored mixed-mode delamination. In these studies [2–5, 7], successive ex situ CT scans were used to reconstruct the sequence of damage evolution. In another example, Shor et al. [8] performed single ex situ CT scans to assess delamination in unidirectional and woven laminates loaded in mode I, mode II, and mixed-mode fracture.

In contrast, few studies have explored in situ CT monitoring of delamination in composites. Borstnar et al. [9] were among the first to capture in situ toughening mechanisms during mode I loading using a wedge-loaded double cantilever beam. Their work revealed micro-mechanisms contributing to global fracture resistance. Similarly, Chatziathanasiou et al. [10] performed in situ CT on carbon fibre-reinforced laminates under standard mode I loading, tracking delamination growth through tomogram segmentation—without contrast agents. This is advantageous, as contrast-agent immersion (common in [2–5, 7]) can alter delamination behaviour, and the time required between successive ex situ scans can lead to stress relaxation.

Recently, our group conducted the first in situ CT investigation of delamination growth and migration in fibre-reinforced composites subjected to remote mode II loading [11]. Building on that foundation, the present study aims to capture successive delamination migration phenomena in multidirectional laminates featuring a +45°//−45° delamination interface and ±45° angled plies. For this purpose, a newly developed in-house in situ loading rig is employed. Preliminary results from our ongoing work demonstrate the ability of our method to accurately track the overall delamination path and reveal mesoscale failure mechanisms. These findings contribute to addressing the fundamental question in composite fracture mechanics, regarding how local mesostructure influences the initiation and progression of delamination.

2 MATERIALS AND METHODS

2.1 Materials and specimen preparation

The composite laminate used in this study, also used in [10], was fabricated by SABCA Limburg NV using automated tape laying followed by autoclave curing. The material system consists of Cytec unidirectional prepregs, comprising Tenax HTS40 12k carbon fibres preimpregnated with the CYCOM 977-2 toughened epoxy resin.

The laminate under investigation featured a multidirectional stacking sequence consisting of only ±45° angled plies: $[(+45°/-45°)_5/+45°//-45°/(-45°/+45°)_5]$, where '//' denotes the position of the delamination plane. In this laminate, the +45°//−45° delamination interface and the two successive −45°-plies next to the delamination plane create preferable paths for delamination migration, so we can test the capability of our method to capture this damage phenomenon.

A 12.5-μm-thick Teflon sheet insert was embedded at the mid-thickness interlaminar plane of the laminate during lamination to create an artificial pre-crack [12], in alignment with ASTM D7905 [1]. The prepreg stack was cured in an autoclave under a controlled temperature and pressure cycle, ensuring consistent fibre volume fraction and minimal voids. Before the final cure, intermediate vacuum debulking steps were conducted to ensure minimal void content and optimal fibre volume fraction. These debulking cycles were carried out at room temperature, with the vacuum pressure maintained between 0.5 and 0.7 bar for at least 10 minutes per cycle. These steps serve to remove

entrapped air before high-temperature consolidation. Final autoclave curing followed the manufacturer's recommended curing cycle, applying a temperature of 180 °C and a pressure of 6 bar. Subsequent CT inspection of the cured laminate confirmed it was nearly void-free. The thickness of the cured laminate is 4.1 mm (22 plies, nominal ply thickness equal to 186 μm). More details on the manufacturing process can be found in [13].

Rectangular specimens with 10 mm width, 110 mm length, and 50 mm pre-crack length were prepared for the delamination tests. The specimens were extracted from the manufactured laminated plate using water-jet cutting, a process that introduced slight asymmetries in the height of the specimens, as shown in Fig. 1. Each specimen was marked with Tipp-Ex at the pre-crack end and at intervals along its length to retain orientation consistency during post-scan analysis. The thermal curing employed can cause partial fusion of the pre-crack interface, so we needed to perform manual separation of the crack front using a scalpel after specimen cutting and before the experiment.

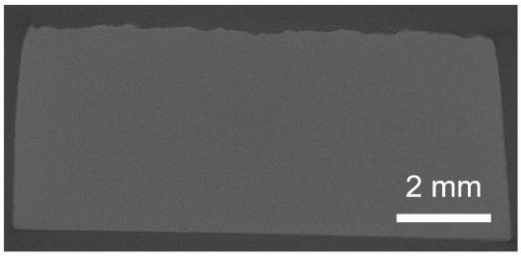

Figure 1: Specimen cross-section, depicting uneven width at the top and bottom surfaces.

2.2 Testing method

To evaluate the interlaminar fracture behaviour of the laminate under remote mode II loading, the four-point end-notched flexure (ENF) test configuration was selected. This method is well established for measuring mode II interlaminar fracture toughness in fibre-reinforced composites, offering several advantages over other testing configurations such as the three-point ENF and end-loaded split tests [14]. For example, in the four-point ENF setup, the crack front is positioned inside a region of pure bending [15] between the two inner loading noses, which reduces frictional effects and distributes the stresses more evenly [14]. Moreover, the four-point ENF test provides a more uniform and well-defined mode II loading field, while the existence of a double-span configuration improves sensitivity to crack growth and reduces excessive deflections in the test specimen. The four-point ENF configuration is also compatible with pre-inserted artificial cracks and allows for both more stable initiation and crack growth [15], making it suitable for qualitative and quantitative fracture analysis in both unidirectional and multidirectional layups.

2.3 In situ testing

Mechanical loading was applied using an in-house developed four-point bending rig, which was mounted on the rotating stage inside a lab-scale CT scanner (TESCAN UniTOM XL), as shown in Fig. 2a. The rig had some operational restrictions, including that the load cells (Sensy model 5962 500 N with Mantracourt DSCH4 MOD amplifier) capped the maximum load at 850 N, and geometric constraints imposed by the loading nose configuration, which limited specimen dimensions (see Fig. 2b). The setup featured dual rotating stages, top and bottom. The span lengths between the inner and outer loading noses were 31 mm and 62 mm, respectively.

Each specimen was loaded incrementally to initiate delamination, followed by a short relaxation period before scanning to reduce motion artefacts. Before the first scan of each testing period, a detector normalisation procedure was carried out to correct for beam profile inhomogeneities and ensure more consistent image contrast across scans. The specimens were loaded under load control, and scans were started manually at selected load steps, mostly after a load drop had been noticed. Table 1 provides the main scan parameters.

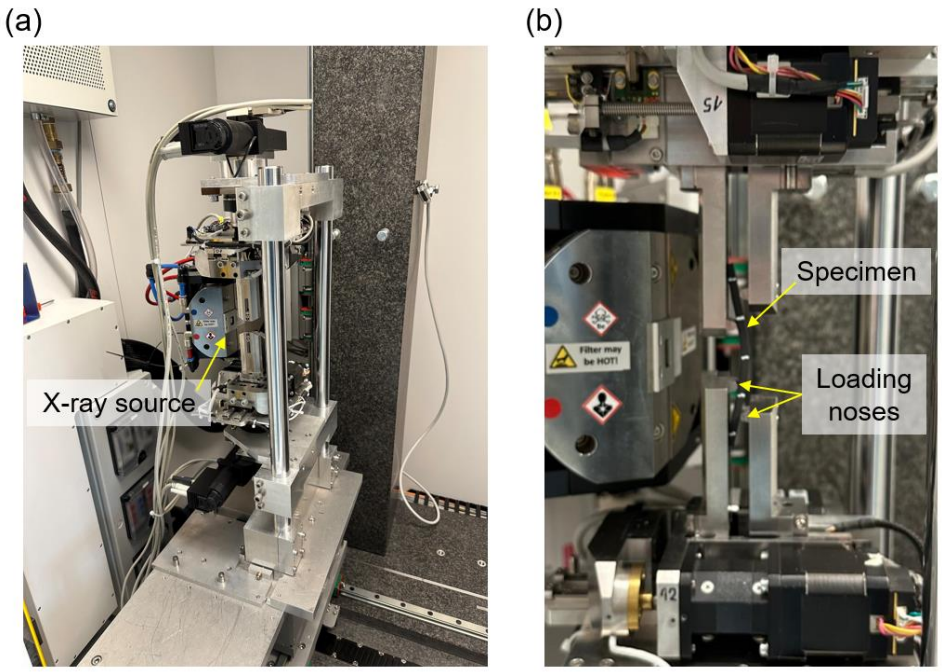

Figure 2: Experimental setup: (a) four-point bending rig mounted onto the rotating stage of the CT scanner and (b) specimen loaded in the in situ bending rig.

Parameter	Value
Tube voltage [kV]	100
Tube current [µA]	150
Power [W]	15
Voxel size [µm]	8.5
Radiographic projections [no.]	4,000
Exposure time per projection [ms]	185
Source-to-object distance [mm]	50
Source-to-detector distance [mm]	882
Scan duration [min]	~13
Pre-scan relaxation time	Until the load was stabilised

Table 1: CT scan parameters.

2.4 Image processing

Each scanned volume was reconstructed into a stack of two-dimensional slices in the TESCAN reconstruction software Panthera. A non-local means filter was applied to reduce image noise, and interactive thresholding to segment the delamination regions (i.e. air phase) from the surrounding composite material was performed in the Avizo 3D 2023.1.1 software (Thermo Fisher Scientific). Due to the similarity in grey values between the carbon fibres and epoxy resin, and too low spatial resolution, segmentation of them was not feasible. Sub-volumes were extracted to exclude rig components and noise caused by them from the field of view as much as possible, and to make the crack visible by excluding the outer layer of air.

3 PRELIMINARY RESULTS

3.1 Capture of successive delamination migrations

Fig. 3 illustrates an example of the 3D reconstructed specimen and delamination in a specific load step. Two successive delamination migration phenomena are visible. The first migration event

occurred just after delamination propagation onset at the end of the pre-cracked region. The crack initiated from the +45°//−45° pre-crack interface, jumped the two successive −45°-plies just above the pre-crack interface, and continued along the new −45°/+45° interface (see Fig. 3a). A second crack migration event was observed in the new +45°/−45° interface (see Fig. 3b), which we could not observe fully developed due to restrictions of our volume of interest.

3.2 Crack length estimations

While the crack front is not easily detectable in 3D volume renderings, the two-dimensional ortho slice views enable a more precise albeit approximate identification. The slice number corresponding to the initial crack edge at the pre-crack end can be identified, along with the slice number where the crack tip ends (both indicated in Fig. 3b). The difference between these two slice numbers is multiplied by the voxel size to obtain the total crack length in the scan volume. This method allows for reasonably accurate estimation of the crack length, despite the presence of some artefacts and the absence of clear 3D crack front segmentation.

In one of the specimens, the initial part of the crack near the pre-crack boundary fell just outside the field of view. However, based on other specimens, it was consistently observed that the crack migration began directly at the end of the pre-crack region.

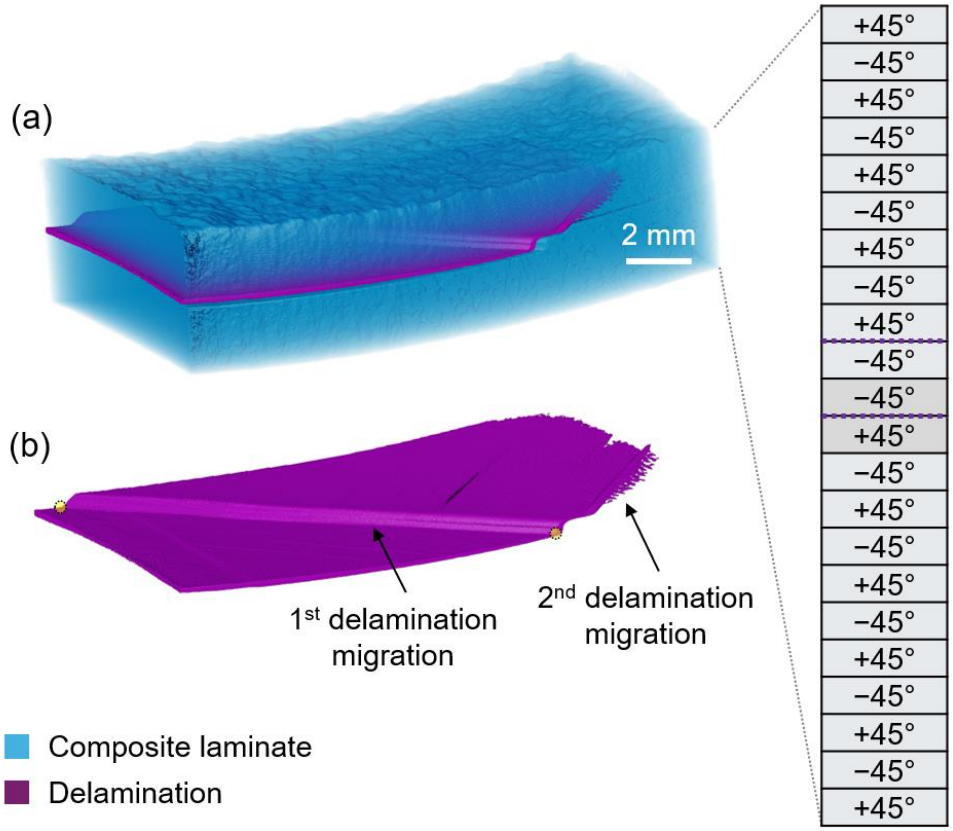

Figure 3: Capture of successive delamination migration events: (a) 3D visualisation of delamination segmentation, and (b) segmented delamination separated from the specimen.

4 CONCLUSION

This study introduced an in situ CT approach to capture successive delamination migration events in ±45° carbon fibre-reinforced laminates subjected to remote mode II loading, using a four-point ENF configuration. A newly developed in situ bending rig was employed to facilitate high-resolution imaging during loading. The results demonstrate the effectiveness of the in situ CT method and loading rig in tracking the bulk evolution of the delamination front, including the observation of two distinct migration phenomena.

Ongoing work focuses on investigating how ply orientation at the delamination interface influences migration behaviour. In addition, we aim to determine the global mode II interlaminar fracture toughness and characterise the mode mixity introduced by factors such as the inherently unsymmetric layup of multidirectional laminates and the progressive stiffness asymmetry in the four-point ENF setup as delamination advances. These efforts will contribute to a deeper understanding of how local mesostructural features govern the initiation and propagation of delamination in composite laminates and their fracture toughness.

ACKNOWLEDGEMENTS

The research leading to these results has been performed within the framework of the INFORM project and has received funding from the European Union's Horizon 2020 research and innovation programme under the Marie Skłodowska-Curie grant agreement No. 101108965. The study was also funded by the KU Leuven Research Council (project C14/21/076). The KU Leuven XCT Core Facility is acknowledged for providing the CT scanner TESCAN UniTOM XL and relevant CT acquisition tools. Technical support from the mechanical workshop and composite laboratory staff from the Department of Materials Engineering at KU Leuven is acknowledged.

REFERENCES

[1] ASTM D7905/D7905M-14, Standard test method for determination of the mode II interlaminar fracture toughness of unidirectional fiber-reinforced polymer matrix composites, ASTM International 2014 (doi: 10.1520/D7905_D7905M-19E01).

[2] Y. Gong, B. Zhang and S.R. Hallett, Delamination migration in multidirectional composite laminates under mode I quasi-static and fatigue loading, *Composite Structures*, **189**, 2018, pp. 160-176 (doi: 10.1016/j.compstruct.2018.01.074).

[3] C. Blondeau, G. Pappas and J. Botsis, Influence of ply-angle on fracture in antisymmetric interfaces of CFRP laminates, *Composite Structures*, **216**, 2019, pp. 464-476 (doi: 10.1016/j.compstruct.2019.03.004).

[4] M. Herráez, N. Pichler, G.A. Pappas, C. Blondeau and J. Botsis, Experiments and numerical modelling on angle-ply laminates under remote mode II loading, *Composites Part A: Applied Science and Manufacturing*, **134**, 2020, 105886 (doi: 10.1016/j.compositesa.2020.105886).

[5] N. Pichler, M. Herráez and J. Botsis, Mixed-mode fracture response of anti-symmetric laminates: experiments and modelling, *Composites Part B: Engineering*, **197**, 2020, 108089 (doi: 10.1016/j.compositesb.2020.108089).

[6] P.J. Withers, C. Bouman, S. Carmignato, V. Cnudde, D. Grimaldi, C.K. Hagen, E. Maire, M. Manley, A. Du Plessis and S.R. Stock, X-ray computed tomography, *Nature Reviews Methods Primers*, **1**, 2021, 18 (doi: 10.1038/s43586-021-00015-4).

[7] Y. Gong, B. Zhang, S. Mukhopadhyay and S.R. Hallett, Experimental study on delamination migration in multidirectional laminates under mode II static and fatigue loading, with comparison to mode I, *Composite Structures*, **201**, 2018, pp. 683-698 (doi: 10.1016/j.compstruct.2018.06.081).

[8] O. Shor, L. Banks-Sills and I. Simon, Quasi-static modes I, II and mixed modes I/II fracture toughness of two laminate composites: Part II — micro-computerized tomography and numerical simulations, *Engineering Fracture Mechanics*, **277**, 2023, 108976 (doi: 10.1016/j.engfracmech.2022.108976).

[9] G. Borstnar, M.N. Mavrogordato, L. Helfen, I. Sinclair and S.M. Spearing, Interlaminar fracture micro-mechanisms in toughened carbon fibre reinforced plastics investigated via synchrotron radiation computed tomography and laminography, *Composites Part A: Applied Science and Manufacturing*, **71**, 2015, pp. 176-183 (doi: 10.1016/j.compositesa.2015.01.012).

[10] T. Chatziathanasiou, J. Soete, J. Vanhulst, D. Carrella-Payan, L. Gorbatikh and M. Mehdikhani, In-situ X-ray computed tomography of mode I delamination in carbon-epoxy composites: the effect of the interface ply orientation, *Composites Part B: Engineering*, **260**, 2023, 110761 (doi: 10.1016/j.compositesb.2023.110761).

[11] P. Tsokanas, T. Chatziathanasiou and Y. Swolfs, 3D observation of delamination in carbon-fibre-reinforced composites under mode II loading through in situ computed tomography, *Composites Part C: Open Access*, **17**, 2025, 100615 (doi: 10.1016/j.jcomc.2025.100615).

[12] K.N. Shivakumar, R. Panduranga, J. Skujins and S. Miller, Assessment of mode-II fracture tests for unidirectional fiber reinforced composite laminates, *Journal of Reinforced Plastics and Composites*, **34**(23), 2015, pp. 1905-1925 (doi: 10.1177/0731684415602335).

[13] M. Mehdikhani, E. Steensels, A. Standaert, K.A.M. Vallons, L. Gorbatikh and S.V. Lomov, Multi-scale digital image correlation for detection and quantification of matrix cracks in carbon fiber composite laminates in the absence and presence of voids controlled by the cure cycle, *Composites Part B: Engineering*, **154**, 2018, pp. 138-147 (doi: 10.1016/j.compositesb.2018.07.006).

[14] R.H. Martin and B.D. Davidson, Mode II fracture toughness evaluation using four point bend, end notched flexure test, *Plastics, Rubber and Composites*, **28**(8), 1999, pp. 401-406 (doi: 10.1179/146580199101540565).

[15] V. Alfred Franklin and T. Christopher, Generation of R-curve from 4ENF specimens: an experimental study, *Journal of Composites*, **2014**, 2014, 956268 (doi: 10.1155/2014/956268).

High-speed X-ray multi-projection and ultra high-speed radiography imaging to capture transverse cracking in glass fibre-reinforced composites

E. Van Vlierberghe, J. Soete, E. M. Asimakopoulou, Z. Yao,
J. Rogalinski, Z. Hu, K. Mom, B. Lukić, **C. Breite**,
P. Villanueva-Perez, Y. Swolfs

ICCM24, August 4, 2025

KU LEUVEN

ESRF The European Synchrotron

fwo

MAX IV

KU LEUVEN XCT CORE FACILITY

LUNDS UNIVERSITET

Composite Materials Group

Transverse cracking in composites

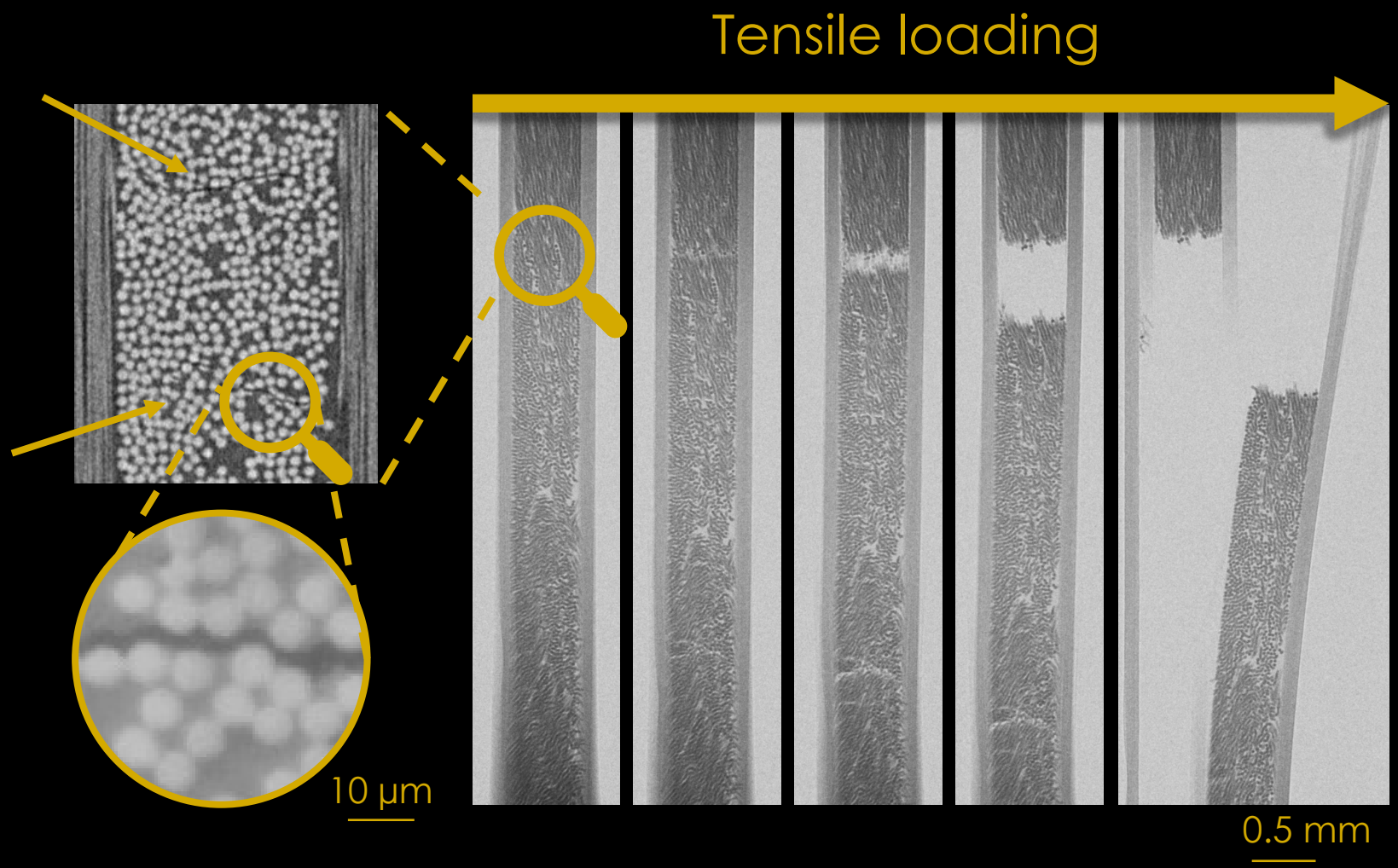



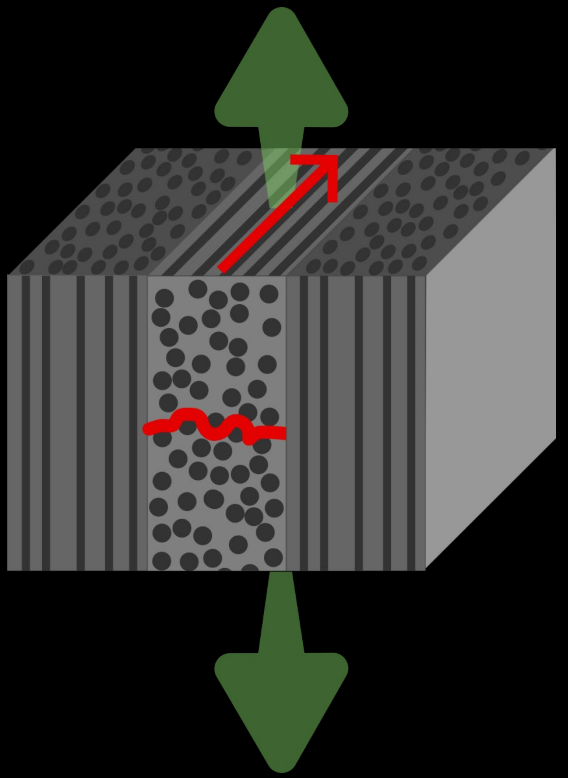

loading rate ↓ ≠ crack propagation speed ↓

Imaging transverse cracking

	3D crack shape	2D crack evolution
Labscale	**XCT** 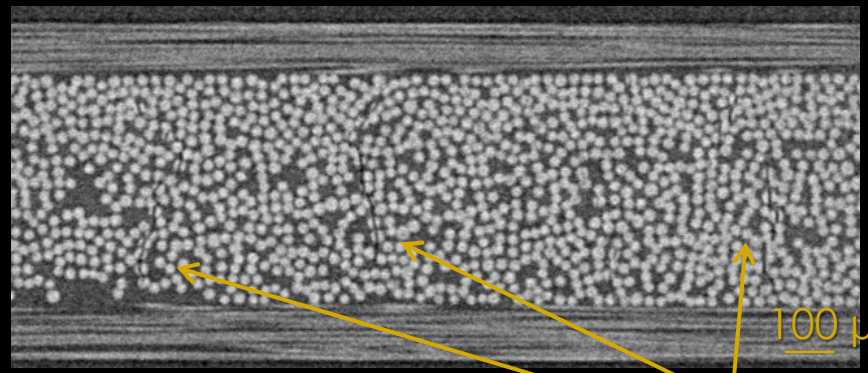 2.9 µm Post-mortem	**Radiography** 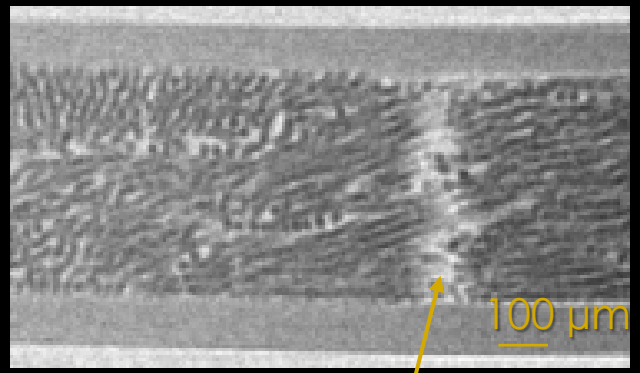 10 Hz + 49.5 µm Lack of contrast Crack opening
Synchrotron	**Fast synchrotron radiation CT (4D-CT)** Garcea et al. (2017). 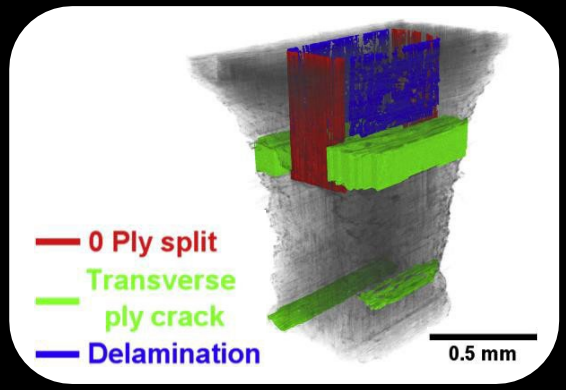 1 Hz + 1.1 µm Rotation stage	**X-ray phase contrast imaging** Pournoori et al. (2023). Damage onset 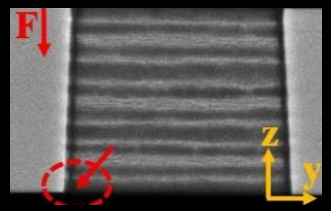 Final crack 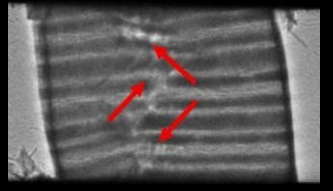 1 MHz + 15.2 µm Triggering strategy

X-ray multi-projection imaging (XMPI)

X-ray tomography requires rotation of the sample

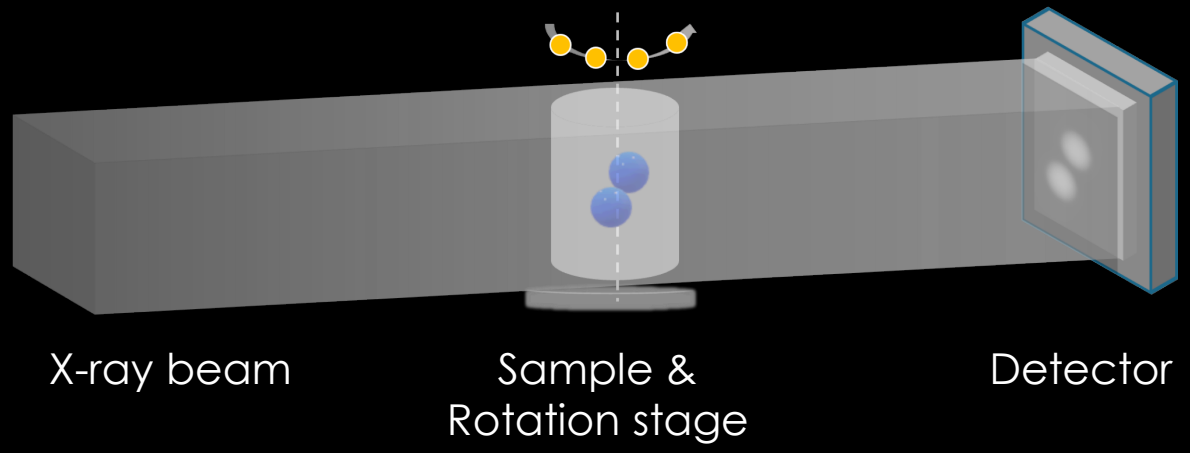

Rotation-free simultaneous projections through XMPI

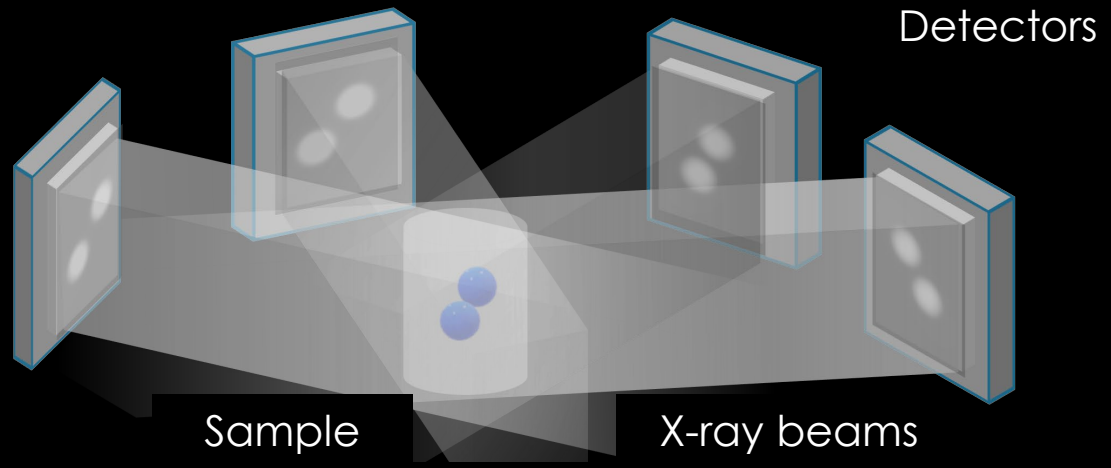

Yao et al. (2025)

XMPI at ID19



kHz acquisition-speed camera (Photron Nova)

Scintillator + 90° mirror

Detectors

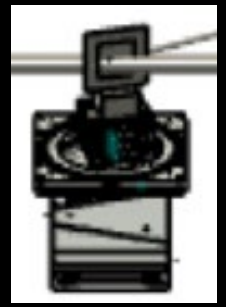

Perfect crystal in Bragg or Laue configuration

Beam-splitter

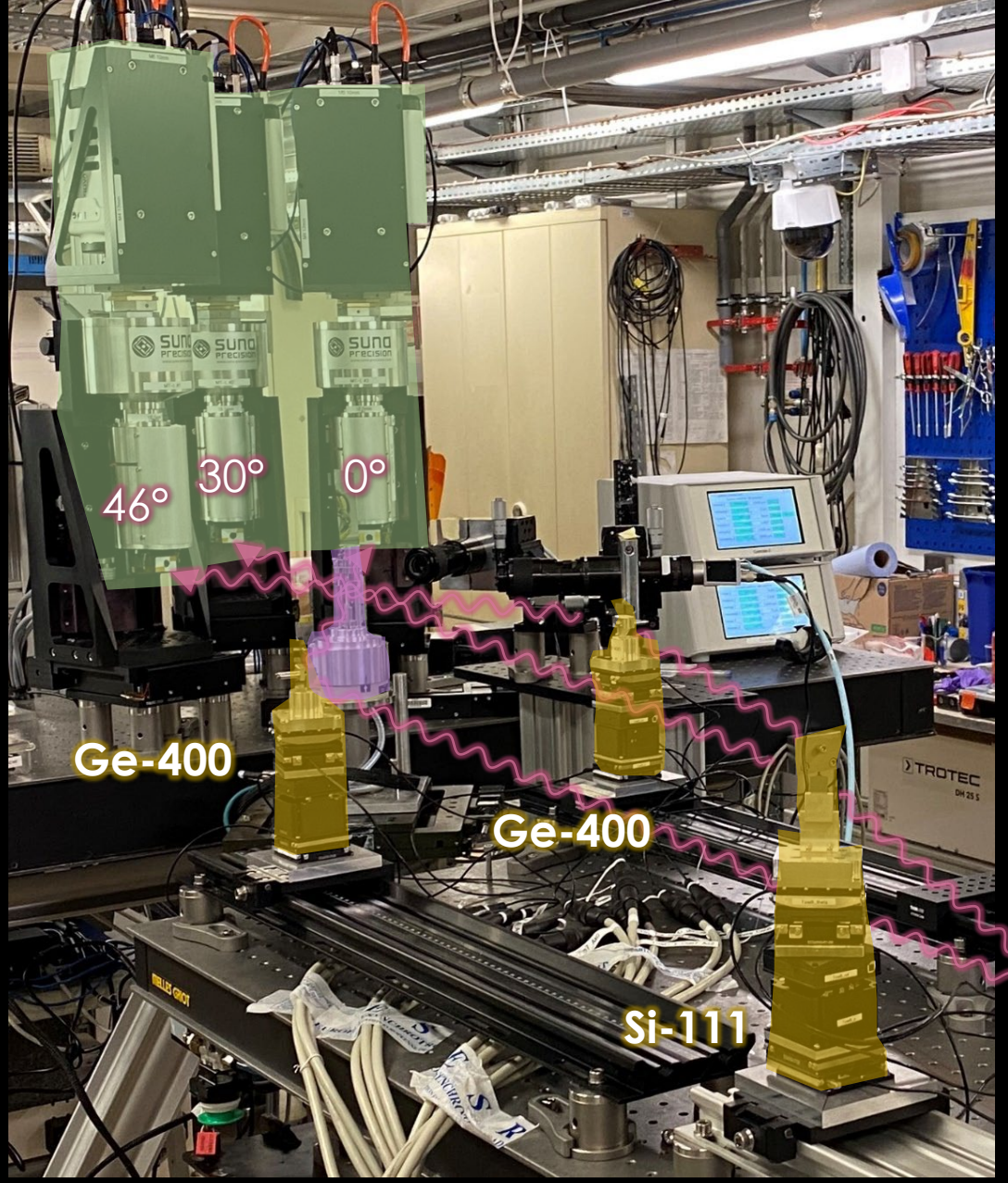

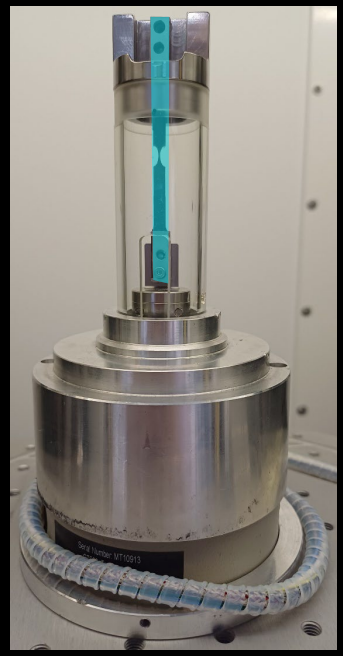

Loading rig

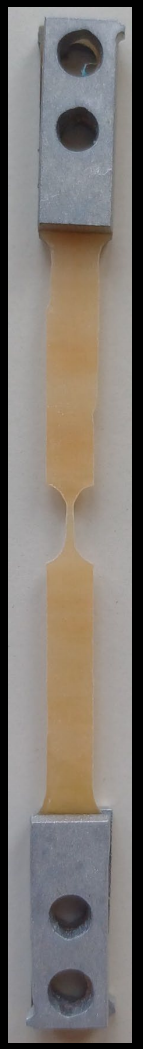

Composite specimen

Sequential damage features imaged at 3 kHz

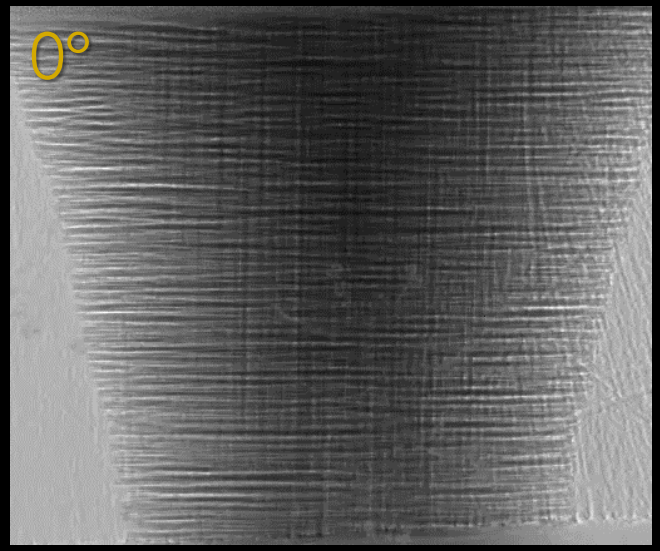

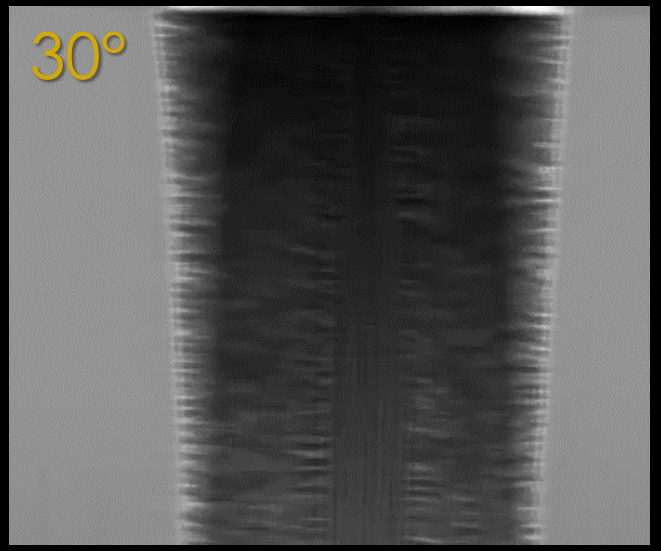

500 µm

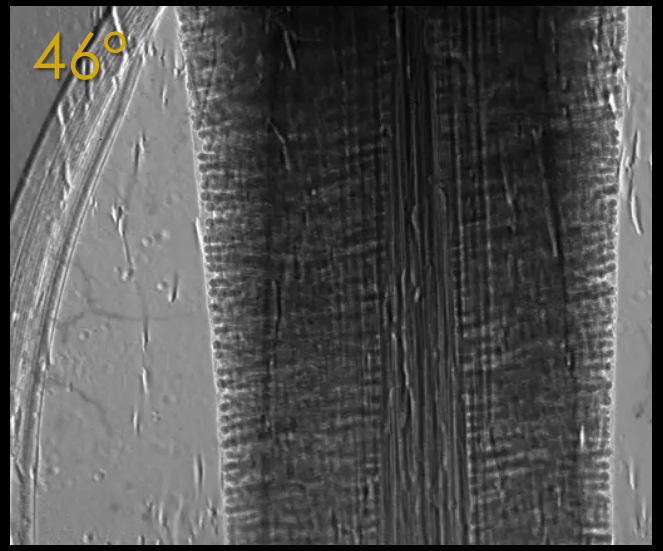

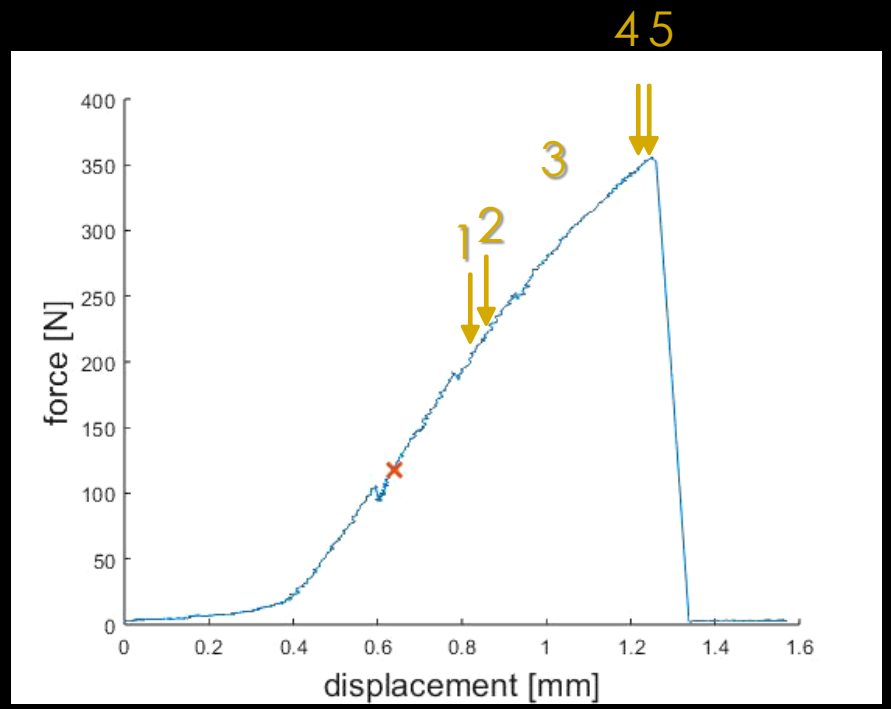

1. Transverse crack
2. Transverse crack
3. Further crack opening
4. Delaminations
5. Final failure 0° plies

Frame subtraction

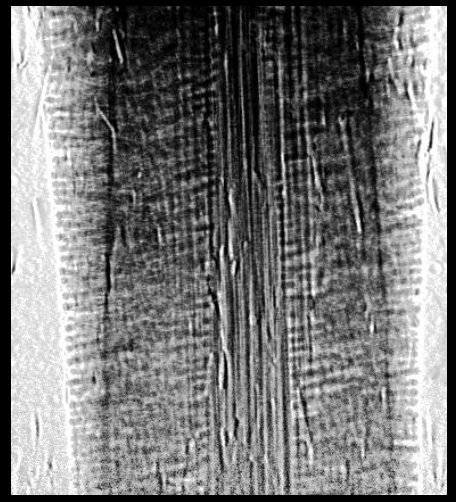

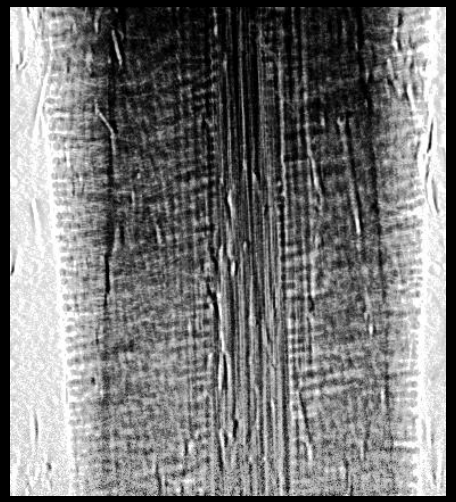

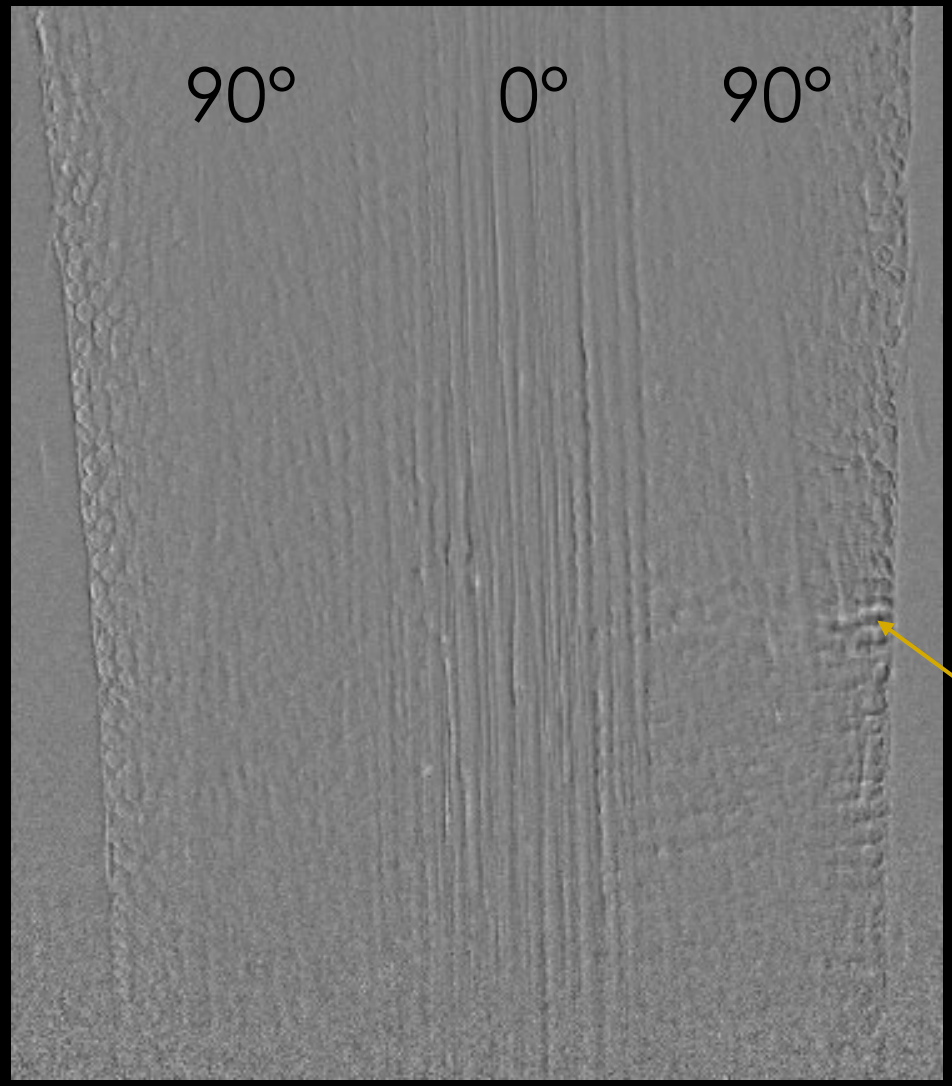

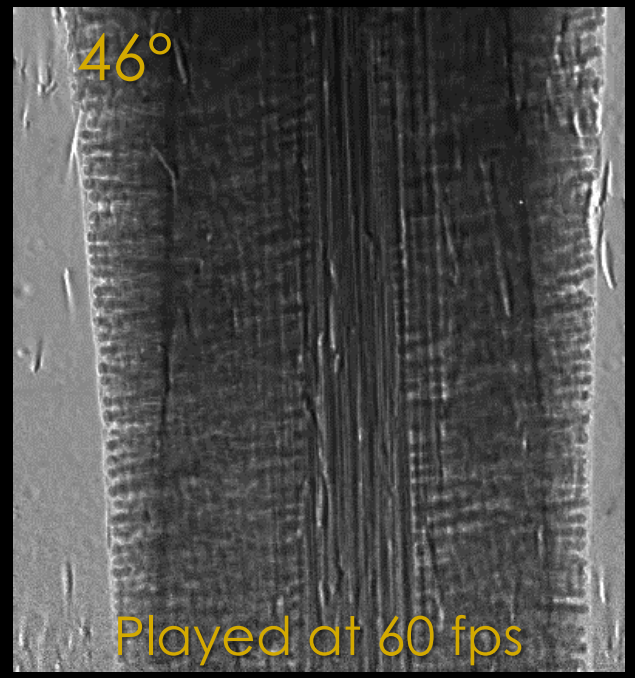

Transverse cracking
58 % UTS

Final failure imaged at 10 kHz



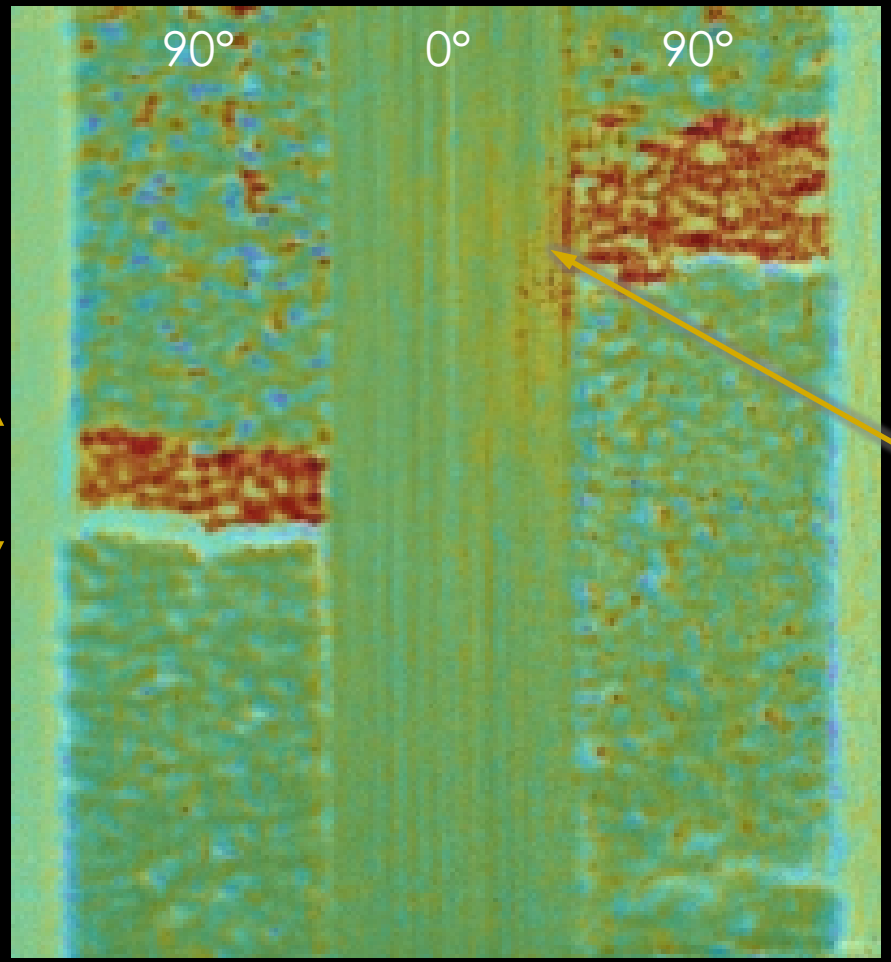

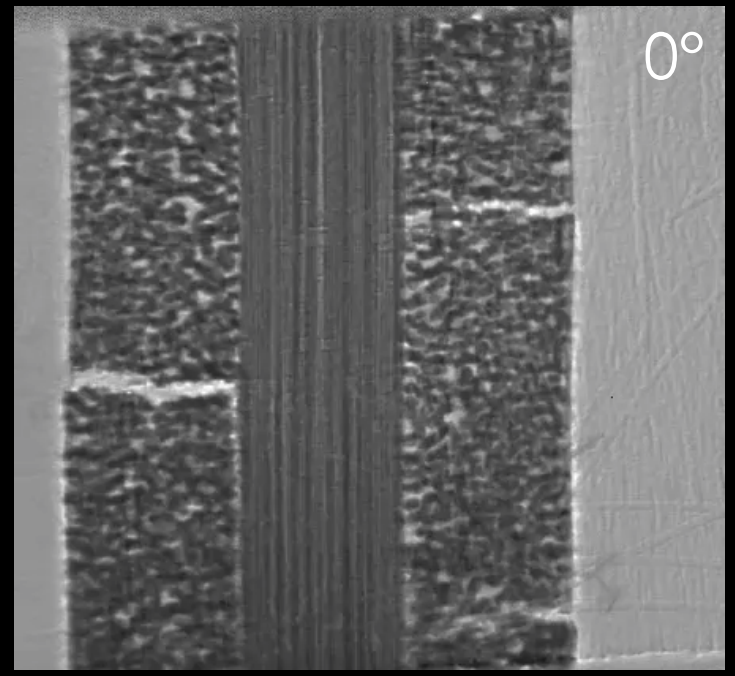

Fast 2D X-ray imaging - Trigger

Goal: Capture crack propagation in 2D up to MHz

Trigger:

- Ultra-short time lapses (256 µs at 1 MHz)
- Non-repetitive event
- Experiment 30 s

Option 1: Conductive coating

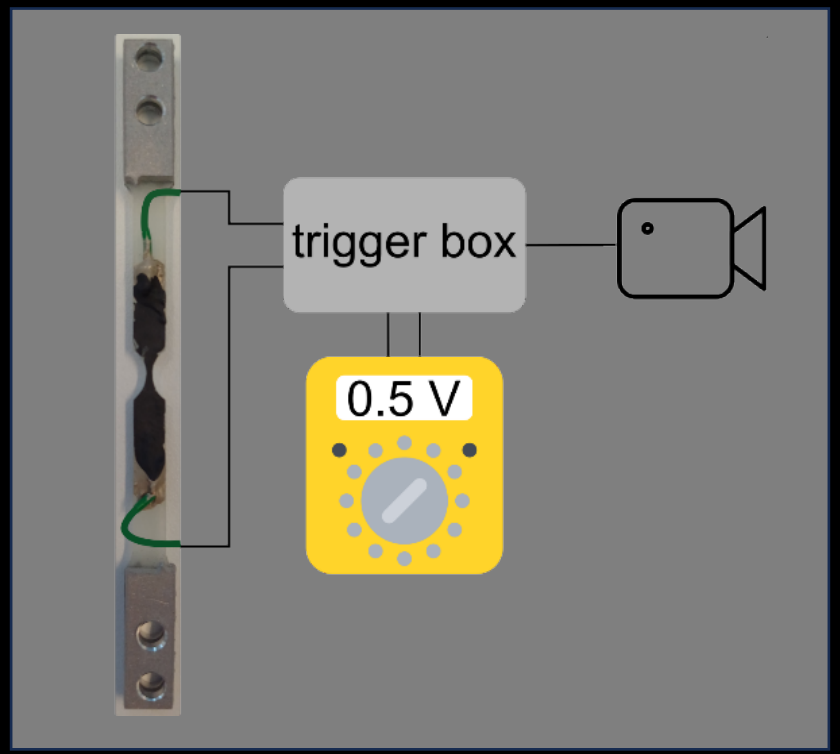

Option 2: Signal from load drop

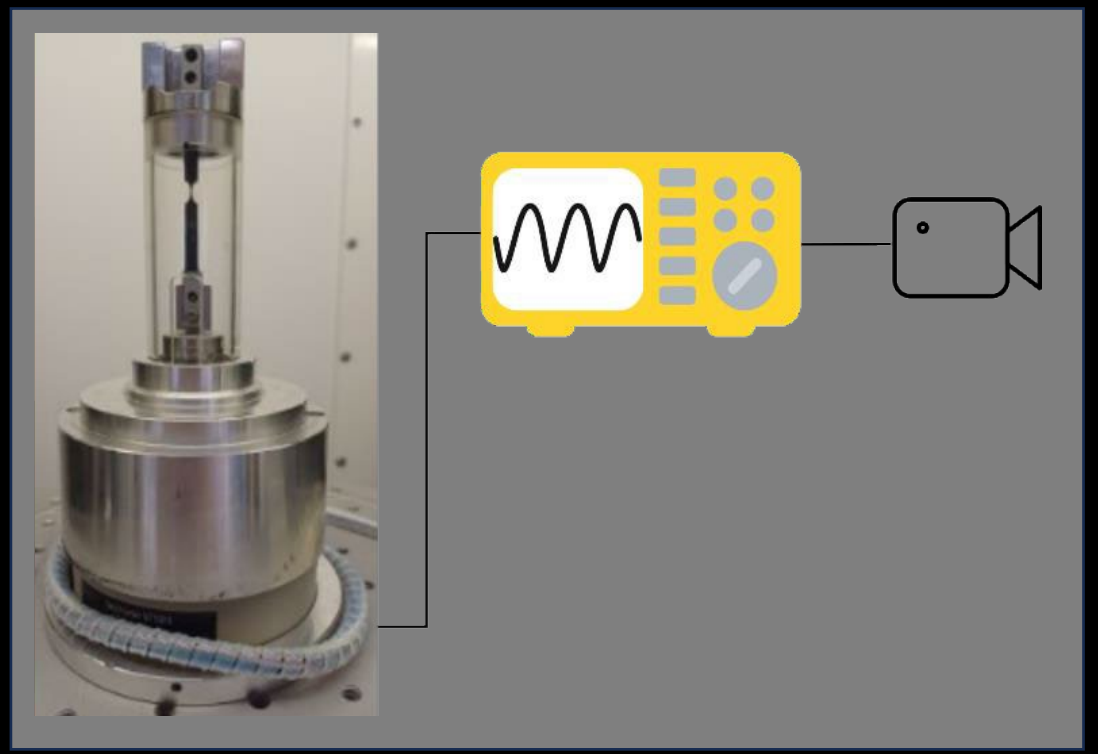

Radiography at ForMAX



MHz acquisition-speed camera
(HPV-X2, Shimadzu)

Microscope

Scintillator + 90° mirror

Detector



1 MHz: 256 µs
vs.
Human reaction time: 250 ms

Trigger

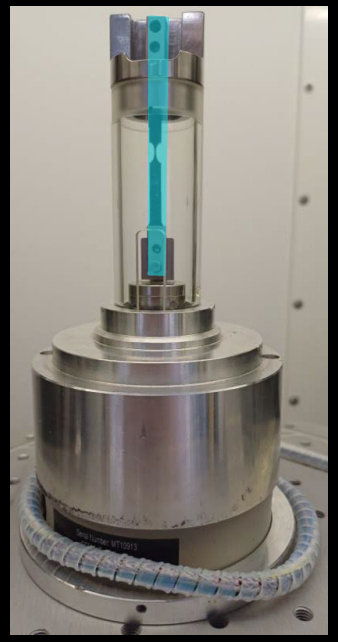

Loading rig



Composite specimen

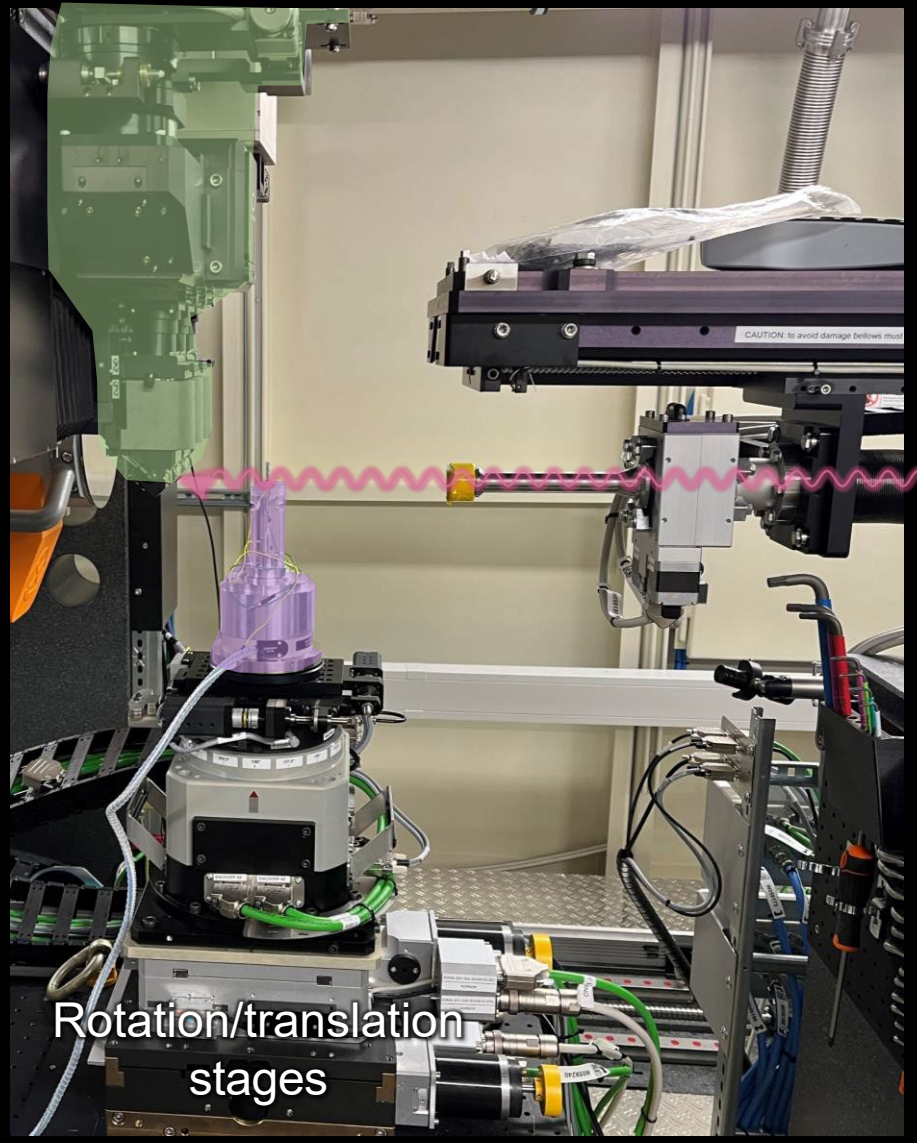

Final failure near transverse crack

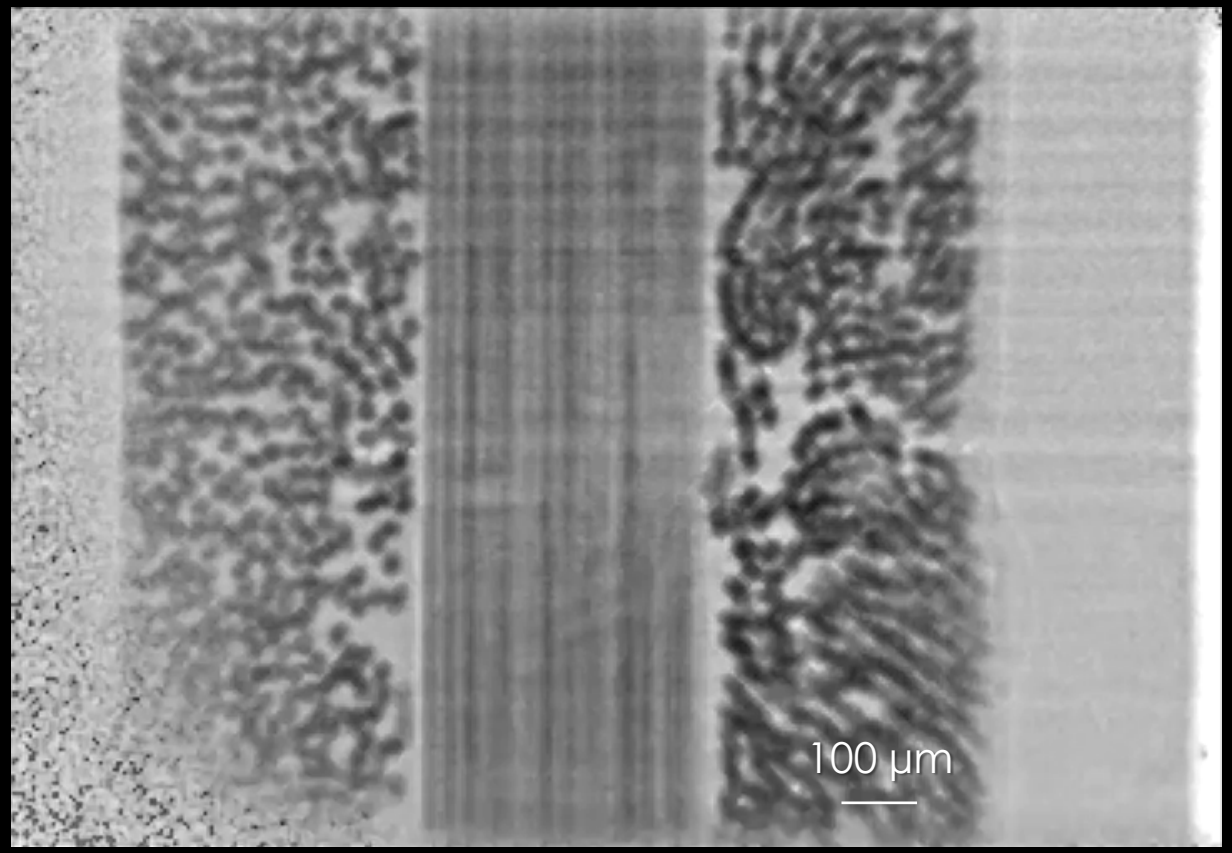

100 kHz (played 1666x slower)

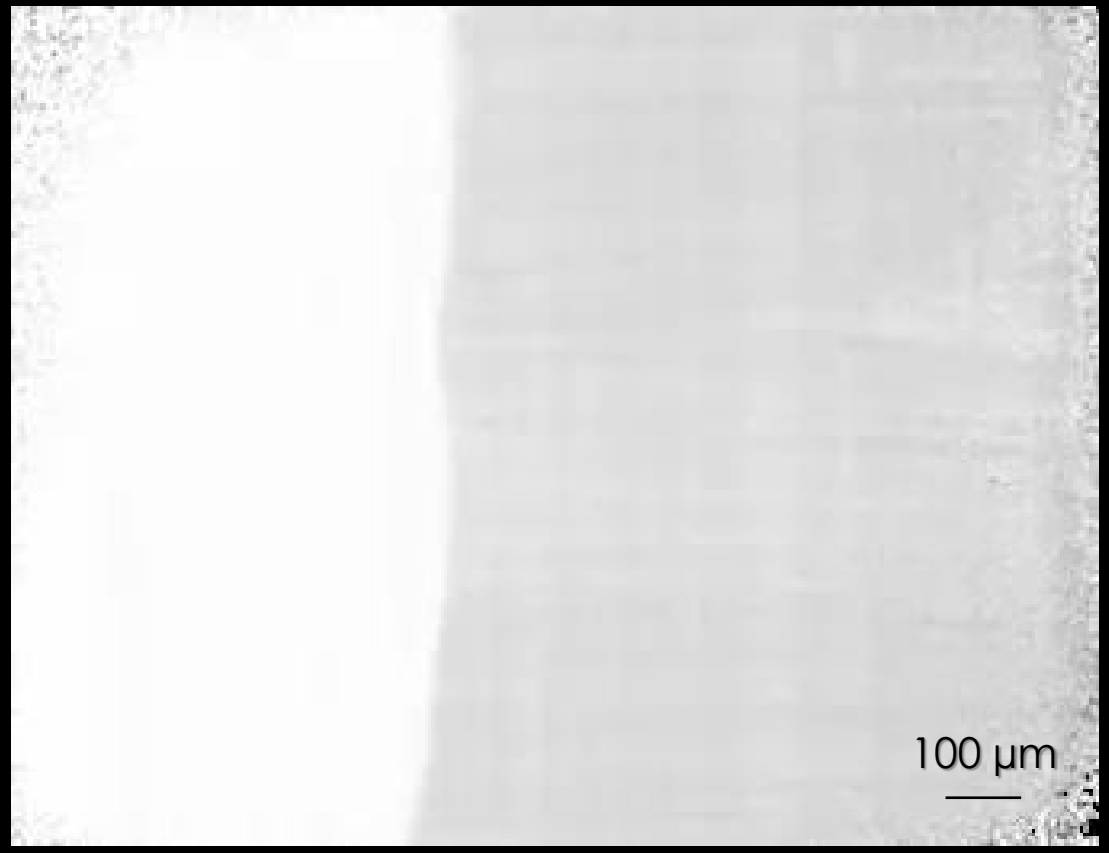

20 kHz (played 333x slower)

Beam-induced sample degradation

Softened matrix

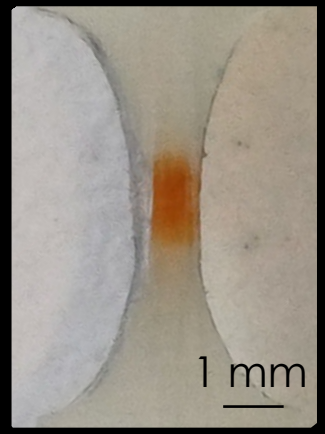

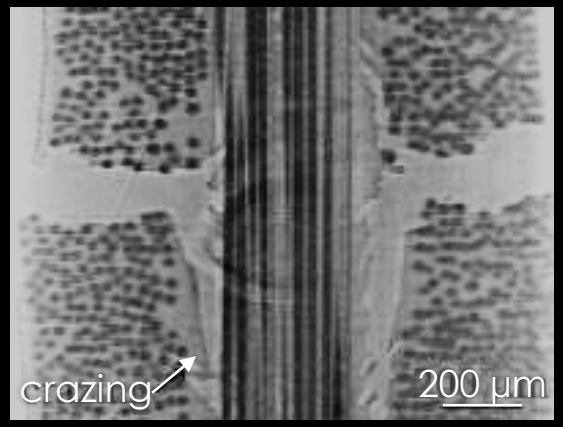

Irradiation glass-epoxy OK

- D = 1.5 MGy
- $D_{degradation}$ = 5 MGy

Wu et al. (2013)

Thermal degradation

Heat load

COMSOL MULTIPHYSICS®

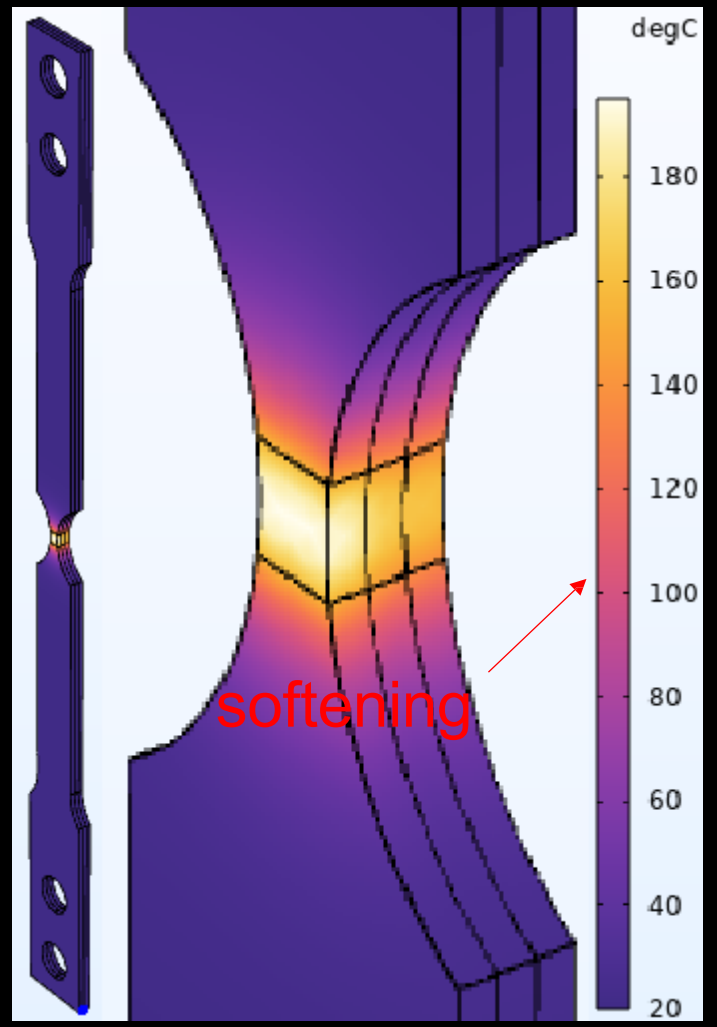

[90,0,90] 10 s at 20 keV with natural convection in tube with slots

Transverse crack segmentation

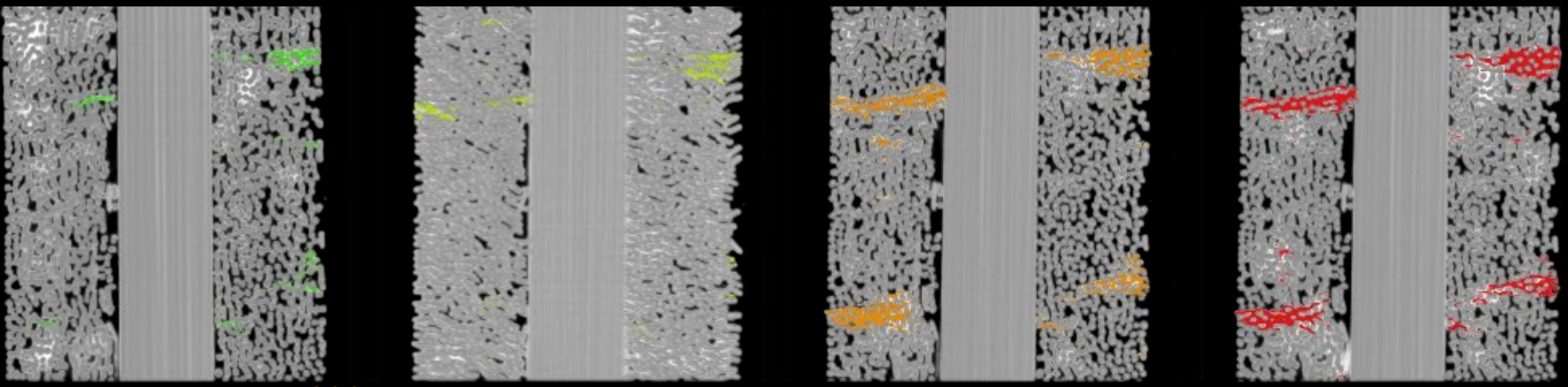



RootPainter

Smith et al. (2022)

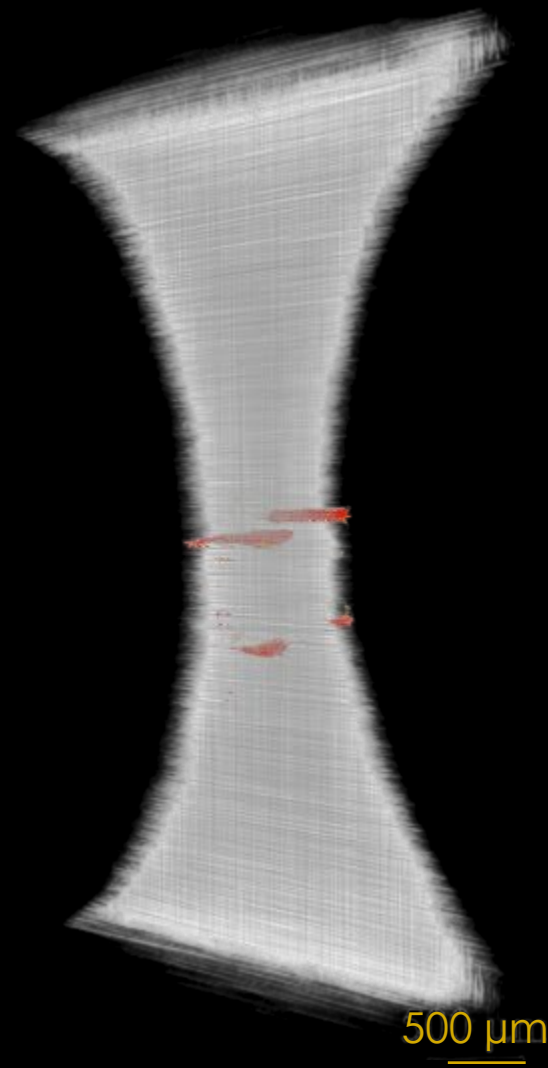

Effect of ply configuration on transverse cracking

E- and S-glass fibre-reinforced epoxy observations

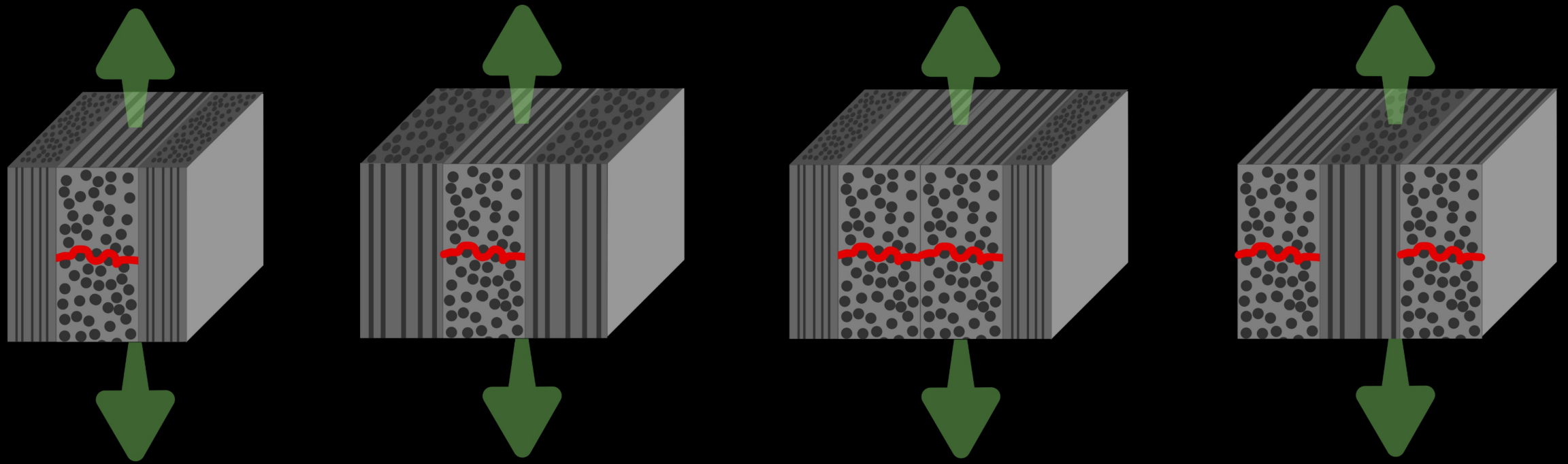

$[0^S,90^E,0^S]$	$[0^E,90^E,0^E]$	$[0^S,90^E,90^E,0^S]$	$[90^E,0^E,90^E]$
Reference layup	≈	$\sigma_2\downarrow$	$\sigma_2\downarrow\downarrow$

Conclusion

Time-resolved synchrotron XMPI

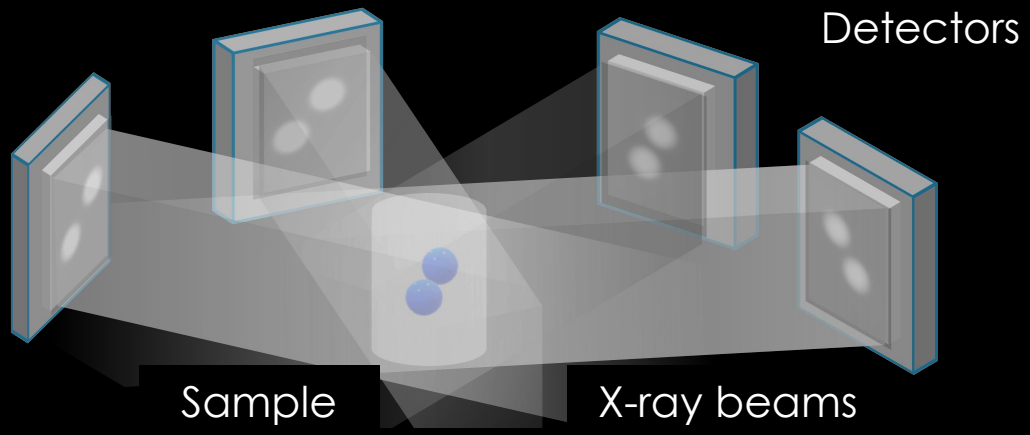

Transverse cracking in 4D

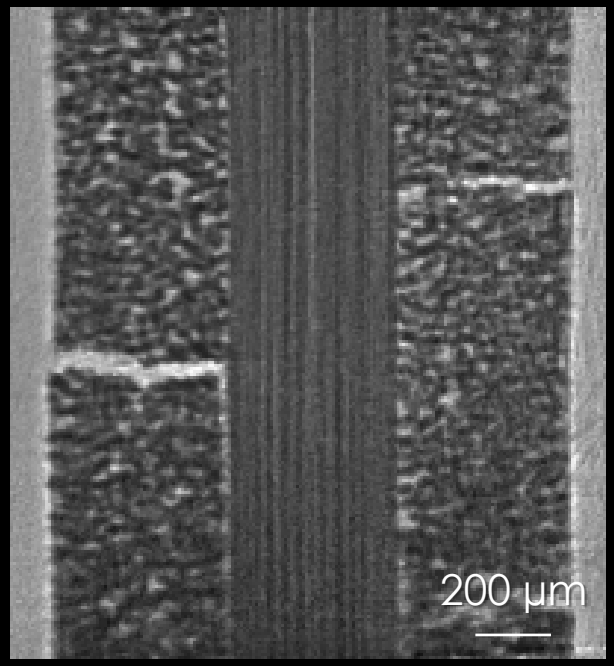

Promising data to reconstruct

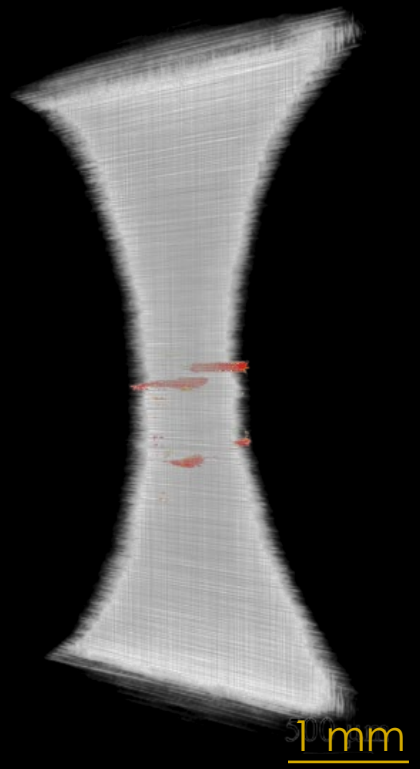

High-speed X-ray multi-projection and ultra high-speed radiography imaging to capture transverse cracking in glass fibre-reinforced composites

E. Van Vlierberghe, J. Soete, E. M. Asimakopoulou, Z. Yao, J. Rogalinski, Z. Hu, K. Mom, B. Lukić, **C. Breite**, P. Villanueva-Perez, Y. Swolfs

ICCM24, August 4, 2025

KU LEUVEN

ESRF The European Synchrotron

fwo

MAX IV

KU LEUVEN XCT CORE FACILITY

LUNDS UNIVERSITET

Composite Materials Group

IN-SITU SYNCHROTRON X-RAY MICROTOMOGRAPHY OF VOID EVOLUTIONS DURING NANOPOROUS NETWORK-ENABLED OUT-OF-AUTOCLAVE MANUFACTURING OF AEROSPACE-GRADE WOVEN COMPOSITE LAMINATES

Jingyao Dai[1,2], Alisa Webb[1], Carina Xiaochen Li[1], Talia Powell[1], Palak Patel[3], Christopher Kwon[1], Shaan Jagani[1], Shweta Sharma[1], Yuying Lin[1], Kwasi Asamoah-Addo[4], Justin Griffin[4], Stephen A. Steiner III[4], Nghia T. Vo[5], and Brian L. Wardle[1,3*]

[1] Department of Aeronautics and Astronautics, Massachusetts Institute of Technology
77 Massachusetts Avenue, Cambridge, MA 02139, USA

[2] School of Aerospace and Mechanical Engineering, University of Oklahoma
865 Asp Avenue, Norman, OK 73019, USA

[3] Department of Mechanical Engineering, Massachusetts Institute of Technology
77 Massachusetts Avenue, Cambridge, MA 02139, USA

[4] Aerogel Technologies, LLC
106B South Street, Hopkinton, MA 01748, USA

[5] National Synchrotron Light Source II, Brookhaven National Laboratory
743 Brookhaven Avenue, Upton, NY 11973, USA

*Corresponding author: Brian L. Wardle (wardle@mit.edu)

Keywords: Composite manufacturing, Nanoporous network, X-ray micro-CT, Synchrotron, In-situ characterization

ABSTRACT

This study presents in-situ synchrotron X-ray computed tomography (SRCT) of the void evolution and resin infusion behavior during a nanoporous network (NPN)-enabled out-of-autoclave (OoA) manufacturing process for aerospace-grade woven composite laminates. During the OoA process, the NPNs could facilitate gas evacuation and promote resin infusion into the interlaminar regions via the induced high capillary pressure. To better understand the underlying mechanisms of the NPN-enabled OoA process, a custom experimental setup employing a thermoelectric module was developed, which allowed active "freezing" of the resin flow during CT scanning while providing heating to promote resin flow between scans. After initial proof-of-concept tests on a lab-scale X-ray micro-CT system, the custom setup was used to scan IM7/8552 woven laminates with and without polymer aerogel NPNs at various stages of a typical composite cure cycle. These scans were conducted using SRCT at the HEX beamline of the National Synchrotron Light Source II (NSLS-II). In these in-situ scans, the baseline laminate exhibited significant void formation and coalescence at elevated temperatures due to volatile release and insufficient resin pressure. On the other hand, the laminate with polymer NPNs showed uniform resin infusion into the interlaminar regions and minimal void development. These results provided direct evidence of the critical role of NPNs in void mitigation during the NPN-enabled OoA process by maintaining open pathways for gas venting and inducing high capillary pressure that promotes resin infusion.

1 INTRODUCTION

Manufacturing of aerospace-grade thermoset composite structures heavily relies on the usage of autoclaves that supply external pressure and convective heating to cure the composite laminates and to achieve minimal void content [1–3]. However, autoclaves often impose significant energy consumption,

equipment cost, and geometric constraints on the manufacturing process for aerospace-grade composites [4]. To overcome these issues, an out-of-autoclave (OoA) manufacturing process utilizing the high capillary pressure induced by nanoporous network (NPN) materials was developed to achieve void-free aerospace-grade composites [5]. When placed at ply-ply interfaces, the NPN materials can provide a pathway for trapped gas to escape while also supplying high capillary pressure to assist resin infusion into the void-prone interlaminar regions (see schematic in Figure 1 (a)). Using this method, void-free unidirectional and woven composite laminates have been successfully fabricated using autoclave-grade prepregs with vacuum-bag-only (VBO) setups using NPNs including vertically aligned carbon nanotubes (CNTs) and polymer aerogels (see Figure 1 (c)) [6–8]. To further understand the NPN characteristics required to enable this OoA manufacturing method, detailed characterizations of the capillary pressure and permeability of various NPN materials have been performed and subsequently informed a 1-D theoretical model developed to predict resin infusion speed in different NPN materials [7,9]. However, there are still many outstanding questions about how voids evolve, and resin infuses into interlaminar regions during the NPN-enabled OoA process as resin viscosity, volatiles, and void content evolve.

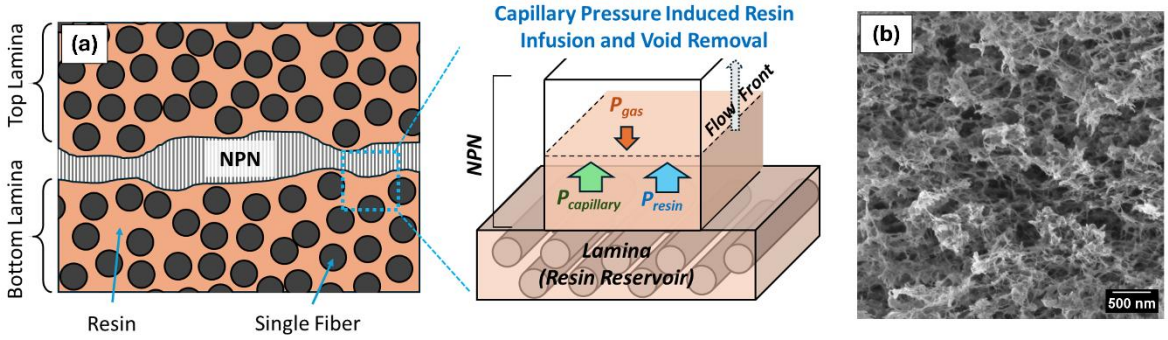

Figure 1: (a) Schematics (recreated from [5]) showing the mechanisms of capillary driven OoA curing of aerospace-grade composites enabled by the nanoporous networks (NPNs) and (b) a representative SEM image of the polymer aerogel NPN used in this study.

To obtain temporal information on the microstructure evolution of the composite laminates during the NPN-enabled OoA process, we developed an in-situ X-ray micro-computed tomography (X-ray micro-CT) experimental setup that can actively freeze the uncured laminates for stable and high-resolution CT scans at different stages of the cure cycles. Proof-of-concept experiments were first conducted on a lab-scale X-ray micro-CT to demonstrate the feasibility of this method. The same testing setup was then adapted for synchrotron radiation computed tomography (SRCT). SRCT scans were performed for IM7/8552 woven laminates with a $[0°]_5$ layup with and without polymer aerogel films as the interlayers using the High Energy Engineering X-Ray Scattering (HEX, 27-ID) beamline at the National Synchrotron Light Source II, Brookhaven National Laboratory. From the reconstructed scans taken at different time steps during a typical cure cycle, significantly different void evolution and resin infusion behavior were observed for the IM7/8552 laminates with and without polymer aerogel NPNs. For the laminate without NPN interlayers, voids can be seen emerging at elevated temperatures while the laminate with the polymer aerogel NPNs exhibited uniform resin infusion into the NPN interlayers without internal void development. The insights obtained from the in-situ SRCT scans will provide valuable learnings on the void evolution and resin infusion behavior during the NPN-enabled OoA process that can help provide a sustainable manufacturing method for high-quality void-free aerospace-grade composites.

2 MATERIAL AND METHOD

2.1 Experimental Setup

To achieve in-situ observation of void evolution and resin infusion behavior during the NPN-enabled OoA process, the resin flow inside the uncured composite laminates must be “frozen” during X-ray CT scans to enable stable and high-resolution imaging. To achieve this objective, we developed a custom

setup (see Figure 2 (a, b)) where a thermoelectric module is used to either heat the laminate to trigger resin flow or cool the laminate to "freeze" any resin motion during imaging by switching the electrodes of the thermoelectric module. To achieve efficient heating/cooling, the thermoelectric module is mounted on an off-the-shelf heat sink that provides a stable temperature near room temperature on the bottom side of the thermoelectric module (see Figure 2 (b)). A sectioned aluminum T-bar is attached on top of the thermoelectric module to conduct heat away or towards the composite laminates while also serving as a rigid and flat surface for the composite layup. Thermal paste was applied between the thermoelectric module and the aluminum support/heat sink to ensure efficient thermal conduction. The backside of the aluminum support was milled thinner to improve the transmission of the X-ray. A K-type thermocouple was mounted on the backside of the aluminum support to measure real-time temperature, which was used as input for a PID temperature controller that controls the heating/cooling of the thermoelectric module. Since the aluminum support provided a rigid and flat surface for the composite layup, a typical vacuum-bag-only setup (see Figure 2 (b)) was used which included all the necessary components, such as cork dams, caul plate, breather, vacuum port, and vacuum bag, and could accommodate laminates with a size of 0.5 inch × 0.5 inch (12.7 mm × 12.7 mm). In this study, all scans were performed on 5-ply $[0°]_5$ IM7/8552 woven laminates. Two sets of laminates were imaged, the baseline samples without any NPN interlayers and laminates with polyimide aerogel films of ~50 µm nominal thickness (supplied by Aerogel Technologies, LLC) as NPNs at every ply-ply interface. Once the layup is completed, the setup is placed on the rotating sample stage for X-ray micro-CT or SRCT imaging (see Figure 2 (c)).

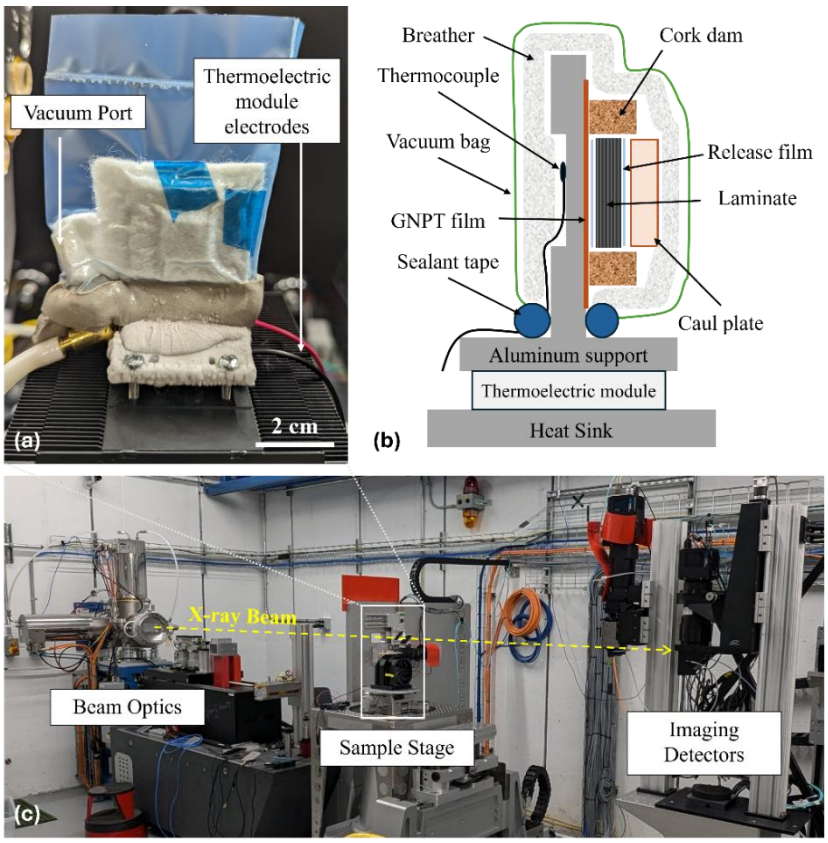

Figure 2: (a, b) Image and schematic showing the experimental setup for in-situ X-ray micro-CT inspection of void evolution within composite laminates during the curing process, and (c) test setup for SRCT at the High Energy Engineering X-ray Scattering (HEX, 27-ID) beamline, National Synchrotron Light Source II

2.2 In-situ X-ray micro-CT and SRCT procedures

Using the custom setup, in-situ X-ray CT imaging was performed using both lab-scale X-ray micro-CT (ZEISS Xradia 620 Versa) and SRCT at the Brookhaven National Laboratory using National Synchrotron Light Source II's High Energy Engineering X-ray Scattering (HEX, 27-ID) beamline. The lab-scale X-ray micro-CT experiments were conducted using the X-ray parameters of 160 keV voltage and 24 W power, with optics being a 4× objective and an HE2 filter. The optics and detector were positioned to result in a 1.6 µm voxel size. To prevent entanglement of the various wiring and vacuum hose, fan scans from -110 to 110 degrees were conducted with 3201 projections and an exposure time of 17 seconds, making the total scanning time roughly 15 hours without considering additional time for stage movement and taking reference scans. For SRCT tests, an X-ray energy of ~70 keV was used with the HEX beamline's optical module B setup, giving a voxel size of 1.3 µm and a field of view of 4.2 mm × 4.2 mm with the high-resolution sensor (3200 × 3200 pixels). Due to the high brilliance of the Synchrotron X-ray light source, a significantly reduced exposure time of 0.375 seconds was used for all the SRCT scans. Fan scans were performed from -90 to 90 degrees with 2401 projections, making each scan last for ~15 minutes.

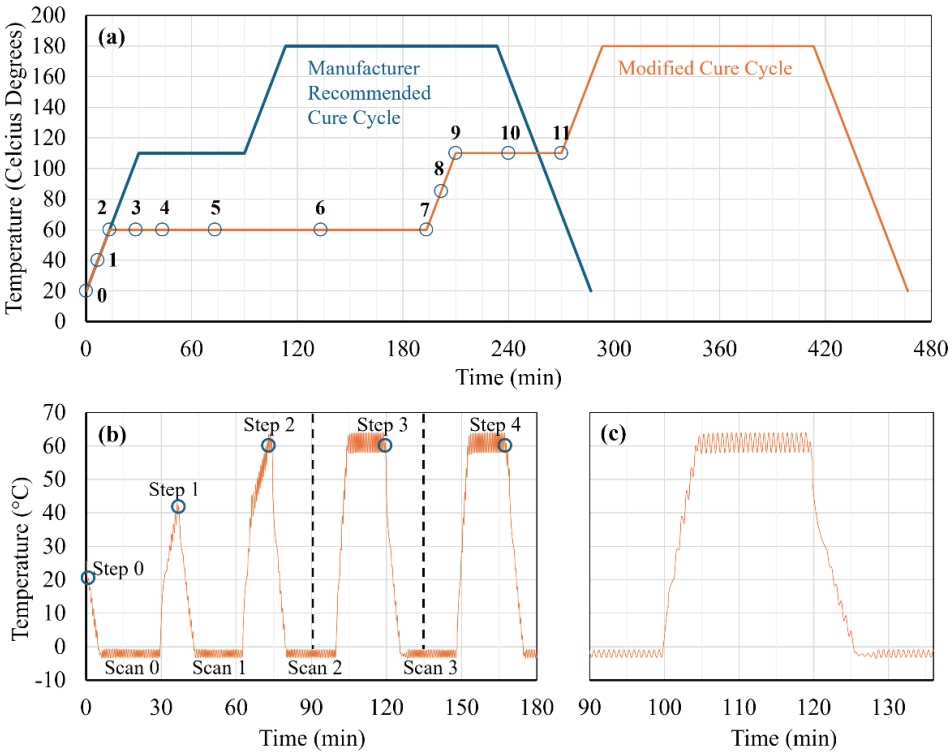

Figure 3: (a) Manufacturer Recommended Cure Cycle (MRCC) for IM7/8552 prepregs and the modified cure cycle with a 3-hour hold at 60 °C and numbered circles indicate time steps where CT inspections were performed, (b, c) representative temperature profiles recorded during the in-situ SRCT experiments.

To monitor resin infusion and void evolution within the composite laminates during the NPN-enabled OoA manufacturing process, scans were carried out at different time steps during a typical cure cycle used for the OoA process (see Figure 3 (a)). A modified cure cycle previously used to achieve void-free IM7/8552 woven composite laminates using polymer aerogel NPNs [6] was used. Compared with the manufacturer-recommended cure cycle (MRCC), the modified cure cycle has an additional 1-hour hold at 60 °C to facilitate the gradual wetting of the NPNs, which allows trapped gas to escape via the open pathway provided by the NPN interlayers. Twelve key time steps (steps 0-11) were selected for SRCT scans, while only selected scans at steps 0, 2, 4, and 5 were conducted on the lab-scale X-ray micro-CT. During the test, the thermoelectric module was controlled by the PID controller with a temperature set

point of -2.5 °C to freeze the resin flow during CT scans. After each scan, the electrodes of the thermoelectric module were reversed to enable heating. The PID setting first allowed the temperature to rise quickly at a rate of ~10 °C/min to the previous temperature step before continuing with the modified cure cycle with either a temperature ramp with a 3 °C/min heating rate or a temperature hold. Measured temperature profiles showed good agreement with the temperature set points with minor oscillations (± 3 °C) due to thermal lag between the aluminum support and the thermoelectric module.

3 RESULTS AND DISCUSSION

3.1 Proof of Concept Results using a Lab-scale X-ray micro-CT

Using the custom in-situ setup, we first obtained 3D volumetric scans of the 5-ply $[0°]_5$ IM7/8552 woven composite laminates with polymer aerogel NPNs using the lab-scale X-ray micro-CT. Scans were performed at steps 0, 2, 4, and 5. The representative slices taken from scans of step 0 (as-bagged) and step 4 (after holding 15 minutes at 60 °C) were compared side by side in Figure 4. In the step-0 scan, the polymer aerogel NPNs can be seen at the ply-ply interfaces, with only one larger void at the interlaminar region. The lack of large voids likely resulted from the open pathways provided by the NPNs for the trapped gas to evacuate to the edges of the laminates. After heating to 60 °C and the 15-minute hold, the voids observed in the step-0 scan disappeared. The thickness of the porous NPN layers was also significantly reduced due to resin infusion into the polymer aerogel NPNs. As a result of resin redistribution, a reduction in laminate thickness from ~1.3 mm to ~1.1 mm was also observed. Through proof-of-concept experiments using the lab-scale X-ray micro-CT, we successfully demonstrated that high-resolution and stable scans can be achieved using our custom in-situ setup to monitor resin infusion and void evolution.

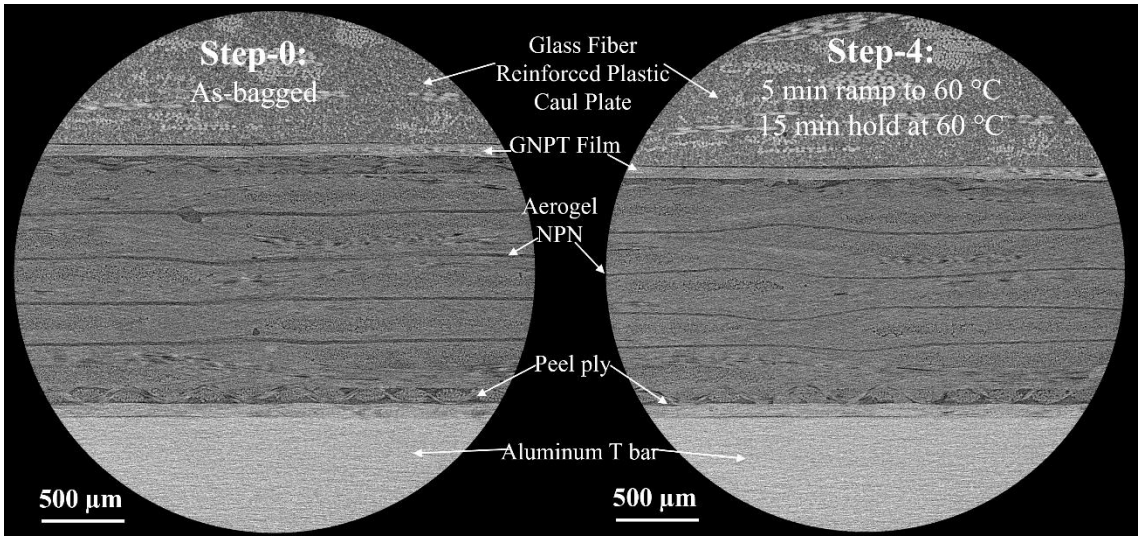

Figure 4: Representative slices taken from reconstructed volumes scanned at step-0 and step-1 for a 5-ply $[0°]_5$ IM7/8552 woven laminate with polymer aerogel NPNs at every interlayer.

3.2 Void Evolution Observation from SRCT Results

After the successful in-situ observation of resin infusion and void evolution using the lab-scale X-ray micro-CT, we performed SRCT scans using the same setup at 12 time steps (see Figure 3(a)) during the modified cure cycle for 5-ply IM7/8552 $[0°]_5$ woven laminates with and without polymer aerogel NPNs. Selected slices taken from steps 1, 5, 7, and 9 for both the baseline laminate and the laminate with polymer aerogel NPNs were shown in Figure 5. For the baseline laminate, small and medium-sized (<100 µm) voids can be observed at the early stage of the cure cycle (step-1, see Figure 5 (a)). These voids are likely air bubbles trapped during the composite layup process. After ramping to 60 °C and holding for one hour, significantly larger voids (~200-500 µm) appeared (see Figure 5 (c)). The void expansion and coalescence may be attributed to the combination of lower resin viscosity and release of

volatiles from the prepregs at elevated temperature [10]. These voids further developed after the 3-hour hold at 60 °C (see Figure 5 (e)), as part of the resin between the fiber tows migrated to fill the intralaminar voids. Once the temperature reached 110 °C (see Figure 5 (g)), large voids with boundaries partially following the contour of fiber tows were observed. These results showcased the difficulty of obtaining void-free aerospace-grade composites without the external pressure supplied by an autoclave. Compared with the baseline laminate, the one with polymer aerogel NPNs exhibited minimal voids throughout the time steps scanned. Small voids present in the early stage of the cure cycle (see Figure 5 (b)) disappeared during the 60 °C hold as the NPNs provided open pathways for the gas to escape and were not fully saturated even after 1 hour at 60 °C (see Figure 5 (d)). After the 3-hour hold (Figure 5 (f)), the NPN layers were fully saturated with resin, and a surface void developed as the resin migrated to fill the intralaminar voids within fiber tows. No significant change in void morphology was observed after the temperature ramp to 110 °C (see Figure 5 (h)).

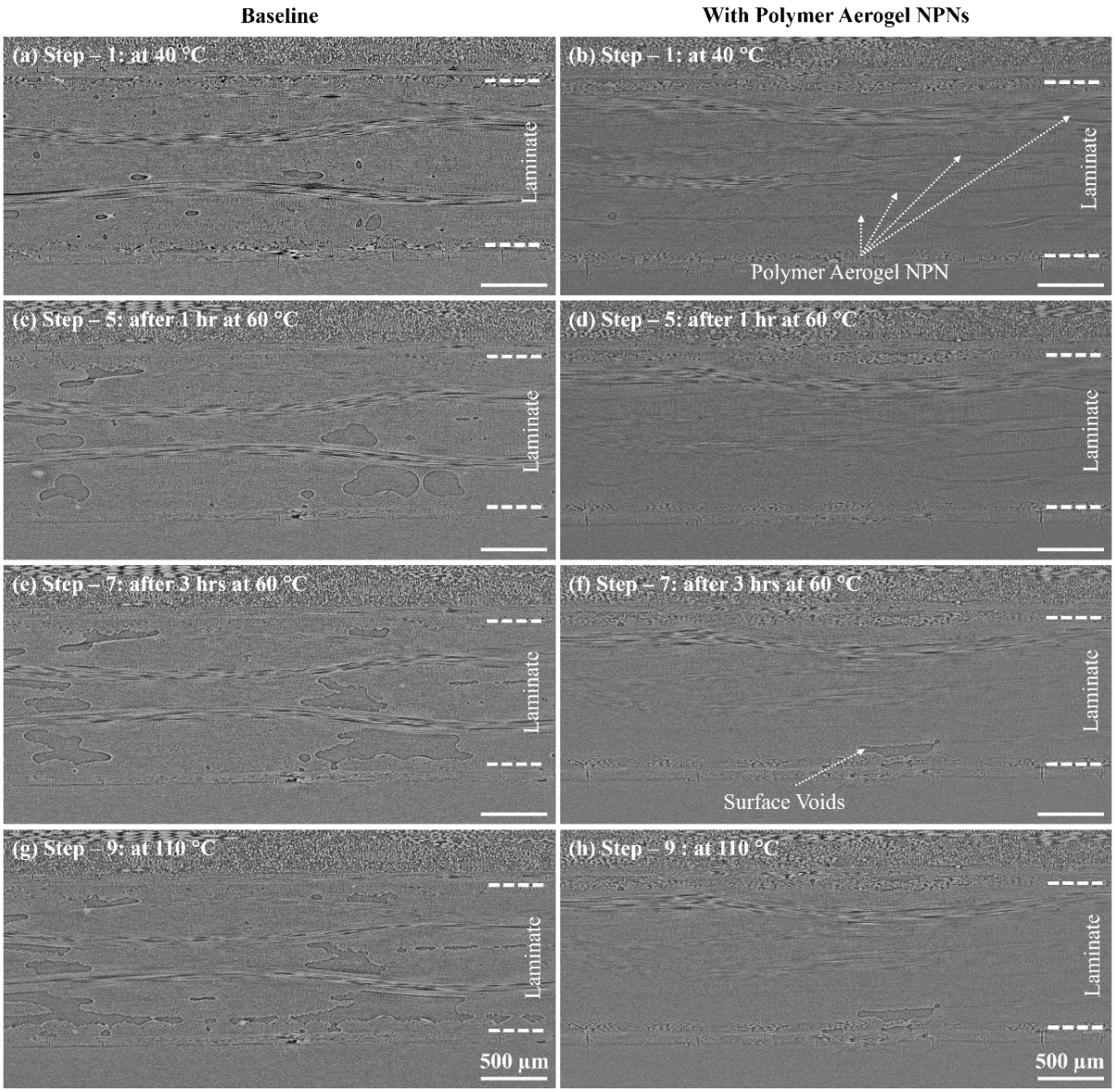

Figure 5: Selected slices from scans at various time steps showing void evolution for (a, c, e, g) the baseline 5-ply $[0°]_5$ IM7/8552 woven laminate and (b, d, f, h) the laminates with polymer aerogel at every interlayer; dashed lines marked the upper and lower surface of the laminates.

4 CONCLUSIONS

In this study, we developed a novel in-situ X-ray tomography setup to monitor resin redistribution and void evolution during the NPN-enabled OoA manufacturing of aerospace-grade composites. Using the thermoelectric module-enabled custom setup, high-resolution and stable volumetric scans of IM7/8552 woven laminates with and without polymer aerogel NPNs were successfully obtained throughout key curing stages using both a lab-scale X-ray micro-CT system and the SRCT using the HEX beamline at NSLS-II. The obtained scans provided time-resolved insights into the resin redistribution and void evolution behavior during the OoA process. Compared with baseline laminates that exhibited significant void formation and coalescence, the laminates with polymer aerogel NPNs demonstrated superior void mitigation and uniform resin infusion into the interlaminar regions. These findings, together with our prior studies on theoretical modeling and measurement of key NPN characteristics, advanced our understanding of mechanisms behind the NPN-enabled OoA manufacturing of void-free aerospace-grade composites and could inform the development and sustainable manufacturing of various aerospace-grade composite systems.

ACKNOWLEDGEMENTS

The work in this paper is partially supported by the U.S Office of Naval Research (ONR) under grant/contract number N00014-20-1-2300, and partially supported by Airbus, ANSYS, Boeing, Embraer, Lockheed Martin, Saab AB, and Teijin Carbon America through MIT's Nano-Engineered Composite aerospace STructures (NECST) Consortium. This research used the High Energy Engineering X-ray Scattering (HEX, 27-ID) beamline of the National Synchrotron Light Source II, a U.S. Department of Energy (DOE) Office of Science User Facility operated for the DOE Office of Science by Brookhaven National Laboratory under Contract No. DE-SC0012704. For the second author, this material is based upon work supported by the National Science Foundation under Grant No. DGE-2141064. This material is based upon work supported in part by the U. S. Army Research Office through the Institute for Soldier Nanotechnologies at MIT, under Cooperative Agreement Number W911NF-18-2-0048. Lab-scale microcomputed tomography instrumentation supported by the Office of Naval Research (ONR) under grant number ONR.N000141712068 through the Defense University Research Instrumentation Program (DURIP) is gratefully acknowledged. The authors gratefully acknowledge Prof. Gregory Rutledge (MIT) and their group for the use of the porometer, and the members of necstlab at MIT for technical support and advice. The first author also gratefully acknowledges the support via the faculty start-up fund by the University of Oklahoma.

REFERENCES

[1] Abliz, D., Duan, Y., Steuernagel, L., Xie, L., Li, D., and Ziegmann, G. "Curing Methods for Advanced Polymer Composites -A Review." *Polymers and Polymer Composites*, Vol. 21, No. 6, 2013, pp. 341–348. https://doi.org/10.1177/096739111302100602.

[2] Mehdikhani, M., Gorbatikh, L., Verpoest, I., and Lomov, S. V. Voids in Fiber-Reinforced Polymer Composites: A Review on Their Formation, Characteristics, and Effects on Mechanical Performance. *Journal of Composite Materials*. 12. Volume 53, 1579–1669.

[3] Clyne, T. W., and Hull, D. "An Introduction to Composite Materials." *An Introduction to Composite Materials*, 2019. https://doi.org/10.1017/9781139050586.

[4] Witik, R. A., Gaille, F., Teuscher, R., Ringwald, H., Michaud, V., and Månson, J. A. E. "Economic and Environmental Assessment of Alternative Production Methods for Composite Aircraft Components." *Journal of Cleaner Production*, Vols. 29–30, 2012, pp. 91–102. https://doi.org/10.1016/J.JCLEPRO.2012.02.028.

[5] Lee, J., Kessler, S. S., and Wardle, B. L. "Void-Free Layered Polymeric Architectures via Capillary-Action of Nanoporous Films." *Advanced Materials Interfaces*, Vol. 7, No. 4, 2020, p. 1901427. https://doi.org/10.1002/ADMI.201901427.

[6] Dai, J., Webb, A., Lee, J., Wardle, B. L., Randaccio, L., Griffin, J., and Steiner, S. A. "Out of Autoclave Manufacturing of Void-Free Woven Aerospace-Grade Carbon Fiber Reinforced

Plastic Composite Laminates Using Capillary Effects of Aerogel Nanoporous Networks." *AIAA SciTech Forum and Exposition, 2023*, 2023. https://doi.org/10.2514/6.2023-0516.

[7] Webb, A., Dai, J., Asamoah-Addo, K., Griffin, J., Steiner III, S., and Wardle, B. L. "Out-of-Autoclave Composite Manufacturing Using Capillary Effects of Electrospun and Aerogel Nanoporous Networks." *Proceedings of 23rd International Conference on Composite Material*, 2023.

[8] Li, C. X., Hank, T. J., Kalfon-Cohen, E., Furtado, C., Lee, J., Cassady, S., Tucker, J., Kessler, S. S., and Wardle, B. L. "Manufacturing Autoclave-Grade Thermoset Carbon Fiber-Reinforced Polymer Aerospace Composites without an Autoclave Using Nanoporous Materials." *ACS Applied Materials & Interfaces*, Vol. 16, No. 19, 2024, pp. 25280–25293. https://doi.org/10.1021/acsami.4c02107.

[9] Dai, J., Webb, A., Lee, J., Asamoah-Addo, K., Griffin, J., Steiner, S., and Wardle, B. L. "Investigation of Void Removal Behavior during Nanoporous Network Enabled Out of Autoclave Manufacturing of Void-Free Aerospace-Grade Carbon Fiber Reinforced Plastic Composites." *AIAA SCITECH 2024 Forum*, 2024. https://doi.org/10.2514/6.2024-1219.

[10] Agius, S. L., Magniez, K. J. C., and Fox, B. L. "Cure Behaviour and Void Development within Rapidly Cured Out-of-Autoclave Composites." *Composites Part B: Engineering*, Vol. 47, 2013, pp. 230–237. https://doi.org/10.1016/J.COMPOSITESB.2012.11.020.

DEEP LEARNING-DRIVEN SEGMENTATION OF RESIN-RICH AREAS IN 3D CT IMAGING OF CFRTP-SMC

Cheng Jin[1], Zihao Zhao[1] , Yi Wan[1] and Jun Takahashi[1]

[1]Department of Systems Innovation, Graduate School of Engineering, The University of Tokyo
7-3-1 Hongo Bunkyo-ku 113-8656 Tokyo, Japan
Email: jincheng-416@g.ecc.u-tokyo.ac.jp

Keywords: CFRTP-SMC, Resin-Rich Area, 3D Microstructural Characterization, Deep Learning Segmentation, X-ray Computed Tomography

ABSTRACT

Carbon fiber-reinforced thermoplastic sheet molding compounds (CFRTP-SMCs) are gaining attention for their combination of high stiffness, formability, and lightweight characteristics. However, local heterogeneities—especially resin-rich areas formed near the edges of fiber tapes—can significantly influence mechanical and functional properties. While these regions are visually distinguishable in X-ray computed tomography (CT) images, their automated identification remains challenging due to subtle boundaries and structural complexity.

This study proposes a deep learning-based approach to automatically segment resin-rich areas in 3D X-ray CT images of CFRTP-SMCs. We first prepared composite specimens using a controlled molding process and acquired high-resolution CT scans capturing detailed internal microstructures. Since no existing methods could reliably identify resin-rich zones, we constructed a ground truth dataset via manual 3D annotation, supported by interpolation techniques. Each data sample consisted of a 3D CT image paired with a binarized label identifying resin-rich regions. We trained a 3D segmentation model using the nnU-Net framework, optimized for material imaging tasks. To enhance generalization and compensate for the limited dataset size, we applied data augmentation, intensity normalization, and cross-validation. The model architecture incorporates convolutional blocks with deep supervision to ensure stable training and accurate feature learning.

Our results demonstrate that the model accurately segmented resin-rich areas, outperforming classical texture-based methods. Crucially, it generalized well to unseen data and supported predictions on larger input volumes, confirming its robustness and scalability. This represents one of the first automated methods for 3D segmentation of resin-rich regions in CFRTP-SMCs using deep learning. The proposed framework enables more efficient and objective internal structure characterization of complex composites, opening the door to automated evaluation of local features that influence macroscopic performance.

1 INTRODUCTION

Carbon fiber reinforced thermoplastic sheet molding compounds (CFRTP-SMCs) are advanced composites composed of long, discontinuous carbon fibers arranged in randomly oriented strands (ROS). These materials exhibit mechanical properties—particularly stiffness—comparable to quasi-isotropic laminates, making them well-suited for stiffness-critical structural designs. Their excellent formability also enables the production of complex, net-shaped components, expanding their applicability in industries requiring lightweight and geometrically intricate parts. In addition, CFRTP-SMCs offer favorable characteristics such as corrosion resistance and cost-efficient processing, positioning them as strong alternatives to metal components in many applications [1,2,3,4].

A notable microstructural feature of CFRTP-SMCs is the presence of resin-rich areas, typically occurring near the edges of fiber tapes. These regions are defined by a local excess of resin and a corresponding lack of fiber reinforcement. Although relatively small in size, they can substantially influence composite properties such as strength, toughness, volume resistivity, and failure strain. Monte Carlo simulations have shown that the region within approximately 2 mm of the tape edge plays a critical role in pull-out behavior, highlighting the importance of accurately identifying these resin-rich areas.

Furthermore, these regions often delineate internal boundaries, offering valuable information about the material's microstructural architecture [5,6].

While human experts can visually identify resin-rich areas in X-ray computed tomography (CT) images, automating this process is difficult due to ambiguous boundaries and structural variability. Existing methods are typically limited to indirect estimation from 2D images, are time-consuming, and lack generalizability across different composite configurations [7,8]. The structural complexity of CFRTP-SMCs presents significant challenges for traditional analysis approaches.

To address this gap, we propose a deep learning-based framework using the nnU-Net model [9] for automatic segmentation of resin-rich areas in 3D X-ray CT images. Our approach demonstrates high segmentation accuracy and strong generalization capability, even with limited training data. This work provides a foundation for comprehensive and automated internal microstructural characterization of CFRTP-SMCs.

2 METHODS

2.1 Specimen Preparation and X-ray CT Scanning

CFRTP-SMC specimens were fabricated using an automatic press molding machine (PINETTE PEI) by stacking 12 plies of carbon fiber prepregs into panels measuring 250 × 125 × 2 mm. To facilitate high-resolution imaging, narrow rectangular specimens were cut to approximately 2 × 2 × 60 mm, optimized for microfocus X-ray CT scanning. Imaging was conducted using a TDM 1000-IS 3D X-ray CT system (Yamato Scientific Co., Ltd.), achieving a voxel resolution sufficient to capture the detailed internal morphology, including individual fiber strands and resin distributions.

2.2 Generating Ground Truth Labels and Datasets

Automating the identification of resin-rich areas in CFRTP-SMCs is complex due to the need to detect un-reinforced pixels, consider the density of adjacent fibers, and the lack of clear boundary definitions. Currently, no existing methods can automatically segment these areas; therefore, we opted for manual labeling to generate ground truth labels.

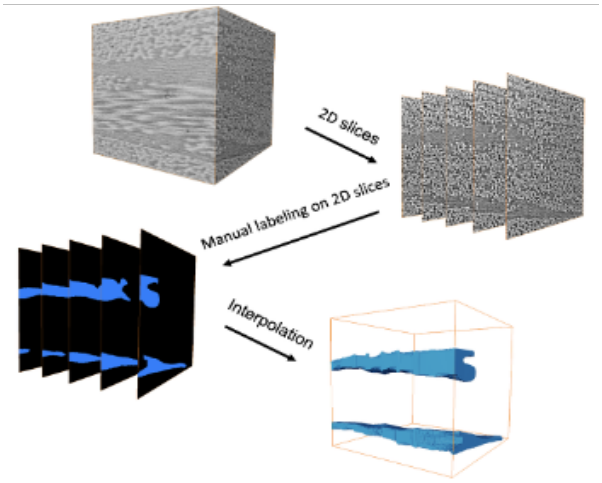

Figure 1: Workflow for manually generating ground truth labels of resin-rich areas for training data. (Scale: 256 × 256 × 256 voxels, 0.425 × 0.425 × 0.425 mm^3.)

Figure 1 illustrates the workflow for manually generating ground truth labels for training data. Raw X-ray CT images were uniformly cropped to dimensions of 256 × 256 × 256 voxels, with each voxel measuring 1.7 μm. The manual segmentation process began with the segmentation of 2D slices. Subsequently, an interpolation method was employed to automatically generate a 3D segmentation map of the resin-rich areas. The final training dataset comprised 26 pairs of 3D images of CFRTP-SMCs, with each pair consisting of a raw grayscale X-ray CT image and a corresponding binarized label image that highlighted the segmented resin-rich areas.

For dataset preprocessing, intensity normalization was applied to ensure consistency in voxel intensities across scans. Given the limited dataset size, data augmentation techniques were employed to enhance model generalization, with augmentations computed on-the-fly by CPU background workers. Additionally, a 5-fold cross-validation split was implemented to provide a robust assessment of the model's performance.

2.3 Model Training

Figure 2 illustrates the 3D U-Net architecture tailored for segmenting resin-rich areas in CFRTP-SMCs. The input patch size was set to 128 × 128 × 128 voxels, cropped from the original 256 × 256 × 256 image volumes. This relatively large patch size enables the network to capture broader contextual features critical for detecting subtle, spatially diffuse patterns such as resin-rich zones. To accommodate memory constraints, the batch size was limited to 2. To ensure stable training with small batches, instance normalization was used instead of batch normalization.

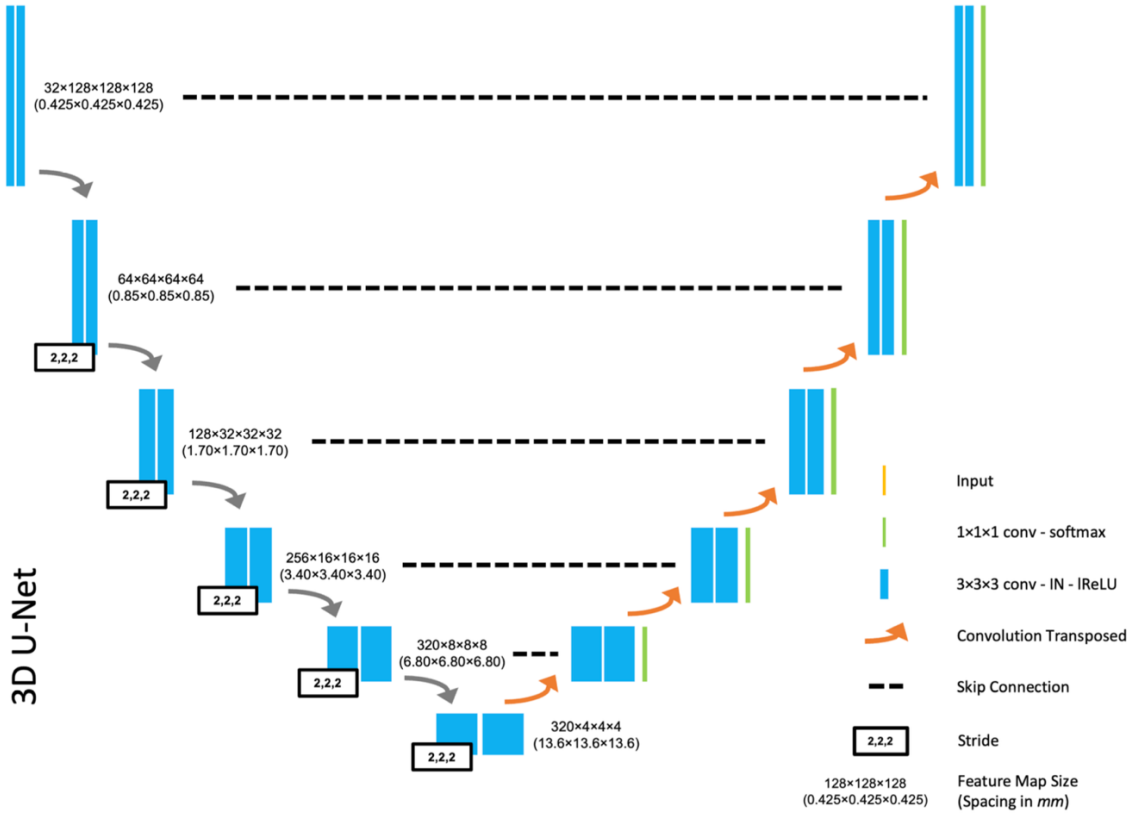

Figure 2: 3D U-Net network architecture for resin-rich areas segmentation.

The architecture consisted of a 3D U-Net with two convolutional blocks per resolution level in both encoder and decoder paths. Each block included a 3×3×3 convolution, instance normalization, and a Leaky ReLU activation with a negative slope of 0.01. Downsampling and upsampling were performed using strided and transposed convolutions, respectively. The number of feature maps started at 32 and increased with each downsampling step, capped at 320.

Training was conducted using stochastic gradient descent with Nesterov momentum ($\mu = 0.99$) and an initial learning rate of 0.01. The learning rate followed a polynomial decay policy. The loss function combined cross-entropy and Dice loss, with deep supervision applied at multiple decoder layers. We employed a 5-fold cross-validation scheme, and each fold was trained for 100 epochs with 250 mini-batches per epoch on an NVIDIA GeForce RTX 4090 GPU.

Performance was monitored using a 'global Dice' score calculated from validation patches. Most folds demonstrated stable training and convergence. One exception was Fold 4, where validation loss fluctuated due to labeling inconsistencies in the validation set.

2.4 Inference

After training, inference was performed using a sliding window strategy with the same patch size as used during training (128 × 128 × 128 voxels). To ensure smooth and accurate predictions across the entire volume, windows were overlapped by 50% in all directions. Because segmentation accuracy tends to degrade near the patch borders, a Gaussian importance weighting scheme was applied. This approach assigns higher weights to the center voxels and reduces the influence of border regions when aggregating softmax outputs.

To further enhance prediction robustness, test-time augmentation was employed by mirroring the input images along each of the three spatial axes. Predictions from each augmented version were averaged to produce the final output.

For final segmentation, we utilized an ensemble of the five models trained during the 5-fold cross-validation. Each model was used to predict on the test set, and their outputs were combined using softmax averaging. This ensemble approach helped reduce prediction variance and improved overall segmentation accuracy. The best-performing configuration, determined by the average Dice score across training folds, was used for final inference.

3 RESULTS AND DISCUSSION

3.1 Enhanced Predictions Over Manual Labeling

To evaluate the segmentation performance in more detail, Figure 3 presents three cases where the model outperforms manual labeling:

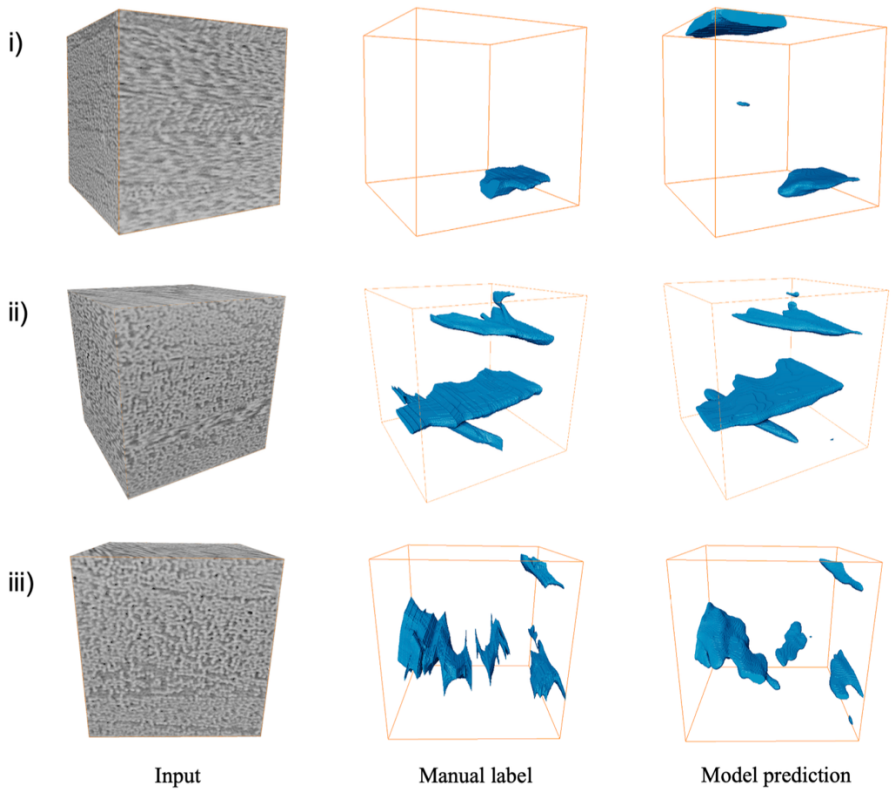

Figure 3: Three cases of the the model input (raw X-ray CT image), the corresponding manual labels of resin-rich areas, and the predicted segmentation map generated by the model. (Scale: 256 × 256 × 256 voxels, 0.425 × 0.425 × 0.425 mm^3.)

Case i: A resin-rich area was missed during manual labeling (false negative), but the model successfully detected it. This highlights the model's higher sensitivity and its ability to mitigate human oversight in identifying subtle resin-rich regions.

Case ii: Manual labeling overestimated the extent of resin-rich areas (false positives), incorrectly marking non-defective regions. The model, though slightly conservative, produced more precise segmentations with fewer false positives, particularly beneficial for identifying resin-rich zones between fiber tapes.

Case iii: For irregularly shaped resin-rich areas, manual segmentation produced coarse, discontinuous boundaries due to the limitations of 2D-based interpolation. The model, leveraging 3D analysis, achieved smooth and accurate boundary delineation.

3.2 Comparison with Texture Classification

Figure 4 compares the segmentation results of our model with those produced by a classical texture-supervised classification method implemented in Avizo. While the texture method relies on local statistical features, such as variance and histogram-based descriptors, it struggles with the complex nature of resin-rich areas. The results exhibited numerous false positives, especially near the image borders.

In contrast, the deep learning model generated cleaner and more reliable segmentation outputs. This comparison underscores the advantage of learning-based methods in capturing global patterns and spatial context, which are essential for accurately segmenting heterogeneous regions in CFRTP-SMCs.

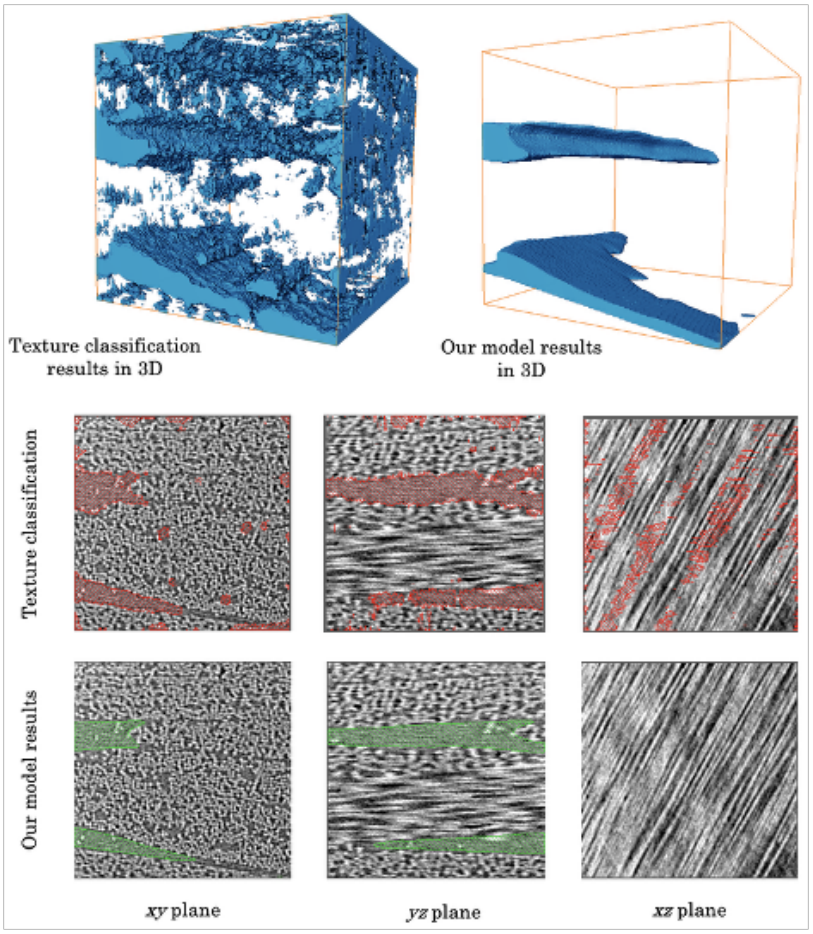

Figure 4: The comparison between the texture classification results and the segmentation of resin-rich areas generated by our model. (Scale: 256 × 256 × 256 voxels, 0.425 × 0.425 × 0.425 mm^3.)

3.3 Verification with Fiber Analysis

To validate the physical relevance of the segmented resin-rich areas, we conducted a fiber orientation analysis based on geometric correlation with parametric cylinder templates. This approach enables the identification and tracing of individual carbon fibers according to their local orientation and spatial continuity. The segmented resin-rich regions consistently coincided with zones of low fiber density, confirming their characterization as fiber-deficient, resin-rich areas. Moreover, these regions frequently appeared between fiber tapes exhibiting distinct orientation patterns, indicating that the model successfully identifies resin accumulations at inter-tape boundaries. These results demonstrate that the model's predictions are not only visually consistent with expert expectations but also structurally meaningful in the context of composite microarchitecture.

3.4 Prediction on Unseen Data

To assess generalization capability, the trained model was applied to a larger, previously unseen CT image with dimensions of 600 × 600 × 600 voxels—over 12 times the size of the training patches. As shown in Figure 5, the model successfully segmented resin-rich areas across multiple planes (xy, yz, xz) and in the full 3D volume.

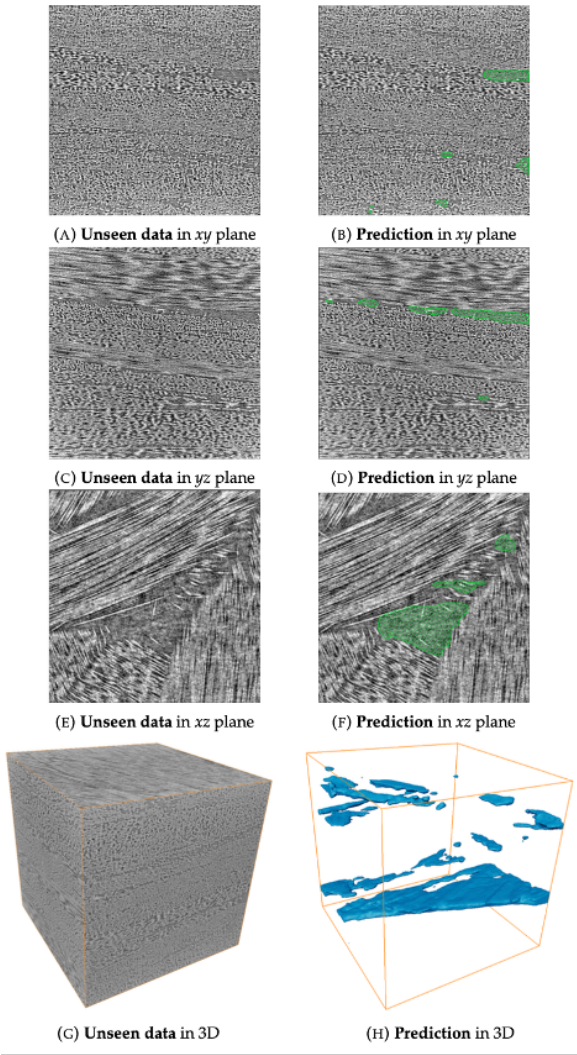

Figure 5: Prediction of resin-rich areas on unseen data. The green hatched regions indicate the model's prediction of resin- rich areas. (Scale: 600 × 600 × 600 voxels, 1 × 1 × 1 mm^3.)

The predicted regions aligned well with visually identifiable resin-rich zones, confirming that the model generalizes effectively beyond the training distribution. This robustness is particularly valuable for real-world applications involving full-scale parts, where input dimensions vary and high-resolution analysis of internal structures is critical.

4 CONCLUSIONS

This study demonstrated the effectiveness of the nnU-Net deep learning framework in automatically segmenting resin-rich areas in 3D X-ray CT images of CFRTP-SMCs. The results reveal several key advantages and implications of the proposed approach:

First, the model successfully automates the segmentation process, reducing reliance on manual labeling and improving both efficiency and consistency. It consistently produces smoother and more accurate boundary delineations than conventional 2D-based manual methods, effectively addressing interpolation artifacts and labeling noise. Moreover, its robust 3D analysis enables accurate segmentation of irregularly shaped resin-rich regions—an area where traditional techniques often fall short.

Second, compared to conventional texture-based classification methods, the nnU-Net model achieves significantly higher segmentation accuracy. While texture-based approaches are limited by local feature dependence and prone to false positives, the deep learning model captures complex structural patterns with superior generalization.

Third, the physical relevance of the predicted resin-rich areas was confirmed through fiber orientation analysis. The model's segmented regions consistently aligned with low fiber density zones and inter-tape boundaries, verifying their structural validity within the composite microarchitecture.

Finally, the model demonstrated strong scalability by accurately predicting resin-rich areas in large, previously unseen CT volumes. This highlights its robustness and practical applicability for high-resolution material characterization at various scales.

In summary, the nnU-Net model provides a reliable, accurate, and scalable solution for segmenting resin-rich areas in CFRTP-SMCs. Its integration into composite materials research holds promise for improving internal structure analysis, enabling advanced material characterization, and supporting automated quality control and performance evaluation.

REFERENCES

[1] Takahashi J, Ishikawa T. Current Japanese activity in CFRTP for industrial application. In *Proceedings of the Leuven: International Conference on Textile Composites, Leuven, Belgium* 2013 Sep (pp. 16-20).

[2] Visweswaraiah SB, Selezneva M, Lessard L, Hubert P. Mechanical characterisation and modelling of randomly oriented strand architecture and their hybrids–A general review. *Journal of Reinforced Plastics and Composites.* 2018 Apr;37(8):548-80.

[3] Wan Y, Takahashi J. Tensile and compressive properties of chopped carbon fiber tapes reinforced thermoplastics with different fiber lengths and molding pressures. *Composites Part A: Applied Science and Manufacturing.* 2016 Aug 1;87:271-81.

[4] Wan Y, Takahashi J. Tensile properties and aspect ratio simulation of transversely isotropic discontinuous carbon fiber reinforced thermoplastics. *Composites Science and Technology.* 2016 Dec 12;137:167-76.

[5] Sacchetti F, Grouve WJ, Warnet LL, Villegas IF. Effect of resin-rich bond line thickness and fibre migration on the toughness of unidirectional Carbon/PEEK joints. *Composites Part A: Applied Science and Manufacturing.* 2018 Jun 1;109:197-206.

[6] Rezasefat M, Mostafavi Y, Ma D, Manes A. A hybrid micro-macro mechanical damage model to consider the influence of resin-rich zones on the transverse tensile behaviour of unidirectional composites. *Composite Structures.* 2023 Mar 15;308:116714.

[7] Li X, Shonkwiler S, McMains S. Detection of resin-rich areas for statistical analysis of fiber-reinforced polymer composites. *Composites Part B: Engineering.* 2021 Nov 15;225:109252.

[8] Fritz NK, Kopp R, Nason AK, Ni X, Lee J, Stein IY, Kalfon-Cohen E, Sinclair I, Spearing SM, Camanho PP, Wardle BL. New interlaminar features and void distributions in advanced aerospace-grade composites revealed via automated algorithms using micro-computed tomography. *Composites Science and Technology.* 2020 Jun 16;193:108132.

[9] Isensee F, Jaeger PF, Kohl SA, Petersen J, Maier-Hein KH. nnU-Net: a self-configuring method for deep learning-based biomedical image segmentation. *Nature methods.* 2021 Feb;18(2):203-11.

PRIOR SHAPE ANALYSIS FOR YARN SEGMENTATION IN XCT IMAGES

Hafsa El Herichi [1,2,3], Arturo Mendoza [1], Yanneck Wielhorski [1], Hugues Talbot [2] and Stéphane Roux [3]

[1]Safran Group
Email: hafsa.el-herichi@safrangroup.com , arturo.mendoza-quispe@safrangroup.com, yanneck.wielhorski@safrangroup.com

[2] Univ. Paris-Saclay, CentraleSupélec, INRIA, CVN
9 Rue Joliot Curie, 91190 Gif-sur-Yvette, France
Email: hugues.talbot@centralesupelec.fr

[3] Univ. Paris-Saclay, CentraleSupélec, ENS Paris-Saclay, CNRS, LMPS
4, avenue des Sciences 91190 Gif-sur-Yvette, France
Email: stephane.roux@ens-paris-saclay.fr

Keywords: 3D woven composites, XCT, segmentation, yarns

ABSTRACT

This study addresses the automatic segmentation of textile reinforcements in fan blades using X-ray CT imaging at resolutions above 120 µm. The proposed approach is a scalable analysis orthogonal to the main yarn orientations (warp and weft), involving the identification of yarn centers and cross-sections on a 2D plane.

The method statistically characterizes three properties: the standard shape of yarn cross-sections using Principal Component Analysis (PCA), the continuity of each yarn path, and their arrangement relative to neighbouring yarns. These properties are exploited in a variational formulation for optimal yarn positions, displacement from previous planes, and neighbour arrangements.

Yarn center positions are determined over successive planes perpendicular to the mean yarn orientation, successfully tracking around 1,500 yarns over 900 slices with a 95\% success rate for annotated yarns. Then the process iteratively refines segmentation by erasing and re-segmenting yarns. This method shows potential for large-scale textile annotation.

1 INTRODUCTION

This work addresses the automatic segmentation of textile reinforcements in aircraft engine fan blades, imaged with X-ray CT at resolutions above 120 µm with lengths in the tens of centimeters. Previous works have used a variety of approaches ranging from image processing [1], variational methods [2, 3], and deep learning [4, 5, 6].

Yet, these studies focused on smaller samples with simpler geometries and used much higher resolutions.

Applying these approaches to the current problem is not feasible because they would require better image characteristics or expensive initialization, or the computation time would be excessive. Hence, a simple and highly scalable method is proposed based on 2D analysis orthogonal to the main yarn orientations (warp and weft).

2 APPROACH

Here, the segmentation involves identifying the yarn centers and cross sections on a 2D plane based on the known yarn positions from the previous 2D plane. For this study, because of the time-consuming nature of the task, only a subset of yarn centers for a fan blade were manually sparsely annotated.

The proposed method statistically characterizes three specific properties of the material. The first property is the "standard" shape of each yarn cross section (for each yarn type).

For this, a Principal Component Analysis is used on small images centered on the yarn centers. The obtained eigenmodes encapsulate unique, learnable features, leading to the identification of the dominant shape and some of its subtler variations. Hence, cross-correlation between the first eigenmode of each yarn type and the CT images generates a heatmap where higher values correspond to likely yarn centers.

To re-adjust the probable central positions, an alignment between the tomographic image and the principal mode is done by minimizing the squared difference between them, considering both the image and its partial derivatives. Only the positive part of the difference is used to focus on the yarn, ignoring the surrounding background in the image before squaring.

The second property of interest describes the continuous path that each yarn follows. Histograms of contiguous yarn center annotations (for each yarn) are used to model the yarn path "displacement" from one plane to the next. The third property is the specific arrangement of a yarn with respect to its (same type) neighbors. In-plane yarn center annotations are used to model this arrangement. It is observed that parallel yarns follow well-defined orderings. From the above statistics, a variational formulation that includes three energies (figure. 1) is built: the optimal position for each yarn according to the 1 eigenmodes, the most likely displacement from the previous 2D plane, and the position that considers the arrangements between neighboring yarns.

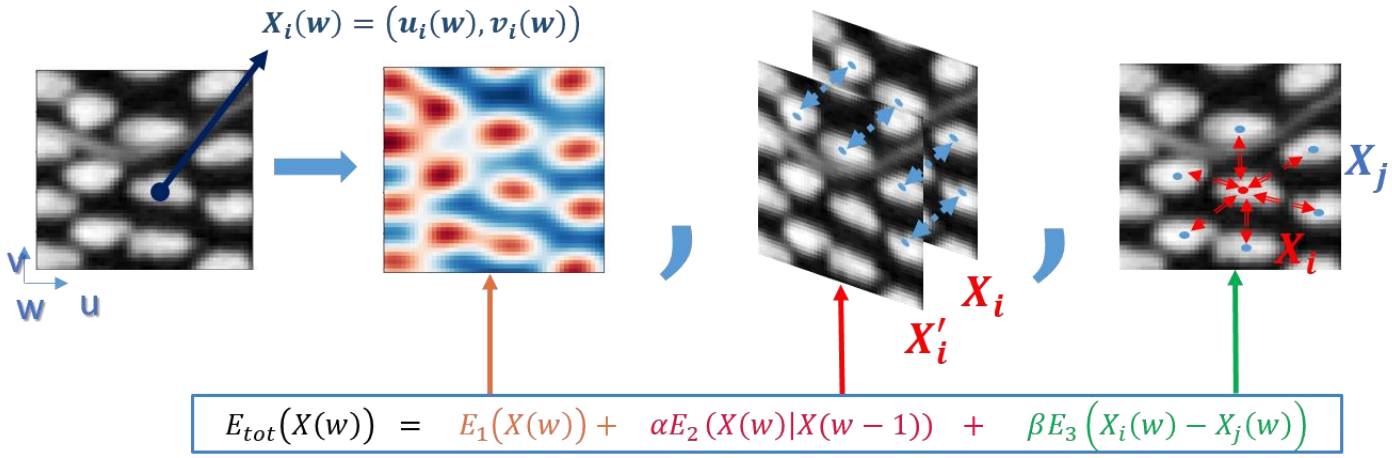

Figure 1: Variational Formulation

Then, an iterative greedy approach is used for successive planes to obtain the new yarn center positions. The initial positions are taken from the previous 2D plane, and at each iteration, the displacement to be applied to each yarn center is computed until convergence.

3 RESULTS

This approach is first applied to warp yarns. Tracking around 1,500 yarns across over 900 slices, with an average success rate of 95% for nearly 400 yarns that have available manual annotations.

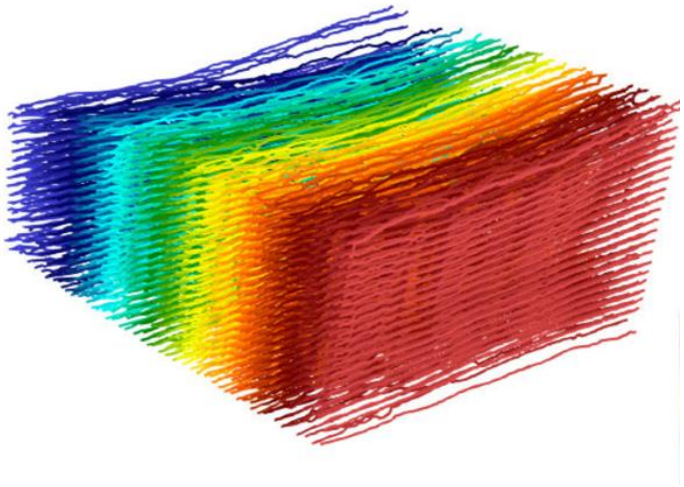

Figure 2: Computed warp yarn paths.

The estimated warp yarn paths (figure. 2) are then erased (figure. 3) from the initial CT image, isolating the weft yarns and highlighting segmentation errors, such as yarns lost during tracking. After addressing these issues, the erased image is used to segment the weft yarns using the same procedure. Then, the warp yarns are re-segmented after erasing the weft yarns, and so on. This fixed-point optimization that progressively improves the yarn segmentation is carried out until stationarity is achieved for both yarn directions.

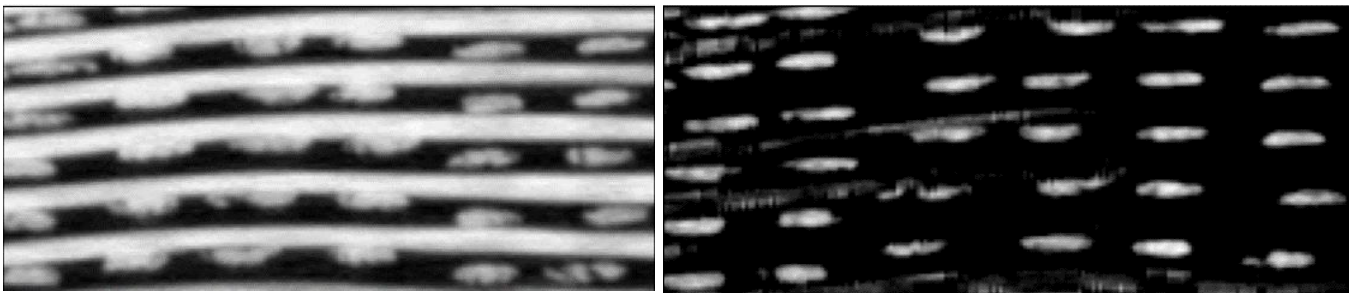

figure (a): original tomography **figure (b): erased warp yarns tomography**

Figure 3: Erasing warp yarns in tomographic image.

Finally, 1,500 warp yarns were automatically annotated and tracked over 900 slices, which amounts to 1,350,000 yarn centers. Considering that 11,460 yarn centers were used as initialization (0.85%), the method shows its potential for automatically annotating large-scale textiles. The next development phase will focus on refining the tracking process of weft yarns after the erasure of the retrieved warp paths that currently interfere with accurate tracking. This adjustment is essential to improve the tracking of yarns, ensuring that the algorithm can correctly distinguish and follow weft yarns.

References

[1] Naouar N. et al., Meso-scale FE analyses of textile composite reinforcement deformation based on X-ray computed tomography, Composite Structures 116 (2014).

[2] Bénézech J. et al., Variational segmentation of textile composite preforms from X-ray computed tomography, Composite Structures 230 (2019).

[3] Pidou-Brion V. et al., Active yarn meshes for segmentation on x-ray computed tomography of textile composite materials at the mesoscopic scale, Composite Structures 281 (2022).

[4] Ali M.A. et al., Deep learning based semantic segmentation of µCT images for creating digital material twins of fibrous reinforcements, Composites Part A 139 (2020).

[5] Sinchuk Y. et al., Automatic yarn path extraction of large 3D interlock woven fabrics with confidence estimation, Composites Part A 186 (2024).

[6] Zheng J. et al., Reverse reconstruction of geometry modeling and numerical verification of 2.5D woven composites based on deep learning, Composite Structures 329 (2024).

ROBUST IMAGE REGISTRATION FOR PERIODIC MATERIALS: APPLICATION TO 3D WOVEN TEXTILES

Aurélie Pillet[1], Kamel Aftisse[1], Jan Neggers[1], Arturo Mendoza[3], Julien Schneider[2] and Stéphane Roux[2]

[1]Univ. Paris-Saclay, CentraleSupélec, ENS Paris-Saclay, CNRS, LMPS, France

[2]Safran Aircraft Engines, France

[3]Safran Tech, France

Keywords: Woven composites, Image registration, Large-scale textiles, Textile periodicity

ABSTRACT

This work introduces a robust finite element-based Digital Volume Correlation (FE-DVC) method tailored for the accurate registration of large-scale textile samples. By detecting and correcting shifted periodic regions, the method enables the precise alignment of sample pairs, making it possible to identify subtle textile differences such as those caused by varying weaving parameters. The proposed approach is applied to textile reinforcements used in aircraft engine fan blades, demonstrating robustness and effectiveness in addressing the challenges of complex textile registration tasks.

1 INTRODUCTION

Comparing different measurements (images) can be a challenging task when these are not expressed in the same reference frame. Image registration aims to identify the transformation that best aligns pairs of images. Various techniques exist for this purpose, but FE-based Digital Image Correlation (DIC) in 2D and its 3D counterpart Digital Volume Correlation (DVC) [1] are popular in experimental mechanics for composite materials [2]. DVC, in particular, has been used on woven composites to highlight differences between pairs of samples [3]. In this context, the found transformations inform on any textile difference between samples (e.g., different weaving parameters). These previous studies have shown some potential but have been limited to small samples.

2 METHOD

Registration on larger textiles tends to fail due to the periodicity of the material, which creates local minima that tend to localize into “regions”. Hence, the goal of the present work is to develop a general and robust FE-DVC method for registering large-scale textiles. The largest identified region is heuristically determined to be correct, while the remaining regions are considered shifted. The goal is then to find the displacement (a multiple of the textile period) that corrects the unwanted shift for each misaligned region. The proposed strategy consists in first characterizing all 3D textile periodicities (along warp, weft, and thickness directions) from the image and testing different integer multiples of these shifts which can be ranked according to the induced registration error. If any shift that reduces the registration error is found, it is used to correct the region; otherwise, the found displacement for the region is discarded and a simple extrapolation is used, starting from the largest region, to define a placeholder displacement field. After treating all shifted regions, the new complete transformation is used as initialization for another complete registration process. This process is repeated until no region boundaries remains (i.e., no more shifted regions).

3 RESULTS

The method was applied to multiple large-scale samples of textile reinforcements from aircraft engine fan blades. In all studied cases, no more than three iterations were required to identify the complete correct transformation. As an illustration, the figure below depicts a transversal view of one such textile reinforcement behind an overlay of the longitudinal strain (deformation), computed from the

displacement field obtained from registering two samples. The illustrated field shows highly localized regions in which the warp yarn columns (orthogonal to the image plane) are further apart in the moving (source) image than in the reference (target) one. These results demonstrate the robustness and generality of the proposed method. Indeed, registering different samples serves as a more challenging registration problem than the traditional task encountered in experimental mechanics of registering of the same sample subjected to an external load. Moreover, not only is the proposed method simple to implement it also is non-intrusive, thus it can be used alongside any existing registration method.

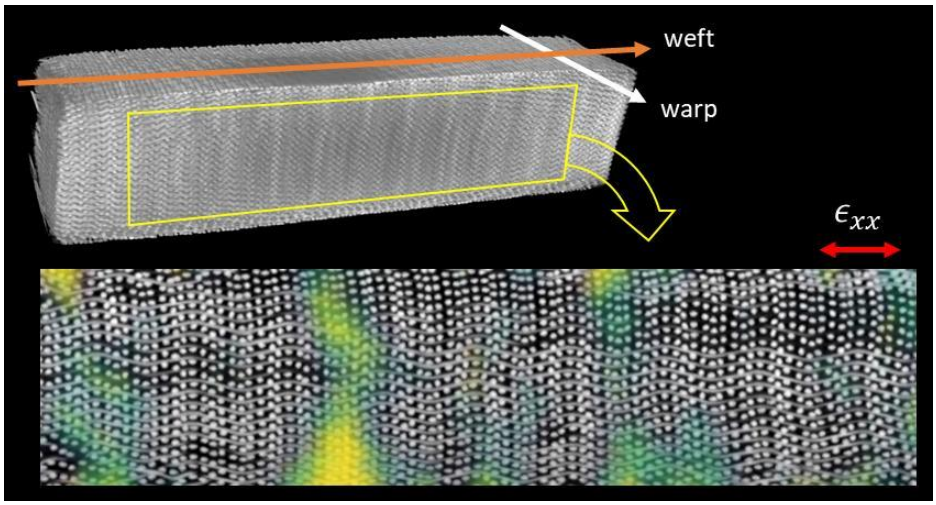

Figure 1 Visualization of the horizontal normal strain for a given region of interest

REFERENCES

[1] S. Roux et al. (2008). Three-dimensional image correlation from X-ray computed tomography of solid foam. Composites Part A.

[2] J. Holmes et al. (2023). Digital image and volume correlation for deformation and damage characterisation of fibre-reinforced composites: A review. Composite Structures.

[3] A. Mendoza et al. (2019). The correlation framework: Bridging the gap between modeling and analysis for 3D woven composites. Composite Structures.

Local and Global Strain and Defect Analysis of Discontinuous Glass Fiber Reinforced Polymers

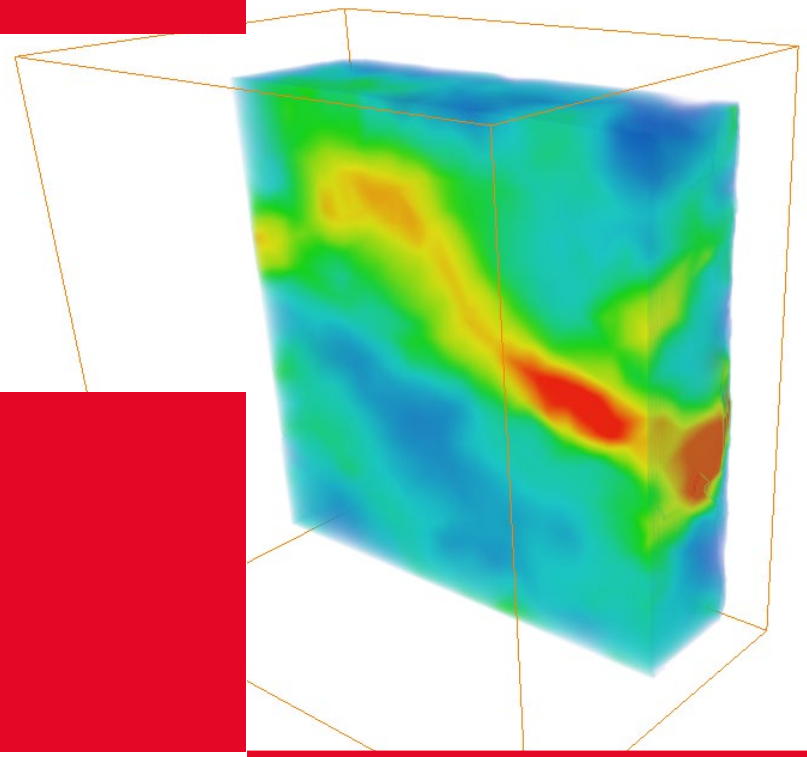

Julia Maurer[1], Dietmar Salaberger[2], Michael Jerabek[2], Zoltán Major[3], Johann Kastner[1]

[1]University of Applied Sciences Upper Austria, Wels, Austria
[2]Borealis Polyolefine GmbH, Linz, Austria
[3]Johannes Kepler University, Linz, Austria

24th International Conference on Composite Materials (ICCM24)
Baltimore, Maryland (USA)
August 4, 2025

Motivation

1. **Material Development** (microscale analysis ⇔ FE simulations)
2. **Application development** (experiments on the macroscale ⇔ component design)

Motivation

Short glass fibres (PPSGF)

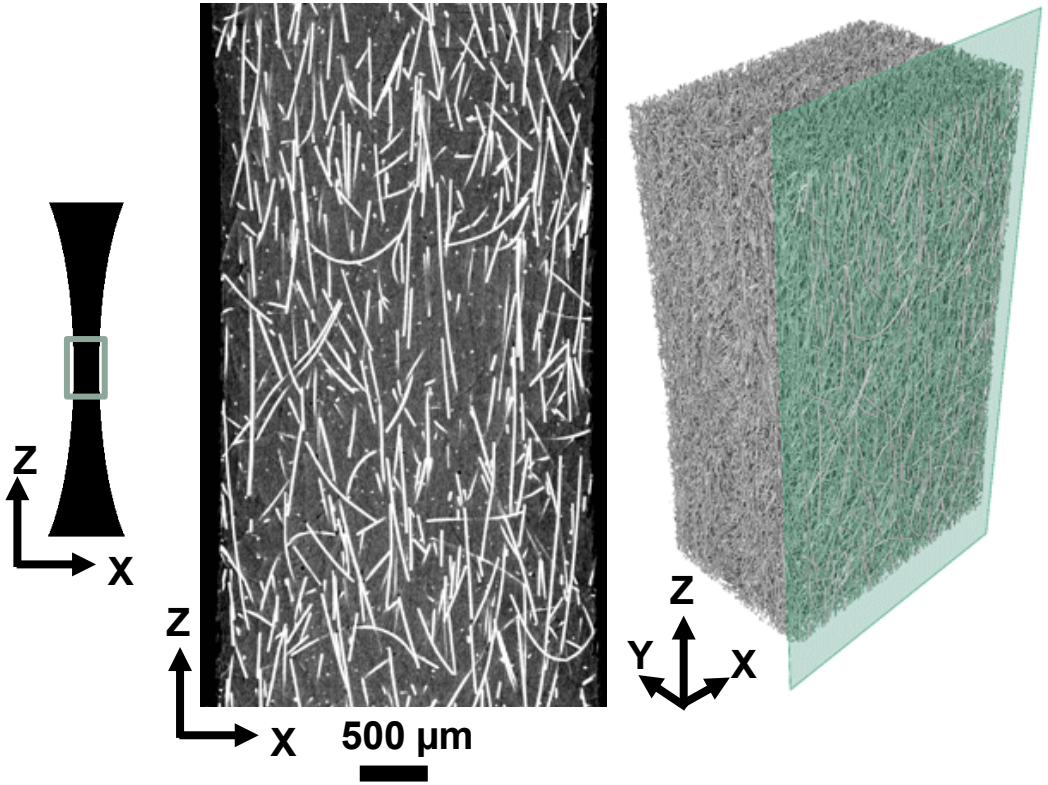

nominal fibre diameter **13 µm**
mean fibre length approx. **470 µm**

Long glass fibres (PPLGF)

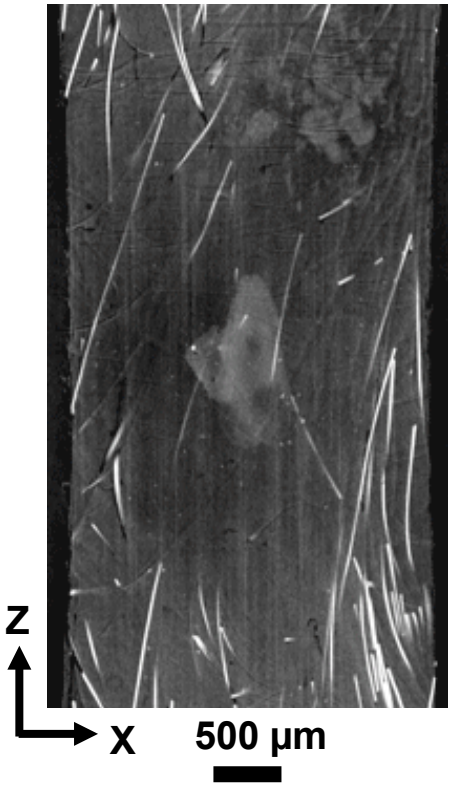

nominal fibre diameter **17 µm**
mean fibre length approx. **1000 µm**

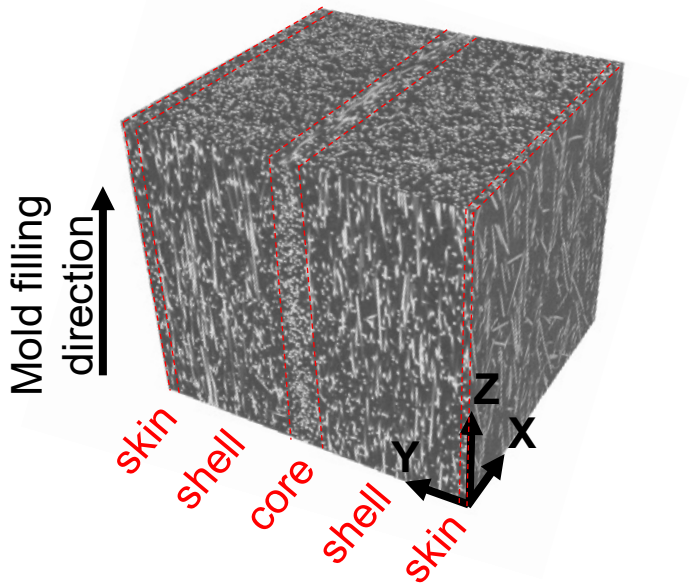

- Highly oriented
- Skin/shell/core layers
- Curved fibres
- Fibre bundles
- Local differences in fibre content

What differences arise in the defect behaviour?

Motivation

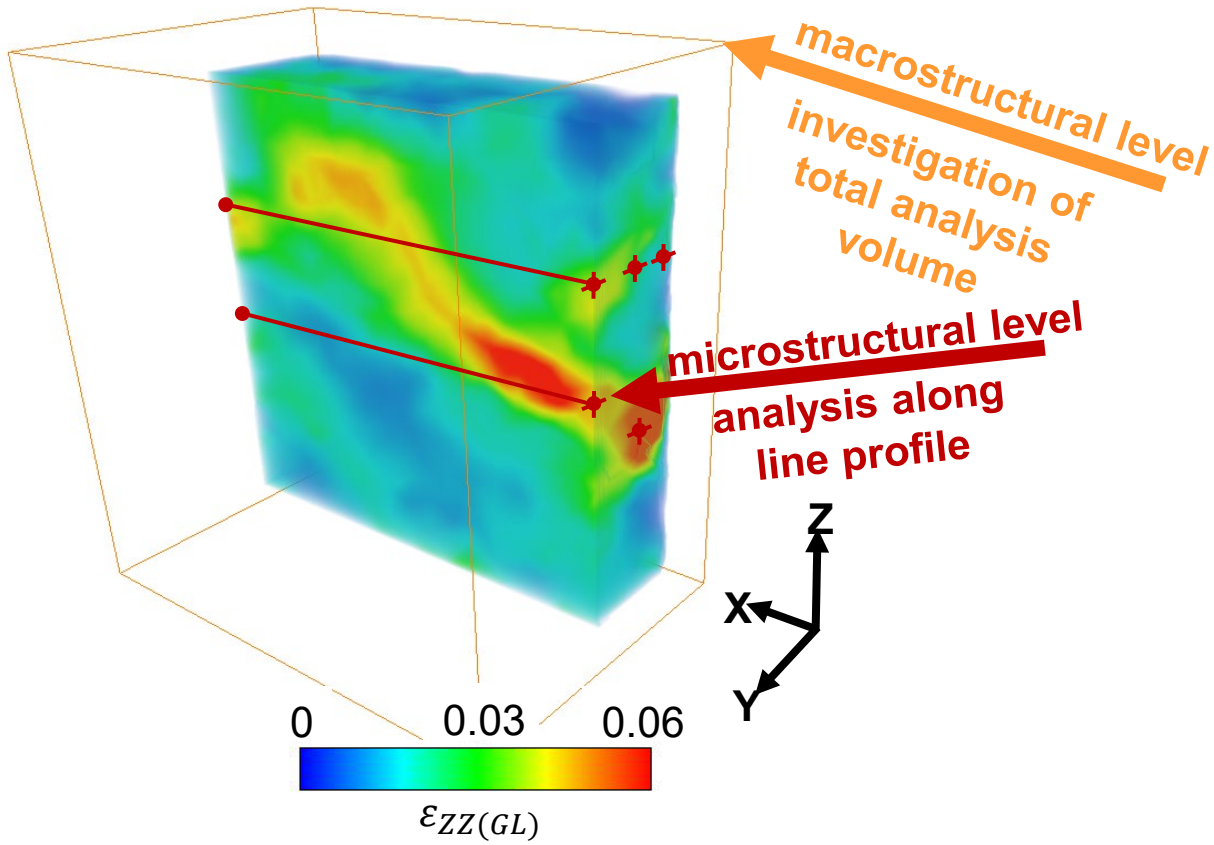

What differences in the strain formation and distribution with regard to fibre structure, fibre orientation and specimen geometry can be identified?

Maurer et. al (submitted)

Materials & Methods

UNIVERSITY OF APPLIED SCIENCES UPPER AUSTRIA
OBERÖSTERREICH

- **Two different materials:**
  - **Polypropylene** with 24 wt.% **short glass fibres** (**PPSGF**):
    nominal fibre diameter 13 µm, mean fibre length approx. 470 µm
  - **Polypropylene** with 24 wt.% **long glass fibres** (**PPLGF**):
    nominal fibre diameter 17 µm, mean fibre length approx. 1000 µm
- **Two** different **specimen geometries** (**CR** – constant radius, **DENT** – double edge notched) cut out from injection moulded GF-Multitool at **three** different **orientations**

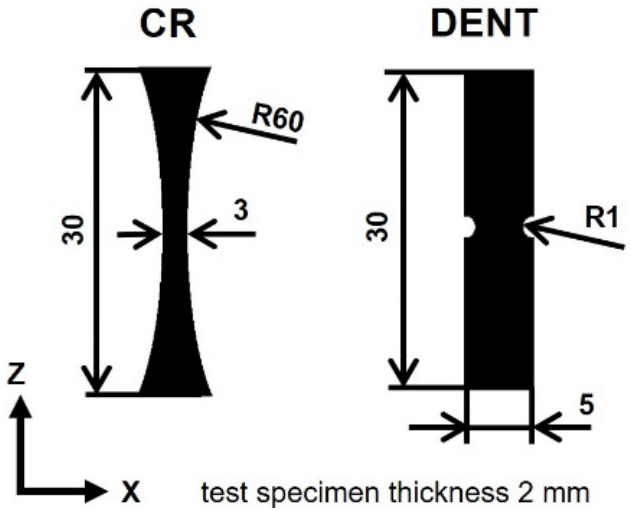

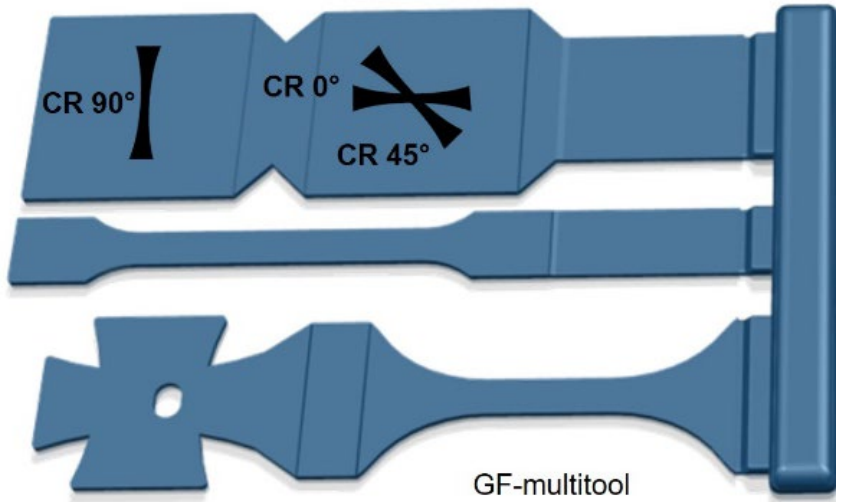

Maurer et. al (2024)

Materials & Methods

UNIVERSITY OF APPLIED SCIENCES UPPER AUSTRIA

Interrupted in situ tensile testing

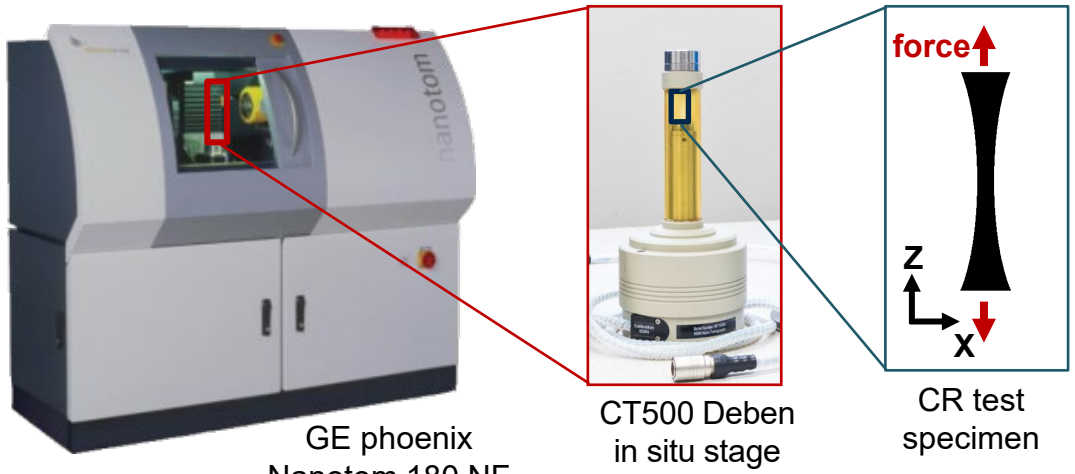

GE phoenix Nanotom 180 NF

CT500 Deben in situ stage

CR test specimen

load application in displacement-controlled manner

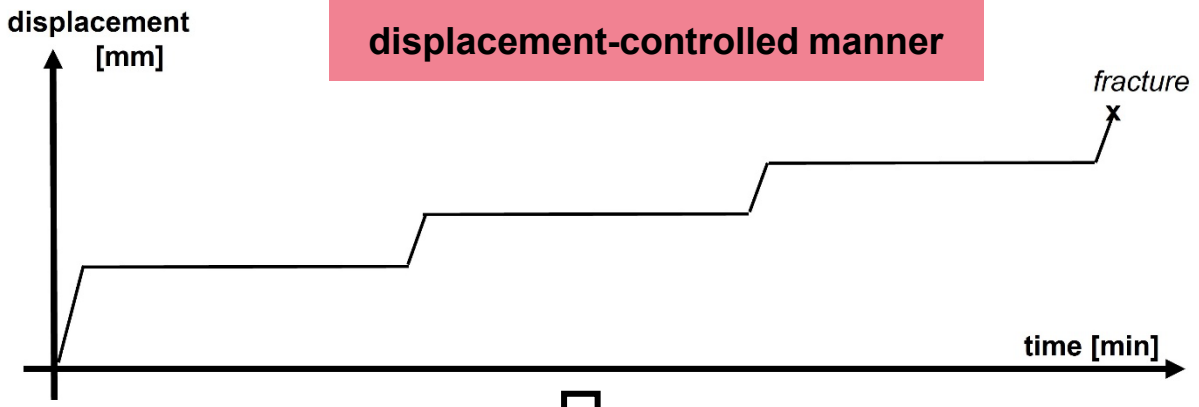

material response

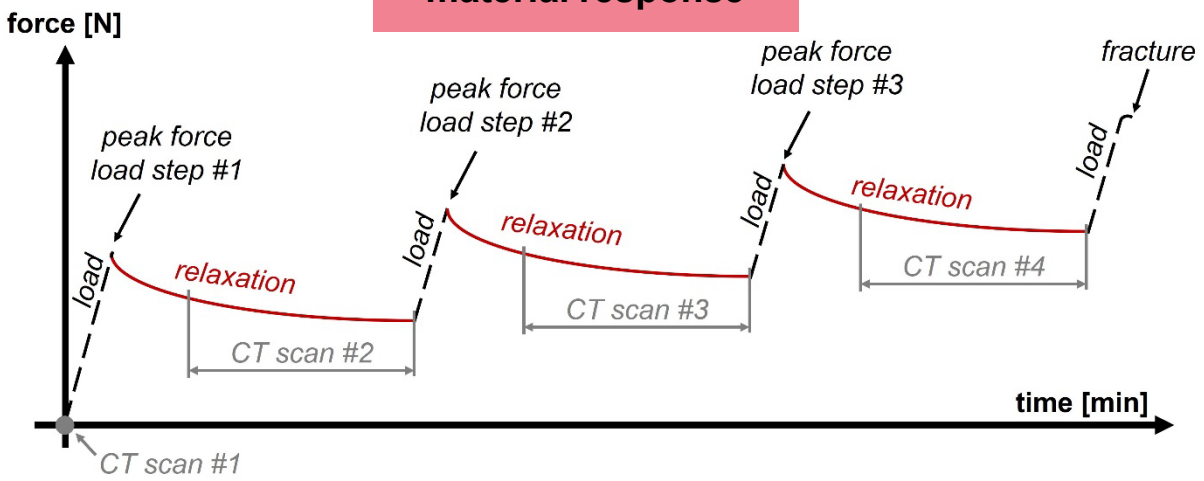

CT data aquisition:

- Voxel edge length:
  PPSGF 2 µm
  PPLGF 2.5 µm
- Scan time: ~ 1h
- Voltage: 80 kV
- Current: 400 µA

Load step definition:

- Based on the maximum tensile force evaluated with pre-evaluations
- starting at 30% followed by 52% and increasing in 8% steps until fracture

Maurer et. al (2022)

Materials & Methods

UNIVERSITY OF APPLIED SCIENCES UPPER AUSTRIA
OBERÖSTERREICH

CT-data evaluation

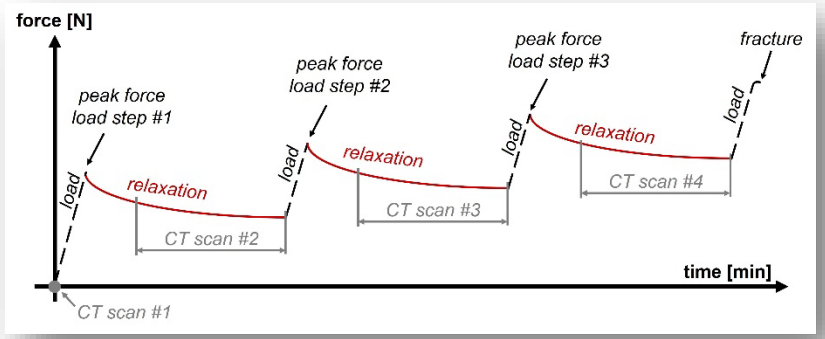

Strain analysis

DVC tool, Avizo Software 2020.1

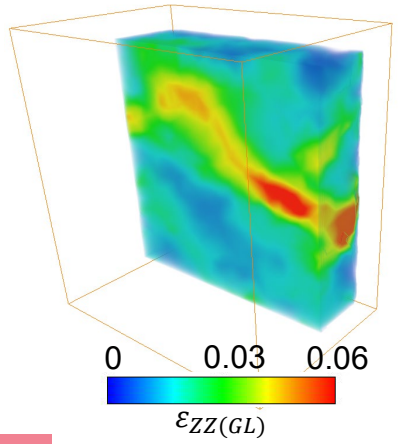

Displacement vector
Strain tensor
Volumetric strain
Poisson‘s ratio
Prediction of fracture surface

Defect analysis

Amirkhanov et al. (2016), Rao et al. (2017), Maurer et al. (2019)

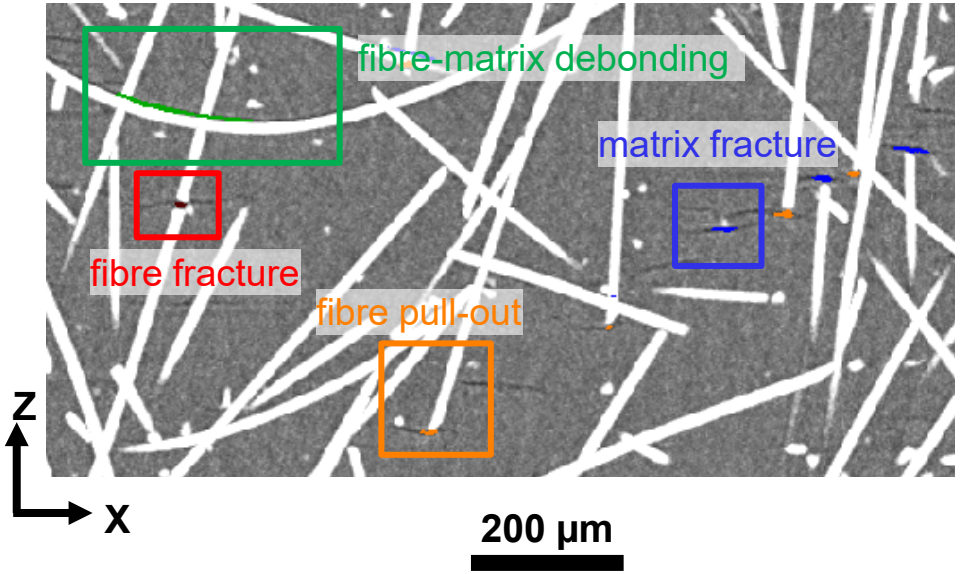

Defect type
Defect number
Defect size
Defect formation

Results

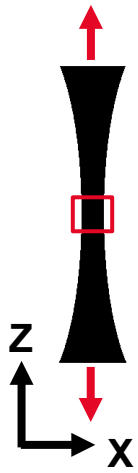

PPSGF - CR 0°
LS 7 – 92 % of $F_{max\ 0°}$

PPSGF - CR 90°
LS 6 – 84 % of $F_{max\ 90°}$

PPSGF - CR 45°
LS 5 – 76 % of $F_{max\ 45°}$

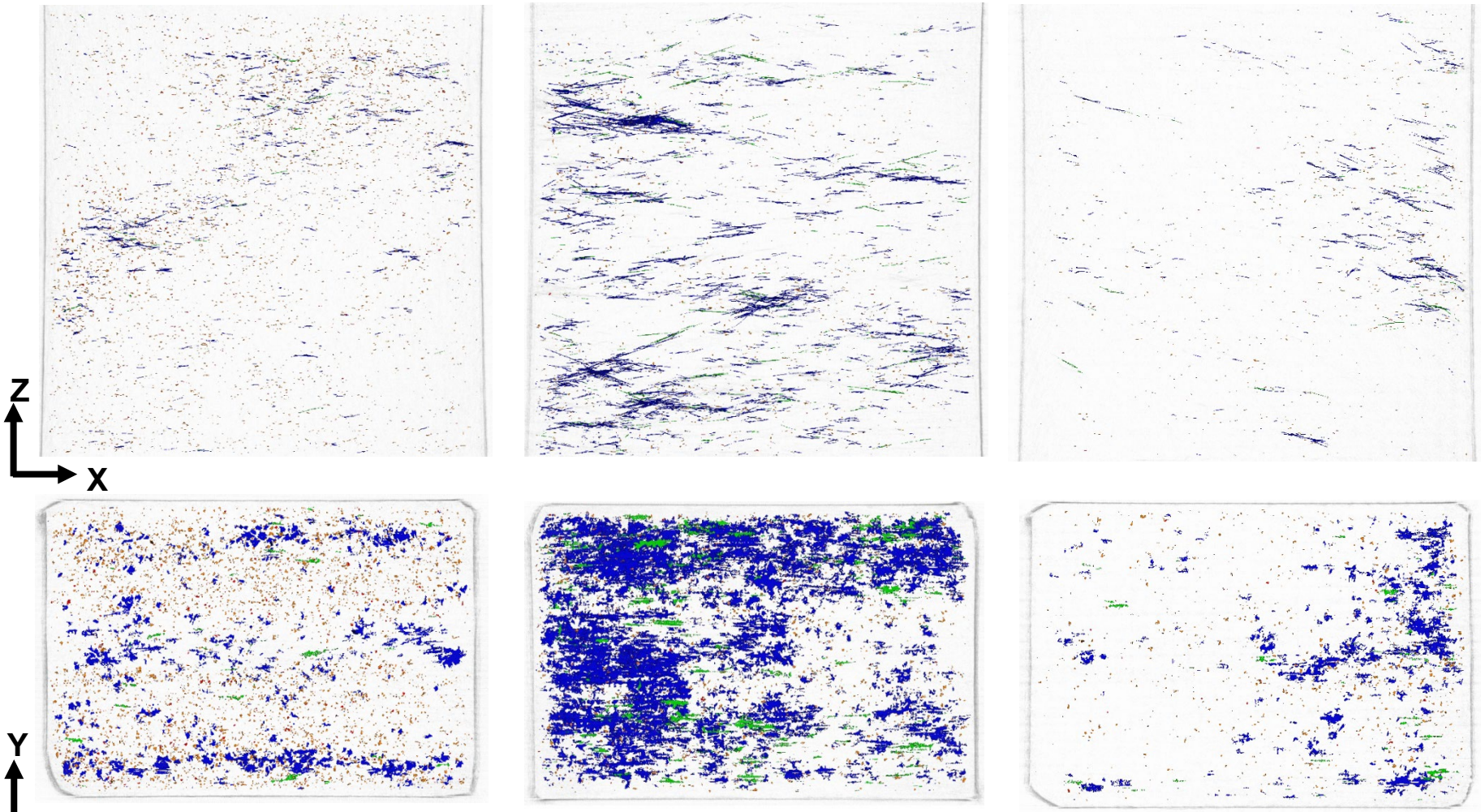

Defects at LAST load step before fracture

- matrix fracture
- fibre-matrix debonding
- fibre pull-out
- fibre fracture

Matrix fracture dominating

Distribution of defect types due to local fibre orientation

Maurer et. al (2022)

Results

UNIVERSITY OF APPLIED SCIENCES UPPER AUSTRIA

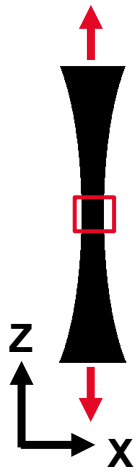

PPSGF - CR 0°
LS 7 – 92 % of $F_{max\ 0°}$

PPSGF - CR 90°
LS 6 – 84 % of $F_{max\ 90°}$

PPSGF - CR 45°
LS 5 – 76 % of $F_{max\ 45°}$

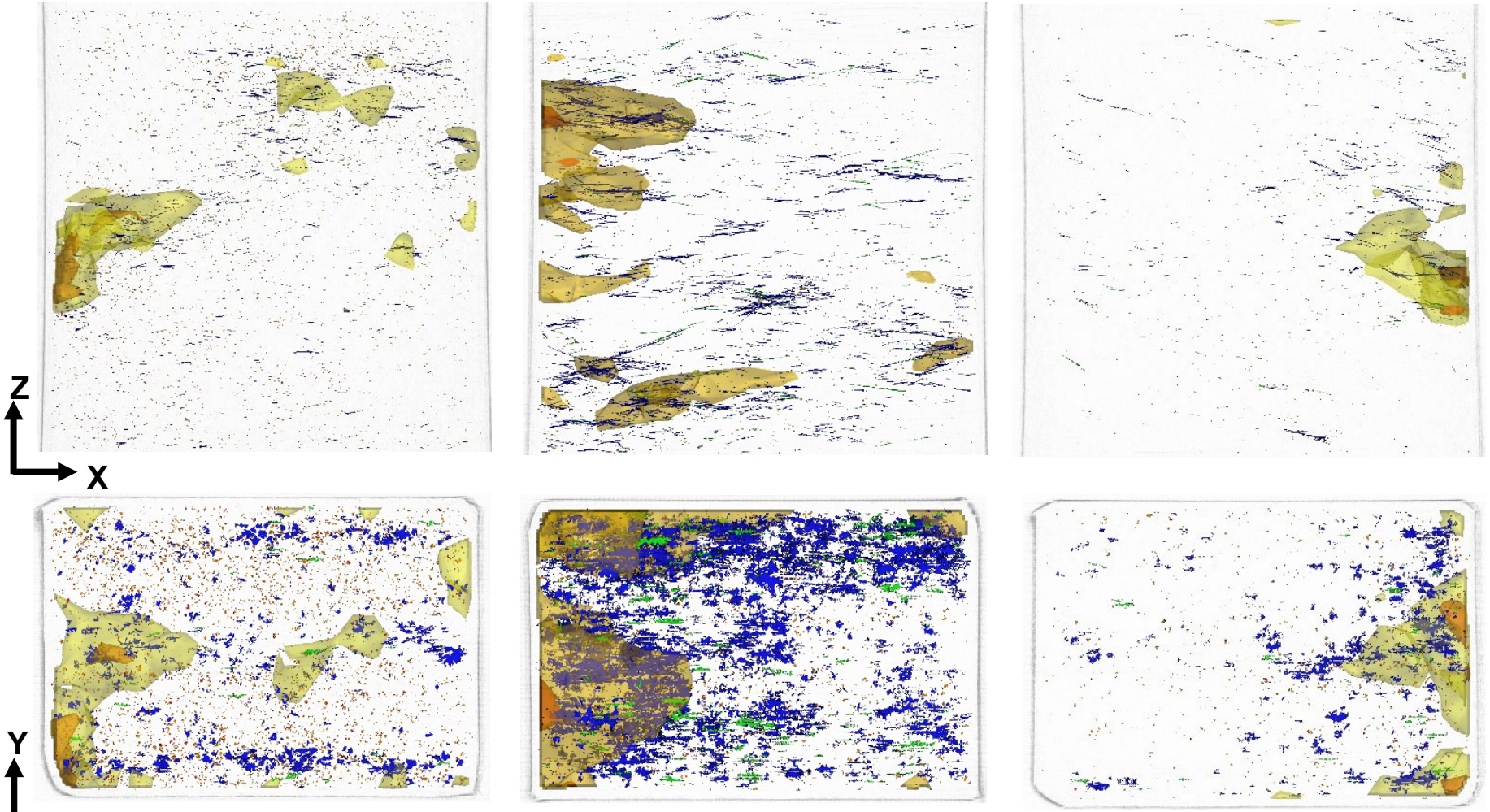

Defects and strain at LAST load step before fracture

- matrix fracture
- fibre-matrix debonding
- fibre pull-out
- fibre fracture

0.05 — 0.15
ε_{zz}

Local strain hotspots indicating positions of fracture onset and correlate well with defect hotspots

500 µm

Maurer et. al (2022)

Results

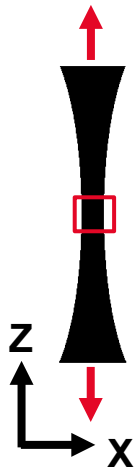

PPLGF - CR 0°
LS 5 – 76 % of $F_{max\ 0°}$

PPLGF - CR 90°
LS 4 – 68 % of $F_{max\ 90°}$

PPLGF - CR 45°
LS 5 – 76 % of $F_{max\ 45°}$

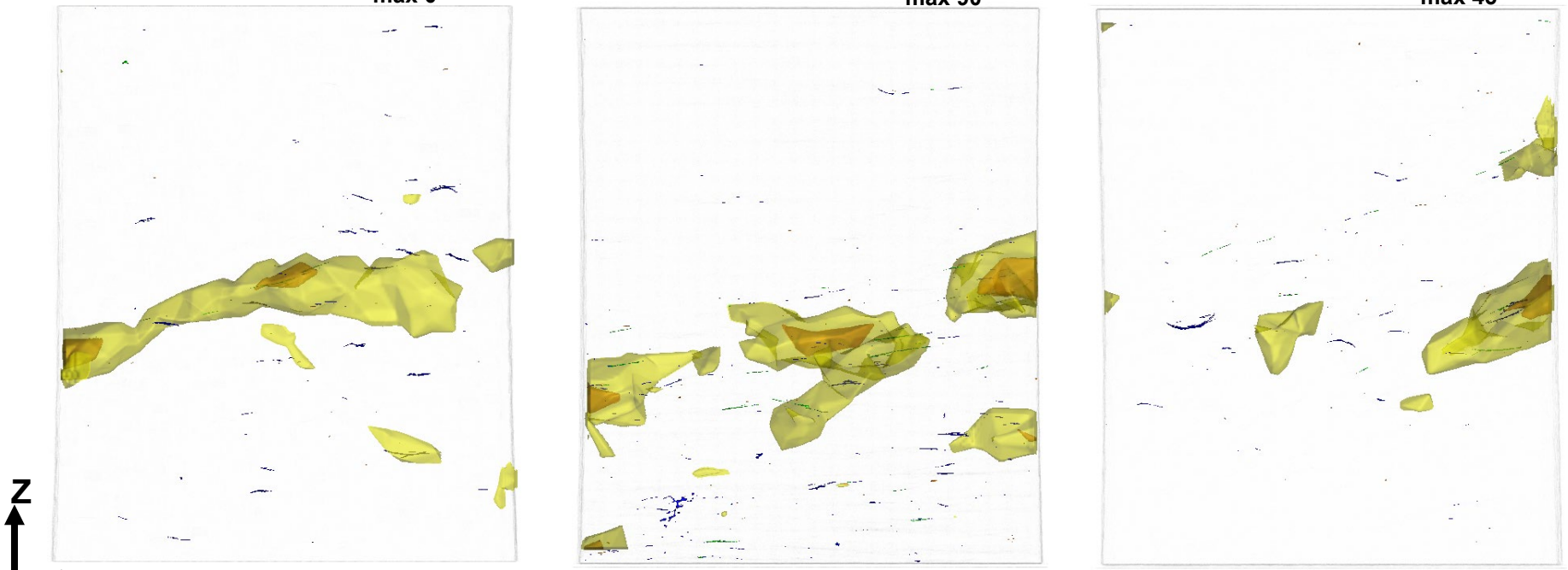

Defects and strain at LAST load step before fracture

- matrix fracture
- fibre-matrix debonding
- fibre pull-out
- fibre fracture

0.04 — 0.07
ε_{zz}

Less defects and smaller strain values for all orientations

Results

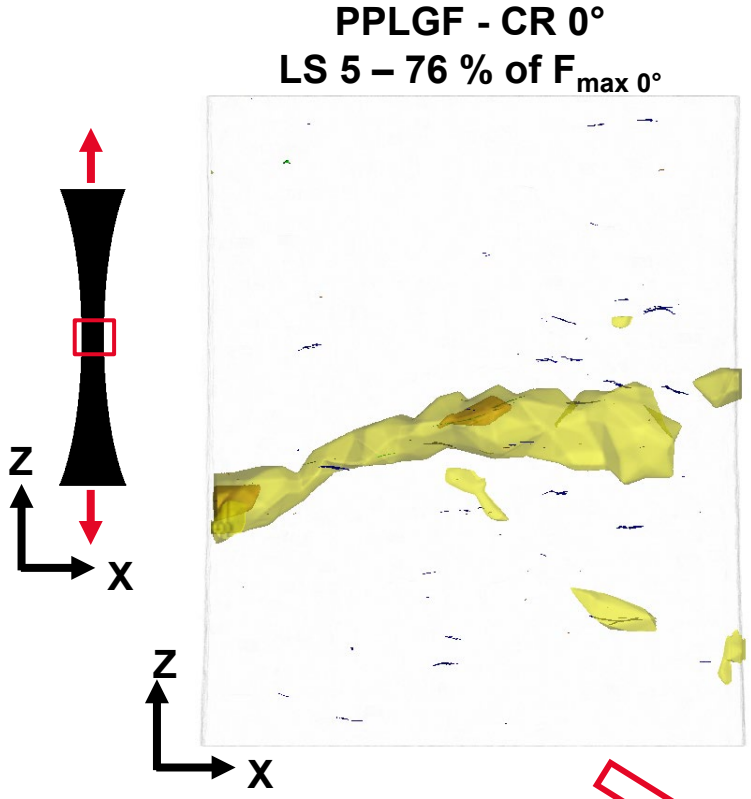

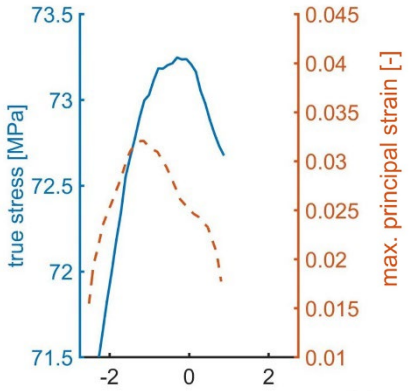

fracture not necessarily at smallest cross section

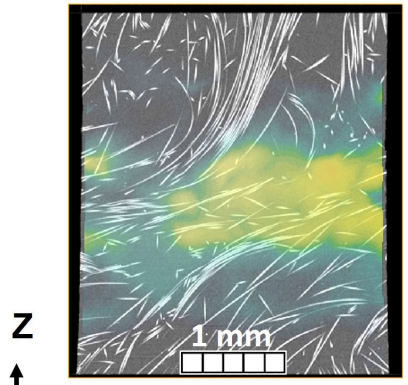

no strain hot spots at first load step

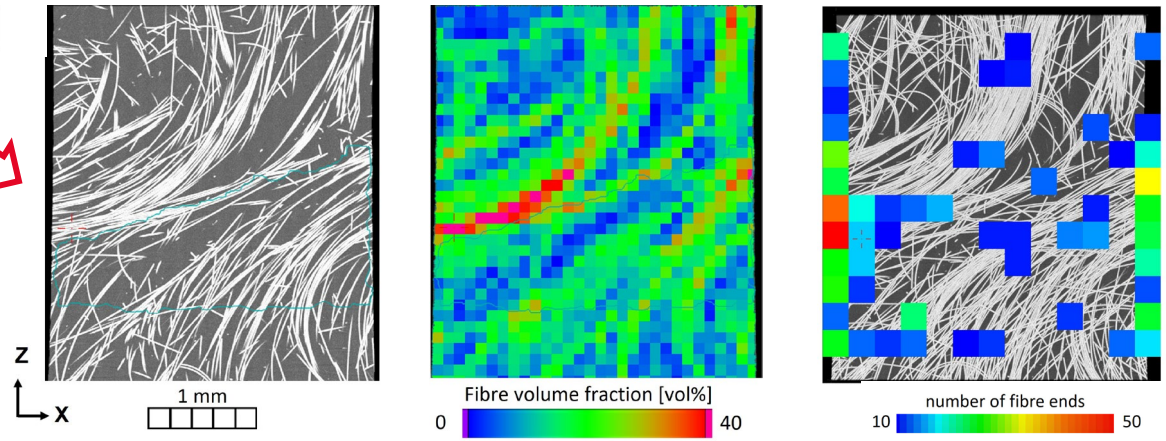

local microstructure significantly influence onset of fracture

Indicating the fracture surface respectively one fragment of the tested specimen

Maurer et. al (2024)

Results

UNIVERSITY OF APPLIED SCIENCES UPPER AUSTRIA
OBERÖSTERREICH

Strain along a line profile at the smallest cross section and the center of the specimen

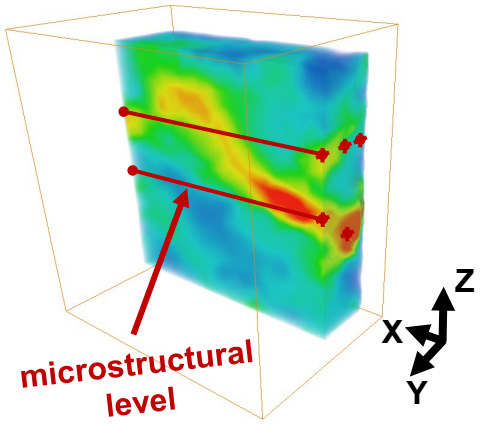



PPSGF-CR0°

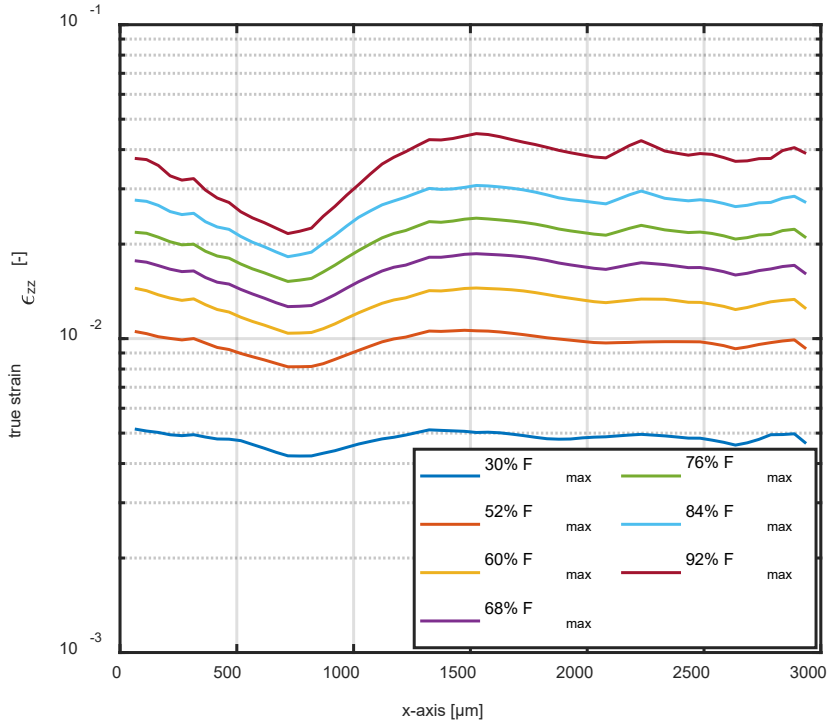

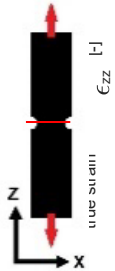

PPSGF-DENT0°

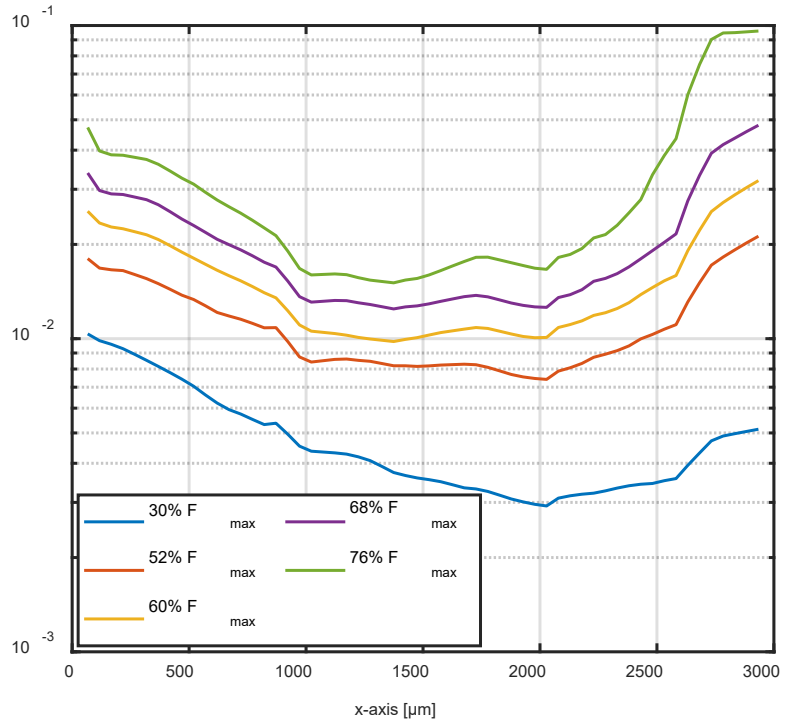

Shape of the strain distribution already apparent at first load step

Strong influence of the notch

Maurer et. al (submitted)

Results

UNIVERSITY OF APPLIED SCIENCES UPPER AUSTRIA
OBERÖSTERREICH

Strain analysis of the total volume – comparison of specimen geometry

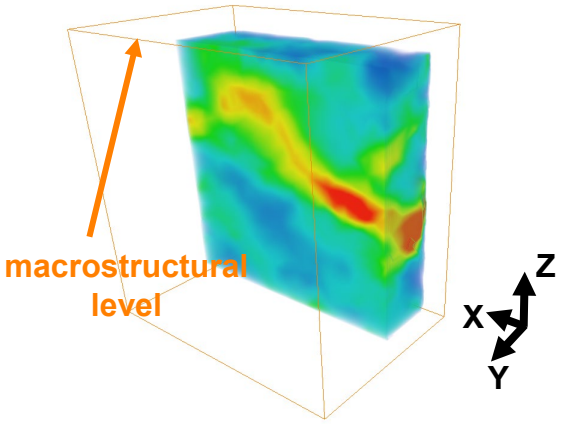

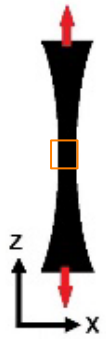

PPSGF-CR0°

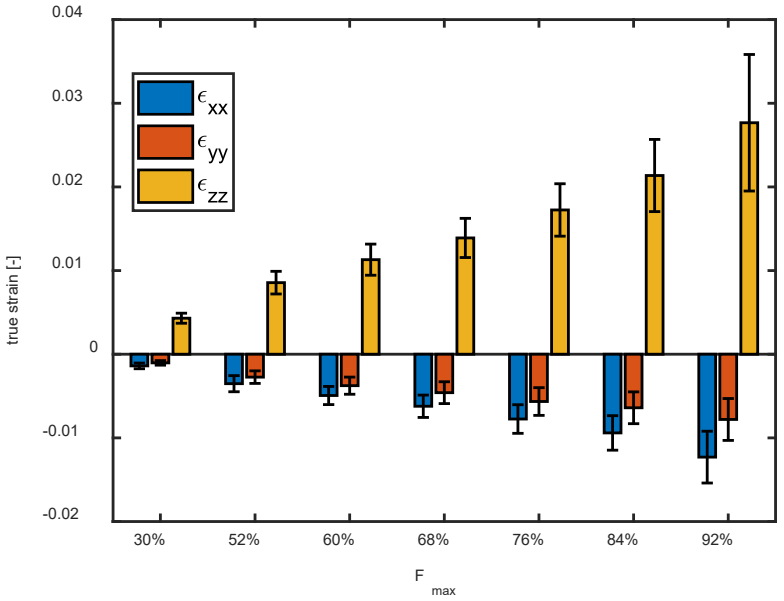

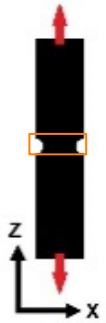

PPSGF-DENT0°

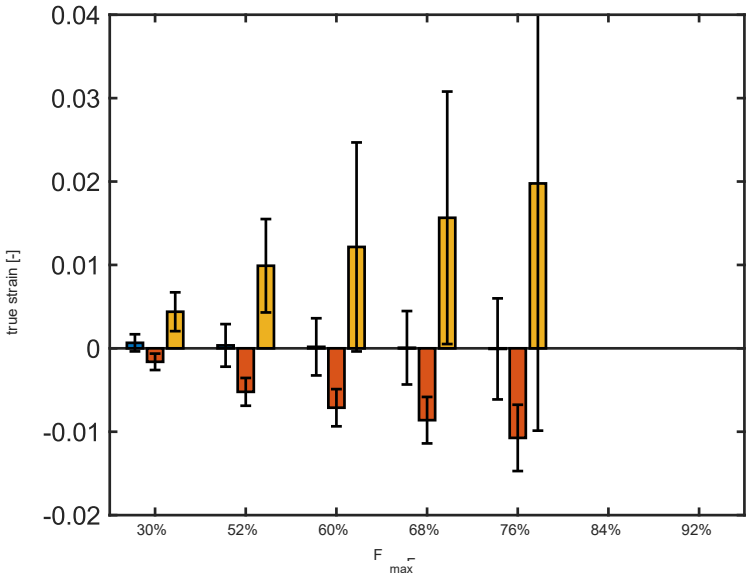

plane strain state
due to bigger width than height

Maurer et. al (submitted)

Results

UNIVERSITY OF APPLIED SCIENCES UPPER AUSTRIA

Strain analysis of the total volume – comparison of main fibre orientation

Poisson's ratio $\nu = -\frac{\varepsilon_{trans}}{\varepsilon_{axial}}$

strain perpendicular to direction of load

strain in direction of load

anisotropic material

$\nu_{XZ} = -\frac{\varepsilon_{XX}}{\varepsilon_{ZZ}}$ $\nu_{YZ} = -\frac{\varepsilon_{YY}}{\varepsilon_{ZZ}}$

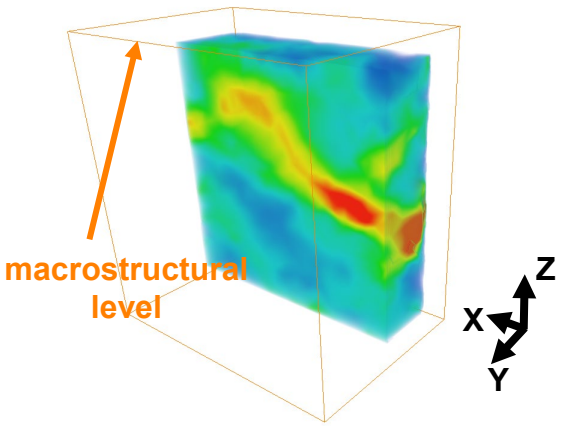



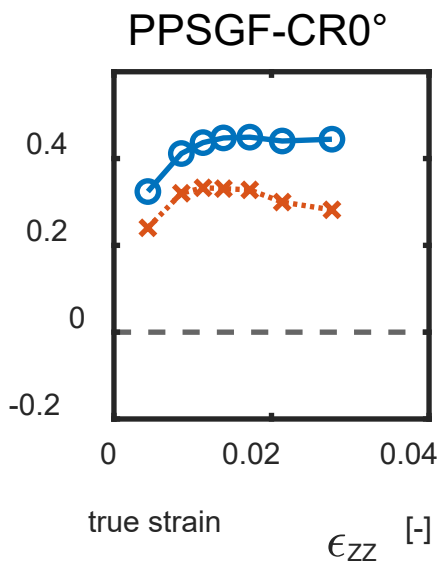

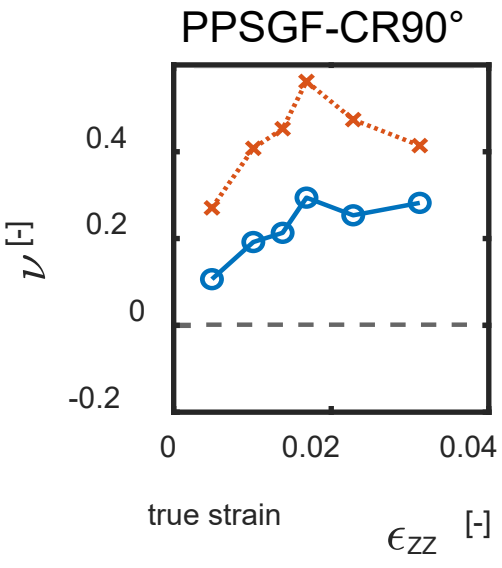

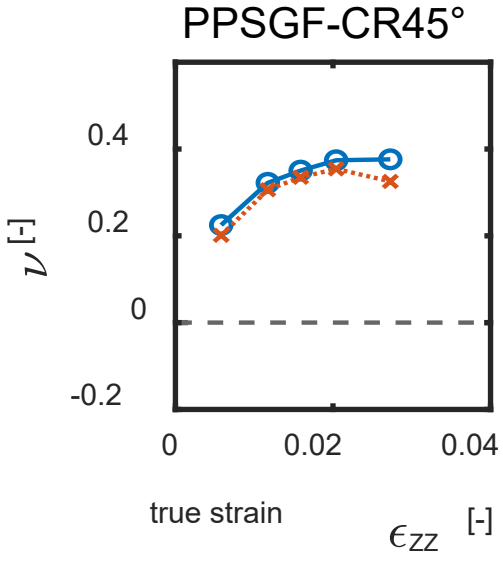

strong dependence on main fibre orientation

Maurer et. al (submitted)

Results

Comparison of different stress and strain states

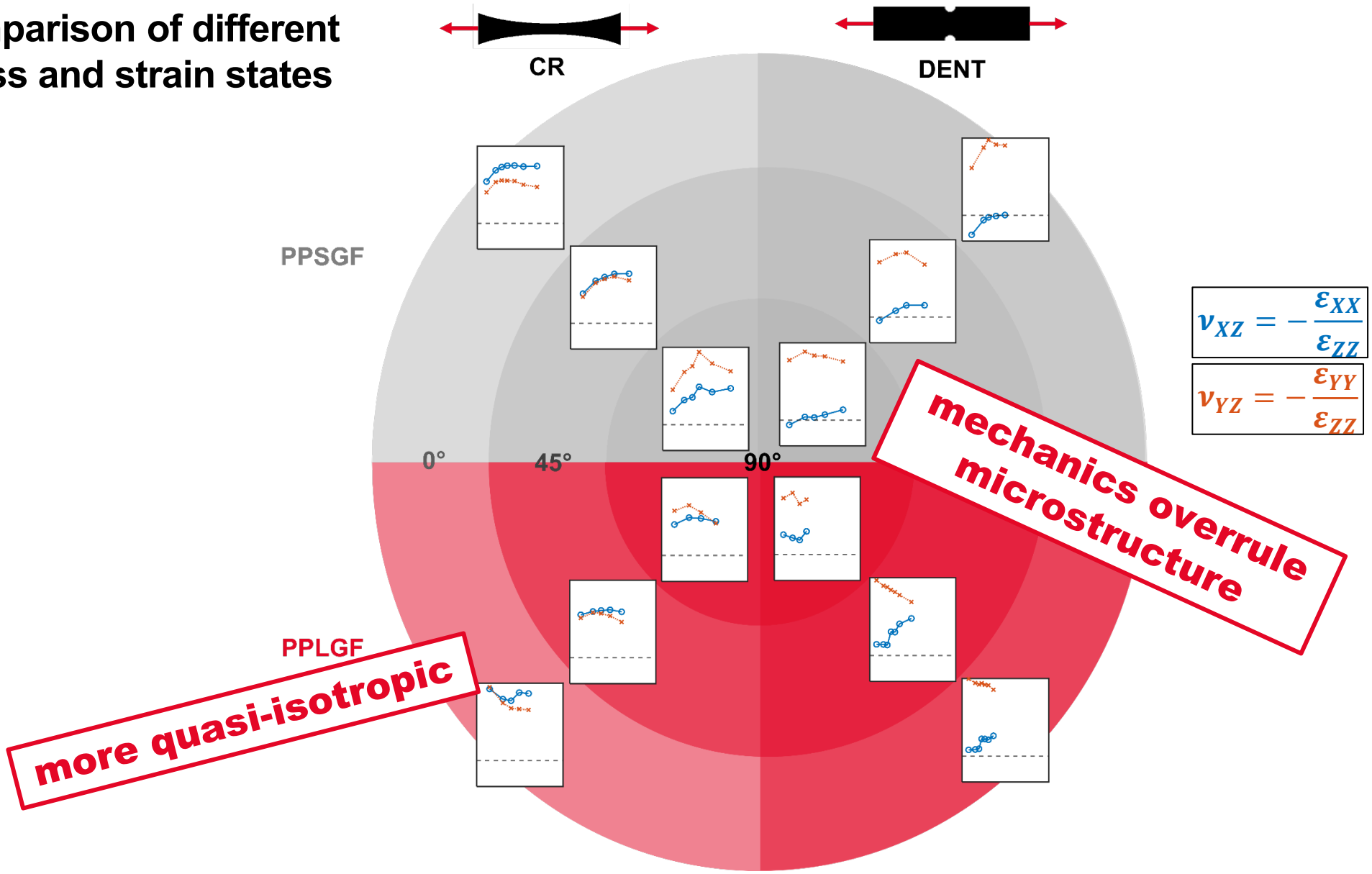

Conclusion

UNIVERSITY OF APPLIED SCIENCES UPPER AUSTRIA
OBERÖSTERREICH

- Short fibre reinforced polypropylene:
  - Defect formation and defect type depend on fibre orientation
  - Major reason for ultimate failure: matrix fracture
- Long glass fibre reinforced polypropylene:
  - No clear correlation between fibre orientation and defect type
  - Strong influence of the strength on the local microstructure (fibre bundles, curved fibres, …)
  - More quasi-isotropic behavior
- Mechanics (induced by sample geometry) overrule microstructure
- Gained results enable better understanding and (in certain cases) a prediction of the damage behaviour from a 3-dimensional perspective

Thank you!

julia.maurer@fh-wels.at

We acknowledge financial support for the project sustaiNDT (grant nr. 909801) funded within the framework "Production & Materials" of Austrian Research Promotion Agency (FFG).

Bibliography

D. Salaberger, “Micro-structure of discontinuous fibre polymer matrix composites determined by X-ray Computed Tomography”, Ph.D. dissertation, Vienna University of Technology, 2019.

A. Amirkhanov, A. Amirkhanov, D. Salaberger, J. Kastner, M. E. Gröller, and C. Heinzl, “Visual Analysis of Defects in Glass Fiber Reinforced Polymers for 4DCT Interrupted In situ Tests”, *Computer Graphics Forum*, vol. 35, pp. 201–210, 3, 2016. doi: https://doi.org/10.1111/cgf.12896.

G. Rao, A. Amirkhanov, D. Salaberger, C. Heinzl, and J. Kastner, “Damage characterization in SFRP using X-ray computed tomography after application of incremental and interrupted in situ quasi static tensile loading”, in *Proceedings of the 7th Conference on Industrial Computed Tomography (iCT 2017)*, Leuven, Belgium, 2017.

J. Maurer, C. Hannesschläger, B. Plank, and J. Kastner, “Damage characterisation of short glass fibre reinforced polyamide with different fibre content by an interrupted in-situ X-Ray computed tomography test”, in *Proceedings of the International Symposium on Digital Industrial Radiology and Computed Tomography (DIR 2019)*, Fürth, Germany, 2019.

Manual: Avizo XDigitalVolumeCorrelation Extension, English, version Version 2019.02, Amira-Avizo Thermo Fisher Scientific, Inc., 2019.

J. Maurer, M. Jerabek, D. Salaberger, M. Thor, J. Kastner, and Z. Major, “Stress relaxation behaviour of glass fibre reinforced thermoplastic composites and its application to the design of interrupted in situ tensile tests for investigations by X-ray computed tomography”, *Polymer Testing*, vol. 109, p. 107 551, 2022. doi: https://doi.org/10.1016/j.polymertesting.2022.107551.

J. Maurer, D. Salaberger, M. Jerabek, J. Kastner, and Z. Major, “Quantitative investigation of local strain and defect formation in short glass fibre reinforced polymers using X-ray computed tomography”, *Nondestructive Testing and Evaluation*, vol. 37, no. 5, pp. 582–600, 2022. doi: https://doi.org/10.1080/10589759.2022.2075865.

J. Maurer, D. Salaberger, M. Jerabek, B. Fröhler, J. Kastner, and Z. Major, “Fibre and failure characterization in long glass fibre reinforced polypropylene by X-ray computed tomography”, *Polymer Testing*, vol. 130, p. 108 313, 2024. doi: https://doi.org/10.1016/j.polymertesting.2023.108313.

J. Maurer, M. Jerabek, D. Salaberger, J. Kastner, and Z. Major, “Discontinuous glass fibre reinforced polypropylene – a macro- and microstructural comparison of the mechanical response for different fibre lengths and test geometries”, manuscript submitted for publication.

Mechanical characterisation of carbon fibre-reinforced sheet moulding compounds and introduction to X-Ray in-situ biaxial testing of composite materials

Salaheddine Madi, Yentl Swolfs, Jeroen Soete, Stepan Lomov, Martine Wevers, Materials Engineering, **KU Leuven**

Yi Wan, Jun Takahashi, Department of Systems Innovation, School of Engineering, **The University of Tokyo**

Kamel Madi, **3Dmagination**

Guillaume Bravais, Barbara Fayard, **NOVITOM**

ICCM24
24TH INTERNATIONAL CONFERENCE ON COMPOSITE MATERIALS

04/08/2025

Objectives

- Understanding spatial strain distribution of SMC-CFRTP material

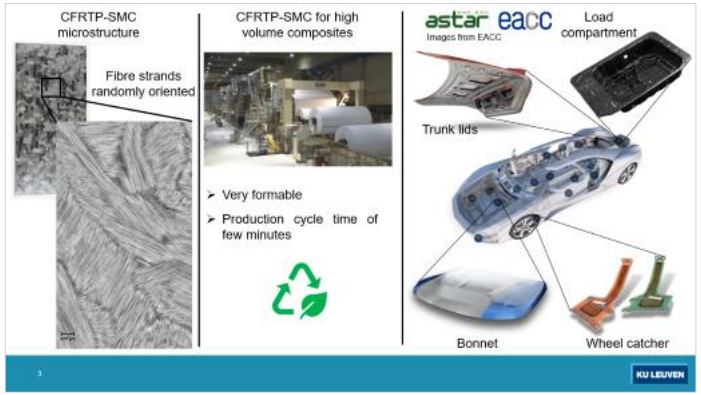

- Propose a new testing method to improve composites failure models

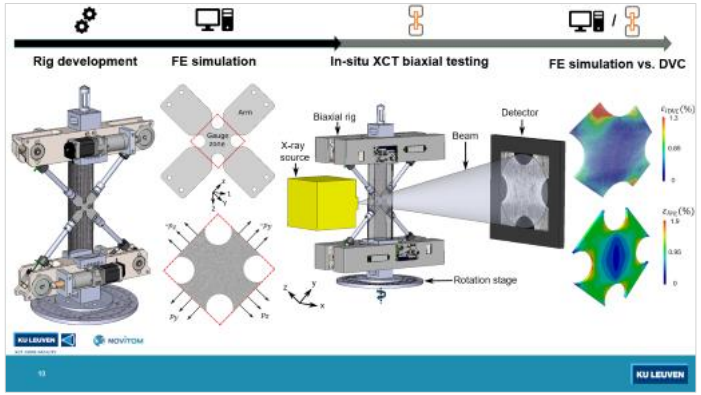

CFRTP-SMC microstructure



Fibre strands randomly oriented

CFRTP-SMC for high volume composites



- Very formable
- Production cycle time of few minutes

Load compartment

Images from EACC

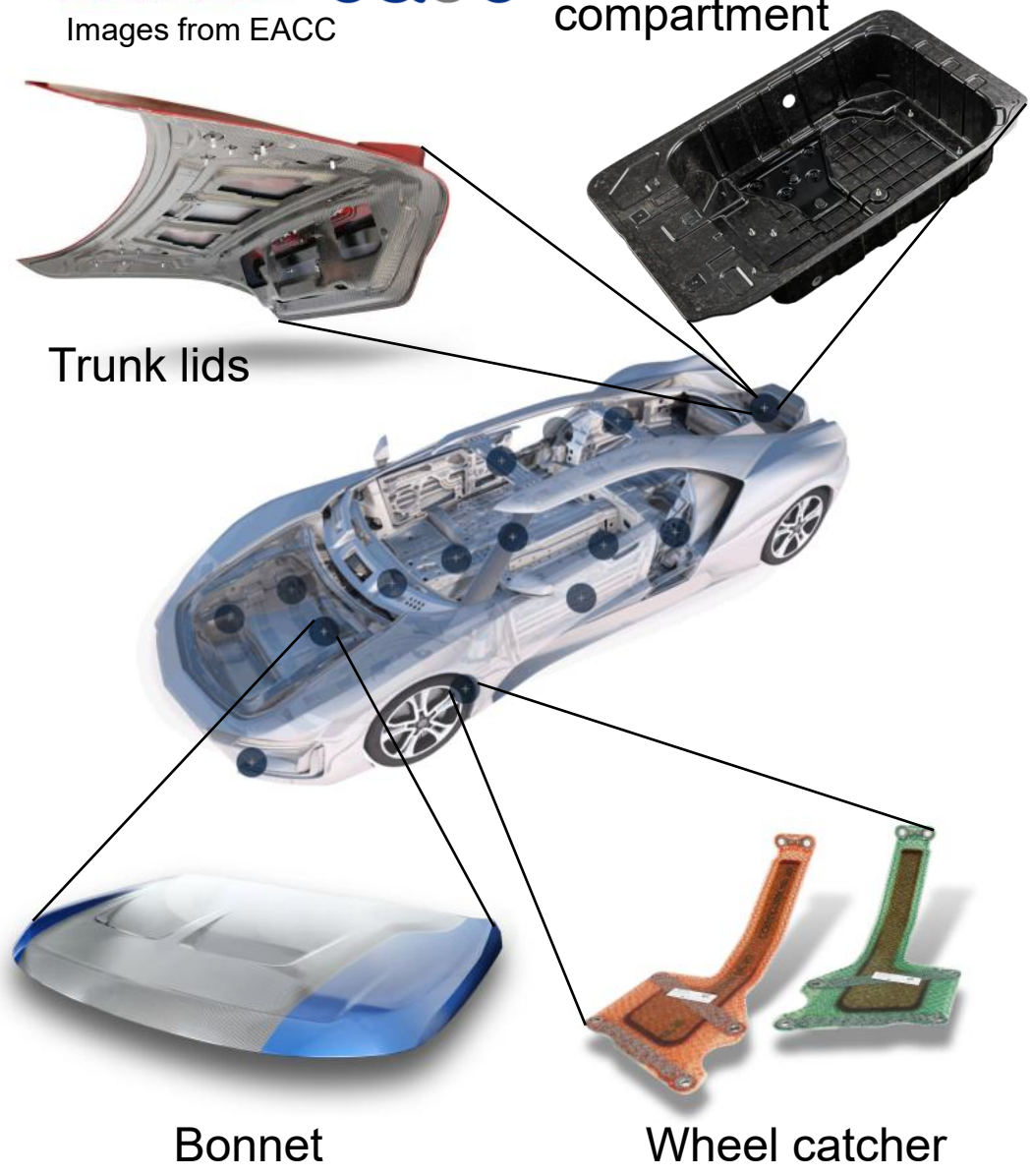

Trunk lids

Bonnet

Wheel catcher

Methodology

XCT in-situ stepwise tensile test



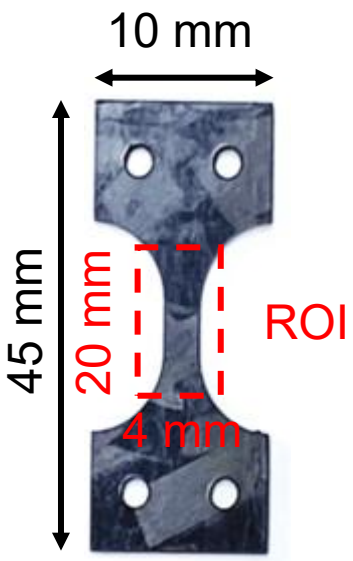

CFRTP-SMC
tensile specimen

- Voltage: 60 kV
- Voxel size: 4 µm

Digital Volume Correlation (DVC)

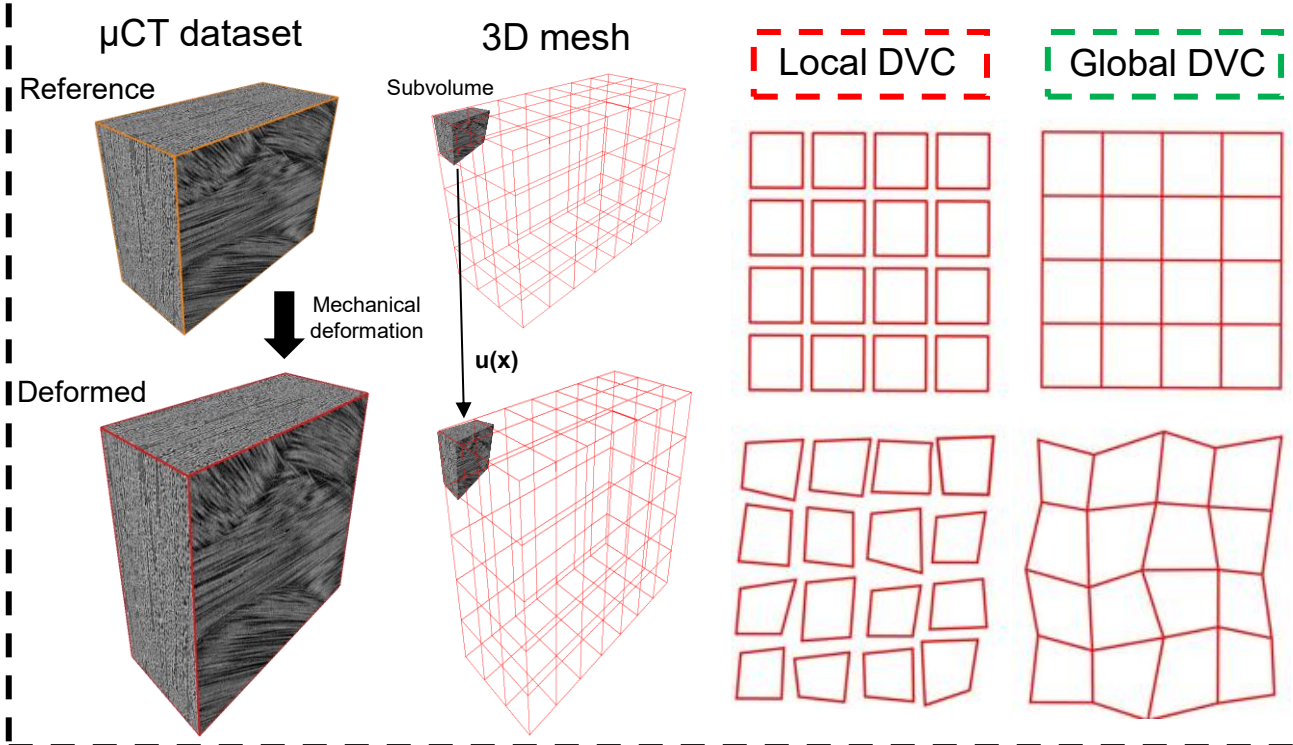

- Two-step DVC approach:
  - subset approach
  - global FE approach
- A 3D FE-based mesh is used to compute the displacements and strains

KU LEUVEN

Correlation residuals

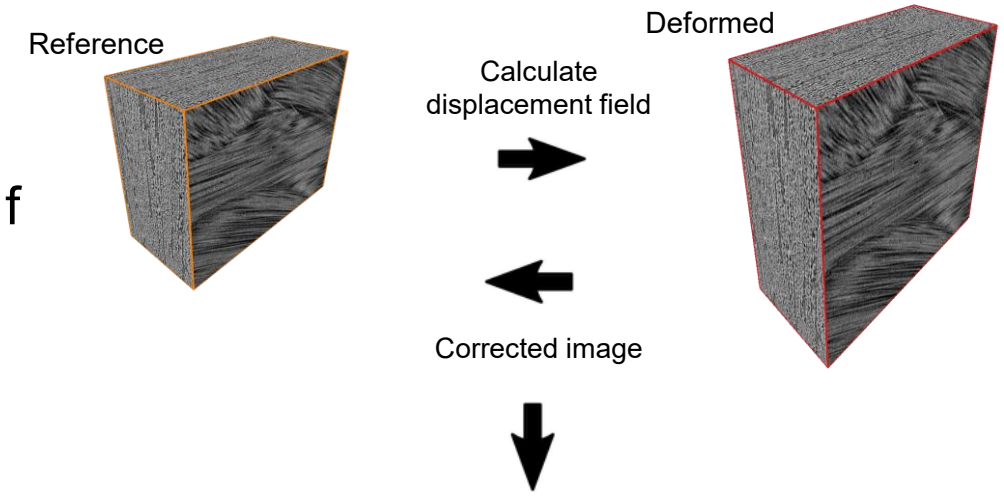

f

g

Correlations residuals = f - g

- Source of errors:
  - Reconstruction artefacts
  - Imaging noise
  - Damage

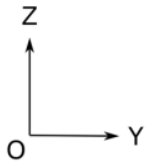

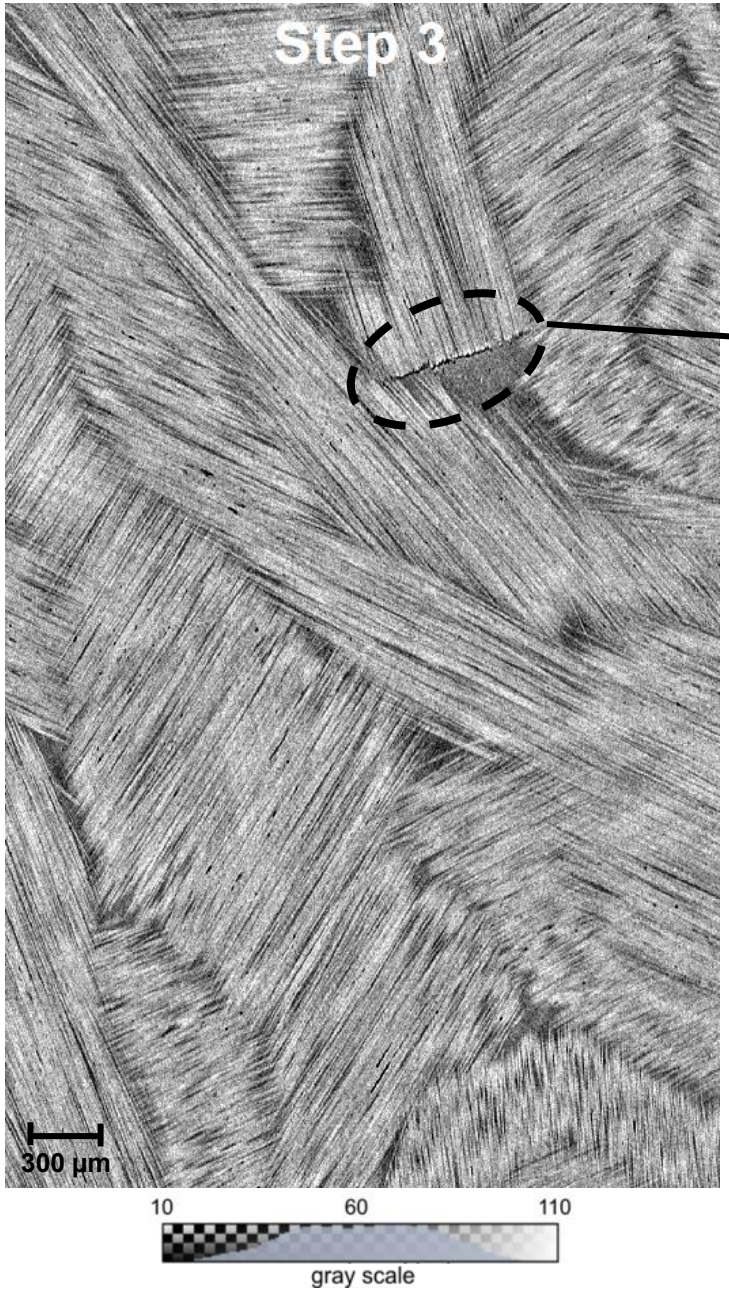

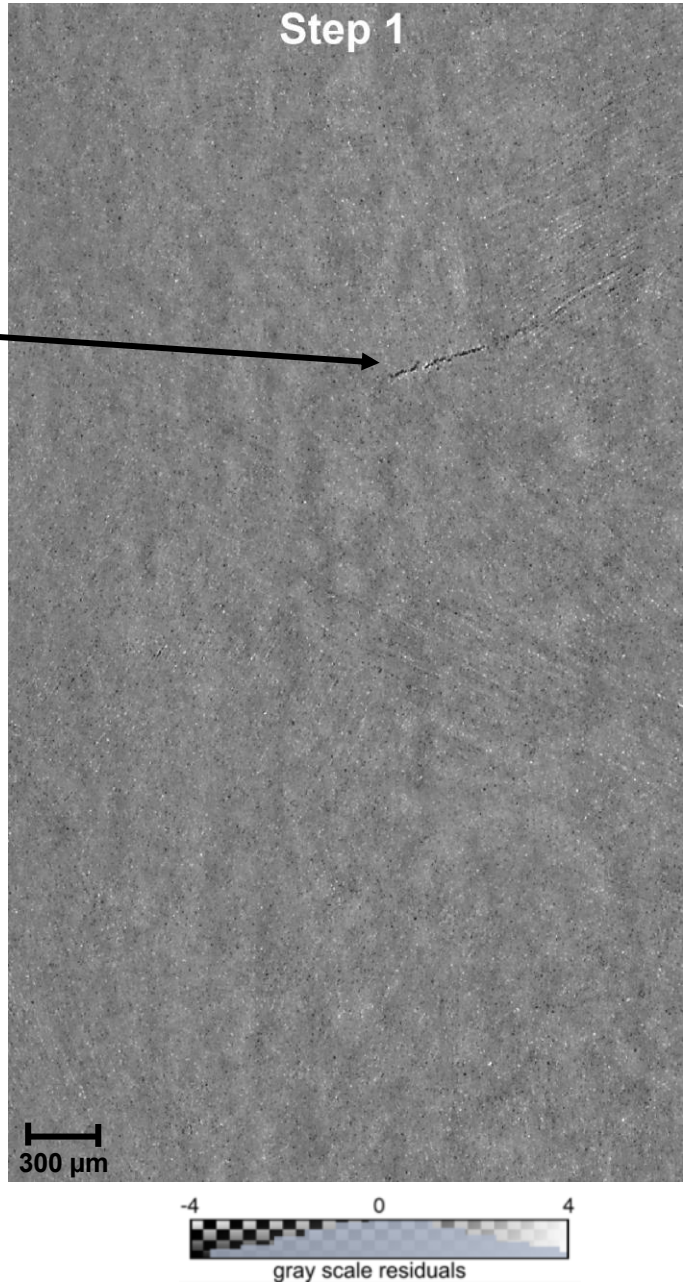

KU LEUVEN

Damage analysis

First principal strain

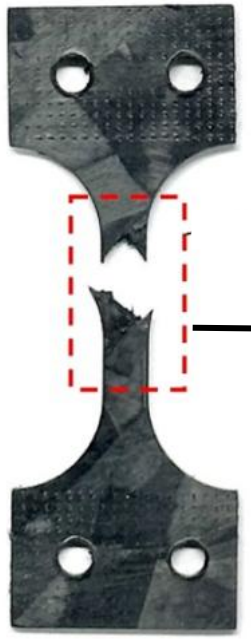

Failed specimen

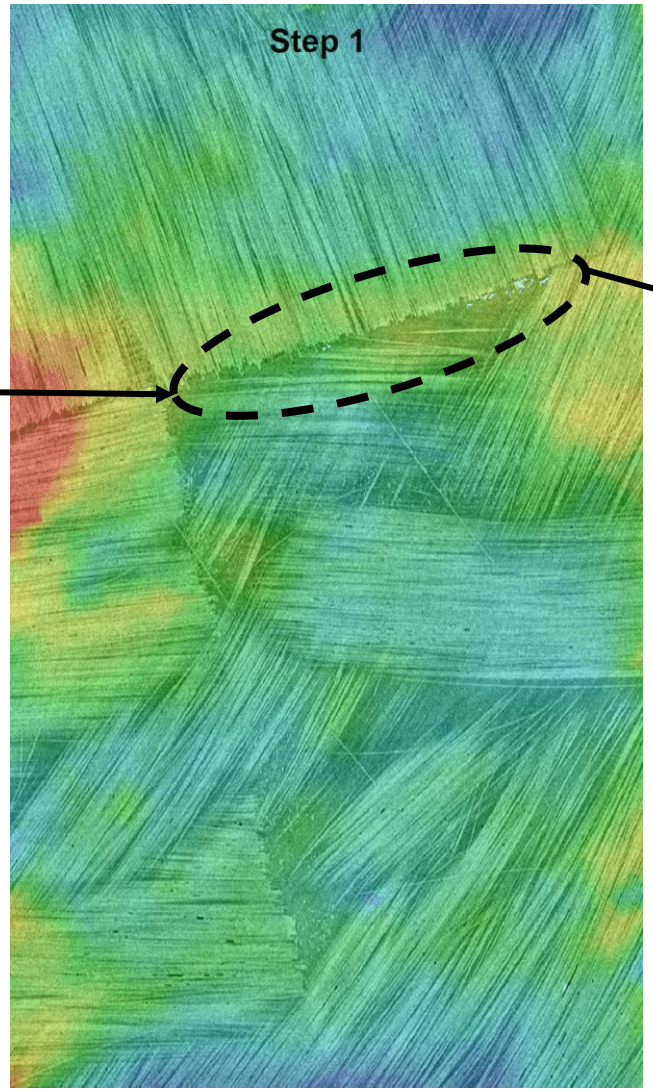

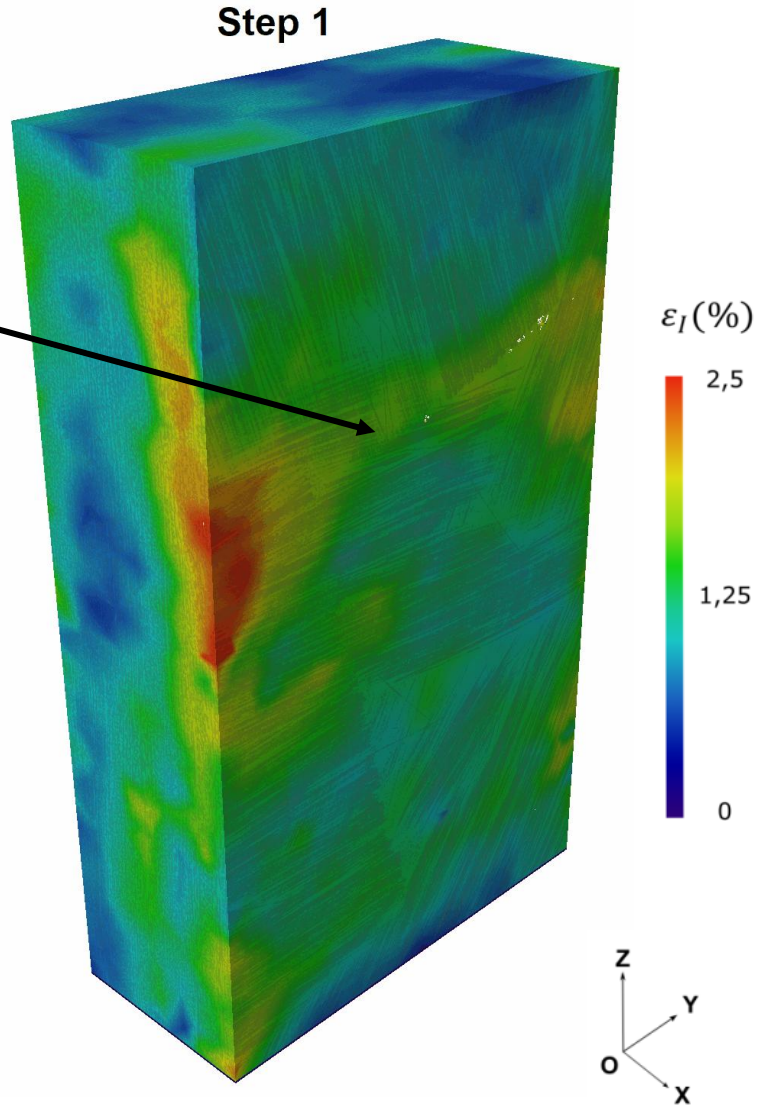

- Microcrack formation in region of high tensile strain

KU LEUVEN

DVC and fibre strand orientation

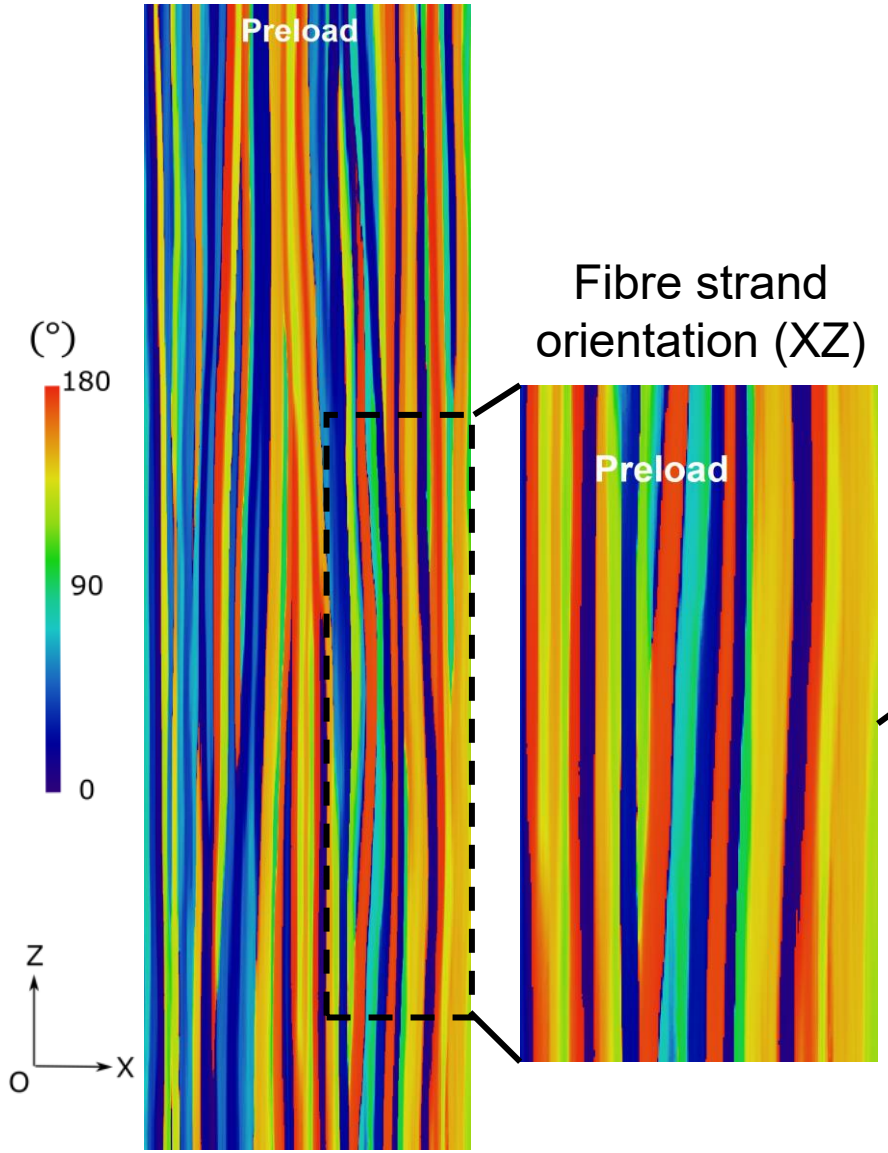

Fibre strand orientation (XZ)

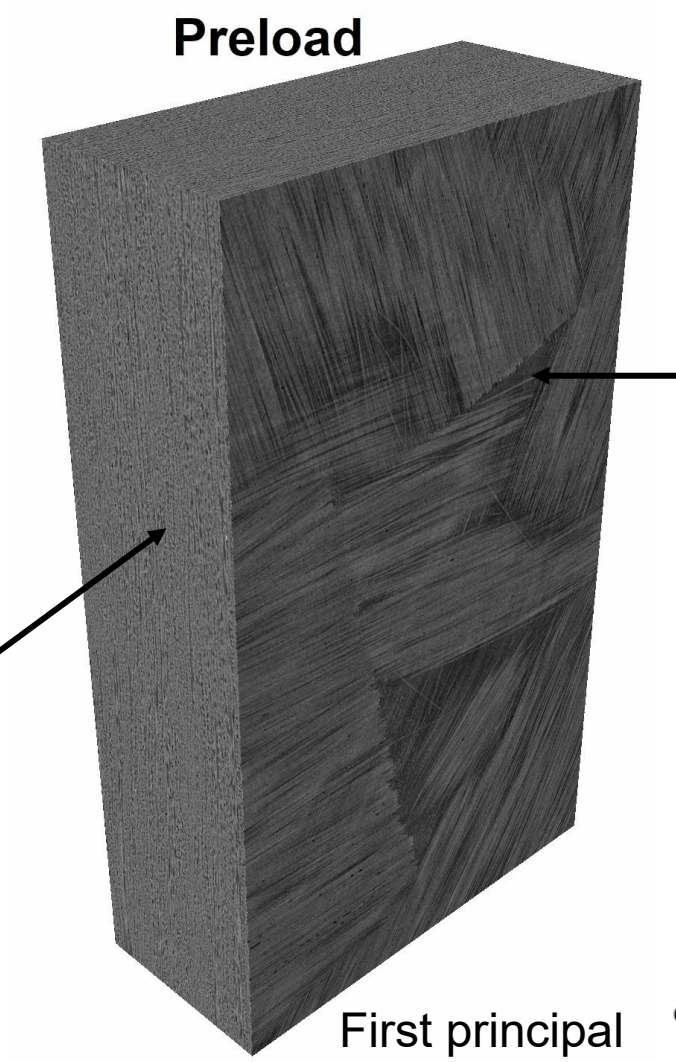

First principal strain



Fibre strand orientation (YZ)

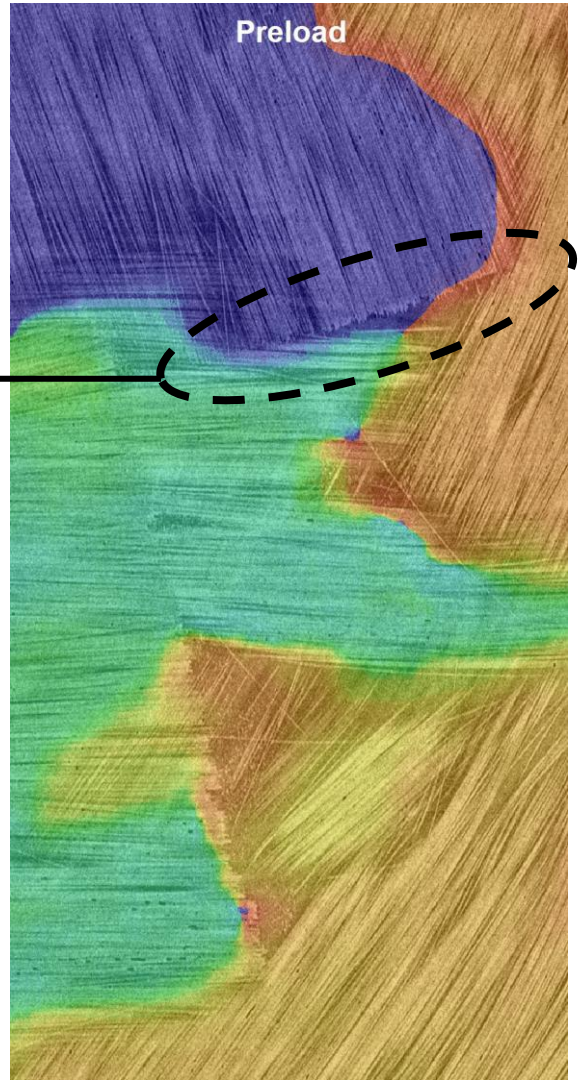

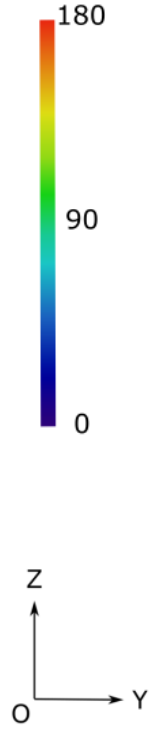

KU LEUVEN

Link with microstructure

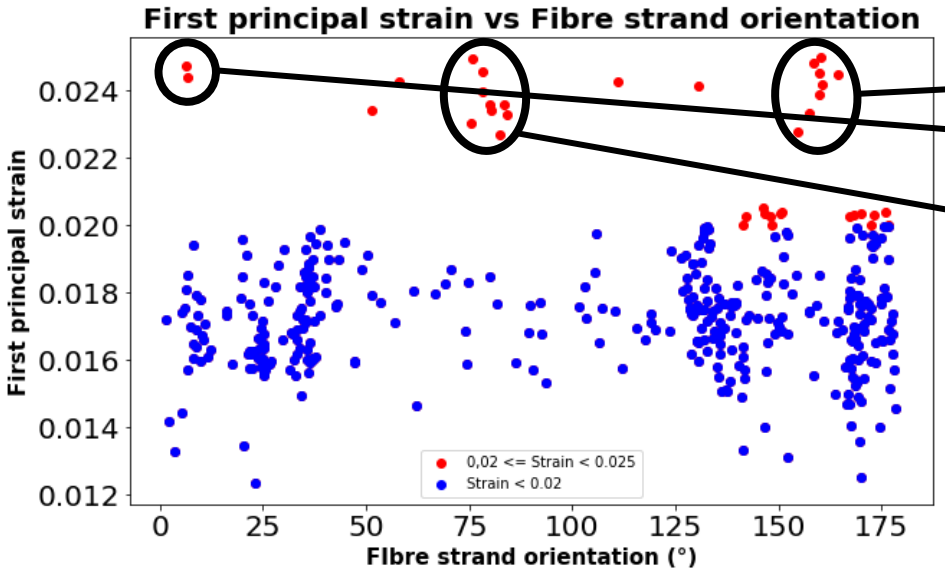

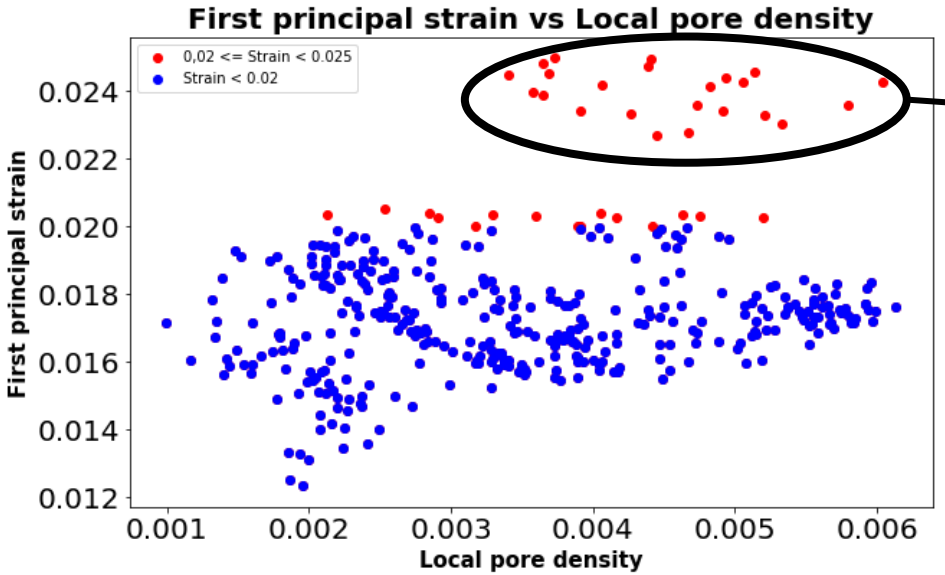

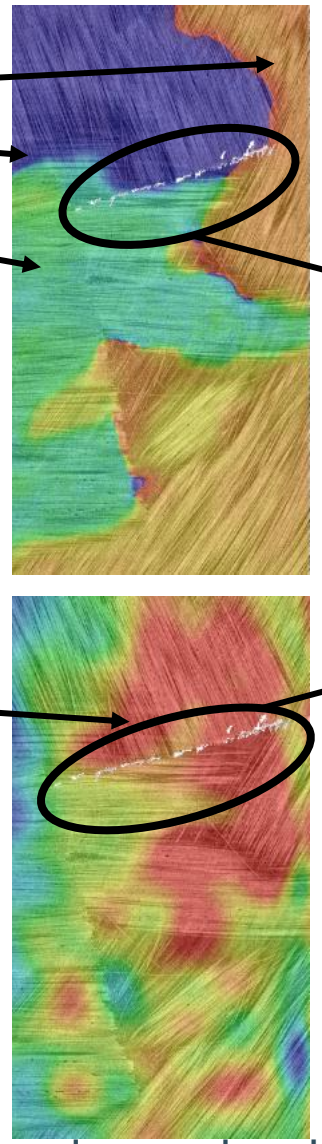

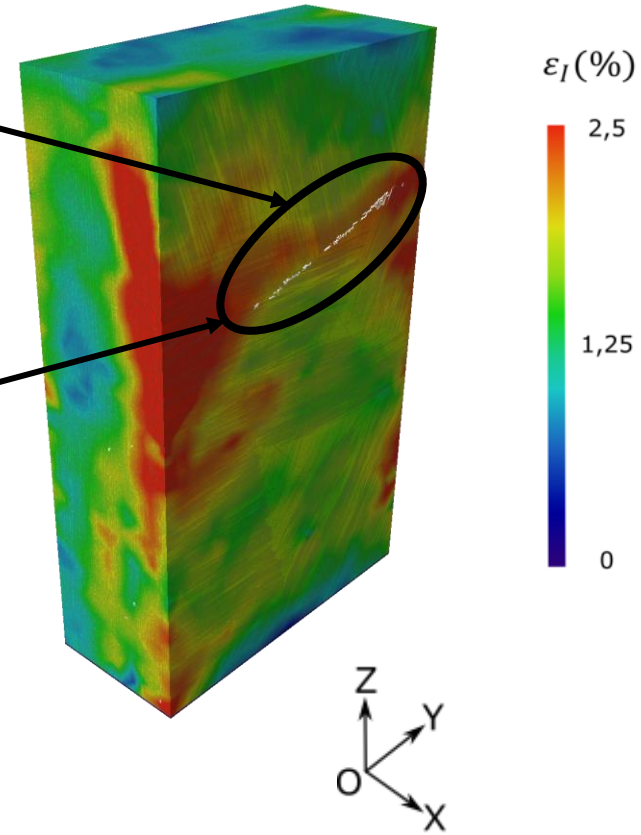

KU LEUVEN

SMC mechanical behaviour

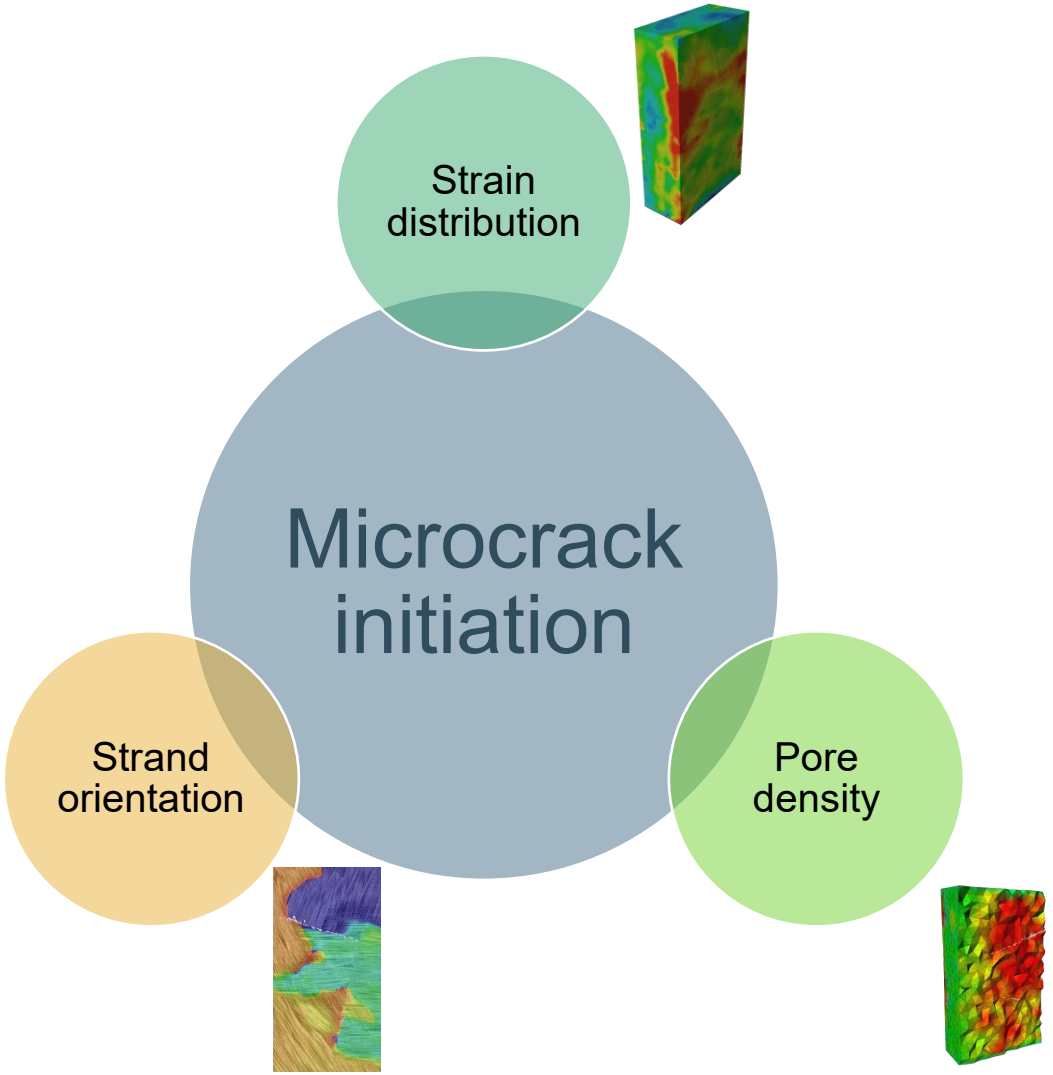

Internal morphology irregularities

Material's mechanical behaviour understanding

Journal Article

ThermoFischer Avizo post

KU LEUVEN

Rig development | **FE simulation** | **In-situ XCT biaxial testing** | **FE simulation vs. DVC**

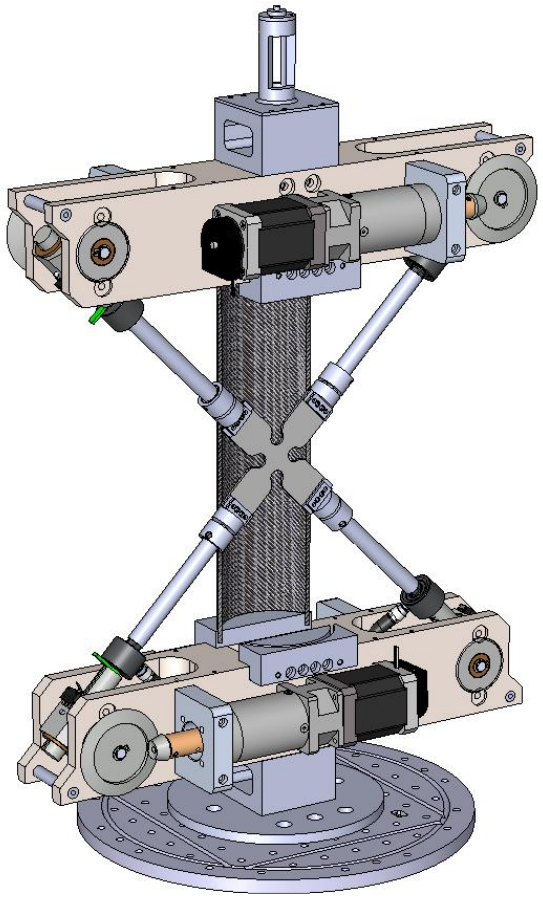

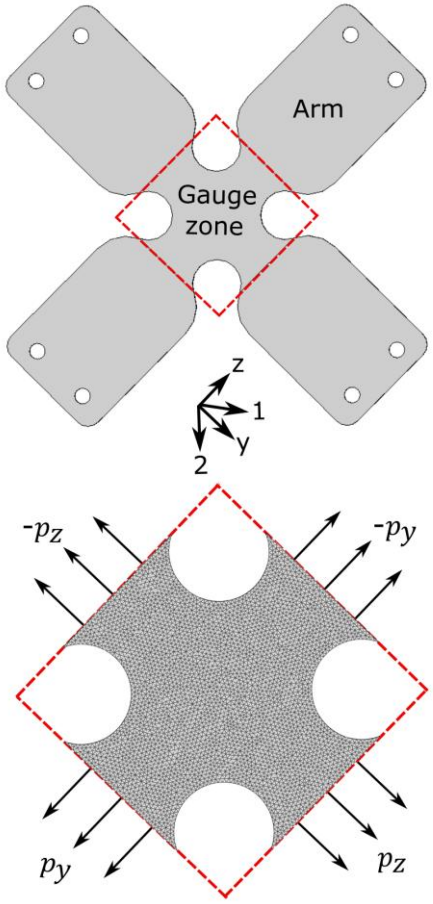

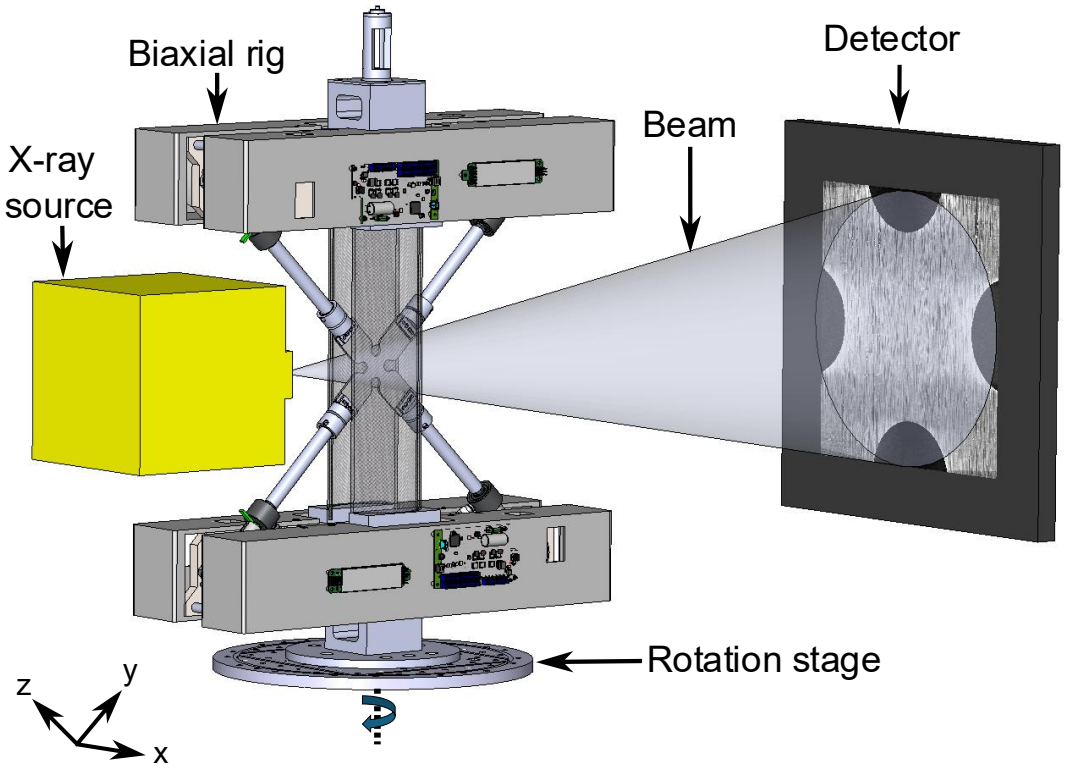

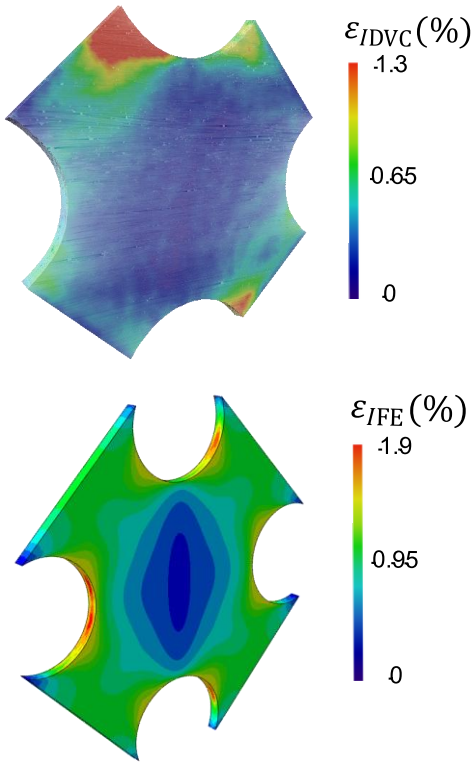

KU LEUVEN XCT CORE FACILITY

NOVITOM

KU LEUVEN

Biaxial setup

- Voxel size down to 4 µm
- Max force: 5 kN
- Max stroke: 20 mm
- Synchrotron extensible

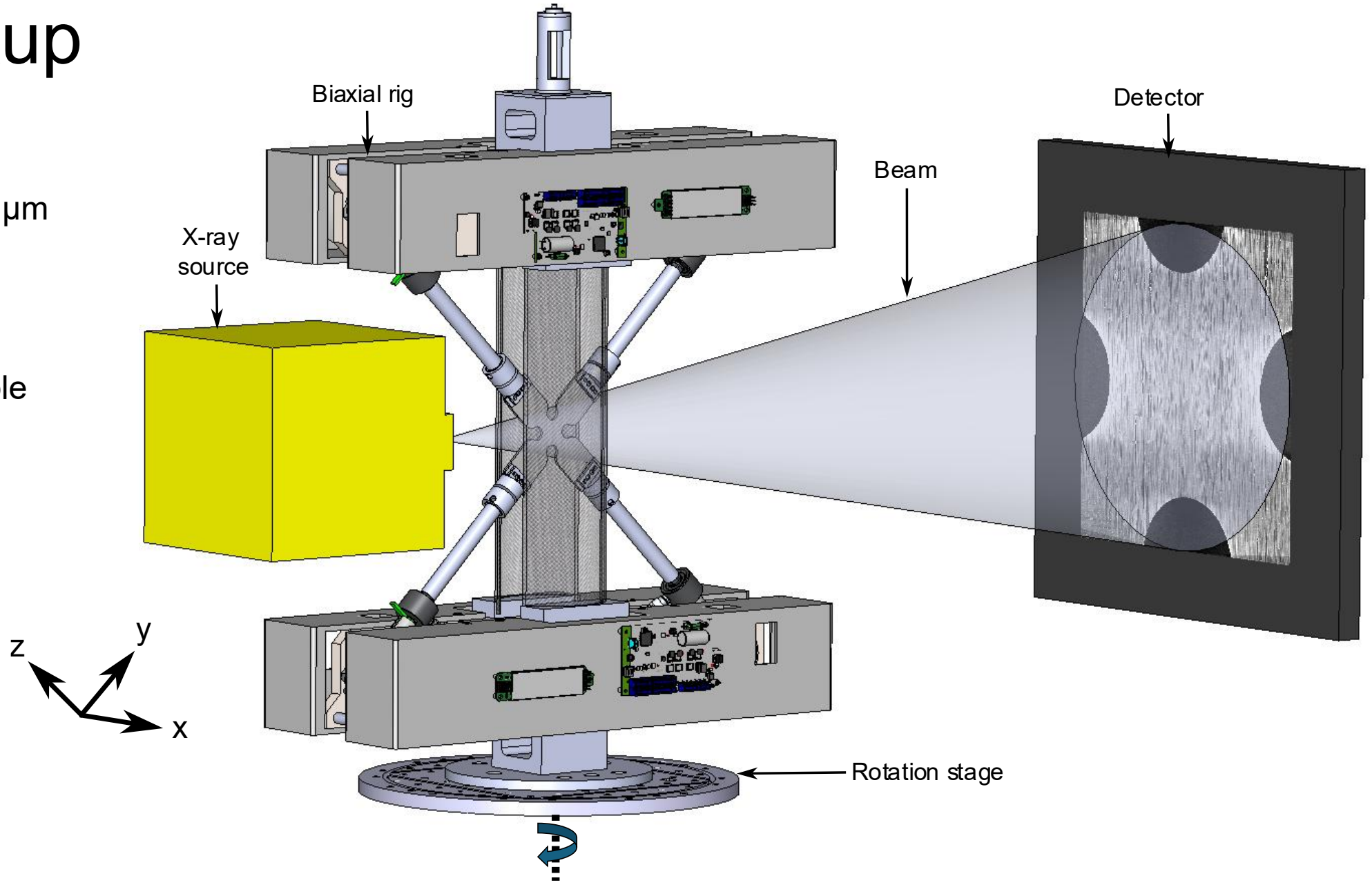

KU LEUVEN

Biaxial specimen

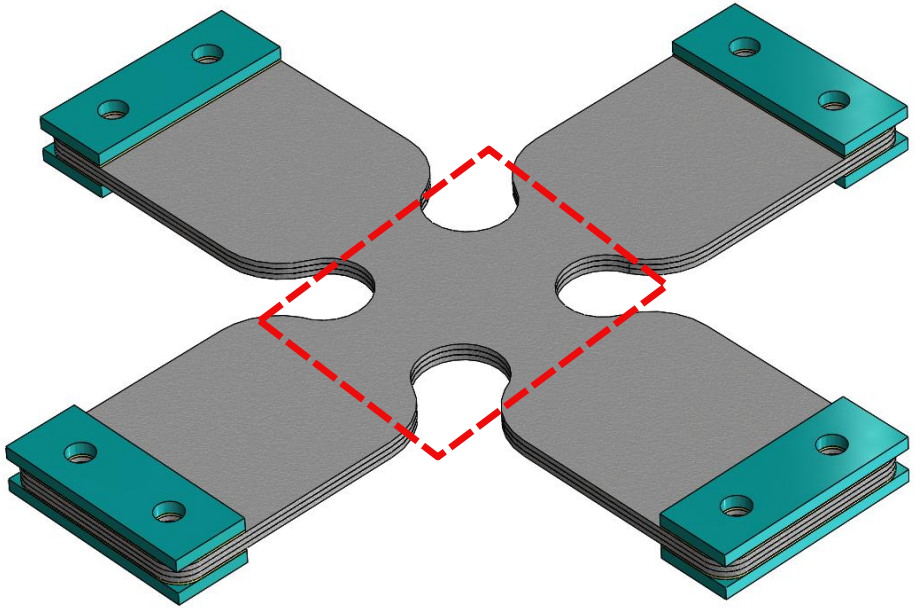

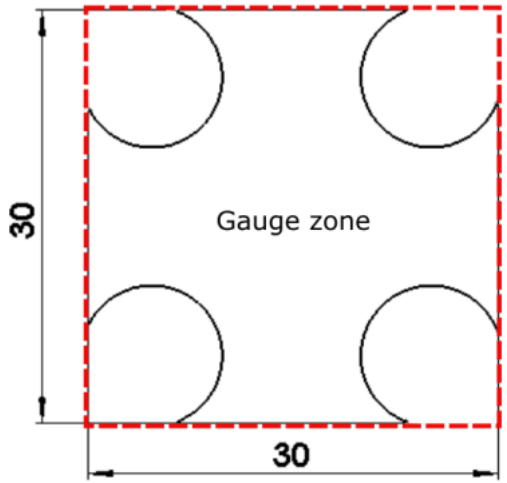

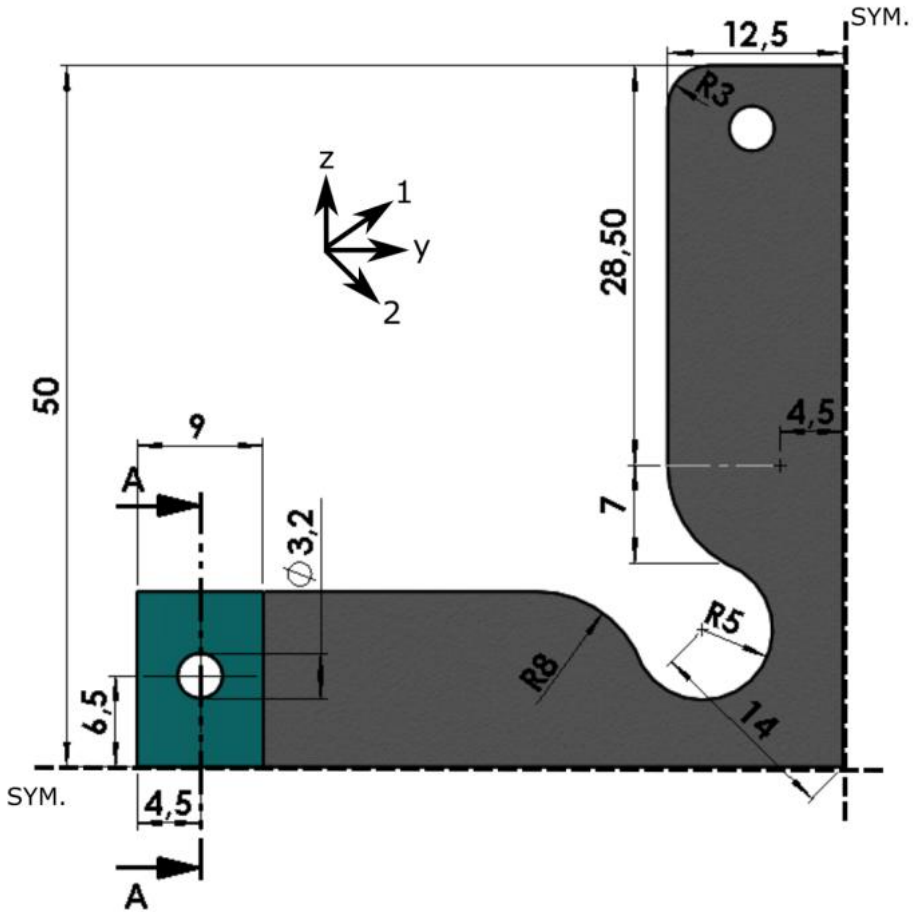

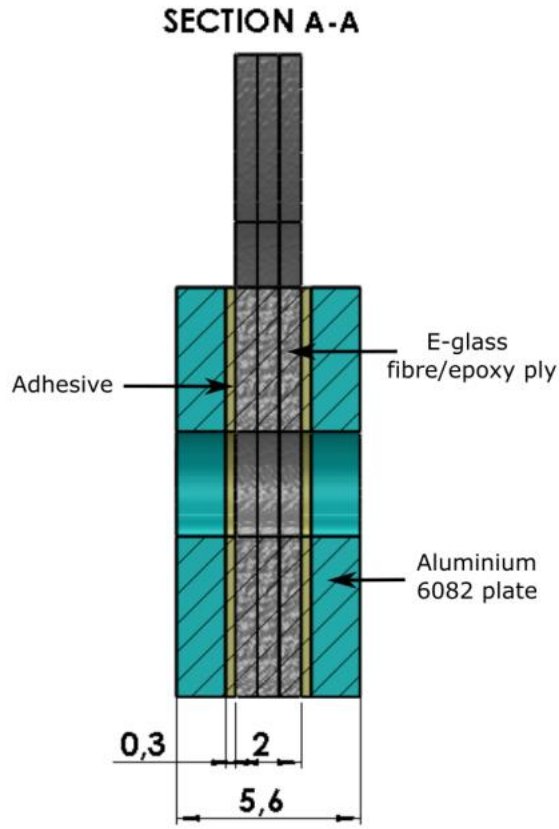

- Advantex R25HX14 E-glass/epoxy ply (fibre diameter: 24 µm)
- [+45/−45/+45] layup
- Section reduction for failure in the gauge zone
- Aluminium end tab at the grips for a better load introduction

KU LEUVEN

FE strains distribution

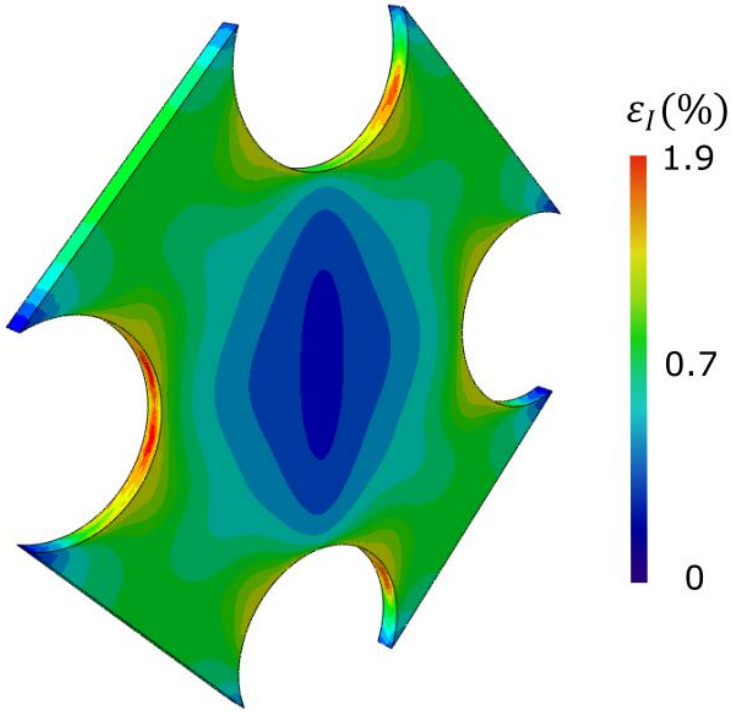

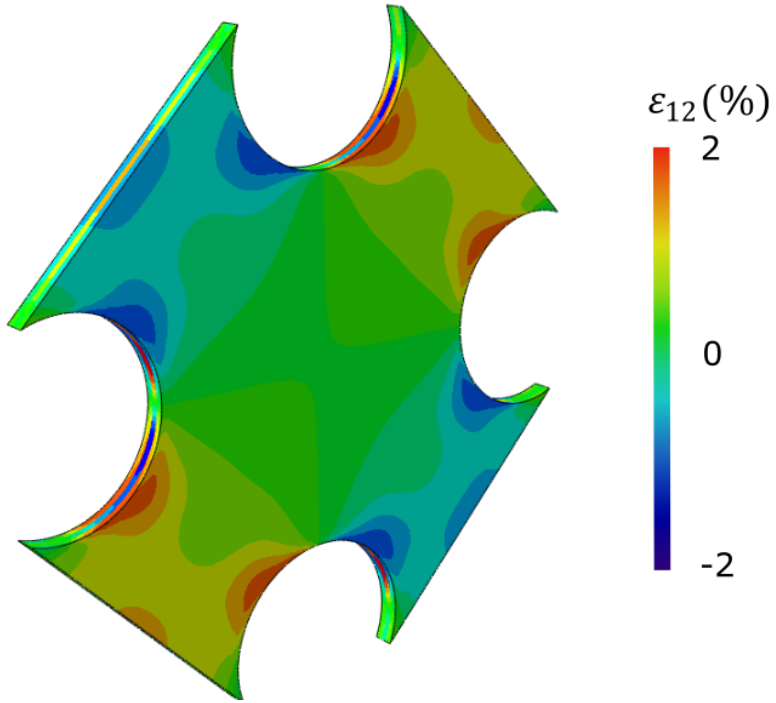

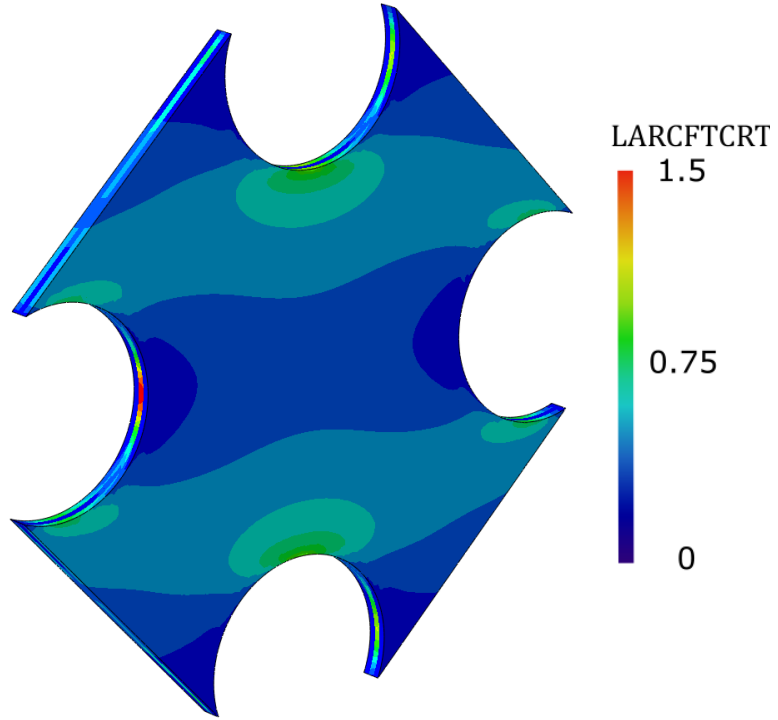

- Uniformity in shear strain
- Failure should initiate in the gauge zone

KU LEUVEN

In-situ XCT time-lapse biaxial testing



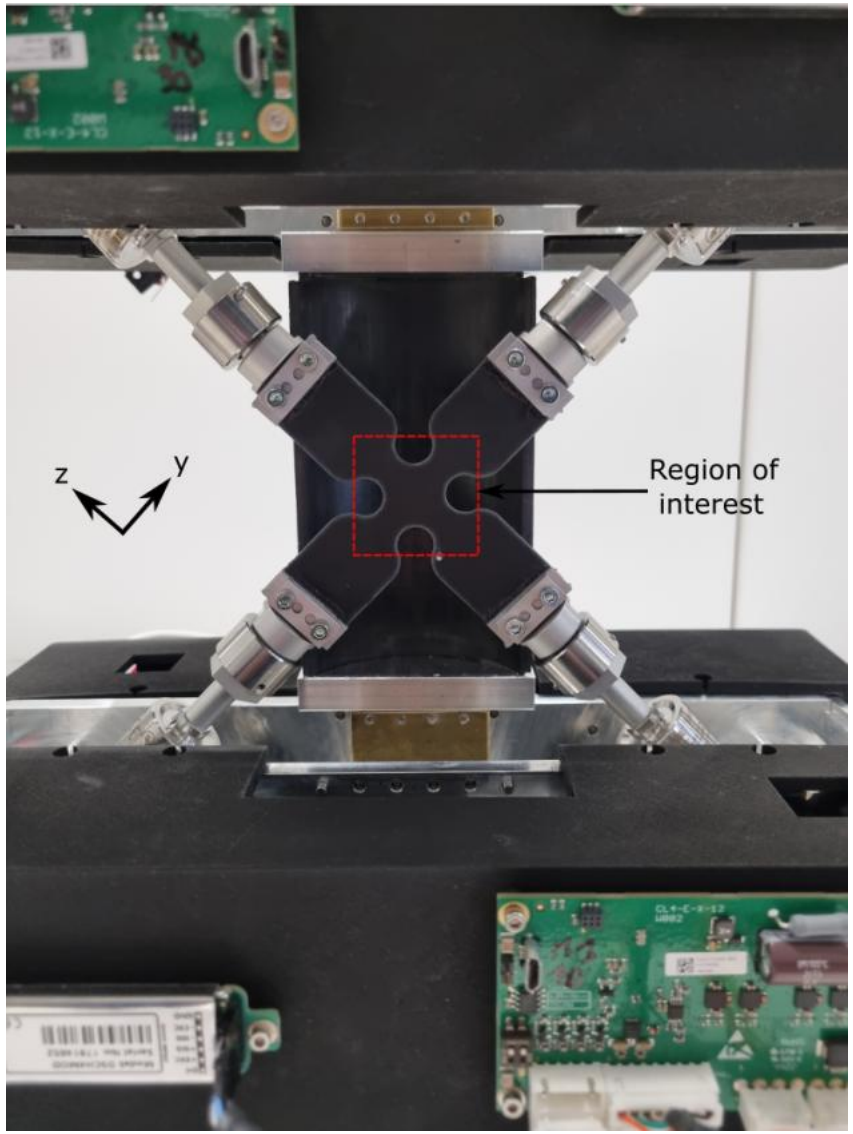

- Tube voltage: 120 kV
- Voxel size: 14 µm
- Fibre diameter: 24 µm

Load strategy

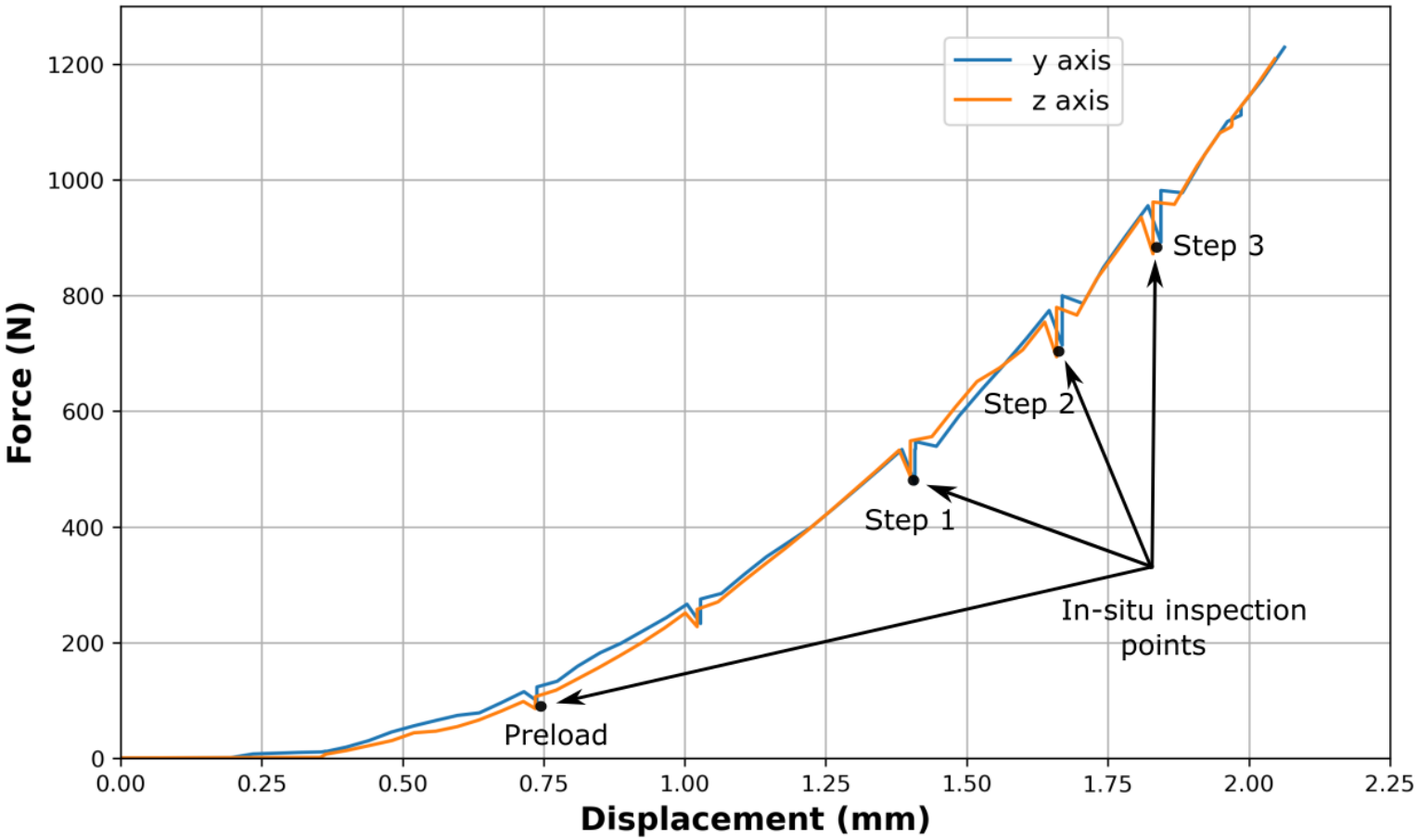

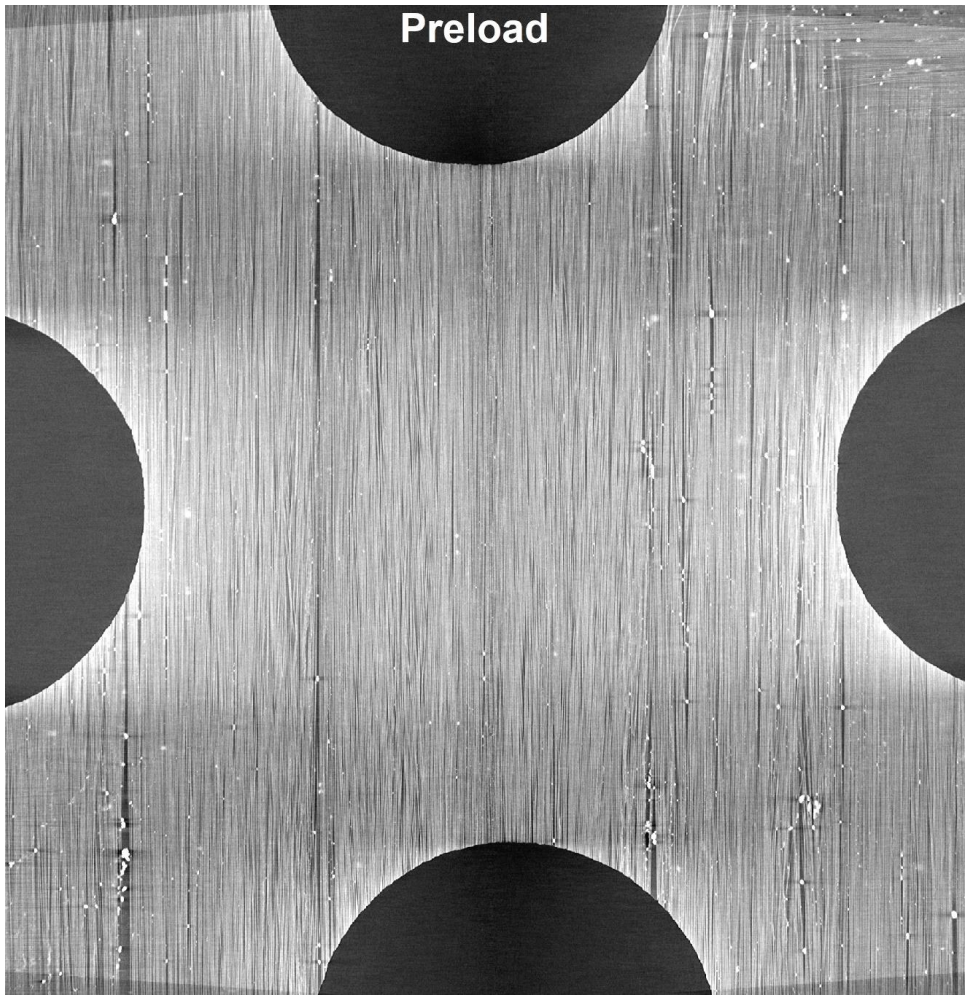

KU LEUVEN

Full strain fields

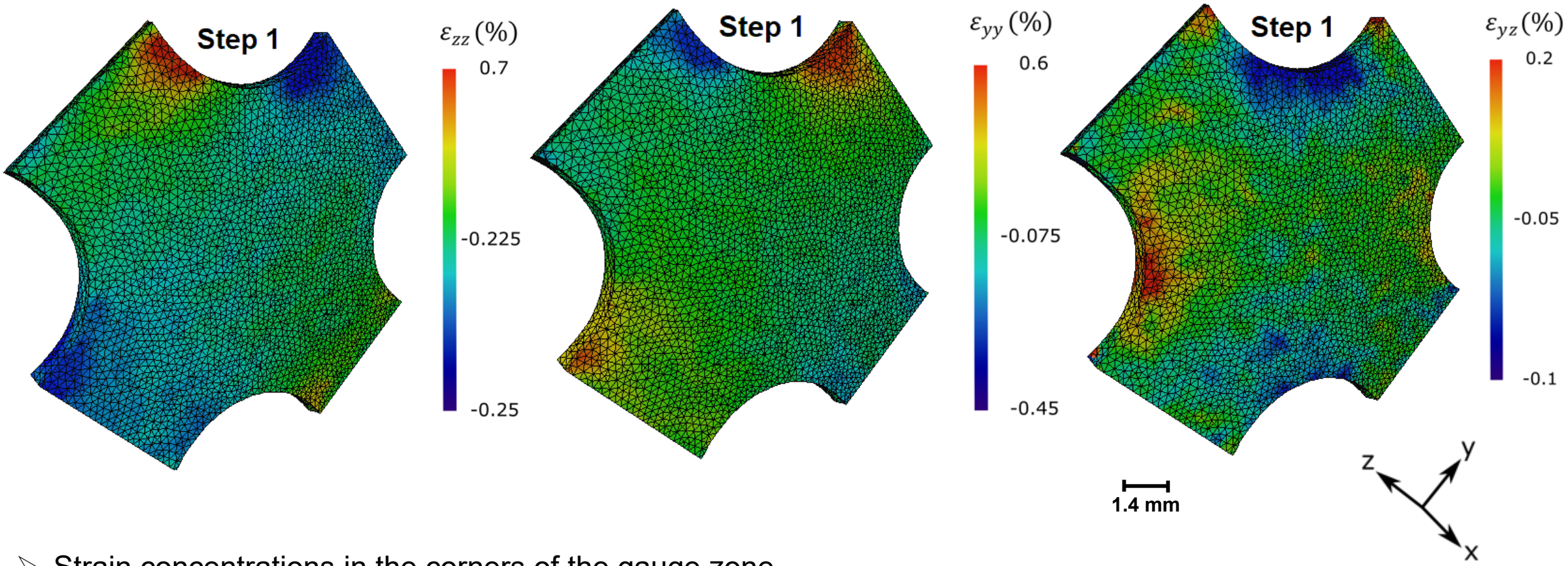

- Strain concentrations in the corners of the gauge zone

KU LEUVEN

Damage investigation

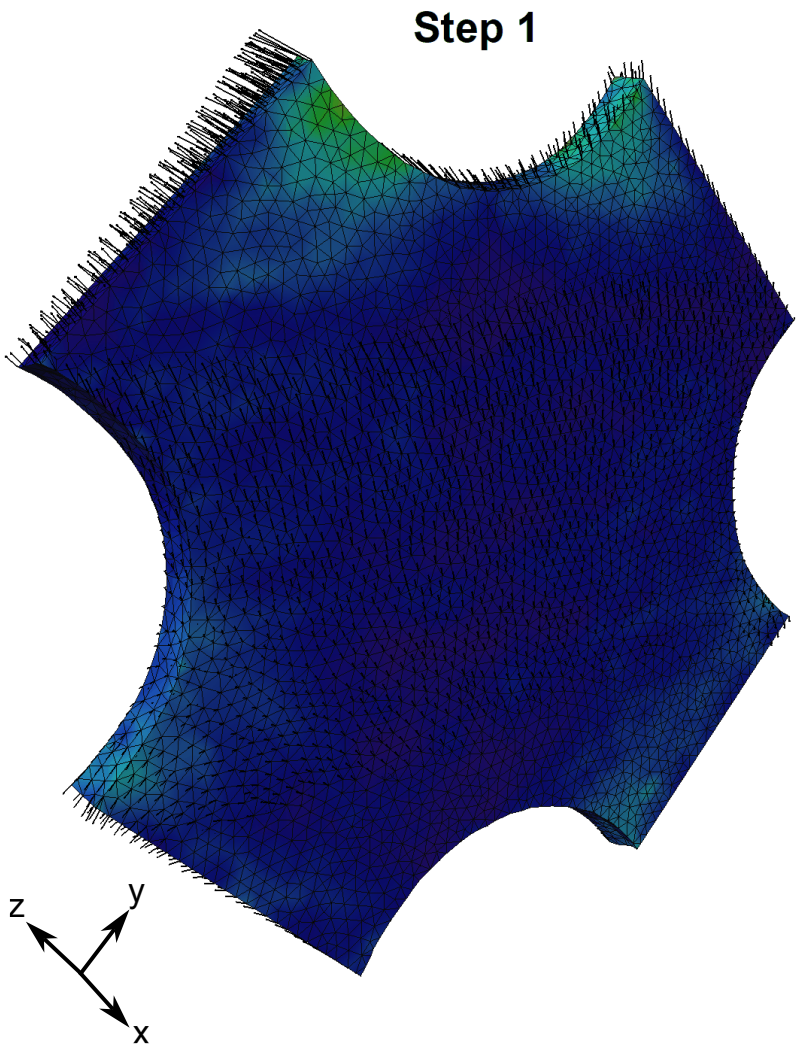

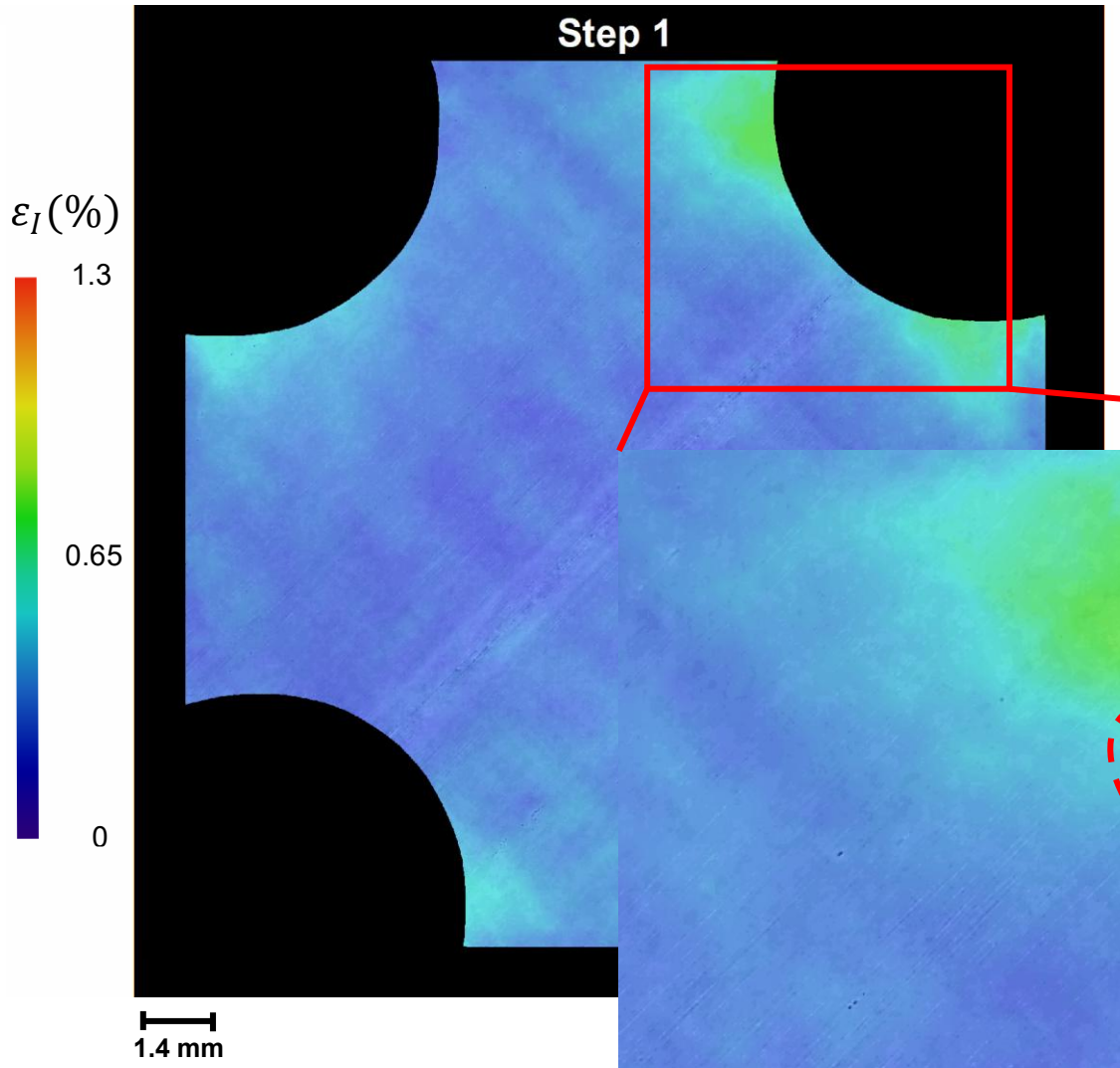

- Residuals images to detect microcrack development

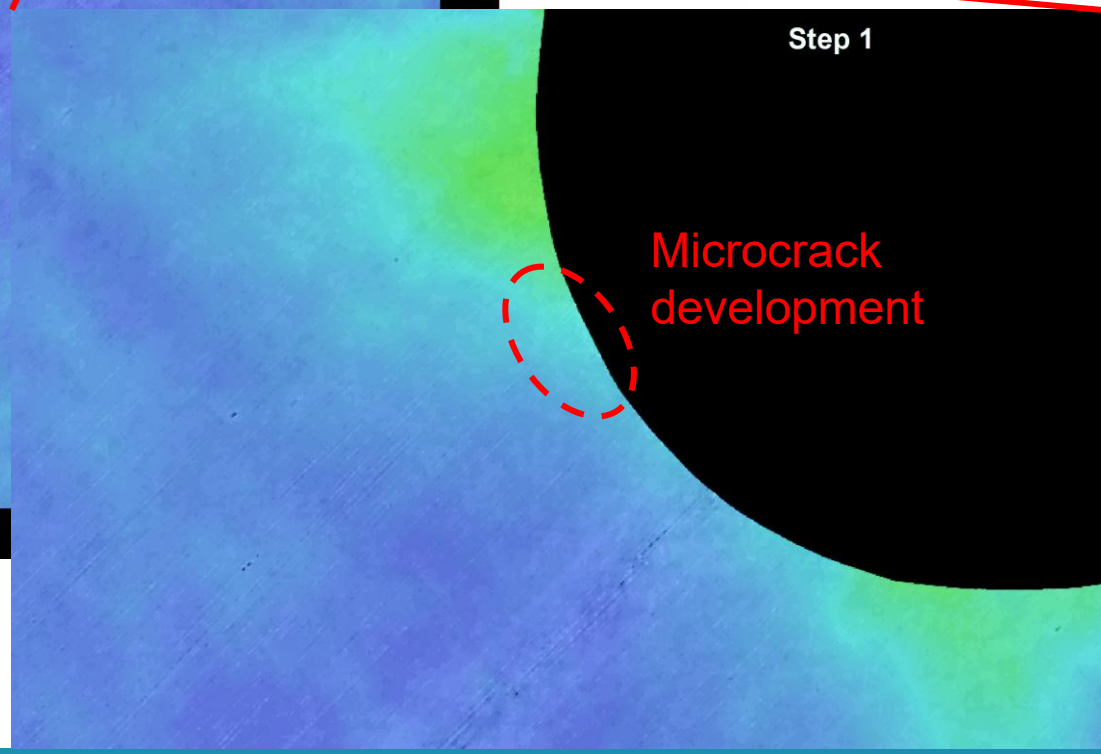

- Strain localisations in the corners

KU LEUVEN

FE vs. DVC

- Similar failure zones
- FE overestimates strain
- DVC integration improves accuracy

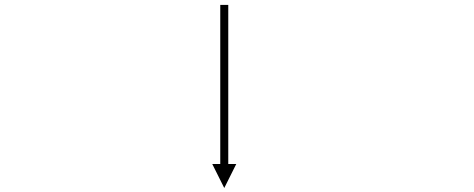

- More data to improve the failure models

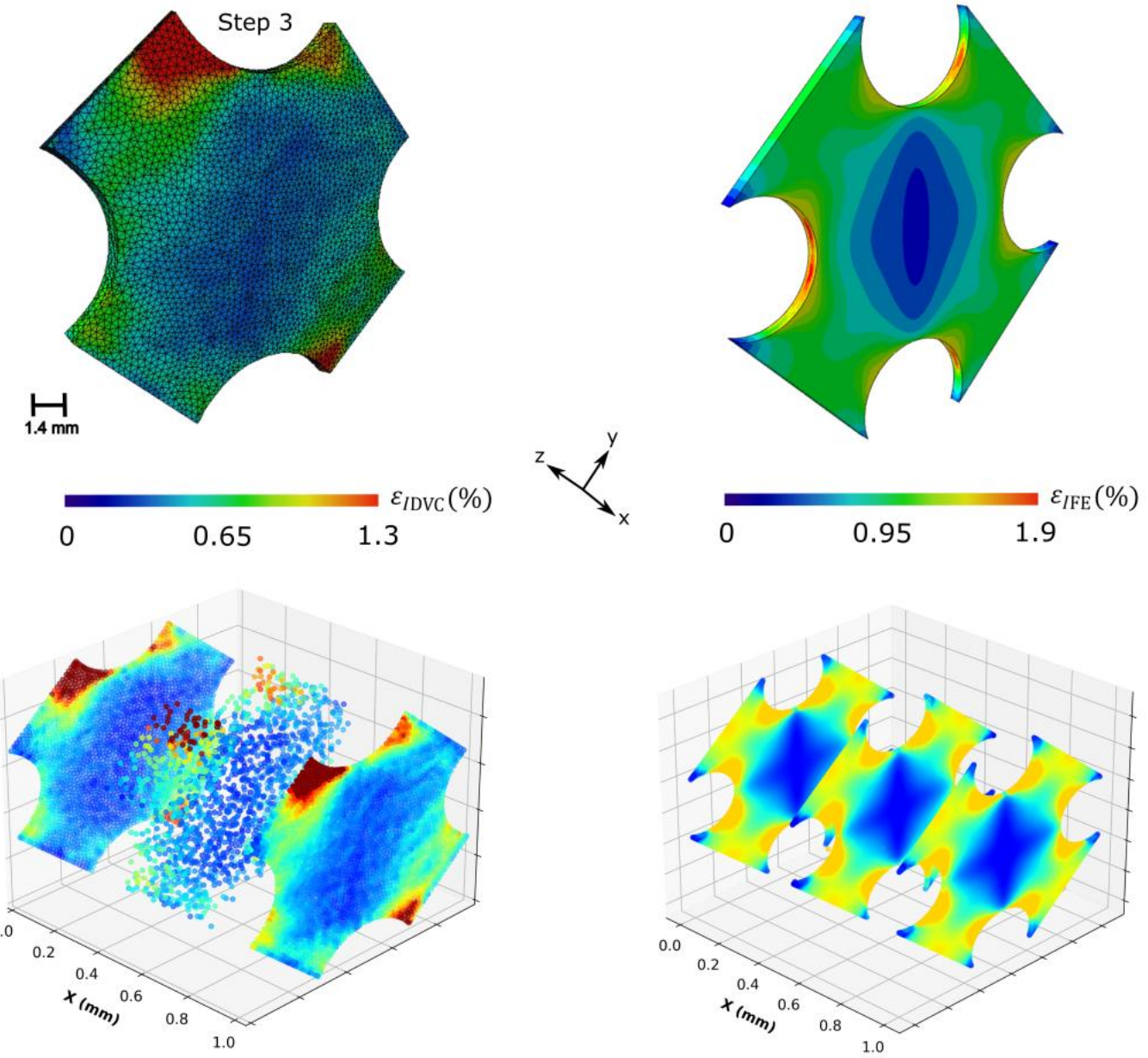

KU LEUVEN

Questions?

salaheddineemine.madi@kuleuven.be

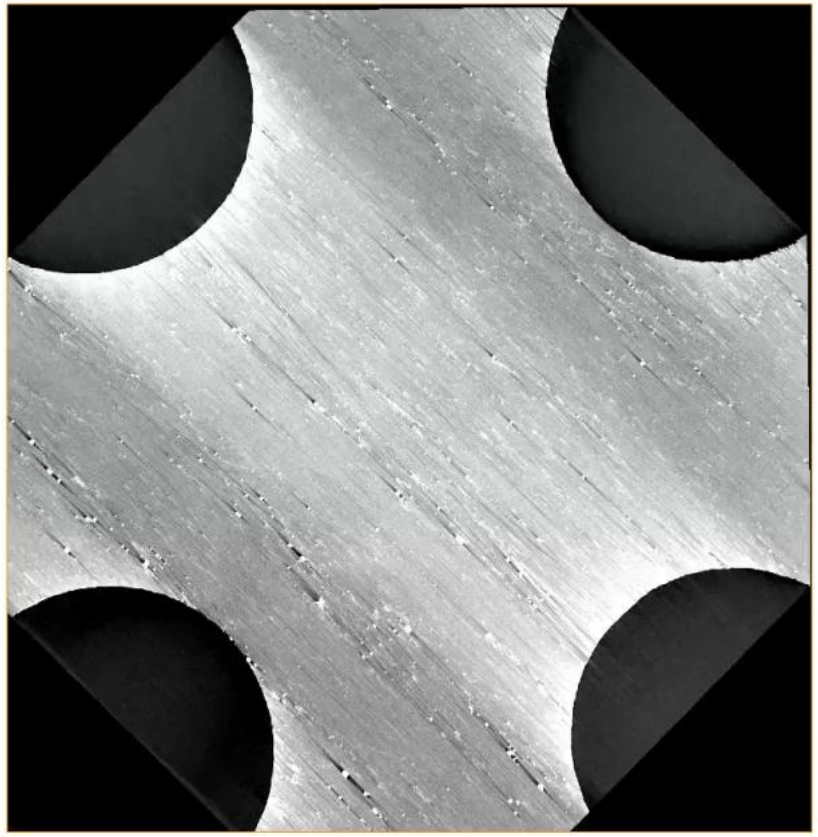



FibreSimulator: An Open-source Python tool for Generating Fiber Phantoms

Mary Chris Roperos Go | ICCM
Co-authors: Daniel Pelt, Anirudh Kohli, Philip J Withers, K Joost Batenburg











Understanding FRPs Starts Inside

- Fiber-reinforced polymers (FRPs) are critical for high-performance industries
- Strength and reliability depend on the **internal fiber structure**
- However, visualizing the internal is **challenging**
- **Tomographic imaging** is the key!

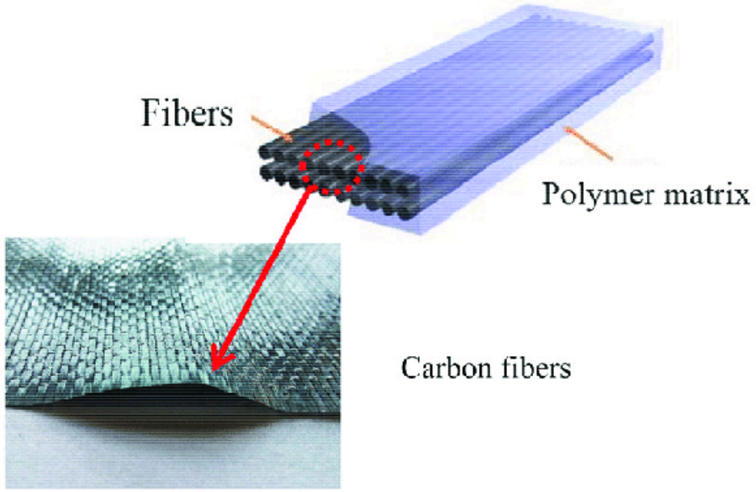

Fiber components: fiber and resin *

> But **high-quality datasets** for developing tomographic algorithms are hard to access!

* Khan, Nazrul & Halder, Sudipta. (2020). Self-healing fiber-reinforced polymer composites for their potential structural applications. 10.1016/B978-0-12-818450-9.00015-5.

Challenges in FRP imaging

- Acquiring high-quality CT datasets is **expensive** & **time-consuming.**
- Existing datasets are often **private** or **not diverse** enough for algorithm development.
- Existing simulators (e.g., PuMA, TexGen, WiseTex) are **rigid** — limited ability to model different fiber features or scanning conditions.

A Flexible Python Fiber Simulator

Top 3 advantages of what FibreSimulator can offer!

2

Generate synthetic FRP volumes with **customizable features & defects**.

1

Built in **Python** for maximum flexibility & easy extension.

FibreSimulator

3

Simulate CT scanning conditions through **ASTRA Toolbox**.

Provides realistic data for **testing** and **improving** tomographic methods.

Outline

Methods

How *FibreSimulator* builds phantom volumes

Conclusion

Key Takeaways

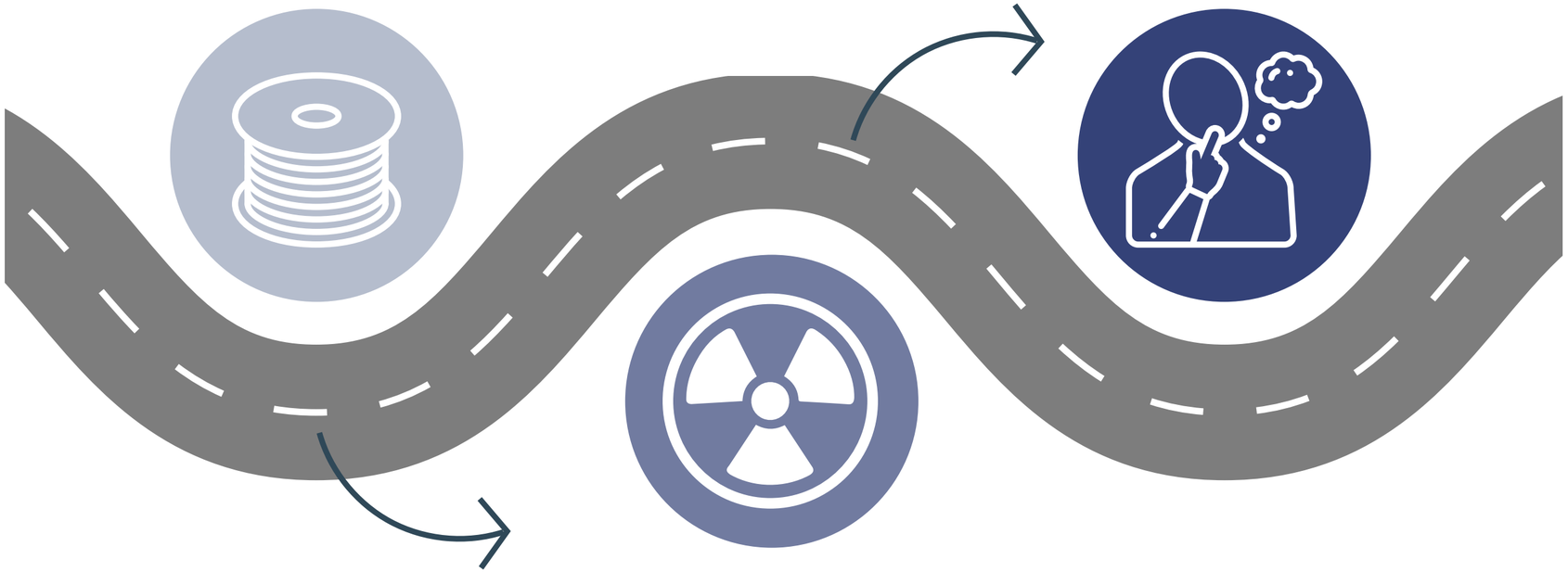

Experiments

How different parameters affect imaging

Outline

Methods

How *FibreSimulator* builds phantom volumes



Experiments

How different parameters affect imaging



Conclusion

Key Takeaways



Methods

In real-world X-ray CT scans of FRPs:

- fiber appears as elongated cylinders
- the volume has the material classes:
  - air
  - resin
  - fiber

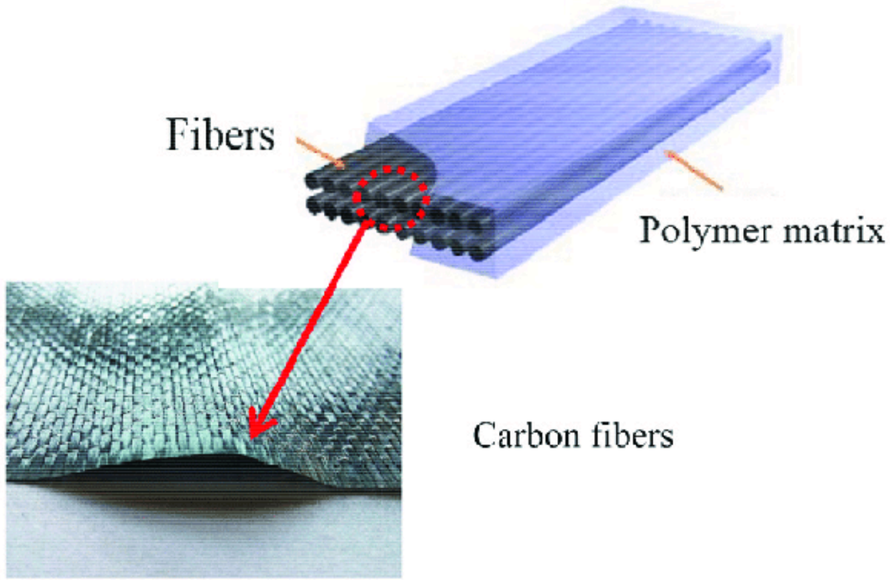

Fiber components: fiber and resin [1]

[1] Khan, Nazrul & Halder, Sudipta. (2020). Self-healing fiber-reinforced polymer composites for their potential structural applications. 10.1016/B978-0-12-818450-9.00015-5.

Notations & Concepts

- We define a fiber phantom as a set of fibers:

$$\mathcal{P} = \{F_1, F_2, \ldots, F_{N_f}\}$$

- Each fiber is a sequence of points:

$$\{p_n\}_{n=1}^{N_s} \subset \mathbb{R}^3$$

- Therefore, a single fiber is written as:

$$F_m = \{(p_1, r), (p_2, r), \ldots, (p_{N_s}, r)\}$$

- The total volume is:

$$V_{fibers} = \bigcup_{m=1}^{N_f} V_m = \bigcup_{m=1}^{N_f} \bigcup_{n=1}^{N_s} B(p_n, r)$$

This final equation defines the whole volume as a union of fibers where each fiber is a union of midpoints.

This continuous volume serves as the geometric model of the fiber phantom before discretization.

Voxel Representation

- Once all the fibers are generated in continuous space, they are converted onto voxel grid:

$$V \in \mathbb{R}^{V_x \times V_y \times V_z}$$

  where each voxel holds a scalar intensity value [0, 255].
- CT attenuation coefficients: resin, material, air

Given a volume where fibers are growing inside a pipe, a voxel is marked as fiber if its center lies inside any sphere the defines a fiber. Voxels outside the pipe are assigned the air value, while voxels in the pipe that do not contain fibers are filled with resin value.

Single Fiber Generation

a) composition of single straight fiber: **overlapping 3D spheres**

b) **schematic representation** of an axial slice of a fiber phantom

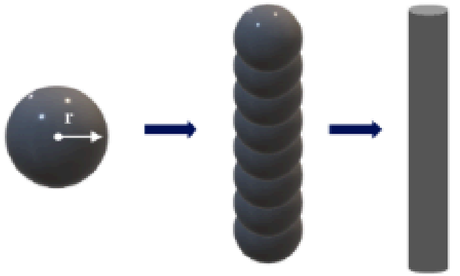

(a)

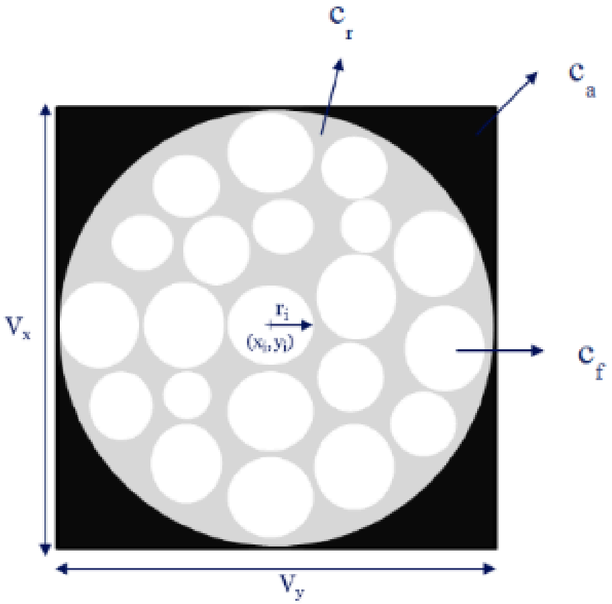

(b)

> Why use this design? It offers in **flexibility in choosing** the next point

Since the workflow of building a fiber involves growing it step by step, the user can choose the direction of growth, demonstrating flexibility.

Fiber Phantom Volume Generation

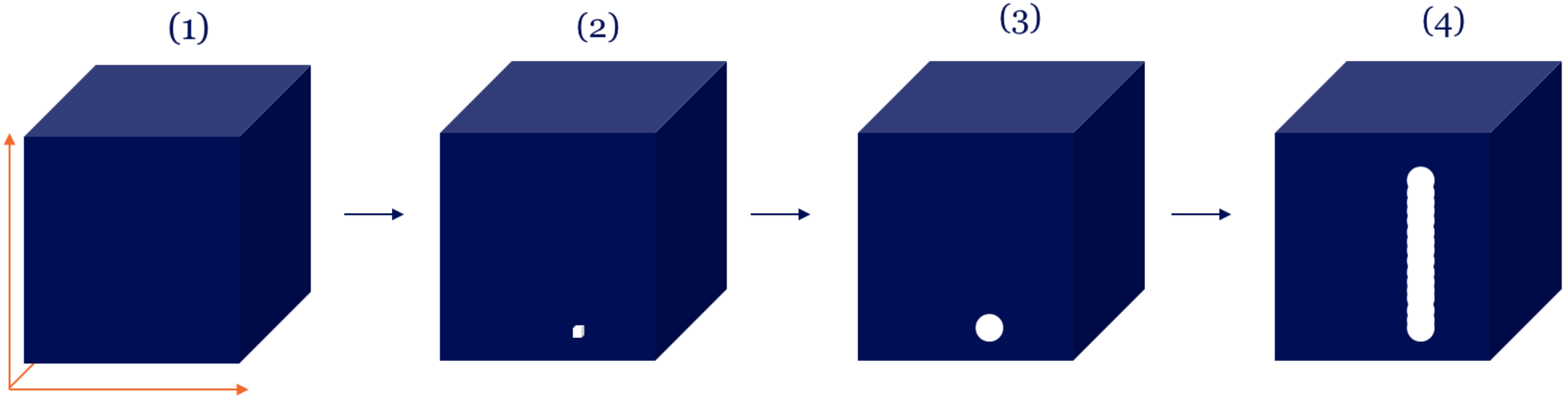

(1) Start with an empty volume.
(2) Initialize a starting point.
(3) Check if the point lies within the volume and ensure that a sphere with the given radius does not overlap with existing fibers.
(4) Grow the fiber and repeat the process until N fibers are generated.
(5) Discretize the volume and label the voxels.

repeat until N fibers are generated & fill unoccupied p_i to resin

For the sake of simplicity, we grow a straight fiber in this example, meaning the next point will just be either +x or -x axis.

Fiber Phantom Volume Example

- Real composite materials:
  - wide range of structural variations
  - differences in fiber diameters
  - presence of manufacturing defects
- size of [800 x 800 x 800] showing:
  - hole
  - kinking
  - variation in fiber diameter

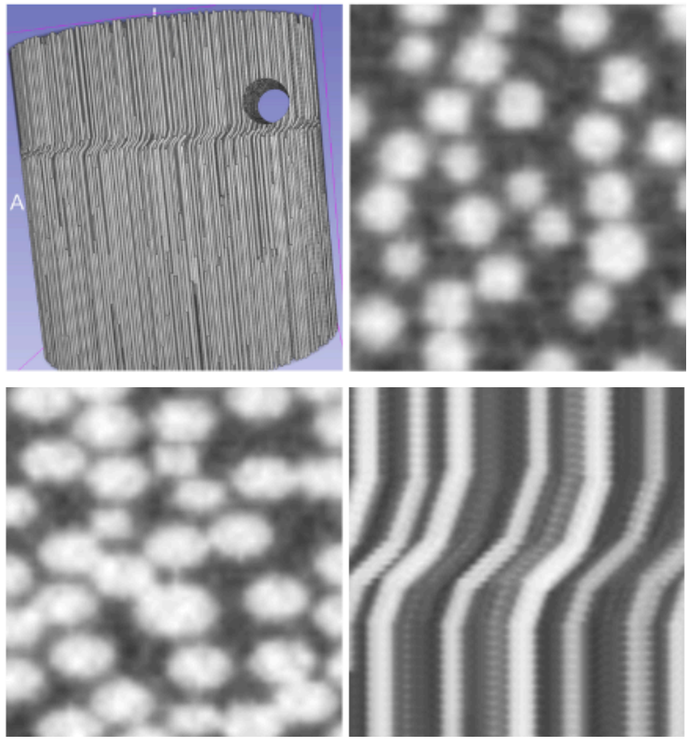

Visualization of a reconstructed phantom volume w/ kinking & a hole

Other features

Fiber Orientation, voids

kink | full-wave | half-wave

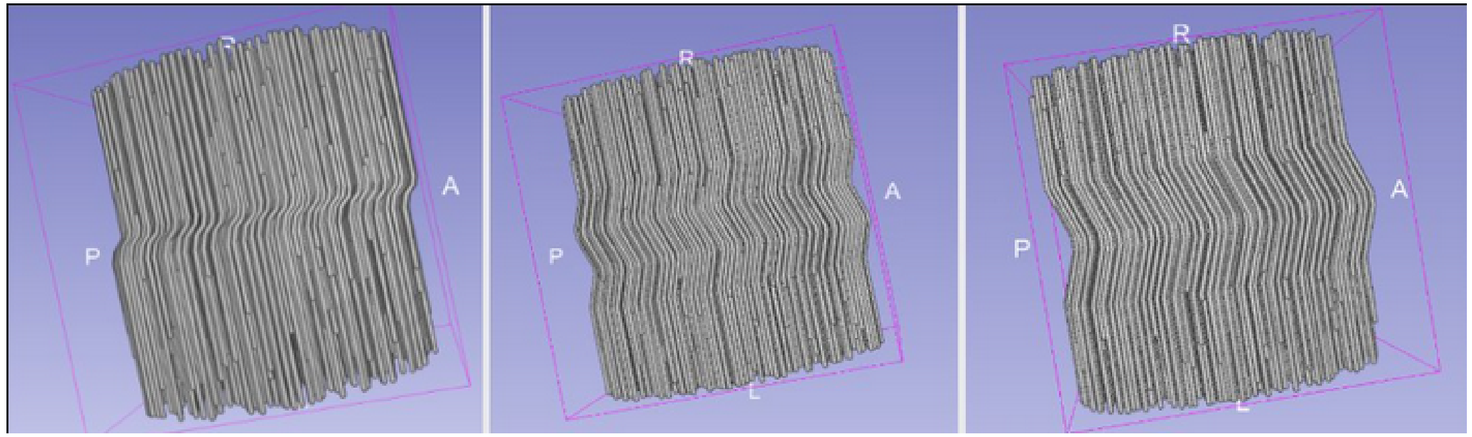

voids

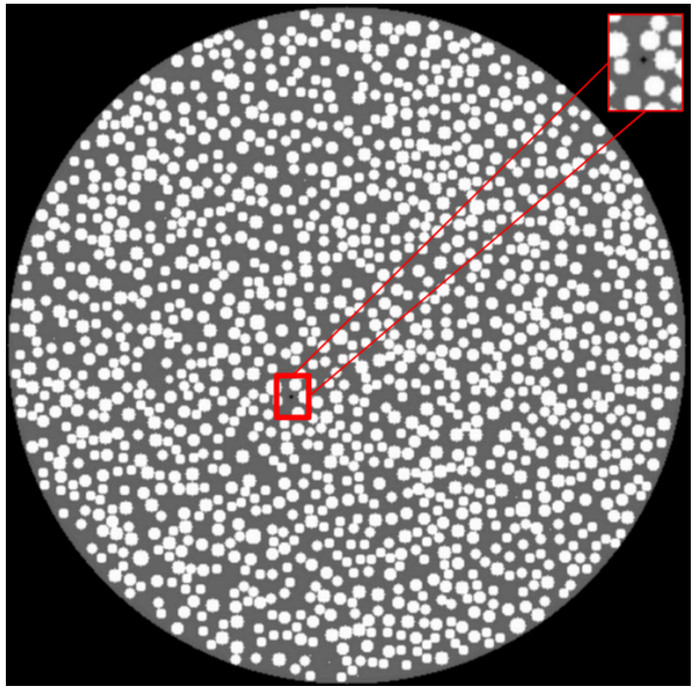

These features are commonly observed in manufactured composites and play a critical role in determining their mechanical performance. To account for this, we incorporated the simulation of these features, aiming to generate more realistic phantoms that reflect imperfections.

Other features

Geometrical Features

These types of features were prioritized for modeling due to the availability of real-world data, enabling qualitative comparison. But because of the flexibility of FibreSimulator, users can generate their own geometrical feature.

hole

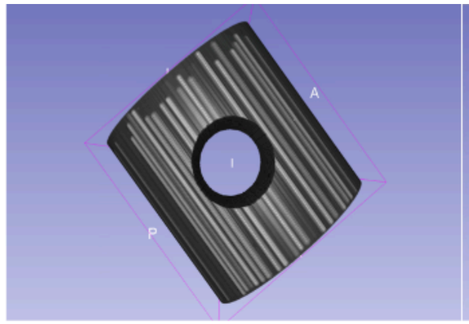

square-notch

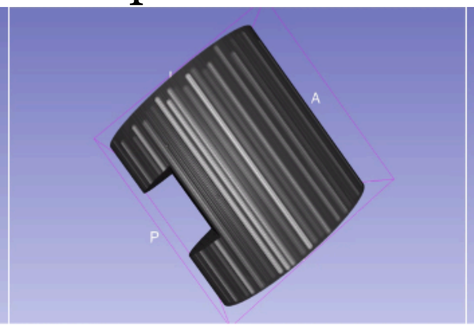

v-notch

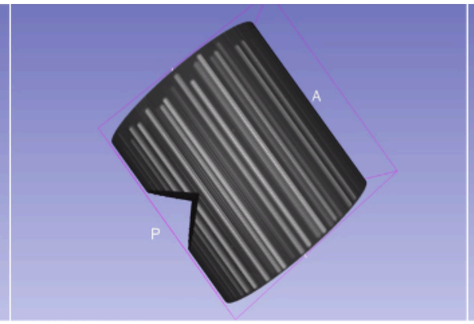

reduced

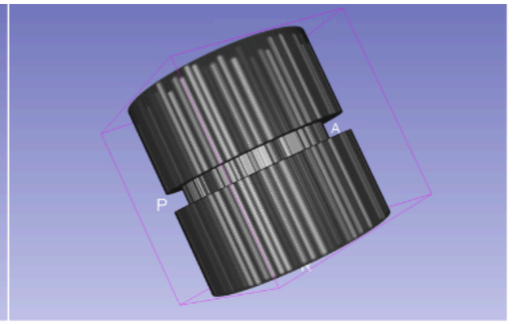

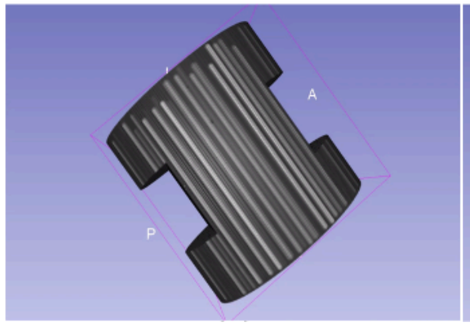

double square-notch

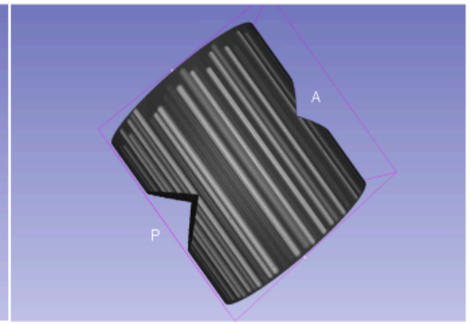

double square-notch

Volume & Scanning Parameters

Detailed description of these parameters can be found on the Github page.

Volume Generation	Tomographic Simulation
# of volumes	# of angles
Volume dimensions	Geometry type
# of fibers	Detector pixel distance
Fiber radius	Detector count
Max. and min. length of fibers	Initial intensity of X-ray beam
Fiber orientation	Reconstruction algorithm
Defects	Distance of source to origin to detector

Tomographic parameters from ASTRA toolbox

Outline

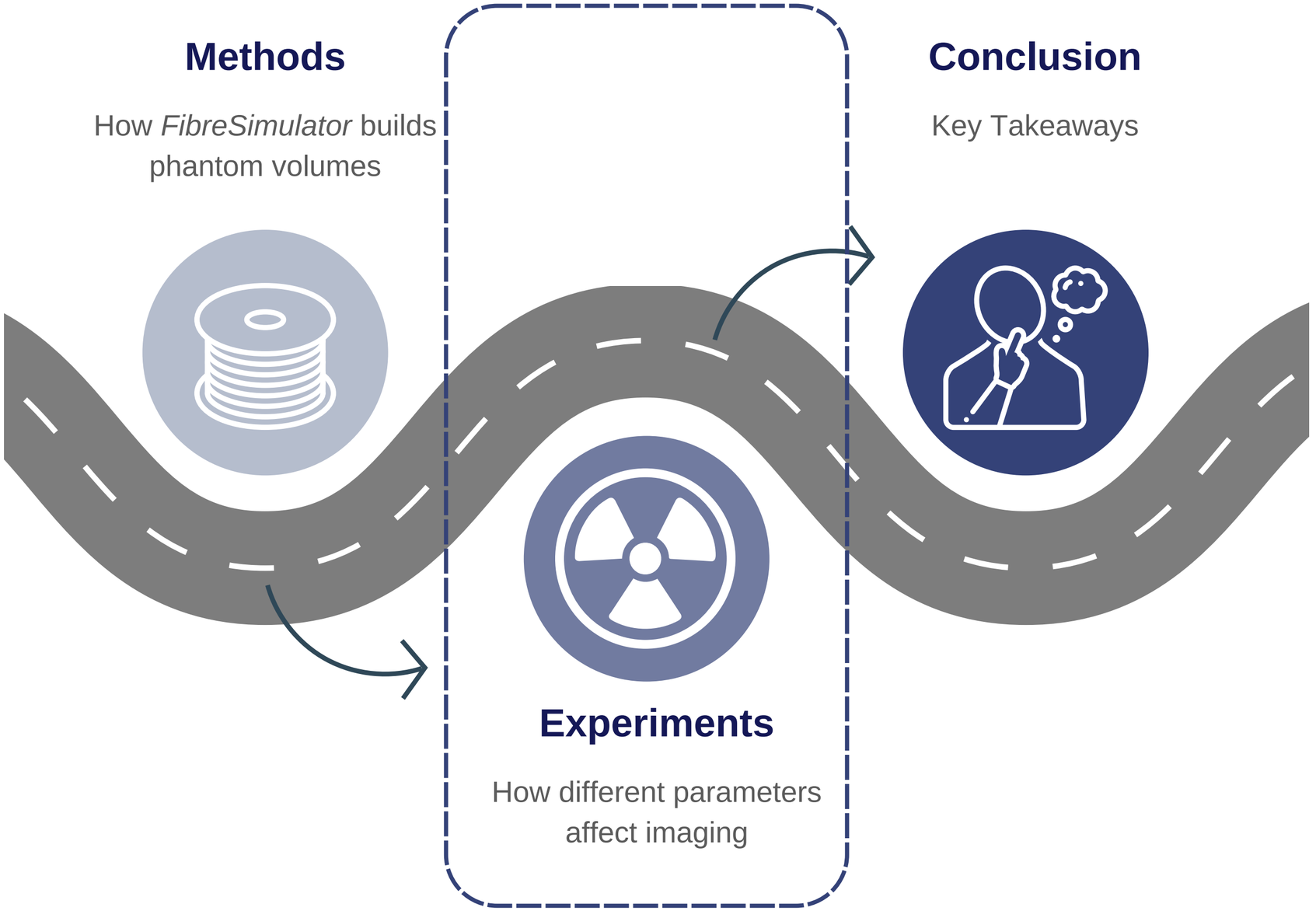
Methods
How *FibreSimulator* builds phantom volumes
Conclusion
Key Takeaways
Experiments
How different parameters affect imaging

Reconstruction Examples

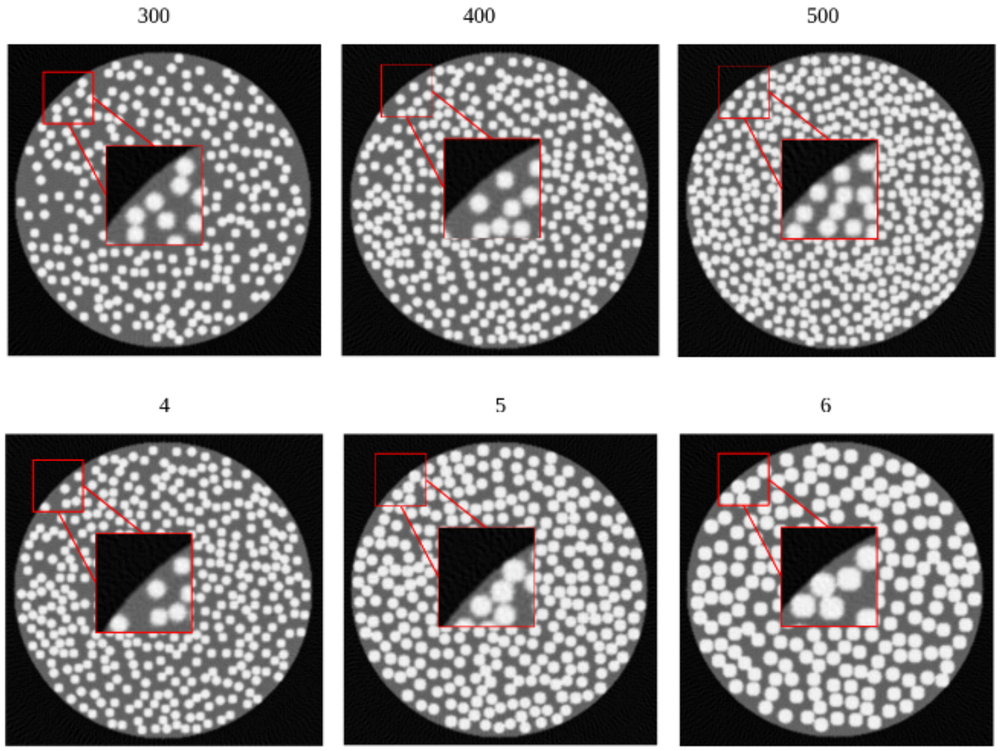

Middle axial slices of increasing # of fibers & increasing voxel radius

These examples demonstrate how the fiber volume fraction (FVF) can be varied in two distinct ways: adjusting # of fibers within a fixed volume (upper row) and altering voxel radius of the fibers (lower row).

Reconstruction Examples

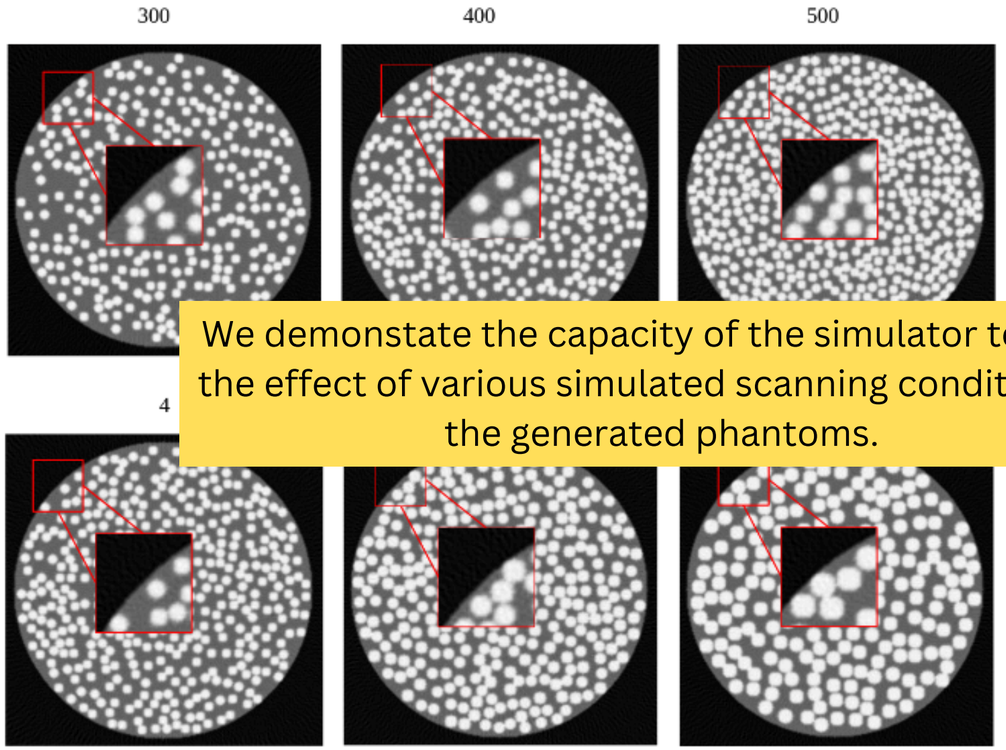

We demonstate the capacity of the simulator to show the effect of various simulated scanning conditions to the generated phantoms.

Middle axial slices of increasing # of fibers & increasing voxel radius

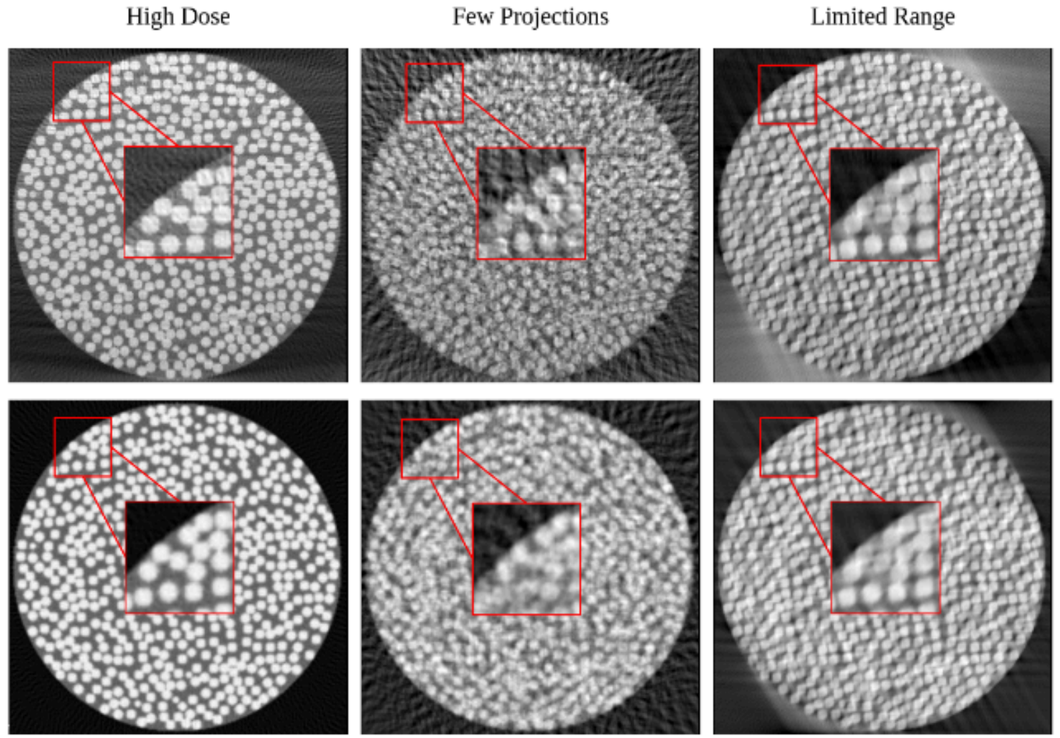

Reconstructed middle axial slices of various experimental conditions: 55e3 dose, 50 projections, & 120° limited angular range.

Reconstruction Examples

Real-world data is taken by Zeiss Xradia Vars 520 scanner, conducted with 4 501 projections using a binning factor of 2.

- a) & b) real-world X-ray CT Scans of a carbon FRP
  - estimate the paramaters through visualization
- c) & d) generated phantom volume without noise
- e) & f) generated phantom volume with Poisson noise

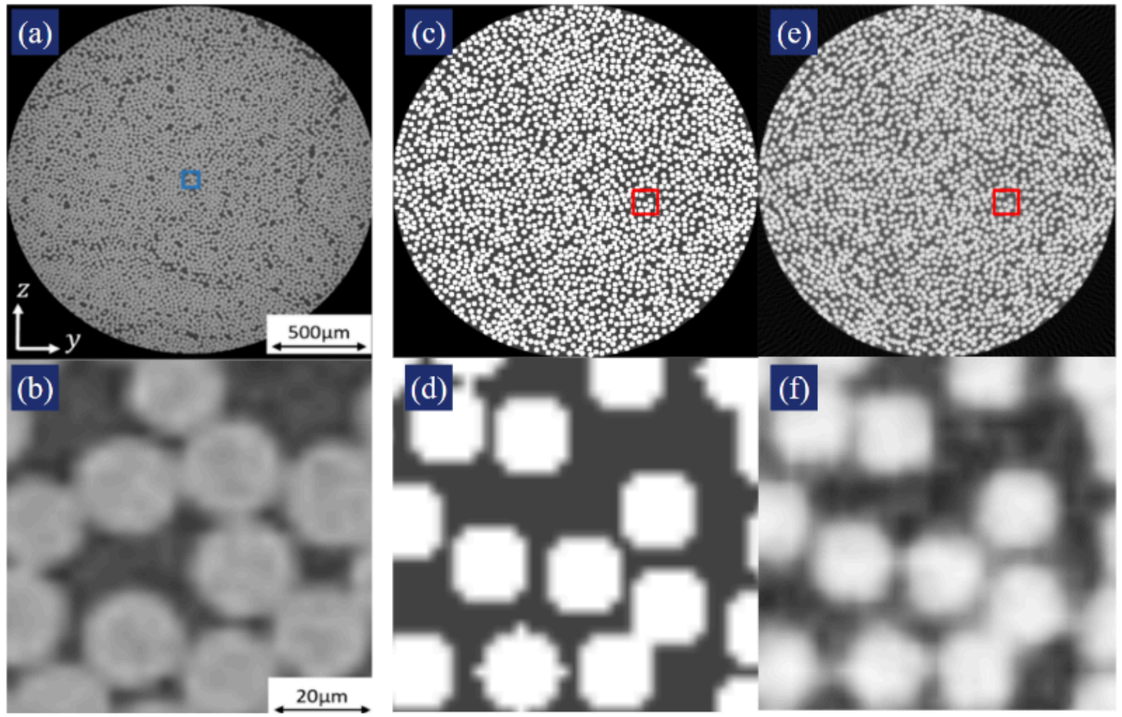

Comparison of real-world data vs FibreSimulator phantom volume *

*F.B. Salling, N. Jeppesen, M.R. Sonne, J.H. Hattel, and L.P. Mikkelsen. Individual fibre inclination segmentation from x-ray computed tomography using principal component analysis. Journal of Composite Materials, 56:83–98, 2022.

Varying tomographic imaging conditions

These are axial reconstruction images of a [256 x 256 x 256] volume acquired using a parallel beam and reconstructed using the SIRT algorithm.

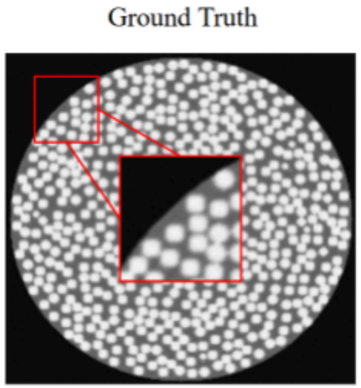

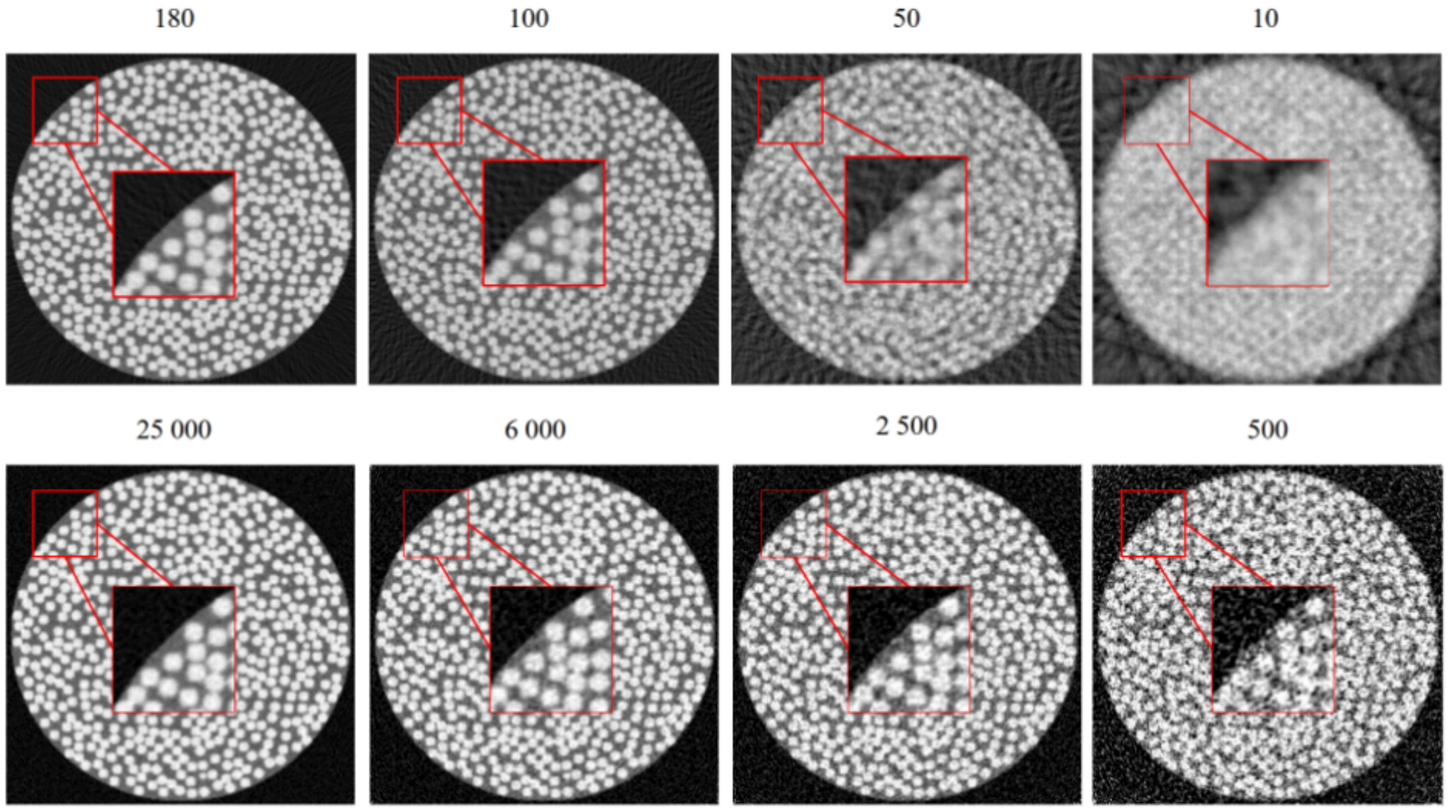

Comparison of reconstructed middle axial slices at varying **number of projections** (top row) and **noise levels** (bottom row)

By fine-tuning the parameters in a simulated environment, users can observe their effects on image quality and make informed adjustments.

With this workflow, it ensures that actual scanning is carried out using an optimized set of conditions.

Varying tomographic imaging conditions

Effect on average diameter & # of fibers detected:

- Decreasing # of projections

As the # of projections decreases, average fiber diameter increases. We can hardly differentiate the boundaries of the fiber, resulting in adjacent fibers appearing fused together.

- Decreasing initial intensity of X-ray beam

A decrease in the initial intensity of the X-ray beam leads to a noisier image. At higher intensities, the average diameter stabilizes close to the ground truth.

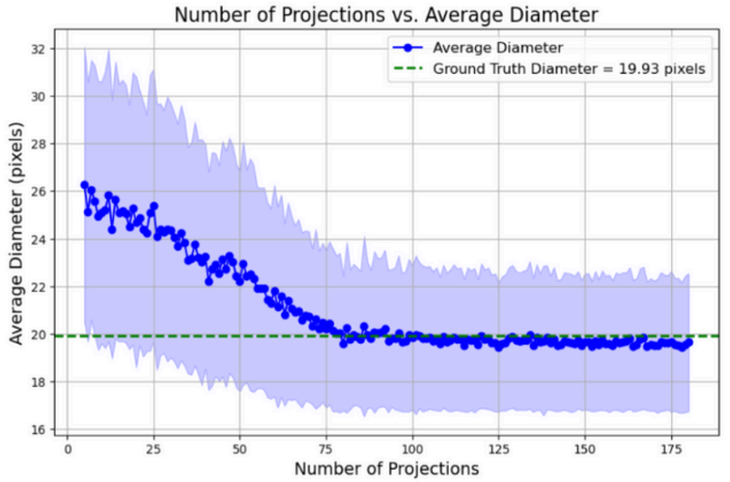

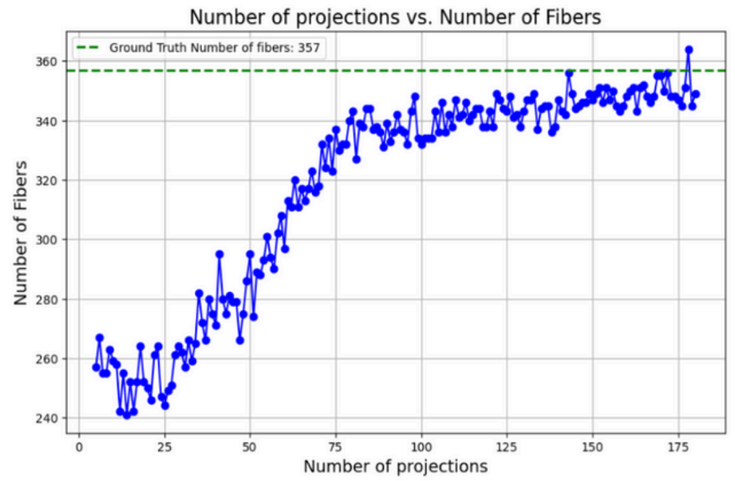

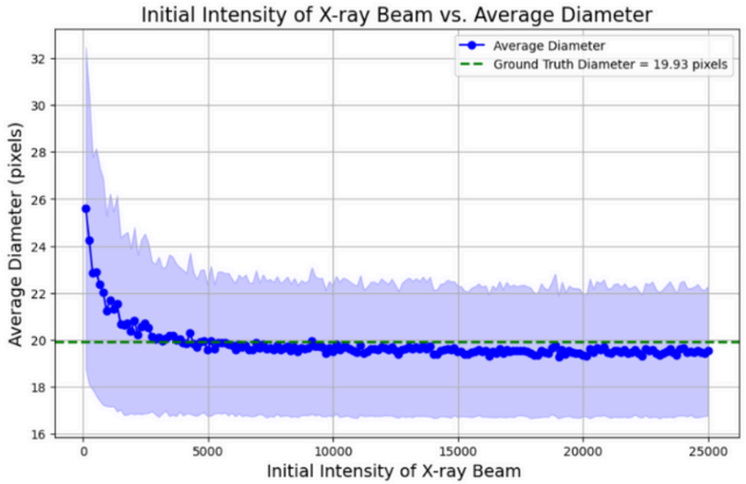

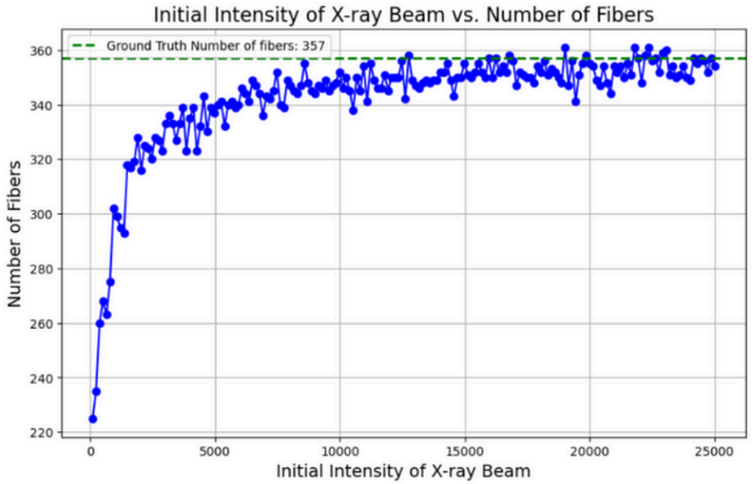

Varying fiber characteristics

The rise in error can be attributed to overlapping streak artifacts, which occur when fibers are densely packed.

- Effect of increasing fiber volume fraction (FVF) to the detected # of fibers in a 120° scan
- Interestingly, the error rate follow a non-linear trend w.r.t. FVF

> Showcases the simulator as **flexible** & **adaptable tool** for studying how sample features affect fiber detectability.

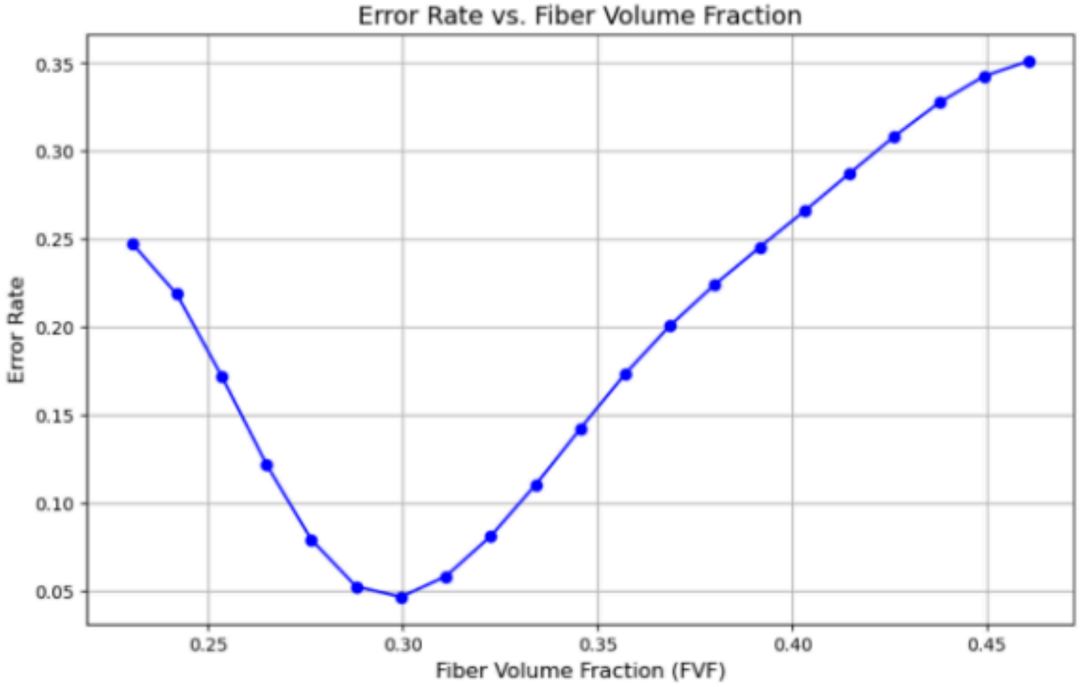

Effect of varying fiber volume fraction on the detected # of fibers

Outline

Methods

How *FibreSimulator* builds phantom volumes



Experiments

How different parameters affect imaging

Conclusion

Key Takeaways

Conclusions

FibreSimulator is a tool that can asses scanning configurations, establishing its potential as a benchmark for data-driven tomographic algorithms

We **introduced** a simulator that:

- Generates **realistic** & **customizable** fiber phantoms
- Integrated with **ASTRA toolbox** for CT simulation
- Written in **Python** for flexibility

We **showed** how it can show:

- **relationships** between noise, number of projections, and reconstruction quality
- **impact of fiber density** on fiber detectability

> Future Work: simulation of additional imaging artifacts (source characteristics, beam hardening effects, and detection defect)

Thank you!

Mary Chris Roperos Go | ICCM
Co-authors: Daniel Pelt, Anirudh Kohli, Philip J Withers, K Joost Batenburg











ICCM24
AUGUST 4-8, 2025
BALTIMORE CONVENTION CENTER
BALTIMORE, MARYLAND, USA

No Technical Paper Submission for:

Ankita Bisht

No Technical Paper Submission for:

Soraia Pimenta

Direct approach for experimental determination of mixed-mode cohesive laws of composites with large-scale fibre bridging



Ruben Erives,
Bent F. Sørensen and
Stergios Goutianos

Overview

- Motivation
- Derivation of cohesive law
- Experimental Characterisation
- Results
- Concluding remarks
- Questions & discussion

Motivation

Why is it important to measure cohesive laws?

1. While the implementation of cohesive zone models is increasing rapidly, research in determining cohesive law of composites has stalled.

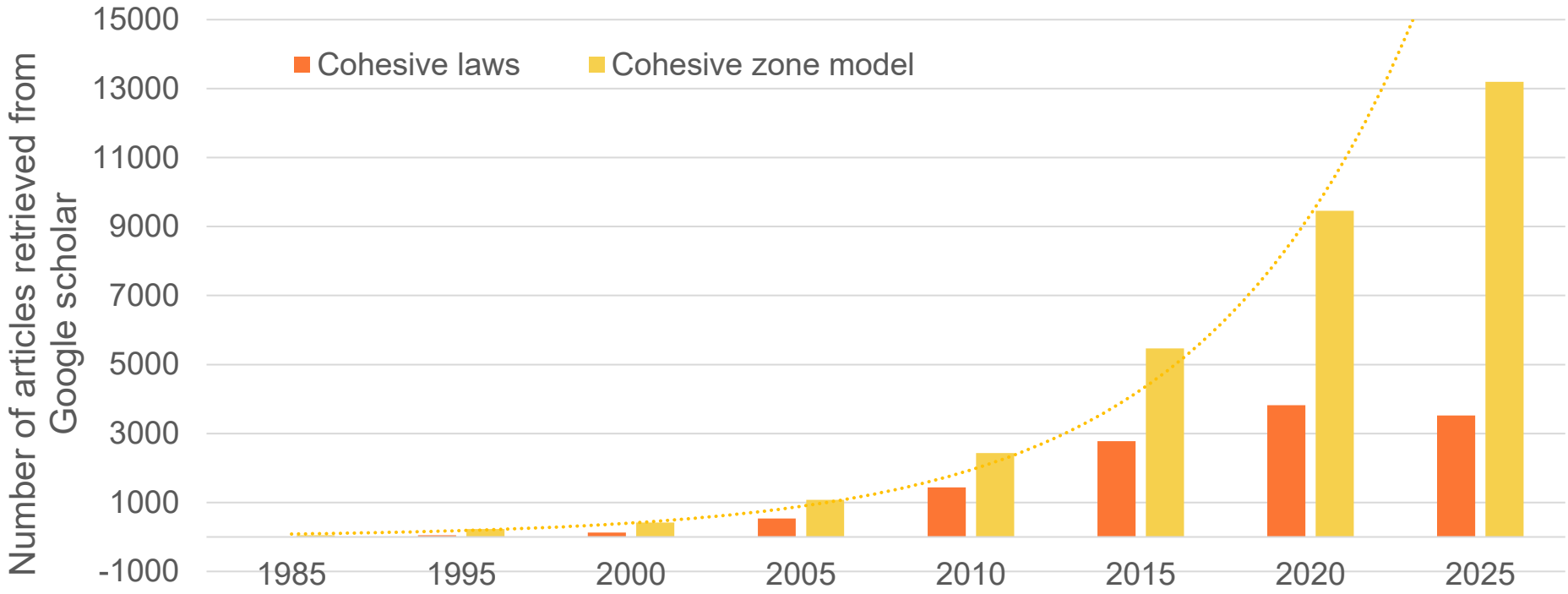

Motivation

Why is it important to measure cohesive laws?

1. *Idealised cohesive* laws have several shortcomings
    1. For bi-linear cohesive laws, the traction separation law is fully determined by the combined work of the peak traction and a critical opening. Then the shape (and peak traction) are predefined
    2. Difficult or not possible to recover R-curves from pre-defined/idealised cohesive laws
2. The *shape of the cohesive traction* conveys important information of the *fracture behaviour* of a material such as failure mechanisms, the coupling between tractions, and crack growth stability among other

Derivation of cohesive law

Definition of end-openings and phase angle

End-opening

$$\delta^* = \sqrt{\delta_n^* + \delta_n^*}$$

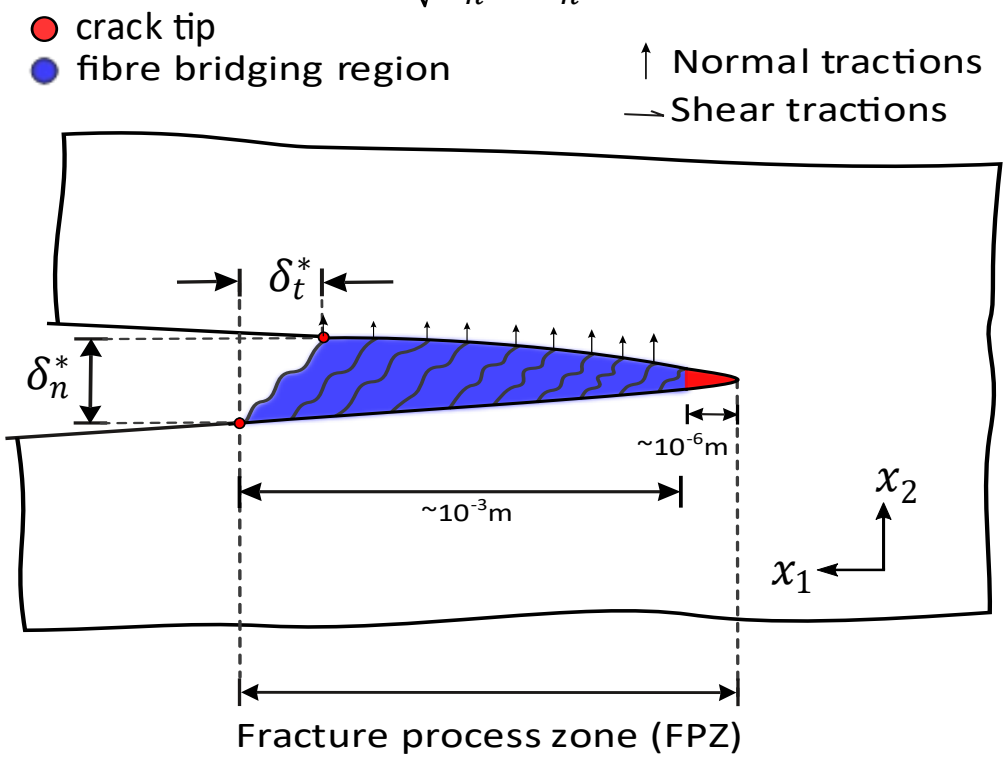

Phase angle of end-openings

$$\varphi^* = tan^{-1}\left(\frac{\delta_t^*}{\delta_n^*}\right)$$

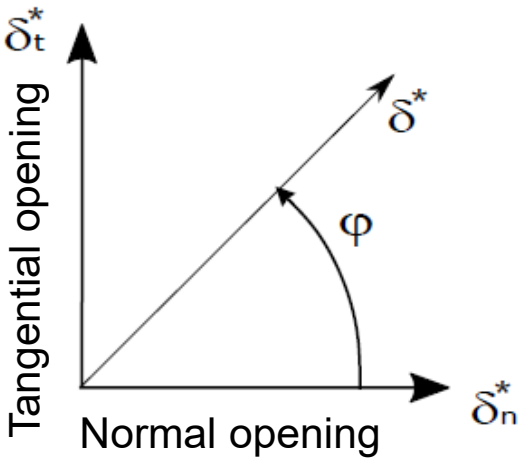

Phase angle of stress intensity factors

$$\Psi = tan^{-1}\left(\frac{K_{II}}{K_I}\right)$$

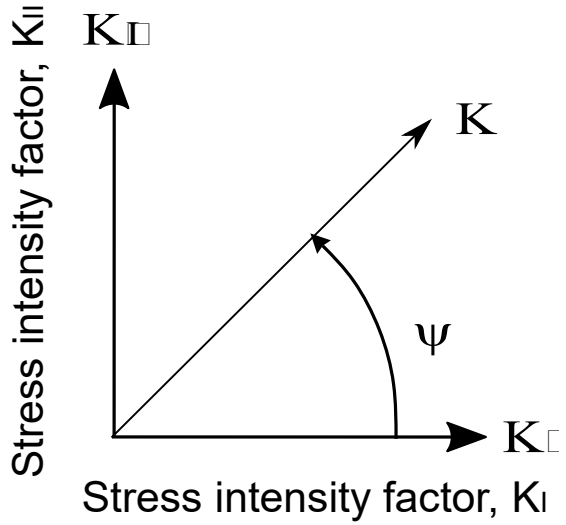

Derivation of a fully coupled potential based cohesive law

J-integral approach

Evaluate the J-integral around the path Γ_{loc} then:

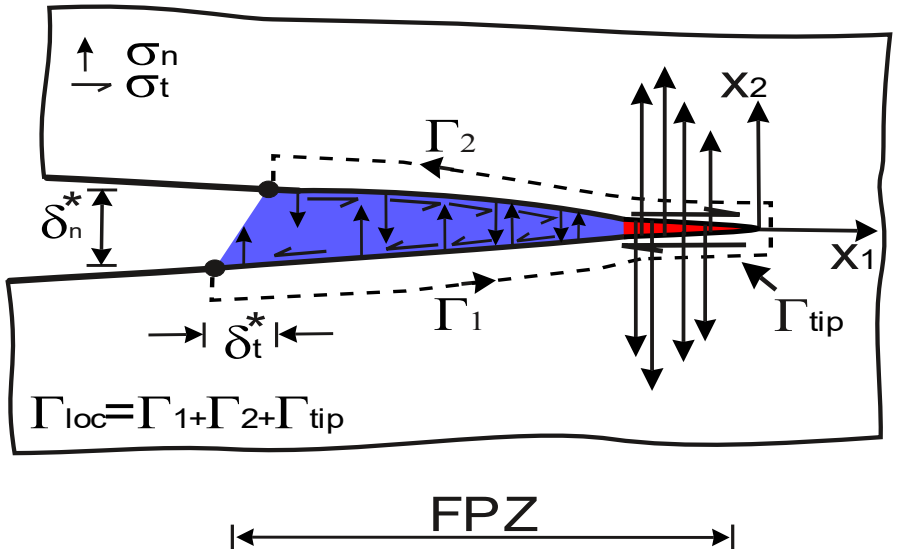

$$J_{loc} = \int_0^{\delta_n^*} \sigma_n(\delta_n, \delta_t) d\,\delta_n + \int_0^{\delta_t^*} \sigma_t(\delta_n, \delta_t) d\,\delta_t$$

[Sørensen and Kirkegaard, 2006]

Relates Φ to R-curves → $J_R = J_{loc} = \Phi(\delta_n^*, \delta_t^*)$

Assuming that the cohesive tractions can be derived from a potential function, Φ, then

Path-independent → $\Phi = \Phi(\delta_n, \delta_t)$

$$\Phi(0,0) = 0$$

So that,

Mixed mode coupled cohesive tractions

Cartesian	Cylindrical
$\sigma_n(\delta_n, \delta_t) = \frac{\partial \Phi(\delta_n, \delta_t)}{\partial \delta_n}$	$\sigma_n(\delta, \varphi) = \cos(\varphi)\frac{\partial \Phi}{\partial \delta} - \frac{\sin(\varphi)}{\delta}\frac{\partial \Phi}{\partial \varphi}$
$\sigma_t(\delta_n, \delta_t) = \frac{\partial \Phi(\delta_n, \delta_t)}{\partial \delta_t}$	$\sigma_t(\delta, \varphi) = \sin(\varphi)\frac{\partial \Phi}{\partial \delta} + \frac{\cos(\varphi)}{\delta}\frac{\partial \Phi}{\partial \varphi}$

Derivation of cohesive law

Piece-wise, cylindrical potential function

- The potential function is defined in a piece-wise function:

$$\Phi(\delta,\varphi)=\begin{cases}\Phi_{CT}(\delta,\varphi), & 0<\delta^*\leq\delta_0\\ \Phi_B(\delta,\varphi), & \delta_0<\delta^*\leq\delta_{ss}\end{cases}$$

$$\Phi_{CT}(\delta^*,\varphi^*)=C_4\delta^{*4}+C_3\delta^{*3}+C_2\delta^{*2}+C_1\delta^*+C_0$$

$$\Phi_B(\delta^*,\varphi^*)=\Phi_0+(\Phi_{ss}-\Phi_0)\left(\frac{\delta^*-\delta_0}{\delta_{ss}}\right)^{\zeta}$$

- Parameters:

$$\Phi_0(\varphi),\Phi_{ss}(\varphi),\delta_0(\varphi),\delta_{ss}(\varphi),\zeta(\varphi)$$

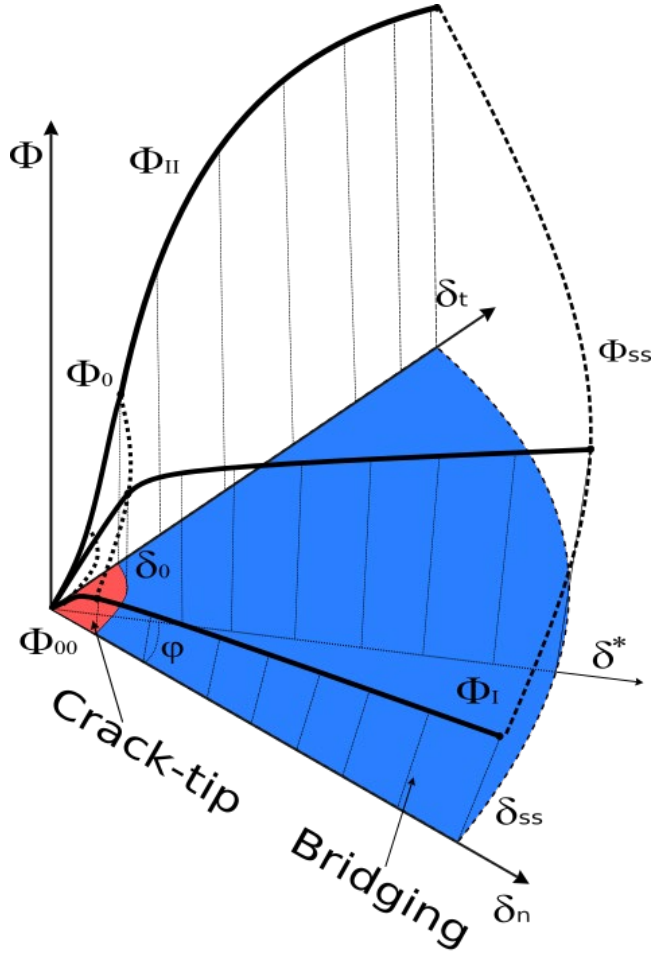

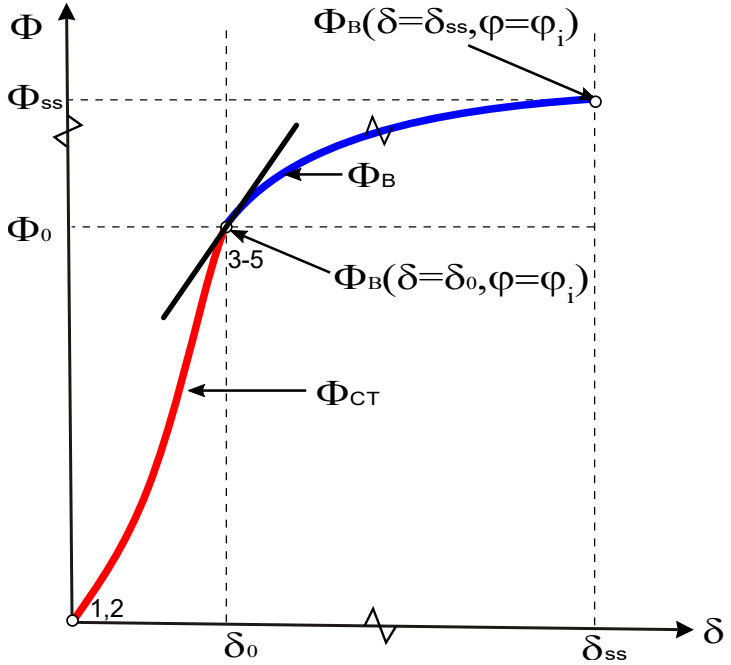

Experimental characterisation

Specimens and test groups

- Lay-up: 20 UD-layers (backing facing downwards on all layers – Not symmetrical)
- Fabric type: UD= E-E-1182 Saertex
- Matrix: Epoxy Hexion RIMR 035c / RIMH 037 100/28
- Curing procedure: 12h@40C+10h@80C
- VF of 55%

DCB specimen geometry

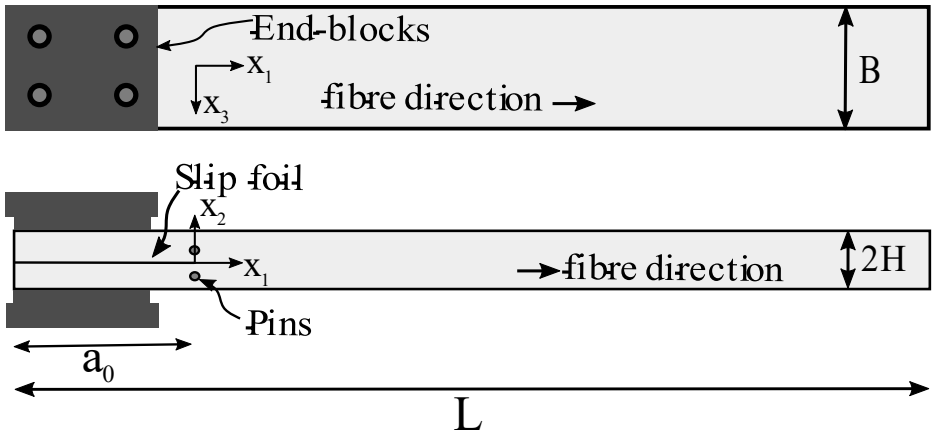

Table 2: Elastic properties of UD glass/epoxy laminate

Prop.	value	Unit
E_1	46.3	GPa
ν_{12}	0.26	-
E_2	12.92	GPa
G_{12}	4.3	GPa

Table 3: Geometric properties of standard DCB specimen

Prop.	value	Unit
a_0	70	mm
L	500	mm
B	30	mm
$2H$	20	layers
	~17	mm

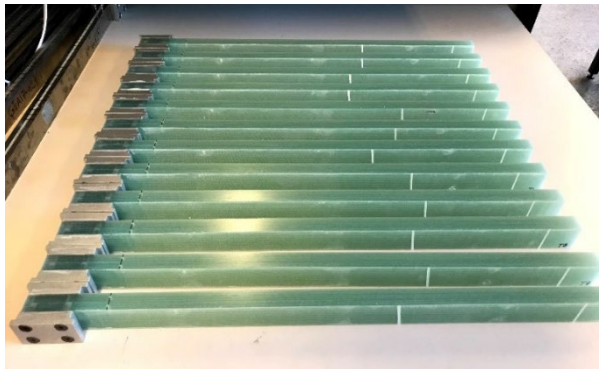

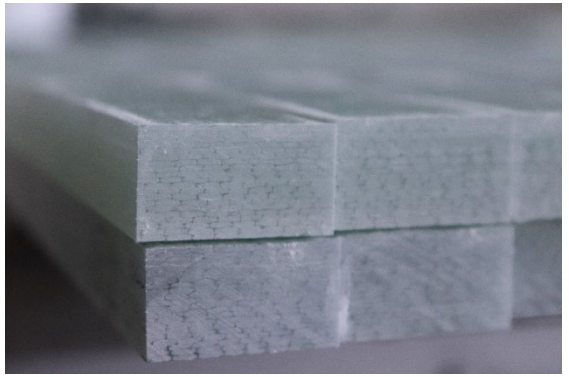

Experimental setup

Double cantilever beam under uneven bending moments DCB-UBM

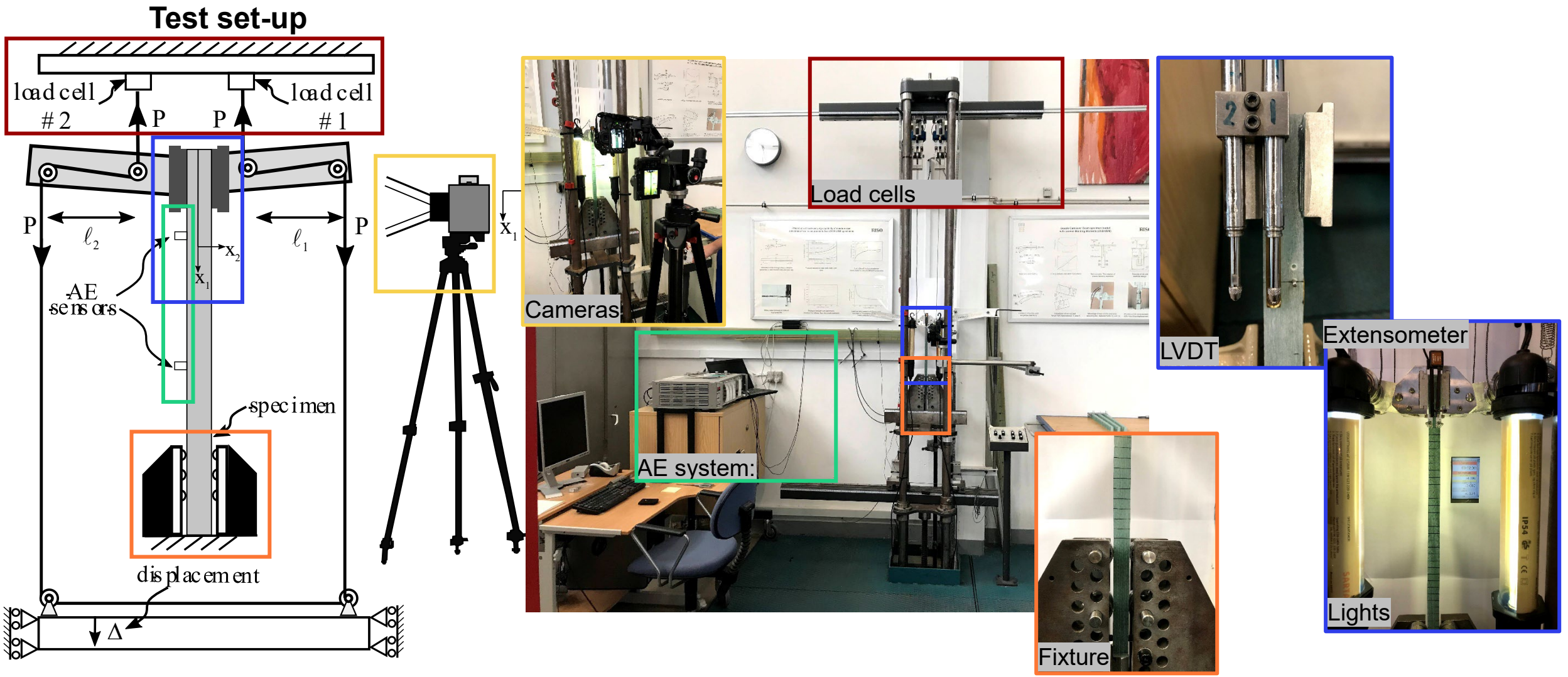

Experimental characterisation

Specimens and test groups

Table 1: List of different mixed-mode tests

M_1/M_2 [-]	φ^* [Deg.]	Ψ [Deg.]
-1.00	0.0 +/- 0.0	0
-0.66	2.7 +/- 1.1	13.6
-0.41	4.9 +/- 0.7	26.8
0.00	8.8 +/- 3.0	50
0.12	9.9 +/- 0.1	56.6
0.50	23.5 +/- 2.8	74.4
0.805	43.5 +/- 13.1	86.7
0.87	50.6 +/- 5.2	89.3
0.96	64.9 +/- 2.8	89.7

Nominal mode I ($M_1 = -M_2$)

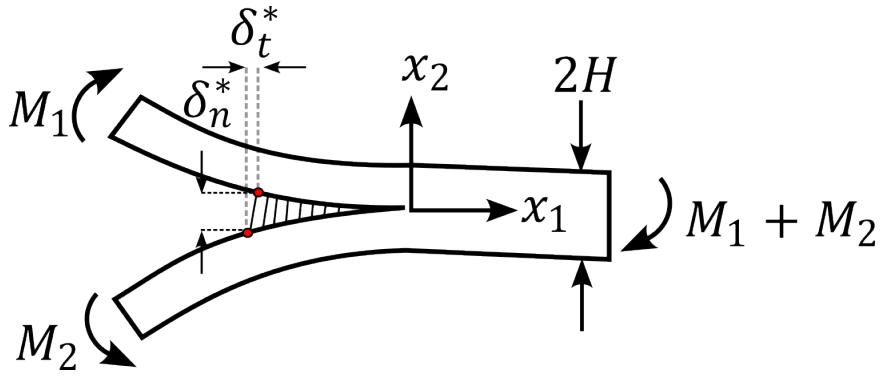

Nominal mode II ($M_1 = M_2$)

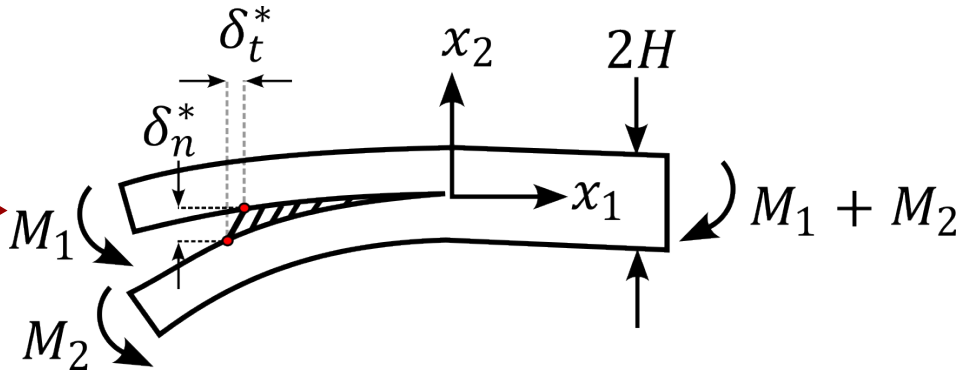

Experimental characterisation

Data processing

Fracture resistance using J-integral:

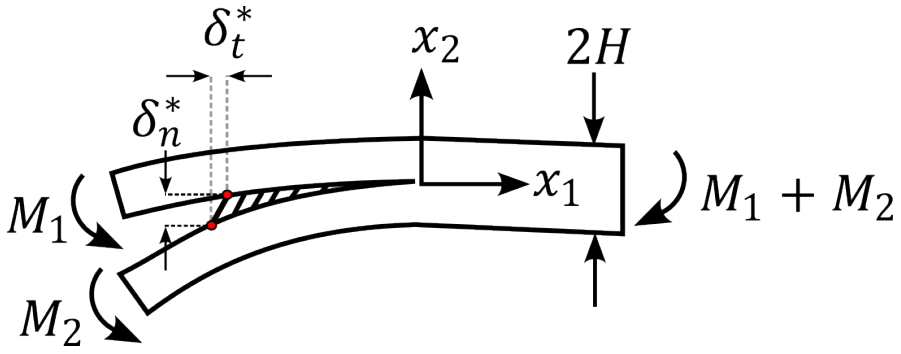

$$J_R = \frac{21(M_1^2 + M_2^2) - 6M_1M_2}{4B^2H^3E^*}$$

Normal and tangential end-openings

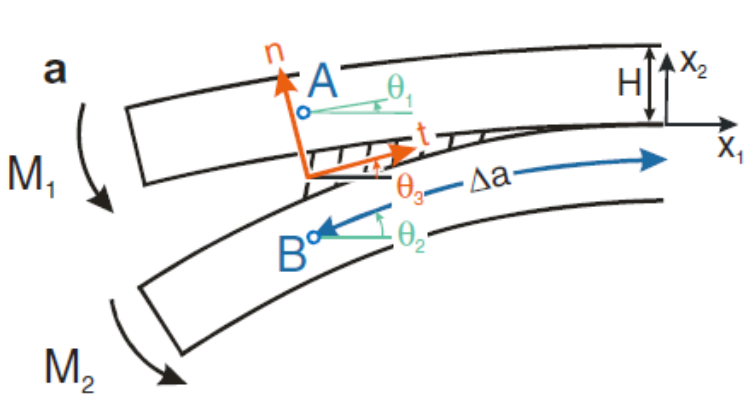

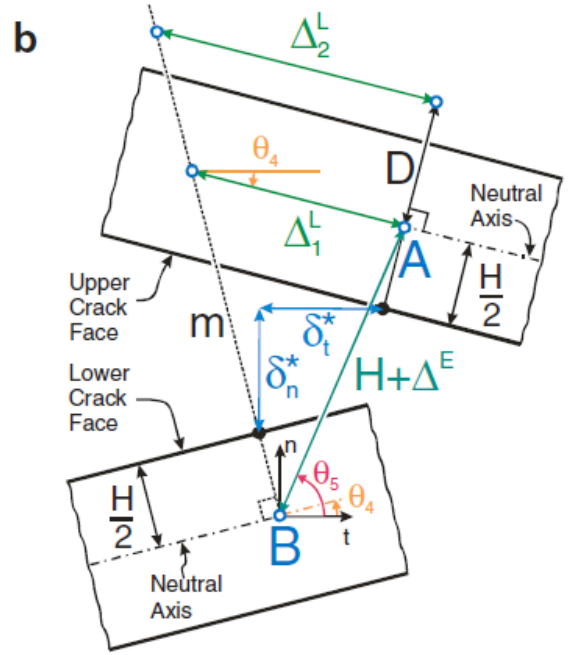

Figures from Sørensen and Jacobsen 2009

$$\delta_n^* = (H + \Delta_E)sin\theta_5 - H \cdot cos\theta_4$$

$$\delta_t^* = (H + \Delta_E)cos\theta_5$$

Experimental characterisation

Extraction of parameters: Phase angle of openings

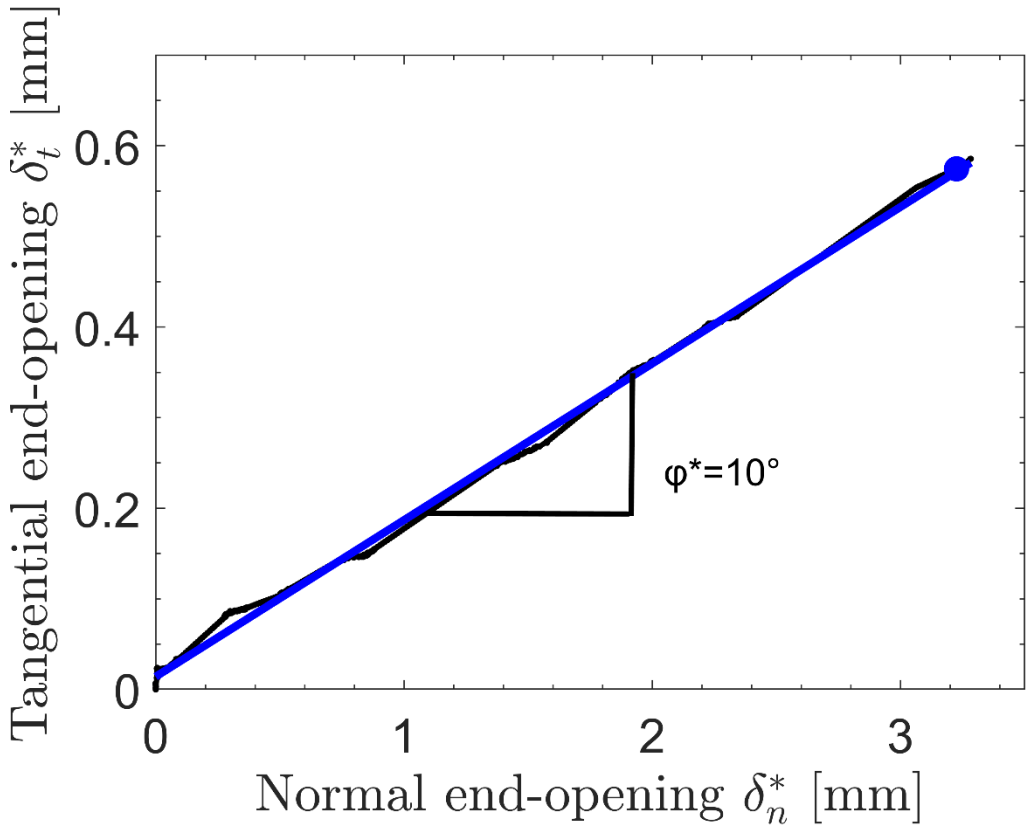

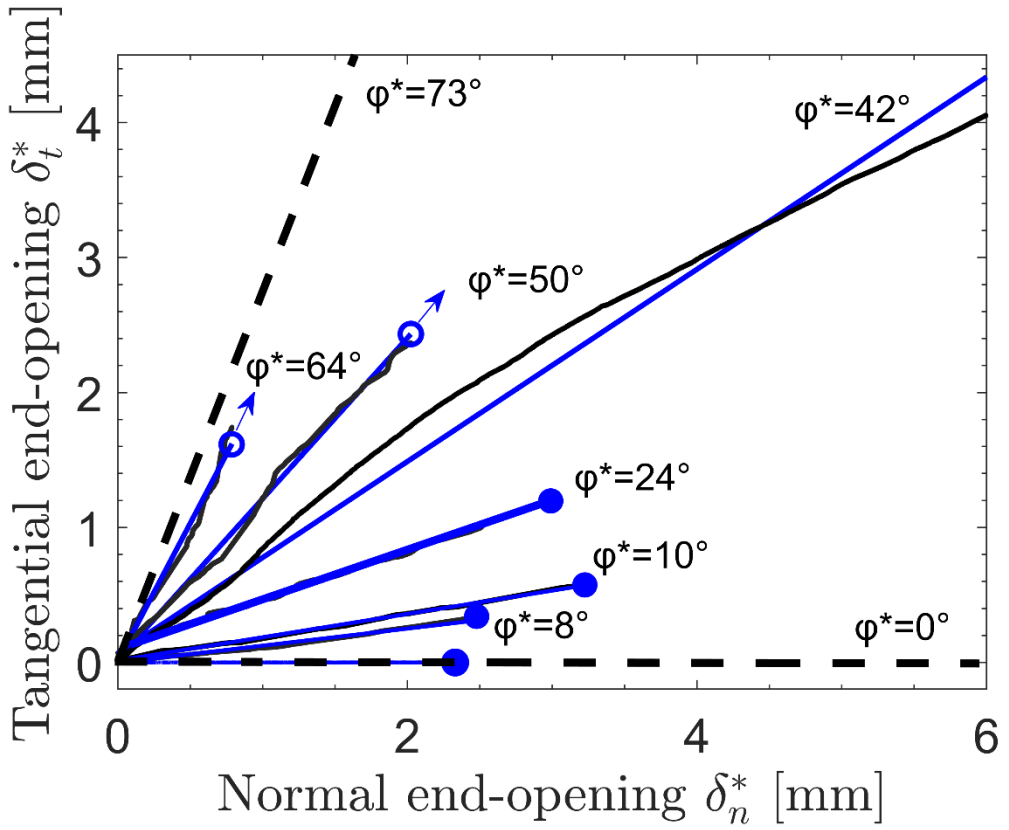

Figures adapted from Erives R. 2023

Experimental characterisation

Extraction of parameters

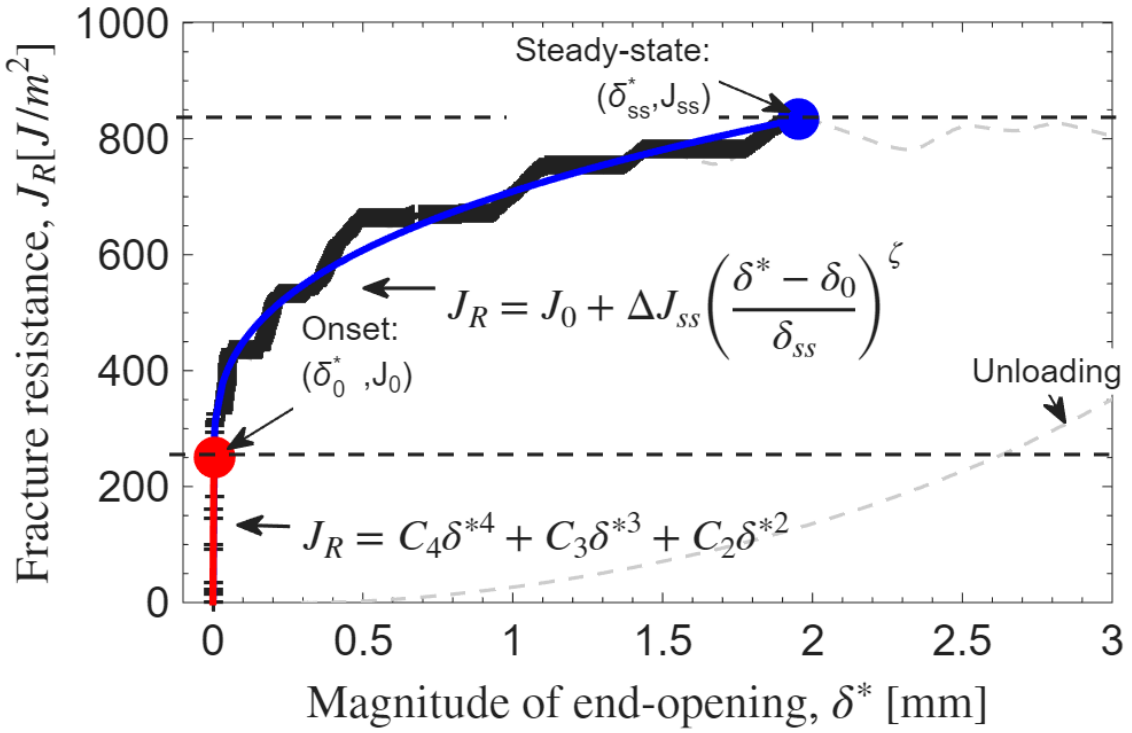

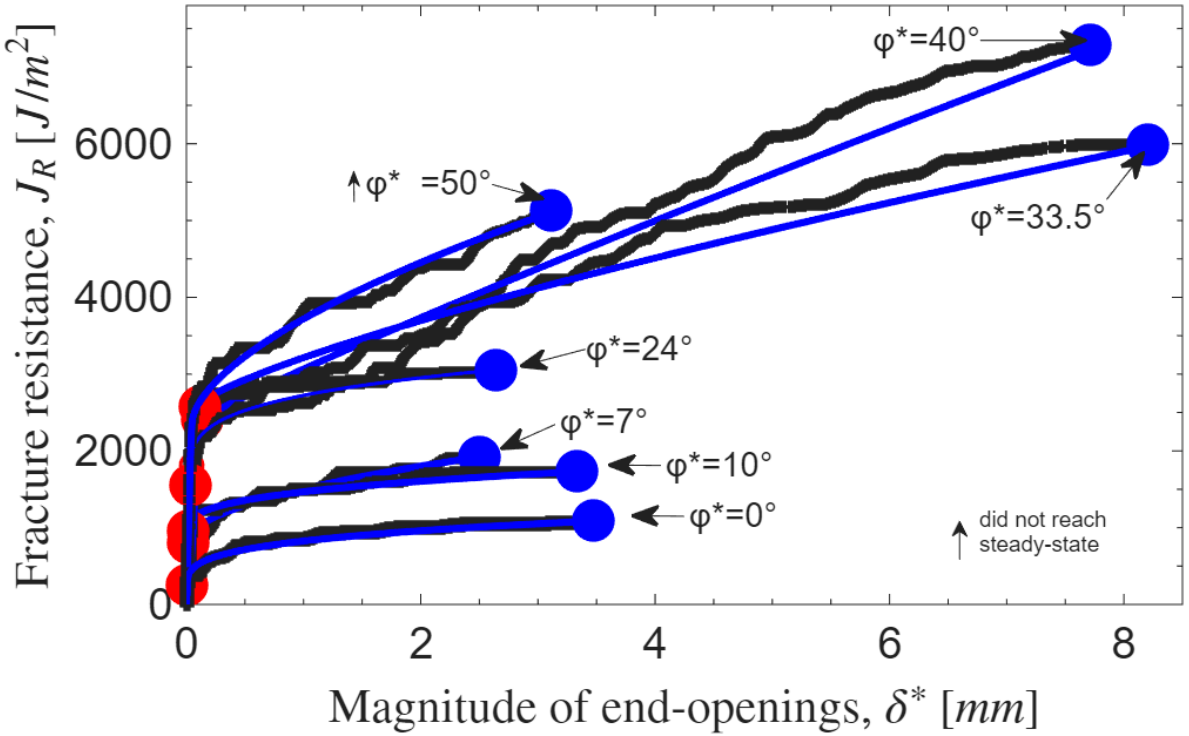

Figures adapted from Erives R., et al 2023

Experimental characterisation

Interpolation of onset parameters: J_0 and δ_0

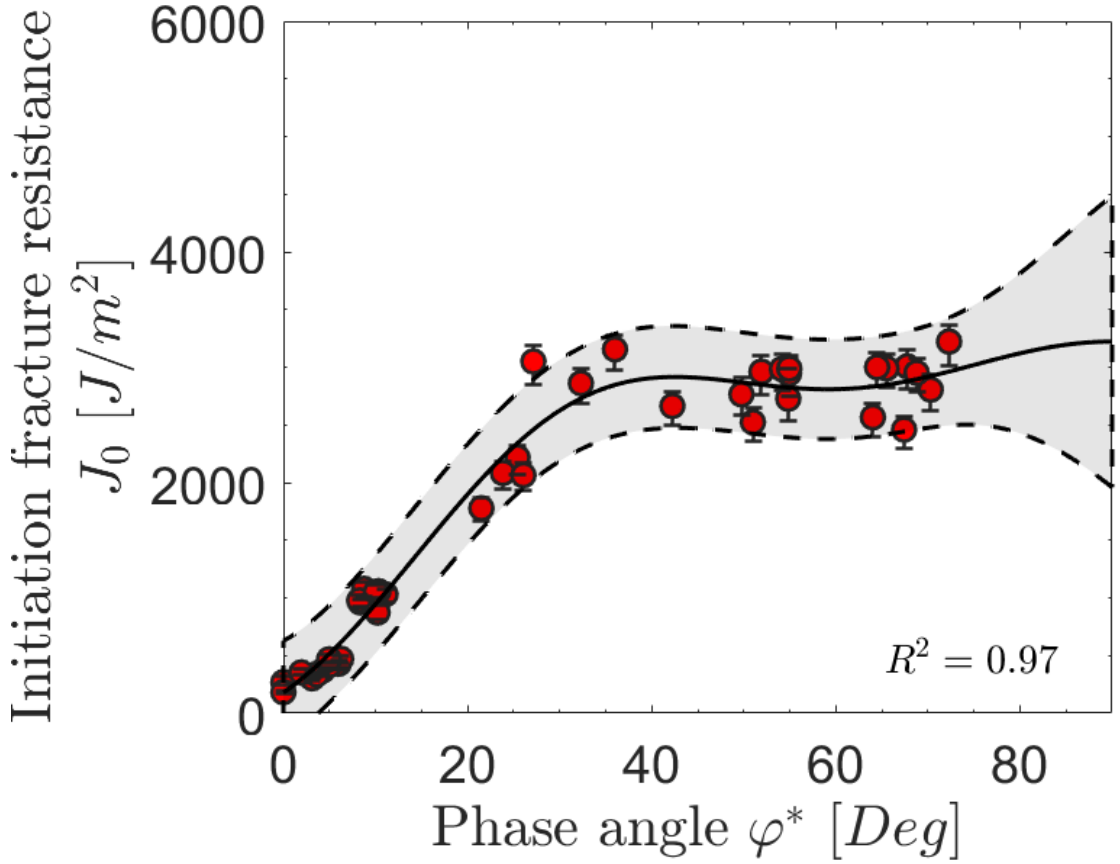

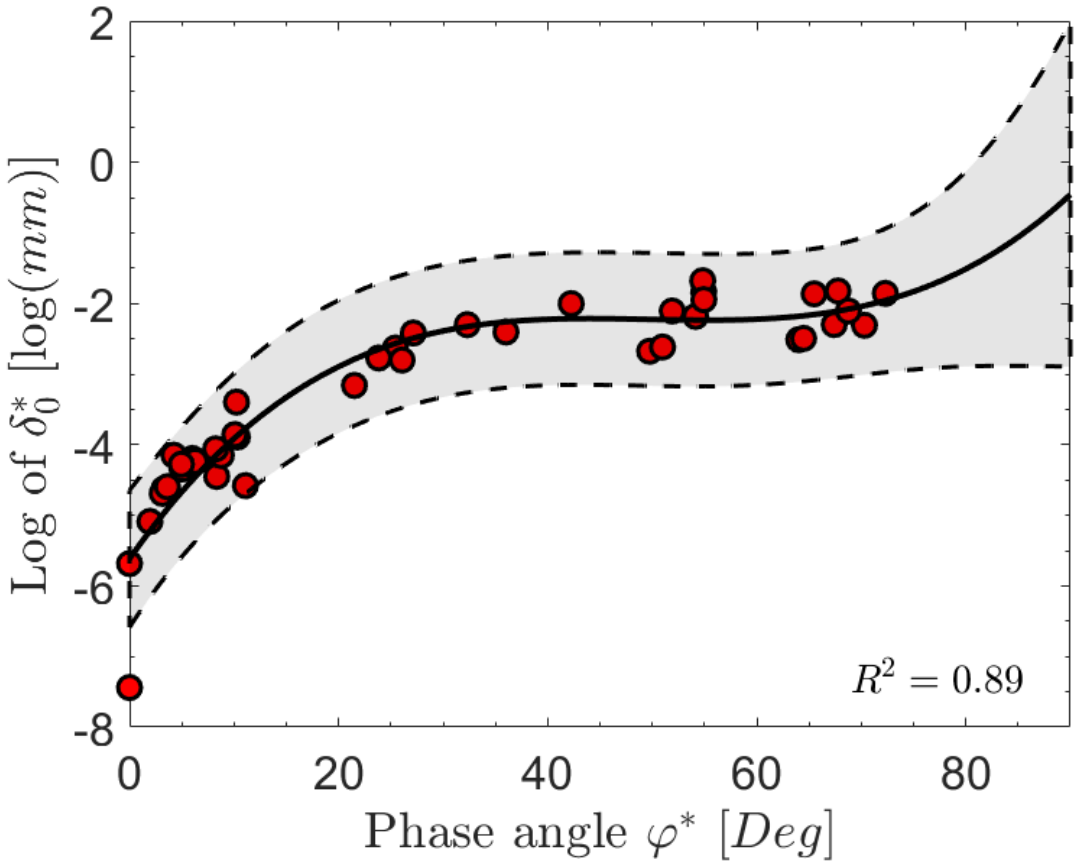

Figures adapted from Erives R. et al 2023

Experimental characterisation

Interpolation of parameters at steady-state: J_{ss} and δ_{ss}

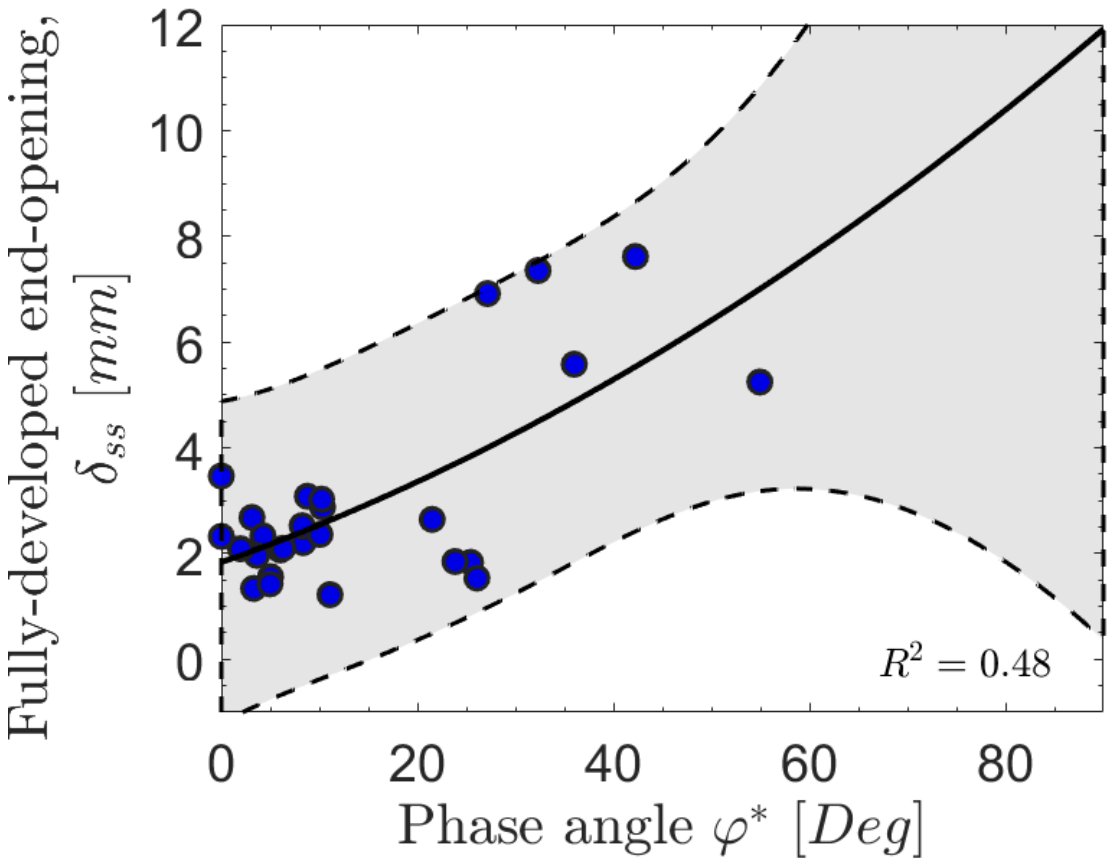

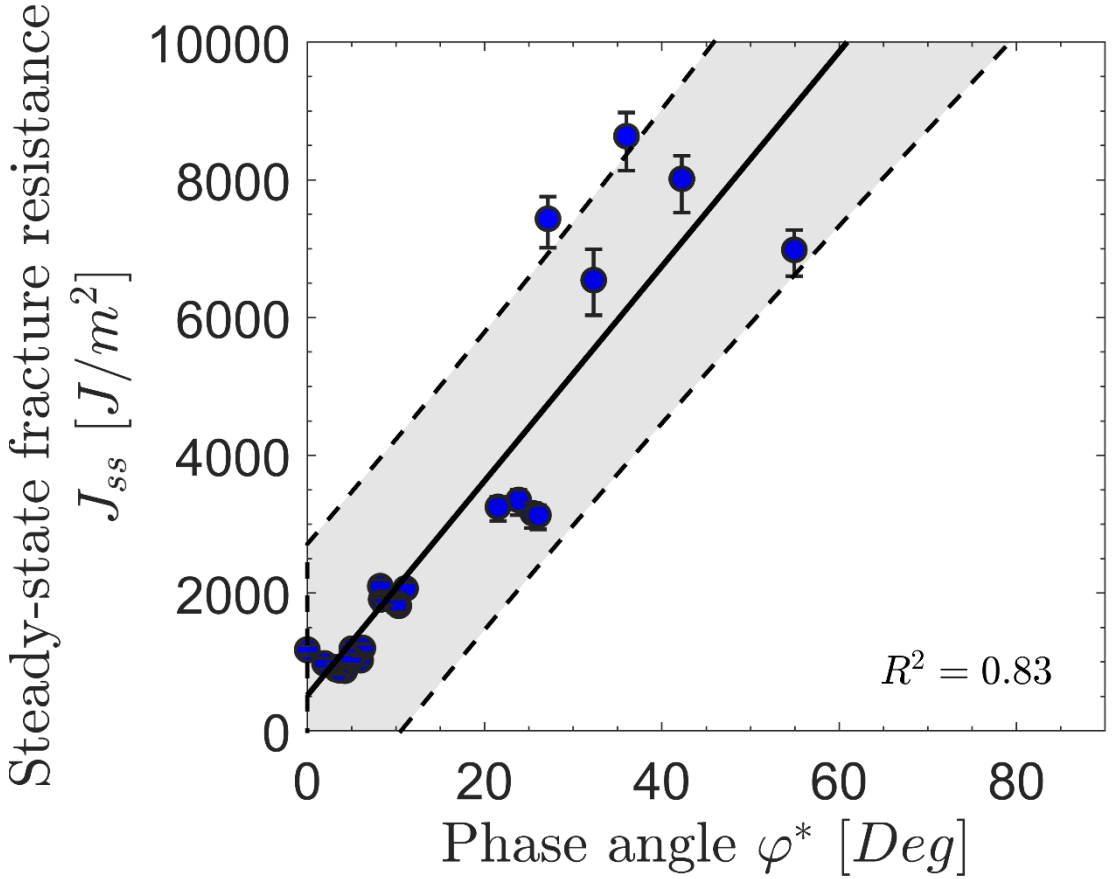

Figures adapted from Erives R. et al 2023

Experimental characterisation

Interpolation of shape parameter: ζ

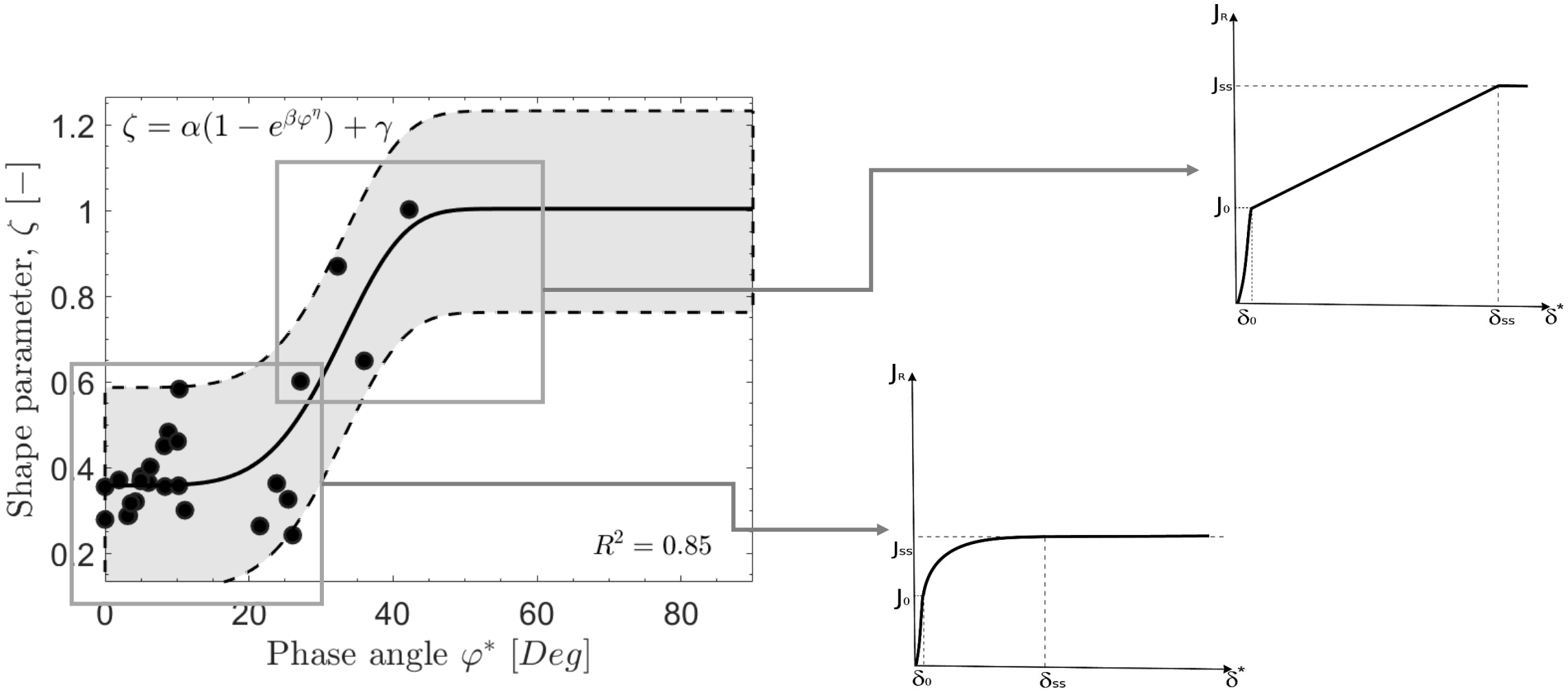

Figures adapted from Erives R. et al 2023

Experimental characterisation

Fitting of fracture resistance

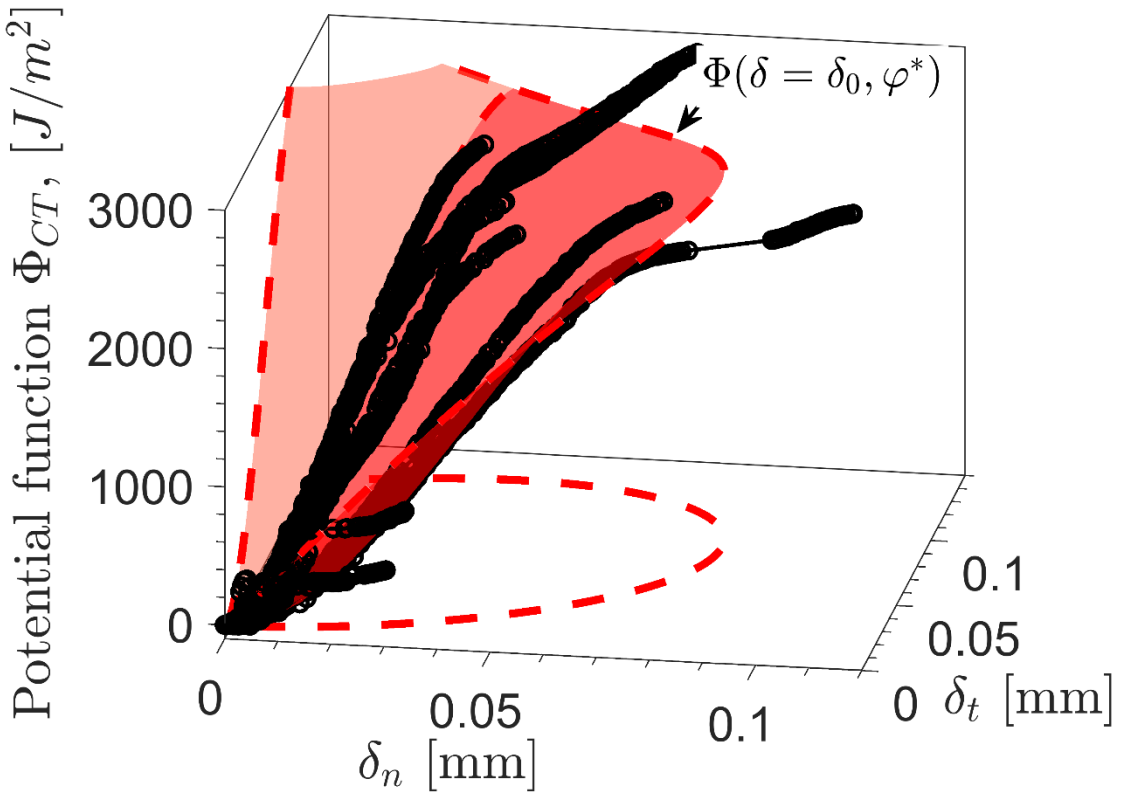

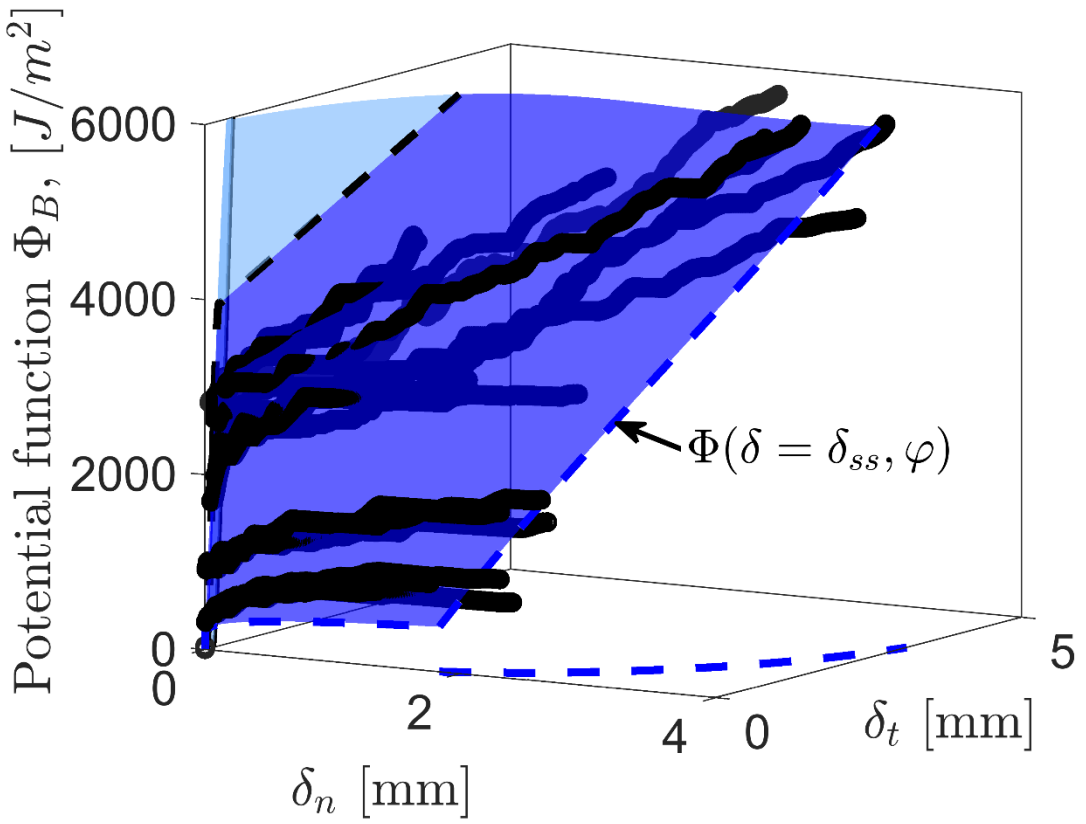

Figures adapted from Erives R. et al 2023

Results

Cohesive tractions – Normal traction

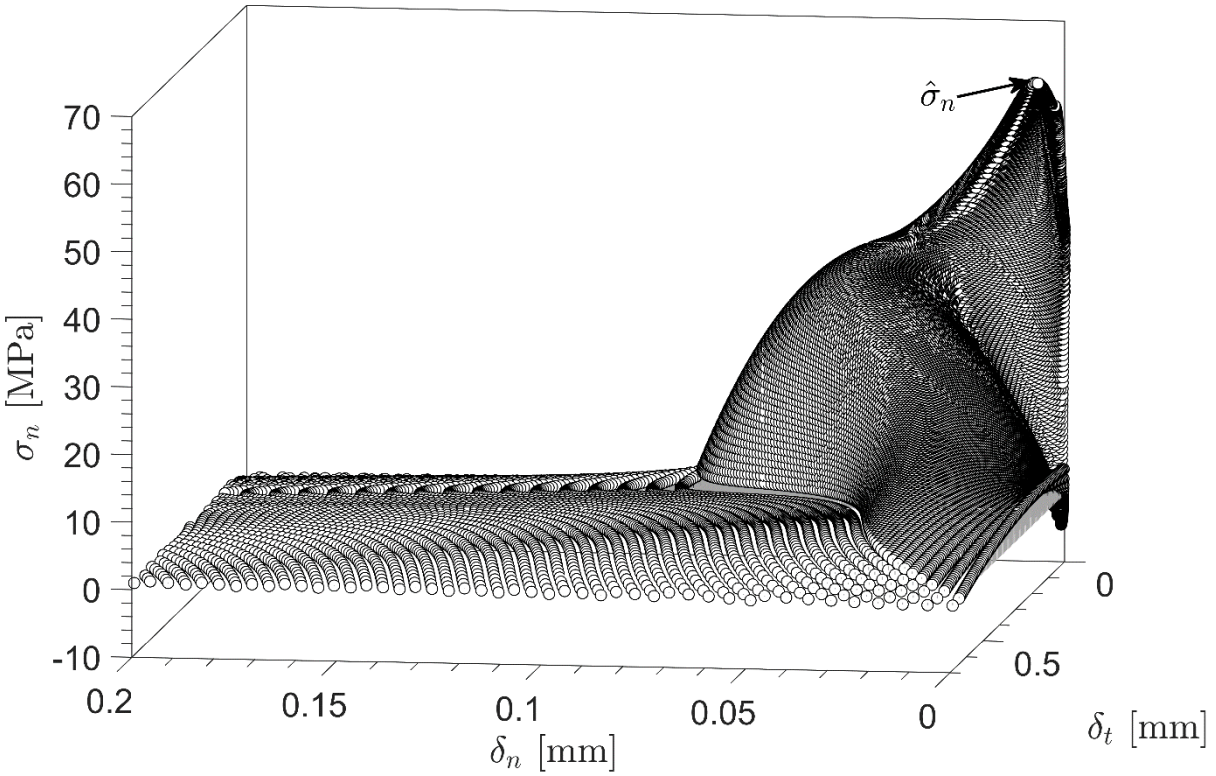

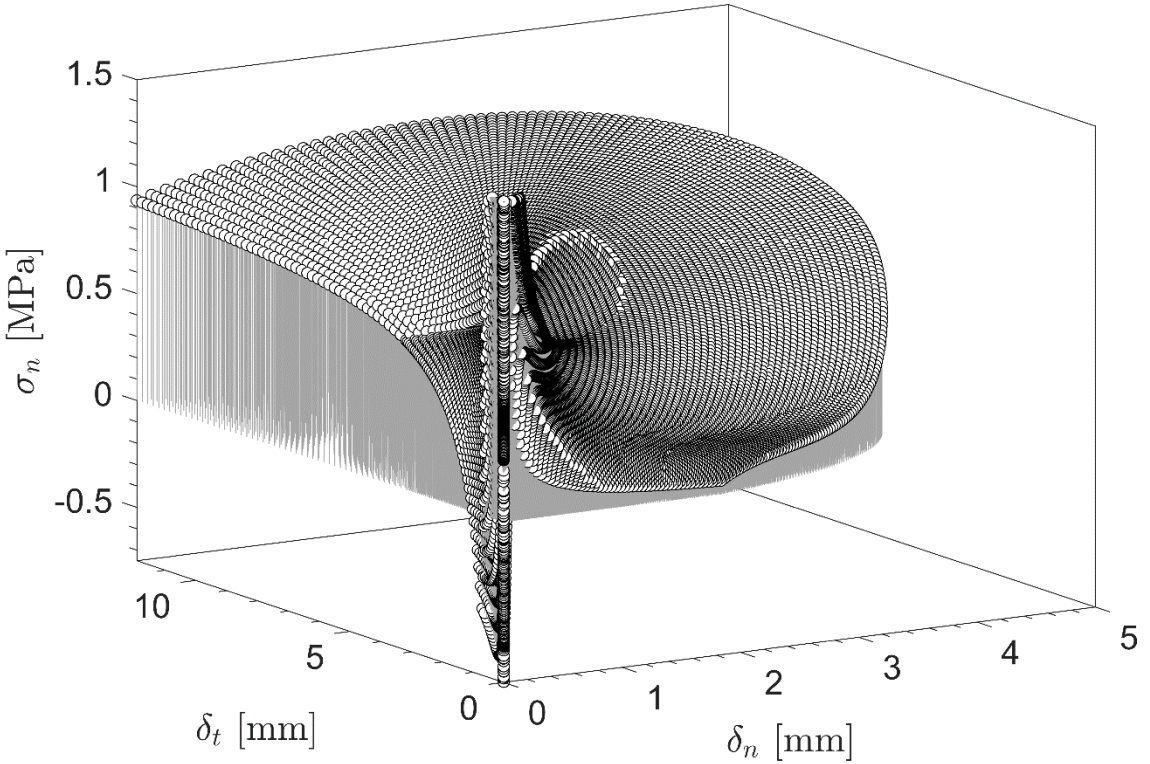

Non-zero normal traction for $\delta_n = 0$
Negative normal traction for large φ

Figures adapted from Erives R. et al 2023

Results

Cohesive tractions – Shear traction

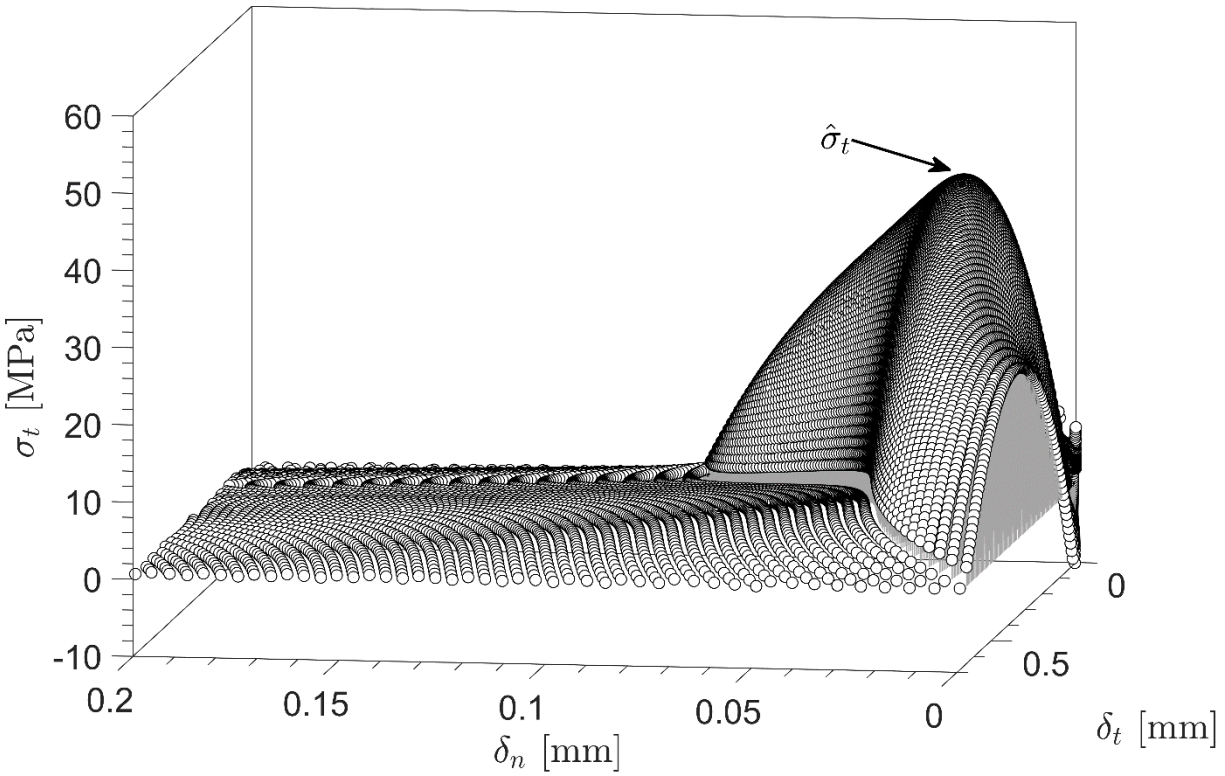

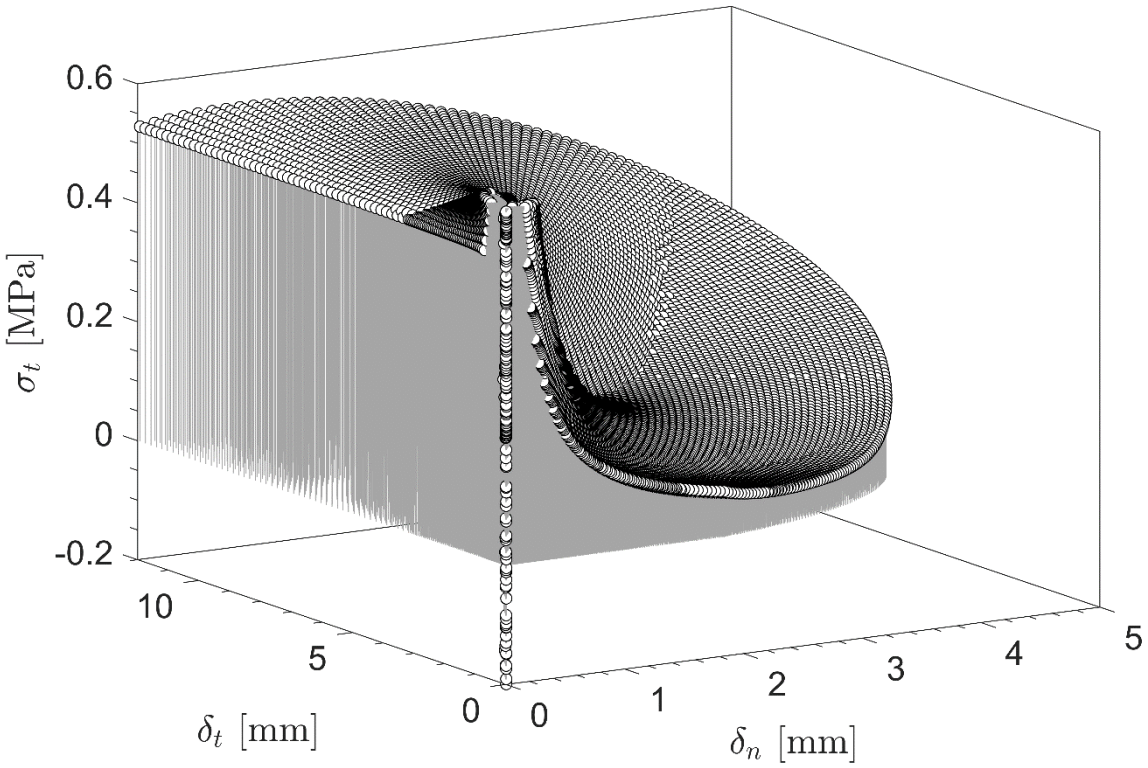

Figures adapted from Erives R. et al 2023

Results

Mixed-mode cohesive tractions

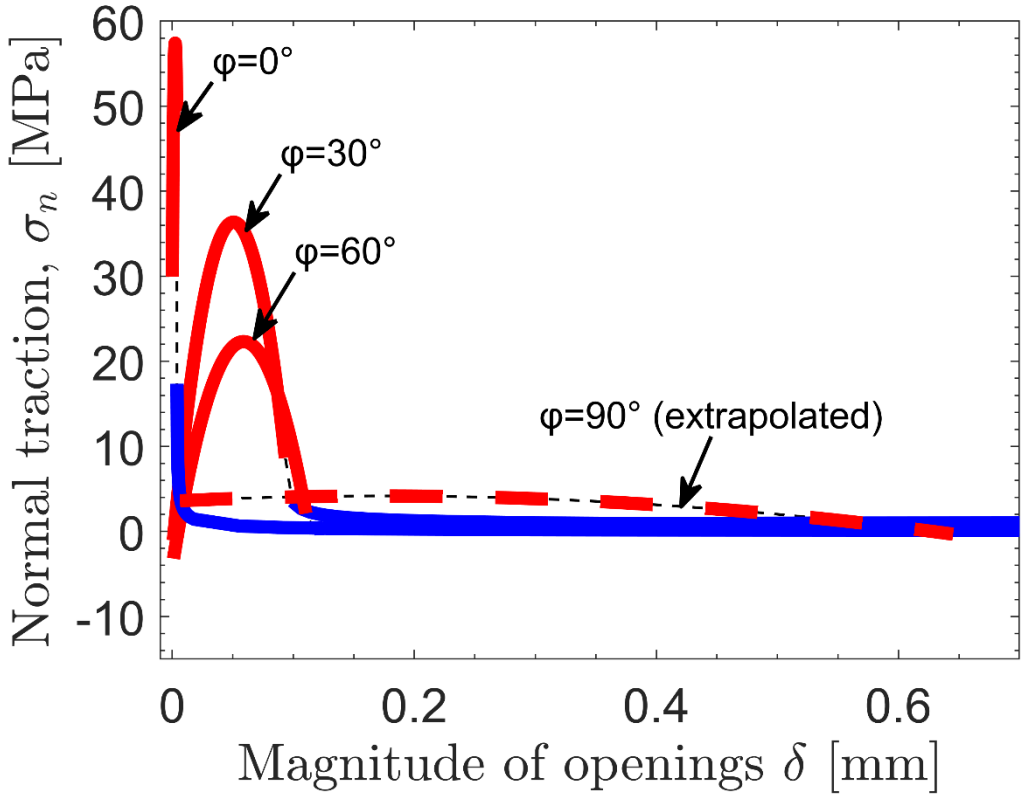

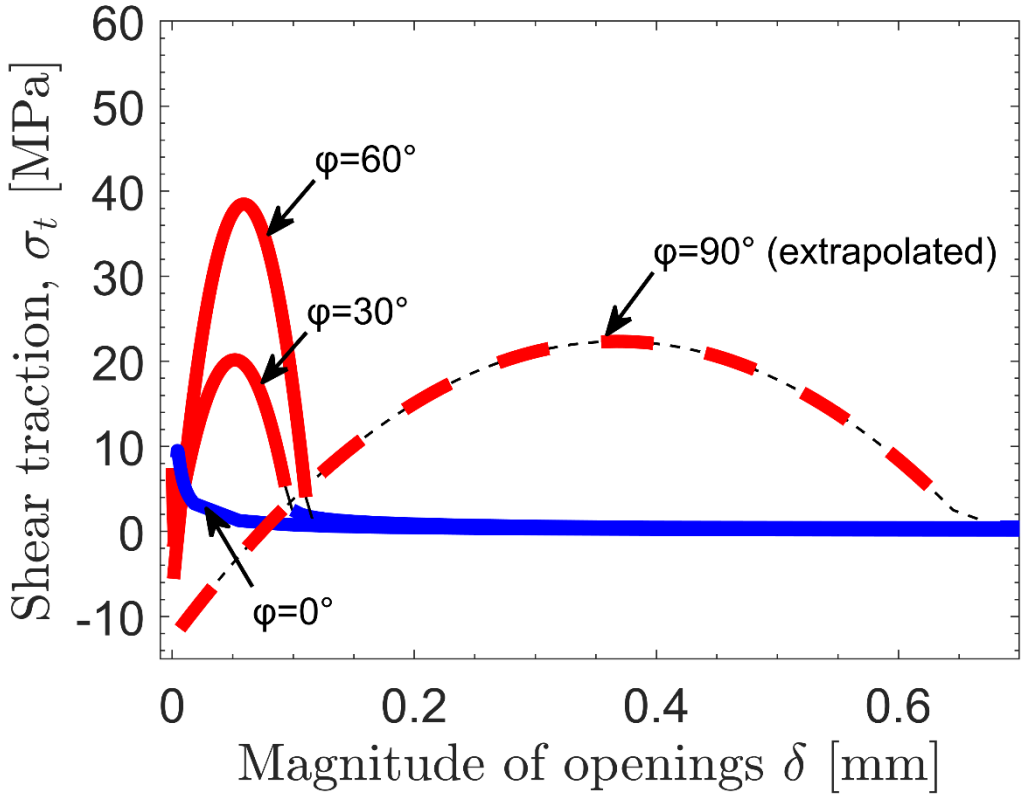

Figures adapted from Erives R. et al 2023

Results

Peak traction at the crack tip and at bridging region

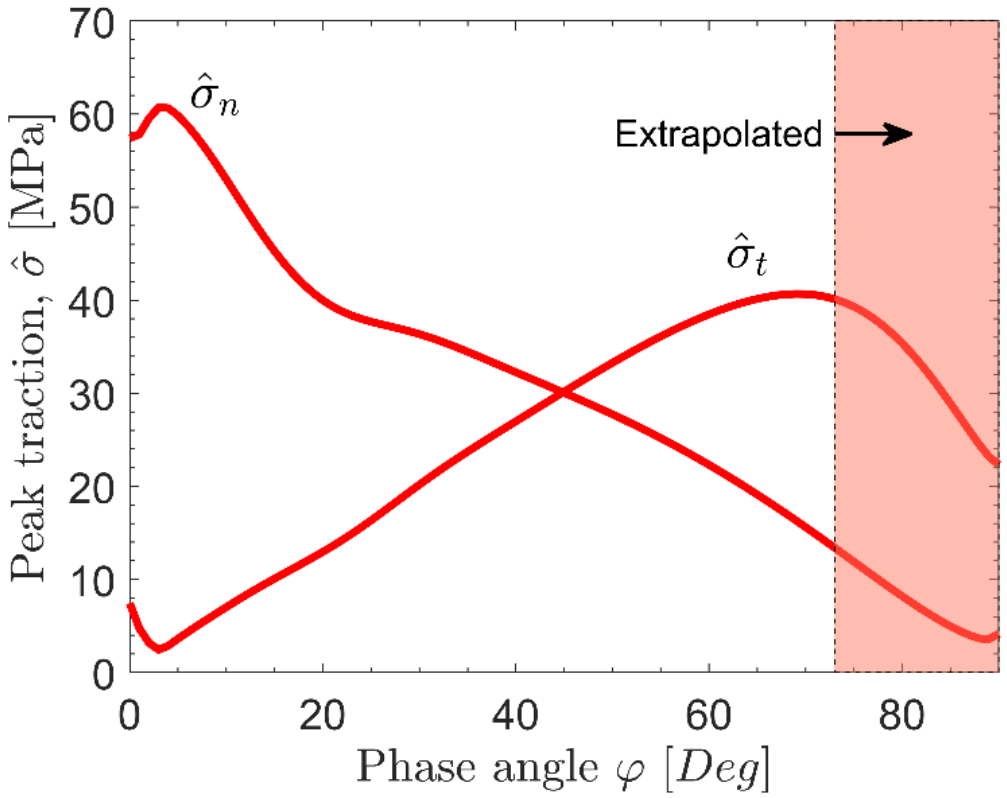

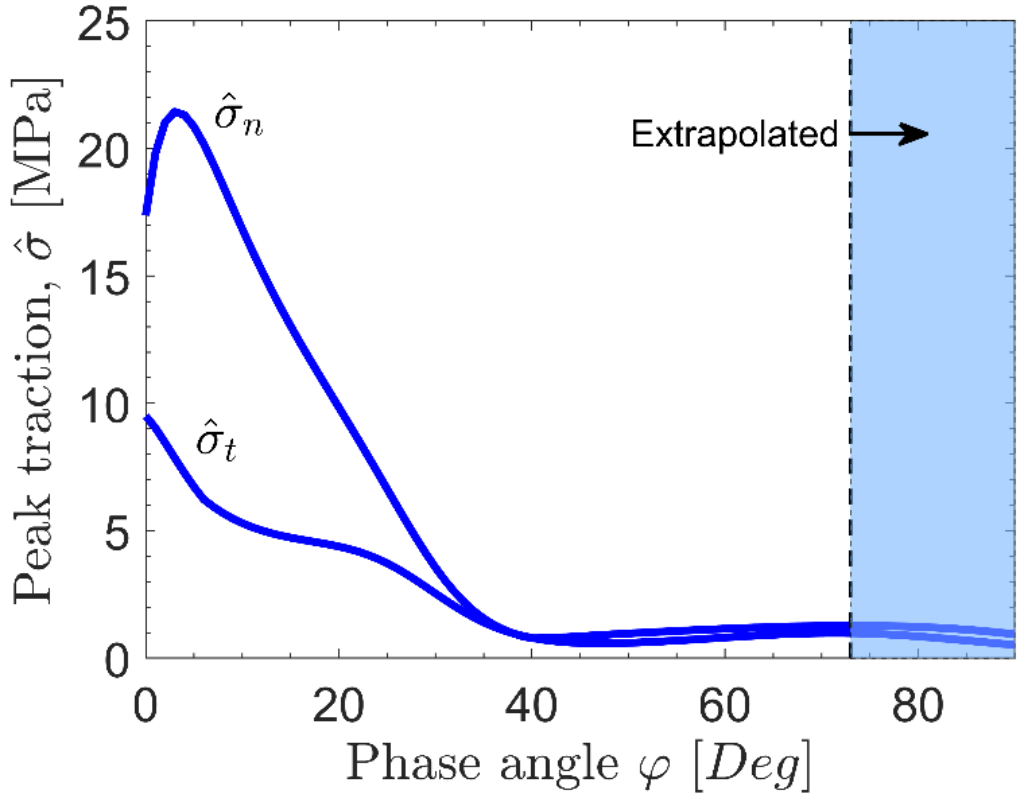

Figures adapted from Erives R. et al 2023

Results

Relationship between external and local phase angle

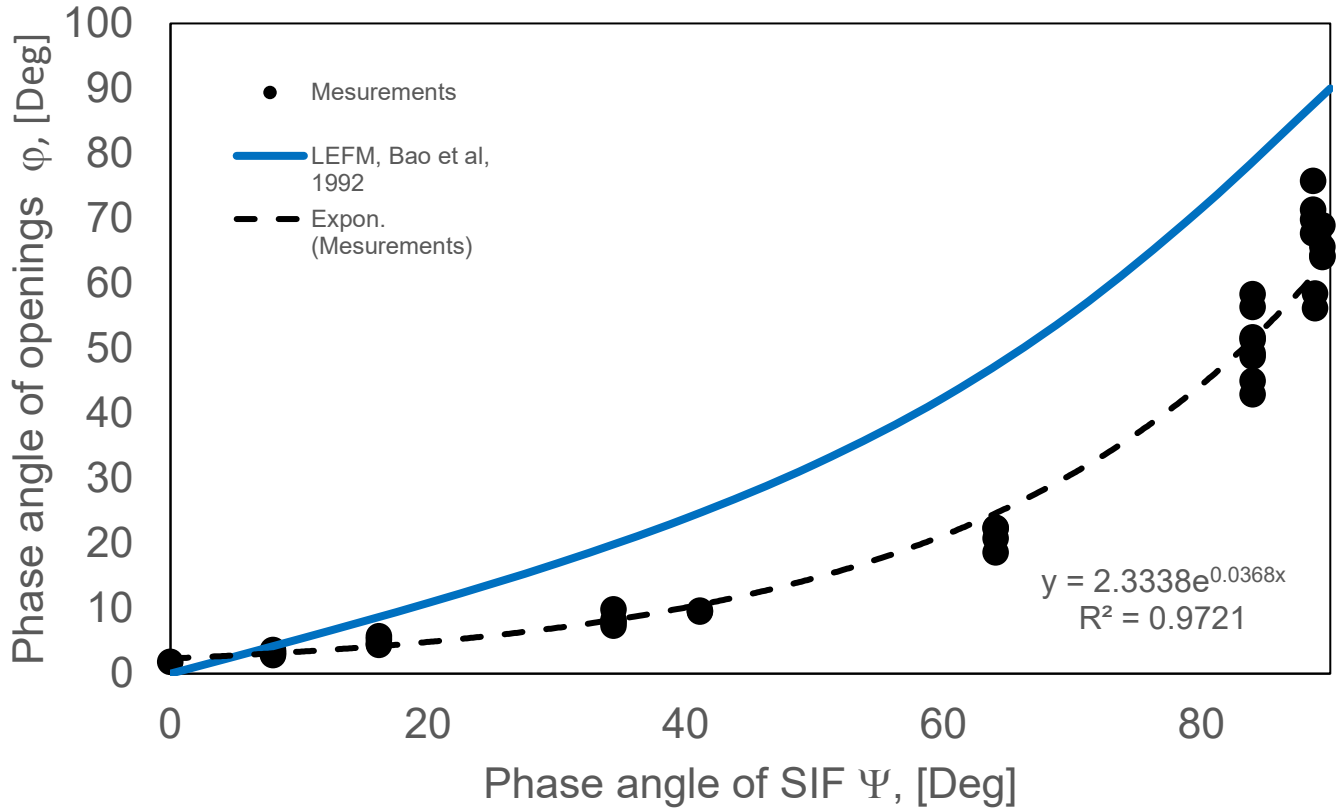

Concluding remarks

1. A framework to extract cohesive laws of composites under large scale fiber bridging is presented
2. Extracted cohesive laws depend on physical parameters directly extracted from experimental R-curves, thus ensuing extracted cohesive laws conform to R-curve behavior
3. The measured cohesive laws resulted on *fully coupled* normal and shear tractions
4. In general, non-monotonic variation of fracture resistance and cohesive tractions can be observed for a fixed opening value



Questions & Discussion

ICCM24
AUGUST 4-8, 2025
BALTIMORE CONVENTION CENTER
BALTIMORE, MARYLAND, USA

No Technical Paper Submission for:

Ashish Kumar Bangaru

ICCM24
AUGUST 4-8, 2025
BALTIMORE CONVENTION CENTER
BALTIMORE, MARYLAND, USA

No Technical Paper Submission for:

Aravind Premanand

INVESTIGATION OF THERMO-MECHANICAL BEHAVIOUR OF COMPOSITES UNDER VIBRATION FATIGUE TESTING

D. Di Maio[1], F. Oude Tanke[2]

[1]Department of Applied Mechanics & Data Analysis, University of Twente
Drienerlolaan 5, 7522 NB Enschede, The Netherlands
Email: d.dimaio@utwente.nl, web page: http://www.utwente.nl

[2] Department of Applied Mechanics & Data Analysis, University of Twente
Drienerlolaan 5, 7522 NB Enschede, The Netherlands
Email: f.oudetanke@utwente.nl, web page: http://www.utwente.nl

Keywords: Fatigue behaviour, High Cycle Fatigue (HCF), High-frequency testing, Thermo-mechanical coupling, Aerospace components, Master curves, Accelerated Testing.

ABSTRACT

While carbon fibre reinforced polymer composites are well-known for their high strength-to-weight ratio, their fatigue behaviour is difficult to predict. Fatigue of composites is generally considered one of the most challenging physical phenomena due to its multi-physics and stochastic behaviour. One of the most challenging aspects of exploring fatigue properties is the extensive time required for fatigue testing. To determine the fatigue life of a test specimen, the number of required load cycles ranges up to millions. The limitation of testing frequency is caused by the viscoelastic properties of the matrix material, which result in self-heating at high testing frequencies. The objectives of XCTE within the DSTANDART project are to increase the rate of mechanical testing by utilising the High Cycle Fatigue (HCF) testing technique and to understand how to measure, analyse, and decouple the thermo-mechanical forces under high rates of cyclic loading. Fatigue testing can be significantly accelerated when high-frequency testing methods are employed. This paper reports the technological advancement achieved through high-frequency testing on two aerospace components: a) a scaled turbine fan and b) a representative aero demonstrator. Both structures embed a typical design feature, ply termination, to change the thickness from the root to the aerofoil of the blade. Those terminations create resin pockets, which are known to be localised stress raisers leading to the onset of fatigue damage. The paper reports on high-frequency experiments conducted in two testing facilities. The first experiment was executed at the Rolls-Royce Mechanical Testing Operational Centre (MTOC) in Berlin (DE), the second experiment was conducted at the NLR testing facility in Marknesse (NL). High-frequency testing and analysis are now a key technology of the spin-off XCTE, which was born thanks to the D-STANDART European project.

1 INTRODUCTION

Composite structures are known to exhibit complex fatigue behaviour due to their stacking sequence and embedded features, such as fibre discontinuity, waviness, resin pockets, and voids, among others. Therefore, any composite laminate requires mechanical testing to determine the material and fatigue properties. The latter properties can be very time-consuming when the number of excitation cycles is large, and the excitation frequency is set lower than five cycles/sec to avoid any self-heating caused by the viscoelastic properties of the resin in the composites. There are numerous research studies examining the environmental and self-heating temperature effects on fatigue life [1,2,3,4,5], which suggest a substantial reduction in residual life due to the coupling between mechanical and thermal loads during fatigue cycles. Temperature-dependent material properties are of no use for engineers who develop fatigue models, assuming a constant entropy behaviour during the development of fatigue damage. The temperature effect(s) are modelled via superposition principles by using test data generated using low excitation rates under different temperature conditions. The result is that a significant amount of time is invested in generating fatigue test data to feed fatigue damage models, even when any aerospace structure can naturally be subjected to oscillatory motions exceeding five cycles per second and

environmental conditions (temperature and moisture). Within the D-STANDART project, the consortium partners investigate the effects of temperature and humidity, with one partner focusing on high-frequency testing under various environmental conditions. These tests indicate how the loss of stiffness correlates with the increase in self-heating temperature in the cross-laminate made of IM7-8552. The research will be published after the ICCM event, so it is advisable to monitor the upcoming literature.

The high-frequency tests were developed and proven in several research studies [1,2,3,4], which are briefly summarised in this paragraph. The composite sample is held by a specific fixture consisting of two rods that support the sample during the excitation of the first bending motion, allowing the structure to rotate at the clamping region. A ply-drop, or cut-ply, features the cross-ply laminate to generate a stress away from the clamping region. That stress raiser is typically placed a few tens of millimetres away from the clamp. The test is executed at a constant excitation frequency, corresponding to the pristine resonance frequency, during the fatigue test. The frequency response phase is measured by the ratio between the input stimulus (typically a base acceleration) and the output response, as measured by a laser Doppler vibrometer (LDV). The vibration amplitude is maintained constant during the fatigue test, thus achieving a displacement control test (noting that the velocity measured by the LDV is converted into displacement). The loss of stiffness as a function of the excitation cycles is measured by the frequency response phase rather than the change of the natural frequency of the test object. The phase is calculated from the inverse tangent of the ratio between the natural frequency and the drive frequency (constant). Consequently, a minimal natural frequency change is transformed into a significant phase deviation due to the tangent function. The temperature (measured by an IR camera) and vibration measurements are synchronised, with the temperature reading sampled every N elapsed cycles to avoid overloading the PC hard drive. The experiments are typically conducted inside an environmental chamber to control the ambient temperature, which scales up or down the effect of self-heating temperatures. The fatigue test data consist of frequency response phase, peak surface temperature (in the region of the ply-drop), and base acceleration versus excitation cycles. These plots will be presented in the following sections.

The experimental technique introduced in the previous paragraph to characterise the fatigue behaviour is applied to two test structures made of composite materials. The first structure is a scaled turbine fan made of a composite material, the type of which and stacking sequence were unknown to the authors [2]. The second structure is an aero demonstrator developed in the D-STANDART consortium. The demonstrator is a quasi-isotropic stacking sequence made of IM7-8552 material. The two experiments were conducted in two different industrial testing facilities. This paper will present the experiments performed and the output generated by the fatigue tests.

2 EXPERIMENTAL SETUP

This section describes the experimental setup, which is common to both experiments, despite being executed in different years. The first experiment was conducted in Rolls-Royce MTOC in 2015, while the second experiment was conducted in NLR in 2025.

The experimental setup is presented in Figure 1. The test structure is mounted on a slip table, which is connected to an electromagnetic shaker that exerts the excitation force. An accelerometer is attached to the slip table to measure the input base acceleration to the test structure. A strain gauge is mounted near the root of the test structure and is used for calibration between the input acceleration, output strain, and output displacement. The LDV and the IR camera are installed in front of the test structure. The XCTE sniper control panel is a custom-made software to control the sensors and exciter. The control panel can perform force or displacement control, depending on the test definition. Moreover, the frequency or phase lock loop at constant amplitude is yielded by a Proportional Integral Derivative (PID) control scheme.

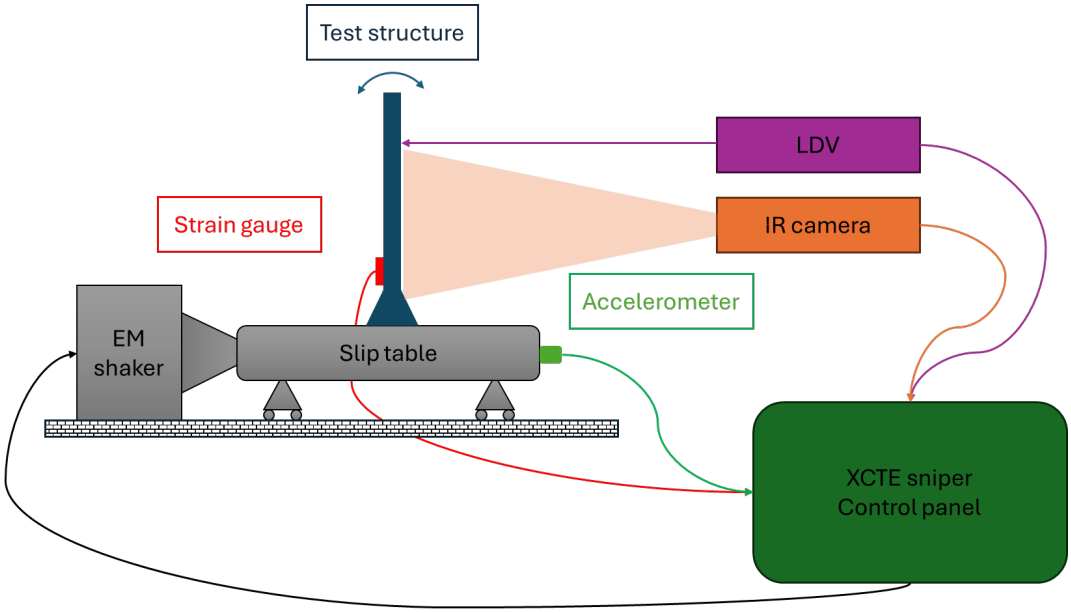

Figure 1: Test setup used for the two experiments.

The first task to accomplish is a frequency check before performing any High Cycle Fatigue with the High Frequency tests. The frequency check is a simple test where the excitation sweeps a frequency range to identify the resonances of the test structure. This step is essential to determine the first bending resonance for which a calibration step is required. In both experiments, the first mode of vibration was the target mode; however, any other fundamental mode can be tested similarly.

Once the frequency check is completed, the second task is to calibrate the base acceleration, the strain gauge, and the LDV laser output. This procedure ensures that a relationship is established between the three sensors, which typically exhibits nonlinearity due to large deformation. This calibration mustn't overload the structure; therefore, it is advisable to avoid large input forces.

At this point, the excitation frequency (resonance) and calibration are known; the final step is to set up the type of force or displacement control for the HCF test. Having decided the kind of control, the HCF can be started, and the frequency response phase is continuously tracked to monitor the loss of stiffness. At the same time, the sniper control panel measures and stores the output of the other sensors, but the strain gauge, whose wire has been cut, is not included.

Figure 2 shows a close-up of the test setup where the blade can be seen vibrating in its test fixture. Note that the test fixture was specifically designed to match the blade root. Figure 3 illustrates the complete measurement setup, as schematically depicted in Figure 1.



Figure 2: Close-up of the test setup.

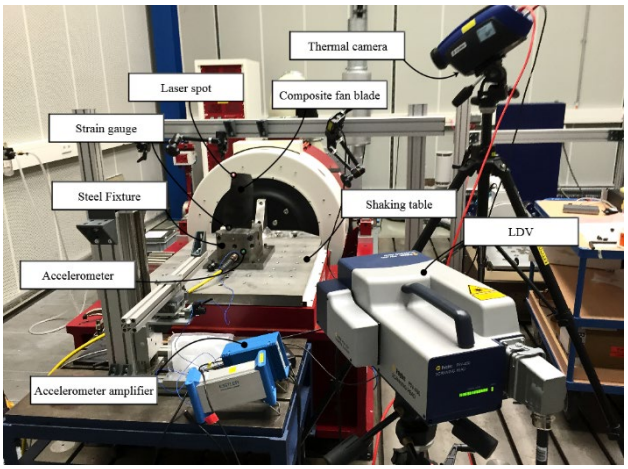

Figure 3: Blade test set up.

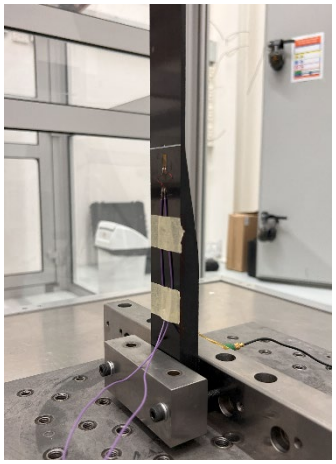

Figure 4: Close-up of the test setup with strain gauge.



Figure 5: DST aero demonstrator test set up.

Although the two experiments were conducted in different years, the modus operandi remains the same. The setup can be adapted to what the test facility can provide, as long as it can be realised as described in Figure 1. XCTE technology enables the setup, performance, and analysis of fatigue test data in hours rather than days.

The following section presents the experimental test data and how the test data from the second experiment are used to evaluate a global master curve of fatigue onset damage growth. It is worth mentioning that the first experiment could be executed using only one fan blade; hence, it was a single shot that could not be missed. The second experiment could be executed using three aero demonstrators, which allowed verifying the repeatability of the results across the three test structures. The comparison between the first and second experiments is not presented in this paper.

3 EXPERIMENTAL RESULTS

This section will present the experimental results obtained from the two experiments. It is worth explaining briefly hereafter why and what the objectives of the experiments were.

The first experiment of the composite blade had two objectives. The first objective was to prove that the fatigue behaviour observed from cross-ply laminate embedding ply drops [2,3,4] at the University of Bristol laboratory was not case-dependent. Hence, similar fatigue behaviours could be observed from scaled fan blades. The second objective was to demonstrate that such a fatigue behaviour could be reproduced and tested in an industrial testing facility.

The second experiment on the DST aero demonstrators also had two objectives. The first objective was to demonstrate that the first experiment on the fan blade was not a fortunate test case, but rather one that could be reproduced years later. The second objective was to evaluate a master curve based on the fatigue onset damage. The second goal was achieved due to the availability of three test structures and the novel testing technique used to obtain the master curve.

3.1 Calibration base acceleration, strain and displacement

Once the frequency check is executed to identify the target resonance, the calibration between the input base acceleration and the output strain and displacement responses is performed using a simple stepped sine test. The procedure consists of exciting under steady-state conditions a frequency near the resonance peak for multiple acceleration amplitude levels. The nought-to-peak of the vibration signals measured from each sensor is processed. Figure 6 shows the relationship between strain and displacement obtained from the fan blade calibration exercise. A linear relationship can be observed. However, a nonlinear behaviour might appear if the strain vs base acceleration or displacement vs base acceleration is plotted. Therefore, the calibration performed for the aero demonstrator retained the use of the three signals, rather than the two used for the fan blade.

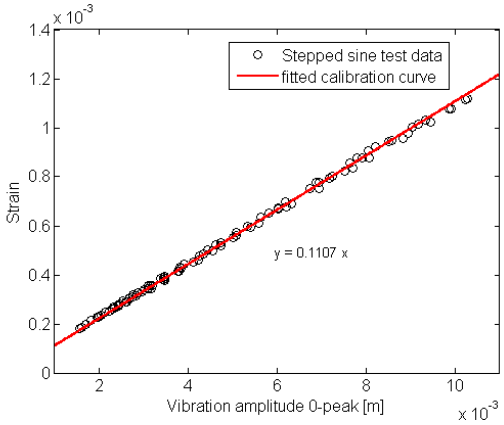

Figure 6: Fan blade strain-displacement calibration.

Figure 7 shows the relationship between the input base acceleration and the output strain for the aero demonstrator. The calibration was performed up to 5 (g) to avoid overloading the test structure. However, it is visible that nonlinear behaviour, which is extrapolated up to 15 (g), where the fatigue behaviour is expected to develop. The nonlinear behaviour is expected because of the large deformation achieved under steady-state vibrations. It is essential to perform this experimental characterisation to avoid setting up incorrect vibration amplitudes during the HCF tests.

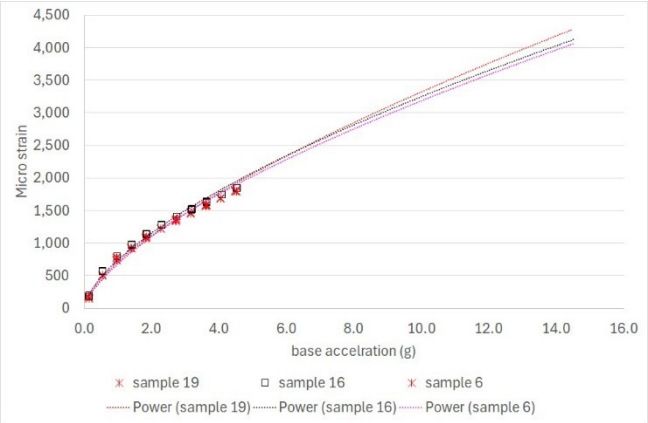

Figure 6: Aero demonstrator strain - base acceleration calibration.

3.2 Test results

This section describes the HCF test data obtained from the fan blade and the aero demonstrator. The type of HCF test is displacement control, which involves using a single excitation frequency and vibrating the target point at a constant amplitude throughout the entire duration of the HCF trial. This procedure is also applied to the aero demonstrator, using a slightly different approach, which will be described later.

The first test results presented are from the fan blade. As previously introduced, the expectation was to observe similar fatigue behaviour already observed with small coupons tested in a university laboratory. The results of the HCF test demonstrated that the experimental procedure was valid for both small coupons and scaled fan blades, thereby meeting the objectives. Figure 7 shows a plot that reproduces three curves: the frequency response phase, the base acceleration, and the surface peak temperature. It is essential to note the correlation between phase decay and the increase in acceleration. This occurs because the mechanical system loses stiffness due to fatigue, and thus, fatigue damage is initiated by the combined mechanical and thermal loads. Both the phase and the acceleration have a specular behaviour. At the same time, the surface peak temperature follows a trend similar to the

acceleration towards the end when a temperature hot spot develops. Figure 8 shows two pictures from the IR camera at two different time instants, when the surface peak temperature reveals a stress concentration (point a) in Figure 7) and when the temperature hot spot is fully developed (point b) in Figure 7).

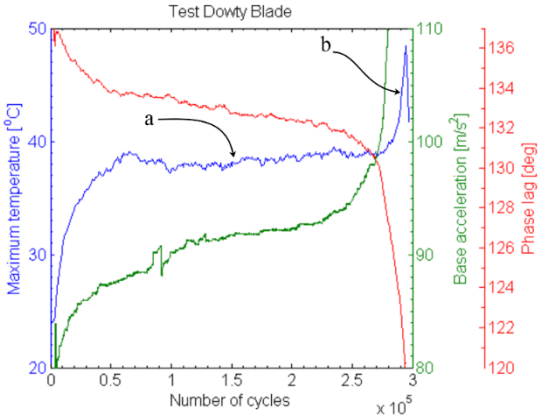

Figure 7: Frequency response phase, base acceleration and surface temperatures of the fan blade.

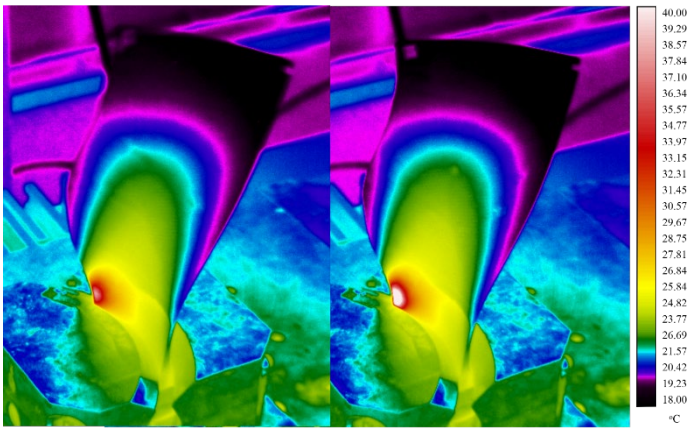

Figure 8: Surface temperature profile in point a) and b) of figure 7.

The main difference with the test carried out with the aero demonstrator was (i) to perform two HCF tests increasing the amplitudes every *N* number of cycles, instead of running a single amplitude, and (ii) to perform one HFC test at a higher amplitude than the previous two HCF tests. The latter goal was to demonstrate that one test structure was sufficient to extract a master curve capable of predicting the results of a different HCF test conducted using a new test structure.

Therefore, one aero demonstrator was tested at a very low amplitude of vibrations, which were incremented every 100,000 cycles. The test was interrupted every 100k cycles to perform nonlinear modal testing. The motivation of that modal test was to observe the change of the nonlinear dynamic response as a function of the increased fatigue behaviour. The modal test was conducted using the last HCF amplitude and was carried out quickly to minimise excessive exposure to dynamic loads. At the end of each HCF test, the frequency response phase, acceleration and surface temperature were stored for analysis. These test sequences were executed for two of the three test structures; the last one was tested to HCF using a single amplitude, which was higher than the one set up for the other two demonstrators.

The HCF test data stored from the first test structure were processed into a master curve based on the onset of fatigue damage. To achieve this, the frequency response phase curves were processed using a specific data analysis toolset to extract the loss of stiffness per unit cycle, described as $d\Phi/dN$, as a function of the input base acceleration. The same procedure was applied to the single frequency response phase curves obtained from the HCF test and plotted on the graph. Figure 9 shows the power law curve extracted from the aero demonstrator tested at several amplitudes, along with a single data point from the other test structure. The single data point (in blue) in Figure 9 lies not far off the power law curve.

Finally, Figure 10 shows the infrared image of the test structure with a fully developed temperature hot spot caused by fatigue delamination.

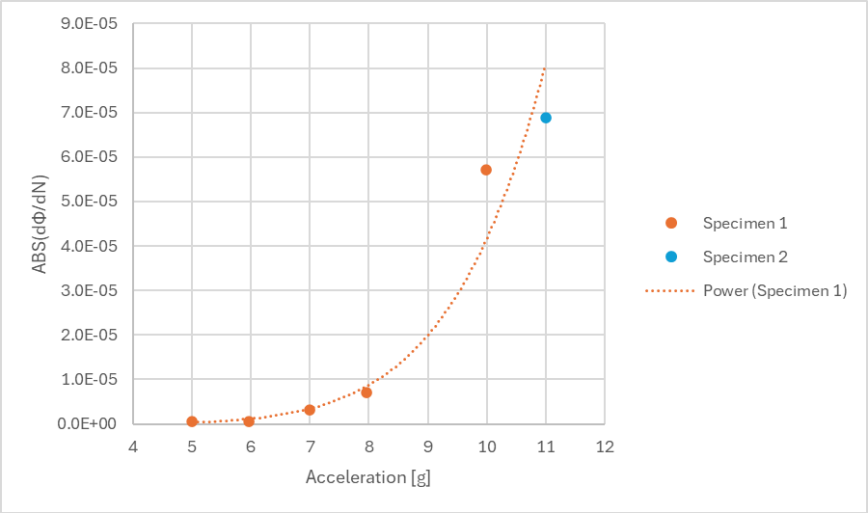

Figure 9: Master curve of the fatigue damage onset generated by specimen 1.

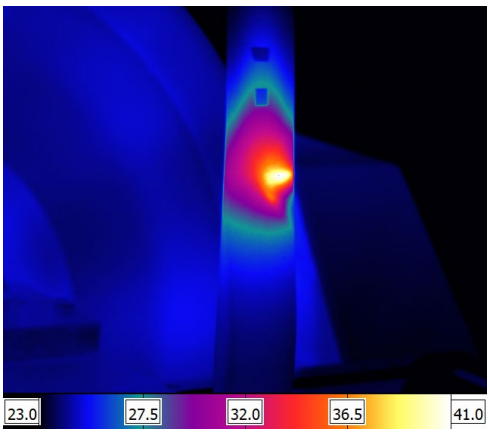

Figure 10: Infrared picture of specimen 1 with developed temperature hot spot.

There are many positive outcomes from this experimental campaign in NLR. The experimental procedure is repeatable and robust. Experiments conducted in two different environments and with two additional test structures indicate that the method for tracking the loss of stiffness is valid regardless of the geometry and material properties. Moreover, the experiments using the aero demonstrator show what was not possible with the fan blade. A single test structure can be used to evaluate a power law function that describes the loss of stiffness per unit excitation cycle as a function of the input load. In this example, the base acceleration was used instead of the strain load; however, the calibration curve allows the references to be interchangeable. Ultimately, the XCTE team had 60 hours to perform the HCF tests with three aero demonstrators in NLR. Despite the self-heating condition, which affected the residual life, the results showed that the fatigue behaviour of the aero demonstrator is a matter of hours rather than days. Finally, any analyst can commission such an experimental test to verify if the design choice delivers the expected durability or not.

4 CONCLUSIONS

This short paper presents some new developments in the area of accelerated fatigue testing developed by XCTE, as part of the D-STANDART EU Horizon project. The testing technology proved to be robust and adaptable to different laboratory environments. Two test cases were presented in the paper; one was an experiment on a composite fan blade conducted in 2015 at a facility in Berlin, and the other was a more recent experiment on an aero demonstrator. The first experiment shows the type of testing setup

and test data generated during an HCF test. The second experiment shows how the HCF test data can be converted into a power law describing the loss of stiffness as a function of the input base acceleration. The scientific value is auspicious because one test structure is sufficient to evaluate a power law describing the fatigue behaviour. The scientific impact will enable engineers to utilise XCTE testing technology to probe structures and assess the most robust design. Moreover, the effectiveness of the proposed HCF tests is demonstrated by their time-saving and potentially cost-saving benefits. The second experiment was conducted over a 60-hour time frame, which is considerably shorter than the standard mechanical tests executed at low excitation cycle rates. Hence, engineers will be able to probe their design optimisations in a very short time. The time savings will enable optimal optimisation towards the standard route of validation and verification.

ACKNOWLEDGEMENTS

Funded by the European Union under GA No. 101091409. Views and opinions expressed are however those of the author(s) only and do not necessarily reflect those of the European Union. Neither the European Union nor the granting authority can be held responsible for them.

REFERENCES

[1] Di Maio, D. and Magi, F., 2015. Development of testing methods for endurance trials of composites components. Journal of Composite Materials, 49(24), pp.2977-2991.

[2] Magi, F., Di Maio, D., Sever, I.: Damage initiation and structural degradation through resonance vibration: Application to composite laminates in fatigue. Composites Science and Technology 132, 47-56 (2016) https://doi.org/10.1016/j.compscitech.2016.06.013

[3] Voudouris, G., Di Maio, D., Sever, I.A.: Experimental fatigue behaviour of CFRP composites under vibration and thermal loading. International Journal of Fatigue 140, 105791 (2020) https://doi.org/10.1016/j.ijfatigue.2020.105791

[4] Di Maio, D., Voudouris, G., Sever, I.A.: Investigation of fatigue damage growth and self-heating behaviour of cross-ply laminates using simulation-driven dynamic test. International Journal of Fatigue 155, 106617 (2022) https://doi.org/10.1016/j.ijfatigue.2021.106617

[5] Katunin, A., Wronkowicz, A.: characterisation of failure mechanisms of composite structures subjected to fatigue dominated by the self-heating effect. Composite Structures 180, 1-8 (2017) https://doi.org/10.1016/j.compstruct.2017.07.101

THE DISCRETE MODEL FOR COMPOSITES DM4C: MESOSCALE MODELING OF COMPOSITES VIA PHYSICS-BASED DISCRETE MATHEMATICAL MODELS OF FIBERS AND MATRIX

Marco Salviato[1,3], Sean Phenisee[2], Antonio Deleo[2], Daniele Pelessone[2], Mark Flores[2],

[1]William E. Boeing Department of Aeronautics and Astronautics, University of Washington
Guggenheim Hall, 3940 Benton Lane NE, Seattle, WA 98195-2400, USA
Email: salviato@aa.washington.edu,

[2]ES3 Inc.
600B Street San Diego, CA 92101-4507, USA

[3]Advanced Composites Center (ACC), University of Washington
7561 63rd Ave NE, Seattle, WA, 98115, USA

Keywords: Composite Modeling, Mesoscale Simulation, Fiber Kinking, Matrix Cracking, Discrete Modeling

ABSTRACT

Fiber-reinforced composites have become integral to lightweight structural applications across aerospace, automotive, and renewable energy sectors. Accurately simulating their mechanical response remains a formidable challenge due to the intricate damage mechanisms governed by micro- and mesostructural features. This paper presents the Discrete Model for Composites (DM4C), a physics-based mesoscale simulation framework that explicitly represents fibers and matrix interactions. By modeling fibers as Timoshenko beams and employing vectorial traction-separation and frictional laws on facet surfaces derived from tetrahedral meshes, DM4C eliminates the need for artificial softening in compression or element erosion. The model is benchmarked against experimental data for IM7/977-3 and demonstrates strong predictive capability across various loading conditions, including longitudinal and transverse loading, as well as off-axis tension.

1 INTRODUCTION

Composite materials offer high specific strength and stiffness and are increasingly applied in mission-critical structures [1,2]. Despite their advantages, predicting their failure remains challenging due to their anisotropy and heterogeneous damage evolution. Traditional continuum-based homogenized models often misrepresent the underlying physical mechanisms, relying heavily on empirical calibration and complex constitutive forms. These models struggle to reproduce essential failure modes like fiber kinking or matrix-dominated microcracking.

To overcome these challenges, the Discrete Model for Composites (DM4C) has been developed as a physics-driven, mesoscale simulation tool [3-5]. In this formulation, DM4C represents fibers explicitly using Timoshenko beam elements, while matrix behavior is captured by discrete constitutive laws defined on interfacial facets of a tetrahedral mesh. This facet-based formulation facilitates a direct simulation of fracture and delamination without relying on damage heuristics or eroding elements, enabling high-fidelity prediction of complex failure phenomena.

2 MESOSCALE MODELING FRAMEWORK

In DM4C, laminate generation starts from the mesoscale. As Figure 1 shows, fibers or bundles of fibers are modeled as Timoshenko beams, offering rotational degrees of freedom and capturing bending and shear deformations. Then, a Delaunay tetrahedralization is performed to connect the nodes of each beam. The result is the three-dimensional tet mesh shown in Figure 1b. After the tets are generated, Voronoi tessellation is used to identify surfaces, called “facets”, that are orthogonal to each edge of the tets. This way, each fiber is surrounded by a set of facets that are orthogonal to the edge

connecting the beam nodes. An orthonormal coordinate system can be defined on each facet. This enables the definition of normal and shear strains and normal and shear stresses through the constitutive laws. Hence, the constitutive behavior of the matrix connecting the fibers becomes vectorial instead of tensorial. This makes it easy compared to tensorial model to simulate phenomena such as cohesive failure or friction which are very important mechanisms for polymer composites which is one of the main advantages of the microplane model developed by Bažant and collaborators for the modelling of complex damage and fracture mechanisms in quasibrittle materials [6-10].

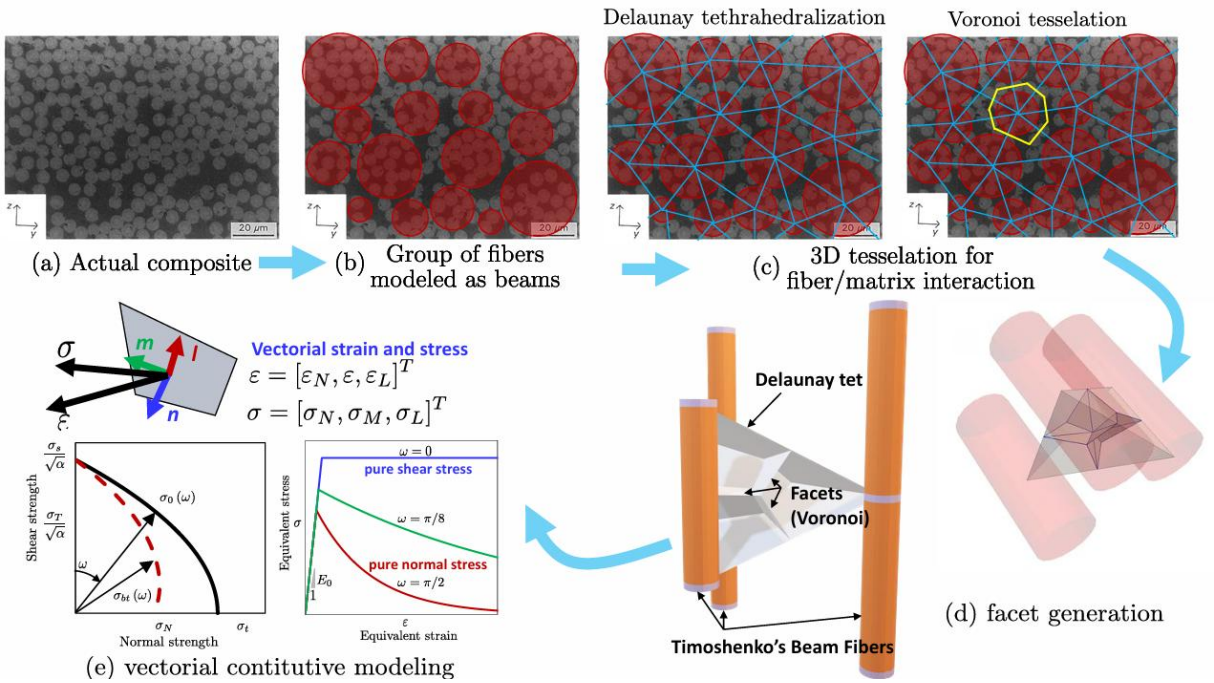

Figure 1: Schematic representation of the DM4C framework for the description of fibers and matrix in fiber composites.

In a tetrahedral element, each facet divides the domain into four subregions, with each subregion containing one of the element's nodes. At every node:
- Three edges converge.
- Each edge is shared by two associated facets.

Within each subregion, a kinematic relation is defined. These local kinematic relations allow for the computation of strain vectors corresponding to the facets of the tetrahedral element.

The displacement field $u(x)$ inside each element is defined following the kinematic relation of nodes as follows:

$$u(x) = u_i + \theta_i \times (x - x_i) = A_i(x) Q_i \tag{1}$$

where:

$$\boldsymbol{A_i(x)} = \begin{bmatrix} 1 & 0 & 0 & 0 & x_3 - x_{3i} & x_{2i} - x_3 \\ 0 & 1 & 0 & x_{3i} - x_3 & 0 & x_1 - x_{1i} \\ 0 & 0 & 1 & x_2 - x_{2i} & x_{1i} - x_1 & 0 \end{bmatrix} \tag{2}$$

The vector $\boldsymbol{x}$ is the Cartesian coordinate inside the element, and the vector $\boldsymbol{x_i}$ represents the coordinate of node *i*. The vector $Q_i^T = [\, u_i^T,\ \theta_i^T \,]$ is the ordered pair of the vector $u_i^T = [\, u_{1i},\ u_{2i},\ u_{3i} \,]$ and the vector $\theta_i^T = [\, \theta_{1i},\ \theta_{2i},\ \theta_{3i} \,]$ which are the translational and rotational degrees of freedom of node *i*.

Stress and strain vectors are defined at individual facets formulated from a Voronoi tessellation process in the tetrahedral mesh as described in the Lattice Discrete Particle Model (LDPM) [13, 14]. The strain components in each projected facet are computed leveraging the following equations:

$$\varepsilon_{Nk} = B_N^{jk}\boldsymbol{Q}_j - B_N^{ik}\boldsymbol{Q}_i \tag{3}$$

$$\varepsilon_{Mk} = \boldsymbol{B}_M^{jk}\boldsymbol{Q}_j - \boldsymbol{B}_M^{ik}\boldsymbol{Q}_i \tag{4}$$

$$\varepsilon_{Lk} = \boldsymbol{B}_L^{jk}\boldsymbol{Q}_j - \boldsymbol{B}_L^{ik}\boldsymbol{Q}_i \tag{5}$$

Once the stress vector for each facet is obtained through the constitutive relation, the nodal forces can be computed via the Principle of Virtual Work (PVW), which imposes that the total external work applied should be identical to the sum of internal work from all the facets. This leads to the following equation defining the internal energy associated with the facet *k*:

$$\boldsymbol{\delta}W_k = \ell_k A_k \sigma_k^T \delta\varepsilon_k = \ell_k A_k(\sigma_{Nk}\delta\varepsilon_{Nk} + \sigma_{Mk}\delta\varepsilon_{Mk} + \sigma_{Lk}\delta\varepsilon_{Lk}) \tag{6}$$

where A_k is the area of a projected facet *k*.

By substituting the relations between strain components and the nodal degrees of freedom to Eq. (6), the nodal force vectors, $\mathrm{F_{ik}}$ and $\mathrm{F_{ik}^T}$, for nodes *i* and *j* associated to the facet *k* can be computed as follows:

$$\boldsymbol{\delta}W_k = \boldsymbol{F}_{ik}^T\boldsymbol{\delta Q}_i + \boldsymbol{F}_{jk}^T\boldsymbol{\delta Q}_j, \text{ where} \tag{7}$$

$$\boldsymbol{F}_{ik}^T = -\ell_k A_k\left(\sigma_{Nk}\boldsymbol{B}_N^{ik} + \sigma_{Mk}\boldsymbol{B}_M^{ik} + \sigma_{Lk}\boldsymbol{B}_L^{ik}\right) \tag{8}$$

$$\boldsymbol{F}_{jk}^T = \ell_k A_k\left(\sigma_{Nk}\boldsymbol{B}_N^{jk} + \sigma_{Mk}\boldsymbol{B}_M^{jk} + \sigma_{Lk}\boldsymbol{B}_L^{jk}\right) \tag{9}$$

2.1 Fiber Constitutive Law

In DM4C, fibers, groups of fibers, and tows are explicitly represented as Timoshenko beam elements; therefore, the constitutive law is described in the integration points of a beam element.

The axial stresses are evaluated at the integration points in the cross-section of a beam element. In the elastic regime, the axial stress is linearly proportional to the axial strain as follows:

$$\sigma_f = E_f\varepsilon_f \tag{10}$$

where $\mathrm{E_f}$ is the parameter associated to the modulus of the fiber bundle and is calibrated to match the longitudinal modulus of a composite material.

When the axial stress reaches the strength limit σ_c it follows a linear softening as defined by the following equation:

$$\sigma_f(\delta) = \max\left[0, \sigma_c\left(1 - \frac{\delta-\delta_c}{\delta_f-\delta_c}\right)\right] \tag{11}$$

where δ is the elongation of a beam element, $\delta_c = \sigma_c\, L_0 / E_f$, with L_0 being the length of the beam element, is the elastic limit displacement which determines the initiation of the linear softening. Complete failure occurs when the elongation of the beam element becomes greater of $\delta_f = (2\, G_f)/\sigma_c$ where G_f is the fracture energy of fibers. In such a case, the axial stress calculated via Eq. (11) becomes zero.

2.1 Matrix Constitutive Law

The constitutive behavior of the matrix is defined at the facet level via vectorial stress-strain relationships. The equations for the elastic and inelastic behaviors are described in the following sections.

Elastic Behavior

The elastic relation for each component of strain and stress vectors resembles the Hooke's law in one-dimension:

$$\sigma_N = E_0 \varepsilon_N \tag{12}$$

$$\sigma_M = \alpha E_0 \varepsilon_M \tag{13}$$

$$\sigma_L = \alpha E_0 \varepsilon_L \tag{14}$$

where E_0 is effective mesoscale normal modulus, and α is a shear-normal coupling parameter. E_0 and α are the DM4C-matrix properties defined at the facet level that are calibrated to match the macroscopic elastic properties of a composite material in the transverse direction which is dominated by the properties of the matrix.

Tensile failure

When a facet deforms under positive normal strain, fracturing behavior determines the softening of the stress components. This behavior is characterized with the effect strain, ε, and the effective stress, σ, as defined in the following equations:

$$\varepsilon = \sqrt{\varepsilon_N^2 + \alpha(\varepsilon_M^2 + \varepsilon_L^2)} \tag{15}$$

$$\sigma = \sqrt{\sigma_N^2 + (\sigma_M^2 + \sigma_L^2)/\alpha} \tag{16}$$

The effective stress incrementally increases proportionally to the effective strain until it reaches the tensile boundary σ_{bt}. As expressed in Eq. (17), the tensile boundary σ_{bt} has an exponential relationship with the normal-shear ratio variable ω and the history-dependent maximum effective strain ε_{max} following the Macaulay's notion: $< x >= \max(x, 0)$:

$$\sigma_{bt}(\varepsilon, \omega) = \sigma_0(\omega) \exp\left(-H_0(\omega) \frac{<\varepsilon_{max} - \varepsilon_0(\omega)>}{\sigma_0(\omega)}\right) \tag{17}$$

The normal-shear ratio variable ω is computed as

$$\tan\omega = \frac{\varepsilon_N}{\sqrt{\alpha}\varepsilon_T} \tag{18}$$

where $\varepsilon_T = \sqrt{\varepsilon_M^2 + \varepsilon_L^2}$. This variable indicates the degree of interaction between shear and normal load in a facet.

In Eq. (17), $\sigma_0(\omega)$ represents the strength limit of the effective stress and expressed as:

$$\sigma_0(\omega) = \sigma_t \frac{-\sin(\omega) + \sqrt{\sin^2(\omega) + 4\alpha\cos^2(\omega)/r_{st}^2}}{2\alpha\cos^2(\omega)/r_{st}^2} \tag{19}$$

where $r_{st} = \sigma_s/\sigma_t$ is the ratio between the shear strength σ_s and the tensile strength σ_t. The elastic limit $\varepsilon_0(\omega)$ is obtained by $\sigma_0(\omega)/E_0$.

The rate of decay of the tensile boundary $H_0(\omega)$ is also dependent on ω and is defined as:

$$H_0(\omega) = H_t \left(\frac{2\omega}{\pi}\right)^{n_t} \tag{20}$$

where $H_t = 2E_0/(l_t/l - 1)$ and $l_t = 2E_0G_t/\sigma_t^2$. G_t is associated to the fracture energy of the matrix, and l is the edge length of the tetrahedron element related to the facet in the evaluation.

Frictional behavior

Facets with compressive normal stress exhibit frictional behavior which increases the shear strength. The effective shear stress:

$$\sigma_T = \sqrt{\sigma_M^2 + \sigma_L^2} \tag{21}$$

increases incrementally until it reaches the shear boundary σ_{bs} defined as follows:

$$\sigma_{bs} = \sigma_s + \alpha(\mu_0 - \mu_\infty)\sigma_{N0} - \alpha\mu_\infty\sigma_N - \alpha(\mu_0 - \mu_\infty)\sigma_{N0}\exp\left(\frac{\sigma_N}{\sigma_{N0}}\right) \tag{22}$$

where σ_s is the shear strength of a facet under pure shear loading condition, and σ_{N0} is the parameter related to the σ_N at which the initial friction coefficient μ_0 transitions to the asymptotic friction coefficient μ_∞.

Property	Value
Fiber strength limit, σ_c, (MPa)	4850
Fiber fracture energy, G_f, (N/m)	65000
Normal modulus, E_0, (MPa)	10570
Shear-normal coupling, α	0.25
Matrix tensile strength, σ_t, (MPa)	50.0
Matrix shear strength, σ_s, (MPa)	45.0
Tensile Characteristic Length, ℓ_t, (mm)	5
Softening exponent, n_t	0.3
Initial friction coefficient, μ_0	0.36
Asymptotic friction coefficient, μ_∞	0.36
Transitional stress, σ_{N0}, (MPa)	500
Compressive yielding strength, σ_{c0}, (MPa)	500
Initial hardening modulus ratio, H_{c0}/E_0	0.5
Transitional strain ratio, $\varepsilon_{c1}/\varepsilon_{c0}$	10.0
Deviatoric strain threshold ratio, κ_{c1}	1.0
Deviatoric damage parameter, κ_{c2}	5.0

Table 1: DM4C parameters calibrated for IM7/977-3

3 CALIBRATION

The DM4C formulation was calibrated against experimental results on IM7/977-3 provided by Clay and Knoth [11]. The whole gauge area of the specimen for each test was modeled using DM4C framework. To resemble the boundary conditions of the experiments, the nodes at the bottom surface were fixed in both translational and rotational degrees of freedom, and the nodes at the top surface were fixed in lateral direction so that the axial displacement is only allowed as a loading condition.

For the modeling of the gauge region, circular ``super fibers" with a diameter of 100 μm were generated and distributed in a rectangular cross-section reaching approximately 60% of fiber volume fraction. The resulting calibrated DM4C parameters are listed in Table 1.

4 RESULTS

In this section, a comparison study between the DM4C simulation results and experimental data is presented.

4.1 Longitudinal Tension

The nominal stress-strain response from the simulation is shown in fig. 2(a). As a calibration result, the longitudinal tensile strength from DM4C model is in good agreement with the experimental data.

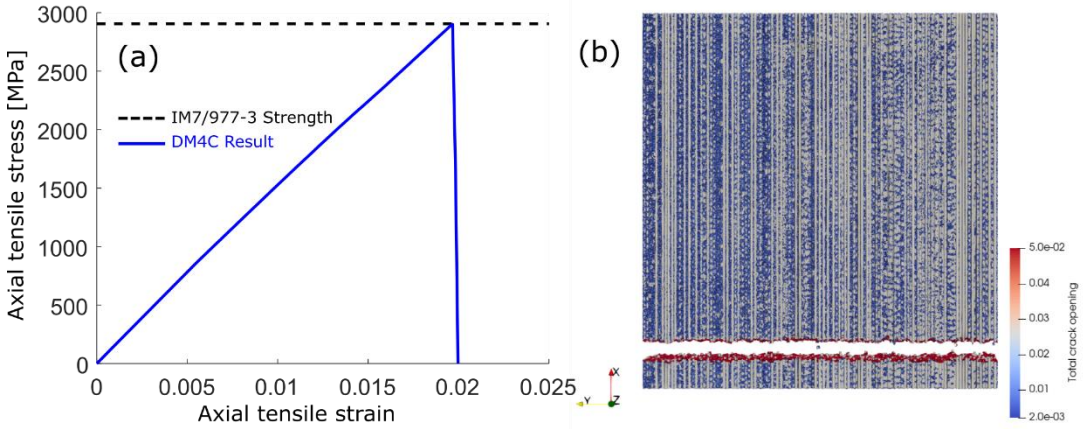

Figure 2. Longitudinal tension: (a) stress-strain curve, (b) damage morphology predicted by DM4C

In the DM4C simulation, fiber failure is the dominant mode of failure leading to the load drop under the tensile load in longitudinal direction as shown in fig. 2(b).

4.2 Longitudinal Compression

It is well-known that imperfections in fiber alignment, introduced during the composite manufacturing process, create local regions of elevated shear stress. Under compressive loading conditions, these regions of high shear stress can rapidly approach the matrix yield strength, triggering local instabilities around the fibers. Consequently, this localized reduction in shear stiffness causes fiber buckling and the subsequent formation of fiber kink bands [12].

Within the DM4C framework, artificial softening of fiber beams under compression is not employed. Instead, the primary damage mechanism causing the load drop is the localized instability resulting from a combination of fiber alignment imperfections and matrix plastic deformation. Therefore, accurately modeling these alignment imperfections is critical for calibrating the compressive strength in the longitudinal direction. The mesoscale nature of the DM4C framework allows for an explicit representation of fiber waviness induced during manufacturing.

In this study, fiber imperfection is modeled as a sinusoidal wave $y = a\cos(\pi x/\lambda)$ following Kyriakides et al. [13]. The amplitude and the half wave-length are calibtrated to match the longitudinal compressive strength of IM7/977-3. The calibrated parameters normalized by the super fiber diameter ($d = 100\sim\mu$m) of a fiber are: $a/d = 0.2$ and $\lambda/d = 27$. The slope of the sinusoidal wave characterized by the resultant parameters stays in the slope range observed in Kyriakides et al. [13].

Figure 3(a) presents the nominal stress-strain response derived from the simulations. The results demonstrate that the longitudinal compressive strength predicted by the DM4C model aligns closely with the experimental observations.

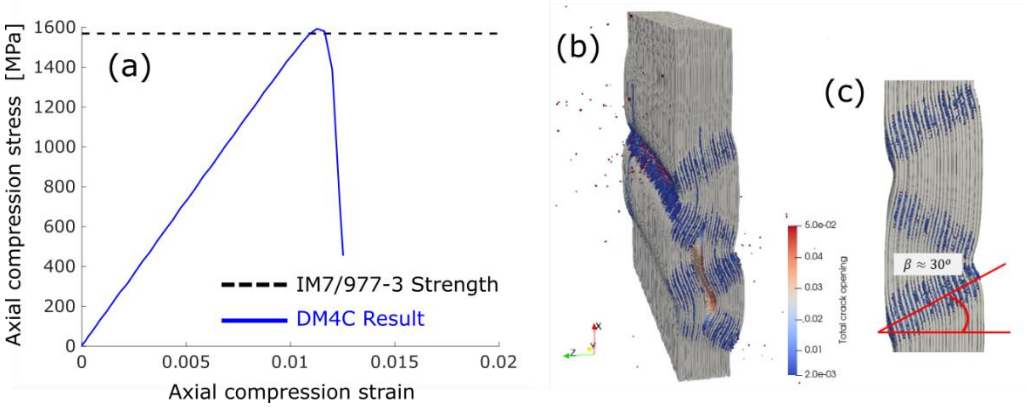

Figure 3. Longitudinal compression: (a) stress-strain curve, (b) damage morphology predicted by DM4C, (c) close up of a kink band.

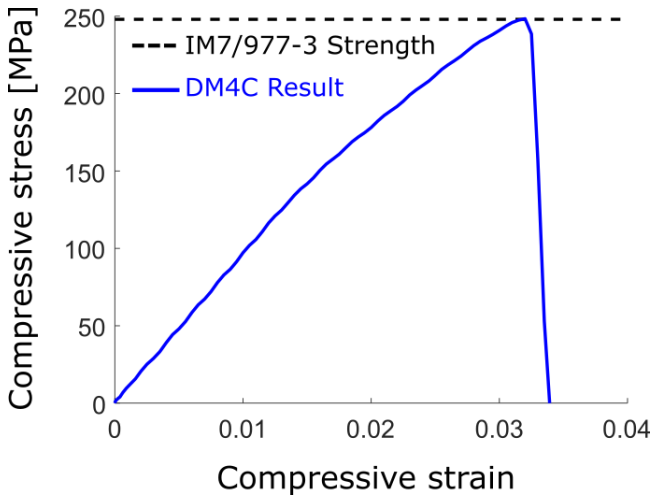

Figure 4. Transverse compression: comparison between experiments and DM4C simulations.

As illustrated in Fig. 3(b), fiber kink bands develop once the nominal stress surpasses the critical threshold. It is also important to highlight that the matrix surrounding the buckled fibers undergoes damage, further reducing local shear stiffness.

The angle of the primary kink band at the onset of load drop was measured, as depicted in Fig. 3(c). Literature indicates that kink band angles typically range between 20 and 35 degrees [14]. The kink band morphology predicted by the DM4C model closely matches this experimentally reported range.

4.3 Transverse Compression

For transverse compression loading, the nominal stress-strain response obtained from the simulation is presented in Fig. 4. The calibrated transverse compressive strength predicted by the DM4C model demonstrates good agreement with the experimental data.

Within the DM4C simulations, shear band formation emerges as the primary failure mode, leading to load drop under transverse compression. The applied boundary conditions simulate a clamped scenario, permitting only axial displacement.

Unconfined compression tests (UCT) are commonly utilized to study matrix cracking under transverse compression. Previous studies [15,16] report the crack plane angles under transverse compression to typically range between 50 and 60 degrees. Figure 5 illustrates the resultant crack plane angle as predicted by DM4C, which closely aligns with the experimentally observed range reported in the literature [15,16].

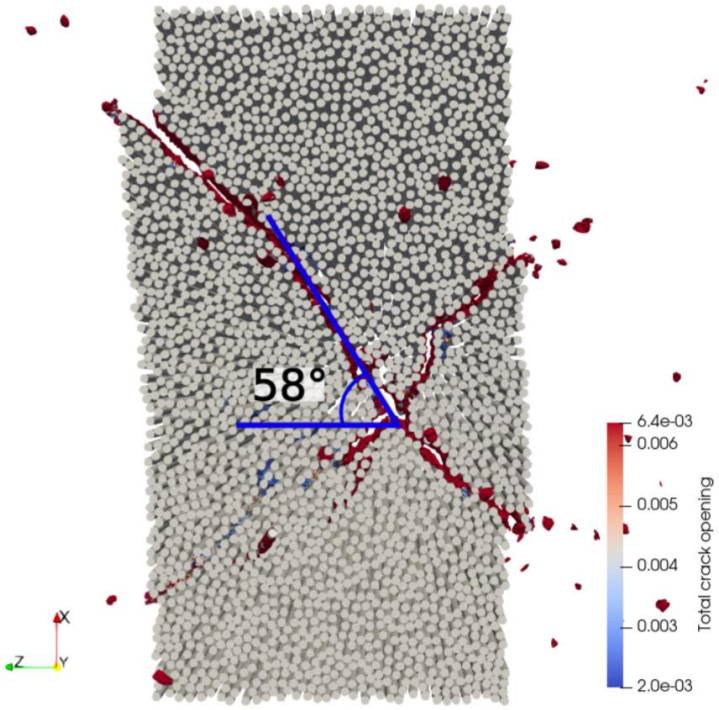

Figure 5. Transverse compression: damage morphology predicted by DM4C.

5 CONCLUSIONS

This work presented an innovative discrete modeling framework designed to accurately capture the mechanical behavior of fiber-reinforced composites. Through detailed comparisons with experimental results, our mesoscale simulations demonstrate the significant advantages of explicitly modeling fibers and matrix constituents. This explicit representation ensures that material parameters within the constitutive laws possess clear physical interpretations, simplifying calibration to match both elastic and strength characteristics of advanced composite materials like IM7/977-3. Moreover, the mesoscale approach excels at simulating complex and critical damage phenomena, including matrix micro-cracking induced by local shear stresses and fiber kink band formation resulting from fiber buckling. This modeling capability opens exciting possibilities for predicting and understanding composite material behavior under diverse loading conditions with unprecedented accuracy.

ACKNOWLEDGMENTS

The authors wish to acknowledge the financial support of the U.S. Air Force Research Laboratory (AFRL).

REFERENCES

[1] I.M., Daniel, O., Ishai, *Engineering mechanics of composite materials*, New York: Oxford university press, 1994.

[2] E.J., Barbero, *Introduction to composite materials design*. CRC press, 2010.

[3] M., Salviato, S., Phenisee, A.A., Deleo, D., Pelessone, and M., Flores, October. A novel discrete, mesoscale modeling framework for the simulation of the damaging and fracturing behavior of composites. *In Proceedings of the ASME International Mechanical Engineering Congress and Exposition* (Vol. 86717, p. V009T12A015). American Society of Mechanical Engineers, 2022.

[4] S.E., Phenisee, A.A, Deleo, D., Pelessone, M. Flores, M., Salviato. Discrete, Meso-Scale Modeling of Fiber-Reinforced Composites (DM4C): Application to Additive Manufacturing of

Continuous Fiber Composites. *In Proceedings Of The American Society For Composites-Thirty-Seventh Technical Conference*, 2022.

[5] M., Salviato, S., Phenisee, A.A., Deleo, D., Pelessone, and M., Flores, To the mesoscale and beyond! capturing complex damage mechanisms in composites via simple, physics-based, discrete mathematical models of fibers and matrix. *In Proceedings Of The American Society For Composites-Thirty-Seventh Technical Conference*, 2023.

[6] Z.P., Bažant, J.L., Le, M., Salviato, 2021. *Quasibrittle fracture mechanics and size effect: A first course*. Oxford University Press, 2021.

[7] Z.P., Bažant, B.H., Oh, Microplane model for progressive fracture of concrete and rock. *Journal of Engineering Mechanics*, 111(4), pp.559-582, 1985.

[8] F.C., Caner, Z.P., Bažant, Microplane model M7 for plain concrete. I: Formulation. *Journal of Engineering Mechanics*, 139(12), pp.1714-1723, 2013.

[9] K., Kirane, M., Salviato, Z.P., Bažant. Microplane triad model for simple and accurate prediction of orthotropic elastic constants of woven fabric composites. *Journal of Composite Materials*, 50(9), pp.1247-1260, 2016.

[10] K., Kirane, M., Salviato, Z.P., Bažant, Microplane-triad model for elastic and fracturing behavior of woven composites. *Journal of Applied Mechanics*, 83(4), p.041006, 2016.

[11] S.B., Clay, P.M., Knoth, Experimental results of quasi-static testing for calibration and validation of composite progressive damage analysis methods. *Journal of Composite Materials*, 51(10), pp.1333-1353, 2017.

[12] A.S., Argon, Fracture of composites. *Treatise on materials science and technology*, 1, pp.79-114, 2013.

[13] S., Kyriakides, R., Arseculeratne, E.J., Perry, K., Liechti, K., On the compressive failure of fiber reinforced composites. *International journal of solids and structures*, 32(6-7), pp.689-738, 1995.

[14] P., Díaz-Montiel, S., Venkataraman, H., Kim, The effects of plasticity mechanisms on micromechanics of composites with fiber waviness defects under compression. *Mechanics of Advanced Materials and Structures*, pp.1-16, 2021.

[15] C., González, J., LLorca, Mechanical behavior of unidirectional fiber-reinforced polymers under transverse compression: Microscopic mechanisms and modeling. *Composites Science and Technology*, 67(13), pp.2795-2806, 2007.

[16] M., Flores, A., Sharits, R., Wheeler, N., Sesar, D., Mollenhauer, Experimental analysis of polymer matrix composite microstructures under transverse compression loading. *Composites Part A: Applied Science and Manufacturing*, 156, p.106859, 2022.

FATIGUE SIMULATION OF LAMINATED COMPOSITES UNDER MIXED MODE CYCLIC LOADING USING A DAMAGE-MECHANICS-BASED FATIGUE ACCUMULATION MODEL

Rong-Can Hong[1], Ryo Higuchi[2], Xin Lu[3] and Tomohiro Yokozeki[4]

[1]Department of Aeronautics and Astronautics, The University of Tokyo
Eng. Building No. 7, 7-3-1 Hongo, Bunkyo-ku, Tokyo 113-0033, Japan
Email: rchong@g.ecc.u-tokyo.ac.jp, web page: http://www.aastr.t.u-tokyo.ac.jp

[2]Department of Aeronautics and Astronautics, The University of Tokyo
Eng. Building No. 7, 7-3-1 Hongo, Bunkyo-ku, Tokyo 113-0033, Japan
Email: higuchi@aastr.t.u-tokyo.ac.jp, web page: http://www.aastr.t.u-tokyo.ac.jp

[3]Department of Aeronautics and Astronautics, The University of Tokyo
Eng. Building No. 7, 7-3-1 Hongo, Bunkyo-ku, Tokyo 113-0033, Japan
Email: xinlu@g.ecc.u-tokyo.ac.jp, web page: http://www.aastr.t.u-tokyo.ac.jp

[4]Department of Aeronautics and Astronautics, The University of Tokyo
Eng. Building No. 7, 7-3-1 Hongo, Bunkyo-ku, Tokyo 113-0033, Japan
Email: yokozeki@aastr.t.u-tokyo.ac.jp, web page: http://www.aastr.t.u-tokyo.ac.jp

Keywords: Fatigue, Damage mechanics, Laminates, Carbon fibre, Finite element analysis, Numerical analysis

ABSTRACT

This paper introduces a damage-mechanics-based fatigue model to simulate fatigue damage accumulation in composite laminates. Unlike typical Paris-law-based models, which assume pre-existing cracks and cannot predict crack initiation, the adopted model by Yashiro and Okabe employs a single constitutive equation covering the entire fatigue process—from initiation to propagation—providing a unified understanding of damage evolution. Originally developed for single-mode loading, the model is extended here to mixed-mode conditions using a new interpolation function. Mixed-mode fatigue parameters are derived from calibrated pure-mode parameters. The study involves two main stages. First, finite element calibration is performed using standard fatigue delamination onset tests, including double cantilever beam and end-notched flexure specimens. Unlike conventional approaches focused solely on propagation data, this work establishes a link between the damage-mechanics-based model and the Paris law, validating the model across both initiation and propagation phases. Simulation results align well with experimental ranges, and the model's propagation trend corresponds with the slope of the Paris law, confirming the reliability of the calibrated pure-mode parameters. In the second stage, the extended model is applied to mixed-mode fatigue using mixed-mode bending tests. Simulations are conducted to derive G-N curves across various mode mixities. The predicted fatigue behavior shows strong agreement with experimental data, with less than 6.86% deviation in the fitted G-N curve parameters. These results validate the proposed mixed-mode formulation. Overall, this study demonstrates the capability of the extended Yashiro-Okabe model to predict fatigue crack initiation and propagation under mixed-mode loading. The proposed method offers a convenient and reliable framework for simulating delamination fatigue in composite laminates across all crack growth phases.

1 INTRODUCTION

Carbon fiber reinforced plastic (CFRP) materials, renowned for their remarkable structural integrity and lightweight properties, have seen an increasing prevalence in aerospace applications. Despite offering superior strength compared to conventional metallic materials, the assessment of their fatigue life has become a crucial concern, given their growing usage in long-term service applications. Previous

research [1] indicates that damage patterns at stresses below the static strength significantly differ from those at static failure loads. Nevertheless, due to the intricate nature of composite materials and fatigue behaviors, characterizing fatigue evolution in CFRPs remains a relatively underdeveloped field [2, 3]. Given that no fatigue accumulation model can encompass all factors, the numerical method for assessing fatigue accumulation in composite structures remains a challenging topic. The primary aim of this paper is to introduce a numerical framework for investigating the intricate mechanisms of fatigue accumulation in CFRPs.

In order to account for the discontinuous feature of material fracture, the cohesive zone model (CZM) has emerged as a popular approach for evaluating damage in structures with plastic properties. Dugdale [4] and Barenblatt [5] laid the foundational concepts of CZM, describing the yielding behavior of stresses around the crack tip. Based on the notion of yielding stress, Hillerborg et al. [6] introduced a traction-displacement relationship for fracture energy within the cohesive zone. Numerous constitutive equations for CZM have been developed [7, 8]. In this paper, Geubelle and Taylor's model [7] is adopted as the damage model for CFRP structures, as further detailed in the subsequent section.

Concerning the prediction of fatigue damage, fatigue accumulation law combined with CZM stands as the primary tool in related research. Generally, fatigue evolution models can be categorized into two primary groups: Paris-law-based and micromechanical models. The Paris law [9], originally proposed for metallic fatigue, has proven to be suitable for predicting fatigue crack growth in FRP ma-terials [10, 11]. Several studies [12–14] have developed modified versions of the Paris law to predict damage evolution under cyclic loading, incorporating cohesive elements. However, Paris-law-based methods cannot predict crack initiation and necessitate additional initiation criteria, as they assume the presence of cracks. Additionally, integrating the Paris law with CZM requires the use of a characteristic length [12–14] to calculate damage accumulation within the damaged area. However, both the characteristic length and mesh size can significantly influence the simulation results. Recognizing the limitations of the Paris law, damage-mechanics-based models have been developed to characterize all phases of fatigue growth. Nojavan et al. [15] introduced a microscopic model considering local states of cohesive stresses and displacement jumps of CZM. Okabe and Yashiro [16] also proposed a damage-mechanics-based fatigue law applicable to delamination and in-ply matrix cracking. An extended model based on Okabe and Yashiro's equation is integrated into the numerical framework presented in this paper.

However, the original model was developed for single-mode loading and does not account for the complexities of mixed-mode loading. In this case, sets of fatigue parameters of different modes needs to be conducted once the loading condition is changed, but implementing mixed mode loading tests is expensive and time-consuming. Considering the inconvenience, obtaining mixed mode parameters from the results of pure mode tests is an important work for establishing an easy-to-use fatigue simulation program. In this study, the fatigue parameters of extended Yashiro-Okabe model are calibrated by delamination onset data. After the FE calibrations, the fatigue propagation simulations are also performed to investigate the fracture behavior after crack initiation. The simulation data is compared to the experimental results in the phase of Paris law. Using simulation results in initiation and propagation, our extended fatigue model can be proved applicable in all phases of fatigue growth.

2 NUMERICAL METHOD

2.1 Numerical Program

The fatigue simulation program in this paper is established upon the work by Nagashima and Sawada [17], as illustrated in Fig. 1. Cohesive elements are employed to simulate delamination on the interfaces. In the quasi-3D program, FE models are established on a 2D-based mesh and subsequently extended into 3D elements along the thickness direction using level set functions. Detailed equations of the numerical framework can be found in [17-19].

2.2 Constitutive Equation of CZM

In this paper, we incorporate Geubelle and Taylor’s model [7] as the constitutive equation for CZM within the numerical program. To assess damage in the cohe-sive zone, a damage variable D is defined

as follows:

$$D = \max\left(D_{\max}, \min\left(1, \sqrt{\left(\frac{\delta_I}{\delta_{IC}}\right)^2 + \left(\frac{\delta_{II}}{\delta_{IIC}}\right)^2}\right)\right) \tag{1}$$

Here, δ_I and δ_{II} represent the relative displacements in mode I and mode II, respectively, and D_{max} signifies the maximum D stored at each integration point. The traction-separation law of CZM can be expressed as:

$$\tau_i = \frac{(1-D)}{D}\frac{\tau_{iC}}{\delta_{iC}}\delta_i \tag{2}$$

In Eq. (2), τ_{iC} and δ_{iC} represent the cohesive strengths and critical relative dis-placements, respectively. The use of the maximum function ensures that D mono-tonically increases and cannot decrease. Once D reaches 1, the integration point on the cohesive element fails and separates, indicating the crack growth.

2.3 Fatigue Accumulation Law

This paper introduces an extended version of the fatigue accumulation law originally proposed by Okabe and Yashiro [16]. In this fatigue model, the damage variable D is treated as a function of the number of loading cycles, N. Consequently, the fatigue accumulation law is expressed in the form of the accumulation rate, dD/dN, as follows:

$$\frac{dD}{dN} = \alpha_m \frac{F^{\beta_m}}{(1-D)^{\gamma_m}} \tag{3}$$

In this equation, α_m, β_m, and γ_m are mixed mode fatigue parameters that are determined through FE calibration using experimental data. Typically, these parameters can only be obtained from mixed mode experiments when using Okabe and Yashiro's model. However, in this study, we propose an interpolation equation for mixed mode loading based on pure mode parameters:

$$\alpha_m = \sqrt{\left(\alpha_I \frac{\delta_I}{\delta_m}\right)^2 + \left(\alpha_{II} \frac{\delta_{II}}{\delta_m}\right)^2} \tag{4}$$

Here, α_I and α_{II} represent α under pure mode I and II, respectively. Using Eq. (4), α_m can be determined using data from pure mode tests, providing a more practical approach to determine the mixed mode parameters. Similarly, β_m and γ_m are calculated in a similar manner as in Eq. (4). In Eq. (3), a dimensionless variable of stress state, F, is introduced for evaluating the states of stresses in cohesive zone:

$$F = \sqrt{\left(\frac{\tau_{Imax}}{\tau_{IC}}\right)^2 + \left(\frac{\tau_{IImax}}{\tau_{IIC}}\right)^2} \tag{5}$$

Here, τ_{Imax} and τ_{IImax} represent the maximum local cohesive stresses in mode I and II, respectively, and they are stored at each integration point. By storing the local stresses and displacements in data arrays, the damage rate of the cohesive zone can be calculated for each computed cycle.

2.4 Cycle jump strategy

To enhance the computational efficiency of fatigue simulations, a cycle jump strategy, adapted from [15, 19], has been incorporated into the numerical framework. The simulation starts at cycle number N = 1, utilizing an implicit static solver. The applied loading on the model is linearly ramped up until reaching the maximum loading. Subsequently, the increment for the next cycle, ΔN, is deter-mined using the following equation:

$$\Delta N = \frac{\Delta D_{max}}{\left(\frac{dD_i}{dN}\right)_{max}} \tag{6}$$

Here, $\left(\frac{dD_i}{dN}\right)_{max}$ represents the maximum $\frac{dD_i}{dN}$ among all integration points in the cohesive elements and XFEM segments. Once ΔN is determined, the array of the damage variable can be updated as follows:

$$D_i = D_{i-1} + \Delta N \left(\frac{dD_i}{dN}\right)_{i-1} \tag{7}$$

As the cycle number increases ($N > 1$), the external loading applied to the simulation model remains constant, forming a load envelope for the core implicit solver of the fatigue numerical program. This updating process is repeated within the fatigue simulation loop until the maximum cycle number is reached.

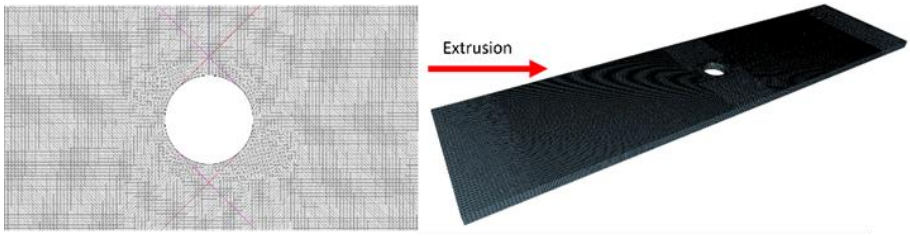

Figure 1: A scheme of modelling and extrusion process for the quasi-3D FE program.

3 NUMERICAL MODELS

To demonstrate the utility of the proposed fatigue accumulation model, we have selected the double cantilever beam (DCB), end-notched flexure (ENF) and mixed mode bending (MMB) tests as the focus of this study. For comparison with simulation results, we utilize the experimental data of fatigue progression in IM7/8552 by Murri [20], O'Brien et al. [21] and Ratcliffe et al. [22]. The numerical analysis can be broken down into the following steps:

1. Calibration of α_I, β_I, and γ_I through the DCB simulation with experimental data.
2. Calibration of α_{II}, β_{II}, and γ_{II} through the ENF simulation with experimental data.
3. Fatigue propagation simulations of DCB and ENF with the calibrated parameters
4. Development of a fatigue OHT model employing the calibrated parameters.

3.1 Calibration of Mode I Fatigue Parameters

Experimental data from the technical report by Murri [20] were introduced for the calibration of mode I parameters. The fatigue double cantilever beam (DCB) test on IM7/8552 was conducted following the ASTM D6115 standard [23]. In this study, fatigue parameters were identified using the G-N curve, which de-scribes the correlation between the maximum energy release rate under fatigue loading and the onset of crack growth cycles. For the finite element (FE) model, an initial static DCB simulation was conducted to determine the maximum dis-placement of the static DCB test. Subsequently, displacements corresponding to various residual percentages were applied for fatigue loading. This approach enabled the determination of the comprehensive G-N curve through FE analysis, and the parameters were established by fitting the simulation data to the experimental curve via a trial-and-error procedure.

The material properties of unidirectional IM7/8552 for the simulations are listed in Table 1. The geometry and boundary conditions of the FE model are depicted in Fig. 2. The fatigue DCB test model exhibited dimensions of 178 mm in length, 25.4 mm in width, 4.5 mm in thickness, and an initial crack length of 50.8 mm. Fig. 3 displays the fatigue simulation data alongside the experimental G-N curve. The solid line represents the curve fitted to the experimental data [20], while the dots represent the simulation results, accompanied by a fitted dotted curve. Through the calibration process, the mode I

parameters were determined, resulting in $\alpha_I = 0.1689$, $\beta_I = \gamma_I = 22.495$.

3.2 Calibration of Mode II Fatigue Parameters

Experimental data from the technical report authored by O'Brien et al. [21] served as the basis for mode II calibration. The fatigue end-notched flexure (ENF) test of IM7/8552 was conducted, incorporating extension from both ASTM D7905 [24] and ASTM D6115 [23], as there is no standardized mode II fatigue test. The methodology for mode II calibration followed the same process as outlined in Section 3.1.

The geometry and boundary conditions of the finite element (FE) model are visualized in Fig. 4. Utilizing the geometric specifications provided in [21], the fatigue ENF test model had dimensions of 101.6 mm in length, 25.0 mm in width, 4.445 mm in thickness, and an initial crack length of 25.4 mm. Fig. 5 presents the fatigue simulation data alongside the experimental G-N curve. The solid line represents the curve fitted to the experimental data [21], while the dots represent the simulation results, accompanied by a fitted dotted curve. Through the calibration process, the mode II parameters were determined, resulting in $\alpha_{II} = 0.11$ and $\beta_{II} = \gamma_{II} = 12.5$.

Properties		Magnitudes
E_{11}	[GPa]	161.0
E_{22}	[GPa]	11.38
G_{12}	[GPa]	5.17
G_{23}	[GPa]	3.92
ν_{12}		0.32
ν_{23}		0.45
G_{IC}	[GPa]	0.2399
G_{IIC}	[GPa]	0.739
τ_{IC}	[GPa]	60.0
τ_{IIC}	[GPa]	90.0

Table 1: Material properties of IM7/8552.

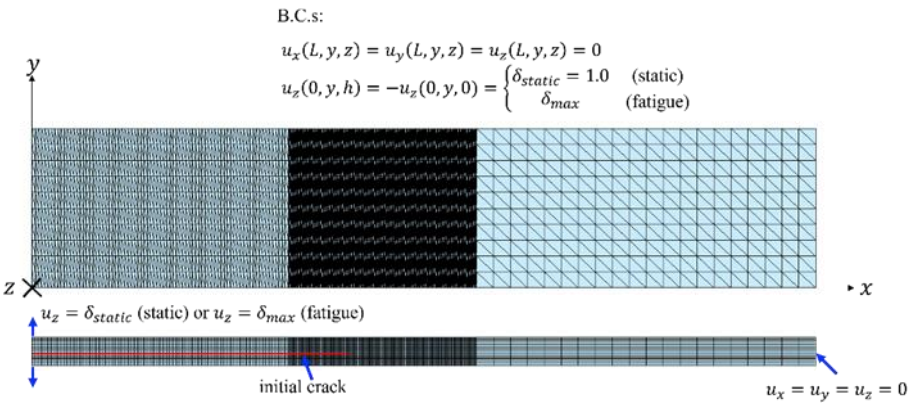

Figure 2: FE model of fatigue DCB test.

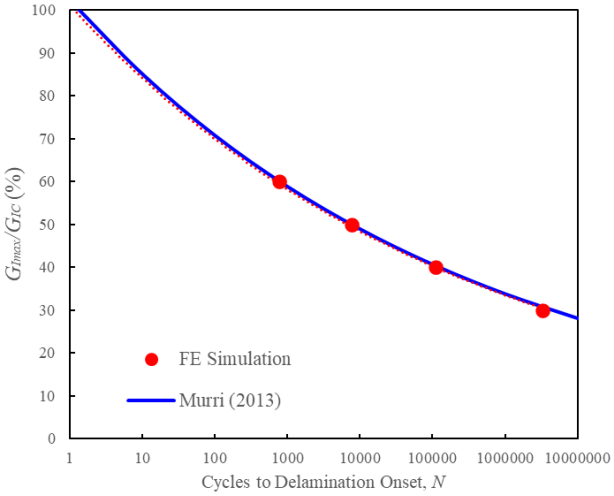

Figure 3: G-N curve of IM7/8552 under mode I loading.

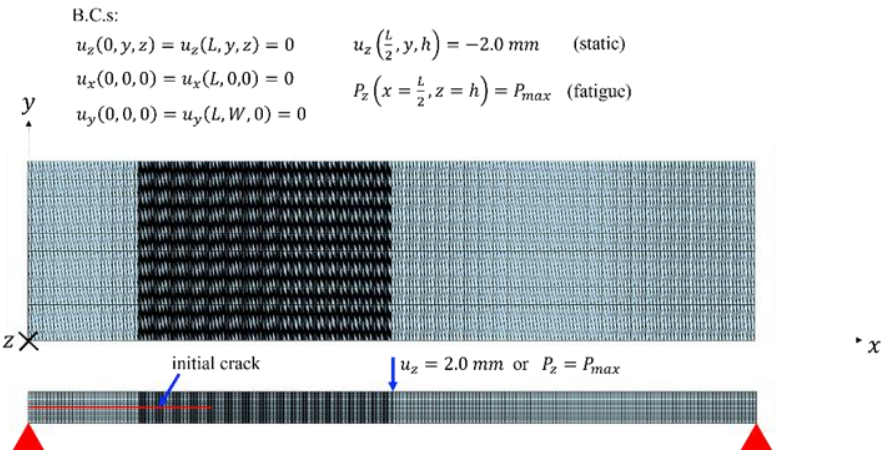

Figure 4: FE model of fatigue ENF test.

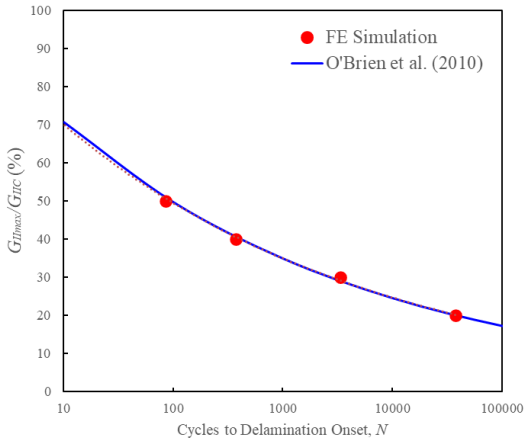

Figure 5: G-N curve of IM7/8552 under mode II loading.

3.3 Mesh sensitivity study

In Section 3.1 and 3.2, the process of calibrating mode I and II fatigue parameters are demonstrated. However, the sensitivity of mesh size to the results of FE calibration is also important. The issue of mesh convergence could result in a huge impact on the fatigue program if the simulation data is highly dependent on the element size. In Section 3.3, simulations are performed with different FE models with different element sizes. Table 2 and 3 listed the element size and number of elements for fatigue DCB and ENF simulation, respectively. In Table 2 and 3, the line with bold text is the original element size utilized in Section 3.3. The 2D views of FE models are also illustrated in Fig. 6 and 7. The G-N curves from fatigue DCB and ENF simulations across all element sizes are depicted in Fig. 8 and 9. These figures demonstrate that the delamination onset curves align with the trend of fitted experimental curves. The variations in onset cycles across different element sizes remain within a narrow range, confirming mesh convergence in the fatigue simulations using the Yashiro-Okabe model.

Element size (mm)	Number of Elements	Number of Solid Elements	Number of cohesive Elements
0.0625	257400	132000	125400
0.1	163800	84000	79800
0.125	**132600**	**68000**	**64600**
0.2	85800	44000	41800
0.25	70200	36000	34200

Table 2: Element size and number for fatigue DCB simulation.

Element size (mm)	Number of Elements	Number of Solid Elements	Number of cohesive Elements
0.0625	277290	142200	135090
0.1	195390	100200	95190
0.125	**168090**	**86200**	**81890**
0.2	115440	59200	56240
0.25	97890	50200	47690

Table 3: Element size and number for fatigue ENF simulation.

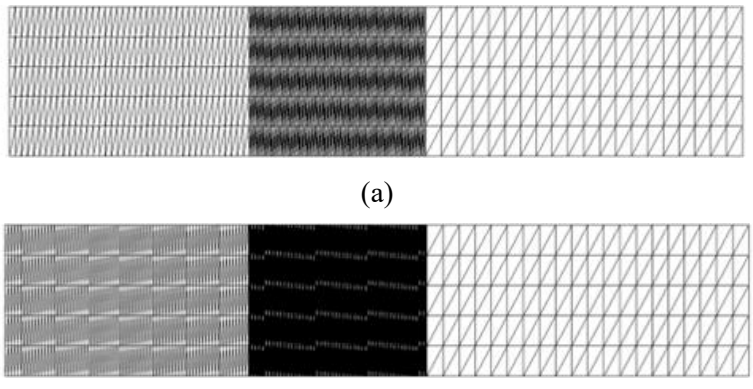

(a)

(b)

Figure 6: FE models for fatigue DCB with the element size of (a) 0.25 mm (b) 0.125 mm.

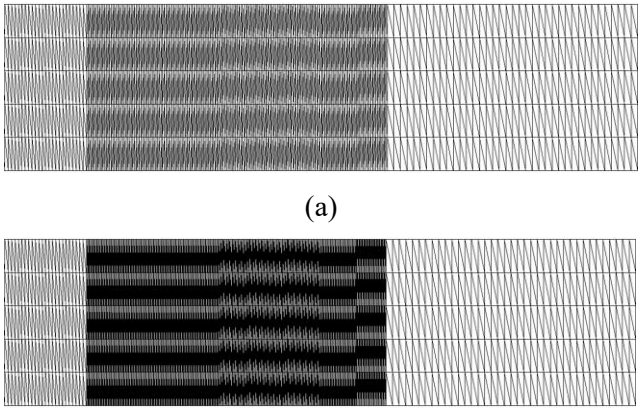

(a)

(b)

Figure 7: FE models for fatigue ENF with the element size of (a) 0.25 mm (b) 0.125 mm.

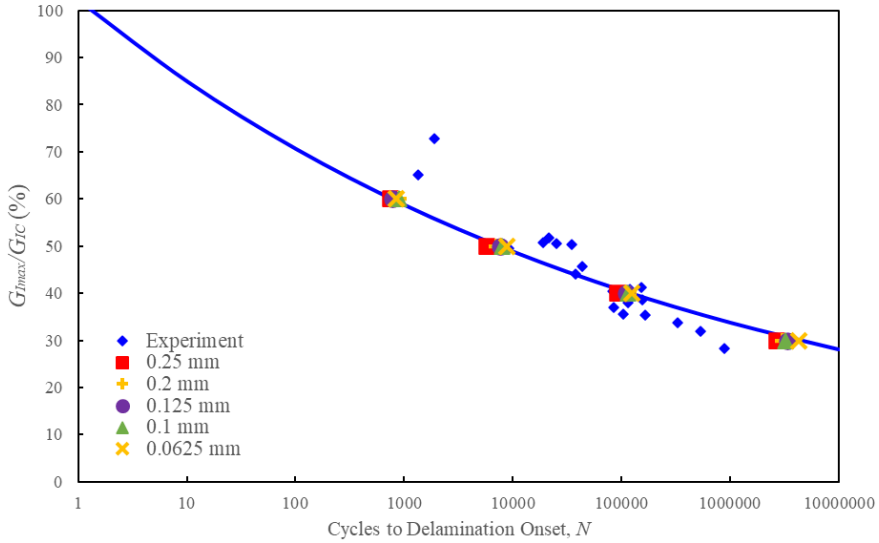

Figure 8: G-N curves of delamination onset in fatigue DCB across different element sizes.

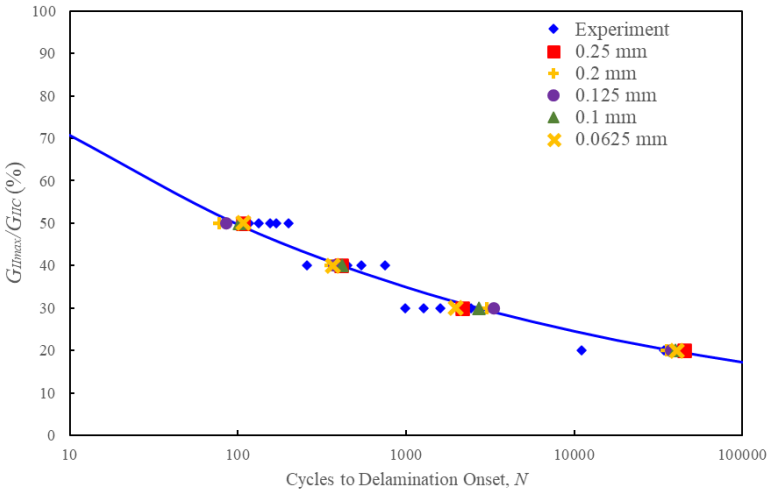

Figure 9: G-N curves of delamination onset in fatigue ENF across different element sizes.

4 NUMERICAL ANALYSES OF FATIGUE PROPAGATION

Using the fatigue parameters calibrated in Section 3, the simulations of fatigue propagation are performed after the fatigue onset. The curves of fatigue propagation rate relative to the input energy release rate are established. A comparative analysis of numerical results and experimental data is shown in Fig. 10, where the simulation results are represented by a blue line, experimental data by grey dots, and the fitted Paris law curve by a black line. As indicated in Fig. 10, the simulation data fits well within the range of the experimental data, and the trend of the simulation curve closely matches the slope of the fitted Paris law curve. The results depicted in Fig. 10 confirm that the pure mode fatigue parameters calibrated from the initiation tests are effectively applicable in the fatigue propagation phase.

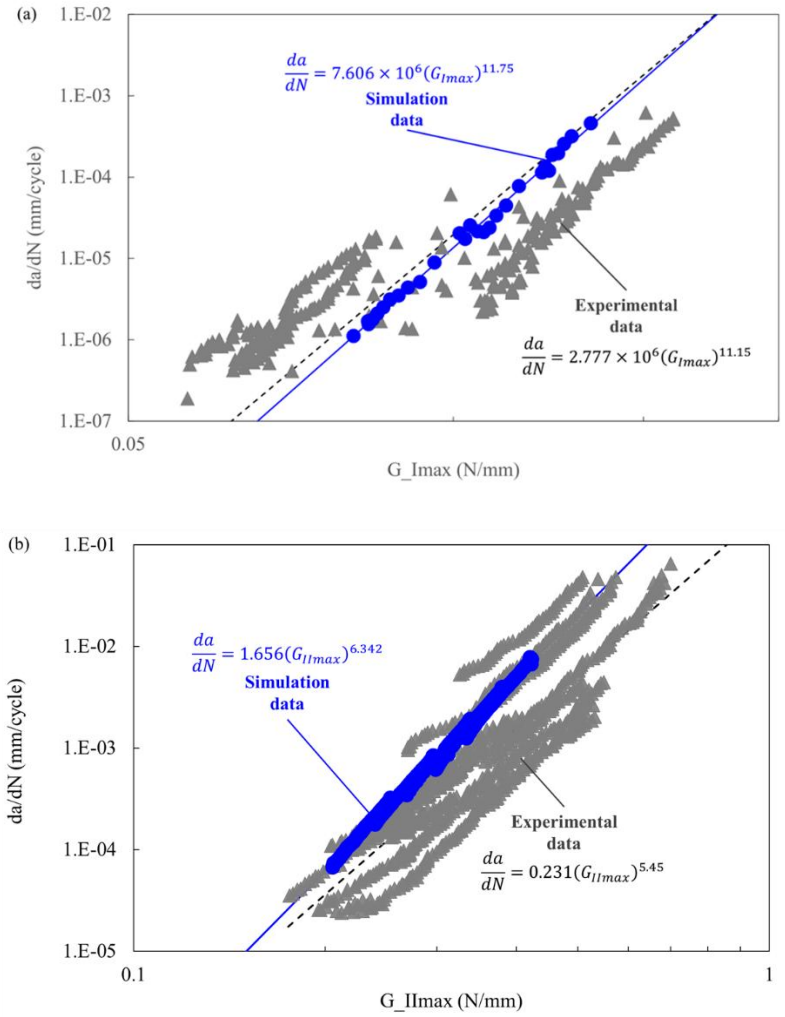

Figure 10: Curve of fatigue propagation rate to the residual energy release rate in (a) fatigue DCB and (b) fatigue ENF test and simulation.

5 VALIDATION OF FATIGUE BEHAVIOR PREDICTION FOR MODE MIXITY

The applicability of the proposed model to crack initiation and propagation under pure modes is validated in Sections 3 and 4. For mixed-mode loading, Eq. (4) is introduced as an extension of Yashiro and Okabe's model [16], and requires validation using experimental mixed-mode data. In this subsection, a finite element model of the fatigue mixed-mode bending (MMB) test is developed to predict fatigue behavior. The numerical results are compared with experimental data reported by Ratcliffe and Johnston

[22]. Simulations are performed at various levels of G_{max}, corresponding to 50%, 40%, 35%, 30%, and 25% of the static critical energy release rate G_C, defined as the sum of G_I and G_{II} at the static critical load.

Following the workflow in Sections 3.1 and 3.2, the compliance of the MMB model is monitored during the simulation to construct the G–N curves. These curves, corresponding to different mixed-mode ratios, are obtained from numerical analysis and compared with the experimental data. The FE model geometry and boundary conditions are shown in Fig. 11. Mixed-mode parameters are calculated at each cycle using the calibrated pure-mode parameters and Eq. (4). The simulation results are presented in Fig. 12, where triangular markers denote numerical results, while circular markers and dashed lines represent experimental data from [22]. As shown, the predicted fatigue life aligns closely with the experimental curves, confirming the validity of the proposed mixed-mode extension.

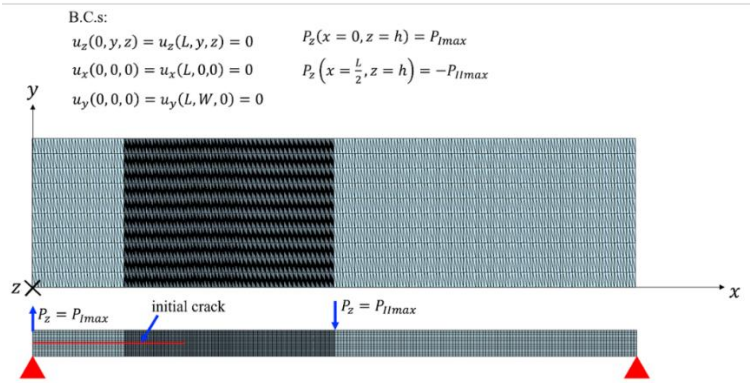

Figure 11: FE model of fatigue MMB test.

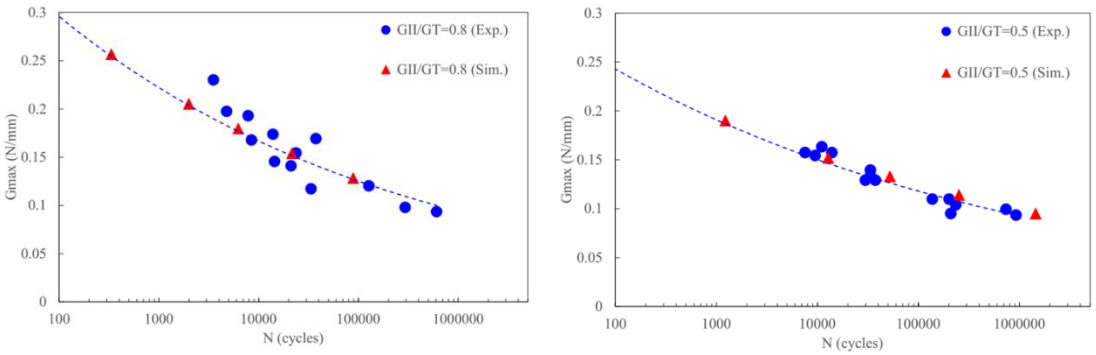

(a) (b)

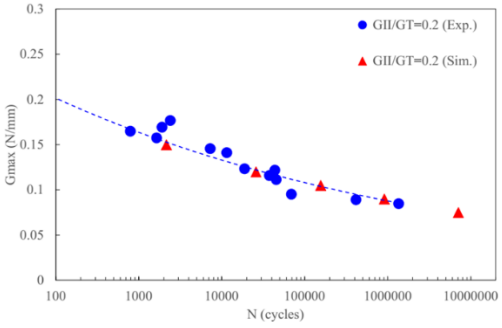

(c)

Figure 12: G-N curve of IM7/8552 under mixed mode loadings (a) Mixed mode ratio of 0.8 (b) Mixed mode ratio of 0.5 (c) Mixed mode ratio of 0.2.

6 CONCLUSIONS

This paper presents a numerical scheme that combines cohesive elements with a damage-mechanics-based approach to predict fatigue evolution in laminated composites. The proposed framework effectively captures both crack initiation and propagation under cyclic loading. An extended version of the fatigue accumulation law, based on the work of Yashiro and Okabe [16], is implemented within the numerical program. The calibration methodology developed in this study enables the derivation of mixed-mode fatigue parameters from pure mode tests, with a proposed interpolation equation that simplifies the process. This extension facilitates the application of the fatigue CZM to cases involving varying mode mixities.

The numerical scheme is validated against experimental results from DCB, ENF, and MMB tests, showing good agreement with the observed fatigue behavior [20-22]. In summary, this study provides a convenient and reliable approach that leverages a damage-mechanics-based model to simulate progressive fatigue damage in composite laminates.

REFERENCES

[1] S.M. Spearing and P.W.R. Beaumont, Fatigue damage mechanics of composite materials. I: Experimental measurement of damage and post-fatigue properties, *Composites Science and Technology*, 44(2), 1992, pp. 159–168.

[2] B.L.V. Bak, C. Sarrado, A. Turon and J. Costa, Delamination under fatigue loads in composite laminates: A review on the observed phenomenology and computational methods, *Applied Mechanics Reviews*, 66(6), 2014.

[3] P. Alam, D. Mamalis, C. Robert, C. Floreani and C.M. Ó Brádaigh, The fatigue of carbon fibre reinforced plastics – A review, *Composites Part B: Engineering*, 166, 2019, pp. 555–579.

[4] D.S. Dugdale, Yielding of steel sheets containing slits, *Journal of the Mechanics and Physics of Solids*, 8(2), 1960, pp. 100–104.

[5] G.I. Barenblatt, The mathematical theory of equilibrium cracks in brittle fracture, *Advances in Applied Mechanics*, 7, 1962, pp. 55–129.

[6] A. Hillerborg, M. Modéer and P.-E. Petersson, Analysis of crack formation and crack growth in concrete by means of fracture mechanics and finite elements, *Cement and Concrete Research*, 6(6), 1976, pp. 773–781.

[7] P.H. Geubelle and J.S. Baylor, Impact-induced delamination of composites: a 2D simulation, *Composites Part B: Engineering*, 29(5), 1998, pp. 589–602.

[8] P.P. Camanho, C.G. Davila and M.F. de Moura, Numerical simulation of mixed-mode progressive delamination in composite materials, *Journal of Composite Materials*, 37(16), 2003, pp. 1415–1438.

[9] P.C. Paris, M.P. Gomez and W.E. Anderson, A rational analytical theory of fatigue, *The Trend of Engineering*, 13, 1961, pp. 9–14.

[10] R.L. Ramkumar and J.D. Whitcomb, Characterization of mode I and mixed-mode delamination growth in T300/5208 graphite/epoxy, *Delamination and Debonding of Materials*, ASTM STP 876, American Society for Testing and Materials, 1985, pp. 315–335.

[11] C. Dahlen and G.S. Springer, Delamination growth in composites under cyclic loads, *Journal of Composite Materials*, 28(8), 1994, pp. 732–781.

[12] P. Robinson, U. Galvanetto, D. Tumino, G. Bellucci and D. Violeau, Numerical simulation of fatigue-driven delamination using interface elements, *International Journal for Numerical Methods in Engineering*, 63(13), 2005, pp. 1824–1848.

[13] A. Turon, J. Costa, P.P. Camanho and C.G. Dávila, Simulation of delamination in composites under high-cycle fatigue, *Composites Part A: Applied Science and Manufacturing*, 38(11), 2007, pp. 2270–2282.

[14] P.W. Harper and S.R. Hallett, A fatigue degradation law for cohesive interface elements – Development and application to composite materials, *International Journal of Fatigue*, 32(11), 2010, pp. 1774–1787.

[15] S. Nojavan, D. Schesser and Q.D. Yang, An in situ fatigue-CZM for unified crack initiation and propagation in composites under cyclic loading, *Composite Structures*, 146, 2016, pp. 34–49.

[16] S. Yashiro and T. Okabe, Numerical prediction of fatigue damage progress in holed CFRP laminates using cohesive elements, *Journal of Solid Mechanics and Materials Engineering*, 3(11), 2009, pp. 1212–1221.

[17] T. Nagashima and M. Sawada, Development of a damage propagation analysis system based on level set XFEM using the cohesive zone model, *Computers & Structures*, 174, 2016, pp. 42–53.

[18] R. Higuchi, T. Okabe and T. Nagashima, Numerical simulation of progressive damage and failure in composite laminates using XFEM/CZM coupled approach, *Composites Part A: Applied Science and Manufacturing*, 95, 2017, pp. 197–207.

[19] R.-C. Hong, R. Higuchi, X. Lu and T. Yokozeki, Numerical analysis of fatigue evolution of laminated composites using cohesive zone model and extended finite element method, *Composites Part A: Applied Science and Manufacturing*, 190, 2025, 108653 (doi: 10.1016/j.compositesa.2024.108653).

[20] G.B. Murri, Evaluation of delamination onset and growth characterization methods under mode I fatigue loading, *NASA/TM-2013-217966*, 2013.

[21] R. Krueger, I.L. Paris, T.K. O'Brien and P.J. Minguet, Fatigue life methodology for bonded composite skin/stringer configurations, *ARL-TR-2432*, 2001.

[22] J.G. Ratcliffe and W.M. Johnston, Influence of mixed Mode I–Mode II loading on fatigue delamination growth characteristics of a graphite epoxy tape laminate, *Proceedings of the American Society for Composites Technical Conference*, La Jolla, CA, 2014.

[23] American Society for Testing and Materials, *ASTM D6115-97: Standard test method for mode I fatigue delamination growth onset of unidirectional fiber-reinforced polymer matrix composites*, ASTM International, 2011.

[24] American Society for Testing and Materials, *ASTM D7905-14: Standard test method for determination of the mode II interlaminar fracture toughness of unidirectional fiber-reinforced polymer matrix composites*, ASTM International, 2011.

ICCM24
AUGUST 4-8, 2025
BALTIMORE CONVENTION CENTER
BALTIMORE, MARYLAND, USA

No Technical Paper Submission for:

Chihaya Hoshikawa

ICCM24 24TH INTERNATIONAL CONFERENCE ON COMPOSITE MATERIALS
AUG 4-8, 2025 • BALTIMORE CONVENTION CENTER • BALTIMORE, MARYLAND

STRENGTH EVALUATION OF TWILL WOVEN LAMINATED STRUCTURE, CONSIDERING KNEE-POINT

M. Kawaguchi[1], Y. Suzuki[1], K. Tanaka[1] and K. Watanabe[1]

[1]Department of Biomedical Engineering, Doshisha University
IN115N, 1-3, Miyakodani, Tatara, Kyotanabe-shi, Kyoto, Japan
Email: maskawag@mail.doshisha.ac.jp, web-page: https://www.doshisha.ac.jp

Keywords: CFRP, Strength evaluation, Tensile test, Finite element method, Knee-point, twill weave

ABSTRACT

Carbon fiber reinforced plastic (CFRP) is characterized by high specific strength and stiffness, so applying it to structures is expected to reduce weight. Due to its high formability, woven CFRP is used in various structures. Woven CFRP is so complex to make numerical model due to its dense structure, that homogenization methods, whose modeling cost is expensive, have been used for analysis. On the other hand, modeling with orthogonal anisotropy is considered to be simple and potentially effective in strength evaluation. Currently, strength design and evaluation of structures using CFRP is not widespread enough for industrial companies, so strength evaluation is performed by testing using actual structures. Because of the high cost of tests using actual structures, it is necessary to propose a method for evaluating strength by analysis. In this study, twill woven structure is modeled as a superposition of orthogonal anisotropic materials to simplify its modeling, assuming strength evaluation could be based on the knee point, which is the maximum point that can be approximated linearly in bending behavior. On our analysis, knee point is calculated by assuming that the layer in the laminated structure that reached the breaking strength for each direction of the twill woven prepreg is broken. In this study, two types of laminates are prepared using twill woven prepregs, and the specimens are subjected to three-point bending tests and loading tests of semi-cylindrical structures. In addition, finite element analysis is applied to reproduce these tests in order to verify the validity of the strength evaluation. These results indicate that the strength evaluation of twill woven composite structures can be available considering the strength for the weakest direction of CFRP, using orthogonal anisotropy modeling.

1 INTRODUCTION

Carbon fiber reinforced plastic (CFRP) is characterized by high specific strength and stiffness, so applying it to structures is expected to reduce weight [1-2]. Due to its high formability, woven CFRP is used in various structures such as automobiles, aircraft, and wind power generation blades [3-5]. Woven CFRP is so complex to make numerical model due to its dense structure, that homogenization methods, whose modeling cost is expensive, have been used for analysis. On the other hand, modeling with orthogonal anisotropy is considered to be simple and potentially effective in strength evaluation [6-8].

Currently, strength design and evaluation of structures using CFRP is not widespread enough for industrial companies, so strength evaluation is performed by testing using actual structures [9]. Because of the high cost of tests using actual structures, it is necessary to propose a method for evaluating strength by analysis. In this study, twill woven structure is modeled as a superposition of orthogonal anisotropic materials to simplify its modeling, assuming strength evaluation could be based on the knee point, which is the maximum point that can be approximated linearly in bending behavior. On our analysis, knee point is calculated by assuming that the layer in the laminated structure that reached the breaking strength for each direction of the twill woven prepreg is broken. In this study, two types of laminates are prepared using twill woven prepregs, and the specimens are subjected to three-point bending tests and loading tests of semi-cylindrical structures. In general, knee point strength is said to be 50-60% of breaking strength, so strength evaluation on the knee point is considered effective. In addition, finite element analysis is applied to reproduce these tests in order to verify the validity of the strength evaluation. These results indicate that the strength evaluation of twill woven composite structures can be available considering the strength for the weakest direction of CFRP, using orthogonal anisotropy modeling.

2 STRENGTH OF COMPOSITE SHEET

2.1 Preface

In this study, strength evaluation is focused on knee point. Knee point is the maximum point that can be approximated linearly on the stress-strain diagram, as shown in Fig. 1. The knee point is assumed to be caused by the rupture of the weakest layer of the laminated composite. Tensile strength of the composite sheet before laminate forming is experimentally determined as breaking stress, and the strength is evaluated based on this breaking stress.

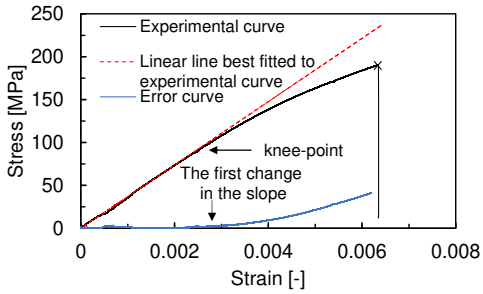

Figure 1: Composite sheet tensile test specimen.

2.2 Tensile test

Twill composite sheet of 0.25 mm thickness is used as the test material. The warp direction of twill structure is set at 0°, and the composite sheet is cut at oblique angles of 0°, 45°, and 90°.
Test specimens are prepared as shown in the Fig. 2 and aluminum tabs are adhered. Strain gauges are attached to the center, and strain measurements are performed using a measuring device. Uniaxial tensile load is applied using Autograph. Stress-strain diagrams from tensile tests of composite sheets are shown in Fig. 3. The results of breaking stress and modulus of elasticity at oblique angles of 0°, 45° and 90° are shown in Fig. 4 and Fig. 5. Both the breaking stress and modulus are lowest in the 45° oblique sheet, where the fibers are not aligned.

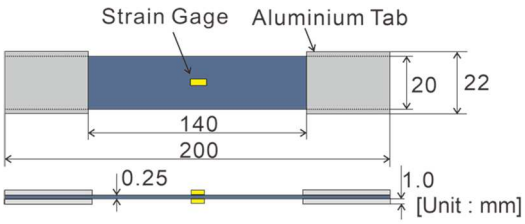

Figure 2: Composite sheet tensile test specimen.

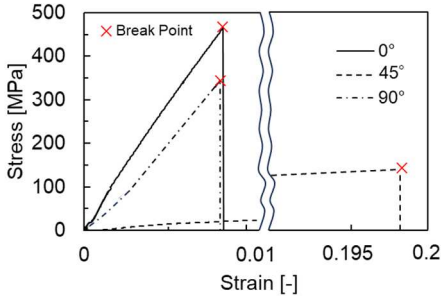

Figure 3: Stress-strain diagram for tensile testing of composite sheets.

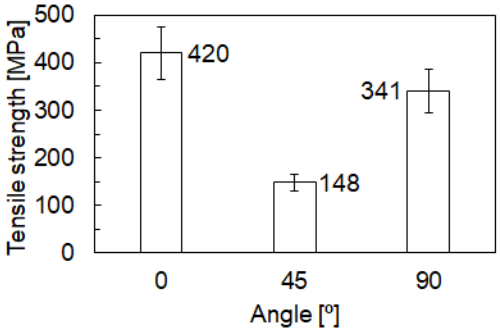

Figure 4: Tensile strength of composite sheets.

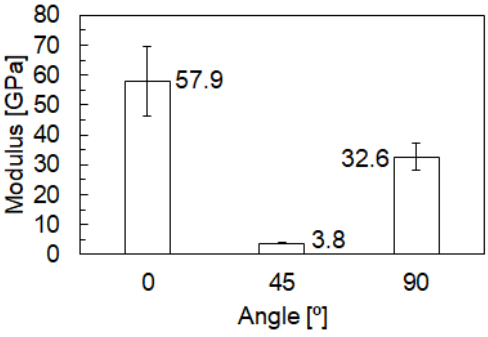

Figure 5: Modulus of composite sheets.

2.3 Tensile Analysis

The composite sheet is treated as an approximated model consisting of a unidirectional V material with only the warp component and a unidirectional H material with only the weft component, superimposed as shown in Fig. 6. The longitudinal modulus of elasticity in the L and T directions of the V material is E_{LV} and E_{TV} ($=\alpha E_{LV}$), and the transverse modulus of elasticity in the LT direction is G_{LTV}, where α is the coefficient of elasticity. Similarly, the coefficients of longitudinal elasticity in the L and T directions for the H material are E_{LH} and E_{TH} ($=\alpha E_{LH}$), and the coefficient of transverse elasticity in the LT direction is G_{LTH}. The elastic properties of the twill weave at angles of 0° and 90° are approximated by the superposition of orthogonal anisotropic materials as shown in Equation (1) below. The value of α is set to 0.032 from literature values, and the Poisson's ratio is also set to the general value of 0.3 from the same paper.

$$E_0=E_{LV}+E_{TH}=E_{LV}+\alpha E_{LH} \qquad (1)$$
$$E_{90}=E_{LH}+E_{TV}=E_{LH}+\alpha E_{LV}$$

The theoretical value of the elastic modulus of the twill woven material is also obtained by superposition of orthogonal anisotropic materials. The modulus of elasticity of the XY coordinate system tilted by an angle θ shown in Fig. 7 from the LT coordinate of the unidirectional material is obtained from equation (2) to (4), and the sum of the V and H materials is used to obtain the modulus of elasticity at that angle. ($\because l = \cos\theta$, $m = \sin\theta$)

$$\frac{1}{E_x}=\frac{1}{E_L}l^4+(\frac{1}{G_{LT}}+\frac{2\nu_{LT}}{E_L})l^2m^2+\frac{1}{E_T}m^4 \qquad (2)$$

$$\frac{1}{E_y}=\frac{1}{E_L}m^4+(\frac{1}{G_{LT}}+\frac{2\nu_{LT}}{E_L})l^2m^2+\frac{1}{E_T}l^4 \qquad (3)$$

$$\frac{1}{G_{xy}}=2(\frac{2}{E_L}+\frac{2}{E_T}+\frac{4\nu_{LT}}{E_L}-\frac{1}{G_{LT}})l^2m^2+\frac{1}{G_{LT}}(l^4+m^4) \qquad (4)$$

The composite sheet is modeled in FEMAP with NX Nastran as shown in Fig. 7. Shell elements are used and divided into 1mm × 1mm rectangular elements. The left end is fully constrained, and the other nodes are free only in the translational XY directions. The load of 1 N is applied to the right end of the model. The physical property values are obtained from Equation 1, and the elastic modulus of the V and H materials are shown in Table 1. Tensile analysis is performed using these physical properties. The distribution of the modulus of elasticity with each angle is shown in Fig. 8. The elastic modulus from the analysis is in qualitative agreement with the theoretical equation. The analytical values are slightly larger than the theoretical values, which may be due to the fact that the V and H materials suppress each other's deformation.

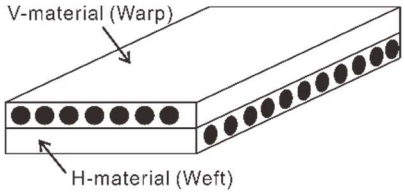

Figure 6: Twill model using orthotropic anisotropy.

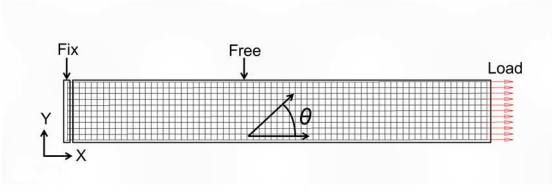

Figure 7: Analysis model of bending specimen.

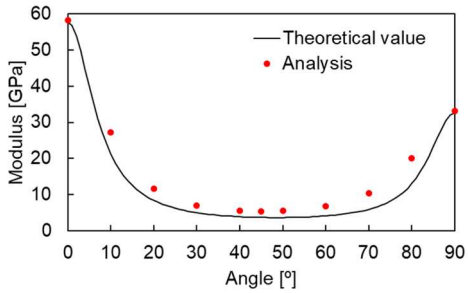

Figure 8: Distribution of elastic modulus at each angle.

Engineering constant		V	H
E_L	[GPa]	57.0	30.8
E_T	[GPa]	1.8	0.9
E_{45}	[GPa]	2.5	1.3
G_{LT}	[GPa]	0.9	0.5

Table 1: Physical properties of V and H materials.

3 STRENGTH OF LAYERED COMPOSITE MATERIAL

3.1 Bending Test

Two types of laminated boards are made by the same composite sheet. Press molding machine (STIP05-05) is used, with molding conditions set at a pressure of 2 MPa, a molding time of 5 minutes, and a molding temperature of 275°C. The laminated board are defined as Type-A $[0°/+45°/-45°/90°]_s$ and Type-B $[+45°/0°/90°/-45°]_s$. Test specimens are cut from the laminated board and three-point bending test is conducted as shown in the Fig. 9. The load-strain diagram obtained from the bending test are shown in the Fig. 10. The knee point loads obtained from the experiments are shown in Table 2. The average load at the knee point was 100 N for Type A and 86 N for Type B.

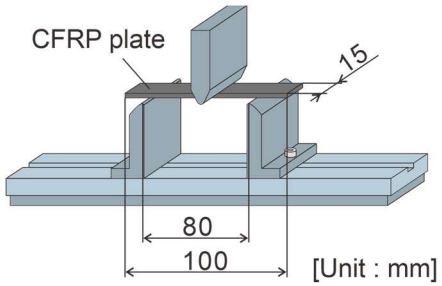

Figure 9: Diagram of 3-point bending test.

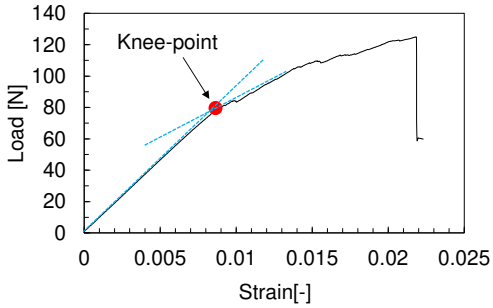

Figure 10: Load-strain curve of 3-point bending tests.

	Type-A[N]	Type-B[N]
No.1	75	108
No.2	107	87
No.3	88	76
No.4	118	62
No.5	113	97
Ave±S.D.	100±18	86±18

Table 2: Knee point load in bending test.

3.2 Finite element analysis

The specimen shown in the Fig. 11 is modeled using stacked layup in FEMAP with NX Nastran. As shown in Fig. 11, the restraint conditions are as follows: the fulcrum of the 3-point bending test is constrained in the direction of translational Y and rotational X and Z direction, while the rest of the specimen is free, that is, in the translational X and Z directions and in the direction of rotation of the Y-axis.

Unit load (1 N) is applied in the negative direction of the Y-axis in the center of the specimen. In this study, the stress is analyzed by 1° with respect to the fiber direction as shown in Fig. 12 for each layer, and the load at which the composite sheet reached the breaking stress at each angle is considered as the knee-point load. The results of tensile tests are used for the rupture stress, and the rupture stress at other angles is assumed to be correlated with the longitudinal modulus of elasticity, resulting in the distribution shown in the Fig. 13. Stress contour plots of the outermost layers of both types are shown in Fig. 14. For both types, the maximum stress occurred at the loaded portion of the specimen. Therefore, the stress at the center of the loaded portion is evaluated.

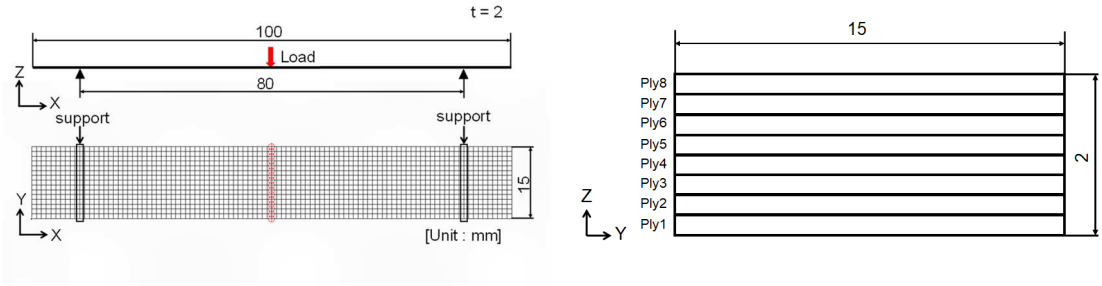

(a) Specimen (b) Layer

Figure 11: Analysis model of bending specimen.

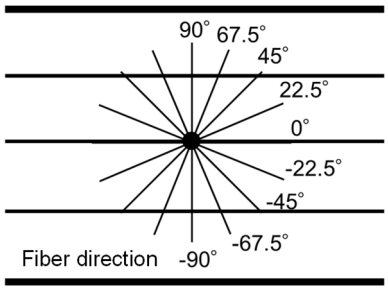

Figure 12: Evaluation angle from fiber direction.

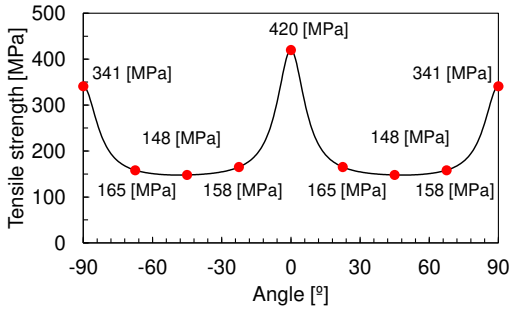

Figure 13: Assumed distribution of fracture stress at each angle.

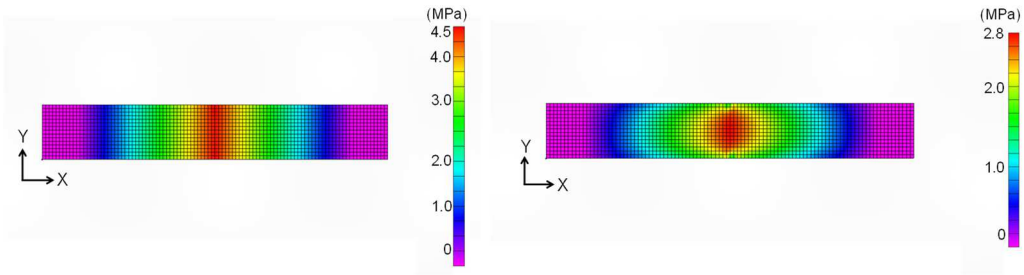

(a)Type-A (b) Type-B

Figure 14: Stress contour of bending test.

3.3 Strength evaluation

In laminated boards, 22.5° pitch direction, where the fibers are not oriented, is considered to be the weakest and most susceptible to fracture, so the stress in 22.5° direction is evaluated. Tables 3 and 4 show the stress in 22.5° direction occurring in each layer of both types. In both types, the stress occurring in Ply 1 and Ply 2 is higher than that in other Plys. In addition, the maximum stress occurred in the 0° material in both types. In this study, stresses are evaluated in 1° increments, and the fracture loads for each direction are determined. Since the stresses in Ply 1 and Ply 2 are higher than those in other plies, resulting in lower fracture loads, Fig 15 shows the distribution of fracture loads for each angle in Ply 1 and Ply 2.

Ply	Angle(°)	Evaluation angle (°)	22.5°directional stress (MPa)	Tensile strength (MPa)
1	0	22.5	1.89	165
2	45	-22.5	0.78	165
3	-45	67.5	0.28	158
4	90	-67.5	0.08	158
5	90	-67.5	-0.08	158
6	-45	67.5	-0.28	158
7	45	-22.5	-0.78	165
8	0	22.5	-1.89	165

Table 3: Analyzed stress of each ply in 22.5° direction (Type-A).

Ply	Angle(°)	Evaluation angle (°)	22.5°directional stress (MPa)	Tensile strength (MPa)
1	45	-22.5	1.36	165
2	0	22.5	1.79	165
3	90	-67.5	0.47	158
4	-45	67.5	0.10	158
5	-45	67.5	-0.10	158
6	90	-67.5	-0.47	158
7	0	22.5	-1.79	165
8	45	-22.5	-1.36	165

Table 4: Analyzed stress of each ply in 22.5° direction (Type-B).

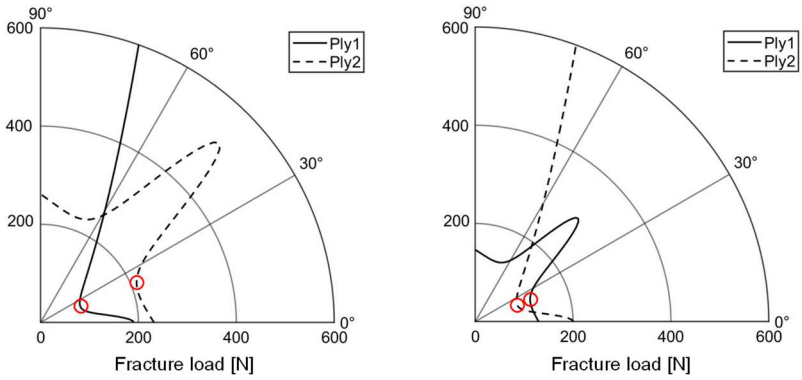

(a) Type-A (b) Type-B

Figure 15: Distribution of fracture load at each angle in three-point bending analysis.

The knee point load is 87 N (= 165/1.89) for Type A and 92 N (= 165/1.79) for Type B, corresponding to 87% (= 87/100) and 107% (= 92/86) of the experimental values, respectively. The knee point loads in 22.5° direction are plotted in Fig. 15. They locate at about the smallest area of the distribution of the knee point load and the average load of Type-A looks larger than Type-B.

4 STRENGTH OF STRUCTURAL SAMPLE

4.1 Loading test

Laminated boards used in three-point bending tests are also used. Diaphragm molding is used to mold test sample. As shown in the Fig. 16, the laminated plate is heated to 275°C for 500 seconds using an IR oven (DIR631), and the softened laminated plate is pressed into a semicylindrical mold with a diameter of 100 mm and a length of 200 mm. A diaphragm molding machine (MEMBRA6, LEIBROCK CO.) is used to mold the sample with a molding pressure of 0.4 MPa and a vacuum time of 15 seconds to produce a semicylindrical sample. As shown in the figure, the sample is fixed to the fixtures at both ends using epoxy adhesive (Three Bond 2082C), and the test is conducted using a fixture that could apply load only to the central part of the sample shown as Fig. 18.With a test speed of 0.25 mm/min and a support distance of 175 mm, as shown in the Fig. 17. A strain gauge is attached directly below the load

application point to measure the circumferential strain. The load-strain diagram measured by the test is shown in the Fig. 19. Table 5 shows the knee point loads for both types obtained in the test. The average load at the knee point is1867 N for Type-A and 1269 N for Type-B.

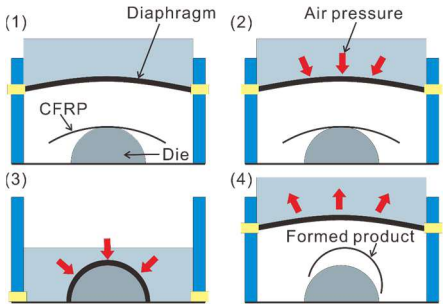

Figure 16: Sample preparation method using diaphragm molding.

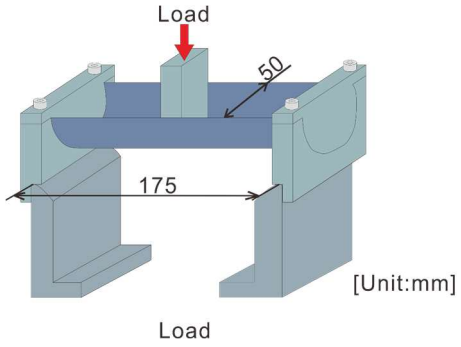

Figure 17: Diagram of loading test of structural sample.

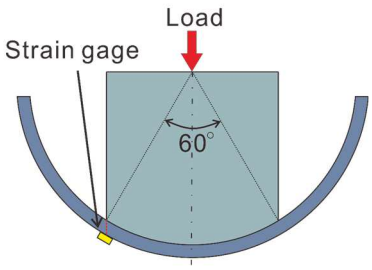

Figure 18: Location of load-bearing parts and strain gauge.

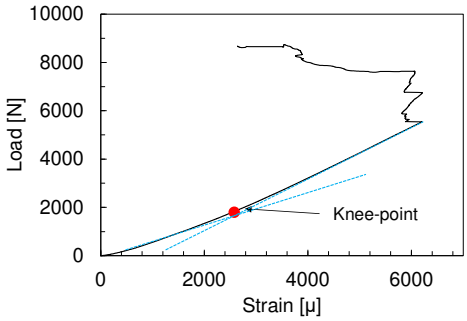

Figure 19: Load-strain curve of structural samples.

	Type-A[N]	Type-B[N]
No.1	1764	1462
No.2	1710	1425
No.3	2125	920
Ave±S.D.	1867±226	1269±302

Table 5: Knee point load in Loading tests of structural sample.

4.2 Finite element analysis

The analytical model of the structural sample is created in FEMAP with NX Nastran, using shell rectangular elements with a mesh size of 1 mm. As shown in Fig. 20, a rigid element is used to apply a unit load of 1 N in the negative direction of the Z axis, with the load point as an independent node free only in the translational Z direction and all degrees of freedom dependent on the dependent node on the structural sample side. The support points at the ends are free only in the direction of rotation around the X axis as independent nodes, and the dependent nodes on the structural sample side are subordinated in all degrees of freedom. Stress contour diagrams of the outermost layers of both types are shown in Fig. 21. For both types, there is a tendency for stress concentration at the edge location of loading fixture as Fig. 18. Therefore, stress evaluation is conducted at the stress concentration area for both types. In this study, the stress is transformed by 1° with respect to the fiber direction in each layer, and the load, at which the composite sheet reached breaking stress at each angle, is taken as the knee point load.

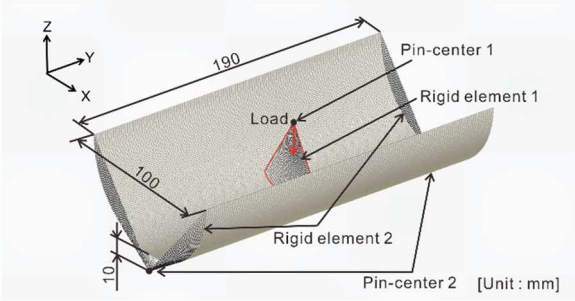

Figure 20: Analysis model of structural samples.

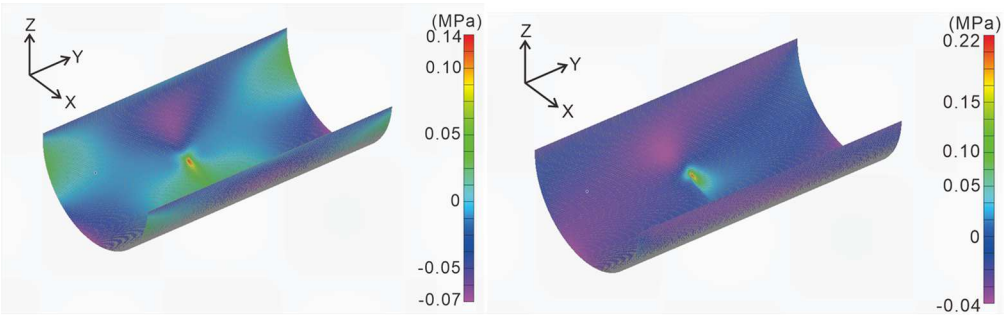

(a) Type-A (b) Type-B

Figure 21: Analysis model of structural samples.

4.3 Strength evaluation

Considering that the direction in which the fibers are not oriented is the weakest and most susceptible to breakage, the stress in 67.5° direction is evaluated. Tables 6 and 7 show the stress generated in 67.5° direction for both types. In both cases, the largest value is observed in the outermost layer. The stress obtained from the structural sample analysis is similarly converted 1° at a time from the fiber direction, and the stress generated in each direction is calculated. Similarly, the distribution of angles and fracture loads in Ply1 and Ply2 is shown in Fig. 22.

Ply	Angle(°)	Evaluation angle (°)	67.5°directional stress (MPa)	Tensile strength (MPa)
1	0	67.5	0.076	158
2	45	22.5	0.074	165
3	-45	112.5	0.035	158
4	90	-22.5	0.067	165
5	90	-22.5	0.035	165
6	-45	112.5	-0.001	158
7	45	22.5	-0.025	165
8	0	67.5	-0.021	158

Table 6: Analyzed stress of each ply in 67.5° direction (Type-A).

Ply	Angle(°)	Evaluation angle (°)	67.5°directional stress (MPa)	Tensile strength (MPa)
1	45	22.5	0.085	165
2	0	67.5	0.060	158
3	90	-22.5	0.081	165
4	-45	112.5	0.023	158
5	-45	112.5	0.013	158
6	90	-22.5	0.019	165
7	0	67.5	-0.003	158
8	45	22.5	-0.033	165

Table 7: Analyzed stress of each ply in 67.5° direction (Type-B).

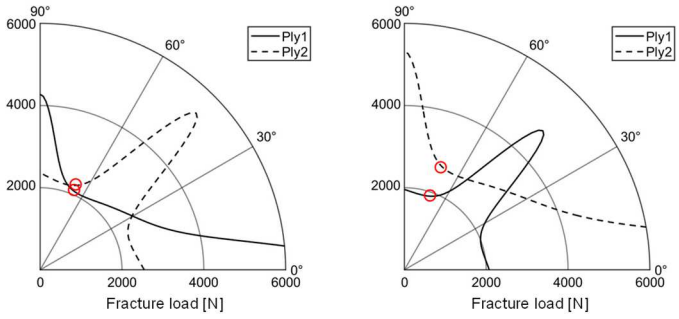

(a)Type-A (b)Type-B

Figure 22: Distribution of fracture load at each angle in structural sample loading analysis.

In the structural sample analysis, the knee point is defined as the point of failure of the weakest layer, and the minimum fracture load is taken as the knee point load. The knee point loads are 2079 N (= 158/0.076) for Type-A and 1941 N (= 165/0.085) for Type-B, corresponding to 111 % (=2079/1867) and 153 % (= 1941/1269) of the experimental values, respectively. As same as bending test, the knee point loads in the weakest direction are plotted in Fig. 22. The plots of Type-A locate at about the smallest area, and also the plots of Type-B locate at the smallest area.

5 CONCLUSIONS

Tensile tests of composite sheets (CF/PA66 twill weave), flexural tests of laminated composites and loading tests of laminated structure samples, and finite element analysis are conducted to predict the initial failure load using a strength evaluation index based on the knee point of laminated composite material. The following is a summary of the findings.

- The knee point load can be predicted by obtaining the stress in each direction by 22.5° pitch in the analysis of a laminated composite bending specimen. For the laminated composite in this test, the knee point load can be predicted with the error within 13 % for the experimental value.
- The knee point load can be predicted by obtaining the stress in each direction by 22.5° pitch in the structural sample loading analysis. The laminated composite in this test can predict the knee point load with the error within 53% from the experimental value.

REFERENCES

[1] T. Okabe, Reducing the weight of transport aircraft using carbon fiber-reinforced plastics, *Journal of The Japan Society of Mechanical Engineers*, Vol.116, No.1132, p.201, 2013.

[2] Y. Izuka, Application to industrial use (6), aerospace applications, *Journal of The Society of Fiber Science and Technology, Japan*, Vol.78, No.11, pp.514-516, 2022.

[3] X. Zhang, Y. Chen and J. Hu, Recent advances in the development of aerospace materials, *Progress in Aerospace Sciences*, Vol.97, pp.22-34, 2021.

[4] M. Nakajima, Manufacturing technology of airframe structure, *Journal of The Japan Society for Precision Engineering*, Vol.75, No.8, pp.862-871, 2014.

[5] R. McKenna, P. Ostman v.d. Leye and W. Fichtner, Key challenges and prospects for large wind turbines, *Renewable and Sustainable Energy Reviews*, Vol.53, pp.1212-1221, 2016.

[6] J. H. Sinclair and C. C. Chamis, Fracture modes in off-axis fiber composites, *Polymer Composites*, Vol.2, No.1, pp.45-52, 1981.

[7] M. Kawai and T. Taniguchi, Off-axis fatigue behavior of plain weave carbon epoxy fabric laminates at room and high temperatures and its mechanical modeling, *Composites Part A*, Vol.37, No.2, pp.243-256, 2006.

[8] M. Kawaguchi, Y. Suzuki, E. Suzuka, K. Tanaka and K. Watanabe, Introduction on strength evaluation of twill weave laminated composite considering knee point, *Journal of the Society of Materials Science, Japan*, Vol.74, No.1, pp.47-54, 2025.

[9] D. Hijikuro, Y. Kanno, K. Shiraishi and T. Hayashi, The structural strength tests of transport aircraft C-2, *The Japan Society for Aeronautical and Space Science*, Vol.66, No.11, pp.338-340, 2013.

High Temperature Fatigue Performance Evaluation of Fibre-Reinforced Polymer Composites Utilizing Monotonic and DMA Tests

Shoab Ahmed Chowdhury, Ph.D.
Applications Scientist

TA Instruments

Fictional Case Study – Material Failure Analysis

An automotive component manufacturer has had an unacceptably high failure rate of their cutting edge new Glass Fiber Reinforced Polymer (GFRP) component. They had done significant development and testing of their design in simulation and in the real world environment, but they are still having failures.

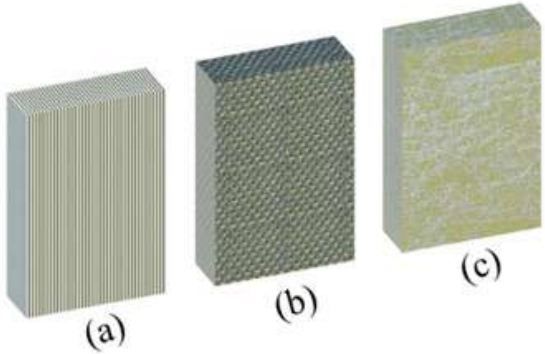

©2022 Waters Corporation

Failure Characteristics: Key Observations

Waters™ | TA Instruments

Failure Characteristics

- Random and usually after long duration
- Significantly more often at elevated temperatures
- No obvious manufacturing defects
- Signs of flexural failure



The failure occurring across the part in a long flat section.

©2022 Waters Corporation

Investigation for Source of Failure

Waters™ | TA Instruments

Operating Temperature 80 to 100 °C → Within Range

Max flexural stress level of 250 MPa → Below Rated Strength

Cyclic stress/cycles 5000 cycles @ 225 MPa Flexural Stress → Below S-N curve

	G-10
Tensile Strength (MPa)	240-345
Flexural Strength (MPa)	310-413
Max Temperature (° C)	130

* no specification for fatigue strength is available

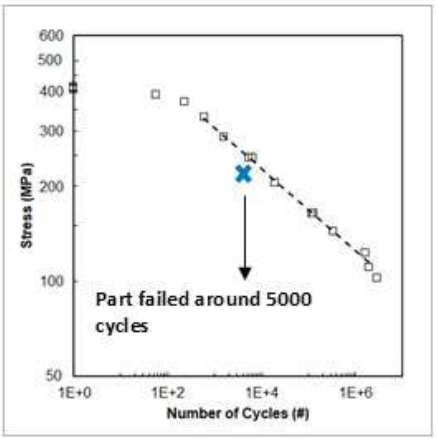

No significant errors were discovered from strength and temperature data!

©2022 Waters Corporation

Hypothesis #1:
The supplied material doesn't meet the reported specification

- **Proposed Test:** Monotonic Four-Point Bending which reflects the in-service loading conditions

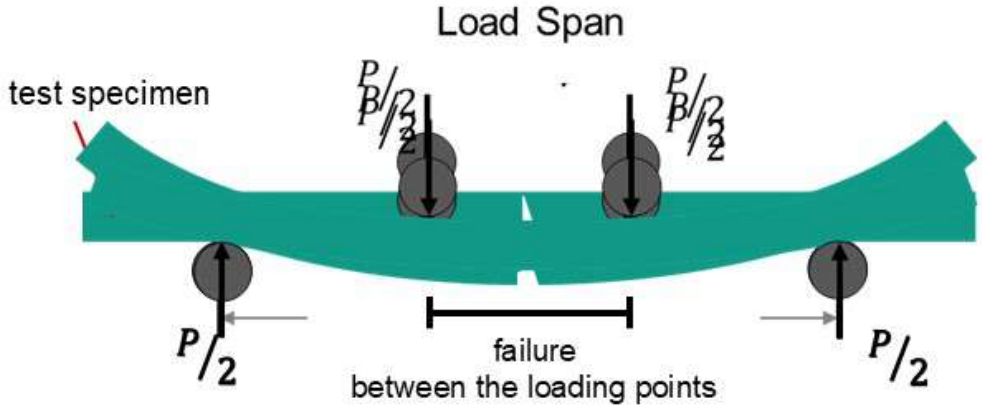

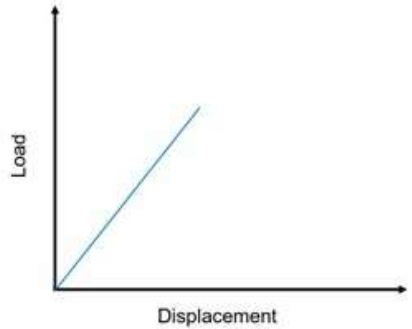

Sample is deformed a under quasistatic ramp loading up to failure

©2022 Waters Corporation

Flexural Properties (Monotonic Test)

- Results are in agreement with the material properties reported by the supplier

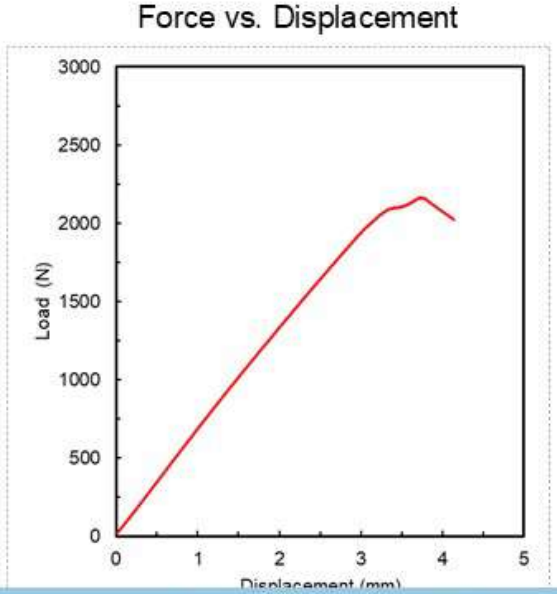

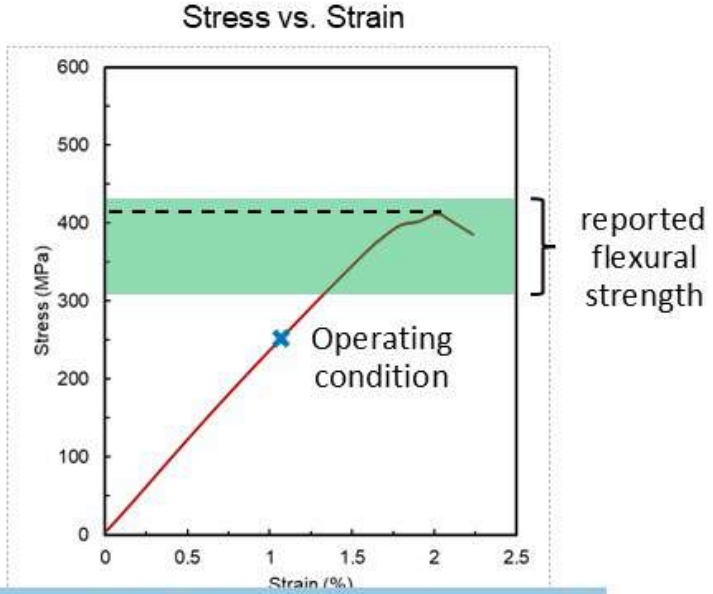

Its not a design issue and its not the vendor's fault, what could it be?

Hypothesis 2:
Material underperforms at the higher operating temperature

Reasoning → The failed components have a highest operating temperature of 100C

- **Proposed Test:** DMA Temperature Ramp

Example Waveform Pattern

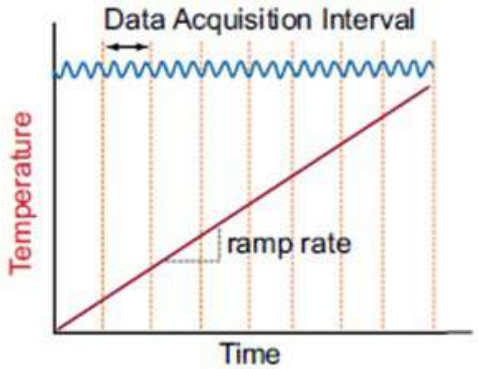

→ **Utilized for the qualitative assessment of the effect of temperature on the material**

©2022 Waters Corporation

DMA Temperature Ramp

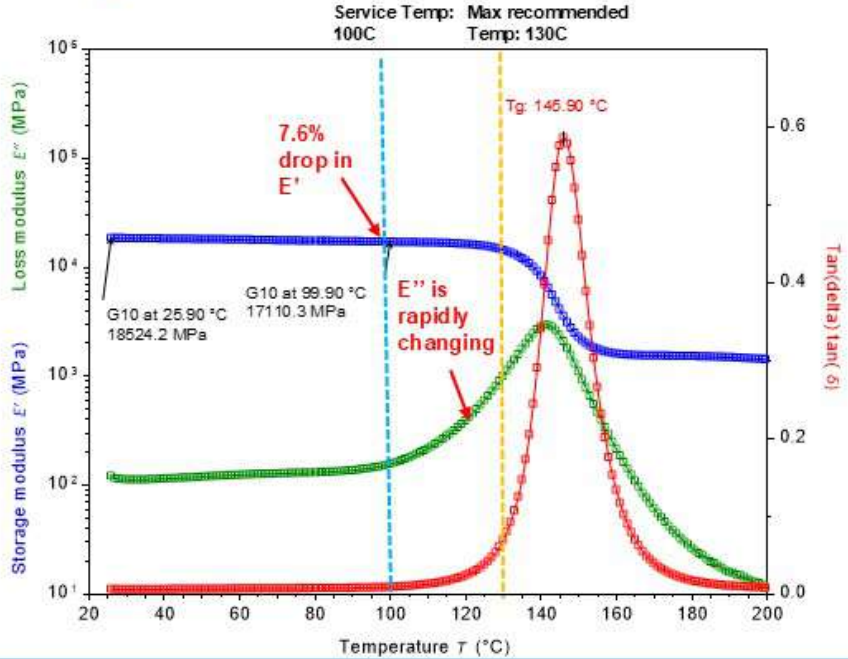

A drop in storage modulus may indicate reduced strength and fatigue life

Flexural Properties (Monotonic Test at Elevated Temperature)

Lower strength may indicate a lower fatigue life at an elevated temperature of 100 °C

Force vs. Displacement

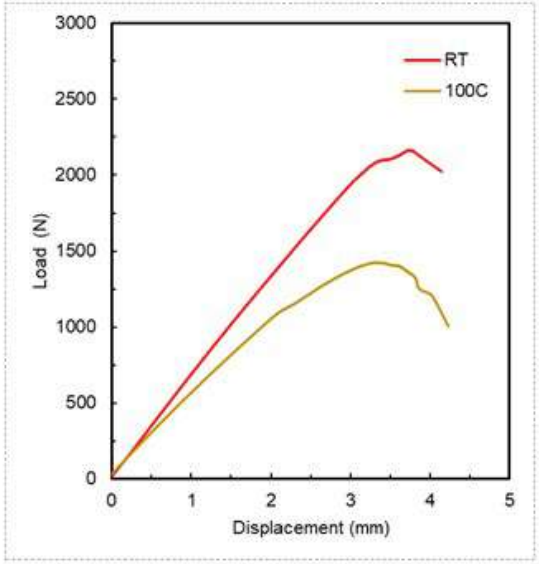

Stress vs. Strain

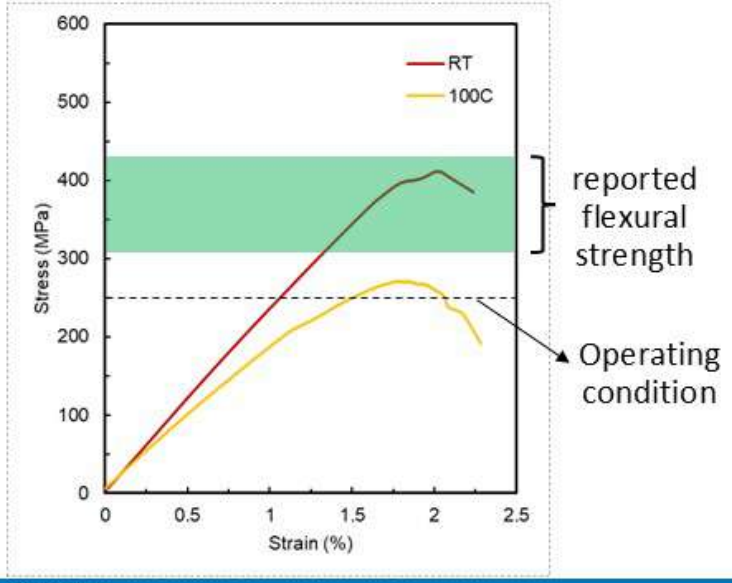

©2022 Waters Corporation

Determination of Dynamic Fatigue Properties in Flexure

- **Test Method**: Specimen is cyclically loaded between two specific stress or strain levels (< ultimate strength of the material) at a uniform frequency until failure
- **Failure**: Specimen is deflected cyclically until rupture occurs or the maximum strain is reached

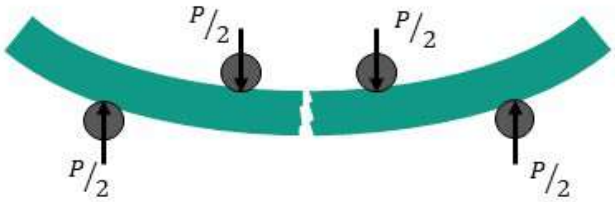

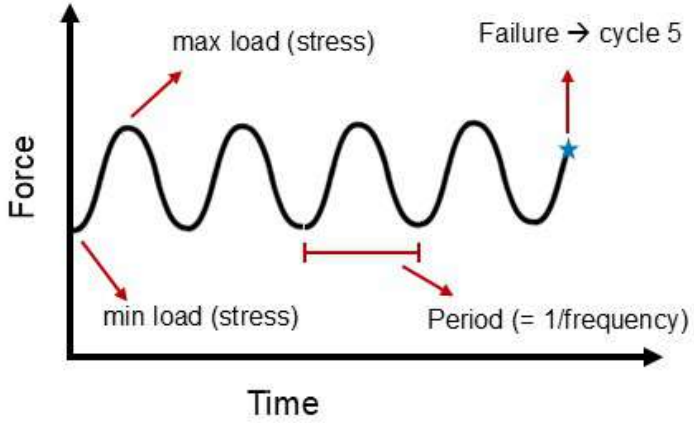

©2022 Waters Corporation

Flexural Fatigue Properties - Cyclic Loading

Waters™ | TA Instruments

There is a significant drop in fatigue life at a higher temperature of 100 °C

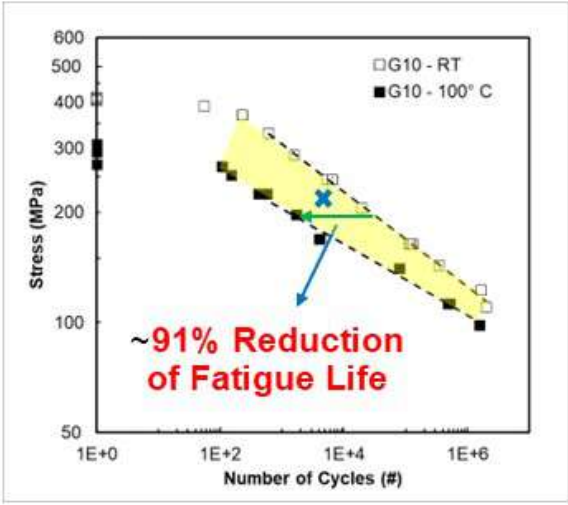

Consideration Point

↓

Not reasonable to lower service condition temperatures

Proposed Solution

↓

An alternative material with a higher temperature rating

©2022 Waters Corporation

New Material vs Current Material

The New Material , G11 demonstrates superior strength and fatigue life at continuous operating temperatures of 100 °C

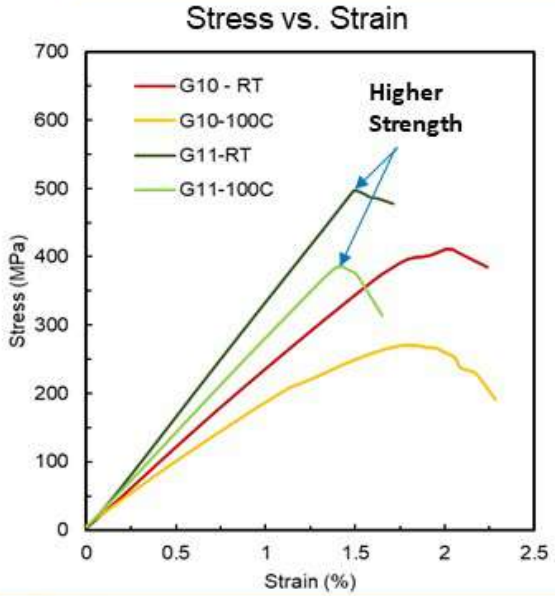

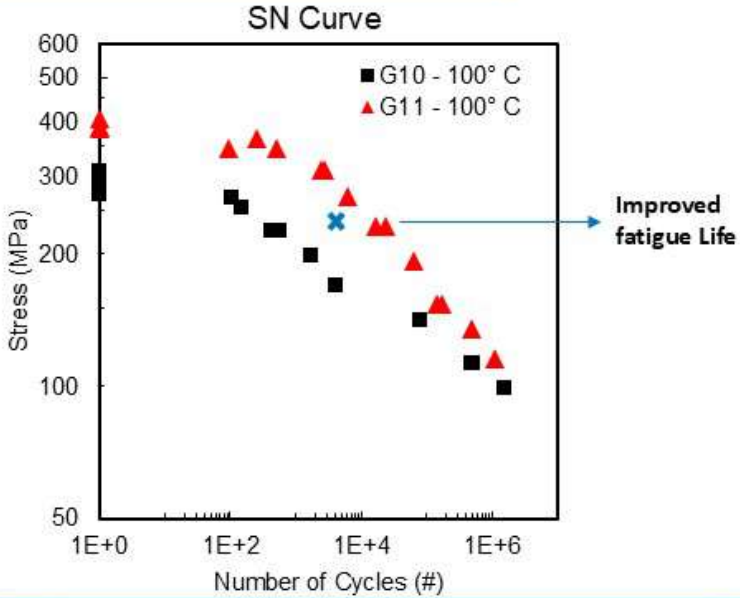

©2022 Waters Corporation

Case Study Takeaways

Waters™ | TA Instruments

DMA Test	→	7.6% reduction in storage modulus at 100C
Monotonic Test at 100 C	→	29% Reduction in strength
Fatigue Test at 100 C	→	91% Reduction in service life

The strength and max rated temperature data may not be enough!

©2022 Waters Corporation

Waters™ | TA Instruments

Questions!

MECHANICAL CHARACTERIZATION OF MWCNT BASED BASALT FIBER-REINFORCED POLYMER (BFRP) COMPOSITE BY USING THE MODE I AND MODE II METHODS

Kalyan Kumar Singh[1*], Hemant Priyadarshi[1]

[1]*Indian Institute of Technology (ISM), Dhanbad, Jharkhand, India*

[*]**Corresponding author***: kksingh@iitism.ac.in*

Abstract

Basalt fiber-reinforced polymer (BFRP) composites contain attention for their potential in high-performance structural applications due to their favourable mechanical properties and environmental benefits. This study investigates the fracture behaviour of BFRP composites under Mode I and Mode II loading with a comparative analysis of neat BFRP and doped with 1%, 2% and 3% multi-walled carbon nanotubes (MWCNT). The results shows the differences in fracture toughness, and specimens reinforced with MWCNT performed better compared to neat BFRP. The MWCNT reinforcement's configuration demonstrates synergistic effects, providing enhanced resistance to crack propagation and superior mechanical behaviour. These results demonstrate the potential utility of MWCNT doped BFRP composites in enhancing strength and stiffness for current applications.

Keywords- BFRP, Mode I, Mode II & MWCNTs.

1. Introduction

Basalt fibre-reinforced polymer (BFRP) composite is one of the high strengths to weight ratio, natural and resistance to high temperature material, which BFRP has become popular to be used as the structural and aerospace applications [1]. However, their poor fracture and delamination resistant behavior to different types of loadings are the great challenges. To solve this problem, the researchers working on the incorporation of nanomaterials in the polymer matrix, for example, multi-walled carbon nanotubes (MWCNTs), to enhance the fracture characteristics have been studied [2]. MWCNTs with excellent mechanical properties, such as tensile strength and high aspect ratio can serve as an effective reinforcement for improvement of crack bridging, energy absorption, and interfacial bonding [3]. Fracture mechanics is an essential part of the failure analysis of the advanced engineering materials of fibre reinforced polymer (FRP) composite. As strong as these materials are with excellent strength to weight properties and mechanical capabilities, they are faced with the risk of delamination or an interlaminar failure mechanism that renders structural integrity largely hampered. Composites fracture behavior is typically classified to have three possible modes: Mode-I (opening), Mode-II (sliding) and Mode III (tearing) each with a particular displacement of the fracture surface with respect to the crack front [4]. The most known among them are Mode-I and Mode-II delamination because they apply to service-related failures cases. Mode-I fracture is usually defined by the crack growing under the action of the tensile stress that acts perpendicular to the crack plane, and it is preferably observed in the Double Cantilever Beam (DCB) test. This technique delivers the Mode-I interlaminar fracture toughness G_{IC} and this measures the amount of energy to open and extend a crack [3]. Mode-II fracture, on the contrary, presents in-plane shear stresses have a parallel direction to the crack plane and is determined by the End-Notched Flexure (ENF) test, where the Mode-II fracture toughness G_{IIC} can be obtained [5]. In order to enhance interlaminar performance, recent researches have been conducted with the supplement of the nanofillers that includes multi-walled carbon nanotubes (MWCNTs)

which is capable of providing very good mechanical strengthening and interfacial bonding arrays [6] & [7]. Nevertheless, the effects of the MWCNT reinforcement largely depend on its dispersion and optimum concentration in the matrix. This article examines how loading MWCNT affects the Mode-I and Mode-II fracture toughness of basalt fibre-reinforced polymer (BFRP) laminates, to provide an answer to the best nanoparticle amount that yields the highest delamination-resistance [8].

2. Material selection and specimen fabrication

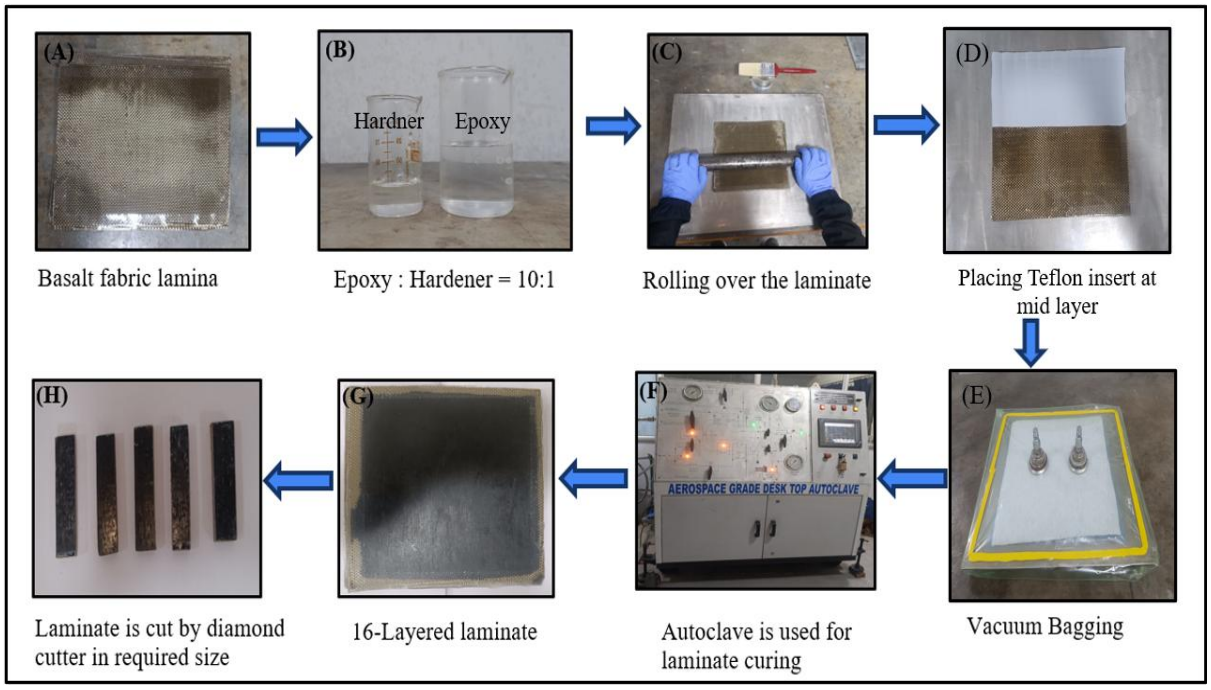

Figure 1. Fabrication process of BFRP laminate

In this study, 380 GSM woven basalt fabric was primarily used as the reinforcement material. The fabric exhibited bi-directional characteristics, with fiber diameters ranging from 12 µm to 24 µm. The basalt fabric was procured from CF Composite, Delhi, India. Woven fabrics are generally preferred for reinforcement due to their balanced in-plane properties and ease of handling during the fabrication process. As the matrix material a thermosetting epoxy resin system HY-951 epoxy and LY-556 hardener both provided by CF Composite were used. All these elements were combined at room temperature [9]. The cross-linked structure generated between the epoxy resin and the hardener improved the adhesive, mechanical properties of the matrix system. The MWCNTs was pure with 99.9 % purity were procured from the AdNano technologies at Bangalore, India. Uniform dispersion of MWCNTs in the epoxy was the objective, which was achieved with the help of a two-stage dispersion method as shown in figure 1. To begin with, the MWCNTs were added to 50 ml of acetone, mixed together with the help of the magnetic stirrer within 30 minutes in order to get a uniform mixture [10]. This was preceded by ultrasonication in a probe-type sonicator at 30 min in order to de-agglomerate the nanotubes further and improve dispersion [11]. Further, 200 ml of epoxy resin solution was added to MWCNT-acetone solution. The mixture that came about was stirred magnetically during a period of 15 minutes, and then an additional probe-style ultrasonication of 15 minutes was carried out. To remove residual acetone, the mixture was placed in an air oven at 60°C for 10 minutes. A curing agent was then added to the epoxy-MWCNT mixture in a 10:1 ratio (resin to hardener), providing a gel time of approximately 20 minutes, as recommended by the supplier, to regulate the curing process effectively [12]. Laminates were fabricated using woven

basalt fabric sheets cut to 240 × 240 mm² dimensions. The layup sequence followed a quasi-isotropic and symmetric stacking order of $[0°/\pm45°/90°]_s$. The hand lay-up technique was employed for fabrication, where the epoxy-MWCNT-hardener mixture was uniformly applied between the layers using a soft brush to ensure even distribution. Composite laminate specimens were precisely cut using Abrasive Water Jet Machining (AWJM), which utilizes a high-pressure stream of water mixed with abrasive particles. Basalt fibre laminates (200 mm × 200 mm) were firmly fixed to the machine bed to ensure stability during cutting. The process was performed at Polymer composite lab (Mechanical testing and damage analysis), Mechanical Engineering Department, IIT (ISM) Dhanbad. A CNC-controlled jet followed a programmed path to shape the specimens as per ASTM standards ASTM D5528 140 mm × 25 mm × 5 mm for Mode I and ASTM D7905 180 mm × 25 mm × 5 mm for Mode II testing [13] & [14]. The high-velocity jet removed material efficiently with minimal thermal effects, ensuring clean cuts and maintaining the structural integrity of the composites.

3. Testing and Characterization of BFRP composite laminate

All experimental investigations were carried out using a Hounsfield H50KS Universal Testing Machine (UTM) with a load capacity of 50 kN, located at the Strength of Materials (SOM) Laboratory, Mechanical Engineering Department, IIT Dhanbad. The UTM system was employed to evaluate mechanical properties of Basalt Fibre Reinforced Polymer (BFRP) laminates, including flexural strength. For each experimental test, five specimens were fabricated in accordance with the ASTM standards. A constant crosshead displacement rate of 2 mm/min was maintained throughout the tests. To monitor damage evolution in the specimens, a Celestron digital microscope with a 5 Mega pixel camera and 20–200× magnification range was utilized for real-time visual inspection during testing.

3.1 Mode-I Interlaminar Fracture Toughness (ILFT) Analysis

The figure 2 illustrates the process of Mode-I Interlaminar Fracture Toughness **(**ILFT) testing was performed following the ASTM D5528 standard, using a Double Cantilever Beam (DCB) configuration [15]. Each DCB specimen measured 140 mm × 25 × 5 mm, and an initial delamination of 63 mm was introduced during the hand lay-up process using a 50 µm thick Teflon insert placed at the mid-plane [16]. To facilitate the application of load, piano hinges were bonded to the top and bottom surfaces of the specimens using Araldite standard epoxy adhesive. To track crack propagation during the test, the specimen's side surfaces were coated with white marker and marked at 1 mm intervals. The DCB specimens were loaded under displacement control at a crosshead speed of 2 mm/min in the opening (positive) direction.

The toughness calculation was done with the following equation 1,

$$\mathbf{G_{IC}} = \frac{\mathbf{3(A1)(A2)}}{\mathbf{2}\boldsymbol{B}} \qquad \ldots\ldots (1)$$

Where, $C = \frac{u}{Pc}$;

$$ln(A1) = \left(\frac{1}{n}\right)[(-3\sum \ln a\ ) + \sum \ln C]$$

$$ln(A2) = \left(\frac{1}{n}\right)[(\sum \ln a\ ) + \sum \ln Pc]$$

u = Displacement (mm) -Vertical distance.

P_c =Critical load (N);

a =Crack length (mm);

B = Specimen thickness (mm);

C= compliance



Figure 2. The experimental setup for the Mode-I fracture toughness test.

3.2 Mode-II Interlaminar Fracture Toughness (ILFT) Analysis

Mode-II fracture behaviour was investigated following ASTM D7905, utilizing the End Notched Flexure (ENF) specimen configuration. The ENF specimens measured 180 mm × 25 mm × 5 mm, and a 50 mm pre-crack was introduced at the mid-plane using a 50 µm Teflon insert during lay-up. Tests were performed under displacement control at a crosshead speed of 2 mm/min in the negative (shear) direction as shown in figure 3. Similar to Mode-I, the side surfaces were marked at 1 mm intervals using white correction fluid to track crack growth and layer sliding. The Mode-II test configuration is shown in Figure. The critical Mode-II strain energy release rate, G_{IIC}, was calculated using the following expression based on simple beam theory for an ideally clamped ENF specimen:

The toughness calculation was done with the following equation 2,

$$G_{IIC} = \frac{9P_c^2 C\, a^2}{2B(2L^3+3a^3)} \qquad \text{..... (2)}$$

Where, P_c = maximum value of force, in the load-extension graph, a= delamination length used in fracture test, B = specimen width

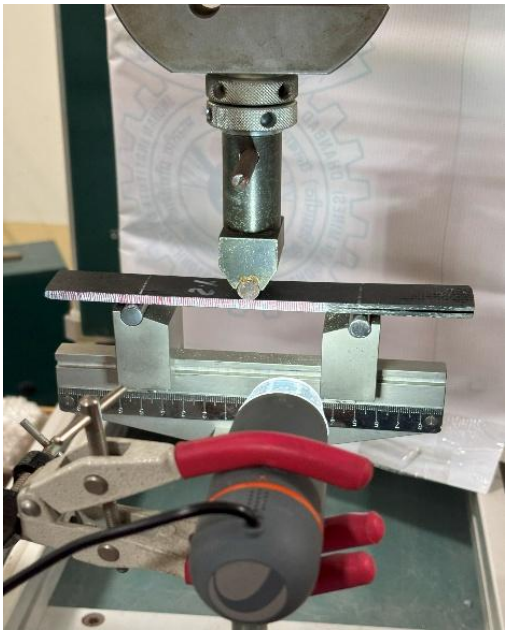

Figure 3. The experimental setup for the Mode-II fracture toughness test.

4. Results and Discussions:

4.1 Mode I Interlaminar fracture toughness

The load–displacement graph illustrates the Mode-I fracture behaviour of basalt fibre-reinforced polymer (BFRP) composites doped with varying concentrations of multi-walled carbon nanotubes (MWCNTs), revealing that the addition of MWCNTs significantly influences crack resistance [17]. Among the tested configurations, the composite with 1 wt% MWCNT exhibits the highest peak load (~39 N) and the largest displacement, indicating superior energy absorption and enhanced fracture toughness due to effective crack-bridging, pull-out, and deflection mechanisms introduced by the well-dispersed nanotubes. The 2 wt% MWCNT sample also demonstrates improved performance over pristine BFRP (~30 N peak load), although the benefit is reduced, likely due to initial signs of MWCNTs agglomeration [18]. As shown in figure 4 (a) & (b) In contrast, the 3 wt% MWCNT composite performs worse than the pristine sample, with a lower peak load (~20 N), suggesting that excessive MWCNT content leads to dispersion challenges and cracking nature of the polymers that act as failure initiation sites. The bar chart displays the Mode-I critical strain energy release rate G_{IC} of basalt fibre-reinforced polymer (BFRP) composites with different concentrations of multi-walled carbon nanotubes (MWCNTs), demonstrating the impact of nanotube incorporation on fracture toughness. The BFRP samples with 1 wt% MWCNTs composite exhibit the highest G_{IC} value (~520 J/m²), nearly doubling that of pristine BFRP (~270 J/m²), due to effective crack-bridging, nanotube pull-out, and improved interfacial strength. While the 2 wt% MWCNT sample also shows an increase in G_{IC} , a decline is observed at 3 wt%, indicating that excessive MWCNT loading may lead to agglomeration and defect formation, adversely affecting fracture resistance.

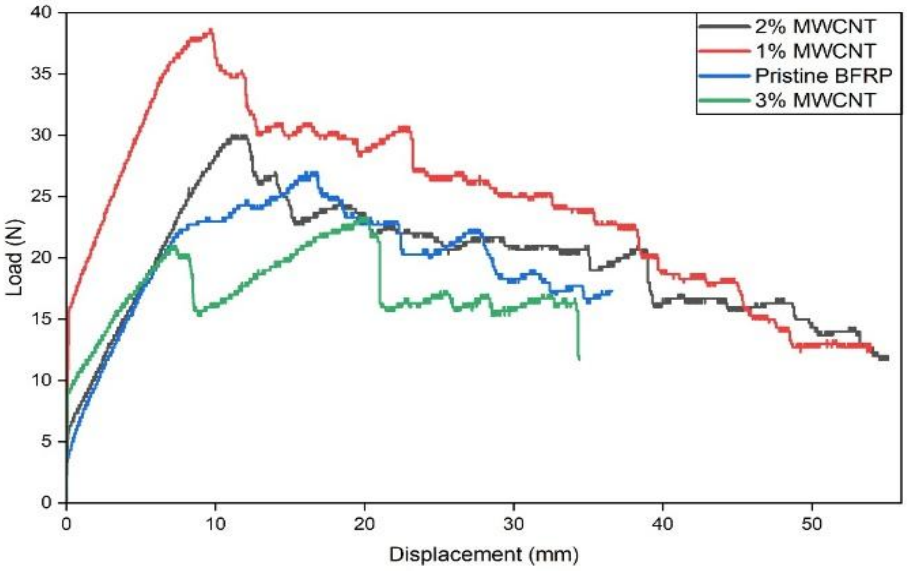

Figure 4 (a). Typical load vs displacement curves of DCB specimen.

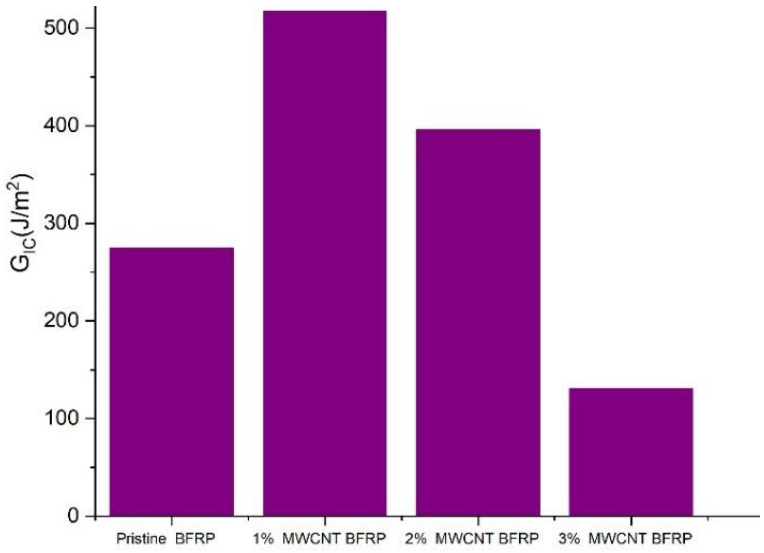

Figure 4 (b) Comparison of Mode I interlaminar fracture toughness with varying MWCNTs

Table 1. Mode1 experimental results

MWCNT wt%	**G_{IC} (J/m^2)**
Pristine BFRP	274.28
1% MWCNT BFRP	517.28
2% MWCNT BFRP	396.16
3% MWCNT BFRP	130.76

4.1 Mode II Interlaminar fracture toughness

The Figure 5 (a) & (b) illustrates Mode-II of load displacement characteristics of basalt fibre reinforced polymer (BFRP) composites, that were loaded with different amounts of multi-walled carbon nanotubes (MWCNTs) indicate a great change in the interlaminar shear strength due to the optimum number of nanotubes added. Composite with 1 wt% MWCNT has maximum load-bearing capacity, and displacement meaning that it could withstand delamination because of shear effects more due to the increase of the interface adhesion, crack-bridging mechanism, and energy dissipation mechanism because of the well-dispersed MWCNTs [19]. Comparatively, the 2% wt MWCNT sample material is also performing better than the pristine BFRP, whilst the 3 wt% MWCNT sample illustrates premature failure indicating plentiful nanotube material results in agglomerate clusters and cracking nature of the polymers that weaken the structural integrity. In the bar chart, the Mode-II critical strain energy release rate G_{IIC} is displayed as it correlates the BFRP composites of different contents of the MWCNT which demonstrates the substantial enhancement of interlaminar fracture toughness of the optimised nanotube inclusion [20]. The highest G_{IIC} value was found in the 1 wt% MWCNT BFRP composite (~1850 J/m²), and this material shows better resistance to delamination than pristine BFRP (~750 J/m²) because of the increased number of interfaces caused by MWCNT relative to the other composites, and further addition of 2 wt% MWCNTs fracture toughness was found in between 1 wt% and pristine whereas 3 wt% of MWCNT shows a decreased toughness as compare to pristine there are likely agglomerations and clumps of MWCNT.

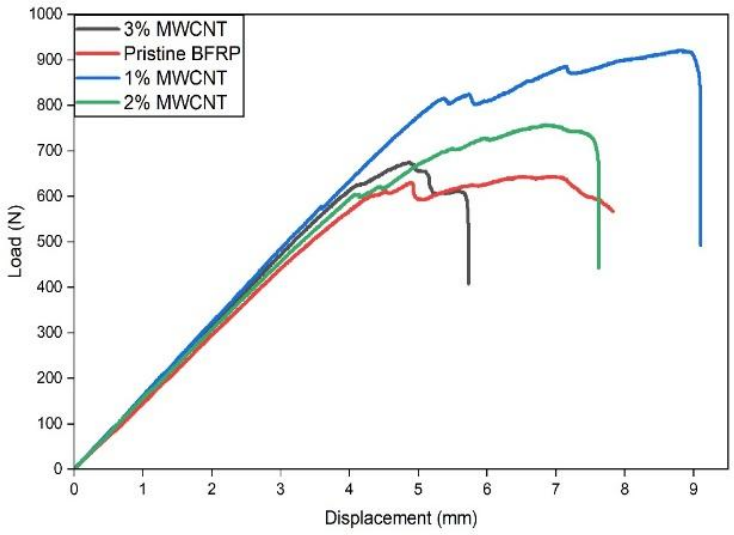

Figure5. (a). Typical load vs displacement curves of ENF specimen.

Table 2. Mode II experimental results

MWCNT wt%	G_{IIC} (J/m²)
Neat BFRP	754.00
1% BFRP	1852.20
2% BFRP	1165.05
3% BFRP	702.00

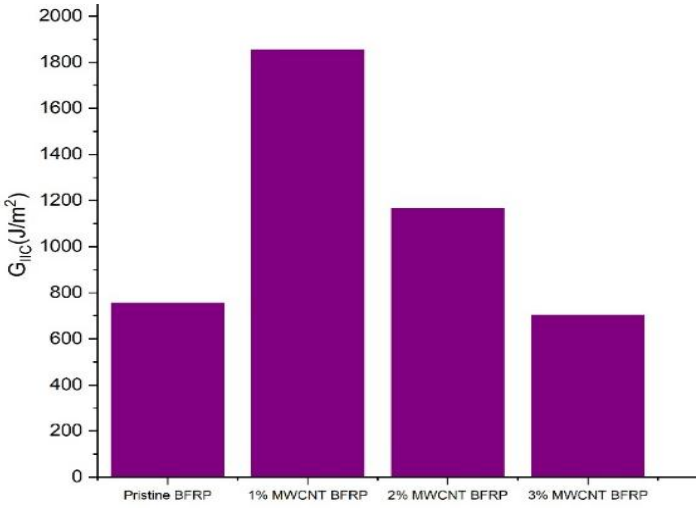

Figure 5 (b) Comparison of Mode II interlaminar fracture toughness with varying MWCNTs

5. Conclusions:

This experimental studied shows the effect of different % of MWCNTs on basalt fiber composites based on mode I and mode II Fracture toughness test and observations are given below:

- Multi-walled carbon nanotubes (MWCNTs) immersion into basalt fibre-reinforced polymer (BFRP) composites has a profound effect on Mode-I fracture toughness G_{IC}, and the performance varies hugely according to the nanotube concentration.
- BFRP with 1 wt % MWCNT exhibited the best fracture performance, with Mode-I and Mode-II fracture toughness values of approximately 520 J/m² and 1850 J/m² respectively, indicating optimal reinforcement and energy dissipation.
- BFRP with 2 wt % MWCNT showed moderate improvement over pristine BFRP, with G_{IC} around 390 J/m² and G_{IIC} about 1250 J/m².
- BFRP with 3 wt % MWCNT resulted in a decline in performance, with reduced fracture toughness $G_{IC} \approx 150$ J/m², $G_{IIC} \approx 700$ J/m²), attributed to MWCNT agglomeration and stress concentration effects.
- The pristine BFRP composite recorded the lowest toughness values $G_{IC} \approx 270$ J/m², $G_{IIC} \approx 750$ J/m²), confirming that 1 wt% MWCNT is the optimal concentration, provided the dispersion is well controlled for structural efficiency.

6. References.

[1] V. Fiore, T. Scalici, G. Di Bella, and A. Valenza, "A review on basalt fibre and its composites," *Compos B Eng*, vol. 74, pp. 74–94, Jun. 2015, doi: 10.1016/j.compositesb.2014.12.034.

[2] R. Shrivastava and K. K. Singh, "Mechanical property characterization of glass/epoxy composite with varying fiber percentage and mid-plane ply orientation," *Journal of the Brazilian Society of Mechanical Sciences and Engineering*, vol. 44, no. 4, Apr. 2022, doi: 10.1007/s40430-022-03402-4.

[3] T. A. Sebaey, N. Blanco, J. Costa, and C. S. Lopes, “Characterization of crack propagation in mode I delamination of multidirectional CFRP laminates,” *Compos Sci Technol*, vol. 72, no. 11, pp. 1251–1256, Jun. 2012, doi: 10.1016/j.compscitech.2012.04.011.

[4] R. Shrivastava and K. K. Singh, “Interlaminar Fracture Toughness Characterization of Laminated Composites: A Review,” Jul. 02, 2020, *Taylor and Francis Inc.* doi: 10.1080/15583724.2019.1677708.

[5] P. Jadhav, “Modeling of mode 1 delamination behavior in laminated composite structures for aerospace applications,” in *Materials Today: Proceedings*, Elsevier Ltd, 2023, pp. 61–67. doi: 10.1016/j.matpr.2022.11.341.

[6] P. Karapappas, A. Vavouliotis, P. Tsotra, V. Kostopoulos, and A. Paipetis, “Enhanced fracture properties of carbon reinforced composites by the addition of multi-wall carbon nanotubes,” in *Journal of Composite Materials*, May 2009, pp. 977–985. doi: 10.1177/0021998308097735.

[7] H. Priyadarshi and K. K. Singh, “Enhancing low-velocity impact resistance of basalt/epoxy laminates through MWCNT nanoparticle incorporation,” *Compos Interfaces*, 2025, doi: 10.1080/09276440.2025.2496018.

[8] R. Hemanth and B. Naresh, “DELAMINATION BEHAVIOUR AND EXPERIMENTAL VALIDATION OF GLASS FABRIC/EPOXY MATRIX AND CARBON FABRIC/EPOXY COMPOSITES IN MODE-1 LOADING,” 2014.

[9] D. Quan, J. L. Urdániz, and A. Ivanković, “Enhancing mode-I and mode-II fracture toughness of epoxy and carbon fibre reinforced epoxy composites using multi-walled carbon nanotubes,” *Mater Des*, vol. 143, pp. 81–92, Apr. 2018, doi: 10.1016/j.matdes.2018.01.051.

[10] G. T. Truong and K. K. Choi, “Effect of short multi-walled carbon nanotubes on the mode I fracture toughness of woven carbon fiber reinforced polymer composites,” *Constr Build Mater*, vol. 259, Oct. 2020, doi: 10.1016/j.conbuildmat.2020.119696.

[11] I. D. G. A. Subagia, A. H. Yuwono, and Y. Kim, “Effect of interlaminated carbon and basalt fiber reinforced hybrid composites on mode i fracture toughness,” in *IOP Conference Series: Materials Science and Engineering*, Institute of Physics Publishing, Nov. 2019. doi: 10.1088/1757-899X/553/1/012035.

[12] X. Zhang *et al.*, “Interfacial microstructure and properties of carbon fiber composites modified with graphene oxide,” *ACS Appl Mater Interfaces*, vol. 4, no. 3, pp. 1543–1552, Mar. 2012, doi: 10.1021/am201757v.

[13] “Test Method for Mode I Interlaminar Fracture Toughness of Unidirectional Fiber-Reinforced Polymer Matrix Composites,” Nov. 15, 2021, *ASTM International, West Conshohocken, PA*. doi: 10.1520/D5528_D5528M-21.

[14] “Test Method for Determination of the Mode II Interlaminar Fracture Toughness of Unidirectional Fiber-Reinforced Polymer Matrix Composites,” Mar. 15, 2019, *ASTM International, West Conshohocken, PA*. doi: 10.1520/D7905_D7905M-19E01.

[15] Z. Liu, Y. Xia, and S. Guo, “Characterization methods of delamination in a plain woven CFRP composite,” *J Mater Sci*, vol. 54, no. 20, pp. 13157–13174, Oct. 2019, doi: 10.1007/s10853-019-03847-4.

[16] M. T. Bashar, U. Sundararaj, and P. Mertiny, “Mode-I interlaminar fracture behaviour of nanoparticle modified epoxy/basalt fibre-reinforced laminates,” *Polym Test*, vol. 32, no. 2, pp. 402–412, 2013, doi: 10.1016/j.polymertesting.2012.10.012.

[17] M. del Pilar de Urquijo-Ventura, J. Alejandro Rodríguez-González, and C. Rubio-González, “Mode I delamination monitoring in carbon nanotubes-glass fiber/epoxy composites using simultaneous electrical self-sensing and acoustic emission techniques,” *Compos Struct*, vol. 351, Jan. 2025, doi: 10.1016/j.compstruct.2024.118608.

[18] Y. Ou, L. Wu, X. Yi, and D. Mao, “Understanding Mode I interlaminar toughening of unidirectional CFRP laminates interleaved with aligned ultrathin CNT fiber veils: Thickness and orientation effects,” *Compos B Eng*, vol. 254, Apr. 2023, doi: 10.1016/j.compositesb.2023.110578.

[19] B. Yenigun, M. S. Chaudhry, E. Gkouti, and A. Czekanski, “Characterization of Mode I and Mode II Interlaminar Fracture Toughness in CNT-Enhanced CFRP under Various Temperature and Loading Rates,” *Nanomaterials*, vol. 13, no. 11, Jun. 2023, doi: 10.3390/nano13111729.

[20] Y. Ou, C. González, and J. J. Vilatela, “Understanding interlaminar toughening of unidirectional CFRP laminates with carbon nanotube veils,” *Compos B Eng*, vol. 201, Nov. 2020, doi: 10.1016/j.compositesb.2020.108372.

[21] M. del Pilar de Urquijo-Ventura, J. Alejandro Rodríguez-González, and C. Rubio-González, “Mode I delamination monitoring in carbon nanotubes-glass fiber/epoxy composites using simultaneous electrical self-sensing and acoustic emission techniques,” *Compos Struct*, vol. 351, Jan. 2025, doi: 10.1016/j.compstruct.2024.118608.

A mechanism-based reaction-diffusion model for frontal polymerization (FP): Toward rapid prediction of FP macro-observables

Donald Bistri

Postdoctoral Research Associate

Beckman Institute for
Advanced Science and Technology

University of Illinois Urbana-Champaign

Regenerative Energy-Efficient Manufacturing of Thermoset Polymeric Materials

ICCM Conference
August 2025







TeamWork

On the application of thermosetting polymers and composites: Perspective and Limitations

Projected Market Value



Study by Market Research Future Article



Aerospace and Defense



Wind Energy



Transportation



Electronics

> 3% → 0 – 3 %

Limitations

Manufacturing – Labor and Capital Intensive



Autoclave for curing large composite structures



Heated mold for wind turbine blades

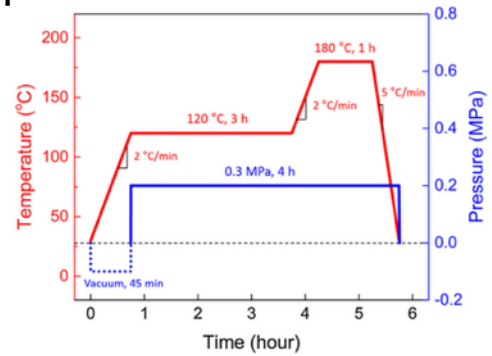

Kim et al. Composites Part A, (2019)

Energy Efficiency – Large continuous energy input

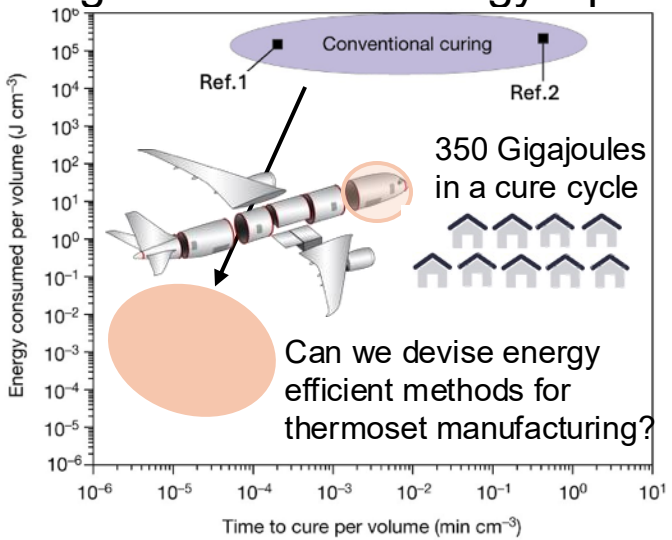

Recyclability – Lack of end-of-life strategies

Covalent network in thermosets limits ability to deconstruct/recycle

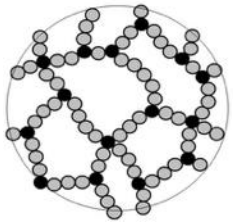



Bloomberg (2020) Article

[1] Timmis, Andrew J., et al. The International Journal of Life Cycle Assessment 20 (2015.
[2] Witik, Robert A., et al.. Journal of Cleaner Production 29

Frontal Ring-Opening Polymerization: An energy-efficient self-sustaining polymerizat route

Monomer + Latent Catalyst

Polymer

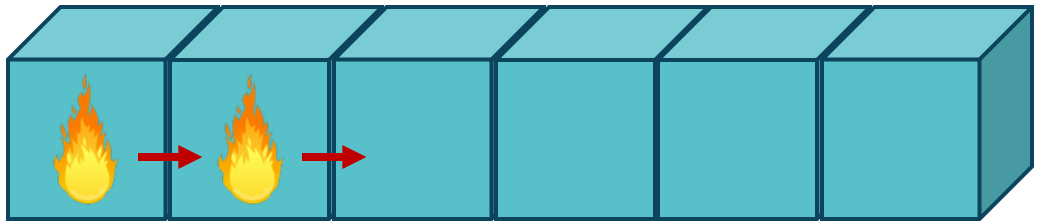

Ring-opening energy release mechanism

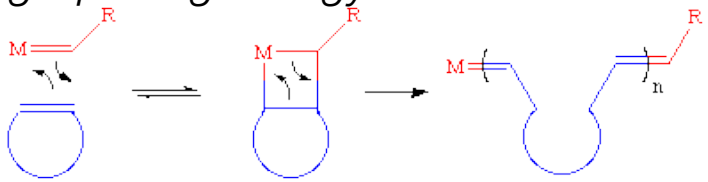

- Requirements
  - Low rate of reaction at initial temperature
  - Very high rate of exothermic reaction at higher temperature
  - Rate of heat production >> rate of heat loss

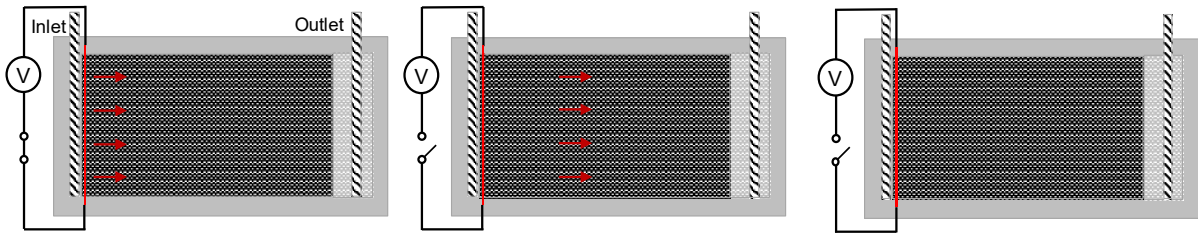

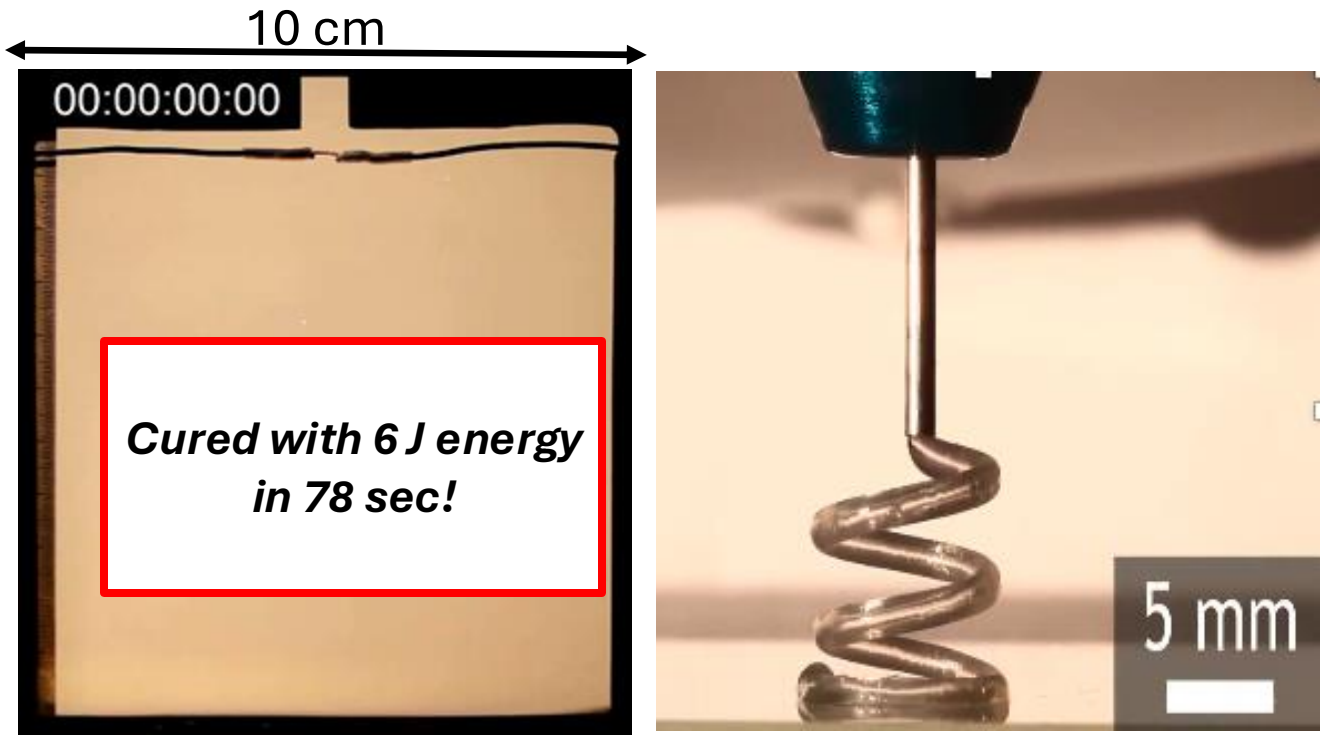

Robertson et al. Nature (2018)

Curing a 10 cm × 20 cm panel in 2 min

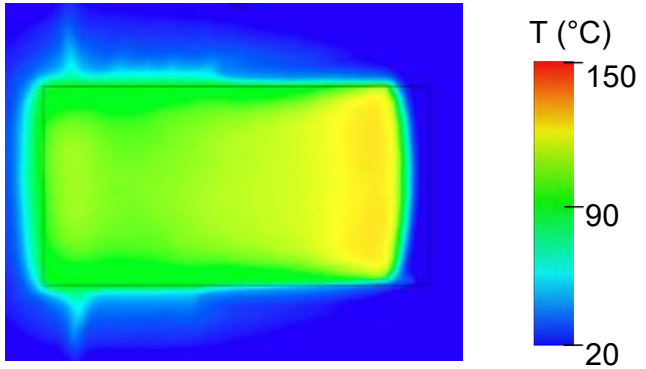

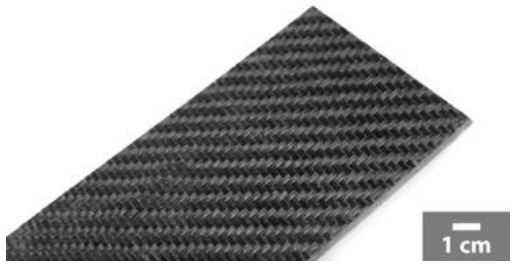

FP Modeling: Phenomenological Reaction-Diffusion Models

$$\begin{cases} \kappa \nabla^2 T + \rho H_r \frac{\partial \alpha}{\partial t} = \rho C_p \frac{\partial T}{\partial t} \\ \frac{\partial \alpha}{\partial t} = A \exp(-\frac{E}{RT}) g(\alpha) \end{cases}$$

- Challenges
  - Coupled multi-physics equations
  - Nonlinear, transient
  - Sharp gradients in temperature and degree of cure in vicinity of propagating front

Convection-Driven Instabilities

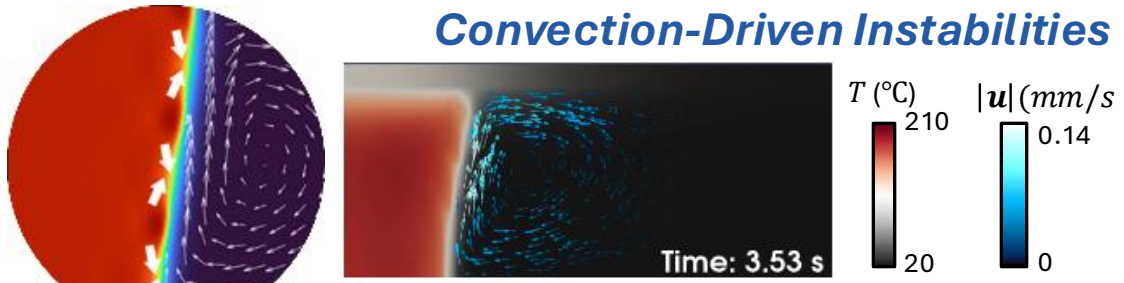

Gao et al., PRL (2023)

Mechanically-Driven Surface Patterning

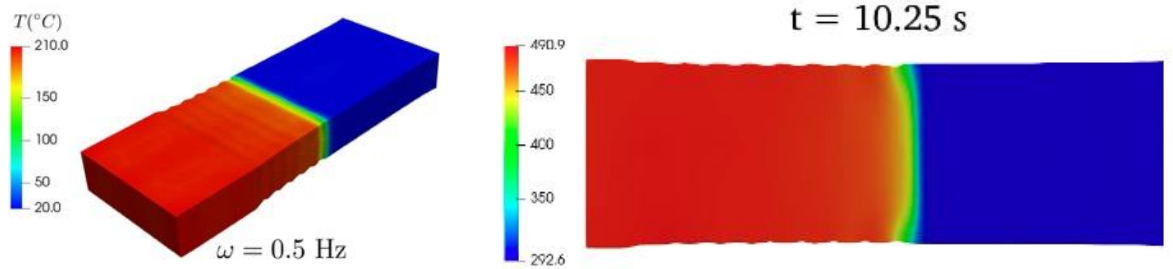

Kumar et al., JMPS (2023)

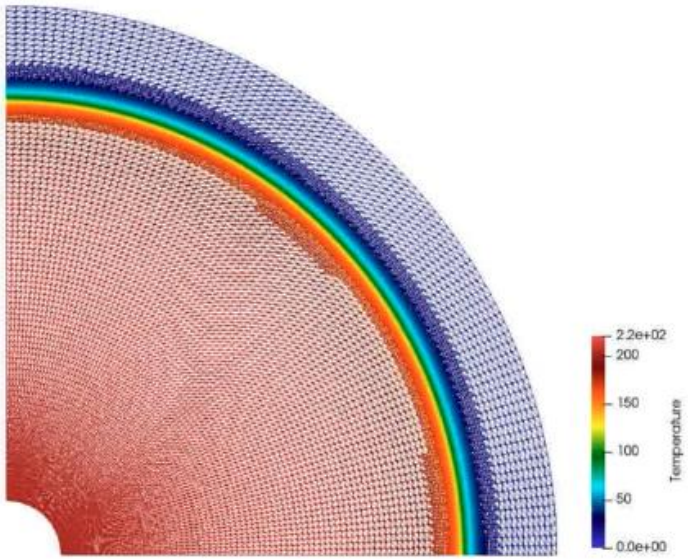

$$\theta = \frac{T - T_0}{T_{max} - T_0}$$

$$T_{max} = T_0 + \frac{H_r}{C_p}$$

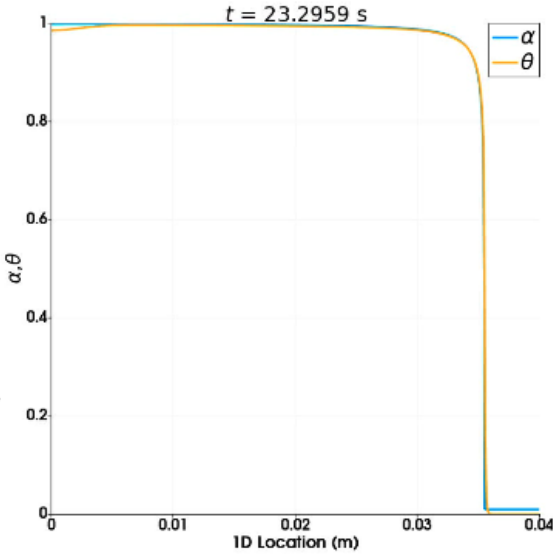

Direct-Ink Write

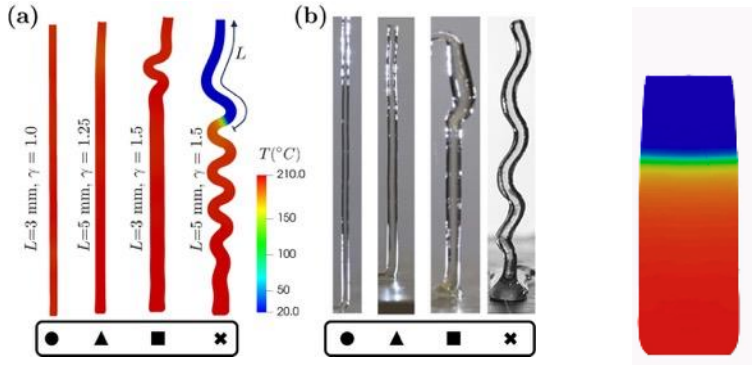

Kumar et al., AM (2024)

FP Modeling: Phenomenological Model Limitations

$$\begin{cases} \kappa\nabla^2 T + \rho H_r \frac{\partial \alpha}{\partial t} = \rho C_p \frac{\partial T}{\partial t} \\ \frac{\partial \alpha}{\partial t} = A\ \exp(-\frac{E}{RT}) g(\alpha) \end{cases}$$



Chemically non-predictive owing to its empirical nature and application to a ***single resin formulation***



Time costly *due to strict reliance on multiple DSC data (~ 30 minutes/DSC test)*



Limited utility, ***one-way experiments-to-simulations workflow.***

Experiments to Simulations Workflow

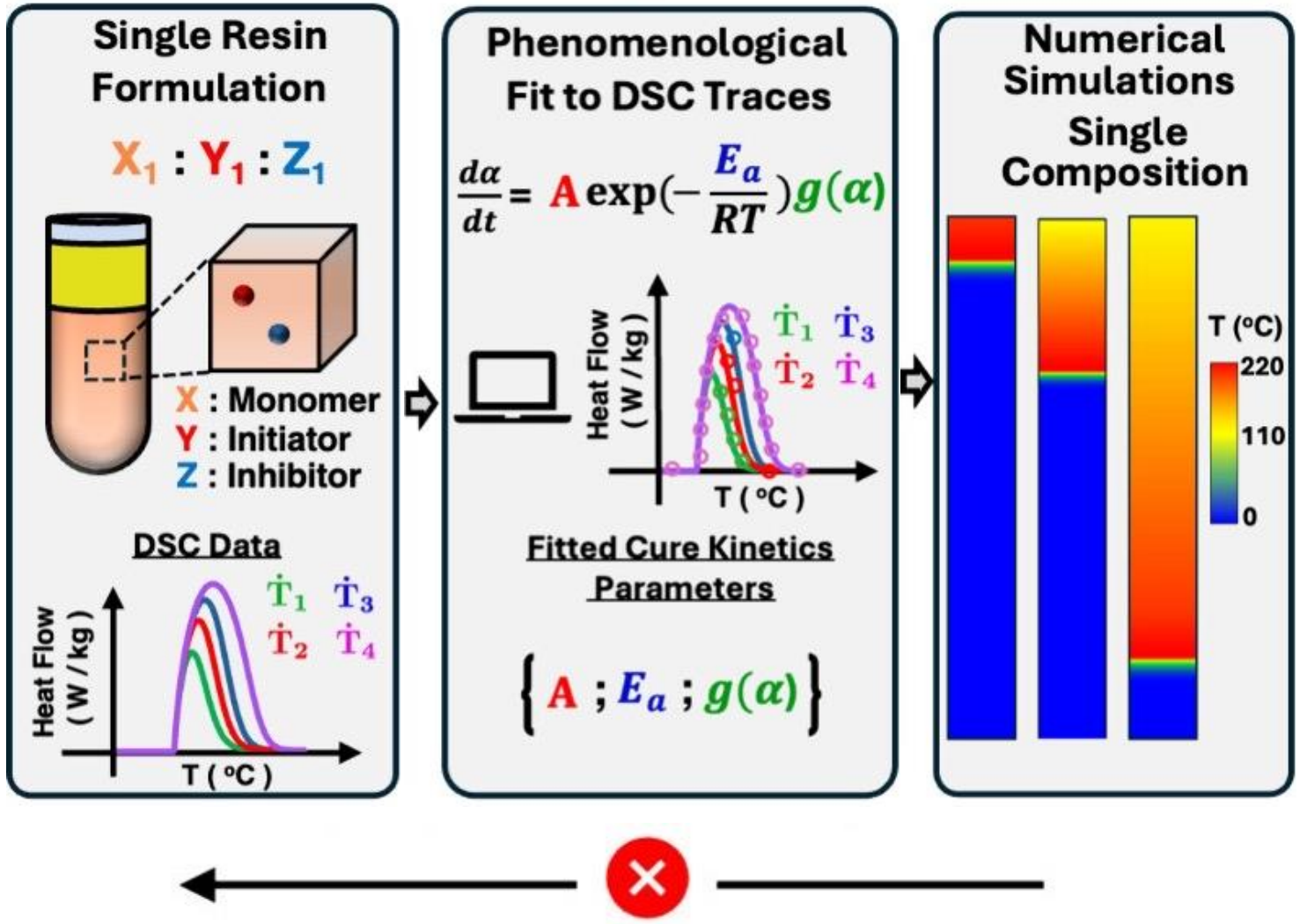

Simulations to Experiments

FP Modeling: A three-step mechanism-based reaction-diffusion model

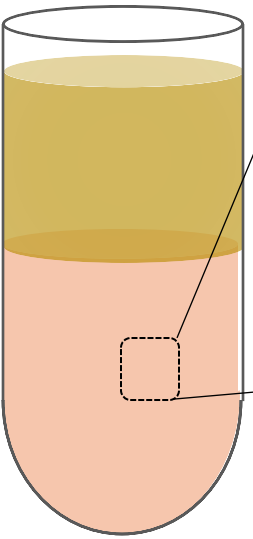

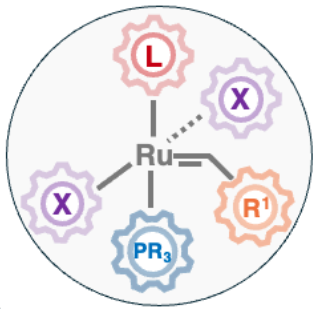

Inactive Initiator



Inhibitory Ligand

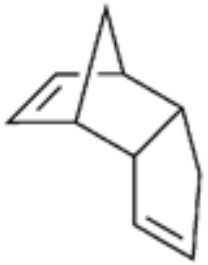

Monomer

Step 1 : Dissociation of the inhibitory ligand

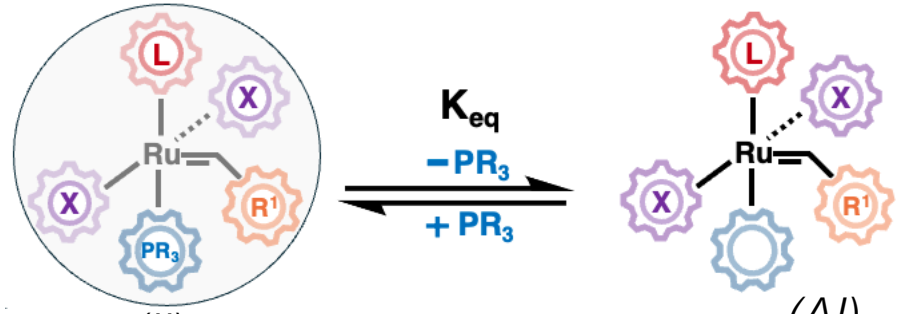

(II) (AI)

$$K_{eq} = \exp\left(-\frac{dH^o}{RT} + \frac{dS^o}{R}\right)$$

Active Initiator Production

$$[\mathrm{AI}+] = -\frac{[\mathrm{AI}_0] + [\mathrm{PR}_3^0] + K_{eq}}{2} + \frac{1}{2}\sqrt{([\mathrm{AI}_0] + [\mathrm{PR}_3^0] + K_{eq})^2 - 4([\mathrm{AI}_0][\mathrm{PR}_3^0] - K_{eq}[II]_0)}$$

Step 2 : Single ring-opening of monomer

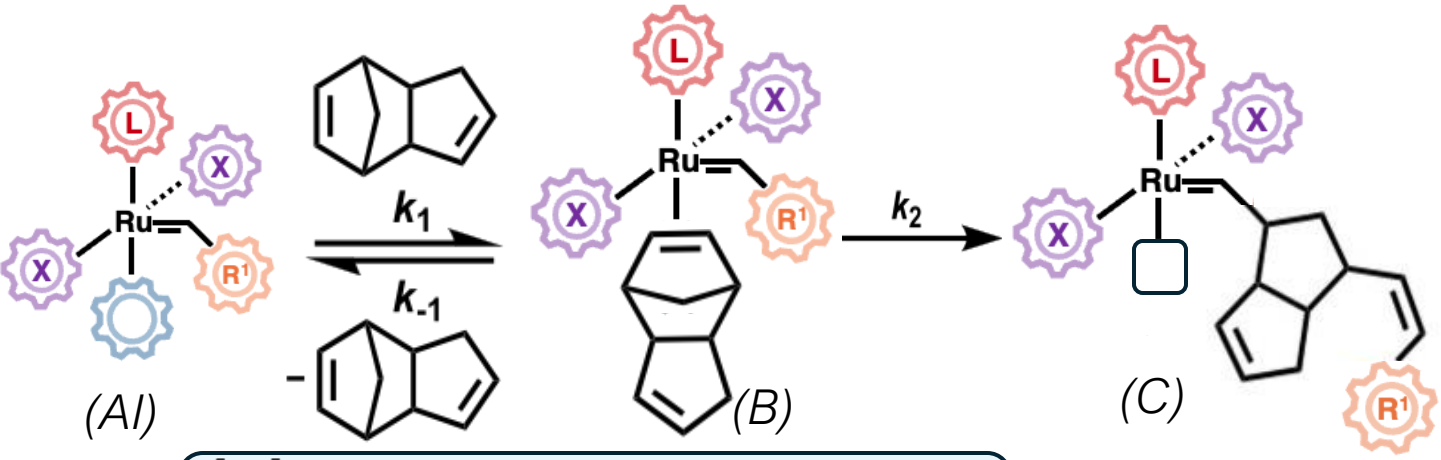

(AI) (B) (C)

$$\frac{d[C]}{dt} = A_i \cdot \exp(-\frac{E_i}{RT})[\mathrm{AI}][1-\alpha]$$

Step 3 : Chain growth polymerization

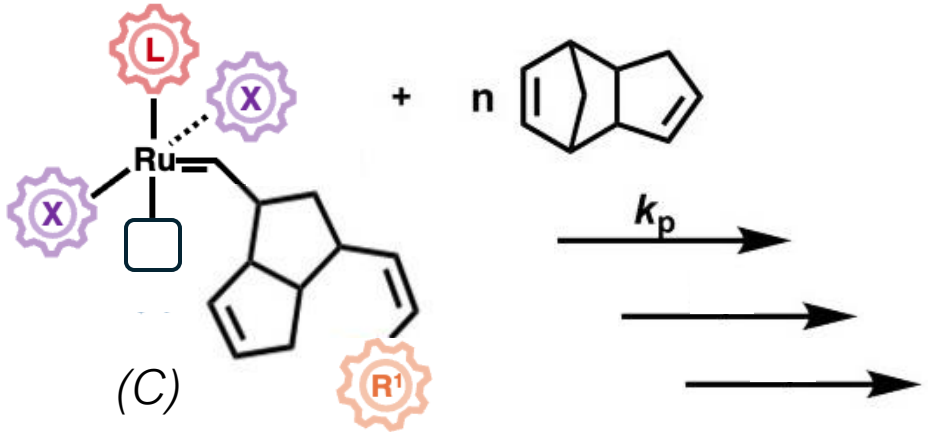

(C)

$$[\mathrm{M}_0]\frac{d\alpha}{dt} = A_p \cdot \exp(-\frac{E_p}{RT})[\mathrm{C}][1-\alpha]$$

FP Modeling: A three-step mechanism-based reaction-diffusion model

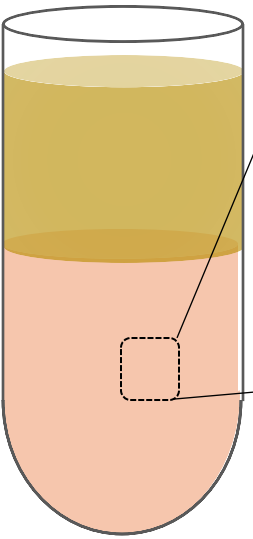



Step 1 : Dissociation of the inhibitory ligand

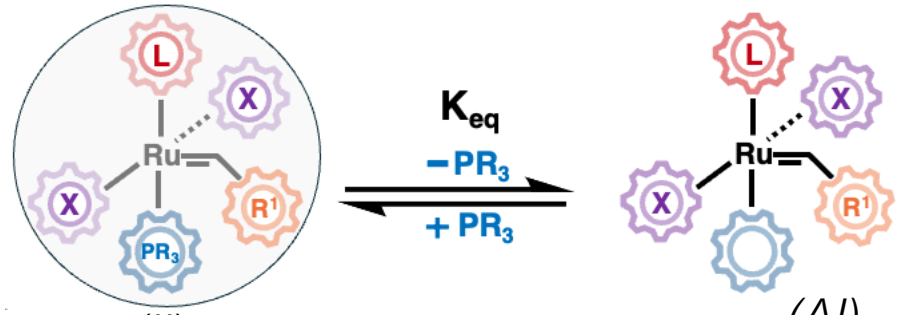

$$K_{eq} = \exp\left(-\frac{dH^o}{RT} + \frac{dS^o}{R}\right)$$

Active Initiator Production

$$[\mathrm{AI}+] = -\frac{[\mathrm{AI}_0] + [\mathrm{PR}_3^0}{2}$$

$$\mathrm{PR}_3^0] - K_{eq}[II]_0)$$

$$\{dS^o, dH^o, A_i, A_p, E_i, E_p\}$$

DFT extractable parameters rooted in the principles of reaction kinetics

Step 2 : Single ring-opening of monome

…th polymerization

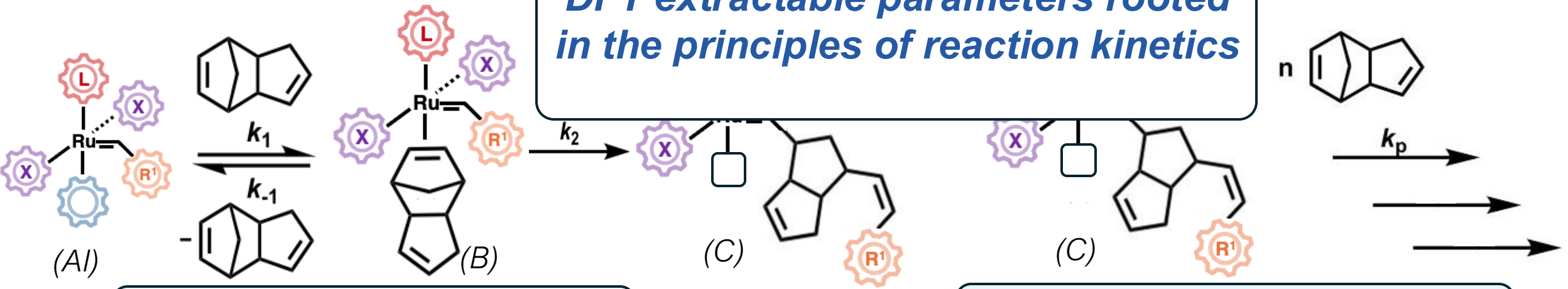

$$\frac{d[C]}{dt} = A_i \cdot \exp(-\frac{E_i}{RT})[\mathrm{AI}][1-\alpha]$$

$$[\mathrm{M}_0]\frac{d\alpha}{dt} = A_p \cdot \exp(-\frac{E_p}{RT})[\mathrm{C}][1-\alpha]$$

FP Modeling: A three-step vs. Phenomenological Model Performance

Polymerization front velocity over a large range of compositions

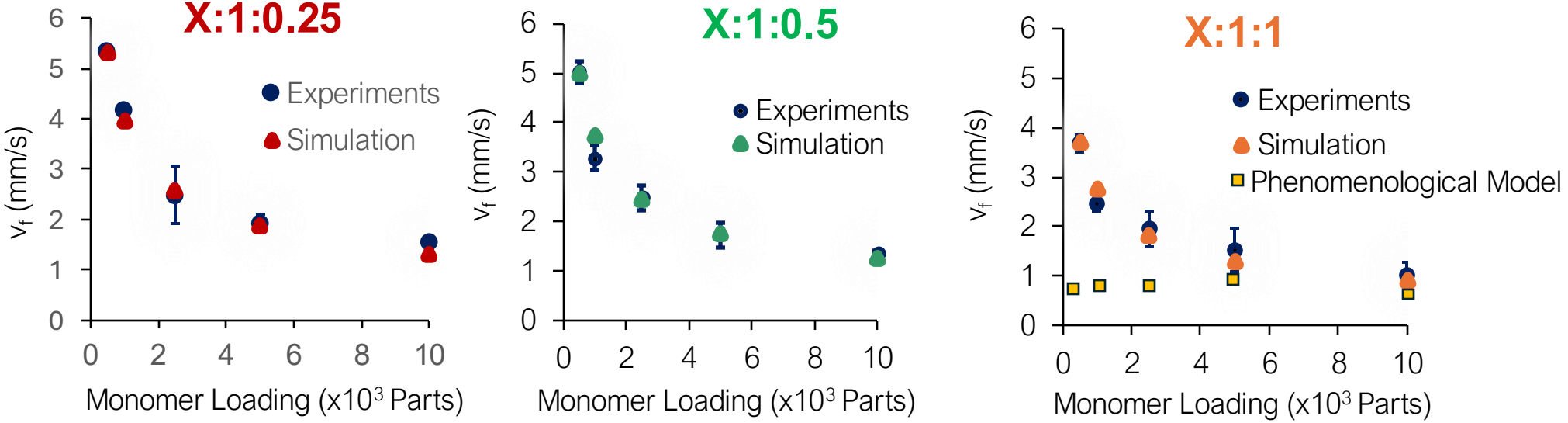

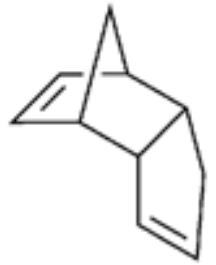

DCPD

Polymerization front velocity with change in both resin composition and processing conditions

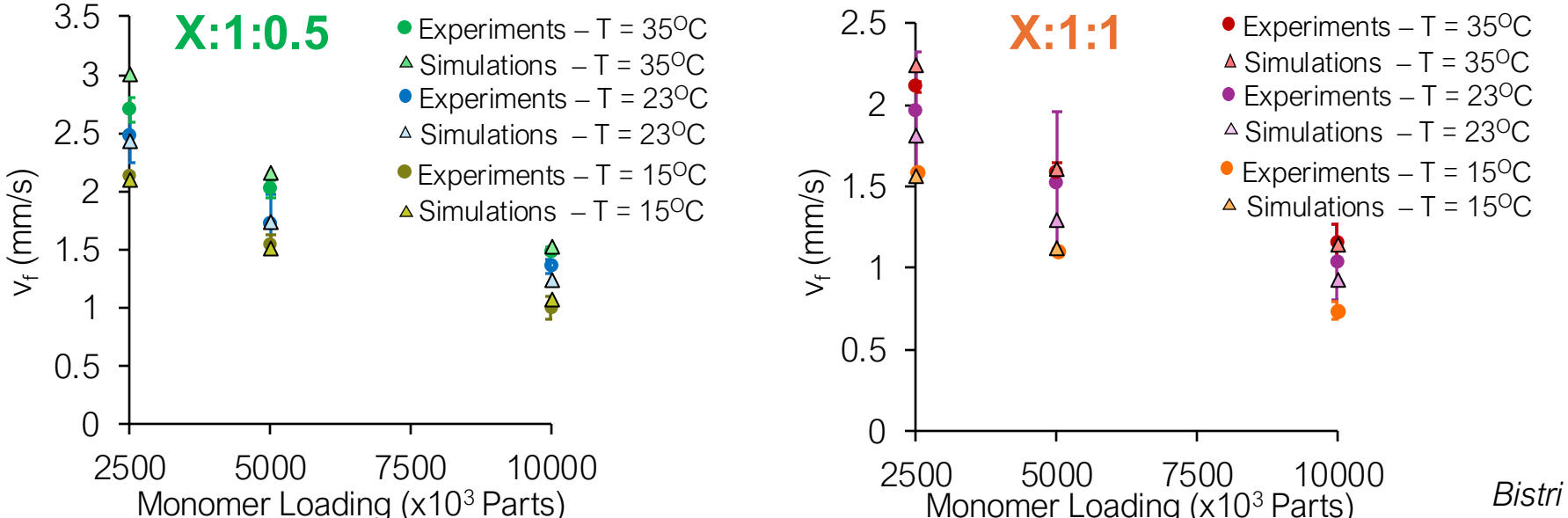

Bistri et al. JACS (2024)

Frontal Polymerization Morphogenic Patterning: From the lens of a mechanism-based model

Emergent behavior in numerous natural systems is attributed to competing reaction-transport phenomena, giving rise to symmetry breaking events.

Biological Matter





Animal Skin Markings

Nature




Sand Ripples, Cloud Patterns

Material Science



Phase-Separating Materials



Oscillatory chemical reactions

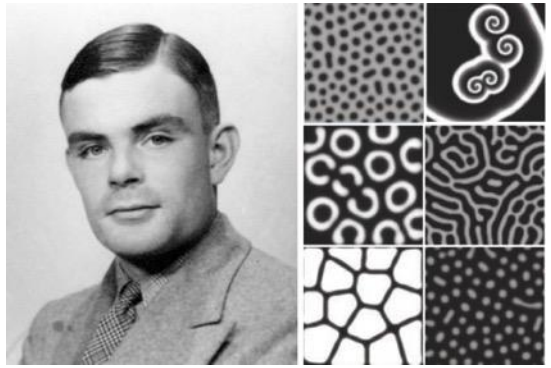

"The chemical basis of morphogenesis" A.M. Turing (1951)

Frontal Polymerization Morphogenic Patterning: From the lens of a mechanism-based model

Emergent behavior in numerous natural systems is attributed to competing reaction-transport phenomena, giving rise to symmetry breaking events.

Biological Matter



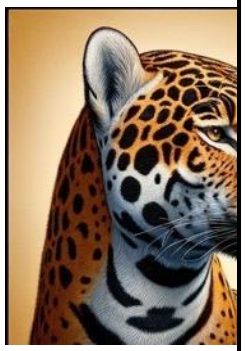

Animal Skin Mar

Can we explore similar concepts to produce emergent behavior in FP – synthetic materials?

Nature





es, Cloud Patterns

Material Science



Phase-Separating Materials



Oscillatory chemical reactions

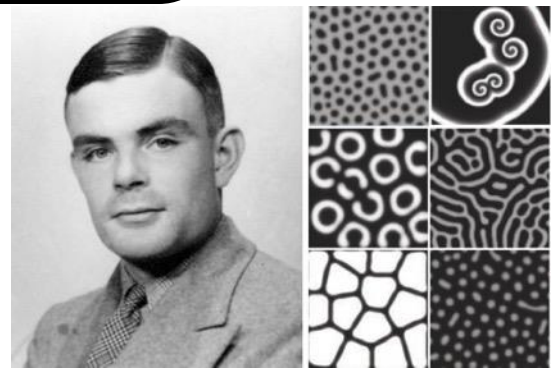

"The chemical basis of morphogenesis" A.M. Turing (1951)

Frontal Polymerization Morphogenic Patterning: A time lapse

Open mold spontaneous patterning: Study by Loyd et al. (ACS Central Science, 2021)

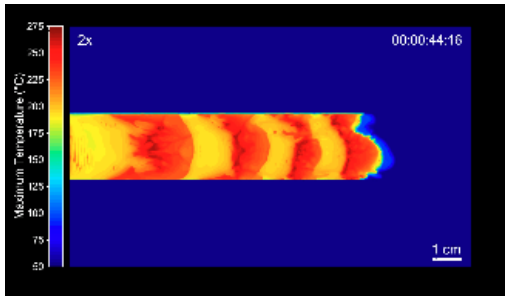

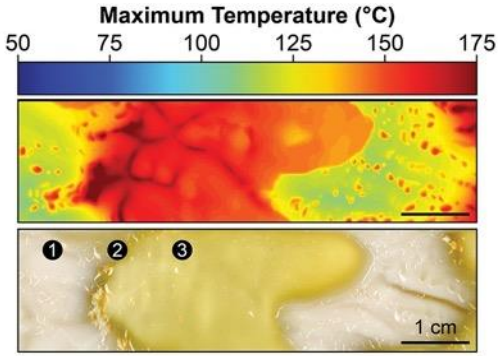

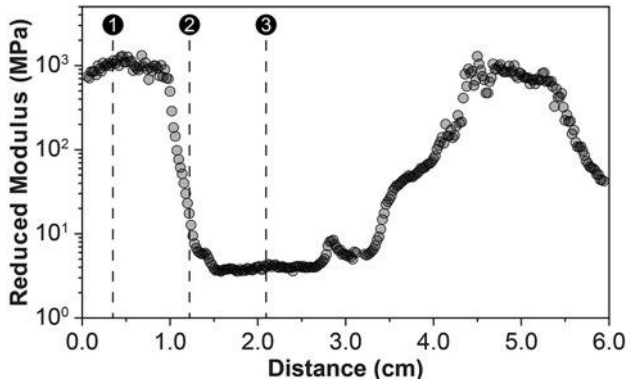

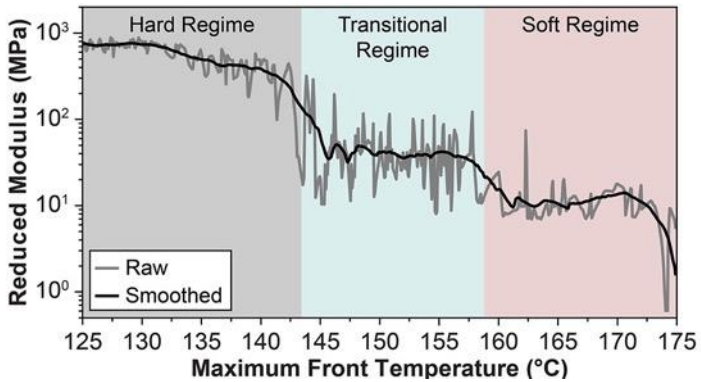

Time

Limited understanding of the controlling mechanisms

Controlled patterning by frontal polymerization: Study by Paul et al. (Nature, 2024)

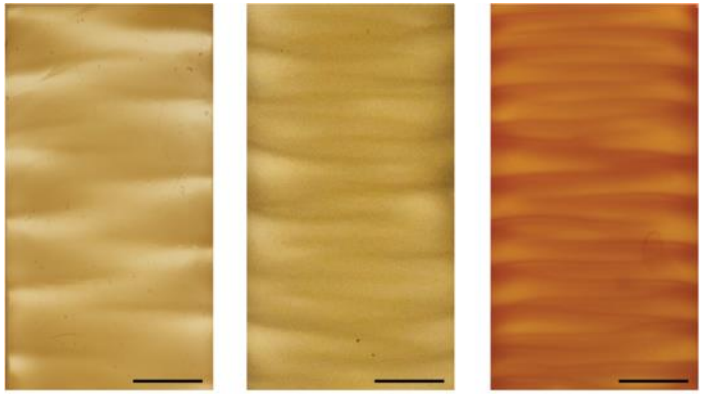

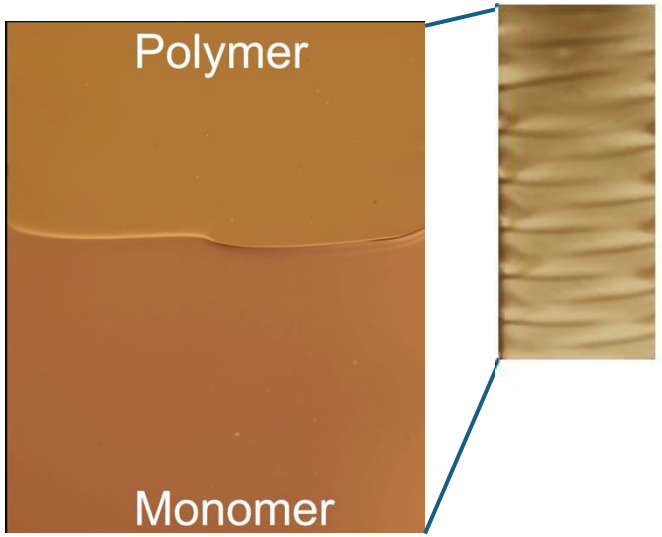

Ru-1

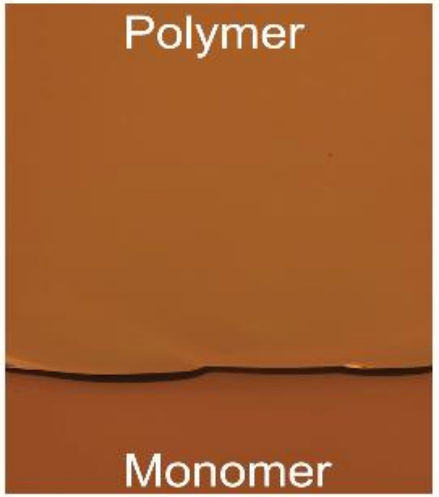

Ru-2

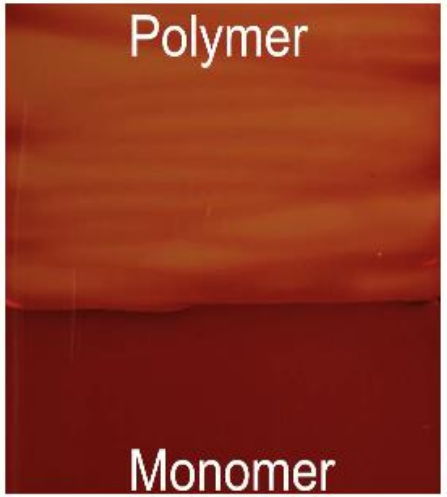

Ru-3

Controlled patterning by frontal polymerization: Study by Paul et al. (Nature, 2024)

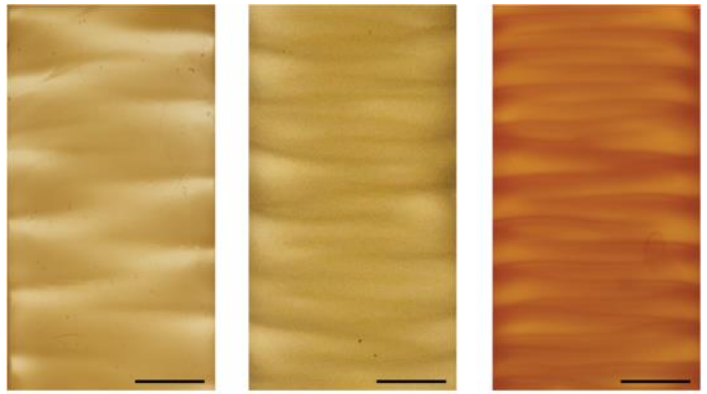

1

Increased propensity for patterning

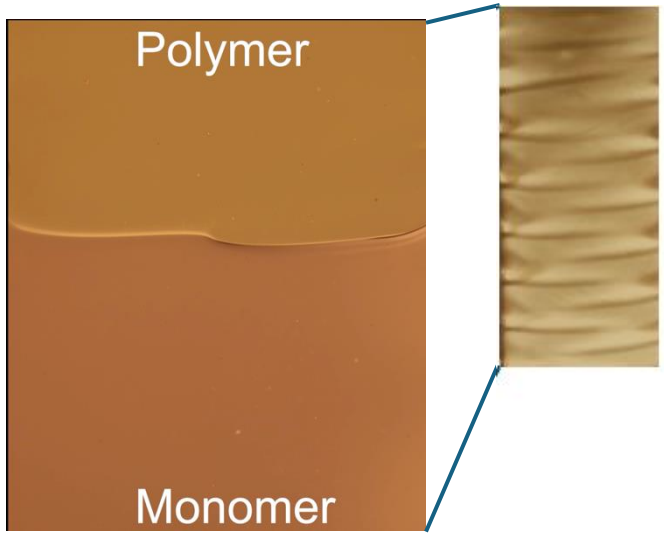

Ru-1

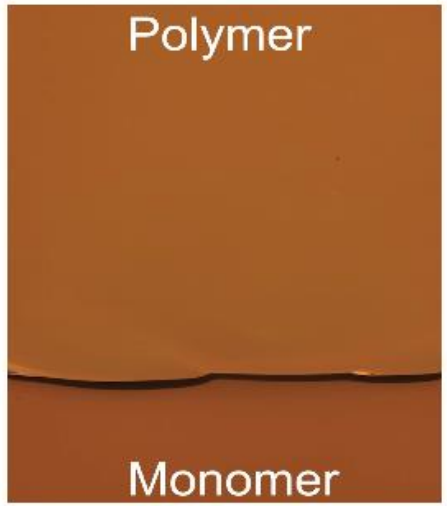

Ru-2

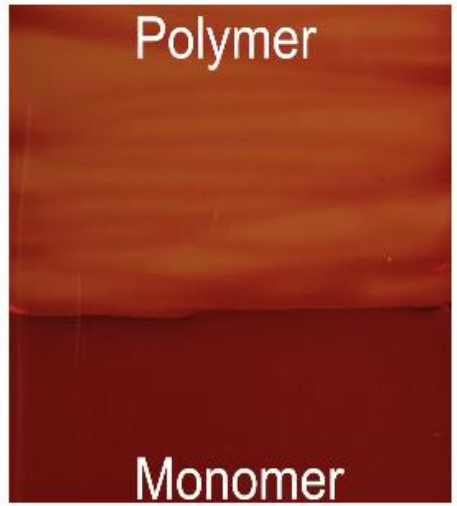

Ru-3

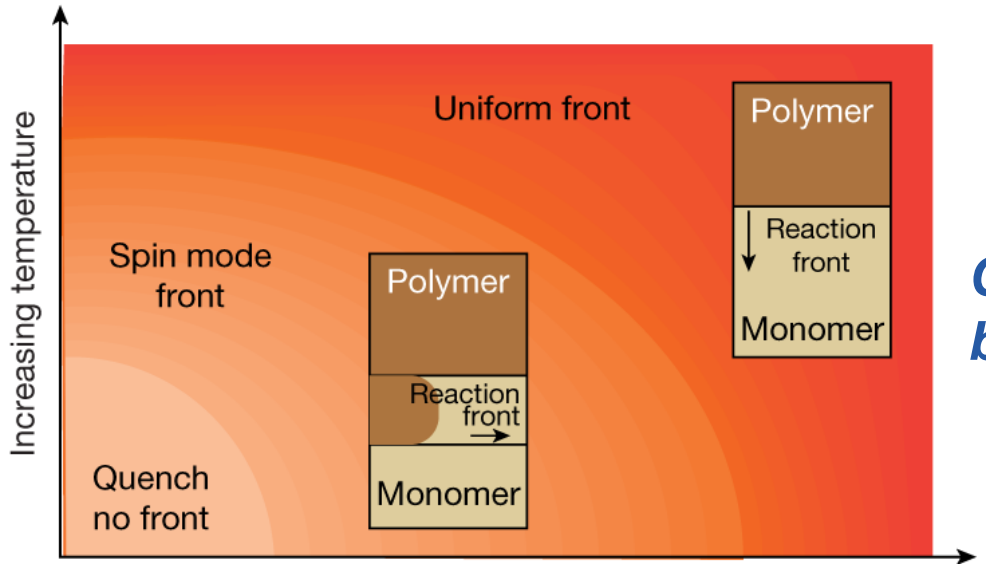

2

Can we provide a mechanistic-guided understanding behind these observations?

On the origins of emergent behavior in frontally-polymerized systems: A mechanism-based model guided understanding

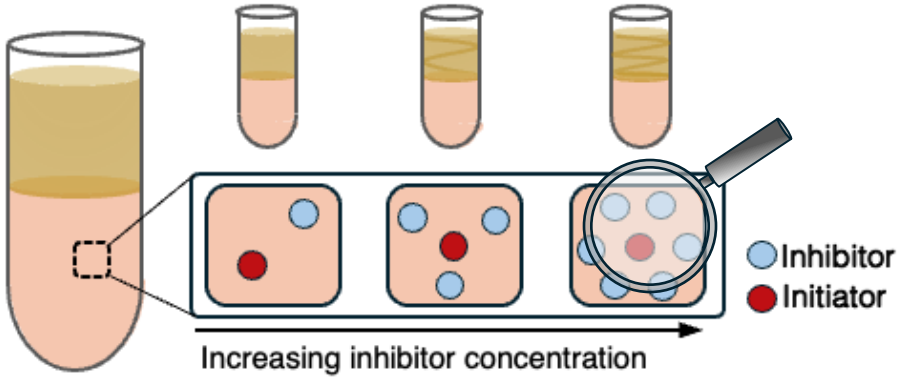

$$[\mathrm{AI}+] = -\frac{[\mathrm{AI}_0] + [\mathrm{PR}_3^0] + K_{eq}}{2} + \frac{1}{2}\sqrt{([\mathrm{AI}_0] + [\mathrm{PR}_3^0] + K_{eq})^2 - 4([\mathrm{AI}_0][\mathrm{PR}_3^0] - K_{eq}[II]_0)}$$

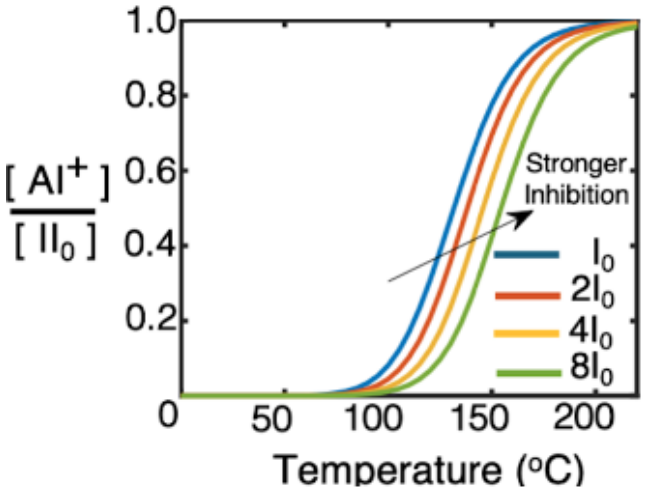

Delayed activation/supply

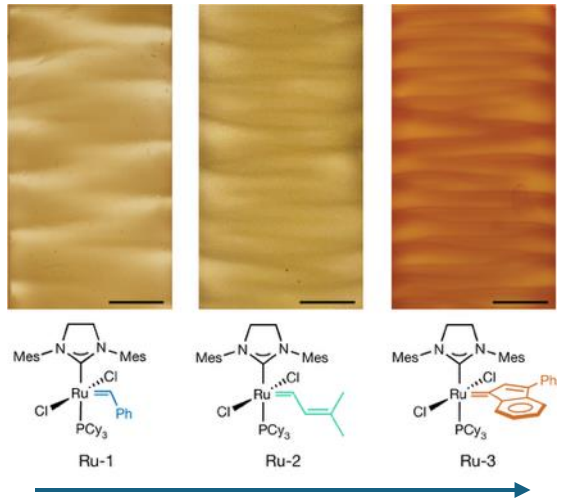

Increased propensity for emergent behavior

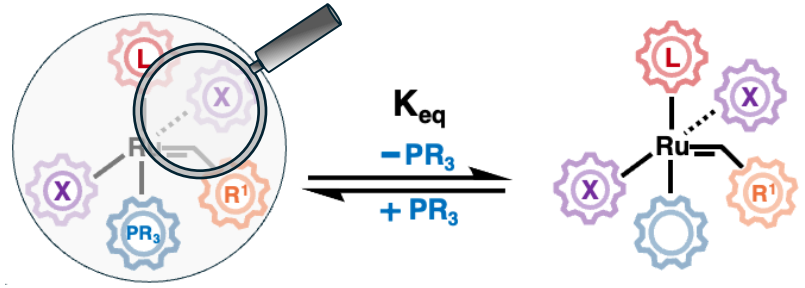

$$K_{eq} = \exp\left(-\frac{dH^o}{RT} + \frac{dS^o}{R}\right)$$

Different ligand substituents alter the dissociation thermodynamics

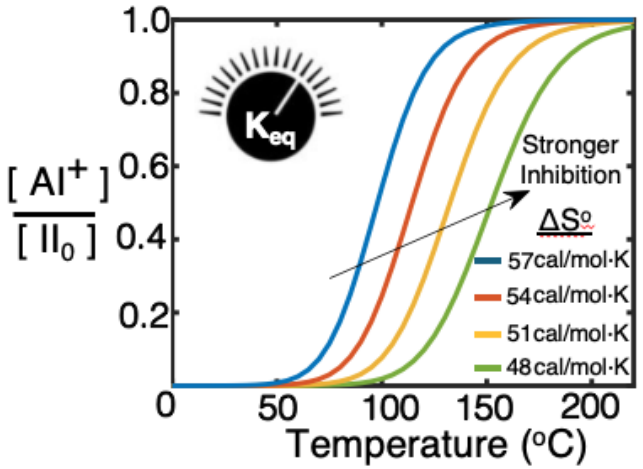

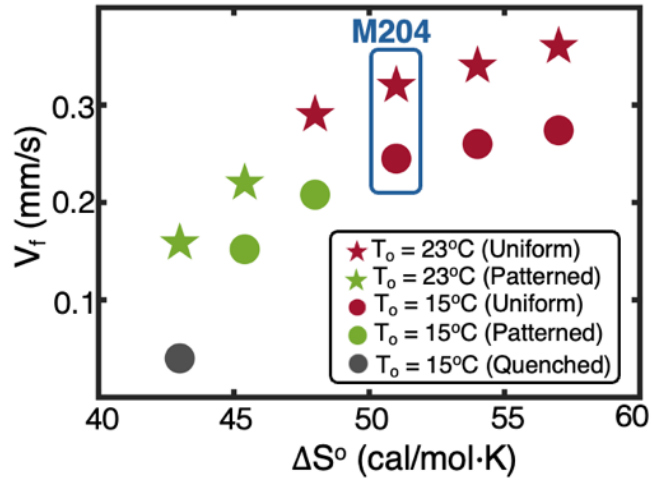

Bistri et al. PNAS (2025)

On the origins of emergent behavior in frontally-polymerized systems: A mechanism-based model guided understanding

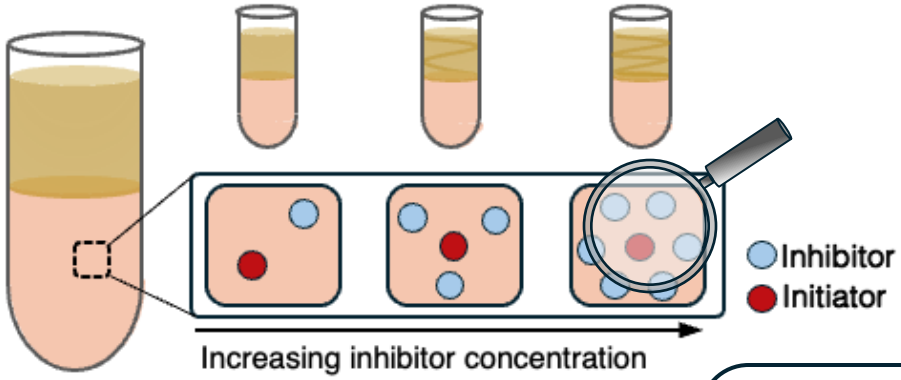

$$[\mathrm{AI}+] = -\frac{[\mathrm{AI}_0] + [\mathrm{PR}_3^0] + K_{eq}}{2} + \frac{1}{2}\sqrt{([\mathrm{AI}_0] + [\mathrm{PR}_3^0] + K_{eq})^2 - 4([\mathrm{AI}_0][\mathrm{I}}$$

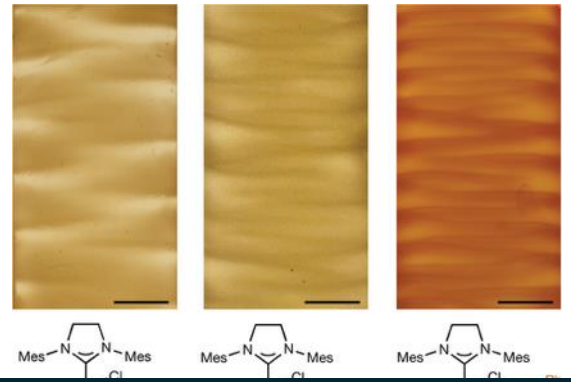

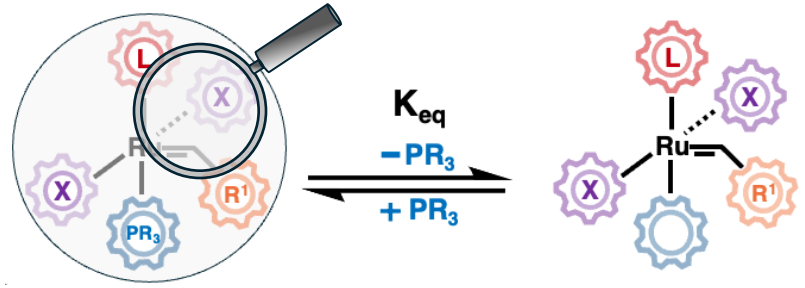

$$K_{eq} = \exp\left(-\frac{dH^o}{RT} + \frac{dS^o}{R}\right)$$

Different ligand substituents alter the dissociation thermodynamics

These results seem to point to the presence of an inhibition-limited dissociation equilibrium

$[\mathrm{AI}^+]$ ✗ 🔥

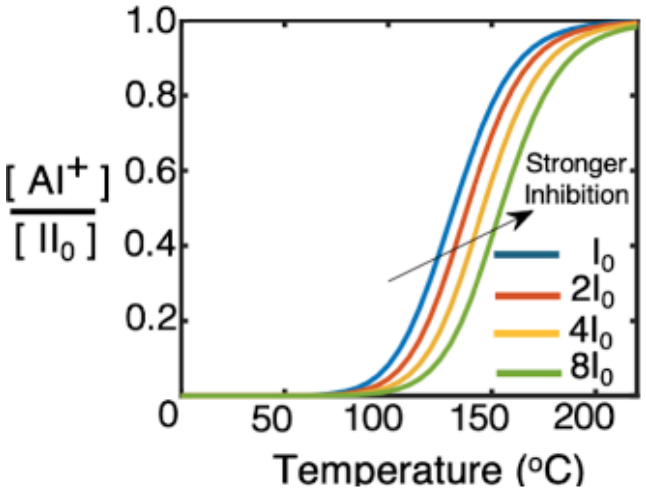

activation/supply

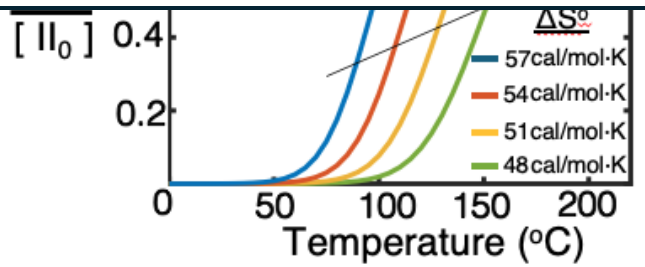

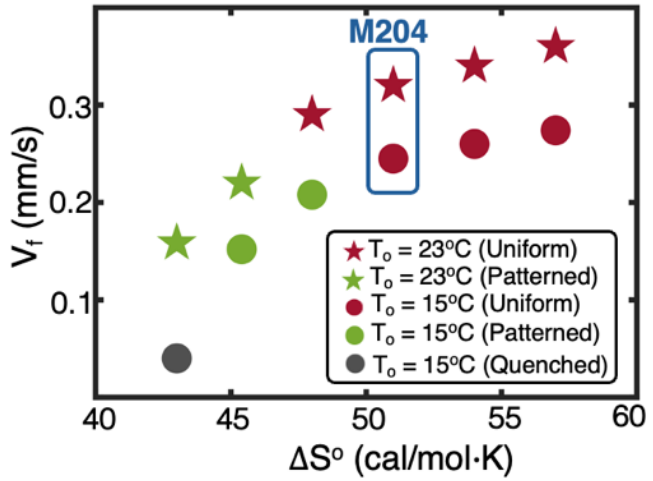

Bistri et al. PNAS (2025)

A systematic exploration of the hypothesis

If the hypothesis is to hold true, ***a saturation front velocity must be attained with decreasing monomer loading*** (i.e., increasing inhibitor concentration)

Specialize for a COD monomer + Ru-1 baseline demonstration



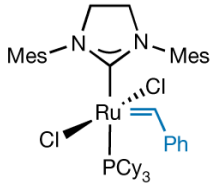

Ru-1

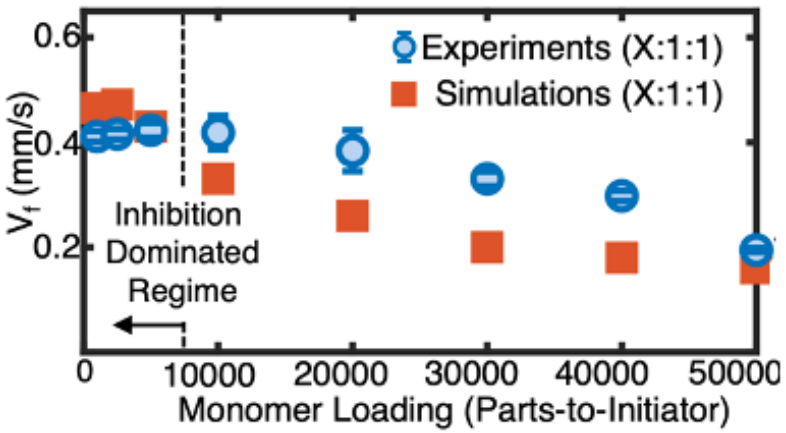

Increasing inhibitor + initiator

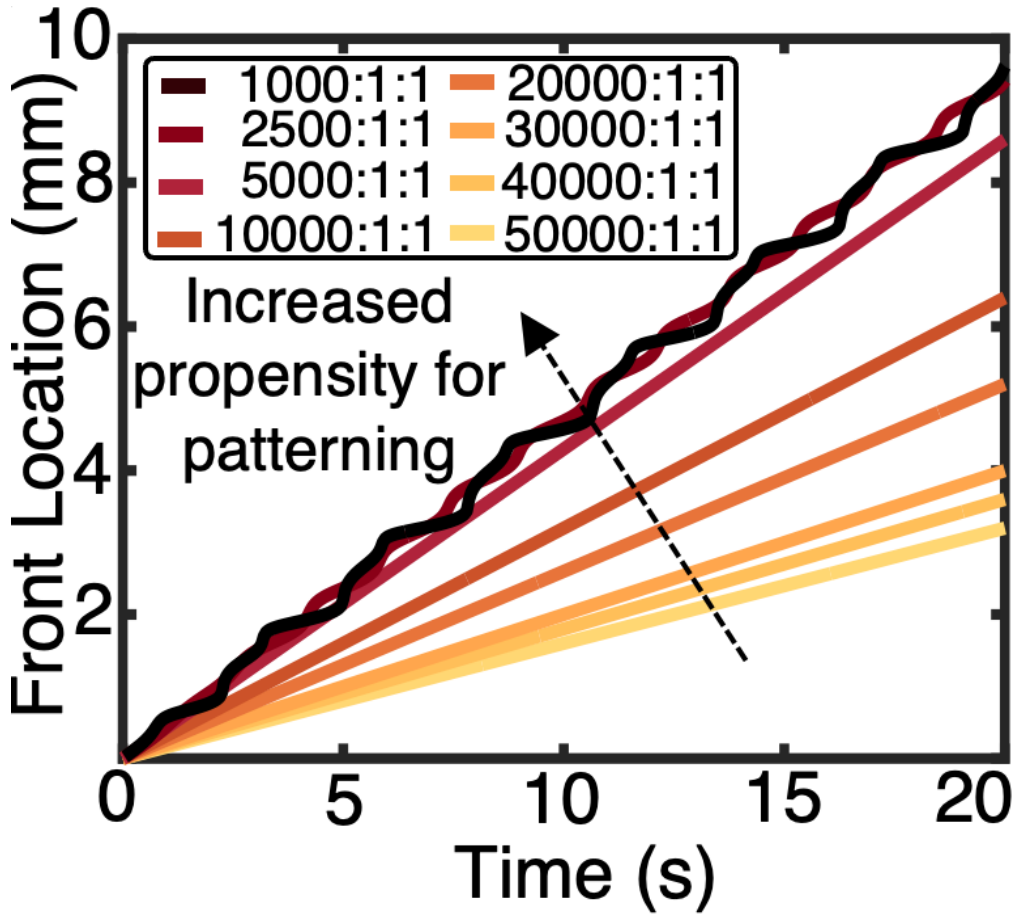

Bistri et al. PNAS (2025)

A systematic exploration of the hypothesis

If the hypothesis is to hold true, ***a saturation front velocity must be attained with decreasing monomer loading*** (i.e., increasing inhibitor concentration)

Specialize for a COD monomer + Ru-1 baseline demonstration



But existing literature states that patterns arise close to front quenching…



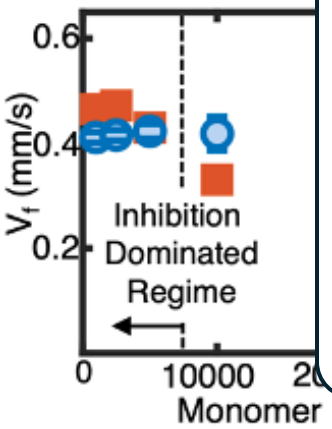

Increasing inhibitor + initiator

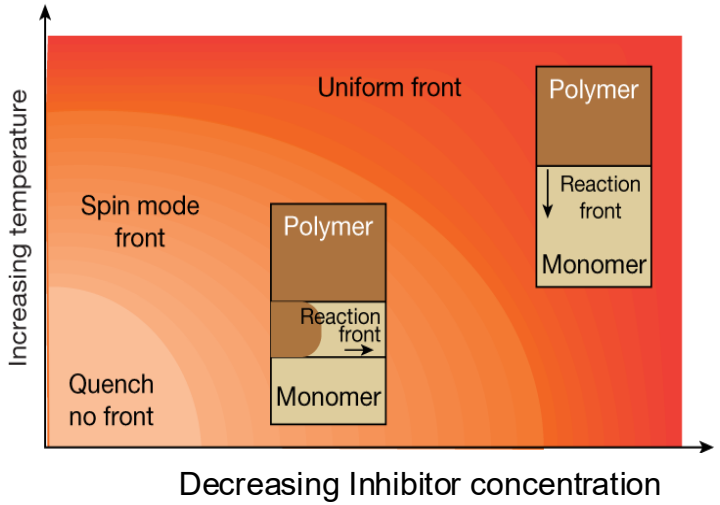

Bistri et al. PNAS (2025)

Experimental map of emergent behavior as a function of composition

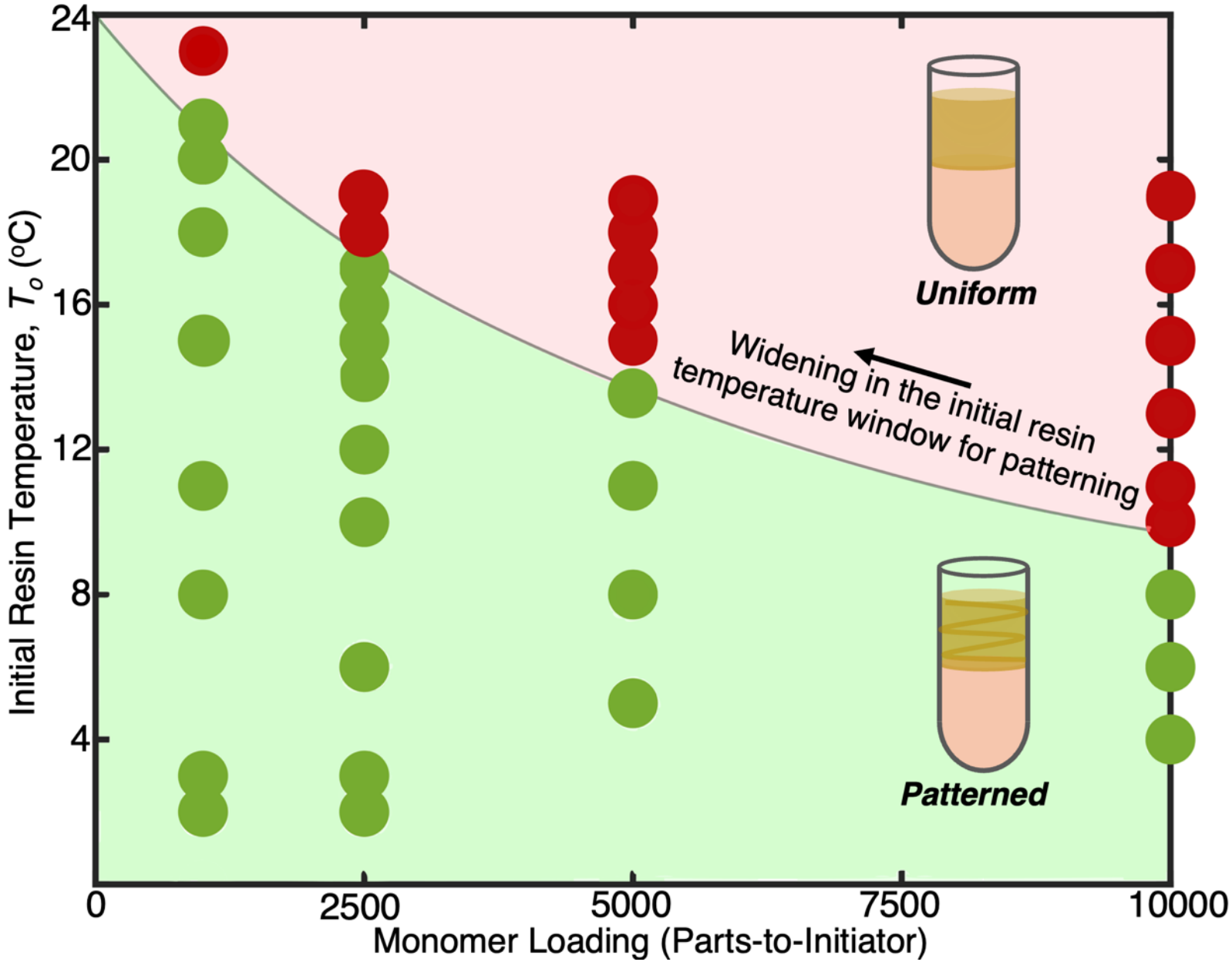



Before

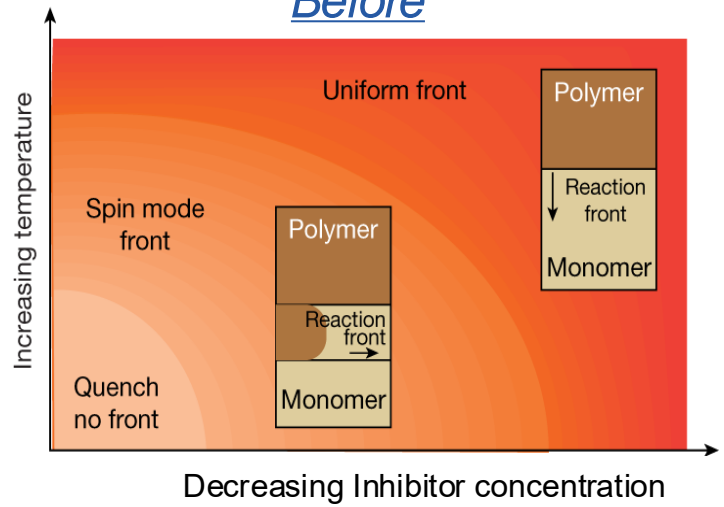

! *This work*

Expanded Design Envelope

Ability to pattern + Good Curing Speeds

Bistri et al. PNAS (2025)







COD

+

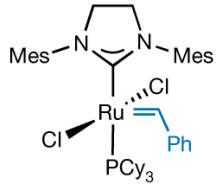

Ru-1

Ability to map emergent behavior over a wide range of compositions + processing conditions

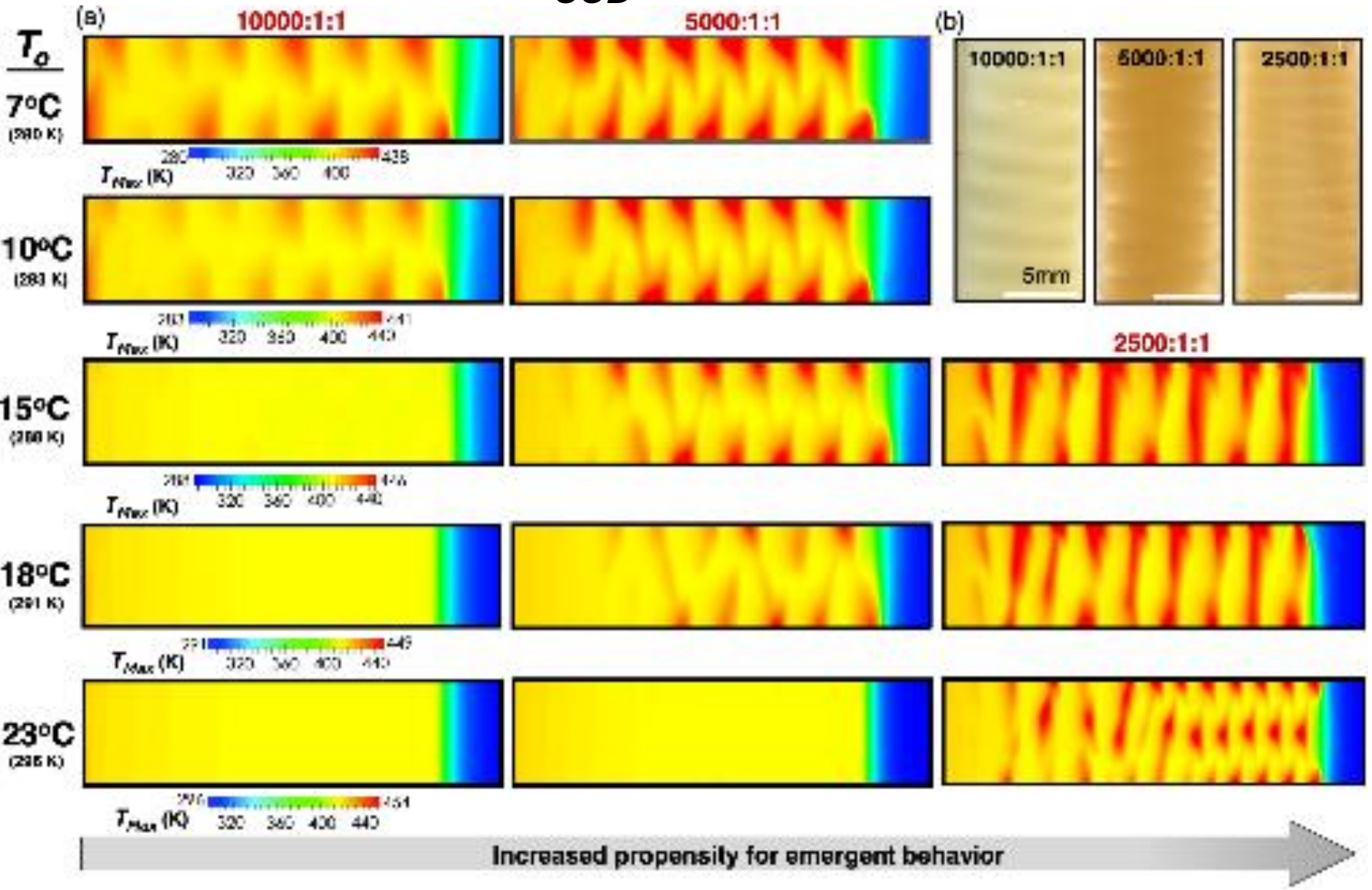

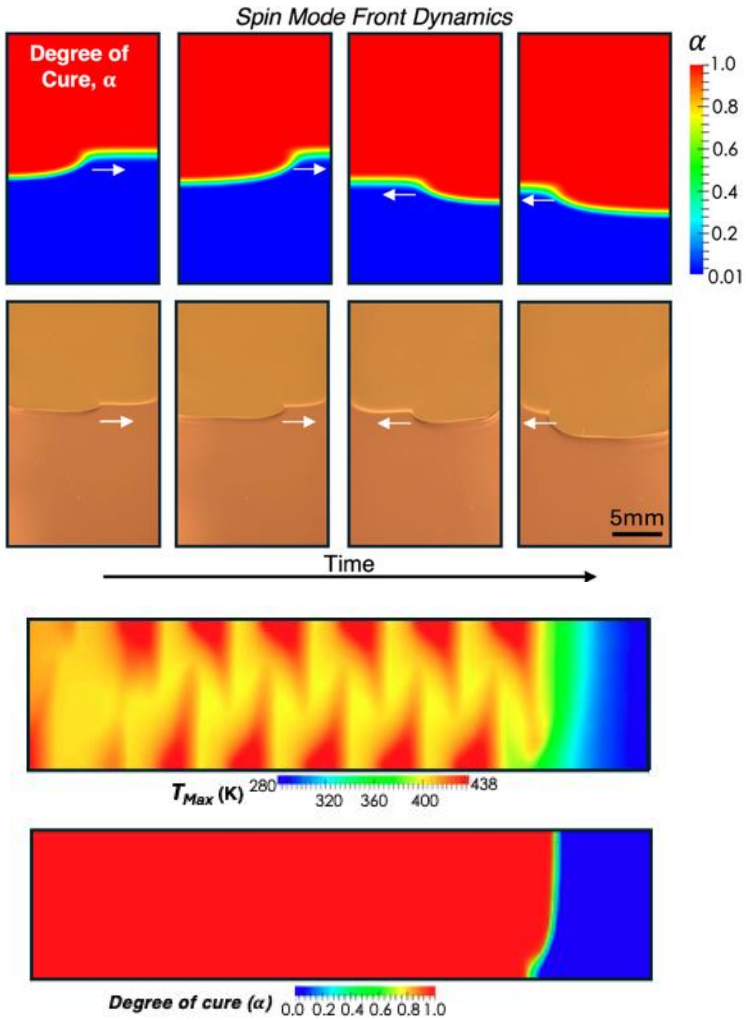

Simulations performed in open-source FEniCS platform

Bistri et al. PNAS (2025)

Mapping Emergent Behavior with Variation in Resin Chemistry

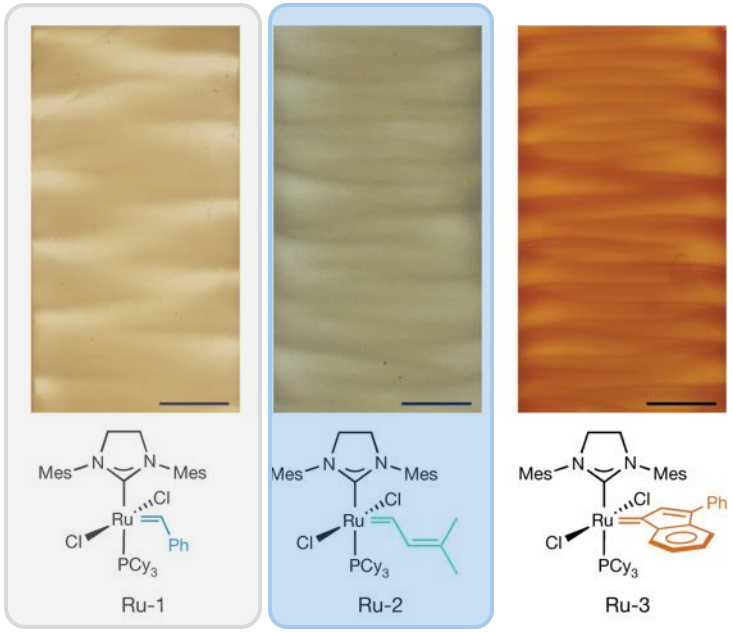

$$K_{eq} = \exp\left(-\frac{dH^o}{RT} + \frac{dS^o}{R} \right)$$

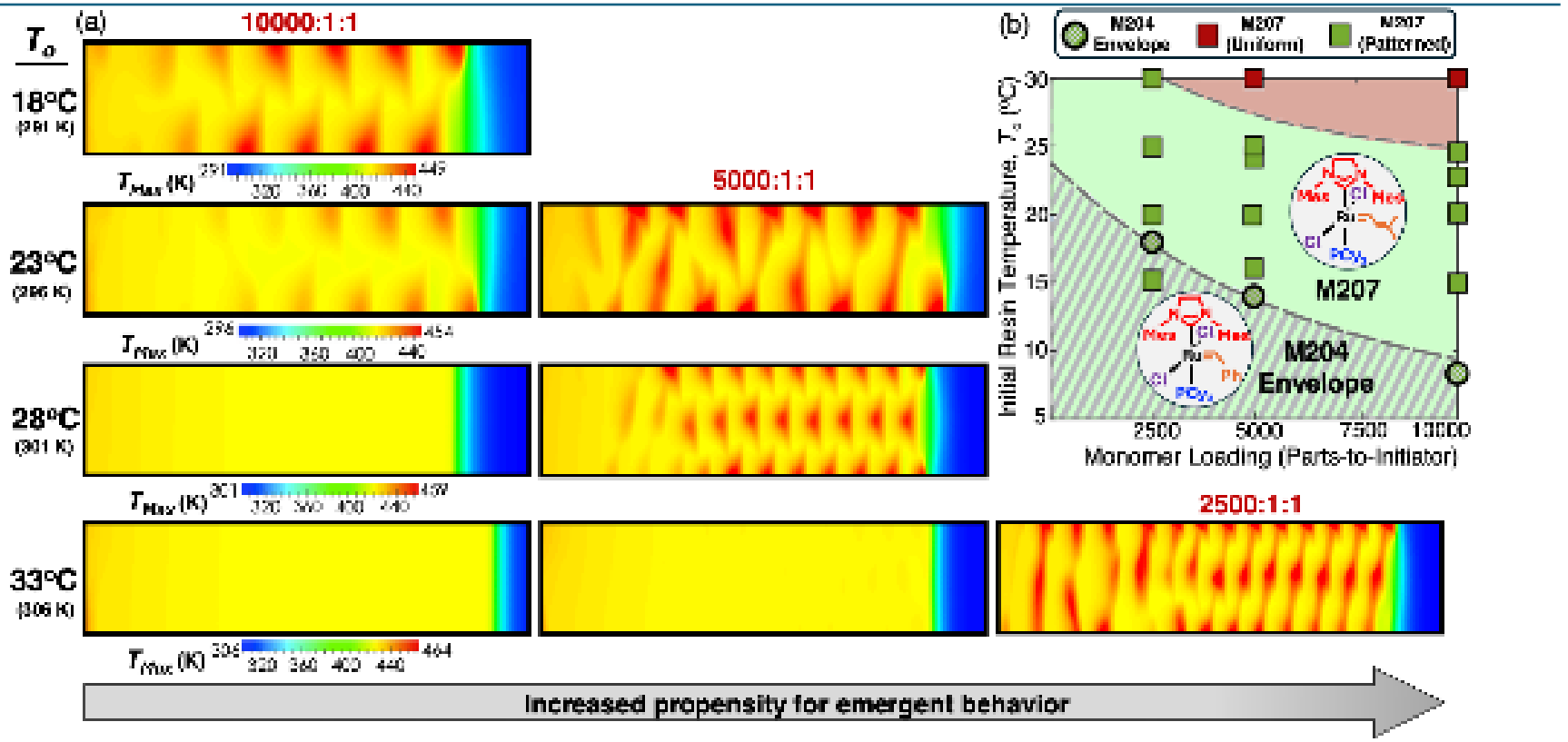

A roadmap for controlling emergent behavior by precise control of chemistry

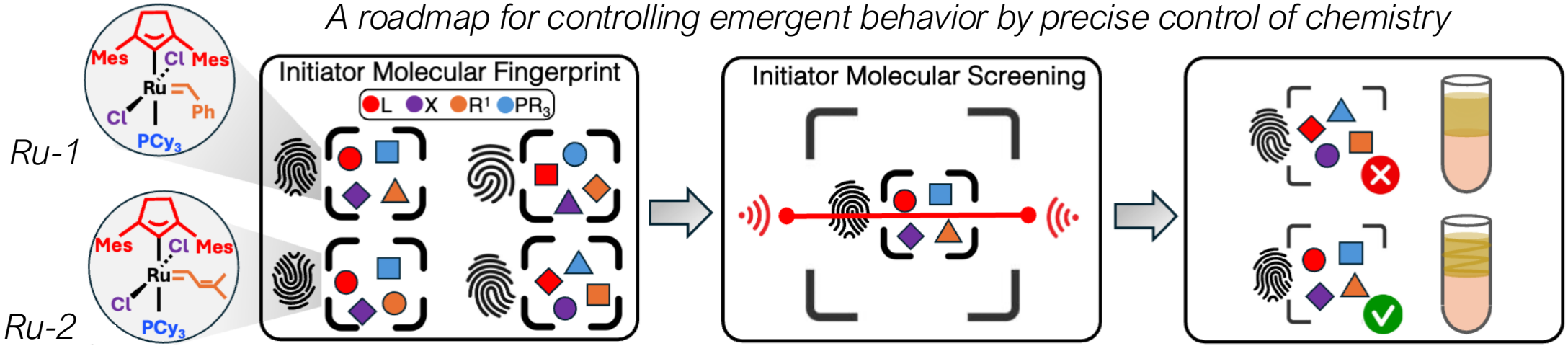

Summary

1. Developed a mechanism-based reaction-diffusion framework to model the coupled three-step sequence of FROMP reaction kinetics.
2. Demonstrated the capacity of the framework to capture macroscopic FROMP observables (i.e., front velocity, maximum front temperature, front propagation mode) over a wide range of compositions + processing conditions
3. Numerically informed *a novel paradigm for emergent behavior in frontally-polymerized synthetic materials* with spatially varying mechanical properties.
4. Demonstrated the ability to map emergent behavior over a wide range of compositions + processing conditions

Thank you for your attention!

Happy to take any questions





AMS Group, Beckman Institute



Computational Solid Mechanics Group

Influence of Kinetic Models on the Simulation of Frontal Polymerization

Ke Wang, Brecklyn Groce, Guy Van Assche

Sustainable Materials Engineering, Vrije Universiteit Brussel, Brussel, Belgium

ICCM24, Baltimore, Maryland, USA

August 4, 2025

Motivation

Frontal Polymerization:

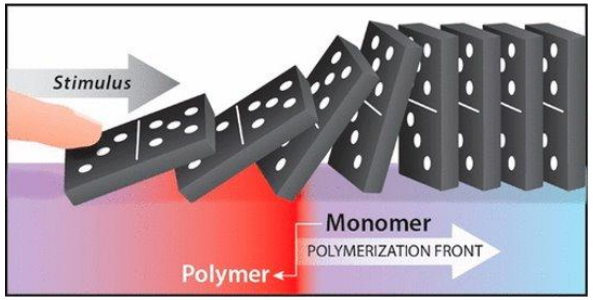

✓

- Fast & energy efficient
- Longer pot-life

? → study with modelling methods

- Require precise balance of heat
  - *Premature (bulk) polymerization*
  - *Quenching of fronts*
- Instabilities

  Comes from rapid change of temperature & properties

Reaction kinetics model:

Phenomenological	Mechanistic
$\frac{d\alpha}{dt} = k(1-\alpha)^n$ *n-th order*	$A + B \xrightarrow{k} C$
α: conversion	$\frac{d[C]}{dt} = k[A][B]$

Phenomenological compared to mechanistic:

Less computation resource required

Less explanatory in mechanism, rely more on experimental data

Parameters are specific to a single formulation

Aim of this study: Propose a rational mechanistic kinetic model for **radical induced cationic polymerization (RICP)** and implement to a frontal polymerization simulation.

Chemistry

Mechanistic kinetic models with FP simulation:

Goldfeder, P. M., et al. (1997): free radical polymerization

Bistri, Donald, et al. (2024): ring-opening metathesis polymerization

Radical induced cationic polymerization (RICP): Mariani, Alberto, et al. (2004)

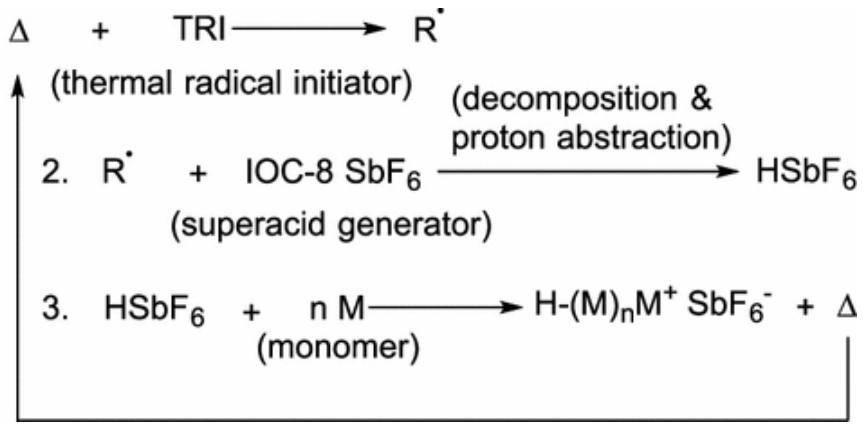

Duo-initiator configuration: radical & cation

- Less sensitive to oxygen (as inhibitor), no termination (by combination)
- No limit on UV penetration depth (compare with cationic photopolymerization)

Groce, Brecklyn R., et al. 2023

Chemistry

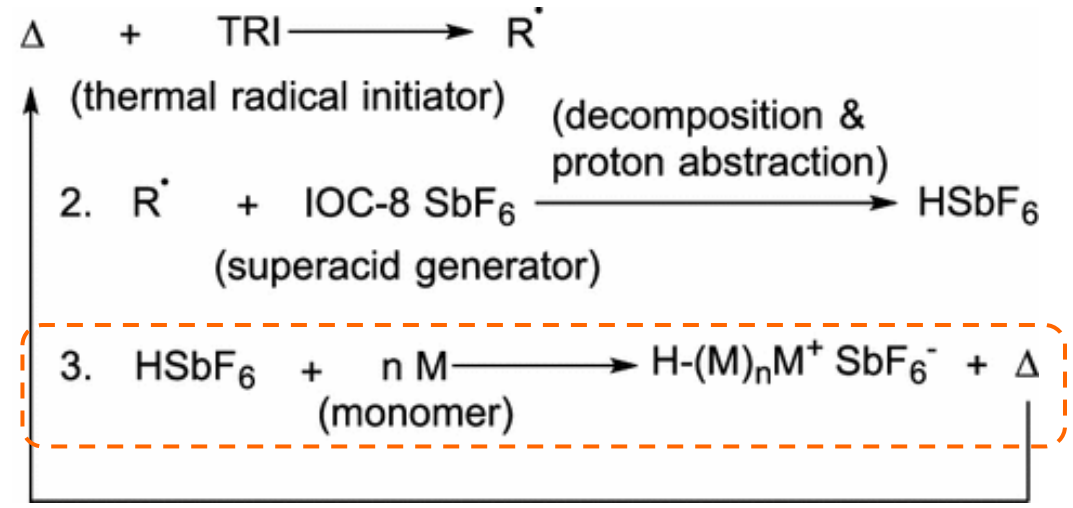

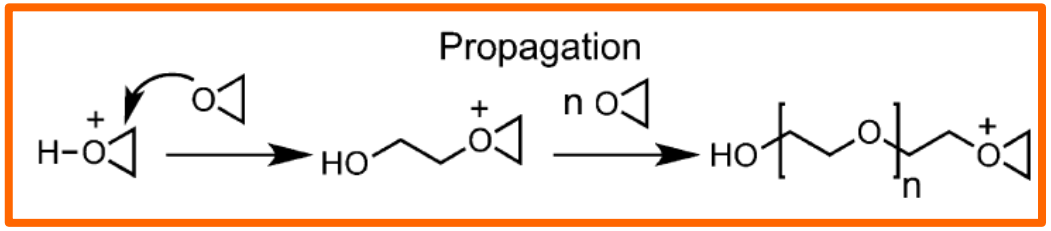

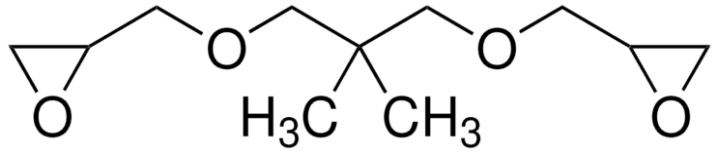

Neopentyl glycol diglycidyl ether
as monomer (E)

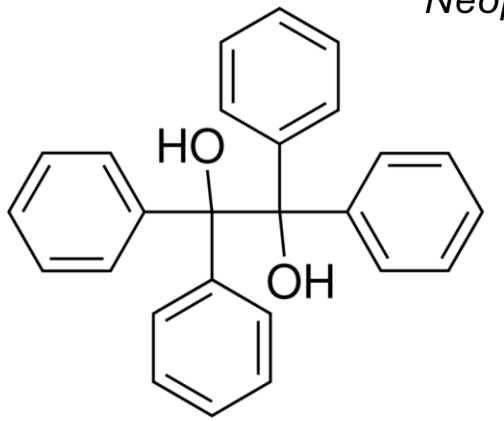

Benzopinacol
as thermal initiator (I)

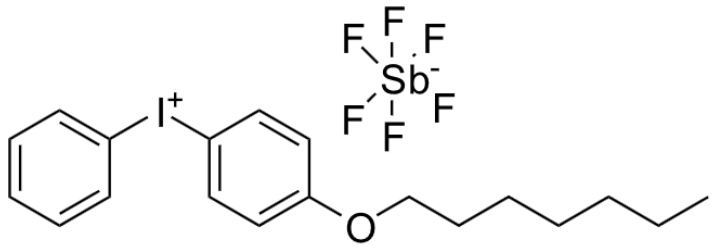

p-(octyloxyphenyl)phenyliodonium hexafluoroantimonate (IOC8)
as superacid generator (A)

Vidil, Thomas, et al. 2016

Mechanistic Model

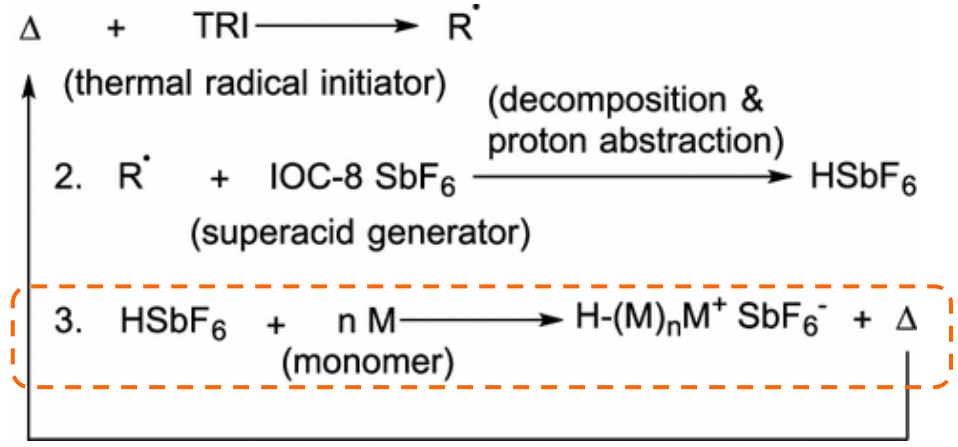

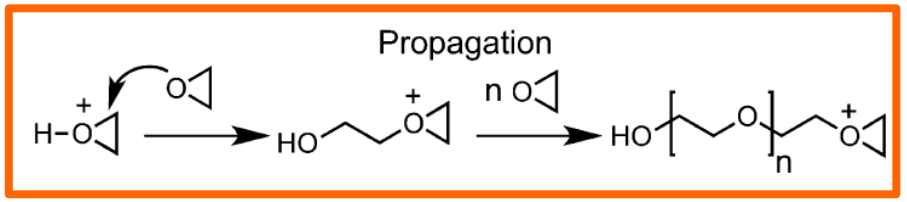

$I \xrightarrow{k_d} R$ thermal decomposition

$R + A \xrightarrow{k_a} SA$ superacid activation

$R + Z \xrightarrow{k_z} D$ inhibition

$SA + e \xrightarrow{k_i} c$ active chain initiation

$c + e \xrightarrow{k_p} c$ active chain propagation

R: radicals c: cations e: epoxy functional groups

$$k = A \cdot \exp(-\frac{E}{RT})$$

Mechanistic Model - Simplifications

Simplifications:

$$I \xrightarrow{k_d} R$$

$$R + A \xrightarrow{k_a} SA$$

$$R + Z \xrightarrow{k_z} D$$

$$SA + e \xrightarrow{k_i} c$$

$$c + e \xrightarrow{k_p} c$$

1. Omit superacid (SA)

$$I \xrightarrow{k_d} R$$

$$R + A \xrightarrow{k_a} c$$

$$R + Z \xrightarrow{k_z} D$$

$$c + e \xrightarrow{k_p} c$$

2. Rewrite inhibition step

$$I \xrightarrow{k_d} R$$

$$R + A \xrightarrow{f_l \cdot k_a} c$$

$$c + e \xrightarrow{k_p} c$$

with f_l: logistic factor

3. Rewrite R and c based on the material balance

$$c = A_0 - A$$

$$R = (I_0 - I) - (A_0 - A)$$

$$\frac{dI}{dt} = -k_d \cdot I$$

$$\frac{dA}{dt} = -f_l \cdot k_a \cdot A \cdot (2 \cdot f \cdot (I_0 - I) - (A_0 - A))$$

$$\frac{de}{dt} = -k_p \cdot e \cdot (A_0 - A)$$

3 steps model

Validation with DSC

Modelling and DSC measurements with varying formulation and thermal conditions

Solving and parameters fitting in MATLAB

100 monomer (in weight): IOC8 – Benzopinacol

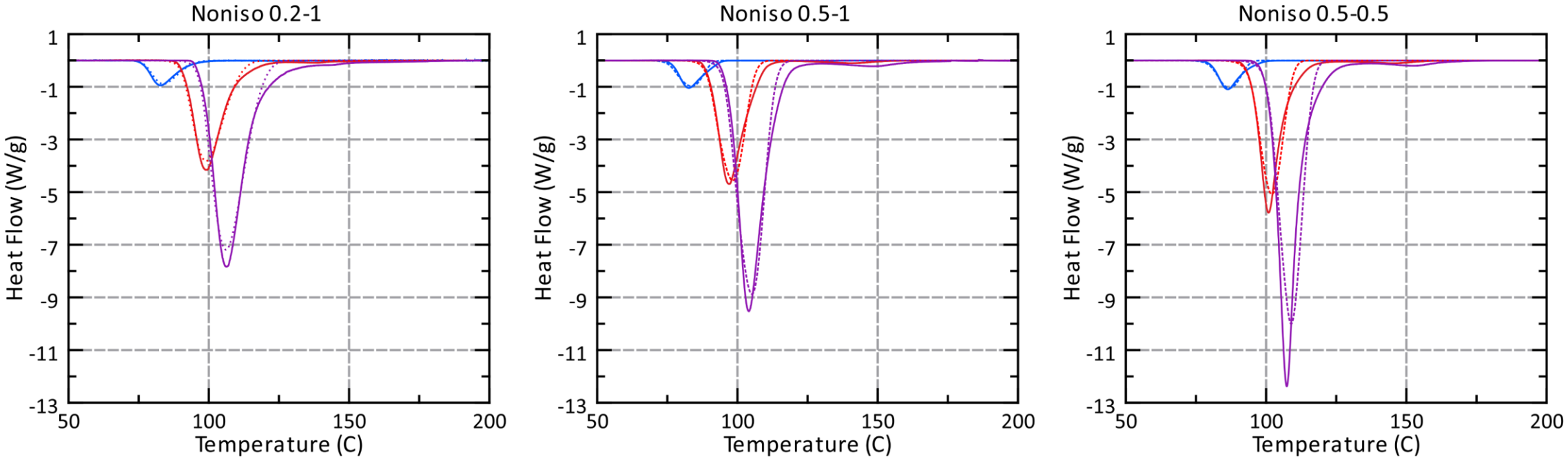

Solid line: experiments
Dash line: 3 steps model

Heating at: 1 K/min, 5 K/min, 10 K/min

↓ exothermic down

Validation with DSC

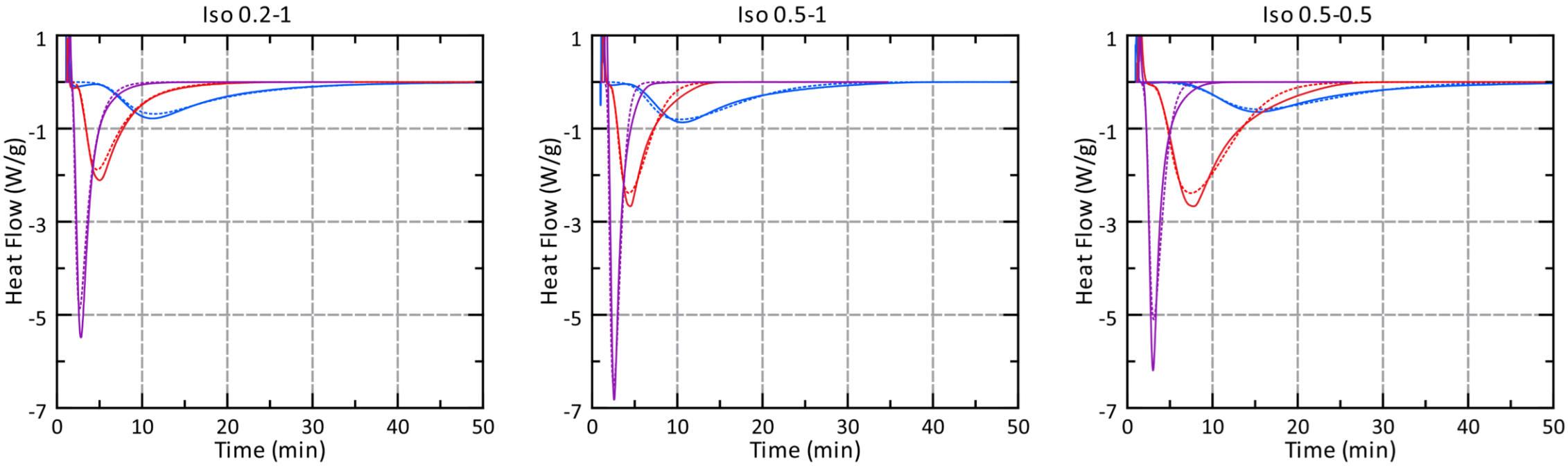

Isothermal at: 80 °C, 90 °C, 100 °C

$$\alpha = 1 - \frac{e}{e_0} \qquad \text{Heat Flow} = \frac{dQ}{dt} = H_r \frac{d\alpha}{dt} = -\frac{H_r}{e_0}\frac{de}{dt}$$

Finite elements modelling

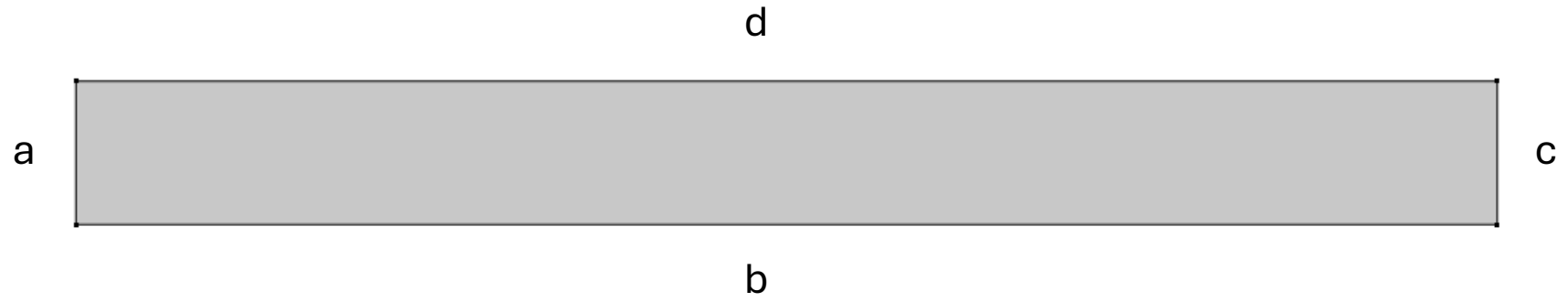

$$\rho C_p \frac{\partial T}{\partial t} = \nabla(\lambda \nabla T) + \rho H_r \frac{\partial \alpha}{\partial t}$$

Width: 6 cm; Height: 0.6 cm Solid domain, without flow & diffusion

ρ (density)* = $1130\ \frac{\mathrm{kg}}{\mathrm{m^3}}$ λ (thermal conductivity)* = $0.2688\ \frac{\mathrm{W}}{\mathrm{m \cdot K}}$ $\mathrm{C_p}$ (thermal capacity) = $1.14\ \frac{\mathrm{J}}{\mathrm{g \cdot K}}$

a: constant temperature 200 °C **d**: Convective heat transfer with external environment at 20 °C.

with heat transfer coefficient $\mathrm{h} = 5\ \frac{\mathrm{W}}{\mathrm{m^2 \cdot K}}$

$k_d,\ k_a,\ k_p,\ \mathrm{H_r} = 420\ \mathrm{J \cdot g^{-1}}$ from kinetic model

*Ma, Yating, et al. Advanced Manufacturing: Polymer & Composites Science 11.1 (2025): 2497106.

FP experiments

Silicon Mold cast with Mold Max™ 60

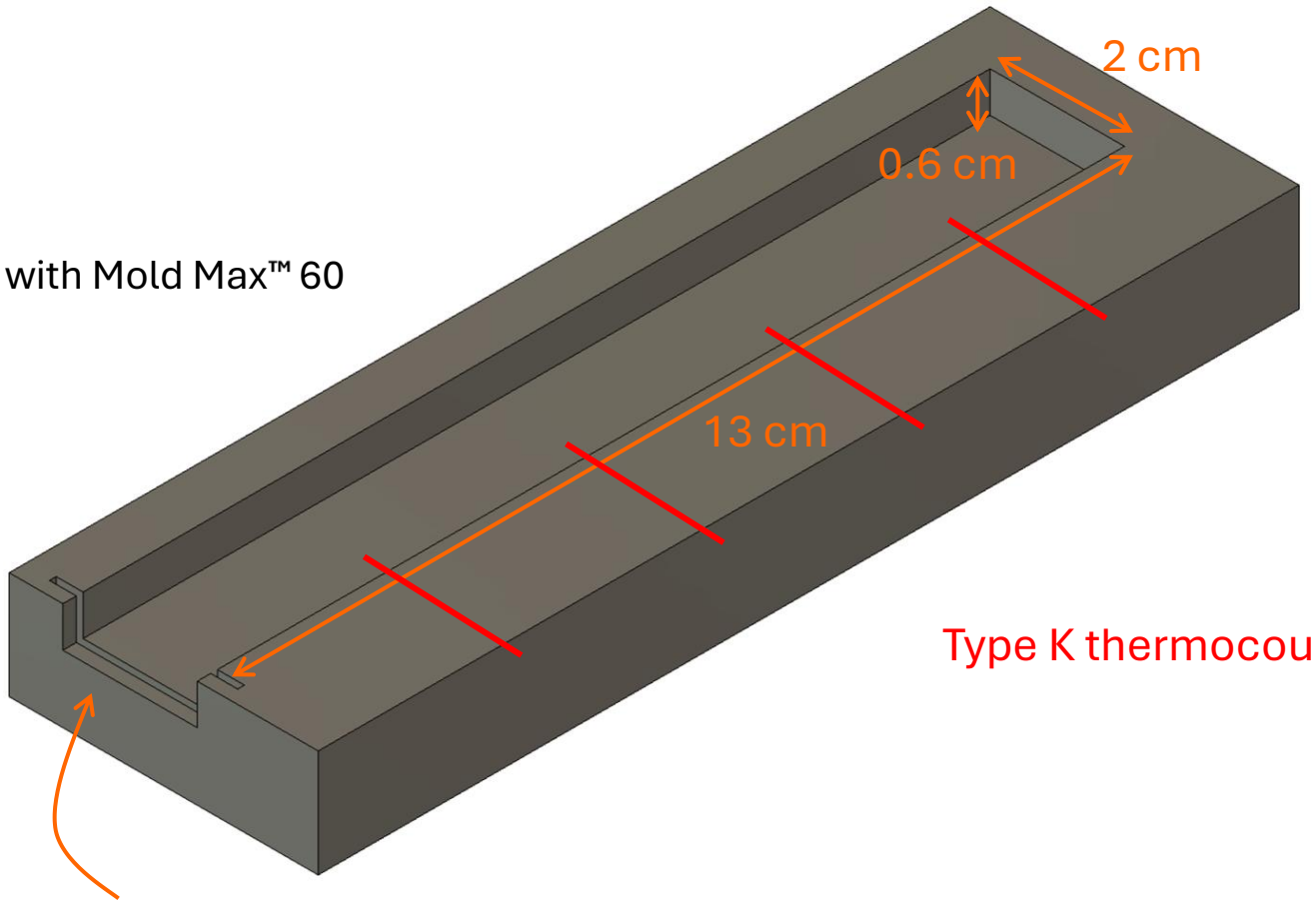

Type K thermocouples

Fronts initiate with hot plate

Finite elements modelling

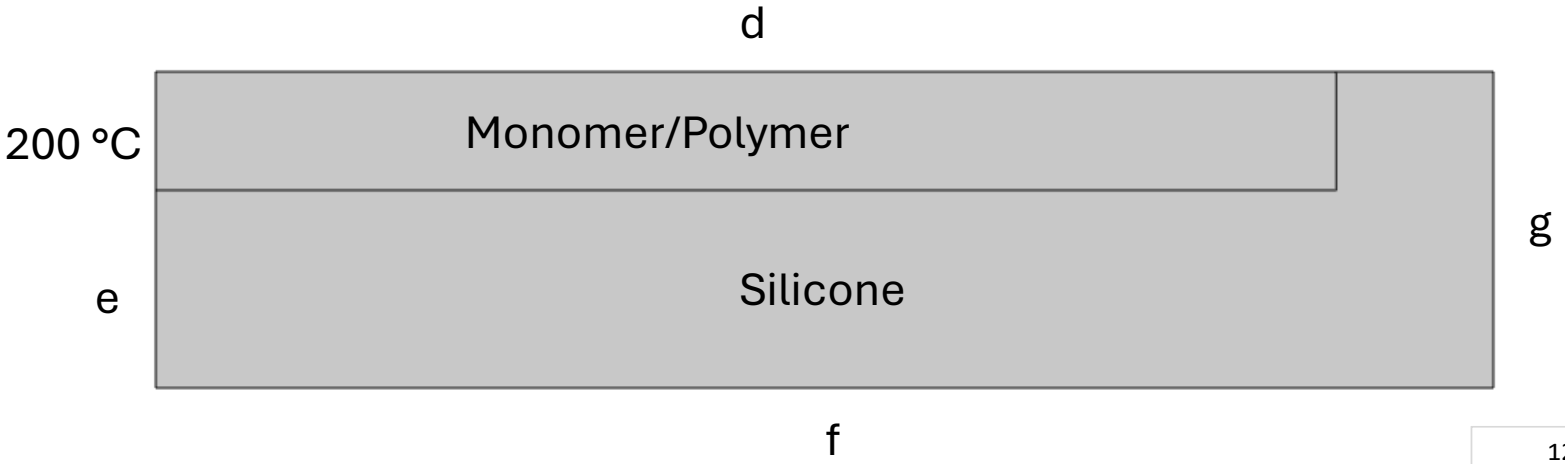

$$q_{radiation} \propto \varepsilon(T^4 - T_{amb}^4)$$

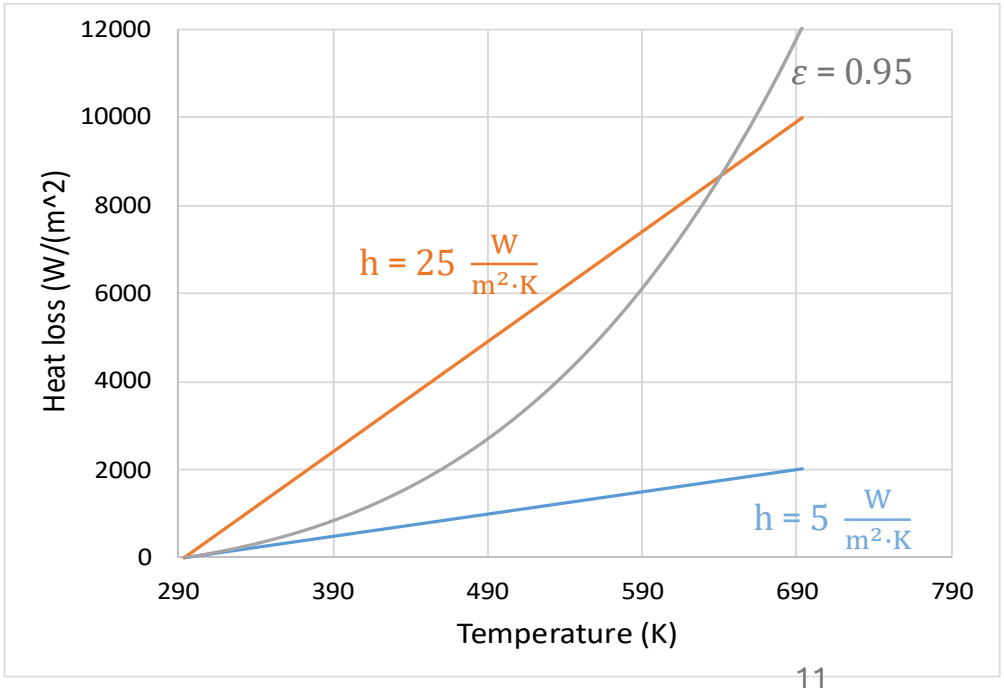

e&g: thermal insulation

f: constant temperature at 20 °C

d: Convective heat transfer with external environment at 20 °C.

+ radiative heat transfer with emissivity 0.95.

thermal conductivity of silicone mold = 0.347 ×1.5 $\frac{W}{m \cdot K}$

Finite elements modelling

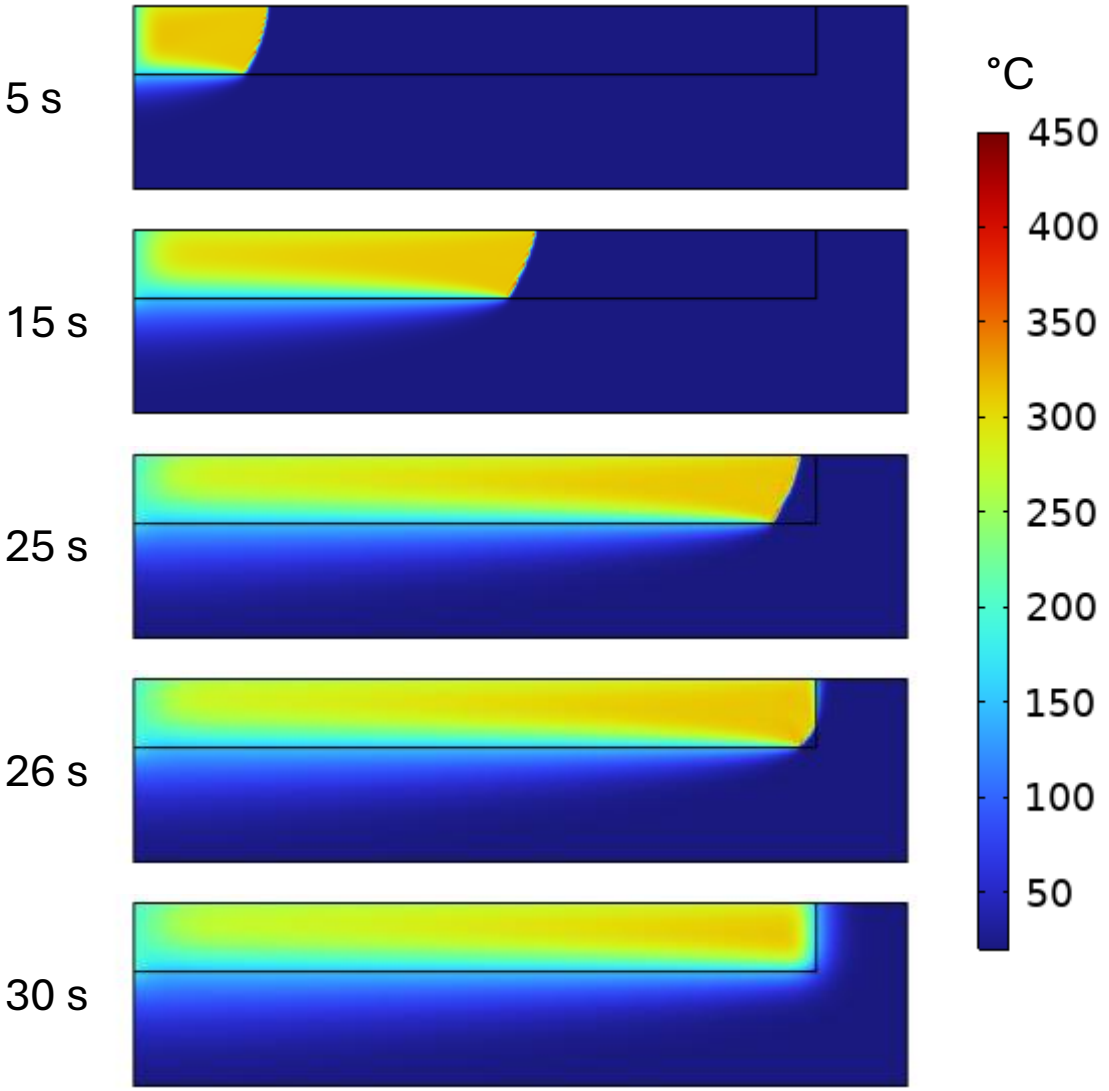



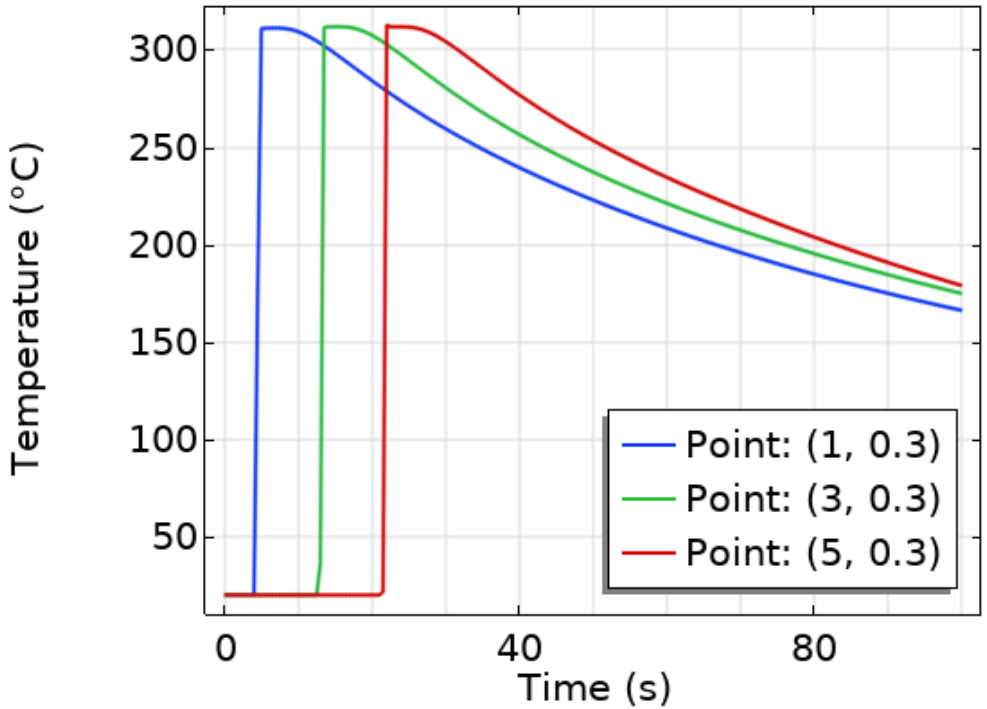

Acknowledgements



The resources and services used in this work were provided by the VSC (Flemish Supercomputer Center), funded by the Research Foundation – Flanders (FWO) and the Flemish Government.

PolyFront(G0A3723N)

Controlled Frontal Polymerization and Direct Writing of Cyclooctadiene-based Inks

Brandon R. Clarke, Jeffrey S. Moore, and Jennifer A. Lewis

ICCM24
08/04/2025

Harvard John A. Paulson School of Engineering and Applied Sciences

REMAT
Regenerative Energy-Efficient Manufacturing of Thermoset Polymeric Materials EFRC

UNIVERSITY OF ILLINOIS URBANA-CHAMPAIGN

Frontal Ring-Opening Metathesis Polymerization

Continuous 3D Printing and Frontal Polymerization of a pDCPD Helix

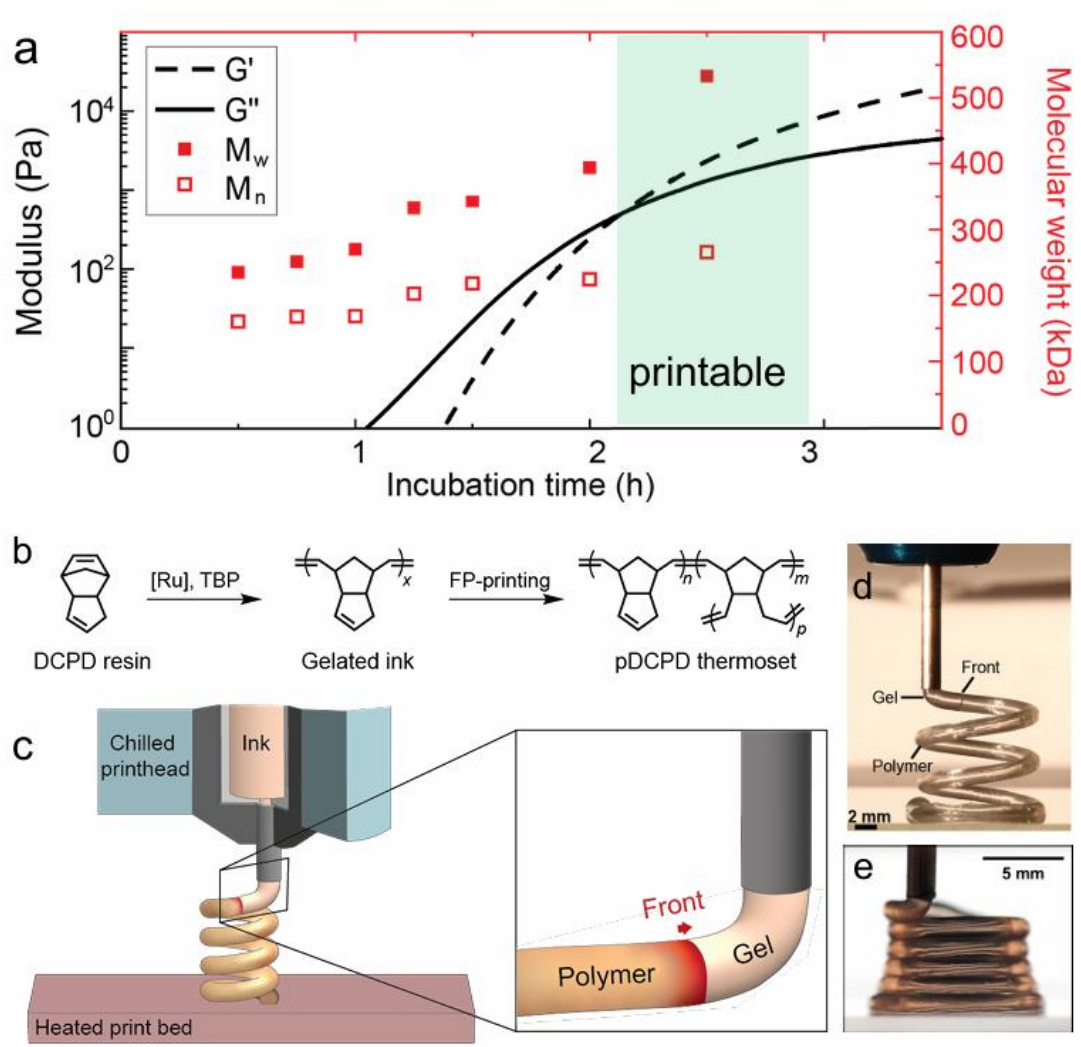

Taken From REMAT Grant Proposal

Nature. **2018**, *557*, 223-227.

COD/DCPD Copolymers

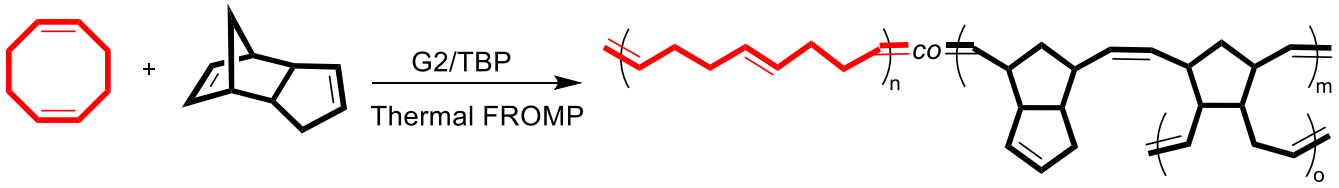

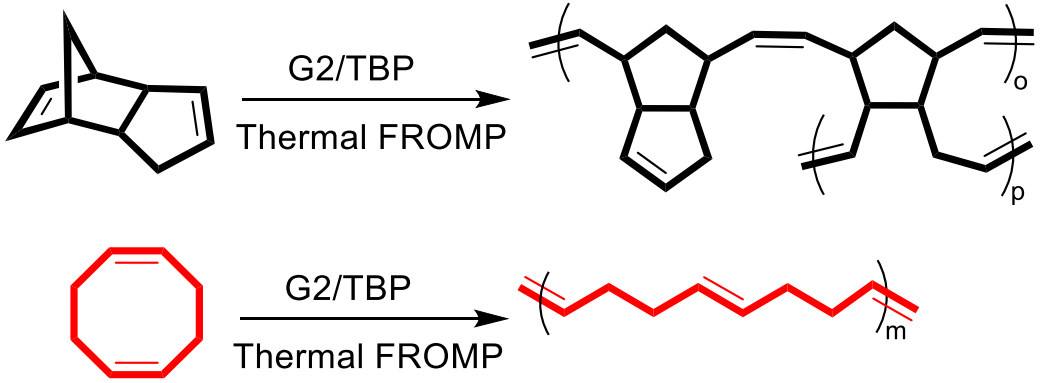

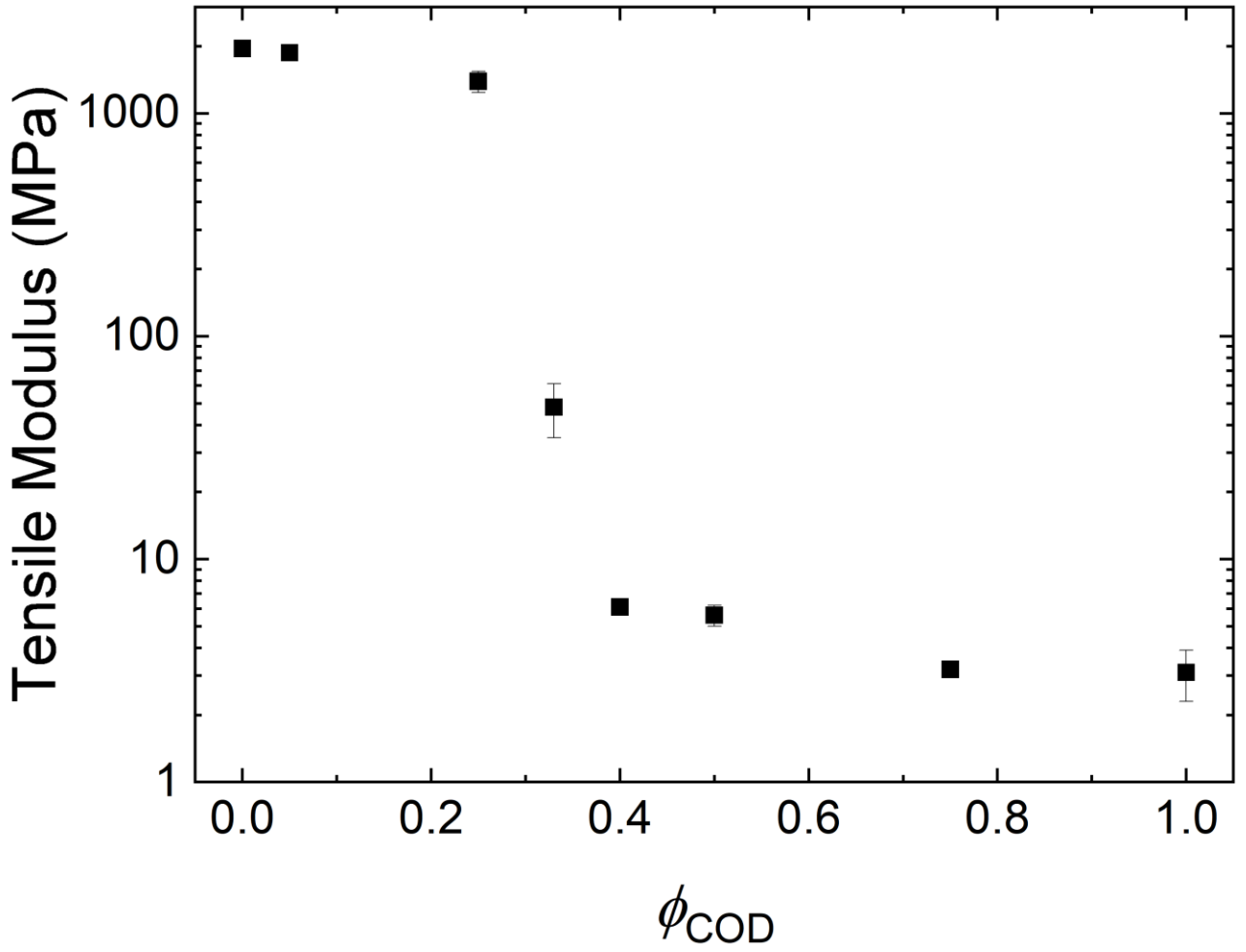

*Dean, *et al*. *ACS Macro Lett.* **2020**, *9*, 819-824.

Problems with Spontaneous Polymerization

COD



DCPD

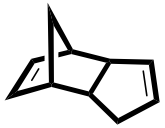

Monomer(s)	Energy Density	Stability
Cyclooctadiene (COD)	7.4 kcals/mol	Prone to Spontaneous FROMP
Dicyclopentadiene (DCPD)	27.2 kcals/mol	Stable against Spontaneous FROMP
COD/DCPD Copolymers	Mixed	Prone to Spontaneous FROMP

Why do COD formulations frequently SP while DCPD homopolymer formulations rarely do?

Polymerization of DCPD

Chain 1 Coordinates to Secondary Ring π Electrons on Chain 2

Secondary Ring-Opening Initiates

Chains Continue to Propagate with DCPD Monomers

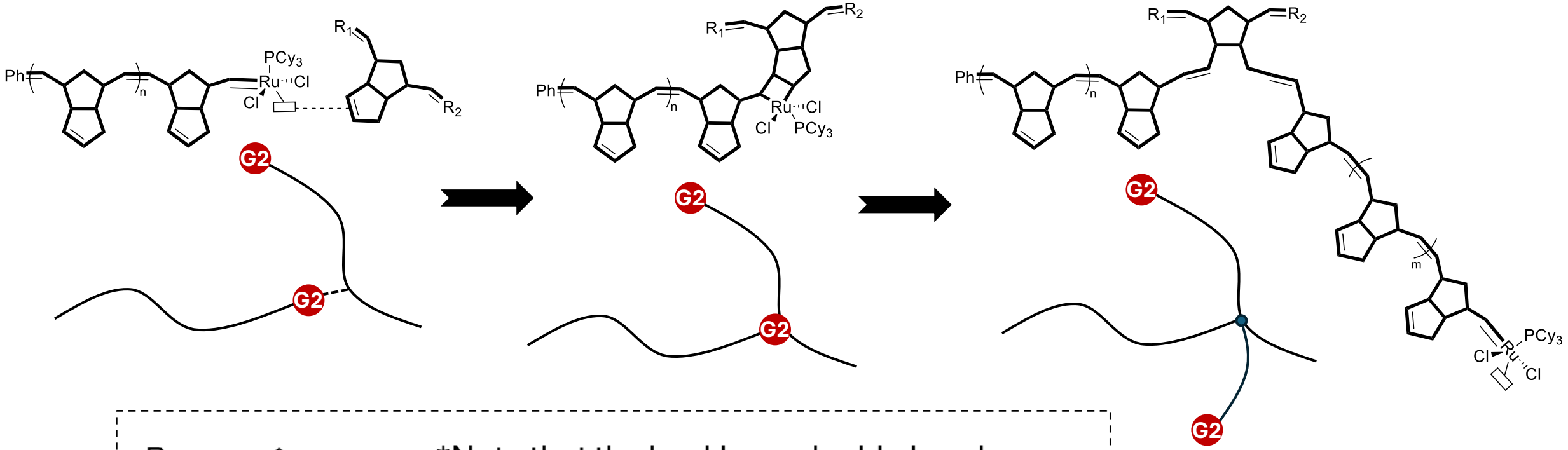

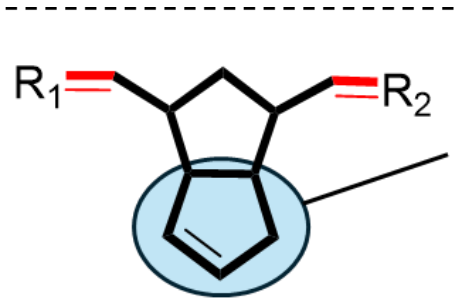

Note that the backbone double bonds are inaccessible to catalyst because of the steric blocking effect imposed by DCPD's secondary ring!

COD Polymerization

Chain 1 Coordinates to Secondary Ring π Electrons on Chain 2

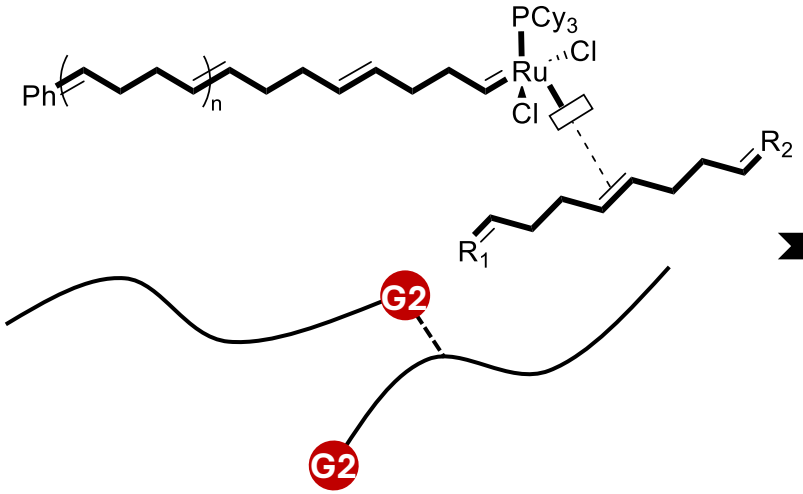

Linear Metathesis Initiates

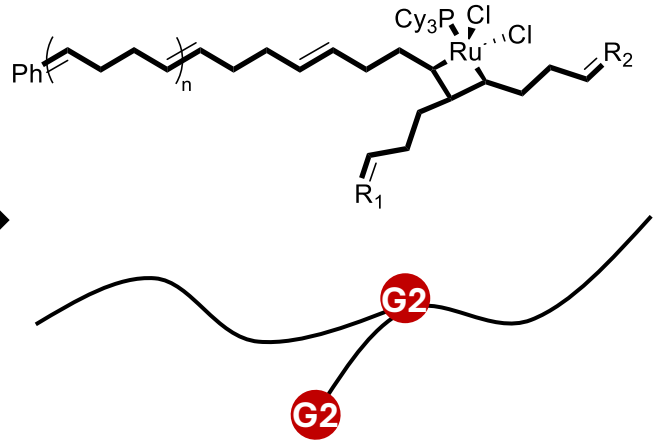

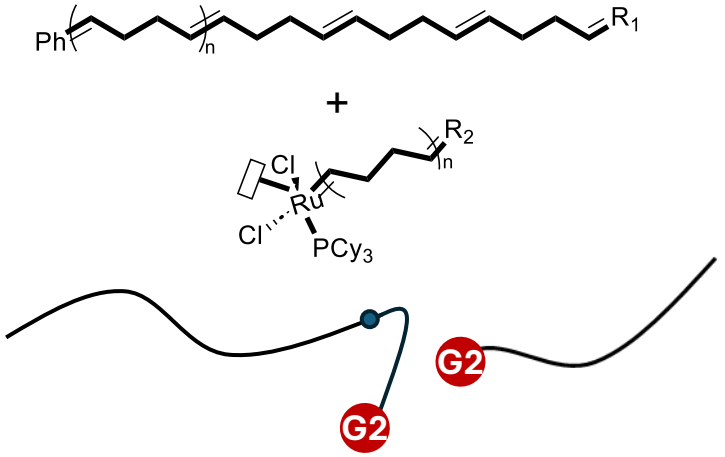

Chain 2 acts as "Chain Transfer Agent" and Chains Split!

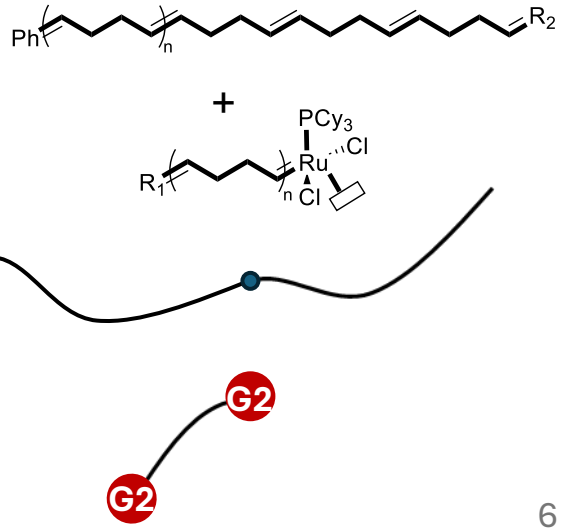



Backbone double bonds are active towards metathesis!

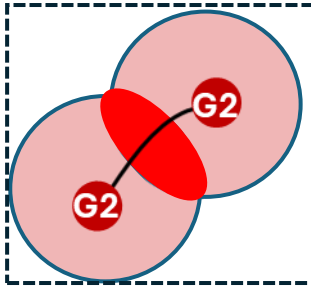

Overlapping fronts result in temperature spikes.

Free Chain End Excluded Volume

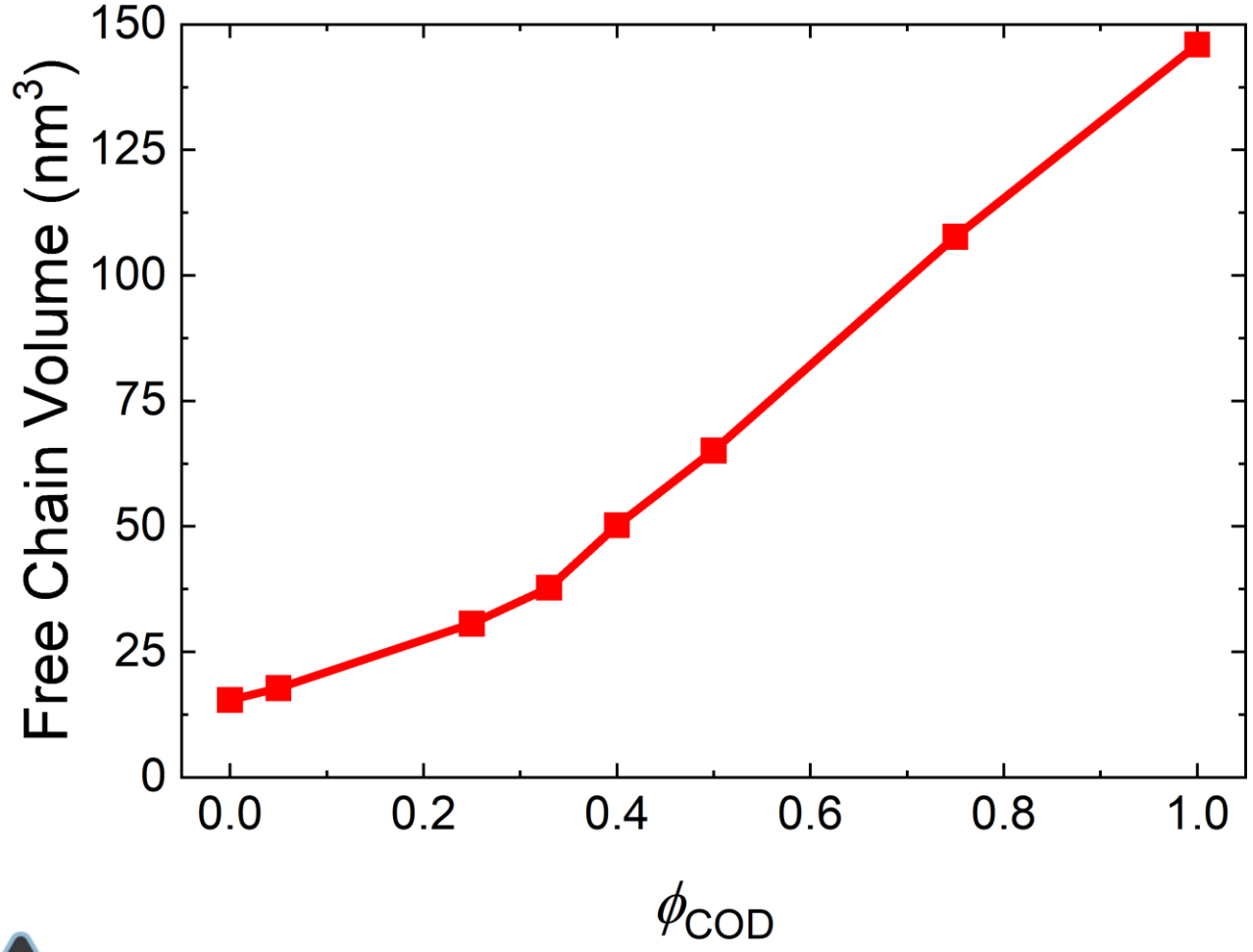

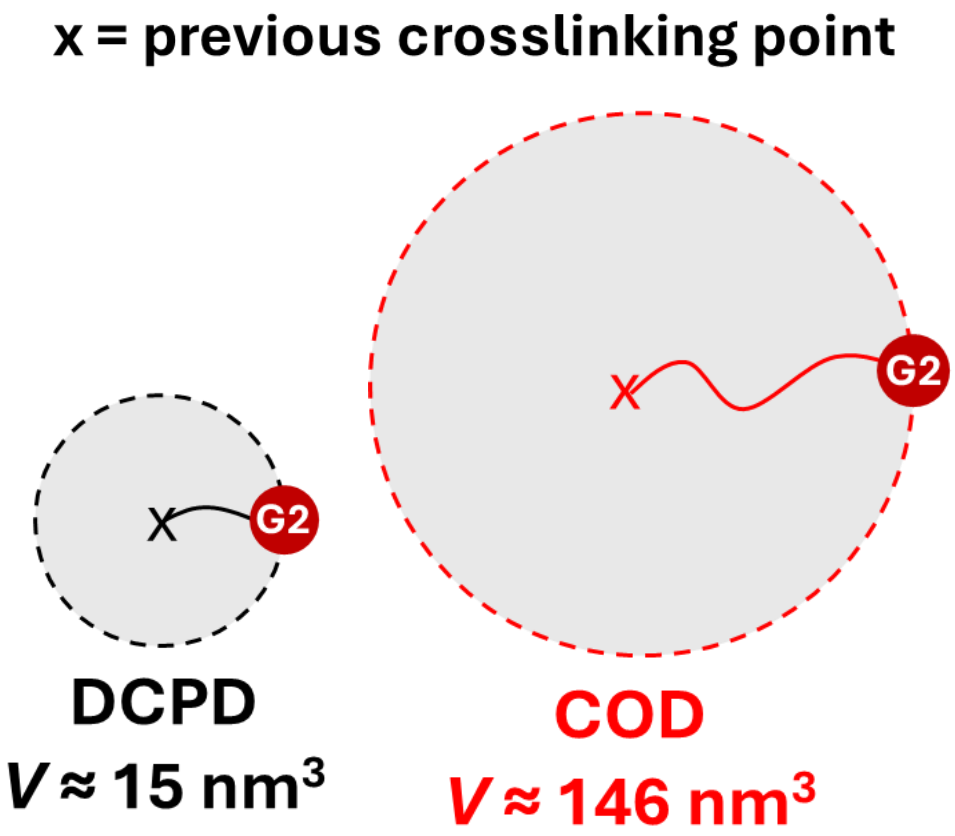

Strategies to Limit Spontaneous Polymerization

- **Shorter Primary Chains**
- **Lowered Temperatures**
- **Fewer Transfer Sites**

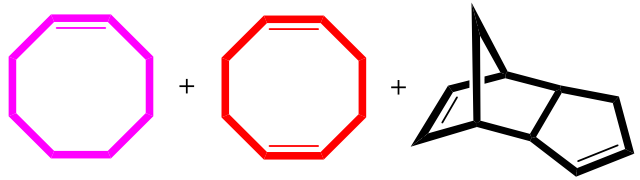

- **“Shackled” Chains**

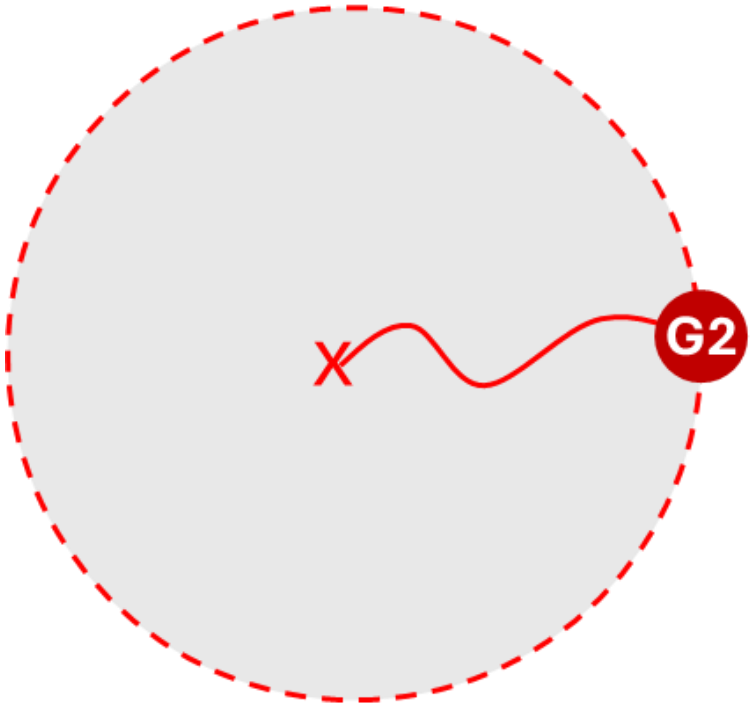

$$V = \langle R^2 \rangle^{3/2}$$

COD

$V \approx 146\ nm^3$

Shackling Chains

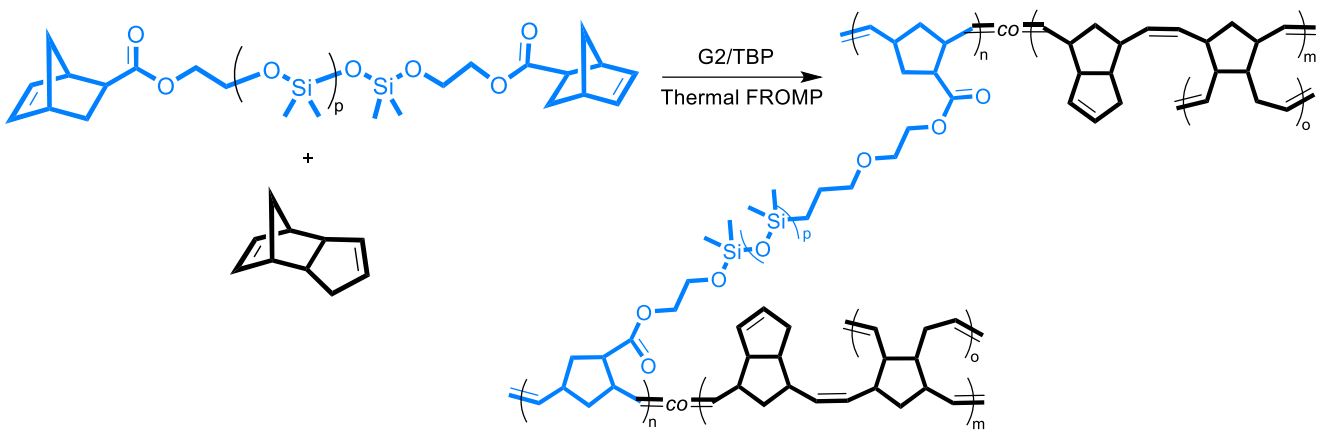

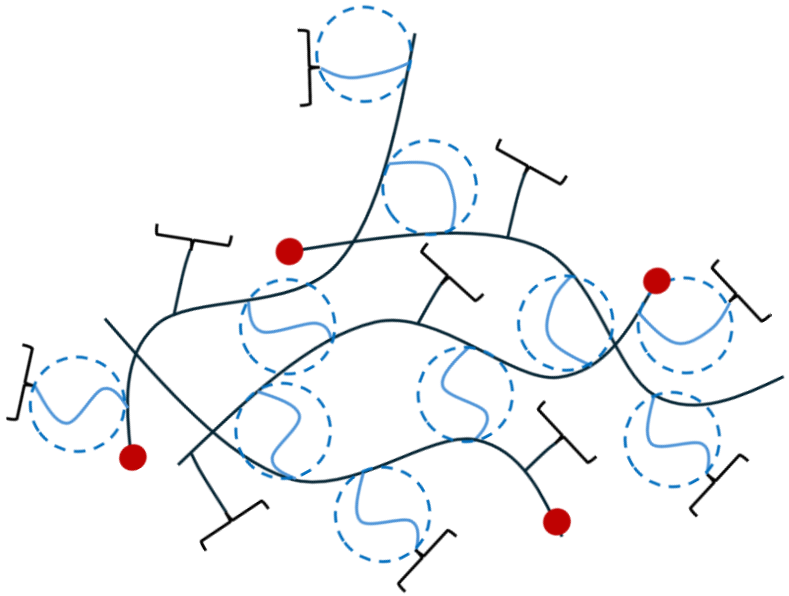

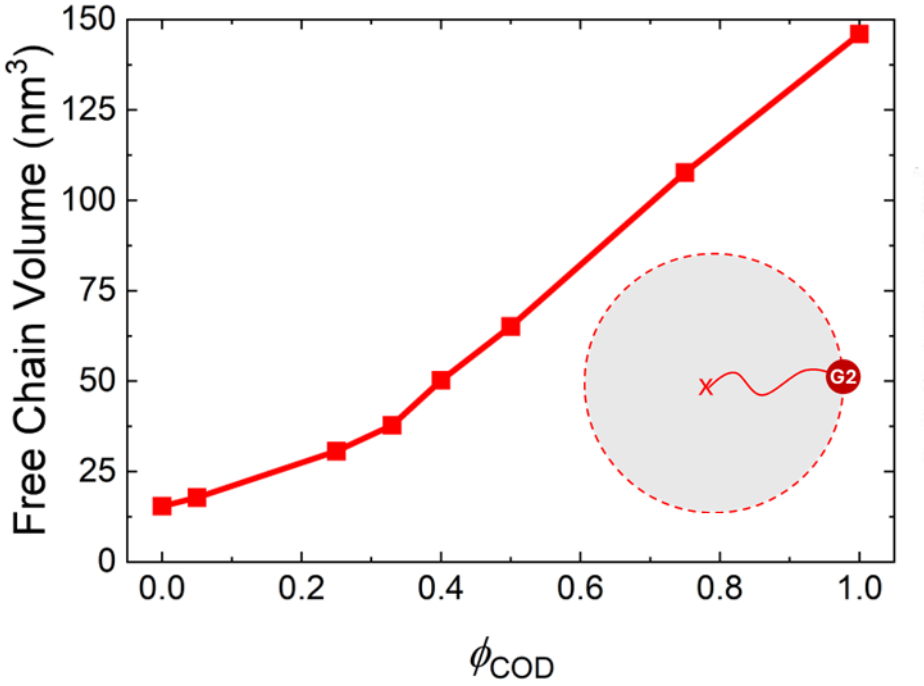

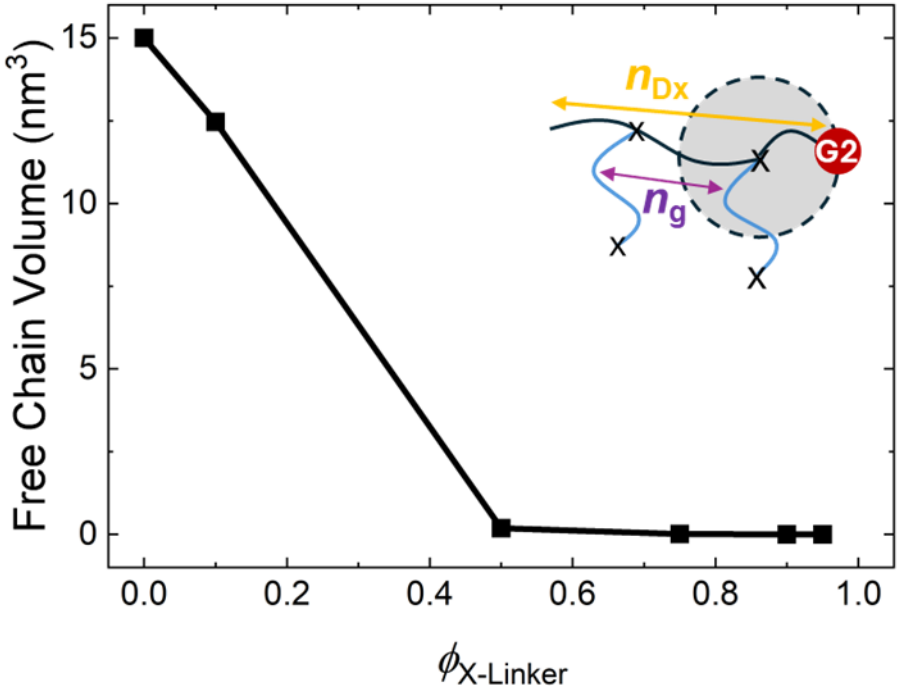

Shackling Chains

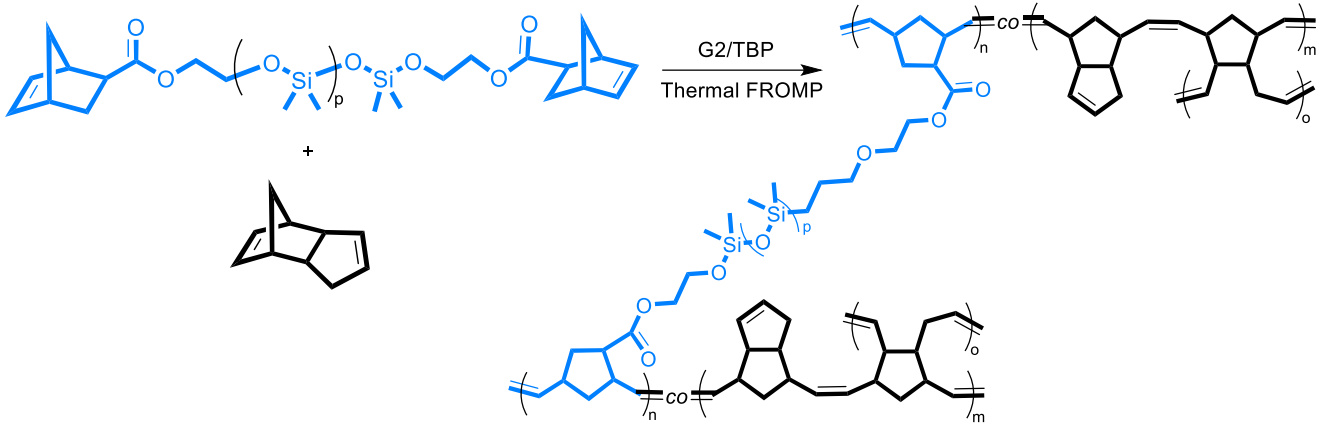

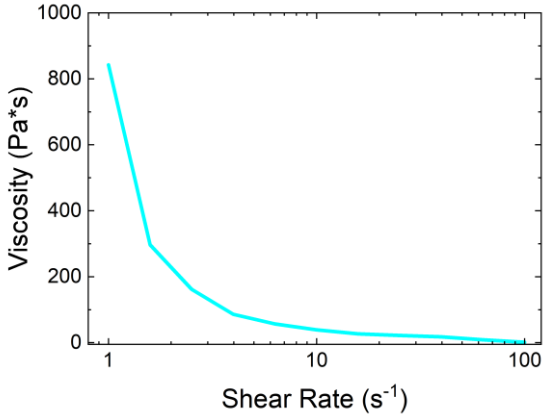



Shear-Thinning Organogel

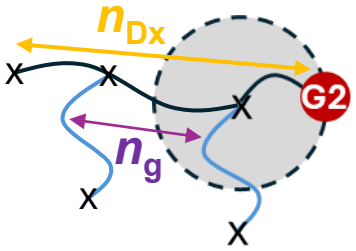

Freely-Jointed Chain Length **Graft Density** **DP between DCPD Crosslinks**

$$V = \left(n_f l^2\right)^{3/2}, n_f = \begin{cases} n_g, n_g < n_{Dx} \\ n_{Dx}, n_g > n_{Dx} \end{cases}$$

Shackling Chains

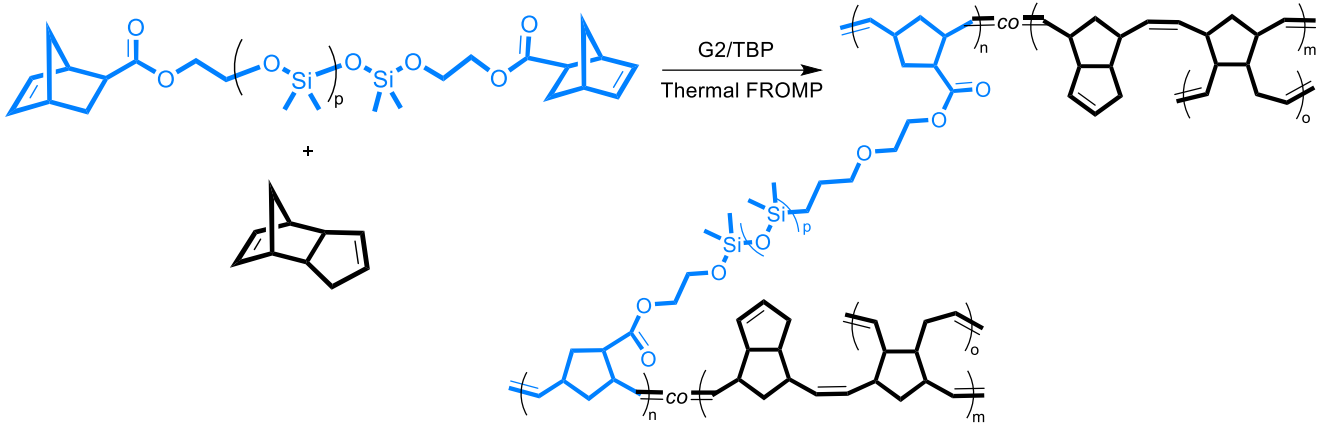

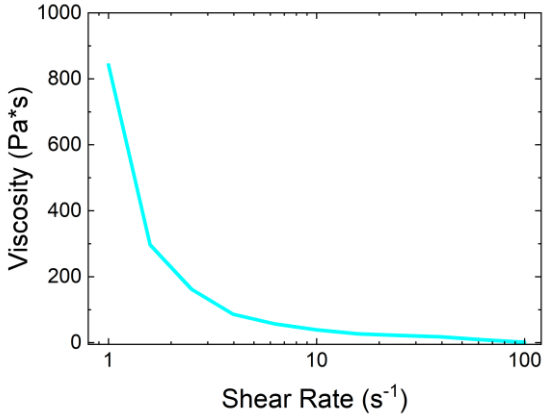



Shear-Thinning Organogel

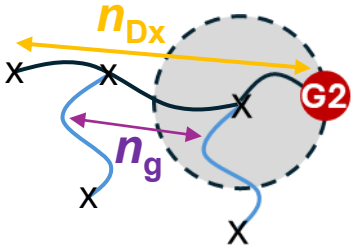

Freely-Jointed Chain Length **Graft Density** **DP between DCPD Crosslinks**

$$V = \left(n_f l^2\right)^{3/2}, n_f = \begin{cases} n_g, n_g < n_{Dx} \\ n_{Dx}, n_g > n_{Dx} \end{cases}$$

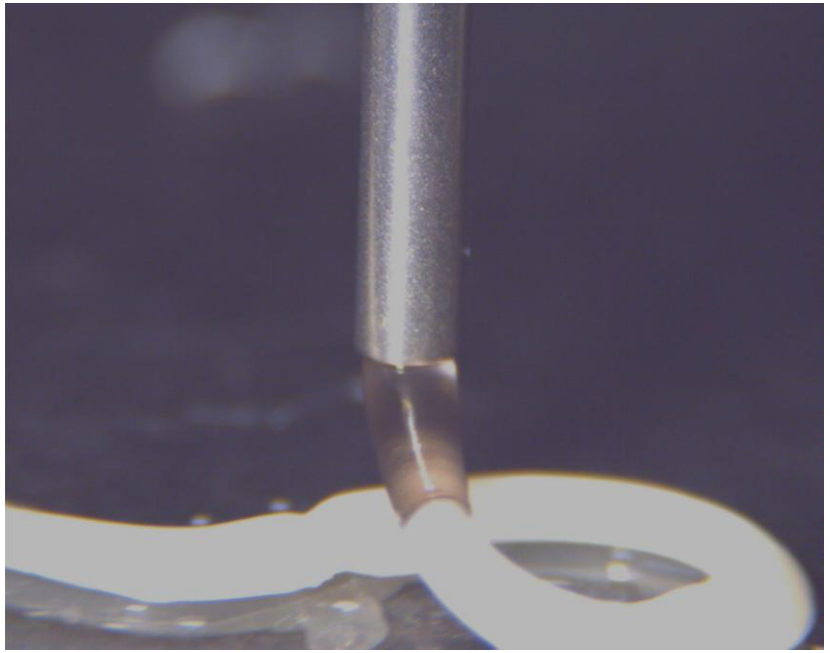

Extension to COD Inks

"Shackled" Chains

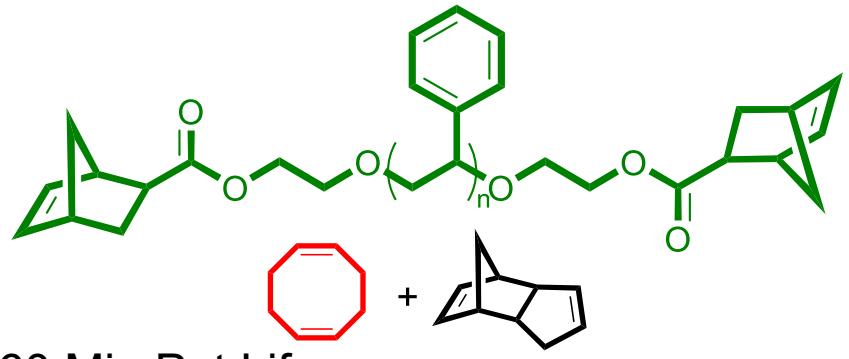

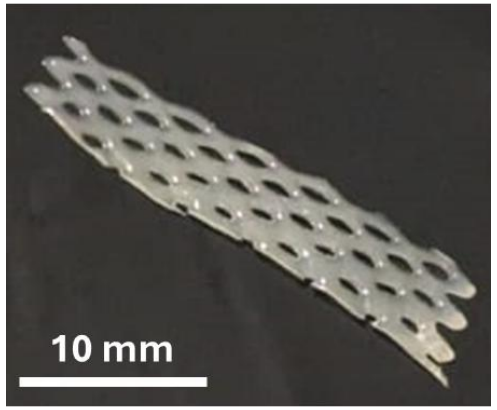

~60 Min Pot Life

Fewer Transfer Sites

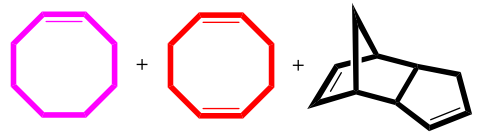



~60 Min Pot Life

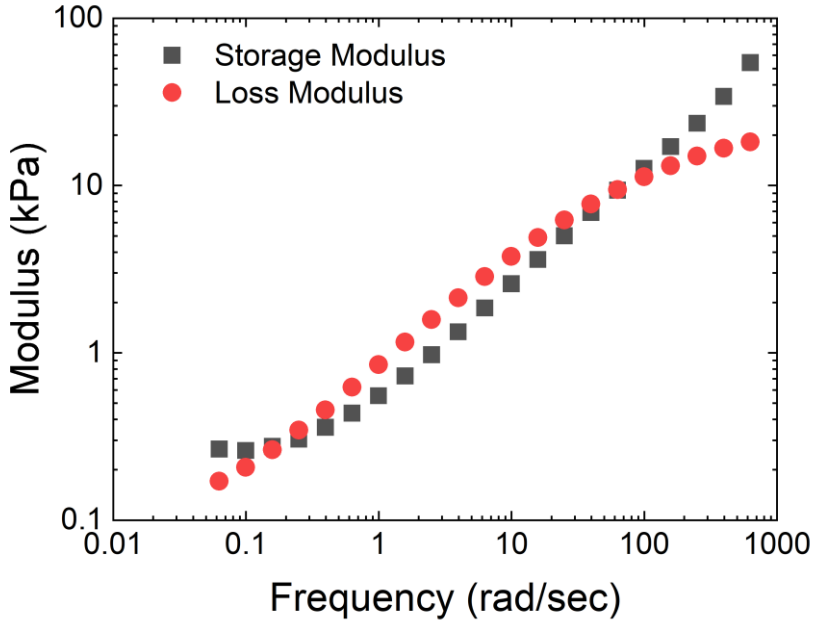

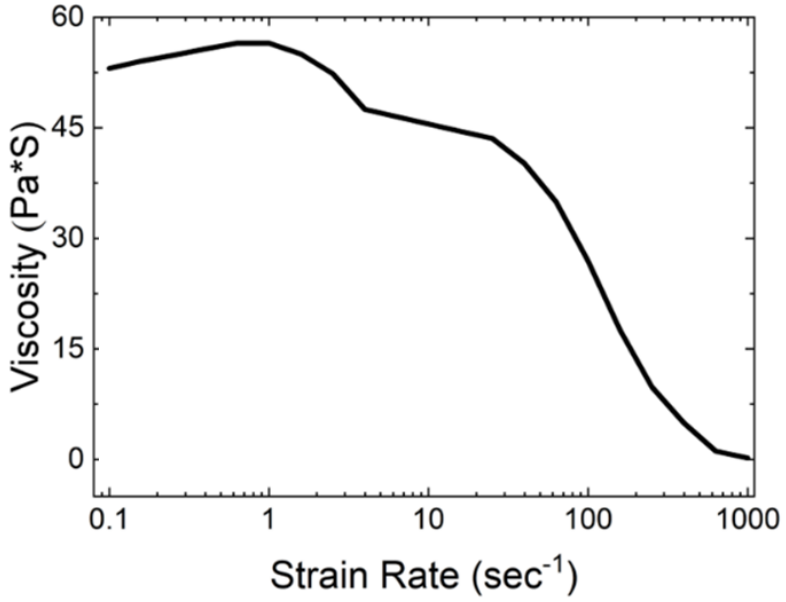

Acknowledgments





UNIVERSITY OF ILLINOIS URBANA-CHAMPAIGN

REMAT

Harvard John A. Paulson School of Engineering and Applied Sciences

Questions?

ICCM24
AUGUST 4-8, 2025
BALTIMORE CONVENTION CENTER
BALTIMORE, MARYLAND, USA

No Technical Paper Submission for:

Philippe Geubelle

ICCM24
AUGUST 4-8, 2025
BALTIMORE CONVENTION CENTER
BALTIMORE, MARYLAND, USA

No Technical Paper Submission for:

Clement Broggi

CURING TIME-ENERGY OPTIMIZATION OF FRONTAL POLYMERIZATION OF FIBER-REINFORCED POLYMER COMPOSITES

Sanghun Shin[1], Nawaf Rasheed[1,2], Sagar K. Vyas[3], Tyler C. Price[1,4], Zheyuan Zheng[1,3], Jeffery W. Baur[1,3], Nancy R. Sottos[1,4], Philippe H. Geubelle[1,3], and Sameh H. Tawfick[1,2,†]

[1]Beckman Institute for Advanced Science and Technology, University of Illinois Urbana-Champaign, Urbana, IL 61801, USA, Web: https://beckman.illinois.edu/
[2]Department of Mechanical Science and Engineering, The Grainger College of Engineering, University of Illinois Urbana-Champaign, Urbana, IL 61801, USA, Web: https://mechse.illinois.edu/
[3]Department of Aerospace Engineering, The Grainger College of Engineering, University of Illinois Urbana-Champaign, Urbana, IL 61801, USA, Web: https://aerospace.illinois.edu/
[4]Department of Materials Science and Engineering, The Grainger College of Engineering, University of Illinois Urbana-Champaign, University of Illinois Urbana-Champaign, Urbana, IL 61801, USA, Web: https://matse.illinois.edu/
[†]Corresponding author (tawfick@illinois.edu)

Keywords: Thermosetting resin, Carbon fibre, Polymer-matrix composites(PMCs), Computational modelling, Cure, Cure behaviour, Process monitoring

ABSTRACT

Frontal ring-opening metathesis polymerization (FROMP) is a promising thermoset composite curing process for thermoset composites, enabling rapid and energy-efficient manufacturing through a self-energized exothermic reaction. Once initiated, the polymerization front spatially propagates through the resin matrix. Among various frontal polymerization curing strategies, through-thickness curing offers potential for scalable carbon-fiber-reinforced polymer (CFRP) composite fabrication. However, manufacturing large composite structures via through-thickness curing requires the analysis of the trade-offs among curing energy and speed, as well as new strategies for scaling up the equipment and tooling required for the heating and pressure applications. To address this issue, incremental curing methods use a fixed area tool for applying pressure and heat to initiate a through-thickness front, followed by removing the pressure and feeding the composite forward to cure the following section of the composite. This process must be optimized to maintain high cure quality while minimizing energy input to fabricate large composite structures. In this study, we develop a computational and experimental approach to optimize and validate the thermal management of incremental through-thickness FROMP for CFRP. A one-dimensional reaction-diffusion model including cure kinetics is implemented to simulate the thermal and chemical reaction with different heating profiles. Using this simple model, parametric optimization with different FROMP initiation parameters is applied to find optimal thermal management cycles to reduce energy and curing time simultaneously. In addition, the simulations consider the influence of adjacent preheated domains from previous cycles to reflect thermal conditions. Experimental validation confirms that the derived optimized curing cycles produce fully cured composite segments with consistent glass transition temperatures by the dynamic mechanical analysis, comparable to those from conventional high-energy processes. The work demonstrates the feasibility of the scalable and low-cost CFRP manufacturing via incremental through-thickness FROMP, supporting the application of future large composite structure manufacturing industries such as aerospace and automotive.

1 INTRODUCTION

Energy-efficient and fast manufacturing of thermoset polymer composites is critical for next generation high-performance materials in aerospace, transportation, marine, and energy industries [1–4]. However, conventional curing methods for thermoset polymers, such as epoxy resins, use large ovens or autoclaves for curing cycles which take many hours, requiring a significant amount of energy and time [5,6]. Here, we use frontal ring-opening metathesis polymerization (FROMP) as a promising fast, energy-efficient curing method to produce carbon-fiber-reinforced poly-dicyclopentadiene. This curing reaction is driven by the exothermic heat generated during the polymerization of the DCPD monomer in the presence of Grubbs catalyst. In the FROMP process, the exothermic reaction is spatially localized near a propagating front, which is triggered thermally at one starting location, enabling fast and low-energy manufacturing [5,7]. In composites, the front can propagate longitudinally along the fibers, or through the thickness if triggered by heat from a heated mold brought in contact with the surface of the composite. However, if insufficient energy is present at the front, for instance due to heat loss to the surrounding or fast heat conduction ahead of the front by the carbon fibers, undesired front quenching might occur [8,9]. For this reason, through-thickness curing is often preferred when large volume fraction composites are desired, as quenching is avoided with through-thickness curing [10,11]. Therefore, it is important to investigate an optimized thermal heating profile that fully cures the polymer with the desired curing time and energy simultaneously. To achieve this, understanding of the curing behavior in response to different thermal trigger profiles through theoretical and numerical modeling of FROMP is essential.

In this study, we develop a numerical optimization process for the cyclic through-thickness FROMP curing of carbon fiber-reinforced polymer (CFRP) composites to realize rapid and low-energy manufacturing of large composites. The cyclic curing enables the use of a small footprint oven to cure large area composites by cyclic feeding and through-thickness front curing in a stepped manner. Due to the exothermic heat generation, continuous external thermal energy supply throughout the process is unnecessary, allowing for various curing profiles depending on the heating method. Furthermore, in the repeated FROMP processes, changes in the initial conditions for subsequent cycles due to high-temperature regions from previous cycles require additional analysis for an optimized thermal management cycle. To address these issues, computational models considering thermo-chemical reaction-diffusion equations are utilized, providing insights into FROMP. In addition, a combination of numerical modeling and experimental validation can further enhance the reliability of FROMP manufacturing.

As shown in Figures 1(a) and 1(b), we model the frontal polymerization of CFRP and apply a gradient-based optimization process to derive an optimized low-energy-consuming heating cycle. For the modeling, we consider three different domains: heater, CFRP, and insulator. DCPD and carbon fiber are used as monomer and reinforcement in the CFRP for reaction-diffusion analysis. The simulation allows us to derive temperature changes and degree of cure variations in the domains with different heating power profiles, enabling the analysis of the impact of thermal management in cyclic curing processes. In the optimization stage, a parametric optimization algorithm is applied to the design variables (e.g., heating, cooling, feeding time, and heating power) to minimize energy consumption while achieving the desired process time and degree of cure conditions. Finally, through experiments, we analyze the curing results and demonstrate the incremental CFRP curing process of a long composite structure using a small footprint oven with lower energy consumption compared to conventional curing conditions by applying the heating cycle proposed by the model and algorithm, as shown in Figure 1(c). Based on the results obtained from this study, the optimized curing strategies can be applied to large-scale manufacturing processes by implementing energy-efficient, low-cost FROMP cycles. This result supports the advancement of sustainable manufacturing for high-performance thermoset polymers and composite materials in various applications.

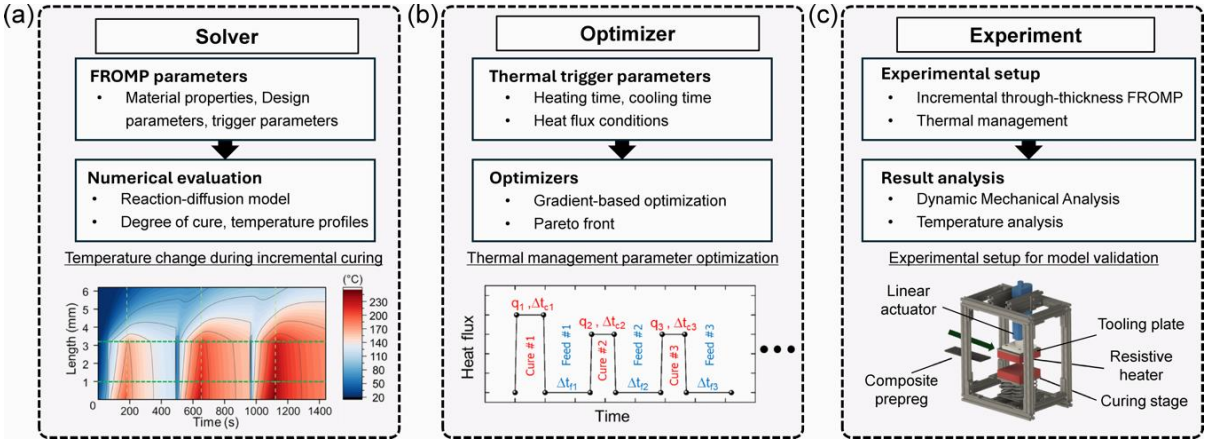

Figure 1: Proposed computational and experimental study for thermal management optimization: (a) numerical modeling for reaction-diffusion equations and cure kinetics, (b) optimization process for the heating cycle, and (c) experiment to demonstrate the optimized FROMP process.

2 MODELING OF COMPOSITE MANUFACTURING

2.1 Reaction-diffusion equation for incremental curing model

For the FROMP-based incremental composite model, we develop a 1D transient finite element model implemented in the FEniCS open-source finite element framework. During the manufacturing process, an insulation layer and a heater domain are required to apply pressure to the composite and initiate through-thickness FROMP, respectively. Therefore, three domains including insulation, composite, and heater layers were applied for the simulation, as illustrated in Figure 2(a). To capture the exothermic reaction and heat transfer, reaction-diffusion relations and heat conduction equations in through-thickness direction (x) were applied, as shown in Equations (1)–(4)[7,12]. Specifically, a phenomenological $g(\alpha)$ model based on the Prout-Tompkins formulation[12] was used to describe the cure kinetics as follows:

$$\overline{\rho C_p}\frac{\partial T}{\partial t} = \bar{k}\frac{\partial^2 T}{\partial x^2} + \rho_m(1-\phi)H_r\frac{\partial \alpha}{\partial t} \tag{1}$$

$$\frac{\partial \alpha}{\partial t} = A\exp\left(-\frac{E}{RT}\right)g(\alpha) \tag{2}$$

$$g(\alpha) = (1-\alpha)^n\alpha^m\left(\frac{1}{1+\exp(c_d(\alpha-\alpha_d))}\right) \tag{3}$$

$$\rho_i C_{p_i}\frac{\partial T}{\partial t} = k_i\frac{\partial^2 T}{\partial x^2}\ (i=1,2) \tag{4}$$

where $\overline{\rho C_p}$ $(J/(m^3K))$ is the homogenized volumetric heat capacity of the composite derived using the rule of mixtures, and $\bar{k}$ $(W/(m\,K))$ is effective thermal conductivity of the composite. The temperature, time, matrix density, fiber volume fraction, enthalpy of the FROMP reaction, and degree of cure are denoted by $T(K)$, $t(s)$, $\rho_m(kg/m^3)$, ϕ, $H_r(365000\,J/kg)$, and α respectively. Regarding Equation (2), time constant, activation energy, and universal gas constant are respectively denoted by $A(8.55e+15\,1/s)$, $E(110750\,J/mol)$, $R(8.314\,J/(mol\,K))$. In Equation (3), the constants used in the Prout-Tompkins model are given by $n=1.72$, $m=0.77$, $c_d=14.48$, and $\alpha_d=0.41$. Since no curing reaction occurs in the insulation ($i=1$) and heater ($i=2$) domains, only Equation (4) is applied to those regions. Other material properties used in the simulation are summarized in Table 1[7].

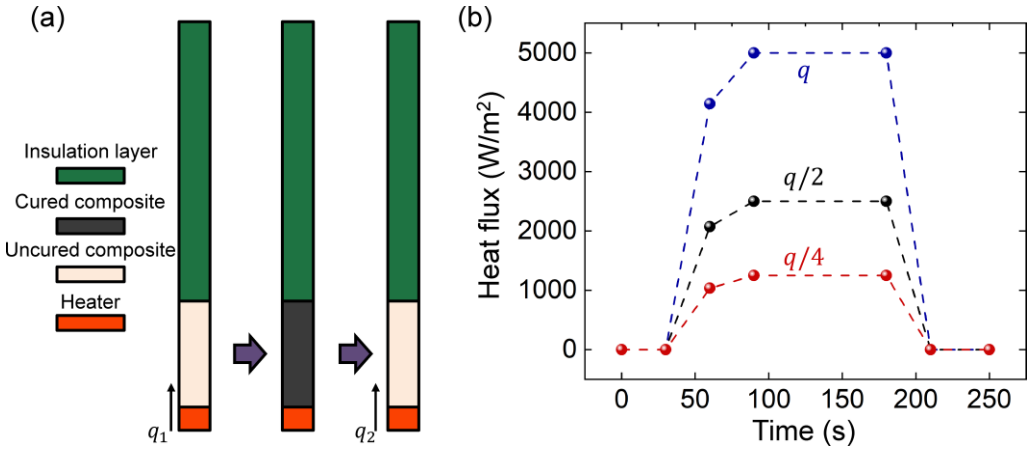

Figure 2: (a) Simulation geometry for incremental curing model, and (b) example of applied heat flux over time for initiation frontal polymerization in composite manufacturing
initial frontal polymerization for composite manufacturing

		Thermal conductivity $(W/(m\,K))$	Density (kg/m^3)	Specific heat $(J/(kgK))$
Carbon fiber	DCPD	0.15	980	1600
	AS4	10.45	1760	795
Insulation	PTFE	0.03	2200	970
	Calcium silicate	0.10	232.27	840
Heater	PI	0.12	1420	1090
	Silicone rubber	0.3	1200	1100

Table 1: Material properties of carbon fiber, insulation, and heater

For the incremental curing process, a heat flux profile $q_1(t)$ is applied in the first cycle to initiate the curing reaction in the CFRP. After the initial CFRP section is cured, a new uncured CFRP is fed into the system, and the second curing cycle begins with a heat flux profile of $q_2(t)$. This process is repeated for multiple curing cycles (see Figure 2(a)). Notably, due to residual heat from the previous cycle, the insulation and heater domains are preheated, which allows the subsequent curing cycle to achieve a fully cured result with a reduced energy input. Figure 2(b) shows examples of the applied heat flux profiles used to initiate the first curing cycle. In all simulations, the initial conditions were set as $\alpha_0 = 0.01$ and $T_0 = 20°C$.

2.2 Curing behavior under different thermal conditions

As shown in Figure 2(b), the area under the heat flux-time plots represents the energy input per unit area (J/m^2). In these examples, the applied surface energy inputs for three different cases (i.e., profiles of q, q/2, and q/4) are 724.3, 362.1, and 181.1 kJ/m^2, respectively. By using these thermal boundary conditions in the curing system, spatiotemporal distributions of temperature and degree of cure under three different curing conditions were obtained. The x-axis represents time, while the y-axis indicates spatial position through the three domains (heater, composite, and insulation), allowing observation of the temperature and cure distribution across each layer.

The thickness values of the heater, composite, and insulation layers are set to 1, 2.2, and 25.4 mm, respectively. In addition, the materials are applied as silicone, rubber, DCPD/AS4 with a fiber volume fraction of 0.65, and PTFE, respectively. We use spatiotemporal plots as a representation of the temperature evolution, represented by colored contours, along the 1-D domain during the curing as shown in Figure 3. We also construct similar contour plots for the degree-of-cure. This type of plot represents the evolution in space and time and hence a single plot replaces a 1-D movie of the curing process, obtained via numerical simulations. As shown in Figures 3(a) and 3(d), the curing is initiated

near the heater and propagates through the composite toward the insulation layer. The degree of cure eventually reaches ~0.98, indicating that full cure is achieved. Assuming 0.95 as the threshold for complete cure, this result suggests that cure time and energy input can be further optimized using a slightly lower heat flux or shorter heating duration.

On the other hand, Figures 3(b) and 3(e) show that while the FROMP is initiated with a reduced energy input, it cannot sustain propagation due to heat loss to surrounding domains, resulting in incomplete cure. Furthermore, in Figures 3(c) and 3(f), the supplied energy is insufficient even for the initiation of FROMP, and the degree of cure at the end of the composite remains at 0.23. These results highlight the importance of proper thermal management (heat flux and heating duration) to ensure complete and energy-efficient curing of composite materials.

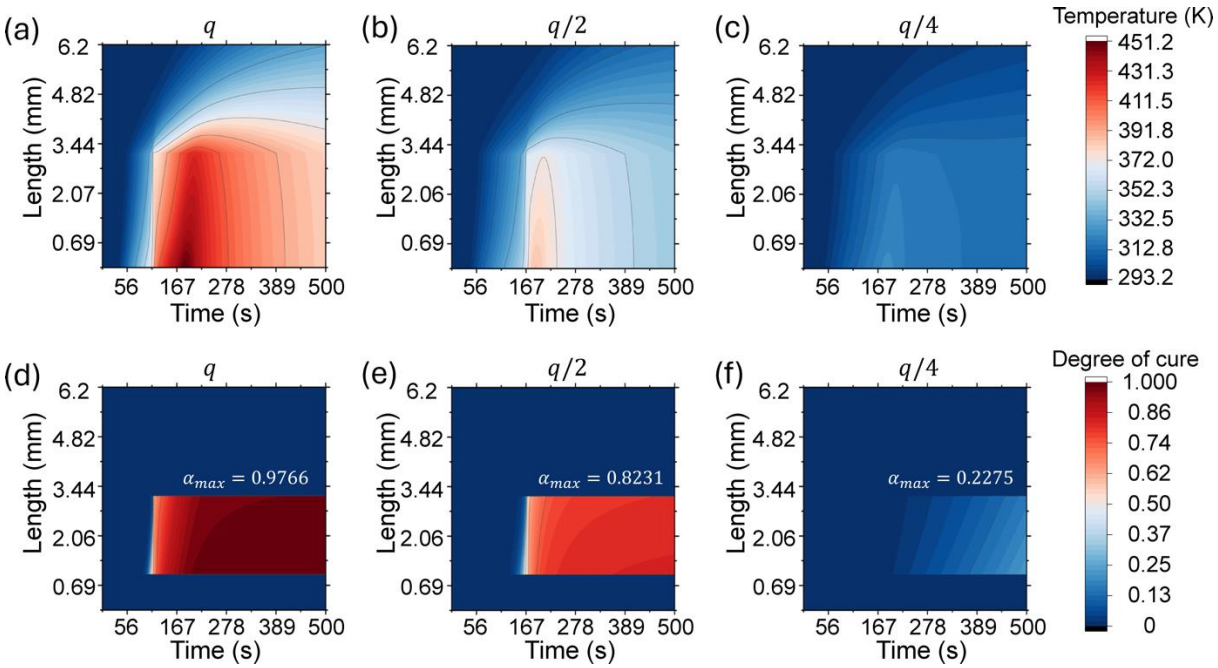

Figure 3: Saptiotemporal simulation results of temperature and degree of cure under different thermal trigger conditions: temperature distributions for (a) *q*, (b) *q/2*, and (c) *q/4*, and degree of cure distributions for (d) *q*, (e) *q/2*, and (f) *q/4*

2.3 Thermal cycle optimization

Figure 4(a) presents the results of a parametric study in which random constant heat flux values (q_h) and heating durations (t_h) are applied. For each case where the degree of cure at the end of the composite (through-thickness direction) reaches 0.95, the required time is defined as the curing time (t_c). The corresponding energy input is calculated based on a surface area of 0.012 m^2. Two cases are considered for comparison. For Case 1, heat flux is applied continuously until the composite is fully cured ($t_h = t_c$), while heat flux is terminated earlier ($t_h < t_c$), allowing the remaining cure to proceed through exothermic FROMP reaction in Case 2. These two cases are shown in different colors in Figure 4(a). As a result, a clear distinction between the two cases is identified. Overall, Case 1 uses more energy than Case 2, indicating that FROMP-based composite manufacturing can be significantly more energy-efficient. For instance, comparing the data points highlighted with green dashed lines, both cases require similar curing times, but Case 2 achieves approximately 22.12% energy savings compared to Case 1.

In addition, Case 2 demonstrates a trade-off relationship between curing time and energy input. Achieving shorter curing time requires more energy consumption, whereas longer curing time leads to lower energy input during the curing cycle. To further explore this relationship, a genetic algorithm (GA) is employed to minimize the energy consumption. The optimization result shows that compared to Case 1, energy consumption can be reduced by 33.27%, although the corresponding curing time increases from 87 to 296 s. Therefore, by evaluating a wide range of conditions, a Pareto front can be identified to balance both energy and curing time, providing guidance for the thermal profile design of the first

cycle. Moreover, since the surrounding domains are preheated by the previous cycle, subsequent cycles require less energy input. As illustrated in Figure 4(b), this concept is applied by scaling down the heat flux in the following cycles to achieve incremental curing with reduced energy input.

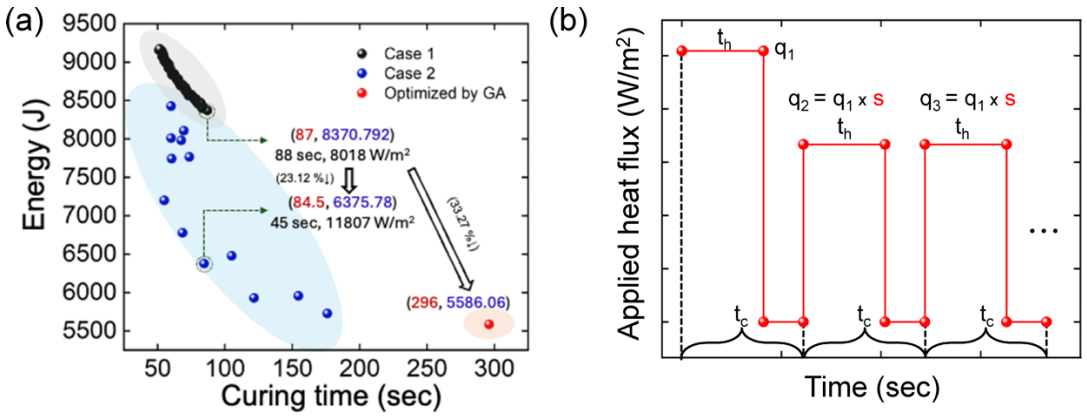

Figure 4: (a) Fully cured state and corresponding thermal conditions of curing time and supplied energy. (b) Numerical approach for determining the optimized incremental curing thermal cycle.

3 EXPERIMENTAL SECTION

3.1 Materials

For the resin system, DCPD, which is solid at room temperature, is mixed with 5 wt% ethylidene norbornene (ENB) to liquify it at room temperature and enable infusion into the carbon fibers. We refer to this mixture as DCPD in the following formulation. A molar ratio of 10000:1:1 of DCPD, second-generation Grubbs catalyst (GC2), and tributyl phosphite (TBP) was mixed using sonication to ensure uniform dispersion. For the carbon fiber layup, an AS4 carbon fiber fabric with the stacking sequence of unidirectional/biaxial/biaxial/unidirectional was used. The prepared resin was then infiltrated into the fabric preform, which was sealed in a nylon vacuum bag. To prevent premature curing at room temperature, the prepregs were stored in a freezer prior to the curing process.

3.2 Experimental setup

Figure 5(a) shows the experimental setup used to validate the optimized curing process. The temperature profiles of the heater and the composite were derived from the optimized heat flux-based thermal profile. To implement this, a K-type thermocouple and a high-sampling-rate PID controller were employed. In addition, an actuator and a calcium silicate insulation layer were used to apply a pressure of ~35 psi. Furthermore, a spring stage and microswitch were introduced to monitor and maintain consistent pressure during all curing cycles. The pressure was controlled by the displacement of the mechanical springs supporting the lower tooling plate as shown in Figure 5. An infrared camera was used to monitor the temperature of the entire system and ensure consistent initial thermal conditions.

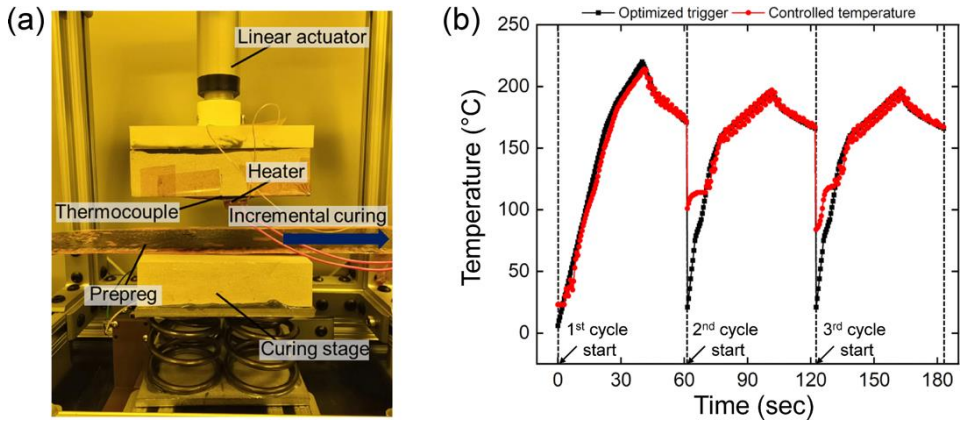

Figure 5: (a) Experimental setup for through-thickness frontal polymerization-based composite manufacturing. (b) Temperature results of three curing cycles based on the optimized curing profile

4 RESULTS AND DISCUSSION

We selected the experimental validation conditions from the Pareto front data points obtained from the simulations of the thermal profile parameters of heat flux (q_h) and heating time (t_h). Specifically, we selected 15267 W/m^2 and 41 s as the optimized thermal cycle for the first section, respectively. In addition, based on the simulation, the expected curing time (t_c) was 61 s for a single curing segment. For the following curing cycles, a scale factor of 0.56 was applied to the heating profile based on numerical fitting for the experimental validation. As shown in Figure 5(b), the intended temperature profiles were successfully applied in each curing section through precise PID control. Notably, the proposed curing cycle required only 61 s per cycle, and a composite panel of 228.6 mm × 50 mm was successfully fabricated using only 3 min and 5.05 kJ of energy.

Figure 6 presents optical images and the thermomechanical analysis of the incrementally cured composite. Before the curing process, the resin remained in a liquid state, as observed in the uncured regions, seen in Figure 6(a). The cured composite was characterized via 3-point bend dynamic mechanical analysis (DMA). As shown in Figure 6(b), the cured composite exhibited a storage modulus onset glass transition temperature (T_g) of 148 °C, which are comparable to previously reported values for fully cured systems [7,10]. These results experimentally validate the thermal profile derived from the proposed numerical approach and demonstrate its potential applicability for large-scale incremental composite curing.

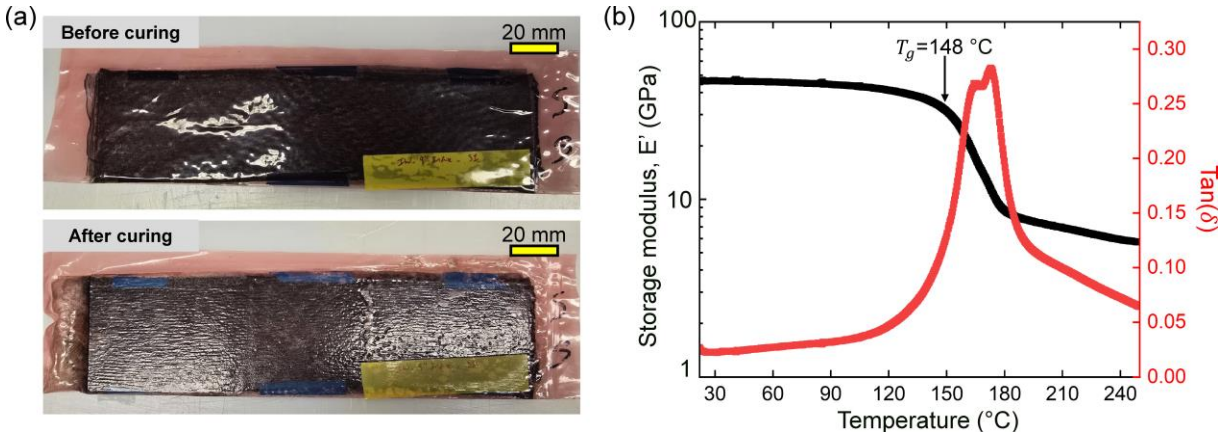

Figure 6: Composite curing using low energy and rapid curing cycle. (a) Optical images of composite before and after curing. (b) DMA test results of the cured composite.

5 CONCLUSION

In this work, the optimization of a FROMP-based incremental composite curing process was investigated numerically and experimentally towards enabling rapid and energy-efficient manufacturing. Through numerical simulations, various heating conditions were explored to find the Pareto front representing the trade-off between energy consumption and total curing time. Subsequently, an optimized first curing cycle condition was selected and extended to multiple curing cycles. In addition, the obtained curing cycle for the incremental curing was validated through experimental method. In conclusion, a 228.6 mm × 50 mm composite with a high glass transition temperature of 148 °C was successfully fabricated using only 5.05 kJ of energy in 3 min. The proposed approach demonstrates potential for scalable, rapid, and energy-efficient manufacturing of fiber-reinforced composites, specifically for applications in aerospace, space, and the automotive industry.

ACKNOWLEDGEMENTS

The authors acknowledge support from Defense Advanced Research Projects Agency (DARPA), United States as part of the NOM4D program through Award HR001122C0057. T. Price acknowledges support from the Beckman Institute for Advanced Science and Technology Graduate Fellows program with support from the Arnold and Mabel Beckman Foundation.

REFERENCES

[1] Traiforos N, Turner T, Runeberg P, Fernass D, Chronopoulos D, Glock F, et al. A simulation framework for predicting process-induced distortions for precise manufacturing of aerospace thermoset composites. Compos Struct 2021;275:114465. https://doi.org/10.1016/j.compstruct.2021.114465.

[2] Zhang Z, Liu R, Li W, Liu Y, Luo H, Zeng L, et al. Direct writing of continuous carbon fibers/epoxy thermoset composites with high-strength and low energy-consumption. Addit Manuf 2021;47:102348. https://doi.org/10.1016/j.addma.2021.102348.

[3] Abouhamzeh M, Sinke J. Effects of fusion bonding on the thermoset composite. Compos Part A Appl Sci Manuf 2019;118:142–9. https://doi.org/10.1016/j.compositesa.2018.12.031.

[4] Crawford S, Lungu CT. Influence of temperature on styrene emission from a vinyl ester resin thermoset composite material. Science of The Total Environment 2011;409:3403–8. https://doi.org/10.1016/j.scitotenv.2011.05.042.

[5] Robertson ID, Yourdkhani M, Centellas PJ, Aw JE, Ivanoff DG, Goli E, et al. Rapid energy-efficient manufacturing of polymers and composites via frontal polymerization. Nature 2018;557:223–7. https://doi.org/10.1038/s41586-018-0054-x.

[6] Timmis AJ, Hodzic A, Koh L, Bonner M, Soutis C, Schäfer AW, et al. Environmental impact assessment of aviation emission reduction through the implementation of composite materials. Int J Life Cycle Assess 2015;20:233–43. https://doi.org/10.1007/s11367-014-0824-0.

[7] Vyas S, Parikh NA, Price TC, Patel DP, Le TB, Geubelle PH, et al. Through-thickness frontal polymerization: Process development and optimization. Compos Part A Appl Sci Manuf 2024;180:108084. https://doi.org/10.1016/j.compositesa.2024.108084.

[8] Suslick BA, Hemmer J, Groce BR, Stawiasz KJ, Geubelle PH, Malucelli G, et al. Frontal polymerizations: From chemical perspectives to macroscopic properties and applications. Chem Rev 2023;123:3237–98. https://doi.org/10.1021/acs.chemrev.2c00686.

[9] Goli E, Gai T, Geubelle PH. Impact of boundary heat losses on frontal polymerization. J Phys Chem B 2020;124:6404–11. https://doi.org/10.1021/acs.jpcb.0c03107.

[10] Abdullah AM, Zakoworotny M, Zhang C, Geubelle PH, Baur JW. Rapid out-of-oven lamination (ROL) for energy-efficient manufacturing of carbon fiber reinforced composites. Compos Part A Appl Sci Manuf 2025;194:108873. https://doi.org/10.1016/j.compositesa.2025.108873.
[11] Hmeidat NS, Zakoworotny M, Kim YS, Le TB, DeBrun G, Shah R, et al. Reactive extrusion of frontally polymerizing continuous carbon fiber reinforced polymer composites. Compos Part A Appl Sci Manuf 2025;190:108609. https://doi.org/10.1016/j.compositesa.2024.108609.
[12] Goli E, Parikh NA, Yourdkhani M, Hibbard NG, Moore JS, Sottos NR, et al. Frontal polymerization of unidirectional carbon-fiber-reinforced composites. Compos Part A Appl Sci Manuf 2020;130:105689. https://doi.org/10.1016/j.compositesa.2019.105689.

ICCM24
AUGUST 4-8, 2025
BALTIMORE CONVENTION CENTER
BALTIMORE, MARYLAND, USA

No Technical Paper Submission for:

Michael Zakoworotny

UV CURING OF NON-TRANSPARENT FIBRE REINFORCED PLASTICS IN LIQUID COMPOSITE MOULDING PROCESSES

Jens Take[1*], Agnesa Bejic[1], Stefan Carosella[1], Peter Middendorf[1]

[1]Institute of Aircraft Design, University of Stuttgart
Pfaffenwaldring 31, DE-70569 Stuttgart, Germany
Email: take@ifb.uni-stuttgart.de, web page: Universität Stuttgart

Keywords: UV-Curing, RTM, Radical Polymerisation, Energy-Efficient, VARI

ABSTRACT

This research presents an innovative approach that combines ultraviolet (UV) radiation curing with Liquid Composite Moulding (LCM) to enable a fast, energy-efficient, and digitally controllable manufacturing process for glass and carbon fiber-reinforced plastics. Conventional curing of fiber-reinforced polymers (FRPs) involves long cycle times and high temperatures, leading to elevated energy demand and tooling inefficiencies, which this work aims to overcome by targeting faster, more energy-efficient processes in line with industry needs for lightweight design, sustainability, and cost reduction [1,2]. To characterize the quality of the manufactured composites with non-transparent fibers, four-point bending tests, tensile tests, and fiber volume fraction (FVF) measurements were performed. In addition, the degree of crosslinking was analyzed, and microscopic imaging was conducted to evaluate the fiber–matrix interaction. All samples were produced using the developed UV-RTM tool, where the cavity is transparent for the UV irradiation. The bending tests showed minimum and maximum forces of 300 Pa and 320 Pa the while the tensile tests yielded ultimate loads ranging from 170 MPa to 270 MPa. The degree of cross-linking across the layer thickness was measured and had an average of 84 %. These tests were carried out for two different materials. Pure glass fiber (GF) samples served as reference samples for the samples with embroidered non-transparent carbon fiber (CF). Overall, this study demonstrates the potential of UV-based curing in LCM processes to enable a scalable, cost-effective, and sustainable manufacturing method for high-performance composite parts.

1 INTRODUCTION

Fiber-reinforced polymer composites have become a foundational material system in aerospace, automotive, and wind energy sectors due to their high specific strength, corrosion resistance, and design flexibility [3]. In the field of FRP manufacturing, conventional thermal curing processes still predominate. These methods rely on high temperatures and long processing times, making them energy-intensive and often associated with significant demands on tooling and thermal management [4]. As an alternative, UV-assisted curing is gaining increasing attention.

UV curing, an alternative method widely used in the coating and printing industries, offers rapid polymerization through radical photoinitiation [5]. While UV curing has been applied to glass fiber composites, carbon fiber's opacity poses a significant barrier to deep matrix polymerization.

Radical UV curing processes also face significant challenges that must be addressed to ensure effective polymerization. A major issue is oxygen inhibition, where the presence of oxygen interferes with the radical polymerization reaction, leading to incomplete curing at the material surface. To overcome this, curing typically needs to be performed in closed or inert environments, which complicates the process design. Alternatively, novel tooling solutions must be developed that allow sufficient UV light penetration while maintaining the necessary environmental control. Additionally, the use of non-transparent fibers poses further limitations, as their opacity prevents effective UV transmission through the composite, restricting the achievable curing depth and uniformity.

Considering these factors, this research focuses on investigating a UV-cured composite manufactured

via the LCM process, with particular attention to how variations in process parameters affect the degree of cure and mechanical properties, while aiming for a time- and energy-efficient production method that meets industry demands for lightweight construction, cost efficiency, and sustainability.

Achieving energy-efficient and cycle time-optimized curing of FRP using UV requires its integration into LCM processes and subsequent optimization. Several interdependent parameters must be considered to realize this goal. To effectively control these interactions, their influences must be systematically investigated and validated, enabling a stable and controllable process.

For good material properties, UV-intransparent CF is integrated into the process and cured. To date, it has only been possible to cure GF up to a maximum thickness using UV radiation, depending on the set process parameters and process technology. The maximum achievable thickness is influenced by the fiber volume content, the type of reinforcement fibers, the resin chemistry, and the characteristics of the UV emitter [6].

A special focus is placed on the UV-curing of CF, integrated through the Tailored Fiber Placement (TFP) process in load-path-optimized orientations, as part of the overall process development and the characterization of the resulting composite material [7]. Critical process parameters such as FVF, resin chemistry, fiber type, and emitter characteristics are investigated to develop a reliable and controllable curing system. Since UV curing does not require thermal energy input to initiate or complete polymerization, heating of thermally inert molds is no longer necessary.

This work investigates the feasibility of UV curing for carbon fiber-reinforced composites using LCM processes. Key questions include whether sufficient crosslinking can be achieved within and beneath the carbon fiber roving and whether the resulting laminates exhibit acceptable mechanical performance.

2 MATERIALS AND METHODS

2.1 Materials

All samples were produced using the resin system RAYLOK ® C1100 from Allnex GmbH (Drogenbos, Belgium) in combination with a glass fiber fabric (600 g/m²) supplied by R&G Faserverbundwerkstoffe GmbH (Waldenbuch, Germany). The composite parts were manufactured using the developed resin transfer molding (RTM) tool with an injection pressure of 2 bar. An embroidered carbon fiber roving (Tenax®-E, HTS40, X030, 12K, 800 tex, V2) was used for a higher stiffness.

The RAYLOK ® C1100 resin system is specifically designed for the production of glass fiber-reinforced composites cured by UV radiation. The curing behavior of this system is based on the free-radical polymerization of acrylate and vinyl ester groups, initiated by UV exposure. In contrast to thermally cured epoxy systems, RAYLOK ® C1100 is a single-component system offering on-demand curing. It remains stable in its liquid state until UV activation, which then triggers immediate polymer network formation.

The RAYLOK ® C1100 resin system is a styrene-free vinyl ester formulation. Its high reactivity under UV radiation enables rapid curing within seconds to minutes, offering a significant reduction in cycle time compared to conventional thermally cured systems. A notable advantage of the system is its long pot life prior to UV exposure (1-K System), which allows for extended processing windows, increased flexibility during layup or infusion, and reduced material waste.

The mechanical performance of the cured system, measured according to standard ASTM protocols, is summarized in Table 1:

Property	Value
Tensile modulus	~2.3 GPa
Tensile strength	~50 MPa
Elongation at break	~2.3 %
Flexural modulus	~2.8 GPa
Flexural strength	~80 MPa
Glass transition temperature (Tg)	~102 °C

Table 1: Material Properties RAYLOK ® C1100 [8].

2.2 Manufacturing of UV-cured composites

The RTM process was employed to manufacture specimens for mechanical characterization, enabling the production of large-scale samples (358 × 258 mm²) incorporating a multilayer glass fiber preform with an embroidered carbon fiber roving. The RTM mold consists of two rigid mold halves, sealed at the parting plane and clamped together with bolts. The cavity is enclosed on both the upper and lower sides by tempered safety glass (ESG), providing transparency for UV curing while ensuring mechanical stability and an effective seal during the infiltration process, see Figure 1. Before processing, the mold is cleaned with isopropanol and air pressure, followed by the application of a release agent (HP7, Marbocote) in three layers with degassing steps between applications. The injection and evacuation hoses are installed afterwards. The injection hose is connected to a pressure vessel, which is later filled by the resin for the infusion process, while the evacuation hose is attached to a resin trap and a vacuum pump.

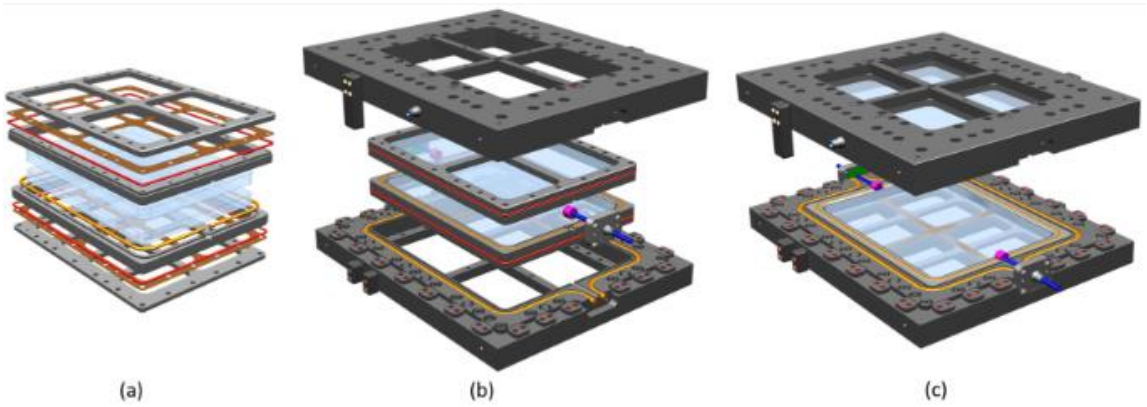

Figure 1: (a) Explosion view of glass plates and glass plate frame assembly, (b) explosion view of assembled glass plate frames and mold frames, and (c) assembled mold in open (charge) position [9].

The fiber preform is prepared by stacking three layers of glass fiber fabric, onto which a carbon fiber roving is embroidered on one Layer of glass fiber using a fine polyester thread (Serafil, 300tex, 10) on a TFP embroidery machine TCWM 102 (Tajima Industries Ltd., Nagoya, Aichi Prefecture, Japan). The embroidered fabric is cut to match the dimensions of the other layers and then positioned within the lower mold cavity (Figure 2).

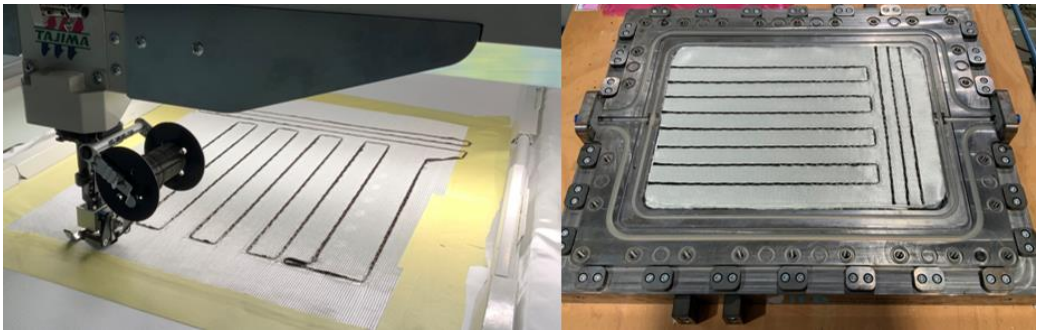

Figure 2: Embroidered machine TCWM 102 and the RTM tool with prepared Preform

Sealing plugs are installed at the resin inlet and outlet ports, and the mold halves are assembled and clamped. The resin system RAYLOK ® C1100 is injected under controlled pressure (initially 800 mbar) through the cavity, which is tilted by 45 ° to enhance air evacuation. The infiltration process was continuously adjusted to maintain a constant flow rate as the flow front progressed, resulting in a concave flow front profile due to faster resin movement near the cavity edges, see (Figure 3). The pressure is gradually decreased to 30 mbar by the end of infiltration.

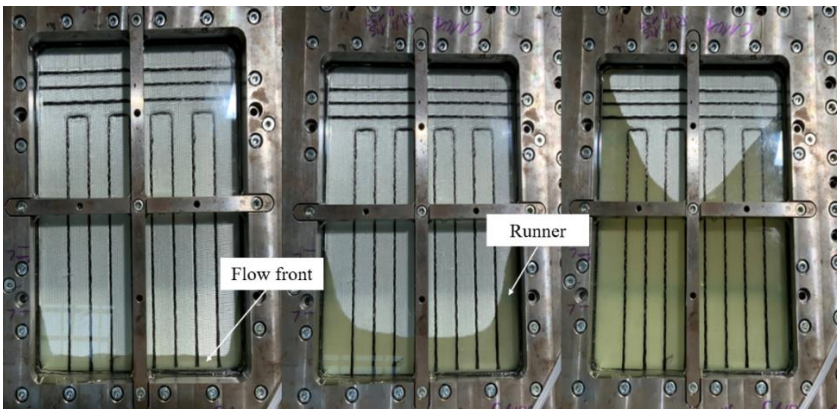

Figure 3: Flow front in the cavity of the RTM mold

Curing was conducted immediately after infiltration by irradiating the entire cavity surface through the transparent mold plate for 120 seconds using an air-cooled MZ80-395 nm UV-LED (IST INTECH Ltd, Banbury, Oxfordshire, United Kingdom), manually positioned close to the mold surface due to the window thickness.

2.3 Material characterization methods

Fourier Transform Infrared Spectroscopy (FT-IR)

The degree of cross-linking across the laminate thickness is measured using a LUMOS II FT-IR microscope (Bruker Optics GmbH & Co. KG, Ettlingen, Germany), performing measurements at 45 discrete points along the thickness direction of the samples. FT-IR analysis was conducted by comparing the C=C absorption peak intensity before and after UV curing, allowing the degree of conversion to be determined based on the reduction of reactive double bonds.

Differential Scanning Calorimetry (DSC)

The reaction enthalpy of the resin systems is analyzed using a UV-DSC 3500 Sirius (NETZSCH Group, Selb, Germany). The DSC system measures the exothermic heat flow during UV-induced

curing, enabling the analysis of reaction kinetics, curing rate, and degree of conversion in real time.

Microscopic Analysis

For microscopic analysis of the specimen cross-sections, samples were initially embedded in an epoxy resin (Struers EpoFix Resin, Struers GmbH, Willich, Germany). Subsequent grinding and polishing were performed using a Struers TegraPol-11 polishing machine (Struers GmbH, Willich, Germany). Wet grinding was conducted with diamond suspensions (Struers DiaPro, 3 µm and 9 µm), while final polishing employed alumina suspensions (Buehler MasterPrep, 0.05 µm, ITW Test & Measurement GmbH, Esslingen am Neckar, Germany) applied on appropriate adhesive discs (Struers MD-Plan and MD-Dur for diamond grinding, and Buehler Master Tex MD Rondo for alumina polishing). Microscopic investigations are conducted using a Keyence VHX-7000 digital microscope with the VH-Z20R objective (Keyence Corporation, Osaka, Japan).

Fiber Volume Content Analysis

The specimens were first dried to ensure consistent measurement conditions. For this purpose, they were placed in numbered crucibles and heated in a drying oven (BINDER, BD/ED/FD (E2)) at 70 °C for 24 hours. After drying, the samples were cooled for 15 minutes in a desiccator over silica gel. Once the specimens reached room temperature (23 °C), both the sample and the empty crucible were weighed. (DIN 29971 Sept. 1989)

Subsequently, the specimens were returned to the crucibles and heated at 600 °C for 24 hours in a muffle furnace (Heraus, KM 170, Hanau, Germany). During this process, the cured resin was thermally decomposed, leaving only the heat-resistant glass fibers. The crucibles containing the remaining glass fibers were then transferred to a desiccator to cool to room temperature. Once cooled, the crucibles with the remaining fibers were weighed again.

Mechanical Testing

The tensile properties of the UV-cured samples are evaluated according to DIN EN ISO 527-4 (Type 2) using the Hegewald & Peschke Universal Testing Machine Inspekt 250 kN (Hegewald & Peschke Meß- und Prüftechnik GmbH, Am Gründchen, Germany). The bending tests were conducted according to DIN EN ISO 14125 (Class 1) using the Hegewald & Peschke 20-1 (20 kN) testing machine (Hegewald & Peschke Meß- und Prüftechnik GmbH, Am Gründchen, Germany). The tensile test specimens have dimensions 250 mm × 25 mm x 2,6 mm. The 4th point bending test specimens measured 80 mm× 15 mm× 2.6 mm. Each specimen type is tested at least seven times. The test setup for the four-point bending and tensile tests is shown in Figure 4 (a-c).

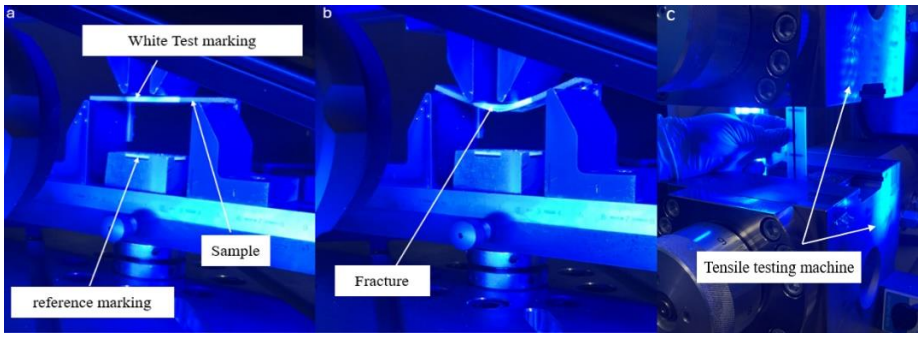

Figure 4: a) Bending test before the test, b) Bending test after fracture failure, c) Tensile testing machine with clamped sample.

3 RESULTS

For the determination of the C=C double bond conversion, cross-sectional samples were prepared in the same manner as for the microscopic analysis. The preparation process ensures consistent positioning and surface quality for accurate spectroscopic measurements. The measurement setup and a representative sample are shown in Figure 5.

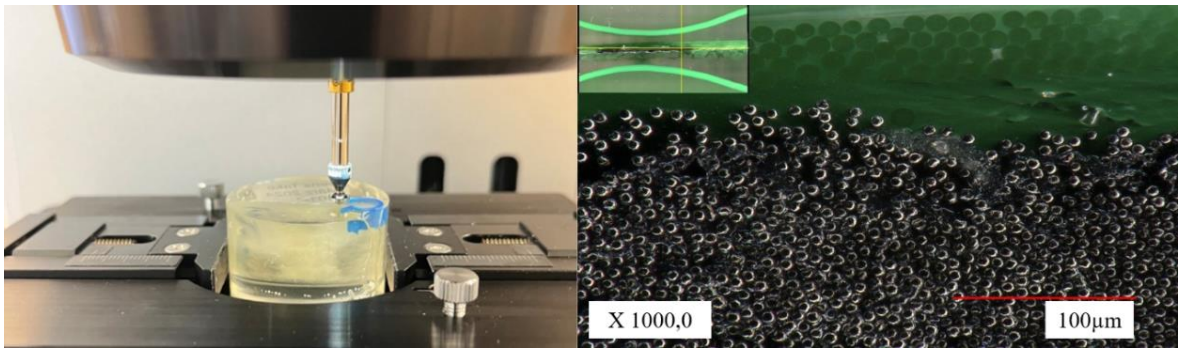

Figure 5: On the left, a measurement setup using FT-IR spectroscopy is shown. On the right, a cross-section of a sample is displayed.

Figure 6 illustrates the measurement of C=C double bond conversion in the thickness direction of the GFRP sample. An average conversion rate of 84 % is determined, excluding the top and bottom regions of the sample from the evaluation. A decrease of approximately 10 % is observed at both the top and bottom regions of the sample. This reduction is presumed to result from oxygen diffusion into the RTM mold, which may inhibit polymerization in these areas due to the oxygen inhibition effect in radical curing. To assess the spatial distribution of the conversion, three measurement series were conducted in the thickness direction of the sample. These are represented in green, yellow, and red curves on the right side of the figure, corresponding to different vertical positions within the specimen. The sample is shown in a horizontal orientation, with light exposure applied from the left side (x = 0.0 mm)**.** The right side of the figure (x = 2.4 mm) represents the bottom surface of the sample. This layout provides a clear depiction of the depth-dependent curing behavior across the composite thickness.

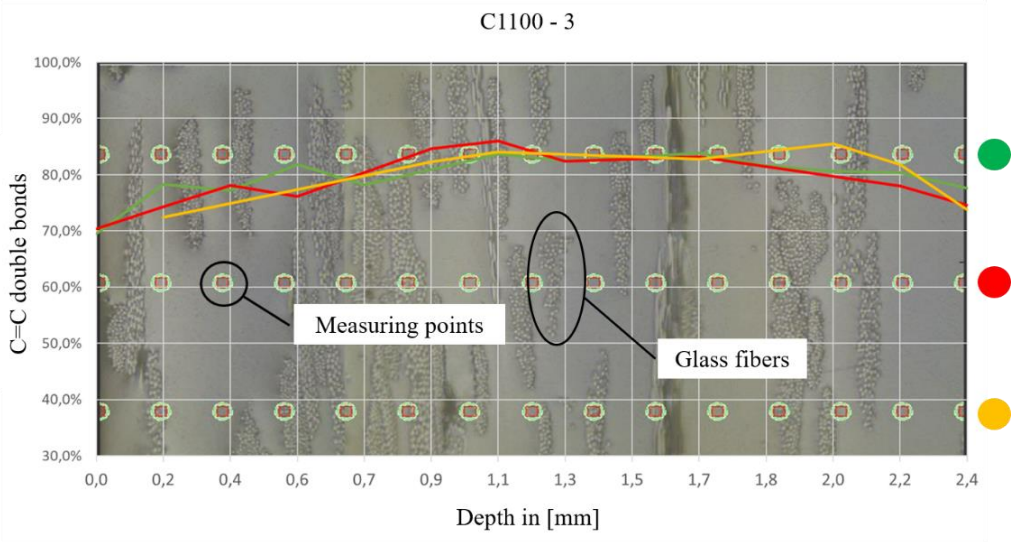

Figure 6: C=C double bond measurement of a GFRP sample, achieving an average value of 84 %.

To investigate the effect of irradiation time on the C=C double bond conversion, four samples containing the 12 K carbon fiber were prepared and subjected to different exposure durations. For the longest irradiation time of 120 seconds, a conversion rate of 84 % is achieved, corresponding to the

reference value obtained without the roving. The nine measurement points were placed above**,** within, and below the roving to evaluate the curing behavior in its immediate vicinity. (Figure 7)

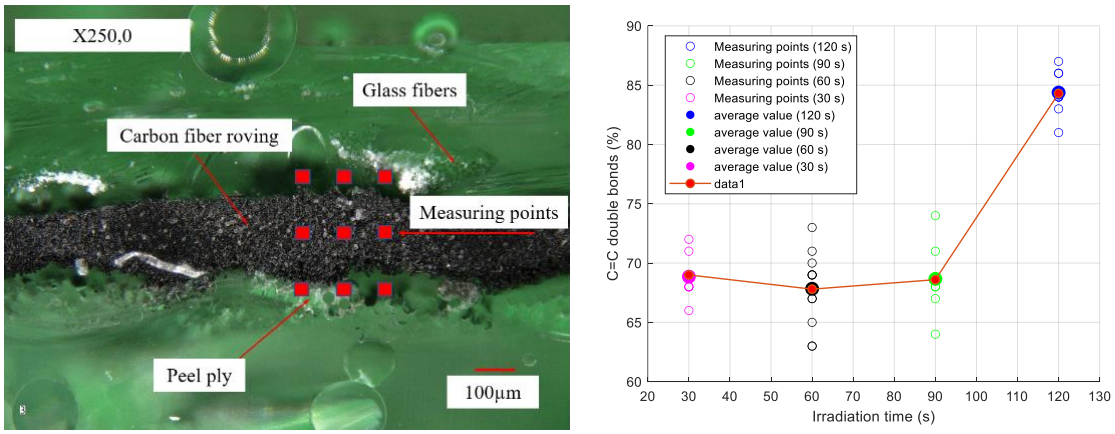

Figure 7: Sample with embedded C-Roving and marked measurement points used for determining the C=C double bond conversion and the Evaluation of the measuring points with the mean value.

The Table 2 lists the mean values of the respective samples with the corresponding irradiation times:

Sample	Irradiation Duration [s]	Mean value C=C double bonds [%]
A	30	70
B	60	68
C	90	69
D	120	84

Table 2: Measurements of the average value C=C double bonds of the samples with different irradiation times

The FVF and porosity of the seven tested samples are summarized in Table 3. The FVF ranged from 36.07 % to 37.86 %, with a mean value of 36.61 % and a standard deviation of 0.60 %. The corresponding porosity values ranged from –0.85 % to 4.76 %, with an average of 0.48 % and a standard deviation of 1.97 %. Negative porosity values are attributed to measurement uncertainty and indicate negligible or absent pore content in the respective samples.

Sample	Fiber volume content					
	Fiber			Pores		
	FVF	average	Standard deviation	Sample	average	Standard deviation
	%	%	%	%	%	%
CFK 1	36,13	36,61	0,60	0,77	0,48	1,97
CFK 2	36,50			-0,50		
CFK 3	36,67			4,76		
CFK 4	36,64			-0,85		
CFK 5	36,39			-0,55		
CFK 6	36,07			-0,51		
CFK 7	37,86			0,22		

Table 3: Measured fiber volume fractions and porosity values of the tested specimens.

The force-deflection behavior of six specimens under three-point bending is illustrated in Figure 8. All samples exhibit a comparable mechanical response, characterized by an initial linear-elastic region up to approximately 7–8 mm deflection, followed by nonlinear deformation until reaching the maximum force. The fracture loads lie between approximately 300 Pa and 320 Pa, demonstrating good

repeatability and uniformity across the specimens. After reaching the peak load, the force drops abruptly, indicating sudden failure of the specimen. Minor deviations in stiffness and ultimate load may result from local variations in fiber alignment or porosity. Overall, the results confirm consistent flexural performance of the tested composite samples.

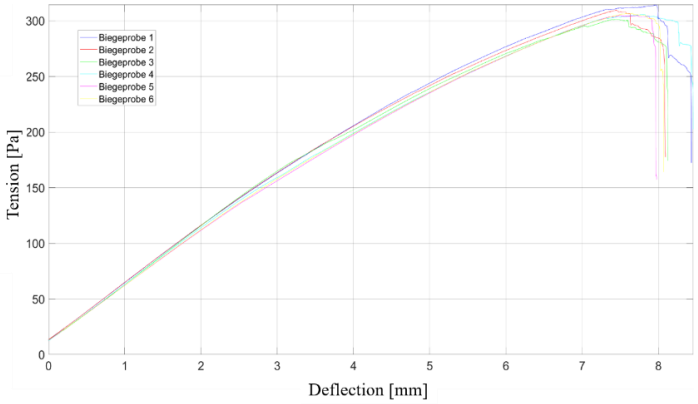

Figure 8: Force–deflection curves of six specimens from three-point bending tests, showing consistent peak loads and failure behavior.

Figure 9 presents the force-elongation curves of seven glass fiber specimens, each reinforced with an embroidered roving. The majority of specimens display a linear-elastic response up to failure, typical of fiber-reinforced composite materials. The specimens fail abruptly upon reaching their maximum load, indicating brittle fracture behavior.

Maximum forces range from approximately 170 MPa and 270 MPa, with elongations at failure between 1.0 % and 1.8 %. Specimen 6 achieved the highest load and strain before failure, suggesting improved load transfer or local reinforcement effects due to the roving structure. The similarity among most curves indicates good repeatability and consistency in material behavior and test conditions.

However, specimen 3 deviates significantly from the others, showing almost no force development and a flat response across the strain axis. This anomaly suggests a testing error, misalignment, or possible damage in the specimen before loading. Given this, it should be excluded from the statistical evaluation.

The abrupt force drops after reaching peak load confirm a brittle failure mode, as expected for glass fiber composites. The embroidered roving appears to have contributed positively to the tensile performance, though the scatter in the maximum loads indicates some variability in the stitching or local fiber alignment.

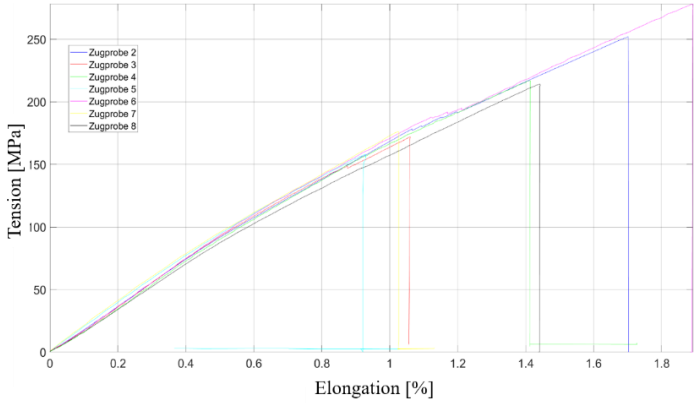

Figure 9: Tensile test results of glass fiber specimens with embroidered roving.

4 CONCLUSIONS AND DISCUSSION

This study investigated the feasibility of UV curing glass fiber-reinforced polymer (GFRP) components, locally stiffened with non-transparent stitched carbon fiber CF, manufactured via LRI processes using UV radiation. Complementary characterization was conducted to assess the degree of cure, the material characteristics, the fiber volume content, and the fiber–matrix interfacial quality.

The highest degree of cure was observed in specimens manufactured via the RTM process after 120 seconds of UV exposure, reaching approximately 84 %. Mechanical testing of RTM-manufactured specimens irradiated for 120 seconds revealed mechanical performance comparable to that of conventionally cured CFRPs. These findings confirm the viability of UV curing for CFRP components under the conditions studied.

However, the samples examined featured a relatively low carbon fiber content. Therefore, the transferability of results to structural CFRP components with higher fiber volume fractions and without glass fibers is limited. Further investigations focusing on preforms made solely from carbon fiber fabrics are recommended to evaluate the broader applicability of UV curing for structural applications.

The UV curing durations in this study were limited to four discrete intervals (30, 60, 90, and 120 s). It is plausible that intermediate exposure times could also yield cure degrees exceeding 84 %. Future research should aim to identify the optimal irradiation time with finer time resolution, particularly to better understand the inflection point in cross-linking behavior within the 90–120 s range.

Cross-sectional analysis showed consistent FVF across all samples, with an average of 36.61 % and minimal variation (standard deviation of 0.60 %). Porosity was generally low, averaging 0.48 %, although some negative values were recorded due to measurement uncertainty, indicating negligible pore content.

Mechanical testing under three-point bending showed highly consistent force–deflection behavior across six samples. Peak loads ranged between 300 Pa and 320 Pa and all specimens exhibited brittle failure after reaching maximum force. The close agreement between the curves suggests uniform fiber distribution and good reproducibility of the manufacturing process.

The tensile tests show a consistent linear-elastic behavior across all samples up to failure, with fracture forces ranging from approximately 170 MPa to 270 MPa. The elongation at break lies between 1.1% and 1.7%, indicating a brittle fracture behavior typical for fiber-reinforced thermosetting composites. The variation in fracture force may result from local differences in fiber distribution or matrix-fiber interaction quality.

The combination of high cure conversion, stable fiber volume content, low porosity, and consistent mechanical performance confirms the quality and reliability of the produced CFRP laminates.

Overall, UV curing demonstrates significant promise as a fast and energy-efficient alternative to thermal curing in composite manufacturing. The reduced curing time, combined with lower energy demand and the use of LED technology, supports the potential for more sustainable and scalable production of fiber-reinforced composites.

ACKNOWLEDGEMENTS

The authors would like to express their sincere gratitude to IST METZ GmbH & Co. KG for the excellent collaboration and for providing access to their laboratory analysis equipment, which significantly contributed to the success of this work.

We would like to thank the Baden-Württemberg Ministry of Science, Research, and the Arts for its financial support of the InnovationCampus Future Mobility.

REFERENCES

[1] Karl-Heinz Füller: “Performance carbon fiber rear wall concept for the Mercedes-AMG S-Class”: In JEC composite magazine 110, 2017.

[2] Heudorfer, K., Carosella, S., and Middendorf, P: “Nasspressen als Alternative zum RTM “: 25. Stuttgarter Kunststoffkolloquium, den 22.03.- 23.03.2017.

[3] Schürmann, 2007; Lengsfeld et al., 2020

[4] Zhilyaev, Igor; Brauner, Christian; Queloz, Sawsane; Jordi, Hans; Lüscher, Rolf; Conti, Silvio; Conway, Roy (2021): Controlled curing of thermoset composite components using infrared radiation and mathematical modelling. In *Composite Structures* 259, p. 113224. DOI: 10.1016/j.compstruct.2020.113224.

[5] Rosenberg, P.: Entwicklung einer RTM Prozessvariante zur kavitätsdruckgeregelten Herstellung von Faserverbundstrukturbauteilen. Stuttgart 2019.

[6] Faserverbundbauweisen. Fertigungsverfahren mit duroplastischer Matrix. Berlin, Heidelberg 1999.

[7] Carosella, Stefan; Hügle, Sebastian; Helber, Florian; Middendorf, Peter (2024): A short review on recent advances in automated fiber placement and filament winding technologies. In *Composites Part B: Engineering* 287, p. 111843. DOI: 10.1016/j.compositesb.2024.111843.

[8] Allnex GmbH. (2024) Technical data sheet RAYLOK ® C1100, Drogenbos, Belgium

[9] Heudorfer, K.; Bauer, J.; Caydamli, Y.; Gompf, B.; Take, J.; Buchmeiser, M. R.; Middendorf, P.: Method of Manufacturing Structural, Optically Transparent Glass Fiber-Reinforced Polymers (tGFRP) Using Infusion Techniques with Epoxy Resin Systems and E-Glass Fabrics. In: Polymers 15 (2023) 9.https://doi.org/10.3390/polym15092183

UNIVERSITÉ LIBRE DE BRUXELLES

NONLINEAR PHYSICAL CHEMISTRY UNIT

Buoyancy-driven Convection in Adiabatic Horizontal Frontal Polymerization

Laurence Rongy*, John A. Pojman**, Reda Tiani*

*Non Linear Physical Chemistry Unit, Université libre de Bruxelles (ULB)
** Department of Chemistry, Louisiana State University (LSU)

24th International Conference on Composite Materials – ICCM2025
Session on Frontal Polymerization
Baltimore, August 4, 2025

Motivation

Frontal polymerization results from the coupling between ***thermal autocatalysis*** and ***heat diffusion***.

- *Monomer:* trimethylolpropane triacrylate (TMPTA)

- *Initiator:* Luperox 231

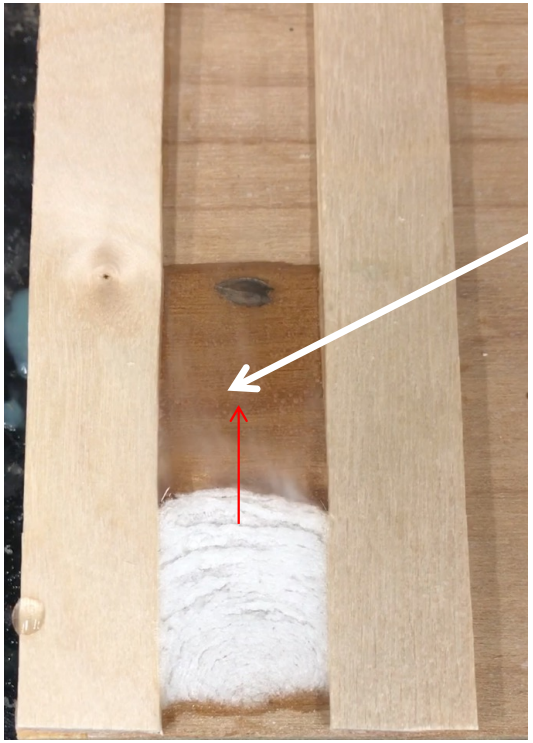

Reactants
(monomer + initiator)
cold

Polymer
hot

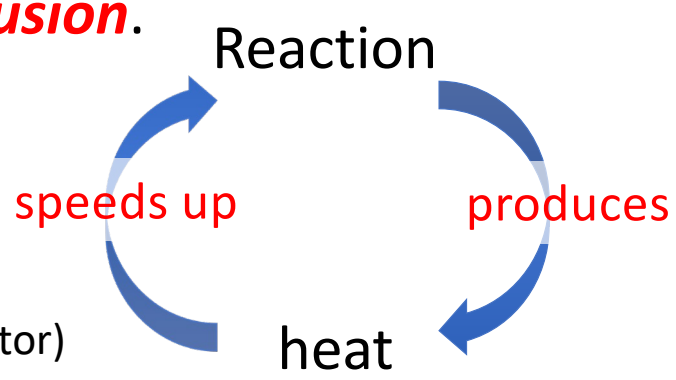

Motivation

Frontal polymerization provides a ***greener*** and more ***efficient*** route for the synthesis of materials.

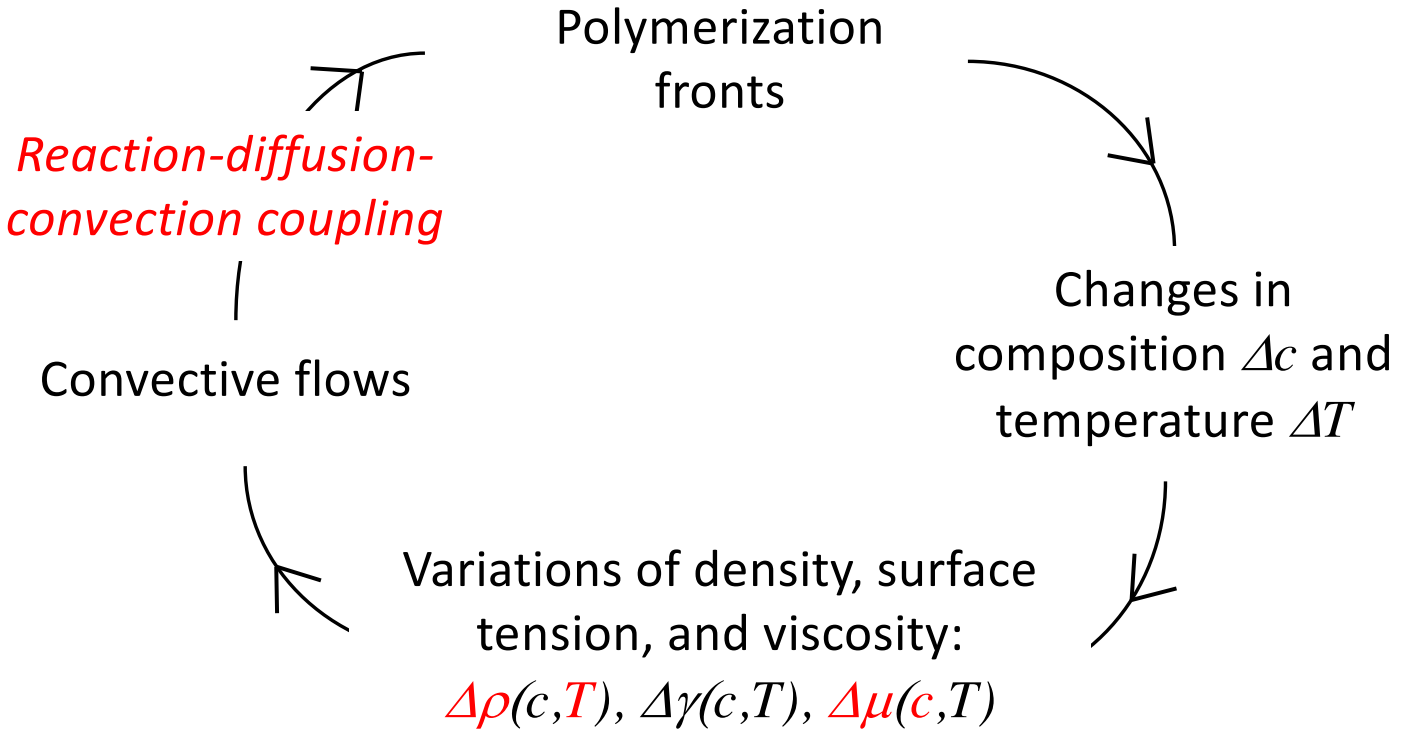

LETTER

https://doi.org/10.1038/s41586-018-0054-x

Rapid energy-efficient manufacturing of polymers and composites via frontal polymerization

Ian D. Robertson[1,2,7], Mostafa Yourdkhani[1,7], Polette J. Centellas[1,3], Jia En Aw[1,3], Douglas G. Ivanoff[1,4], Elyas Goli[1,5], Evan M. Lloyd[1,6], Leon M. Dean[1,4], Nancy R. Sottos[1,4], Philippe H. Geubelle[1,3], Jeffrey S. Moore[1,2] & Scott R. White[1,3]*

Robertson *et al.*, Nature, 557 (2018), 223

Our ***objective***: characterize front propagation with ***2D models*** accounting for ***natural convection***.

2D one-step FP model* coupled to Navier-Stokes equations

$$\frac{\partial M}{\partial t} + \underline{v}.\underline{\nabla}M = D_M \nabla^2 M - k(T)M$$

$$\rho_0 c_p \left(\frac{\partial T}{\partial t} + \underline{v}.\underline{\nabla}T\right) = \lambda \nabla^2 T - \Delta H \; k(T)M$$

$$\rho_0 \left(\frac{\partial \underline{v}}{\partial t} + (\underline{v}.\underline{\nabla})\underline{v}\right) = -\underline{\nabla}p + \underline{\nabla}.\underline{\tau} + \rho(T)\underline{g}$$

$$\text{div}\, \underline{v} = 0$$

$$\boldsymbol{k(T)} = k_{\text{eff}}^0 e^{-E_{\text{eff}}/(RT)}$$

$$\boldsymbol{\rho(T)} = \rho_0 + \frac{\partial \rho}{\partial T}(T - T_0)$$

$$\underline{\tau} = \boldsymbol{\mu}\left(\underline{\nabla} \otimes \underline{v} + (\underline{\nabla} \otimes \underline{v})^T\right)$$

$$\text{M} \rightarrow \text{P}$$

Monomer concentration: $M(x,z,t)$
Temperature: $T(x,z,t)$
Fluid velocity: $\underline{v}(x,z,t)$
Pressure: $p(x,z,t)$

Ambient temperature $T_0 = 293$ K
Effective rate constant $k_{\text{eff}}{}^0 = 10^{10}$ s^{-1} at T_0
Activation energy E_{eff} = 85.0 kJ/mol
Thermal conductivity: $\lambda = 0{,}100$ W/(m K)
Solution density at T_0 : $\rho_0 = 800$ kg/m^3
Solution viscosity: μ
Specific heat capacity: c_p = 600 J/(K kg)
Monomer diffusion coefficient $D_M = 10^{-9}$ m^2/s
Reaction enthalpy: $\Delta H = -75.0$ kJ/mol

*Volpert, *in Self-Assembly, Pattern Formation and Growth Phenomena in Noanosystems*, Springer (2006).

2D one-step FP model* coupled to Navier-Stokes equations

$$\frac{\partial M}{\partial t} + \underline{v}.\underline{\nabla} M = D_M \nabla^2 M - k(T) M$$

$$\rho_0 c_p \left(\frac{\partial T}{\partial t} + \underline{v}.\underline{\nabla} T \right) = \lambda \nabla^2 T - \Delta H \; k(T) M$$

$$\rho_0 \left(\frac{\partial \underline{v}}{\partial t} + (\underline{v}.\underline{\nabla})\underline{v} \right) = -\underline{\nabla} p + \underline{\nabla}.\underline{\tau} + \rho(T)\underline{g}$$

$$\text{div}\, \underline{v} = 0$$

Monomer concentration: $M(x,z,t)$
Temperature: $T(x,z,t)$
Fluid velocity: $\underline{v}(x,z,t)$
Pressure: $p(x,z,t)$

- Initial conditions $T_0 = 293$ K, $M_0 = 1$ mol/L ; no flow

- **Adiabatic** boundary conditions

$$\underline{v} = 0 = \frac{\partial M}{\partial x} \quad x = 0, x = L_x; \quad \frac{\partial T}{\partial x} = 0 \quad x = L_x$$

$$\underline{v} = 0 = \frac{\partial M}{\partial z} \quad z = 0, z = L_z$$

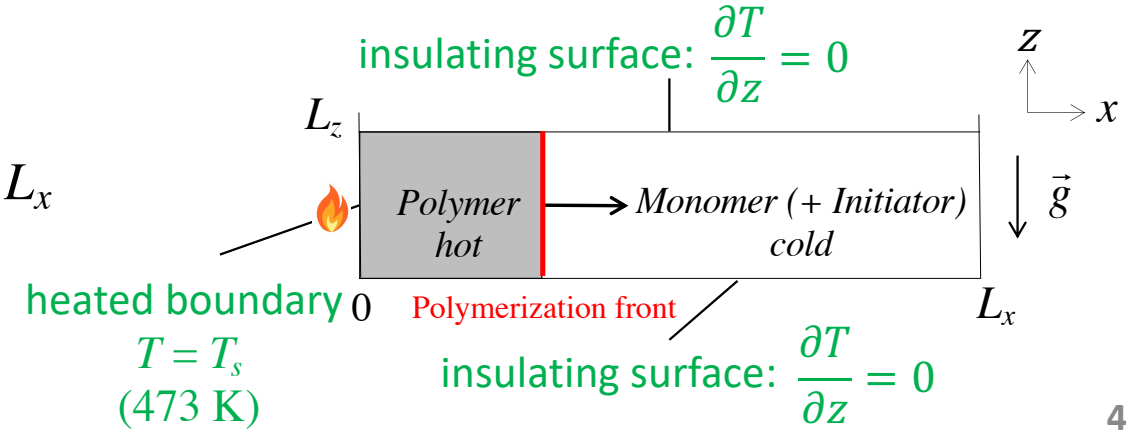

1. Front propagation with constant viscosity

Infinitely large viscosity (reaction-diffusion front)

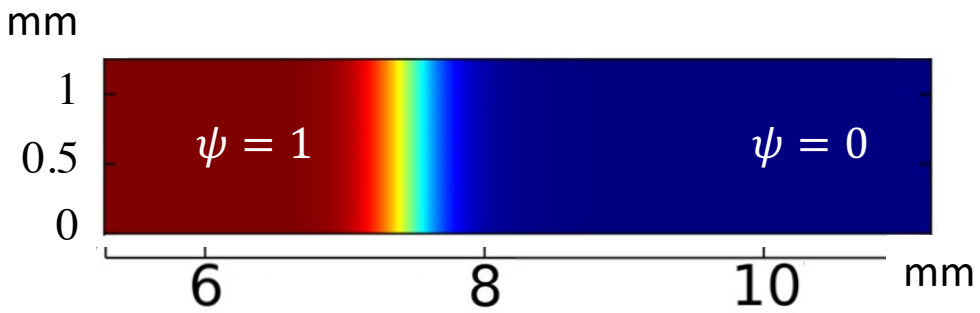

degree of cure

$$\psi = \frac{(M - M_0)}{M_0}$$

Time = 40 s, propagation speed ~ 0.2 mm/s, width ~ 2 mm.
Regime with no thermal instabilities.

1. Front propagation with constant viscosity

degree of cure

$$\psi = \frac{(M - M_0)}{M_0}$$

Time = 40 s, $\frac{\partial \rho}{\partial T} = -0.05$ kg/(m^3 K)

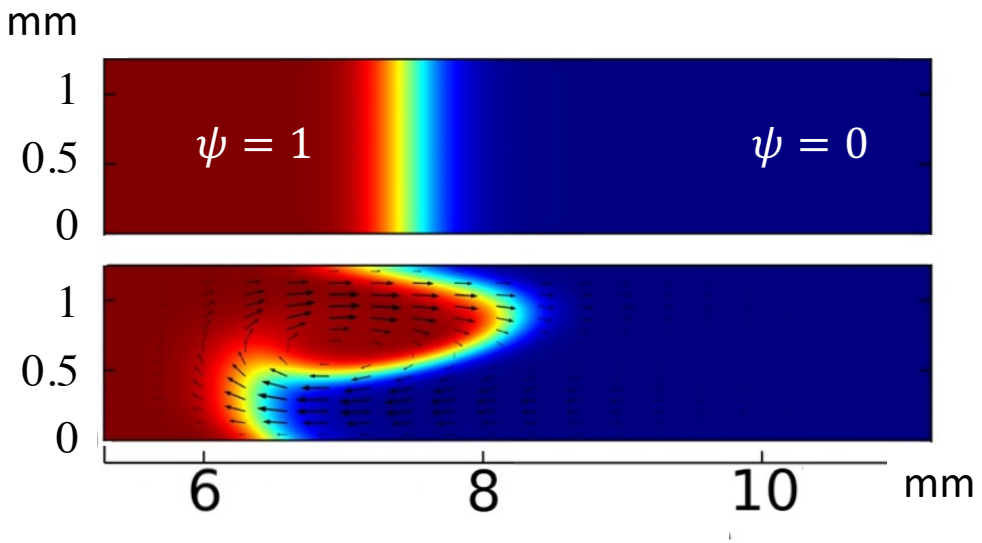

Infinitely large viscosity
(reaction-diffusion front)

$\mu_0 = 1.5$ mPa.s
$L_z = 1.25$ mm

Deformation of the front by buoyancy-driven convection arising from ***thermal gradients***.

1. Front propagation with constant viscosity

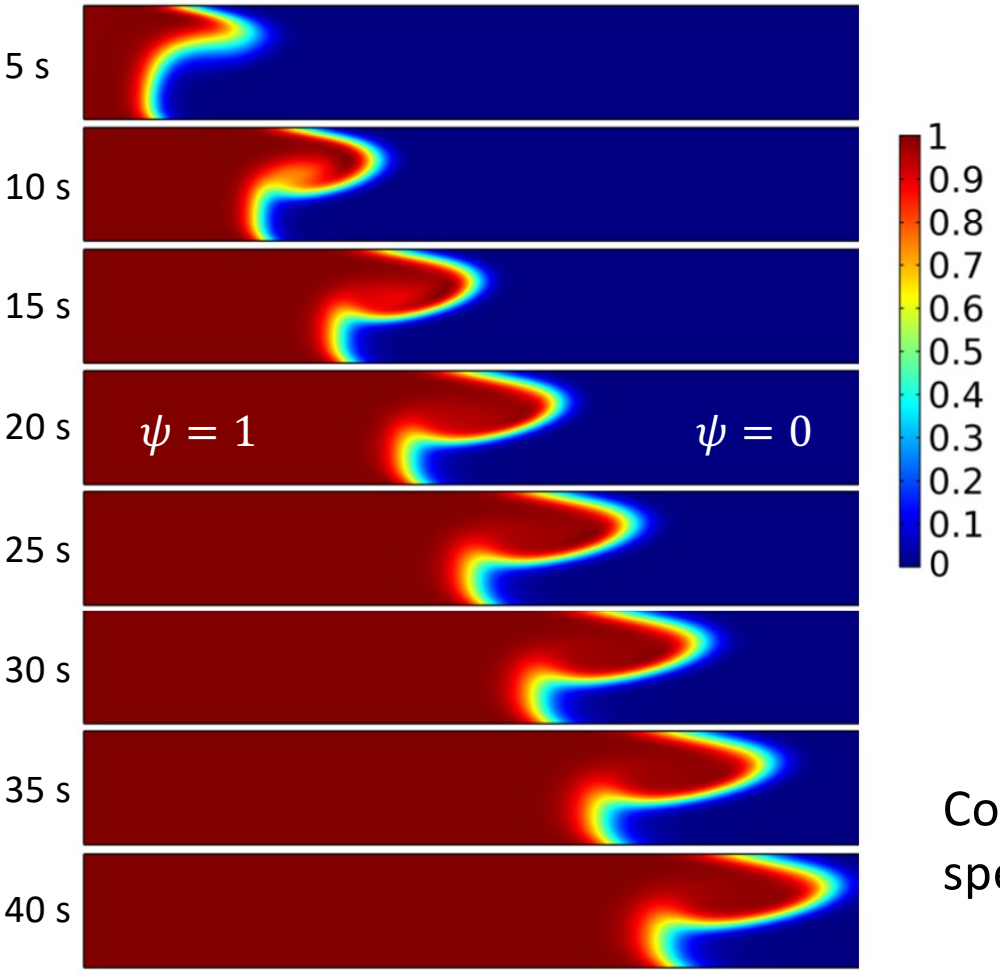

degree of cure

$$\psi = \frac{(M - M_0)}{M_0}$$

$\mu_0 = 1.5$ mPa.s

$L_z = 1.25$ mm

Constant propagation speed ~ 0.12 mm/s

1. Front propagation with constant viscosity

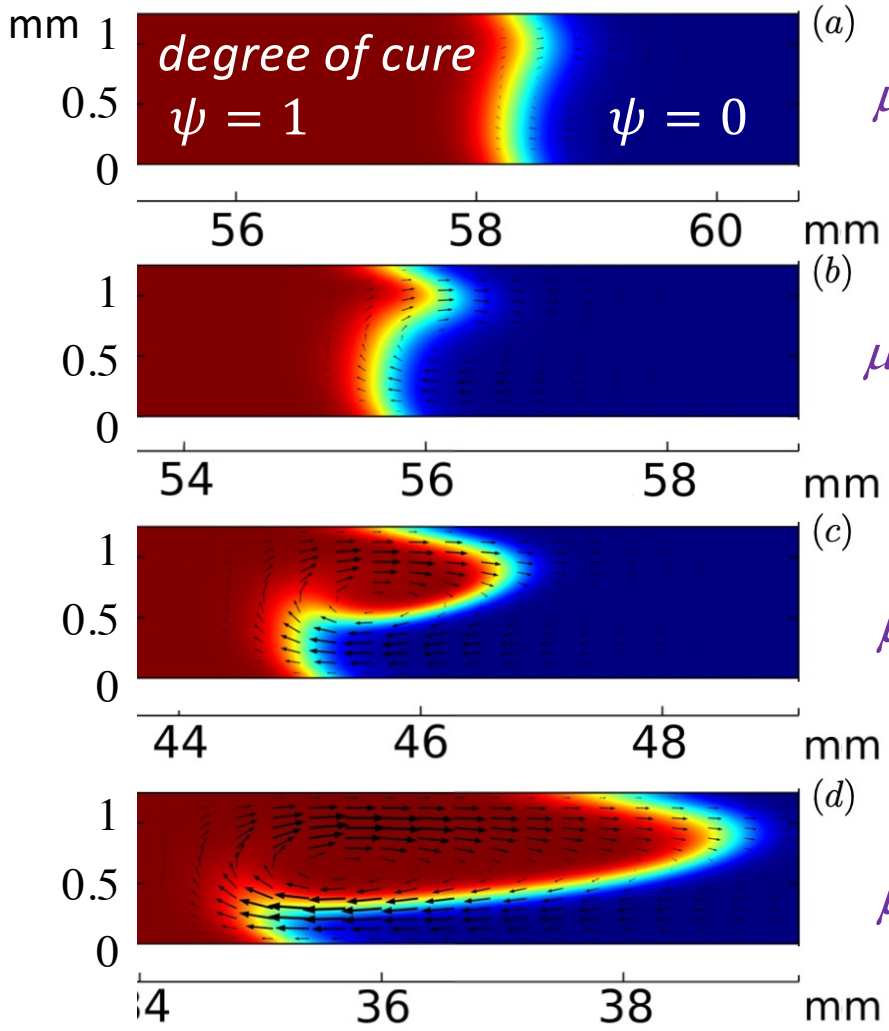

$L_z = 1.25$ mm

$\mu_0 = 6.0$ mPa.s

$\mu_0 = 3.0$ mPa.s

$\mu_0 = 1.5$ mPa.s

$\mu_0 = 0.75$ mPa.s

$\mu_0 \searrow$

Convection ↗
Deformation ↗

Propagation speed ↘

Time = 300 s
(asymptotic shape)

1. Front propagation with constant viscosity

The reaction zone propagates as a **hot spot**.

$L_z = 1.25$ mm

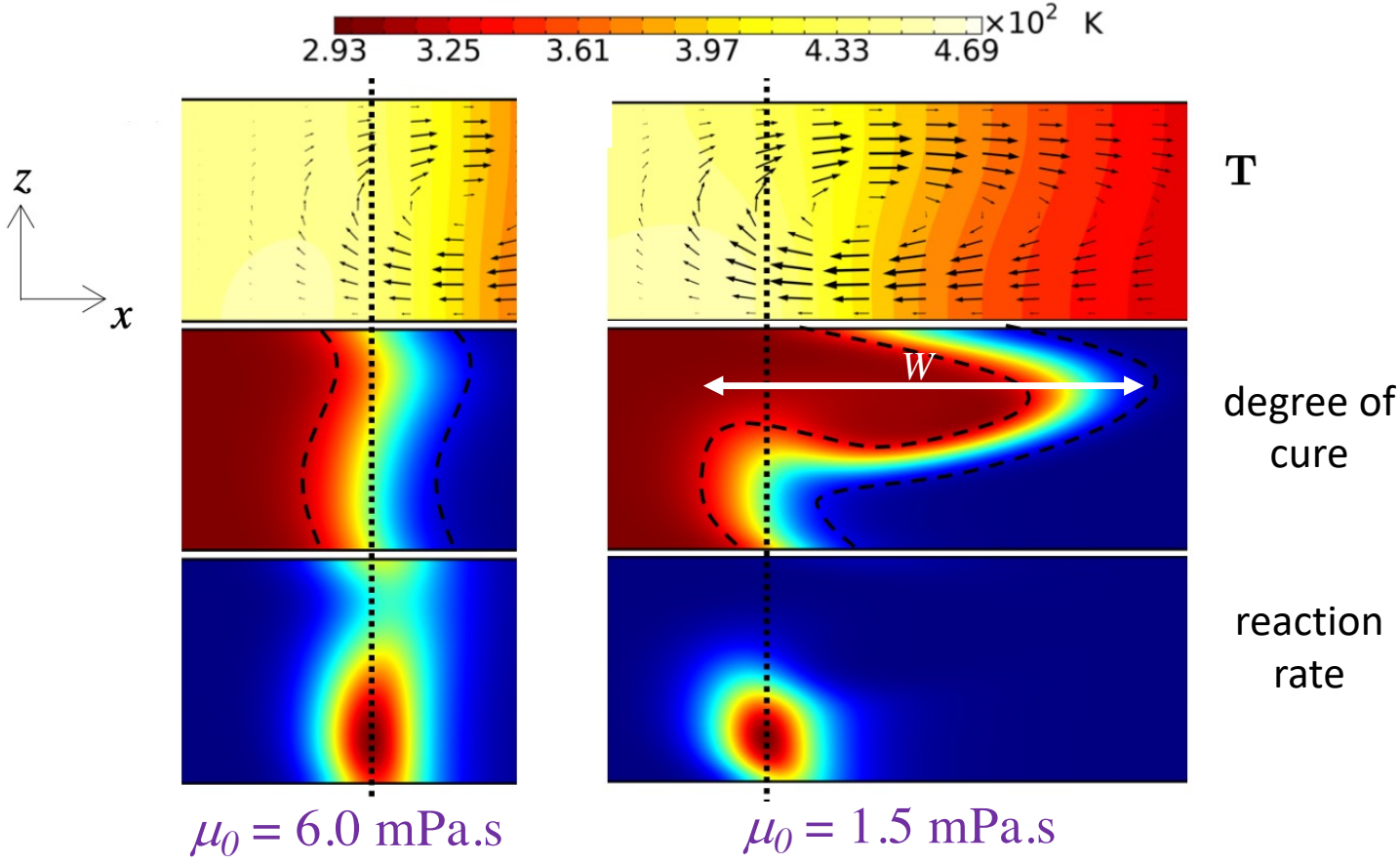

1. Front propagation with constant viscosity

The front reaches an **asymptotic dynamics**.

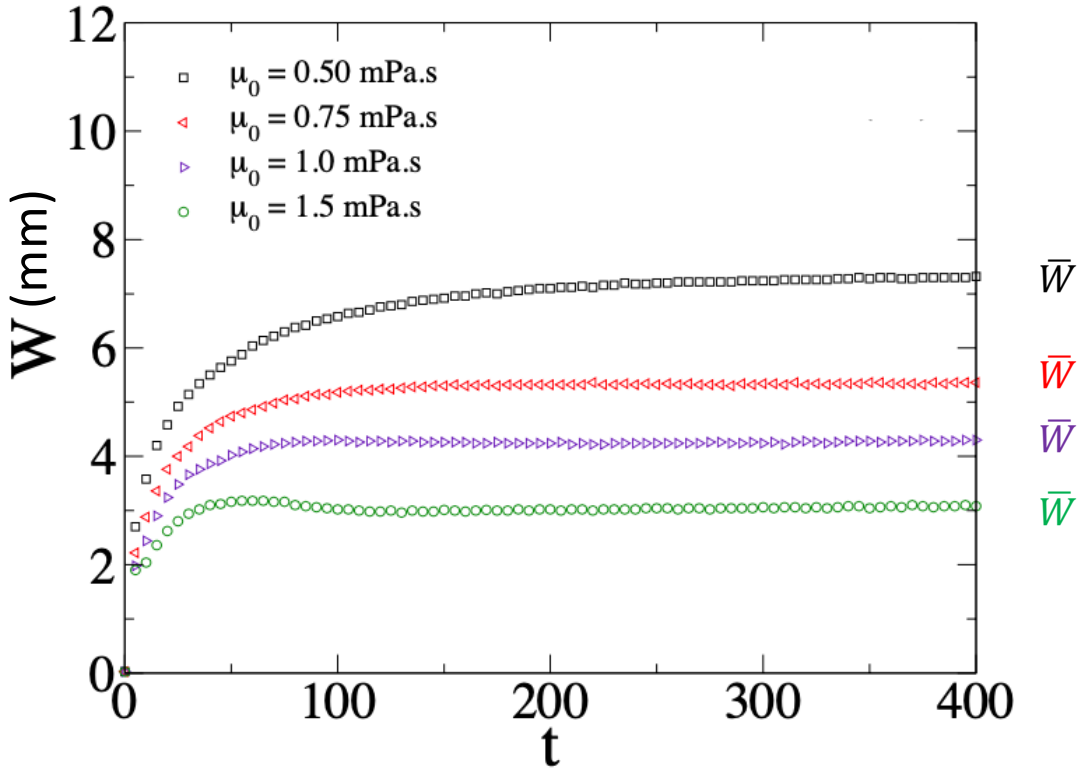

$\mu_0 \searrow$

Convection ↗

Deformation ↗

$L_z = 1.25$ mm

1. Front propagation with constant viscosity

The front reaches an asymptotic dynamics, **two regimes** are observed depending on the viscosity μ_0

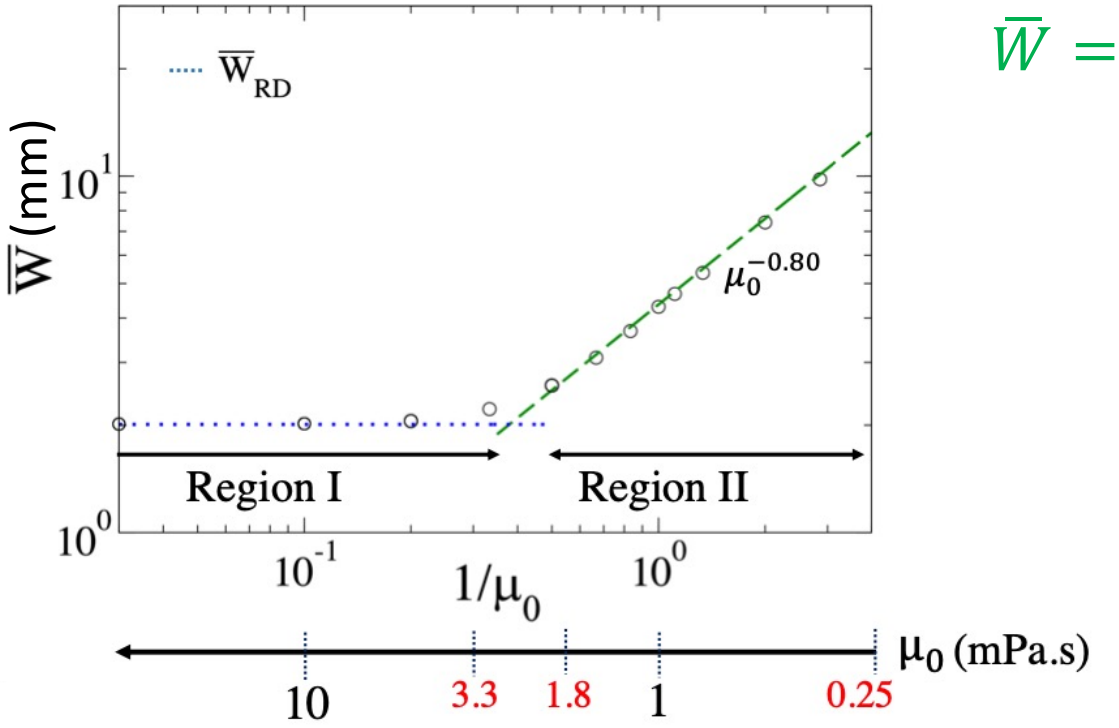

$\overline{W}$ = steady deformation

$L_z = 1.25$ mm

1. Front propagation with constant viscosity

The front reaches an asymptotic dynamics, **two regimes** are observed depending on the viscosity μ_0

$L_z = 1.25$ mm

$\bar{u}_{\max}$ = maximum horizontal flow velocity

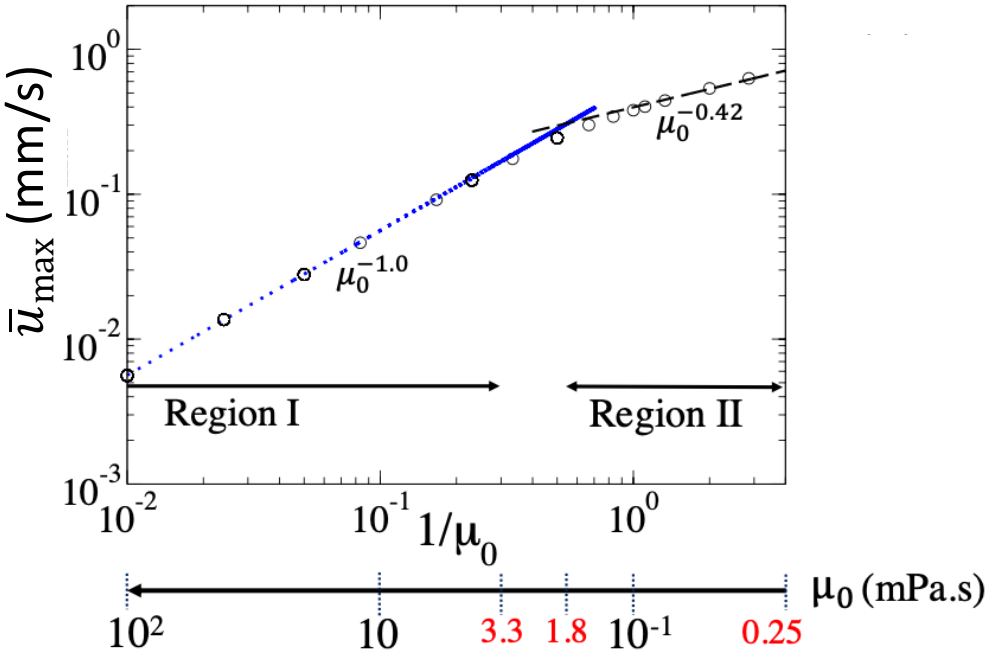

$\bar{V}$ = constant propagation speed

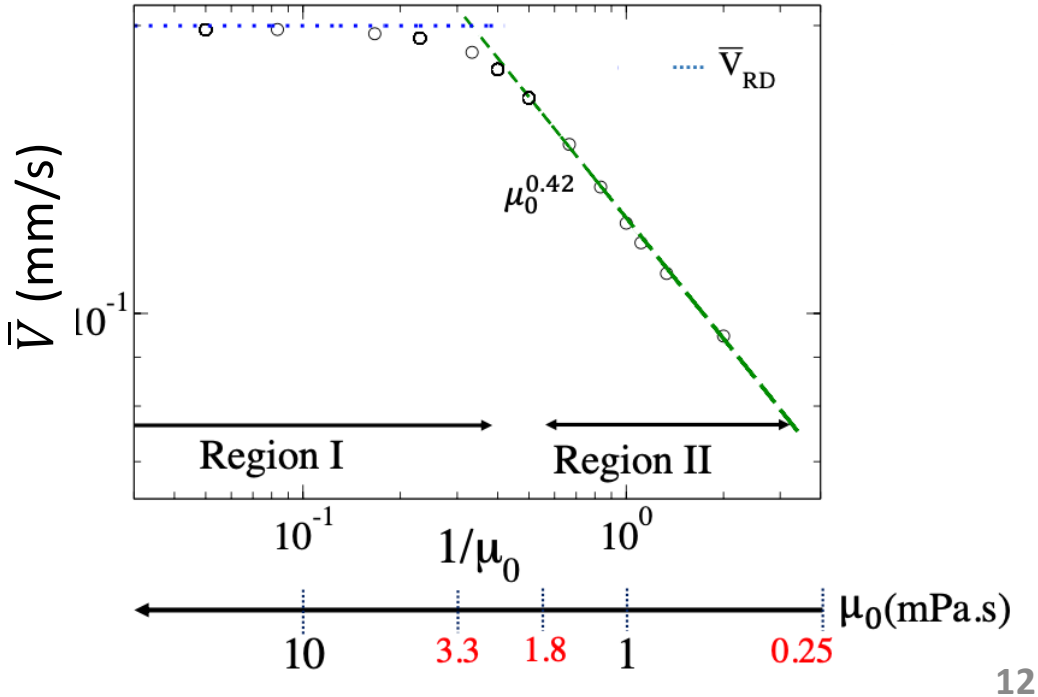

1. Front propagation with constant viscosity

The front reaches an asymptotic dynamics, **two regimes** are observed depending on the viscosity μ_0

$L_z = 1.25$ mm

	Viscosity range	$\bar{u}_{max}$	$\overline{W}$	$\overline{V}$
Region I	$\mu_0 \geq 3.3$ mPa.s	μ_0^{-1}	μ_0^{0}	μ_0^{0}
Region II	0.25 mPa.s $\leq \mu_0 \leq 1.8$ mPa.s	$\mu_0^{-2/5}$	$\mu_0^{-4/5}$	$\mu_0^{2/5}$

Characteristic horizontal convective time scale:

$$t_c \sim \frac{\overline{W}}{\bar{u}_{max}} \sim \frac{\mu_0^{-4/5}}{\mu_0^{-2/5}} \sim \mu_0^{-2/5}$$

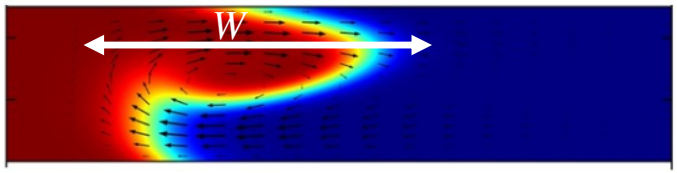

$\mu_0 \searrow$: flow and deformation $\nearrow$ but $t_c \nearrow \Longrightarrow \bar{V} \searrow$

*Different from **isothermal autocatalytic fronts** where convection increases mass transfer rates.*

Tiani, De Wit, Rongy, Adv. Colloid Interf. Sci. 225 (2018).

1. Front propagation with constant viscosity

The front reaches an asymptotic dynamics, **two regimes** are observed depending on the layer thickness L_z (mm)

$\mu_0 = 1.5$ mPa.s

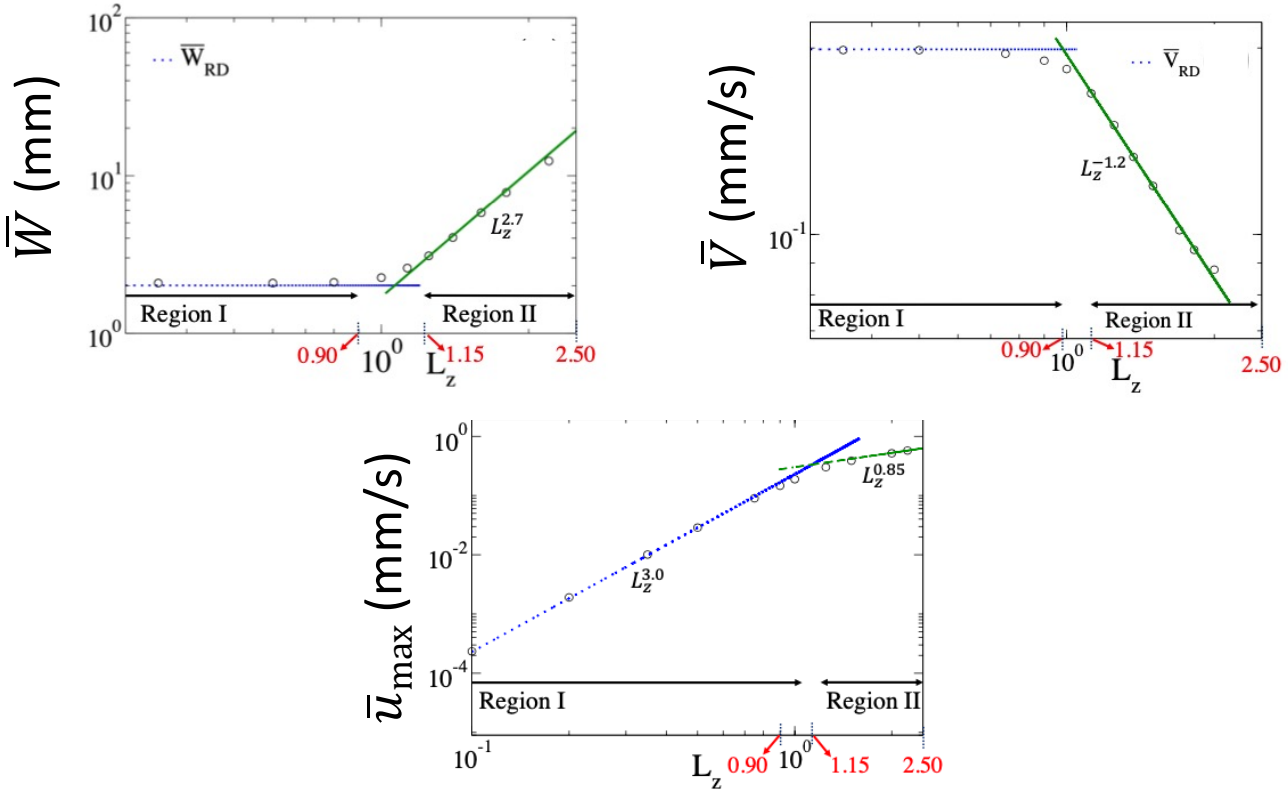

1. Front propagation with constant viscosity

Summary

The front reaches an asymptotic dynamics with steady shape $\bar{W}$, constand speed $\bar{V}$, steady vortex

CONVECTION ↗ $\mu_0 \searrow$ or $L_z \nearrow$

"PASSIVE" REGIME

$\bar{W} \sim W_{RD}$

$\bar{V} \sim V_{RD}$ *(cf: reaction-diffusion)*

$u_{\max} \sim \frac{L_z^3}{\mu_0}$

"ACTIVE" REGIME

$\bar{W} \nearrow$

$\bar{V} \searrow$

$u_{\max} \nearrow$ but more weakly (smaller scaling exponents)

2. Front propagation with varying viscosity $\mu = \mu_0 e^{C\psi}$

The viscosity increases with the degree of cure ψ.
When C increases, the deformation decreases and $\bar{V} \rightarrow V_{RD}$.

$L_z = 1.25$ mm
$\mu_0 = 1.5$ mPa.s

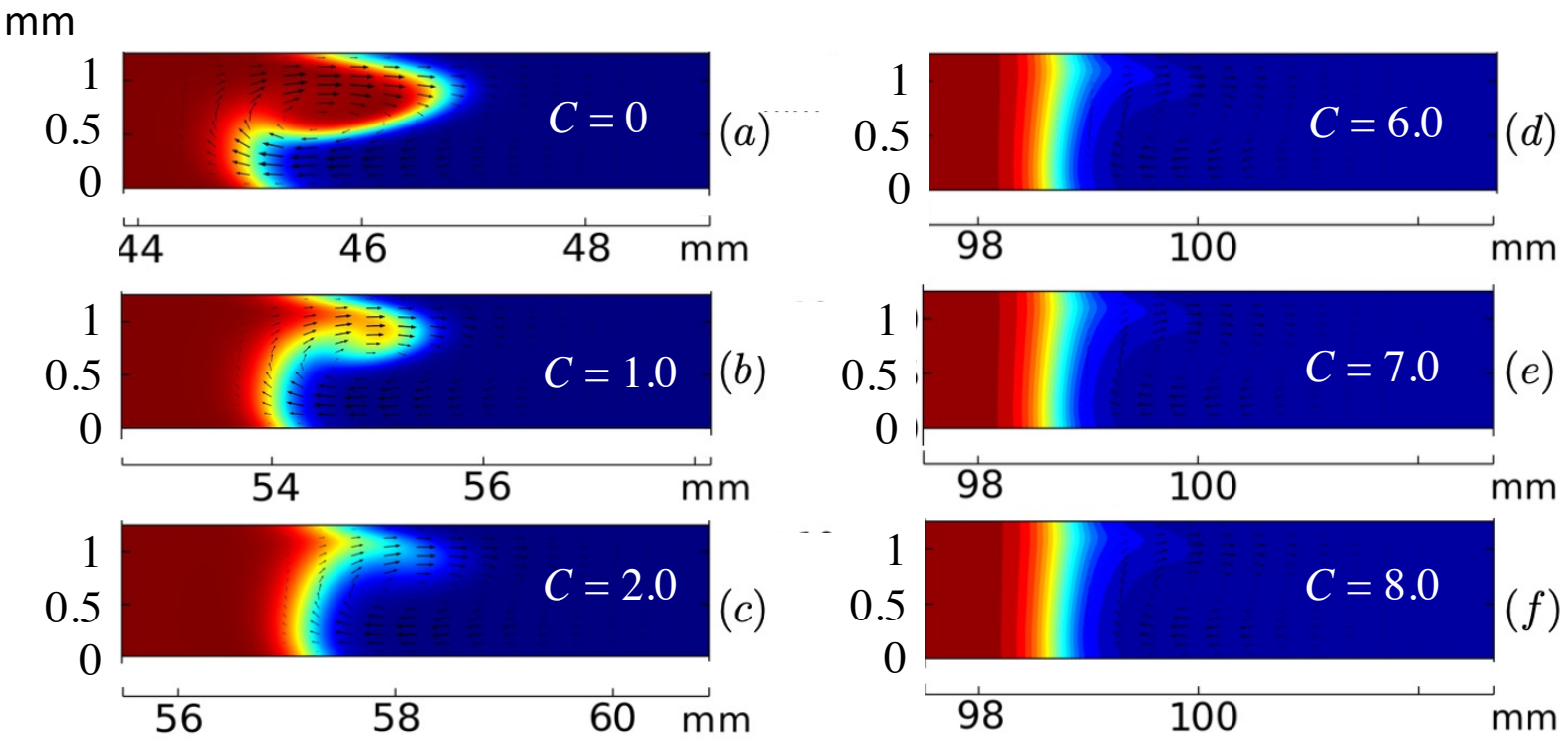

2. Front propagation with varying viscosity $\mu = \mu_0 e^{C\psi}$

The viscosity increases with the degree of cure ψ.
When C increases, the deformation decreases and $\bar{V} \rightarrow V_{RD}$.

$L_z = 1.25$ mm
$\mu_0 = 1.5$ mPa.s

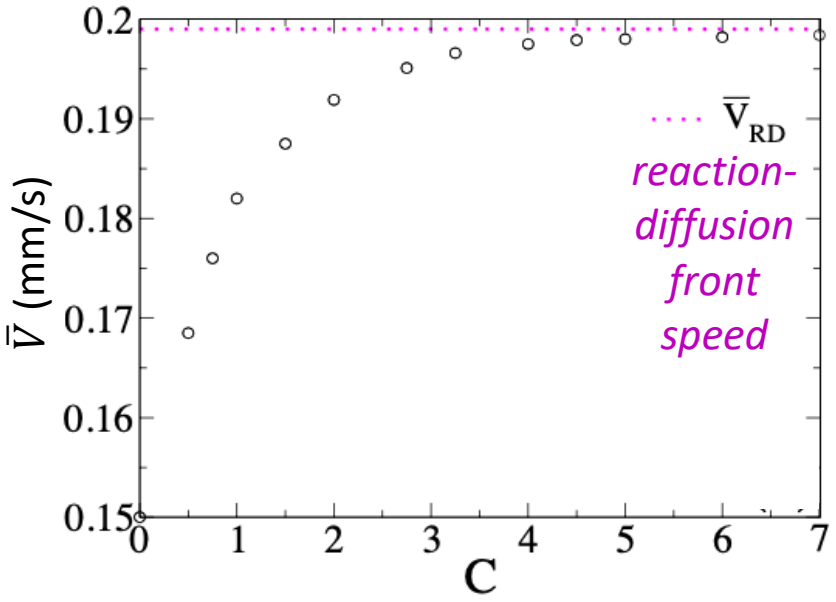

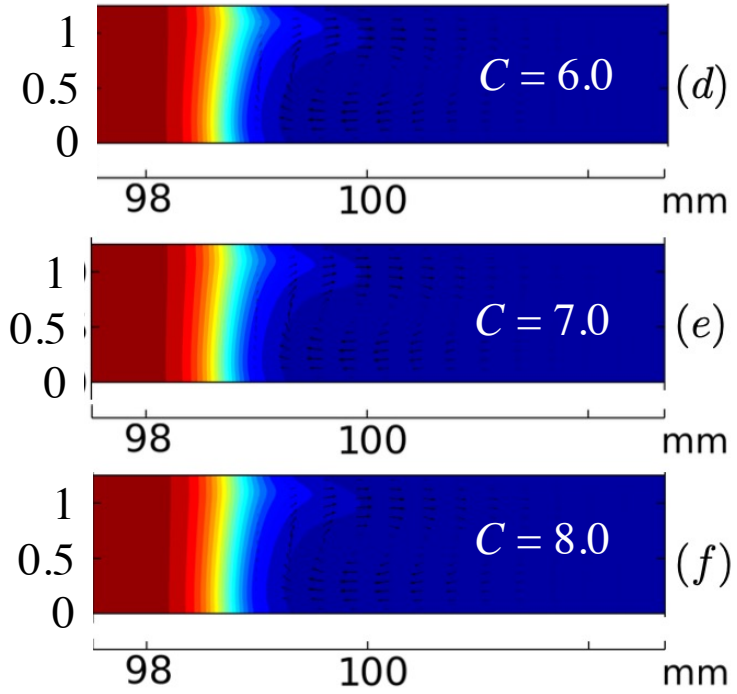

2. Front propagation with varying viscosity $\mu = \mu_0 e^{C\psi}$

The viscosity increases with the degree of cure ψ.
When C increases, the deformation decreases.

cf: Gao, Paul, Chen, Hong, Chamorro, Sottos, Geubelle, PRL 130 (2023).

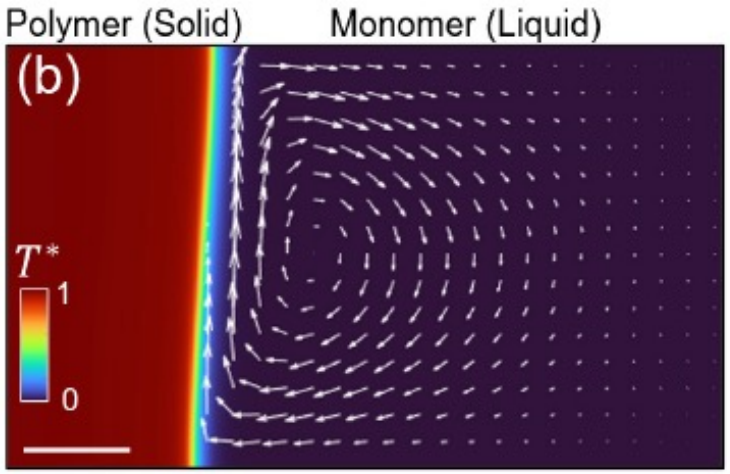

$C = 8.0$

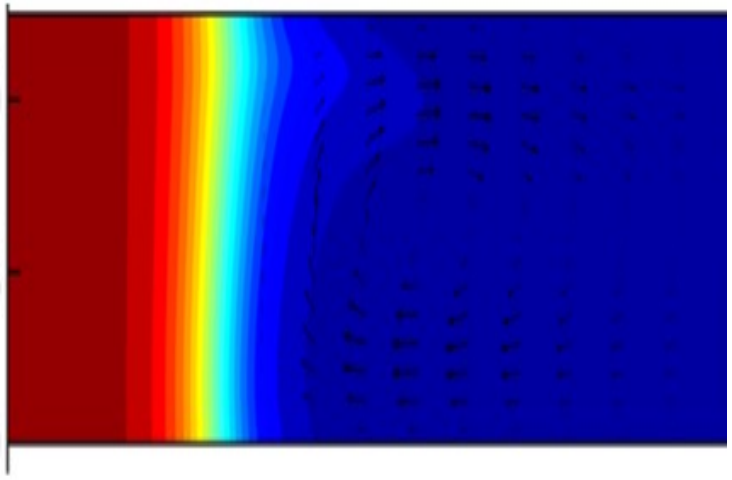

Conclusions

- **Buoyancy-driven convection** arises from **thermal gradients** across polymerization front.

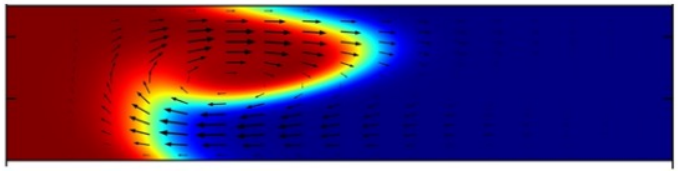

- Convection strengthens when the **monomers' viscosity** is decreased or the **layer thickness** increases.
- **Asymptotic dynamics** with constant deformation ($\bar{W}$ ↗ with flow), constant speed ($\bar{V}$ ↘ with flow).
- Transition between a **"passive" regime (RD + hydro)** and an **"active" regime (chemo-hydrodynamic coupling)**.
- Viscosity increasing during reaction: flow ahead of reaction zone.

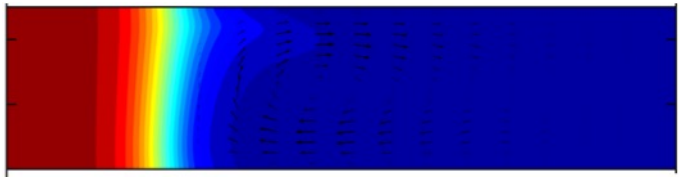

R. Tiani, J.A . Pojman, and L. Rongy, J. Chem. Phys. 162, 124903 (2025).

Scaling Up the Efficient Manufacturing of Carbon Fiber Epoxy Composites Using Frontal Polymerization

Amirreza Tarafdar[1], Ian D. Hosein[2] and Yeqing Wang[1]

[1]Department of Mechanical & Aerospace Engineering, Syracuse University, Syracuse, NY 13244,
[2]Department of Biomedical and Chemical Engineering, Syracuse University, Syracuse, NY 13244, USA

Composite Materials Laboratory

Presentation at the ICCM24 conference, Baltimore Convention Center, Baltimore, Maryland, August 4-8, 2025

Syracuse University
College of Engineering & Computer Science

Background

UV-induced frontal polymerization mechanisms:

- Reduce curing time from hours to few seconds or minutes
- Significant reductions in cost & energy
- Compatible with opaque FRP laminates

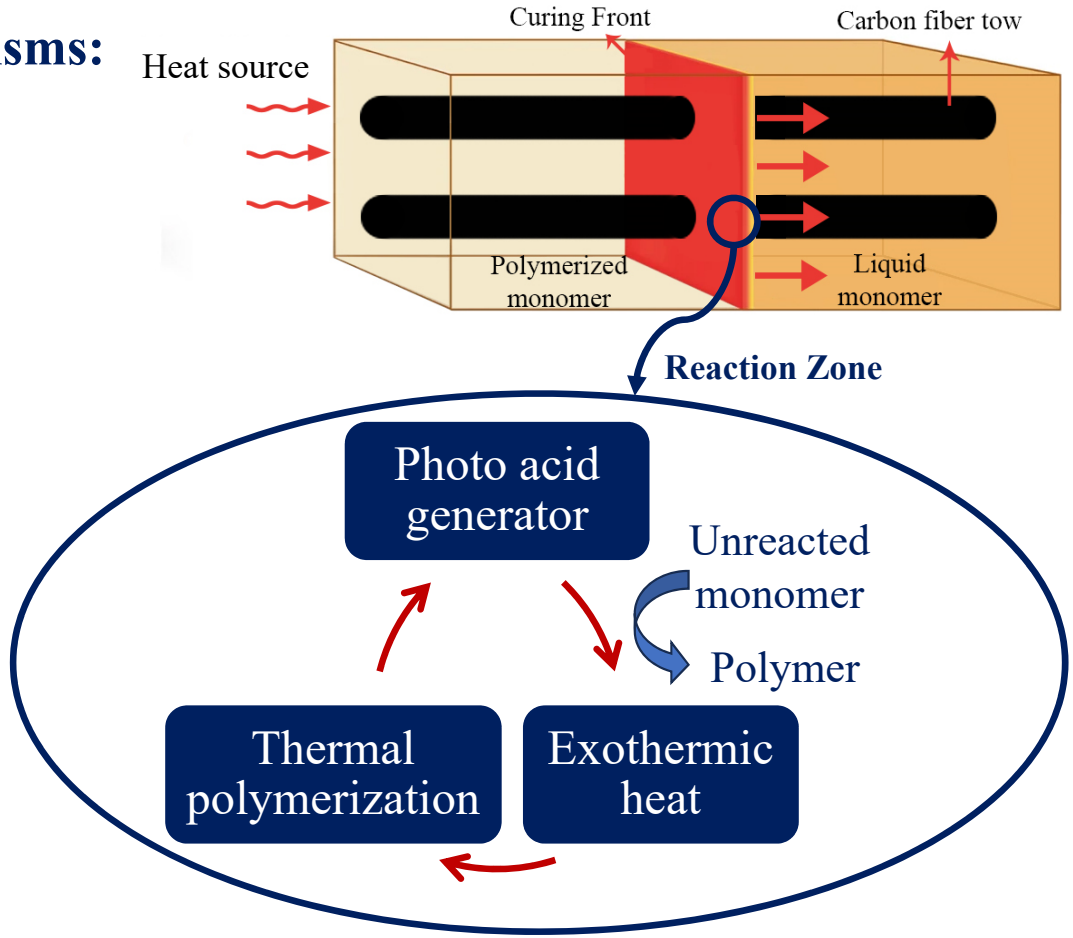

UV-induced frontal polymerization for CFRP composites

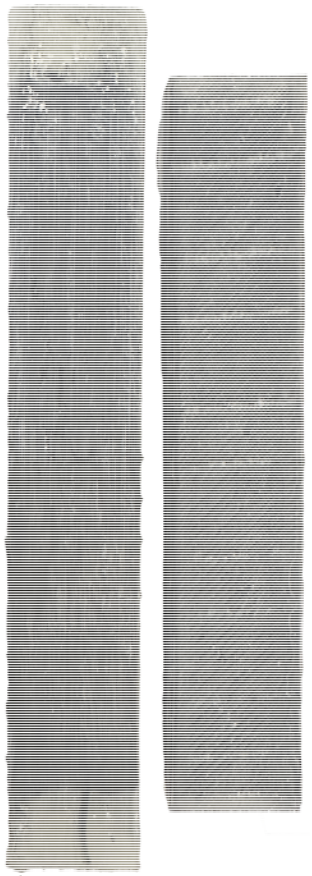



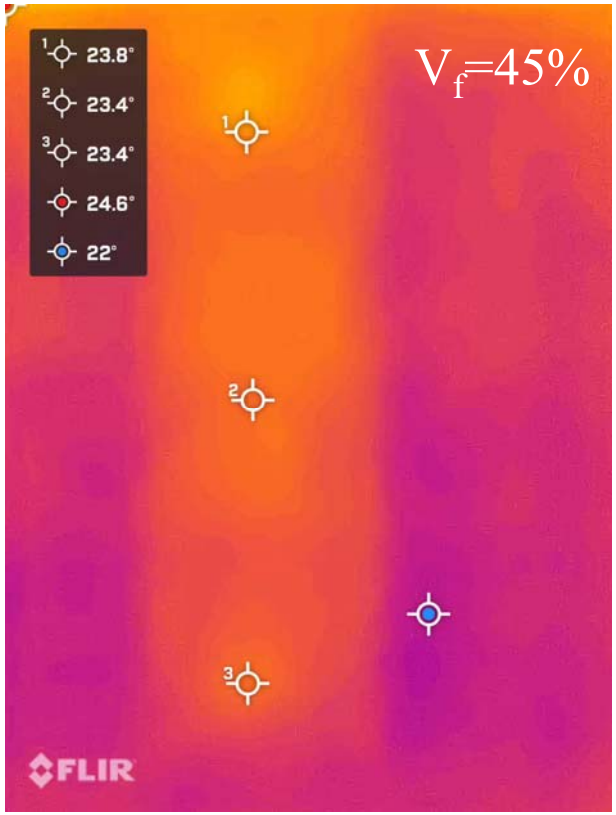

Curing time dropped from 15 hours to only 66-83 seconds!

Modeling of Frontal Polymerization in Carbon Fiber Composites

Experimental Data [1]
(Optical Measurements)

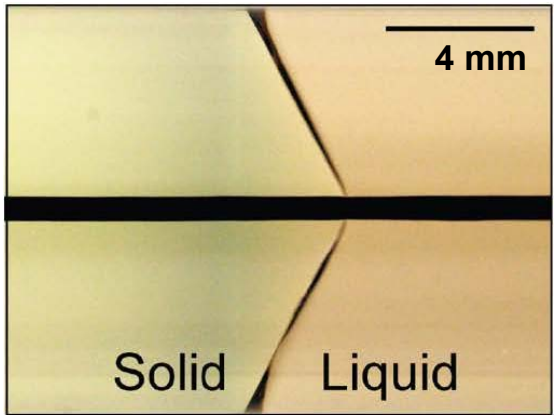

2D Model Simulations [1]

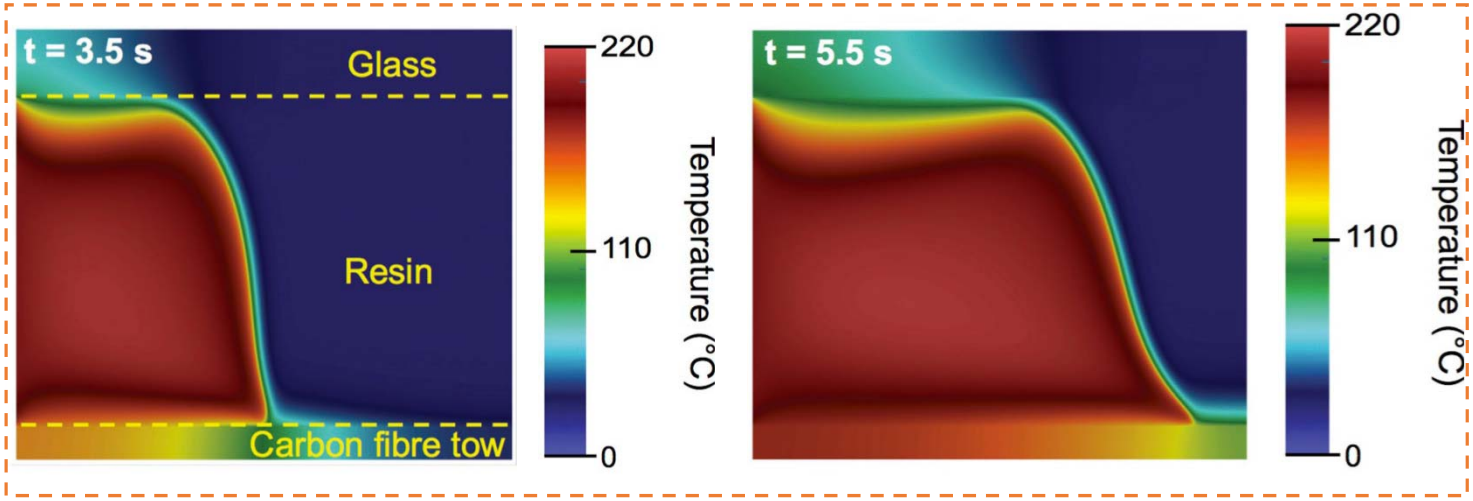

Existing models mainly focused on 1D and 2D configurations

Need to develop 3D models to study the effect of composite layups (e.g., unidirectional, cross-ply) and triggering directions for practical applications!

[1] . Robertson ID, et al. Rapid energy-efficient manufacturing of polymers and composites via frontal polymerization. Nature. 2018;557(7704):223-7.

Part 1:

3D Modeling of Heat-Triggered Frontal Polymerization in CFRP

Problem Formulation

- Heat is generated by an enthalpic reaction during the frontal polymerization process:

$$k\left(\frac{\partial^2 T}{\partial x^2}+\frac{\partial^2 T}{\partial y^2}+\frac{\partial^2 T}{\partial z^2}\right)+\rho H_r\frac{\partial \alpha}{\partial t}=\rho C_P\frac{\partial T}{\partial t},$$

- The curing kinetics is described by Arrhenius equation with the classical Prout-Tompkins (PT) autocatalytic model:

$$\frac{\partial \alpha}{\partial t}=A\,exp(-\frac{E}{RT})(1-\alpha)^n\alpha^m\frac{1}{1+\exp\left[\mathrm{C}(\alpha-\alpha_c)\right]}$$

Numerical Implementation

- Finite element analysis using Abaqus with: HETVAL + USDFLD user subroutines

Monomer:
Dicyclopentadiene (DCPD) resin

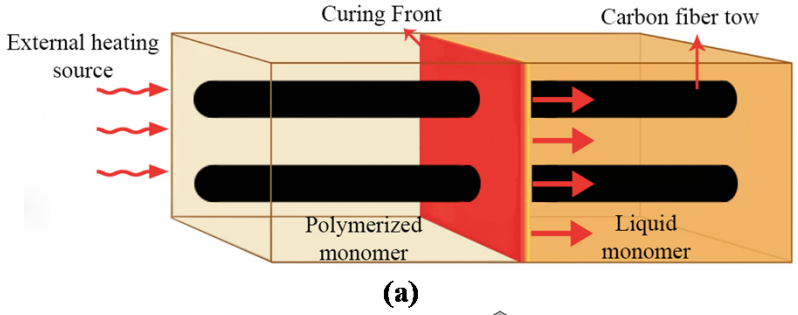

8-node linear heat transfer quadrilateral brick elements

Unidirectional

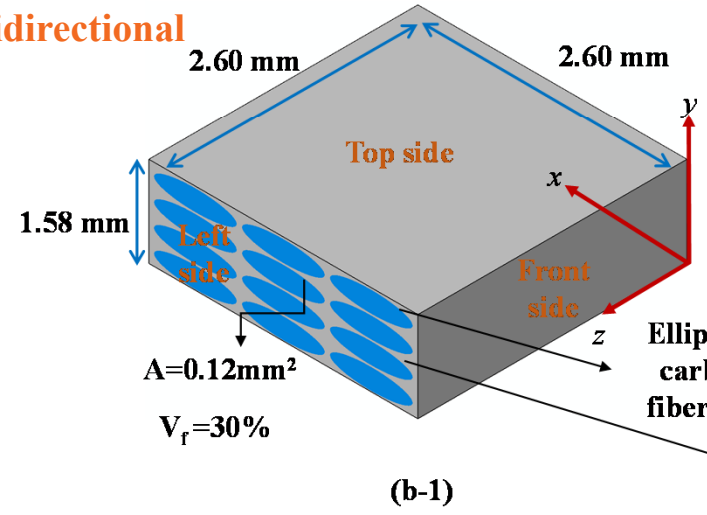

Cross-ply

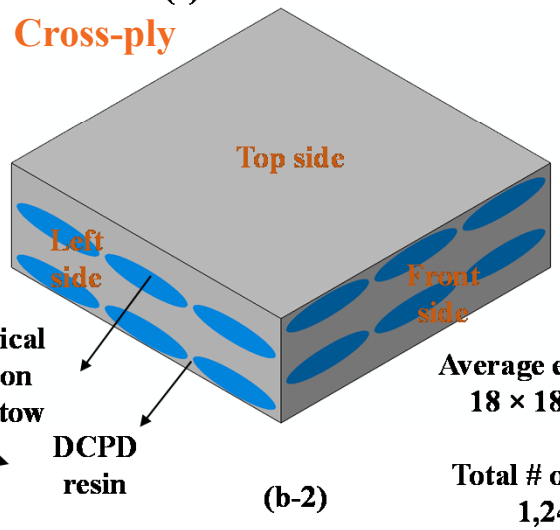

Mesh

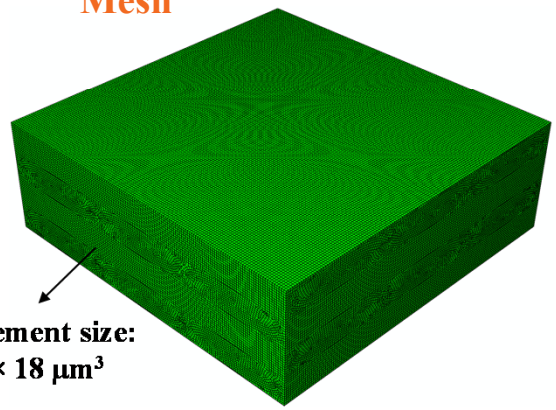

Model Validation

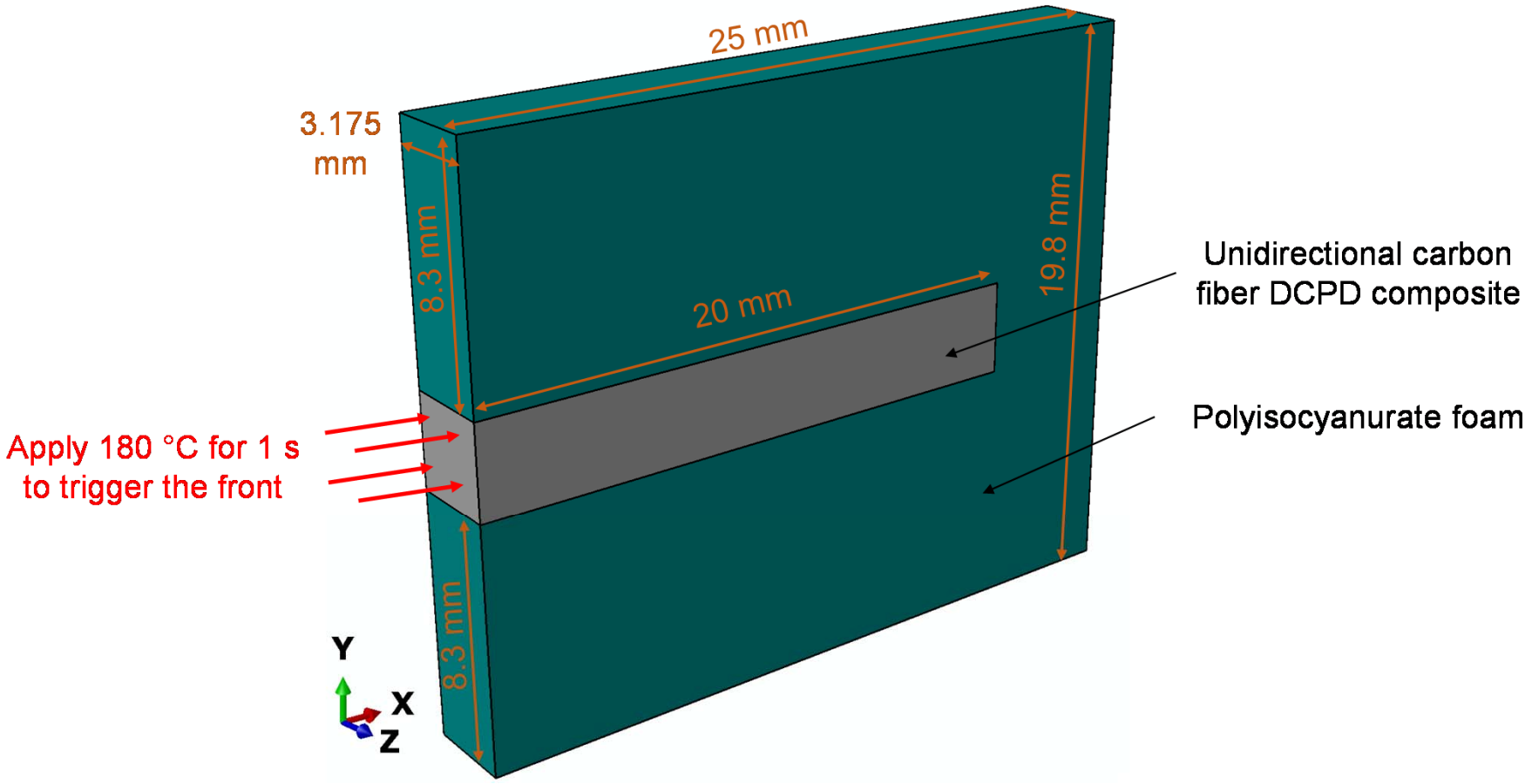

Model Validation

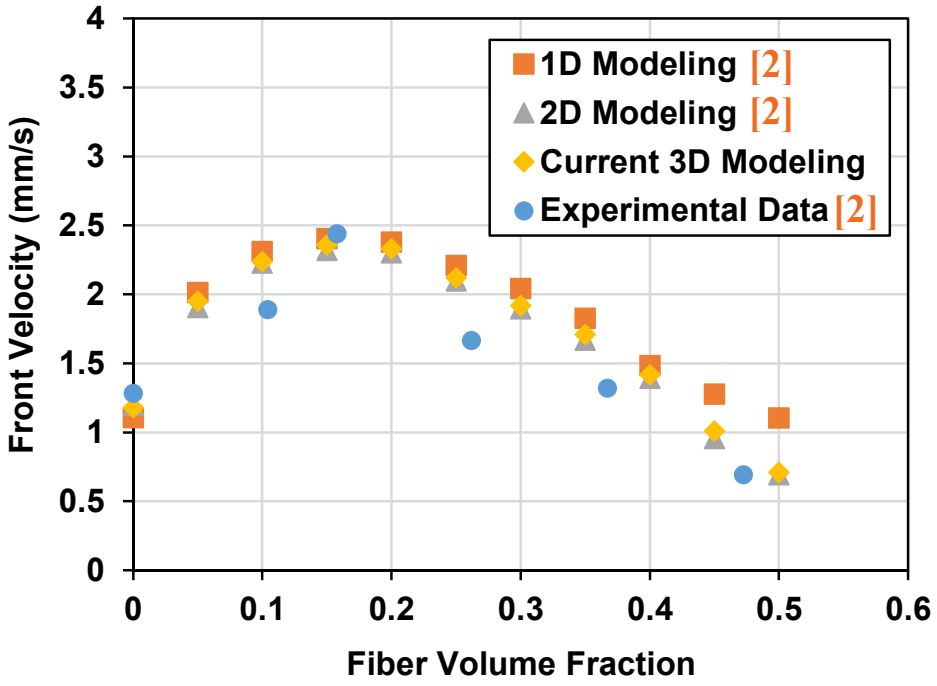

(a)

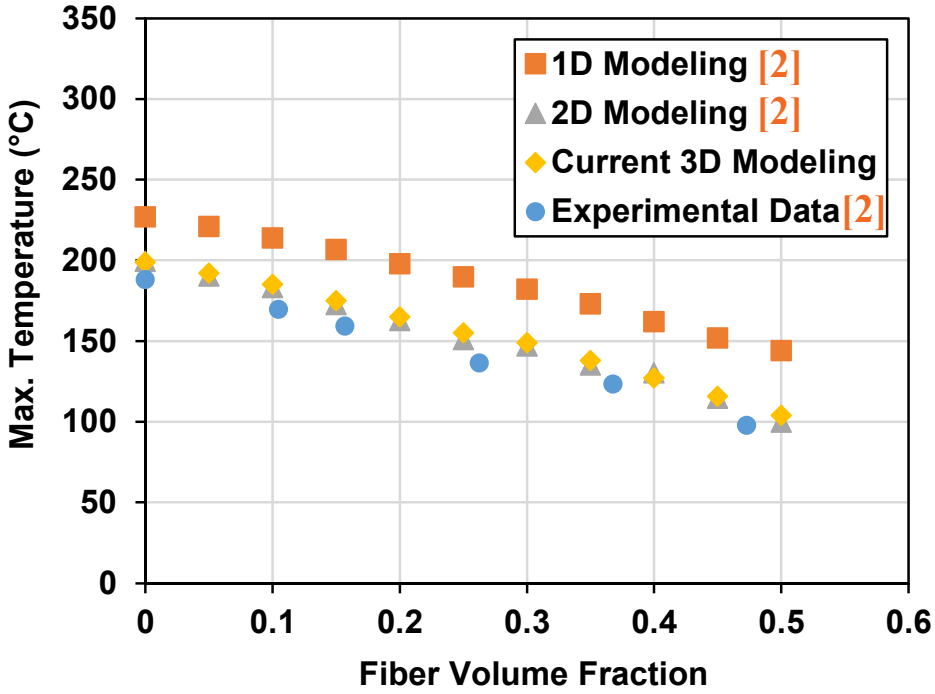

(b)

[2] Goli E, et al. Frontal polymerization of unidirectional carbon-fiber-reinforced composites. Composites Part A: Applied Science and Manufacturing. 2020;130:105689.

Results: Frontal Triggered from the Top Surface

Unidirectional

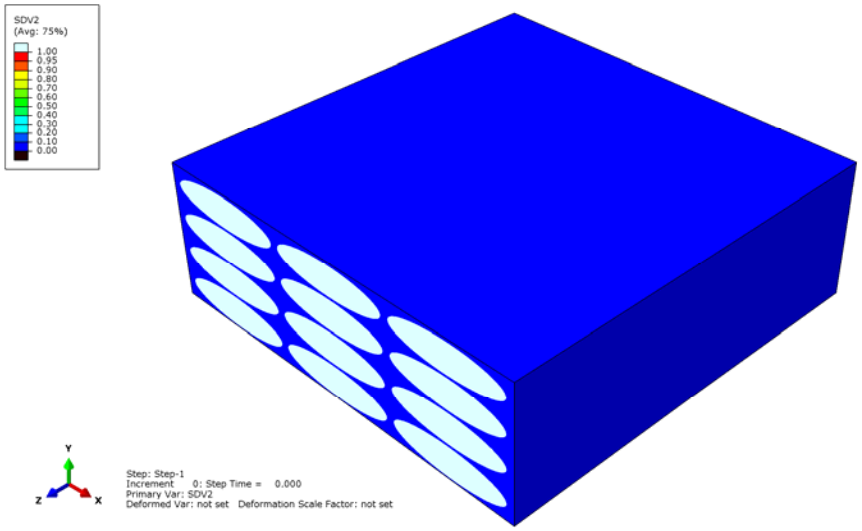

Cross-ply

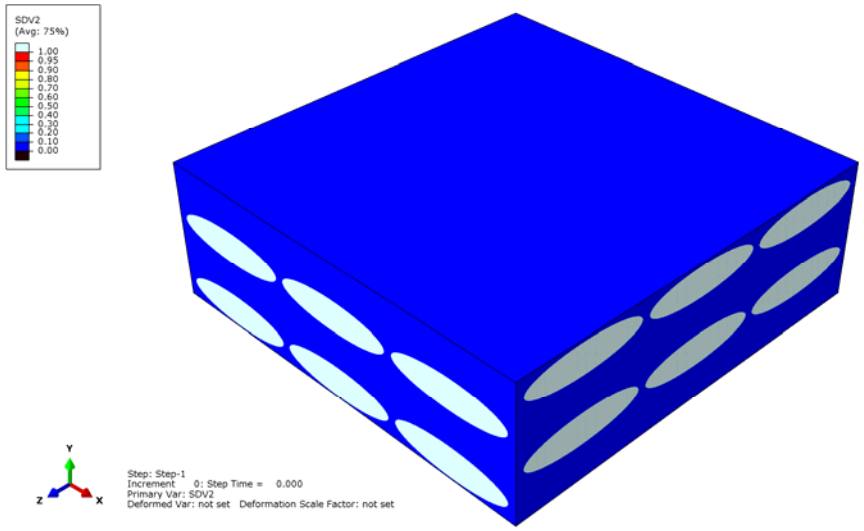

Results: Frontal Triggered from One Side

Unidirectional

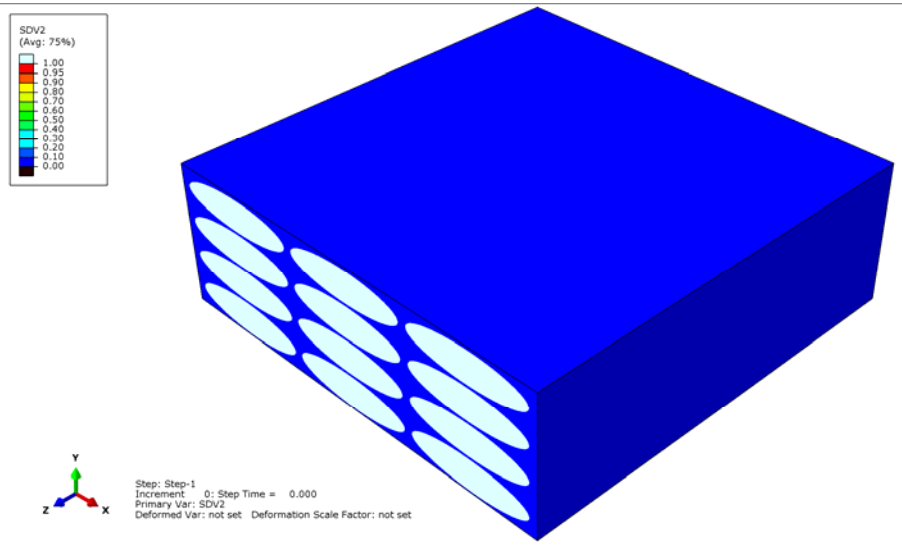

Cross-ply

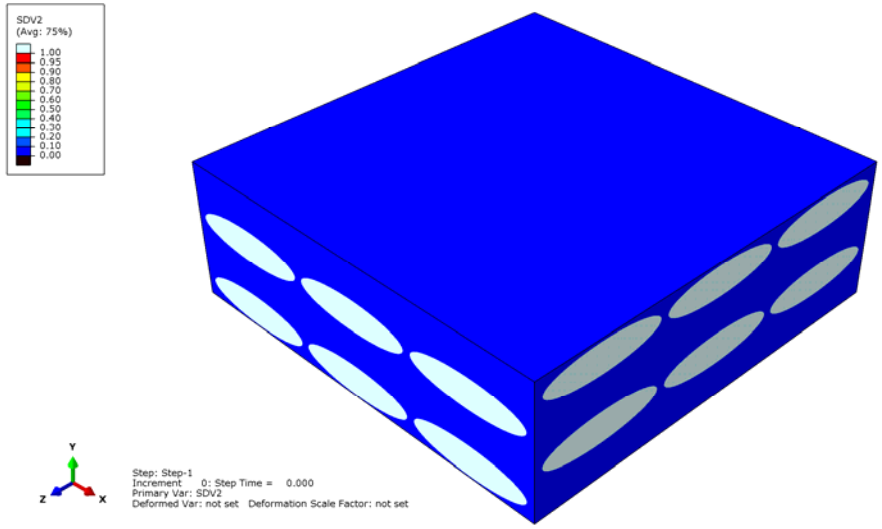

Results: Frontal Triggered from Two Sides

Unidirectional

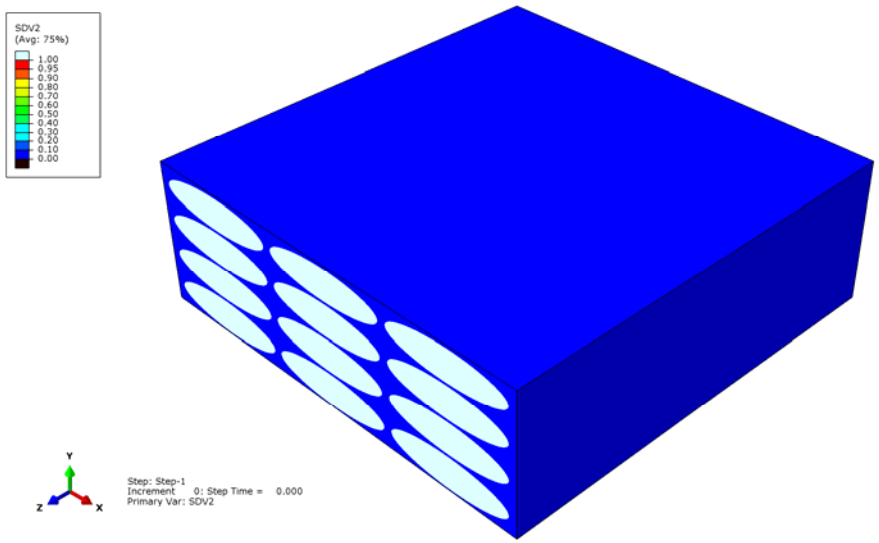

Cross-ply

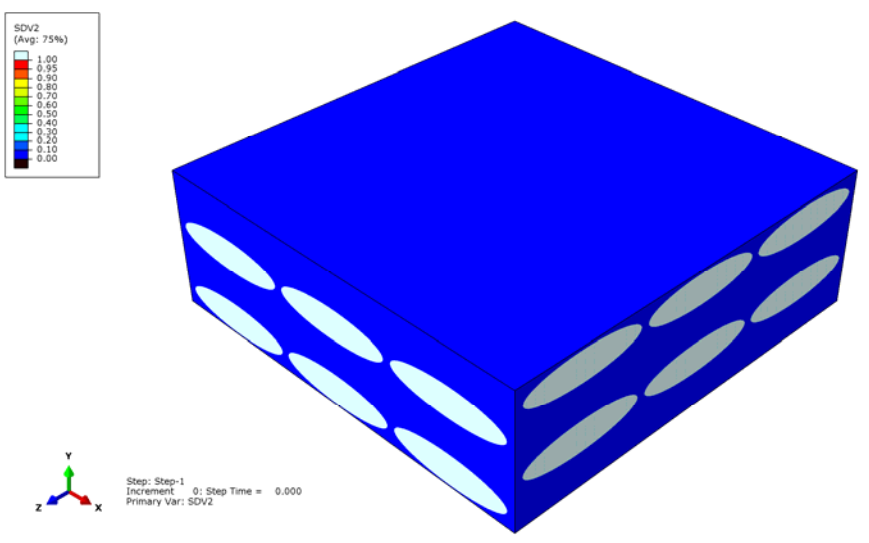

Results: Frontal Triggered from Front (Perpendicular to Fiber Direction)

Unidirectional
(triggered from front surface)

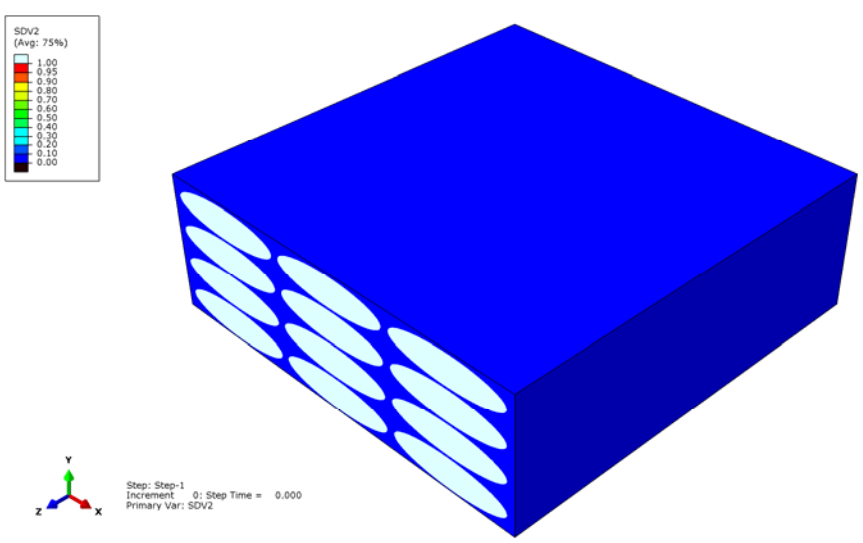

Unidirectional
(triggered from front & back surfaces)

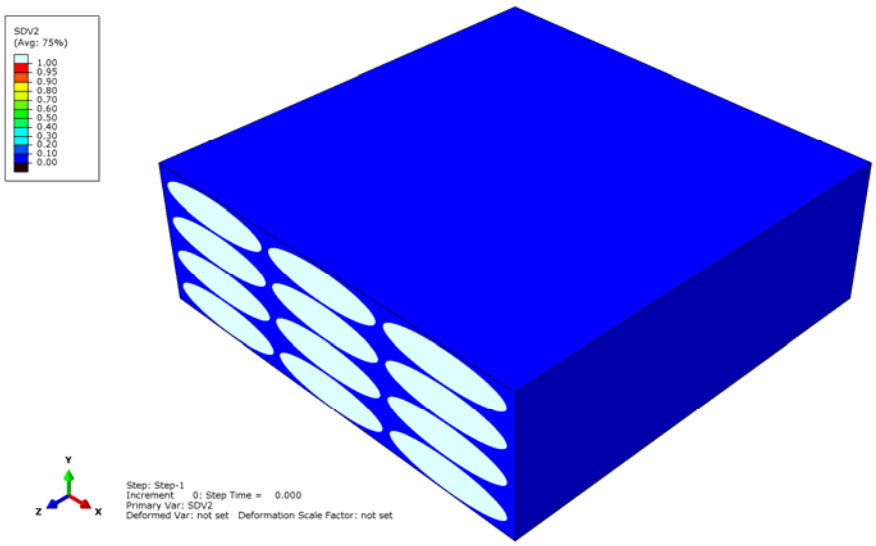

Results – Unidirectional Layup

- Triggering parallel to the fiber direction leads to a faster frontal propagation and higher degree of cure
- Triggering from two sides accelerates the frontal propagation

Specimen	Initial curing duration (s)	Average front velocity (mm/s)	Average degree of cure (%)
UT	0.48	1.80	94.30
UL	0.42	6.17	95.30
ULR	0.14	9.13	99.50
UF	Not fully cured	0.27	24.80
UFB	1.11	1.16	77.30

Results – Unidirectional Layup

- Thermal spike forms when the two fronts merge if triggered from both sides
- May indicate wavy patterns or non-uniform degree of cure

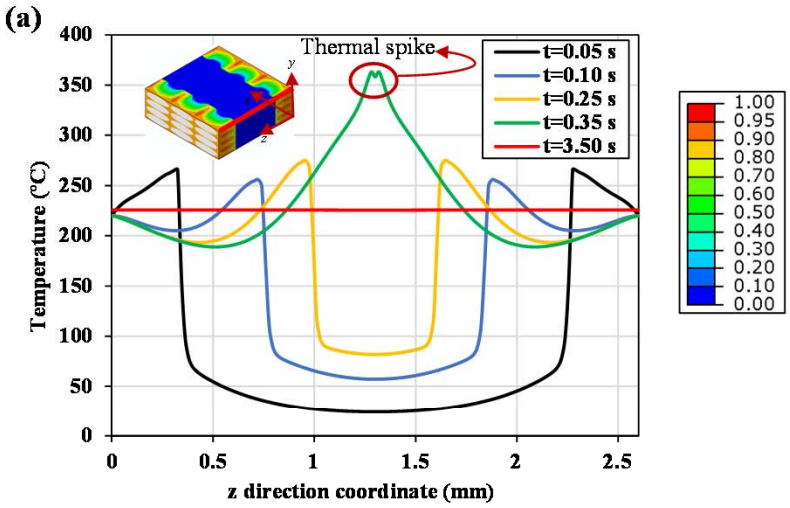

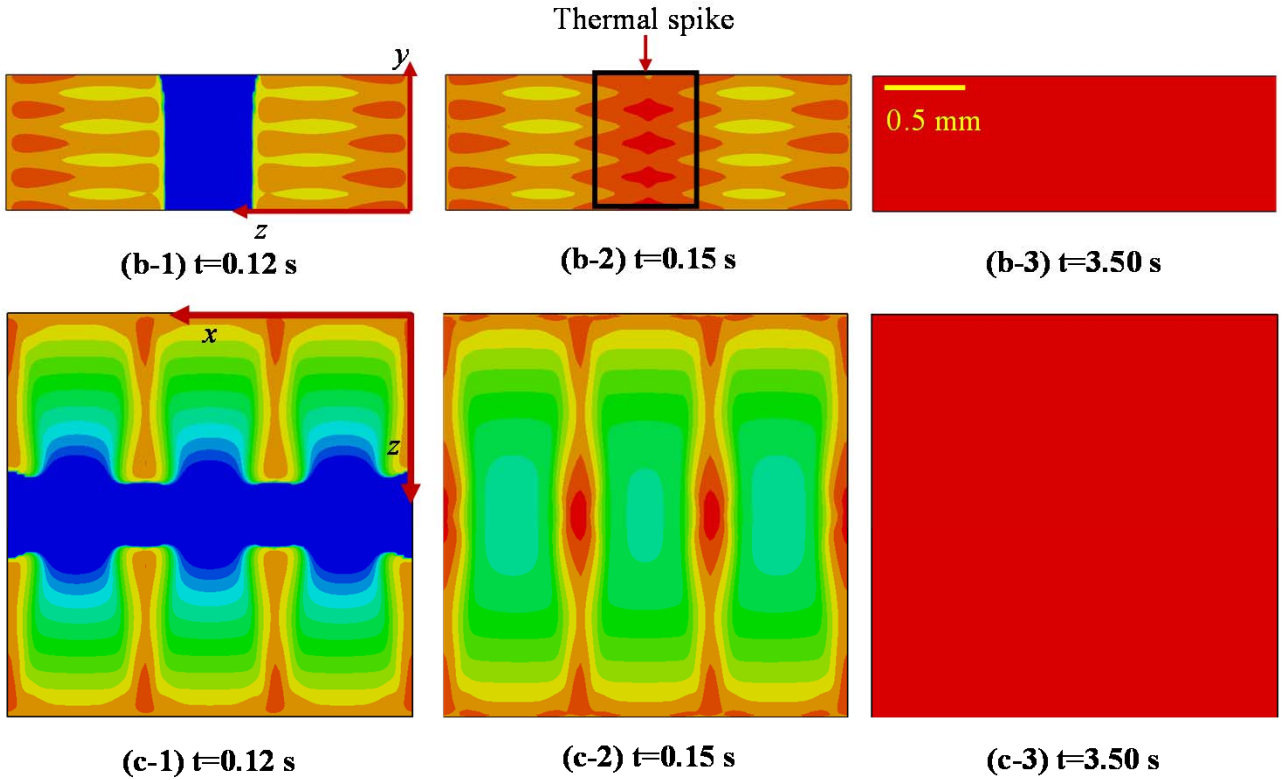

Results – Cross-Ply Layup

- Triggering parallel to the fiber is still preferred
- Triggering from both sides accelerates the frontal polymerization and leads to an overall higher degree of cure

Specimen	Initial curing duration (s)	Average front velocity (mm/s)	Average degree of cure (%)
CT	0.54	1.58	94.00
CL	0.56	4.59	87.80
CLR	0.17	7.27	99.40

Results – Cross-Ply Layup

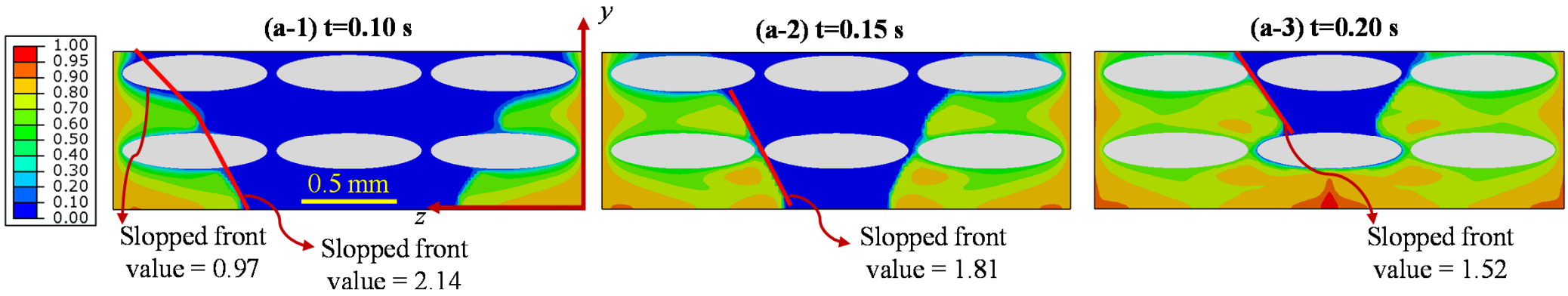

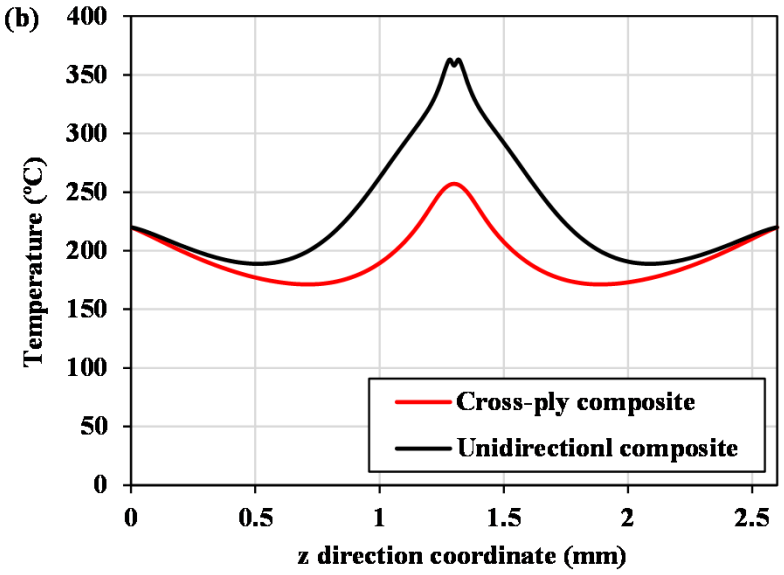

- Thermal spike still exists in cross-ply laminates if triggered from two sides
- The temperature at the thermal spike is 100 degrees lower in cross-ply when compared to unidirectional laminates

Results – Unidirectional vs. Cross-Ply

- Front propagates faster in unidirectional laminates
- Front velocity changes as the front propagates, especially in UL and CL cases

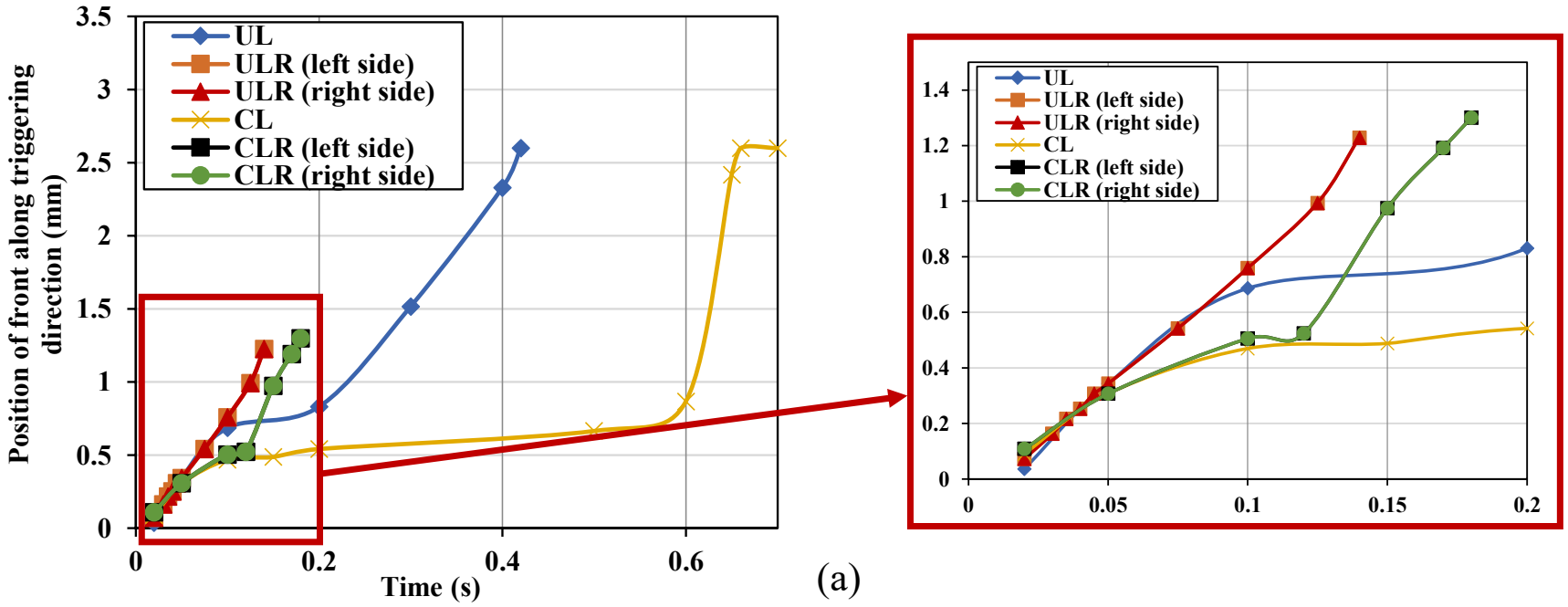

Results – Unidirectional vs. Cross-Ply

- Front velocity changes as the front propagates
- Cross-ply laminate CT case exhibits a lower front velocity in different times than the UT case

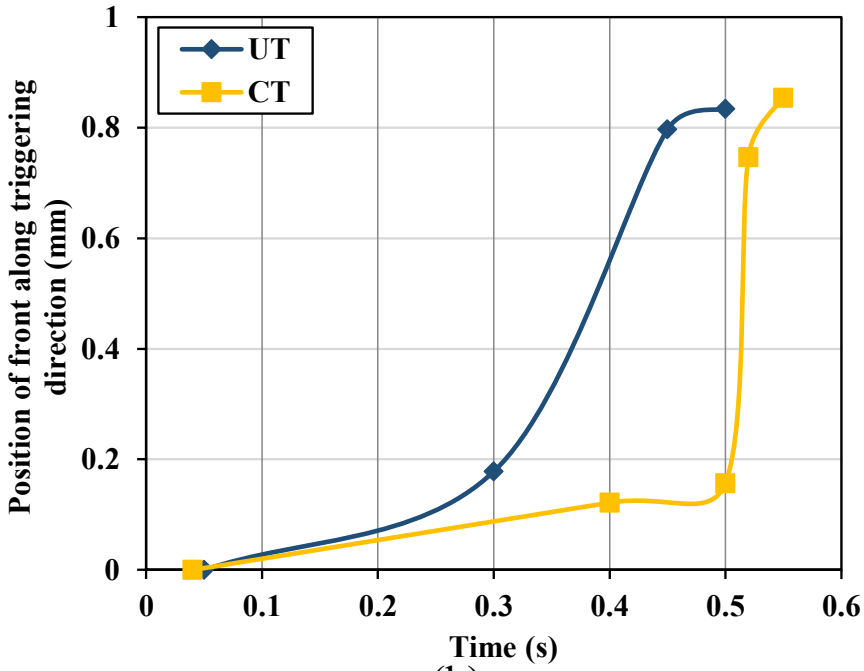

(b)

Results – Effect of Fiber Thermal Conductivity

- Three different types of fibers: 10.45 W/m·K (for carbon fiber); 1.14 W/m·K (for glass fiber); 0.04 W/m·K (for Kevlar fiber).
- Front velocity drastically decreases as the thermal conductivity decreases

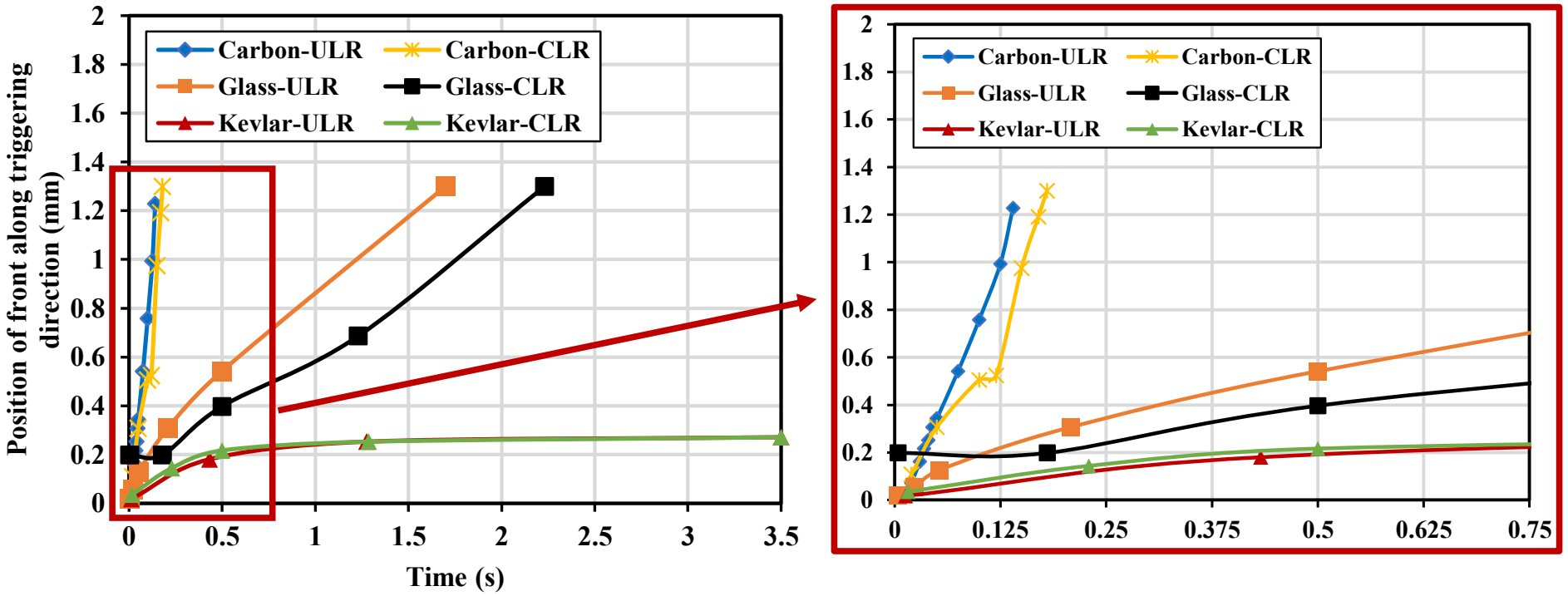

Results – Effect of Fiber Thermal Conductivity

- Thermal spike temperature dropped from 255 °C and 355 °C for the carbon fiber CLR and ULR cases to only 133 °C and 117 °C for the glass fiber ULR and CLR cases
- For cases with the Kevlar fiber, the thermal spike is not formed

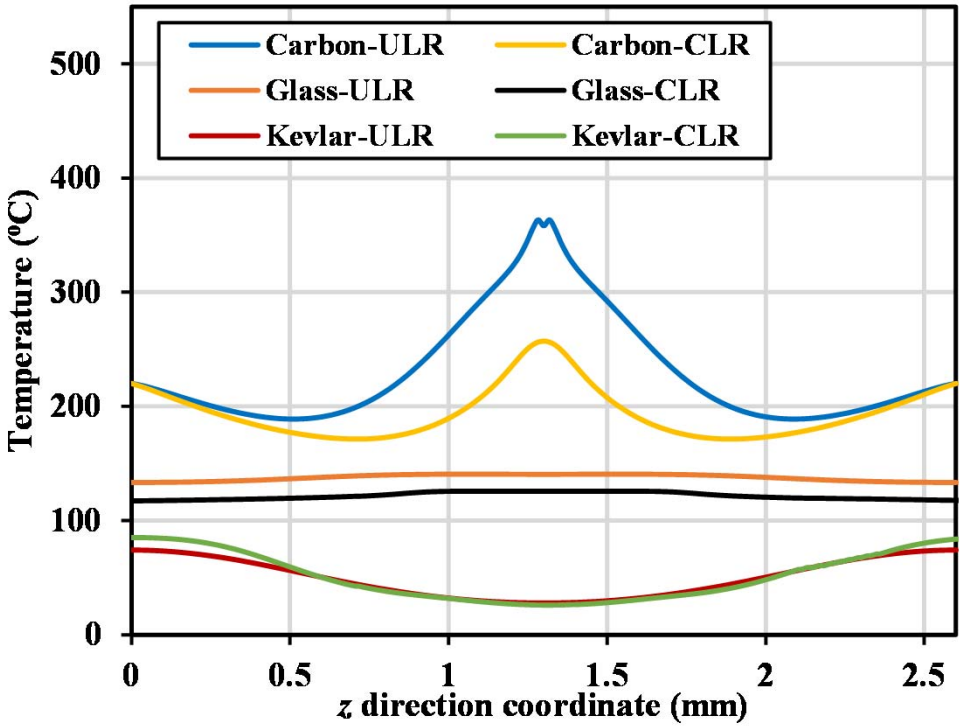

Part 2:

Modeling of UV-induced Frontal Polymerization in CFRP (On-going work)

Problem Setup & Objective

- 2D model for unidirectional CFRP composite with epoxy frontal resin

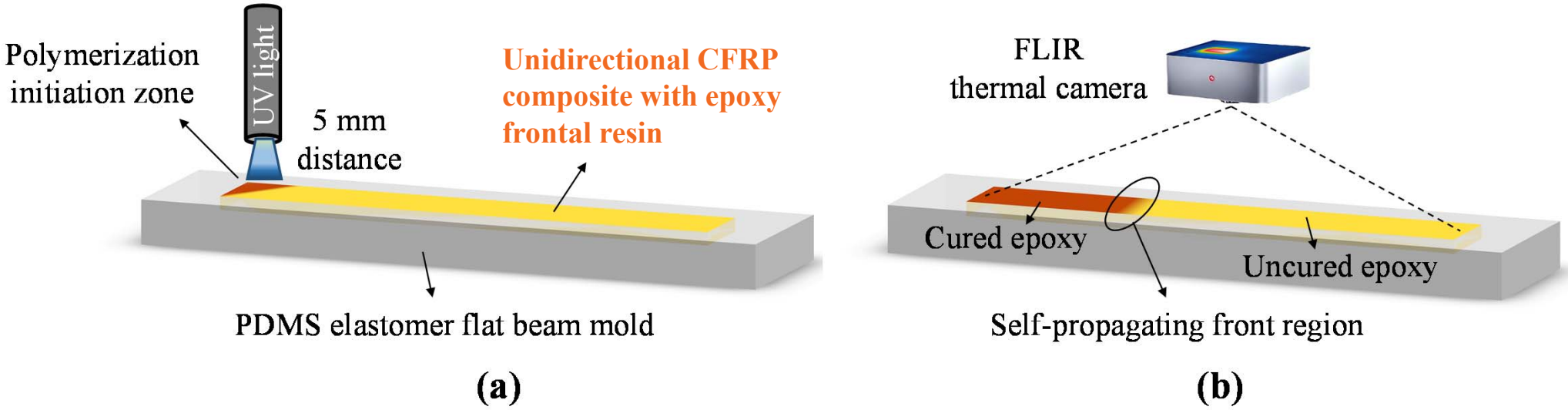

- **Objective:** Investigate how the UV light parameters, including UV light intensity, spot size, wavelength, and distance to the specimen surface affect the frontal polymerization process

Challenges:

- Determine the accurate curing kinetics of the epoxy-based frontal resin
  - Traditional DSC does not provide the exact same UV-induced polymerization environment
  - One possible solution is to use UV-DSC to get more accurate curing kinetics

UV-indced frontal polymerizable material system	
Frontal monomer	(3,4-epoxycyclohexane)-methyl-3,4-epoxycyclohexyl carboxylate (**ECC**)
Photo-initiator (PI)	p-(octyloxyphenyl)phenyl iodonium hexafluorostibate (**IOC-8 SbF6**)
Thermal-initiator (TI)	**benzopinacol**

Preliminary Results



Conclusion

1. 3D models of heat triggered frontal polymerization have been used to investigate the effects of laminate layup, triggering direction, and fiber types
   - We recommend to trigger the frontal polymerization along the fiber direction as much as possible
   - We should anticipate a slower frontal propagation in cross-ply laminates
   - Triggering from multiple locations will result in thermal spikes, which could indicate occurrence of high thermal residual stresses, wavy surface patterns, and/or non-uniform degree of cure

2. A simple UV-induced frontal polymerization model for CFRP composites with epoxy-based frontal resin was modeled in a 2D configuration. Currently, we face challenges in:
   - Characterization of the curing kinetics of epoxy-based frontal resin under UV conditions
   - Can be potentially solved using the UV-DSC

Syracuse University
College of Engineering
& Computer Science

National Science Foundation under Award No. CMMI-2208130

Composite Materials Laboratory



Amirreza Tarafdar



Dr. Ian Hosein

INDUCTION HEATING OF THERMOSETTING CFRP MOLDS FOR COMMINGLED PP/GF COMPOSITE FORMING

Eunjung Kim[1,2], Cheol-Hee Ahn[2], Woong-Ryeol Yu[2]*, Wonjin Na[1]*

[1]Composite Materials Applications Research Center, Korea Institute of Science and Technology (KIST), Jeonbuk 55324, Republic of Korea

[2]Department of Materials Science and Engineering and Research Institute of Advanced Materials (RIAM), Seoul National University, Seoul 08826, Republic of Korea

Email: t20468@kist.re.kr, web page: https://sites.google.com/view/scmrl/home
Email: chahn@snu.ac.kr, web page: https://nbml.snu.ac.kr/
Email: woongryu@snu.ac.kr, web page: http://nscm.snu.ac.kr/
Email: namossi@kist.re.kr, web page: https://sites.google.com/view/scmrl/home

Keywords: Polymer-Matrix Composites (PMCs), Electrical Properties, Finite Element Analysis, Process Monitoring

ABSTRACT

This study focuses on the development of an optimized coil pattern for uniform temperature distribution during induction heating of thermoplastic composite PP/GF using a thermoset CFRP mold. While CFRP molds offer advantages in lightweight structure and reduced heating and cooling times, they have limitations in achieving uniform heating due to anisotropy. To address this, various coil patterns were designed and analyzed for heating efficiency, resulting in a pattern capable of maintaining uniform temperature distribution even in complex geometries. The PP/GF composite produced using the optimized pattern is expected to achieve high quality without compromising mechanical properties, as compared to conventional molding methods. This research is anticipated to enhance the industrial feasibility of induction heating-based molding processes.

1 INTRODUCTION

TInduction heating is a process that generates induced currents within a conductor through electromagnetic induction, thereby heating the conductor due to resistive losses [1, 2]. When a high-frequency alternating current flows through the coil of an induction heating device, a fluctuating magnetic field is created within the coil, forming a strong magnetic flux around it. When a conductor is placed within this magnetic field, eddy currents are generated within the conductor, flowing in a direction that opposes the change in the magnetic field, according to the law of electromagnetic induction [3]. The induced currents within the conductor produce Joule heating due to electrical resistance, resulting in rapid heating. This method of induction heating is known for its high energy efficiency, as it allows precise heating of specific regions, thereby reducing processing time [4]. Additionally, as the heating process is contactless, it does not damage the surface of the conductor. The skin effect due to high-frequency currents enables uniform temperature control in targeted areas, contributing to improved product quality [5]. Moreover, since no combustion is involved, induction heating provides a clean and safe working environment, making it a preferred heating method for mass production and automation, and an environmentally friendly solution [6].

Metal molds have traditionally been widely used in various manufacturing processes due to their high strength and thermal conductivity, but they have recently shown limitations in weight and thermal inefficiency [7]. Consequently, CFRP molds with lightweight properties and excellent thermal stability have emerged as an attractive alternative [8]. CFRP molds are lighter than metal molds and can be fabricated in thin layers, which shortens heating and cooling times and significantly reduces energy consumption [9]. Additionally, CFRP has a low coefficient of thermal expansion, which minimizes thermal deformation at high temperatures, making it suitable for precision processing, especially in

processes requiring repeated high-temperature heat treatments. Thus, CFRP molds offer a viable alternative to metal molds by addressing their limitations and proving effective in high-temperature processing applications.

Despite these advantages, CFRP molds present inherent challenges during the heating process due to their anisotropic nature [10]. The electrical and magnetic properties of CFRP vary according to the fiber orientation within the material, making it difficult to achieve uniform electromagnetic field distribution, which complicates even heating with standard coil arrangements [11]. Specifically, the induced currents generated by electromagnetic induction are often deflected or concentrated in certain directions within the CFRP, creating zones of interference where the currents cancel each other out. In these interference zones, heat transfer may be insufficient or overly concentrated, making it challenging to achieve a uniform temperature distribution across the entire mold [12]. This uneven temperature distribution can lead to inconsistencies in the quality and uniformity of processed products.

Therefore, this study aims to design a novel coil pattern that minimizes interference zones in the electromagnetic field and achieves more uniform heating by considering the anisotropic properties of CFRP molds. To accomplish this, various coil patterns were simulated, analyzing temperature distribution and magnetic field density to derive an optimal coil design. The developed pattern was successfully applied to uniformly heat CFRP molds. Subsequently, the heated CFRP mold was used to fabricate thermoplastic composites composed of commingled PP/GF, with plans to perform mechanical property tests on these composites. Through this approach, the study seeks to present an effective solution to the anisotropic challenges of CFRP molds, enhancing reliability and quality in thermoplastic composite molding processes.

2 MODELING AND NUMERICAL ANALYSIS

Induction heating of the CFRP mold was numerically simulated to optimize coil placement. The CFRP model was a plate measuring 250×300×6 mm^3, with Litz wires comprising 1,500 strands of copper wire, each 0.12 mm in diameter. The working distance (WD) between the CFRP and the coil was set to 1 mm. The coil placement was tested in three configurations: a zigzag pattern (Figure 1a), a spiral pattern (Figure 1b), and a zig-spiral hybrid coil pattern (Figure 1c) newly developed in this study. In the zig-spiral hybrid coil pattern, adjacent coils were arranged with opposite current directions, and 180° turns were also oriented to maintain opposite current directions with neighboring coils. The spacing between coils was 20 mm, with a radius (R) of 20 mm for 90° turns and 10 mm for 180° turns. If the outermost coil (last coil) reached a higher temperature than preceding coils, uniform heating could be achieved by either decreasing the spacing from the previous coil or increasing the WD of the last coil. Additionally, to prevent excessive heating between the input and output of the coil, the spacing was minimized (approximately 0.5 mm) or eliminated altogether. The operating frequency and current were set to 152 kHz and 100.8 A, respectively.

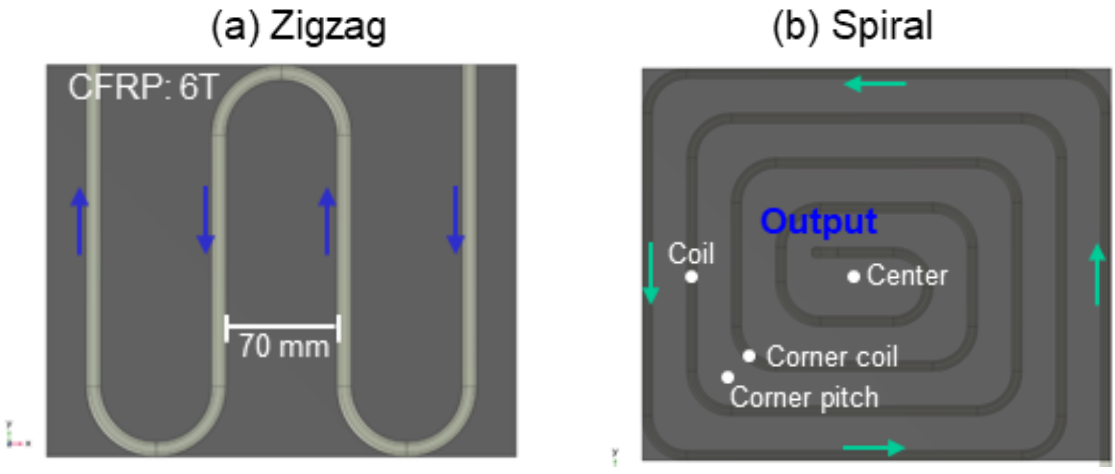

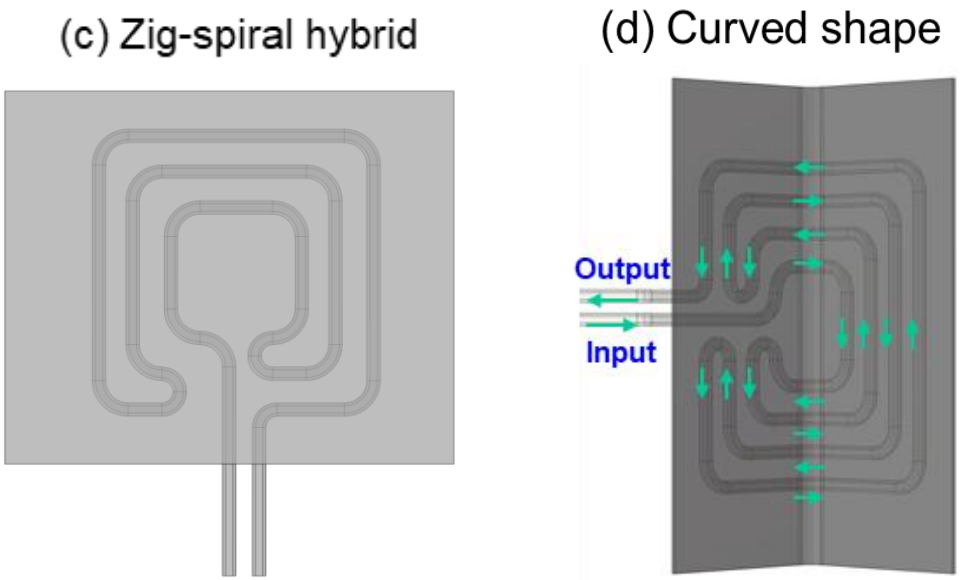

Figure 1: Coil pattern geometries: (a) Zigzag, (b) Spiral, (c) Zig-spiral hybrid, (d) Curved-shape.

COMSOL Multiphysics V6.2 software (COMSOL, USA) was used to calculate the multiphysics of the electromagnetic field, electromagnetic induction, and heat transfer. Maxwell's equation was computed in the magnetic field interface, followed by heat transfer in the solid interface, to calculate Fourier's heat transfer law. A magnetic field interface was applied to the workpiece, induction coil, and air domain. Heat transfer in a solid interface was applied to the workpiece and coil domain. A heat flux boundary condition was added for convection in air, with a heat transfer coefficient of 10 W/m2·K.

Property	Parallel	Vertical
Electrical conductivity (S/m)	3.25×10^4	0.0325
Thermal conductivity (W/m·K)	2.4	0.59
Heat capacity (J/kg·K)	820	820
Density (kg/m³)	1780	1780
Relative permeability	1	1
Relative permittivity	2156	1640

Table 1: This is the example of a table.

3 EXPERIMENTAL

3.1 Manufacturing of CFRP mold

The CFRP molds were fabricated using a high-temperature-resistant resin (LAS200M, KGF) and carbon-fiber fabric (Toray T300 plain-woven fabric, areal weight 200 g/m²) through an autoclave process. The resin was impregnated into the carbon-fiber fabric using the hand lay-up method, with 16 or 32 layers laminated on a mold of the desired shape. The resin-impregnated fabric was placed between release films and breathers, both above and below the mold, then wrapped in a nylon film and sealed under vacuum. Curing was performed at 175℃ and 7 bar pressure in an autoclave for 2 hours, following the resin's curing conditions. After demolding, the mold underwent post-curing in an oven at 200℃ for at least 2 hours. Three types of molds were fabricated: a 3 mm thick flat plate, a 6 mm thick flat plate, and a 3 mm thick plate with a 45° curvature.

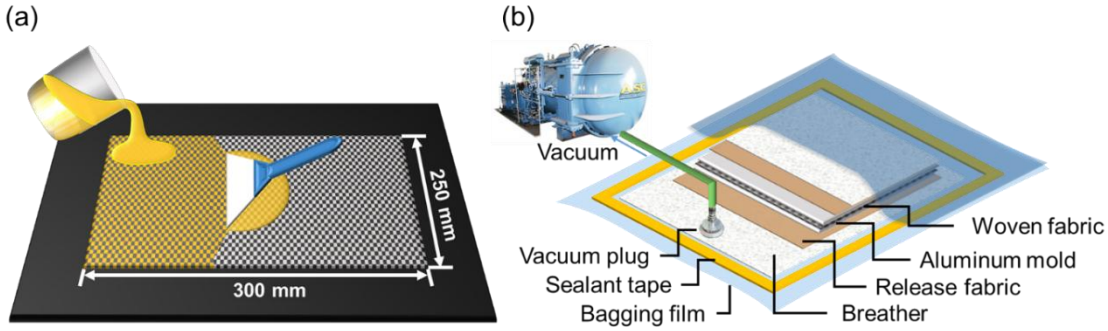

Figure 2: Hand lay-up process (a) and vacuum bagging setup (b) for CFRP mold curing.

4 RESULTS AND DISCUSSION

4.1 Optimization of coil pattern design

In the zigzag pattern (Figure 3a), the coil reached a high temperature of 404℃ at the 180° bends due to the magnetic field reinforcement effect, resulting in a non-uniform temperature distribution. For the spiral pattern (Figure 3b), the center was heated to 58.8℃, while the pitch and coil sections in the cancellation zone reached 73.3℃ and 89.6℃, respectively, and the linear coil section reached 106℃, indicating significant temperature variations across different sections. In contrast, the zig-spiral hybrid pattern (Figure 3c) exhibited a relatively uniform temperature distribution, with the center at 93.3℃, the pitch (between coils) at 108℃, the area directly above the coil at 145℃, and the last coil at 154℃, maintaining a difference of approximately 40-50℃. Temperature comparisons were illustrated in a graph after heating for 3600 seconds.

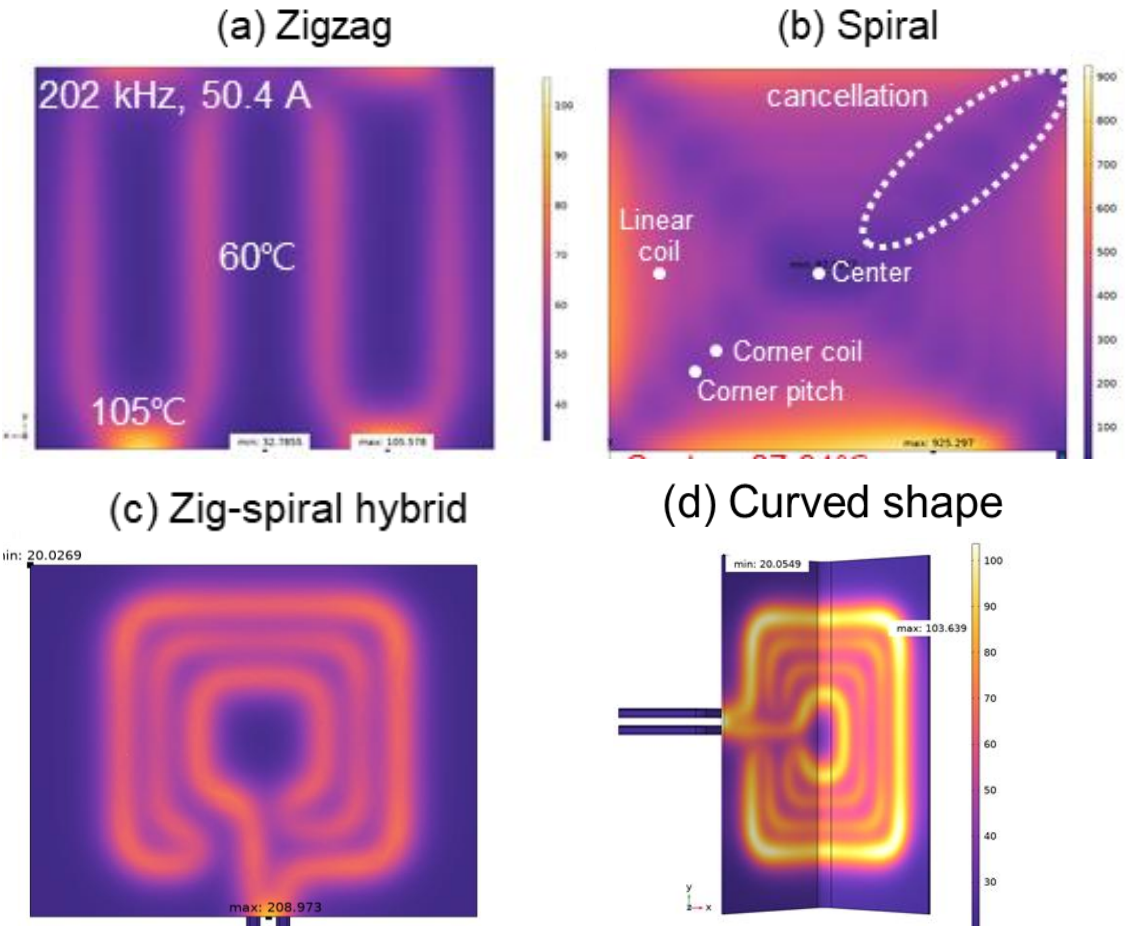

Figure 3: Temperature distribution for (a) zigzag, (b) spiral, (c) zig-spiral hybrid, (d) Curved-shape.

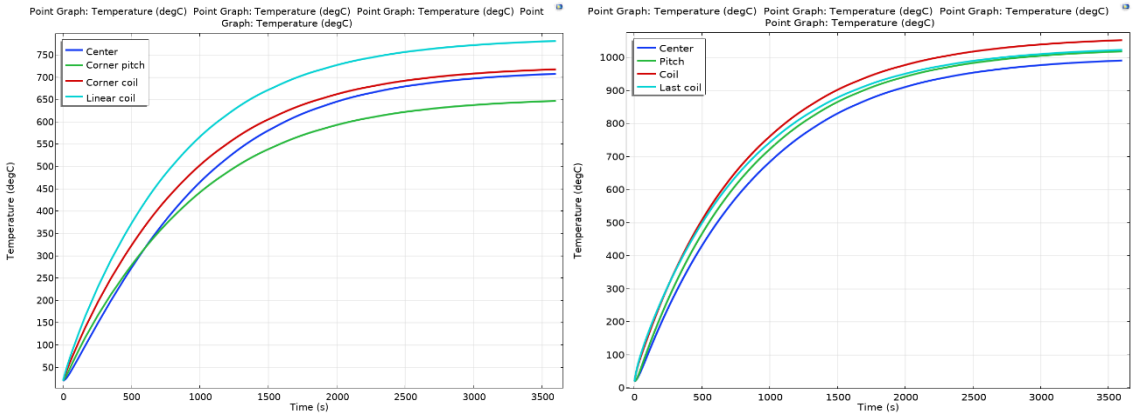

Figure 4: Temperature profiles: (a) spiral coil, (b) zig-spiral hybrid coil over 3600s heating.

5 CONCLUSIONS

An optimized zig-spiral hybrid coil pattern was proposed and validated for the induction heating of CFRP molds, addressing the challenge of uneven heating caused by the anisotropic properties of CFRP materials. Through simulation and experimental verification, the proposed design demonstrated significantly improved temperature uniformity compared to conventional zigzag and spiral configurations.

This improved uniformity is expected to reduce internal stresses, minimize defects, and enhance the quality of thermoplastic composite parts molded using CFRP tooling. The successful application of the coil pattern in heating CFRP molds and subsequent forming of commingled PP/GF composites confirms the feasibility of this approach for industrial use.

Furthermore, this study highlights the importance of coil design in electromagnetic heating applications and provides a scalable methodology that can be adapted for molds of various geometries and composite systems.

Future work will include mechanical testing of the molded composites to quantitatively evaluate property enhancement, and the development of closed-loop control systems for real-time heating uniformity monitoring. This research lays the groundwork for broader adoption of induction-based smart mold systems in high-performance thermoplastic composite manufacturing.

REFERENCES

[1] Sharma GK, Pant P, Jain PK, et al. Numerical and experimental analysis of heat transfer in inductive conduction based wire metal deposition process. Proc Inst Mech Eng C. 2022;236(5):2395-2407.

[2] Patil M, Kumar Choubey R, Kumar Jain P. Influence of coil shapes on temperature distribution in induction heating process. Mater Today Proc. 2023;72:3029-3035.

[3] Vishnuram P, Ramachandiran G, et al. Overview of power converter topologies for induction heating applications. Int Trans Electr Energy Syst. 2020;30(10):e12554.

[4] Sharma GK, Pant P, Jain PK, et al. Suitability of induction heating system for metal additive manufacturing. Proc Inst Mech Eng B. 2021;235(1-2):219-229.

[5] Szychta E, Szychta L. Effectiveness of Resistance and Induction Turnout Heating. Energies. 2020;13(20):5262.

[6] Oskolkov AA, Trushnikov DN, Bezukladnikov II. Induction heating in FDM/FFF 3D manufacturing. J Phys Conf Ser. 2021;1730(1):012005.

[7] Kan M, Ipek O. Thermal behavior of permanent metal molds with new cooling designs. Int J Metalcasting. 2022;16(2):699-712.

[8] Rudolf R, Mitschang P, Neitzel M. Induction heating of continuous CF-reinforced thermoplastics. Compos Part A. 2000;31(11):1191-1192.
[9] Shrivatsaan MM, GB N, Palka R, et al. Electric motor cooling and lightweighting review. Proc Inst Mech Eng C. 2024;238(5):1732-1746.
[10] Zhao F, Liu Z, Chen R, et al. Temperature effects on CF/TP composites in shaping. Int J Adv Manuf Technol. 2022;121(11):7569-7589.
[11] Lundström F, Frogner K, Andersson M. Temperature in weave-based CFRP via induction. Compos Part B. 2021;223:109153.
[12] Fu T, Xu J, Hui Z. Induction heating temp field in plain weave CFRP. Appl Compos Mater. 2021;28(1):149-163.

ICCM24 24TH INTERNATIONAL CONFERENCE ON COMPOSITE MATERIALS
AUG 4-8, 2025 • BALTIMORE CONVENTION CENTER • BALTIMORE, MARYLAND

CHARACTERISING THE INTER-PLY BEHAVIOUR OF NON-CRIMP FABRICS DURING SINGLE DIAPHRAGM FORMING EXPERIMENT

Yilong Li[1], Guy Lawrence[2], Lee Harper[3] and Michael Sutcliffe[4]

[1]Department of Engineering, University of Cambridge
Engineering Dept, Trumpington St, CB2 1PZ, Cambridge, UK
Email: yl895@cam.ac.uk, web page: https://www.cam.ac.uk/

[2]Composites Research Group, University of Nottingham
Advanced manufacturing Building, Jubilee Campus, NG7 2GW, Nottingham, UK
Email: guydlawrence@gmail.com, web page: https://www.nottingham.ac.uk/

[3]Composites Research Group, University of Nottingham
Advanced manufacturing Building, Jubilee Campus, NG7 2GW, Nottingham, UK
Email: lee.harper@nottingham.ac.uk, web page: https://www.nottingham.ac.uk/

[4]Department of Engineering, University of Cambridge
Engineering Dept, Trumpington St, CB2 1PZ, Cambridge, UK
Email: mpfs@eng.cam.ac.uk, web page: https://www.cam.ac.uk/

Keywords: Fabrics, Preform, RTM, Process monitoring, FEA

ABSTRACT

The Single Diaphragm Forming (SDF) process has received limited attention in the literature compared with the Double Diaphragm Forming (DDF). However, its advantages in multi-layer preforming have led to its adoption in certain manufacturing contexts. To facilitate a more comprehensive investigation of the SDF process, a compact experimental rig capable with various tool geometries was designed and constructed. Previous research has highlighted the critical influence of friction between fabric plies in forming defects during the preforming of multi-ply diaphragms. Inter-fabric sliding has been introduced as an additional quantitative metric to establish a connection between interface friction and preforming quality to enable more effective monitoring of fabric behaviour during preforming. In the SDF experiments, the opacity of both the diaphragm and fabric poses a significant challenge to direct visual tracking of the lower fabric plies using photographic or videographic methods. Consequently, an indirect measurement technique has been developed by applying pre-painted grease dots to the fabric surface and subsequently tracking their deformed configurations post-forming. This methodology has been implemented across a range of tool geometries within the SDF experiments. By comparing the experimental sliding data with results obtained from finite element (FE) simulations, the sliding metric provides valuable insights into the dynamics between fabric layers and an evaluation of the current simulation models in terms of fabric interface behaviour. Future work will focus on employing this integrated approach to further investigate the correlation between friction, inter-ply sliding and preforming defects, and on extending the sliding tracking methodology to the study of the DDF process.

1 INTRODUCTION

Diaphragm forming is an open-moulding preforming technique developed for shaping dry textile reinforcements into complex geometries before resin infusion in liquid composite moulding (LCM) processes. Compared to conventional closed-moulding or draping methods, the diaphragm forming process offers a balance between efficiency and preforming quality [1]. Owing to its compatibility with automation and scalability, the diaphragm forming process is increasingly adopted in high-rate manufacturing sectors such as aerospace and automotive, where geometric complexity and production efficiency are critical requirements. Based on the number of diaphragms involved in each manufacture,

the diaphragm forming process can be further classified into single diaphragm forming (SDF) and double diaphragm forming (DDF). By slightly compromising processing stability, the SDF reduces the complexity of the manufacturing rig and material requirements compared to the DDF. Moreover, the SDF process allows for sequentially preforming operations, thereby enabling the manufacturing of thicker fabric structures [2].

Non-Crimp Fabric (NCF) is a class of dry fibre reinforcements used extensively in the manufacture of high-performance composite materials. Unlike traditional woven fabrics, in which yarns are interlaced, NCF is composed of multiple layers of unidirectional (UD) fibres that are stitched or bound together without any crimping, which achieves better mechanical performance in the final products [3]. NCF materials can be classified in various ways, allowing for more precise descriptions based on the orientation of the UD layers, the number of plies, or the style of interlayer connection.

Numerous experimental setups have been designed and fabricated to investigate the processing mechanisms of preforming and to optimise both the procedure and product quality. Viisainen et al. [4] explained the mechanism of wrinkle generation through the draping experiments with the aid of digital image correlation (DIC) technology. Lawrence et al. [5] explored the contact situation of fabric samples under high compaction force, as well as the effect of the variability of vacuum pressure with the micro-CT devices. Yu et al. [6] discussed the effect of inter-ply sliding during multi-ply DDF under both lubricated and unlubricated conditions. Meanwhile, the finite element (FE) method has been widely applied to simulate the preforming process from both meso-level and macro-level [7-9].

This study proposes a novel design for an SDF experimental rig, upon which a new experimental methodology is developed. The method exploits the fluidity of grease on the fabric surface to monitor interply sliding between the fabric sample during the SDF process by measuring the deformation of pre-applied grease marks. A selection of experimental results derived from the proposed rig and methodology is also presented to demonstrate the applicability and effectiveness of the approach.

2 SINGLE DIAPHRAGM FORMING EXPERIMENT RIG

The SDF process, as one form of diaphragm forming, offers methodological advantages such as a simpler structure and more convenient operation compared with the DDF process. Though with higher variability, the SDF experiments can comprehensively represent the behaviour of the fabric and diaphragm under vacuum force in the DDF process. Therefore, a lab-level SDF rig has been designed and assembled to achieve rapid experiment methodology validation and simulation model validation at a lower cost.

The SDF experiment rig is designed for dry fabric preforming only, without the involvement of resin injection and heating systems. The schematic of the SDF experiment process is shown in Figure 1. By generating a vacuum between the diaphragm and rig base, the flat fabric plies are formed into 3D structures by vacuum pressure. The edge of the diaphragm is sealed against the edge of the rig base to form an enclosed chamber, after which air is evacuated from the system.

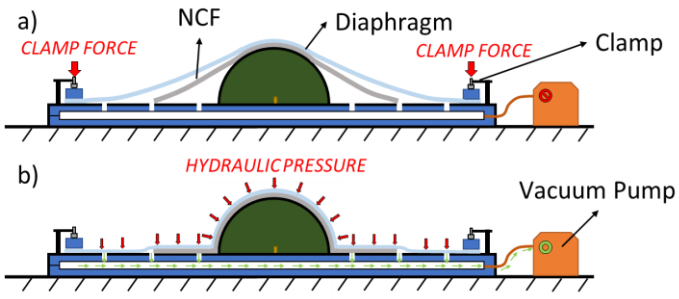

Figure 1: The scheme for the SDF process: a) Material preparation and diaphragm boundary clamping, and b) Vacuum forming

2.1 Materials

The target material in the SDF process is a biaxial ±45° NCF fabric with pillar stitch manufactured by Hexcel under the name 'HiMax™ CGL4790 - FCIM359 NCF'. The mechanical property of this material has been previously characterised through a standard picture frame test, while a shell-membrane element has been created and validated for the simulation of the NCF with the FE method [10]. The tribological properties of the NCF have been measured using the lap shear friction test developed by Lawrence et al. [5].

The StretchLon® HT-350, a high-elongation vacuum film with an elongation at break of 550% and a temperature resistance of up to 162 °C, was selected as the diaphragm material for the experiments. This vacuum film shows good ductility during stretching, which allows more deformation and maintains good vacuum integrity during the SDF process [11]. BR180 is a 140 gsm non-woven polyester felt fabric used as a breather layer during the vacuum forming of fabric laminates, which avoids the formation of bubbles and ensures the uniform application of vacuum force. Other materials and components applied in the diaphragm forming rig and experiment design are listed in Table 1.

Description	Manufacturer	Type	Reusability
Biaxial NCF	Hexcel®	HiMax™ FCIM359	No
Vacuum Diaphragm	Tygavac Ltd UK	StretchLon® HT-350	No
Lithium Grease	MG Chemicals	No. 8461 Lithium Grease	No
Breather	AeroFilm®	BR180 Breather Cloth	Yes
Vacuum Pump	DVP Vacuum Tech	VP-EC4-UK	Yes
Vacuum Gauge	Vac Checker®	VE-VCG	Yes

Table 1: The components and materials used in the single diaphragm forming rig and experiment.

2.2 The Design of the Single Diaphragm Rig

The rig contains four main components: base, blank holder, detachable tool, and vacuum system with pressure gauge, as shown in Figure 2 a). The vacuum port is located on the side of the rig base and is connected to the pressure gauge through tubes. The digital vacuum gauge connecting the rig inlet and the gauge delivers reliable pressure measurements in the range of 1100 to 0.00 mbar and with a resolution of 0.01 mbar. The base is fixed to the experiment table with screws to avoid instability during experiments. The base is assembled with three parts: a top board with ventholes, a middle frame and a bottom board. The vacuum port is placed on the middle frame, while these components are assembled through screws near the edge and sealed with the vacuum tape and the multi-purpose sealant.

To ensure a uniform vacuum pressure, 72 ventholes with a 10 mm diameter are evenly drilled on the top baseboard except for the tool region, as shown in Figure 2 b). Breathers are laid between the tool edge and the ventholes to avoid air cavities near the junction between the tool and the rig base. The sealing strips are added between the bed and the blank holder. Under the clamp force from the blank holder, the strips deform elastically to secure good sealing during the preforming.

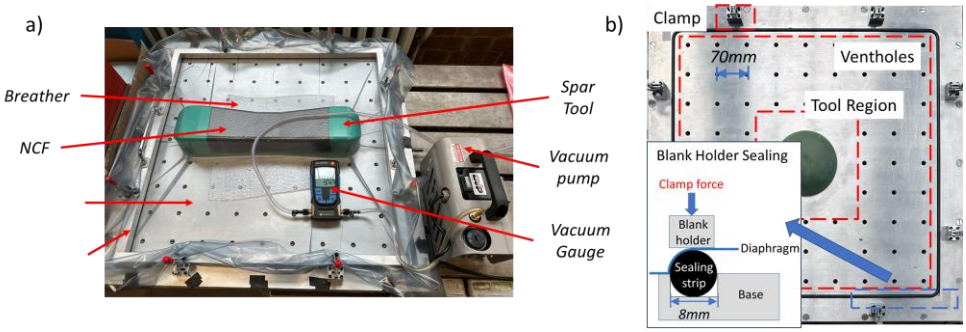

Figure 2: a) Assembly of SDF rig system with fabric samples, b) the structure of the top base board

3 THE INTER-PLY SLIDING TRACKING METHODOLOGY

In previous research, various parameters and methodologies have been introduced to monitor and understand the behaviour of fabrics during the preforming process as detailed in the introduction. One area of research focuses on dynamically tracking the visible surfaces with videos or photos to explain the correlation between deformation and defect. Other research topic concentrates on statistically analysing the preforming results with various methods. For example, digital image correlation and micro-CT scanning are widely used for dynamic and static research, respectively. However, both processes are not sufficient to dynamically monitor the fabric behaviour in the multi-ply forming. Therefore, a novel methodology is proposed for the indirect measurement of interply sliding between fabrics by tracking the changes in marker points, which helps build a bridge between the manufacturing setup and the preform quality.

3.1 Methodology Introduction

In industrial production, grease is used to label the surface of carbon fabrics, as it provides stable and long-lasting markings with good clarity. For a period following the painting process, the grease retains a certain degree of fluidity and viscosity. Consequently, when relative motion occurs between the two contacting surfaces, the shape of the grease undergoes deformation. This inspired an experimental methodology to track the interply sliding through the deformation of painted marks between the fabrics.

The method is presented in Figure 3. Before the experiments, the grease dots are placed on the fabric sheet as marks, which are sandwiched between the interested fabric interface in the experiment. During the diaphragm forming process, the fabric plies have relative motion, while the grease dots are flattened by the compaction of fabric sheets, accompanied by the sliding-induced shape elongation. By evaluating the final shape of the grease marks, the sliding distance on the marked position is indirectly measured.

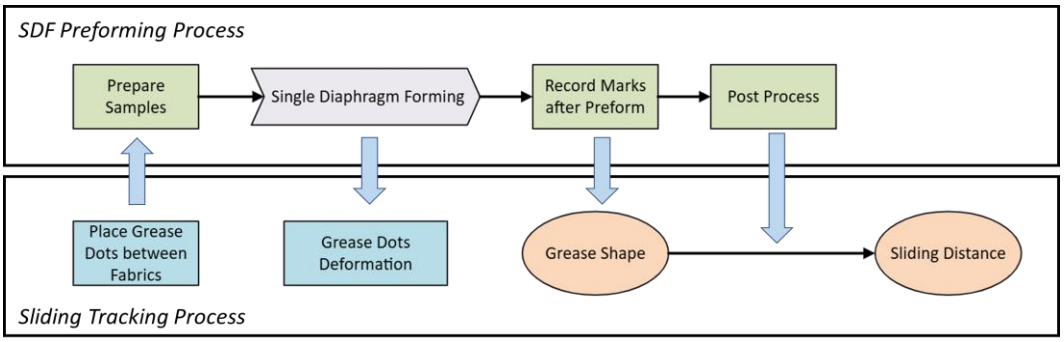

Figure 3: Flowchart of the method for measuring relative inter-ply sliding based on grease marks.

To ensure the consistency of the grease dots applied during the experiments, a PVC board with precision-drilled holes was employed as a mould for dot placement. The thickness of the mould board is 1.6 mm, while the diameter of the holes is 4 mm. The painting process is shown in Figure 4. After filling the mould hole with grease, a flat blade is used to remove the excess grease on the top of the mould. Vertically lifting the mould, the grease dot is placed on the fabric surface with the shape of a 1.6 mm high cylinder because of the viscosity and surface tension.

3.2 Method Consistency

To validate the feasibility of the proposed method, two well-designed experiments were conducted. The first assessed the stability of the grease quantity of the grease dots, while the second evaluated the morphological stability of the grease dots under pure compaction.

The weight consistency test focuses on verifying whether the quantity of grease within the dots remains uniform, assuming their external shapes are geometrically ideal. The experimental result is

shown in Figure 5. The difference in the amount of grease within each dot is mainly induced by operational errors in the experimental procedures. Therefore, the external shape of the grease dots is first evaluated and classified into two groups: dots with an ideal external shape (ideal dot) and dots with defects (defect dot). The ideal dots have an ideal cylindrical shape, while the dots with obvious grease loss or other problems (asymmetric, non-circular, etc.) are marked as defective dots.

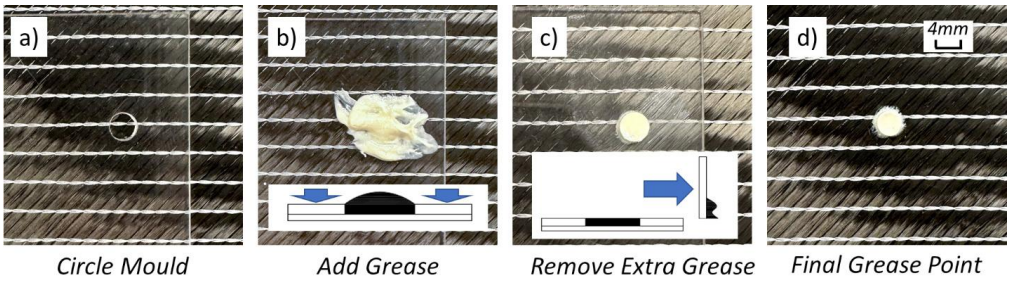

Figure 4: Fabric grease painting process with 4 mm plastic mould

The ideal dots are directly used in the experiments, while the defective dots are removed and repainted. By dot classification and replacement/discarding of defective dots, the grease weight consistency is improved. As shown in Figure 5, the coefficient of variation of the dot weight (ideal dots only) is reduced to 5.6%, which is acceptable for the following diaphragm forming experiments.

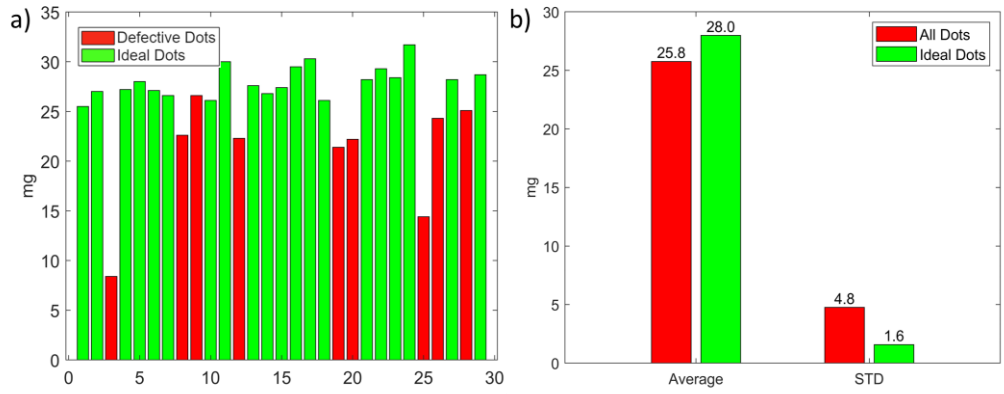

Figure 5: Grease weight consistency experiment result: a) Weight of every grease point, and b) statistical data for grease weight

The deformation of the grease shape is influenced not only by the original placement of the grease dots but also by the fabric interface properties, such as fabric direction and interface compaction force. To quantify these factors, an experiment for the grease marks with pure compaction is designed to quantify the mark shape with different fabric directions. In the experiments, the prepared fabric stacks have been sealed into a vacuum bag, while the bag is vacuumed to imitate the vacuum compaction in the diaphragm forming.

The mark shape after compaction is tracked through images, while the ideal shape of a grease dot under pure compaction was derived based on the averaged geometry of these shapes. As shown in Figure 6, the shape of the grease dots is influenced by the relative orientation of the fibre tows. In the 90° case, the grease tends to form a circular mark, while in the 45° and 90° cases, the grease shape is elongated towards the direction of the bisector of the acute angle between the tows. Among all fibre setups, the shape of the grease mark after pure compaction exhibited good stability across repeated experiments. This ensures that any subsequent changes in the grease mark morphology can be attributed solely to the sliding motion between fabric plies during the experiment, rather than to the inherent variability of the grease itself.

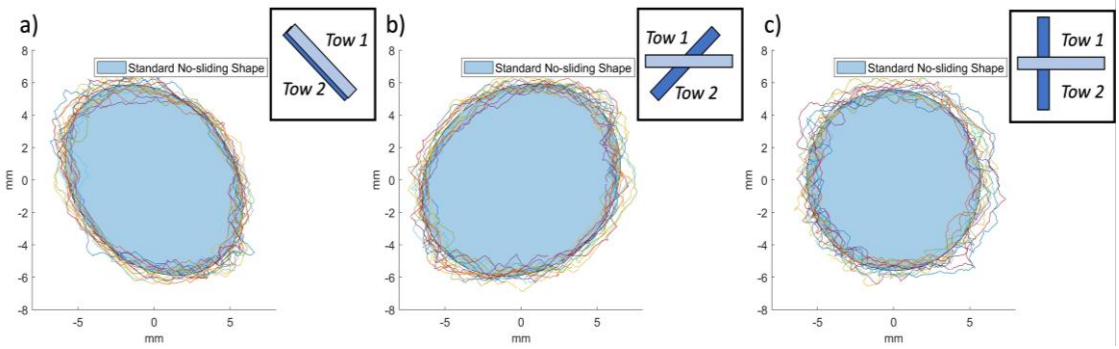

Figure 6: Standard no-sliding grease shape with Ø 4 mm mould under different tow directions

3.3 The Post-Processing of Experiment Results

In the post-processing, the shape of the grease marks is recorded through photography, as shown in Figure 7 a). The red points in the grease marks are the pre-drawn reference points to locate the original position of the mark. The reference points are painted with solvent-based markers, which dry out rapidly before the grease painting. The post-process involves mark boundary tracking and the sliding calculation. Subsequently, the boundary and initial mark centre are selected from the photos, as shown in Figure 7 b).

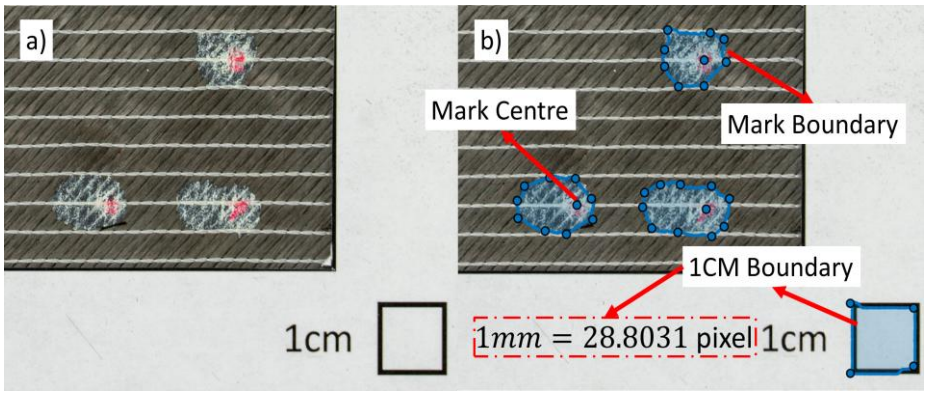

Figure 7: The image record and boundary track of the grease marks after diaphragm forming experiments.

The mark shape after sliding is similar to the trajectory of an elliptical dot translating on the plane, as shown in Figure 8 a). The selected original centre of the grease dot is marked as point B on the grease. The chord AC is the longest line segment on the figure that is intercepted by the line passing through point B. The length L1 is the sum of the grease elongation length and the radius of the no-slip mark shape in the sliding direction, while the length L2 is the radius of the no-slip mark shape in the opposite direction of sliding. As the no-slip shape is centre symmetry, the grease elongation length can be calculated as the difference between L1 and L2.

While the actual sliding distance and the measured elongation length of the grease were generally not equivalent across most experiments, a linear relationship was consistently observed between them. Based on a series of overlap tests performed at 1 bar pressure [5], the linear correlation between the two parameters is described by the following equation, as shown in Figure 8 b):

$$\textit{Grease Elongation Length} = 0.85 \times \textit{Sliding Distance} \tag{1}$$

Based on the aforementioned procedure and equation, the relative interply sliding at the grease dot position during the preforming can be derived.

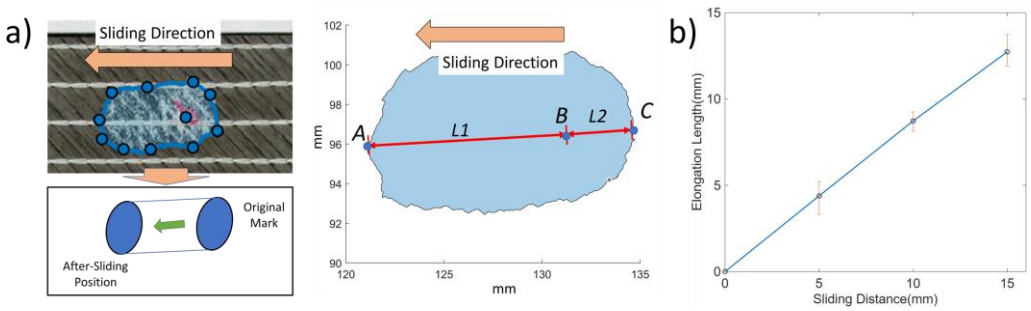

Figure 8: a) Sliding calculation for tracked grease mark shape in the post-process. b) Correlation between grease elongation length and sliding distance

4 RESULTS AND DISCUSSION

To validate the effectiveness of the aforementioned method and to enhance understanding of the SDF process, a series of experiments were conducted using the previously described SDF rig, employing the grease technique to track the sliding of specific positions. The experimental results were compared with those from finite element (FE) simulations [11], enabling an analysis of the limitations inherent in the current experimental methods and simulation models.

Four different tool geometries are included in the experiments: a hemisphere tool, a double dome tool and two spar tools with different ramp angles [4]. The hemisphere tool and the double dome tool, known as the benchmark geometries, are widely used in the preforming research on woven and NCF fabrics. In addition to wrinkling, which is the primary focus of this study, bridging is another common defect encountered during preforming. Although the impact of bridging on the manufacturing process is less severe and it can typically be eliminated in subsequent processing steps, bridging still affects the fabric behaviour during processing and therefore needs to be taken into consideration. Among the experiments conducted with the four tools, bridging is expected to occur in the benchmark tools, whereas it does not appear in the experiments using the spar tools.

4.1 The Experiment Result with Different Tools

In the experiment with spar tools, 15 grease dots were applied at designated points, maintaining a minimum spacing of 2 cm between each to prevent mutual interference. A total of 12 dots were placed at the corners of the sample, two dots were positioned along the edges, and one dot was placed in the centre as a control, in Figure 9 a). The formed fabric samples are shown in Figure 9 b) and c).

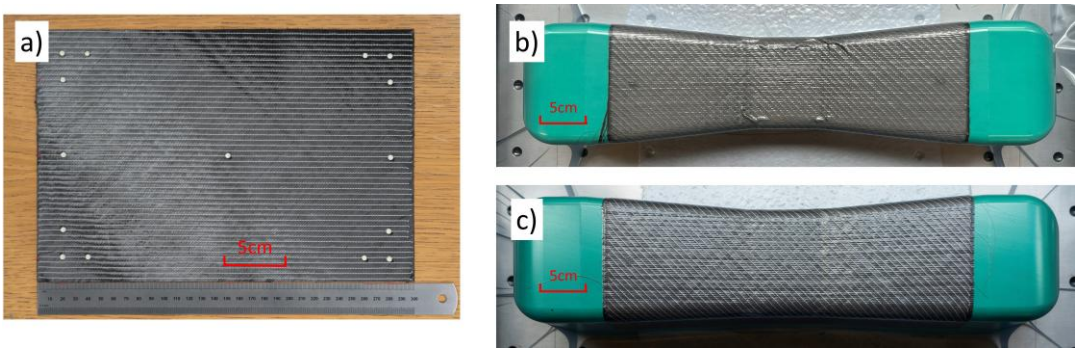

Figure 9: The SDF experiments with the spar tools: a) the prepared fabric sample with grease dots, b) the formed fabric sample with the high ramp spar tool and c) the formed fabric sample with the low ramp spar tool.

The processed sliding distances from the grease method are compared with the FE simulation result, as shown in Figure 10. The comparison shown in the figure indicates that, in both the high ramp spar and low ramp spar experiments, the sliding directions of the tracked data points closely

correspond with the predicted directions. However, the predicted sliding distances are consistently larger than the distances observed in the experiments.

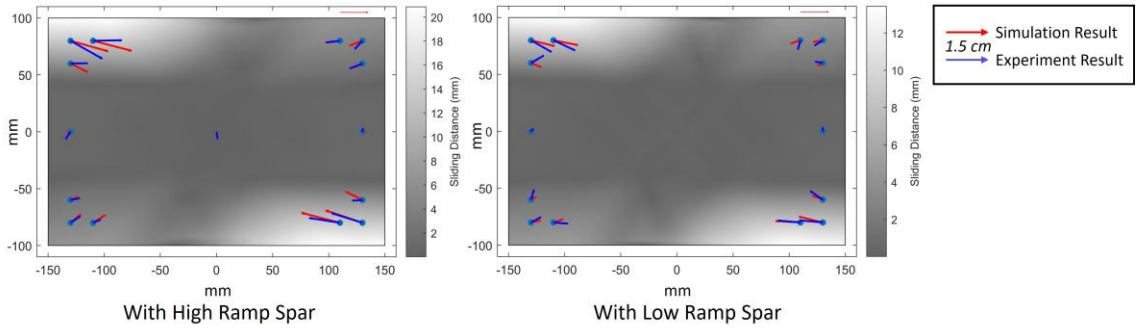

Figure 10: The sliding measurement result for the SDF experiments with the spar tools, where the sliding vectors are marked by arrows on the grease mark positions.

In the experiments with the benchmark tools, 17 grease dots were applied at designated points, maintaining a minimum spacing of 3 cm between each to prevent mutual interference. A total of 12 dots were placed at the corners of the sample, four dots were positioned along the edges, and one dot was placed in the centre as a control, as shown in Figure 11 a). The formed fabric samples are shown in Figure 11 b) and c).

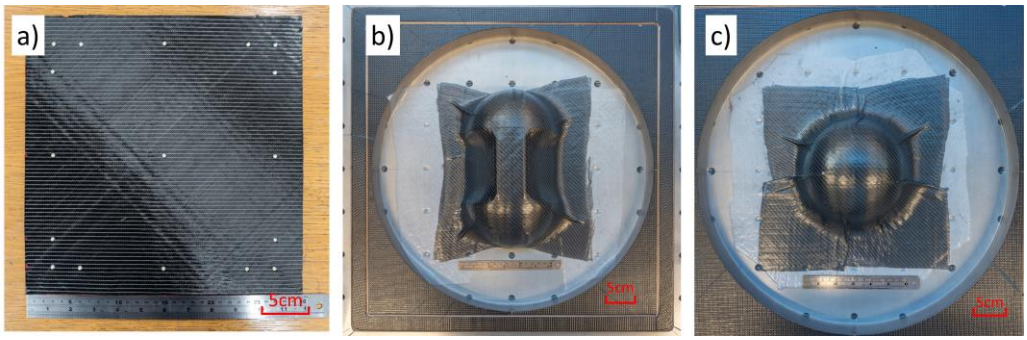

Figure 11: The SDF experiments with the benchmark tools: a) the prepared fabric sample with grease dots, b) the formed fabric sample with the double dome tool, and c) the formed fabric sample with the hemisphere tool.

The processed sliding distances are compared with the FE simulation result, as shown in Figure 12 respectively. In the figure, the sliding vectors from the grease dots in the low sliding regions show certain differences from the simulation results in both direction and magnitude.

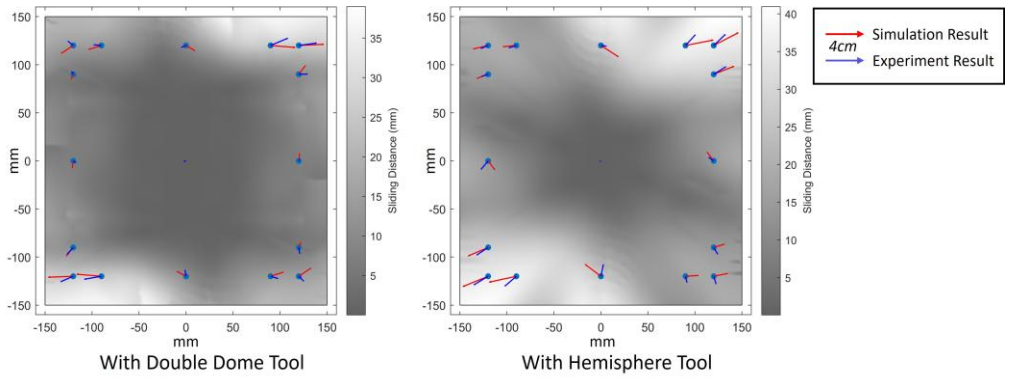

Figure 12: The sliding measurement result for the SDF experiments with the benchmark tools, where the sliding vectors are marked by arrows on the grease mark positions

In the high sliding regions (top-right and bottom-left corners), the experimental results show a good agreement with the prediction from the simulation results in the direction, while the sliding distances from the simulation are longer than those measured in the experiment, similar to the situation in the spar experiments. Overall, in the experiments conducted with the benchmark tool, the discrepancy between the experimental and simulation results was greater in both direction and magnitude.

4.2 Discussions

The application of the grease mark method in SDF experiments proved to be an effective means of tracking the sliding behaviour in specific regions. Adding additional grease dots has a negligible impact on the preforming result. A comparison between the experimental and simulation results reveals a good level of agreement in the prediction of relative sliding, particularly in regions where the sliding distance exceeds 8 mm. The current simulation model tends to overestimate the sliding distance during the SDF process, while the experimental method exhibits considerable uncertainty in capturing small-scale sliding displacements.

The error associated with the experimental methodology primarily arises from three sources. Firstly, the accuracy of sliding measurement relies on the intimate contact between the upper and lower surfaces. However, the relative opening between the fabric plies exists in the diaphragm forming process, especially for the SDF experiment, because of the lack of compaction. Secondly, the sliding trajectory is assumed to be linear, while tow twisting is ignored to reduce the complexity of the grease shape. This assumption may introduce a certain degree of error in the calculation of sliding distance, particularly in regions affected by wrinkling, where the fabric undergoes higher levels of in-plane shear. Finally, as indicated in the pure compaction experiments, even under identical experimental conditions, the grease shape exhibited in repeated trials is not entirely consistent. This is attributed to the uneven surface of the NCF material, where the irregularities caused by stitching and fabric tows affect the flow of the grease. Although this influence is not severe, it nevertheless leads to instability in the results when the sliding distances are small.

Although the above analysis highlights certain limitations of the current experimental method, it remains highly effective in tracking large interply sliding. The simulation model employed at this stage has not yet undergone specific validation or optimisation concerning sliding behaviour. As such, the discrepancies currently observed between experimental and simulation results are primarily attributed to shortcomings in the simulation model. In future work, the experimental results obtained in this study will be used to refine the simulation model to achieve more accurate predictive capability.

5 CONCLUSIONS

This paper presents the development of an experimental system, together with a methodology for tracking inter-ply sliding during forming. The experimental rig incorporates an interchangeable tooling design, enabling flexible investigation of various tool geometries and their influence on fabric deformation. Building upon the established diaphragm forming experimental procedure, a method using grease marks was developed to track interply sliding at designated locations. When the initial weight and geometry of the grease marks are controlled, identical marks exhibit comparable elongation lengths under equivalent sliding distances, with only minor variations. By calibrating the relationship between grease elongation and sliding distance through an overlap test, both the magnitude and direction of inter-ply sliding can be calculated from the deformed shape of the grease marks.

A series of SDF experiments with different tools have been conducted using the sliding tracking method, while the results were compared with finite element simulation results. Based on the comparison results, an analysis was conducted regarding the applicability, effectiveness, and associated errors of the current method. The method has been validated to be effective for tracking the long sliding distance of more than 5 mm. The sliding tracking methodology has shown its potential in simulation model validation and modification. With certain optimisation, this method can be extended

to DDF experiments and even further applied to other studies involving relative interply motion of fabric materials.

ACKNOWLEDGEMENTS

This research is funded by the Engineering and Physical Sciences Research Council, via an EPSRC Doctoral Training Partnership (DTP) studentship and grant number EP/P006701/1, as part of the EPSRC Future Composites Manufacturing Research Hub. The trip to present at ICCM 24 is supported by the Jost Foundation via the Peter Jost Travel Fund.

REFERENCES

[1] J. Krebs, K. Friedrich, and D. Bhattacharyya, "A direct comparison of matched-die versus diaphragm forming," (in English), *Composites Part A: Applied Science and Manufacturing,* vol. 29, no. 1, pp. 183-188, 1998/01/01/ 1998, doi: https://doi.org/10.1016/S1359-835X(97)82706-6.

[2] A. Schnabel and T. Gries, "1 - Production of non-crimp fabrics for composites," in *Non-Crimp Fabric Composites*, S. V. Lomov Ed.: Woodhead Publishing, 2011, pp. 3-41.

[3] S. Lomov, "Introduction," in *Non-Crimp Fabric Composites*, S. V. Lomov Ed.: Woodhead Publishing, 2011, pp. xvi-xix.

[4] J. V. Viisainen, A. Hosseini, and M. P. F. Sutcliffe, "Experimental investigation, using 3D digital image correlation, into the effect of component geometry on the wrinkling behaviour and the wrinkling mechanisms of a biaxial NCF during preforming," *Composites Part A: Applied Science and Manufacturing,* vol. 142, p. 106248, 2021/03/01/ 2021, doi: https://doi.org/10.1016/j.compositesa.2020.106248.

[5] G. D. Lawrence, S. Chen, N. A. Warrior, and L. T. Harper, "The influence of inter-ply friction during double-diaphragm forming of biaxial NCFs," *Composites Part A: Applied Science and Manufacturing,* vol. 167, 2023, doi: 10.1016/j.compositesa.2023.107426.

[6] F. Yu, S. Chen, L. T. Harper, and N. A. Warrior, "Investigation into the effects of inter-ply sliding during double diaphragm forming for multi-layered biaxial non-crimp fabrics," *Composites Part A: Applied Science and Manufacturing,* vol. 150, p. 106611, 2021/11/01/ 2021, doi: https://doi.org/10.1016/j.compositesa.2021.106611.

[7] F. Yu, S. Chen, J. V. Viisainen, M. P. F. Sutcliffe, L. T. Harper, and N. A. Warrior, "A macroscale finite element approach for simulating the bending behaviour of biaxial fabrics," *Composites Science and Technology,* vol. 191, p. 108078, 2020/05/03/ 2020, doi: https://doi.org/10.1016/j.compscitech.2020.108078.

[8] J. P. H. Belnoue and S. R. Hallett, "A rapid multi-scale design tool for the prediction of wrinkle defect formation in composite components," (in English), *Mater Design,* vol. 187, p. 108388, 2020/02/01/ 2020, doi: https://doi.org/10.1016/j.matdes.2019.108388.

[9] W. Huang *et al.*, "A Fourier based reduced model for wrinkling analysis of circular membranes," (in English), *Comput Method Appl M,* vol. 345, pp. 1114-1137, 2019/03/01/ 2019, doi: https://doi.org/10.1016/j.cma.2018.09.012.

[10] F. Yu, S. Chen, L. T. Harper, and N. A. Warrior, "Simulating the effect of fabric bending stiffness on the wrinkling behaviour of biaxial fabrics during preforming," *Composites Part A: Applied Science and Manufacturing,* vol. 143, p. 106308, 2021/04/01/ 2021, doi: https://doi.org/10.1016/j.compositesa.2021.106308.

[11] F. Yu, "The prediction of wrinkle formation in non-crimp fabrics during double diaphragm forming," University of Nottingham, 2022.

THERMOFORMING OF LOAD-PATH-OPTIMISED, RECYCLED THERMOPLASTIC COMPOSITES: DEVELOPMENT OF AN AI-SUPPORTED EMITTER TECHNOLOGY AND PROCESS EVALUATION

Matthias Froning[1], Maximilian Backenstos[2], Lisa Richter[2], Mesut Cetin[1,3], Thomas Gries[4]

[1]Institut für Textiltechnik Augsburg gGmbH,
Am Technologiezentrum 5, DEU-86159 Augsburg, Germany
Email: mf@ita-augsburg.de, mc@ita-augsburg.de, web page: www.ita-augsburg.com

[2]DatenBerg GmbH, Haid-und-Neu-Straße 7, DEU-76131 Karlsruhe, Germany
Email: maximilian.backenstos@datenberg.eu, lisa.richter@datenberg.eu,
web page: www. Datenberg.eu

[3]Technische Hochschule Augsburg, An der Hochschule 1, DEU-86161 Augsburg, Germany
Email: mesut.cetin@tha.de, web page: www.tha.de

[4]Institut für Textiltechnik of RWTH Aachen University,
Otto-Blumenthal-Straße 1, DEU-52074 Aachen, Germany
Email: thomas.gries@ita.rwth-aachen.de, web page: www.ita.rwth-aachen.de

Keywords: Automation, Heat treatment, Recycling, Tape, Thermoplastic resin

ABSTRACT

The hybrid moulding process is a combination of thermoforming and injection moulding. It enables the fully automated production of highly integrated, ready-to-install lightweight structural components based on organo-sheet semi-finished products and therefore fulfils the prerequisites for a high-volume, economical production process for lightweight components.

The paper describes the development of an emitter technology that processes modern, load-path-compatible tailored organo-sheets in which the mass utilisation in the component has been optimised. Tailored organo-sheets in particular offer the possibility of CO_2 savings through resource efficiency and substitution. By developing a high-resolution radiator field, the tailored organo-sheets can be heated homogeneously with a discontinuous wall thickness. The high-resolution radiator field is controlled via an AI-supported control system. This simplifies product changeovers and assembly work can be reduced thanks to the universal emitter field. The explanatory AI also helps to build up an understanding of the process. This increases the efficiency and flexibility of the process.

As part of a process evaluation, the influence of the developed emitter technology on the quality of the heating process, cycle times and energy efficiency will be analysed in detail. Specific key figures such as the temperature homogeneity within the organo-sheets, the heating rate and the thermal efficiency are recorded and analysed. The evaluation shows how the combination of optimised emitter technology and AI control contributes to the development of a robust, energy-efficient and high-quality thermoforming process.

1 INTRODUCTION

In the following paper, the CRISP-DM method is used as a structured framework to systematically accompany the development and evaluation of an AI-supported control system for the thermoforming process. The method is divided into six successive phases (figure 1). It begins with business understanding, in which the overarching objectives are analyzed from an application-related perspective and translated into a data-based problem definition. This is followed by Data Understanding, in which available data is collected and examined in terms of quality, structure and information content. In the Data Preparation phase, the raw data is converted into a format suitable for

modeling through selection, transformation and cleansing. This is followed by the Modeling phase, in which suitable algorithms are selected, parameterized and applied to the prepared data. This is followed by the Evaluation phase, in which the quality of the model is checked with regard to the original objectives and the procedure is critically reflected upon. Finally, the Deployment phase involves transferring the developed solution to the practical application context, for example by integrating it into existing systems or by creating usable results for the end user. [1]

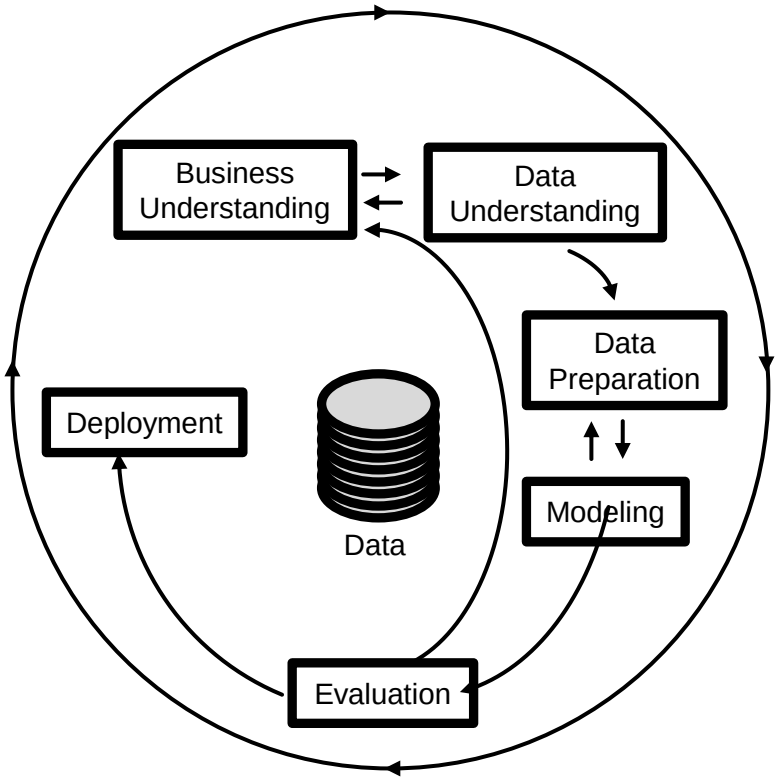

Figure 1: The six phases of the CRISP-DM method [1]

2 BUSINESS UNDERSTANDING

For ecological and economic reasons, the reduction of CO_2 emissions is a key objective in industrial production. In the context of the hybrid molding process (Figure 2), tailored organo sheets offer a promising approach to support this goal through resource-efficient lightweight construction. These are fiber-reinforced thermoplastics with specifically varied wall thicknesses or locally differentiated fiber reinforcement. This material optimization enables needs-based reinforcement along the load paths while reducing the amount of material used and thus the carbon footprint. These tailor-made semi-finished products are processed using the hybrid molding process, which combines thermoforming and injection molding and enables the highly automated production of functionally integrated lightweight components.

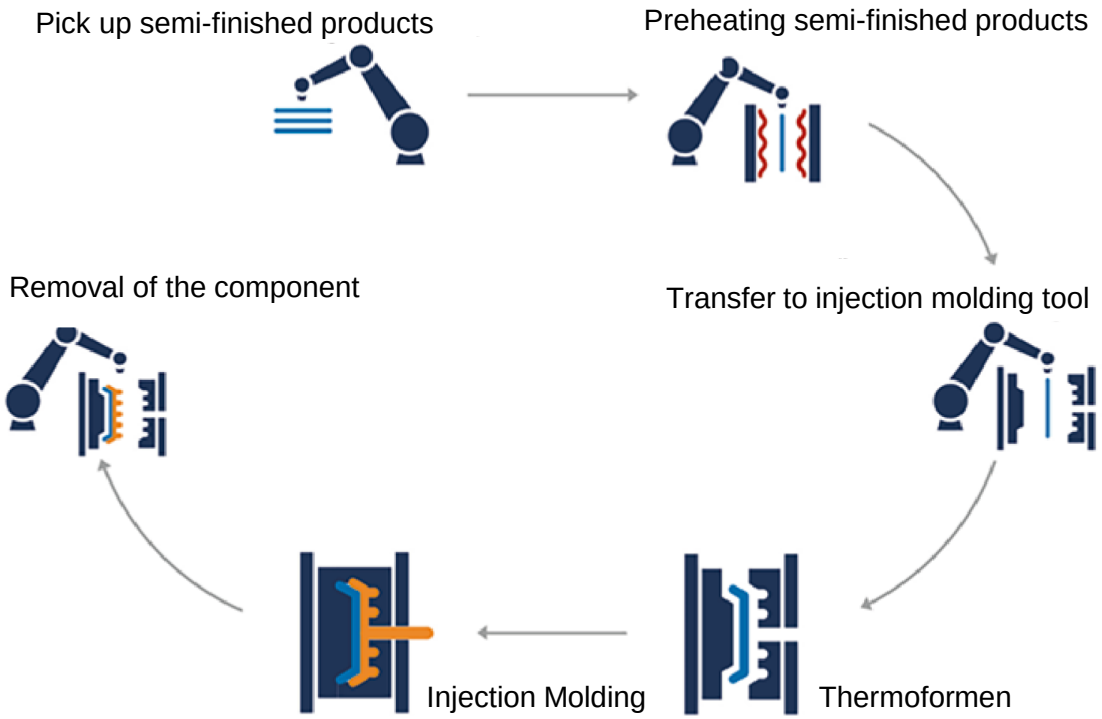

Figure 2: Process steps of the hybrid molding process [2]

However, the processing of such complex semi-finished products requires precise and locally adapted heating. The current state of the art uses large-area infrared emitters, which cannot ensure homogeneous temperature distribution in tailored organo sheets due to their low spatial resolution. This leads to local overheating or underheating and thus to quality losses in the subsequent thermoforming process. In order to make the quality of the heating process visible, a thermal imaging camera is used to analyze and evaluate the temperature distribution on the surface of the semi-finished products.

The solution presented here is based on a high-resolution infrared radiator field consisting of a large number of compact spot heaters. The resulting heating field resolution exceeds conventional systems by a factor of 25 (Figure 3). Due to the large number of individual emitters, manual parameterization is not practicable. Therefore, an automated, AI-supported power distribution is being developed with the aim of ensuring uniform temperature distribution in the semi-finished product. This uniform heating is the prerequisite for a reproducible and tool-friendly thermoforming process.

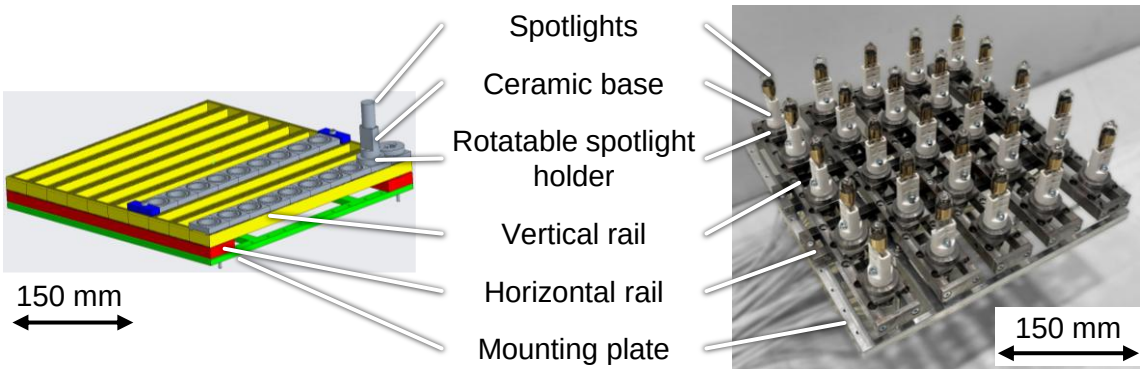

Figure 3: The high-resolution radiator field as a CAD model (left) and real image (right)

The main users of the technology are machine operators who monitor the process. As this is a further development of existing system concepts, existing interfaces must be taken into account and simple integration into established control systems must be made possible.

3 DATA UNDERSTANDING

Various data sources, including both process and sensor data, were used to develop and validate the AI-supported heating concept. The central data basis is an infrared camera that provides thermal images of the tailored organo sheet in the form of CSV files (Figure 4). These images are taken immediately after passing through the radiator field, but before insertion into the forming tool. This positioning allows potential disturbance variables that occur during transportation from the furnace to the tool (e.g. convection influences or temperature fluctuations due to radiation) to be recorded and taken into account in the analysis.

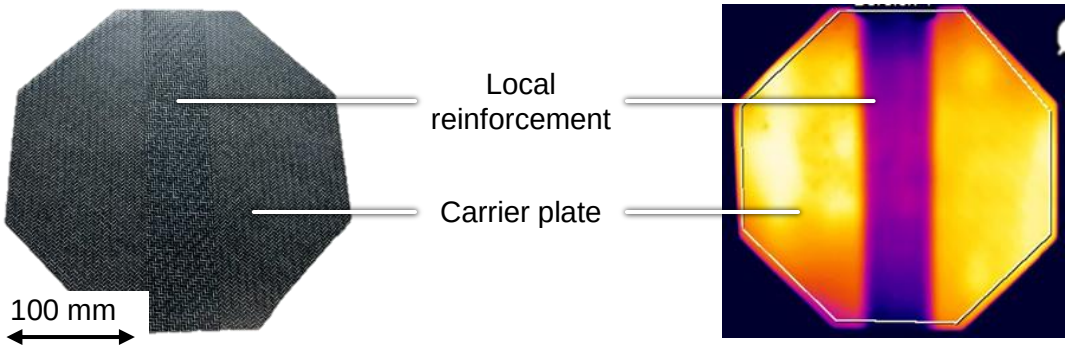

Figure 4: Tailored Organo Sheet as real image (left) and in IR image (right)

In addition to thermographic detection, non-contact temperature measurement is carried out during the heating process in the oven using a pyrometer, which is integrated into a classic control system on a PLC (Figure 5). The individual emitters are controlled via pulse width modulation, with the relative duty cycle within a network phase serving as the control variable. The control system accesses a material-specific database that contains setpoints, maximum temperatures and upper and lower specification limits for the respective organic sheet material.

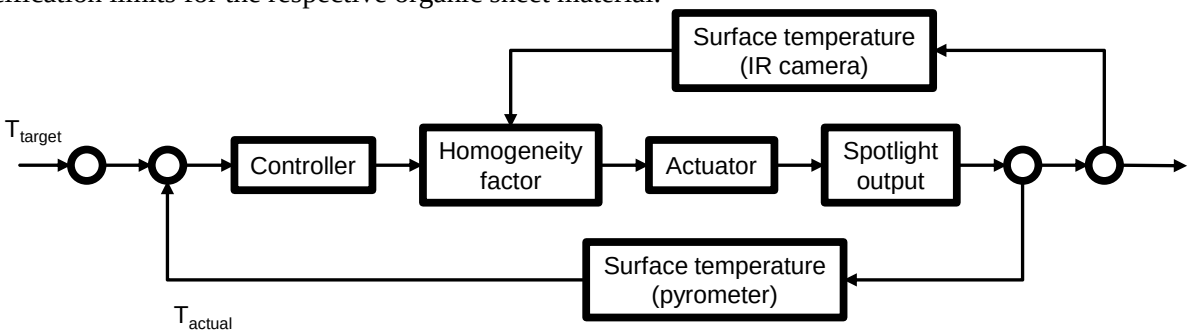

Figure 5: Controller architecture

Based on the evaluation of the thermal image data, a maximum switch-on time for the following heating cycle is specified for each spot heater via an OPC UA interface. This indirect control leads to a system-related latency between temperature detection and power adjustment, which must be taken into account when allocating data over time.

The data is collected using an adapted test setup based on a conventional IR oven, which has been expanded to include the newly developed high-resolution radiation field and thermographic measurement technology. To reduce material consumption and increase reproducibility, the heating process is carried out several times on one and the same tailored organo sheet (PA matrix with glass fiber reinforcement). The target temperature is limited to 100 °C in order to ensure thermal stress below the melting point. A defined cooling time of ten minutes is maintained between the heating cycles to ensure identical initial conditions.

Another technical aspect concerns the power supply: Due to high switch-on currents with cold infrared radiators, there is a risk of overloading the fuses. For this reason, a cascaded switch-on procedure was implemented as part of the project, which staggers the switch-on times of individual

emitters and thus enables stable operation.

The analysis of the data obtained shows a high degree of variance in the temperature distribution, particularly in areas with variable wall thickness. This heterogeneity forms the starting point for the subsequent development of a model for targeted radiator power distribution.

4 DATA PREPARATION

The central data source for modeling is the thermal image of the heated organic sheet. This is available in CSV format for each heating cycle and contains the temperature values as a pixel matrix. A threshold value method is used to separate the relevant image areas (organosheet) from the background: All pixels with temperatures above a defined threshold value are assigned to the organosheet, while pixels below this value are classified as background and excluded from further analysis. This procedure makes it possible to dispense with the product-dependent transfer of geometry information (e.g. CAD files or wall thickness curves), which simplifies system integration and increases generalizability.

To quantitatively evaluate the temperature distribution in the heated semi-finished product, the standard deviation of the temperature values within the detected component area is calculated for each image. This key figure serves as a direct measure of the homogeneity of the heating and at the same time forms the target value for the optimization model.

The data was collected as part of a systematically planned experimental setup in which the duty cycles of selected heaters were varied according to a design-of-experiment (DoE). This created a controlled variation of the heating power with the aim of investigating its influence on the resulting temperature distribution. Missing or incorrect data sets, for example due to software crashes of the IR camera, were replaced as far as possible by repeating the affected experiment. These measures made it possible to create a consistent and complete data basis for the subsequent modeling.

5 MODELING

The modeling phase comprises three consecutive steps, each of which maps specific aspects of the heating process and is linked together to enable precise prediction and optimization of the temperature distribution in the organic sheet.

In the first step, a regression-based model is set up that describes the relationship between individual radiators and their local temperature influence on the surface of the component (Figure 6). This model is furnace-specific and was determined on a reference organo sheet without local reinforcement structures. For each emitter, the extent to which its power contributes to the temperature increase in defined areas of the thermographic image is quantified. To ensure sufficient model accuracy, at least one test run is required for each emitter used. By spatially limiting the potential influence zones based on the results of this step, the test effort can be significantly reduced in the second step.

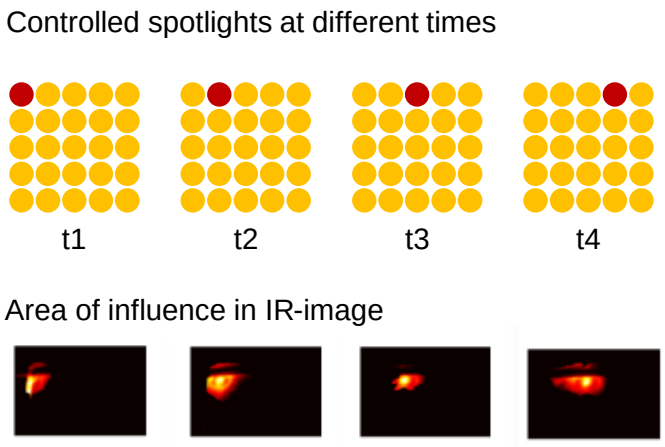

Figure 6: Correlation between emitter and IR image

The second step involves modeling the organic sheet itself. The aim is to map the thermal reaction

patterns of the semi-finished product as a function of geometry, wall thickness distribution and material behavior. Based on the radiator influence model learned in the first step, a simulation can be created that predicts a complete thermal image of the component from a given radiator switch-on scenario (Figure 7). This simulated thermography serves as the basis for subsequent optimization.

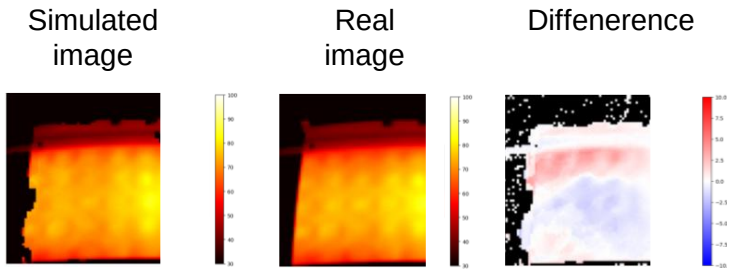

Figure 7: Comparison of simulated IR image and real recorded IR image based on the emitter parameters

In the third step, the radiator power distribution is optimized with the aim of achieving the most homogeneous temperature distribution possible across the component surface. The standard deviation of the temperature distribution within the detected organic sheet serves as the target value. A genetic algorithm is used for optimization, which strives for a global solution in the high-dimensional parameter space by iteratively varying the radiator switch-on times. The use of a simulation-based prediction model makes it possible to carry out this optimization process efficiently and in a material-friendly manner without having to carry out large-scale real test series.

This three-stage model structure allows both the physical properties of the system and data-based correlations to be taken into account. At the same time, it ensures that the final model combines high forecasting quality with realistic feasibility in process control.

6 EVALUATION

A pilot production was carried out to validate the developed model architecture. A cruiser skateboard was used as a demonstrator, which is provided with targeted local reinforcement in the area between the axles. This constructive measure enables a weight-saving design of the component and at the same time places increased demands on temperature homogeneity during the heating process. Different material systems were used to evaluate the generalizability: a laminate consisting of an organic sheet with a unidirectional tape made of hemp and polypropylene as well as another laminate based on glass fibre and polyamide. The geometry remained constant so that the influence of the material properties on the temperature behavior could be analyzed in isolation.

To validate the model, the simulated temperature image generated by the genetic algorithm was compared with real thermal images. Table 1 shows examples of the deviations between simulated and measured data based on the parameters mean value, standard deviation, minimum and maximum temperature. The differences are less than 1 K in all cases, with the mean temperature deviation being only 0.39 K. The standard deviation is particularly relevant as a target value for optimization: with a difference of only 0.83 K, there is a good match between simulation and real behavior.

Table 1: Comparison of characteristic values based on simulated and real IR images

	Average [°C]	Standard deviation [K]	Minimum [°C]	Maximum [°C]
Simulated image	70,42	4,95	50,64	78,13
Real image	70,03	5,78	50,10	79,00
Difference	0,39	0,83	0,54	0,87

An interactive dashboard was used in the pilot environment to make the model decisions comprehensible for the operating personnel and to increase practical suitability (Figure 8). This visualizes the resulting spotlight settings and enables the machine operator to understand and manually adjust the suggestions. As a result, the human operator retains the decision-making authority and a human-in-the-loop approach is implemented, which both creates trust in the AI application and increases process reliability.

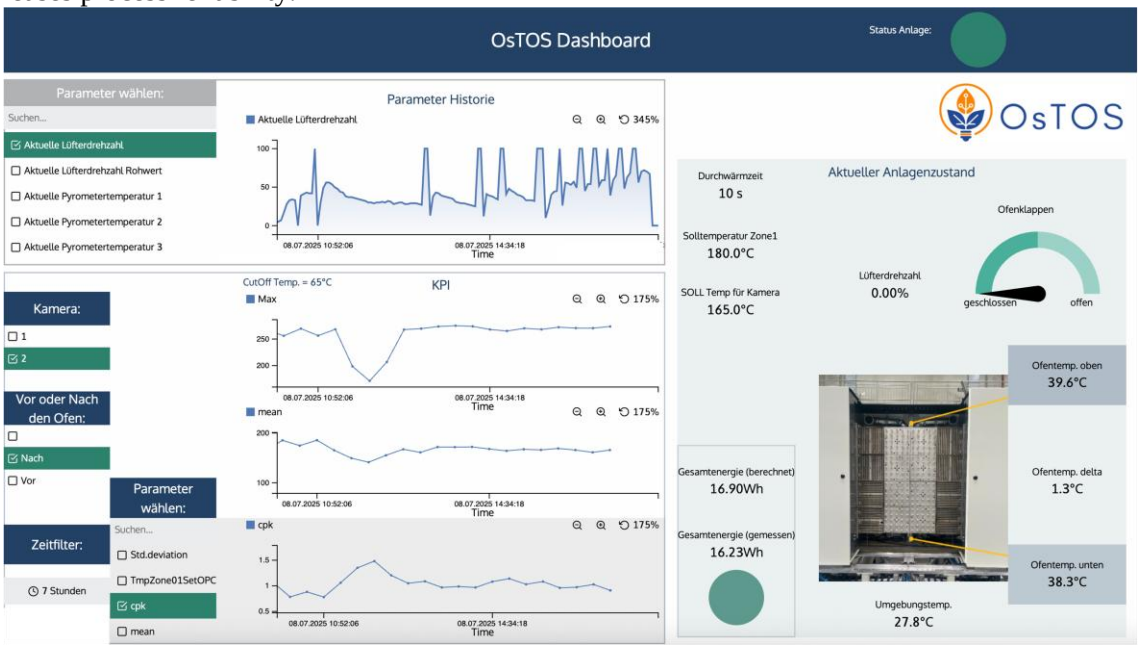

Figure 8: Dashboard for process visualization

The evaluation confirms that the model is able to predict the desired temperature distribution with high accuracy and thus fulfills the objective of developing a robust, AI-supported control concept for homogeneous heating of tailored organo sheets. In addition, the tested solution enables material-specific adaptation without the need for changes to the model structure. This ensures practical applicability in varying industrial scenarios.

7 DEPLOYMENT

The thermographic images are evaluated on an external industrial PC, which communicates with the machine control system via a standardized OPC UA interface. The AI model is executed cyclically in the production process: For each heating cycle, the relevant process data, in particular the individual duty cycles of the spot heaters, are buffered in the PLC and used for control in the following cycle. This buffered procedure allows the system to react continuously without jeopardizing the real-time capability of the control system.

The system architecture is designed in such a way that the operator can actively intervene in the process at any time. The dashboard already used in the evaluation context will continue to be used during operation. It is used to visually display the control suggestions generated by the model, to make them comprehensible and to modify them manually if necessary. In this way, humans remain an integral part of the control loop, in the sense of a human-in-the-loop approach that combines automation with operational responsibility and strengthens trust in AI-supported processes.

The deployment is currently in the final implementation phase. Initial integration tests have demonstrated the functionality of the communication and control chain as well as the practicality of the model-based control system. Specially designed demonstrator tailored organo sheets were manufactured in order to further test the generalizability and resilience of the system under realistic conditions. These consist of high-temperature resistant PAEK with carbon fiber reinforcement. (Figure

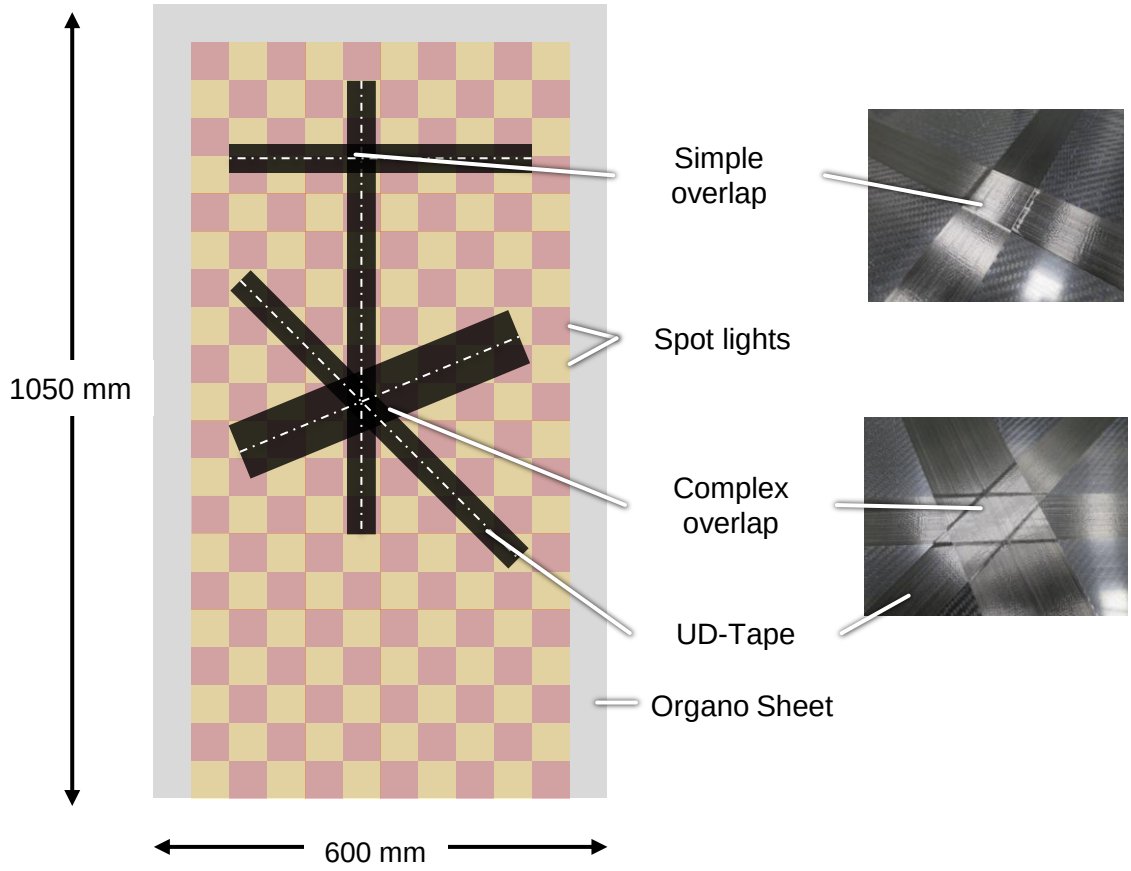

Figure 9: Tailored Organo Sheet Demonstrator with different UD-Tape reinforcements

ACKNOWLEDGEMENTS

The fabrication of the tailored organo sheet demonstrators was made possible through the collaboration with Coriolis Composites, particularly Mr. Yohan Bouyssière, and the Fraunhofer IGCV, with support from Mr. Florian Jennemann. Many thanks for their valuable support.

This work is part of the research project Oven system for Tailored-Organo-Sheets (OsTOS) and funded by the Federal Ministry for Economic Affairs and Climate Action (BMWK) as part of the Technology Transfer Programme for Lightweight Construction (TTP LB) under funding code 03LB3027. The project is supervised by Project Management Jülich (PTJ). The author is responsible for the content of this publication.

Supported by:
Federal Ministry for Economic Affairs and Climate Action
on the basis of a decision by the German Bundestag
Projektträger Jülich Forschungszentrum Jülich

REFERENCES

[1] P. Chapman, J. Clinton, R. Kerber, T. Khabaza, T. Reinartz, C. Shearer and R. Wirth, The CRISP-DM User Guide, CRISP-DM Consortium, 2000. Available: https://web.archive.org/web/20200912023158/https://www.the-modeling-agency.com/crisp-dm.pdf

[2] Cetin, M., Thienel, M. Großserienfertigung von thermoplastischen Türmodulträgern. Lightweight Des 12, 12–17 (2019). https://doi.org/10.1007/s35725-019-0056-0

ICCM24
AUGUST 4-8, 2025
BALTIMORE CONVENTION CENTER
BALTIMORE, MARYLAND, USA

No Technical Paper Submission for:

Takumi Morishima

ICCM24
AUGUST 4-8, 2025
BALTIMORE CONVENTION CENTER
BALTIMORE, MARYLAND, USA

No Technical Paper Submission for:

Ehshan ul-Haq

August 4-8, 2025
ICCM24, 24th International Conference on Composite Materials

Viscoelastic bi-scale modeling of process-induced deformation in non-crimp fabric composite

[a] **Sera Koo**, [a]Yamato Hoshikawa, [b]Yoshiaki Kawagoe,
[a]Kazuki Ryuzono, [a,c,d]Tomonaga Okabe

[a] Graduate school of Engineering, Tohoku University
[b] The University of Tokyo
[c] Department of Materials Science and Engineering, University of Washington, USA
[d] Polymer Matrix Hybrid Composite Materials Group, National Institute for Materials Science, Japan

Today’s topic

Process-induced residual stress in non-crimp fabric composites: experimental and numerical evaluation considering viscoelasticity (S. Koo and Y. Hoshikawa, et al., 2025, status: accepted)

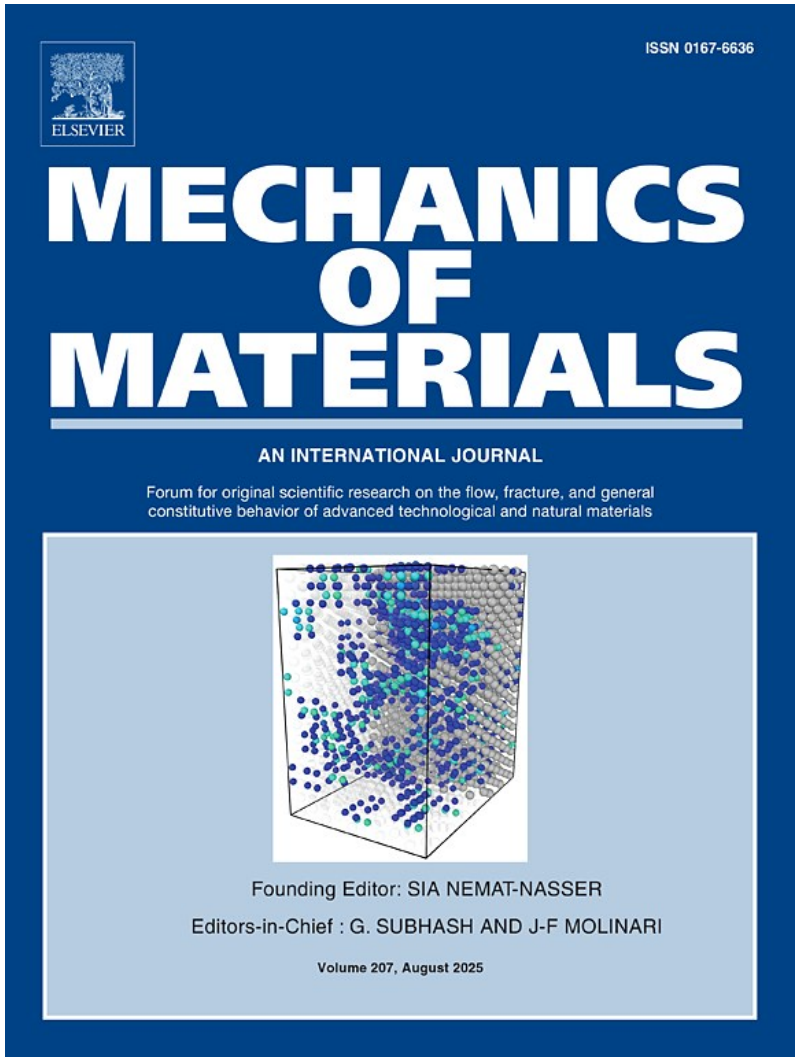

Introduction: manufacturing composite materials and its problem

Fiber reinforced plastic (FRP)

✓ Manufacturing characteristics

Thermosetting resin	**Thermoplastic resin**
Cured (chemical reaction)	Mold/Remold by heating
High reliability	High productivity
Low productivity	Complex molding mechanism

Problems with FRP composites processing

✓ Process-induced residual stress → dimensional change

➢ Thermomechanical mismatch between layers, between fiber/matrix

➢ Stress relaxation by viscoelasticity

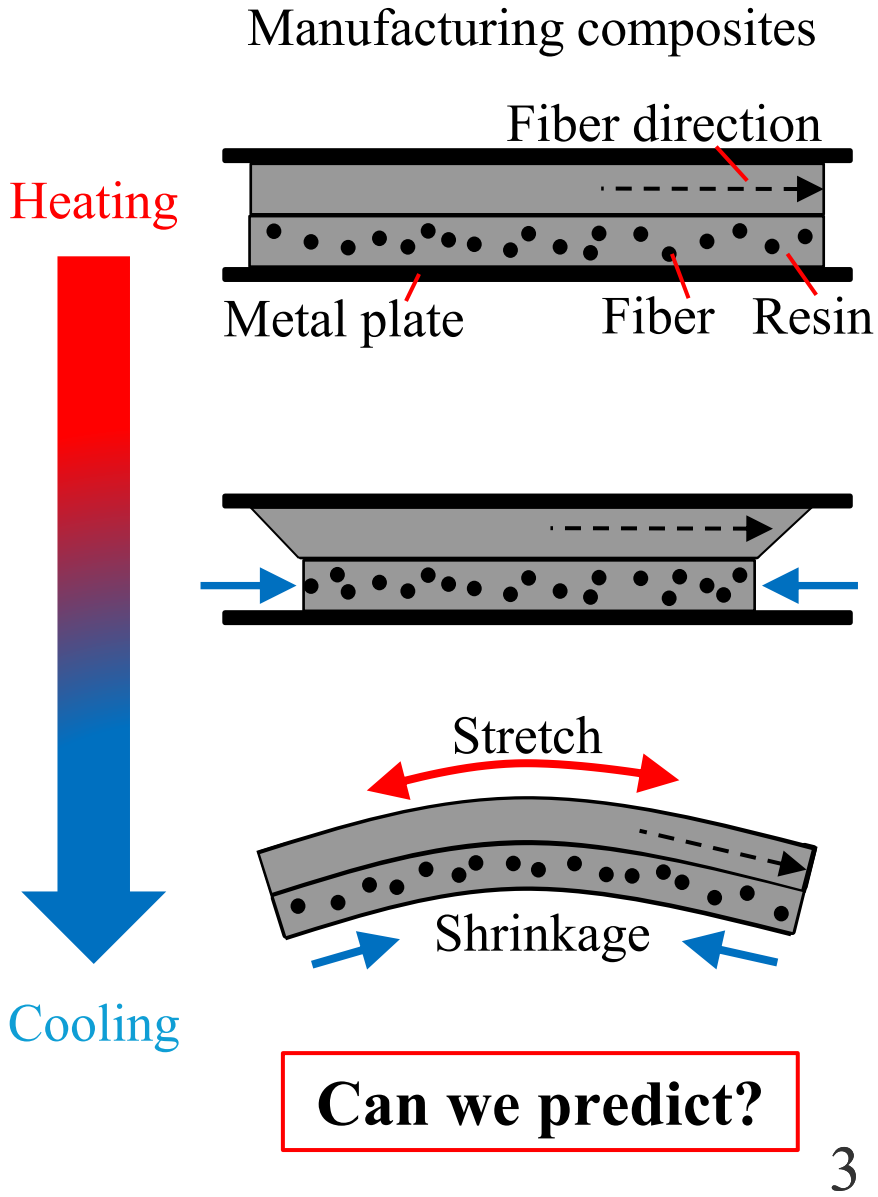

Introduction: outline

- ✓ Mechanism investigation of process-induced deformation (**PID**) in NCF composites using **a bi-scale FEA.**
- ✓ **Different resin types** (thermosetting, thermoplastic) were compared and verified

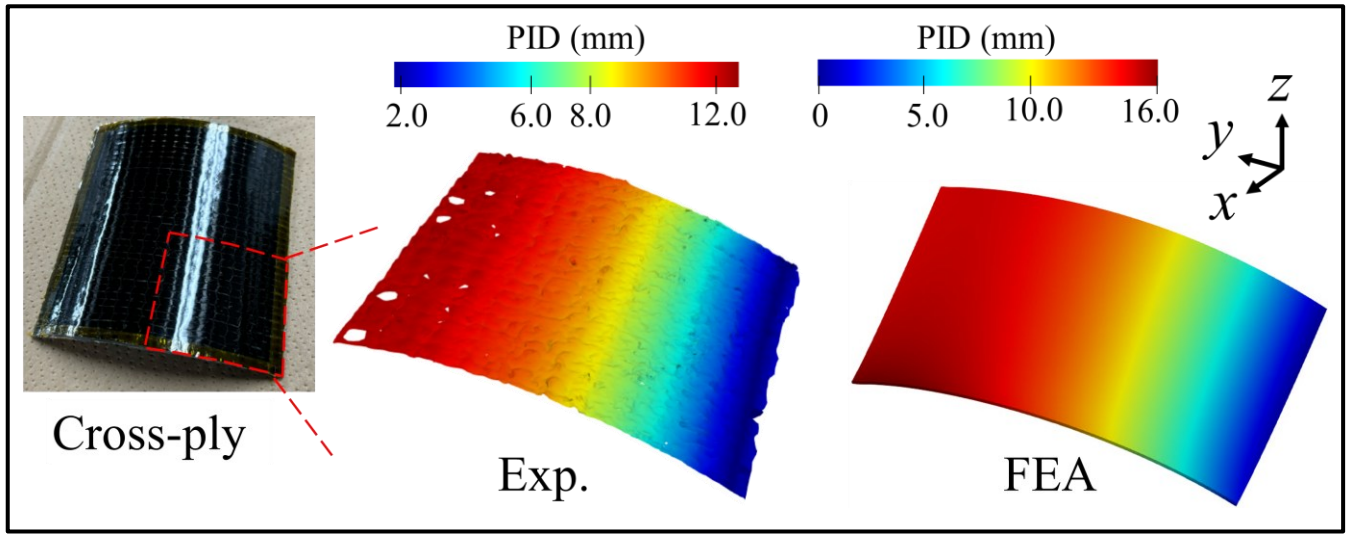

Macro-scale

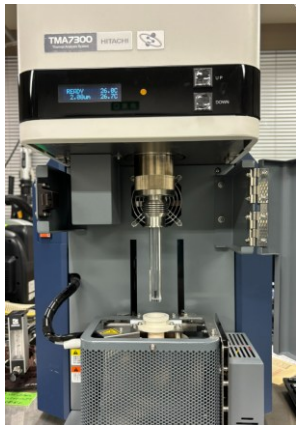

TMA

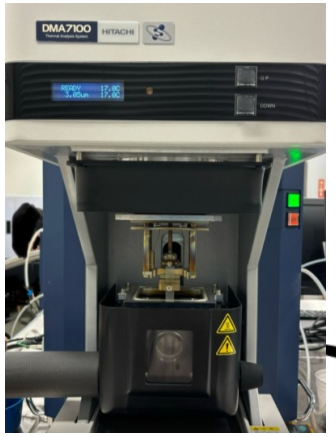

DMA

Resin properties

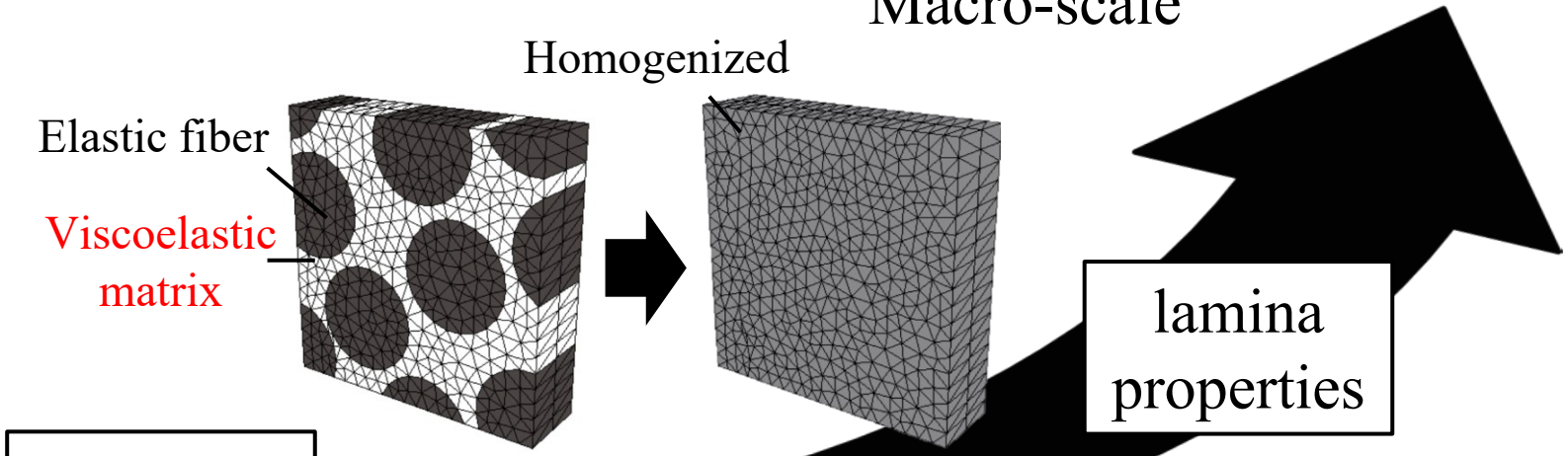

Micro-scale

lamina properties

Experiment: NCF cross-ply laminate

Materials used



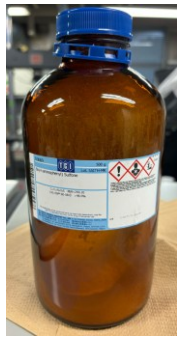

DGEBA/4,4'-DDS
(**Epoxy**, thermosetting)

OR



Nylon 6
(**PA6**, thermoplastic)

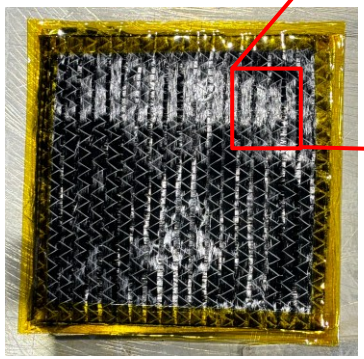

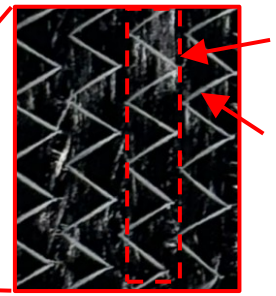

Cross-ply NCF

Cross-ply laminate of non-crimp fabric (NCF) composite

✓ 90° layer (top) ≠ 0° layer (bottom)

Necessary to consider resin-gap and viscoelasticity in evaluation of PID



Top layer



Bottom layer

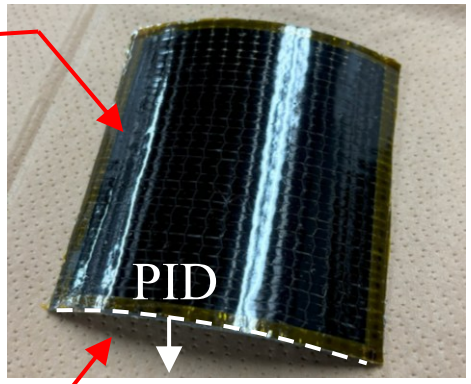

Experiment: fabrication of NCF cross-ply laminate

Hot press (Toyoseiki, mini test press MP-WCL)

- Specimen: [90/0] cross-ply laminate, 100×100 mm^2
- Method: hot press curing

➢ Measure PID with a 3D scanner

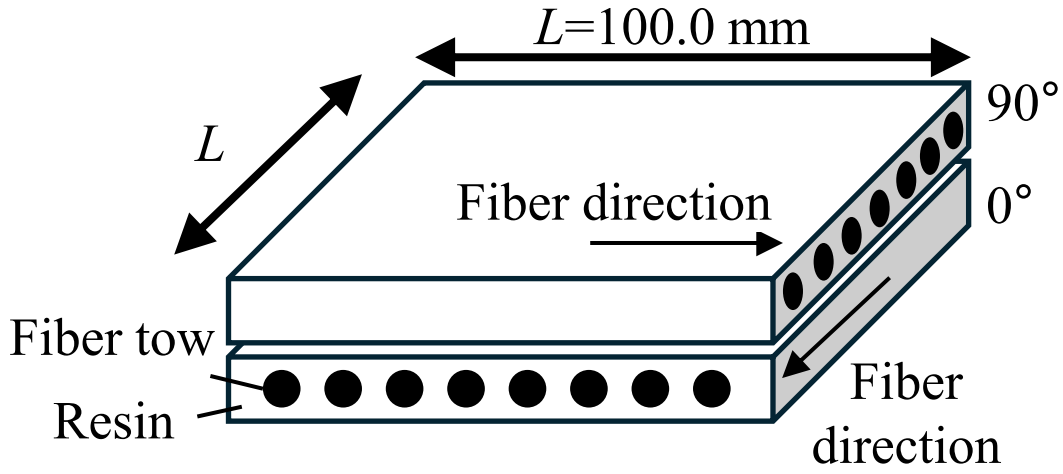

Cross-ply configuration

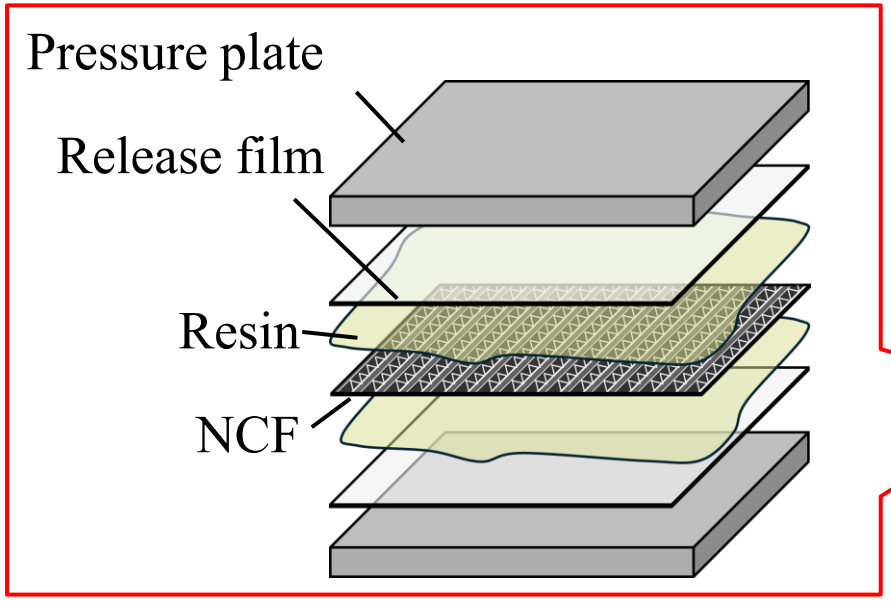

1. Cross-ply molding



2. Hot press curing

Demold

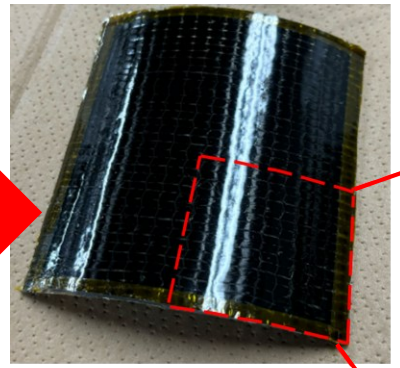

3. PID record

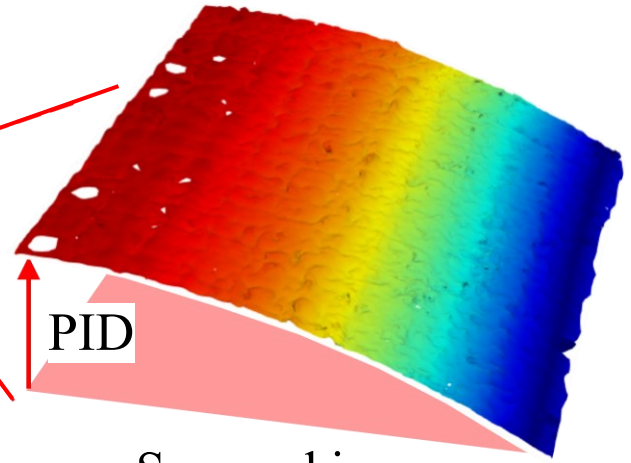

Scanned image

Experiment: evaluation of resin viscoelasticity with DMA test

Dynamic mechanical analysis (DMA)

Material	Temperature	Frequency
Epoxy, PA6	25℃~220℃	0.1~10 Hz

- Construct master curve applying time-temperature superposition principle (TTSP):

$$\log(t_{\text{ref}}) + \log(\alpha^{\text{T}}) = \log(t)$$

- Generalized Maxwell Model (GMM):

$$C_{ij}(t) = C_{ij}^{0} - \sum_{k=1}^{\text{N}} C_{ij}^{k}\left[1 - \exp\left(-\frac{t}{\alpha_{ij}^{\text{T}}\tau_{ij}^{k}}\right)\right]$$

t_{ref} :	Reference time
t :	Time of interest
α_{ij}^{T}:	Shift factor from reference temperature T_{ref}
$C_{ij}(t)$:	Relaxation stiffness matrix
τ_{ij}^{k} :	Relaxation time
N :	Number of maxwell model parameter

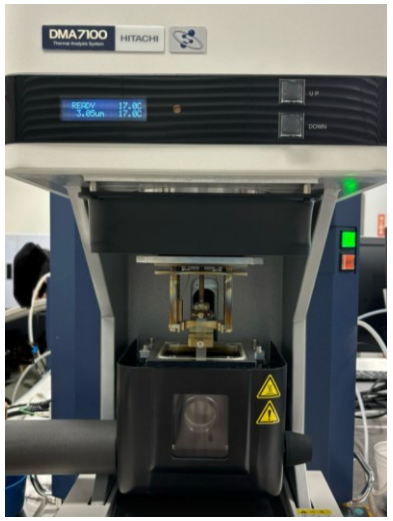

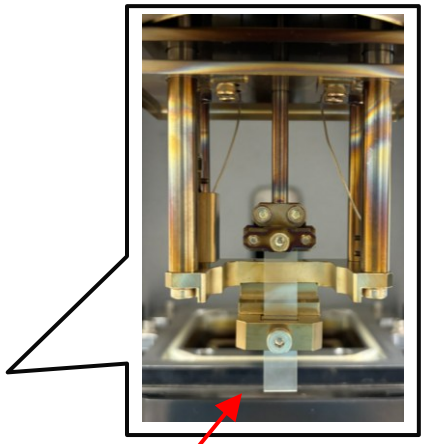

10.0 x 50.0 x 1.0 mm³

DMA tension mode

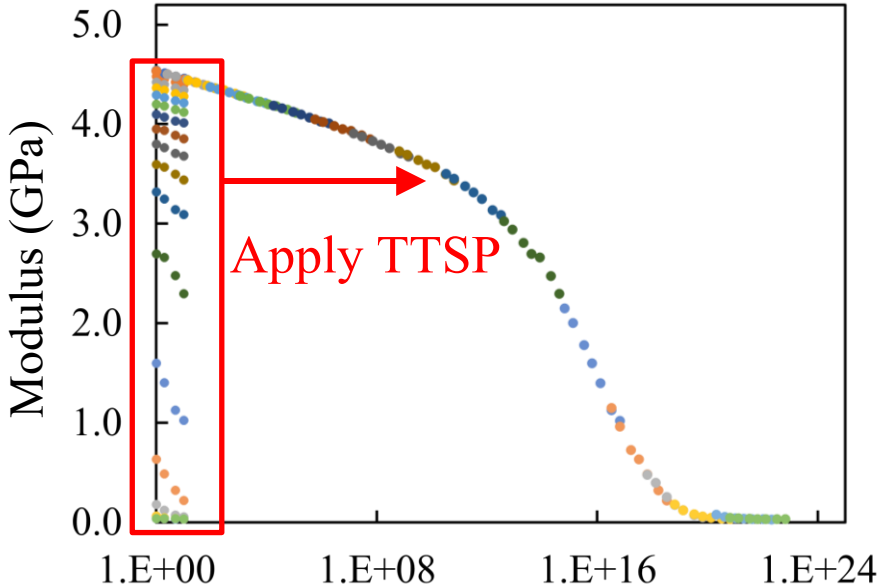

DMA data to master curve

Simulation: micro-scale Fiber/Resin PUC model

Stress update in periodic unit cell (PUC) analysis

Total stress:

$$ {}^{t}\boldsymbol{\sigma} = {}^{t}\boldsymbol{\sigma}^{\mathrm{e}} - {}^{t}\boldsymbol{\sigma}^{\mathrm{v}} $$

$$ {}^{t_{n+1}}\boldsymbol{\sigma}^{\mathrm{e}} = {}^{t}\boldsymbol{\sigma}^{\mathrm{e}} + \boldsymbol{C}^{\mathrm{e}}\Delta\boldsymbol{\varepsilon} $$

$$ {}^{t_{n+1}}\boldsymbol{\sigma}^{\mathrm{v}} = {}^{t}\boldsymbol{\sigma}^{\mathrm{v}} + \Delta\boldsymbol{q} $$

Nonequilibrium stress increment $\Delta\boldsymbol{q}^{k}$ [1]:

$$ \Delta\boldsymbol{q} = \sum_{k=1}^{\mathrm{N}} \sum_{j=1}^{6} \Delta q^{k}_{(\mathrm{m}),ij}(t_{n+1}) $$

Viscoelastic matrix

$$ \Delta q^{\mathrm{k}}_{\mathrm{m},ij}(t_{n+1}) = \left[1 - \exp\left(-\frac{\Delta t}{\alpha^{\mathrm{T}}_{ij}\tau^{k}_{ij}}\right)\right]\left[C^{k}_{\mathrm{m},ij}\left(\varepsilon_{j}(t_{n}) + \frac{\Delta\varepsilon_{j}(t_{n+1})}{2}\right) - \Delta q^{k}_{\mathrm{m},ij}(t_{n})\right] $$

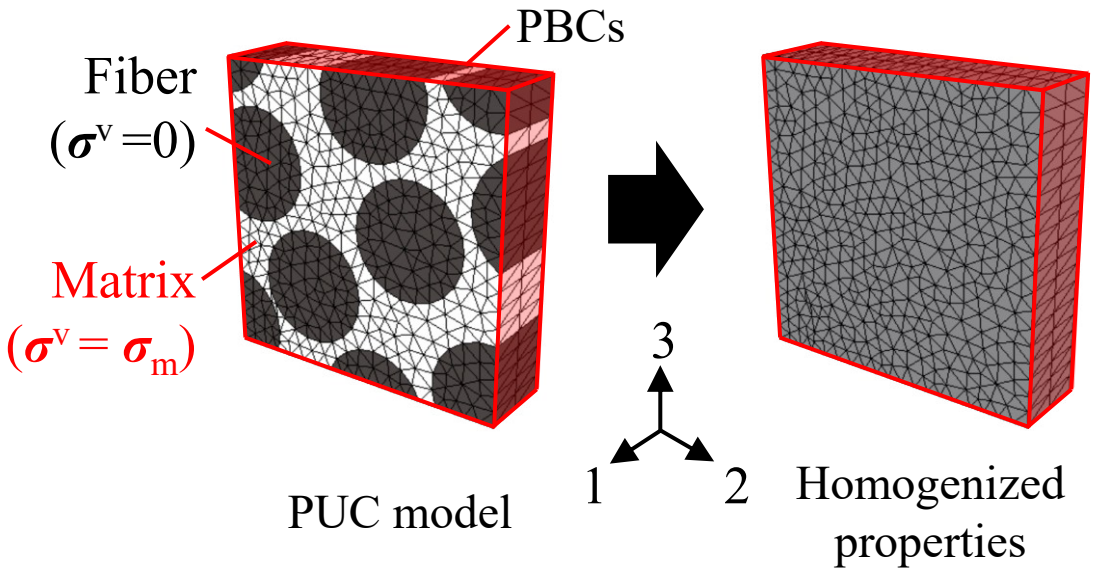

t :	Time
dt :	Time increment
Δ :	Incremental component
$\boldsymbol{\sigma}$:	Stiffness matrix
$\boldsymbol{\varepsilon}$:	Internal force vector
$[\ ]_{\mathrm{m}}$:	Matrix component
$[\ ]_{\mathrm{f}}$:	Fiber component
$[\ ]^{\mathrm{e}}$:	Elastic component
$[\ ]^{\mathrm{v}}$:	Nonequilibrium component

[1] Hoshikawa et al., International Journal of Damage Mechanics, 2024.

Simulation: homogenized unidirectional (UD) viscoelastic properties

Fiber/Epoxy

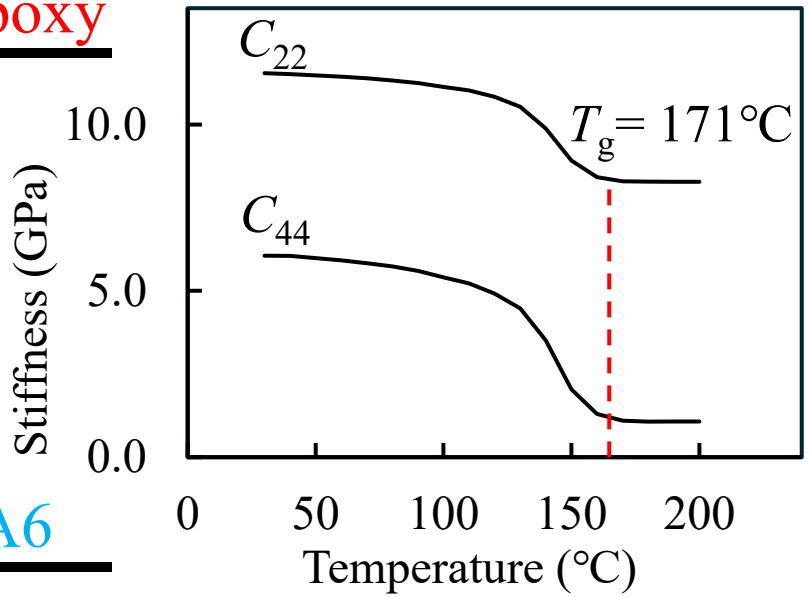

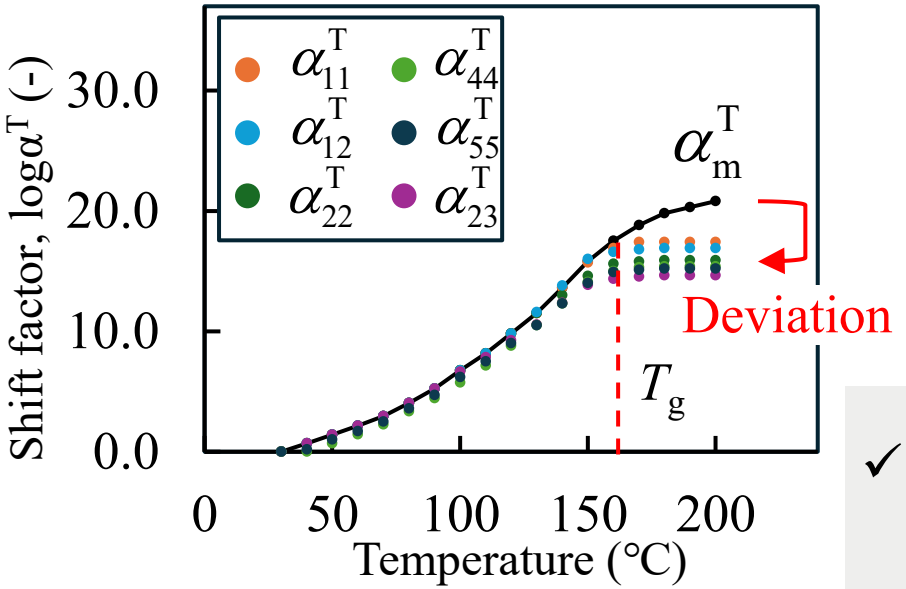

Fiber/PA6

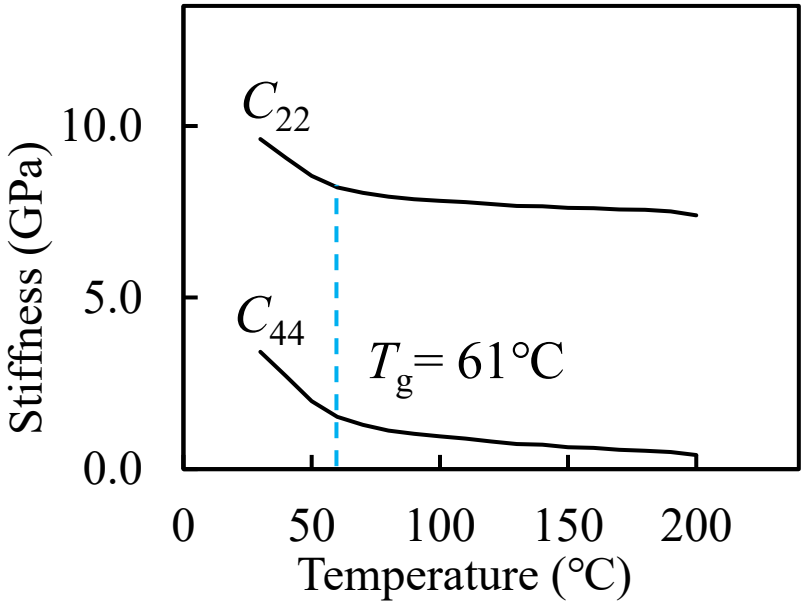

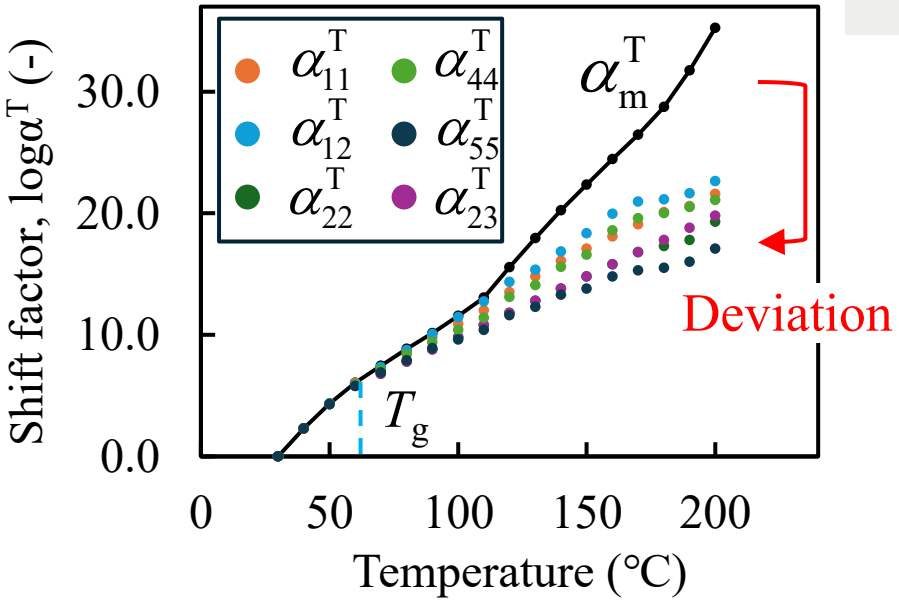

✓ **Smaller shift factor**

⇔ **Faster relaxation**

Simulation: stress distribution during PUC simulation

Fiber/Epoxy

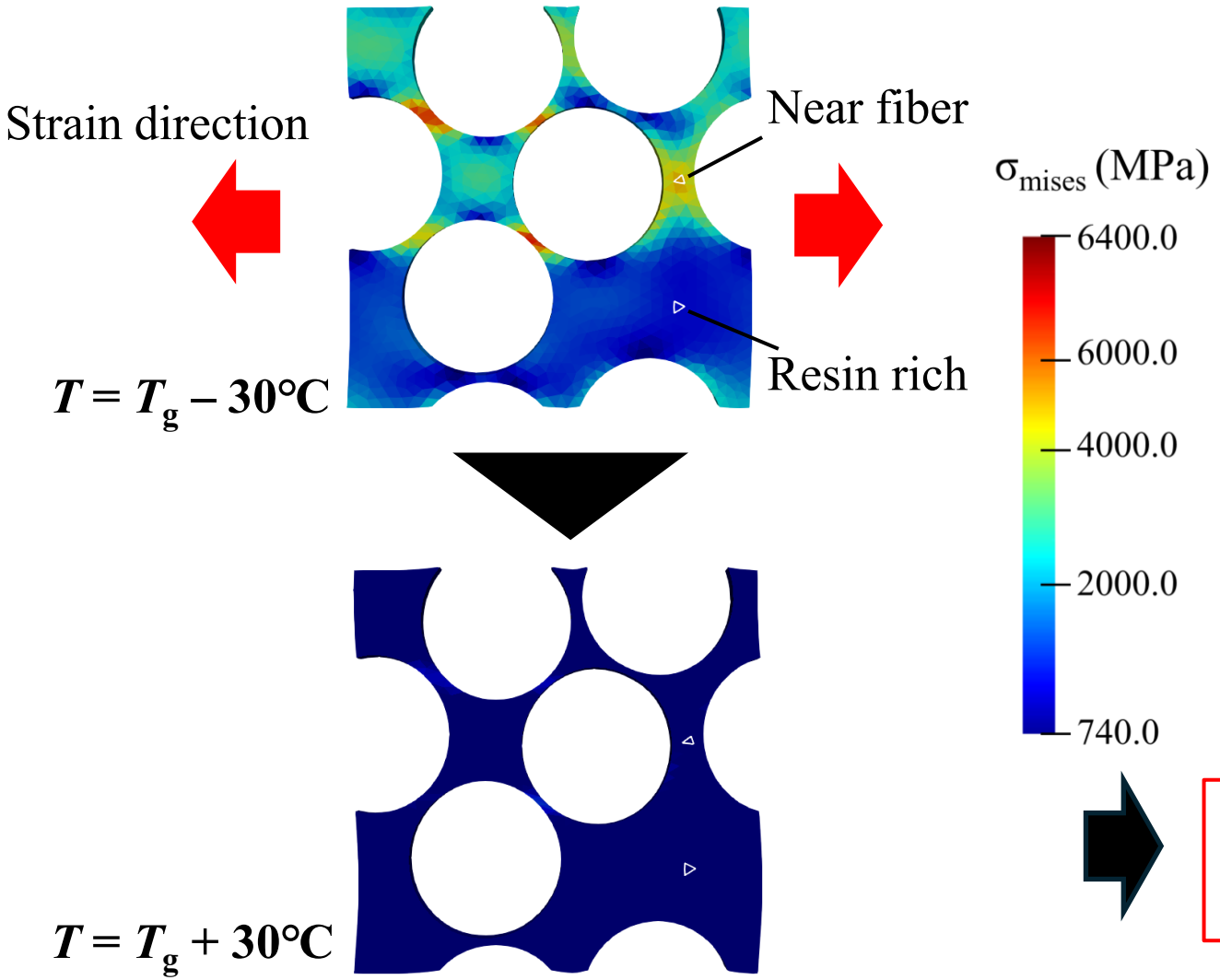

- ✓ Faster relaxation
- ✓ Smaller amount of relaxation

Position	Relaxation amount
Near fiber	84%
Resin rich	97%

Application of homogenized properties to **PID prediction with macro-scale FEA**

Simulation: macro-scale PID model

Numerical model for PID simulation

- Quarter modeling (symmetry at $x = 0$ and $y = 0$)
- Boundary conditions: symmetry, fix base
- Mesh: 20-node Hex element

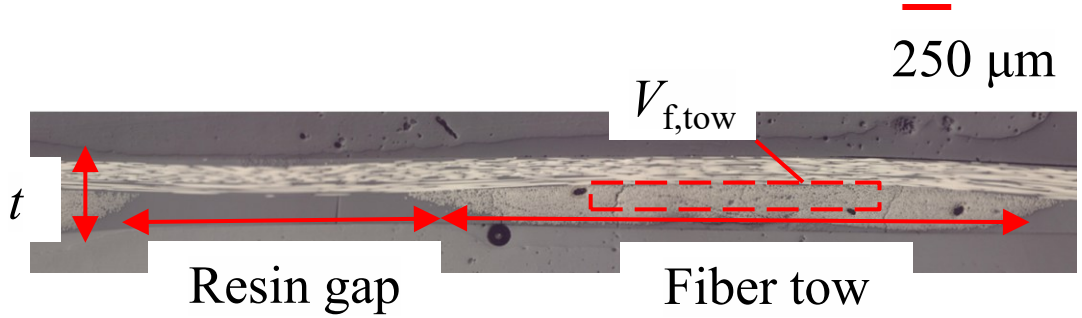

Cross-section view of NCF/Epoxy
($V_{f,tow}$: fiber-volume fraction)

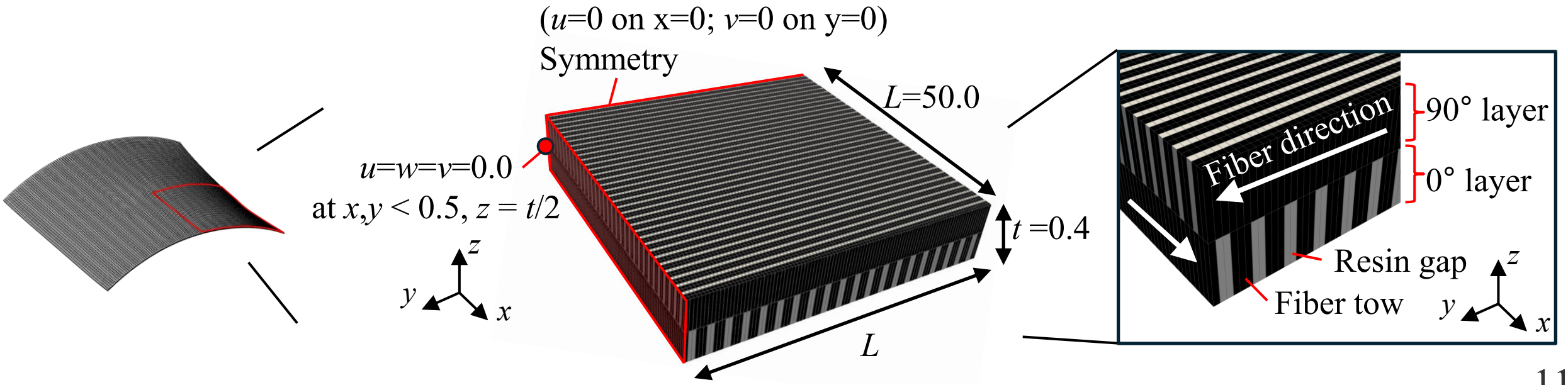

Simulation: macro-scale PID model

Classical total Lagrangian method [2]

Implicit Newton-Raphson's scheme:

- Cure shrinkage and thermal shrinkage

$$\boldsymbol{K}^{(iter)}\Delta\boldsymbol{U}^{(iter)} = \boldsymbol{F}_{\mathrm{ex}} - \boldsymbol{Q}_{\mathrm{int}}^{(iter)} + \boldsymbol{Q}_{\mathrm{nm}}$$

$$\boldsymbol{Q}_{\mathrm{nm}} = \sum_{e}\int \boldsymbol{B}^{\mathrm{T}}(\boldsymbol{C}^{0}\Delta\boldsymbol{E}^{\mathrm{nm}})dV$$

$$\Delta\boldsymbol{E}^{\mathrm{nm}} = \begin{cases} \Delta\boldsymbol{E}^{\mathrm{sh}} = [\Delta E_1^{\mathrm{sh}} \quad \Delta E_2^{\mathrm{sh}} \quad \Delta E_3^{\mathrm{sh}} \quad 0 \quad 0 \quad 0]^{\mathrm{T}} \\ \Delta\boldsymbol{E}^{\mathrm{th}} = [\Theta_1\Delta T \quad \Theta_2\Delta T \quad \Theta_3\Delta T \quad 0 \quad 0 \quad 0]^{\mathrm{T}} \end{cases}$$

$\boldsymbol{Q}_{\mathrm{nm}}$	: Non-mechanical internal force vector
$\boldsymbol{K}$	: Total stiffness matrix
$\Delta\boldsymbol{U}$	: Displacement vector
$\boldsymbol{F}_{\mathrm{ex}}$	: External force vector
$\boldsymbol{Q}_{\mathrm{int}}$	: Internal force vector
$(iter)$	: Newton-Raphson iteration
n	: Simulation steps

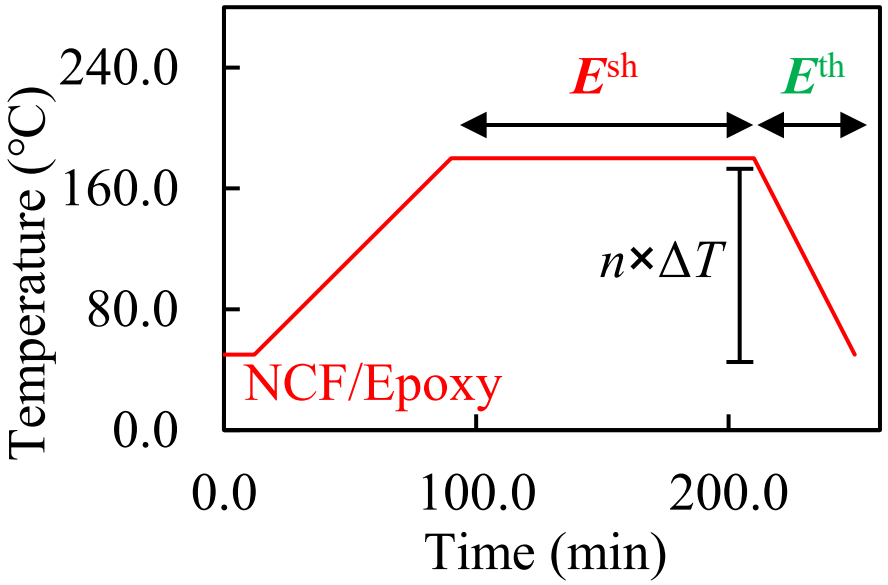

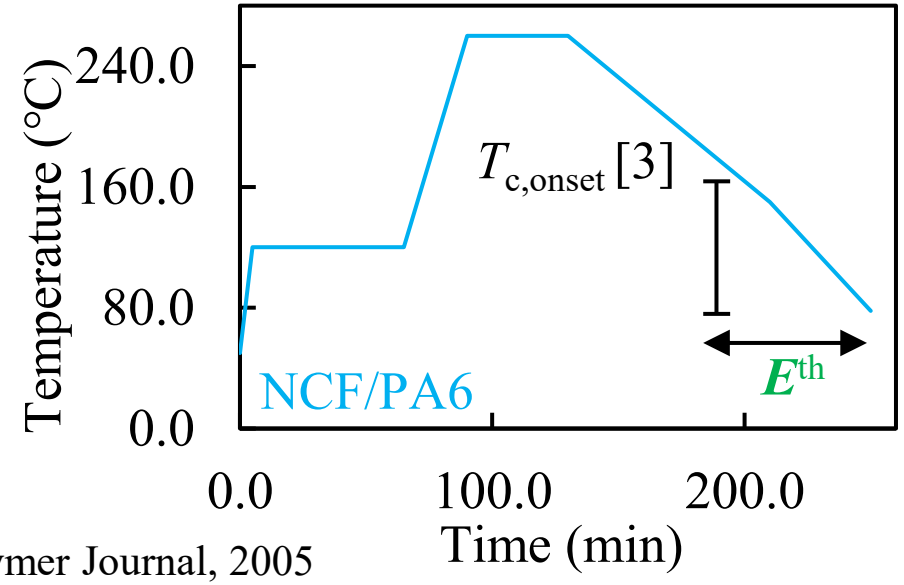

[2] Kawagoe et al., Mechanics of Materials, 2022. [3] Pesetskii et al., European Polymer Journal, 2005

Simulation: macro-scale PID model

Stress update and consistent tangent matrix [1]

$$(\Delta S_i)^{(iter)}(t_{n+1}) = (\Delta S_i^{\mathrm{e}})^{(iter)}(t_{n+1}) - (\Delta S_i^{\mathrm{v}})^{(iter)}(t_{n+1})$$

Same as PUC

$$\Delta S_i^{\mathrm{e}} = C_{ij}^{0}(\Delta E_j^{\mathrm{e}} - \Delta E_j^{\mathrm{nm}})$$

$$D_{ij}^{(iter)}(t_{n+1}) = \frac{1}{2}\sum_{k=1}^{N}\left[1 - \exp\left(-\frac{\Delta t}{\alpha_{ij}^{T}\tau_{ij}^{k}}\right)\right]$$

$\boldsymbol{S}(t)$: 2nd Piola-Kirchhoff stress
$\boldsymbol{E}(t)$: Green Lagrange strain
$\boldsymbol{D}(t)$: Consistent tangent matrix

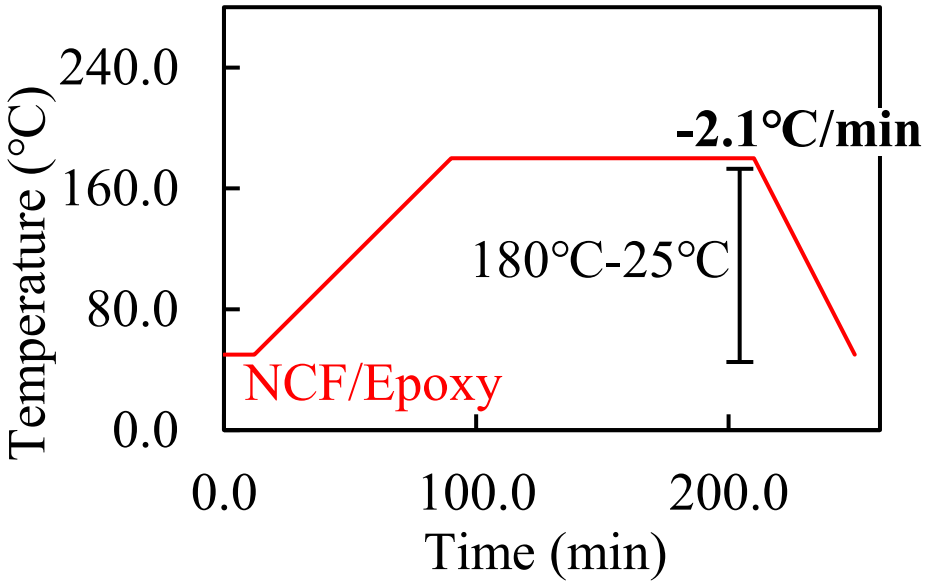

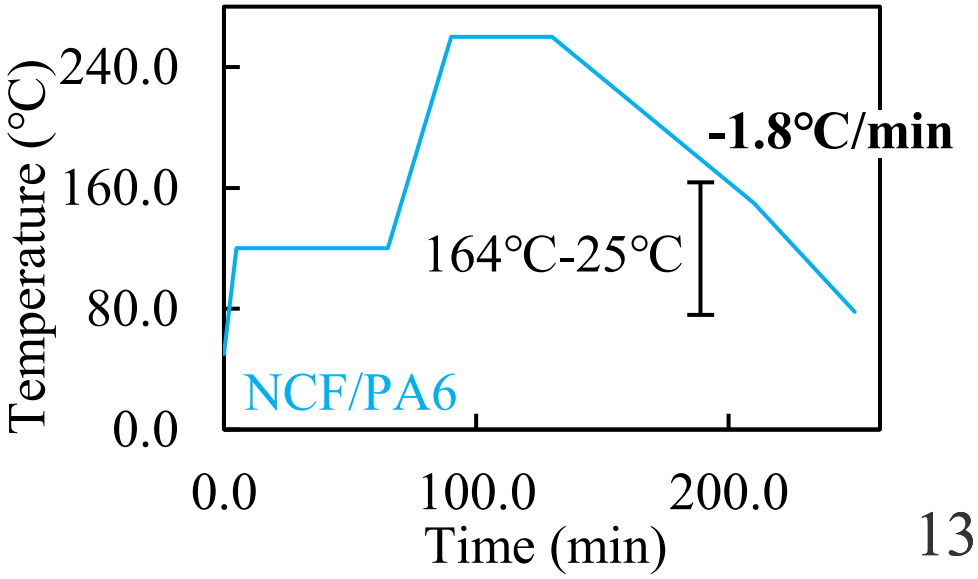

[1] Hoshikawa et al., International Journal of Damage Mechanics, 2024.

Simulation: validation of proposed model

Quantitative/ Qualitative evaluation

NCF/Epoxy

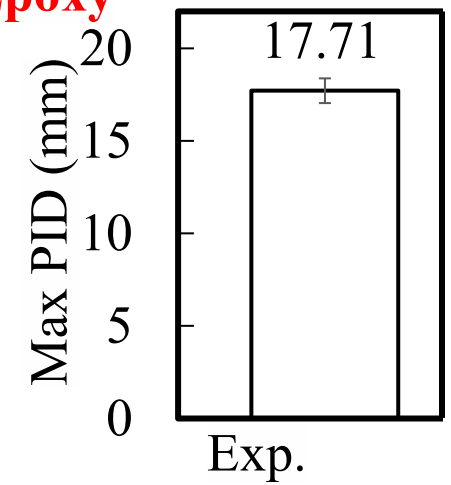

NCF/PA6

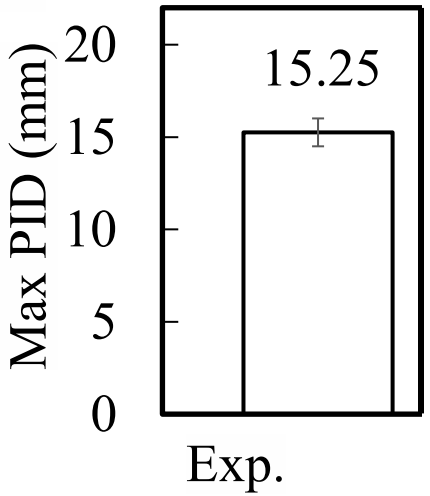

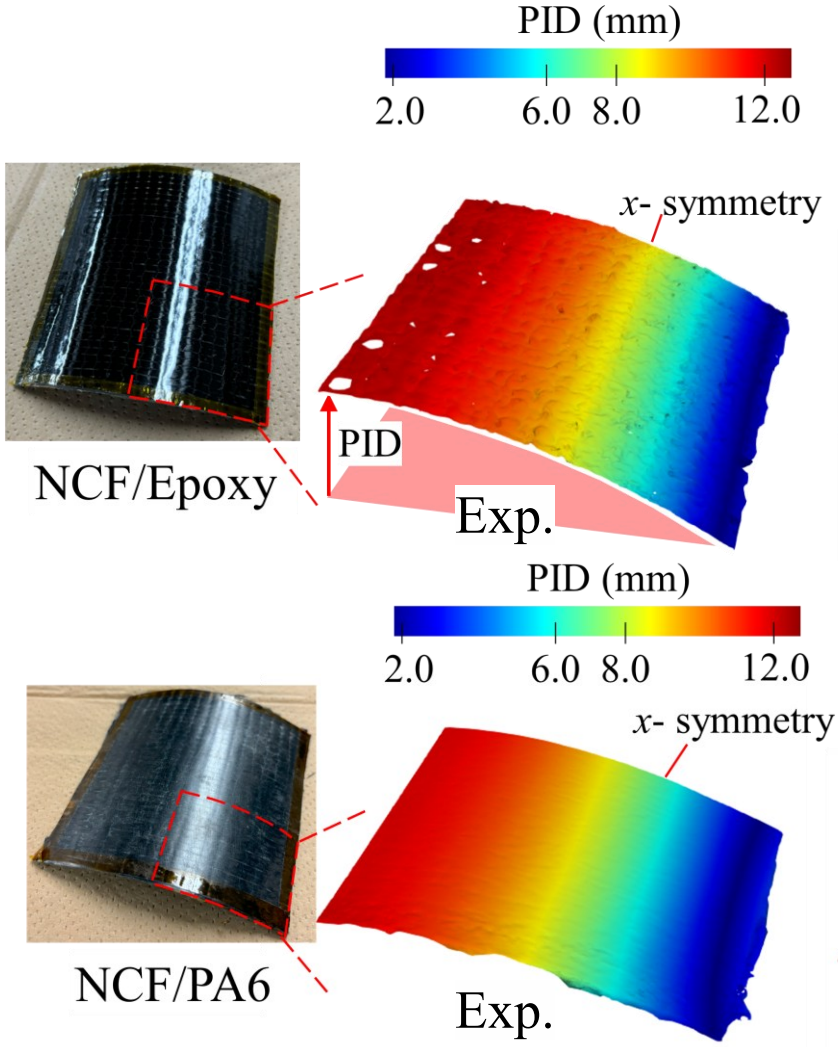

Experiment: similar PIDs despite curing patterns

Simulation: validation of proposed model

Quantitative/ Qualitative evaluation

NCF/Epoxy

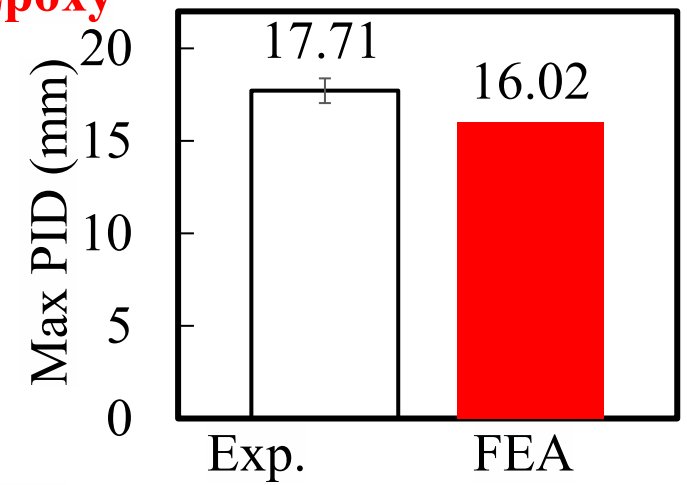

NCF/PA6

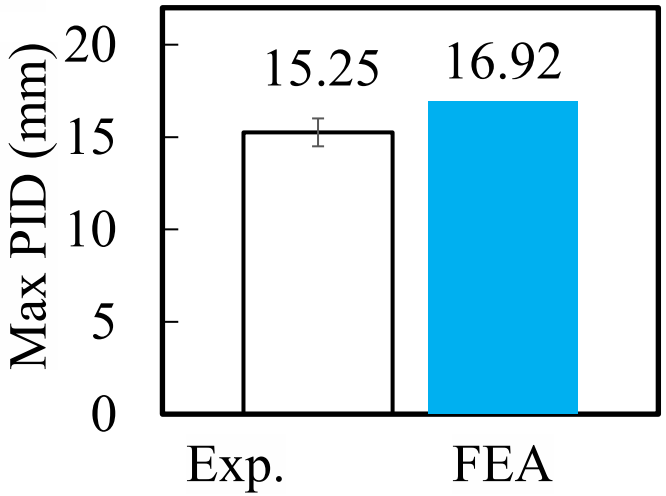

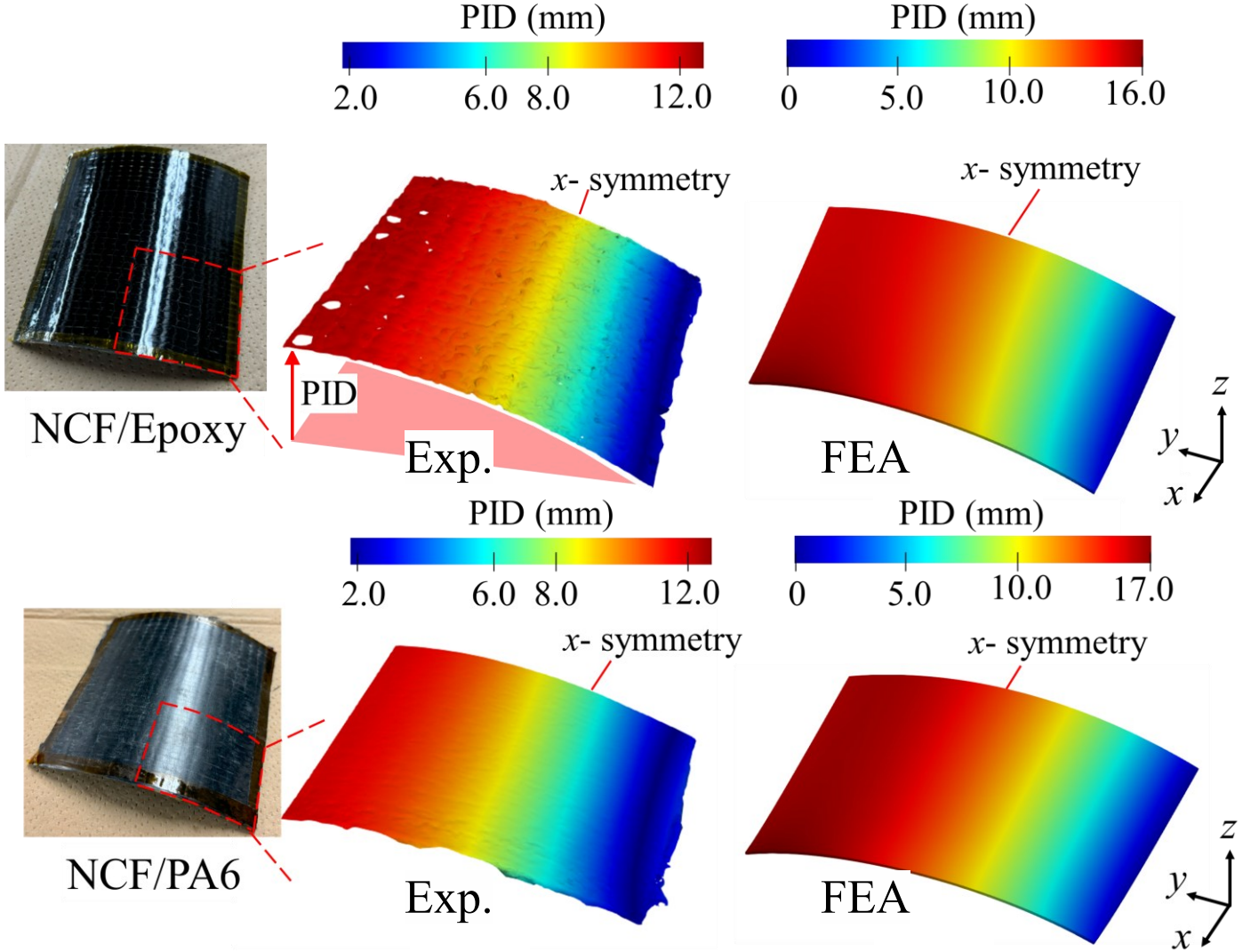

Experiment: similar PIDs despite curing patterns
FEA: well reproduced PIDs

Simulation: validation of proposed model

NCF/Epoxy

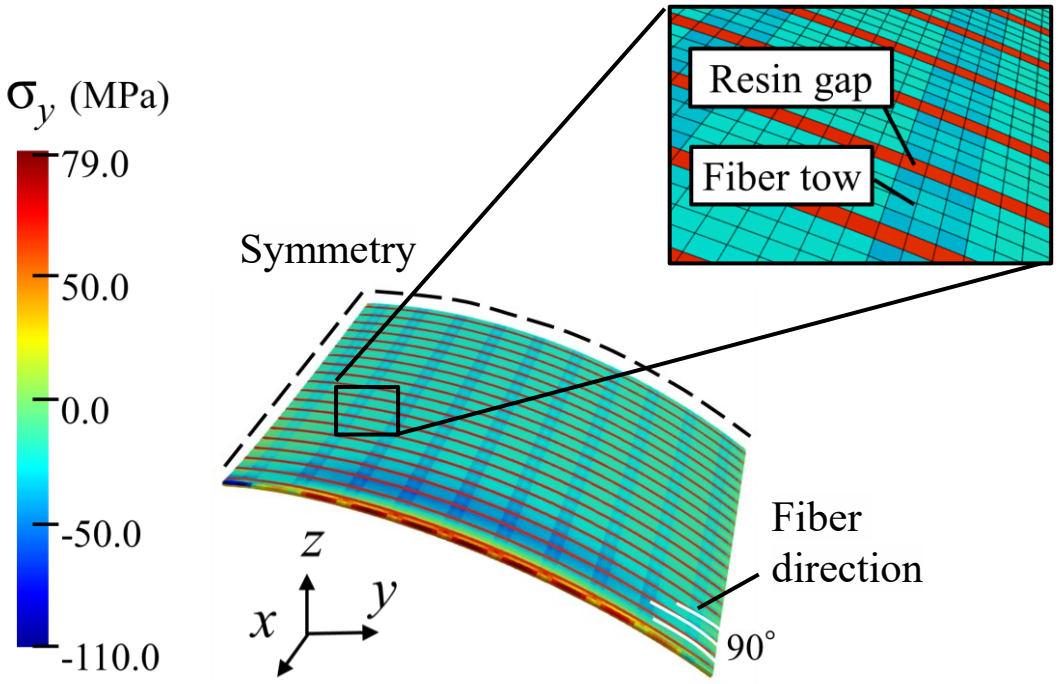



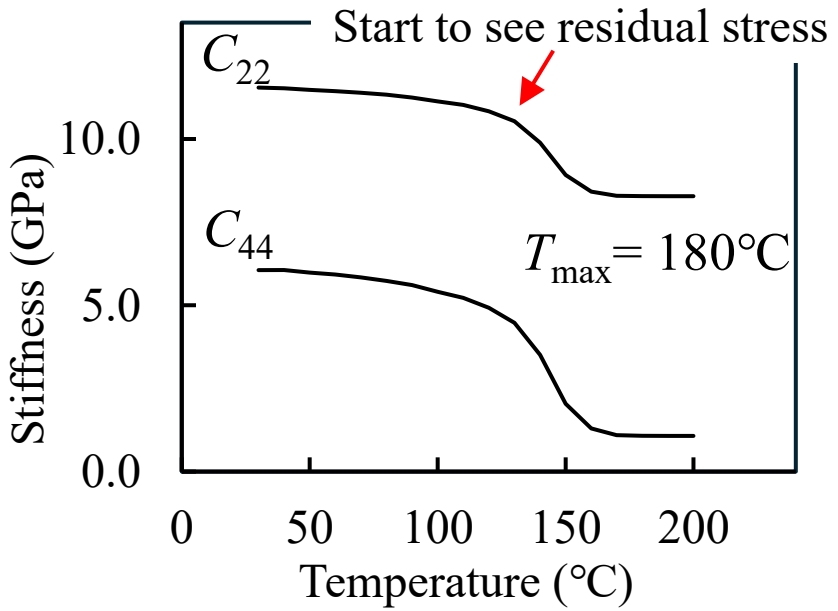

Residual stress development

Simulation: validation of proposed model

Residual stress distribution

- ✓ **Localized stress in resin gap:** reaction force causes tensile stress
- ✓ **Out-of-plane PIDs:** shrinkage of 0° layer in y-direction

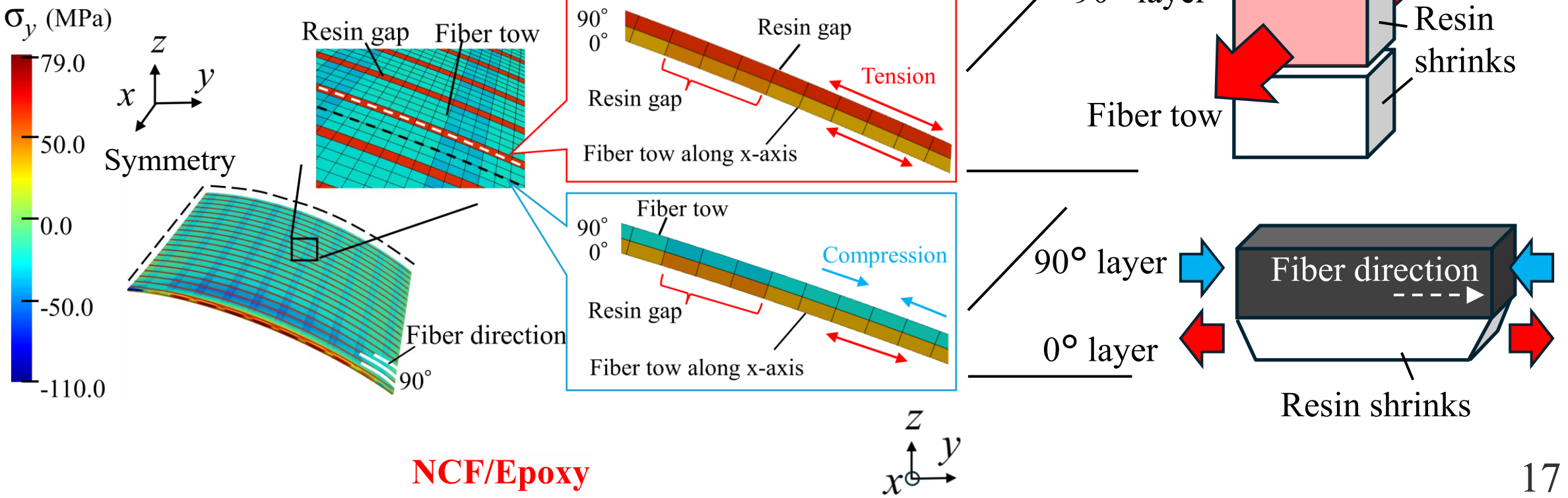

Summary

- **Experimental and bi-scale numerical FEA study on PID of thermosetting and thermoplastic NCF composites** were conducted
  - ✓ NCF resin-gap was captured in numerical model
  - ✓ Stress relaxation during processing was predicted using **pure resin** by GMM viscoelastic framework
- **Residual stress distribution** was reproduced by FEA, caused by thermomechanical mismatches
  - ✓ **The effect of thermal stress development and stress relaxation was captured**

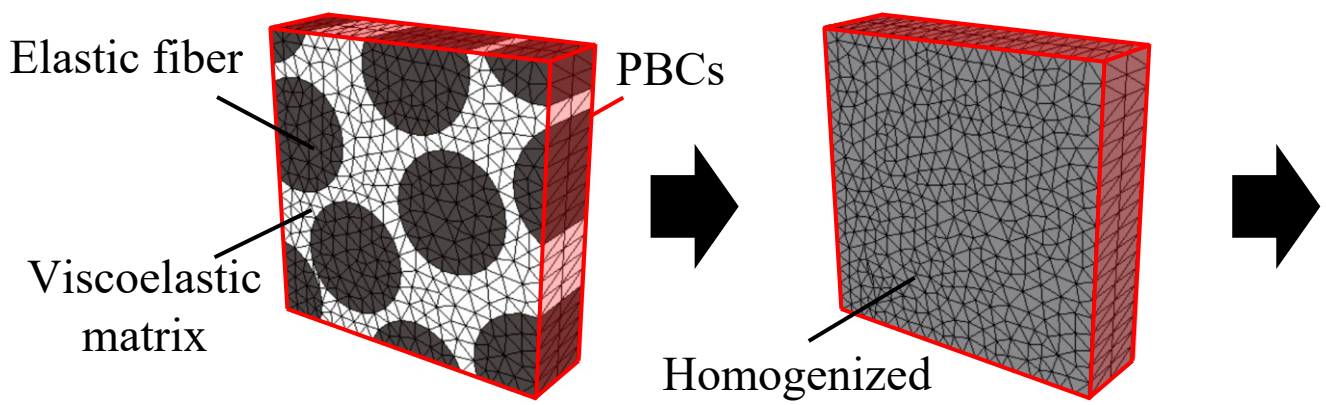

1. Micro-scale analysis

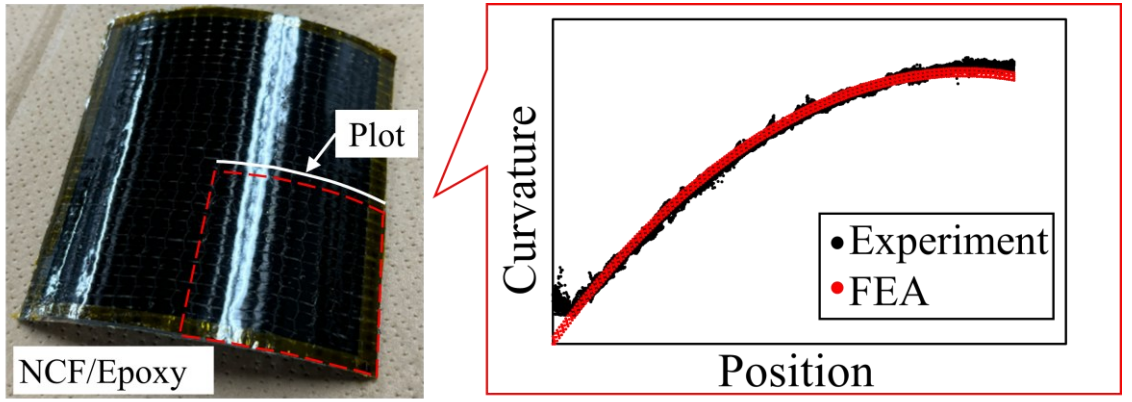

2. Macro-scale analysis

ICCM24
AUGUST 4-8, 2025
BALTIMORE CONVENTION CENTER
BALTIMORE, MARYLAND, USA

No Technical Paper Submission for:

Kaiho Zhang

Dr. Richard Rydin, CTO

Building Composites, LLC



Photo Courtesy of HITT Contracting

Insights on Expanding the Role of Structural Composites in Construction

ICCM 24 – RR/1

Acknowledge Where “Impacts” Matter

Typical Medium Scale Ultra-Low Energy Residential Building

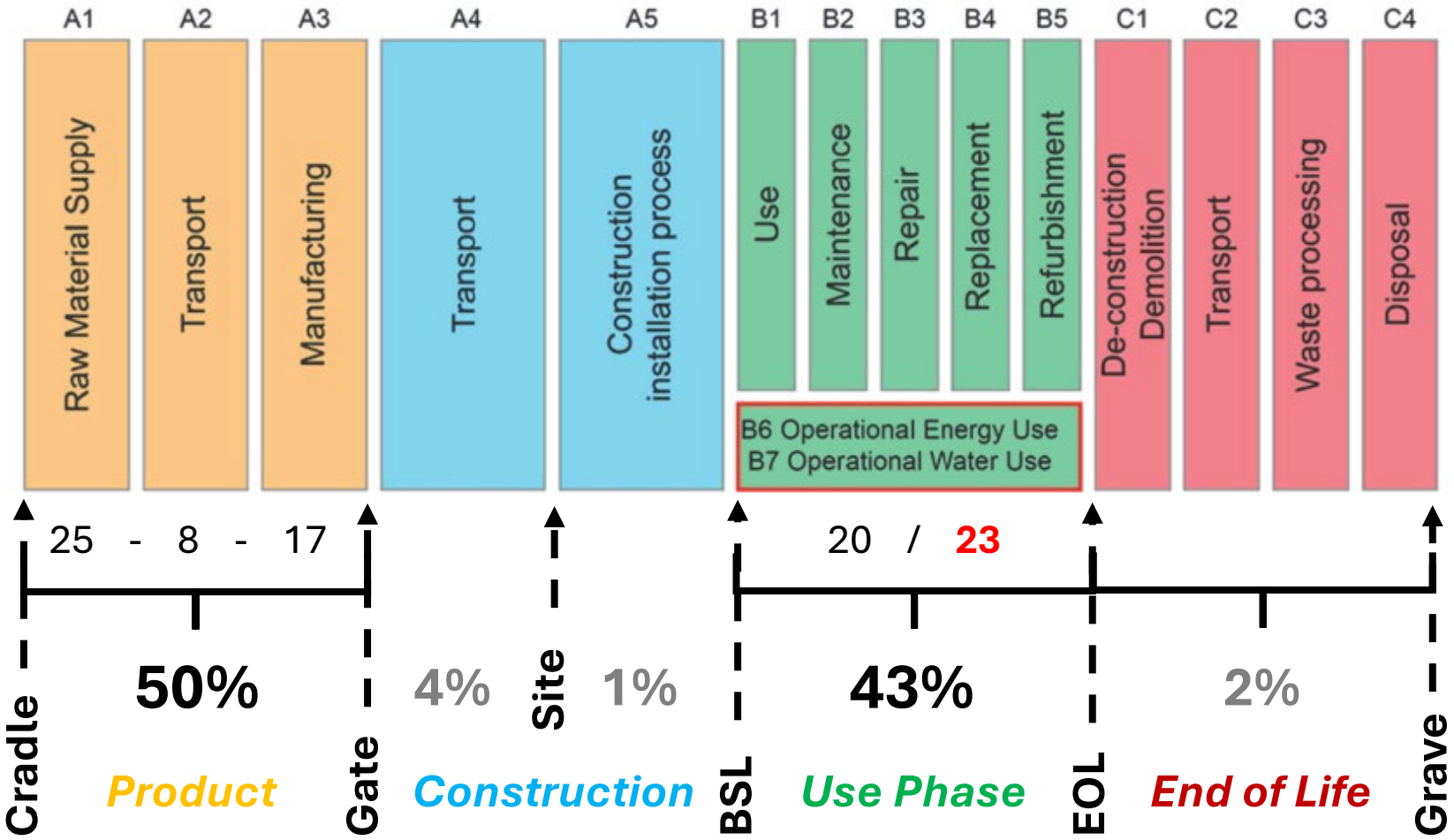

Source: The Institution of Structural Engineers – ***How to Calculate Embodied Carbon***, 2020

Practice Competitive Sustainability

Exterior Building Wall Technology is Evolving

State of the Art	Precast Concrete Wall Panels	FRP Response
Insulated Sandwich Structures	Typical PIC: structural wythe / polystyrene insulation / exterior architectural wythe	We've Got This
Smart Assemblies	Embedded sensors on IoT platform for real time monitoring of temps, RH, strains	Mostly Translates
Digital Fabrication	Rapid prototyping of custom frameworks to create complex architectural features	Translates
Sustainable Materials	Standard supplements include fly ash, slag, silica fume and even carbon capture tech	Adopt Circularity
BIM and Digital Twins	Facilitates clash detection, scheduling, logistics and life cycle performance tracking	Required
Design Standards	PCI Design Handbook defines fire, seismic, connection design and build procedures	ASTM, NFPA ACMA
Construction Logistics	Just in time panelized construction, self aligning connections, integrated lift systems	Translates

Stay Focused on Reducing Product Weight

Wall Panel	Outer Wall	Core	Inner Wall	Areal Mass (#/sq ft)	Typ Dims (sq ft)	Panel Mass (#)	Mass Factor
High Density PIC 150 #/cu ft	3" Wythe	3-5" PS	6" Wythe	112	300	33,600	**> 6 x**
Low Density PIC 110#/cu ft	3" Wythe	3-5" PS	6" Wythe	83	300	24,900	**~ 5 x**
Typical FRP Sandwich Panel	0.5" FRP	2-12" PISO	0.5" FRP	17	300	5,100	**x**

The ***Extra Mass*** of a Building's Foundation and Steel Framing required to support a heavier Envelope materially impacts:

Project Delivery Time, Cost and Carbon Footprint

Coupon Level Testing for Design Data

Determined by Nuances of Fabric Reinforcement

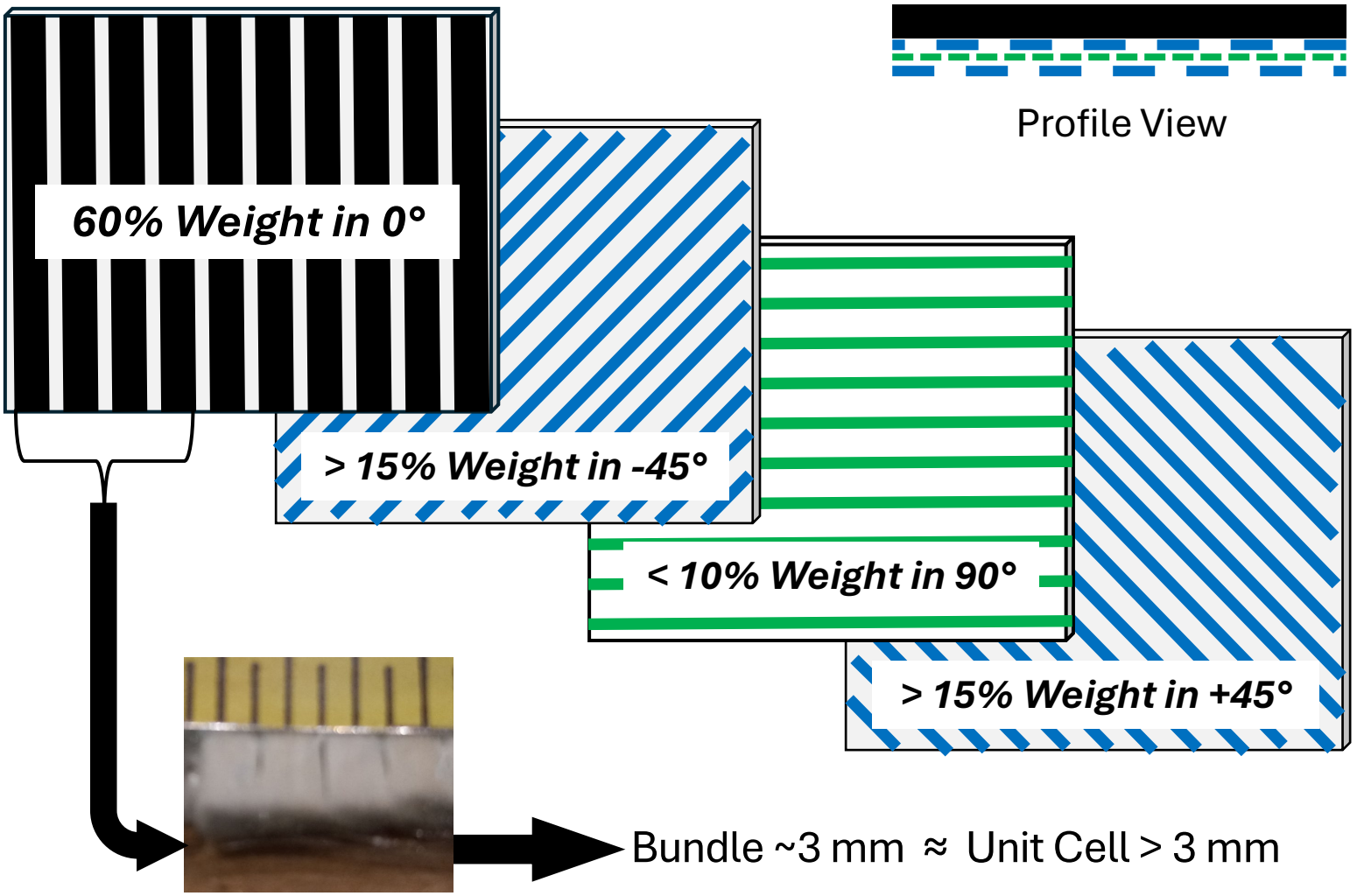

Single Ply of Heavy Quad-Axial Fabric

Asymmetric & Anisotropic



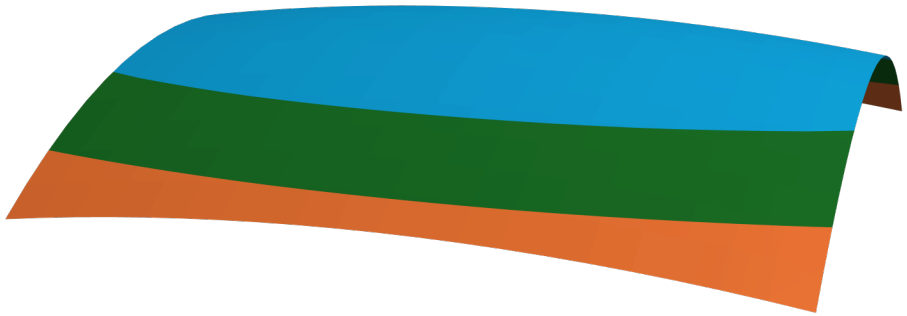

[B] ≠ 0

Typical Response to Reduced Temperature

Double Ply of Heavy Quad-Axial Fabric

Symmetric & Orthotropic

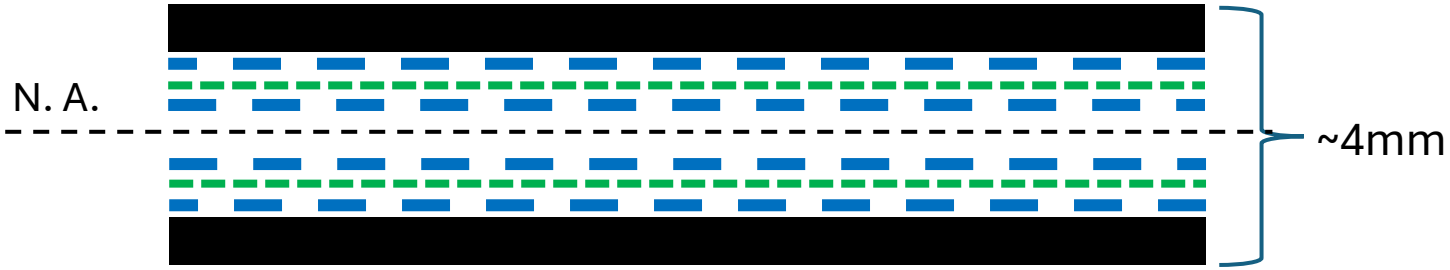

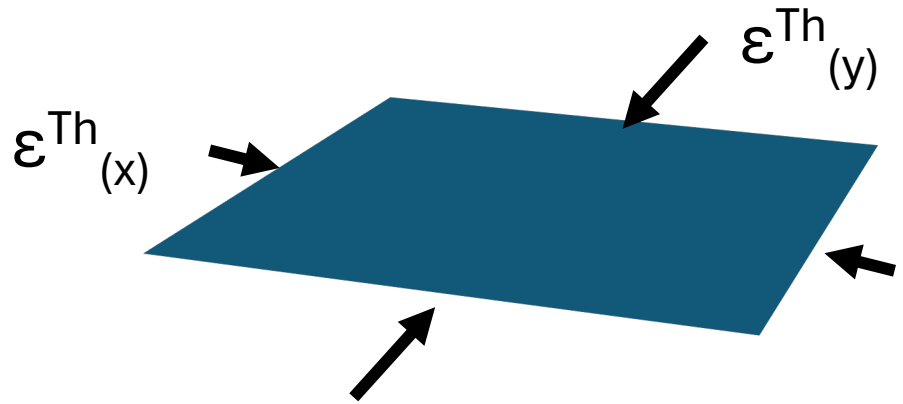

[B] = 0

$\varepsilon^{Th}_{(x)} \neq \varepsilon^{Th}_{(y)}$

Typical Response to Reduced Temperature

Double Ply of Heavy Quad-Axial Fabric

Asymmetric & Quasi-Isotropic

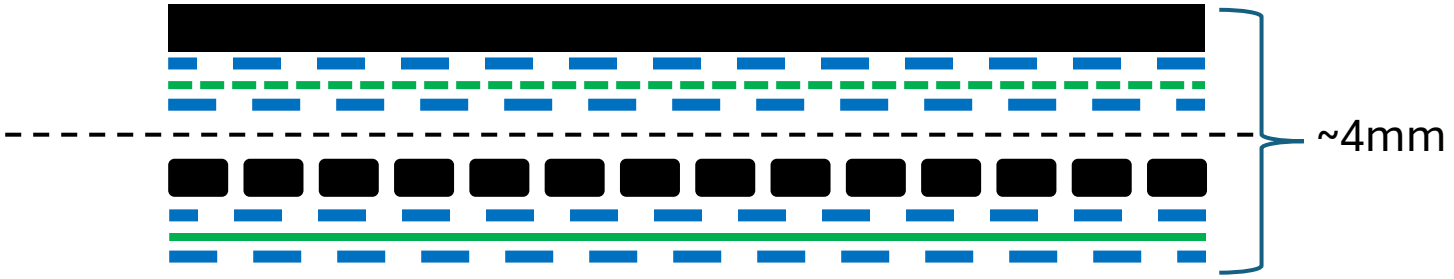



[B] ≠ 0

Typical Response to Reduced Temperature

Quad Ply of Heavy Quad-Axial Fabric

Symmetric & Quasi-Isotropic

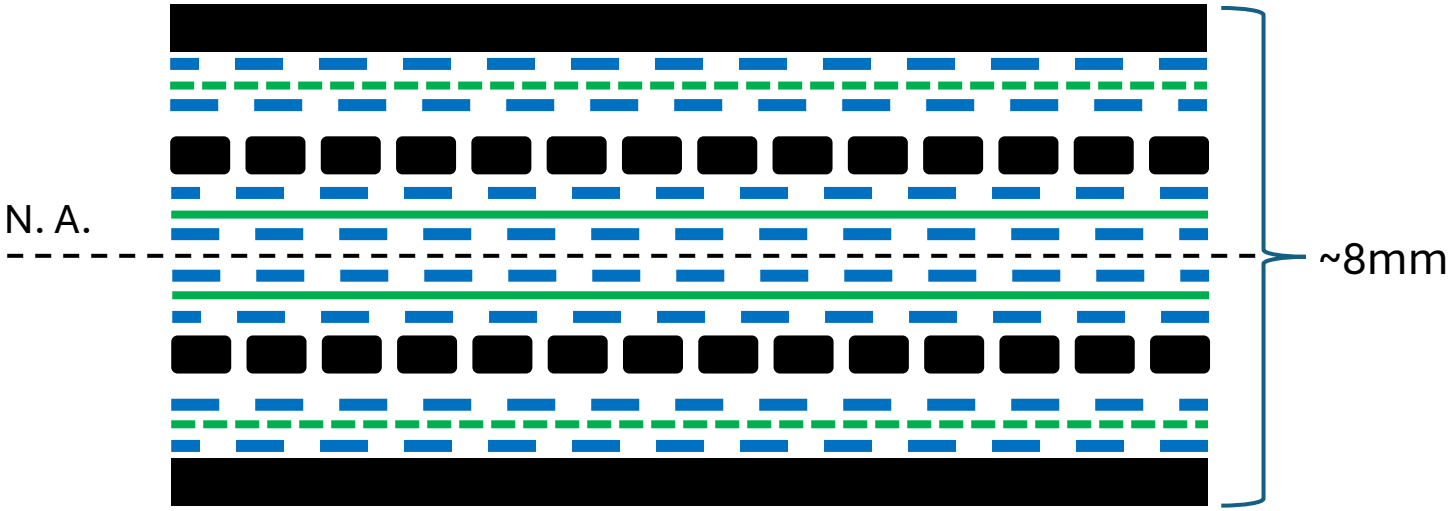

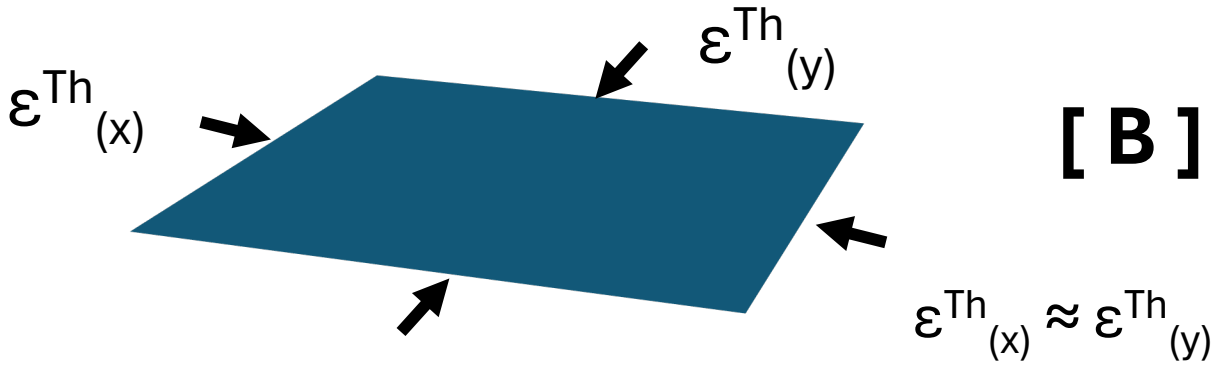

[B] = 0

Typical Response to Reduced Temperature

Standard CTE Test Method Options

Method	**TMA** ASTM E831	**Dilatometry** ASTM D228	**Optical Comparator** ISO 11359-2	**Strain Gauges** ASTM D5335
Typical Materials	Polymers Thin Films	Bulk Materials Composites	Metals, Polymers Composites	Rocks Composites
Temp Range	−120°C to 900°C	−180°C to 900°C	-50°C to 300°C	20°C to 260°C
Sample Width	Up to 10 mm	Std 12.7 mm	10 to 50 mm	Gauge Dependent
Direction	Uniaxial	Uniaxial	Full Field	Gauge Alignment
Surface Prep	Smooth & Flat Parallel Ends	Smooth & Flat Parallel Ends	Clear Speckling Good Lighting	Flat Bondable Surface
Equipment Cost	$50 to $100K	$60 to $120K	$80 to $250K	$10 to $30K

Determining In-Plane CTE Per ASTM D5335

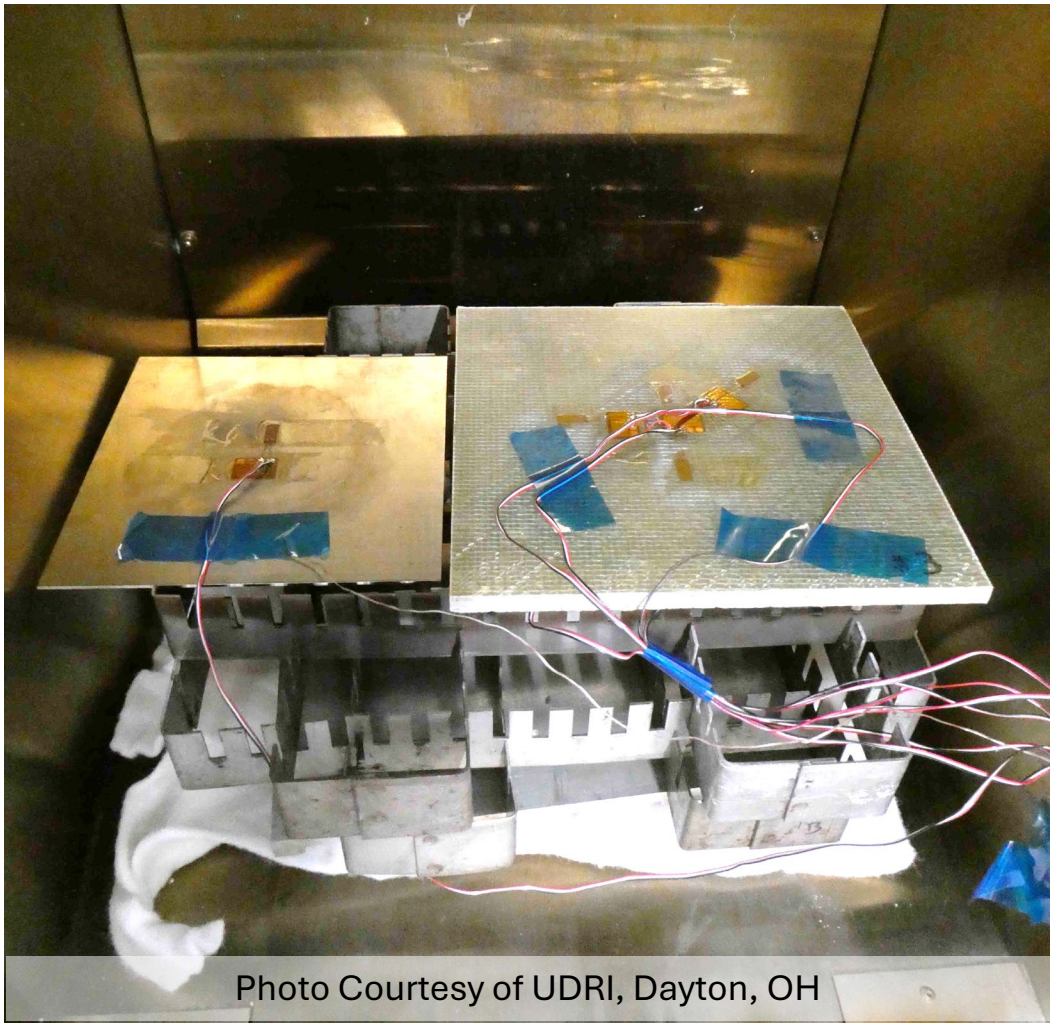

Reference Gauge on Standard Panel Occupies ¼ of Wheatstone Bridge

Separate Circuits Constructed for the Upper and Lower Faces

Assembly Testing of Exterior Wall Panels



- Air Penetration
- Water Penetration
- Sound Transfer
- Heat Transfer
- Smoke Evolution
- Flame Spread
- Environmental

A Very Early NFPA 285 Test Specimen

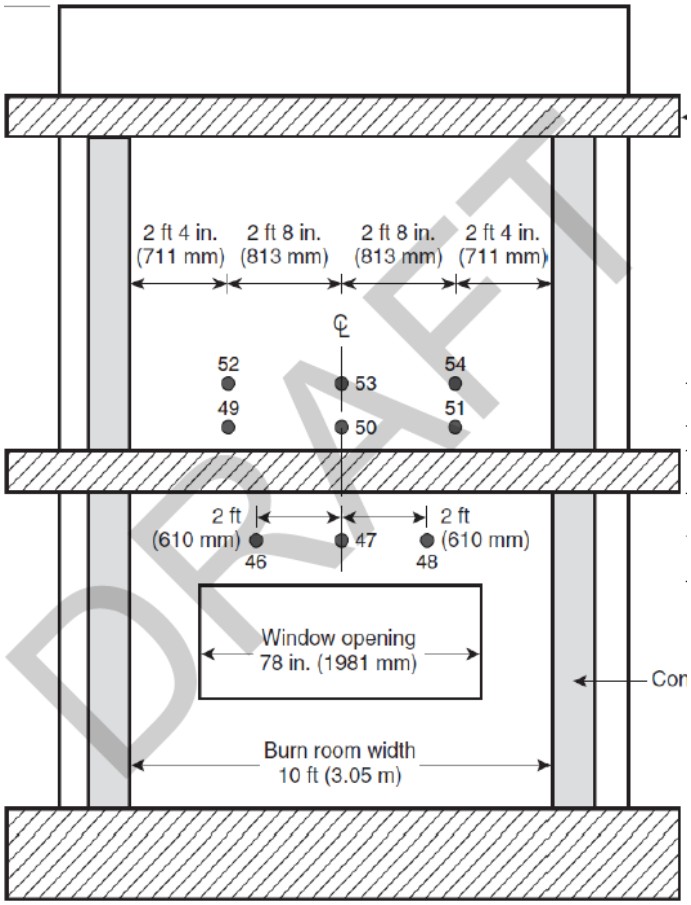

TC Location Schematic

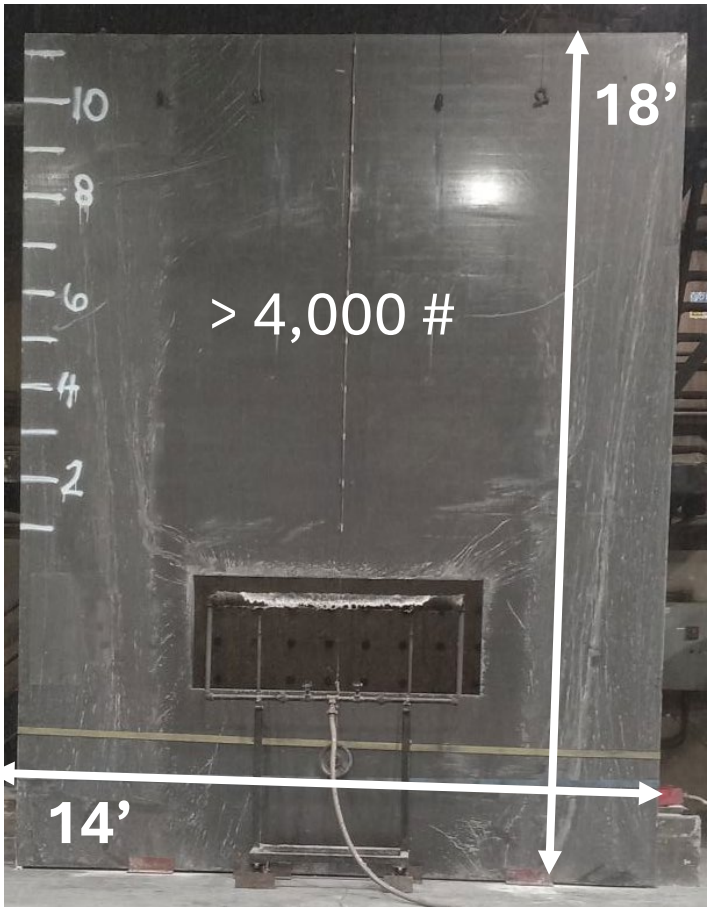

Unitary Sandwich Panel

NFPA 285 – A Sequence of Intensifying Fluxes

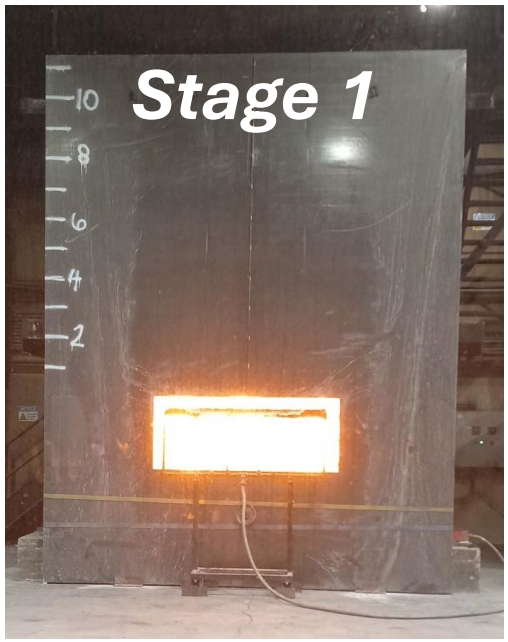

Room Burner is Activated

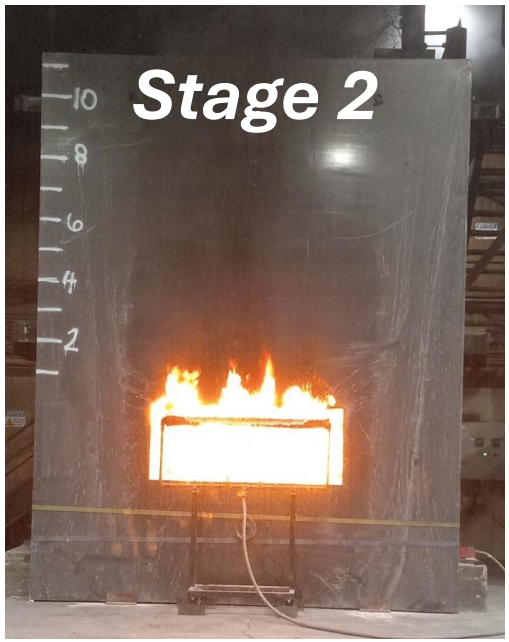

Window Burner Is Activated



Combined Burners Ramp Up Heat

Stage	1	2	3	4	5	6
Time (min)	0 - 5	5 -10	10 – 15	15 – 20	20 – 25	25 - 30
Room Gas (CFM)	35.50	35.50	43.75	43.58	43.58	47.37
Window Gas (CFM)	0.00	4.30	5.60	8.10	11.00	15.60

Understand the Intent of Standards

A Unitary Wall Panel is Not Anticipated by NFPA 285



Horizontal and Vertical Joints are Required in the Fire Zone

Revised NFPA 285 Wall Assembly Specimen



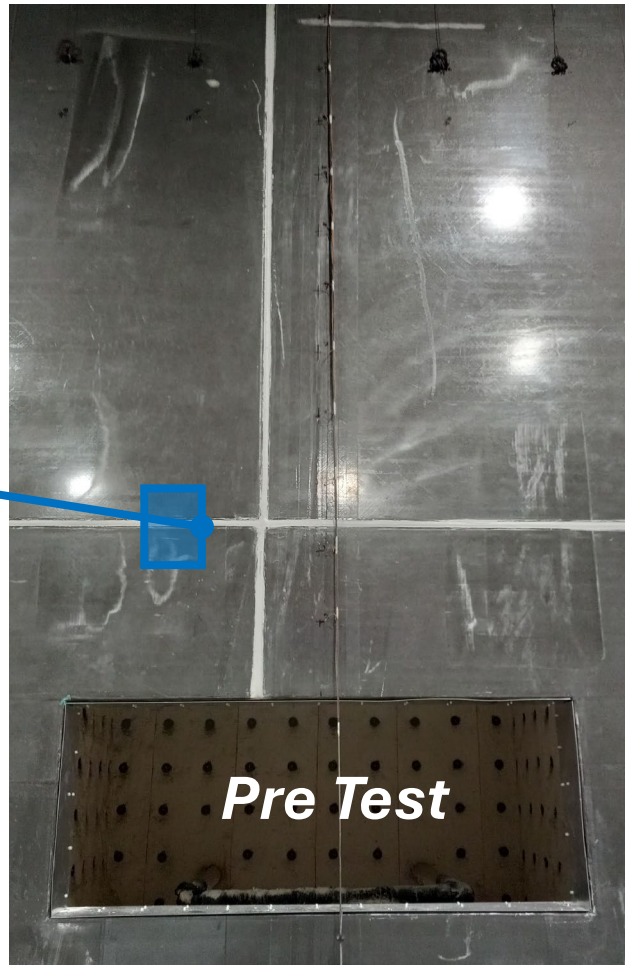

Places Panel Edges, Specified Sealant & Backer Rod in Fire Zone

Combining Reductive & ADM on 3/2 CNC

Offers Architectural Freedom w/Inflexible Schedules



Rough Cut Foam Backer



Coat Shaped Foam w/ Paste

Combining Reductive & ADM on 3/2 CNC

Requires BIM / REVIT / CAD / FEA / CAM Inter-Operability



Cure Paste Coating Layer



Rough & Final Finish Plug/Tool

It's Costly Not to Manage Waste Streams





Pragmatic Circularity

Create Clean Streams

Homogenize & Densify

Green Stocks

Efficient Trash

Options to Re-Use Closed Cell Foam Scrap

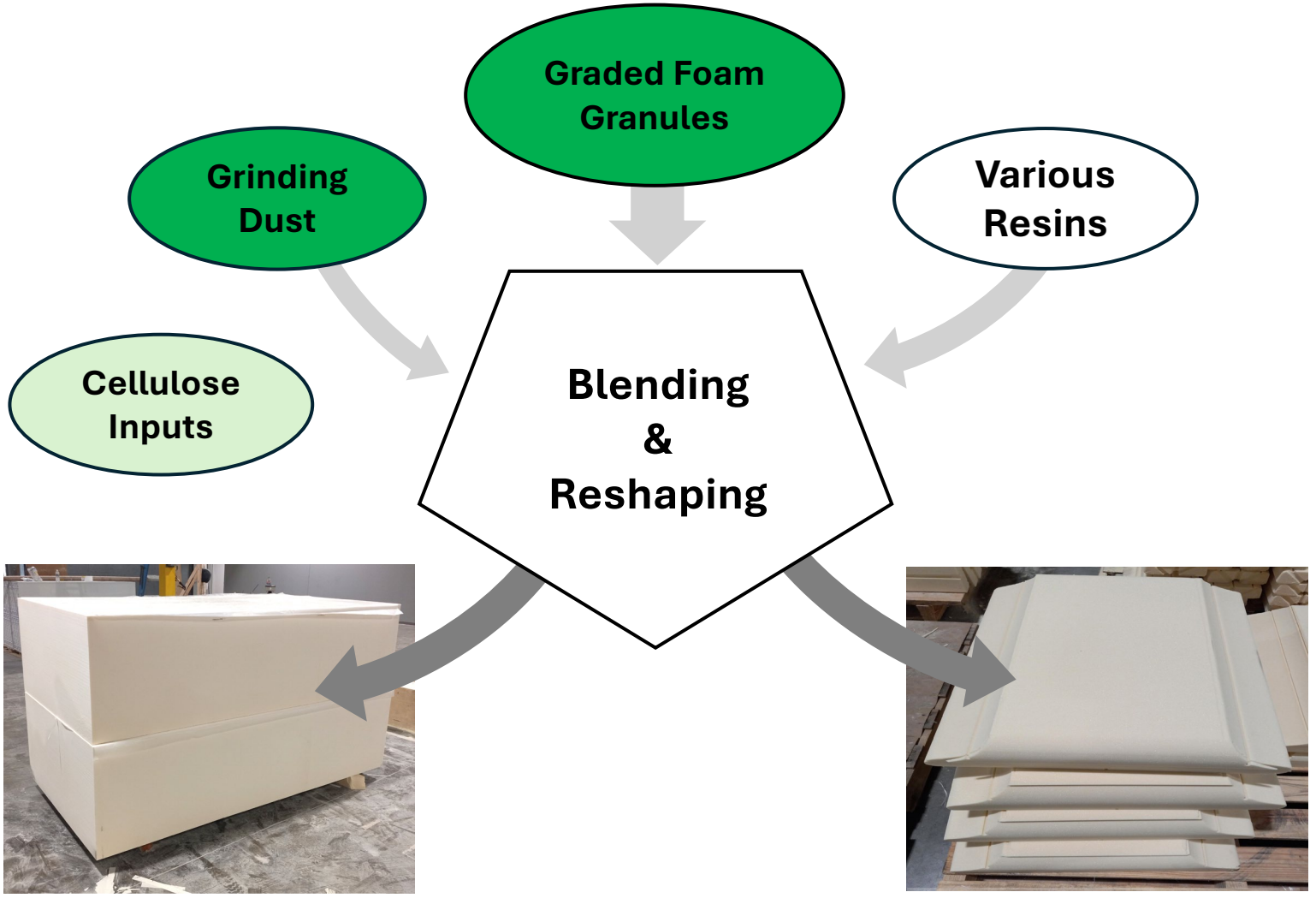

rrydin@building-composites.com



Questions ?

Photo Courtesy of Building Composites

ICCM24
AUGUST 4-8, 2025
BALTIMORE CONVENTION CENTER
BALTIMORE, MARYLAND, USA

No Technical Paper Submission for:

Alex Vanarelli

ICCM24
AUGUST 4-8, 2025
BALTIMORE CONVENTION CENTER
BALTIMORE, MARYLAND, USA

No Technical Paper Submission for:

Jimmy Jean

NUMERICAL ANALYSIS OF MACROVOID FORMATION PROCESS IN A SINGLE-LAYERED WOVEN FIBRE BUNDLE CONFINED BETWEEN PARALLEL PLATES

M. Inagawa[1], T. Ito[1], S. Yamashita[1+] and I. Ueno[2]

1 Division of Mechanical & Aerospace Engineering, School of Science & Technology, Tokyo University of Science 2641, Yamazaki, Noda, Chiba 278-8510, Japan
2 Department of Mechanical & Aerospace Engineering, Faculty of Science & Technology, Tokyo University of Science, 2641 Yamazaki, Noda, Chiba 278-8510, Japan

* Corresponding author: I. Ueno (ich@rs.tus.ac.jp)
+ Original affiliation: Division of Mechanical Engineering (affiliation name was changed after the graduation)

Keywords: Resin transfer moulding (RTM), Wettability, Fibres, Numerical analysis

ABSTRACT

We numerically analyse macrovoid formation in a single-layer woven fibre bundle confined between parallel plates, focusing on the effects of capillary number (Ca) and wettability. The volume-of-fluid (VOF) method is employed to capture the interface, and the continuum surface force method (CSF) is applied to treat the surface tension as the body force. The simulation captures the dynamic evolution of the flow front, showing that low Ca and small contact angles induce non-uniform impregnation and frequent snap-off events, resulting in forming macrovoids. Detailed analysis of velocity and shear stress distributions reveals abrupt interface deformation and local shear stress increases near snap-off regions. These localized dynamics strongly influence the progression and coalescence of flow fronts. The final macrovoid fraction decreases with increasing Ca, fibre–liquid contact angle (θ_f), and wall–liquid contact angle (θ_w). The observed dependence on a modified capillary number is consistent with previous experimental results.

1 INTRODUCTION

Void formation during the impregnation process in fibrous reform has been widely recognized as a critical issue in composite manufacturing, decreasing the mechanical properties of the final product [1-3]. The volume fraction of voids is known to depend sensitively on the capillary number $Ca = \mu \cdot U/\sigma$ [4-6], which characterizes the balance between viscous stress and surface tension. It must be emphasized that the optimal value of Ca to minimize the formation of macro- and microvoids is not universal, but rather depends on the specific geometric and wetting properties of the specific systems [7,8]. Consequently, the development of a generalized predictive model remains difficult. This system-dependent nature of void formation necessitates a more detailed investigation into the local dynamics of interface deformation and fluid displacement mechanisms, especially in terms of snap-off event which is important for the entrapment of non-wetting phase fluids in porous media [9,10].

Previous numerical simulations of impregnation process in RTM and VARTM have employed Darcy-scale models to predict the pressure and flow fields within the fibrous preform [11-13]. Whist such models are computationally efficient and provide valuable insights into macroscopic flow behavior, their formulation based on averaged quantities poses limitations in capturing local interfacial dynamics at the pore scale. In particular, detailed mechanisms such as dynamic wetting, curvature-driven pressure difference, and snap-off-induced interface redistribution are often beyond the resolution of Darcy-based approaches [14]. Consequently, predicting the precise formation processes of individual voids remains a nontrivial task within this modeling framework. Whist, investigations in soil and petroleum engineering have suggested that snap-off events—where the non-wetting phase becomes disconnected due to capillary instabilities—can influence fluid entrapment behavior, even in single-scale porous media [9,10]. These findings imply that the interaction between local pore geometry and interfacial dynamics may be more relevant than previously assumed, particularly in the context of multiphase

displacement.

In this study, we address this issue by modeling the flow field within a single-layer woven fibre bundle between parallel plates, instead of using the previous Darcy-scale approach. Using key parameters such as the capillary number (Ca), which represents the impregnation velocity of the liquid, and the wettability between the liquid and fibres, as well as between the liquid and the top and bottom walls, we analyze the behavior of the flow front and the flow field within the liquid, focusing on macrovoid formation processes.

2 METHOD

The analysis domain considered in this study is shown in Fig. 1. We simulate a single-layer woven fibre bundle enclosed by parallel plates, with the domain dimensions $(L_x\, L_y\, L_z)$ [μm] = $(9500, 700, 4600)$. The main-flow-direction length of the unit cell L_u is of 4600 μm. The distance between the warp and weft fibre bundles (or, size of inter-bundle region in the x and z directions) is set at 1.1 mm. The fibre diameter D_f is of 320 μm, and the distance between fibres d_f is of 397.5 μm = 1.242 D_f . Given the difficulty in reproducing the accurate geometry of the experimental fibres at the spatial scale of the analytical domain, the fibre volume fraction within the fibre bundle is maintained to the corresponding experimental systems, providing a relatively large fibre diameter. A no-slip boundary condition is provided to the fibre surfaces and the top and bottom walls ($(x, y = 0, z)$; $(x, y = L_y, z)$), whist mirror boundary conditions are provided to the side walls ($(x, y, z = 0)$; $(x, y, z = L_z)$). At the inlet ($x = 0, y, z$), the velocity condition $(u, v, w) = (U_\mathrm{in}, 0, 0)$ is provided, and a convective boundary condition is provided at the outlet ($x = L_x, y, z$). The properties of the liquid and gas are applied as those of 350-cSt silicone oil and air, respectively, to simulate the experiments [4]. All simulations are conducted under zero gravity acceleration $g = 0$ kg/s. The capillary number Ca is defined as $\mathrm{Ca} = \mu_\mathrm{l} \cdot U_\mathrm{in}/\sigma$, where μ_l and σ represent the viscosity of liquid and surface tension, respectively. To track the gas-liquid interface the volume of fluid (VOF) method [15] is applied, whist surface tension effects are described using the continuum surface method (CSF) [16], treating surface tension as a body force. In this study, the simulation is conducted using the `interFoam` solver of the OpenFOAM ver. 9.

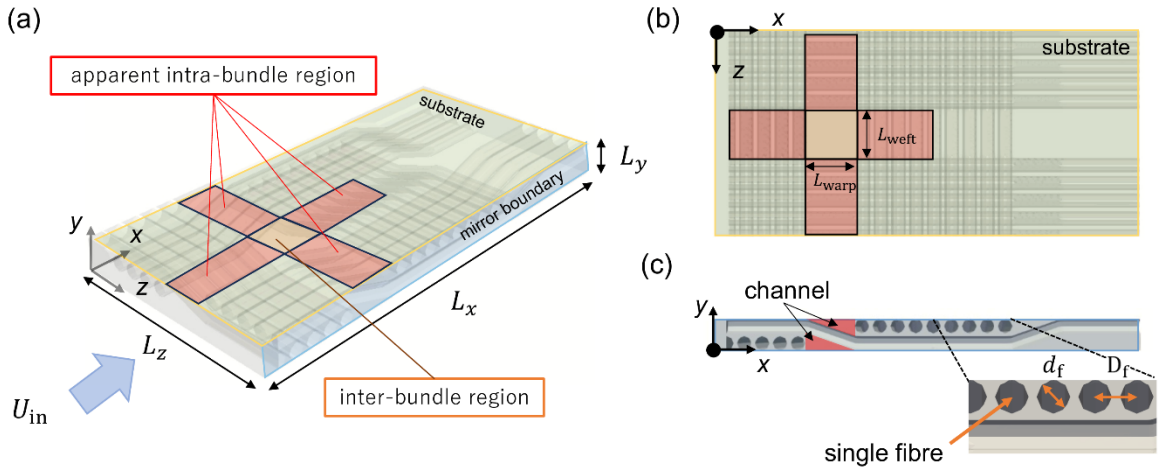

Fig. 1 Computational domain for infiltration of a viscous fluid into a single-layer woven fibre bundle confined between parallel plates: (a): bird view, (b): top view, and (c): side view.

3 RESULTS AND DISCUSSION

3.1 General impregnation process

Figures 2 (a) and (b) show the temporal variations of the permeating behaviour for $\theta_\mathrm{f} = \theta_\mathrm{w} = 20°$ via the present numerical simulation under different Ca conditions. This figure represents how the impregnating liquid (shown in deep grey) permeates a single-layer woven fibre bundle (shown in semi-

transparent light grey) under (a) Ca = 0.001, and (b) Ca = 0.01. For the sake of visibility, the flow fronts near the bottom wall (thin line) and near the top wall (thick line) are also illustrated. The normalized time, t^*, is defined as $t^* = \frac{\sigma}{\mu_l L} \cdot t$, where L is the length of the inter-bundle region in the warp direction.

In the case of (a) Ca = 0.001, the flow front advances non-uniformly near both top and bottom walls. The liquid advances preferentially in the intra-bundle region, whist significant delay occurs in the inter-bundle region. Due to this lead-lag behaviour with different spatial scales, the snap-off events occur in the apparent intra-bundle region in the downstream side of the inter-bundle region near the top wall (thick line (in blue) at $t^* = 2435$ in Fig. 2 (a)). Subsequently, another snap-off event occurs near the bottom wall (thin line (in red) at $t^* = 2675$ in Fig. 2 (a)), resulting in complete trap of the non-wetting fluid in the inter-bundle region (at $t^* = 2938$ in Fig. 2 (a)).

In the case of a higher Ca ((b) Ca = 0.01), the influence of viscous forces becomes more significant than those in the case of Fig. 2 (a), and the flow fronts near the top and bottom walls advance relatively uniformly in both of the inter-bundle and intra-bundle regions (at $t^* = 101.7$ in Fig. 2 (b)). No snap-off is observed near either wall, and the inter-bundle regions are completely filled with the permeating liquid (at $t^* = 186.4$ in Fig. 2 (b)). Under this condition, both snap-off and macrovoid formation are completely avoided. Further, the present numerical results show a qualitative agreement with the findings of previous studies using woven fibre bundles [4-7,17].

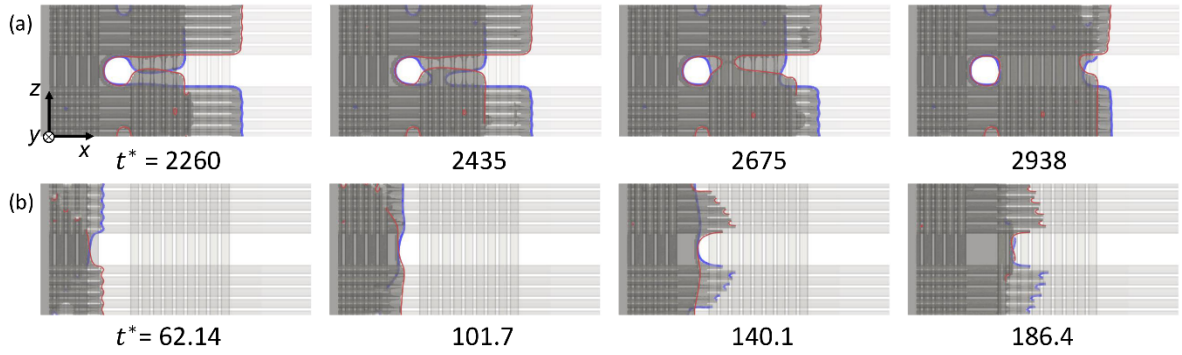

Fig. 2 Temporal variation of impregnation behavior of permeating liquid for $\theta_f = \theta_w = 20°$ under (a) $Ca = 0.001$ and (b) 0.01. Observations are made from bottom wall side. In each panel, permeating liquid is represented in dark grey, whist fibres and air are represented semi-transparently light grey. Thin- (in red) and thick- (in blue) lines denote flow fronts near bottom wall (at $y = 50$ μm and near top wall (at $y = 650$ μm), respectively.

3.2 Velocity and shear stress distributions

We discuss the effects of Ca on the impregnation process. We focus on the distributions of velocity and shear stress within the permeating liquid. Figure 3 presents successive images of distributions of the streamwise velocity (Row I), the spanwise velocity (Row II), and the shear stress in the streamwise direction (Row III) near the flow front on a plain near the bottom wall at $(x, y = 50\ \mu m, z)$. The streamwise and spanwise velocities within the permeating liquid are normalized by the inlet velocity, U_{in}, and the shear stress is normalized by the dynamic pressure $\rho_l U_{in}^2$. We first examine the effect of Ca on the velocity and shear stress distributions via Panels (a) and (b) in Fig.3.

In the case of (a) $Ca = 0.001$, when the flow front or the gas-liquid interface advances within the fibre bundle in the warp direction (at $t^* = 1525$ in Row (I)), high U_x is realized within the warp as well as in the apparent intra-bundle region, whereas low U_x is realized within the wefts. As a result, the flow front progresses non-uniformly in the spanwise direction. The liquid permeates significantly along the weft, whilst it is prevented to advance by the weft toward the streamwise direction. As time elapses, the flow front changes its advancing direction, and the encountering flow fronts merge and coalesce, causing the snap-off events (see region (A) at $t^* = 2675$). That is, in this region, there exist two gas-liquid interfaces advancing opposite directions in the streamwise direction after the snap-off: Negative

component of the streamwise velocity is distributed in the upstream side near the of upstream-side interface, whist its positive velocity component is distributed in the downstream side of the downstream-side interface. As a result, a residual bubble, or the void, is formed (at $t^* = 3164$) as demonstrated by previous experimental [7,16,18] and numerical [7-10] works. From the distribution of the spanwise velocity U_z near the snap-off region (region (A) at $t^* = 2675$ in Row (II) in Fig. 3 (a)), the liquid permeates from the spanwise direction toward this region. Then the shear stress τ_x near the snap-off region (region (A) at $t^* = 2685$ in Row (III) in Fig. 3 (a)) locally increases drastically. As the snap-off event occurs, the permeating liquid is driven further by the Young-Laplace pressure difference acting on the regions near the interfaces with different curvatures, resulting in the significant variations of velocity and shear stress.

In the case of (b) $\mathrm{Ca} = 0.01$, the gas-liquid interface advances without being held at the edge of bundles forming the inter-bundle: The absolute value of the shear stress under this condition (see Row (III)) is uniformly lower compared to Fig. 3 (a). These results indicate that Ca significantly governs the liquid mobility and the corresponding shear stress within the permeating liquid.

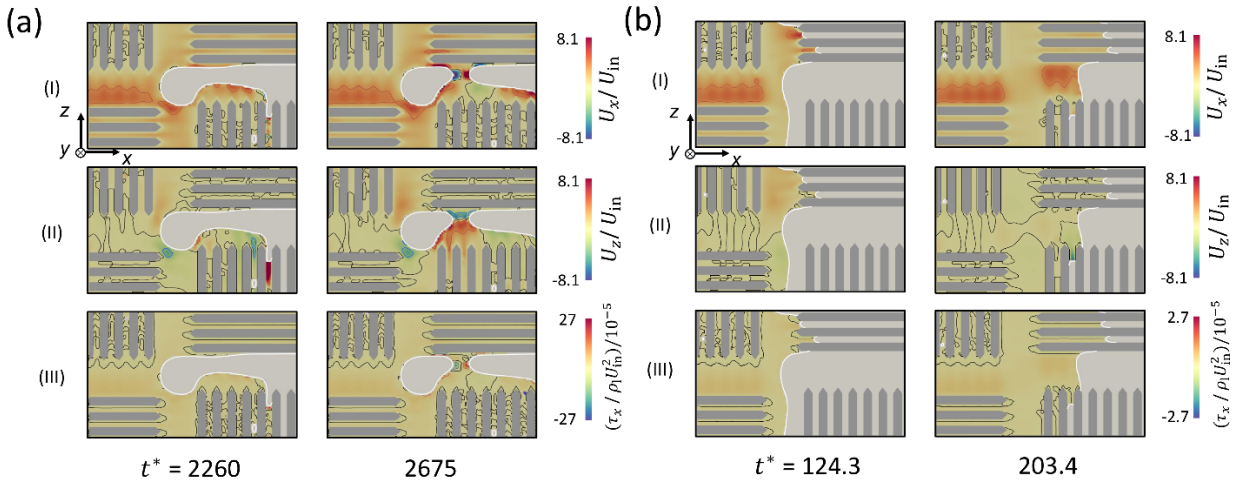

Fig. 3 Effect of Ca on velocity and shear stress distributions at $\mathrm{y} = 50$ μm. Rows (I)--(III) indicate streamwise velocity, spanwise velocity, and shear stress in streamwise direction, respectively. Conditions of Panel (a) and (b) correspond to those in Fig. 2:(a) $(\mathrm{Ca}, \theta_\mathrm{f}, \theta_\mathrm{w}) = (0.001, 20°, 20°)$ and (b) $(0.01, 20°, 20°)$.

3.3 Macrovoid fraction

We demonstrate that the snap-off event is crucial and governing factor on the entrapment of non-wetting fluid, or the void formation. In this section, we examine the correlation between the contact angles, θ_f and θ_w, and the apparent macrovoid fraction. The apparent macrovoid fraction is evaluated at each time step as the ratio of the gas volume in the mold gap to the initial gas volume in the unit cell. In other words, it represents the void fraction excluding voids formed within the fibre bundles (microvoids). Hereafter, this is referred as the macrovoid for the sake of brevity. Left panel of Fig. 4 illustrates the typical example of temporal variation of the macrovoid fraction in the unit cell from the start of impregnation under different Ca. The macrovoid fraction decreases as time elapses as indicated in the previous studies [8,11,12,17,18]. The macrovoid fraction significantly drops and converges more rapidly as the capillary number (inlet velocity) increases [8,11,12]. Under the condition $(\mathrm{Ca}, \theta_\mathrm{f}, \theta_\mathrm{w}) = (0.001, 20°, 20°)$, a macrovoid is formed, resulting in a final macrovoid fraction greater than zero. To evaluate the macrovoid fraction after a sufficient time following the completion of impregnation, the end of impregnation is defined as the point at which the variation rate of macrovoid fraction falls below $0.05\%/\mathrm{s}$ in this analysis. The macrovoid fraction at this fully developed point is referred to as the final macrovoid fraction hereafter. Figure 4 presents the final macrovoid fraction against the modified

capillary number, $\mathrm{Ca}' = \frac{\mu U}{\gamma \cos\theta_\mathrm{f}}$ [9]. The shape of symbols represents the contact angle between the liquid and the fibres, whist the hollow or filled symbols indicate the contact angles between the liquid and the walls. It is remarked that the modified capillary number, proposed by Patel et al., (1995), would not accurately measure the effect of wettability because it collapses under $\theta_\mathrm{f} = 90°$ nonetheless the flow front advances. For the sake of comparison with previous research, it is temporarily utilized. For lower modified capillary numbers ($\mathrm{Ca}' \sim 0.001$), the final macrovoid fraction decreases as either θ_f or θ_w increases. At intermediate modified capillary numbers ($\mathrm{Ca}' \sim 0.002$), an increase in θ_f suppresses the macrovoid formation altogether. At higher modified capillary numbers ($\mathrm{Ca}' \sim 0.01$), no macrovoid forms, even under small θ_f and θ_w. These findings demonstrate that the final macrovoid fraction is highly sensitive to the variation in θ_f, consistent with previous studies [7,8,19]. It is emphasized that, even under low Ca' conditions, the macrovoid fraction decreases by increasing θ_w for woven fibre bundles installed near the walls. The final macrovoid fraction decreases under larger θ_w, notwithstanding this effect is less pronounced than that of θ_f.

Through this study, we have focused on the impregnation and the void formation in a narrow space between parallel walls, and have clarified the dynamics and development process of the impregnation and void formation. We measure the influence of the dynamic wettability between the impregnating liquid and the fibre, and that between the impregnating liquid and the walls. It must be emphasized that, when forming larger-scale composite material especially in the thickness direction, the proportion of near-wall area decreases relatively, and it is essential to understand the snap-off phenomenon between and/or among fibre bundles. Furthermore, if we consider woven fibre bundles as a porous media consisting of multiple characteristic scale in space, understanding the spatio-temporal behavior of the formed voids, in addition to the impregnation and void formation processes, will definitely make an important contribution, not only to the material processing, but also to the application to separation and mixing processes of multiphase systems. Accumulation of knowledge in dynamics on the impregnation in a larger area and on the movement of the formed voids [7] is essential for comprehensive understanding and developing engineering technologies that handle multiphase fluid systems in porous media.

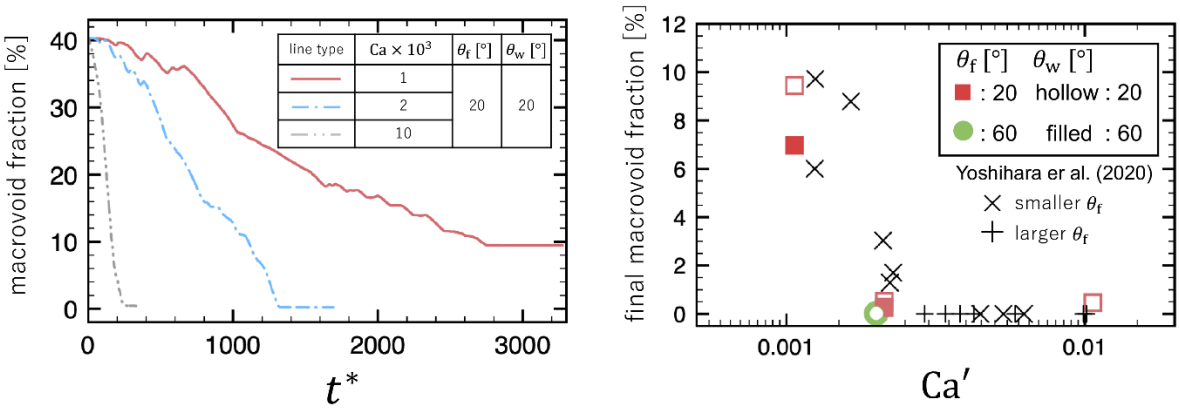

Fig. 4 Typical example of temporal evolution of macrovoid fraction for various Ca conditions under $(\theta_\mathrm{f}, \theta_\mathrm{w}) = (20°, 20°)$ (left), and correlation between macrovoid fraction in developed state and modified capillary number Ca' (right). Symbol shape in Right panel represents contact angle between liquid and fibre: square for 20° and circle for 60°. Filled style indicates contact angle between liquid and walls: Hollow (unfilled) symbols for $\theta_\mathrm{w} = 20°$ and filled symbols for 60°. Experimental data from Yoshihara et al., (2020) are also plotted in the Right panel, with crosses (×) and plus signs (+) corresponding to conditions with smaller and larger contact angle between liquid and fibre, respectively.

4 CONCLUSIONS

Displacement events of the non-wetting fluid during the impregnation process in woven-fibrous porous media are investigated, experimentally and numerically, focusing on the effects of the capillary

number (Ca) and wettability. We indicate that lower Ca not only leads to a more uneven movement of the flow front, making snap-off events more likely to occur, but also affects the mobility of the flow front. When a snap-off event occurs, the velocity of the permeating liquid increases rapidly near the snap-off occurrence region due to gas-liquid interface deformation, and the shear stress locally rises.

The influence of these factors is evident not only in the nature and behaviour of the displacement events but also in the final macrovoid fraction. A lower Ca and smaller contact angles promote snap-off events, leading to increased void trapping, whereas a higher Ca and larger contact angles favor more uniform flow and pore-filling events. The correlation between the modified capillary number and the final macrovoid fraction is particularly noteworthy, as it aligns with findings from previous studies [4,8], validating the robustness of present results.

These findings provide significant insights, not only for optimizing composite manufacturing processes to achieve more uniform impregnation and reduced void formation, but also for broader applications dealing with two-phase flow with free surface: Controlling water flow in fuel cell catalysts and managing gas/liquid separation in porous media with complex flow paths, such as in environmental control systems for orbital structures [20-23]. The ability to fine-tune flow behaviour in such systems highlights the broader impact and applicability of this research in advanced engineering and scientific fields.

ACKNOWLEDGEMENTS

This research was partially supported by the Grant-in-Aid for scientific Research (B) (Grant No.: 24K00824) from the Japan Society for the Promotion of Science (JSPS). One of the authors, MI, acknowledges the Advanced Centre for Computational Materials Science (ACCMS), Kyoto University, for providing their supercomputer resources (JFY2024 & 2025) for the part of the present simulations.

REFERENCES

[1] J. Varna, R. Joffe, L.A. Berglund, T.S. Lundström, Effect of voids on failure mechanisms in RTM laminates, Compos. Sci. Technol. 53 (1995) 241–249.

[2] L.F. Nielsen, Composite Materials: Properties as Influenced by Phase Geometry, Springer, 2005.

[3] K.K. Chawla, Composite materials: Some recent developments, JOM 35 (1983) 82–87.

[4] V. Rohatgi, N. Patel, L.J. Lee, Experimental investigation of flow‐induced microvoids during impregnation of unidirectional stitched fibreglass mat, Polym. Compos. 17 (1996) 161−170.

[5] G.W. Lee, K.J. Lee, Mechanism of void formation in composite processing with woven fabrics, Polym. Polym. Compos. 11 (2003) 563–572.

[6] E. Ruiz, V. Achim, S. Soukane, F. Trochu, J. Bréard, Optimization of injection flow rate to minimize micro/macro-voids formation in resin transfer molded composites, Compos. Sci. Technol. 66 (2006) 475–486.

[7] H. Teixidó, B. Caglar, V. Michaud, Effect of wettability and textile architecture on fluid displacement and pore formation during infiltration of carbon fibrous preforms, Compos. Part A Appl. Sci. Manuf. 174 (2023) 107733.

[8] K. Yoshihara, Y. Kamei, A. Mizuno, H. Ohgaki, T. Hori, I. Ueno, Effect of wettability on viscous fluid impregnation in single-layer woven-fibre bundles driven by pressure difference, Compos. Part A Appl. Sci. Manuf. 138 (2020) 106049.

[9] K. Singh, H. Menke, M. Andrew, Q. Lin, C. Rau, M.J. Blunt, B. Bijeljic, Dynamics of snap-off and pore-filling events during two-phase fluid flow in permeable media, Sci. Rep. 7 (2017) 5192.

[10] K. Singh, T. Bultreys, A.Q. Raeini, M. Shams, M.J. Blunt, New type of pore-snap-off and displacement correlations in imbibition, J. Colloid Interface Sci. 609 (2022) 384–392.

[11] C. DeValve, R. Pitchumani, Simulation of void formation in liquid composite molding processes, Compos. Part A Appl. Sci. Manuf. 51 (2013) 22–32.

[12] N. Patel, L.J. Lee, Modeling of void formation and removal in liquid composite molding. Part II: Model development and implementation, Polym. Compos. 17 (1996) 104–114.

[13] J.S.U. Schell, M. Deleglise, C. Binetruy, P. Krawczak, P. Ermanni, Numerical prediction and experimental characterisation of meso-scale-voids in liquid composite moulding, Compos. Part A Appl. Sci. Manuf. 38 (2007) 2460–2470.

[14] W. Lei, X. Lu, W. Gong, M. Wang, Triggering interfacial instabilities during forced imbibition by adjusting the aspect ratio in depth-variable microfluidic porous media, Proc. Natl. Acad. Sci. USA 120 (2023) e2310584120.

[15] C.-W. Hirt, B.-D. Nichols, Volume of fluid (VOF) method for the dynamics of free boundaries, J. Comput. Phys. 39 (1981) 201–225.

[16] J.-U. Brackbill, D.-B. Kothe, C. Zemach, A continuum method for modeling surface tension, J. Comput. Phys. 100 (1992) 335–354.

[17] N. Patel, V. Rohatgi, L.J. Lee, Micro scale flow behavior and void formation mechanism during impregnation through a unidirectional stitched fibreglass mat, Polym. Eng. Sci. 35 (1995) 837–851.

[18] Y. Fu, X. Yao, X. Gao, Micro-mesoscopic prediction of void defect in 3D braided composites, Compos. Part A Appl. Sci. Manuf. 147 (2021) 106450.

[19] H. Teixidó, J. Staal, B. Caglar, V. Michaud, Capillary effects in fibre reinforced polymer composite processing: a review, Front. Mater. 9 (2022) 809226.

[20] M.M. Weislogel, H.D. Ross, Surface settling in partially filled containers upon step reduction in gravity, NASA Report No. E-4998, 1990.

[21] Y. Chen, M.M. Weislogel, C.L. Nardin, Capillary-driven flows along rounded interior corners, J. Fluid Mech. 566 (2006) 235–271.

[22] R. Wheeler, L. Tang, S. Wambolt, E. Golliher, J. Agui, Demonstration of Nautilus Centripetal Capillary Condenser Technology, 46th Int. Conf. Environ. Syst. (2016).

[23] M.M. Weislogel, J.T. McCraney, The symmetric draining of capillary liquids from containers with interior corners, J. Fluid Mech. 859 (2019) 902–920.

ICCM24
AUGUST 4-8, 2025
BALTIMORE CONVENTION CENTER
BALTIMORE, MARYLAND, USA

No Technical Paper Submission for:

Kieran Guoite

Prepreg Surface Morphology: A Key Factor in Minimizing Interfacial Air and Interlaminar Voids

August 4, 2025

Jaewoong Kim, Jeho Jin, Hanguk Lee, Jeonyoon Lee

Korea Advanced Institute of Science and Technology
Department of Aerospace Engineering

ICCM24
24TH INTERNATIONAL CONFERENCE ON COMPOSITE MATERIALS

Contents

1. Introduction

2. Research objective

3. Surface morphology of prepreg

4. Correlation between prepreg surface and interlaminar void

5. Conclusion

Introduction

Void formation and elimination in laminate

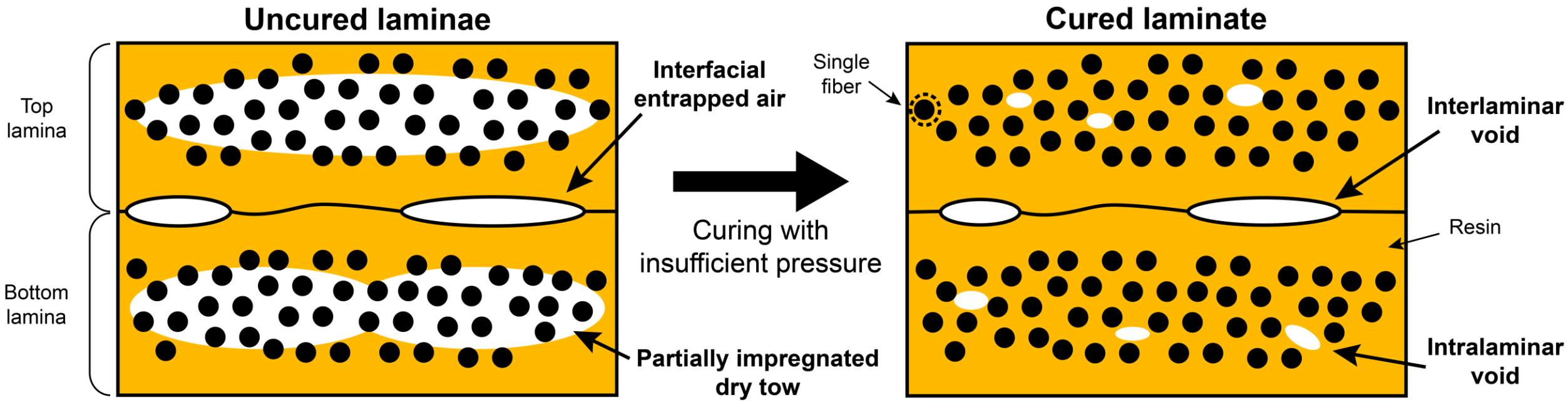

Schematic of interlaminar, intralaminar void formations in laminate

- When insufficient pressure is applied during curing, voids form within the laminate
- Partially impregnated dry tows disappear under vacuum-bag-only curing (i.e., **0.1 MPa** of pressure)[1]
- Complex techniques are used to eliminate interfacial entrapped airs but all have limitations[2-6]

[1] J. Lee et al., Advanced Materials Interfaces, 2020.
[2] F. C. Campbell, Manufacturing Technology for Aerospace Structural Materials, 2006.
[3] T. Centea et al., Composites Part A: Applied Science and Manufacturing, 2015.
[4] P. Hubert et al., Comprehensive Composite Materials II, 2018.
[5] A. N. Webb et al., *ICCM23*,2023.
[6] C. X. Li et al., in *AIAA SCITECH 2023 Forum*, 2023.

Curing with autoclave for high pressure

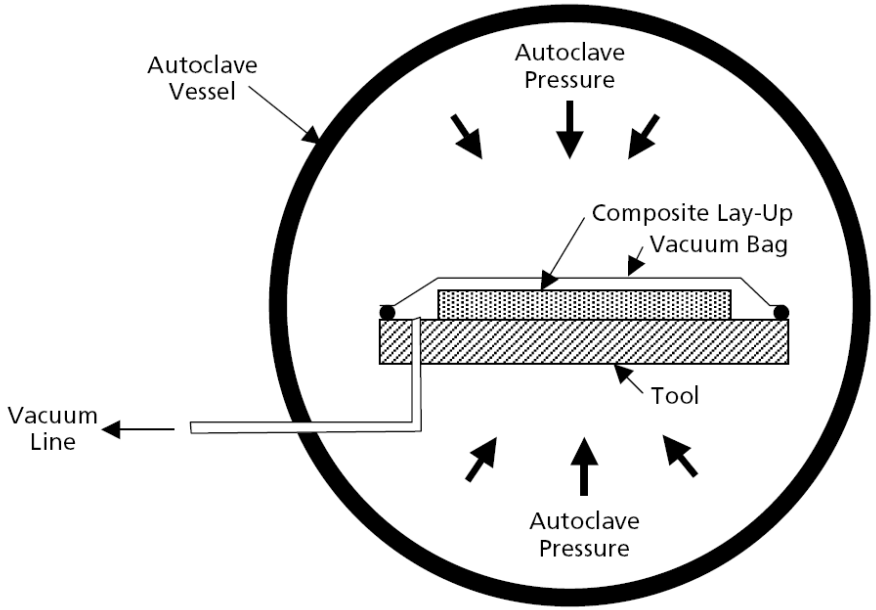

Schematic of autoclave curing[10]



Autoclave for Boeing 777X

- Autoclave uses **high pressure** to prevent entrapped air expansion[2]
- **Limitations** of autoclave:
  - **Capacity** of the autoclave **limits** the size and design of the parts[4,7]
  - Cost during a curing process accounts for **26%** of the total composite acquisition costs[8]

[2] F. C. Campbell, Manufacturing Technology for Aerospace Structural Materials, 2006.
[4] P. Hubert et al., *Comprehensive Composite Materials II*, 2018.
[7] L. Nele et al., *Procedia CIRP*, 2016.
[8] Lee, J. PhD diss., Massachusetts Institute of Technology, 2018.

Alternative of the autoclave: Out of Autoclave (OoA) prepreg

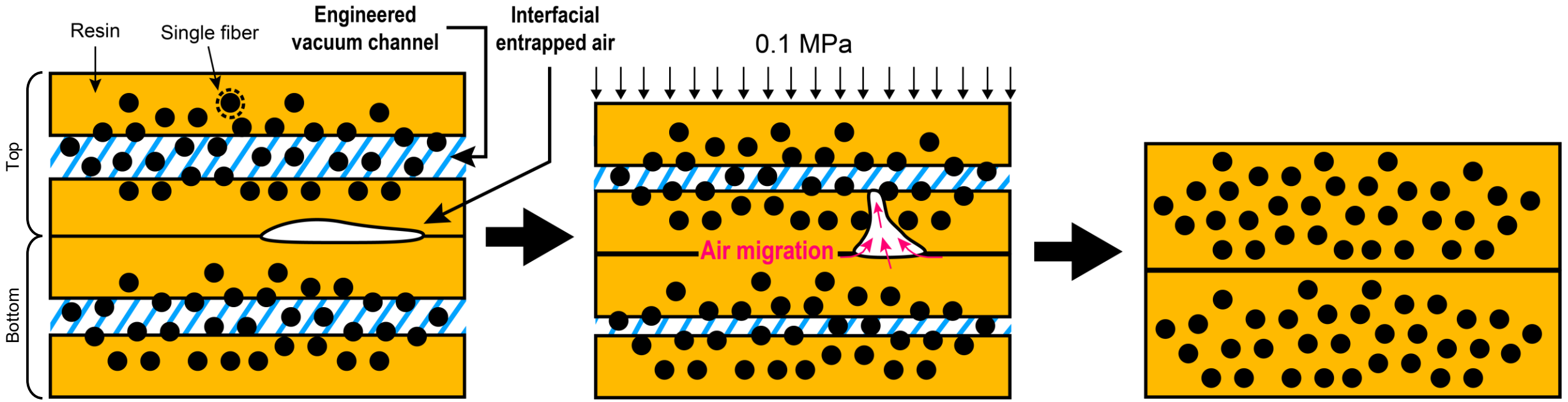

Schematic of OoA prepreg curing process

- Debulking process is performed after every 1-3 plies for air evacuation[4]
- Engineered vacuum channels are created **intentionally** for easy air migration[4]
- **Limitations** of OoA prepreg[1,3]:
  - For high resin flow, resin composition is altered from autoclave prepregs ⇨ **low reliability**
  - Numerous factors (moisture, out-time, etc) affect void-free curing ⇨ **low stability**

[1] J. Lee et al., Advanced Materials Interfaces, 2020.
[3] T. Centeaet al., Composites Part A: Applied Science and Manufacturing, 2015.
[4] P. Hubert et al., Comprehensive Composite Materials II, 2018.

OoA manufacturing strategies for next-generation layup processes

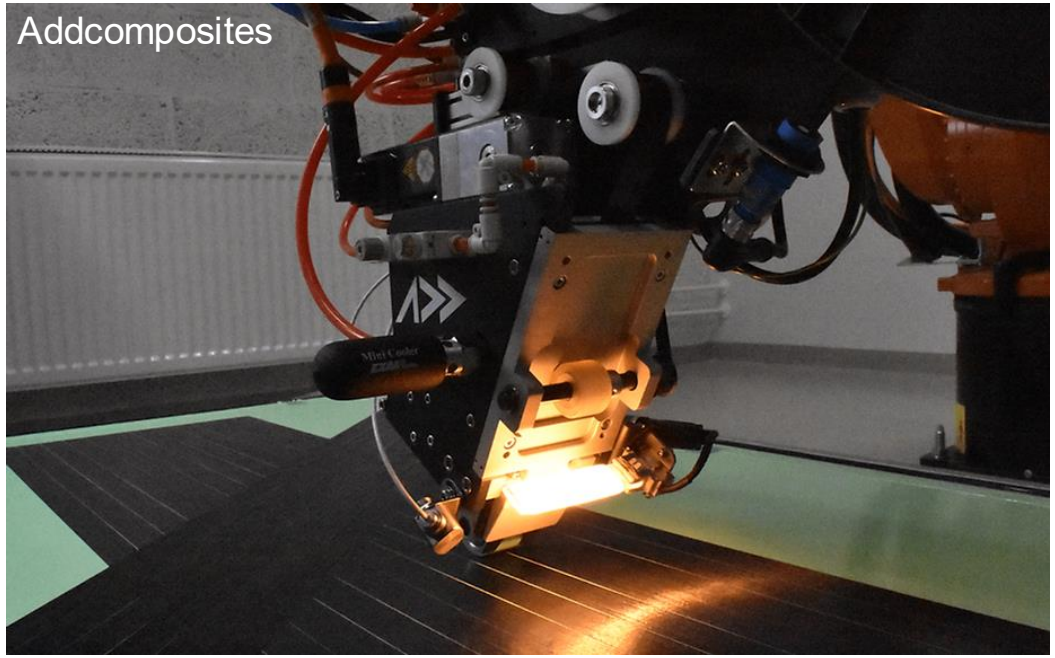

Automated Fiber Placement (AFP)

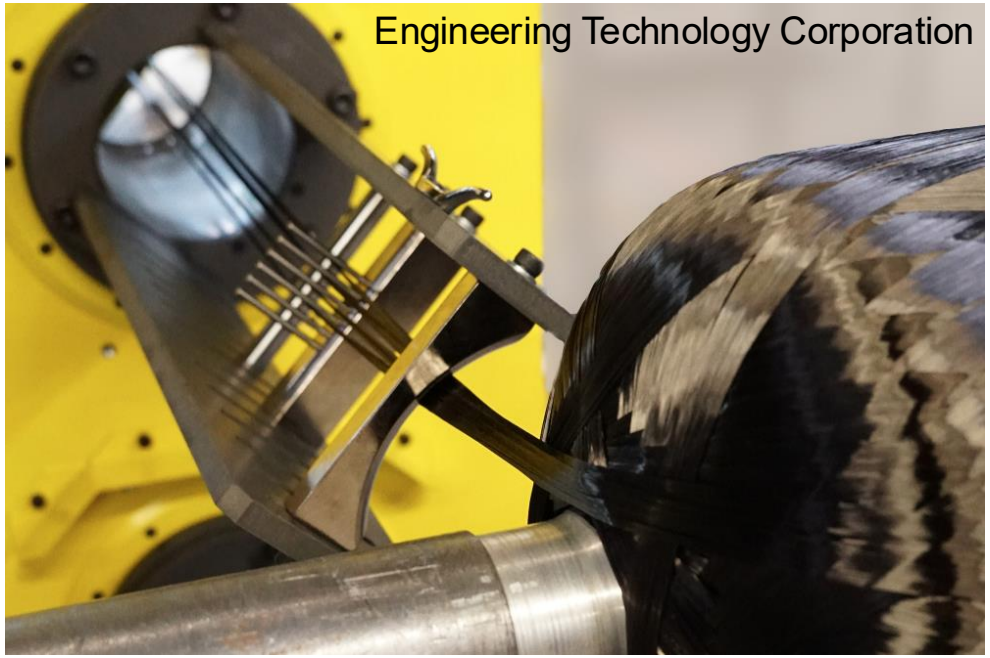

Filament Winding (FW)

- AFP and FW are automated layup processes using robotics, offering high time and cost efficiency[9]
- Since debulking is not applicable, **high compaction pressure and fiber tension** are being studied as alternatives in these processes[10,11]
- However, excessive pressure and tension may cause resin squeeze-out or fiber misalignment[11]

[9] S. Carosella et al., Composites Part B: Engineering, 2024.
[10] M. E. Bello et al., Advanced Manufacturing: Polymer & Composites Science, 2022.
[11] A. Błachut et al., Composite Structures, 2023.

Relation between prepreg surface and interlaminar void

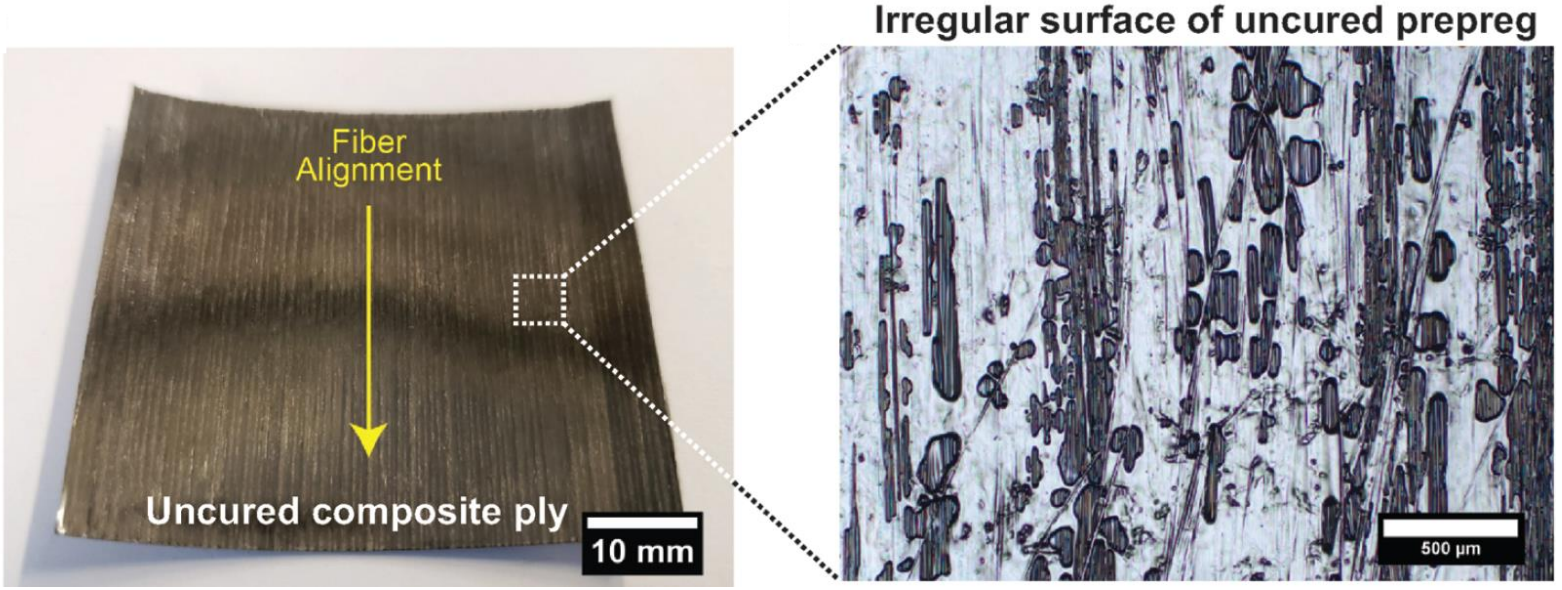

Optical image of prepreg surface[1]

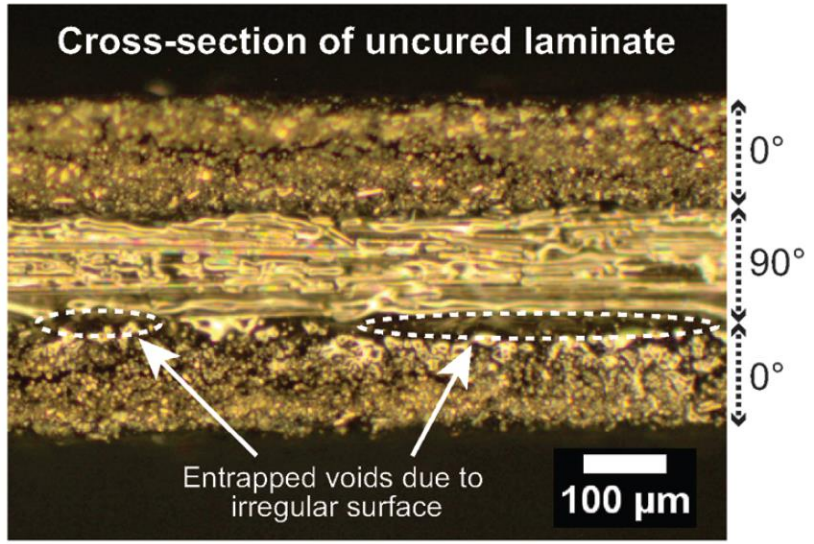

Cross-section of laminae[1]

- Rather than *compressing after layup*, eliminating the **cause of air entrapment** before layup can be more effective
- Recent study suggests that the prepreg surface may be **primary factor** in formation of the interfacial entrapped air and interlaminar void[1]

➢ Research topic: relation between **prepreg surface** and **interlaminar void** through experiments

[1] J. Lee et al., Advanced Materials Interfaces, 2020.

Research objective

To examine relation between **prepreg surface** and **interlaminar void**, these topics need to be understood:

1. Analysis of irregular surface morphology of prepreg

2. Study of correlation between prepreg surface and interlaminar void

Surface morphology of prepreg

Top and bottom side surfaces of prepreg show different textures

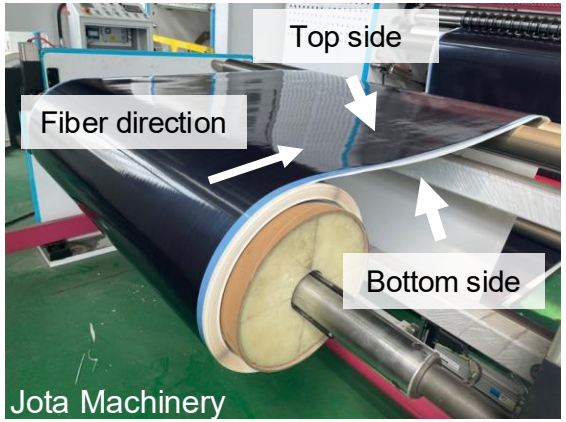

Typical unidirectional prepreg roll

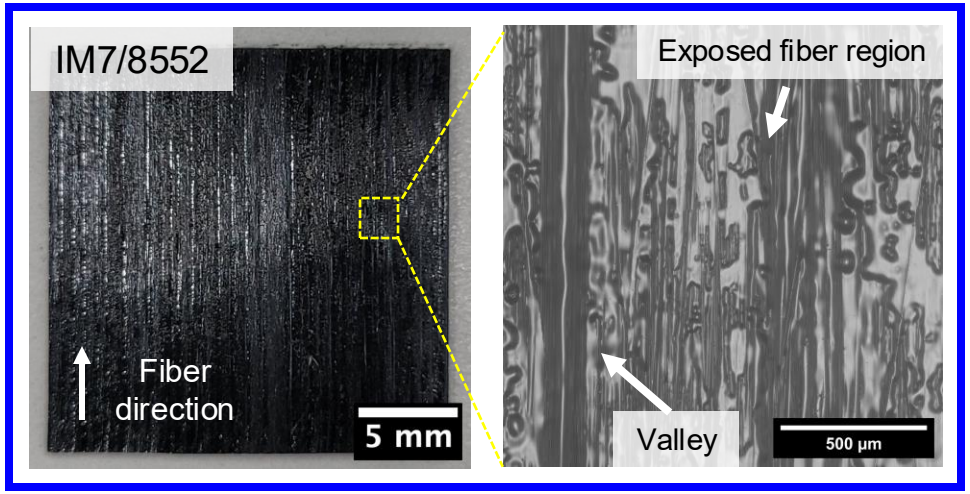

Top side prepreg surface

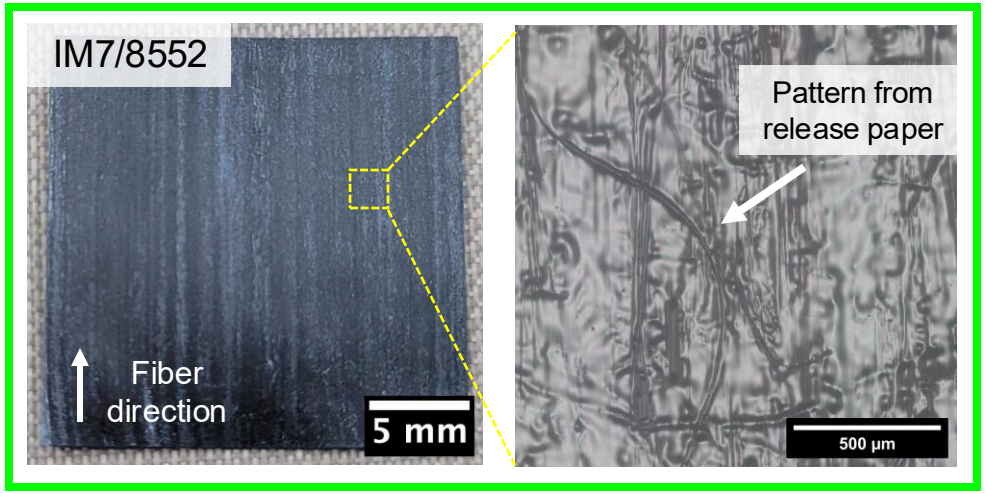

Bottom side prepreg surface

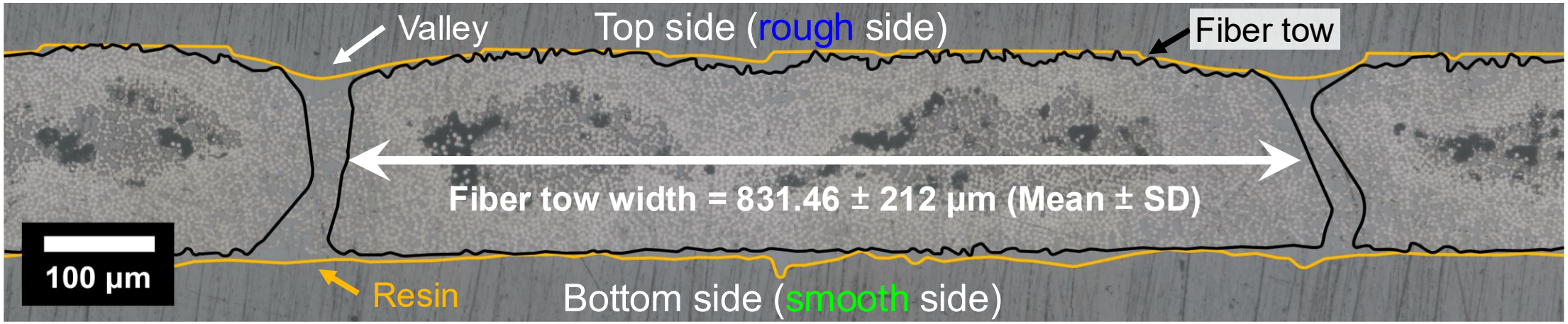

Prepreg cross-section

Height measurement of the prepreg surface

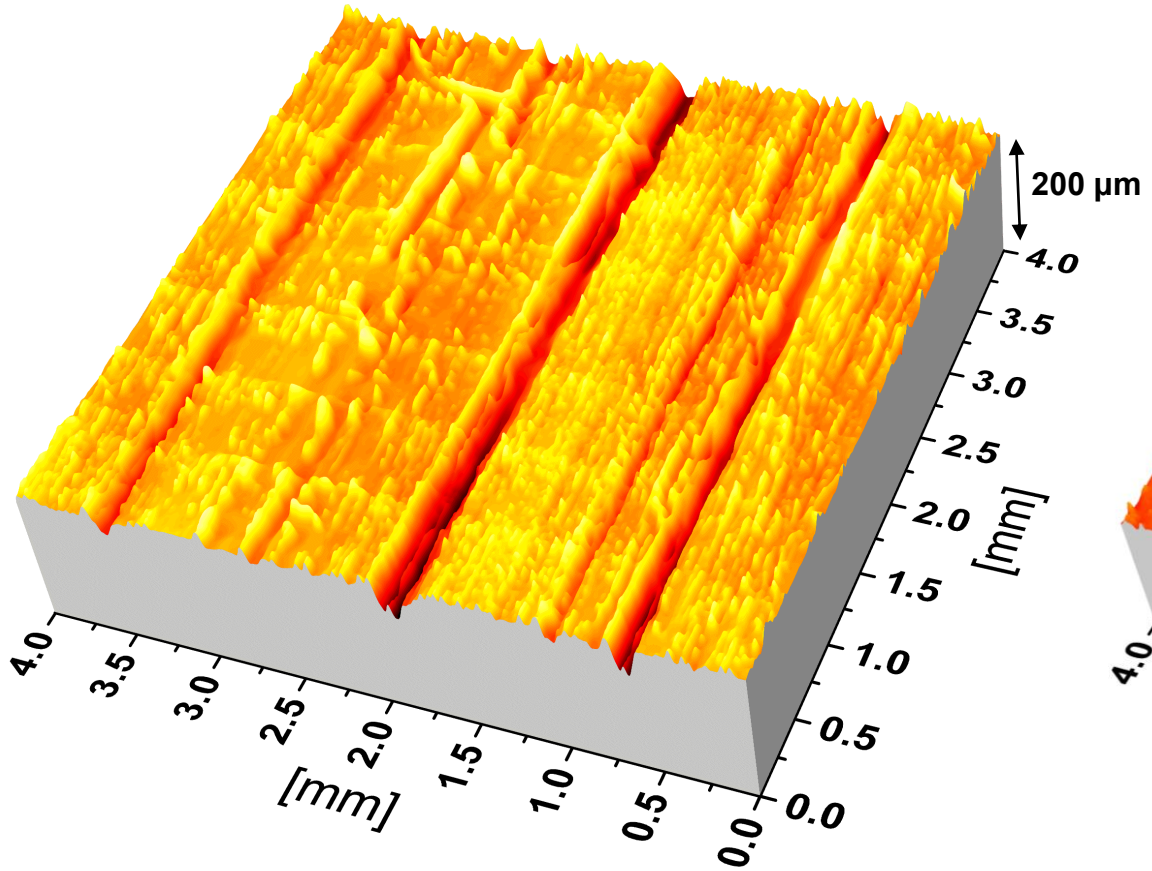

Rough side surface

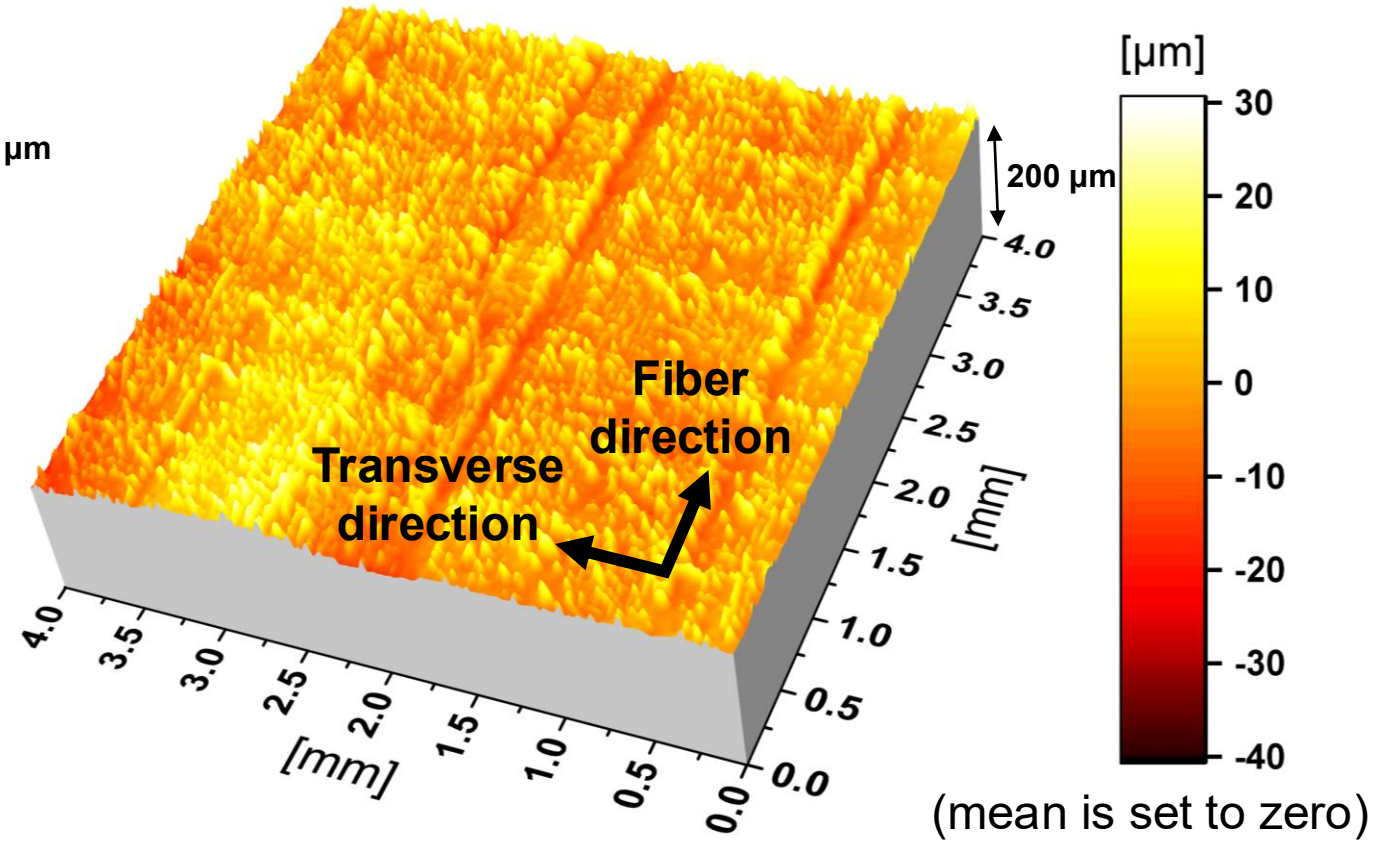

(mean is set to zero)

Smooth side surface

Transverse direction of rough surface has high roughness

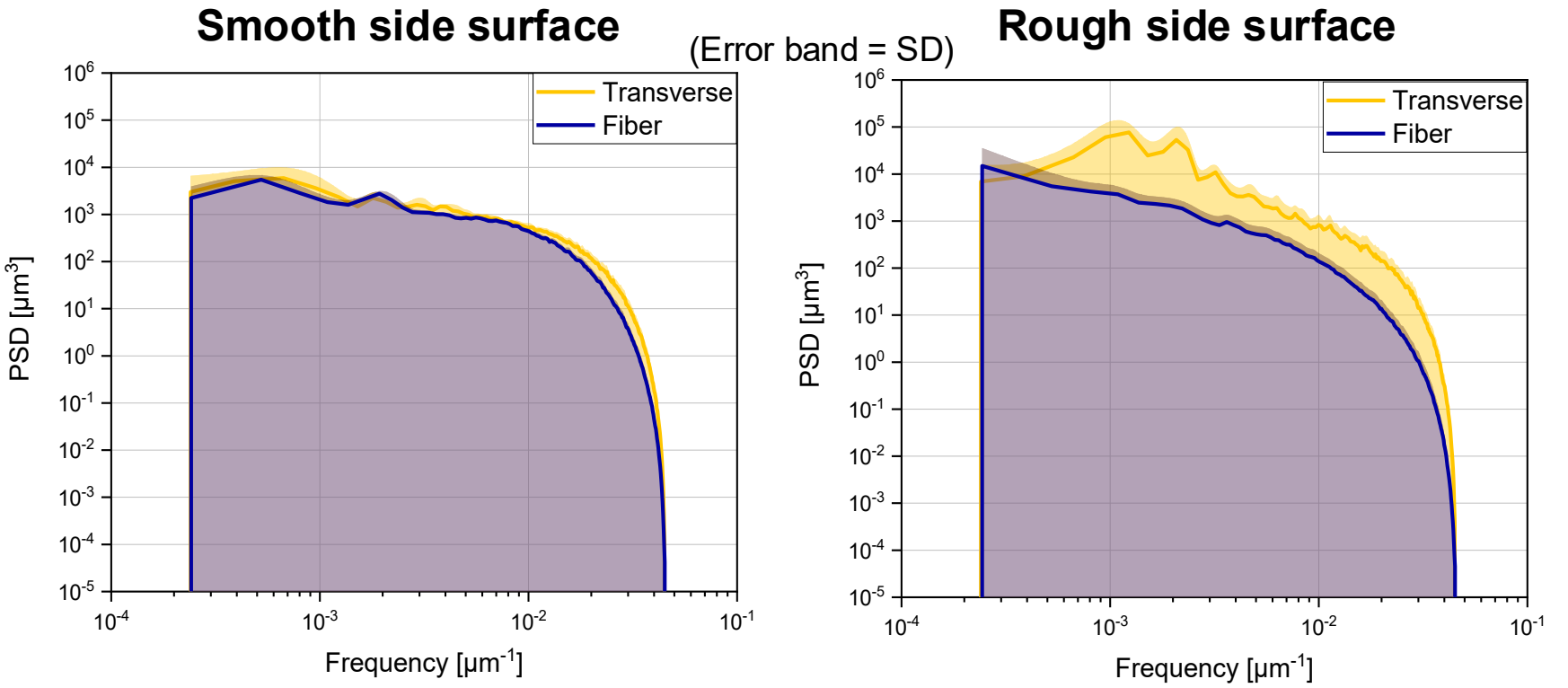

PSD curves of rough and smooth side surface

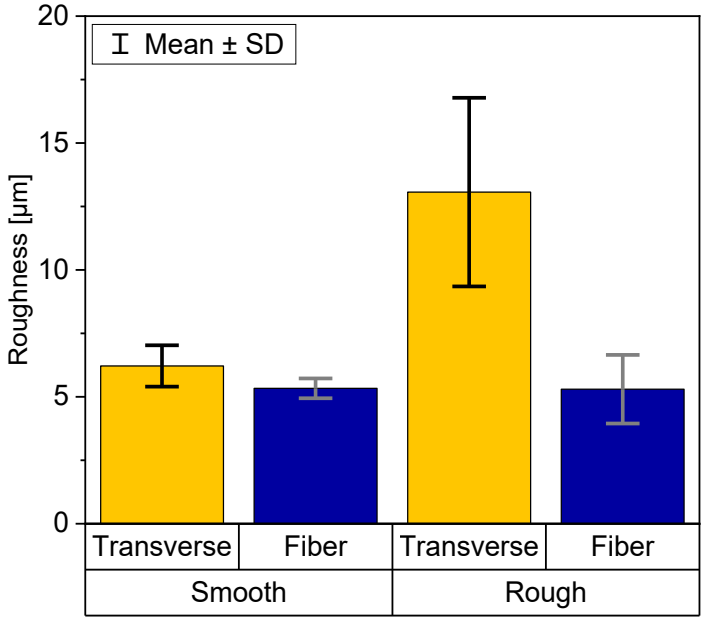

Roughnesses of each surfaces

- Power Spectral Density (PSD) represents the power of **frequencies** composing a surface[12,13]
- Area under the PSD curve is related to the surface roughness
- Transverse direction of the rough side contributes to difference in roughness between two surfaces

[12] B N J Persson et al., J. Phys.: Condens. Matter 17 R1, 2004
[13] N. Youngworth et al., Optical Manufacturing and Testing VI, 2005.

Roughness difference is caused by periodicity of surface valley

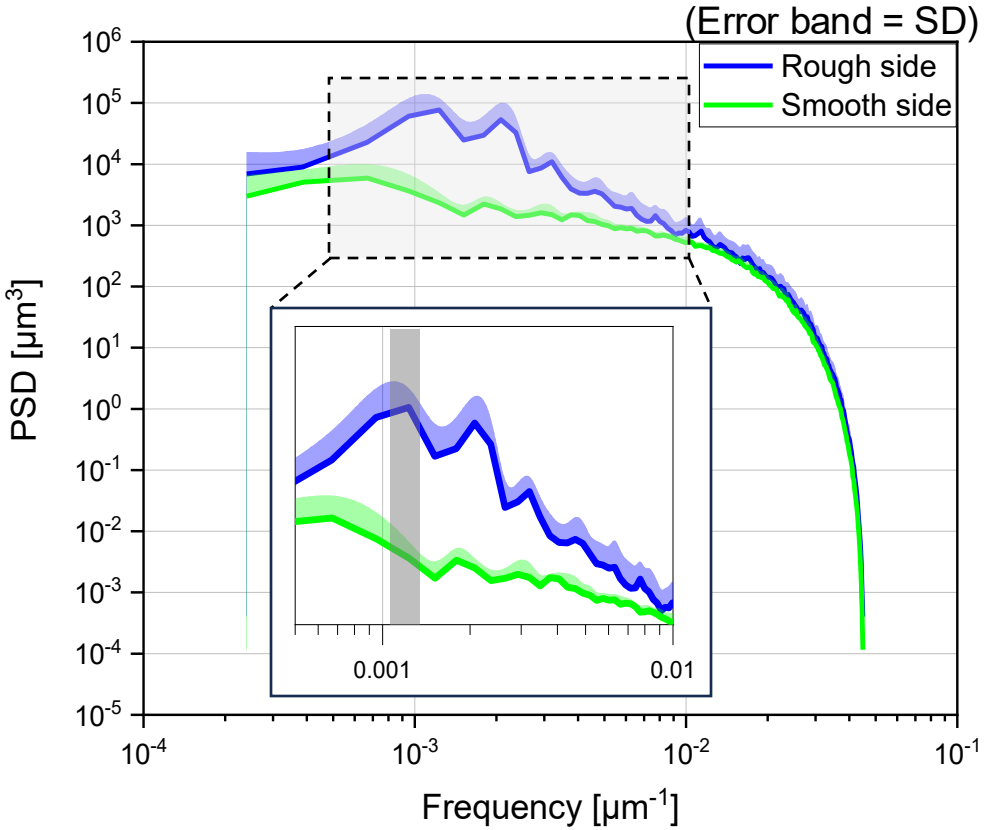

PSD curves in transverse direction

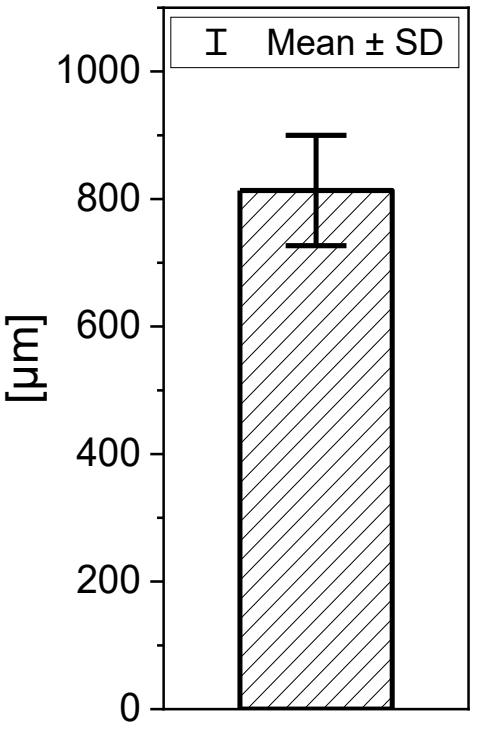

Fiber tow width

- Peak in the PSD curve indicates prominence of specific frequency component in the surface
- Rough side surface shows peak, reflecting the **periodic surface valleys**
- Roughness difference between the two surfaces arises from surface valleys at tow-tow junction

Correlation between prepreg surface and interlaminar void

Method for preserving laminae's shape: Cold-ammonia resin solidifying



Bent laminae due to gravity at room temperature

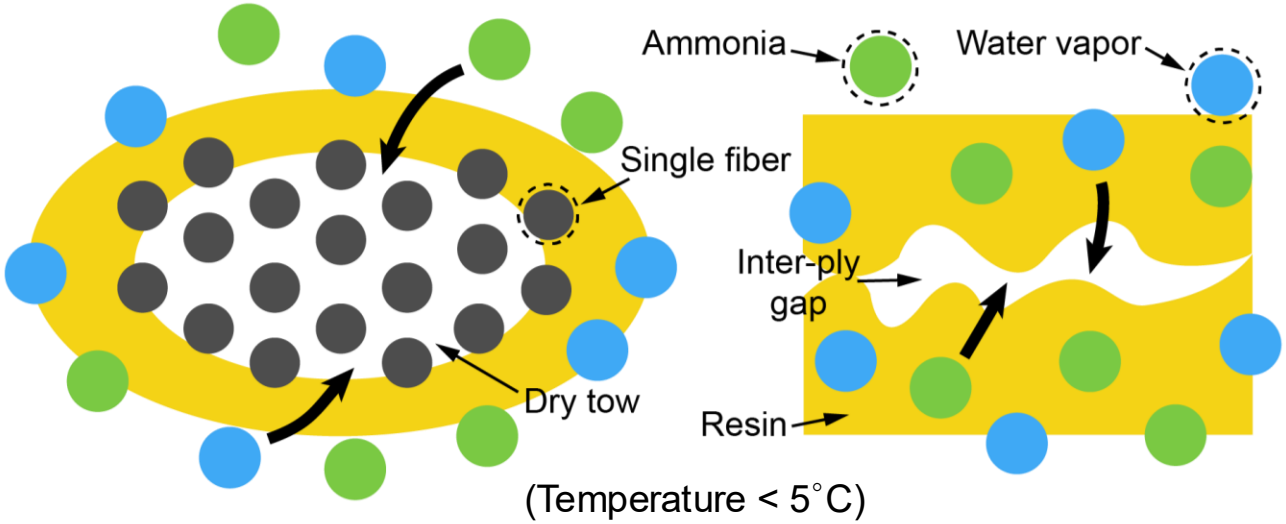

Schematic of cold-ammonia solidifying

- Since resin **deforms** at room temperature, it must be **fixed in shape** for precise imaging
- When **ammonia** and **water vapor** meet amine-curing epoxy, crosslinking is **promoted**[14]
- Maintaining temperature **below 5 ˚C** can **minimize** movement of resin[15]
- Keeping sample for 1 week at 5 ˚C, then 1 week at room temperature, can **fix** the resin

[14] I. T. Smith, *Polymer*, 1961.
[15] S. Howard, *Proceedings of the SAMPE 2016 technical conference*, 2016.

Lamina surfaces with different roughness forms different interfacial entrapped airs

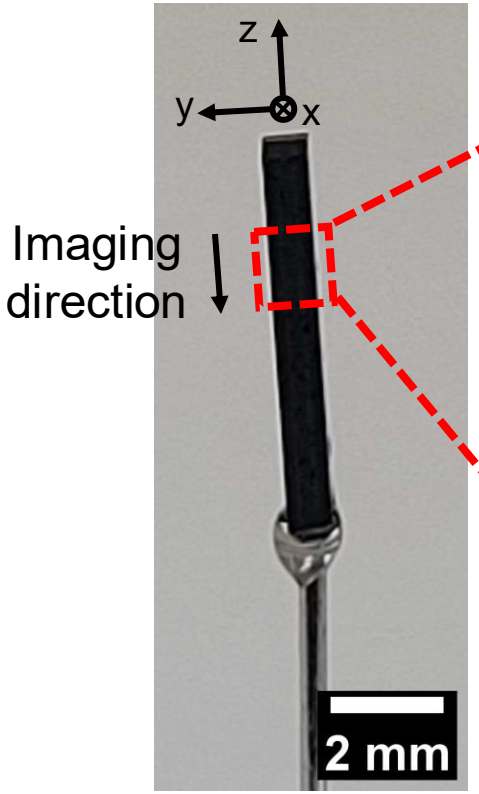

Micro-CT sample

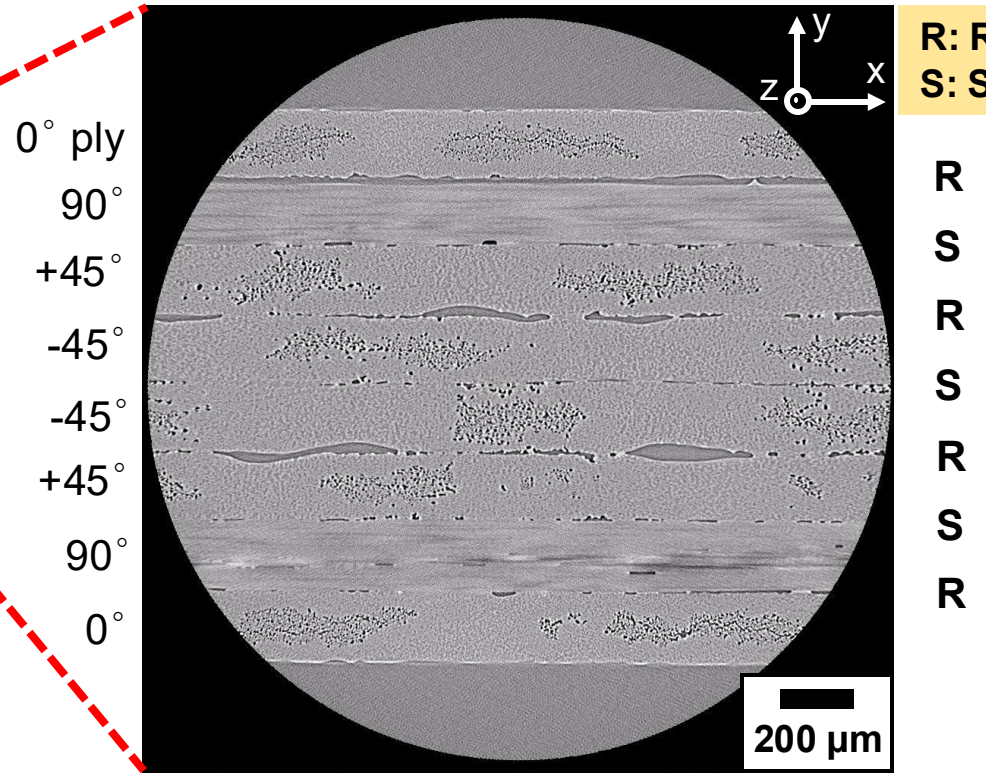

Micro-CT image sequence of laminae

R: Rough-Rough interface
S: Smooth-Smooth interface

R
S
R
S
R
S
R

- Uncured laminae and cured laminate are stacked with three interface cases:
  - **Rough-Rough**, **Rough-Smooth**, **Smooth-Smooth**
- Dark regions in the micro-CT image sequence represent entrapped airs

Entrapped air and interlaminar void show weak correlation

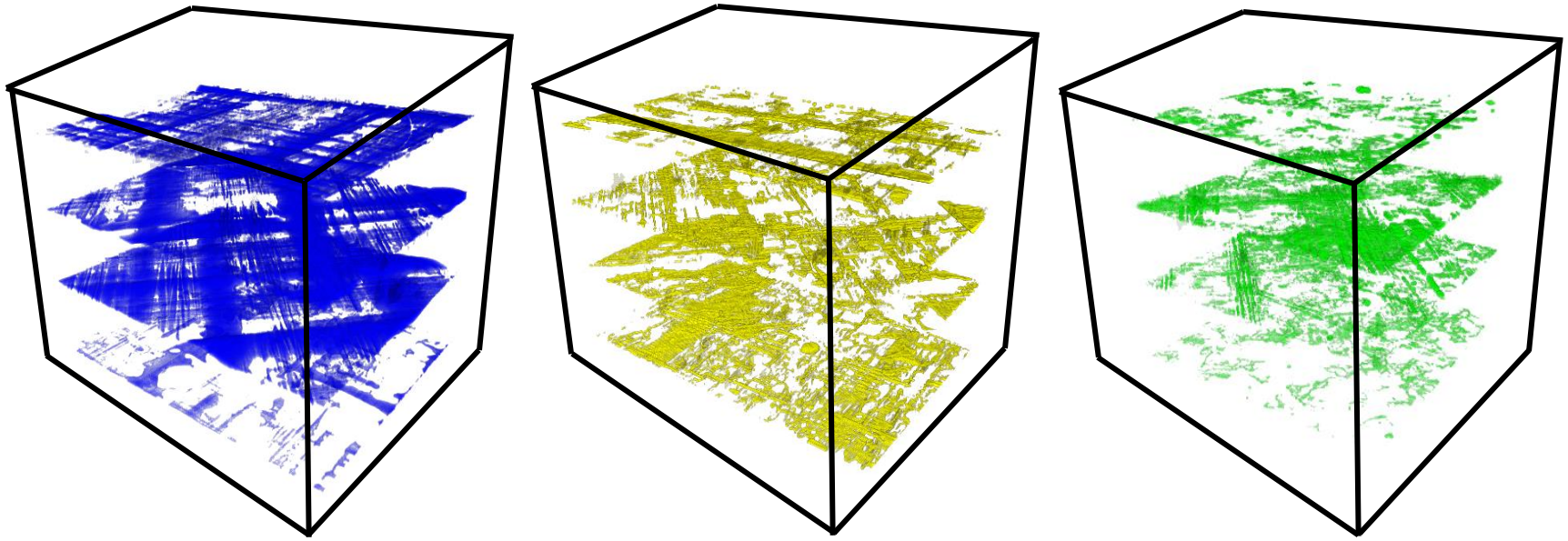

Rough-Rough, **Rough-Smooth**, **Smooth-Smooth**
interfacial entrapped airs

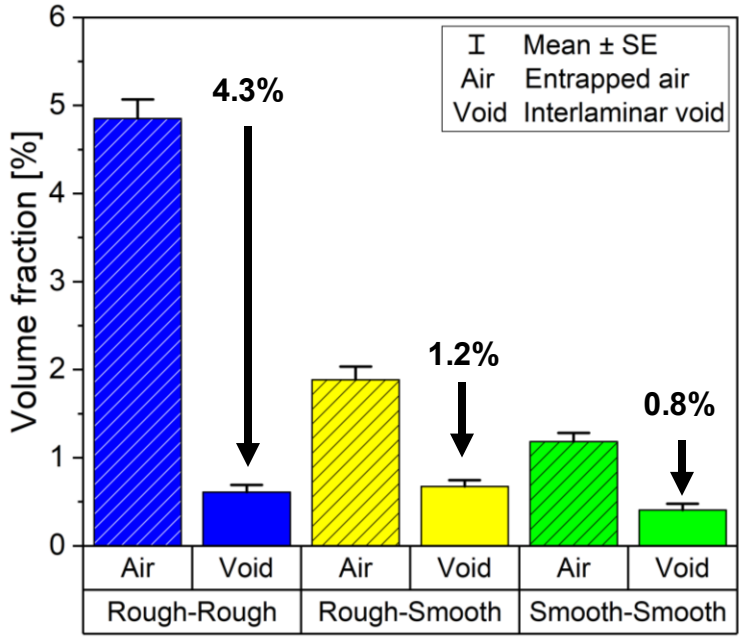

Void removal in each interface cases

- Entrapped air is removed during curing across all types of interfaces
- The greatest amount of removal occurs at the **Rough-Rough** interface

Surface valley affects connectivity of entrapped airs

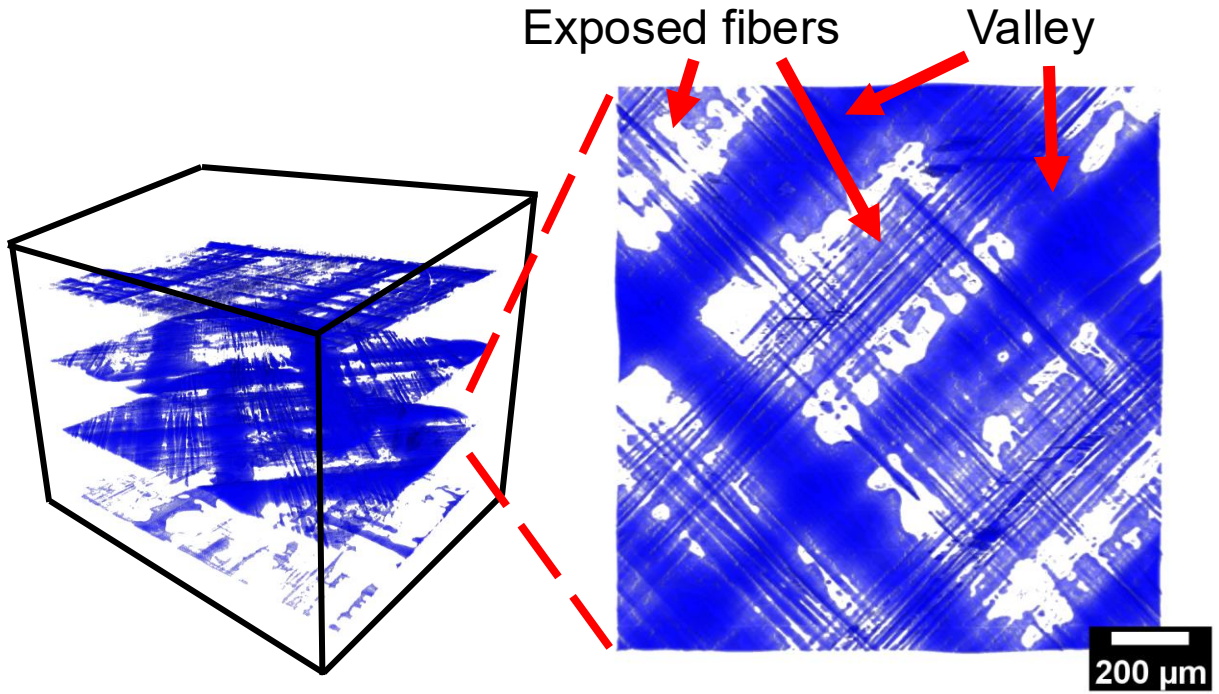

Single layer of
Rough-Rough entrapped air

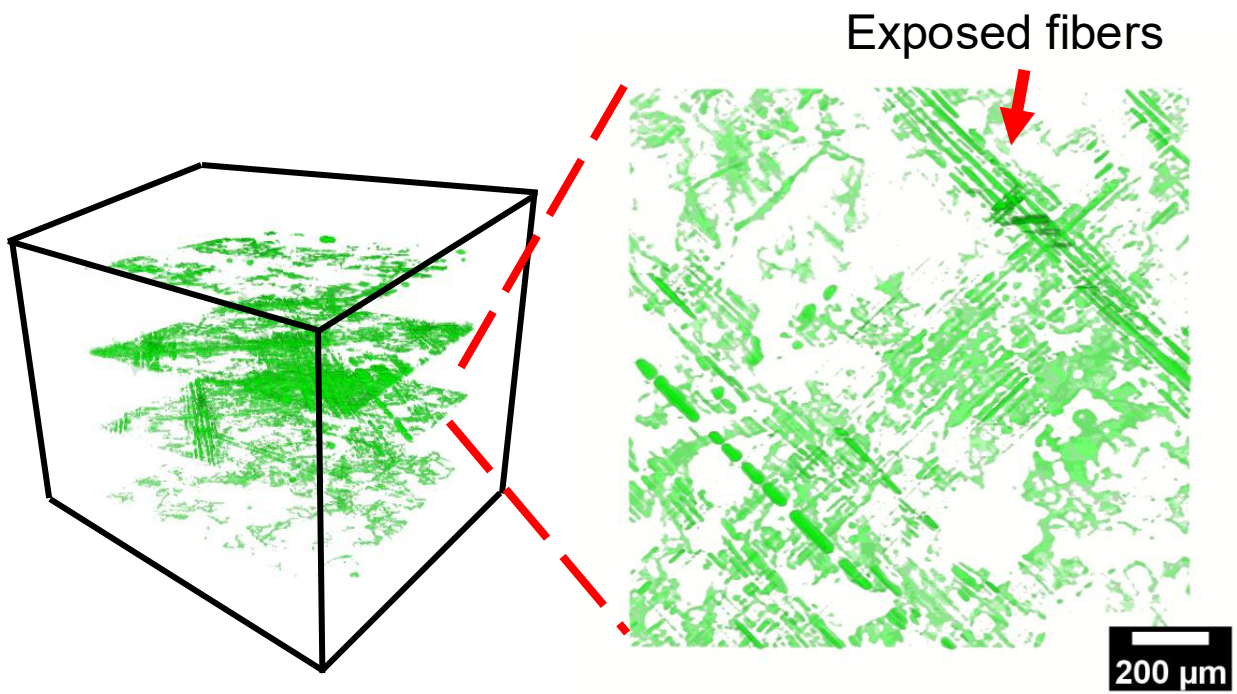

Single layer of
Smooth-Smooth entrapped air

- In Rough-Rough entrapped air layer, valley induced entrapped airs are **connected** in the layer
- In Smooth-Smooth entrapped air layer, entrapped airs are **not fully connected** each other

➢ **Air permeability difference** would **affect** void morphology change during curing

Absence of surface valley can reduce interlaminar voids

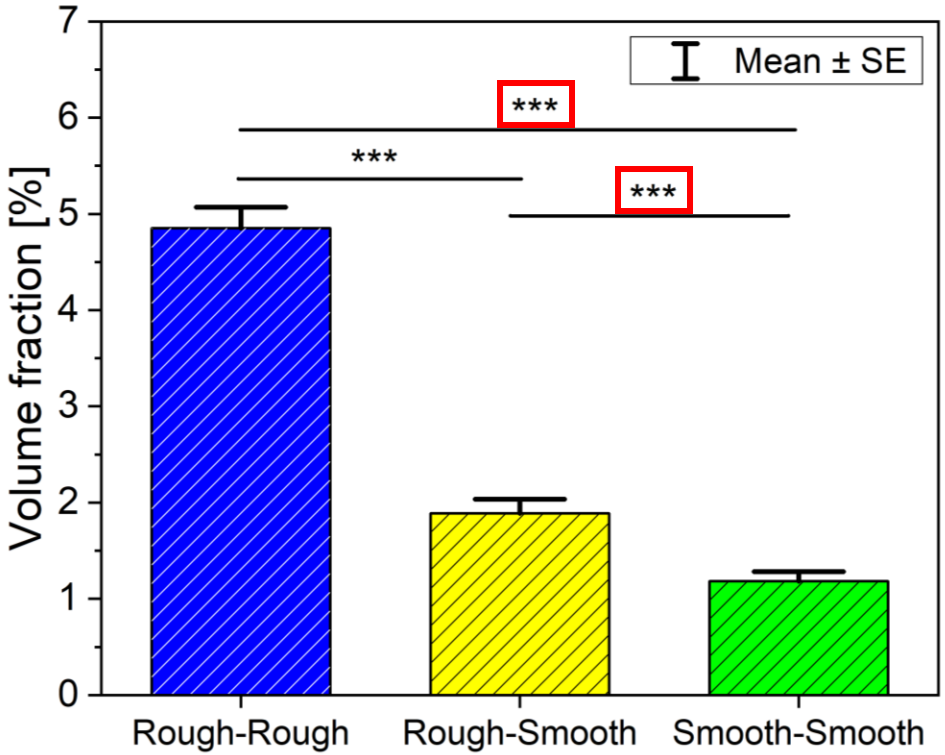

Entrapped airs in each interface cases

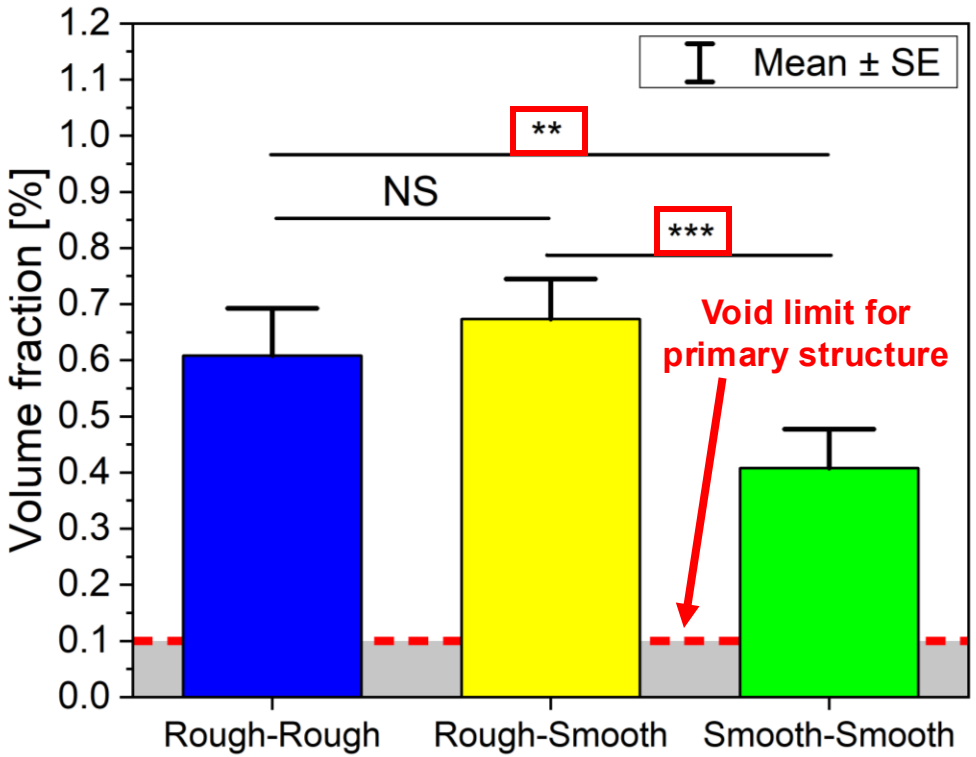

Interlaminar voids in each interface cases

- The Kruskal-Wallis ANOVA is performed to analyze the differences among the three interface types
- **Smooth-Smooth** interface shows clear difference compared to the other two interfaces

➢ Removing surface valleys can lead to fewer interlaminar voids

Conclusion

Conclusion

- **Valleys** formed at tow-tow junctions are the major difference between both side surfaces of the prepreg
- Interfacial entrapped airs are mainly formed at **valleys** on the prepreg surface
- Minimizing prepreg surface **valleys** can reduce the amount of interlaminar void

Thank you for your attention



ICCM24
AUGUST 4-8, 2025
BALTIMORE CONVENTION CENTER
BALTIMORE, MARYLAND, USA

No Technical Paper Submission for:

George Holiday

ICCM24
AUGUST 4-8, 2025
BALTIMORE CONVENTION CENTER
BALTIMORE, MARYLAND, USA

No Technical Paper Submission for:

Christian Lauter

DUAL-SURFACE ENGINEERING OF CARBON FIBERS BY GRAFTING CARBON NANOTUBES AND CHEMICAL FUNCTIONALIZATION

Hassan A. Almousa[1], Yunze Jiang[2], Hugo G. De Luca[3], David B. Anthony[4], Emile S. Greenhalgh[5], Alexander Bismarck[6], and Milo S.P. Shaffer[7]

[1]Department of Materials, Imperial College London, London, UK
South Kensington Campus, London, SW7 2AZ, United Kingdom
h.almousa19@imperial.ac.uk, https://www.researchgate.net/profile/hassan-almousa-5

[2]Chemistry Department, Imperial College London
White City Campus, London, WC12 0BZ, United Kingdom
yunze.jiang23@imperial.ac.uk

[3]Materials Department, Imperial College London
South Kensington Campus, London, SW7 2AZ, United Kingdom
hugo.de-luca14@imperial.ac.uk, https://www.researchgate.net/profile/hugo-de-luca

[4]Chemistry Department, Imperial College London
White City Campus, London, WC12 0BZ, United Kingdom
d.anthony08@imperial.ac.uk, https://profiles.imperial.ac.uk/d.anthony08

[5]Aeronautics Department, Imperial College London
South Kensington Campus, London, SW7 2AZ, United Kingdom
e.greenhalgh@imperial.ac.uk, https://profiles.imperial.ac.uk/e.greenhalgh

[6]Institute of Materials Chemistry, Faculty of Chemistry, University of Vienna
Währinger Strasse 42, 1090, Vienna, Austria
alexander.bismarck@univie.ac.at,
https://mc.univie.ac.at/polymer-composite-engineering-group/people/head-of-the-group

[7]Chemistry Department and Materials Department, Imperial College London
White City Campus, London, WC12 0BZ, United Kingdom
m.shaffer@imperial.ac.uk, https://profiles.imperial.ac.uk/m.shaffer

Keywords: Carbon fiber; Carbon nanotubes; Interface/interphase; Chemical vapor deposition (CVD); Surface treatments; Pultrusion; Micro-mechanics

ABSTRACT

Carbon fiber-reinforced polymer (CFRP) composites, performance remains constrained by fiber–matrix adhesion due to the chemically inert and smooth surfaces of the untreated fibers (CFs). Chemical compatibility is usually improved by electro-oxidation followed by sizing to improve the mechanical properties, particularly in epoxy-matrix composites. Grafting carbon nanotubes (CNTs) onto CFs by chemical vapour deposition (CVD) improves mechanical interlocking but generates a chemically inert surface. This study shows that combining CNT grafting with a simple chemical treatment (sizing or epoxidation) activates the surface and maximises interfacial strength between epoxy matrix and modified fibers. Surface analysis confirmed increased oxygen content and polarity from these treatments. Single-fiber pull-out tests demonstrated that sized CNT-g-CF in an epoxy matrix achieved up to 60% higher interfacial shear strength than both unsized CFs and as-produced (unsized) CNT-g-CF. Flexural testing of unidirectional fiber reinforced epoxy composite rods (40% V_f) showed a 30% increase in flexural strength compared to unsized CFs and an 8% gain over as-produced (unsized) CNT-

g-CFs. These results highlight that chemical modification is essential to fully exploit the potential of CNT-enhanced interfaces in epoxy-based matrices.

1 INTRODUCTION

In carbon fiber-reinforced polymer (CFRP) composites, the fiber–matrix interface governs load transfer and stress distribution, directly influencing strength and toughness. However, untreated carbon fibers (CFs) have chemically inert surfaces, low surface energy, and minimal roughness, which limit bonding with polymer matrices such as epoxy-based matrices and lead to poor load transfer and reduced mechanical performance [1,2]. Conventional methods such as chemical modification (oxidation or sizing) or nanoscale roughening (grafting carbon nanotubes (CNTs), nanorods, or whiskers) can improve fiber–matrix adhesion but each has drawbacks. Strong oxidative treatments, for example, enhance surface reactivity but can degrade CF tensile strength, creating a trade-off between reactivity and structural integrity [3]. Grafting CNTs improves interfacial properties through mechanical interlocking and a larger interphase interaction volume [4], yet the high temperatures used in chemical vapour deposition (CVD) can damage the CF structure. Recent developments have enabled the continuous production of uniformly CNT-grafted CF tows, avoiding any fiber damage. However, to maximise the benefits of CNT-grafted-CFs (CNT-g-CF), chemical compatibility with the epoxy matrix must also be considered, since the as grown CNTs are chemically inert and the CVD growth conditions strip the oxide groups form the CF surface. After grafting, epoxy-based CNT-g-CF composites have a complex hierarchical structure, consisting of three coupled interfaces, as illustrated in Figure 1: CNT/CF, CNT/matrix, and CF/matrix, compared to the traditional single planar CF/matrix interface.

To identify which interface limits efficient stress transfer, each must be considered. Reported interfacial shear strength (IFSS) values in the literature vary widely (30–270 MPa) for CNT-epoxy interfaces [5], depending on factors such as CNT diameter, length, and surface defects, which enhance mechanical interlocking, together with experimental measurement difficulties. The CNT/CF junctions, formed during CVD growth, can achieve bond strengths approaching 200 MPa which far exceeds the van der Waals limit [6]. In contrast, the CF/epoxy interface is often the weakest region in unsized carbon fiber reinforced systems, with IFSS typically ranging from 30–60 MPa due to the chemically inert CF surface [2]. Note if the whole system is considered, CNT-g-CF/epoxy interfaces values also vary widely and can be affected by matrix choice (between different epoxies) and the method used to determine IFSS (~30–166 MPa) [7]. For this reason, it is often good practice to evaluate these modified fibers with an appropriate baseline and consider relative improvements.

As significant portion of the CNT-g-CF surface includes this CF/epoxy interface, any improvements to the CF/epoxy interphase region is likely to produce overall improvements in IFSS for CNT-g-CF/epoxy systems. The effect of post-treatment on any as-produced CNT-g-CFs has not been reported in relation to the IFSS in an epoxy matrix. Therefore, combining CNT grafting (mechanical) with chemical post-treatments could further improve these interfacial characteristics. An optimal fiber–matrix interface combines chemical bonding and mechanical interlocking to fully exploit the primary reinforcing fiber (CF in this instance) strength. This study demonstrates that integrating CNT-g-CFs with sizing or epoxidation achieves dual-surface engineering, demonstrating a synergistic improvement in CFRP interfacial properties.

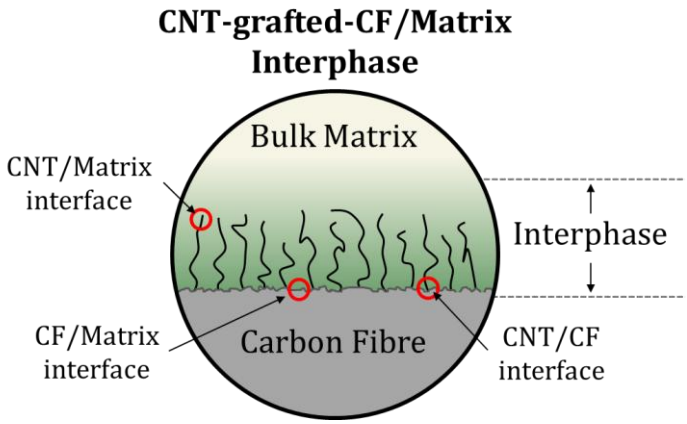

Figure 1: Schematic of CNT-reinforced interphase and its constituent interfaces.

2 MATERIALS AND METHODS

Unsized as-received carbon fibers (AS4-12K-7D, HS-CP-5000 grade, Hexcel) and as-produced CNT-g-CFs (prepared using a continuous CVD process described elsewhere [8]) were used. For the sizing treatment, a solvent-based epoxy sizing was prepared by dissolving 1.25 wt.% PRIME 27 epoxy resin (Gurit) in acetone (≥99.5%, Sigma-Aldrich); fibers were held under tension and dipped for ~2 min and then dried overnight at room temperature. Epoxidation involved immersing fibers in a 1 wt.% meta-chloroperoxybenzoic acid (≥77%, Sigma-Aldrich) solution in dichloromethane (≥99.5%) at room temperature for 3 h, rinsing in pure dichloromethane for 1 h, and drying at 80 °C for 30 min. Composite rods were fabricated by continuous fiber pultrusion. The fibers were tensioned on a spool, pulled through a bath of bisphenol A-based PRIME 27 epoxy resin with extra slow PRIME 27 hardener (Gurit), and guided through a 1.2 mm nozzle to control fiber volume fraction. Tension was applied during curing to maintain rod shape. Composites were cured at room temperature for 24 h, cut to length, and post-cured at 50 °C for 16 h.

Fiber morphology was examined using a Zeiss Sigma 300 field emission scanning electron microscope (SEM) operated at 5 kV with an in-lens detector; samples were mounted on aluminium stubs with conductive silver paint. Fiber surface chemistry was analysed by X-ray photoelectron spectroscopy using a Thermo Fisher K-Alpha+ system with a monochromated Al Kα source, keeping the chamber pressure below 5×10^{-7} mbar; fibers were cut to 10 mm, mounted on Cu-based holders with carbon double-sided tape and metallic clips. Interfacial shear strength (IFSS) was determined by single-fiber pull-out test. Single filament were embedded in epoxy droplet, with embedded lengths controlled below 80 µm to avoid fiber breakage, then pre-cured at 150 °C for 10 min, followed by room temperature curing for 24 h and post-curing at 50 °C for 16 h (following manufacturers recommendations). Single-fiber pull-out tests were performed using a KISTLER 9207 piezoelectric force sensor and a PICA P-216.9S actuator (180 µm travel, 50 N capacity); fibers were aligned and glued to the actuator needle with Born2Bond cyanoacrylate, UV-cured for 20 s, and pulled at 250 $nm.s^{-1}$. Flexural strength of composite rods was measured by three-point bending test using a Linkam MFS modular force stage with a 200 N load cell; samples (60 mm long) were tested on a 30 mm support span at 1 $mm.min^{-1}$ rate until failure.

3 RESULTS

3.1 Surface morphology and chemistry

Surface morphology is crucial for the fiber-matrix interphase, contributing through mechanical interlocking. SEM analysis (Figure 2) shows that sizing introduced noticeable surface changes. Both CFs and CNT-g-CFs were uniformly coated with resin, indicating effective wetting. In sized CNT-g-CFs, the CNT network was embedded in the resin. To quantify these effects, average roughness (Ra) was measured from SEM images as semi-quantitative method using Equation 1 through ImageJ software

(version 1.54m). The examined profiles were taken from regions less than 1 μm in length and 15% in diameter to minimize curvature effects, keeping sampling consistent to ensure comparability. Histogram stretching was also applied to enhance contrast. The CNT-g-CFs showed higher roughness (Ra = 21.4) due to the grafted nanotube network (Table 1). Sizing reduced surface roughness in both fibers. For CFs, the change was minimal, likely from resin filling surface features. In contrast, CNT-g-CFs showed a more noticeable decrease in Ra, aligning with the collapse and embedding of the CNT network in the sizing layer. This smoothing could impact resin infiltration, fiber packing, and interfacial mechanics in composite fabrication.

$$Ra = \frac{1}{N}\sum_{i=1}^{N}|y_i - \bar{y}| \tag{1}$$

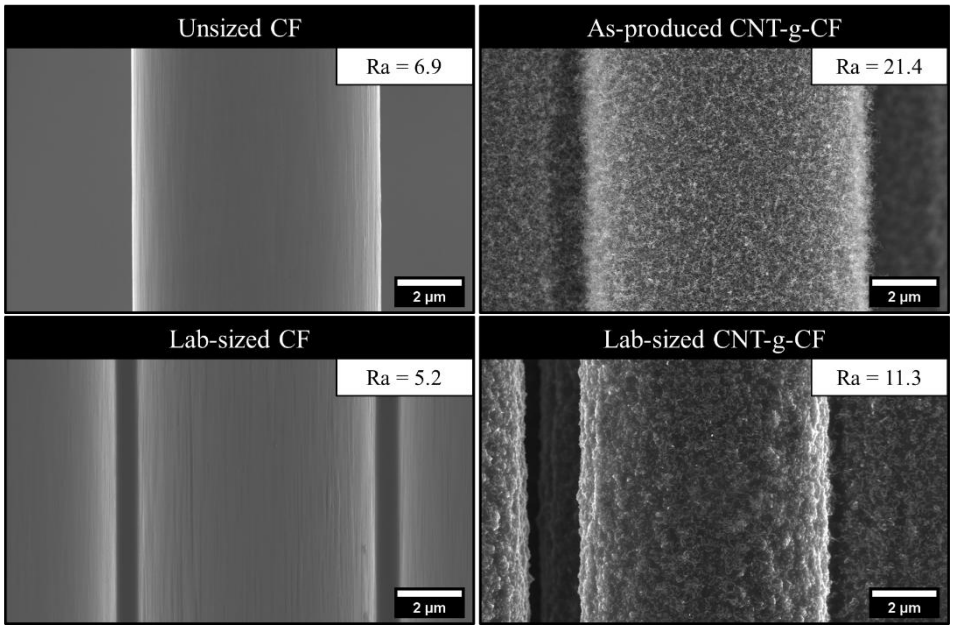

Figure 2: SEM micrographs of baseline carbon fibers and after sizing surface treatment in comparison to CNT-g-CF.

Table 1: X-ray photoelectron spectroscopy for surface composition of carbon fiber-based samples.

Element (at. %)	As-received unsized CF	Epoxidized CF	Lab-sized CF	As-produced CNT-g-CF	Epoxidized CNT-g-CF	Lab-sized CNT-g-CF
Oxygen	5.9	23.4	37.8	3.6	17.2	35.4
Carbon	94.1	76.6	62.2	96.4	82.8	64.6

3.2 Interfacial performance

The apparent IFSS (Figure 3) was calculated based on Equation 2 where one-way analysis of variance (ANOVA) test showed no significant IFSS differences between as-produced CNT-g-CFs and unsized CFs, indicating CNT grafting process did not necessarily enhance interfacial performance in the Prime 27 epoxy. Likely, the loss of reactivity of the previously oxidised CF, led to a weak CF/matrix interface and premature debonding, counteracting any benefit of the mechanical interlocking effect. Lab-sized CFs increased IFSS by 35%, demonstrating the sizing benefits for compatibility with thermosetting matrices. While epoxidation did not show great benefit with unsized CF, the epoxidized CNT-grafted-

CFs improved IFSS by 28% over as-produced (unsized) CNT-g-CF, with oxidative treatment facilitating matrix interaction. This exploitation of surface modification using CNT-g-CFs was even stronger with sizing, achieving over 60% IFSS increase (lab-sized CNT-g-CF). In low-reactivity epoxies like Prime 27, the resin bonds weakly to CF, so CNT functionalisation adds active sites that improve interfacial adhesion and load transfer. Without functionalization, CNTs mainly act as topographical elements, underlining the synergy between mechanical interlocking by CNTs and chemical compatibility from sizing.

$$IFSS = \frac{F_d}{\pi d l_{emb}} \tag{2}$$

3.3 Flexural properties

To evaluate composite flexural performance, three-point bending tests were performed on pultruded rods (40% V_f, void content below 3%), which subjects specimens to combined tensile, compressive, and shear stresses. This configuration captures how interfacial enhancements translate to macroscopic bending behavior, which involves different failure mechanisms than local fiber pull-out. The flexural strength is calculated using Equation 3 and results were normalized to the nominal composite diameter (Figure 3). Lab-sized CNT-g-CF reinforced composites exhibited a 30% increase in flexural strength compared to unsized CF reinforced composites, demonstrating that combining CNT grafting with sizing improves fiber–matrix bonding and multiscale stress transfer. Sizing also enhanced flexural strength in CF reinforced composites, although the effect was more pronounced with CNT grafting due to the additional mechanical interlocking and stiffening of matrix. In contrast, epoxidation improved interfacial shear strength but did not significantly increase flexural strength under these conditions, highlighting that strong fiber–matrix adhesion alone is insufficient without optimized matrix wettability and improved interfacial properties.

$$\sigma_f = \frac{FL}{\pi R^3} \tag{3}$$

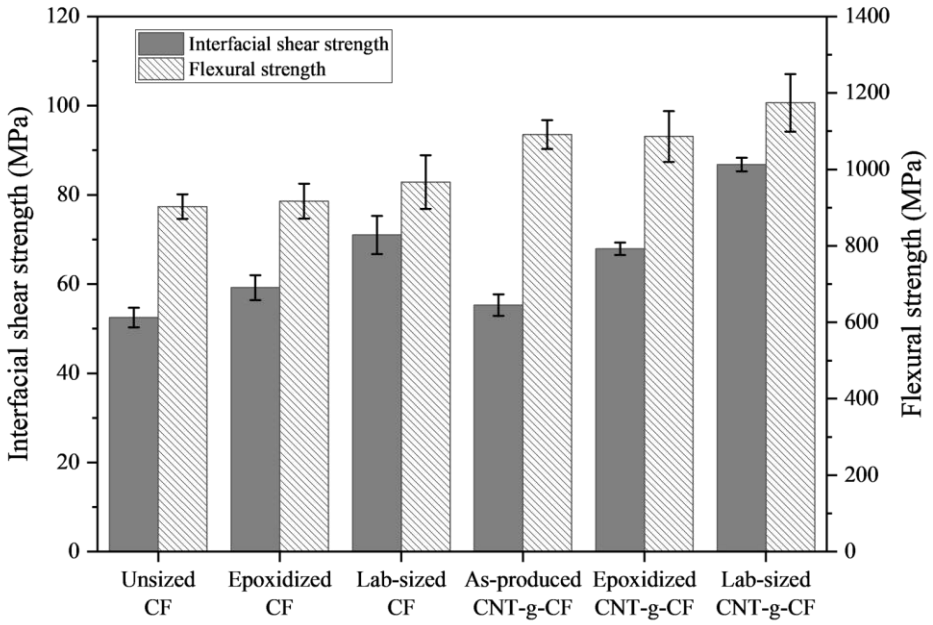

Figure 3: For corresponding modified carbon fibers interfacial shear strength was determined through single-fiber pullout test in an epoxy matrix, and flexural strength via 3-point bending test (40% V_f unidirectional epoxy composite rods).

4 CONCLUSIONS

This work demonstrates that carbon nanotube grafting alone does not fully overcome the limitations of untreated carbon fibers due to their inert surfaces in composites. Combining carbon nanotube-grafted-carbon fibers with targeted chemical treatments, such as sizing, creates a dual-surface engineered interface that improves the overall fiber–matrix adhesion and enables more efficient stress transfer. This synergy provided up to 60% higher interfacial shear strength and ~30% greater flexural strength compared to unsized carbon fibers. These results highlight the importance of integrating chemical compatibility and mechanical interlocking to maximize the performance of hierarchical interfaces in carbon fiber reinforced polymer composites.

ACKNOWLEDGEMENTS

The authors kindly acknowledge the funding for this research provided by UK Engineering and Physical Sciences Research Council (EPSRC) programme Grant EP/T011653/1, Next Generation Fiber-Reinforced Composites (NextCOMP): a Full Scale Redesign for Compression a collaboration between Imperial College London and the University of Bristol. For the purpose of open access, the authors has applied a Creative Commons Attribution (CC BY) license to any author accepted manuscript version arising.

REFERENCES

[1] M. Sharma, S. Gao, E. Mäder, H Sharma, L.Y. Wei and J. Bijwe, Carbon fiber surfaces and composite interphases. *Composites Science and Technology*, **102**, 2014, pp. 35–50. https://doi.org/10.1016/j.compscitech.2014.07.005

[2] H. Zheng, W. Zhang, B. Li, J. Zhu, C. Wang, G. Song, G. Wu, X. Yang, Y. Huang and L. Ma, Recent advances of interphases in carbon fiber-reinforced polymer composites: A review. *Composites Part B: Engineering*, **233**, 2022, 109639. https://doi.org/10.1016/j.compositesb.2022.109639

[3] D.J. Eyckens, F. Stojcevski, A. Hendlmeier, J.D. Randall, D.J Hayne, M.K. Stanfield, B. Newman, F. Vukovic, T.R. Walsh and L.C. Henderson, Carbon fiber surface chemistry and its role in fiber-to-matrix adhesion. *Journal of Materials Chemistry A*, **9** (47), 2021, pp.26528–26572. https://doi.org/10.1039/D1TA07151C

[4] R. Sahu, S.A. Ponnusami, C. Weimer and D. Harursampath, Interface engineering of carbon fiber composites using CNT: A review. *Polymer Composites*, 2023, pp.1–34. https://doi.org/10.1002/pc.27772

[5] Y. Chandra, F. Scarpa, S. Adhikari, J. Zhang, E.I. Saavedra Flores and H.X. Peng, Pullout strength of graphene and carbon nanotube/epoxy composites. *Composites Part B: Engineering*, **102**, 2016, pp.1–8. https://doi.org/10.1016/j.compositesb.2016.06.070

[6] K.J. Kim, G. Lee, S.D. Kim, S Kim, J.H. Youk, J. Lee, Y Kim and Yu, W. R. Bond strength of individual carbon nanotubes grown directly on carbon fibers. *Nanotechnology*, **27**(40), 2016, 405704. https://doi.org/10.1088/0957-4484/27/40/405704

[7] D. Anthony, X. Sui. I. Kellersztein, H. De Luca, E. White, H. Wagner, E. Greenhalgh, A. Bismarck and M. Shaffer, Continuous carbon nanotube synthesis on charged carbon fibers. *Composites Part A: Applied Science and Manufacturing*, **112**, 2018, pp.525-538. https://doi.org/10.1016/j.compositesa.2018.05.027

[8] H.A. Almousa, H.G. De Luca, D.B. Anthony, E.S. Greenhalgh, A. Bismarck and M.S.P. Shaffer, Dynamic snapshot of continuous carbon nanotube growth on carbon fibers: From Sparse to Uniform and Controlled Growth, *In preparation*, 2025.

ELECTROSPUN NANOFIBROUS INTERLEAVES FOR IMPROVING THE PERMEABILITY RESISTANCE OF CRYOCYCLED COMPOSITE LAMINATES

Othman Laban[1], Garth Pearce[2], Jin Zhang[3], Mohammad S. Islam[4]

School of Mechanical and Manufacturing Engineering, University of New South Wales, Sydney, NSW, 2052, Australia
[1]Email: o.abu_laban@unsw.edu.au, web page: https://www.unsw.edu.au/

[2]Email: g.pearce@unsw.edu.au, web page: https://www.unsw.edu.au/

[3]Email: jin.zhang6@unsw.edu.au, web page: https://www.unsw.edu.au/

[4]Email: m.s.islam@unsw.edu.au, web page: https://www.unsw.edu.au/

Keywords: Electrospinning; Interleaving; Cryogenic microcracking; Discrete damage modelling; Permeability

ABSTRACT

Interleaving is a common technique used to provide localised toughening in laminated composites, improving impact and fatigue damage resistance. However, little research has explored their effectiveness in cryogenic conditions, especially under cyclic loadings. This study presents an integrated experimental and numerical approach to evaluate the capability of ultra-thin electrospun veils in delaying the onset of localised delamination areas formed at crack junctions in cryogenically cycled laminates. Cross-ply laminates were interleaved with five-micron-thick veils at each asymmetric interface and cryogenically cycled. An indirect assessment of the degree of damage was carried out by measuring the helium permeability coefficients, and the crack networks were examined using micro-computed tomography scanning and scanning electron microscopy techniques. Compared to the baseline laminates, the sudden increase in permeability after cryocycling was damped in toughened laminates, yielding a lower coefficient by one order of magnitude after the first cryo-cycle and 40% after the second cycle. A finite element modelling approach with an integrated 3-D cohesive network was used to simulate the progressive discrete crack damage in cross-ply laminates subjected to cyclic thermomechanical loading. When the thermomechanical loading is high, the interleaves will show more resistance to damage growth due to their substantial R-curve effect. When the cyclic loads are low, the damped interfaces will tend to fatigue faster because of the increased stress from resisting the opening of transverse cracks. This work can be forecasted to assess the veil's performance in quasi-isotropic laminates with asymmetric interface angles and to explore the possibility of encapsulating nanofillers into the electrospun nanofibers to promote synergic toughening effects.

1 INTRODUCTION

The heterogeneous nature of composite laminates makes them susceptible to premature cracking due to the inherent mismatch in the coefficient of thermal expansion (CTE) between the composite constituents [1]. Fibre reinforcements have extremely small CTE, while matrix CTE is relatively larger. At cryogenic conditions, the fibres tend to expand slightly and the matrix attempts to contract, promoting thermal strains at the microscopic level. At the macroscopic scale, varying ply orientations lead to differential expansion in different directions, driven by the stiff fibres within each lamina. This differential expansion generates multiaxial thermal strains, causing the matrix to go into tension and, ultimately, the initiation of microcracks.

The developed microcracks do not have sufficient energy to break the fibres, so they propagate along them longitudinally and through the thickness of the lamina [2]. The microcracks get arrested as

they approach an interface with a dissimilar ply orientation. The tip of the arrested microcrack acts as a stress raiser and induces localised delamination at the interlaminar region. These zones are the junctions that interconnect the crack network, which has direct implications for the gas leakage rates through damaged laminates. This delamination area grows as the number of service cycles increases, and subsequently, the crack opening displacement (COD) increases, leading to higher gas leakage rates [3, 4]. Delaying the onset and growth of these localised delaminations will improve the gas barrier performance of linerless composite tanks [5].

Interleaving techniques are known to provide localised interlaminar toughening effects without necessarily compromising the laminate's global response [6, 7]. These processes involve placing additional layers of materials, usually made of soft thermoplastics, between the individual plies of the composite laminate. For instance, HexPly M21 and Toray 3900-2B prepregs were toughened with polyamide particles and used to build primary structures in Airbus A350 and Boeing 777 aircraft [8-10].

Overall, the effectiveness of the interleaves in enhancing damage resistance has been extensively demonstrated in impact and mechanical fatigue problems [11]. However, there is a lack of understanding and knowledge regarding their toughening effects at cryogenic temperatures, particularly compared to the toughness enhancements achieved with thermoplastic-thermoset blends. Further investigation is needed to understand their potential use for improving the delamination resistance in composite laminates for cryogenic applications.

2 EXPERIMENTAL PROGRAM

2.1 Methodology

An epoxy resin system was used in this study, consisting of three components: bisphenol A diglycidyl ether (DGEBA, Huntsman Araldite® LY1564), methyl tetrahydrophtalic anhydride curing agent (MTHPA, Huntsman Aradur® 917-1), and tertiary amine co-hardener (accelerator 960-1). For the manufacture of composite laminates, Torayca T300 CK-12 unidirectional carbon fibre reinforcement with an areal weight of 200 gsm was utilised. Polyethersulfone (PES, Ultrason® E1010 NAT, 1.37 g/cc, BASF-Germany) was selected as the thermoplastic toughening agent. An organic solvent, N,N-Dimethylformamide (DMF, purity>99%), was used to synthesise the polymer solution for electrospinning, as demonstrated by [12]. During the electrospinning process, PES nanofibres were directly deposited onto a dry carbon fabric that was mounted onto the drum-collector. After the electrospinning process was completed, the fabric with the deposited PES nanofibres was dried in a vacuum chamber at 100 °C overnight to ensure the evaporation of any residual DMF solvent from the electrospun PES nanofibres.

Cross-ply composite laminates, having a layup sequence of $[0_3/90_3]_s$, were manufactured for a cryogenic cycling test. Two laminates were made, with and without electrospun PES veils. The toughened laminate was interleaved only at the 0/90 interfaces with a single five-micron-thick veil. The vacuum bag resin infusion technique was used to minimise the void content in the laminates. The laminate underwent curing in an ASC autoclave under an absolute vacuum pressure of negative 800 mbar inside the bag and atmospheric external pressure throughout the process. The curing schedule comprised three segments. Firstly, the laminate was dwelled at 60 °C for one hour to facilitate diffusion between the PES-veil and epoxy resin. During the second segment, the cross-linking reaction commenced as the temperature increased to 120 °C and was maintained for four hours. Finally, after consolidation, the temperature was gradually reduced to 50 °C at a rate of 5 °C per minute. The cured laminates were 250×250 mm^2 and 2.5 ± 0.04 mm thick. Each laminate was sectioned into four 100 mm squared samples with a diamond cut-off wheel on the Axitom-5TM from Struers.

The baseline and interleaved cross-ply samples were cryogenically cycled from room temperature to the liquid nitrogen (LN_2) temperature for five cycles to determine their resistance to microcracking. Direct submersion in LN_2 was avoided to minimise thermal shocks, and instead, the specimens were subject to a gradual three-stage precooling process. Initially, the specimens were placed in a freezer at -28 °C for at least an hour and then chilled at approximately -100 °C in a chamber containing LN_2 beneath the samples. After another hour, the samples were removed from the chamber and immediately immersed in LN_2 for 10 minutes. The reverse order of this process was followed for warming up the samples to room temperature. Finally, they were allowed to dry at 60 °C for two hours to remove condensed moisture before further cycling or permeability testing.

Permeability measurements are frequently used as a quantitative assessment of the progressive damage state in laminates [13, 14]. Permeability tests were performed to measure the helium leakage rates through the cross-ply laminates as a function of the number of cryogenic cycles. These tests were conducted at room temperature in compliance with the ISO 15105 standard for determining gas transmission rate (***GTR***) by the differential pressure method. The ***GTR*** can be expressed as a physical property, called the gas permeability coefficient (***P***), by taking its product with the average laminate thickness. It should be noted that ***P*** is commonly reported in the literature in metric units as standard cubic centimetres times metre per square metre times day times atmosphere ($scc \cdot m/m^2 \cdot day \cdot atm$). The standard conditions for measuring the gas volume are set to room temperature and atmospheric pressure [14]. The ASTM D1434 provides multiple factor tables for converting the permeance or gas permeability from one unit system to another.

The ***GTR*** measurements were taken using the Manometric Permeability Meter Mk VI acquired from Versaperm. The equipment setup is illustrated in Figure 1. The cross-ply sample was mounted in a gas transmission cell between a pressurised chamber and a vacuumed downstream chamber. The gas transmission area was 1/200 m^2, and the testing temperature was set to 298 K. Helium gas permeated through the laminate from the high-pressure chamber to the downstream chamber. The rate of pressure increase in the downstream chamber was recorded every second. A moving average of 50 points was applied to reduce the noise in the test data. Each sample was tested under three different gas supply gauge pressures of 1, 2, and 3 bars in order to check the consistency of permeance measurement because of potential gas leakages from the barrier seals. Measurement time varied according to the leakage rate through the damaged laminates. All the runs were continued until the time limit of one thousand minutes was reached or the pressure build-up in the downstream chamber exceeded 900 mbar to avoid damaging the low-pressure transducer. The uncycled samples reached the time limit, whereas the cycled ones had higher leakage rates and met the second test stop criterion.

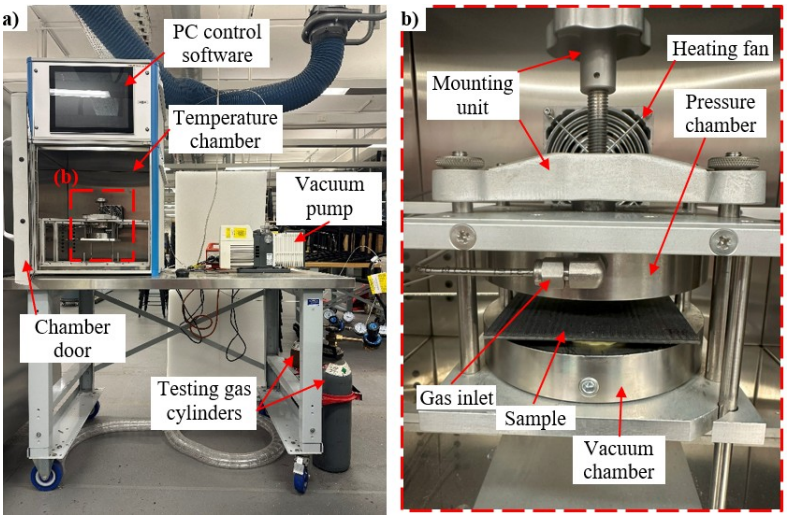

Figure 1: (a) Gas permeability tester and (b) the sample clamping fixtures located inside the temperature chamber.

Non-destructive X-ray micro-computed tomography (micro-CT) scanning is a 3-D visualisation technique that is used for the detection of internal damage in structures. Micro-CT imaging was conducted on the HeliScanTM microCT from ThermoFisher, which had a 160kV/16W Hamamatsu X-ray tube with diamond windows. The flatbed detector size was 3072×3072 pixels, and the readout rate was 3.75 fps. To achieve high voxel resolutions, down to one micron in size, the samples were carefully sectioned into small 3×3 mm pieces. This allows the sample to sit closer to the X-ray source for higher magnification. One sample was sectioned and inspected after one cryogenic cycle, and another sample after five cycles. Avizo software was used for image data processing, segmentation, and visualisation analysis.

Although the CT-scan voxel resolution was refined to detect the transverse microcracks, capturing the localised delaminations was challenging. The crack opening displacement of these delaminations was at sub-micron levels after the sample reached room temperature after cryogenic cycling. Therefore, scanning electron microscopy (SEM) was primarily used to inspect the localised delaminations at the tips of the transverse cracks identified under the microscope. For SEM analysis, the sample's edge was coated with a 40 nm thick platinum layer, and then it was examined using the FEI Nova nanoSEM-230 equipment.

2.2 Helium permeability measurements

A comparison between the determined ***GTR*** of the baseline and interleaved laminates as a function of the number of cryogenic cycles is given in Figure 2(a). The presented ***GTR*** values were averaged between the samples of each set for each gas supply pressure. The ***GTR*** results are consistent between the different pressure levels, indicating no significant gas leakage from the transmission cell during the measurements. The highest standard deviation was 7.7×10^{-14} scc/m^2·day·atm, which occurred for the uncycled specimens because the mean ***GTR*** was very low, making the measurements more sensitive to variation in specimen thicknesses. The ***GTR*** increased by two orders of magnitude after the first cryogenic cycle and systematically increased afterwards with subsequent cycles. The helium permeability coefficients of the baseline and interleaved samples are presented in Figure 2(b) versus the number of cryogenic cycles.

The permeability of uncycled samples from both sets measured a value of 8.1×10^{-16} scc·m/m^2·day·atm, which is within the same range as the results reported in [15]. After the first cryogenic cycle, the permeability of the baseline samples increased by three orders of magnitude to 1.6×10^{-13} scc·m/m^2·day·atm. In contrast, the interleaved laminates were one order of magnitude lower than the baseline, measuring 3.5×10^{-14} scc·m/m^2·day·atm. Even after two cycles, the permeability of interleaved samples was 40.6% lower than the baseline value, measuring 1.7×10^{-13} versus 2.8×10^{-13} scc·m/m^2·day·atm of the baseline.

The permeability of the baseline samples plateaus from the second cycle to roughly 3.4×10^{-13} scc·m/m^2·day·atm. A 71% increase in permeability occurred in the fifth cycle, suggesting the potential initiation of a new crack. The permeability of interleaved samples plateaus as well from the third cycle and onwards to 2.2×10^{-13} scc·m/m^2·day·atm. The error bars during this plateau overlap with those of the baseline samples. These results suggest that the interleaving technique damped damage evolution after onset during the initial stages of cryogenic cycling. With subsequent cyclic loadings, the damage reaches a saturation point in laminates with or without interleaves until a new crack forms, causing a sudden increase in the permeability coefficient. These observations are in agreement with those reported by Choi and Sankar [16], where the permeability of blocked $[0/90]_s$ laminate increased by two orders of magnitude in the first cycle and remained constant afterwards till 20 cycles.

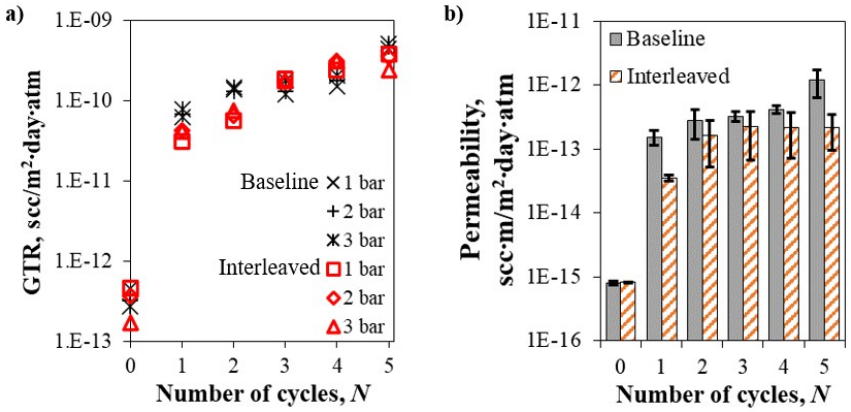

Figure 2: (a) The determined gas transmission rates (GTR) at three gas supply pressures (1-3 bars) as a function of cryogenic cycles, and (b) the corresponding average gas permeability coefficients of the baseline and interleaved cross-ply laminates.

2.3 Examination of the crack networks

Image processing was carried out to create a 3-D reconstruction of the laminate sample pieces and segment different phases within the structure, as shown in Figure 3. The network of polyester stitches was captured and illustrated in the figure. However, the attempt to reconstruct a similar network for the cracks was not successful because the crack opening displacements (CODs) were too small to trace fully. An example of a detected internal crack in a baseline laminate after one cryogenic cycle is illustrated in Figure 4. The voxel resolution of the scan was one micron. The maximum COD was determined to be 5.7 μm under the SEM, and it was reduced to submicron at the initiation and arrestment stages of the crack, making it difficult to detect. In addition, the polyester stitches had significantly higher contrast than the fibres and the matrix, resulting in blurry voxels near the stitches due to beam hardening artifacts. Micro-CT scanning of carbon fibre-based laminates is generally known to be more challenging compared to other types of fibre reinforcements [17]. Therefore, the collected scan data was primarily used to detect the locations of the cracks and their propagation path.

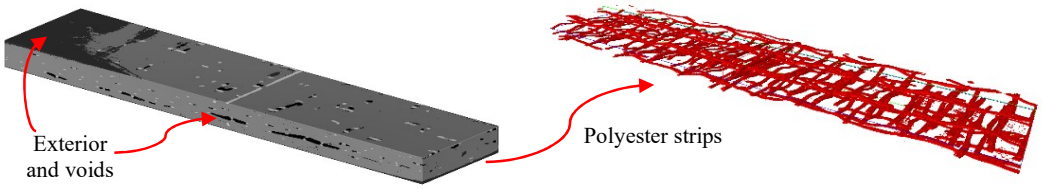

Figure 3: 3-D reconstruction and segmentation of micro-CT scan images of a section of a baseline cross-ply sample.

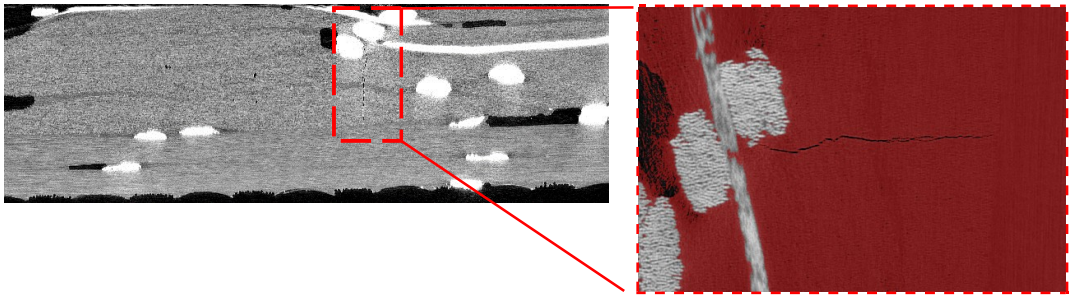

Figure 4: A 2-D X-ray image of a sectioned piece of a baseline cross-ply laminate showing a single inner transverse crack.

The micro-CT scans of cryogenically cycled laminates reveal that cracks tend to initiate from voids and polyester stitches, as in the case in Figure 4. The extension of the cracks across the sample width followed the voids and was deflected around the stitches. The minimum spacing between two fully developed sequential cracks was considered for measuring the crack density. The spacing between the inner cracks was about two times higher than the outer cracks, measuring 1.36 and 3.38 mm, respectively. In contrast, a single inner crack was detected in a 7 mm long sample and no outer cracks. This is a significant increase in the crack density versus the number of cycles, and it explains the increase in the gas permeability in the baseline laminates at the fifth cycle. However, the permeability increase ratio between the uncycled laminates and those with one cycle is significantly higher. This suggests that the increase in the permeability is not solely proportional to the crack density, but potentially the existence of delaminations as well, which were not detected in the micro-CT scans.

Upon examination under the microscope and SEM analysis, short-length delaminations in samples after one and five cycles were observed. The onset of localised delaminations occurs when the tip of the transverse crack terminates at the interface. However, this is not always the case when the singular stress field in its vicinity is not intense enough to overcome the corrected critical fracture toughness, depending on the relative thicknesses between 90°/0° [18]. The SEM micrograph in Figure 5 shows a transverse crack in an interleaved sample after one cycle. The crack initiated from the outer surface and propagated through a void located at a polyester stitch and arrested at the 90°/0° interface. Similar crack arrestment behaviour was observed on baseline samples as well after one cryogenic cycle. Fibre breakage near the arrested crack tip in the neighbouring 0° ply was not observed as reported in similar studies in [18].

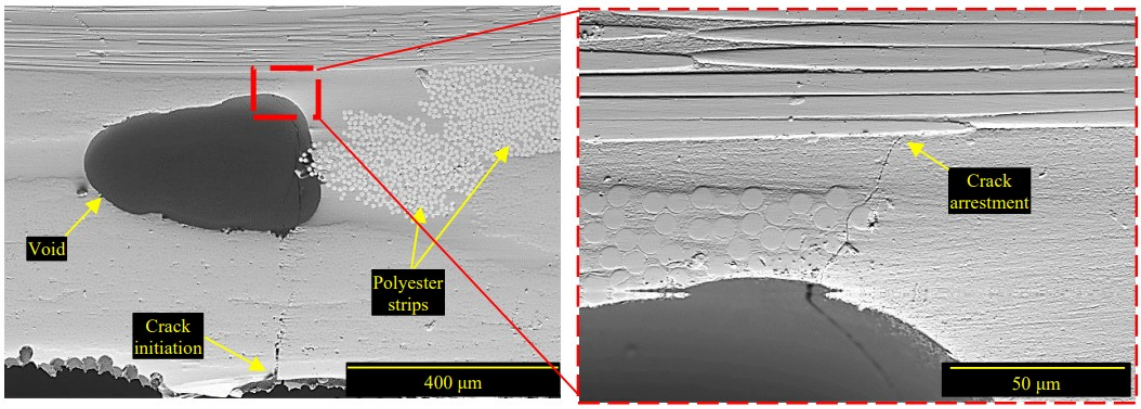

Figure 5: SEM micrograph of an interleaved sample after one cryogenic cycle, showing the initiation of a transverse crack from the outer laminate surface, its propagation through a void, and its arrestment at the interface of the adjacent ply.

Overall, no localised delaminations were observed to be induced from the tips of outer cracks, even after five cycles. For inner cracks, however, a few localised delaminations with random lengths were detected. The representative SEM micrographs in Figure 6 are of a baseline sample after five cycles, showing the branching of a transverse crack and propagating through the 90°/0° interface. The delamination propagation path seems to follow the interface of fibre/matrix. Another behaviour was noticed and illustrated in Figure 6(b) where the crack branches out before approaching the 90°/0° interface. The branched crack propagation eventually got arrested at the interface.

The process of developing these localised delaminations at the crack tips is thought to contribute to the slight increments in the gas permeability coefficient with repeated cycling after the initial cycle. However, the reason for the variation between the gas permeability trends of the baseline and interleave laminates was not clear after examining the cracks. The generation of transverse cracks was triggered by the voids, which caused a scatter in the crack densities observed between the samples. In

addition, delamination lengths were difficult to detect and quantify due to the inconsistency in their occurrence along the interfaces. This is a common challenge, and researchers tend to rely solely on counting the transverse cracks and measuring their opening displacement to explain differences in laminate permeability [13, 19]. Therefore, numerical modelling is generally used to analyse the evolution of interconnected crack networks and their potential effect on gas permeability [5, 20].

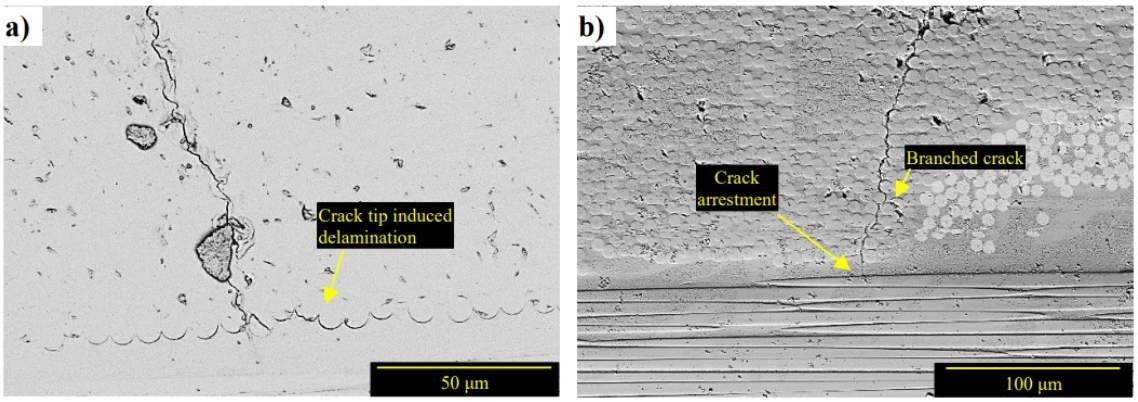

Figure 6: SEM micrographs of a baseline sample after five cryogenic cycles, showing (a) the transformation of a transverse crack into a localised delamination and (b) full arrestment of the transverse crack propagation at the interface. The crack in (b) branched out before approaching the interface.

3 NUMERICAL INVESTIGATION

3.1 Modelling approach

The ability to predict intraply discrete cracks, interlaminar delaminations, and their interactions is useful for analysing the possible ways to delay or suppress the damage in composite laminates. The cohesive network technique was employed to simulate progressive damage and map crack junctions for potential gas leakage routes. The model utilises the brick-and-mortar concept, originally proposed by Begley et al. [21], to simulate the initiation and diffusion of discrete cracks without the need to have a pre-crack. The bricks represent the continuum elements, and the cohesive elements (CEs) are regarded as the mortar.

The discrete crack locations must be predetermined to insert CEs along potential paths within continuum elements. These coordinates can be predetermined since matrix-dominant intralaminar cracks propagate along the fibre direction under thermomechanical cyclic loading. Fibre breakage appears as the final stage of failure only if the mechanical stresses are substantially high enough, causing the ultimate fracture of the structure [22]. In this study, fibre breakage was not considered a potential failure consequence of the presented thermomechanical loading case. The CEs were inserted parallel to the fibre orientation and at the interfaces to represent two premature failure modes, namely, transverse matrix cracking and interface delaminations. Contact connections were defined between adjacent strips and interlaminar regions to represent potential intralaminar cracks and delaminations, respectively. More details on the implementation of this approach and the cyclic bilinear cohesive zone model are presented in [23]. User-defined Python scripts were used within the Ansys pre-processor to automate the process of constructing a laminate model and integrating the network of CEs. A total of five Python scripts were coded to automate the process of embedding CEs within composite laminates in Ansys Mechanical software

The temperature-dependent mechanical properties and interface properties are given in Table 1 and Table 2, respectively. These properties were obtained by calibrating simple coupon models against testing data presented in [12]. The interface properties of the interlaminar and intralaminar regions differ owing to the increased surface area of the intralaminar cracks as they deflect around the

randomly distributed fibres. For simplicity, they are commonly presumed to be identical [18]. Applying this assumption herein should not influence the conclusions of this study because the delaminations are under investigation, and the transverse interface properties are identical between baseline and interleaved models. It should also be noted that the effect of asymmetric interface angles on interlaminar fracture toughness was not considered because the collected test data is limited to unidirectional samples. This limitation is not expected to produce biased results towards one of the models, but it will affect the prediction accuracy. In reality, the interleaving technique shows better toughness improvements under mode I and mode II in woven composites than in unidirectional [24].

Description	Symbol	Value at 293 K	Value at 77 K	Units
Young's modulus	E_{11}	125	135	GPa
	$E_{22} = E_{33}$	9.09	9.57	GPa
Shear modulus	$G_{12} = G_{13}$	2.77	2.98	GPa
	G_{23}	1.10	1.20	GPa
Poisson's ratio	$\nu_{12} = \nu_{13}$	0.34	0.34	-
	ν_{23}	0.48	0.48	-
Coefficients of thermal expansion	α_{11}	-0.06	-0.11	ppm/K
	$\alpha_{22} - \alpha_{33}$	29.3	23.98	ppm/K

Table 1: Material properties for T300/Araldite 1564/Aradur 917.

Cohesive property	Baseline laminate		Interleaved laminate		Units
	293 K	77 K	293 K	77 K	
Intralaminar zones					
σ_c	60.8	81.1	60.8	81.1	MPa
τ_c	62.6	99.3	62.6	99.3	MPa
G_{Ic}	0.19	0.18	0.19	0.18	kJ/m^2
G_{IIc}	0.85	0.91	0.85	0.91	kJ/m^2
Interlaminar regions					
σ_c	60.8	81.1	60.8	81.1	MPa
τ_c	62.6	99.3	62.6	99.3	MPa
G_{Ic}^{ini}	0.19	0.18	0.19	0.18	kJ/m^2
G_{Ic}^{prop}	0.69	0.34	0.69	0.34	kJ/m^2
G_{IIc}^{ini}	0.85	0.91	0.85	0.91	kJ/m^2
G_{IIc}^{prop}	1.2	0	1.26	0	kJ/m^2
Fatigue parameters					
ε	0.09	0.45	0.1	0.5	
η	0.98	0.98	0.98	0.98	
p	2	2	2	2	

Table 2: Temperature-dependent intralaminar and interlaminar interface properties used in modelling.

3.2 A single transverse crack under uniaxial static loading

The cohesive properties, namely the interface strengths and the critical strain energy release rates, are expected to impact the initiation of matrix cracks and the onset of delaminations. This impact is sensitive to the thickness ratio of the 90° ply relative to the 0° plies, as suggested in [18]. To investigate these effects, a 3D FE model of a cross-ply laminate under uniaxial tension was developed. The model includes two pre-existing transverse cracks at each end and one prospective crack in the middle of the span length. Three symmetry planes were prescribed to reflect the following symmetries: through-thickness mid-plane (x-z) at the bottom surface of the 90° ply, longitudinal cross-sectional plane (x-y) on all the side faces, and transverse cross-sectional plane (z-y) on the face of the 0° ply. A

3% longitudinal tensile strain along the x-axis was prescribed onto the face of the 0° ply opposite the x-y symmetry plane. The ply size was 5×10 mm and 0.2 mm in thickness. Three layup sequences were modelled, having a different number of transverse plies, namely $[90_2/0_2]_s$, $[90_4/0_2]_s$, and $[90_8/0_2]_s$. The corresponding 90° block thicknesses (t_{90}) are 0.4, 0.8, and 1.6 mm. The intralaminar contact region was prescribed the neat interface properties, whereas three sets of interlaminar cohesive properties were defined: a) the neat properties, b) interleaved properties, and c) neat properties with a 50% increase in the interface strengths (σ_n, τ_s).

The normal stresses in the 0° ply were three orders of magnitude higher than those generated in the 90° ply. Typical curves of the maximum normal stress and maximum in-plane shear stress in the laminate versus the applied longitudinal strain are given in Figure 7. The figure compares the laminate responses with the three different interlaminar contact properties. The laminate's initial linear behaviour corresponds to the elastic material properties. All curves show a small step at about 0.9% strain, and then the curve trends continue to increase linearly. This step corresponds to the initiation of the transverse crack. A shear-lag effect is observed owing to the presence of pre-cracks at the ends of the 90° ply. The thickness of the ply has a direct effect on the shear-lag distribution, where the thinner it is, the quicker the stress is transferred from the outer 0° ply to the 90° ply. The laminate configuration with the thickest transverse ply block requires higher applied strains to initiate transverse cracks. Therefore, under mechanical fatigue loadings, the characteristic crack density is expected to increase as the 90° decreases [22]. However, the normal stress severity increases in thinner transverse plies, meaning thicker blocks of transverse plies are more susceptible to microcracking at early loading stages, but the overall crack density is lowered with repeated loadings. For gas barrier applications, the use of alternating thin plies was recommended to delay the initiation of matrix cracking [16].

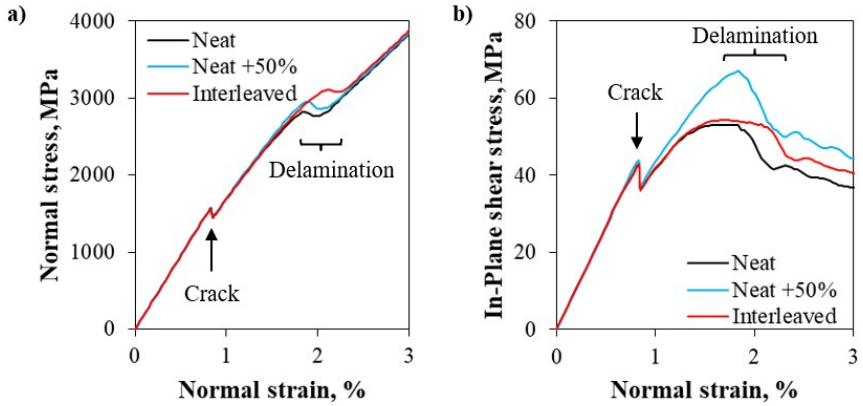

Figure 7: Typical curves of (a) the maximum normal stress and (b) the maximum in-plane shear stress in $[90_8/0_2]_s$ laminate with different interface properties at the interlaminar region.

The subsequent failure after transverse cracking is the onset of delamination, which corresponds to the second step in Figure 7. The strain to onset delaminations is delayed, as shown on the laminate normal stress response in Figure 7(a). The normal stress kept rising linearly since the 0° ply still carried the loads elastically. The delamination lengths of the models with the three different sets of interlaminar properties are illustrated in Figure 8. The figure also compares the delaminations in $[90_2/0_2]_s$ and $[90_8/0_2]_s$ laminates for each interface property set. In all the models, the delamination onset began simultaneously from all three transverse cracks owing to the uniformity of the loading and geometry. The cohesive process zone of the interleaved model was the largest due to the higher critical toughness compared to the others, which, in turn, enlarges the cohesive zone envelope. The corresponding delamination length was 21% shorter than the reference neat model. The 50% increase in the neat interface strengths reduced the convergence efficiency of the model due to the narrower cohesive process zone. It also increased the delamination length by 14% compared to the neat model. The delamination propagation length and cohesive process length were insensitive to variations in the transverse ply thickness.

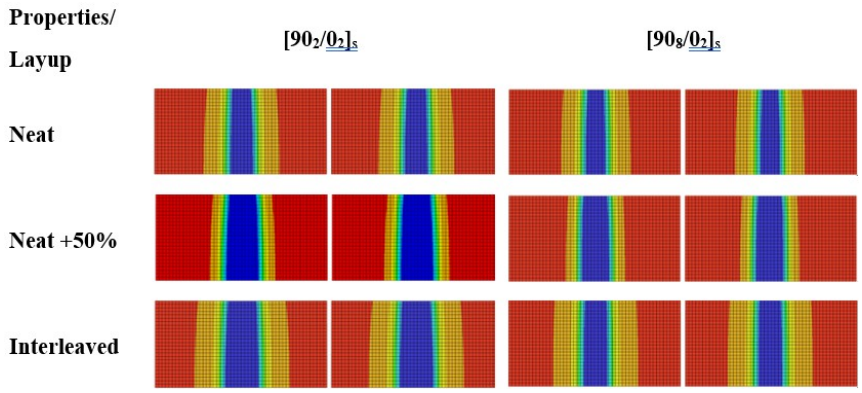

Figure 8: Top view of the models showing the sensitivity of the delamination area and process zone to the interlaminar cohesive properties relative to the min-max thicknesses of the transverse ply.

3.3 A cross-ply laminate under biaxial fatigue loading

Two $[0_3/90_3]_s$ laminate models were constructed, one with the baseline interlaminar interface properties and the second with interleaved properties. Since the mesh and contact patterns were uniform, the Gaussian (normal) distribution was used to randomise the interface strengths and the critical strain release energies, allowing the damage to onset at random locations, which was necessary to avoid convergence difficulties. Randomisation techniques are commonly employed to simulate multiple delaminations [5, 19]. To avoid creating biased results, the contact properties at each intralaminar contact region were identical between the baseline and interleaved models. The laminates were loaded for 15 cycles with a differential body temperature from 293 to 77 K. To accelerate the damage evolution, an equal biaxial tension strain of 0.1% was applied with a load ratio of 0.1. A dynamic viscous regulation coefficient of 1×10^{-3} to resolve convergence difficulties when encountered.

The predicted damage evolution in the baseline and interleaved laminates after 15 cycles is illustrated in Figure 9. After two cycles, the first fully developed matrix crack occurred in the 90° ply. The crack propagated through the thickness before extending rapidly across the width of the laminate. The initiation of this crack caused a relaxation in the 90° ply, and subsequently, the other intralaminar interfaces were undamaged. In contrast, four adjacent 0° interfaces were experiencing cohesive fatigue damage. The outer intralaminar interfaces tend to soften near the fully developed crack. The tip of a transverse crack acts as a stress raiser that triggers the formation of a stitch crack in the adjacent ply. The softening regions propagated transversely through the thickness before advancing longitudinally along fibres. That is, the energy release rate is twice as high in the transverse direction than in the longitudinal [25]. Such cracks are thin in nature, and they grow unstably in the transverse direction, quickly occupying the lamina's thickness [26]. After that, the partially developed 0° crack had no choice but to propagate longitudinally when the strain energy rate exceeded the critical fracture toughness.

Cohesive softening at the interlaminar region along the fully developed crack is observed in the enlarged image in Figure 9. The adjacent 0° ply resisted the crack openings of the damaged 90° lamina and produced high levels of interlaminar normal and shear stresses. These stresses were severe enough to overcome the interface strength of the interlaminar region. However, the energy release rate was not sufficient to onset delaminations. This explains the rare occurrence of localised delaminations at the crack tips of the laminates when examined under the SEM. The transverse matrix cracking pattern between the baseline and interleaved laminate was identical. A sudden increase in the damage occurred when the first transverse cracks initiated after two cycles. The toughened interface damped this jump in damage by 20.4% compared to the baseline. Both interfaces were linearly softening afterwards with subsequent cycling. The final damage value of the interleaved model was 16.1% lower than the reference. This indicates that the damage growth was higher in interleaved interfaces, which is

driven by the localised stress state. This stress severity was higher due to the damage effect while resisting the transverse crack opening displacements.

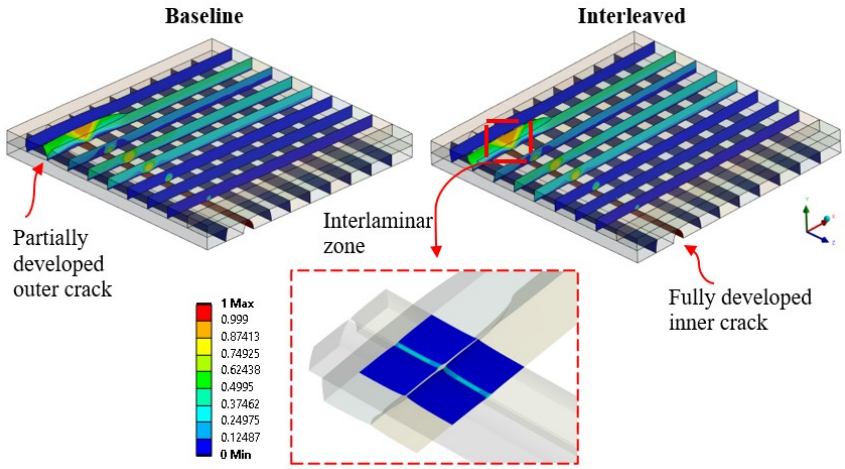

Figure 9: Predicted damage evolution in the baseline and interleaved cross-ply laminates. The enlarged region shows the softening of the interlaminar zone at the junction between two transverse cracks. The legend represents the damage parameter, where one means a fully damaged element.

4 CONCLUSIONS

The effectiveness of the interleaving technique in minimising the interconnections in a crack network, and thus permeability coefficients, was explored in this study. Electrospun PES veils were used to toughen cross-ply laminates. Helium gas permeability rates through these laminates were measured as a function of the number of cryo-cycles. Compared to the baseline samples, the interleaving technique significantly reduced the permeability coefficient by one order of magnitude after the first cryo-cycle and by 40% after the second cycle. This suggests that the toughening effects seen in the coupon testing data have effectively reduced the crack network size. With subsequent loadings, the growth in the crack network reached a saturation point.

Examination of the cracks with micro-CT scanning and SEM techniques revealed that the inner plies had a higher crack density than the outer plies. Transverse cracks tend to extend from trapped voids in the matrix near the stitches, causing variability in crack density measurements. The majority of these cracks were arrested at the interface of the adjacent ply without branching into localised delaminations. The observed delaminations were short and random in their occurrence.

The finite element model was employed to provide a supporting analysis of these observations and to highlight the impact of the interleaving technique. The model demonstrated how PES veils delay the onset of delaminations and slow their growth rate. These effects were apparent in cross-ply laminates with multiple inner ply thicknesses. The improvement levels were consistent relative to the untoughened model as the ply thickness reduced. The onset of delamination was suppressed in all the models till a later stage of uniaxial leading when the 90° ply thickness reduces. The results from the gas permeability measurements and modelling predictions favour using the interleaving technique to improve the damage resistance in cryo-cycled laminates.

To summarise, the use of interleaves is beneficial in damping the initial evolution of damage networks. If the thermomechanical loading is high, the interleaves will show more resistance to damage growth due to their substantial R-curve effect, which was assessed experimentally in the previous chapters. When the cyclic loads are low, the damped interfaces will tend to fatigue faster because of the increase in the stress state from resisting the opening of transverse cracks.

ACKNOWLEDGEMENTS

This research has been supported by a University International Postgraduate Award from the University of New South Wales. The authors would also like to acknowledge Omni Tanker Pty Ltd, Australia, for supplying the epoxy resin, and the Tyree X-ray CT Facility, X-ray Analysis Facility, Mark Wainwright Analytical Centre, UNSW Sydney, for the acquisition of the 3D μXCT images.

REFERENCES

1. Kratmann, K.K., et al., *A novel image analysis procedure for measuring fibre misalignment in unidirectional fibre composites.* Composites Science and Technology, 2009. **69**(2): p. 228-238.
2. Ochoa, O.O., et al., *Finite element analysis of composite laminates*. 1992: Springer.
3. Nair, A. and S. Roy, *Modeling of permeation and damage in graphite/epoxy laminates for cryogenic tanks in the presence of delaminations and stitch cracks.* Composites Science and Technology, 2007. **67**(11-12): p. 2592-2605.
4. Roy, S. and M. Benjamin, *Modeling of permeation and damage in graphite/epoxy laminates for cryogenic fuel storage.* Composites Science and Technology, 2004. **64**(13-14): p. 2051-2065.
5. Grogan, D., C.Ó. Brádaigh, and S. Leen, *A combined XFEM and cohesive zone model for composite laminate microcracking and permeability.* Composite Structures, 2015. **120**: p. 246-261.
6. Zhang, J., T. Lin, and X. Wang, *Electrospun nanofibre toughened carbon/epoxy composites: Effects of polyetherketone cardo (PEK-C) nanofibre diameter and interlayer thickness.* Composites science and technology, 2010. **70**(11): p. 1660-1666.
7. Li, G., et al., *Inhomogeneous toughening of carbon fiber/epoxy composite using electrospun polysulfone nanofibrous membranes by in situ phase separation.* Composites Science and Technology, 2008. **68**(3-4): p. 987-994.
8. Zbed, R.S., S. Le Corre, and V. Sobotka, *Process-induced strains measurements through a multi-axial characterization during the entire curing cycle of an interlayer toughened Carbon/Epoxy prepreg.* Composites Part A: Applied Science and Manufacturing, 2022. **153**: p. 106689.
9. Odagiri, N., H. Kishi, and M. Yamashita, *Development of TORAYCA prepreg P2302 carbon fiber reinforced plastic for aircraft primary structural materials.* Advanced Composite Materials, 1996. **5**(3): p. 249-254.
10. Joudon, V., et al., *Experimental procedure to characterize the mode I dynamic fracture toughness of advanced epoxy resins.* Engineering Fracture Mechanics, 2014. **126**: p. 166-177.
11. Brugo, T., et al., *Study on Mode I fatigue behaviour of Nylon 6, 6 nanoreinforced CFRP laminates.* Composite Structures, 2017. **164**: p. 51-57.
12. Laban, O., et al., *A comparative study of the cryogenic performance of CFRP composites with polyethersulfone/epoxy blends and electrospun polyethersulfone interleaves.* Composites Part A: Applied Science and Manufacturing, 2024. **178**: p. 108000.
13. Bechel, V.T., J.D. Camping, and R.Y. Kim, *Cryogenic/elevated temperature cycling induced leakage paths in PMCs.* Composites Part B: Engineering, 2005. **36**(2): p. 171-182.
14. Murray, B.R., et al., *Helium permeability of polymer materials as liners for composite overwrapped pressure vessels.* Journal of Applied Polymer Science, 2016. **133**(29).
15. Saha, S., R.W. Sullivan, and M.L. Baker, *Gas permeability of three-dimensional stitched carbon/epoxy composites for cryogenic applications.* Composites Part B: Engineering, 2021. **216**: p. 108847.
16. Choi, S. and B.V. Sankar, *Gas permeability of various graphite/epoxy composite laminates for cryogenic storage systems.* Composites Part B: Engineering, 2008. **39**(5): p. 782-791.
17. Zwanenburg, E., et al., *Effective X-ray micro computed tomography imaging of carbon fibre composites.* Composites Part B: Engineering, 2023. **258**: p. 110707.
18. Carraro, P.A., et al., *Delamination onset in symmetric cross-ply laminates under static loads: Theory, numerics and experiments.* Composite Structures, 2017. **176**: p. 420-432.
19. Grogan, D.M., et al., *Damage and permeability in tape-laid thermoplastic composite cryogenic tanks.* Composites Part A: Applied Science and Manufacturing, 2015. **78**: p. 390-402.
20. Hamori, H., et al., *Numerical and experimental evaluation of the formation of leakage paths through CFRP cross-ply laminates with leak barrier layers.* Composite Structures, 2019. **230**: p. 111530.
21. Begley, M.R., et al., *Micromechanical models to guide the development of synthetic 'brick and mortar' composites.* Journal of the Mechanics and Physics of Solids, 2012. **60**(8): p. 1545-1560.
22. Nairn, J.A., *Matrix microcracking in composites.* Polymer matrix composites, 2000. **2**: p. 403-432.
23. Laban, O., et al. *Prediction of discrete crack network formation in composite laminates subjected to cyclic thermomechanical loading conditions*. in *11th Australasian Congress on Applied Mechanics (ACAM2024)*. 2024. Engineers Australia Brisbane.
24. Brugo, T. and R. Palazzetti, *The effect of thickness of Nylon 6, 6 nanofibrous mat on Modes I–II fracture mechanics of UD and woven composite laminates.* Composite Structures, 2016. **154**: p. 172-178.
25. Dvorak, G.J. and N. Laws, *Analysis of progressive matrix cracking in composite laminates II. First ply failure.* Journal of Composite Materials, 1987. **21**(4): p. 309-329.
26. Barbero, E.J., *Introduction to composite materials design*. 2017: CRC press.

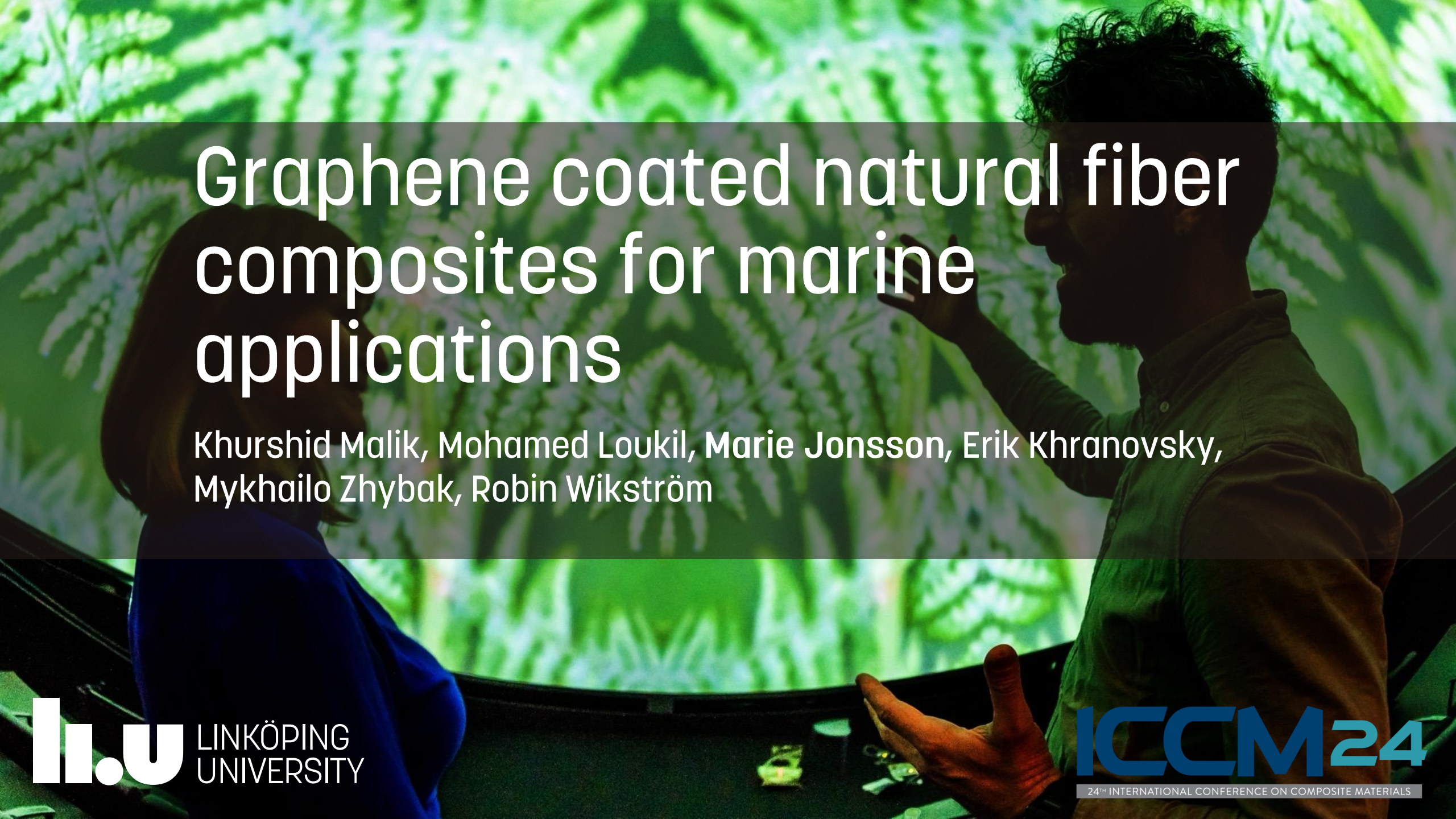

Graphene coated natural fiber composites for marine applications

Khurshid Malik, Mohamed Loukil, **Marie Jonsson**, Erik Khranovsky, Mykhailo Zhybak, Robin Wikström

LINKÖPING UNIVERSITY

ICCM24
24TH INTERNATIONAL CONFERENCE ON COMPOSITE MATERIALS

Motivation



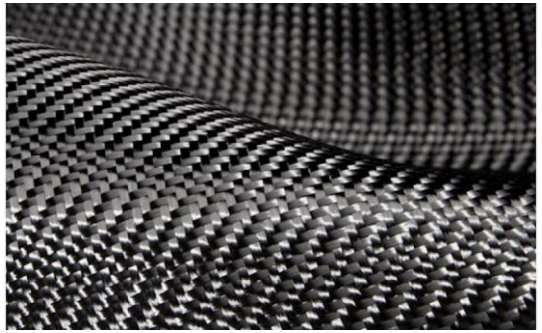

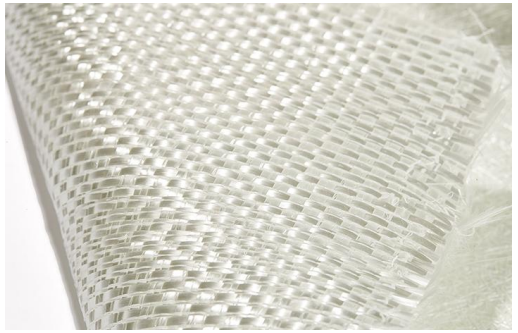

Sustainability



Natural fibers:
Flax Fibers

Very sensitive to water and humidity

Med stöd från
VINNOVA Sveriges innovationsmyndighet
Energimyndigheten
FORMAS
Strategiska innovationsprogram

Project Aim

Investigate how coating natural fibers with graphene affects their sensitivity to water and performance.

A complete study from the microscale to the macroscale level

- Material Selection
- Manufacturing
- Testing
- Material characterization



2023-03-01 G3 2025-02-28 G3-Demo 2026-05-30

Med stöd från VINNOVA Sveriges innovationsmyndighet, Energimyndigheten, FORMAS, Strategiska innovationsprogram

Outline

Cupon tests

Purpose: Impact of graphene coating in surface layers of full.

- Water absorption
- Visual inspection

Graphene amount comparison (coupon)

Purpose: Optimise graphene amount

- Water absorption
- Visual inspection
- Mechanical testing
- SEM

Small hatch demonstrator

Purpose: Scalability

- Water absorption
- Visual inspection

LINKÖPING UNIVERSITY GRAFREN Innovative Materials Arena RI SE Trifilon X SHORE
Med stöd från VINNOVA Sveriges innovationsmyndighet Energimyndigheten FORMAS Strategiska innovations-program
ICCM24 24th INTERNATIONAL CONFERENCE ON COMPOSITE MATERIALS

Composite design

Coating:

- Graphene flakes coating by Grafren AB purification technology

Material System

- Flax Fiber weaves
- Polymer matrix: SR InfuGreen (Bioresin)

Manufacturing

- Vacuum Infusion

Testing and Analysis

- Physical : Fiber volume fraction and Voids
- Mechanical: Flexural, Tensile, ILSS
- Failure: Visual, SEM
- Hot Salted Water, 50°C

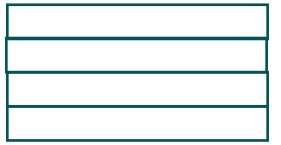

No Coated
0% coated



Surface Layers Coated
25% coated



All Coated
100% coated

Med stöd från
VINNOVA Sveriges innovationsmyndighet
Energimyndigheten
FORMAS
Strategiska innovationsprogram

Graphene coating process

(propriatery Grafren AB)

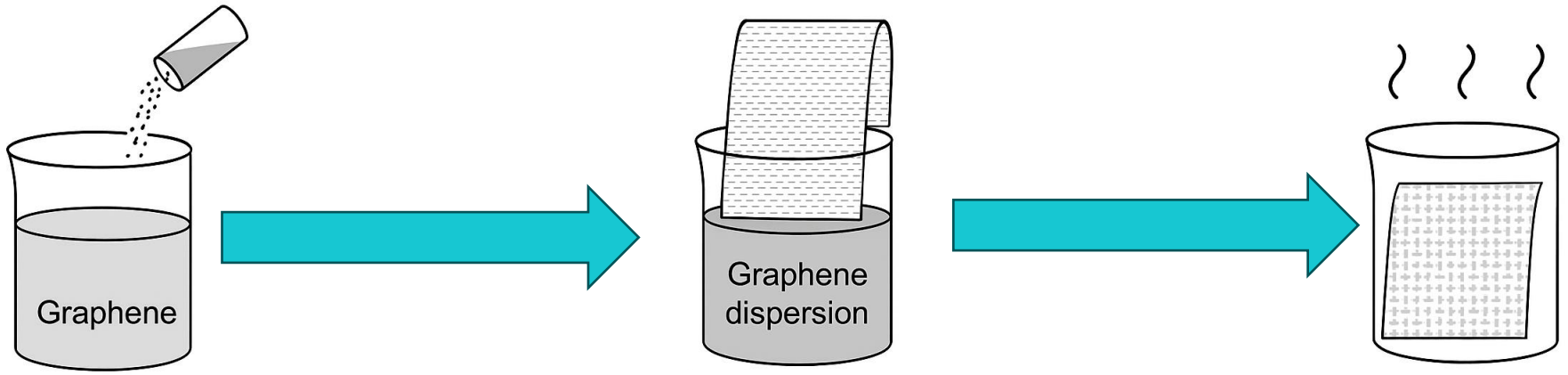

1.
Aqueous dispersions of few-layer graphene flakes (graphene powder in deionized water without any surfactants or chemical binders). Ultrasonic homogenization for 30–60 minutes.

2.
Flax fabric immersion at room temperature. Graphene flakes adhere to the fiber surfaces through van der Waals interactions, forming a non-continuous but conformal coating.

3.
Fibers are removed and air-dried under ambient conditions or oven-dried at 60 °C to remove residual moisture.

Reference:
https://patents.google.com/patent/SE544448C2/fr

Composite manufacturing

Quasi-isotropic [+45/-45/0/90]s
Infusion

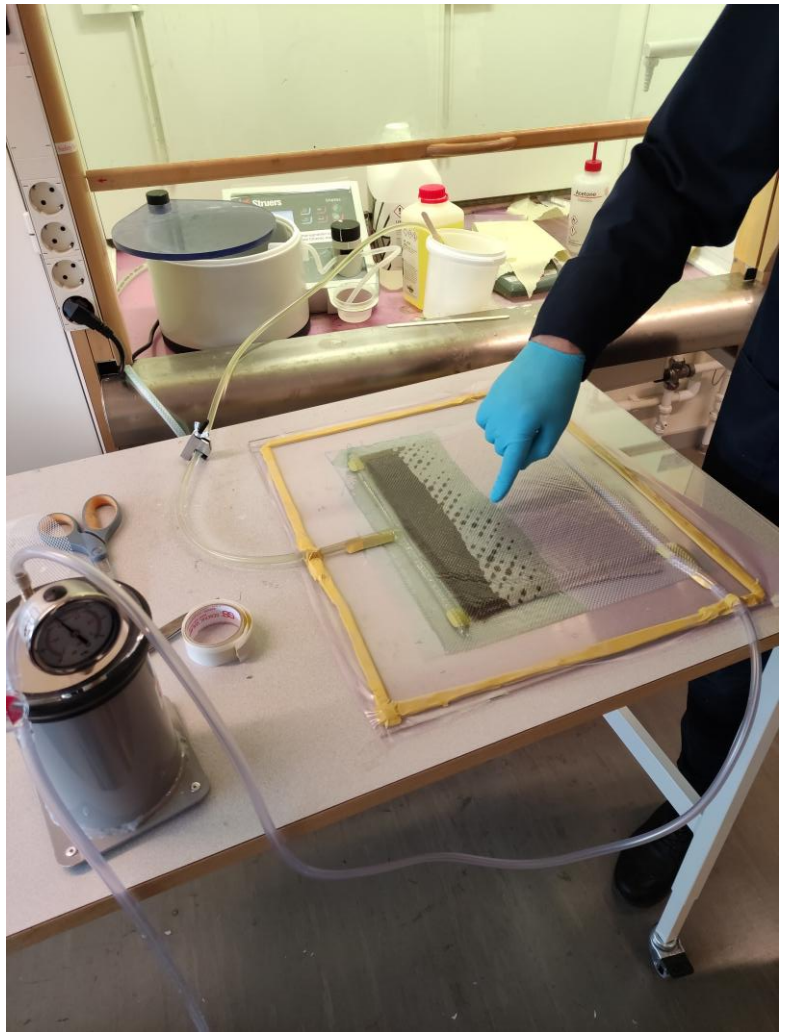

Med stöd från
VINNOVA Sveriges innovationsmyndighet
Energimyndigheten
FORMAS
Strategiska innovationsprogram

Water absorption properties

Salt water 50 ˚C

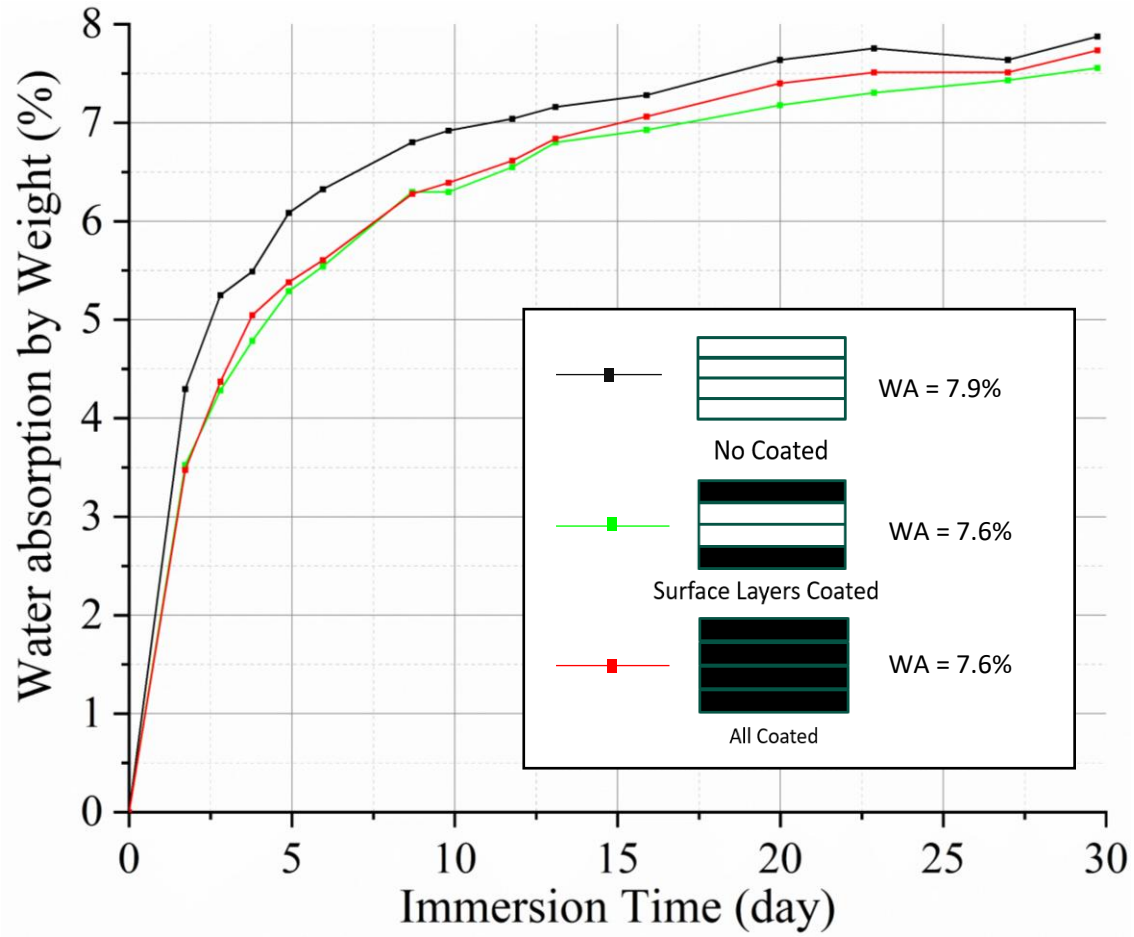

Fiber swelling/ degradation



No Coated

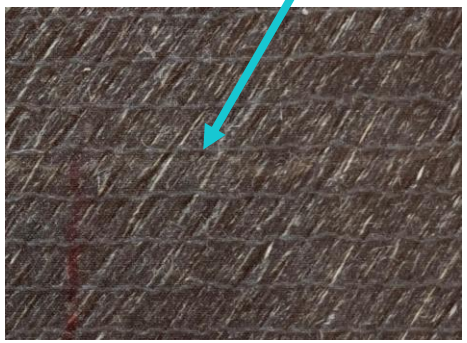

No Coated-Conditioned

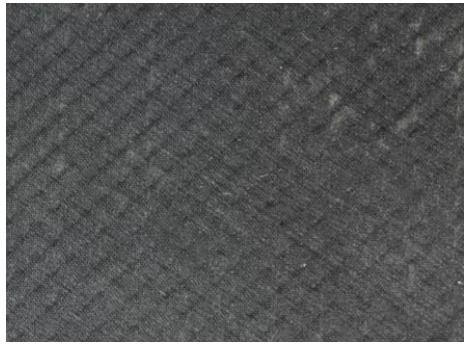

All Coated

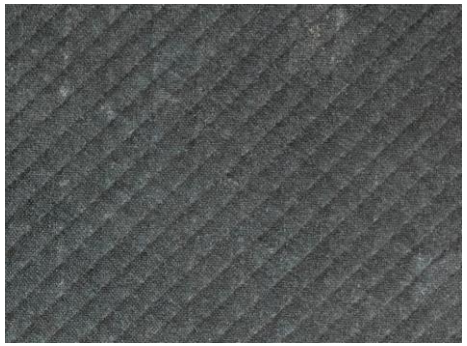

All Coated-Conditioned

-> Water resistance were improved slightly incoated laminates.

Med stöd från
VINNOVA Sveriges innovationsmyndighet
Energimyndigheten
FORMAS
Strategiska innovations-program

Graphene Amount comparison

Lay-up: (±45/±45/±45/±45)

Plate size: 250 x 160 mm2

Graphene (wt.%) at 4 different concentrations:

- 0%
- 0.5%
- 1.0%
- 1.5%

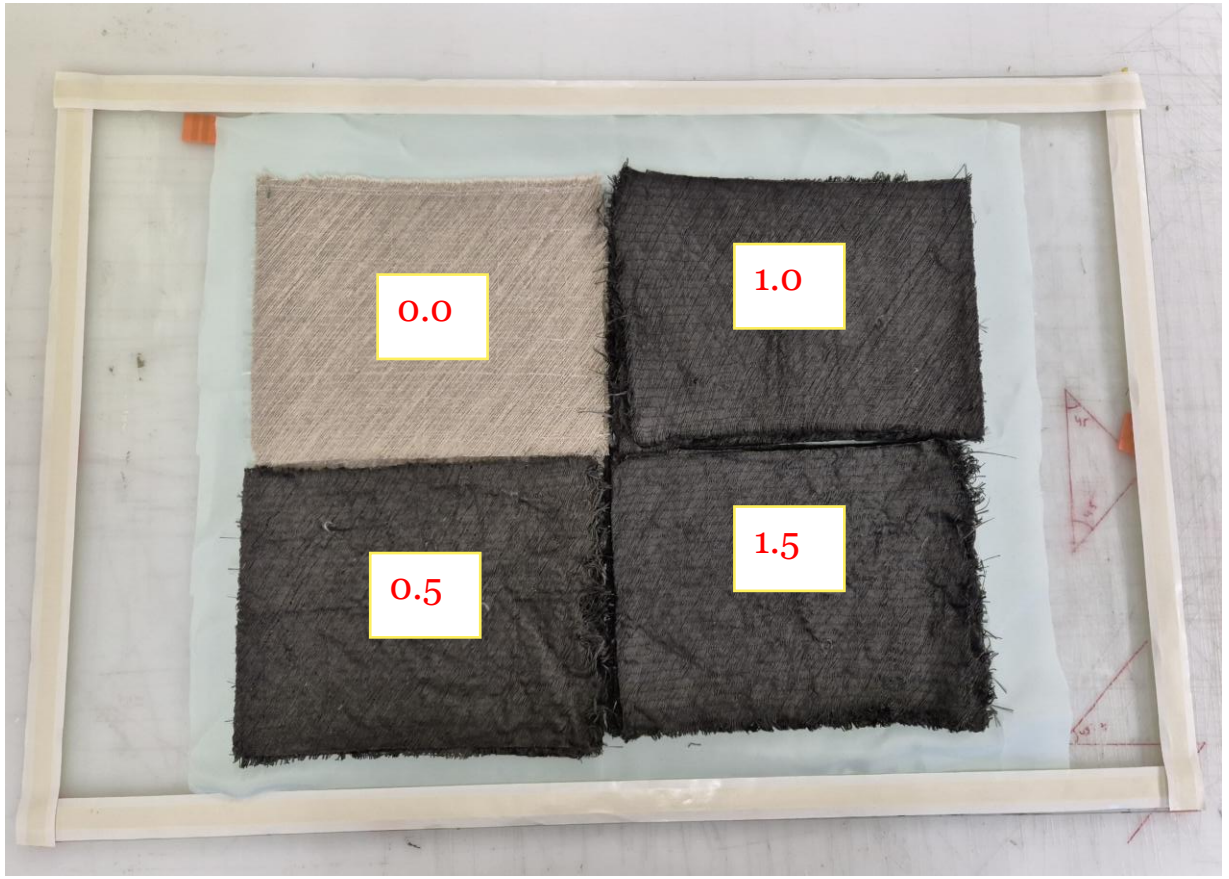

Med stöd från
VINNOVA Sveriges innovationsmyndighet
Energimyndigheten
FORMAS
Strategiska innovations-program

Flexural Properties for Different Graphene Amounts

Sample Name		FS (MPa)	Strain (%)	FM (GPa)
Pure	0.0	105.6±0.2	5.4±0.6	3.9±0.1
Full Graphene	0.5	87.1±0.4	4.6±0.3	3.9±0.1
Full Graphene	1.0	72.8±3.0	5.3±0.9	2.8±0.2
Full Graphene	**1.5**	**145.4±13.3**	**4.2±0.5**	**5.8±0.3**

FS: Flexural Strength, FM: Flexural Modulus

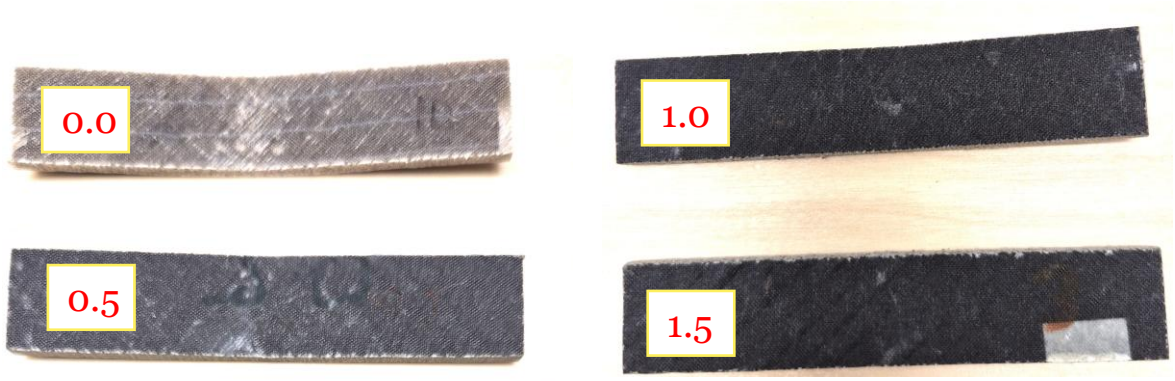

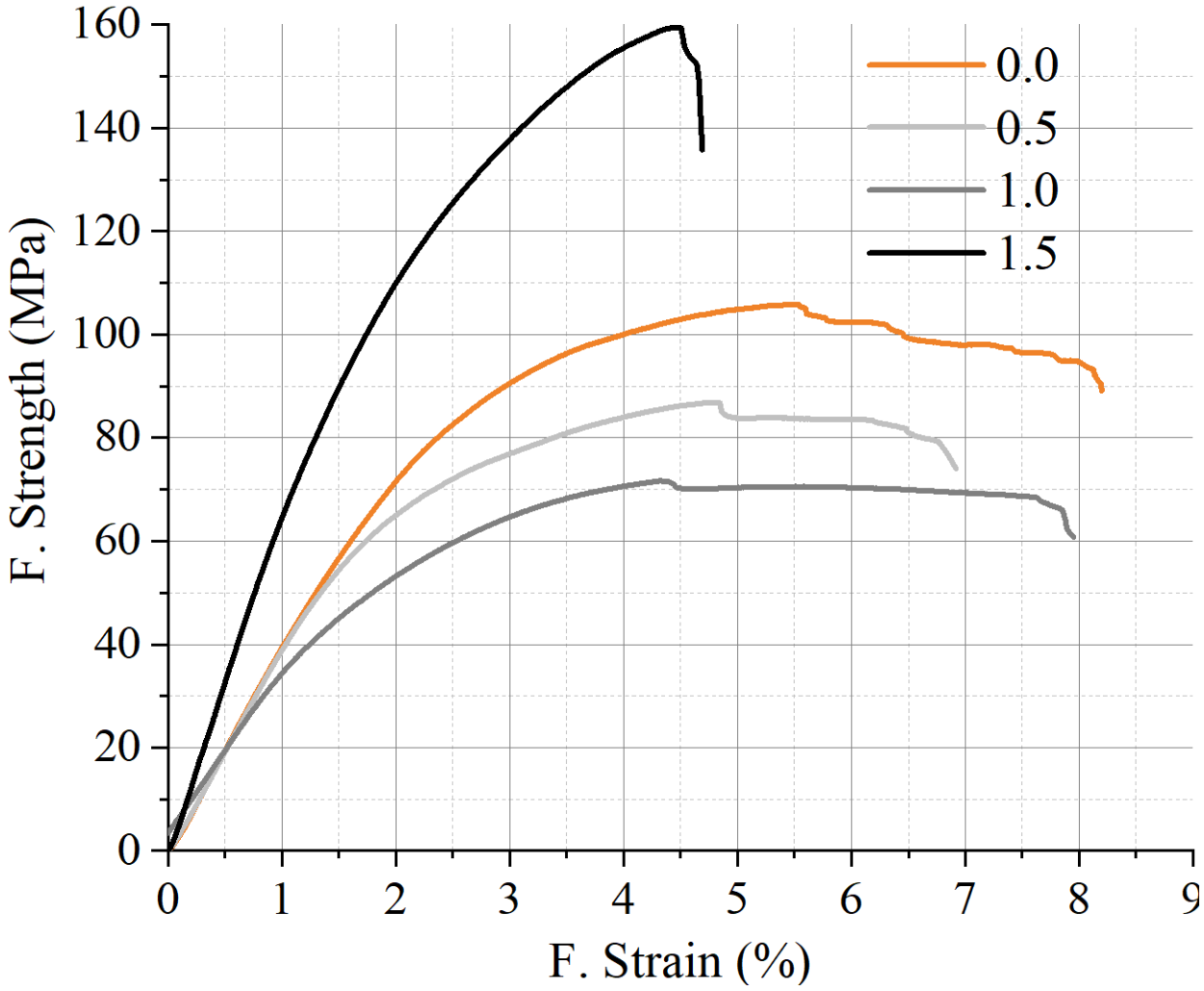

SEM analysis - fibers

Smooth surface

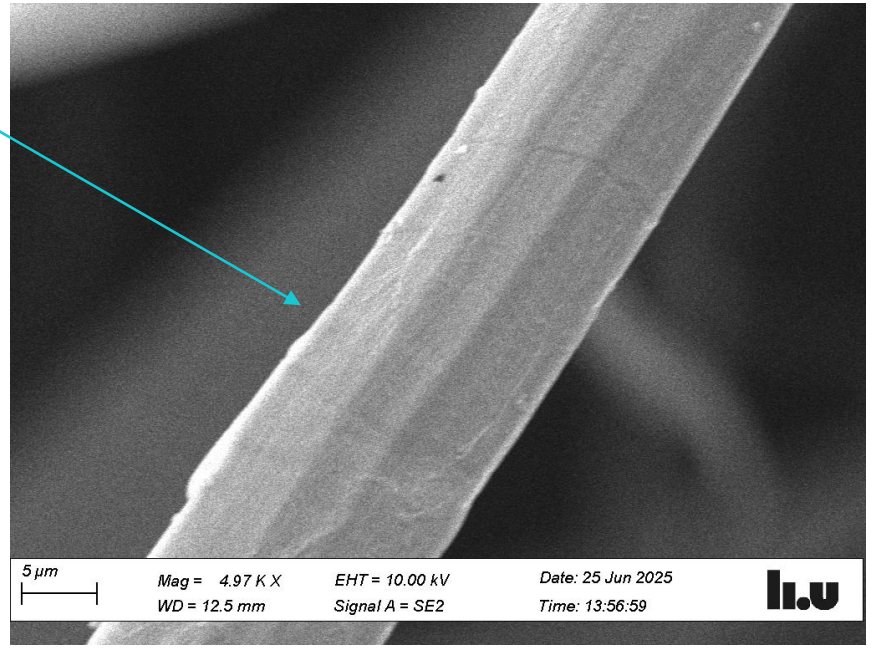

0% graphene

Uniform coating

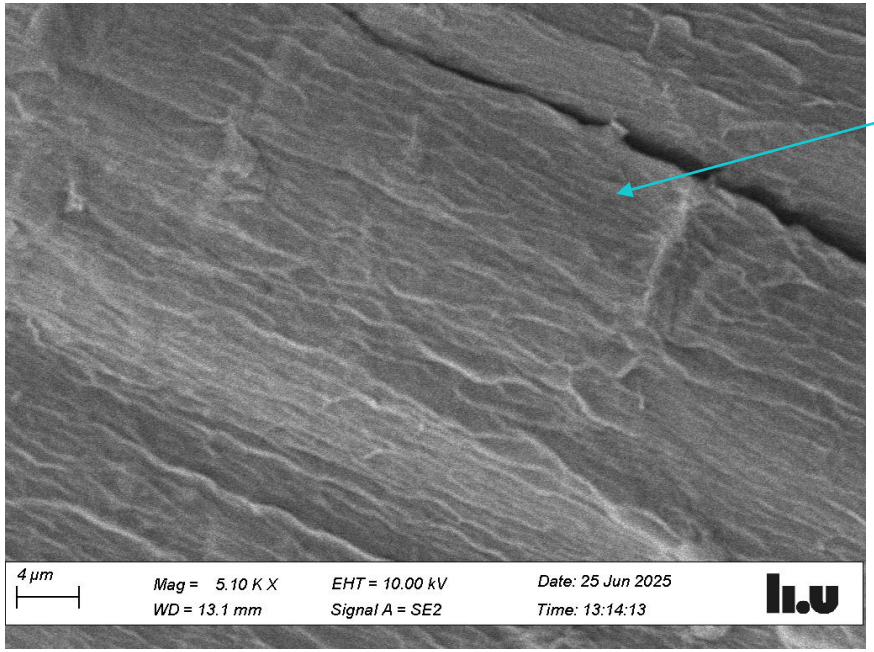

1.5% graphene

1.5% of Graphene: The fibers were fully coated without any sign of detachment of graphene flakes

LINKÖPING UNIVERSITY GRAFREN Innovative Materials Arena RI.SE Trifilon X SHORE
Med stöd från VINNOVA Sveriges innovationsmyndighet Energimyndigheten FORMAS Strategiska innovations-program
ICCM24 24TH INTERNATIONAL CONFERENCE ON COMPOSITE MATERIALS

SEM analysis – composite laminate

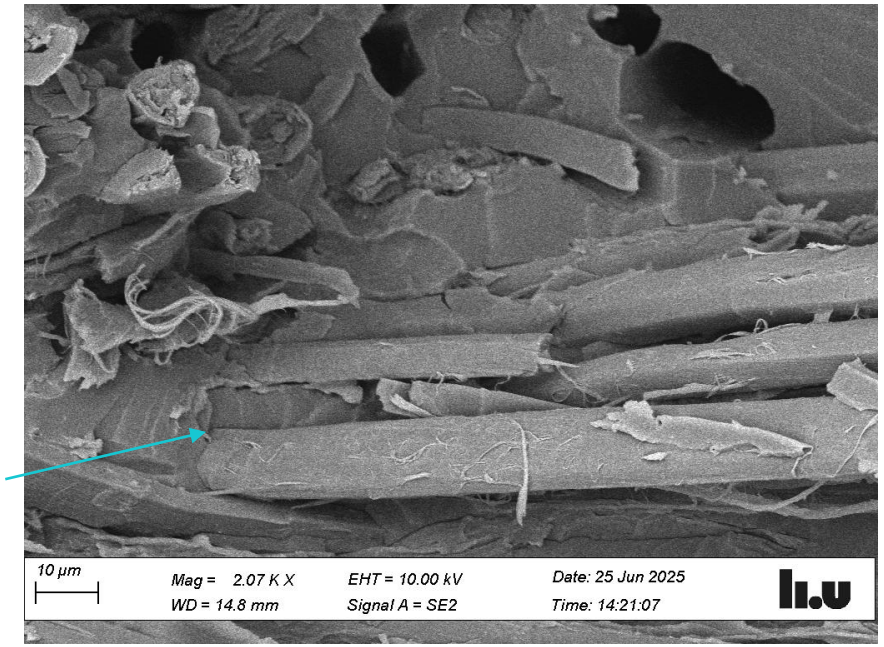

Interfacial binding

0% graphene

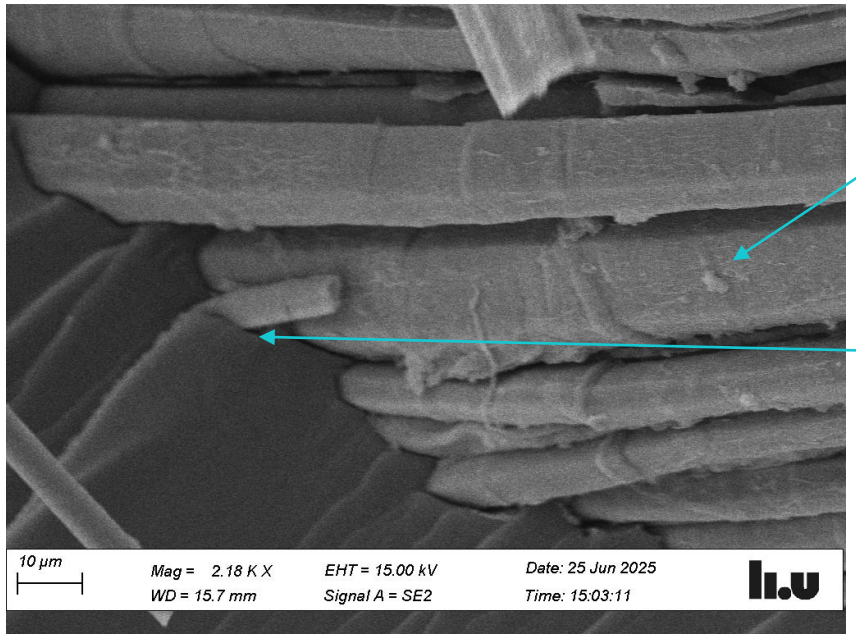

Uniform coating

Interfacial binding

1.5% graphene

Med stöd från
VINNOVA Sveriges innovationsmyndighet
Energimyndigheten
FORMAS
Strategiska innovationsprogram

Small Demonstrator (Hatch)

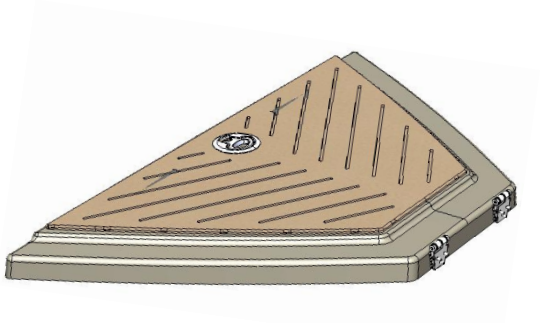



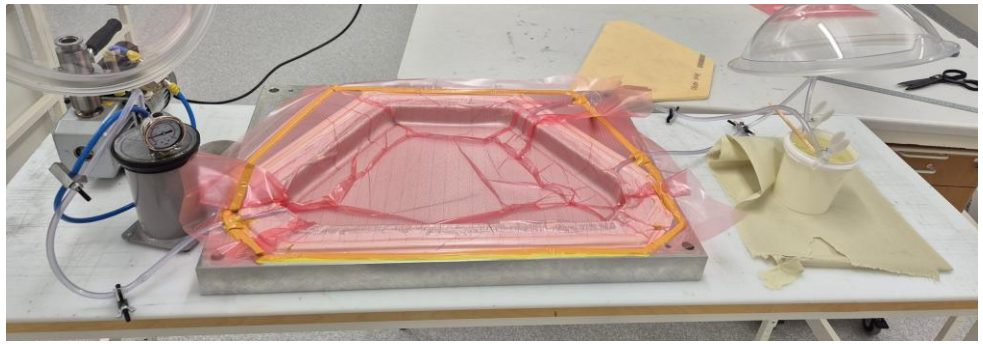

Manufacturing setup



Not Coated



100% coated fibers (1.5%)

Med stöd från
VINNOVA Sveriges innovationsmyndighet
Energimyndigheten
FORMAS
Strategiska innovationsprogram

Hatch demo testing (salt water immersion)

Before water absorption test



After water absorption test

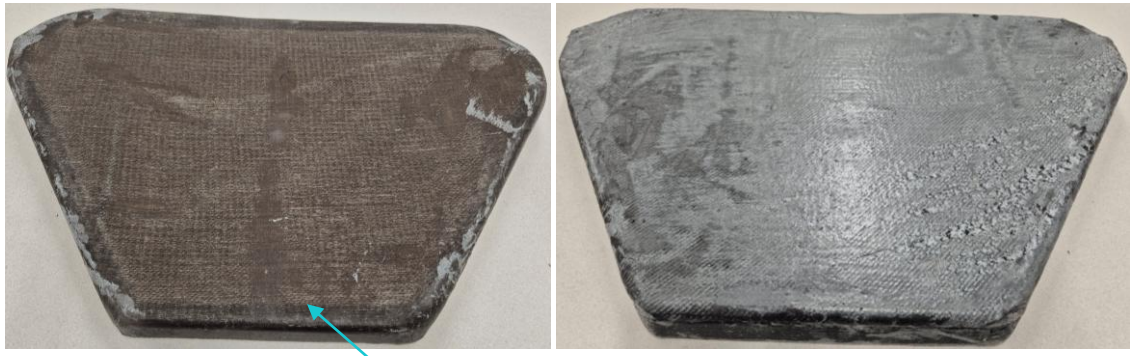

Uncoated

Coated

Fiber swelling/ degradation

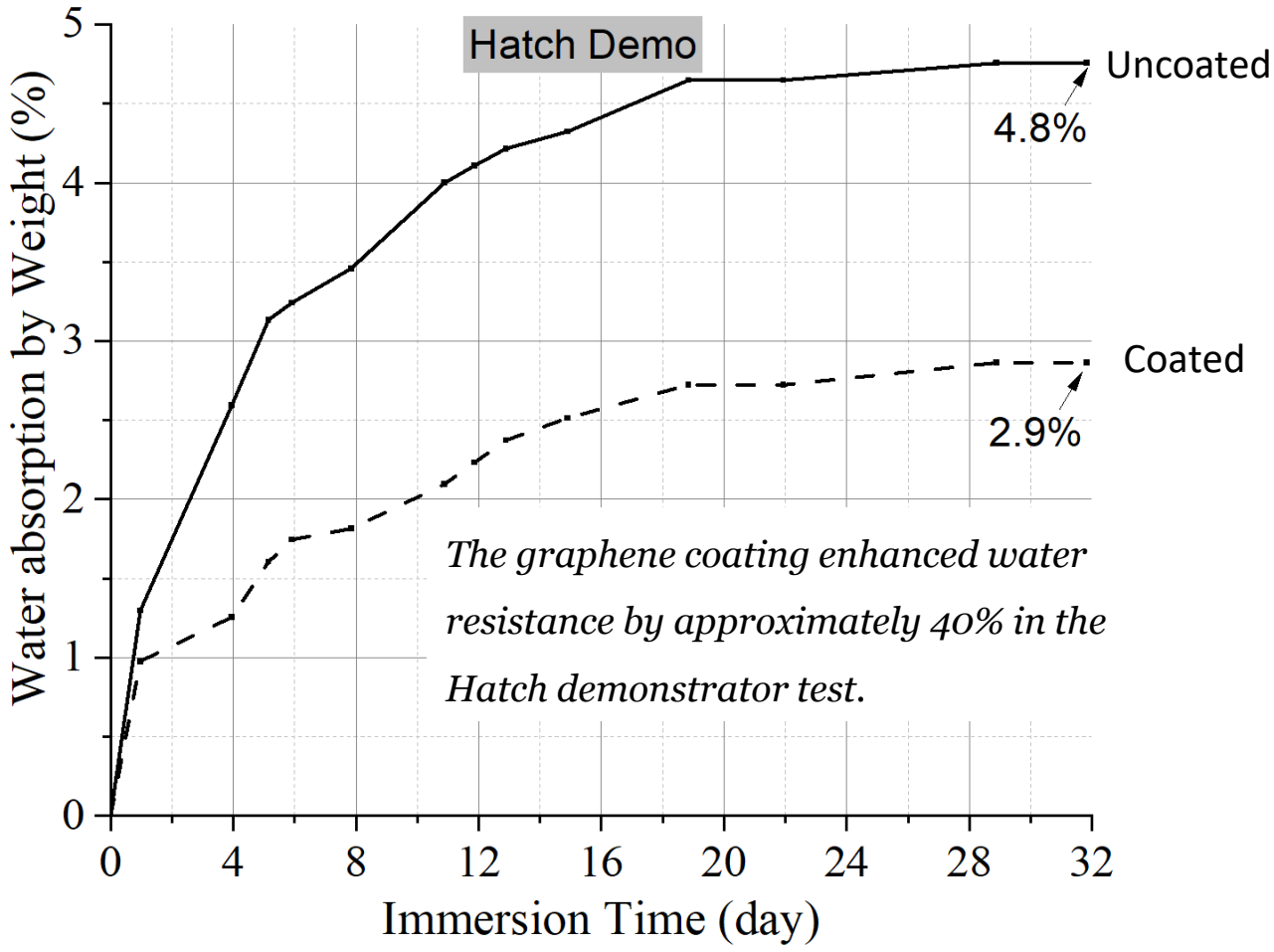

Med stöd från
VINNOVA Sveriges innovationsmyndighet
Energimyndigheten
FORMAS
Strategiska innovations-program

Conclusions and future prospects

- Graphene coating successfully applied to flax fiber, enhancing composite performance.
- 1.5 wt.% graphene coating resulted in approximately 38% increase in flexural strength and a 48% rise in flexural modulus.
- The testing at the demonstrator level (Hatch) confirmed around 40% improvement in water resistance.
- To fully harness the potential of graphene in bio-composites, the following key factors are currently under investigation:
  - Graphene size, thickness, concentration and surface area
  - Desired coating thickness and Post-coating drying process
- Larger demonstrator will be manufactured
  - The fabrication process will utilize prepreg to ensure consistency and quality.

LINKÖPING UNIVERSITY GRAFREN Innovative Materials Arena RI SE Trifilon X SHORE
Med stöd från VINNOVA Sveriges innovationsmyndighet Energimyndigheten FORMAS Strategiska innovations-program
ICCM24 24th INTERNATIONAL CONFERENCE ON COMPOSITE MATERIALS

Acknowledgements

- **Linköping University**: Khurshid Malik, Mohamed Sahbi Loukil, Mikael Segersäll
- **RISE**: Stephanie Nunes, Erik Sandlund
- **Grafren**: Mykhailo Zhybak, Erik Khranovsky
- **X Shore**: Robin Wikström
- **Trifilon**: Martin Lidstrand, Dimitrios Georgouvelas
- **IMA**: Andreas Johansson
- **University of Sfax, Tunisia**: Sami Boufi, Makki Abdmouleh

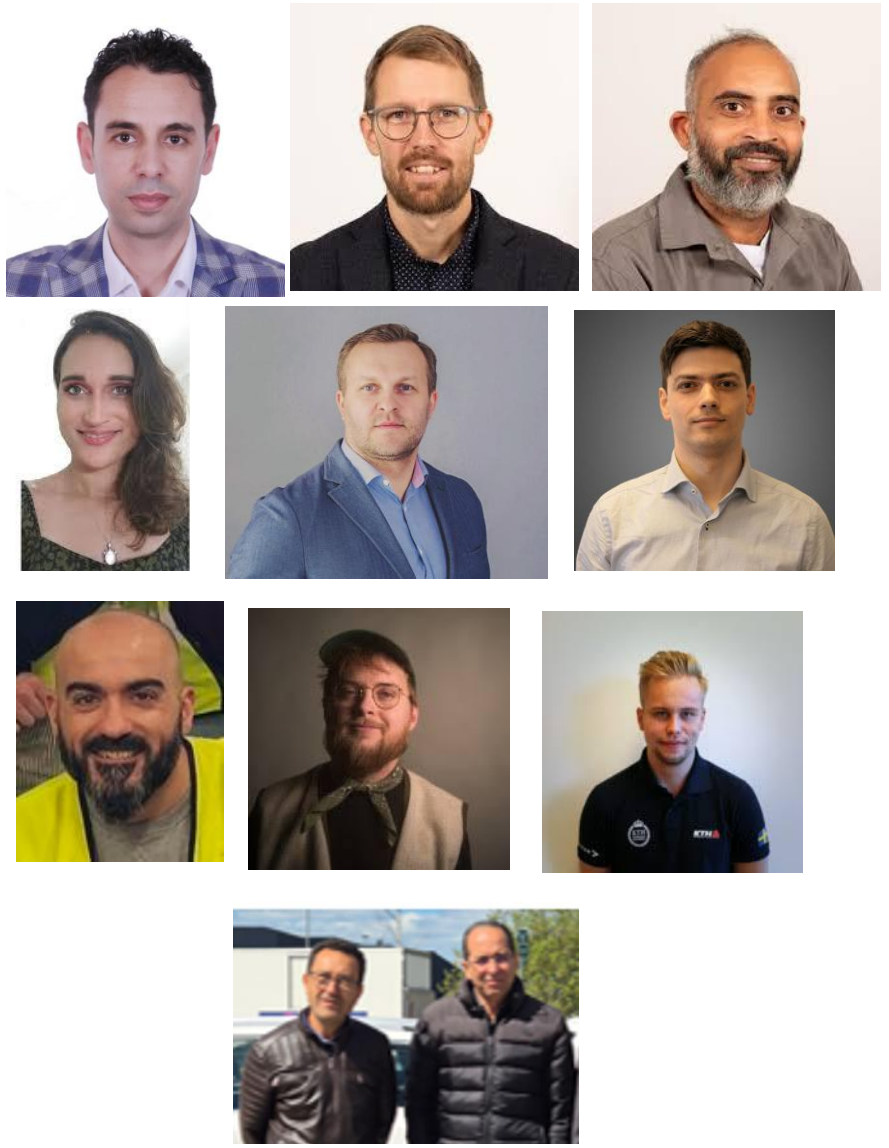

Med stöd från VINNOVA Sveriges innovationsmyndighet, Energimyndigheten, FORMAS, Strategiska innovationsprogram

Thanks!

ICCM24

24TH INTERNATIONAL CONFERENCE ON COMPOSITE MATERIALS

Med stöd från
VINNOVA Sveriges innovationsmyndighet
Energimyndigheten
FORMAS
Strategiska innovationsprogram

Contact:
Marie Jonsson, marie.s.jonsson@se (Presenter)
Khurshid Malik khurshid.malik@liu.se (Post-doctoral researcher)
Mohamed Sahbi Loukil mohammad.loukil@liu.se (Principal investigator)

Image generated using ChatGPT and the iput "Baltimore"

ELECTRON BEAM AND GAMMA RAY RADIATION TREATMENTS TO ACHIEVE HIGH STRENGTH IN CARBON NANOTUBE LAMINATES

Cecil Evers[1,2], Jin Gyu Park[1,2], Britannia Vondrasek[3,4], Christopher Johnson[1,2], Terrencia Martin[1,2], Mike Czabaj[4], Gregory Odegard[5], and Richard Liang[1,2*]

[1]FAMU-FSU College of Engineering, Florida State University
2025 Pottsdamer St, Tallahassee FL, USA
*Email: liang@eng.famu.fsu.edu

[2]High Performance Materials Institute, Florida State University
2005 Levy Ave, Tallahassee FL, USA

[3]Aerospace Engineering Department, United States Naval Academy
Annapolis, MD, USA

[4]Department of Mechanical Engineering, University of Utah
Salt Lake City, UT, USA

[5]Mechanical Engineering – Engineering Mechanics
Michigan Technological University, Houghton, MI, USA

Keywords: Carbon Nanotubes, CNT, Gamma Ray, Electron Beam

ABSTRACT

Gamma ray and electron beam irradiation are used to improve the tensile properties of scalable ultra-high volume fraction laminates made from continuous carbon nanotube (CNT) yarns. Radiation treatments simultaneously induce crosslinking and surface activation, enhancing load transfer. Yarns are treated with doses ranging from 50 kGy to 1200 kGy (gamma ray) and 40 Mrad to 300 Mrad (electron beam). Gamma ray treatment yields up to a 5% increase in specific modulus and 4.7% in specific strength, while electron beam treatment achieves increases of up to 10% and 8.9%, respectively. Surface modification is assessed via DCAT which showed a lower contact angle after irradiation, indicating the addition of functional groups. Raman spectroscopy is also used to evaluate surface changes by comparing I_D and I_G peaks. Laminate-scale specimens assess the combined impact on tensile and surface properties. Unidirectional laminates with ~80 wt.% CNTs are fabricated. The 700 kGy gamma ray laminate achieved a specific modulus of 258 GPa g^{-1} cm^3, and the 40 Mrad electron beam laminate achieved a specific strength of 2.29 GPa g^{-1} cm^3. Results demonstrate that radiation treatments enhance load transfer in CNT yarn laminates, with crosslinking playing a critical role in achieving performance beyond state-of-the-art CFRPs.

1 INTRODUCTION

Carbon nanotubes (CNTs) have mechanical and transport properties beyond current state-of-the-art materials, however achieving nanoscale properties at the macro scale remains a challenge. A key limitation of CNT-based laminates is the weak interface between CNT bundles and polymer resin systems [1], [2], [3], [4].

Crosslinking and functionalization by irradiation may mitigate this issue [5], [6], [7], [8], [9]. Other functionalization approaches have limited effectiveness on commercially available CNT yarns due to their dense and aligned networks and large diameters relative to carbon fiber [10]. Additionally. The graphitic nature of CNT yarns has resulted in very low interface strengths, with fracture usually occurring within the CNT yarns themselves [3]. Radiation techniques like gamma ray or electron beam may penetrate the dense CNT networks and provide not only surface functionalization but also

crosslinking in the interior structure [11]. There is a theoretical limit where damage to the CNT structures will become greater than effects from crosslinking and functionalization; thus a range of treatments are necessary [12].

This work compares the effects of electron beam and gamma ray treatments on highly aligned MRIALON® high strength 2-ply CSY CNT yarns, manufactured by Nanocomp Technologies, Inc. (now part of Huntsman Advanced Materials). Tensile testing of single CNT yarns is used to evaluate the effectiveness of treatment methods on improving tensile properties of the CNT materials. Dynamic contact angle testing (DCAT) is used to evaluate the effectiveness of treatment methods on improving the interface of CNT yarns. Changes to both tensile and interface properties are evaluated by comparing laminate-scale specimens made with treated yarns and CYCOM® 5250-4 bismaleimide resin, supplied by Syensqo.

2 METHODS

2.1 Electron Beam Treatment

CNT yarn was wrapped around aluminum mandrel and exposed to a high-energy electron beam with 1.5 MeV. Electron beam dose depends on the exposure time; operation was paused between each 20 Mrad dose to avoid excessive temperature increase in the sample area. CNT yarns were treated with doses of 40, 200, and 300 Mrad. Additional batches of yarns were treated at 40 and 300 Mrad for manufacturing into CNT yarn laminates.

2.2 Gamma Ray Treatment

Gamma ray irradiation was conducted at the Radiation Center, Oregon State University, using the Co60 isotope with 1.13 and 1.33 MeV photon energies. The CNT yarns were wrapped around a plastic tube and placed at the center of the irradiation chamber. The dose was controlled by the irradiation time. Six different doses were applied: 50 kGy, 100 kGy, 200 kGy, 400 kGy, 700 kGy, and 1200 kGy. Composite laminates were made from 200, 700 and 1200 kGy samples.

2.3 Ozone Treatment

Yarns were wound on a truss and placed in a container for even ozone flow. An LG-7 CD Laboratory Ozone Generator was used at 9 V output at 5 L min^{-1}. The treatment was controlled by exposing yarns for 1 hour and 3 hours.

2.4 Yarn Tensile Testing

CNT yarns were tested at large gauge lengths of 120 mm according to a previously published paper [13]. A Shimadzu Autograph AGS-X mechanical test system using Grip-Engineering Thümler GmbH TH76-1+Ko capstan grips with 2.5 cm diameter and a 500 N load cell were used. The loading rate was 3 N min^{-1}, and strain was calculated by crosshead displacement between 0.5 – 1.0%. Crosshead extension was used for the modulus calculations presented in this work due to the small size of the yarns. This makes direct comparison of modulus values with the laminate-scale specimens unsuitable; however, we assume that the trends remained consistent regardless of if an extensometer was used.

2.5 Dynamic Contact Angle Testing

Dynamic contact angle was measured using a Dataphysics DCAT15. The sample was advanced into and receded from deionized water at 1 mm min^{-1} speed with an immersion depth of 3 mm, which was repeated for 5 cycles. A wetted length was used for DCA calculations based on the measured perimeter of the yarns using a digital microscope.

2.6 Laminate Manufacturing

Unidirectional CNT yarn composite laminates were fabricated using a filament winder and confined mold as shown in Figure 1a-d. Yarns were wrapped in the recessed area of the mold, shown in Figure

1a, then densified (1b), then a thin film of CYCOM® 5450-4 BMI is applied to the densified yarn stack (1c) and cured for 6 hours at 204 °C in a hot press [10]. The resultant laminate is shown in Figure 1d.

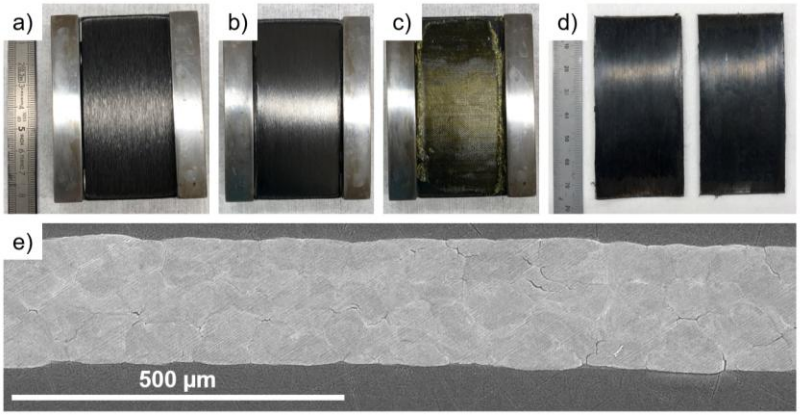

Figure 1: (a) CNT yarns wound on recessed mold, (b) yarns after densification, (c) resin applied to yarns, and (d) The laminates after curing. (e) shows a cross section image of the laminate.

The laminates manufactured with this technique have extremely high reinforcement concentrations, of over 80 wt.% CNTs. Figure 1e shows an SEM micrograph of the cross section of a laminate embedded in mounting resin. Typical composite cross sections have clear distinctions between the reinforcement and the matrix, but the densification step plastically deforms the CNT yarns together and limits resin content to an extremely low amount between adjacent yarns. This allows for favorable reinforcement-dominated properties when compared with state-of-the-art carbon fiber composites. Moreover, the high degree of densification and mechanical interlock mitigates the low interface strength of CNTs with polymer resins [10].

2.7 Laminate Tensile Testing

The CNT yarn composite laminates were cut to 2-3 mm wide by 80 mm long tensile test coupons and an aluminum jig was used to obtain a consistent gauge length of 25 mm. An Instron 5969 load frame equipped with a 50 kN load cell and MTS 646 hydraulic collet grips were used and tested at 0.3 mm min^{-1}. Strain was calculated with an Epsilon One optical extensometer. The modulus was taken via loading, unloading, and reloading cycles over the range from 400 MPa to 1200 MPa [14].

3 RESULTS AND DISCUSSION

Specimens from a single roll of yarns were sent for electron beam and gamma ray treatment to minimize any effects of roll-to-roll variation. The effects of treatment on mechanical properties were measured by tensile testing individual CNT yarns, while functionalization was measured with DCAT and Raman spectroscopy. Both effects were evaluated by fabricating laminate scale specimens with polymer resin to form a comprehensive assessment of the viability of irradiation treatment techniques. Due to the large quantity of yarn required for laminate fabrication, each laminate was made with a different roll of yarn from the same lot.

3.1 Electron Beam Treatment

Measuring the cross-section area of CNT yarns is impractical at scale, so the SI units of linear density were used: tex (g km^{-1}). Linear specific tensile strength, reported in units of (N/tex) is dimensionally equivalent to volumetric specific strength units of (GPa g^{-1} cm^3).

Results from tensile testing of CNT yarns are shown in Figure 2. Tex, shown in Figure 2a, tended to increase with temperature, except for the lowest treated specimen of 40 Mrad which was below the control. Figure 2b compares how the ultimate force varied with treatment, with no clear linear trend ($r = 0.45$). Therefore, the specific properties are dominated by the changes in linear density, resulting in the 40 Mrad yarn demonstrating an increase in both specific strength and specific stiffness while the 200

Mrad dose was most like the control and the higher mass of the 300 Mrad specimens caused it to have the lowest specific properties.

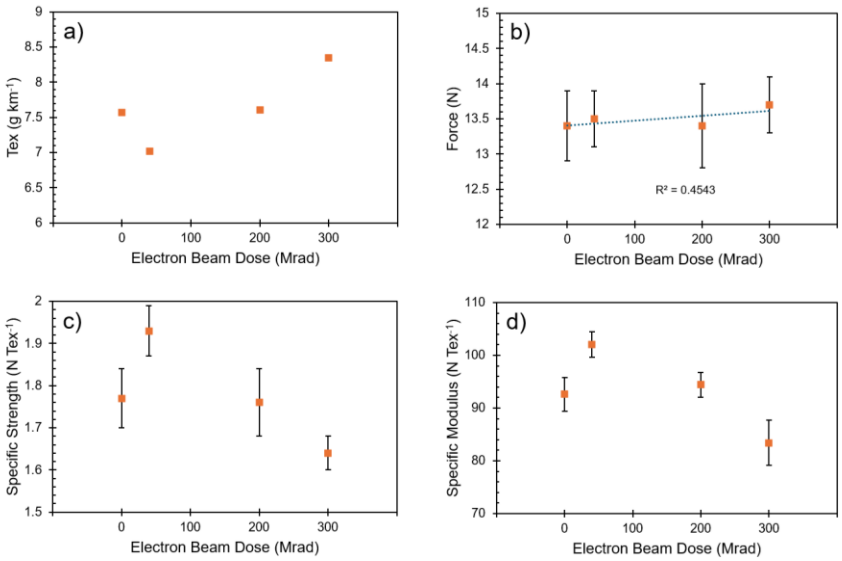

Figure 2. Electron beam treated CNT yarn tensile results. (a) compares linear density in units of tex (g km^{-1}), (b) compares ultimate force, (c) specific strength, and (d) specific modulus.

Raman spectroscopy was used to evaluate the ratio of the I_D band to I_G band. Increases in disorder related I_D band indicate potential functional sites after electron beam treatment. Figure 3a shows a significant increase in the I_D band in a randomly oriented CNT network, while Figure 3b shows the trend holds for the CNT yarns. The I_D band at 300 Mrad treatment is most similar to a gamma ray treatment of 50 kGy, shown in Figure 3b.

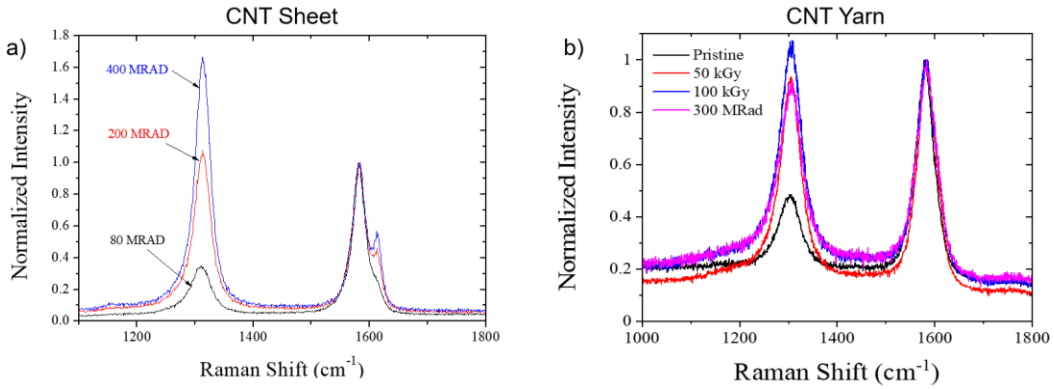

Figure 3. Raman spectroscopy comparing I_D and I_G of (a) randomly oriented CNT sheet treated with electron beam, and (b) CNT yarns treated with electron beam or gamma ray.

Figure 2 shows decreasing specific tensile properties with treatment, while Figure 3 suggests increasing interface properties. Therefore, a laminate scale specimen which relies on both is needed to gain a comprehensive assessment of the effectiveness of electron beam treatment. Interestingly, the higher properties at lower dose shown in Figure 2c and 2d are also present in the laminate scale specimens in Figure 4a and 4b. The most significant improvement was in the specific strength at a treatment of 40 Mrad, which reflects the yarn tensile results. However, the improved interface may be responsible for the slight increase in both specific strength and modulus at 300 Mrad, since those properties decreased in the yarn tensile test.

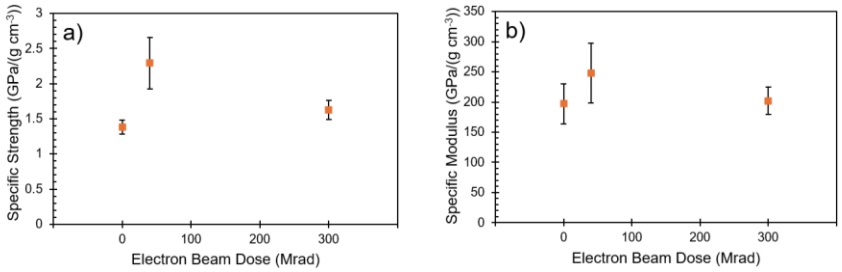

Figure 4. Electron beam treated CNT yarn laminates (a) specific strength and (b) specific modulus.

3.2 Gamma Ray Treatment

Gamma rays cause damage to CNT walls, opening sites for cross linking between adjacent CNT bundles and functional groups on the outer surface. The dose was controlled by altering the time the specimen was exposed to the source, allowing for a large quantity of yarn to be treated.

Figure 5 compares how the tensile properties of the yarns evolved with treatment. As the dosage increased so did the mass of the yarns and therefore also the linear density, shown in Figure 5a. This effect was more pronounced at higher dosage. Figure 5b shows a concurrent increase in ultimate force which increased linearly with treatment ($r = 0.955$), unlike the electron beam. However, the increase in force was less than the increase in tex, so the specific strength, expressed in units of N tex^{-1}, decreased at the higher levels of treatment, shown in Figure 5c. The 200 kGy specimen had the highest specific strength, and while this may be due to the low tex measurement, it also had the highest specific modulus, shown in Figure 5d.

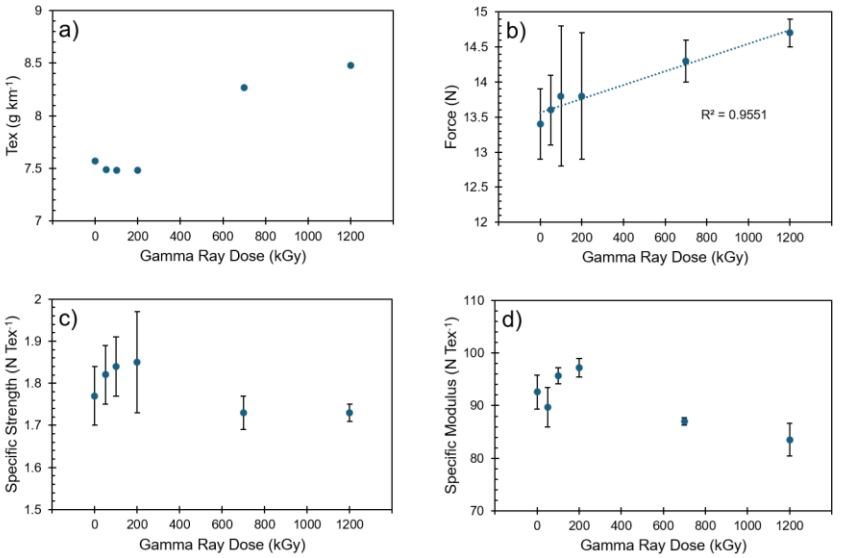

Figure 5. Gamma ray treated CNT yarn (a) linear density, and tensile results. (b) shows ultimate force, (c) specific strength, and (d) specific modulus.

Dynamic contact angle measures both the initial interaction with the liquid, in this case deionized water, and the effect of advancing and receding through the medium. The average contact angle of the yarns which were later used for laminate scale specimens is reported in Figure 6. There is a clear inverse relationship between treatment and contact angle, indicating the presence of functional groups which will likely increase the interface between treated CNT yarns and various polymer resin systems.

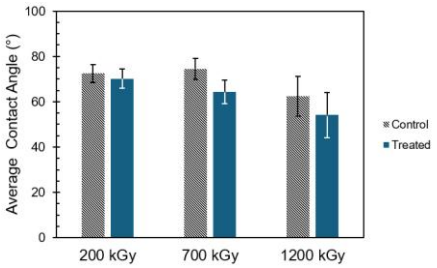

Figure 6. Average dynamic contact angle of the CNT yarns used for the gamma ray treated laminates.

There exists an optimal dose which combines the ideal amount of cross linking and surface functionalization, therefore treated CNT yarns were fabricated into laminate scale specimens. These specimens combine the effects on mechanical properties of the yarns in Figure 5 with the interface properties in Figure 6. Each treated laminate had greater specific strength and modulus than the control, shown in Figure 7a and 7b, respectively. The optimal combination for proved to be the 700 kGy treatment, due to combining the effects of increased specific mechanical properties and increased interface properties.

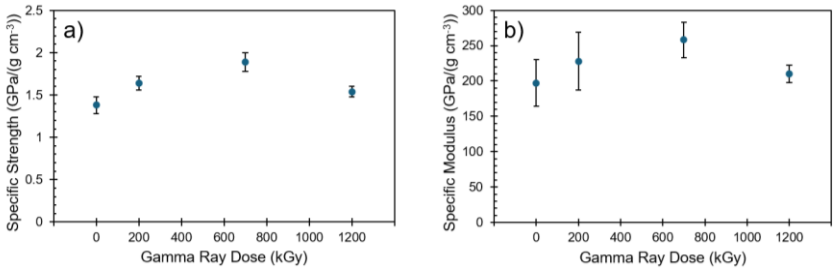

Figure 7. Gamma ray treated laminate tensile (a) specific strength and (b) specific modulus.

3.3 Ozone Treatment

The primary goal of ozone treatment is to functionalize the surface of the CNTs to improve bonding with resin. Like other treatments, the linear density slightly increased with exposure to ozone, shown in Figure 8a. Unlike other treatments, the ultimate force steadily decreased ($r = 0.997$) with treatment because ozone does not crosslink the dense CNT network but damage the CNT structures. Accordingly, Figure 8c shows the treatment resulted in decreased specific strength, while the specific modulus (Figure 8d) was relatively unaffected.

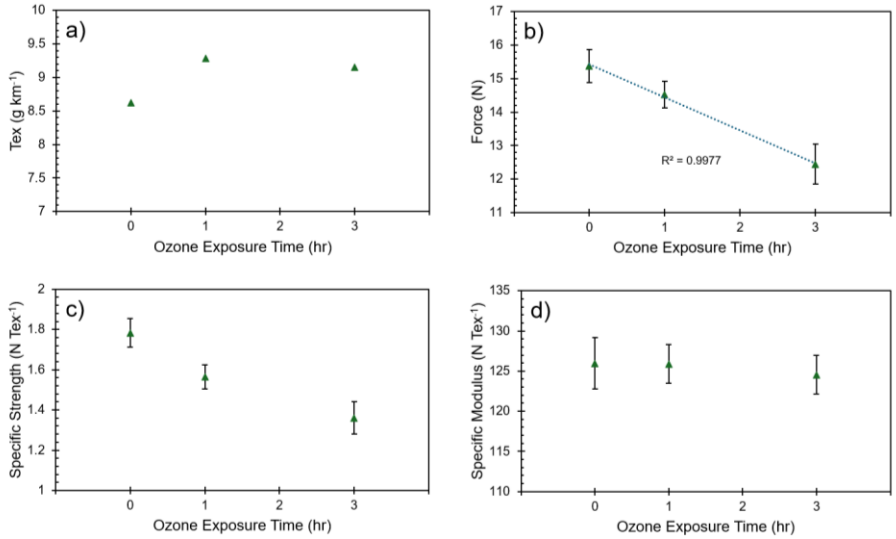

Figure 8. Ozone treated CNT yarn tensile results including (a) linear density, (b) ultimate force, (c) specific strength, and (d) specific modulus.

Figure 9 shows the advancing, receding, and average contact angle of ozone treated yarns and deionized water. While both treatments decreased the contact angle, the difference between one hour and three hour treatment was minimal.

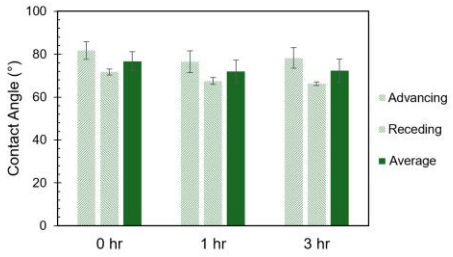

Figure 9. DCAT of yarns exposed to ozone for varying times.

4 CONCLUSIONS

Figure 10 shows how radiation treated CNT composites compare with state-of-the-art unidirectional carbon fiber composites. Laminate properties seem to depend on both crosslinking and surface activation. Gamma ray and electron beam treatments improved both specific strength and modulus over the control laminate; there was an optimal dose of 40 Mrad for the electron beam treatment and 700 kGy for the gamma ray. While ozone treatment may be easier to implement, it was likely not as effective in adding functional groups to improve the interface as the radiation techniques. Additionally, the lack of crosslinking means that ozone treatment by itself will likely have limited success in improving CNT yarn laminate mechanical properties.

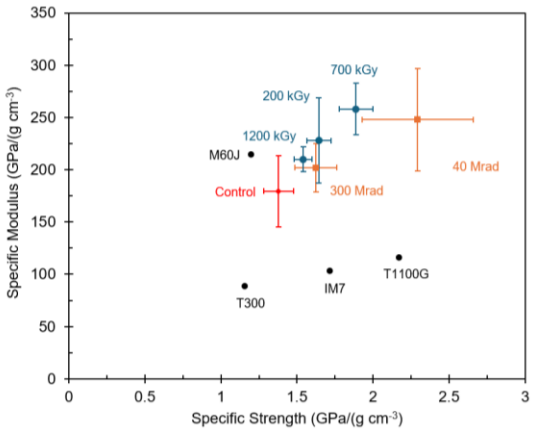

Figure 10. Chart comparing specific strength and specific modulus of radiation treated CNT yarn laminates and state-of-the-art unidirectional composites.

The laminate results show that both interface properties and tensile properties must be considered when using single yarn-scale specimens to predict the performance of composite specimens. The optimal dose in both cases was a treatment that improved both mechanical and interface properties, with lower doses not having as much improvements, or higher doses reducing mechanical properties.

ACKNOWLEDGEMENTS

This work was supported by the Institute for Ultra-Strong Composites by Computational Design (US-COMP, NASA NNX17AJ32G, a NASA Space Technology Research Institute (STRI)). TEM work was performed at the National High Magnetic Field Laboratory, which is supported by National Science Foundation Cooperative Agreement No. DMR-1644779 and the State of Florida. We would like to thank

Syensqo and Huntsman for providing nanotube and resin materials. We appreciate the support of the Syensqo Doctorial Fellowship. The views expressed in this article are those of the authors and do not reflect the official policy or position of the U.S. Naval Academy, Department of the Navy, the Department of Defense, or the U.S. Government.

REFERENCES

[1] A. De Leon, M. Tank, and R. Sweat, "A scalable fiber bundle pullout manufacturing method for data-driven interfacial shear strength measurements of micro and nanomaterials," *Compos. Sci. Technol.*, vol. 222, p. 109375, May 2022, doi: 10.1016/j.compscitech.2022.109375.

[2] M. H. Kirmani, G. Sachdeva, R. Pandey, G. M. Odegard, R. Liang, and S. Kumar, "Cure Behavior Changes and Compression of Carbon Nanotubes in Aerospace Grade Bismaleimide-Carbon Nanotube Sheet Nanocomposites," *ACS Appl. Nano Mater.*, vol. 4, no. 3, pp. 2476–2485, Mar. 2021, doi: 10.1021/acsanm.0c03013.

[3] J.-W. Kim *et al.*, "Modifying carbon nanotube fibers: A study relating apparent interfacial shear strength and failure mode," *Carbon*, vol. 173, pp. 857–869, Mar. 2021, doi: 10.1016/j.carbon.2020.11.055.

[4] J. Bourdeau, K. J. Mintz, B. Jony, M. H. Kirmani, K. Gupta, and S. Kumar, "Improvement of apparent IFSS and specific modulus of CNT yarns," *Compos. Part B Eng.*, vol. 284, p. 111683, Sep. 2024, doi: 10.1016/j.compositesb.2024.111683.

[5] M. C. Evora *et al.*, "Single-step process to improve the mechanical properties of carbon nanotube yarn," *Beilstein J. Nanotechnol.*, vol. 9, pp. 545–554, Feb. 2018, doi: 10.3762/bjnano.9.52.

[6] S. G. Miller *et al.*, "Increased Tensile Strength of Carbon Nanotube Yarns and Sheets through Chemical Modification and Electron Beam Irradiation," *ACS Appl. Mater. Interfaces*, vol. 6, no. 9, pp. 6120–6126, May 2014, doi: 10.1021/am4058277.

[7] J. Y. Cai *et al.*, "Enhanced mechanical performance of CNT/Polymer composite yarns by γ-irradiation," *Fibers Polym.*, vol. 15, no. 2, pp. 322–325, Feb. 2014, doi: 10.1007/s12221-014-0322-9.

[8] M. C. Evora, D. Klosterman, K. Lafdi, L. Li, and J. L. Abot, "Functionalization of carbon nanofibers through electron beam irradiation," *Carbon*, vol. 48, no. 7, pp. 2037–2046, Jun. 2010, doi: 10.1016/j.carbon.2010.02.012.

[9] M. H. Kirmani *et al.*, "Using a carbon fiber sizing to tailor the interface-interphase of a carbon nanotube-polymer system," *Compos. Part B Eng.*, vol. 247, p. 110284, Dec. 2022, doi: 10.1016/j.compositesb.2022.110284.

[10] C. E. Evers *et al.*, "Scalable High Tensile Modulus Composite Laminates Using Continuous Carbon Nanotube Yarns for Aerospace Applications," *ACS Appl. Nano Mater.*, p. acsanm.3c01266, Jun. 2023, doi: 10.1021/acsanm.3c01266.

[11] J. G. Park *et al.*, "Gamma-ray irradiation to achieve high tensile performance of unidirectional CNT yarn laminates," *Carbon*, vol. 216, p. 118530, Jan. 2024, doi: 10.1016/j.carbon.2023.118530.

[12] V. Skákalová, "Effect Of Gamma-Irradiation on Single-Wall Carbon Nanotube Paper," in *AIP Conference Proceedings*, Kirchberg, Tirol (AUSTRIA): AIP, 2003, pp. 143–147. doi: 10.1063/1.1628005.

[13] Y.-S. Dessureault *et al.*, "Tensile performance and failure modes of continuous carbon nanotube yarns for composite applications," *Mater. Sci. Eng. A*, vol. 792, p. 139824, Aug. 2020, doi: 10.1016/j.msea.2020.139824.

[14] B. Vondrasek, C. Evers, C. Jolowsky, G. M. Odegard, Zhiyong Liang, and M. Czabaj, "Characterization of multidirectional carbon-nanotube-yarn/bismaleimide laminates under tensile loading," *Compos. Part B Eng.*, vol. 280, p. 111465, Jul. 2024, doi: 10.1016/j.compositesb.2024.111465.

ICCM24
24TH INTERNATIONAL CONFERENCE ON COMPOSITE MATERIALS

Plasma Treated PET Nanofiber Veils: A Novel Interface Enhancement for Cryogenic Composite Applications

Jeho Jin[1], Jaejun Bae[1], Sunghwan Park[2], Jaeho Yun[2], and Jeonyoon Lee[1†]

[1] Department of Aerospace Engineering, Korea Advanced Institute of Science and Technology

[2] Technologies R&D Team 2, Launch Vehicle R&D Center, Hanwha Aerospace

† : Corresponding Author

2025. 08. 04

KAIST Laboratory for Advanced Materials and Processes

한화에어로스페이스 Hanwha Aerospace

Contents

1. Research Background
2. Materials & Methods
3. Results & Discussion
4. Conclusion & Future Work

Research Background

Conventional Autoclave Manufacturing for High Pressure

- Composites are typically manufactured using autoclaves, which apply **heat** and **pressure** to cure the material and produce a **void-free structure**.
- However, autoclaves have several **limitations**, including **high energy consumption**, **large space requirements**, and their tendency to become a **bottleneck** in the production process [1].

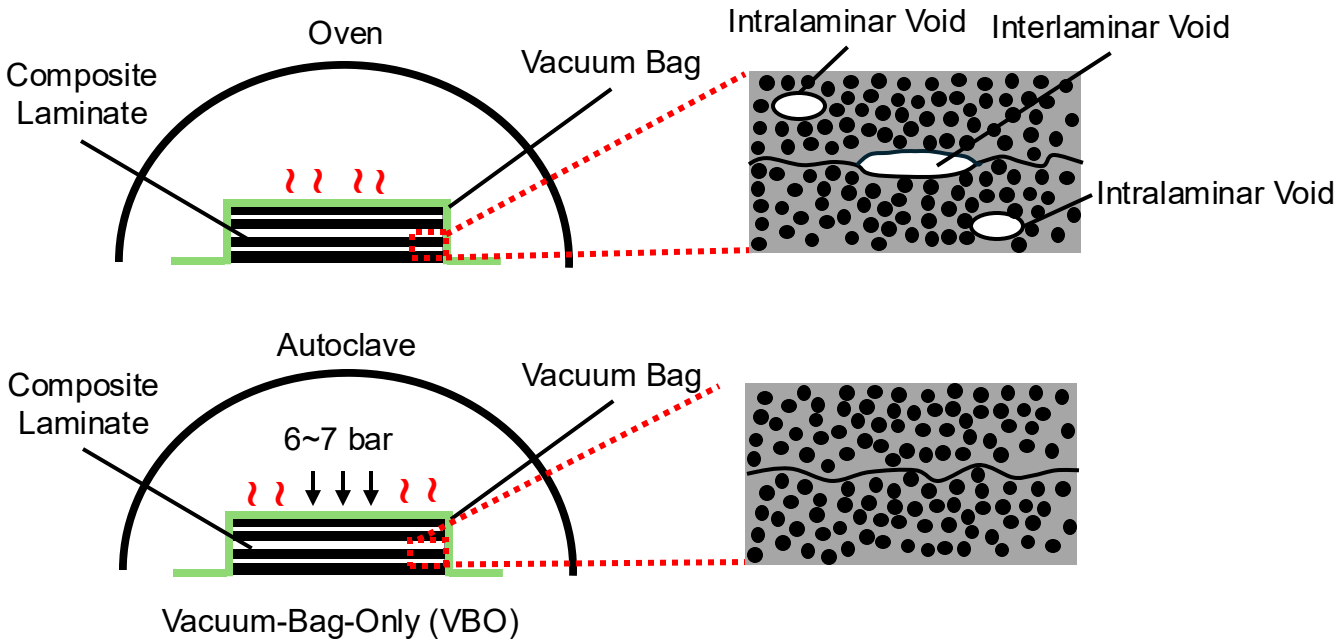

<Void Content Difference Between VBO and Autoclave>

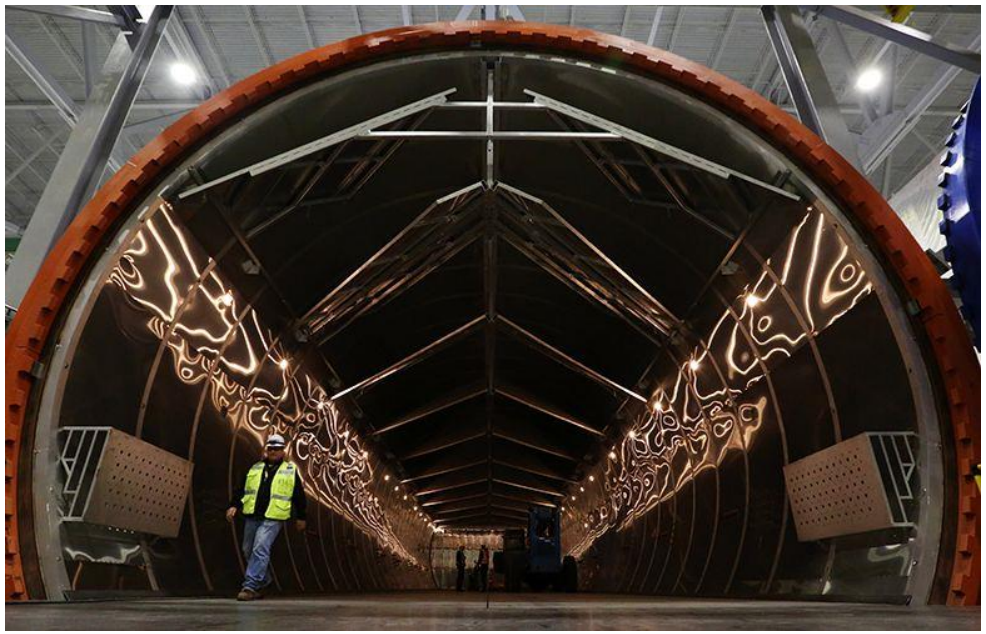

<Autoclave for Boeing 777X Composite Wings [2]>

[1] Hubert, Pascal, et al. "Out-of-autoclave prepreg processing." Comprehensive composite materials II 2 (2018): 63-94.
[2] https://www.seattletimes.com/business/boeing-aerospace/boeing-shows-off-new-777x-wing-center/

Effect of Voids on Mechanical Properties

- **Minimizing voids** is critical, as voids significantly degrade the mechanical properties of the final product.
- Therefore, there is a **need for Out-of-Autoclave (OoA)** manufacturing processes that can ensure **void-free composites**.

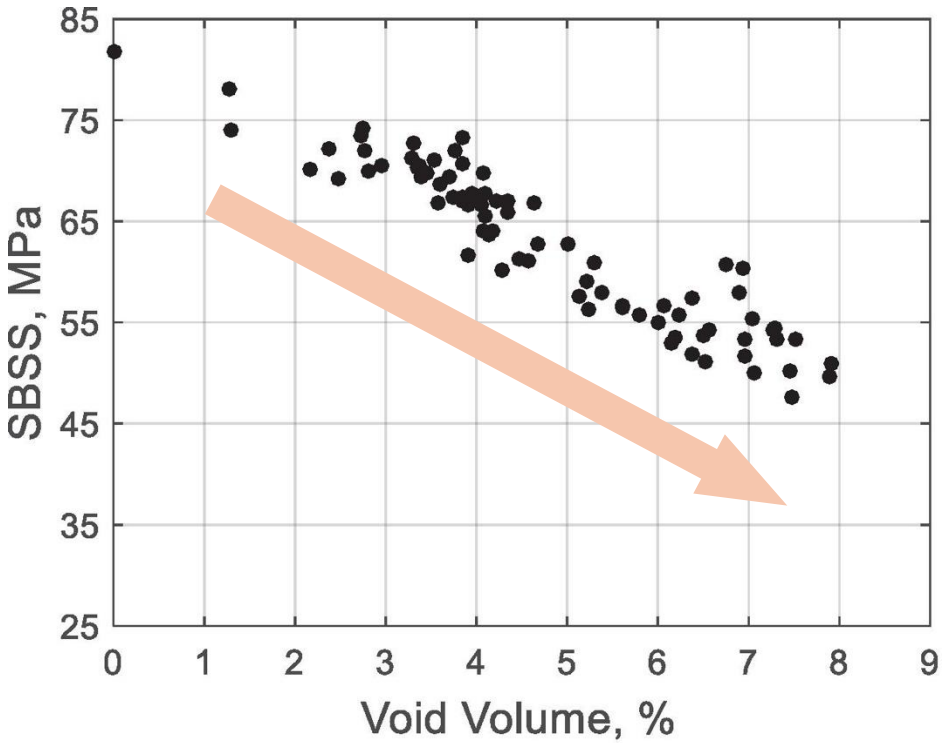

<Void Content and the Change in Short Beam Shear Strength [3]>

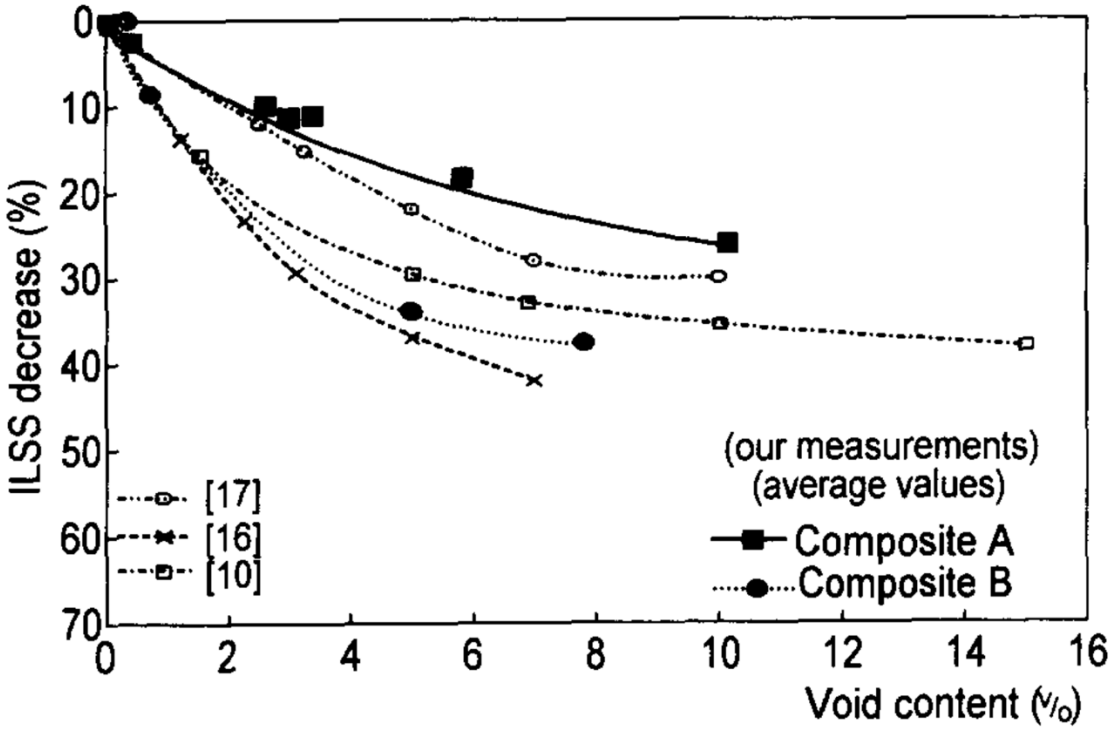

<Void Content and the Change in Interlaminar Shear Strength [4]>

[3] Tretiak, Iryna, Luiz F. Kawashita, and Stephen R. Hallett. "Predicting short beam shear strength reduction in carbon/epoxy laminates containing voids." Composite Structures 290 (2022): 115472.
[4] Serrano, Léonard, Philippe Olivier, and Jacques Cinquin. "Compaction behavior of out-of-autoclave prepreg materials." AIP Conference Proceedings. Vol. 1896. No. 1. AIP Publishing, 2017.

Use of Nano-Porous Networks – Alternative to Autoclaves

- One solution is to **interleave nanoporous networks** within the composite prior to curing, allowing them to conform to and fill the rough interfaces between adjacent prepreg layers [5].
- Additionally, these nanoporous networks generate **capillary pressure** during curing, which can partially **substitute** external pressure provided by an autoclave [6].
- Furthermore, the nanoporous networks can **enhance toughness** by acting as a **buffer** for coefficient of thermal expansion (CTE) mismatches, which arise from the differing orientations of prepreg plies [7].

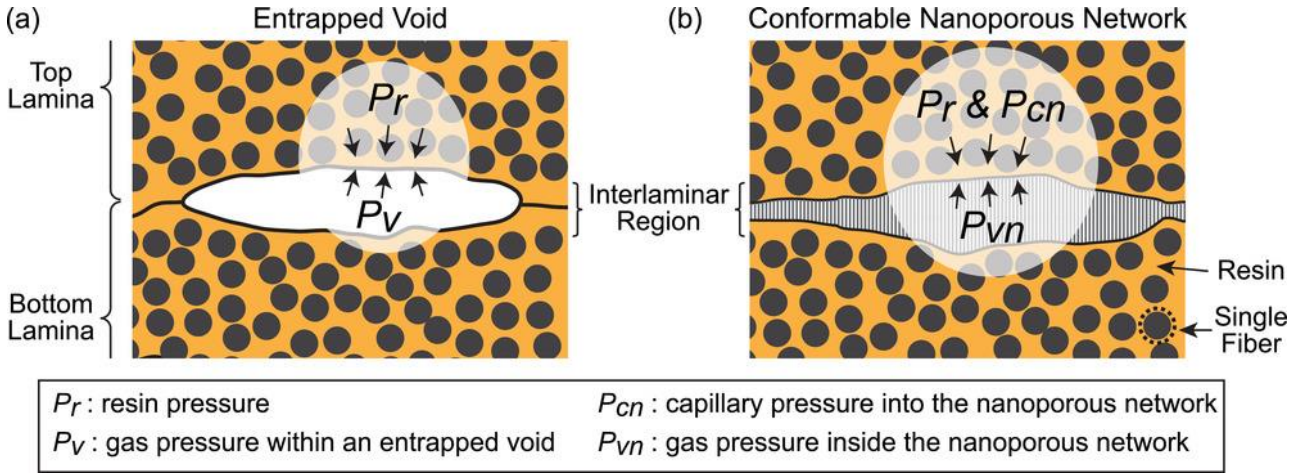

<Schematic of Composite Curing w/ & w/o Nano-Porous Networks [5]>

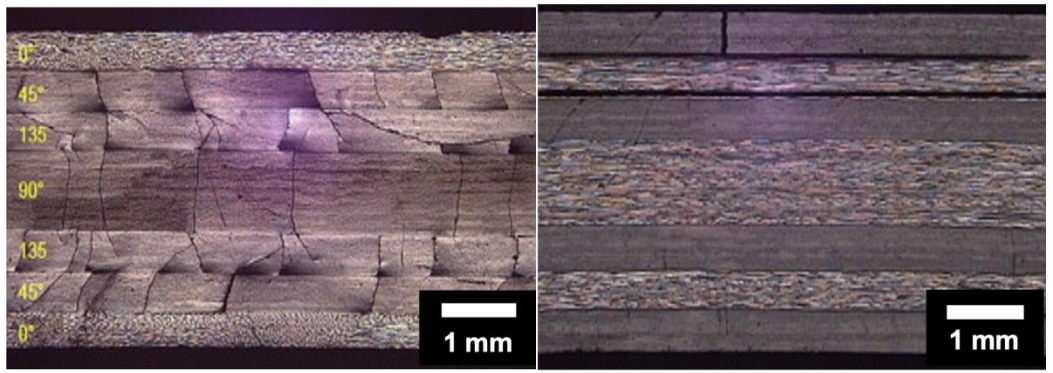

Microcracks **Delamination**

<Microcracks and Delamination Caused by CTE Mismatch [8]>

KAIST Laboratory for Advanced Materials and Processes
[5] Lee, Jeonyoon, Seth S. Kessler, and Brian L. Wardle. "Void-Free Layered Polymeric Architectures via Capillary-Action of Nanoporous Films." Advanced Materials Interfaces 7.4 (2020): 1901427.
[6] Masoodi, Reza, and Krishna M. Pillai, eds. Wicking in porous materials: traditional and modern modeling approaches. Crc Press, 2012.
[7] Bae, Jaejun. "Effect of Polyamide Electrospun Nanofiber Architectures on Gas Permeability and Mechanical Properties of Carbon Fiber Reinforced Polymer." Korea Advanced Institute of Science and Technology, 2025.
[8] Grogan, David M., et al. "Damage characterisation of cryogenically cycled carbon fibre/PEEK laminates." Composites Part A: Applied Science and Manufacturing 66 (2014): 237-250.

Candidates for Nano-Porous Network - Polymers

- Engineering polymers are promising candidates for nanoporous networks due to their **high strain capacity** and **toughness**, making them effective CTE buffers.
- **Polyamide** (PA) -based composite reinforcements—such as XLB from Nanolayr—are already **commercially available**.
- However, some high-toughness engineering polymers, including PEEK, HDPE, and UHMWPE, **cannot be easily fabricated into nanostructured forms** [9,10].

Material	Modulus (Gpa)	Tensile strength (Mpa)
Polyethylene (PE)	0.88	35
Polyurethane (PU)	0.02	35
Polytetrafluoroethylene (PTFE)	0.5	27.5
Polyacetal (PA)	2.1	67
Polymethylmethacrylate (PMMA)	2.55	59
Polyethylene terephthalate (PET)	2.85	61
Polyether ketone (PEEK)	8.3	139
Silicone rubber (SR)	0.008	7.6
Polysulfone (PS)	2.65	75

<Mechanical Properties of Engineering Polymers [11]>

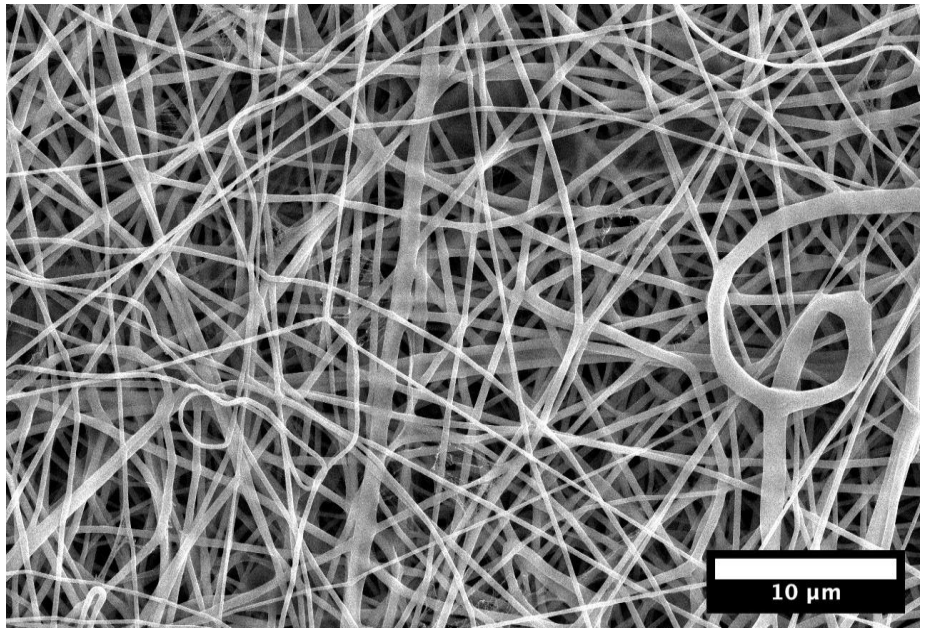

<PA Composite Reinforcement (Nanolayr XLB)>

[9] Rein, D. M., et al. "Electrospinning of ultrahigh-molecular-weight polyethylene nanofibers." Journal of Polymer Science Part B: Polymer Physics 45.7 (2007): 766-773.
[10] Nayak, Prajesh, Anup K. Ghosh, and Naresh Bhatnagar. "Preparation and characterization of electrospun mat of ultra-high molecular weight polyethylene/high-density polyethylene blends." Fibers and Polymers 24.10 (2023): 3421-3433.
[11] Ghalme, Sachin G., Ankush Mankar, and Yogesh Bhalerao. "Biomaterials in hip joint replacement." *Int. J. Mater. Sci. Eng* 4.2 (2016): 113-125.

Importance of Cryogenic Properties in Aerospace Composites

- **Mechanical performance at cryogenic temperatures** is critical, particularly with the growing use of cryogenic fuels and composite overwrapped pressure vessels (COPVs).
- However, **PA exhibit poor mechanical properties under cryogenic conditions**, limiting their applicability in such environments.



<Composite Overwrapped Pressure Vessel [12, 13]>

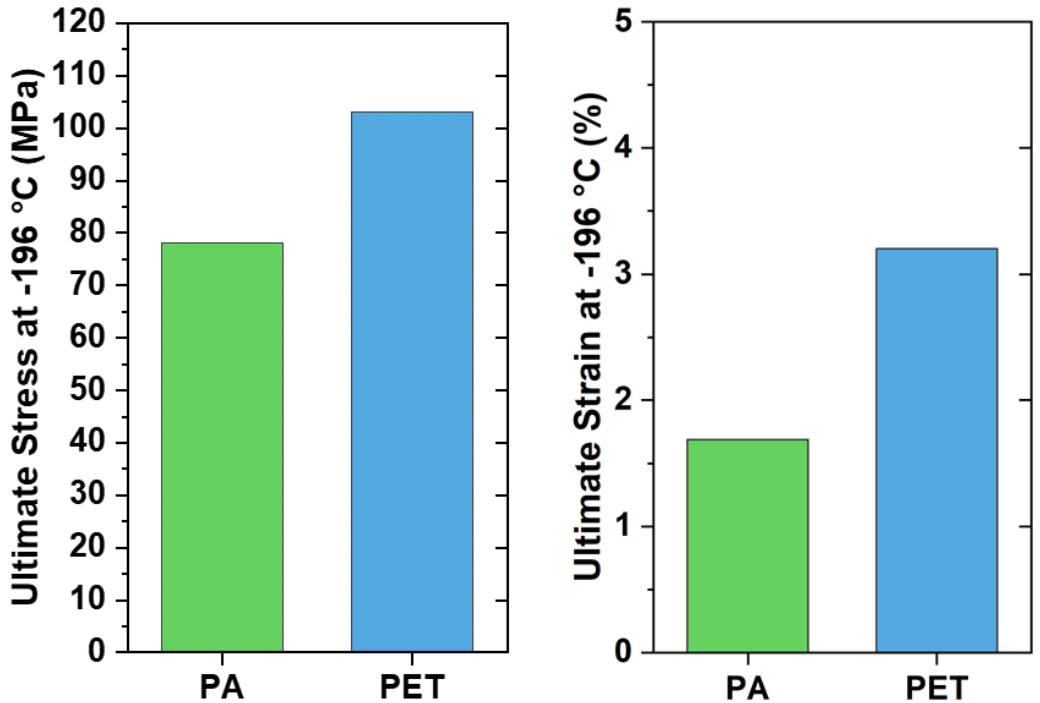

<Mechanical Properties of PA [14] & PET [15] at -196 °C>

[12] https://www.l3harris.com/all-capabilities/arde-pressure-vessels-and-propellant-tanks
[13] https://www.compositesworld.com/articles/spacex-announces-copvs-role-in-sept-rocket-explosion
[14] Marcos, A. C. I. N., and Emiliano Frulloni. "A reinforced thermoplastic cryostat for a high temperature superconductor." U.S. Patent Application No. 18/832,585.
[15] C. D. Armeniades, I. Kuriyama, J. M. Roe & Eric Baer (1967) Mechanical behavior of poly(ethylene terephthalate) at cryogenic temperatures, Journal of Macromolecular Science, Part B, 1:4, 777-791, DOI: 10.1080/00222346708212361

Limitation of PET – Poor Adhesion with Composites

- PET exhibits **poor adhesion to epoxy**, which limits its effectiveness as a reinforcing material in composites [16].
- Composites interleaved with PET veils demonstrated **no significant improvement in toughness** [17].

- This study focuses on **plasma treatment** to enhance PET's adhesion to epoxy, enabling its use as a **nanofiber reinforcement** and potentially improving **cryogenic toughness.**

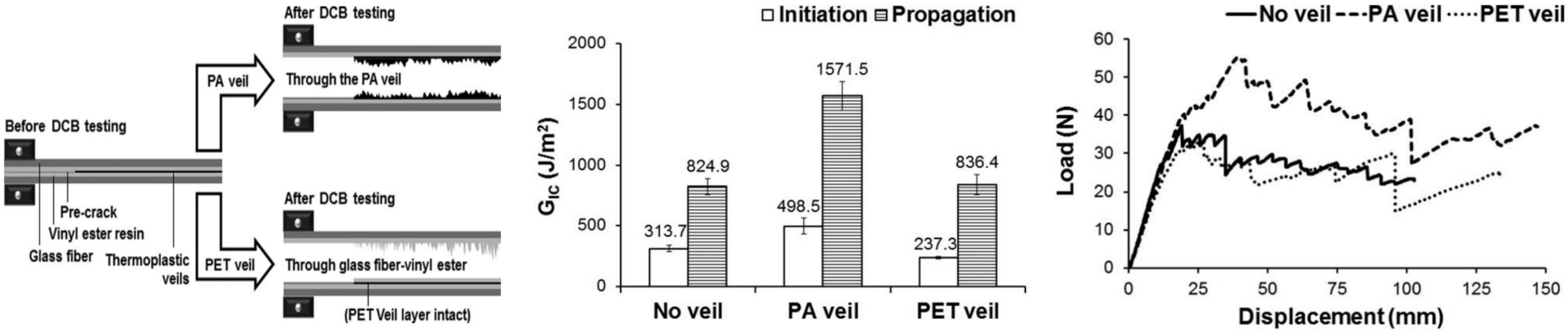

<Mode I Test Schematic & Results for PA & PET Interleaved Composites [16]>

[16] Quan, Dong, et al. "Mode-II fracture behaviour of aerospace-grade carbon fibre/epoxy composites interleaved with thermoplastic veils." Composites Science and Technology 191 (2020): 108065.
[17] Del Saz-Orozco, Belén, Dipa Ray, and Walter F. Stanley. "Effect of thermoplastic veils on interlaminar fracture toughness of a glass fiber/vinyl ester composite." Polymer Composites 38.11 (2017): 2501-2508.

Material & Methods

Synthesizing Nanofibers - Electrospinning

- Electrospinning is a technique that uses a high-voltage electric field to draw a polymer solution into fine fibers, which solidify as they reach a grounded collector [18].
- This enables the fabrication of **nanoscale fibers**, offering enhanced mechanical properties across a range of polymers [18].
- Fiber diameter is controlled by **adjusting key process parameters** such as voltage, flow rate, and solution concentration [19].

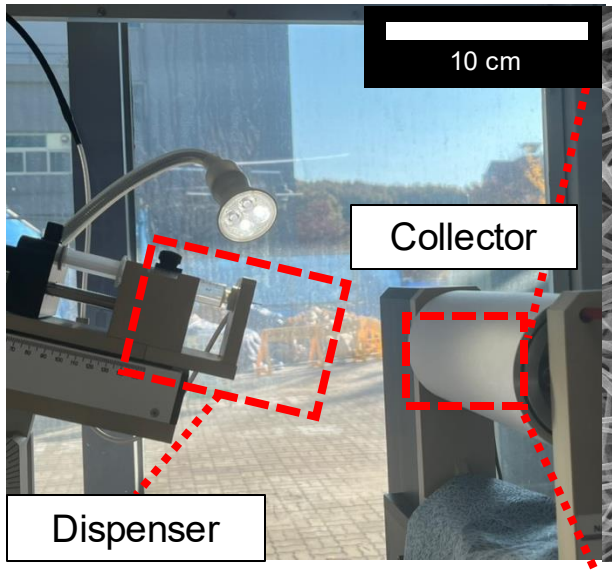

<Electrospinning Machine>

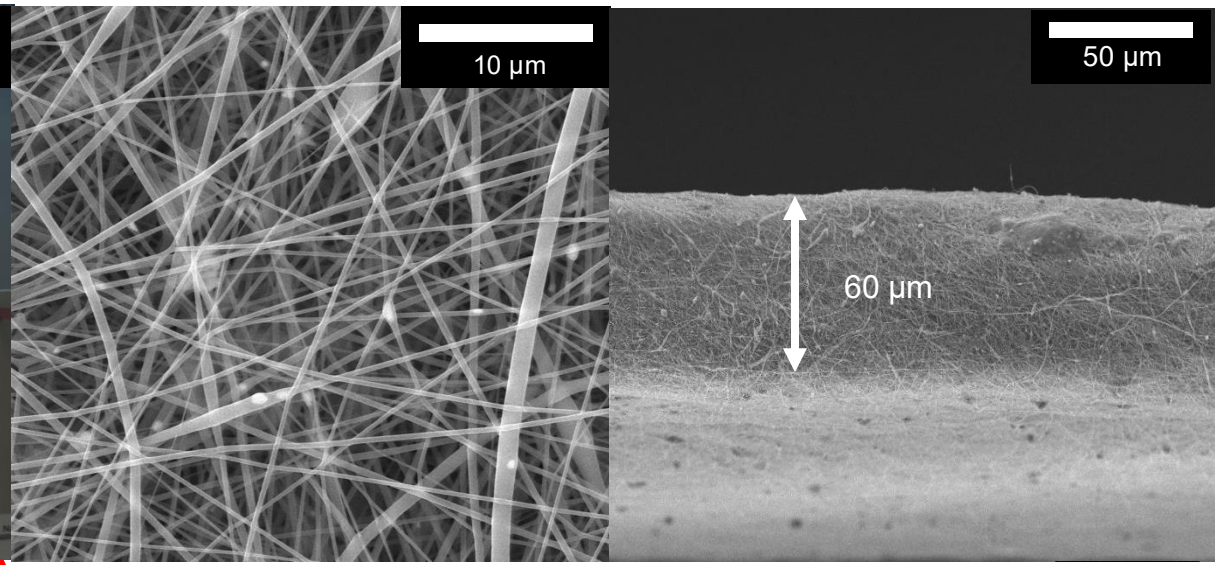

<SEM Image of Electrospun PET Nanofibers (Top & Side view)>

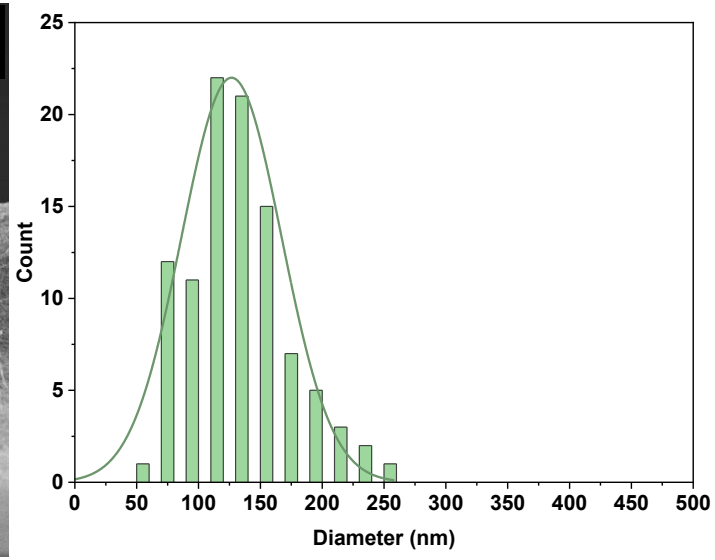

<Distribution of Nanofiber Diameters>

[18] Ji, Dongxiao, et al. "Electrospinning of nanofibres." Nature Reviews Methods Primers 4.1 (2024): 1.
[19] Teo, Wee E., and Seeram Ramakrishna. "A review on electrospinning design and nanofibre assemblies." Nanotechnology 17.14 (2006): R89.

Plasma Treatment for Improving PET Adhesion

- Plasma treatment has been widely employed in previous studies as an effective method to enhance the surface adhesion of PET to epoxy [20,21].
- However, the application of atmospheric plasma treatment to **improve adhesion of nanofibers** is being explored for the **first time** in this research.

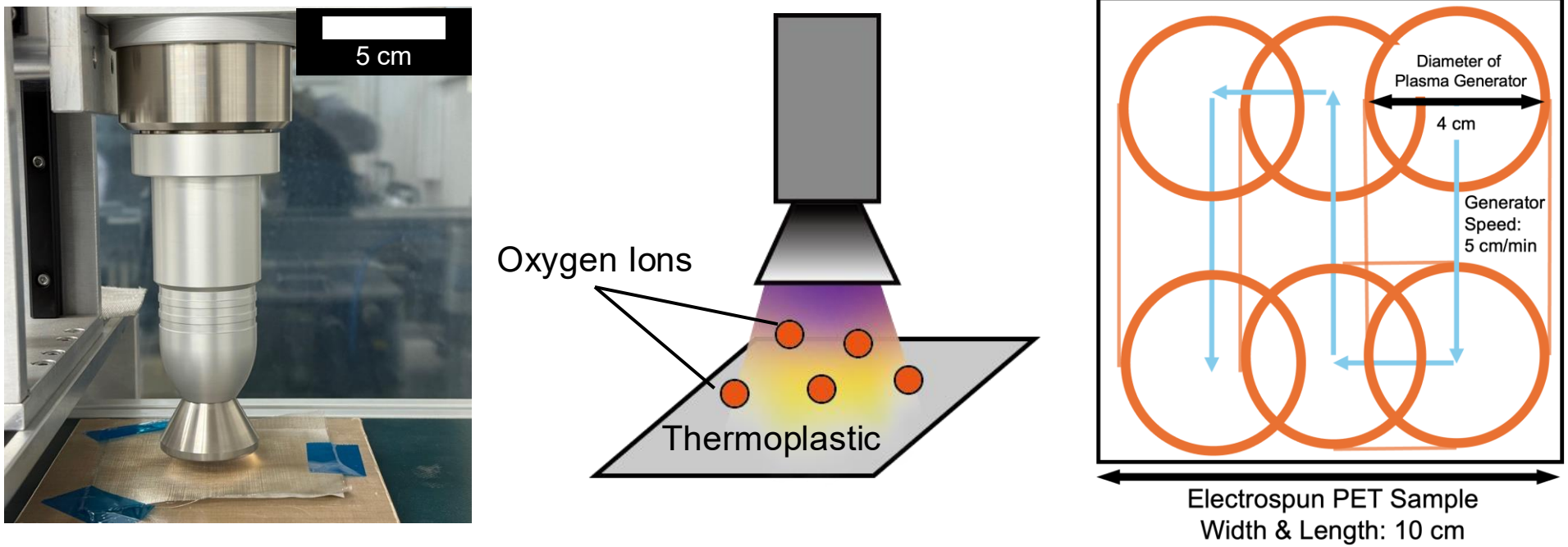

<Atmospheric Plasma Generator & Schematic of Plasma Treatment>

[20] Jiang, Wei, et al. "Interlaminar fracture properties of carbon fibre/epoxy matrix composites interleaved with polyethylene terephthalate (PET) films." Polymers and Polymer Composites 9.2 (2001): 141-145.
[21] Oh, Chang-Bin, Byeong-Joo Kim, and Man Young Lee. "Synergistic interlaminar strengthening of unidirectional carbon fiber-reinforced composites using carbon nanofiber-modified sizing on the surface of PET interleaves." Composites Part B: Engineering 264 (2023): 110929.

Use of Metal Mesh to Prevent Shedding of Nanofibers

- High air pressure (6 bar) generated by atmospheric plasma can **dislodge nanofibers**, reducing their effectiveness.
- A **metal mesh** support (60 & 2500) enables **closer** and **longer plasma exposure** while preventing nanofiber shedding.
- With a 1 cm nozzle-to-sample distance, both mesh prevented nanofiber shedding, while achieving comparable plasma treatment efficiency.

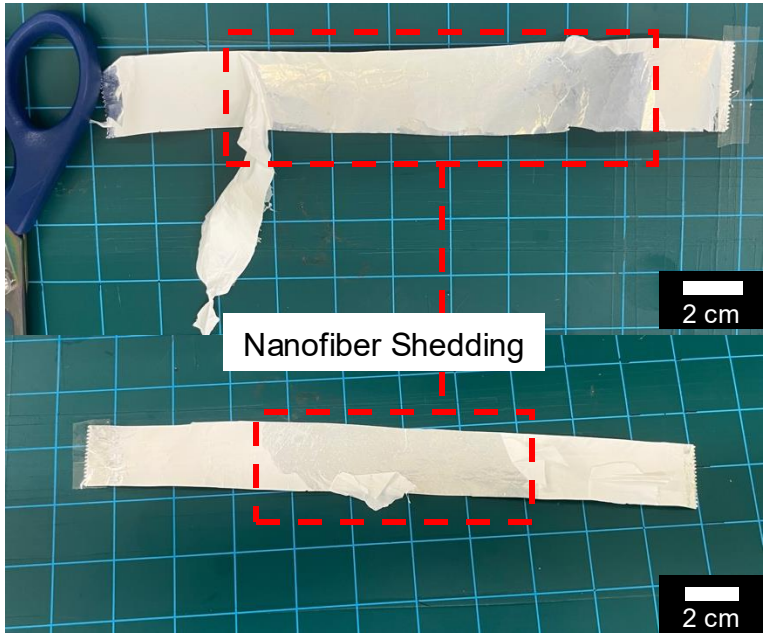

<Shedding of Nanofibers due to Plasma Treatment>

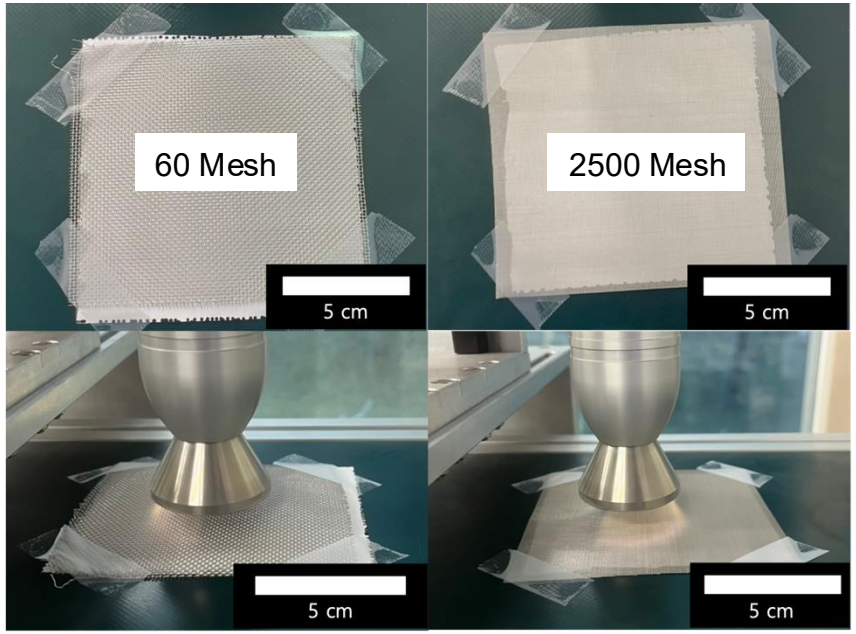

<Use of 60 Mesh & 2500 Mesh to Prevent Shedding>

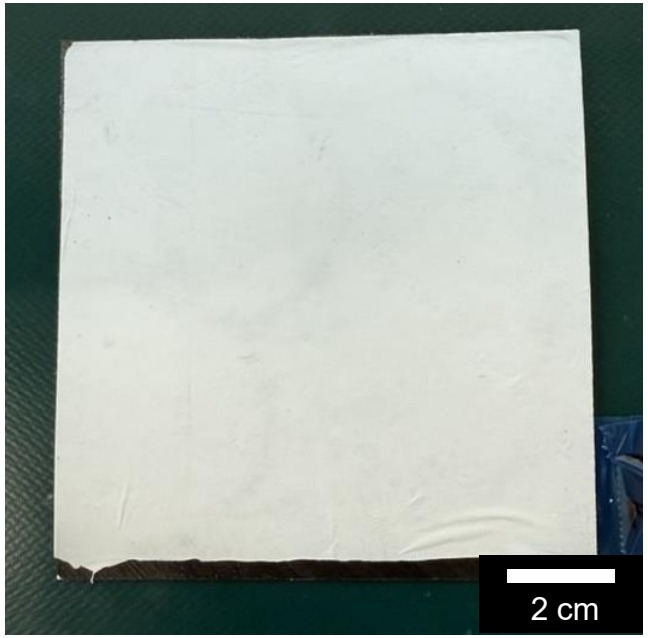

<PET Nanofibers Transferred to Composites after Plasma Treatment>

Composite Curing Process with Interleaved Nanofibers

- After plasma treatment, PET nanofibers are **interleaved between each lamina** during the prepreg layup process.
- The laminates are then cured using a **Vacuum-Bag-Only (VBO)** method, following the standard cure cycle for IM7/8552.
- Three sample types were prepared: baseline (no interleaved nanofibers), As-spun PET, and Plasma-treated PET.

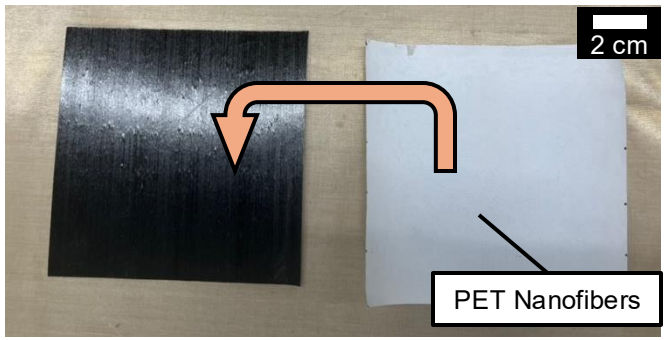

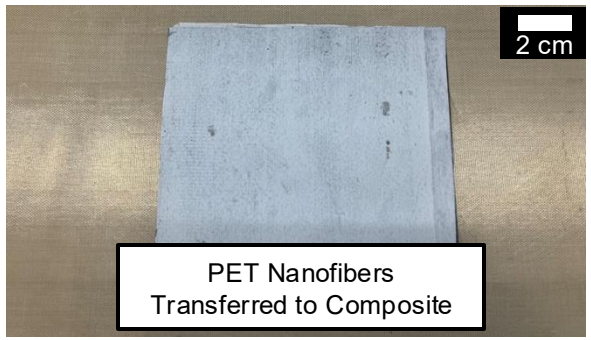

<Composite Laminate Interleaved with PET Nanofibers>

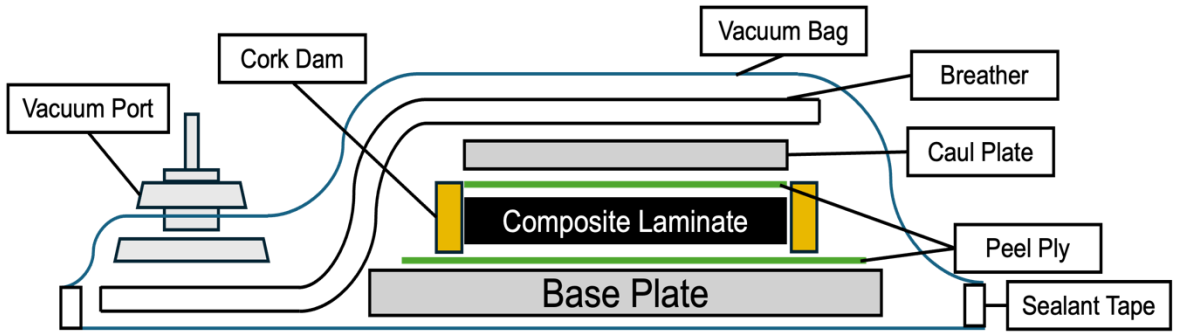

<Schematic of Composite Curing Setup>



<Vacuum-Bag-Only>

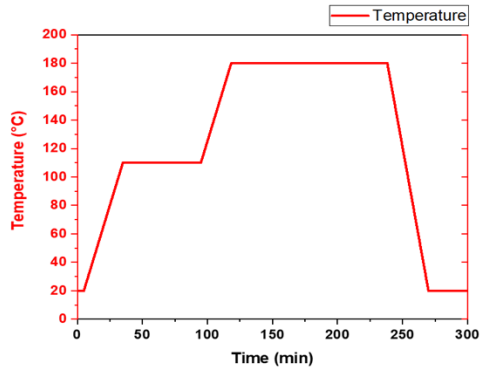

<Cure Cycle>

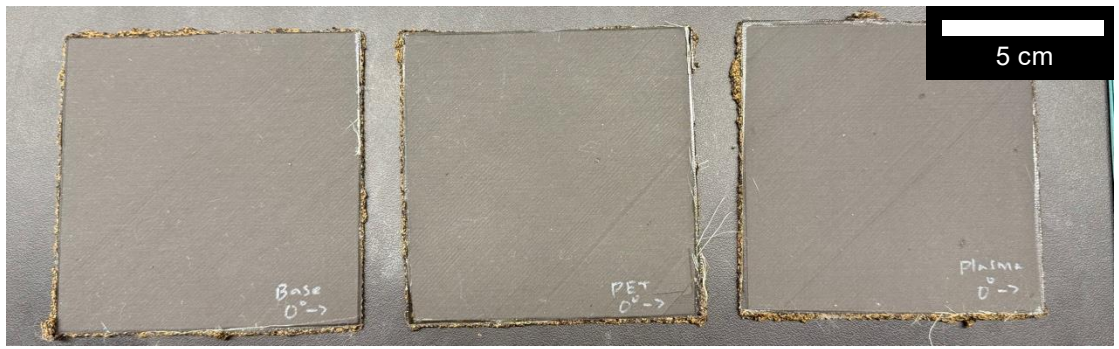

<Composite Laminates after Cure>

Results & Discussion

Morphological & Chemical Composition Change after Plasma Treatment

PET Nanofiber Morphology Change after Plasma Treatment

- Despite **6 bar of air pressure** and **120 °C gas temperature** involved in plasma treatment, SEM analysis confirms that **nanofiber structure** remains **intact**.
- The use of a metal mesh enables effective plasma exposure while preserving the **integrity of the nanofibers**.
- These findings indicate that even after plasma treatment, PET nanofibers can act as **nanoporous networks** that help **eliminate voids** in composite materials.

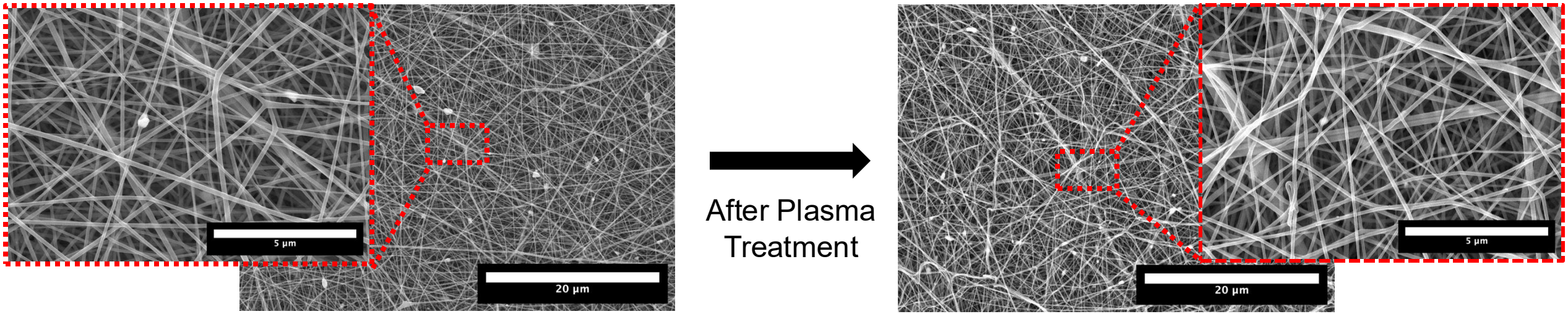

<SEM Images of Electrospun PET Nanofibers Before & After Atmospheric Plasma Treatment>

Surface Energy Increase via Plasma (Contact Angle Analysis)

- Contact angle analyzer was used to assess change in the wettability of PET nanofibers.
- Reduced contact angle with deionized water indicates **increased hydrophilicity**, confirming a **rise in surface energy**.
- Consistent with previous studies on PET films, plasma treatment enhances the hydrophilicity of PET nanofibers, demonstrating its **effectiveness even in nanostructures**.
- For more detailed and quantitative analysis on increased hydrophilicity, X-ray Photoelectron Spectroscopy (XPS) was conducted.

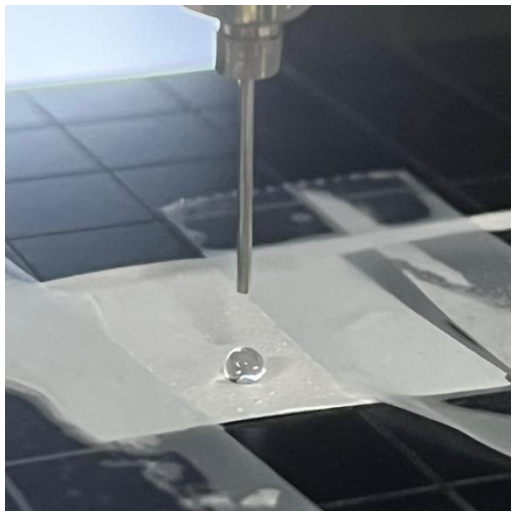

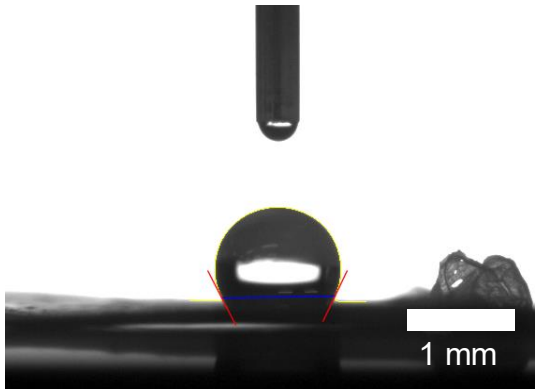

Before Treatment:
120° with DI water

Plasma
Treatment

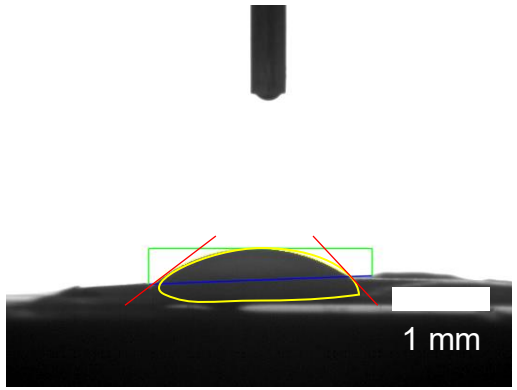

After Treatment:
30° with DI water

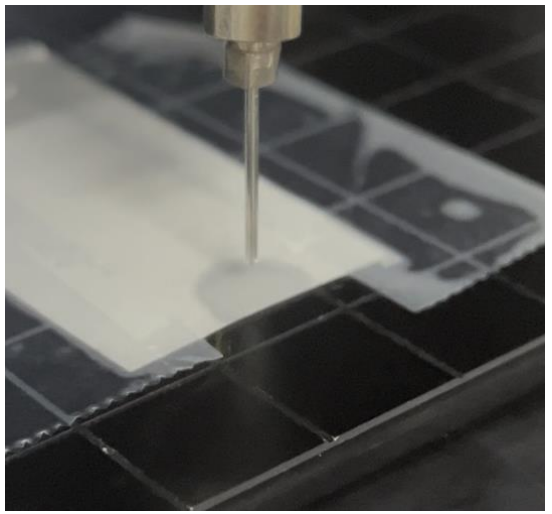

<Contact Angle Difference Before & After Plasma Treatment>

Surface Energy Increase via Plasma (XPS Analysis)

- Atomic composition showed a 15% decrease in carbon content and a 12% increase in oxygen content.
- High-resolution C-scan revealed **40% reduction in phenyl** (C–C, C=C) bonds, while O-scan showed a **45%** increase in organic C=O and a **61.5%** increase in C–O bonds, explaining the **enhanced hydrophilicity** and **increased surface energy**.
- These indicate a **potential enhancement in adhesion to epoxy**, which will be assessed through Short Beam Shear (SBS).

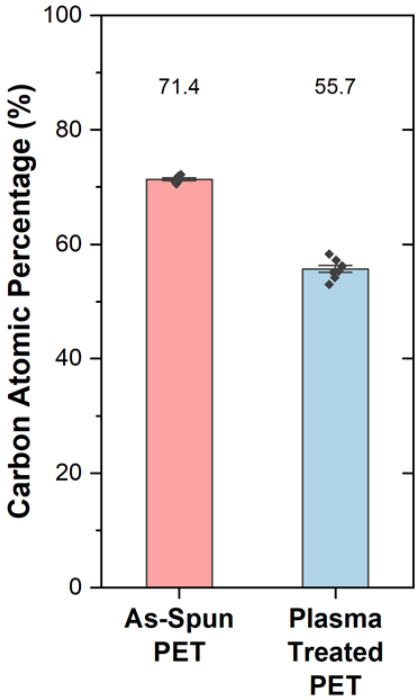

<Carbon Percentage>

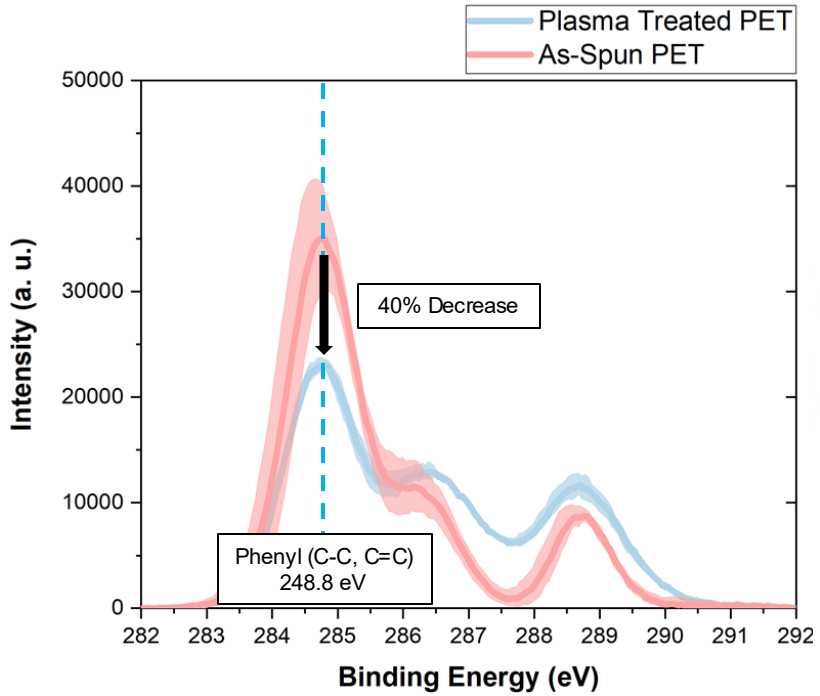

<Carbon Region Scan>

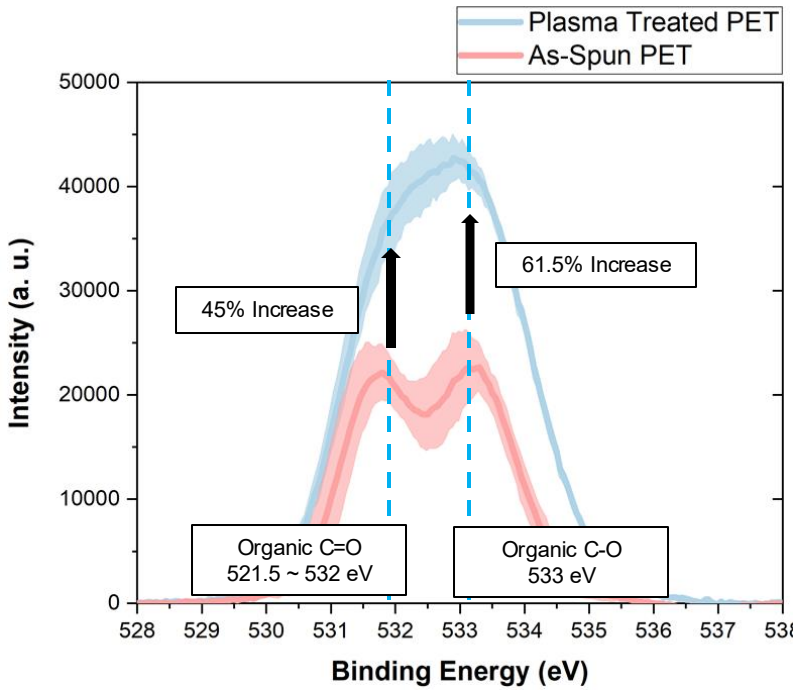

<Oxygen Region Scan>

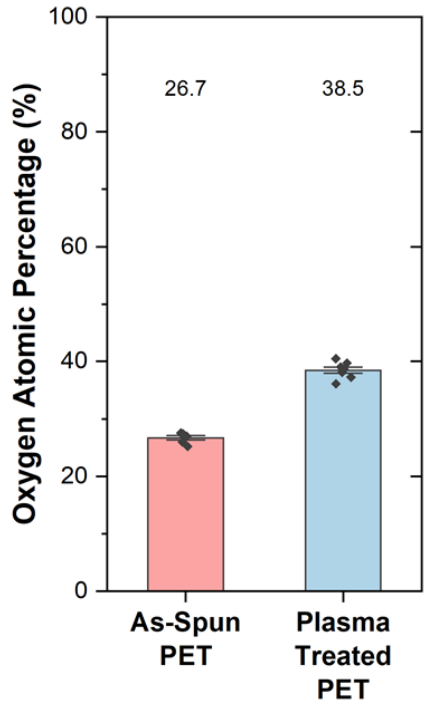

<Oxygen Percentage>

<XPS Results Comparison for PET and Plasma Treated PET Nanofibers>

Void Elimination using Nanofiber Interleaved Composites

- Void content were analyzed using **IM7/8552 prepregs** (Hexcel) with $[45/0/-45/90]_{2s}$ layup cured with **VBO method**.
- Void content of 1.6% present in the baseline samples were **eliminated** in both PET-interleaved composites.
- Plasma-treated PET nanofibers are capable of generating sufficient capillary pressure during curing also confirming the conservation of nanofibers.

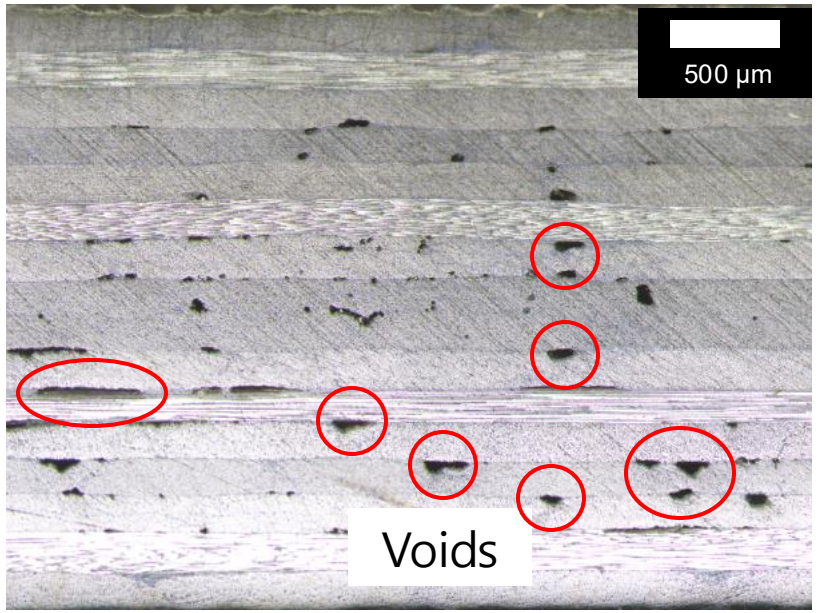

<Baseline Composite>

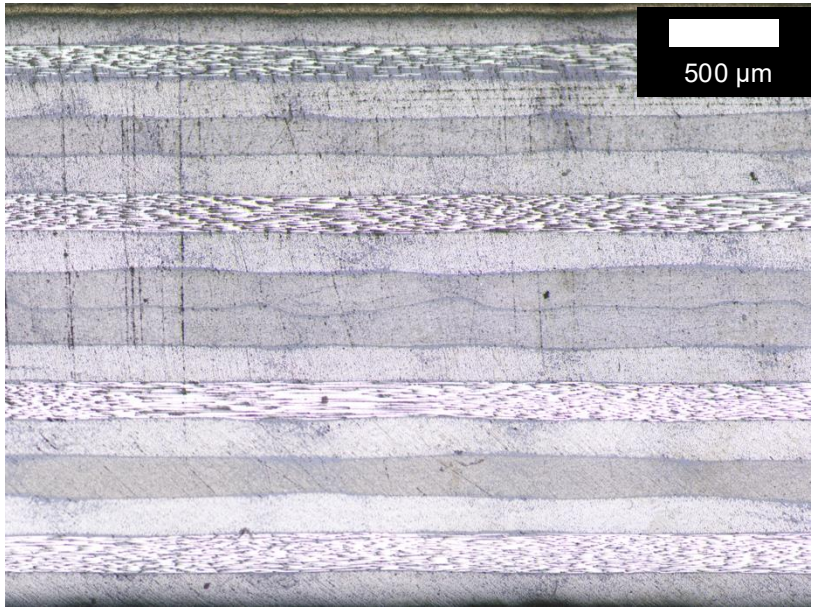

<As-Spun PET Composite>

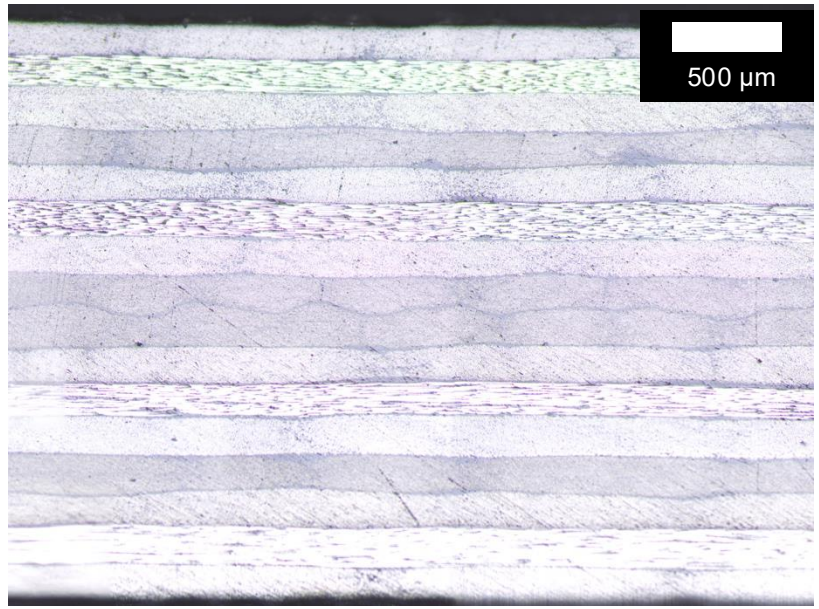

<Plasma PET Composite>

Short Beam Shear (SBS) Tests for Analyzing the Toughening Effect of PET Nanofibers

Short Beam Shear (SBS) Test Setup – ASTM D2344

- To evaluate the reinforcing effect of plasma-treated PET, SBS tests were conducted on three types of composites: **Baseline, As-spun PET, and Plasma-treated PET**.
- SBS tests were performed in accordance with **ASTM D2344**, using **IM7/8552** prepregs (Hexcel).
- **$[45/0/-45/90]_{2S}$** layup configuration was employed, and samples were fabricated using **both VBO and autoclave processes**.
- This layup structure **enables comparison with reference data** from the National Center for Advanced Materials Performance **(NCAMP)**.

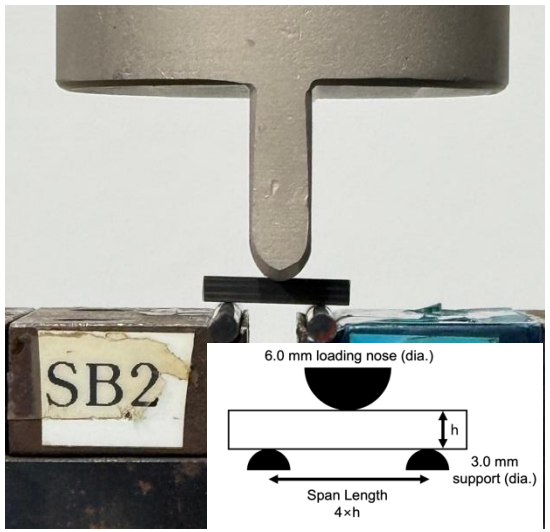

<Schematic & Setup for SBS>

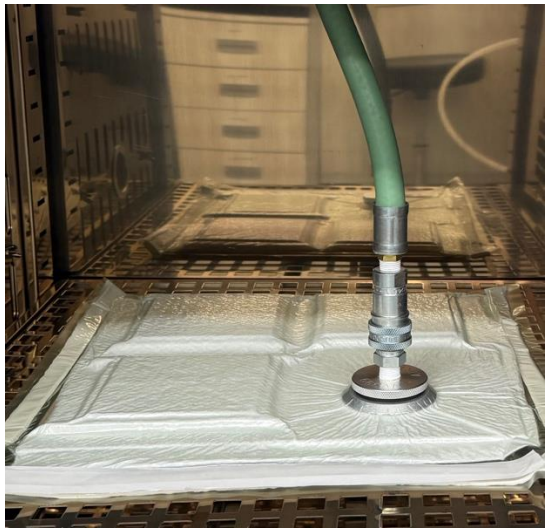

<VBO Curing>



<Autoclave Curing>

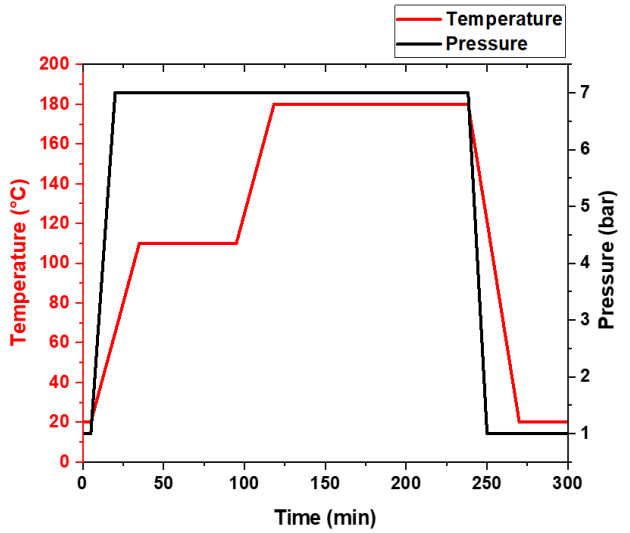

<Manufacturer Recommended Cure Cycle for IM7/8552>

Short Beam Shear (SBS) Result Comparison

- Plasma-treated PET composites exhibited **improved Short Beam Strength** compared to their respective baselines.
- Although the SBS value of Plasma PET (VBO) was lower than that of the Baseline (Autoclave) sample, this difference is likely attributed to **variations in specimen thickness**.

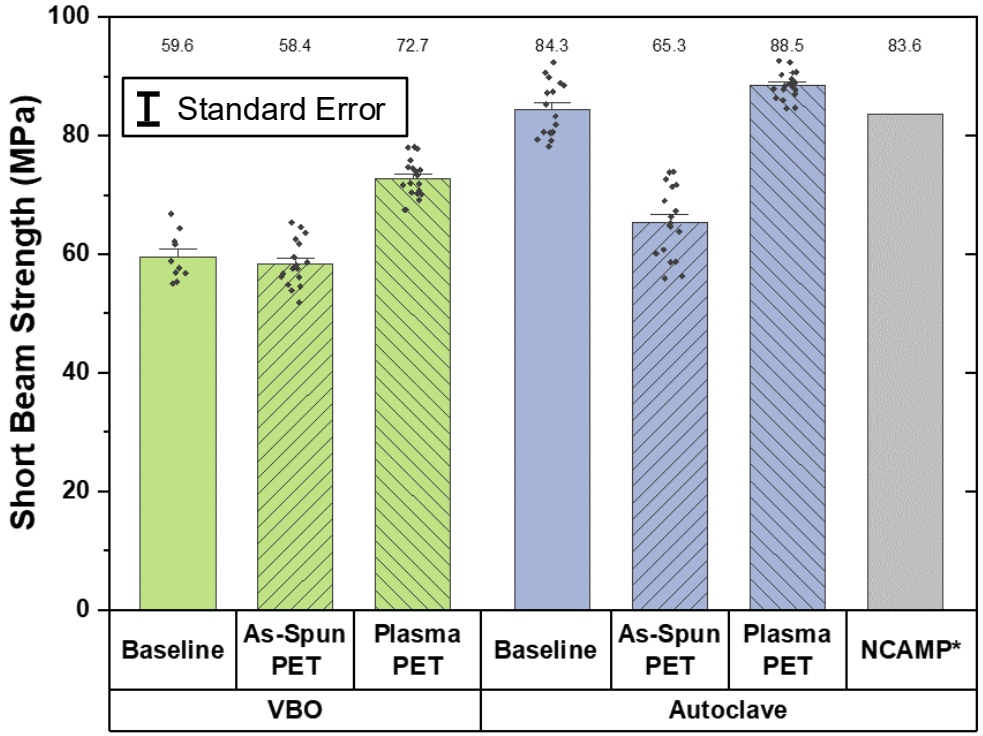

<Short Beam Strength Comparison>

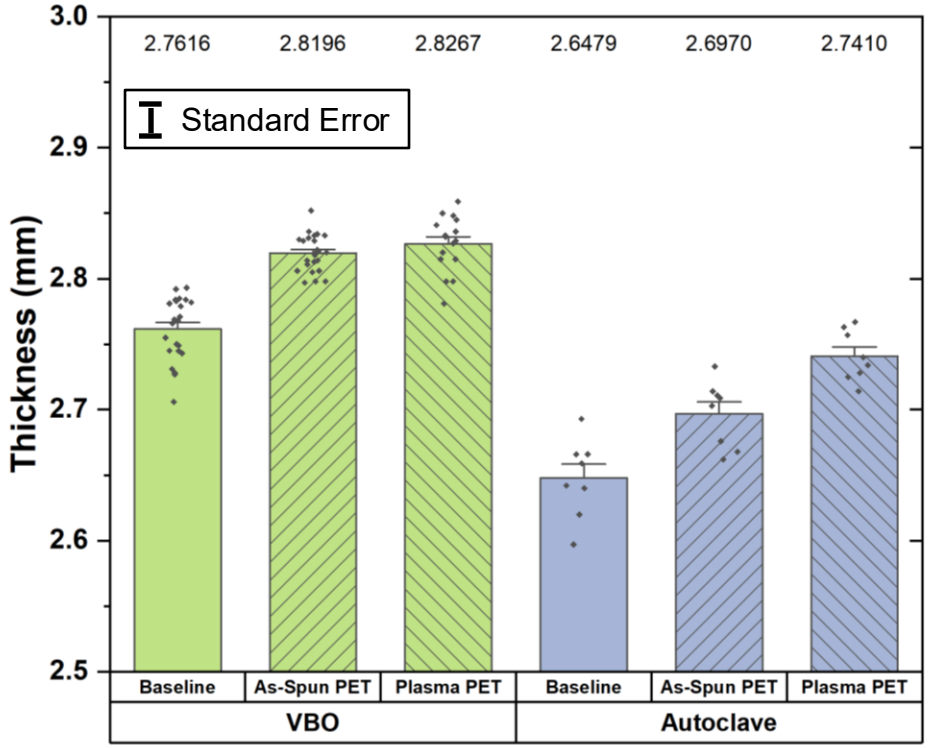

<Thickness Comparison>

KAIST Laboratory for Advanced Materials and Processes

NCAMP* : National Center for Advanced Materials Performance IM7/8552 Datasheet

ICCM24 24TH INTERNATIONAL CONFERENCE ON COMPOSITE MATERIALS

Short Beam Shear (SBS) – Load v. Displacement

- Furthermore, load v. displacement curve shows **no significant difference in maximum load** between the Baseline (Autoclave) and Plasma PET (VBO) specimens.
- While both show similar maximum load, Short Beam Strength of the VBO specimen appear lower due to its greater thickness.

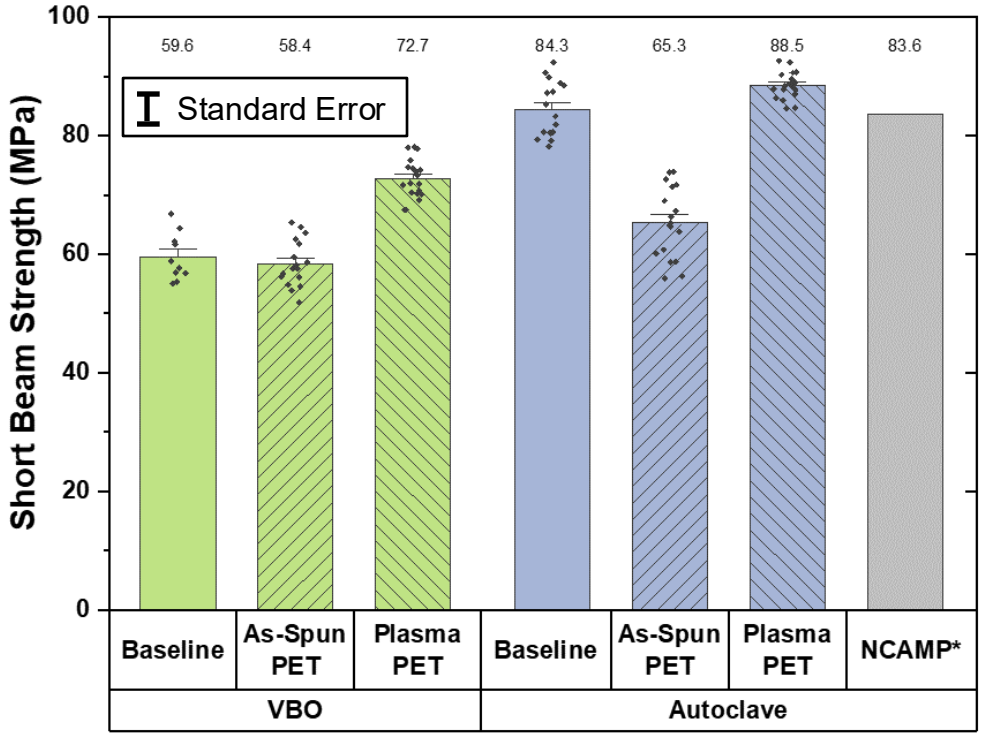

<Short Beam Strength Comparison>

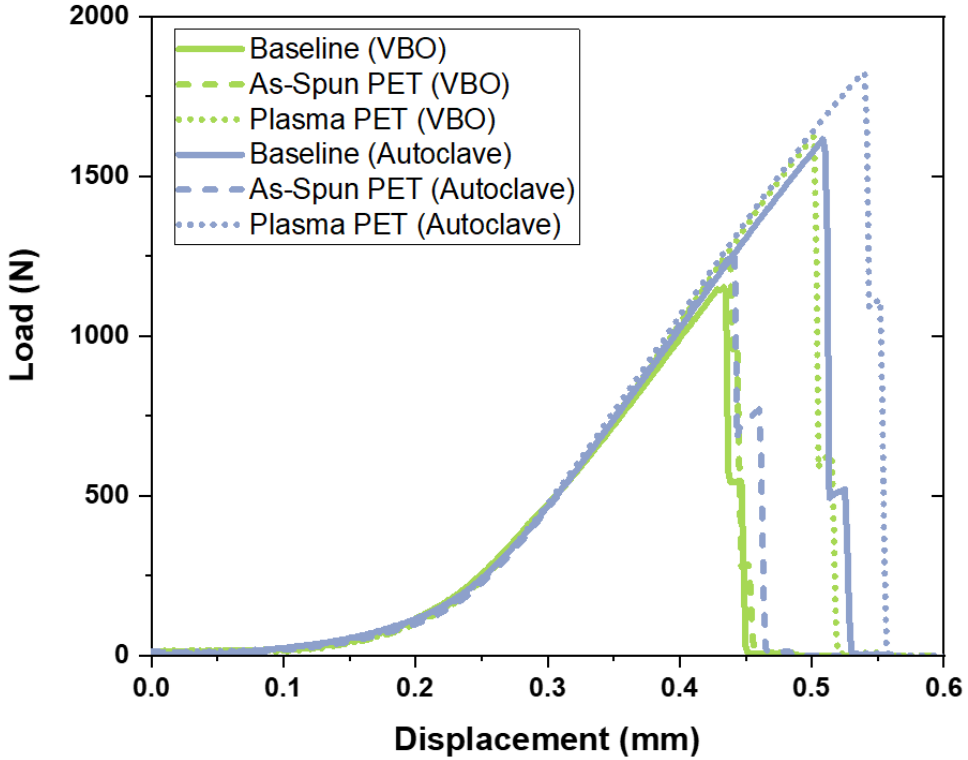

<Load v. Displacement Curve >

NCAMP* : National Center for Advanced Materials Performance IM7/8552 Datasheet

Short Beam Shear (SBS) – Load v. Displacement

- In contrast, **both As-spun PET** specimen showed Short Beam Strength values **comparable to Baseline (VBO)**.
- **Low adhesion of PET** did not contribute to composite reinforcement and may have **behaved similarly to voids**.
- Additionally, comparison with NCAMP* reference values confirmed that the Short Beam Strength value of the Baseline (Autoclave) specimen closely matched the standard, **validating the reliability of the experimental results**.

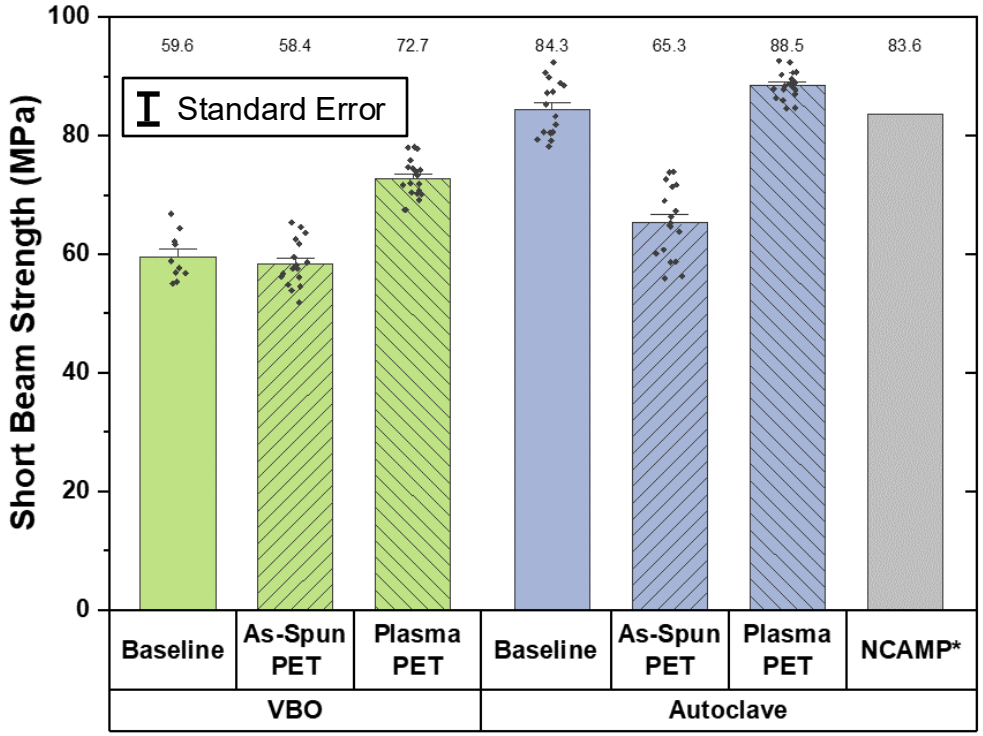

<Short Beam Strength Comparison>

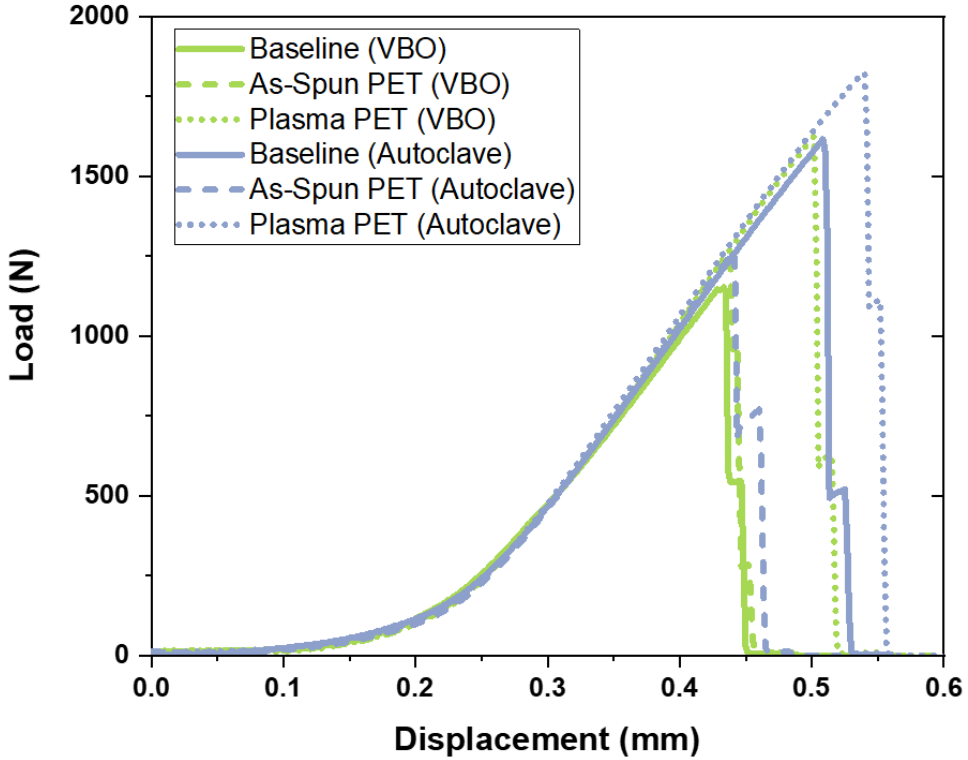

<Load v. Displacement Curve >

KAIST Laboratory for Advanced Materials and Processes

NCAMP* : National Center for Advanced Materials Performance IM7/8552 Datasheet

ICCM24 24th INTERNATIONAL CONFERENCE ON COMPOSITE MATERIALS

SBS Result Comparison – Crack Analysis (VBO)

- Optical microscopy revealed that Plasma-treated PET composites exhibited more frequent occurrences of **“ply-jumps”** compared to untreated PET composites.
- The increased number of ply-jumps suggests that plasma treatment enhances PET adhesion [22], thereby contributing to more **effective composite reinforcement**.
- Also, the higher surface area created from the crack indicates a higher energy flux [23], indicating toughening of plasma treated PET nanofibers compared to As-spun PET nanofibers.

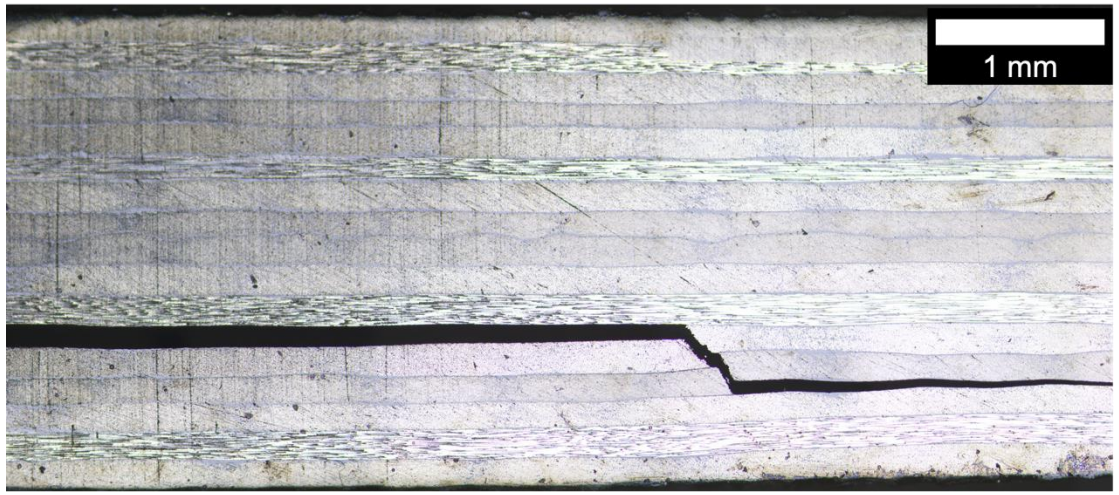

<As-Spun PET interleaved Composites after SBS>

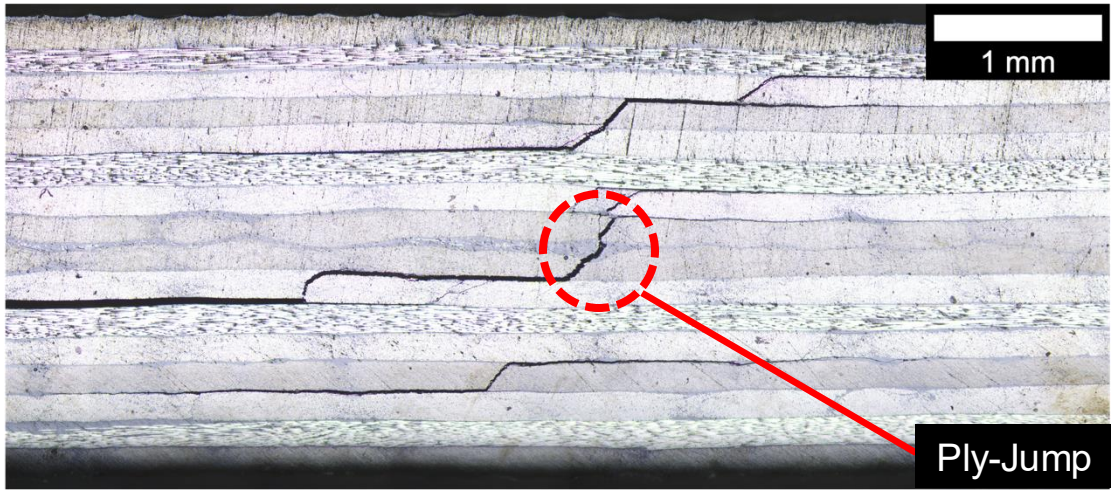

<Plasma Treated PET interleaved Composites after SBS>

[22] Borstnar, G., et al. "Interlaminar fracture micro-mechanisms in toughened carbon fibre reinforced plastics investigated via synchrotron radiation computed tomography and laminography." *Composites Part A: Applied Science and Manufacturing* 71 (2015): 176-183.
[23] Sharon, Eran, Steven P. Gross, and Jay Fineberg. "Energy dissipation in dynamic fracture."Physical review letters 76.12 (1996): 2117.

SBS Result Comparison – Crack Analysis (Autoclave)

- **Similar increases in ply-jump frequency** were observed in Baseline (Autoclave) and Plasma-treated PET (Autoclave), whereas As-spun PET—even when processed via autoclave—showed no ply-jump formation.
- These results, along with SBS values, confirm the **reinforcing effect** of plasma-treated PET in composites.
- Furthermore, the observed intralaminar failure suggests that plasma-treated PET nanofibers enhance composite toughness not only by eliminating voids but also by **directly strengthening the interlaminar region**.

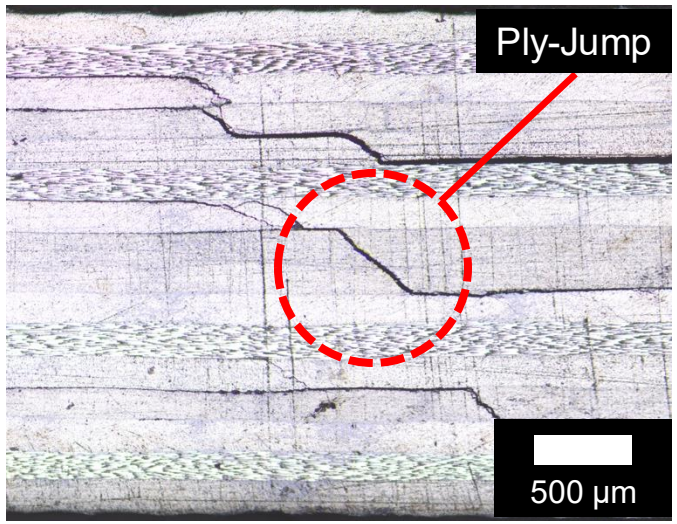

<Baseline Composites after SBS>

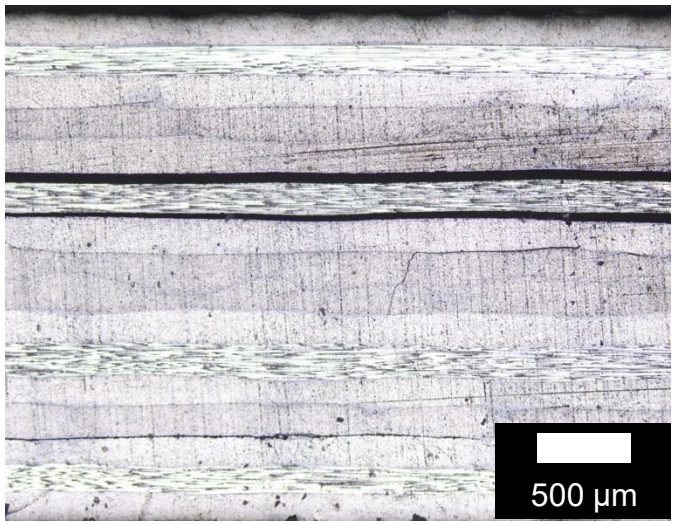

<As-Spun PET Interleaved Composites after SBS>

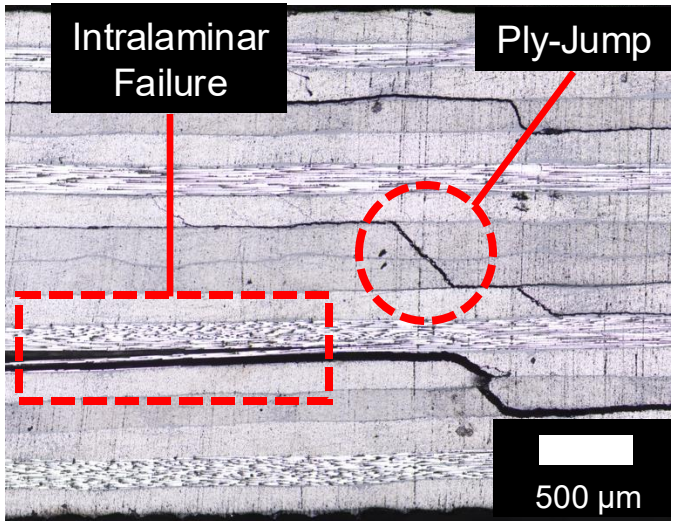

<Plasma Treated PET interleaved Composites after SBS>

SBS Result Comparison – Crack Analysis (VBO, SEM)

- To perform a more detailed analysis of the fracture surfaces, the interlaminar regions of VBO composites containing As-spun PET and Plasma Treated PET were examined using SEM, both before and after SBS testing.
- In composites with As-spun PET, the fracture path propagated linearly through the interlaminar region.
- In contrast, composites with plasma-treated PET exhibited a more complex fracture path, propagating through both interlaminar and intralaminar regions, **indicating increased adhesion** from non-linear, more tortuous fracture behavior.

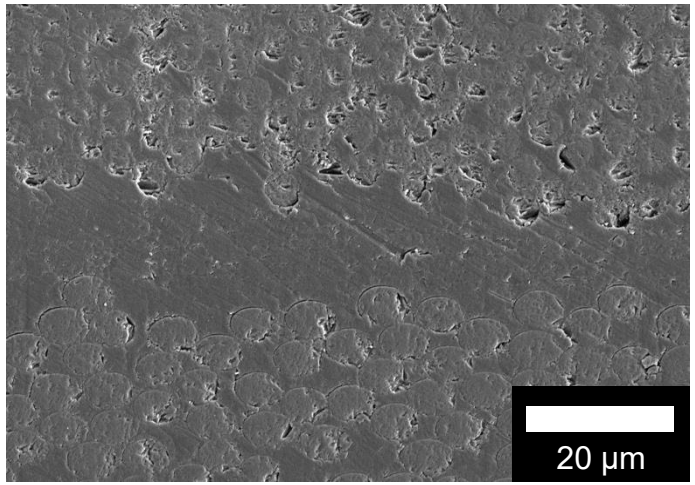

<PET Nanofiber Region Before SBS>

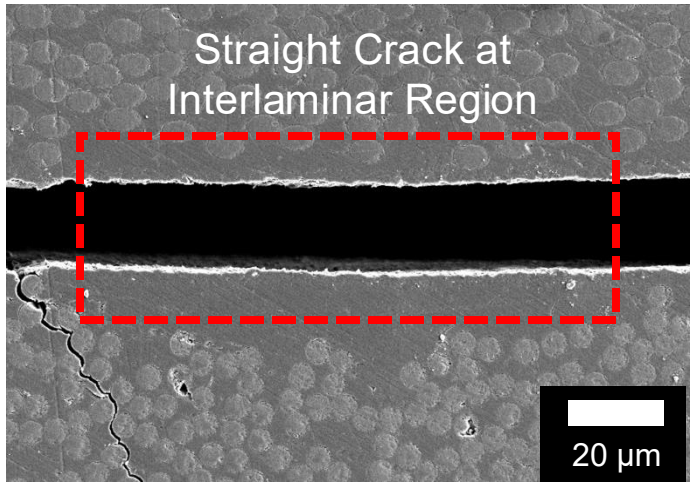

<As-Spun PET Composites after SBS>

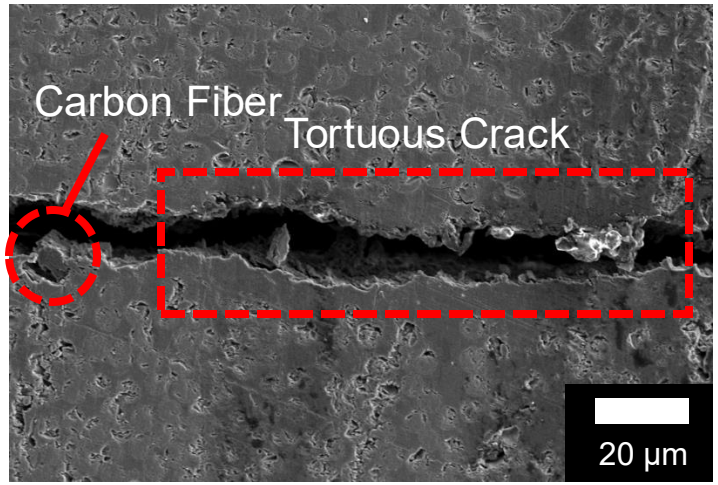

<Plasma Treated PET interleaved Composites after SBS>

Conclusion & Future Work

Conclusion

- This research has:
  1. Developed an atmospheric plasma treatment method that **functionalizes nanofibers without damaging their morphology**, **enabling previously unused materials as nanoporous networks** for void elimination.
  2. Shown that plasma-treated PET nanofibers markedly increase short beam shear strength, **overcoming their adhesion with epoxy,** and **reinforcing composites**.

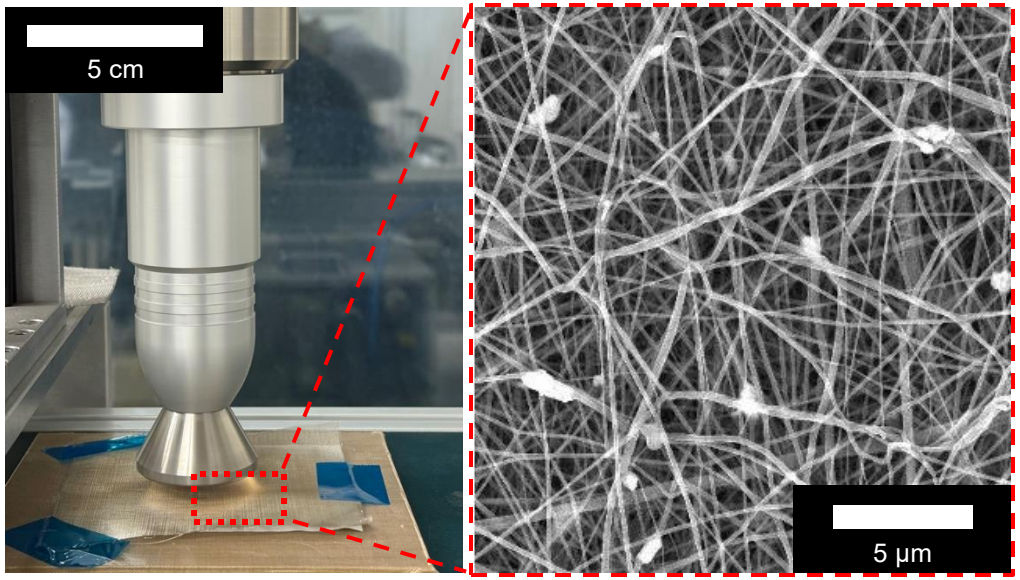

<Retention of Nanofibers after Plasma Treatment>

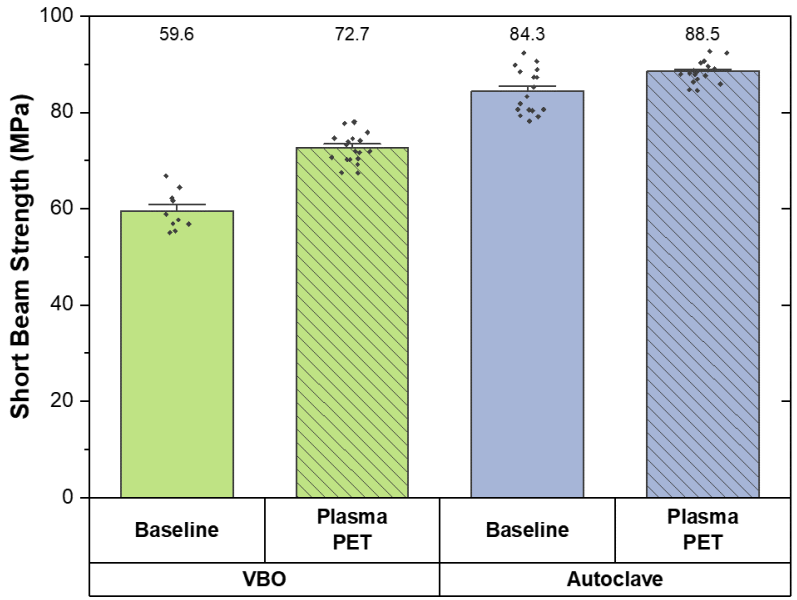

<Increased Short Beam Shear Strength with Plasma PET>

Future Work – Dynamic Mechanical Analysis (DMA)

- Dynamic Mechanical Analysis (DMA) in **dual-cantilever mode** will be conducted to evaluate composite modulus.
- Temperature sweep from –100 °C to 300 °C compared the **low-temperature modulus and glass-transition temperature (T_g)** of baseline, PET-interleaved laminates, and **PA-interleaved laminate** (Xantulayr, XLB) will be added for comparison.
- DMA measurements will be repeated after 500 liquid-nitrogen cryogenic cycles to assess modulus retention.
- **$[0/90]_{4S}$** layup with IM7/8552 prepreg is chosen to maximize coefficient-of-thermal-expansion mismatch during cycling.

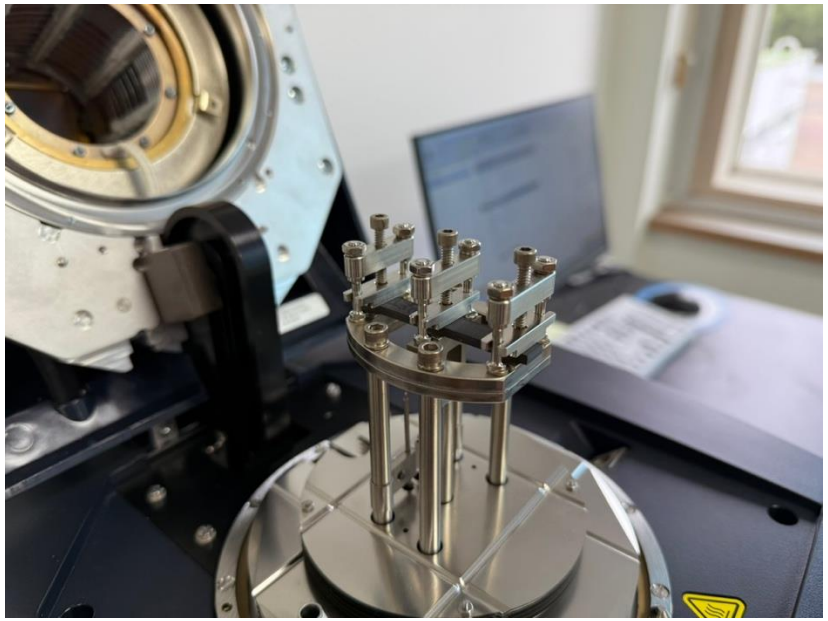

<DMA 850 (TA) – Dual Cantilever>

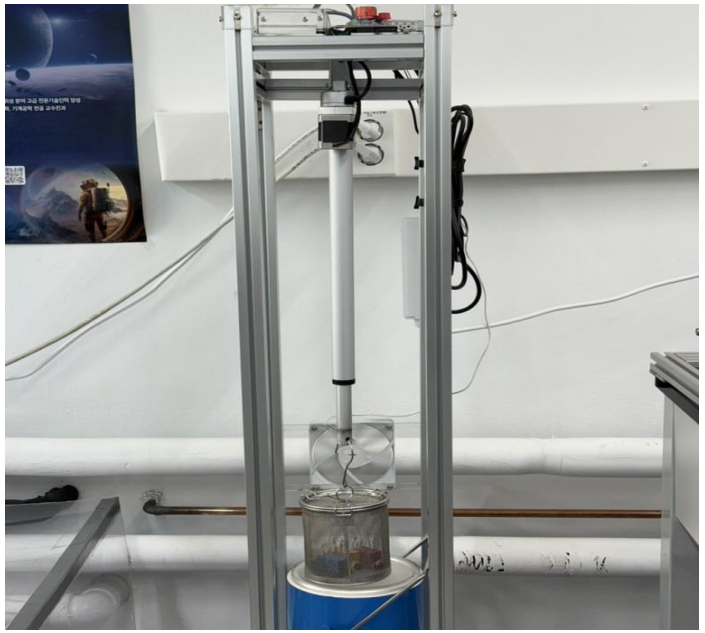

<Cryogenic Cycle>

Future Work – Permeability Measurements

- Higher **post-cycling storage modulus** of PET-interleaved laminates compared to baseline laminates demonstrates their **suitability for reusable space-launch structures**.
- Future work will focus on **permeability tests of PET interleaved composites** for use in **Type V composite overwrapped pressure vessel** (COPV), focusing on **low hydrogen permeability of PET** while being **capable of multiple use**.

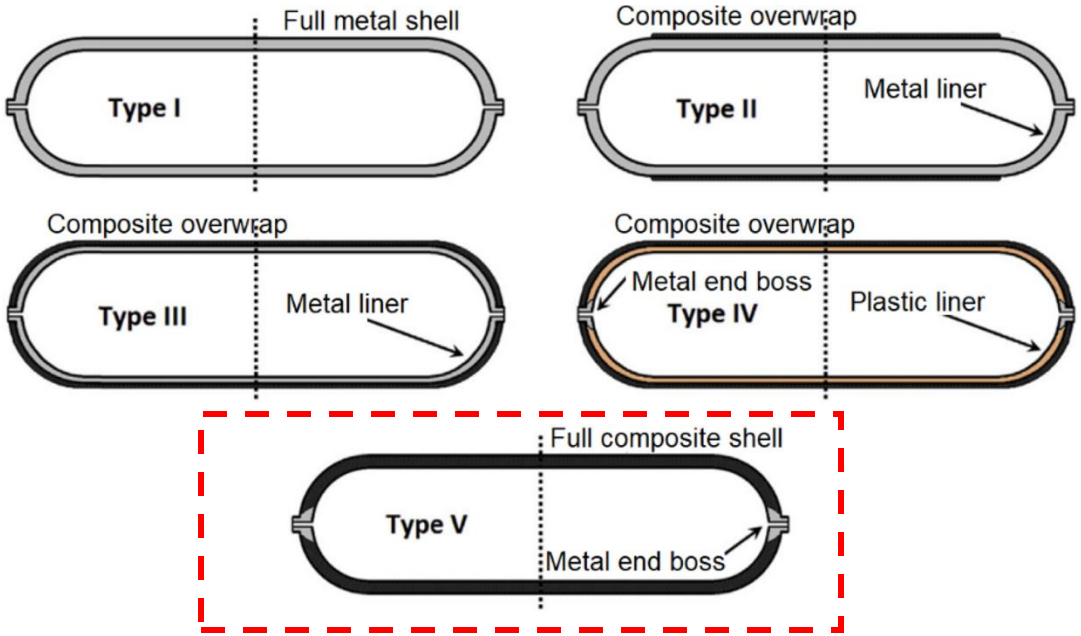

<Types of COPV [24]>

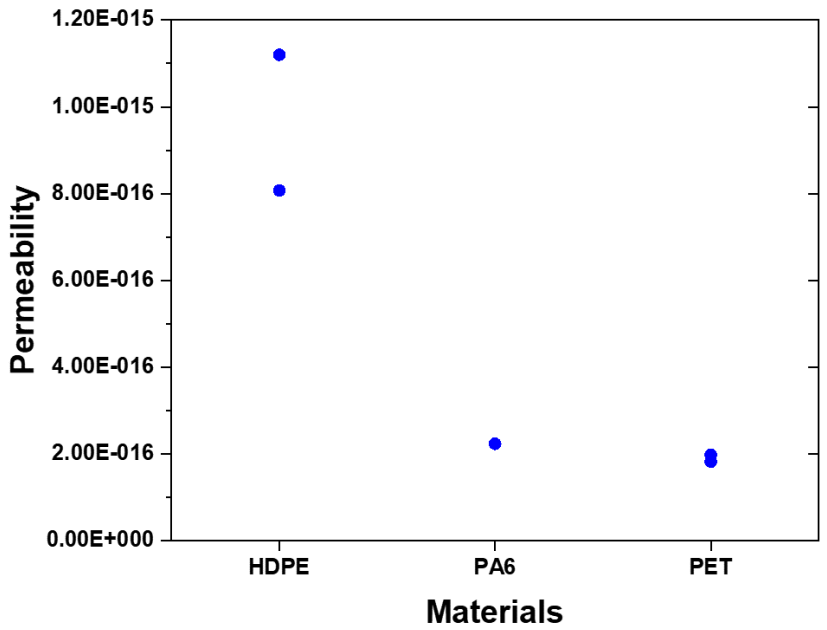

<Hydrogen Permeability for Different Thermoplastic Materials [25]>

[24] Avcu, Adem, et al. "Characterizing the effects of liner and fiber-reinforced resin composite shell on fracture energy in type-III high-pressure composite tanks." Journal of the Brazilian Society of Mechanical Sciences and Engineering 46.1 (2024): 13.
[25] Schultheiß, Daniel. "Permeation barrier for lightweight liquid hydrogen tanks." (2007).

Acknowledgements

This research was supported by Hanwha Space Hub and the KAIST Space Institute.
Part of the experimental work was performed using the facilities of the KAIST Analysis Research Advancement (KARA).

ICCM24
24TH INTERNATIONAL CONFERENCE ON COMPOSITE MATERIALS

Thank You

Contact email: jlee@kaist.ac.kr

KAIST

Laboratory for Advanced Materials and Processes

한화에어로스페이스
Hanwha Aerospace

Multifunctional Carbon Nanotube-based Composite Carbon Fibers for Enhanced Mechanical Properties

Junghwan Kim[1], So Jeong Heo[1], Seo Gyun Kim[1], and Bon-Cheo Kur[1]

[1]Composite Materials Research Center, Institute of Advanced Composite Materials, Korea Institute of Science and Technology, Republic of Korea
92 Chudong-ro, Bongdong-eup, Wanju-gun, Jeollabuk-do,
Email: seogyun.kim@kist.re.kr and cnt@kist.re.kr

Keywords: Nanocarbon fibers, Mechanical properties, Electrical conductivity, Thermal conductivity

ABSTRACT

In this work, we demonstrate an alternative strategy for enhancing the mechanical performance of carbon fibers by incorporating polyphenylene sulfide (PPS) into carbon nanotube (CNT)-based systems via a CSA-assisted wet-spinning approach. PPS, typically insoluble and highly crystalline, was successfully processed to form composite fibers, which exhibited significant improvements in tensile properties following thermal treatment. The results indicate the effectiveness of PPS incorporation without traditional stabilization steps. This method may provide a scalable and cost-effective route for multifunctional carbon fiber production.

1 INTRODUCTION

Carbon nanotube (CNT) fibers have gained recognition as a potential next-generation carbon fiber due to their outstanding mechanical and electrical properties [1-6]. Efforts to enhance CNT fiber performance have primarily focused on increasing CNT length or crystallinity, but these strategies face thermodynamic and practical limitations [7-8]. As an alternative, researchers have begun incorporating other carbon materials or polymers into CNT fibers to leverage synergistic effects and reduce reliance on costly CNTs [9-11].

Wet-spinning of CNT fibers using chlorosulfonic acid (CSA) offers a versatile platform, as CSA can not only dissolve CNTs but also sulfonate otherwise insoluble polymers [10-16]. This enables the co-processing of CNTs with sulfonated polymers into composite fibers. These sulfonated polymers are advantageous in that they can generate radicals during pyrolysis, which in turn form covalent bonds with CNTs—either between CNTs themselves or between CNTs and polymer chains [17-20]. This radical-mediated crosslinking enhances the structural cohesion and mechanical integrity of the resulting carbon fibers [21-24].

Carbon nanotube (CNT) fibers have attracted considerable attention as a new class of carbon fiber materials due to their exceptional electrical, thermal, and mechanical properties. However, their broad commercialization remains constrained by high production costs and technical limitations related to CNT alignment and interfacial bonding. Recent approaches have explored hybridization with polymers to enhance spinnability, reduce cost, and improve mechanical integrity.

Among these, poly(p-phenylene sulfide) (PPS) presents a promising option due to its aromatic backbone and high carbon yield upon pyrolysis. Despite its poor solubility in most solvents, PPS can be sulfonated and processed in chlorosulfonic acid (CSA), forming anisotropic liquid crystalline dopes in combination with CNTs [25-30]. This co-processing enables the fabrication of CNT–PPS composite fibers via wet-spinning. Upon carbonization, the composite fibers benefit from radical-mediated crosslinking between PPS and CNTs, potentially improving the mechanical integrity of the final carbon fiber.

In this study, we examine the structural and mechanical evolution of CNT–PPS fibers as a function of PPS content and heat-treatment temperature. Our goal is to establish processing–structure–property relationships that support the design of high-performance CNT-based carbon fibers using PPS as a functional additive and carbon source.

2 RESULTS AND DISCUSSION

The wet-spinning process allowed for uniform mixing of CNTs and sulfonated PPS (sPPS), forming composite fibers with smooth morphology and good spinnability even at high PPS loadings. Following drying and heat treatment, structural transformations such as de-sulfonation and crosslinking led to noticeable changes in fiber morphology and density.

Thermal analysis revealed that sPPS enhanced the thermal stability and char yield of the composite fibers. This was attributed to the generation of radicals during thermal decomposition, which promoted covalent bonding within the fiber structure. These interactions supported better structural coherence and higher carbon retention.

Mechanical testing showed that the incorporation of PPS improved tensile strength and modulus after carbonization. An optimal PPS content of around 30 wt% yielded the best performance, balancing reinforcement from PPS-derived carbon with effective load transfer through CNT-PPS bonding. Excessive PPS content, however, led to turbostratic structures and reduced mechanical integrity due to misalignment and void formation.

Small-angle and wide-angle X-ray scattering analyses confirmed that increasing PPS disrupted CNT alignment, which impacted the modulus. Transmission electron microscopy further visualized turbostratic carbon domains originating from sPPS, which were distinguishable from CNT regions.

Overall, the combination of PPS and CNTs, processed through CSA-assisted wet-spinning and tailored heat treatment, enabled the production of carbon fibers with improved mechanical properties and structural integrity. The findings highlight the importance of optimizing composite composition and processing conditions to maximize performance.

3 FIGURES AND TABLES

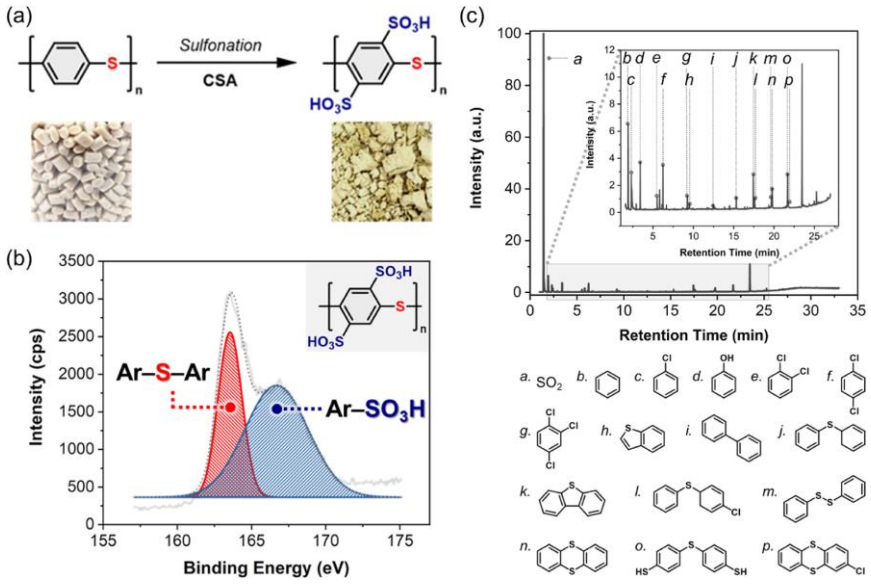

Figure 1: (a) The possible structure of sPPS using CSA, (b) XPS of sPPS, (c) GC-MS of sPPS and possible molecules corresponding to each peak of MS. Reprinted from *Carbon* 219 (2024) 118814

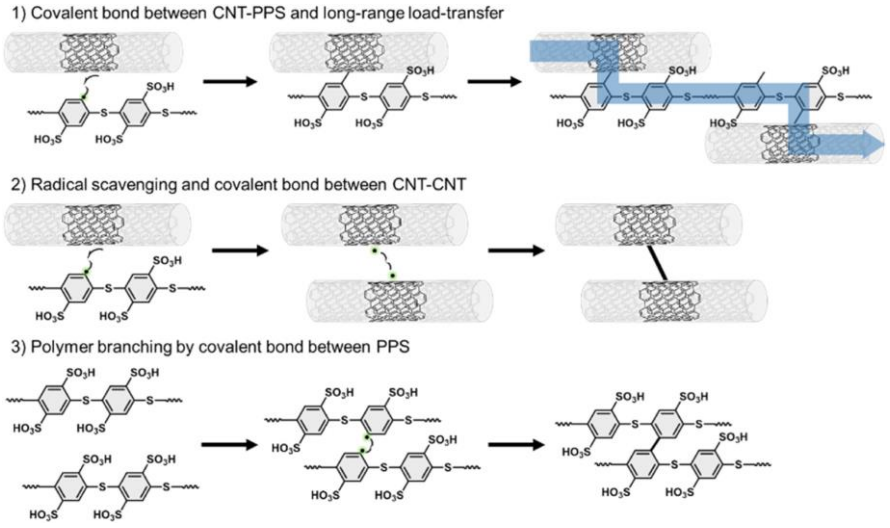

Figure 2: Proposed mechanisms of interaction between radical from sPPS and CNT. Reprinted from *Carbon* 219 (2024) 118814

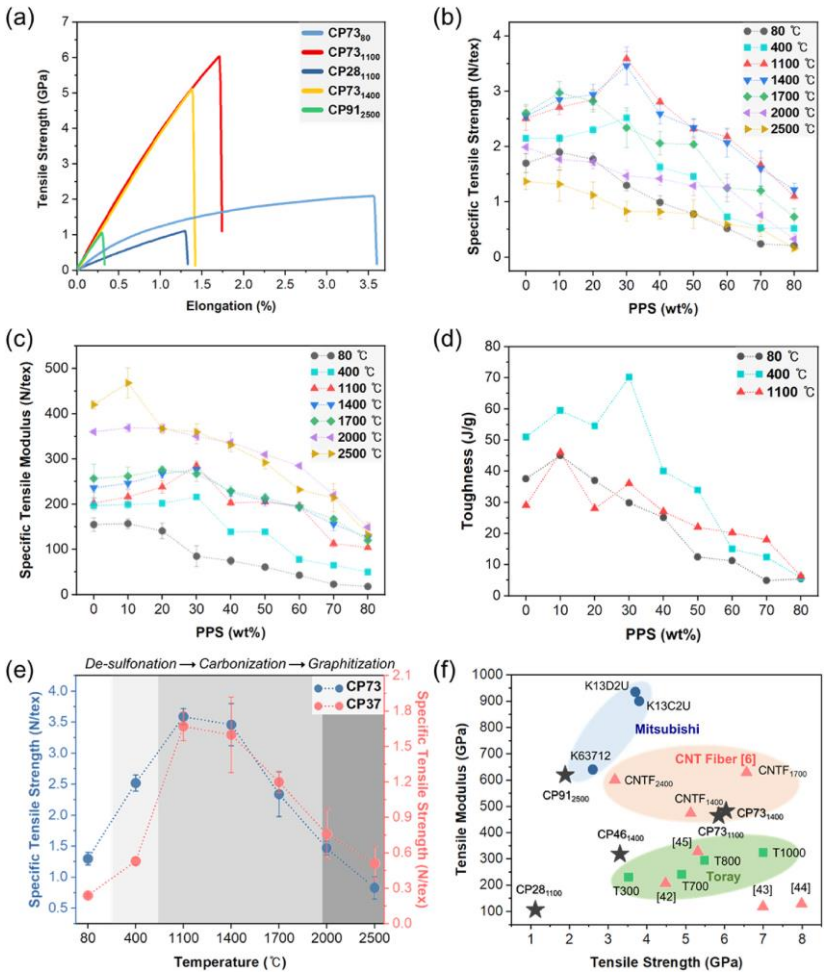

Figure 3: (a) Stress-strain curves (b) Specific tensile strength, (c) Specific tensile modulus and (d) Toughness of CNT-PPS composite fibers and their heat-treated fibers, (e) Specific tensile strength of CP73 and CP37 depending on heat-treatment temperature, (f) Comparison of CNT-PPS fibers with other CNTFs [30-34] and commercial CFs. Reprinted from *Carbon* 219 (2024) 118814

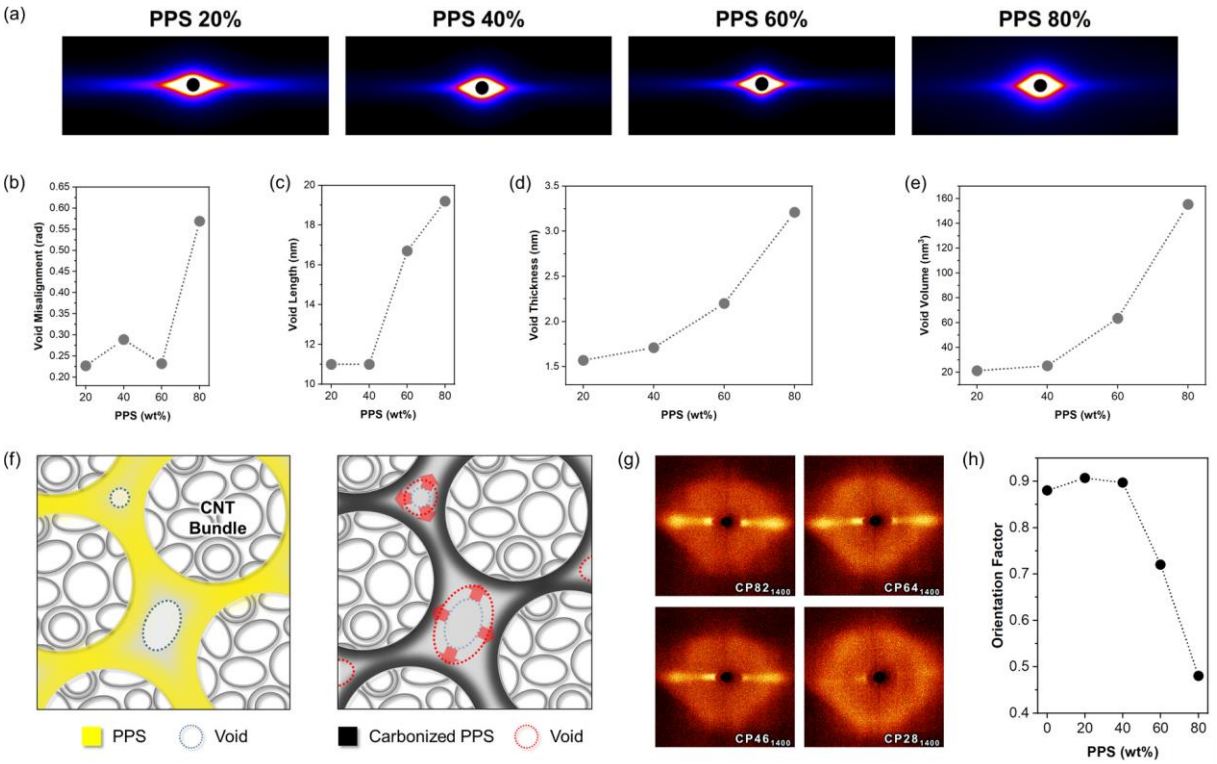

Figure 4: (a) 2D SAXS patterns, (b) Misalignment, (c) Length, (d) Thickness and (e) Volume of 1400 ˚C-carbonized CNT–PPS composite fibers, (f) Schematic diagram of enlargement of voids in the fibers after carbonization, (g) WAXS pattern images of 1400 ˚C-carbonized CNT–PPS composite fibers, (h) CNT orientation factor alongthe fiber axis. Reprinted from *Carbon* 219 (2024) 118814

4 CONCLUSIONS

This study demonstrated a practical route for manufacturing CNT-based composite carbon fibers by incorporating sulfonated PPS through a liquid crystalline wet-spinning process. The fibers exhibited improved mechanical properties after controlled thermal treatment, attributed to enhanced carbon yield and covalent interaction between CNTs and PPS. The optimized composites balanced CNT alignment with polymer-derived carbon reinforcement, resulting in high-performance structural materials. This approach holds promise for scalable and cost-effective production of next-generation carbon fibers

ACKNOWLEDGEMENTS

This work was supported by grants from the institutional program (2E32632) and K-Lab (2E32635) of the Korea Institute of Science and Technology (KIST). This work was also supported by the program (RS- 2023-00258521) of development of high-performance carbon nanocomposites fiber funded by the Ministry of Trade, Industry and Energy (MOTIE).

REFERENCES

[1] N. Behabtu, C.C. Young, D.E. Tsentalovich, O. Kleinerman, M. Pasquali, et al., Strong, light, multifunctional fibers of carbon nanotubes with ultrahigh conductivity, Science 339 (2013) 182–186.

[2] X. Zhang, W. Lu, G. Zhou, Q. Li, Understanding the mechanical and conductive properties of carbon nanotube fibers for smart electronics, Adv. Mater. 32 (2020) 1902028.

[3] D. Lee, S.G. Kim, M. Pasquali, J.J. Vilatela, B.C. Ku, et al., Ultrahigh strength, modulus, and conductivity of graphitic fibers by macromolecular coalescence, Sci. Adv. 8 (2022) eabn0939.

[4] M. Adnan, R.A. Pinnick, Z. Tang, L.W. Taylor, S.S. Pamulapati, G.R. Carfagni, M. Pasquali, Bending behavior of CNT fibers and their scaling laws, Soft Matter 14 (2018) 8284–8292.

[5] L.W. Taylor, O.S. Dewey, R.J. Headrick, N. Komatsu, N.M. Peraca, F. Wehmeyer, J. Kono, M. Pasquali, Improved properties, increased production, and the path to broad adoption of carbon nanotube fibers, Carbon 171 (2021) 689–694.

[6] D. Lee, S.J. Heo, S.G. Kim, B.-C. Ku, A review of high-performance carbon nanotube-based carbon fibers, Funct. Compos. Struct. 5 (2023) 45007–45032.

[7] J.J. Vilatela, J.A. Elliott, A.H. Windle, A model for the strength of yarn-like carbon nanotube fibers, ACS Nano 5 (2011) 1921–1927.

[8] B.D. Jensen, J.W. Kim, G. Sauti, K.E. Wise, L. Dong, Toward ultralight high strength structural materials via collapsed carbon nanotube bonding, Carbon 156 (2020) 538–548.

[9] S. Zhang, A. Hao, N. Nguyen, A. Oluwalowo, Z. Liu, et al., Carbon nanotube/carbon composite fiber with improved strength and electrical conductivity via interface engineering, Carbon 144 (2019) 628–638.

[10] S.G. Kim, S.J. Heo, D. Lee, H.G. Chae, B.C. Ku, et al., Ultrastrong hybrid fibers with tunable macromolecular interfaces of graphene oxide and carbon nanotube for multifunctional applications, Adv. Sci. 9 (2022) 2203008–2203018.

[11] S.G. Kim, S.J. Heo, H.C. Kim, H.G. Chae, B.C. Ku, et al., Ultrahigh strength and modulus of poylimide-carbon nanotube based carbon and graphitic fibers with superior electrical and thermal conductivities for advanced composite applications, Compos. B Eng. 247 (2022) 110342–110350.

[12] V.A. Davis, A.N.G. Parra-Vasquez, M.J. Green, P.K. Rai, M. Pasquali, et al., True solutions of single-walled carbon nanotubes for assembly into macroscopic materials, Nat. Nanotechnol. 4 (2009) 830–834.

[13] R.J. Headrick, D.E. Tsentalovich, J. Berdegue, E.A. Bengio, L. Liberman, O. Kleinerman, et al., Structure-property relations in carbon nanotube fibers by downscaling solution processing, Adv. Mater. 30 (2018) 1704482–1704489.

[14] H.D. Jeong, S.G. Kim, M. Park, B.C. Ku, H.S. Lee, Theoretical and experimental investigation of the wet-spinning process for mechanically strong carbon nanotube fibers, Chem. Eng. J. 412 (2021) 128650–128660.

[15] S.G. Kim, G.M. Choi, H.D. Jeong, D. Lee, S. Kim, K.H. Ryu, et al., Hierarchical structure control in solution spinning for strong and multifunctional carbon nanotube fibers, Carbon 196 (2022) 59–69.

[16] C.A. Idibie, S.A. Abdulkareem, C.H. Pienaar, S.E. Iyuke, L. van Dyk, Mechanism and kinetics of sulfonation of polystyrene-butadiene rubber with chlorosulfonic acid, Ind. Eng. Chem. Res. 49 (2010) 1600–1604.

[17] D.R. Gudgell, M. Day, J.D. Cooney, Thermal degradation of poly(phenylene sulfide) as monitored by pyrolysis–GC/MS, Polym. Degrad. Stabil. 43 (1994) 109–115.

[18] J.M. Younker, T. Saito, M.A. Hunt, A.K. Naskar, A. Beste, Pyrolysis pathways of sulfonated polyethylene, an alternative carbon fiber precursor, J. Am. Chem. Soc. 135 (2013) 6130–6141.

[19] P. Balding, R. Cueto, P.S. Russo, W.R. Gutekunst, Synthesis of perfectly sulfonated sodium polystyrene sulfonate over a wide molar mass range via reversible deactivation radical polymerization, J. Polym. Sci. 57 (2019) 1527–1537.

[20] G. Lee, S.I. Park, H.Y. Shin, S.S. Kim, S. Lee, et al., Simultaneous reactions of sulfonation and condensation for high-yield conversion of polystyrene into carbonaceous material, J. Ind. Eng. Chem. 122 (2023) 426–436.

[21] A. Galano, Carbon nanotubes as free-radical scavengers, J. Phys. Chem. C 112 (2008) 8922–8927.

[22] M.J. Martinez-Morlanes, P. Castell, P.J. Alonso, M.T. Martinez, J.A. Puertolas, Multi-walled carbon nanotubes acting as free radical scavengers in gamma irradiated ultrahigh molecular weight polyethylene composites, Carbon 50 (2012) 2442–2452.

[23] T. Shimizu, R. Kishi, T. Yamada, K. Hata, Radical scavenging activity of carbon nanotubes: toward appropriate selection of a radical initiator, RSC Adv. 10 (2020) 29419–29423.

[24] Y. Wang, Z. Chen, H. Huang, D. Wang, D. Liu, et al., Organic radical compound and carbon nanotube composites with enhanced electrical conductivity towards high performance p-type and n-type thermoelectric materials, J. Mater. Chem. A 8 (2020) 24675–24684.

[25] H.N. Beck, Solubility characteristic of poly(etheretherketone) and poly(phenylene sulfide), J. Appl. Polym. Sci. 45 (2003) 1361–1366.

[26] Z. Jiang, L.A. Gyurova, A.K. Schlarb, K. Friedrich, Z. Zhang, Study on friction and wear behavior of polyphenylene sulfide composites reinforced by short carbon fibers and sub-micro TiO2 particles, Compos. Sci. Technol. 68 (2008) 734–742.

[27] J. Gu, J. Du, J. Dang, W. Geng, S. Hu, Thermal conductivities, mechanical and thermal properties of graphite nanoplatelets/polyphenylene sulfide composites, RSC Adv. 42 (2014) 22101–22105.

[28] J. Gu, Y. Guo, X. Yang, C. Liang, W. Geng, et al., Synergistic improvement of thermal conductivities of polyphenylene sulfide composites filled with boron nitride hybrid fillers, Compos. – A: Appl. Sci. Manuf. 95 (2017) 267–273.

[29] M. Choi, J. Kim, S. Ryu, N.H. You, B.C. Ku, et al., Surface modification of sulfur assisted reduced graphene oxide with poly(phenylene sulfide) for multifunctional nanocomposites, Polymers 14 (2022) 732–747.

[30] D. Lee, S.G. Kim, M. Pasquali, J.J. Vilatela, B.C. Ku, et al., Ultrahigh strength, modulus, and conductivity of graphitic fibers by macromolecular coalescence, Sci. Adv. 8 (2022) eabn0939.

[31] J. Lee, D.M. Lee, Y. Jung, H.S. Jeong, S.M. Kim, et al., Direct spinning and densification method for high-performance carbon nanotube fibers, Nat. Commun. 10 (2019) 2962–2971.

[32] D. Yan, J. Di, Z. Zhang, Z. Gao, J. Zhang, et al., Carbon nanotube-directed 7 GPa heterocyclic aramid fiber and its application in artificial muscles, Adv. Mater. 2306129 (2023).

[33] H.L. Shi, Q.Q. Shi, H. Zhan, J.J. Ai, Y.T. Chen, et al., High-strength carbon nanotube fibers from purity control by atomized catalytic pyrolysis and alignment improvement by continuous large prestraining, Nano Lett. 23 (2023) 10739–10747.

[34] D. Lee, S.G. Kim, J. Kim, D.S. Lee, B.C. Ku, et al., Highly conductive and mechanically strong metal-free carbon nanotube composite fibers with self-doped polyaniline, Carbon 213 (2023) 118308–118315.

UNRAVELLING THE EFFECT OF THE ADDITION OF A NEW CARBON ALLOTROPE IN POLYMERIC COMPOSITES: INVESTIGATION OF ELECTRICAL PROPERTIES

S.Zecchi[1,2*], E.Piatti[1], G.Ghigo[1], D.Torsello[1], L.Lavagna[1,2], M.Etzi[3], M. C. Belduque Correa[4], A.Tagliaferro[1,2,5], F.C. Robles Hernandez[4,6*], M. Bartoli[2,3*]

[1]Department of Applied Science and Technology, Politecnico di Torino, C.so Duca degli Abruzzi 24, 10129 Turin, Italy Email: silvia.zecchi@polito.it, erik.piatti@polito.it, gianluca.ghigo@polito.it, daniele.torsello@polito.it, luca.lavagna@polito.it, alberto.tagliaferro@polito.it, web page: https://www.disat.polito.it/

[2]Consorzio Interuniversitario Nazionale per la Scienza e Tecnologia dei Materiali (INSTM), Via G. Giusti 9, 50121 Florence, Italy

[3]Center for Sustainable Future Technologies @POLITO, Istituto Italiano di Tecnologia, Via Livorno 60, 10144 Turin, Italy Email: marco.etzi@iit.it, mattia.bartoli@iit.it , web page: https://www.iit.it/it/csft-polito

[4] Cullen College of Engineering, Materials Science and Engineering, University of Houston, Houston, TX, 77204-4020, USA Email: fcrobles@central.uh.edu, mbelduqu@cougarnet.uh.edu, web page: https://www.uh.edu/

[5]Faculty of Science, OntarioTech University, Simcoe Street North, Oshawa, ON L1G 0C5, Canada

[6]Cullen College of Engineering, Technology Division, University of Houston, Houston, TX, 77204-4020, USA Email: fcrobles@central.uh.edu, web page: https://www.uh.edu/

Keywords: morphed graphene, DC electrical properties, surface properties, electrical properteis

ABSTRACT

The discovery of new carbon allotropes has led to major advancements in materials science, as each new form of carbon has unique properties that can lead to new applications. The variety of structures and characteristics existing in carbon allotropes provides unprecedented mechanical, electrical, and thermal properties. However, even though these new forms are revolutionary, their synthesis process is difficult. The production processes are complex and often need extreme conditions or highly specialized production techniques, which make their production and application challenging.

A recent milestone in this field has been the identification of the hexagonal carbon allotrope RH6-II developed through a novel morphing mechanism in graphene nanostructures, which represents a significant shift from traditional sp^2-bonded carbon structures, introducing a hybrid bonding configuration of sp^2 and sp^3 carbons. This new structure showed unique atomic arrangements that differentiate it from conventional graphene or diamond structures. In this work, we build upon these findings by investigating the effect of the incorporation of RH6-II allotrope within polymeric composites. Given the increasing electrical conductivity with RH6-II content, these nanostructures hold potential for applications in structural composites, where both mechanical reinforcement and enhanced electrical properties are desirable. Future improvements in RH6-II production yield could further facilitate its use in various composite applications.

1 INTRODUCTION

The research for innovative carbon-based reinforcements for structural and functional purposes is one of the most advanced frontiers of materials science. During the past half century, the discovery of fullerenes [1], carbon nanotubes (CNTs) [2] and graphene related materials [3] has dramatically changed the world of research. Nevertheless, the carbon family has recently grown by adding a new carbon allotrope named morphed graphene [4-6]. Morphed graphene, shown in Figure 1, is composed of

distorted covalently cross-linked graphene layers bonded with a sp^2 hybridization but a sp^3-like arrangement. Among its phases, morphed graphene RH6-II phase is a rippled structure emerging when graphene sheets undergo mechanical deformation induced by compressive strain promoted by ball milling [4]. RH6-II phase is formed as a result of energy minimization under strain when the pristine graphene buckles rather than stretches further or tear. This structural change decreases the overall elastic energy of the system leading to a stable, non-planar configuration. Though the atomic connectivity of graphene remains intact, the out-of-plane deformation significantly alters its physical properties. Electronically, the RH6-II morphology can induce changes in the band structure of graphene. Local curvature generates strain fields that open small bandgaps or produce pseudomagnetic effects, which are absent in pristine graphene.

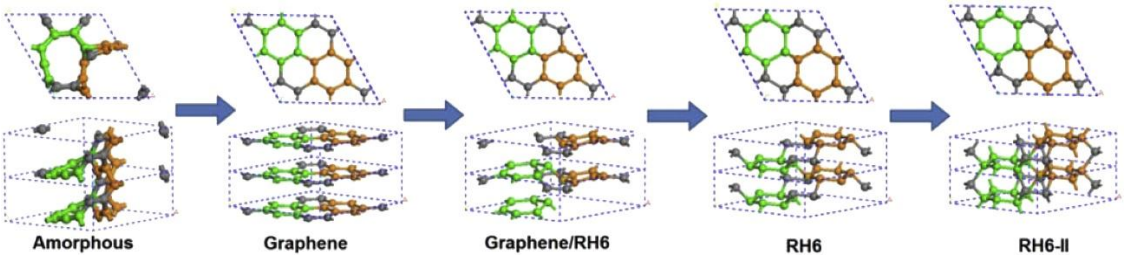

Figure 1: Mechanical synthesis of morphed graphene. Reprinted with permission.

Morphed graphene is characterized by astonishing properties as mechanical reinforcement agent in a wide range of matrices in concentrations ranging from 1 wt% up to 5 wt.% [7-10] showing mechanical properties improvements of up to 2 orders of magnitude with an increase of 73%, 25% and 250% in elastic energy ratio, hardness and toughness [7-11]. On the other hand, morphed graphene electrical properties are not well described and actually neglected in the composite science. Accordingly, this work will investigate the electrical properties of morphed graphene containing polymeric composites in both DC and AC regimes also considering how the surface properties are changing in a wide range of filler concentration.

2 MATERIALS AND METHODS

2.1. MATERIALS

The morphed graphene was manufactured using PetCoke a very abundant oil-and-gas soot byproduct. The PetCoke was ground in a Nutribullet® for periods of 1 minute at a time until fine powder (-150 mesh) was produced. The fines are collected and milled for periods of 1 h to 10 h in a Spex mill. The final product is morphed graphene (MG). The Spex procedure was previously reported in [4, 5, 12].

Poly(vinylbutyral)(PVB) was purchased by Sigma Aldrich and used without any further purification.

Composites were prepared by mechanically mixing morphed graphene with PVB in acetone and cast into molds until the solvent was evaporated.

2.2 CHARACTERIZATIONS

Raman spectroscopy was performed using a Renishaw inVia spectrometer (H43662 model, Gloucestershire, UK) equipped with 514 nm laser line with a 100× objective. Raman spectrum was recorded in the range from 250 cm^{-1} to 4000 cm^{-1}. Raman spectrum was fitted by using the methodology proposed by Tagliaferro et al. [13].

Morphed graphene morphology was studied by using a field emission scanning electron microscope (FESEM, Zeis SupraTM40, Oberkochen, Germany) equipped with an energy dispersive X-ray detector (EDX, Oxford Inca Energy 450, Oberkochen, Germany).

XRD analysis were run on a powder sample using aPanalytical X'PERT PRO PW3040/60 diffractometer, with Cu K αradiation at 40 kV and 40 mA, Panalytical BV, Almelo in the 2θ range from 10 to 80 °with a step size of 0.013 °.

The wetting properties were investigated by optical contact angle (OCA) measurements with the sessile drop technique, using an OCAH 200 (DataPhysic Instruments). Two different liquid probes were used: water (H_2O) and diiodomethane (CH_2I_2). Each liquid drop (1 µL in volume) was dispensed, and the image of the drop on the sample was acquired with the integrated high-resolution camera. The drop profiles were extracted and fitted with dedicated software (SCA20) using the Young-Laplace method, and contact angles at the liquid-solid interface between fitted function and baseline were calculated. For each sample and each liquid probe, the contact angle measurement was repeated three times on different areas. The polar and dispersive components if the surface energy were evaluated by applying the Owens-Wendt method [14].

The DC electrical conductivity of the composites was measured at room temperature (295 K) by electrically contacting the composite samples in the four-point van der Pauw configuration by using thin gold wires and conducting silver paste (RS Components, Sesto San Giovanni, Italy). The resistance of each van der Pauw configuration was measured using the four-probe resistance option of a 34410 multimeter (Keysight Technologies, Santa Rosa, CA, USA). The conductivity was then calculated as $\sigma = R_s^{-1}t^{-1}$, where R_s is the sheet resistance obtained by solving the van der Pauw equation, and t is the thickness of the material.

The complex permittivity of the samples was measured in the GHz range by means of a cylindrical coaxial cell (EpsiMu toolkit [15]), containing the sample as a spacer between inner and outer conductors, whose diameters are 0.6 cm and 1.3 cm, respectively. Two conical parts link the cell to standard connectors, allowing it to keep the characteristic impedance to 50 W, thus avoiding mismatch and energy loss. The cell is connected to a ZVK Vector Network Analyzer (Rohde & Schwarz GmbH, Munich, Germany), suitably calibrated, and measurements are analyzed with a two-port transmission line technique. The electromagnetic properties of the sample are determined by de-embedding and the Nicolson-Ross-Weir transmission/reflection algorithm [16, 17].

3 RESULTS

3.1 Physico-chemical properties of MG and related composites

Morphed Graphene was analyzed using Raman spectroscopy in the range from 250 cm^{-1} to 4000 cm^{-1} as reported in Figure 2.

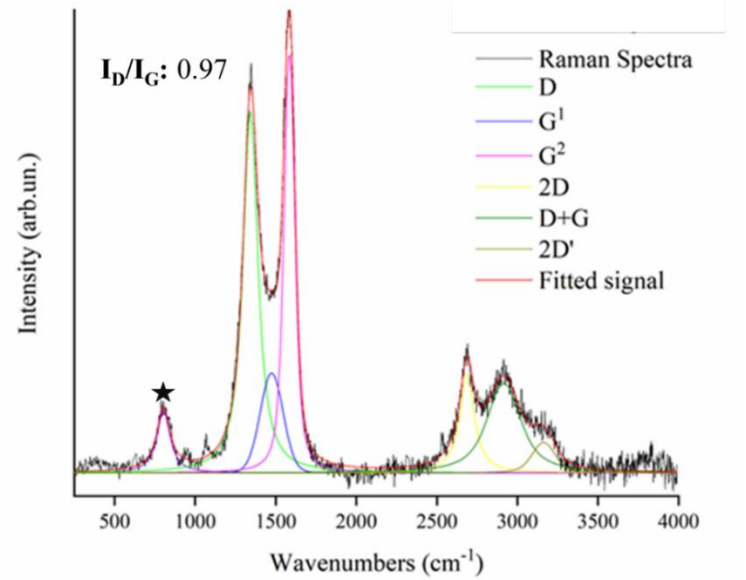

Figure 2: Raman spectra of morphed graphene in the range from 250 cm^{-1} to 4000 cm^{-1} fitted accordingly with the procedure reported by Tagliaferro et al.[13]

As shown in Figure 2, the D and G peaks are represented by a component (named D) centered at 1343 cm^{-1} and two components named G^1 and G^2 centered at 1480 cm^{-1} and 1580 cm^{-1} respectively [18]

while the 2D region is composed by three components known as 2D, D+G, 2D centered at 2687, 2915 and 3163 cm^{-1} respectively. According to Shimoidara et al. [19], the G^2 peak is originated from graphitic domains characterized by a high order of bond angle while G^1 arises from amorphous domains with greater disorder. The ration between G^1 and G^2 can be used for the evaluation of bond angle disorder and morphed graphene is characterized by a value of 0.41 inferior that is considerably lower than non-activated carbon black that is close to 0.6 [19]. This suggest that the milling process promotes a greater angular order, as also evidenced by the ID/IG ratio of 0.97. Such a value suggests the presence of a long-range structural order, comparable to that observed in non-graphitizable carbon treated at high temperatures [20-29]. Moreover, the calculated volumetric crystallite size L_a is 17.2 nm [30]. It is also noticed the presence of a peak centered at 863 cm^{-1} (marked with a star) due to iron oxide trace or organic-rich residue from the original pet coke [31].

Morphed Graphene was analyzed using XRD spectroscopy in the range from 10° to 80° as reported in Figure 3.

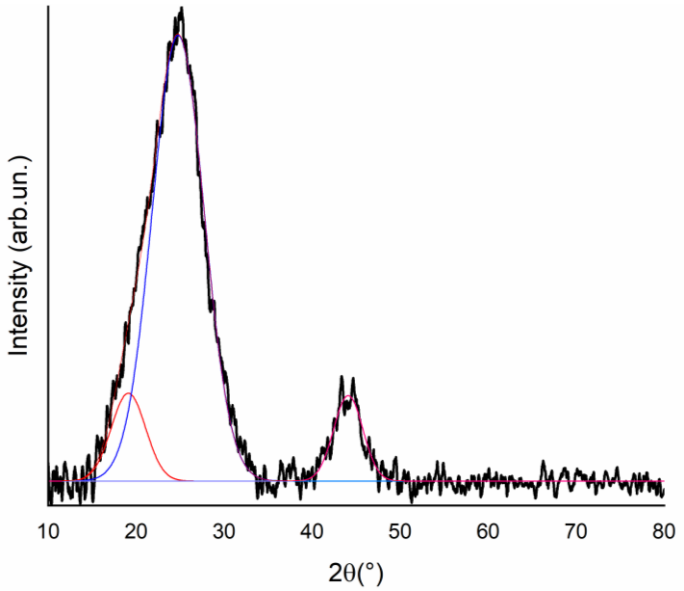

Figure 3: XRD spectra of morphed graphene between 10 to 80°.

XRD spectra show three large components centered at 19.1, 24.7 and 44.1° respectively as reported by Calderon et al. [4] due to different lattice modes. Using the component at 24.7° (basal lattice mode), RH6-IIa phase with a crystallite size of 1.52±0.29 nm calculated using Scherrer equation [32] in agreement with TEM data reporter by Calderon et al. [4].

The morphological analysis reported in Figure 4 showed the presence of round shaped particles with an average size of 41±6 nm and a carbon content of up to 90.2 wt.% and an oxygen amount of 9.8.

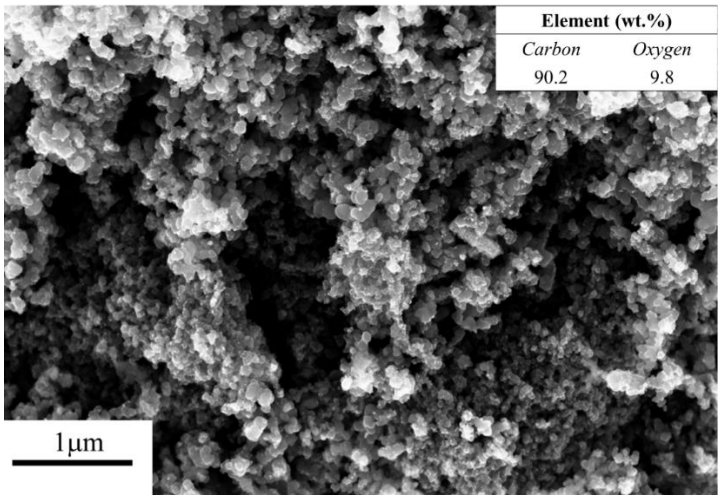

Figure 4: Morphological and elemental analysis of RH6-II.

For both atmosphere (air and argon, see Figure 5) the TGA of morphed graphene have a weight loss between 25 and 100 °C due to the moisture of the sample. In air atmosphere there is a significant weight loss starting around 350 °C, with a rapid decomposition occurring up to approximately 550 °C, after which the weight stabilizes, indicating complete degradation of the combustible components. This sharp weight loss suggests oxidative degradation. In contrast, under an argon atmosphere, the weight loss is more gradual and continues over the entire temperature range. This indicates that in the absence of oxygen, the material decomposes more slowly, likely through pyrolysis rather than combustion. Overall, the data highlights the strong influence of the atmospheric environment on the thermal degradation behavior of the material.

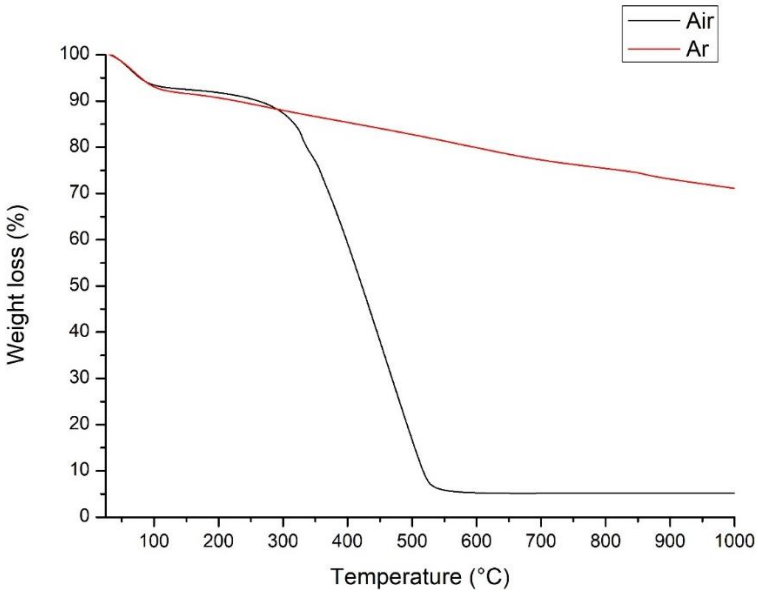

Figure 5: Thermogravimetric analysis (TGA) of morphed graphene in argon and air condition.

As shown in Figure 6, the superficial energy of the composite system, determined from contact angle measurements showed a two-regime behavior as a function of RH6-II content. In the low concentration range up to 40 wt.%, the superficial energy remains almost constant at 40 mN/m, indicating that the addition of RH6-II does not significantly alter the wettability of the composite surface. This suggests that RH6-II particles were either well embedded within the PVB matrix or did not form a continuous

surface layer that modifies the overall surface chemistry. Above a threshold concentration of 50 wt.%), a sharp increment in superficial energy was observed together with a strong linear dependence on RH6-II content ($R^2 \approx 0.98$). This drastic change supported a percolation-like behavior where RH6-II particles begin to dominate the surface properties. The structure of RH6-II, characterized by a hierarchical arrangement of conductive domains and amorphous regions, plays a crucial role in this transition. At low concentrations, the polymer matrix drives the surface properties whereas at high concentrations, RH6-II's intrinsic surface chemistry, including its potential oxygen-containing functional groups and rough morphology, enhance the surface energy.

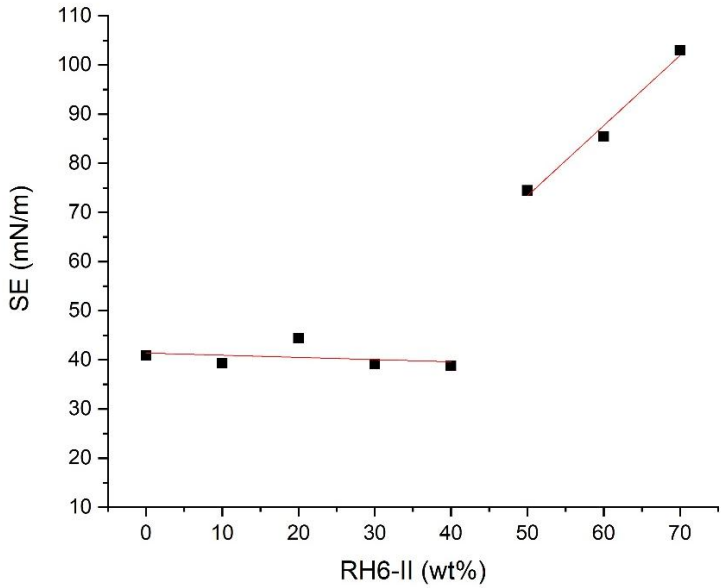

Figure 6: Contact angle measurement of RH6-II loaded PVB composites.

As shown in Figure 7, the DC electrical conductivity measurements revealed clear percolative behavior in the PVB-based composites containing RH6-II as a conductive filler. For RH6-II loadings lower than 10 wt.%, no measurable conductivity values were obtained, and therefore these points are not reported in the figure. This suggests that at such low filler content, the RH6-II particles remain too isolated to establish conductive paths, and the composite maintains an insulating behavior similar to that of neat PVB (1×10^{-13} S m^{-1} {Roy, 2014 #500}) due to the too dispersed filler particles being unable to form percolating conductive pathways. A dramatic increase in DC conductivity by nearly 10 orders of magnitude ($6.6\pm2.7\times10^{-4}$ S m^{-1}) was observed at a RH6-II loading of 10%, which indicates the successful establishment of a percolative conductive network across the sample. Increasing the filler content up to a RH6-II loading of 50% results in a further increment of the DC conductivity by another order of magnitude (up to a value of $8.9\pm0.4\times10^{-4}$ S m^{-1}) with no sign of saturation. Indeed, the inset to Figure 6 shows that the experimental conductivity values as a function of the filler concentration are in fair agreement with the expected behavior for a percolative network

$$\sigma \propto (x - x_c)^{\beta}$$

where σ is the DC conductivity, x is the concentration of conductive particles, x_c is the critical concentration for percolation, and β is the percolation exponent. The fit to our experimental data gives $\beta \approx 1.5$, as expected for a standard three-dimensional network {Kirkpatrick, 1973 #501} and indicates that the improvement in conductivity can be largely ascribed to an increment in the percolation probability in the entire RH-II loading range. As the filler content exceeds 50 wt.%, conductivity may approach saturation, resembling the behavior of a conductive network with an insulating phase dispersed within it. Compared to other conductive fillers, RH6-II provides distinct advantages: whereas graphene offers high conductivity, its dispersion in polymer matrices is challenging, and sedimentation can disrupt electrical continuity. Carbon black, on the other hand, consists of nanometric spherical particles with lower intrinsic conductivity than RH6-II, requiring higher loadings to achieve percolation. The observed

percolative behavior in RH6-II-based composites confirms its potential as an effective conductive filler, with possible applications in electromagnetic shielding, EMI attenuation, and flexible electronics.

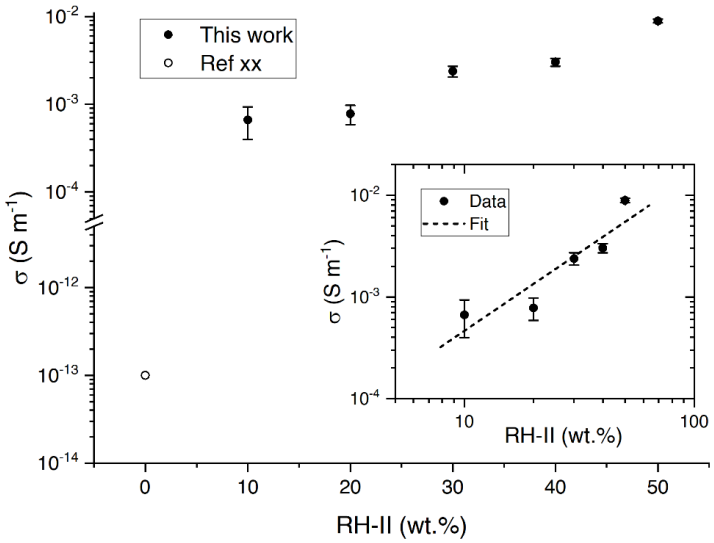

Figure 7: DC electrical conductivity of RH6-II loaded PVB composites in ambient conditions (filled circles) and literature value for neat PVB (hollow circle) {Roy, 2014 #500}. Inset shows the same data in bilogarithmic scale (filled circles) with the fit to standard percolation theory (dashed line).

3.2 Modelling of shielding properties of MG containing composites

The electromagnetic shielding properties in the GHz frequency range can be modelled starting from the microwave characterization, in terms of the complex permittivity $\varepsilon = \varepsilon' - j\varepsilon''$. The real part of the permittivity for the reference PVB is shown as a function of frequency in the lower panel of Figure 8, while its increments $\Delta\varepsilon'$ in composites with different RH6-II contents – with respect to the neat material – are shown in the upper panel.

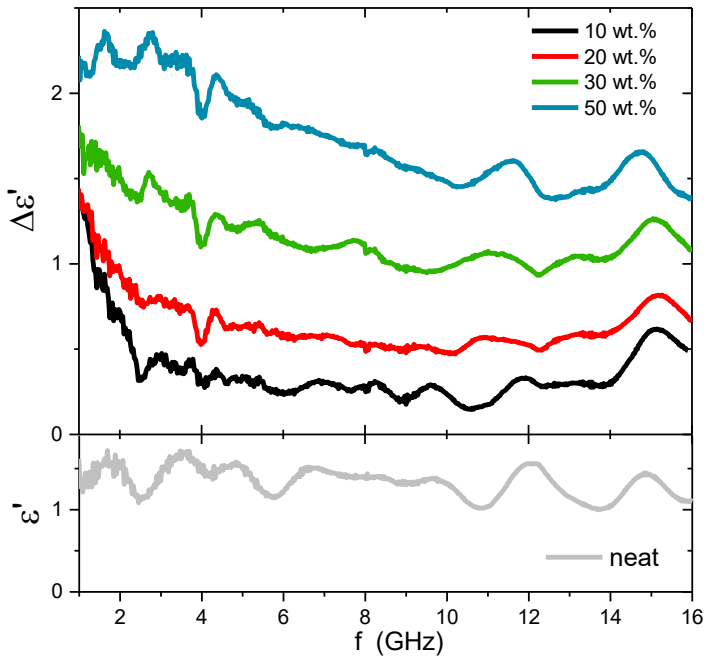

Figure **8**: Real part of the complex permittivity for the reference PVB sample (lower panel) and its increments in composites with different RH**6**-II contents (upper panel).

The AC conductivity σ is related to the imaginary part of the permittivity by $\varepsilon'' = \sigma/\omega\varepsilon_0$. In Figure **9**, the AC conductivity as a function of the RH**6**-II content, obtained at different frequencies, is compared to the DC conductivity already reported in Figure 7.

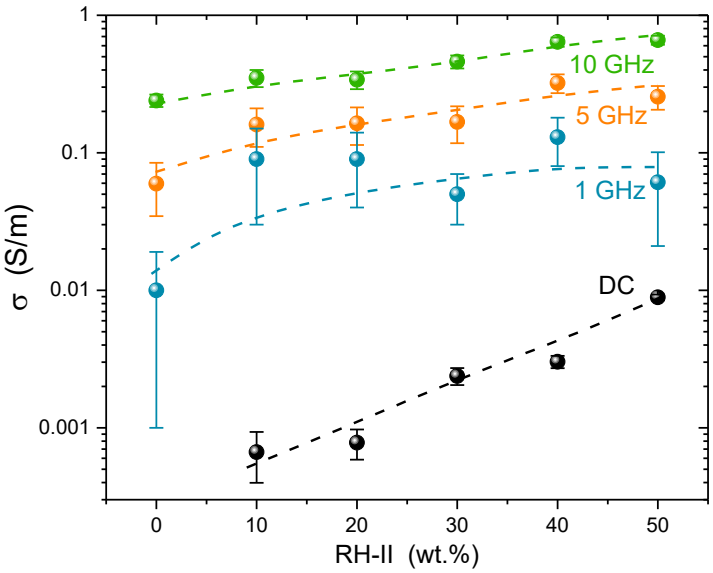

Figure **9**: DC and AC conductivity for composites with different RH-II contents. Lines are guides to the eye.

Finally, the ratio of the imaginary to the real part of the complex permittivity gives the loss tangent, that can be used together with the conductivity in the formulae reported in Ref. 28 to calculate the overall electromagnetic shielding efficiency

$$\boldsymbol{SE = 10\, log_{10}\left(\frac{P_i}{P_t}\right)}$$

as a sum of absorption, reflection, and multiple-reflection contributions (here, $\boldsymbol{P_i}$ and $\boldsymbol{P_t}$ are the incident power and the power transmitted through the shield, respectively). It turns out that the dominant term is the absorption one, and that a significant shielding efficiency can be obtained at frequencies above about 3 GHz (Figure 10).

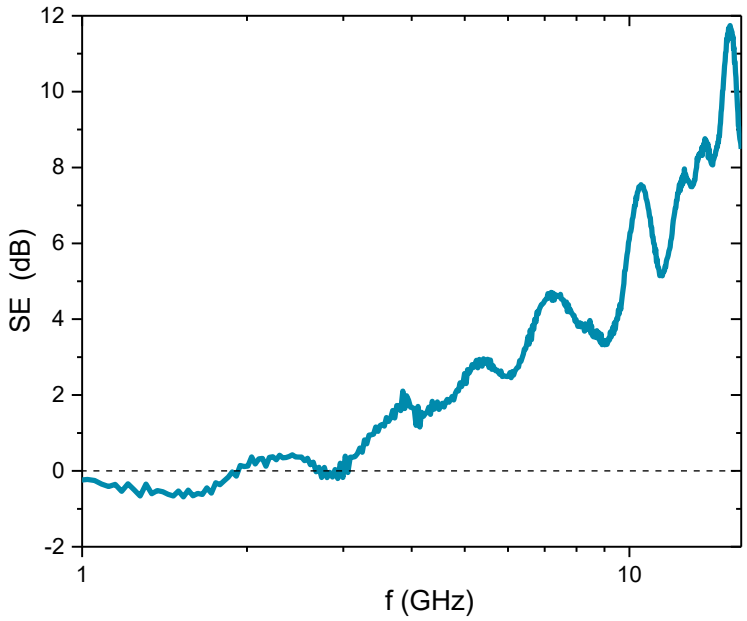

Figure 10: shielding efficiency for a 10-mm-thick composite with RH6-II content of 50 wt.%, as a function of frequency.

4. CONCLUSIONS

In this study, we investigated the electrical properties of RH6-II in both AC and DC regimes by incorporating morphed graphene into a filmable polymeric matrix. The analysis of physicochemical properties allowed us to draw a complete picture of the exotic RH6-II supporting our further considerations based on solid structural insights. Electrical analysis highlighted a stable charge transport mechanism over the examined frequency domain with SE dominated by absorption mechanism. The evaluation on a 10 mm RH6-II based composite showed that SE increased significantly above 3 GHz supporting the utilization of these species for high-frequency electromagnetic interference in which multiple layers of the composites are added. Accordingly, these materials can be used in aerospace layered composites as engineered connection layers between structural ones or in advanced communication devices such as those operating using 5G technology and electronic components that demand robust EMI protection without requirements of thickness. Furthermore, the combination of mechanical flexibility and processability of these composites together with their SE properties can find application in smart devices for biomedical applications including in vivo sensors due also to the high surface energy that can prevent the proliferation of bacterial biofilm.

ACKNOWLEDGEMENTS

Erik Piatti acknowledges funding by the European Union - Next Generation EU as part of the PRIN 2022 PNRR project “Continuous THERmal monitoring with wearable mid-InfraRed sensors” (P2022AHXE5).

REFERENCES

[1] H.W. Kroto, J.R. Heath, S.C. O'Brien, R.F. Curl, R.E. Smalley, C60: Buckminsterfullerene, nature, 318 (1985) 162-163.
[2] L. Radushkevich, V.á. Lukyanovich, O strukture ugleroda, obrazujucegosja pri termiceskom razlozenii okisi ugleroda na zeleznom kontakte, Zurn Fisic Chim, 26 (1952) 88-95.
[3] K.S. Novoselov, A.K. Geim, S.V. Morozov, D.-e. Jiang, Y. Zhang, S.V. Dubonos, I.V. Grigorieva, A.A. Firsov, Electric field effect in atomically thin carbon films, science, 306 (2004) 666-669.
[4] H.A. Calderon, I. Estrada-Guel, F. Alvarez-Ramírez, V.G. Hadjiev, F.C. Robles Hernandez, Morphed graphene nanostructures: Experimental evidence for existence, Carbon, 102 (2016) 288-296.
[5] H. Calderon, F.A. Ramírez, I.E. Guel, V. Hadjiev, F.R. Hernandez, Electron Microscopy of Morphed Graphene Nanostructures Synthesized by Mechanical Milling, Microscopy and Microanalysis, 22 (2016) 1250-1251.
[6] H. Calderon, A. Okonkwo, I. Estrada-Guel, V. Hadjiev, F. Alvarez-Ramírez, F. Robles Hernández, HRTEM low dose: the unfold of the morphed graphene, from amorphous carbon to morphed graphenes, Advanced Structural and Chemical Imaging, 2 (2016) 1-12.
[7] H. Calderon, F.A. Ramirez, D. Barber, V. Hadjiev, A. Okonkwo, R.O. Olivares, I.E. Guel, F.R. Hernandez, Enhanced elastic behavior of all-carbon composites reinforced by in-situ synthesized morphed graphene, Carbon, 153 (2019) 657-662.
[8] O. Velazquez-Meraz, J.E. Ledezma-Sillas, C. Carreño-Gallardo, W. Yang, N.M. Chaudhari, H.A. Calderon, I. Rusakova, F.C. Robles Hernandez, J.M. Herrera-Ramirez, Improvement of physical and mechanical properties on bio-polymer matrix composites using morphed graphene, Composites Science and Technology, 184 (2019) 107836.
[9] A. Raghatate, F.D. Cortes Vega, O. Velazquez Meraz, K. Ahmadi, N.M. Chaudhari, D. Solanki, A.B. Puthirath, N. Castaneda, P.M. Ajayan, J.M. Herrera Ramirez, Sustainable biocomposites for structural applications with environmental affinity, ACS Applied Materials & Interfaces, 14 (2022) 17837-17848.

[10] J.M. Mendoza-Duarte, I. Estrada-Guel, F.C. Robles-Hernandez, C. Carreño-Gallardo, C. López-Meléndez, R. Martínez-Sánchez, Mechanical and microstructural response of an aluminum nanocomposite reinforced with carbon-based particles, Materials Research, 19 (2016) 13-19.
[11] O. Velazquez-Meraz, J. Ledezma-Sillas, C. Carreño-Gallardo, W. Yang, N. Chaudhari, H. Calderon, I. Rusakova, F.R. Hernandez, J. Herrera-Ramirez, Improvement of physical and mechanical properties on bio-polymer matrix composites using morphed graphene, Composites Science and Technology, 184 (2019) 107836.
[12] H. Calderon, A. Okonkwo, I. Estrada-Guel, V. Hadjiev, F. Alvarez-Ramírez, F.R. Hernández, HRTEM low dose: the unfold of the morphed graphene, from amorphous carbon to morphed graphenes, Advanced Structural and Chemical Imaging, 2 (2017) 10.
[13] A. Tagliaferro, M. Rovere, E. Padovano, M. Bartoli, M. Giorcelli, Introducing the novel mixed gaussian-lorentzian lineshape in the analysis of the raman signal of biochar, Nanomaterials, 10 (2020) 1748.
[14] D.K. Owens, R. Wendt, Estimation of the surface free energy of polymers, Journal of applied polymer science, 13 (1969) 1741-1747.
[15] D. Ba, P. Sabouroux, Epsimu, a toolkit for permittivity and permeability measurement in microwave domain at real time of all materials: Applications to solid and semisolid materials, Microwave and optical technology letters, 52 (2010) 2643-2648.
[16] A. Nicolson, G. Ross, Measurement of the intrinsic properties of materials by time-domain techniques, IEEE Transactions on instrumentation and measurement, 19 (1970) 377-382.
[17] J. Baker-Jarvis, E.J. Vanzura, W.A. Kissick, Improved technique for determining complex permittivity with the transmission/reflection method, IEEE Transactions on microwave theory and techniques, 38 (1990) 1096-1103.
[18] A. Orlando, F. Franceschini, C. Muscas, S. Pidkova, M. Bartoli, M. Rovere, A. Tagliaferro, A comprehensive review on Raman spectroscopy applications, Chemosensors, 9 (2021).
[19] N. Shimodaira, A. Masui, Raman spectroscopic investigations of activated carbon materials, Journal of Applied Physics, 92 (2002) 902-909.
[20] R. Arrigo, M. Bartoli, G. Malucelli, Poly(lactic Acid)-biochar biocomposites: Effect of processing and filler content on rheological, thermal, and mechanical properties, Polymers, 12 (2020).
[21] M. Bartoli, D. Duraccio, M.G. Faga, E. Piatti, D. Torsello, G. Ghigo, G. Malucelli, Mechanical, electrical, thermal and tribological behavior of epoxy resin composites reinforced with waste hemp-derived carbon fibers, Journal of Materials Science, 57 (2022) 14861-14876.
[22] M. Bartoli, M. Giorcelli, C. Rosso, M. Rovere, P. Jagdale, A. Tagliaferro, Influence of commercial biochar fillers on brittleness/ductility of epoxy resin composites, Applied Sciences (Switzerland), 9 (2019).
[23] M. Bartoli, M.A. Nasir, P. Jagdale, E. Passaglia, R. Spiniello, C. Rosso, M. Giorcelli, M. Rovere, A. Tagliaferro, Influence of pyrolytic thermal history on olive pruning biochar and related epoxy composites mechanical properties, Journal of Composite Materials, 54 (2020) 1863-1873.
[24] M. Bartoli, D. Torsello, E. Piatti, M. Giorcelli, A.C. Sparavigna, M. Rovere, G. Ghigo, A. Tagliaferro, Pressure-Responsive Conductive Poly(vinyl alcohol) Composites Containing Waste Cotton Fibers Biochar, Micromachines, 13 (2022).
[25] M. Bartoli, M. Troiano, P. Giudicianni, D. Amato, M. Giorcelli, R. Solimene, A. Tagliaferro, Effect of heating rate and feedstock nature on electrical conductivity of biochar and biochar-based composites, Applications in Energy and Combustion Science, 12 (2022).
[26] A. Bifulco, M. Bartoli, I. Climaco, M.C. Franchino, D. Battegazzore, R.A. Mensah, O. Das, H. Vahabi, G. Malucelli, A. Aronne, C. Imparato, Coffee waste-derived biochar as a flame retardant for epoxy nanocomposites, Sustainable Materials and Technologies, 41 (2024).
[27] S. Lepak-Kuc, M. Kiciński, P.P. Michalski, K. Pavlov, M. Giorcelli, M. Bartoli, M. Jakubowska, Innovative biochar-based composite fibres from recycled material, Materials, 14 (2021).
[28] D. Torsello, M. Bartoli, M. Giorcelli, M. Rovere, R. Arrigo, G. Malucelli, A. Tagliaferro, G. Ghigo, High frequency electromagnetic shielding by biochar-based composites, Nanomaterials, 11 (2021).
[29] D. Torsello, G. Ghigo, M. Giorcelli, M. Bartoli, M. Rovere, A. Tagliaferro, Tuning the microwave electromagnetic properties of biochar-based composites by annealing, Carbon Trends, 4 (2021).

[30] F. Tuinstra, J.L. Koenig, Raman Spectrum of Graphite, The Journal of Chemical Physics, 53 (1970) 1126-1130.
[31] C. Phillippi, K. Mazdiyasni, Infrared and Raman spectra of zirconia polymorphs, Journal of the American Ceramic Society, 54 (1971) 254-258.
[32] A. Monshi, M.R. Foroughi, M.R. Monshi, Modified Scherrer equation to estimate more accurately nano-crystallite size using XRD, World journal of nano science and engineering, 2 (2012) 154-160.

OPTIMIZING HIERARCHICAL CARBON NANOTUBE-GRAFTED CARBON FIBER PRODUCTION

Hassan A Almousa[1], David B Anthony[2], Diana-Ioana Bratilescu[3], Hugo G De Luca[4], Emile S Greenhalgh[5], Alexander Bismarck[6], Milo SP Shaffer[7]

[1] Materials Department, Imperial College London
South Kensington Campus, London, SW7 2AZ, United Kingdom
h.almousa19@imperial.ac.uk, https://www.researchgate.net/profile/hassan-almousa-5

[2] Chemistry Department, Imperial College London
White City Campus, London, WC12 0BZ, United Kingdom
d.anthony08@imperial.ac.uk, https://profiles.imperial.ac.uk/d.anthony08

[3] Institute of Materials Chemistry, Faculty of Chemistry, University of Vienna
Währinger Strasse 42, 1090, Vienna, Austria
diana-ioana.bratilescu@univie.ac.at, https://www.researchgate.net/profile/diana-bratilescu

[4] Materials Department, Imperial College London
South Kensington Campus, London, SW7 2AZ, United Kingdom
hugo.de-luca14@imperial.ac.uk, https://www.researchgate.net/profile/hugo-de-luca

[5] Aeronautics Department, Imperial College London
South Kensington Campus, London, SW7 2AZ, United Kingdom
e.greenhalgh@imperial.ac.uk, https://profiles.imperial.ac.uk/e.greenhalgh

[6] Institute of Materials Chemistry, Faculty of Chemistry, University of Vienna
Währinger Strasse 42, 1090, Vienna, Austria
alexander.bismarck@univie.ac.at,
https://mc.univie.ac.at/polymer-composite-engineering-group/people/head-of-the-group

[7] Chemistry Department and Materials Department, Imperial College London
White City Campus, London, WC12 0BZ, United Kingdom
m.shaffer@imperial.ac.uk, https://profiles.imperial.ac.uk/m.shaffer

Keywords: Carbon fiber; Nano-structures; Fiber/matrix bond; Surface properties; Statistical properties/methods; Chemical vapor deposition (CVD)

ABSTRACT

The promise of state-of-the-art-fiber reinforced composites containing carbon nanotube-grafted-carbon fibers has been in development since the early 90s. The main hurdle to manufacturing a hierarchical reinforced composite coupon/component, is the volume of modified fibers required. This requirement, is in turn dependent on repeatable, well-controlled and robust growth regime to ensure that the carbon nanotube coverage is uniform and consistent along the fibers, and subsequently throughout the composite. Failure to ensure that the modification is constant can result in stress concentrations in the regions of the fibers with variable length/coverage. Whilst there has been some limited development in woven fabrics being modified by growing carbon nanotubes in closed chemical vapor deposition (CVD) tubular reactors; to achieve a route towards industrial scale-up modification of the fiber tow is required, as well an open CVD reactor to facilitate the fibers being passed through the reactor unimpeded making the process continuous. The production of spool-to-spool open CVD on whole carbon fiber tows has been reported previously, but with limited evidence of prolonged and robust conditions, or a constant carbon nanotube-grafted-carbon fiber product over tens or more meters. Presented here are results of optimizing the carbon nanotube growth process on carbon fiber 12K tow in a bespoke open CVD reactor.

1 INTRODUCTION

The incorporation of high-performance nanomaterials like carbon nanotubes (CNTs) at the critical fiber-matrix interface in composites have been proposed to address an inherent weakness. One method to introduce these nanomaterials at this particular interfacial region is to produce hierarchical fibers (exhibiting two length scales of reinforcement), for example carbon nanotubes grafted/grown on the surface of carbon fibers (CNT-g-CFs). Particularly promising is the improved apparent interfacial shear strength of the fiber-matrix interphase of CNT-g-CFs with thermoplastic matrices shown at the single fiber level (+53%, polypropylene) when compared to an unsized carbon fiber baseline [1].

Yet, the increased production of hierarchical fibers is a challenge due to growth conditions for CNTs necessitating high temperatures and an inert environment, further complicated because carbon fibers are susceptible to damage in the process [2]. Parameters were identified to synthesize CNT-g-CF without loss of performance of the underlying fiber at the 12K tow level and in a continuous process (spool-to-spool) [3], and attention turned to increasing the scale of production. CNT chemical vapor deposition (CVD) growth conditions are notoriously sensitive to activation/reduction gases, availability of carbon feedstock as well as the catalysts composition/loading on the substrate, additionally influenced by the temperature on reaction rates and catalyst wettability kinetics; and in a continuous in-line process the fiber pull-through rate which is linked to dwell duration in reduction/growth regions. Achieving robust production of CNT-g-CFs for a prolonged duration and to modify a significant length of tow has therefore been difficult.

We present our latest work using a reaction snap-shot methodology developed from [4], which was employed to glean information at various positions inside the reactor. With these insights, reactor conditions were altered and extended CNT-g-CF production achieved with controlled lengths of 300 to 1000 nm growth of multiwalled CNTs with diameters ~10 nm (+30 m 12K tow, 16 h in a single session). To fully evaluate the CNT-g-CF we developed a protocol which was reliable and provided an unbiased evaluation (using sections of up to 10 m long 12K tow). The protocol included a machine learning evaluation script inspecting electron micrographs and determining if CNTs were present on the fiber surface and the whole tow was examined to determine intra-tow regions (and full coverage of nanotubes). Average CNT coverage (uniformity) along the length of tow was evaluated through global methods for example, additional weight gain from CNT growth which was correlated to gas sorption analytical analysis (specific surface area). Mechanical properties of composites made wholly from CNT-g-CFs will also be presented at the conference.

2 MATERIALS AND METHODS

- Polyacrylonitrile (PAN)-based unsized carbon fiber (AS4-12K-7D, HS-CP-5000 grade) with diameter of 7.1 μm was supplied by Hexcel Composites (Duxford, GB), and used as a continuous tow of 12K fibers.

- The precursor bi-catalyst solution for carbon nanotube synthesis consisted of nickel (II) acetylacetonate (≥98%, VWR, GB) and iron (III) nitrate nonahydrate (≥98% ACS reagent, Merck, DE) in ethanol (96%, Brenntag, AT) in a 1:0.64 mol, respectively.

- The carbon source, reduction, and carrier gases for the reactions was acetylene in nitrogen (1.3 vol.% in 98.7 vol.%, respectively), hydrogen in nitrogen (2.4 vol.% in 97.6 vol.%, respectively), and nitrogen (99.998 vol.%), respectively. All gases were purchased from BOC gases, GB.

The equipment for CNT deposition and synthesis on carbon fibers is detailed elsewhere [3] and open CVD reactor shown in Figure 1. In short, unsized CFs were used as received, and then pre-deposited at a rate of 20 m/h with an in-line plasma oxidation pre-treatment, a bi-catalyst with a residence duration of 1 min and dried at 40 °C and 70 °C, producing approx. 200 m of treated tow. The collected and spooled precursor bi-catalyst deposited CFs were then passed, in inert conditions, through an open chemical vapor deposition reactor at 550 °C at varied at pull-through speeds of 1.92 m/h and 3.36 m/h

and subjected to reaction gases. After an initial inert gas sleeve, sequential regions of reaction gases for reduction (to activate the bi-catalyst), and a carbon rich gas (to grow the carbon nanotubes), and finally a second inert gas sleeve where the modified fibers were collected on a motorized spool. Fiber morphology was characterized by scanning electron microscopy (SEM), using a Zeiss Sigma 300 (DE) at an operating voltage 5 keV where whole 12K section of carbon fiber samples were sampled. ImageJ software (version 1.52p, NIH) [6] was used for image analysis. The specific surface area of samples was characterized following ISO 9277 Standard with gas sorption isotherms using nitrogen using a Quantachrome NOVAtouch gas sorption analyser (Anton Paar gmbH, AT) with Quantachrome TouchWin software (version 1.22, Anton Paar gmbH, AT) and BET (Brunauer, Emmett and Teller) method used to analyze collected data.

3 RESULTS

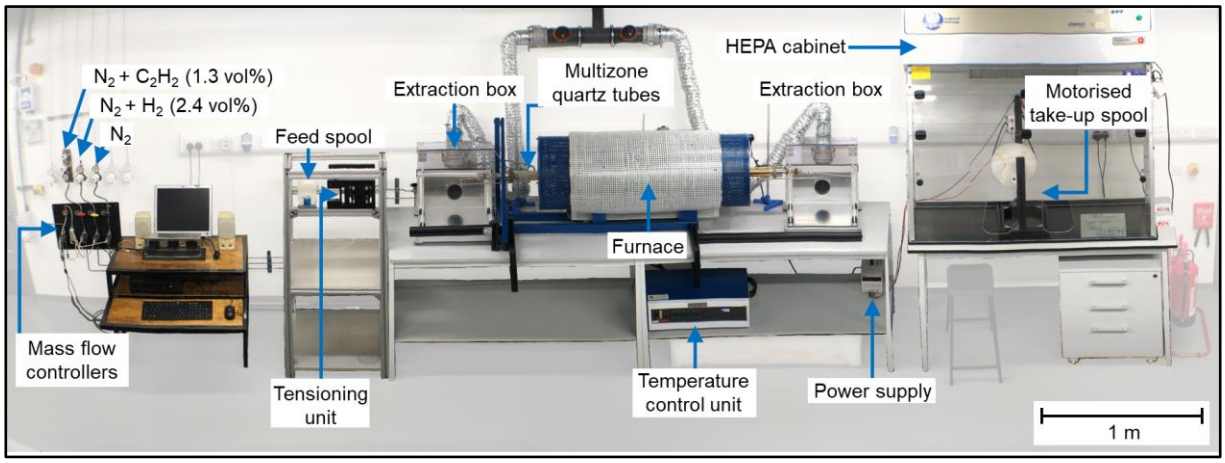

Figure 1: Overview of open CVD reactor showing continuous spool-to-spool configuration.



Figure 2: An example spool of CNT-g-CF used to determine the weight percentage of carbon nanotubes on the fiber after synthesis on open CVD line (12 m).

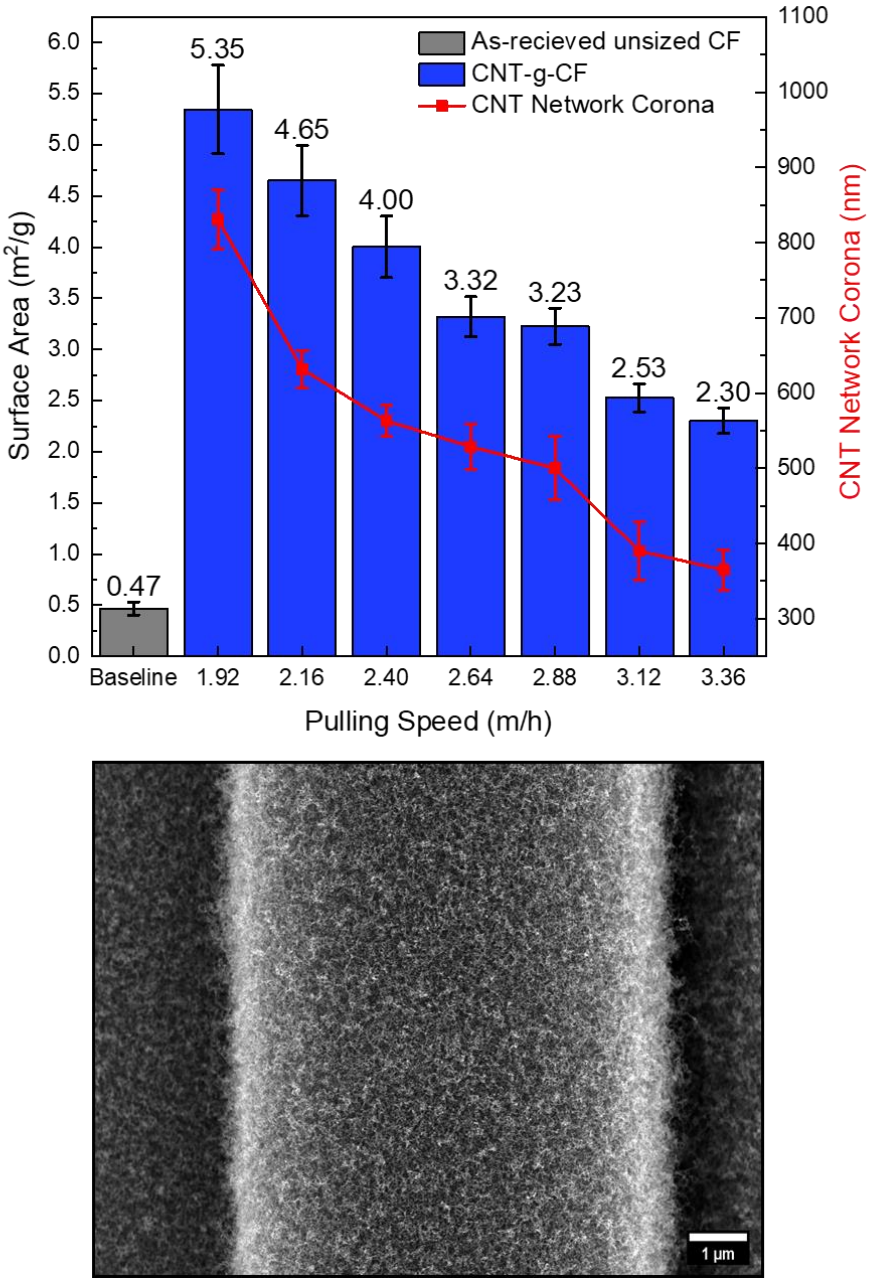

Figure 3: Top, Specific surface area measurements and CNT network corona length as a function of varying pull-through speeds, and Bottom, SEM micrograph of CNT-g-CF at a pulling speed of 1.92 m/h. Adapted from [5].

Sample	Specific surface area (m^2/g)	CNT weight percentage (wt. %)	CNT perpendicular thickness to fibre/corona (nm)
As-received unsized carbon fibre	0.47 ± 0.05	NA	NA
CNT-g-CF (1.92 m/h)	5.35 ± 0.38	2.9 †	856 ± 91
CNT-g-CF [ref. 3, y2020]	0.53 ± 0.05	0.1 *	126 ± 69

Table 1: Comparison between as-received fiber and previous CNT-g-CFs with optimized CNT-g-CF growth. Specific surface area determined BET analysis, relative increase in CNTs grown on the fiber surface as a weight percentage with † weight percentage determined though weighting spool using a balance and +10 m of modified 12K tow, * from ref. 3 weight percentage using specific surface area and geometric considerations and a specific surface area estimate of CNTs of 260 m^2/g to determine relative CNT loading (sample length ~0.15 m), and CNT length determined through scanning electron microscopy analysis.

4 DISCUSSIONS

The open CVD reactor conditions including reactive gas flow rates/relative concentrations, temperature, and pull-through speed were changed to determine a stable growth regime of CNTs on the carbon fiber [7]. Further details on the protocols including a machine learning evaluation script inspecting electron micrographs and determining if CNTs are present will also be included in this publication. Stable CNT growth was achieved for a standard modulus commercially available unsized 12K carbon fiber tow over a length +30 m with the specific surface area and weight uptake (Figure 2), and an extensive microscopy analysis was completed. A uniform growth at the currently optimized synthesis parameters produced a CNT-g-CF with perpendicular CNT forest growth ca. 850 nm, which for a ~7 µm fiber diameter will not impact the potential fiber volume fraction in a composite considering ideal hexagonal packing [3, detailed in supplementary information]. Once a baseline set of conditions was established, a second test to determine the effect of varying pull-through rate was performed with CNTs length and specific surface area of the resultant CNT-g-CFs characterized (Figure 3, Table 1). Note that due to the arrangement of the reactor, altering the pull-through rate changed the relative catalyst reduction duration as well as the CNT synthesis duration (inherently linked), which in turn also altered the overall dwell duration in the reactor (in a fixed configuration). When the pull-through speed is altered it is clear that this impacts both the corona length (perpendicular forest height from the fiber surface), and the surface area. These two properties are fundamentally linked as the growth of CNTs provides the main contribution of the specific surface area. Considering that the reduction and the growth duration are currently altered, modification to the CVD parameters for CNT growth could be altered further to increase CNT growth (corona length) or conversely increase pull-through speed for a desired CNT corona length.

A comparison to the previously published results [3], which detailed the initial concept and reactor design, clearly indicates that an improved CNT growth has been achieved, with an increase in CNT weight percentage on the order 250% and an increase in corona length of about 5 times.

5 CONCLUSIONS

The results presented are another step towards the scaled production of carbon nanotube-grafted-carbon fibers. The continued development to increase production of these hierarchical fibers over the past 5 years is clear, and a more robust growth regime with better understanding of the critical carbon nanotube open chemical vapor deposition synthesis parameters have been confirmed. The next stage of development for manufacturing carbon nanotube-grafted-carbon fibers should be directed toward implementation into larger furnaces and full tension creel-controlled systems. Further investigations into hierarchical fiber reinforcement should be made in parallel with larger coupons, and their performance in a range of matrices including thermoplastic and thermoset.

ACKNOWLEDGEMENTS

The authors kindly acknowledge the funding for this research provided by UK Engineering and Physical Sciences Research Council (EPSRC) programme Grant EP/T011653/1, Next Generation Fibre-Reinforced Composites (NextCOMP): a Full Scale Redesign for Compression a collaboration between Imperial College London and the University of Bristol. For the purpose of open access, the authors has applied a Creative Commons Attribution (CC BY) license to any author accepted manuscript version arising.

REFERENCES

[1] J. Wang, D.B. Anthony, C.A. Fuentes, H.G. De Luca, D. Zhang, A. Bismarck, A. Willem Van Vuure, M.S.P. Shaffer and D. Seveno, Wettability of carbon nanotube-grafted carbon fibers and their interfacial properties in polypropylene thermoplastic composite, *Composites Part A: Applied Science Manufacturing*, **159**, 2022, 106993, (doi: 10.1016/j.compositesa.2022.106993).

[2] H. Qian, A. Bismarck, E.S. Greenhalgh, G. Kalinka and M.S.P. Shaffer, Hierarchical Composites Reinforced with Carbon Nanotube Grafted Fibers: The Potential Assessed at the Single Fiber Level, *Chemistry of Materials*, **20**(5), 2008, pp. 1862-1869, (doi: 10.1021/cm702782j).

[3] D. Anthony, X. Sui. I. Kellersztein, H. De Luca, E. White, H. Wagner, E. Greenhalgh, A. Bismarck and M. Shaffer, Continuous carbon nanotube synthesis on charged carbon fibers. *Composites Part A: Applied Science and Manufacturing*, **112**, 2018, pp. 525-538 (doi: 10.1016/j.compositesa.2018.05.027).

[4] J. Qin, C. Wang, Z. Yao, Z. Ma, Q. Gao, Y. Wang, Q. Wang and H. Wei, Growing carbon nanotubes on continuous carbon fibers to produce composites with improved interfacial properties: A step towards commercial production and application, *Composites Science and Technology*, **211**, 2021, 108870, (doi: 10.1016/j.compscitech.2021.108870).

[5] H.A. Almousa, H.G. De Luca, D.B. Anthony, E.S. Greenhalgh, A. Bismarck and M.S.P. Shaffer. How can hierarchical composites with carbon nanotube-grafted carbon fibres enhance compression performance?, *Proceedings of the 21st European Conference on Composite Materials (ECCM21), Nantes, France, July 2-5, 2024,* Volume 8, Paper KCBE4, pp. 734-740, (doi: 10.60691/yj56-np80).

[6] C.A. Schneider, W.S. Rasband and K.W. Eliceiri, NIH Image to ImageJ: 25 years of image analysis, *Nature Methods*, **9**, 2012, pp. 671–675 (doi: 10.1038/nmeth.2089).

[7] H.A. Almousa, H.G. De Luca, D.B. Anthony, E.S. Greenhalgh, A. Bismarck, M.S.P. Shaffer, Dynamic Snapshot of Continuous Carbon Nanotube Growth on Carbon Fibers: From Sparse to Uniform and Controlled Growth, *In preparation*, 2025.

No Technical Paper Submission for:

Phoung Le

SIMULTANEOUS ELECTRO-MECHANICAL TESTING OF A STRUCTURAL BATTERY

T.E. Tay[1]*, K. Raju[1], V.B.C. Tan[1]
[1] Department of Mechanical Engineering, National University of Singapore, Singapore
*Corresponding author: mpetayte@nus.edu.sg

Keywords: 3-point bend test, structural battery composites, concurrent electrochemical-mechanical testing, composite current collectors

ABSTRACT

Structural batteries [1] combine structural load bearing capabilities with electrochemical functionalities. In order to achieve this dual purpose, the battery must be able to function electrically while sustaining mechanical loads. This work presents a simultaneous electromechanical (SEM) testing of a structural battery pouch cell under three-point flexural load while electrochemical testing. An important component is the current collectors, which are expected to function as conveyors of the electric current generated by the battery's electrochemical reactions, as well as possessing mechanical stiffness. This presentation also describes the selection of carbon fiber-based collectors considering the tensile properties and electrical resistivity of the fabricated current collectors. Current collectors fabricated using 5% PVDF (Polyvinylidene Fluoride) as the polymer matrix is used to fabricate PEO solid electrolyte based structural battery pouch cells employing Lithium Iron Phosphate (LFP) cathode and Lithium Titanium Oxide (LTO) anode, with a cellulose separator. In addition to conventional electrochemical testing of pouch cells, SEM tests are carried out to demonstrate the working of the cell under mechanical load and demonstrate the effect of mechanical loads on electrochemical performance. It is hoped that this and similar SEM tests will contribute to the development of eventual standards for the evaluation of structural batteries.

1 INTRODUCTION

Structural batteries are multi-functional material systems designed to store electro-chemical energy while serving as structural load bearing members of a system such as an electric vehicle. Structural batteries are a potential solution to improve drive range of electric vehicles, drones, etc. According to a study [2], the drive range of an electric car may be increased by 70% with the introduction of structural batteries while maintaining the weight of a vehicle.

Most structural battery prototypes published today employ liquid [3,4] or bicontinuous electrolytes [5–7]. Bicontinuous electrolytes suffer from the ionic conducting liquid phase squeezed out under certain loading conditions such as compression, as reported by Tavano *et al* [8]. In this work, a Polyethylene Oxide (PEO) based solid electrolyte [9] is used for developing the structural batteries. Carbon fibre is widely employed as an electrode in many prototypes and when carbon fibre is employed as an electrode, issues such as the high first cycle capacity loss make it difficult to balance charge capacity of the electrodes which is essential to fabricate full cells. In this work, carbon fibre is employed only as a current collector and Lithium Titanium Oxide (LTO) is used as the anode with Lithium Iron Phosphate (LFP) as the cathode.

Most structural battery research do not report the effect of mechanical loads on electrochemical cycling. This work aims to illustrate the importance of demonstrating the working and quantifying the effect of mechanical loads of structural battery prototypes. First, a suitable current collector is developed and selected for fabricating structural battery pouch cells with PEO based solid electrolyte and LFP and LTO electrodes. The developed prototype is tested in bending to demonstrate the effect of flexural loads on the electrochemical performance of the pouch cell.

2 METHODOLOGY

The development of current collectors by optimizing for the amounts of PVDF and electrically conductive carbon nanotubes (CNT) are discussed in section 2.1. The pouch cell fabrication and electrochemical testing is discussed in section 2.2. The simultaneous flexural and electrochemical testing of the pouch cells is reported in section 2.3

2.1 Current collector fabrication and testing

The carbon fibre based current collectors are fabricated from T300 unidirectional (UD) carbon fibres. The current collector needs to efficiently conduct current and bear loads. In this work since loose carbon fibres are not efficient in bearing various loads, a polymer matrix Polyvinylidene Fluoride (PVDF) is used to develop current collectors in this work termed as CF-PVDF current collectors. PVDF is used since it is a commonly used binder in battery electrode slurries, and known to not have any adverse side-reactions with other chemicals used in battery fabrication. However, PVDF is an insulator, so the quantity of the PVDF deposited must be optimized. Similarly, carbon nanotube suspensions (TUBALL^{TM}) used for improving battery electrode slurries are also applied on bare T300 carbon fibres to fabricate CF-CNT current collectors. The different current collectors fabricated are listed in Table 1.

Table 1: Fabricated composite current collectors

Materials	Sample label
pure Carbon fiber	CF
CF-PVDF made with 1%PVDF-DMF (Dimethylformamide) solution	1%CF-PVDF
CF-PVDF made with 5%PVDF-NMP (N-Methyl-2-Pyrrolidone) solution	5%CF-PVDF
CF-CNT coated twice	CF-CNT-2c
CF-CNT coated once	CF-CNT-1c
CF-CNT coated once and deposited PVDF	CF-CNT-PVDF

The various carbon fibre current collectors were fabricated and tested for their resistance and tensile behaviour as shown in the flowchart in Figure 1 below. The fabrication, testing methods and the development of current collectors are reported in more detail in [10]. The results of the resistance and tensile measurements are summarised in section 3.1 to guide the selection of the current collector.

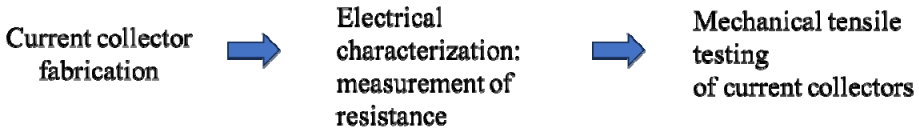

Figure 1: Current Collector development workflow

2.2 Pouch cell fabrication and testing

The LFP and LTO slurries and the PEO slurries are prepared as per the recipes in appendices A1 and A2 respectively. Once the slurries and the electrolyte are prepared, a battery can be fabricated with any of the current collectors described above. In this work, the 5% CF-PVDF current collector was used to fabricate pouch cells and carry out the simultaneous testing of electrochemical and mechanical loads since it exhibited relatively good electrical conductivity, tensile properties and is suitable for pouch cell fabrication, as explained later in section 3.1. Two current collectors (cut to 30-40 mm in length and 10-15mm width) are then coated with LFP and LTO slurries as shown in the leftmost images in Figure 2 and dried in an oven. A cellulose separator is coated with the PEO electrolyte on both sides and dried in an oven. The anode, the cellulose separator infused with the PEO electrolyte and cathode are assembled and placed in a pouch cell film which is partially sealed and vacuum dried at 80°C overnight to remove moisture. The dried pouch cell is then vacuum sealed. The whole fabrication procedure is shown in Figure 2.

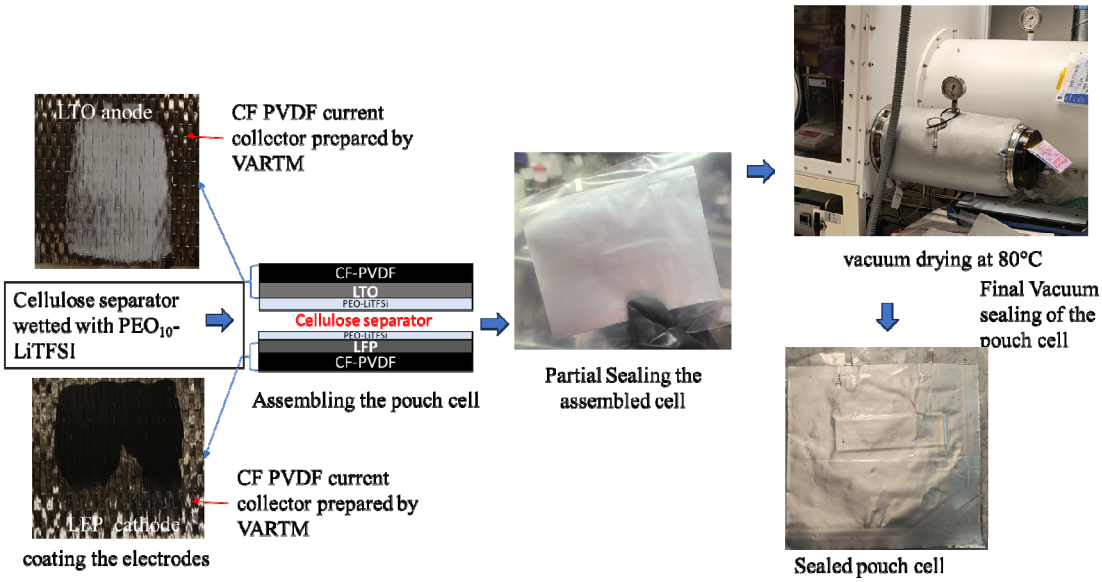

Figure 2: Pouch cell fabrication

The fabricated pouch cell was electrochemically tested at constant current magnitudes corresponding to rates of 0.1C and 0.2C at 60°C. The pouch cells were charged and discharged between 1 and 2.5V. The high temperature electrochemical performance is also compared to the cell's electrochemical performance at room temperature.

2.3 Simultaneous Electro-Mechanical (SEM) testing

Most research work [3–7,11] follows a sequential workflow of designing structural batteries, demonstrating the electrochemical performance of the battery and evaluate the mechanical behaviour (with tensile testing) of the structural battery as shown in Figure 3(c). The demonstration of electrochemical and mechanical performance in isolation (isolated multifunctionality) does not quantify and determine the electrochemical performance of the structural battery under mechanical loads (simultaneous multi-functionality). If structural batteries are to be practically realized, simultaneous electro-mechanical tests as shown in the flowchart in Figure 3(d) are essential to demonstrate that the structural battery can operate under mechanical loads. However simultaneous tests are challenging since the time scales involved in the electrochemical tests (at low charging currents) are long compared to time scales of typical mechanical tests and the lack of test standards.

This work aims to demonstrate the effect of mechanical three-point bend loads on electrochemical performance [12] and that the fabricated structural battery prototype continued operating after the test. The simultaneous electro-mechanical (SEM) testing of the cell was carried out with a set-up shown in Figure 3(a). The set-up comprises a universal testing machine Instron 5848 and NEWARE battery tester. The cell was loaded to an extent such that the pouch cell does not mechanically fail (indicated by a load drop) or electrically short to demonstrate the operation of the cell under load. The loading pin was held at the constant cross head displacement during the SEM test and then subsequently unloaded. The pouch cell with the encapsulation intact loaded in 3 point bending is shown in Figure 3(b).

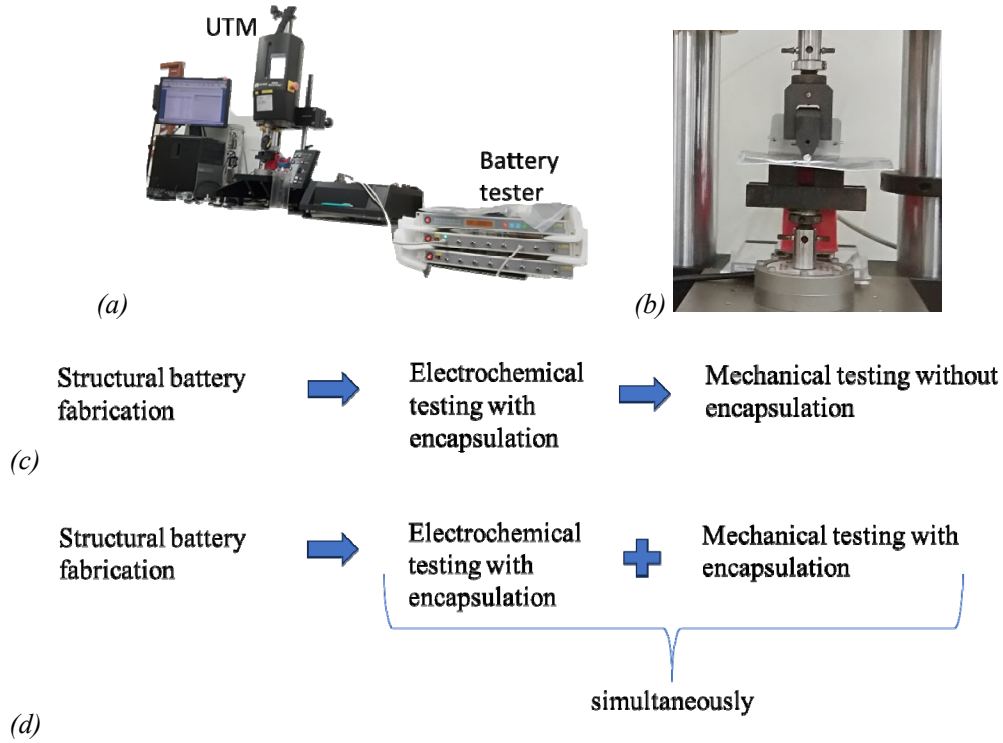

Figure 3: (a) Simultaneous electrochemical-flexural testing experimental set-up;(b) A pouch cell undergoing a 3-point bend test; (c) research work flow of structural battery found in literature; (d) Simultaneous electro-mechanical testing

3 RESULTS AND DISCUSSION

3.1 Current collector selection

In this section, the current collector selection is justified based on the resistivity measurements and the tensile behaviour of the current collectors[10]. The tensile behaviour and resistivity measurements of various current collectors are summarized below.

Current collector tensile behaviour

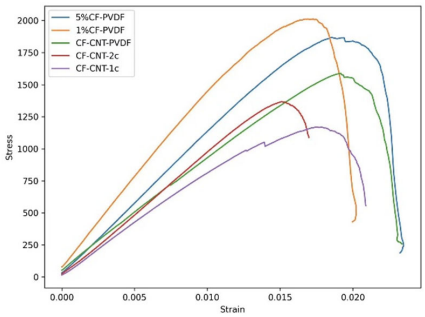

Figure 4: Tensile stress-strain behaviour of different current collectors

The tensile stress-strain behaviour of various current collectors is shown in Figure 4 and the tensile strength and modulus are tabulated in Table 2. The CF-PVDF current collectors exhibit a higher tensile strength and tensile modulus compared to the CF-CNT current collectors.

Table 2 Tensile properties of various current collectors

Sample	Strength(MPa)	Young's Modulus(GPa)
1%CF-PVDF	1970.9	140.1
5%CF-PVDF	1649.1	104.5
CF-CNT-1c	1246.8	88.5
CF-CNT-2c	1172.9	89.9
CF-CNT-PVDF	1601.2	91.5

Current collector resistivity

The resistivities of various current collectors are tabulated in Table 3. Despite PVDF being an electrical insulator, the CF-PVDF current collectors exhibit a lower longitudinal (along the fibre direction) and through thickness resistivity compared to the CF-CNT samples. This might be because the CF-CNT current collectors do not have a uniform distribution of the electrically conductive CNTs through the thickness.

Table 3 Electrical resistivity of current collectors along the fibre (longitudinal direction) and the thickness direction

Sample label	Longitudinal resistivity (Ωmm)	Through thickness resistivity(Ωmm)
CF	0.021	48.092
1%CF-PVDF	0.032	22.593
5%CF-PVDF	0.041	24.505
CF-CNT-2c	0.057	38.254
CF-CNT-1c	0.053	46.939
CF-CNT-PVDF	0.070	75.211

Comparison of current collectors

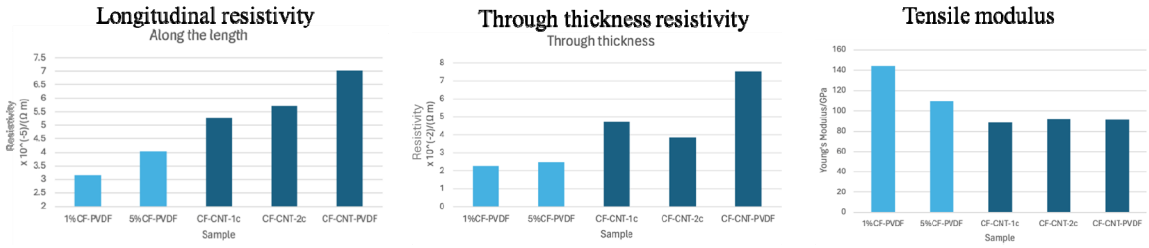

(a) (b) (c)

Figure 5 Comparison of (a) Longitudinal resistivity;(b) through thickness resistivity and (c) Young's modulus across fabricated composite current collector samples

The various current collectors are compared in terms of longitudinal resistivity, through thickness resistivity and tensile modulus in Figure 5. The 1% CF-PVDF current collector exhibit the least resistivity and highest tensile modulus. However, since the various tows of the 1%CF-PVDF current collector samples were not well bonded to one another (Figure 10 in the appendix), it was difficult to fabricate pouch cells with the 1%CF-PVDF current collectors. Instead, 5% CF-PVDF current collectors were used to fabricate the structural battery pouch cells whose electrochemical performance is discussed in the next section.

3.2 Pouch cell electrochemical performance

The pouch cells fabricated were electrochemically tested as described in section 2.2 by charging and discharging between 1 and 2.5V at 0.1C and 0.2C charging rates. The voltage capacity graph of a single pouch cell at room temperature and at 60°C are shown in Figures 6(a) and (b), respectively. The capacity at room temperature is lower than the capacity at 60°C since the ionic conductivity of the PEO based solid electrolyte is sub-optimal at room temperature. The pouch cells' performance at 60°C shows reasonable repeatability as observed from the voltage-specific capacity graphs of three pouch cells in Figure 7, indicating a repeatable battery fabrication process. The capacity fading observed in the prototypes' performance at 60°C is similar to the PEO cells cycled at high temperature reported in literature [13].

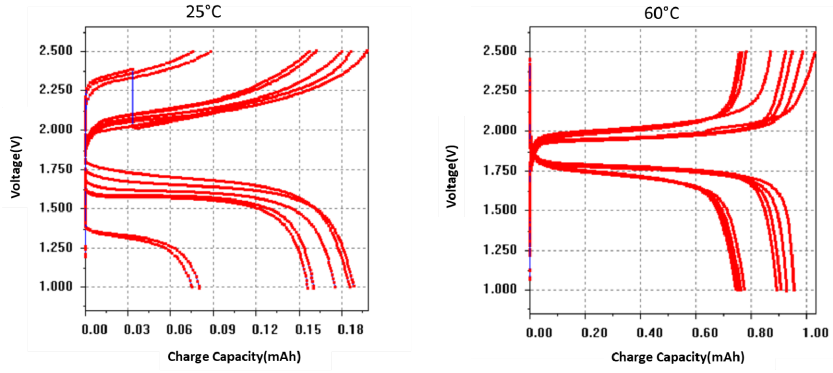

(a) (b)

Figure 6: Voltage-capacity behaviour of structural battery pouch cell of the configuration shown in Figure 2 at (a) 25 °C; (b) 60°C

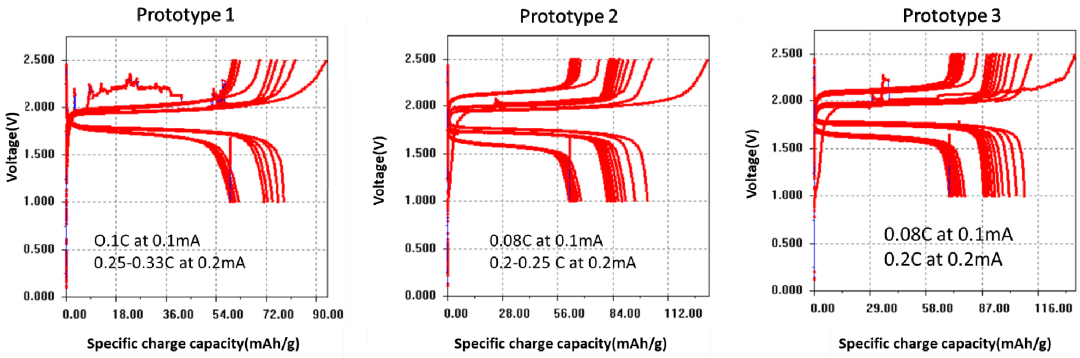

Figure 7: The voltage capacity graphs for three pouch cell prototypes cycled at 60°C

3.3 Simultaneous electro-mechanical testing

Simultaneous Electro-Mechanical (SEM) testing of a pouch cell was carried out as described in section 2.3. The voltage specific capacity of the cell before loading is shown in Figure 8(a) by the blue curve. The cell was loaded to about 40N in three-point bending (as seen in Figure 3(b)) corresponding to 1mm cross head displacement as shown in Figure 8(b). The loading pin was held at the same position after loading the cell. The load decreased after the initial loading but was not recorded and therefore not reported here. Although the load is not constant, but the loading pin position is held stationary during the SEM test.

Since the test is carried out at room temperature, the capacity is lower and a higher charging rate is used to decrease the total testing time. The voltage decreases upon loading during charging as can be seen in the loaded box in Figure 8(a) This most likely is due to the decreased resistance upon loading due to better contact during the loading of the pouch cell. The cycle shown in orange in Figure 8(a) was charged during the application of the three-point bending (i.e. the orange curve between the loaded and unloaded boxes) The lower voltage observed in the charging phase of the cycle in orange is due to application of the mechanical load. Subsequently, the voltage is seen to increase upon unloading during the charging phase.

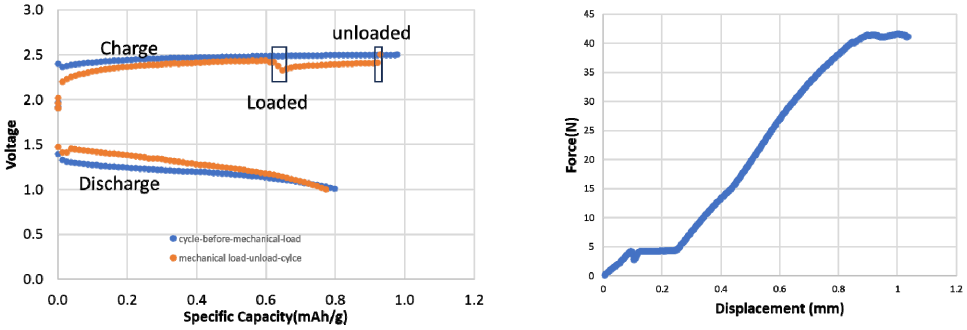

(a) (b)

Figure 8: (a) Voltage vs specific capacity of cell before and after applying a bending load. The voltage decreases upon application of load most likely due to decreased resistance because of improved contact. The SEM test is conducted during the charging phase represented by the orange curve between the “loaded” and “unloaded” boxes. (b) Force-displacement graph during the application of load (i.e. “Loaded” box) in Figure 8(a).

Figure 9 shows the subsequent three cycles after the initial cycles plotted in Figure 8(a). The performance of the cell improved in the immediate cycle (grey plot in Figure 9) after the SEM test depicted in Figure 8(a) as evident from the increased capacity. This suggests that the pouch cell is in an improved state of contact (leading to decreased cell resistance) during the

1st (grey plot in Figure 9) and 2nd cycles (yellow plot in Figure 9) after SEM. However, by the third cycle (red plot in Figure 9) after the SEM test, the capacity of the cell returned to the pre-SEM level (blue plot). In conventional battery testing, these type of contact effects are avoided, and the best possible electrochemical performance is obtained by using a fixture shown in Figure 11 in the appendix. This demonstrates the need for simultaneous electro-mechanical testing of structural battery pouch cells since the effect of load on electro-chemical performance is quantified and simultaneous multi-functionality is demonstrated. Structural battery research needs to progress from an isolated multi-functionality evaluation (Figure 3(c)) to simultaneous multi-functionality evaluation (Figure 3(d)) as discussed in this work for practical realization of structural batteries.

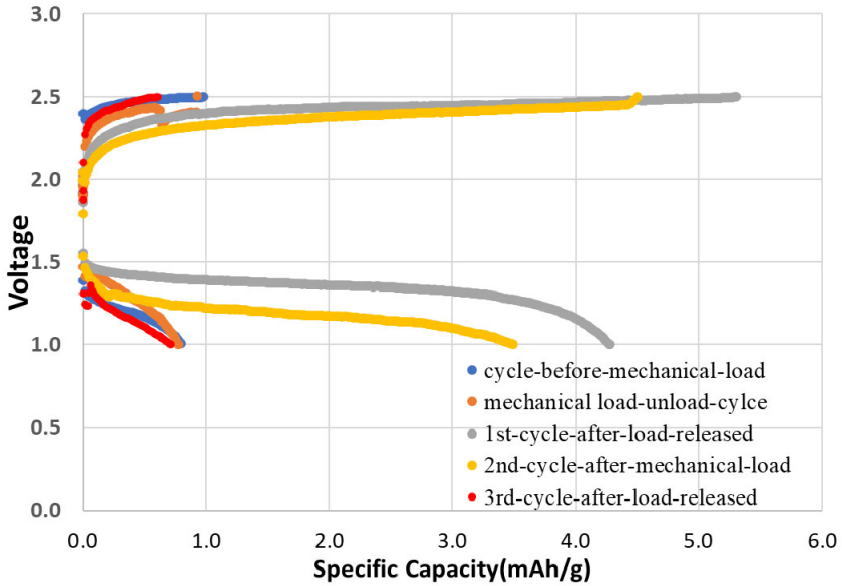

Figure 9 The comparison of the voltage vs specific capacity after the mechanical 3-point bending test. The orange and blue curves are the same cycles from ***Error! Reference source not found.***. The subsequent cycle displays an increase in charge and discharge capacity that decreases in the subsequent cycles suggesting that the improved contact that was established during loading relaxes with time returning back to the previous state (See 3rd cycle after load released (red curve) and cycle before mechanical load (blue curve)).

4 CONCLUSION

Carbon fibre based current collectors are used to develop PEO solid electrolyte based structural battery prototypes. The current collector with 5% PVDF solution was used to make the prototypes even though 1% PVDF samples exhibited the least resistivity and higher tensile properties since 1% CF PVDF current collectors are not suitable for making large pouch cell prototypes (as explained in section 3.1). The optimum amount of PVDF is indicated to lie between 1% and 5% CF-PVDF as observed from the measurements.

Pouch cells made with LFP and LTO electrodes with PEO solid electrolyte were successfully demonstrated to cycle electrochemically at room temperature and 60°C. These prototypes have been demonstrated to be fabricated with reasonable amount of repeatability as indicated in the performance of 3 pouch cells. Finally, a proposed Simultaneous Electro-Mechanical (SEM) flexural test has been performed. The battery could operate during and

after the test. The batteries exhibited higher capacities in the subsequent cycles mostly due to improved contact but eventually relaxed and returned to pre-SEM capacity.

Research and development of standards for these and similar simultaneous electromechanical tests and exploring alternate time-efficient methods to demonstrate simultaneous multi-functionality is necessary for the evaluation of structural batteries.

ACKNOWLEDGEMENT

The support of A*Star under Structural power for portable and electrified transportation; grant no. A20H3b0140 is gratefully acknowledged.

APPENDIX

A.1 Anode and cathode slurry preparation:

LFP + C : 88:5 mass ratio of LFP powder and Carbon (C65) Black Powder are mixed using a pestle and mortar for cathode.

(a) 1 g of LFP + C mixed above

(b) 1.2 g of DMF (N, N Dimethylformamide) solvent

(c) 4.5 g of PEO10-LiTFSI-DMF solution

(d) 4 g of 5% PVDF-DMF solution (a 5:95 mass ratio of PVDF-DMF solution)

(e) 2 g of 0.4%Single Walled Carbon Nanotube (SWCNT) 2% PVDF in NMP (N-Methyl pyrrolidone)

The above ingredients are added in glass bottle as per the weights one by one and centrifuged at 2000rpm for two minutes after the addition of each component from (b) to ensure uniformity of the slurry.

For the anode, LTO + C: 90:5 mass ratio of LTO powder and Carbon (C65) Black Powder is mixed with a pestle and mortar and replaces the LFP+C in the above recipe

A.2 PEO_{10}-LiTFSI solid electrolyte preparation:

Add 1 g of LiTFSI (Lithium bis(trifluoromethanesulfonyl)imide) and 1.533 g of PEO(poly(ethylene) oxide) in glass bottle inside a glovebox to avoid moisture absorption. Add DMF(Dimethylformamide) solvent such that the total solid content (PEO + LiTFSI) is 10% of the total mass after adding DMF. Place a stirrer bar and place in oil bath at 80°C and stir at 500 rpm for 12 hours to prepare the electrolyte.



Figure 10: 1% CF-PVDF fabricated sample with disconnected individual tows- makes it difficult to assemble cells

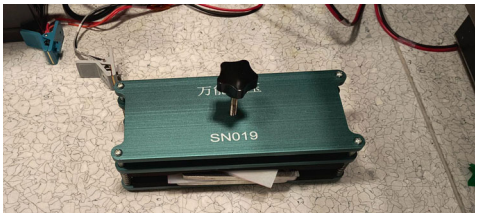

Figure 11: Fixture used in conventional pouch cell testing to ensure proper contact within the cell and ensure the best battery performance

REFERENCES

[1] L.E. Asp, E.S. Greenhalgh, Structural power composites, Compos. Sci. Technol. 101 (2014) 41–61. https://doi.org/https://doi.org/10.1016/j.compscitech.2014.06.020.

[2] D. Carlstedt, L.E. Asp, Performance analysis framework for structural battery composites in electric vehicles, Compos. Part B Eng. 186 (2020) 107822. https://doi.org/https://doi.org/10.1016/j.compositesb.2020.107822.

[3] Q. Jiang, A. Beutl, H. Kühnelt, A. Bismarck, Structural composite batteries made from carbon fibre reinforced electrodes / polymer gel electrolyte prepregs, Compos. Sci. Technol. 244 (2023) 110312. https://doi.org/https://doi.org/10.1016/j.compscitech.2023.110312.

[4] G.J.H. Lim, R. Chua, J.J. Koh, K.K. Chan, E.J.J. Tang, V. Teh, M. Srinivasan, Structural and conformable designs for aqueous multifunctional batteries, Mater. Today Energy 33 (2023) 101255. https://doi.org/https://doi.org/10.1016/j.mtener.2023.101255.

[5] L.E. Asp, K. Bouton, D. Carlstedt, S. Duan, R. Harnden, W. Johannisson, M. Johansen, M.K.G. Johansson, G. Lindbergh, F. Liu, K. Peuvot, L.M. Schneider, J. Xu, D. Zenkert, A Structural Battery and its Multifunctional Performance, Adv. Energy Sustain. Res. 2 (2021) 2000093. https://doi.org/https://doi.org/10.1002/aesr.202000093.

[6] R. Chaudhary, J. Xu, Z. Xia, L.E. Asp, Unveiling the Multifunctional Carbon Fiber Structural Battery, Adv. Mater. 36 (2024) 2409725. https://doi.org/https://doi.org/10.1002/adma.202409725.

[7] K. Bouton, L. Schneider, D. Zenkert, G. Lindbergh, A structural battery with carbon fibre electrodes balancing multifunctional performance, Compos. Sci. Technol. 256 (2024) 110728. https://doi.org/https://doi.org/10.1016/j.compscitech.2024.110728.

[8] R. Tavano, M. Spagnol, N. Al-Ramahi, R. Joffe, J. Xu, L.E. Asp, Mechanical characterisation of a structural battery electrolyte, Polymer (Guildf). 312 (2024) 127646. https://doi.org/https://doi.org/10.1016/j.polymer.2024.127646.

[9] N. Ding, S.W. Chien, T.L.D. Tam, X. Li, G. Wu, W.J. Lee, S.Y. Chiam, Y.S. Meng, D.W.H. Fam, Revealing Phase Transitions in Poly(Ethylene Oxide)-Based Electrolyte for Room-Temperature Solid-State Batteries, Adv. Energy Mater. 14 (2024) 2402986. https://doi.org/https://doi.org/10.1002/aenm.202402986.

[10] K. Raju, S. Dong, T.-E. Tay, Developing Carbon Fibre Composite Current Collectors for Structural Battery Applications, (2024). https://doi.org/10.1115/IMECE2024-146111.

[11] K.K. Chan, G.J.H. Lim, N.A.A. Sutrisnoh, K. Raju, M. Srinivasan, Toward a Safe and High Performance Quasi-Solid-State Structural Battery, ACS Appl. Energy Mater. 7 (2024) 9098–9109. https://doi.org/10.1021/acsaem.4c00981.

[12] K. Raju, T.-E. Tay, V.B.C. Tan, Multi-functional performance evaluation of carbon fibre structural battery composite prototypes with flexural mechanical loading, in: 21st Eur. Conf. Compos. Mater., The European Society for Composite Materials (ESCM) and the Ecole Centrale de Nantes., Nantes, 2024: p. Volume 6: 355-362. https://doi.org/10.60691/yj56-np80.

[13] G. Homann, L. Stolz, J. Nair, I.C. Laskovic, M. Winter, J. Kasnatscheew, Poly(Ethylene Oxide)-based Electrolyte for Solid-State-Lithium-Batteries with High Voltage Positive Electrodes: Evaluating the Role of Electrolyte Oxidation in Rapid Cell Failure, Sci. Rep. 10 (2020) 4390. https://doi.org/10.1038/s41598-020-61373-9.

ICCM24
24TH INTERNATIONAL CONFERENCE ON COMPOSITE MATERIALS
AUG 4-8, 2025 BALTIMORE CONVENTION CENTER - BALTIMORE, MARYLAND, USA
HOSTED BY: UNIVERSITY OF DELAWARE CENTER FOR COMPOSITE MATERIALS Celebrating 50 Years

Self-healing of Structural Damage in Thermoplastic Composite Laminates via Incorporated Nano-engineered Heating Architecture

Hyungmin Kim, Sumin Lee, Jeonyoon Lee

August 4th, 2025

Korea Advanced Institute of Science and Technology
Department of Aerospace Engineering

Contents

1. Research background
2. Design of the Nano-engineered heating architecture
3. Mechanical test methods for quantifying the self-healing effect
4. Analyzing the morphological results and the mechanical properties
5. Conclusion and future work

Research Background

The Growing Importance of Composites in the Aerospace Industry

- Composites are a good choice for maximizing payloads and aircraft performance due to high strength-to-weight ratio
  - Reduced aircraft weight leads to lower operational costs
  - Usage of composites are rising both in commercial and military applications

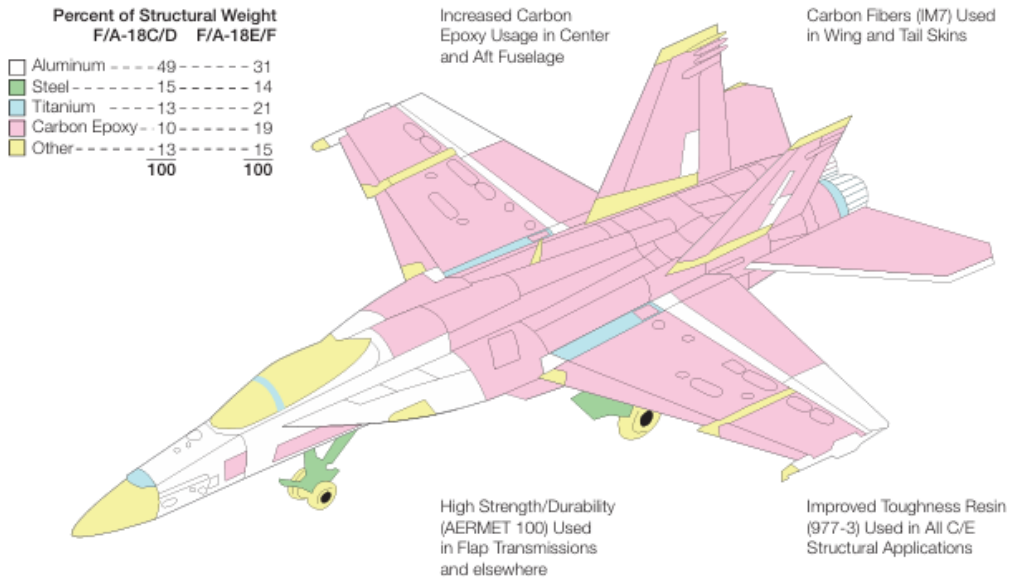

<Wide use of composite materials in Boeing fighter jets F/A-18C/D and F/A-18E/F [1]>

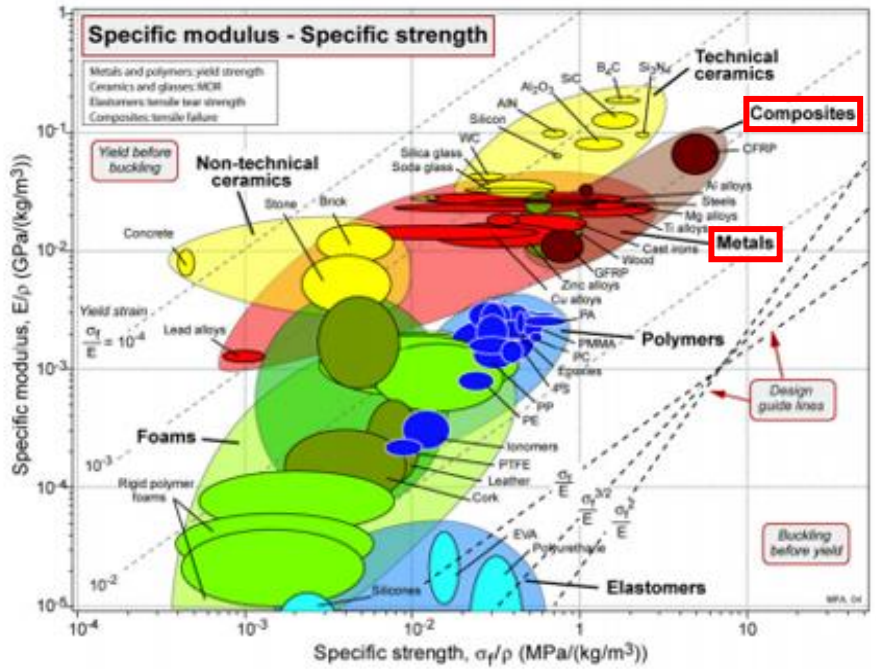

<Composites vs. Metals: Specific stiffness and Specific strength[2]>

[1] Quilter, Adam. "Composites in aerospace applications." *IHS White Paper* 444.1 (2001): 264.
[2] Ashby, Michael F., Hugh Shercliff, and David Cebon. *Materials: engineering, science, processing and design*. Butterworth-Heinemann, 2018.

Existing Repairing Mechanisms of Composites

- In-situ inspection and direct addition of composite material into the damaged region is currently utilized
- Repair techniques and researches of thermoset matrix composites are more common

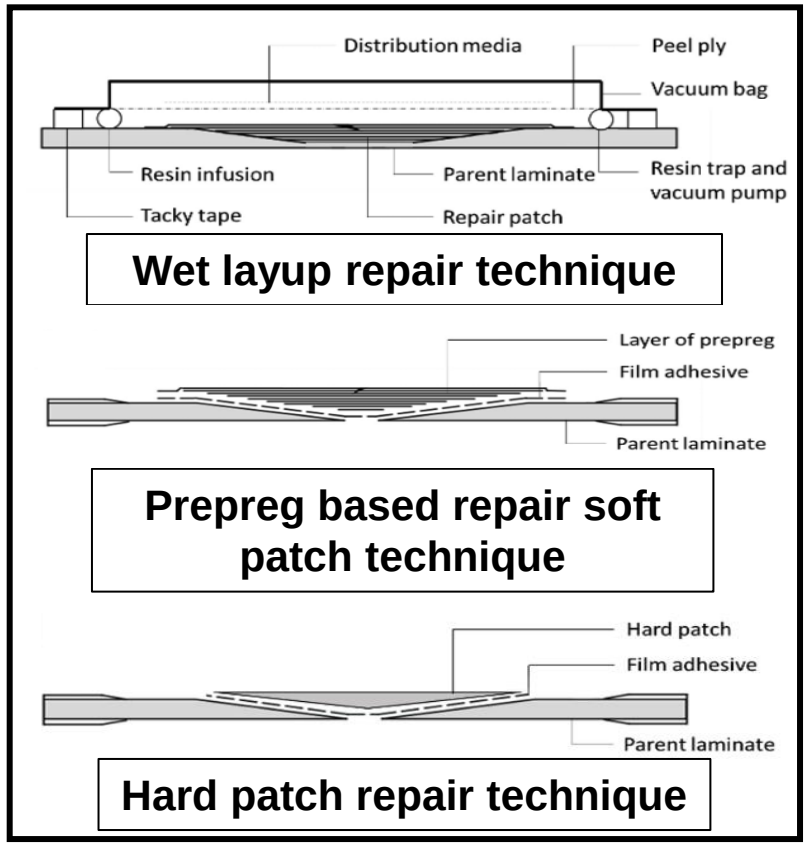

<Scarfing Repair Techniques[1] >

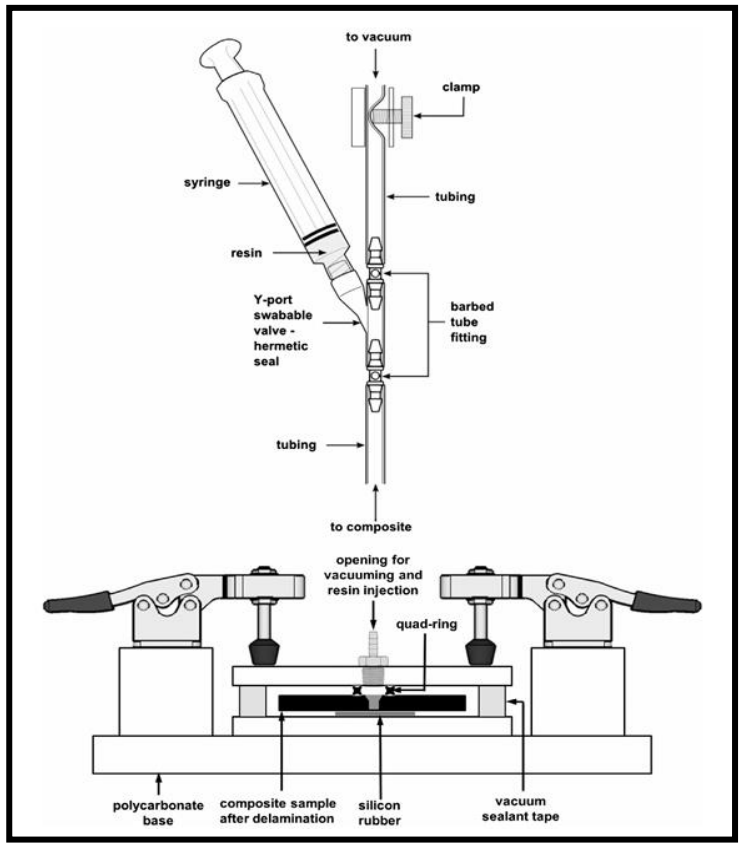

<Injection Repair Technique[2] >

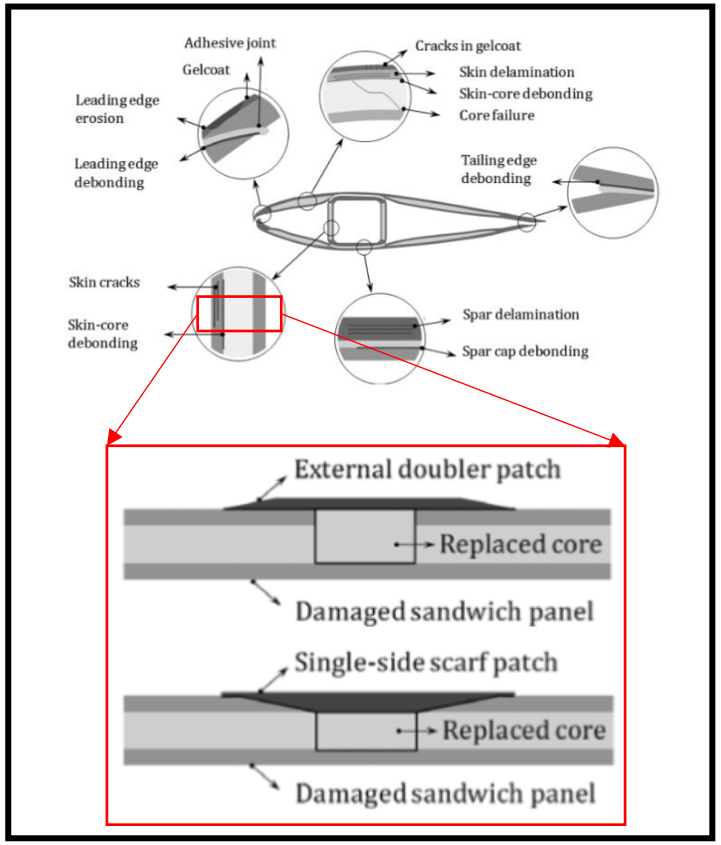

<Doubler Patch Repair[3] >

[1] Balakrishnan, Venkateswaran Santhanakrishnan, and Holger Seidlitz. "Potential repair techniques for automotive composites: A review." *Composites Part B: Engineering* 145 (2018): 28-38.
[2] Thunga, Mahendra, et al. "Low viscosity cyanate ester resin for the injection repair of hole-edge delaminations in bismaleimide/carbon fiber composites." *Composites Part A: Applied Science and Manufacturing* 52 (2013): 31-37.
[3] Katnam, K. B., et al. "Composite repair in wind turbine blades: an overview." *The Journal of Adhesion* 91.1-2 (2015): 113-139.

Rising Solution: Self-healing via Joule Heating

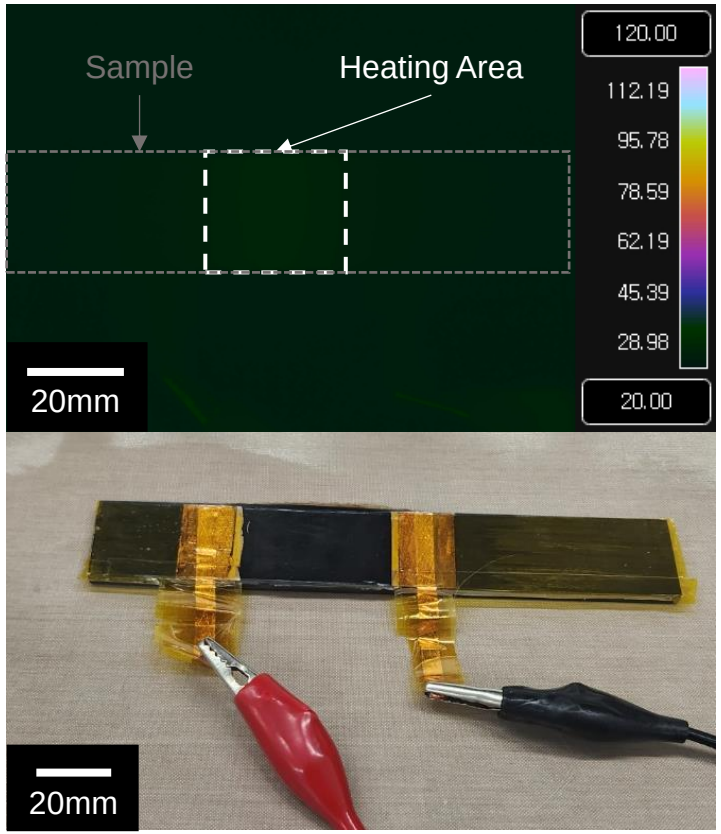

<IR Recording of the CNT Heater>

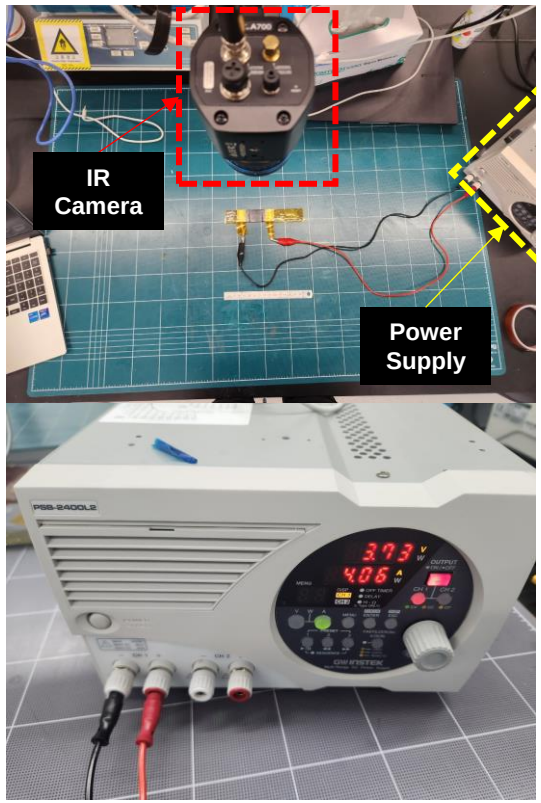

<Measured Voltage(3.73V) and Current(4.06A)>

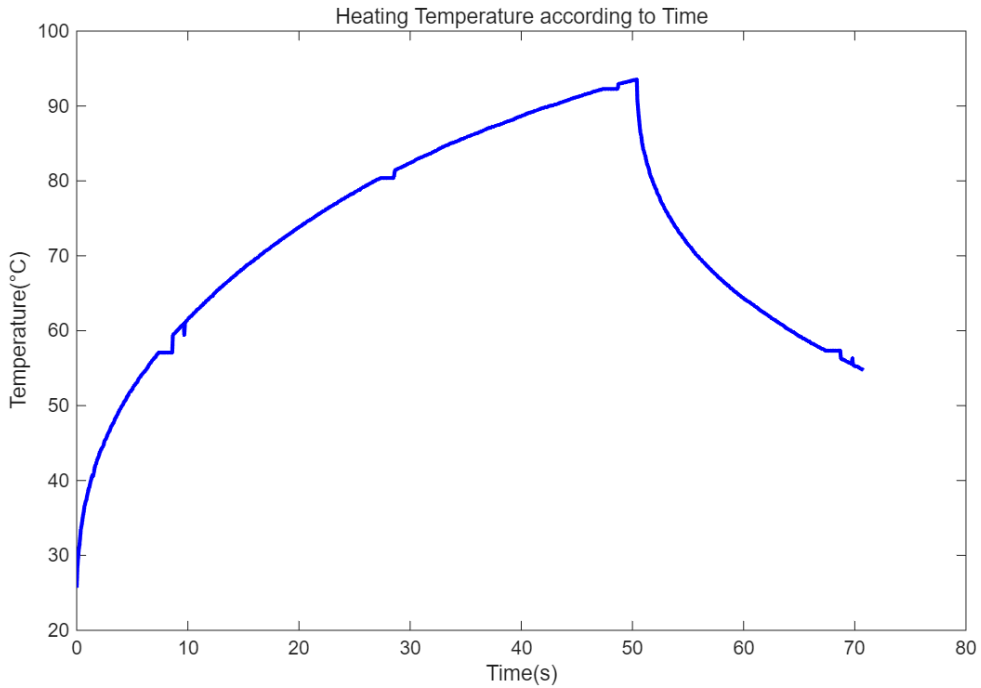

<Temperature-Time Plot>

- CNT bucky paper based heater possesses Joule heating capabilities to ~100℃ in 50s with $3.73V \times 4.06A = 15.1438W$ and the aspect ratio of 25mm(width)/40mm(length) = 0.625
- Thermoplastic resin can be reconsolidated into the damage cracks with the heat from the CNT bucky paper

Further Research Required for the Self-healing Architecture

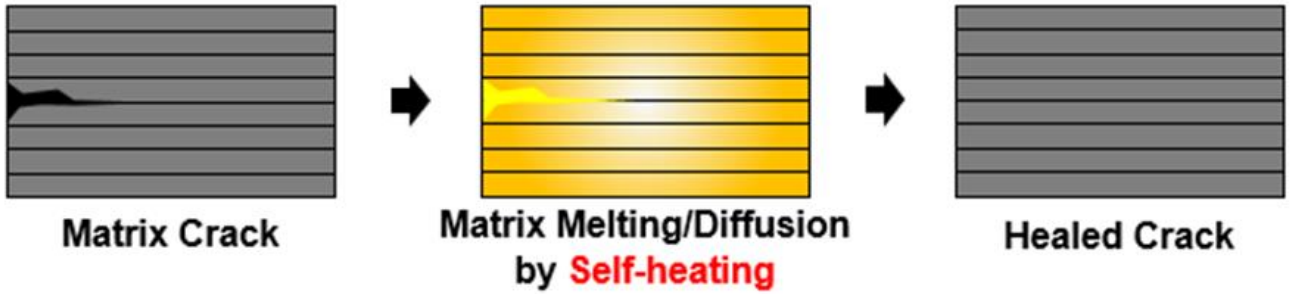

<Schematic of the Self-healing process>

① **Sustainable self-healing structure and method throughout the entire temperature cycle**

- Self-healing cycle based on manufacturer's instructions
- The nanoarchitecture must be free of electrical shorts via sufficient electrical insulation

② **Consistent mechanical test methods for self-healed composites testing**

- Finding the appropriate mechanical test for thermoplastic matrix based composites
- Sufficient amount of test data for such materials is required for further self-healing research

Thesis Objectives

1) Design of **CNT heater-based nano-engineered heating architecture**

   - Targeting on structurally incorporated nanocomposite integration

2) **Short Beam Shear(SBS)** and **End-Notched Flexural(ENF) Testing** of nanocomposite-integrated structure for self-healing efficiency

   - Stiffness analysis via the SBS test

   - Mode II Toughness analysis via the ENF test

3) **Morphological analogy** of the self-healing effects on the nanocomposites

   - Visual effects of the CNT-heater self-healing via the optical microscope

   - CT, Crystallinity(Thermophysical) N/A

Design of the Nano-engineered Heating Architecture

Design of Composite Surface Incorporated Heater Architecture

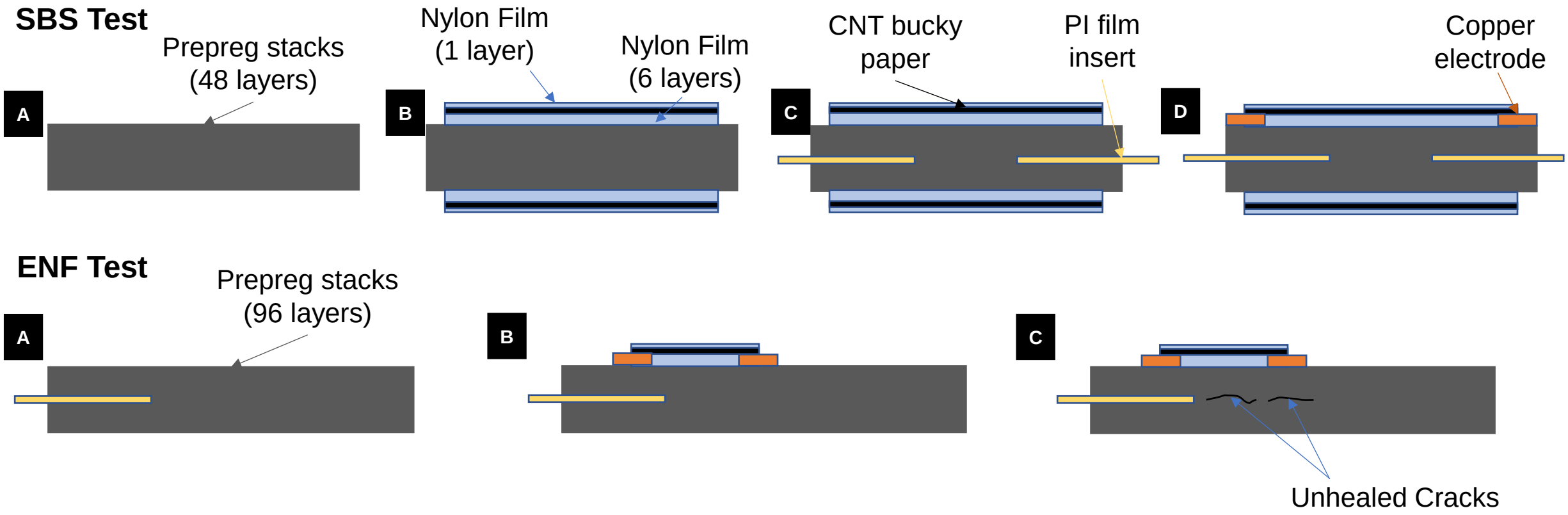

- CNT bucky paper is added on both top and bottom of the SBS sample groups B, C, D to control the structural conditions that might affect the mechanical properties
- The PI film insert is removed after initial curing(manufacturing) for mechanical testing
- ENF Sample C is equal to Sample B after mechanical testing(cracks propagated)

Manufacturing the Specimens for Mechanical Testing

SBS

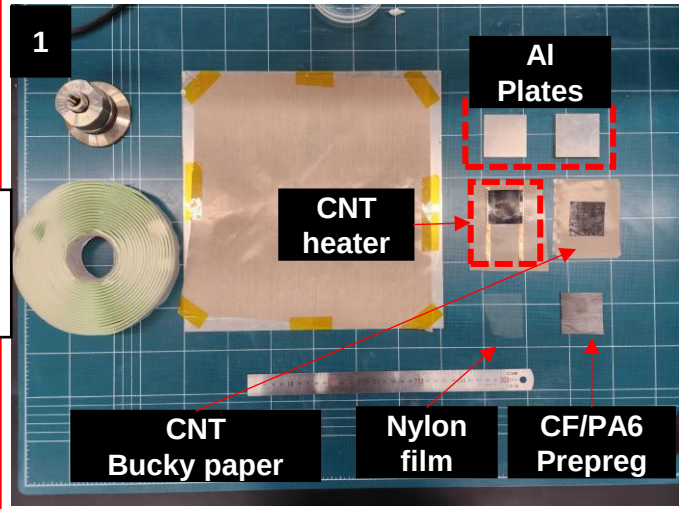

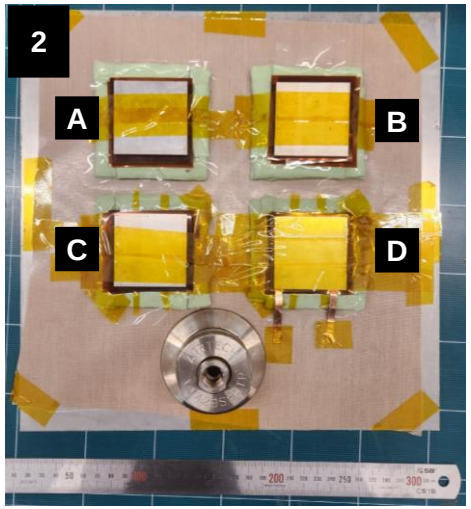

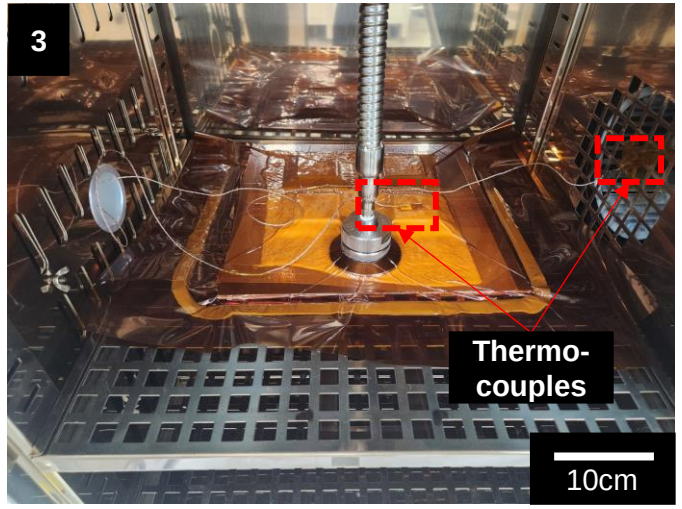

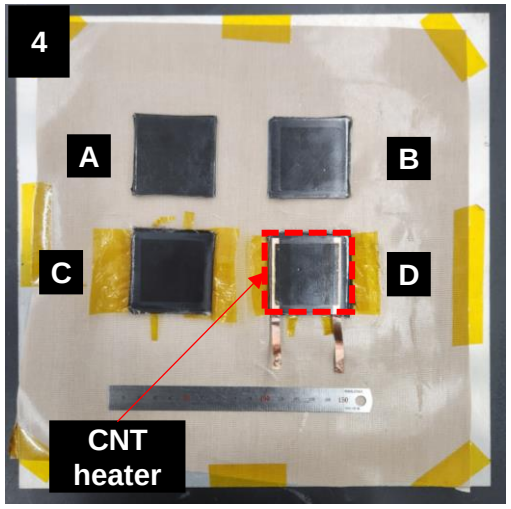

ENF

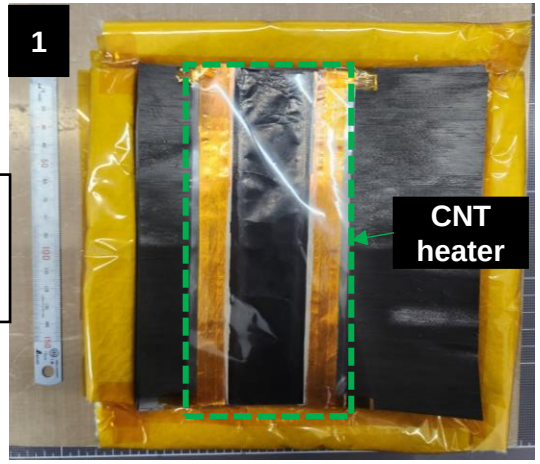

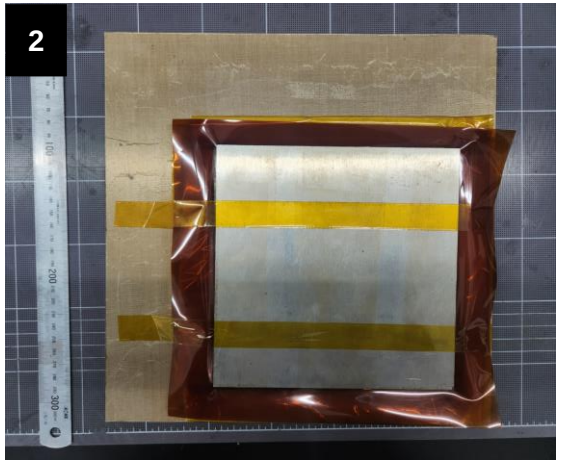

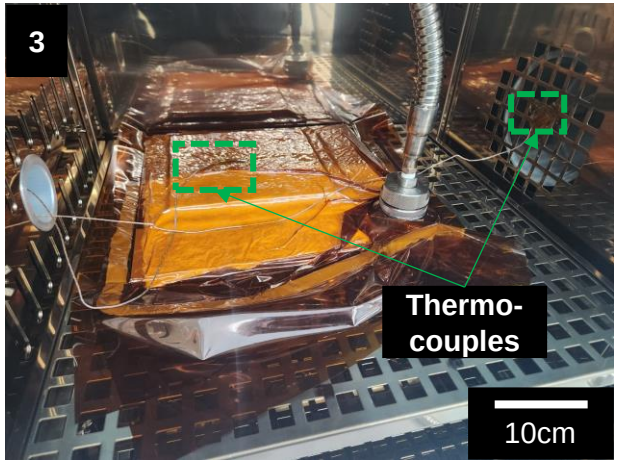

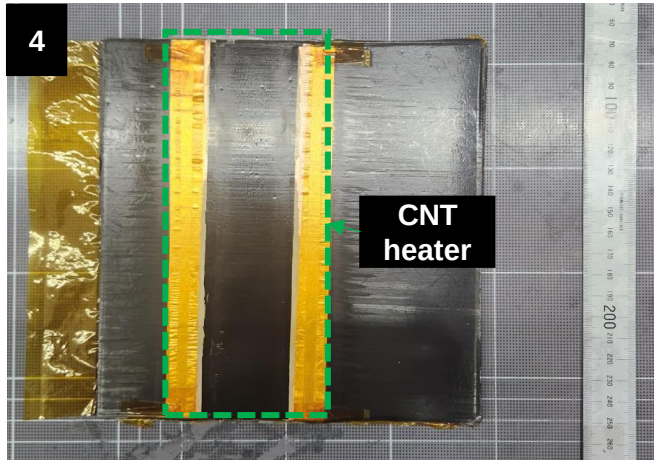

Manufacturing the Specimens for Mechanical Testing

SBS Test

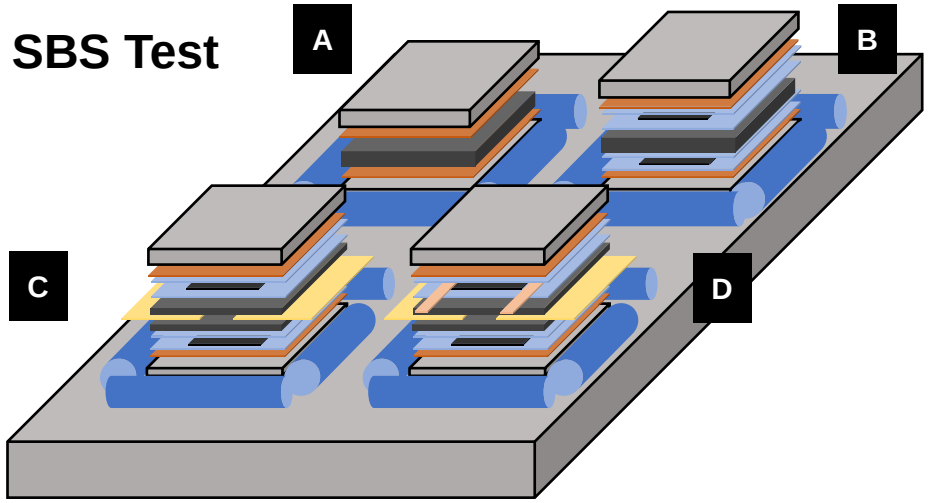

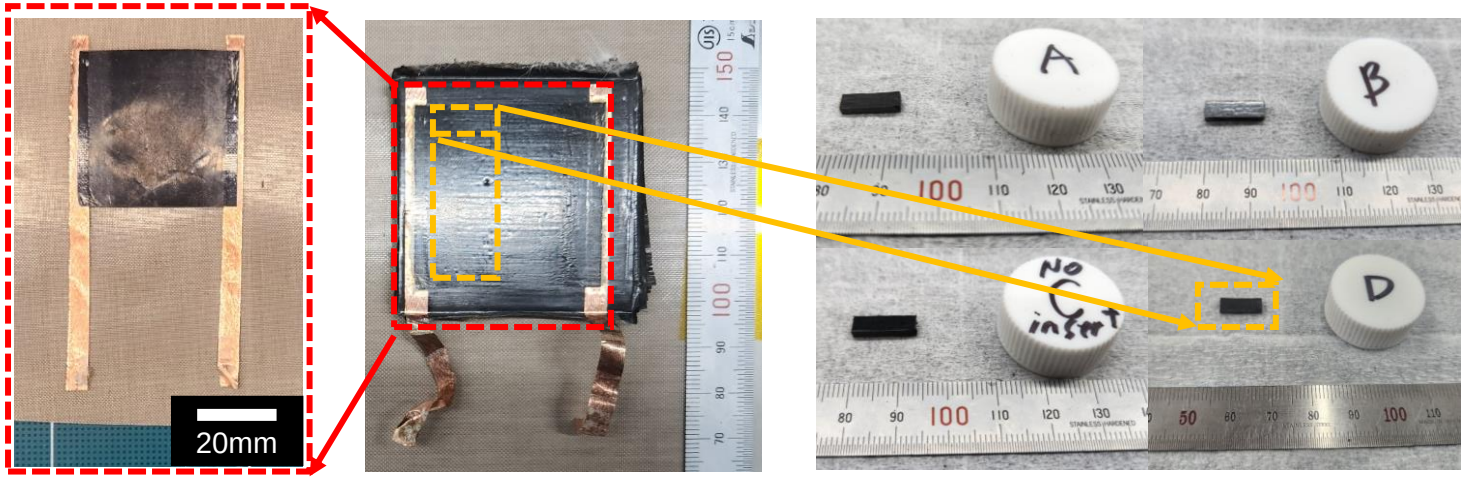

ENF Test

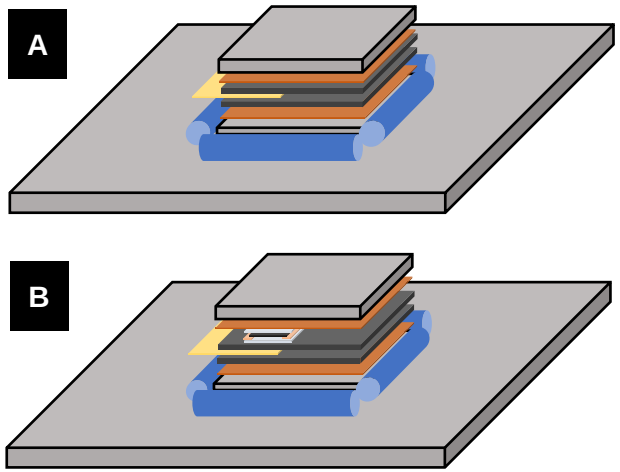

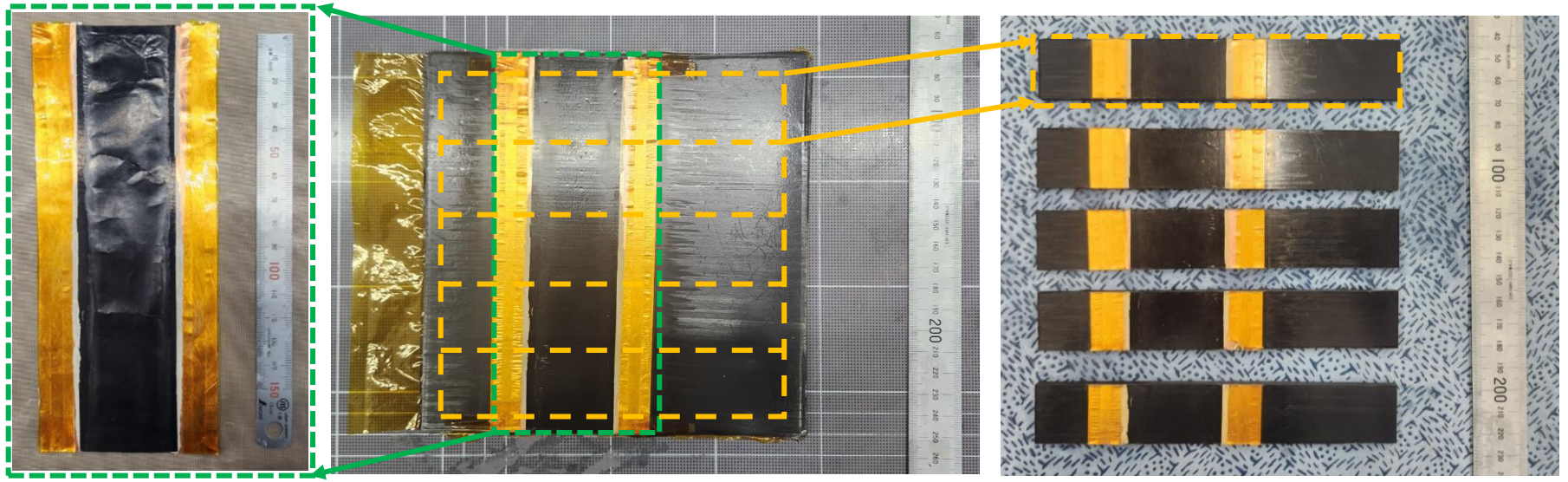

Self-healing the Specimens for Mechanical Testing

SBS Test

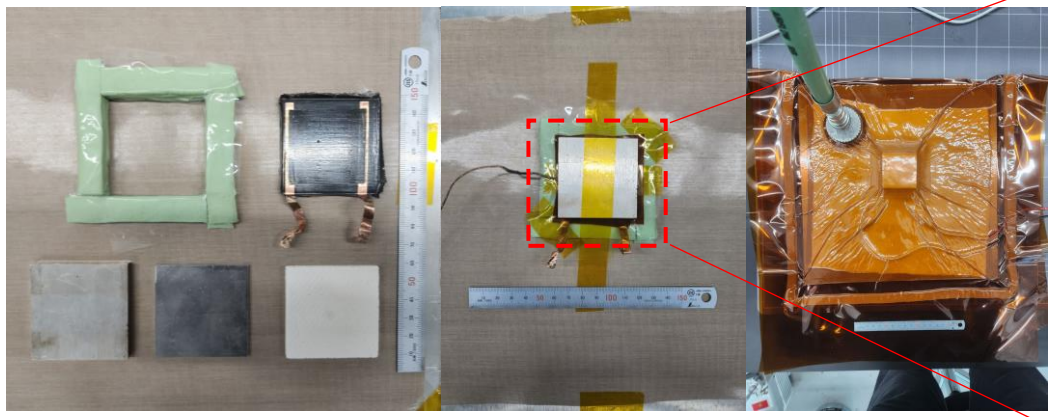

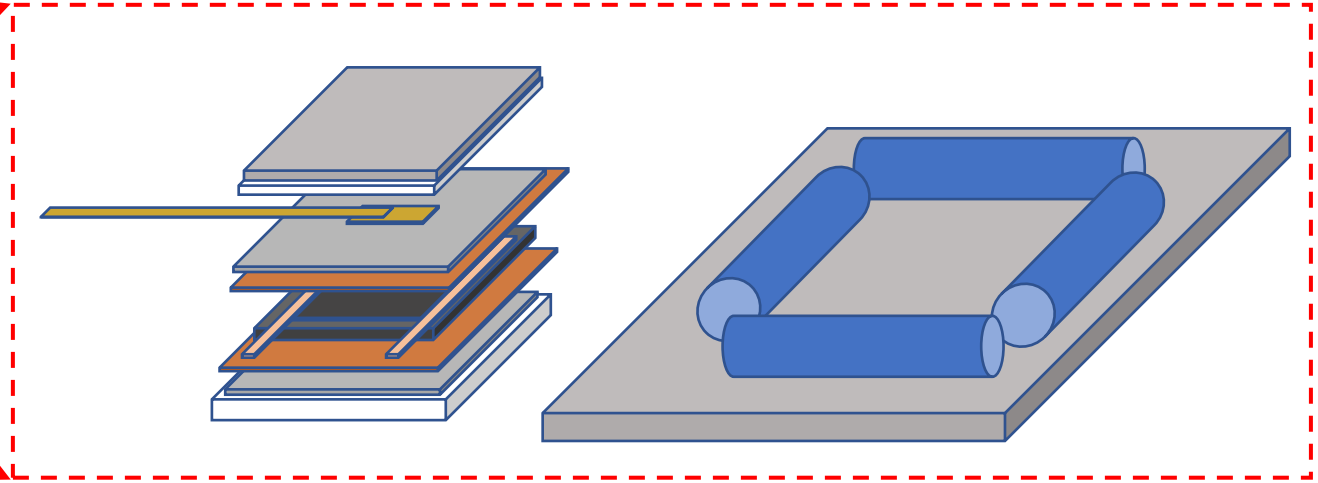

ENF Test(Spacer method)

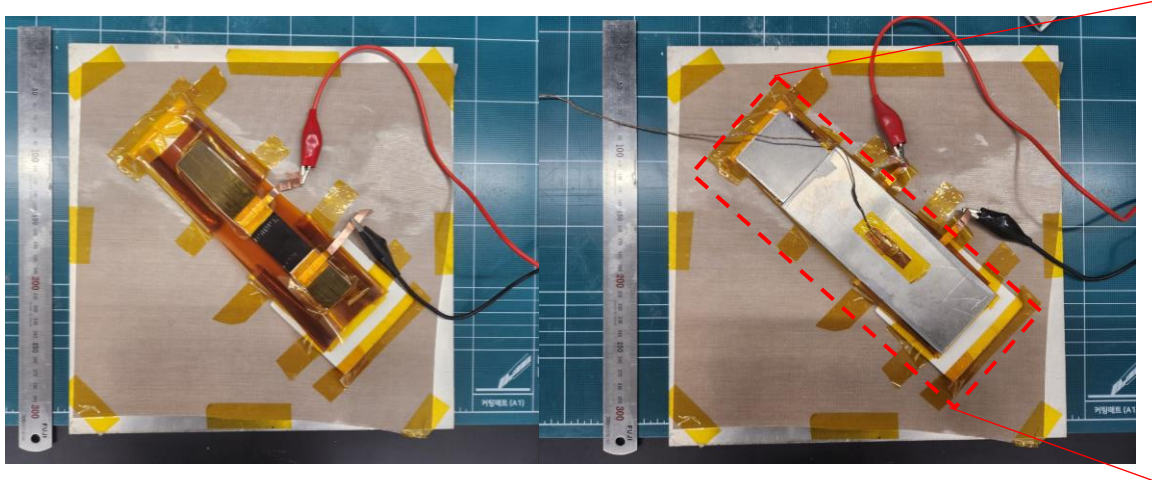

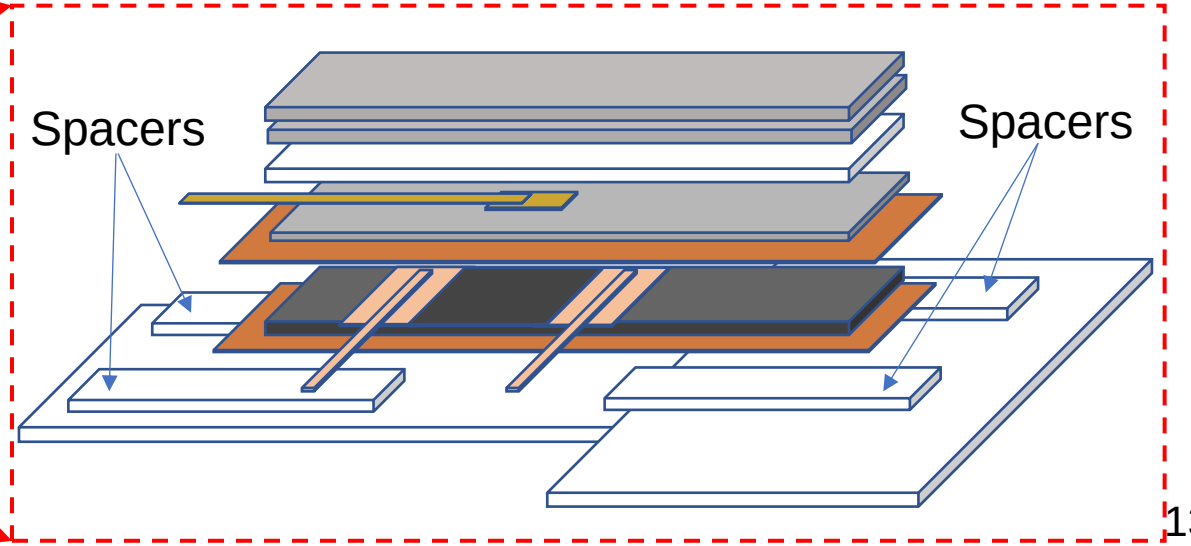

Self-healing the Specimens for Mechanical Testing

ENF Test(Double-sample method)

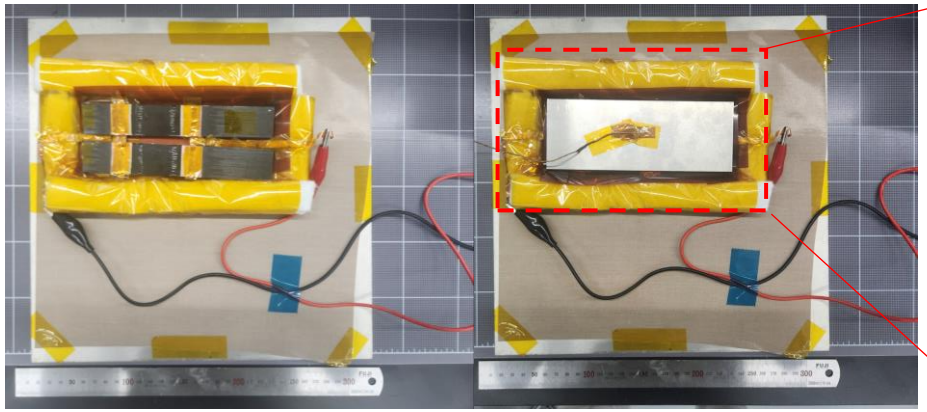

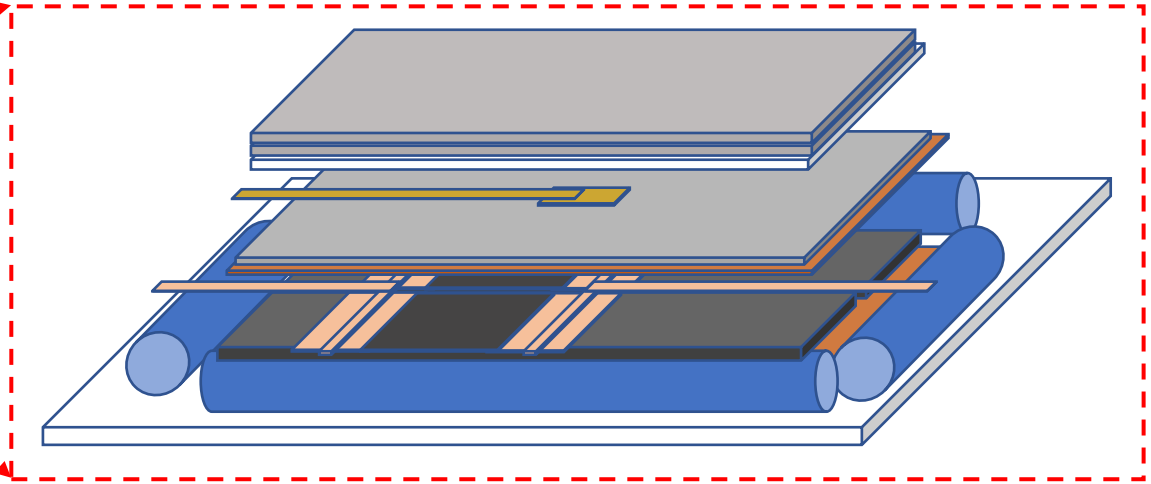

ENF Test(Metal mold method)

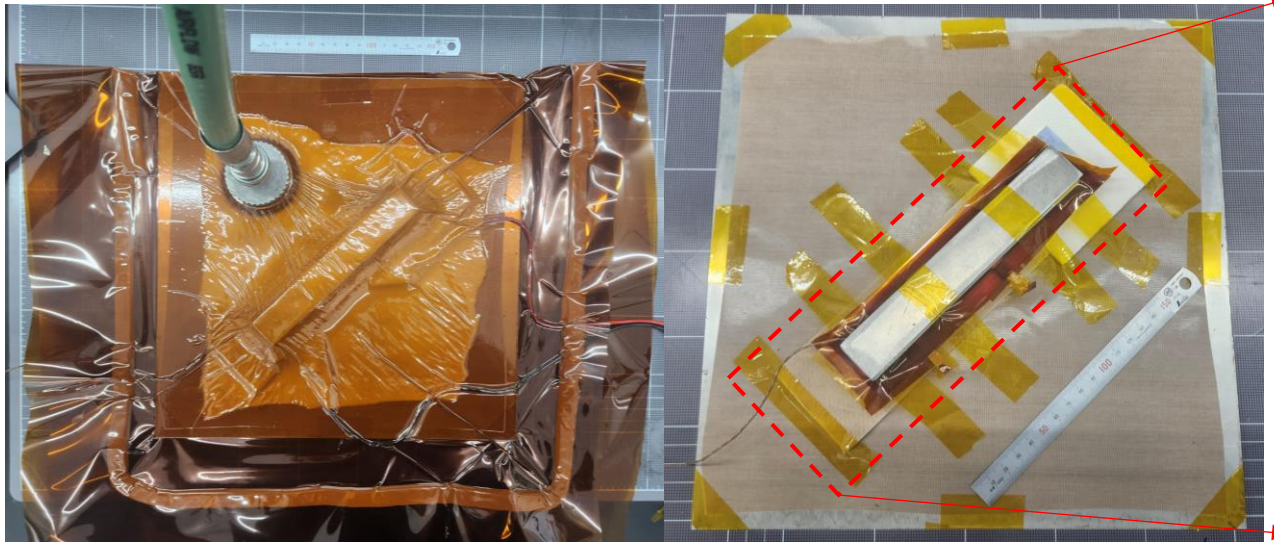

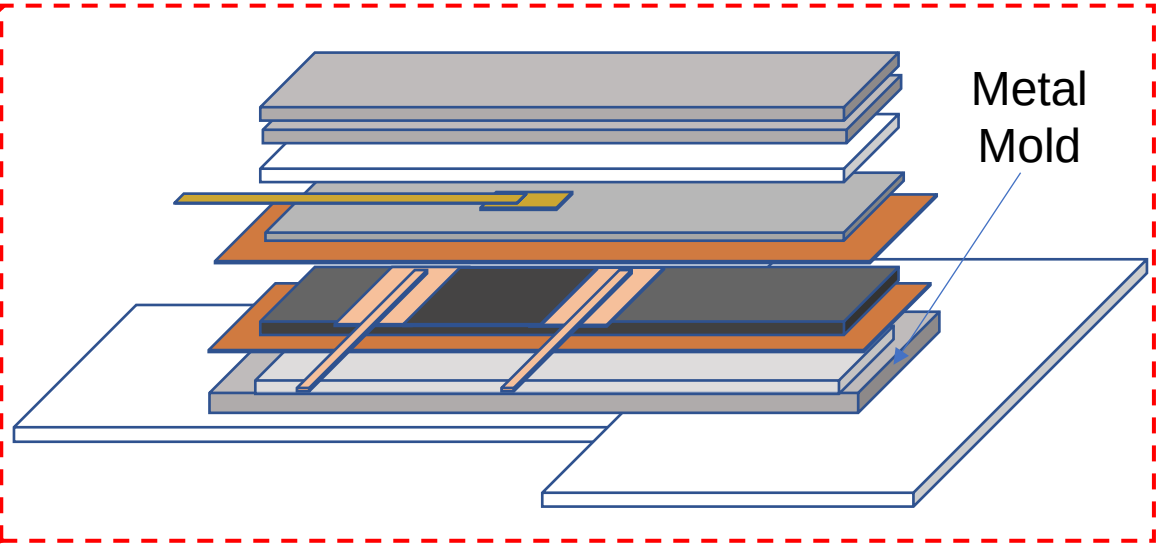

Mechanical Test Methods for Quantifying the Self-healing Effect

Short Beam Shear Testing(SBS) for Self-Healing Effects on the Stiffness

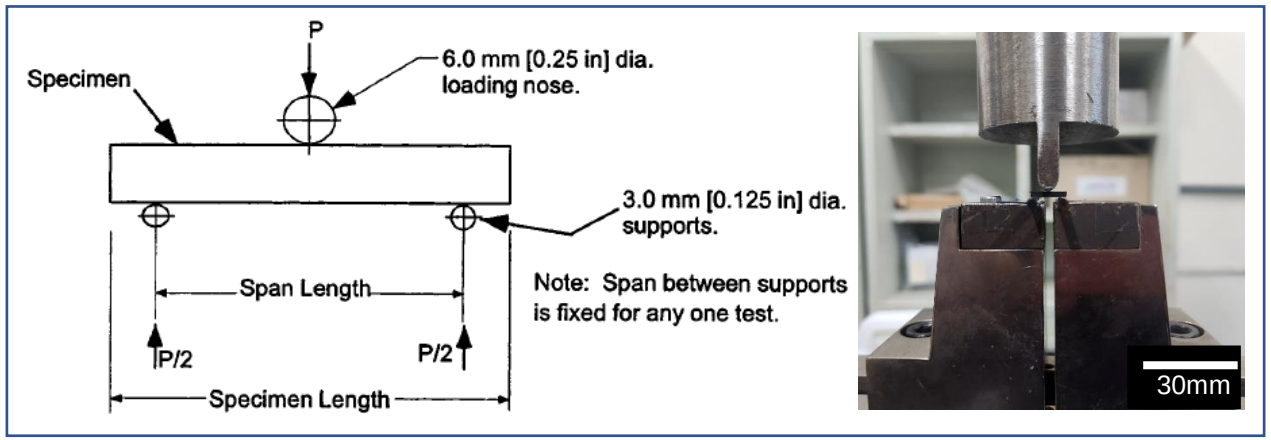

<SBS Test Setup Design(Left) & Actual Photo(Right)>

Specification

- Thickness(h) : ~2mm
- Width(b): ~4mm(b = 2t)
- Length(l): ~12mm
- Loading nose radius (r_1): 3mm
- Supports radius (r_2): 1.5mm
- Span Length(s): 8mm
- Loading speed: 1mm/min

- Termination condition
  - 30% Load drop off
  - The loading nose travel distance exceeds the sample nominal thickness
  - 2-piece failure
- Short beam strength calculation(Peak load = P_{max})
  - $F_{sbs} = 0.75 \times \frac{P_{max}}{bh} (b = specimen\ width, h = specimen\ thickness)$

End-Notched Flexural Testing(ENF) for Self-Healing Effects on the Mode II Toughness

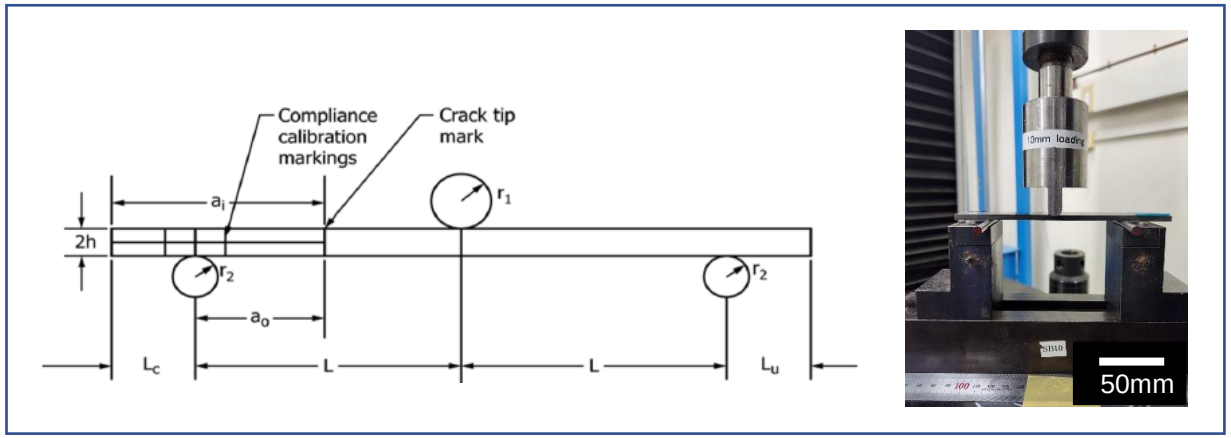

<ENF Test Setup Design(Left) & Actual Photo(Right)>

Specification

- Thickness(2h) : 3.4-4.7mm
- Pre-crack length (a_i): ~45mm
- Left supports – crack tip length(a_0): 20mm, 40mm(Compliance Calibration), 30mm(Fracture Test)
- Loading nose radius(r_1), Supports radius (r_2): 5mm, 3mm
- Total Sample Length, Width: ≥160mm, 19-26mm
- Span Length(2L): 100mm
- Loading speed, Unloading speed: 0.5mm/min, 0.5mm/min

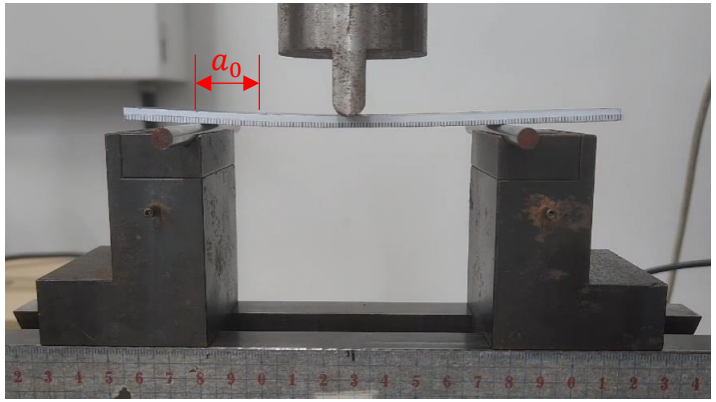

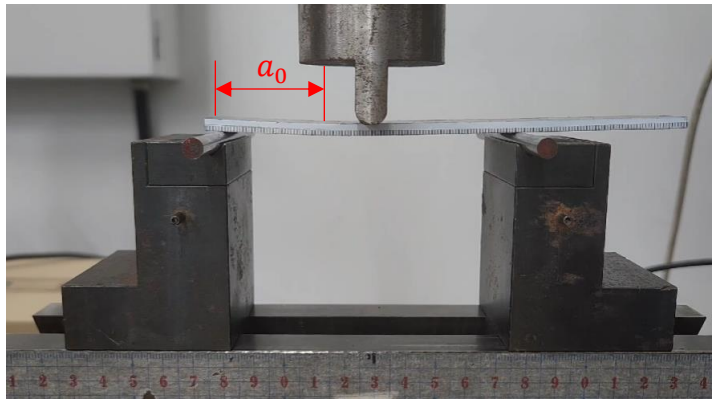

<Compliance Calibration Tests(Left: $a_0 = 20mm$, Right: $a_0 = 40mm$)>

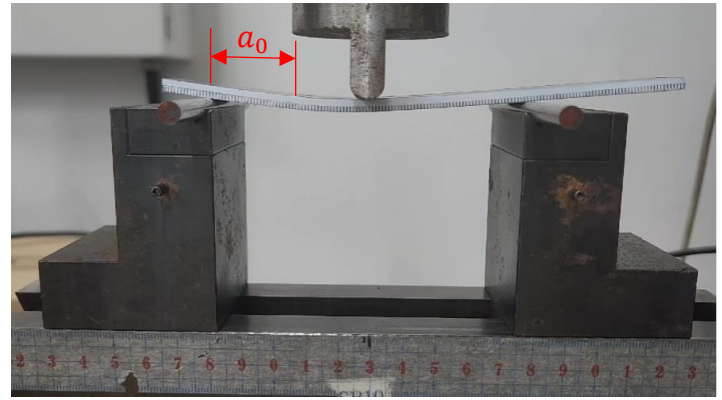

<Fracture Tests($a_0 = 30mm$)>

End-Notched Flexural Testing(ENF) for Self-Healing Effects on the Mode II Toughness

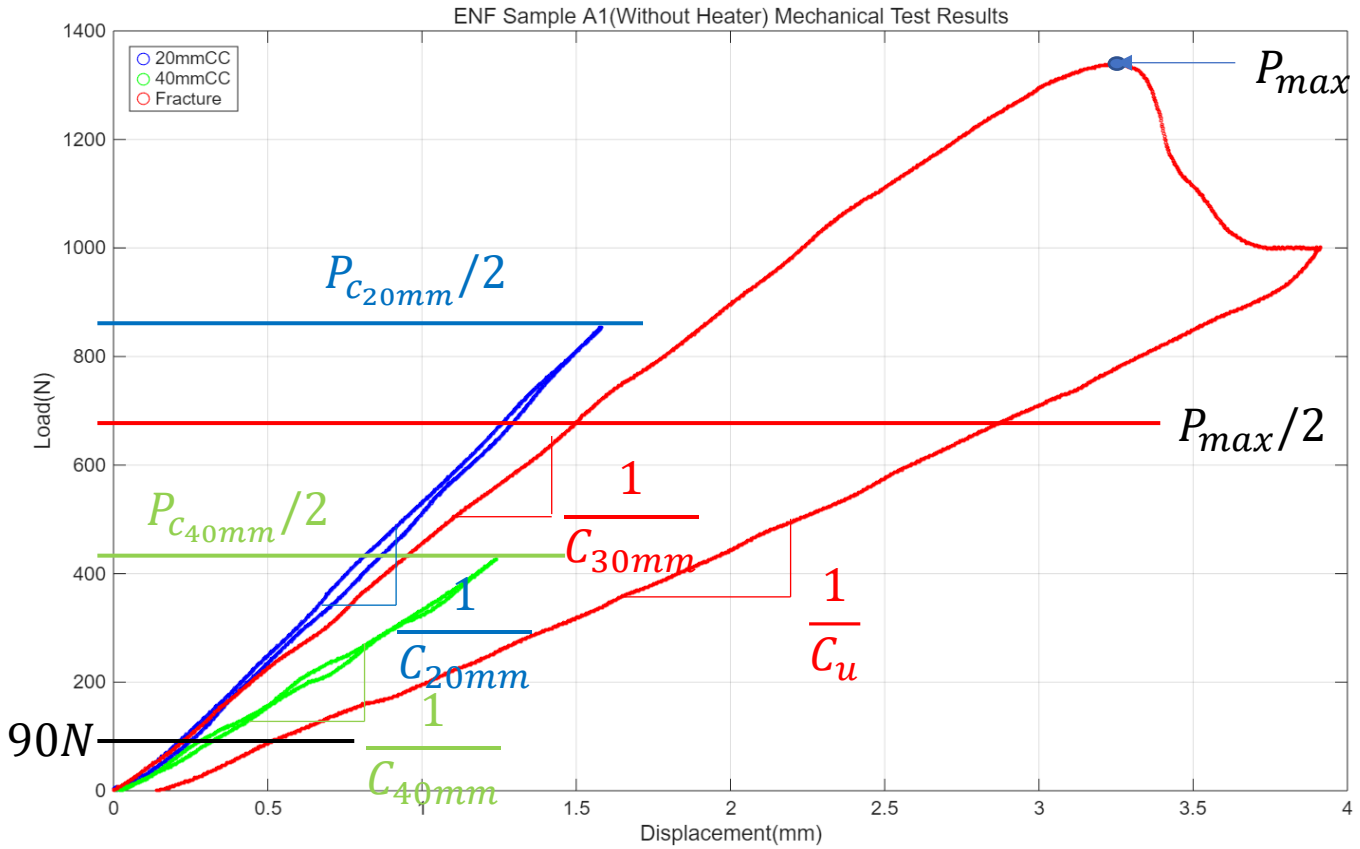

<Calculating the Compliances from the Load-Displacement Curve>

$$P_{c_{a_0}}(\mathrm{a_0 = 20mm, 40mm}) = \frac{4B}{3a_0}\sqrt{G_{IIc}E_{11}h^3}\ a_0^3$$

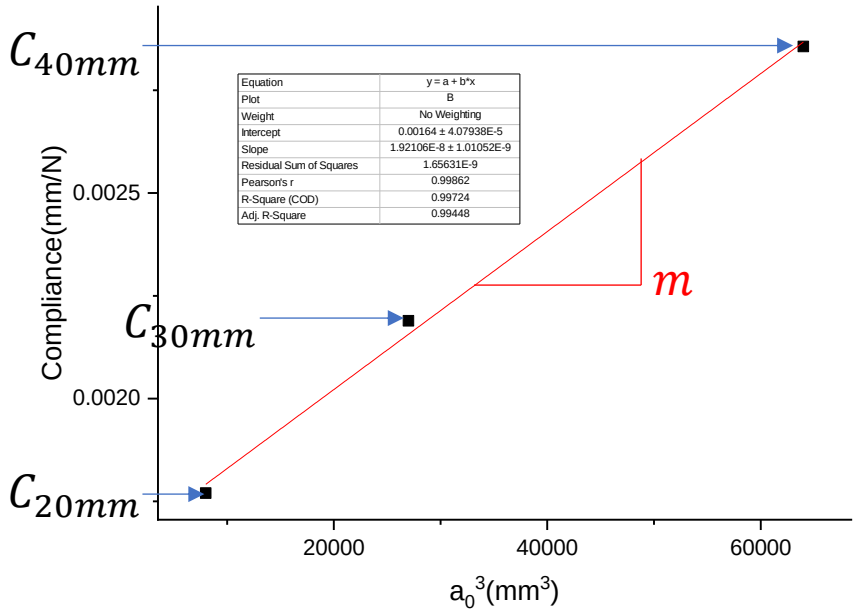

<Calculating the slope of the Compliance-Crack length(a_0) linear fit>

$$G_Q = \frac{3mP_{max}^2a_0^2}{2B}\ (a_0 = 30mm, Fracture\ Test)$$

$$\text{If } 0.15 \le \left(\frac{P_{c_{a_i}}a_i}{P_{max}a_0}\right)^2 \le 0.35\ (\mathrm{a_i = 20mm, 40mm}),$$

$$\mathbf{G_Q = G_{IIc}}$$

Specimen Morphology and the Mechanical Test Results

Morphological Analysis of SBS Specimen

- Visible crack by the film insert is completely reconsolidated in the self-healed Sample D specimen
- Morphologically the self-healing effect is confirmed

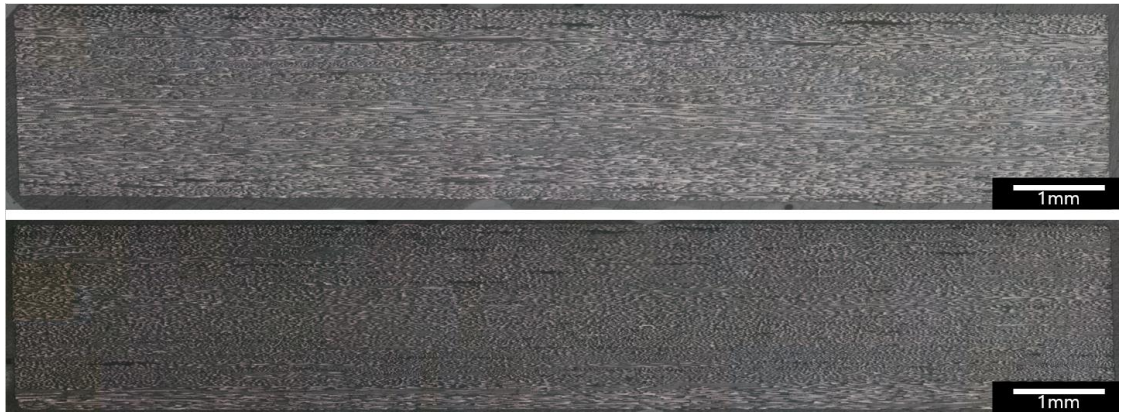

<Sample A(Length X Thickness)>

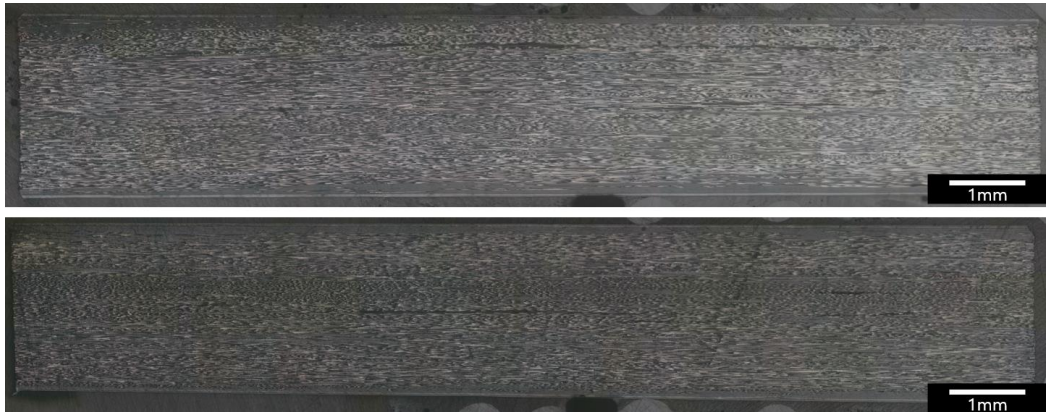

<Sample B(Length X Thickness)>

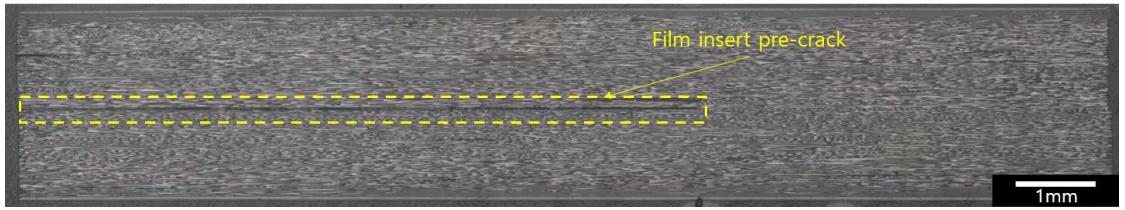

<Sample C(Length X Thickness)>

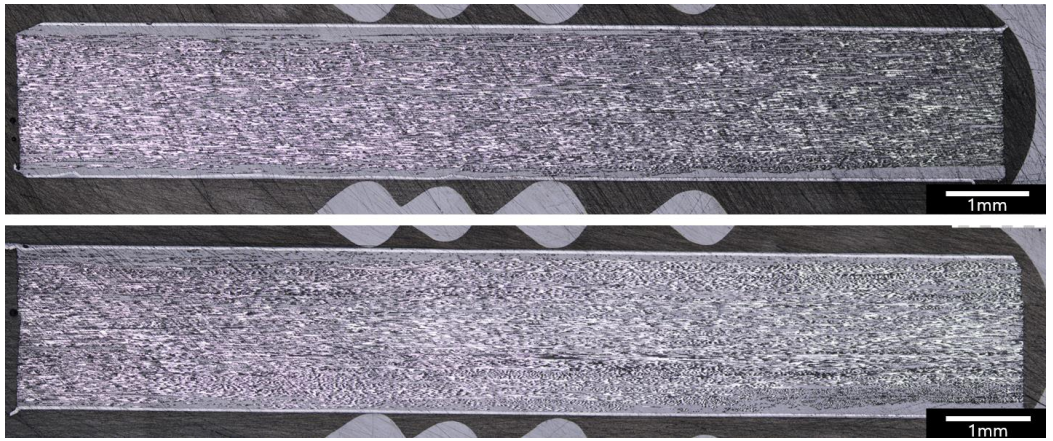

<Sample D(Length X Thickness)>

Stiffness Comparison Results of SBS Specimen

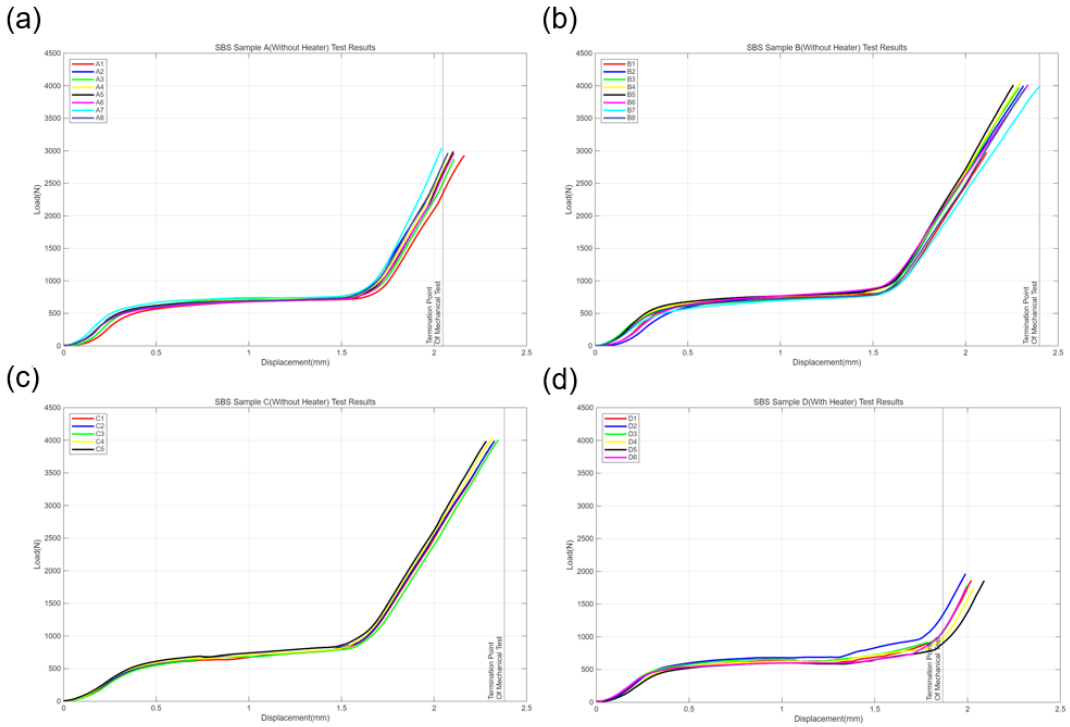

<Load-Displacement Curves of all specimens>

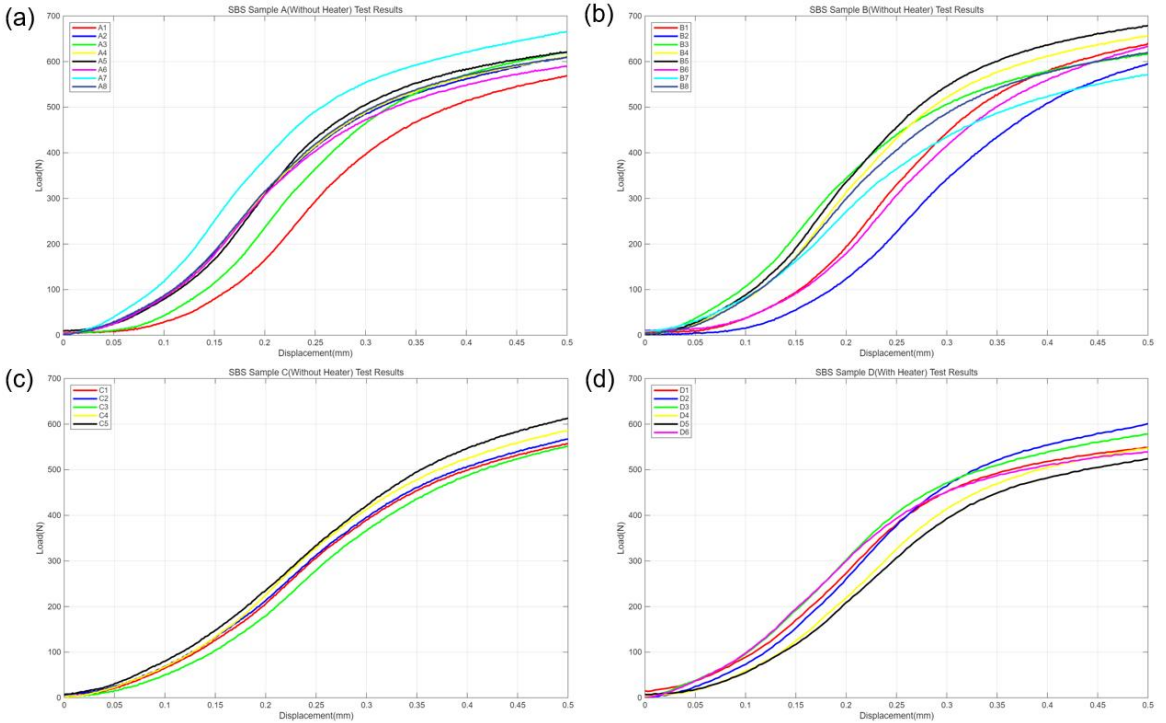

<The Initial load increasing region of the load-displacement curves>

- Maximum derivative value of the initial load-increasing region is selected to represent the bending stiffness
- The calculated bending stiffness is normalized by the second moment of area

Stiffness Comparison Results of SBS Specimen

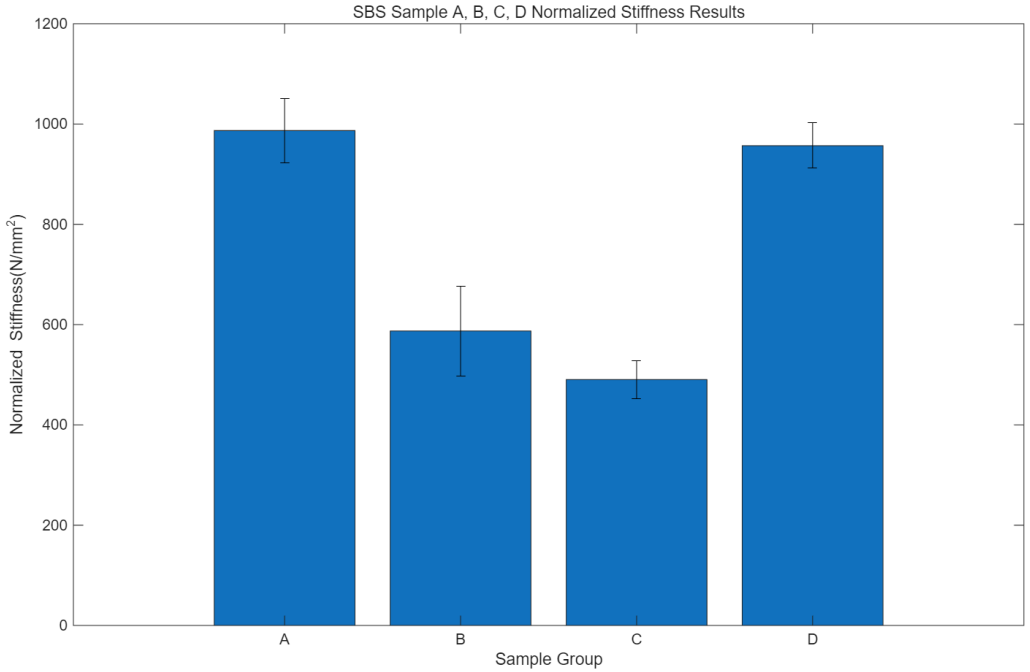

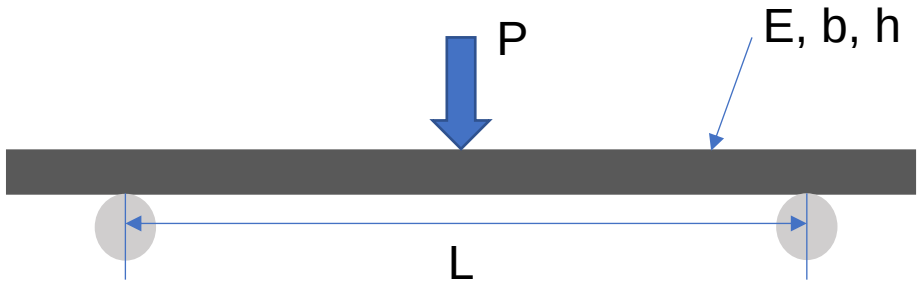

$$K(bending\ stiffness) = \frac{48EI}{L^3}, I = \frac{bh^3}{12}$$

Sample Group	A	B	C	D
Normalized Stiffness(N/mm^2)	986.9234 ± 64.3291	587.3051 ± 89.5869	490.4462 ± 37.9087	956.8082 ± 45.1380

- The bending stiffness is normalized according to the 3-point bending beam theory
- The order of magnitude for bending stiffness is A > D > B > C, with A and D showing similar values

$$K_{normalized} = \frac{1}{12}E = \frac{L^3}{48bh^3}$$

Explanation of Each Stiffness Comparison (A > B)

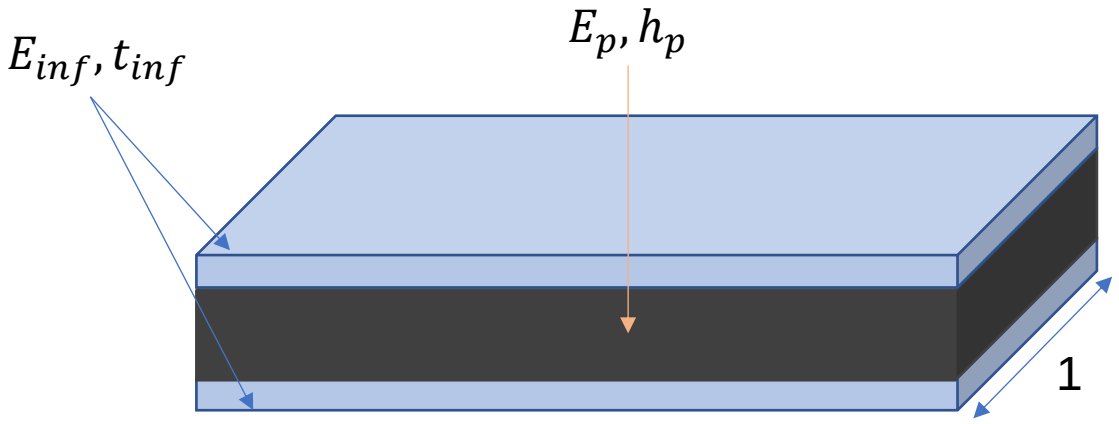

<A sandwich-structured composite material>

*per unit width

$$(EI)_{total} = E_{inf}\frac{1}{12}\left[(h_p + 2t_{inf})^3 - h_p^3\right] + E_p\frac{1}{12}h_p^3$$

$$= \frac{E_{inf}t_{inf}h_p^2}{2}\left(1 + 2\frac{t_{inf}}{h_p} + \frac{4}{3}\left(\frac{t_{inf}}{h_p}\right)^2 + \frac{1}{6}\frac{E_p h_p}{E_{inf}t_{inf}}\right)$$

$$I_{total} = \frac{(h_p + 2t_{inf})^3}{12}$$

- Sample group B resembles a sandwich-structured composite panel material, with the bucky paper-nylon infusion layer as the outer skin
- The Young's modulus of the sample group B specimens are calculated theoretically, and compared with the values of the sample group A specimens
- The ratio of the sample group B to sample group A experimentally turned out to be 0.595, while the theoretical ratio based on parameters obtained through morphology turned out to be 0.61638

Explanation of Each Stiffness Comparison (B > C)

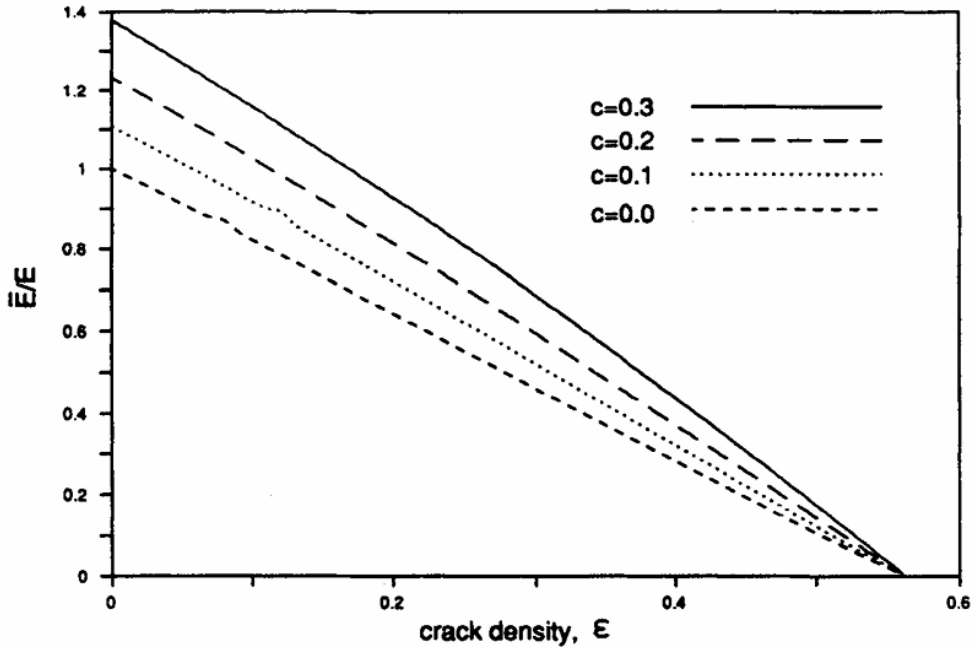

<Ratio of effective Young's modulus with randomly distributed microcracks to the plain Young's modulus[1]>

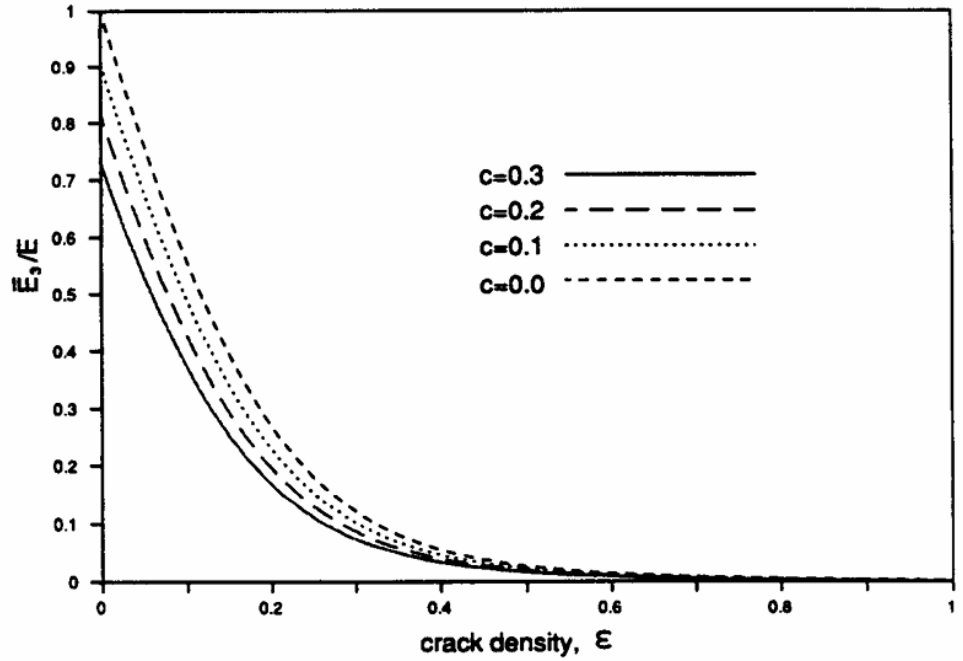

< Ratio of effective Young's modulus with parallel layered microcracks to the plain Young's modulus[1]>

- Intuitively the presence of the pre-crack should decrease the mechanical properties(Young's modulus, or normalized bending stiffness)
- Y Huang et al. showed that the presence of micro-cracks, such as in this research, possess a decreasing effect in the total effective modulus value

[1] Huang, Y., K. X. Hu, and A. Chandra. "The effective elastic moduli of microcracked composite materials." *International journal of solids and structures* 30.14 (1993): 1907-1918.

Explanation of Each Stiffness Comparison (A > D > B)

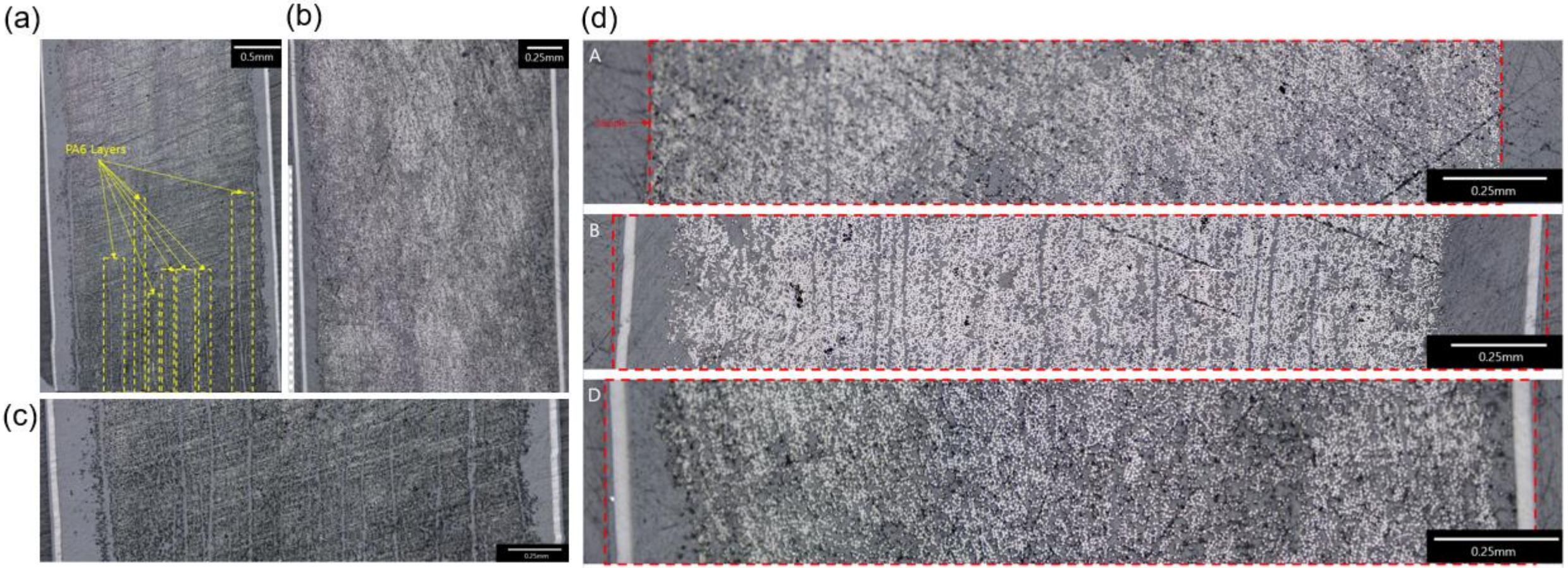

Morphological Analysis of ENF Specimen

(a)

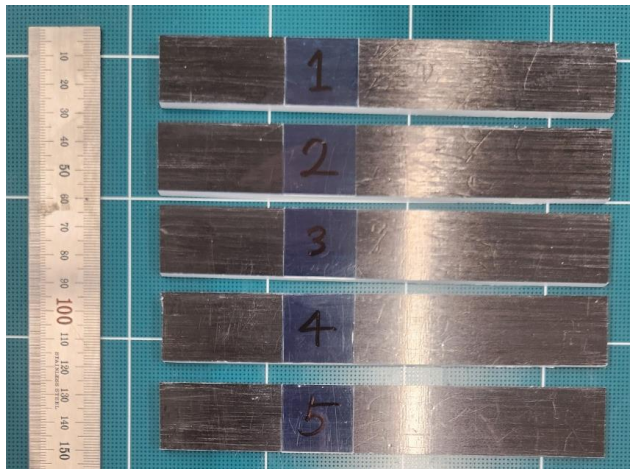

(b)

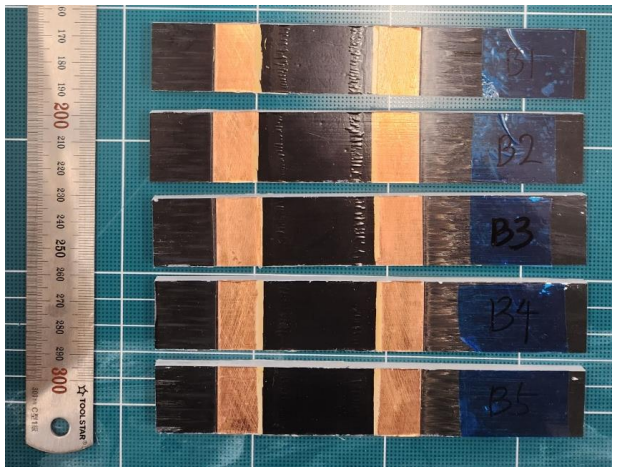

(c1)

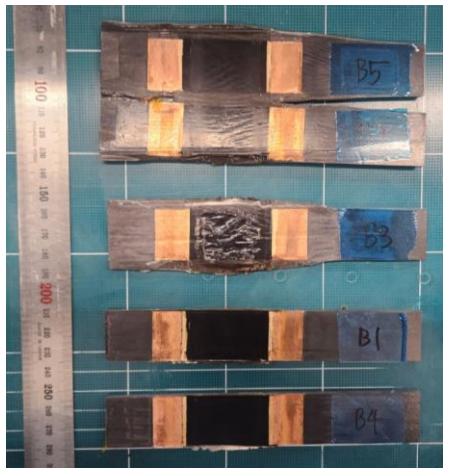

(c2)

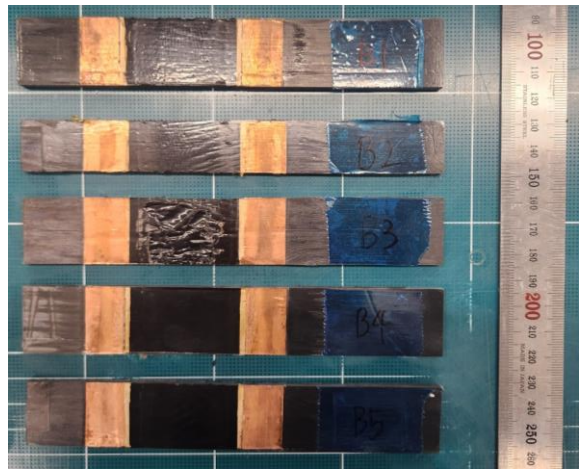

- Specimens in sample group A showed uniform geometry as a baseline control group (a)
- Specimens B2, B3, B5 in sample group B (b) showed deformations after self-healing (c1)
- All specimens in sample group C(after self-healing) were trimmed into a parallel rectangular shape for the ENF testing (c2)

Morphological Analysis of ENF Specimen

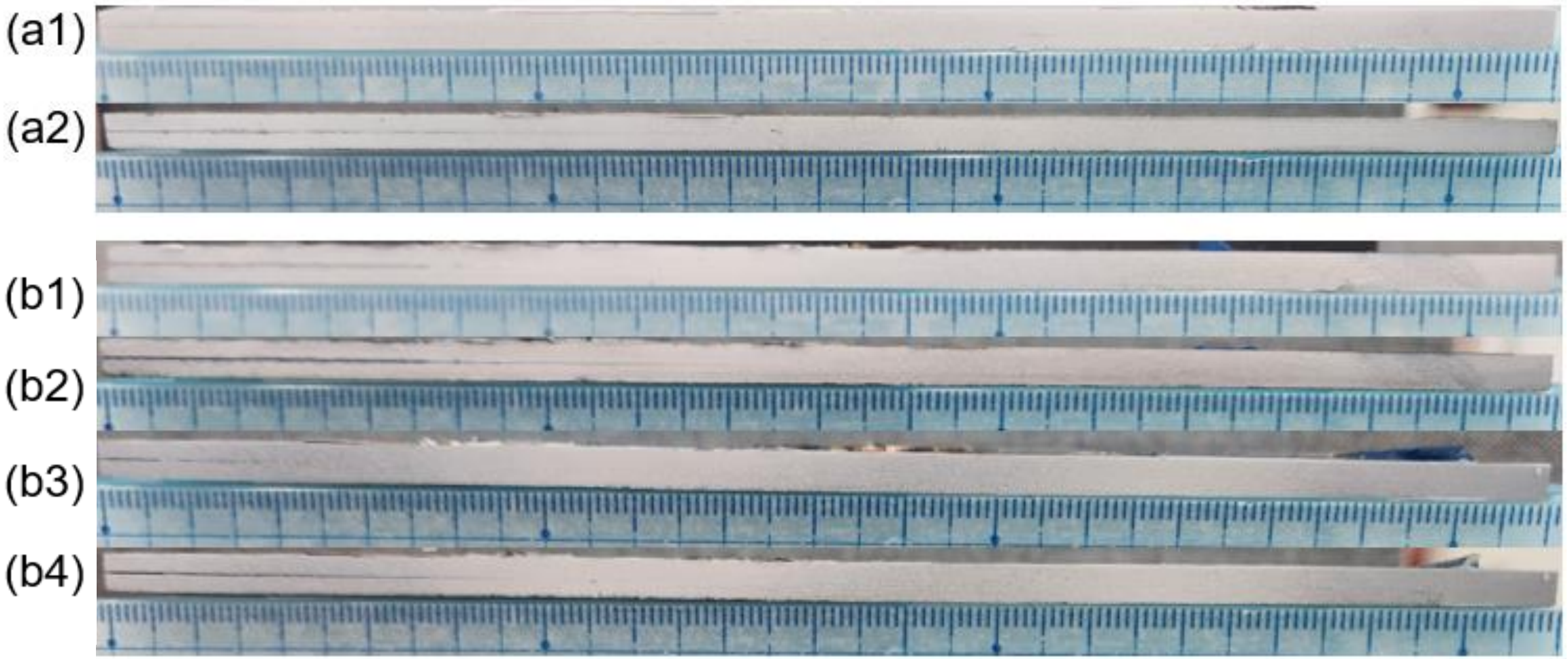

Load-Displacement Curves of all ENF Specimens

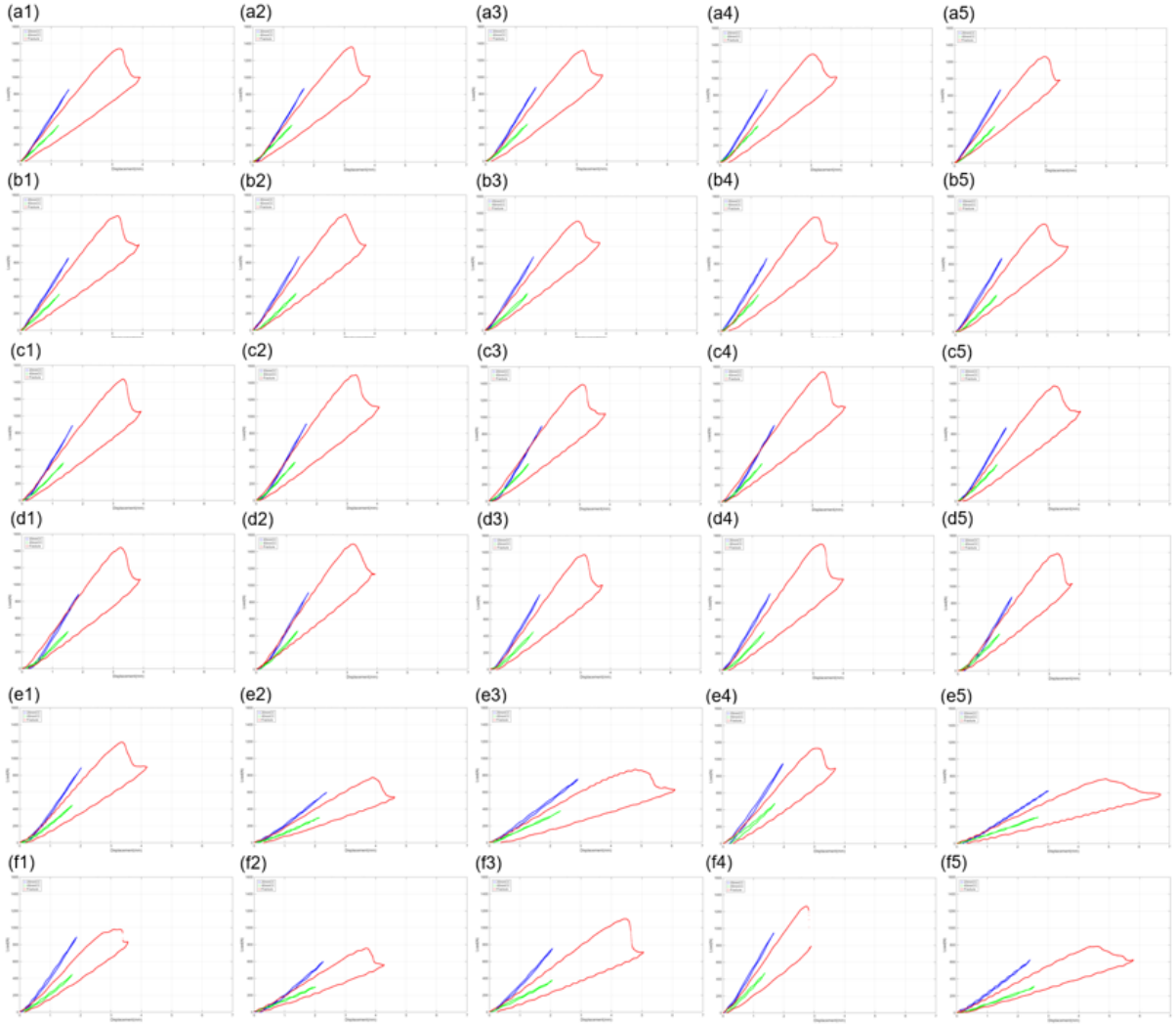

- Specimens in sample group A and B showed consistent and resembling load-displacement curves
- Variations occurred for sample group C specimens, due to the geometry deformations of each specimens via the self-healing process
- The mode II toughness was calculated based on the compliance data obtained via linear fit of each curves

$$G_{IIC} = \frac{3mP^2a^2}{2b} (ASTM\ D7905)$$

Mode II Toughness Comparison Results of ENF Specimen

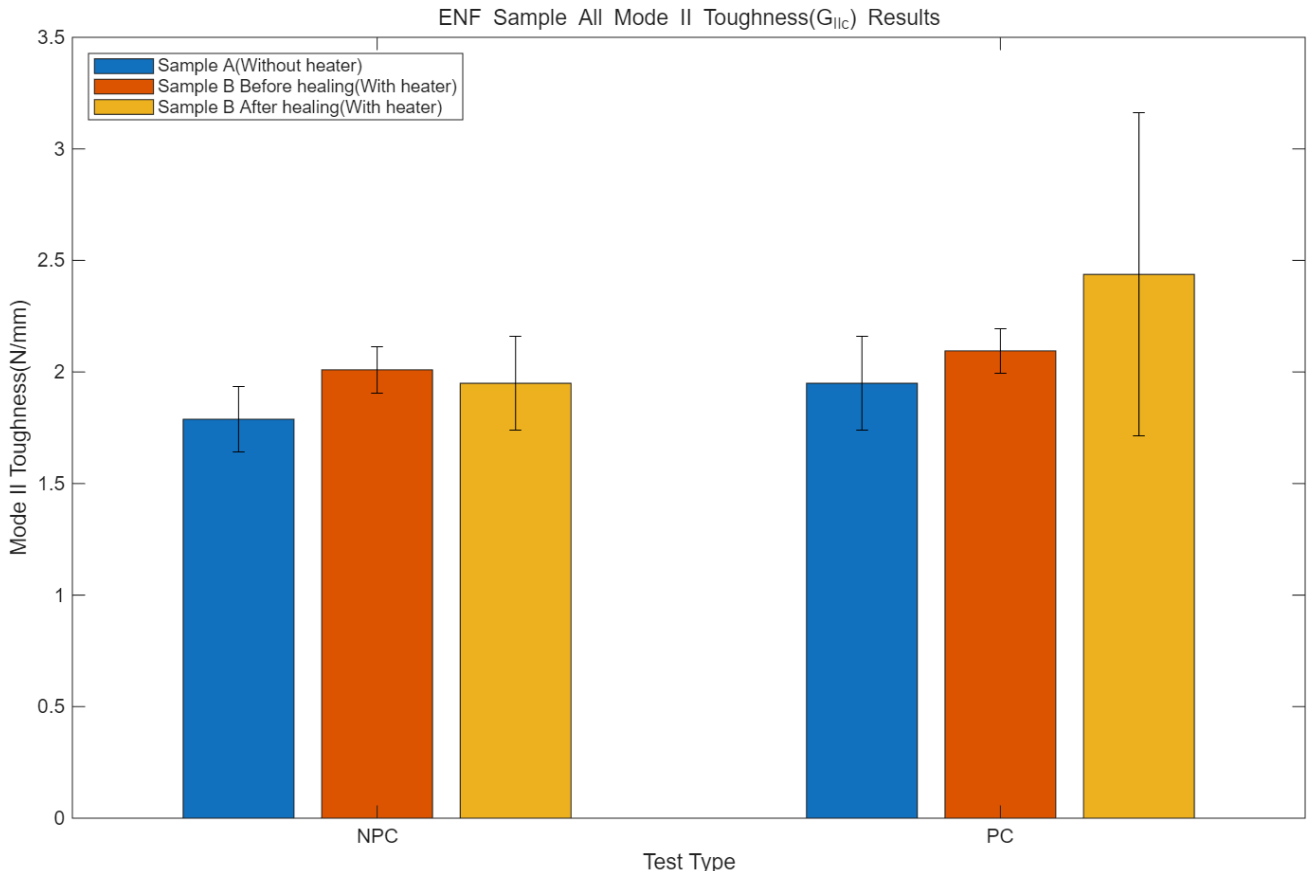

Sample Group	A	B	C
G_{IIC}(NPC)	1.7882 ± 0.1463	2.0095 ± 0.1036	1.9494 ± 0.2094
G_{IIC}(PC)	1.9494 ± 0.2094	2.0946 ± 0.1006	2.4373 ± 0.7253

Mode II Toughness Comparison Results of ENF Specimen: Experiment vs. Theory

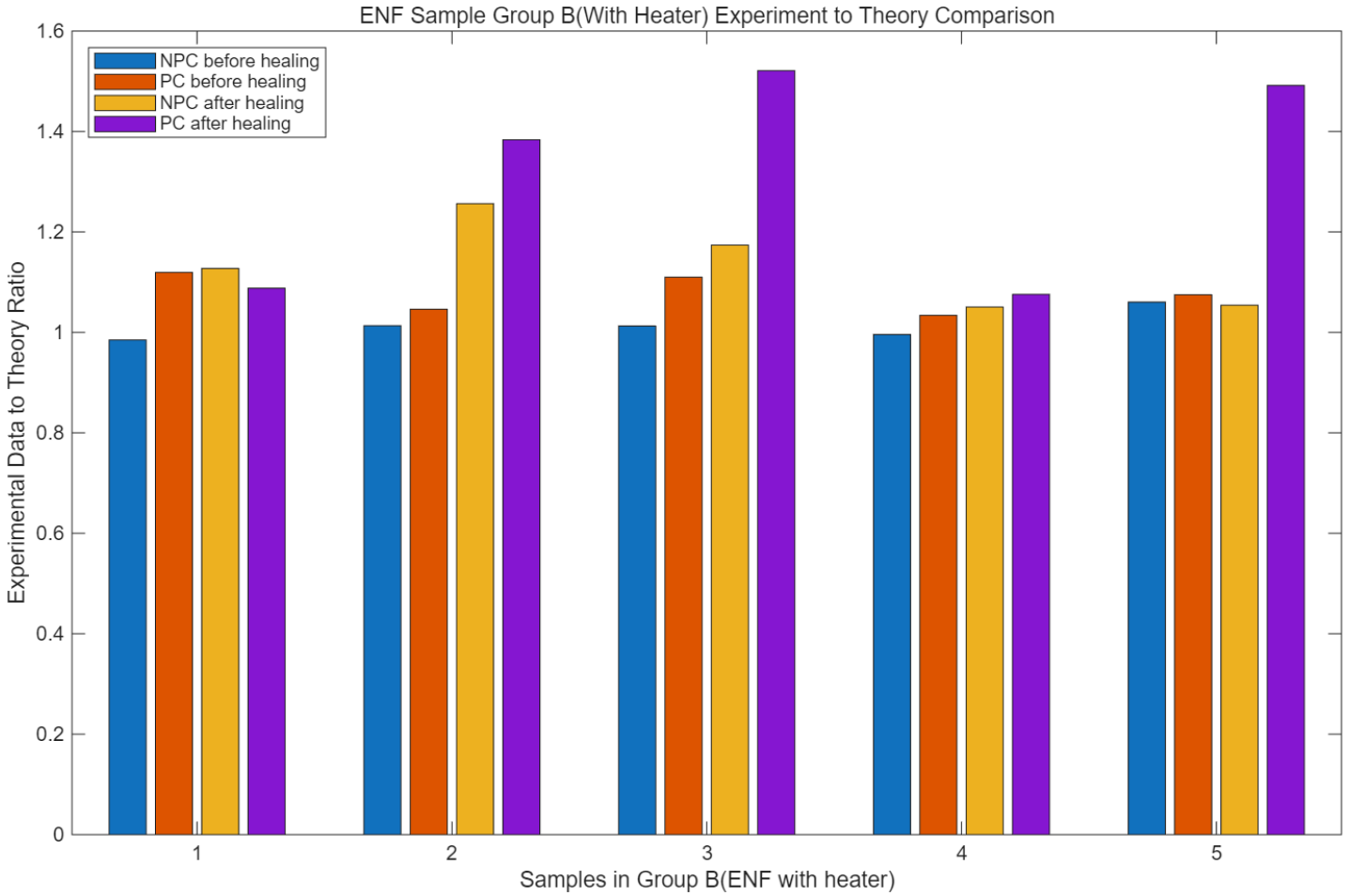

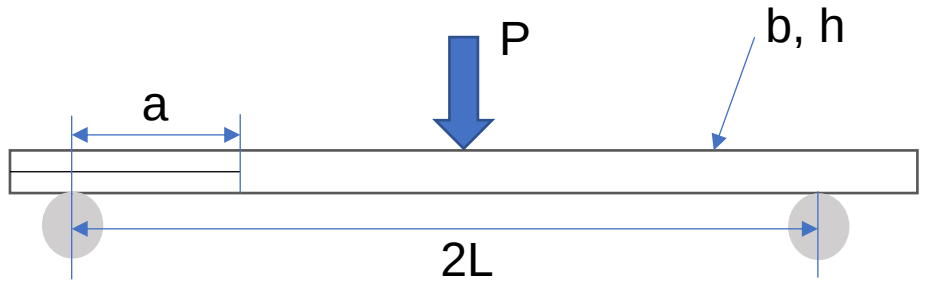

$$G_{II} = \frac{9CP^2a^2}{2b(2L^3 + 3a^3)} (Theory, [1])$$

$$G_{IIC} = \frac{3mP^2a^2}{2b} (ASTM\ D7905)$$

$$\frac{Experiment}{Theory} = \frac{m}{\frac{3C}{2L^3 + 3a^3}}$$

[1] Yoshihara, Hiroshi, and Masamitsu Ohta. "Measurement of mode II fracture toughness of wood by the end-notched flexure test." *Journal of wood science* 46 (2000): 273-278.

Conclusion and Future Work

Conclusion

1) Morphology presents the self-healing is successful for both SBS and ENF specimen

   - Pre-crack(SBS) and propagated crack(ENF) shown reconsolidation

2) Short Beam Shear(SBS) specimens showed around 90% bending stiffness recovery compared to the baseline specimen

   - Self-healing results in the composite parts resembling that of the plain specimen without the nano-engineered architecture

3) End-Notched Flexural(ENF) specimens showed around 90% mode II toughness recovery after self-healing compared to before self-healing

   - Average recovery rates of form-preserved specimens showed around 80% recovery rate
   - More form-preserved specimen data required

Future Work

1) Increasing the Mode II toughness data of the ENF test specimens
   - Utilizing the form-preserving technique via the metal mold

2) Finding the temperature cycle for 100% self-healing efficiency
   - Increasing the holding time or the cooling phase
   - Adjusting the other temperature cycle parameters

3) Developing the self-healing technique without the vacuuming procedure
   - Different polymer matrices without discoloration with oxygen exposure as for PA6
   - Raising the self-healing convenience and efficiency

Thank you for your attention



ICCM24
AUGUST 4-8, 2025
BALTIMORE CONVENTION CENTER
BALTIMORE, MARYLAND, USA

No Technical Paper Submission for:

William Martin

ICCM24
AUGUST 4-8, 2025
BALTIMORE CONVENTION CENTER
BALTIMORE, MARYLAND, USA

No Technical Paper Submission for:

Zachary Phillips

MULTIFUNCTIONAL GRAPHENE-BASED NANOCOMPOSITES WITH SYNERGISTIC EFFECTS OF CHEMICAL AND PHYSICAL INTERACTIONS

Seira Morimune-Moriya*, Satoshi Ito, Kozue Miura

Department of Applied Chemistry, College of Engineering, Chubu University, Matsumoto, Kasugai 487-8501, Japan
Email: seiram@fsc.chubu.ac.jp,

Keywords: PMCs, Mechanical properties, Thermal properties

ABSTRACT

Here in, polyamide 66 nanocomposites with graphene-based nanofillers were prepared and the structure and the properties were investigated. In order to achieve the high dispersibility of the nanofillers, the nanocomposites were prepared by in-situ polymerization. As graphene-based nanofillers, graphene oxide and the chemically modified GO were used. It was revealed that the mechanical properties and the thermal properties significantly increased by the incorporation of graphene-based nanofillers. The nanocomposites with chemically modified GO showed higher Young's modulus, tensile strength and thermal properties. These results indicates that the synergistic effects of chemical and physical interfacial interactions in the nanocomposites achieved the excellent reinforcement effects.

1 INTRODUCTION

Since the first development of polymer nanocomposites by Toyota Central R&D Labs., Inc., research on polymer nanocomposites has intensively been conducted for various applications. So far, many types of nanomaterials have been investigated as nanofillers for polymer nanocomposites, such as nanocarbons, nitride compounds, nanofibers and so on. Among them, nanofillers with high aspect ratio have been revealed to show excellent reinforcement effect to achieve the significant improvement in the properties of polymer materials. Graphene is a single layer of graphite with one-atom-thickness and has high aspect ratio. Graphene have attracted great attention because of itsexcellent mechanical properties, thermal properties, electrical properties and so on since Geim et al. won the Nobel Prize in physics for discovering and identifying its unique properties.

In this study, graphene-based polyamide 66 (PA66) nanocomposites were prepared by in-situ polymerization. In the process of in-situ polymerization, polymerization proceeded under the presence of fillers. Therefore, the dispersibility of a filler in a solvent can be maintained even in the nanocomposites. In addition, fillers can chemically react with polymer matrices during the polymerization, resulting in the strong interfacial interactions through covalent bonds. We used two types of graphene, graphene oxide (GO) and the chemically modified GO (GO-DDA) and investigated the effect of the surface functional groups of graphene oxide (GO) and the chemically modified GO (GO-DDA) on the structure and the properties of the nanocomposites.

2 SAMPLE PREPARATION

GO aqueous suspension or GO-DDA was dispersed in pure water. The amount of filler was controlled to be 0.1 wt% in the suspension. The suspension was ultrasonicated for 90 min in water bath to obtain the high exfoliation of GO or GO-DDA. The GO or GO-DDA suspension was added to the mixture of hexamethylenediamine and sodium hydroxide solution and then stirred for 1 h (mixture 1). The organic chloride mixture which contained adipoyl chloride and carbon tetrachloride (mixture 2) was prepared in the other beaker. The mixture 1 was slowly added to the top of the mixture 2 using a glass rod. The condensation polymerization of PA66 was proceeded at the interface between mixture 1 and mixture 2

under the presence of GO or GO-DDA. The reaction product was wound on the glass rod, followed by washing with water and ethanol for several times. For the purification, re-precipitation with phenol and methanol was carried out to remove the unreacted solvents and low-molecular-weight products. After vacuum filtration, the product was washed with water, dried at 40 °C for 48 h and then in vacuum at 40 °C for 72 h. The dried product was put between aluminum plates with a spacer and then melt pressed at 270 °C to obtain the PA66/GO nanocomposite or PA66/GO-DDA nanocomposite with a thickness of 0.2 mm.

3 RESULTS AND DISCUSSION



Figure 1 Optical images of PA66, PA66/GO nanocomposites and PA66/GO-DDA nanocomposites.

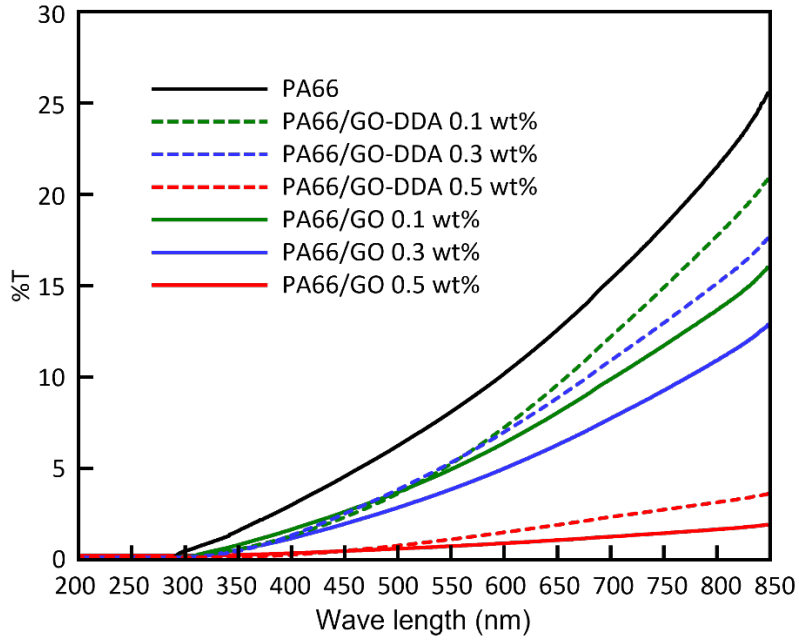

Figure 2 UV-vis spectra of PA66, PA66/GO nanocomposites and PA66/GO-DDA nanocomposites.

Figure 1 and Figure 2 shows the optical images and UV-vis spectra of PA66, PA66/GO nanocomposites and PA66/GO-DDA nanocomposites, respectively. The nanocomposites exhibited the favorable transparency, indicating the homogeneous dispersion of the fillers. Compared to the nanocomposites with GO, the nanocomposites with GO-DDA shows higher transparency. It was suggested that the dispersibility in PA66 was improved by the chemical modification of GO.

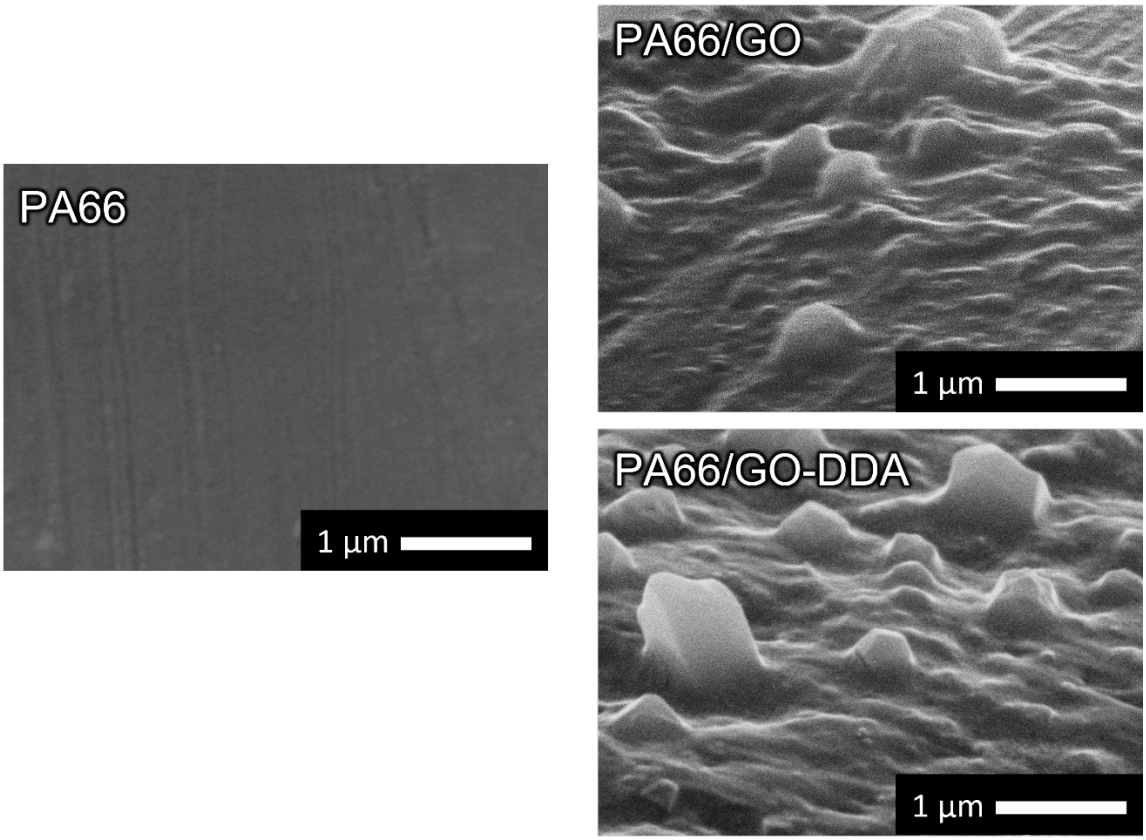

Figure 3 SEM images of PA66, PA66/GO nanocomposites (0.5 wt%) and PA66/GO-DDA nanocomposites (0.5 wt%).

Figure 3 shows SEM images of the cross section of PA66, PA66/GO nanocomposites and PA66/GO-DDA nanocomposites. The filler content was 0.5 wt%. It was revealed that the fillers were homogeneously dispersed and highly aligned in the in-plane direction of the nanocomposites.

Figure 4 shows XRD profiles of PA 66, PA66/GO nanocomposites and PA66/GO-DDA nanocomposites. All the profiles show the characteristic peaks of (100) and (010)/(110) of PA66 at 2 theta of 20.9 ˚ and 24.2 ˚, respectively. Since there is no shift in peak position, there is no change in d-spacing by the addition of GO or GO-DDA. The crystallinity estimated from the profiles are inserted in Figure 4. The crystallinity of the nanocomposites increases with the addition of GO or GO-DDA. It is well known that nanofillers can act as crystallization nuclei in polymer nanocomposites. At the same time, nanofillers can increase the viscosity of composite suspensions/solutions and cause the low molecular mobility which decrease the crystallinity. These counter effects can also occur in PA66/GO nanocomposites and PA66/GO-DDA nanocomposites. It is assumed that the former effect might be slightly dominant in the present nanocomposites.

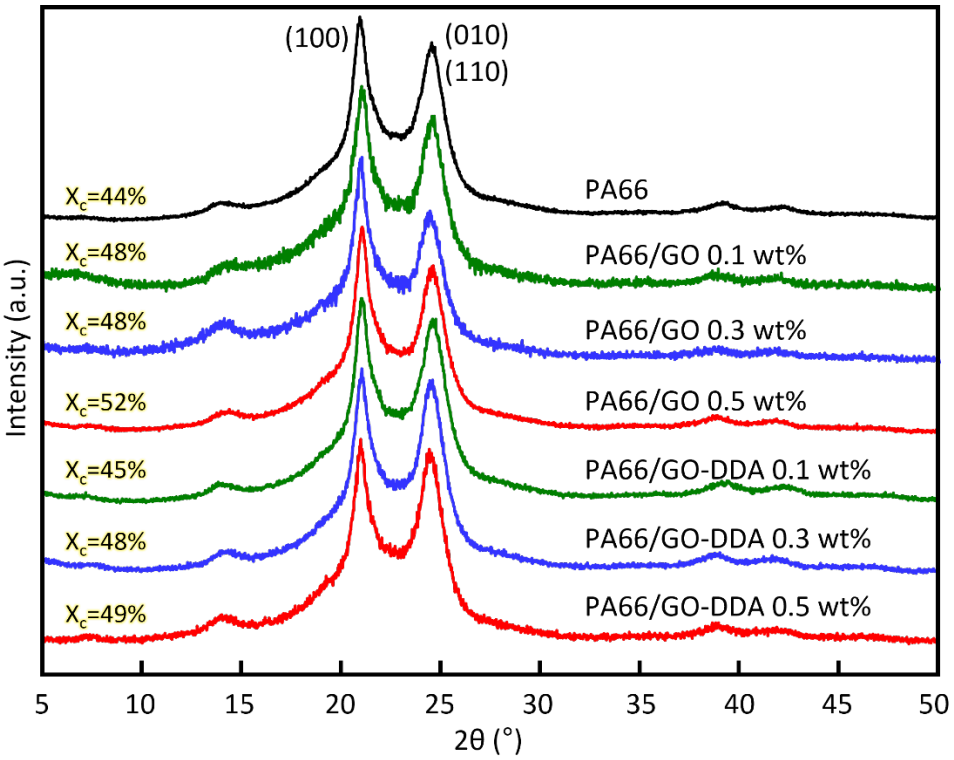

Figure 4 X-ray diffraction profiles of PA66, PA66/GO nanocomposites and PA66/GO-DDA nanocomposites.

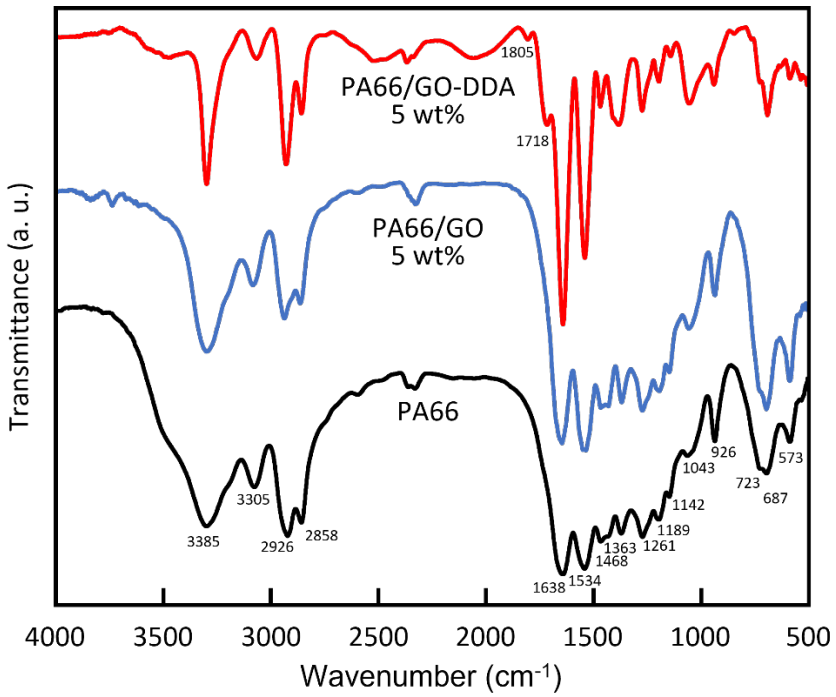

Figure 5 ATR-FTIR spectra of PA66, PA66/GO nanocomposites and PA66/GO-DDA nanocomposites.

Figure 5 shows the ATR-FTIR spectra of PA66, PA66/GO nanocomposites and PA66/GO-DDA nanocomposites. The characteristic bands derive from amide bonds in PA66 are observed for all the spectra. Both of the bands at 3385 cm^{-1} and 3305 cm^{-1} are attributed to N-H stretching vibration, while the lower wavenumber indicates the effects of intermolecular or intramolecular hydrogen bonds of PA66. The intensity of the bands at 3305 cm^{-1} of the PA66/GO-DDA nanocomposites is weaker than that of the PA66/GO nanocomposites, indicating the decrease of hydrogen bonds due to the substitution of carboxy groups to DDA on GO surface. Furthermore, the PA66/GO nanocomposite had the highest amide bond content, followed in the order of PA66/GO-DDA nanocomposites > PA66. It is revealed that the formation of amide bonds is facilitated in the process of the *in-situ* polymerization of the nanocomposites.

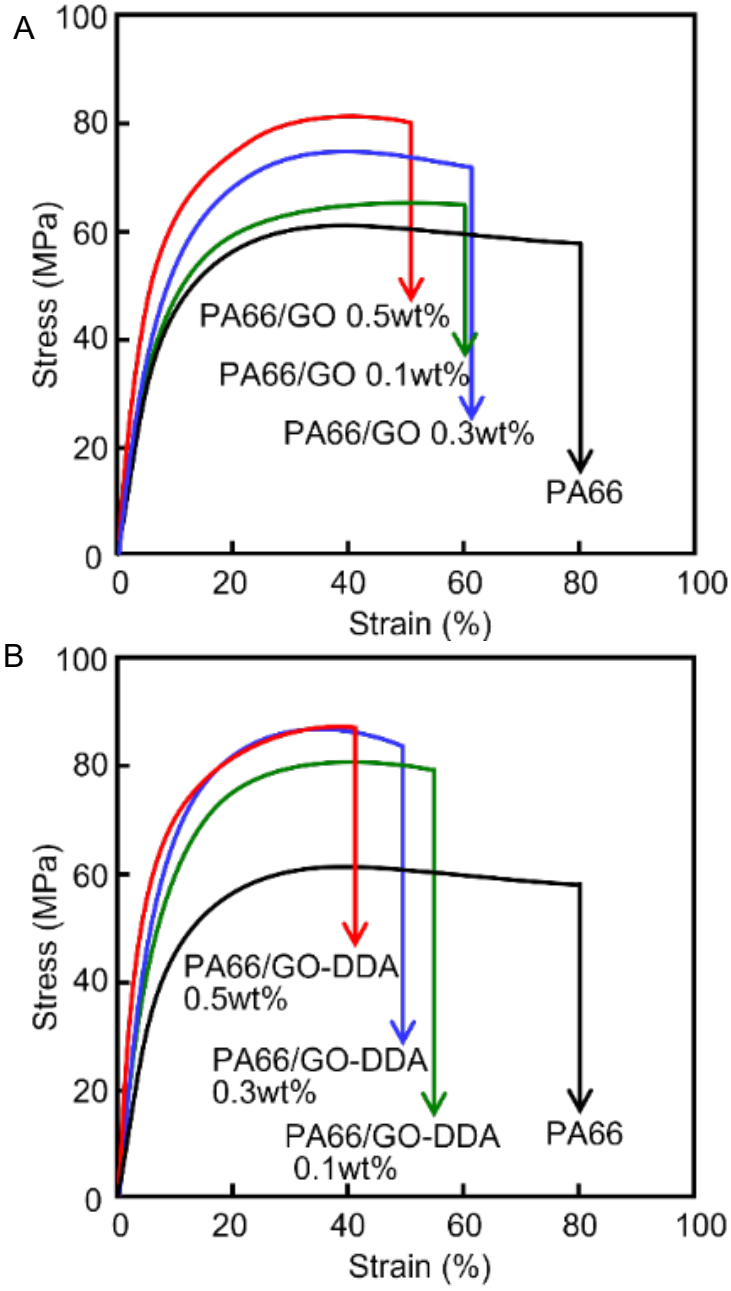

Figure 6 Stress-strain curves of (A) PA66/GO nanocomposites and (B) PA66/GO-DDA nanocomposites

Figure 6 shows stress-strain curves of (A) PA66/GO nanocomposites and (B) PA66/GO-DDA nanocomposites. It was revealed that the Young's modulus increased by 75% and 100% by the addition of 0.5 wt% of GO and GO-DDA, respectively. The strong reinforcement effects of the fillers were successfully imparted to the nanocomposites by the strong interfacial interactions and the high dispersibility with in-plane alignment. From the theoretical analysis using Halpin-Tsai model, the Young's modulus of the PA66/GO-DDA nanocomposites was revealed to be higher than that of the theoretical value at all the filler content. It was assumed that the physical interactions between PA66 and DDA molecular chains on GO-DDA played the important role in the reinforcement of the nanocomposites.

As for the thermal properties, the nanocomposites showed excellent thermal resistance. For example, the thermal decomposition temperature increased by 26 ˚C and 31 ˚C by the addition of 0.5 wt% of GO and GO-DDA, respectively. The molecular motion of PA66 was restricted by the highly dispersed/ aligned fillers with strong interfacial interactions. In addition, generation of volatile decomposition products were effectively barriered by the 2D fillers aligned to the in-plane direction.

In conclusion, the synergistic effects of chemical and physical interfacial interactions of the graphene-based nanocomposites lead the superior reinforcement effect in the mechanical and thermal properties at low content.

4 CONCLUSIONS

In this study, PA66/GO nanocomposites and PA66/GO-DDA nanocomposites were prepared by in-situ polymerization. As a result, the high dispersibility with in-plane alignment of the fillers was achieved in the nanocomposites. The crystallinity increase by the incorporation of GO or GO-DDA, indicating the nucleation effects by these nanofillers. ATR-FTIR spectra indicate that amide bonds are formed at the interfaces between PA66 and the fillers for both PA66/GO nanocomposites and PA66/GO-DDA nanocomposites. The excellent reinforcement effects on the mechanical and thermal properties are revealed. Compared to PA66, the Young's modulus increases by 92% for the nanocomposites at only 0.3 wt% loading of GO-DDA, while it increases by 42% for the nanocomposites with GO at the same content. In addition, the thermal decomposition temperature of the PA66/GO-DDA nanocomposite at 0.3 wt% is 31 ˚C higher than that of PA66. It is assumed that the synergetic effect of chemical and physical interfacial interactions lead the superior reinforcement effects of the PA66/GO-DDA nanocomposites at low content.

SOFT COMPOSITES FOR CHARGE TRANSPORT AND STORAGE TO SYNERGISTICALLY ENHANCE ENERGY HARVESTING PERFORMANCE OF TRIBOELECTRIC GENERATORS

Ziyan Gao[1], Yang Zhou[1], Zhao Sha[1], Vahid Mohabbati[1,2,3], Mohammadkazem Papan[2,3,4], Shuai He[1], Shuhua Peng[1], Chun Hui Wang[1]*

[1] School of Mechanical and Manufacturing Engineering, University of New South Wales, Sydney, NSW 2052, Australia

[2] Sydney Pain Management Centre, Sydney, NSW 2150, Australia

[3] Sydney Pain Research Centre, Sydney, NSW 2076, Australia

[4] School of Natural Sciences, Macquarie University, Sydney, NSW 2109, Australia

*Corresponding author (chun.h.wang@unsw.edu.au)

Keywords: Triboelectric Nanogenerator; Multilayer Structure; Surface Potential; Volume Charge Distribution

ABSTRACT

The incorporation of interlayers between the charge-generating layers and current collectors of triboelectric nanogenerators (TENGs) has been found as an effective strategy to significantly increase power output, indicating their critical role in charge retention. However, there is a lack of direct experimental evidence of charge distribution in the interlayers. We introduce herein a novel approach of self-bonding and de-stacking to quantitatively characterize volume charge distributions within the interlayers as well as the charge-generating layers. The total charge within each layer is determined by measuring their surface potential. Applying this method on multilayer TENGs composed of different materials shows that the charge-generating layer holds roughly the same amount of charge independent of the interlayer characteristics, while the interlayer can store electrical charges depending on its conductivity and dielectric constant. At an optimal balance between these properties, a 220% increase in electrical output has been found compared to conventional TENGs without interlayers and a 50% increase over those with only one interlayer.

1 INTRODUCTION

Triboelectric nanogenerators (TENGs) have emerged as a promising technology, which are operated through the coupling effects of triboelectrification and electrostatic induction. It offers several advantages, including large range of material selection, lightweight, low-cost, high-power output, making them highly adaptable for diverse applications. Several studies have shown good potential of integrating TENGs into medical and therapeutic application [1-3]. However, the development of triboelectric materials with high power output performance are crucial to power medical devices. Various methods have been previously explored to enhance the performance of TENG by improving permittivity of composite materials, performing surface engineering [4, 5] and so on. The above methods have contributed significantly to improving the output performance of the TENGs.

However, the performance of TENGs is largely influenced by the surface charge density of the triboelectric material.[6] Unfortunately, surface charges tend to decay quickly due to factors such as air breakdown, ambient humidity and charge diffusion which can significantly reduce the output.[7] Delaying the surface charge decay time is particularly important to improve the output performance of TENGs. Triboelectric charge drift or diffusion is one of major factor causing triboelectric charges decay.

During continuous operation of TENG, the negative triboelectric layer captures negative triboelectric charges from the positive triboelectric layer, accumulating them on its surface. At the same time, the bottom electrode beneath the negative triboelectric layer generates induced positive charges via electrostatic induction establishing an upward electric field.[8] Consequently, triboelectric charge decay occurs through charge drift and diffusion. The drift is driven by the electric field, and the diffusion driven by the electron's concentration gradient.

To mitigate triboelectric charge dissipation in TENG, an effective strategy involves employing composite films that incorporate high-permittivity fillers within the triboelectric layer. For instance, Tantraviwat et al enhanced the dielectric constant by incorporating PDMS with $BaTiO_3$ which significantly boosted the output performance.[9] Furthermore, conductive fillers have also been incorporated into composites because of its great charge storage capacity to enable charge transport deeper within the film and boost performance.[10] For example, Sun et al. used a conductive MWCNT network in TPU film, significantly enhancing output current by dispersing surface charges into the TPU layer's interior.[11]

Another effective strategy to reduce charge diffusion and drift involves embedding an intermediate layer between the triboelectric layer and electrode, which can transport, storage and block charges. High-permittivity materials such as TiO2[12, 13] and BTO[14] have been developed as charge-blocking layers to enhance TENG output. For example, Park et al. showed that incorporating a TiOx electron-blocking layer with high permittivity enhanced TENG output power by 25 times, owing to its combined electron-blocking and polarization effects [13]. Similarly, Wu et al. introduced a SiO_2 layer to trap charges on hydrophobic fluoropolymer surfaces, leading to the development of a novel charge-trapping nanogenerator[15]. Furthermore, Jiang et al. demonstrated that placing a charge-trapping-blocking intermediate layer composed of rGO and Ag nanoparticles between the triboelectric layer and the electrode can significantly boost the output performance.[16]

Although interlayers have been shown to be effectively enhanced the power outputs of TENGs, direct experimental evidence regarding how the charges are distributed beneath the surface of the charge generating layer remains limited. This leaves a significant gap in understanding the volume charge distributions within the interior of various interlayer types, such as transporting layer,[11] storage layer,[16] and blocking layer.

In this study, we present a novel approach for quantifying the electrical charge distribution beneath the charge-generating surface using a stacking and de-stacking technique. To investigate the influence of dielectric constant and conductivity on charge distribution, we developed a composite tri-layer TENG comprising a PDMS-based charge generating layer, a charge-transporting layer (PDMS nanocomposite with multi-wall carbon nanotube MWCNT) and a charge-storage layer (PDMS nanocomposite with $BaTiO_3$). By adjusting the concentrations of nanofillers, we tuned the electrical conductivity and dielectric constant of the interlayers to determine the optimal combination for maximizing output performance. Enabled by a commercially scalable fabrication process, the composite tri-layer TENG holds strong potential for advancing high performance, self-powered wearable and implantable medical devices.

2 RESULTS AND DISCUSSION

Figure 1 provides a schematic overview of the multilayer composite TENG device structure including intermediate layers. In this configuration, a thin PDMS film acts as the negative triboelectric

layer, while the bottom aluminum film serves as the electrode. The top aluminum film functions both as the positive triboelectric layer and as an additional electrode. To enhance performance of the TENG, intermediate layers were introduced between the PDMS and aluminum electrode. An $MWCNT/PDMS$ hybrid layer was incorporated as a charge transport layer, while a $BaTiO_3/PDMS$ hybrid layer served as a charge-storage layer. As illustrated in **Figure 1a-c**, three designs were developed: Design A, consisting of a pristine PDMS thin layer; Design B, featuring a PDMS layer with a $BaTiO_3/PDMS$ hybrid layer inserted between the PDMS and the aluminum electrode; and Design C, which included both an MWCNT/PDMS hybrid layer and a $BaTiO_3/PDMS$ hybrid layer inserted between the PDMS and the aluminum electrode.

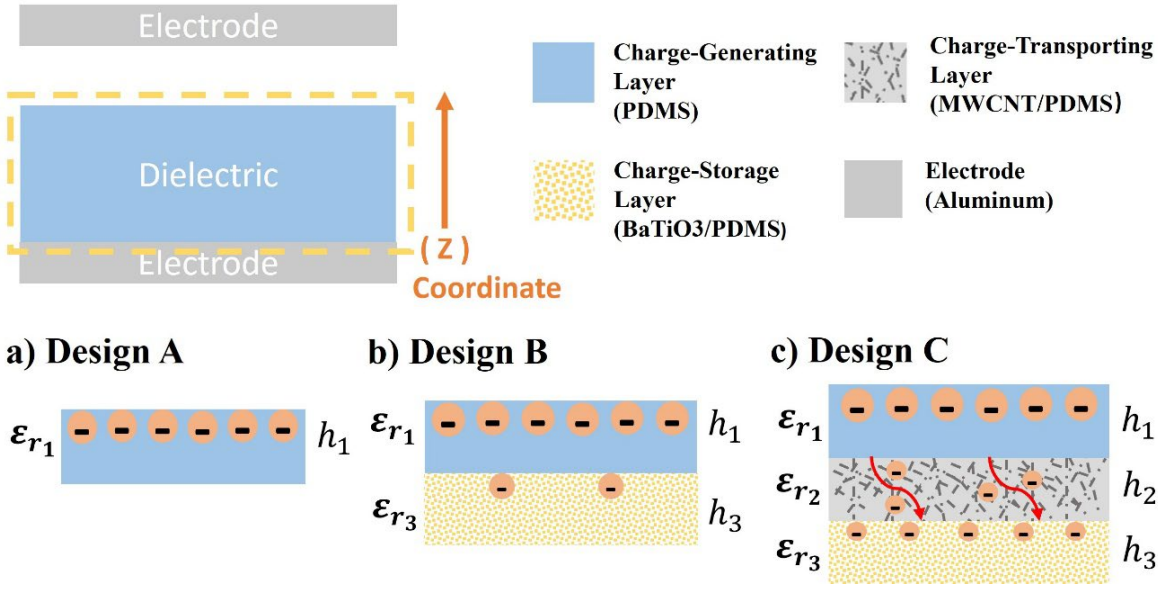

Figure 1: Multilayer TENG Configurations. a) Design A features a single PDMS layer. b) Design B includes one intermediate $BaTiO_3/PDMS$ layer as charge-storage layer. c) Design C incorporates two intermediate layers: MWCNT/PDMS as charge-transporting layer and $BaTiO_3/PDMS$ as charge-storage layer.

2.1 ELECTRICAL CHARACTERIZATION OF DIFFERENT MULTILAYER COMPOSITE TENGS

Based on the prepared composite films, the electrical output performance of samples was tested in the vertical contact-separation mode during the experiment. **Figure 2a** demonstrated the working principle of the multilayer composite TENG. The electricity generation cycle is governed by the combined effects of contact electrification and electrostatic induction. When the aluminium film contacts the PDMS surface, electrons transfer between the two-contacting surface due to their different electron affinities (**Figure 2a(i)**). As the aluminium film moves away from the PDMS, a potential difference is established, driving electrons through the external circuit from the top electrode to the bottom one (**Figure 2a(ii)**). This current continues until an equilibrium is reached at the point of maximum separation (**Figure 2a(iii)**). When the aluminium film returns toward the PDMS surface, the process reverses: electrons flow from the bottom to the top electrode (**Figure 2a(iv)**). Through repeated contact and separation, the multilayer composite TENG generates alternating current (AC) electricity,

which can be rectified and stored in a battery or capacitor to power electronic devices. During this cycle, electric charges also flow through the PDMS and the charge-transporting layer (**Figure 2a(ii)**), driven by the internal electric field. This charge flow continues from the generation surface to the storage layer until a new equilibrium is reached.

Figure 2b-d plots the output performance of different multilayer composite TENGs working at the frequency of 2 Hz. The pristine TENG without the additional layer shows a peak open-circuit voltage (V_{oc}) of 243 V, peak short-circuit current (I_{sc}) of 1.2 μA and transferred charge (Q_{sc}) of 33 nC. Later, Design B with a $BaTiO_3$/PDMS hybrid layer exhibits enhanced output, with the V_{oc}, I_{sc} and Q_{sc} of 575 V, 3 μA and 54 nC respectively. Design C with the MWCNT/PDMS and $BaTiO_3$/PDMS hybrid layers demonstrate further enhancement in output performance with V_{oc} of ~1103 V, I_{sc} of 6.18 μA and Q_{sc} of 73 nC respectively. Accordingly, the enhancement of the output I_{sc} with the MWCNT/PDMS and $BaTiO_3$/PDMS hybrid layers is almost 5 times that of the pristine TENG.

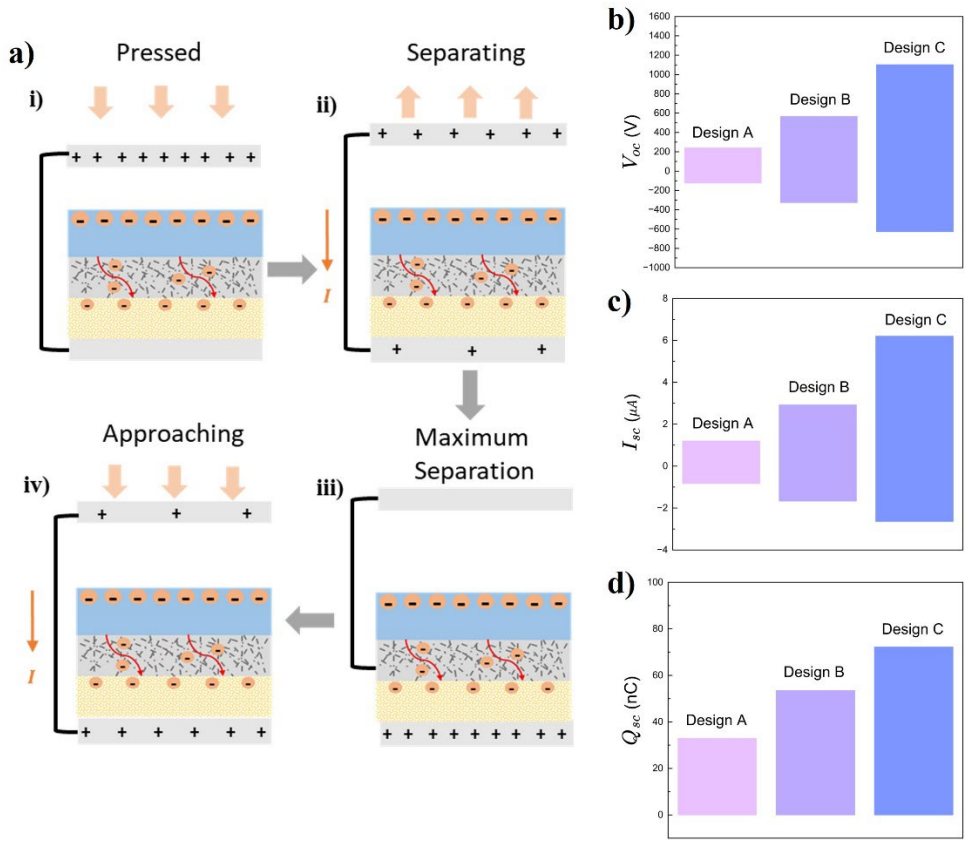

Figure 2: Electrical Characterization of different multilayer composite TENGs. a) Working mechanism of the tri-layer TENG. b) V_{oc} of TENGs. c) I_{sc} of TENGs. d) Q_{sc} of TENGs.

As electrons accumulate on the contact surface, they induce positive charges on the bottom electrode, forming a vertically upward built-in electric field between the surface and the electrode. This field initiates two modes of electron transport: drift which is driven by the electric field, and diffusion which is caused by the concentration gradient of electrons. Both mechanisms can lead to the recombination of triboelectric electrons with the induced positive charges on the electrode, resulting in charge loss. Moreover, triboelectric electrons may also recombine with adsorbed positively charged ions or air particles, further contributing to the performance degradation observed in conventional TENGs.[17]

To overcome these limitations, we incorporate a charge transport layer and a charge storage layer between the triboelectric layer and the bottom electrode. The charge transport layer provides a conductive pathway, enabling efficient migration of triboelectric charges away from the surface. This mitigates repulsive interactions with incoming charges, thereby improving charge accumulation efficiency.[11] The charge storage layer, characterized by strong electron-trapping capability, suppresses recombination between electrons and induced positive charges.[13] Additionally, embedding high-permittivity fillers into these layers enhances the overall dielectric constant, further boosting the output performance of the composite tri-layer TENG.[9]

To evaluate the charge accumulation performance of three multilayer composite TENGs, a series of contact-separation tests were conducted using a linear motor with a 1 mm displacement, 100 N contact force, and 2 Hz frequency. The electrical performance of three test samples was compared. The corresponding open-circuit voltage and maximum charge transfer density for each design are presented in **Figure 3a-b**. Design A showed a moderate voltage increase from 97 V to 243 V. Design B demonstrated greater improvement, with V_{oc} rising from 230 V to 575 V, attributed to the enhanced permittivity and electron-trapping capability of the $BaTiO_3$/PDMS layer.[18] In Design C, the incorporation of a conductive intermediate layer with the MWCNT/PDMS transport layer enable an V_{oc} of 238 V and then eventually saturating at 1103 V. The sharp rise in voltage suggests effective charge storage within the composite tri-layer TENG. Design C reached a maximum charge transfer density of 3.3 nC/cm^2, which is 3 times compared with that of Design A, which did not include intermediate layers. This improvement is primarily attributed to the charge transport layer, which facilitates the movement of triboelectric charges away from the surface. By alleviating charge repulsion during subsequent cycles, it significantly boosts the device's overall performance.

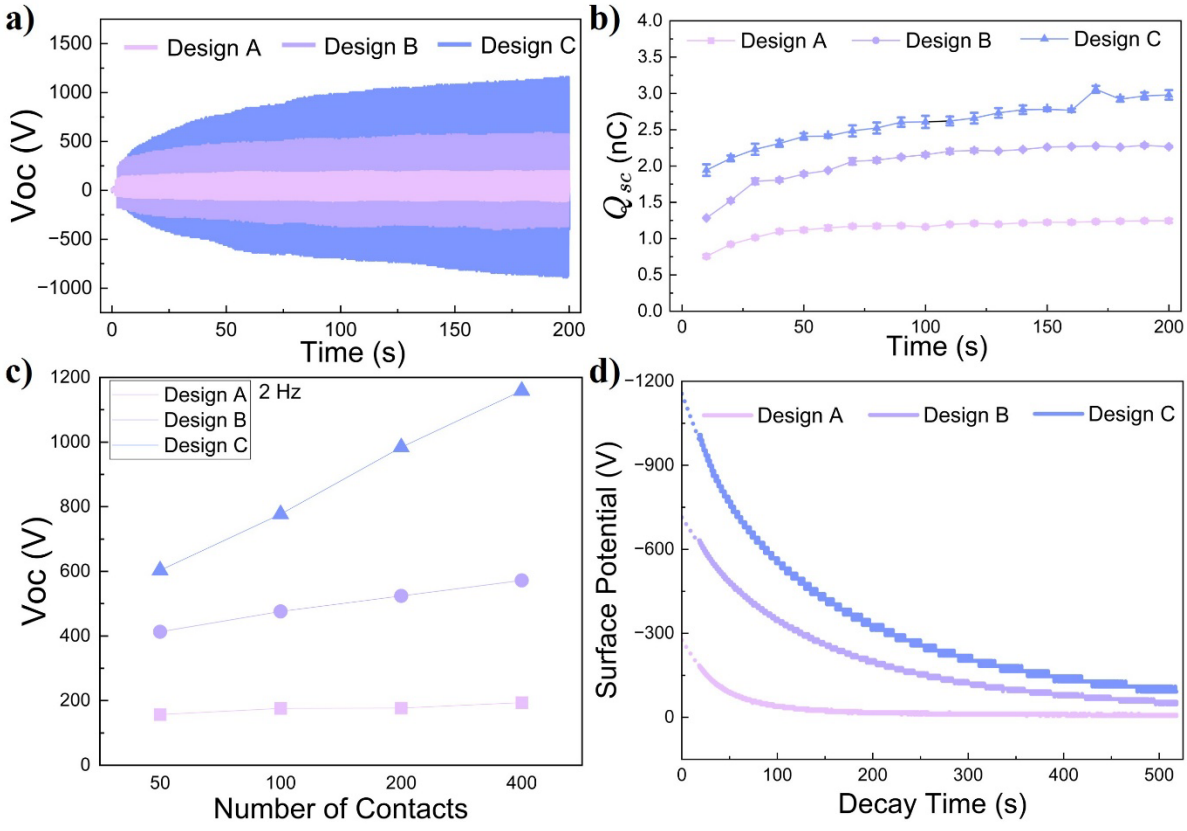

Figure 3: Charge accumulation of multilayer composite TENGs. a) V_{oc} (open circuit current). b) Q_{sc} (transferred charge density). c) after-contact surface potential of different designs. d) Surface potential decay of different designs.

2.2 SURFACE POTENTIAL CHARACTERIZATION FOR DIFFERENT MULTILAYER COMPOSITE TENGS

The origin of surface charge is a fundamental aspect of TENG, essential for visualizing and quantifying the creation and dissipation processes of triboelectric charges during contact and separation movements[19]. To better understand this, we systematically investigated the performance of Designs A, B, and C using surface potential measurements, with the aim of confirming the advantages of the MWCNT/PDMS charge-transporting layer and the $BaTiO_3$/PDMS charge-storage layer. Any residual charges on the surface of each test layer were neutralized before measurement to ensure a zero-surface potential which is verified by the electrostatic voltmeter. The surface potential was then measured at 3 mm to accurately assess the charge characteristics on the nanocomposite surface. These measurements were performed after driving the TENG samples using a linear motor operating at a frequency of 2 Hz and a force of 100 N.

As shown in **Figure 3c**, the surface potential trends are similar with those of the V_{oc} across all designs, with potential values increasing as the tapping time rose. This correlation indicates that the surface potential is directly tied to the contact-separation numbers. For Design A, the surface potential stabilized around -300 V after 50 s tapping time, indicating a limitation in net charge accumulation due to contact electrification. In comparison, the surface potential of Design B continued to rise after 25 s of tapping, eventually stabilizing at approximately -700 V after 100 s. This enhancement is contributed by the $BaTiO_3$/PDMS layer, whose high dielectric constant and strong electron-trapping ability effectively reduce electron recombination, thereby improving both charge retention and surface potential.[9, 20]. As a result, the elevated surface charge enhanced electrostatic induction at both electrodes, leading to increases in V_{oc}, I_{sc}, and Q_{sc}. With the addition of an intermediate MWCNT/PDMS transporting layer, Design C exhibited a continuous rise in surface potential from approximately -870 V to -1160 V which is nearly four times compared with that of Design A. The charge transporting layer enables deeper migration of charges away from the surface, reducing electrostatic repulsion on incoming charges and promoting more efficient charge accumulation at the top interface. This improvement not only enhances the charge storage capacity but also increases the depth of charge retention within the triboelectric material.

To evaluate the charge-storage capabilities of the TENGs, surface potential decay was measured following 200 seconds of tapping. Due to an 18s delay between the linear motor halting and the positioning of the electrostatic voltmeter probe, surface potentials were estimated by extrapolating the measured data to time zero using a double-exponential fitting function: $V = Ae^{-\frac{x}{\tau}} + Be^{-\frac{x}{\tau}}$, as shown in **Figure 3d**. The extrapolated surface potentials after 200 s of tapping were approximately -300 V, -700 V, and -1160 V for Designs A, B, and C, respectively. Designs B and C exhibited prolonged surface potential retention compared to Design A, with Design C maintaining a measurable potential for over 8 minutes after continuous contact cycles. Design A experienced a more rapid decay, whereas Designs B and C displayed nearly identical and slower decay rates. These findings confirm that the integration of MWCNT/PDMS and $BaTiO_3$/PDMS interlayers play a crucial role in stabilizing and enhancing the

output performance of the TENG.

To further investigate the charge distribution the mechanisms contributing to the enhanced output performance and particularly the effects of the conductive filler (MWCNT) and the high-permittivity filler ($BaTiO_3$), we conducted additional experiments to examine the surface potential of each individual layer in Designs A, B, and C.

As illustrated in **Figures 4**, each design was fabricated layer-by-layer. Design A served as the baseline and did not contain any fillers. Design B incorporated a layer-by-layer assembly with a pure PDMS triboelectric layer and an additional layer containing the dielectric filler $BaTiO_3$. Design C included a triboelectric layer, a charge-transporting layer, and a charge-storage layer. To ensure consistent testing, a linear motor was employed to ensure 200s tapping time at 2 Hz frequency and 100 N force for all three designs. Furthermore, we measured the surface potential layer by layer using a peeling method which allowed for a precise assessment of each layer's contribution to the overall charge distribution. Surface potentials for the layers were measured using an electrostatic voltmeter setup as presented in **Figure 4b**, where the measurement probe was set at 3 mm above a separated PDMS layer that was placed on the ground plane. The probe of an electrostatic voltmeter detects the electric field and measures voltage relative to the ground plane on which the dielectric layer is placed.

Surface potential measurements were conducted layer by layer using a peeling method, as illustrated in **Figure 4a**, enabling precise evaluation of each layer's contribution to the overall charge distribution. As shown in **Figure 4c**, Design C exhibited the highest total surface potential among the three configurations. The surface potentials of the PDMS charge-generating layers in Design B (~334 V) and Design C (~350 V) were slightly higher than that in Design A (~300 V), suggesting that the interlayers contributed to the increased potential in Design C. The charge-transporting layer in Design C showed a relatively low surface potential (~200 V), indicating its limited charge retention capacity due to high conductivity which an attribute that facilitates efficient charge transfer to deeper layers. Notably, the surface potential of the charge-storage layer in Design C was significantly higher than in Design B, confirming that the addition of a charge-transporting layer between the PDMS and $BaTiO_3$/PDMS layers enhanced charge transfer and accumulation, thereby improving the surface potential of the charge-storage layer.

Based on the measured surface potentials, the volume charge density can be determined using Gauss's law. For a single dielectric layer with cross-sectional area S and thickness d, placed on a grounded plane at $z = 0$, the total enclosed charge between z and $z = d$ can be expressed in terms of the volume charge density ρ

$$Q_{enclosed} = S\int_z^d \rho dz = S\rho(d-z) \quad [1]$$

The electric displacement field *D* at a distance z above the ground plane can be expressed as:

$$D = \frac{Q_{enclosed}}{S} = \rho(d-z) \quad [2]$$

The resulting electric field within the dielectric material is:

$$E(z) = \frac{D(z)}{\varepsilon_0\varepsilon_r} = \frac{\rho(d-z)}{\varepsilon_0\varepsilon_r} \quad [3]$$

where ε_0 represents the permittivity of air, ε_r is the relative permittivity of the dielectric material.

The surface potential at the top surface ($z = d$) is determined by integrating the electric field from a position z up to *d*:

$$V(d) = -\int_z^d Edz = -\frac{d^2-\frac{1}{2}d^2}{\varepsilon_0\varepsilon_r} = -\frac{\rho d^2}{2\varepsilon_0\varepsilon_r} \quad [4]$$

Using Equation [4], the volume charge densities of the three individual layers in the tri-layer PDMS stack were calculated to be 920.634 nC/cm^3, 501.816 nC/cm^3, and 648.587 nC/cm^3, as depicted in **Figure 4d**. These values highlight the variation in charge distribution across the different material layers.

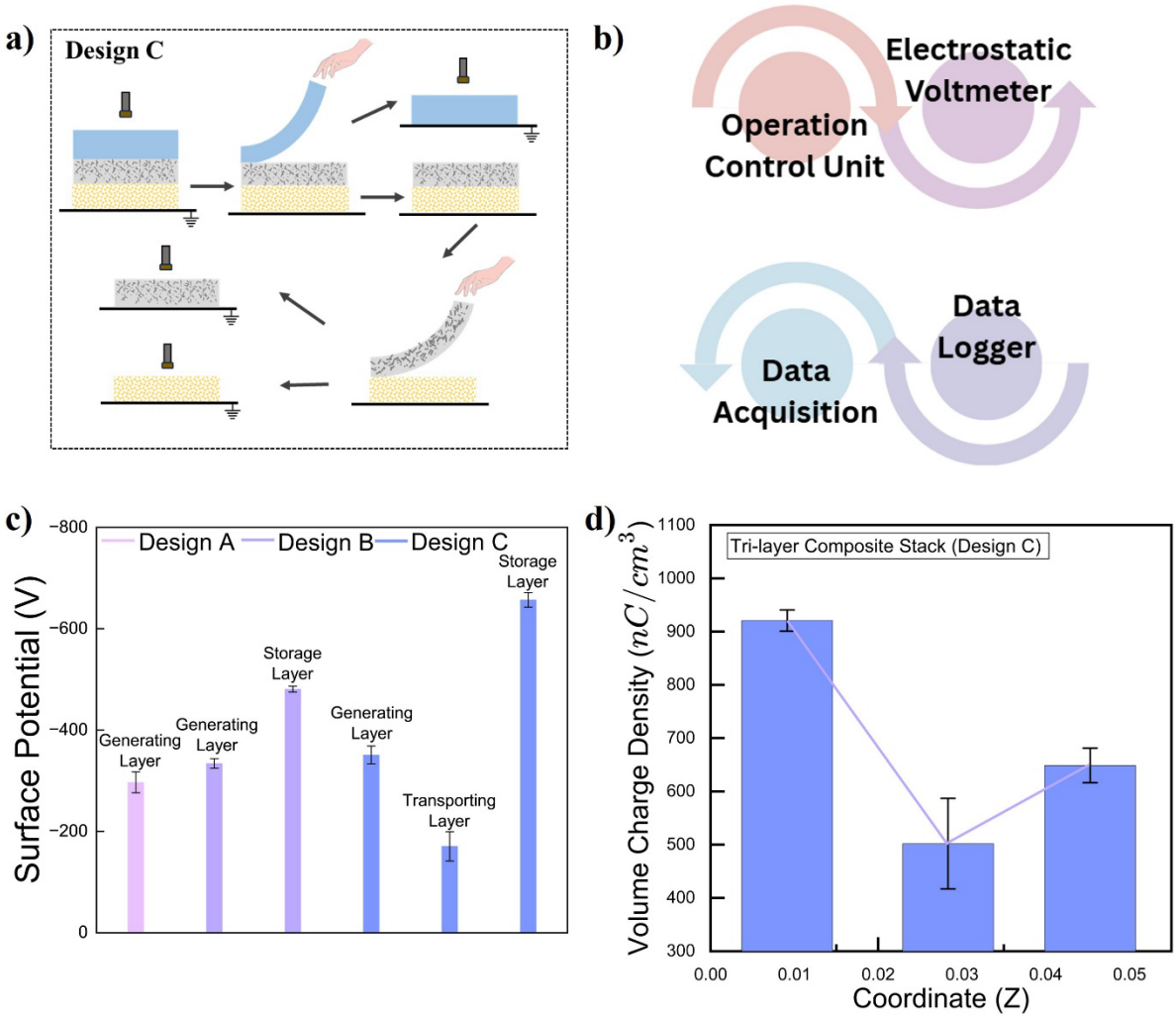

Figure 4: Surface potential measurement and volume charge density analysis in multilayer TENG with composite materials. a) Schematic representation of the surface potential measurement procedure for different TENG design layers. b) Illustration depicting the steps involved in surface potential measurement. c) Experimental results showing the measured surface potential across layers in various TENG configurations. d) Trend of volume charge density within the multilayer composite stack.

The relationship between TENG output and external resistance under a 2 Hz excitation frequency and 100 N contact force is shown in **Figure 5**. As expected by Ohm's law, the output voltage increased with external resistance, while the current correspondingly decreased. The peak power density of the composite tri-layer TENG was observed across varying load resistances, reaching a maximum of 1.22 W/m^2 at 300 MΩ. This level of output is sufficient to power many wireless wearable and implantable medical devices, highlighting the strong potential of the composite tri-layer TENG. Nevertheless, extending the operational lifespan of wearable and implantable medical devices will

require not only efficient power generation but also optimized power management systems and reduced device power consumption.

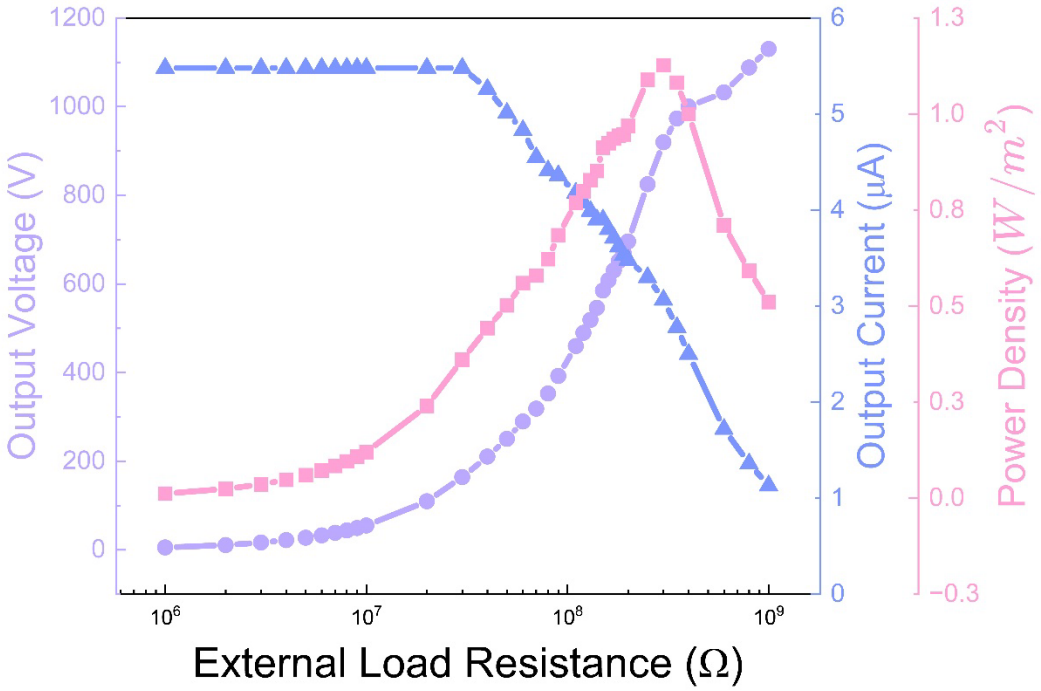

Figure 5: Effect of external load resistance on the output characteristics of the TENG, showing the variations in voltage, current, and power density.

3 CONCLUSIONS

This study introduces a novel approach for measuring and understanding charge distribution beneath the friction surface, utilizing a tri-layered composite TENG stack design. By examining the individual layers of this stack, we quantified the charge distributions within the individual layers of the TENG. These results were achieved through in-depth investigation of the enhancement mechanisms, including physical characterizations and detailed electrical measurements. For the first time, we visualized the surface potential of layers beneath the triboelectric layer, shedding light on charge distribution below the surface and confirming the effectiveness of the MWCNT/PDMS charge-transporting layer and the $BaTiO_3$/PDMS charge-storage layer using surface potential measurements.

Based on these findings, a high-performance tri-layered composite TENG was developed featuring a structural design that incorporates intermediate layers. These layers are composed of MWCNT/PDMS and $BaTiO_3$/PDMS hybrid films, serving as the charge-transporting layer and charge-storage layer respectively. This combination enabled electrical charges to be stored in the dielectric component without affecting the charges in the generating layer, significantly increasing the TENG's transferred charge density to 3.3 nC/cm^2 and a maximum power density of 1.2 W/m^2. The new tri-layered composite TENG demonstrates significant potential for integration into self-powered medical devices. Future research will focus on optimizing the materials and device architecture to enhance durability, efficiency, and pave the way for broader adoption in medical and consumer electronics.

REFERENCES

[1] G. Jian *et al.*, "Biodegradable triboelectric nanogenerator as a implantable power source for embedded medicine devices," *NPG Asia Materials,* vol. 16, no. 1, 2024, doi: 10.1038/s41427-023-00528-2.

[2] Q. Zheng *et al.*, "In vivo powering of pacemaker by breathing-driven implanted triboelectric nanogenerator," *Adv Mater,* vol. 26, no. 33, pp. 5851-6, Sep 3 2014, doi: 10.1002/adma.201402064.

[3] H. Ouyang *et al.*, "Symbiotic cardiac pacemaker," *Nat Commun,* vol. 10, no. 1, p. 1821, Apr 23 2019, doi: 10.1038/s41467-019-09851-1.

[4] C. Lee, S. Yang, D. Choi, W. Kim, J. Kim, and J. Hong, "Chemically surface-engineered polydimethylsiloxane layer via plasma treatment for advancing textile-based triboelectric nanogenerators," *Nano Energy,* vol. 57, pp. 353-362, 2019, doi: 10.1016/j.nanoen.2018.12.051.

[5] Y. Liu, X. Wang, Y. Yan, Z. Rao, H. Chen, and T. Guo, "A novel post-processed surface modified double-network polymer layer for a triboelectric nanogenerator," *Journal of Materials Chemistry A,* vol. 8, no. 13, pp. 6328-6336, 2020, doi: 10.1039/d0ta01070g.

[6] H. Yang, F. R. Fan, Y. Xi, and W. Wu, "Design and engineering of high-performance triboelectric nanogenerator for ubiquitous unattended devices," *EcoMat,* vol. 3, no. 2, 2021, doi: 10.1002/eom2.12093.

[7] C. Zhang *et al.*, "Surface charge density of triboelectric nanogenerators: Theoretical boundary and optimization methodology," *Applied Materials Today,* vol. 18, 2020, doi: 10.1016/j.apmt.2019.100496.

[8] N. Cui *et al.*, "Dynamic Behavior of the Triboelectric Charges and Structural Optimization of the Friction Layer for a Triboelectric Nanogenerator," *ACS Nano,* vol. 10, no. 6, pp. 6131-8, Jun 28 2016, doi: 10.1021/acsnano.6b02076.

[9] D. Tantraviwat, M. Ngamyingyoud, W. Sripumkhai, P. Pattamang, G. Rujijanagul, and B. Inceesungvorn, "Tuning the Dielectric Constant and Surface Engineering of a BaTiO(3)/Porous PDMS Composite Film for Enhanced Triboelectric Nanogenerator Output Performance," *ACS Omega,* vol. 6, no. 44, pp. 29765-29773, Nov 9 2021, doi: 10.1021/acsomega.1c04222.

[10] J. H. Choi, Y. Ra, S. Cho, M. La, S. J. Park, and D. Choi, "Electrical charge storage effect in carbon based polymer composite for long-term performance enhancement of the triboelectric nanogenerator," *Composites Science and Technology,* vol. 207, 2021, doi: 10.1016/j.compscitech.2021.108680.

[11] Q. Sun *et al.*, "Charge Dispersion Strategy for High-Performance and Rain-Proof Triboelectric Nanogenerator," *Adv Mater,* vol. 36, no. 8, p. e2307918, Feb 2024, doi: 10.1002/adma.202307918.

[12] Y. Nan *et al.*, "Synergistic effects of charge transport and trapping in tribomaterials for boosted triboelectric nanogenerators," *Nano Energy,* vol. 110, 2023, doi: 10.1016/j.nanoen.2023.108345.

[13] H.-W. Park *et al.*, "Electron blocking layer-based interfacial design for highly-enhanced triboelectric nanogenerators," *Nano Energy,* vol. 50, pp. 9-15, 2018, doi: 10.1016/j.nanoen.2018.05.024.

[14] Y. Park *et al.*, "Ferroelectric Multilayer Nanocomposites with Polarization and Stress Concentration Structures for Enhanced Triboelectric Performances," *ACS Nano,* vol. 14, no. 6, pp. 7101-7110, Jun 23 2020, doi: 10.1021/acsnano.0c01865.

[15] H. Wu, N. Mendel, S. van der Ham, L. Shui, G. Zhou, and F. Mugele, "Charge Trapping-Based Electricity Generator (CTEG): An Ultrarobust and High Efficiency Nanogenerator for Energy Harvesting from Water Droplets," *Adv Mater,* vol. 32, no. 33, p. e2001699, Aug 2020, doi: 10.1002/adma.202001699.

[16] H. Jiang *et al.*, "Charge-trapping-blocking layer for enhanced triboelectric nanogenerators," *Nano Energy,* vol. 75, 2020, doi: 10.1016/j.nanoen.2020.105011.

[17] R. Wen, J. Guo, A. Yu, J. Zhai, and Z. l. Wang, "Humidity-Resistive Triboelectric Nanogenerator Fabricated Using Metal Organic Framework Composite," *Advanced Functional Materials,* vol. 29, no. 20, 2019, doi: 10.1002/adfm.201807655.

[18] X. Chen *et al.*, "Electron trapping & blocking effect enabled by MXene/TiO2 intermediate layer for charge regulation of triboelectric nanogenerators," *Nano Energy,* vol. 98, 2022, doi: 10.1016/j.nanoen.2022.107236.

[19] Y. Liu *et al.*, "Quantifying contact status and the air-breakdown model of charge-excitation triboelectric nanogenerators to maximize charge density," *Nat Commun,* vol. 11, no. 1, p. 1599, Mar 27 2020, doi: 10.1038/s41467-020-15368-9.

[20] X. Kang, C. Pan, Y. Chen, and X. Pu, "Boosting performances of triboelectric nanogenerators by optimizing dielectric properties and thickness of electrification layer," *RSC Adv,* vol. 10, no. 30, pp. 17752-17759, May 5 2020, doi: 10.1039/d0ra02181d.

Australian Government
Department of Defence
Defence Science and Technology Group

Designing Novel Composite Structural Supercapacitors with Discrete Carbon Nanotube Electrodes

Alex B. Harman, Benjamin J. Mapleback, Andrew N. Rider, and Patrick C. Howlett

Platforms Division
Defence Science and Technology Group

Defending Australia and its National Interests
www.defence.gov.au

PUBLIC RELEASE

Composite Structural Supercapacitors (SSCs)

- Improvement in Size, Weight, and Power (SWaP) energy storage to mobile devices or transportation vehicles
- Electrode and electrolyte materials have been well developed for SSCs
- However, little work has focused on developing materials for the SSC separator layer
  - Common materials: cellulose filter paper, glass fibre fabric, aramid fibre fabrics, porous polymer membranes
- Non-conductive porous materials such as boron nitride nanotubes (BNNTs) can be incorporated to one surface of the electrode material, removing the need for the separator layer altogether

PUBLIC RELEASE

Boron Nitride Nanotubes (BNNTs)

- Strong, light weight and chemically resilient
- Thin film materials that possess high structural integrity and porosity
- Dimensionally stable and capable of withstanding high temperature
- High potential for high-power composite structural supercapacitors applications

This work combines commercially available carbon nanotube (CNT) mat with BNNTs coating to produce a high-performance fibre-reinforced polymer composite using industrial autoclave curing techniques.

PUBLIC RELEASE

BNNTs Coating Method

Stable dispersed mixture of BNNTs, achieved using sonicated ozonolysis. Sonication reduces the size of large BNNT agglomerates and cleaves BNNTs to decrease their average length.

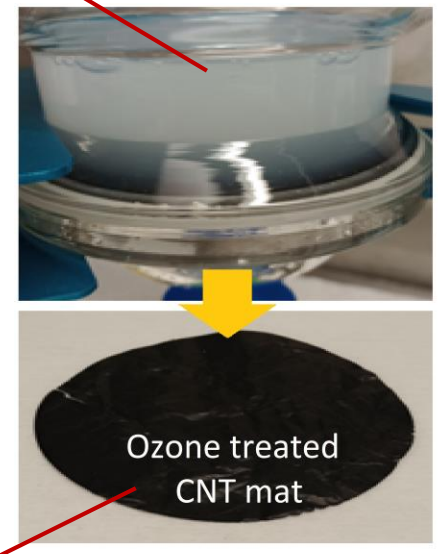

Oxygen-functionalised CNT Mats, treated for 6h prior to BNNT coating. This process enhances the water permeability for better vacuum filtration.

Porous support underneath CNT Mat can be tailored using a glass fibre filter paper to control coating homogeneity.

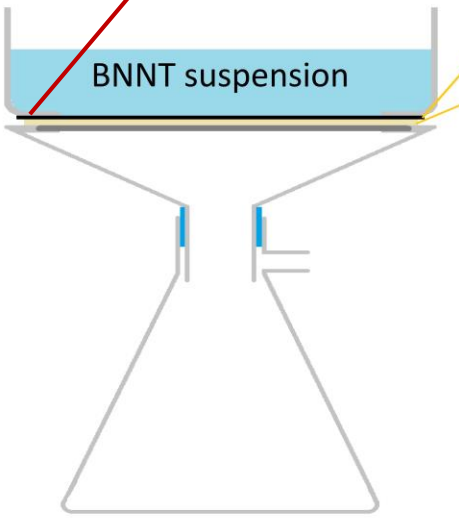

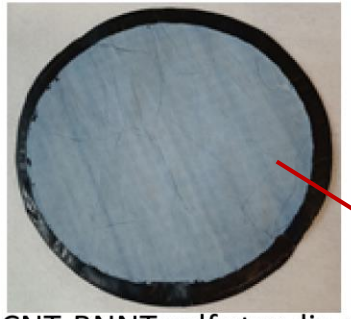

CNT-BNNT self standing electrode and separator

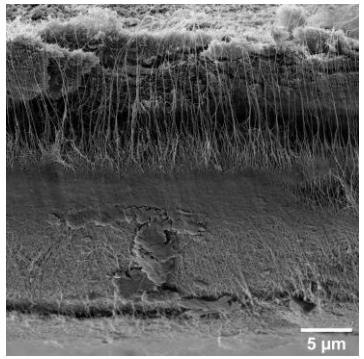

Dried CNT-BNNT film. Polymeric binder can also be combined in the BNNT suspension before vacuum filtration for more uniform coating.

Coating Characterisation

- Four different binders were used: PEG, PVP, PEI, PBDT
- Addition of PEG, PVP and PBDT has significantly improved coverage of CNT mat creases
- Some agglomerates (white spots) can form during deposition due to dispersion instability
- Addition of polymeric binders leads to micro-scale network
- BNNT-PBDT coating demonstrated the best overall characteristics, with homogeneous coverage and limited agglomerate formation

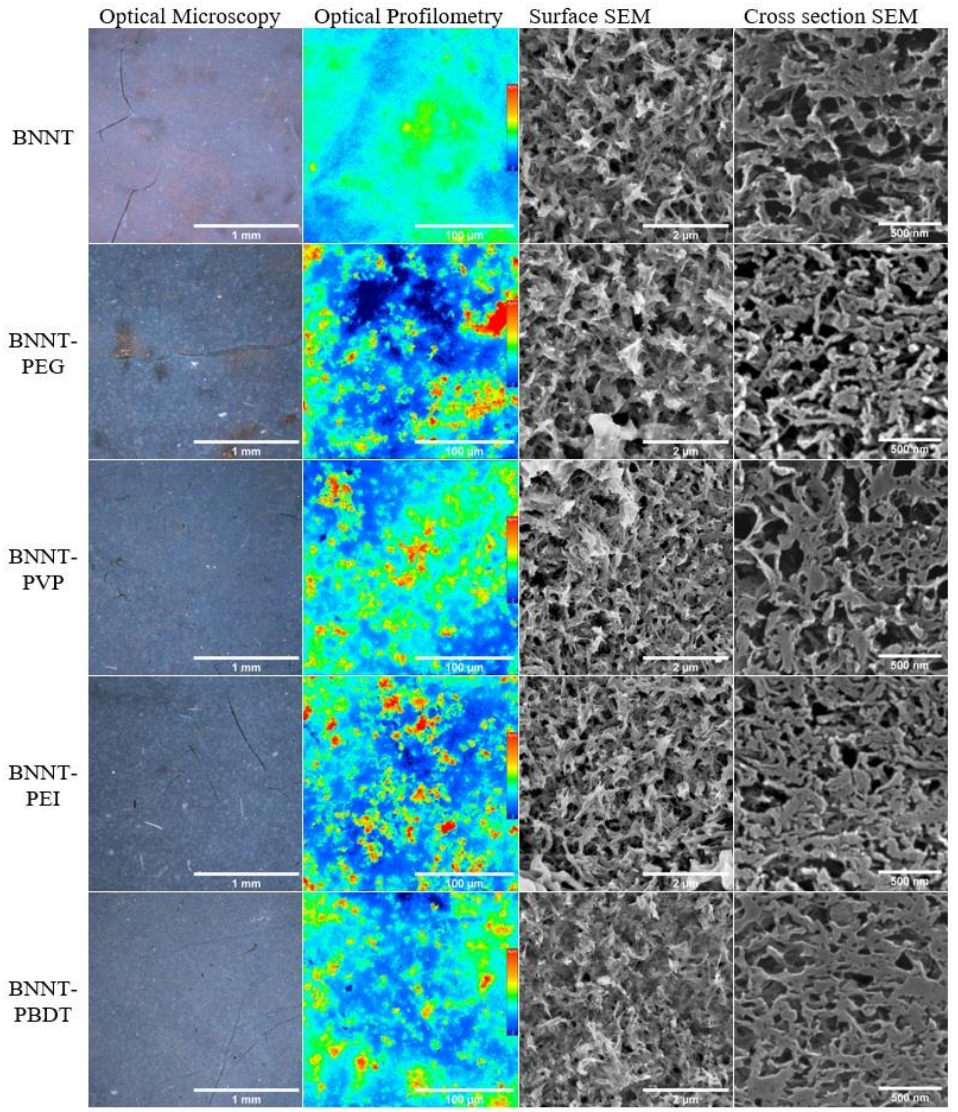

Coating Electrochemical Performance

- 2016 Coin cell with CNT-BNNT as electrodes
- EMIM TFSI ionic liquid as the electrolyte
- BNNT-PBDT
  - Best performance at low cycling rates
  - Excellent capacity retention
  - Coulombic efficiency above 98%
- BNNT-PVP and BNNT-PEI: deterioration and loss in capacitance after 2,000 cycles

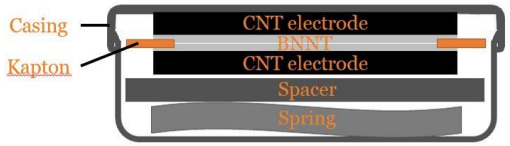

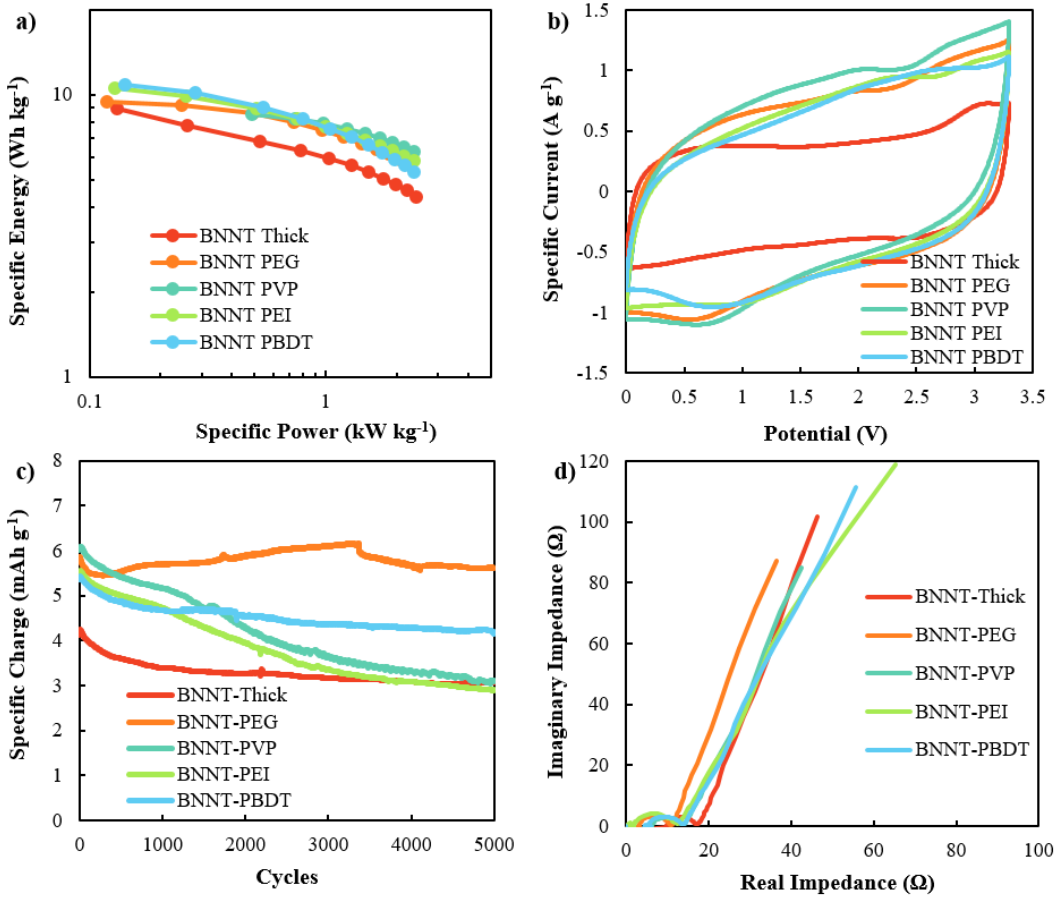

BNNT-PBDT Electrochemical Performance

- Best microstructure and all round electrochemical performance with EMIM TFSI electrolyte
- Stable operation up to 4V
- Pyrrolidinium electrolytes have higher specific energies at low charge-discharge rate, but worse performance at higher cycling rate, which decreases further with extended cycling.
- Alternative polymer systems required to improve the performance of the pyrrolidinium electrolytes

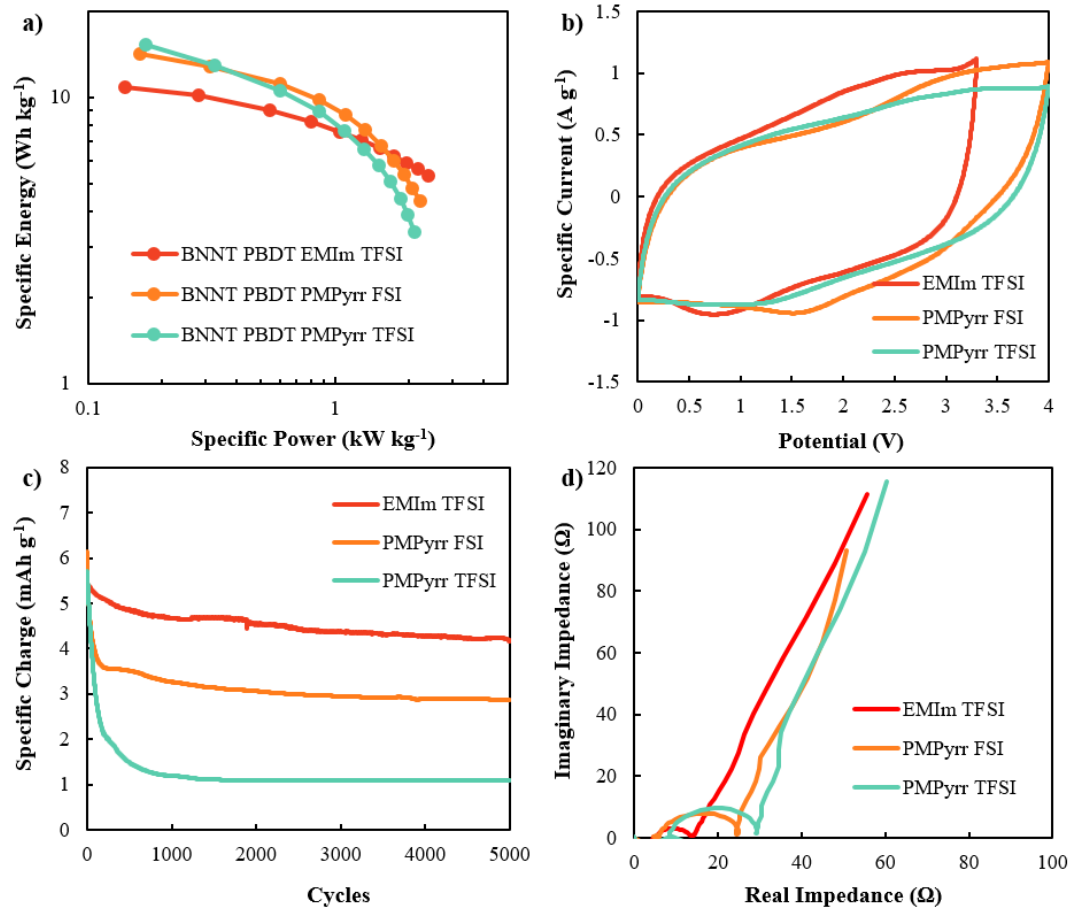

Composite SSC using CNT-BNNT

- Manufactured using industry standard vacuum-bag and autoclave-cure techniques
- Composite device demonstrated better performance than the coin cell, with 12.8 $Wh.kg^{-1}$ at 0.0984 $kW.kg^{-1}$
- Good capacitance observed from CV curve
- High coulombic efficiency maintained after extended cycling (above 94%)
- Highly suitable for integration into composite structures

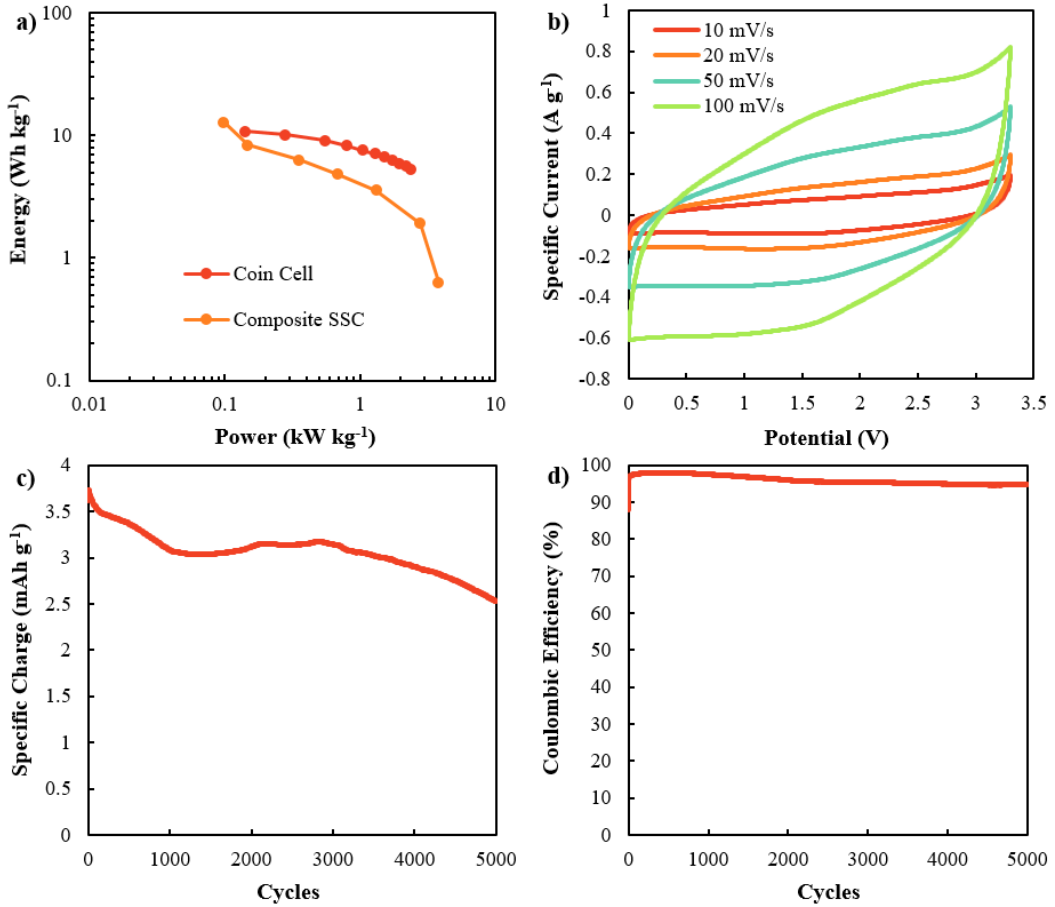

Conclusions

- CNT-BNNT coatings were produced using four different polymeric binders: PEG, PVP, PEI, PBDT
- Coin-cell testings demonstrated good performance with selected binders
  - PBDT showed the best overall electrochemical results
  - High specific energy up to 15.2 $Wh.kg^{-1}$
- Composite structural supercapacitor performance exceeded the coin cell performance
- Strong viability of CNT-BNNT coatings for integration into large-scale composite structures

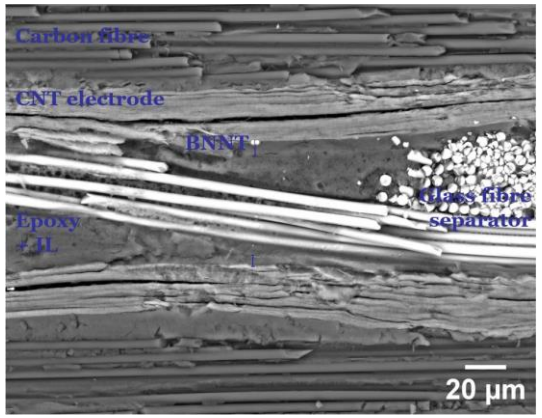

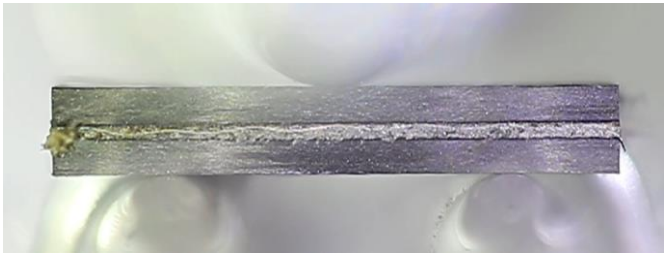

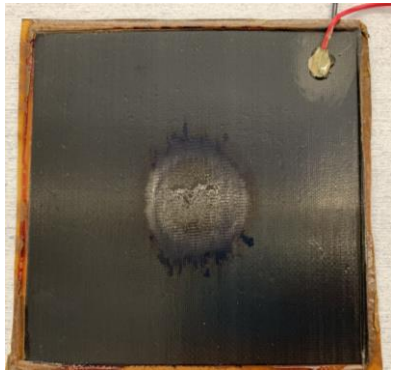

Acknowledgements

- storEnergy – The ARC Training Centre for Future Energy Storage Technologies
- Deakin University
- Dr Vu Dao, Defence Science and Technology Group





ICCM24
AUGUST 4-8, 2025
BALTIMORE CONVENTION CENTER
BALTIMORE, MARYLAND, USA

No Technical Paper Submission for:

Yon Tae Park

ICCM24
AUGUST 4-8, 2025
BALTIMORE CONVENTION CENTER
BALTIMORE, MARYLAND, USA

No Technical Paper Submission for:

Hongxu Guo

EVALUATION OF CRYO TMA/DMA FOR DETERMINING THE STIFFNESS PROPERTIES OF ADHESIVES AT CRYOGENIC TEMPERATURES

Patrick Nowakowski[1], Adli Dimassi[1], David May[1]
Jörn Jaschinski[2], Ilja Koch[2], Maik Gude[2]
Timo Stöven[3]

[1]Faserinstitut Bremen e.V. (FIBRE), University of Bremen, Bremen, Germany
[2]TUD Dresden University of Technology, Institute of Lightweight Engineering and Polymer (ILK) Technology (ILK), Dresden, Germany
[3]Airbus Operations GmbH, Hamburg, Germany

Keywords: Adhesive, Cryogenic, TMA, CTE, Tensile Strength

ABSTRACT

Two epoxy paste adhesives, one polyurethane paste-adhesive and one epoxy film adhesive, were tested for their ability to operate in bonded carbon composites joints which are exposed to a cryogenic environment as it is existent in a liquid hydrogen storage tank. Due to different coefficient of thermal expansion (CTE), a thermal mismatch occurs between the composite and adhesive layers which can lead to thermally induced cracks. Therefore, for the design of the bonding area the thermal and mechanical properties, including the CTE, of the adhesives are considered as key elements. The CTE of the adhesives was measured in a cryogenic TMA according to the ISO 11359-2 at temperatures from 4 K up to 350 K. The tensile properties of the adhesives were determined according to the DIN EN ISO 527-2 at 296 K and in liquid nitrogen (LN_2) at 77 K. In addition, the viscoelastic properties of the adhesives were determined in a temperature range from 173 K up to 473 K by dynamic mechanical analysis (DMA). All in all, the results show a quite similar thermo-mechanical behavior of the tested adhesives, with an increasing stiffness and a significantly decreasing thermal expansion coefficient with decreasing temperature.

1 INTRODUCTION

The demand for emission-free aviation is increasing and liquid hydrogen (LH_2) has a high potential as propellant for emission-free aircrafts. Therefore, intensive research into liquid hydrogen storage systems has begun, as weight-optimized storage is a key element in the implementation of emission-free aviation. Due to its lower specific density and the possibility for load-adapted fiber orientation, the structural weight of a liquid hydrogen tank can be significantly reduced by using carbon fiber reinforced plastics (CFRP). [1] However, the assembly of such CFRP based components to an LH_2 storage tank is challenging in several ways such as by structure, tightness and other constraints, which become effective especially at the typical LH_2 storage temperature of 20 K. [2]

The thermo-mechanical behaviour of adhesives in cryogenic conditions has not been sufficiently investigated yet. There is a minor of studies, which deal with the determination of mechanical and fracture behaviour of adhesives for LH_2 steel and CFRP-Tank structures. [3, 4, 5] Furthermore, test methods for determination of mechanical properties of epoxy based composite materials in cryogenic conditions are not standardized yet and will be developed within the framework of this study [6, 7].

The main objective of this project is to develop resource-efficient processing, joining and assembly methods for CFRP LH_2 tanks based on simulation- and test-based verification of cryogenic bonded joints. Two epoxy paste adhesives, one polyurethane paste-adhesive and one epoxy film adhesive, were tested for their ability to bond CFRP composites, in the context of cryogenic hydrogen storage. The design of the bonding area requires consideration of the adhesives thermal and mechanical properties, including the coefficient of thermal expansion (CTE).

2 METHODOLOGY

2.1 Test specimen preparation

The manufacturing and preparation of test specimens was conducted at Airbus Materials laboratory. While the processing of the film adhesive and prepreg adherent substrates was conducted using established standard procedures, the fabrication of test coupons made from adhesive pastes had to be optimized to reduce air entrapment and void formation within the adhesive bulk material. Figure 1 shows the preparation of the specimen for CTE, tensile strength test and DMA measurement.

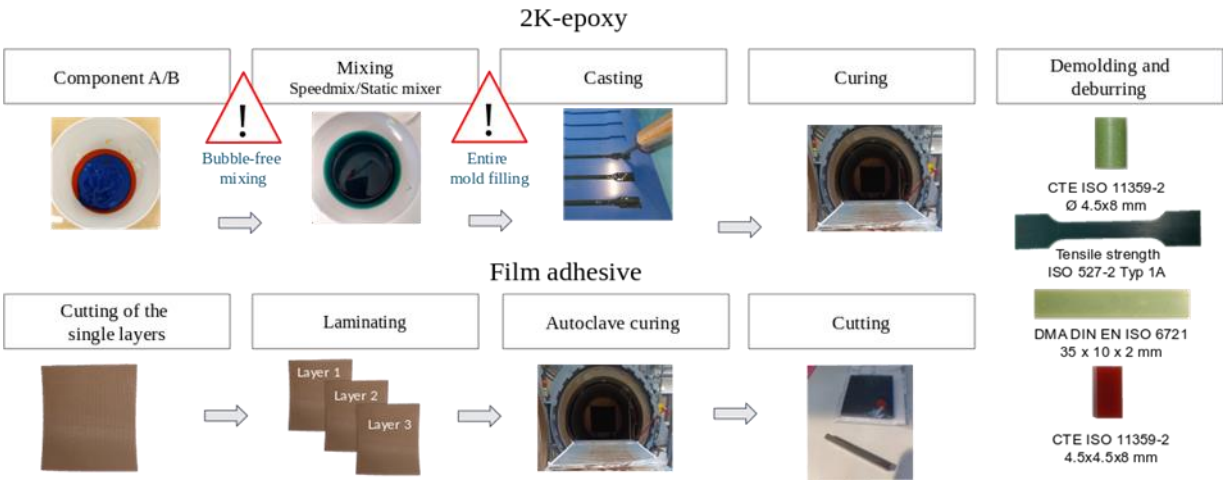

Figure 1: Specimens manufacturing and preparation

Four variants of adhesives are tested having the following characteristics:

ID	Chemistry	Curing characteristics	Typical field of application
1	2-part epoxy paste	Hot curing	Structural bonding of composites
2	2-part epoxy paste	Cold & hot curing	Shimming & Bonding
3	2-part polyurethane paste	Cold curing & tempering	Multi-purpose e.g. insulation of cryo tanks
4	1-part epoxy film	Hot curing	Structural bonding of composites

Table 1: Variants of adhesives

2.2 Tensile Testing

Tensile tests were performed according to DIN EN ISO 527-2 for the evaluation of strength, stiffness and poisons ratio of the adhesive bulk material at the ILK of the TUD. For the testing at room temperature the majority of test specimens were mounted on a ZwickRoell Z2.5 testing machine equipped with a 2.5 kN load cell, a video extensometer and pneumatic clamps. However, a few specimens exposed such a high yield strength that the testing of those adhesive candidates required a switch to a Z250 testing machine with a 10 kN load cell and wedge sample holders.
Test speeds for 296 K are 1 mm/min (modulus up to 0.25 % elongation), then switch to 5 mm/min (strength, adhesive 1, 2 and 4) or 50 mm/min (strength adhesive 3, due to high elongation at break).
The tensile test at 77 K was performed on a Zwick 1475 universal testing machine using a 10 kN load cell with a specially developed test setup (Figure 2, left).

Cryogenically suitable strain gauges (HBM 1.5/350 XC11) on both sides of the specimen were used for strain measurement. The specimen is clamped using a knurled specimen holder, and the clamping force is achieved by two screws tightened to a nominal torque appropriate to the material – typically 8 Nm. This test setup thermally decouples the specimen environment from the testing machine and ensures testing with the specimen completely immersed in liquid nitrogen. After filling the fixture with nitrogen, the test has only been started when minimal nitrogen evaporation is observed, i.e., when all parts of the clamping system and the specimen have reached the test temperature of 77 K (see Figure 3). Due to the very low strains to fracture observed under cryogenic conditions, the test speed at 77 K was set to 1 mm/min for the entire test, contrary to the standard.

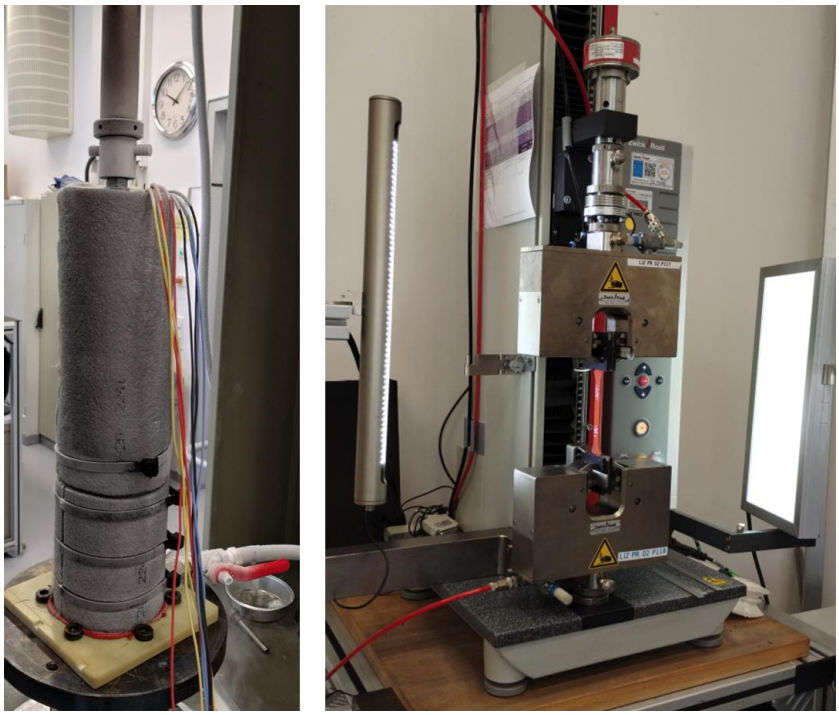

Figure 2: Testing device for tests at 77 K (left) and testing machine for tests at 296 K (right)

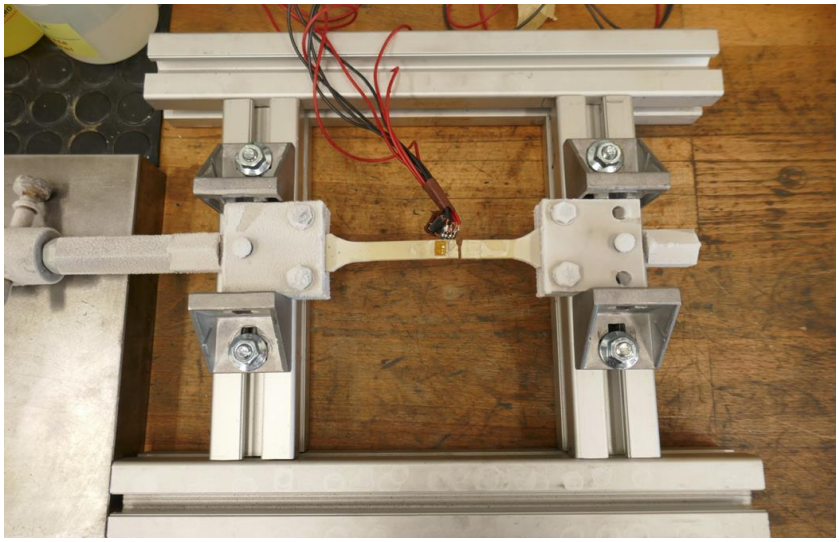

Figure 3: Clamps in assembly device after test

2.3 Thermo-mechanical analysis (TMA)

At FIBRE, the CTE was determined using expansion-probe TMA in a standard and cryogenic conditions following the ISO 11359-2 at temperatures from 4 K up to 350 K (see Figure 4). To ensure the cold temperatures during testing, the measurement chamber is placed in a helium closed loop cryostat. This requires a three times longer dilatometer than in a standard TMA. To compensate for this, an up to ten times higher load than described in the ISO standard has to be applied to the specimen. This again requires extreme care concerning the mechanical contact of the quartz glass dilatometer to the specimen. A controlled cooling rate of 0.5 K/min and a heating rate at 1 K/min were applied in order to get insights on the temperature-dependence.

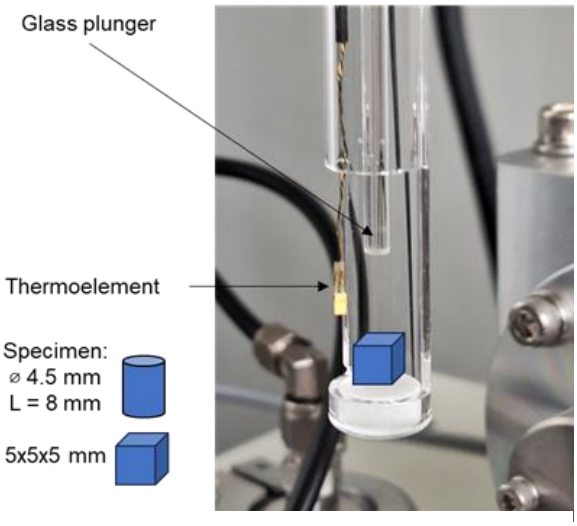

Figure 4: Cryo-TMA test stand and specimen

All specimens were preconditioned in a standard TMA Q800 from TA Instruments. The preconditioning was conducted as follows:

1. Apply a load of 25 mN
2. Cool and equilibrate at 223 K
3. Heating run at 5 K/min to 343 K
4. Hold isotherm for 5 min
5. Cooling run at 5 K/min to 223 K
6. End of measurement

The samples were weighed before and after each conditioning step and each measurement to determine the changes in moisture content. The results show, that the moisture content has an influence above around 263 K, but not below. Nevertheless, the preconditioning was used to ensure equal conditions of the specimen before the cryogenic CTE measurement.

2.4 Dynamic mechanical analysis (DMA)

The temperature-modulus behavior tests (see Figure 5) were conducted using an Anton Paar MCR-502s rheometer in torsion mode according to ISO 6721-7 [8].
To perform the tests following settings have been used:

- Testing instrument: MCR-502s rheometer (Anton Paar Germany GmbH)
- Specimen shape: Rectangular bar with a gauge length of approximately 22 mm, a width of approximately 10 mm, and a thickness of approximately 2.2 mm
- Heating rate: 4 K/min
- Test atmosphere: Air
- Amplitude of the dynamic angular displacement θ_A: 0.1 %
- Test frequency: 1 Hz
- 5 Tests per material

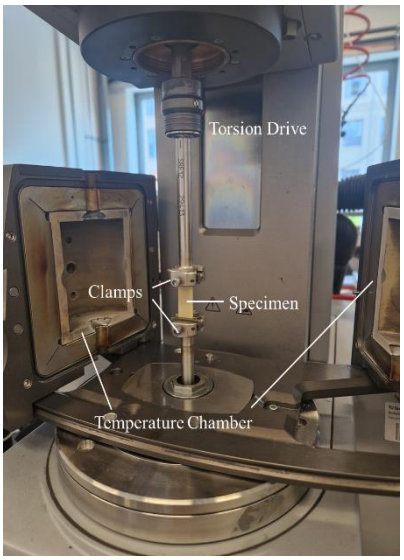

Figure 5: DMA test setup

3 RESULTS

3.1 Tensile Testing

The results show a significant difference in the Young's modulus, which increases significantly with decreasing temperature. The strengths also tend to increase, but less significantly and not for all adhesives tested. The graphs in Figure 6 show the average values of the results from seven samples.

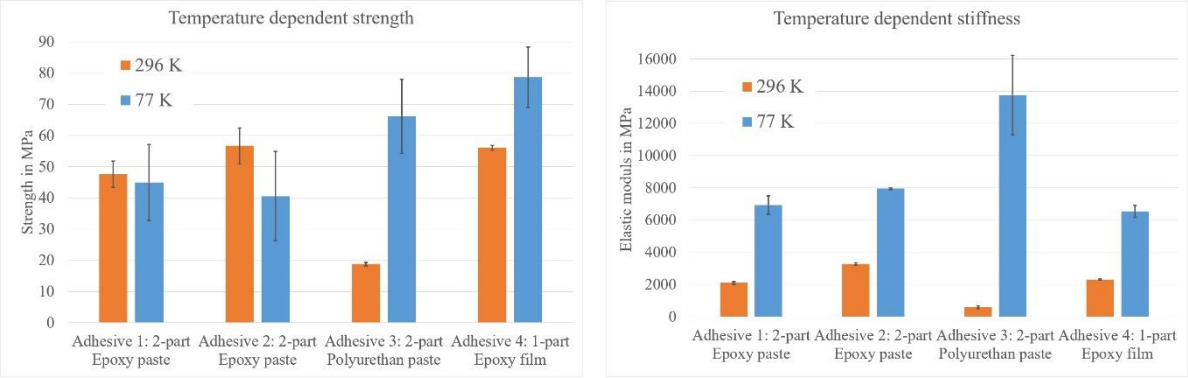

Figure 6: Temperature dependent strength and stiffness of adhesives at 296 K and 77 K

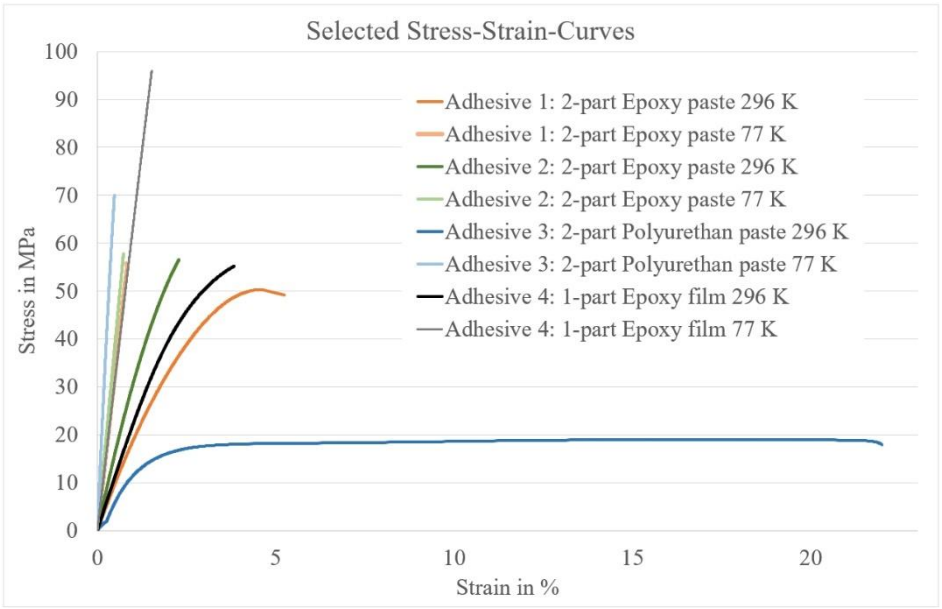

Figure 7: Representative stress-strain-curves at 296 K and 77 K

3.2 Thermo-mechanical analysis

The CTE results show a comparable decrease of the CTE with decreasing temperature, while the difference of the value is decreasing with lower temperature. In addition, at temperatures below 73 K a smaller decrease is visible, and the CTE of the various adhesives is similar. At temperatures below 93 K the CTE is remains almost constant for all adhesives.
Due to the higher load of 500 mN a delayed measurement signal in the area around the glass transition temperature (Tg) is generated, which leads to an incorrect output (see Figure 8, adhesive 3). Therefore, the determination of the CTE and glass transition must be decoupled. This means, in the cryogenic TMA the CTE is measured from 4 K up to T_g of each adhesive. Above T_g the CTE is determined in a standard TMA according to the ISO 11359-2. The glass transition temperature is shown in the results of the DMA in the following chapter.

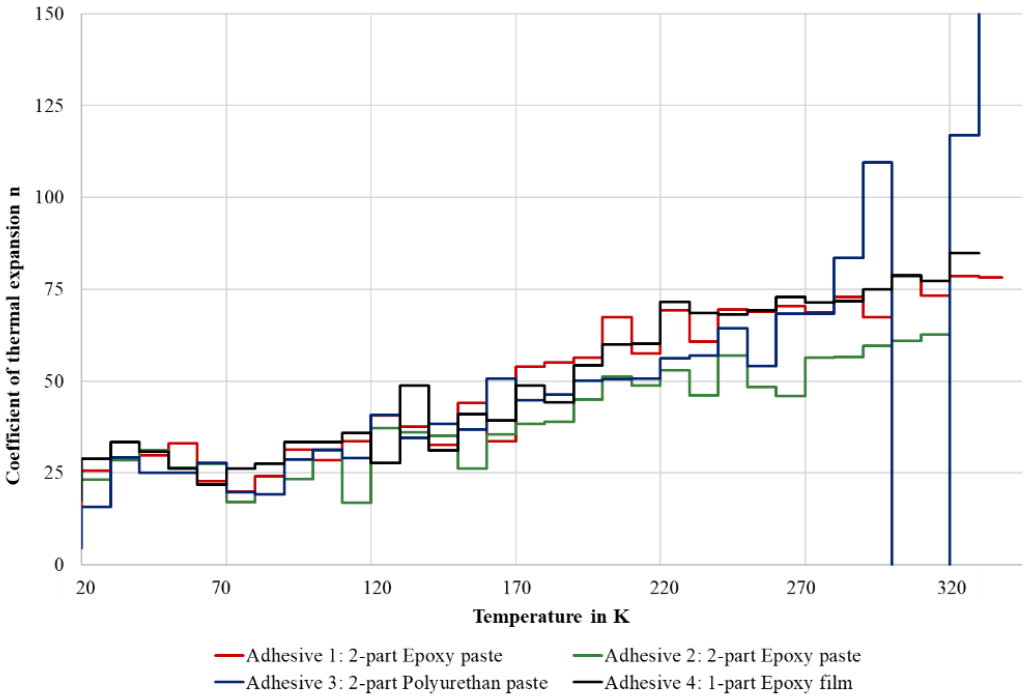

Figure 8: Coefficient of thermal expansion of 4 adhesives

3.3 Dynamic mechanical analysis

Representative curves selected from the five result curves for the respective adhesive are shown in Figure 9. The typical glass transition temperatures are clearly visible. The glass transition temperature of the polyurethane adhesive is only slightly above room temperature, whereas the epoxy resins exhibit significantly higher glass transition temperatures. It is also clearly evident that the elastic moduli of all polymers increase with decreasing temperature; it should be noted that the scale is non-linear. This clearly supports the results of the tensile tests conducted at two selected temperatures.

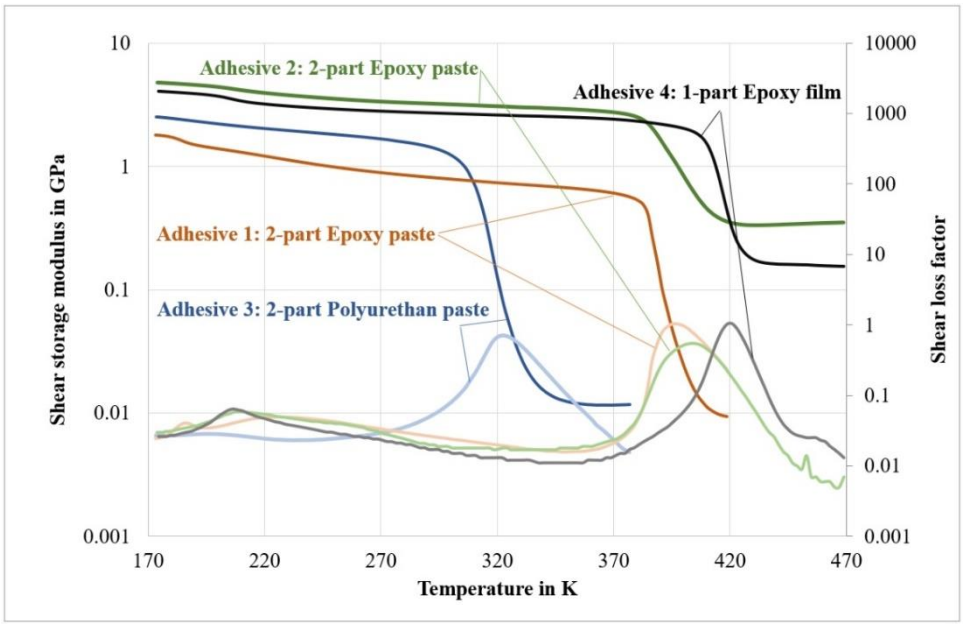

Figure 9: Results of DMA test for 4 adhesives, representative curve of 5 samples selected

4 CONCLUSIONS

The stiffness properties of various epoxy adhesives were successfully determined using novel cryogenic testing procedures. In general, the results show a quite similar thermo-mechanical behavior of the tested epoxy adhesives at cryogenic temperatures. As the temperature decreases, all tested adhesives exhibit an increase in stiffness, with the polyurethane-based adhesive showing a particularly pronounced stiffening effect. While the epoxy adhesives respond in a very much comparable manner under cryogenic conditions, significant differences in individual properties remain. Most notably, the elongation at break decreases considerably for all materials, indicating increased brittleness at low temperatures. In contrast, the strength results are inconsistent, and display no clear trend across the different adhesives. These findings highlight the importance of carefully considering the response of individual materials when selecting adhesives for cryogenic applications.

ACKNOWLEDGEMENTS

The author would like to thank the Federal Ministry of Economic Affairs and Climate Action of the German government for funding the project HyTank (funding reference: 20W2214).

REFERENCES

[1] W. Suwaileh, Y. Bicer, S. Al Hail, S. Farooq, R. Mohamad Yunus, N. Nabila Rosman, I. Karajagi, *Exploring hydrogen fuel as a sustainable solution for zero-emission aviation: Production, storage, and engine adaptation challenges, International Journal of Hydrogen Energy, 2025*

[2] Development of a composite liquid hydrogen tank for commercial aircraft, https://www.compositesworld.com/articles/development-of-a-composite-liquid-hydrogen-tank-for-commercial-aircraft, 05.06.2025

[3] S. Takayuki, J. He, S. Aso: *Study of Cryogenic Mechanical Strength and Fracture Behavior of Adhesives for CFRP Tanks of Reusable Launch Vehicles,* Memoirs of the Faculty of Engineering, Kyushu University. 66, 2006

[4] C.S. Bang, J.G. Kim, D.G. Lee, *Cryogenic Performance of Adhesively Bonded Metal Joints for LNG Containment System, Journal of Adhesion Science and Technology 26* (2012) 969– 986. https://doi.org/10.1163/156856111X593667.

[5] G. Blugan, G. Mata-Osoro, S. Fecht, J. Janczak-Rusch, J. Kuebler, Torsional shear strength of steel joined with high performance aerospace adhesives at cryogenic and elevated temperatures, PLoS One 13 (2018) e0206981. https://doi.org/10.1371/journal.pone.0206981.

[6] S.H. Yoon, J.G. Kim, Y.J. Hwang, D.G. Lee, *Fracture Toughness Measurement of Adhesively Bonded Joints at Cryogenic Temperatures*, Journal of Adhesion Science and Technology 26 (2012) 987–1001. https://doi.org/10.1163/156856111X593676.

[7] Y. Liu, G. Yang, H.-M. Xiao, Q.-P. Feng, S.-Y. Fu, *Mechanical properties of cryogenic epoxy adhesives: Effects of mixed curing agent content*, International Journal of Adhesion and Adhesives 41 (2013) 113–118. https://doi.org/10.1016/j.ijadhadh.2012.10.006.

[8] M. Müller-Pabel, J. Alberto Rodríguez Agudo, M. Gude, *Measuring and understanding cure-dependent viscoelastic properties of epoxy resin: A review*, Polymer Testing, Volume 114, 2022, 107701, ISSN 0142-9418, https://doi.org/10.1016/j.polymertesting.2022.107701.

University of Nottingham
UK | CHINA | MALAYSIA

Characterisation of heterogeneous permeability in LCM processes using stochastic inversion and neural surrogates

M.E. Causon[a], M.A. Iglesias[a], M.Y. Matveev[b], A. Endruweit[b], M.V. Tretyakov[a]

[a] School of Mathematical Sciences, University of Nottingham, UK

[b] Faculty of Engineering, University of Nottingham, UK

Motivation

"Conventional" permeability testing (as in ISO 4410)

- Flow experiments
- Simple geometries
- Uses analytical solution for relation between flow velocity and pressure gradient
- Results in one permeability value or a set of principal permeability values at a nominal fibre volume fraction
- Does not really work if there are local variations in permeability or edge effects (racetracking)

Idea

Recover local distributions of fibre volume fraction and permeability in specimens with non-uniform properties in real time; potentially in the presence of racetracking.

Method

Domain for flow analysis

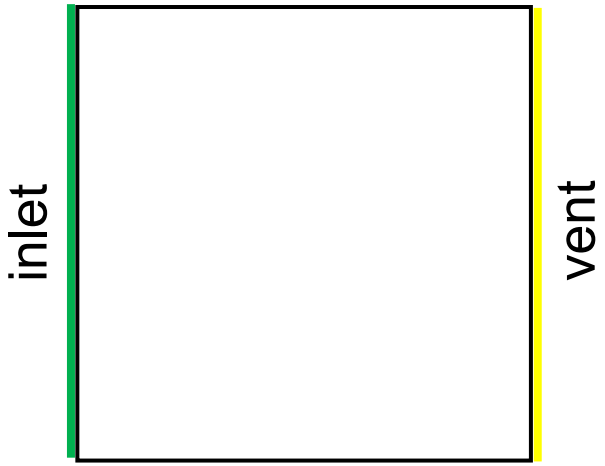

- $300\ \text{mm} \times 300\ \text{mm}$
- linear inlet and vent
- constant pressure difference
- constant viscosity

Partitioning of domain

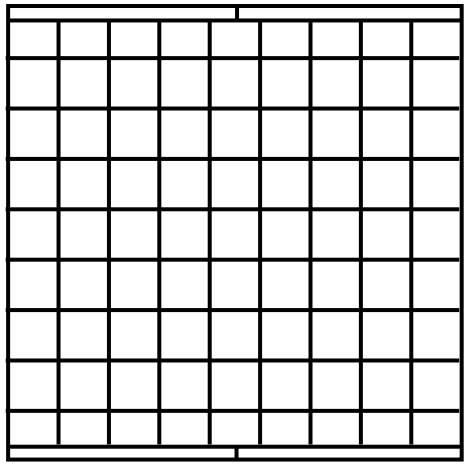

$9 \times 9 + 2 \times 2$ (racetracking)

➡ 85 unknown values of permeability and porosity

Virtual pressure sensors

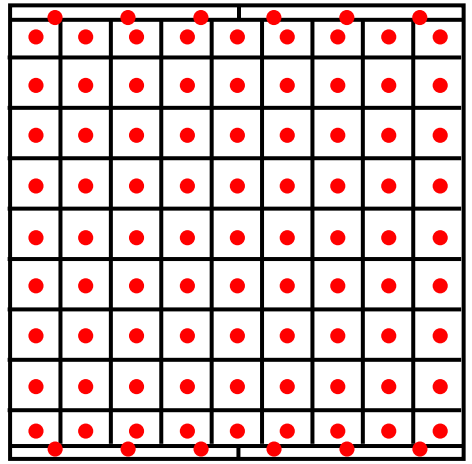

record pressure as a function of time

- for all sensors
- or for subsets

Method: Inversion

(Unknown) true distribution of permeability and porosity

$\log K^{\dagger}$

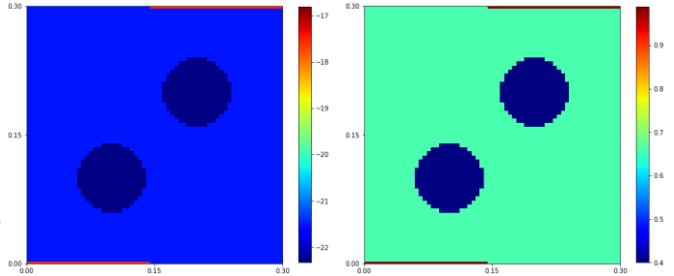

$\Phi^{\dagger}$

experiment

Recorded pressure-time curves

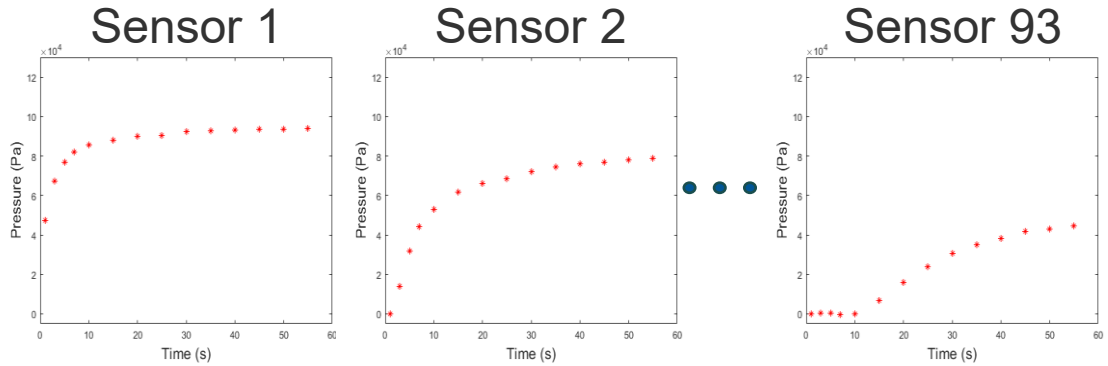

Recover local properties

Ensemble of J samples

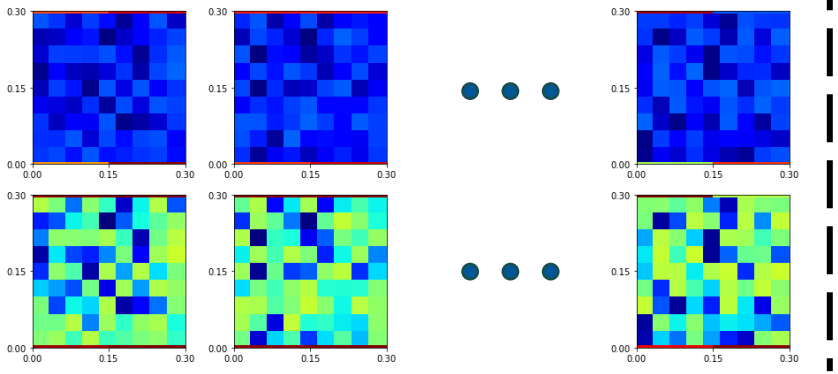

Mean

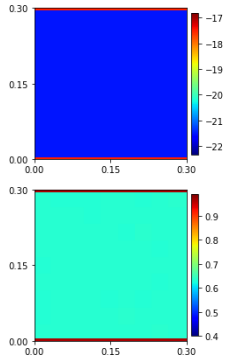

First guess (“prior”)

CVFEM simulations

Results from all J samples

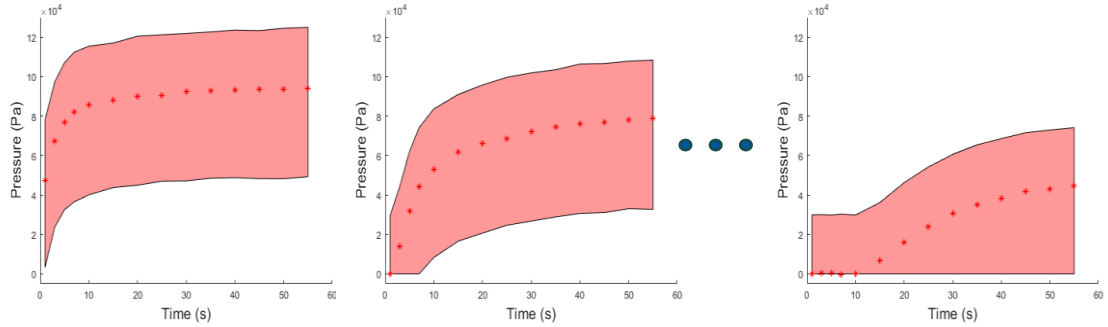

Not a good match with recorded data

Update ensemble

University of Nottingham
UK | CHINA | MALAYSIA

Method: Inversion

(Unknown) true distribution of permeability and porosity

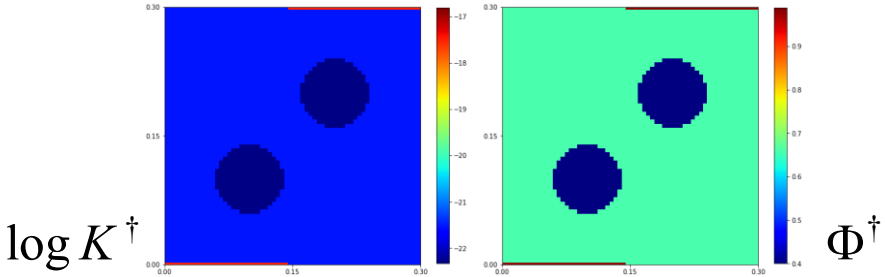

experiment

Recorded pressure-time curves

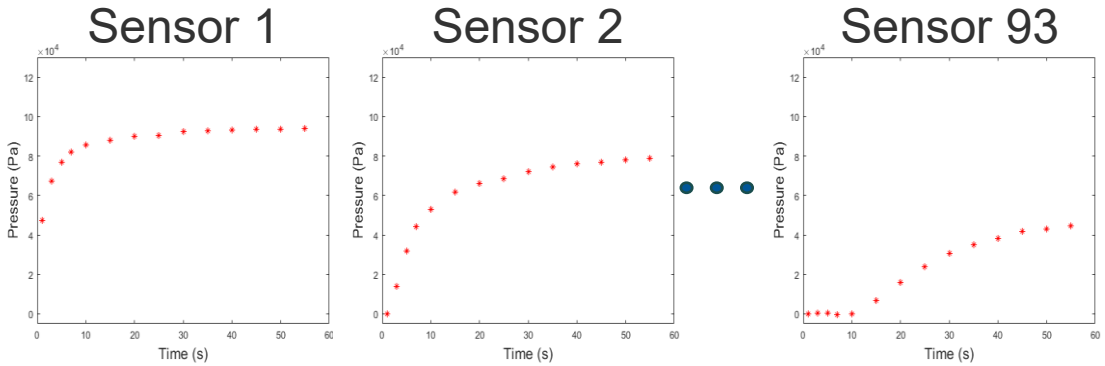

Recover local properties

Ensemble of J samples

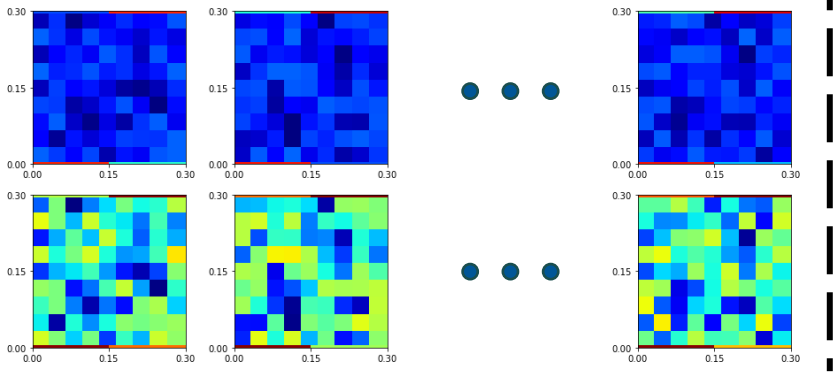

Mean

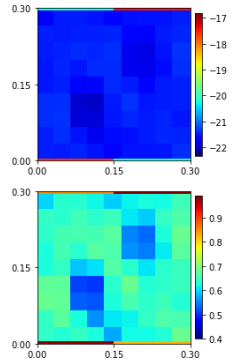

updated

CVFEM simulations

Results from all J samples

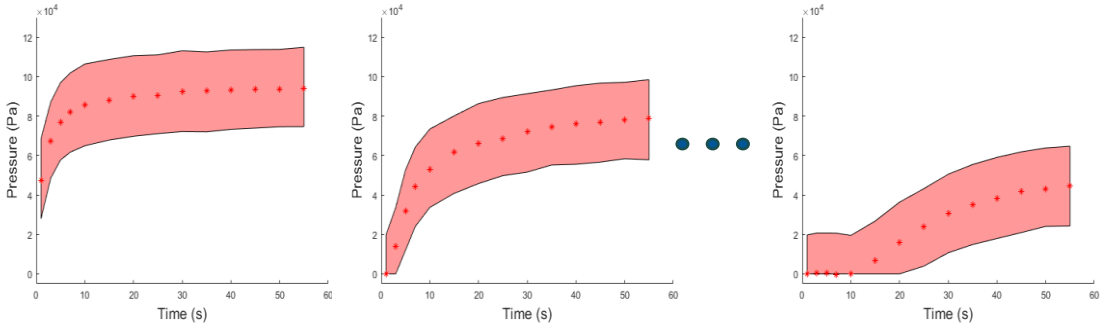

Improved, but still not a good match

Update ensemble

Method: Inversion

(Unknown) true distribution of permeability and porosity

$\log K^{\dagger}$

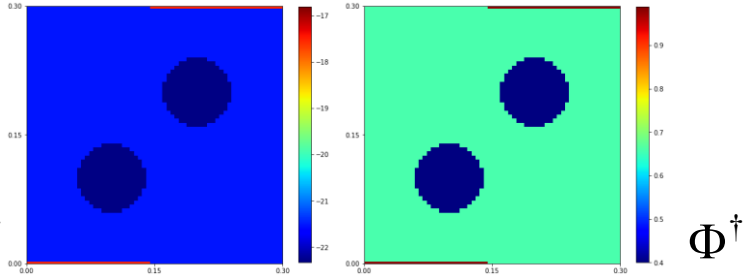

$\Phi^{\dagger}$

experiment

Recorded pressure-time curves

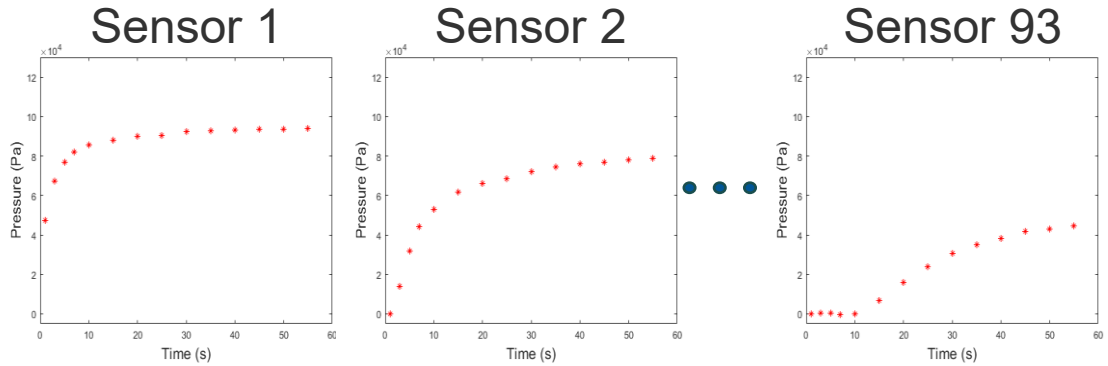

Recover local properties

Ensemble of J samples

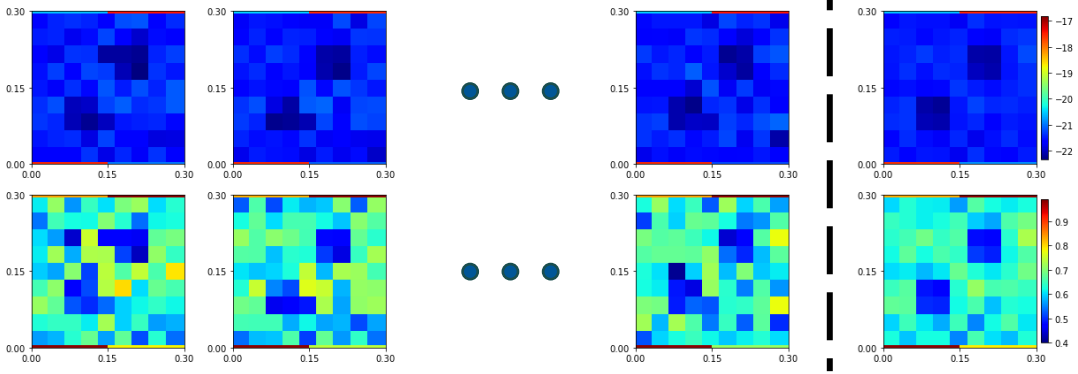

updated

Mean

CVFEM simulations

Results from all J samples

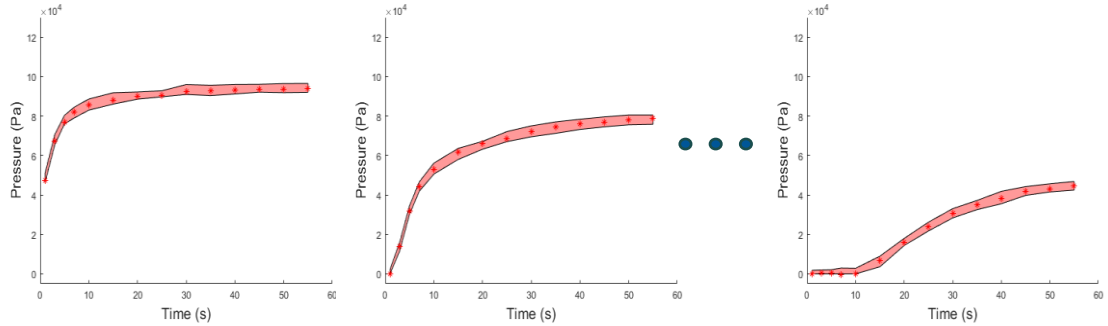

Acceptable match

➡ Ensemble is “posterior” approximation

Method: Surrogate

Run time for each CVFEM simulation ~100 s

Simulations for thousands of samples required.

➡ Even with parallel computing, finding posterior approximation takes hours.

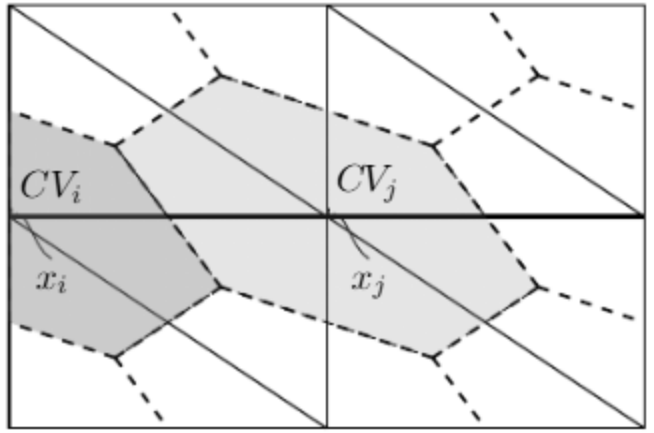

Wells, H., Park, M., Matveev, M., & Tretyakov, M. (2024). RTM-Flow: Control volume FEM solver for 2D moving boundary problems (v2.0). Zenodo. https://doi.org/10.5281/zenodo.12583662

To speed up inversion:

Generate a data set based on CVFEM simulation for 50,000 samples, all with different properties.

Use Artificial Neural Network as surrogate to interpolate outputs for unseen parameter sets, near-instantaneously.

Method: Surrogate

85 values of
- permeability
- porosity

Injection pressure
Viscosity

One hidden layer,
1000 nodes

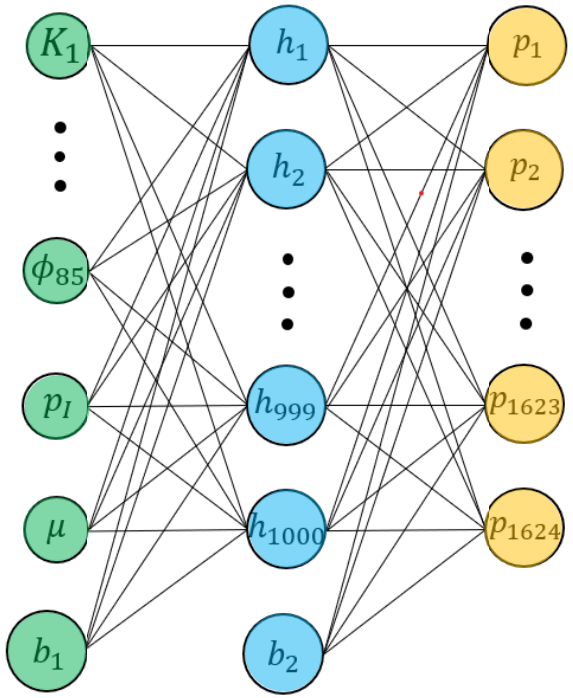

Pressure values
- all sensors
- 14 observation times

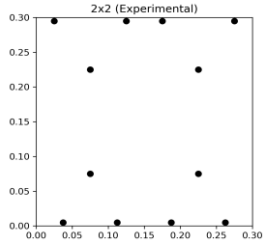

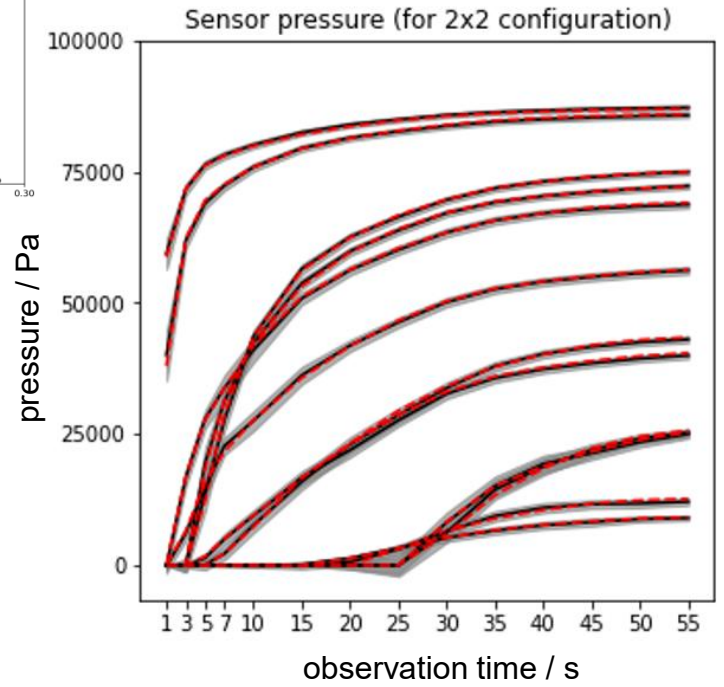

Red: CVFEM simulation
Black: Neural network prediction
Grey: surrogate uncertainty

	Relative error (average)	Execution time (average)
CVFEM	-	109 s
Surrogate	1.15 %	3.52×10^{-4} s

University of Nottingham
UK | CHINA | MALAYSIA

Virtual experiments: Results

"Truth"

Log-permeability

Observed flow front shapes and recovered local permeability and porosity.

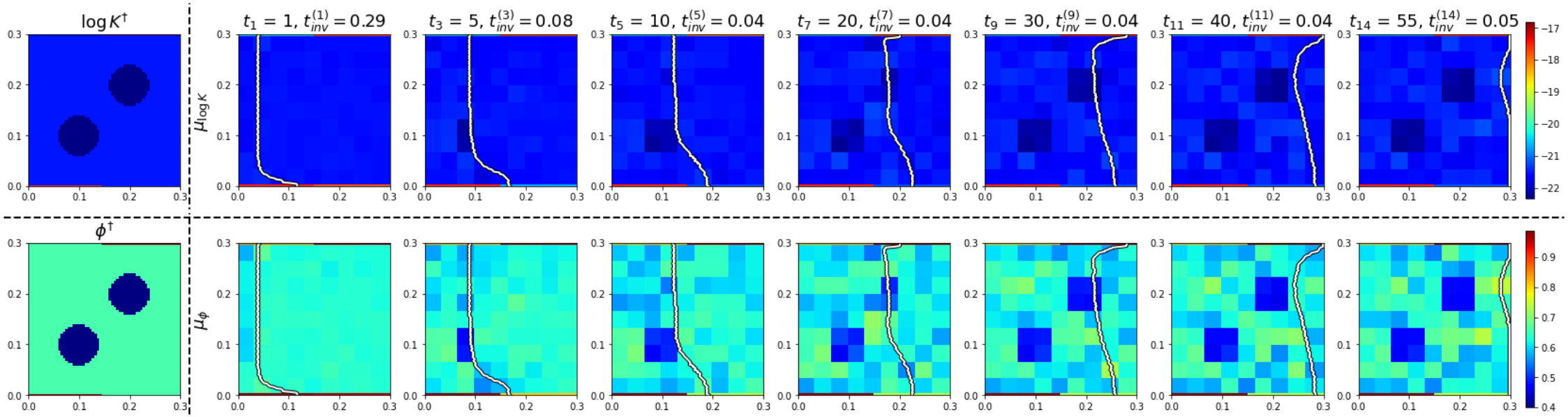

Porosity

Increasing levels of detail are recovered as the flow front propagates.

Virtual experiments: Results

Permeability and porosity

- recovered at end of impregnation process;
- averaged on sub-domains identified as “background”, “inclusions” and “racetracking channels”.

	background		inclusions		racetracking channels	
	K / m^2	Φ	K / m^2	Φ	K / m^2	Φ
“truth”	4.50×10^{-10}	0.66	2.05×10^{-10}	0.40	2.50×10^{-8}	0.98
recovered	4.65×10^{-10}	0.64	2.18×10^{-10}	0.45	2.39×10^{-8}	0.98
Δ	+ 3 %	- 3 %	+ 6 %	+ 12 %	- 4 %	± 0 %

Quantitatively, porosity and permeability can be recovered with acceptable accuracy.

Virtual experiments: Results

Number of sensors considered in inversion

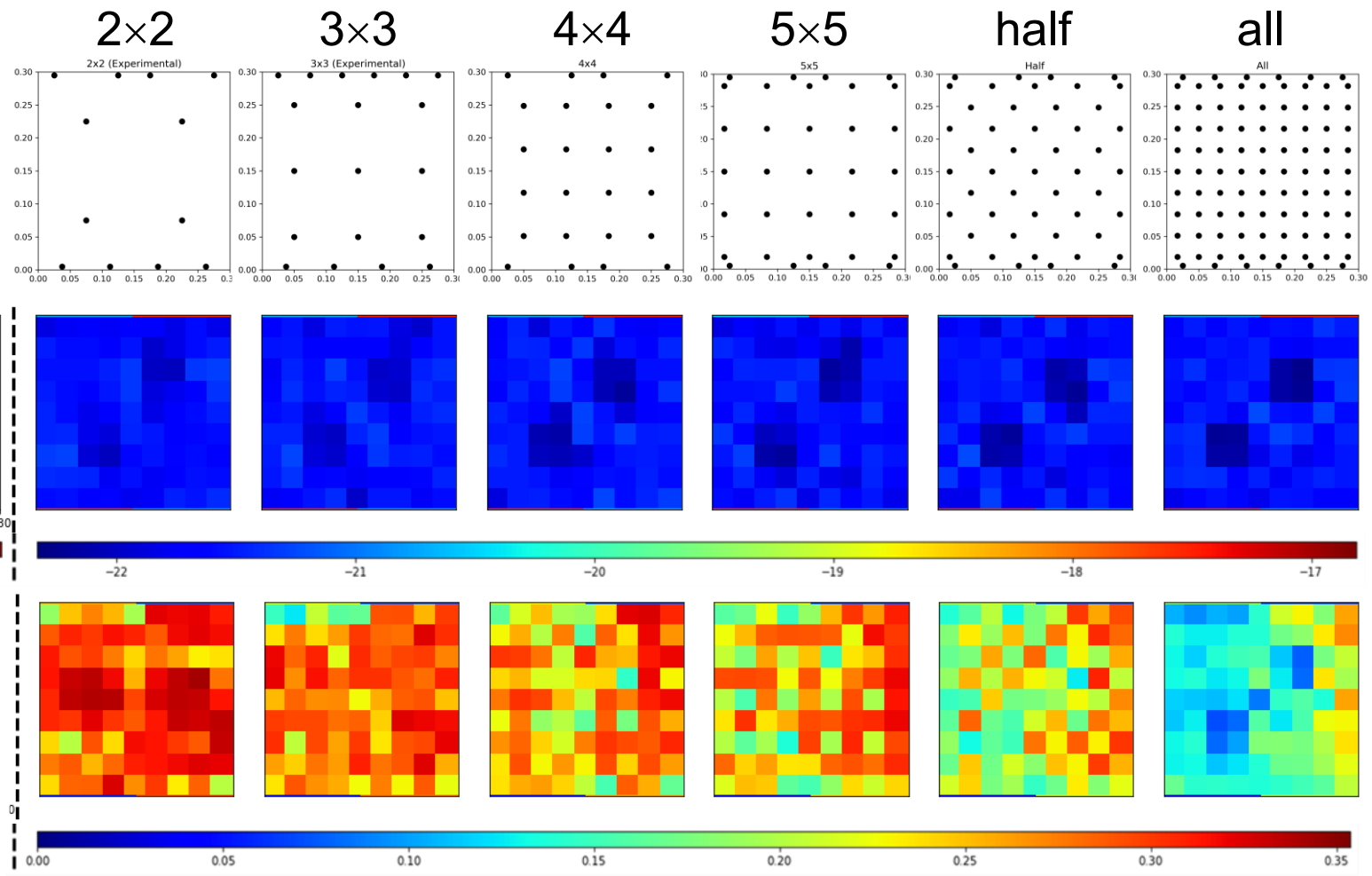

Uncertainty in recovered permeability decreases with increasing number of sensors.

Lab experiments: Set-up

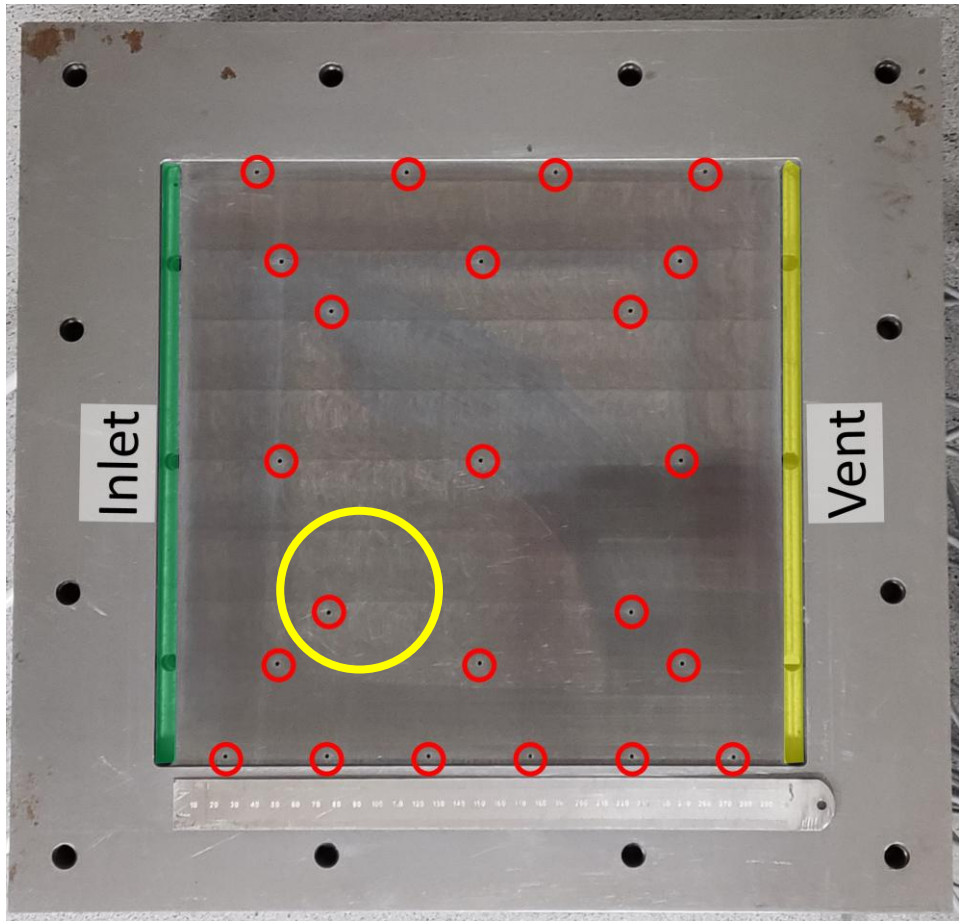

- 300 mm × 300 mm, 2.1 mm height
- 23 pressure sensors
- transparent lid for flow front tracking

Reinforcement:
Random glass fibre mat;
$S_0 = (210 \pm 15)\ \mathrm{g/m^2}$

Example lay-up:
- 7 layers (background)
- 10 layers, 80 mm diameter (inclusion)

Test fluid:
Synthetic engine oil; $\eta \approx 0.1$ Pa.s

Pressure difference:
$\Delta p \approx 10^5$ Pa

University of Nottingham
UK | CHINA | MALAYSIA

Lab experiments: Results

Recovery of porosity and permeability as flow front propagates

Visual flow front tracking

Log-permeability

Porosity

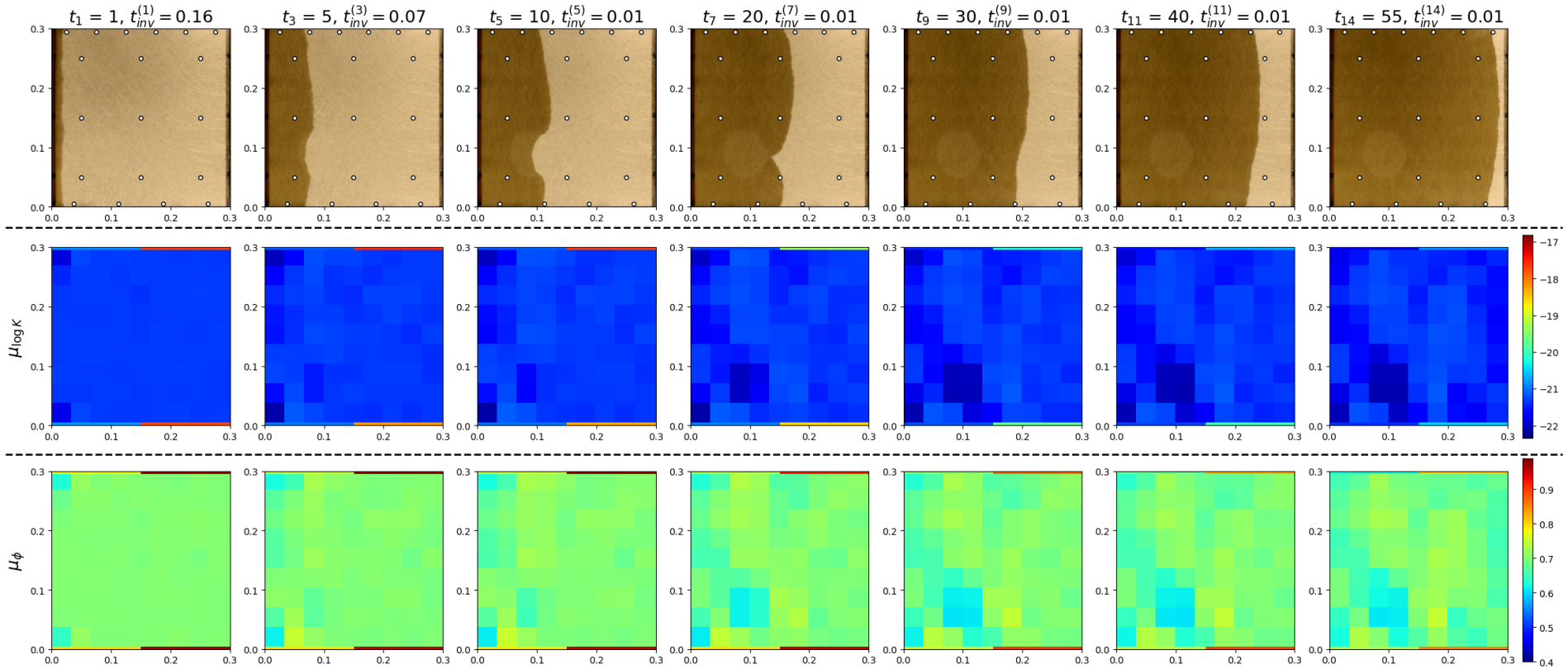

Note: 19 sensors considered here (2×2 omitted)

Lab experiments: Results

Permeability and porosity

Comparison with results from “conventional” permeability testing (uniform, at comparable number of layers, n, and cavity height, h)

	background		inclusion	
	K / m^2	Φ	K / m^2	Φ
conv.	6.29×10^{-10}	0.73	3.77×10^{-10}	0.61
recovered	5.86×10^{-10}	0.72	3.34×10^{-10}	0.57
Δ	- 7 %	- 1 %	- 11 %	- 8 %

$$\Phi = 1 - \frac{n S_0}{\rho h}$$

K interpolated at Φ based on “conventional” test series

Quantitatively, recovered porosity and permeability are reasonably consistent with results from “conventional” testing.

Note: Results from “conventional” testing are affected by uncertainty as well.

Conclusions

An Artificial Neural Network surrogate was combined with a stochastic inversion algorithm to estimate local reinforcement permeability and porosity in real time based on in-process data.

Virtual and lab experiments indicate that

- positions and shape of inclusions and racetracking channels can be identified correctly;
- recovered values of permeability and porosity are generally in good agreement with the corresponding “true” values.

As the reinforcement properties can be recovered in real time, integration of this algorithm within active process control systems is feasible.

Outlook

Recover local permeabilities for more complex geometries

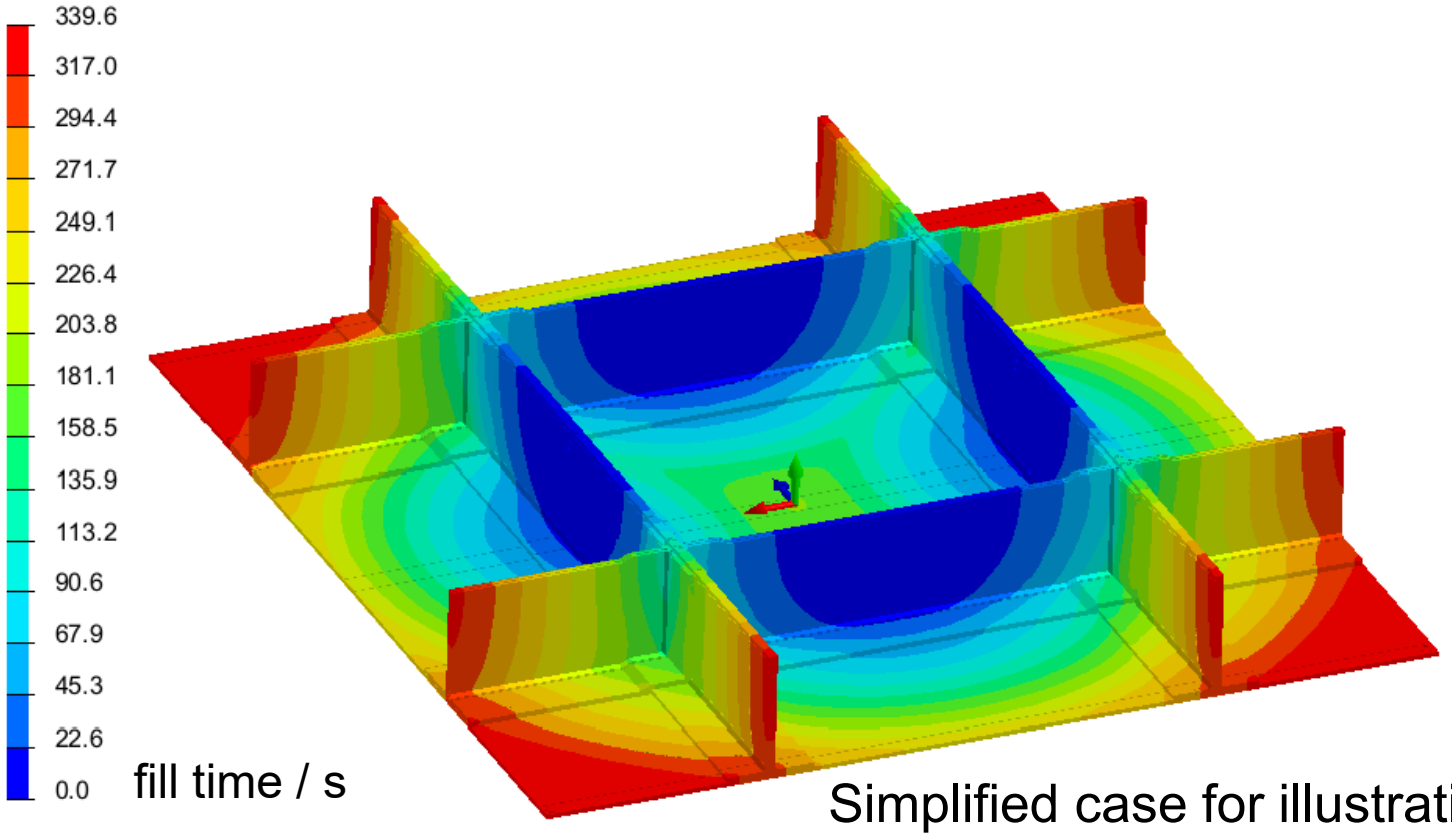

Simplified case for illustration

Example: “stiffened panel”

complex overlap configuration
+ noodle regions
+ racetracking

4 inlets, 5 vents

20 pressure sensors,
visual monitoring on flat side

University of Nottingham
UK | CHINA | MALAYSIA

Acknowledgement

This work was supported by the Engineering and Physical Sciences Research Council, UK, through the EPSRC Future Composites Manufacturing Research Hub [EP/P006701/1].

Technical University of Leoben

In-Plane Permeability of VARI Consumables: A Comparison of Experimental and Virtual Estimation Methods

E. Fauster, T. Schmidt, S. Cassola, C. Obertscheider, M. Bender, C. Lira, M. Duhovic, D. May

24th International Conference on Composites Materials (ICCM24), August 4, 2025, Baltimore

Move mountains

Contents

- Motivation
- Materials
- Experimental Work
- Results
- Conclusions
- Future Work

Motivation

- Vacuum-Assisted Resin Infusion (VARI):
  - Highly inhomogeneous setup of:
    - fibrous reinforcement in combination with
    - single layers of peely ply and flow distribution media
  - Significant differences in permeability

- Aim
  - Full coverage of flow related mechanisms in flow simulation software
  - Methodological comparison of methods for estimating in-plane permeability

VARI Consumable Materials

- Flow distribution media (FM)
  - Airtech Knitflow 105 HT
  - Polyester knitted fabric
  - Areal weight: 105 g/m²

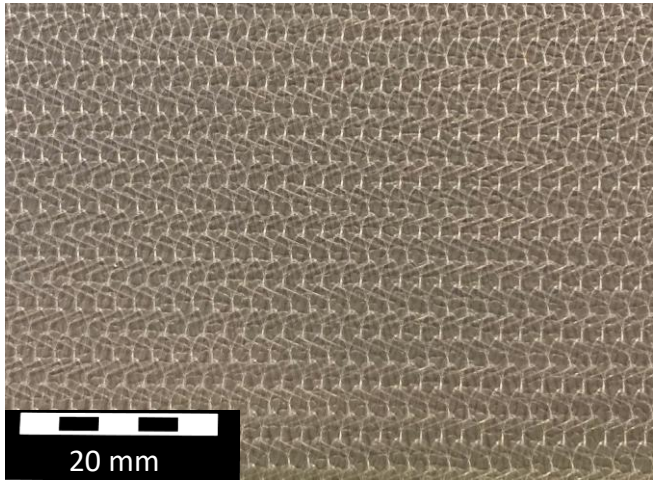

- Peel ply (PP)
  - Airtech 60BR
  - Nylon woven fabric, silicone coating
  - Areal weight: 60 g/m²

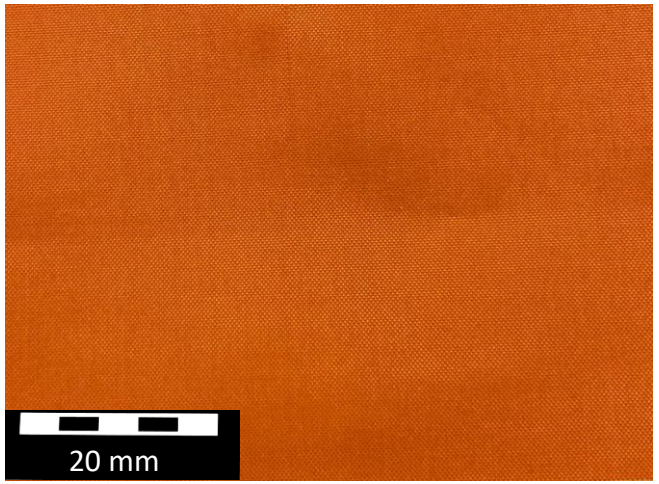

Determination of Ply Thickness

- Compressibility tests @ MUL
  - Loading at $0.01\ mm/min$
  - Holding at constant force (equivalent to $1\ \mathrm{bar}$ of vacuum pressure) for $15\ min$
  - Unloading at $0.01\ mm/min$

- Ply thickness (5 rep.)
  - FM: $0.573 \pm 0.015\ mm$
  - PP: $0.096 \pm 0.001\ mm$



Experimental Work

- In-plane permeability estimation
  - Experimental approach
  - Reverse engineering approach
  - Virtual approach

Experimental Approach - Workflow

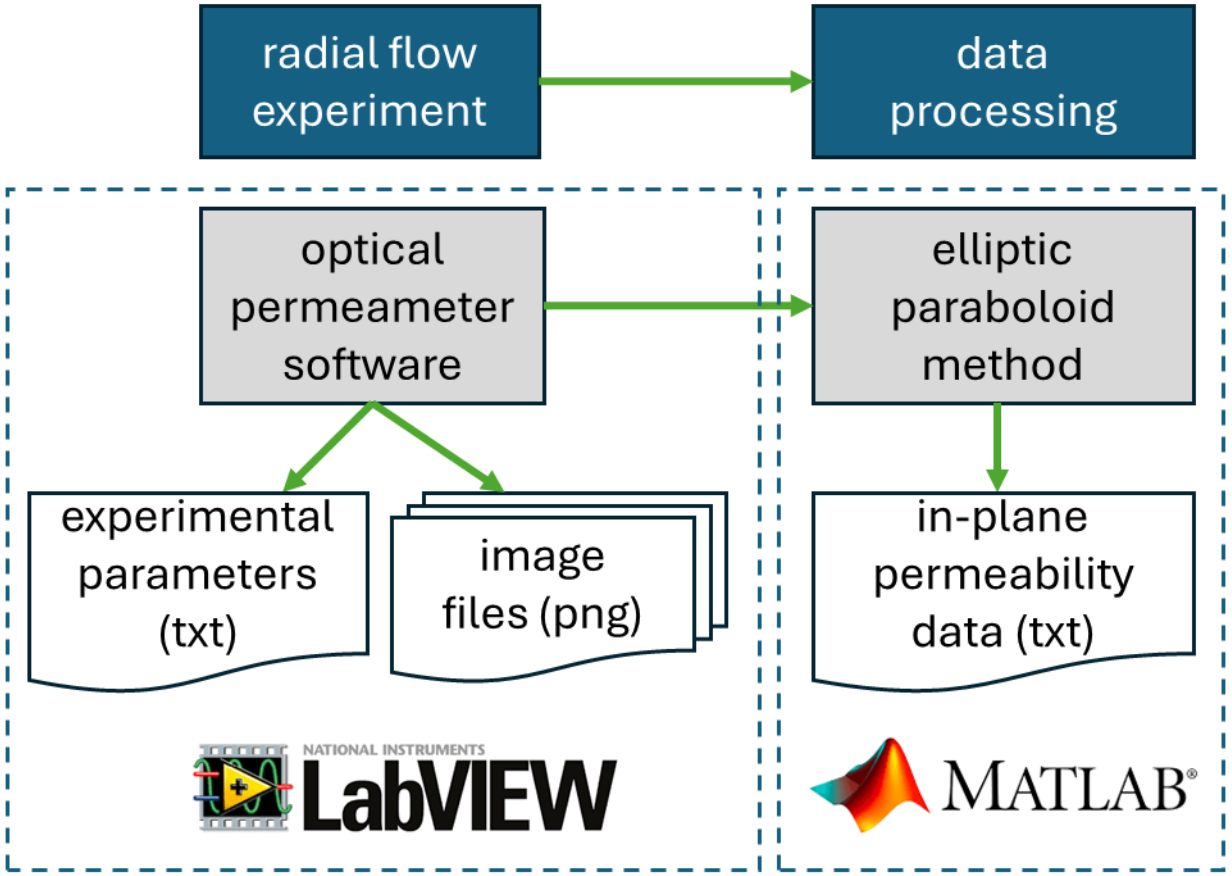

Experimental Approach

- Experiments @ MUL
  - Radial flow experiments with optical tracking of flow front advancement
  - Plant oil with dynamic viscosity of about $65\ mPas$ at $21\ °C$
  - Measurement of fluid pressure and temperature in the feed line

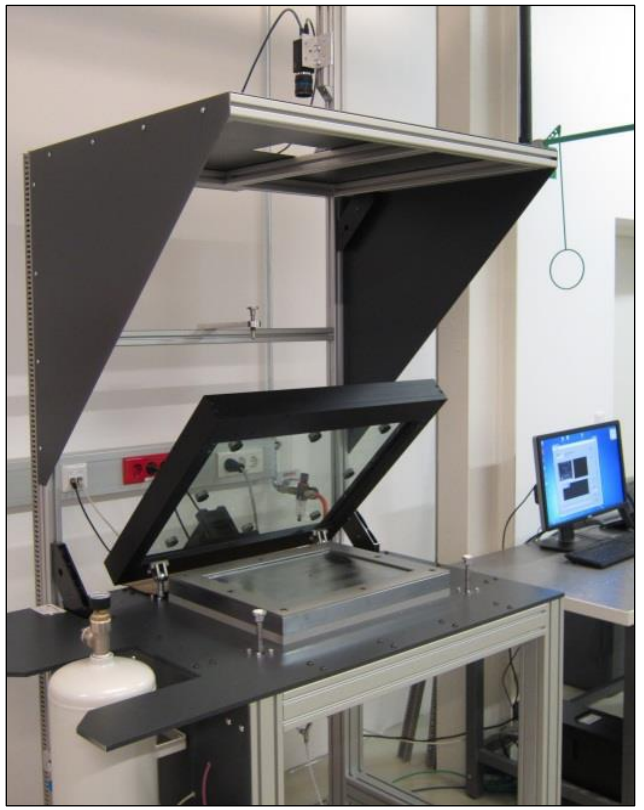

- Cavity height and fiber volume content
  - FM: $h_{DM} = 0.57\ mm$ $\varphi_{DM} = 13.20\ \%$
  - PP: $h_{PP} = 0.09\ mm$ $\varphi_{PP} = 61.35\ \%$

Experimental Approach

- Digital image processing @ MUL

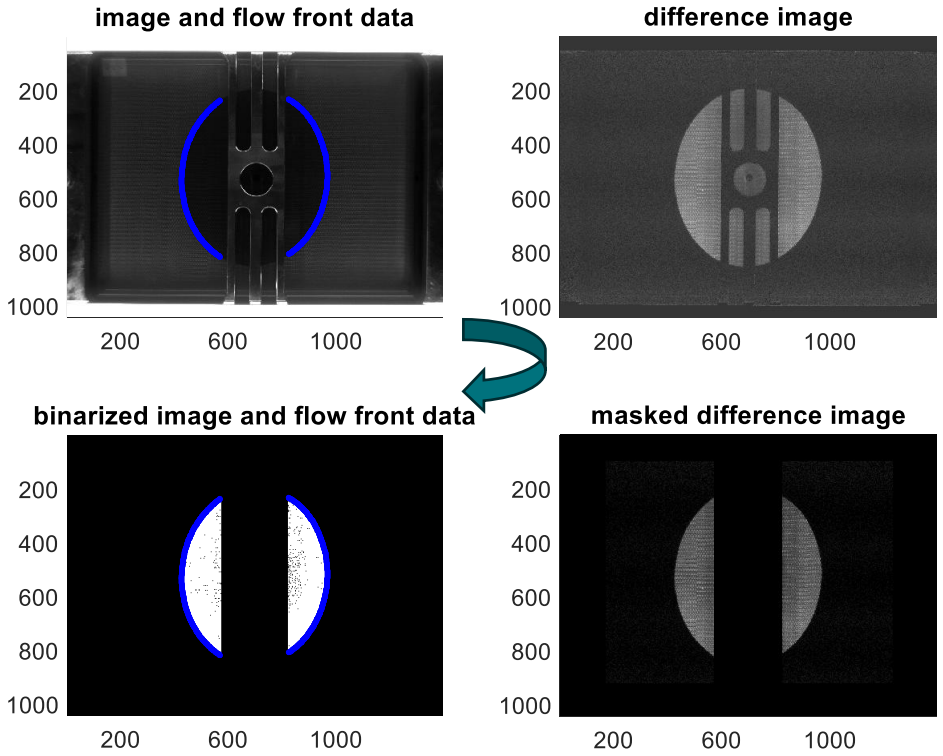

Evaluation of a test on a FM sample

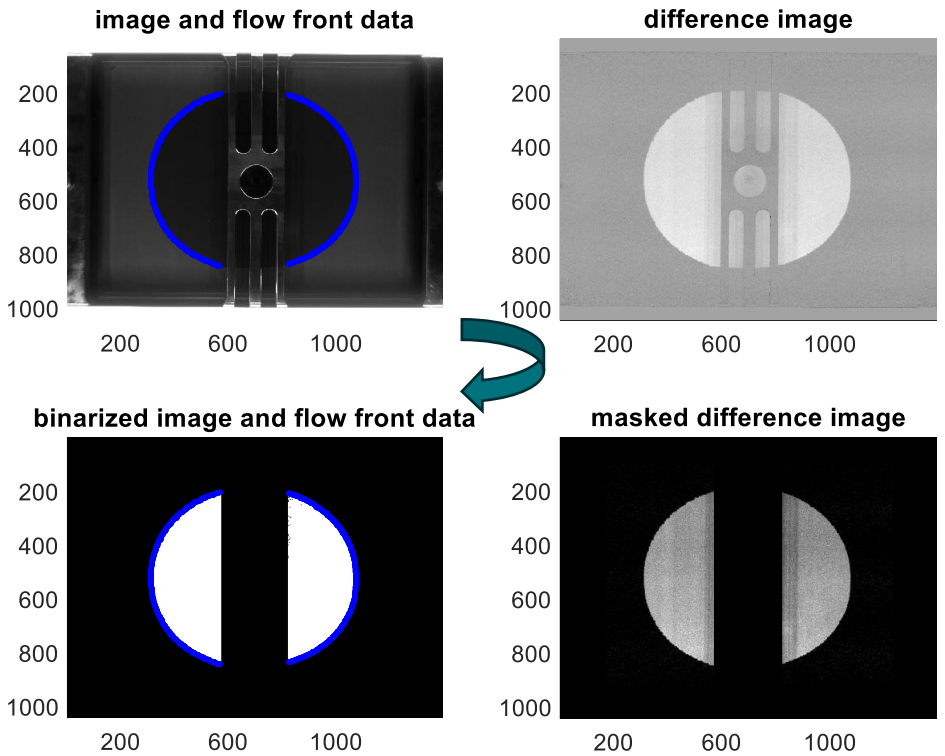

Evaluation of a test on a PP sample

Experimental Approach

- Data processing @ MUL
  - Elliptic paraboloid method

- In-plane permeability of FM (3 rep.)
  - $k_1 = 10.32\ 10^{-9}\ m^2$
  - $k_2 = \ \ 7.01\ 10^{-9}\ m^2$

- In-plane permeability of PP (3 rep.)
  - $k_1 = 91.81\ 10^{-12}\ m^2$
  - $k_2 = 69.95\ 10^{-12}\ m^2$

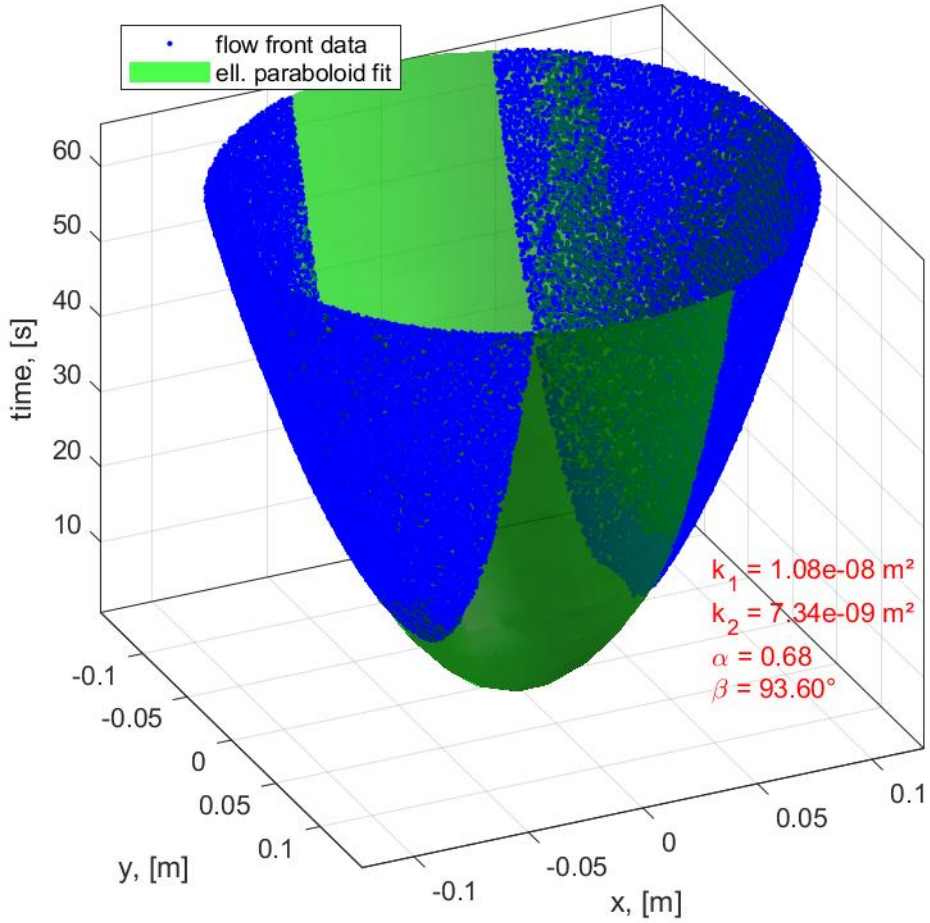

Results of a test on a FM sample

Reverse Engineering - Workflow

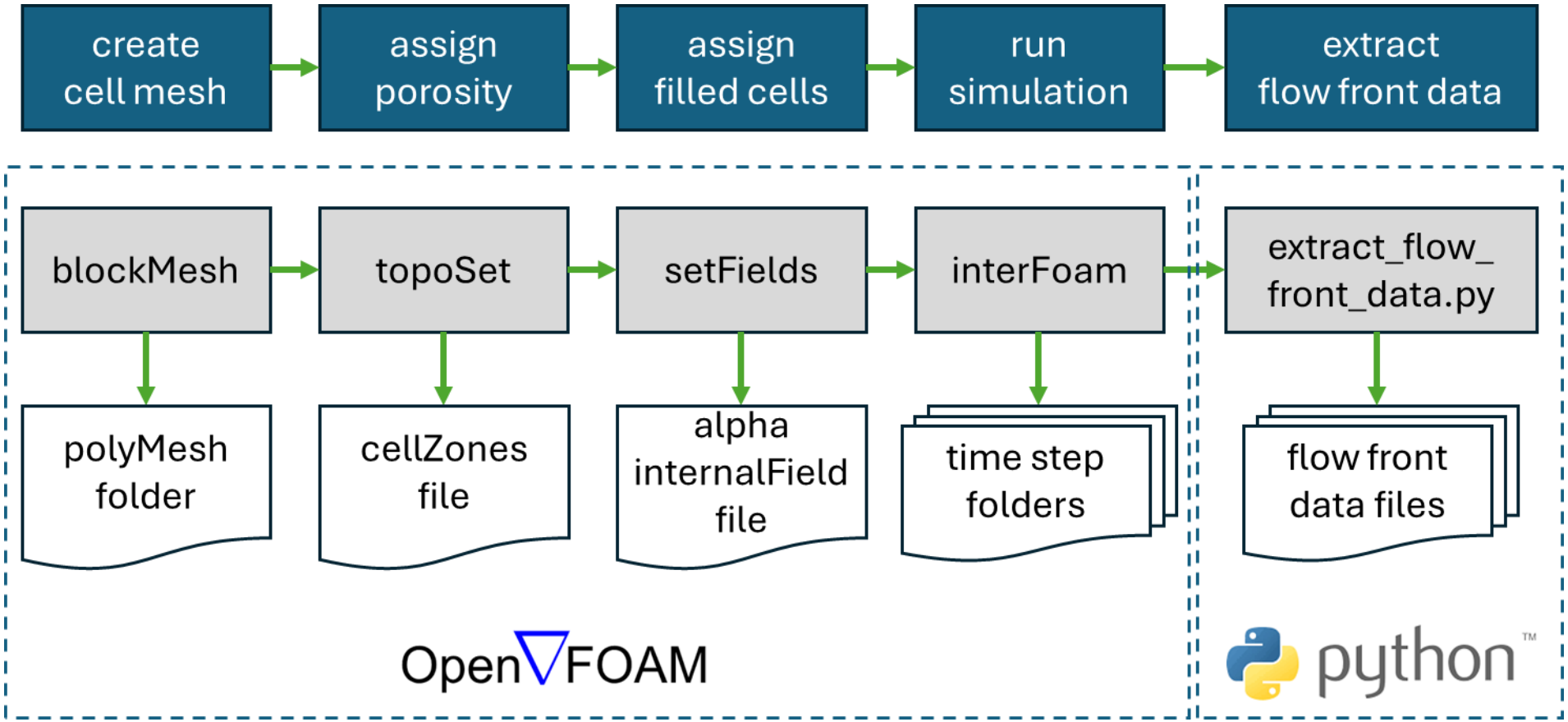

Reverse Engineering - Geometry

- Flow simulations @ IVW
  - Input data from radial flow experiments @MUL

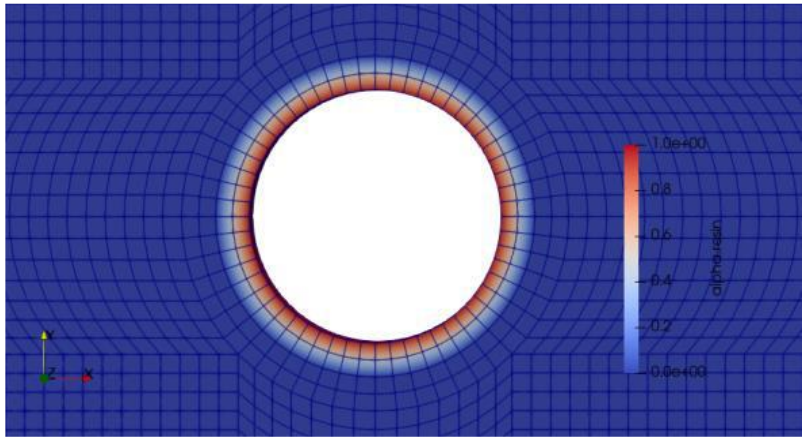

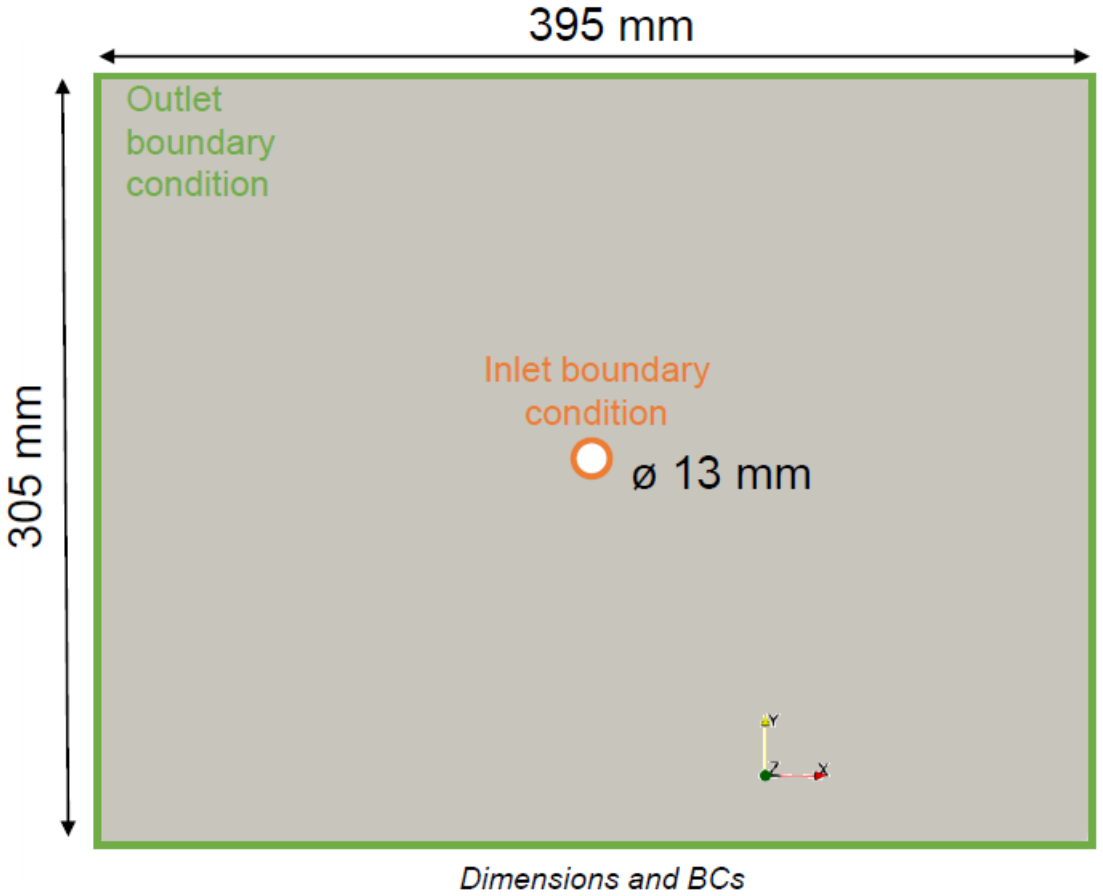

Dimensions and BCs

Reverse Engineering - Data Processing

- Data processing @ MUL
  - Elliptic paraboloid method

- In-plane permeability of FM
  - $k_1 = 10.23\ 10^{-9}\ m^2$
  - $k_2 = \quad 6.91\ 10^{-9}\ m^2$

- In-plane permeability of PP
  - $k_1 = 88.72\ 10^{-12}\ m^2$
  - $k_2 = 68.36\ 10^{-12}\ m^2$

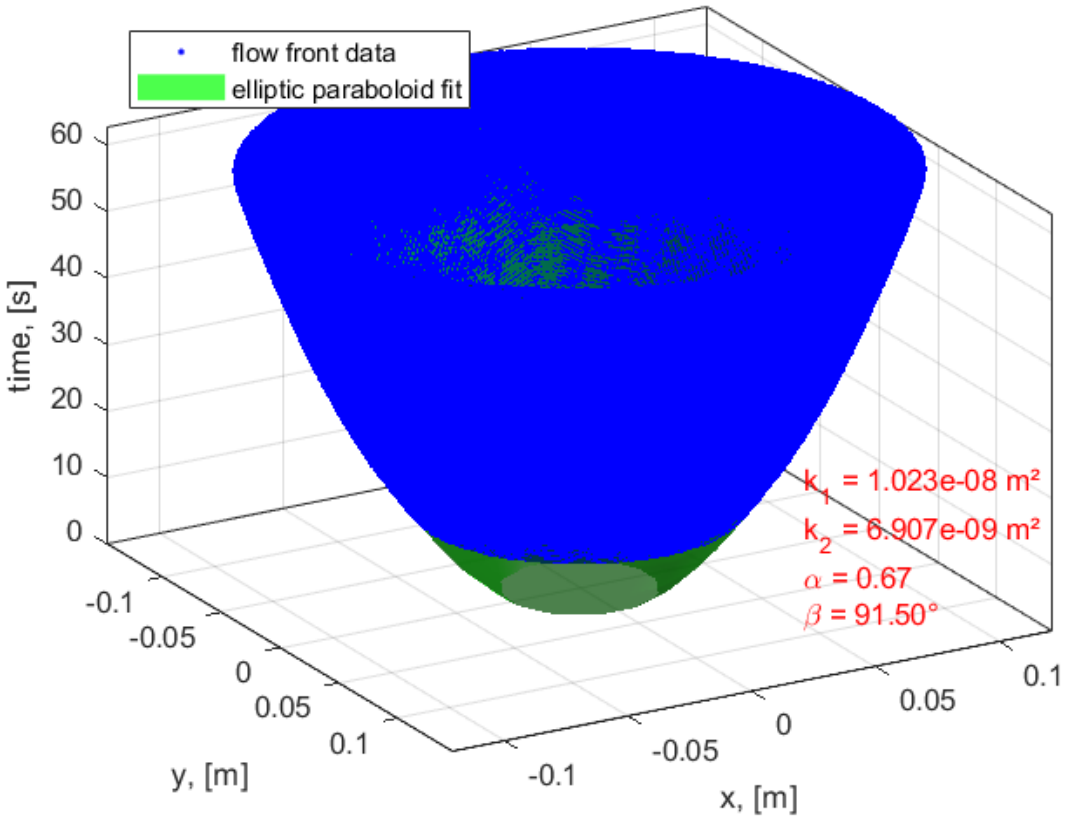

Results from simulation run on FM

Virtual Approach

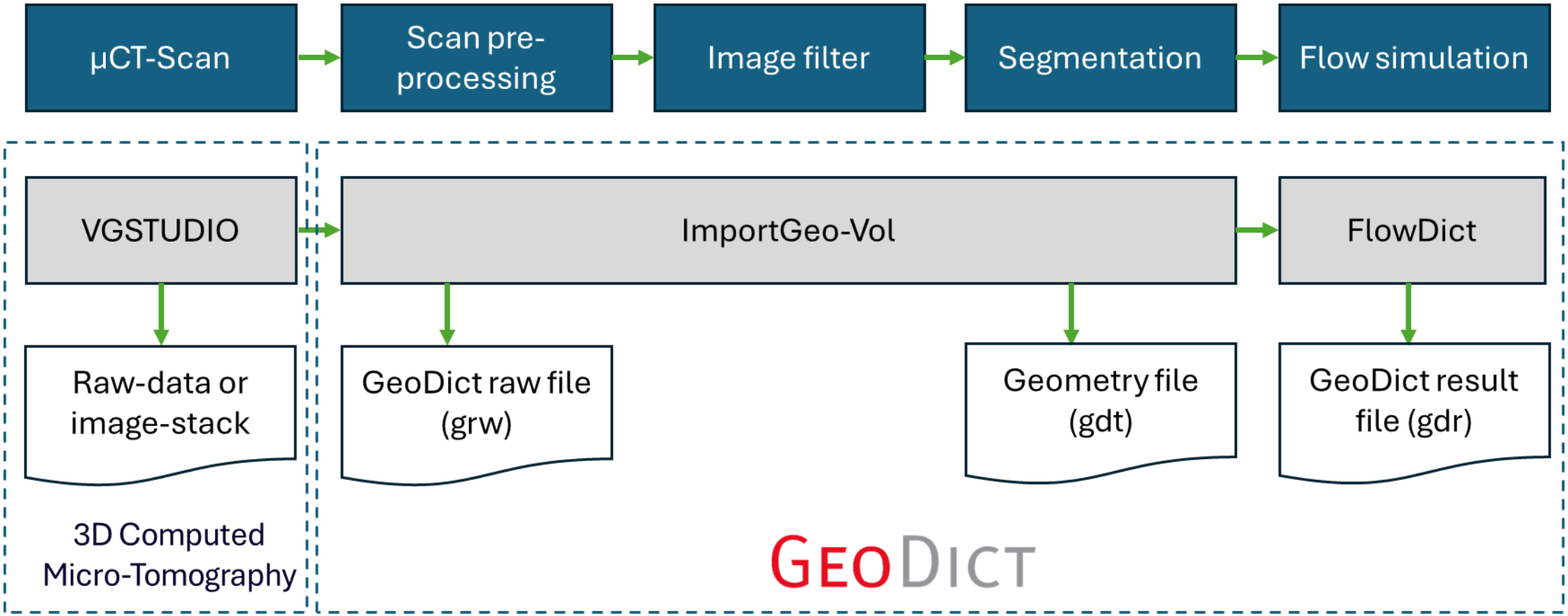

Virtual Approach

- µCT scans @ IVW

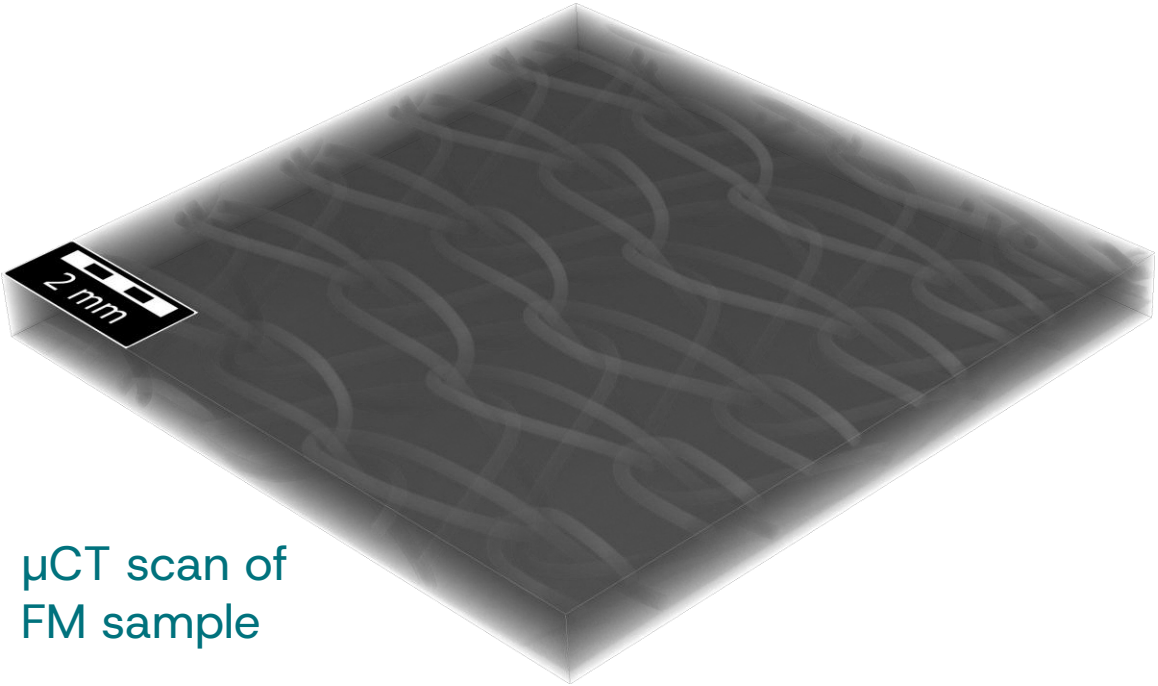

µCT scan of
FM sample

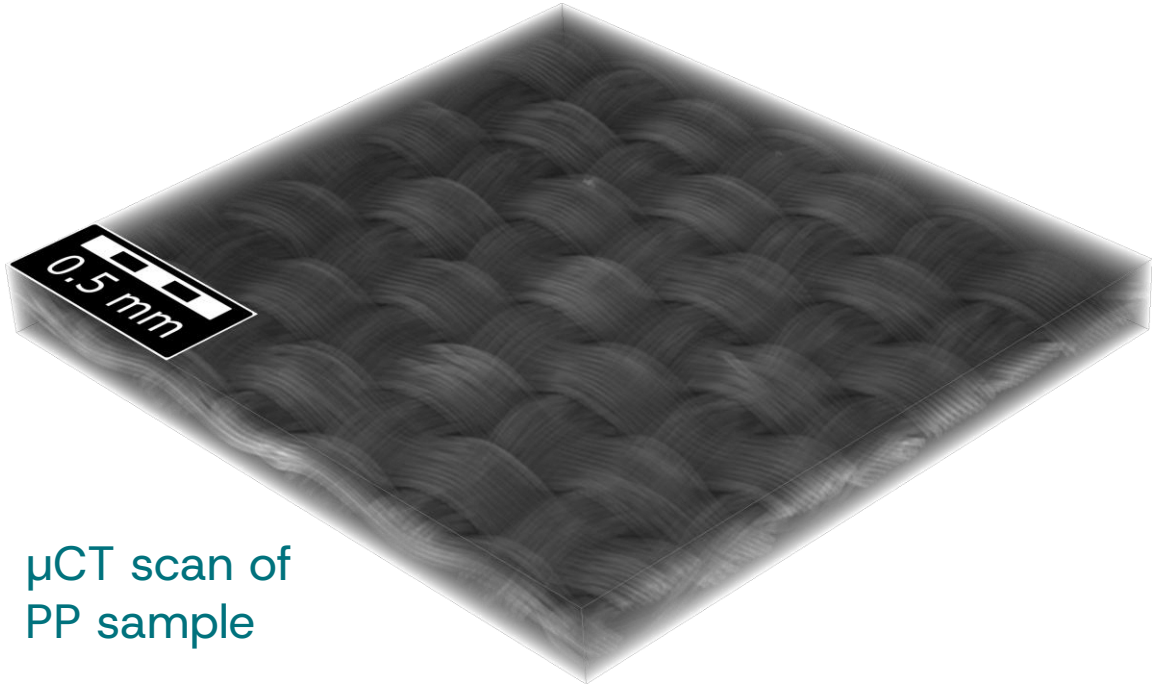

µCT scan of
PP sample

Virtual Approach - Models

- Virtual material models

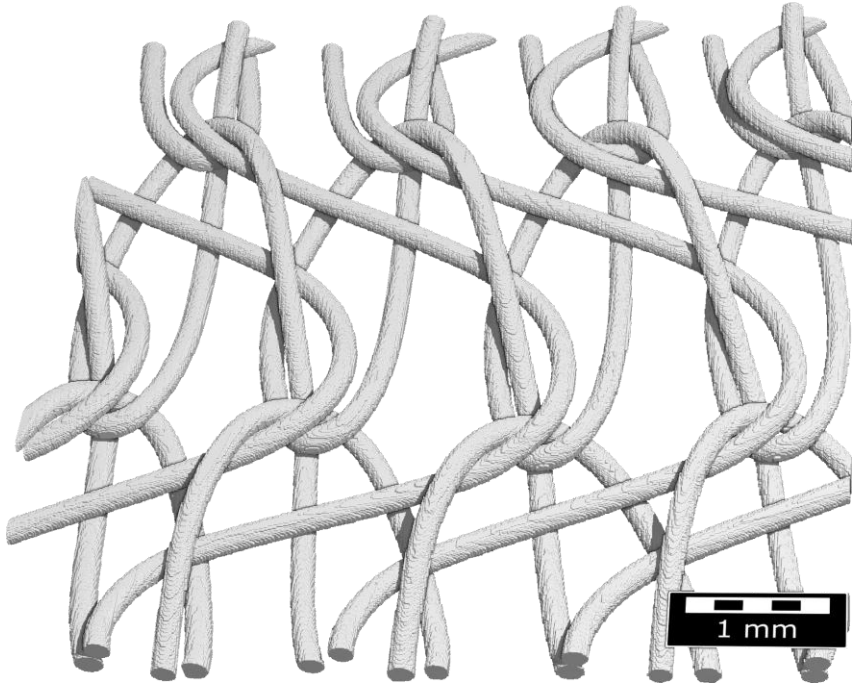

FM sample

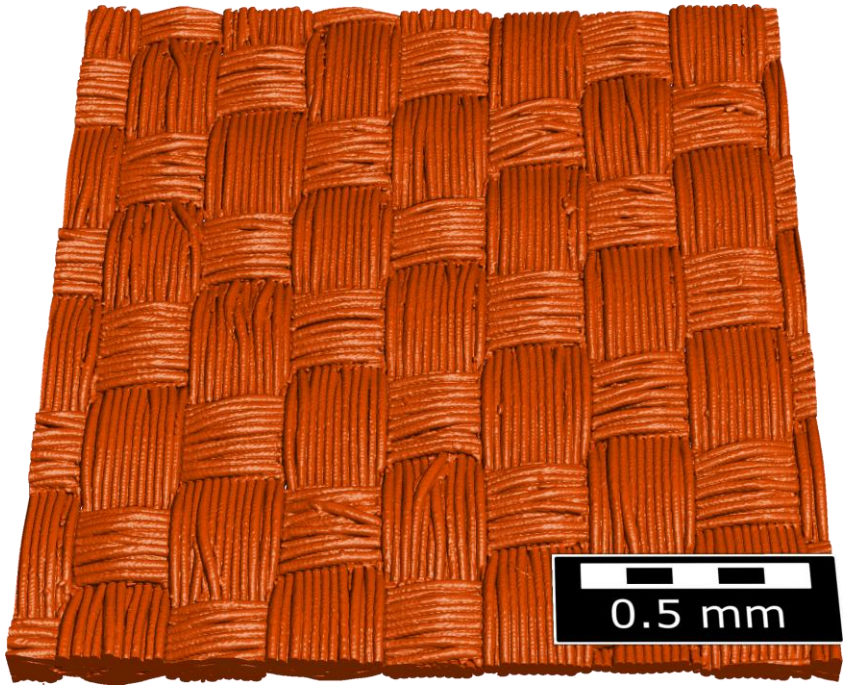

PP sample

Virtual Approach – Data Processing

- Flow simulations @ IVW
  - Flow velocity fields in x and y
- In-plane permeability of FM
  - $k_1 = 11.76\ 10^{-9}\ m^2$
  - $k_2 = \ \ 6.84\ 10^{-9}\ m^2$
- In-plane permeability of PP
  - $k_1 = 32.00\ 10^{-12}\ m^2$
  - $k_2 = 24.00\ 10^{-12}\ m^2$

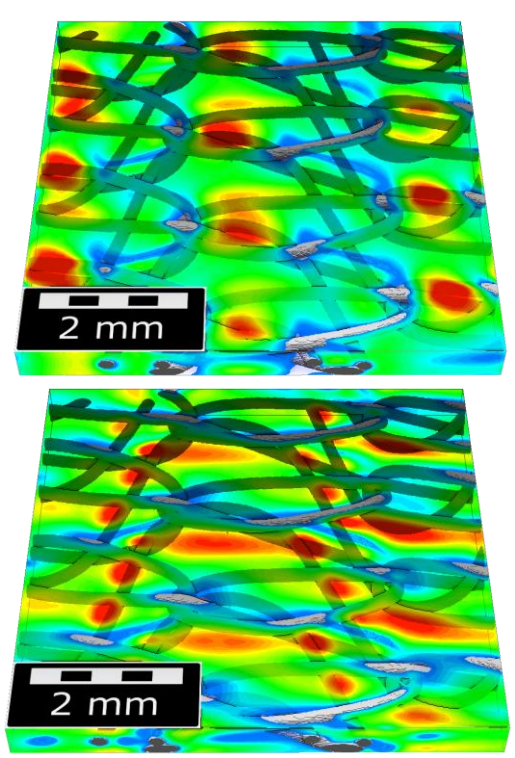

FM sample

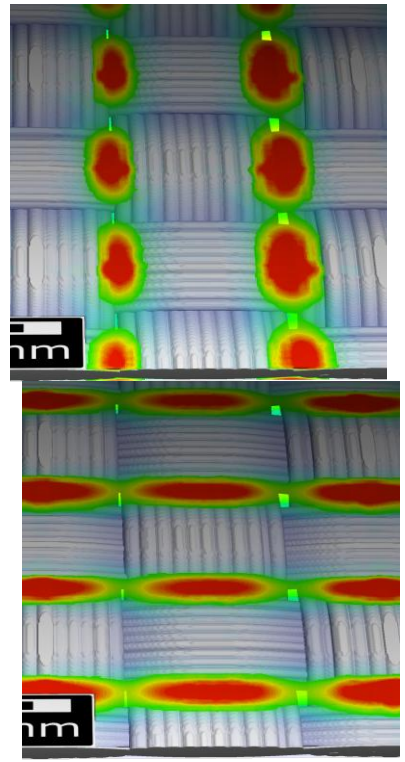

PP sample

Results

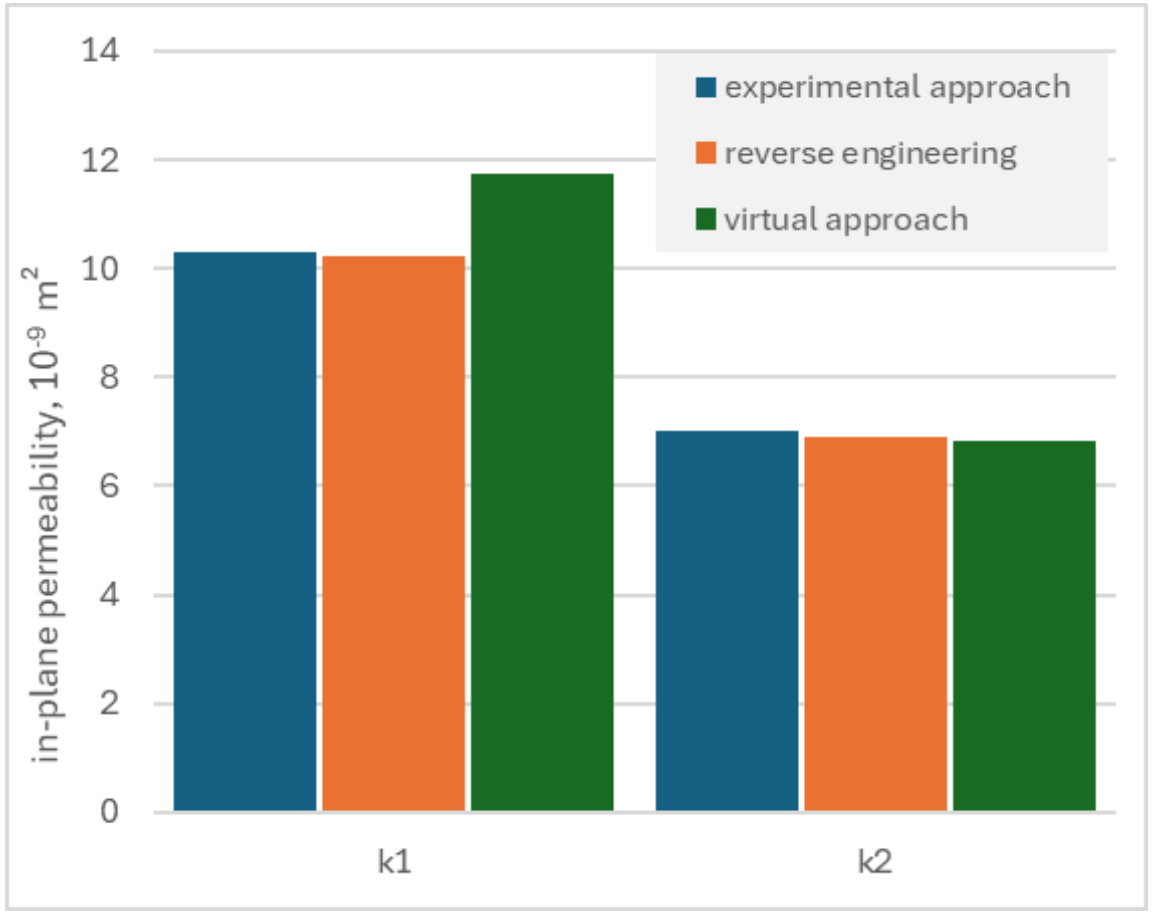

In-plane permeability of FM

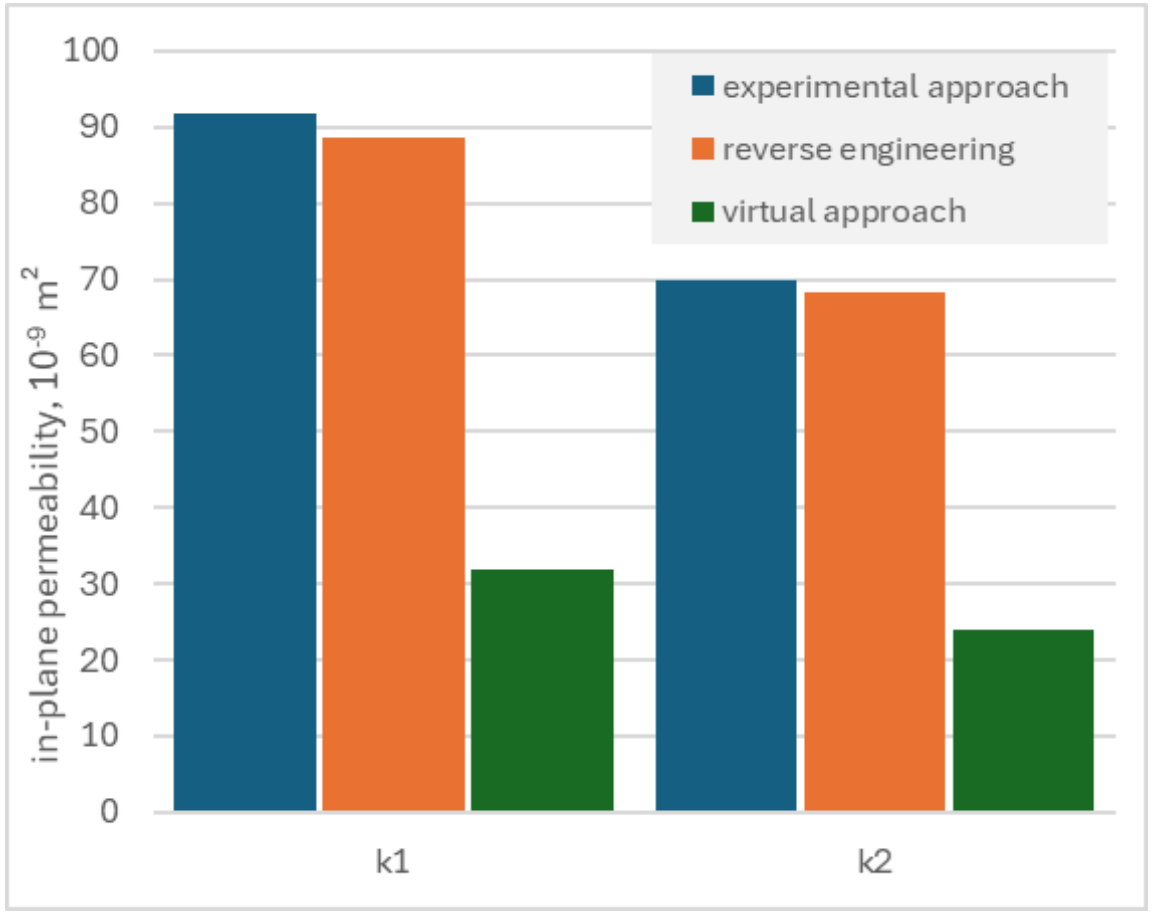

In-plane permeability of PP

Conclusions

- Experimental approach and reverse engineering approach show well comparable results
- Virtual approach shows agreement with other approaches for the model of the flow distribution media only
- In the peel ply model, insufficient level of data segmentation leads to significant deviations

Future Work

- Improving virtual models by enhancing the level of fidelity in the data segmentation

- Extension of the comparison to stacks of FM and PP
  - Incorporation of flow effects in transverse direction

Technical University of Leoben

ewald.fauster@unileoben.ac.at

Thanks for your attention!

ICCM24
AUGUST 4-8, 2025
BALTIMORE CONVENTION CENTER
BALTIMORE, MARYLAND, USA

No Technical Paper Submission for:

Mayur Godbole

NPL
National Physical Laboratory

A Practical Approach to Uncertainty and Validation of Process Simulation for LCM Manufacture

Dr Ana Yong

National Physical Laboratory

Background

- In the manufacture of composites by liquid composite moulding (LCM), a liquid resin is infused through a textile reinforcement within a mould that provides the shape and thickness of the component being made. To ensure the efficient and complete saturation of the reinforcement, simulation can be used as part of the design of the manufacturing process.
- One of the key data inputs used in the simulation of the manufacturing process is the permeability of the reinforcement, K. Here, Darcy's Law is applied to measure how well a fluid will flow through the reinforcement. Following several decades of study and interlaboratory trials, a standardised method for the experimental measurement of the in-plane permeability is available (ISO 4410:2023).
- While extensive research has been carried out into both the determination of permeability and simulation of manufacture, industry uptake of these tools remains low due to lack of familiarity and confidence in the application and resulting data.



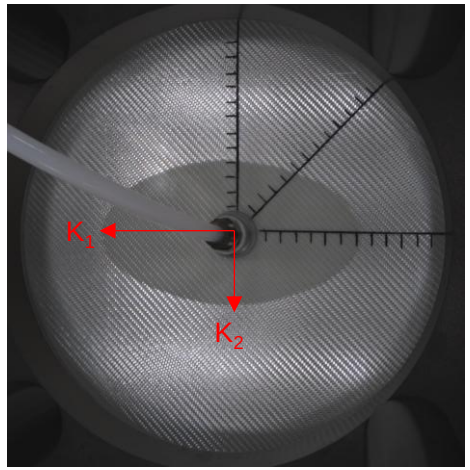

The in-plane permeability can be measured by injecting a model fluid into a dry textile specimen and monitoring the flow front progression with respect to time. The major and minor permeability values (K_1 and K_2) are then calculated using Darcy's Law:

$$v = -\frac{K}{\eta} \cdot \frac{\Delta P}{\Delta L}$$

K = permeability (m^2); ΔP = pressure drop; ΔL = flow length; v = flow velocity; η = fluid viscosity

Objectives

- The work presented here was carried out with the aims of bringing together the knowledge of how to simulate the manufacture of a composite part via LCM, and the experimental measurement of permeability as one of the major data inputs for simulation.

- The final goal is to increase industry use of these tools, in support of the development of manufacturing processes that are time and cost efficient and result in high quality parts.

- The work will test the robustness of these tools and provide an assessment of the expected level of accuracy of the process from characterisation through to simulation, in order to build more trust in the data outputs and enhance their useability.

- The work will provide an understanding of the main contributors to uncertainty, and how these can be mitigated or managed.

- The final outcomes will provide a source of open access information that can be used by anyone to understand the tools, where a lot of previous knowledge has been commercially protected.

Preliminary case study: flat panel

- An initial case study was carried out as an initial proof of concept of how the accuracy of the permeability can influence the result of the simulation and the basis of the next phase of work.
- An FE model of the NPL RTM tool was created using Abaqus CAE. The filling of the tool was simulated using LIMS. Permeability values used in the simulation were taken from values experimentally measured following the standard test procedure described in ISO 4410:2023 and supporting research. [1][2]
- An interlaboratory comparison exercise, carried out as the precursor to ISO 4410:2023, showed that data between sites can vary as much as 40%. To assess the impact of this level of uncertainty, the simulation was rerun using permeability data 40% higher and lower than the experimentally obtained values. The results are summarised in Table 1.
- The comparison of the simulated to the experimental values is given in Table 2.

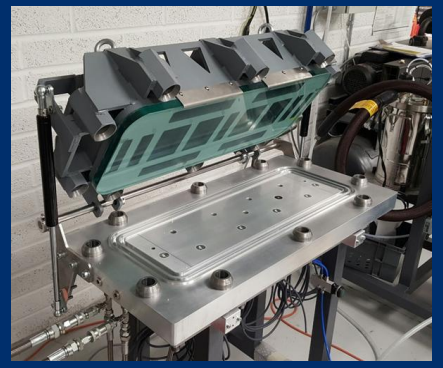



Table 1. Effect of permeability variation on simulated fill time

	Kxx (m^2)	Kyy (m^2)	Fill time (min:s)
Original	2.3e-11	4.24e-12	19:47
Higher	2.76e-11	5.088e-12	16:29
Lower	1.84e-11	3.392e-12	24:43

Table 2. Comparison of simulated to experimental fill times

Simulated	Test 1	Test 2	Test 3
19:47	12:35	12:50	11:00

Second case study: complex shape

- Following the preliminary work, a second case study was carried out following the same steps of (1) measure the permeability; (2) simulate the mould filling and (3) compare the simulation to experimental values.
- In this second case study, a more complex shape was used. Here, the experimental work and simulations were carried out on a double-dome shape (Fig. 5). This shape is commonly used in the study of composites manufacture as it allows for the examination of the effects of a number of different geometrical features.
- Here, as the fabric is now draped over a 3D shape, the draping results in different areas of shear. The shearing of the fabric is known to change the permeability in localised areas, where opening up of the tows provides for easier flow and a higher permeability.
- The effect of simulating the mould filling using locally different permeability values was studied by first measuring the permeability of specimens that had undergone controlled degrees of shear, with the aim of applying these to the model for increased accuracy.



Fig. 5. Double dome mould

Sheared permeability measurement

- The permeability of sheared specimens was measured using a specially designed frame as shown in Fig. 6. Here, the specimens were clamped along two parallel edges of the frame. The frame was able to move in a scissor movement, allowing for a pure shear condition.
- Specimens were made from 3 layers of fabric and tested at a cavity height of 0.7 mm to provide a fibre volume fraction of 0.5. The number of layers used here reflected the setup used in the double-dome mould experiments. This is fewer layers than would typically be used in an in-plane permeability measurement, however keeping the number of layers low provided the additional benefit of minimising any differences in shear angle between each layer.
- The frame was used with the top part of NPL's radial permeameter.
- Flow front data was processed using NPL's flow front detection algorithm, which tracks the elliptical flow front and automatically calculates the in-plane permeability.

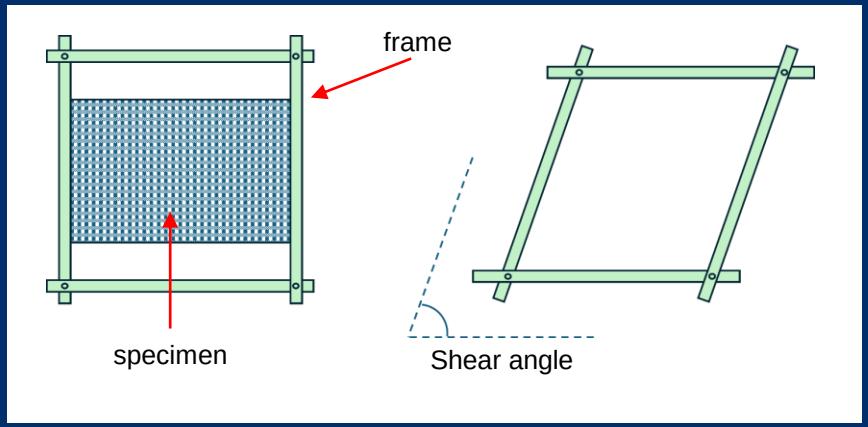

Fig. 6. Schematic diagram of shear frame

Sheared permeability test results

- As seen in the example in Fig. 7, the shearing of the fabric resulted in a flow front that was not perfectly elliptical. It should be noted that the algorithm used to calculate the permeability continuously fits the moving flow front to a perfect ellipse, which resulted in a reduced applicability here. At present, radial permeability measurement is always based on an assumed elliptical flow, so this remains the most current solution available.
- The permeability values were plotted against the known angle of shear of the specimens and plotted against the fit established in previous works. As seen in Fig. 8 and Fig. 9, the data showed a reasonable fit to the expected trend.

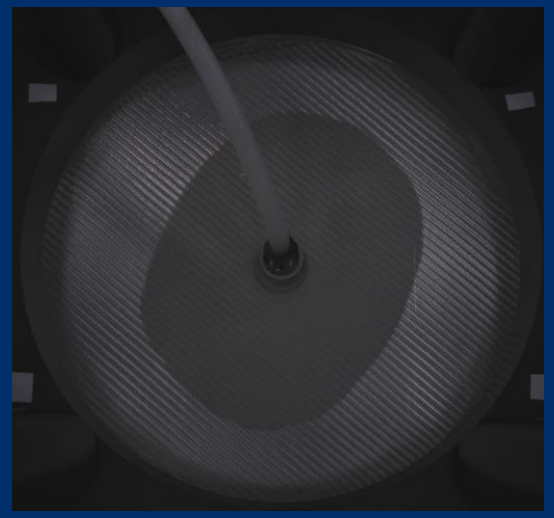

Fig. 7. Example flow through sheared specimen

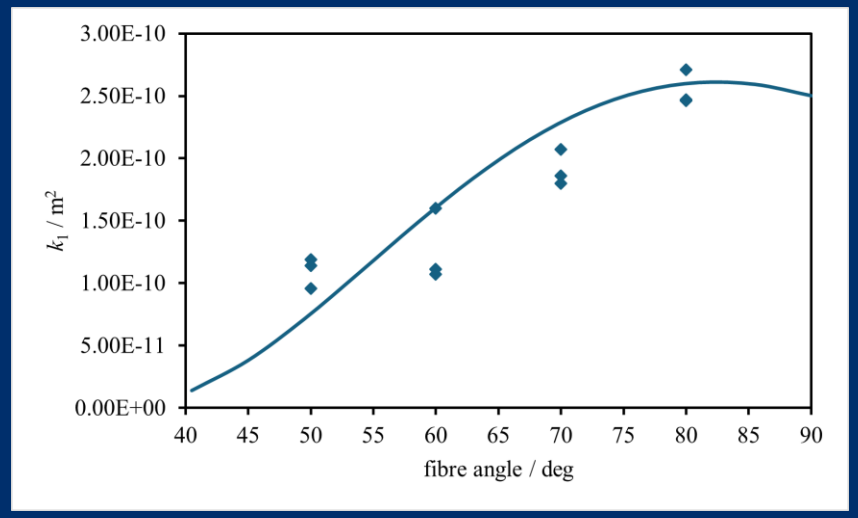

Fig. 8. k_1 values against shear angle

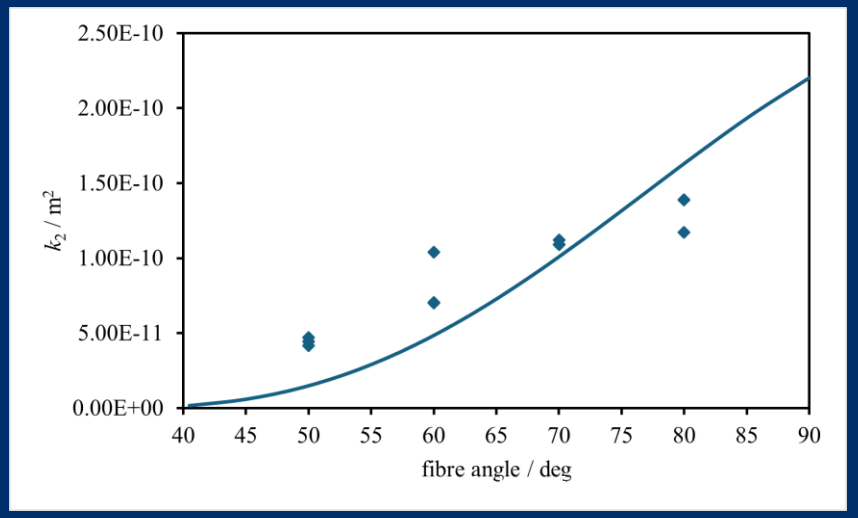

Fig. 9. k_2 values against shear angle

Simulation of the mould filling

- Flow through the mould was simulated using uniform permeability values taken from measurements carried out following the standard method, i.e. a flat and unsheared specimen (Fig. 11)
- The drape of the fabric over the mould was then modelled (Fig. 10) to obtain the localised shear angle of the fabric at different parts of the model component. This was used to apply localised permeability values taken from the sheared specimen tests. The flow was then modelled as shown in Fig. 12. Here we can see the change in predicted flow front.

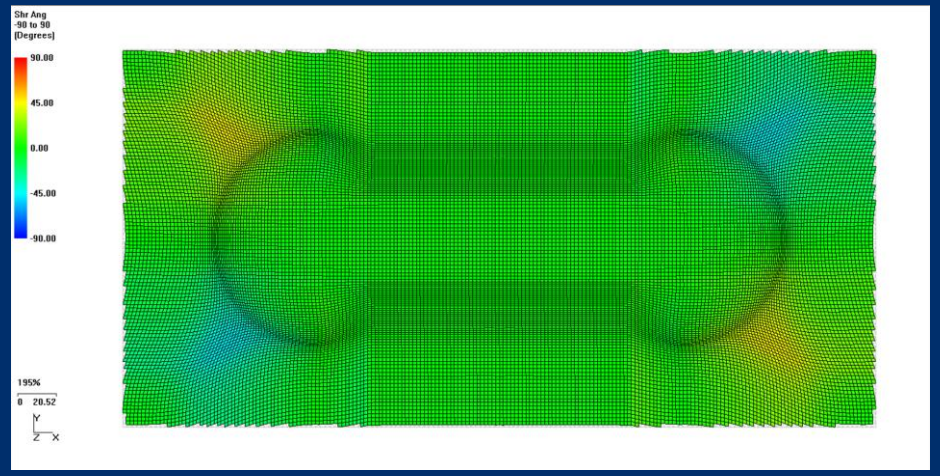

Fig. 10. Model of fabric drape in mould

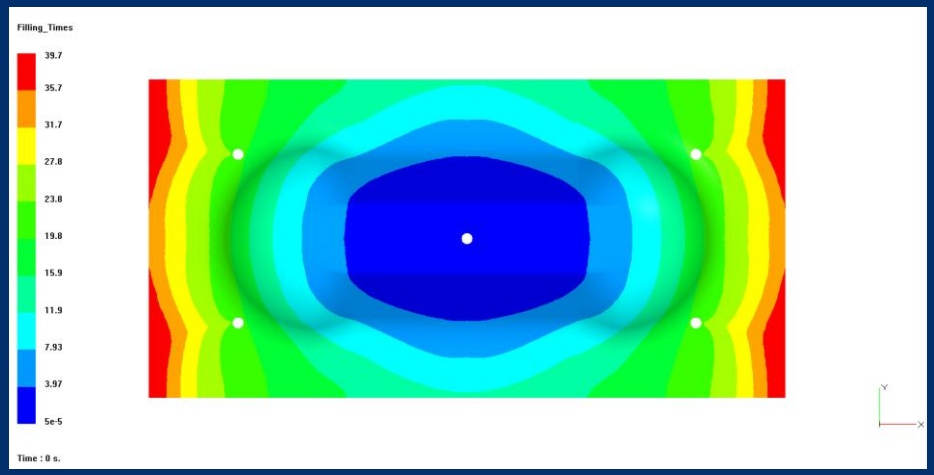

Fig. 11. Simulated mould filling using uniform permeability values

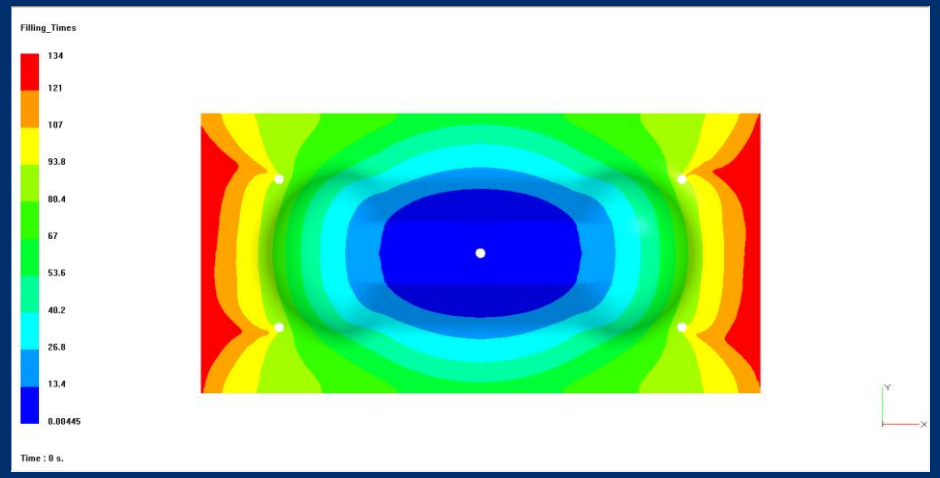

Fig. 12. Simulated mould filling using non-uniform permeability values

Infusion into the double-dome mould

- Laboratory-scale infusions were carried out using the double-dome mould at the University of Nottingham. The fabric was the same Hexcel 2/2 twill woven fabric as characterised in the permeability measurements and engine oil was used as a model fluid. Injections were carried out at 0.1 MPa
- Using video footage of the experiments, the movement of the flow front was tracked using NPL's automated system. These data were used to generate colour maps of the flow front progression
- The scale of the colour map was programmed to produce clear and readable isolines. An example output is shown in Fig. 13.

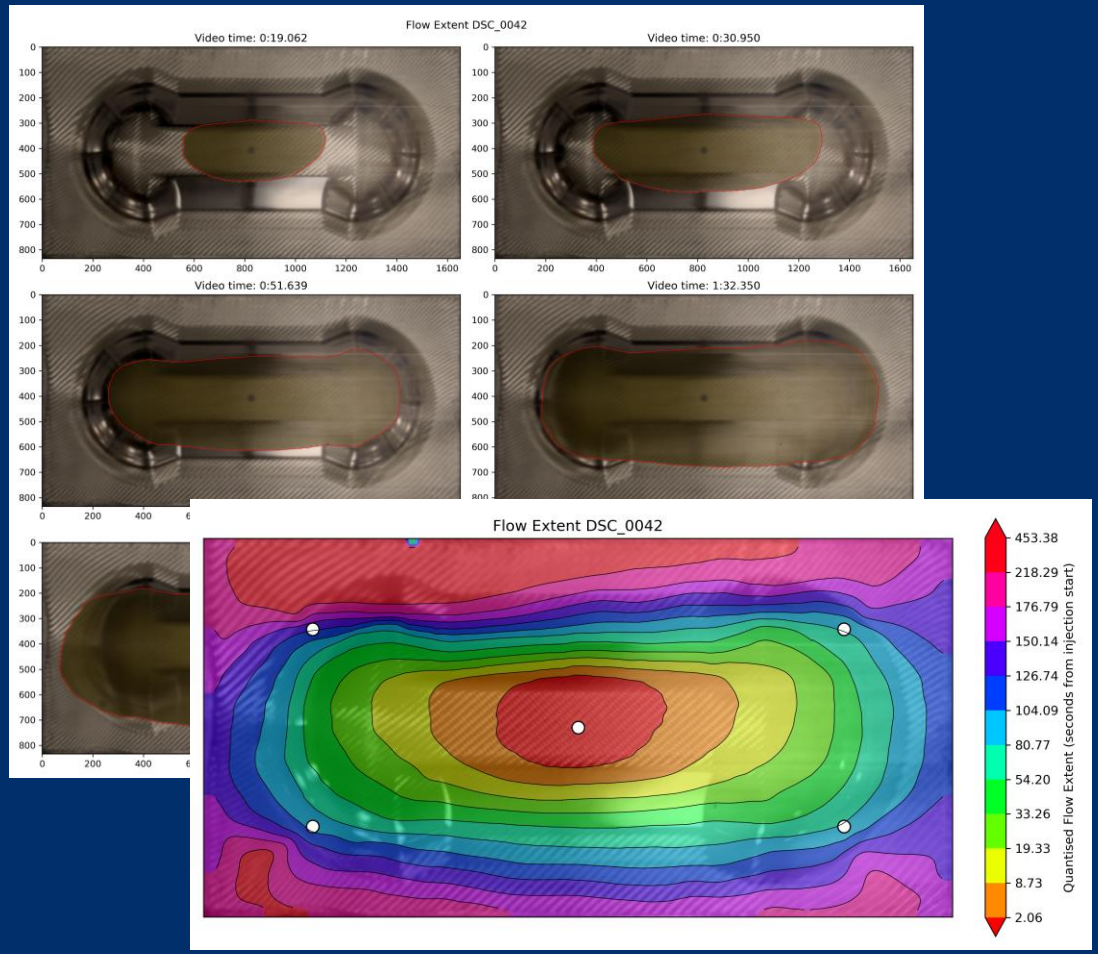

Fig. 13. Generation of colour maps of flow front progression

Time-stamping the flow front progression

- In order to be able to compare the experimental values to simulated data it was necessary to time stamp the images using a means that would be comparable to the simulation. Homography transformation (projective transformation) was used to align the video images to the simulated images, using the inlet and vent holes as the reference.
- Markers were placed on the cardinal axes at the time bounds of the simulated images to enable comparison with the flow arrival time from the experimental measurements (Fig 14). A representative graph is given in Fig. 15 of the progression of the flow from the experimental data. For increased accuracy, in further work these points will be taken from the mesh of the simulation in order to assign a scale to the distance markers. The next step will be to fine tune the simulation for comparison to these experimental data.

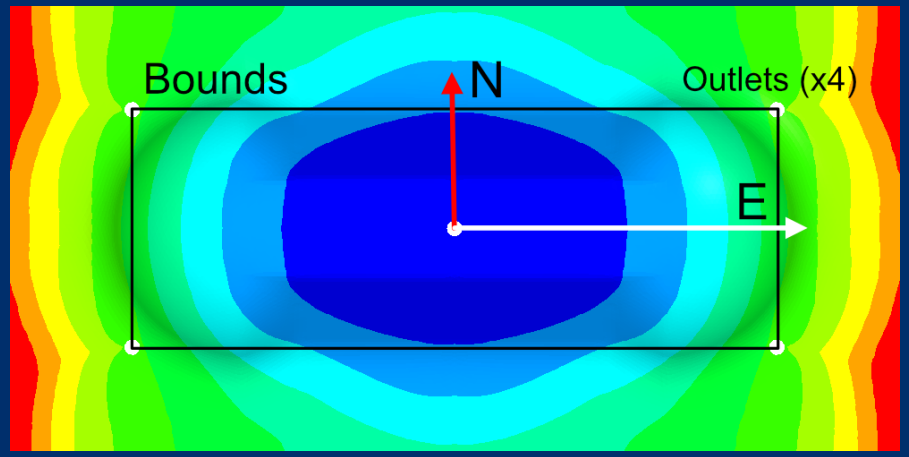

Fig. 14. Cardinal axes

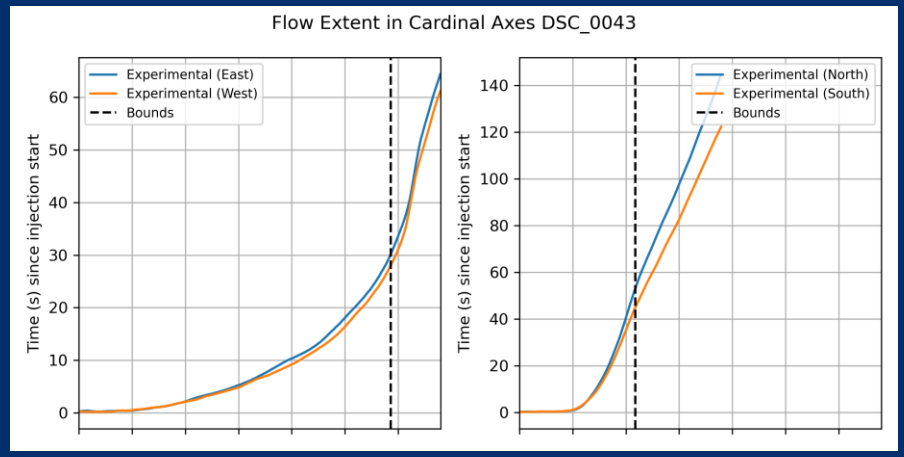

Fig. 15. Flow front progression

Accuracy of permeability

- In order to ensure the most accurate simulation, the permeability input data need to be precise. As shown in the preliminary case study, changes in the permeability input data can have a significant impact on the simulation of even a simple shape. Throughout this work, a number of areas of improvement have been identified for further development, including:
  - The low number of layers used in the measurement of the permeability of sheared specimens was beneficial in ensuring that any difference in the degree of shear between the layers was minimised, however this may affect accuracy of permeability measurement in other ways such as increased impact of surface effects of the tool on the volume fraction, e.g. parallelism of the top and bottom plates and any features of the tool such as sensor placement.
  - The compliance correction required for cavity height settings was proportionally quite high – 0.2 mm correction for a 0.7 mm thickness setting. Ensuring the correction is carried out is essential to accurate reporting of the volume fraction.
  - It was noted that care was required during loading and unloading of specimens with respect to any fluid remaining in the system. If fluid remained, it would leak prematurely onto the specimen, prior to the start of the controlled injection and potentially contain bubbles. Therefore, the best course of action was to begin each test with an emptied inlet tube.
  - The tool used to measure the sheared specimen permeability had been significantly modified from the method used to measure the permeability following the standard method, effectively resulting in what could be considered a “different” tool. Interlaboratory trials have shown variability between different tools which can significantly impact mould filling simulations.
  - Benchmarking trials using nominally the same fabric have shown that there is batch to batch variability in the architecture at scales relevant to permeability measurement. Different values were measured on different batches of the “same” fabric. [3][4]

Uncertainty of measurement

- In order to further understand the accuracy of the permeability measurements, measurement uncertainty evaluation was performed by identifying and quantifying the sources:
  - Injection pressure
  - Fluid viscosity
  - Radius of injection port
  - Volume fraction
  - Flow front position
  - Time

- Using Monte Carlo simulation, it was possible to quantify the uncertainty for each measurement at 95% CI at 11% for K_1 and 12% for K_2 (Fig. 16).

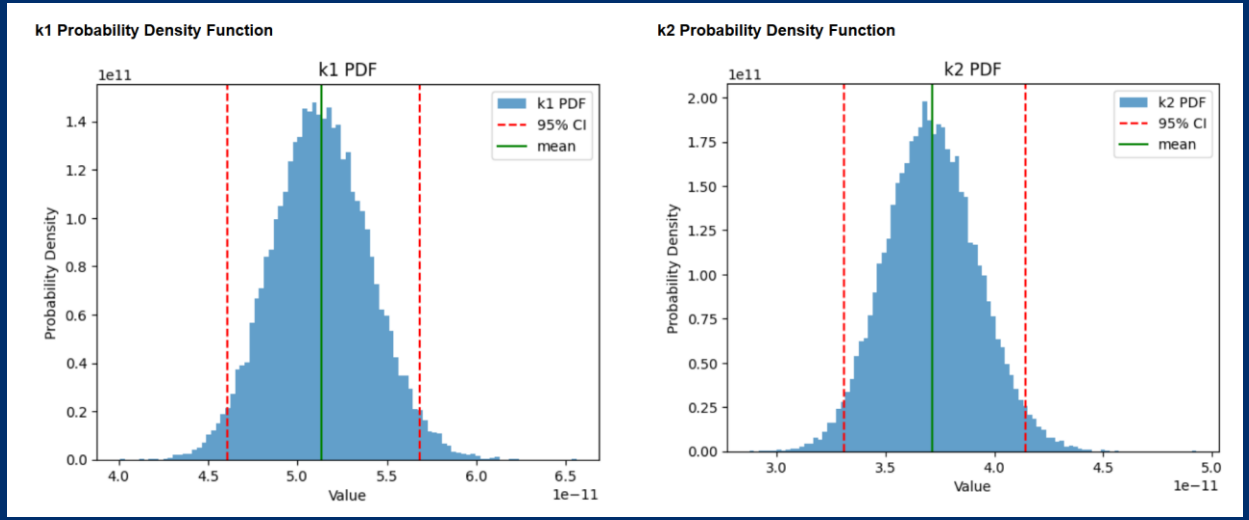

Fig. 16. Histogram showing measurement uncertainty

Proposed next steps and concluding remarks

- The two case studies presented here show a preliminary effort to assess the accuracy of mould filling simulations and the impact of permeability values as an input parameter.
- The permeability of sheared specimens was successfully measured, and the influence of mapping a non-uniform permeability onto simulations of the mould filling vs using a uniform value was shown.
- In the next steps, following refinements to the simulations, these results will be put together to form a complete picture and provide an accessible understanding of the process of characterising textile reinforcements and simulating the manufacture of a composite part.
- Here, some of the complexity of this process has been shown, highlighting the importance of putting these methods through their paces at all stages from fabric characterisation through to simulation and manufacture.
- Ongoing work is being carried out into the virtual characterisation of permeability, which may pave the way for a suitable alternative to experimental measurements [ref].

Acknowledgements

Research carried out with the support of Dr Andreas Endruweit at the University of Nottingham, who contributed the simulated data and collaborated on the experimental measurements using the double dome mould provided by the university.

Further information on this work is available at: https://eprintspublications.npl.co.uk/

References

[1] May D, Aktas A, Advani SG, Berg DC, Endruweit A, Fauster E, Lomov SV, Long A, Mitschang P, Abaimov S,Abliz D et al. In-plane permeability characterization of engineering textiles based on radial flow experiments: A benchmark exercise. Composites Part A: Applied Science and Manufacturing, 2019; 121: 100-114.

[2] May D, Advani SG, Duhovic M, Endruweit A, Fauster E, George A, Liotier PJ, Lira C, Lomov SV, Pucci MF, Schmeer S et al. A new ISO standard for the experimental characterization of in-plane permeability of fibrous reinforcements. Composites Part A: Applied Science and Manufacturing, 2025; 190: 108592

[3] Yong AXH, Endruweit A, George A, May D, Aksoy YA, Ali MA, Allen T, Baral P, Betteridge C, Brauner C, Caglar B et al. Towards standardisation of the out-of-plane permeability measurement for reinforcement textiles. Composites Part A: Applied Science and Manufacturing, 2025; 190: 108630.

[4] Yong AXH, Aktas A, May D, Endruweit A, Advani S, Hubert P, Abaimov SG, Abliz D, Akhatov I, Ali MA, Allen T et al. Out-of-plane permeability measurement for reinforcement textiles: A benchmark exercise. Composites Part A: Applied Science and Manufacturing, 2021; 148: 106480.

[5] E. Syerko, T. Schmidt, D. May, C. Binetruy, S.G. Advani, S. Lomov, et al. Benchmark exercise on image-based permeability determination of engineering textiles: Microscale predictions, Composites Part A: Applied Science and Manufacturing, 2023; 167: 107397

MATERIAL CHARACTERIZATION FOR PARTICLE-FILLED RTM IN 3D FIBROUS PREFORMS

L. Marchand[1,2], S. Comas-Cardona[1], C. Binetruy[1] and A. Hautefeuille[2]

[1]Nantes Université, Ecole Centrale Nantes, CNRS, GeM, UMR 6183, F-44000 Nantes, France
1 rue de la Noë, Nantes, 44321, France
Email: leonie.marchand@ec-nantes.fr, sebastien.comas@ec-nantes.fr and christophe.binetruy@ec-nantes.fr , web page: https://gem.ec-nantes.fr/

[2]ArianeGroup SAS
Les Cinq Chemins, 5 Rue de Touban, 33185, Le Haillan, France
Email: alexandre.hautefeuille@ariane.group, web page: https://ariane.group/

Keywords: 3D reinforcement, Physical properties, Microstructure, Filtration, Retention

ABSTRACT

In the case of severe thermo-mechanical loads, the composite materials of this study are manufactured through Resin Transfer Molding process in which a particle-filled thermosetting resin is injected into a 3D fibrous preform.

The challenge is to control the process by building a model that couples flow in porous media, particle filtration, and material properties' evolution induced by the filtration phenomenon. Such a model requires material properties related to particle-filled resin rheology and fibrous preform permeability as inputs.

Experimental methods were used in order to characterize the materials of the study taking into account the fibrous preform architecture. An initial phase consisted in characterizing the particle-filled fluid with experimental tests and determining the preform microstructure with micro-tomography. In a second phase, a new non-destructive method was developed to measure the three-dimensional permeability of a 3D anisotropic fibrous reinforcement using an air-flow bench.

The material data generated from the characterization will further be implemented in the coupled flow-filtration model.

1 INTRODUCTION

3D fiber-reinforced composite materials are often used for thermal protection systems (TPS) that are exposed to severe thermo-mechanical loads. The 3D composites investigated in this study are manufactured through RTM (Resin Transfer Molding) process in which a thermosetting resin is injected into a 3D fibrous preform (Fig. 1). The 3D composites are further functionalized by two means: (i)

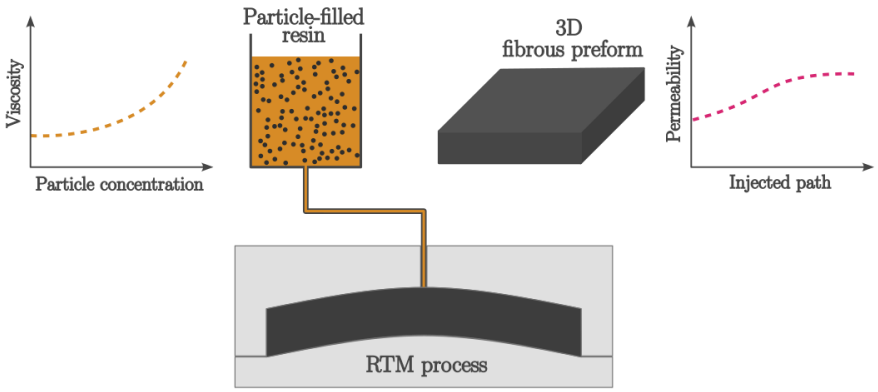

Figure 1: Study process overview.

adding fillers to the resin and (ii) generating a fillers' content gradient in the fibrous preform. Therefore, the challenge consists in controlling this process, which involves the flow of particle-filled resin through a three-dimensional fibrous preform.

In order to control the particle content during the injection, one must build a model that couples flow in porous media, particle filtration, and material properties' (e.g., viscosity and permeability) evolution induced by the filtration phenomenon [1], [2], [3], [4]. Such a model requires material properties related to particle-filled resin rheology and fibrous preform permeability as inputs. Literature showed that the resin viscosity increases with the particle concentration. Because of the addition of particles, the particle-filled fluid may exhibit different behaviours than the neat fluid [1], [4]. Previous studies developed different experimental methods for fibrous reinforcement permeability measurement. These methods are usually destructive and apply to 2D reinforcements [5].

This work aims to extend the understanding of the flow behaviour and architecture of the three-dimensional fibrous network geometries during Resin Transfer Moulding. Experimental methods were used in order to characterize the materials of the study taking into account the fibrous preform architecture.

An initial phase of the work consisted in characterizing the particle-filled fluid and determining the preform microstructure. The rheology of the particle-filled fluid was analysed in order to determine the influence of filler content on the viscosity. Then, micro-computed tomography was used to analyse the three-dimensional fibrous preform architecture. In a second phase, a new non-destructive method was developed to measure the three-dimensional permeability of the fibrous reinforcement using an air-flow bench. Using an inverse method, the preform permeability 3D tensor is determined from experimental and numerical simulation results

2 MATERIALS

A first phase of the work consisted in characterizing the materials of the study. The particle-filled fluid rheology was determined and the 3D fibrous preform microstructure was analyzed.

2.1 Suspension characterization

A model suspension was chosen in order to develop experimental methods by fluid flow. Glycerin SOLVAGREEN® from Carl Roth was mixed with ethanol at a percentage of 65/35% by mass. The glycerin-ethanol is then mixed with carbon blacks using the T25 digital Ultra-Turrax disperser to homogenize the suspension. The model suspension of the study is studied with variable particle contents to measure the viscosity as a function of particle concentration as shown in figure 2.

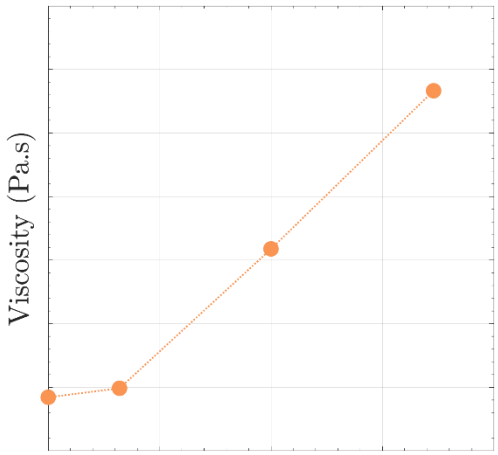

Figure 2: Evolution of the suspension viscosity as a function of the particle content.

2.1 Fibrous preform morphology

The 3D fibrous preform architecture is obtained by non-woven horizontal ply stacking made of carbon fibers whose orientations vary periodically in a balanced way. The three-dimensional structure is built by transferring fibers in the vertical direction, i.e. through the thickness. Samples of the dry fibrous preform were analyzed by micro-tomography to better examine its microstructure. The micro-tomography tests were conducted with a XRadia XCT-400 to obtain images of the fibrous preform slices through its thickness. According to the sample size, the image resolution varies from ~40µm to ~6µm.The 3D volume were reconstructed from the micro-tomography images (Fig. 3 left) and the fiber orientations was analyzed by image treatment. As shown in figure 3 (right), in-plane images were segmented by fiber orientation using the ImageJ plugin OrientationJ.

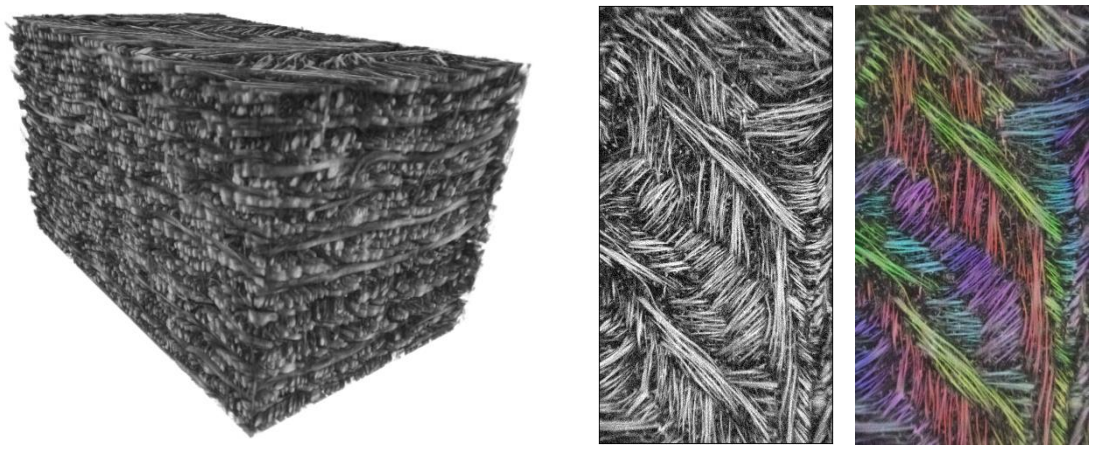

Figure 3:3D reconstruction of the fibrous preform (left) and image segmentation by fiber orientation (right) of micro-tomography images. The color map indicates the orientations of the fibers.

3 A NEW NON-DESTRUCTIVE 3D PERMEABILITY METHOD FOR ANISOTROPIC 3D FIBROUS PREFORM

Accurate measurement of the three-dimensional permeability tensor of fibrous preforms is essential for the prediction and optimization of resin flow in Liquid Composite Molding processes. In 3D fibrous reinforcements, resin can flow not only in the in-plane directions but also through the thickness, due to the presence of fibers transferred in the transverse direction. Moreover, because the fibrous preform presents an anisotropic three-dimensional architecture, the determination of the 3D permeability tensor becomes more complex.

To this day, different experimental methods of fibrous reinforcement permeability measurement exist [5]. While experimental methods to measure 1D, 2D or 3D permeability of fibrous reinforcements are commonly used, they are often limited to destructive methods since liquid is used to saturate the fiber bed. Non-destructive methods such as gas-based permeability measurement offer a cleaner, relatively faster alternative. By imposing gases like air to flow through dry preforms, pressure or flow rate difference is measured to determine permeability values [6], [7]. However, these experimental methods are typically constrained to 1D and 2D flows.

We thus propose a new experimental method to determine the 3D permeability tensor of a thick anisotropic fibrous preform using a transient air flow using an inverse method. This method has the advantage to be non-destructive, to limit the number of sample to the to-be-processed preform and of not requiring the sealing of the material.

3.1 Description of the experimental setup

The test rig (Fig. 4) consists in a cavity, where the fibrous preform is placed, formed by a bottom plate, a frame and a top plate. The cavity is sealed with the two plates above and below the preform (in

contact), leaving the side faces free. Depending on the preform thickness, the frame can be adapted. The bottom plate presents several locations in order to place pressure sensors according to the measurement configuration and the preform geometry. Moreover, the top plate presents one pressure sensor location. On the bottom plate, an air inlet is connected to a vacuum pump allowing imposing pressure in the cavity for the measurement. During a measurement, a transient air flow is thus imposed inside the cavity where the fibrous preform is, from an initial pressure P_0 to P_{end}. An automated data acquisition line saves the pressure sensor measurement. It is possible to conduct the experiments by raising pressure method (RPM) or dropping pressure method (DPM). These tests were conducted using the RPM method where the pressure of the cavity during the measurement goes from $P_0 = P_{vacuum}$ to $P_{end} = P_{atm}$ by opening the inlet to ambient air.

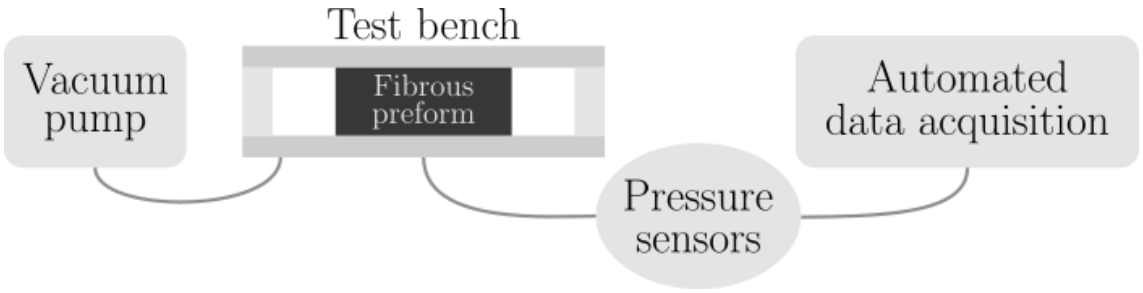

Figure 4: Schematic diagram of the experimental setup.

The aim of the experiment is to measure the pressure difference at several locations of the fibrous preform during the imposed transient air flow. This pressure difference between sensors allows determining each component of the 3D permeability tensor. This experimental method is decoupled in two steps (Fig. 5): (step 1) in-plane flow and (step 2) transverse flow.

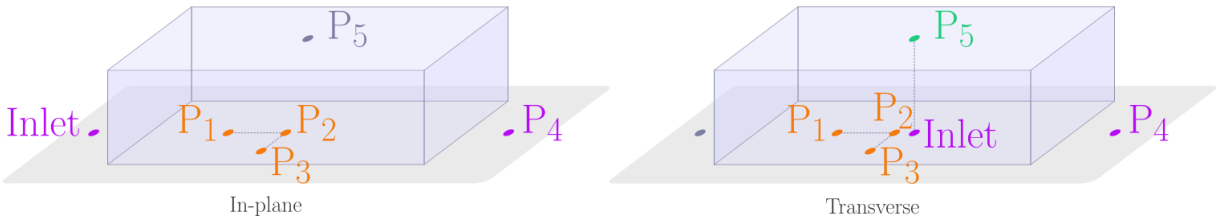

Figure 5: Schematic diagrams of the in-plane (step 1, sensor P5 is not active) and transverse (step 2) measurement configurations.

During step 1, air flows in through the inlet point and the pressure in the cavity (out of the preform) is measured by the sensor P4. This measurement represents the pressure imposed on the lateral sides of the fibrous preform because the pressure in the cavity is considered to be homogenised quasi instantaneously. Then, air flows through the fibrous preform and the pressure is measured at points P1, P2 and P3.

During step 2, a transverse airflow is imposed by letting the air in at the centre of the preform, on the bottom plate side. The pressure measurement by sensor P5 is added, which is located on the upper plate, on the top face of the preform and above the inlet. In this way, air flows within the entire preform and the pressure sensors P1, P2 and P3 measure the in-plane pressure as in step 1. In addition, the sensor P4, placed in the cavity, measures the pressure outside the preform to be implemented as a boundary condition applied at the lateral sides of the preform.

Figure 6 shows the experimental pressure measured by the sensors in both configurations (step 1 and step 2). The transient phase of the pressure curves is observed and can be distinguished between sensors. This transient part of the curves highlights the delay between sensors, which will is used for numerical resolution and the permeability identification.

During these measurements, only one material sample is tested and the fibrous preform remains intact after each test. Thus, the tests can be repeated as many times as necessary.

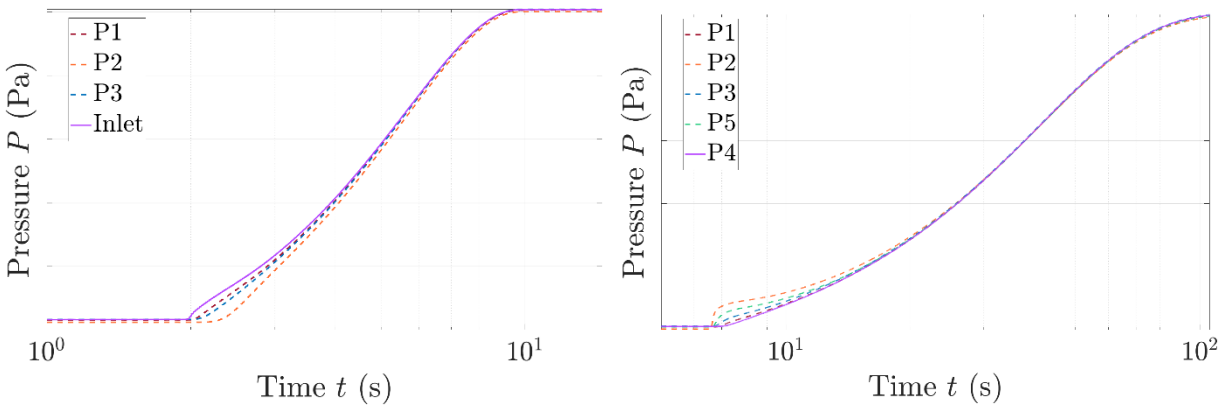

Figure 6: Experimental results of pressure sensors in both configurations: step 1 in-plane (left) and step 2 transverse (right)

3.2 Numerical model

Because of non-linearity and the three-dimensional flow, numerical model is needed to extract the permeability tensor components. The simulation tool COMSOL Multiphysics® is used to implement air flow through the 3D fibrous preform. Two distinct numerical models are established replicating both experimental measurement steps.

Three governing equations are necessary to solve for the pressure inside the fibrous preform as the three unknowns of this problem are the fluid pressure, velocity and density. In the case of viscous flow [6], the equations are: (1) the fluid mass conservation (assuming the preform does not deform while the fluid moves inside), (2) the momentum equation (Darcy's law) and (3) equation of state of an ideal gas. They result in equation (4) that is implemented in the numerical model solved for the pressure.

$$\frac{\partial \rho}{\partial t} + \nabla \cdot (\rho v) = 0 \tag{1}$$

$$v = \frac{\overline{\overline{K}}}{\phi \mu} \cdot \nabla P \tag{2}$$

Where ρ and μ are the fluid density and viscosity, respectively, ϕ is the preform porosity and v is the pore-scale fluid velocity.

In the case of anisotropic porous media, the permeability $\overline{\overline{K}}$ is a symmetric third second order tensor:

$$\overline{\overline{K}} = \begin{bmatrix} K_{xx} & K_{xy} & K_{xz} \\ K_{yx} & K_{yy} & K_{yz} \\ K_{zx} & K_{zy} & K_{zz} \end{bmatrix}$$

$$pV = nRT \tag{3}$$

$$\frac{\partial P}{\partial t} = \nabla \cdot \left(\frac{\overline{\overline{K}}}{\phi \mu} \cdot P \nabla P \right) \tag{4}$$

In this study, the permeability tensor principal axes (*1,2,3*) are considered aligned with the experimental bench axes (*x,y,z)* so that the permeability tensor is simplified as a diagonal tensor such as:

$$\bar{\bar{K}} = \begin{bmatrix} K_1 & 0 & 0 \\ 0 & K_2 & 0 \\ 0 & 0 & K_3 \end{bmatrix}$$

To identify the permeability tensor by inverse method, two models (Fig. 7) are build according to the experimental configurations:

- **Step 1** (in-plane flow): a 2D model where the initial pressure condition reads the initial pressure P0 applied to the 2D preform domain. As a Dirichlet boundary condition, the transient inlet pressure that is measured by the cavity sensor (P4) is applied around the 2D preform domain. The pressure P is then solved for $K_1$and K_2 intervals to get pressure located in points P1, P2 and P3 used in identification of the in-plane permeability components $K_1$and K_2 by the inverse method.

- **Step 2** (transverse flow): a 3D model where the initial pressure condition reads the initial pressure P0 applied to the 3D preform domain. There is a no flow condition applied to the top and bottom faces of the domain. As Dirichlet boundary conditions, the centre point on the bottom face is set as the inlet and the cavity transient pressure (measured by P4) is applied to the four lateral faces. The in-plane permeability components $K_1$and K_2 previously identified are set as model parameters and the pressure is solved for a K_3 interval. Pressure located in points P1, P2, P3 and P5 are saved to be used in identification of the transverse permeability component K_3 by the inverse method.

Both models are initialize with the preform dimensions, the material parameters such as the fluid (air) viscosity μ and the fibrous preform porosity ϕ.

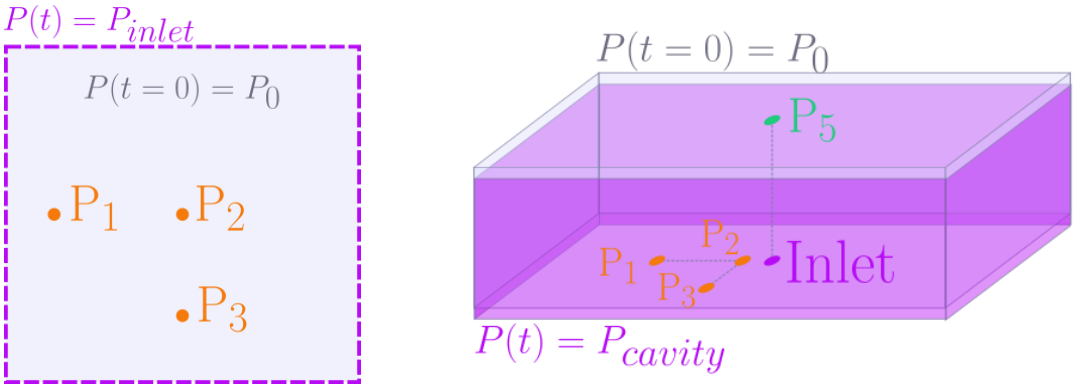

Figure 7: Boundary conditions applied to the step 1 (left) and step 2 (left) numerical models

3.3 $\bar{\bar{K}}$ determination by inverse method

The full 3D permeability tensor of the fibrous preform $\bar{\bar{K}}$ is determined with an inverse method illustrated in the figure 8. First, the in-plane components $K_1$and K_2 are identified by minimizing a cumulated error ϵ (equation (5)) by time step on each pressure sensor measurement and for each $K_1$and K_2 couple, between experimental measurement P_{exp} (step 1) and the corresponding numerical solution P_{sim} (2D model of step 1).

$$\epsilon(K_1, K_2) = \sqrt{\frac{1}{N_t}\sum_t \left(\frac{P_{1_{exp}} - P_{1_{sim}}}{P_{1_{exp}}}\right)^2 + \left(\frac{P_{2_{exp}} - P_{2_{sim}}}{P_{2_{exp}}}\right)^2 + \left(\frac{P_{3_{exp}} - P_{3_{sim}}}{P_{3_{exp}}}\right)^2} \quad (5)$$

The couple (K_1, K_2) is solution of the minimum cumulated error ϵ, such as shown in figure 9.

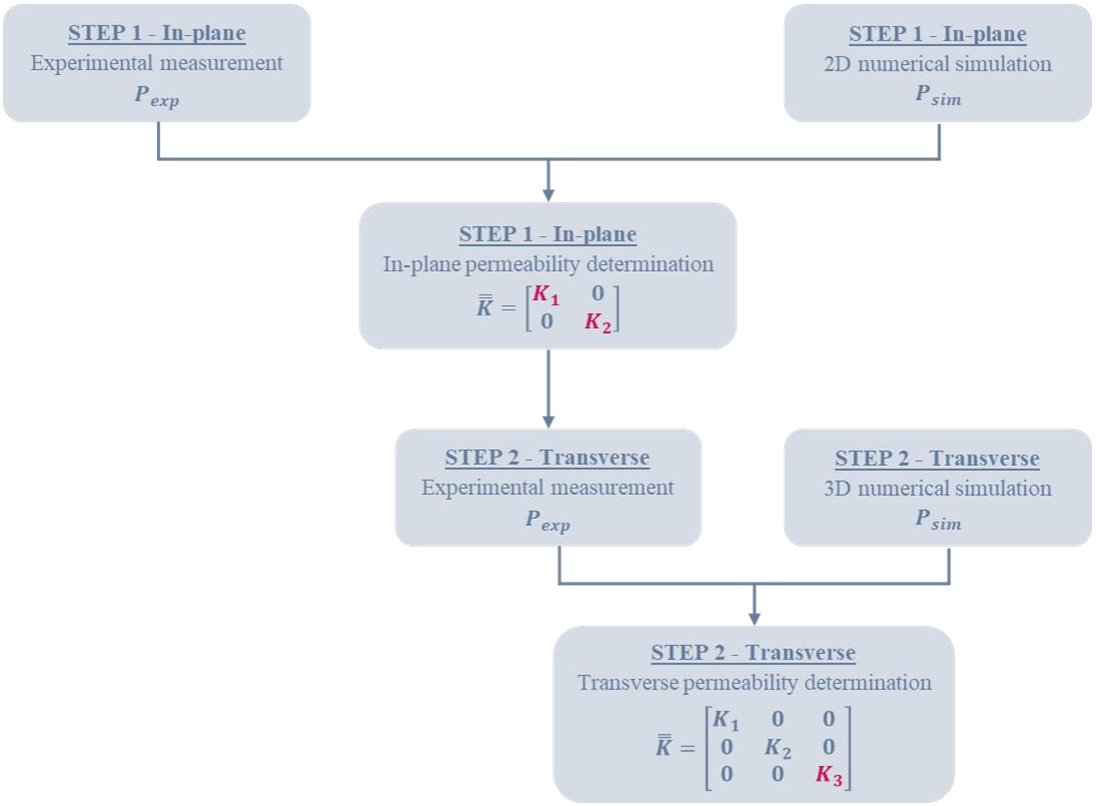

Figure 8: Schematic of the inverse method used to determine the 3D permeability tensor of an anisotropic 3D fibrous preform.

Secondly, the 3D numerical model for step 2 is solved with the identified in-plane permeability $K_1$and K_2 as parameters for a set of K_3values. Then, the transverse component K_3 is identified by minimizing the cumulated error (K_3) (Fig. 9), as in equation (6), between experimental measurement P_{exp} (step 2) and the corresponding numerical solution P_{sim} (3D model of step 2).

$$\epsilon(K_3) = \sqrt{\frac{1}{N_t}\sum_t \left(\frac{P_{1_{exp}} - P_{1_{sim}}}{P_{1_{exp}}}\right)^2 + \left(\frac{P_{2_{exp}} - P_{2_{sim}}}{P_{2_{exp}}}\right)^2 + \left(\frac{P_{3_{exp}} - P_{3_{sim}}}{P_{3_{exp}}}\right)^2 + \left(\frac{P_{5_{exp}} - P_{5_{sim}}}{P_{5_{exp}}}\right)^2} \quad (6)$$

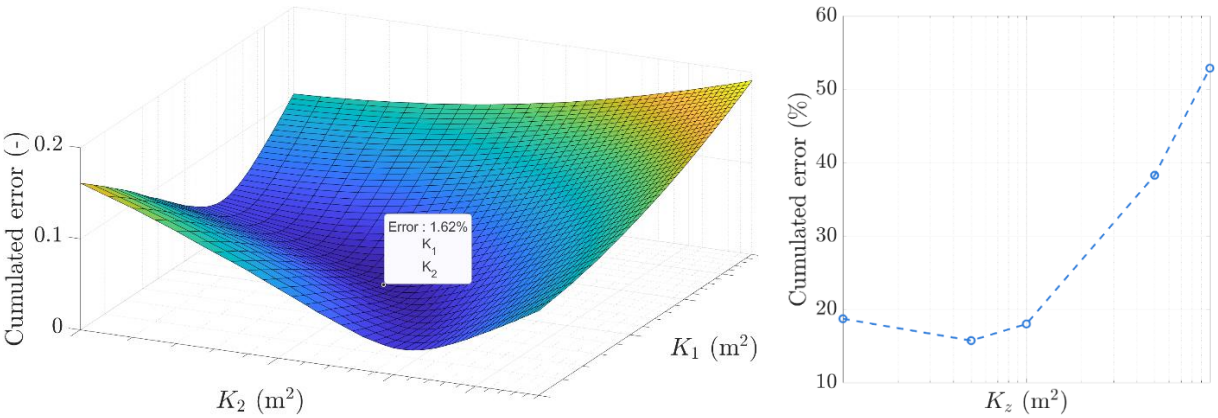

Figure 9: Plots of the cumulated errors $\epsilon(K_1, K_2)$ for in-plane (left) and $\epsilon(K_3)$ for transverse (right) permeability tensor components identification.

5 CONCLUSIONS

To control particle-filled RTM in 3D fibrous preforms, a model should be built so as to couple flow in porous media, particle filtration, and material properties' evolution induced by the filtration phenomenon. Such a model requires material properties related to particle-filled resin rheology and fibrous preform permeability as inputs. To do so, a material characterization work was conducted, which consisted first in the study of particle-filled fluid rheology, also in the understanding of the 3D fibrous preform using micro-tomography and then in the preform permeability determination.

A new experimental methodology to measure a 3D anisotropic fibrous preform permeability tensor using a transient air flow has been described. This fast and non-destructive method is based on the gas pressure measurement at different locations of the preform during the transient air flow. By decoupling the measurements into two distinct steps, in-plane and transverse, the 3D permeability tensor components can be identified by an inverse method. To do so, a cumulated error by time steps and between the experimental pressure sensor measurements and numerical pressure solution is minimized. First, the in-plane permeability tensor components $K_1$and K_2 are identified by solving a 2D numerical model. Then, a 3D numerical model, replicating the second step of the experiment, is solved with the identified $K_1$and K_2 as inputs to determine the remaining transverse component K_3.

The material data generated from the characterization will further be implemented in the coupled flow-filtration model. Perspectives are to assess and validate the model with experimental protocol.

ACKNOWLEDGEMENTS

This research is co-funded by the French Ministry of Defence - Defence Innovation Agency. For the purpose of open access, the author has applied a CC-BY public copyright licence to any Author Accepted Manuscript (AAM) version arising from this submission.

REFERENCES

[1] S. P. Fernberg, E. J. Sandlund, and T. S. Lundstrom, Mechanisms Controlling Particle Distribution in Infusion Molded Composites, *Journal of Reinforced Plastics and Composites*, vol. 25, no 1, p. 59-70, 2006, doi: 10.1177/0731684406055455.

[2] N. A. A. Siddig, Experimental and numerical modeling of the impregnation of fibrous media by suspensions in LCM processes, PhD thesis, Université Le Havre Normandie, 2021.

[3] H. A. Barnes, J. F. Hutton, and K. Walters, An Introduction to Rheology. Elsevier, 1989.

[4] D. Lefèvre, Étude expérimentale, modélisation et simulation de la filtration lors de l'écoulement d'une résine chargée de particules à travers un renfort fibreux dans les technologies LCM, PhD thesis, Ecole des Mines de Douai, 2007.

[5] S. Sharma and D. A. Siginer, Permeability Measurement Methods in Porous Media of Fiber Reinforced Composites, *Applied Mechanics Reviews*, vol. 63, no 020802, 2010, doi: 10.1115/1.4001047.

[6] Y. Hou, S. Comas-Cardona, C. Binetruy, and S. Drapier, Gas transport in fibrous media: Application to in-plane permeability measurement using transient flow, *Journal of Composite Materials*, vol. 47, no 18, p. 2237-2247, 2013, doi: 10.1177/0021998312455676.

[7] B. Laine, Influence des déformations d'un renfort fibreux sur sa perméabilité : modélisations et expériences, PhD thesis, Arts et Métiers ParisTech, 2008, https://pastel.hal.science/pastel-00004533

On the international benchmarking of permeability predictions in anisotropic reference porous media:

Insights from a multi-participant computational study

Coordination:
Masoud Bodaghi (Luxembourg Institute of Science and Technology (LIST))
Mostafa Nikzad (Swinburne University of Technology)
Cristian Lira (NCC - UK)
Supported and presented by:
Andreas Endruweit (University of Nottingham)

AUTHORS

Masoud Bodaghi[a], Mostafa Nikzad[b], Cristian Lira[c], Andreas Endruweit[d], I. Afgan[e] ,A.B. Albayraktar[f], C. Binetruy[g,o], S. Cassola[h] ,D. Droste[i], M. Duhovic[h], M.Faizan[e], S. Guessesma[j], L. Kärger[k], S.Kperegueni[l], A. Leitão[m], S.V. Lomov[n], S.M. Mokli[j], P. Mulye[o], D. May[i], M. Matveev[d], J. Machado[m], C.H. Park[l], M.Rouhi[p], S. Schlegel[k], T. Schmidt[h], M. Shakoor[l], E. Syerko[g], E.M. Sozer[f], R. Umer[e], D.Weitze[k]

[a] Luxembourg Institute of Science and Technology (LIST), Sustainable Composite Materials & Manufacturing (SCMM) Innovation Centre
[b] Swinburne University of Technology, Melbourne, Australia
[c] National Composites Centre (NCC), United Kingdom
[d] University of Nottingham, Faculty of Engineering, Nottingham, United Kingdom
[e] Khalifa University of Science and Technology, Abu Dhabi, UAE
[f] Koç University, Istanbul, Turkey
[g] Ecole Centrale de Nantes, Nantes, France
[h] Leibniz-Institut für Verbundwerkstoffe GmbH, Kaiserslautern, Germany
[i] Faserinstitut Bremen e.V., University of Bremen, Bremen, Germany
[j] INRAE, National Research Institute for Agriculture, Food and Environment, France
[k] Karlsruhe Institute of Technology (KIT), Karlsruhe, Germany
[l] IMT Nord Europe, Institut Mines-Télécom, Univ. Lille, Centre for Materials and Processes, F-59000 Lille, France
[m] INEGI, Campus da FEUP, Porto, Portugal
[n] Department of Materials Engineering, KU Leuven, Leuven, Belgium
[o] Quantiflex Simulations SAS, France
[p] RISE Research Institutes of Sweden, Composite Technology Unit, Mölndal, Sweden

PARTICIPANTS AND SOFTWARE TOOLS OVERVIEW

Calculation of permeability benchmark		
Entry ID	**Organisation**	**Software, software version**
B	Faserinstitut Bremen e.V. (FIBRE), University of Bremen, Germany	OpenFOAM,Version 9
C	IMT Nord Europe, Institute Mines-Telecom, Center for Materials and Processes, Lille, France	FEMS,4.3
D	Institute of Science and Innovation in Mechanical and Industrial Engineering (INEGI), Porto, Portugal	ANSYS,2023 R2; OpenFOAM,v202406
E	Koc University, Istanbul, Türkiye	ANSYS,2024 R1
F	Khalifa University of Science and Technology, Abu Dhabi, UAE	OpenFOAM,v202406
G	KU Leuven, Department of Materials Engineering, Belgium	FlowTex,
H	Leibniz-Institut für Verbundwerkstoffe GmbH, Kaiserslautern, Germany	GeoDict, (voxel 100),SP1 for Windows, Revision 82612; ESI OpenCFD Release v2312
J	University of Nottingham, Nottingham, UK	ANSYS,2024 R1
K	INRAE, 147, rue de l'Université, Paris Cedex, France	Comsol
L	Quantiflex Simulations SAS, Nantes, France	PORESPY,2.4.2+2.8.2; OpenFOAM,Version 8
M	Karlsruhe Institute of Technology (KIT), Karlsruhe, Germany.	OpenFOAM,Version 6
N	Nantes Universite, Ecole Centrale Nantes, Nantes, France	

REFERENCE MEDIUM

Unit cell

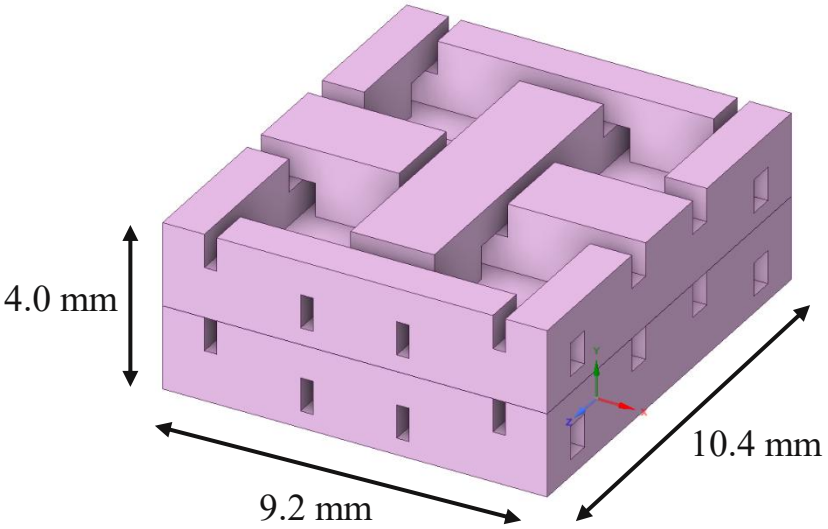

Periodic assembly

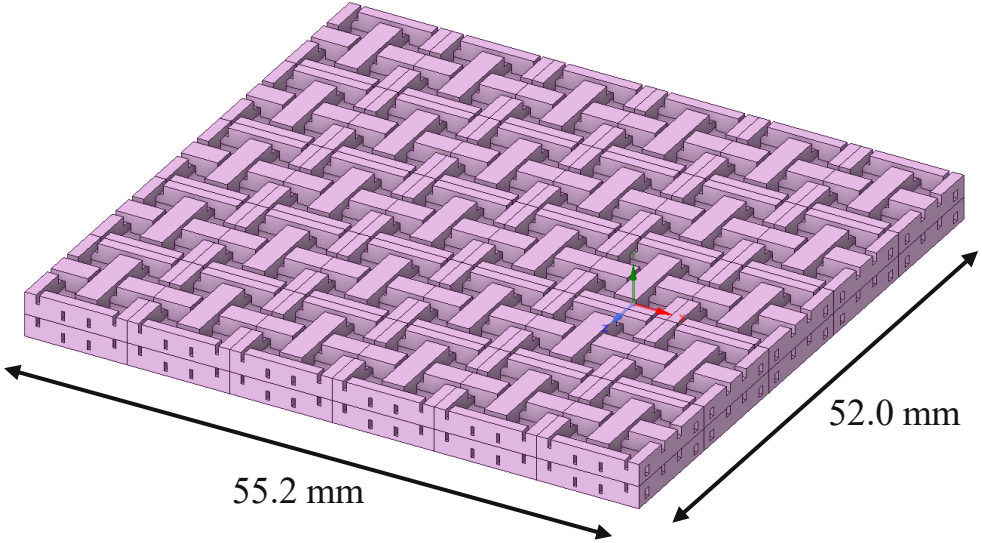

OVERVIEW & OBJECTIVES

Overview

- Numerical benchmark study focused on **simulating in-plane (K11(Kxx), K33 (Kzz))** and **through-thickness (K22 (Kyy))** permeability of an **engineered textile-like reference medium**
- The computer-aided design (CAD) file represents a **3D-printable porous structure** intended for **calibration of permeability test rigs**
- Data collected from multiple simulation teams using **identical geometry**

Objectives

- Assess **variability** of permeability prediction by the participants from multiple institutions using the same digital geometry
- Establish **reference values (K11, K22, K33)** based on consensus reported by simulation results
- Support **future calibration** of experimental setups through a **well-characterized, repeatable digital reference medium**

POROSITY FRACT- UNIT CELL

Organisation who calculated K	Porosity (%)
B.1	34.1
B.2	34.1
C.1	34.1
C.2	34.1
D.1	34.1
D.2	34.1
E	34.1
F	34.1
G.1	34.4
G.2	34.1
H.1	34.1
H.2	34.1
H.3	34.1
H.4	34.1
H.6	34.1
J	34.0
K	34.0
L.1	34.0
L.2	34.0
M	34.1
N	34.1

POROSITY FRACTION- PERIODIC ASSEMBLY

Organisation who calculated K	Porosity (%)
B	34.1
C	34.1
D	34.1
E	34.1
F	
G	---
H	34.1
J	34.0
K	34.0
L	34.0
M	34.1
N	34.1

OVERVIEW OF KXX, KYY, KZZ STATISTICS

Component	Typical range	Notes
Kxx	~5.76E-11 to ~1.8E-08	Most values are clustered between 2.4×10^{-9} and 3.0×10^{-9} m^2, with a few outliers on the higher end (notably 1.80×10^{-8} and 9.49×10^{-9} m^2).
Kyy	~4.63E-12 to ~2.424E-9	The most variable component of all three directions. This could reflect asymmetric flow pathways, differences in mesostructural alignment, or artifacts from simulation resolution.
Kzz	~1.49E-11 to ~8.79E-09	Relatively consistent compared to Kyy, with many values close to 6–7 $\times 10^{-10}$ m^2 Outliers (e.g., 8.79×10^{-9} and 4.22×10^{-9}) suggest localized channels or voxel resolution effects.

PERMEABILITY COMPARISON: UNIT CELL VS PERIODIC ASSEMBLY

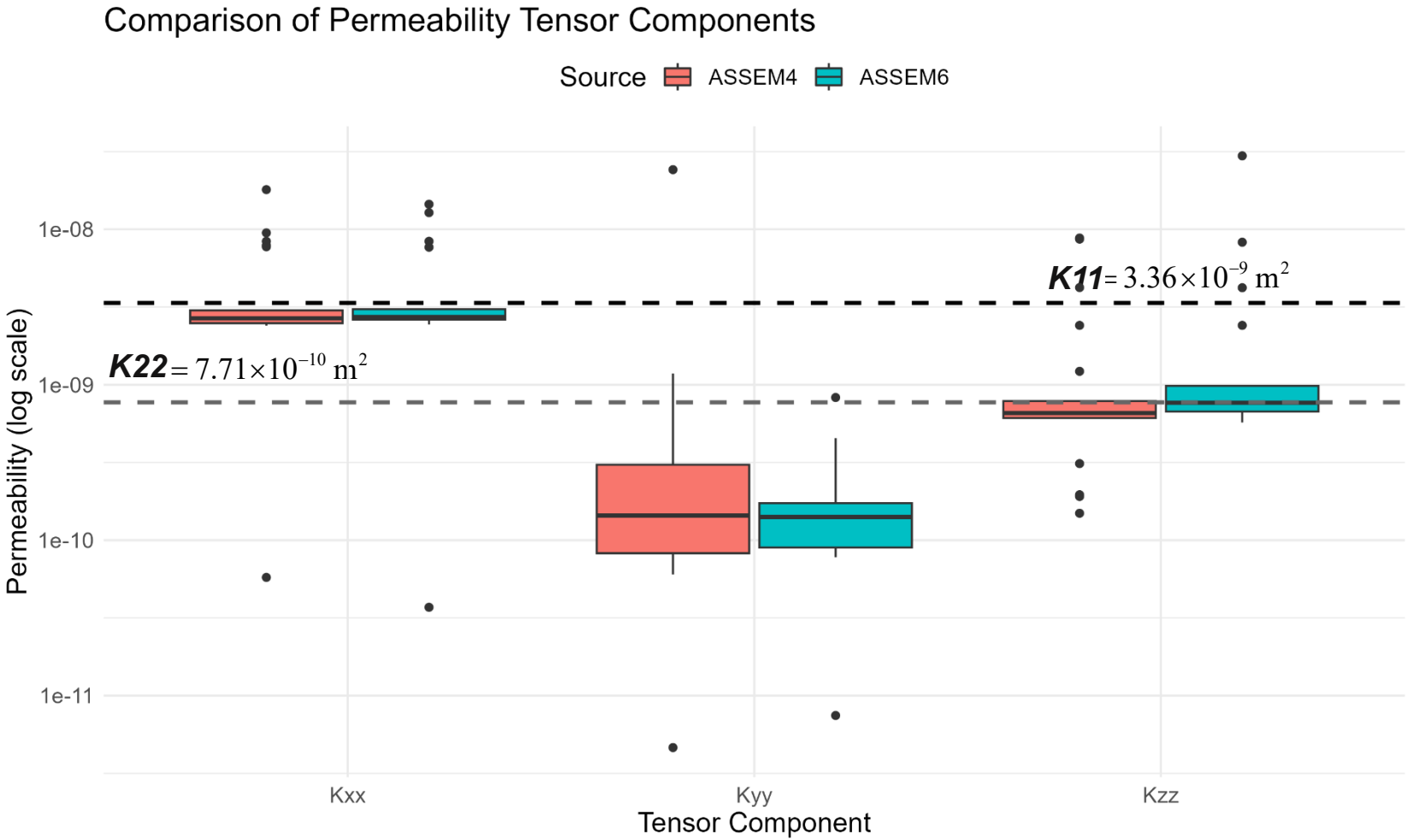

CORRELATION

- Kxx and Kzz may have moderate correlation.
- Off-diagonal terms are negligible; cross-correlation with diagonal terms is insignificant

SYMMETRY CONSISTENCY

Looking at whether **K12 = K21**, **K13 = K31**, etc.

Cross-term symmetry	Pattern
Y/Y/Y (Symmetric)	Reported by OpenFOAM (B) and FEMS (C) runs
N/N/N (Asymmetric)	Reported by GeoDict and many others: may reflect minor numerical asymmetries or anisotropy.

OBSERVATIONS

- Anisotropy is evident, with Kxx consistently larger than Kyy and Kzz in most samples.
- Outliers in Kyy and Kzz suggest localized flow instabilities or non-uniform compaction..
- Measurement robustness is acceptable for Kxx and Kzz; however, Kyy data would benefit from increased replicates or better control of preform architecture.
- Off-diagonal terms (K12, K13, K23) are generally very small or zero, indicating near-symmetry and negligible coupling effects.
- Symmetry indicators (K12=K21 etc.) mostly “Y” but some “N” or “N (diff X%)” showing small asymmetries.
- Porosity mostly consistent around 34%.

FUTURE WORK / NEXT STEPS

Investigate the effect of geometric scale on permeability predictions

- Perform CFD simulations on scaled versions of the current RVE geometry:
  RVE × 0.1 and **RVE × 0.01**
- Analyze whether the **permeability tensor K** remains clustered (directionally consistent and within the same order of magnitude) across scales
- Document any shifts in anisotropy or permeability magnitude due to scale changes

Motivation:

- Understanding scale dependence is crucial for **validating CFD results** when extrapolating from microscale geometries to macroscale behaviors
- Although physical 3D printing and experimental validation of very small-scale RVEs may not be feasible, simulation outcomes can still inform:
  - Limitations of current CAD-based permeability predictions
  - Guidelines for scale selection in future digital calibration designs

Broader impact:

- Enhances the **robustness of digital twin strategies** for permeability benchmarking
- Supports development of **scalable reference materials** for various rig sizes and flow regimes

PHASE II: ENLARGED RVE ANALYSIS

- New geometry scaled ×2.8 used for experimental validation
- Participants to simulate and report **Kxx, Kyy, Kzz**

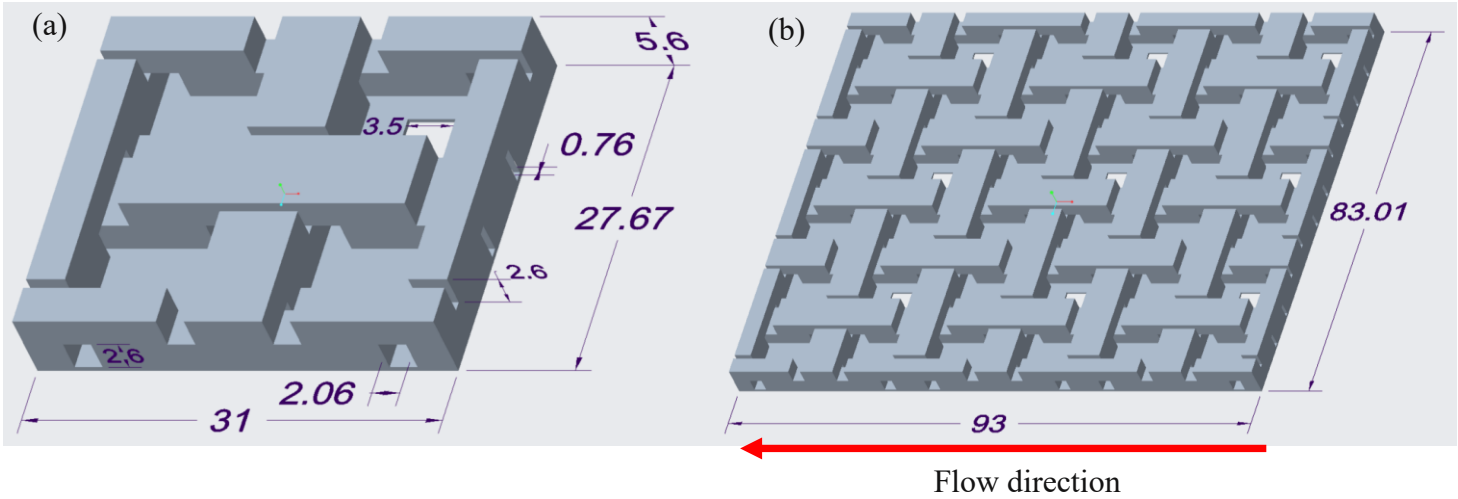

(a) Unit cell CAD design with all channels, (b) CAD model of the full-scale interconnecting channel (All dimensions are in mm).

KEY REFERENCES FOR PERMEABILITY BENCHMARK

1. May et al., 2024

A new ISO standard for the experimental characterization of in-plane permeability of fibrous reinforcements
Composites Part A: Applied Science and Manufacturing, Vol. 190, 108592, doi.org/10.1016/j.compositesa.2024.108592

2. Annamalai et al., 2025

On the extension of in-plane permeability calibration to out-of-plane measurements: Advancements in additively manufactured textile-structured porous media for liquid composite moulding
Composites Part A: Applied Science and Manufacturing, Vol. 193, 108863, doi.org/10.1016/j.compositesa.2025.108863

3. Machado et al., 2023

On the understanding of bubble dynamics through a calibrated textile-like porous medium using a machine learning based algorithm
Composites Part A: Applied Science and Manufacturing, Vol. 177, 107955, doi.org/10.1016/j.compositesa.2023.107955

4. Bodaghi et al., 2021

Surface quality of printed porous materials for permeability rig calibration, Journal of Composite Materials, Pages 548-558, doi.org/10.1080/10426914.2021.1960994

5. Bodaghi et al., 2020

Additively manufactured three dimensional reference porous media for the calibration of permeability measurement set-ups
Composites Part A: Applied Science and Manufacturing, Vol. 139, 106119,doi.org/10.1016/j.compositesa.2020.106119

Determination of Mechanical Properties of Polyimide - Silica Nanocomposite Using Micromechanical Modeling

August 4th, 2025

Nithin Kaliyath Parambil, Sagar Doshi, John Gillespie Jr.

UNIVERSITY OF DELAWARE
CENTER FOR COMPOSITE MATERIALS
Celebrating 50 Years

Motivation

- The demand for high-speed electronics is rapidly increasing, leading to more demanding printed wiring board (PWB) requirements.
  - 5G Communication Devices
  - Solid-State Drives (SSDs)
  - Microprocessors etc.
- A typical PWB is made by bonding dielectric films like polyimide to electrically conductive copper foil, such as rolled annealed (RA) copper.
- PWBs are expected to become thinner, more flexible, durable, and compatible with high-frequency 5G performance.
- Polyimide films naturally have a higher coefficient of thermal expansion (CTE) than copper foils, which results in a mismatch and causes residual thermal stresses.

To reduce the CTE mismatch, silica nanoparticles can be added to the polyimide films to lower their CTE.

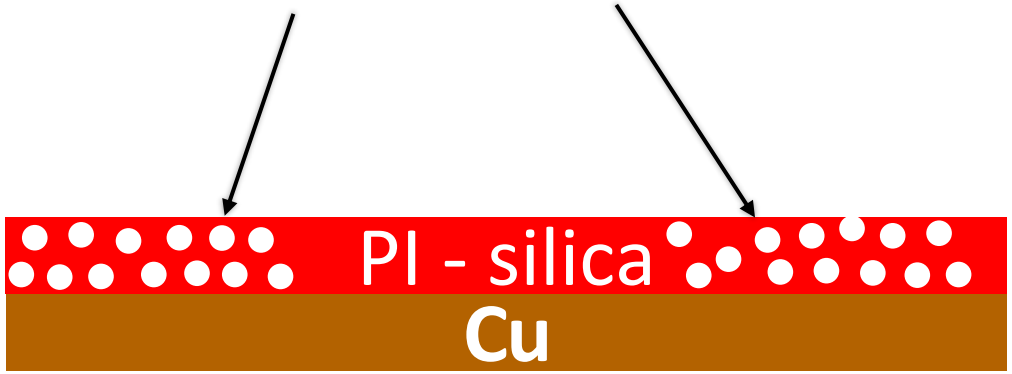

The focus of this work is to understand crack propagation in the PI-Silica substrate

90° Peel Test – Current Configuration

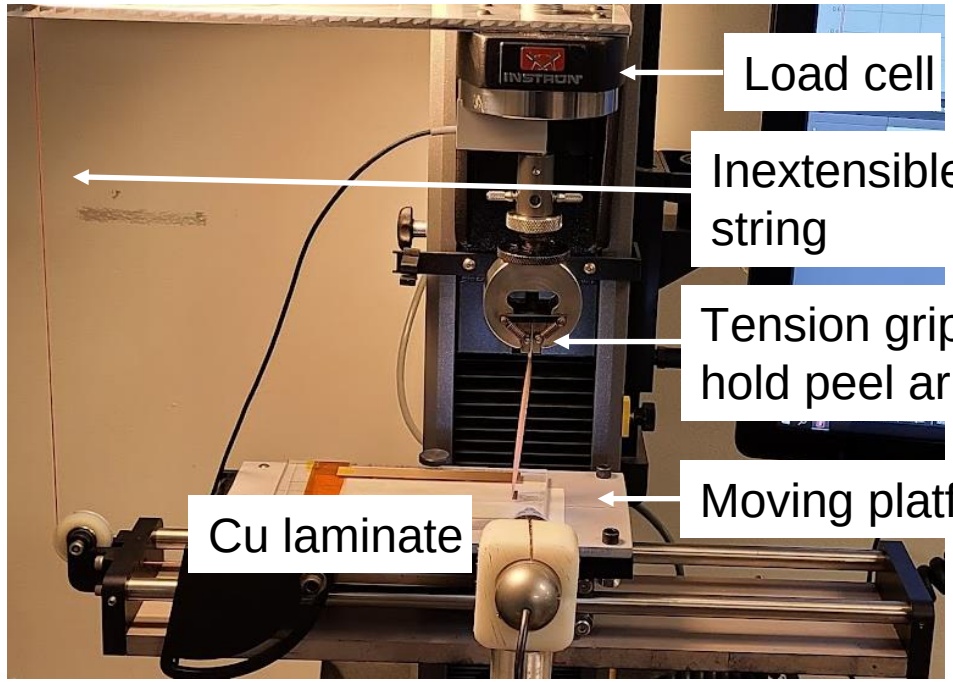

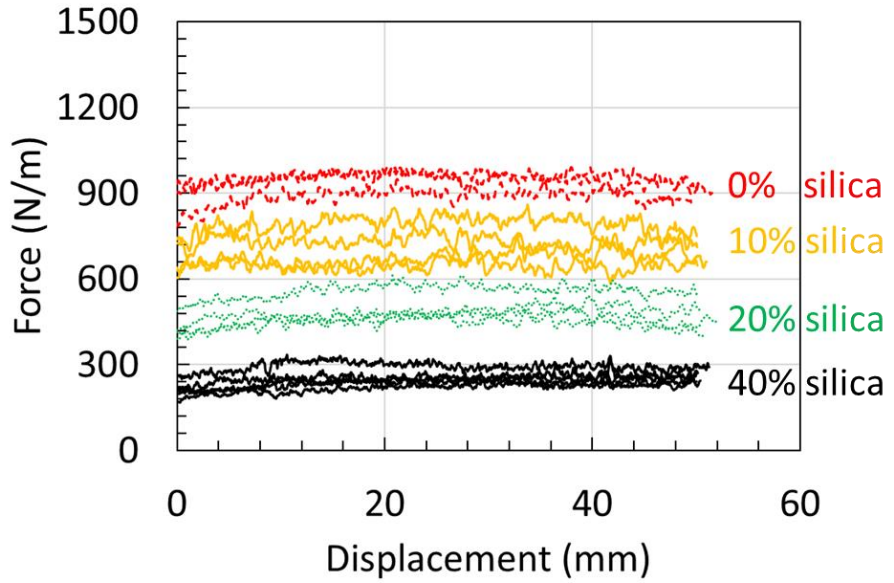

Force – displacement curve

Plastic deformation of copper after the peel test



- The force-displacement curve obtained from the peel test does not accurately represent the adhesion properties of Cu-PI.
- To capture the adhesion properties of Cu-PI, it is necessary to separate all other deformation energies from the materials, such as the plastic deformation of copper.

*2024 ACS Materials and Interfaces, Doshi, Parambil, Gillespie et al.

Crack Propagate Through PI Film (XPS Experiment)

UNIVERSITY OF DELAWARE
CENTER FOR COMPOSITE MATERIALS
Celebrating 50 Years

Surface of Cu side and PI side after peel test

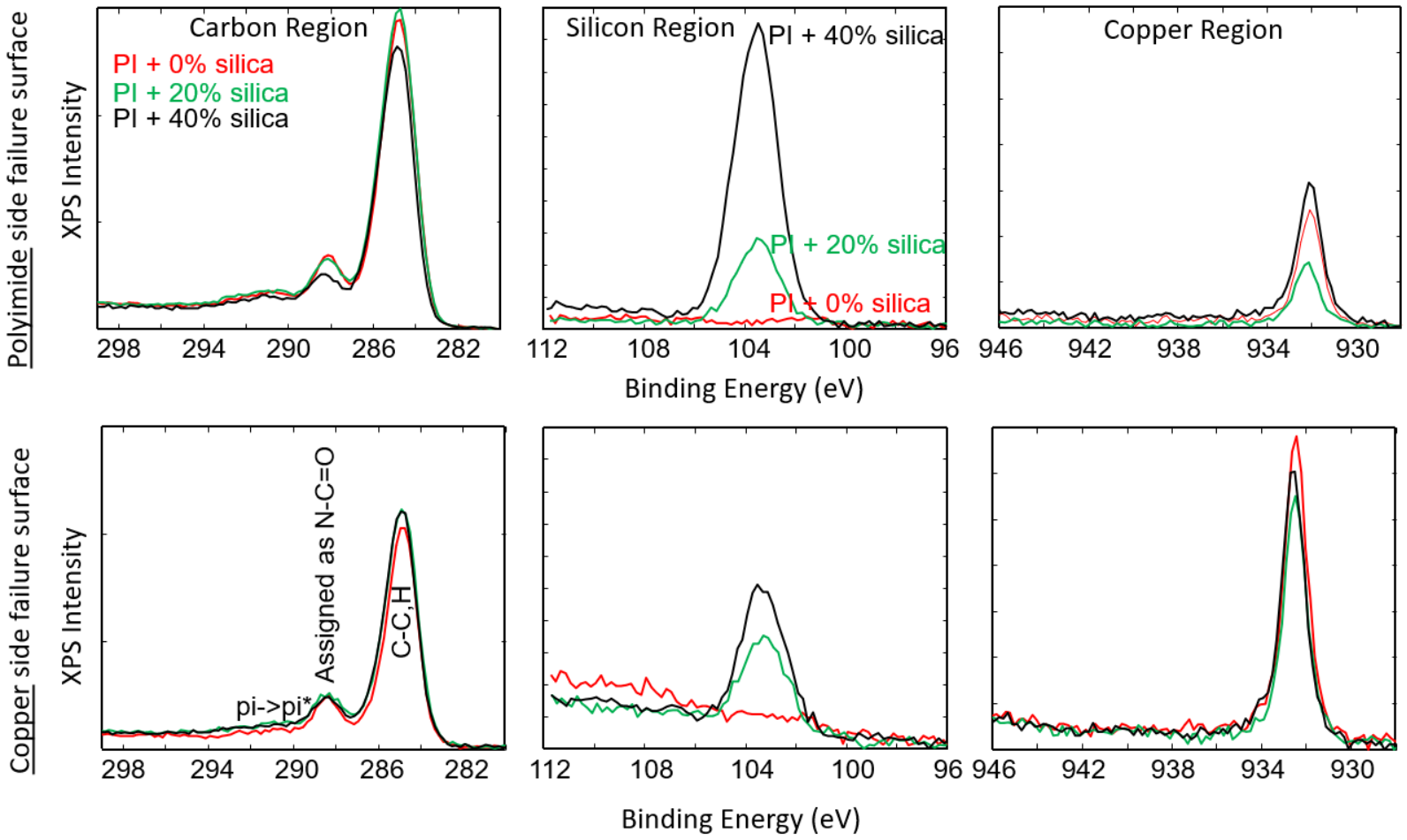

- XPS (X-ray Photoelectron Spectroscopy) was used to analyze each side of the failure interface.
- The surface analysis reveals that crack interpenetration is occurring within the PI film.
  - PI material is present on both sides of the crack surface.
  - This indicates that the crack does not propagate along the PI–Cu interface, but rather through the bulk of the PI film.
  - Further investigation is needed to understand the role of embedded particles within the PI.

*2024 ACS Materials and Interfaces, Doshi, Parambil, Gillespie et al.

Finite Element Analysis (Bridging length scales)

- Establishing RVE
  - Residual stress (polyimide/silica)
  - Inelastic properties of polyimide
  - Traction law (polyimide/silica) (from MD modeling)
  - Predict the effective properties
    - Relate to particle debonding/cracking

- Copper bulk properties
- Traction law (copper/surface of polymer (MD modeling))

Failure mode could be at the interface or cracking through the polyimide depending on level of adhesion

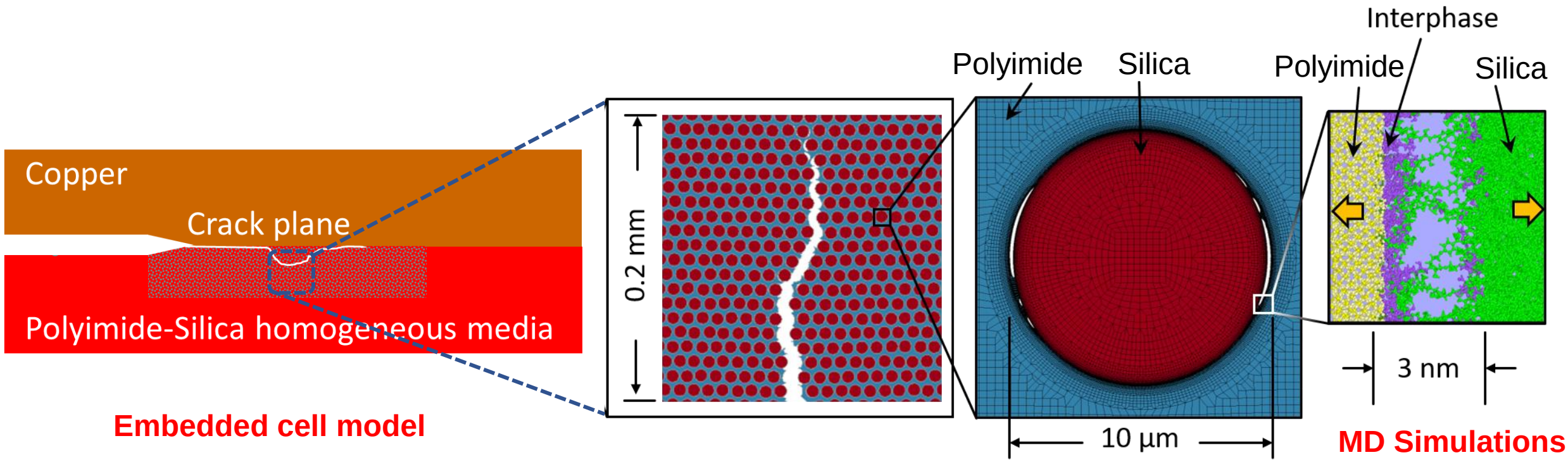

*2021 JCOMB, Meyer and Gillespie

Embedded Cell Method

- Embedded cell modeling approach (Canal et al., CST 2012) – embed fiber-matrix microstructure into continuum
- Assembled microstructure from randomly selected unit cells from 17 realizations (MATLAB)
- This ensured 60% FVF, no fibers touching (causes very small finite elements, drives down timestep)

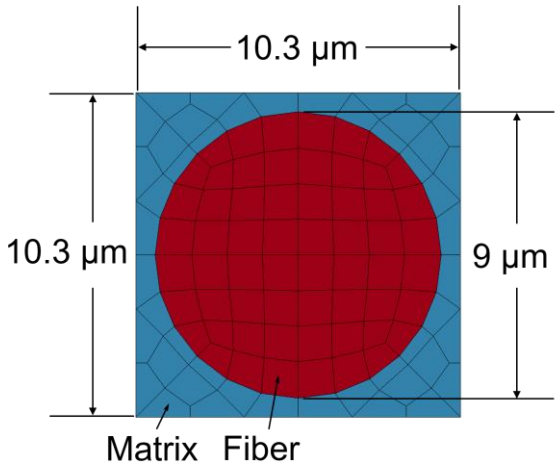

60% FVF Unit Cell

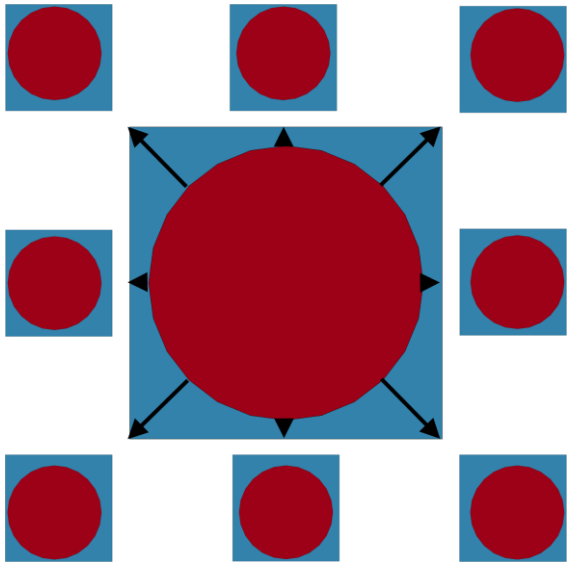

16 DOF

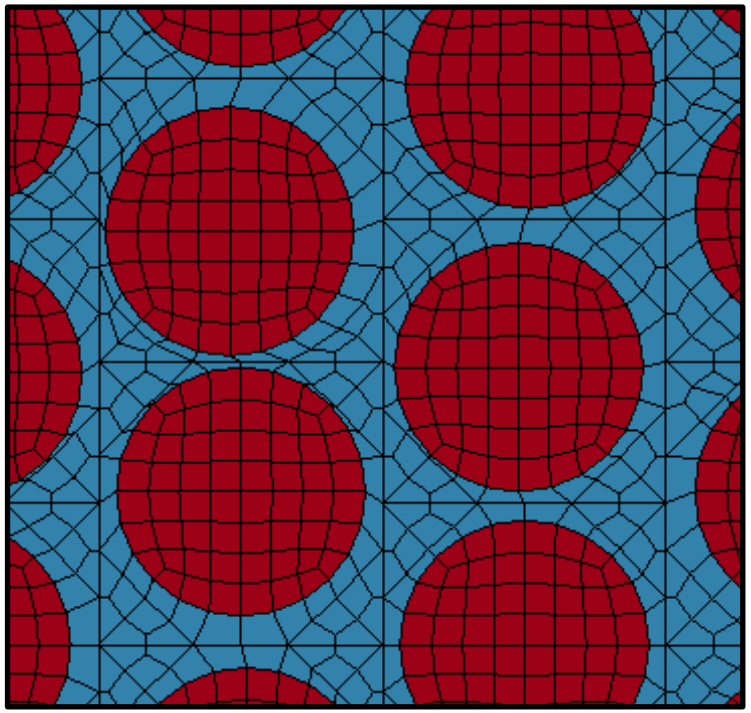

*2021 JCOMB, Meyer and Gillespie

Materials Properties and FE Model

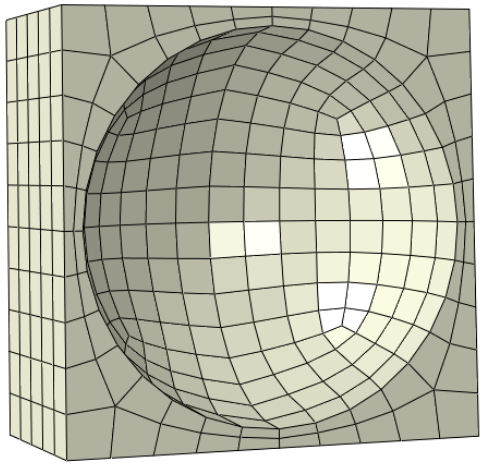

Polyimide (PI)

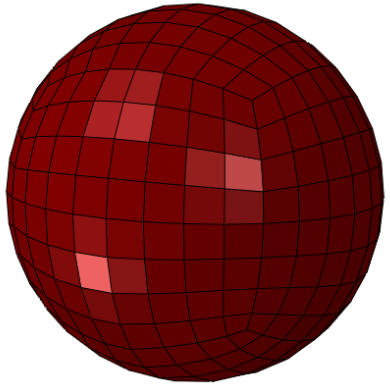

Silica Nanoparticle (SNP)

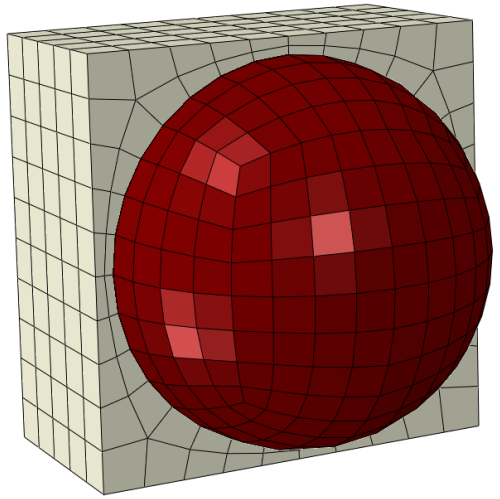

Single particle composite (cut section for better view)

$$V_s = \frac{4}{3}\pi R^3$$

$$V_r = L^3$$

$$V_p = \frac{V_s}{V_r}$$

Maximum V_p when $L = 2R; V_p = \frac{\pi}{6} = 0.52$

Mechanical properties

	Modulus (GPa)	Yield stress (MPa)	Poisson's Ratio	CTE (ppm/°C)
Polyimide (PI)	3.81 ± 0.05	76 ± 1	0.34	20
Silica	73		0.17	0.52

- Volume fraction V_p= 5.7, 12 and 26.5%

Theories for Elastic modulus

- Einstein's equation
  - Based on the rigid particle assumption

$$\frac{E_c}{E_m} = 1 + 2.5V_p$$

- Guth's equation
  - Added a particle interaction term in the Einstein equation

$$\frac{E_c}{E_m} = 1 + 2.5V_p + 14.1V_p^2$$

- Halpin and Tsai's equation
  - Semi-empirical relationship

$$\frac{E_c}{E_m} = \frac{1 + A_1 B_1 V_p}{1 - B_1 V_P} \qquad B_1 = \frac{\frac{E_p}{E_m} - 1}{\frac{E_p}{E_m} + A_1}$$

  - A_1=1

- Assumption of theoretical model
  - Perfect bonding between interface
  - No residual stress
  - Both fiber and matrix are elastic

- Kerner's equation
  - $E_p >> E_m$

$$\frac{E_c}{E_m} = 1 + \frac{V_p}{(1-V_P)} \frac{15(1-\nu_m)}{(8-10\nu_m)}$$

- Mooney's equation

$$\frac{E_c}{E_m} = exp\left(\frac{2.5V_p}{1 - sV_P}\right)$$

  - s = 1.43

- Lower bound

$$E_c^{lower} = E_p E_m / \left[E_p(1 - V_P) + E_m V_p\right]$$

- Upper bound

$$E_c^{upper} = \left[E_p V_P + E_m(1 - V_p)\right]$$

Effective Modulus at Different V_p

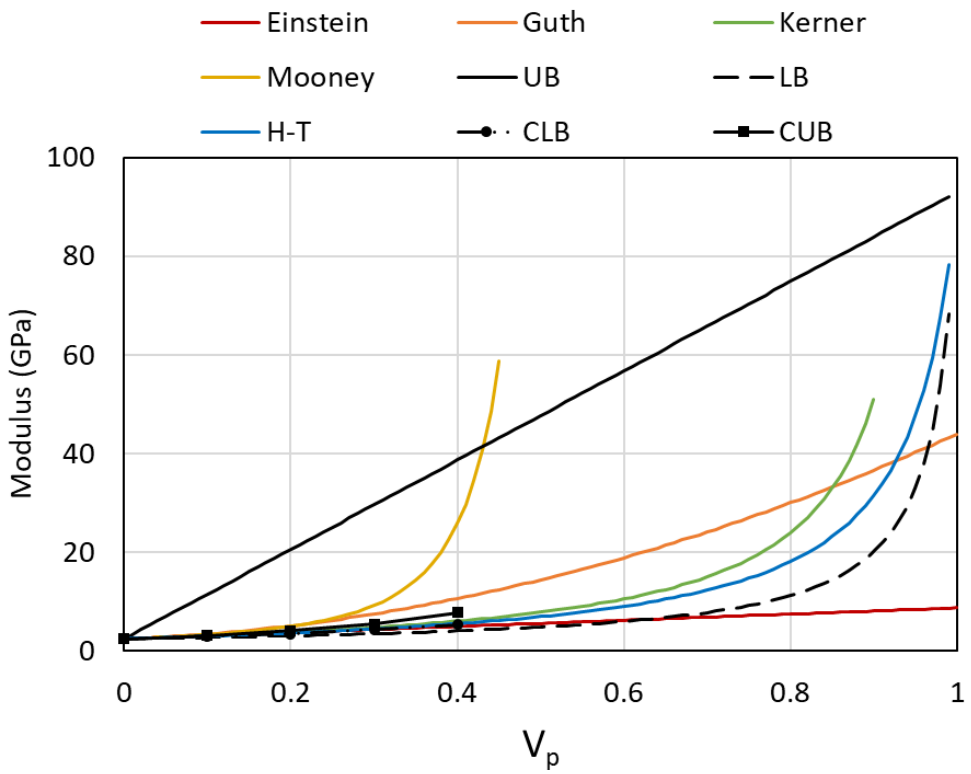

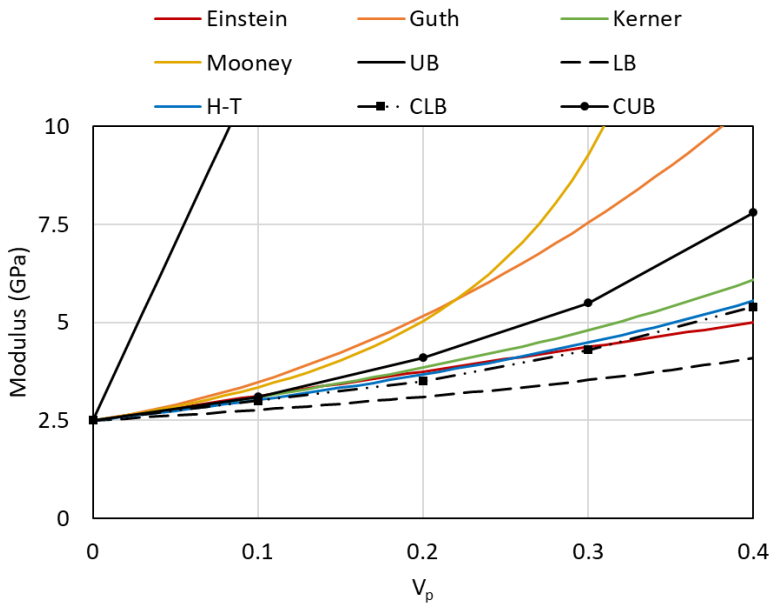

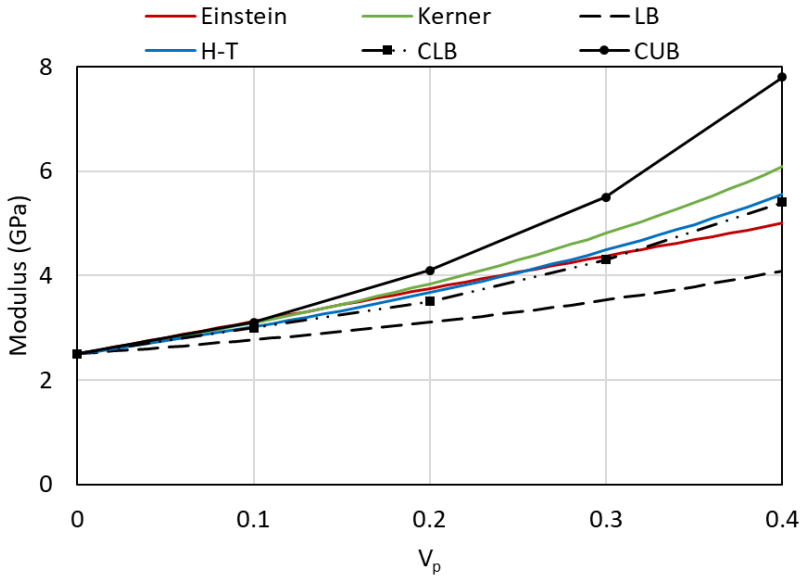

- Experimental comparison is needed to determine the best fit for the model.

Comparison of CTE with Theoretical Model

- Results from various analytical models are compared with the proposed FE model.
- Kerner's model shows strong correlation with the FE model.
- The bounds for the CTE of copper is 16 - 18 ppm/°C
- PI (polyimide) CTE values considered: 20 ppm/°C (room temperature) and 40 ppm/°C (higher temperature).
- The required silica Vp is determined to be approximately 0.125 at room temperature and 0.5 at the higher service temperature range.

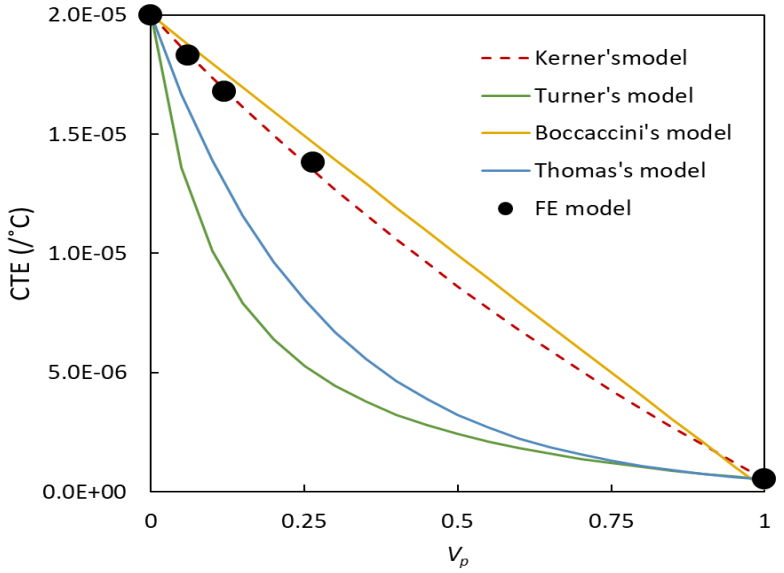

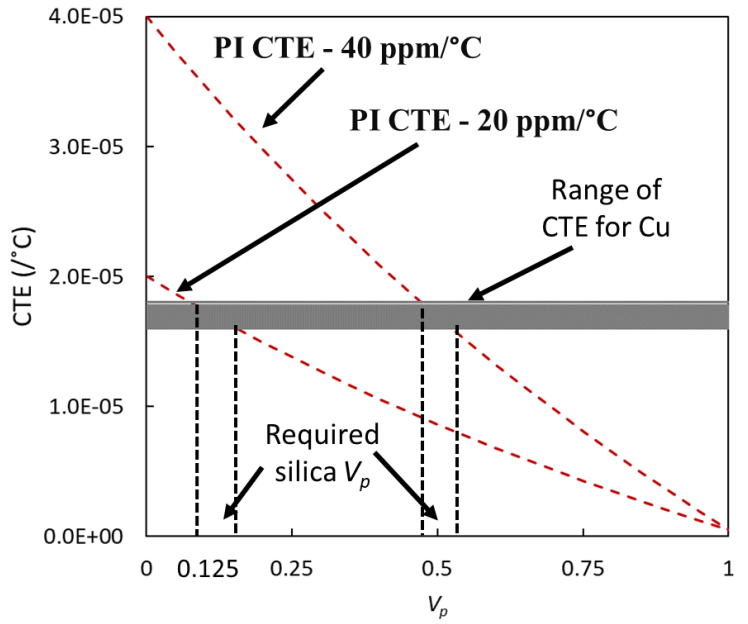

Boundary Conditions for FE Model

UNIVERSITY OF DELAWARE
CENTER FOR COMPOSITE MATERIALS
Celebrating 50 Years

Constant Displacement (CD) BC

$$\varepsilon_y = \frac{\Delta v}{L} \qquad \varepsilon_z = \frac{\Delta w}{W}$$

$$\nu = -\frac{\varepsilon_z}{\varepsilon_y} \qquad E = \frac{\sigma_y}{\varepsilon_y}$$

$$\sigma_y = \frac{average\ force}{area}$$

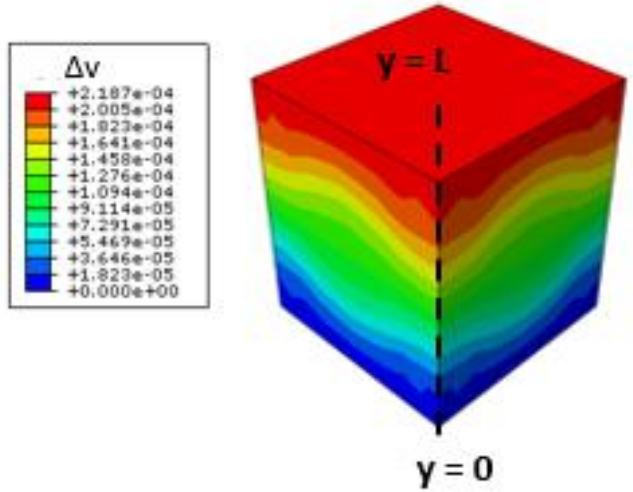

Tensile loading in y direction

Constant Pressure (CP) BC

$$\varepsilon_y = \frac{\Delta v}{L} \qquad \varepsilon_z = \frac{\Delta w}{W}$$

$$\nu = -\frac{\varepsilon_z}{\varepsilon_y} \qquad E = \frac{\sigma_y}{\varepsilon_y}$$

$\Delta v = Average\ displcament$

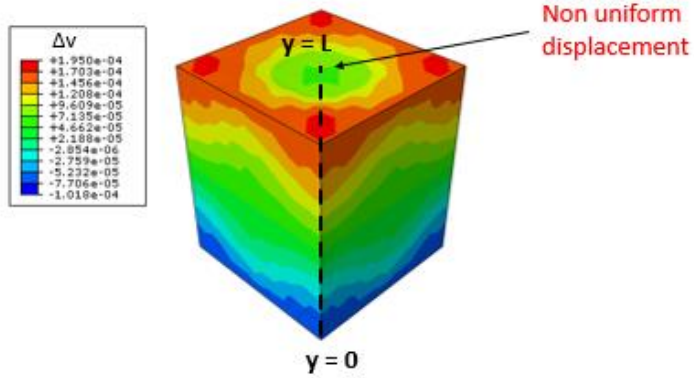

Tensile loading in y direction

- The 3D generalized plane strain boundary condition is not straight forward in Abaqus
- Plane surface should be plane
  - Edges are shared with two planes
  - Vertices are shared between three planes
- "Equation" option in Abaqus is suitable for applying multiple DOF constraints
- Both the resin and particles are modeled using three-dimensional eight-node elements (C3D8).
- For the elastic analysis, a converged mesh size of 2 nm was obtained.

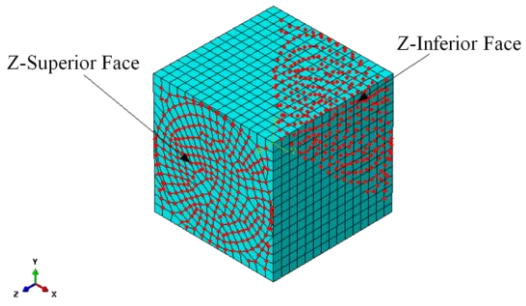

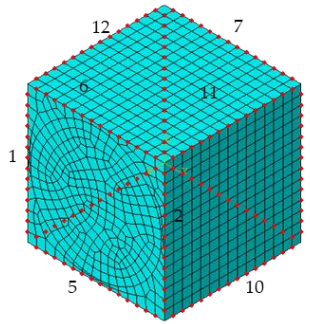

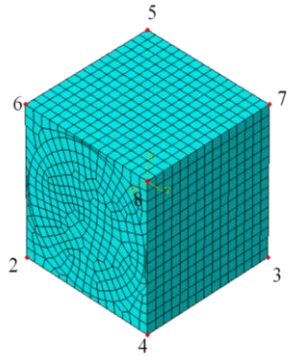

Effective CTE and Modulus Calculation

In put

	Modulus (GPa)	Yield stress (MPa)	Poisson's Ratio	CTE (ppm/°C)
Polyimide (PI)	3.81 ± 0.05	76 ± 1	0.34	20
Silica	73		0.17	0.52

Effective CTE - Simulation result

V_p(%)	5.7	12	26.5
CTE (ppm/°C)	18.3	16.8	13.8

Elastic modulus – simulation result and validation

V_p (W_p) (%)	5.7 (10)	12 (20)	26.5 (40)
Experiment (MPa)	4407 ± 96	4948 ± 159	6417 ± 102
FE model - CD (MPa)	4280	4898	7748
FE model - CP (MPa)	4197	4618	5908

- Strains in all three directions are equal

$$CTE = \frac{\varepsilon_x}{\Delta T} = \frac{\varepsilon_y}{\Delta T} = \frac{\varepsilon_z}{\Delta T}$$

$$\varepsilon_y = \frac{\Delta v}{L}$$

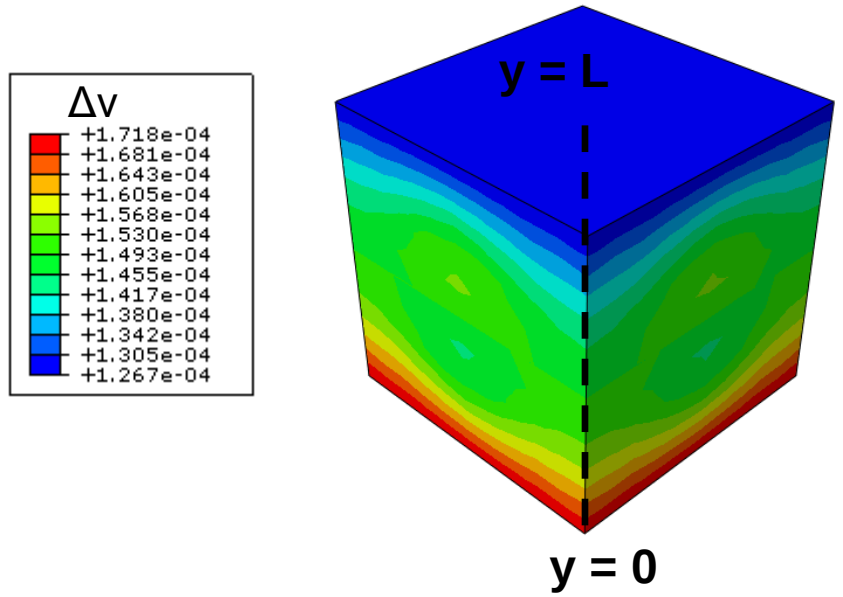

Stress-Strain Curve of Neat PI

› Stress-strain curve of PI is fitted to a Ramberg-Osgood equation in terms of strain:

$$\sigma = \frac{E\varepsilon}{\left(1 + \left(\frac{E\varepsilon}{\sigma_0}\right)^a\right)^{\frac{1}{a}}}$$

$$a = 2.7$$

$$\sigma_0 = 138\ MPa$$

$$E = 1.4\ GPa$$

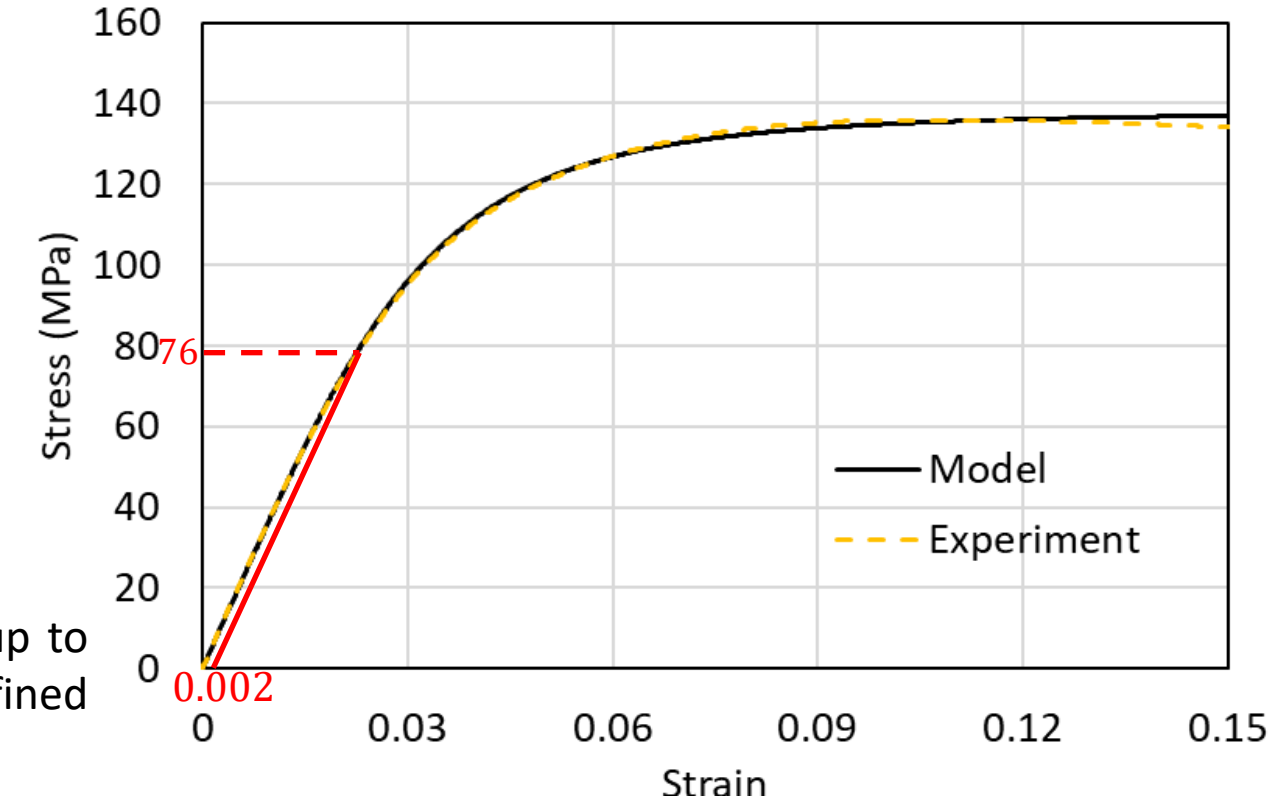

- In Abaqus, the resin is modeled as linear elastic up to the yield stress, and the nonlinear behavior is defined using the tabular input method.
- Resin failure is modeled as ductile damage using a strain-based failure criterion.

Mechanical Properties of Cu and PI (with silica)

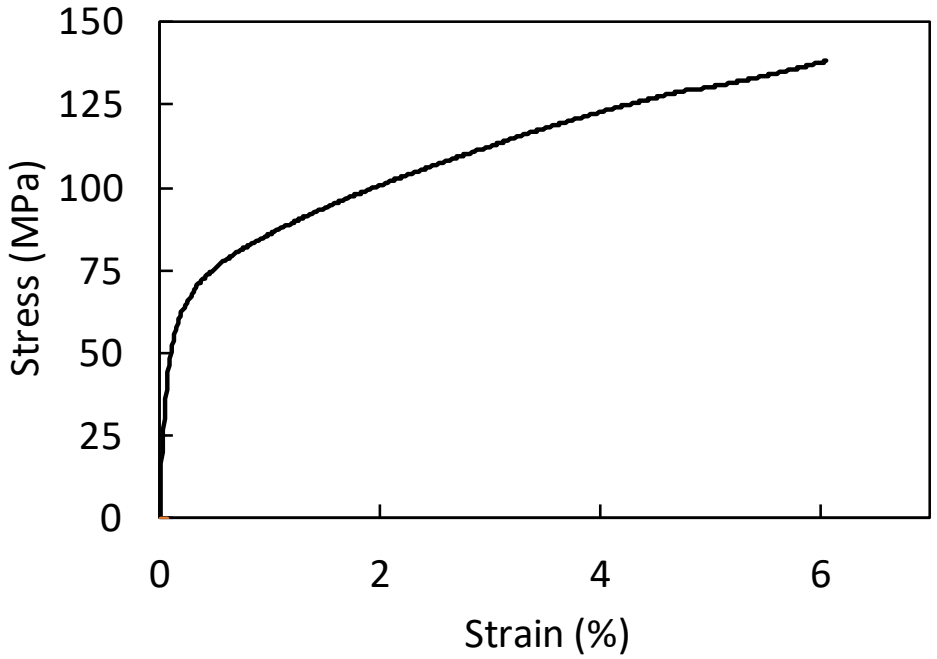

Property of copper considering the processing conditions

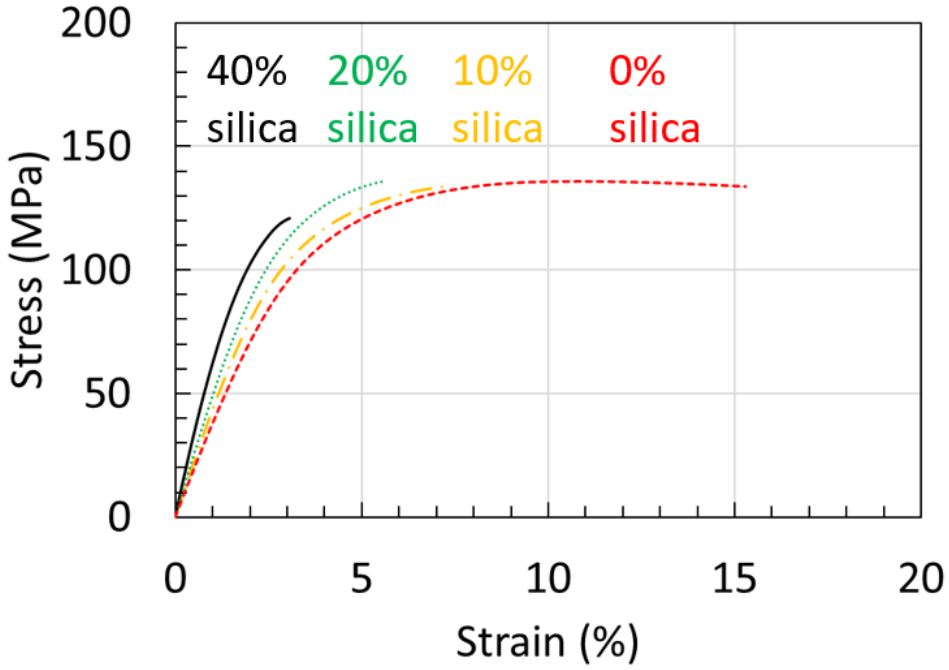

Property of PI – Silica films at different silica weight fraction

Mesh Convergence Study – Constant Displacement (V_p = 26.5%)

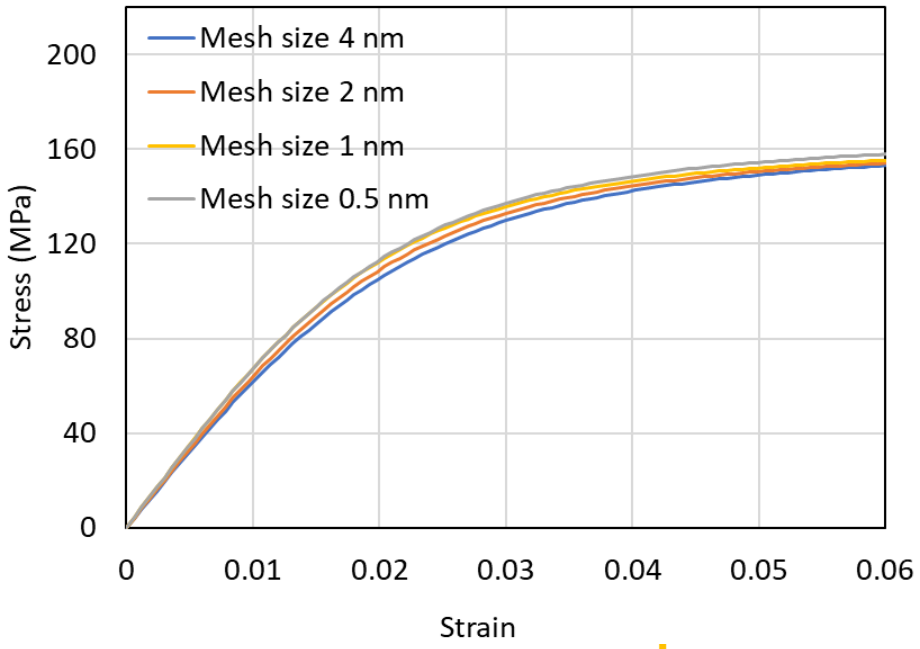

- Mesh convergence studies were conducted with different sizes ranging from 4 nm to 0.5 nm.
- Both global and local properties were studied.
- It was observed from the plot that, after a mesh size of 2 nm, both elastic and plastic solutions converged within a 5% error.

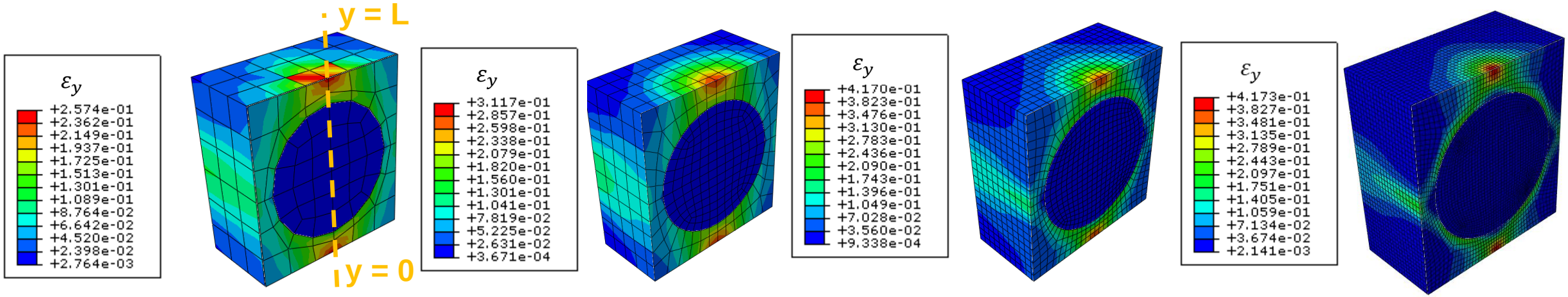

Stress – Strain Curves at Different V_p

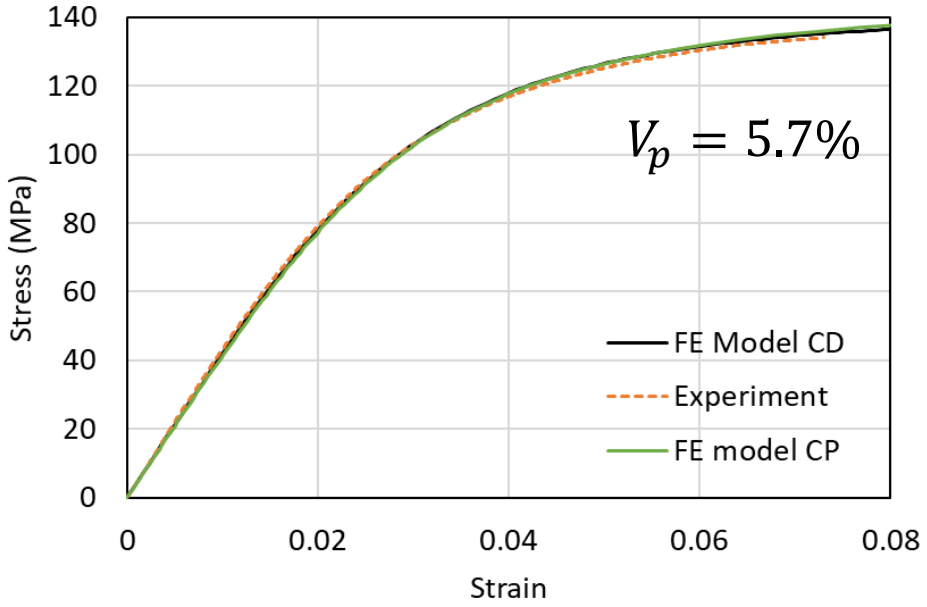

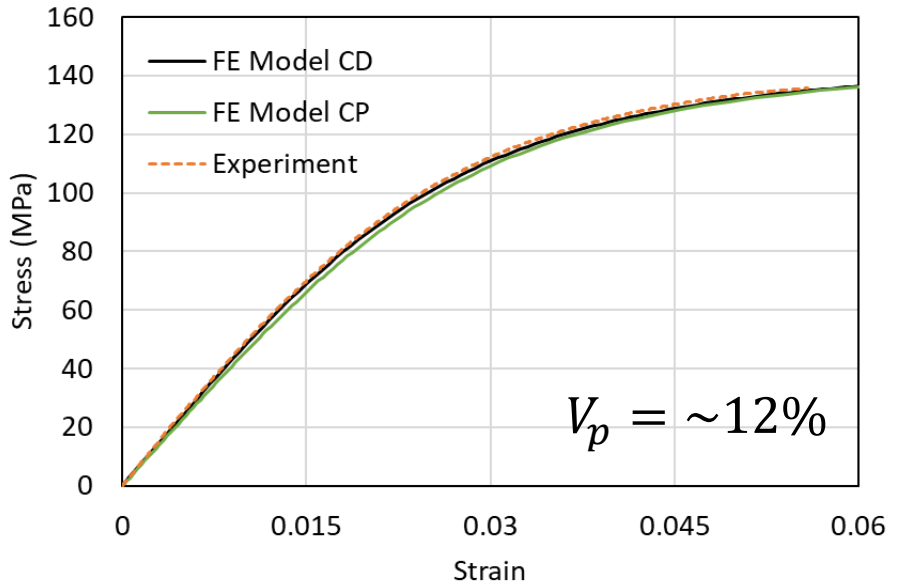

- Inputting the stress – strain curve of PI and changing the V_p
- Comparing FE results with experiment
- With out considering thermal loading

Constant Displacement (CD)
Constant Pressure (CP)
Frictionless (FL)

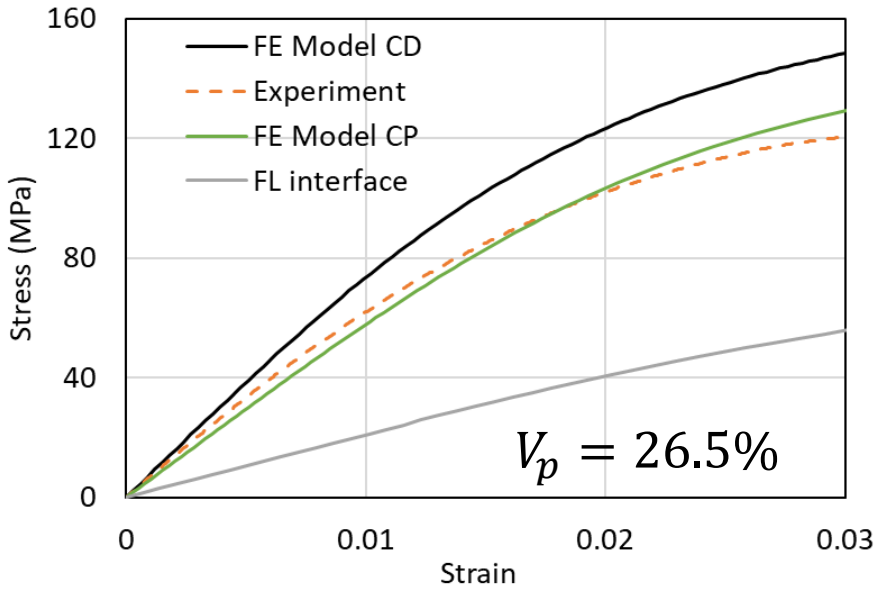

- At lower V_p, FE results has good correlation with experiments
- At V_p = 26.5% experimental stress – strain curve is close to the FE model with constant pressure BC
- Perfect bonding is the upper bond and FL is the lower bond.
  - Need to include residual stress, frictional sliding and include traction law to predict debonding between interface

Mesh Convergence Studies with Damage (CD)

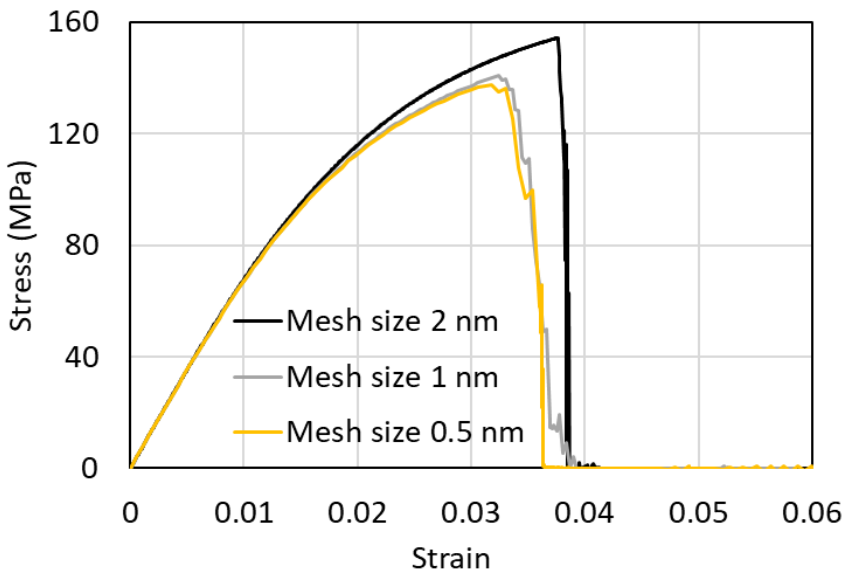

- Inputting the stress – strain curve of PI and strain to failure from experiment (~15%)
- V_p = 26.5%
- Perfect bonding between PI and Silica interface
- With out considering thermal loading
- Both failure stress and energy (area under the stress – strain curve) are very sensitive to mesh
- It is observed from the plot, after mesh size of 1 nm both failure stress and energy are converged with in the 5% error

mesh size = 1 nm

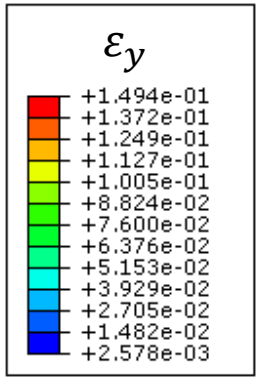

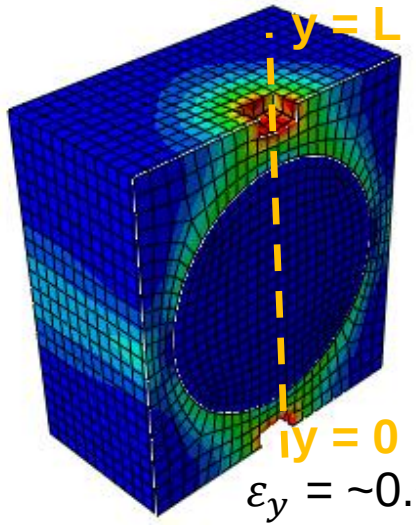

ε_y = ~0.035

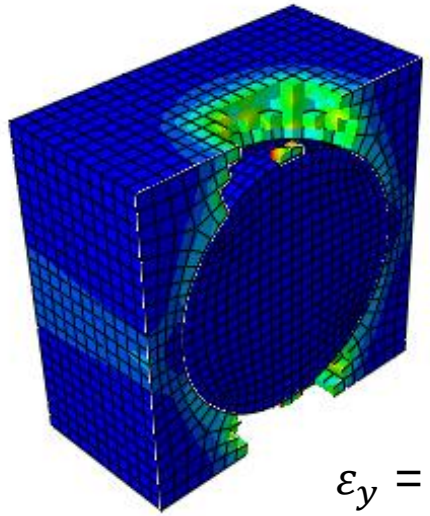

ε_y = ~0.037

Effect of Failure Strain (CD)

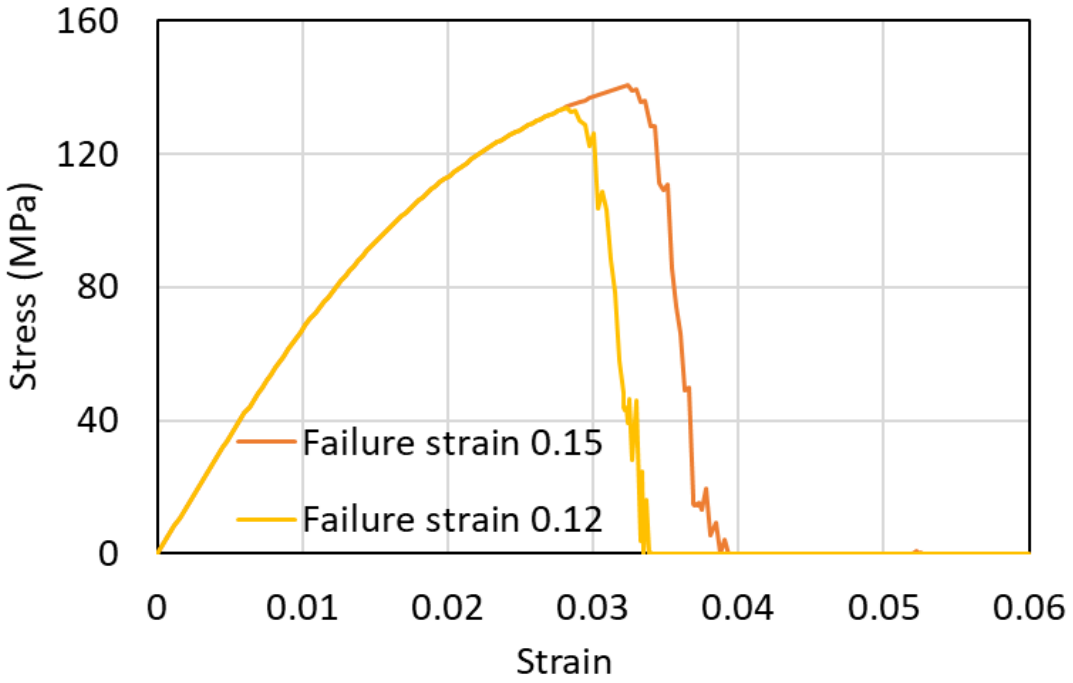

Plastic strain to failure from experiment = ~0.13 and ~0.10

- Inputting the stress – strain curve of PI and varying strain to failure (15% to 12%)
- V_p = 26.5%
- Perfect bonding between PI and Silica interface
- With out considering thermal loading

- Damage initiation/propagation may change if we consider other damage mechanisms in the model

Considering Three Particles RVE (CD)

mesh size = 1 nm

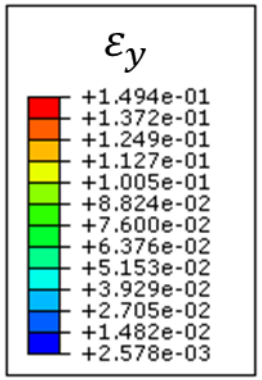

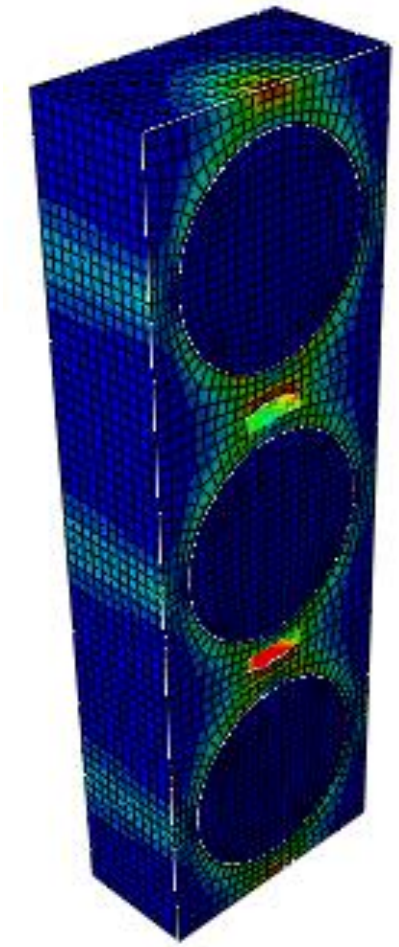

ε_y = ~0.035

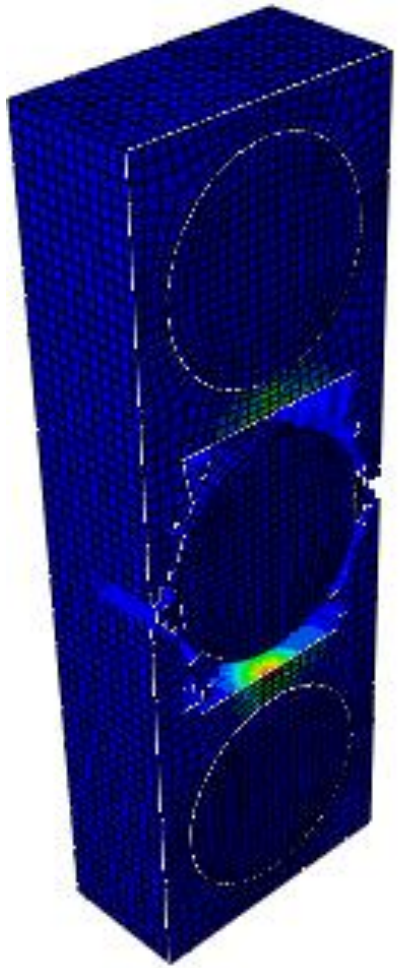

ε_y = ~0.038

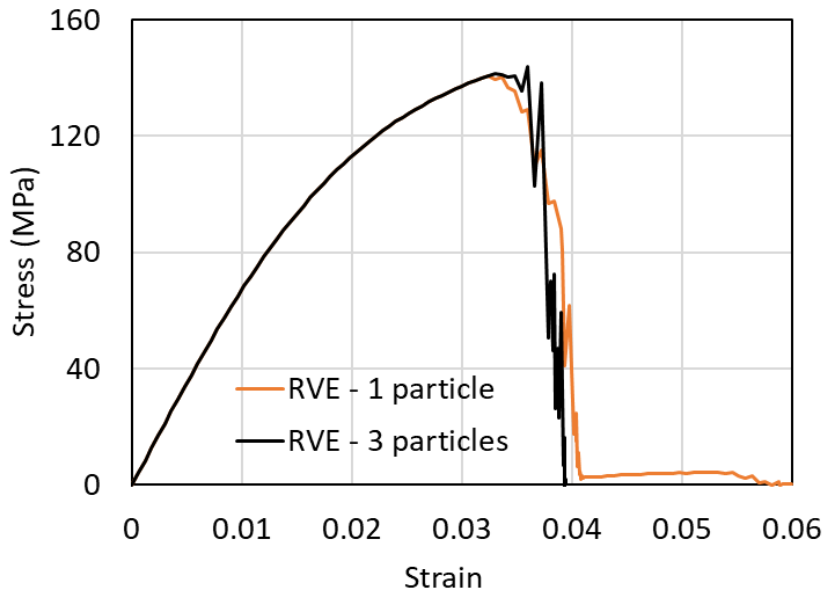

- Considering three particles in the RVE as the first step of building cell model
- Inputting the stress – strain curve of PI and strain to failure from experiment (~15%)
- V_p = 26.5%
- Perfect bonding between PI and Silica interface
- With out considering thermal loading
- Only middle region has failure criteria

Considering Three Particles RVE (CP)

mesh size = 1 nm

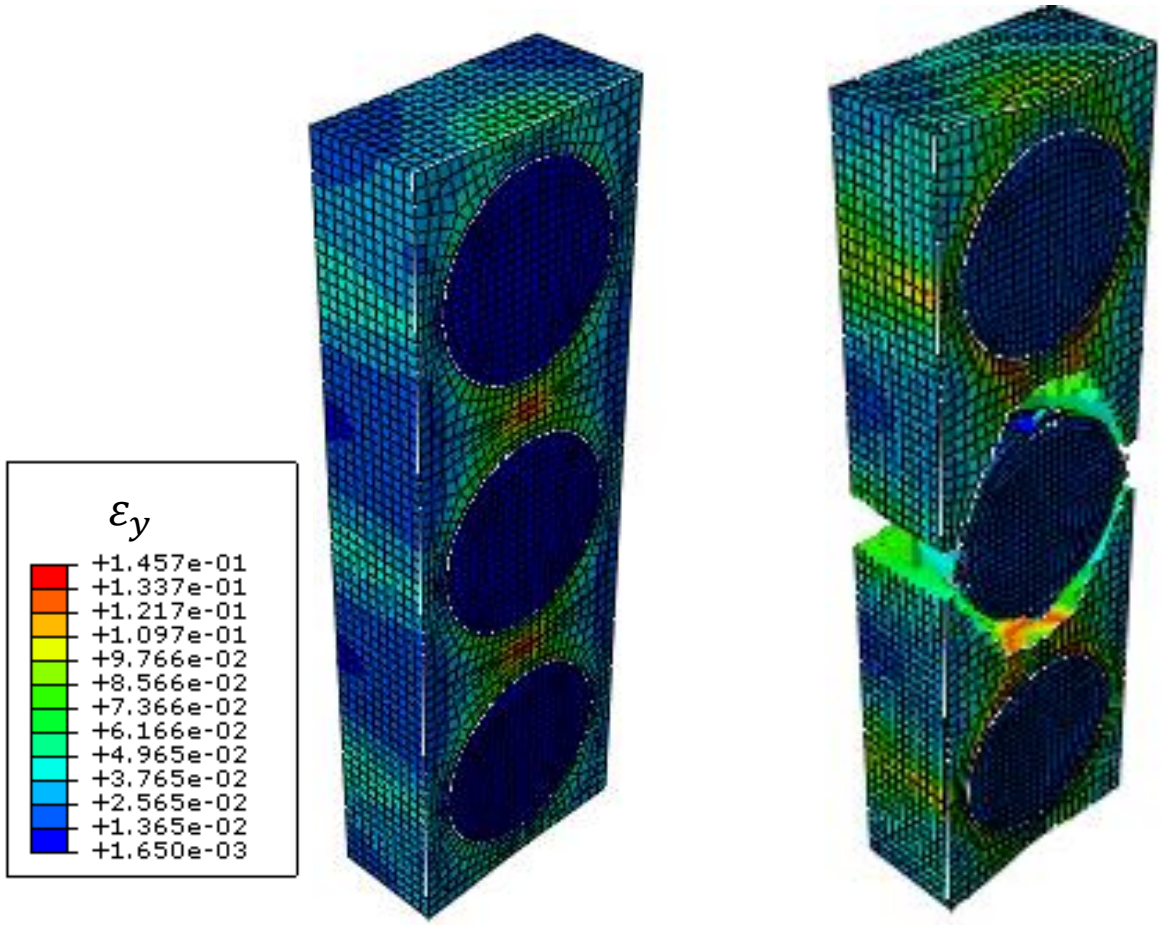

$Applied\ pressure = \sim 135\ MPa$

$Applied\ pressure = \sim 140\ MPa$

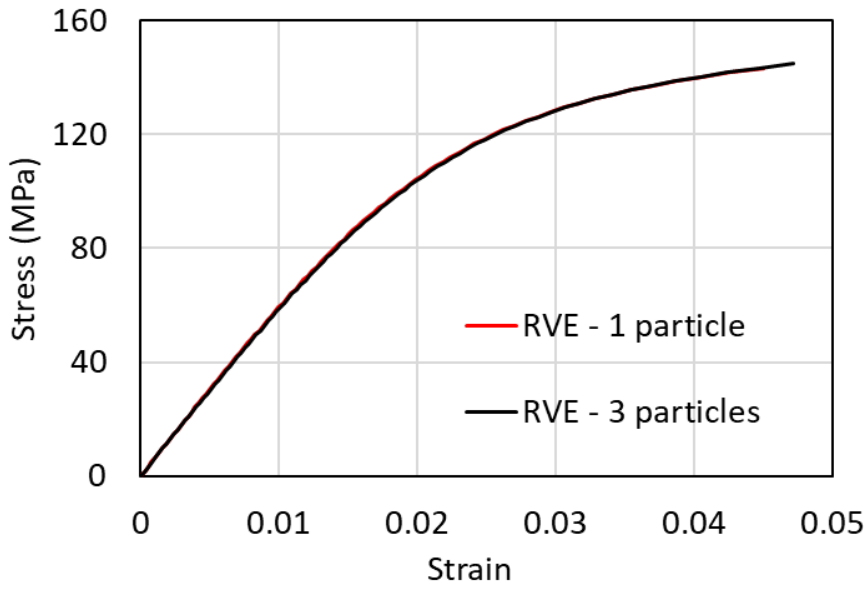

- Considering three particles in the RVE as the first step of building cell model
- Inputting the stress – strain curve of PI and strain to failure from experiment (~15%)
- V_p = 26.5%
- Perfect bonding between PI and Silica interface
- With out considering thermal loading
- Only middle region has failure criteria

Conclusion and Discussion

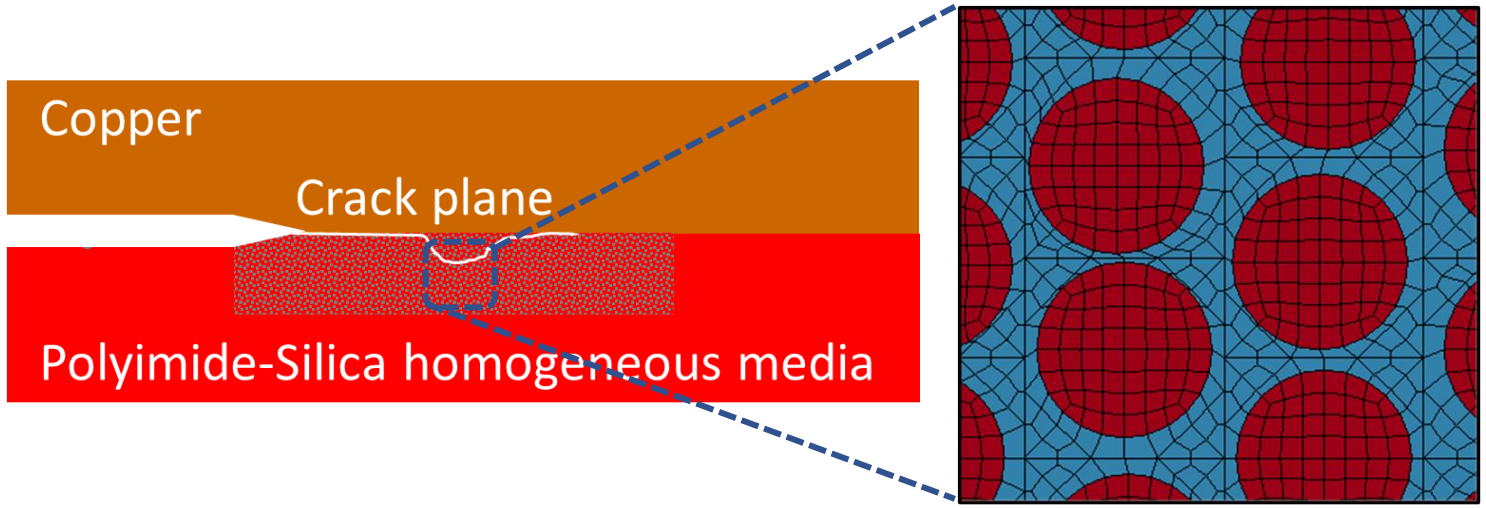

- Single RVE study has completed and compared with experiment.
- Including CTE and different damage mechanisms study the RVE at different loading conditions and volume fractions.
- Develop the cell model by inputting the properties of the constituents and stacking the RVE with a random distribution.
  - Residual stress
  - Resin Plasticity
  - Frictional sliding and interface debonding
- Next, measure the peel strength of copper/polyimide laminates to understand the underlying mechanism.

Acknowledgments

- The project was funded by DuPont Specialty Materials, USA.
- Special thanks Dr. Nicholas Shevchenko for his assistance in manufacturing the 90° peel test setup and Dr. Steve Sauerbrunn for helping with thermal characterization.
- Discussions with Dr. Joseph Deitzel on SEM micrographs and thermal analysis results were valuable in understanding the key mechanisms.
- Comments and suggestions from DuPont team members during biweekly meetings are greatly appreciated.

MICRO-SCALE SIMULATION FOR NONLINEAR STRESS–STRAIN BEHAVIOR OF UNIDIRECTIONAL CARBON FIBER/ PHENYL–ETHYNYL TERMINATED POLYIMIDE TRIA-X COMPOSITES

Tatsuya Kobayashi [1], Satoru Yoshikawa [1], Toshio Ogasawara [1]
Yuichi Ishida [2], Mio Sato [2], Masahiko Miyauchi [3]

[1] Tokyo University of Agriculture and Technology,
2-24-16 Naka-cho, Koganei-shi, 184-8588, Tokyo, Japan
Email: s252316r@st.go.tuat.ac.jp, ogasat@cc.tuat.ac.jp

[2] Japan Aerospace Exploration Agency (JAXA),
6-13-1 Osawa, Mitaka-shi, 181-0015, Tokyo, Japan

[3] Kaneka Co.,
5-1-1 Torikainishi, Setsu-shi, 566-0072, Osaka, Japan

Keywords: Polymer-matrix composites (PMCs), Thermosetting resin, Mechanical properties, Analytical modelling, High-temperature properties

ABSTRACT

TriA-X, a phenylethynyl-terminated polyimide resin with a Kapton-type structure, has a glass transition temperature of 350°C or higher and is a promising matrix resin for heat-resistant CFRP (Carbon Fiber Reinforced Plastics). This study attempted to predict the mechanical behavior of carbon fiber/TriA-X composites (CF/TriA-X) using micro-scale analysis. Based on the experimentally obtained mechanical properties of the cured resin, the constitutive model for linear viscoelasticity and viscoplasticity were applied individually, and the time and temperature dependent mechanical behaviors were taken into consideration. The viscoelastic parameters were determined from the results of creep tests without residual strain, while the viscoplastic parameters were obtained by subtracting the viscoelastic strain from the total strain of the creep tests that produced residual strain. Using microscale models consisting of fiber and matrix, the nonlinear mechanical behavior of unidirectional CF/TriA-X (UD-CFRP) under off axis tension was calculated using finite element analysis code Digimat FE (Hexagon) considering the viscoelastic and viscoplastic behavior. As a result, the stress-strain curves of off-axis UD-CF/TriA-X composites at room temperature were good agreement with the experimental results.

1 INTRODUCTION

In recent years, carbon fiber reinforced plastic composites (CFRP), which have high specific strength and stiffness, were widely applied to airframe structures to reduce aircraft weight and maintenance costs. Most of the CFRP for aircrafts consists of an epoxy resin matrix, with operating heat resistance temperatures limited to 120°C. By contrast, CFRP consisting of heat-resistant resins such as bismaleimide and polyimide have higher operating temperature of 200 to 300°C, which is superior to that of epoxy resins. Among heat-resistant resins, polyimide resin has a high glass transition temperature (Tg), excellent mechanical properties, chemical stability, and low thermal expansion coefficient. Therefore, it is expected to be used as a matrix resin for heat-resistant CFRP to be applied to parts requiring high heat resistance, such as turbofan engine parts and the airframe of supersonic aircrafts, which have been difficult to apply with conventional epoxy-based CFRP [1-3].

Generally, addition-type (thermosetting type) polyimide resins have high heat resistance, corrosion resistance, mechanical strength, and good moldability, however, they tend to have poor toughness [4]. Furthermore, heat-resistant resins, including polyimide, are generally not easy to mold because it is difficult to obtain low viscosity enough to enable melt molding even in high-temperature environments. To solve this problem, a phenyl-ethynyl terminated addition polyimides (PETI) had been studied, mainly

by NASA. However, the glass transition temperature of typical polyimide resin PETI-5 is only 260-270°C, and it has been difficult for a long time to achieve both heat resistance and mechanical properties [5-9]. Yokota et al. successfully developed for synthesizing an addition-type polyimide (Triple A (TriA) polyimide) with both heat resistance, toughness, and moldability using an asymmetric chemical structure for the polymer main chain. Based on this concept, Miyauchi [6] et al. developed an additive polyimide TriA-X (TripleA-X), having the chemical structure shown in Scheme 1. Cured TriA-X polyimide has high heat resistance and good mechanical properties. TriA-X has higher toughness and heat resistance than conventional polyimide resins, having a softening temperature of 350-370°C and an average strain at break of about 11% for cured resin [10]. TriA-X is expected to be used as a matrix resin for heat-resistant CFRPs, however the mechanical properties of the resin or of composites have not sufficiently understood.

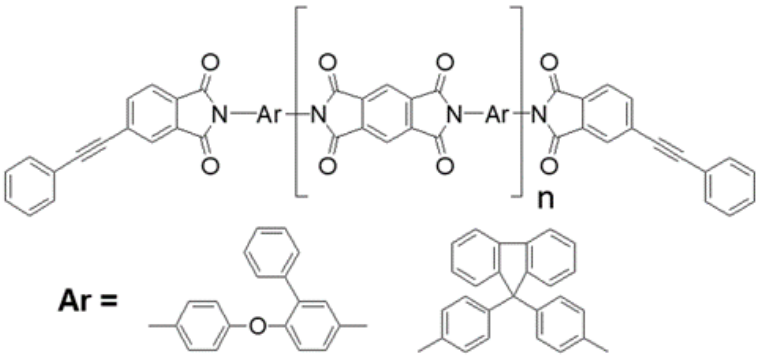

Scheme 1: Chemical structure of TriA-X imide oligomer [6].

Meanwhile, unidirectional CFRP (UD-CFRP) is known to exhibit nonlinear stress-strain behavior because of viscoelastic deformation of matrix resin in the off-axis tensile test. Furthermore, the nonlinear stress-strain behavior of CFRP has time- and temperature-dependence. In polyimide-based CFRP, studies have also been conducted to predict nonlinear behavior by theoretical equations based on experimental results [11]. In structural design using heat-resistant CFRPs, it is necessary to evaluate the mechanical properties at various temperatures, however obtaining material strength data by experimental methods is costly and time-consuming. For this reason, it is expected to establish a technique to predict various mechanical properties of CFRP at a wide range of temperatures based on the properties of resin obtained from experiments.

The aim of this study is to predict the mechanical behavior of UD-CFRP with thermosetting polyimide TriA-X as a matrix at elevated temperatures from the experimentally obtained material properties of matrix resin. In this paper, the mechanical properties of cured neat TriA-X resin are evaluated to model its stress-strain behavior, and the nonlinear mechanical behavior of UD-CFRP is predicted from stress analysis of a unit cell model consisting of fiber and matrix.

2 MECHANICAL PROPERTIES OF POLYIMIDE RESIN TRIA-X

2.1 Material and specimen

Cured resin plates were obtained from imide oligomer TriA-X powder (n=4). The curing temperature was 370°C. After curing, strip-shaped specimens (120 × 10 × t 2.8 [mm^3] and 140 × 10 × t 2 [mm^3]) were cut from each resin plate using a cutting machine and provided to tensile testing. The glass transition temperature of the cured resin was about 350°C, obtained from the change in storage modulus by dynamic viscoelasticity (DMA) measurement.

2.2 Experimental procedure

Tensile tests including creep/recovery tests were conducted for cured resin specimens. A servo-hydraulic testing machine (Model 8804, Instron, USA) equipped with a convection type environment chamber (oven) was used for tensile testing. A 5 kN load cell was used to measure the load.

Monotonic tensile tests were conducted under a constant displacement of 1 mm/min until final failure. A contact-type extensometer (Model 633.11C-14, MTS Systems Co.) with a gauge length of 25 mm was used to measure the longitudinal strain. Test temperatures were set to be 23°C, 200°C and 250°C.

Creep/recovery tests were conducted under constant displacement and load-controlled conditions. The holding loads were 20, 30, 40, 60, and 80 MPa, and the time holding was 1 hour, followed by 3 hours of no load (0 MPa). The loading rate up to the holding load was 35 N/min.

Loading/unloading tensile tests were conducted under a constant displacement rate of 0.1 mm/min or 10 mm/min. When the crosshead displacement reached 1, 2, and 3 mm, the load was unloaded to 0 N and then reloaded, respectively. The test temperatures for the creep recovery and loading/unloading tests are 23°C and 200°C, respectively.

2.3 Experimental Result

Stress-strain curves obtained from monotonic tensile testing at 23, 200, and 250°C are shown in Fig. 1, and the initial elastic modulus of and strength at break calculated in the strain range 0.05-0.25% are summarized in Table 1. A significant decrease in stiffness with increasing temperature was observed.

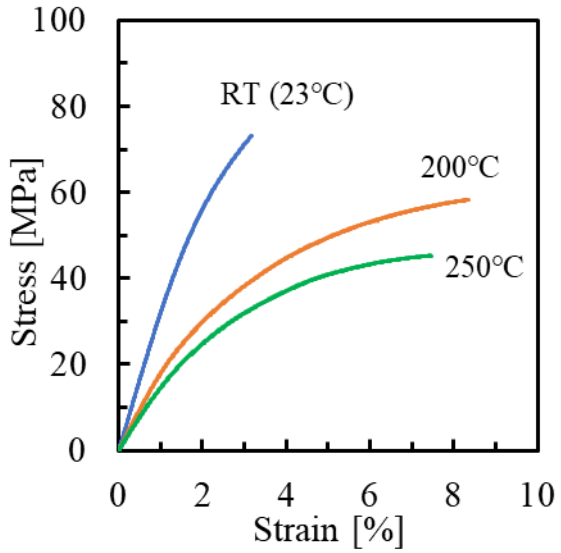

Fig. 1: Stress-strain curves of cured TriA-X polyimide specimens.

Table 1: Initial elastic modulus and rupture strength of cured TriA-X.

Temperature	Young modulus [GPa]	Rupture strength [MPa]
RT (23°C)	3.28	78.0
200°C	1.91	58.2
250°C	1.59	45.2

Fig. 2 (a) and (b) present the strain-time curves obtained by the creep/recovery tests. The results show viscoelastic behavior (creep and recovery behavior) at all stress levels [12]. In room temperature, residual strain was not observed at room temperature at holding stresses of 20 and 30 MPa, while residual strain due to viscoplasticity or plasticity was seen at stresses above 40 MPa. It was also confirmed that the creep strain increased with increasing temperature, even at the same holding stress.

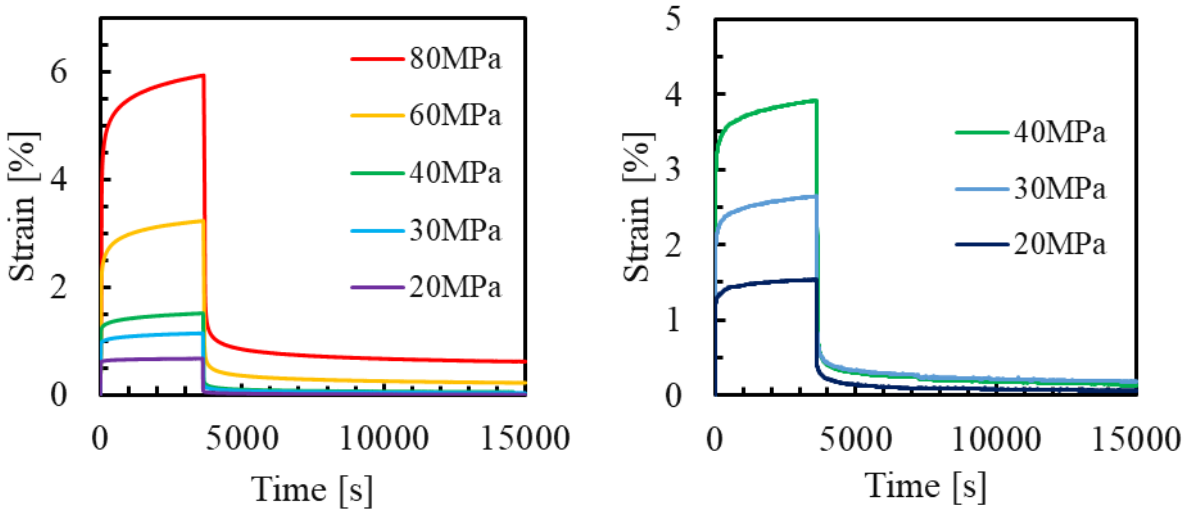

(a) 23°C. (b) 200°C.

Fig. 2: Strain-time curves of cured TriA-X polyimide specimens at 23°C and 200°C.

Fig. 3 (a) and (b) show the stress-strain curves obtained by the loading/unloading tests. Hysteresis behavior in the nonlinear region is observed for all test conditions. Also, the relation between the residual strain after every load-unloading test cycle and the maximum stress during each cycle is depicted in Fig. 4. As shown in Fig. 4, significant residual strain is observed from the third cycle at 23°C and from the second cycle at 200°C. Additionally, residual strain increased rapidly with maximum stress, and the degree of increase was more pronounced at higher temperatures and slower loading rates. The hysteresis behavior and the decrease in stiffness with decreasing loading rate indicate that the resin exhibits remarkable viscoelastic behavior.

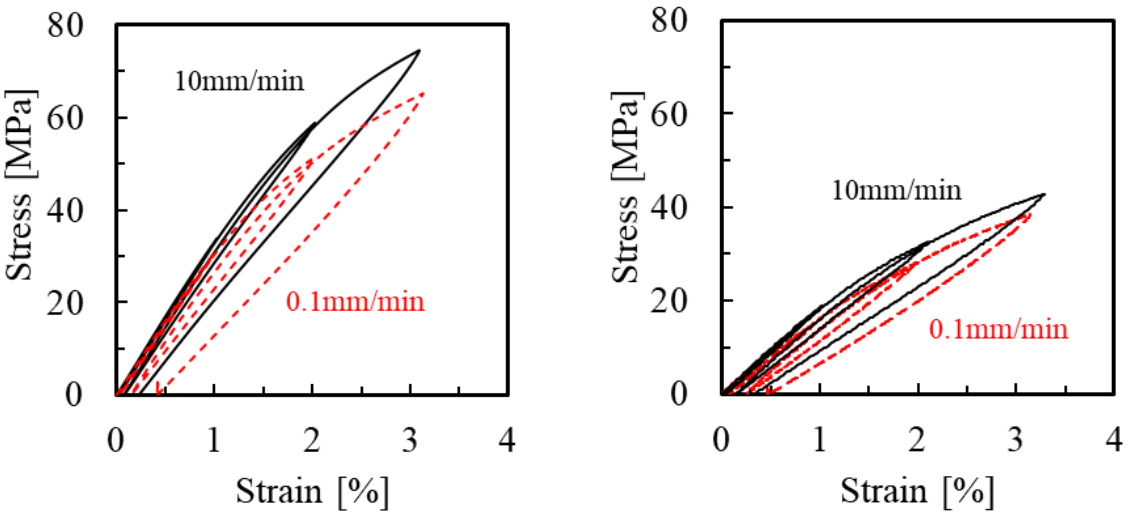

(a) 23°C. (b) 200°C.

Fig. 3: Stress-strain curves of cured TriA-X polyimide specimens at 23°C and 200°C under load/unload tests.

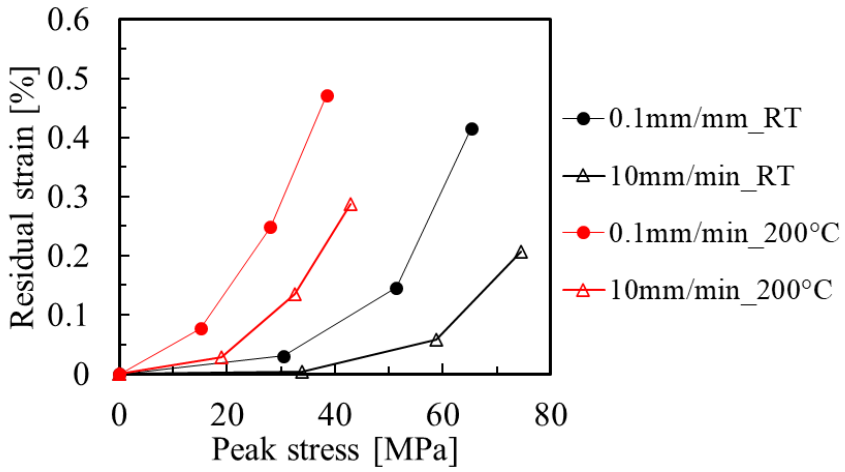

Fig. 4: Residual strain-peak stress curves of cured TriA-X polyimide specimens at RT (23°C) and 200°C under loading/unloading testing.

3 MECHANICAL MODELING OF CURED TRIA-X POLYIMIDE RESIN

3.1 Viscoelastic model

The experimental results of cured TriA-X resin suggest that the nonlinear behavior at room and elevated temperatures cannot be expressed using a simple viscoelastic model. Therefore, strictly speaking, it is considered appropriate to use nonlinear viscoelastic and plastic (or viscoplastic) modeling. In this study, we focus only on the time dependence of monotonic loading, and attempt to model the nonlinear stress-strain behavior in the loading using linear viscoelastic and viscoplastic models approximately.

In the viscoelastic-viscoplastic model, the total strain ε is expressed as the sum of the viscoelastic strain ε^{VE} and the viscoplastic strain ε^{VP}.

$$\begin{aligned} \varepsilon &= \varepsilon^{VE} && (\sigma_{eq} < \sigma_Y) \\ \varepsilon &= \varepsilon^{VE} + \varepsilon^{VP} && (\sigma_{eq} > \sigma_Y) \end{aligned} \tag{1}$$

The viscoelastic strain ε^{VE} is 0 when the Mises equivalent stress σ_{eq} is lower than the yield stress σ_Y, which means only viscoelastic deformation. The viscoelastic constitutive model is defined as follows.

$$\sigma(t) = G(t):\varepsilon(0) + \int G(t-\tau):\dot{\epsilon^{ve}}(\tau)d\tau \tag{2}$$

$$\text{with } \varepsilon(0) = \lim_{\substack{t\to 0 \\ t>0}} \varepsilon(t) \text{ and } G(t) = 2G_R(t)I^{dev} + K_R(t)1 \otimes 1 \tag{3}$$

The shear modulus $G_R(t)$ and bulk modulus $K_R(t)$ are described using the generalized Maxwell model.

$$G_R(t) = G_0\left[1 - \sum_{i=1}^{n} e_i\left(1 - e^{-\frac{t}{\Lambda_k}}\right)\right] \tag{4}$$

$$K_R(t) = K_0\left[1 - \sum_{i=1}^{n} e_i\left(1 - e^{-\frac{t}{\Lambda_k}}\right)\right] \tag{5}$$

where G_0 is the initial shear modulus, and K_0 is the initial bulk modulus. To conduct a finite element analysis, the relaxation modulus (Prony series e_k, Λ_k) in equations (4) and (5) must be obtained from the results of creep tests for the cured TriA-X resin. In this research, the relaxation modulus was determined as follows. First, the creep test results at 20 MPa, where almost no residual strain occurs

after unloading, were fitted with a generalized Voigt model (n=3) as shown in Fig. 5. Next, the Prony series (n=3) was obtained by the Laplace transform for the Voigt model [13]. The determined Prony series are shown in Table 2.

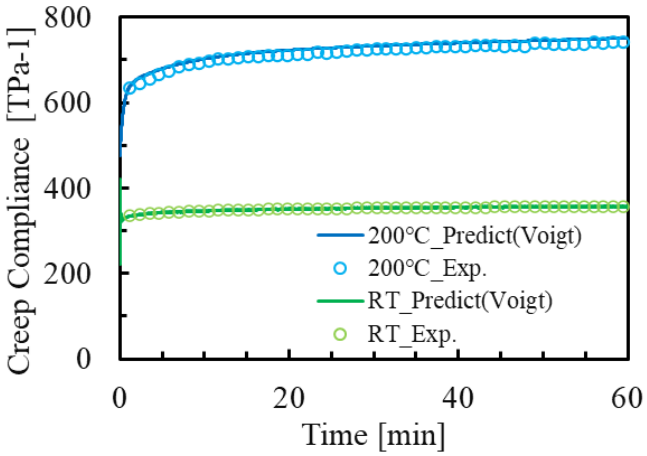

Fig. 5: Relationship between creep compliance and time of TriA-X polyimide specimens at 23°C and 200°C.

Table 2: Prony series.

		23°C	200°C
Λ_1	[min]	1.91×10^{-1}	4.02×10^{-1}
Λ_2	[min]	6.07	5.44
Λ_3	[min]	1.14×10^{2}	1.08×10^{2}
e_1	[-]	8.30×10^{-2}	1.76×10^{-1}
e_2	[-]	4.10×10^{-2}	9.02×10^{-2}
e_3	[-]	5.66×10^{-2}	9.20×10^{-2}

The initial shear modulus G_0 and initial bulk modulus K_0 were calculated from Young's modulus E obtained in the monotonic tensile test using the following relationships.

$$K = \frac{E}{3(1-2\nu)} \tag{6}$$

$$G = \frac{E}{2(1+\nu)} \tag{7}$$

where ν is Poisson's ratio, which is 0.37. The initial shear modulus and initial bulk modulus at each temperature are shown in Table 3.

Table 3: Initial shear modulus, G_0 and initial bulk modulus, K_0.

	23°C	200°C
G_0 [MPa]	1.20×10^{3}	6.98×10^{2}
K_0 [MPa]	4.20×10^{3}	2.45×10^{3}

3.2 Viscoplastic model

When the Mises stress σ_{eq} exceeds the yield stress σ_Y, plastic deformation occurs. The viscoplastic strain ε^{VP} was represented using the J_2 plasticity model as a time-dependent viscoplastic constitutive equation as follows;

$$\sigma_{eq} = \sigma_Y + R(p) \tag{8}$$

where $R(p)$ and p are hardening stress, and accumulated plastic strain, respectively. In this study, uniaxial tensile analysis is treated, therefore the Mises stress, σ_{eq} is equal to the axial stress, σ_{11} . $R(p)$ is approximated by the following power law.

$$R(p) = kp^{m_1} \tag{9}$$

where k is the hardening modulus and m_1 is the hardening exponent. The viscoplastic stress f is defined as follows.

$$f = \sigma_{eq} - \sigma_Y - R(p) \tag{10}$$

The accumulated plastic strain rate $\dot{p}$ is expressed by the equation (11).

$$\dot{p} = \frac{\sigma_Y}{\eta}\left(\frac{f}{\sigma_Y}\right)^{m_2} \tag{11}$$

where η is the viscoplasticity coefficient, m_2 is the viscoplasticity index, σ_{eq} is the equivalent stress, and σ_Y is the yield stress. Substituting equations (9) and (10) into equation (11) and arranging,

$$\dot{p} = \frac{\sigma_Y}{\eta}\left(\frac{\sigma_{eq} - \sigma_Y - kp^{m_1}}{\sigma_Y}\right)^{m_2} \tag{12}$$

The constants k, m_1, η and m_2 in Eq. (12) were determined by simultaneously fitting the experimental results of monotonic tensile tests, loading/unloading tests, and creep tests for cured TriA-X resins. As described in Chapter 2, TriA-X resin exhibits nonlinear viscoelastic behavior over a certain stress level, however, since only the monotonic loading is considered in this paper, linear viscoelasticity and viscoplasticity are applied in the model. Viscoplastic strain was calculated by subtracting the viscoelastic strain obtained from the 20 MPa test results from the creep strain measured at 60 MPa and 40 MPa at 23°C (RT) and 200°C, respectively. Table 4 shows the constants k, m_1, η, m_2 and yield stress σ_Y obtained at room temperature and 200°C.

Table 4: Viscoplastic parameter.

	23°C	200°C
Hardening modulus, k [MPa]	211	230
Hardening exponent, m_1 [-]	0.465	0.615
Creep coefficient, η [MPa · s]	6.00×10^3	3.40×10^4
Creep exponent, m_2 [-]	2.8	13
Yield stress, σ_Y [MPa]	36.9	16.5

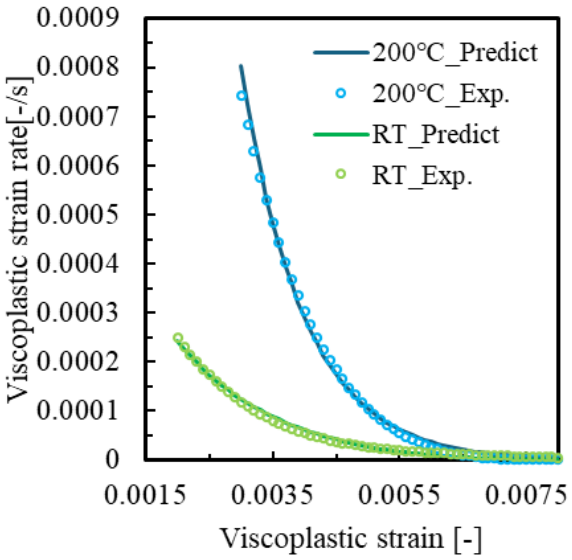

Fig. 6: Fitting of viscoplastic strain rate - viscoplastic strain curves at RT (23°C) and 200°C.

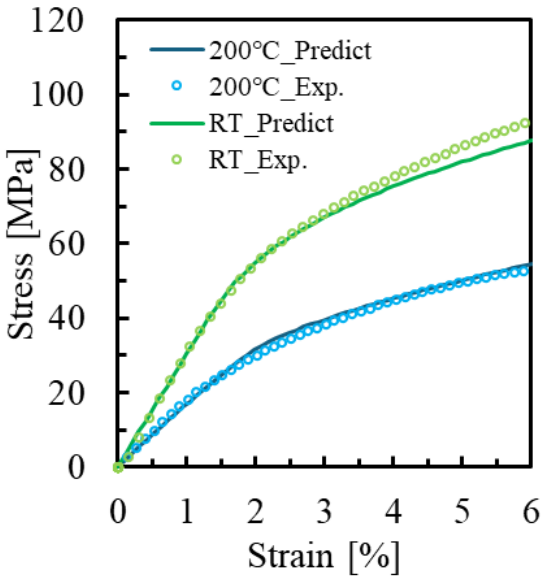

Fig. 7: Fitting of Stress Strain curves in 1 mm/min at RT (23°C) and 200°C.

4 NUMERICAL SIMULATIONS FOR NONLINEAR STRESS–STRAIN BEHAVIOR OF UNIDIRECTIONAL CFRP LAMINATES

4.1 Numerical Analysis Method

Tensile analysis of unidirectional reinforced CFRP in off-axis direction is conducted at 23°C and 200°C using a microscale representative volume element (RVE) model composed of matrix resin and fibers to predict the nonlinear stress-strain behavior of UD-CF/TriA-X. Digimat-FE (MSC Software, Hexagon) was used to make finite element model and set boundary conditions. Also, MS/Marc (MSC Software, Hexagon), standard solver of Digimat, was used for the finite element analysis (FEA). In order to simulate the tensile strength of unidirectional CFRP in the 30°, 45° and 90° directions, the REV models shown in Fig. 8 were made. The sizes of each model are presented in Table 5. All models are voxel meshes with hexahedral brick elements applied.

Table 5: RVE size and number of elements/nodes.

	30°	45°	90°
X (mm)	0.0154	0.0108	0.0764
Y (mm)	0.00889	0.0108	0.0764
Z (mm)	0.0133	0.0132	0.0132
Number of elements	125000	125000	125000
Number of nodes	132651	132651	132651

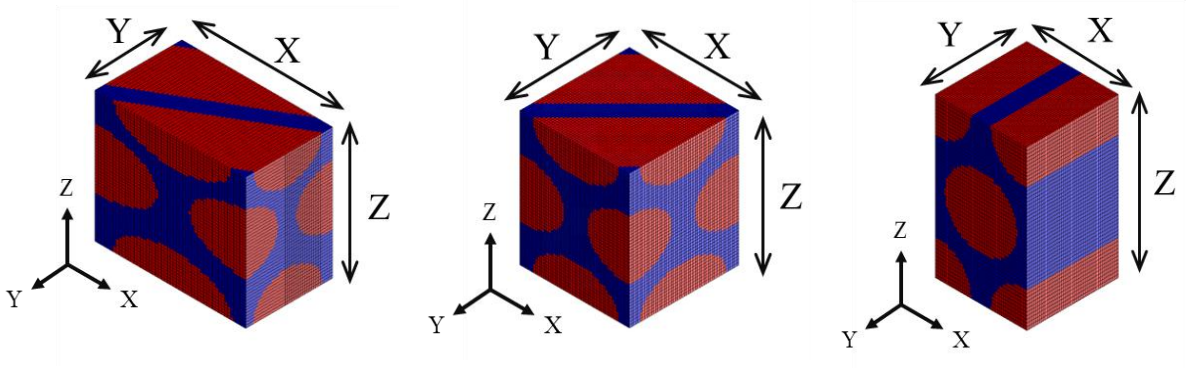

(a) Fiber angle 30°. (b) Fiber angle 45°. (c) Fiber angle 90°.

Fig. 8: Unit cell (RVE) model for microscale analysis.

Table 6: Material properties of carbon fiber, MR50 (Mitsubishi Chemical).

		Value
Fiber diameter	[mm]	0.006
Axial young's modulus E_{11}	[GPa]	2.95×10^2
In-plane young's modulus E_{22}	[GPa]	14
In-plane Poisson's ratio ν_{12}	[-]	0.2
Transverse Poisson's ratio ν_{23}	[-]	0.25
Transverse shear modulus G_{12}	[GPa]	27.6
Thermal expansion coefficient α_{carbon}	[K^{-1}]	-4×10^{-7}

Table 6 shows the mechanical properties of the PAN-based carbon fiber (MR50, Mitsubishi Chemical Corporation) used in the calculations. The fibers were treated as isotopic elastic material. The fiber volume fraction is 0.56, in agreement with the experimental results. For the matrix resin, the viscoelastic/viscoplastic model defined in the previous section is applied, and it is assumed to be an isotropic material. The periodic boundary conditions are applied to each surface. The test condition in the analysis was strain control. To have the same strain rate as the experimental data, the loading rate was set to 0.0002083 [1/s]. Calculations were performed under the following two conditions (Case 1 and Case 2) for load and temperature to investigate the effect of thermal residual stress.

1. Mechanical load (Enforced displacement (strain) 1%) is applied at constant temperature (23℃, 200℃).
2. After giving the same temperature change of 370°C to 23°C as during processing, the temperature is maintained at the test temperature (23°C) and mechanical load (Enforced displacement (strain) 1%) is applied.

For the analysis of Case 2, the time-temperature superposition principle (TTSP) was applied to the viscoelastic model as follows;

$$\sigma(t) = \int_{-\infty}^{t} E(\tau - \acute{t}, T) : \frac{\partial \varepsilon^{ve}}{\partial \acute{t}} d\acute{t} \tag{13}$$

$$\text{With } E(t,T) = 3K_R(t,T)J + 2G_R(t,T)K \tag{14}$$

$$\Delta(t) = \int_0^t \frac{d\acute{t}}{A_T\big(T(\acute{t})\big)} \Rightarrow \frac{d\Delta}{dt} = \frac{1}{A_T\big(T(t)\big)} \tag{15}$$

where A_T is the shift function in the time-temperature conversion law, using the Arrhenius law. Applying Eq. (15) to Δ_k in Eqs. (4) and (5), the temperature dependence of the relaxation modulus can be taken into account. The activation energy used in the Arrhenius equation was estimated from the master curve of the storage modulus at 30°C using the results of dynamic viscoelasticity (DMA) tests of resins from 30°C to 390°C. The estimated activation energy was 160 kJ/mol. In addition, the coefficient of thermal expansion (CTE) of the cured TriA-X is 6×10^{-5} K^{-1}[14].

4.1 Numerical Analysis Result

Stress-strain curves obtained from stress analysis for the 30°, 45°, and 90° directions and experimental results at room temperature obtained in the previous study are depicted in Fig. 9 (a), (b) and (c). The analytical results at room temperature were generally in good agreement with the experimental results, confirming that the analytical model was approximately valid.

A contour plot of plastic strain is presented in Fig. 10, immediately after cooling in Case 2. For all fiber orientation angles analyzed in this study, plastic strain was observed in the resin at close fiber spacing. In Fig. 9, when comparing the stress-strain curves at 23°C without (Case 1) and with (Case 2) thermal residual stress, significant differences were not observed. The possible reason for this is that in the model considering the thermal residual stress, although plastic deformation occurs once in the resin due to the difference in thermal shrinkage between the resin and the fiber, the time of increase in plastic strain is the same as in the model not considering the thermal residual stress. From these results, it is expected that there is little need to consider thermal residual stress at room temperature as well as 200°C, which is closer to the process temperature than room temperature.

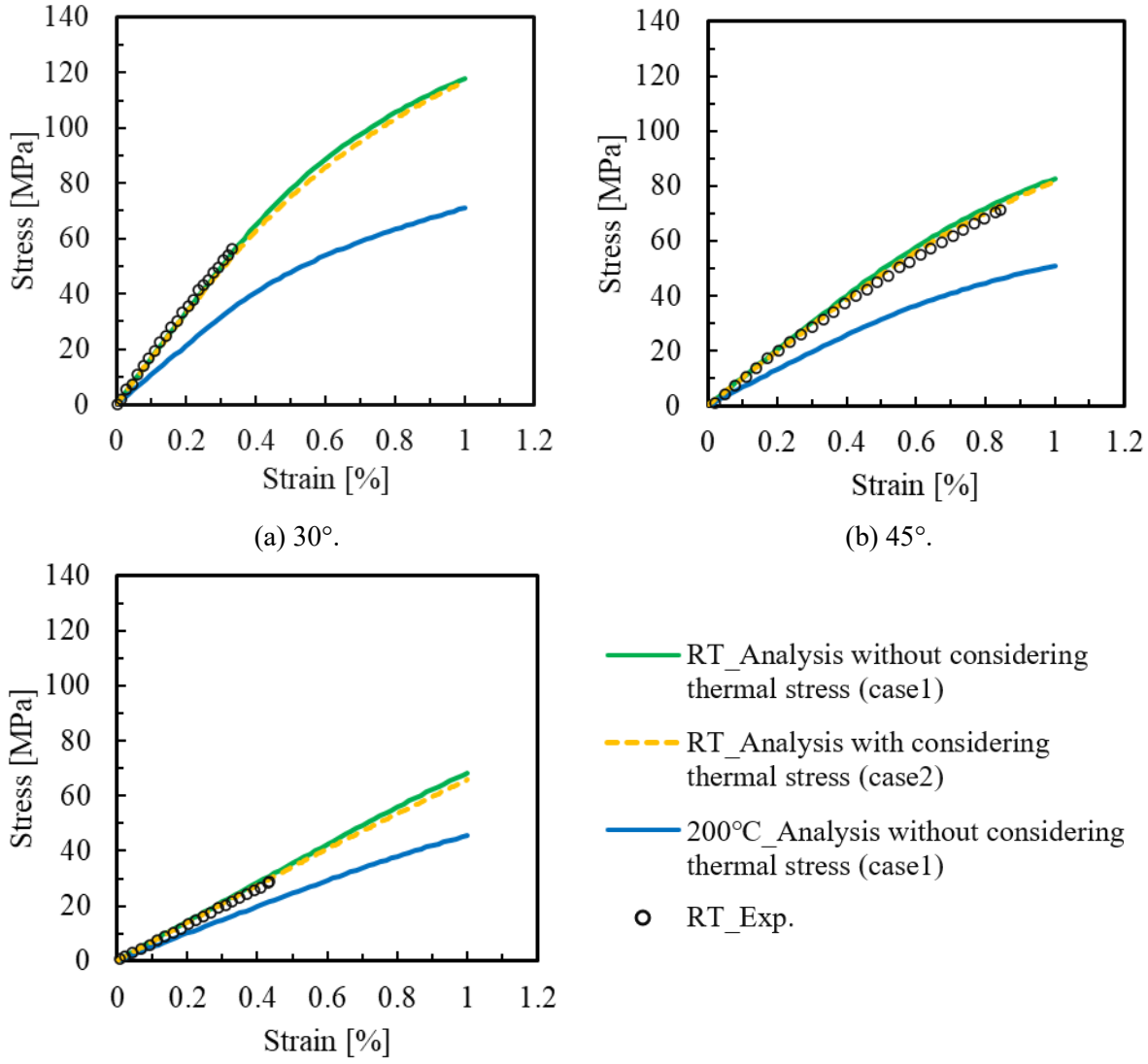

(a) 30°. (b) 45°.

(c) 90°.

Fig. 9: Numerical and experimental results of stress-strain curves of carbon fiber/TriA-X composites for 30°, 45°, 90° tensile test at 23°C and 200°C.

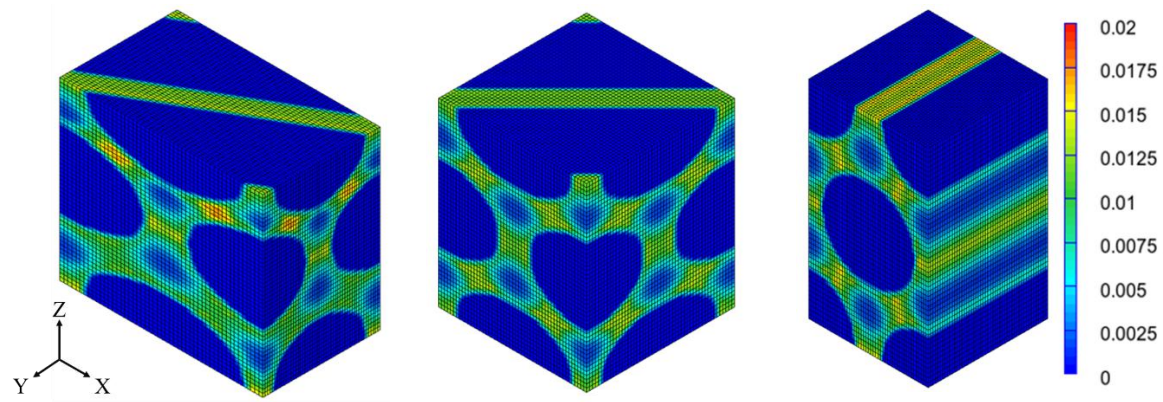

(a) Fiber angle 30°. (b) Fiber angle 45°. (c) Fiber angle 90°.

Fig. 10: Contour plot of plastic strain after cooling.

5 CONCLUSIONS

The mechanical properties of cured neat TriA-X resin are evaluated to model its stress-strain behavior, and the nonlinear mechanical behavior of UD- CF/TriA-X is predicted from stress analysis of a unit cell model consisting of fiber and matrix. The results obtained are as follows.

(1) The viscoelastic-viscoplastic constitutive equation was applied to the cured TriA-X resin, and the necessary material parameters were determined from the tensile test results. The resin model created accurately reproduced the experimental results at both 23°C and 200°C.

(2) The micro-scale analysis was conducted for the representative volume element model consisting of fiber and TriA-X matrix with applying the viscoelastic-viscoplastic model. The numerical results showed good agreement with the experimental results at room temperature. It was also confirmed that the effect of thermal residual stress during processing was relatively small for the tensile test results.

REFERENCES

[1] M. K. Ghosh, and K. L. Mittal, *Polyimides: Fundamental and Applications*, Marcel Dekker, New York, 1996.

[2] M. I. Bessonov, and V. A. Zubkov, *Polyamic Acids and Polyimides: Synthesis, Transformations and Structure*, CRC Press, Boca Raton, 1993.

[3] C. Feger, M. M. Khojasteh, and S. E. Molis, *Polyimides: trends in Materials and Applications*, Society of Plastic Engineers, Mid Hudson Section, New York, 1996.

[4] M. Tomoi, Fundamentals of thermosetting resin, *Journal of the institute of Electronics*, 4, 6, 2001, pp. 537-542.

[5] T. T. Serafini, *Polyimides; Synthesis, Characterization, and Applications*, Vol. 2. Mittal, K. L, New York, Plenum, 1984.

[6] M. Miyauchi, et al., Novel phenylethynyl-terminated PMDA-type polyimides based on KAPTON backbone structures derived from 2-phenyl-4,4’-diaminodiphenyl ether, *Journal of Polymer*, 44, 2012, pp. 959-965.

[7] G. W. Meyer, B. Tan, J. E. McGrath, Solvent resistant polyetherimide network systems via phenylethynyl phthalic anhydride endcapping, *Journal of High Performance Polymers*, 6, 1994, pp. 423-435.

[8] T. V. Holland, T. E. Glass, J. E. McGrath, Investigation of the thermal curing chemistry of the phenylethynyl group using a model aryl ether imide, *Polymer*, 41, 2000, pp. 4965-4990.

[9] T. Takekoshi, J. M. Terry, High temperature thermoset polyimides containing disubstituted acetylene end groups, *Polymer*, 35, 1994, pp. 4874.

[10] T. Ogasawara, Y. Ishida, and R. Yokota, Journal of the Japan Society for Aeronautical and Space Sciences, Vol. 54, 2006, pp. 161-167.

[11] R. Minegishi, T. Ogasawara, T. Aoki, Y. Ishida, Nonlinear stress–strain behavior of unidirectional carbon fiber/ phenyl–ethynyl terminated KAPTON-type polyimide, TriA-X, composites at elevated temperatures, *Advanced Composite Materials*, 30, 2021, pp. 24-38.

[12] J. N. Antonakakis, P. Bhargava, K. C. Chuang, A. T. Zehnder, Linear Viscoelastic Properties of HFPE-II-52 Polyimide, *Journal of Applied Polymer Science*, 100, 2006, pp. 3255-3263.

[13] S. P. Marques, G. J. Creus, *Computational viscoelasticity,* Springer Science & Business Media , 2012.

[14] M. Sato, et al., Temperature dependence of interfacial strength of carbon-fiber-reinforced temperature-resistant polymer composites, *Composite Structure*, 202, 2018, pp. 283-289.

ICCM24
24TH INTERNATIONAL CONFERENCE ON COMPOSITE MATERIALS
AUG 4-8, 2025 • BALTIMORE CONVENTION CENTER • BALTIMORE, MARYLAND
KIMS 한국재료연구원 Korea Institute of Materials Science

Prediction and Validation of Crush Behaviors in Advanced Glass Mat Thermoplastic Tubes Using Innovative Simulation Technology

Geunsu Joo[1)], Youngchul Kim[1)], Hong-Kyu Jang[1)], Jinbong Kim[1)], Mungyu Jeong[1)]

[1)] **Korea Institute of Materials Science**

Aug. 4th , 2025



KIMS 한국재료연구원
Korea Institute of Materials Science

ICCM24

목차

Contents

Introduction

Material Characterization

Material Modeling

Crush test & simulation

Conclusions



ICCM24

chapter 01

Introduction

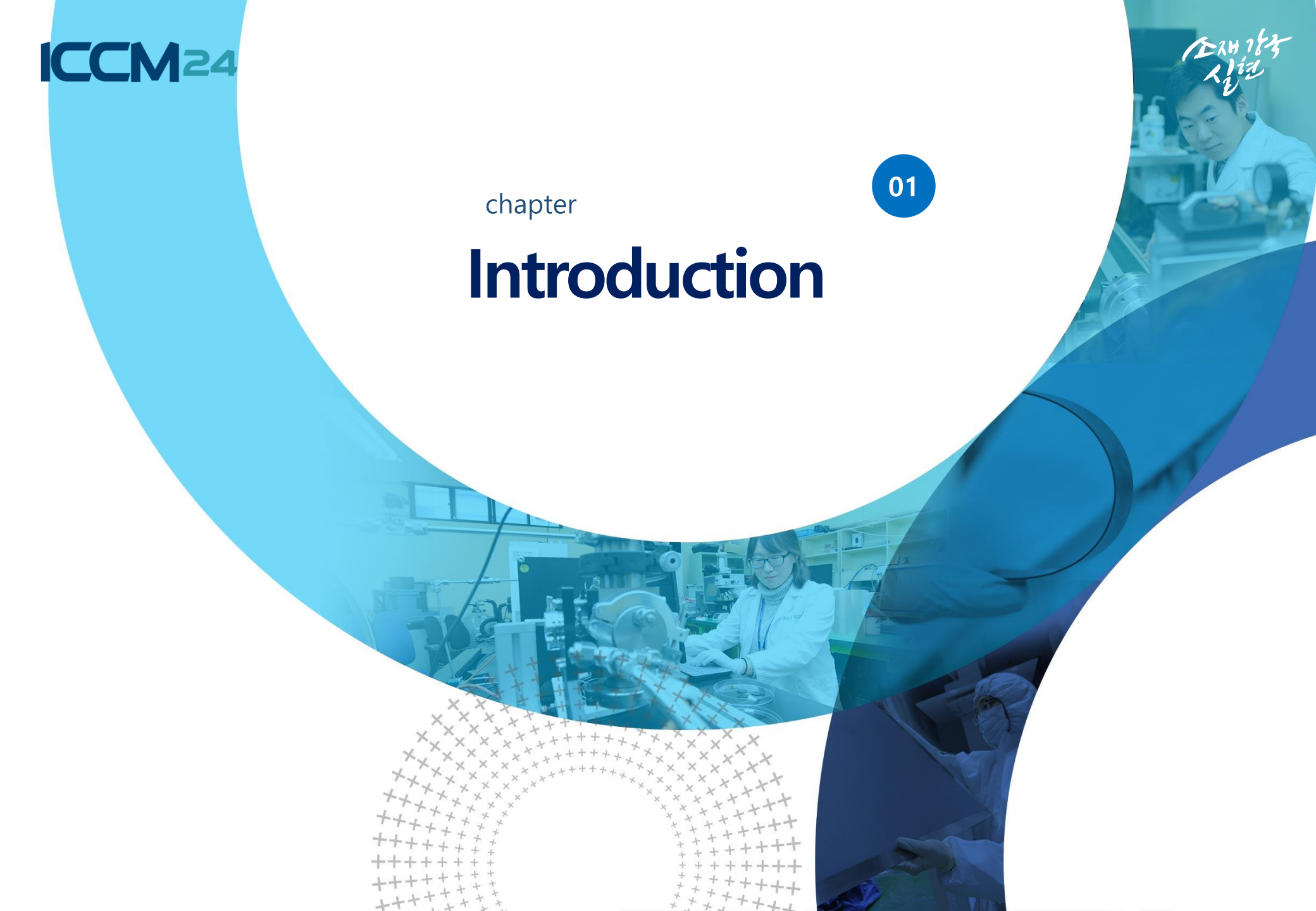

Introduction

Motivation & Background

☑ What is GMT (Glass Mat Thermoplastics)?

- lightweight composite material that uses thermoplastic resin as a matrix and glass fiber mat as a reinforced skeleton

☑ Key Advantages

- High specific strength, Excellent impact resistance
- Good formability for complex shapes
- Recyclability suitable for sustainable applications.

Glass Mat Thermoplastic(GMT) Composites for Automotive Applications

*Source: https://ilucku.com/

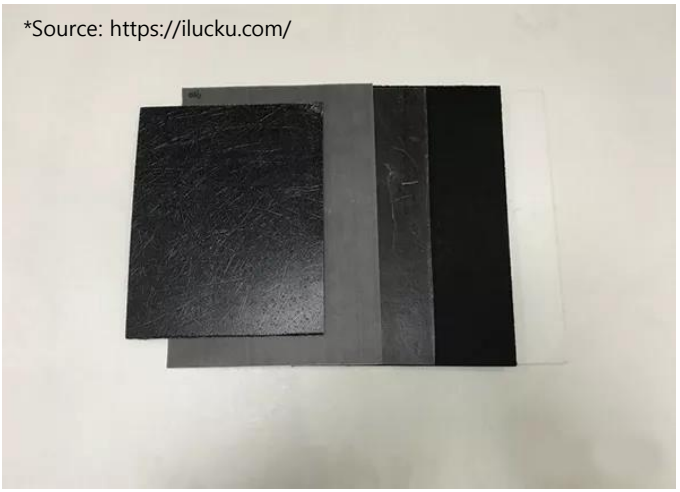

❑ Glass Mat Thermoplastic Sheets

*Source: https://www.fiberglassfiber.com/



❑ Application to automotive parts

- Bumper System
- Battery enclosures
- Under body
- Crash boxes
- Seat frames
- Dashboard
- Others

Motivation & Background

☑ **Failure mode & Crashworthiness of GMT tubes**

- **Stable progressive splaying failure mode** enabled by high toughness of thermoplastic matrix.
- Enhanced **crash energy absorption** significantly

☑ **Modeling & Simulation Requirements**

- **Material modeling** for progressive failure in GMT tube with random fiber orientation
- **Efficient FE modeling** to replicate **both the splaying failure** and **energy absorption response**

☑ **Aim of this study**

- **Analysis of failure and energy absorption behavior** of Advanced GMT Tubes
- **Proposal** of **a practical crash simulation framework** for GMT tubes

	Thermoset composites tube	Thermoplastic composites tube(GMT)
Comparison of Failure modes	 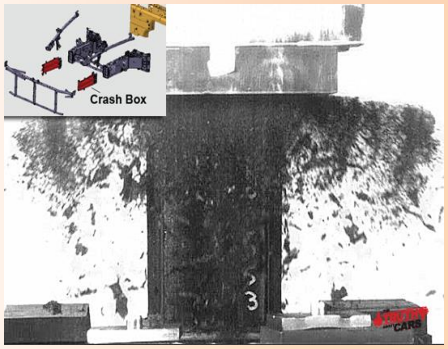	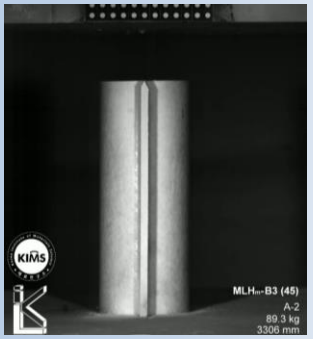 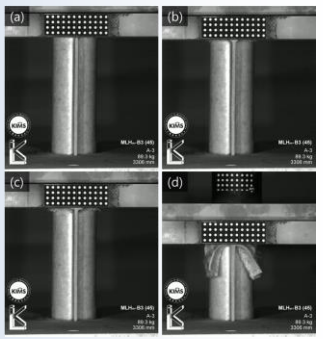
	• Transverse shearing & Fragmentation Mode	• Lamina bending & Splaying Failure Mode

ICCM24

소재강국 실현

chapter 02

Material Characterization

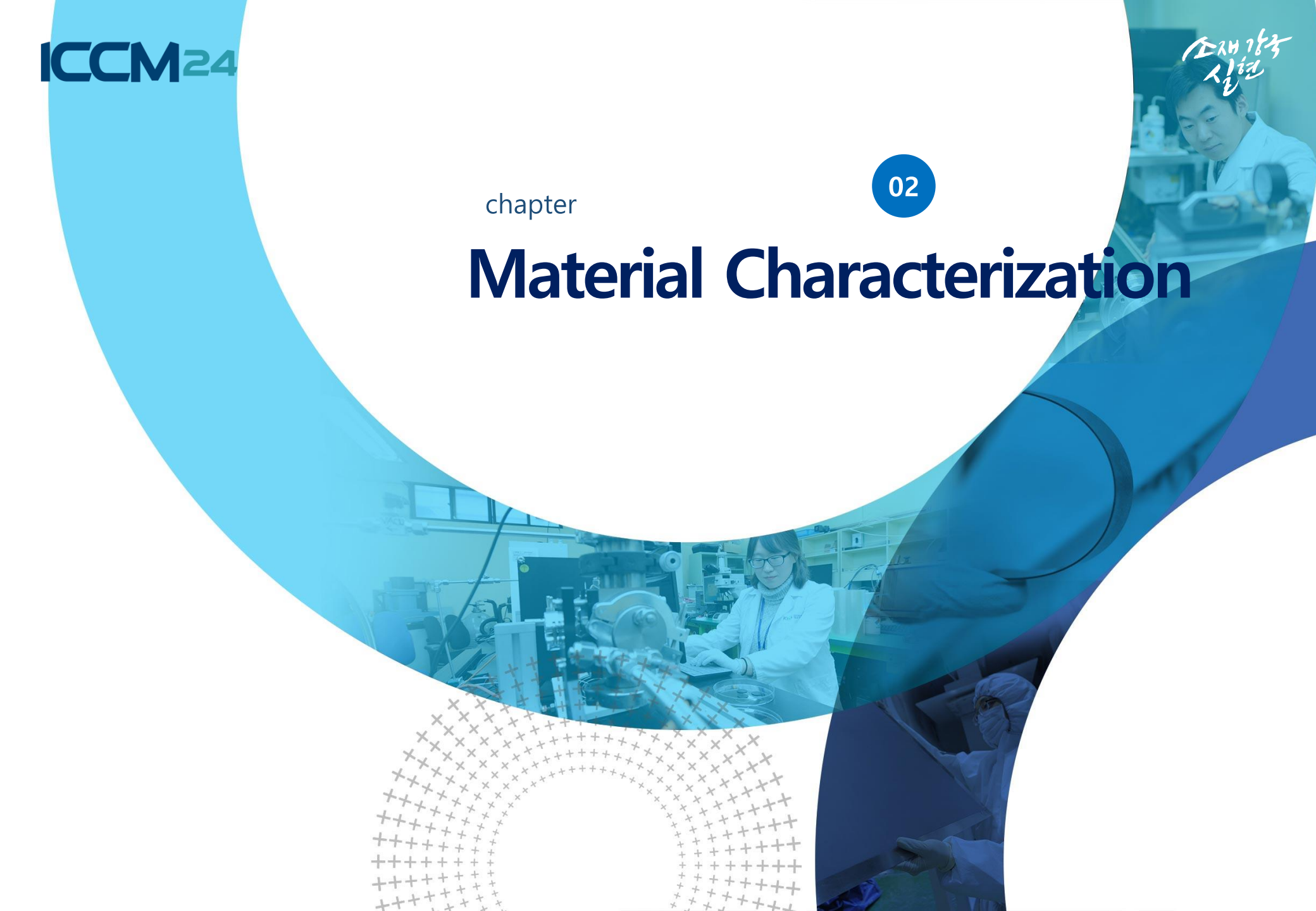

Advanced Glass Mat Thermoplastic

☑ Multi-layered Hybrid(MLH) Mat

- Fabricated by **alternately stacking resin films and chopped long glass fibers**
- **Minimized the resin flow path** improving **the impregnation quality** of high-viscosity **thermoplastic resin**

☑ Fabrication of MLH-mat composites

- GF/PA6 MLH-mat ▶ **Glass fiber mat – 125 g/m², PA6 resin films – 33 g/m²**
- 26 plies stacked to form MLH-mat composite plates ▶ **Total thickness : 2.4 mm , Fiber volume : 40 % vol.**

Multi-layered Hybrid(MLH) mat – Advanced Glass Mat Thermoplastic

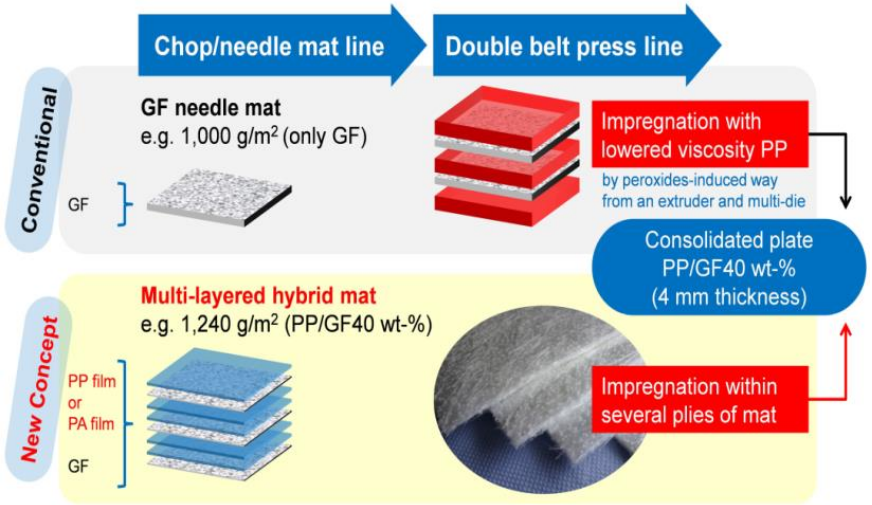

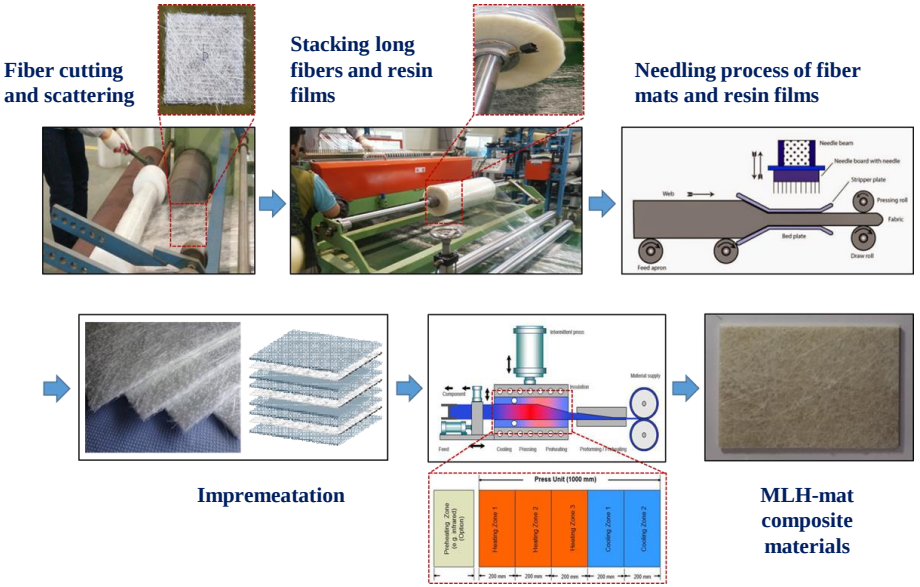

❑ Comparison of conventional GMT and MLH-mat

Mechanical properties and Fracture toughness evaluation

☑ Static mechanical properties

- Tensile, Compressive and In-plane shear Tests results

Static mechanical properties

Tension – ASTM D3039

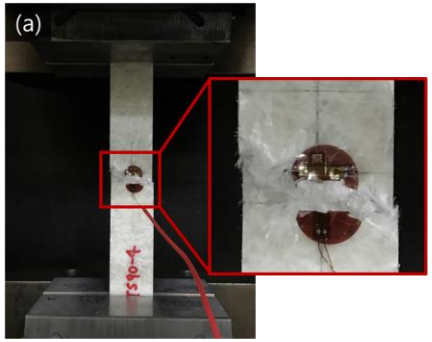

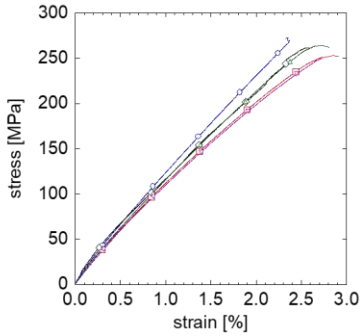

Compression – ASTM D3410

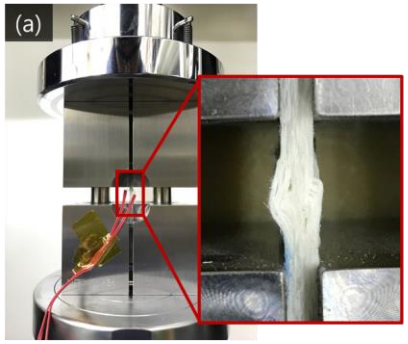

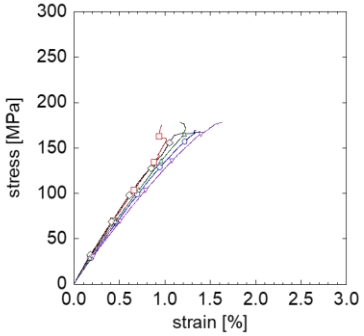

Property	Strength [MPa]	Modulus [GPa]	Poisson's Ratio
Tension in longitudinal dir.	250	13.1	0.32
Tension in transverse dir.	260	12.5	0.32
Compression in longitudinal dir.	174	15.1	-
Compression in transverse dir.	162	14.9	-
In-plane shear	132	5.0	-

Material Characterization

Mechanical properties and Fracture toughness evaluation

☑ Fracture toughness evaluation

- **Inter**-laminar fracture toughness : ❶ Mode I (DCB tests) = 2.74 kJ/m^2 | ❷ Mode II (ELS tests) = 2.34 kJ/m^2
- **Intra**-laminar fracture toughness : ❶ Compact Tension = 37.4 kJ/m^2 | ❷ Compact Compression = 40.2 kJ/m^2

Inter-laminar fracture toughness tests



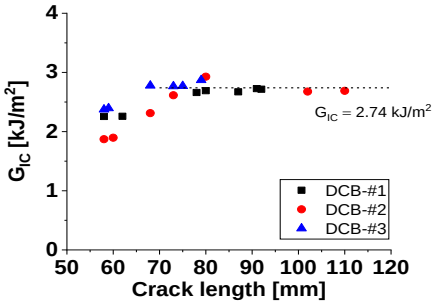

❑ Mode I(Double Cantilever Beam) tests results

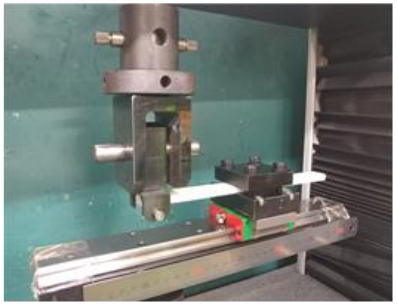

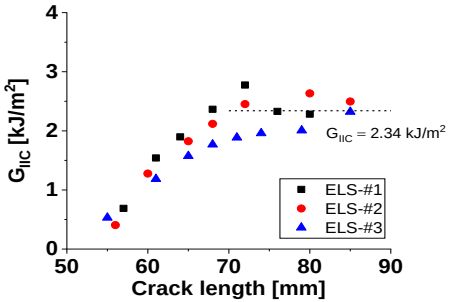

❑ Mode II(End-Loaded Split) tests results

Intra-laminar fracture toughness tests



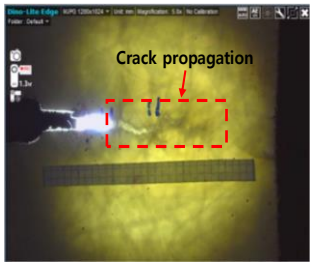

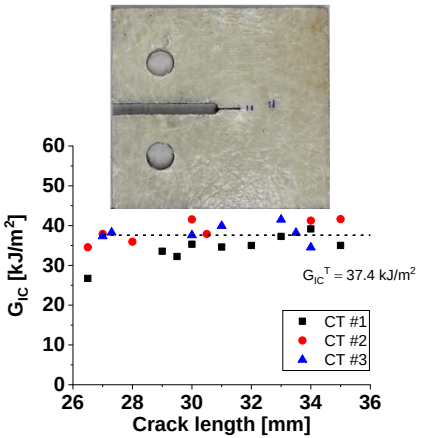

❑ Compact tension

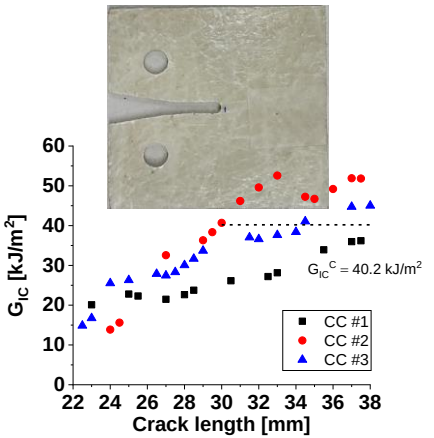

❑ Compact compression

ICCM24

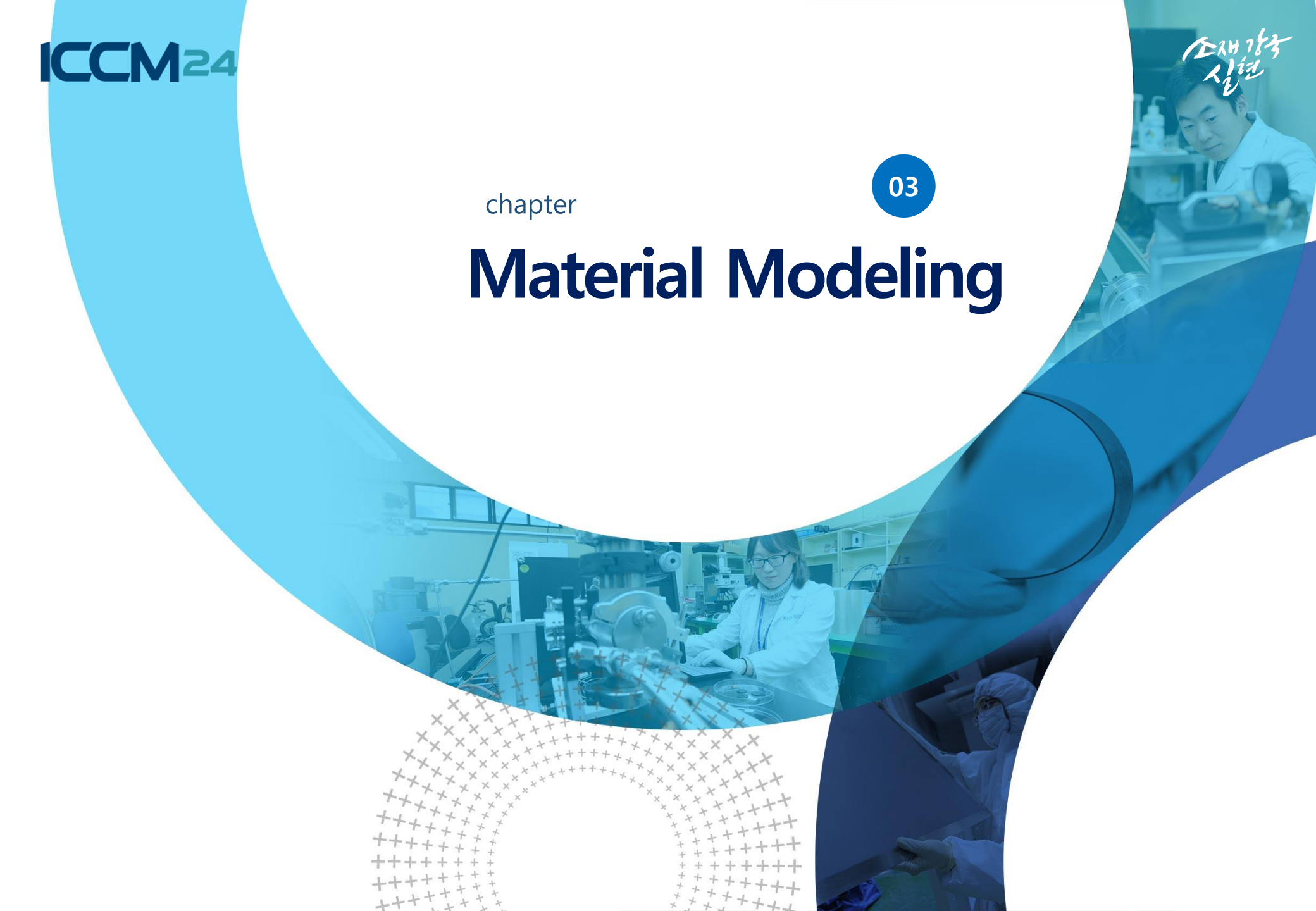

chapter 03

Material Modeling

3D Progressive damage model for MLH-mat composites

☑ Motivation for material modeling of MLH-mat composites

- Requirement for a material model **suitable for randomly oriented fiber-reinforced composites**
- Need for a damage mechanics-based model incorporating experimentally measured fracture toughness

☑ Modeling Strategy – Damage initiation

- Modification of **the 3D Hashin-type failure criterion** for randomly oriented fiber-reinforced composites
- Inclusion of shear stress effects in all directions to reflect matrix-dominated failure

Material modeling for MLH-mat composites

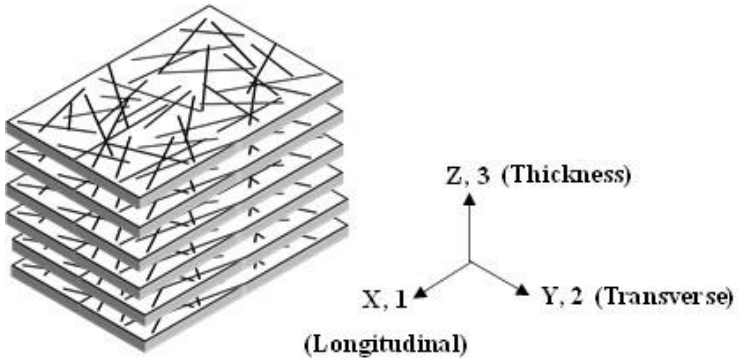

❑ **Schematic diagram of randomly oriented fiber composites**

Failure mode	Damage initiation criteria
$\sigma_{11} \geq 0$	$f_{1T} = \left(\frac{\sigma_{11}}{X_{1T}}\right)^2 + \left(\frac{\sigma_{12}}{S_{12}}\right)^2 + \left(\frac{\sigma_{13}}{S_{13}}\right)^2$
$\sigma_{11} < 0$	$f_{1C} = \left(\frac{\sigma_{11}}{X_{1C}}\right)^2 + \left(\frac{\sigma_{12}}{S_{12}}\right)^2 + \left(\frac{\sigma_{13}}{S_{13}}\right)^2$
$\sigma_{22} \geq 0$	$f_{2T} = \left(\frac{\sigma_{11}}{X_{2T}}\right)^2 + \left(\frac{\sigma_{12}}{S_{12}}\right)^2 + \left(\frac{\sigma_{13}}{S_{13}}\right)^2$
$\sigma_{22} < 0$	$f_{2C} = \left(\frac{\sigma_{11}}{X_{2C}}\right)^2 + \left(\frac{\sigma_{12}}{S_{12}}\right)^2 + \left(\frac{\sigma_{13}}{S_{13}}\right)^2$
$\sigma_{33} \geq 0$	$f_{3T} = \left(\frac{\sigma_{11}}{X_{3T}}\right)^2 + \left(\frac{\sigma_{12}}{S_{12}}\right)^2 + \left(\frac{\sigma_{13}}{S_{13}}\right)^2$
$\sigma_{33} < 0$	$f_{3C} = \left(\frac{\sigma_{11}}{X_{3C}}\right)^2 + \left(\frac{\sigma_{12}}{S_{12}}\right)^2 + \left(\frac{\sigma_{13}}{S_{13}}\right)^2$
Shear failure in 1-2 plane	$f_{12} = \left(\frac{\sigma_{12}}{S_{12}}\right)^2$
Shear failure in 2-3 plane	$f_{23} = \left(\frac{\sigma_{23}}{S_{23}}\right)^2$
Shear failure in 1-3 plane	$f_{13} = \left(\frac{\sigma_{13}}{S_{13}}\right)^2$

❑ **Modification of the 3D Hashin-type damage initiation criterion**

3D Progressive damage model for MLH-mat composites

☑ Modeling Strategy – Damage evolution

- Adoption of **a constitutive model** based on the **Continuum Damage Mechanics(CDM)**
- Simulation of **gradual stiffness degradation** during progressive damage evolution
- Incorporation of **intra-laminar fracture toughness** for realistic simulation of **complex damage mechanisms** in composite structures
- Implementation of the 3D progressive damage model into **LS-DYNA solver** using **UMAT subroutine**

Material modeling for MLH-mat composites

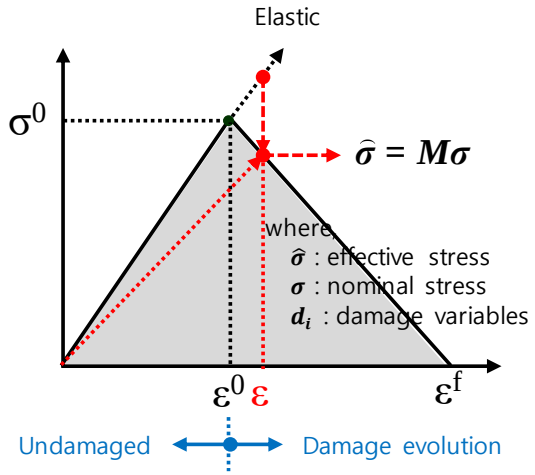

$$\varepsilon = S : \hat{\sigma} = S : M : \sigma = H\sigma \;\Rightarrow\; \sigma = H^{-1}\varepsilon = C_d\varepsilon$$

$$C_d = \begin{bmatrix} C_{11} & C_{12} & C_{13} & 0 & 0 & 0 \\ & C_{22} & C_{23} & 0 & 0 & 0 \\ & & C_{33} & 0 & 0 & 0 \\ & & & C_{44} & 0 & 0 \\ & \textit{Symmetric} & & & C_{55} & 0 \\ & & & & & C_{66} \end{bmatrix} \Rightarrow$$

$$\begin{aligned}
C_{11} &= (1-d_1)E_1[1-(1-d_2)(1-d_3)v_{32}v_{23}]/\Delta \\
C_{22} &= (1-d_2)E_2[1-(1-d_1)(1-d_3)v_{13}v_{31}]/\Delta \\
C_{33} &= (1-d_3)E_3[1-(1-d_1)(1-d_2)v_{12}v_{21}]/\Delta \\
C_{12} &= (1-d_1)(1-d_2)E_1[v_{21}+(1-d_3)v_{31}v_{23}]/\Delta \\
C_{13} &= (1-d_1)(1-d_3)E_1[v_{31}+(1-d_2)v_{21}v_{32}]/\Delta \\
C_{23} &= (1-d_2)(1-d_3)E_2[v_{32}+(1-d_1)v_{12}v_{31}]/\Delta \\
C_{44} &= (1-d_{12})G_{12} \\
C_{55} &= (1-d_{23})G_{23} \\
C_{66} &= (1-d_{13})G_{13}
\end{aligned}$$

$$\Delta = 1-(1-d_2)(1-d_3)v_{32}v_{23}-(1-d_1)(1-d_3)v_{31}v_{13}-(1-d_1)(1-d_2)v_{21}v_{12}-2(1-d_1)(1-d_2)(1-d_3)v_{13}v_{21}v_{32}$$

❑ **progressive constitutive model based on continuum damage mechanics**

ICCM24

chapter 04

Crush Test & Simulation

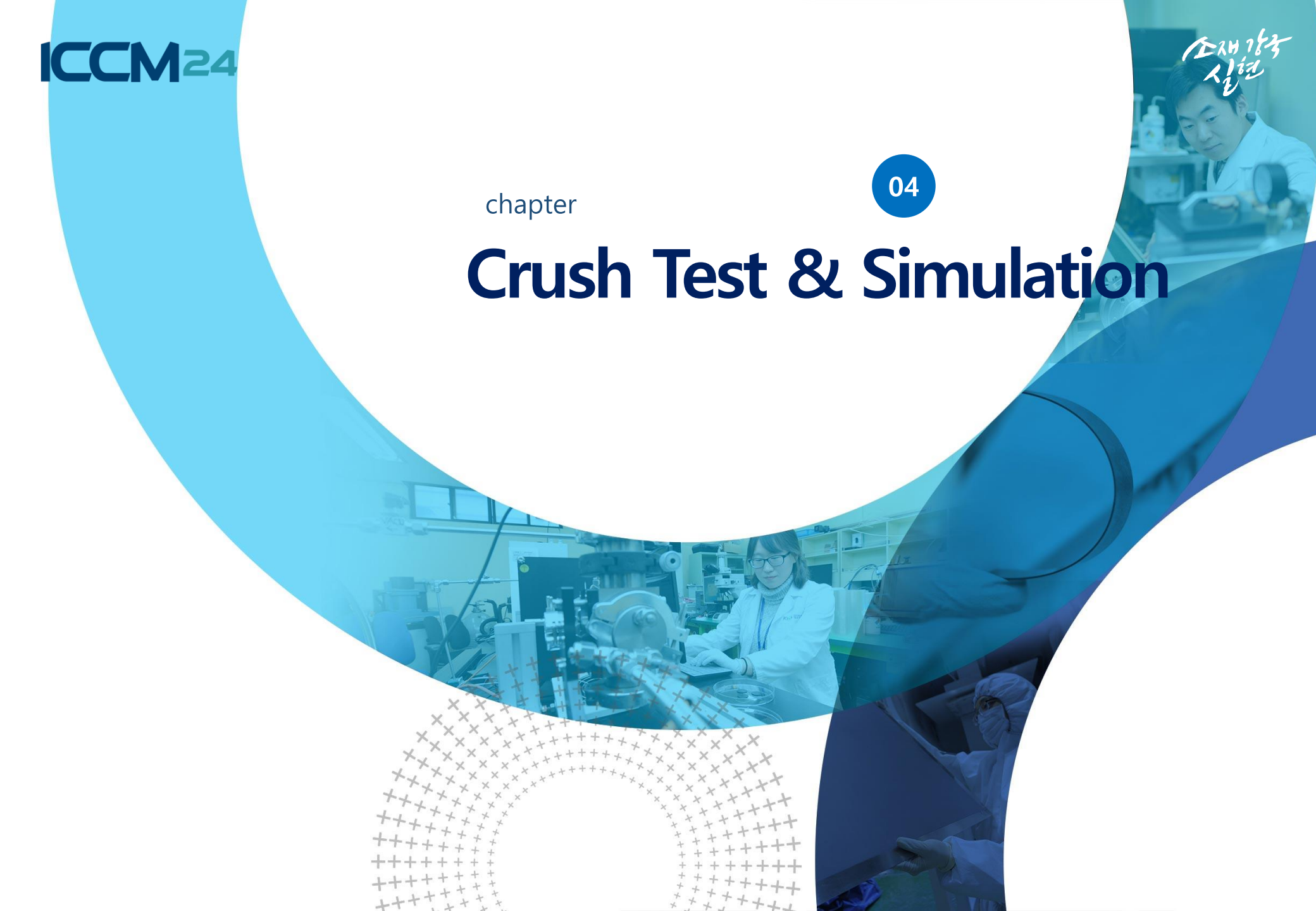

Crush Test & Simulation

ICCM24

Crush tests of the MLH-mat Tubes

☑ Specimen preparation

- **Shape** : A circular cylindrical shell with flat vertical flanges on both sides
- **Fabrication process** : Hot forming of two half-shells with flat flanges, followed by thermal fusion bonding along the flanges

☑ Test Conditions & Results

- **Test conditions** : ❶ Impactor Mass = 90.9 kg | ❷ Impact velocity = 7.86 m/s
- **Test Results(Ave.) :** ❶ Specific Energy Absorption(SEA) = 48.9 J/g | ❷ Crush depth = 57.9 mm

Crush Tests of the MLH-mat Tubes

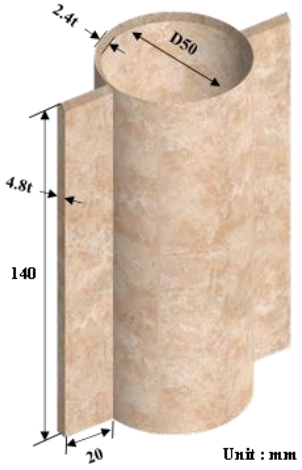

❑ **Specimen dimension**

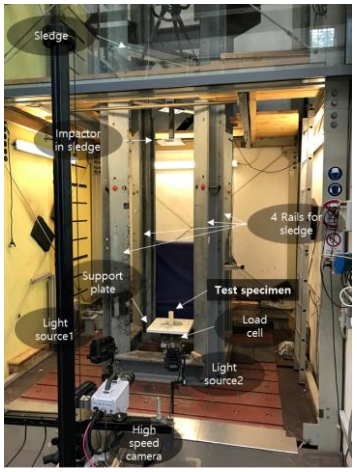

❑ **Crush test setup**

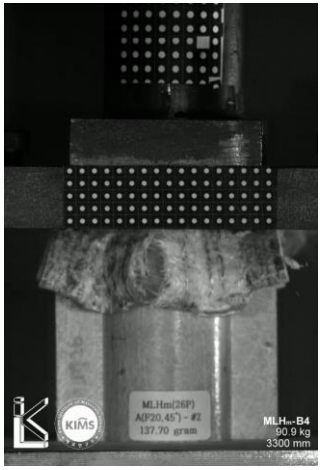

❑ **Crush test results (Final shape | Force–displacement curves)**

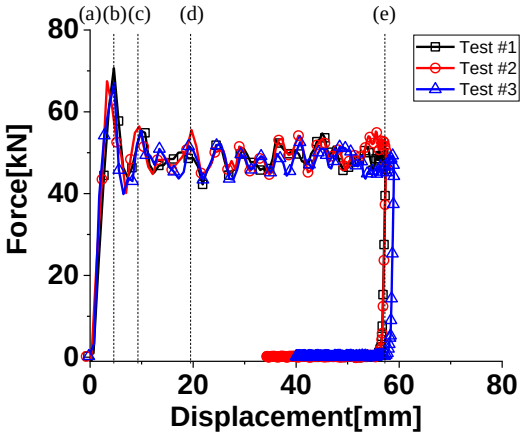

KIMS 한국재료연구원 Korea Institute of Materials Science

Crush Test & Simulation

Crush Simulation of MLH-mat Tubes

☑ FE model of the MLH-mat tube

- **Solid elements with four layers along the thickness direction** to enhance computational efficiency
- **Cohesive elements** embedded **at the mid-plane of the MLH-mat tube** to enable **the splaying failure mode**
- Rigid body elements used for the impactor, matching the conditions of the physical crush test

☑ Material model

- **MLH-mat material** ⇒ Proposed 3D Progressive damage model
- **Interlaminar behavior** ⇒ Cohesive material model (MAT_COHESIVE_MIXED_MODE in LS-DYNA)

Crush Tests of the MLH-mat Tubes

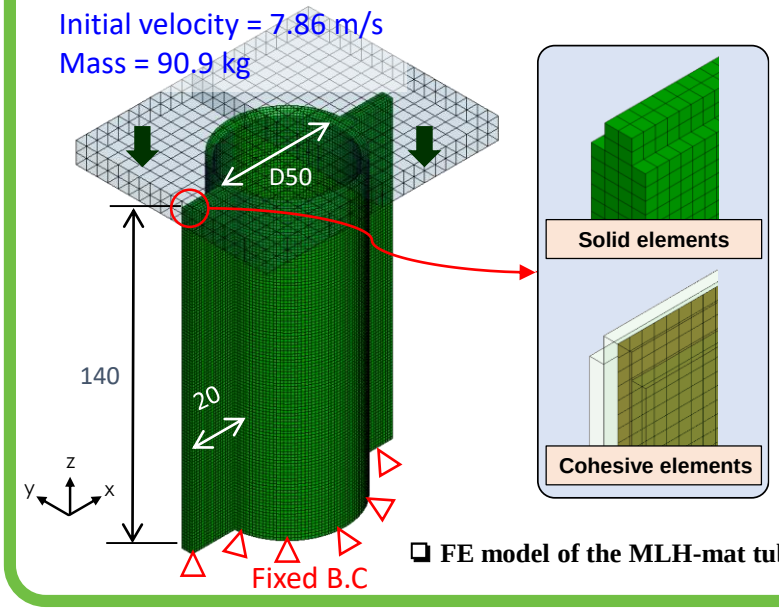

❑ FE model of the MLH-mat tube

Stiffness	E_1 [MPa]	E_2 [MPa]	E_3 [MPa]	G_{12} [MPa]	G_{23} [MPa]	G_{13} [MPa]	v_{12}	v_{23}	v_{13}
	13,100	12460	12460	5032	5032	5032	0.32	0.32	0.32
Strength	$X1T$ [MPa]	$X1C$ [MPa]	$X2T$ [MPa]	$X2C$ [MPa]	$X3T$ [MPa]	$X3C$ [MPa]	S12	S23	S13
	250	174	260	162	260	162	132.8	132.8	132.8
Fracture toughness	G1T[kJ/m²]	G1C [kJ/m²]	G2T [kJ/m²]	G2C [kJ/m²]	G3T [kJ/m²]	G3C [kJ/m²]			
	112.9	37.9	112.9	37.9	112.9	37.9			

Intra-laminar fracture toughness

❑ Material parameters of the proposed 3D progressive damage model

1	MID	RO [g/m³]	ROFLG	INTFAIL	EN	ET	GIC	GIIC
	3	3.30e-5	1.0	1.0	3,000	3,000	2.88 (To be Calibrated)	2.30 (To be Calibrated)
2	XMU	T	S	UND	UTD	GAMMA		
	1.0	80.0	80.0	0	0	1.0		

Inter-laminar fracture toughness

❑ Material parameters of the cohesive material model

Crush Test & Simulation

Crush Simulation of MLH-mat Tubes

☑ Initial simulation result

- **Observation of a stable splaying failure mode** enabled by **cohesive element deletion** under impact loading
- **Underestimation of energy absorption performance** due to **simplified modeling of interlaminar fracture**
  - **FE simulation** → Interlaminar fracture **only considered at the mid-plane of the tube** for **computational efficiency**
  - **Actual test** → Interlaminar fracture **observed at multiple ply interfaces** throughout the thickness
- **Necessary to calibrate interlaminar fracture toughness** to match the **experimental energy absorption performance**

Crush Simulation Results before calibration

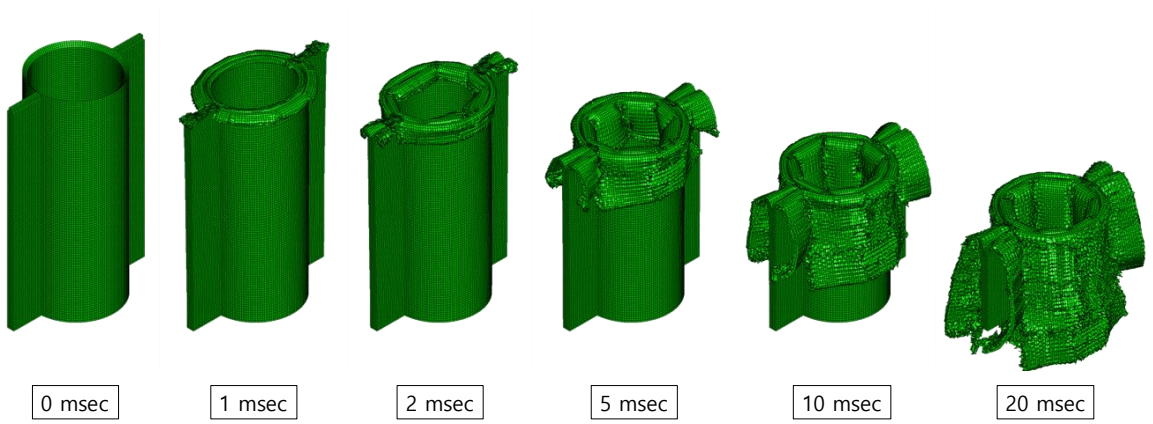

❑ **Sequential images of the MLH-tube in the initial crush simulation**

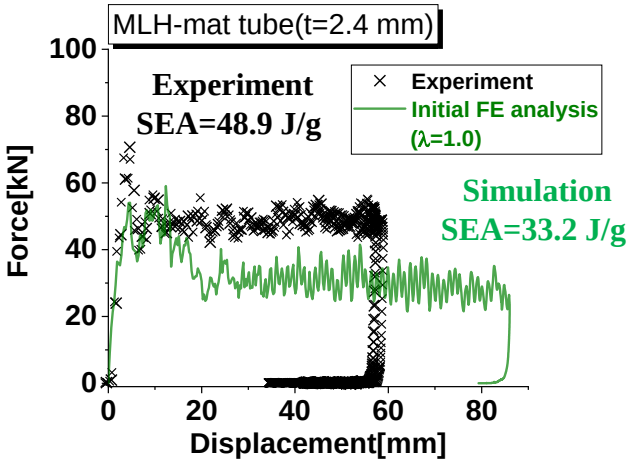

❑ **Force–displacement curve of crush simulation before calibration**

Crush Test & Simulation

Crush Simulation of MLH-mat Tubes

☑ Calibration for interlaminar fracture toughness

- **Proposal of a fracture toughness correction factor (λ)** to adjust the **interlaminar fracture toughness value** for crash analysis
- **Definition of λ** as a **multiplier** applied to **Mode I and Mode II fracture toughness** from **experimental tests**
- **Establishment of an objective function** based on the **difference between force–displacement curves from test and simulation**
- **Optimization of λ** using LS-OPT with the **response surface method**, finally **converged to 6.87**

Crush Simulation Results before calibration

❑ **Fracture toughness correction factor(λ)**

$$G_{IC}^{FEA} = \lambda \cdot G_{IC}^{Exp}$$

$$G_{IIC}^{FEA} = \lambda \cdot G_{IIC}^{Exp}$$

❑ **Definition of object function**

Find λ

To minimize

$$f(\lambda) = \sqrt{\frac{1}{n}\int_{i=0}^{n}\left(y(x_i) - \hat{y}_\lambda(x_i)\right)^2}$$

Subjected to $\mathbf{1 \le \lambda \le 10}$

$y(x_i)$: Force from simulation
$\hat{y}_\lambda(x_i)$: Force from tests

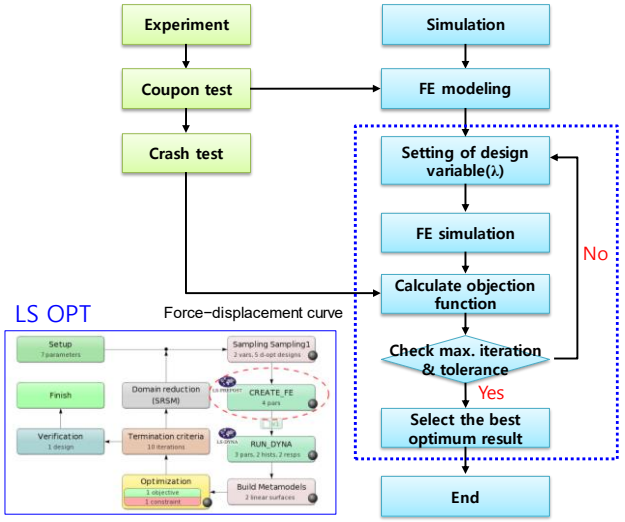

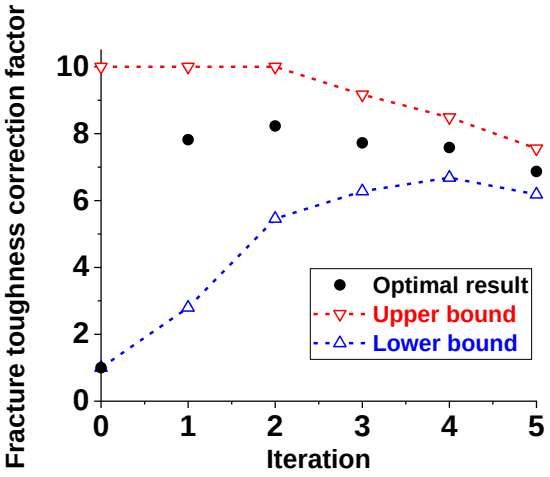

❑ **Optimization of calibration parameter for interlaminar fracture toughness using LS-OPT**

Crush Test & Simulation

Crush Simulation of MLH-mat Tubes

☑ Simulation results after calibration

- **Visualization of stable crushing** and **complete energy absorption** in the **optimized crush analysis**
- **Increase in mean crash force** and **energy absorption,** reaching values **comparable with experimental results**
  ⇒ **Prediction Results :** ❶ SEA = 48.4 J/g | ❷ Crush depth = 60.3 mm
- **Excellent agreement** with experimental results, with **small deviation** of **1.02% for SEA,** and **4.14% for crush depth**
- **Confirmation of λ as a critical factor** in **improving prediction accuracy** of crash energy absorption for the MLH-mat tube

Crush Simulation Results after calibration

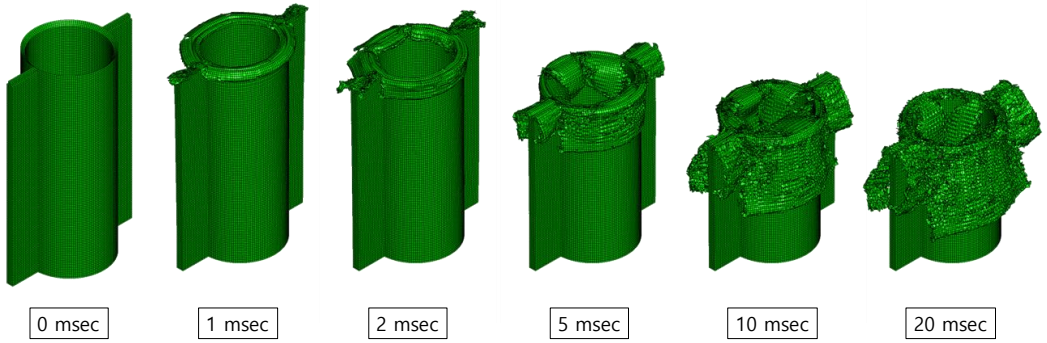

❑ **Sequential images of the MLH-tube in crush simulation after calibration**

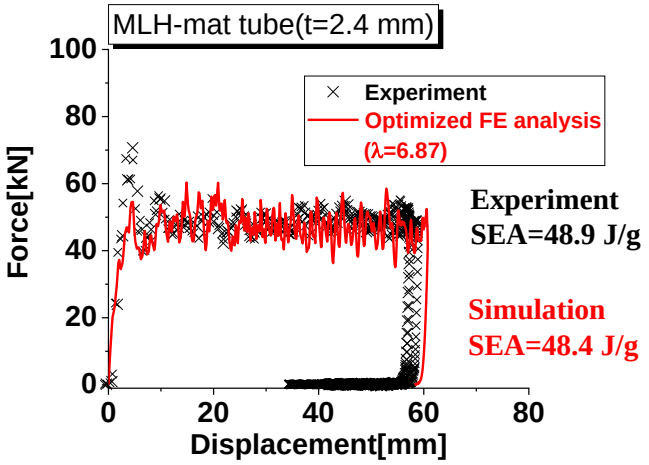

❑ **Force–displacement curves of crush simulation after calibration**

Crush Test & Simulation

Crush Simulation of MLH-mat Tubes

☑ Failure mechanism and energy absorption

- **Identification** of the **splaying failure mechanism** through optimized crush simulation and comparison with test results
- **Observation of Mode I delamination** as the **dominant cause of splaying**, triggered by **debris wedge formation** at the crash front
- **Quantitative analysis** showing **interlaminar failure contributes to 39.4%** and **intralaminar failure to 61.6%** of total absorbed energy
- **Emphasis on** the critical role for **accurate estimation** of **energy absorption by interlaminar failure**

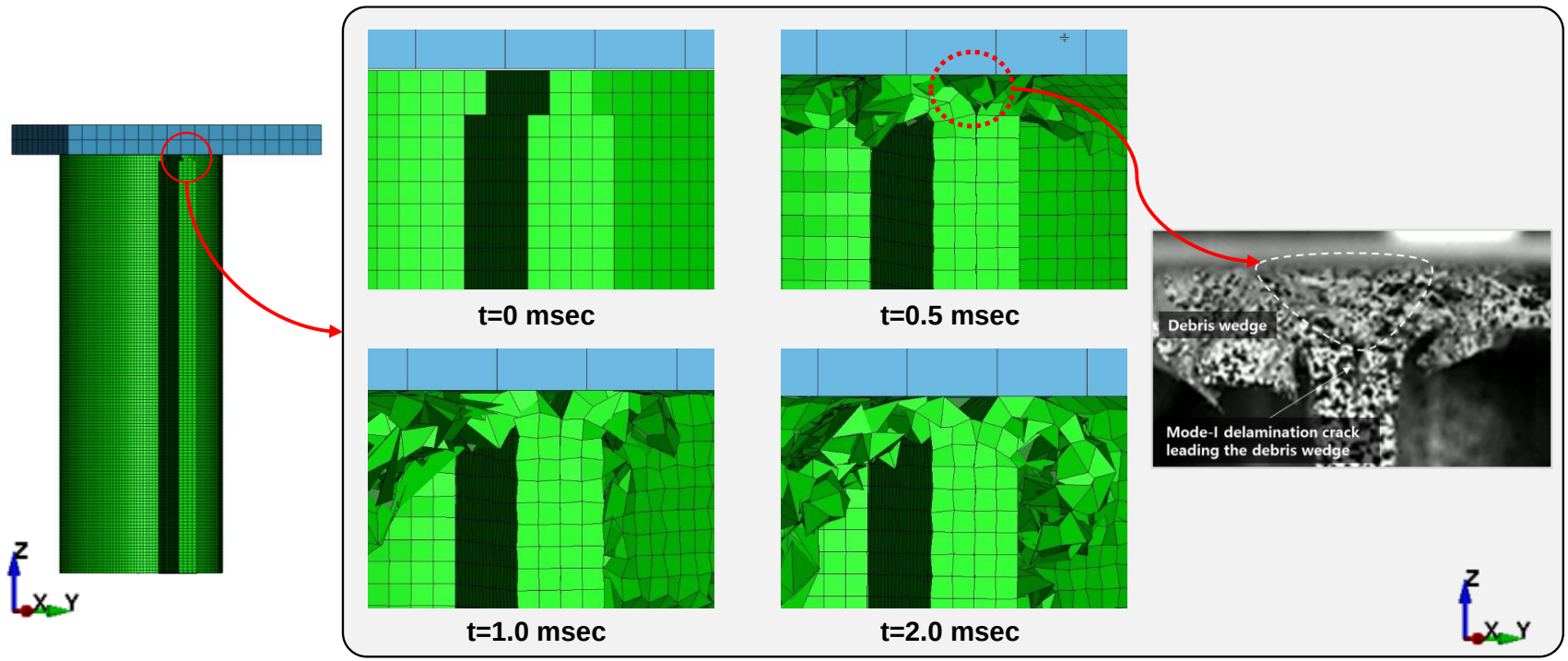

Crush Test & Simulation

Crush Simulation of MLH-mat Tubes

☑ Validation under geometry variation

- **Necessary to validate applicability** of the proposed crush **simulation method** under **tube geometry variation**
- **Application of the same correction factor (λ = 6.87)** to **tubes** with **2.3 mm** and **3.1 mm** thickness
- **Consistent crush simulation results** with **test results** within **deviation of 5.1%** for **SEA** and **crush depth**
- **Demonstration of reliability and applicability for the proposed method** under **moderate geometric changes** without **re-calibration**

Validation of the proposed method for dimensional variation



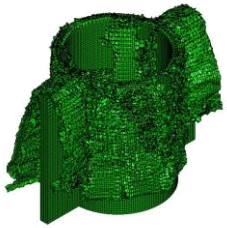

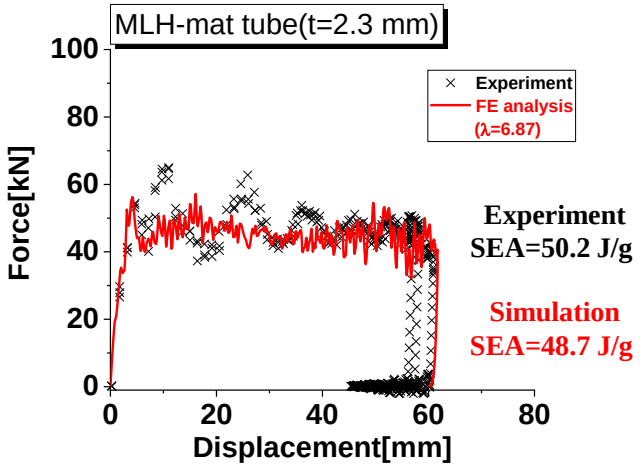

❑ Crush test and simulation results (Thickness = 2.3 mm)



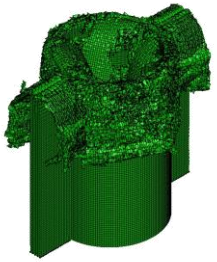

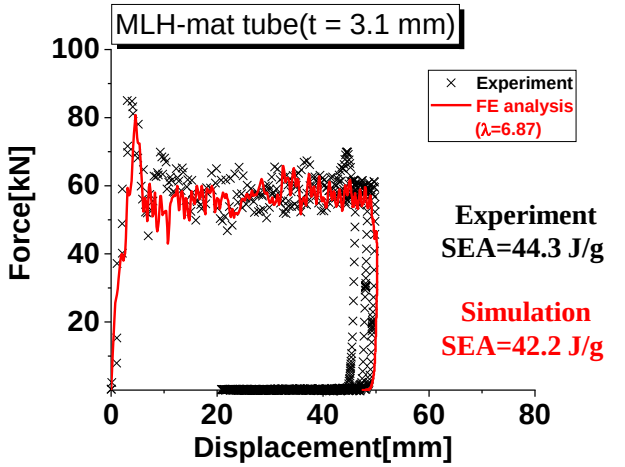

❑ Crush test and simulation results (Thickness = 3.1 mm)

ICCM24

chapter 04

Conclusion

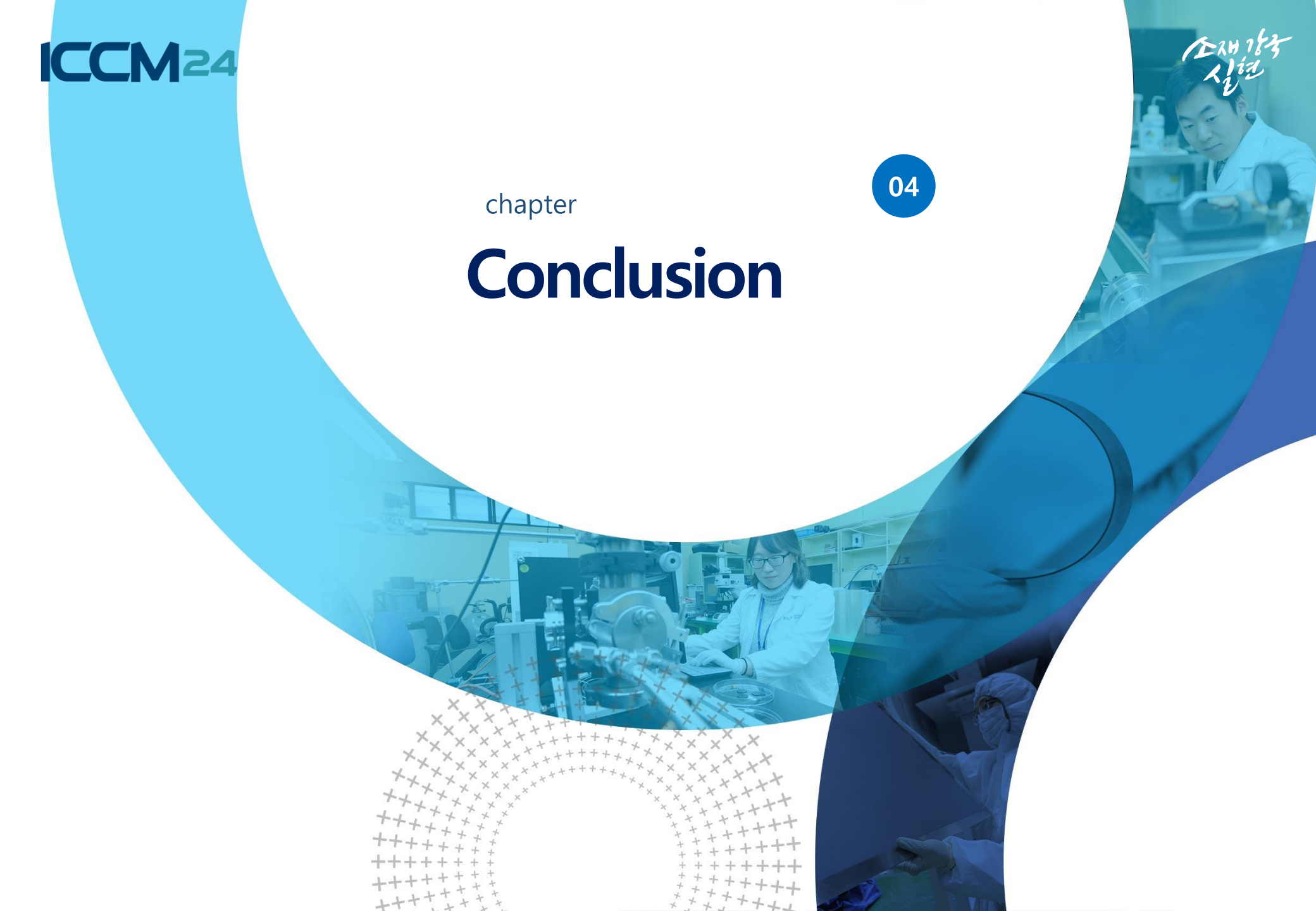

Conclusions

☑ **Characterized** the mechanical properties and fracture toughness of **the MLH-mat material**, confirming its quasi-isotropic behavior due to **random fiber orientation**

☑ **Developed** a crash analysis method using a **3D progressive damage model** and **mid-plane cohesive elements** to **simulate splaying failure**

☑ **Introduced** a **fracture toughness correction factor (λ)** and optimized it to ensure **accurate prediction of energy absorption**

☑ **Proposed a practical crush analysis framework** for industrial application, demonstrating **reliable performance** under **moderate geometric variation.**

ICCM24

24TH INTERNATIONAL CONFERENCE ON COMPOSITE MATERIALS

AUG 4-8, 2025 • BALTIMORE CONVENTION CENTER • BALTIMORE, MARYLAND

KIMS 한국재료연구원
Korea Institute of Materials Science

Thanks for your kind attention



ICCM24
AUGUST 4-8, 2025
BALTIMORE CONVENTION CENTER
BALTIMORE, MARYLAND, USA

No Technical Paper Submission for:

Paul Dason Samuel

ICCM24
AUGUST 4-8, 2025
BALTIMORE CONVENTION CENTER
BALTIMORE, MARYLAND, USA

No Technical Paper Submission for:

Marco Salviato

U.S. ARMY

U.S. ARMY COMBAT CAPABILITIES DEVELOPMENT COMMAND ARMY RESEARCH LABORATORY

Influence of Consolidation Pressure on Tensile Strength of Ultra High Molecular Weight Polyethylene Composites

27 JUNE 2025

Molla Ali, Travis A. Bogetti, Michael Yeager,
Joseph M. Deitzel, Jack Gillespie

Distribution Statement A: Approved for public release: distribution is unlimited.

Background



https://www.army-technology.com/contractors/personal/dsm-dyneema/





https://www.samsonrope.com/resources/defense/air



https://www.freepik.com/premium-photo/fully-equipped-special-forces-military-unit-tactical-gear-wartime-ai_42288360.htm

- Ultra High Molecular Weight Polyethylene UHMWPE is unique for its low density and high tensile strength
- It is light weight and provides higher protection
- This is used in high velocity impact resistant applications: protective shields, armored vehicles, helmets, bulletproof vests, short arrest systems for aircraft

Goal of the Program

Goal: Understand how consolidation process variables Temperature(T), Pressure(P) and time (t) control composite microstructure (*Reduce voids, Increase fiber volume fraction, Minimize filament damage*) to improve composite performance (*Reduce weight, Maintain Performance, Reduce dynamic deflection, Maximize energy absorption*).



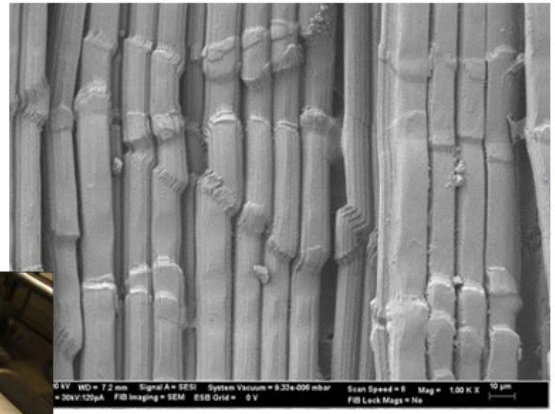

Scale



Virgin SK99 Fibers

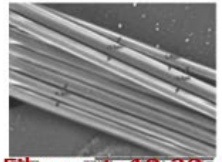

AFM Images of Microtomed Post-Draw Fibers

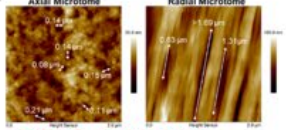

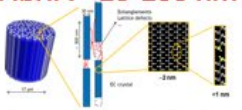

Objectives and Approach

OBJECTIVES:

- Study the tensile strength of UHMWPE composites as a function of consolidation pressure
- Study the void fraction and thickness reduction as a function of consolidation pressure
- Study the consolidation pressure induced micro damage on the UHMWPE sheet composites
- To understand the tension failure modes and damage mechanisms
- To have a correlation of fiber strength to [0/90/0/90] sheet strength taking void and compressive strain into account
- To have insight on how to improve the Tension performance of this material

APPROACH:

- To develop an experimental methodology for tension test of UHMWPE composites
- To develop lab scale consolidation of UHMWPE following the exact thermal and pressure profile prescribed by DSM Dyneema
- To perform tension test on unconsolidated HB210 WHMWPE thin sheets and composites consolidated at various pressures [1ksi, 2ksi,3ksi, 6.5ksi,8.25ksi & 10ksi]
- Consolidation pressure induced micro damage analysis
- Results and discussions

Overview of the Test Methods

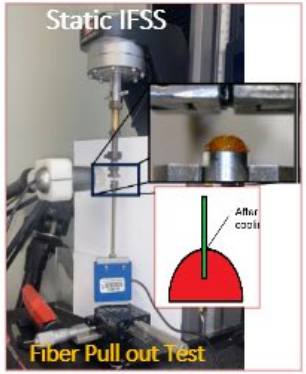

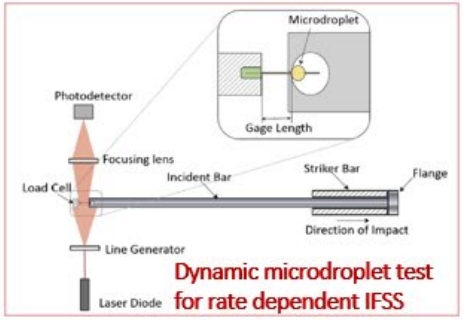

IFSS: Interfacial shear strength

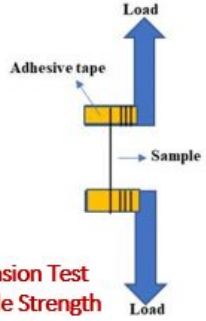

Fiber Tension Test
for Tensile Strength

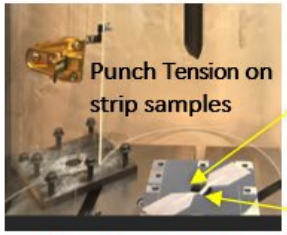

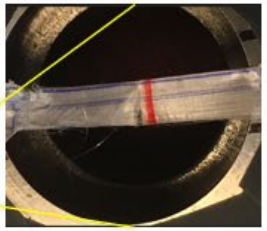

- Vertical load applied
- Specimen failed in tension
- Include tension and in plane shear



- Include tension, in plane shear, punch shear which are useful for studying mixed loading that occurs during impact



- Tension properties can be achieved directly from axial tension of sheets
- It enables effects of consolidation pressure on microstructure and tension properties to be quantified
- Challenge is the slippage in the grip

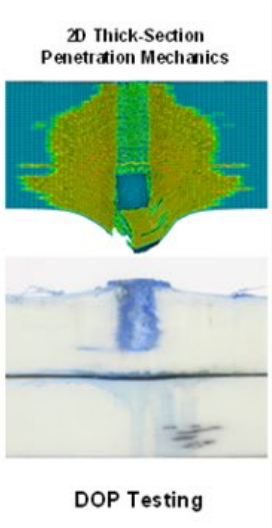

Development of Tension Experiment

UNIVERSITY OF DELAWARE
CENTER FOR COMPOSITE MATERIALS
Celebrating 50 Years

- Instron: 1331
- Load cell: 100kN
- Grips: Hydraulic
- Clamp Pressure: 2ksi
- Displacement rate = 0.05 in/min

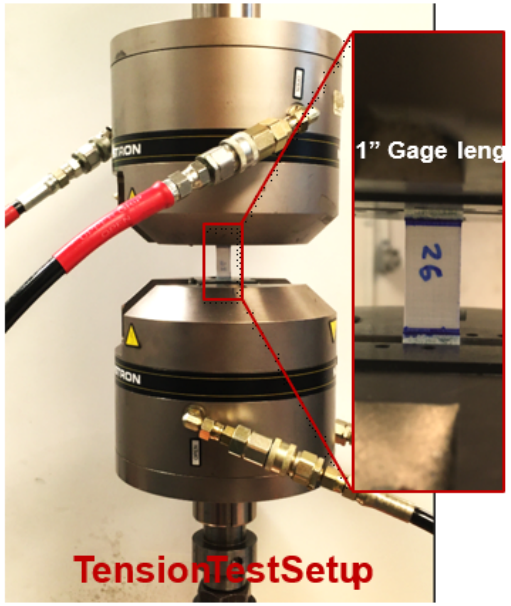

Specimen prep

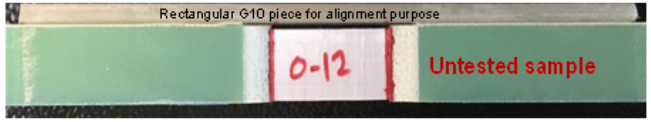

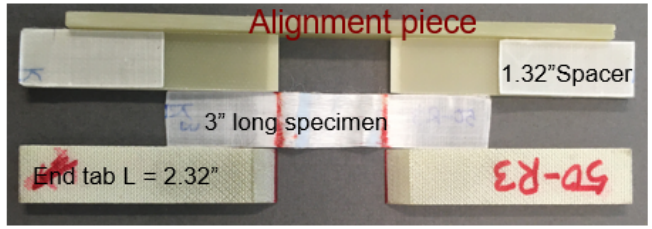

All pieces have been assembled and kept in place with the help of tape

Specimen Dimensions:

- Specimen Length : L = 5.64" [1.32" Spacer + 3" Sample + 1.32" Spacer]
- Width W = 0.5"
- Thickness T = 0.157 ± 0.006 mm
- Tab: L = 2.32"
  W = 0.6"
- Gage Length = 1"
- Specimen & Spacers are Consolidated at same Pressure

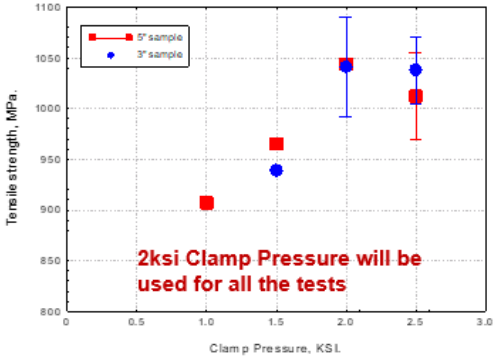

Tensile Strength vs Clamp pressure

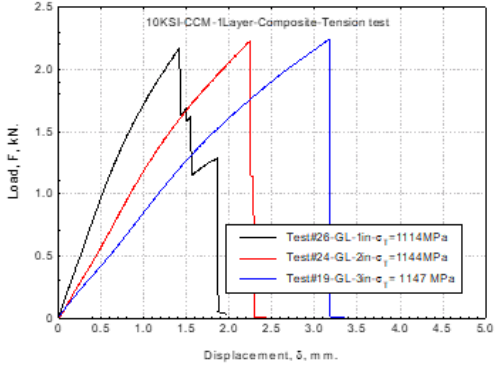

Load vs Displacement of Tension Test with Gage Length GL = 1", 2" & 3"

Consolidation Process of 1L Dyneema Sheets

UNIVERSITY OF DELAWARE
CENTER FOR COMPOSITE MATERIALS
Celebrating 50 Years

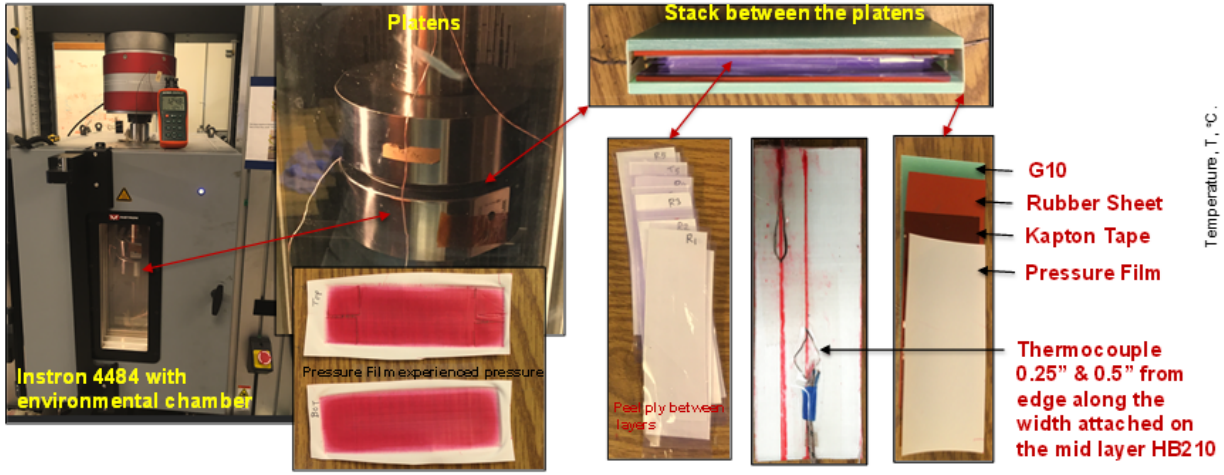

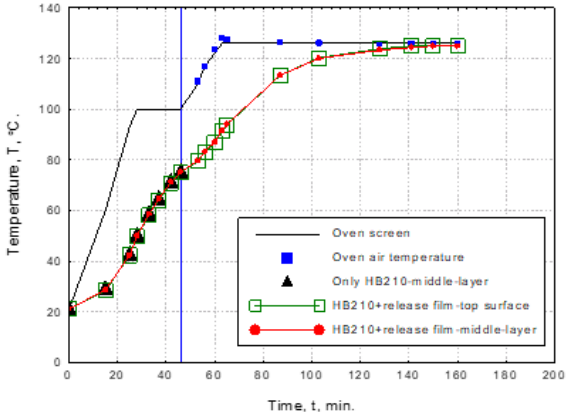

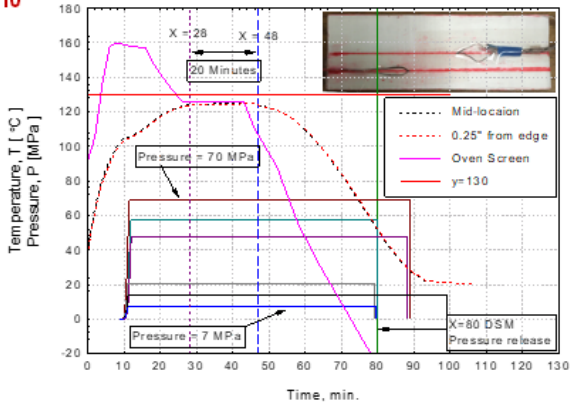

- Pressure Source: Instron 4484, Load Cell: 150kN
- Heat source: Environmental Chamber
- Two identical Metal platens have been used on top and bottom
- Both the setup and the material stack arranged in a symmetric way
- No noticeable temperature gradient through the thickness of the stack with & without separation film [release film]
- Oven air temperature is recorded to validate oven screen temperature and found to be identical
- Temperature along the width of the sample recorded 0.25" &0.5" inside from the edge location of the middle layer and found to be the same
- Pressure films have been used on the top & bottom layer which show uniform pressure distribution

Material Under Study: Dyneema HB210

UNIVERSITY OF DELAWARE
CENTER FOR COMPOSITE MATERIALS
Celebrating 50 Years

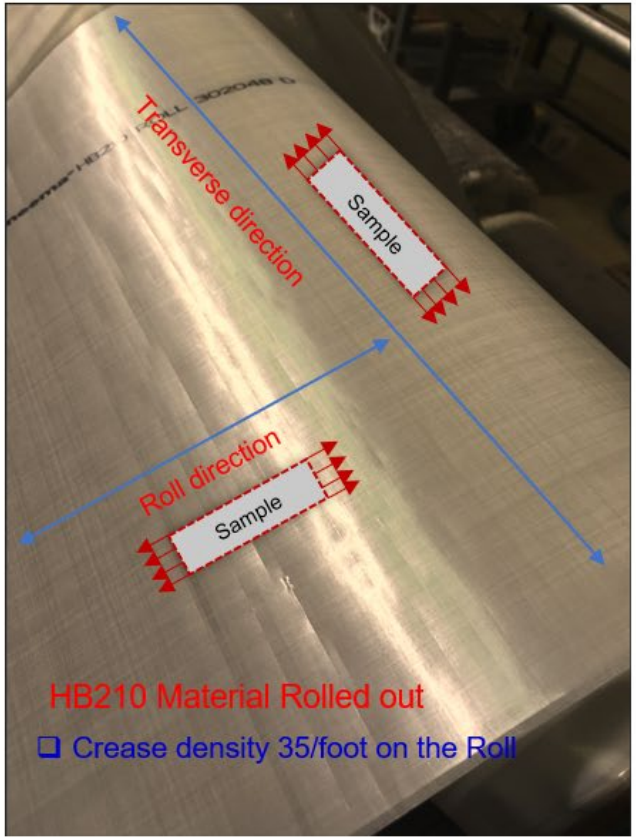

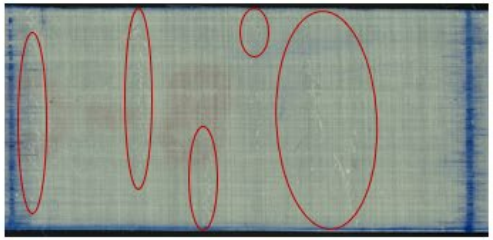

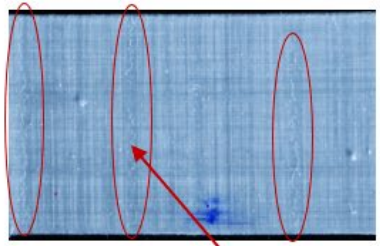

Every crease is not similarly severe & all the creases are not continuous from one edge to the other in the gage section of the samples

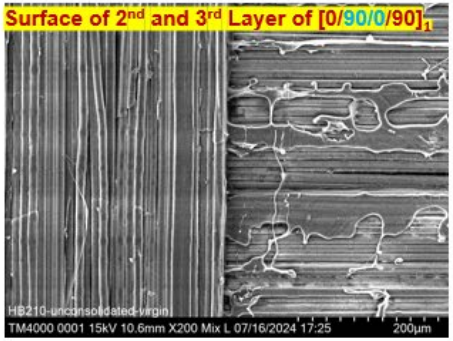

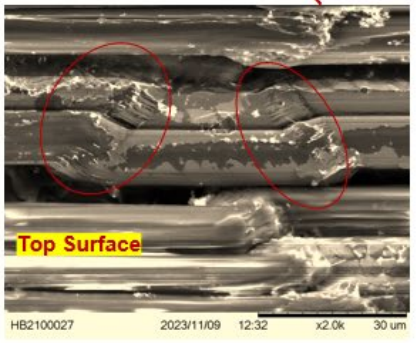

- ❑ Lots of Crease visible on the unconsolidated Dyneema HB210 surface
- ❑ Crease density 4/inch on a 3" X 1" sample
- ❑ Crease direction is parallel to transverse direction
- ❑ Roll samples have crease defects but not transverse samples
- ❑ Crease kinks introduce more voids in the material
- ❑ Resin Reach & resin Lean Areas are Observed inside the $[0/90/0/90]_1$ Sheet

Representative Failure modes in Videos

Roll direction test video

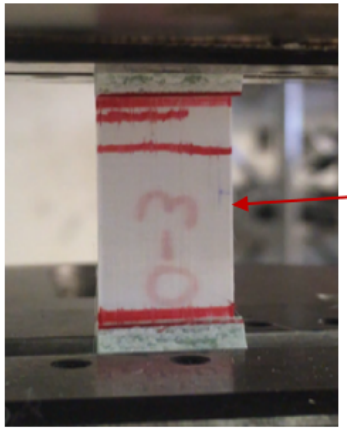

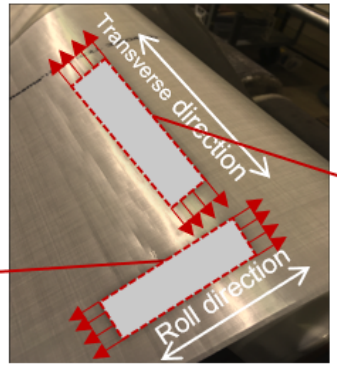

Transverse direction test video



- Transverse samples have been picked to study the effect of consolidation pressure on tensile strength to avoid the effect of original crease defects

- Fails progressively [these samples have crease effect]
- Fibers fail in a cluster at a location then another location, then another location & eventually catastrophic failure happens at the end

- Roll direction samples show 7% strength reduction due to creases
- Transverse sample is least sensitive for creases

- Fails instantaneously [these samples don't have crease defect in the load carrying fibers]
- In some cases, fiber failure initiates in a cluster at a location but in a moment catastrophic failure happens all over

Representative Failure Modes in Pictures

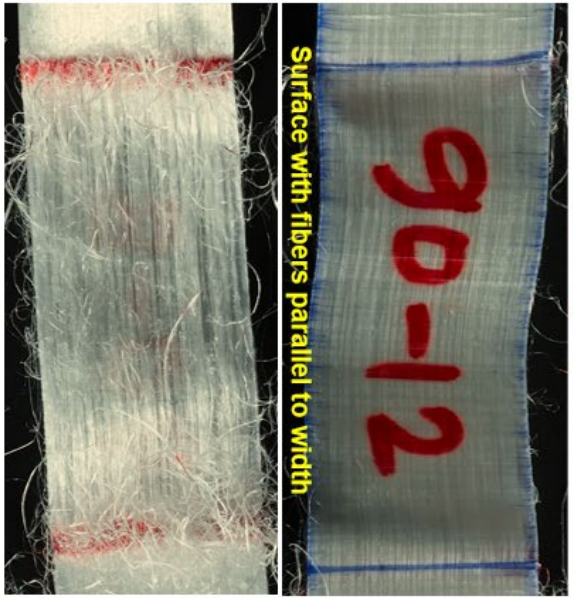

Transverse direction tested sample



Tested sample pulled in loading direction separates into two pieces as above pictures

- Sample surface with fibers parallel to the loading direction shows catastrophic failure
- but surface with fibers perpendicular to loading direction don't show failure as they don't carry load



Roll direction tested sample

Load vs Displacement & Stress vs Strain Plots of UHMWPE

Load vs Displacement

Stress Vs Strain

Unconsolidated

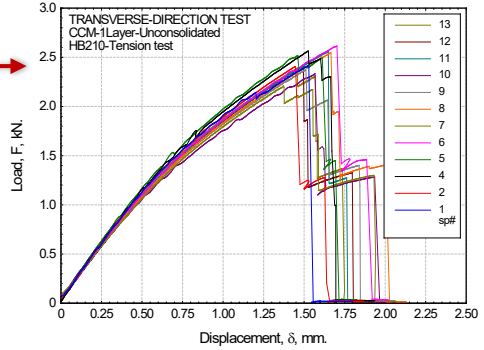

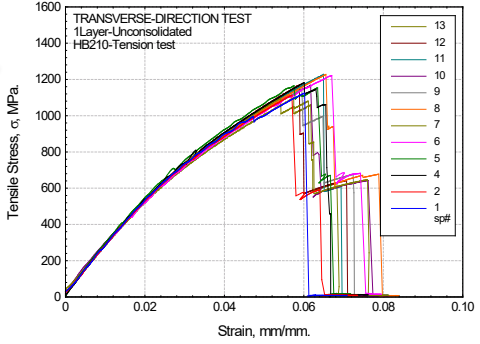

Consolidated @3ksi

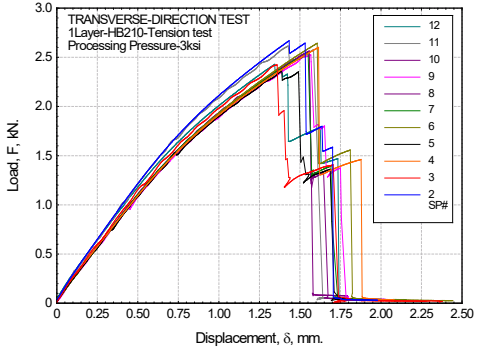

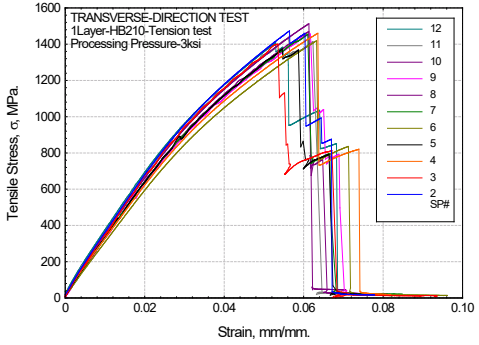

Consolidated @10ksi

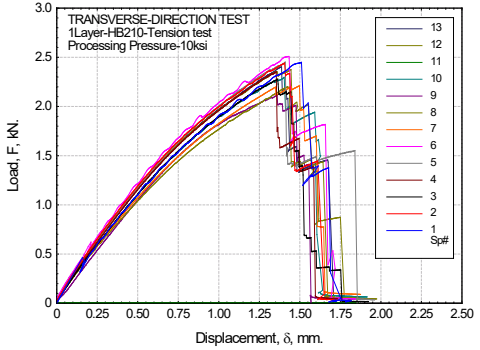

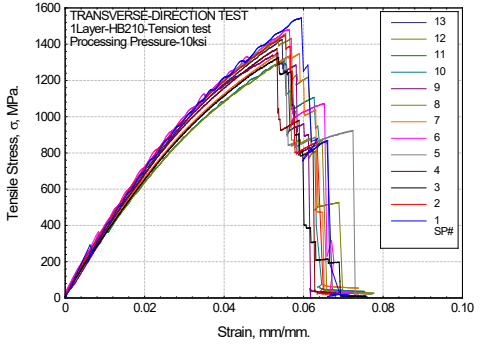

More Progressive Failure Happens to Materials Consolidated at Higher Pressure

Sheet Surface Roughness Study

UNIVERSITY OF DELAWARE
CENTER FOR COMPOSITE MATERIALS
Celebrating 50 Years

Thickness of 1 Layer sheet – 2* surface roughness = Roughness free thickness of the sheet

3ksi-top-surface Rz = 51 um

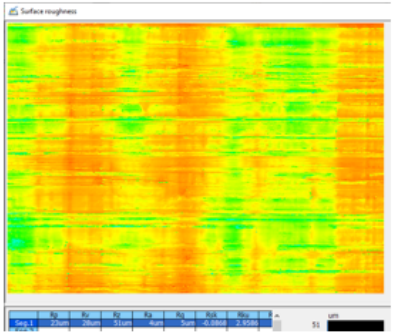

3ksi-bot-surface Rz = 56 um

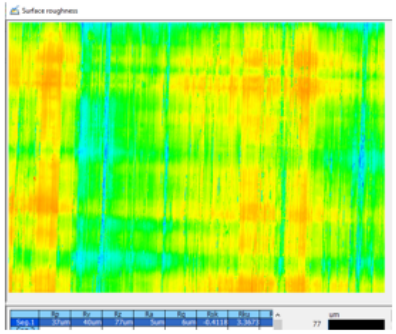

Micrometer T = 157 um

- Confocal roughness Rz of HB210 sheet shows that the surface has hills and valleys
- roughness free thickness is required to get accurate tensile strength
- Micrometer measurement of thickness includes the surface roughness

- Thickness of 24 Layer stack includes 2 rough surfaces
- Total thickness of 24 counts of 1 individual Layer sheet has 48 rough surfaces
- Average roughness of one surface can be calculated from the above two micrometer measurements

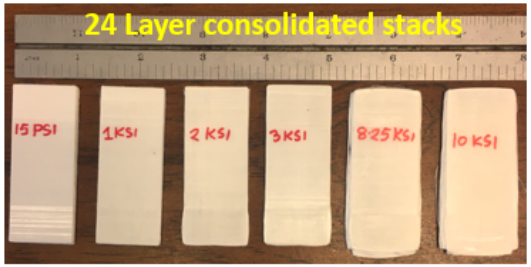

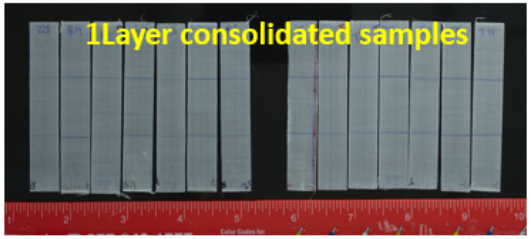

Consolidation Pressure	[Unconsolidated]	1ksi	2-ksi	3-ksi	8.25-ksi	10-ksi
Single sheet roughness, $R_{avg.}$, microns	24 ± 5	22 ± 4	23 ± 3	20 ± 5	16 ± 5	19 ± 5
Roughness free thickness, um	167 ± 7	146 ± 4	140 ± 4	135 ± 4	135 ± 5	130 ± 3

Thickness Reduction & Void fraction with Consolidation Pressure

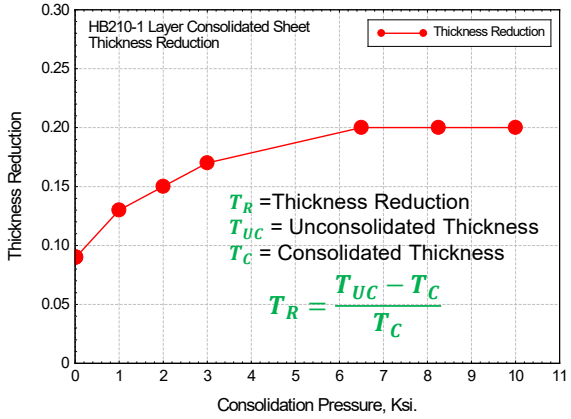

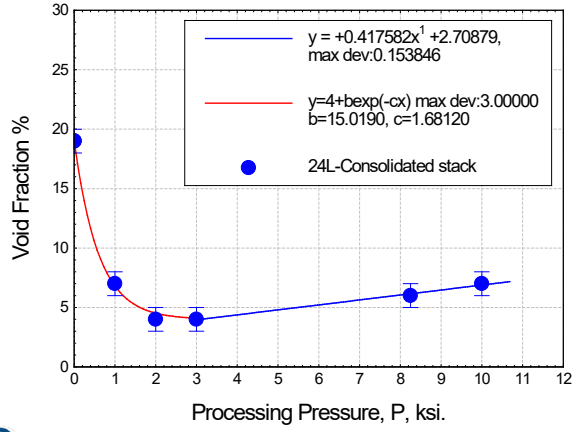

- Gas Pycnometer provides Skeletal volume
- Archimedes method provides external volume
- Void fraction can be calculated from these two volume

Challenges with Archimedes' Principal:

- TPU is hydrophilic
- Sample sucks in water
- external volume gets compromised

consolidation Pressure	Void Fraction	uncertainity of Void Fraction
1ksi	7	1
2ksi	4	1
3ksi	4	1
8.25ksi	6	1
10ksi	7	1
Unconsolidated	19	1

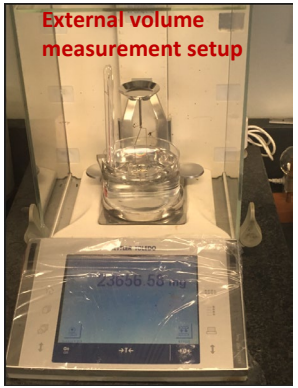



Solution:

- Applying paraffin coat on the material to prevent water suction
- The volume of a piece of glass slide has been measured using Archimedes principal to validate the process



Tensile Strength & Evolution of Pressure Induced Damage

UNIVERSITY OF DELAWARE
CENTER FOR COMPOSITE MATERIALS
Celebrating 50 Years

Strength $\sigma = \frac{1}{2}V_f X_f (1-V_V)$

[Contribution of matrix in not included in the equation]

where

σ = Tensile strength of 4 layer sheet

V_f = fiber volume fraction

V_V = the void fraction

X_f = Fiber tensile strength

- **Processing condition that guarantees higher void and thickness reduction without any pressure induced denting, flattening, spilliting may increase tensile strength to some extent**

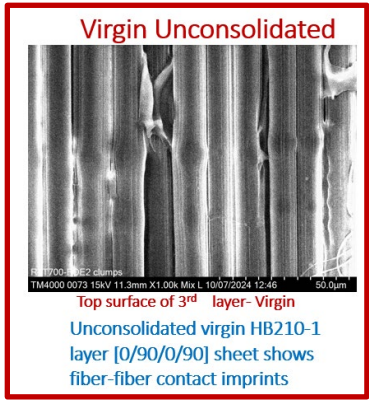

Fiber layers of [0/90/0/90] sheets have been peeled off and looked under SEM

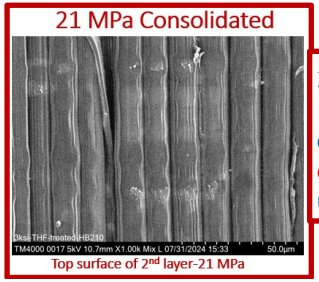

21 MPa consolidated HB210-1 layer [0/90/0/90] sheet shows fiber-fiber contact imprints which is in the form of dents are more frequent and severe than unconsolidated material

- **Void reduction benefits get defeated by pressure induced damage in fibers for consolidation pressure more than 21 Mpa**

50% Fiber failure strength has been used in the calculation

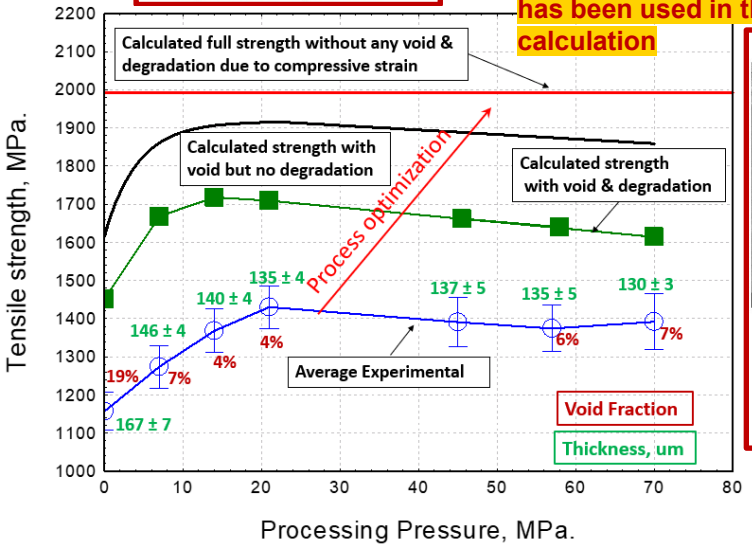

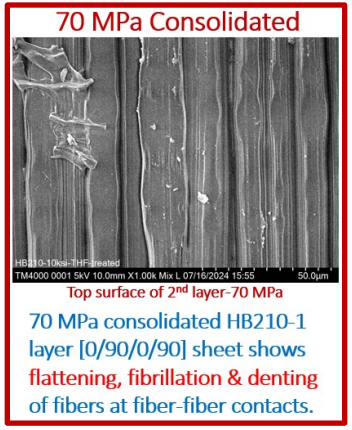

Consolidation pressure, MPa	[Unconsolidated]	7	14	21	46	58	70
Experimental Avg. strength, MPa	1157±50	1274±56	1368±57	1430±56	1391±64	1374±61	1392±73
Calculated Strength, MPa	1454	1668	1703	1705	1662	1640	1617

Fiber damage analysis as a function of Processing Pressure

Measurement of fiber width growth & fiber surface flattening

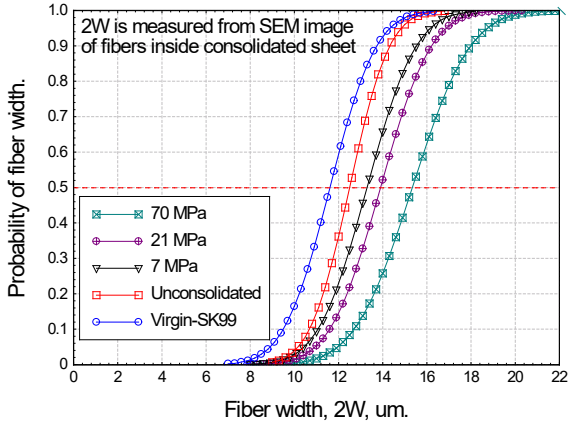

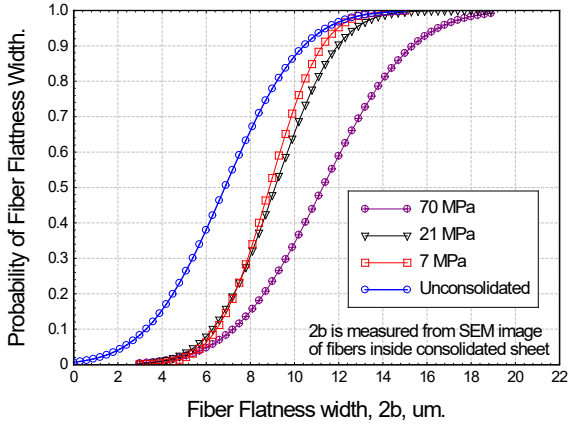

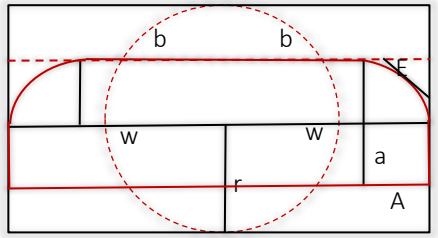

- 2W = Width of the compressed fiber in the sheet
- 2b = Flatness width on the surface of a fiber in the sheet

Material	Avg. 2b, um	Avg. 2W, um
SK-99 fibers	0	11.61 ± 1.65 [200+]
Unconsolidated	6.85 ± 2.79[17]	12.50 ± 1.42[250+]
7 MPa	8.87 ± 1.87 [180+]	13.29 ± 1.74[220]
21 MPa	9.12 ± 2.21[150+]	13.90 ± 1.80[250+]
70 MPa	11.28 ± 3.17 [150+]	15.34 ± 2.06 [340+]

NOTE: [count of measurements]

- Width 2w of a fiber & the flatness 2b on the surface of a fiber inside the [0/90/0/90] sheet grows as a function of consolidation pressure
- Growth of fiber width is restricted by adjacent fibers and matrix
- Growth in width causes splitting and separation of fibril bundles in a fiber which may result is early failure there

Fiber damage analysis as a function of Processing Pressure

Measurement of Imprints & Surface deformation

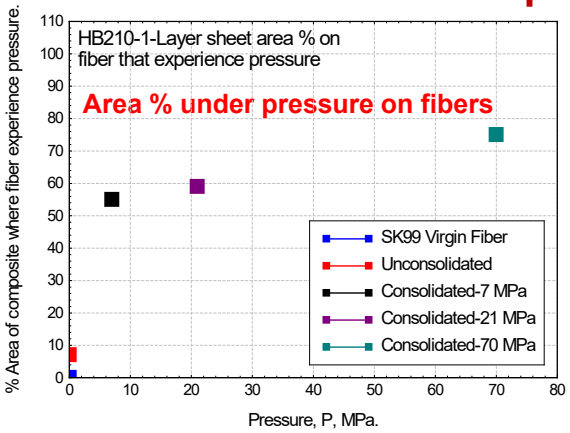

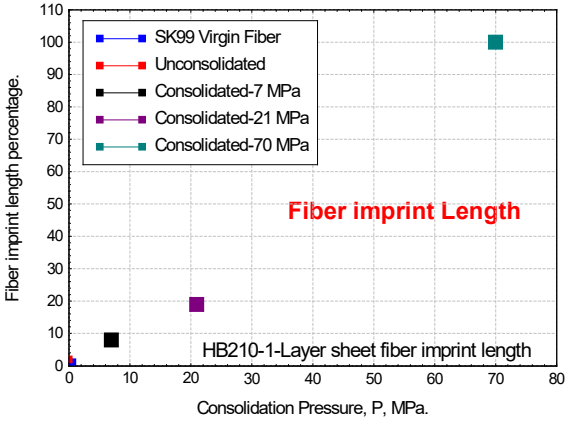

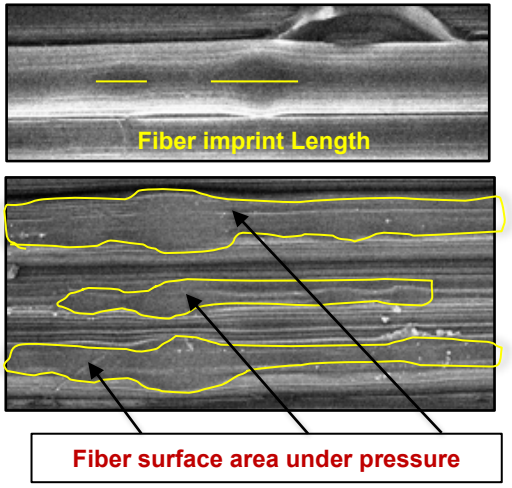

Fiber layers of [0/90/0/90] sheets have been peeled off and looked under SEM & all measurements are conducted on the SEM images

Material	Area % under pressure on fibers	Length % having imprint
SK-99 Virgin fiber	0	0
Unconsolidated	7	2 [17]
7 MPa	55	8 [250+]
21 MPa	59	19 [250+]
70 MPa	75	0

NOTE: [count of measurements]

- Percentage of the length occupied by all imprints on all the fibers in an image has been calculated and plotted as a function of consolidation pressure which shows a linear increase and it is 100% at 70 MPa
- The area percentage on the fiber surface inside a sheet that experience pressure is counted and found to increase as a function of consolidation pressure. 75 % of the total area experience pressure at 70 MPa

Determination of Sheet Strength Using Void fraction & Strain

UNIVERSITY OF DELAWARE
CENTER FOR COMPOSITE MATERIALS
Celebrating 50 Years

Residual Tensile Strength as a Function of Fiber Compressive Strain

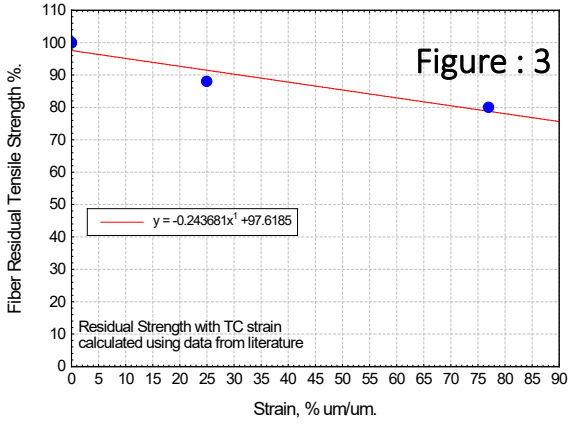

Fiber Strain distribution @ different Processing Pressure

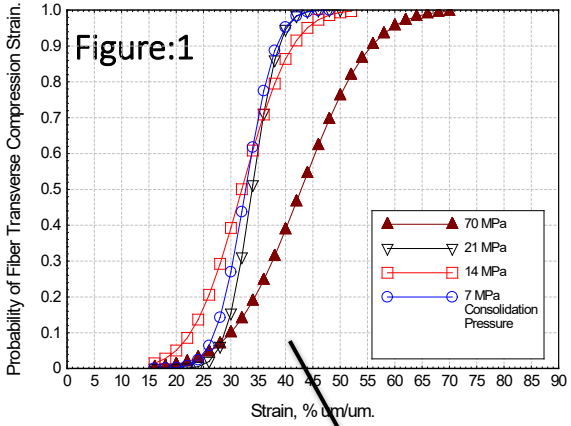

- Fiber strain has been calculated using the deformation geometry of the compressed fibers
- Figure:1 shows the strain distribution @ different processing pressure
- Figure : 2 uses 50% fiber strain from Figure : 1
- Figure : 3 uses UHMWPE fiber residual strength data from literature
- Figure : 2, Figure : 3, Figure : 4 have been used to calculate sheet tensile strength

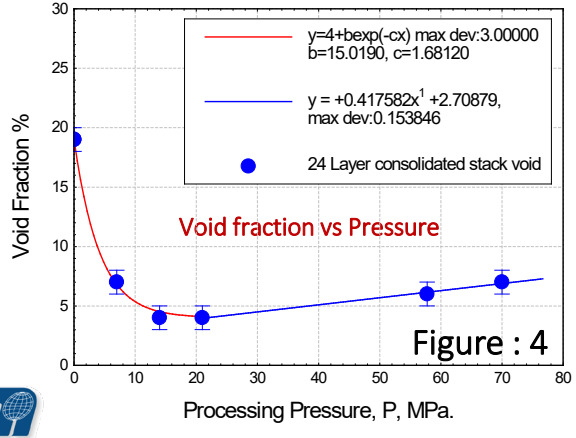

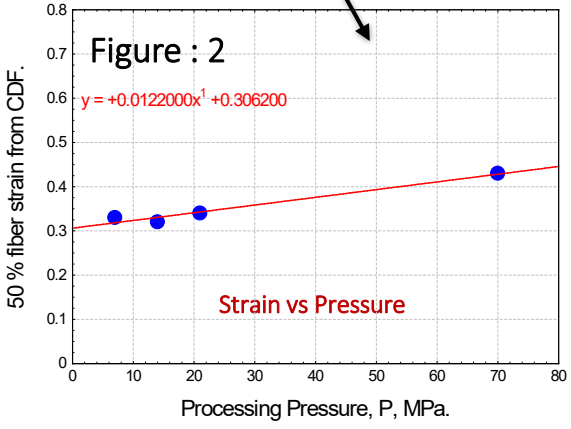

	Fiber strength						
	at 50% failure probability			4800	Mpa		
		Vf		0.83			
				Sheet Strength =		½VfXf (1-VV)	
processing pressure	processing pressure			Vf (1-VV) correspon	fiber residual strength %	fiber residual strength Xf	sheet tensile strength
ksi	Mpa	void %	strain %	FVF			Mpa
0	0	0.19	0.306	0.672	0.90	4327.54	1454
0.1	0.7	0.17	0.307	0.691	0.90	4326.11	1496
0.2	1.4	0.15	0.309	0.708	0.90	4324.68	1530
0.3	2.1	0.13	0.310	0.722	0.90	4323.25	1560
0.4	2.8	0.12	0.311	0.733	0.90	4321.83	1584
0.5	3.5	0.10	0.312	0.743	0.90	4320.40	1605
0.6	4.2	0.09	0.314	0.751	0.90	4318.97	1623
0.7	4.9	0.09	0.315	0.758	0.90	4317.55	1637

Sheet Tensile Strength @ % of Fiber Failure

UNIVERSITY OF DELAWARE
CENTER FOR COMPOSITE MATERIALS
Celebrating 50 Years

$0.50*X_f$

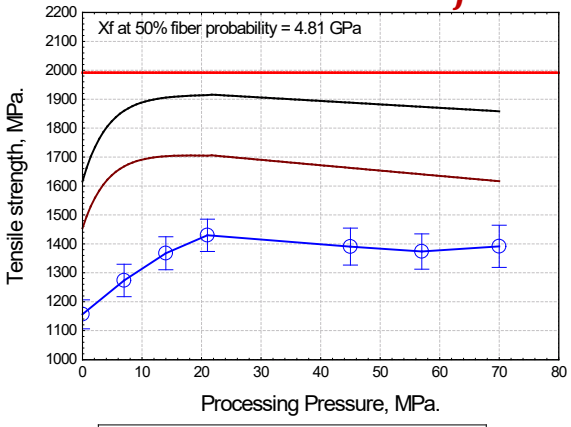

$0.20*X_f$

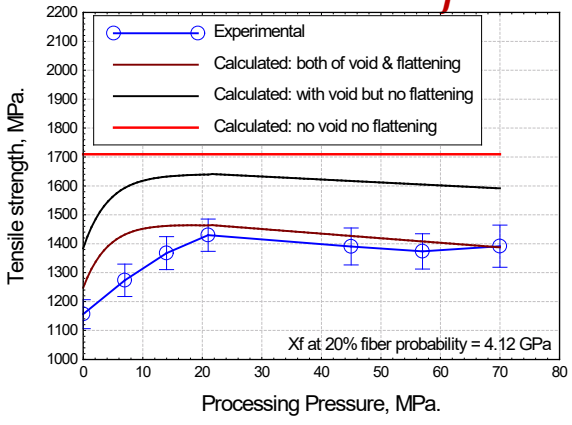

$0.18*X_f$

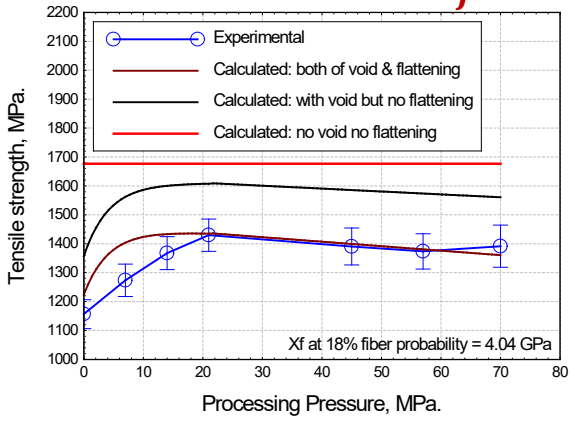

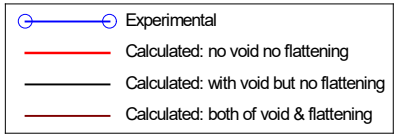

- Sheet tensile strength has been calculated using different % of fiber failure probability

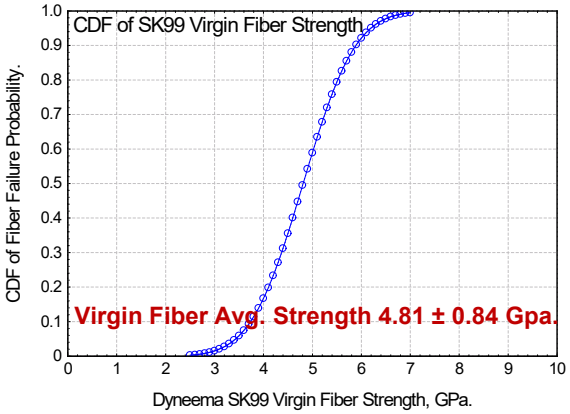

- Fiber failure strength at 18% failure probability estimates sheet strength matching to experimental data
- This indicates that 18% fibers failure initiates catastrophic failure in the sheet
- There could be other mechanism responsible for lower experimental strength at consolidation pressures less than 21 MPa

SUMMARY AND FUTURE WORKS

Summary & Conclusion:

- An Experimental methodology for tension test of Dyneema thin composites has been developed
- A lab-scale manufacturing technique has been developed to make Dyneema composites following the exact DSM provided thermal and pressure profile
- Void fraction as a function of consolidation has been determined
- Evolution of micro damage inside the sheet as a function of consolidation pressure has been studied
- A competing mechanism is found where tensile strength increases with increase in consolidation pressure due to void reduction and thickness reduction but it shows a reduction at higher pressure due to pressure induced damage like flattening, splitting, denting
- A correlation has been established to get UHMWPE sheet tensile strength using single fiber strength taking sheet void reduction and fiber compressive strain into account as a function of consolidation pressure
- Processing condition that guarantees higher void and thickness reduction without any pressure induced denting, flattening, splitting may increase tensile strength to some extent

Acknowledgements: Army Research Laboratory (ARL) through Pitt Program

Dr. Ahmad Abuobaid, Dr. Sagar Doshi, Steven Sauerbrunn PhD. John Thiravong, Touy, Ted Lake, Art & all of CCM Family

QUESTIONS ?

ICCM24
AUGUST 4-8, 2025
BALTIMORE CONVENTION CENTER
BALTIMORE, MARYLAND, USA

No Technical Paper Submission for:

Shubham Shubham

ICCM24
AUGUST 4-8, 2025
BALTIMORE CONVENTION CENTER
BALTIMORE, MARYLAND, USA

No Technical Paper Submission for:

Tobias Laux

IMPROVING THE COMPUTATIONAL EFFICIENCY OF IMPACT SIMULATIONS ON WOVEN FRP COMPOSITE PLATES

Jakov Ratković[1] and Darko Ivančević[2]

[1]Department of Aeronautical Engineering, University of Zagreb Faculty of Mechanical Engineering and Naval Architecture, Ivana Lučića 5, 10000 Zagreb, Croatia
Email: jakov.ratkovic@fsb.unizg.hr, web page: http://www.fsb.unizg.hr

[2]Department of Aeronautical Engineering, University of Zagreb Faculty of Mechanical Engineering and Naval Architecture, Ivana Lučića 5, 10000 Zagreb, Croatia
Email: darko.ivancevic@fsb.unizg.hr, web page: http://www.fsb.unizg.hr

Keywords: Impact Simulation, FEM Numerical Analysis, Progressive Damage, Woven Composites, Computational Efficiency

ABSTRACT

This study investigates several strategies to improve the computational efficiency of numerical simulations aimed at predicting impact damage in woven fibre reinforced composites. Utilisation of homogenised ply-scale modelling, performed using a VUMAT user-defined material model, was justified for plain weave woven laminates. The commercial finite element software Abaqus/Explicit was used for progressive damage modelling in woven carbon fibre reinforced epoxy laminates. Along stress-based failure initiation criteria and energy-driven damage evolution, complete loss of load-bearing capability is captured by effective failure strain-based element removal, thus enabling the accurate assessment of full perforation energy margin. Validation of the numerical model was performed through impact simulations at two energy levels in which steel spherical impactors induce damage in composite plates made of plain weave CFRP with the layup $[45, 0, 45, 0, 45]_s$. The results have shown that in this study the homogenised approach has performed well, and that careful implementation of simplifications in the model leads to significant improvement in computational efficiency while retaining the accuracy level. Namely, a remarkable total time reduction of over 75 % was achieved from initial model. Thus, the final model is rendered much more suitable for practical, industrial purposes in which large structural components are examined.

1 INTRODUCTION

Utilization of composite materials in aeronautical, automotive, military and other major industry segments is well established. Due to many advantages, such as more balanced properties, enhanced impact resistance and improved ease of handling [1], woven carbon fibre reinforced plastic (CFRP) composites are seeing continuous increase in utilization in important structural elements. However, based on the available references, it can be concluded that woven CFRP materials are significantly less investigated compared to their unidirectional (UD) CFRP counterparts [2]. Thus, the uncertainties concerning the assumptions and simplifications introduced in modelling that are still existent even regarding the UD composites, are projected to the woven composites as well, and are perhaps even more pronounced.

Research studies focused on woven CFRP are usually performed at the microscale, e.g. [3], due to their complex microstructure. The microstructural geometry of these materials consists of interlaced and interconnected fibre bundles in warp and weft directions, potential voids, resin pockets or resin-rich zones and interfaces between fabric bundles and matrix. For the same reasons, micromechanical modelling of woven composites is significantly more challenging than that of UD composites [2]. The microscale approach enables capturing the behaviour of the micro-geometrical features of the woven material in the most accurate manner. However, this capability is accompanied with an enormous computational cost, deeming the micromechanical approach inapplicable for engineering problems. In

the microscale modelling approach, a single unit cell that would be represented by a single finite element in the homogenised approach, is discretized using many finite elements with explicit contact interactions between them. This level of detail dramatically increases the computational cost compared to the homogenised ply-scale approach.

However, despite capturing many microscopic features of woven fabrics, these detailed models still rely on certain assumptions and are subject to uncertainties—particularly concerning void content and the simplified representation of bonding between individual fibres and the matrix, as well as between fibre bundles and the matrix [2]. Additionally, the need to impose idealised boundary conditions introduces further sources of uncertainty in the analysis.

Multiscale methods enable application of micromechanical approaches in the engineering applications. However, these models contain algorithms that analyse the material at various scales and are thus even more complex. Furthermore, multiscale models for woven composites require calculations on some of the analysed regions to be performed multiple times, i.e., at different scales. Consequently, although multiscale approaches offer improved computational efficiency compared to microscale models, they are still too computationally demanding for engineering applications. This is particularly the case in transient dynamic analyses, where explicit finite element simulations require extremely small time increments.

In contrast, well-defined ply-level homogenisation approaches can simplify complex numerical simulations, offering considerably increased computational efficiency. The selection of the material segment used to construct a homogenised volume element (referred to as HVE in this work) can vary based on its size and location, allowing flexibility for different woven fabric architectures. The HVE strategy proposed in this work is based on the experimentally determined properties of woven composites. As the internal geometry of the fabric is not considered explicitly, the need for specifically defined boundary conditions is eliminated. Instead, the approach assumes that the finite element boundaries align with the interlacing regions of the woven fabric. The HVE discretisation approach is explained visually in Fig. 1. As shown, the possible HVEs in woven composites differ by the boundary conditions corresponding to neighbouring fibre bundle interlacings causing variances in stiffness and strengths. In finite element modelling, this variety can be reduced by limiting the average in-plane size of the finite elements employed to the width of a single fibre bundle or, alternatively, to a specified natural number of fibre bundles. Figure 1 presents the Plain Weave, 2x2 Twill and 4H Satin weave fabrics with various HVEs obtained by identifying different 1 x 1 (blue squares) and 2 x 2 (magenta squares) fibre bundle elements. For the clarity of the display, not all existing variants of 2 x 2 HVEs were marked on Figure 1 for the Twill and Harness Satin weaves.

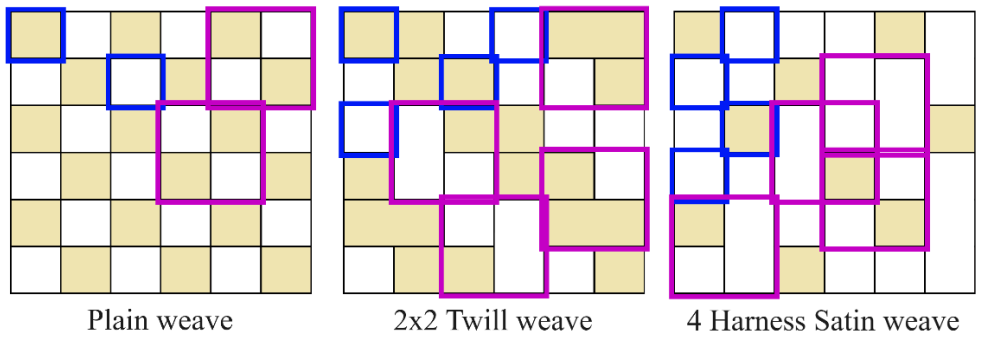

Figure 1. Various possible homogenised volume elements (HVEs) for Plain weave, 2x2 Twill weave and 4 Harness Satin weave woven fabrics: 1 x 1 (blue) and 2 x 2 (magenta) fibre bundle sized HVEs

By increasing the HVE dimensions, the numerical problems are simplified as the microstructural geometry is more homogeneous and the overall number of degrees of freedom is reduced. However, a compromise between accuracy and computational efficiency has to be made to simulate engineering problems. Even in the case of utilization of the smallest HVE (1 x 1 fibre bundle size), the computational efficiency of homogenized approaches is still superior compared to the micromechanical or multiscale approaches.

Despite having the most interlacings and thus potentially the highest quantities of resin-rich zones, resin pockets and voids – all of which reduce their strength, Plain weave fabrics have the most balanced properties when considering the HVEs of the material. Moreover, with the correct size of the homogenised finite element modelling, plain weave fabrics are the only fabric type that can be discretised by only a single variant of HVE. This is shown in Figure 1, in which for the Plain weave fabric two of all of the HVE sizes (1 x 1 and 2 x 2) are marked. However, their boundary conditions, number and position of interlacings in these sets of two HVEs are the same, hence rendering the same properties, with the assumption that warp and weft fibre bundles are equal.

Furthermore, various positions of the, e.g., 3 x 3 HVEs are obtainable. Of all of the possible HVEs in the Plain weave fabric, the only ideally balanced and homogenised, i.e. presumably orthotropic, are the ones that are perfectly cut along the fibre bundle boundaries and the ones cut exactly in the middle of warp and weft fibre bundles.

Clearly, it is impractical to try to fit the HVEs discretising the model to correspond to the exact positions of the fibre bundles in the real structure to be modelled. However, it is evident that the largest error, i.e., discrepancy, in the position between the utilized HVE and the closest one of the ideal cases is half of the width of the fibre bundle. Moreover, the larger the HVE, the less significant this error is. For example, for a 2 x 2 HVE, the maximum error in position is 25 % of the length of the homogenised element, whereas for the 5 x 5 HVE, the error is 10 % of the length of the homogenised element. Despite the large percentage of these errors defined in this manner, it is evident that it is practically negligible considering the overall length of the structure. For example, for a structure with a 100 mm length in the examined direction, considering a 1 mm fibre bundle width, for any chosen size of the HVE, this error in the shifting of the position of the HVEs is, at maximum, only 0.5 %.

In this study, the homogenised ply-scale approach is utilized, mainly for computational efficiency, as it is by far the most efficient approach and the only practical solution for applications in explicit dynamic analyses as elaborated previously. In the light of the aforementioned problems with homogenised ply-level discretization of woven fabric plies, to reduce uncertainties and retain physical meaningfulness of the model, application of this model is restricted to plain-weave woven fabric plies. Furthermore, the in-plane dimensions of the finite elements modelling the woven fabric composite structures are defined by and restricted to the width of the fibre bundles, thus rendering the approximately 1 x 1 x 0.21 mm solid finite elements.

2 METHODOLOGY

The material behaviour is assumed to be elastic orthotropic prior to any damage initiation. Additionally, for all three shear modes, a non-linear behaviour is modelled. Because of the assumed orthotropy of the material, shear behaviour is decoupled from normal behaviour, simplifying the implementation of shear non-linearity.

2.1 Shear Non-Linearity

Non-linearity is especially pronounced in the shear response of woven composites. This nonlinear behaviour is introduced according to the stress to strain relation proposed by Coles et al. [4]:

$$\tau_{ij} = S_{ij} \cdot \left[1 - \exp\left\{-\frac{G_{ij}^0 \cdot \gamma_{ij}}{S_{ij}}\right\}\right],\ i,j = 1,2,3, i \neq j. \quad (1)$$

In Eq. (1), S_{ij} is the shear strength, G_{ij}^0 is the shear modulus and γ_{ij} is the instantaneous engineering shear strain. The shear stress vs. shear strain plot obtained by the non-linear formulation provided in Eq. (1) for the values of shear strength $S_{ij} = 100$ MPa and shear modulus $G_{ij}^0 = 4$ GPa respectively, is shown in Figure 2.

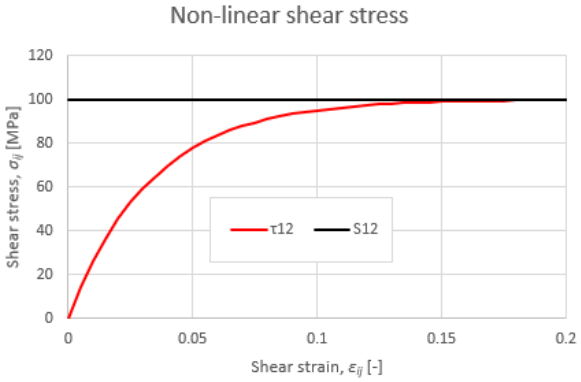

Figure 2. Non-linear shear behaviour: stress-strain plot

2.2 Failure criteria

The in-plane failure initiation corresponding to fibre rupture is modelled using the interactive stress criteria adopted from the study [4] for warp (FF1) and weft (FF2) direction in tensile (T) and compressive (C) loading conditions:

$$FF1T = \left(\frac{\sigma_{11}}{X_t}\right)^2 + \left(\frac{\tau_{12}}{S_{12}}\right)^2 + \left(\frac{\tau_{13}}{S_{13}}\right)^2 \geq 1, \tag{2}$$

$$FF1C = \left(\frac{\sigma_{11}}{X_c}\right)^2 + \left(\frac{\tau_{12}}{S_{12}}\right)^2 + \left(\frac{\tau_{13}}{S_{13}}\right)^2 \geq 1, \tag{3}$$

$$FF2T = \left(\frac{\sigma_{22}}{Y_t}\right)^2 + \left(\frac{\tau_{12}}{S_{23}}\right)^2 + \left(\frac{\tau_{23}}{S_{23}}\right)^2 \geq 1, \text{ and} \tag{4}$$

$$FF2C = \left(\frac{\sigma_{22}}{Y_c}\right)^2 + \left(\frac{\tau_{12}}{S_{23}}\right)^2 + \left(\frac{\tau_{23}}{S_{23}}\right)^2 \geq 1. \tag{5}$$

In Eqs. (2) - (5), σ_{11}, σ_{22}, τ_{12}, τ_{13} and τ_{23} are the stress components, whereas X_t, X_c, Y_t, Y_c are the warp and weft tensile and compressive strengths, respectively, while S_{12}, S_{13} and S_{23} are the shear strengths of the material.

Matrix micro-cracks forming and coalescing into larger cracks is exhibited by shear non-linear material behaviour, according to e.g. [5, 6]. Interactive quadratic stress criteria are used for evaluating intralaminar matrix tensile (MFT) and compressive (MFC) damage initiation. Matrix failure is defined using the through-thickness normal and all three shear stress components, while the failure mode is predicted based on the sign of the through-thickness stress:

$$MFT = \left(\frac{\sigma_{33}}{Z_t}\right)^2 + \left(\frac{\tau_{12}}{S_{12}}\right)^2 + \left(\frac{\tau_{13}}{S_{13}}\right)^2 + \left(\frac{\tau_{23}}{S_{23}}\right)^2 \geq 1, \tag{6}$$

$$MFC = \left(\frac{\sigma_{33}}{Z_c}\right)^2 + \left(\frac{\tau_{12}}{S_{12}}\right)^2 + \left(\frac{\tau_{13}}{S_{13}}\right)^2 + \left(\frac{\tau_{23}}{S_{23}}\right)^2 \geq 1. \tag{7}$$

2.3 Progressive Damage Evolution

Progressive damage evolution is modelled by the degradation of material stiffness through modification of the stiffness matrix. The damage variable d can be considered as an internal parameter describing the reduction of the load bearing material surface from the undamaged state to the current, instantaneous state, as proposed in the early studies by Murakami [7], Matzenmiller et al. [8] and Zako et al. [9]. The stress reduction related to material damage can be described by the following simplified general relation:

$$\sigma = (1 - d) \cdot \sigma' = (1 - d) \cdot \mathbf{C}\varepsilon = \mathbf{C}_d\varepsilon, \tag{8}$$

in which σ' is the nominal, undamaged stress vector determined by the Hooke's law from the undamaged stiffness matrix $\mathbf{C}$ and strain vector ε while assuming the orthotropic linear elasticity of the material. In

Eq. (8), the damaged stiffness matrix $\mathbf{C}_d$ has been introduced by combining the damage vector d consisting of warp direction d_{f1} and weft direction d_{f2} damage variable with the undamaged stiffness matrix $\mathbf{C}$. This can be expanded for the first three, i.e., normal, coupled components as:

$$\mathbf{C}_d^N = \frac{1}{\Delta}\begin{bmatrix} d_{f1}E_{11}(1-d_{f2}\nu_{23}\nu_{32}) & d_{f1}d_{f2}E_{11}(\nu_{21}+\nu_{23}\nu_{31}) & d_{f1}E_{11}(\nu_{31}+d_{f2}\nu_{21}\nu_{32}) \\ d_{f1}d_{f2}E_{11}(\nu_{12}+\nu_{32}\nu_{13}) & d_{f2}E_{22}(1-d_{f1}\nu_{13}\nu_{31}) & d_{f2}E_{22}(\nu_{32}+d_{f1}\nu_{12}\nu_{31}) \\ d_{f1}E_{11}(\nu_{13}+d_{f2}\nu_{12}\nu_{23}) & d_{f2}E_{22}(\nu_{23}+d_{f1}\nu_{21}\nu_{13}) & E_{33}(1-d_{f1}d_{f2}\nu_{12}\nu_{21}) \end{bmatrix}. \quad (9)$$

Damage in the shear components is modelled as:

$$\mathbf{C}_d^S = \frac{1}{\Delta}\begin{bmatrix} d_{f1}d_{f2}G_{12}^0\Delta & 0 & 0 \\ 0 & d_{f2}G_{23}^0\Delta & 0 \\ 0 & 0 & d_{f1}G_{31}^0\Delta \end{bmatrix}. \quad (10)$$

When damage is initiated, the initial, intact shear moduli G_{ij}^0 in the Eq. (1), should be replaced by the corresponding damaged stiffness matrix components introduced in Eq. (10). In the above equations, the remaining unintroduced variables are:

$$\begin{gathered} \Delta = 1 - d_{f1}d_{f2}\nu_{12}\nu_{21} - d_{f2}\nu_{23}\nu_{32} - d_{f1}\nu_{13}\nu_{31} - 2d_{f1}d_{f2}\nu_{12}\nu_{21}\nu_{21}, \\ d_{f1} = (1-d_{11}^t)(1-d_{11}^c), \text{ and} \\ d_{f2} = (1-d_{22}^t)(1-d_{22}^c). \end{gathered} \quad (11)$$

The parameters $d_{ii}^{t/c}$ in Eq. (11) are the four different damage variables. These variables, corresponding to fibre tensile and compressive (upper index t/c) damage in warp and weft directions (lower index ii) are calculated according to, e.g., [10], by the relation:

$$d_{ii}^{t/c} = \frac{\varepsilon_{ii}^f \cdot (\varepsilon_{ii} - \varepsilon_{ii}^0)}{\varepsilon_{ii} \cdot (\varepsilon_{ii}^f - \varepsilon_{ii}^0)}. \quad (12)$$

In Eq. (12), ε_{ii}^0 is the corresponding equivalent strain at failure initiation, ε_{ii} is the instantaneous equivalent strain value, while ε_{ii}^f is the strain value of total rapture. The total rapture strain is determined depending on the corresponding fracture energy Γ_{ii}, corresponding equivalent stress at the point of failure initiation according to the failure initiation criteria in Eqs. (2) – (5), σ_{eq}, and the characteristic finite element length as: $\varepsilon_{ii}^f = 2 \cdot \Gamma_{ii}/(\sigma_{\text{eq}} \cdot L_c)$. The characteristic finite element length is introduced to ensure mesh-objectivity in the strain softening constitutive behaviour.

The presented formulation is a modification and a combination of the approaches presented by Hu et al. [11] and Coles et al. in [4] that represents a reasonable and physically sound approach to the modelling of the materials stiffness degradation.

Element deletion due to damage is employed in certain specific conditions. A total loss of load bearing capability is considered to occur only if fibre laid in both in-plane directions (warp and weft) have undergone total rupture. Thus, the finite element is removed when either tensile or compressive damage variables in both warp ($d_{11}^{t/c}$) and weft ($d_{22}^{t/c}$) directions reach their maximum defined value, which is chosen to be 0.98 to avoid numerical problems associated with excessive distortion of degraded finite elements.

Furthermore, to prevent large distortions and unphysical deformations of degraded finite elements, as well as to capture the matrix failure, along with enabling the accurate simulation of perforation behaviour of the laminated structures, the effective failure strain (EFS) element removal criterion is implemented. This criterion is defined as:

$$\varepsilon_{\text{eff}} \leq \varepsilon_{\text{eff}}^{\max}, \quad (13)$$

where $\varepsilon_{\text{eff}}^{\max}$ is the semi-empirical material parameter, defining the maximum effective strain that a material point, i.e. single finite element with reduced integration could sustain, above which complete

material failure is expected. In the Eq. (13), effective strain ε_{eff} is calculated based on the deviatoric strain components e_{ij} as:

$$\varepsilon_{\text{eff}} = \sqrt{2 \cdot e_{ij}^2/3}. \tag{14}$$

The maximum effective strain $\varepsilon_{\text{eff}}^{\text{max}}$ is taken to be 0.3 in this study. This value is in similar to the values employed by other researchers, such as in [12], when using similar failure strain element removal criteria.

2.4 Interlaminar behaviour

Zero-thickness cohesive finite elements (COH3D8) were used to model the ply interfaces. To capture delamination phenomena, the Abaqus built-in decoupled traction-separation cohesive material model was used in this study. The model employs quadratic traction failure initiation criterion, and the B-K energy driven delamination propagation, with the B-K factor set to η = 2. Furthermore, the interface stiffness parameters were estimated according to the relationship suggested in [13]: $K_{nn} = E_{33}/h_0$, $K_{ss} = G_{13}/h_0$ and $K_{tt} = G_{23}/h_0$, where E_{33}, G_{13} and G_{23} are the matrix material elastic properties, and h_0 is the assumed thickness of the interface. As proposed in [13, 14] the interface thickness h_0 can be taken as 1/10 of the thickness of the ply.

Cohesive element removal was set when the damage variable reaches the value of 0.98 for stability reasons.

3 NUMERICAL MODEL

Numerical simulations of the impact experiments in [14] have been used in this study to validate the model. Thus, a 12.7 mm diameter spherical steel impactor with the total falling mass of the drop weight apparatus equal to 1.573 kg was simulated to impact the plain weave woven CFRP plates. Simulations of two impact energies (16 J and 28 J) were performed.

Several FE modelling strategies were investigated. The rectangular plate with the dimensions 100 x 150 mm has been modelled with solid (C3D8R) elements in Abaqus. The layup is $[45, 0, 45, 0, 45]_s$ layup, resulting in the 2.1 mm total thickness. A single finite element has been employed in the thickness direction for each composite ply. Thus the numerical model consists of a total of 150,000 C3D8R finite elements. At all interfaces of the composite plies a total of 135,000 zero-thickness cohesive COH3D8 finite elements were utilized for delamination modelling. Results obtained using this modelling strategy are further denoted as “Full” simulation results.

The plate is simply supported along all edges at its backside. The steel impactor was modelled as a discretely rigid body, and all of its degrees of freedom were constrained, except for the vertical movement. General contact algorithm was employed with hard normal and tangential contact with a defined penalty frictional coefficient of 0.3. The model is schematically represented in Figure 3.

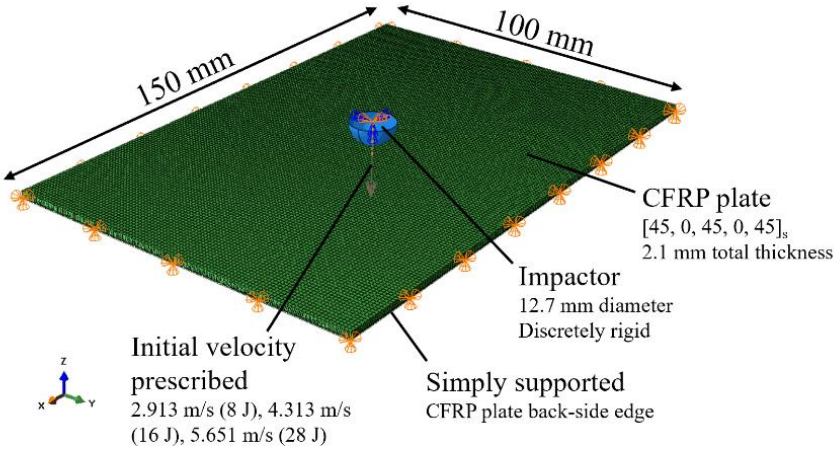

Figure 3. Numerical model with boundary conditions and loading

The mechanical intralaminar and interlaminar properties were taken from [14], and the already mentioned related study [13] of the same research group. All of the necessary intralaminar stiffness constants, strengths and fracture energies are listed in Tables 1, 2 and 3, respectively.

Table 1. Intralaminar elastic properties of the plain weave CFRP ply

property	E_1	E_2	E_3	G_{12}	$G_{13} = G_{23}$	ν_{12}	$\nu_{13} = \nu_{23}$
unit	[GPa]	[GPa]	[GPa]	[GPa]	[GPa]	[-]	[-]
reference	[14]	[14]	[14]	[14]	[13]	[14]	[4]*
value	60.8	58.25	2.97	4.55	1.08	0.07	0.35

* Value calculated based on the value in [4], according to the ratio of η_{12} values from [14] and [4]

Table 2. Intralaminar strengths of the plain weave CFRP ply, taken from [14]

property	X_t	X_c	Y_t	Y_c	S_{12}	$S_{13} = S_{23}$
unit	[MPa]	[MPa]	[MPa]	[MPa]	[MPa]	[MPa]
value	621	760	594	707	125	150

Table 3. Intralaminar fracture energies of the plain weave CFRP ply, taken from [14]

property	G_{ft}	G_{fc}	G_{mt}	G_{mc}	G_{sh}
unit	[kJ/m^2]	[kJ/m^2]	[kJ/m^2]	[kJ/m^2]	[kJ/m^2]
value	75	25	2.5	2.5	2.25

The interlaminar fictitious penalty stiffness constants are K_I = 141430 N/mm^3, K_{II} = 216670 N/mm^3 and K_{III} = 514290 N/mm^3, based on the values of shear moduli reported in [13]. The remaining interlaminar model properties are taken directly from [14] and are as follows: N = 75 MPa, S_{II} = 125 MPa, S_{III} = 150 MPa, G_I = 0.6 kJ/m^2, G_{II} = 5.5 kJ/m^2, G_{III} = 5.5 kJ/m^2.

To investigate the effect of the employed cohesive elements on the computational efficiency, a modelling strategy without cohesive elements at the ply interfaces was performed. Consequently, this model consists only of the solid finite elements of the composite plies, without the ability to simulate the delamination failure mode. The results obtained by this simulation type are remarked as the "Bulk" simulation results.

The next modelling strategy consists of a hybrid approach that was tested for increasing the computational efficiency while retaining the capability to accurately assess both intralaminar and interlaminar damage. In this model, the VUMAT user-defined material is employed only on the central 50 x 50 mm part of the composite plate, whereas on the remaining, outer portion of the plate, the Abaqus built-in orthotropic material with the same elastic properties was employed. Furthermore, the cohesive interface model with zero-thickness cohesive finite elements was included only on the central 50 x 50 mm portion of the plate as well. Hence, the outer part of the plate is incapable of assessing any failure and damage mode. This model is in the Results section denoted as "Hybrid" simulation model and results.

Figure 4 schematically presents the employed meshing strategy in the transition zone from the outer composite plate area (Abaqus built-in orthotropic material model without damage) to the inner area of specific interest (VUMAT material model + cohesive zone for delamination) for impact analyses.

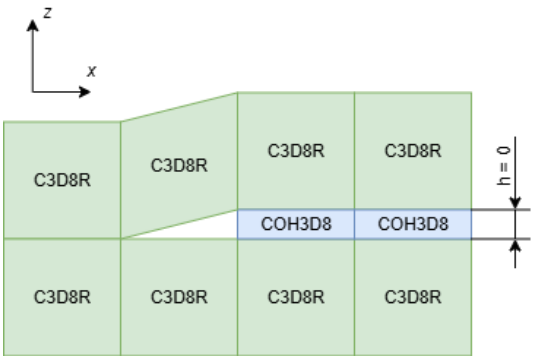

Figure 4. Meshing strategy in the transition zone from outer to inner plate area

All simulations were performed on a desktop workstation using 22 2.2 GHz processors. The details on the finite element meshes for the three simulation modelling approaches are summarized in Table 4.

Table 4. Details of the finite element meshes for different modelling approaches

	"Full"	"Bulk"	"Hybrid"
Total number of nodes, [-]	305,020	167,761	191,170
Total number of elements, [-]	285,000	150,000	172,500
VUMAT elements, [-]	150,000	150,000	25,000
Cohesive elements, [-]	135,000	0	22,500

4 RESULTS

Figure 5 shows the comparison of numerical to experimental impactor displacement history and contact force history for the impact energy of 16 J. Both graphs contain results obtained by employing the presented three modelling approaches, namely: "Full", "Bulk" and "Hybrid".

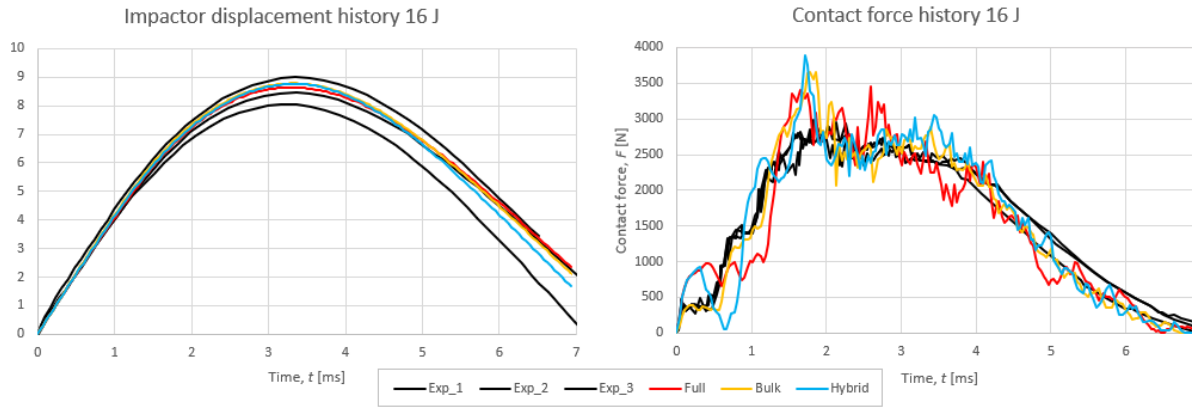

Figure 5. Comparison of numerical to experimental results [14] for the 16 J impact: contact force and impactor displacement

The results in Figure 5 indicate that, overall, the simulation results correspond well with the experimental data in both plots. A more pronounced difference is observed in the contact force history, where all three models similarly overestimate its magnitude. This tendency to overpredict the contact force may be related to an underestimation of the plate's final absorbed energy and additional investigation will have to be performed to identify the source. Additionally, the lower predicted absorbed energy could result from insufficient estimation of interlaminar damage, which will be examined in the continuation of this work. The overall slope of the numerical curves matches the experimental curve slope reasonably well. The contact force history graph shows that the "Bulk" simulation results align more closely with the experimental data. Contrarily, the simulations incorporating cohesive elements

("Full" and "Hybrid" models) show oscillatory behaviour. Additionally, the oscillation frequency is higher in the "Hybrid" simulation. This is likely related to the smaller area covered by cohesive elements in that case, which reduces the time needed for stress waves to reflect from the boundaries of the delamination modelling region. Figure 6 shows a comparison between experimental and numerical delamination areas for the two investigated impact energies. The red outlines (profiles) were derived from C-scan images presented in [14], while the orange and blue regions indicate the areas where cohesive elements were completely removed in the "Full" and "Hybrid" simulations. In the lower part of the figure, the green and purple regions correspond to solid intralaminar elements exhibiting tensile or compressive matrix damage in the "Full" and "Hybrid" models.

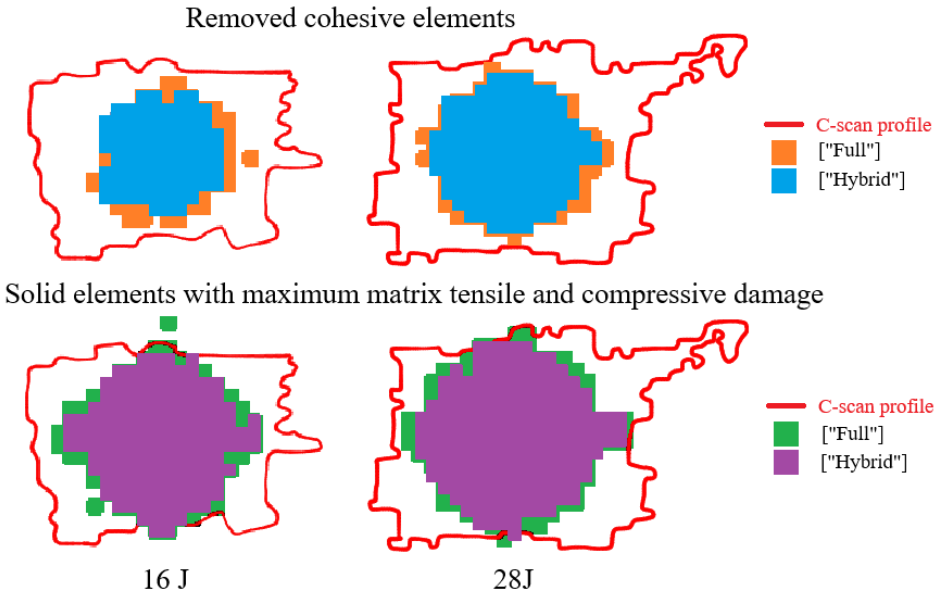

Figure 6. Comparisons of "Full" and "Hybrid" simulations' numerically and experimentally [14] obtained delamination areas for impacts of 16 J and 28 J

Figure 6 shows that the simulated delamination areas are smaller compared to the experimental results. Furthermore, the comparison indicates that including elements with matrix damage (tensile or compressive) leads to a better match with experimental results. As discussed in [15] and [16], increasing load causes matrix micro-cracks to merge into larger intralaminar cracks. When such a crack extends to the ply boundaries (interfaces between the plies) it leads to initiation and growth of delamination, explaining the motivation for the comparison presented in Figure 6. From the perspective of the experimental findings in the existing studies such as [15, 16] and their confirmation from Figure 6, it seems that the phenomenological approach of connecting the interlaminar damage initiation to the propagation of intralaminar matrix damage in the adjacent plies could lead to improved overall delamination extent predictions. This is one of the main objectives of the authors' current effort to develop a joint, combined VUMAT for both intralaminar and interlaminar composite progressive damage modelling.

For the computationally efficient "Hybrid" simulation, the discrepancy between numerical and experimental area in Figure 6 is barely larger than the one found in the comprehensive "Full" simulation model in which both intralaminar and interlaminar damage assessment is available for the whole volume of the composite plate. For the 16 J and 28 J impact cases, the "Hybrid" simulations' results predict slightly lower extent of interlaminar damage compared to the "Full" simulations.

Finally, Table 5 summarizes the computational times for both investigated impact energy levels using all three simulation models, along with the corresponding percentages in reduction.

Table 5. Summary of all computational times - all three simulation strategies employed at both impact energies

	Time analysed, [ms]	"Full", [min]	"Bulk", [min]	Reduction from "Full", [%]	"Hybrid", [min]	Reduction from "Full", [%]
16 J	7	2893	424	85.34	604	79.12
28 J	4	1882	404	78.53	410	78.21

From Table 5, it is clear that a significant increase in computational efficiency is achieved by both strategies: I) removing the interlaminar damage modelling from the model in "Bulk" simulations and II) reducing the zone of interest of the composite plate in which both intralaminar and interlaminar damage evaluation is available only to the central region of the composite plate in "Hybrid" simulations. It is visible that the reduction of computational time is constant in the case of "Hybrid" simulations.

On the other hand, different time savings were achieved by employing the "Bulk" simulations. These differences are attributed to different numbers of semi-detached cohesive finite elements which do not constructively contribute to the analysis model but deteriorate the stable time increment (STI). These highly distorted elements are a byproduct of removal of adjacent intralaminar solid elements of the plies above and below the interface. Because some of their nodes are free-floating, these semi-detached elements do not bear any load and thus could not be effectively removed from the simulation by reaching the maximum defined load driven, i.e., displacement driven damage variable value. The number of semi-detached cohesive finite elements is a function of, among other factors, the intensity of loading conditions and subsequent rate of removal of adjacent intralaminar solid finite elements.

Hence, it is expected that further improvements in the computational efficiency could be achieved by effectively removing any semi-detached cohesive elements from the simulation. This is another objective of the aforementioned key future agenda goal – development of the joint VUMAT user-defined material that is constituted of both intralaminar and interlaminar progressive damage material models.

9 CONCLUSIONS

In this study, several FE modelling strategies have been investigated in the impact damage simulations in woven CFRP structures. Validation of the numerical model and the investigated modelling strategies was performed using experimental results of impact damage. The investigation is focused on plain weave woven architectures.

The numerical results overall demonstrated good agreement with experimental data for the simulated impact energies. Application of the VUMAT material model and interlaminar damage modelling to the central interior region of the plate ("Hybrid" simulations), it was possible to maintain satisfactory accuracy of the simulations at significantly lower computational time. However, this approach requires careful application, particularly regarding the accurate definition of the zone of interest or the anticipated damage region. A preliminary, faster simulation without interface modelling, e.g. using the "Bulk" simulations used in this work, can help identifying the likely extent of intralaminar damage before performing the detailed analysis.

The presented results are part of an ongoing investigation aimed at developing accurate numerical models for impact simulations in engineering problems As stated throughout the Results section, future work will be focused on integrating the user-defined material behaviour of the plies and ply interfaces into a single VUMAT subroutine, which is considered to be a direction for further improvements in both accuracy and computational efficiency. Furthermore, as the constitutive model of the cohesive models will be user-defined, strain rate effects will be included in the subsequent models to additionally improve accuracy in the impact damage prediction.

ACKNOWLEDGEMENTS

The research is fully funded by the Croatian Science Foundation (HRZZ) within the project "Computational Modelling of Composite Structures Impact Damage" (CONCORDE), grant number UIP-HRZZ-2020-02-9317.

REFERENCES

[1] O.I. Okoli, The effects of strain rate and failure modes on the failure energy of fibre reinforced composites, *Composite Structures*, **54**, 2001, pp. 299-303 (doi: 10.1016/S0263-8223(01)00101-5).

[2] M.H. Kashani, and A.S. Milani, Damage Prediction in Woven and Non-woven Fabric Composites, In book *Non-woven Fabrics* (Ed. H.-Y Jeon), Ch. 10: pp. 233-262, IntechOpen, 2016.

[3] N. Tran, J. Berthe, M. Brieu, Characterization of High Strain Rate Dependency of 3D CFRP Materials, *Conference Proceedings of the Society for Experimental Mechanics Series: Dynamic Behavior of Materials, Vol. 1 (Eds. D. Casem, L. Lamberson, J. Kimberley), Costa Mesa, California, USA, June 8-11, 2015*. Springer, Cham, 2017, pp. 111-116.

[4] L.A. Coles, A. Roy, V. Silberschmidt, Ice Vs. Steel: Ballistic Impact of Woven Carbon/epoxy Composites. Part II – Numerical Modelling, *Engineering Fracture Mechanics*, **225**, 2020, e106297 (doi: 10.1016/j.engfracmech.2018.12.030).

[5] F. Martínez-Hergueta, D. Ares, A. Ridruejo, J. Wiegand, N. Petrinic, Modelling the inplane strain rate dependent behaviour of woven composites with special emphasis on the non-linear shear response. *Composite Structures*, **210**, 2019, pp. 840–857 (doi: 10.1016/j.compstruct.2018.12.002).

[6] J.M. Rodriguez-Sereno, J. Pernas-Sánchez, J.A. Artero-Guerrero, J. López-Puente, A constitutive model for rate-dependency analysis of open hole woven composites under compression loading, *Composite Structures*, **343**, 2024, e118274. (doi: 10.1016/j.compstruct.2024.118274).

[7] S. Murakami, Mechanical Modeling of Material Damage, *Journal of Applied Mechanics*, **55**, 1988, pp. 280-286 (doi: 10.1115/1.3173673).

[8] A. Matzenmiller, J. Lubliner, R.L. Taylor, A constitutive model for anisotropic damage in fiber-composites, *Mechanics of Materials*, **20**, 1995, pp. 125-152 (doi: 10.1016/0167-6636(94)00053-0).

[9] M. Zako, Y. Uetsuji, T. Kurashiki, Finite element analysis of damaged woven fabric composite materials, *Composite Science and Technology*, **63**, 2003, pp. 507-516 (doi: 10.1016/S0266-3538(02)00211-7).

[10] L. Raimondo, L. Iannucci, P. Robinson, P.T. Curtis, A progressive failure model for mesh-size-independent FE analysis of composite laminates subject to low-velocity impact damage, *Composite Science and Technology*, **72**, 2012, pp. 624–632 (doi: 10.1016/j.compscitech.2012.01.007).

[11] X. Hu, J. Tang, W. Xiao, K. Qu, A Strain Rate Dependent Progressive Damage Model for Carbon Fiber Woven Composites under Low Velocity Impact, *Journal of Physics: Conference Series, 2021 The 2nd International Conference on Mechanical Engineering and Materials (ICMEM 2021) 19-20 November 2021, Beijing, China*, **2101**, 2021, e012073 (doi: 10.1088/1742-6596/2101/1/012073).

[12] I. Goda, J. Girardot, Numerical modeling and analysis of the ballistic impact response of ceramic/composite targets and the influence of cohesive material parameters, *International Journal of Damage Mechanics*, **30**, 2021, pp. 1079–1122 (doi: 10.1177/1056789521992107).

[13] D. Bürger, A.R. de Faria, S.F.M. de Almeida, F.C.L. de Melo, M.V. Donadon, Ballistic impact simulation of an armour-piercing projectile on hybrid ceramic/fiber reinforced composite armours, *International Journal of Impact Engineering*, **43**, 2012, pp. 63-77 (doi: 10.1016/j.ijimpeng.2011.12.001).

[14] P.A.A.E. Mendes, M.V. Donadon, Numerical prediction of compression after impact behavior of woven composite laminates, *Composite Structures*, **113**, 2014, pp. 476-491 (doi: 10.1016/j.compstruct.2014.03.051).

[15] T. Ouyang, W. Sun, R. Bao, R. Tan, Effects of matrix cracks on delamination of composite laminates subjected to low-velocity impact, *Composite Structures*, **262**, 2020, e113354 (doi: 10.1016/j.compstruct.2020.113354).

[16] M. McElroy, W. Jackson, R. Olsson, P. Hellström, S. Tsampas, M. Pankow, Interaction of delamination and matrix cracks in a CFRP plate, Part I: A test method for model validation. *Composites Part A*, **103**, 2017, pp. 314-326 (doi: 10.1016/j.compositesa.2017.09.011).

TOWARDS AN ACCELERATED NONLINEAR SOLUTION METHOD INSPIRED BY MULTISCALE AND MULTIGRID METHODS

Ryan Whitehead[1], Keith Ballard[2]

[1]AV, Inc.
Email: ryan.whitehead.4.ctr@us.af.mil

[2]Air Force Research Laboratory
Email: michael.ballard.28@us.af.mil

Keywords: Computational Modelling, Numerical Analysis, FEA

ABSTRACT

Numerical modelling of nonlinear behavior in composites represents a significant computational challenge, which this paper seeks to address. We are developing a family of numerical methods capable of efficiently and accurately solving general nonlinear multiscale problems. The essential components of the method are described along with possible future variations. The results of a preliminary implementation of the basic method are shown for simple linear and nonlinear elasticity. These demonstrate the capability of this approach to produce fine scale results in a scalable fashion.

1 INTRODUCTION

All engineered structures exhibit structural variation across length scales. Material structures at small length scales lead to emergent responses at larger length scales, which complicates modeling the behavior of a material without experimentally testing the response at the relevant length scale. Composite materials exacerbate this challenge by extending the range of possible variation due to the multiple constituents, which simultaneously offers many potential advantages for material design. The phenomenon of progressive failure introduces additional unique challenges as failure modes at small scales eventually coalescence to form a dominant crack at a larger length scale, bridging length scales as failure evolves. These challenges have motived significant effort towards the development of multiscale modeling methods that each aim to strike a particular balance between computational efficiency, which favors modeling at coarser scales, and accuracy, which favors modeling at finer scales.

One collection of popular approaches are the various homogenization and homogenization-adjacent methods, which tend toward computational efficiency over local fine scale accuracy. While these can vary in the details, from asymptotic perturbation approaches [1] to variational techniques [2] to other simplifying assumptions [3, 4], the underlying principle is that the microstructure has sufficient regularity, typically periodic or statistically periodic, that one can consider a small number of local microscale problems, which are generally regarded as infinitesimal compared to the macroscopic domain. Regardless of the specific method, the responses from these microscale problems are then used to determine effective macroscopic properties, with each local problem contributing to the properties of a specific subset of the domain. These models are effective within the assumptions about periodicity and scale separation, such as in a unidirectional fiber composite sheet under loads well within the elastic regime. They can even accommodate moderate deviations from these assumptions, and with further model complexity, their applicability can be extended [1, 3, 5]. However, their effectiveness significantly diminishes when these fundamental assumptions are entirely violated. This limitation is particularly evident in phenomena like discrete fracture, where highly localized fine-scale details and their macroscopic effects pose a significant challenge for homogenization methods.

On the other side of the spectrum are methods which still produce a global fine scale solution but use various techniques to try to accelerate that solution over just directly solving on a global fine mesh. These techniques include domain decomposition [6, 7], multigrid methods [8, 9], and the MsFEM approach [10, 11, 12]. In the first, subdomain problems are alternated with the global problem, while in the second, coarser representations of the problem are alternated with the fine scale representation. In

Distribution Statement A. Approved for public release: distribution is unlimited. Case number: AFRL-2025-3173

both cases, the goal is to save effort on the global fine problem, making progress with other, faster alternatives and somehow incorporating that progress into the global fine solution. The third case does not alternate but instead produces a full set of multiscale basis functions on a relatively coarse grid, which are determined using local solutions on a much finer grid. This frontloads a large amount of effort on a finer grid, but the later solution process involves much fewer degrees of freedom (DoFs), despite a solution with nominally fine grid resolution. While there are technical difficulties that must be addressed in all these cases, especially around discontinuities and nonlinearity, and these methods will in general require more effort than a homogenizing approach, the fact that these methods produce a global fine solution is appealing for complex geometries where the fine detail of the stress and strain is potentially critical anywhere in the component.

A third class of methods are global-local methods, which in some sense combine features of the previous two classes. For much of the domain, a relatively coarse, typically homogenized, method is applied, while at specific regions of interest, typically geometric features like corners and holes which induce stress concentration, a much finer method, possibly just a direct solve on a fully resolved grid, is used [13]. This is feasible as it involves only a smaller portion of the domain. The fine scale solve is then incorporated into the global domain, involving additive error correction, basis enrichment [14] (similar to MsFEM but with a specific solution rather than a general fine basis), or a connection between the fine and coarse solutions through boundary conditions along the fine-coarse boundary. The key to these methods is generally that the fine scale problem is only tackled on small portions of the domain, and hence the effort is minimized while still producing fine detail at the regions of interest.

However, as geometries and microstructures grow both more complex and defy length scale separation, it becomes difficult to determine the location of critical stress concentrations *a priori*. In the most challenging cases, stress concentrations and eventually fracture initiation can form across much of the domain, rendering the traditional global-local ideas irrelevant. In this paper, we describe a method which is applicable to fracture in complex aperiodic geometries, requiring the capability to produce a solution at the finest scale. The method presented combines concepts from multigrid techniques and global-local methods to produce a method that is adapted for efficiency in nonlinear problems and flexibility for a variety of material models.

2 METHODOLOGY

Our proposed method broadly takes the structure of a multigrid method, with the displacement field solved on a hierarchy of meshes of different characteristic sizes, and with corrections passed between them. Nonlinearity is addressed primarily by formulating the coarse grid correction in terms of the Full Approximation Scheme (FAS), in which the right-hand side of the coarsened equations receives a correction term relative to just the coarsening of the original right-hand side. Briefly, given a fine displacement field at iteration n, u_n^f, with residual function r^f, the coarse problem to solve is $r^c(u^c) = r^c\left(P\, u_n^f\right) - P\, r^f(u_n^f)$, where r^c is a suitably defined coarse residual and P is the matrix that maps from a vector on the fine mesh to the corresponding vector on the coarse mesh. The FAS correction is the two terms on the right side, rather than just solving $r^c(u^c) = 0$. Approximately solving this coarser problem hopefully smooths the longer wavelength error components, and the result is used to correct the fine problem, with $u_{n+1}^f = u_n^f + Q(u^c - Pu_n^f)$ where Q is the matrix which maps a coarse vector to its corresponding fine vector. The definitions of r^c, P, Q are what characterize the specific multigrid approach and are discussed below, with particular focus on ensuring that the computational cost of r^c scales appropriately with the mesh size for a nonlinear problem.

The primary distinguishing feature in our approach is the extensive incorporation of operations on an overlapping set of patches covering the domain into the operators r^c, P, and Q. By performing patch-local operations, and blending the results across the overlap regions, globally consistent fields can be obtained without needing to handle globally sized arrays, while also easing parallelism of the method. It also should allow for some degree of adaptivity in the future, where computation is only required for patches where nonlinearity is evolving while leaving the remaining patches unmodified.

Distribution Statement A. Approved for public release: distribution is unlimited. Case number: AFRL-2025-3173

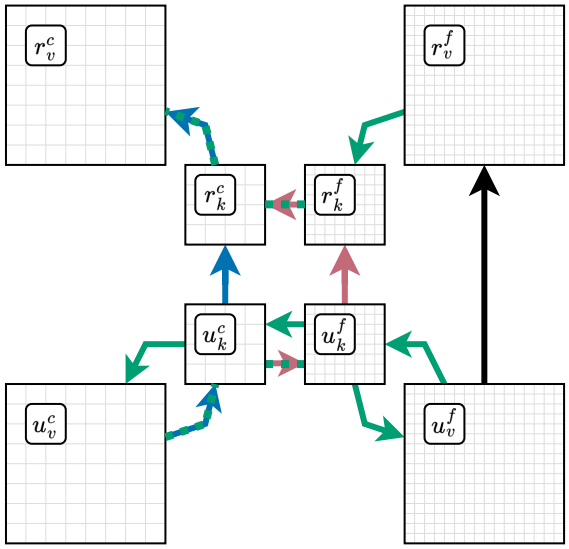

Figure 1: Schematic showing the functional links between patch and global meshes (large and small squares), coarse and fine meshes (left and right sides), and displacements and residuals (bottom and top squares). Blue and red arrows indicate chains of functions over which are autodifferentiated. Green arrows (or arrows with green dashes) are the functions which are composed into the global coarsening and refining maps.

In order to work effectively with unstructured meshes at each scale, none of which necessarily nest with each other, we define our grid transfer operations in terms of L^2 projections between the Finite Element spaces on the respective meshes. Such non-nested meshes greatly increase flexibility in mesh generation while still allowing for each mesh to conform to the features which are present at that scale, so it was important to be able to handle them. However, since a projection defined on the entire domain would quickly become computationally intractable, involving the inversion of a fine-mesh-sized mass matrix $M_{ij}^f = \int \phi^i \phi^j dV$, we instead use projections restricted to the aforementioned patches, which collectively cover the entire domain. The resulting patch projections can then be smoothly blended into a global result. The diagonal and horizontal arrows in green in Figure 1 illustrate the component operations of the overall P and Q (right to left and left to right respectively): splitting from a global array to a collection of patch arrays, projecting the patch arrays, and reassembling the patch arrays into a single global array. Note that we omitted any arrows for refining of the residual, as that is not something required in multigrid. One factor that must be kept in mind with non-nested meshes is the potential for issues along the boundary. When a coarse element barely intersects the fine domain, projection of the "ghost" nodes outside the domain will be poorly conditioned. We are continuing to explore more rigorous bounds on when this ill-conditioning will prevent or impair convergence, but provided the grids are chosen appropriately, it can be mitigated.

The remaining operator to define is the coarse residual. Since for nonlinear problems, the constant re-evaluation of a Galerkin coarse residual $r_g^c(\cdot) = P\, r^f(Q\,\cdot)$ is as expensive as re-evaluating the fine residual itself, even slightly more expensive with the projections, we required a faster approximation. Note that there is no such issue for linear problems, as the coarse matrix can be evaluated once, with subsequent matrix-vector products only involving coarse-mesh-sized arrays. The key is a residual which does not directly invoke the fine problem, and its fine-mesh-sized operations. Our solution was to locally expand this residual as a Taylor series around the current reference displacement, then store the first couple of Taylor coefficient arrays instead. These can be used for a few iterations of nonlinear smoothing, converging towards the zero of the truncated residual, before moving the solver iterations to another scale, eventually returning with an improved reference displacement about which to recompute the coefficient arrays. This still provides meaningful progress towards the exact solution, at a much lower computational cost, before moving to the next scale. Note that the general principle of a multigrid method is that at each scale a portion of the error is smoothed, and the progress is passed either up or down to smooth a different portion of the error. As the reference displacement converges towards the solution, the accuracy of the root of this truncated residual improves, and hence we can still attain similar

Distribution Statement A. Approved for public release: distribution is unlimited. Case number: AFRL-2025-3173

accuracy to the case where we had used the Galerkin residual throughout the process.

A further improvement in speed is possible by performing the Taylor expansion on individual patches and blending the resulting patch residuals into a global residual. While this introduces inaccuracy along the patch boundary nodes, by applying the blending weights to these patch residuals at the fine scale before projecting back, in the "Patch Galerkin" residual whose derivatives are being examined, the resulting errant nodes receive a weight of zero, so accuracy is comparable to the globally computed coefficients. Additionally, the global Jacobian in this approach, while never explicitly formed due to the use of matrix-free global solvers, is markedly sparser due to the coupling of nodes only within patches and more amenable to parallelization. Figure 1 illustrates this patch-wise Taylor coefficient breakdown, with coefficients computed based on the derivatives along the red path and then used for residual evaluation along the blue path. Currently, we are leveraging the automatic differentiation abilities of the JAX library both to automatically compute and cache the derivatives along the red path, as well as to obtain Jacobian-vector products along the blue path for use in a matrix-free solver.

While effort on the coarse mesh dramatically reduces the effort required on the fine mesh, the final component of our proposed method addresses the fact that a multigrid method benefits from smoothing the fine error on the fine mesh. Operating on the entire fine domain is not cheap, but working on each patch independently at the fine scale will in general require less effort, since it scales linearly with the number of patches. Importantly, when applying a smoother at the fine scale, the solution on a patch will likely be inaccurate near the patch boundary, since the solution is fixed based on the solution projected from the coarse scale to ensure well-posedness. However, since the various patch results are blended to obtain the global fine solution, where the edges of each patch receive blending weights of zero, these inaccurate values along patch boundaries contribute little to the resulting fine-scale displacement field. Moreover, by cycling between patch-level iterations at the fine scale and iterative corrections at the coarse scale, according to the principle of multigrid methods, the solution along the boundary of patches at the fine scale improve with each cycle. We will show in the next section that such a cyclic approach can achieve errors well below that of just the coarse grid, while not yet as accurate as a global fine solution. The technique is partly inspired by the GFEM^{gl} technique of Duarte et al [15, 14], although that method was applied only to specific subsets of the domain and incorporated the fine information as a basis enrichment rather than a multigrid correction.

The approach laid out above forms the foundation for a family of patch-based multigrid approaches that we foresee exploring in the future. We could more directly adapt the GFEM^{gl} approach by using the patch solutions as basis enrichment functions. The method could be made at least partly adaptive, with fine scale computational effort only done on those patches in which the coarse solution changed by some threshold. The approach also opens many questions, such as the choice of which scales to act on patch-wise and which to handle as a single global domain or decisions about tradeoffs around the number of iterations on each scale. We will explore these questions and more variations in the future as the general technique is applied to larger, more complex problems.

3 RESULTS

The current implementation of proposed method has not been optimized, so the discussion here will focus on the error convergence performance both on a per-iteration and limiting basis, but we expect that effort on the coarse scale will reduce fine scale effort such that the total time is reduced. This should especially be true as the problem begins to scale up, which given the lack of optimization is not something that has been done at this point. For a rough idea, in the nonlinear sample problem below both the fine scale smoothing across all patches and solving the global coarse problem using already-computed Taylor coefficients took on the order of 30ms, while a global fine scale solution took on the order of 2 seconds. Computing the coefficients is currently the bottleneck, taking multiple seconds as well. However, these times are based on a single CPU, whereas the eventual plan is to work on GPUs, which is straightforward in JAX and which will greatly improve the efficiency of the autodifferentiation. It should also be emphasized that coefficient computation time scales primarily with patch size, which can be fixed independent of problem size, whereas the time for a direct fine scale solve scales with domain size.

The following examples consider an elastic body with nonuniform material properties. Body force

Distribution Statement A. Approved for public release: distribution is unlimited. Case number: AFRL-2025-3173

and boundary conditions were imposed to produce a known non-constant solution, and the displacement field was initialized to a zero solution on both the fine and coarse scales. The fine mesh was composed of 1054 linear triangle elements tiling a rhomboid shape, while the coarse mesh was a structured grid of 113 regular quadrilateral elements that covers the fine domain. The meshes were divided into 9 overlapping patches in a 3 by 3 layout. Figure 2 shows the global meshes on the left, with the overlapping bands highlighted in green. On the right, both meshes are split out onto individual patches, illustrating the boundary mismatch between the two.

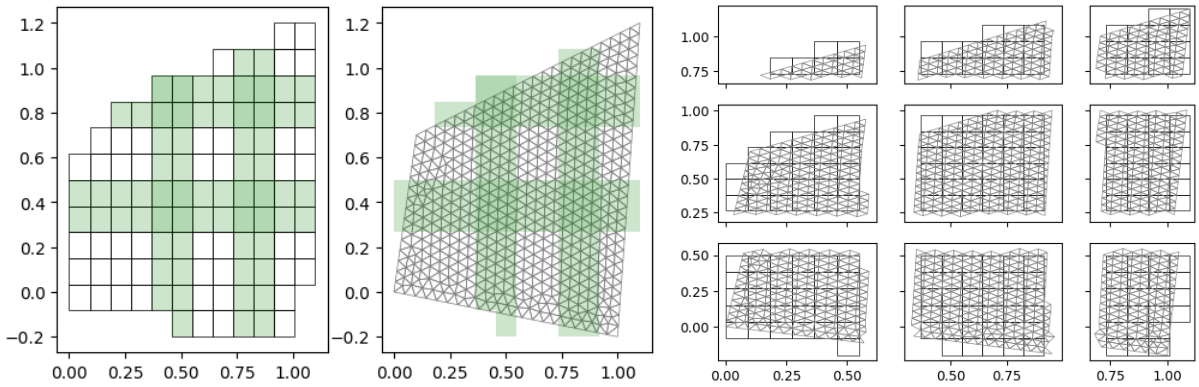

Figure 2: Trial problem mesh structure for coarse (left) and fine (middle) meshes. Green bands denote the overlap regions between neighboring patches. Individual patches are shown on the right.

Dirichlet boundary conditions were enforced directly in the residual function through the Taylor coefficients, and consequently, the coarse mesh received no explicit boundary conditions. However, boundary conditions were explicitly imposed on the fine solution after every fine update. Figure 3 shows the magnitude of the constructed exact solution used in the following problems alongside its coarse projection.

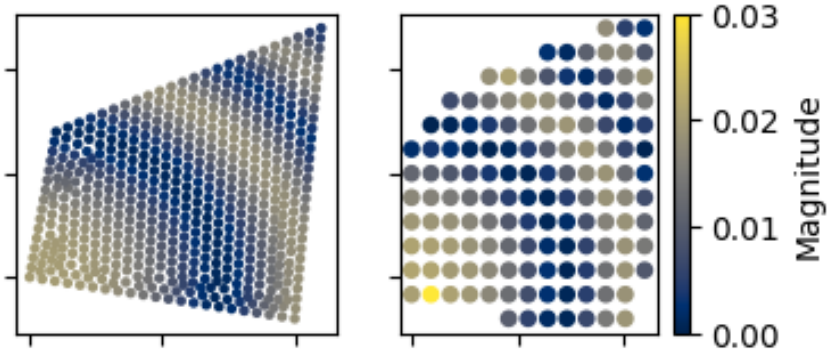

Figure 3 Manufactured fine grid solution (left) and the patch-wise projection onto the coarser grid (right) using the patches shown in Figure 2

3.1 Solving Exclusively on the Coarse Mesh

Figure 3 shows the evolution of the L^2 error of a linear elastic and geometrically nonlinear elastic problem solved only on the coarser grid, with the only fine mesh action being implicit in the re-computing of Taylor coefficients periodically. Each odd tick on the x-axis corresponds to a global solve on the coarse mesh. For the nonlinear case, that involved four Newton iterations using one set of Taylor coefficients, while for the linear case a single use of a direct solver suffices. In both cases, the required linear system solves were done to machine precision. Each even tick on the x-axis denotes an update of the Taylor coefficients, which in the linear case amounts to changing the right-hand side of the FAS equation since the higher order coefficients are constant.

Distribution Statement A. Approved for public release: distribution is unlimited. Case number: AFRL-2025-3173

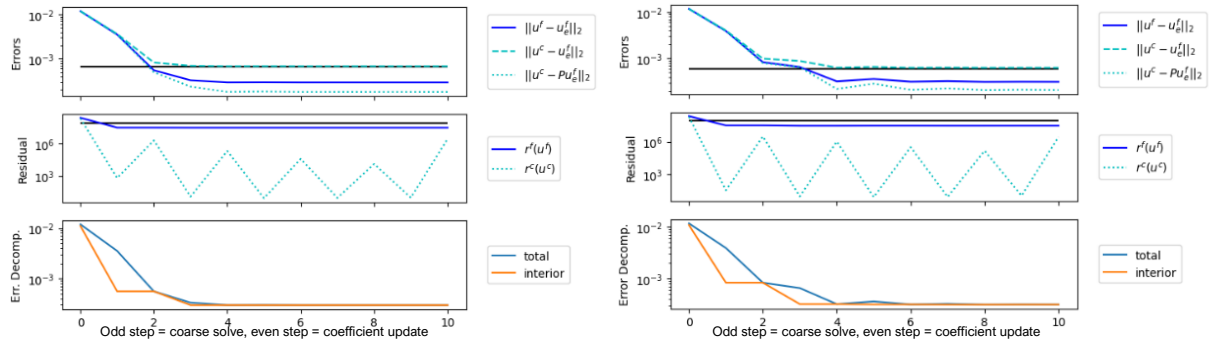

Figure 4: Error and residual convergence for linear (left) and nonlinear (right) elastic materials, alternating coarse iterations with coefficient updates.

The horizontal line in black for the error indicates the "coarsening error", that is $\left\|Pu_{ex}^{f} - u_{ex}^{f}\right\|_2$. Since in a multigrid FAS cycle, the coarse solution will converge to Pu_{ex}^{f}, this is in some sense the best case for the coarse solution, and indeed the error of the coarse solution against the fine bottoms out there. However, even though we are at no point solving the fine problem, just using these coarse updates and imposing the Dirichlet conditions is sufficient to produce a fine solution that is slightly more accurate. This is further illustrated by the first few pairs of steps in the third plot, which separates the error specifically on interior nodes. It should also be pointed out that the coarse residual is not actually oscillating between multiple orders of magnitude. Since each even step updates the coefficients, we are using a new, theoretically more accurate, residual function on the same coarse displacement, and thus seeing some of the remaining error in the coarse solution.

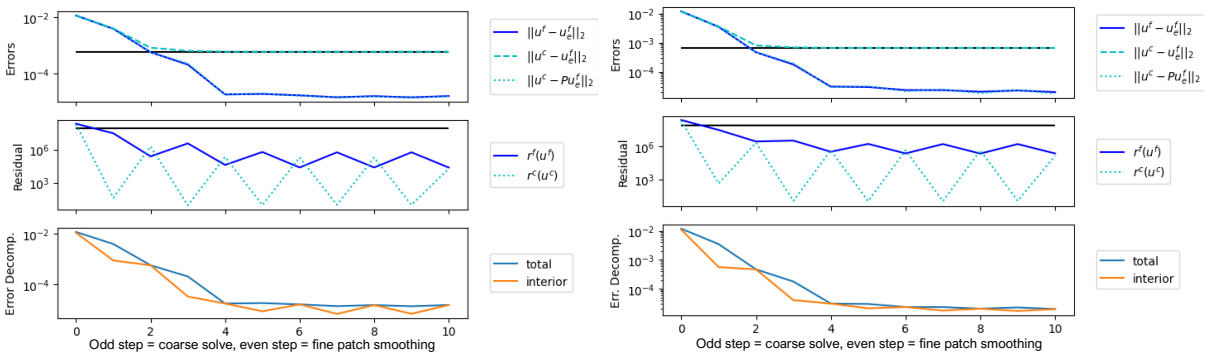

Figure 5: Error and residual convergence for linear (left) and nonlinear (right) elastic materials, alternating coarse iterations with fine patch iterations.

3.2 Incorporating a Smoother on Fine Scale Patches

In the previous section, solves are only performed on the coarse mesh using the projected Taylor coefficients from the fine mesh, but in this section, we illustrate the effect of alternating between coarse scale solutions and fine patch smoothing for the same two problems. Figure 5 shows the error and residual information as before, which shows that the fine scale smoothing dramatically improve the limiting accuracy of the solution. Interestingly, the rate of convergence is similar for the first few cycles compared to the case of exclusively using coarse solves in the previous section. However, the convergence does bottom out abruptly after the second cycle. The third row of plots in Figure 8 separately shows the error within the interior of the domain and the total error, which shows that the interior error fluctuates without affecting the total error. While numerical precision contributes to this issue, this also suggests that solves on the coarse mesh improve interior nodes while also negatively impacting the error along the boundary. It is therefore possible that better handling of the boundary could further improve the asymptotic level of convergence. Further simulations have also shown that the asymptotic convergence level is sensitive to the details of the patch layout in ways that are not yet fully

Distribution Statement A. Approved for public release: distribution is unlimited. Case number: AFRL-2025-3173

clear. However, we anticipate being able to reduce the asymptotic error significantly further.

4 CONCLUSIONS

We have implemented a novel multigrid technique which takes influence from a variety of existing multiscale methods to enable rapid solution of complex multiscale nonlinear problems. In principle, it can be applied directly to any nonlinear phenomenon for which we can model the fine scale behavior. We have demonstrated the capacity to solve nonlinear elastic problems to well below the error level of a coarse mesh using solely coarse solves and patch-local smoothing. Interestingly, the nonlinear and linear cases demonstrated similar convergence rates and asymptotic levels. As this study considered only geometrically nonlinear hyperelasticity, which is smooth in nature, it remains to be seen whether more complex nonlinearity, particularly highly localized nonlinearity such as cohesive fracture, exhibits a similar behavior.

Moving forward, we are prioritizing transitioning the implementation to GPUs. This will be simplified greatly by the fact that the current implementation is built in JAX, which can be adapted to GPUs nearly transparently. The GPU transition will allow for significant scaleup in feasible problem size, allowing for the exploration of larger meshes, deeper mesh hierarchies, and three-dimensional domains. The other main priority is expanding the breadth of physical phenomena under consideration, especially incorporating fracture. As noted above, this only requires implementing the fine scale model of these phenomena in our JAX-based framework, as the coarser levels incorporate the nonlinear physics through the Taylor coefficients, independent of the underlying mechanisms.

ACKNOWLEDGEMENTS

We thank AFOSR Program Officer Dr. Greg Abate for support through LRIR 24RXCOR005. We are also grateful to Professors Mike Kirby and Varun Shankar at University of Utah for their insights in the course of our regular discussions, as well as Professor Hari Sundar at Tufts University for his expertise in Multigrid methods.

REFERENCES

[1] A. Bacigalupo, "Second-order homogenization of periodic materials based on asymptotic approximation of the strain energy: formulation and validity limits," *Meccanica,* pp. 1407-1425, 2014.

[2] W. Yu and T. Tang, "Variational asymptotic method for unit cell homogenization of periodically heterogeneous materials," *International Journal of Solids and Structures,* pp. 3738-3755, 2007.

[3] R. Haj-Ali and J. Aboudi, "Nonlinear micromechanical formulation of the high fidelity generalized method of cells," *International Journal of Solids and Structures,* pp. 2577-2592, 2009.

[4] S. Arnold, B. Bednarcyk and J. Aboudi, "Comparison of the computational efficiecy of the original and reformulated high-fidelity generatlized method of cells," NASA, 2004.

[5] L. Zhang, W. Yu, J. Fernandez and A. Bergan, "Nonlinear Homogenization of Finitely Deformed Viscoelastic-Viscoplastic Composites Using Mechanics of Structure Genome," in *AIAA Scitech 2021 Forum*, 2021.

[6] C. Farhat and F. Roux, "A method of finite element tearing and interconnecting and its parallel solution algorithm," *International Journal for Numerical Methods in engineering,* pp. 1205-1227, 1991.

[7] C. Farhat, M. Lesoinne and P. LeTallec, "FETI-DP: a dual-primal unified FETI method -- part I: A faster alternative to the two-level FETI method," *International Journal for Numerical Methods in Engineering,* pp. 1523-1544, 2001.

[8] A. Brandt and O. Livne, Multigrid Techniques: 1984 Guide with Applications to Fluid Dynamics, Revised Edition, SIAM, 2011.

[9] V. Henson, "Multigrid methods nonlinear problems: an overview," *Computational Imaging,* pp.

Distribution Statement A. Approved for public release: distribution is unlimited. Case number: AFRL-2025-3173

36-48, 2003.

[10] T. Hou and X. Wu, "A Multiscale Finite Element Method for Elliptic Problems in Composite Materials and Porous Media," *Journal of Computational Physics,* pp. 169-189, 1997.

[11] P. Henning and D. Peterseim, "Oversampling for the Multiscale Finite Element Method," *Multiscale Modeling & Simulation,* pp. 1149-1175, 2013.

[12] Y. Efendiev, J. Galvis and T. Hou, "Generalized Multiscale Finite Element Methods (GMsFEM)," *Journal of Computational Physics,* pp. 116-135, 2013.

[13] D. Kim, J. Pereira and C. Duarte, "Analysis of three-dimensional fracture mechanics problems: A two-scale approach using coarse-generalized FEM meshes," *International Journal for Numerical Methods in Engineering,* pp. 335-365, 2010.

[14] B. Mazurowski, P. O'Hara and C. Duarte, "On-the-fly multiscale analysis of composite materials with a Generalized Finite Element Method}," *Finite Elements in Analysis and Design,* pp. 1-26, 2024.

[15] A. Duarte, D. Kim and I. Babuška, "A Global-Local aproach for the construction of enrichment functions for the generalized FEM and Its Application to Three-Dimensional Cracks," in *Advances in Meshfree Techniques*, Dordrecht, 2007.

Distribution Statement A. Approved for public release: distribution is unlimited. Case number: AFRL-2025-3173

ICCM24
AUGUST 4-8, 2025
BALTIMORE CONVENTION CENTER
BALTIMORE, MARYLAND, USA

No Technical Paper Submission for:

Richard Butler

Influence of the fiber curvature on the mechanical properties of long fiber reinforced composites

Celine Lauff, Matti Schneider, Thomas Böhlke | 04.08.2025, ICCM 2025



Motivation

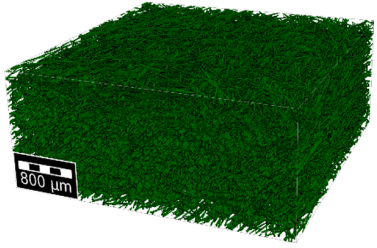

(Andrä et al., 2014)

Information on real microstructures, e.g., from μCT-scans

Microstructure generation

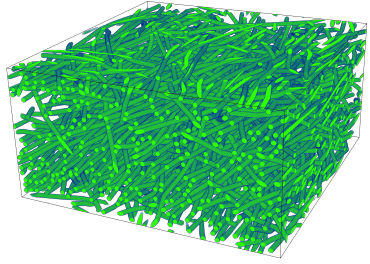

Synthetic microstructures

State of the art - selected literature

Modeling the fibers as straight cylinders:

- Sequential insertion algorithms:
  - Random sequential addition (RSA) algorithm
    (Feder, 1980; Widom, 1966)
  - Extensions of the RSA algorithm
    (Chen et al., 2019; Lauff et al., 2023; Tian et al., 2015, 2021)
- Collective rearrangement algorithms:
  - Mechanical contraction method (MCM)
    (Williams et al., 2003)
  - Sequential addition and migration (SAM) algorithm
    (Mehta et al., 2022, 2024; Schneider, 2017)

↯ limited to short fiber-reinforced microstructures

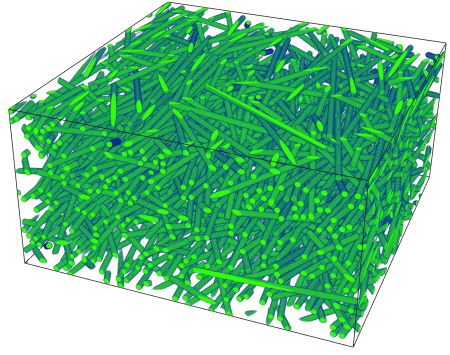

State of the art - selected literature

Modeling the fibers with curvature:

- RSA and compression in thickness direction
  (Fliegener et al., 2014)
  - \+ Enables industrial fiber packings
  - \- Computationally complex finite element analysis is necessary
- Fused sequential addition and migration algorithm
  (Lauff et al., 2025a, 2024)
  - \+ Computationally efficient
  - \+ Enables industrial fiber packings

↯ no fiber curvature control

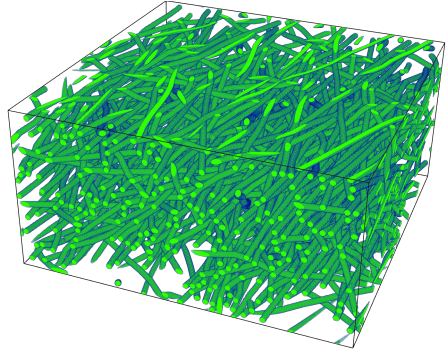

Overview

1 Description of discontinuous long fiber-reinforced microstructures

2 fSAM algorithm for long and curved fibers

3 Extension of the fSAM algorithm for curvature control

4 Computational investigations

Description of discontinuous long fiber-reinforced microstructures

Curved fiber

- Fiber described by curve:

$$\boldsymbol{c}_i : [0, L_i] \longrightarrow Q,$$
$$Q = [0, Q_1] \times [0, Q_2] \times [0, Q_3]$$

- Parametrization by arc length:

$$\|\boldsymbol{c}_i'(s)\| = 1, \quad s \in [0, L_i]$$

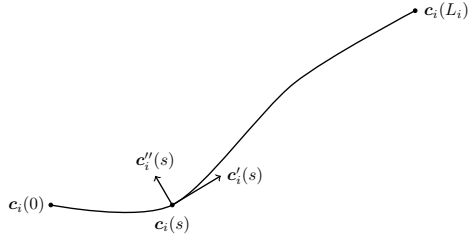

description of a curved fiber

(Schneider, 2022)

Description of discontinuous long fiber-reinforced microstructures

Fiber orientation tensors

(Advani et al., 1987)

$$\mathbb{A}_{\langle k \rangle} = \frac{1}{L} \sum_{i=1}^{N} \int_0^{L_i} \boldsymbol{c}_i'(s)^{\otimes k} \, \mathrm{d}s$$

$$\boldsymbol{A} \equiv \mathbb{A}_{\langle 2 \rangle}, \quad \mathbb{A} \equiv \mathbb{A}_{\langle 4 \rangle}, \quad L = \sum_{i=1}^{N} L_i$$

Description of discontinuous long fiber-reinforced microstructures

Fiber orientation tensors

(Advani et al., 1987)

$$\mathbb{A}_{\langle k \rangle} = \frac{1}{L} \sum_{i=1}^{N} \int_0^{L_i} \boldsymbol{c}_i'(s)^{\otimes k} \, \mathrm{d}s$$

$$\boldsymbol{A} \equiv \mathbb{A}_{\langle 2 \rangle}, \quad \mathbb{A} \equiv \mathbb{A}_{\langle 4 \rangle}, \quad L = \sum_{i=1}^{N} L_i$$

Fiber volume fraction

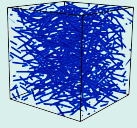

$\phi = 5\%$

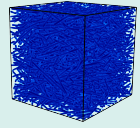

$\phi = 20\%$

$$\phi = \frac{V_f}{V}$$

Description of discontinuous long fiber-reinforced microstructures

Fiber orientation tensors

(Advani et al., 1987)

$$\mathbb{A}_{\langle k \rangle} = \frac{1}{L} \sum_{i=1}^{N} \int_0^{L_i} \boldsymbol{c}_i'(s)^{\otimes k} \, \mathrm{d}s$$

$$\boldsymbol{A} \equiv \mathbb{A}_{\langle 2 \rangle}, \quad \mathbb{A} \equiv \mathbb{A}_{\langle 4 \rangle}, \quad L = \sum_{i=1}^{N} L_i$$

Fiber volume fraction

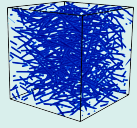

$\phi = 5\%$

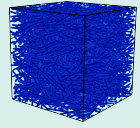

$\phi = 20\%$

$$\phi = \frac{V_f}{V}$$

Fiber length distribution

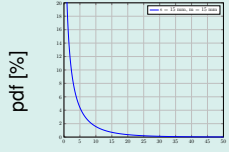

aspect ratio:

$$r_a = \frac{L_{\text{mean}}}{D}$$

Description of discontinuous long fiber-reinforced microstructures

Fiber orientation tensors

(Advani et al., 1987)

$$\mathbb{A}_{\langle k \rangle} = \frac{1}{L} \sum_{i=1}^{N} \int_0^{L_i} \boldsymbol{c}_i'(s)^{\otimes k} \, \mathrm{d}s$$

$$\boldsymbol{A} \equiv \mathbb{A}_{\langle 2 \rangle}, \quad \mathbb{A} \equiv \mathbb{A}_{\langle 4 \rangle}, \quad L = \sum_{i=1}^{N} L_i$$

Fiber volume fraction

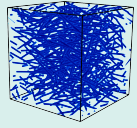

$\phi = 5\%$

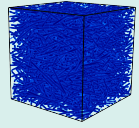

$\phi = 20\%$

$$\phi = \frac{V_f}{V}$$

Fiber length distribution

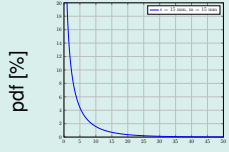

aspect ratio:

$$r_a = \frac{L_{\text{mean}}}{D}$$

Size of the unit cell

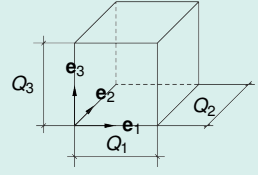

$$V = Q_1 Q_2 Q_3$$

Overview

1 Description of discontinuous long fiber-reinforced microstructures

2 fSAM algorithm for long and curved fibers

3 Extension of the fSAM algorithm for curvature control

4 Computational investigations

fSAM algorithm for long and curved fibers

Discretization for long and curved fibers

- Parametrization:

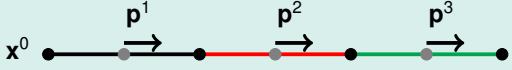

starting point $\mathbf{x}^0$
directions $\mathbf{p}^a$
lengths $\ell = \frac{L}{n}$

$\Big\}\ a = 1, \ldots, n$

fSAM algorithm for long and curved fibers

Discretization for long and curved fibers

- Parametrization:

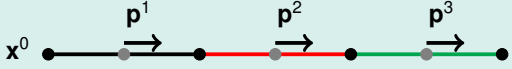

starting point $\mathbf{x}^0$
directions $\mathbf{p}^a$
lengths $\ell = \frac{L}{n}$

$\Big\}\ a = 1, \dots, n$

- Coordinate vector:

$$\mathbf{q} = \left[\left(\hat{\mathbf{x}}^0\right)^{\mathsf{T}} \quad \left(\mathbf{p}^1\right)^{\mathsf{T}} \quad \cdots \quad \left(\mathbf{p}^n\right)^{\mathsf{T}} \right]^{\mathsf{T}}$$

with normalization:

$$\hat{\mathbf{x}}^0 = \hat{\mathbf{Q}}^{-1}\,\mathbf{x}^0 \quad \text{with} \quad \hat{\mathbf{Q}} = \mathtt{diag}(Q_1, Q_2, Q_3)$$

fSAM algorithm for long and curved fibers

Discretization for long and curved fibers

- Parametrization:

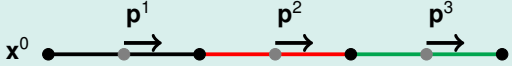

starting point $\mathbf{x}^0$
directions $\mathbf{p}^a$
lengths $\ell = \frac{L}{n}$
$\Big\}\ a = 1, \dots, n$

- Coordinate vector:

$$\mathbf{q} = \left[\left(\hat{\mathbf{x}}^0\right)^\mathsf{T} \quad \left(\mathbf{p}^1\right)^\mathsf{T} \quad \cdots \quad \left(\mathbf{p}^n\right)^\mathsf{T} \right]^\mathsf{T}$$

with normalization:

$$\hat{\mathbf{x}}^0 = \hat{\mathbf{Q}}^{-1}\,\mathbf{x}^0 \quad \text{with} \quad \hat{\mathbf{Q}} = \mathtt{diag}(Q_1, Q_2, Q_3)$$

Configuration space

$$\mathcal{R} = \left\{ \mathbf{q} \in \mathbb{R}^{3(n+1)} \mid \boldsymbol{\Phi}_1(\mathbf{q}) = \mathbf{0} \right\},$$

$$\boldsymbol{\Phi}_1(\mathbf{q}) \mathrel{\hat{=}} \left[\Phi_1^1(\mathbf{q}) \quad \cdots \quad \Phi_1^n(\mathbf{q}) \right]^\mathsf{T} \quad \text{with} \quad \Phi_1^a(\mathbf{q}) = \frac{1}{2}\left(\|\mathbf{p}^a\|^2 - 1 \right), \quad a = 1, \dots, n$$

fSAM algorithm for long and curved fibers

Minimization problem

$$F(\mathbf{q}_1, \ldots, \mathbf{q}_n) \longrightarrow \min_{\mathbf{q}_1,\ldots,\mathbf{q}_n} \quad \mathbf{q}_i \in \mathcal{R}_i$$

$$F(\mathbf{q}_1, \ldots, \mathbf{q}_n) \mathrel{\hat{=}} \underbrace{\frac{1}{2} \sum_{i,j=1}^{N} \sum_{a=1}^{n_i} \sum_{b=1}^{n_j} \left(\delta_{ij}^{ab}\right)^2 + \frac{w_{\mathbb{A}}}{8} \|\mathbb{A} - \mathbb{A}^{\mathrm{r}}\|^2}_{\text{non-overlap condition and fiber orientation tensor}}$$

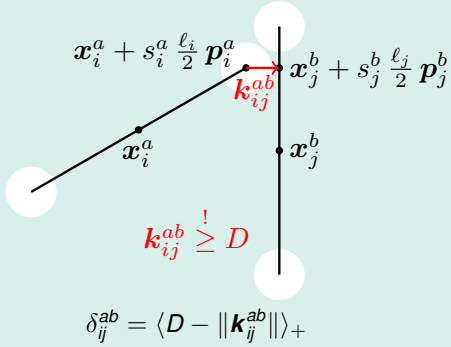

fSAM algorithm for long and curved fibers

Minimization problem

$$F(\mathbf{q}_1, \ldots, \mathbf{q}_n) \longrightarrow \min_{\mathbf{q}_1,\ldots,\mathbf{q}_n} \quad \mathbf{q}_i \in \mathcal{R}_i$$

$$F(\mathbf{q}_1, \ldots, \mathbf{q}_n) \mathrel{\hat{=}} \underbrace{\frac{1}{2} \sum_{i,j=1}^{N} \sum_{a=1}^{n_i} \sum_{b=1}^{n_j} \left(\delta_{ij}^{ab}\right)^2 + \frac{w_{\mathbb{A}}}{8} \|\mathbb{A} - \mathbb{A}^{\mathrm{r}}\|^2}_{\text{non-overlap condition and fiber orientation tensor}}$$

$$+ \underbrace{\frac{w_\rho}{2} \sum_{i=1}^{N} \sum_{a=1}^{n_i - 1} \left(\rho_i^a\right)^2}_{\text{angle constraint}}$$

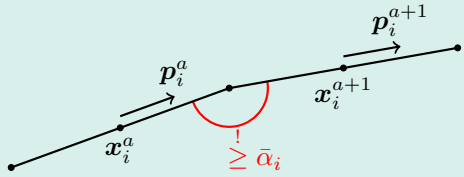

$$\rho_i^a = \left\langle \cos\alpha_i - \boldsymbol{p}_i^{a+1} \cdot \boldsymbol{p}_i^a \right\rangle_+$$

Overview

1 Description of discontinuous long fiber-reinforced microstructures

2 fSAM algorithm for long and curved fibers

3 Extension of the fSAM algorithm for curvature control

4 Computational investigations

Extension of the fSAM algorithm for curvature control

Quantifying the fiber curvature of a single fiber

- Fiber orientation of a single fiber:

$$\boldsymbol{A}_f = \frac{1}{L} \int_0^L \boldsymbol{c}'(s) \otimes \boldsymbol{c}'(s) \, \mathrm{d}s$$

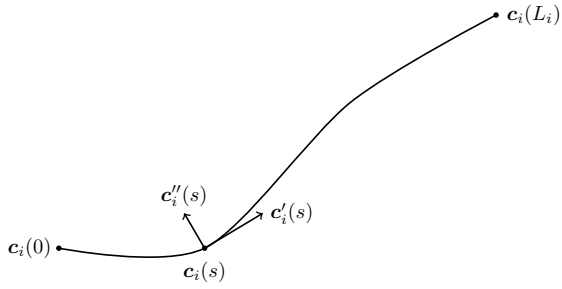

description of a curved fiber

(Schneider, 2022)

Extension of the fSAM algorithm for curvature control

Quantifying the fiber curvature of a single fiber

- Fiber orientation of a single fiber:

$$\boldsymbol{A}_f = \frac{1}{L}\int_0^L \boldsymbol{c}'(s) \otimes \boldsymbol{c}'(s)\,\mathrm{d}s$$

- Deviation from straight curve (DSC):

$$K_f = \mathrm{tr}\left(\frac{1}{L}\int_0^L \left(\boldsymbol{A}_f - \boldsymbol{c}'(s) \otimes \boldsymbol{c}'(s)\right)^{\otimes 2}\,\mathrm{d}s\right)$$
$$= 1 - \|\boldsymbol{A}_f\|^2$$

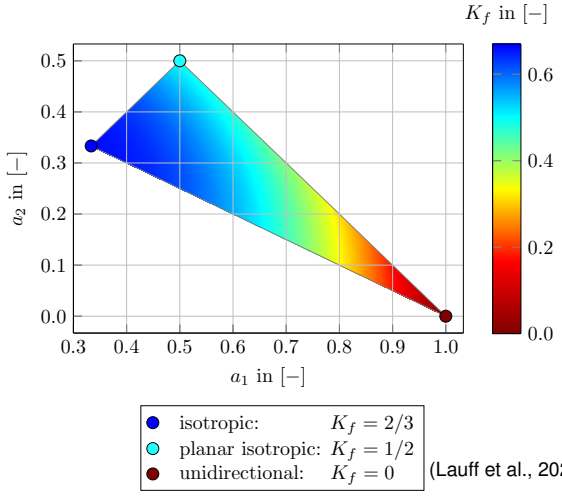

(Lauff et al., 2025b)

Extension of the fSAM algorithm for curvature control

Quantifying the fiber curvature of a single fiber

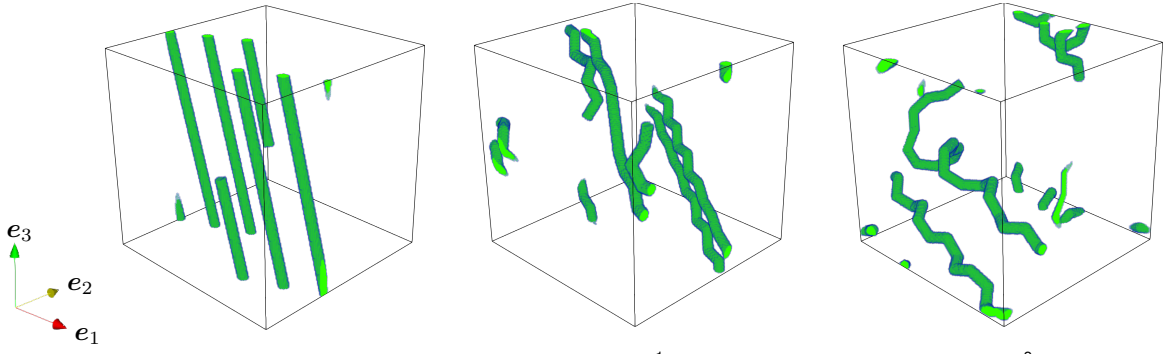

(a) $K_f = 0$ (b) $K_f = \frac{1}{3}$ (c) $K_f = \frac{2}{3}$

(Lauff et al., 2025b)

Extension of the fSAM algorithm for curvature control

Volume-averaged DSC:

$$\bar{K} = \frac{1}{L_{\text{total}}} \sum_{i=1}^{N} L_i \, K_f^i,$$

Objective function with extended curvature control

$$F(\mathbf{q}_1, \ldots, \mathbf{q}_n) \longrightarrow \min_{\mathbf{q}_1, \ldots, \mathbf{q}_n} \quad \mathbf{q}_i \in \mathcal{R}_i$$

$$F(\mathbf{q}_1, \ldots, \mathbf{q}_n) \hat{=} \underbrace{\frac{1}{2} \sum_{i,j=1}^{N} \sum_{a=1}^{n_i} \sum_{b=1}^{n_j} \left(\delta_{ij}^{ab}\right)^2 + \frac{w_{\mathbb{A}}}{8} \|\mathbb{A} - \mathbb{A}^{\mathrm{r}}\|^2}_{\text{non-overlap condition and fiber orientation tensor}} + \underbrace{\frac{w_\rho}{2} \sum_{i=1}^{N} \sum_{a=1}^{n_i - 1} \left(\rho_i^a\right)^2}_{\text{angle constraint}} + \underbrace{\frac{w_{\bar{K}}}{8} n_s \left(\bar{K} - \bar{K}^{\mathrm{r}}\right)^2}_{\text{DSC}}$$

Overview

1 Description of discontinuous long fiber-reinforced microstructures

2 fSAM algorithm for long and curved fibers

3 Extension of the fSAM algorithm for curvature control

4 Computational investigations

Computational investigations

Algorithmic Choices

- Relative error of the fiber orientation state < 10^{-4}
- Relative error of the DSC state < 10^{-3}
- Minimum distance: $2.0 \mu m$
- Maximum segment length: $\bar{\ell} = 25 \mu m$
- Maximum bending angle: $\bar{\alpha} = 30°$
- Closure approximation: Exact closure
  (Montgomery-Smith et al., 2011a,b)

Computational investigations

Algorithmic Choices

- Relative error of the fiber orientation state $< 10^{-4}$
- Relative error of the DSC state $< 10^{-3}$
- Minimum distance: $2.0 \mu m$
- Maximum segment length: $\bar{\ell} = 25 \mu m$
- Maximum bending angle: $\bar{\alpha} = 30°$
- Closure approximation: Exact closure
  (Montgomery-Smith et al., 2011a,b)

Material

- $Q_i = 400 \mu$m
- $D = 10 \mu m$
- $L = 1000 \mu$m
- $\boldsymbol{A} \hat{=} \texttt{diag}\,(0.75, 0.15, 0.1)$

Computational investigations

Algorithmic Choices

- Relative error of the fiber orientation state < 10^{-4}
- Relative error of the DSC state < 10^{-3}
- Minimum distance: $2.0\mu m$
- Maximum segment length: $\bar{\ell} = 25\mu m$
- Maximum bending angle: $\bar{\alpha} = 30°$
- Closure approximation: Exact closure
  (Montgomery-Smith et al., 2011a,b)

Material

- $Q_i = 400\mu$m
- $D = 10\mu m$
- $L = 1000\mu$m
- $\boldsymbol{A} \hat{=} \mathtt{diag}\,(0.75, 0.15, 0.1)$

Homogenization with an FFT-Solver (Schneider, 2021; Zeman et al., 2010)

- Approximation of the **orthotropic** engineering constants
- Polypropylene matrix: $E = 1.25$ GPa, $\nu = 0.35$ (DOW® Chemical Company, 2003)
- E-glass fibers: $E = 72.0$ GPa, $\nu = 0.22$ (PPG Fiber Glass, 2013)

Computational investigations

Generated microstructures with varying fiber curvature

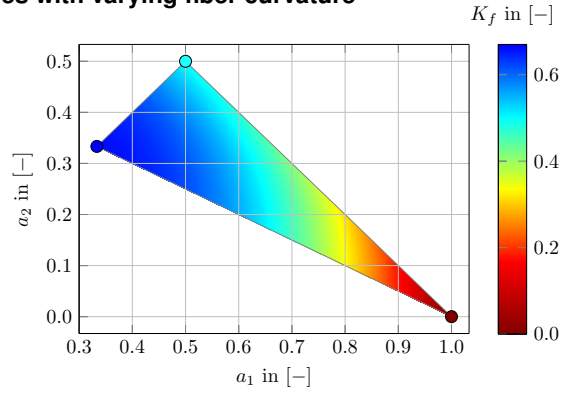

isotropic:	$K_f = 2/3$
planar isotropic:	$K_f = 1/2$
unidirectional:	$K_f = 0$

(Lauff et al., 2025b)

Computational investigations

Generated microstructures with varying fiber curvature

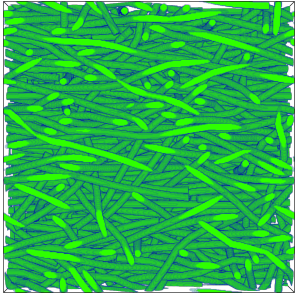

(a) $\bar{K} = 0.06$

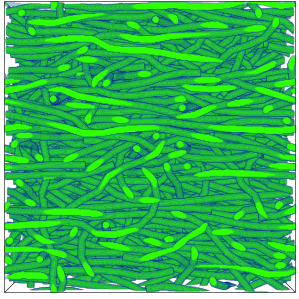

(b) $\bar{K} = 0.15$

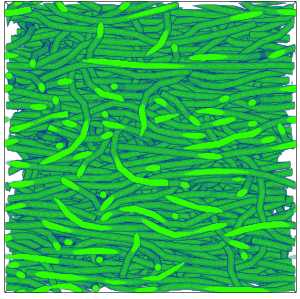

(c) $\bar{K} = 0.25$

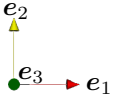

(Lauff et al., 2025b)

Computational investigations

Runtime for the microstructure generation

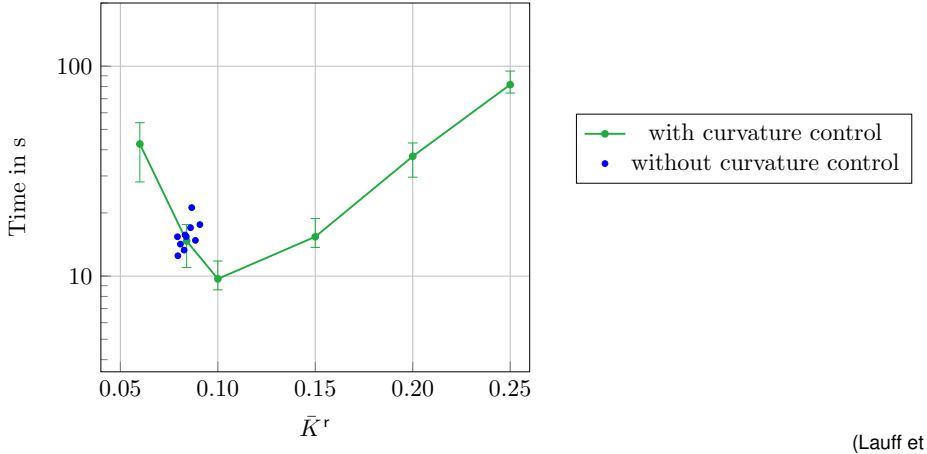

(Lauff et al., 2025b)

Computational investigations

Effect of the fiber curvature on the mechanical properties

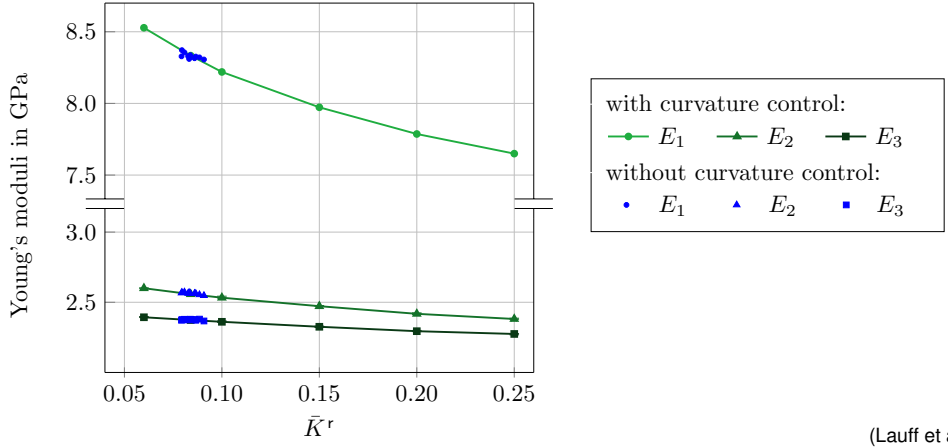

(Lauff et al., 2025b)

Computational investigations

Effect of the fiber curvature on the mechanical properties

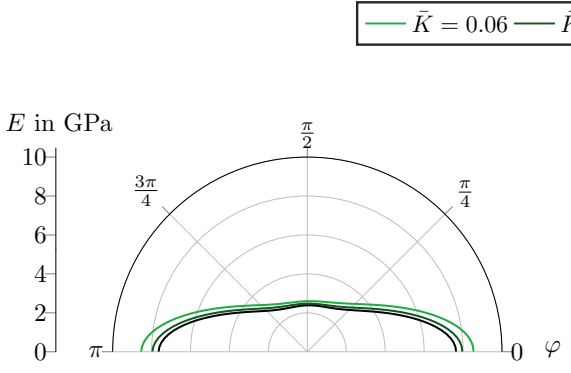

Computational investigations

Effect of the fiber curvature on the mechanical properties

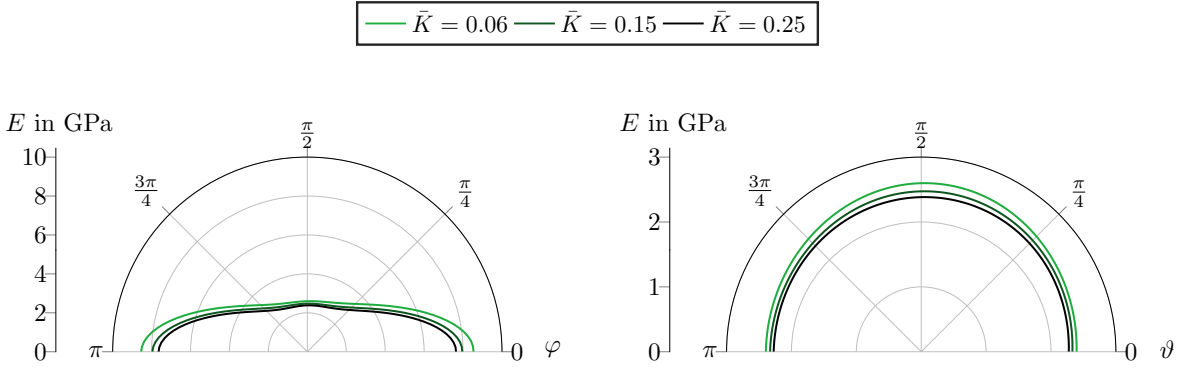

Computational investigations

Study on the maximum segment length

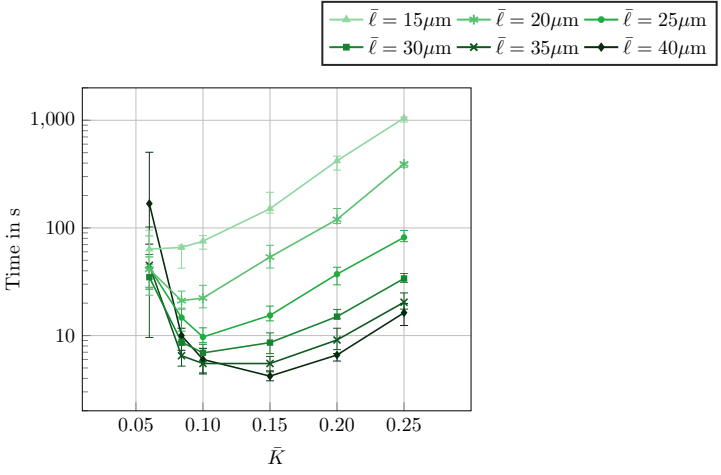

(Lauff et al., 2025b)

Computational investigations

Study on the maximum segment length

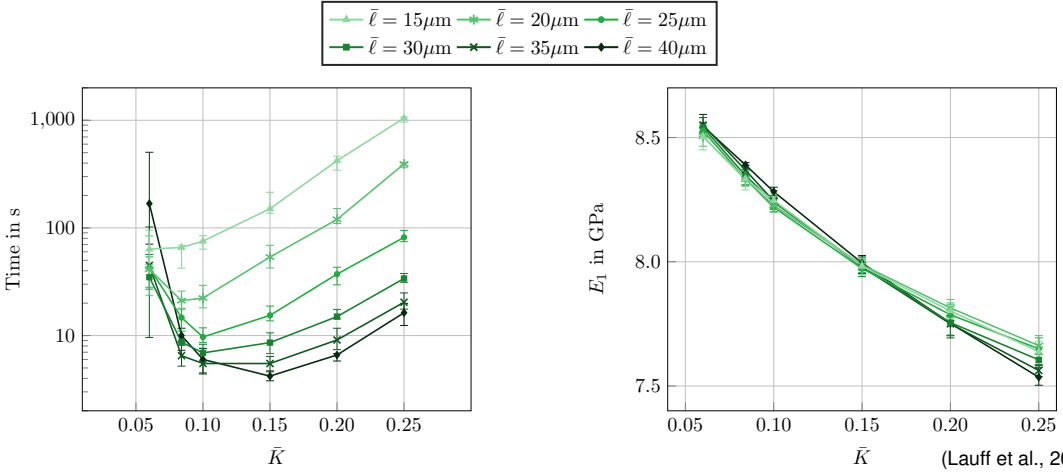

(Lauff et al., 2025b)

Conclusion

- fSAM algorithm with **fiber curvature control**
  - Novel measure to quantify the fiber curvature: **deviation from straight curve** (DSC)
  - Extension of the objective function

Conclusion

- fSAM algorithm with **fiber curvature control**
  - Novel measure to quantify the fiber curvature: **deviation from straight curve** (DSC)
  - Extension of the objective function
- Computational investigations
  - fSAM algorithm is capable of realizing a **wide spectrum of curvatures**
  - Significant **Young's moduli reduction** for increased fiber curvature

Karlsruhe Institute of Technology

CoDiCo FRP

Thank you for your attention!

The research documented in this presentation has been funded by the German Research Foundation (DFG), project number 255730231, within the International Research Training Group “Integrated engineering of continuous-discontinuous long fiber-reinforced polymer structures” (GRK 2078). The support by the German Research Foundation is gratefully acknowledged.

FAST · IAM Institut für Angewandte Materialien · wbk · FM · IFM · IPEK Institut für Produktentwicklung am KIT · Fraunhofer IWM · Fraunhofer ICT

Western International Composites Research Centre (ICRC) · University of Windsor · University of Toronto · McGill University · University of Waterloo · MMRI McMaster Manufacturing Research Institute · FPC @ Western

Literature I

Advani, S. G. and C. L. Tucker III (1987). “The Use of Tensors to Describe and Predict Fiber Orientation in Short Fiber Composites”. In: *Journal of Rheology* 31.8, pp. 751–784.

Andrä, H. et al. (2014). “Geometric and Mechanical Modeling of Fiber-Reinforced Composites”. In: *Proceedings of the 2nd International Congress on 3D Materials Science*. Cham: Springer International Publishing, pp. 35–40.

Chen, L. et al. (2019). “Study of the Effectiveness of the RVEs for Random Short Fiber Reinforced Elastomer Composites”. In: *Fibers and Polymers* 20.7, pp. 1467–1479.

DOW® Chemical Company (2003). *C711–70RNA Polypropylene Resin. Product Information*.

Feder, J. (1980). “Random Sequential Adsorption”. In: *Journal of Theoretical Biology* 87.2, pp. 237–254.

Fliegener, S., M. Luke, and P. Gumbsch (2014). “3D Microstructure Modeling of Long Fiber Reinforced Thermoplastics”. In: *Composites Science and Technology* 104, pp. 136–145.

Lauff, C., M. Schneider, and T. Böhlke (2025a). “Microstructure Generation of Long Fiber Reinforced Hybrid Composites Using the Fused Sequential Addition and Migration Method”. In: *Journal of Thermoplastic Composite Materials* Online First.

Literature II

Lauff, C. et al. (2023). “An Orientation Corrected Shaking Method for the Microstructure Generation of Short Fiber-Reinforced Composites with Almost Planar Fiber Orientation”. In: *Composite Structures* 322, p. 117352.

— (2024). “Generating Microstructures of Long Fiber Reinforced Composites by the Fused Sequential Addition and Migration Method”. In: *International Journal for Numerical Methods in Engineering* 125.22, e7573.

Lauff, C. et al. (2025b). “On the Influence of the Fiber Curvature on the Stiffness of Long Fiber Reinforced Composites”. In: *Submitted*.

Mehta, A. and M. Schneider (2022). “A Sequential Addition and Migration Method for Generating Microstructures of Short Fibers with Prescribed Length Distribution”. In: *Computational Mechanics* 70.4, pp. 829–851.

— (2024). “A Maximum-Entropy Length-Orientation Closure for Short-Fiber Reinforced Composites”. In: *Computational Mechanics* 74.3, pp. 615–640.

Montgomery-Smith, S., D. A. Jack, and D. E. Smith (2011a). “The Fast Exact Closure for Jeffery’s Equation with Diffusion”. In: *Journal of Non-Newtonian Fluid Mechanics* 166.7-8, pp. 343–353.

Literature III

Montgomery-Smith, S. et al. (2011b). “Exact Tensor Closures for the Three-Dimensional Jeffery’s Equation”. In: *Journal of Fluid Mechanics* 680, pp. 321–335.

Petersen, P. (2016). *Riemannian Geometry*. Vol. 171. Graduate Texts in Mathematics. Cham: Springer International Publishing.

PPG Fiber Glass (2013). *Data Sheet - TufRov® 4575*.

Schneider, M. (2017). “The Sequential Addition and Migration Method to Generate Representative Volume Elements for the Homogenization of Short Fiber Reinforced Plastics”. In: *Computational Mechanics* 59.2, pp. 247–263.

— (2021). “A Review of Nonlinear FFT-based Computational Homogenization Methods”. In: *Acta Mechanica* 232.6, pp. 2051–2100.

— (2022). “An Algorithm for Generating Microstructures of Fiber-reinforced Composites with Long Fibers”. In: *International Journal for Numerical Methods in Engineering* 123.24, pp. 6197–6219.

Tian, W. et al. (2015). “Representative Volume Element for Composites Reinforced by Spatially Randomly Distributed Discontinuous Fibers and Its Applications”. In: *Composite Structures* 131, pp. 366–373.

Literature IV

Tian, W. et al. (2021). “An Advanced Method for Efficiently Generating Composite RVEs with Specified Particle Orientation”. In: *Composites Science and Technology* 205, p. 108647.

Widom, B. (1966). “Random Sequential Addition of Hard Spheres to a Volume”. In: *The Journal of Chemical Physics* 44.10, pp. 3888–3894.

Williams, S. R. and A. P. Philipse (2003). “Random Packings of Spheres and Spherocylinders Simulated by Mechanical Contraction”. In: *Physical Review E* 67.5, p. 051301.

Zeman, J. et al. (2010). “Accelerating a FFT-based Solver for Numerical Homogenization of Periodic Media by Conjugate Gradients”. In: *Journal of Computational Physics* 229.21, pp. 8065–8071.

fSAM algorithm for long and curved fibers

Solving the minimization problem

$$F(\mathbf{q}) \longrightarrow \min_{\mathbf{q} \in \mathcal{R}}$$

- Gradient descent approach
  - ↯ Standard gradient descent approach: **q** may leave its configuration space

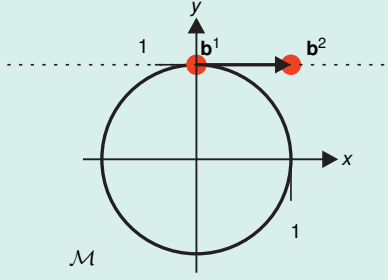

fSAM algorithm for long and curved fibers

Solving the minimization problem

$$F(\mathbf{q}) \longrightarrow \min_{\mathbf{q} \in \mathcal{R}}$$

- Gradient descent approach
  - ↯ Standard gradient descent approach: **q** may leave its configuration space

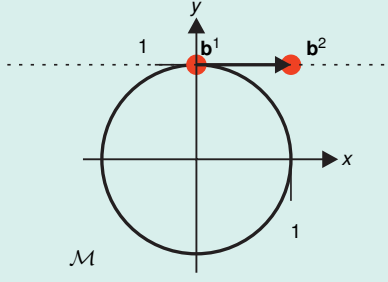

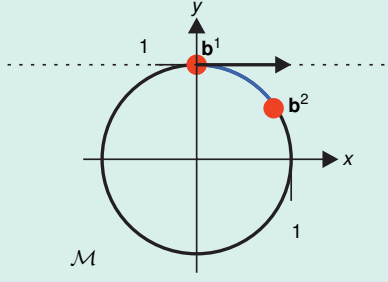

fSAM algorithm for long and curved fibers

Moving along the geodesics

- Geodesic (Petersen, 2016):
  - Shortest path between two points on a manifold
  - Minimizing the energy functional

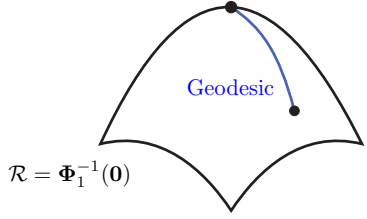

fSAM algorithm for long and curved fibers

Exponential mapping

- For the geodesically complete Riemannian manifold $(\mathcal{R}, \mathbf{G})$:
  - Input:
    - Tangent vector $\mathbf{v} \in T_{\mathbf{q}}\mathcal{R}$
    - Point on the manifold $\mathbf{q} \in \mathcal{R}$
  - Output:

$$\exp_{\mathbf{q}}(\mathbf{v}) = \mathbf{q}_v(1)$$

    - $\mathbf{q}_v : [0, 1] \to \mathcal{R}$: unique geodesic with $\mathbf{q}_v(0) = \mathbf{q}$ and $\dot{\mathbf{q}}_v(0) = \mathbf{v}$

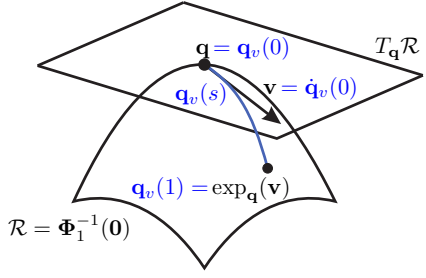

fSAM algorithm for long and curved fibers

Exponential mapping

- For the geodesically complete Riemannian manifold $(\mathcal{R}, \mathbf{G})$:
  - Input:
    - Tangent vector $\mathbf{v} \in T_{\mathbf{q}}\mathcal{R}$
    - Point on the manifold $\mathbf{q} \in \mathcal{R}$
  - Output:

$$\exp_{\mathbf{q}}(\mathbf{v}) = \mathbf{q}_v(1)$$

  - $\mathbf{q}_v : [0, 1] \to \mathcal{R}$: unique geodesic with $\mathbf{q}_v(0) = \mathbf{q}$ and $\dot{\mathbf{q}}_v(0) = \mathbf{v}$

Adapted gradient descent approach

$$\mathbf{q}^{k+1} = \exp_{\mathbf{q}^k}\left(-\tau_k \nabla_{\mathbf{q}} F\left(\mathbf{q}^k\right)\right), \quad k = 0, 1, \ldots,$$

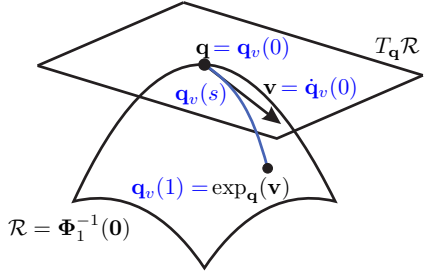

ICCM24
AUGUST 4-8, 2025
BALTIMORE CONVENTION CENTER
BALTIMORE, MARYLAND, USA

No Technical Paper Submission for:

Jack Turicek

ICCM24

24TH INTERNATIONAL CONFERENCE ON COMPOSITE MATERIALS

UFRN

UNIVERSIDADE FEDERAL DO RIO GRANDE DO NORTE

BAM

Bundesanstalt für Materialforschung und -prüfung

Influence of the addition of thermoplastic healing agent to epoxy resin

Ana Paula C. Barbosa[1], Allana A. do Nascimento[1], Lina Pavasaryte[2], José Daniel D. Melo[1], Volker Trappe[2]

1 Federal University of Rio Grande do Norte (UFRN), Department for Materials Engineering, Av. Senador Salgado Filho 3000, Natal-RN, Brazil

2 Federal Institute for Materials Research and Testing (BAM), Unter den Eichen 87, 12205, Berlin, Germany

Index

- Motivation
- Self-healing in epoxy and epoxy-matrix composites
- Influence of thermoplastic particles in epoxy
- Conclusions and outlook

Motivation

- Composite materials
  - ✓ Exposure to environmental factors and mechanical loading may lead to the formation of microcracks
    - *Microcracks difficult to detect*
    - *Costly repairs / failure*

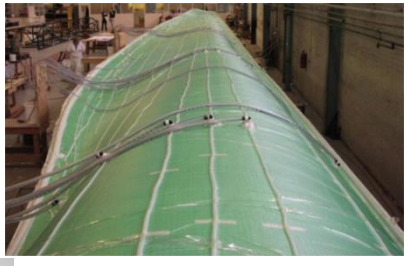

www.reinforcedplastics.com



www.energes.com.br



Superstrata Bike



www.nauticexpo.com



www.asdnews.com





Self-healing materials

- Alternative to conventional repair methods to heal microcracks in the structure
  - ✓ Extension of service life
  - ✓ Reduction of maintenance cycles
  - ✓ Increase reliability

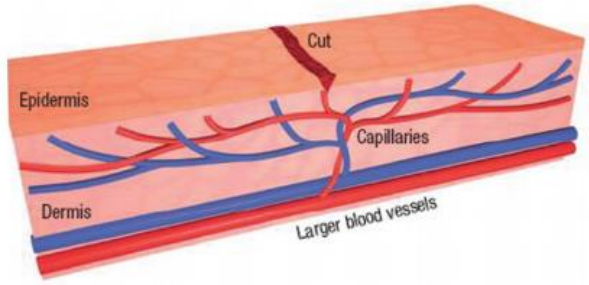

Bio-inspired

- Repair associated to restoration of properties:

$$\text{Healing efficiency} = \frac{\textit{Property value}_{\,healed}}{\textit{Property value}_{\,initial}} \times 100$$

Self-healing in epoxy and epoxy composites

- Thermoplastic healing agents

  - ✓ Addition of thermoplastic particles to epoxy matrix
  - ✓ Heating during healing cycle allows increase in mobility of thermoplastic material and flow to damaged areas
  - ✓ Thermoplastic as a crack filler capable of re-bonding fracture surfaces.

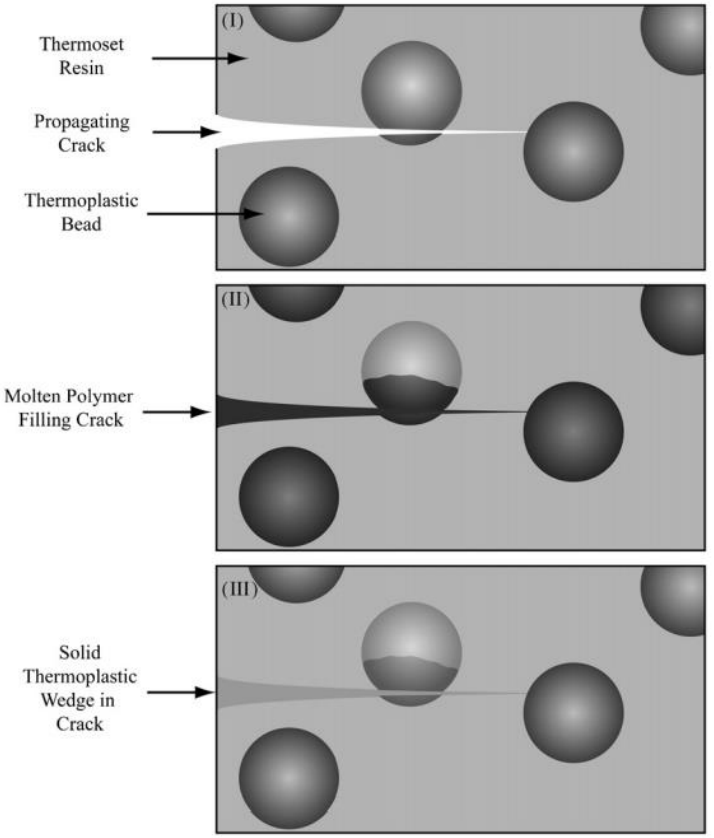

D. Y. Wu et al, Prog. Polym. Sci. 33 (2008) 479–522

Self-healing in epoxy and epoxy composites

MEURE; WU; FURMAN, 2009:

- Addition of 15 wt.% of thermoplastic particles (polyethylene-co-methacrylic acid) (EMAA) to epoxy resin
  - ✓ Decrease in modulus + increase in fracture strength
  - ✓ Recovery = 85% (TDCB) and 100% (SENB)

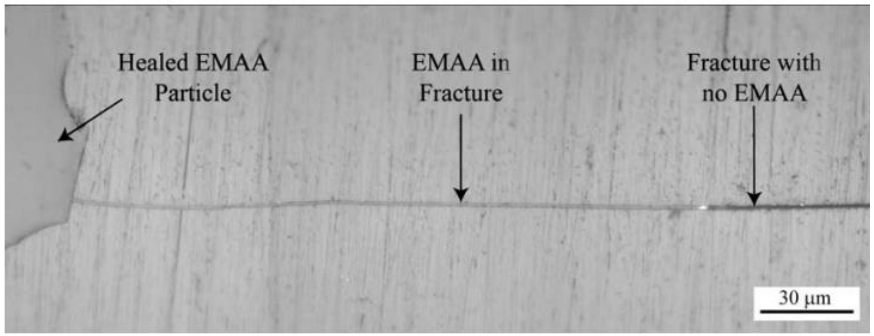

healed SENB showing the fracture plane

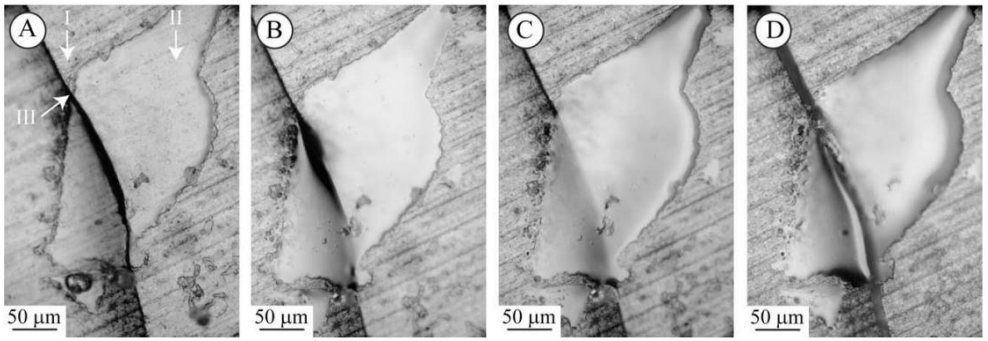

(I) epoxy resin, (II) an EMAA particle and (III) crack

EMAA particle healing and formation of an adhesive EMAA layer between adjacent epoxy fracture surfaces

S. Meure et al., Acta Materialia 57 (2009) 4312–4320

Polymer Testing 117 (2023) 107863

Contents lists available at ScienceDirect

Polymer Testing

journal homepage: www.elsevier.com/locate/polytest

Fatigue behavior of self-healing glass fiber/epoxy composites with addition of poly (ethylene-co-methacrylic acid) (EMAA)

Allana Azevedo do Nascimento [a,*], Volker Trappe [b], José Daniel Diniz Melo [a], Ana Paula Cysne Barbosa [a]

[a] Federal University of Rio Grande do Norte (UFRN), Av. Senador Salgado Filho 3000, CEP, 59078-970, Natal, RN, Brazil
[b] Federal Institute for Materials Research and Testing (BAM), Unter den Eichen 87, 12205, Berlin, Germany

Fatigue behaviour and self-healing

- Composites with 2 wt% and 5 wt% of EMAA were manufactured by resin infusion using glass fibers impregnated with EMAA
- Healing efficiency: number of cycles to failure of specimens subjected to cyclic loading
- No significant effect on glass transition temperature, tensile strength or modulus of elasticity

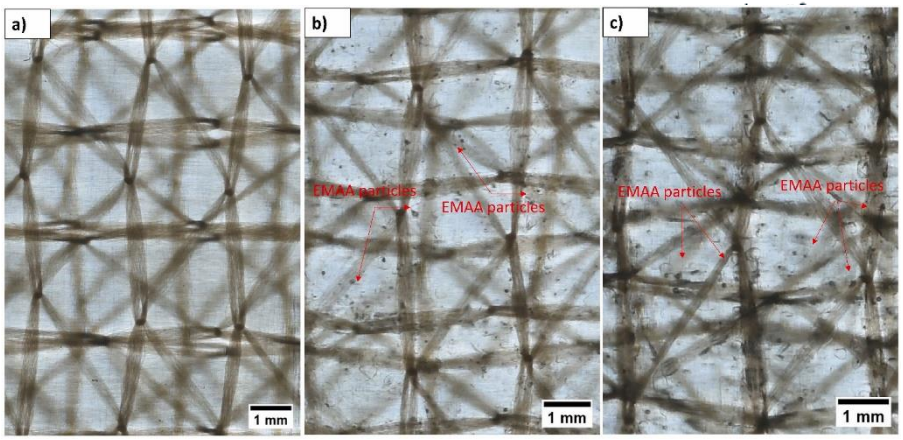

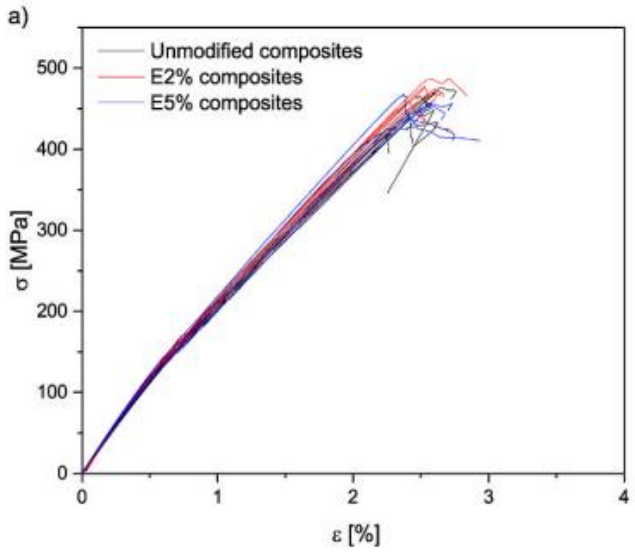

Allana A. do Nascimento, Volker Trappe, José D. D. Melo, Ana P.C. Barbosa, Polymer Testing 117 (2023) 107863

Fatigue behaviour and self-healing

- 5 wt% of EMAA: reduction of the fatigue life
- 2 wt% of EMAA: slight increase in life
- greatest number of cycles to failure of composites: with 2 wt% of EMAA
- greatest healing efficiency: healing cycle after 10^3 loading cycles, as compared to 10^4 loading cycles: healing can be more efficient if activated in early stages of damage.

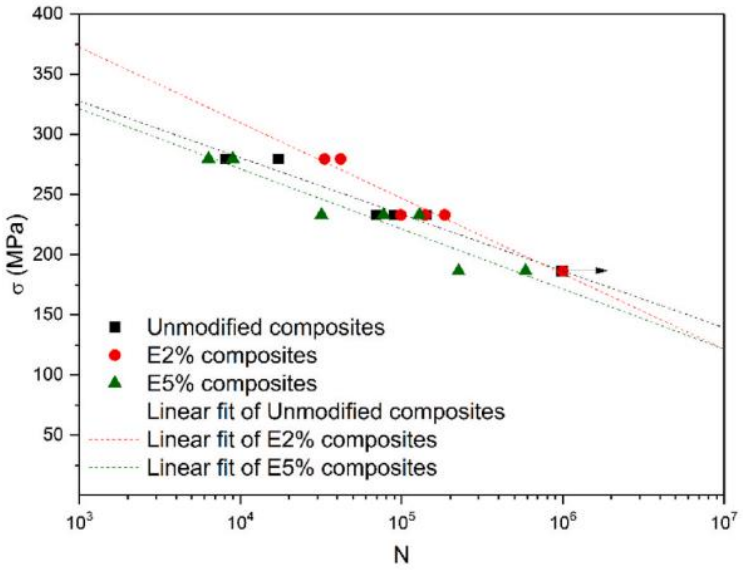

Table 3. Average healing efficiency of unmodified and modified composites.

Sample	η (%)	
	10^3	10^4
Unmodified composites	105.9	31.2
E2% composites	102.1	27.4
E5% composites	199.6	37.7

Allana A. do Nascimento, Volker Trappe, José D. D. Melo, Ana P.C. Barbosa, Polymer Testing 117 (2023) 107863

Received: 12 September 2023 | Revised: 23 April 2024 | Accepted: 27 April 2024

DOI: 10.1002/app.55677

RESEARCH ARTICLE

Journal of Applied Polymer Science WILEY

Effects of particle size and particle concentration of poly (ethylene-co-methacrylic acid) on properties of epoxy resin

Allana Nascimento[1] | **Volker Trappe**[2] | **Lina Pavasaryte**[2] | **José Melo**[1] | **Ana Paula Cysne Barbosa**[1]

[1]Department of Materials Engineering, Federal University of Rio Grande do Norte (UFRN), Natal, RN, Brazil

[2]Graduate Program in Materials Science and Engineering, Federal Institute for Materials Research and Testing (BAM) Unter den Eichen 87, Berlin, Germany

Effects of particles in epoxy

- addition of EMAA: reduction in tensile strength and modulus of elasticity of epoxy resin

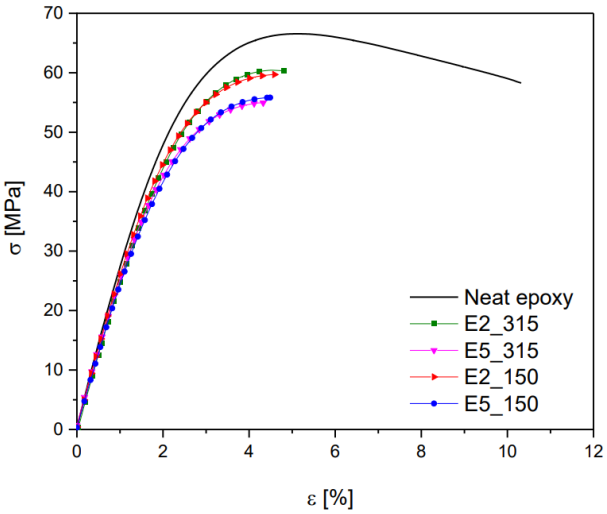

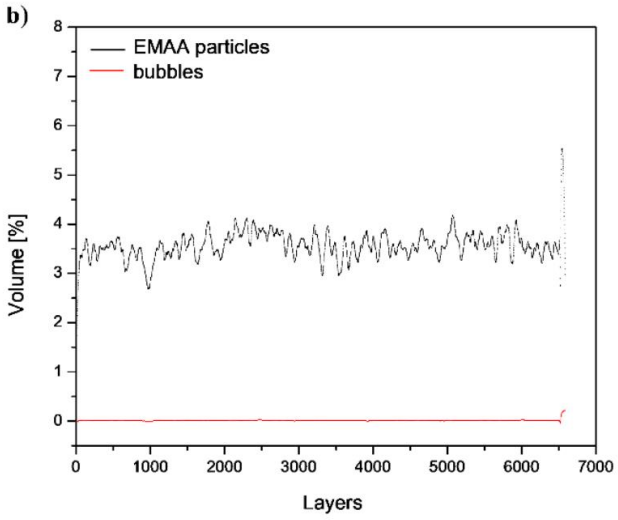



- EMAA particle dispersion along the length of samples was not homogenous: X-CT studies

NASCIMENTO, ALLANA ; TRAPPE, VOLKER ; PAVASARYTE, LINA ; MELO, JOSÉ ; BARBOSA, ana paula cysne . Effects of particle size and particle concentration of poly (ethylene-co-methacrylic acid) on properties of epoxy resin. JOURNAL OF APPLIED POLYMER SCIENCE

Effects of particles in epoxy

- lower EMAA concentration with smaller particle sizes may be optimal condition, considering the maintenance of base tensile properties of epoxy and homogeneity in particle distribution
- trade-off between healing efficiency and the reduction of mechanical properties must be considered and adjusted by the selection of particle concentration and particle size of the healing agent

BAM

Menu Specialized portals

Sicherheit in Technik und Chemie

Paper of the month of August: Material

Effects of particle size and particle concentration of poly (ethylene-co-methacrylic acid) on properties of epoxy resin

Home › News › Papers of the month

› Effects of particle size and particle concentration of poly (ethylene-co-methacrylic acid) on properties of epoxy resin

NASCIMENTO, ALLANA ; TRAPPE, VOLKER ; PAVASARYTE, LINA ; MELO, JOSÉ ; BARBOSA, ana paula cysne . Effects of particle size and particle concentration of poly (ethylene-co-methacrylic acid) on properties of epoxy resin. JOURNAL OF APPLIED POLYMER SCIENCE

Preliminary results on crack propagation

- Crack propagation in SET samples investigated for neat epoxy and epoxy with 5 wt.% of thermoplastic (EMAA) particles, with 2 different particle sizes

- Preliminary results indicate that cracks seems to propagate faster for neat epoxy than for epoxy modified with thermoplastic material

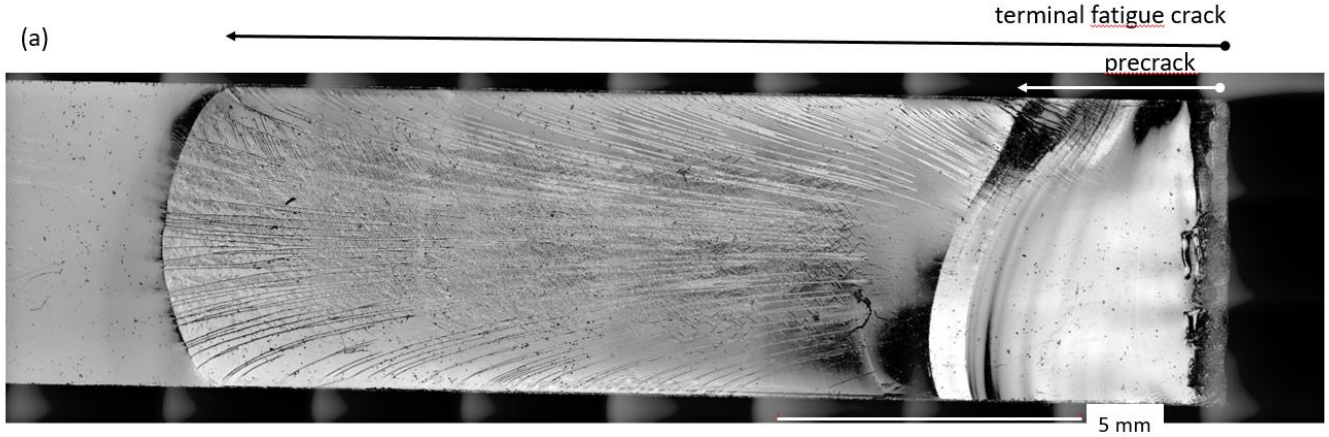

Fracture surface of neat epoxy SET sample

Conclusions and outlook

- Self-healing with thermoplastic particles as alternative to heal material and extend service life
- Healing can be more efficient if activated in early stages of damage
- Trade-off between healing efficiency and the reduction of mechanical properties must be considered
- Ongoing studies on crack propagation of epoxy with and without thermoplastic particles

Acknowledgements

- Financial and administrative support

CAPES

CNPq

UFRN | PROPESQ Pró-Reitoria de Pesquisa

UFRN | PPG Pró-Reitoria de Pós-Graduação

Funpec Fundação Norte-Rio-Grandense de Pesquisa e Cultura



Thank you!
Obrigada!

SELFHEALING COMPOSITES: INFLUENCE OF AGENT FRACTION

Odila Cioffi[1], Yuri Chuves[2], Francisco Monticeli[3], Ana Barbosa[4] and Herman Voorwald[1]

[1] São Paulo State University (Unesp) - Materials and Technology Department - Fatigue and Aeronautic Materials Research Group, Av. Ariberto Pereira a Cunha, 333 – 12516-410 Guaratinguetá - SP, Brazil
Email: odila.cioffi@unesp.br, h.voorwald@unesp.br, web page: https://www.feg.unesp.br

[2] Alltec Composites – R&D Laboratory - Rua Moxotó, 456, Chácaras Reunidas 12238-320 SJ. Campos – SP, Brazil
Email: yuri.chuves@allteccompositescom.br, web page: https://allteccomposites.com.br/site/

[3] Department of Aerospace Structures and Materials, Faculty of Aerospace Engineering, Delft University of Technology, Kluyverweg 1, 2629 HS, Delft, the Netherlands
Email: F.m.monticeli@tudelft.nl, web page: https://www.tudelft.nl/lr

[4] Department of Materials Engineering, Federal University of Rio Grande Do Norte, Natal, RN, Brazil
Email: ana.cysne@ufrn.br, web page: https://www.ufrn.br/institucional/reitoria

Keywords: Composite plates, Modal analysis, Identification, Properties, Finite elements

ABSTRACT

Polymer composites used in structural applications are subjected to dynamic loads that can generate fatigue-induced microcracks. As these microcracks grow and merge, they lead to material failure, thereby reducing the service life of the component. To address this challenge, a promising strategy involves the development of smart self-healing polymers that, similar to biological systems, respond to damage by activating self-repair mechanisms, effectively enhancing the durability and lifespan of the material. This study investigates the interlaminar shear behavior of 5HS carbon fiber/epoxy composites containing varying amounts of the self-healing agent EMAA, processed via RTM. It examines the influence of agent content on mechanical performance and confirms, through thermal analysis, the feasibility of laminate fabrication, though particle dispersion may limit agent volume. ANOVA results show that EMAA content has a higher effect on mechanical response than internal dispersion. Weibull analysis indicates a linear decrease in shear strength with increased EMAA due to reduced stiffness from its ductile nature. Healing was most effective in interlaminar regions, achieving up to 62% recovery in shear strength, 106% in toughness, and 57% crack area reduction. Predictive modeling supports optimizing healing agent levels to meet design needs while reducing experimental effort and cost.

1 INTRODUCTION

Carbon fiber-reinforced polymer (CFRP) composites with continuous fibers are extensively employed in aerospace applications. From 1980s, the AV-8B aircraft incorporated CFRP in 27% of its components, followed by the Boeing 787 that increased to 50% in its fuselage structure in 2000. More recently, advancements in urban air mobility (UAM) have been directed toward achieving fully fiber-reinforced structural designs, aiming for 100% composite reinforcement [1].

The use of RTM process for manufacturing high fiber volume fraction composite parts replacing autoclave manufacturing is quickly gaining momentum [2-3]. RTM manufactured components can also be co-cured with stiffener and rib structures. Although this reduces assembly time it opens up the possibility of poor mechanical properties in through the thickness direction [4] with damage usually occurring at the fiber/matrix interface in the form of microcracks or micro delamination [5], influencing adversely the fracture toughness [6].

Micro cracks can compromise the structural integrity of a vehicle and can reduce the vehicle life or result in a potentially injury of passenger safety. In recent years many repair techniques have been developed by transportation industry, and the goal of these repair methods is to fix visible damages on

composite polymer structure, however, for invisible damage inside the component during service life, traditional methods of repairing are not effective [7].

One emerging approach for mitigating or preventing damage is the use of healing agents, especially considering the high costs associated with replacing failed components. Incorporating self-healing agents offers the potential to enhance the safe operational lifespan of structural parts [8-10].

Since 2008, thermoplastic polymers have been explored as self-healing agents in high-performance composites, with the goal of addressing microcracks generated under mechanical stress [11]. These polymers act by interpenetrating into the damaged regions and forming chemical bonds at the crack surfaces, thereby helping to prevent failure. Meure et al. [12] incorporated EMAA (polyethylene-co-methacrylic acid) into an epoxy matrix, producing particles around 250 μm in size via cryogenic grinding and impact milling. Although this approach reduced the energy needed for activation, it also compromised the mechanical integrity of the healing material. The same researchers later examined the influence of pressure on healing, using EMAA films in epoxy systems. They identified gas bubble formation and chemical interactions involving oxirane, amine, and hydroxyl groups, and applied increased pressure to suppress the bubbles [13].

Further work by Varley et al. [14] revealed that ionomers in EMAA could effectively repair impact damage, triggered by ionic activation and reversible thermal behavior. Additives were shown to enhance plasticization and ion cluster mobility, which improved healing performance. Additionally, EMAA and EMA (polyethylene-co-methyl acrylate) have been utilized as co-polymeric healing agents in prepreg-based composites, where they were converted from pellets into thin films through hot pressing [15].

However, the presence of the self-healing agent in the polymeric resin introduces a new phase into the matrix, which can significantly alter the elastic behavior of the composite, which raises the following question: what is the influence of the healing agent fraction on the mechanical behavior of the material? Then, there is a requirement to know about the material's post-repair properties, analyzing the distribution of the agent within the material regions, and employing statistical tools to validate the results and predict the materials behavior, aiming to reduce both project time and cost.

2 EXPERIMENTAL PROCEDURES

The manufacturing process employed was the resin transfer molding (RTM) Radius 2100cc RTM Injector according to the Figure 1



Figure 1 – RTM system

The self-healing thermoplastic agent was cryogenically milled using a high-energy grinder, then sieved through a 100-mesh screen to obtain a fine particle as it can see in the Fig. 2, which were subsequently blended with the resin prior to molding. This mixture was injected into the fiber reinforcement within closed mold under regulated thermal and pressure conditions.

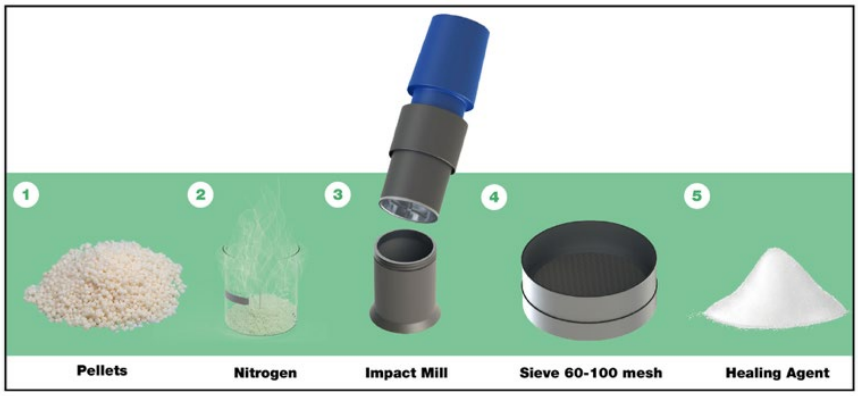

Figure 2 - Schematic steps of the thermoplastic self-healing process. (1) Pellets; (2) frozen pellets with liquid N2; (3) impact mill; (4) sieve, and (5) self-healing powder (150–250 μm) [16]

Processing parameters settled for both laminates are shown in Table 1.

Table 1 – Processing parameters

Laminate	Injection pressure MPa	Vacuum level [MPa]	Injection temperature (°C)	Curing cycle (min)
A and B	*0.2*	0.05	125	180-240

The fiber preforms consisted of eight symmetrically arranged layers, achieving a fiber volume fraction of 55%. Composite samples were sectioned using a metallographic cutter from allied high-tech products, equipped with a diamond blade, following the dimensional specifications outlined in ASTM D2344. For microscopy evaluation, specimens were embedded in Bakelite and cure at 170°C for 7.5 min, polished with diamond suspensions (9 μm to 1 μm) and finished with 0.05 μm alumina suspension. Cross-sectional image was performed using a Tescan Vega 3 scanning electron microscope., according to the ref. [17].

3 RESULTS

The average and standard deviation measurement data of self-healing fraction in the laminates composite processed by RTM is shown in Table 2. The reference composite is called A without adding a healing agent (i.e., 0%). The C-B laminate represents a composite with 2.41% of self-healing agent, while the C–C represents a laminate with 9.79% of self-healing agent average fraction. Through the image treatment, it was possible to measure the diameter size distribution of self-healing particles along the C–B and C–C composites, as shown in the histogram of Fig. 3a. Both composite families had the same processing procedures, modifying only the EMAA particle fraction. For specimen C–B, the largest diameter concentration is found in the range 20–30 μm (i.e., 41.73%), with a low fraction for particles >100 μm (3.98%).

Table 2: Agent fraction data.

Healing agent Fraction		
laminate	Average	Standard deviation
A	2.41	1.60
B	9.79	2.30

The self-healing particle diameter distribution in A and B coposites was measured and it was seen that in A, most particles fall within the 20–30 µm range (41.73%), with few exceeding 100 µm (3.98%). In contrast, increasing the thermoplastic content in B shifts the peak to 60–70 µm (31.08%) and raises the >100 µm fraction to 17.29%. This suggests higher particle agglomeration in B, increasing size variation and standard deviation. Higher healing agent content led to particle coalescence during manufacturing, enlarging particles and reducing dispersion uniformity. This inhomogeneity can affect self-healing efficiency, as a more uniform particle distribution improves the likelihood of crack interaction and closure through thermoplastic flow and reconnection [18].

Irregular shapes were no significant—0.05% in A and 0.09% in B laminates. As with diameter distribution, B showed higher morphological variation due to particle coalescence. Despite this, circular and elliptical shapes remained consistent across both laminates, indicating that coalescence increased particle size in B without altering morphology. While larger particles may improve localized healing, they reduce macro-healing effectiveness by concentrating the agent in fewer regions, limiting its interaction with diverse cracks [19].

The fig. 3 presents the ILSS curves for the reference laminates (no self-healing agent), the laminate with 2.41% healing agent before (A) and after repair (AB), and with 9.79% agent before (B) and after repair (RB).

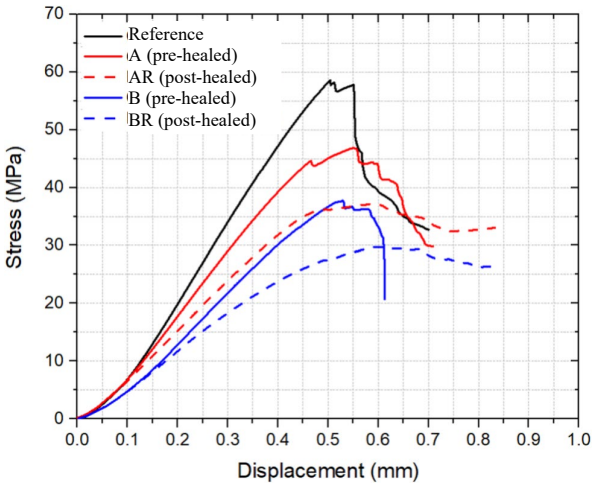

Figure 3 - ILSS curves [1].

The stress–displacement curve (Fig. 3) shows a reduced stiffness attributed to the addition and increasing EMAA content comparred the reference. After testing, self-healing samples were heated at 150 °C for 30 min. activate healing. The post-healing curves exhibit smoother behavior and lower load capacity, reflecting the ductile nature of the thermoplastic agent compared to the highly crosslinked epoxy matrix [20].

ANOVA was performed to assess the contribution of the self-healing agent fraction to the variability in mechanical properties and to test the null hypothesis (H_0) of no significant difference between fractions. The alternative hypothesis (H_1) assumes the agent fraction affects mechanical performance. Analysis was conducted in Minitab 18 with $\alpha = 0.05$ and 95% confidence, comparing between-group variance (agent fraction) to within-group variance (test repeatability).

The equations used in the ANOVA method to calculate the F-factor are shown in Table 3, where *n* is the number of data points, *C* is the group number, *xi* is the group mean, *x* is the overall mean, *xji* is each individual value, and the F-factor indicates whether the self-repair fraction's variation has higher variance than the mechanical response's standard deviation. The p-value is tabulated based on the degrees of freedom and F-value.

Table 3 - Structured form of the ANOVA model

Variation	SS-total	DF	MS	F-factor
Between-groups	$S_a = \sum_{i=1}^{c} n(\bar{x}_i - \bar{x})^2$	$V_a = C - 1$	$SM_a = \frac{S_a}{V_a}$	$F = \frac{SM_a}{V_a}$
Whithin-groups	$S_b = \sum_{i=1}^{c} \sum_{j=1}^{n} (\bar{x}_{ji} - \bar{x})^2$	$V_b = n - 1$	$SM_b = \frac{S_b}{V_b}$	

n *= number of experimental observations;* ***C*** *= group identifier (or group index);* $\bar{x}_i$ *mean of the* i*-th group;* $\bar{x}$ *= grand mean (overall mean across all groups);* $\bar{x}_{ji}$ *= individual observation* j *within group* i*;* ***F*** *= F-statistic, representing the ratio of the between-group mean square to the within-group mean square*

The variation in interlaminar shear strength was characterized using a two-parameter Weibull distribution, as presented in Equation (1) [20]. This distribution enables the estimation of failure probability across different reliability levels and is widely adopted for analyzing the variability in brittle failure of composite materials. Linearization of the Weibull distribution was performed using Equation (2), allowing for the estimation of the shape parameter (m) and the scale parameter (X_U).

$$P(\bar{x}) = \bar{e}\left[-\frac{x_c}{X_u}\right]^m \tag{1}$$

$$ln\left[\left(\frac{1}{1 - P(\bar{x})}\right)\right] = m.ln(x_c) - m.ln(x_u) \tag{2}$$

In addition to the probabilistic approach, Response Surface Methodology (RSM) was applied to model and predict the mechanical behavior as a function of key processing parameters, specifically the self-healing agent fraction (*SH, in %*) and displacement (*D, in mm*). This approach enabled the development of predictive models for both the pre-healing condition (σ_N) and the post-healing condition (σ_R), as described in Equation (3).

$$Y = \beta_0 + \sum_{i=1}^{k} \beta_i \bar{x}_i + \sum_{j=1}^{k} \beta_j \bar{x}_j + \sum_{i=1}^{k} \beta_{ii} \bar{x}_i^2 + \sum_{j=1}^{k} \beta_{jj} \bar{x}_j^2 + \sum_{j=i}^{k} \beta_{ji} \bar{x}_i \bar{x}_j \tag{3}$$

Where *Y* represents the predicted response, an the variables *xi* and *xj* correspond to the levels of the processing parameters, the beta coefficients (β) represent the constant term, the linear effects, and the interaction effects between the variables.

An analysis of variance (ANOVA) was conducted to assess the influence of the self-healing agent fraction on the mechanical properties. Prior to the healing process (Table 4), the between-group variance was found to be statistically significant (**F > Fcritical, p < 0.05**), indicating that variations in the self-healing agent fraction have a substantial effect on the mechanical response. The contribution percentage (PC) of the between-group variance reached **87.6%**, whereas the within-group variance accounted for only **12.4%**, confirming the dominant influence of the healing agent fraction on the composite's performance.

Table 4. ANOVA pre-repair action

Variance	*SS*	*DF*	*MS*	*F-ratio*	*p-values*	*Fcrítico*	*%*
within-group	65.213	5	13.04	0.72	0.620	3.32	12.40
between-group	460.67	2	230.34	12.79	0.001	4.10	87.60
Total	525.89	10					-

Sum of Squares (SS); Degrees of Freedom (DF); Mean Square (MS); Variation between sample means / Variation within samples (F – F-ratio) and Percentage Contribution ***(%)***

Following the healing process (Table 5), an inverse trend was observed. The within-group variance increased substantially (**% = 76.56%**), while the between-group contribution decreased (**% = 23.43%**). Moreover, both F-values were lower than Fcritical, with p-values exceeding 0.05, indicating that the effect of the self-healing agent fraction became statistically insignificant post-repair. This behavior is attributed to the inherent variability in crack propagation and closure, as well as the stochastic nature of damage localization after failure, which introduced higher dispersion in the post-healing mechanical results.

Table 5. ANOVA post-repair action.

Variance	*SS*	*DF*	*MS*	*F-factor*	*p-value*	*Fcrítical*	*%*
Within-group	45.56	5	9.11	0.45	0.79	5.05	76.56
Between-group	13.94	1	13.94	0.69	0.44	6.60	23.43
Total	59.50	6					

Sum of Squares (SS); Degrees of Freedom (DF); Mean Square (MS); Variation between sample means / Variation within samples (F – F-ratio) and Percentage Contribution ***(%)***

Weibull distribution modeling (Figure 4) demonstrated an excellent fit to the experimental data, both before and after the healing process, with a coefficient of determination $\mathbf{R^2 > 0.99}$.

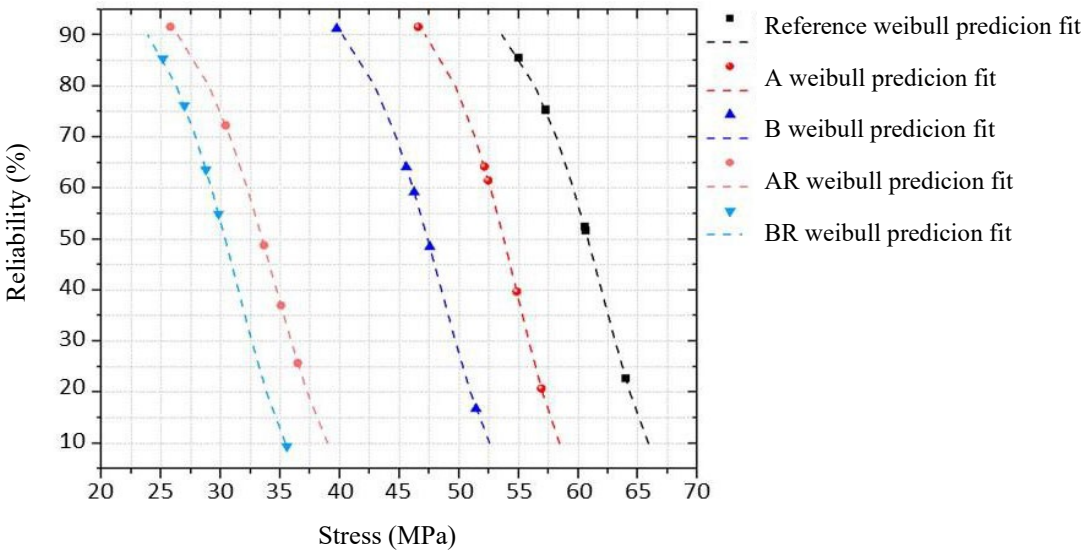

Fig. 4 - Sensitivity analysis of the predicted ultimate shear stress pre- and post-healing.

The analysis revealed that increasing the self-healing agent fraction led to a progressive reduction in maximum interlaminar shear strength at a given reliability level. This reduction is associated with particle agglomeration effects and lower fracture consolidation efficiency at higher healing agent concentrations.

A three-dimensional Response Surface Methodology (RSM) surface was also generated, effectively describing the mechanical response as a function of SH and D, enabling predictive capabilities beyond experimentally tested conditions. The models presented a maximum error of less than **3.9%**, with **R^2 > 0.93**, demonstrating robust predictive accuracy. The resulting predictive equations are as follows 3 and 4:

- **Pre-healing mechanical behavior**:

$$\sigma_N = -7.33 - 1.11SH + 195.46D + 0.067SH^2 - 179.25D^2.D \quad (3)$$

- **Post-healing mechanical behavior**:

$$\sigma_R = -3.11 - 0.28SH + 126.23D - 0.037SH^2 - 99.90D^2 - 0.63SH.D \quad (4)$$

These predictive models provide a valuable tool for design optimization of self-healing laminated composites, supporting the selection of the optimal healing agent fraction to balance mechanical performance and repair efficiency. Additionally, the generated response surfaces contribute to reducing experimental efforts, time, and costs associated with mechanical testing.

The findings highlight that although the inclusion of self-healing agents enhances damage tolerance, excessive fractions lead to a notable reduction in mechanical properties without proportional gains in repair efficiency. Therefore, optimizing the healing agent content is essential for maintaining a balance between structural integrity and autonomous repair functionality.

4 CONCLUSIONS

It was evaluated the influence of thermoplastic self-healing agent fraction on the shear behavior of CFRP through comprehensive mechanical and statistical analyses. The distribution of self-healing particles, morphology, and repair performance were characterized. Key findings include:

- Stiffness values is reduced with the addition of the self-healing agent due to reduced bond density in the thermoplastic within the thermoset matrix;
- Higher agent fractions lowered repair efficiency, attributed to intralaminar fracture and thermoplastic coalescence (larger particle size), indicating a threshold for injection processing;
- ANOVA revealed that the agent fraction had a higher influence than internal variation among similar laminates prior to repair;
- Self-healing achieved average recoveries of 62% in shear strength, 106% in toughness modulus, and a 57% reduction in crack size;
- Predictive modeling of interlaminar shear behavior identified optimal agent fractions that meet design goals while reducing time and cost.

REFERENCES

[1] Y. P. Chuves, F. Monticeli, A. A. Nascimento, A. A. C. Barbosa, H. J. C. Voorwald and M. O. H. Cioffi. The Efect of Self-Healing Agent Fraction on CFRP Mechanical Behavior: Statistical Analysis Approach. *Fibers and Polymers*, **24**, 2023, pp. 729–740. https://doi.org/10.1007/s12221-023-00103-0

[2] A. Woo-Jin, K. Cheol-Hwan, C. Jin-Ho, K. Jin-Hwe. Static strength of RTM composite joint with I-fiber stitching process. Composite Structures **210**, 2019, 348–353. https://doi.org/10.1016/j.compstruct.2018.11.072

[3] Y. Geng, J. Jiang, N. Chen. Local impregnation behavior and simulation of non-crimp fabric on curved plates in vacuum assisted resin transfer molding. Composite Structures. **208**, 15, 2019, 517-524. https://doi.org/10.1016/j.compstruct.2018.10.054

[4] C. Kracke, A. Nonn, C. Koch, M. Nebe, E. Schmidt, S. Bickerton, T. Gries, P. Mitschang. Interaction of textile variability and flow channel distribution systems on flow front progression in the RTM process Composites: Part A **106**, 2018, 70–81. https://doi.org/10.1016/j.compositesa.2017.12.010

[5] M. Ducousso, A. Dalodière, A. Baillard. Evaluation of the thermal aging of aeronautical composite materials using Lamb waves. Ultrasonics **94**, 2019, 174-182. https://doi.org/10.1016/j.ultras.2018.09.014

[6] López-Menéndez J. Viña A. Argüelles I. Viña S. Rubiera. Analysis of mode III interlaminar fracture toughness of laminated composites using a novel testing device Engineering Fracture Mechanics **173**, 2017, 55-63. https://doi.org/10.1016/j.engfracmech.2017.01.021

[7] D. Y. Wu, S. Meure, D. Solomon. Self-healing polymeric materials: A review of recent developments. Progress in Polymer Science (Oxford), **33**, 5, 2008, 479– 522. https://doi.org/10.1016/j.progpolymsci.2008.02.001

[8] V. Kostopoulos, A. Kotrotsos, A. Sousanis, G. Sotiriadis, Fatigue behaviour of open-hole carbon fbre/epoxy composites containing bis-maleimide based polymer blend interleaves as self-healing agent. Compos. Sci. Technol. **171**, 2019, 86–93. https://doi.org/10.1016/j.compscitech.2018.12.013

[9] A. Azevedo do Nascimento, F. Fernandez, S. da Silva, P.C.E. Ferreira, J.D. José, A.P. Cysne Barbosa, Addition of poly (ethylene-co-methacrylic acid) (EMAA) as self-healing agent to carbon-epoxy composites. Compos. Part A Appl. Sci. Manuf. **137**, 2020, 106016. https://doi.org/10.1016/j.compositesa.2020.106016

[10] D.G. Bekas, K. Tsirka, D. Baltzis, A.S. Paipetis, Self-healing materials: A review of advances in materials, evaluation, characterization and monitoring techniques. Compos. Part B **87**, 2016, 92–119 https://doi.org/10.1016/j.compositesb.2015.09.057

[11] J. Lee, D. Bhattacharyya, M.Q. Zhang, Y.C. Yuan ᶜ Mechanical properties of a self-healing fibre reinforced epoxy composites. Composites Part B: Engineering, **78**, 2015, 515-519 https://doi.org/10.1016/j.compositesb.2015.04.014

[12] S. Meure, D. Y. Wu, S. Furman, Polyethylene-co-methacrylic acid healing agents for mendable epoxy resins. Acta Mater. 57,14, 2009, 4312-4320. https://doi.org/10.1016/j.actamat.2009.05.032.

[13] S. Meure, R. J. Varley, D. Y. Wu, S. Mayo, K. Nairn, S. Furman, Confirmation of the healing mechanism in a mendable EMAA–epoxy resin. Eur. Polym. J., **48**, 2012, 524. https://doi.org/10.1016/j.eurpolymj.2011.11.021

[14] R. J. Varley, S. Shen, S. Van der Zwaag. The effect of cluster plasticisation on the self healing behaviour of ionomers. Polymer, **51**, 3, 2010, 679-686. https://doi.org/10.1016/j.polymer.2009.12.025

[15] C. H. Wang, K. Sidhu, T. Yang, J. Zhang, R. Shanks. Interlayer self-healing and toughening of carbon fibre/epoxy composites using copolymer films. Compos. Part A: Appl. Sci. Manuf. **43**, 3, 2012, 512-518. https://doi.org/10.1016/j.compositesa.2011.11.020

[16] M. O. H. Cioffi, A. S. Bomfim, V. Ambrogi, S. Advani. A review on self-healing polymers and polymer composites for structural applications. **43**, 2022, 7643-7668. https://doi.org/10.1002/pc.26887

[17] F.M. Monticeli, H.L. Ornaghi, H.J.C. Woorwald, M.O.H. Ciof, Three-dimensional porosity characterization in carbon / glass fiber epoxy hybrid composites. Compos. Part A Appl. Sci. Manuf. **125**, 105555 (2019). https://doi.org/10.1016/j.compositesa.2019.105555

[18] S.Y. Kim, N.R. Sottos, S.R. White, Self-healing of fatigue damage in cross-ply glass/epoxy laminates. compos. sci. technol. **175**, 2019, 122–127. https://doi.org/10.1016/j.compscitech.2019.03.016

[19] I.S. Vintila, S. Draghici, H.A. Petrescu, A. Paraschiv, M.R. Condruz, L.R. Maier, A. Bara, M. Necolau, Evaluation of dispersion methods and mechanical behaviour of glass fbre composites with embedded self-healing systems. Polymers **13,** 1, 2021, 1642. https://doi.org/10.3390/polym13101642
[20] ASHRAFI, B. *et al.* Enhancement of mechanical performance of epoxy/carbon fiber laminate composites using single-walled carbon nanotubes. Composites Science and Technology, Barking, **71**, 13, 2011, 1569–1578. https://doi.org/10.1016/j.compscitech.2011.06.015
[21] AO, X. G.; OY, J. A. J. A Weibull stress model to predict cleavage fracture in plates containing surface cracks. **Fatigue & Fracture of Engineering Materials & Structures (FFEMS)**, Oxford, v. 22, n. 6, p. 481–493, 1999. Disponível em: https://onlinelibrary.wiley.com/doi/10.1046/j.1460-2695.1999.00202.x

ACKNOWLEDGEMENTS

This research was financially supported by the Sao Paulo Research Foundation (FAPESP, Sao Paulo-Brazil) Grant no. 2006/02121-6 and 2019/04412-8.

EXPERIMENTAL AND NUMERICAL COMPRESSION ANALYSIS OF 3D X-RAY CT SCANNED UNI-DIRECIONAL PULTRUDED CARBON FIBER COMPOSITES

Pinelopi Mageira[1], Konstantinos Poulios[2], Jens W. Andreasen[3], Vedrana A. Dahl[4] and Lars P. Mikkelsen[5]

[1,5]Department of Wind and Energy Systems, Technical University of Denmark
Frederiksborgvej 399, DK-4000 Roskilde, Denmark
Email: [1] pinma@dtu.dk, [5] lapm@dtu.dk, web page: http://www.dtu.dk

[2]Department of Civil and Mechanical Engineering, Technical University of Denmark
Koppels Allé, 404, DK-2800 Kgs. Lyngby, Denmark
Email: kopo@dtu.dk, web page: http://www.dtu.dk

[3]Department of Energy Conversion and Storage, Technical University of Denmark
Fysikvej, 310, Building 403, DK-2800 Kgs. Lyngby, Denmark
Email: jewa@dtu.dk, web page: http://www.dtu.dk

[4]Department of Applied Mathematics and Computer Science, Technical University of Denmark
Richard Petersens Plads, 324, DK-2800 Kgs. Lyngby, Denmark
Email: vand@dtu.dk, web page: http://www.dtu.dk

Keywords: Mechanical properties, Plastic deformation, Compressive strength, Finite element analysis (FEA), Mechanical testing

ABSTRACT

This work presents a numerical prediction of the compressive strength of pultruded carbon composite profiles. Predictions based on input data acquired through 3D X-ray computed tomography scanning. The X-ray data are derived from real uni-directional pultruded samples and used for the determination of the fiber orientation distribution of the composite through the structure tensor analysis mathematical method. The fiber and matrix material properties are determined through experimental testing both of composite samples derived from the same pultruded profiles as the ones of the X-ray scanned specimens and of matrix samples. The compressive strength of the composite is acquired and compared to the numerically obtained values. Apart from the fiber and matrix properties, the fiber orientation distribution, the voxel size and the fiber diameter serve as input for the model. The model is two-dimensional, subjected to compressive loading, while material homogenization of the fibers and matrix is performed. The formulation ensures that the model is mesh independent. Apart from the prediction of the compressive strength, the numerical model provides information on the kink band formation in the material sample. The results show the effect of each X-ray scanned slice's fiber orientation distribution to the material's strength. It is also shown that the numerical compressive strength values could serve as a prediction for the actual ones in the case that the fiber orientation distribution is the sole material variation found in a pultruded composite. This study forms the basis for a more extensive investigation presented in ongoing work.

1 INTRODUCTION

Pultruded unidirectional carbon fiber composites are commonly used as structural elements in wind turbine blades, particularly in the load carrying spar cap, where high compressive strength is required [1-4]. Due to the nature of the manufacturing process, pultrusion is related with enhanced fiber straightness and constant cross section of the manufactured composite. However, small deviations in fiber orientation can significantly reduce the material's capacity to sustain compressive loads and trigger kink band formation [5]. This study introduces a numerical modelling approach to predict the

compressive strength of such composites, using fiber orientation distribution extracted from X-ray computed tomography (CT) scans as the primary input.

Fiber orientations will lead to shear loads in the matrix material. When the matrix shear loading capacity is reached, excessive fiber rotation occurs resulting in the formation of kink bands [5]. Researchers have used extensively 3D X-ray scanning techniques to develop three-dimensional methods to estimate the fiber orientation distribution in real composite materials [6, 7]. Volumetric data of composite sample acquired by X-ray CT scanning can be used as an input for the structure tensor analysis, an image analysis mathematical method for the determination of the fiber orientation, as described by Jeppesen et al. [8, 9]. The structure tensor analysis, used in this work as well, allows for the calculation of the local gradient of intensity in a neighbourhood around each voxel of the examined scanned volume, and is stored in a matrix. Through eigenvalue decomposition of this matrix, the dominant fiber orientation can be found and, subsequently, being mapped to the integration points of a finite element (FE) model's mesh [10].

Kyriakides et al. [11] and Vogler et al. [12] developed a two-dimensional discretized model to study the mechanisms of compression of unidirectional fiber composites, including fiber orientation variations. The kink band formation was investigated while it was found that fiber non-uniformity affects greatly the compressive limit load. A two-dimensional numerical model was developed by Christoffersen and Jensen [13, 14] to study the kink band formation on composites. The material was described by an elastic-plastic constitutive law, while homogenization was applied on the constitutive properties. Ferguson et al. [7, 15] adapted the method above and, after extracting the fiber orientation distribution from X-ray CT scanned composite data by using the structure tensor analysis and mapping it to the model, was able to predict the compressive strength and the initiation of the kink band formation. The solution acquired following this approach is mesh dependent [16].

Fleck and Shu [17] presented a theoretical homogenized numerical model. In the model, the fiber microrotation was described by introducing a scalar kinematic variable θ, the fiber diameter served as length scale and the fiber bending's effect on the stiffness was included. Poulios and Niordson [17, 18] developed a similar homogenized numerical model. It also included a kinematic variable θ, but contrary to the one mentioned above this is a vector. Two independent constitutive material laws described the composite's components, with the fibers and the matrix following hyperelastic and hyperelastoplastic behavior respectively. Similar as above, the fiber diameter was used as length scale and the fiber bending effect on the stiffness was included. This FE model was used for the study of composite materials under compressive loading following the assumption of idealized fiber orientation imperfections. The kink band formation was thoroughly investigated and, after comparing the fiber-matrix homogenized micromechanical model with the corresponding fiber-matrix discrete one, the former was found accurate and in good agreement. Mageira et al. [20] first studied a real composite case with the method described above. Carbon fiber composite data acquired through X-ray CT scanning served as input for the model.

The presented work continues the method built in [20] by adding experimental testing to compare and evaluate the numerical obtained values of the compressive strength of real composite samples with the corresponding experimentally obtained ones. To the knowledge of the authors, a comparison between experimental and numerical values based on real data using the homogenized model developed by Poulios and Niordson is introduced for the first time here. The method includes the acquisition of 3D X-ray data from samples from a carbon composite pultruded profile. By using the structure tensor analysis, the fiber orientation distribution can be determined and serve, along with the material properties obtained after experimental compression testing, as an input for the FE model. The two-dimensional numerical model from [17, 18], built in the finite element library GetFEM, has been adapted to include the extracted fiber orientation data. The results show the kink band formation in the examined sample and the prediction of the compressive strength of it; the latter is compared with the corresponding experimental values. The work presented here are part of a larger framework, which is further developed in an extended study [21]. This study contributes to the improvement of the numerical prediction of the compressive strength of unidirectional composites by integrating real fiber orientation data with a mesh-independent homogenized finite element model.

2 THEORY

The two-dimensional numerical model is an implementation of the composite material homogenized formulation developed by Poulios and Niordson [18]. Key points of the formulation include the decomposition of the homogenized composite's kinematics into the ones of the fiber and the matrix. Apart from the displacement variable $\boldsymbol{u}$, an additional kinematic filed variable, $\boldsymbol{d}$, is introduced. Both are two-dimensional vectors, while a plastic multiplier scalar variable ξ_m is also used. It describes a scaled version of the increment $\Delta\gamma_m$ of the accumulated plastic strain γ_m, between two consecutive time steps. Considering the above, there are five degrees of freedom in total per node (u_1, u_2, d_1, d_2, ξ_m). The method results in the model's mesh independence, meaning that the element size does not affect the results. A detailed description of the homogenized formulation can be found on [19], while more information on the presented implementation, including the calculation steps, is available on [21].

The fibers' behavior is described by standard isotropic hyper-elasticity defined by the Young's modulus E_f and the Poisson's ratio ν_f. The matrix's behavior is described by standard isotropic hyper-elastoplasticity, with the matrix's hyper-elasticity defined in a similar manner as above (by the Young's modulus E_m and the Poisson's ratio ν_m). The plasticity of the model's material is depicted through the Ramberg-Osgood constitutive law applied on the matrix. This material model can capture the non-linear strain hardening relationship, described by two fitting parameters, $\sigma_{0,m}$ and n_m. The Ramberg-Osgood material model is:

$$\varepsilon_{eq,m} = \frac{\sigma_{eq,m}}{E_m} + \frac{3}{7}\left(\frac{\sigma_{eq,m}}{\sigma_{0,m}}\right)^{n_m} \tag{1}$$

where $\varepsilon_{eq,m}$ is the effective von Mises strain and $\sigma_{eq,m}$ the effective von Mises stress for the matrix. Apart from the aforementioned fitting parameters and fiber and matrix properties, the model requires the fiber volume fraction V_f and the fiber diameter h_f as an input. The latter enables the model to account for the fiber's bending effect. The numerical model was built in GetFEM [22], an open-source FE library with interface for Python.

3 METHOD AND RESULTS

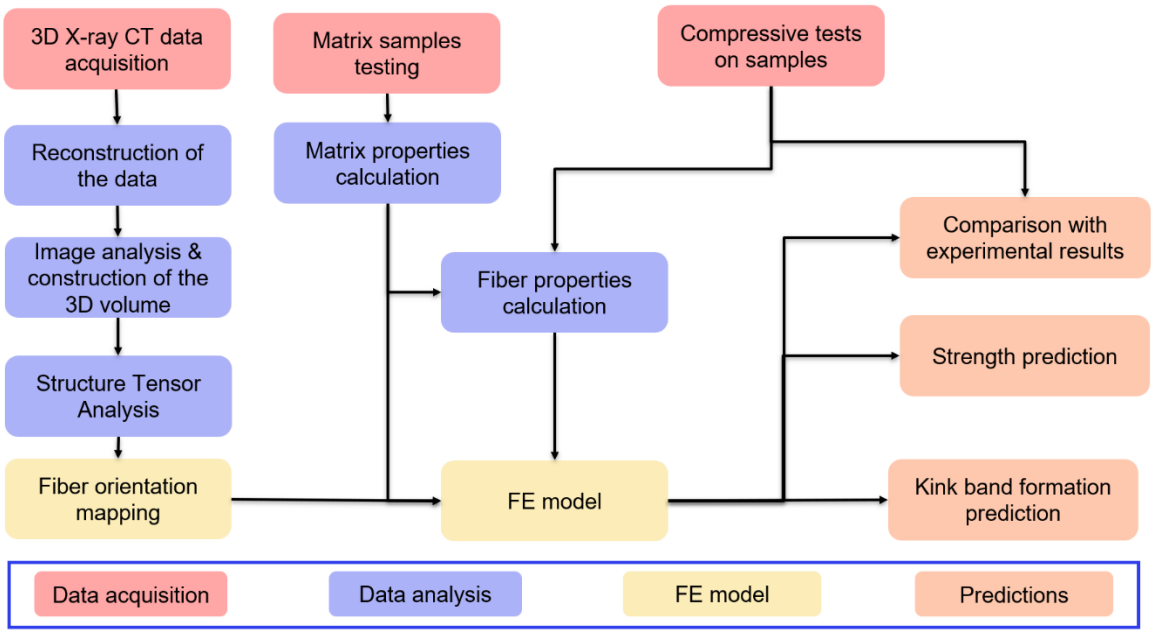

Figure 1: The developed methodology used in this work, described in a flow chart.

The methodology followed in this work, presented in Figure 1, started with the acquisition of the X-ray CT data of the unidirectional carbon composites, their analysis and, subsequently, the calculation of the fiber orientation distribution and its mapping on the FE model. Material characterization was carried out for the fibers, the matrix and the whole composite (it should be noted that in this work, the term fiber corresponds to what is considered filament, as it is widely used in similar articles). Along with the fiber orientation distribution, the extracted material properties served as the input for the numerical model. In this way, the predictions of the compressive strength and the kink band formation could be obtained. Mageira et al. [21] provides a more thorough description on the whole process and results.

3.1 X-ray CT data acquisition and results

Three samples were cut from a pultruded carbon profile. Their geometry was cylindrical as can be seen in Figure 2, with a diameter and length of 1 mm and 20 mm respectively. The samples were X-ray fully scanned at DanMAX beamline of the MAX IV synchrotron facility. The projection field was 1.2 x 1.2 x 1.2 mm^3 and the voxel size was equal to 0.55 μm. Considering that the average size of the single carbon fiber diameter is 7 μm, this voxel size ensured clear capture of the data, as it can be seen in the zoomed detail of Figure 2b. For the demonstration of the method and due to page limitations, only the results of the sample numbered six are presented in this work.

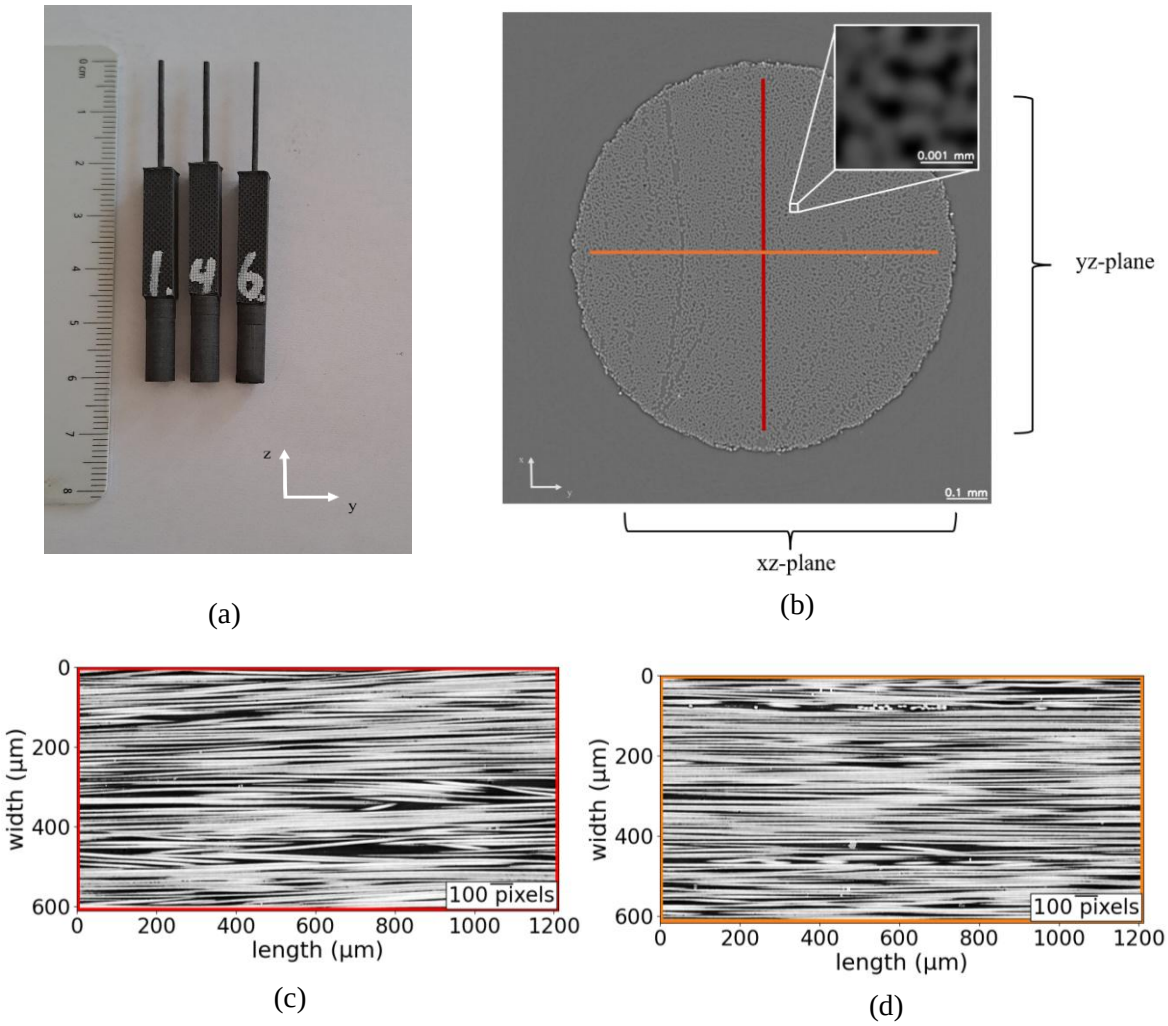

Figure 2: (a) The scanned unidirectional carbon composite samples. Each sample is fixed on a base used for mounting during 3D X-ray scanning. (b) Representative slice showing the cross section of one of the examined samples, as it is after reconstruction. The zoomed image shows the level of detail and quality of the scan. The characteristic kidney-shaped cross section of carbon fibers can be observed.

The two planes are annotated. The coloured lines represent the top view of the slices showing the longitudinal direction of the fibers, that can be seen in the bottom of the figure, for the yz-plane (c) and the xz-plane (d). These slices serve as an input for the structure tensor analysis.

Figure 2b show a slice of the scanned sample after reconstruction, showing the cross section of it. The images representing the slices were cropped and stacked accordingly to create a digital subvolume of the total scanned samples' volume. The subvolume had a thickness corresponding to 100 slices. Through its creation, the slices related to the planes that show the longitudinal direction of the fibers could be acquired. These slices and their corresponding subvolumes were essential for using the three-dimensional structure tensor analysis for the determination of the fiber orientation distribution. In Figure 2, the two planes, xz- and yz-, are annotated. Five slices were considered in this work, per orientation. An example of each plane's slice showing the longitudinal direction of the fibers can be seen at the bottom of the figure; these two slices and their corresponding results are the ones thoroughly presented in this work.

3.2 Material results

The material properties that serve as an input for the numerical model and thus need to be determined experimentally are the Young's moduli and Poisson's ratios of the fiber and the matrix, the fiber volume fraction and average diameter and the fitting parameters of the Ramberg-Osgood model for the matrix system. The first step was the determination of the mechanical properties of the composite material. To achieve this, samples were cut from the same pultruded profile from which the scanned samples were acquired. These samples were subjected to compressive testing. The Universal Testing Machine used had a load cell of 250 kN, and the applied testing speed was 1 mm/min. The strain range considered for the calculation of the composite's Young's modulus was 0.05 - 0.25 %, according to ISO-14126 [23]. As it can be seen in Figure 3, most of the samples broke outside their gauge area, due to the shear control of the failure [7]. For that reason, the acquired values of the compressive strength should be considered conservative.



(a)



(b)

Figure 3: (a) The examined dogbone-shaped samples, after the compression test. (b) The failure outside the gauge area of most of them can be noted. For the development of the kink band outside the gauge area, please refer to [7].

The matrix was vinyl ester, with its stress-strain curve shown in Figure 4, and the values of its Young's modulus and Poisson's ratio in Table 1. As mentioned in the Theory section, the Ramberg-Osgood material model was used to describe the behavior of the matrix numerically. The values of the parameters are $\sigma_{o,\,m}$ = 104.37 MPa and n_m = 2.35, and were found by fitting the Ramberg-Osgood material model on the matrix stress strain curve, as shown in Figure 4. The Young's modulus of the fibers was determined through back calculation by using the rule of mixture, since the matrix and composite material properties were already known. The detailed description and analysis of the material data are presented on [24].

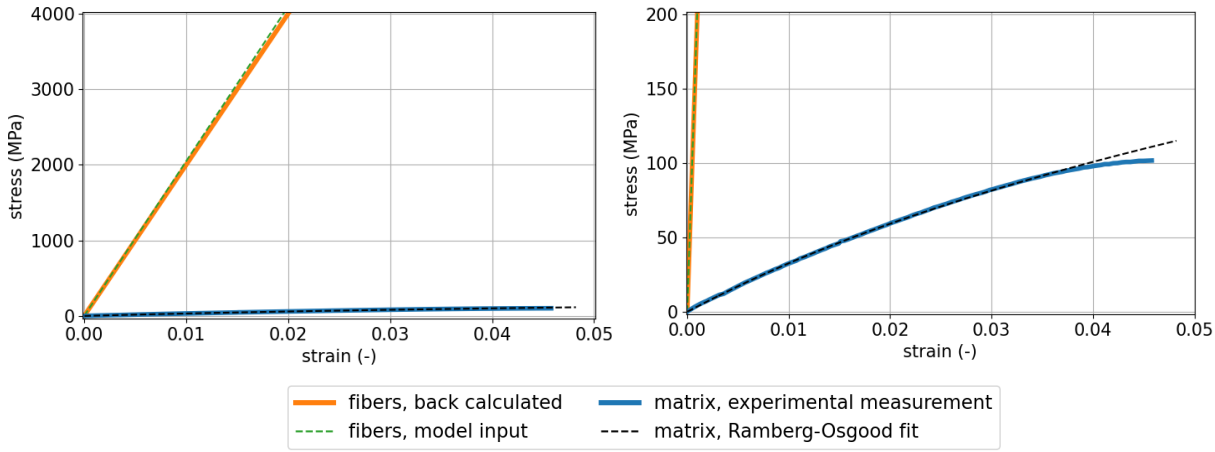

Figure 4: The stress-strain curves for the fibers and the matrix (left). A zoomed area of the graph is included (right). The fit of the Ramberg-Osgood material model for the matrix can be observed, as well the numerical model's material input for the fibers.

The average values of the calculated properties are presented on the following table:

Magnitude		Composite	Matrix	Fiber
Young's modulus E	[GPa]	137.5 ± 1.7	3.55	204.8 ± 4.1
Poisson's ratio v	[–]	–	0.4	0.26
Volume fraction	[%]	–	33.6 ± 0.9	66. 2 ± 0.8
Fiber's diameter	[μm]	–	–	7

Table 1: The mechanical properties and material parameters acquired after characterization of the composite, the fiber and the matrix.

3.3 Fiber orientation distribution results

The structure tensor analysis was used to determine the fiber orientation distribution. A short description of the method is included in the introduction, along with references regarding where to find details on it. For information on how it was applied on this dataset, please refer to [21].

After the decomposition of the eigenvalues, the corresponding eigenvectors were calculated, and the dominant fiber orientation was found. For the two-dimensional model used, the representation of the fiber orientation is a two-dimensional projection of the eigenvector $\boldsymbol{r}_1$ to the yz- or xz-plane, respectively. The subscript 1 identifies the dominant fiber orientation. To show the fiber orientation, the elevation angle φ was used, formed and calculated as shown in Figure 5. In the same figure, the elevation angle distribution on a slice is presented.

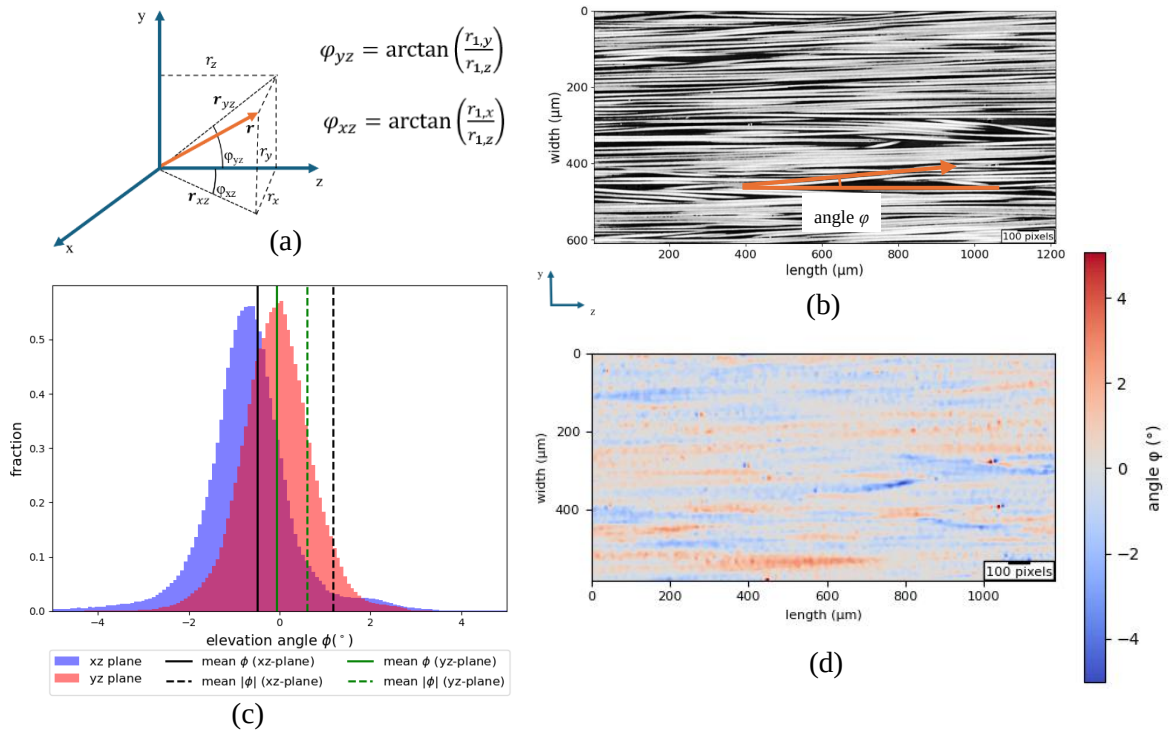

Figure 5: (a) The coordinates system used for this work, along with the dominant eigenvector $\boldsymbol{r}_1$, its projections at the yz- and xz-planes and the corresponding elevation angle for each case. Right next to it, the equations for the calculation of the elevation angle, per plane. (b) A yz-plane slice used for the 3D structure tensor analysis, with the elevation angle for a fiber shown. (d) The distribution of the elevation angle of the same slice as in figure 5b. (c) Distribution of the elevation angles for one slice per plane. The slices used are same as in Figure 2.

Figure 5 shows also the histogram of the distribution of the elevation angle's values for each examined plane. In the same figure, the values of the mean elevation angle φ, as well as of the mean absolute elevation angle, $|\varphi|$, are presented. The mean absolute elevation angle is chosen as a single value to represent both the magnitude and the scatter of the fiber orientation distribution [7, 24, 25]. For both planes, the vast majority of the values of the elevation angle ranged between -3° and 3°, something that is due to the unidirectionality of the pultruded material and the high quality of this manufacturing process. For the xz-plane, the mean elevation angle φ = -0.50° and the mean absolute elevation angle $|\varphi|$ = 1.17°. For the yz-plane, the corresponding value of the mean φ = -0.07°, and for the mean $|\varphi|$ = 0.61°.

3.4 Mapping of the fiber orientation distribution

The fiber orientation distribution serves as an input for the numerical model by its mapping to the integration points of the elements. A file containing the distribution of the elevation angle φ regarding the undeformed slice modelled is read by the FE code. The cosine and sine of each value of the elevation angle are calculated and saved as the following unit vectors, $\boldsymbol{N}$ and $\boldsymbol{T}$:

$$\boldsymbol{T} = \begin{Bmatrix} \cos(\varphi_0) \\ \sin(\varphi_0) \end{Bmatrix} \text{ and } \boldsymbol{N} = \begin{Bmatrix} -\sin(\varphi_0) \\ \cos(\varphi_0) \end{Bmatrix} \quad (2)$$

Each pair of $\boldsymbol{N}$ and $\boldsymbol{T}$ is mapped on an integration point. The unit vector $\boldsymbol{T}$ describes the direction parallel to the fibers, while the unit vector $\boldsymbol{N}$ the direction perpendicular to the fibers. The number of the mesh elements corresponds to the size of the examined slice, through the coupling of an elevation angle value with an integration point.

3.5 Numerical results

The numerical model was built in GetFEM. The coordinate system of the simulation is similar to the one related to the X-ray CT scanned samples presented on Figure 2. The model was two dimensional and was subjected to compression.

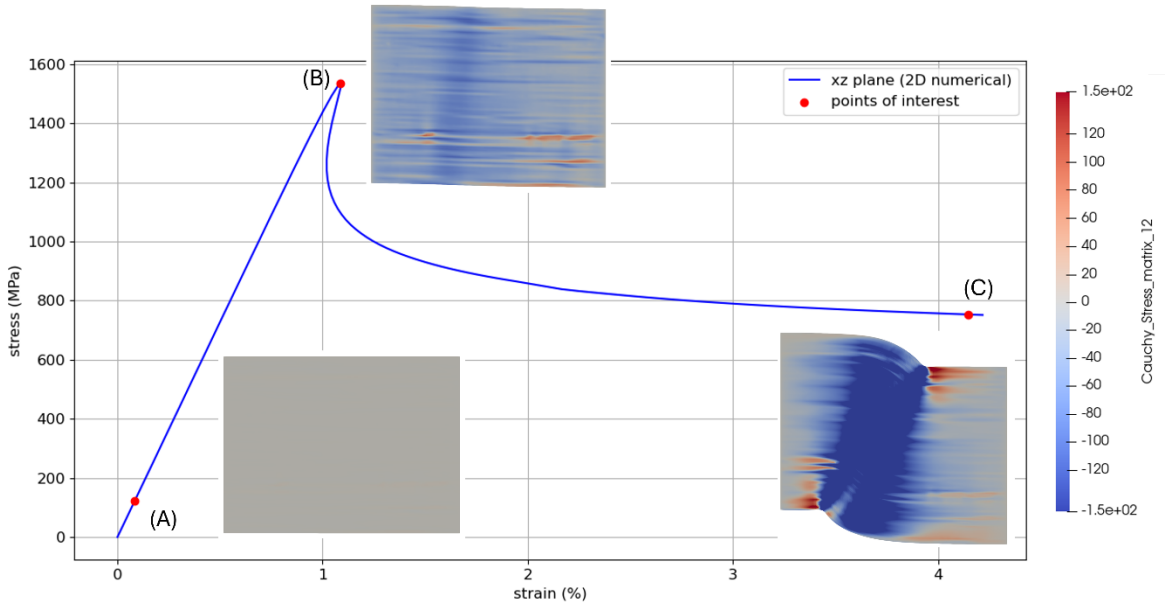

Figure 6: The stress-strain curve, for a single numerical case (xz-plane). Three points of interest are annotated as (A): just after the start of the compressive loading, (B): at maximum compressive stress and (C): at the latest stages of the simulation. For the same points, the distribution of the matrix's Cauchy shear stresses on the examined slice is shown, with the related scale bar included on the right of the graph.

Figure 6 shows the predicted stress-strain curve of one simulated slice. In addition, the distribution of the matrix's Cauchy shear stresses at the early loading stages, at the point of failure and after it can be observed, along with the gradual formation of the kink band. The stress-strain curve follows an almost linear trend, until the maximum stress value is reached and thus failure occurs. During the compressive failure of a composite, particularly when it is unidirectional, the material's limit load is reached in an area of localized strain [27], leading to the abrupt and excessive bending of the fibers, and subsequently to the kink band formation.

In the numerical model, the stress-strain curve follows a snap-back trend, which is a characteristic of the unidirectional composite's kink band formation during a FE simulation [25]. The snap back behavior is due to the localized fiber rotation leading in a load drop which results in elastic unloading in the material outside the kink-band region.

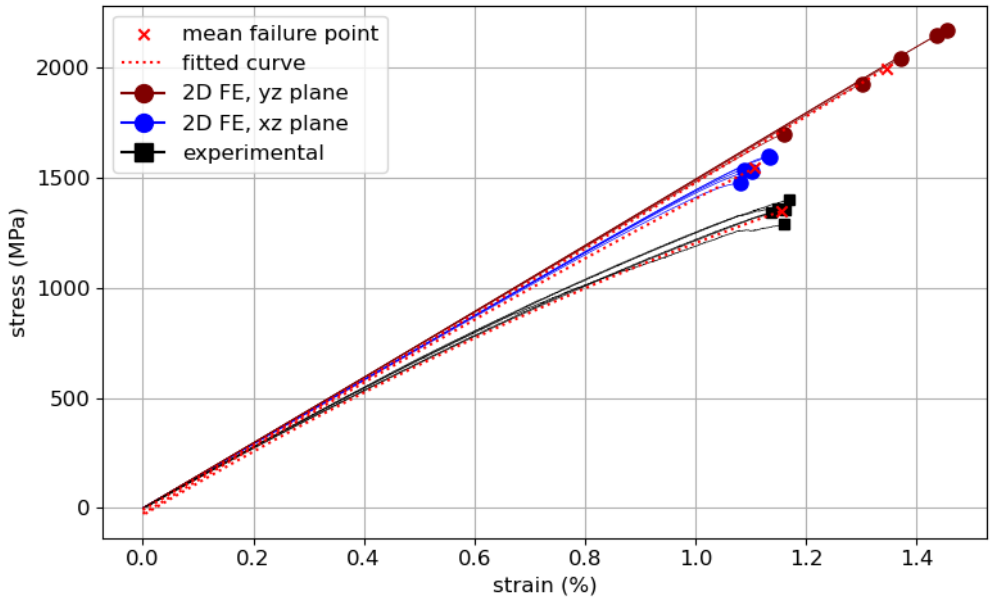

Figure 7: The stress-strain curves of the numerical data, for both planes examined, along with the results acquired through experimental testing. The maximum stress value is marked, for each case. A fitted curve for both the numerical and the experimental response, along with the mean failure point of each case, are included.

In Figure 7, the stress-strain curves for both the experimental and the numerical (for both planes) results is shown. The initial part of the experimental and numerical curves follows a similar trend. After this, however, the trend of the experimental measurements follows a curvature, govern by the non-linearity of the fiber material [28]. The numerical results show a stiffer response, which, as argued by Ferguson et al. in [7], is expected for a two-dimensional plane strain numerical model [25].

In the same figure, the value of the mean maximum stress (annotated as mean failure point) is included. For the numerical simulations, this value is 1546 MPa (xz-plane) and 1997 MPa (yz-plane). The corresponding experimental value is 1349 MPa. These results, along with the Young's moduli, average strain, mean elevation angle and mean absolute elevation angle are presented on Table 2. The compressive strength on yz-plane was on average 29% larger than the one of the xz-plane, and the compressive strength of xz-plane was 15% larger than the experimental values, on average. The Young's moduli of the numerical simulations were close to the experimental value, being 6% different for the yz-plane and 8% for the xz-plane.

Magnitude		Numerical, yz-plane	Numerical, xz-plane	Experimental
Young's modulus E	[GPa]	145.5 ± 0.2	148.0 ± 0.2	137.5 ± 1.0
Strength σ_{max}	[MPa]	1997 ± 110	1546 ± 29	1349 ± 23
Strain ε at max load	[%]	1.35 ± 0.07	1.11 ± 0.02	0.98 ± 0.02
Mean angle φ	[°]	0.19 ± 0.10	-0.63 ± 0.15	–
Mean absolute angle $\lvert\varphi\rvert$	[°]	0.63 ± 0.05	1.24 ± 0.07	–

Table 2: Average values of strength, strain, mean elevation angle and mean absolute elevation angle regarding the numerical results, along with the average values for stress and strain obtained through experimental testing.

The difference between the experimental and numerical compressive strengths can be attributed to

several factors. Geometry and loading conditions of the tested samples may have introduced local stress concentrations [7], with some samples failing outside the gauge area due to shear, which the model does not capture. In addition, the volume fraction of the fibers and the matrix were considered constant in the model, while, according to Kyriakides et al. [11] and Jensen [29], the varying volume fraction leads to a decrease in the sample's ability to resist kink band formation, and thus probably to a slightly reduced compressive strength. The fiber-matrix interface, which affects load transfer, and thus the compressive strength, is also not included. Finally, as a two-dimensional model, it cannot capture out-of-plane variations in fiber orientation distribution, possibly leading to a higher numerical value of compressive strength.

Considering the above, the compressive strength predicted by the numerical model can represent the potential strength of the composite, accounting for its fiber orientation distribution, under pure compression where shear effects are negligible.

4 CONCLUSIONS

In this work, X-ray CT images of pultruded carbon fiber reinforced composite samples were used to predict the compressive strength of the material by using a built numerical model. Key part of the two-dimensional, mesh independent, homogenized model was the inclusion of the composite's real fiber orientation distribution. The numerical results of the predicted compressive strength were compared with the corresponding experimental values, with the former being higher than the latter ones. This difference was expected, mostly due to the model being two-dimensional, the effect of shear during the experimental testing and any potential imperfections of the tested samples. Thus, the numerical results could serve as the prediction of the compressive strength of a composite considering its fiber orientation distribution. Through this work, the effect of fiber orientation distribution, dependent on pultrusion parameters, on the composite's compressive strength is shown. Based on these findings, adjustments to the pultrusion process could be made to improve the mechanical properties of wind turbine composite blades.

ACKNOWLEDGEMENTS

This study was funded by EU Horizon MSCA 2021 DN Reliance: REaL-tIme characterization of ANisotropic Carbon-based tEchnological fibers, films and composites, grant no. 101073040.

REFERENCES

[1] J. Tang, X. Chen, and K. Yang, Evaluating Structural Failure of Load-Carrying Composite Box Beams with Different Geometries and Load Conditions, *Applied Composite Materials*, vol. 26, no. 4, 2019, (doi: 10.1007/s10443-019-09776-4).

[2] R. Nijssen and G. D. De Winke, Developments in materials for offshore wind turbine blades, in *Offshore Wind Farms: Technologies, Design and Operation*, 2016, (doi: 10.1016/B978-0-08-100779-2.00005-2).

[3] D. Penumadu, M. E. Kant, J. Spanovich, G. Girolomini, R. E. Norris, and C. D. Jackson, Low cost pultruded carbon fiber composites development for spar cap applications in wind turbine blades, in *CAMX 2015 - Composites and Advanced Materials Expo, Dallas TX, United States, October 26-29*, 2015.

[4] P. S. Veers *et al.*, Trends in the design, manufacture and evaluation of wind turbine blades, 2003, (doi: 10.1002/we.90).

[5] B. Budiansky and N. A. Fleck, Compressive failure of fibre composites, *J Mech Phys Solids*, vol. 41, no. 1, 1993, (doi: 10.1016/0022-5096(93)90068-Q).

[6] M. J. Emerson, K. M. Jespersen, A. B. Dahl, K. Conradsen, and L. P. Mikkelsen, Individual fibre segmentation from 3D X-ray computed tomography for characterising the fibre orientation in unidirectional composite materials, *Compos Part A Appl Sci Manuf*, vol. 97, 2017, (doi: 10.1016/j.compositesa.2016.12.028).

[7] O. V. Ferguson, S. P. H. Skovsgaard, H. M. Jensen, and L. P. Mikkelsen, Compressive strength prediction of carbon fiber-reinforced pultruded profiles including realistic volumetric fiber orientations, *European Journal of Mechanics, A/Solids*, 2023, (doi: 10.1016/j.euromechsol.2023.105011).

[8] N. Jeppesen, L. P. Mikkelsen, A. B. Dahl, A. N. Christensen, and V. A. Dahl, Quantifying effects of manufacturing methods on fiber orientation in unidirectional composites using structure tensor analysis, *Compos Part A Appl Sci Manuf*, vol. 149, 2021, (doi: 10.1016/j.compositesa.2021.106541).

[9] N. Jeppesen, V. A. Dahl, A. N. Christensen, A. B. Dahl, and L. P. Mikkelsen, Characterization of the fiber orientations in non-crimp glass fiber reinforced composites using structure tensor, in *IOP Conference Series: Materials Science and Engineering*, 2020, (doi: 10.1088/1757-899X/942/1/012037).

[10] R. M. Auenhammer, L. P. Mikkelsen, L. E. Asp, and B. J. Blinzler, Automated X-ray computer tomography segmentation method for finite element analysis of non-crimp fabric reinforced composites, *Compos Struct*, vol. 256, 2021, (doi: 10.1016/j.compstruct.2020.113136).

[11] S. Kyriakides, R. Arseculeratne, E. J. Perry, and K. M. Liechti, On the compressive failure of fiber reinforced composites, *Int J Solids Struct*, vol. 32, no. 6–7, 1995, (doi: 10.1016/0020-7683(94)00157-R).

[12] T. J. Vogler, S. Y. Hsu, and S. Kyriakides, On the initiation and growth of kink bands in fiber composites. Part II: Analysis, *Int J Solids Struct*, vol. 38, no. 15, 2001, (doi: 10.1016/S0020-7683(00)00175-X).

[13] J. Christoffersen and H. M. Jensen, Kink band analysis accounting for the microstructure of fiber reinforced materials, *Mechanics of Materials*, vol. 24, no. 4, 1996, (doi: 10.1016/S0167-6636(96)00052-X).

[14] H. M. Jensen and J. Christoffersen, Kink band formation in fiber reinforced materials, *J Mech Phys Solids*, vol. 45, no. 7, 1997, (doi: 10.1016/S0022-5096(96)00126-3).

[15] O. V. Ferguson and L. P. Mikkelsen, Three-dimensional finite element modeling of anisotropic materials using X-ray computed micro-tomography data[Formula presented], *Software Impacts*, vol. 17, 2023, (doi: 10.1016/j.simpa.2023.100523).

[16] L. P. Mikkelsen, K. D. Sørensen, and H. M. Jensen, "User Subroutine for Compressive Failure of Composites," in Proceedings of 2009 SIMULIA Customer Conference, London, United Kingdom, 2009, pp. 618–632.

[17] N. A. Fleck and J. Y. Shu, Microbuckle initiation in fibre composites : A finite element study, *J Mech Phys Solids*, vol. 43, no. 12, 1995, (doi: 10.1016/0022-5096(95)00057-P).

[18] K. Poulios and C. F. Niordson, Accounting for fiber bending effects in homogenization of long fiber reinforced composites, in *ICCM International Conferences on Composite Materials, , Copenhagen, Denmark, July 19-24*, 2015.

[19] K. Poulios and C. F. Niordson, Homogenization of long fiber reinforced composites including fiber bending effects, *J Mech Phys Solids*, vol. 94, 2016, (doi: 10.1016/j.jmps.2016.04.010).

[20] P. Mageira, O. V. Ferguson, K. Poulios, K. Nelms, P. J. Withers, and L. P. Mikkelsen, Finite Element Predictions of In-Situ 3D X-Ray CT Determined Compression Failure of Uni-Directional Composites, in *Proceedings of ECCM21 – 21st European Conference on Composite Materials: Special Sessions (Vol. 8, pp. 385-392), Nantes, France, July 2-5*, European Society for Composite Materials, 2024.

[21] P. Mageira, K. Poulios, J. W. Andreasen, V. A. Dahl, and L. P. Mikkelsen, Experimental and numerical analysis of uni-directional carbon fiber composites in compression using a mesh independent homogenization model and real fiber orientation distribution, 2025, Available: under preparation.

[22] J. Pommier and Y. Renard, GetFEM++, An Open Source Generic C++ Library for Finite Element Methods, 2016.

[23] Iso 14126, Fibre-reinforced plastic composites - Determination of compressive properties in the in-plane direction, *International Standard*, vol. 2001, 1999.

[24] P. Mageira and L. P. Mikkelsen, Understanding the mechanical properties of carbon fiber reinforced composites used for X-ray CT scanning, 2025, Accessed: Jan. 30, 2025, Available: (under preparation).

[25] L. P. Mikkelsen *et al.*, Numerical 2D prediction of the compression strength of pultruded carbon fiber profiles with mapped X-ray determined fiber orientations, 2025, Available: (under preparation).

[26] R. Thirumalai, D. Prabhakaran, H. Lilholt, F. Aviles, T. Løgstrup Andersen, and H. Knudsen, Fibre waviness and misalignment measurement of unidirectional glass / LPET commingled composites – Effect on mechanical properties, *Risoe International Symposium on Materials Science, Roskilde, Denmark, September 2-5, 2013, Proceedings*, vol. 34, 2013.

[27] V. Tvergaard and A. Needleman, On the localization of buckling patterns, *Journal of Applied Mechanics, Transactions ASME*, vol. 47, no. 3, 1980, (doi: 10.1115/1.3153742).

[28] R. Kumar, L. P. Mikkelsen, H. Lilholt, and B. Madsen, Understanding the mechanical response of glass and carbon fibres: Stress-strain analysis and modulus determination, in *IOP Conference Series: Materials Science and Engineering*, 2020. (doi: 10.1088/1757-899X/942/1/012033).

[29] H. M. Jensen, Residual stress effects on the compressive strength of unidirectional fibre composites, *Acta Mater*, vol. 50, no. 11, 2002,(doi: 10.1016/S1359-6454(02)00114-3).

International Committee on Composite Materials

Student Status Confirmation Form for the ICCM Tsai Award

May 26th, 2025

I, Lars Pilgaard Mikkelsen, hereby confirm that Pinelopi Mageira, who applied for the ICCM Tsai Award, was, at the date of the abstract submission November 15th, 2024, a PhD student under my supervision at Technical University of Denmark.



_____ (signature)

Lars Pilgaard Mikkelsen
Associate Professor
Technical University of Denmark
Department of Wind Energy
Frederiksborgvej 399
Building 101
4000 Roskilde
Denmark
Direct +45 46774709
Mobile +45 21325406
lapm@dtu.dk
https://orbit.dtu.dk/en/persons/lars-pilgaard-mikkelsen

International Committee on Composite Materials

Authors Contributions

Manuscript title: EXPERIMENTAL AND NUMERICAL COMPRESSION ANALYSIS OF 3D X-RAY CT SCANNED UNI-DIRECIONAL PULTRUDED CARBON FIBER COMPOSITES

Please describe the contributions of each author, referring to the taxonomy below.

Author 1 (Tsai Award Applicant): Pinelopi Mageira

- ☒ Conception
  Specify contribution in more detail (optional; no more than one sentence)
- ☒ Data curation
  Specify contribution in more detail (optional; no more than one sentence)
- ☒ Formal Analysis
  Specify contribution in more detail (optional; no more than one sentence)
- ☒ Investigation
  Specify contribution in more detail (optional; no more than one sentence)
- ☒ Methodology
  Specify contribution in more detail (optional; no more than one sentence)
- ☒ Software
  Specify contribution in more detail (optional; no more than one sentence)
- ☒ Validation
  Specify contribution in more detail (optional; no more than one sentence)
- ☒ Visualization
  Specify contribution in more detail (optional; no more than one sentence)
- ☒ Wrote the paper (original draft)
  Specify contribution in more detail (optional; no more than one sentence)
- ☒ Wrote the paper (review and editing)
  Specify contribution in more detail (optional; no more than one sentence)
- ☐ Other contribution
  Specify contribution in more detail (required; no more than one sentence)

Author 2: Konstantinos Poulios

- ☐ Conception
  Specify contribution in more detail (optional; no more than one sentence)
- ☐ Data curation
  Specify contribution in more detail (optional; no more than one sentence)
- ☐ Formal Analysis
  Specify contribution in more detail (optional; no more than one sentence)
- ☐ Investigation
  Specify contribution in more detail (optional; no more than one sentence)
- ☒ Methodology
  Specify contribution in more detail (optional; no more than one sentence)
- ☒ Software
  Specify contribution in more detail (optional; no more than one sentence)
- ☐ Validation
  Specify contribution in more detail (optional; no more than one sentence)
- ☐ Visualization
  Specify contribution in more detail (optional; no more than one sentence)
- ☐ Wrote the paper (original draft)
  Specify contribution in more detail (optional; no more than one sentence)
- ☐ Wrote the paper (review and editing)
  Specify contribution in more detail (optional; no more than one sentence)
- ☐ Other contribution
  Specify contribution in more detail (required; no more than one sentence)

Author 3: Jens Wenzel Andreasen

- ☐ Conception
  Specify contribution in more detail (optional; no more than one sentence)
- ☐ Data curation
  Specify contribution in more detail (optional; no more than one sentence)
- ☒ Formal Analysis
  Specify contribution in more detail (optional; no more than one sentence)
- ☐ Investigation
  Specify contribution in more detail (optional; no more than one sentence)
- ☐ Methodology
  Specify contribution in more detail (optional; no more than one sentence)
- ☐ Software
  Specify contribution in more detail (optional; no more than one sentence)

☐ Validation
Specify contribution in more detail (optional; no more than one sentence)

☐ Visualization
Specify contribution in more detail (optional; no more than one sentence)

☐ Wrote the paper (original draft)
Specify contribution in more detail (optional; no more than one sentence)

☐ Wrote the paper (review and editing)
Specify contribution in more detail (optional; no more than one sentence)

☐ Other contribution
Specify contribution in more detail (required; no more than one sentence)

Author 4: Vedrana Andersen Dahl

☐ Conception
Specify contribution in more detail (optional; no more than one sentence)

☐ Data curation
Specify contribution in more detail (optional; no more than one sentence)

☒ Formal Analysis
Specify contribution in more detail (optional; no more than one sentence)

☐ Investigation
Specify contribution in more detail (optional; no more than one sentence)

☐ Methodology
Specify contribution in more detail (optional; no more than one sentence)

☐ Software
Specify contribution in more detail (optional; no more than one sentence)

☐ Validation
Specify contribution in more detail (optional; no more than one sentence)

☐ Visualization
Specify contribution in more detail (optional; no more than one sentence)

☐ Wrote the paper (original draft)
Specify contribution in more detail (optional; no more than one sentence)

☐ Wrote the paper (review and editing)
Specify contribution in more detail (optional; no more than one sentence)

☐ Other contribution
Specify contribution in more detail (required; no more than one sentence)

Author 5: Lars Pilgaard Mikkelsen

☒ Conception
Specify contribution in more detail (optional; no more than one sentence)

☒ Data curation

Specify contribution in more detail (optional; no more than one sentence)

☒ Formal Analysis
Specify contribution in more detail (optional; no more than one sentence)

☒ Investigation
Specify contribution in more detail (optional; no more than one sentence)

☒ Methodology
Specify contribution in more detail (optional; no more than one sentence)

☐ Software
Specify contribution in more detail (optional; no more than one sentence)

☐ Validation
Specify contribution in more detail (optional; no more than one sentence)

☐ Visualization
Specify contribution in more detail (optional; no more than one sentence)

☐ Wrote the paper (original draft)
Specify contribution in more detail (optional; no more than one sentence)

☒ Wrote the paper (review and editing)
Specify contribution in more detail (optional; no more than one sentence)

☐ Other contribution
Specify contribution in more detail (required; no more than one sentence)

Conceptualization
Ideas; formulation or evolution of overarching research goals and aims.

Data Curation
Management activities to annotate (produce metadata), scrub data and maintain research data (including software code, where it is necessary for interpreting the data itself) for initial use and later reuse.

Formal Analysis
Application of statistical, mathematical, computational, or other formal techniques to analyze or synthesize study data.

Investigation
Conducting a research and investigation process, specifically performing the experiments, or data/evidence collection.

Methodology
Development or design of methodology; creation of models.

Software
Programming, software development; designing computer programs; implementation of the computer code and supporting algorithms; testing of existing code components.

Validation

Verification, whether as a part of the activity or separate, of the overall replication/reproducibility of results/experiments and other research outputs.

Visualization
Preparation, creation and/or presentation of the published work, specifically visualization/data presentation.

Writing – Original Draft Preparation
Creation and/or presentation of the published work, specifically writing the initial draft (including substantive translation).

Writing – Review & Editing
Preparation, creation and/or presentation of the published work by those from the original research group, specifically critical review, commentary or revision – including pre- or post-publication stages.

PARTIALLY CARBONISED CARBON FIBRES AS AN IMPROVED MULTIFUNCTIONAL STRUCTURAL BATTERY ELECTRODE

Ruben Tavano[1*], Johanna Xu[1], Claudia Creighton[2], James D. Randall[2], Luke C. Henderson[2], Leif E. Asp[1]

[1]Industrial and Materials Science, Chalmers University of Technology, 41296 Göteborg, Sweden

[2]Institute of Frontier Materials, Deakin University, Geelong Waurn Ponds Campus, VIC 3216, Australia

* Corresponding author (ruben.tavano@chalmers.se)

Keywords: *Carbon fibre; Smart materials; Multifunctionality*

Abstract

Carbon fibres are increasingly explored for use in structural battery electrodes due to their ability to combine mechanical strength and stiffness with electrochemical functionality. The properties of carbon fibres are largely governed by their microstructure, which is shaped by the processing conditions—particularly the carbonisation temperature. This study focuses on exploring how partial carbonisation during manufacture influences the multifunctional performance of carbon fibres. The manufactured fibres are subjected to mechanical and electrochemical tests to evaluate their tensile properties, and reversible capacity. The results confirm previously reported multifunctionality trade-offs: when comparing to conventional intermediate modulus carbon fibres, by reaching a maximum temperature of 900 °C (compared to the usual 1500 °C) the electrochemical capacity increases at the expense of mechanical performance. Up to a 50% reduction in tensile modulus is observed alongside a 40% improvement in electrochemical capacity. These findings highlight the potential to greatly expand the achievable multifunctionality window for carbon fibres by adjusting the maximum carbonisation temperature, enabling a versatile design of active materials for structural energy-storing applications.

Introduction

The development of multifunctional materials is paving the way for significant changes in energy storage solutions for transportation and portable devices. One of the most promising concepts are structural battery composites (SBCs), which combine structural functions with the ability to store electrical energy. By embedding energy storage directly into load-bearing components, such as those in electric vehicles, designers can reduce weight, increase efficiency and consequently extend driving range. Structural battery composites embody this dual functionality, enabling materials to perform as both batteries and composite panels. Typically, a structural battery features a configuration where a thin-ply carbon fibre tow acts as the negative electrode, layered with a separator and a counter electrode[1–6]. These layers are infused with a structural battery electrolyte (SBE), which provides load transfer capabilities and ionic transport[7–11]. Due to their multifunctionality, carbon fibres not only provide structural reinforcement but also serve as lithium hosts and electron conductors.

While the mechanical properties of commercial carbon fibres are well-characterised, owing to their established role in composite reinforcement, their electrochemical behaviour remains less understood. Works by Jacques et al. and Duan et al. helped shed light on how lithium insertion alters the physical and mechanical characteristics of these fibres[12–15]. Additional investigations by Kjell et al. evaluated the electrochemical performance of widely used PAN-based carbon fibres[16], and Hagberg et al. examined the capacity and coulombic efficiency of intermediate modulus (IM) fibres (such as T800 and IMS65) in contrast to high modulus (HM) fibres like M60J, using precise coulometry techniques[17]. IM fibres generally exhibited superior electrochemical capacity, though the exact mechanisms behind this disparity were not initially clear.

Fredi et al. employed high-resolution transmission electron microscopy and in-situ Raman spectroscopy to uncover the underlying lithiation processes in T800, IMS65, and M60J fibres[18]. Their findings revealed that IM fibres behave somehow similarly to amorphous carbon during lithium insertion, with each fibre displaying unique performance characteristics. Conversely, the HM fibre followed a graphite-like staging mechanism, which was hindered by defects in its large crystalline domains. This structural obstruction contributed to its lower lithium capacity. Further insights into the performance differences between IM fibres were offered by Johansen et al., who investigated the role of heteroatoms in the carbon fibre microstructure[19]. They discovered notable variations in nitrogen content: IMS65 contained 20.5% pyridinic and pyrrolic nitrogen compared to just 14.2% in T800. These nitrogen configurations typically appear at defect sites and facilitate lithium coordination, suggesting that the higher concentration of these species in IMS65 may account for its enhanced capacity.

Asp et al. demonstrated the potential of intermediate modulus (IM) carbon fibres for multifunctional energy applications by integrating T800 fibres into a laminated structural battery composite, where the fibres functioned as the negative electrode[20]. Their prototype achieved an energy density of 24 Wh/kg alongside a mechanical stiffness of 25 GPa, exemplifying the material's dual structural and electrochemical roles. More recently, by using carbon fibres coated with lithium iron phosphate as the active material for the positive electrode, Chaudhary et al. managed to realise the first all-fibre structural battery. They boosted the structural battery performance leading to a significant improvement in the mechanical performance, with a tensile modulus of 76 GPa and a slight decrease in the energy density to 30 Wh/kg[21,22].

Despite such advancements, significant challenges remain. Commercially available carbon fibres have traditionally been optimised solely for mechanical properties, particularly strength and stiffness, without consideration for electrochemical functionality. This presents complications for multifunctional applications, not only because critical details such as the precursor materials and processing conditions are often proprietary, but also because the fibres are typically coated with sizing agents whose chemical composition is unknown, potentially interfering with their performance in electrochemical applications.

In an effort to better understand how lithium interacts with carbon fibres and to identify which microstructural characteristics enhance electrochemical performance, Xu et al. and Tavano et al. manufactured custom-made carbon fibres. The same PAN-based precursor was used in both cases, but each study introduced distinct modifications during fibre processing. Xu et al. varied the tensile force applied during the stabilisation stage, while Tavano et al. adjusted the carbonisation temperature profiles. These deliberate alterations allowed them to systematically investigate the effects of processing conditions on the resulting fibre properties. Their findings revealed a fundamental trade-off between mechanical properties and electrochemical performance. As the electrochemical capacity of the fibres improved, a corresponding decline in mechanical performance was observed, highlighting the inherent antagonistic character between these two functional objectives in carbon fibres. Furthermore, it was shown that fibres with a less ordered microstructure, specifically those with reduced crystalline carbon content, smaller crystallite sizes, and increased interlayer spacing within the crystalline regions, exhibited superior lithium storage capabilities. These results suggest that while high structural order favours mechanical strength, a more disordered carbon structure can be advantageous for lithium intercalation, pointing to the need for careful optimisation when designing carbon fibres for multifunctional applications.

In the current study, we investigate a custom-made carbon fibre manufactured only by a partial carbonisation step. The resulting carbonaceous microstructure attributes peculiar properties to the fibres, enabling us to further expand the design window for structural battery composites. Previous studies have focused on HM and IM carbon fibres. HM fibres have high mechanical performance but almost non-existent lithium storing capabilities. IM fibres show a good multifunctionality compromise. With partially carbonised carbon fibres, the mechanical properties are significantly decreased but unmatched reversible

electrochemical capacity is reached. These types of fibres can prove useful for applications that need energy storage at low mechanical requirements, and can guide the development of a new category of multifunctional fibres.

Experimental

Materials: Carbon fibres were produced at Carbon Nexus, Institute for Frontier Materials at Deakin University, Australia, using a research-grade production line. The production process followed similar criteria as in the previous studies by Xu et al. and Tavano et al.[23,24]. The precursor material was a 24 K tow of polyacrylonitrile (PAN) fibres sourced from Bluestar Ltd (China). Following stabilisation, the fibres were subjected to a carbonisation process only in the low temperature carbonisation furnace (LT furnace), reaching a maximum temperature of 900 °C. During production, the fibre line operated at a speed of 30 m/h, resulting in residence times of approximately 2 h in the stabilisation step and 2.5 minutes in the low-temperature carbonisation furnace. Throughout the oxidation phase, the fibres were subjected to an average tension of 2300 cN. This tension was adjusted in the carbonisation stage, with values maintained at 1200 cN during the low-temperature carbonisation. After exiting the LT furnace, the carbon fibres were directed to a winder for collection.

For the electrochemical characterisation, half-cells were assembled. Glass fibre separator (Whatman GF/A, ~260 µm thick), lithium metal foil (99.9%, 0.75 mm thick), lithium bis(trifluoromethanesulfonyl)imide (LiTFSI, anhydrous, 99.99%), propylene carbonate (PC, ≥99%, acid <10 ppm, H_2O <10 ppm), and ethylene carbonate (EC, 99% anhydrous) were all purchased from Sigma Aldrich (USA). The copper foil, nickel foil and silver glue used for the cell assembly were purchased from Ted Pella, Inc. (USA).

Physical properties: Fibre density was assessed using a Ultrapyc 1200e pycnometer (Quantachrome, Austria), with three replicate measurements. The fibre diameter was obtained combining the fibre density with the vibrational analysis conducted via a Favimat+ single fibre tensile test machine (Textechno, Germany) prior to mechanical testing. Conductivity was evaluated via the four-point probe method, with ten measurements carried out to ensure reproducibility and consistency. Surface area measurements were obtained using Brunauer–Emmett–Teller (BET) analysis, conducted on an inverse gas chromatography surface energy analyser (Surface Measurement Systems, UK) with octane gas adsorption at 30 °C. Complementary imaging of the carbon fibre surfaces was performed using a field emission scanning electron microscope LEO-1550 (Zeiss, Germany) to reveal surface texture and morphology.

Raman spectroscopy: Raman spectra were recorded using a WITec alpha300 R spectrometer (WITec GmbH, Germany), equipped with a confocal microscope Zeiss LSM (Zeiss, Germany) and a 50× magnification objective lens Zeiss EC Epiplan (NA = 0.75) (Zeiss, Germany). All measurements were carried out at room temperature (23 °C) using a 532 nm laser excitation source. The laser, focused to approximately 300 nm spot size, enabled detailed analysis of individual carbon fibres. Data acquisition was performed in backscattering geometry, using a 100 µm slit, a 600 lines/mm diffraction grating, and no optical filters. The spectra were collected using a charge-coupled device (CCD) detector. To enhance the signal-to-noise ratio (S/N), each spectrum was composed of 60 accumulations, each with an exposure time of 1 second. Post-processing of the spectra was performed using the software Project FIVE (WITec GmbH, Germany). A linear baseline was subtracted to correct for background fluorescence, and Savitzky-Golay smoothing was applied to further reduce noise. Spectral peaks were analysed in terms of Raman shift, intensity, area, and full width at half maximum (FWHM), using Lorentz function fitting. For visual comparison, all spectra were normalised to the most intense peak.

Mechanical Properties: Mechanical properties, including tensile strength, elastic modulus, and strain to failure, were characterised using single filament tensile testing with a Favimat+ machine (Textechno, Germany), equipped with a 210 cN load cell and a 20 mm gauge length. Tests were performed according

to ASTM D3822-07 at a constant strain rate of 1 mm/min. Seventy-five individual fibres were tested for each fibre type.

Electrochemical properties: Electrochemical characterisation involved the preparation of electrode samples using 24K tows of carbon fibres. To facilitate the electrode performance and repeatability, the tows were divided into two 12K tows prior to assembly. To establish electrical contact, copper strip current collectors were bonded to the carbon fibres using silver paint. Nickel foil was used as a current collector in the counter electrode. The assembled carbon fibre electrodes were dried under vacuum at 50 °C overnight before transfer to an argon-filled glovebox (with H_2O and O_2 levels <1 ppm).

The electrochemical testing employed a two-electrode pouch cell configuration. Lithium metal foil served as both counter and reference electrode. Glass microfiber separator was used to insulate the two electrodes. The liquid electrolyte was then added to the cell prior to sealing it. The complete cell was sealed in a pouch bag prior to testing. Galvanostatic charge/discharge cycles were conducted to determine specific capacity, coulombic efficiency, and first-cycle losses. Testing was carried out on a Neware CT-4008-5V10mA-164 battery cycler (Neware, China). For half-cell cycling studies, the voltage window was set from 0.01 V to 1.50 V versus Li/Li^+. The applied current densities were based on graphite's theoretical capacity (372 mAh g^{-1}), corresponding to 0.05C (for the conditioning cycles), 0.1C, 0.2C, and 0.4C. The sequence included ten cycles at 0.05C, followed by five each at 0.1C, 0.2C and 0.4C, and concluding with twenty-five additional cycles at 0.1C. A resting period of two hours was applied after each charge/discharge phase.

Results and Discussion

For comparison purposes, we report the results of the partially carbonised fibre, labelled PC900, and two IM carbon fibres investigated in previous studies. These are commercially available T800 carbon fibres and the cool temperature profile (CP) carbon fibres from Tavano et al. (which are referred to as fully carbonised (FC) in the coming sections)[24]. The importance of comparing the fibres from this study to the FC fibres lies in the almost identical manufacturing process. The only difference was a passage in the high-temperature carbonisation furnaces for the FC fibres, which made them similar to other IM carbon fibres. This difference attributes peculiar microstructural differences to the two fibres.

Physical Properties:

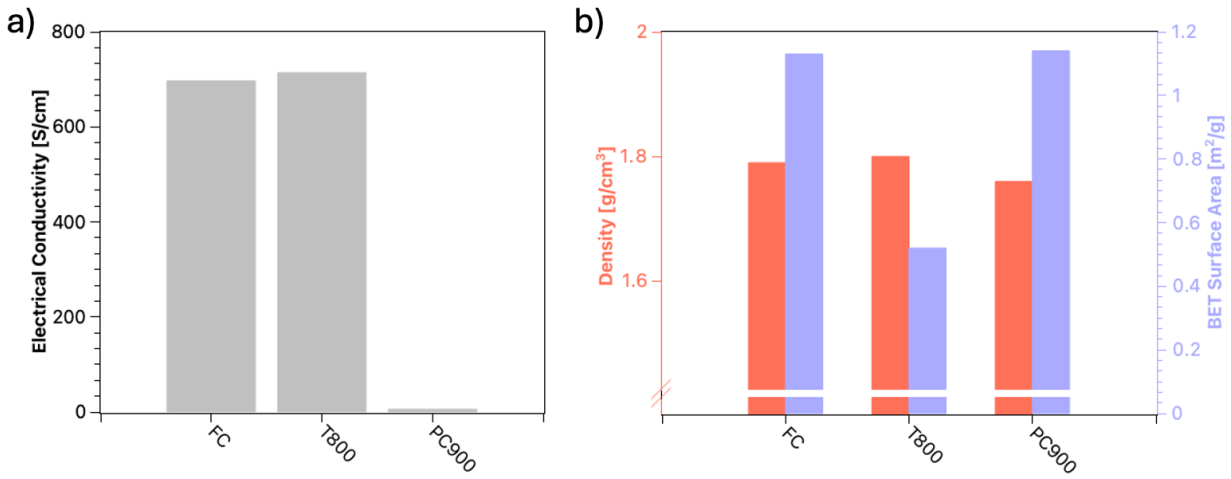

Figure 1 Physical, mechanical and electrochemical properties overview for two IM carbon fibres (FC and T800) and the partially carbonised carbon fibre (PC900). a) Electrical conductivity; b) Density and BET surface area.

Electrical conductivity is needed for energy storage applications since the active material needs to be conductive enough to transport electrons to and from the current collector. No clear requirements in terms of minimum conductivity have been reported in the literature. In Figure 1a, a comparison of the three

fibres is shown for the electrical conductivity. Values more than two orders of magnitude lower were measured for the PC900 fibres compared to the IM fibres.

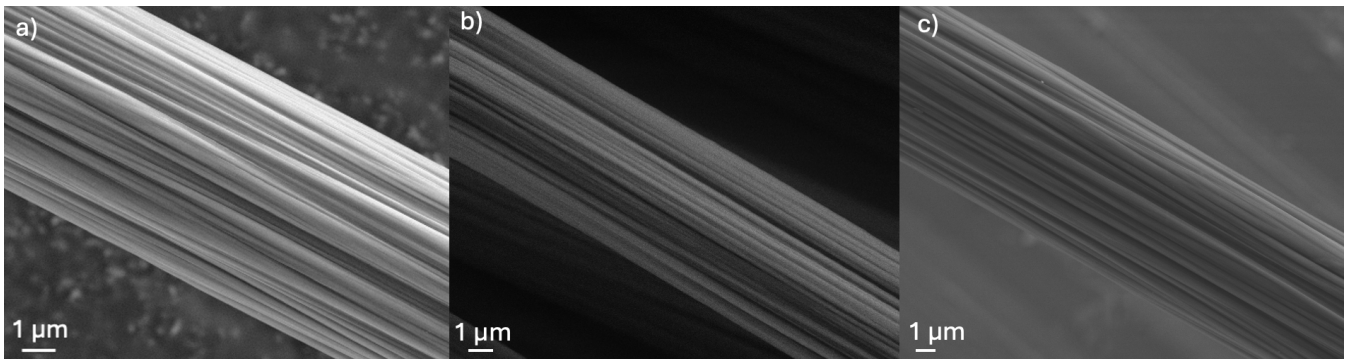

Figure 2. SEM surface images of the three carbon fibres at x10k magnification of the. a) FC fibres from Tavano et al[24]; b) T800 fibres; c) PC900 fibres manufactured in the current study.

A comparison of density and BET surface area for the three fibres is shown in Figure 1b. Comparable densities were measured for the two IM carbon, while slightly lower values were measured for the PC900 fibre. The BET surface area is highly influenced by the type of precursor fibre used for the manufacturing. The values measured for all the fibres were very low, below 1.2 m^2 g^{-1}, and comparable, indicating that the precursor was produced with a similar wet spinning process[25–27]. These results are confirmed by the SEM images shown in Figure 2a-c, where no significant differences are evident. Similar crenulations along the fibre length are visible for all fibre types.

Raman Spectroscopy: The three fibre types were characterised via Raman spectroscopy to obtain information about the carbonaceous microstructure and its possible differences due to the different carbonisation process. Different spectra were obtained for the three fibres, with different intensities of the D and G peaks along with differences in the Raman shift values.

In Figure 3a, the three spectra are shown in the 500-2500 cm^{-1} Raman shift range with a zoomed-in view of the D and G peaks in the inset. Similar G' peaks were observed in all the samples, indicating a low degree of crystallisation, small domains and a turbostratic or amorphous microstructure[28]. For the IM fibres, the intensity is similar for the D and the G peaks, resulting in a ratio between the intensity of the two equal to 1.0 and 0.9 for FC and T800, respectively. This is most likely due to the FC fibre being carbonised at a slightly lower temperature compared to the commercial T800 fibre. For the partially carbonised fibre, the intensity of the D peak is significantly higher, consistent with a more disordered, less graphitised carbonaceous microstructure of this fibre type. In this case, a ratio of 1.2 was calculated between the intensity of the D and G peaks. Additionally, by using the Tuinstra-Koenig approach, the average crystal length in the carbon fibres could be estimated from the peak intensity ratio[29]. Smaller crystallites were calculated for PC900 fibres compared to the two IM fibres with an average crystal length equal to 42 Å, compared to approximately 52 Å for IM fibres. Furthermore, the D and G peaks for the PC900 fibres are slightly shifted towards smaller Raman shifts compared to IM fibres, as can be seen in Figure 3b. This could be caused by residual strains in the microstructure due to the partial carbonisation, as well as a higher amount of heteroatoms and structural disorder[18].

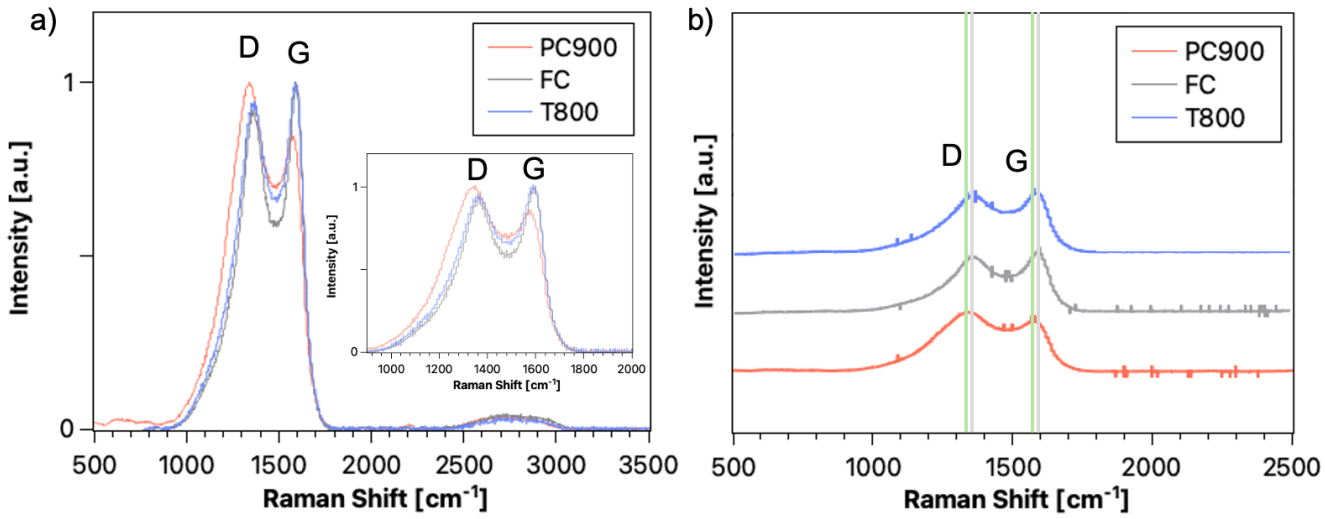

Figure 3 Raman spectroscopy results for IM fibres FC and T800, and partially carbonised fibre PC900. a) Full Raman spectra in the 500-3500 cm^{-1} Raman shift range, with zoomed-in view of the D and G peaks in the inset; b) View of the spectra with movement along the vertical direction. The D and G peaks are slightly shifted towards higher Raman shifts for the IM fibres.

Mechanical Properties: The mechanical properties of carbon fibres are mainly influenced by the tension applied during the stabilisation step and the temperature reached in the carbonisation step[30]. T800 carbon fibres showed the highest mechanical performance with a strain to failure, breaking strength and tensile modulus between 10% and 20% higher than FC fibres. This is most likely due to the maximum reached temperature in the carbonisation step, which was 1300 °C for FC fibres and is unknown for T800 fibres. However, the differences are small when compared to the values measured for PC900 fibres, with a tensile modulus around half that of IM fibres and a breaking strength and strain to failure 40% and 70% lower compared to IM fibres, respectively. All the mechanical properties are shown in Table 1.

Table 1. Mechanical properties for FC, T800 and PC900 carbon fibres.

Sample	Tensile modulus [GPa]	Tensile strength [GPa]	Strain to failure [%]
FC	204.5	2.8	1.4
T800	241.4	3.9	1.7
PC900	99.2	1.0	1.1

Mechanical properties are known to be affected by crystallite size and orientation[18,31]. For partially carbonised carbon fibres, as evidenced by the Raman spectra, smaller crystalline domains were achieved. The difference in the intensity between D and G peaks also suggests that PC900 fibres have a more disordered and less graphitised microstructure, which is further confirmed by the lower mechanical properties compared to IM fibres.

Electrochemical properties: For simplicity purposes and since the differences in the electrochemical behaviour between the FC and T800 fibres were reported to be small, in the following section, the partially carbonised PC900 fibres will only be compared to T800 fibres.

In Figure 4a-f the voltage profiles for charge and discharge for the two fibre types are depicted for various cycles at different current rates. For all the current rates, the PC900 fibres reached a higher specific capacity compared to the IM fibres, here illustrated for the T800 fibre. For the first conditioning cycle in Figure 4a, differences between the two fibres were very conspicuous, especially for the discharging part of the profile. Furthermore, the shapes of the charge and discharge curves were very different, with a

more linear trend observed for PC900. For the other voltage profiles in Figure 4b-e, the differences were more significant for the charging phase, while the discharging phase showed a similar trend. The difference between the curves was also influenced by the current rate used: by increasing the current rate, the voltage curve for T800 fibres got closer to that of PC900 fibres, almost overlapping at a specific current of 150 mA g^{-1} (0.4C rate). In Figure 4f, the reversibility of the behaviour is demonstrated. The 15th and 30th cycles overall, performed at a specific current of 35 mA g^{-1} (0.1C rate), showed an almost perfect overlapping of the curves, indicating reversibility of the lithium insertion/extraction process.

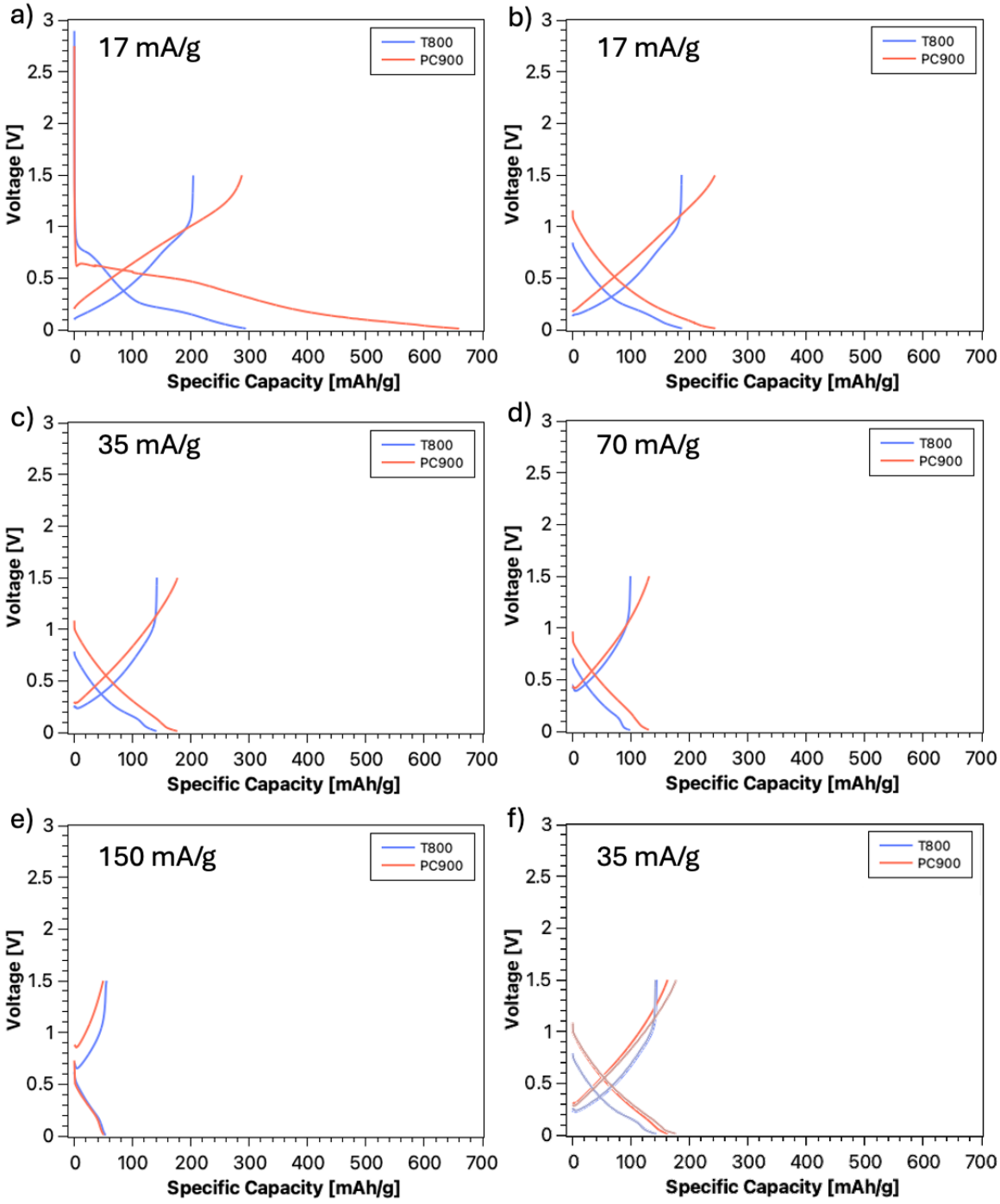

Figure 4. Charge/discharge voltage profiles for T800 and PC900 fibres. a) 1st conditioning cycle at 0.05C rate; b) 10th conditioning cycle at 0.05C rate; c) 5th cycle at 0.1C rate; d) 5th cycle at 0.2C rate; e) 5th cycle at 0.4C rate; f) 30th cycle and 15th cycle (overlayered in grey colour, same as b)) at 0.1C rate.

In Figure 5a, the specific capacities for both fibre types are shown for the different current rates. As expected, with increased current rates, lower specific capacities were measured. However, significant differences in specific capacities were observed between the two fibres, with PC900 performing better at all the current rates and equalling the specific capacity of T800 only at the fastest 0.4C rate. Additionally, the previously mentioned good reversibility of the capacity was observed, as well, when returning to a 0.1C rate after the 25th cycle.

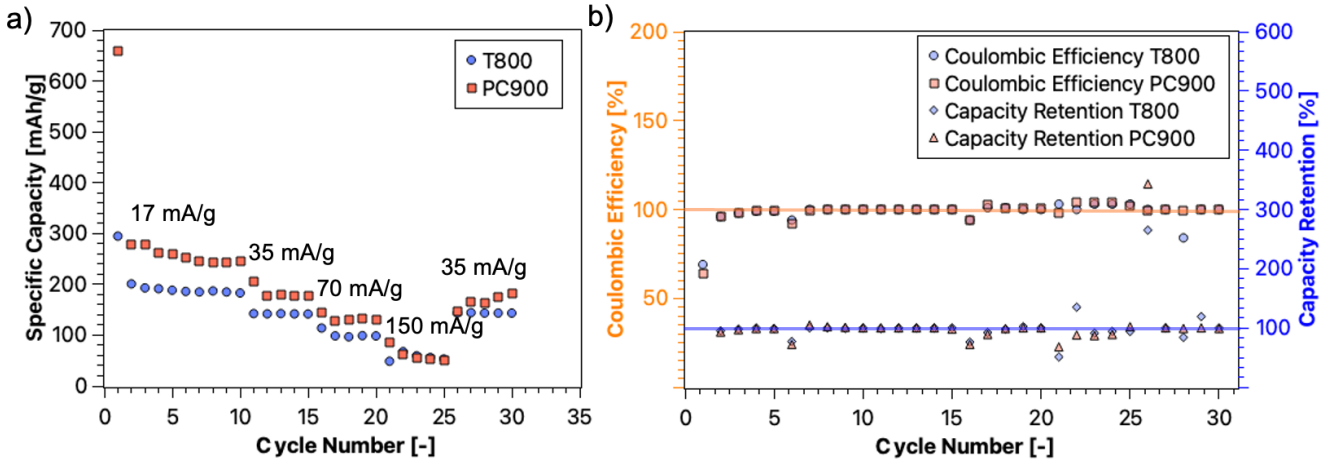

Figure 5 Overall view of the electrochemical cycling results. a) Specific capacity at different current rates at different cycle numbers for T800 and PC900; b) Coulombic efficiency and capacity retention for T800 and PC900.

For the partially carbonised PC900 fibre, an unmatched 1st cycle capacity was measured at more than double the value for T800 fibres. This was accompanied by a much larger 1st cycle loss for PC900 (56% compared to 36%). The reason for this is likely related to more of the inserted lithium ions remaining trapped in the active material due to the more disordered microstructure, as previously reported by Johansen et al.[32]. Furthermore, the results of the electrochemical characterisation are in line with previous studies and the Raman spectroscopy results[18,23,24,33–35]. Previous studies have shown that carbon fibres with a turbostratic microstructure and small crystallite size exhibit lithium storage behaviour similar to that of amorphous carbon. However, unlike fully amorphous materials, these fibres retain some graphitic domains where limited lithium intercalation can still occur. In what is referred to as the "single-layer model," amorphous regions surrounding the disordered crystalline structures impede lithium insertion into graphitic layers. As a result, lithium ions are primarily stored in the amorphous areas and at structural defects such as nanocavities. A prevalence of amorphous domains, more defects and nanocavities, and small crystalline domains in the partially carbonised carbon fibres could explain the better electrochemical performance. In the case of PC900 fibres, higher reversible capacities, with up to 40% better performance for the slower current rates, were observed compared to T800 fibres.

In Figure 5b, the good reversible behaviour for the electrochemical cycling is further evidenced. Comparable Coulombic efficiencies and capacity retentions were measured for both fibres**.** Coulombic efficiency serves as an indicator of how effectively the cell recovers its stored charge, calculated as the proportion of discharge capacity relative to the charge input within a single cycle. In contrast, capacity retention tracks the stability of performance over time by comparing each cycle's discharge capacity to that of the cycle immediately before it. This provides a detailed view of how the cell responds to changing current rates. During the initial cycle, a noticeable decline in efficiency was observed, primarily due to irreversible lithium loss associated with SEI formation and trapped ions. However, from the second cycle onward, Coulombic efficiency rapidly stabilised near 100%, signalling minimal parasitic reactions and excellent reversibility. Capacity retention data further showed that the electrodes maintain consistent performance even when subjected to fluctuations in current rates. Minor dips were correlated with current rate changes but recovered swiftly in the subsequent cycles. This behaviour underscores the

electrochemical reliability of both fibres under dynamic operating conditions. Together, the near-perfect Coulombic efficiency and strong capacity retention present compelling evidence for the durability and reliability of these carbon fibre-based structural anodes in longer-term cycling scenarios. Long-term cycling experiments (i.e. up to 1000 cycles) were not included in this study, in line with previous methodologies that focused on coulombic efficiency as an initial metric. Full-cycle durability testing will be carried out in future investigations once these fibres are integrated into structural full cells, where system-level longevity becomes a central concern[23].

Conclusion

In this study, partially carbonised carbon fibres have been characterised to assess their possible use as active material in a structural negative electrode. Partially carbonised fibres demonstrate an electrical conductivity more than two orders of magnitude lower than IM fibres. Nonetheless, the low conductivity is still sufficient for the electrochemical functioning. The lower temperature used during carbonisation of the partially carbonised fibre resulted in a lower number of graphitic domains and smaller crystallites. As a consequence, the mechanical properties of the partially carbonised fibres were reduced, with a tensile modulus reaching less than half of the IM fibres' value. In contrast, the electrochemical performance highly benefited from the achieved microstructure, with specific capacity values which were up to 40% higher compared to IM fibres. These results confirm what was previously observed, with a clear trade-off in terms of multifunctionality. The results from this study expand the previous results from Xu et al. and Tavano et al., highlighting how the multifunctionality window can be enormously expanded by using less conventional production methods[23,24].

Acknowledgements

The authors would like to thank the following entities for funding this research: United States Air Force (USAF), USA, Award Number FA8655-21-1-7038, Office of Naval Research (ONR), USA, Award Numbers N62909-22-1-2037 and N62909-22-1-2052, Swedish National Space Agency, Contract 2020-00256, Swedish Energy Agency, Contract 46598-1, 2D TECH VINNOVA Competence Center, Contract 2019-00068. This work was partly performed at the Chalmers Material Analysis Laboratory (CMAL).

The authors would also like to thank Mr. John Herron, Dr. Maxime Maghe and Mr. Scott Anderson at Carbon Nexus for manufacturing the carbon fibres analysed in the current study.

References

(1) Asp, L. E.; Greenhalgh, E. S. Structural Power Composites. *Compos. Sci. Technol.* **2014**, *101*, 41–61. https://doi.org/10.1016/j.compscitech.2014.06.020.

(2) Asp, L. E.; Johansson, M.; Lindbergh, G.; Xu, J.; Zenkert, D. Structural Battery Composites: A Review. *Funct. Compos. Struct.* **2019**, *1* (4), 042001. https://doi.org/10.1088/2631-6331/ab5571.

(3) Jin, T.; Singer, G.; Liang, K.; Yang, Y. Structural Batteries: Advances, Challenges and Perspectives. *Mater Today* **2023**, *62*, 151–167. https://doi.org/10.1016/j.mattod.2022.12.001.

(4) Johannisson, W.; Zenkert, D.; Lindbergh, G. Model of a Structural Battery and Its Potential for System Level Mass Savings. *Multifunct. Mater.* **2019**, *2* (3), 035002. https://doi.org/10.1088/2399-7532/ab3bdd.

(5) Meng, C.; Muralidharan, N.; Teblum, E.; Moyer, K. E.; Nessim, G. D.; Pint, C. L. Multifunctional Structural Ultrabattery Composite. *Nano Lett.* **2018**, *18* (12), 7761–7768. https://doi.org/10.1021/acs.nanolett.8b03510.

(6) Moyer, K.; Meng, C.; Marshall, B.; Assal, O.; Eaves, J.; Perez, D.; Karkkainen, R.; Roberson, L.; Pint, C. L. Carbon Fiber Reinforced Structural Lithium-Ion Battery Composite: Multifunctional Power Integration for CubeSats. *Energy Storage Mater* **2020**, *24*, 676–681. https://doi.org/10.1016/j.ensm.2019.08.003.

(7) Cattaruzza, M.; Fang, Y.; Furó, I.; Lindbergh, G.; Liu, F.; Johansson, M. Hybrid Polymer–Liquid Lithium Ion Electrolytes: Effect of Porosity on the Ionic and Molecular Mobility. *J. Mater. Chem. A* **2023**, *11* (13), 7006–7015. https://doi.org/10.1039/D3TA00250K.

(8) Ihrner, N.; Johannisson, W.; Sieland, F.; Zenkert, D.; Johansson, M. Structural Lithium Ion Battery Electrolytes *via* Reaction Induced Phase-Separation. *J. Mater. Chem. A* **2017**, *5* (48), 25652–25659. https://doi.org/10.1039/C7TA04684G.

(9) Schneider, L. M.; Ihrner, N.; Zenkert, D.; Johansson, M. Bicontinuous Electrolytes via Thermally Initiated Polymerization for Structural Lithium Ion Batteries. *ACS Appl. Energy Mater.* **2019**, *2* (6), 4362–4369. https://doi.org/10.1021/acsaem.9b00563.

(10) Larsson, C.; Larsson, F.; Xu, J.; Runesson, K.; Asp, L. E. Effects of Lithium Insertion Induced Swelling of a Structural Battery Negative Electrode. *Composites Science and Technology* **2023**, *244*, 110299. https://doi.org/10.1016/j.compscitech.2023.110299.

(11) Tavano, R.; Spagnol, M.; Al-Ramahi, N.; Joffe, R.; Xu, J.; Asp, L. E. Mechanical Characterisation of a Structural Battery Electrolyte. *Polymer* **2024**, *312*, 127646. https://doi.org/10.1016/j.polymer.2024.127646.

(12) Jacques, E.; H. Kjell, M.; Zenkert, D.; Lindbergh, G. The Effect of Lithium-Intercalation on the Mechanical Properties of Carbon Fibres. *Carbon* **2014**, *68*, 725–733. https://doi.org/10.1016/j.carbon.2013.11.056.

(13) Jacques, E.; Hellqvist Kjell, M.; Zenkert, D.; Lindbergh, G.; Behm, M. Expansion of Carbon Fibres Induced by Lithium Intercalation for Structural Electrode Applications. *Carbon* **2013**, *59*, 246–254. https://doi.org/10.1016/j.carbon.2013.03.015.

(14) Jacques, E.; Kjell, M. H.; Zenkert, D.; Lindbergh, G.; Behm, M.; Willgert, M. Impact of Electrochemical Cycling on the Tensile Properties of Carbon Fibres for Structural Lithium-Ion Composite Batteries. *Compos Sci Technol* **2012**, *72* (7), 792–798. https://doi.org/10.1016/j.compscitech.2012.02.006.

(15) Duan, S.; Iyer, A. H. S.; Carlstedt, D.; Rittweger, F.; Sharits, A.; Maddox, C.; Riemschneider, K.-R.; Mollenhauer, D.; Colliander, M.; Liu, F.; Asp, L. E. Effect of Lithiation on the Elastic Moduli of Carbon Fibres. *Carbon* **2021**, *185*, 234–241. https://doi.org/10.1016/j.carbon.2021.09.037.

(16) Kjell, M. H.; Jacques, E.; Zenkert, D.; Behm, M.; Lindbergh, G. PAN-Based Carbon Fiber Negative Electrodes for Structural Lithium-Ion Batteries. *J. Electrochem. Soc.* **2011**, *158* (12), A1455. https://doi.org/10.1149/2.053112jes.

(17) Hagberg, J.; Leijonmarck, S.; Lindbergh, G. High Precision Coulometry of Commercial PAN-Based Carbon Fibers as Electrodes in Structural Batteries. *J. Electrochem. Soc.* **2016**, *163* (8), A1790. https://doi.org/10.1149/2.0041609jes.

(18) Fredi, G.; Jeschke, S.; Boulaoued, A.; Wallenstein, J.; Rashidi, M.; Liu, F.; Harnden, R.; Zenkert, D.; Hagberg, J.; Lindbergh, G.; Johansson, P.; Stievano, L.; Asp, L. E. Graphitic Microstructure and Performance of Carbon Fibre Li-Ion Structural Battery Electrodes. *Multifunct. Mater.* **2018**, *1* (1), 015003. https://doi.org/10.1088/2399-7532/aab707.

(19) Johansen, M.; Schlueter, C.; Tam, P. L.; Asp, L. E.; Liu, F. Mapping Nitrogen Heteroatoms in Carbon Fibres Using Atom Probe Tomography and Photoelectron Spectroscopy. *Carbon* **2021**, *179*, 20–27. https://doi.org/10.1016/j.carbon.2021.03.061.

(20) Asp, L. E.; Bouton, K.; Carlstedt, D.; Duan, S.; Harnden, R.; Johannisson, W.; Johansen, M.; Johansson, M. K. G.; Lindbergh, G.; Liu, F.; Peuvot, K.; Schneider, L. M.; Xu, J.; Zenkert, D. A Structural Battery and Its Multifunctional Performance. *Adv Energy Sustain Res* **2021**, *2* (3), 2000093. https://doi.org/10.1002/aesr.202000093.

(21) Chaudhary, R.; Chetry, A.; Xu, J.; Xia, Z.; Asp, L. E. Structural Positive Electrodes Engineered for Multifunctionality. *Advanced Science* **2024**, *11* (33), 2404012. https://doi.org/10.1002/advs.202404012.

(22) Chaudhary, R.; Xu, J.; Xia, Z.; Asp, L. E. Unveiling the Multifunctional Carbon Fiber Structural Battery. *Advanced Materials* **2024**, *36* (48), 2409725. https://doi.org/10.1002/adma.202409725.

(23) Xu, J.; Creighton, C.; Johansen, M.; Liu, F.; Duan, S.; Carlstedt, D.; Mota-Santiago, P.; Lynch, P.; Asp, L. E. Effect of Tension during Stabilization on Carbon Fiber Multifunctionality for Structural Battery Composites. *Carbon* **2023**, *209*, 117982. https://doi.org/10.1016/j.carbon.2023.03.057.

(24) Tavano, R.; Xu, J.; Creighton, C.; Liu, F.; Dharmasiri, B.; Henderson, L. C.; Asp, L. E. Influence of Carbonisation Temperatures on Multifunctional Properties of Carbon Fibres for Structural Battery Applications. *Batteries & Supercaps* **2024**, *7* (8), e202400110. https://doi.org/10.1002/batt.202400110.

(25) Minus, M.; Kumar, S. The Processing, Properties, and Structure of Carbon Fibers. *JOM* **2005**, *57* (2), 52–58. https://doi.org/10.1007/s11837-005-0217-8.

(26) Zhang, S.; Wang, R.; Liao, Y. A Comparative Study of Two Kinds of T800 Carbon Fibers Produced by Different Spinning Methods for the Production of Filament-Wound Pressure Vessels. *New Carbon Materials* **2019**, *34* (6), 578–586. https://doi.org/10.1016/S1872-5805(19)60033-8.

(27) Liu, C.; Miao, L.; Zhao, R.; Yang, F.; Unnikrishnan, V.; Rana, R.; Deng, N.; Ghandehari Ferdowsi, M. R.; Chao, Q.; Kang, W.; Razal, J. M.; Miao, L.; Naebe, M.; Li, Q. In-Situ Fabrication of Multifunctional N-Doped Hybrid Carbon Nanotube@carbon Fiber by Recycling Gaseous Effluents of Carbon Fiber Production. *Carbon* **2022**, *193*, 368–380. https://doi.org/10.1016/j.carbon.2022.03.046.

(28) Melanitis, N.; Tetlow, P. L.; Galiotis, C. Characterization of PAN-Based Carbon Fibres with Laser Raman Spectroscopy: Part I Effect of Processing Variables on Raman Band Profiles. *JOURNAL OF MATERIALS SCIENCE* **1996**, *31* (4), 851–860. https://doi.org/10.1007/BF00352882.

(29) Tuinstra, F.; Koenig, J. L. Raman Spectrum of Graphite. *The Journal of Chemical Physics* **1970**, *53* (3), 1126–1130. https://doi.org/10.1063/1.1674108.

(30) Park, S.-J. Precursors and Manufacturing of Carbon Fibers. In *Carbon Fibers*; Park, S.-J., Ed.; Springer Series in Materials Science; Springer: Singapore, 2018; pp 31–67. https://doi.org/10.1007/978-981-13-0538-2_2.

(31) Johnson, D. J. Structure-Property Relationships in Carbon Fibres. *J. Phys. D: Appl. Phys.* **1987**, *20* (3), 286–291. https://doi.org/10.1088/0022-3727/20/3/007.

(32) Johansen, M.; Singh, M. P.; Xu, J.; Asp, L. E.; Gault, B.; Liu, F. Unravelling Lithium Distribution in Carbon Fibre Electrodes for Structural Batteries with Atom Probe Tomography. *Carbon* **2024**, 119091. https://doi.org/10.1016/j.carbon.2024.119091.

(33) Endo, M.; Nishimura, Y.; Takahashi, T.; Takeuchi, K.; Dresselhaus, M. S. Lithium Storage Behavior for Various Kinds of Carbon Anodes in Li Ion Secondary Battery. *J Phys Chem Solids* **1996**, *57* (6), 725–728. https://doi.org/10.1016/0022-3697(95)00339-8.

(34) Endo, M.; Kim, Y. A. Chapter 25 - Applications of Advanced Carbon Materials to the Lithium Ion Secondary Battery. In *Carbon Alloys*; Yasuda, E., Inagaki, M., Kaneko, K., Endo, M., Oya, A., Tanabe, Y., Eds.; Elsevier Science: Oxford, 2003; pp 417–433. https://doi.org/10.1016/B978-008044163-4/50025-5.

(35) Endo, M.; Kim, C.; Karaki, T.; Fujino, T.; Matthews, M. J.; Brown, S. D. M.; Dresslhaus, M. S. In Situ Raman Study of PPP-Based Disordered Carbon as an Anode in a Li Ion Battery. *Synthetic Metals* **1998**, *98* (1), 17–24. https://doi.org/10.1016/S0379-6779(98)00141-6.

24th International Conference on Composite Materials
Baltimore Convention Center
August 4-8, 2025

Moisture Effects on Impact Strength and Recovery in Carbon Fiber Reinforced Vitrimers

Jun Young Choi[1], Jennifer Callanga[1], Esther Gil[1], Ji Ho Jeon[2*],and Sung-Hoon Ahn[1,3*]

[1]Department of Mechanical Engineering, Seoul National University, Seoul, South Korea
[2]School of Mechanical, Aerospace, and Manufacturing Engineering, University of Connecticut, Connecticut, United States
[3]Institute of Advanced Machines and Design, Seoul National University, Seoul, South Korea

*Corresponding Authors: jiho.jeon@uconn.edu, ahnsh@snu.ac.kr

2025.8.4

Table of Contents

01 Introduction

Vitrimers as Matrix for Composites

02 Methods

Fabrication of Vitrimer Composites, Impact Tests, Environmental Conditioning

03 Results

Impact Strength, Moisture, Repair Analysis

04 Conclusions

Summary & Future Works

Utilization of Composites

Driving Factors for Utilization of Composites

- For future mobility to integrate with existing infrastructure, lightweight components are required for maximized driving range
- Pressure is placed on car manufacturers to satisfy legal regulations to alleviate greenhouse gas (GHG) emissions

Potential of Composites

- In 2021, composites market was valued at $88.8 billion, and the market is forecasted to expand to $144.5 billion by 2028
- With composition of metals for automobiles being 63% by weight, 10% weight reduction can increase fuel efficiency by 6-10%

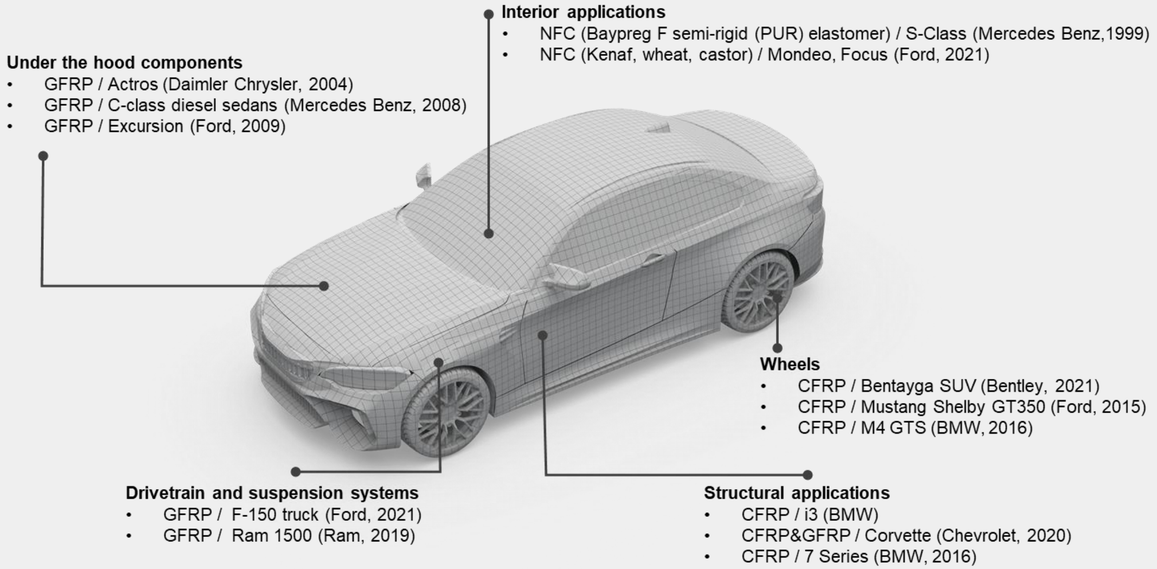

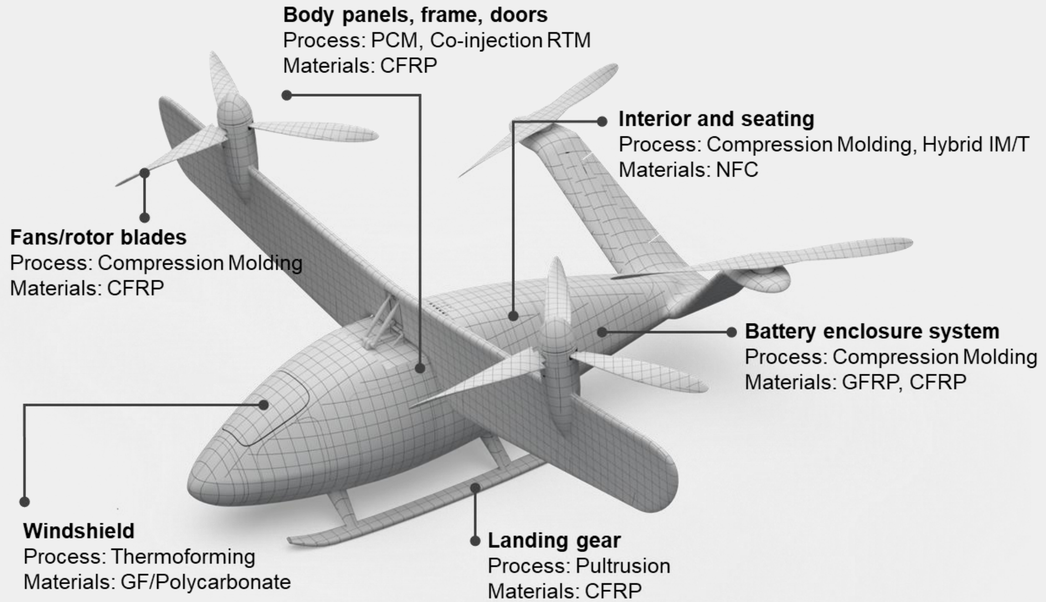

Choi, Jun Young, et al. “Current Applications and Development of Composite Manufacturing Processes for Future Mobility.” International Journal of Precision Engineering and Manufacturing-Green Technology, vol. 10, no. 1, Jan. 2023, pp. 269–91.

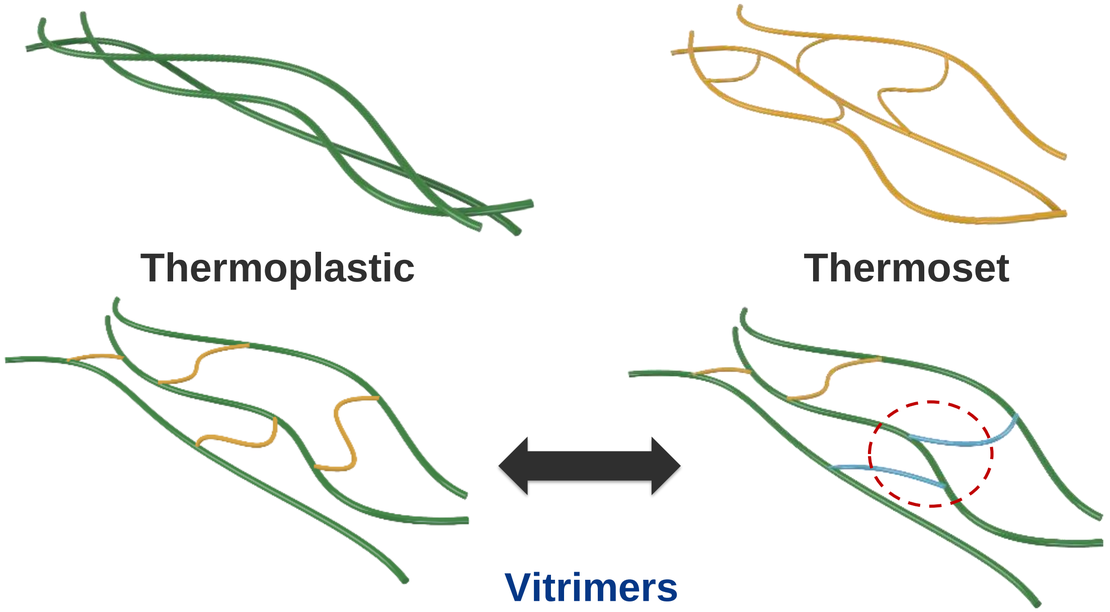

Property	Thermoset	Thermoplastic	Vitrimer
Strength	High (crosslinked network)	Moderate to High	High (similar to thermoset)
Reshapability	✗ Permanent shape after cure	✓ Heat-softenable and reshaped	✓ Reprocessable via bond exchange (no melting)
Repairability	✗ Difficult; requires scarfing + long thermal cycles	✗ Poor; needs melting and reprocessing	✓ Fast healing via heat/stimulus; no structural prep needed
Recyclability	✗ Incineration or grinding (energy-intensive, fiber loss)	✓ Re-meltable and reusable	✓ Chemically recyclable; enables clean fiber separation for reuse

Vitrimers: A New Matrix for Composites

What Are Vitrimers?

- A specific class of polymer materials with dynamic covalent bonds for reversible cross-linking
- Discovered in 2011 by French researcher Ludwik Leibler

Key Characteristics of Vitrimers

- Like thermosets, can crosslink at certain temperatures
- Like thermoplastics, can be softened and reformed at higher temperatures

Vitrimers in Composite Manufacturing

- Vitrimers can be used to make fiber reinforced composites
- Potential to use reversible cross-linking ability for efficient material recycling

Problem Statement

- Vitrimer composites offer self-healing and reshaping, but impact behavior remains underexplored
- Existing studies neglect real-world factors like moisture exposure (e.g., seawater, humidity)
- Environmental moisture can degrade composite properties by lowering impact strength
- Current protection methods (coatings) are vulnerable to aging or mechanical damage
- Repairability post-environmental aging is unclear, especially for fiber-reinforced vitrimers.

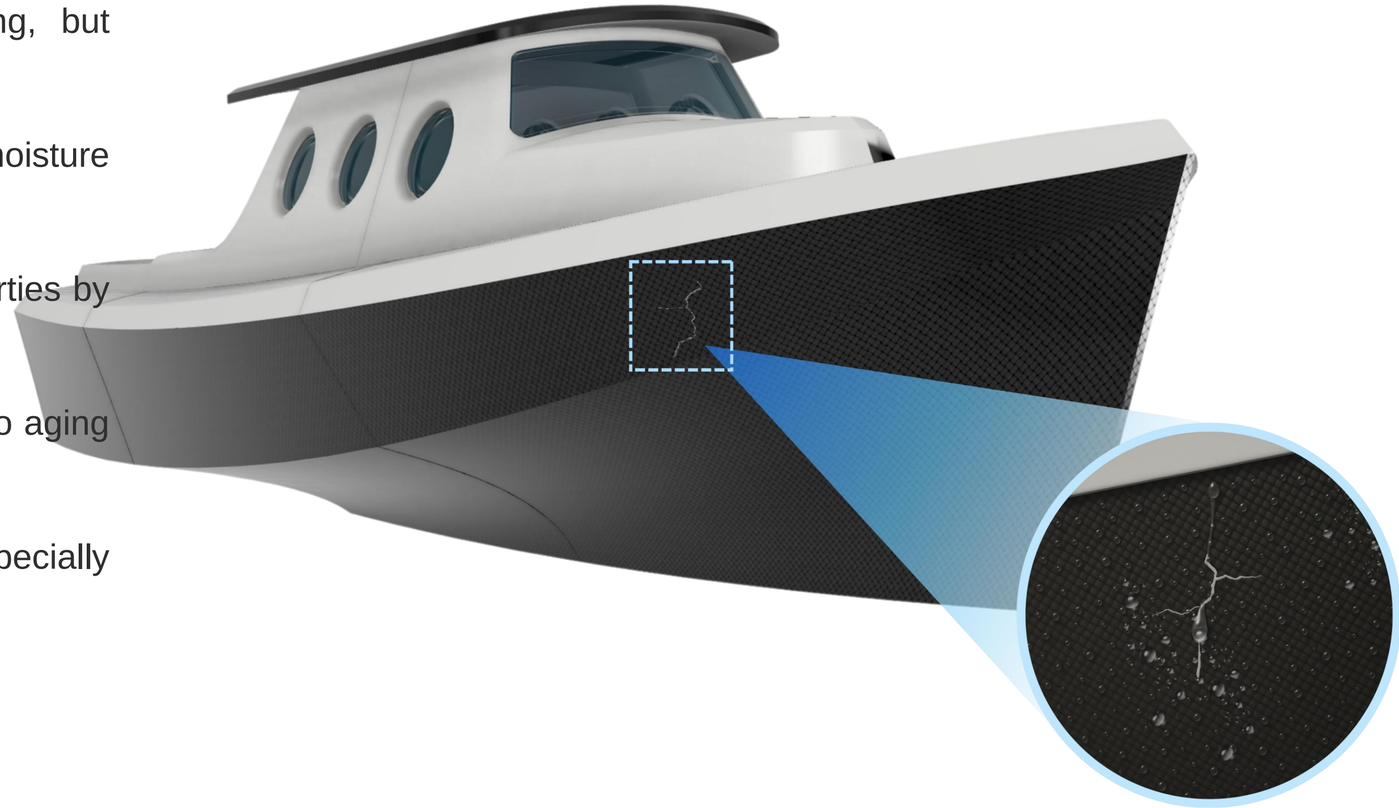

Fabrication of Vitrimer Composites

- **Reinforcement Types**: Milled (60 μm), Forged (6 mm), and Woven (3K fabric) carbon fibers used at 8%, 15%, and 40% V_f
- **Resin System:** Vitrimax T100™ epoxy + hardener; hardener preheated at 80 °C for 2 h
- **Milled, Forged CFRV:** Fibers dispersed in epoxy, hardener added, degassed at 1 MPa for 1 min
- **Woven CFRV:** 12 layers (259.2 g) for 40% V_f
- **Molding:** Compression molded at 130 °C, 0.8 MPa for 4 h in 300 × 300 × 4 mm mold

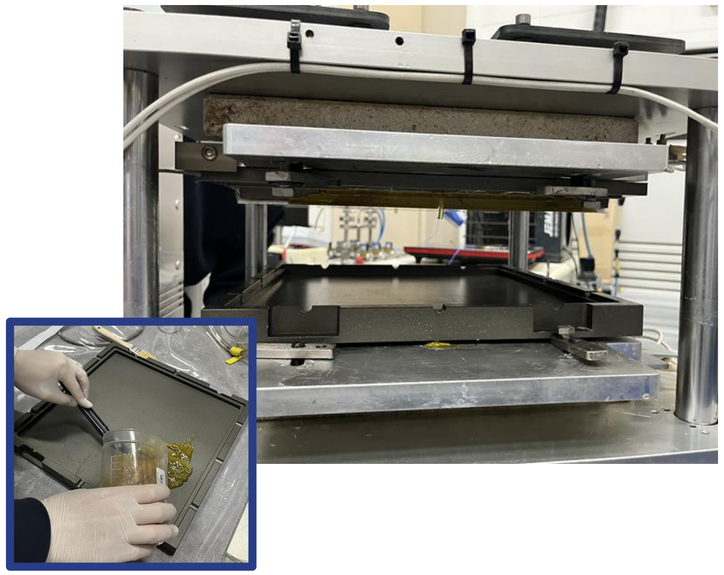





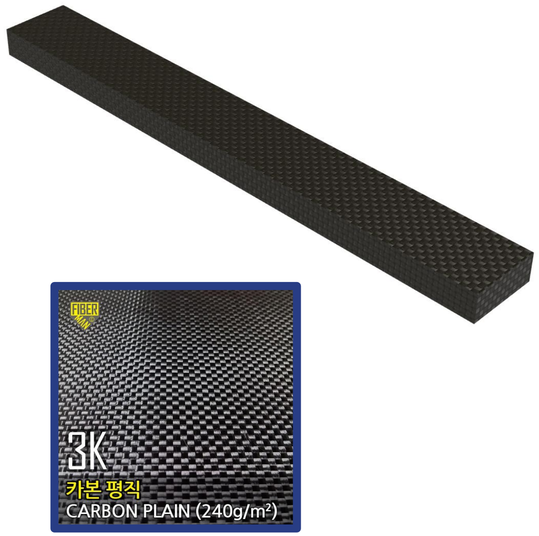

Impact Testing

- **Equipment:** QM700A digital tester with 1.114 kg pendulum, 0.3 m arm
- **Specimens:** 80 × 10 × 4 mm, tested in edgewise parallel and flatwise normal orientations
- **Purpose:** Edgewise simulates interlaminar failure; flatwise tests through-thickness resistance.



$$v = \sqrt{2gH}$$

$$H = L_p\left(1 - cos\theta_i \frac{\pi}{180}\right)$$

$$E = mgL_p\left(cos\theta_f \frac{\pi}{180} - \cos\theta_i \frac{\pi}{180}\right)$$

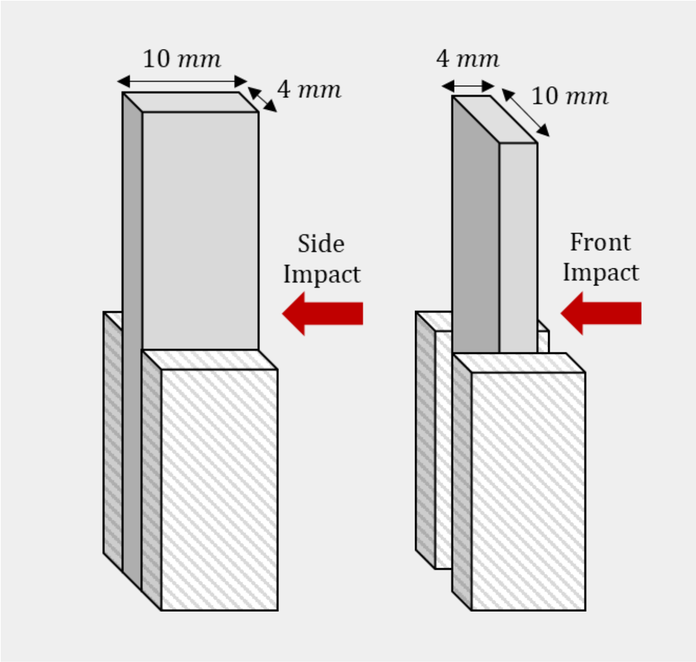

Environmental Conditioning

- **Pre-conditioning:** All specimens oven-dried at 50 °C for 24 h to set dry mass baseline
- **Aging Protocols:**
  - Seawater: Immersion at 25 °C and 50 °C using synthetic salt mix (~33.3 g/L)
  - Humidity: 90% Relative Humidity (RH) at 25 °C and 50 °C per ISO 6270-2 CH standard
- **Fickian Modeling:** 10-term Fickian diffusion series; *D* extracted via nonlinear least-squares fit (MATLAB)
- **Key Estimate:** $t_{95}\%$ ≈ 19 days (25 °C), 2 days (50 °C) for 4 mm thickness.

Material Type	Environment	Temperature (°C)	RH (%)	Duration (h)
Milled, Forged, Woven	Seawater Immersion	25, 50	–	1, 2, 4, 24, 48, 72
Milled, Forged, Woven	Humidity Exposure	25, 50	90	1, 2, 4, 24, 48, 72

$$\frac{M(t)}{M_\infty} = 1 - \Sigma \sum_{n=0}^{\infty} \frac{8}{\pi^2(2n+1)^2} exp\left(-\frac{\pi^2(2n+1)^2 Dt}{4h^2}\right)$$

$$\frac{M(t)}{M\infty} \approx 1 - \frac{8}{\pi^2} exp\left(-\frac{\pi^2 Dt}{4h^2}\right) \qquad t_{95}\% \approx \frac{4h^2}{\pi^2 D}$$

$$D(T) = D^0 exp\left(-\frac{E_a}{RT}\right)$$









Effect of Orientation on Impact Damage

- ❑ Milled Composites: Very low impact strength (4.1 kJ/m² flat, 2.3 kJ/m² edge); brittle fracture due to short, random 7 µm fibers.
- ❑ Forged Composites: Moderate strength (~18.5/16.7 kJ/m²); isotropic behavior with delamination and full fiber breakage.
- ❑ Woven Composites: Highest strength (~128.6/115.6 kJ/m²); flatwise impact resisted better due to fiber face exposure.
- ❑ Fracture Observations:
  - Flatwise: partial fiber fracture + bulging → high energy absorption
  - Edgewise: fiber pull-out, interlayer fracture

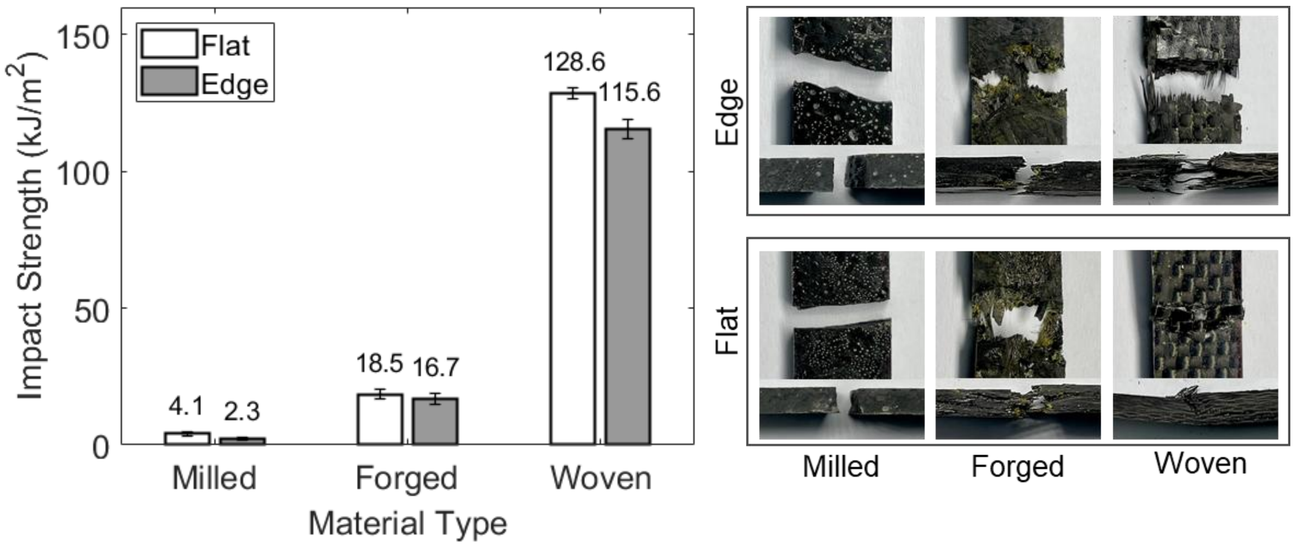

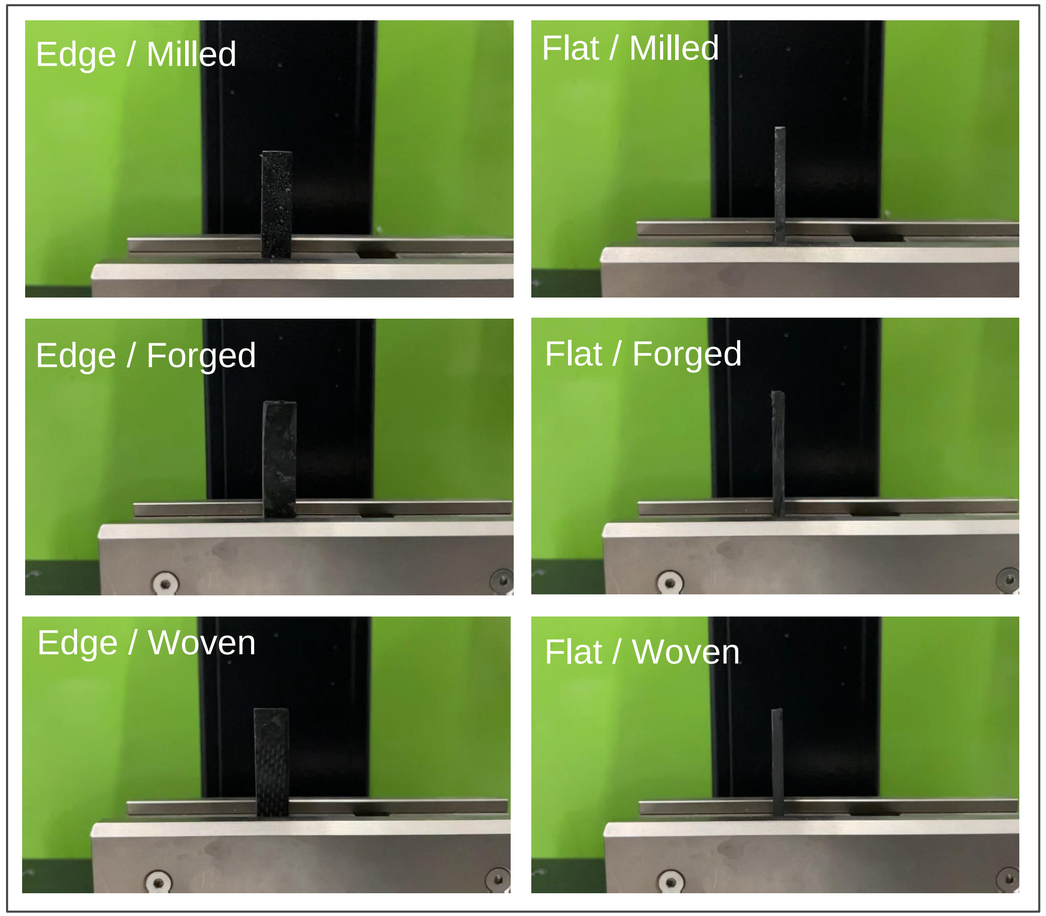

Moisture Uptake of Carbon Fiber Reinforced Vitrimer Composites

- Milled, forged, and woven CFRVs aged in 25 °C/50 °C under humidity (90% RH) and seawater immersion.
- **Fickian Fit Results:** humidity *D* ↑ with *T*, seawater *D* showed anomalies (25 °C > 50 °C in some cases).
- Seawater → faster uptake than humidity
- 50 °C → higher total absorption despite some lower *D* values
- *Forged CFRVs:* Highest uptake (~3.8%) due to voids and microcracks → capillary-driven diffusion.
- Early-time *D* estimates affected by microgram-scale fluctuations; trends remain consistent and meaningful.

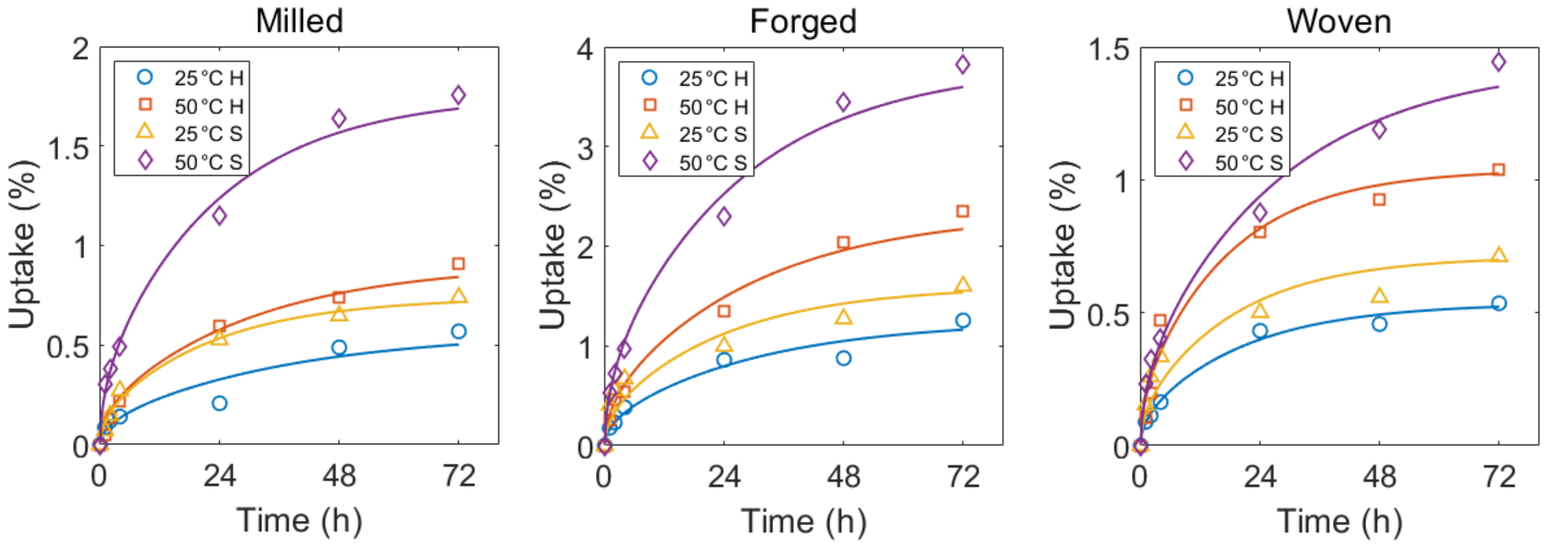

Type	Condition	Temperature (°C)	D (m²/s)
Milled	Humidity	25	1.19×10^{-11}
		50	1.57×10^{-11}
	Seawater	25	1.94×10^{-11}
		50	1.87×10^{-11}
Forged	Humidity	25	1.47×10^{-11}
		50	1.50×10^{-11}
	Seawater	25	1.91×10^{-11}
		50	1.64×10^{-11}
Woven	Humidity	25	2.07×10^{-11}
		50	2.37×10^{-11}
	Seawater	25	2.34×10^{-11}
		50	1.57×10^{-11}

Effect of Moisture on Impact Damage

Humidity Exposure

- ❑ Sharp declines after 4 h; no recovery observed at 72 h
- ❑ Milled: −81.4%, Forged: −65.7%, Woven: −54.0% (4 h vs. 24 h)

Seawater Immersion

- ❑ Initial drop (4–24 h), followed by partial recovery at 72 h
- ❑ Milled: -40.6%, Forged: -58.1%, Woven: -11.9% (4 h vs. 24 h)
- ❑ Recovery attributed to moisture-induced plasticization enhancing ductility and energy absorption.

Fracture Observation

- ❑ • Forged: surface degradation, mold-like appearance
- ❑ • Woven: multilayer fractures, visible resin flow with time

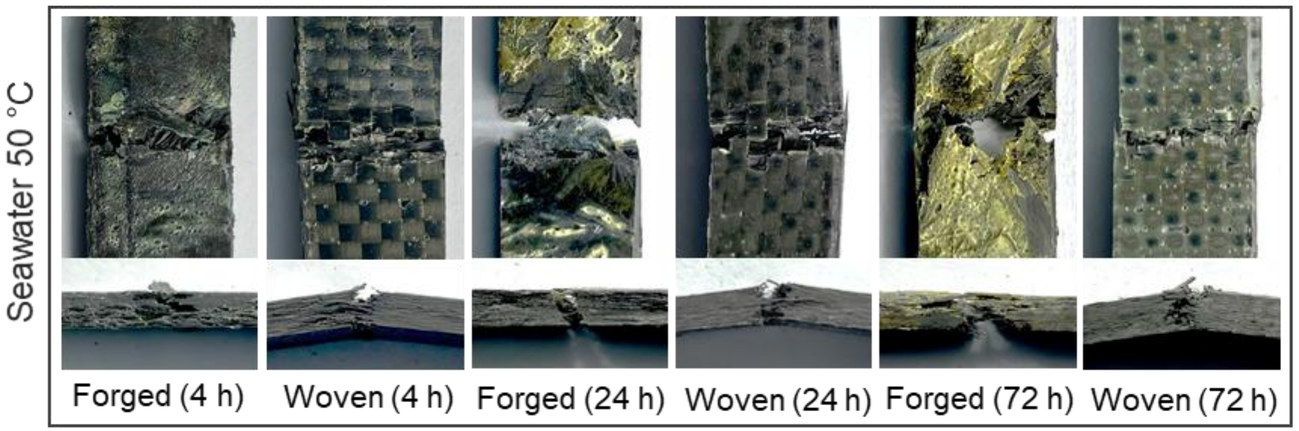

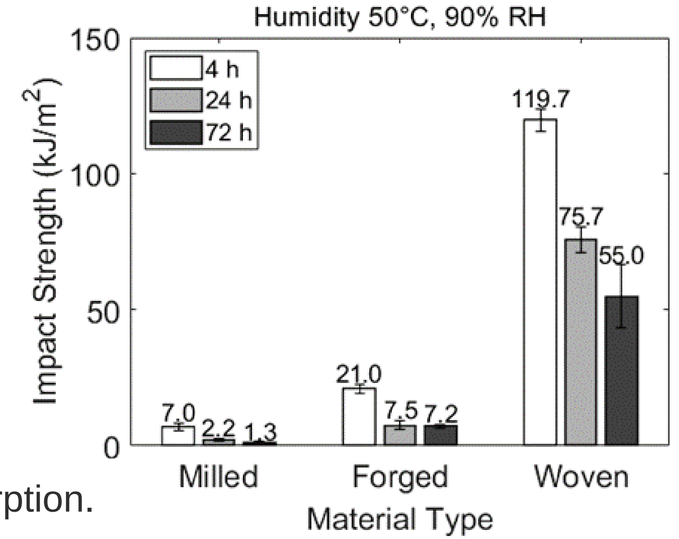

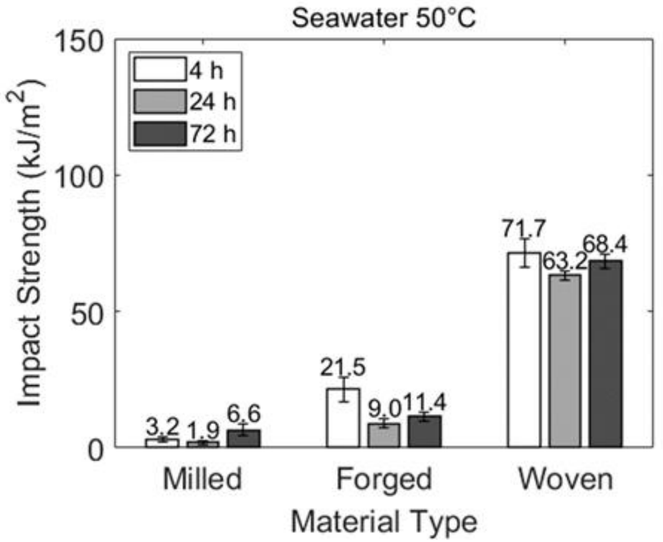

Effect of Moisture on Impact Damage

Milled

- ❑ T_g ↑ from 91.5 °C (dry) → 102 °C (humidity)
- ❑ T_g ↓ to 90.5 °C (seawater); large endothermic peak → plasticization dominant

Forged

- ❑ T_g consistently ↑ from 101.9 °C → 108.2 °C (humidity) → 116.1 °C (seawater)
- ❑ Suggests post-curing or plasticizer loss, leading to stiffer network

Woven

- ❑ T_g ↑ to 110 °C (humidity), then ↓ to 94.6 °C (seawater)
- ❑ Indicates initial curing, followed by strong plasticization due to deep moisture ingress

Note: Deepest endothermic peaks in seawater → confirms high moisture absorption and enthalpic relaxation

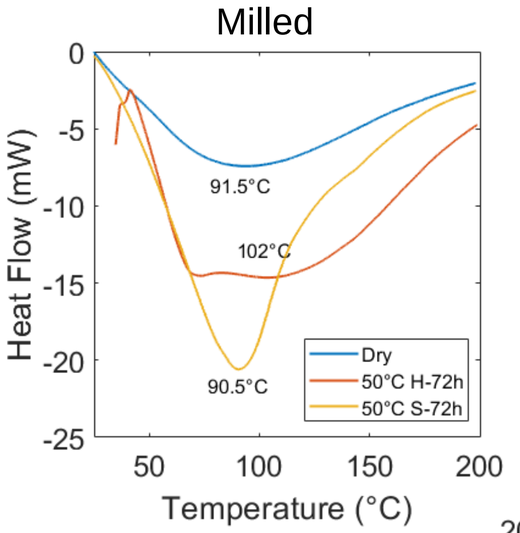

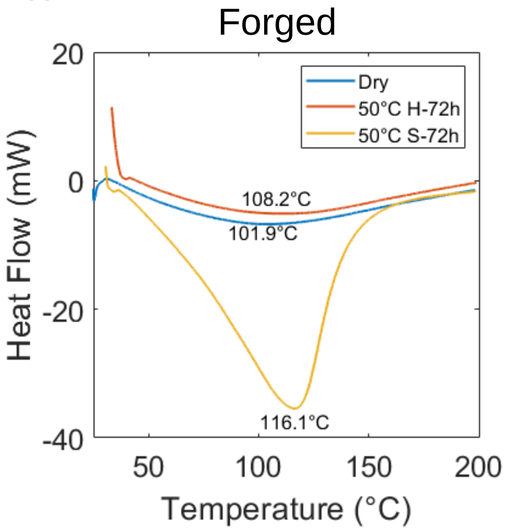

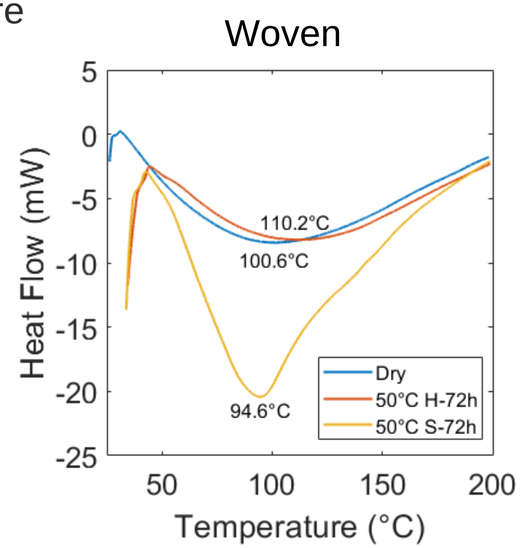

Effect of Moisture on Recovery from Impact

Milled CFRV

- ❑ High recovery (89–111%) across all conditions → resilient structure
- ❑ Seawater-induced voids seen, but minimal strength loss

Forged CFRV

- ❑ Excellent dry recovery (125%) from heat-press compaction
- ❑ Seawater severely reduced recovery (~38%) → fiber–matrix debonding
- ❑ Humidity: moderate recovery (77–85%)

Woven CFRV

- ❑ Limited dry recovery (61%); no recovery post moisture → fiber fracture irreversible
- ❑ **Oven-Drying:** Removed moisture (0.3–2.2% mass loss), but did not restore mechanical integrity → damage is structural, not just moisture retention
- ❑ **Fracture Surfaces:** Seawater → more porosity; woven → visible delamination and unrecoverable breakage

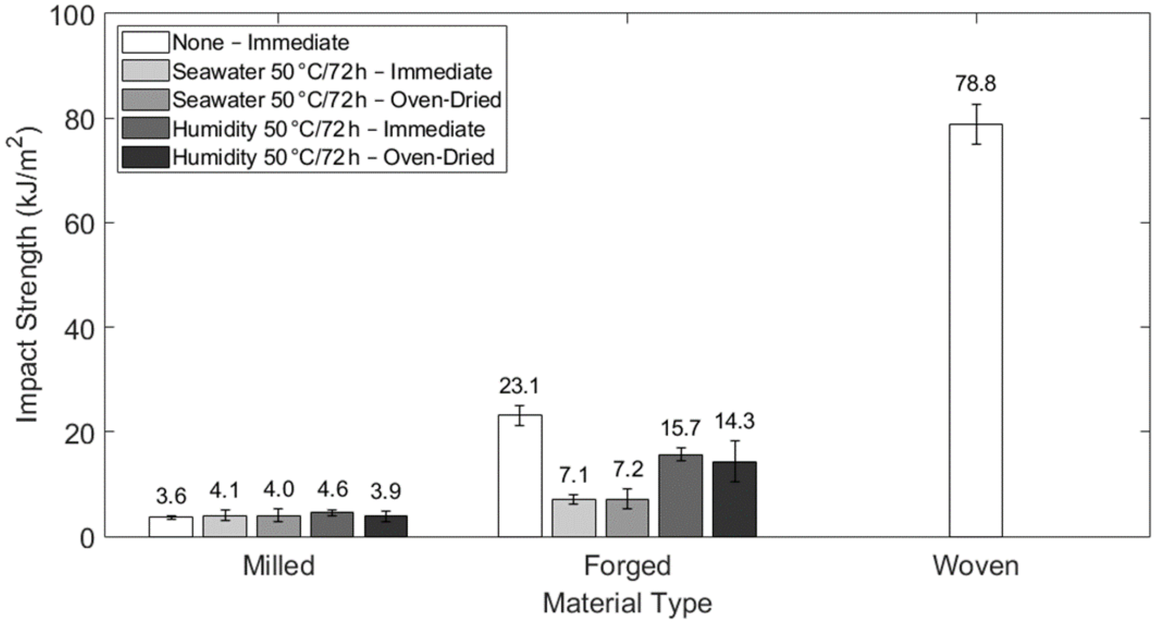

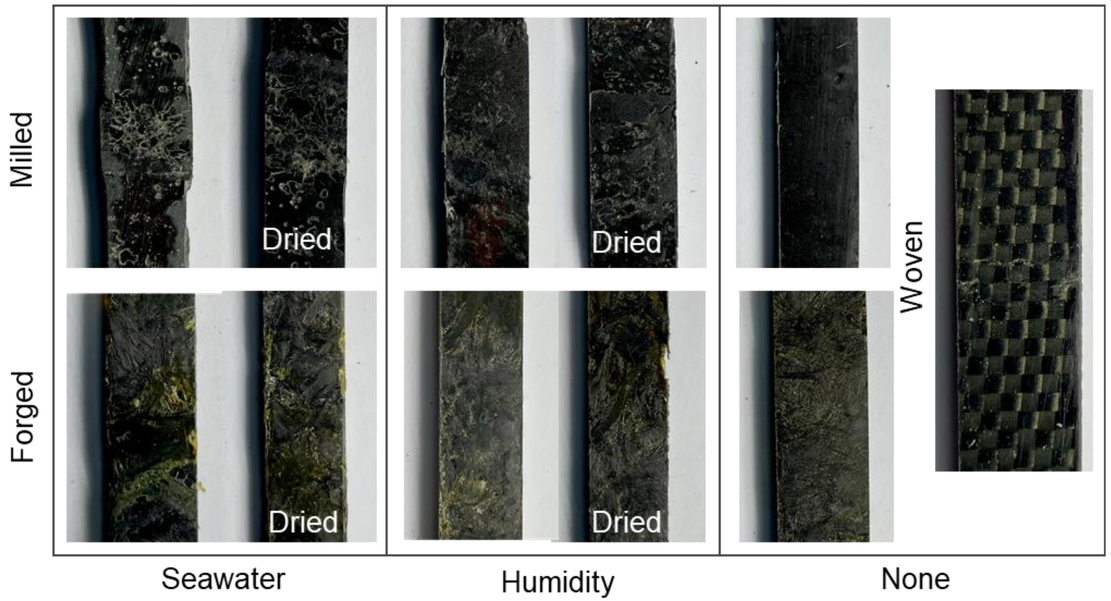

Conclusions

- Moisture exposure significantly degrades impact strength, especially under prolonged seawater or humidity at elevated temperatures.
- Forged CFRVs absorbed the most moisture, leading to severe mechanical deterioration due to voids and microcracks.
- Woven CFRVs showed irreversible damage post-immersion, with minimal repair recovery due to continuous fiber fracture.
- Milled CFRVs exhibited the most stable performance, showing high recovery and low moisture uptake.
- T_g shifts revealed competing effects of plasticization and post-curing, influenced by fiber type and environment.

THANK YOU FOR LISTENING

Presenter vCard

AUTHORS



Jun Young Choi
Ph.D. Candidate



Jennifer Callanga
Ph.D. Student



Ester Gil
M.S. Candidate



Ji Ho Jeon
Professor



Sung-Hoon Ahn
Professor

A STRUCTURE-INTEGRATED NANOCOMPOSITE SENSOR SYSTEM CAPABLE OF SIMULTANEOUS MEASUREMENT OF OMNIDIRECTIONAL STRAIN AND TEMPERATURE

Sumin Lee[1], Jeonyoon Lee[1]

[1]Department of Aerospace Engineering, Korea Advanced Institute of Science and Technology
291, Daehak-ro, Yuseong-gu, Daejeon, Republic of Korea
Email: jlee@kaist.ac.kr, web page: lamp.kaist.ac.kr

Keywords: Nanocomposite sensor, Omnidirectional, Carbon nanotubes, Structural health monitoring

ABSTRACT

Strain-based structural health monitoring (SHM) is essential for composite structures due to their complex and unpredictable failure mechanism. However, conventional strain sensors are inherently limited by their unidirectional sensitivity and their inability to distinguish strain from temperature effects without additional sensors, leading to complex configurations and extensive wiring. To address these challenges, a carbon nanotube (CNT)-based omnidirectional sensing system was developed, designed as a structurally integrated nanocomposite surfacing layer for composites. This novel sensor system enables the detection of strain in all directions using a single nanocomposite sensor, while simultaneously measuring temperature to isolate its effects. Experimental validation demonstrated that the sensor accurately measured the full in-plane strain tensor under tensile loading, closely matching the output of a 3-element strain gauge rosette. It also achieved high temperature sensing accuracy, with a maximum error of just 0.3%. By maintaining reliable strain and temperature measurement capabilities while simplifying system architecture, this CNT-based sensor system offers a promising solution for efficient and multifunctional SHM in aerospace and other advanced applications.

1 INTRODUCTION

Advanced composite materials have become widely adopted in engineering applications due to their high mechanical performance and low density [1,2]. In the aerospace industry, where minimizing structural weight is of paramount importance, fiber-reinforced polymer (FRP) composites are increasingly replacing conventional metals in primary load-bearing structures [3]. However, the heterogeneous composition of FRP—comprising distinct fiber and matrix phases—leads to more complex failure mechanisms than those observed in metallic structures [4,5]. This complexity, which includes failure modes such as matrix cracking, delamination, and fiber breakage, complicates accurate failure prediction [6]. As a result, structural health monitoring (SHM) plays a more critical role in composites than in metals, enhancing structural reliability and life-cycle management. Moreover, the inherently brittle characteristic of FRP composites makes early damage detection essential to mitigate degradation and prevent failure. Real-time SHM technologies capable of identifying damage at its onset are vital for reducing maintenance costs and avoiding catastrophic events. Although non-destructive inspection (NDI) methods such as ultrasonics, acoustic emission, and infrared thermography have shown effectiveness [7,8], their applicability to in-service structures—such as aircraft during operation—is limited [8].

Real-time SHM systems operate by tracking physical parameters through permanently embedded sensors. Strain is one of the most informative parameters, directly reflecting deformation and potential damage under load. Metallic strain gauges are commonly used in traditional SHM systems due to their low cost and ease of integration [9]. Fiber Bragg grating (FBG) sensors, embedded in composite laminates, have also gained popularity in aerospace structures for their high-resolution strain monitoring and minimal intrusion [3,10–14]. However, both metallic and FBG sensors are inherently unidirectional, measuring strain along a single axis [10,15]. To capture full in-plane strain states, at least three sensors oriented in different directions are required. Furthermore, their sensitivity to temperature necessitates an

additional sensor, such as a thermocouple, for thermal compensation, which increases system complexity and sensor count. In wired SHM systems, sensor cabling alone can constitute over 75% of the total installation time and around 25% of the system cost [16].

Carbon nanotube (CNT)-based nanocomposite sensors have attracted increasing interest due to their high conductivity and low weight since their discovery [17]. When dispersed into polymers, conductive nanofillers like CNTs yield nanocomposites with piezoresistive properties. Their electrical response can be tuned through material composition and filler ratio, enabling applications in both structural strain monitoring [18–24] and flexible wearable sensors [17,25–27]. Moreover, nanocomposite sensors possess an omnidirectional piezoresistive characteristic [28-31], a key feature that can be utilized to simplify the SHM systems.

Despite these advantages, the development of multi-directional nanocomposite sensors remains limited. Most studies emphasize high sensitivity and flexibility, often overlooking the importance of omnidirectional sensing. Typically, nanocomposite sensors utilize a two-probe method that only enables unidirectional measurement, restricting their multi-directional sensing potential. Furthermore, the coupled piezoresistive and thermoresistive characteristics of nanocomposites complicates accurate strain measurement under varying temperatures [32]. Most existing approaches isolate one variable while fixing the other, which limits practical implementation. Therefore, developing methods that allow simultaneous or decoupled measurement of strain and temperature is essential.

This study introduces a novel sensing system that enables simultaneous omnidirectional strain and temperature monitoring using a single nanocomposite sensor. The proposed approach incorporates two main innovations: (1) a sensing mechanism that accounts for both piezoresistive and thermoresistive characteristics to extract strain and temperature concurrently, and (2) a multi-directional measurement configuration that captures resistivity in four independent directions from a single sensor with reduced wiring complexity. These features allow for the formulation of four independent equations, enabling the simultaneous determination of the in-plane strain components (ε_x, ε_y, ε_{xy}) and temperature (T).

2 FRAMEWORK OF OMNIDIRECTIONAL STRAIN AND TEMPERATURE SENSING SYSTEM

This section outlines a semi-empirical framework for detecting omnidirectional strain and temperature using a nanocomposite sensor. Initially, a conduction model incorporating both piezoresistive and thermoresistive behaviors of the nanocomposite is introduced and experimentally validated within typical strain and temperature ranges of composite structures. A multi-directional resistivity measurement method is then presented to exploit the sensor's omnidirectional sensitivity. Finally, a system of equations based on the validated conduction model is formulated, enabling the estimation of in-plane strain tensor components and temperature from four electrical properties measurements.

2.1 Conduction model of omnidirectional nanocomposite sensor

Several conduction mechanisms, including tunneling [33] and hopping [34], have been considered for nanocomposite sensing. Among them, the fluctuation-induced tunneling conduction (FITC) model was selected due to its strong correlation with the resistivity behavior of CNT networks under varying strain and temperature conditions [35–38]. The FITC model describes resistivity as a function of temperature affecting tunneling probability, as follows [35]:

$$\rho = \rho_0 \cdot exp\left(\frac{T_b}{T + T_0}\right) \tag{1}$$

, where ρ is the resistivity, ρ_0 is empirical resistivity constant, T_b is the energy required to transport an electron through the tunneling gap, T is the temperature of the nanocomposite, and T_0 is the temperature at which thermally activated voltage is generated. T_b and T_0 are empirically determined by examining the temperature variation in the zero-strain resistivity. Furthermore, the model can be extended by incorporating normal strain, based on the relationship between the junction distance of conductive nanofillers and the occurrence of tunneling effects, as expressed below [36].

$$\rho = \rho(0, T_r) \cdot exp\left(\frac{\varepsilon}{\lambda} + \frac{T_b \cdot \exp(dT_b/d\varepsilon \cdot \varepsilon)}{T + T_0 \cdot \exp(dT_0/d\varepsilon \cdot \varepsilon)} - \frac{T_b}{T_r + T_0}\right) \quad (2)$$

$\rho(0, T_r)$ is the resistivity at room temperature T_r (297 K) with zero strain, and λ is an empirical strain sensitivity constant. ε denotes the strain in the nanocomposite that aligns with the direction of resistivity. The derivatives of $dT_b/d\varepsilon$ and $dT_0/d\varepsilon$ with respect to strain are approximated as $1.48 \cdot T_b$ and $0.020 \cdot T_0$ based on the assumption of image-force corrected rectangular potential barrier [36].

To assess the fit of the FITC model to the resistivity data of the nanocomposite under varying strain and temperature conditions, a CNT/epoxy nanocomposite sensor as fabricated and tested (fabrication details are in the Experimental section). The resistance of fabricated sensor was monitored with two-probe method under conditions of either varying strain or temperature, with the other variables held constant. By fitting the experimental data to determine the empirical parameters of Eq. 2, the resistance of the nanocomposite was accurately predicted with a strain parameter λ of 0.48 (R^2 = 0.9941), and temperature parameters T_b and T_0 of 118.92 K and 10.04 K, respectively (R^2 = 0.9965), as shown in Fig. 1a and b. The FITC model could accommodate strain values up to 0.63%, a range comparable to conventional FBG sensors (0.2% - 1.0%) [39-41]. Beyond 0.63% strain, a sudden increase in resistance was observed, suggesting potential morphological rearrangement in the CNT network or possible delamination of the Cu electrodes from the nanocomposite layer. Of note, a sharp resistance increase indicates possible network rearrangement or electrode delamination, consistent with prior findings [29]. The temperature parameters were fitted up to a maximum of 120°C, aligning with aerospace structure operating conditions [42].

2.2 Resistivity measurement method of nanocomposite sensor

Nanocomposite sensors have traditionally been constrained to detecting unidirectional strain due to limitations in their resistivity measurement methods. The two-probe method, which is the most commonly employed technique, measures resistivity along a single direction between a parallel pair of electrodes. This setup fails to utilize the potential for multidirectional strain detection inherent in nanocomposite materials. To address this limitation, the van der Pauw (vdP) method [43], a well-established four-probe technique for characterizing the resistivity of thin conductive films, was adopted for the nanocomposite sensor system. Among various extensions of the vdP method, the approach developed by Kleiza et al. enables determination of the resistivity tensor in anisotropic materials [44]. Their method allows for calculating the resistivity tensor components ($\rho_x, \rho_y, \rho_{xy}$) of a rectangular conductive medium equipped with four corner-mounted electrodes, as illustrated in Fig. 1c. These tensor elements are derived from four sets of resistance and current measurements (R_1, R_2, I_1, I_2), as demonstrated in Fig. 1d. The calculations are governed by the following equations:

$$\exp\left(-\frac{\pi \cdot d \cdot R_1}{\rho_{iso}}\right) + \exp\left(-\frac{\pi \cdot d \cdot R_2}{\rho_{iso}}\right) = 1 \quad (3)$$

$$\rho_x = \frac{a}{b}\eta\frac{A_{\alpha,k}}{A_{\alpha,1-k}}, \qquad \rho_y = \frac{b}{a}\eta\frac{A_{\alpha,1-k}}{A_{\alpha,k}}, \qquad \rho_{xy} = -\eta\cos(\alpha\pi) \quad (4)$$

Here, d represents the thickness of the conductive layer, while a and b are the side lengths of the rectangular nanocomposite sample shown in Fig. 1c. ρ_{iso} is the determinant of resistivity tensor [45]. The parameters are defined as follows: $\alpha = 1/(1+I_1/I_2)$, $\eta = \rho_{iso}/\sin(\alpha\pi)$, $k = \exp(-\pi \cdot d \cdot R_1/\rho_{iso})$, and $A_{\alpha,k} = \int_0^1 |f_{\alpha,k}(q)| dq$ where $f_{\alpha,k}(q) = q^{\alpha-1} \cdot (1-q)^{-\alpha} \cdot (1-kq)^{\alpha-1}$. By employing the vdP method, the resistivity tensor of the nanocomposite can be comprehensively obtained using only four electrodes positioned on a single sensor. In contrast to conventional applications of the vdP method, which are typically restricted to static characterization of conductive materials, this study implements it in real time to monitor resistivity variations in the nanocomposite under dynamic strain and temperature conditions.

2.3 System of equations determining omnidirectional strain and temperature

Given the omnidirectional piezoresistive behavior of the nanocomposite, the FITC model (Eq. 1) can be generalized to any direction under the assumption that the material is homogeneous and isotropic. By substituting the resistivity measurements taken in four independent directions $(\theta_1, \theta_2, \theta_3, \theta_4)$, obtained via the vdP method into the FITC model, the following system of nonlinear equations is established:

$$\rho_{\theta_i} = \rho(0, T_r) \cdot exp\left(\frac{\varepsilon_{\theta_i}}{\lambda} + \frac{T_b \cdot \exp\left(dT_b/d\varepsilon \cdot \varepsilon_{\theta_i}\right)}{T + T_0 \cdot \exp\left(dT_0/d\varepsilon \cdot \varepsilon_{\theta_i}\right)} - \frac{T_b}{T_r + T_0}\right), \qquad i = 1,2,3,4 \qquad (5)$$

Since the in-plane strain tensor can be fully described by strain components in three independent directions, ε_{θ_4} can be expressed as a function of ε_{θ_1}, ε_{θ_2}, and ε_{θ_3}. Consequently, the four unknowns, the in-plane strain tensor elements and temperature, can be simultaneously determined by solving this system of four independent equations. As summarized in Fig. 1e, the developed nanocomposite sensor system enables the theoretical estimation of both the full in-plane strain tensor and temperature using just four directional resistivity measurements obtained from a single sensor.

Although thermal expansion effects were not explicitly incorporated into this study, the strain measured by the sensor includes both mechanical and thermal contributions. Therefore, future work should aim to extend the FITC model to explicitly account for thermal strain. With this enhancement, the sensor system would be capable of fully decoupling temperature effects from mechanical strain, thereby improving the accuracy and reliability of multidimensional strain sensing.

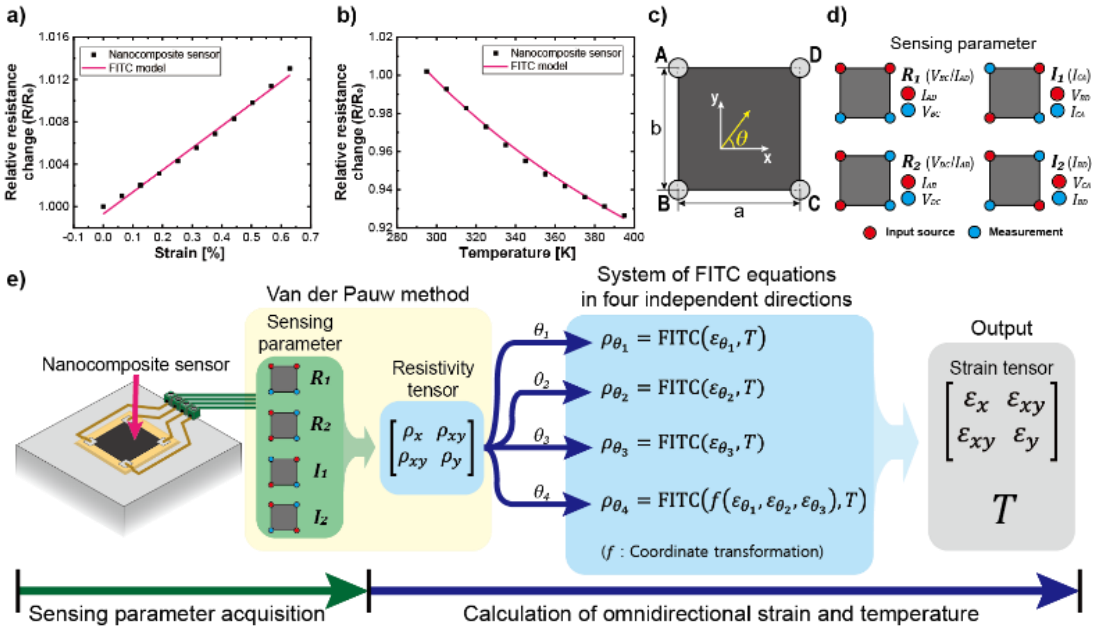

Figure 1: ㄱOmnidirectional strain and temperature sensing system based on nanocomposite sensor. Representation of (a) piezoresistive and (b) thermoresistive characteristics of nanocomposite sensor using the Fluctuation Induced Tunneling Conduction (FITC) model. Schematic of (c) the van der Pauw method applied nanocomposite sensor and (d) four electrical property measurements for in-plane resistivity tensor calculation. (e) Flowchart of the in-plane strain and temperature sensing process.

3 EXPERIMENTAL

To validate the proposed omnidirectional strain and temperature sensing framework, experimental studies were conducted by comparing sensor outputs with reference data from conventional strain and temperature sensors. This section is organized into two subsections: fabrication of the nanocomposite sensor and the experimental setup for measurement using both the nanocomposite and conventional

sensors. The fabrication subsection details the materials and manufacturing process for constructing the CNT/epoxy nanocomposite sensing layer on the composite substrate. The subsequent subsection describes the real-time measurement setup used to record the four sensing parameters of the nanocomposite sensor, along with data acquisition from conventional sensors.

3.1 Materials and fabrication of nanocomposite

A carbon fiber-reinforced-polymer (CFRP), commonly used in aerospace structures, was chosen as the composite substrate for sensor installation. The CFRP laminates were fabricated using unidirectional carbon fiber-reinforced epoxy prepreg (MCP125NS, TB Carbon) with a layup sequence of $[0/90/45/-45]_{2s}$. The fabricated laminates were then cut to dimensions of 250 mm x 25 mm in accordance with ASTM D3039M standards for tensile testing. High-conductivity CNT buckypaper (MWCNTs, US Research Nanomaterials, Inc.), with a purity of 99.9%, a thickness of 50 µm, and an areal density of 30 gsm, was used as the piezoresistive material for the nanocomposite sensor. As shown in Fig. 2a, the CNT buckypaper was cut into square films of different dimensions (10 mm x 10 mm, 20 mm x 20 mm) using a scalpel to assess the size effect of the sensor. Then, the films were attached to the CFRP surface using an epoxy adhesive film (Loctite EA 9695K, Henkel), which infiltrates the CNT network to form a CNT/epoxy nanocomposite surfacing layer during curing. The CNT films were oriented not only at 90° in the tensile direction, but also at 120° for shear strain measurements (See the coordinate axis of the sensor illustrated in Fig. 1c). Four copper films, each 10 µm thick, were then connected to the corners of the buckypaper as electrodes for the vdP method using a one-part silver epoxy (EO-98HT, Hightemp Korea). The assembled specimens were vacuum bagged as shown in Fig. 2c and cured at 120°C for 1.5 h in a convection oven, forming CNT/epoxy nanocomposite layer on the CFRP laminates.

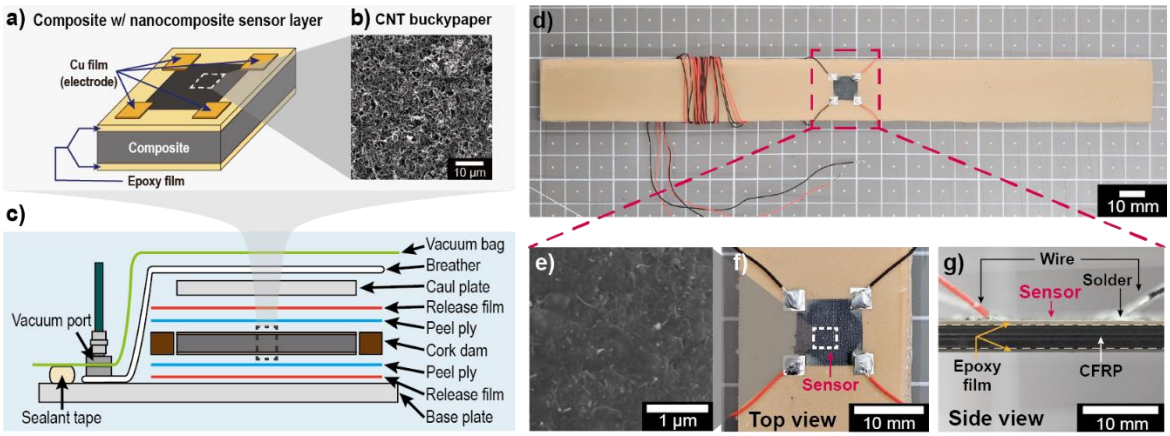

Figure 2: Fabrication of composite integrated carbon nanotube (CNT)/epoxy nanocomposite sensor. (a) Schematic illustration of the structure. (b) Surface image of CNT buckypaper from a scanning electron microscopy (SEM). (c) Manufacturing process of the sensor specimen. (d) Fabricated nanocomposite sensor specimen for tensile test. (e) Cross-section image of nanocomposite sensor using SEM. (f, g) Top and side view of fabricated nanocomposite sensor.

3.2 Measurement setup

The developed omnidirectional strain and temperature sensor system was experimentally validated under uniaxial tensile loading by comparing its measurements with data from conventional strain gauges and an infrared (IR) camera, as shown in Fig. 3. Real-time, automated four-probe resistivity measurements were conducted using a Keithley 2400 sourcemeter which is synchronized with a switch matrix (Keithley 3706A & 3730), enabling real-time measurements with a 0.1-second delay without the need for manual probe switching. Conventional strain data were obtained from metallic strain gauges (FRA 2-11, Tokyo Instruments) configured in a rosette layout to capture strain in three independent directions. These strain gauges were installed on the rear surface of each specimen and connected to a data acquisition system (cDAQ-9174 and NI-9237, National Instruments) with a sampling rate of 2 kHz.

Concurrently, surface temperature data of the nanocomposite sensor were captured using a FLIR A700 infrared camera.

Given that the vdP method assumes a homogeneously conductive layer, the calculated strain tensor reflects an averaged strain across the nanocomposite sensing region. To evaluate the impact of this spatial averaging, digital image correlation (DIC) analysis was performed using VIC 2D software (Correlated Solutions, Inc.). A speckle pattern was airbrushed onto the nanocomposite surface, and high-resolution images were acquired to assess the local strain field. Uniaxial tensile loading was applied using a universal testing machine (INSTRON 4482), while sinusoidal cyclic loads were applied via a servo-hydraulic testing system (INSTRON 1350) to examine dynamic sensing performance across varying frequencies and amplitudes. Each test configuration was repeated with five specimens to compute the average response and standard error.

To further evaluate the sensor's ability to simultaneously detect strain and temperature under varying thermal conditions, additional experiments were conducted. For stress-free conditions, specimens were placed on a programmable hot plate (HP-61A-2, Torrey Pines Scientific) and gradually heated, while both electrical resistance and surface temperature were monitored using the sourcemeter and IR camera, respectively. Under quasi-static tensile loading, external heating was provided via a heat gun, introducing simultaneous changes in strain and temperature. These tests were conducted to validate the sensor's real-time capability in decoupling strain and temperature for structural health monitoring (SHM) applications.

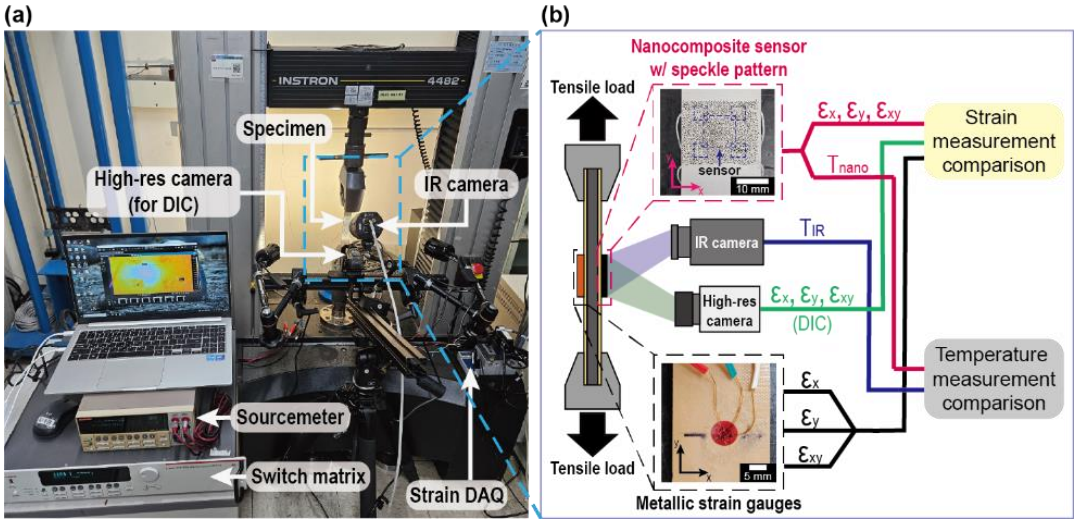

Figure 3: Experimental setup for the validation of nanocomposite sensor system. (a) Image of the real-time measurement setup, including the nanocomposite sensor and references (strain gauge, DIC analysis and IR camera) during the tensile test. (b) Schematic illustrating the validation process of the nanocomposite sensor system by comparing its measurement data with reference data.

4 Results and discussion

This section details the morphological characterization of the fabricated nanocomposite sensor and presents the experimental evaluation of its omnidirectional strain and temperature sensing performance under tensile loading. Performance validation was conducted by comparing the sensor's four outputs with reference measurements obtained from metallic strain gauges and an IR camera. Quasi-static tensile tests were used to assess the sensor's accuracy and operational range, while cyclic tensile tests evaluated its real-time monitoring capability. Additionally, the system's capacity to measure strain and temperature simultaneously under varying thermal conditions was examined both in unloaded states and during uniaxial tension.

4.1 Morphological analysis

Fig. 2b shows a scanning electron microscopy (SEM) image of the commercial MWCNT buckypaper,

revealing a randomly oriented, homogeneous CNT network. The nanotubes, with diameters ranging from 30 to 50 nm, form a nanoporous structure that allows epoxy resin to penetrate during oven curing [46,47]. This ensures complete infiltration of the epoxy into the CNT network without disrupting the random alignment, as confirmed in Fig. 2e. This morphology is critical because isotropic strain sensitivity has been associated with randomly dispersed CNTs [28,29,48], while aligned CNTs tend to produce anisotropic responses [31,49].

To verify the isotropic electrical properties of the buckypaper, resistivity tensor elements were measured using the vdp method. The off-diagonal component ρ_{xy} was approximately zero, and the anisotropy ratio—calculated as the ratio of ρ_x to ρ_y [50]—was calculated to be 0.9817 ± 0.0123 (mean ± SE), indicating near-isotropic behavior. In contrast, aligned CNT films typically exhibit an anisotropy ratio of around 1.44 ± 0.19 [49]. Given this isotropy, a constant gauge factor λ c can be uniformly applied in all directions in the FITC model.

Beyond electrical uniformity, the low thickness (i.e., ~50 µm) and areal density (i.e., 30 gsm) of CNT buckypaper allow it to be embedded into structural surfaces without significantly altering their shape or mass. Accordingly, a CNT/epoxy nanocomposite layer was successfully formed on the CFRP substrate, maintaining the integrity of its surface morphology (see Fig. 2g).

4.2 Omnidirectional strain and temperature monitoring performance under quasi-static tensile loading

Fig. 4 shows the results of quasi-static tensile tests, where the nanocomposite sensor's measurements were compared with those of strain gauges and an IR camera across a strain range of 0.18%. When oriented 90° to the loading axis, the sensor simultaneously captured the full in-plane strain tensor and temperature (Fig. 4a). It accurately recorded both axial tension and transverse compression due to the Poisson effect, with negligible shear strain. The temperature measurement was also highly precise, with a maximum error of only 0.03%.

Slight discrepancies in strain measurement arose from the temporal mismatch between individual electrical readings, due to sourcemeter switching delays. With a sampling time of ~2 seconds, the system showed some limitations in accuracy compared to conventional strain gauges. However, these could be mitigated by employing faster electrical measurement systems. Despite this, the nanocomposite sensor offers a significant advantage by combining multi-directional strain and temperature sensing into a single sensing layer.

When the sensor was rotated to 120°, it was subjected to shear strain, yet it still managed to resolve the strain tensor and temperature (Fig. 4b). Some loss in measurement accuracy was observed due to instability in electrical readings caused by sensor shape distortion under shear strain. This is attributed to the limitations of the vdP method, which assumes rectangular geometry; deformation distorts resistivity calculations. A more advanced version of the vdP method for parallelogram-shaped conductors [51] could address this issue, albeit with added complexity and the need for five probes.

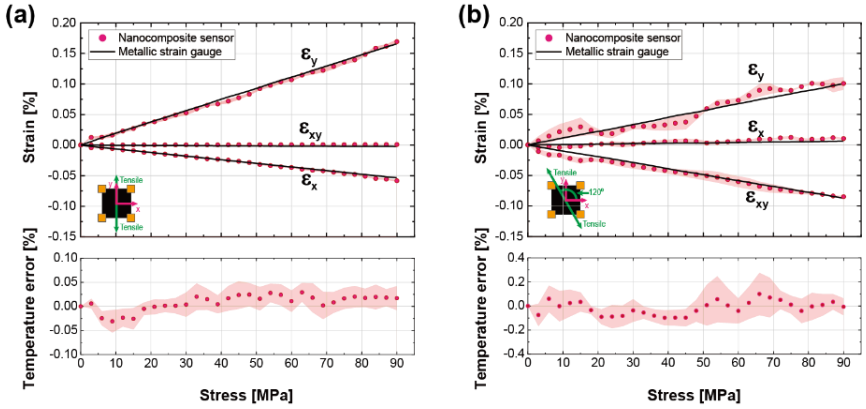

Figure 4: Sensing performance of nanocomposite sensor system monitoring omnidirectional strain and temperature under quasi-static tensile loading. (a-b) Comparison of in-plain strain tensor

measurements with strain gauges and difference in temperature measurements between nanocomposite sensor and IR camera in tensile direction of (a) 90° and (b) 120°, respectively (Mean ± SE). The error bands represent the standard error of the nanocomposite sensor specimens.

4.3 Size effect of nanocomposite sensor

As shown in Fig. 5a-b, sensor specimens of various sizes were subjected to tensile loading under the same conditions as those applied during the quasi-static tensile tests. The strain distribution across the composite surface was evaluated using DIC, as depicted in Fig. 5c-f. The strain patterns observed on the nanocomposite sensor surface were in close agreement with those on the surrounding composite substrate, demonstrating that the sensor accurately reflects the structural surface strain. When the applied tensile strain reached 0.18%, approaching the upper boundary of the sensor's measurement capability, localized strain concentrations were observed near the sensor's electrode regions (Fig. 5e-f). This occurrence is attributed to the relatively poor adhesion of the copper electrodes compared to the structurally embedded CNT buckypaper within the epoxy matrix. Although the nanocomposite sensor's strain estimation based on the FITC model remains valid up to 0.63% strain (as indicated in Fig. 1a), premature delamination caused by weak electrode adhesion may arise before the irreversible rearrangement of the CNT network begins, ultimately limiting the operational strain range of the sensor. This limitation becomes especially critical in failure detection of composite structures, considering that the average yield strain of typical CFRP materials is approximately 1.4% [52]. To overcome this constraint, it is necessary to reinforce the nanocomposite sensor by enhancing the electrode materials and refining the sensor design to reduce strain concentration at the electrode boundaries, as identified through DIC analysis. Furthermore, no discernible differences in strain distribution were observed across nanocomposites of varying sizes, indicating that the presence of the nanocomposite layer does not influence the strain distribution on the epoxy surface layer, regardless of the sensor's size.

Fig. 5 g-h present a comparison between the strain data acquired from the nanocomposite sensor and the average surface strain measured via DIC over the sensor region. The nanocomposite region is outlined with white dashed lines in Fig. 5 c-f, excluding the electrode regions, which are marked with black dashed lines. The sensor system calculates an effective strain tensor by averaging the non-uniform strain field within the nanocomposite layer. This outcome arises from the inherent averaging characteristic of the vdP method, which interprets a heterogeneous resistivity distribution as an equivalent uniform resistivity field [53]. As a result, the piezoresistive nanocomposite sensor determines an effective strain tensor that represents the overall mechanical response of the sensing layer. Due to this averaging mechanism, even when the sensor area was increased by a factor of four, the calculated effective strain tensors under the same tensile conditions remained consistent between sensors, regardless of their dimensions. Moreover, in the quasi-uniform strain field induced during uniaxial tensile loading, the effective strain values measured by the nanocomposite sensor aligned closely with the mean strain over the entire nanocomposite region. This response is analogous to the behavior of conventional metallic strain gauges, where the measured strain corresponds to the average resistance change across the gauge section, with the gauge length defining the effective sensing area.

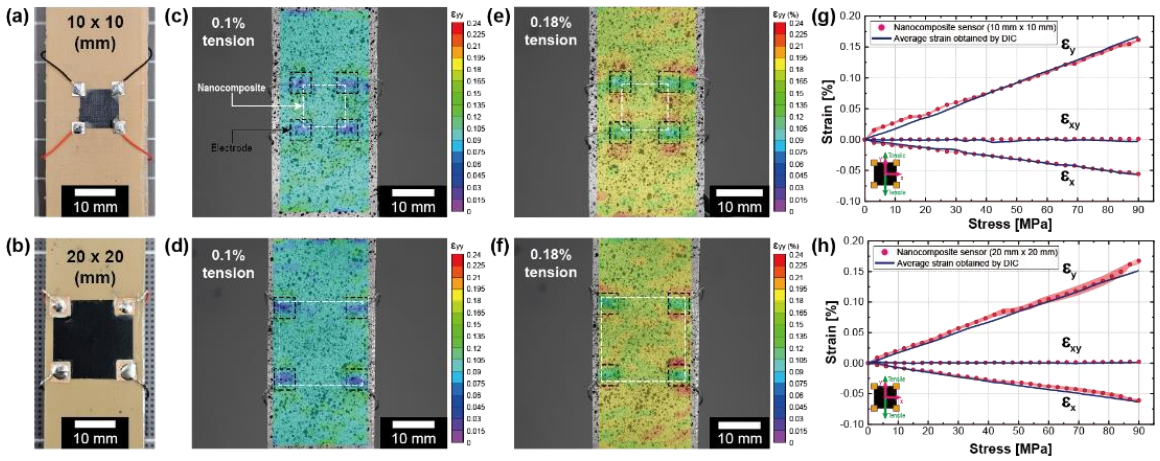

Figure 5: Size and averaging effect of strain measurements for nanocomposite sensor in different side dimensions. (a-b) Top view of nanocomposite sensors with different side lengths of 10 mm and 20 mm. (c-f) Strain distribution obtained by digital image correlation (DIC) in the tensile direction of 90°, under tensile strains of (c-d) 0.1% and (e-f) 0.18%. (g-h) Comparison of strain measurements from the nanocomposite sensors with the average strain of nanocomposite obtained via DIC. The error bands indicate the standard error of the nanocomposite sensor specimens.

4.4 Real-time monitoring performance of nanocomposite sensor

To assess dynamic performance, nanocomposite sensors (oriented 90° to the tensile axis) were preloaded by 0.4 mm (corresponding to strain of 0.55%) to avoid compression during cyclic loading, as they were specifically designed for tensile deformations. Following this pre-stretching, the specimens were then subjected to sinusoidal tension at two conditions: 0.025 Hz with 0.2 mm amplitude for 10 cycles, and 0.0125 Hz with 0.1 mm amplitude for 5 cycles. Measurements were recorded using the nanocomposite sensor, strain gauges, and an IR camera.

The real-time monitoring performance of the nanocomposite sensor specimens is shown in Fig. 6. The nanocomposite sensor reliably tracked all three in-plane strain components in agreement with the strain gauges (Fig. 6a), with average errors of 4.06% for the strain in the tensile direction (ε_y), 8.06% for the strain perpendicular to the tensile direction (ε_x), and approximately zero for the shear strain (ε_{xy}). The average strain error of the nanocomposite sensor is comparable to the reported average measurement errors of FBG sensors embedded in wind turbine blades, which are within 2.25% [54]. Future improvements should aim to enhance measurement accuracy to match that of conventional sensors by refining the calibration of strain and temperature sensitivities or by increasing the sensor's sampling rate. Nevertheless, the nanocomposite sensor maintained a low relative standard error in strain measurements, with a maximum value of 4.68%, demonstrating consistent real-time monitoring performance in all samples.

In addition to strain, the nanocomposite sensor also exhibited precise real-time temperature sensing, with a maximum deviation of only 0.203% from IR camera readings (see Fig. 6b). This accuracy indicates the sensor's ability to successfully decouple thermal effects from piezoresistive responses during dynamic loading. Notably, the temperature error from the nanocomposite sensor showed cyclic fluctuations aligned with the frequency of the applied mechanical loading, particularly at higher frequencies. These periodic variations were not observed in the IR camera data, as illustrated by the comparison in Fig. 6c. A frequency-domain analysis using fast Fourier transform (FFT) revealed distinct peaks at the loading frequencies (0.025 Hz and 0.0125 Hz) in the nanocomposite sensor data, while no such peaks were present in the IR camera data. Since the FITC model concurrently resolves both strain and temperature from the composite's resistive response, calibration mismatches in strain sensitivity may contribute to residual temperature errors, generating synchronized variations in both strain and temperature outputs. As a result, although strain changes are the dominant factor influencing resistivity during loading, minor cyclic variations in temperature data also emerged. Despite these fluctuations, the nanocomposite sensor achieved close agreement with reference sensors, affirming its capability for simultaneous strain and temperature monitoring.

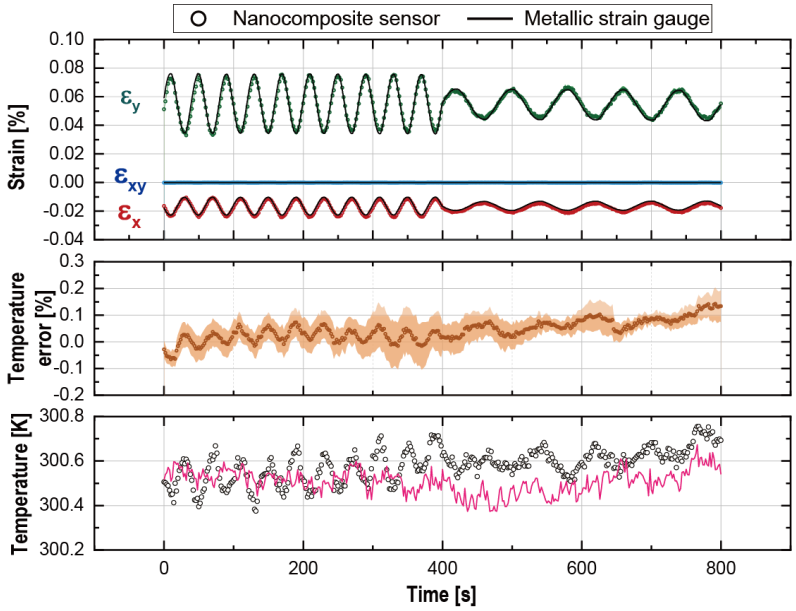

Figure 6: Real-time monitoring performance of nanocomposite sensor system under cyclic tensile loading (Mean ± SE). (a) Comparison of in-plane strain measurements with strain gauges. (b) Difference in temperature measurements between nanocomposite sensor and IR camera. The error bands represent the standard error of the nanocomposite sensor specimens. (c) Comparison of temperature measurements between one of the nanocomposite sensor and IR camera.

While the previous section focused on validation under room temperature with minor thermal variations, Fig. 7 evaluates the sensor's performance under substantial temperature changes induced by external heating. When the sensor's temperature increased by more than 30 K due to a heated plate without mechanical loading, the nanocomposite sensor measured temperature with less than 1% error, and strain readings remained near zero, as shown in Fig. 7a. Since the strain parameter in the FITC model is the sum of mechanical strain and thermal strain, a slight increase in strain measurements was observed in the stress-free condition due to the positive thermal expansion coefficient in the CFRP substrate. However, the strain in the x-direction increased less than in the y-direction unless the substrate was a quasi-isotropic laminate, indicating the presence of errors in strain calculations. As discussed in the cyclic tension test, this mismatch in temperature sensitivity is reflected in the measurement error of strain tensor elements, arising from coupled strain-temperature estimation in the FITC framework.

When convective heating was applied to the nanocomposite sensor during quasi-static tensile loading under the same conditions as depicted in Fig. 4b, the sensor system successfully tracked changes in both strain tensor components and temperature, thereby confirming the decoupling capability between piezoresistive and thermoresistive effects. The heater was activated while the tensile strain ranged between 0.03% and 0.06%, and again between 0.1% and 0.12%, as marked by the orange-shaded regions in the figure. During these heating intervals, strain measurement errors increased, particularly when the temperature ramp rate was relatively high; however, as the ramp rate decreased, the strain measurements closely realigned with the reference data. The rise in measurement error during rapid variations in strain or temperature is attributed to the low sampling rate caused by switching delays in electrical property acquisition. Despite this, the temperature readings from the nanocomposite sensor remained highly accurate, with a maximum deviation of just 1%.

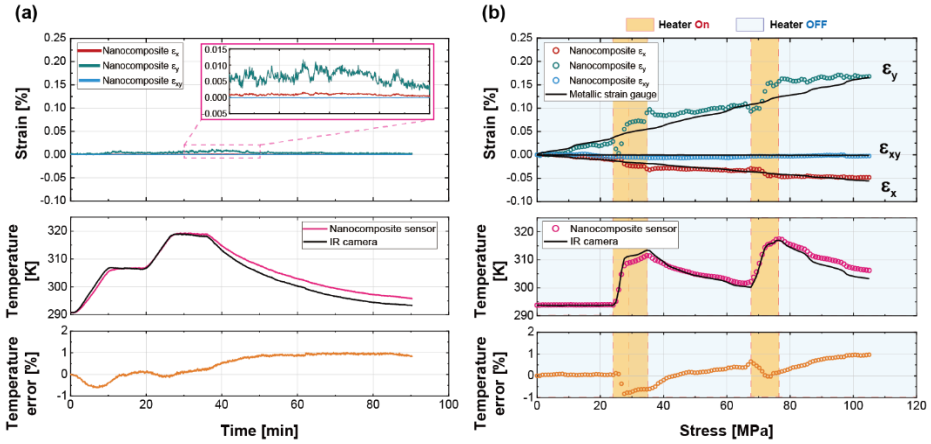

Figure 7: Sensing performance of nanocomposite sensor system monitoring omnidirectional strain and temperature under varying temperature conditions. (a) Stress-free condition. (b) Quasi-static tensile loading.

5 Conclusions

The developed sensor system enables simultaneous monitoring of the in-plane strain tensor and temperature by utilizing the omnidirectional sensitivity of nanocomposites, based on a conduction model that incorporates both piezoresistivity and thermoresistivity, alongside a multi-directional resistivity measurement technique. This strategy significantly reduces the number of required sensors to 25% and cuts down the number of electrodes by 50%, needing only four electrodes per sensor. For system validation, CNT/epoxy nanocomposite sensing layers were fabricated directly onto CFRP substrates. These sensors act as structurally integrated layers on composite surfaces, offering smooth, paintable finishes similar to standard surfacing layers while enabling real-time detection of structural anomalies. SEM-based morphological characterization and resistivity testing verified that the nanocomposites exhibit isotropic piezoresistive characteristic, owing to their uniformly dispersed, randomly oriented CNT networks. Experimental evaluations confirmed the system's accuracy, with strain and temperature measurements closely matching those from traditional metallic strain gauges and IR cameras under both mechanical and thermal loading. Measurement accuracy was particularly high when shear deformation in the sensor was limited. Cyclic tensile tests validated the system's capability for simultaneous strain and temperature monitoring, supporting its application in real-time health monitoring of composite structures. Furthermore, strain distribution assessed via DIC showed that the strain tensors derived from the nanocomposite sensors correspond to the effective strain across the sensor area, regardless of sensor size, and mirrored the surface strain distribution of the structure. These results demonstrate the feasibility of simplifying SHM systems by embedding multi-directional strain and temperature sensing functionalities into a single sensing layer. Additionally, implementing appropriate insulation methods to mitigate electrical interference with the CFRP substrate may enable full structural integration of nanocomposite sensors within CFRP laminates, paving the way for multifunctional composite structures.

ACKNOWLEDGEMENTS

This research was supported by the National Research Council of Science and Technology (NST) [Project ID: CPS22201-110]. The authors gratefully acknowledge Professors Han-Sohl Cho and Minkyun Noh from Korea Advanced Institute of Science and Technology (KAIST) for their helpful advice and valuable discussions. The morphological analysis via SEM was conducted with support from KAIST Analysis center for Research Advancement (KARA).

REFERENCES

[1] M. Balasubramanian, Composite materials and processing, vol. 711, CRC Press, CRC press Boca Raton, 2014.

[2] D.M. Frangopol, T.B. Messervey, Chapter 89 maintenance principles for civil structures, in: Encyclopedia of structural health moni- toring, Encyclopedia of structural health monitoring, 2009.

[3] R. Di Sante, Fibre optic sensors for structural health monitoring of aircraft composite structures: Recent advances and applications, Sensors (Switzerland) 15 (8) (2015) 18666–18713, http://dx.doi.org/10.3390/s150818666.

[4] M. Kashtalyan, C. Soutis, Stiffness and fracture analysis of laminated composites with off-axis ply matrix cracking, Compos. Part A: Appl. Sci. Manuf. 38 (4) (2007) 1262–1269, http://dx.doi.org/10.1016/J.COMPOSITESA.2006.07.001.

[5] L. Gao, E.T. Thostenson, Z. Zhang, T.W. Chou, Sensing of damage mechanisms in fiber-reinforced composites under cyclic loading using carbon nanotubes, Adv. Funct. Mater. 19 (1) (2009) 123–130, http://dx.doi.org/10.1002/adfm. 200800865.

[6] D. Kreculj, B. Rasuo, Impact damage modeling in laminated composite aircraft structures, Sustain. Compos. Aerosp. Appl. (2018) 125–153, http://dx.doi.org/ 10.1016/B978-0-08-102131-6.00007-4.

[7] A. Güemes, A. Fernandez-Lopez, A.R. Pozo, J. Sierra-Pérez, Structural health monitoring for advanced composite structures: A review, J. Compos. Sci. 4 (1) (2020) http://dx.doi.org/10.3390/jcs4010013.

[8] D.M. McCann, M.C. Forde, Review of NDT methods in the assessment of concrete and masonry structures, Ndt & E Int. 34 (2001) 71–84.

[9] D. Jung, G.S. Lee, Strain-sensing characteristics of multi-walled carbon nanotube sheet, J. Sens. Sci. Technol. 22 (5) (2013) 315–320, http://dx.doi.org/10.5369/ jsst.2013.22.5.315.

[10] G.C. Kahandawa, J. Epaarachchi, H. Wang, K.T. Lau, Use of FBG sensors for SHM in aerospace structures, Photonic Sensors 2 (3) (2012) 203–214, http: //dx.doi.org/10.1007/s13320-012-0065-4.

[11] Q. Liang, K. Zou, J. Long, J. Jin, D. Zhang, G. Coppola, W. Sun, Y. Wang, Y. Ge, Multi-component FBG-based force sensing systems by comparison with other sensing technologies: A review, IEEE Sensors J. 18 (18) (2018) 7345–7357, http://dx.doi.org/10.1109/JSEN.2018.2861014.

[12] A. Papantoniou, G. Rigas, N.D. Alexopoulos, Assessment of the strain monitoring reliability of fiber bragg grating sensor (FBGs) in advanced composite structures, Compos. Struct. 93 (9) (2011) 2163–2172, http://dx.doi.org/10.1016/j. compstruct.2011.03.001.

[13] J. Degrieck, W. De Waele, P. Verleysen, Monitoring of fibre reinforced composites with embedded optical fibre bragg sensors, with application to filament wound pressure vessels, NDT & E Int. 34 (4) (2001) 289–296, http://dx.doi.org/10. 1016/S0963-8695(00)00069-4.

[14] K.T. Lau, C.C. Chan, L.M. Zhou, W. Jin, Strain monitoring in compositestrengthened concrete structures using optical fibre sensors, Compos. Part B: Eng. 32 (1) (2001) 33–45, http://dx.doi.org/10.1016/S1359-8368(00)00044-5.

[15] A. Ajovalasit, Advances in strain gauge measurement on composite materials, Strain 47 (4) (2011) 313–325, http://dx.doi.org/10.1111/j.1475-1305.2009. 00691.x.

[16] J. P. Lynch, K. H. Law, E. G. Straser, A. S. Kiremidjian, T. W. Kenny,

[16] J.P. Lynch, K.H. Law, E.G. Straser, A.S. Kiremidjian, T.W. Kenny, The development of a wireless modular health monitoring system for civil structures, in: MCEER Mitigation of Earthquake Disaster By Advanced Technologies (MEDAT-2) Workshop, 2000.

[17] R. Wang, L. Sun, X. Zhu, W. Ge, H. Li, Z. Li, H. Zhang, Y. Huang, Z. Li, Y.F. Zhang, J. Zhao, Q. Xu, H. Lan, Carbon nanotube-based strain sensors: Structures, fabrication, and applications, Adv. Mater. Technol. 8 (1) (2023) http://dx.doi.org/10.1002/admt.202200855.

[18] L. Zhang, Y. Xie, S. Lu, B. Zhang, X. Wang, X. Li, W. Li, X. Wang, Mechanical behavior monitoring of composite hybrid bonded-riveted joints using highstability mxene sensors, Polym. Compos. 45 (8) (2024) 7316–7328, http://dx. doi.org/10.1002/pc.28267.

[19] L. Zhang, X. Wang, S. Lu, X. Liu, B. Zhang, X. Wang, Monitoring the damage evolution of Al 6061-T6 laser welded T-joint structure using nano-carbon tube based buckypaper film sensor, Diam. Relat. Mater. 146 (2024) http://dx.doi.org/ 10.1016/j.diamond.2024.111217.

[20] X. Liu, B. Wei, F.I. Farha, W. Liu, W. Li, Y. Qiu, F. Xu, Densely packed, highly strain sensitive carbon nanotube composites with sufficient polymer penetration, Compos. Part A: Appl. Sci. Manuf. 130 (2020) http://dx.doi.org/10.1016/j. compositesa.2019.105728.

[21] M.K. Njuguna, C. Yan, N. Hu, J.M. Bell, P.K. Yarlagadda, Sandwiched carbon nanotube film as strain sensor, Compos. Part B: Eng. 43 (6) (2012) 2711–2717, http://dx.doi.org/10.1016/j.compositesb.2012.04.022.

[22] X. Cao, X. Wei, G. Li, C. Hu, K. Dai, J. Guo, G. Zheng, C. Liu, C. Shen, Z. Guo, Strain sensing behaviors of epoxy nanocomposites with carbon nanotubes under cyclic deformation, Polymer 112 (2017) 1–9, http://dx.doi.org/10.1016/ j.polymer.2017.01.068.

[23] S.C. Her, W.C. Hsu, Sensing performance and mechanical properties of buckypaper impregnated with epoxy resin, Nanomaterials 10 (11) (2020) 1–11, http://dx.doi.org/10.3390/nano10112258.

[24] A. Sanli, A. Benchirouf, C. Müller, O. Kanoun, Piezoresistive performance characterization of strain sensitive multi-walled carbon nanotube-epoxy nanocomposites, Sensors Actuators, A: Phys. 254 (2017) 61–68, http://dx.doi.org/10.1016/ j.sna.2016.12.011.

[25] H. Liu, H. Xiang, Y. Wang, Z. Li, L. Qian, P. Li, Y. Ma, H. Zhou, W. Huang, A flexible multimodal sensor that detects strain, humidity, temperature, and pressure with carbon black and reduced graphene oxide hierarchical composite on paper, ACS Appl. Mater. Interfaces 11 (43) (2019) 40613–40619, http: //dx.doi.org/10.1021/acsami.9b13349.

[26] T. Yamada, Y. Hayamizu, Y. Yamamoto, Y. Yomogida, A. Izadi-Najafabadi, D.N. Futaba, K. Hata, A stretchable carbon nanotube strain sensor for human-motion detection, Nature Nanotechnology 6 (5) (2011) 296–301, http://dx.doi.org/10. 1038/nnano.2011.36.

[27] J. Huang, X. Yang, J. Liu, S.C. Her, J. Guo, J. Gu, L. Guan, Vibration monitoring based on flexible multi-walled carbon nanotube/polydimethylsiloxane film sensor and the application on motion signal acquisition, Nanotechnology 31 (33) (2020) http://dx.doi.org/10.1088/1361-6528/ab8edd.

[28] L. Zhang, X. Qu, Z. Zhao, H. Zhang, S. Lu, X. Wang, Health monitoring of composite pressure vessels through omnidirectional buckypaper sensor array, Appl. Phys. A: Mater. Sci. Process. 128 (3) (2022) http://dx.doi.org/10.1007/ s00339-022-05316-3.

[29] S. Lu, K. Du, X. Wang, C. Tian, D. Chen, K. Ma, T. Xu, Real-time monitoring of low-velocity impact damage for composite structures with the omnidirection carbon nanotubes' buckypaper sensors, Struct. Heal. Monit. 18 (2) (2019) 454–465, http://dx.doi.org/10.1177/1475921718757937.

[30] S.H. Hwang, H.W. Park, Y.B. Park, Piezoresistive behavior and multi-directional strain sensing ability of carbon nanotube-graphene nanoplatelet hybrid sheets, Smart Mater. Struct. 22 (1) (2013) http://dx.doi.org/10.1088/0964-1726/22/1/ 015013.

[31] A. Santos, L. Amorim, J.P. Nunes, L.A. Rocha, A.F. Silva, J.C. Viana, Ligned carbon nanotube based sensors for strain sensing applications, Sensors Actuators A: Phys. 289 (2019) 157–164, http://dx.doi.org/10.1016/J.SNA.2019.02.026.

[32] M. Nankali, N.M. Nouri, M. Navidbakhsh, N. Geran Malek, M.A. Amindehghan, A. Montazeri Shahtoori, M. Karimi, M. Amjadi, Highly stretchable and sensitive strain sensors based on carbon nanotube-elastomer nanocomposites: The effect of environmental factors on strain sensing performance, J. Mater. Chem. C 8 (18) (2020) 6185–6195, http://dx.doi.org/10.1039/d0tc00373e.

[33] L. Mandelstam, M. Leontowitsch, Zur theorie der Schrödingerschen gleichung, Z. Für Phys. 47 (1) (1928) 131–136, http://dx.doi.org/10.1007/BF01391061, URL https://doi.org/10.1007/BF01391061.

[34] R.M. Hill, Variable-range hopping, Phys. Status Solidi (A) 34 (2) (1976) 601–613, http://dx.doi.org/10.1002/pssa.2210340223.

[35] P. Sheng, E.K. Sichel, J.I. Gittleman, Fluctuation-induced tunneling conduction in carbon-polyvinylchloride composites, Phys. Rev. Lett. 40 (18) (1978) 1197.

[36] E.K. Sichel, P. Sheng, J.I. Gittleman, S. Bozowski, Observation of fiuctuation modulation of tunnel junctions by applied ac stress in carbon polyvinylchloride composites, Phys. Rev. B 24 (10) (1981) 6131.

[37] T. Karlsson, P. Hallander, F. Liu, T. Poot, M. Åkermo, Sensing abilities of embedded vertically aligned carbon nanotube forests in structural composites: From nanoscale properties to mesoscale functionalities, Compos. Part B: Eng. 255 (2023) http://dx.doi.org/10.1016/j.compositesb.2023.110587.

[38] R. Zhang, M. Baxendale, T. Peijs, Universal resistivity-strain dependence of carbon nanotube/polymer composites, Phys. Rev. B - Condens. Matter Mater. Phys. 76 (19) (2007) http://dx.doi.org/10.1103/PhysRevB.76.195433.

[39] M.C.J. Large, L. Poladian, G.W. Barton, M.A. van Eijkelenborg, History and applications of polymer fibres and microstructured fibres, Microstruct. Polym. Opt. Fibres (2008) 1–20.

[40] X. Li, M. Zheng, D. Hou, Q. Wen, Advantageous strain sensing performances of FBG strain sensors equipped with planar UV-curable resin, Sensors 23 (5) (2023) http://dx.doi.org/10.3390/s23052811.

[41] J.M. Kim, C.M. Kim, S.Y. Choi, B.Y. Lee, Enhanced strain measurement range of an FBG sensor embedded in seven-wire steel strands, Sensors (Switzerland) 17 (7) (2017) http://dx.doi.org/10.3390/s17071654.

[42] I. Hamerton, L. Mooring, The use of thermosets in aerospace applications, in: Thermosets, Elsevier, 2012, pp. 189–227.

[43] O. Philips'Gloeilampenfabrieken, A method of measuring specific resistivity and hall effect of discs of arbitrary shape, Philips Res. Rep. 13 (1) (1958) 1–9.

[44] J. Kleiza, V. Kleiza, On the applying of the van der pauw method to anisotropic media, Acta Phys. Pol. A 119 (12) (2011) 148–150.

[45] W.L.V. Price, Extension of van der pauw's theorem for measuring specific resistivity in discs of arbitrary shape to anisotropic media, J. Phys. D: Appl. Phys. 5 (6) (1972) 1127.

[46] R. Masoodi, K.M. Pillai, Wicking in porous materials: traditional and modern modeling approaches, Crc Press, 2012.

[47] J. Lee, S.S. Kessler, B.L. Wardle, Void-free layered polymeric architectures via capillary-action of nanoporous films, Adv. Mater. Interfaces 7 (4) (2020) http: //dx.doi.org/10.1002/admi.201901427.

[48] T. Xu, Q. Qiu, S. Lu, K. Ma, X. Wang, Multi-direction health monitoring with carbon nanotube film strain sensor, Int. J. Distrib. Sens. Networks 15 (2) (2019) http://dx.doi.org/10.1177/1550147719829683.

[49] J. Lee, I.Y. Stein, M.E. Devoe, D.J. Lewis, N. Lachman, S.S. Kessler, S.T. Buschhorn, B.L. Wardle, Impact of carbon nanotube length on electron transport in aligned carbon nanotube networks, Appl. Phys. Lett. 106 (5) (2015) http: //dx.doi.org/10.1063/1.4907608.

[50] I. Kazani, G. de Mey, C. Hertleer, J. Banaszczyk, A. Schwarz, G. Guxho, L. Van Langenhove, Van Der Pauw method for measuring resistivities of anisotropic layers printed on textile substrates, Text. Res. J. 81 (20) (2011) 2117–2124, http://dx.doi.org/10.1177/0040517511416280.

[51] K.A. Borup, K.F. Fischer, D.R. Brown, G.J. Snyder, B.B. Iversen, Measuring anisotropic resistivity of single crystals using the van der pauw technique, Phys. Rev. B - Condens. Matter Mater. Phys. 92 (4) (2015) http://dx.doi.org/10.1103/ PhysRevB.92.045210.

[52] P.D. Mangalgiri, Composite materials for aerospace applications, Bull. Mater. Sci. 22 (3) (1999) 657–664.

[53] T. Matsumura, Y. Sato, A theoretical study on van der pauw measurement values of inhomogeneous compound semiconductor thin films, J. Mod. Phys. 01 (05) (2010) 340–347, http://dx.doi.org/10.4236/jmp.2010.15048.

[54] K.-S. Choi, Y.-H. Huh, I.-B. Kwon, D.-J. Yoon, A tip deflection calculation method for a wind turbine blade using temperature compensated FBG sensors, Smart Materials and Structures 21 (2) (2012) 25008

PREPREG DEVELOPMENT FOR RAPID ON-ORBIT COMPOSITES MANUFACTURING VIA FRONTAL CURING

Tyler Price[1], Po-Wen Wang[2], Jeffrey Moore[3], Sameh Tawfick[4], and Nancy Sottos[5]

[1]Beckman Institute for Advanced Science & Technology and Department of Materials Science & Engineering, Grainger College of Engineering, University of Illinois Urbana-Champaign
3307 Beckman Institute, 405 N Mathews Ave, Urbana, IL, 61801, USA
Email: tylercp2@illinois.edu, web page: https://sottosgroup.matse.illinois.edu/people/tyler-price

[2]Beckman Institute for Advanced Science & Technology and Department of Materials Science & Engineering, Grainger College of Engineering, University of Illinois Urbana-Champaign
3300 Beckman Institute, 405 N Mathews Ave, Urbana, IL, 61801, USA
Email: powenww2@illinois.edu, web page: https://sottosgroup.matse.illinois.edu/people/po-wen-wang

[3]Beckman Institute for Advanced Science & Technology and Department of Chemistry, University of Illinois Urbana-Champaign
3351 Beckman Institute, 405 N Mathews Ave, Urbana, IL, 61801, USA
Email: jsmoore@illinois.edu, web page: https://chemistry.illinois.edu/jsmoore

[4]Beckman Institute for Advanced Science & Technology and Department of Mechanical Science & Engineering, Grainger College of Engineering, University of Illinois Urbana-Champaign
4412 Mechanical Engineering Lab, 105 S Mathews Ave, Urbana, IL, 61801, USA
Email: tawfick@illinois.edu, web page: https://mechse.illinois.edu/people/profile/tawfick

[5]Beckman Institute for Advanced Science & Technology and Department of Materials Science & Engineering, Grainger College of Engineering, University of Illinois Urbana-Champaign
203 Materials Science & Engineering Building, 1304 W Green St, Urbana, IL, 61801, USA
Email: n-sottos@illinois.edu, web page: https://matse.illinois.edu/people/profile/n-sottos

Keywords: Prepreg, Thermosetting resin, Cure, Thermal analysis, Cure behavior, Carbon fibre

ABSTRACT

We develop a novel A-staging approach for manufacturing a stable, frontally curable prepreg, to address the challenges of in-space composite manufacturing. The prepreg achieves room temperature stability through two key innovations: (1) physical separation of the reactive components via microencapsulation of the polymerization initiator and (2) the use of unreacted monomer (i.e. A-stage) resins that are solid at room temperature. A two-step dip-coating and infusion process was developed to manufacture the prepreg. Systematic studies of the dip-coating process reveal predictable and repeatable microparticle uptake that varies linearly with the dip-coating suspension concentration. Leveraging these results, we demonstrate control over the resin composition by achieving a desired initiator:monomer ratio in the prepreg despite introducing them in separate steps. When properly packaged, the prepreg remains below 20% conversion for at least 30 days at room temperature and pressure—a 300-fold improvement in shelf-life compared to B-staged DCPD prepregs.

1 INTRODUCTION

Large space structures, such as the international space station, are currently assembled in space from terrestrially manufactured components. This approach imposes mass and deployment constraints that limit the scale and robustness of space infrastructure.[1, 2] In-space manufacturing (ISM) offers a transformative paradigm to reduce the cost and increase the scale of space structures.[3, 4]

Continuous fiber reinforced composites are well-suited for ISM due to their high specific strength and stiffness.[5-7] However, current composite manufacturing methods and materials are poorly suited

for ISM due to their complex tooling, multi-step processing, energy intensive curing, and/or reactive feedstocks with limited shelf-life. Thermoset prepregs pose the most promising pathway to ISM of composites by eliminating the complexity of resin mixing and infusion on-orbit. A typical thermoset prepreg consists of reinforcement pre-impregnated with resin that is partially gelled or "B-staged."[8, 9] Conventional prepregs such as Hexcel's M21 or Toray's 3960 require high temperature, multi-hour cure cycles and must be stored at sub-ambient temperatures to achieve storage lives longer than 2 months.[10, 11] Highly reactive "snap-cure" prepregs such as Hexcel's M77 series reduce cycle time but suffer from very short shelf-lives, up to 2 months at 0°C, which are incompatible with 6-month launch timelines.[12] New prepreg systems are needed for ISM that combine long term stability at room temperature with rapid, low-energy curing.

Frontal curing (FC) offers a pathway towards stability and rapid conversion of monomer. Frontal curing leverages the heat of polymerization to generate a self-sustaining polymerization front that passes through the material.[13-15] A front can be initiated using a small local stimulus (e.g. UV, heat) which consumes 10^5 to 10^{10} less energy than conventional oven cures.[16] Frontally curable epoxy- and olefin-based resins have found success in composites manufacturing via additive, vacuum infusion, and wet layup methods, though these pose substantial risk for ISM.[17-24]

Shelf-stable FC prepregs remain elusive due to the limited pot life of formulated resins; Parikh developed the first FC prepreg material using dicyclopentadiene (DCPD) resin but found 80% conversion after 8h at room temperature or 14 days at -20°C, likely due to degradation of the phosphite inhibitor.[24, 25] More recently, Davydovich et al. achieved 8 months of stability at room temperature in unreinforced DCPD resins by microencapsulating the polymerization initiator (Hoveyda-Grubbs Second-Generation Catalyst).[26] However, the microencapsulation strategy precludes B-staging as the sequestered Grubbs-type catalyst remains inactive until thermally triggered release, at which point frontal curing begins immediately.

In this work, we introduce a novel frontally curable DCPD prepreg system tailored for ISM of carbon fiber composites. The prepreg (Figure 1) leverages polysulfone-encapsulated Grubbs' Second-Generation Catalyst (G2) and unreacted (i.e. A-stage) monomer that is solid at room temperature. We develop the manufacturing process for this A-stage prepreg and evaluate prepreg stability as well as cured composite performance as a function of storage time at room-temperature.

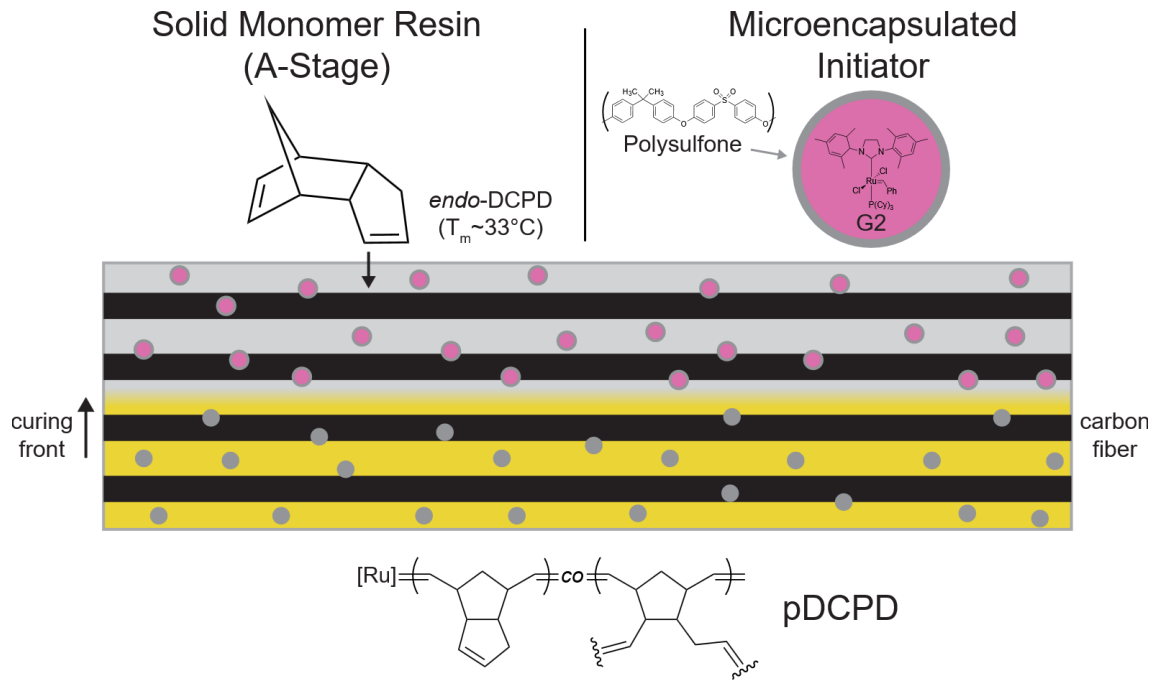

Figure 1: Microparticle Prepreg Strategy. The proposed "A-stage" prepreg material combines high purity endo-dicyclopentadiene resin, which is solid at room temperature, with polysulfone encapsulated Grubbs' Second-Generation Catalyst (G2) to achieve long term stability at ambient

temperature while enabling low-energy on-demand curing via frontal curing due to the thermally triggered release of G2 from the microparticles.

2 MATERIALS AND METHODS

2.1 Constituent Materials

Endo-dicyclopentadiene (DCPD) was purchased from Cymetech Corporation (UltreneTM 99, >99%, T_m=32-34°C). Grubbs' Second-Generation Catalyst (G2) was purchased from Chemscene Corporation. Polysulfone (PSU) was purchased from Sigma Aldrich Corporation. Poly(ethylene-alt-maleic anhydride) (EMA) was purchased from Aurorium (ZemacTM E400). Dichloromethane was purchased from Fischer Scientific. All chemicals were used as received without further purification. The reinforcing phase consisted of 5 plies of T300 2x2 twill weave carbon fiber fabric from Rock West Composites (1300D, 3K tow, 204 g/m^2). The fabric was cut to size (100 mm x 125 mm) and dried in an oven at 110°C for at least 2 hours to remove residual moisture. The plies were cooled and stored in a desiccator prior to use.

2.2 Catalyst Microparticle Preparation and Characterization

PSU microparticles containing G2 (PSU-G2) were manufactured using an oil-in-water emulsion technique similar to the work of Davydovich *et al.*[26] The oil phase was prepared using dichloromethane (56mL), PSU (5g), and G2 (0.7g), and the aqueous phase (200mL) was prepared with the EMA surfactant (7.6g). After emulsification using a homogenizer, the solvent was removed by evaporation. The microparticle-containing emulsion was centrifuged, and the supernatant was decanted. After two subsequent aqueous washing steps to remove EMA, the microparticles were freeze-dried to yield a free-flowing light pink powder (Figure 2A, ~4g, ~70% yield).

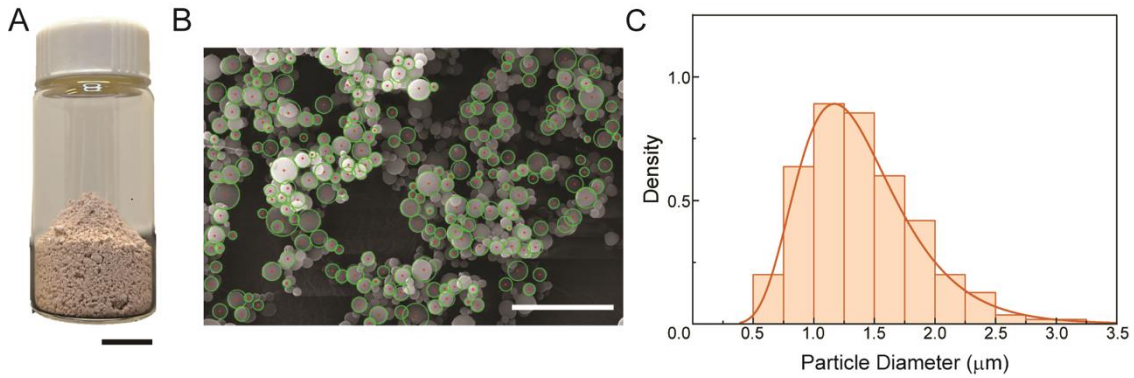

Figure 2. Microparticle Characterization. (A) Image of the PSU-G2 microparticles. Scale bar (black) 1 cm. (B) SEM image of PSU-G2 microparticles after applying an edge detection algorithm to determine microparticle size distribution. Green circles represent detected edges and red denotes the centroid. Scale bar (white) 10 μm. (C) Histogram of microparticle diameter from automated edge detection applied to SEM images with log-normal fit.

^{1}H nuclear magnetic resonance spectroscopy (NMR) was used to determine the average mass ratio of G2 to PSU in microparticles. NMR was conducted on a Bruker CB500. Spectra are referenced to residual $CDCl_3$ (δ=7.26 ppm), with chemical shifts reported in parts per million. The molar ratio of G2 to PSU repeat units was determined by comparing the integration of the peaks corresponding to the benzylidene proton from G2 (δ=19.15 ppm) against the four aromatic protons from polysulfone (δ=7.84 ppm). The mass ratio G2/PSU was calculated from the molar ratio using the molar masses of G2 (848.98 g/mol) and the polysulfone repeat unit (472.60 g/mol).

The morphology and size distribution of the PSU-G2 microparticles were characterized using scanning electron microscopy (SEM). SEM samples were coated with Au/Pd using a Denton Desk II TSC turbo-pumped sputter coater. SEM was performed on a FEI Quanta 450 FEG. The size of individual

PSU-G2 microparticles was measured by applying a custom Hough-circle-transform-based Python script to detect particle edges in the SEM images (Figure 2B).

The PSU-G2 microparticle preparation method produced microparticles with narrower size distribution and lower initiator loading compared to prior work. Replicate preparations exhibited slight variability in G2 loading with average G2/PSU mass ratios of 0.024 and 0.042. In contrast, Davydovich *et al.* reported a higher loading of 0.105 using Hoveyda-Grubbs' Second-Generation Catalyst, which could be due to differences in catalyst structure or encapsulation process.[26] To evaluate particle size, we analyzed SEM images using a custom Hough circle transformation algorithm to identify ca. 220 particles. The resulting size histogram (Figure 2C) follows a log-normal distribution with high correlation. The median particle diameter was 1.34 μm with standard deviation 0.35 μm, representing a significantly narrower distribution than prior work.[26] Moreover, the maximum microparticle diameter was also much smaller in this study. In this work, none exceeded the fiber diameter whereas the largest particles in prior studies exceeded the diameter of carbon fiber.

2.3 Prepreg and Composite Characterization

Differential scanning calorimetry (DSC) was performed in triplicate on prepreg samples and cured laminates at each time point in the longitudinal study. DSC was conducted using a TA Instruments Discovery DSC 2500 on 4-7 mg samples in Tzero pans. Cure kinetics experiments were conducted on prepreg samples from 0-200°C at 10°C/min. Heat-cool-heat post-cure DSC cycles were performed on cured composite samples from 0-250°C at 10°C/min. For both cure kinetics and post-cure DSC, the polymerization exotherm was measured over the range of 50-150°C using TA Trios software. The measured exotherm was corrected for reinforcement mass by burning off the matrix of the DSC samples in a thermogravimetric analyzer (TGA) similar to ASTM D3171 Method I Procedure H.[28] TGA was also conducted on unreinforced polymer to account for carbonization of the matrix as described in the standard. TGA was conducted on a TA Instruments Q500 in platinum pans with a 10°C/min ramp to 600°C and 30-min isothermal hold at 600°C. The degree of cure α was calculated for prepregs and cured laminates using Equation 1 where H_{res} is the observed residual exotherm corrected for reinforcement mass and H_r is the total enthalpy of reaction determined from a freshly prepared prepreg sample corrected for reinforcement mass.

$$\alpha = 1 - H_{res}/H_r \quad (1)$$

Soxhlet extractions were also performed on cured laminates at each point in the longitudinal study to determine the soluble fraction of the cured material. While the DSC provides a reactivity-based measure of curing, extraction provides a mass-based assessment of incorporation which provides valuable insights for space qualification where residual volatile material and off-gassing are critical considerations though the technique is no substitute for thermal vacuum characterization.[29] The extractions were performed under nitrogen over 20h on 25 mm x 50 mm cured samples using dichloromethane (DCM) heated to 65°C. This procedure was selected over the 4h 260°C procedure described in ASTM C613 to minimize the effects of oxidative crosslinking at elevated temperatures which could lead to under-estimation of the unincorporated mass fraction.[30]

Dynamic mechanical analysis (DMA) was performed on cured laminates during the longitudinal study to characterize their thermomechanical performance. DMA was conducted on a TA Instruments RSA-G2 in a 3-point bend configuration using the provided fixture with a 25mm span. Samples were cut and polished to 30 mm x 5 mm x ~1.1 mm. An oscillation heat ramp was applied at 2°C/min from 20-250°C with dynamic loading of 0.01% strain amplitude at 1 Hz. All experiments were conducted in a nitrogen environment. The average glass transition temperature T_g was taken as the peak of the tanδ curve determined using TA Trios software for n=2 samples. The reported error is the range of values.
The fiber volume fraction V_f for each laminate in the longitudinal study was characterized according to ASTM D3171 Method II using Equation 2 where n is the number of plies (5), h is the average laminate thickness, and A_r and ρ_r are the areal (204 g/m^2) and bulk (1.76 g/cm^3) reinforcement densities respectively.[28] The average laminate thickness was determined from n=8 measurements. The reported uncertainty represents the range due to thickness variation in the laminate. The void content V_v of each laminate was characterized using a polished 20 mm cross-section from each laminate. The void area was

manually identified using ImageJ software and V_v taken as the ratio of the void area to the total cross-sectional area.

$$V_f = (A_r n)/(\rho_r h) \quad (2)$$

3 RESULTS AND DISCUSSION

3.1 Prepreg Preparation

The A-stage prepreg was prepared by functionalizing the reinforcement with microparticles then infusing DCPD into the functionalized reinforcement (Figure 3). The dip-coating procedure was developed instead of infusing a pre-mixed microparticle resin to minimize filtering of the microparticles by the reinforcement, ensuring uniform G2 distribution. T300 2x2 twill carbon fiber plies were functionalized with the PSU-G2 microparticles by dip-coating each ply individually in a suspension of PSU-G2 microparticles in deionized water. The functionalized plies were immediately removed after submersion and oven-dried at 110°C for 2h to remove moisture. Microparticles ostensibly adhere to the fiber surface through Van der Waals interactions after drying.

After drying, the functionalized reinforcement was infused with DCPD using the vacuum assisted resin transfer molding (VARTM) setup described in Figure 3C. Resin was infused at 50°C (η~1 cp), which is above the melting temperature of the monomer (T_m~32°C), using a vacuum pressure of at -15 kPa.[27] After infusion, the preform was cooled to room temperature to solidify the DCPD monomer and allow the 5-ply prepreg to be removed from the bagging as a self-supporting solid—unlike liquid DCPD resin, which would immediately de-wet the reinforcement. The molar ratio of G2:DCPD, or resin formulation, was calculated from the G2 and DCPD masses added during dip-coating and infusion, respectively.

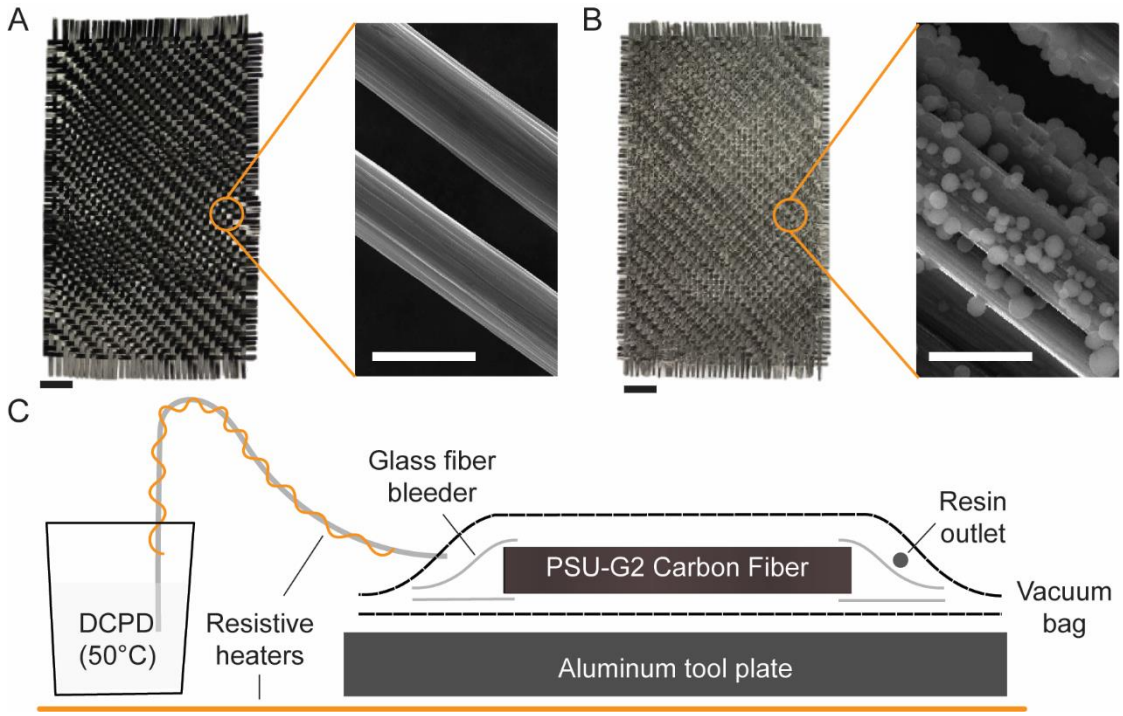

Figure 3. Prepreg Preparation and Curing. Optical and SEM images of reinforcement (A) before and (B) after dip-coating in an aqueous suspension of 5wt% PSU-G2 microparticles. Scale bars 1 cm (black) and 10 µm (white). (C) Schematic of the VARTM infusion of endo-DCPD into PSU-G2 functionalized reinforcement at 50°C to manufacture the A-stage prepreg.

3.2 Reinforcement Microparticle Functionalization

Unlike traditional prepreg processes, this manufacturing scheme introduces the polymerization initiator (G2) and monomer (DCPD) into the reinforcement in subsequent steps: reinforcement functionalization with catalyst microparticles followed by monomer infusion. Consequently, accurately predicting the final resin formulation, defined here as the molar ratio of initiator to monomer, is essential. We investigated the feasibility of this two-step approach in controlling resin formulation by systematically characterizing the dip-coating process.

The aqueous dip-coating procedure delivered reproducible and predictable microparticle uptake by the carbon fiber plies, enabling precise control of the final resin composition. The microparticle mass gain in the reinforcement increased linearly with the microparticle concentration in the dip-coating suspension (Figure 4A), consistent with prior work using different microparticles and reinforcement.[31] Notably, the trend was independent of the G2 loading within the microparticles. Using this data and the mass of DCPD added during infusion, we calculated resin formulation in the prepreg (Figure 4B). The resulting linear relationship allows prediction of the dip-coating suspension concentration needed to achieve a desired resin formulation. However, the predictive power is limited to A-stage DCPD prepregs of identical reinforcement architecture and microparticle composition.

We generalized this relationship for microparticles of arbitrary G2 loading. Since microparticle uptake (Figure 4A) is independent of G2 loading, the linear fit of resin formulation for microparticles containing 0.024 G2/PSU (Figure 4B, blue) can be scaled for other G2/PSU loadings by multiplying by the ratio $x/0.024$ where x is the G2/PSU mass ratio of interest. We validated this approach by targeting 100 ppm G2:DCPD using microparticles with 0.042 G2/PSU. The target ratio of 100 ppm was selected as this formulation has been extensively studied for phosphite inhibited pDCPD composites.[16-21] The calculated suspension concentration of 1.0 wt% PSU-G2 indeed resulted in 100 ± 10 ppm G2:DCPD after infusion (Figure 4B, orange). This demonstrates a single set of experiments (Figure 4, blue) can be extended to predict resin formulation for any G2 loading in PSU microparticles. However, additional studies are required to evaluate the effect of reinforcement architecture for further generalization.

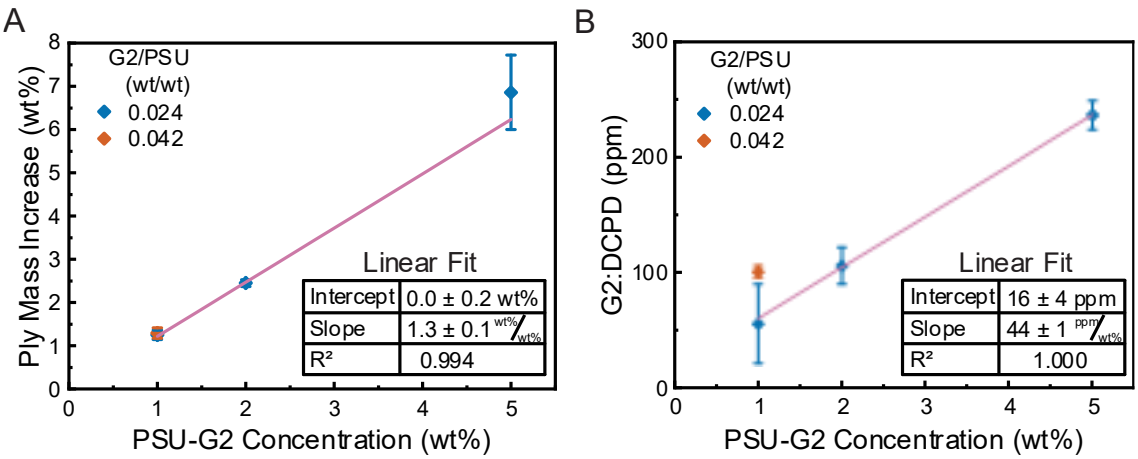

Figure 4. Prepreg Resin Formulation. (A) The PSU-G2 microparticle mass gained by the fabric plies during dip-coating as a function of suspension concentration for microparticles containing different G2 loading. Error bars represent one standard deviation on the mean (n=5). (B) Corresponding resin formulation calculated using the PSU-G2 mass gain in (A), the G2/PSU ratio in the microparticles, and the mass of resin infused into the reinforcement. Error bars represent measurement uncertainty due to mass loss during handling. Pink lines represent linear fits of the data for microparticles containing 0.024 G2/PSU (blue). Orange data points represent the prepreg used in the longitudinal study for which the suspension concentration was determined using (A) to achieve a target formulation of 100 ppm G2 using microparticles containing 0.042 G2/PSU.

3.3 Prepreg Stability

As an initial probe of the prepreg's stability, we examined the resin retention over time. Immediately after infusion, a prepreg sample was removed from the vacuum bagging material and stored in a heat-sealed polyethylene (PE) bag at ambient conditions. After 14 days in the PE bag at room temperature and pressure, 85% of the resin mass was lost (Figure 5A). We attribute this to the volatilization of DCPD monomer, given its moderate vapor pressure of 1.4 mm Hg at 20°C.[32] A systematic study using neat DCPD (Figure 5B) confirmed PE's permeability to DCPD vapor as 20% of the mass was lost within 8 days. However, a typical nylon vacuum bag with sealant tape effectively retained DCPD for the same duration and was used for subsequent longitudinal testing (Figure 5C). In contrast, typical DCPD-based resins that are liquid at room temperature immediately de-wet the reinforcement during re-pressurization and debagging after infusion, prohibiting storage at ambient conditions for any length of time. DCPD's volatility underscores the need for low-volatility monomers, though this limitation can be mitigated by packaging the prepreg in DCPD-impermeable materials.

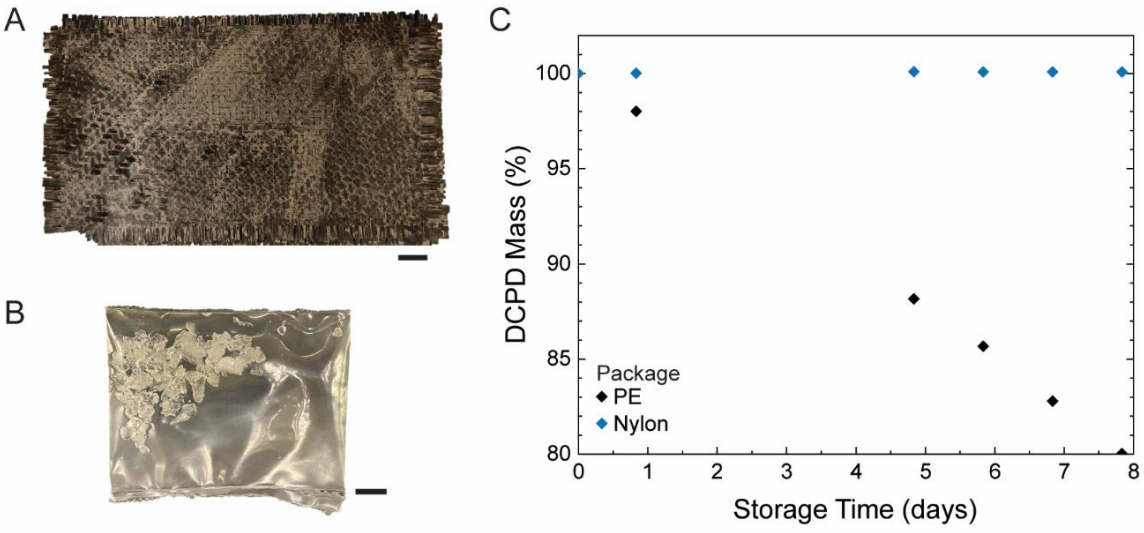

Figure 5. Prepreg Packaging. (A) A prepreg sample after 14 days stored at room temperature in a polyethylene (PE) bag with 85% of the initial resin mass lost to volatilization. (B) A sample of solid endo-DCPD monomer without reinforcement or PSU-G2 used to examine the permeability of packaging materials to volatile DCPD. (C) Comparison of DCPD mass loss in heat-sealed PE and a typical tape-sealed nylon vacuum bag. The tape-sealed nylon bag was used for the longitudinal study.

3.4 Longitudinal Study

The stability of the A-stage prepreg was evaluated through a 30-day longitudinal study examining properties of both the uncured prepreg and a frontally cured composite manufactured at each time point. After manufacturing prepreg, four 50-mm square coupons were cut to size with a rotary cutter and individually packed in a fresh nylon vacuum bag with sealant tape. The thermochemical properties of the prepreg coupons were characterized by differential scanning calorimetry (DSC) after storage at room temperature and atmospheric pressure for 0, 7, 14, and 30 days. At each time point the remaining prepreg material was used to frontally cure a laminate (Figure 6A). The coupons were first consolidated using 345 kPa applied by a hand press before FC was initiated through the thickness of the laminate by a resistive heater (Omega Engineering, 10W/in^2). The curing trigger consisted of a 2.5-min ramp to 180°C followed by a 2.5-min hold at 180°C controlled by a custom Arduino-Uno-based PID. A representative thermal profile measured by the thermocouple during curing is reported in Figure 6B. The cured prepreg coupons (Figure 6C) achieve excellent fiber distribution (Figure 6D).

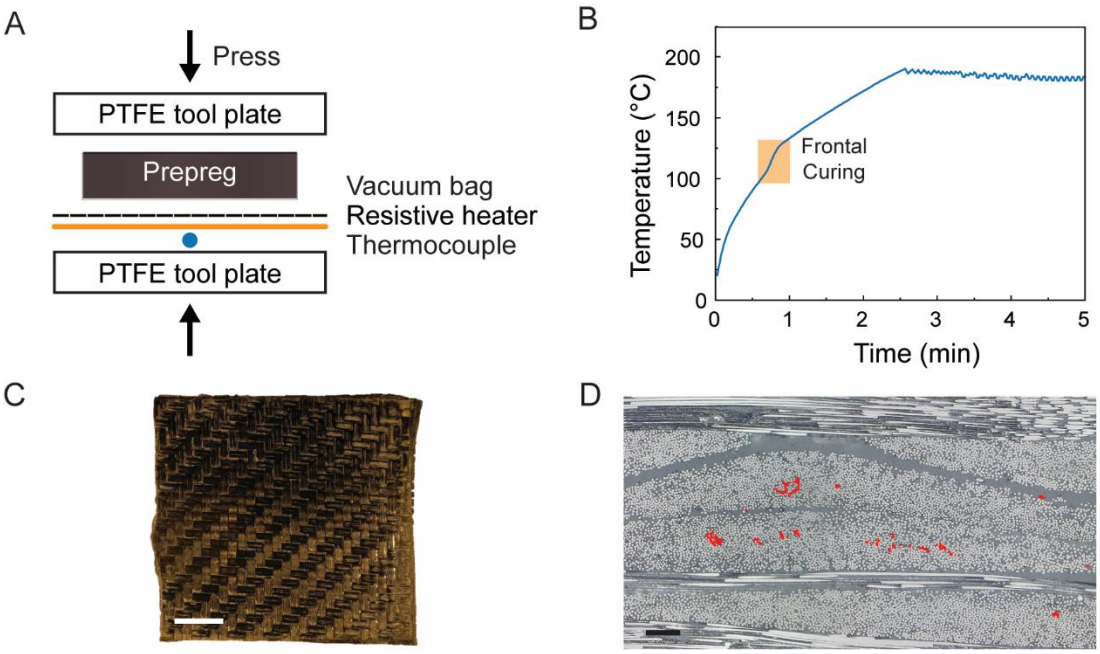

Figure 6. Prepreg Curing. (A) Schematic of through-thickness frontal curing of the A-stage prepreg with external consolidation from a press. (B) A representative temperature profile measured by the thermocouple during the applied cure cycle. (C) A representative cured composite coupon from the A-stage prepreg and (D) corresponding optical micrograph with voids false colored in red (V_v=0.5%). Scale bars 1 cm (white) and 100 μm (black).

The A-stage prepreg maintained α < 20% and frontally cured to achieve α > 99% at all time points in the 1-month study (Figure 7A). This demonstrates the stability of this system compared to B-staged DCPD prepregs, which reach α > 20% within 2 to 4 hours at room temperature.[24] Once cured, the prepreg coupons achieved robust properties summarized in Table 1; the laminates exhibited fiber volume fractions approaching 50% and low void fractions near 2%. The variation in constituents is attributed to variability in hand-pressing and the absence of vacuum during curing. Thermomechanical characterization (Figure 7B) showed glass transition temperatures T_g near 160°C with variation in the storage modulus again attributed to nonuniform consolidation causing local thickness and V_f variation. The extracted fraction of each laminate approximates the maximum possible mass loss due to vacuum in space (Table 1). While not a substitute for standardized thermal vacuum (TVAC) characterization, the screening approach provides valuable insights into the monomer incorporation beyond DSC. Mass loss remained below 2% at each time point, an encouraging preliminary indication of the material's off-gassing stability once cured. Overall, the longitudinal study confirms A-stage retains reactivity when properly packaged as well as its capacity to form high-performance composites via rapid, energy-efficient frontal curing.

Storage time [days]	V_f [%]	V_v [%]	T_g [°C]	Extracted mass [wt%]
0	46 ± 5	2 ± 1	160 ± 1	1.0 ± 0.3
7	48 ± 5	2 ± 1	153 ± 1	1.8 ± 0.6
14	45 ± 6	4 ± 1	163 ± 1	1.5 ± 0.4
30	49 ± 6	2 ± 1	166 ± 2	1.8 ± 0.4

Table 1: Properties of Cured Prepreg Coupons.

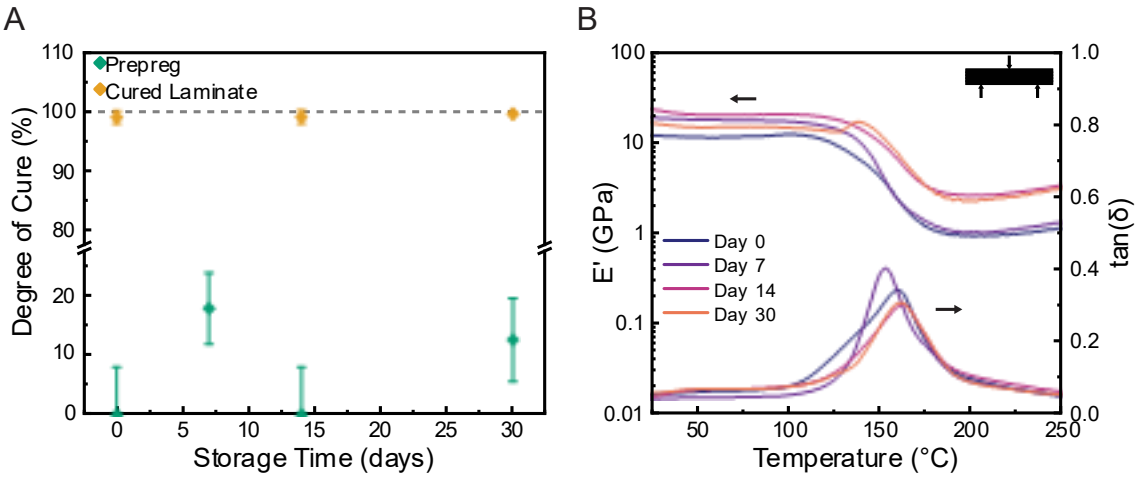

Figure 7. Longitudinal Study. (A) The degree of cure measured by DSC for prepreg after storage at room temperature in nylon bagging before and after frontal curing. (B) Representative DMA curves for laminates manufactured from prepreg after storage for 0 to 30 days at room temperature.

4 CONCLUSIONS

We developed a novel A-staging approach to create a shelf-stable, frontally curable prepreg by physically separating reactive components. Through microencapsulation of the polymerization initiator coupled with unreacted (A-stage) monomer that is solid at room temperature, the A-stage microparticle prepreg achieves long-term stability. We developed a two-step dip-coating and infusion process to manufacture the unique prepreg. Systematic variation of microparticle concentration in the aqueous dip-coating suspension enabled tunable initiator loading on the reinforcement. Importantly, we demonstrated control over the resin formulation by achieving a target initiator-monomer ratio in the final prepreg despite introducing the initiator and monomer in separate processes. The use of solid monomer prevents de-wetting immediately after infusion, though the monomer volatility necessitates careful packaging to prevent de-wetting during long-term storage. When properly packaged, the prepreg retains degree of cure under 20% over one month and successfully undergoes frontal curing, yielding a high-quality composite. The A-stage prepreg method developed in this work represents a 300-fold increase in shelf life over previously reported B-staged frontally curable DCPD prepregs. The A-stage prepreg's combination of months-long stability; low-energy, on-demand curing; and robust composite properties addresses the unique challenges of large-scale in-space manufacturing and marks a pivotal advancement in the viability of composite manufacturing via frontally curable prepregs.

ACKNOWLEDGEMENTS

The authors acknowledge support from DARPA, United States as part of the NOM4D program through Award HR001122C0057. The authors thank the Imaging Technology Group at the Beckman Institute for Advanced Science and Technology and the School of Chemical Sciences NMR laboratory at the University of Illinois Urbana-Champaign for the facilities necessary to complete this work. The authors thank Dr. Zhenchuang Xu for his assistance in conducting NMR experiments. T. Price thanks the Arnold and Mabel Beckman Foundation for financial support.

REFERENCES

[1] Z. Xue, J. Liu, C. Wu and Y. Tong, Review of in-space assembly technologies, *Chinese Journal of Aeronautics*, **34**, 2021, pp. 21–47 (doi: 10.1016/j.cja.2020.09.043).

[2] NASA Office of Inspector General, *NASA's Management of the International Space Station and Efforts to Commercialize Low Earth Orbit*, IG-22-005, NASA, 2021.

[3] E. Gibney, How to build a Moon base, *Nature*, **562**, 2018, pp. 474–478 (doi: 10.1038/d41586-018-07107-4).

[4] H. G. Bhundiya, F. Royer and Z. Cordero, Engineering Framework for Assessing Materials and Processes for In-Space Manufacturing, *Journal of Materials Engineering and Performance*, **31**, 2022, pp. 6045–6059 (doi: 10.1007/s11665-022-06755-y).
[5] NASA Technical Library Branch, *Technology for Large Space Systems*, SP_7046(20), NASA, 1989.
[6] I.M. Daniel and O. Ishai, *Engineering mechanics of composite materials*, Oxford University Press, New York, 2006.
[7] K. Tserpes and I. Sioutis, Advances in Composite Materials for Space Applications: A Comprehensive Literature Review, *Aerospace*, **12**, 2025, pp. 215 (doi: 10.3390/aerospace12030215).
[8] T. G. Gutowski, *Advanced composites manufacturing*, Wiley, New York, 1997.
[9] Clyne, T. W. and D. Hull, *An introduction to composite materials*, Cambridge University Press, New York, 2019.
[10] Toray Composite Materials America Inc., *3960 Prepreg System Product Data Sheet*, 2025.
[11] Hexcel Corporation, *HexPly M21 Product Data Sheet*, 2020.
[12] Hexcel Corporation, *HexPly M77HF Product Data Sheet*, 2022.
[13] B.A. Suslick, J. Hemmer, B. R. Groce, K. J. Stawiasz, P. H. Geubelle, G. Malucelli, A. Mariani, J. S. Moore, J. A. Pojman and N. R. Sottos, Frontal Polymerizations: From Chemical Perspectives to Macroscopic Properties and Applications, *Chemical Reviews*, **123**, 2023, pp. 3237-3298 (doi: 10.1021/acs.chemrev.2c00686).
[14] J. A. Pojman, Cure-on-Demand Composites by Frontal Polymerization, *Encyclopedia of Materials: Plastics and Polymers*, 2022.
[15] D. Bomze, P. Knaack, T. Koch, H. Jin and R. Liska, Radical induced cationic frontal polymerization as a versatile tool for epoxy curing and composite production, *Journal of Polymer Science Part A: Polymer Chemistry*, **54**, 2016, pp. 3751–3759 (doi: 10.1002/pola.28274).
[16] I.D. Robertson, M. Yourdkhani, P. J. Centellas, J. E. Aw, D. G. Ivanoff, E. Goli, E. M. Lloyd, L. M. Dean, N. R. Sottos, P. H. Geubelle, J. S. Moore and S. R. White, Rapid energy-efficient manufacturing of polymers and composites via frontal polymerization, *Nature*, **557**, 2018, pp. 223–227 (doi: 10.1038/s41586-018-0054-x).
[17] P.J. Centellas, M. Yourdkhani, S. Vyas, B. Koohbor, P. H. Geubelle and N. R. Sottos, Rapid multiple-front polymerization of fiber-reinforced polymer composites, *Composites Part A: Applied Science and Manufacturing*, **158**, 2022, pp. 106931 (doi: 10.1016/j.compositesa.2022.106931).
[18] I. Naseri and M. Yourdkhani, Rapid and Energy-Efficient Frontal Curing of Multifunctional Composites Using Integrated Nanostructured Heaters, *ACS Applied Materials & Interfaces*, **14**, 2022, pp. 50215–50224 (doi: 10.1021/acsami.2c15415).
[19] C. Dojan, M. Ziaee, S. Radosevich and M. Yourdkhani, Additive Manufacturing of Carbon Fiber-Reinforced Thermoset Composites via In-Situ Thermal Curing, *Nature Communications*, **16**, 2025, (doi: 10.1038/s41467-025-59848-2).
[20] P. Centellas, M. Garg, Z. Chen, X. Zhang, N. Parikh, P. Geubelle and N. Sottos, Energy-efficient manufacturing of multifunctional vascularized composites, *Journal of Composite Materials*, **57**, 2022, pp. 581-592 (doi: 10.1177/00219983221142353).
[21] S. Vyas, N. A. Parikh, T. C. Price, D. P. Patel, T. B. Le, P. H. Geubelle and N. R. Sottos, Through-thickness frontal polymerization: Process development and optimization, *Composites Part A: Applied Science and Manufacturing*, **180**, 2024, pp. 108084 (doi: 10.1016/j.compositesa.2024.108084).
[22] E. Goli, N. A. Parikh, M. Yourdkhani, N. G. Hibbard, J. S. Moore, N. R. Sottos and P. H. Geubelle, Frontal polymerization of unidirectional carbon-fiber-reinforced composites, *Composites Part A: Applied Science and Manufacturing*, **130**, 2020, p. 105689 (doi: 10.1016/j.compositesa.2019.105689).
[23] N. S. Hmeidat, M. Zakoworotony, Y. S. Kim, T. B. Le, G. DeBrun, R. Shah, J. J. Lessard, J. S. Moore, J. W. Baur, P. H. Geubelle, N. R. Sottos and S. H. Tawfick, Reactive extrusion of frontally polymerizing continuous carbon fiber reinforced polymer composites, *Composites*

Part A: Applied Science and Manufacturing, **190**, 2025, pp. 108609 (doi: 10.1016/j.compositesa.2024.108609)

[24] N.A. Parikh, *Rapid Manufacturing of Thermoset Polymers and Composites Processed by Frontal Polymerization*, University of Illinois Urbana-Champaign, 2023.

[25] I.D. Robertson, L. M. Dean, G. E. Rudebusch, N. R. Sottos, S. R. White and J. S. Moore, Alkyl Phosphite Inhibitors for Frontal Ring-Opening Metathesis Polymerization Greatly Increase Pot Life, *ACS Macro Letters*, **6**, 2017, pp. 609–612 (doi: 10.1021/acsmacrolett.7b00270).

[26] O. Davydovich, A. J. Greenlee, H. D. Root, A. L. Jansen, S. C. Gallegos, M. J. Warner, M. S. Kent, J. A. Cardenas, L. N. Appelhans, D. J. Roach, B. H. Jones and S. C. Leguizamon, Encapsulated Transition Metal Catalysts Enable Long-term Stability in Frontal Polymerization Resins, *Macromolecules*, **56**, 2023, pp. 7543–7550 (doi: 10.1021/acs.macromol.3c01146).

[27] I. Palmová, J. Kosek, J. Schöngut, M. Marek, and K. Štěpánek, Experimental and modeling studies of oligomerization and copolymerization of dicyclopentadiene, *Chemical Engineering Science*, **56**, 2001, pp. 927–935 (doi: 10.1016/S0009-2509(00)00307-9).

[28] ASTM D30 Committee, *ASTM D3171 Test Methods for Constituent Content of Composite Materials*, ASTM International, West Conshohocken, PA, 2022.

[29] Pastore, R., A. Delfini, M. Albano, A. Vricella, M. Marchetti, F. Santoni and F. Piergentili, Outgassing effect in polymeric composites exposed to space environment thermal-vacuum conditions, *Acta Astronautica*, 170, 2020, pp., 466–471 (doi: 10.1016/j.actaastro.2020.02.019).

[30] ASTM D30 Committee, *ASTM C613 Test Method for Constituent Content of Composite Prepreg by Soxhlet Extraction*, ASTM International, West Conshohocken, PA, 2019.

[31] Y.S. Kim, A. R. Jones, N. R. Sottos and S. R. White, Manufacturing of unidirectional glass/epoxy prepreg with microencapsulated liquid healing agents, *Composites Science and Technology*, **153**, 2017, pp. 190–197 (doi: 10.1016/j.compscitech.2017.10.017).

[32] T. E. Daubert and R. P. Danner, *Physical and thermodynamic properties of pure chemicals: data compilation*. CRC Press, 1989.

International Committee on Composite Materials

Student Status Confirmation Form for the ICCM Tsai Award

May 1, 2025

I, Nancy Sottos, hereby confirm that Tyler Price, who applied for the ICCM Tsai Award, was, at the date of the abstract submission 12/10/24, a PhD student under my supervision at the University of Illinois at Urbana-Champaign.



Nancy Sottos
Department Head and Swanlund Chair
University of Illinois
Materials Science & Engineering
1304 W. Green Street
Urbana, IL 61801
217-333-1031
n-sottos@illinois.edu

International Committee on Composite Materials

Authors Contributions

Manuscript title: Prepreg Development for Rapid On-Orbit Composites Manufacturing via Frontal Curing

Please describe the contributions of each author, referring to the taxonomy below.

Author 1 (Tsai Award Applicant): Tyler Price

- ☒ Conception
  Specify contribution in more detail (optional; no more than one sentence)
- ☒ Data curation
  Specify contribution in more detail (optional; no more than one sentence)
- ☒ Formal Analysis
  conducted the analyses of the microparticle size distribution (Fig. 2), dip-coating (Fig. 4), packaging (Fig. 5), and longitudinal study (Fig. 6-7; Table 1) data and contributed to the analysis of the nmr data.
- ☒ Investigation
  Conducted manufacturing, dip-coating, infusion, packaging, and longitudinal studies.
- ☒ Methodology
  Specify contribution in more detail (optional; no more than one sentence)
- ☐ Software
  Specify contribution in more detail (optional; no more than one sentence)
- ☒ Validation
  Verified reproducibility of the prepreg manufacturing/curing and select time points in the longitudinal study.
- ☒ Visualization
  Specify contribution in more detail (optional; no more than one sentence)
- ☒ Wrote the paper (original draft)
  Specify contribution in more detail (optional; no more than one sentence)
- ☒ Wrote the paper (review and editing)
  Specify contribution in more detail (optional; no more than one sentence)
- ☐ Other contribution
  Specify contribution in more detail (required; no more than one sentence)

Author 2: Po-Wen Wang

- ☒ Conception
  Specify contribution in more detail (optional; no more than one sentence)
- ☒ Data curation
  Specify contribution in more detail (optional; no more than one sentence)
- ☒ Formal Analysis
  Contributed to the analysis of the nmr data (Fig. 2)
- ☒ Investigation
  Manufactured catalyst microparticles and conducted SEM imaging.
- ☒ Methodology
  Developed the methodology to manufacture catalyst-containing microparticles.
- ☒ Software
  Contributed to the development of the microparticle SEM image analysis software.
- ☒ Validation
  Conducted validation of the microparticle identification software by manual analysis.
- ☐ Visualization
  Specify contribution in more detail (optional; no more than one sentence)
- ☐ Wrote the paper (original draft)
  Specify contribution in more detail (optional; no more than one sentence)
- ☒ Wrote the paper (review and editing)
  Specify contribution in more detail (optional; no more than one sentence)
- ☐ Other contribution
  Specify contribution in more detail (required; no more than one sentence)

Author 4: Jeffrey Moore

- ☒ Conception
  Specify contribution in more detail (optional; no more than one sentence)
- ☐ Data curation
  Specify contribution in more detail (optional; no more than one sentence)
- ☐ Formal Analysis
  Specify contribution in more detail (optional; no more than one sentence)
- ☐ Investigation
  Specify contribution in more detail (optional; no more than one sentence)
- ☒ Methodology
  Specify contribution in more detail (optional; no more than one sentence)
- ☐ Software
  Specify contribution in more detail (optional; no more than one sentence)
- ☐ Validation

Specify contribution in more detail (optional; no more than one sentence)

☐ Visualization
Specify contribution in more detail (optional; no more than one sentence)

☐ Wrote the paper (original draft)
Specify contribution in more detail (optional; no more than one sentence)

☒ Wrote the paper (review and editing)
Specify contribution in more detail (optional; no more than one sentence)

☐ Other contribution
Specify contribution in more detail (required; no more than one sentence)

Author 5: Sameh Tawfick

☒ Conception
Specify contribution in more detail (optional; no more than one sentence)

☐ Data curation
Specify contribution in more detail (optional; no more than one sentence)

☐ Formal Analysis
Specify contribution in more detail (optional; no more than one sentence)

☐ Investigation
Specify contribution in more detail (optional; no more than one sentence)

☒ Methodology
Specify contribution in more detail (optional; no more than one sentence)

☒ Software
Contributed to the development of the microparticle SEM image analysis software.

☐ Validation
Specify contribution in more detail (optional; no more than one sentence)

☐ Visualization
Specify contribution in more detail (optional; no more than one sentence)

☐ Wrote the paper (original draft)
Specify contribution in more detail (optional; no more than one sentence)

☒ Wrote the paper (review and editing)
Specify contribution in more detail (optional; no more than one sentence)

☐ Other contribution
Specify contribution in more detail (required; no more than one sentence)

Author 6: Nancy Sottos

☒ Conception
Specify contribution in more detail (optional; no more than one sentence)

☐ Data curation
Specify contribution in more detail (optional; no more than one sentence)

☐ Formal Analysis
Specify contribution in more detail (optional; no more than one sentence)

☐ Investigation
Specify contribution in more detail (optional; no more than one sentence)

☒ Methodology
Specify contribution in more detail (optional; no more than one sentence)

☐ Software
Specify contribution in more detail (optional; no more than one sentence)

☐ Validation
Specify contribution in more detail (optional; no more than one sentence)

☐ Visualization
Specify contribution in more detail (optional; no more than one sentence)

☐ Wrote the paper (original draft)
Specify contribution in more detail (optional; no more than one sentence)

☒ Wrote the paper (review and editing)
Specify contribution in more detail (optional; no more than one sentence)

☐ Other contribution
Specify contribution in more detail (required; no more than one sentence)

Author Signatures



Tyler Price

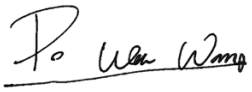

Po-Wen Wang



Jeffrey Moore



Sameh Tawfick



Nancy Sottos

Conceptualization
Ideas; formulation or evolution of overarching research goals and aims.

Data Curation
Management activities to annotate (produce metadata), scrub data and maintain research data (including software code, where it is necessary for interpreting the data itself) for initial use and later reuse.

Formal Analysis
Application of statistical, mathematical, computational, or other formal techniques to analyze or synthesize study data.

Investigation
Conducting a research and investigation process, specifically performing the experiments, or data/evidence collection.

Methodology
Development or design of methodology; creation of models.

Software
Programming, software development; designing computer programs; implementation of the computer code and supporting algorithms; testing of existing code components.

Validation
Verification, whether as a part of the activity or separate, of the overall replication/reproducibility of results/experiments and other research outputs.

Visualization
Preparation, creation and/or presentation of the published work, specifically visualization/data presentation.

Writing – Original Draft Preparation
Creation and/or presentation of the published work, specifically writing the initial draft (including substantive translation).

Writing – Review & Editing
Preparation, creation and/or presentation of the published work by those from the original research group, specifically critical review, commentary or revision – including pre- or post-publication stages.

SURROGATE MODEL-DRIVEN AUTOMATION FOR RVE DESIGN AND VALIDATION OF LONG DISCONTINUOUS CARBON FIBER COMPOSITE STRUCTURES

Akshay Zaveri[1], Hyunsu Lee[1], Mark W. D. Nielsen, Keith D. Humfeld, and Ji Ho Jeon[1*]

[1]School of Mechanical, Aerospace, and Manufacturing Engineering, University of Connecticut, Storrs, Connecticut, USA
*Corresponding author (jiho.jeon@uconn.edu)

Keywords: Carbon fiber, Discontinuous fiber, Finite element analysis, Microstructure, Numerical analysis, Surrogate model

ABSTRACT

A physics-informed surrogate-modeling framework is presented for automated RVE generation, validation, and rapid prediction of effective stiffness in aligned discontinuous carbon fiber composites. A fully Python-driven workflow within Abaqus creates 2D representative volume elements (RVEs) parameterized by fiber length, gap, width, angle, and volume fraction. Convergence studies show that including three repeating units of the fiber-gap pattern within the RVE is sufficient to capture microstructural variability without requiring periodic boundary conditions. A 200 sample 0 degree dataset trains three Random Forest regressors: one each for E_{11} G_{12}, and the Halpin–Tsai shape factor $\xi_{E_{11}}$. Validation on $\theta = 0°$ yields $R^2 > 0.970$ and MAE < 0.07 GPa for E_{22} and G_{12}, while $\xi_{E_{11}}$ achieves $R^2 > 0.975$. Embedding these predictions in a Classical Laminate Theory (CLT) framework enables accurate modulus prediction across arbitrary fiber angles, with E_{11} and E_{22} remaining within 10% of full-FEA across arbitrary fiber angles. This consistency inspires confidence in the FEA data as its trends align with well-established composite analytical models. Beyond prediction, the surrogate model is used to identify and filter anomalous simulations, a particularly important capability for angled fibers, where meshing and loading artifacts frequently corrupt results. By integrating micromechanical models, laminate theory, and machine learning, this hybrid framework bridges physical intuition with data-driven inference. It enables the rapid generation of large, validated property datasets at a fraction of the cost of full FEA. These datasets are well-suited for future inverse design workflows, where optimal discontinuous fiber architectures must be identified for target stiffness requirements.

1 INTRODUCTION

Discontinuous fiber-reinforced composites (DFRCs) combine fiber segments within a polymer matrix, offering scalability and automation advantages over continuous fiber composites (CFRCs). While CFRC processes often involves high labor and tooling costs, DFRCs offer a cost-effective alternative with improved recyclability, and compatibility with complex geometries [1,2]. Recent advances in robotic fiber placement and AI-driven control have significantly enhanced DFRC mechanical performance, bringing tensile strength and stiffness closer to CFRC benchmarks [3,4]. Moreover, aligned DFRCs enable spatial control of stiffness, strength, and energy absorption, allowing mechanical behavior to be tailored to application specific loading through inverse design. The success of such inverse design efforts, aimed at identifying optimal microstructures to achieve target macroscopic properties, relies on the ability to generate large, accurate datasets that reflect the influence of fiber architecture on mechanical response.

Existing FEA based datasets are often constrained by manually generated fiber geometries, inconsistent boundary condition implementations, and limited control over key design parameters such as fiber length, gap, and orientation. Numerous prior studies utilize idealized or overly simplified microstructures, which fail to reflect the parametric complexity of aligned discontinuous fiber configurations. For such systems, accurate prediction of load transfer and stiffness anisotropy demands

precise geometric fidelity and consistent numerical formulations. Furthermore, meshing artifacts and numerical instability, particularly in off axis fiber alignments, result in high simulation failure rates and reduce the reliability of computed property data [5,6]. Automated workflows for representative volume element (RVE) generation and validation in aligned DFRCs remain limited, restricting the scalability and fidelity of data driven inverse modeling.

To address these constraints and enable scalable inverse design, a set of computational tools is being developed in conjunction with a gantry mounted robotic aligned DFRC manufacturing platform engineered to physically implement the methods established in this study. In parallel, a fully automated process for RVE generation, validation, and surrogate model training has been established to overcome modeling limitations associated with manual fiber placement and simulation inconsistency. A Python driven Abaqus workflow generates 2D RVEs parameterized by fiber length, interfiber gap, width, orientation angle, and volume fraction. Convergence studies determine the minimum number of fiber segment repetitions required to capture statistically representative behaviour without the need for periodic boundary conditions. Physics informed validation is performed using micromechanical models, including the Halpin–Tsai formulation for predicting longitudinal stiffness and a series rule model for estimating transverse and shear stiffness components [7–9]. Until the manufacturing platform is fully operational, high fidelity FEA datasets generated within the research group serve as the primary basis for training and validating inverse design methodologies.

Building on this validated dataset, a machine learning surrogate is trained to predict both the Halpin–Tsai shape factor and effective stiffness components from a curated 0 degree dataset. The surrogate is incorporated into Classical Laminate Theory (CLT) calculations to enable rapid and accurate property prediction for arbitrary fiber orientations, significantly reducing computational cost compared to full FEA. In addition, the surrogate aids in simulation quality control by identifying anomalous cases, particularly in angled cases, where mesh distortion and boundary artifacts are common. This automated approach enables scalable, physics informed generation of validated property datasets, supporting efficient inverse design of aligned DFRCs.

2 BACKGROUND AND THEORY

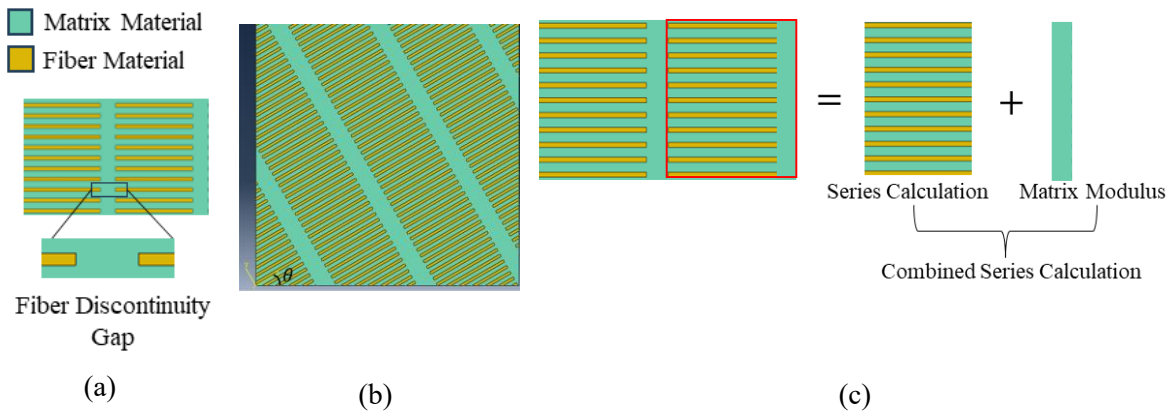

Figure 1: (a) Basic RVE Model (b) RVE with fibers orientated at angle θ (c) Combined series calculation example for E_{22} and G_{12}

In the RVE workflow, two distinct but complementary micromechanical approaches are used to characterize, estimate, and predict composite stiffness under different loading directions: the Halpin–Tsai model for axial modulus E_{11}, and a simple series-rule model for transverse modulus E_{22} and in-plane shear G_{12}. These models are complimented by Classical Laminate Theory (CLT) via the ply-

stiffness matrix Q to rotate those base moduli to arbitrary fiber angles. Each approach is explained below in terms of its mathematical formulation, physical rationale as it relates to the RVE geometry as shown in Figure 1a and 1c, and specific examples of its application within this work.

2.1 Micromechanical Models

The stiffness of the DFRC RVE can be evaluated by analyzing the mechanics of the load transfer through its microstructural constituents. In the fiber axis direction, apart from the localized fiber to fiber gap region, where the fiber gap is small in absolute terms, most structural elements are aligned in parallel with high length to width aspect ratios. Under these conditions, the Halpin-Tsai formulation as shown in Equation 1, accurately captures the composite's longitudinal stiffness [10]**.** In this configuration, each RVE is defined by a global fiber volume fraction V_f, fiber modulus E_{f1}, and matrix modulus E_m, with the parameter η defined in Equation 2.

$$E_{11} = E_m \frac{1 + \xi \eta V_f}{1 - \eta V_f} \tag{1}$$

$$\eta = \left(\frac{E_{f1}}{E_m} - 1 \right) \Big/ \left(\frac{E_{f1}}{E_m} + \xi \right) \tag{2}$$

Here, ξ is a dimensionless shape factor that encapsulates fiber aspect ratio, spacing, and interphase stiffness. As discussed previously, this factor is often determined experimentally based on fiber to fiber interactions [8,10]**.** As ξ approaches zero, the Halpin-Tsai equation predicts a lower bound consistent with the classical Reuss Model [11], while in the limit as ξ approaches infinity, the model converges to an upper bound akin to the Rule of Mixtures. For aligned discontinuous fiber based RVEs, ξ must account not only for the fiber aspect ratio but also for the efficiency of load transfer through the longitudinal matrix gaps between fibers.

In contrast, when the RVE is subjected to transverse loading or in-plane shear, the microscopic load path intersects matrix dominated regions before reaching the fiber reinforced domains. For example, the representative cross-sectional used to determine the transverse modulus E_{22} differs significantly from that used in the longitudinal case, both in geometry and in local stiffness distribution. As a result, applying the same Halpin-Tsai model to E_{22} and G_{12} yields inaccurate predictions, with the lower bound failing to capture the behavior observed in finite element simulations. To address this, a hybrid Reuss series model [7,12] is employed to estimate the transverse and shear moduli by decomposing the RVE into two distinct subregions; one consisting of a fiber and matrix region, and other composed solely of matrix filled fiber gap zones, as described in Equations 3 and 4. In this formulation, E_{f2} denotes the fiber transverse modulus, and the associated microstructural configuration is illustrated in Figure 1c).

$$E_{22} = \left(\frac{f_{stripe}}{E_{22_{stripe}}} + \frac{1 - f_{stripe}}{E_m} \right)^{-1} \tag{3}$$

$$E_{22_{stripe}} = \left(\frac{f_{fiber}}{E_{f2}} + \frac{1 - f_{fiber}}{E_m} \right)^{-1} \tag{4}$$

A similar modeling approach is used to calculate the shear modulus. Since the matrix gaps function as the weakest link under loading, even a modest value of f_{gap}, defined as the length fraction

of transverse fiber gaps as shown in Figure 1a, can significantly reduce both E_{22} and G_{12}, driving them toward the matrix properties E_m or G_m. As a result, rather than using the Halpin–Tsai model, which assumes a uniformly mixed fiber and matrix medium, a simple series model more accurately captures the reduced transverse and shear stiffness observed in RVE data. This series model serves as a physically meaningful baseline estimate and does not require any fitted parameters such as ξ, thereby providing additional confidence in the quality of the initial training data. Nonetheless, machine learning models remain essential to account for the complex nonlinear interactions among geometric and material inputs that are not adequately captured by analytical formulations alone.

2.2 Stiffness Matrix

Once the base-case ply moduli have been determined and validated, they can be extended to RVEs with rotated fiber orientations (Figure 1b) to predict the composite's overall behavior. Using Classical Laminate Theory, the validated values of E_{11}, E_{22} and G_{12} are implemented into the plane-stiffness matrix, Q**,** thereby transforming the 0 degree ply properties into the local coordinate system of an angled fiber system and allowing for the extraction of global moduli [13]. Equations 5-7 detail the basics of this transformation where values of Q_{xy} are functions of the global E_{11}, E_{22} and G_{12} for a 0 degree ply. The Q matrix is then rotated by transposition matrix $T(\theta)$ and inverted into a global compliance matrix **S** which holds the rotated values for E_{11}, E_{22} and G_{12} [11].

$$Q = \begin{bmatrix} Q_{11} & Q_{12} & 0 \\ Q_{12} & Q_{22} & 0 \\ 0 & 0 & Q_{66} \end{bmatrix}, \begin{cases} Q_{11} = \dfrac{E_{11}}{1 - v_{12}v_{21}} \\ Q_{22} = \dfrac{E_{11}}{1 - v_{12}v_{21}} \\ Q_{12} = \dfrac{v_{12}E_{22}}{1 - v_{12}v_{21}} \\ Q_{66} = G_{12} \end{cases} \tag{5}$$

$$\boldsymbol{S} = (T(\theta)QT(\theta)^{-T})^{-1} \tag{6}$$

$$S = \begin{bmatrix} S_{11} & S_{12} & 0 \\ S_{12} & S_{22} & 0 \\ 0 & 0 & S_{66} \end{bmatrix} \begin{cases} E_{11}(\theta) = \dfrac{1}{S_{11}} \\ E_{22}(\theta) = \dfrac{1}{S_{22}} \\ G_{12}(\theta) = \dfrac{1}{S_{66}} \end{cases} \tag{7}$$

These expressions describe how in-plane stiffness of a ply changes as its fibers rotate from 0 degrees to an arbitrary angle θ. In this study, once the stiffness values for plies with 0-degree fiber orientation are validated, they are incorporated into the transformed reduced stiffness matrix Q to estimate the mechanical properties of plies with rotated fibers. This approach enables the validation of more complex FEA geometries involving arbitrary fiber orientations.

3 METHODOLGY

3.1 Automated Representative Volume Element Generation

In this study, RVEs of aligned DFRCs were generated using a fully automated Python-driven workflow within the Abaqus environment. A Python driver script invokes Abaqus to generate 2D unit-cell models of aligned discontinuous fiber composites. Each cell contains a square polymer matrix of

size $L_x \times L_x$ and a prescribed number of straight fiber segments. Each RVE geometry was parameterized by four key microstructural variables: fiber length (L_f), fiber discontinuity gap (F_g), fiber width (F_w), fiber angle (θ) and fiber volume fraction (V_f).

In conventional composite RVE FEA, it is common practice to impose periodic boundary conditions (PBCs). These conditions enforce compatibility of displacement and traction across opposing faces, allowing the RVE to behave as part of an infinite periodic microstructure. This ensures accurate homogenization of effective mechanical properties [14,15]. However, in the present study, PBCs were not applied due to challenges introduced by angled fiber configurations. These configurations result in irregular meshing along the boundaries of RVE, making it impractical to maintain node to node correspondence across opposite faces, which is necessary for enforcing periodicity.

Instead, mechanical properties are extracted from global reaction forces generated by applied boundary conditions. In this approach, one edge of the RVE is fully constrained, while the opposite edge is subjected to a prescribed strain, ε. The resulting reaction forces on the boundaries are used to compute effective stiffness moduli, as shown in Equation 8. The quantity F_i represents the reaction force in either the longitudinal or transverse direction and is used to compute the corresponding modulus. The shear modulus is calculated using the built-in stress and strain volume averaging functionality within the FEA environment.

$$E_i = \frac{F_i * L_x}{\varepsilon} \tag{8}$$

To ensure that the RVE is statistically representative despite the absence of PBCs, a convergence study is conducted. The side length L_x of the RVE is systematically increased according to the relation:

$$L_x = N\left(F_l + F_g\right) + \delta, N = 1, 2, 3, \ldots \tag{9}$$

where δ is a small buffer added to avoid edge truncation artifacts, and N is the number of repeated fiber and gap units included in the simulation domain. Simulations are conducted for each value of L_x at a fiber orientation angle of 0 degrees, and the corresponding moduli E_{11} and E_{22} are tracked. Once the moduli exhibit convergence with increasing L_x, the RVE is considered sufficiently large to capture microstructural variability and yield reliable estimates of bulk mechanical properties. To verify consistency across different configurations, additional simulations are performed using randomly generated angles θ, confirming convergence across all phases of interest.

3.2 Dataset Generation

The driver script functions as the primary tool for dataset generation. It automates the creation of a large set of RVE simulations, specifically targeting 0 degree fiber orientation cases. A master script controls this process by systematically modifying key geometric parameters, L_f, F_g, F_w, and V_f across a wide range of values as shown in Table 1. Sampling these parameter spaces enables the construction of a comprehensive dataset suitable for training predictive models. As discussed in Section 2, the 0 degree ply configuration serves as the baseline case for the modeling framework. These baseline simulations are validated through a combination of analytical predictions using the Halpin–Tsai model and the Reuss series formulations, as well as visual inspection of the simulated fiber and matrix microstructure. This validation process ensures that the generated data accurately captures the governing mechanics and provides a reliable foundation for model development.

In parallel, a second dataset was generated using the same automated workflow, varying the same geometric parameters as before, but with fiber angles assigned within $\theta \in [0°,\ 90°]$. This dataset captures a broader spectrum of microstructural variability and is intended for testing the generalization capability of the surrogate models. Unlike the baseline 0 degree cases, these angled configurations are

not used for training but rather serve as validation and application scenarios. Due to the computational expense associated with running full FEA for thousands of fiber angle combinations and manually validating results, this dataset highlights the necessity of the surrogate modeling approach. The combination of a targeted training dataset at 0 degrees and a broader set including randomized fiber orientations provides both accuracy in model calibration and coverage of geometrically diverse cases. This approach supports efficient property prediction across a wide range of composite configurations while reducing the computational cost associated with full finite element simulations.

Table 1: Key geometric parameters with respective ranges

Geometric Parameter	Variation Range
Fiber Length, (L_f)	5.0 – 40.0 mm
Fiber Discontinuity Gap (F_g)	0.1 – 4.0 mm
Fiber Width (F_w)	0.1 – 4.0 mm
Target Volume Fraction (V_f)	0.1 – 0.55

3.3 Surrogate Model Training and Application

To enable scalable and efficient prediction of effective mechanical properties across a wide range of fiber architectures, a surrogate modeling framework was developed. This framework is based on machine learning models trained exclusively on the high-fidelity simulation results from the 0 degree fiber orientation dataset. The surrogate combines direct regression models with a Classical Laminate Theory formulation to generalize predictions to arbitrary fiber angles, thereby significantly reducing the computational cost associated with full FEA runs. The surrogate model development begins with training three separate regression models to predict transverse modulus E_{22}, in-plane shear modulus G_{12}, and the Halpin–Tsai shape parameter ξ, which governs the longitudinal modulus E_{11} through a physics based equation. While E_{22} and G_{12} are directly predicted by regression models, the prediction of E_{11} requires an additional modeling step. This is due to complex load transfer mechanisms introduced by fiber discontinuities, which limit the ability of purely data driven models to directly capture the relationship between geometric parameters and the longitudinal modulus. Therefore, E_{11} is calculated using the Halpin-Tsai equation with the predicted value of ξ.

The input features for models include the fiber volume fraction, fiber gap length, fiber length, and fiber width. Random Forest Regression was selected due to its ability to capture nonlinear relationships, resistance to overfitting, and minimal hyperparameter sensitivity [16,17]. Each model was trained using standardized input features with an 80 to 20 training and testing split. Model performance was evaluated using the coefficient of determination R^2 and mean absolute error (MAE), with results showing high predictive accuracy and good agreement between model outputs and FEA data. Once trained, the regression models were coupled with Classical Laminate Theory to estimate global stiffness for fiber orientations beyond zero degrees. The predicted values of $E_{11}, E_{22},$ and G_{12} for the base 0 degree case were rotated using transformation matrices (Equations 5 through 7) to compute moduli for arbitrary fiber angles. This approach allows rapid estimation of in-plane moduli for any fiber angle without additional simulation, enabling efficient evaluation of a broad design space.

In addition to property prediction, the surrogate model is also used to detect erroneous data within the larger dataset of randomly oriented fiber configurations. When applied to this broader set, the surrogate helps identify cases that produce nonphysical results or exhibit large deviations from expected trends. These errors result from issues such as poor mesh quality, incorrect material assignment, or fiber placement failures, particularly in angled configurations where boundary conditions are more difficult to apply consistently. Anomalous cases are flagged and removed for further inspection, helping to ensure that only valid simulation results are used in future inverse design tasks. A representative instance of datapoint failure is visualized in Figure 2 showing improper assignment of fiber material to matrix regions, which would result in uncharacteristically high mechanical properties reported by FEA.

Through this entire process, the surrogate model not only accelerates property prediction but also ensures the reliability and physical consistency of the overall dataset.

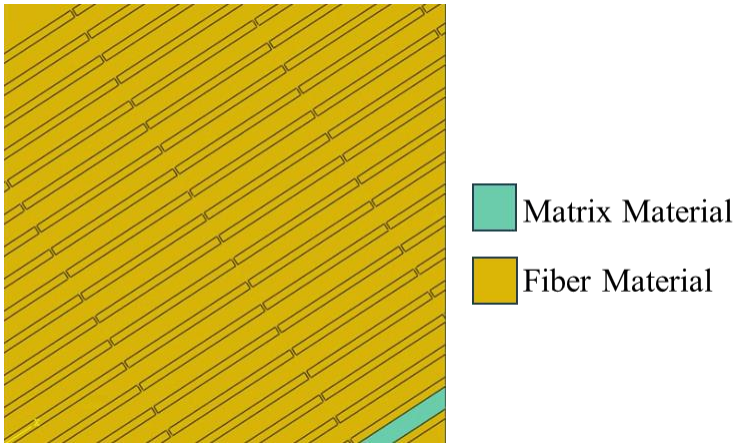

Figure 2: Angled fiber geometry generated with erroneous material assignment

4 RESULTS AND DISCUSSION

As discussed in section 3.1, Figure 3 displays the results of the convergence study used to initially size RVEs for accurate statistical representation. For each N as shown in Equation 9, E_{11}, E_{22}, and G_{12}, were calculated for a variety of permutations of geometric variables. Three representative cases are shown in the figure. As N increased from 1 to 7, all three moduli changed by less than 2% variation beyond $N = 3$ in every trial. Based on this result, $N = 3$ was selected as the minimum RVE size that balances convergence of effective properties with computational efficiency. While the surrogate is trained on baseline FEA simulations and relies on their accuracy, it is also leveraged as a secondary validator when applied to large datasets with random fiber angles. In this role, the surrogate acts as a filter, flagging FEA cases that yield nonphysical or inconsistent results typically due to meshing, fiber placement, or boundary condition errors thereby enforcing dataset quality and reliability.

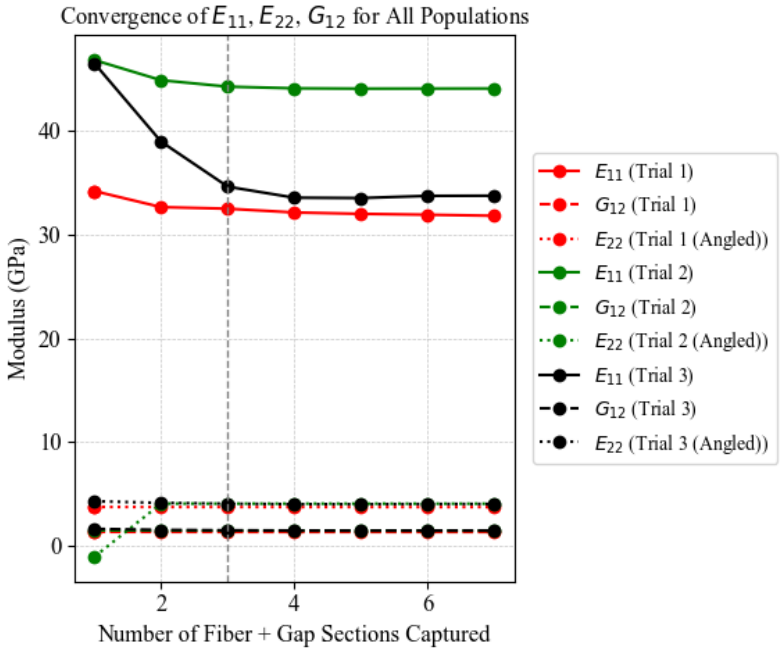

Figure 3: Moduli convergence with variation in number of simulated fiber and gap sections

Following the confirmation of RVE size, a dataset of 200 with 0 degree fiber orientations and varying geometric parameters was generated to train the Random Forest Regression model. Figure 4 presents parity plots illustrating the performance of each surrogate model. Figure 4c and 4d show predicted versus actual values for, E_{22}, and G_{12}, while Figures 4a and 4b display the predicted versus actual values for the Halpin-Tsai shape factor $\xi_{E_{11}}$, with Figure 4a showing the full range and Figure 4b focusing on a zoomed view to better illustrate accuracy in the relevant domain.

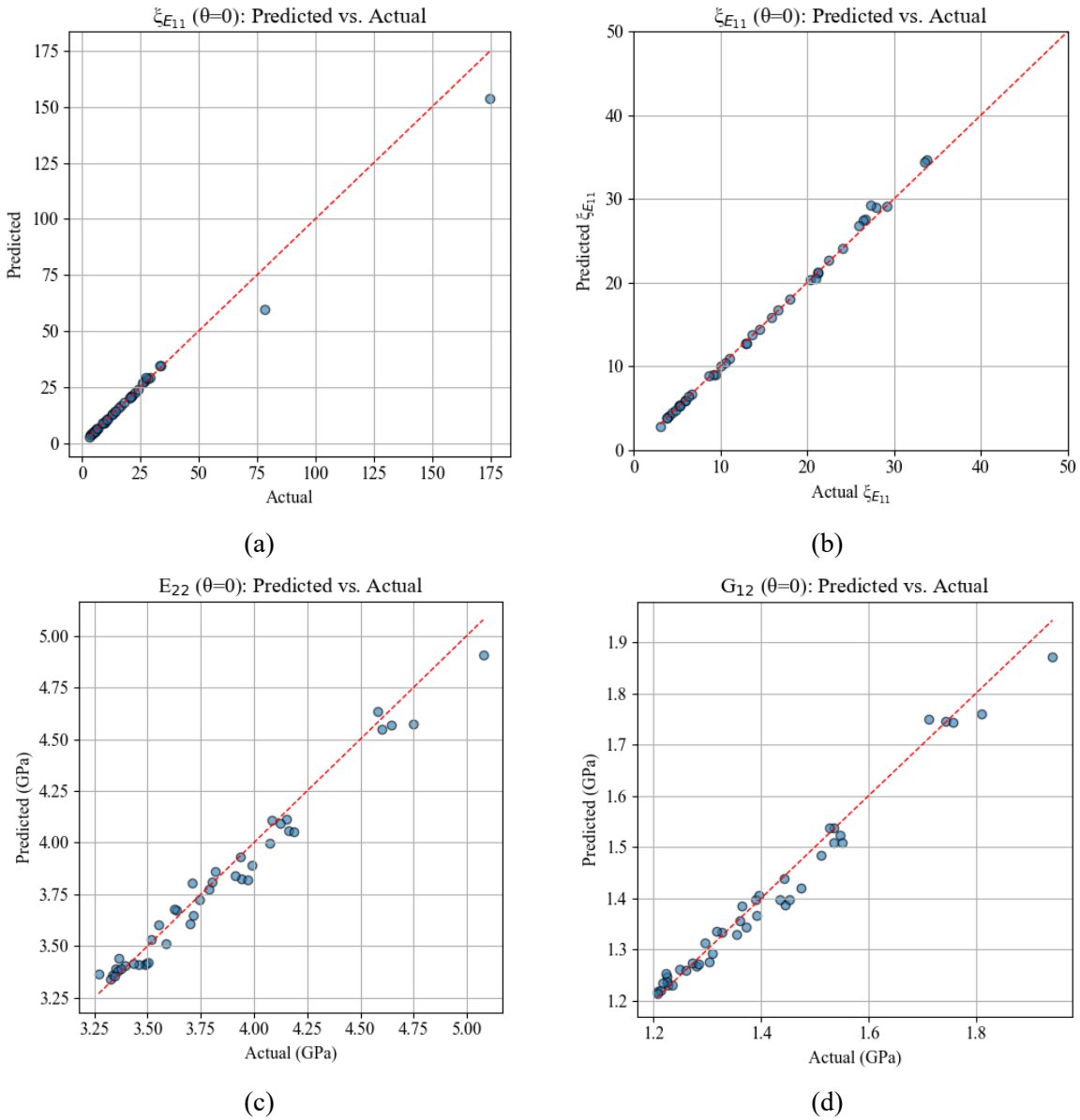

Figure 4: Random Forest parity plots for (a) $\xi_{E_{11}}$ (b) $\xi_{E_{11}}$ with range 0-50 (c) E_{22} and (d) G_{12}

While the full parity plot for $\xi_{E_{11}}$ in Figure 4a reveals a few outliers at higher values, their impact on the predicted E_{11} is minimal. Visual inspection of the corresponding data indicates that these outliers are associated with cases involving very high fiber lengths, where the resulting error in $\xi_{E_{11}}$ translates to deviation of less than 5% in the predicted modulus E_{11}. In the more relevant operational range shown in Figure 4b, the predicted and actual values of $\xi_{E_{11}}$ are nearly perfectly alignment, with overall $R^2 = 0.975$ and $MAE = 1.21$. The parity plots for E_{22}, and G_{12} also show tight clustering around the identity

line, demonstrating strong predictive accuracy. The computed performance metrics are $R^2 = 0.970$ and $MAE = 0.061$ GPa for E_{22} and $R^2 = 0.977$ with $MAE = 0.021$ GPa for G_{12}. Collectively, these results confirm that the Random Forest Regression models, when trained on data with $\theta = 0°$ fiber orientations, are capable of accurately predicting transverse and shear stiffness and of reliably estimating the shape factor $\xi_{E_{11}}$. This estimated shape factor can then be used in the Halpin-Tsai equation to produce a representative value of E_{11}. The high level of agreement between predicted and actual values supports the use of these models in CLT-based validation for fiber angles beyond 0 degrees.

Applying the trained regressors to geometries with fiber orientations different from 0 degrees revealed important insights into the behavior of aligned discontinuous fiber composites under CLT. Initially, any trial in which either E_{11} or E_{22} deviated by more than 10% from the FEA result was discarded. However, this percentage-based criterion incorrectly flagged cases where one modulus was inherently much larger than the other. For example, when fibers are closely aligned with the loading direction, E_{11} may be significantly higher than E_{22}, or when a moderate angle is selected, both moduli may approach their minimum values. In such cases, even a small absolute discrepancy (e.g. 0.5 GPa) in modulus can correspond to a relative error exceeding 10 %. To address this issue, a dual thresholding method was implemented. A trial was retained if the absolute error in E_{11} or E_{22} was below 3 GPa and only excluded if both the percent error exceeded 10% and the absolute error was greater than 3 GPa. This approach ensures that low-modulus cases with small absolute deviations are preserved, while still eliminating predictions with both large relative and large absolute errors.

While this dual-threshold filtering improves the retention of valid data points, it also accepts lower accuracy in directions with inherently low stiffness. This compromise is reasonable for highly anisotropic plies, where structural performance is primarily governed by axial stiffness. It is also applicable to symmetric configurations that exhibits low values of both E_{11} and E_{22}, where accurate predictions across all directions remains essential to fully characterize composite behavior. Across the validation set, the mean absolute error was 0.98 GPa for E_{11} and 2.2 GPa for E_{22}, suggesting a bias introduced by training with 0 degree fiber orientation which favors accurate prediction of E_{11}. Figures 5a and 5b display retained data points for E_{11} and E_{22}, respectively. In conjunction with these plots, Figure 5d illustrates that many of the erroneously discarded points were in fact valid E_{11} or E_{22} dominated cases, or intermediate cases, in which 0.5 GPa error translated to a > 10 % discrepancy.

In contrast, the surrogate model for shear modulus G_{12} performed poorly, with a mean absolute error of 1.35 GPa, even though typical G_{12}values remain below 4 GPa. As shown in Figure 5c, the model consistently overpredicts shear stiffness for aligned discontinuous fiber composites. Further analysis indicates that this discrepancy is not due to surrogate error but rather limitations in the underlying FEA data for rotated plies. Specifically, the simulated G_{12} values show minimal variation across fiber angles, clustering tightly around 1 GPa, despite expectations of greater anisotropy. This suggests that the global shear loading conditions in the current FEA configuration may not effectively engage the angle-dependent shear response of the fiber–matrix system. Importantly, this behavior highlights the surrogate model's utility in identifying and flagging erroneous or unphysical FEA outputs. While G_{12} accuracy remains a limitation, it does not impact the validation of E_{11} and E_{22}, which are the primary moduli of interest in inverse design applications.

Although validation based CLT does not perfectly match FEA results, it provides a reasonable confidence range for E_{11} and E_{22}. In practice, CLT and other analytical methods are inherently approximate and cannot fully capture the complexity of microscale fiber interactions. Nonetheless, their ability to bound trends observed in simulation data lends credibility to the FEA results and justifies their use in inverse modeling where longitudinal and transverse stiffness are primary targets.

Looking ahead, future work must focus on improving both the FEA shear loading methodology and the surrogate model's ability to predict lower stiffness values for E_{11} and E_{22}. This may include a wider range of off-axis fiber configurations and exploring hybrid modeling strategies that more

effectively integrate analytical theory, data-driven methods, and microscale physics.

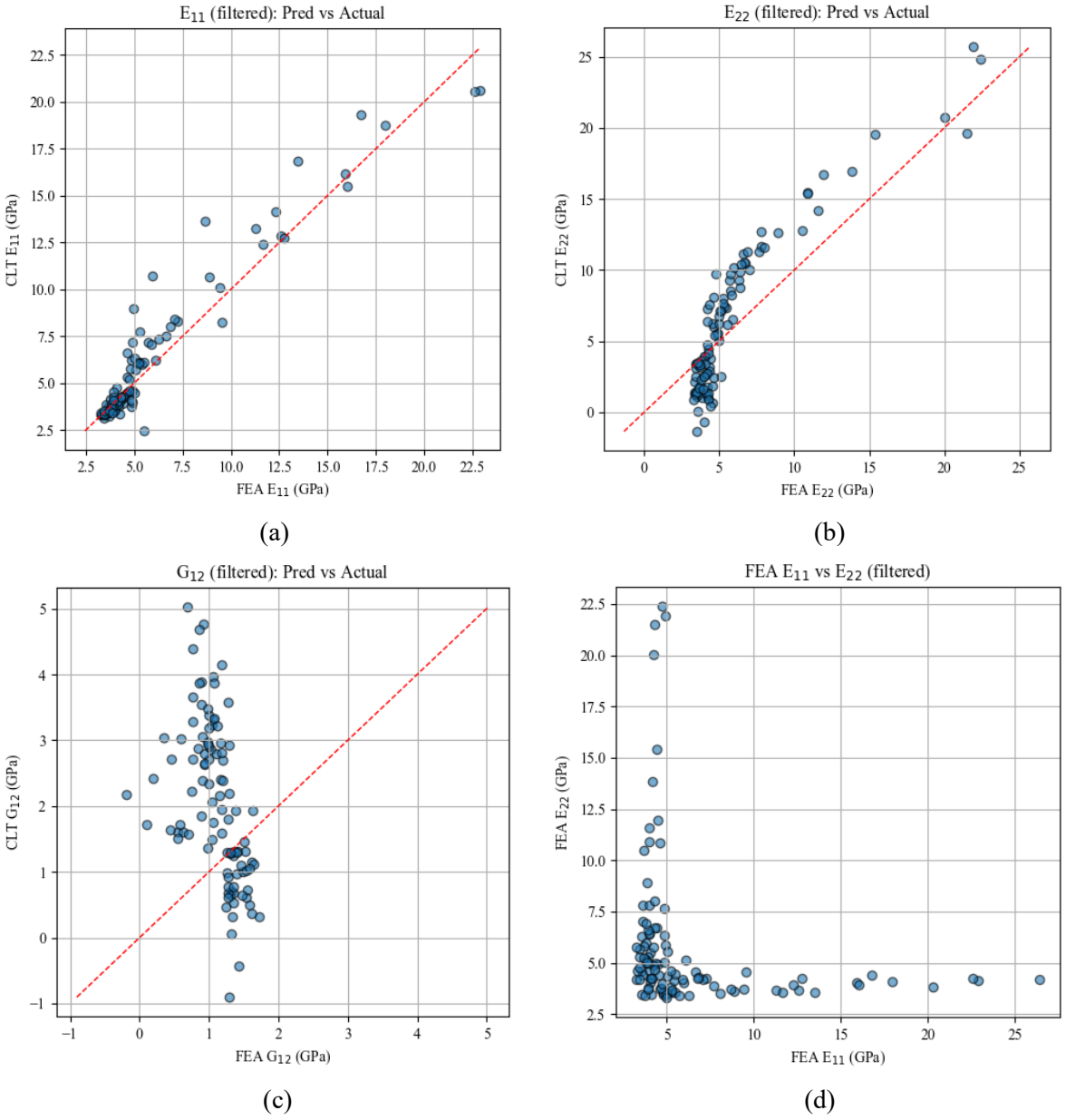

Figure 5: Parity plot of Surrogate Application (a) E_{11} (b) E_{22} (c) G_{12} (d) Filtered Fea Data E_{11}vs E_{22}

6 CONCLUSIONS

An automated, surrogate-model-driven pipeline was demonstrated for generating and validating 2D RVEs of aligned discontinuous carbon fiber composites. Convergence studies confirmed that three repeated fiber gap units are sufficient to capture representative moduli without the use of periodic boundary conditions, offering a practical balance between accuracy with computational efficiency. A training dataset of 200 samples with 0-degree fiber orientation was used to train three Random Forest Regression models to predict transverse modulus $E_{22,}$ shear modulus G_{12}, and the Halpin–Tsai shape factor $\xi_{E_{11}}$. The models achieved $R^2 > 0.97$and MAE < 0.07 GPa on held out test data. The trained regression models were integrated into a Classical Laminate Theory based validation approach, enabling

rapid prediction of longitudinal and transverse moduli across arbitrary fiber orientations. Predictions for most configurations remained within 10% of corresponding FEA results. In addition to property prediction, the surrogate model was applied during post-processing to identify and flag anomalous FEA outputs from large datasets with random fiber orientations. This filtering step removed results that deviated from expected physical behavior, improving consistency and reliability of the dataset.

Together, this approach reduces computational expense by several orders of magnitude while generating a high-fidelity dataset appropriate for inverse design tasks. By combining physics-informed micromechanics with machine learning, it offers a scalable approach for tailoring composite microstructures to target properties. Future work must focus on improving both the FEA shear loading strategy to correctly analyze angle-sensitive G_{12} behavior, and the surrogate model's precision in predicting low moduli E_{11} and E_{22} cases more precisely.

REFERENCES

[1] Cairns DS, Shramstad JD. Evaluation of Hand Lay-Up and Resin Transfer Molding in Composite Wind Turbine Blade Manufacturing. 2000. https://doi.org/10.2172/760737.
[2] Rajak DK, Wagh PH, Linul E. Manufacturing Technologies of Carbon/Glass Fiber-Reinforced Polymer Composites and Their Properties: A Review. Polymers 2021;13:3721. https://doi.org/10.3390/polym13213721.
[3] Feraboli P, Peitso E, Deleo F, Cleveland T, Stickler PB. Characterization of Prepreg-Based Discontinuous Carbon Fiber/Epoxy Systems. Journal of Reinforced Plastics and Composites 2009;28:1191–214. https://doi.org/10.1177/0731684408088883.
[4] Lewis C, Yavuz BO, Longana ML, Belnoue JP-H, Ramakrishnan KR, Ward C, et al. A Review on the Modelling of Aligned Discontinuous Fibre Composites. J Compos Sci 2024;8:318. https://doi.org/10.3390/jcs8080318.
[5] Tian W, Qi L, Chao X, Liang J, Fu M. Periodic boundary condition and its numerical implementation algorithm for the evaluation of effective mechanical properties of the composites with complicated micro-structures. Composites Part B: Engineering 2019;162:1–10. https://doi.org/10.1016/j.compositesb.2018.10.053.
[6] Tian W, Qi L, Zhou J, Liang J, Ma Y. Representative volume element for composites reinforced by spatially randomly distributed discontinuous fibers and its applications. Composite Structures 2015;131:366–73. https://doi.org/10.1016/j.compstruct.2015.05.014.
[7] Landel RF, Nielsen LE. Mechanical Properties of Polymers and Composites. 2nd ed. Boca Raton: CRC Press; 1993. https://doi.org/10.1201/b16929.
[8] Shokrieh MM, Moshrefzadeh-Sani H. On the constant parameters of Halpin-Tsai equation. Polymer 2016;106:14–20. https://doi.org/10.1016/j.polymer.2016.10.049.
[9] Hadi AE, Hamdan MHM, Siregar JP, Junid R, Tezara C, Irawan AP, et al. Application of Micromechanical Modelling for the Evaluation of Elastic Moduli of Hybrid Woven Jute–Ramie Reinforced Unsaturated Polyester Composites. Polymers (Basel) 2021;13:2572. https://doi.org/10.3390/polym13152572.
[10] Affdl JCH, Kardos JL. The Halpin-Tsai equations: A review. Polymer Engineering & Sci 1976;16:344–52. https://doi.org/10.1002/pen.760160512.
[11] Agarwal BD, Broutman LJ, Chandrashekhara K. Analysis and performance of fiber composites. 3rd ed. Hoboken, N.J.: John Wiley; 2006.
[12] Hull D, Clyne TW. An Introduction to Composite Materials. 2nd ed. Cambridge University Press; 1996. https://doi.org/10.1017/CBO9781139170130.
[13] Nettles AT. Basic mechanics of laminated composite plates 1994.
[14] Liu H, Zeng D, Li Y, Jiang L. Development of RVE-embedded solid elements model for predicting effective elastic constants of discontinuous fiber reinforced composites. Mechanics of Materials 2016;93:109–23. https://doi.org/10.1016/j.mechmat.2015.10.011.

[15] Taheri-Behrooz F, Pourahmadi E. A 3D RVE model with periodic boundary conditions to estimate mechanical properties of composites. Structural Engineering and Mechanics 2019;72:713–22. https://doi.org/10.12989/SEM.2019.72.6.713.
[16] Grömping U. Variable Importance Assessment in Regression: Linear Regression versus Random Forest. The American Statistician 2009;63:308–19. https://doi.org/10.1198/tast.2009.08199.
[17] Segal MR. Machine Learning Benchmarks and Random Forest Regression 2004.

ICCM24
AUGUST 4-8, 2025
BALTIMORE CONVENTION CENTER
BALTIMORE, MARYLAND, USA

No Technical Paper Submission for:

Francisco Chinesta

Multiscale and Multiphysics Modelling and Characterisation of Structural Batteries

Professor Leif E. Asp

ICCM24
Baltimore, August 2025



Example – Aircraft Interior



Image: Prof Emile Greenhalgh Imperial College London

Example – Aircraft Interior

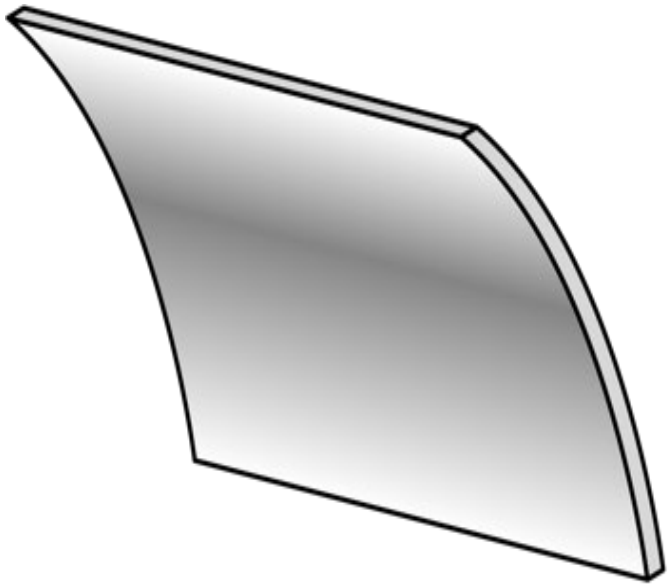

VS.

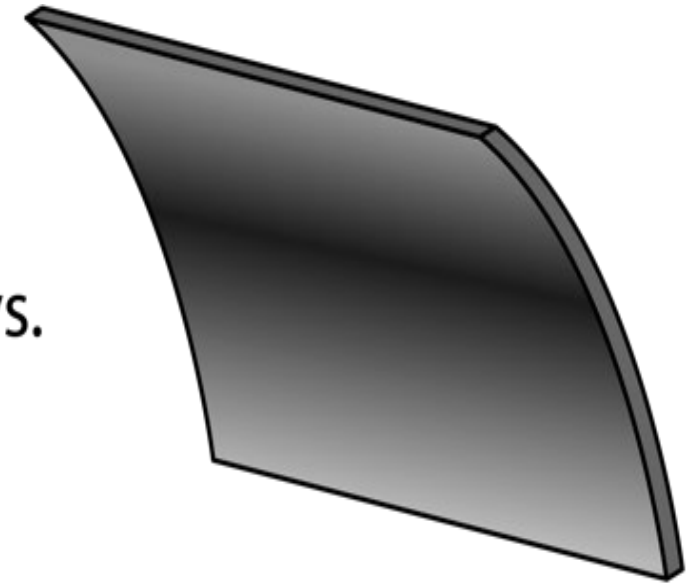

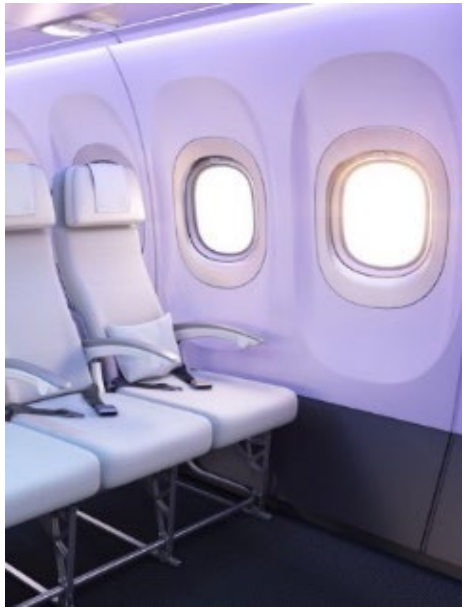

Interior panel, 2 x 1.5 m

Glass fiber / phenolic, mass 2.8 kg

Li-ion battery, mass 0.63 kg

Multifunctional interior panel, 2 x 1.5 m

Structural battery, mass 1.13 kg

Weight saving 67 %

Johannisson *et al*, *Multifunc Mater*, 2, 2019

The All-Carbon Fibre Based Structural Battery

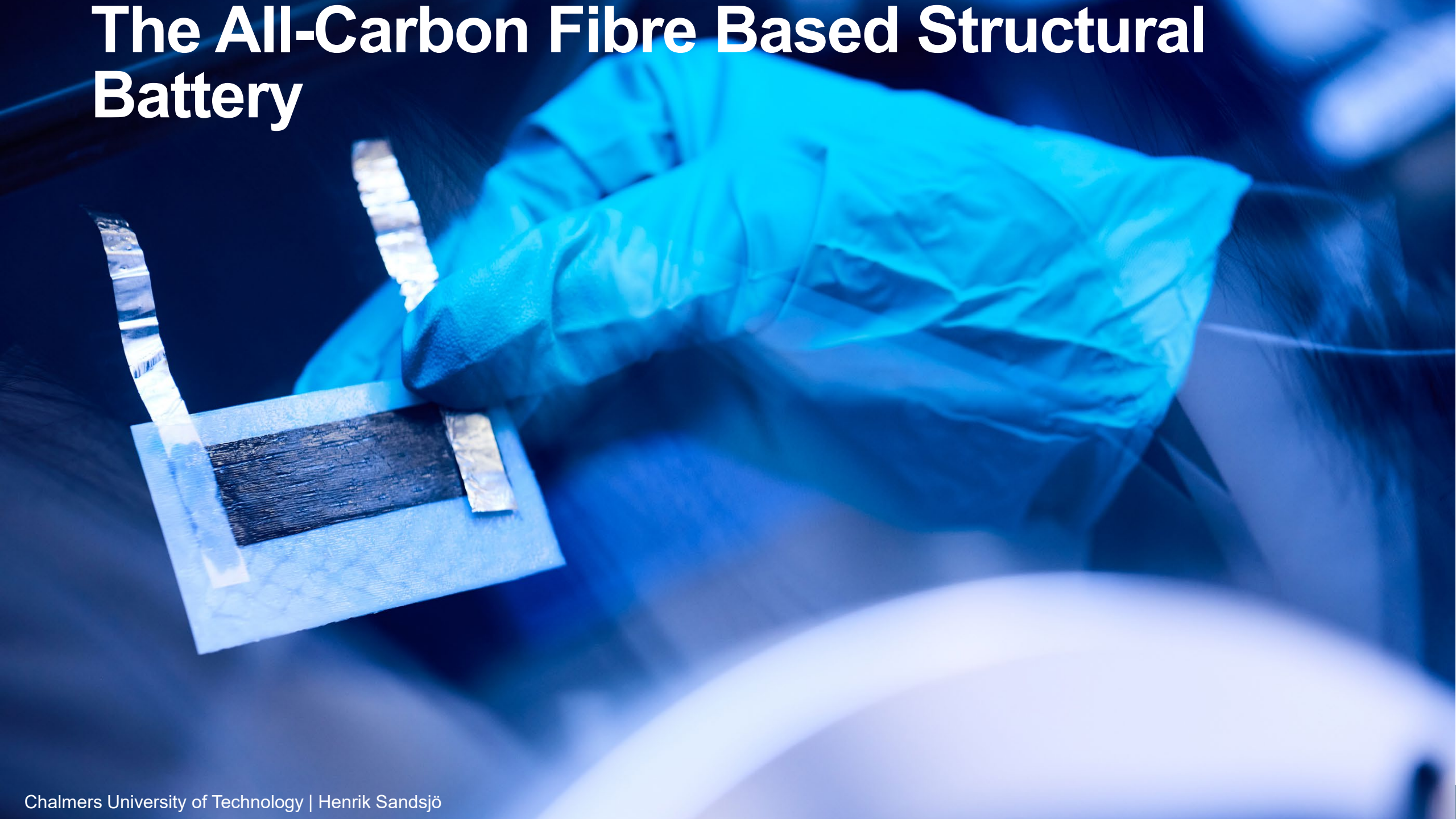

Chalmers University of Technology | Henrik Sandsjö

A laminated structural battery composite

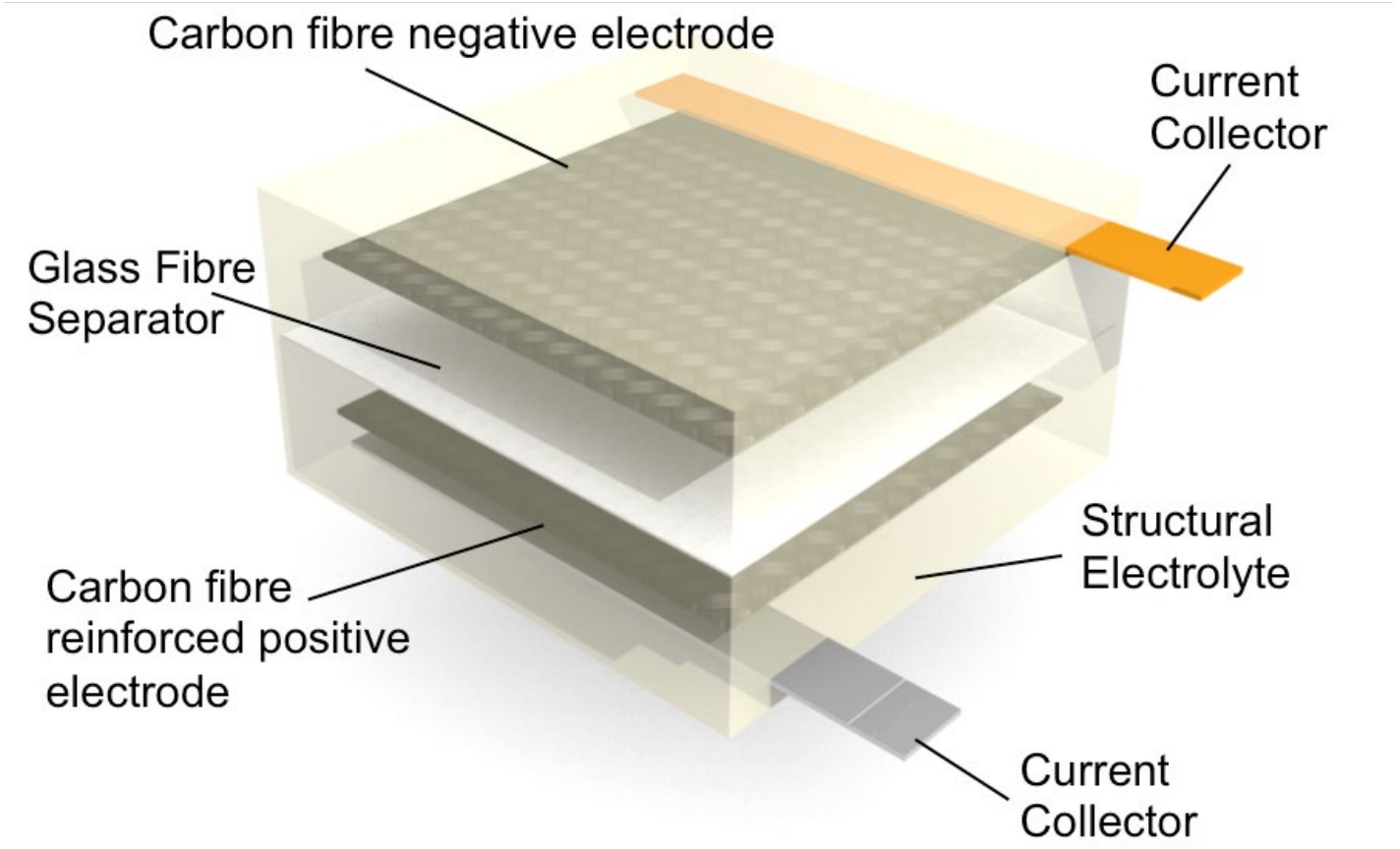

Asp et al. *Funct. Comp. Struct.* **1**, 2019, 042001

Resin-infused cells



The positive electrode

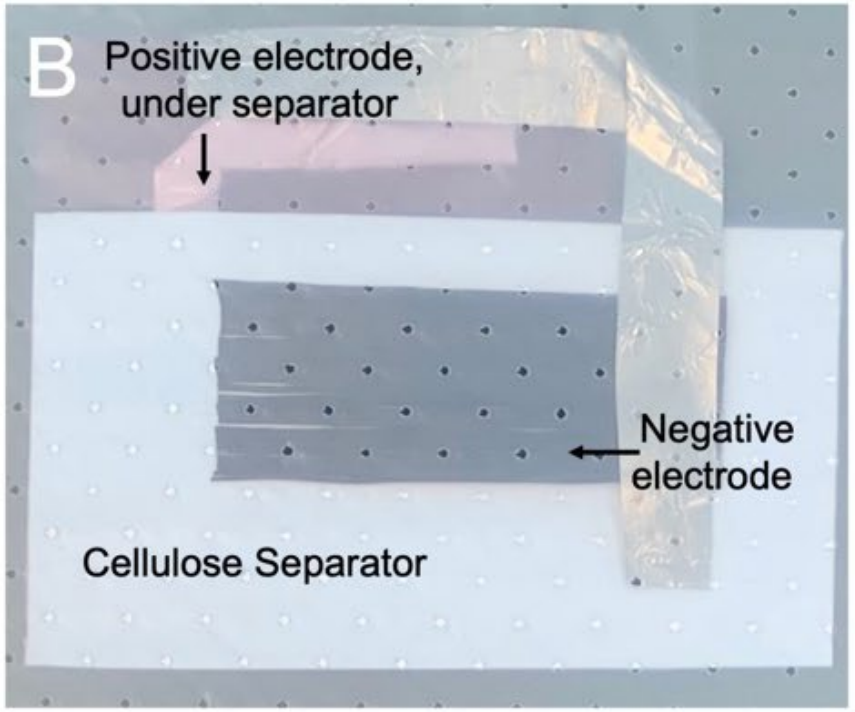

Bagged cell before infusion

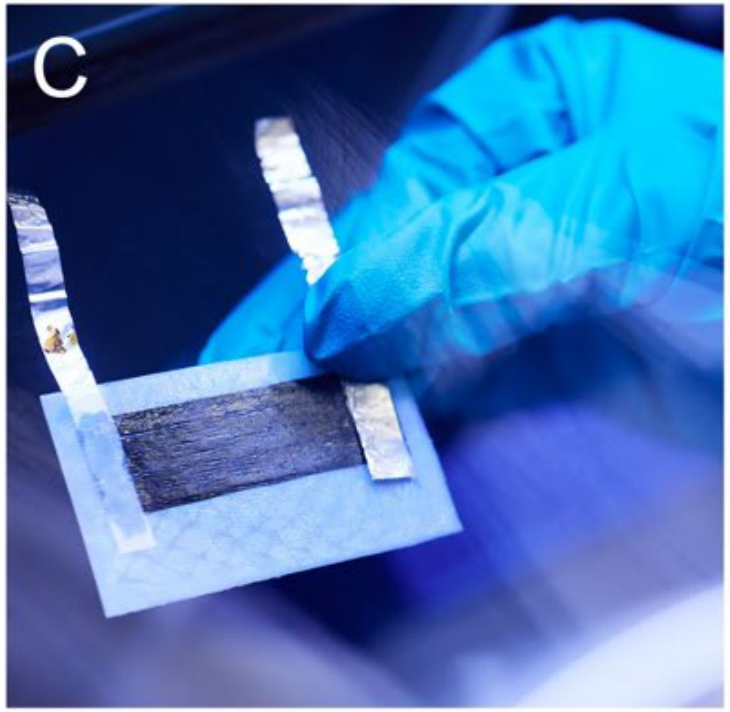

Cured cell

Siraj et al. *Adv. Energy Sustainability Res.*, 2023, 2300109.
Chaudhary et al. *Adv. Mater.* 2024, 2409725

Multifunctional Performance

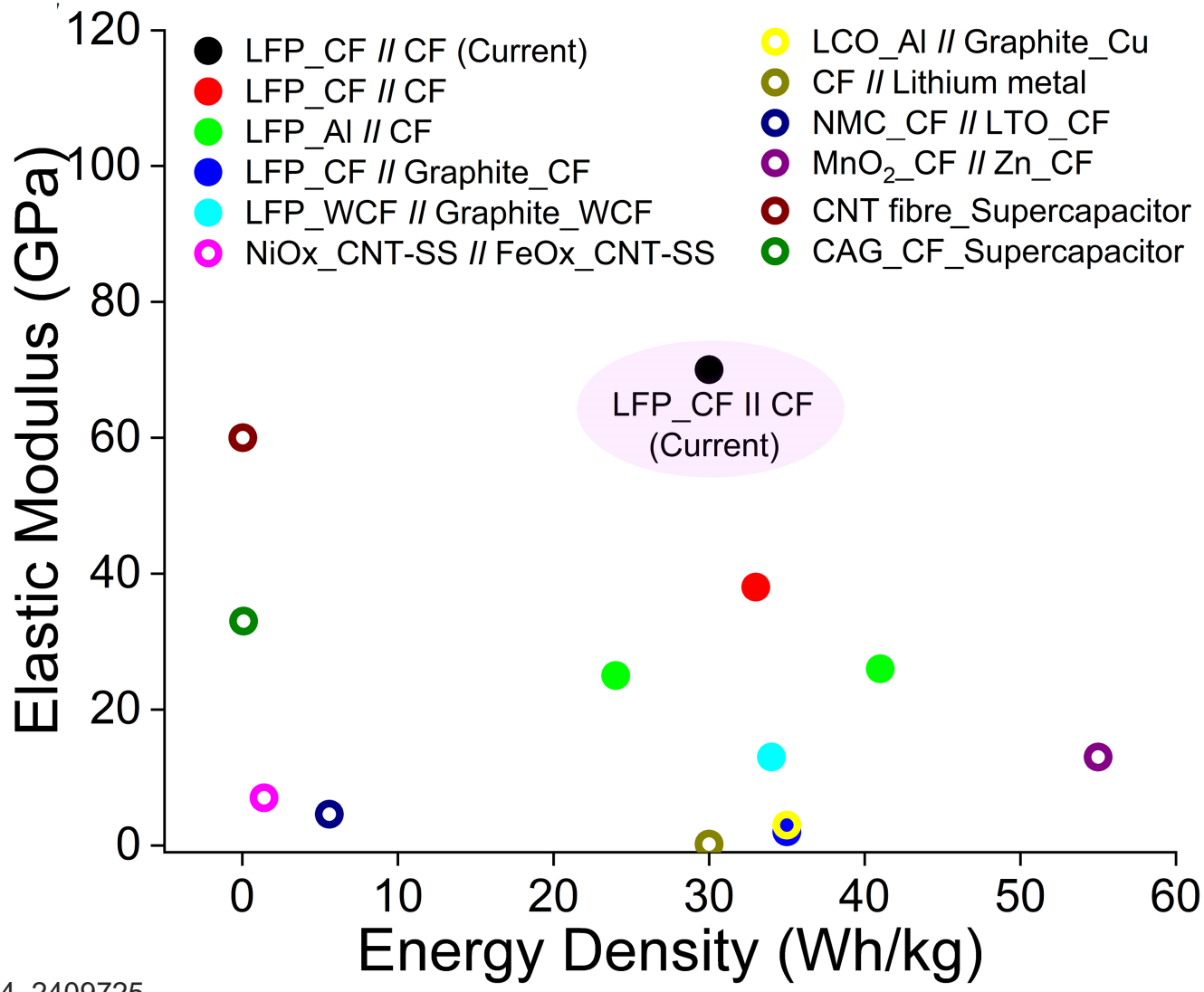

Chaudhary et al. *Adv. Mater.* 2024, 2409725

The Carbon Fiber-Based Electrodes



Chalmers University of Technology | Henrik Sandsjö

Capacity and Coulombic Efficiency of Carbon Fiber Negative Electrodes

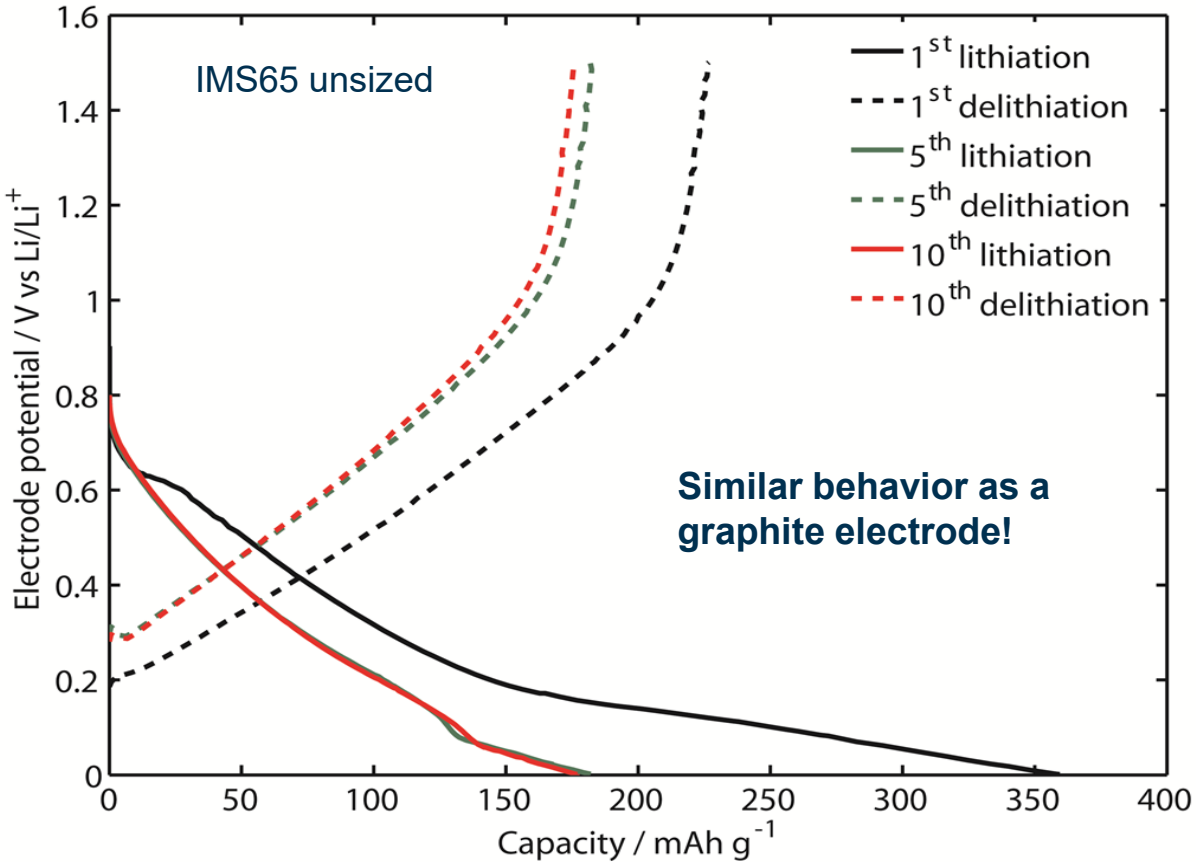

Kjell et al, J Electrochem Soc., 2011

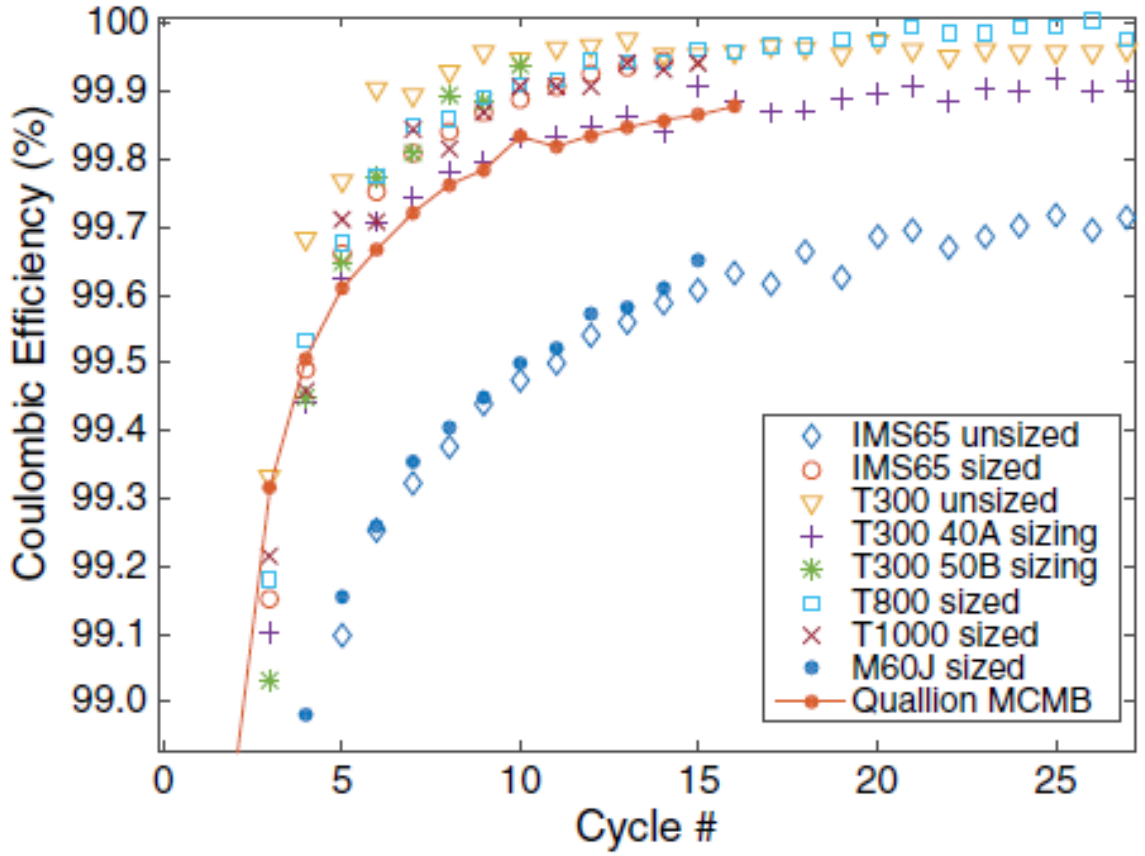

Hagberg et al, ECS., 2016

Effects of lithiation of the Carbon Fiber

Negative half-cell

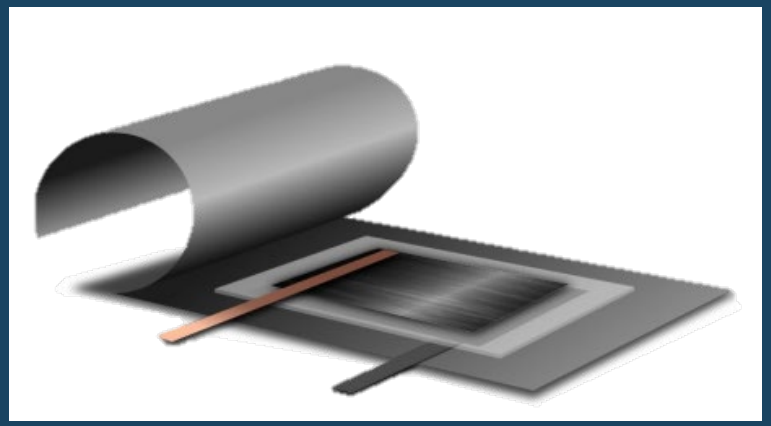

Image courtesy: Marcus Johansen

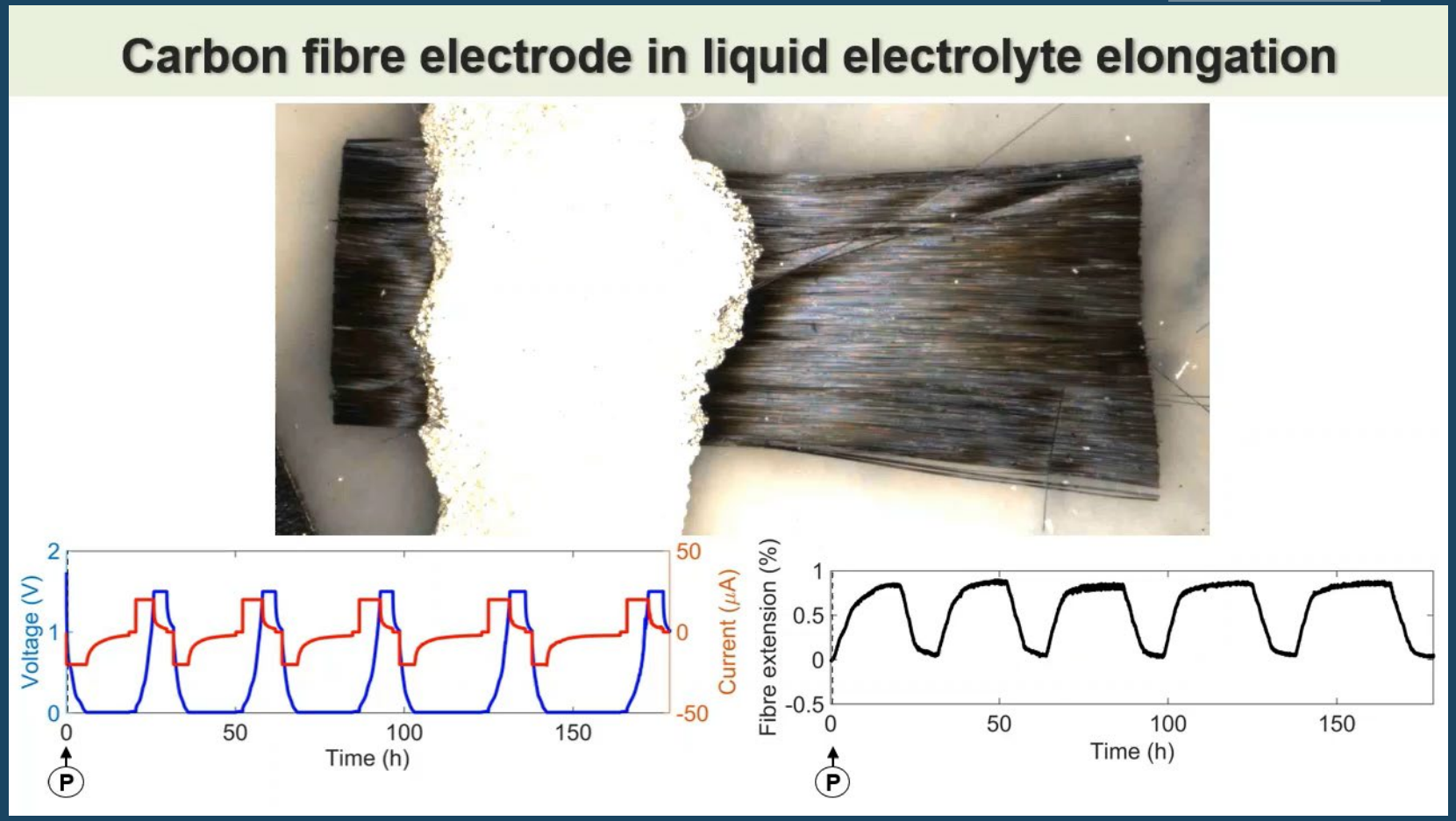

Carlstedt et al. *Composites Science and Technology* 2022

Effect of lithiation on carbon fibre volume and moduli

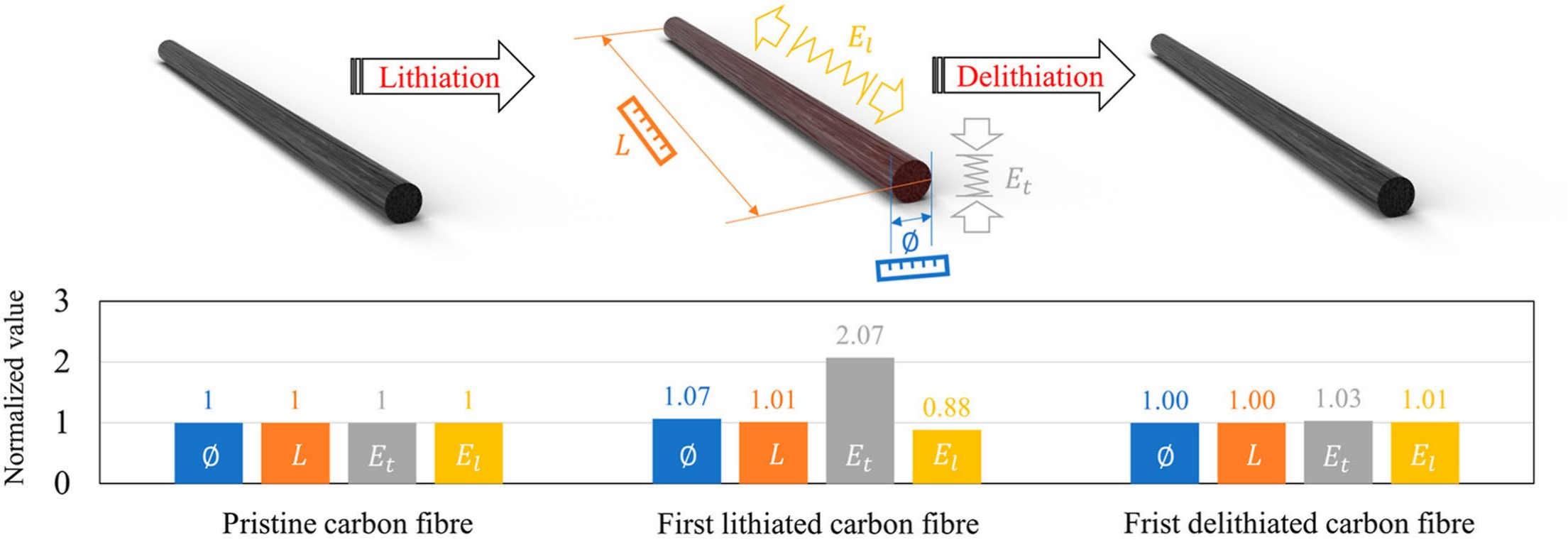

Duan et al. *Carbon* 2021

An electro-chemo-mechanically coupled material

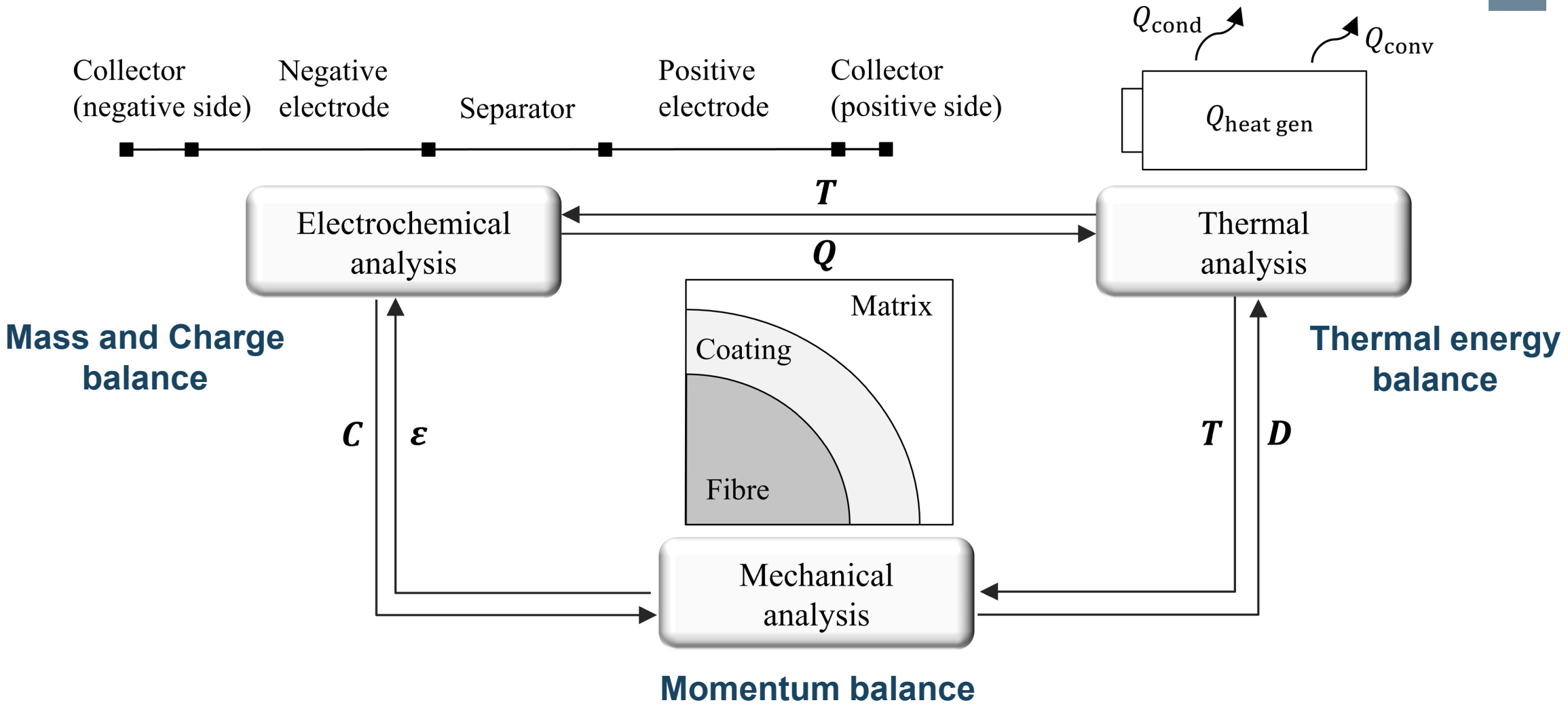

Carlstedt et al. ICCM22, 2019

The negative half-cell

Electro-chemo-mechanically coupled computational modelling of structural batteries

D. Carlstedt, K. Runesson, F. Larsson, J. Xu and L.E. Asp

Multifunctional Materials, Vol. 3, 2020

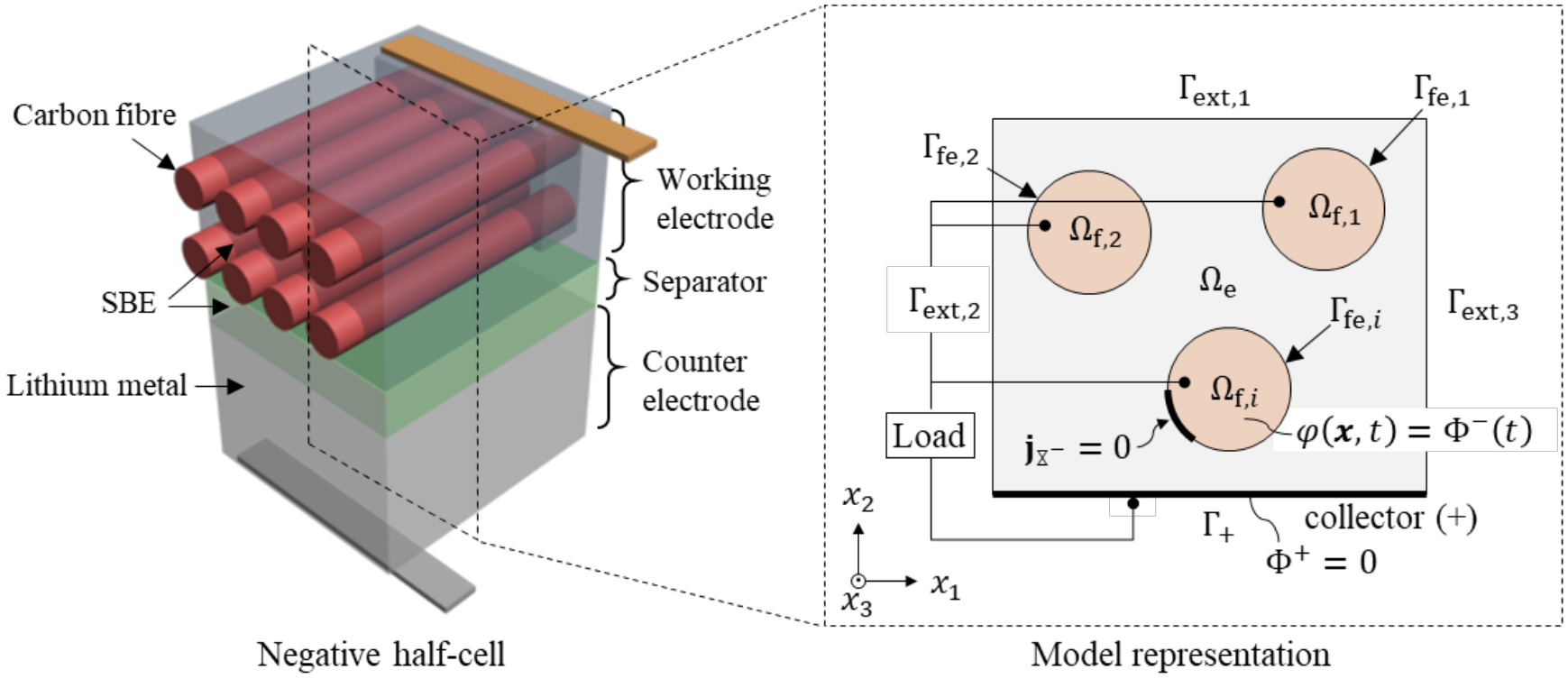

Negative half-cell

Model representation

Half-cell: Governing equations

Electrolyte (SBE)

(M) $$-\boldsymbol{\sigma} \cdot \boldsymbol{\nabla} = \mathbf{0} \text{ in } \Omega_\mathrm{e} \times \mathbb{R}^+$$

(E) $$-\boldsymbol{i}_\mathrm{MAX} \cdot \boldsymbol{\nabla} = 0 \text{ in } \Omega_\mathrm{e} \times \mathbb{R}^+$$

(C) $$-\partial_t c_\mathrm{Li} - \boldsymbol{j}_\mathrm{Li} \cdot \boldsymbol{\nabla} = 0 \text{ in } \Omega_\mathrm{e} \times \mathbb{R}^+$$

(C) $$-\partial_t c_\mathrm{X} - \boldsymbol{j}_\mathrm{X} \cdot \boldsymbol{\nabla} = 0 \text{ in } \Omega_\mathrm{e} \times \mathbb{R}^+$$

Fibres

(M) $$-\boldsymbol{\sigma} \cdot \boldsymbol{\nabla} = \mathbf{0} \text{ in } \Omega_\mathrm{f} \times \mathbb{R}^+$$

(C) $$-\partial_t c_\mathrm{Li} - \boldsymbol{j}_\mathrm{Li} \cdot \boldsymbol{\nabla} = 0 \text{ in } \Omega_\mathrm{f} \times \mathbb{R}^+$$

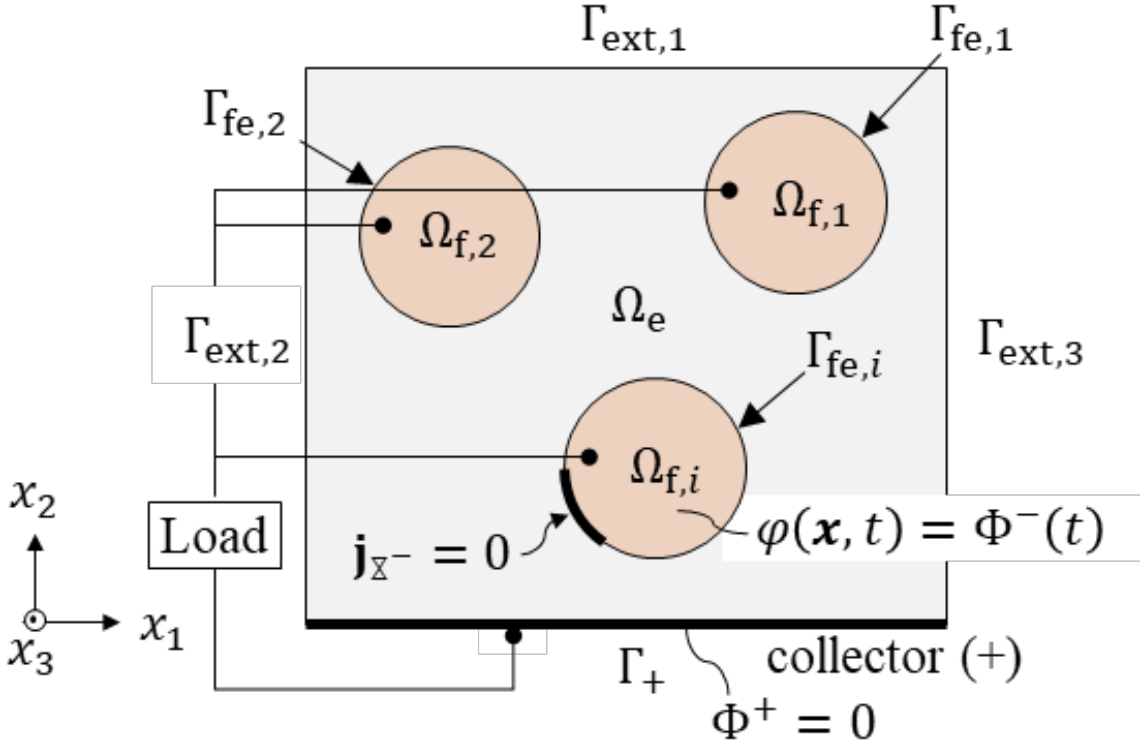

*(M)echanical, (E)lectrical and (C)hemical response

Half-cell: Implementation

Strong format + constitutive relations + BCs

Electrolyte (SBE)

$$-\boldsymbol{\sigma}\cdot\boldsymbol{\nabla}=\mathbf{0}\ \text{in}\ \Omega_\mathrm{e}\times\mathbb{R}^+$$

$$-\boldsymbol{i}_\mathrm{MAX}\cdot\boldsymbol{\nabla}=0\ \text{in}\ \Omega_\mathrm{e}\times\mathbb{R}^+$$

$$-\partial_t c_\mathrm{Li}-\boldsymbol{j}_\mathrm{Li}\cdot\boldsymbol{\nabla}=0\ \text{in}\ \Omega_\mathrm{e}\times\mathbb{R}^+$$

$$-\partial_t c_\mathrm{X}-\boldsymbol{j}_\mathrm{X}\cdot\boldsymbol{\nabla}=0\ \text{in}\ \Omega_\mathrm{e}\times\mathbb{R}^+$$

Fibre

$$-\boldsymbol{\sigma}\cdot\boldsymbol{\nabla}=\mathbf{0}\ \text{in}\ \Omega_\mathrm{f}\times\mathbb{R}^+$$

$$-\partial_t c_\mathrm{Li}-\boldsymbol{j}_\mathrm{Li}\cdot\boldsymbol{\nabla}=0\ \text{in}\ \Omega_\mathrm{f}\times\mathbb{R}^+$$

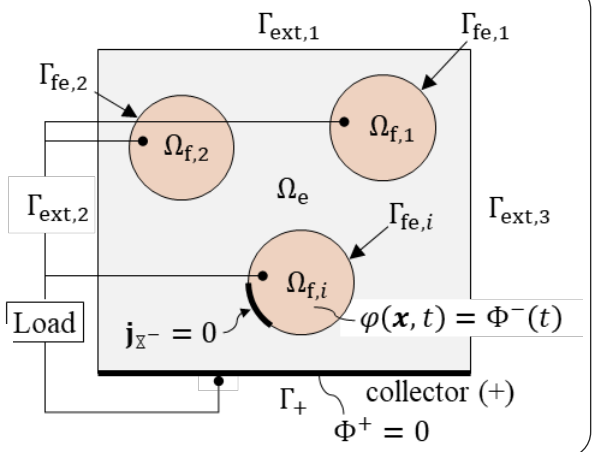

COMSOL Multiphysics

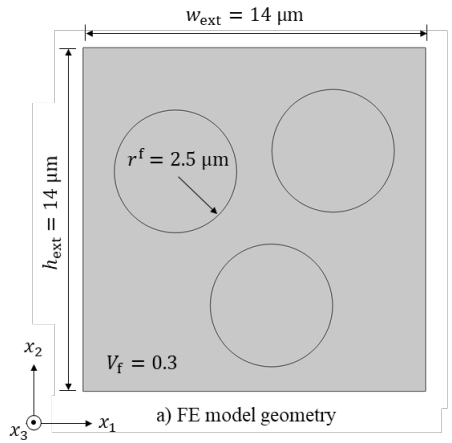

a) FE model geometry

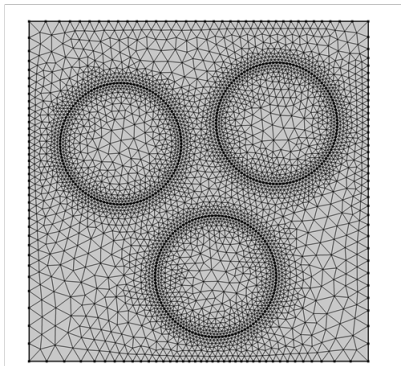

b) Element mesh

Weak format (mixed formulation)

Potentiostatic cycling

$$\int_{\Omega_\mathrm{f}\cup\Omega_\mathrm{e}}\boldsymbol{\sigma}:\boldsymbol{\epsilon}[\delta\boldsymbol{u}]\,\mathrm{d}V=0\qquad\forall\delta\boldsymbol{u}\in\hat{\mathbb{U}}^0$$

$$\int_{\Omega_\mathrm{e}}\boldsymbol{i}_\mathrm{MAX}\cdot\boldsymbol{\nabla}[\delta\varphi]\,\mathrm{d}V+\int_{\Gamma_\mathrm{fe}}i_{\mathrm{Max},n}\delta\varphi\,\mathrm{d}S-\int_{\Gamma_+}i_{\mathrm{Max},n}\delta\varphi\,\mathrm{d}S=0\qquad\forall\delta\varphi\in\hat{\mathbb{F}}^0$$

$$-\frac{1}{\Delta t}\int_{\Omega_\mathrm{f}\cup\Omega_\mathrm{e}}\left[c_\mathrm{Li}-{}^{n-1}c_\mathrm{Li}\right]\delta\mu_\mathrm{Li}\,\mathrm{d}V+\int_{\Omega_\mathrm{f}\cup\Omega_\mathrm{e}}\boldsymbol{j}_\mathrm{Li}\cdot\boldsymbol{\nabla}[\delta\mu_\mathrm{Li}]\,\mathrm{d}V$$

$$+\int_{\Gamma_\mathrm{fe}}j_{\mathrm{Li},n}\,[\![\delta\mu_\mathrm{Li}]\!]\,\mathrm{d}S-\int_{\Gamma_+}j_{\mathrm{Li},n}\,\delta\mu_\mathrm{Li}\,\mathrm{d}S=0\qquad\forall\delta\mu_\mathrm{Li}\in\hat{\mathbb{M}}^0_\mathrm{Li}$$

$$-\frac{1}{\Delta t}\int_{\Omega_\mathrm{e}}\left[c_\mathrm{X}-{}^{n-1}c_\mathrm{X}\right]\delta\mu_\mathrm{X}\,\mathrm{d}V+\int_{\Omega_\mathrm{e}}\boldsymbol{j}_\mathrm{X}\cdot\boldsymbol{\nabla}[\delta\mu_\mathrm{X}]\,\mathrm{d}V=0\qquad\forall\delta\mu_\mathrm{X}\in\hat{\mathbb{M}}^0_\mathrm{X}$$

$$\int_{\Omega_\mathrm{f}\cup\Omega_\mathrm{e}}\left[\mu^\mathrm{en}_\mathrm{Li}-\mu_\mathrm{Li}\right]\delta c_\mathrm{Li}\,\mathrm{d}V=0\qquad\forall\delta c_\mathrm{Li}\in\mathbb{L}_2(\Omega_\mathrm{f}\cup\Omega_\mathrm{e})$$

$$\int_{\Omega_\mathrm{e}}\left[\mu^\mathrm{en}_\mathrm{X}-\mu_\mathrm{X}\right]\delta c_\mathrm{X}\,\mathrm{d}V=0\qquad\forall\delta c_\mathrm{X}\in\mathbb{L}_2(\Omega_\mathrm{e})$$

Electro-chemo-mechanical analysis

Structural battery design

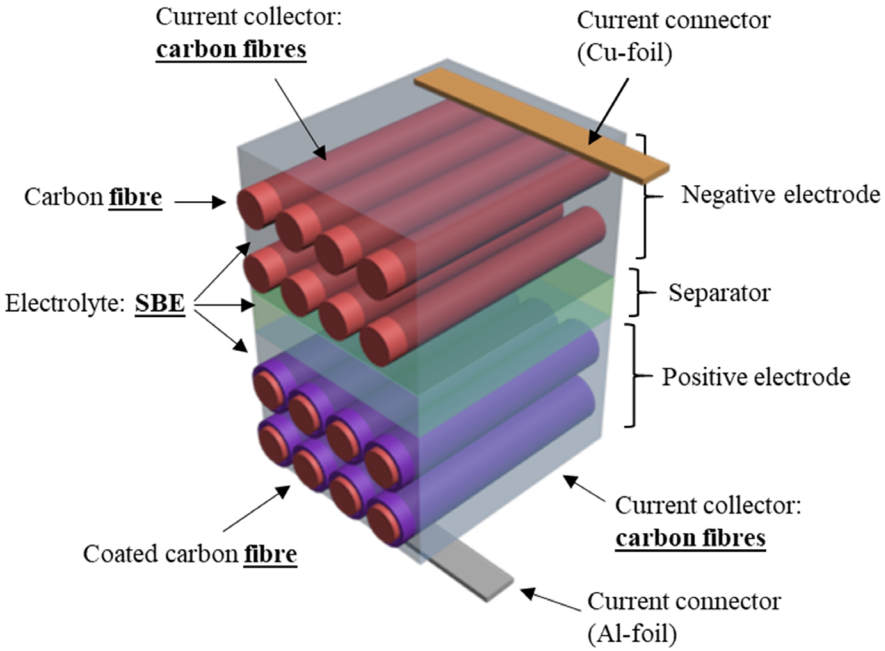

Electro-chemo-mechanical framework

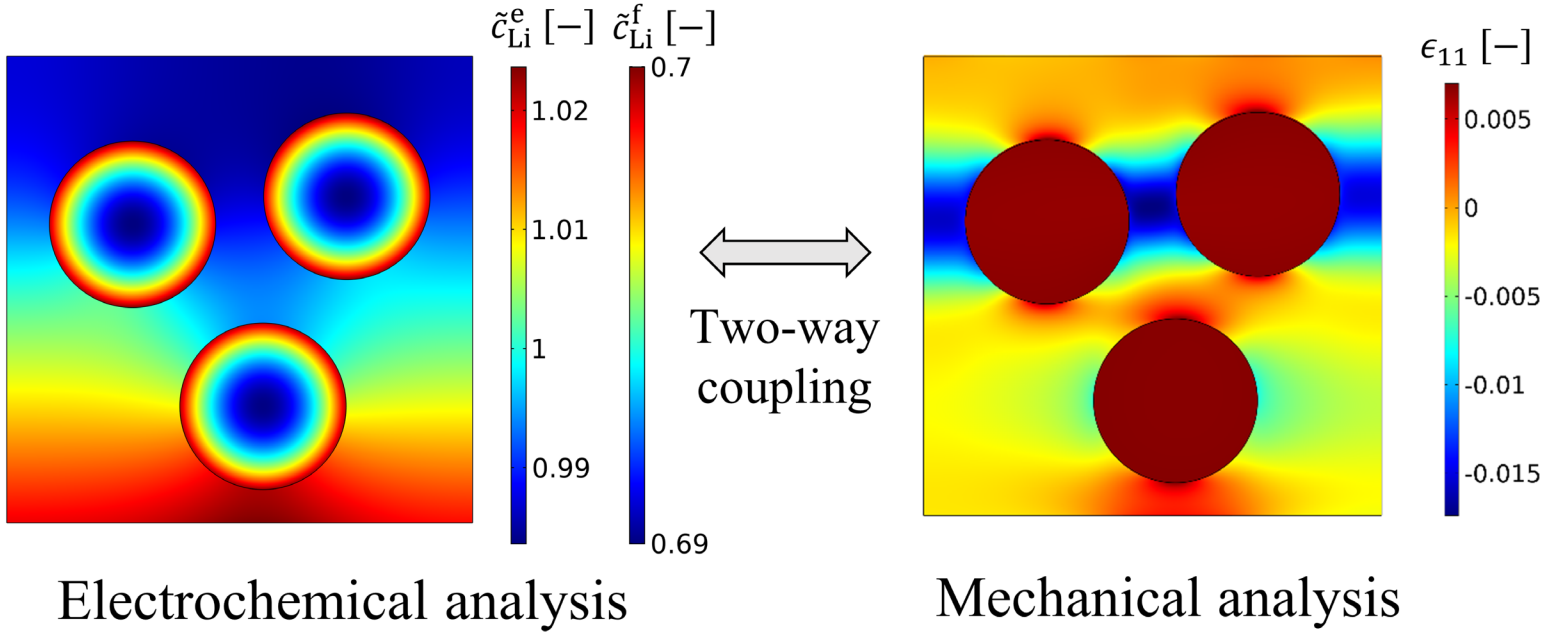

Carlstedt et al. *Multifunc. Mater.* **3**, 2020, 045002

Electro-chemo-mechanical analysis

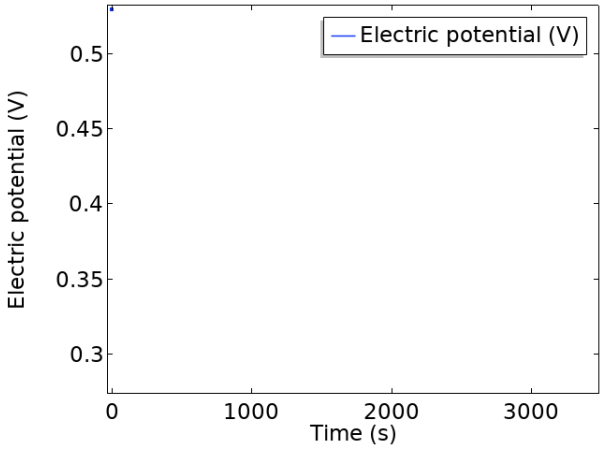

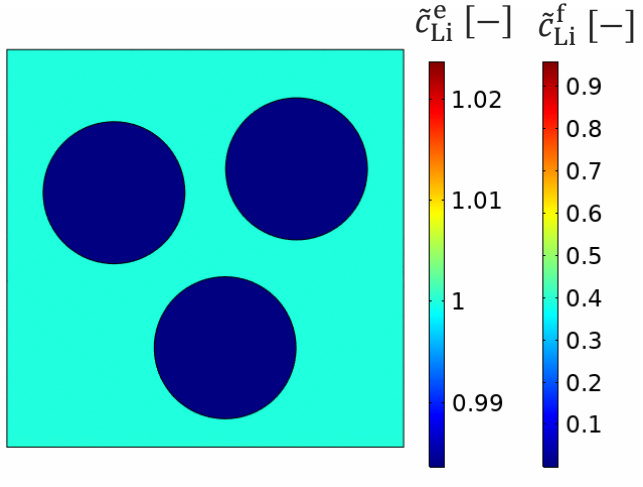

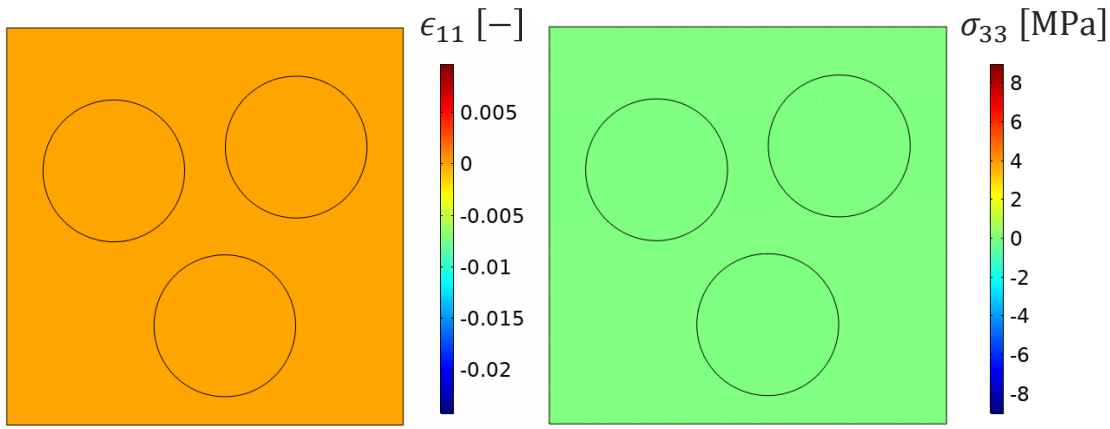

Electrochemical analysis

Two-way coupling

Mechanical analysis

Carlstedt et al. *Multifunc. Mater.* **3**, 2020, 045002

Multiphysics analysis – Internal stresses

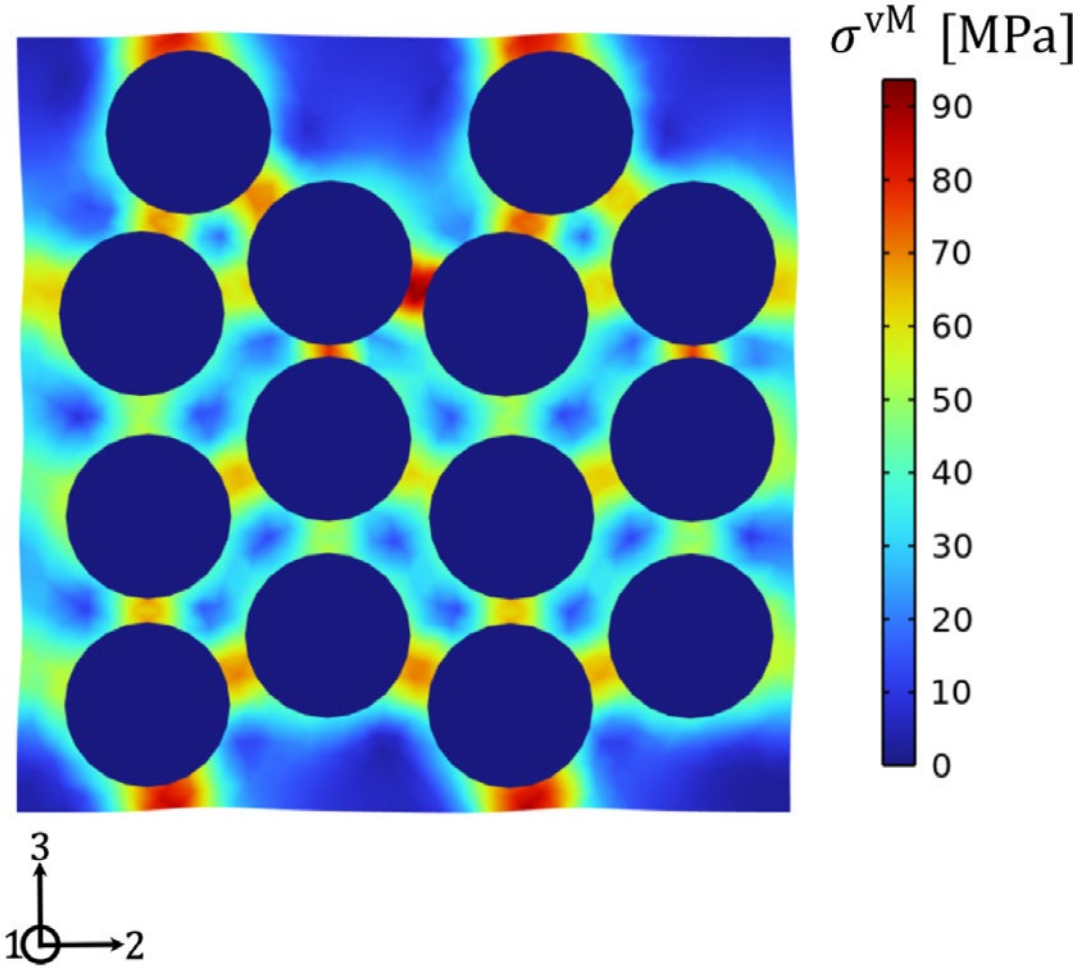

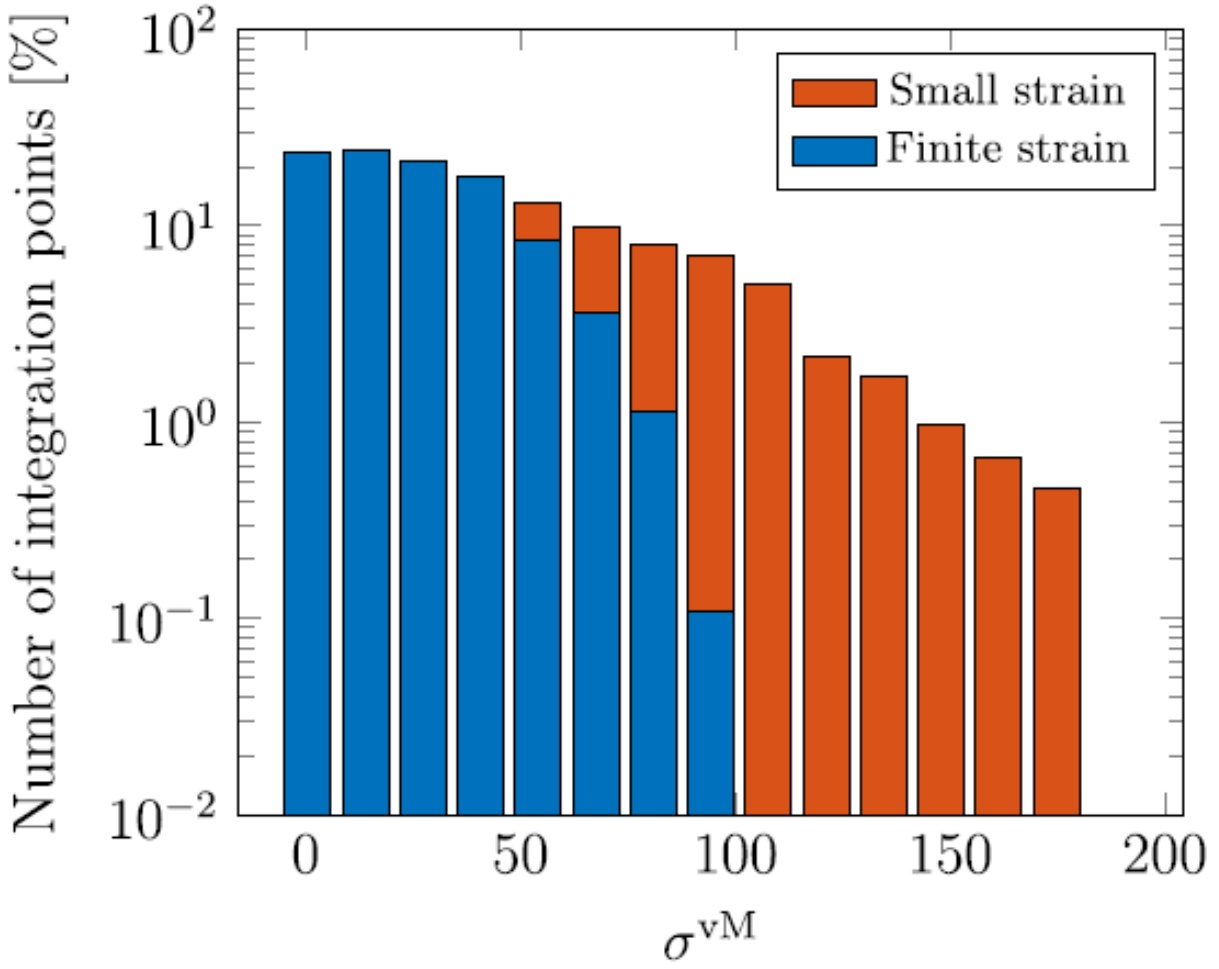

Larsson et al. *Compos. Sci. Technol*. 2023

Coupling between mechanical stress and chemical potential

Example: fibres (active electrode material)

Stresses

$$\boldsymbol{\sigma} = \mathbf{E} : \left[\boldsymbol{\epsilon}[\boldsymbol{u}] - \boldsymbol{\epsilon}^{\mathrm{ch}}(c_{\mathrm{Li}})\right]$$

Mass flux

$$\boldsymbol{j}_{\mathrm{Li}} = -\boldsymbol{M}_{\mathrm{Li}} \cdot \boldsymbol{\nabla}\mu_{\mathrm{Li}}$$

Coupling effects

Chemical potential

$$\text{where } \mu_{\mathrm{Li}} = \boldsymbol{\alpha}^{\mathrm{ch}} : \boldsymbol{\sigma}(\boldsymbol{\epsilon}, c_{\mathrm{Li}}) + \mu^0_{\mathrm{Li}} + k_{\mathrm{B}}\theta_0 \log\left(\frac{f_{\mathrm{Li}}(c_{\mathrm{Li}})c_{\mathrm{Li}}}{f^0_{\mathrm{Li}}c^0_{\mathrm{Li}}}\right)$$

Carlstedt et al. *Multifunc. Mater.* **3**, 2020, 045002

Effect of Mechanical Load on Voltage

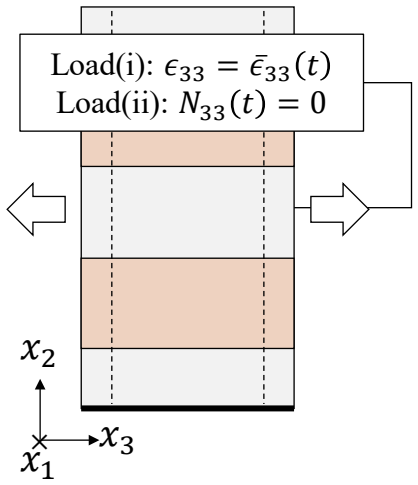

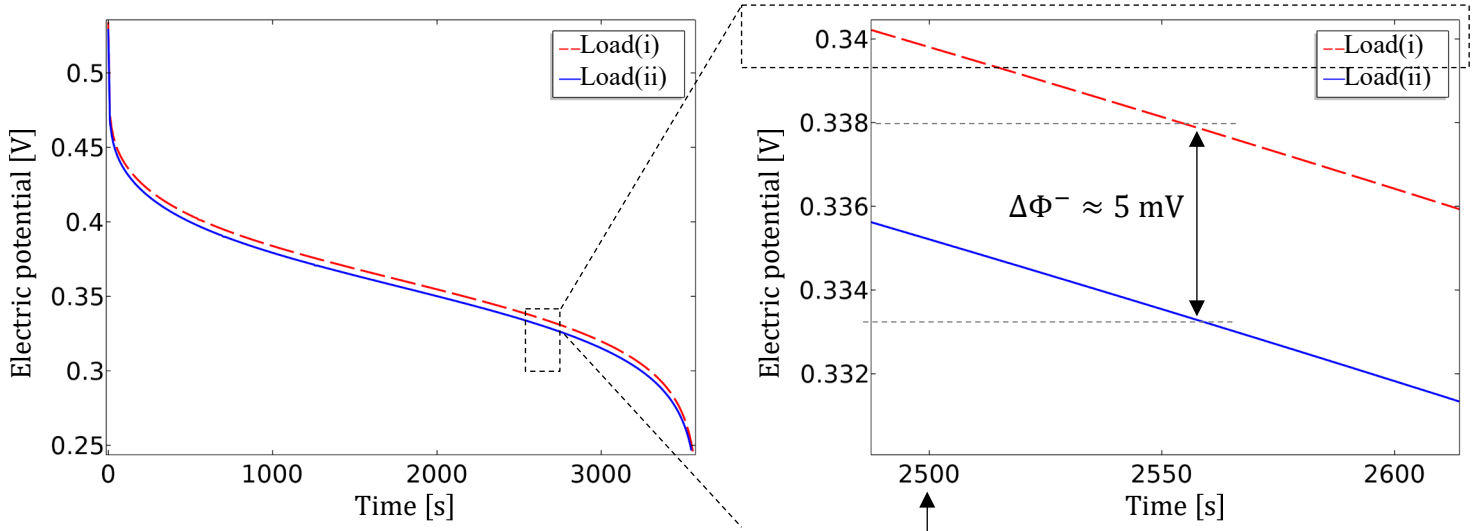

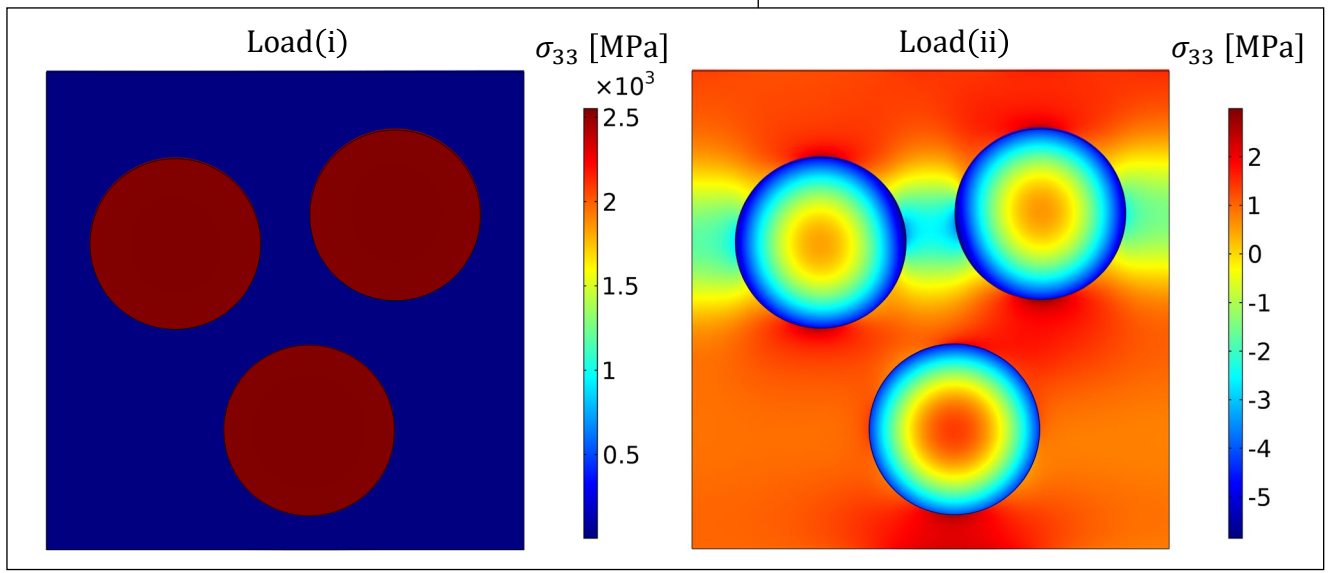

Carlstedt et al. *Multifunc. Mater.* **3**, 2020, 045002

Method in place to characterise performance under combined loads

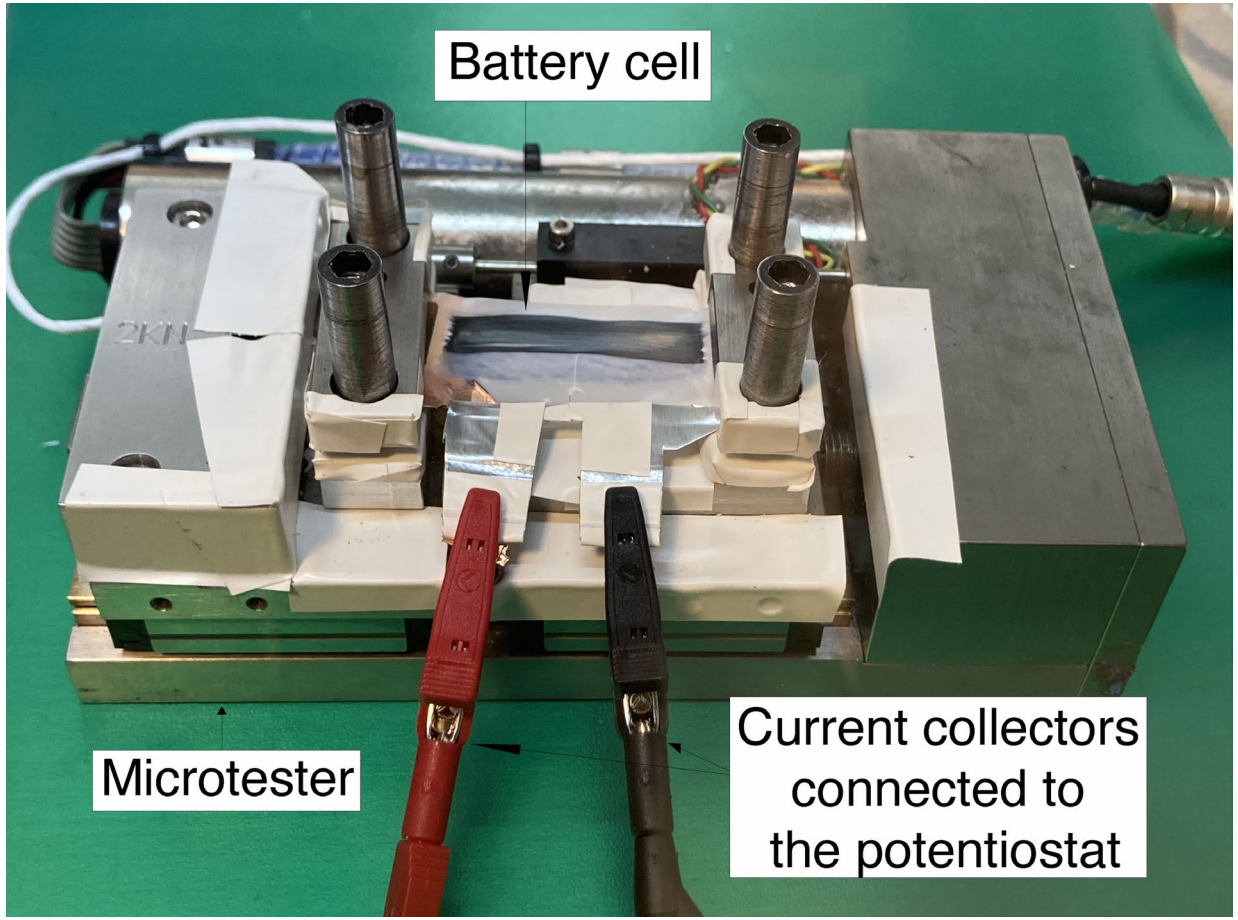

Effect of applied load on electric potential for the structural battery full cell

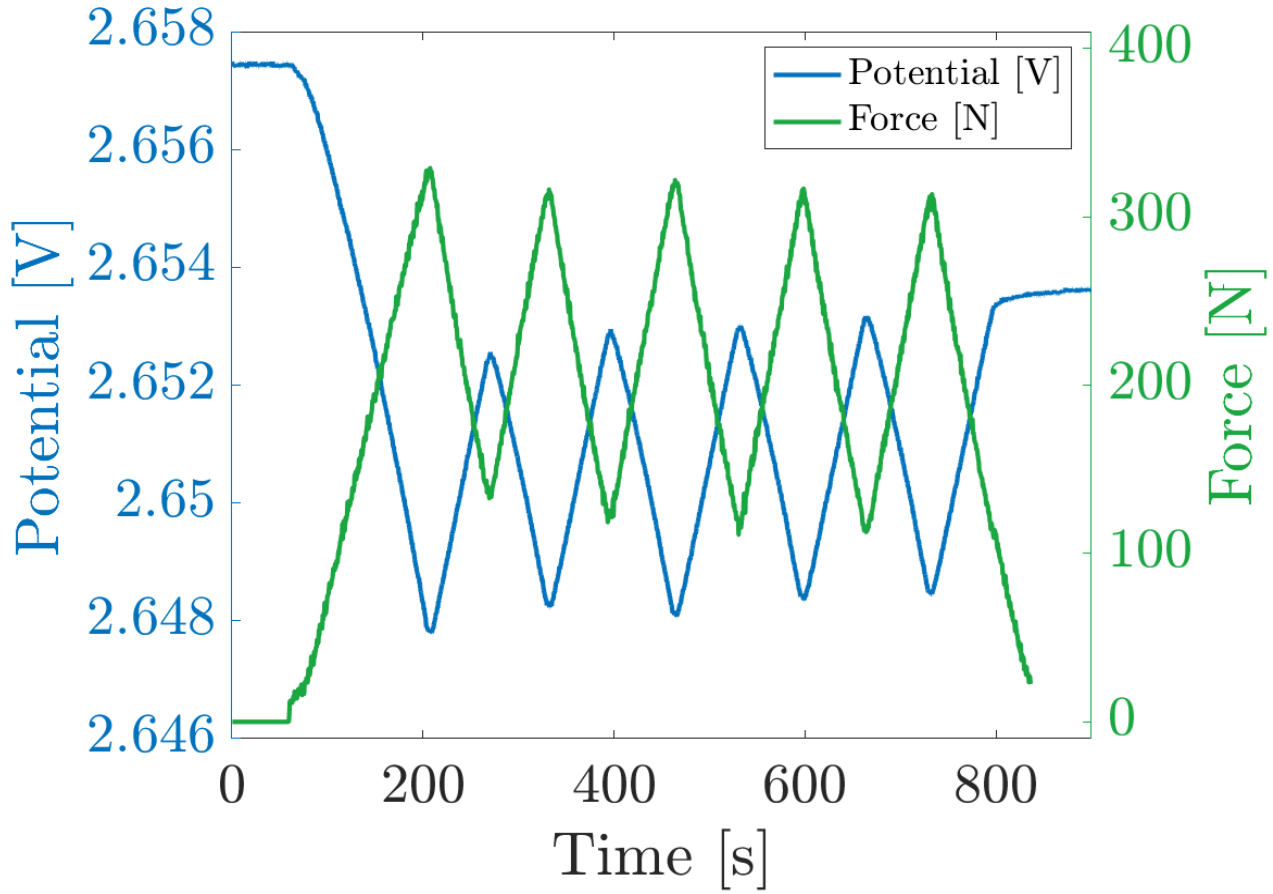

Xu, Dahlberg, Asp. *Submitted*

The Structural Positive Electrode



https://www.eurekalert.org/multimedia/1041190

The LFP-coated Carbon Fiber Electrode

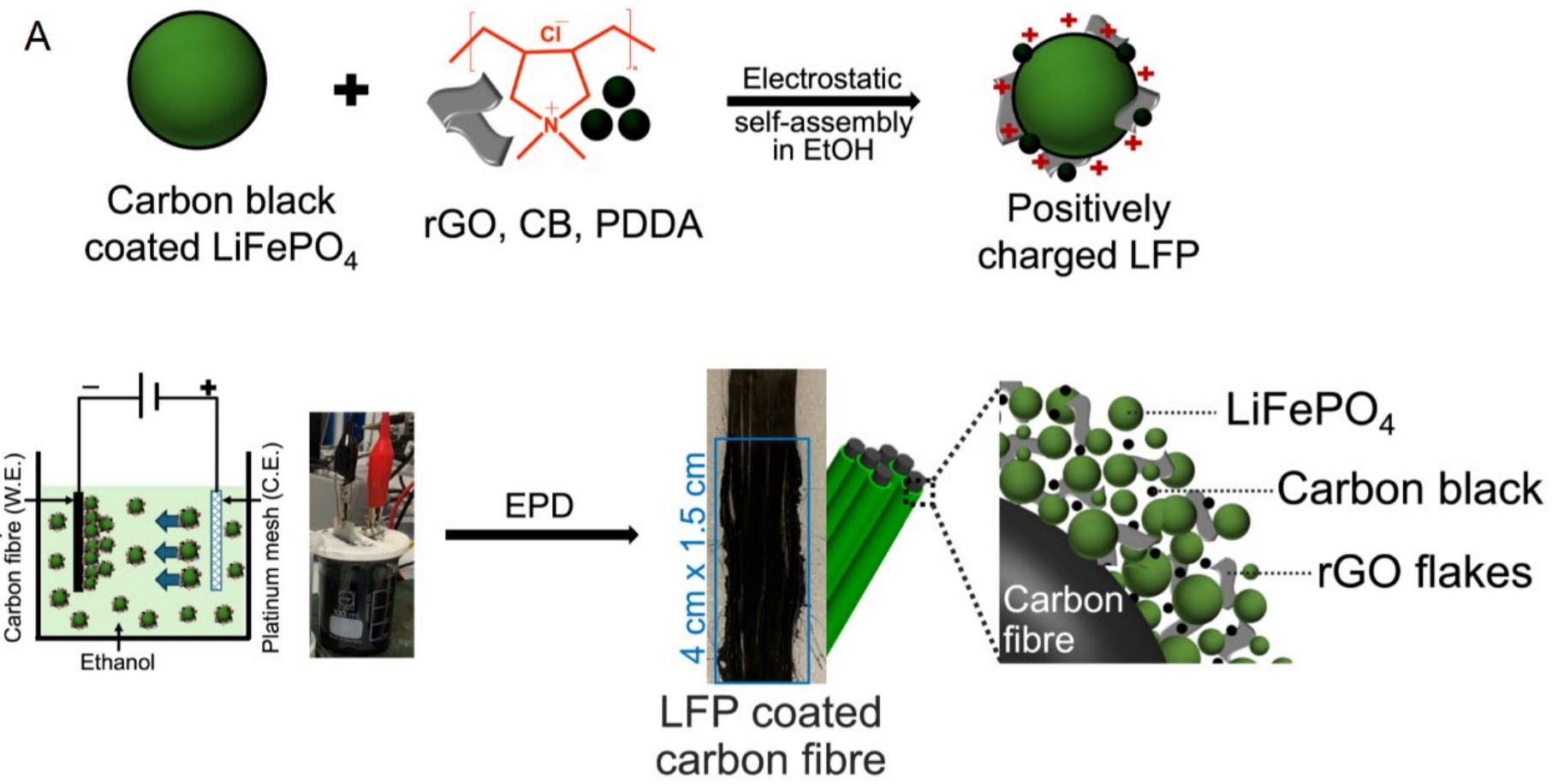

Chaudhary et al. *Adv. Sci.* 2024, 24014012.

The LFP-coated Fibers

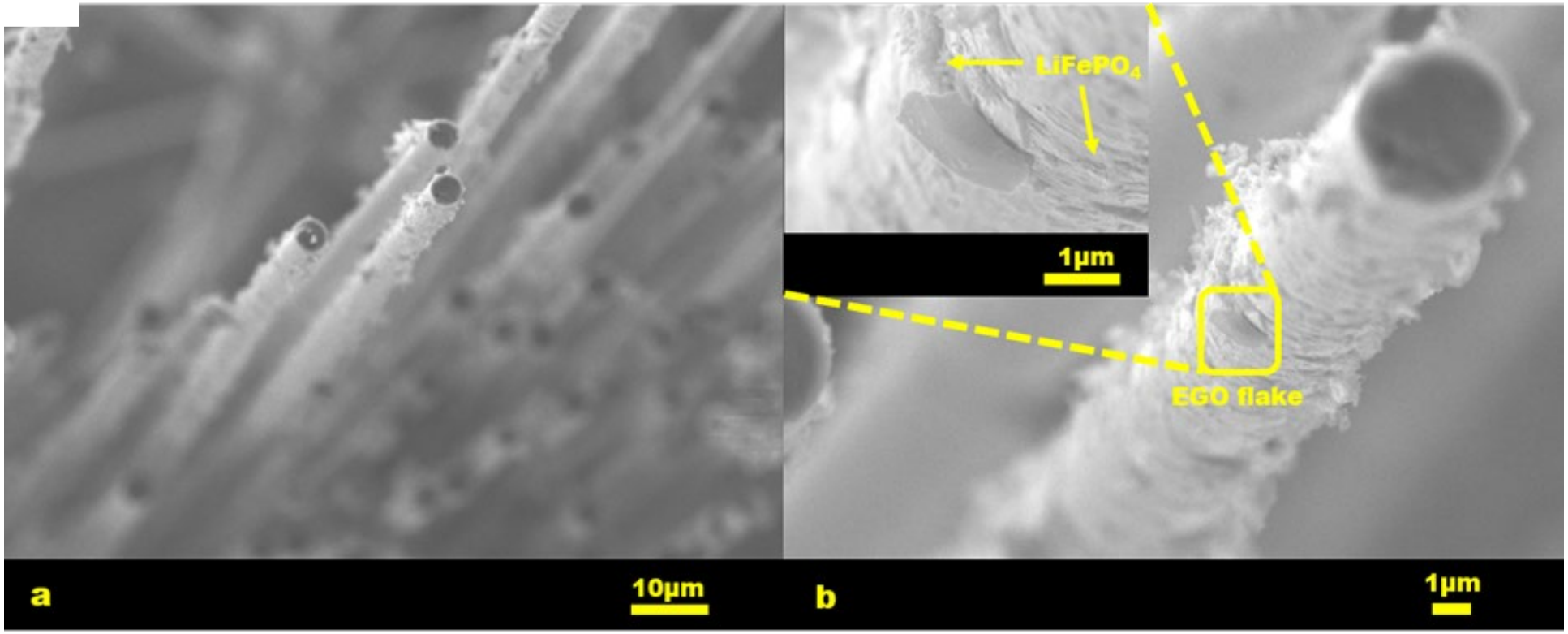

Sanchez et al. *Comp. Sci. Technol.* 208, 2021. 108768

Capacity of the Structural Positive Electrode

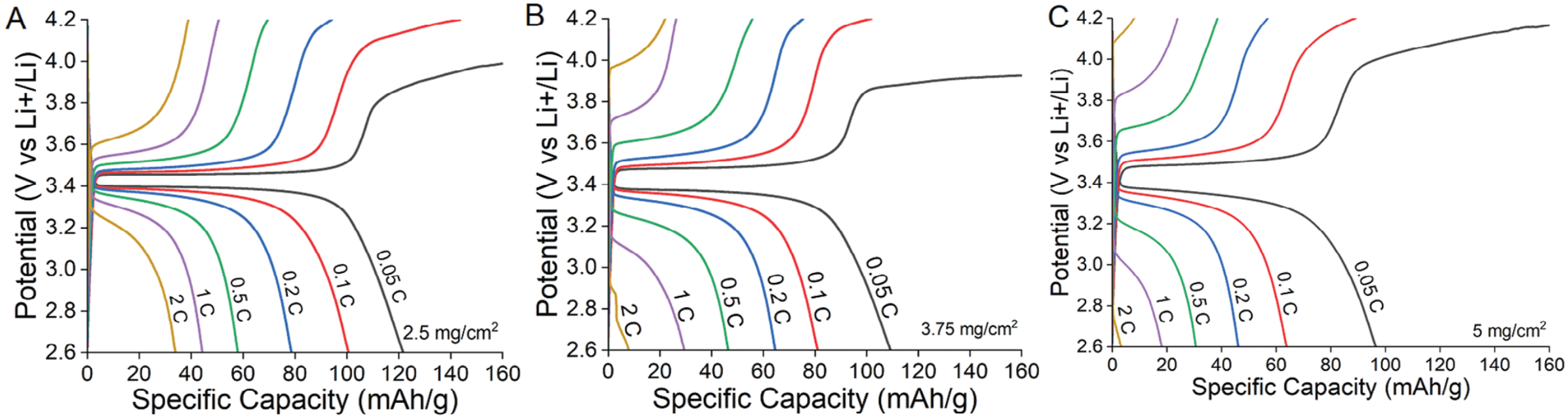

Chaudhary et al. *Adv. Sci.* 2024, 24014012.

Structural Battery Electrolytes

Homogenous systems
- Ion transport depend on polymer chain mobility
- Two competing properties

Inhomogeneous systems
- One phase → Stiffness
- One phase → Conductivity

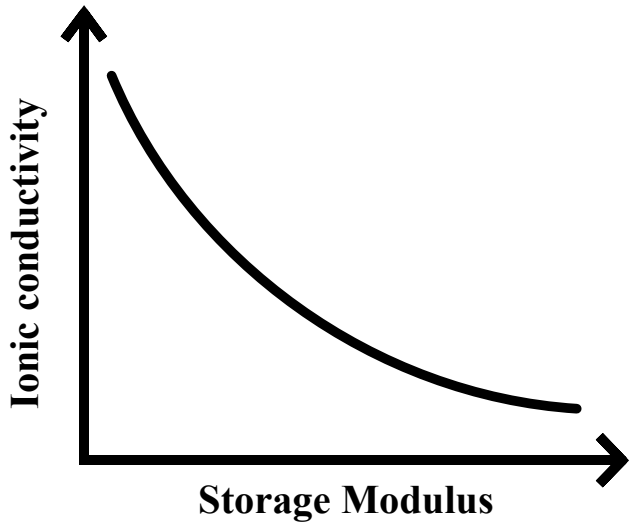

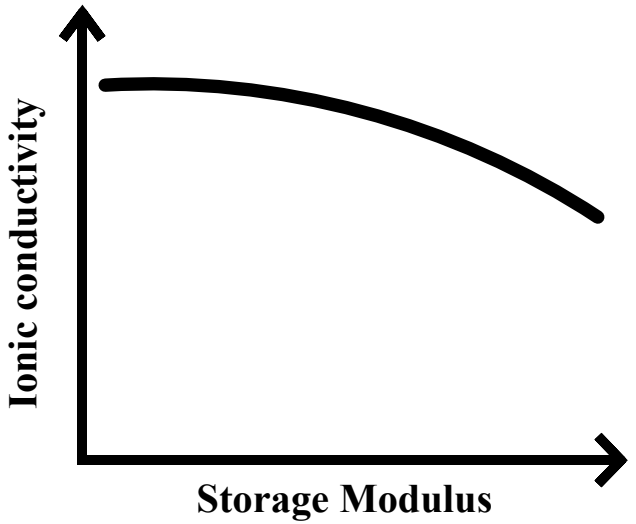

Structural battery electrolyte

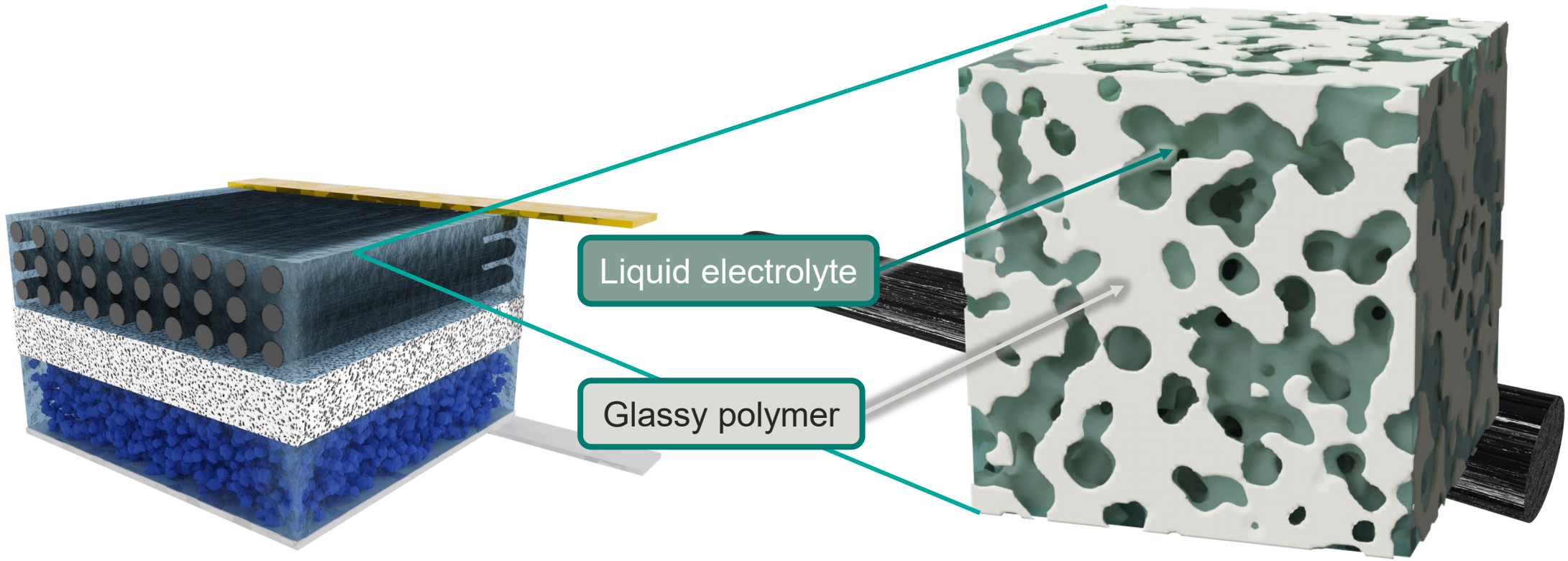

Duan S, et al. *Communications Materials,* 2023, 4:49.

Structural battery electrolyte

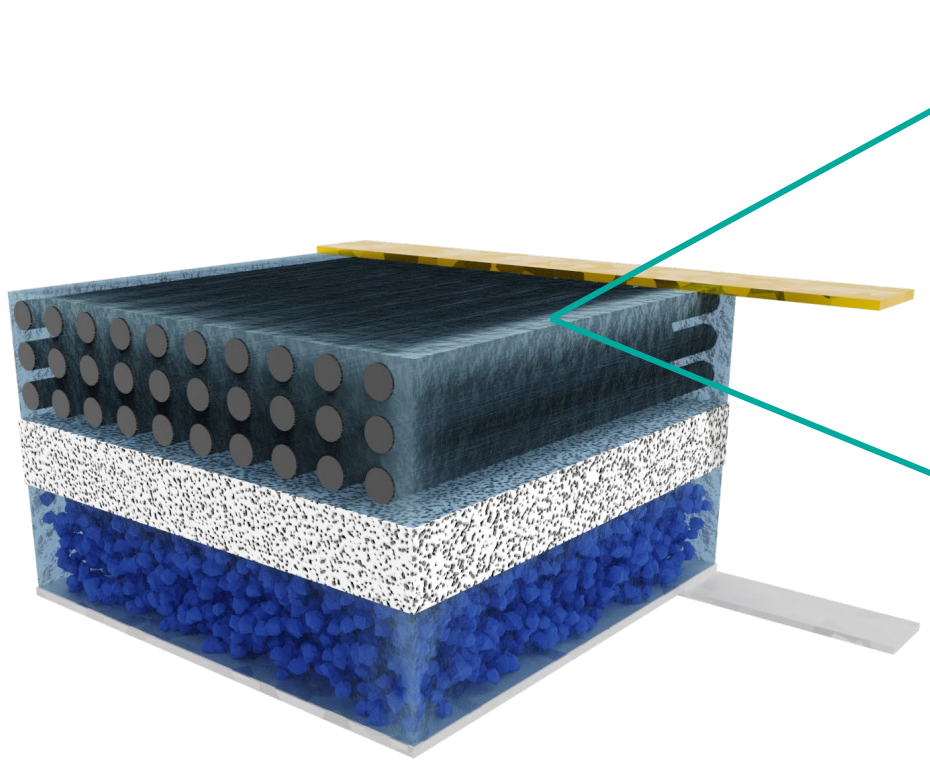

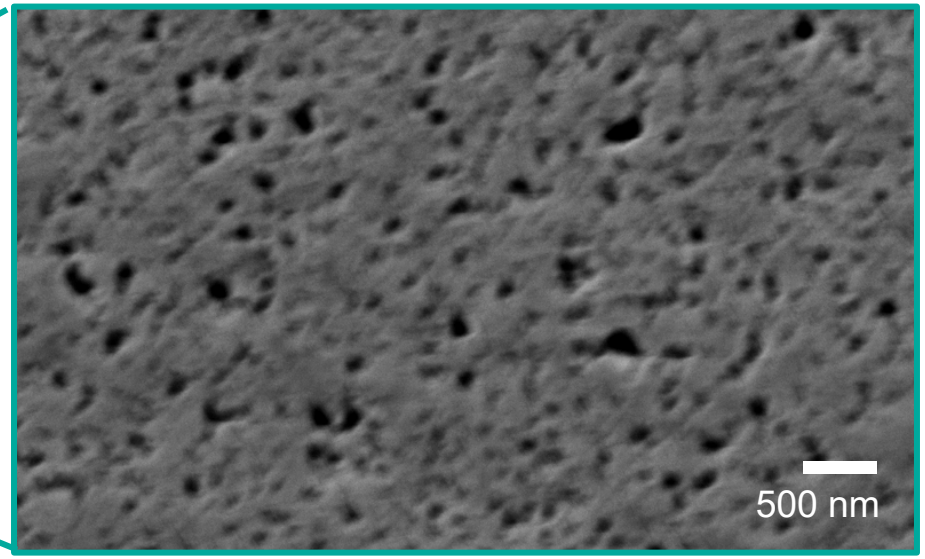

Conventional 2D image is lacking information for a porous system.

Duan S, et al. *Communications Materials,* 2023, 4:49.

FIB

Milling machin

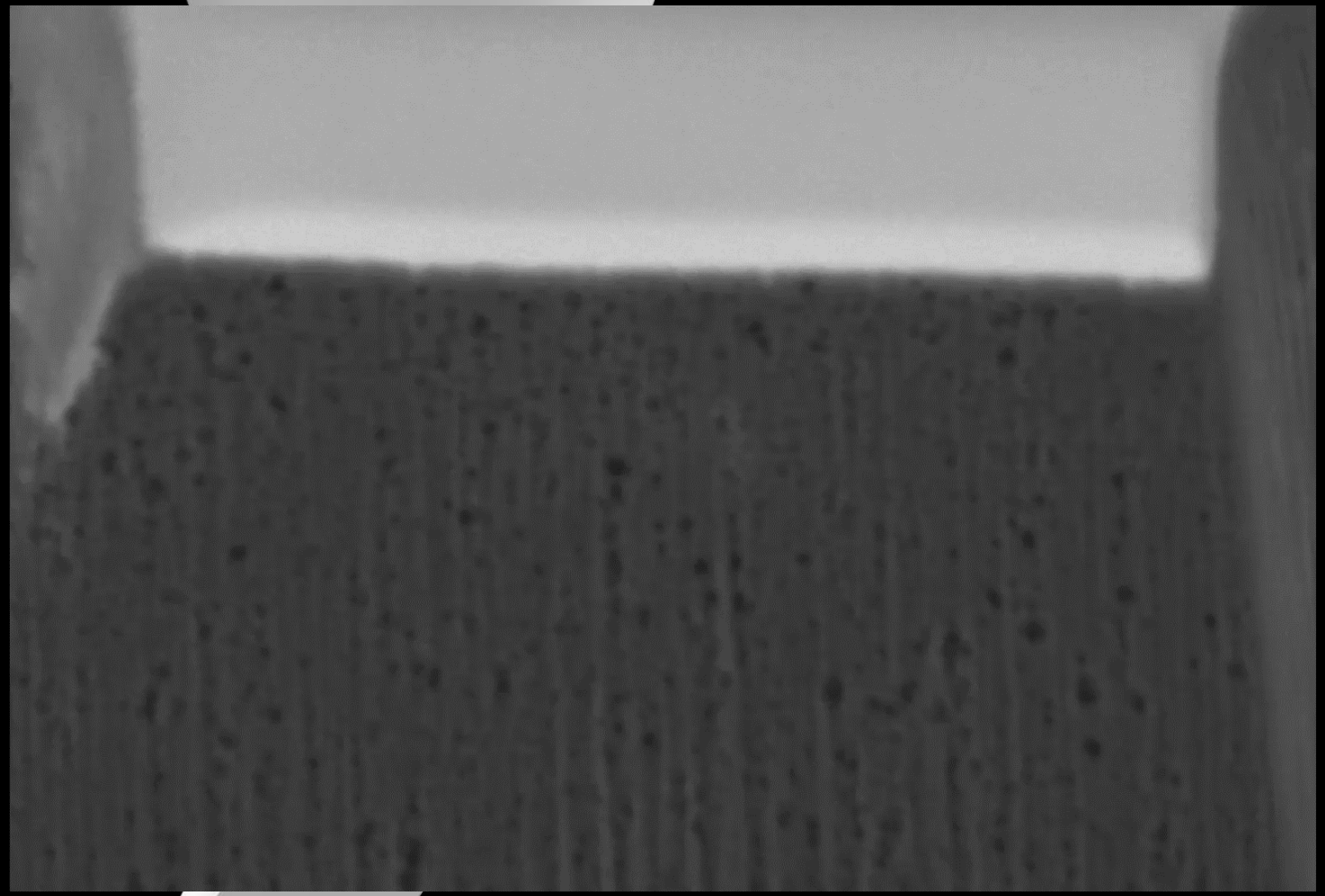

SEM Viewport

Duan S, et al. *Communications Materials,* 2023, 4:49.

Structural battery electrolyte



SBE

Cross section images

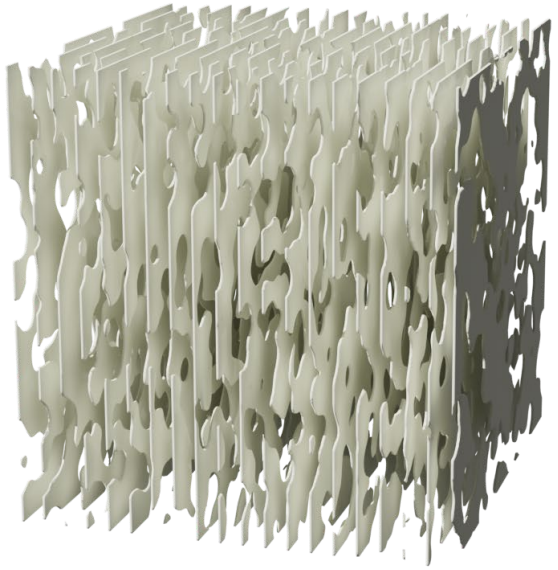

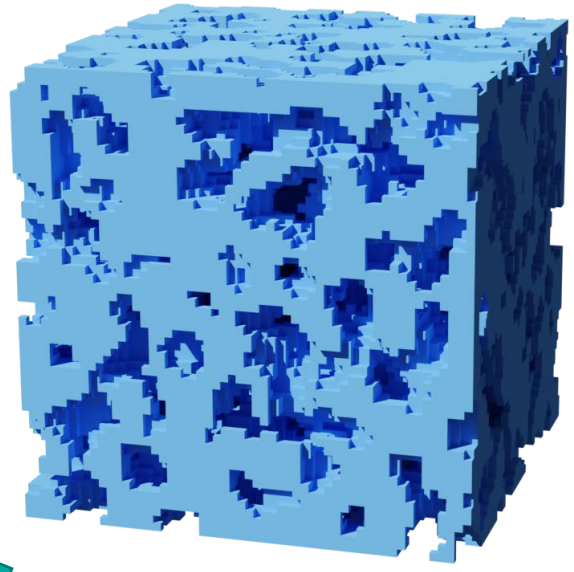

3D model

Topology analysis:

Diameter and volume



Polymer

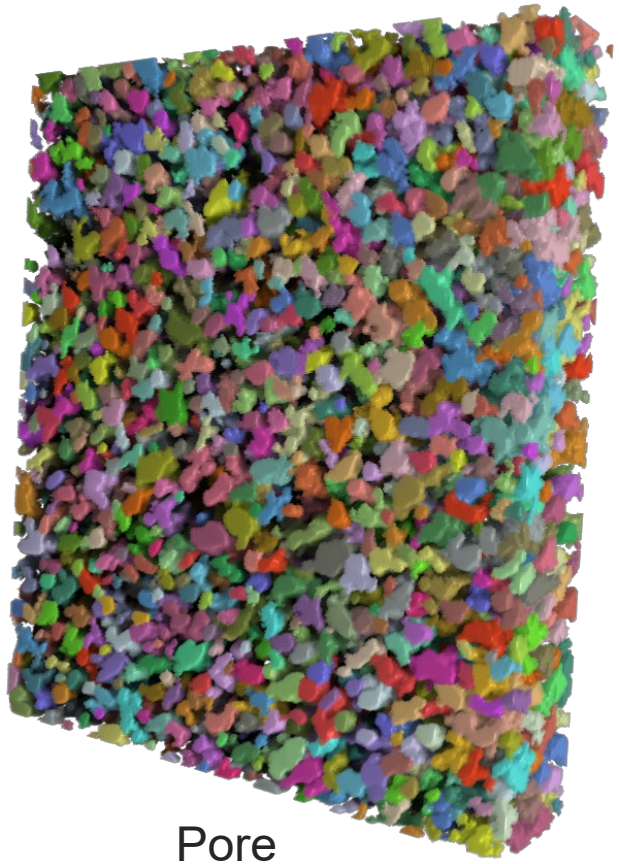

Pore

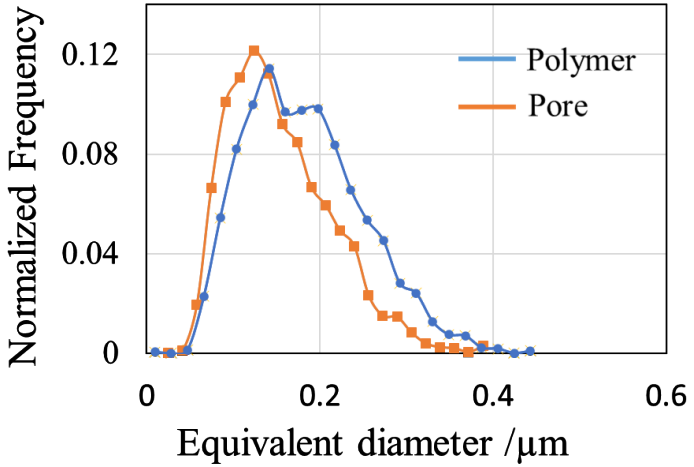

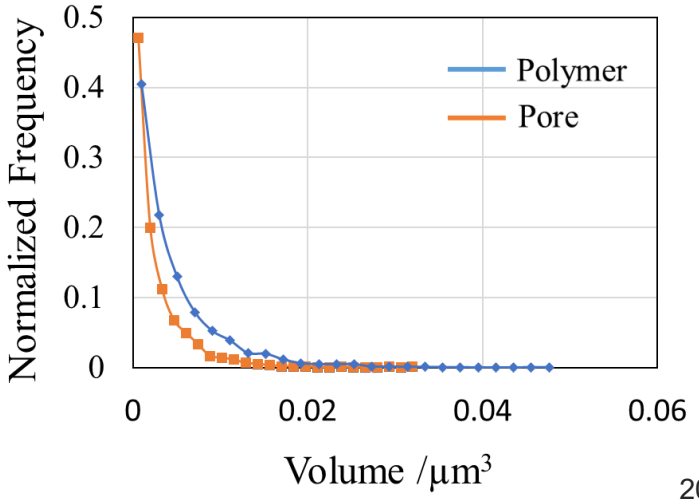

Duan S, et al. *Communications Materials,* 2023, 4:49.

Topology analysis:

Geodesic tortuosity

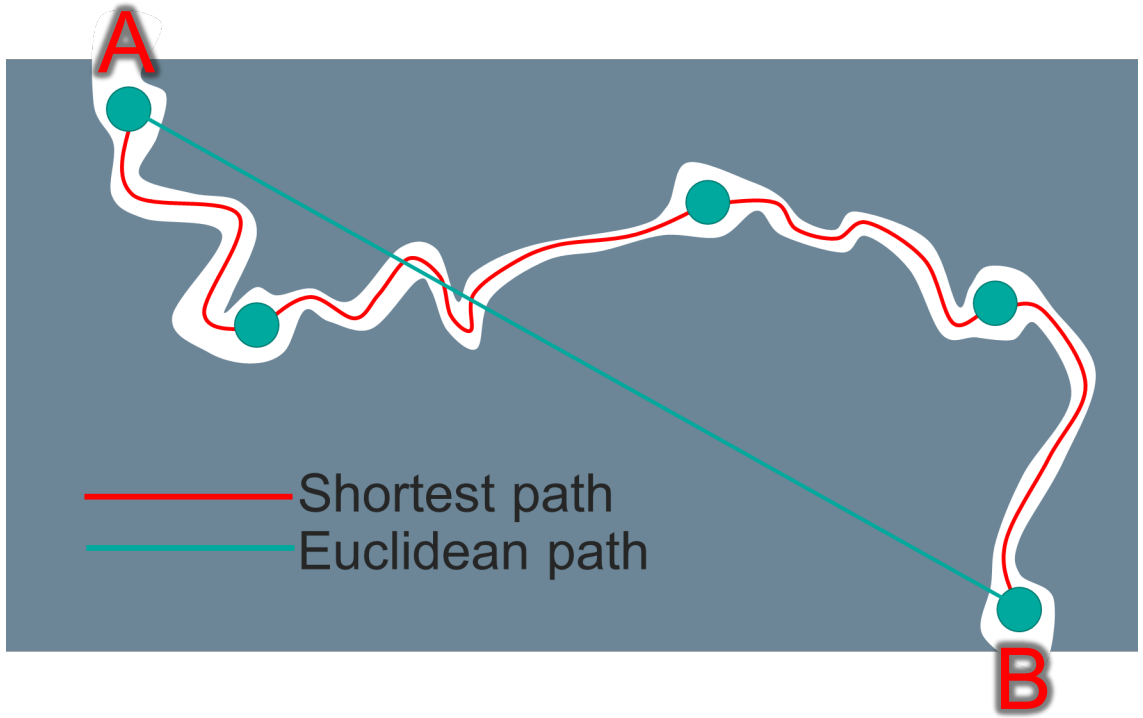

Dense graph in polymer

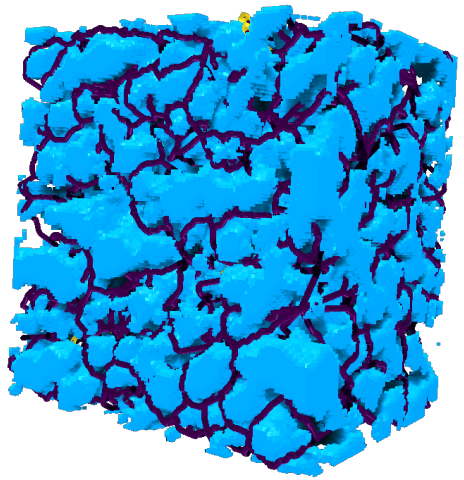

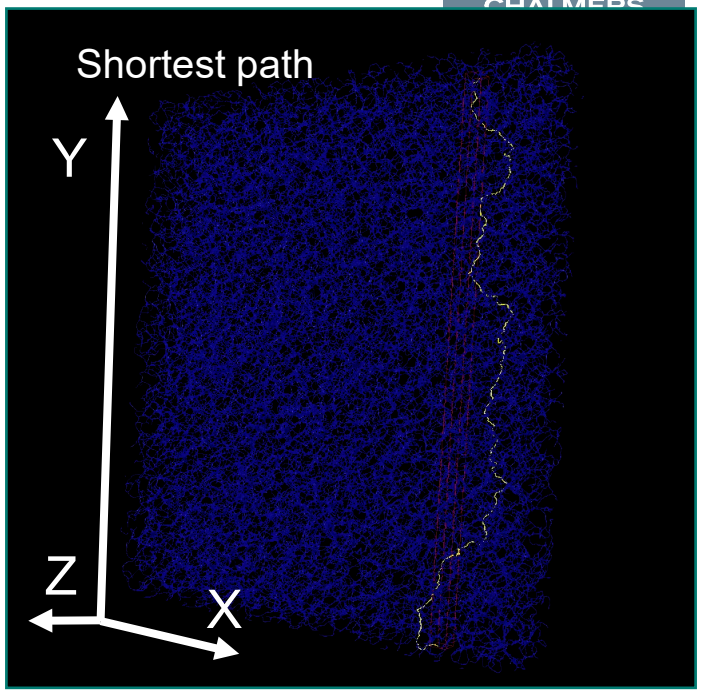

$$\text{Geodesic tortuosity} = \frac{\text{Length of the shortest path}}{\text{Length of the Euclidean path}}$$

	Geodesic tortuosity
x-direction	1.79
y-direction	1.81
z-direction	1.72

Duan S, et al. *Communications Materials,* 2023, 4:49.

FEM Simulation

Comsol

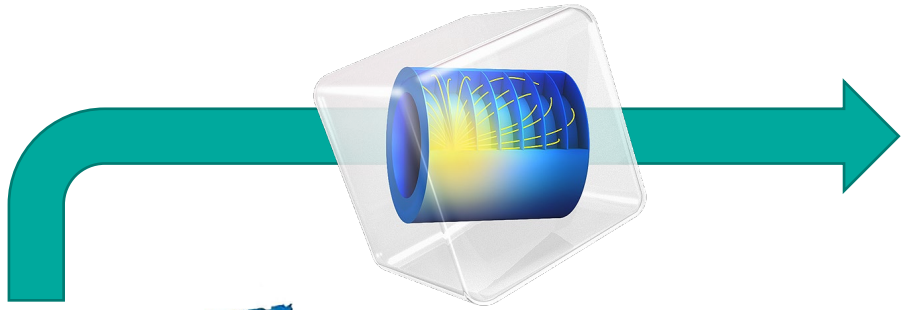

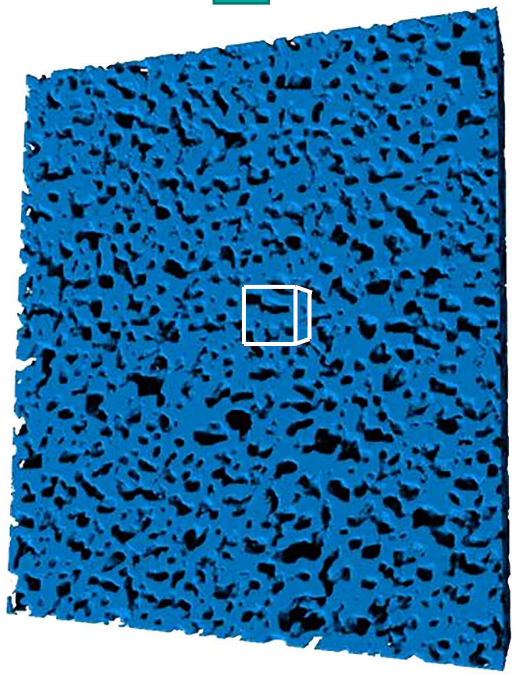

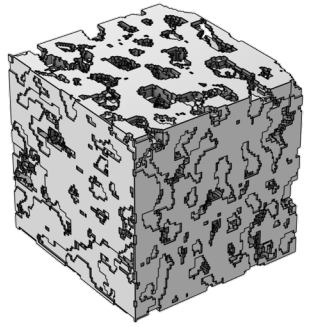

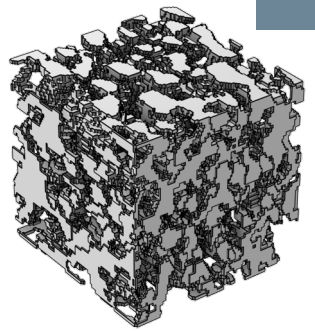

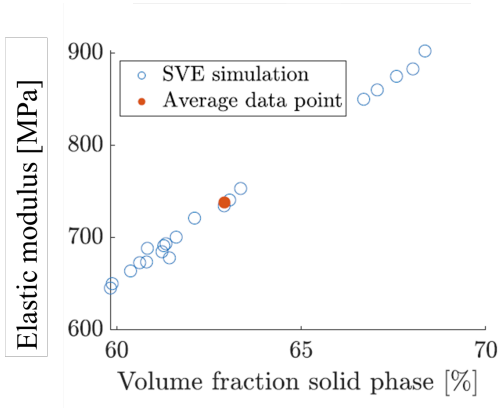

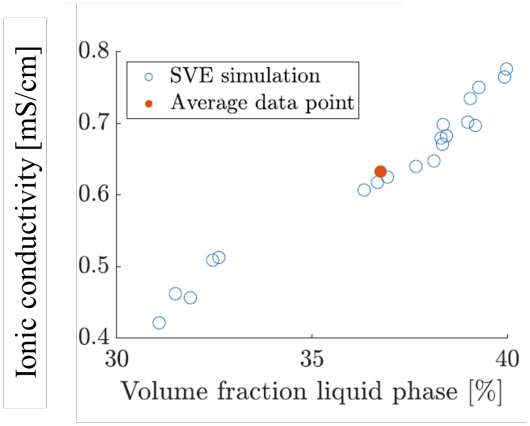

	Measured	Numerical prediction
Elastic modulus [MPa]	611	738
Ionic conductivity [mS/cm]	0.134	0.633

Duan S, et al. *Communications Materials,* 2023, 4:49.

Summary of research activities on structural battery composites @ Chalmers

Structural Battery Cells

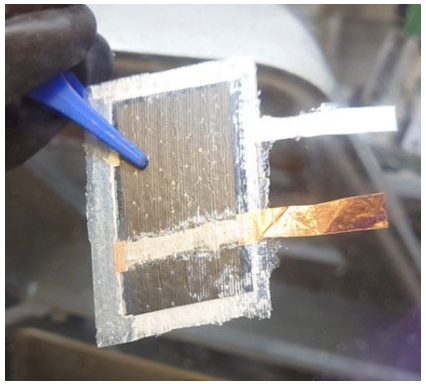

Structural Electrodes



Demonstration

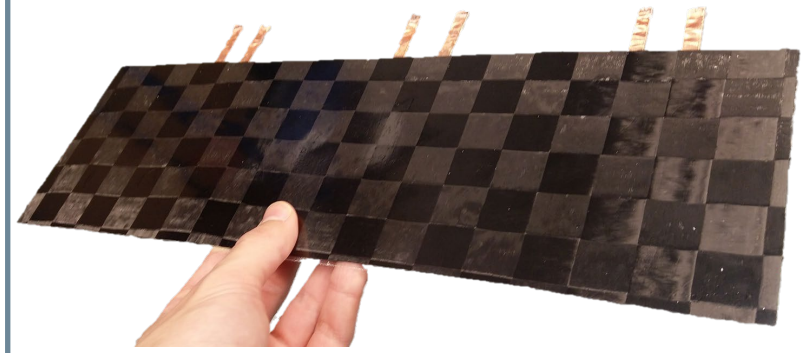

Structural Electrolytes

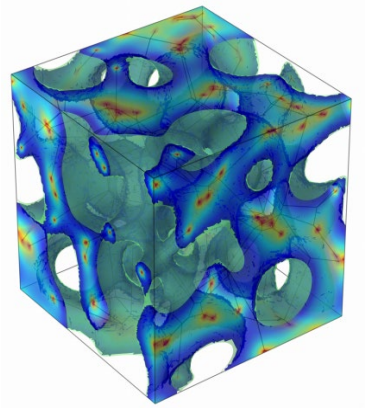

Material Models

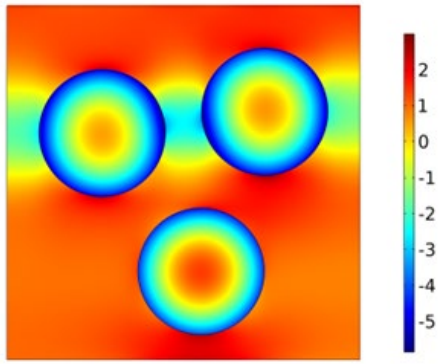

Performance Analysis & LCA

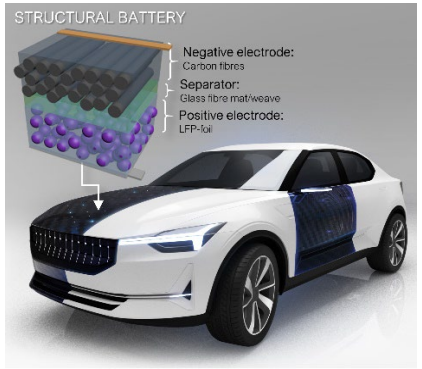

Acknowledgements

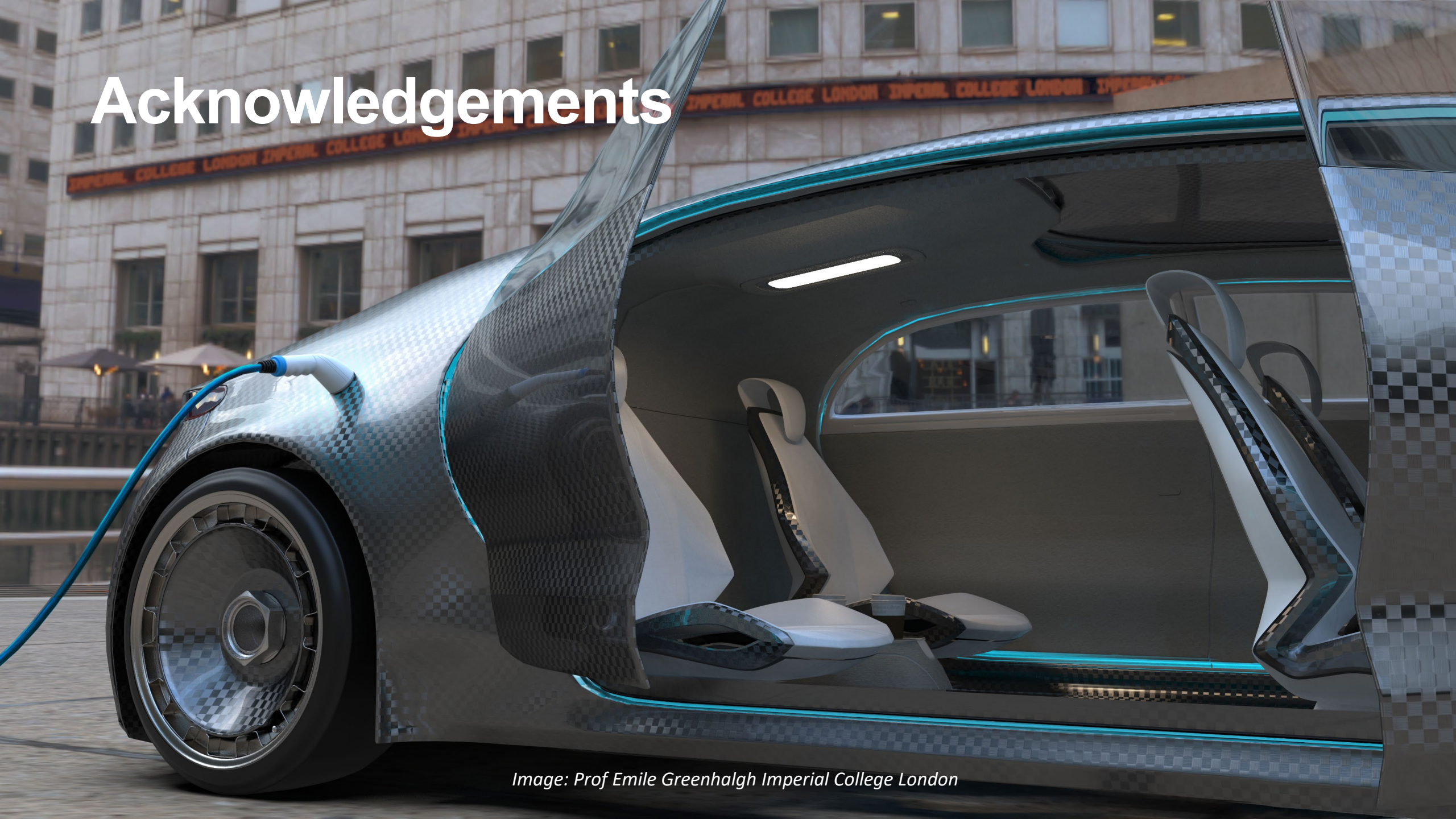

Image: Prof Emile Greenhalgh Imperial College London

The Chalmers team

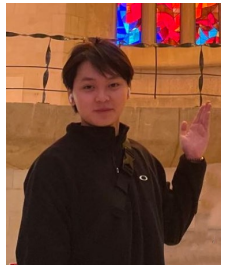
Guokang Li


Emelie Seignér


Prof. F Larsson


Dr M Johansen

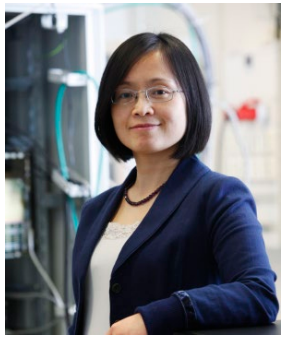
Prof Fang Liu

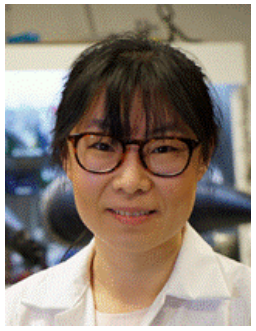
Dr Johanna Xu

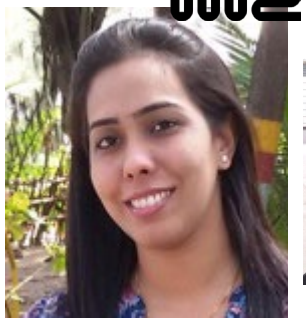
Dr Richa Chaudhary


Dr D Carlstedt


Dr Zhenyuan Xia


Ruben Tavano


Prof K Runesson


Prof Thiringer


Prof Leif Asp


Dr Giulia Fredi


Huixin Chen


Dr Vinh Tu


Dr Shanghong Duan


Siam Siraj


Dr Nicole Abdou


Prof P Johansson


Prof M Svanström


Dr N Sieti

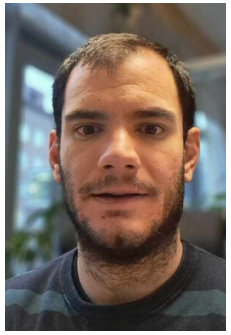
Dr A Pipertzis

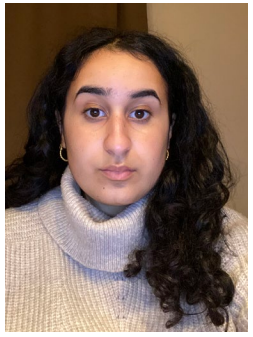
Rauan Al-Emrani


Prof Anna Martinelli


Prof Jan Swenson


Carl Larsson


Dr F Hermansson

Special thanks to



Prof Emile Greenhalgh,
Imperial College London



Prof Dan Zenkert
KTH



Prof Mats Johansson
KTH



Prof Göran Lindbergh
KTH

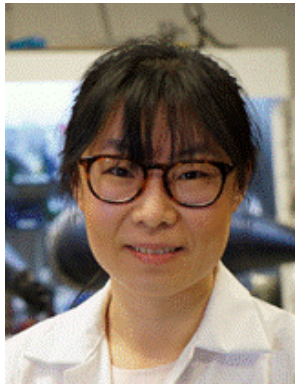

Ass Prof Johanna Xu
Chalmers

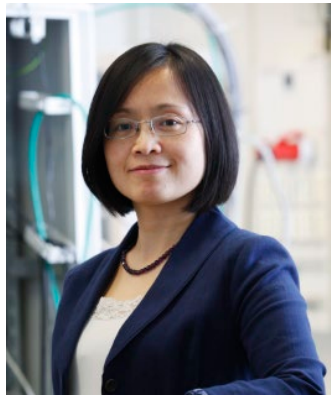

Prof Fang Liu
Chalmers



Prof K Runesson
Chalmers



Prof F Larsson
Chalmers

Vetenskapsrådet

Rymdstyrelsen
Swedish National Space Agency



CHALMERS

ICCM24
AUGUST 4-8, 2025
BALTIMORE CONVENTION CENTER
BALTIMORE, MARYLAND, USA

No Technical Paper Submission for:

Olivier De Almeida

Crystallization hybrid modeling and simulation in robotic 3D printing of continuous carbon fiber reinforced thermoplastic composites

Chady Ghnatios[1], Kazem Fayazbakhsh[2], Reza Vaziri[3]

[1]University of North Florida, Jacksonville, Florida, USA
[2]Toronto Metropolitan University, Toronto, Canada
[3]University of British Columbia, Vancouver, Canada

August 05, 2025







Introduction

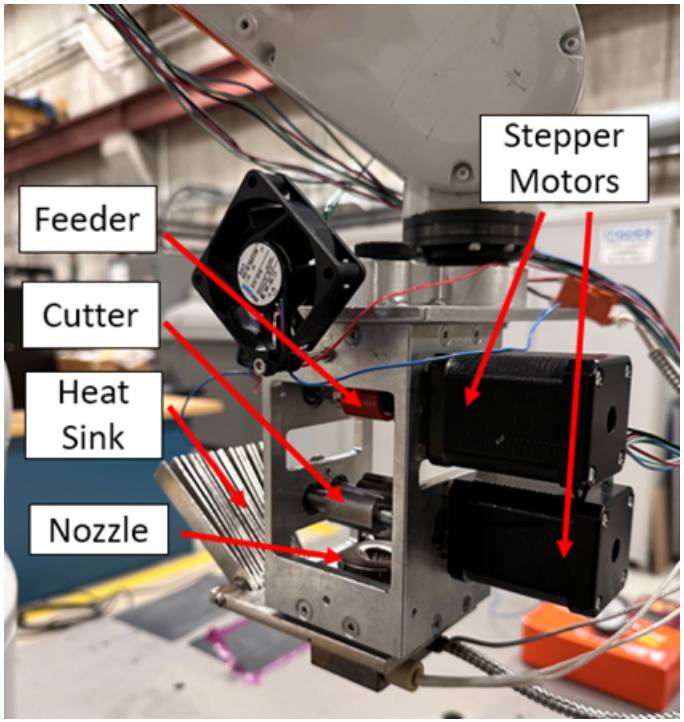



- The prepreg tapes change their dimensions when heated.
- Prepreg tapes contains residual stresses.
- Drying can affect the width.
- Crystallization contributes to the deformation.
- Experimental and digital models are built to investigate those effects

Introduction

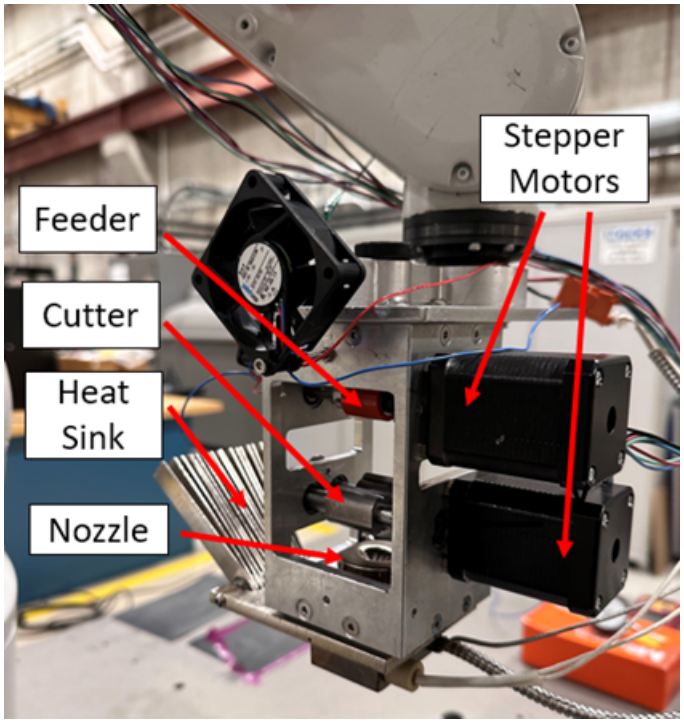



- The prepreg tapes change their dimensions when heated.
- Prepreg tapes contains residual stresses.
- Drying can affect the width.
- Crystallization contributes to the deformation.
- Experimental and digital models are built to investigate those effects

Introduction

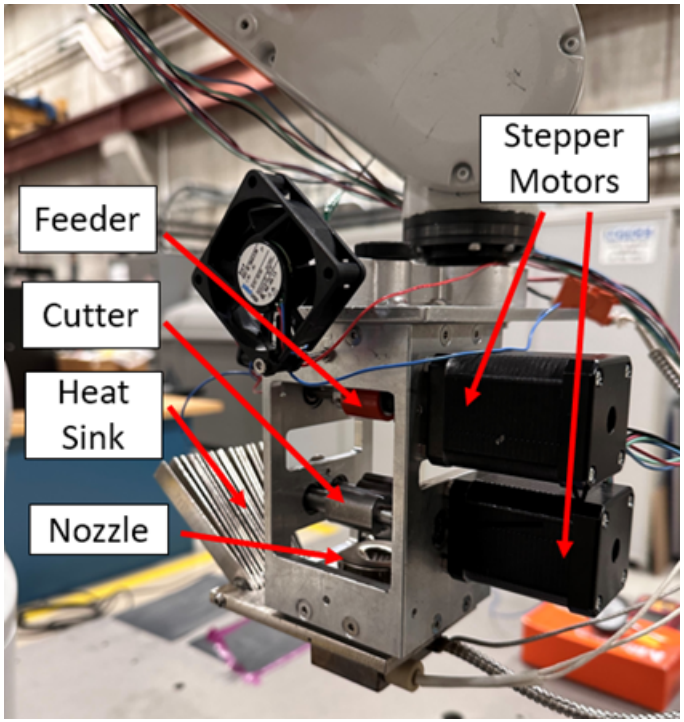



- The prepreg tapes change their dimensions when heated.
- Prepreg tapes contains residual stresses.
- Drying can affect the width.
- Crystallization contributes to the deformation.
- Experimental and digital models are built to investigate those effects

Introduction

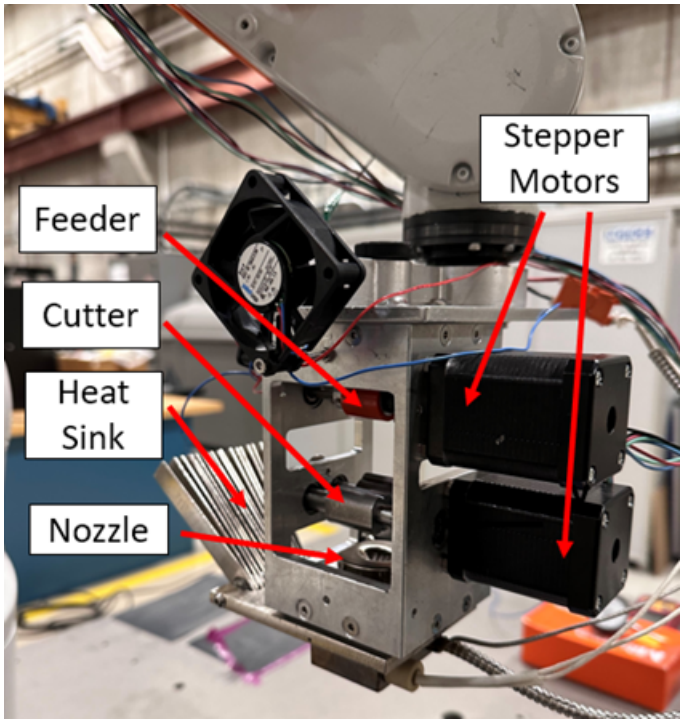



- The prepreg tapes change their dimensions when heated.
- Prepreg tapes contains residual stresses.
- Drying can affect the width.
- Crystallization contributes to the deformation.
- Experimental and digital models are built to investigate those effects

Introduction

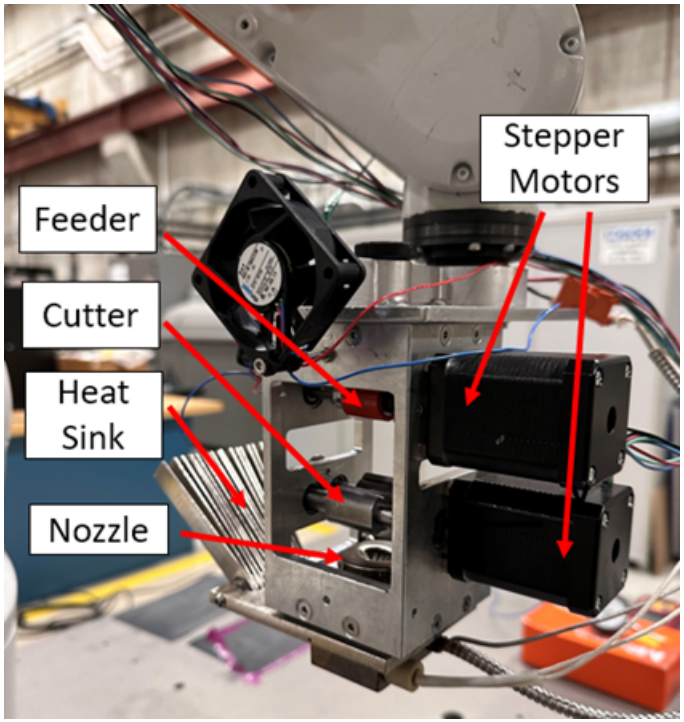



- The prepreg tapes change their dimensions when heated.
- Prepreg tapes contains residual stresses.
- Drying can affect the width.
- Crystallization contributes to the deformation.
- Experimental and digital models are built to investigate those effects

Introduction

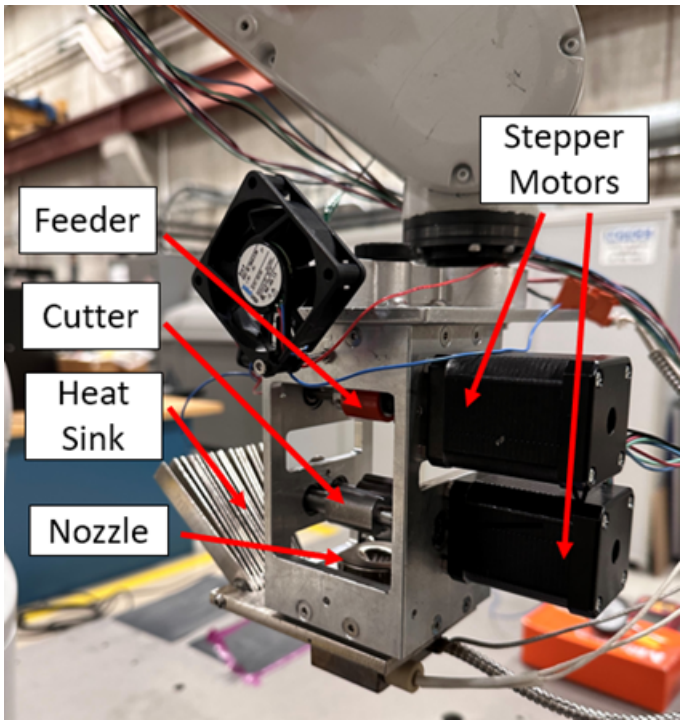



- The prepreg tapes change their dimensions when heated.
- Prepreg tapes contains residual stresses.
- Drying can affect the width.
- Crystallization contributes to the deformation.
- Experimental and digital models are built to investigate those effects

Outline

1. Experiments
2. Viscoelastic modeling of the prepregs
3. Modeling the initial strain release
4. Crystallization strains
5. Conclusion

Experimental setup



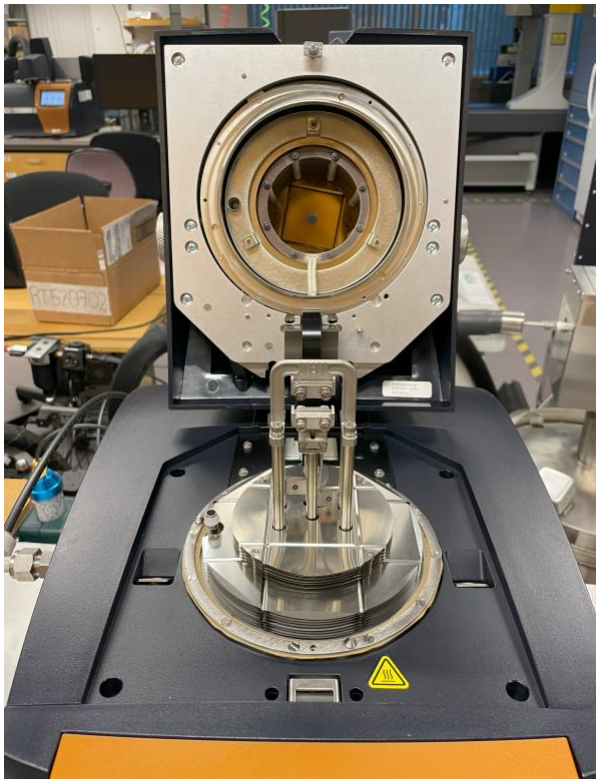

- DMA test with film tensile fixture
- Different heating and cooling rates
- Sufficient time at equilibrium

Experimental setup



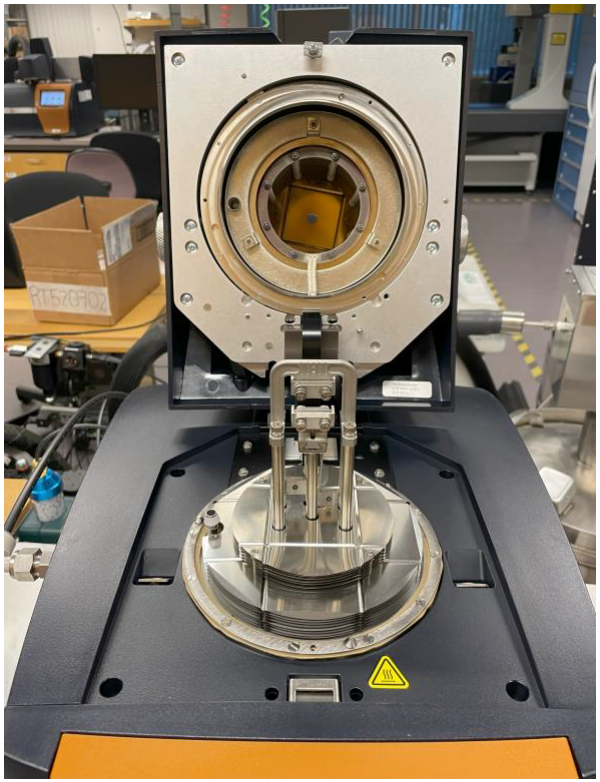

- DMA test with film tensile fixture
- Different heating and cooling rates
- Sufficient time at equilibrium

Experimental setup



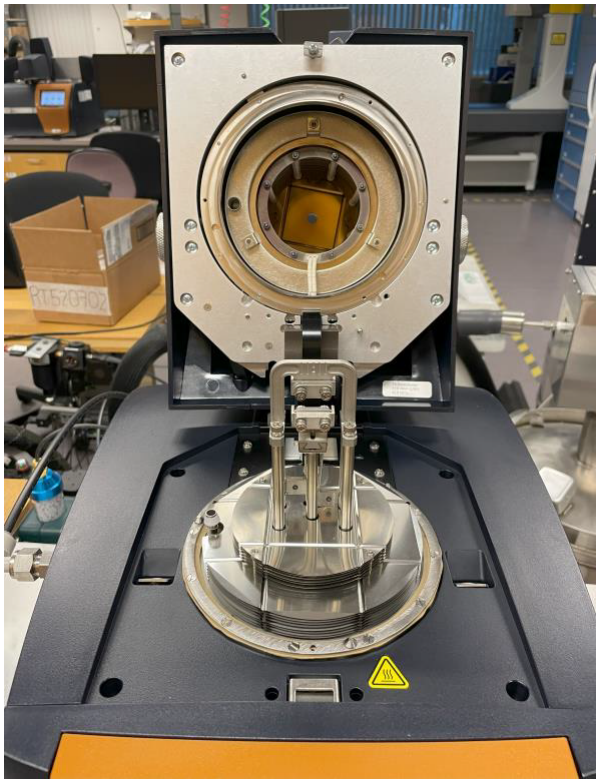

- DMA test with film tensile fixture
- Different heating and cooling rates
- Sufficient time at equilibrium

Experimental setup

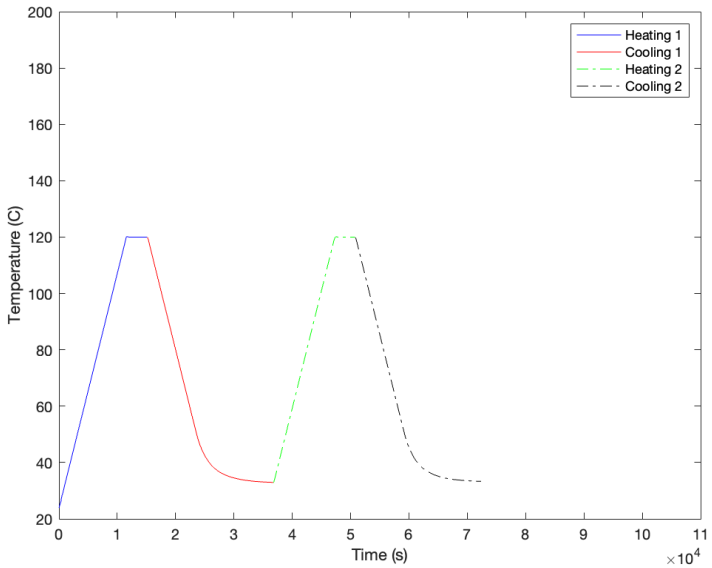

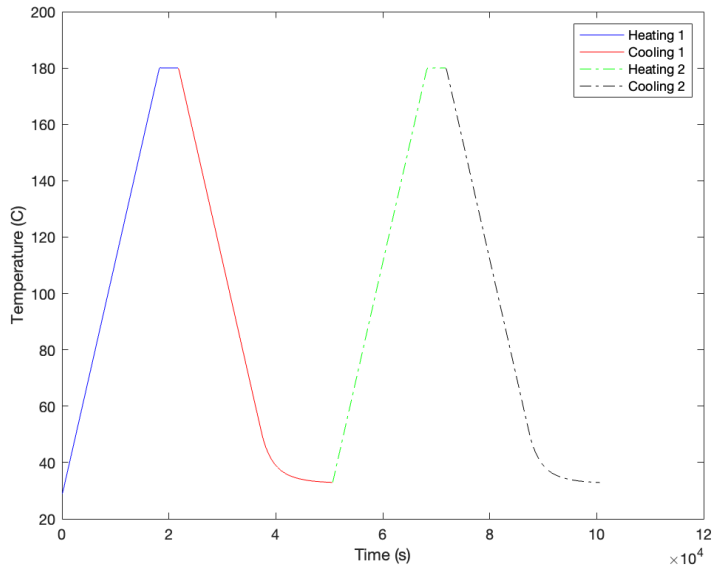

- Viscoelastic characterization is performed using the heating cycles reaching up to 120°C.
- Heating and cooling are performed at 0.5°C per minute.
- Large steady-state period allowing thermal equilibrium.

Experimental setup

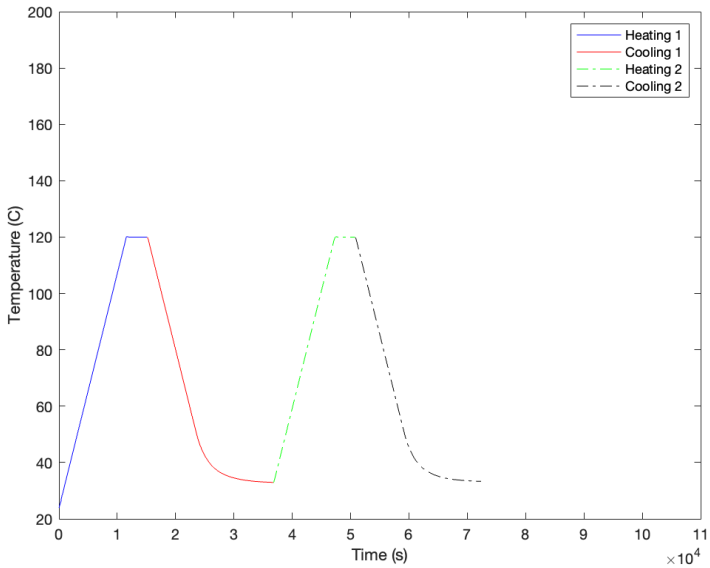

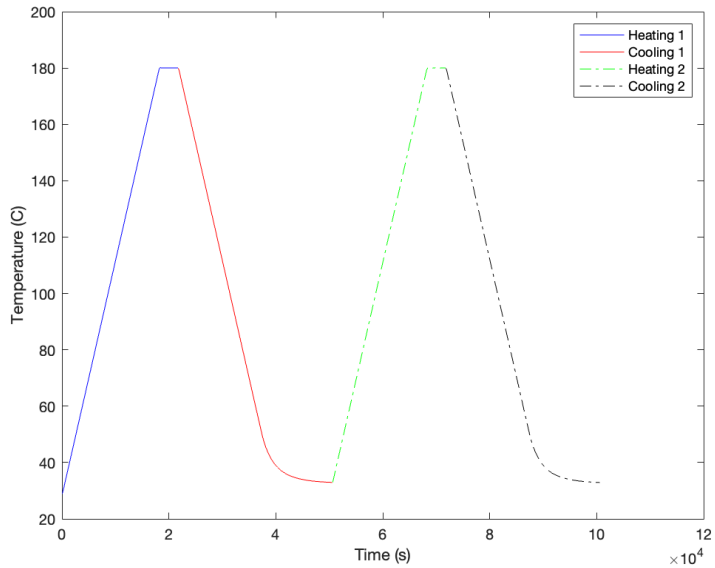

- Viscoelastic characterization is performed using the heating cycles reaching up to 120°C.
- Heating and cooling are performed at 0.5°C per minute.
- Large steady-state period allowing thermal equilibrium.

Experimental setup

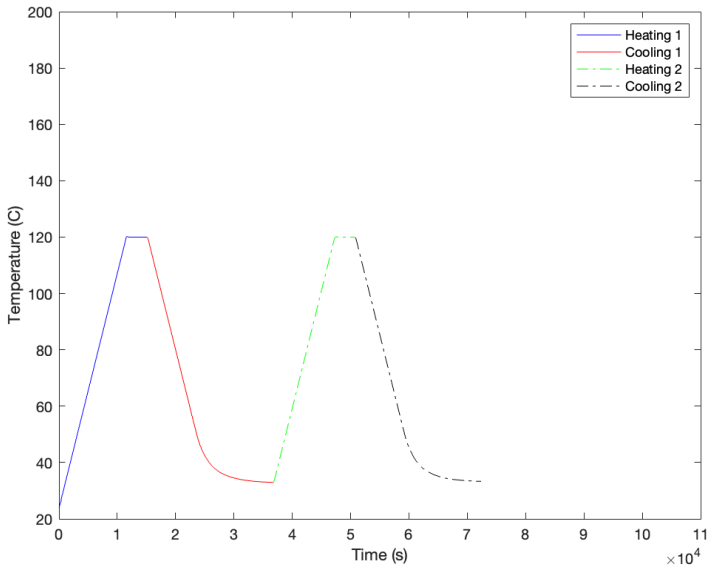

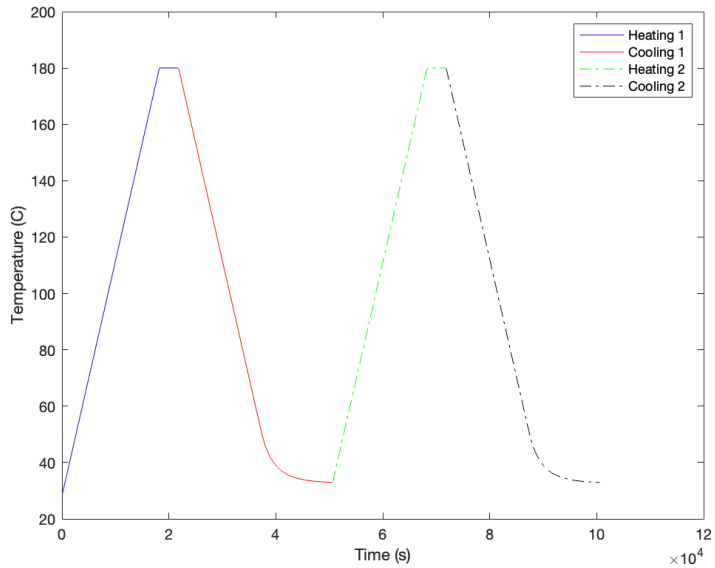

- Viscoelastic characterization is performed using the heating cycles reaching up to 120°C.
- Heating and cooling are performed at 0.5°C per minute.
- Large steady-state period allowing thermal equilibrium.

DSC experiment or composite prepregs

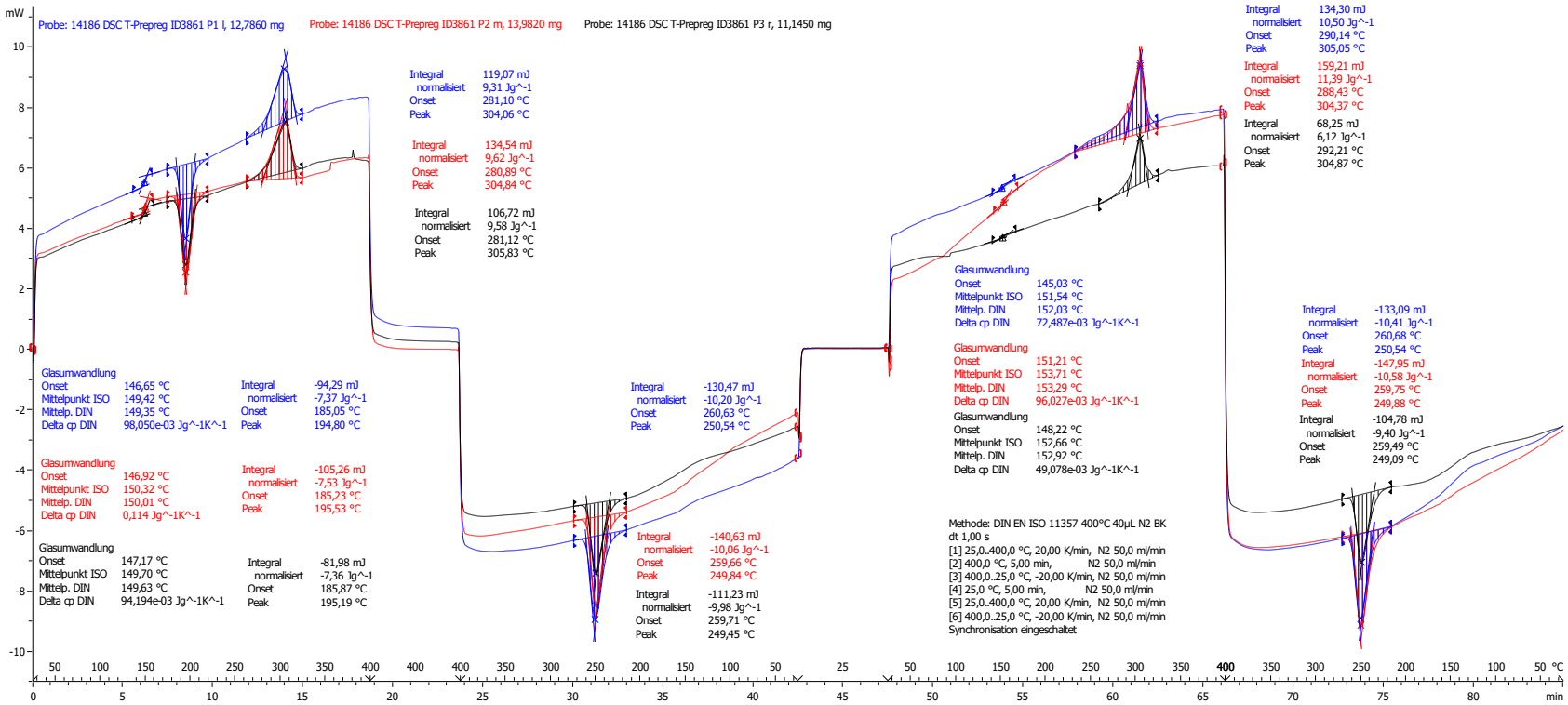

- The onset of glass transition temperature is around 147°C
- No cold crystallization during the second heating phase

DSC experiment or composite prepregs

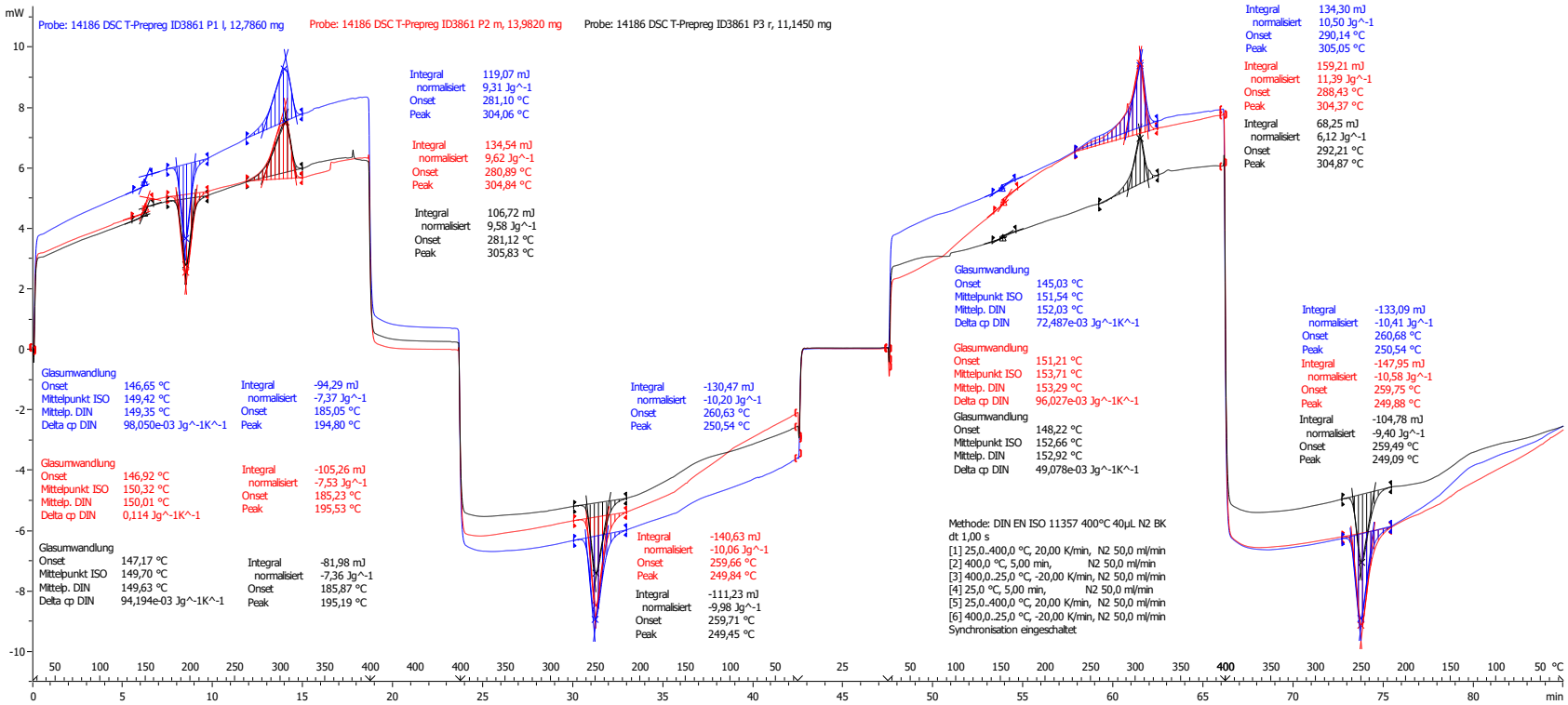

- The onset of glass transition temperature is around 147°C
- No cold crystallization during the second heating phase

Experimental setup

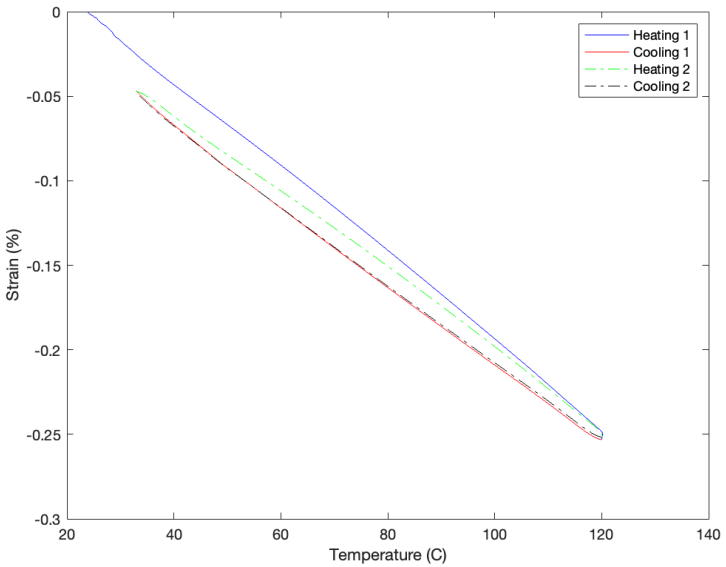

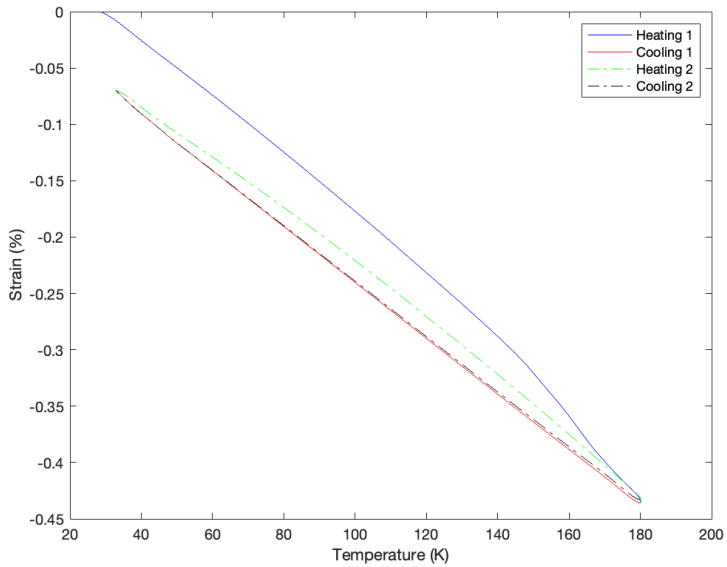

- First experiment characterizes the behavior of the prepreg without further crystallization
- Second experiment identifies the crystallization behavior

Experimental setup

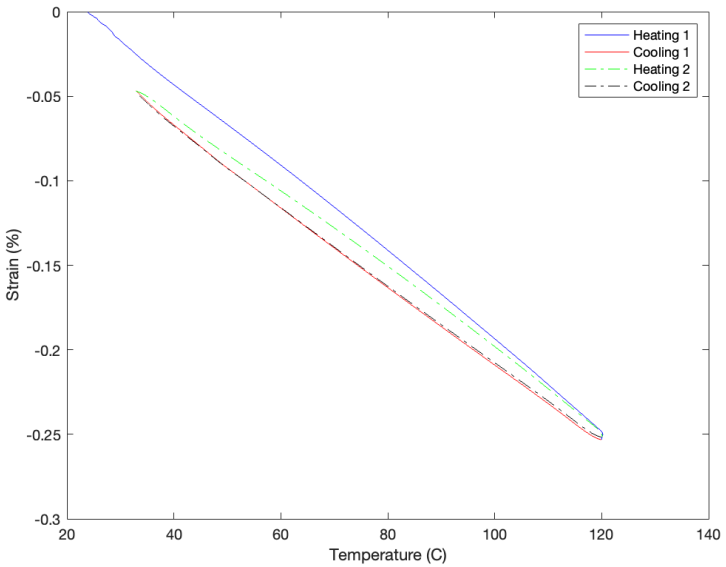

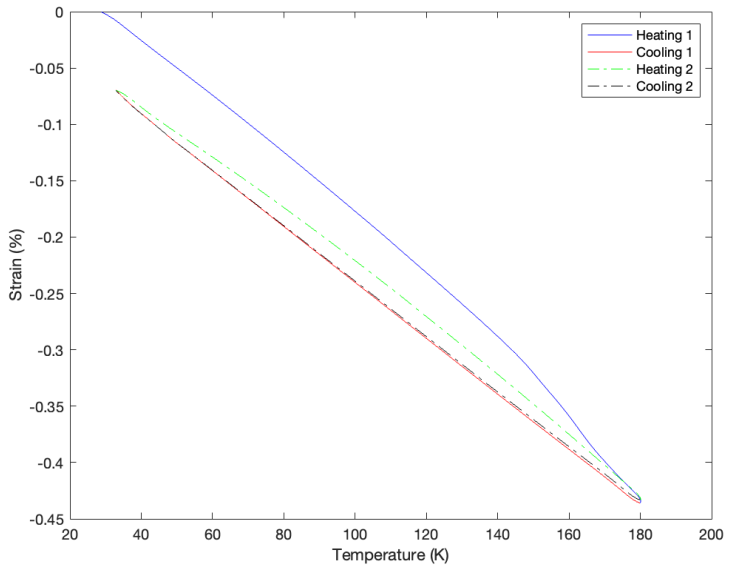

- First experiment characterizes the behavior of the prepreg without further crystallization
- Second experiment identifies the crystallization behavior

Experimental setup

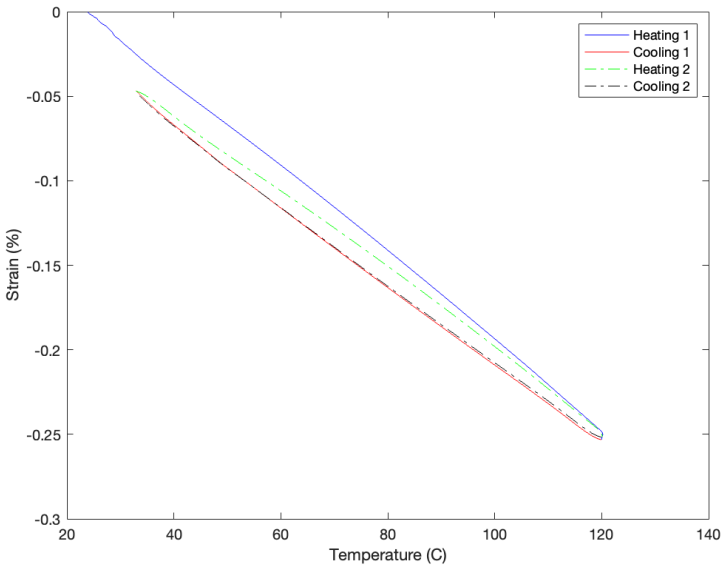

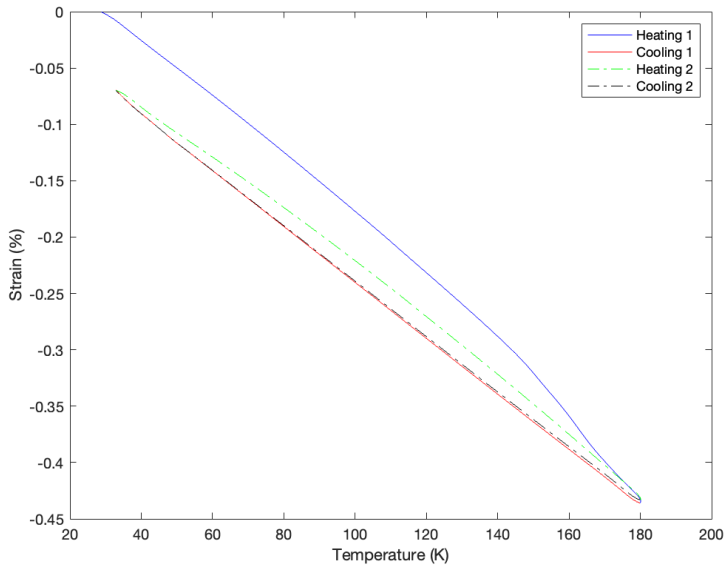

- First experiment characterizes the behavior of the prepreg without further crystallization
- Second experiment identifies the crystallization behavior

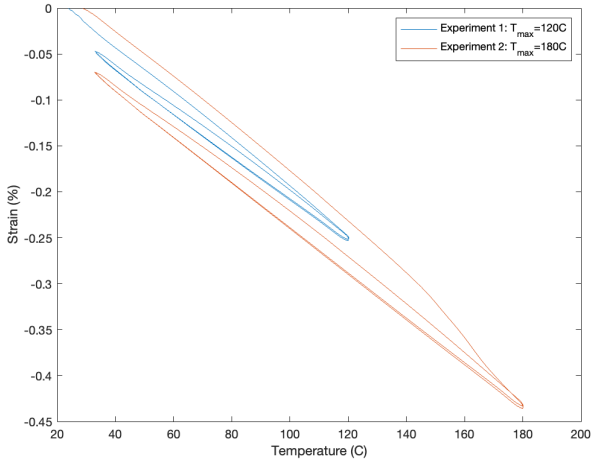

Thermal simulation

$$\rho C_p \frac{\partial T}{\partial t} - \nabla \cdot (\mathbf{K} \nabla T) = 0$$

- The boundary conditions : convection throughout the domain with $h = 25 W/m^2 K$.
- The PGD is used : $T(x, y, z, t) = \sum_{i=1}^{n} F_i(x, y) G_i(t) Z_i(z)$
- The thermal simulation shows a quasi constant temperature through the thickness of the part at every time step.

Thermal simulation

$$\rho C_p \frac{\partial T}{\partial t} - \nabla \cdot (\mathbf{K} \nabla T) = 0$$

- The boundary conditions : convection throughout the domain with $h = 25 W/m^2 K$.
- The PGD is used : $T(x, y, z, t) = \sum_{i=1}^{n} F_i(x, y) G_i(t) Z_i(z)$
- The thermal simulation shows a quasi constant temperature through the thickness of the part at every time step.

Thermal simulation

$$\rho C_p \frac{\partial T}{\partial t} - \nabla \cdot (\mathbf{K} \nabla T) = 0$$

- The boundary conditions : convection throughout the domain with $h = 25 W/m^2 K$.
- The PGD is used : $T(x, y, z, t) = \sum_{i=1}^{n} F_i(x, y) G_i(t) Z_i(z)$
- The thermal simulation shows a quasi constant temperature through the thickness of the part at every time step.

Thermal simulation

$$\rho C_p \frac{\partial T}{\partial t} - \nabla \cdot (\mathbf{K} \nabla T) = 0$$

- The boundary conditions : convection throughout the domain with $h = 25 W/m^2 K$.
- The PGD is used : $T(x, y, z, t) = \sum_{i=1}^{n} F_i(x, y) G_i(t) Z_i(z)$
- The thermal simulation shows a quasi constant temperature through the thickness of the part at every time step.

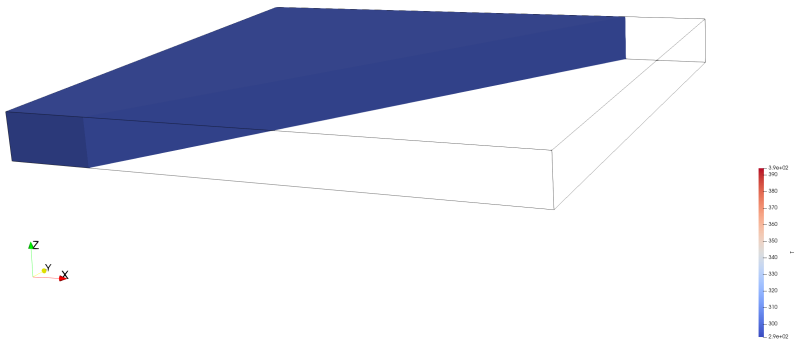

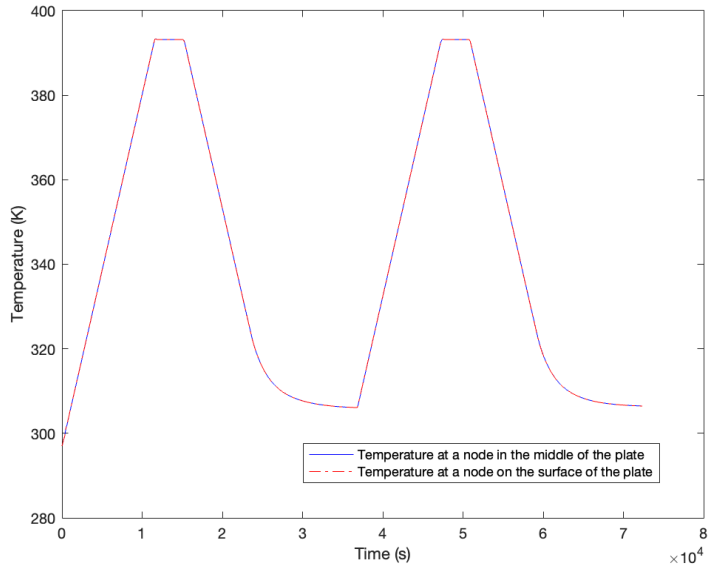

A viscoelastic model

- A Kelvin-Voight viscoelastic model is selected
- Neglecting the acceleration, the equilibrium equations write :

$$\sigma = \mathbb{E}\epsilon + \mu\dot{\epsilon}$$

$$\nabla \cdot (\sigma - \sigma_0) = \mathbf{f}$$

- The gravity constitutes the body force $\mathbf{f}$.
- The thermal stresses are written as :

$$\sigma_0 = \mathbb{E}\epsilon_0$$

$$\epsilon_0 = \alpha\Delta T$$

A viscoelastic model

- A Kelvin-Voight viscoelastic model is selected
- Neglecting the acceleration, the equilibrium equations write :

$$\sigma = \mathbf{E}\epsilon + \mu\dot{\epsilon}$$

$$\nabla \cdot (\sigma - \sigma_0) = \mathbf{f}$$

- The gravity constitutes the body force $\mathbf{f}$.
- The thermal stresses are written as :

$$\sigma_0 = \mathbf{E}\epsilon_0$$

$$\epsilon_0 = \alpha \Delta T$$

A viscoelastic model

- A Kelvin-Voight viscoelastic model is selected
- Neglecting the acceleration, the equilibrium equations write :

$$\sigma = \mathbf{E}\epsilon + \mu\dot{\epsilon}$$

$$\nabla \cdot (\sigma - \sigma_0) = \mathbf{f}$$

- The gravity constitutes the body force $\mathbf{f}$.
- The thermal stresses are written as :

$$\sigma_0 = \mathbf{E}\epsilon_0$$

$$\epsilon_0 = \alpha\Delta T$$

A viscoelastic model

- A Kelvin-Voight viscoelastic model is selected
- Neglecting the acceleration, the equilibrium equations write :

$$\sigma = \mathbf{E}\epsilon + \mu\dot{\epsilon}$$

$$\nabla \cdot (\sigma - \sigma_0) = \mathbf{f}$$

- The gravity constitutes the body force $\mathbf{f}$.
- The thermal stresses are written as :

$$\sigma_0 = \mathbf{E}\epsilon_0$$

$$\epsilon_0 = \alpha \Delta T$$

A viscoelastic model

- The used mechanical properties have the following form :

$$\mathbf{E} = \begin{bmatrix} E_{11} & E_{12} & E_{12} & 0 & 0 & 0 \\ E_{12} & E_{22} & E_{23} & 0 & 0 & 0 \\ E_{12} & E_{23} & E_{22} & 0 & 0 & 0 \\ 0 & 0 & 0 & G_{12} & 0 & 0 \\ 0 & 0 & 0 & 0 & G_{12} & 0 \\ 0 & 0 & 0 & 0 & 0 & G_{23} \end{bmatrix} \quad \mu = \begin{bmatrix} 0 & \mu_{12} & \mu_{12} & 0 & 0 & 0 \\ \mu_{12} & \mu_{22} & \mu_{23} & 0 & 0 & 0 \\ \mu_{12} & \mu_{23} & \mu_{22} & 0 & 0 & 0 \\ 0 & 0 & 0 & 0 & 0 & 0 \\ 0 & 0 & 0 & 0 & 0 & 0 \\ 0 & 0 & 0 & 0 & 0 & 0 \end{bmatrix}$$

- The elasticity properties are computed using Halpin-Tsai equations and the available data sheets.
- The unknown parameters $\mathbf{P}$ are identified using the Proper Generalized Decomposition and the optimization.
- The identification is performed only on the experiment reaching up to 120°C.

A viscoelastic model

- The used mechanical properties have the following form :

$$\mathbf{E} = \begin{bmatrix} E_{11} & E_{12} & E_{12} & 0 & 0 & 0 \\ E_{12} & E_{22} & E_{23} & 0 & 0 & 0 \\ E_{12} & E_{23} & E_{22} & 0 & 0 & 0 \\ 0 & 0 & 0 & G_{12} & 0 & 0 \\ 0 & 0 & 0 & 0 & G_{12} & 0 \\ 0 & 0 & 0 & 0 & 0 & G_{23} \end{bmatrix} \quad \mu = \begin{bmatrix} 0 & \mu_{12} & \mu_{12} & 0 & 0 & 0 \\ \mu_{12} & \mu_{22} & \mu_{23} & 0 & 0 & 0 \\ \mu_{12} & \mu_{23} & \mu_{22} & 0 & 0 & 0 \\ 0 & 0 & 0 & 0 & 0 & 0 \\ 0 & 0 & 0 & 0 & 0 & 0 \\ 0 & 0 & 0 & 0 & 0 & 0 \end{bmatrix}$$

- The elasticity properties are computed using Halpin-Tsai equations and the available data sheets.
- The unknown parameters $\mathbf{P}$ are identified using the Proper Generalized Decomposition and the optimization.
- The identification is performed only on the experiment reaching up to 120°C.

A viscoelastic model

- The used mechanical properties have the following form :

$$\mathbf{E} = \begin{bmatrix} E_{11} & E_{12} & E_{12} & 0 & 0 & 0 \\ E_{12} & E_{22} & E_{23} & 0 & 0 & 0 \\ E_{12} & E_{23} & E_{22} & 0 & 0 & 0 \\ 0 & 0 & 0 & G_{12} & 0 & 0 \\ 0 & 0 & 0 & 0 & G_{12} & 0 \\ 0 & 0 & 0 & 0 & 0 & G_{23} \end{bmatrix} \quad \mu = \begin{bmatrix} 0 & \mu_{12} & \mu_{12} & 0 & 0 & 0 \\ \mu_{12} & \mu_{22} & \mu_{23} & 0 & 0 & 0 \\ \mu_{12} & \mu_{23} & \mu_{22} & 0 & 0 & 0 \\ 0 & 0 & 0 & 0 & 0 & 0 \\ 0 & 0 & 0 & 0 & 0 & 0 \\ 0 & 0 & 0 & 0 & 0 & 0 \end{bmatrix}$$

- The elasticity properties are computed using Halpin-Tsai equations and the available data sheets.
- The unknown parameters $\mathbf{P}$ are identified using the Proper Generalized Decomposition and the optimization.
- The identification is performed only on the experiment reaching up to 120°C.

A viscoelastic model

- The used mechanical properties have the following form :

$$\mathbf{E} = \begin{bmatrix} E_{11} & E_{12} & E_{12} & 0 & 0 & 0 \\ E_{12} & E_{22} & E_{23} & 0 & 0 & 0 \\ E_{12} & E_{23} & E_{22} & 0 & 0 & 0 \\ 0 & 0 & 0 & G_{12} & 0 & 0 \\ 0 & 0 & 0 & 0 & G_{12} & 0 \\ 0 & 0 & 0 & 0 & 0 & G_{23} \end{bmatrix} \quad \mu = \begin{bmatrix} 0 & \mu_{12} & \mu_{12} & 0 & 0 & 0 \\ \mu_{12} & \mu_{22} & \mu_{23} & 0 & 0 & 0 \\ \mu_{12} & \mu_{23} & \mu_{22} & 0 & 0 & 0 \\ 0 & 0 & 0 & 0 & 0 & 0 \\ 0 & 0 & 0 & 0 & 0 & 0 \\ 0 & 0 & 0 & 0 & 0 & 0 \end{bmatrix}$$

- The elasticity properties are computed using Halpin-Tsai equations and the available data sheets.
- The unknown parameters $\mathbf{P}$ are identified using the Proper Generalized Decomposition and the optimization.
- The identification is performed only on the experiment reaching up to 120°C.

Parametric identification

- Optimization cost function :

$$(\mathbf{P}) = \underset{\mathbf{P} \in \mathbb{R}^{+k}}{arg\,\min} \left\{ \sum_{i=2}^{4} \left(\sum_{j=1}^{N_i} \left(\bar{\epsilon}_i^{e,j} - \epsilon_i^{s,j} \right)^2 \right) \right\}, \tag{1}$$

- The optimization is performed on the sections 2 to 4 which are the first cooling, second heating and second cooling.

- The translated strains $\bar{\epsilon}_i^{e,j}$ are derived from the experimental strains $\epsilon_i^{e,j}$ such as the final experimental state and simulated ones superpose.
- The extra strains recovered from section 1 (heating 1) are the residual/drying strains

Parametric identification

- Optimization cost function :

$$(\mathbf{P}) = \underset{\mathbf{P} \in \mathbb{R}^{+k}}{arg\,\min} \left\{ \sum_{i=2}^{4} \left(\sum_{j=1}^{N_i} \left(\bar{\epsilon}_i^{e,j} - \epsilon_i^{s,j} \right)^2 \right) \right\}, \tag{1}$$

- The optimization is performed on the sections 2 to 4 which are the first cooling, second heating and second cooling.
- The translated strains $\bar{\epsilon}_i^{e,j}$ are derived from the experimental strains $\epsilon_i^{e,j}$ such as the final experimental state and simulated ones superpose.
- The extra strains recovered from section 1 (heating 1) are the residual/drying strains

Parametric identification

- Optimization cost function :

$$(\mathbf{P}) = \underset{\mathbf{P} \in \mathbb{R}^{+k}}{arg\,\min} \left\{ \sum_{i=2}^{4} \left(\sum_{j=1}^{N_i} \left(\bar{\epsilon}_i^{e,j} - \epsilon_i^{s,j} \right)^2 \right) \right\}, \tag{1}$$

- The optimization is performed on the sections 2 to 4 which are the first cooling, second heating and second cooling.

- The translated strains $\bar{\epsilon}_i^{e,j}$ are derived from the experimental strains $\epsilon_i^{e,j}$ such as the final experimental state and simulated ones superpose.
- The extra strains recovered from section 1 (heating 1) are the residual/drying strains

Parametric identification

- Optimization cost function :

$$(\mathbf{P}) = \underset{\mathbf{P} \in \mathbb{R}^{+k}}{arg\,\min} \left\{ \sum_{i=2}^{4} \left(\sum_{j=1}^{N_i} \left(\bar{\epsilon}_i^{e,j} - \epsilon_i^{s,j} \right)^2 \right) \right\}, \tag{1}$$

- The optimization is performed on the sections 2 to 4 which are the first cooling, second heating and second cooling.

- The translated strains $\bar{\epsilon}_i^{e,j}$ are derived from the experimental strains $\epsilon_i^{e,j}$ such as the final experimental state and simulated ones superpose.
- The extra strains recovered from section 1 (heating 1) are the residual/drying strains

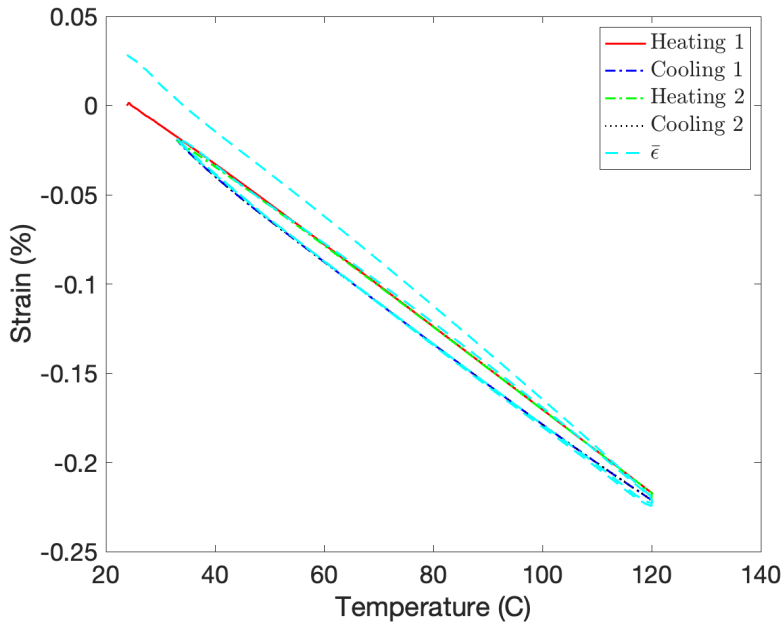

Initial residual and drying strains

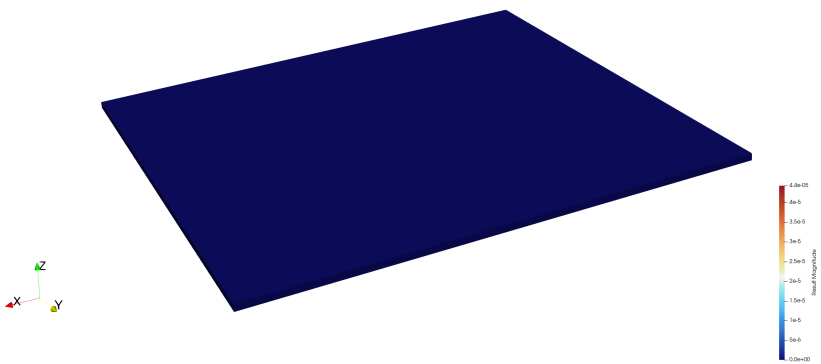

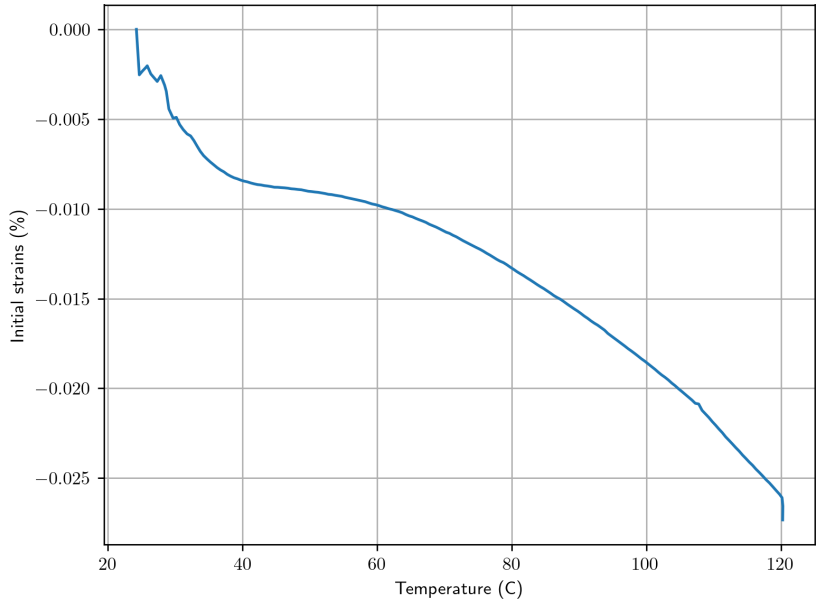

- Residual/drying strains as defined as :

$$\bar{\epsilon}^{ini} = \bar{\epsilon}^{e}_{1} - \epsilon^{s}_{1}$$

- The identified initial irreversible strain release will be modeled using neural Ordinary Differential equations.

Initial strain release

- The initial irreversible strain ϵ^{ini} release can be generated by residual strains and drying of the prepregs.
- Neural Ordinary Differential Equation (Neural ODE) will be used to identify the strain release.

$$\frac{\partial \epsilon^{ini}}{\partial t} = \mathcal{F}(t, \Delta T_0, \epsilon^{ini}, \epsilon^s)$$

- To guarantee stability, the following stabilized neural ODE formulation is

$$\frac{\partial \epsilon^{ini}}{\partial t} = \epsilon^{ini} \cdot \mathcal{G}(t, \Delta T_0, \epsilon^{ini}, \epsilon^s) + \mathcal{H}(t, \Delta T_0, \epsilon^s)$$

- For stability $\mathcal{G}$ is a neural network imposed to output negative values by construction.

Initial strain release

- The initial irreversible strain ϵ^{ini} release can be generated by residual strains and drying of the prepregs.
- Neural Ordinary Differential Equation (Neural ODE) will be used to identify the strain release.

$$\frac{\partial \epsilon^{ini}}{\partial t} = \mathcal{F}(t, \Delta T_0, \epsilon^{ini}, \epsilon^s)$$

- To guarantee stability, the following stabilized neural ODE formulation is

$$\frac{\partial \epsilon^{ini}}{\partial t} = \epsilon^{ini} \cdot \mathcal{G}(t, \Delta T_0, \epsilon^{ini}, \epsilon^s) + \mathcal{H}(t, \Delta T_0, \epsilon^s)$$

- For stability $\mathcal{G}$ is a neural network imposed to output negative values by construction.

Initial strain release

- The initial irreversible strain ϵ^{ini} release can be generated by residual strains and drying of the prepregs.
- Neural Ordinary Differential Equation (Neural ODE) will be used to identify the strain release.

$$\frac{\partial \epsilon^{ini}}{\partial t} = \mathcal{F}(t, \Delta T_0, \epsilon^{ini}, \epsilon^s)$$

- To guarantee stability, the following stabilized neural ODE formulation is used [1]

$$\frac{\partial \epsilon^{ini}}{\partial t} = \epsilon^{ini} \cdot \mathcal{G}(t, \Delta T_0, \epsilon^{ini}, \epsilon^s) + \mathcal{H}(t, \Delta T_0, \epsilon^s)$$

- For stability $\mathcal{G}$ is a neural network imposed to output negative values by construction.

1. Ghnatios et al., Learning Data-Driven Stable Corrections of Dynamical Systems, Application to the Simulation of the Top-Oil Temperature Evolution of a Power Transformer, 2024

Initial strain release

- The initial irreversible strain ϵ^{ini} release can be generated by residual strains and drying of the prepregs.
- Neural Ordinary Differential Equation (Neural ODE) will be used to identify the strain release.

$$\frac{\partial \epsilon^{ini}}{\partial t} = \mathcal{F}(t, \Delta T_0, \epsilon^{ini}, \epsilon^s)$$

- To guarantee stability, the following stabilized neural ODE formulation is used [1]

$$\frac{\partial \epsilon^{ini}}{\partial t} = \epsilon^{ini} \cdot \mathcal{G}(t, \Delta T_0, \epsilon^{ini}, \epsilon^s) + \mathcal{H}(t, \Delta T_0, \epsilon^s)$$

- For stability $\mathcal{G}$ is a neural network imposed to output negative values by construction.

1. Ghnatios et al., Learning Data-Driven Stable Corrections of Dynamical Systems, Application to the Simulation of the Top-Oil Temperature Evolution of a Power Transformer, 2024

Neural ODE model

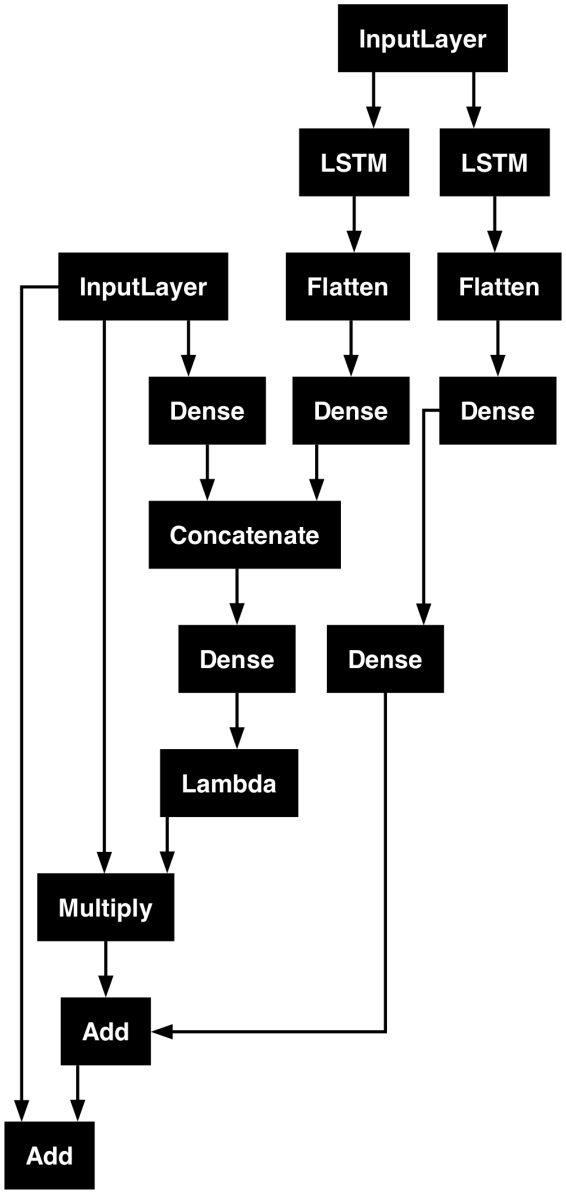

- Training performed over 100 epochs with ADAM algorithm.
- A custom built learning rate update function is used
- the LSTM takes in memory the last two values in the input parameters (t, T, ϵ^s)
- Only the last value of $\bar{\epsilon}^{ini}$ is passed into the next time step

Neural ODE model

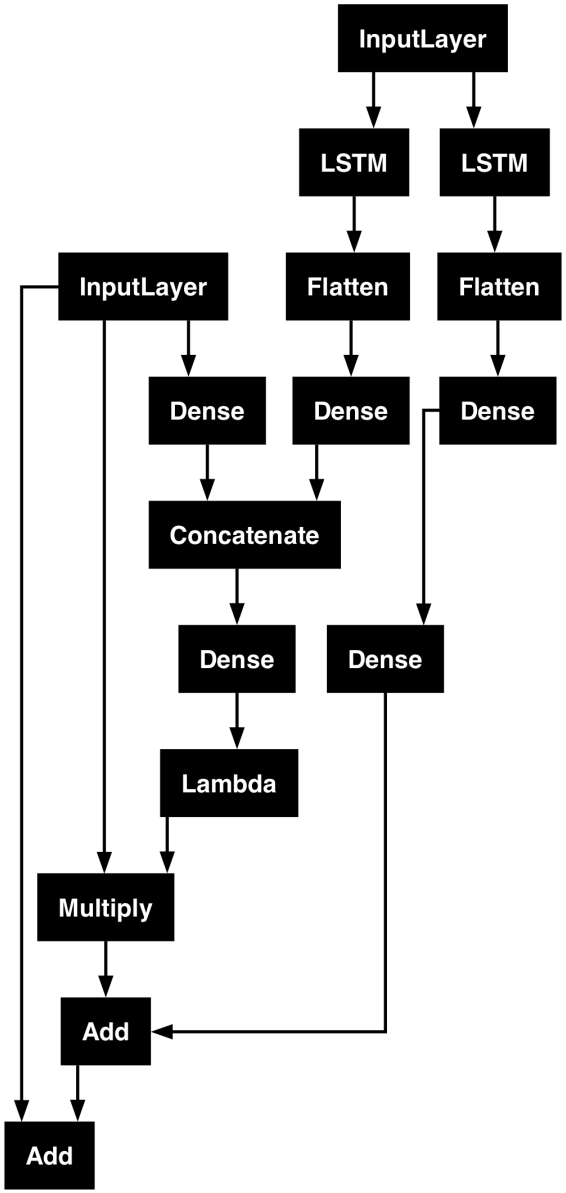

- Training performed over 100 epochs with ADAM algorithm.
- A custom built learning rate update function is used
- the LSTM takes in memory the last two values in the input parameters (t, T, ϵ^s)
- Only the last value of $\bar{\epsilon}^{ini}$ is passed into the next time step

Neural ODE model

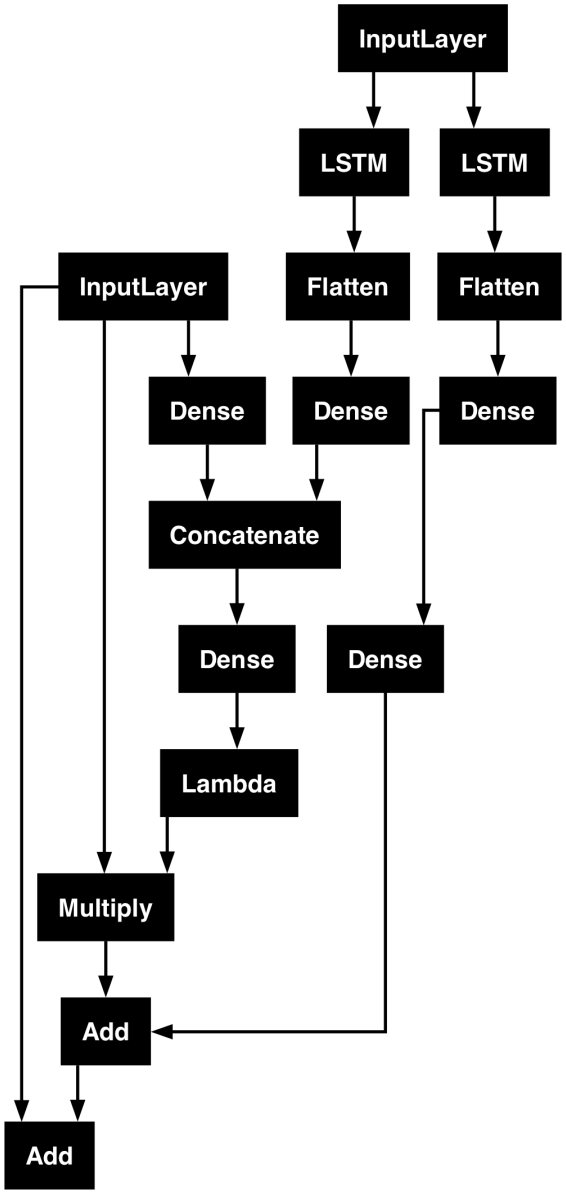

- Training performed over 100 epochs with ADAM algorithm.
- A custom built learning rate update function is used
- the LSTM takes in memory the last two values in the input parameters (t, T, ϵ^s)
- Only the last value of $\bar{\epsilon}^{ini}$ is passed into the next time step

Neural ODE model

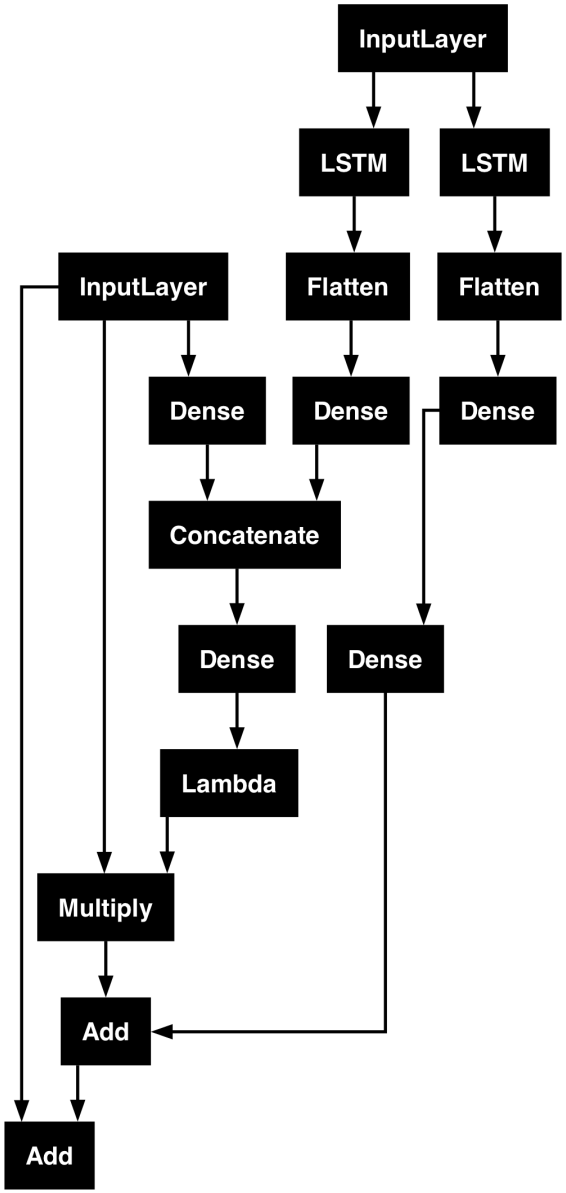

- Training performed over 100 epochs with ADAM algorithm.
- A custom built learning rate update function is used
- the LSTM takes in memory the last two values in the input parameters (t, T, ϵ^s)
- Only the last value of $\bar{\epsilon}^{ini}$ is passed into the next time step

Converged model

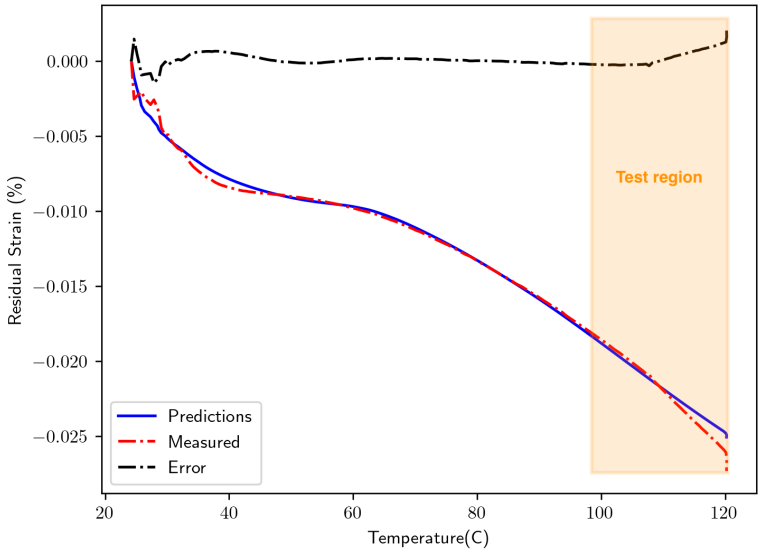

- Absolute errors after convergence :
  - On training region : 0.02% strain
  - On Testing region : 0.07% strain
- The Neural ODE relied the most on the simulated strains from the viscoelastic model.

Converged model

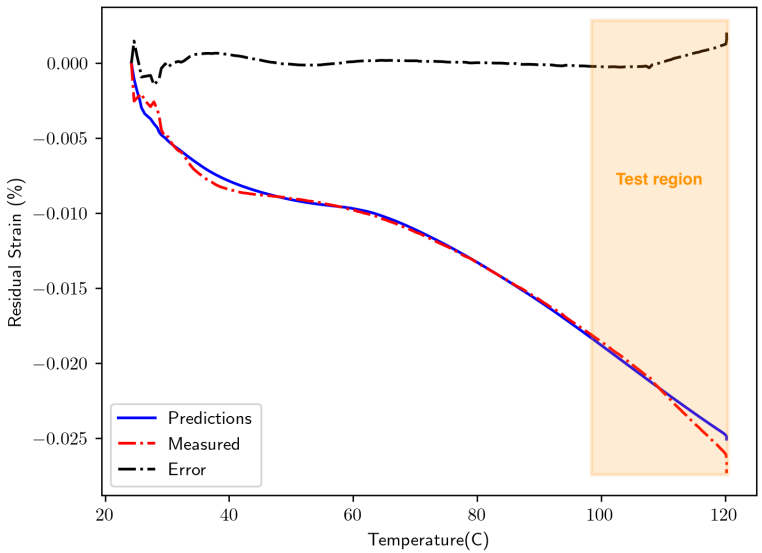

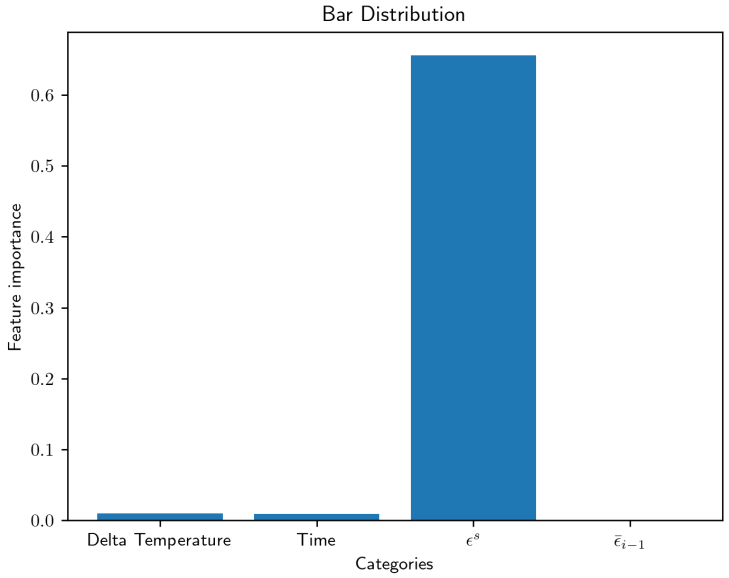

- Absolute errors after convergence :
  - On training region : 0.02% strain
  - On Testing region : 0.07% strain
- The Neural ODE relied the most on the simulated strains from the viscoelastic model.

Converged model

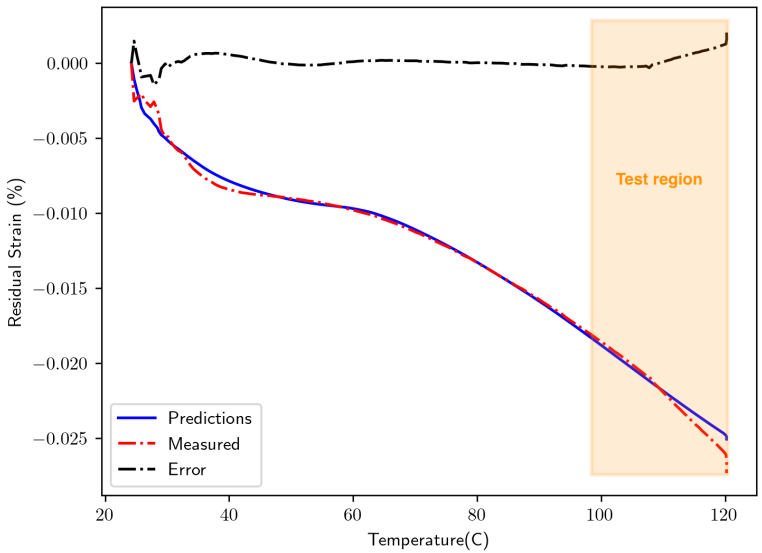

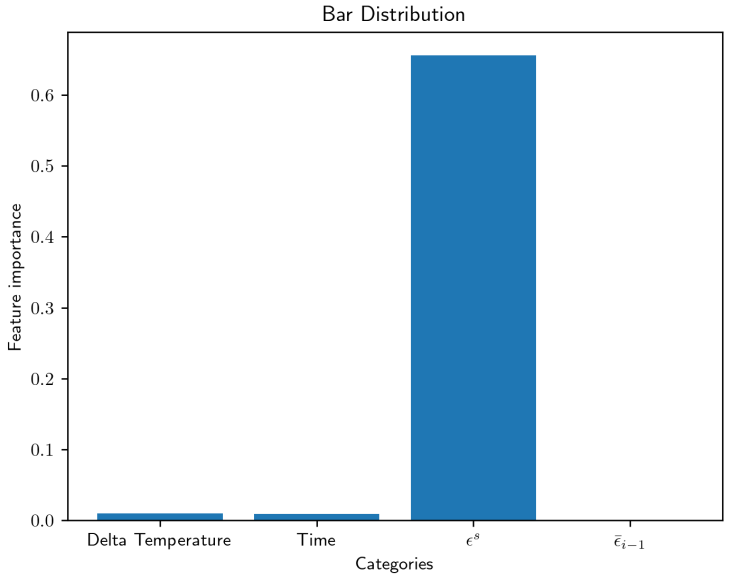

- Absolute errors after convergence :
  - On training region : 0.02% strain
  - On Testing region : 0.07% strain
- The Neural ODE relied the most on the simulated strains from the viscoelastic model.

Derivative functions

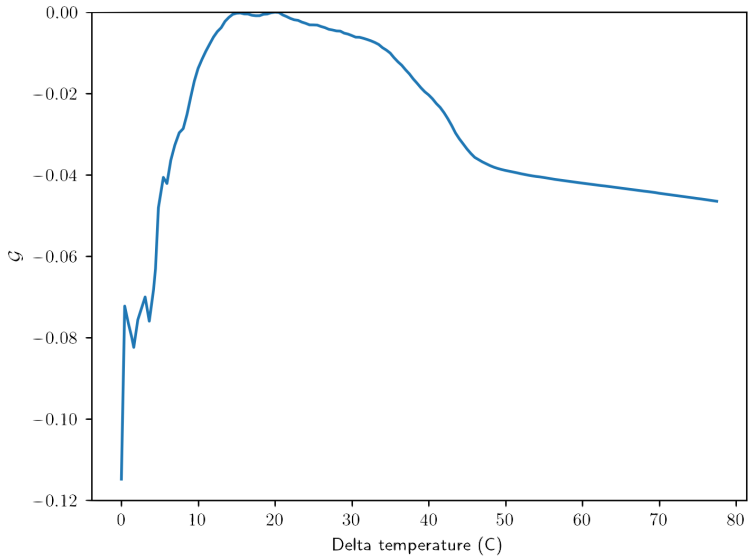

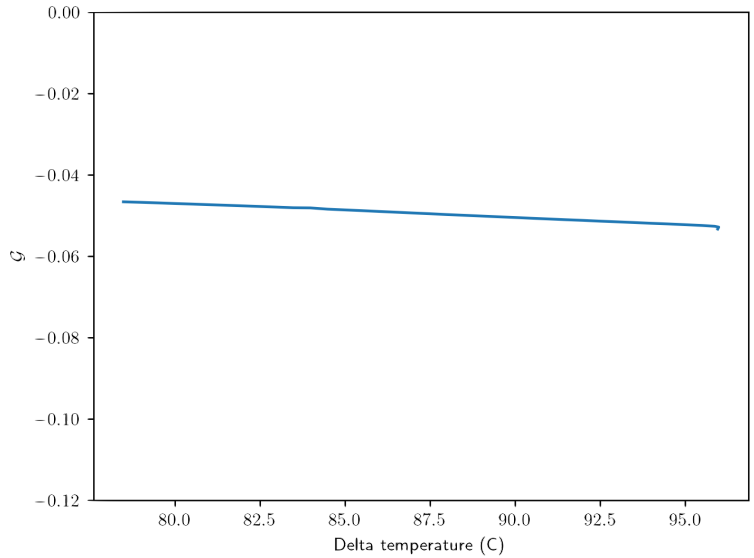

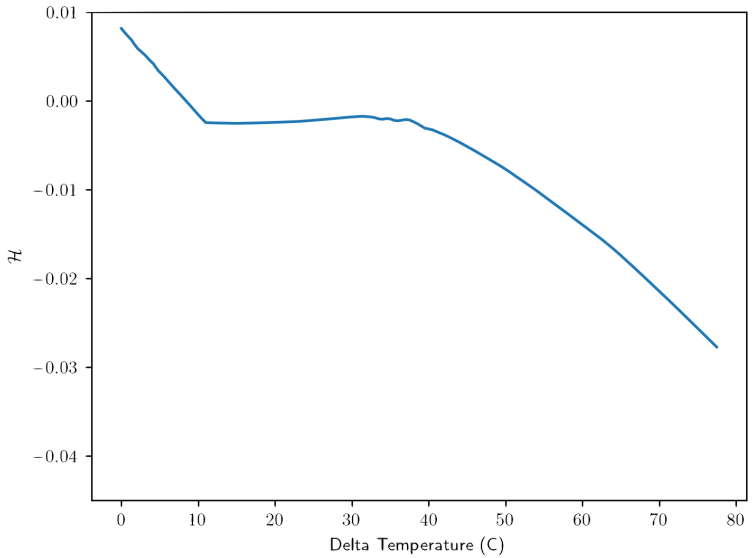

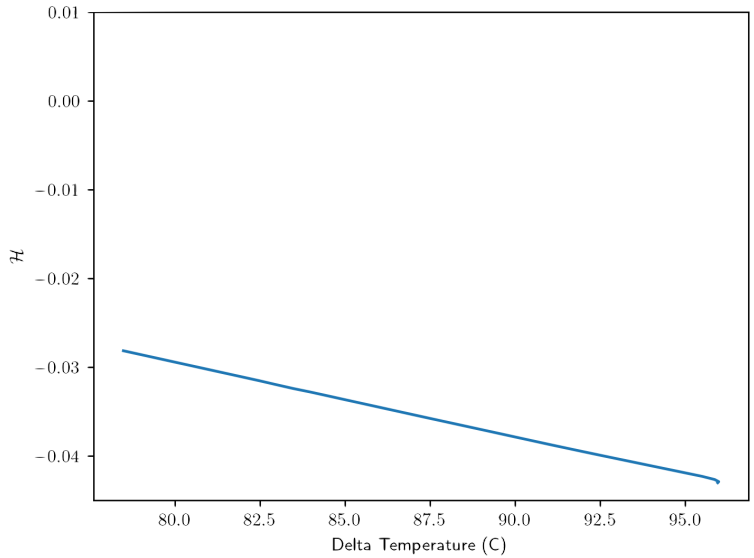

Prediction on the 180C experiment

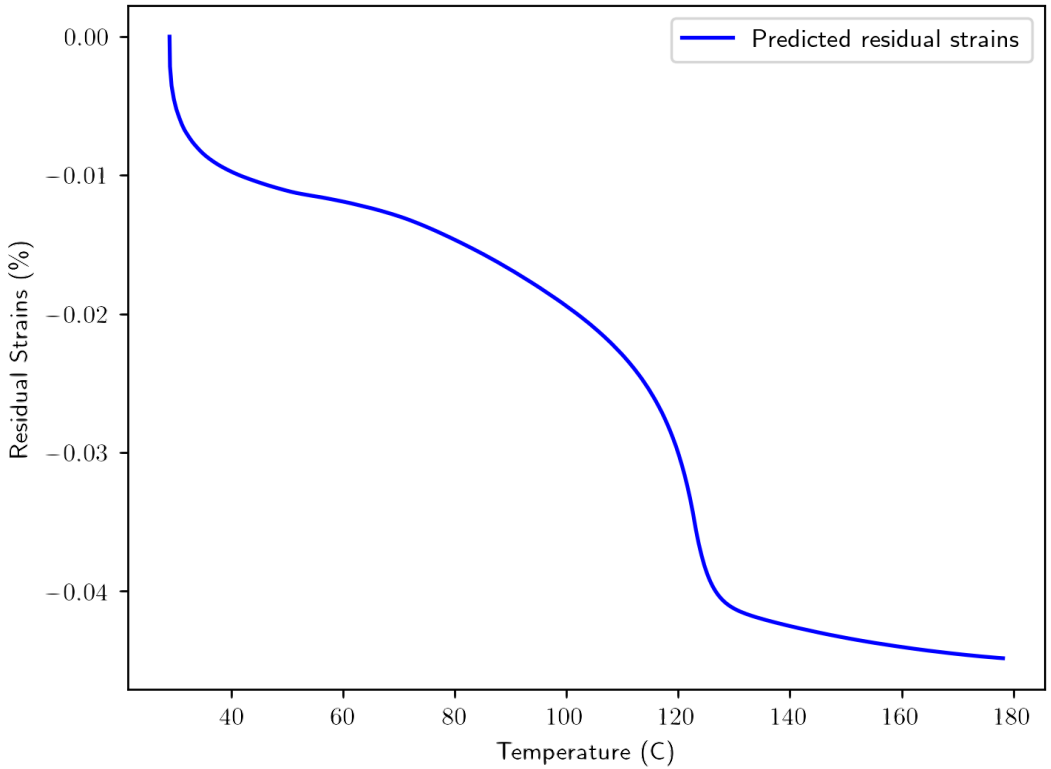

- The prediction can be performed on the experiment with the temperature increasing up to $180C$ on section "heating 1".
- The neural network predicted the saturation of the residual/drying stresses.

Prediction on the 180C experiment

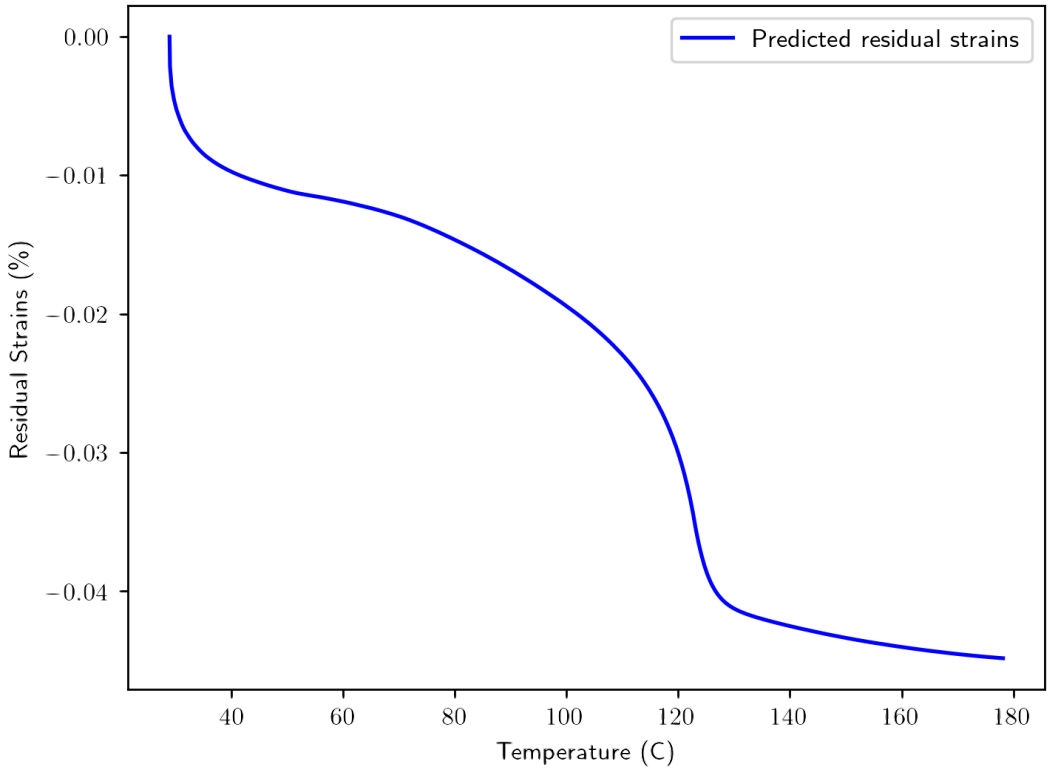

- The prediction can be performed on the experiment with the temperature increasing up to $180C$ on section "heating 1".
- The neural network predicted the saturation of the residual/drying stresses.

Viscoelastic + residual strains model

- The crystallization strains are defined as :

$$\epsilon_{180}^{crys} = \bar{\epsilon}_{180} - \epsilon_{180}^{s} - \epsilon_{180}^{ini}$$

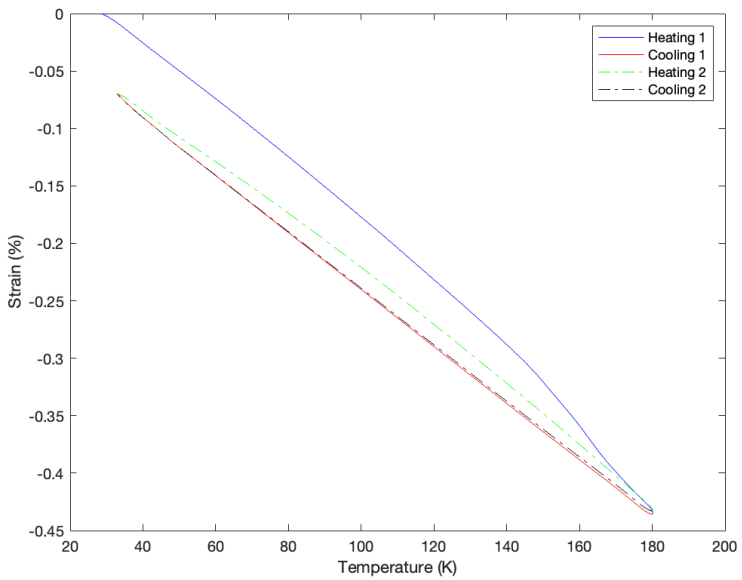

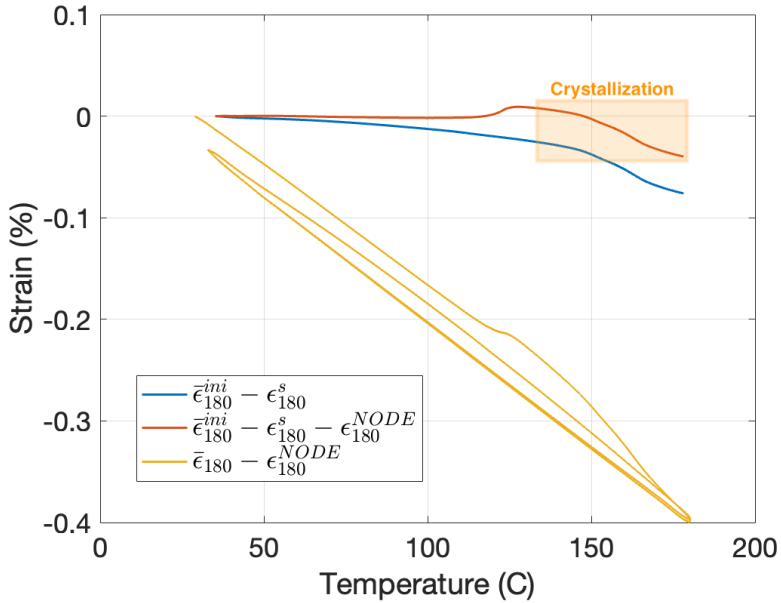

Correlation with DSC experiment

- The DSC experiment shows an glass transition temperature around $146.7^{o}C$ during the first heating phase.
- The strains shows a decrease in value starting $147^{o}C - 148^{o}C$.

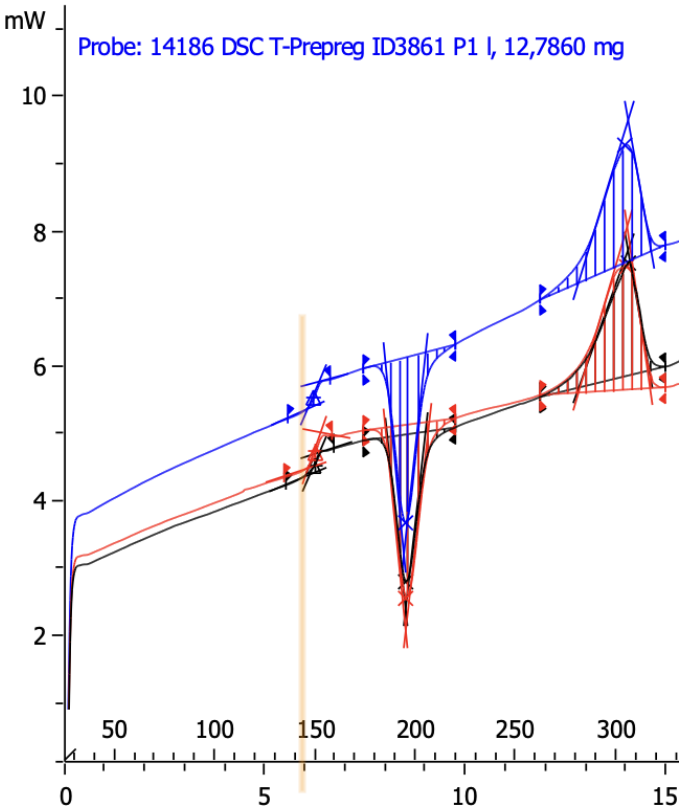

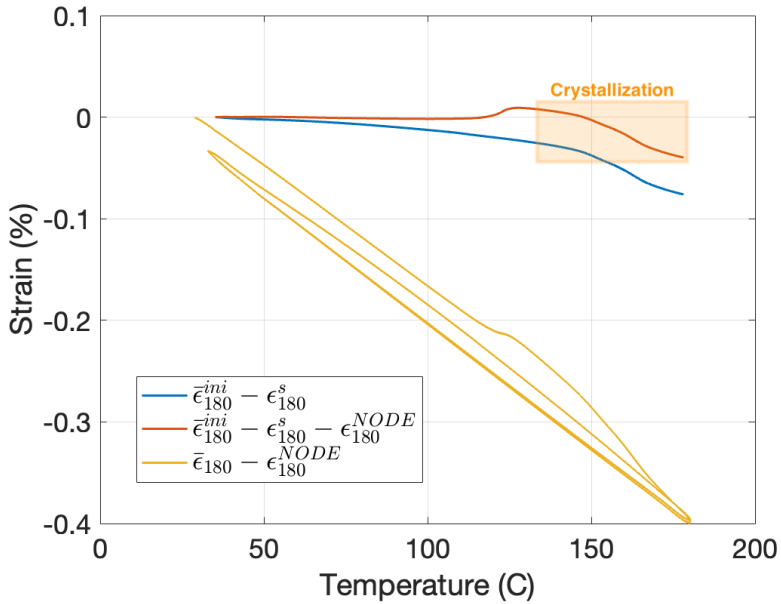

Correlation with DSC experiment

- The DSC experiment shows an glass transition temperature around 146.7^oC during the first heating phase.
- The strains shows a decrease in value starting $147^oC - 148^oC$.

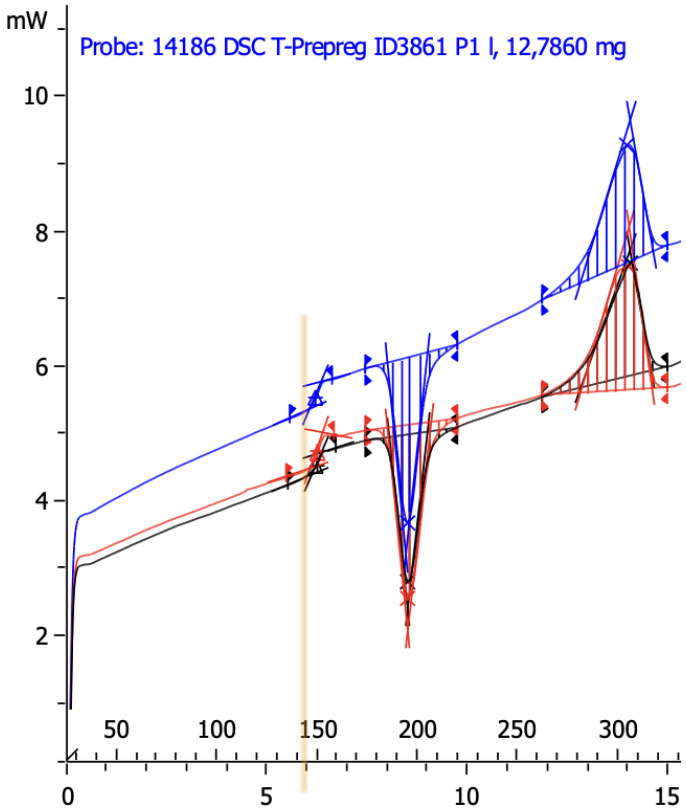

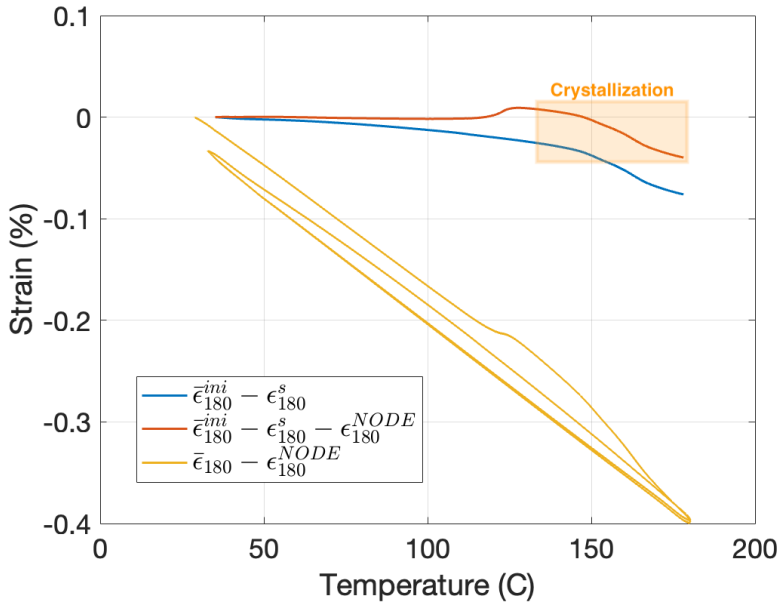

Crystallization Neural ODE

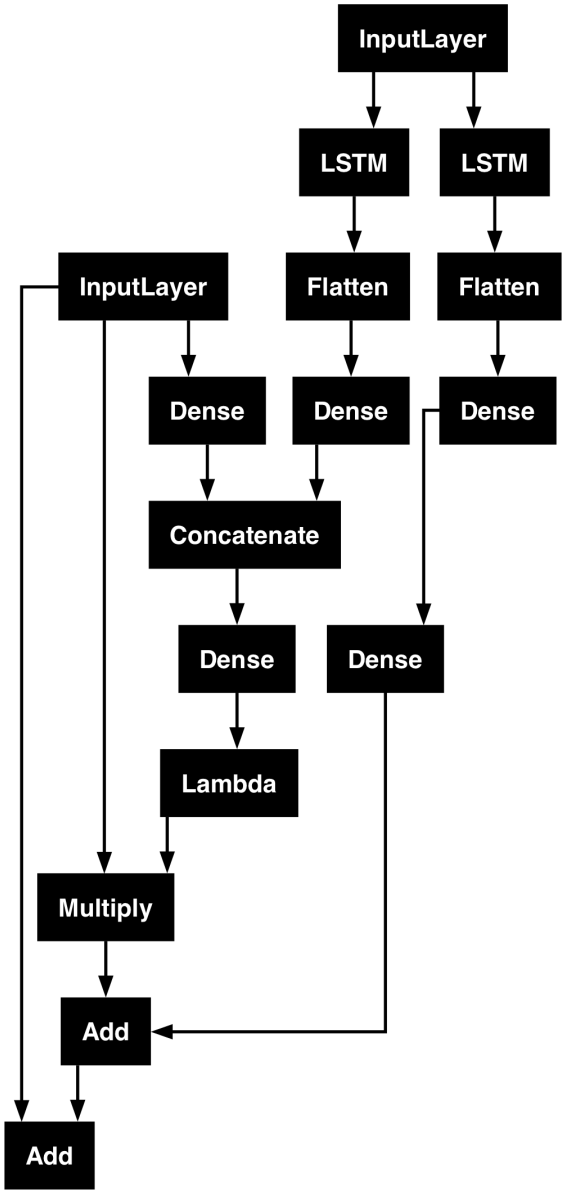

- Training performed over 100 epochs with ADAM algorithm.
- A custom built learning rate update function is used
- LSTM takes as memory input the last two values in the input parameters (t, T, ϵ^s)
- Only the last value of $\bar{\epsilon}^{crys}$ is passed into the next time step

Crystallization Neural ODE

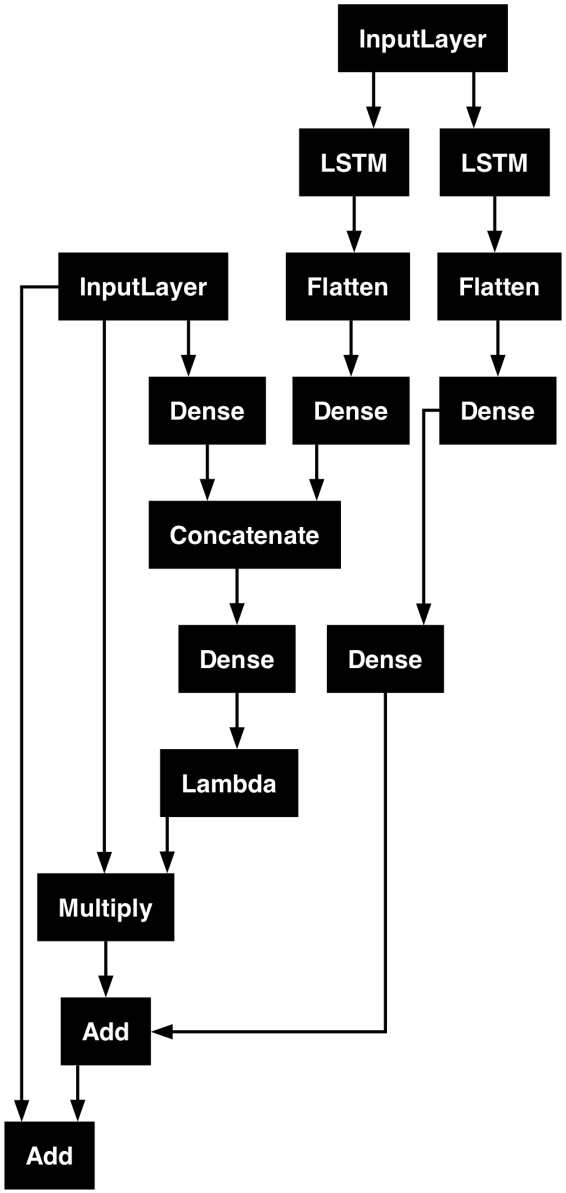

- Training performed over 100 epochs with ADAM algorithm.
- A custom built learning rate update function is used
- LSTM takes as memory input the last two values in the input parameters (t, T, ϵ^s)
- Only the last value of $\bar{\epsilon}^{crys}$ is passed into the next time step

Crystallization Neural ODE

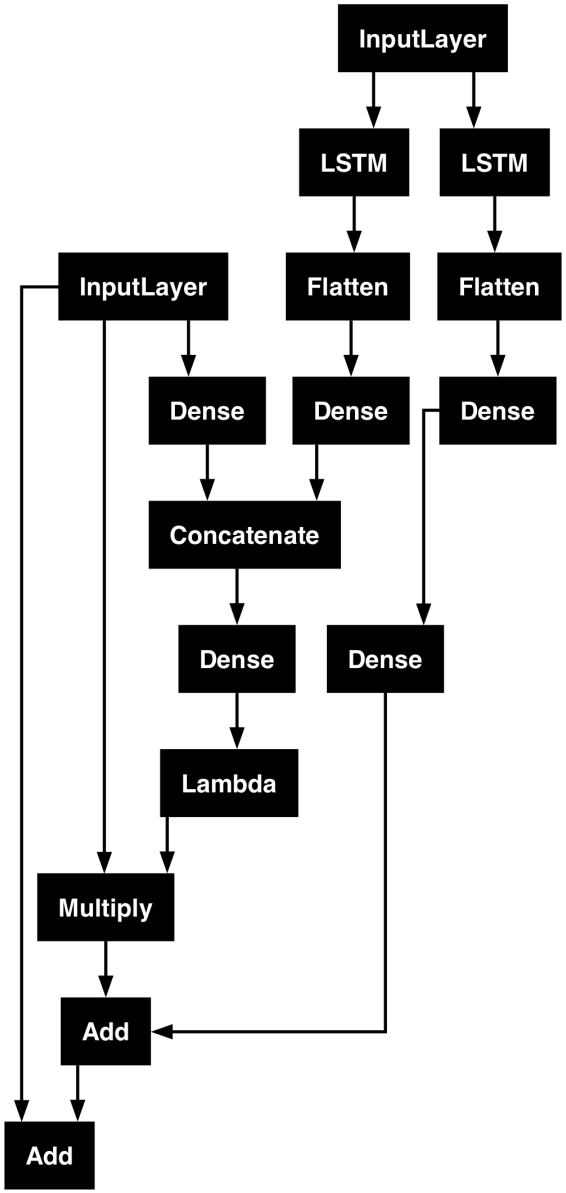

- Training performed over 100 epochs with ADAM algorithm.
- A custom built learning rate update function is used
- LSTM takes as memory input the last two values in the input parameters (t, T, ϵ^s)
- Only the last value of $\bar{\epsilon}^{crys}$ is passed into the next time step

Crystallization Neural ODE

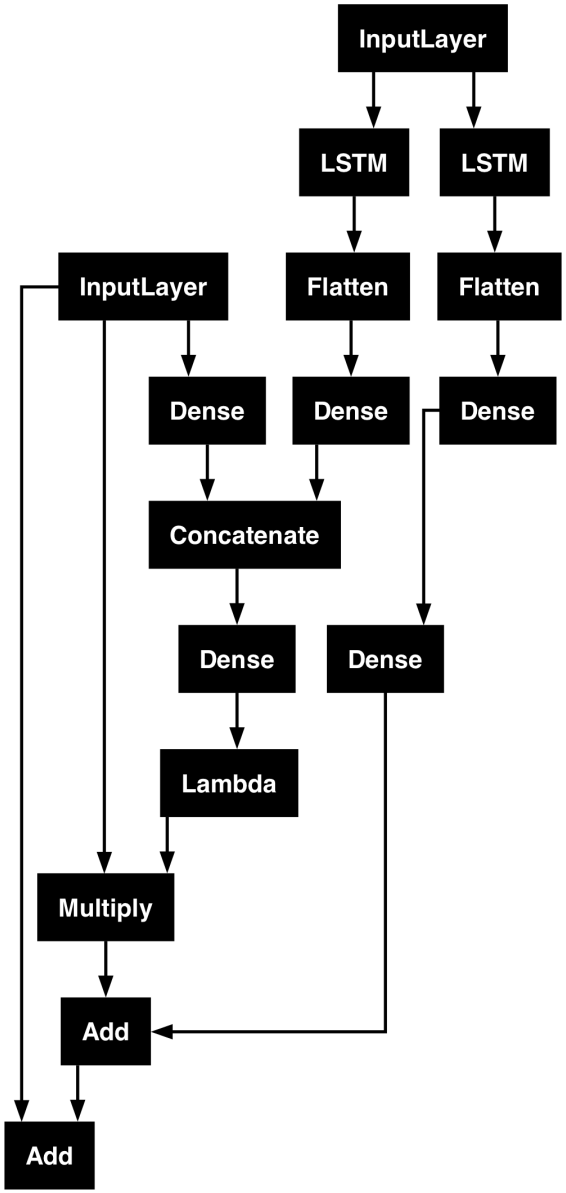

- Training performed over 100 epochs with ADAM algorithm.
- A custom built learning rate update function is used
- LSTM takes as memory input the last two values in the input parameters (t, T, ϵ^s)
- Only the last value of $\bar{\epsilon}^{crys}$ is passed into the next time step

Converged model

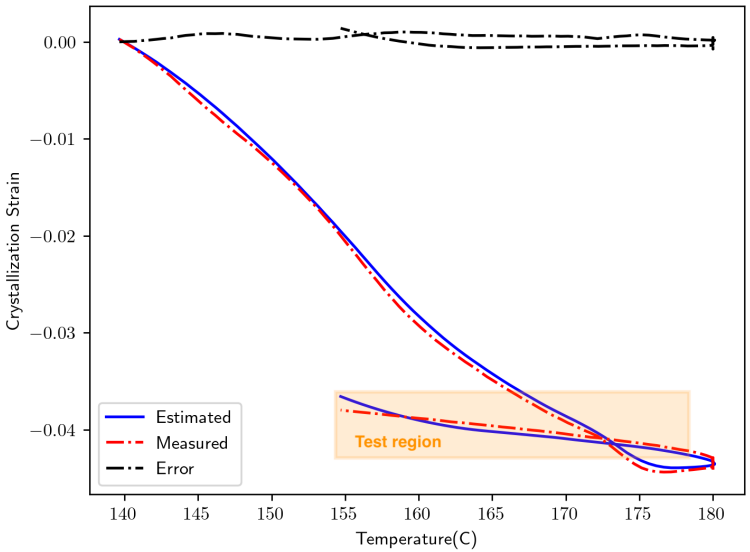

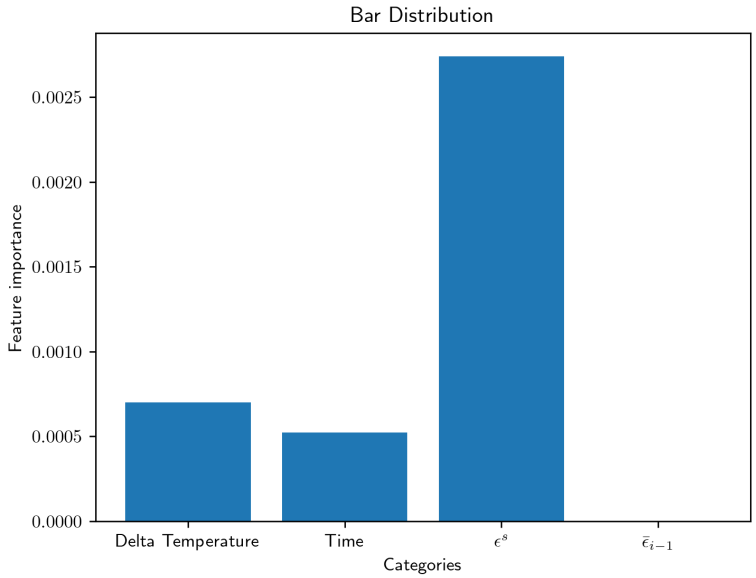

- Relative error of about 10.92% on both testing and integration
- The neural ODE relied mostly on the the simulated strains
- The thermal differential and time are also important in this case, as the evolution direction in time and temperature is important to create a unique input to the Neural ODE.

Converged model

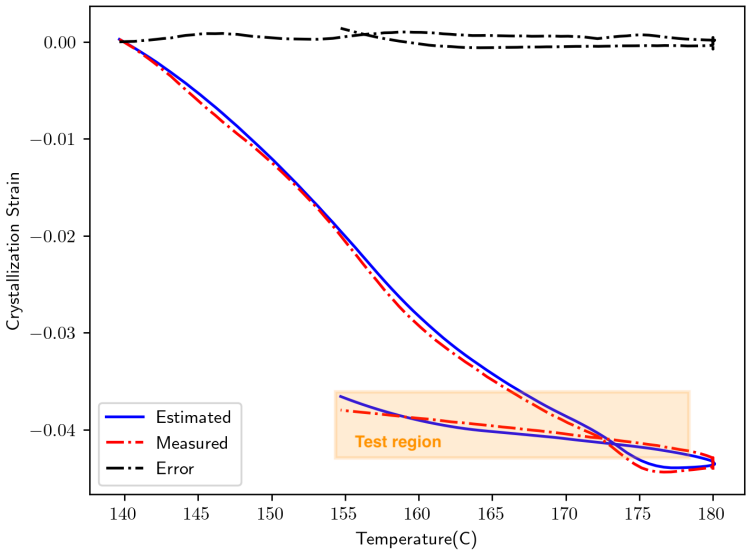

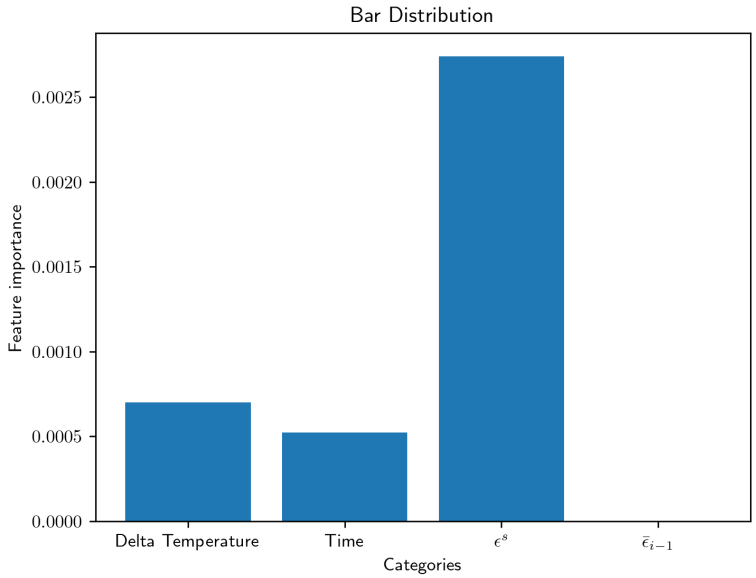

- Relative error of about 10.92% on both testing and integration
- The neural ODE relied mostly on the the simulated strains
- The thermal differential and time are also important in this case, as the evolution direction in time and temperature is important to create a unique input to the Neural ODE.

Converged model

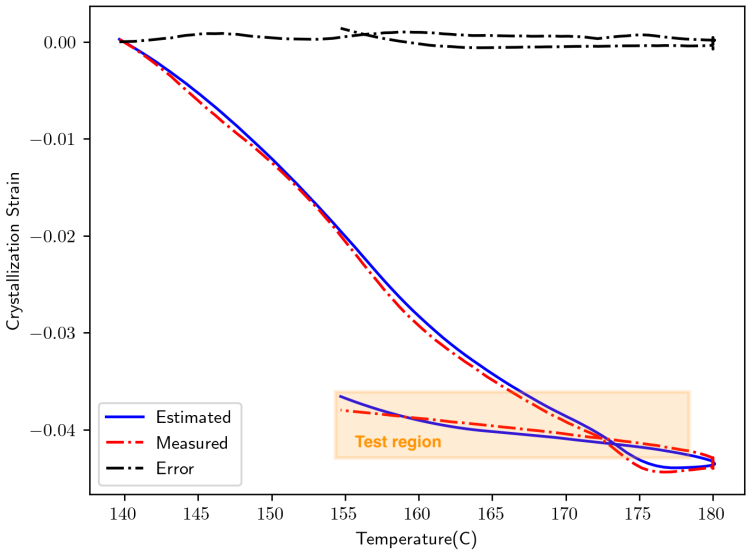

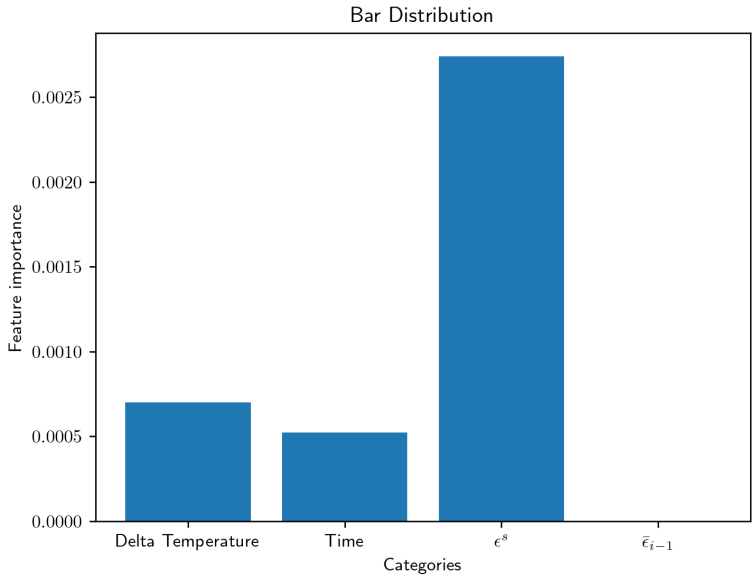

- Relative error of about 10.92% on both testing and integration
- The neural ODE relied mostly on the the simulated strains
- The thermal differential and time are also important in this case, as the evolution direction in time and temperature is important to create a unique input to the Neural ODE.

Crystallization effect

- Crystallization can generate further changes in **E** and α
- To avoid the need to identify the parameters at every cycle, we build a hybrid model
- The modeling compensate the strains using :

$$\epsilon^{cryst}\Big|_{T>T_{cryst}} = \epsilon^{exp}\Big|_{T>T_{cryst}} - \epsilon^{s}\Big|_{T>T_{cryst}}$$

- The same Neural ODE used for crystallization is extended throughout the experiment to predict the effect of the crystallization using :

$$\epsilon^{cryst}\Big|_{T>T_{cryst}} = \epsilon^{cryst}\Big|_{T>T_{cryst}} + \mathcal{N}_{\Theta}(\epsilon^{cryst}, T, \epsilon^{exp}) + \mathcal{N}_{\Theta}(\epsilon^{cryst}, T, \epsilon^{exp})$$

- The training is performed on the first three stages of the experiment, and testing is performed on the last one.

Crystallization effect

- Crystallization can generate further changes in $\mathbf{E}$ and α
- To avoid the need to identify the parameters at every cycle, we build a hybrid model
- The modeling compensate the strains using :

$$\epsilon^{cryst}|_{T>147} = \epsilon^{exp}|_{T>147} - \epsilon^{s}|_{T>147}$$

- The same Neural ODE used for crystallization is extended throughout the experiment to predict the effect of the crystallization using :

$$\epsilon^{cryst}|_{T>147} = \epsilon^{cryst} \cdot \mathcal{G}_2(t, T, \epsilon^s, \epsilon^{cryst}) + \mathcal{H}_2(t, T, \epsilon^s)$$

- The training is performed on the first three stages of the experiment, and testing is performed on the last one.

Crystallization effect

- Crystallization can generate further changes in $\mathbf{E}$ and α
- To avoid the need to identify the parameters at every cycle, we build a hybrid model
- The modeling compensate the strains using :

$$\epsilon^{cryst}\big|_{T>147} = \epsilon^{exp}\big|_{T>147} - \epsilon^{s}\big|_{T>147}$$

- The same Neural ODE used for crystallization is extended throughout the experiment to predict the effect of the crystallization using :

$$\epsilon^{cryst}\big|_{T>147} = \epsilon^{cryst} \cdot \mathcal{G}_2(t, T, \epsilon^s, \epsilon^{cryst}) + \mathcal{H}_2(t, T, \epsilon^s)$$

- The training is performed on the first three stages of the experiment, and testing is performed on the last one.

Crystallization effect

- Crystallization can generate further changes in **E** and α
- To avoid the need to identify the parameters at every cycle, we build a hybrid model
- The modeling compensate the strains using :

$$\epsilon^{cryst}|_{T>147} = \epsilon^{exp}|_{T>147} - \epsilon^{s}|_{T>147}$$

- The same Neural ODE used for crystallization is extended throughout the experiment to predict the effect of the crystallization using :

$$\epsilon^{cryst}|_{T>147} = \epsilon^{cryst} \cdot \mathcal{G}_2(t, T, \epsilon^s, \epsilon^{cryst}) + \mathcal{H}_2(t, T, \epsilon^s)$$

- The training is performed on the first three stages of the experiment, and testing is performed on the last one.

Crystallization model

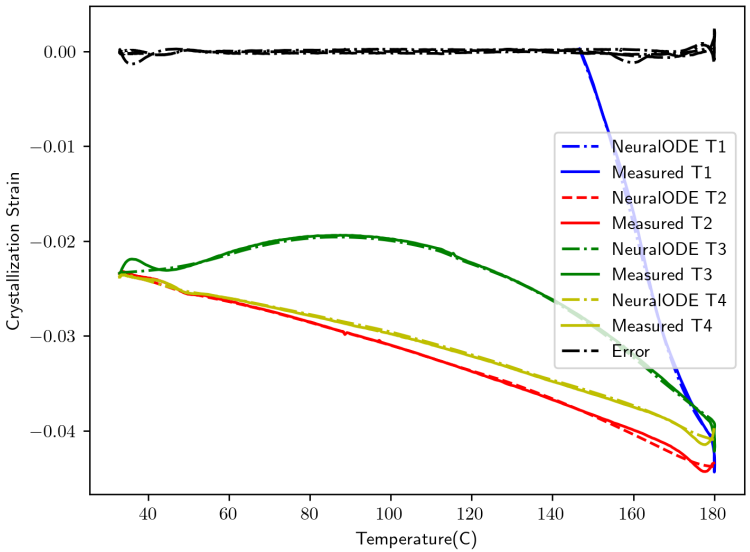

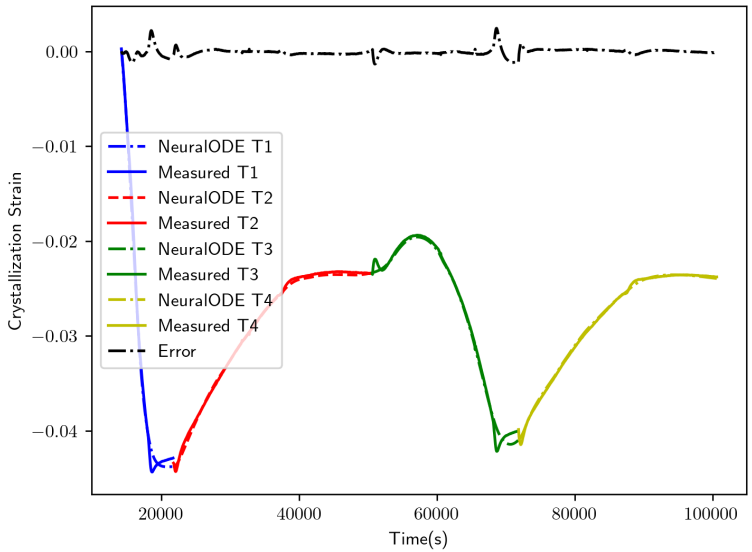

- Beyond the first onset of crystallization the effect becomes limited due to limited changes in material properties
- The errors in the testing region are similar to the ones obtained on the training data.

Crystallization model

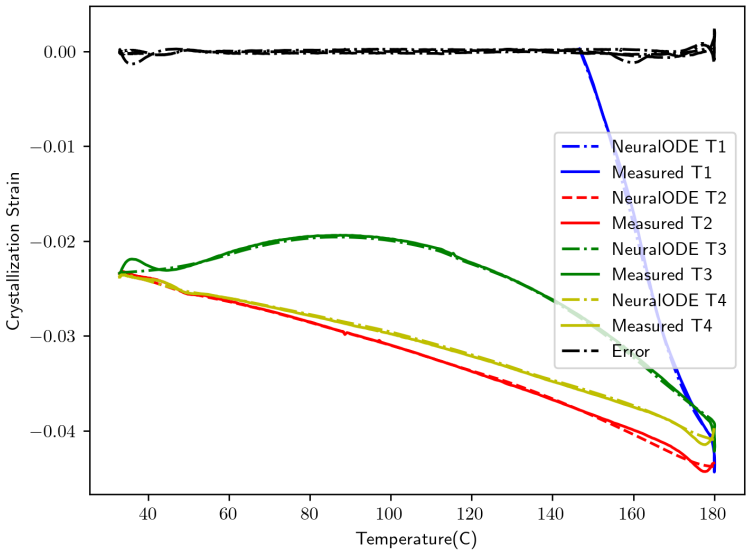

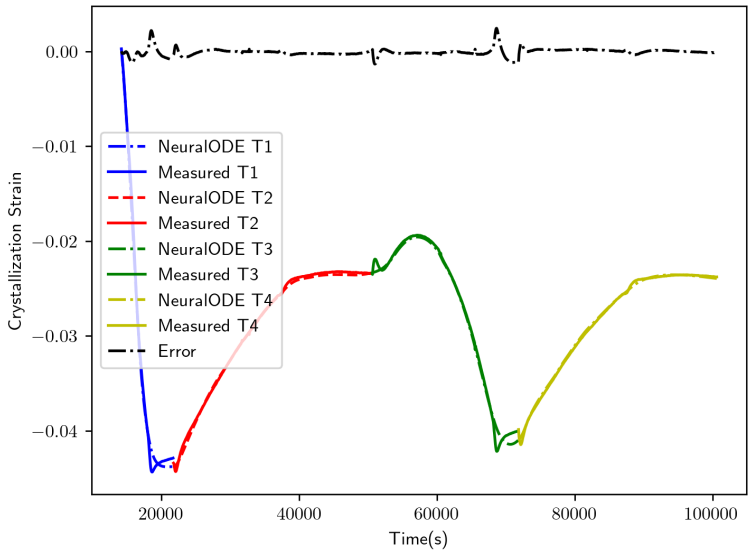

- Beyond the first onset of crystallization the effect becomes limited due to limited changes in material properties
- The errors in the testing region are similar to the ones obtained on the training data.

Crystallization model

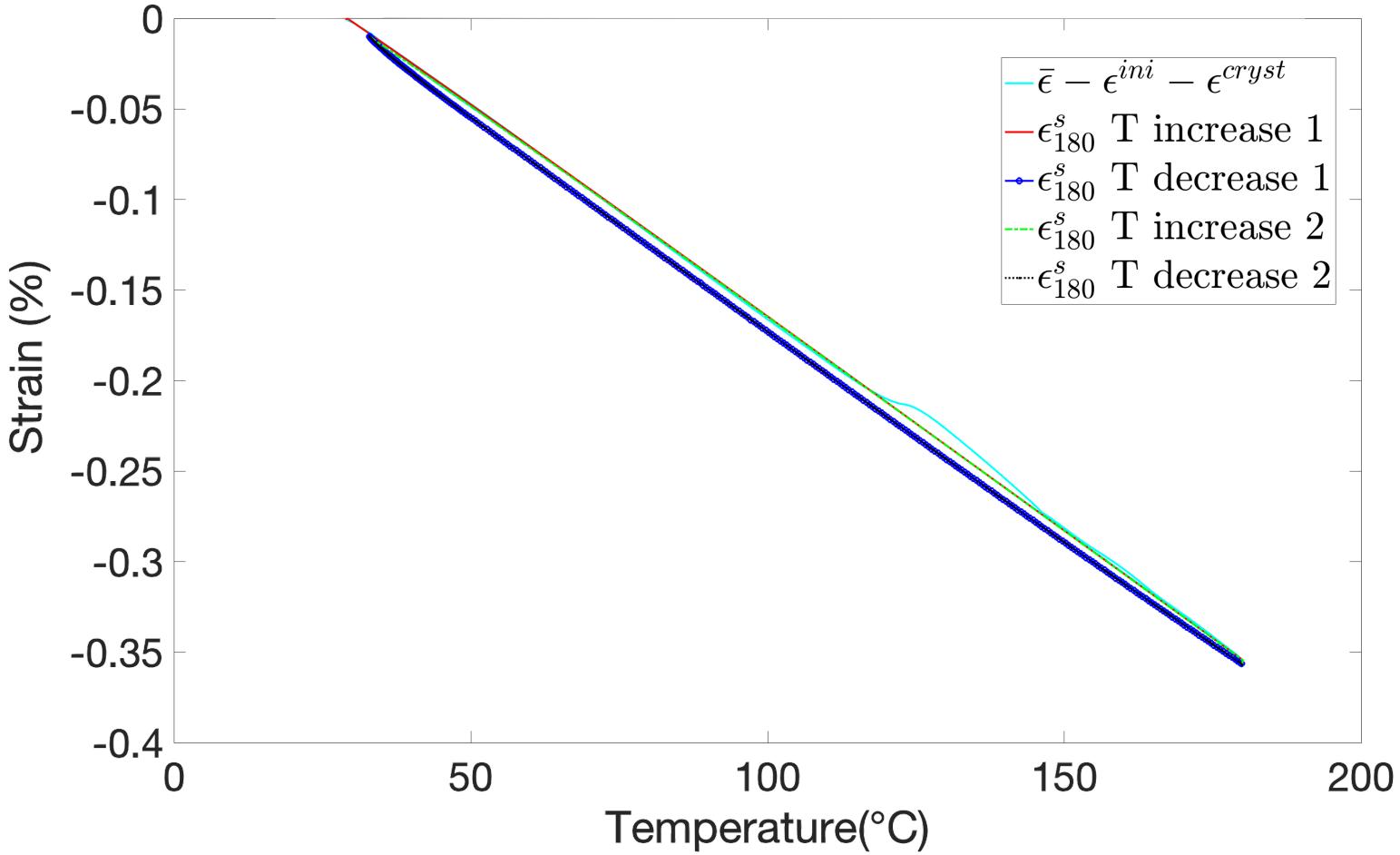

- Final result when accounting for the initial strains and the crystallization effect.

Conclusion

- We can identify the viscoelastic material properties of robotic 3D printed prepregs.
- The effect of drying and residual strains is modeled and used on unseen data.
- The predictions generalize well far beyond the training region.
- The effect of the Crystallization on the trains and material performance is modeled using stabilized Neural ODEs.
- The prediction generalizes outside the training region.
- Stabilized neural ODEs are stable for data applications.

Conclusion

- We can identify the viscoelastic material properties of robotic 3D printed prepregs.
- The effect of drying and residual strains is modeled and used on unseen data.
- The predictions generalize well far beyond the training region.
- The effect of the Crystallization on the trains and material performance is modeled using stabilized Neural ODEs.
- The prediction generalizes outside the training region.
- Stabilized neural ODEs are stable for data applications.

Conclusion

- We can identify the viscoelastic material properties of robotic 3D printed prepregs.
- The effect of drying and residual strains is modeled and used on unseen data.
- The predictions generalize well far beyond the training region.
- The effect of the Crystallization on the trains and material performance is modeled using stabilized Neural ODEs.
- The prediction generalizes outside the training region.
- Stabilized neural ODEs are stable for data applications.

Conclusion

- We can identify the viscoelastic material properties of robotic 3D printed prepregs.
- The effect of drying and residual strains is modeled and used on unseen data.
- The predictions generalize well far beyond the training region.
- The effect of the Crystallization on the trains and material performance is modeled using stabilized Neural ODEs.
- The prediction generalizes outside the training region.
- Stabilized neural ODEs are stable for data applications.

Conclusion

- We can identify the viscoelastic material properties of robotic 3D printed prepregs.
- The effect of drying and residual strains is modeled and used on unseen data.
- The predictions generalize well far beyond the training region.
- The effect of the Crystallization on the trains and material performance is modeled using stabilized Neural ODEs.
- The prediction generalizes outside the training region.
- Stabilized neural ODEs are stable for data applications.

Conclusion

- We can identify the viscoelastic material properties of robotic 3D printed prepregs.
- The effect of drying and residual strains is modeled and used on unseen data.
- The predictions generalize well far beyond the training region.
- The effect of the Crystallization on the trains and material performance is modeled using stabilized Neural ODEs.
- The prediction generalizes outside the training region.
- Stabilized neural ODEs are stable for data applications.

Spoilers

- Link the material properties to the crystallization percentages and shape.

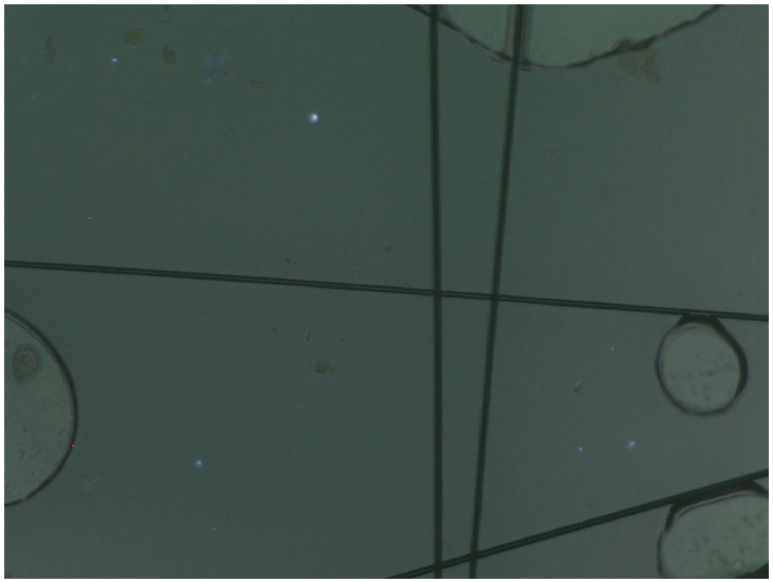

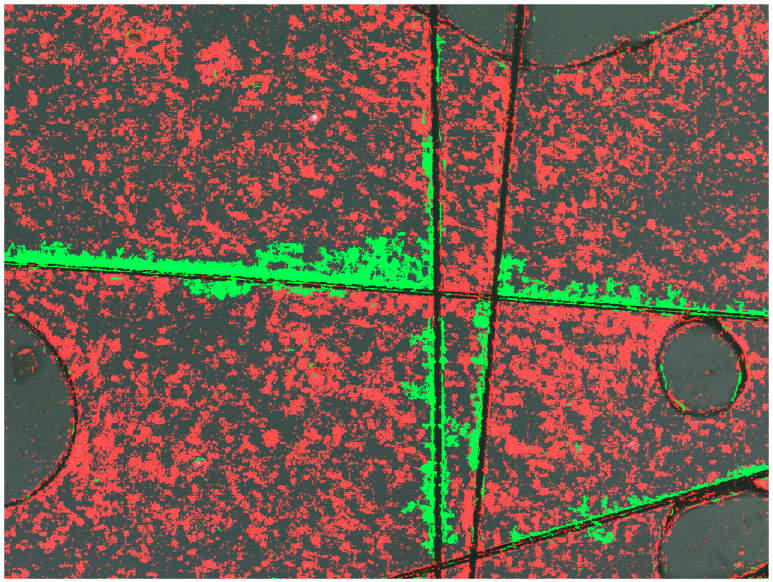

- The crystals radius, volume, and percentage are post processed from videos.

Thank you for your attention

Crystallization hybrid modeling and simulation in robotic 3D printing of continuous carbon fiber reinforced thermoplastic composites

Chady Ghnatios[1], Kazem Fayazbakhsh[2], Reza Vaziri[3]

[1]University of North Florida, Jacksonville, Florida, USA
[2]Toronto Metropolitan University, Toronto, Canada
[3]University of British Columbia, Vancouver, Canada

August 05, 2025







ICCM24
24TH INTERNATIONAL CONFERENCE ON COMPOSITE MATERIALS

Thermoplastic Composites for Demanding Energy Environments: Some current studies

Gilles Lubineau
Mechanics of Composites for Energy and Mobility
KAUST

Mechanics of Composites for Energy and Mobility

جامعة الملك عبدالله للعلوم والتقنية
King Abdullah University of Science and Technology

From corrosion management to corrosion free: the non-metallic path



Courtesy: Novel

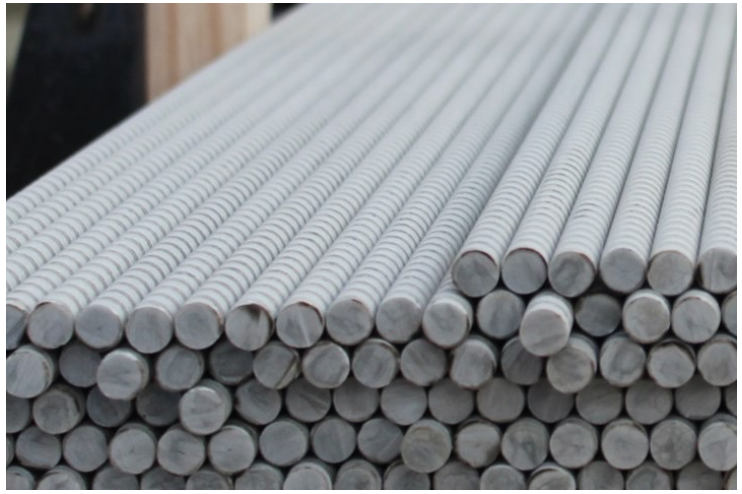

Courtesy: Composite worlds



Courtesy: Calcul Meca – HHR Roof.

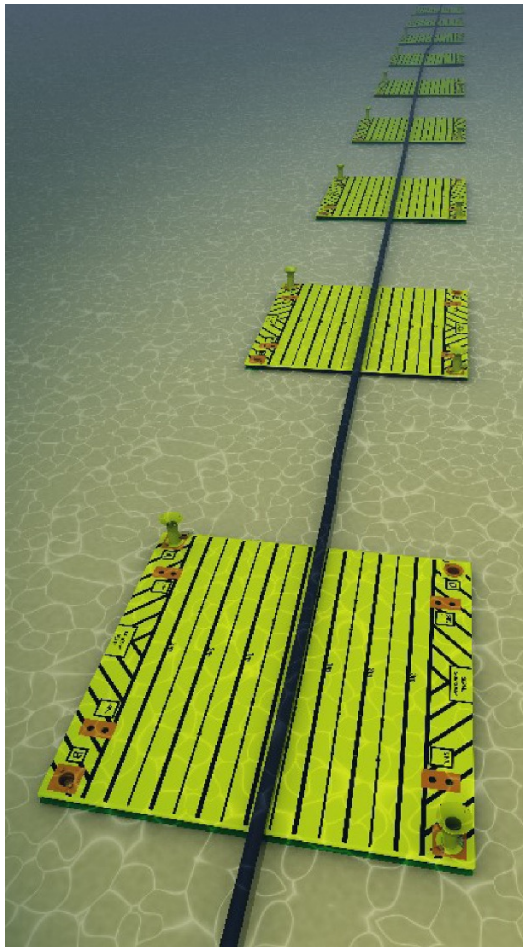

Courtesy: CSUB

From corrosion management to corrosion free: the non-metallic path



Courtesy: Novel

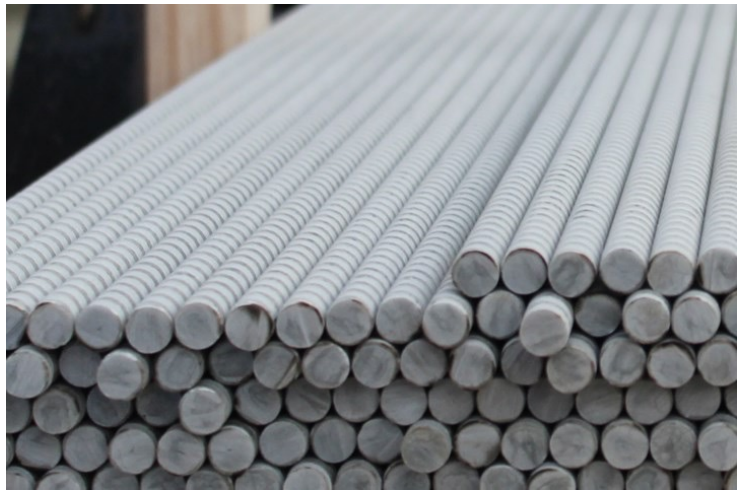

Courtesy: Composite worlds



Courtesy: Calcul Meca – HHR Roof.

- No classical corrosion,
- Ideal for coastal, offshore, sour gas contexts,
- Reduced OPEX, lighter infrastructures,
- Huge potential for localizing the supply chain

Courtesy: CSUB

The non-metallic path: an enabler to sustainability

- Hydrogen value-chain:

  No hydrogen embrittlement

- Carbon capture and storage context:

  Wet CO_2

  CO_2 mixed with impurities (Sox, Nox, etc..)



J. Sonke, W. Bos, and S. Paterson, “Materials challenges with CO2 transport and injection for carbon capture and storage,” Int. J. Greenhouse Gas Control, vol. 114, p. 103601, 2022

Two applications to be discussed

- Compressed hydrogen storage,
- Monitoring of high-performance thermoplastic pipes

Thermoplastics thin-plies for compressed hydrogen storage

Mechanics of Composites for Energy and Mobility

جامعة الملك عبدالله للعلوم والتقنية
King Abdullah University of Science and Technology

Compressed mobile hydrogen storage: a need for the hydrogen value-chain

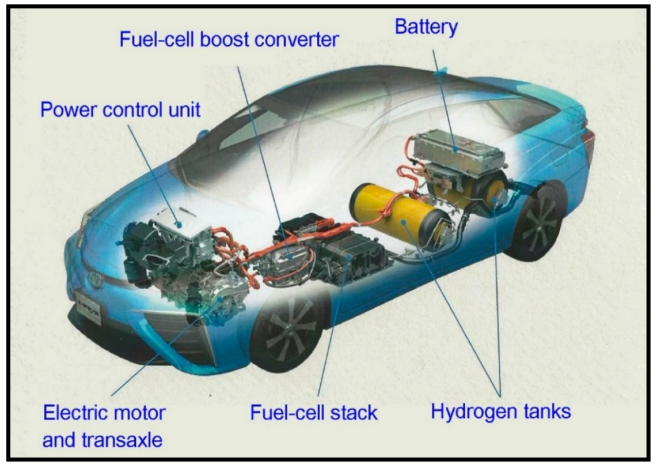

Toyota Mirai car
with hydrogen tanks



Hydrogen power
Jupiter H2 Drone

- Compressed Hydrogen tanks are essential for **mobile applications**,
- Typical conditions:
  - RT, **[300-700] bars**,
  - Multiple refueling cycle,
  - Safe to impact,
  - Maximum leak rate (app. 0.05g/h/Kg H_2)

Getting Compressed hydrogen storage lighter: type IV tank

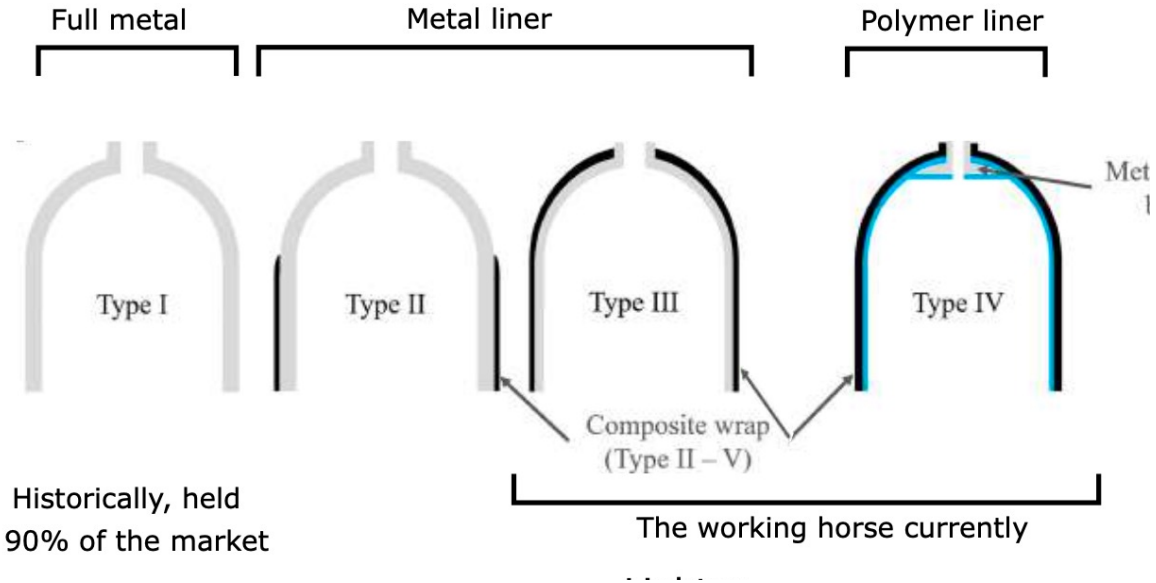

- In all cases, **most of the weight** of a filled tank, **is the tank**,
- Composites enable **larger tank-to-hydrogen weight ratio**:
  - In Type III tanks:
    [~22]
  - In Type IV tanks:
    [~12]

H. Barthélémy, M. Weber, F. Barbier, Hydrogen storage: Recent improvements and industrial perspectives, International Journal of Hydrogen Energy 42 (11 (2017) 7254-7262.

Compressed mobile hydrogen storage: the challenges of type IV tank

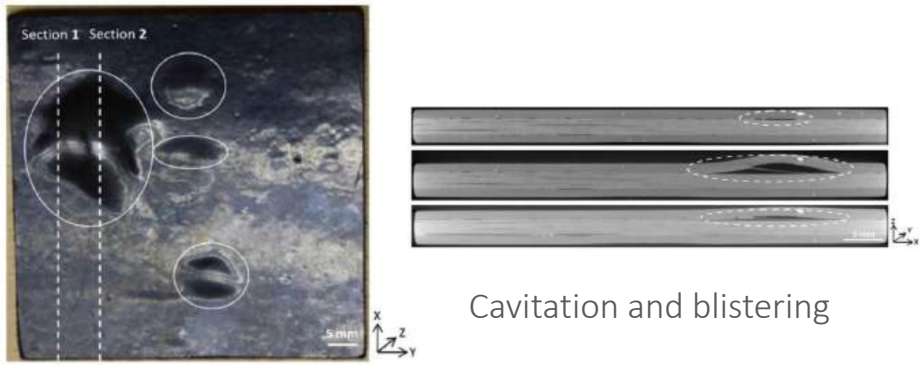

Cavitation and blistering

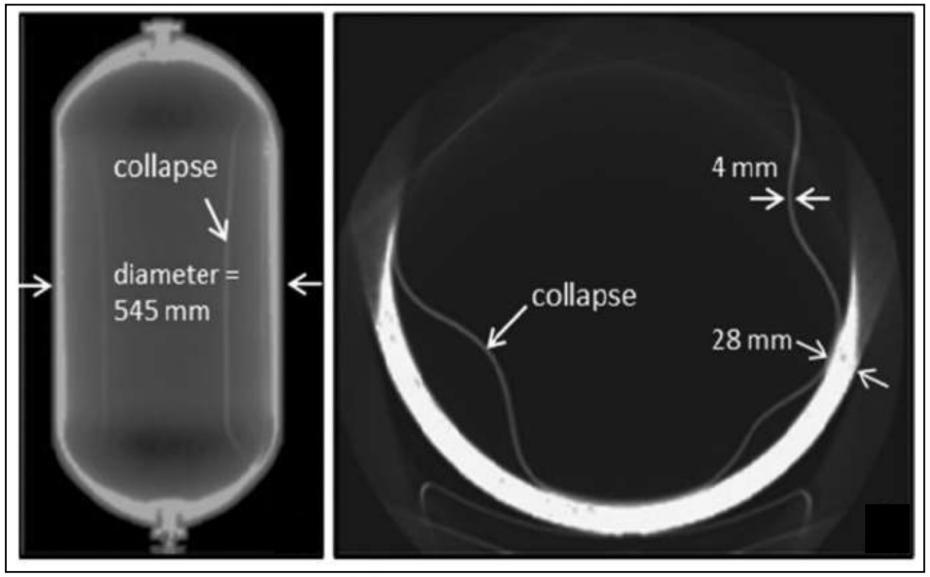

Liner collapse

- **Cavitation** during **depressurization** in the liner or interface,
- **Collapse of the liner** due to
  - Liner/wall interface,
  - Lack of structural bearing capabilities of the liner

How to simultaneously

- Bring more structural stability?
- Save more weight ?

J. Pépin, E. Lainé, J.C. Grandidier, G. Benoit, D. Mellier, M. Weber, C. Langlois, Replication of liner collapse phenomenon observed in hyperbaric type IV hydrogen storage vessel by explosive decompression experiments, International Journal of Hydrogen Energy 42 (9) (2018) 4671-4680.

Getting Compressed hydrogen storage lighter : Moving to Type V tanks

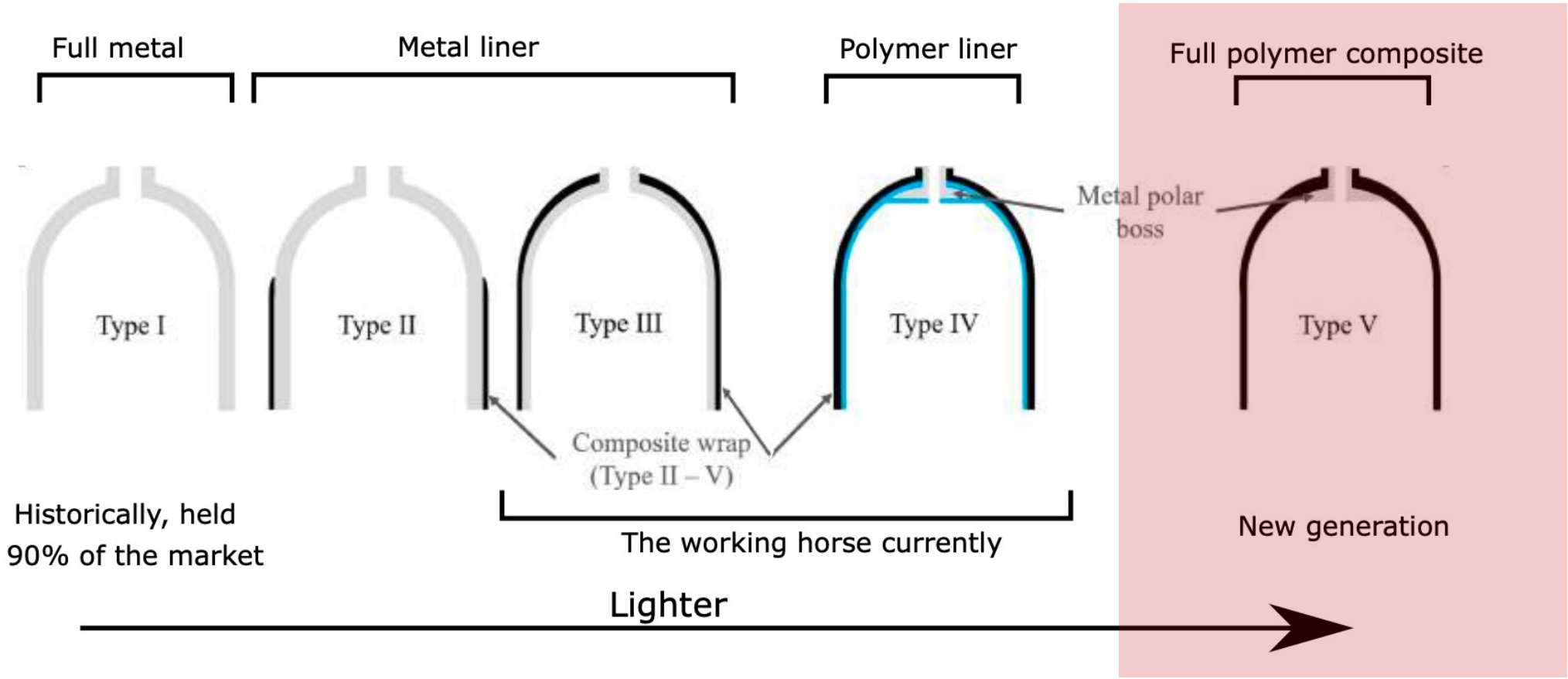

H. Barthélémy, M. Weber, F. Barbier, Hydrogen storage: Recent improvements and industrial perspectives, International Journal of Hydrogen Energy 42 (11 (2017) 7254-7262

Classical type V tanks: thermoset based with classical ply thickness



Mikroni et al. “Design, Analysis and Testing of a Type V Composite Pressure Vessel for Hydrogen Storage”. Polymers, Vol.16, 2024.

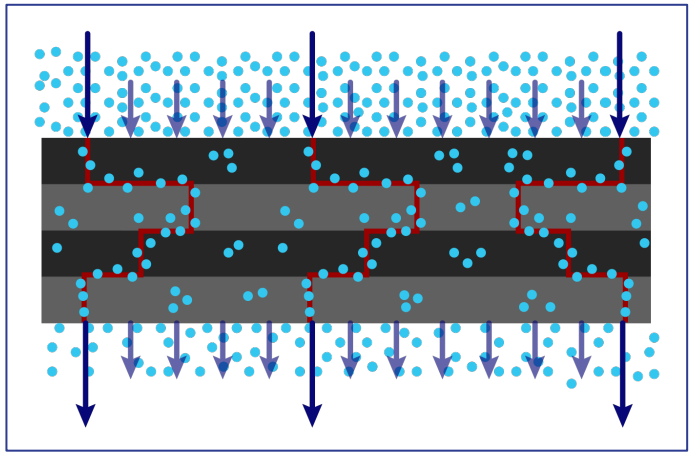

- Prone to **transverse cracking**,
- **Transverse cracking induces local delamination** close to the tips of transverse cracks .
- **Leakage criterion get compromised** due to a percolating network of crack throughout the thickness.
- The percolated regime **is not an acceptable regime, permeability criteria should be met on diffusion regime**
  - Bring more structural stability?

Our study: moving to thin-ply thermoplastics

Unidirectional Carbon-Fiber Prepreg(CF/PA6)

Fiber tensile modulus [GPa]	230	Material configuration	Sheet roll
Fiber areal weight [g/m²]	40	Package configuration	Cardboard with 3" core
Resin areal weight [g/m²]	23	Sheet length [m]	450
Vf [%]	53	Sheet width [mm]	250
RC [%]	36	Matrix resin Melting point [°C]	225
T_g [°C]	50	Thickness [μm]	42

Test items	Test Resalts	Test Method
0° tensile strength [MPa]	2300	JIS K 7165
0° tensile modulus [GPa]	120	JIS K 7165

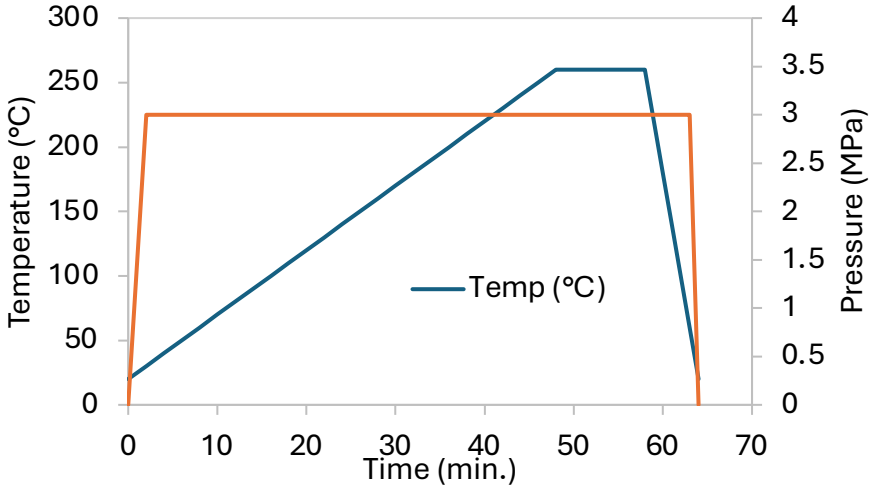

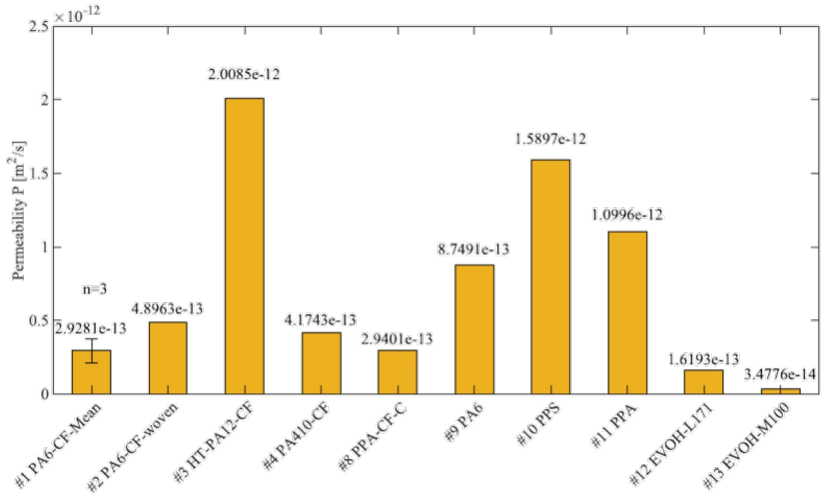

Conde-Wolter et al. "Hydrogen permeability of thermoplastic composites and liner systems for future mobility applications", Composites Part A: Applied Science and Manufacturing, (2023).

Our study: moving to thin-ply thermoplastics

3 advantages:

- 2 from “thin”,
- 1 from “thermoplastics”

Our study: moving to thin-ply thermoplastics

3 advantages:

- 2 from “thin”,
- 1 from “thermoplastics”

Advantage 1:

Thin plies eliminates transverse cracks

- Well-known Finite Fracture Mechanics result,
- Well-accepted observation in thermosets,
- Can be readily extended to thermoplastic laminates.

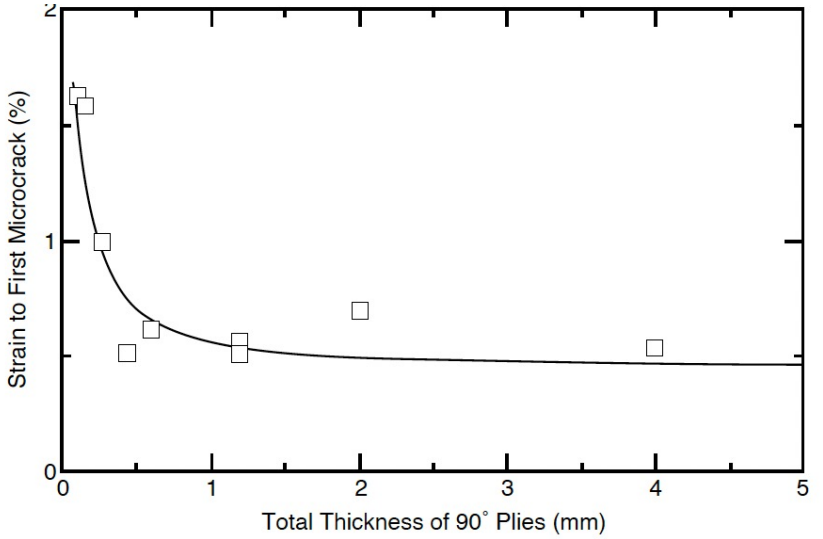

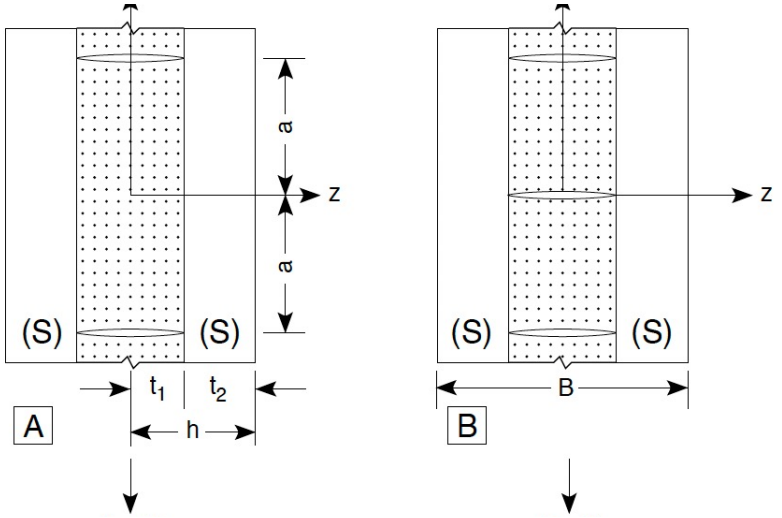

Nairn, Hashin, Parvizi, Hutchinson, Ladevèze and Lubineau [70s,80s,90s]

Our study: moving to thin-ply thermoplastics

3 advantages:

- 2 from “thin”,
- 1 from “thermoplastics”

Advantage 1:

Thin plies eliminates transverse cracks

- Well-known Finite Fracture Mechanics result,
- Well-accepted observation in thermosets,
- Can be readily extended to thermoplastic laminates.

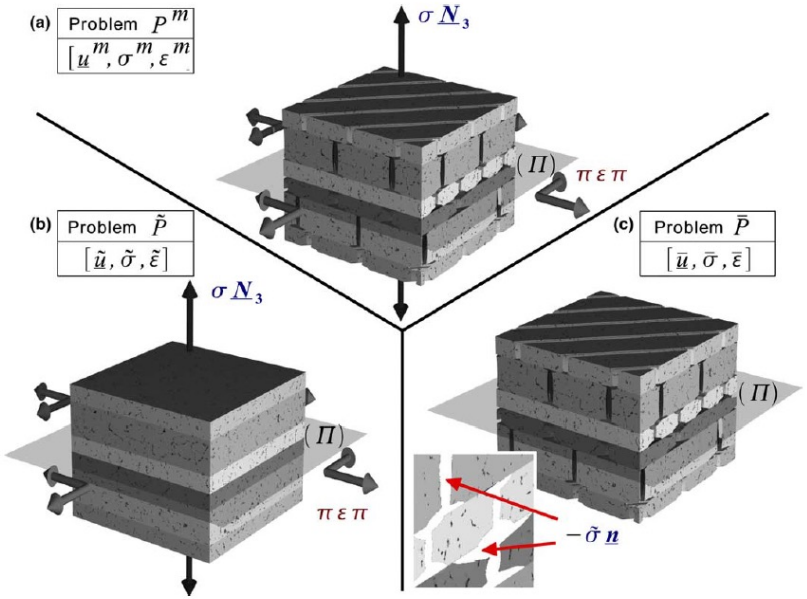

Fig. 4. The fundamental micro–meso link.

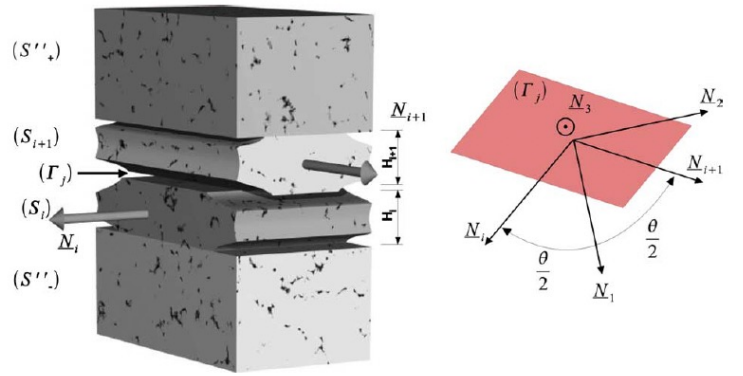

Fig. 5. Problem $\bar{\mathcal{P}}|_{\Gamma_j}$: approximate solution of $\bar{s}$ around an interface Γ_j.

Micro-meso relations
Ladeveze and Lubineau – LMT Cachan
[2000-2009]

Our direction: moving to thin-ply thermoplastics

3 advantages:

- 2 from “thin”,
- 1 from “thermoplastics”

Advantage 1:

Thin plies eliminates transverse cracks

- Well-known Finite Fracture Mechanics result,
- Well-accepted observation in thermosets,
- Can be readily extended to thermoplastic laminates, with additional dissipation sources.

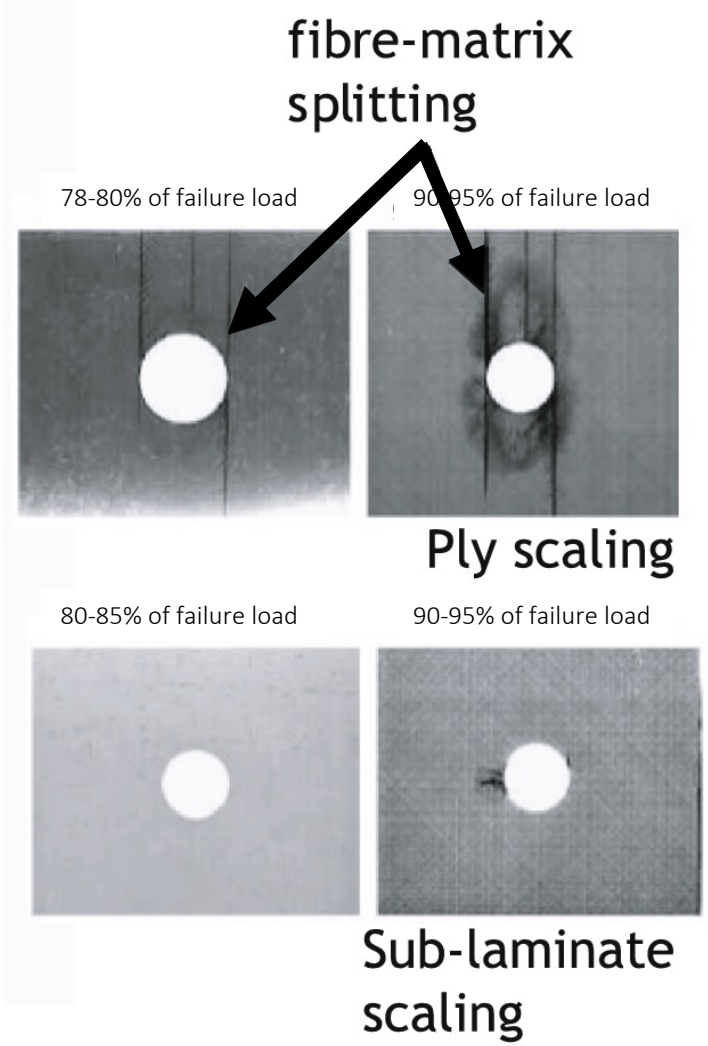

Lee J, Soutis C. Measuring the notched compressive strength of composite laminates: specimen size effects. Compos Sci Technol 2008;68:2359–66.

Our direction: moving to thin-ply thermoplastics

3 advantages:

- 2 from “thin”,
- 1 from “thermoplastics”

Advantage 2:

Thin plies come with “better” microstructures

- Obtained by two spreading,
- Resulting in more “uniform” fiber distribution,
- Might be interesting for permeability.

Classical “Thick” Thermoplastics PP tapes

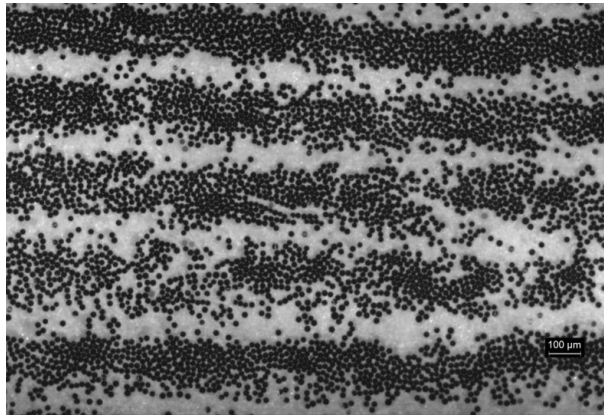

“layered-like” structures

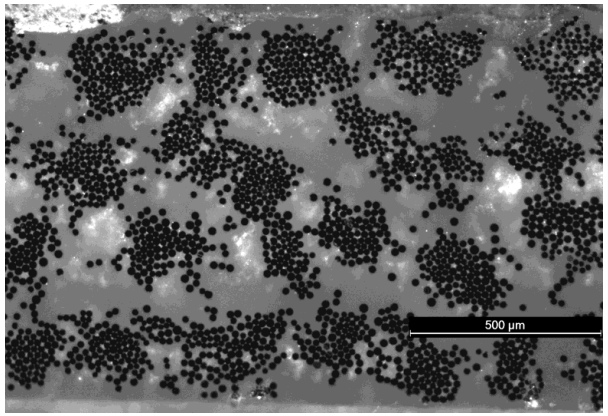

“Bindle” structures

Thin 42 microns tapes

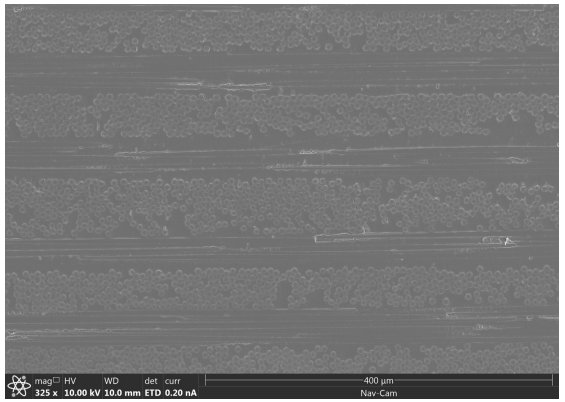

Our direction: moving to thin-ply thermoplastics

3 advantages:

- 2 from “thin”,
- 1 from “thermoplastics”

Advantage 2:

Thermoplastic bring more ductility, leveraging the classical “brittleness” of thin-plies

- Thermoset thin-plies are known to be very brittle,
- Moving to their thermoplastic counterpart brings the best of both worlds.

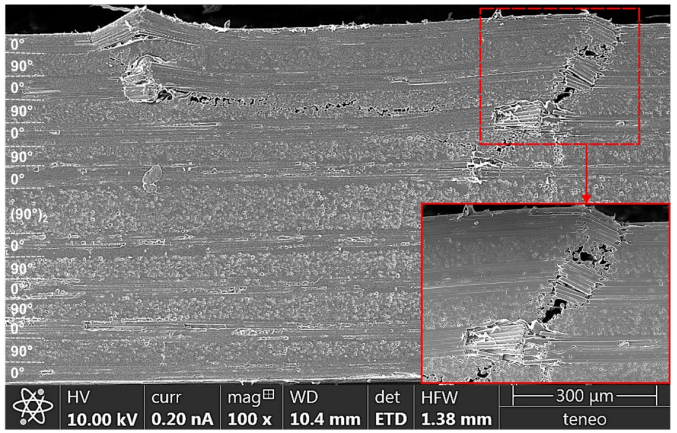

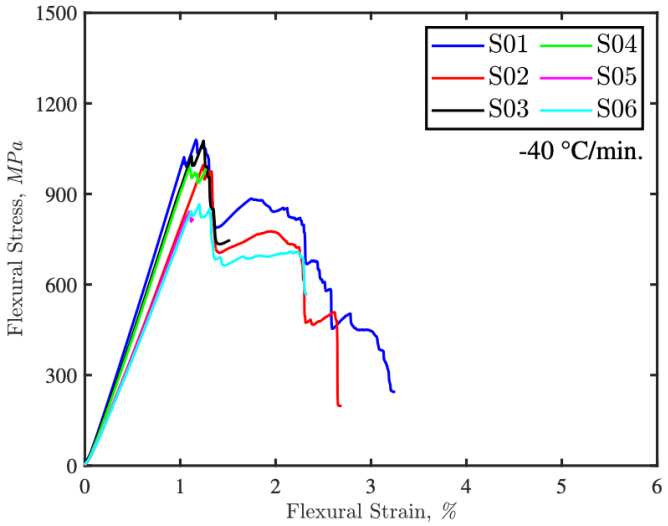

(a) $t_l = 42\ \mu$m

F. Oz, A. Wagih, Y. Kara, M. Bahabri, G. Lubineau, Thin-shell thermoplastic composites with tunable out-of-plane properties: The interplay of layer thickness and cooling rate, Composites Part B: Engineering, 2025, Vol 299, 112381

Our direction: moving to thin-ply thermoplastics

Advantage 2:

Thermoplastic bring more ductility, leveraging the classical “brittleness” of thin-plies

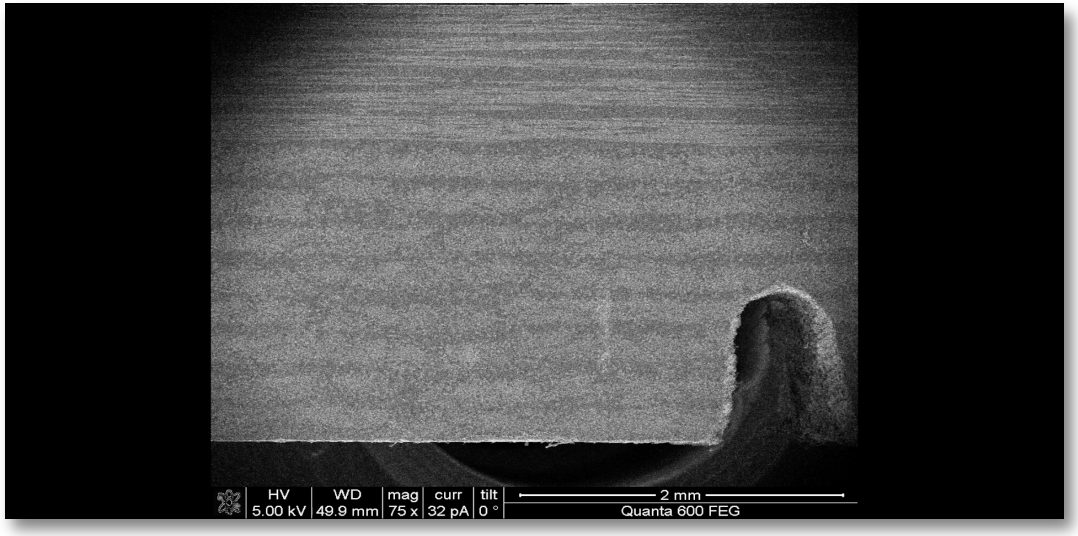

Damage transition in GFPP with Matrix “C” (less ductile)

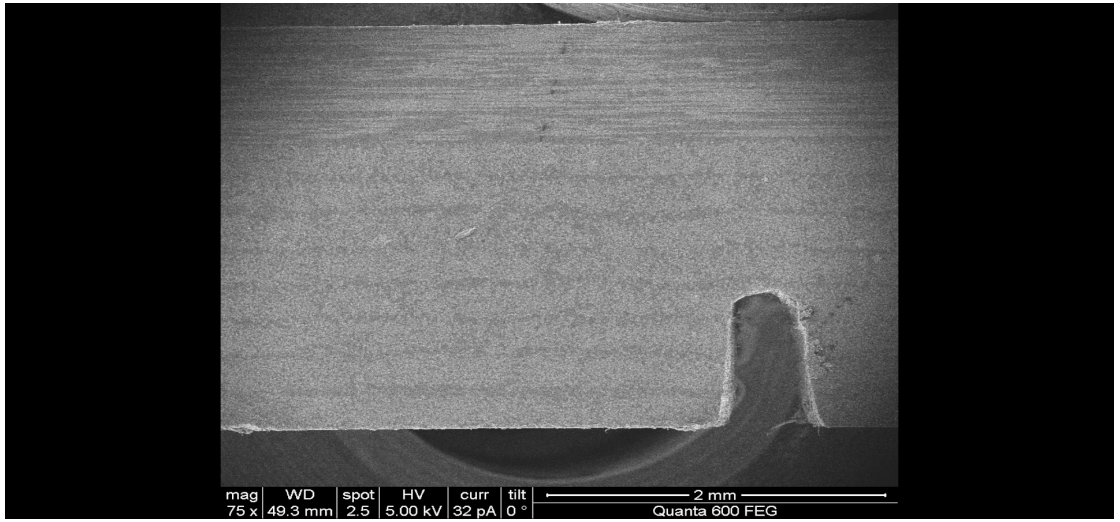

Damage transition in GFPP with Matrix “H” (more ductile)

Insights about Permeability of thin-plies based composites

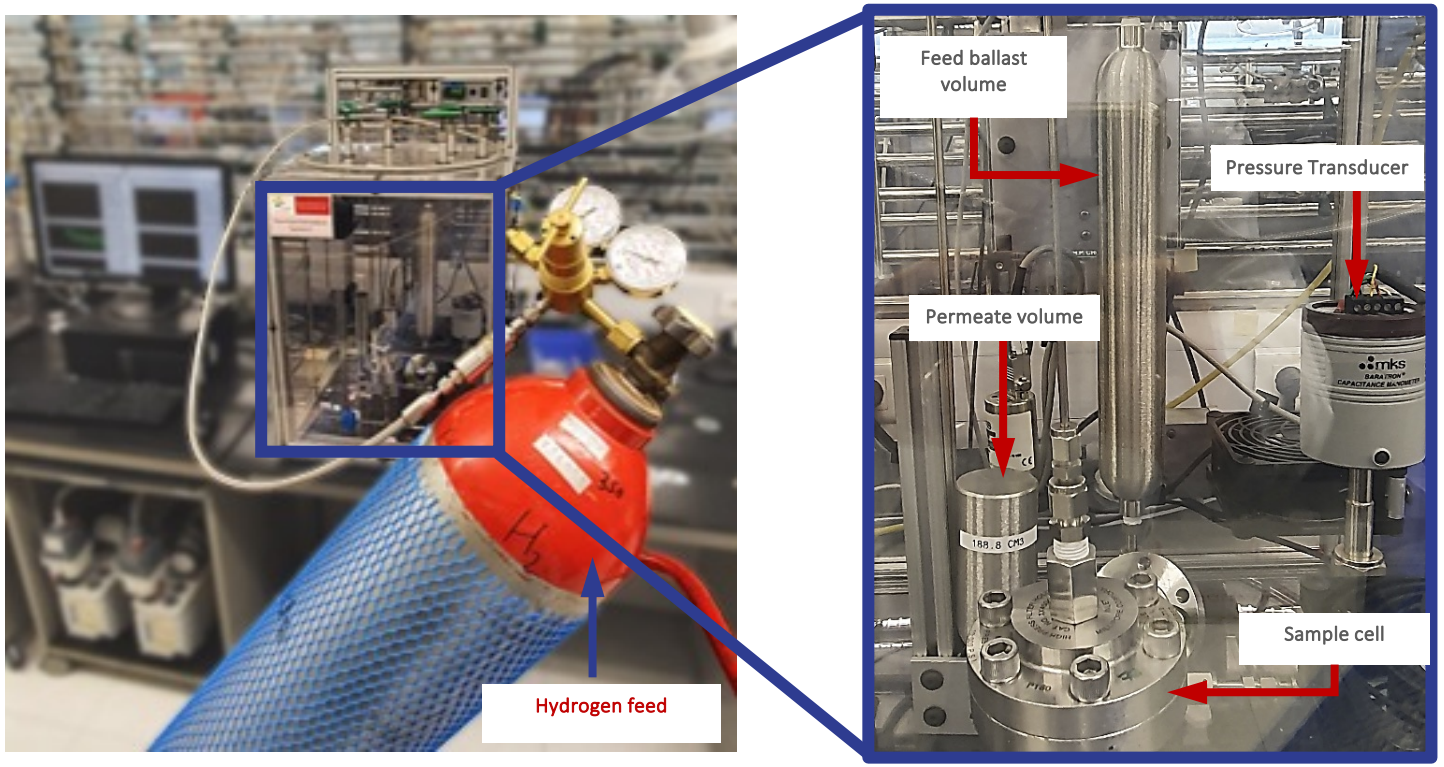

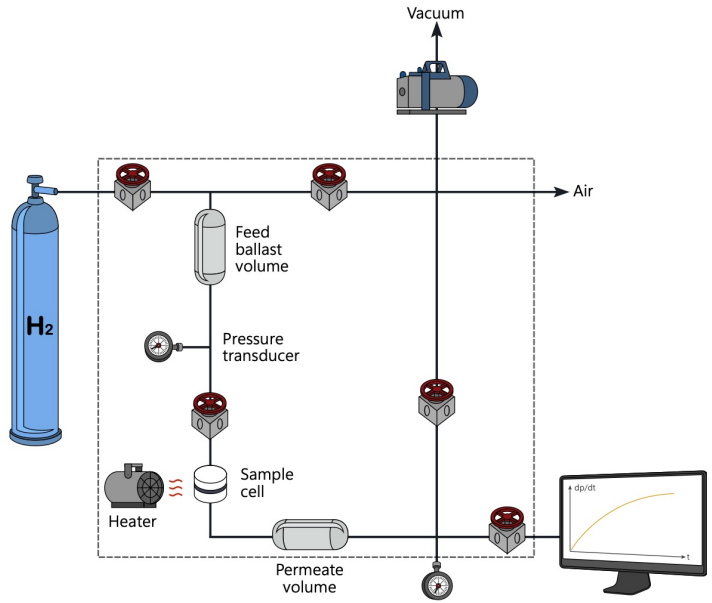

Permeability of thin-plies based composites
Point 1: testing with H_2 (not with helium) is key

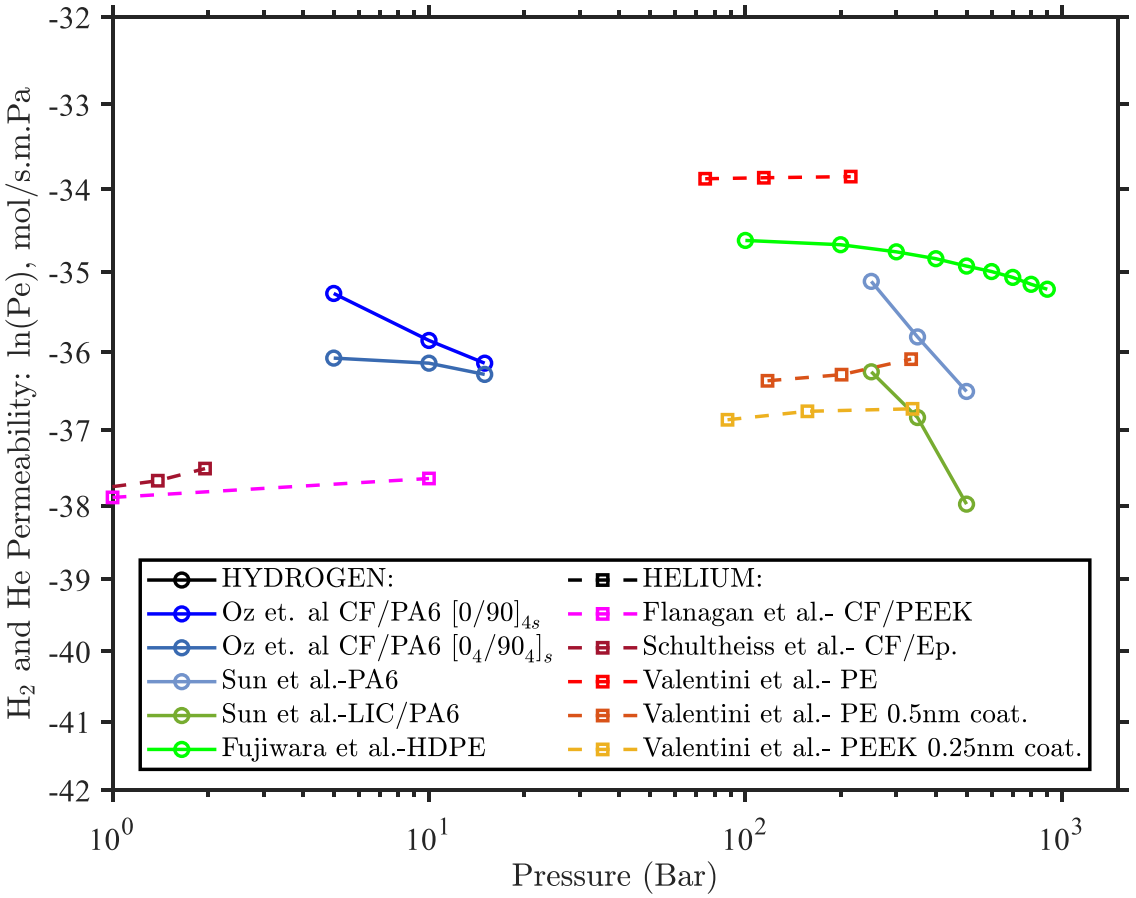

- Many studies use **Helium as a surrogate,**
- This may result in **totally different permeability/pressure trends.**

Hydrogen

- Y. Sun, H. Lv, W. Zhou, C. Zhang, Research on hydrogen permeability of polyamide 6 as the liner material for type IV hydrogen storage tank, International Journal of Hydrogen Energy 45 (46) (2020) 24980-24990.
- H. Fujiwara, H. Ono, K. Onoue, S. Nishimura, High-pressure gaseous hydrogen permeation test method-property of polymeric materials for high-pressure hydrogen devices, International Journal of Hydrogen Energy 45 (53) (2020) 29082-29094.
- F. Oz, A. Wagih, J. Datta, B. Joarder, M. Eddaoudi, G. Lubineau, On hydrogen permeability of thin-ply thermoplastic composites, Proceedings of the 21st European Conference in Composite materials 8 (2024) 1163-1168.

Helium

- L/ Valentini, M. Bellachioma, L. Lozzi, S. Santucci, J. M. Kenny, Helium permeation through a-C: H films deposited on polymeric substrates, Journal of Vacuum Science & Technology A: Vacuum, Surfaces, and Films 20 (50 (2002) 1647-1652.
- M. Flanagan, D. M. Grogan, J. Goggins, S. Appel, K. Doyle, S. B. Leen, C. M. Bradagaigh, Permeability of carbon fibre peek composites for cryogenic storage tanks of future space launchers, Composites Part A: Applied Science and Manufacturing 101 (2017) 173-184
- D. Schultheiß, permeation barrier for lightweight liquid hydrogen tanks, Universität Augsburg, PhD Dissertation (2007)

Permeability of thin-plies based composites

Point 1: testing with H_2 (not with helium) is key

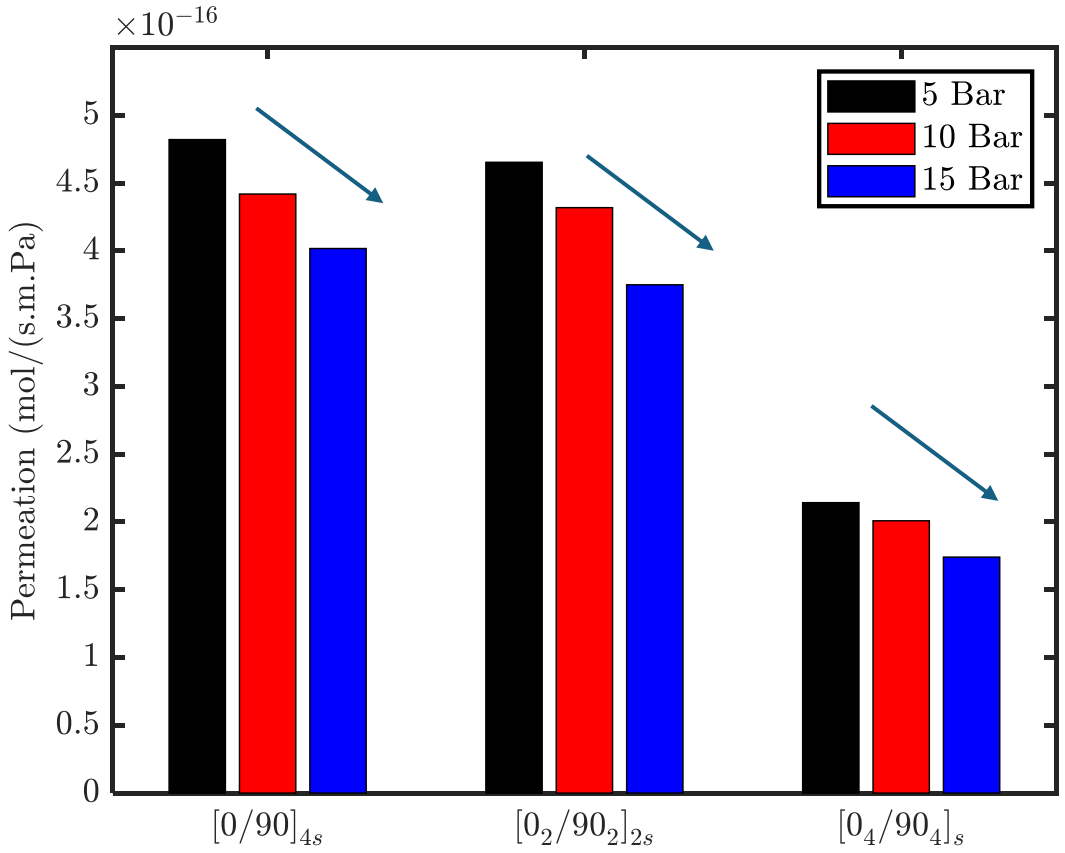

- Permeability **is decreasing with pressure,**
- **True for all tested sequences,**
- Usually attributed to **reduction of free volume under high pressure,**
- **Permeability at low-pressure is a safe design quantity** if no additional damage

Permeability of thin-plies based composites

Point 2: thicker layers result in lower permeability (initially)

Laminate	Layer thickness (μm)
$[0/90]_{4s}$	42
$[0_2/90_2]_{2s}$	84
$[0_4/90_4]_s$	168

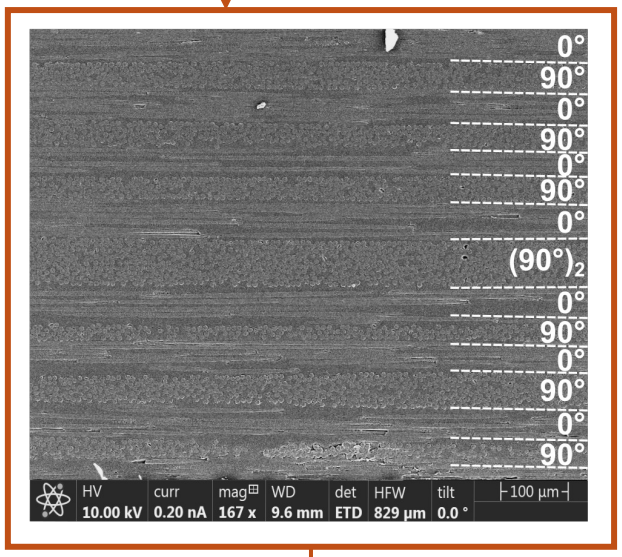

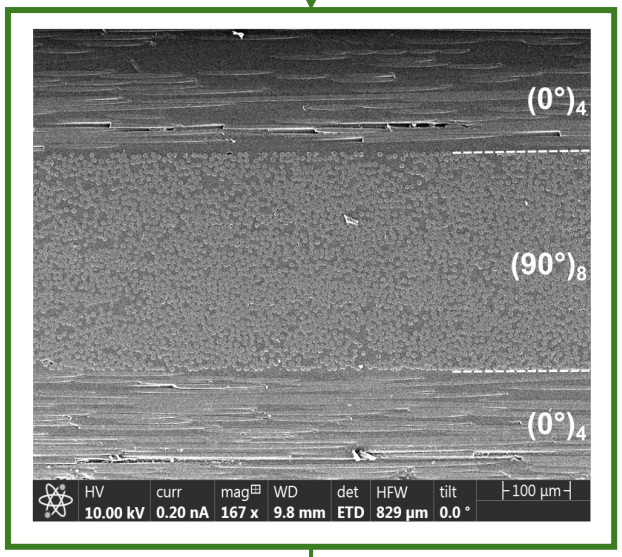

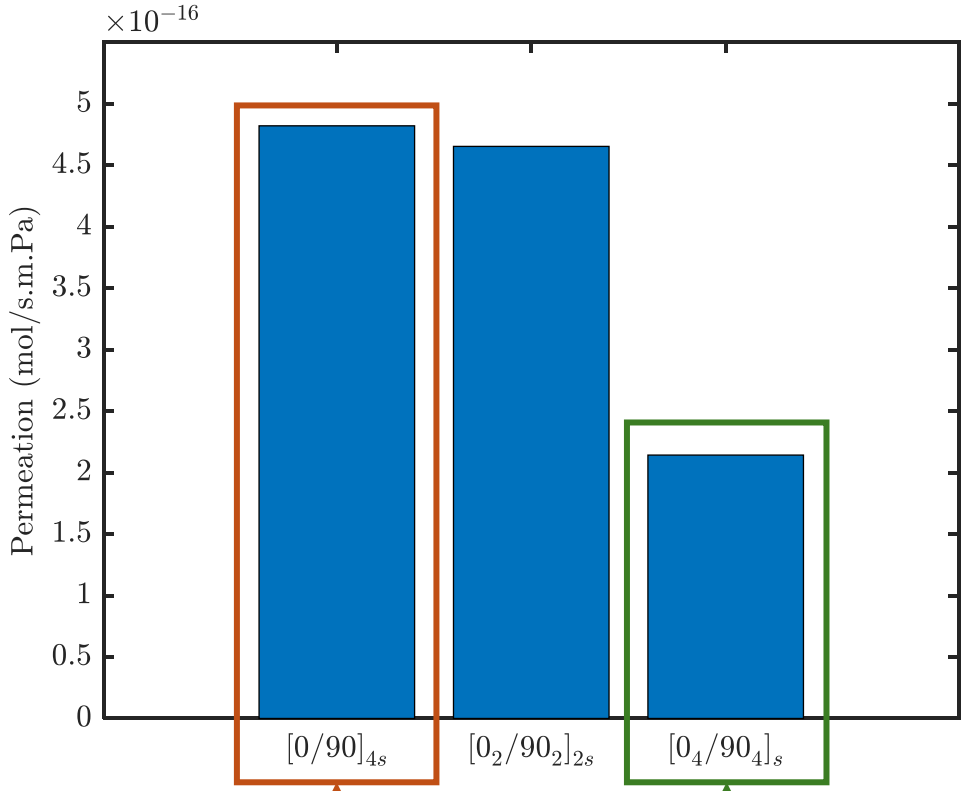

Permeability of thin-plies based composites
Point 2: thicker layers result in lower permeability (initially)

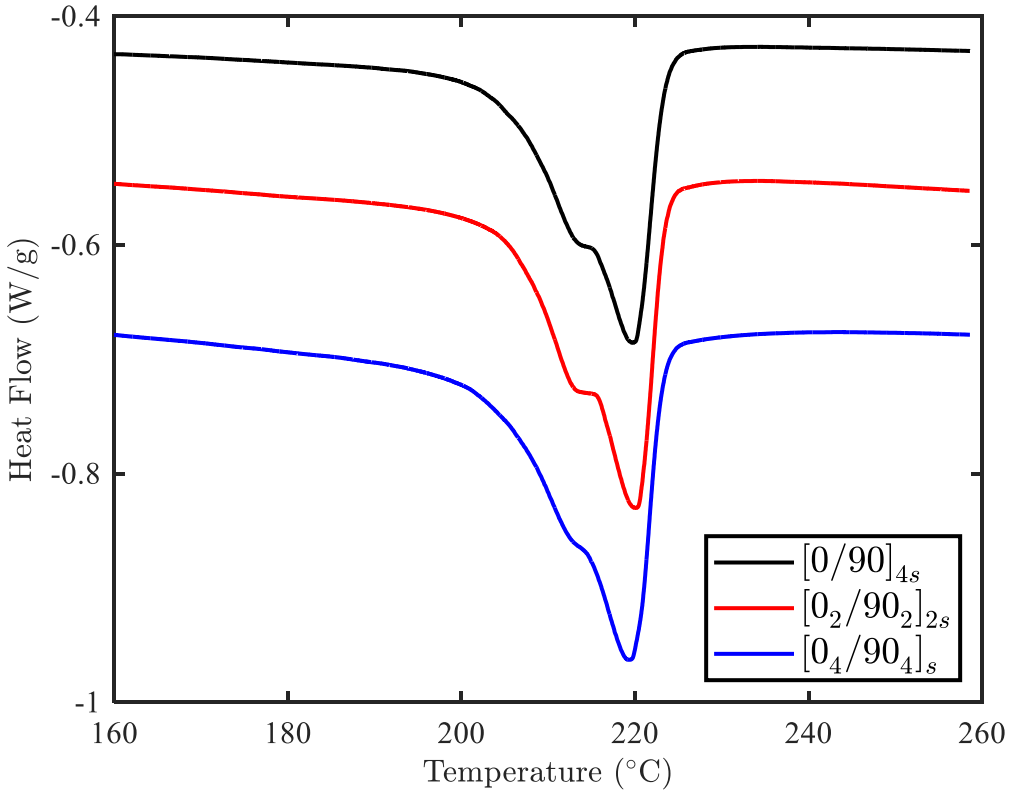

- All samples **have been analyzed by DSC,**
- Observation of **a large proportion of γ phases, meaning that equilibrium was not fully reached,**
- Clearly **more crystallinity in thick samples.**

Permeability of thin-plies based composites

Point 2: thicker layers result in lower permeability (initially)

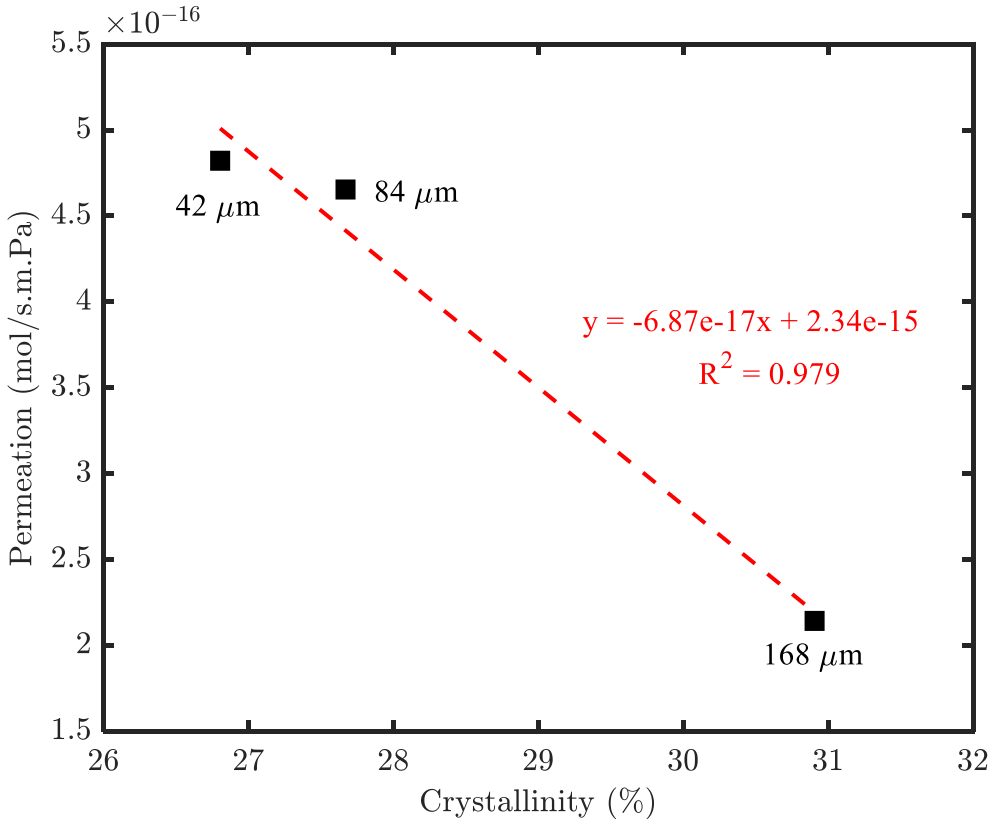

- Permeability is **decreasing quickly with crystallinity,**
- From a strict "permeability" criterion, **thicker layers are better in the pristine state due to high crystallinity**

Permeability of thin-plies based composites

Point 3: think layers will however remain competitive at higher strains

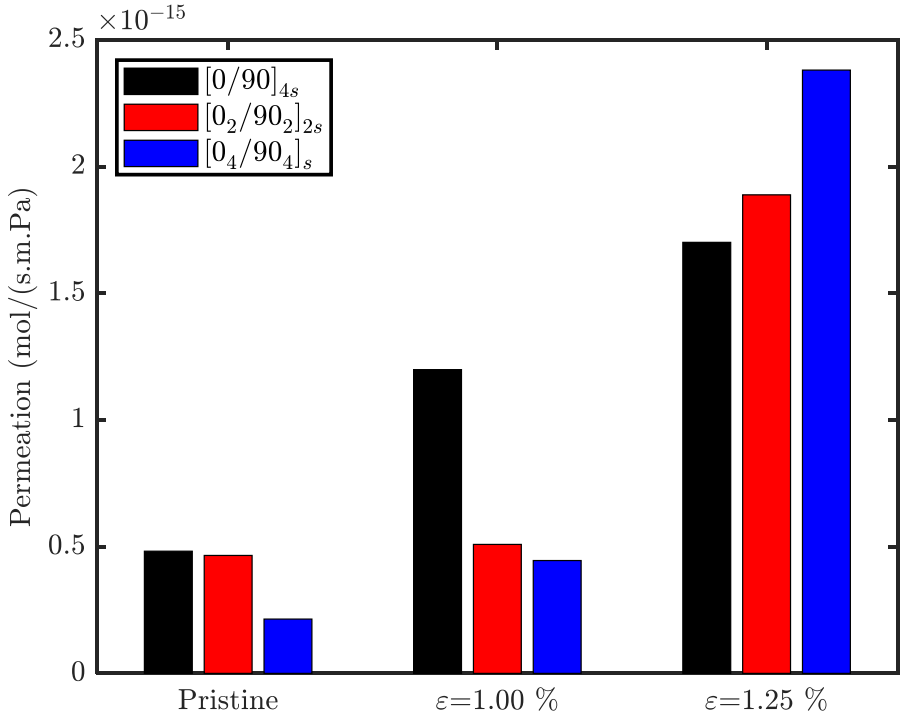

Permeability of thin-plies based composites

Point 3: think layers will however remain competitive at higher strains

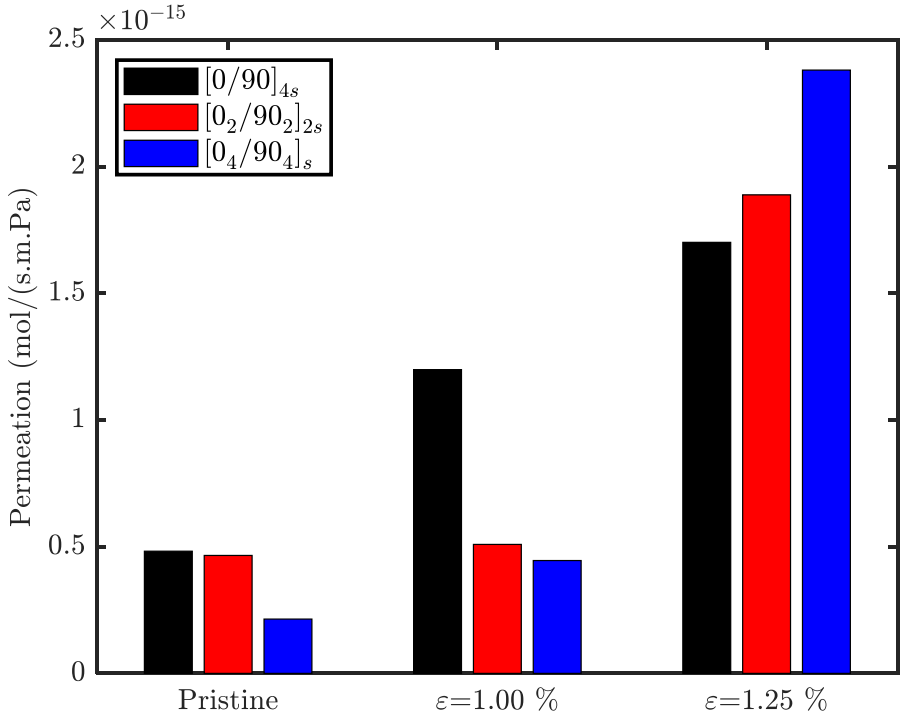

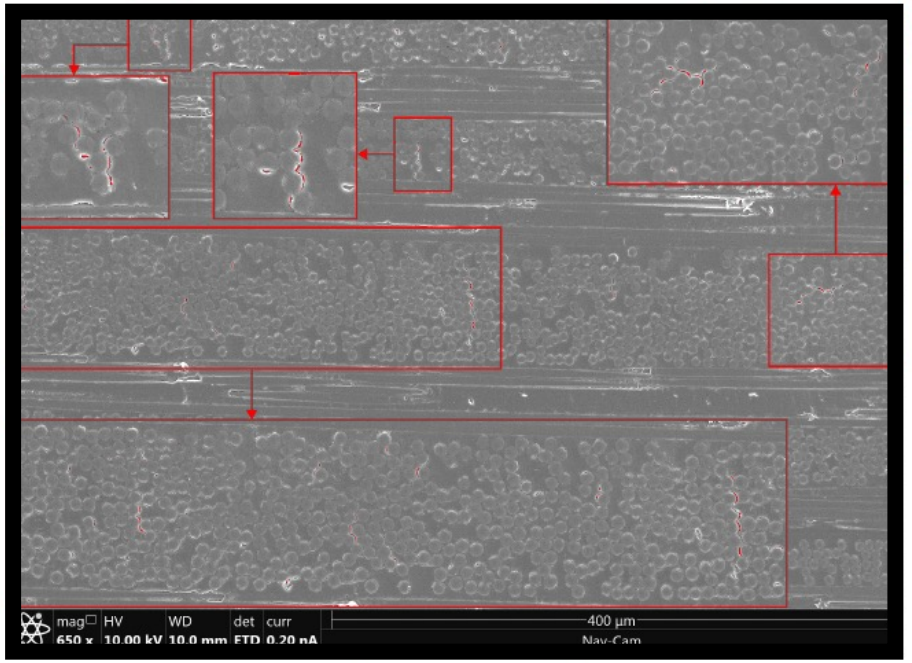

(b) $[0/90]_{4s}$ at 1.25 % strain.

Limited cracking at higher strain with thin plies, as expected

Permeability of thin-plies based composites

Point 3: think layers will however remain competitive at higher strains

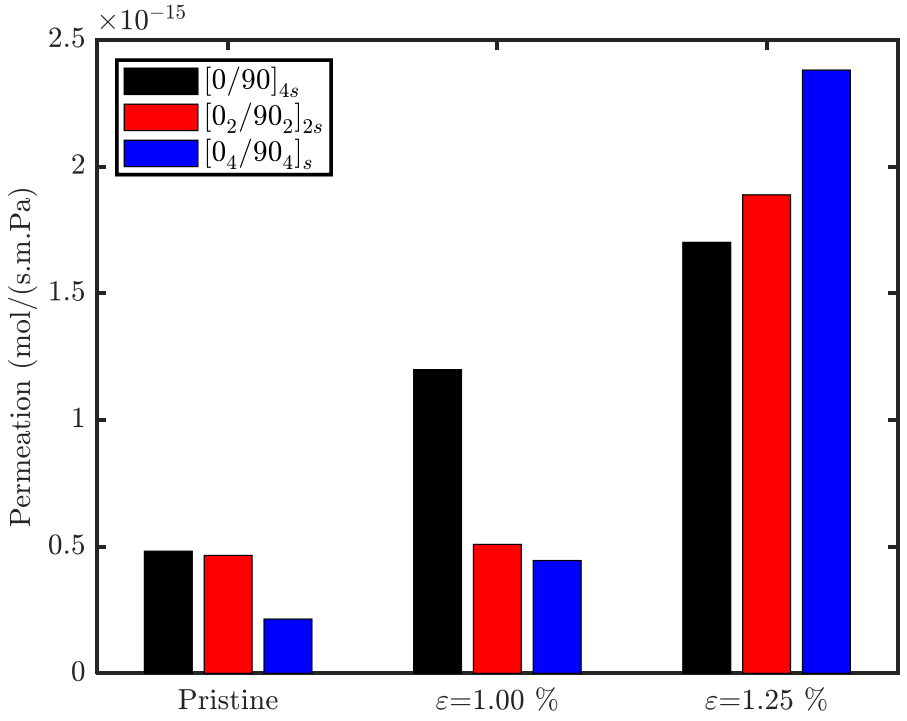

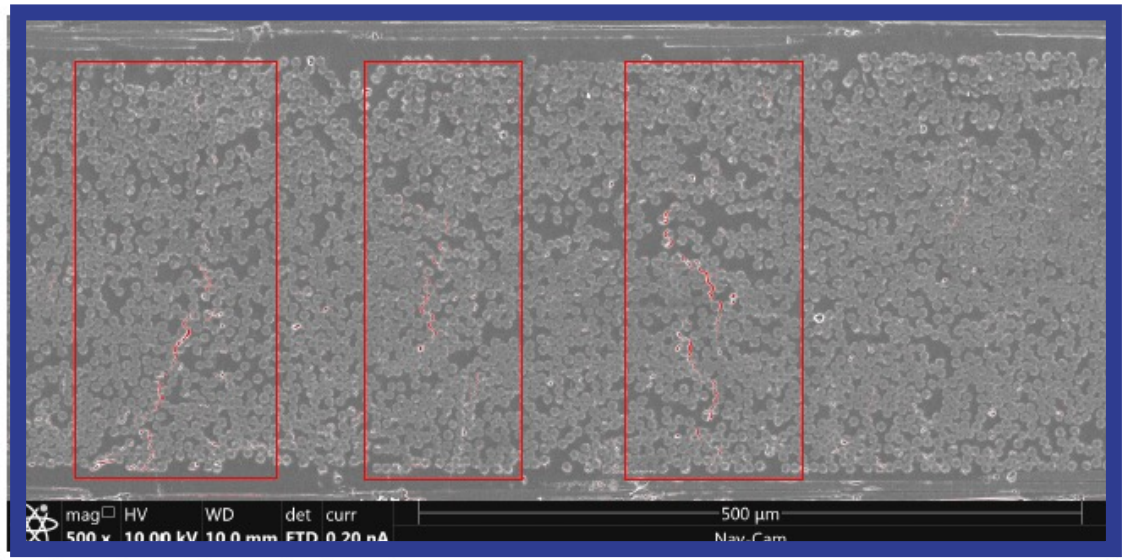

(f) $[0_4/90_4]_s$ at 1.25 % strain.

Even based on thin-plies, **thick layers are more prone to percolating damage.**

Permeability of thin-plies based composites
Point 4: design of a 100 bars thin-plies tank

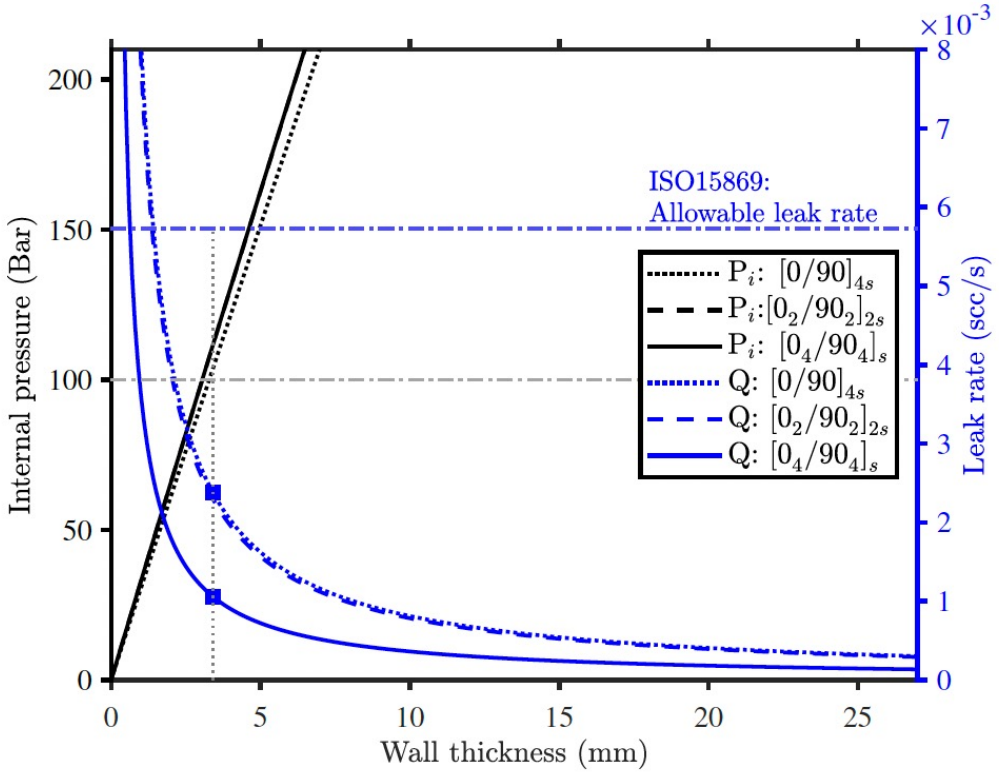

(a) P_i and Q as a function of t_w (pristine).

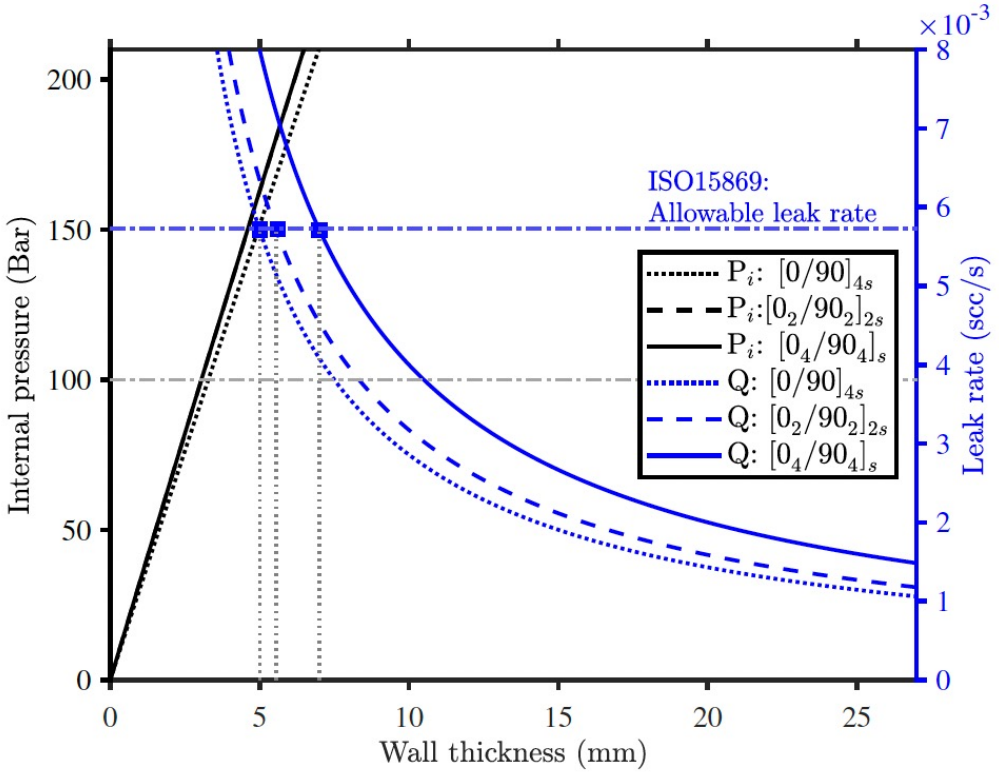

(b) P_i and Q as a function of t_w (compromised).

Permeability of thin-plies based composites
Point 4: design of a 100 bars thin-plies tank

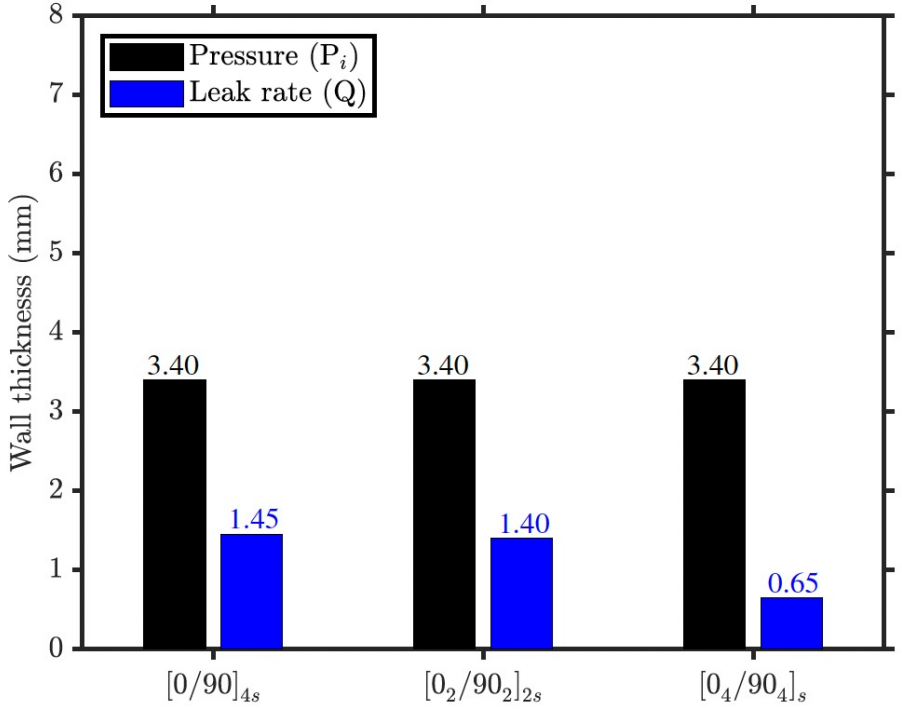

(c) Required t_w for each criteria (pristine).

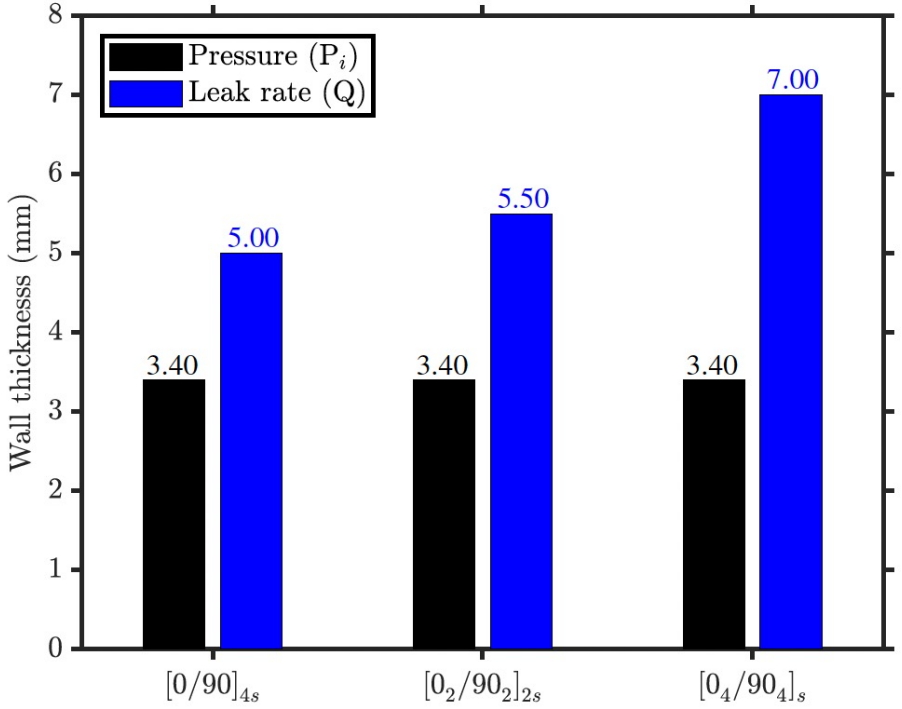

(d) Required t_w for each criteria (compromised).

Quick math about the total wall thickness:

Type IV: ˜8 mm, Type V ”Thick layers Th Pl”: 7 mm, Type 5 “Thin layer Th”: 5-6 mm

Conclusions

- **Moving to type V tank** requires to bring **more stability to the inner lay**er (load-bearing liner) and to avoid permeation through the wall,
- Thin-plies thermoplastics are ideal to **mitigate catastrophic cracking-induced leakage,**
- Processing conditions and lay-up **influence the crystallinity and by then the initial permeability,**
- This-plies used as “thin-plies” reduce the permeability under loading train, showing potential for wall-reduction.

IsoSORP: Gravimetric Gas Sorption Analysis with Magnetic Suspension Balance

Mechanics of Composites for Energy and Mobility

Magnetic Suspension Balance

- High-resolution mass determination under extreme conditions
  - At high pressures: < 700 bars
  - Temperature: -196 °C (77 K) – +1550 °C
  - In corrosive environments
  - Sample weight: < 25 g (10 µg balance resolution)

- Main application area:
  - Measuring gas sorption on porous particles for gas separation and storage
    - ➢ CO_2, H_2, CH_4

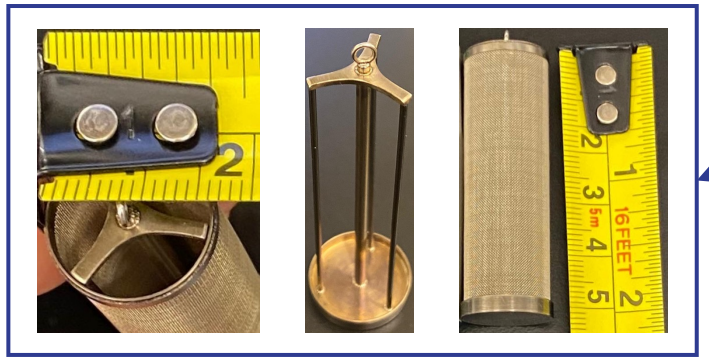

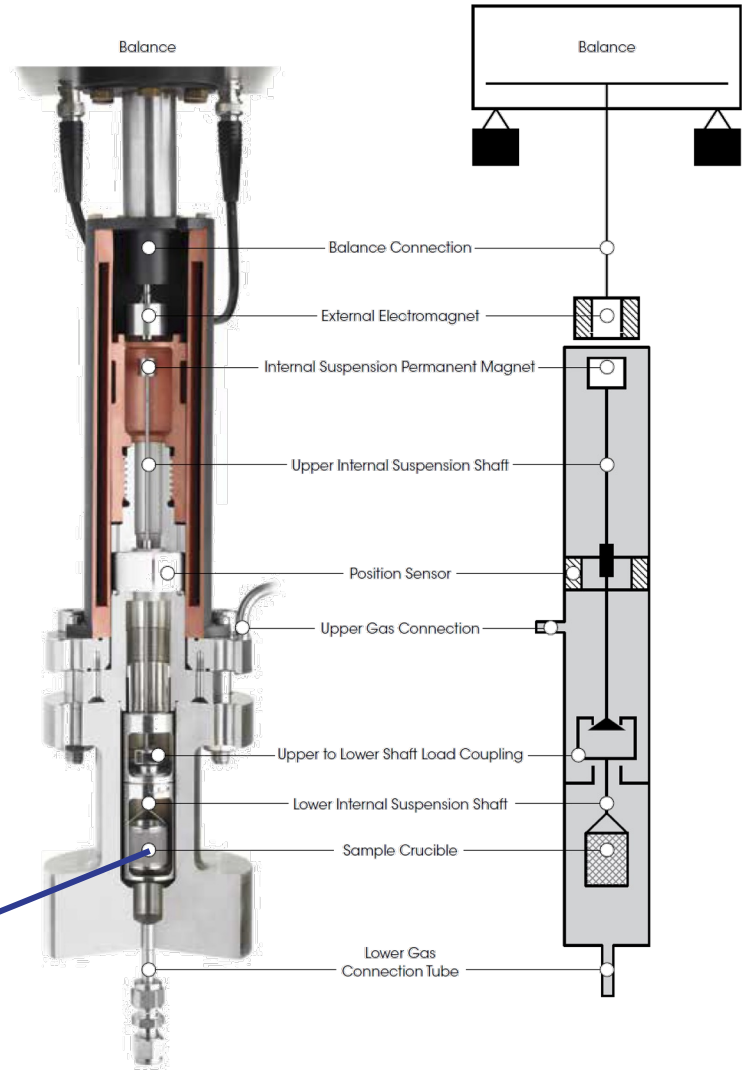

جامعة الملك عبدالله للعلوم والتقنية
King Abdullah University of Science and Technology

Experimental procedure

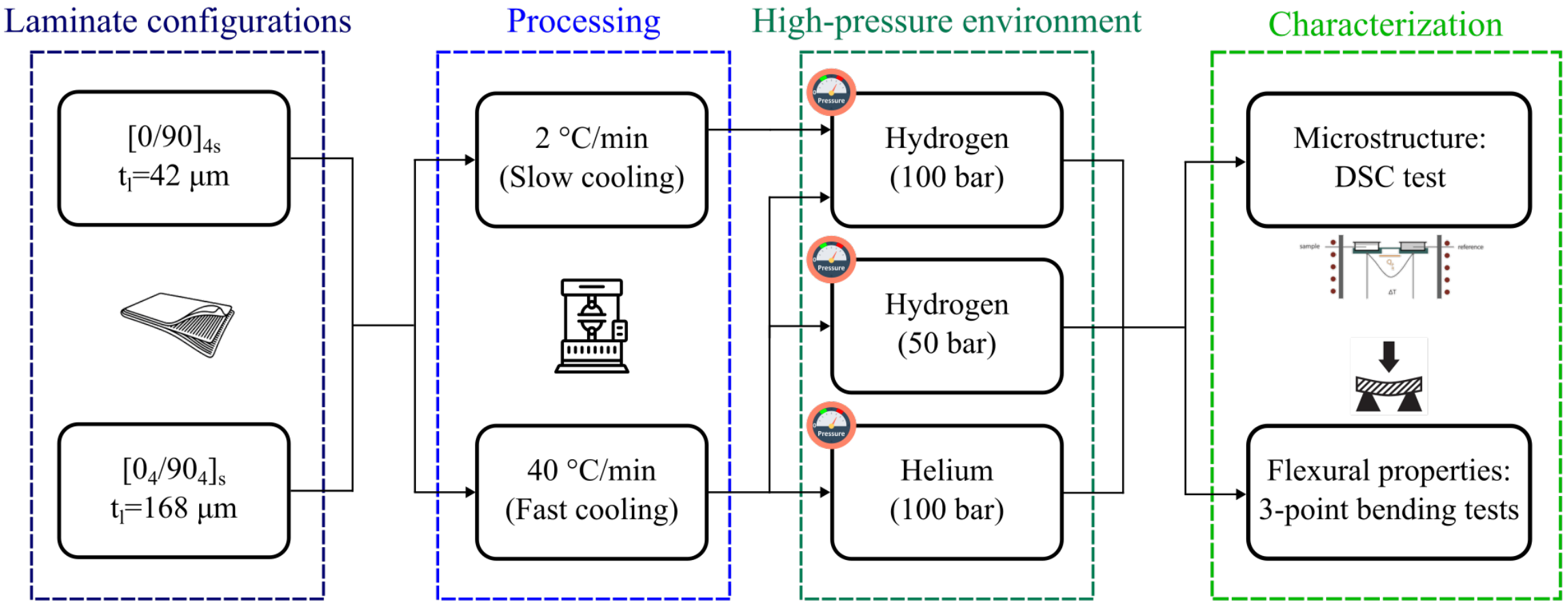

Effect of H2 pressure on microstructure

Fast-cooled laminates:

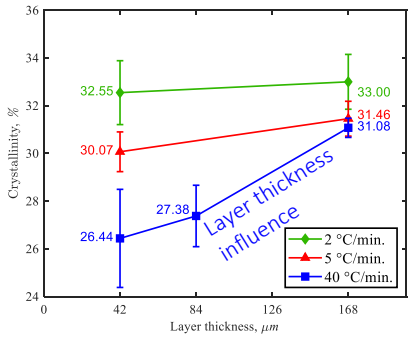

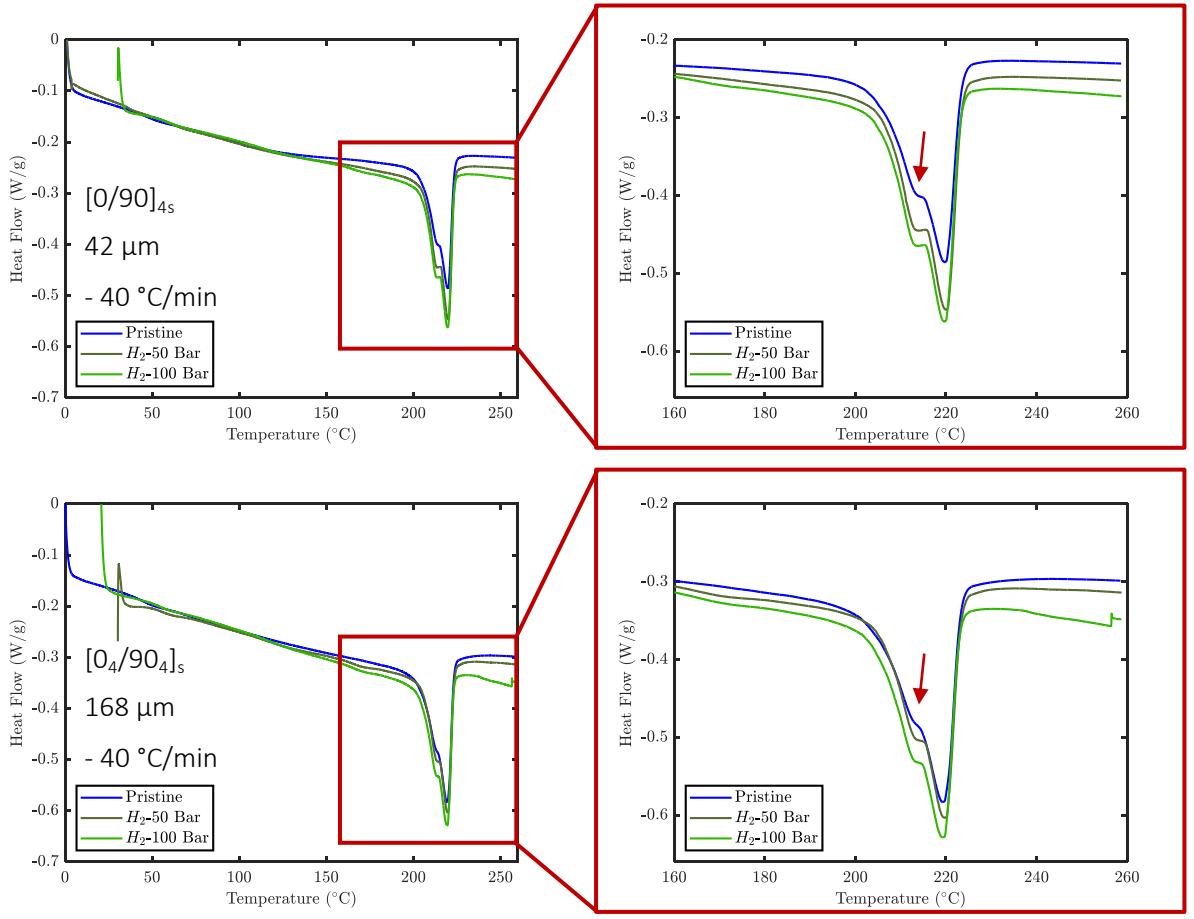

- High-pressure H_2 acts as an annealing agent:
  - Allowing amorphous phases to transform into crystallites
    - ➢ Formation of new unstable γ crystallites
  - Significant increase in crystallinity

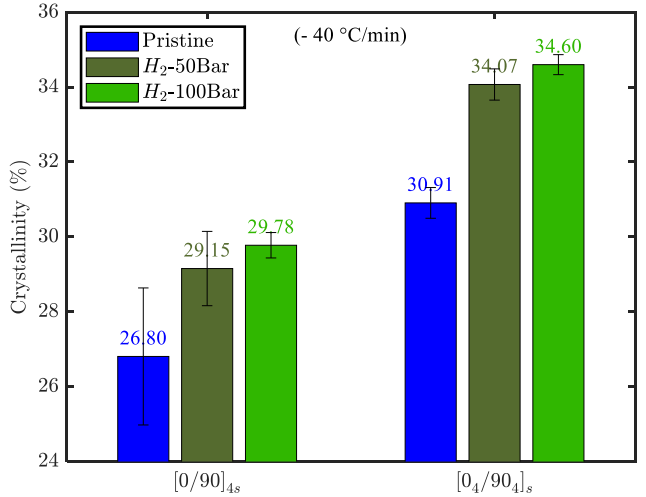

High performance Thermoplastic pipes for O&G

Corrosion: Trillions lost

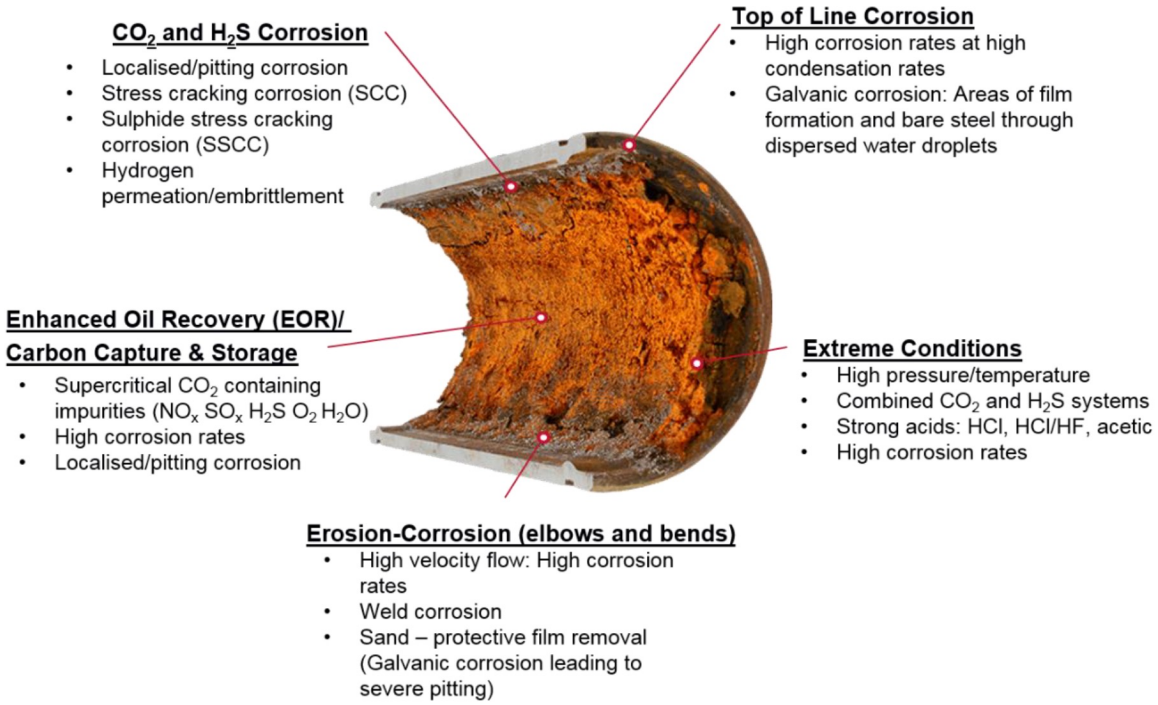

Burkle, D. P. (2017). *Understanding the formation of protective FeCO3 onto carbon steel pipelines during CO2 corrosion* (Doctoral dissertation, University of Leeds).

Energy environment
is particularly aggressive to metal.
(CO_2, H_2S, acids, …)

Resulting in extensive and corrosion:

- Uniform corrosion,
- Pitting,
- Crevice corrosion,
- Galvanic corrosion / stress-assisted corrosion,
- Microbiologically Influenced corrosion…

To simplify, the key consequence is global or localized change in wall thickness

Classical metallic inspections target change in geometry

New materials, new challenges: just 2 examples

Joints in Thermosets

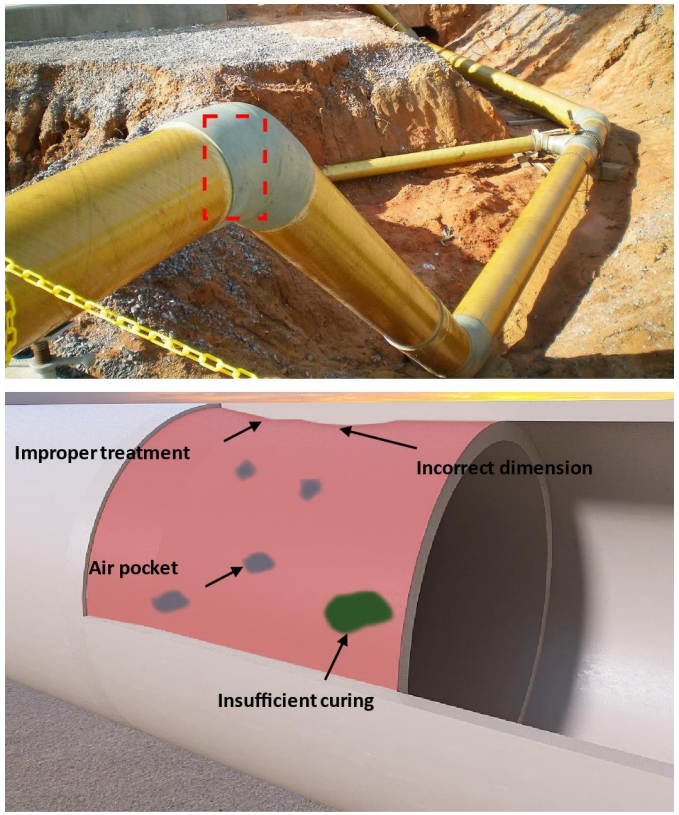

Bulk aging in thermoplastics

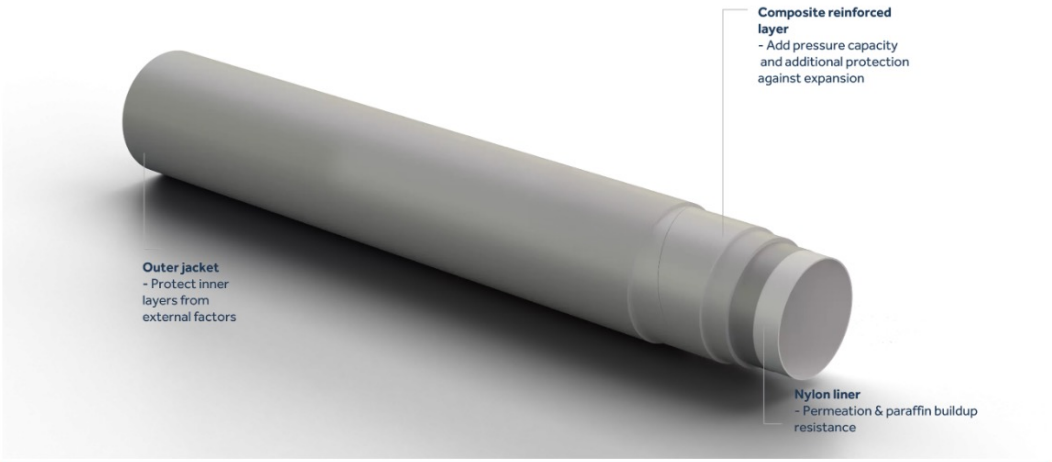

Size	Operational Temperature	Nominal Pressure (psi)	Outside Diameter (in)	Inside Diameter	Max Length Per Reel (ft)	Min Bend Radius (ft)	Reel Size (ft)	Max Reel Weight (lb)
4"	150 F/180 F	750	4.71	3.83	2,110	7.8	14.5	10,396
		1500	4.90	3.83	1,910	8.2	14.5	11,639
6"	150 F/180 F	750	6.87	5.60	870	11.4	14.5	9,550
		1500	7.20	5.60	460	12.0	16.3	9,295
8"	150 F/180 F	750	9.31	7.63	365	15.5	16.3	9,342

New materials, new challenges: just 2 examples

Bulk aging in thermoplastics

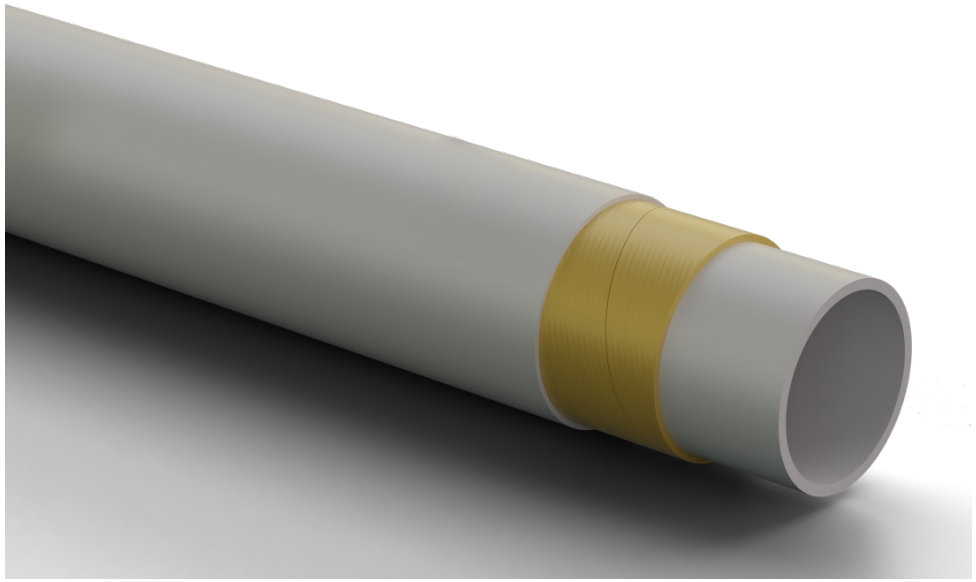

Thermoplastics may evolve in time

Chemical aging
- Thermo-oxydation (heat +Oxygen),
- Photo-oxydation (UV),
- Solvent/stress cracking (bleach, acids)

Physical aging
- Lower molecular weight (chain scission),
- Changes in crystallinity,
- Loss of ductility and mechanical strength

Time/temperature/stress/environment acceleration?

Resulting in bulk changes in:
Ductility, Mechanical strength, Permeability

Sensing technologies available for composite integrity

Many…but few really practical/operational for SHM

What is globally available on the market for composites NDT/SHM?

Far from being as mature as strategies for inspections of metallic infrastructures

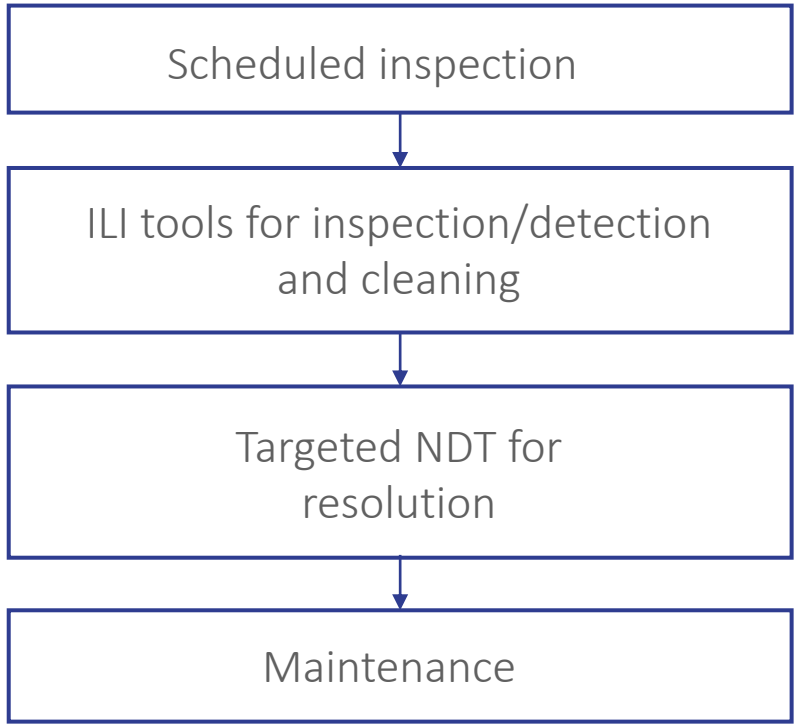

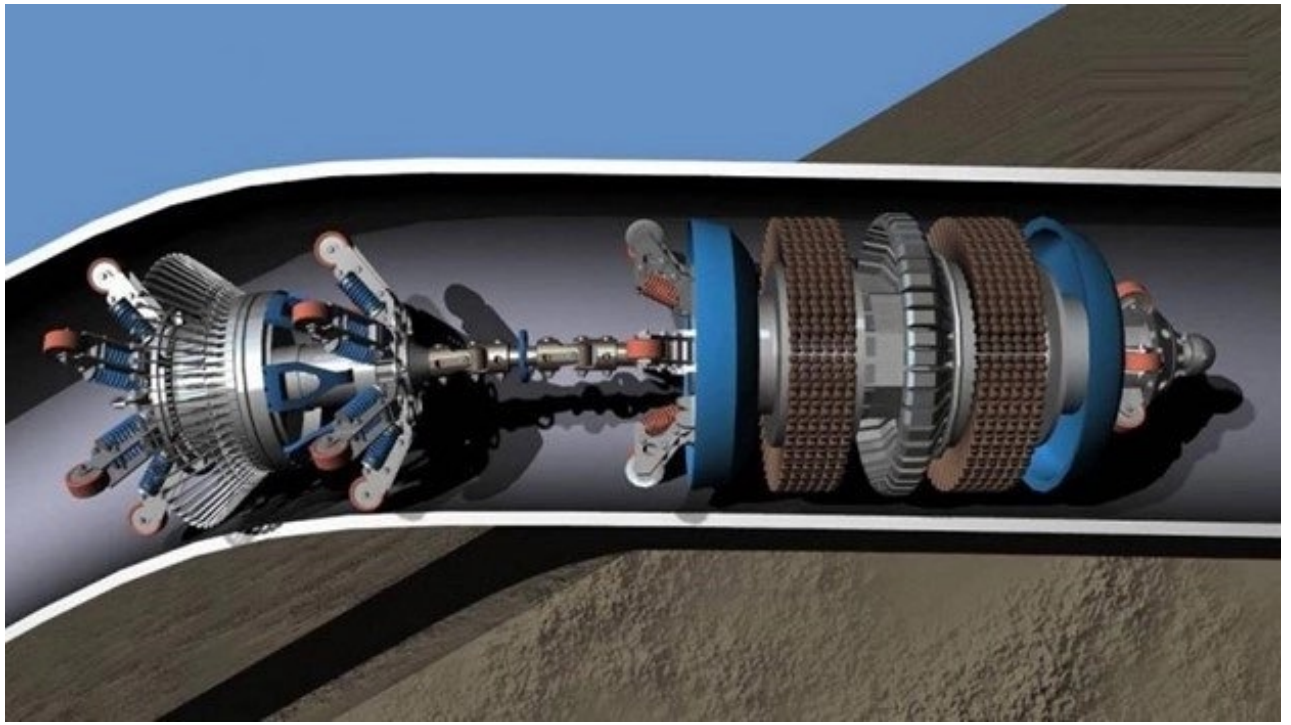

Copyright: assetintegrityengineering.com

New materials, new challenges: the example of permeability

Hydrogen permeation tests of pristine samples conducted at 5-10-15 bars at 35 °C

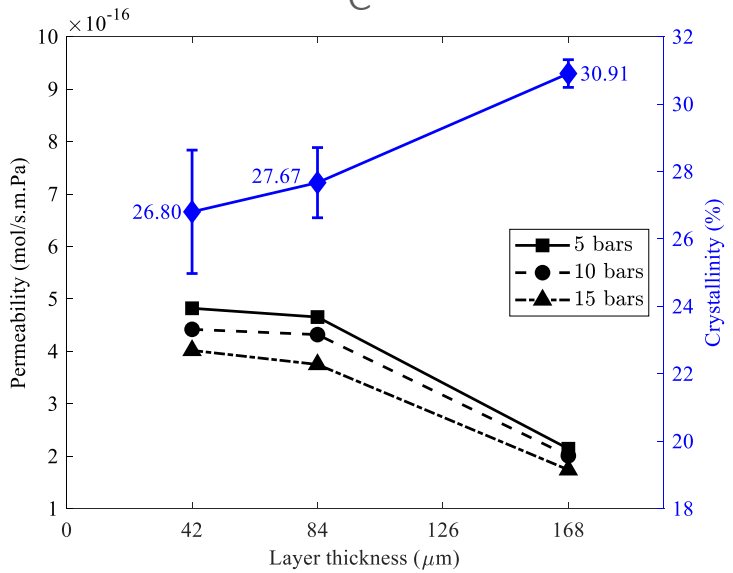

Relation between crystallinity, structure and Permeability in CF/PA6



Hydrogen percolation paths of [0/90]4s laminate after pre-applied tensile loading

Evolution of crystallinity: Pristine samples vs. samples exposed to 100 bars of hydrogen at 35 °C

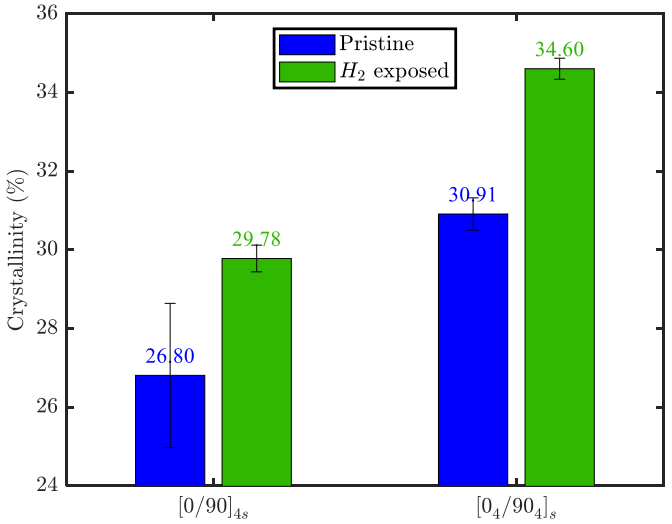

Crystallinity versus time in CF/PA6 laminates Exposed to 100bars at 35°C

An example: In such material, tracking bulk crystallinity is extremely important

Types of energy



Mechanical Energy



Nuclear Energy



Chemical Energy



Electromagnetic Energy



Electric Energy



Thermal Energy

Types of energy



Mechanical Energy



Electromagnetic Energy

NDT&E techniques on the electromagnetic spectrum.

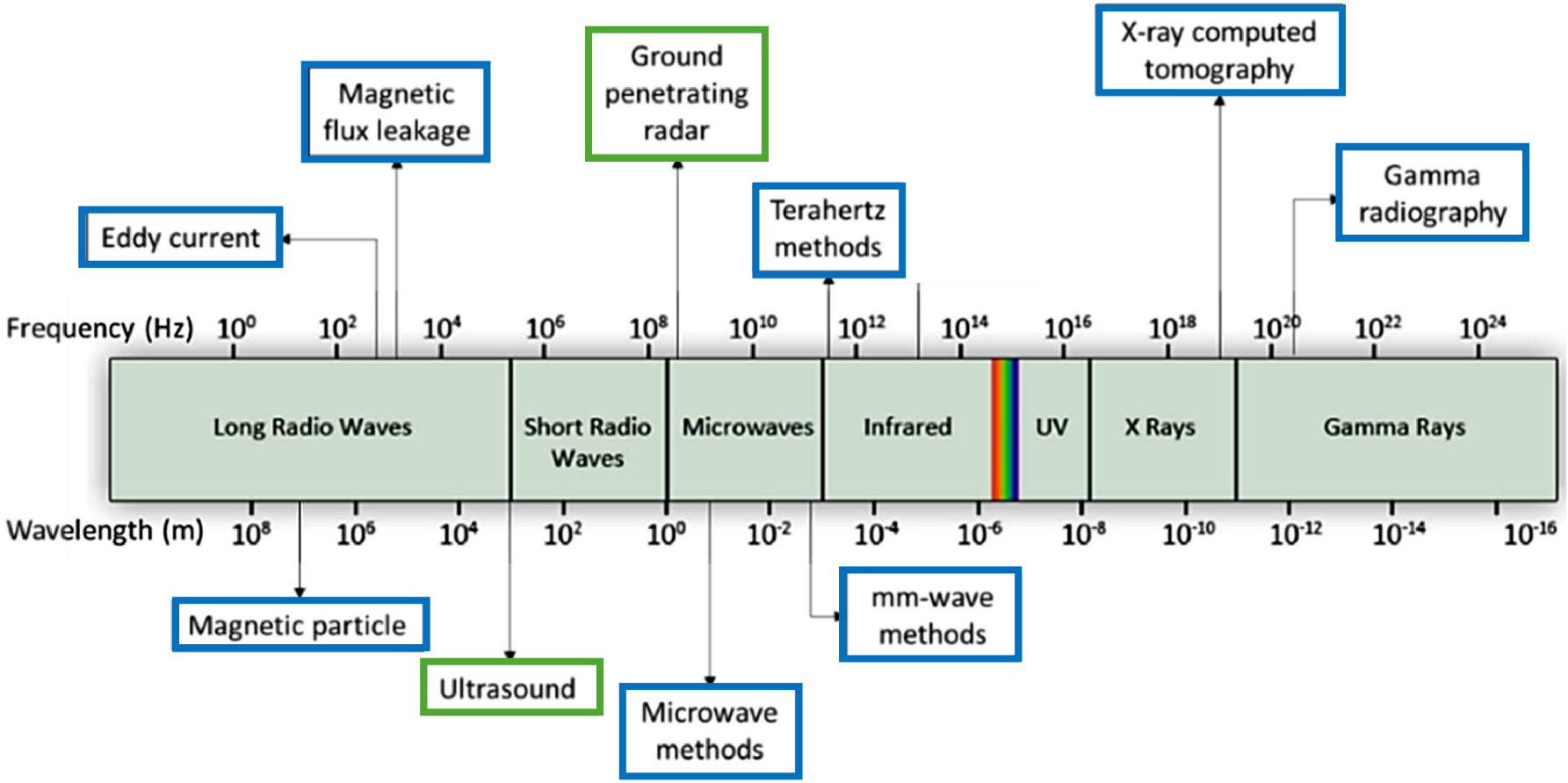

Yao Ren, Robert Skilton. A review of pipe cutting, welding, and NDE technologies for use in fusion devices. Fusion Energy and Design. Vol. 202, May 2024

New materials, new opportunities: leveraging non-metallic innovations

Smart materials

- Integrated sensors
- Printable sensors
- Multi-functional composites

AI generalized diagnosis

- Regularized data-driven technologies
- Direct data to fraud detection/Diagnosis

جامعة الملك عبدالله للعلوم والتقنية
King Abdullah University of Science and Technology

Mechanics of Composites for Energy and Mobility

Sensor Printing

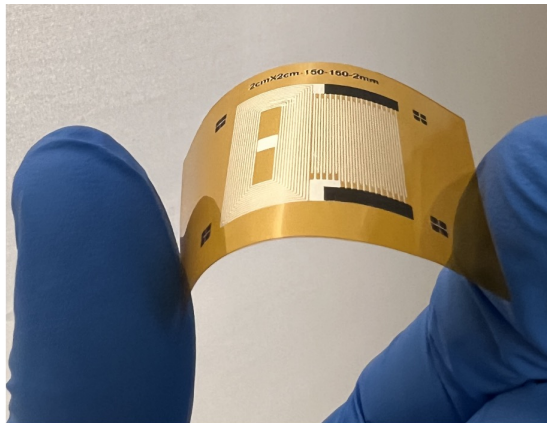

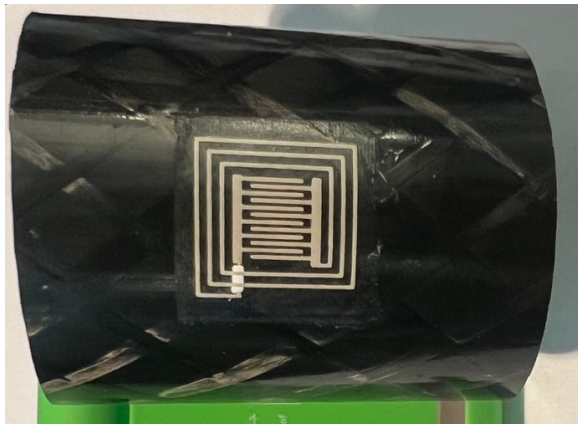

Courtesy: Hassan Mahmoud, MCEM Lab.

New materials, new opportunities

Smart materials

- Integrated sensors
- Printable sensors

AI generalized diagnosis

- Regularized data-driven technologies
- Direct data to fraud detection/Diagnosis



Mechanics of Composites for Energy and Mobility

composites.kaust.edu.sa

@gilleslubineau

جامعة الملك عبدالله للعلوم والتقنية
King Abdullah University of Science and Technology

Thank you!

Gilles Lubineau
gilles.lubineau@kaust.edu.sa

MCEM Website

Mechanics of
Composites
for Energy
and Mobility

PURDUE UNIVERSITY | School of Aeronautics and Astronautics

Composites Manufacturing & Simulation Center™

Shift the Paradigm of Composites Modeling with AI

Wenbin Yu

Milton Clauser Professor, Purdue University

Director, Composites Design and Manufacturing HUB

CTO, AnalySwift LLC

THE NOBEL PRIZE IN PHYSICS 2024

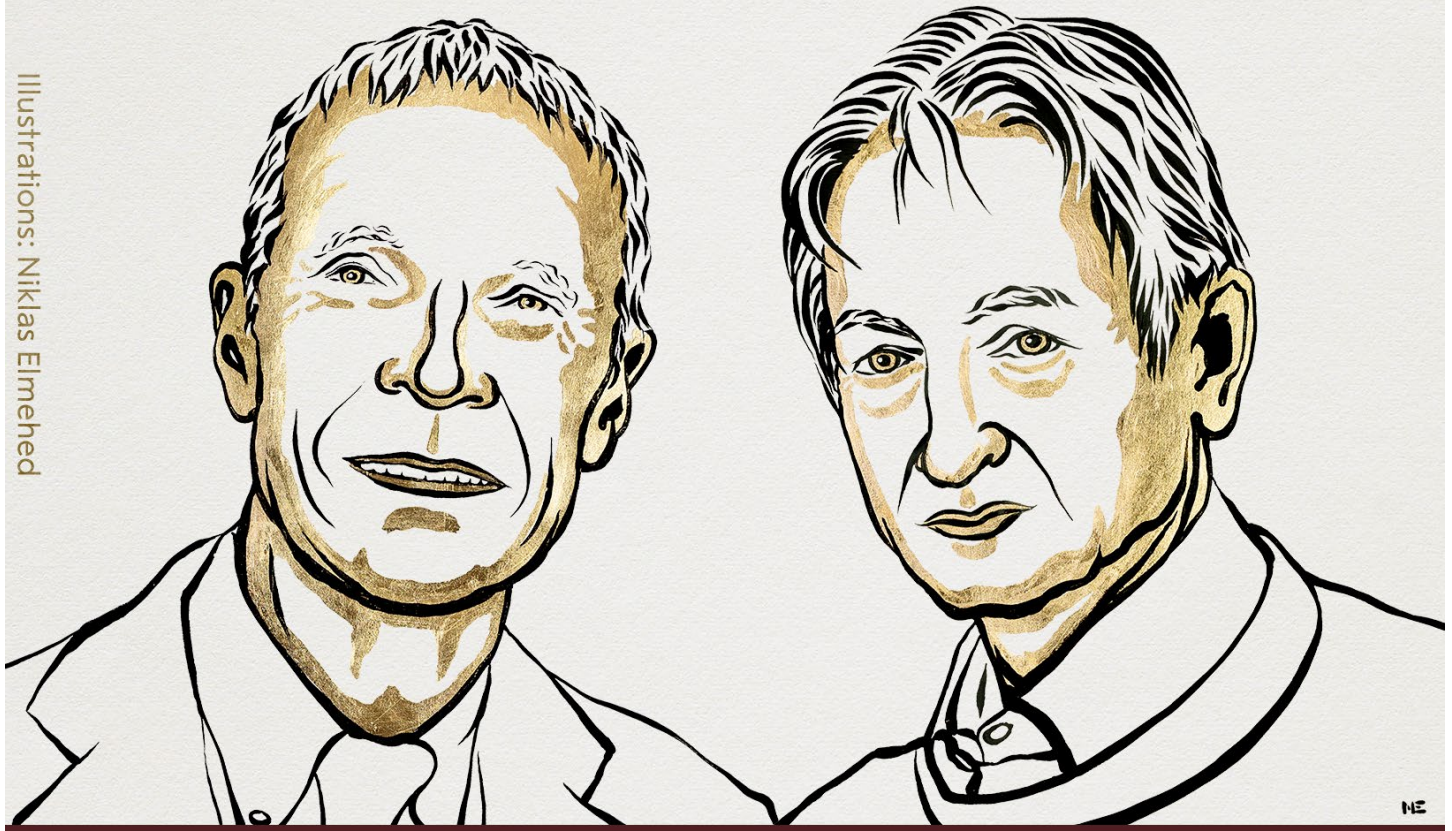

Illustrations: Niklas Elmehed

John J. Hopfield Geoffrey E. Hinton

"for foundational discoveries and inventions
that enable machine learning
with artificial neural networks"

THE ROYAL SWEDISH ACADEMY OF SCIENCES

Is Physics-based Modeling Still Needed?



Tycho Brahe
(1546-1601)

Astronomical & Planetary Observations (Data)



Johannes Kepler
(1571-1630)

Laws of Planetary Motion
(Curve Fitting)

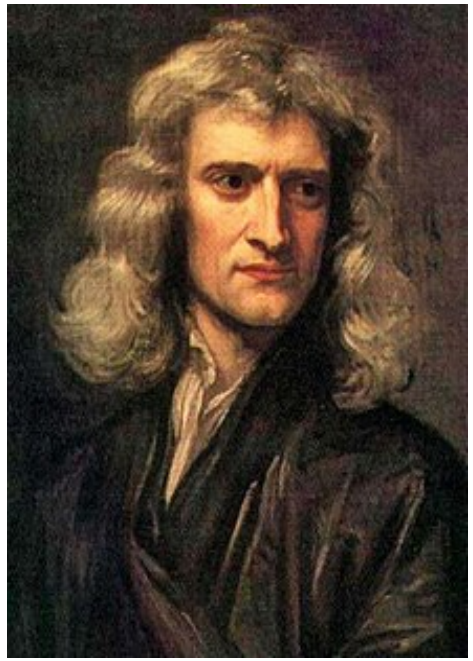

Isaac Newton
(1642-1726)

Laws of Motion & Gravitation
(Modeling)

Challenges: Multiscale/Anisotropy/Heterogeneity



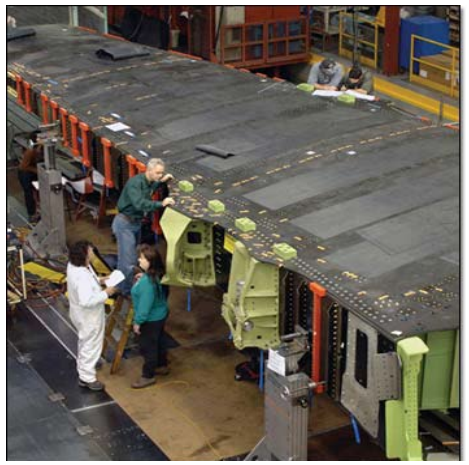





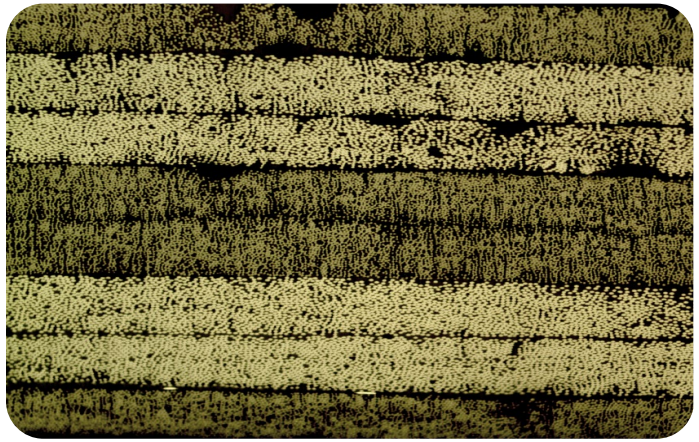

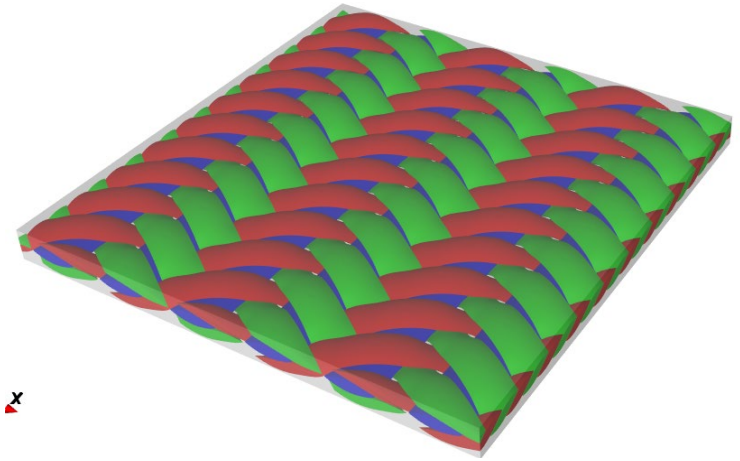

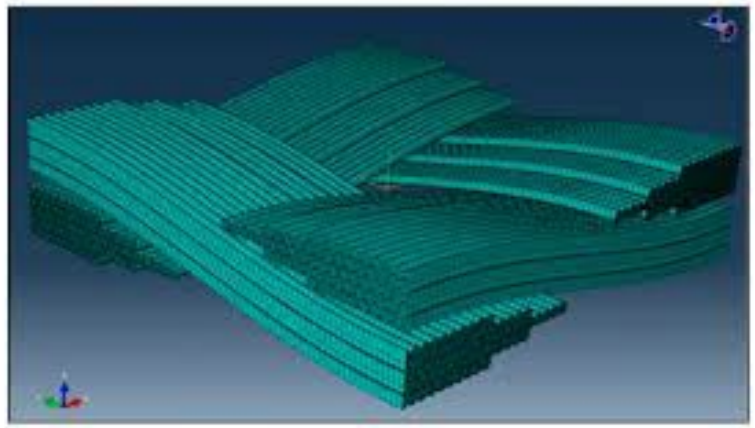

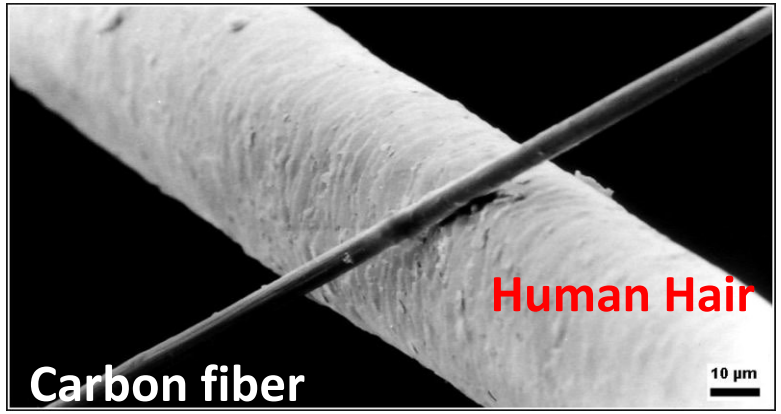

1 mm^3 material block ~ **20 Million DOFs**







MSG: *A top-down modeling framework that **models relevant behavior in terms of microstructural details as needed and affordable**.*

SwiftComp™

A Purdue Technology

Principle of Minimum Information Loss

- Virtual testing of materials/structures
  - Mechanical properties
  - Multifunctional properties
  - Transport properties
- Multiscale modeling of structures
  - Composite structures
  - Stiffened structures
  - Build-up structures
  - Sandwich structures

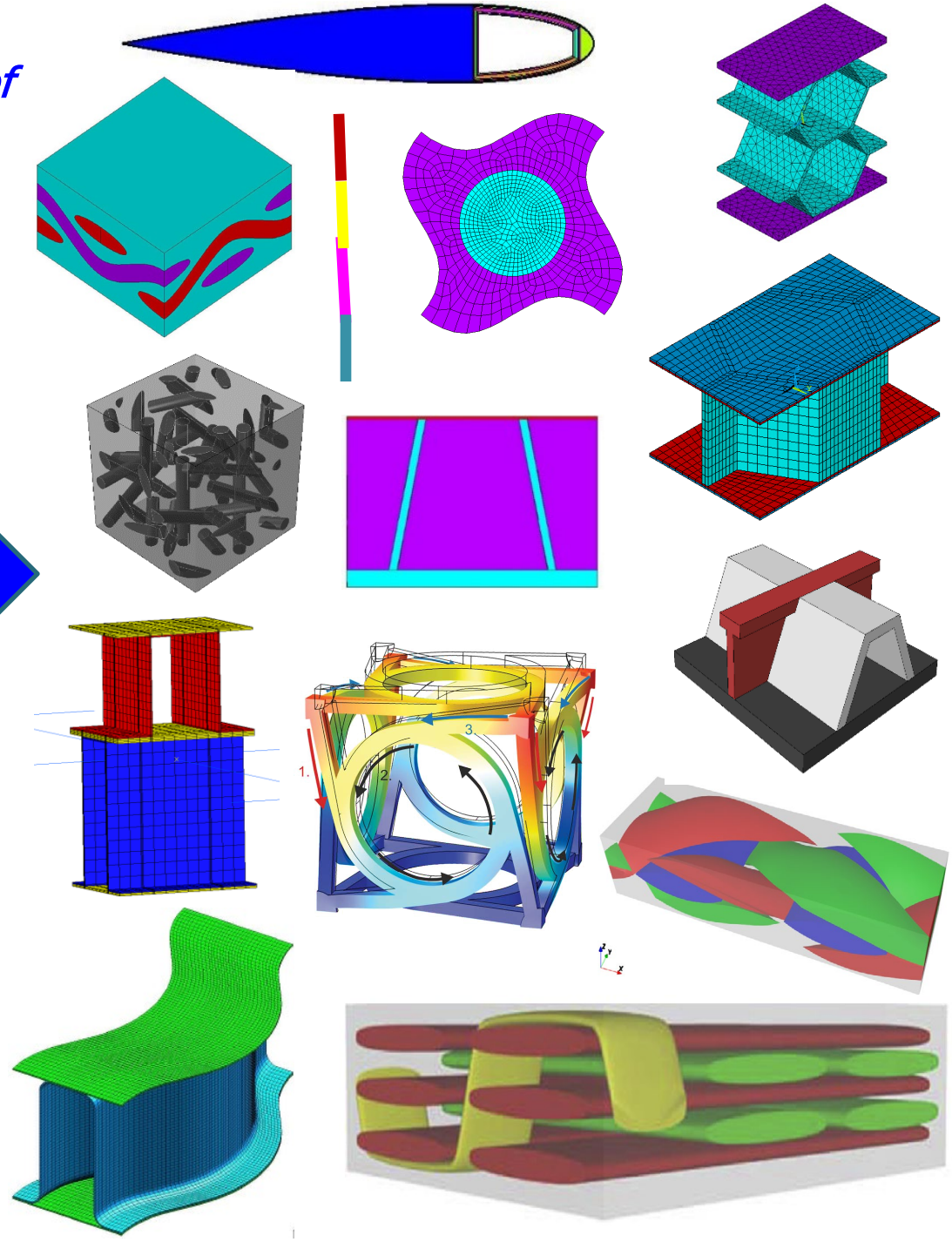

MSG-based Progressive Damage Analysis for Composites

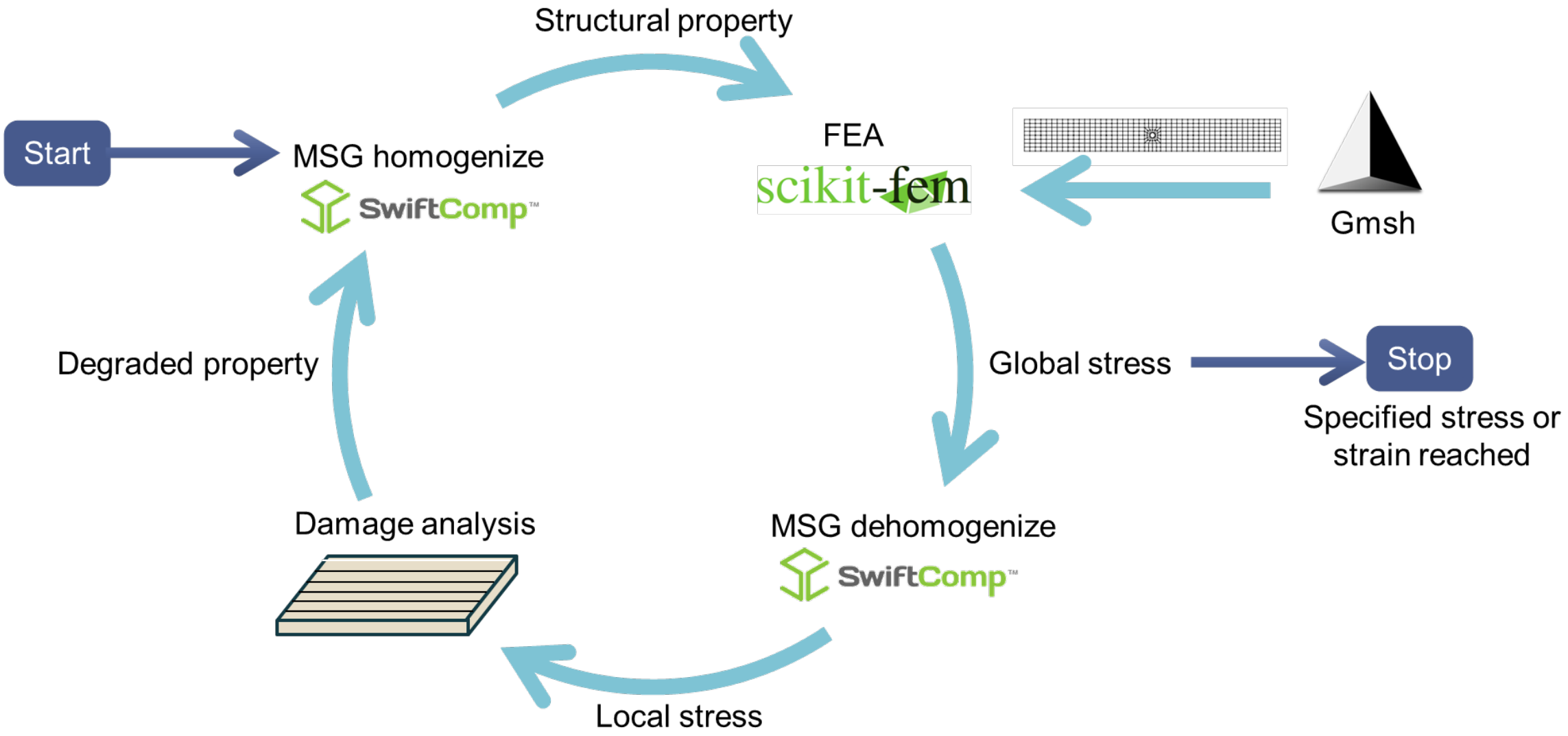

Progressive Damage Analysis of Open-hole Laminate

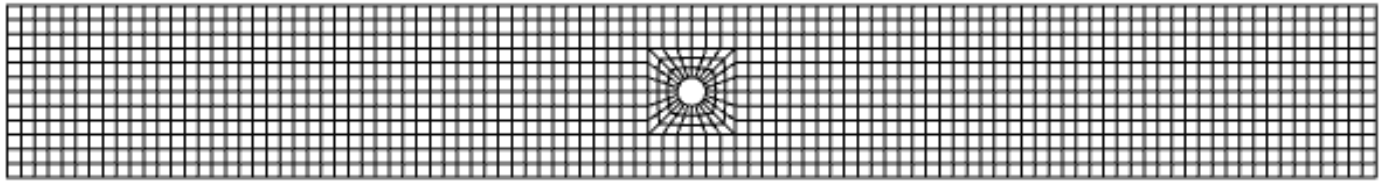

- Material: IM7/8552 laminate
- Layup: $[0/45/90/-45]_{2s}$
- Dimensions: 300 x 38 mm hole diameter 6.35mm
- Mesh: 11800 quad elements
- Material properties:

(a) Lamina elastic properties

E_1	$E_2 = E_3$	$G_{12} = G_{13}$	G_{23}	$\nu_{12} = \nu_{13}$	ν_{23}
171.42 GPa	9.08 GPa	5.29 GPa	4.27 GPa	0.32	0.45

(b) Strength properties (MPa)

X^T	X^C	$Y^T = Z^T$	$Y^C = Z^C$	$S_{12} = S_{13}$	S_{23}
2323.5	1200.1	62.3	253	92.3	107.6

(c) Fracture energy (kJ/m^2)

$G^+_{1,c}$	$G^-_{1,c}$	$G^+_{2,c} = G^+_{3,c}$	$G^-_{2,c} = G^-_{3,c}$
133.3	61	0.28	1.31

Progressive Damage Analysis of Open-hole Laminate

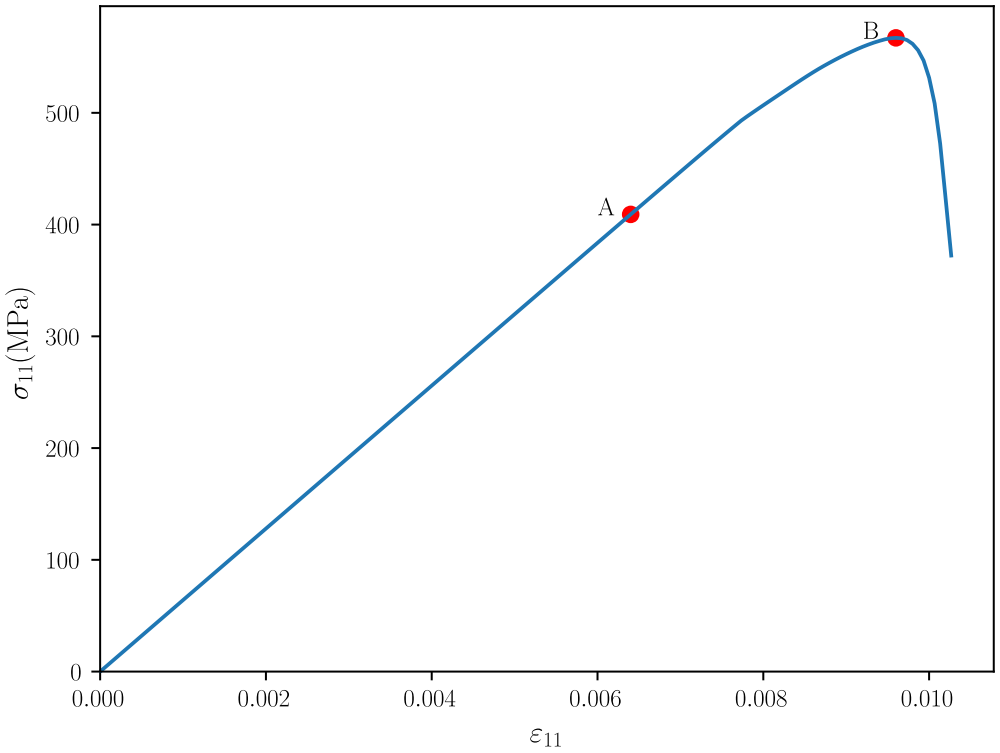

A: initial failure
B: ultimate failure

Damage variable d1 (a)-(d) (Left) and d2 (e)-(h) (Right) at the ultimate failure

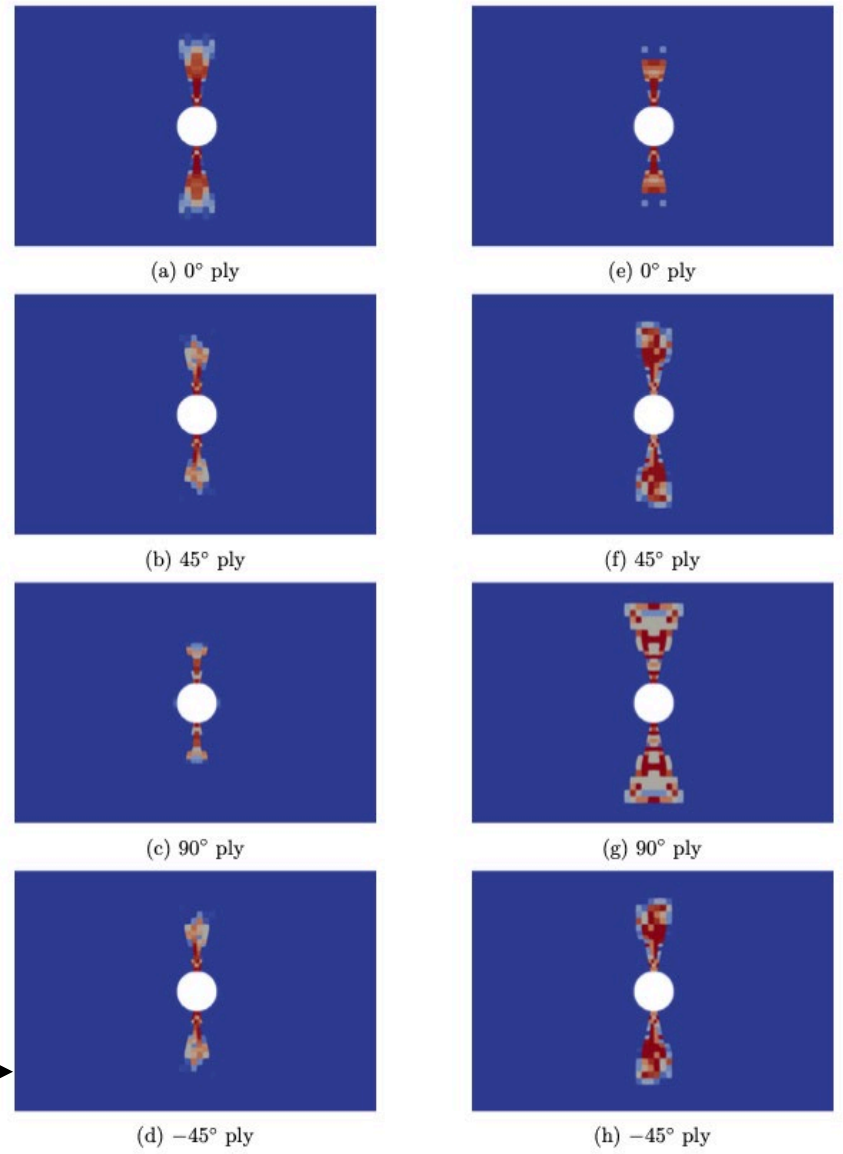

Challenges for Composites Modeling

1. High computational costs for complex 3D microstructures
2. Idealized microstructures
3. Unknown constituent properties and constitutive models
4. Interface with other codes to form the end-to-end simulation
5. Highly specialized training (PhD level) for confidently performing composites simulations, unaffordable for small companies

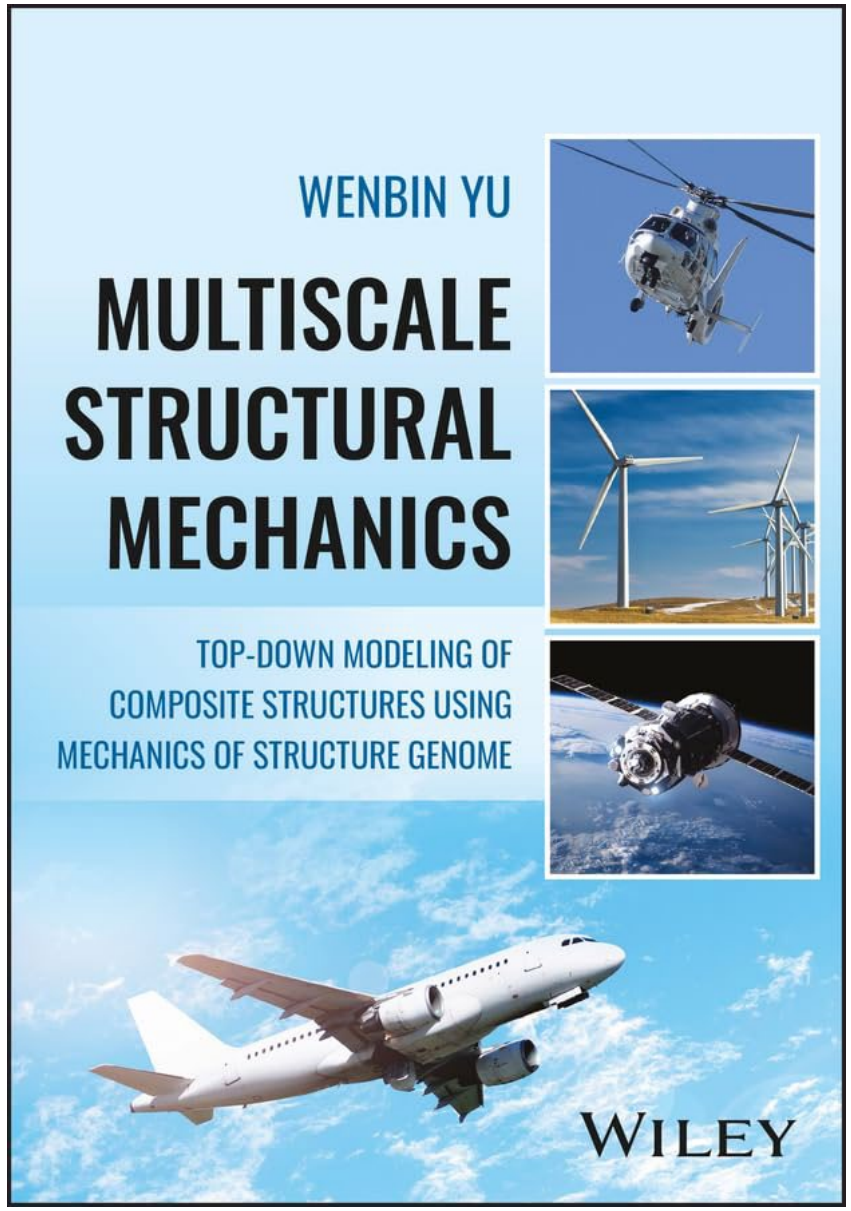

AI-Assisted MSG-based Composites Modeling

1. Create ultra-efficient surrogate models
2. Produce realistic microstructures using image recognition or generation
3. Learn unknown constituent properties & constitutive models
4. Integrate different tools using human language
5. Democratize the use of simulation workflows using a domain-specific LLM

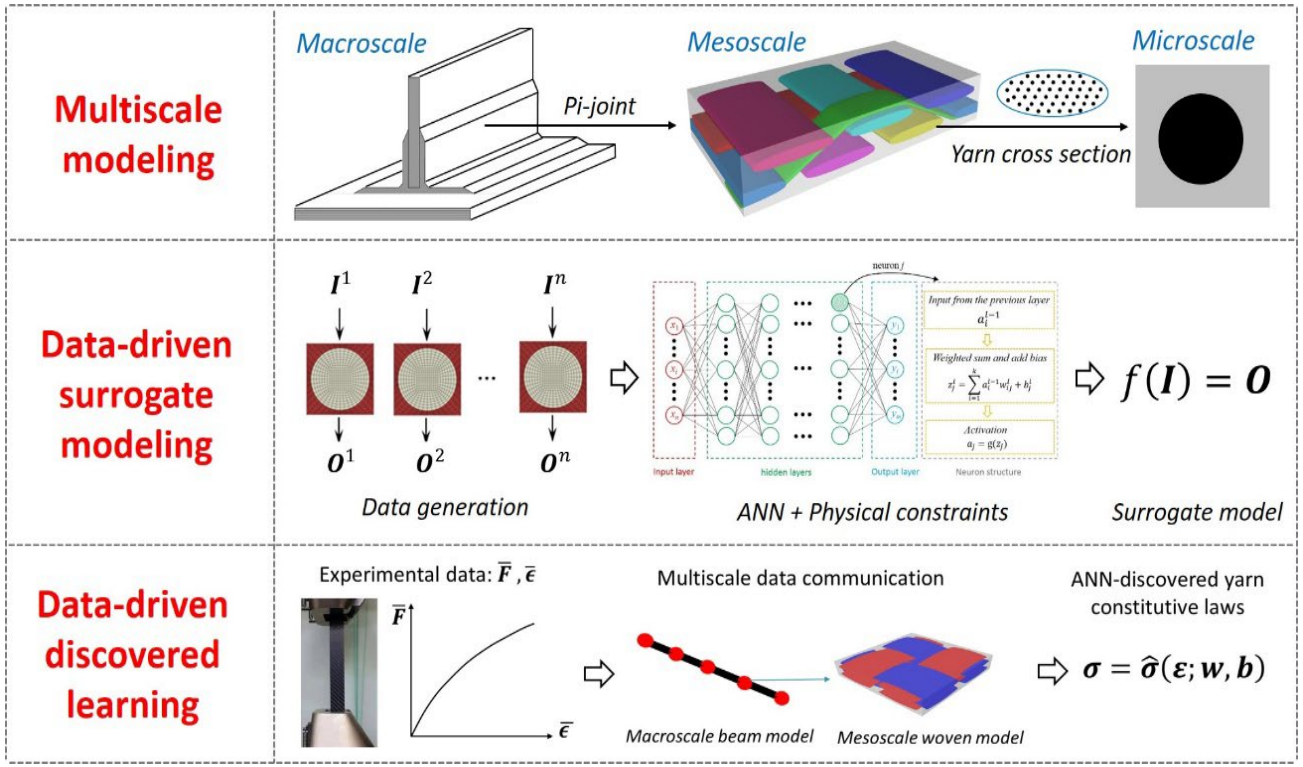

Liu, X., Tian, S., Tao, F. and Yu, W., 2021. *Composites Part B: Engineering*, 224, p.109152.

Effective Thermal Conductivity of Woven Composites

- Deep learning neural network (DNN) model
  - Include both microscale and mesoscale features
  - Mixed continuous (e.g., yarn geometries) and discrete (weave patterns) input data

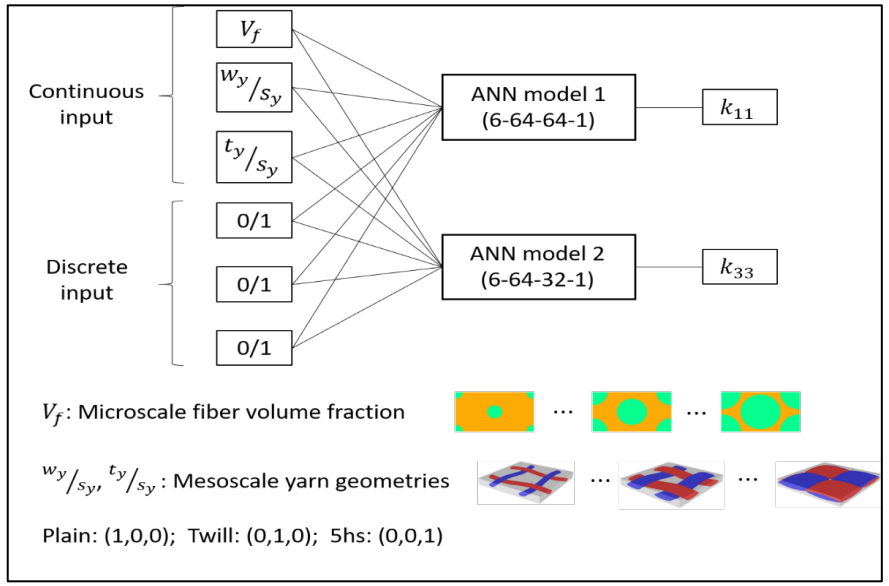

DNN architecture

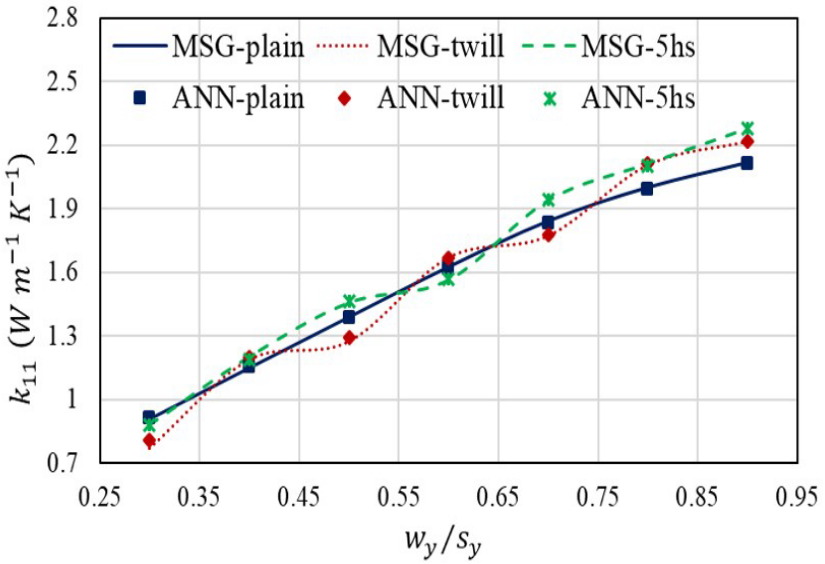

In-plane conductivity vs yarn width

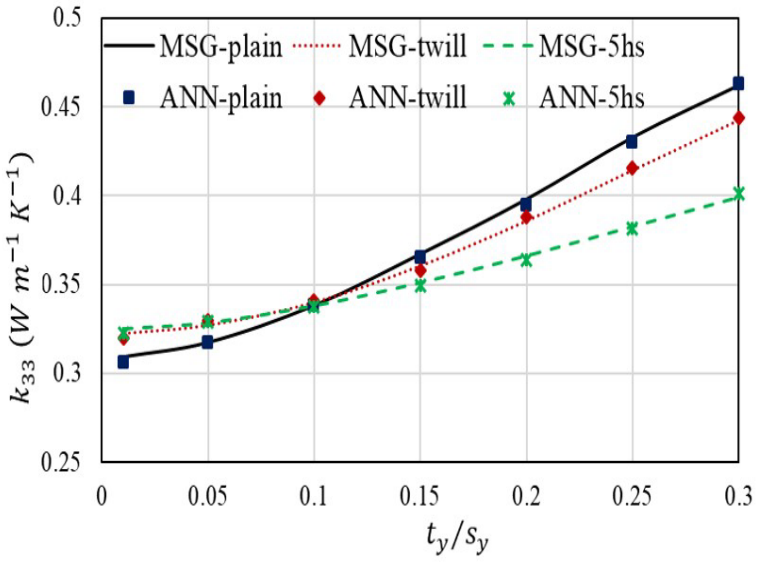

Out-of-plane conductivity vs yarn thickness

Liu, X., Peng, B. and Yu, W., 2021. *International Journal of Heat and Mass Transfer*, 179, p.121673.

Failure Strength Prediction of Woven Composites

➢Data-driven yarn failure criterion

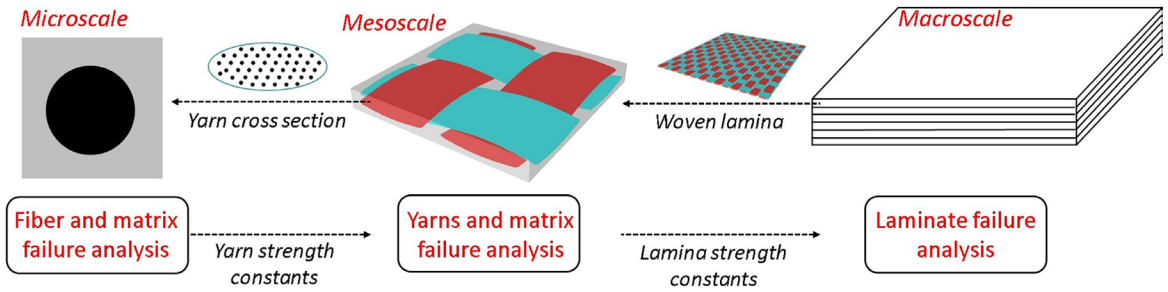

Multiscale failure analysis

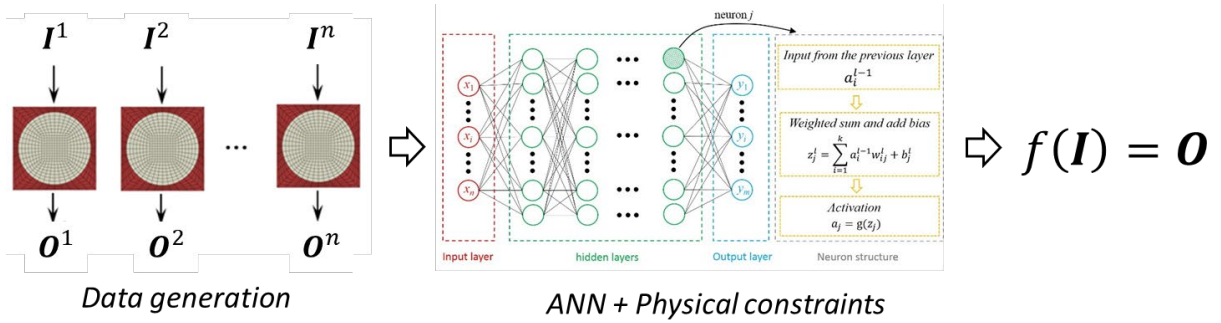

Replace microscale modeling with a DNN model

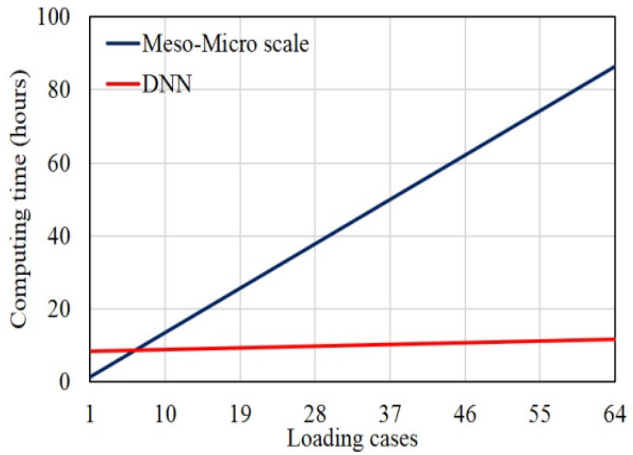

Computing time

Model	Xt	Xc	Zt	Zc	R	S
Two-scale MSG	149.81	294.25	39.91	144.60	22.94	19.10
DL model	148.84	295.74	39.44	140.11	22.78	19.11
Diff(MSG vs DL)	**0.65%**	**0.51%**	**1.18%**	**3.11%**	**0.70%**	**0.05%**

- Good accuracy compared with high-fidelity model
- Significantly improved efficiency

Liu, X., Gasco, F., Goodsell, J. and Yu, W., 2019. *Composite Structures*, 230, p.111505.

AI-Assisted MSG-based Composites Modeling

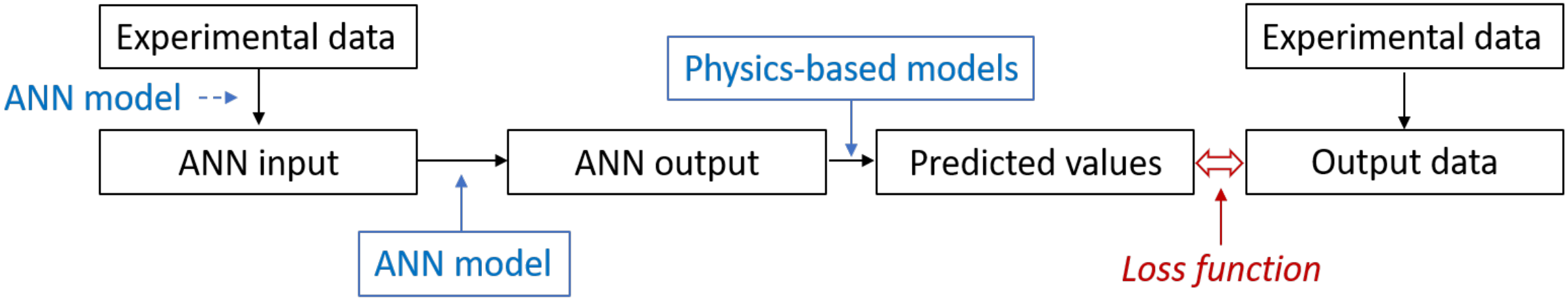

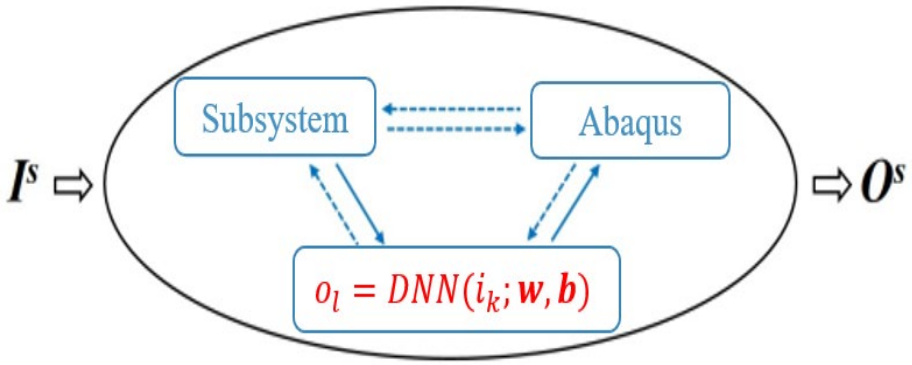

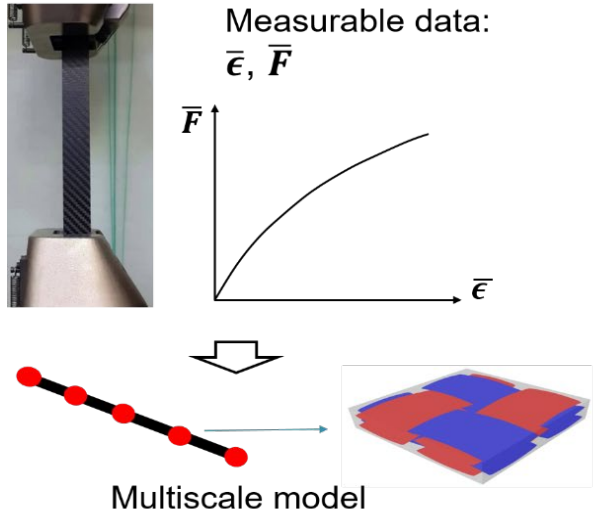

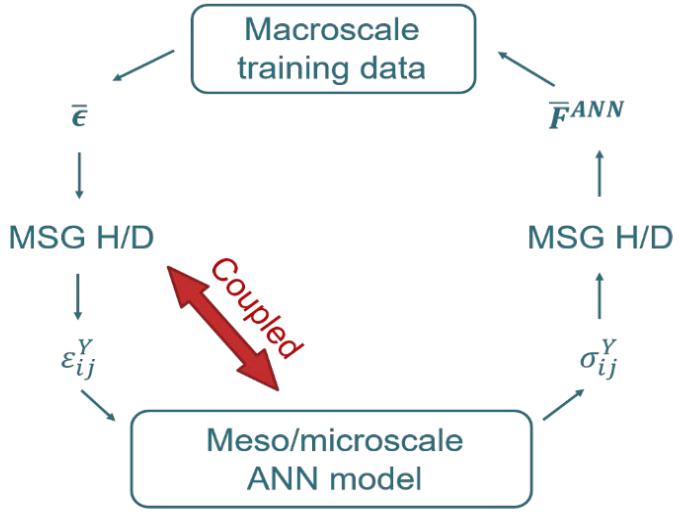

Liu, X., Tian, S., Tao, F. and Yu, W., 2021. *Composites Part B: Engineering*, 224, p.109152.

Hybrid Neural Network – Finite Element Model

➢Train constitutive model with indirectly measurable data

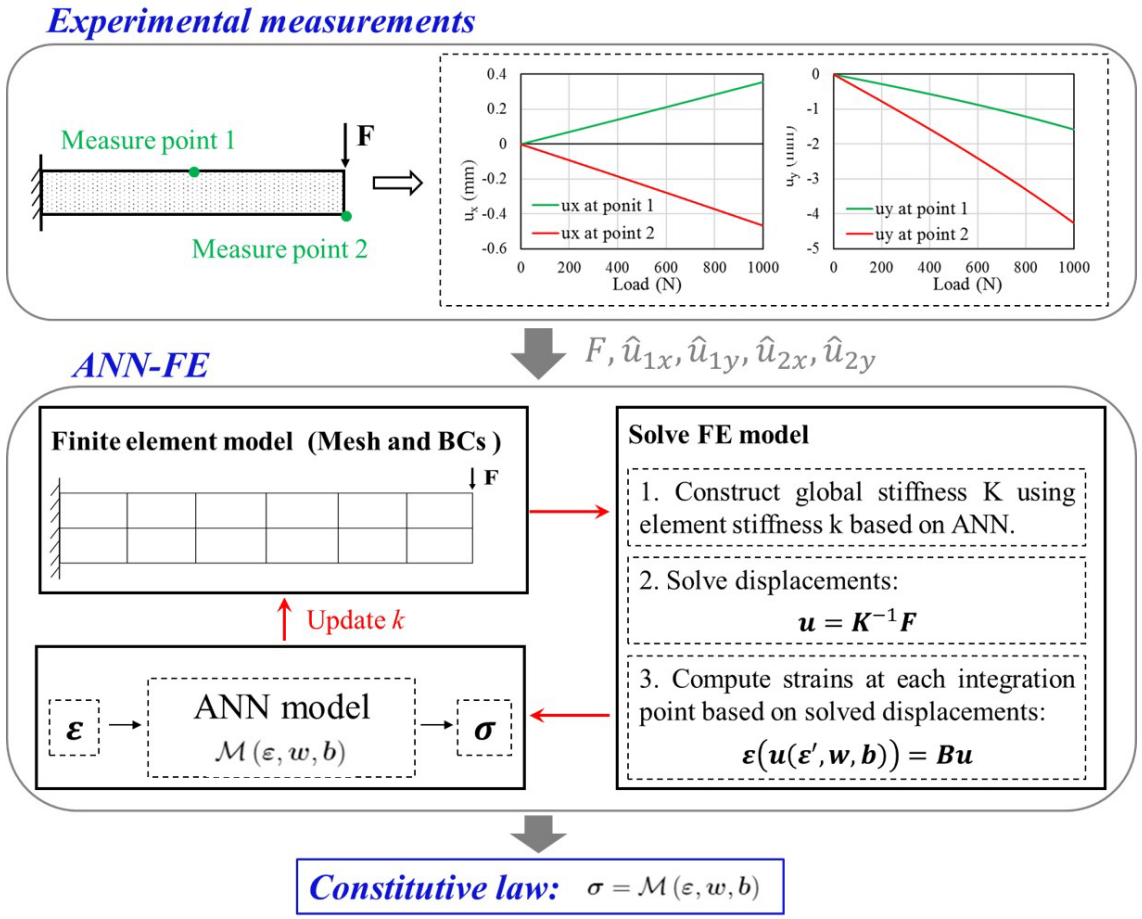

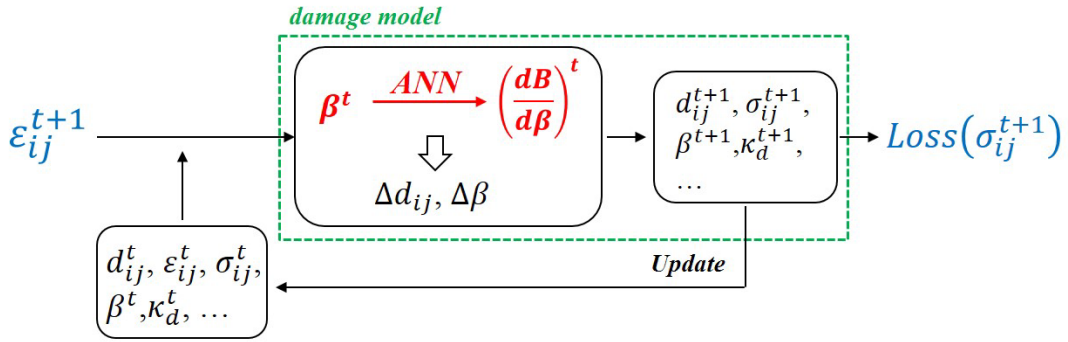

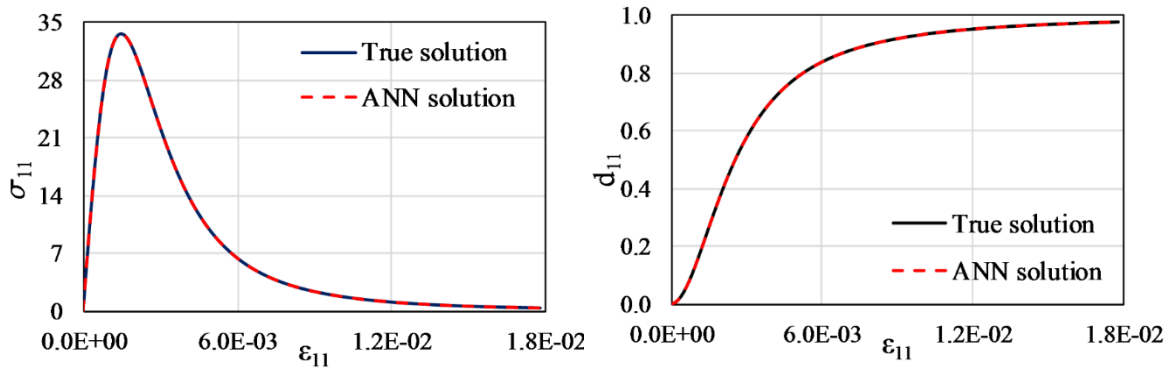

Learn damage based on stress-strain curve

Liu, X., Tao, F., Du, H., Yu, W. and Xu, K., 2020. *Journal of Applied Mechanics*, 87(8), p.081003.

Learn Lamina Constitutive Law Based on Laminate Response

- Couple neural network with Abaqus for model training
  - Training data: Surface displacements
  - Learned model: Stress-strain relation

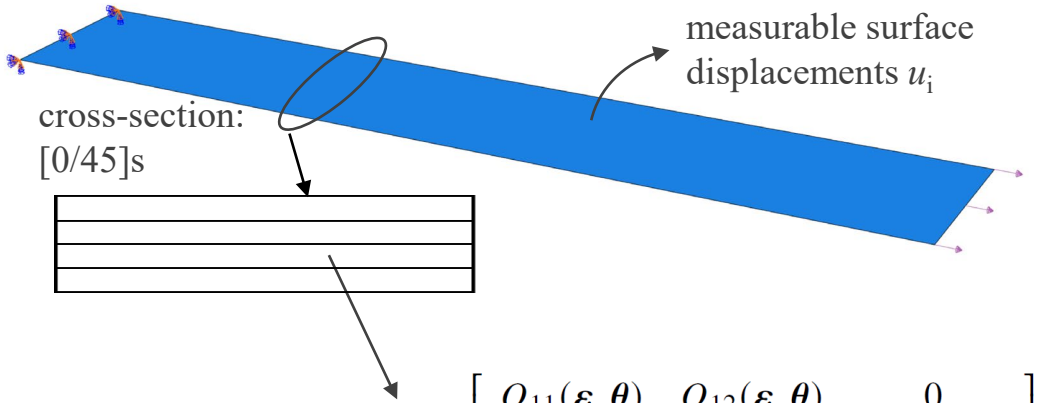

$$\mathcal{M}(\boldsymbol{\varepsilon},\boldsymbol{\theta}) = Q(\boldsymbol{\varepsilon},\boldsymbol{\theta}) = \begin{bmatrix} Q_{11}(\boldsymbol{\varepsilon},\boldsymbol{\theta}) & Q_{12}(\boldsymbol{\varepsilon},\boldsymbol{\theta}) & 0 \\ Q_{12}(\boldsymbol{\varepsilon},\boldsymbol{\theta}) & Q_{22}(\boldsymbol{\varepsilon},\boldsymbol{\theta}) & 0 \\ 0 & 0 & Q_{66}(\boldsymbol{\varepsilon},\boldsymbol{\theta}) \end{bmatrix}$$

Damage material stiffness matrix to be learned

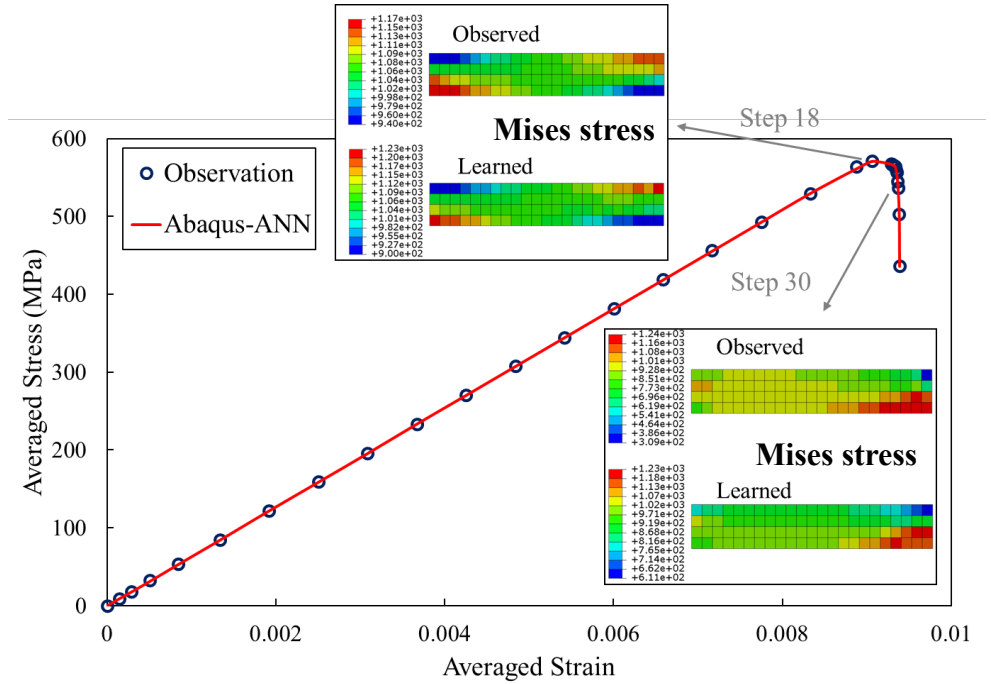

Tao, F., Liu, X., Du, H. and Yu, W., 2021. *Composite Structures*, 272, p.114137.

CompositesAI™: AI-Powered Composites Expert System

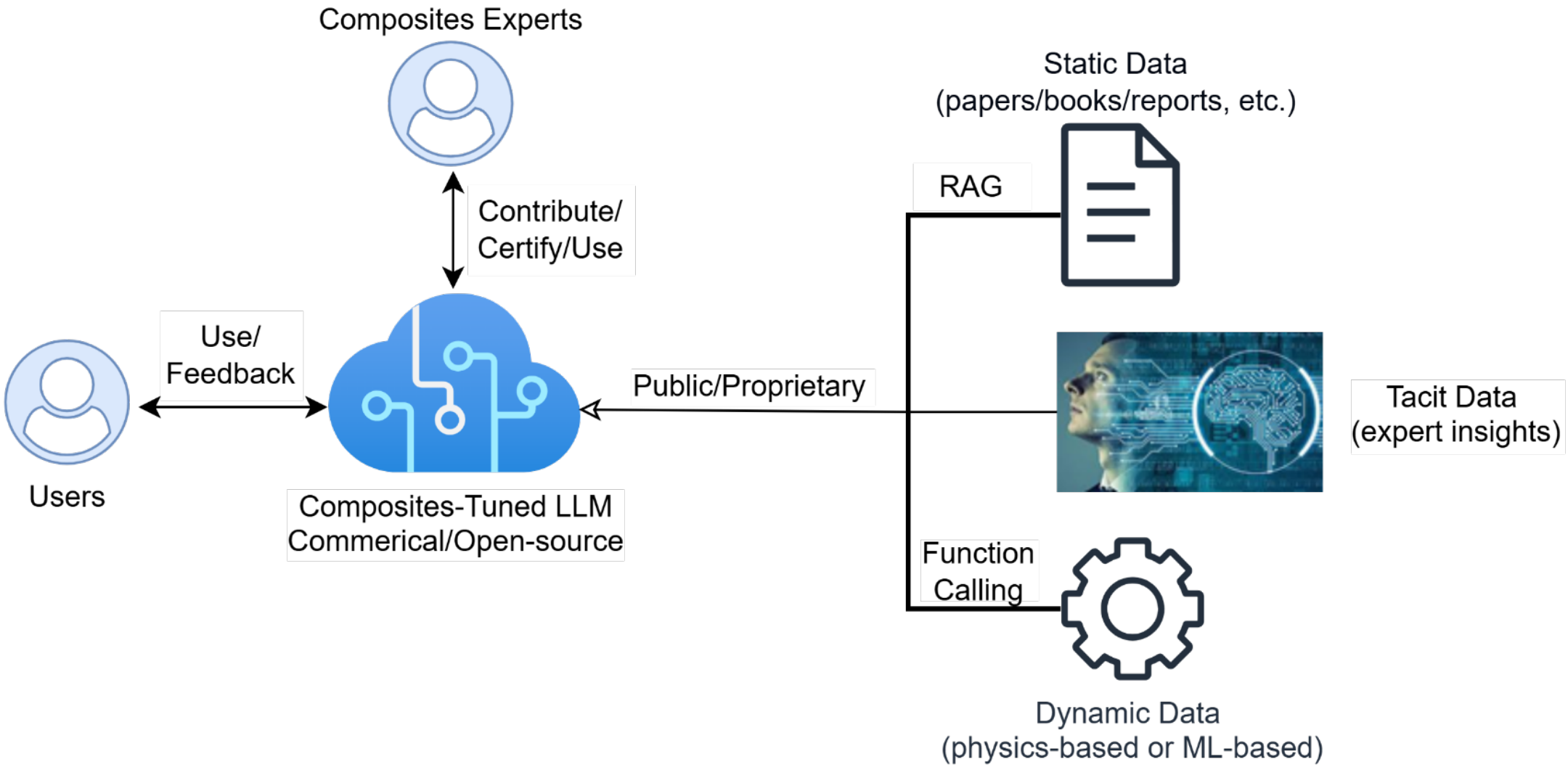

Expert Knowledge Intelligentized in CompositesAI

how to compute the upper bound of young's modulus for a two-phase isotropic composite

CompositesAI

To compute the upper bound of Young's modulus for a two-phase isotropic composite, you generally use the Voigt rule of mixtures. The Voigt upper bound assumes isostrain conditions (i.e., the strain is uniform across the phases). For constituents with equal Poisson's ratios ($\nu_f = \nu_m$), the upper bound is given by:

$$E_V^* = V_f E_f + V_m E_m$$

where:

- E_f and E_m are the Young's moduli of the fiber and matrix (the two phases),
- V_f and V_m are their respective volume fractions.

However, if the two isotropic phases have different Poisson's ratios ($\nu_f \neq \nu_m$), the simple rule above is not the strict upper bound. In this case, the upper bound is obtained by extracting Young's modulus from the effective stiffness matrix calculated according to the Voigt rule, incorporating both moduli and Poisson's ratios. The result is always greater than the simple mixture rule due to the influence of differing Poisson's ratios.

Thus, for most accurate results, when $\nu_f \neq \nu_m$, you should compute the effective stiffness matrix using the Voigt approach and then extract the effective Young's modulus from that matrix, rather than relying solely on the simple mixture formula

Simulation via CompositesAI

- Integrate commercial code SwiftComp for multiscale modeling
  - No need of FE knowledge
  - Execute sophisticated code using natural language
  - Guide the process of preparing input and understand outputs
  - Live on CompositesAI (AC)

for a unidirectional fiber reinforced composites, I would like to know G13 and G23, do you have a tool to help me compute it?

CompositesAI

Yes, I have a specialized tool that can compute the shear moduli G_{13} and G_{23} (as well as other engineering constants) for unidirectional fiber-reinforced composites. This tool requires the following inputs:

Fiber and matrix elastic properties (E, ν or full set if anisotropic)
Fiber volume fraction
Packing arrangement (e.g., hexagonal, square)

If you provide:
Fiber modulus (E_f) and Poisson's ratio (ν_f)
Matrix modulus (E_m) and Poisson's ratio (ν_m)
Fiber volume fraction (V_f)
Packing type (default is hexagonal if not specified)

I can obtain G_{13} and G_{23} for your system. Please supply the above inputs or confirm if you want to use prior examples.

isotropic fiber with E=300 GPa, nu=0.3; isotropic matrix with E=20 GPa, nu =0.4, hexagonal, Vf=68%

CompositesAI

View Result from **homogenize_elastic_constants**

For a unidirectional fiber-reinforced composite with isotropic fibers ($E_f = 300\,\text{GPa},\ \nu_f = 0.3$), isotropic matrix ($E_m = 20\,\text{GPa},\ \nu_m = 0.4$), hexagonal packing, and a fiber volume fraction of 68%, the calculated shear moduli are:

$G_{13} = 28.86$ GPa
$G_{23} = 31.58$ GPa

These values are computed using physics-based homogenization methods appropriate for your specified microstructure and constituent properties.

Your numbers are a bit high. Try Ef = 231 GPa, Poisson's ratio of the fiber is 0.35. Em = 4 GPa, Poisson's ratio of matrix is 0.3.

CompositesAI

View Result from **homogenize_elastic_constants**

For a unidirectional fiber-reinforced composite with the following properties:

Isotropic fiber: $E_f = 231\,\text{GPa},\ \nu_f = 0.35$
Isotropic matrix: $E_m = 4\,\text{GPa},\ \nu_m = 0.3$
Hexagonal packing, fiber volume fraction $V_f = 68\%$

The computed shear moduli are:

$G_{13} = 7.50\,\text{GPa}$
$G_{23} = 7.21\,\text{GPa}$

These values reflect a physically realistic shear response for your specified composite system.

cdmHUB Community: Experts Interact with AI

- Mission: to convene & serve the composites community by creation, education, evaluation, and sharing of resources for composites design & manufacturing
- Live on cdmHUB Community



Composites Modeling in the Era of AI

- Physics-based modeling still needed
  - Rigorously model advanced materials featuring general anisotropy and heterogeneity
  - Provide data and simulation tools for AI
- AI helps
  - Reducing computational cost
  - Creating more realistic microstructures
  - Discovering unknown physics information
  - Consolidating and delivering composites knowledge
  - Distilling experts' insights

CompositesAI.com

community.cdmHUB.com

PROCESS MONITORING FOR DEFECT CONTROL – FROM RTM TO SANDWICH PANEL CO-CURE

Steven Nutt, M. Anders, and T. Centea

M.C. Gill Composites Center, University of Southern California
3651 Watt Way-VHE-406, Los Angeles, CA, 90089, USA
Email: nutt@usc.edu, web page: https://composites.usc.edu

Keywords: Process monitoring, Defects, RTM, Co-cure

ABSTRACT

Insights into process phenomena provide understanding necessary to eliminate manufacturing defects, yet process hardware (autoclaves, moulds, and tools), renders these phenomena opaque. At USC, we have developed instrumented testbeds that replicate common process conditions and afford real-time observation and insights into key phenomena leading to defects. In one example, a lab-scale RTM mould features a transparent window, allowing observation of mould filling and porosity evolution. In a second example, a pressurized cavity replicates autoclave conditions for co-cure of honeycomb panels, providing real-time observations of bond-line formation at core-skin junctions. Such observations were use to support the construction and validation of physics-based process models for co-cure. The combination of conventional systematic characterization of resin properties with the instrumented testbeds provide a method for process optimization, understanding of defect formation, and a basis for developing strategies for defect reduction.

1 INTRODUCTION

Manufacturing defects cause variations in performance levels that lead to knockdowns in property levels used for design. The opacity of production hardware – autoclaves, tooling, and moulds – prevent direct observation of defect formation. As a result, attempts to understand defect origins rely primarily on "post-mortem" analysis of polished sections, leaving ample room for speculation and imagination, but providing scant guidance to adjust process parameters. Instrumented testbeds provide useful insights into defect formation mechanisms, and when combined with resin characterization tools – primarily thermal analysis and rheometry – constitute a framework for analyzing and mitigating defects.

In this work, two case studies are presented that illustrate a methodology that relies on conventional materials characterization complemented by data and observations acquired from lab-scale testbeds that replicate manufacturing conditions. The thermal analysis and rheological data can be presented alongside video observations on a synchronized time axis. Thus, the physical state of the resin (degree of cure, viscosity) can be correlated with flow phenomena, void nucleation, and other phenomena. The combined use of conventional and customized analytical tools provide rich datasets and useful insights into how, when, and where defects arise. These insights can be used to develop and validate process models, and to guide parametric adjustments to reduce/eliminate defects.

The first case study involves an effort to develop a benoxazine-epoxy formulation for liquid molding, specifically for RTM[1]. The formulation included a solvent(s), and increasing the risk of void formation if volatiles left the solution during molding. A lab-scale RTM mold was designed and built to monitor the mold filling and curing processes directly, and the data acquired were combined with the use of a suite of conventional characterization tools, and led to specific recommendations for mitigating process-induced defects. The second case study focuses on co-cure of honeycomb sandwich panels, and attempts to develop physics-based models.[2] The name of the process derives from the simultaneous curing of facesheets and the film adhesive used to attach the core. Despite the appeal of a one-step process, the process is difficult to manage, and the facesheets prevent observation of bondline formation. A customized testbed was designed and built that afforded direct observation of the bondline during co-

cure under autoclave conditions.[3] The project led to process models for co-cure and validation of predictions.

2 EXPERIMENT

The lab-scale RTM tool built for Case Study 1 (CS1) is shown in Figure 1 and described in detail in reference [1]. The main body of the mold was an anodized aluminum block containing inlet and outlet ports with ‘‘line injection” grooves used to generate a one-dimensional flow front. A ‘‘picture frame” plate with a rectangular cavity was placed against the main body to define the thickness (3.2 mm) and in-plane dimensions (76 × 127 mm) of the part. The second tool face was a 20 mm thick tempered glass plate, rated for pressures up to 1200 kPa. This glass plate formed a rigid window that afforded direct *in situ* observation of in-mold phenomena, including air evacuation, preform saturation during injection, and the time and location of any subsequent void formation.

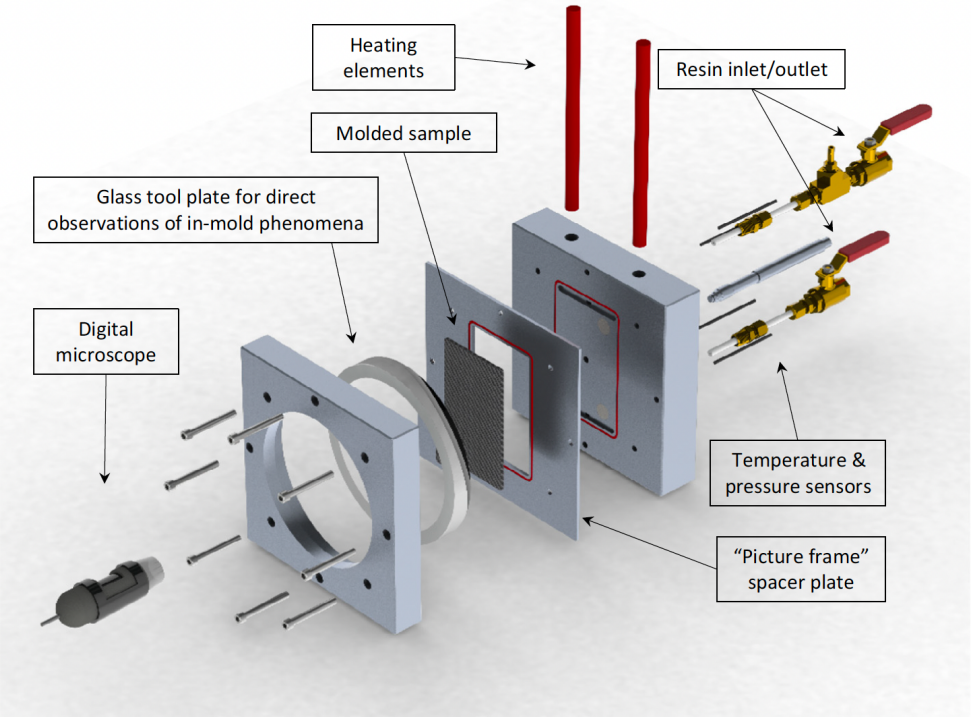

Figure 1: Expanded view of lab-scale RTM tool.[1]

For Case Study 2 (CS2), attention focused on co-cure of sandwich panels under autoclave conditions. The elements to be assembled included a honeycomb core (Nomex), a toughened epoxy film adhesive (Loctite EA 9658 AERO 060UNS, Henkel Corp.), and CF-epoxy prepreg plies (Syensco 5320-1 or Hexcel 8552S). To view phenomena associated with bond-line formation, a cell was designed that replicated autoclave pressure and temperature while affording direct observation of the bondline during co-cure. A half-panel sample was used (one face sheet, one adhesive film, and a core of half-thickness) in a testbed shown in Figure 2. Note that the glass viewport on the lower side allowed video observation of film adhesive redistribution during co-cure, a process called reticulation, that was intended to result in fillet formation at cell wall-facesheet junctions (adhesive remaining between cell walls amounted to parasitic weight).

The reticulation process – which can be performed in several ways [11,31] – results in adhesive located only along the edges of the honeycomb cell walls, with an opening in the film at the center of each cell. Fig. 4 shows the stages of adhesive reticulation. First, the adhesive film was placed onto the top side of the honeycomb core and manually perforated in the center of each honeycomb cell using a ~1mm diameter needle. Then, heated air was blown over the surface of the film using a handheld hot-air gun. As the film softened under the applied heat, surface tension caused the holes to

widen, reshaping the film into an adhesive bead along the edges of the cell walls. Temperatures were monitored using a thermocouple and did not exceed 70 °ΔC. Reticulation was completed in < 3 min, ensuring that the process did not advance the cure of the adhesive.

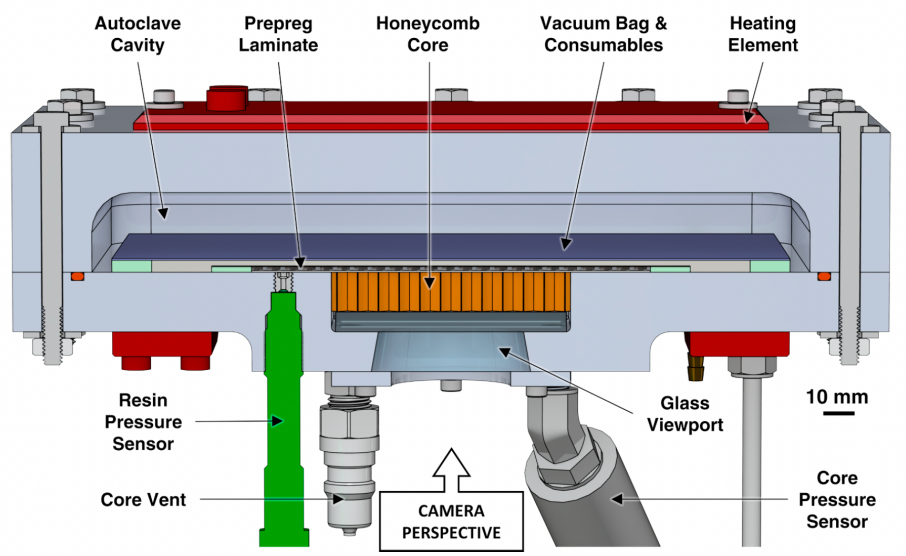

Figure 2: Section view of co-cure fixture with sample and consumables.[3]

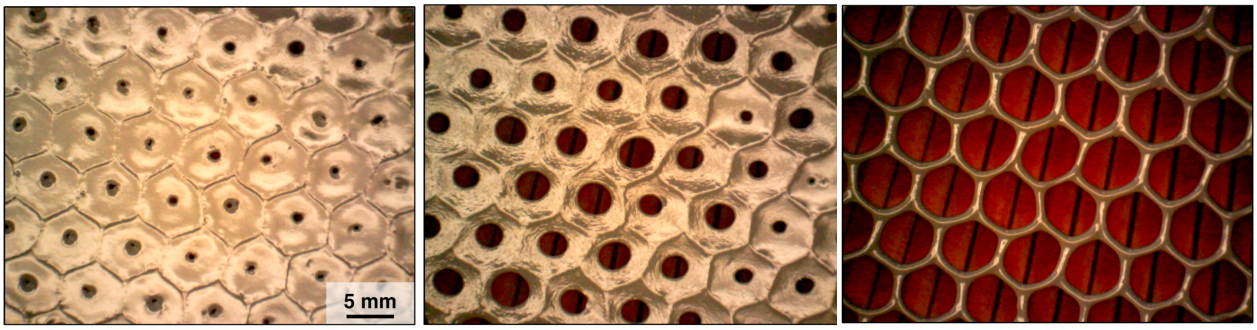

Figure 3. Stages of adhesive reticulation process. Left: film applied to core and perforated. Center: Film softening and perforations expanding due to surface tension. Right: Process completed – adhesive forms a fillet along edges of cell walls.

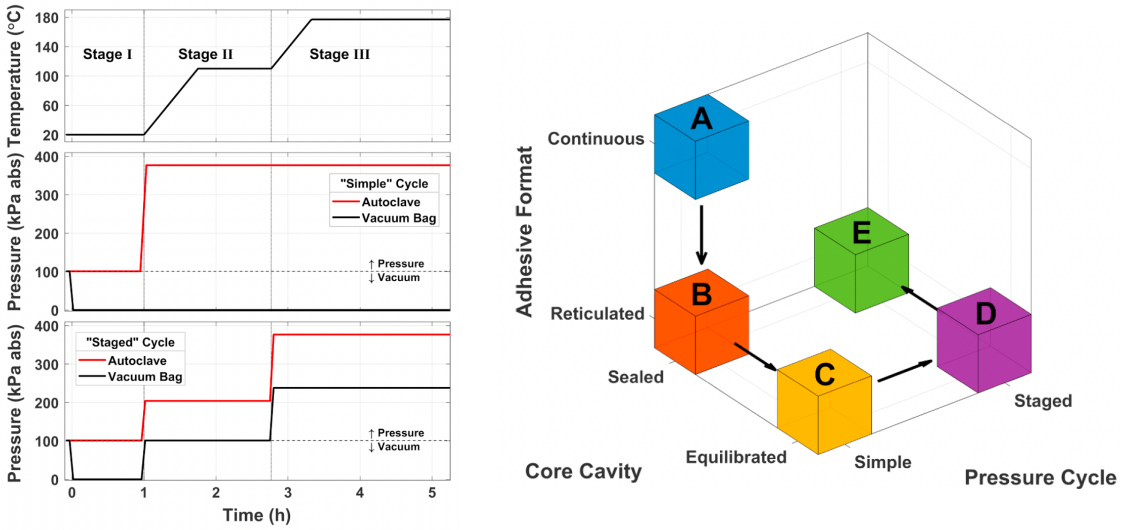

Figure 4. Temperature cycle used for all tests (top left), and the two cycles used for autoclave and vacuum bag pressures. On right, diagram of Cases A-E, where the three axes denote the test variables.

The process parameters for CS 2 are summarized in Figure 4a. The temperature cycle resembles the manufacturer-recommended cure cycle for the prepreg. The three temperature stages – RT, 110C, and 177C, are labeled Stages I, II, and III. Three parameters were varied between cases – the initial adhesive format, the core breathability, and the imposed P_{auto} and P_{bag} pressure cycles. The five test cases are presented as a cube diagram in Figure 5a. Each of the three axes corresponds to one of the varied parameters. (1) The adhesive was applied either as a continuous film or reticulate onto the HC core. (2) The core cavity was either sealed or connected via the "core vent" to equilibrate the gas pressure in the core cavity with that of the vacuum bag. (3) Autoclave and vacuum bag pressures were applied according to either of two cycles – "simple" or "staged" – as shown in Fig. 4a.

5 RESULTS

For CS1, neat resin BOX-e samples were produced without entrapped air during injection. The test results are summarized in Figure **5** as a process map relating cure temperature, imposed mold pressure, and defect growth. Each point represents one sample. Temperature and pressure combinations that resulted in the generation of voids are shown in red, while samples that did not grow voids are shown in blue. In cases when voids did develop, they nucleated on the hottest side of the mold cavity (the tool side that contains the heating elements), grew rapidly, sometimes detached and floated upwards, and eventually were fixed in place when the resin gelled. Application of pressures of 200kPa were sufficient to suppress voids in molded plates of neat-resin.

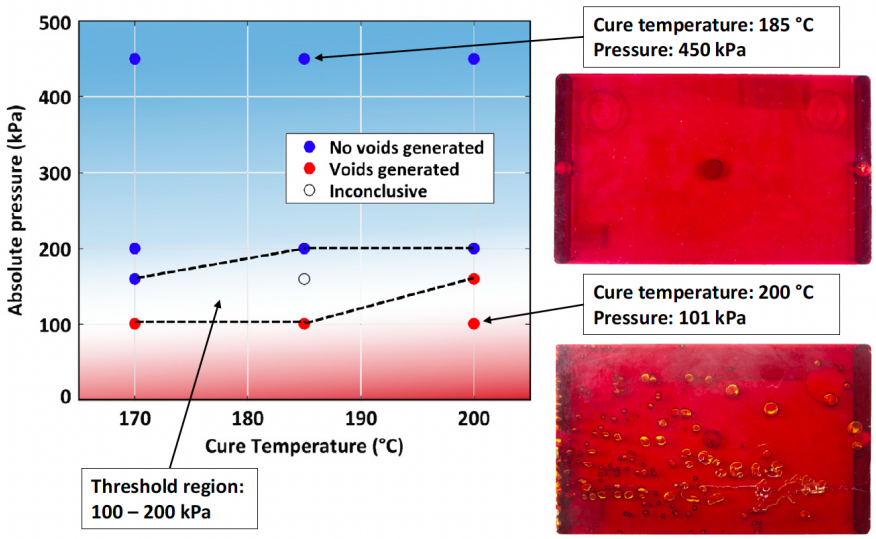

Figure 5: Temperature-pressure map of neat-resin tests. Red (on graph) indicates conditions that lead to void growth, while blue corresponds to conditions that suppress void growth. Points correspond to individual tests and background shading is used to highlight the general trend.

While applied pressures >200kPa sufficed to prevent bulk porosity, surface porosity developed, typically on the cooler side of the mold cavity (with the glass plate). The window in the mold afforded visual confirmation that, initially after injection, the surfaces of all samples were bubble-free. However, porosity developed on the window side during high-temperature dwells late in the cure cycle. The aluminum tool side (which was slightly hotter, since it contained the heating elements) had effectively no defects for all samples, and micrographs of polished cross-sections confirmed that internal porosity was also negligibly low. For this reason, only the quality of the cold sides is considered below.

In situ data and porosity formation mechanisms are revealed from the measured sensor data for a composite sample, shown in Figure 6, for formulation F1 cured under Cycle A, which resulted in 26% surface porosity. The temperature graph consists of the controller temperature (black) and the temperatures of the hot and cold sides of the mold cavity (in red and blue, respectively). The hot side,

being closest to the heating elements, followed the control temperature to within 1°C, while the cold side lagged by roughly 4 min (or, equivalently, 8°C) during ramps and stabilized at 4°C below the hot side at steady-state conditions during high-temperature dwell.

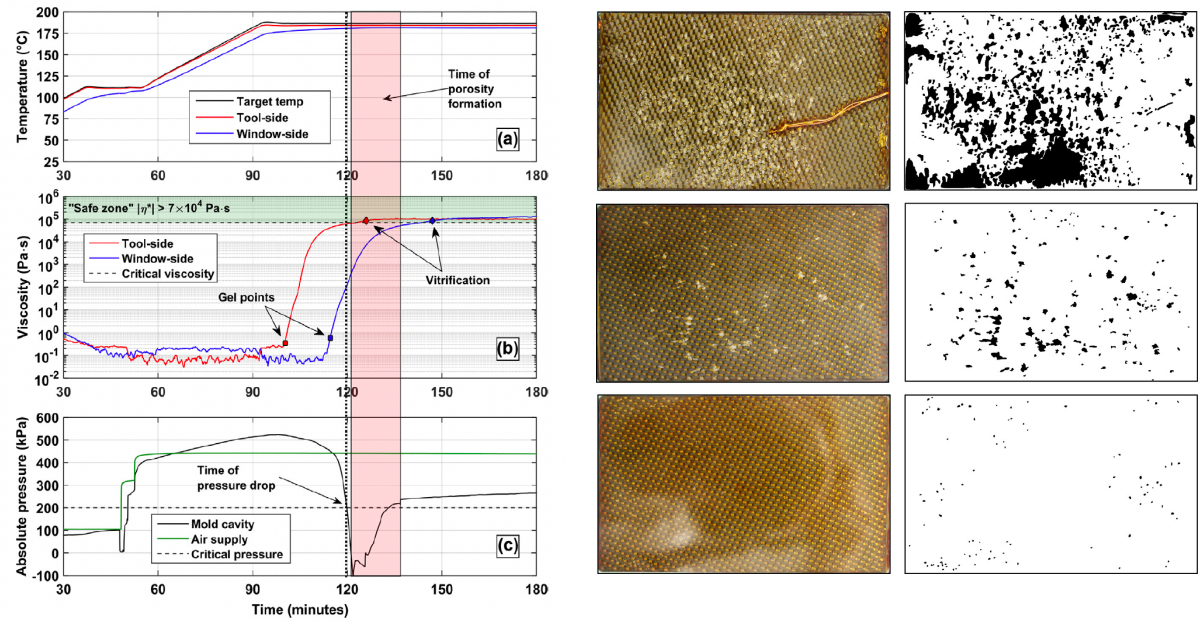

Figure 6: Temperature, viscosity, and pressure for formulation F1, Cycle A. Surface porosity measurements are shown at right, where the top row is formulation F1, Cycle A, the middle row is F2, Cycle A, and bottom row is F2, Cycle B. The thermocouple is visible in the first image.

Surface porosity occurred because of the relative timing of the pressure drop and the increasing viscosity at the coldest location of the mold cavity. The pressure drop occurred when the cold-side viscosity was in the vicinity of 100 Pa·s, which is past the gel point, but far below the critical value of 7 × 104 Pa·s that has been shown to suppress volatile release. The hot-side, meanwhile, had already reached a high viscosity level, and therefore did not off-gas. Once the mold cavity pressure decreased below the critical value, voids began to form at the cold surface. The period of void formation was clearly observable through the window in the mold, and is indicated on Fig. 6a.

Fig. 7 shows a series of images recorded in situ for the same sample, beginning with an initially defect-free surface just before the pressure drop. Almost immediately after the pressure fell below the critical value, voids began to form and continued to grow for 15 min. All void growth finally ceased as the cold-side viscosity reached the ‘‘safe” zone, where the resin was nearly vitrified. In cases of extreme porosity such as in Fig. 7, much of the surface separates from the tool face, clearly manifest through the window because of the change in refractive index (compare Fig. 7c and d), and accompanied by a concurrent spike/drop in measured cavity pressure (see Fig. 6 at 136 min). The volatile gasses are less dense than the liquid resin, so their release at the cold surface relieves the tensile stresses generated by cure shrinkage. This phenomenon can be seen in Fig. 6 by the gradual recovery in pressure during the time of porosity formation. Note that since the pressure drop occurred when most of the resin was already approaching high viscosities (and due to the presence of the fibrous preform), the total volume of volatiles released was much less than for the ambient-pressure neat resin samples (which began to grow bubbles earlier, during the ramp to the high-temperature dwell).

In summary, the tendency of this resin to exhibit surface porosity in RTM processing stems from a combination of two factors: significant potential for volatile release during cure, and rapid, highly temperature-dependent gelation, which increases the material sensitivity to in-mold temperature gradients. Additionally, the distribution of the porosity – concentrated on the cold surface – is determined by the direction of the temperature gradient. Additional information regarding process monitoring with the RTM testbed is included in reference [1].

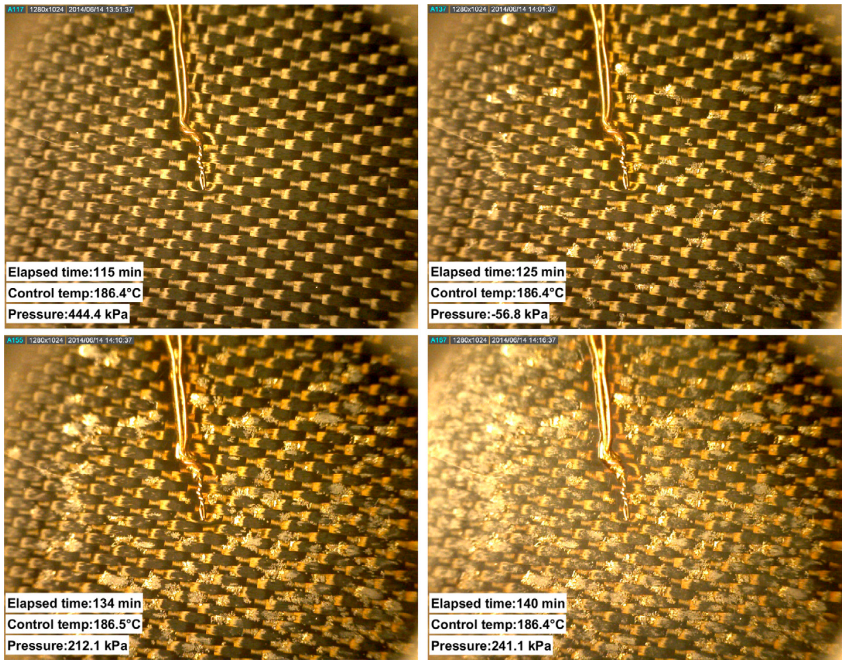

Figure 7: Formation of surface porosity recorded *in situ* for the composite sample with formulation F1, Cycle A. Time labels correspond to the data in Fig. 6. The thermocouple used to measure the window-side temperature history is visible in the frame.

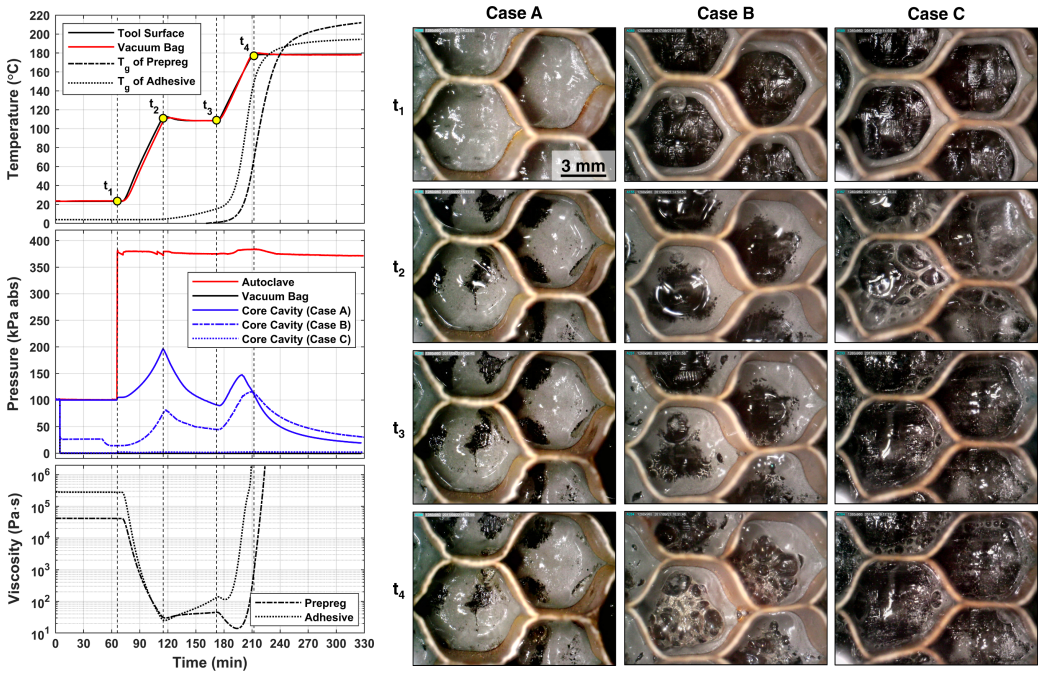

Figure 8: (a) Temperature data for the three cases using the "simple" pressure cycle (A, B, and C). Models for the glass transition temperature and viscosity (for both the prepreg resin and the adhesive) are shown, computed from the temperature history recorded outside the vacuum bag, near the center of the laminate. (b) *In situ* images of the bond-line during processing Columns correspond to Cases A, B, and C (left to right), and rows correspond to the times of interest t_1 though t_4 indicated in (a).

CS2 entails the use of a similar approach to monitor defect evolution during co-cure of sandwich panels in an autoclave, with the expectation that the insights would provide a basis for a process model. Measured data for Cases A, B and C is shown in Fig. 8, and *in situ* images from these tests are shown in Fig. 8b. For Cases D and E, measured data and corresponding in situ images are shown in Figs. 9a and 9b, respectively. To fully appreciate the dynamic behavior captured in the visual data, readers are encouraged to view the timelapse videos from which the images in Figs. 8 and 9 were taken.[1]

Case A. Figure 8(a) shows the measured temperatures (top) and pressures (middle) for Case A, which featured a continuous adhesive film, a sealed core, and the simple pressure cycle. Models were used to compute the glass transition temperature T_g of the prepreg and adhesive, as well as the viscosity μ profiles (bottom graph). The indicated times of interest t1 through t4 correspond to the images in the left column of Fig. 8(b).

Upon application of vacuum in the bag, P_{core} remained unchanged, and the continuous adhesive film acted as a barrier for gas transport. Negligible change was observed visually during Stage I, although flow occurred as the temperature was raised between t_1 and t_2. First, prepreg resin (which appears clear, while the aluminum-powder-filled adhesive is gray) pushed through the adhesive film in a grid-like pattern, clearly emanating from the "pinholes" between the fiber tows in the fabric weave. Additionally, the mixture of adhesive and prepreg resin migrated toward the cell walls, forming fillets. During this period, P_{core} increased to ~200 kPa due to ideal gas law expansion (and likely some volatile generation). During the intermediate temperature dwell, little change was observed, and P_{core} ecayed due to continual application of vacuum to the bag.

During the second temperature ramp (between t_3 and t_4), the adhesive fillets appeared to "inflate" and bubbles appeared in the locations where the prepreg resin had created discontinuities in the film adhesive. After t_4, all motion abruptly ceased, as the adhesive had gelled. Note that during the second temperature ramp, the adhesive viscosity was already rapidly increasing, whereas the prepreg resin was just reaching its minimum viscosity. Thus, during this ramp, bubbles could still nucleate and grow within the prepreg resin. However, they became trapped by the adhesive film. The section view of the sample confirms that the fillet "inflation" was due to the growth and entrapment of bubbles between the adhesive film and the first ply of prepreg. P_{core} followed a similar trend during Stage III as in Stage II, first increasing during the ramp (although to a lesser extent), and decaying during the dwell.

Case A showed that the continuous adhesive film was disrupted by the behavior of the prepreg resin. Specifically, the mismatch in gel times was such that, during the second temperature ramp, the prepreg resin formed bubbles that distorted – and became trapped by – the rapidly gelling adhesive layer. To prevent the adhesive from acting as a barrier for gas transport, the film was reticulated onto the core in Case B.

Case B. Figure 8(a) shows P_{core} (all other temperatures and pressures were identical to Case A). The core evacuation during Stage I, in the absence of a continuous adhesive film, depended on the prepreg permeability. Initial evacuation was rapid, but halted as the skin compacted (analogous to the behavior observed by Kratz [20]). A new pathway for gas transport formed after ~45 min (the delay caused by gradual displacement of the highly viscous prepreg resin), allowing core evacuation to continue. During the remainder of the cycle, P_{core} followed a similar trend as in Case A, although shifted downward due to the lower initial pressure upon heating.

In Fig. 8 (Case B, t_1) the reticulated adhesive is visible along the edges of the cell walls, and the first prepreg ply is visible in the center of each cell. During the room-temperature vacuum hold, minor bubble formation was observed in the adhesive and prepreg resin. As the temperature was increased between t_1 and t_2, the adhesive fillets formed, and a mixture of prepreg resin and bubbles could be seen pushing out from the pinholes in the fabric weave. By t_2, most of the bubbles had disappeared, leaving a layer of resin at the skin/core interface and creating a continuous meniscus with the adhesive. During the dwell between t_2 and $t3$, bubbles gradually reappeared in the prepreg resin. During the final temperature ramp, the bubbles grew, yet none burst before resin gelation, resulting in a large cluster of bubbles at the center of each cell.

Contrasting this behavior to Case A reveals that the bubbles in the bond-line in Case A were not solely due to the adhesive acting as a barrier, but also a consequence of the core pressure. Even

without the barrier (i.e., Case B), Pcore was low enough to allow bubble growth within the resin at the skin/core interface, yet not so low that the bubbles burst. Considering this insight, the modification for Case C was chosen to afford improved control over P_{core}.

Case C. Case C simulated the conditions of a vented sandwich structure – in which P_{core} can equilibrate with P_{bag} – by connecting the core vent to the vacuum line. During the room temperature vacuum hold, thin-walled bubbles grew from the pinholes in the fabric and burst, indicating that air initially trapped between the prepreg plies was evacuating into the core. Previously, in Cases A and B, vacuum was only applied on the upper surface of the skin, so air in the core had to travel upwards through the skin to escape. Conversely, in Case C, the core was evacuated directly and simultaneously with the vacuum bag, so air was not driven through the skin, and air initially entrapped within the skin could evacuate in either direction (up through the perforations in the release film, or down into the core), along the path of least resistance.

Upon initial heating, the vacuum in the core pulled a foamy mixture of gas and resin out from the fabric pinholes. Towards the end of the first ramp (see Fig. 8, t_2), vigorous frothing was observed, with large bubbles growing and bursting repeatedly. Bubble formation slowed during the intermediate-temperature dwell, but, by that point, much of the adhesive had been spattered onto the cell walls, leaving little at the skin/core interface to form fillets (see Fig. 8, t_3). Small bubbles remained along the edges of the cell walls against the skin, which grew during the second temperature ramp and became fixed at gelation (t_4). The section view of this sample provides a complementary perspective of the small, void-filled fillets and the adhesive coating the cell walls.

Case D. The staged pressure cycle used for Case D was designed to avoid the observed defect formation phenomena, by applying positive pressure within the vacuum bag to suppress the release of gasses that could not be evacuated prior to gelation. Stage I was identical to Case C: reticulated adhesive and full vacuum in the bag and core, to maximize air removal from the skin while the resin and adhesive were still at high viscosity ("equilibrated" P_{core} in Case D matched P_{bag} exactly (Fig. 9). During Stage II, to avoid the fillet disruption that occurred in Case C and duplicate the undisrupted flow seen in Case B, the vacuum bag was vented with N_2 to ~100 kPa. To prevent excess resin exuding toward the skin/core interface, P_{auto} was increased to only 205 kPa, maintaining the same compaction pressure ($P_{auto} - P_{bag}$) as in Stage I. Finally, in Stage III, recall that during the second temperature ramp in Cases A and B, a P_{core} range of ~50–150 kPa caused bubbles to grow yet remain sessile until gelation. In Case C, vacuum pressure in the core caused bubbles to burst, but this also caused severe fillet disruption. Therefore, in Case D, the opposite approach was used to prevent defects in Stage III: the application of positive pressure to suppress bubble formation and growth. First, P_{auto} was increased to 377 kPa to maintain compaction on the sample, and then P_{bag} was increased to 239 kPa.

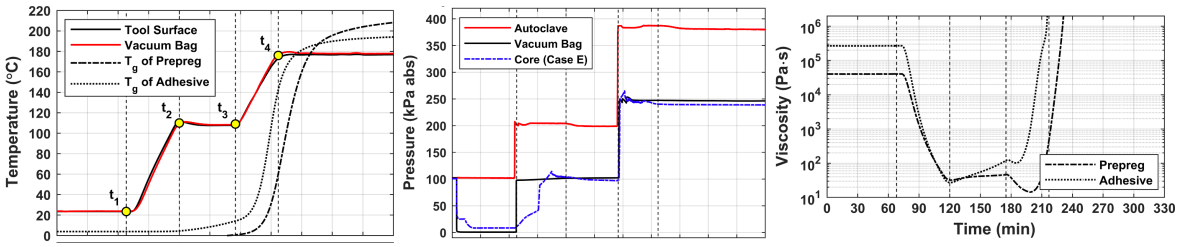

Figure 9: Temperature and pressure data for the cases D and E, using the "staged" pressure cycle. Models for T_g and viscosity (for prepreg resin and adhesive) are computed from temperature history.

The images in the left column of Fig. 10 correspond to the times indicated on Fig. 9. During the initial vacuum hold, thin-walled bubbles similar to Case C appeared and burst, indicating air evacuation from the skin. During the temperature ramp and dwell of Stage II, fillet formation occurred, the flow undisrupted by bubbles (similar to Case B t_2 but without the bubble formation seen at ~50 kPa in Case B t_3). The image captured at t_3 for Case D (Fig. 10) was taken in the brief time after P_{auto} was increased, but before P_{core} was increased. Momentarily, resin containing small bubbles exuded from the fabric pinholes due to the increased compaction pressure. However, once the bag/core

pressure was set to the final value, the excess resin receded into the skin, and the bubbles disappeared. The equal gas pressures on the upper and lower boundaries of the skin (i.e. P_{bag} and P_{core}, respectively) resulted in a hydrostatic condition in which no gas was driven through the skin. Furthermore, the gas pressure in the core/bag imposed a lower bound for the resin pressure in the skin, which prevented the formation of bubbles. The resin and adhesive remained effectively motionless during the second temperature ramp and until gelation (t_4).

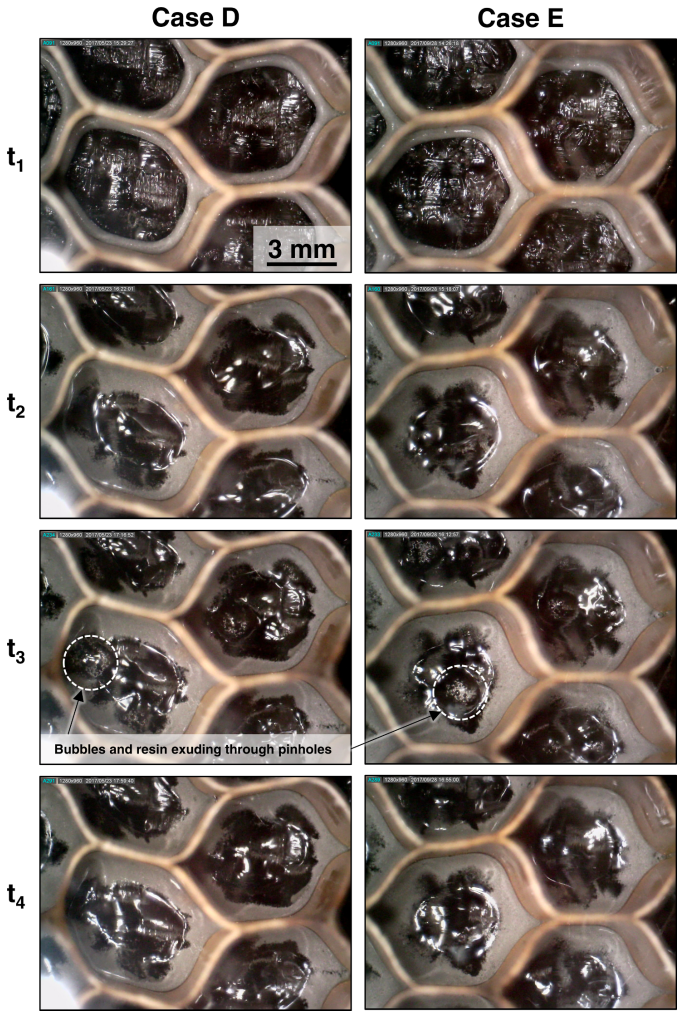

Figure 10: In situ images of the bond-line during processing. Columns correspond to Cases D and E (left to right), and rows (top to bottom) correspond to the times t_1 through t_4 indicated in Fig. 9.

CONCLUSIONS

We have demonstrated a methodology for understanding the origins of defects in composites, and controlling those defects through process modifications. The method relies on process monitoring through the use of instrumented testbeds that afford direct observation of process phenomena. These observations are closely coupled with systematic characterization of resin properties by more conventional methods, such as thermal analysis and rheology. Visual data acquired with these tools revealed the occurrence and timing of defect-formation mechanisms. For CS2, these included (a) gas entrapment by early gelation of the adhesive, (b) bond-line bubble growth at intermediate core pressure, and (c) fillet disruption from the bursting of bubbles at low core pressures. In CS1, the defect formation mechanisms during RTM included pore formation from volatile evolution, surface porosity from cure shrinkage, and the times and temperatures at which these occurred.

The case studies demonstrate the utility of *in situ* visualization for composites manufacturing (for both RTM and autoclave co-cure). Through visual observations, the process conditions corresponding

to defect formation can be identified, informed process modifications can be made, and theories about the relevant physical phenomena can be validated. Altogether, this approach can provide understanding and insight into manufacturing processes that could not be attained by traditional inspection of the structures after manufacturing. Most importantly, much of the guesswork can be eliminated from process troubleshooting, and the interactions between materials and phenomena can be analyzed in realistic conditions.

ACKNOWLEDGEMENTS

The work on RTM process monitoring was supported jointly by the M.C. Gill Composites Center and by Kaneka Corporation. Process monitoring of co-cure of sandwich panels was supported by NASA NRA NNL16AA13C and was undertaken in collaboration with S. Advani of University of Delaware. The work presented was performed by Drs. Mark Anders and Tim Centea.

REFERENCES

[1] [1] "Eliminating Volatile-Induced Surface Porosity During Resin Transfer Molding of a Benzoxazine/Epoxy Blend" M. Anders, J. Lo, T. Centea, and S.R. Nutt, *Compos. A* Jan (2016) DOI

[2] [2] "In situ observations and pressure measurements for autoclave co-cure of honeycomb core sandwich structures" M Anders, D Zebrine, T Centea, and S Nutt, *J Mfg Sci & Engrg* **139** (2017) DOI

[3] [3] "Process diagnostics for co-cure of sandwich structures using *in situ* visualization" M Anders, D Zebrine, T Centea, and S Nutt, *Composites A* **116** 24-35 (2018) DOI

Advanced Biocomposites

High-Performance Cellulose-Based Composites for Sustainable Materials Engineering

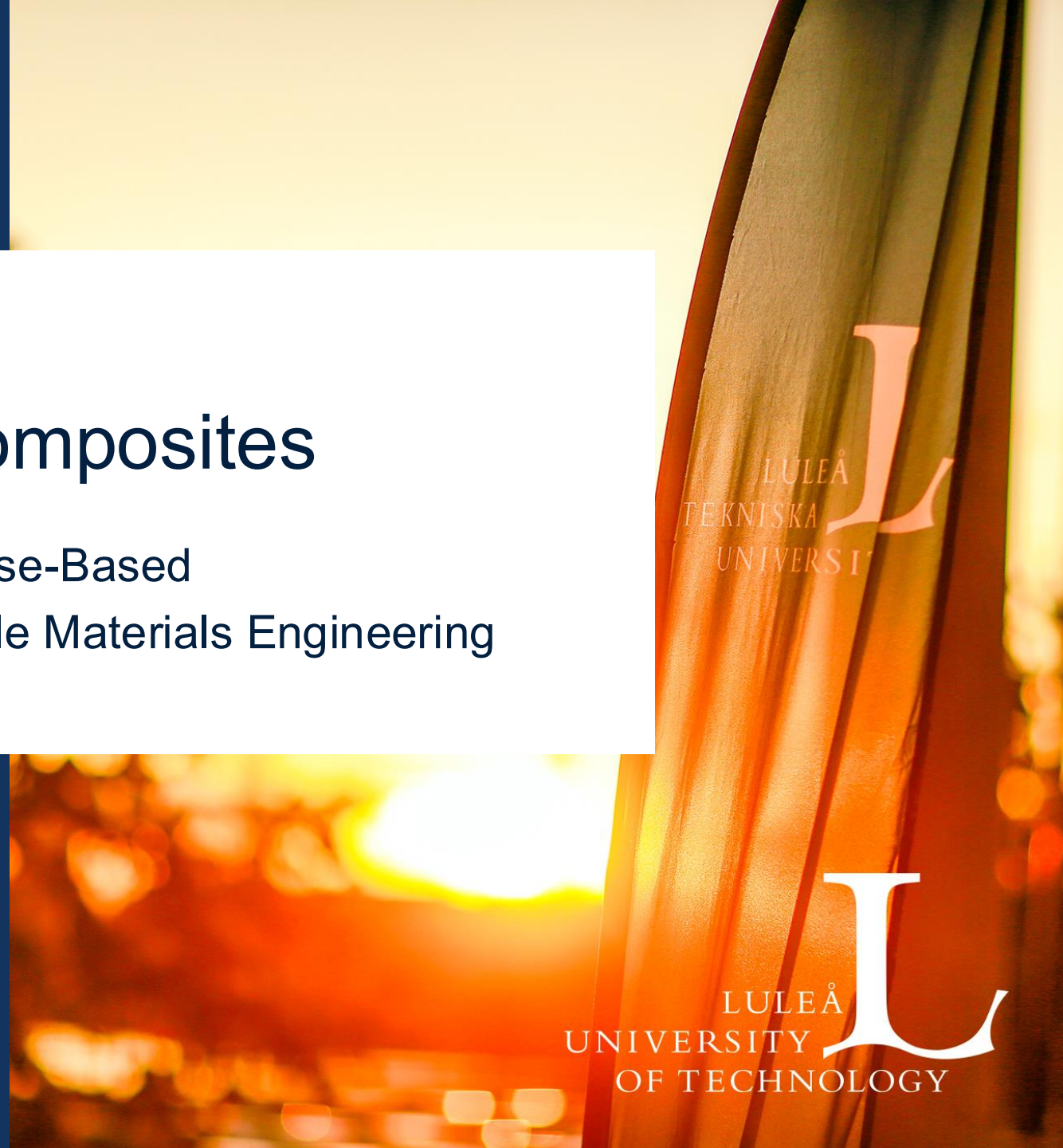

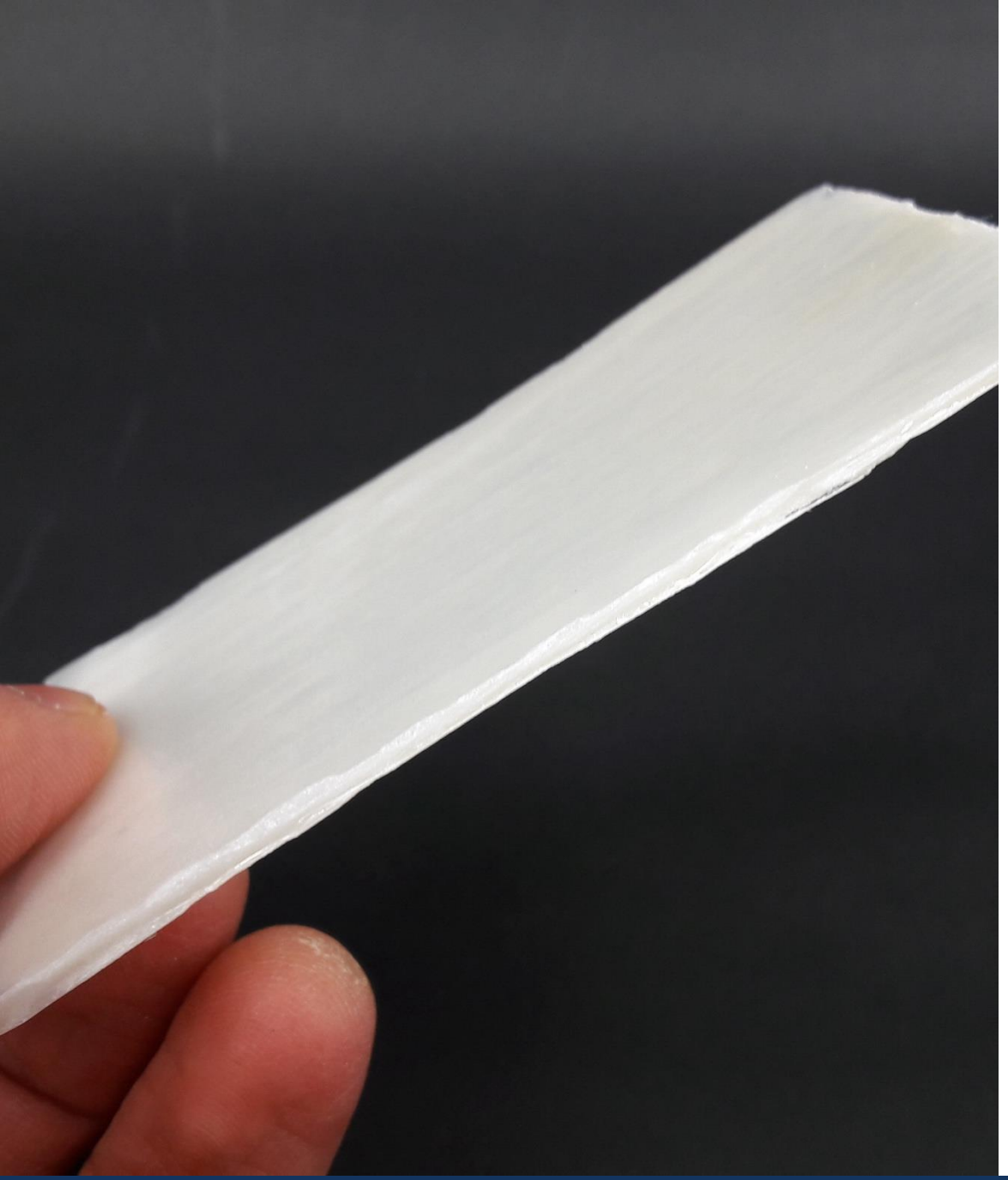

Outline

- Cellulose nanofibers
- Cellulose nanocomposites
- Cellulose filaments with different size scales spun of cellulose nanofiber gels
- Filament properties
- Composite properties,both experimental and estimated
- What challenges do we face in development of composites?



What are cellulose nanofibers?

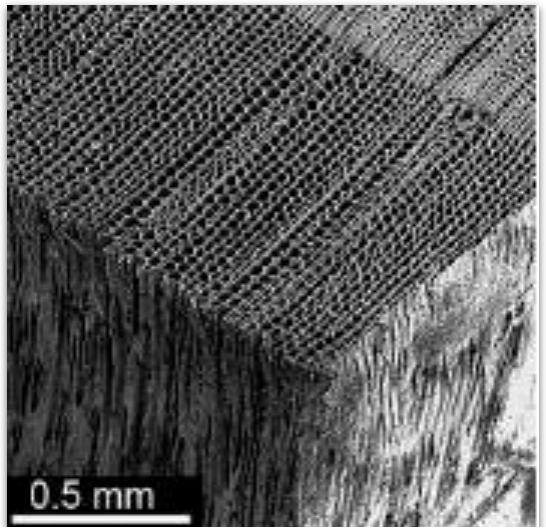

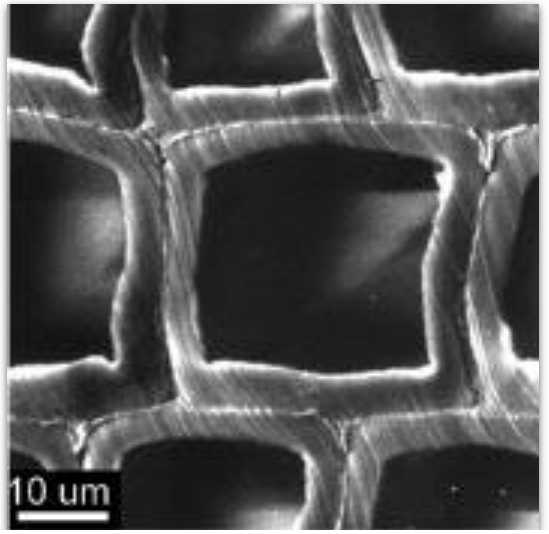

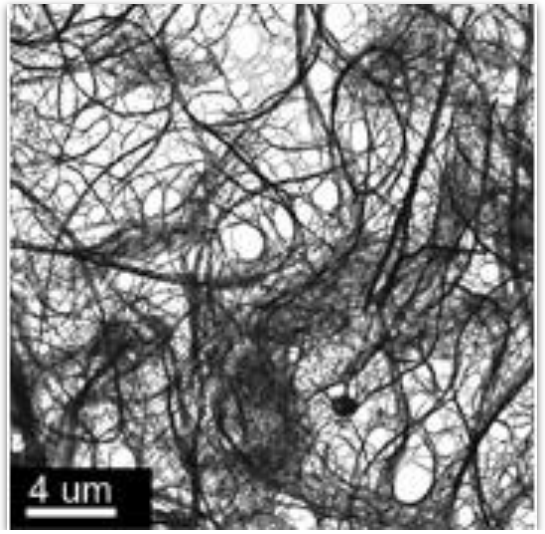

- Soft wood fiber, diam 20-30 µm, length 2-5 mm
- Nanofibers, diam <100 nm, length µm-scale, can be separated from cell wall combining chemical and mechanical methods
- Mechanical properties increases with the decreased size scale
- E-modulus estimated to 140 GPa and strength 10000 MPa compared with soft wood E-modulus 12 GPa and strength 100 MPa

Why cellulose nanofibers?

- Natural resources, and can be extracted from residues
- Sustainable
- High mechanical properties
- Large surface area
- Forming gel in low concentration
- Forming strong network when dried
- Lightweight
- High thermal stability compared to many natural polymers



Cellulose nanofiber network properties

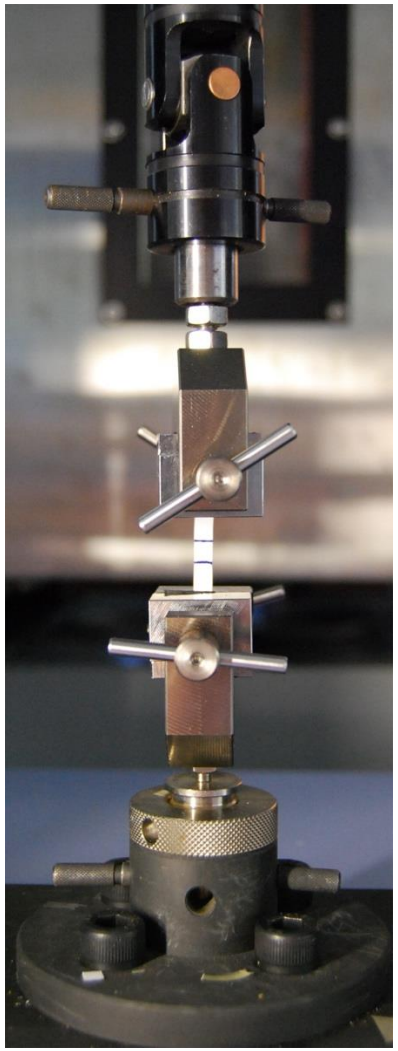

Nanofiber networks are prepared by vacuum filtration and pressing

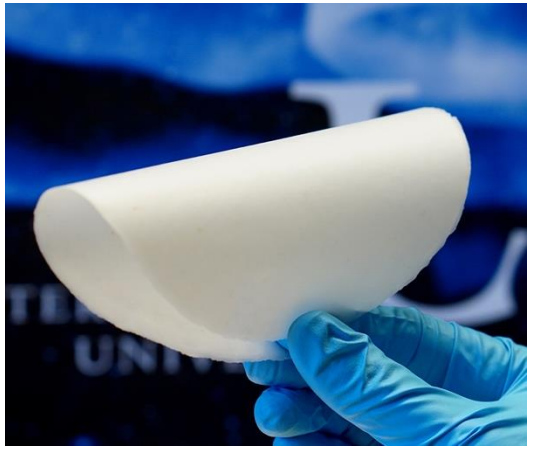

	E-Modulus (GPa)	Strength (MPa)	Strain at break (%)
$Wood_{nanofiber}$	**11.2 ± 0.8**	**183 ± 14**	**5.0 ± 0.9**
*$TEMPO_{oriented}$	**24.6 ± 0.4**	**428 ± 15**	**2.5 ± 0.2**

*Sehaqui et al ACS Appl Matr & Inter 2012

Nanocomposites by impregnation of nanofiber network

- High mechanical properties but the resin impregnation process is challenging and time consuming
- Reduce viscosity of the polymer and / or increase porosity of the network to be able to use conventional composite processing methods such as vacuum infusion
- Is it possible to align the nanofibers?

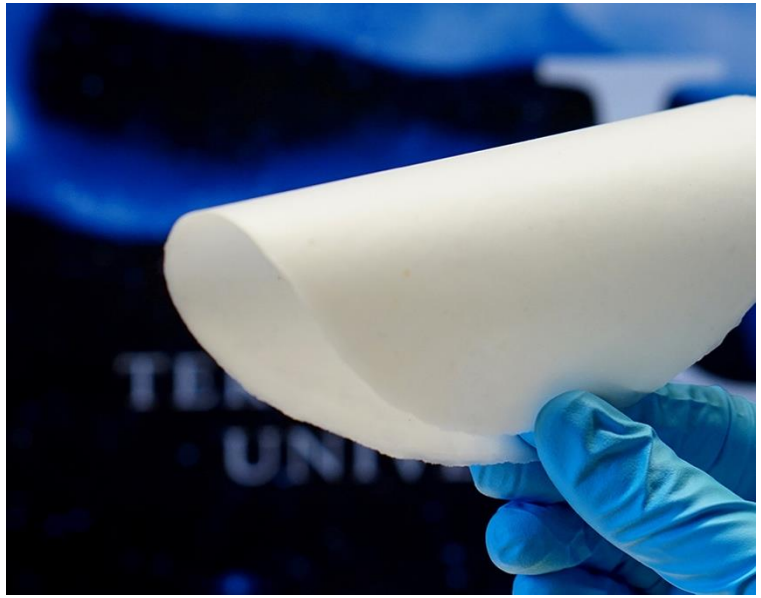

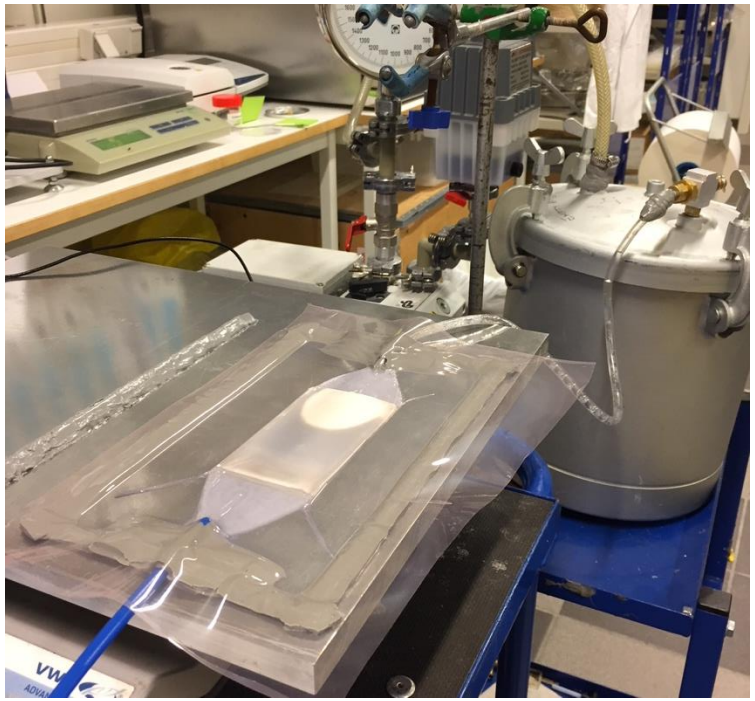



Cellulose nanofiber preforms for resin impregnation

PhD-student Tuukka Nissilä

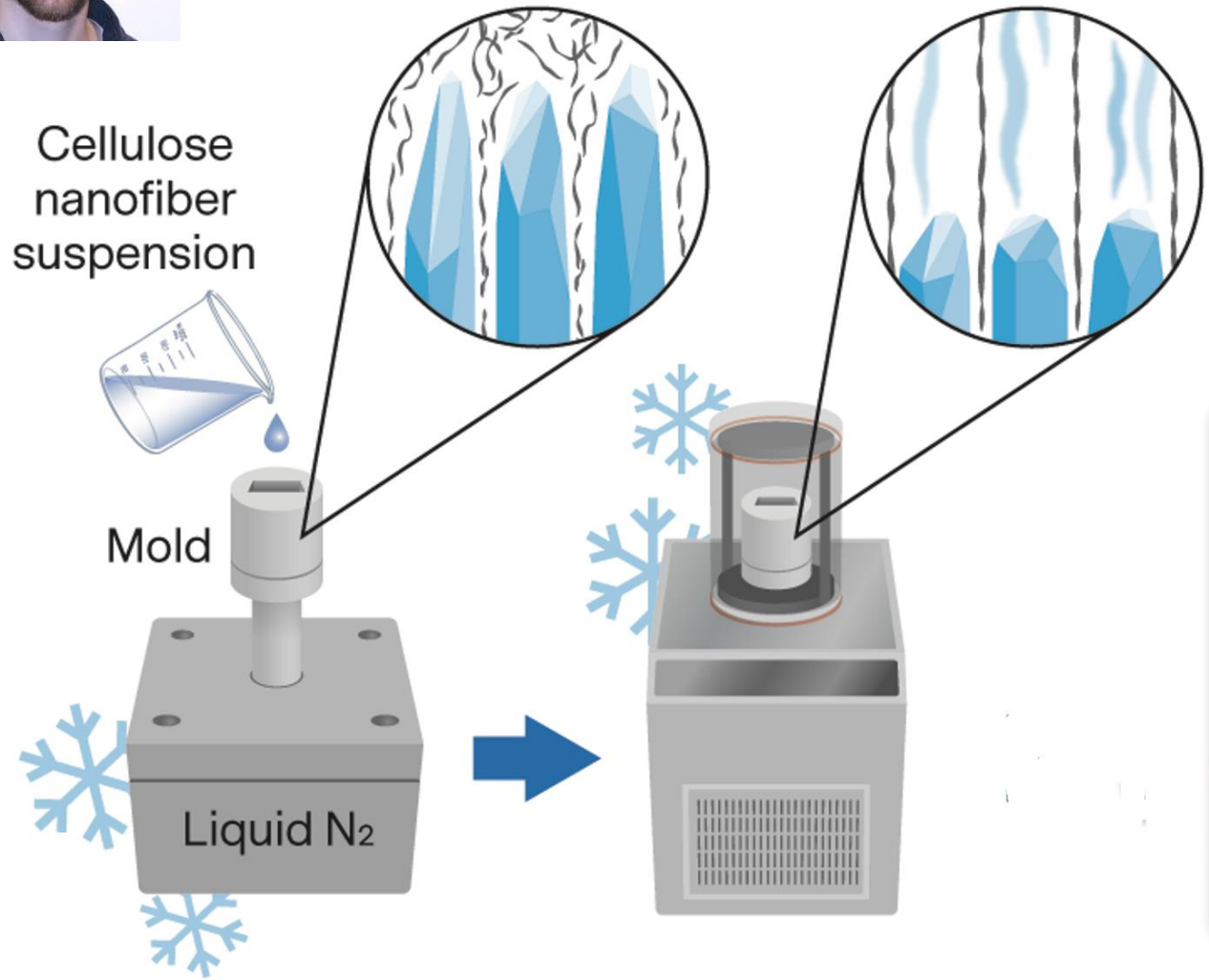

CNF preform



T Nissilä et al Nanomaterials **2021**, *11*(2), 490; doi.org/10.3390/nano11020490

Cellulose filaments and orientation of cellulose

Ice-templating resulted in filaments with width 1 µm

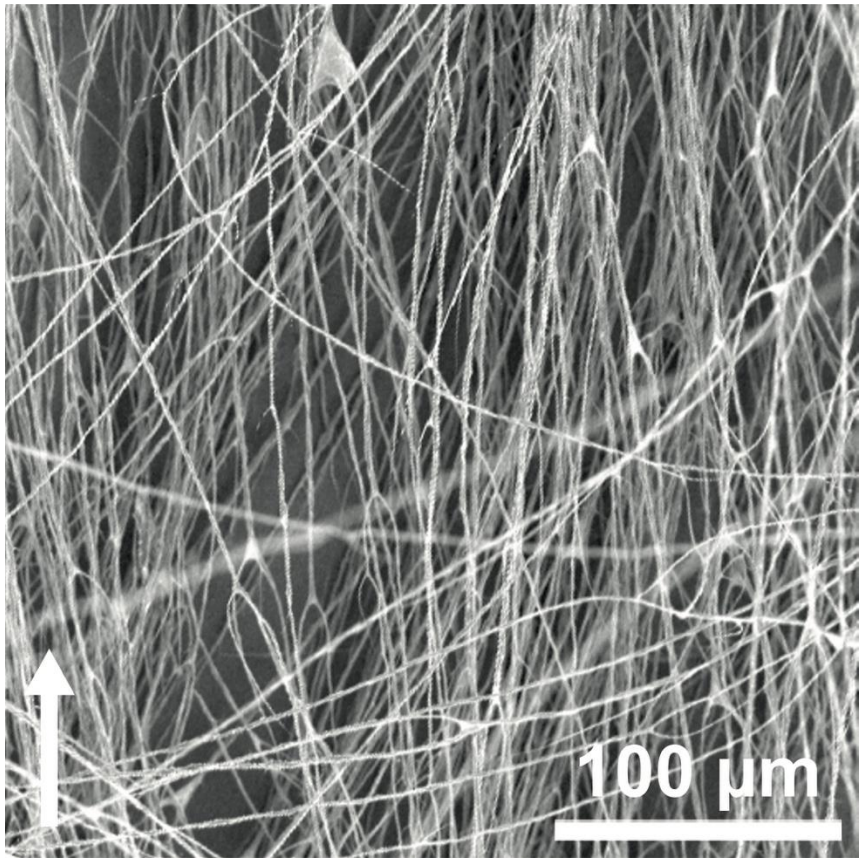

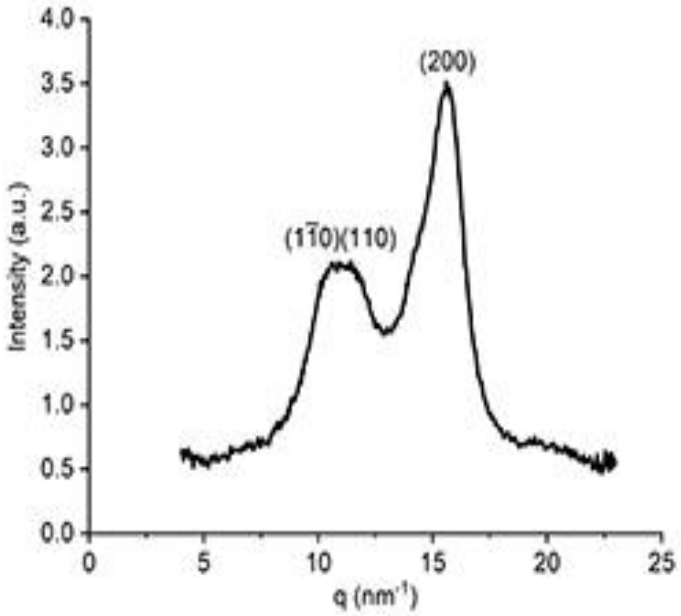

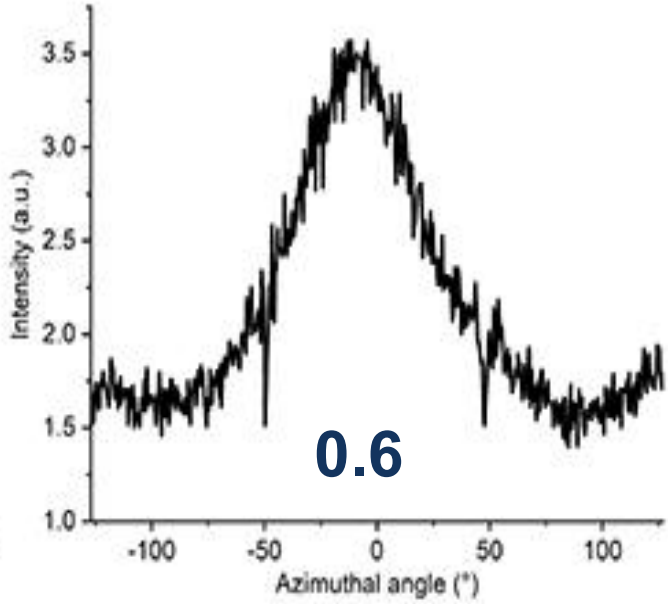

Very difficult sample preparation, low density and thin fibers, 1 µm

TREESEARCH

Nissilä et al Nanomaterials 2021,11(2), 490; doi.org/10.3390/nano11020490

Cellulose filament composites by vacuum infusion

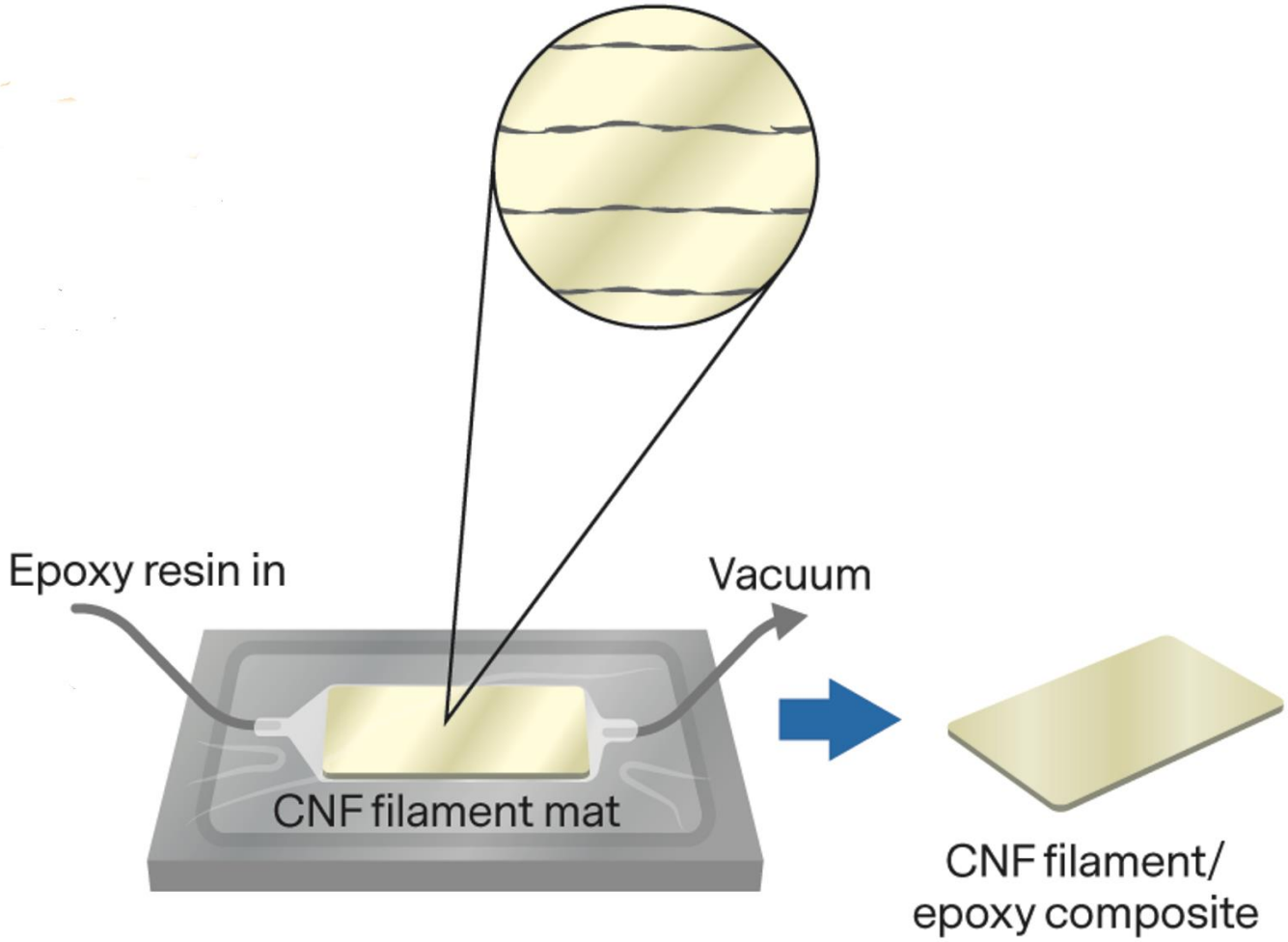

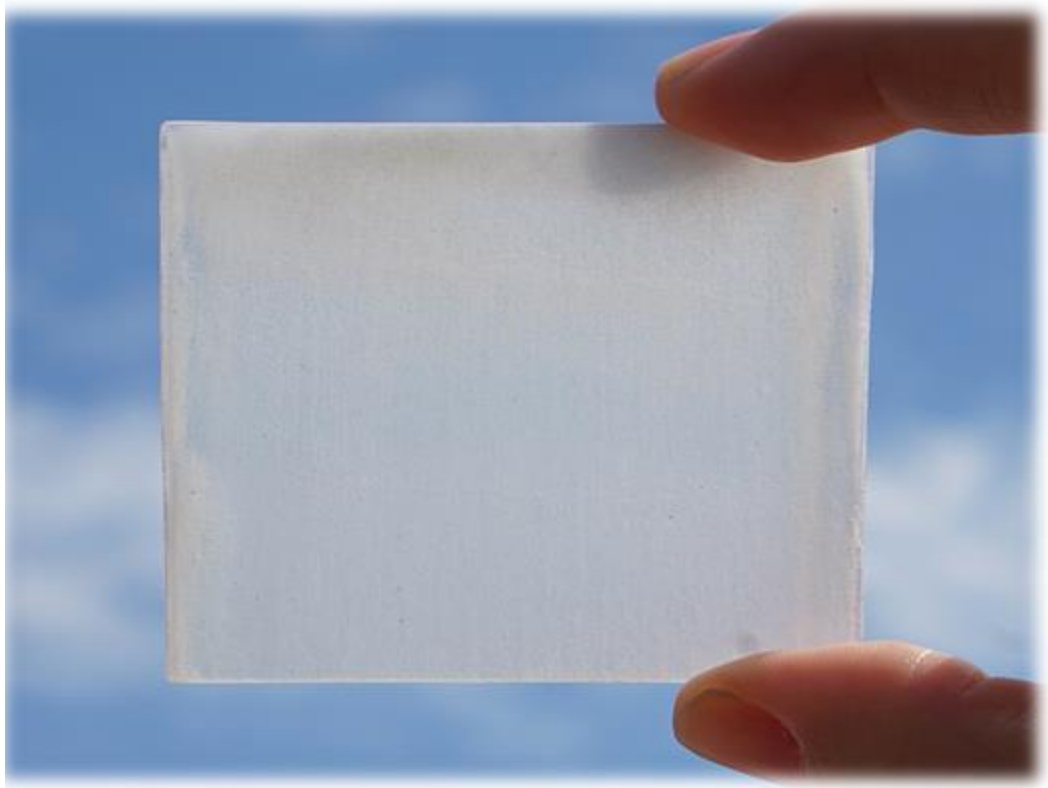

Nissilä et al Nanomaterials **2021**, *11*(2), 490; doi.org/10.3390/nano11020490

Orientation of cellulose in the composite structure

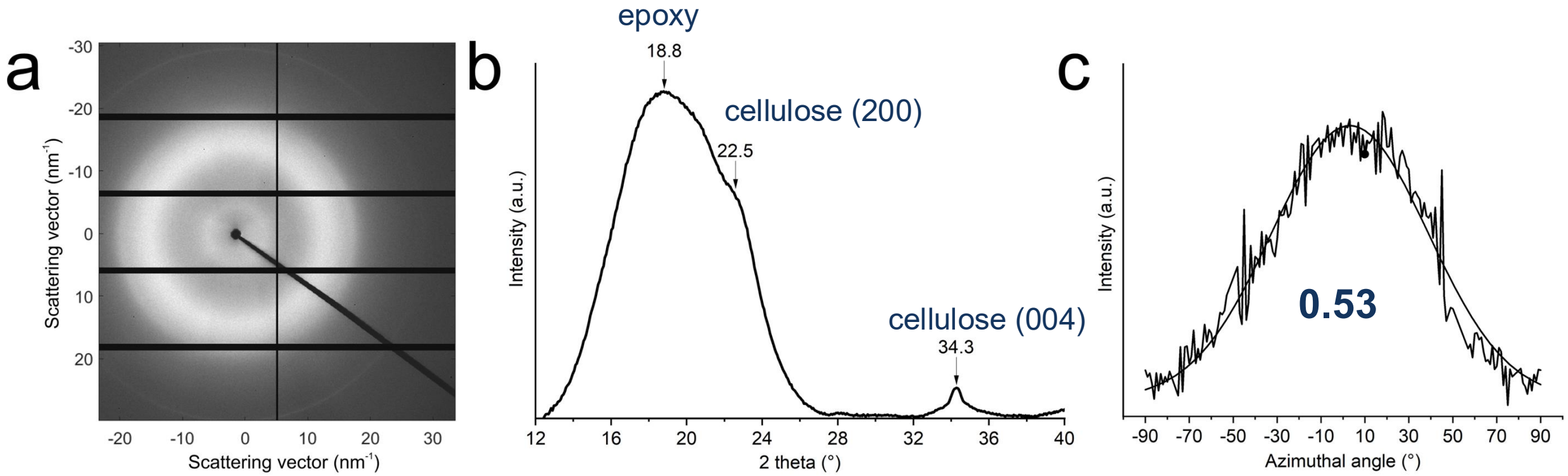

Nissilä et al Nanomaterials 2021,11(2), 490; doi.org/10.3390/nano11020490

Composite properties

- Storage modulus increased from 2.2 to 5.4 GPa with 13 vol% cellulose filament content at room temperature
- Filaments treated with chemical surface deposition of amino silane
- Silane treated filaments resulted in better interaction with the resin as tan delta moved towards higher temperature (73 to 81 ℃)

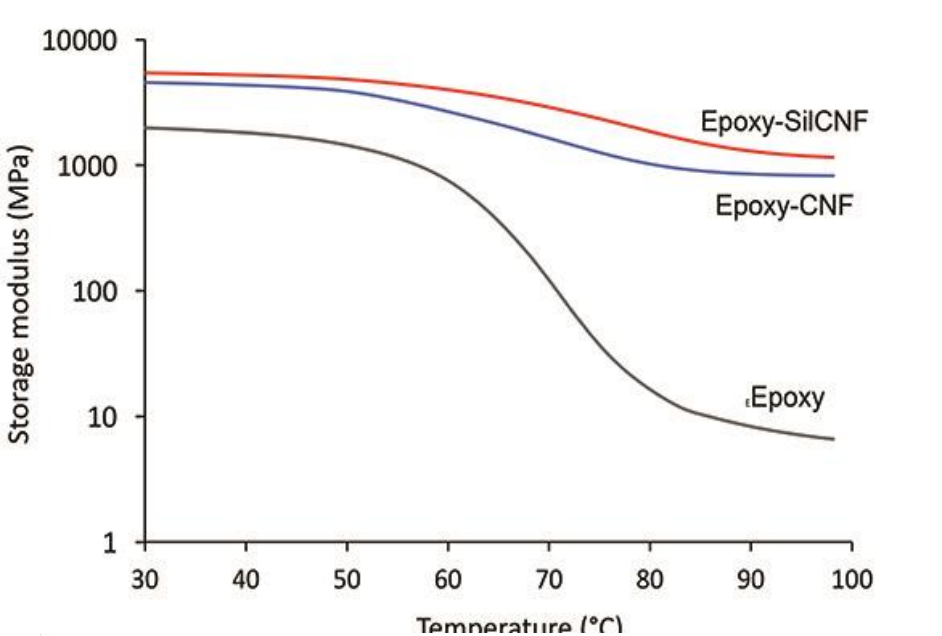

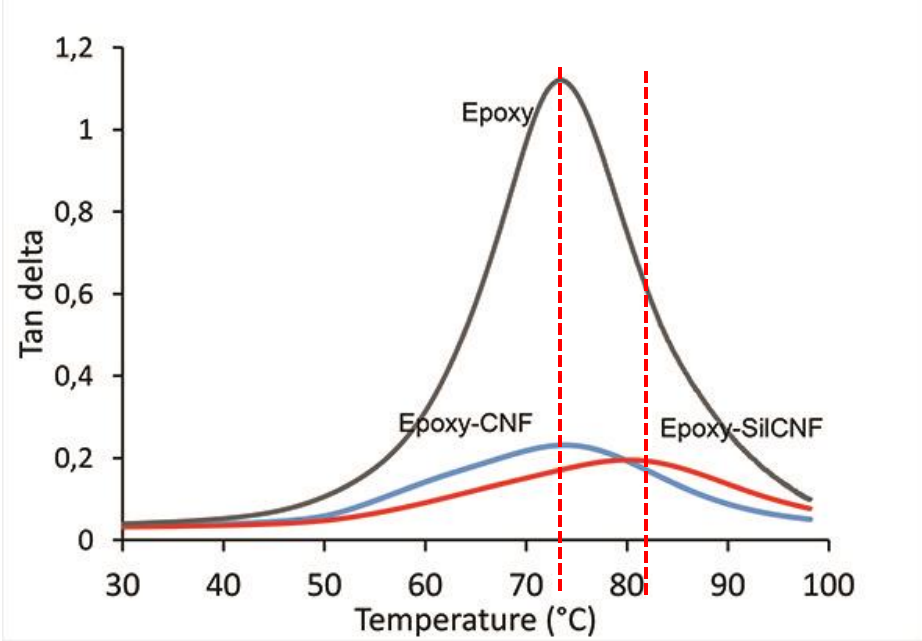

Nanomaterials **2021**, *11*(2), 490; doi.org/10.3390/nano11020490

Conclusions on ice-templated filaments

- Ice-templated nanocellulose filament preforms can be one way to improve the impregnation and ice-templating resulted in oriented preform structure, but it is time consuming and difficult to make large quantities
- Vacuum infusion resulted in cellulose filament content of 13 vol%
- Composites mechanical properties were increased compared to epoxy (2.5 times)
- Cellulose content was limited
- Silane treatment improved the interaction

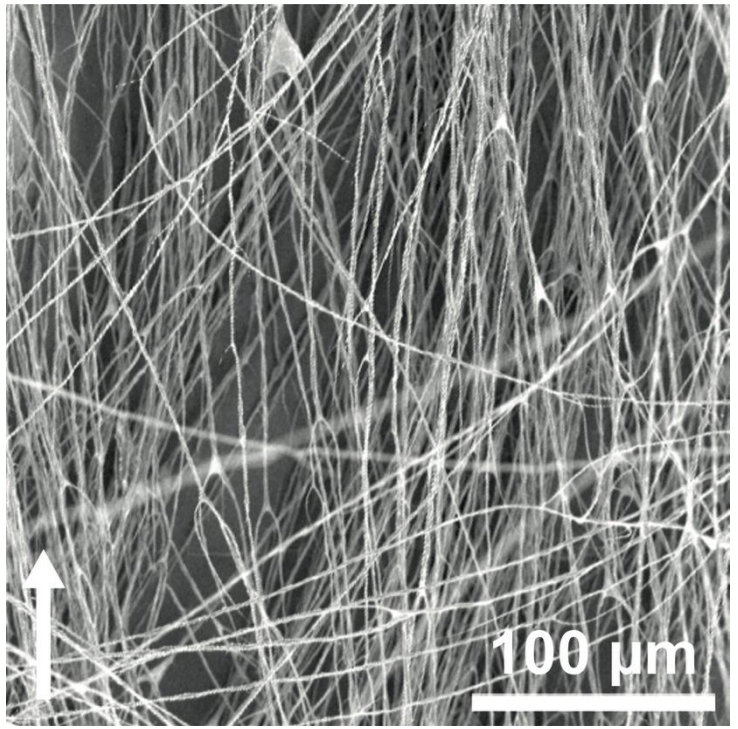

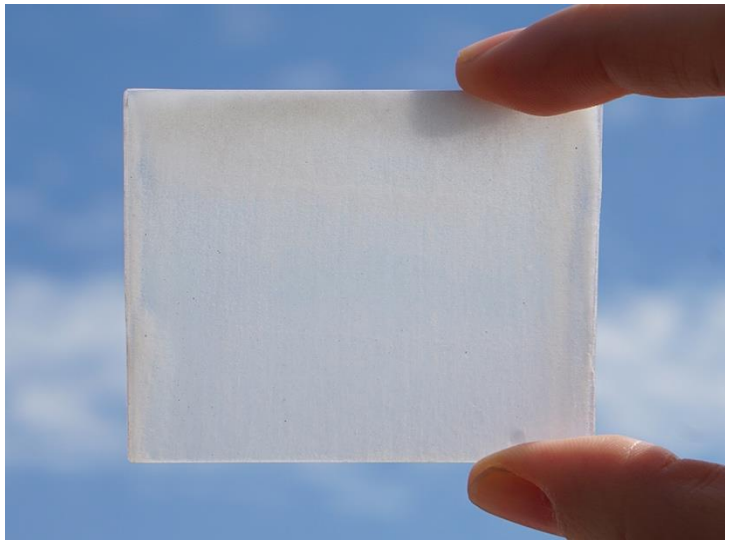

SPINNOVA® Textile Material Innovation Company in Finland



Spun cellulose filaments

- Spun from cellulose nanofiber /microfibril dispersion without harsh chemicals
- Continuous and lightweight
- Sustainable and bio-based
- Can we create high-performance and sustainable biocomposites of cellulose filaments?
- Develop a composite process which is leading to aligned filaments

SPINNOVA®

WWSC
WALLENBERG WOOD SCIENCE CENTER

Motivation

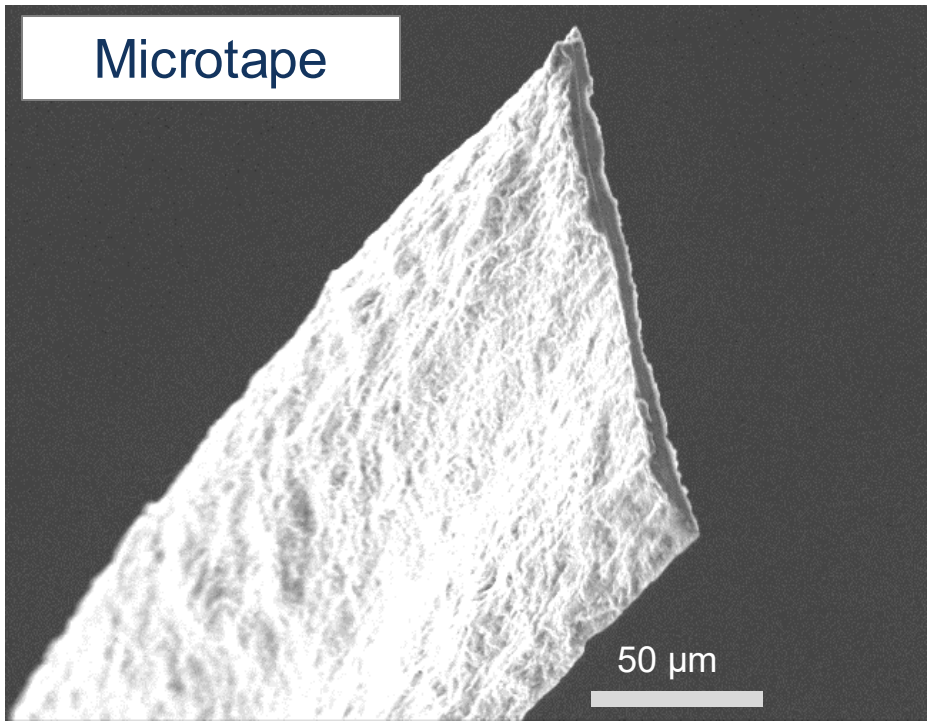

Thickness 2 μm
Width 80 μm

- Unique micro-tape shape
- Stress transfer of microtape-shaped fiber is expected much more efficient
- Performance of microtapes in the composite is also expected to lead better properties compared to circular fibers
- Better packing is expected

Effect of shape for elastic properties

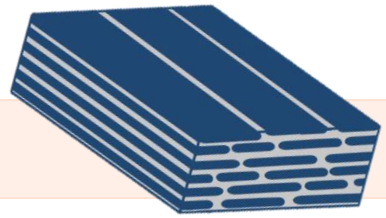

Estimated in-plane transverse modulus

Circular fibers

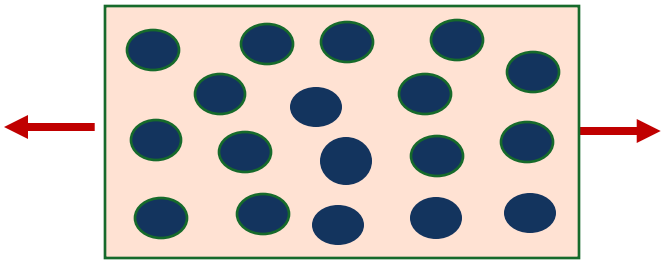

Halpin-Tsai



Random oriented microtapes

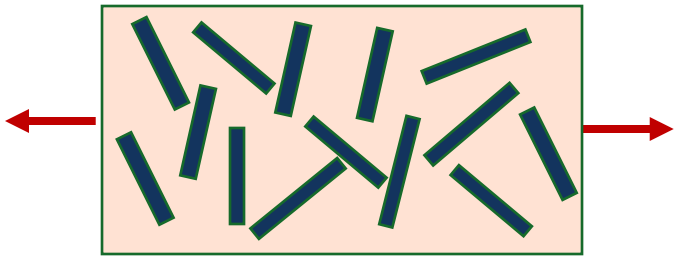

Krenchel's model

$$E_{Trandom} = 3/8 E_f t \eta_l V_f + E_m V_m$$

η_θ: Orientation efficiency.

$E_T^{circular}$ 3.3 GPa

E_T^{random} 3.8 GPa

Aligned microtapes

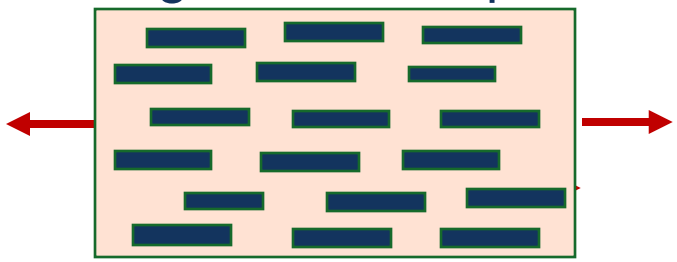

Shear lag model

$$E_T = E_f V_f \eta_l + E_m V_m$$

$$\eta_l = 1 - \frac{2}{\beta_l} tanh \frac{\beta_l}{2} \quad ; \beta_l = \frac{1}{r_f} \sqrt{\frac{4G_m}{E_f ln\, 1/V_f}}$$

η_l: Length correction factor

$E_T^{aligned}$ 6 GPa

Filament properties

- Average filament strength 367 MPa
- Average modulus 33 GPa
- Nanoindentation was used to measure in-plane transverse modulus, 12 GPa (needed for the micromechanical modelling)
- Challenging and time consuming to measure single filaments
- Cross section have large impact and here average cross-section was used
- Nanoindentation and the sample preparation was difficult

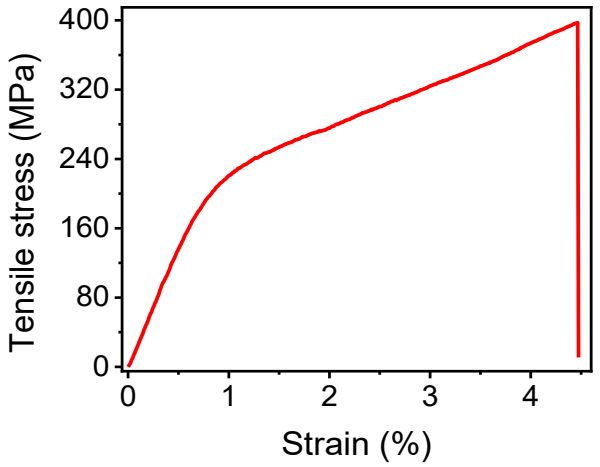

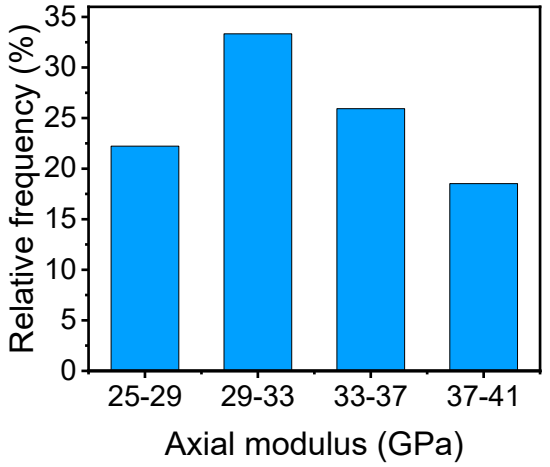

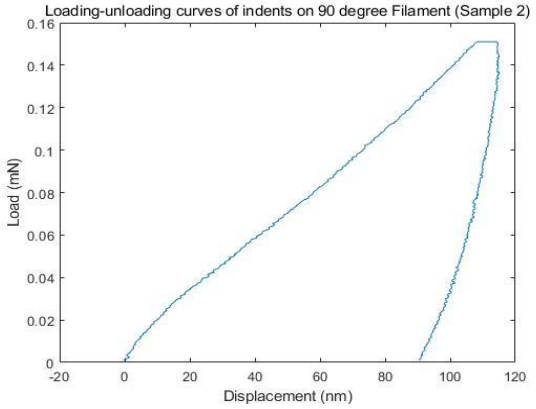

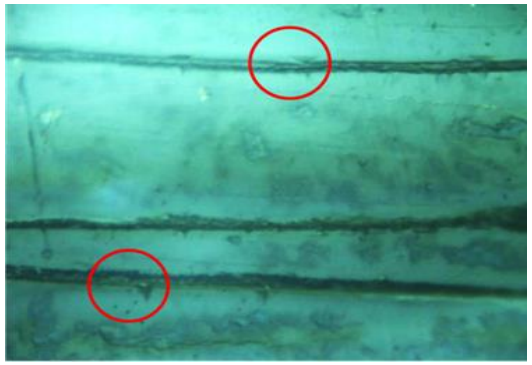

Ben Kahla et al Composites Part A 2025, 109153

Micromechanical modelling of filaments

- Using Halpin-Tsai model we estimated E-modulus would be around 100 GPa, if the cellulose nanofibers are completely oriented (η_f = 1)
- Experimentally measured values are lower
- Factors:
  - Orientation of the cellulose along the filament axis, and their length efficiency
  - Porosity, composition, bond between the nanofibers (G_m), Poisson's ratio
  - Need correct cross section

$$E = \eta_f \, \eta_o \, E_f \, \mathcal{V}_f + \left(1 - \mathcal{V}_f\right) E_m$$

$$\eta_f = 1 - \frac{\tanh(\beta l/2)}{\beta l/2}$$

$$\beta = \frac{1}{r_f} \sqrt{\frac{2G_m}{E_f \ln(R/r_f)}}$$

Orientation of cellulose nanocrystals in the filament measured with Wide Angle X-ray Spectroscopy (WAXS)

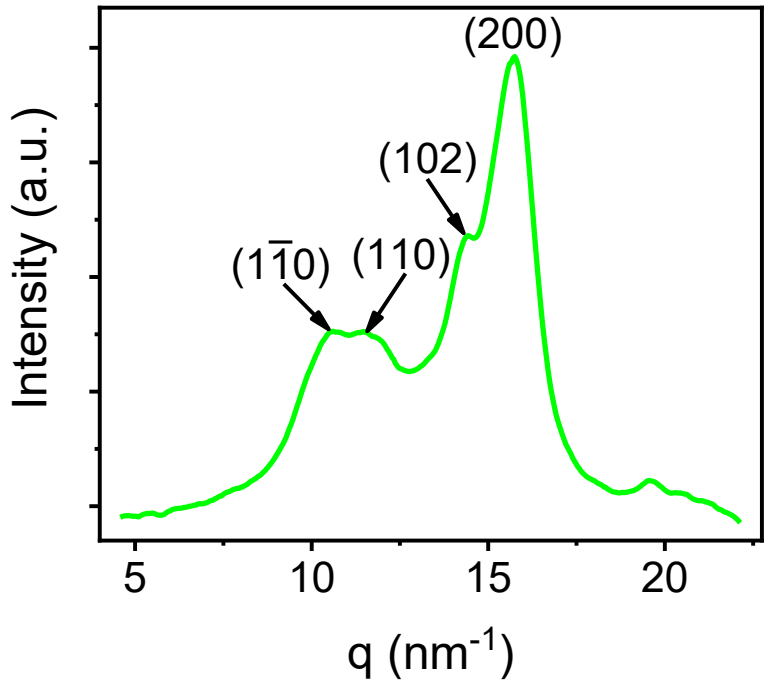

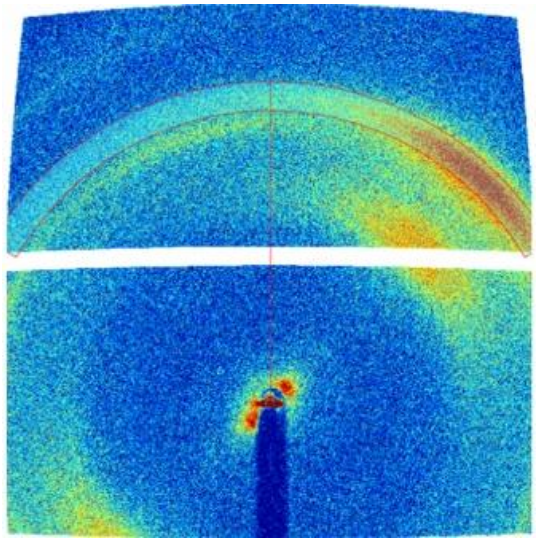

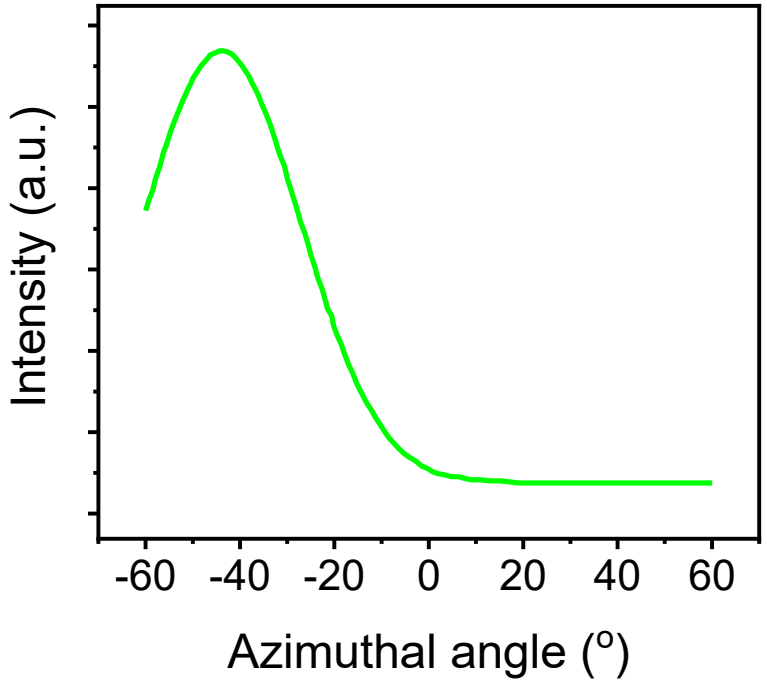

Orientation index 0.78 show that cellulose nanofibers are oriented along the microtape axis (bundle)

TREESEARCH



Unidirectional composites

Postdoc Hiba ben Kahla

- Winding of the filament roving around a metal plate
- Bio-epoxy resin (Super Sap, Entropy Resins), filament content 21-23 vol%



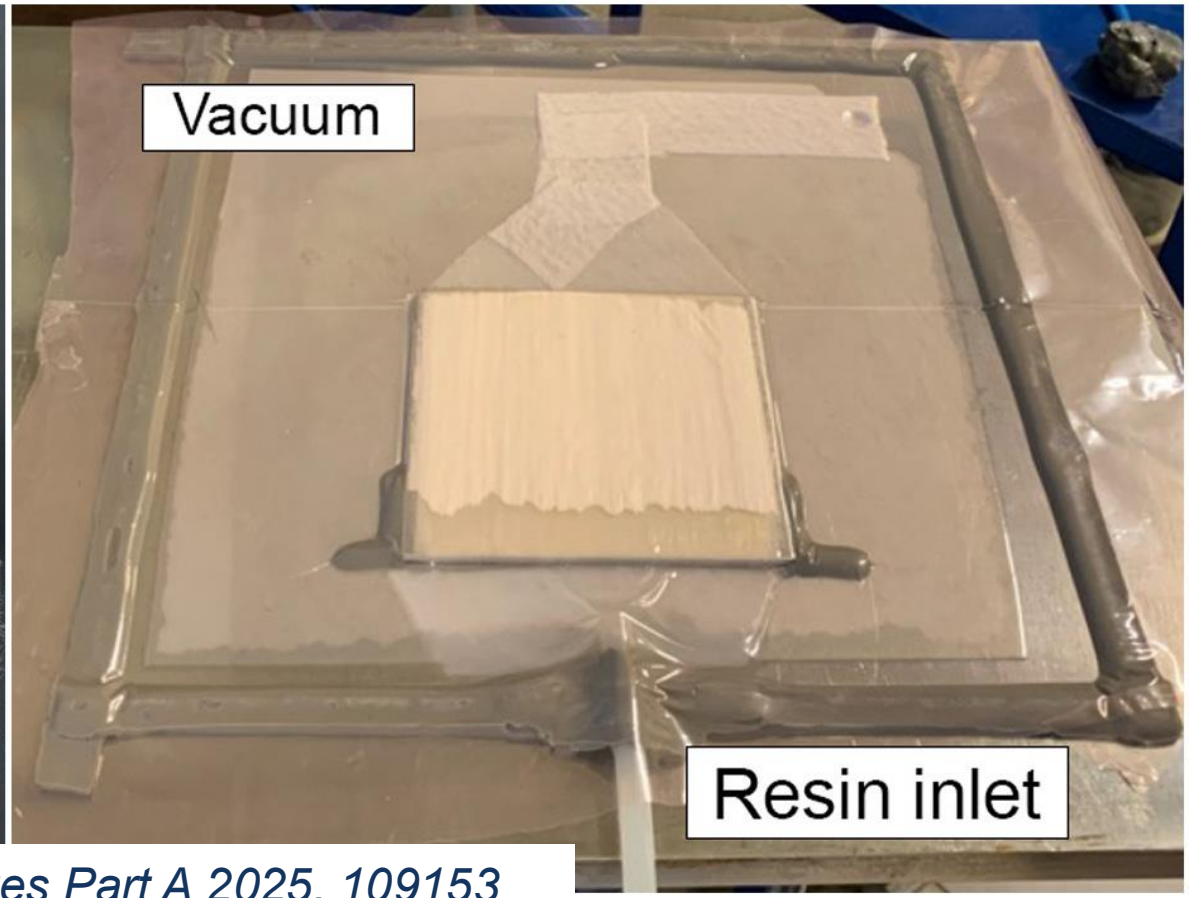

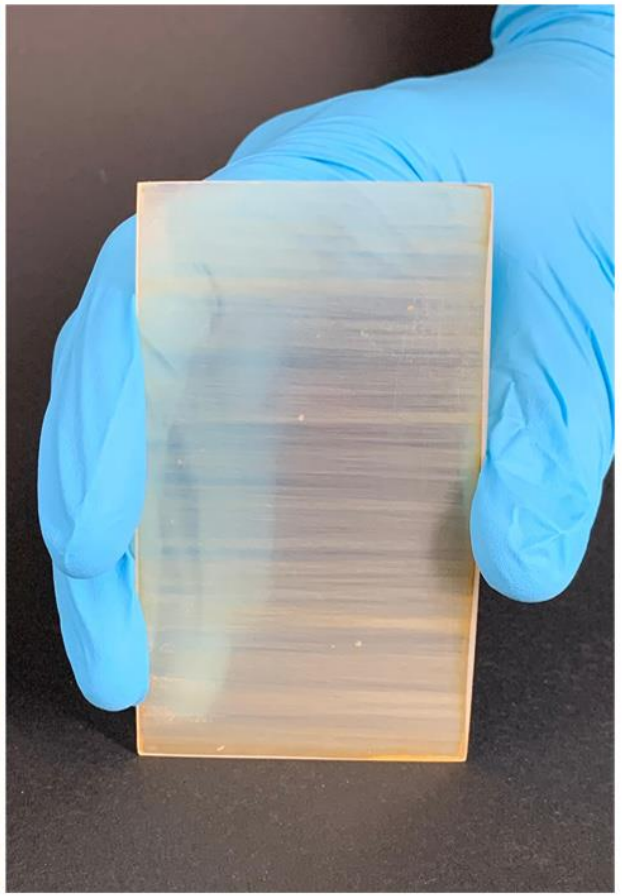

Ben Kahla et al Composites Part A 2025, 109153

Microstructure

- Longitudinal and transverse cross-sections of fracture surfaces
- Filaments are broken, no pull-outs indicating good adhesion
- Some well packed areas, which are expected to be filament bundles, also resin rich area and voids
- Need to understand why we get voids, how are these voids formed?

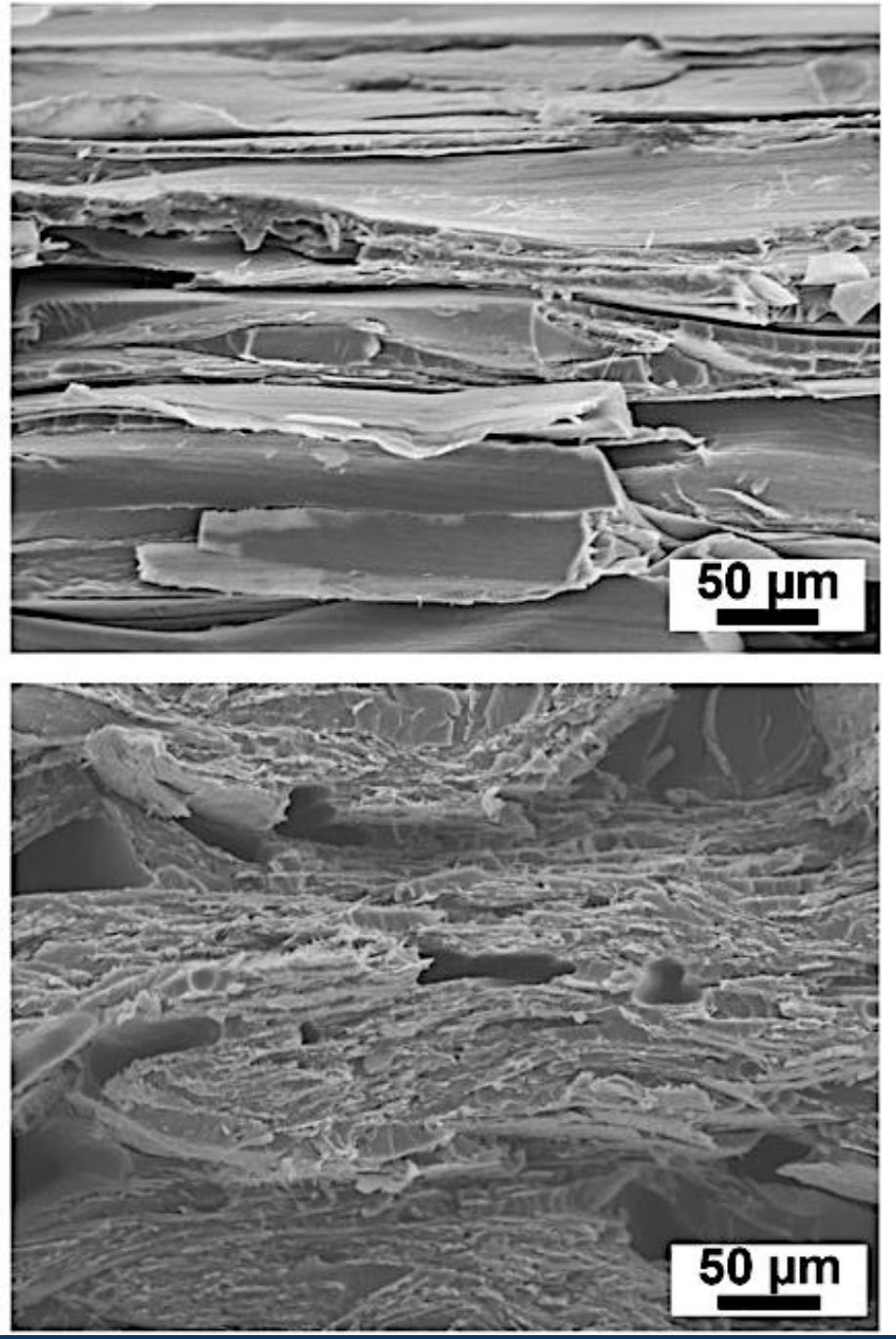

Ben Kahla et al Composites Part A 2025, 109153

Microtomography of composite structure



- Distribution of filaments is not optimal
- Need to improve packing
- Avoid twisting and void formation

Ben Kahla et al Composites Part A 2025, 109153

Mechanical properties

Filament content 21 vol%

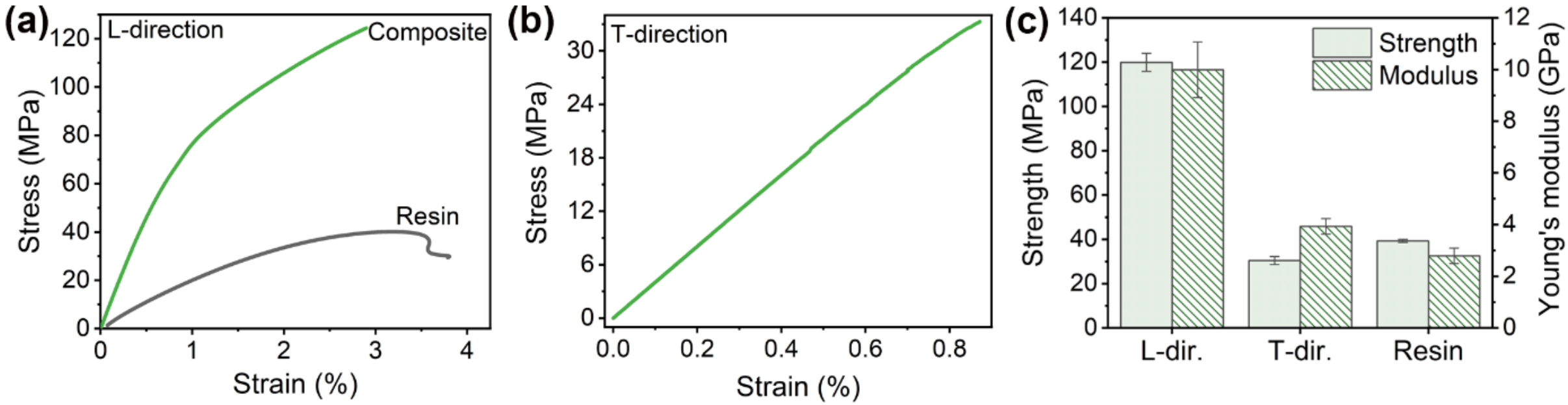

Longitudinal modulus (GPa)	10
Elongation at break (%)	3
Max. strength (MPa)	120

Transverse modulus (GPa)	4.5
Elongation at break (%)	0.8
Max strength (MPa)	27

Ben Kahla et al Composites Part A 2025, 109153

Micromechanical modelling of mechanical properties

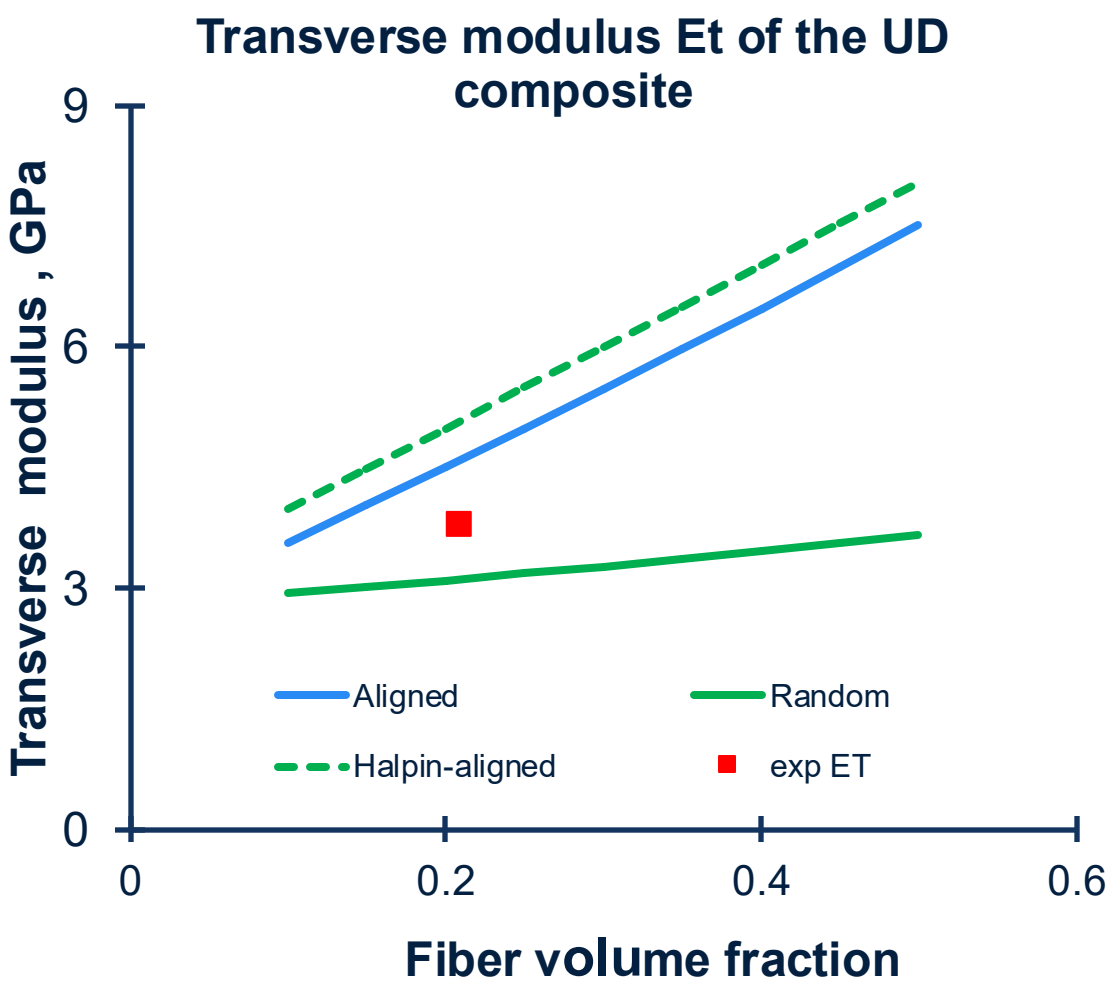

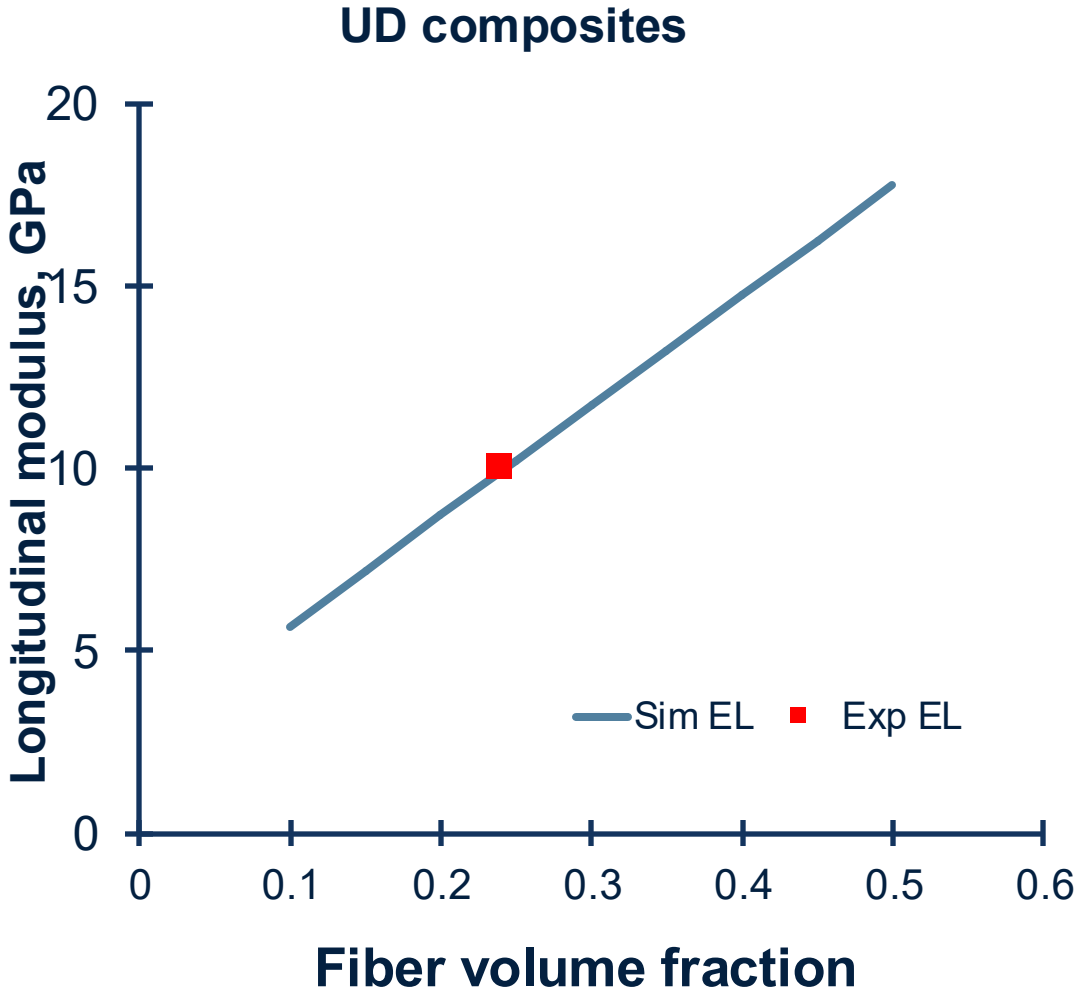

Ben Kahla et al Composites Part A 2025, 109153

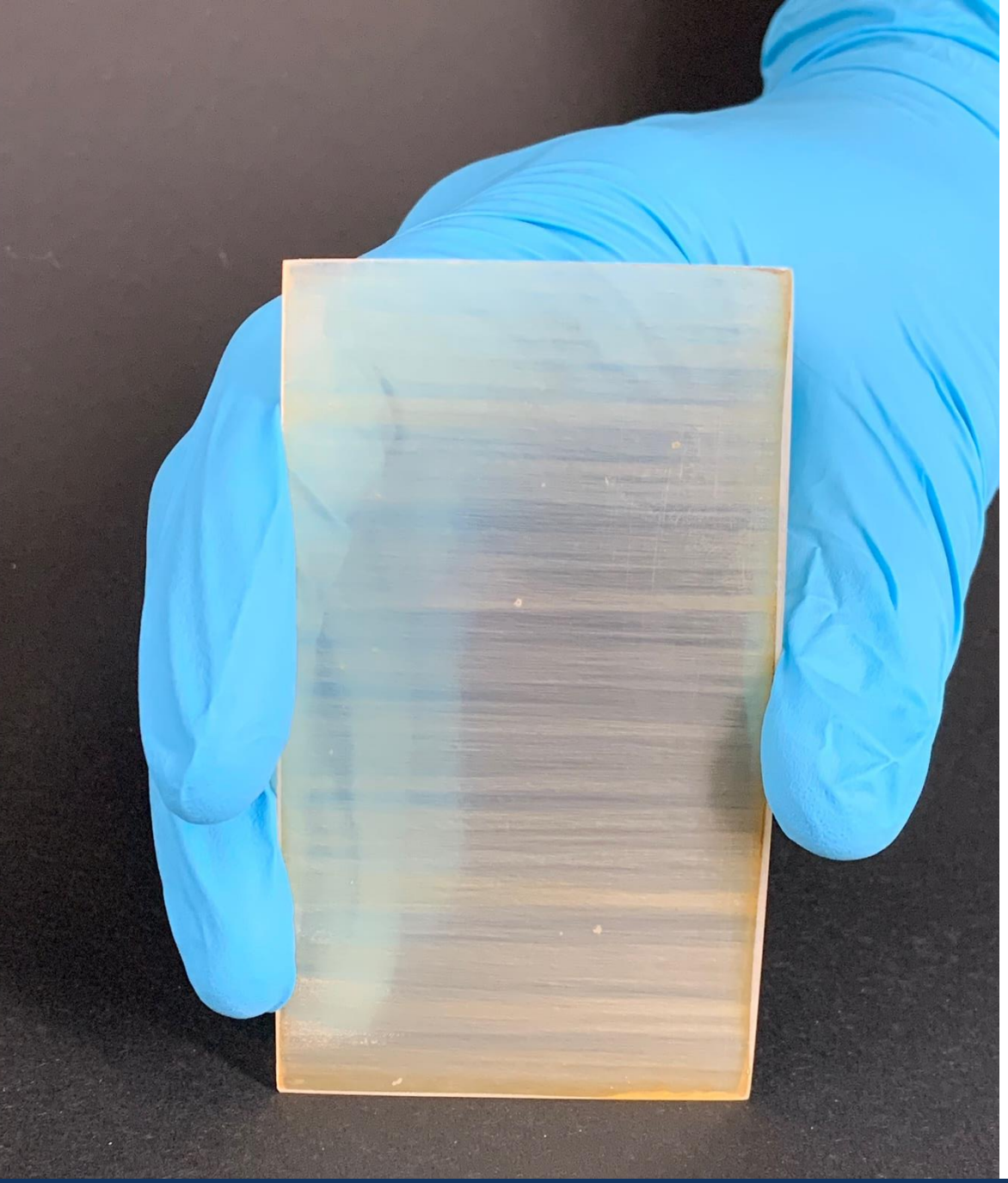

Conclusions

- Promising results, so far and we believe we can improve from this initial study
- We have filaments/fibers which can be further developed for composite use
- Optimize the testing of filaments, measure correct cross-section
- Optimize the composite manufacturing process
  - Control in-plane orientation distribution of the filaments
  - Increase the filament content and decrease void content

Thank you for listening and many thanks to the partners, team members and funders







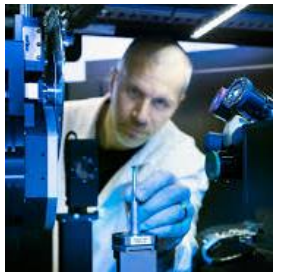


Knut and Alice Wallenberg Foundation

SPINNOVA®

FORSK

TREESEARCH

WWSC
WALLENBERG WOOD SCIENCE CENTER

BUSINESS FINLAND

FIDIPRO Finland Distinguished Professor Programme

MAX IV


LULEÅ
UNIVERSITY
OF TECHNOLOGY

Kelly Prize

Challenges and opportunities in synchrotron computed tomography imaging of composites

Yentl Swolfs
+ Elise Van Vlierberghe, Thanasis Chatziathanasiou,
Sina AhmadvashAghbash, Mahoor Mehdikhani, Christian Breite

05-08-2025

KU LEUVEN

Composite Materials Group

What is computed tomography?

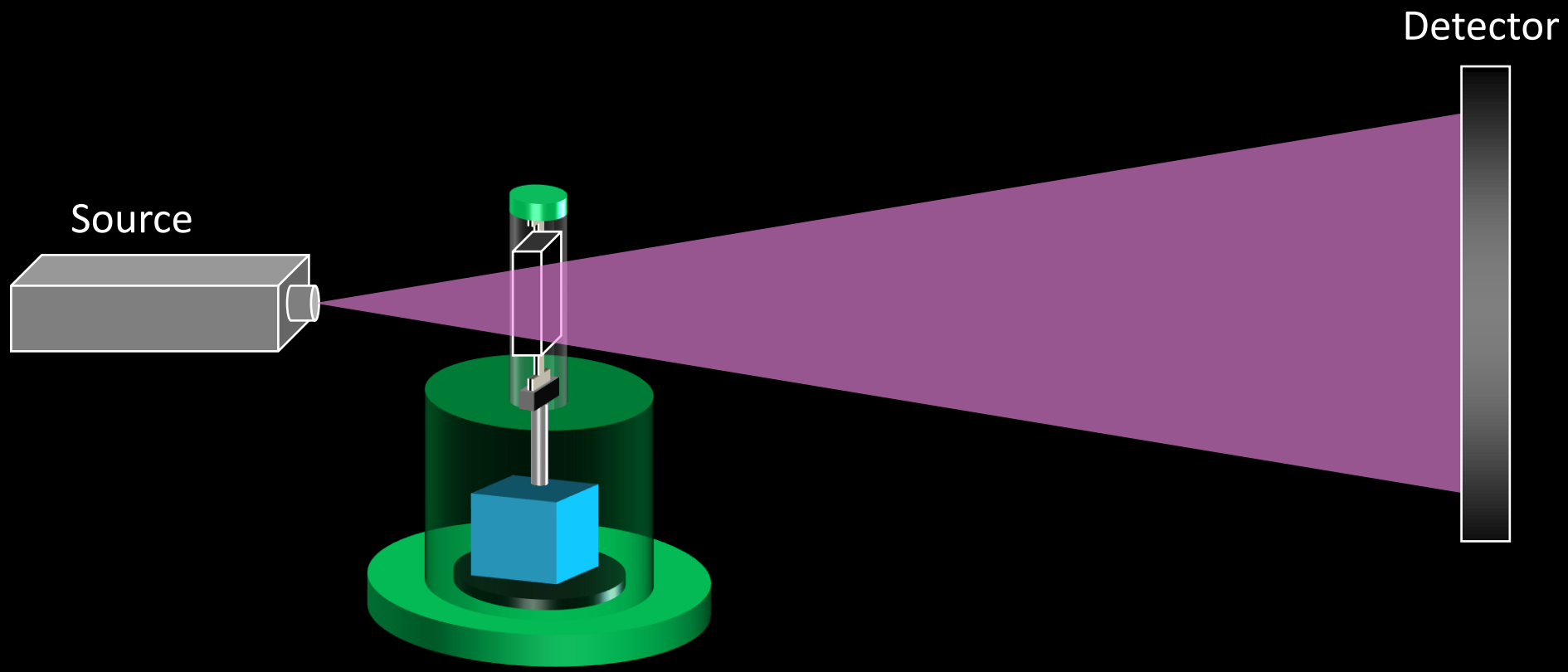

The specific nature of X-ray computed tomography

Getting 3D images = easy

Getting the best possible 3D images efficiently = difficult

What do you need?

- A device suited to your needs/material
- Suitable software
- (Years of) experience

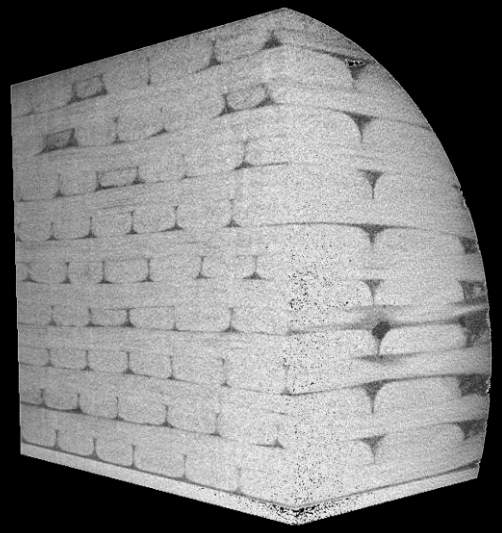

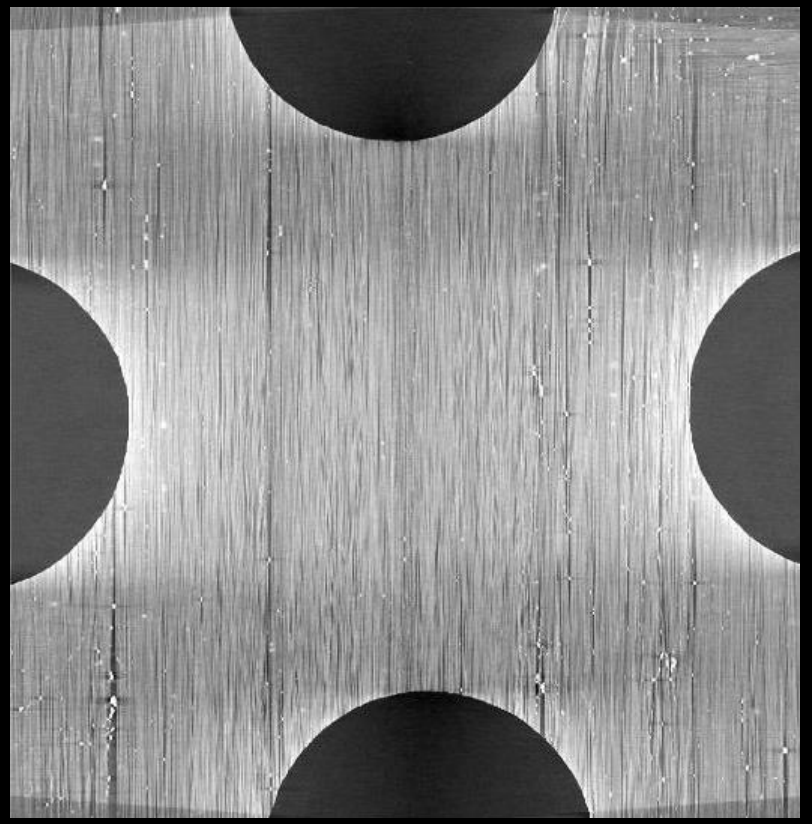

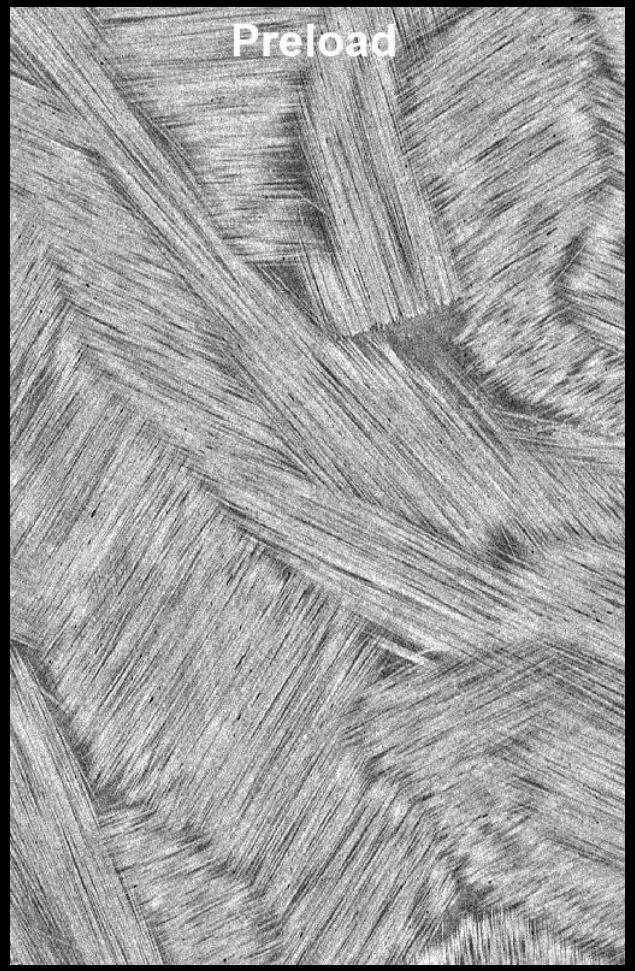

Typical layout of an XCT beamline

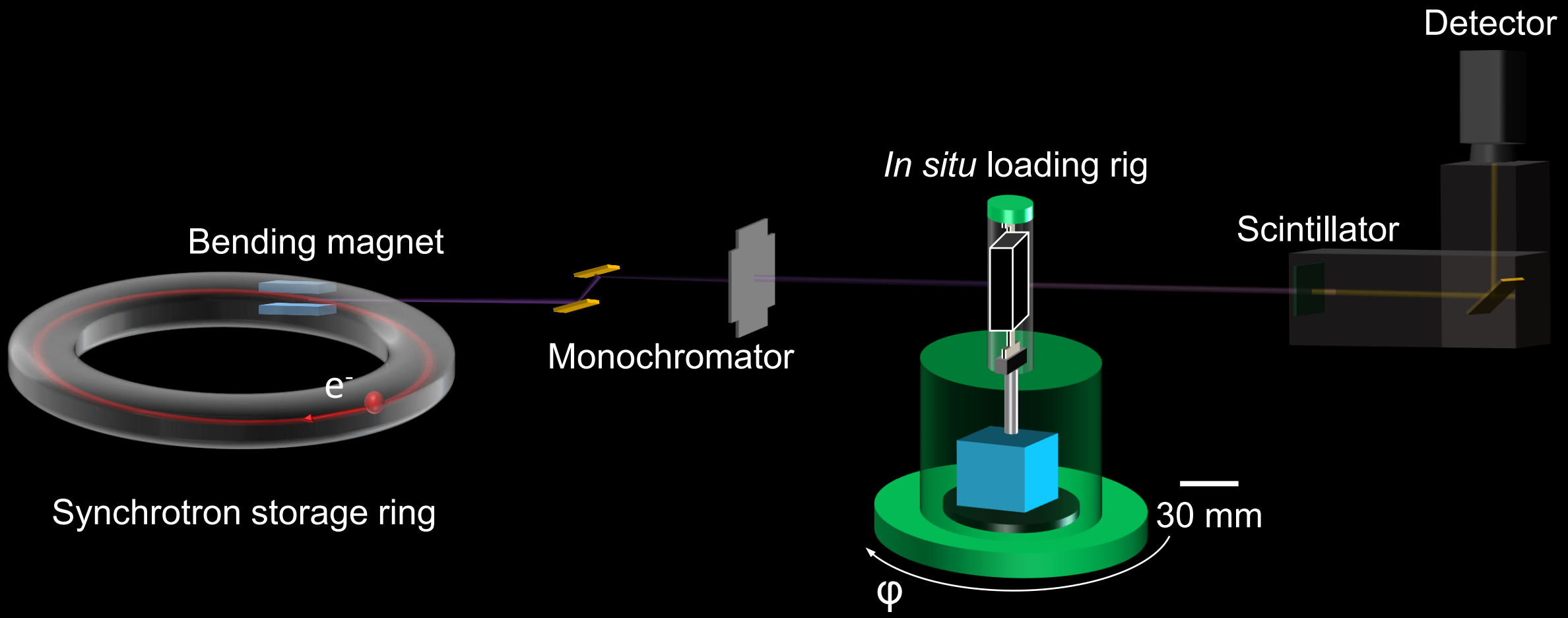

The specific nature of synchrotron computed tomograpy

Mostly parallel beams
- No geometric magnification
- Ample space for load rigs

Voxel size can be smaller
- Not necessarily!

More phase contrast present
- Can be tweaked via propagation distance

Much higher flux
- Faster experiments
- Monochromatic light or pink beam

Three synchrotron techniques

Continuous acquisition | Ultrafast radiography | Holotomography

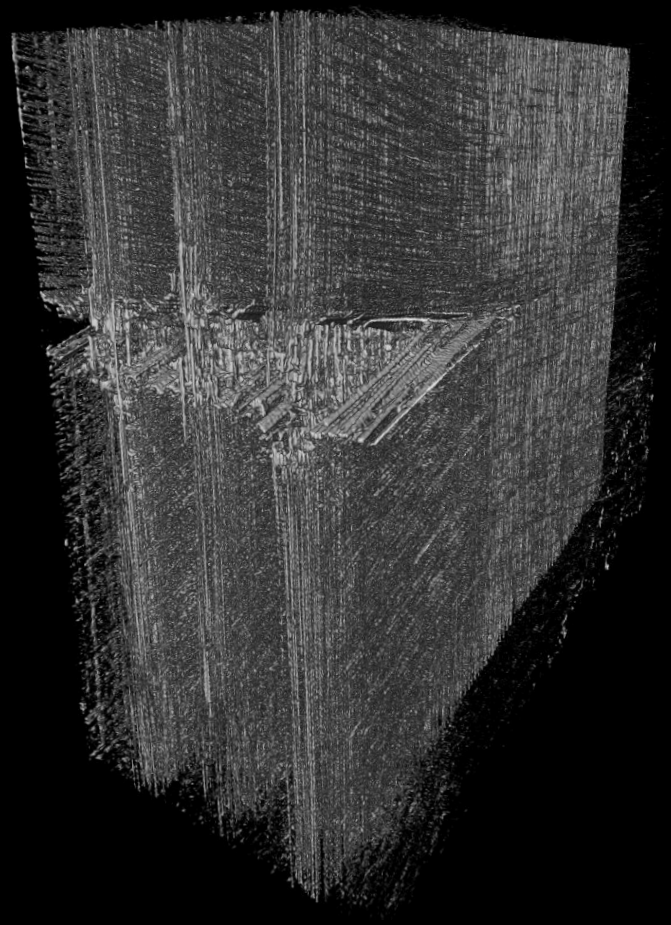

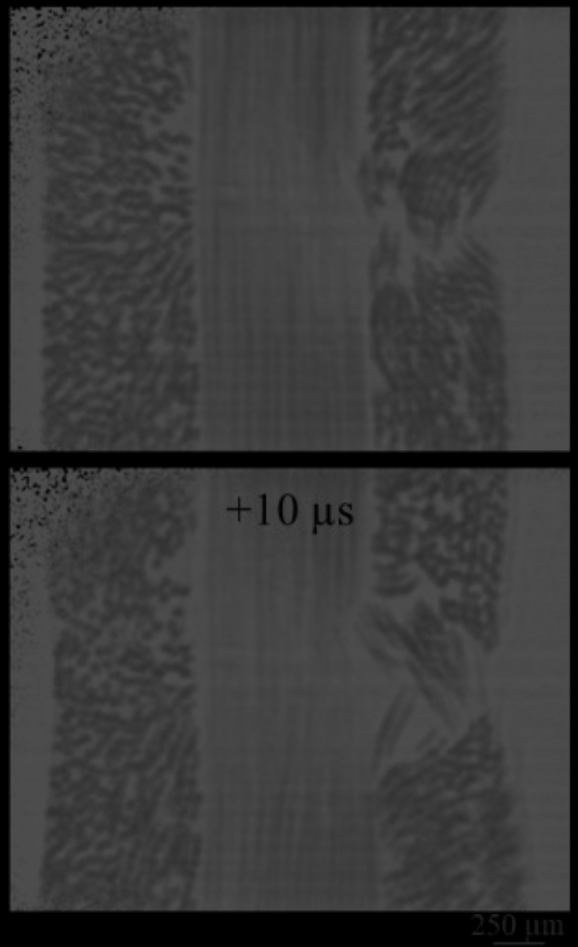

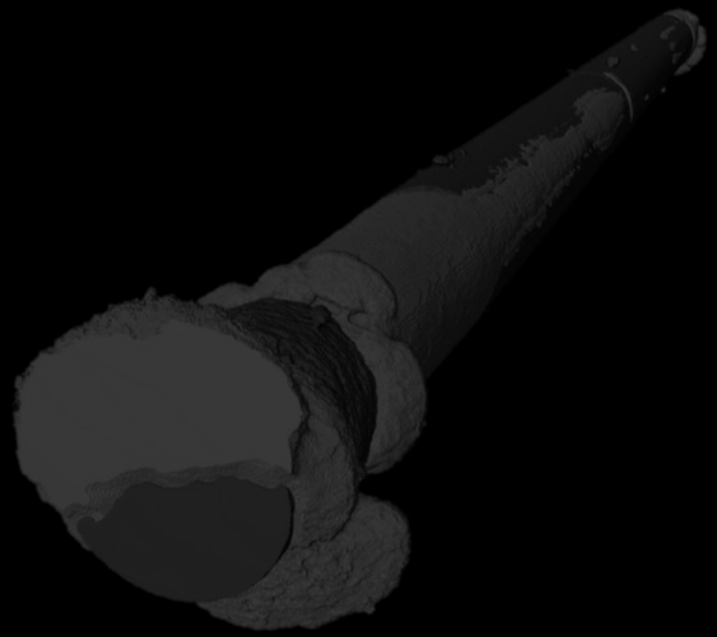

The ply thickness effect for translaminar fracture toughness

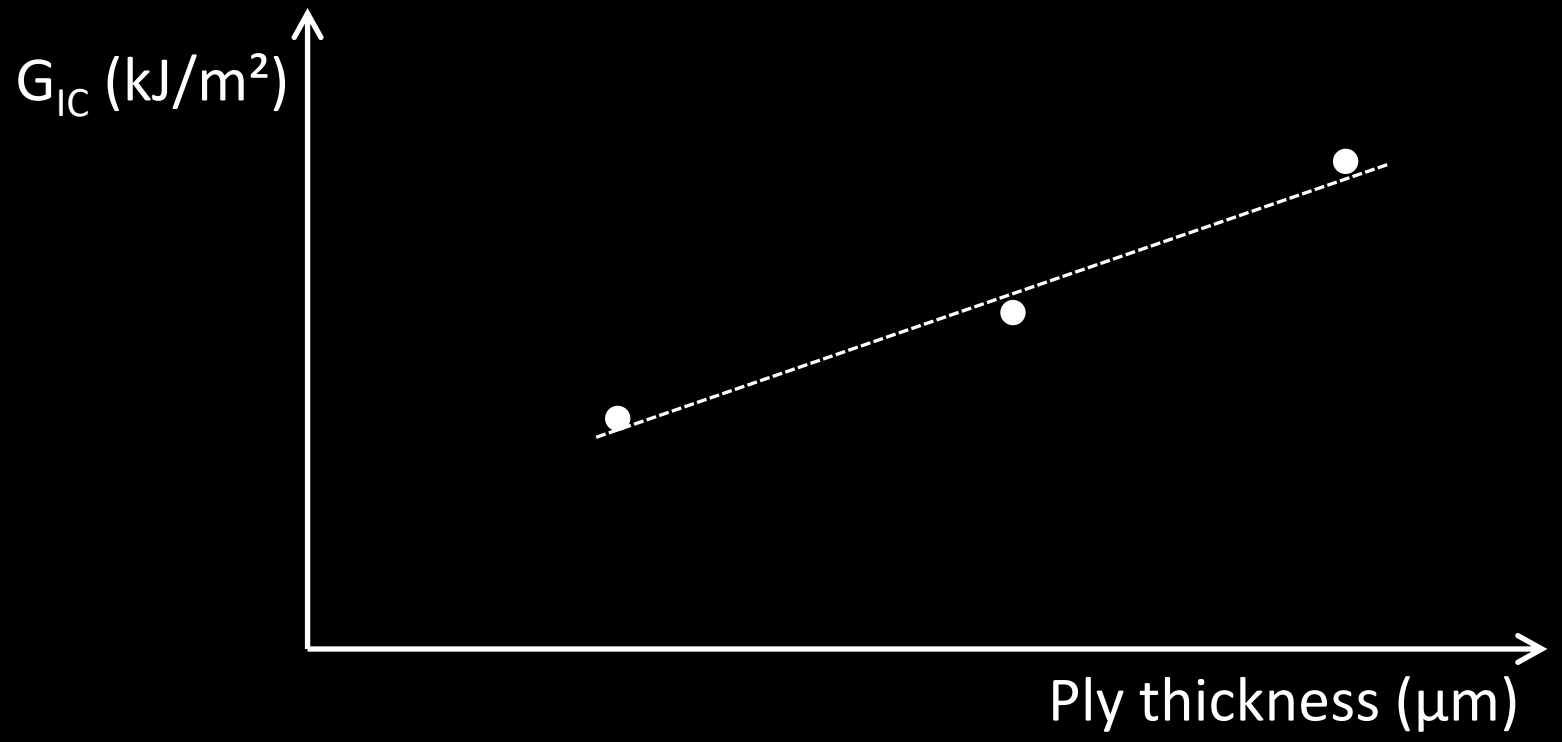

Only one micromechanical model available

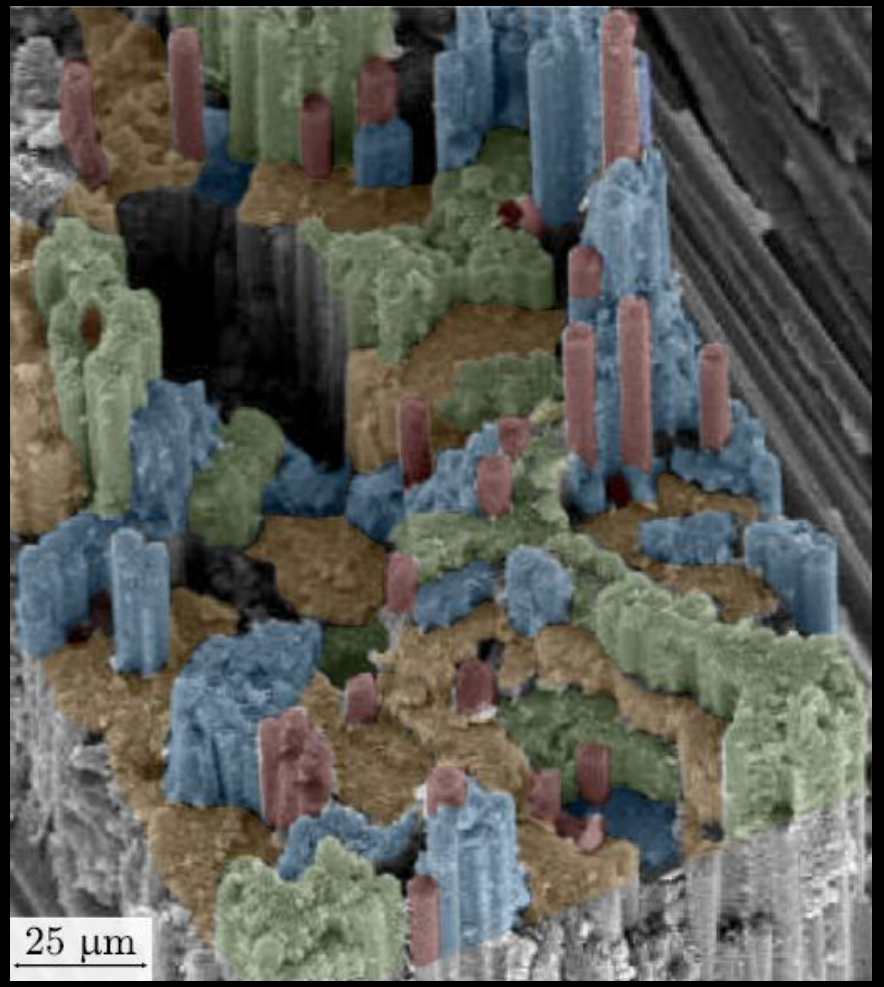

Pimenta and Pinho (2014)

The TOMCAT beamline and GigaFRoST detector

800 nm, 2s per scan

Superfast read-out system:

60.000 radiographs in 2 min

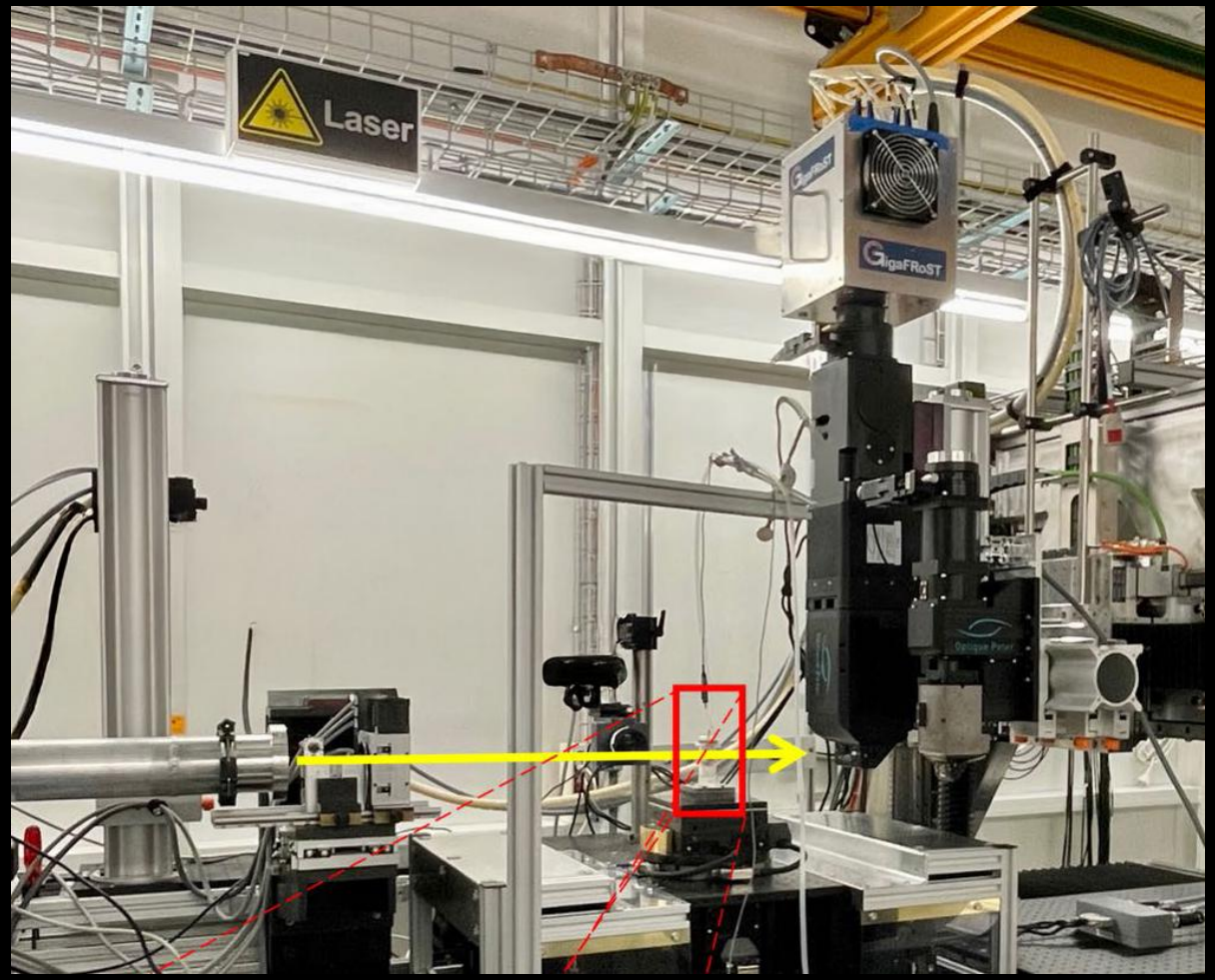

Ivanovic et al. (2024)

Miniaturised compact tension specimen

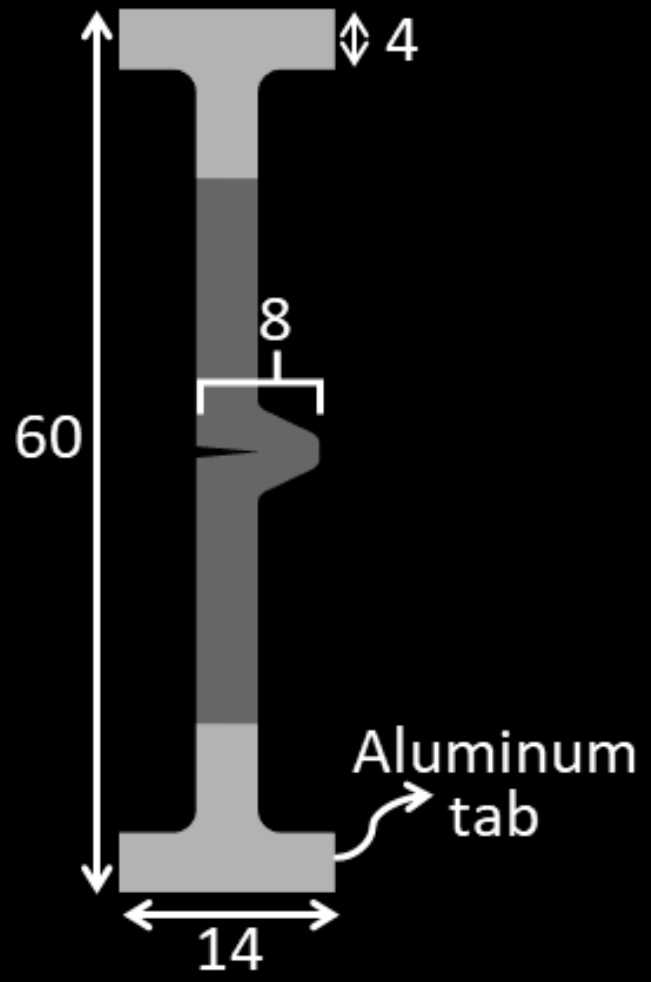

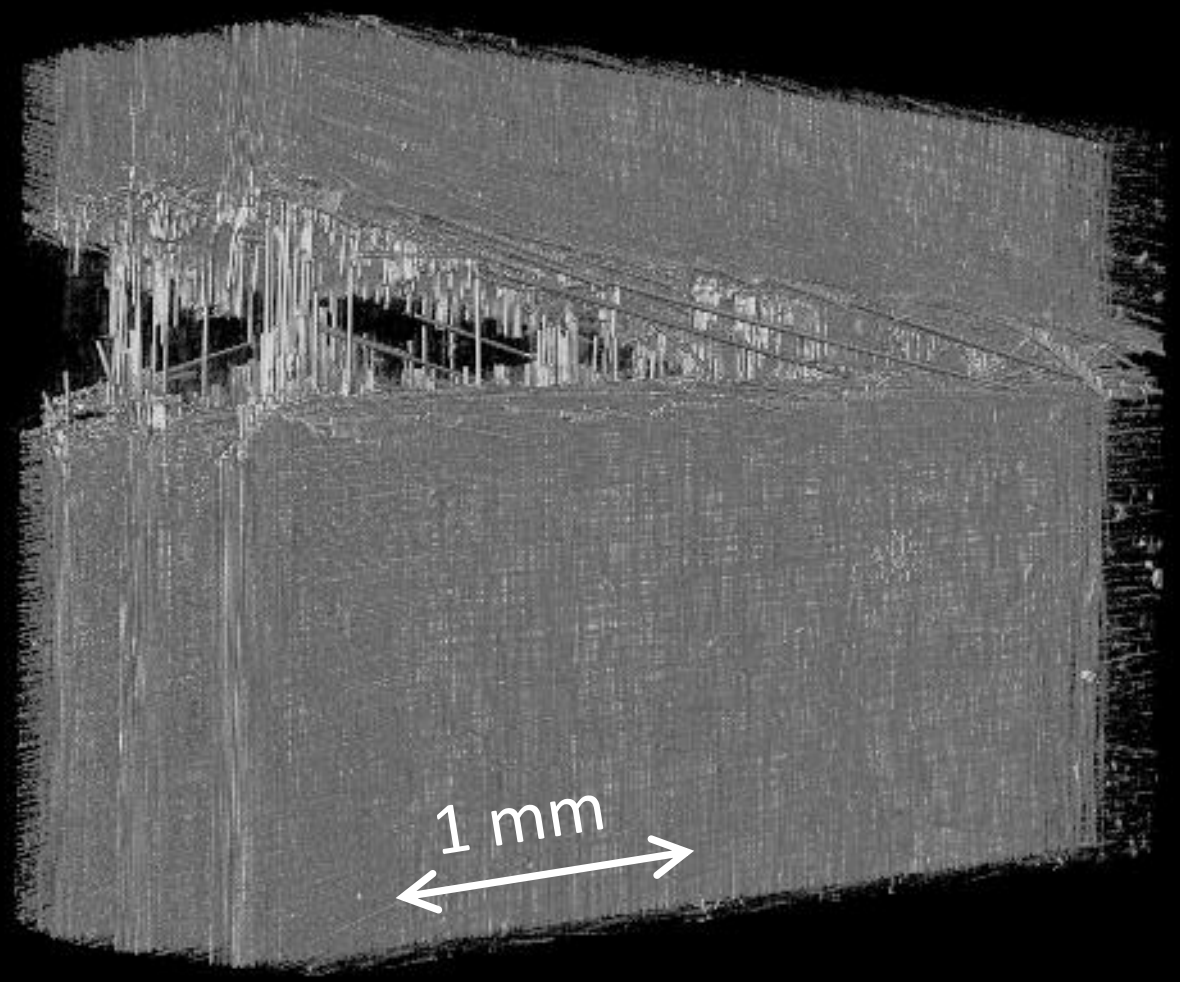

Complex fracture morphology

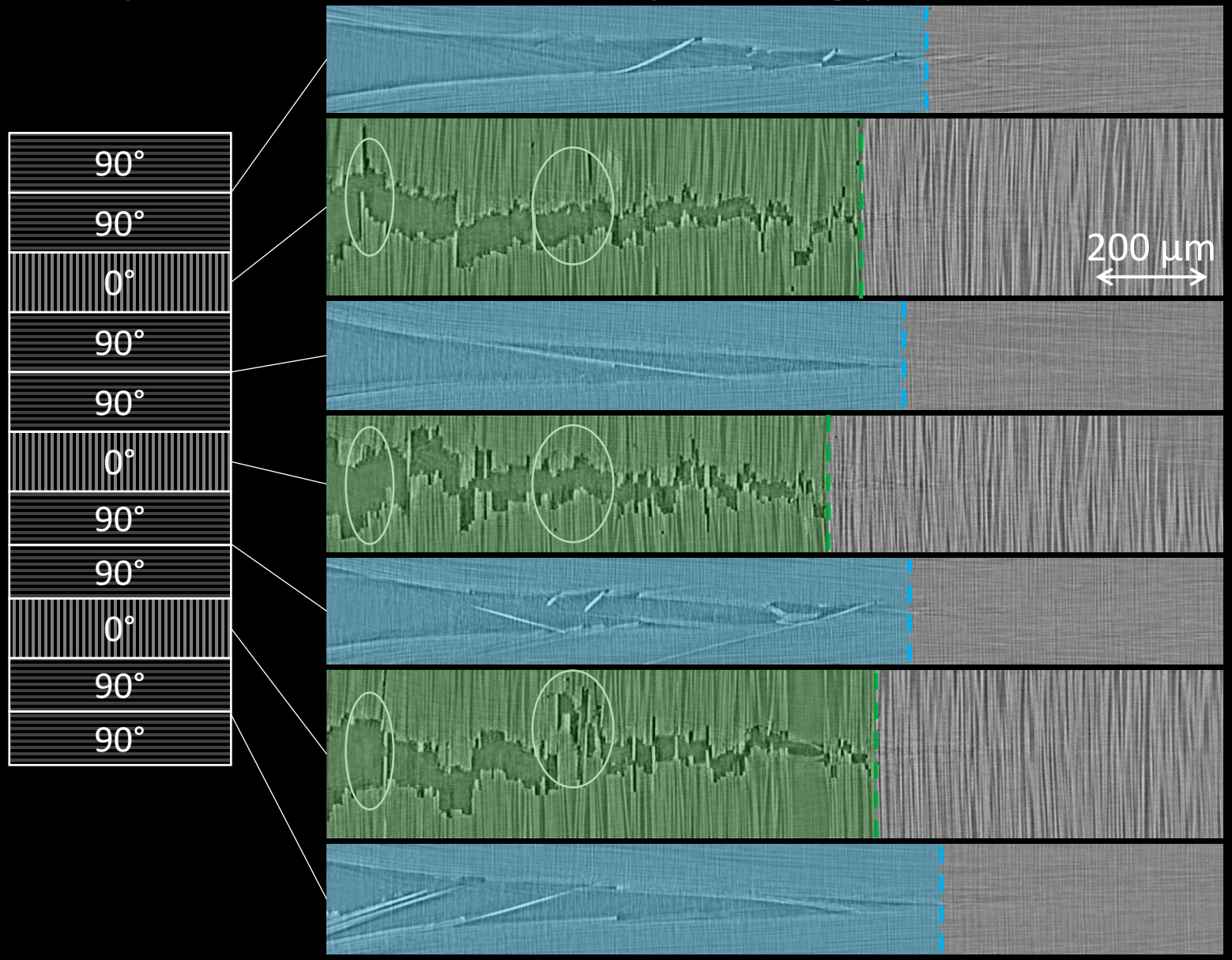

Detailed pull-out characterisation

Independent 0° cracks

90° cracks ahead of 0° cracks

Fibre breaks near crack tip

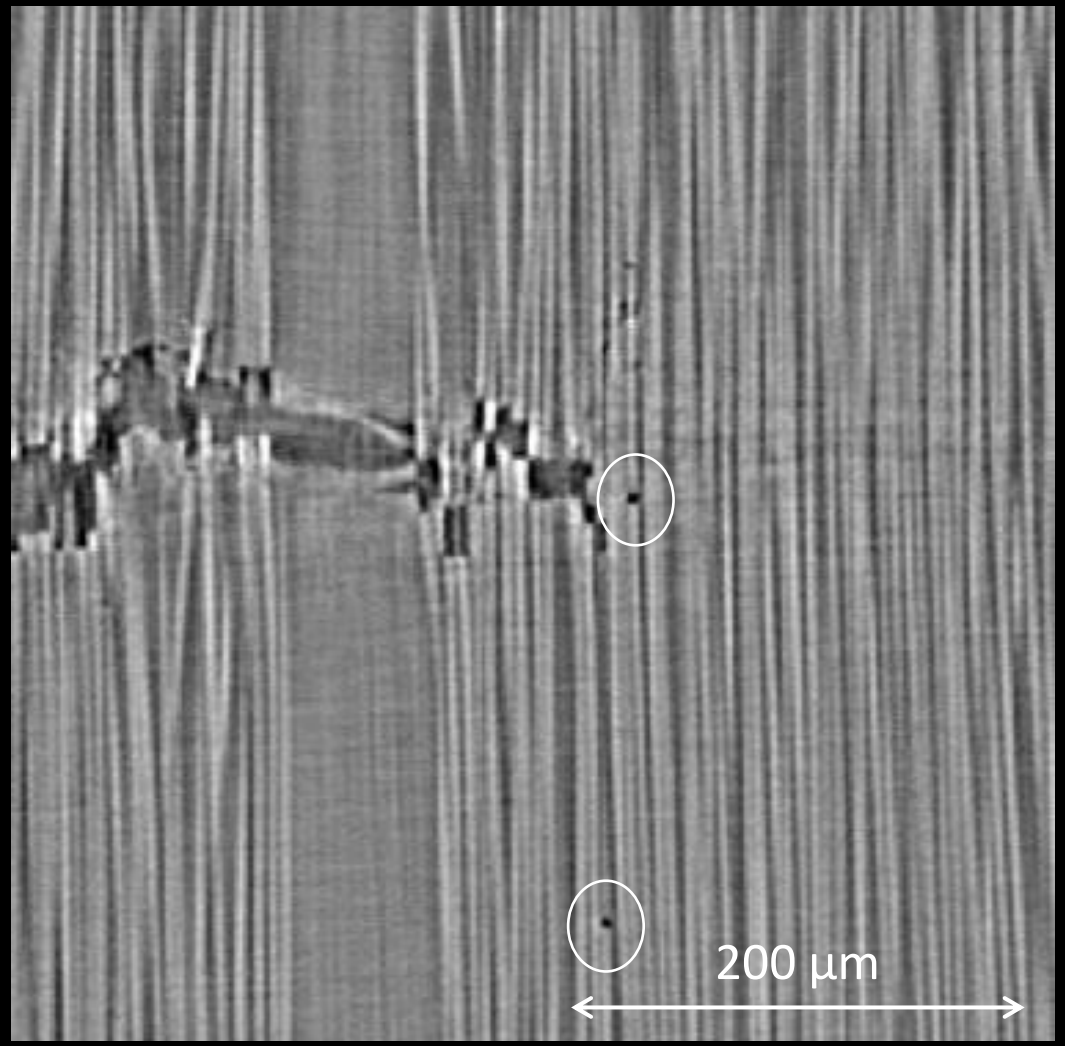

Future challenges and opportunities

Challenges:

- Unique camera only available at TOMCAT beamline
- Fast rig rotations → stability concerns

Opportunities

- Swiss Light Source 2.0 upgrade → brighter
- 2 TOMCAT beamlines

Three synchrotron techniques

Continuous acquisition | **Ultrafast radiography** | Holotomography

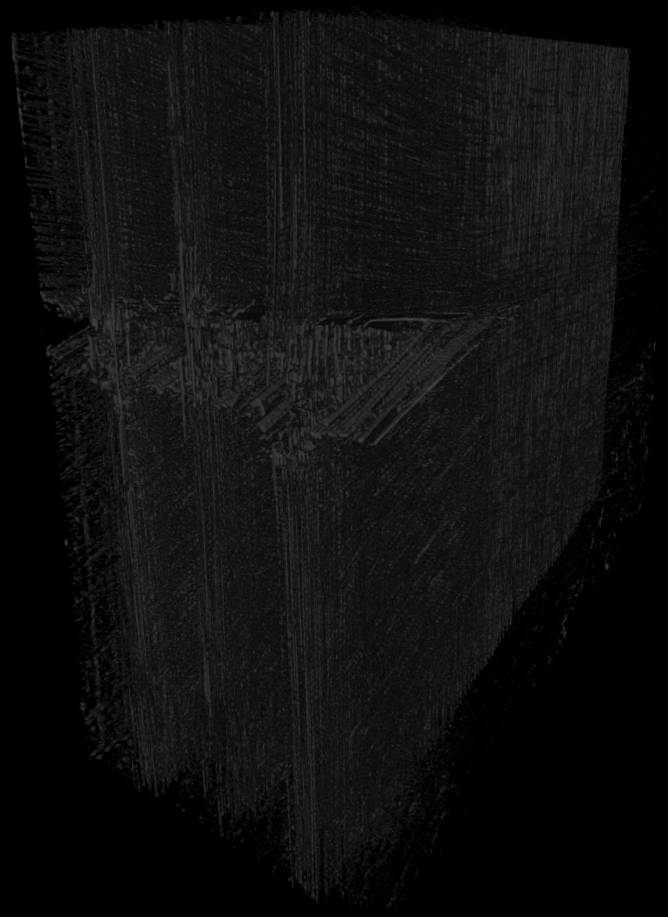

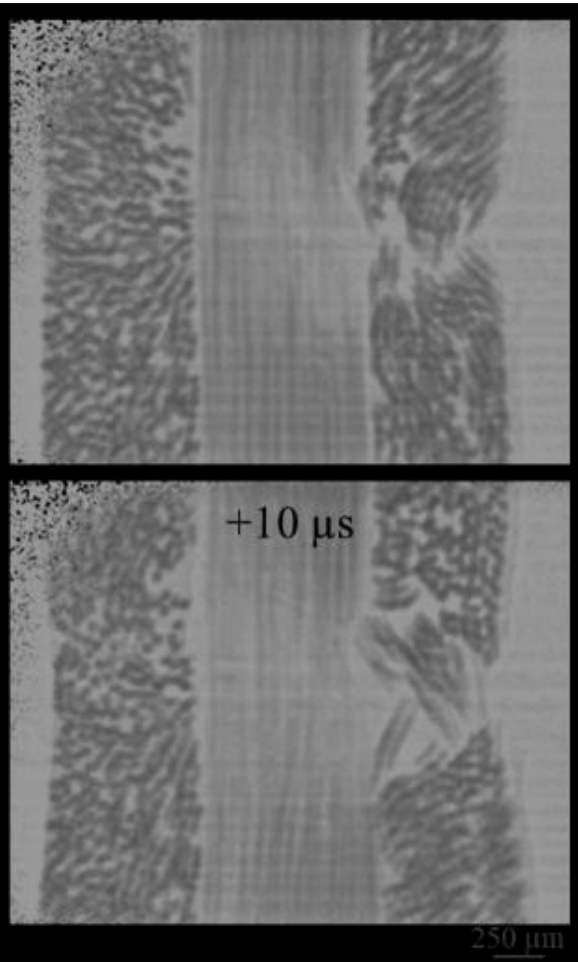

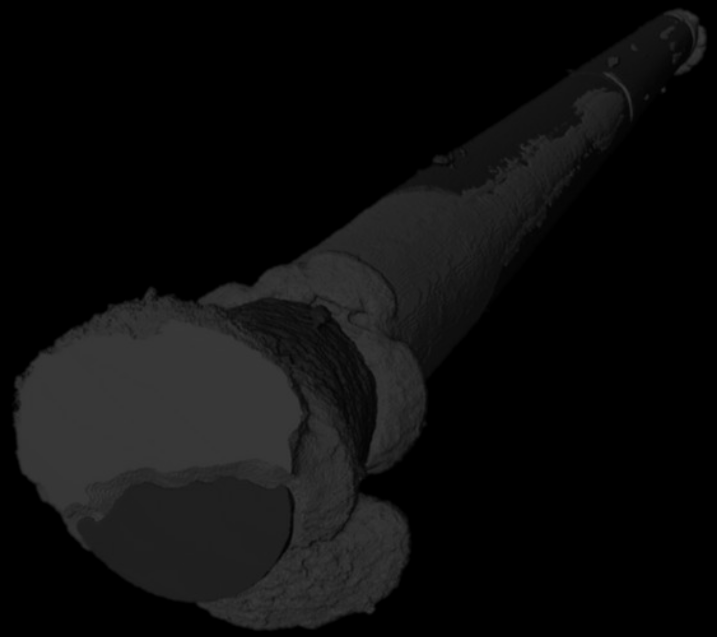

Ultrafast camera

Shimadzu HPV-X2

- Up to 10 MHz
- Up to 256 frames
- 250x400 pixels



Setup at FORMAX

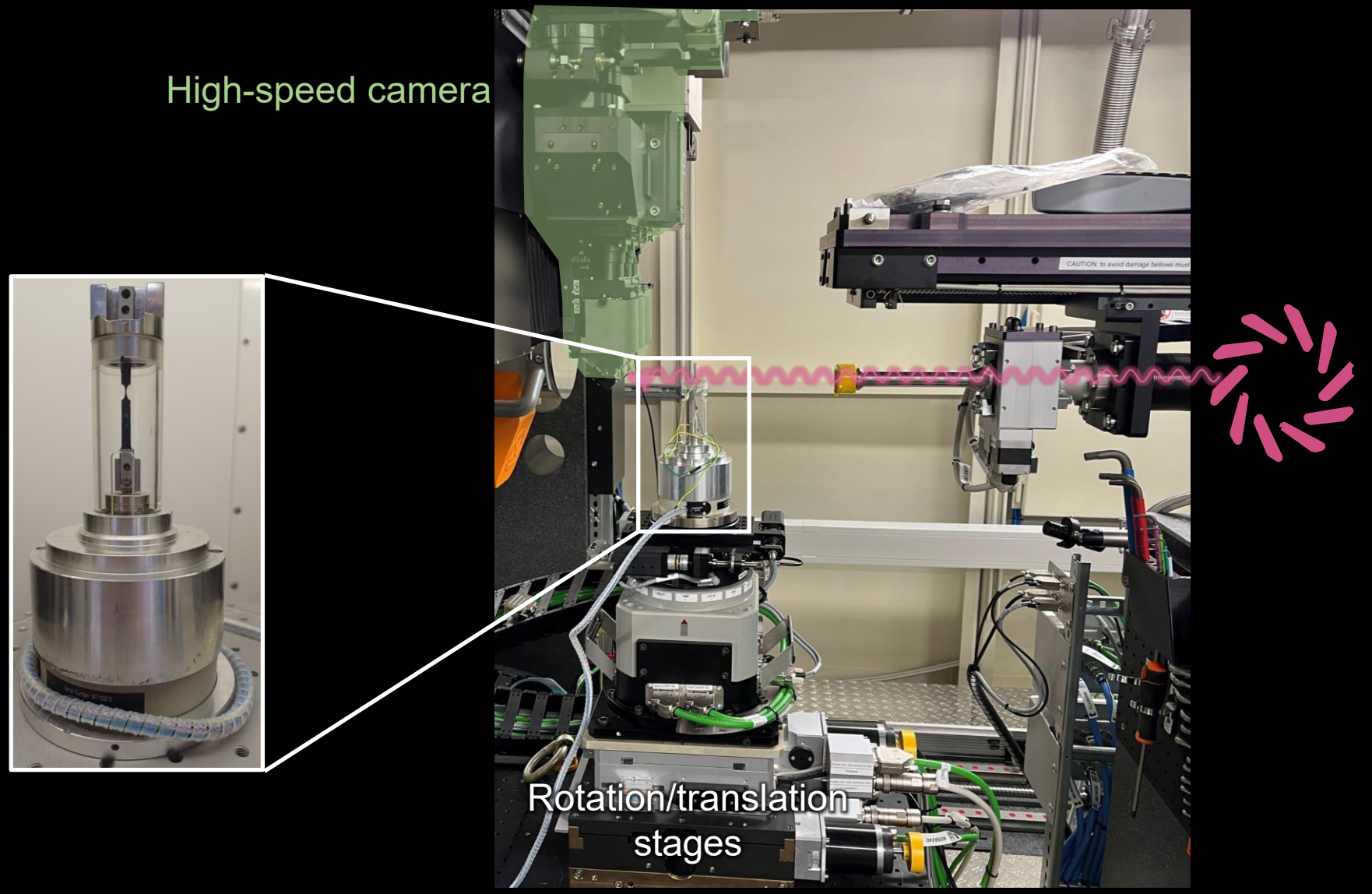

Specimen degradation

Imaged at 0.1-1 MHz ➔ 256-2560 µs

Degradation due to dose

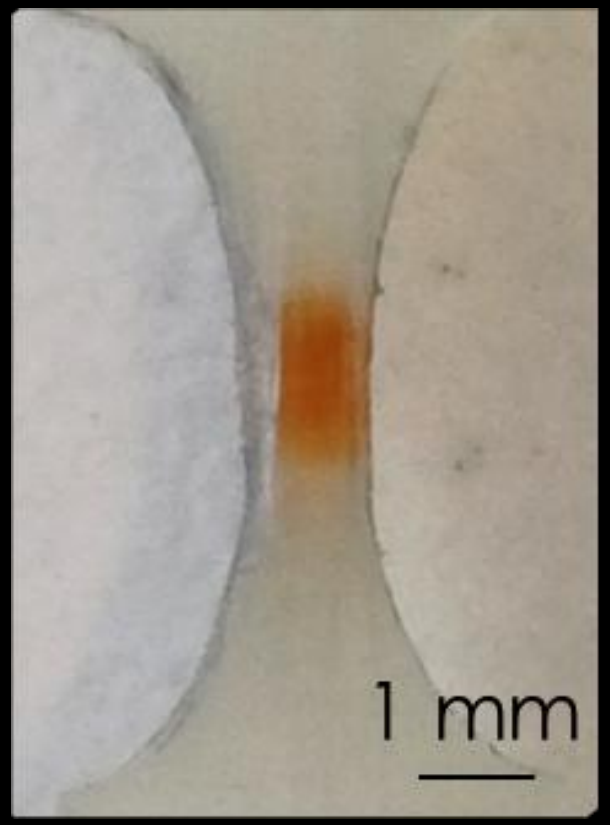

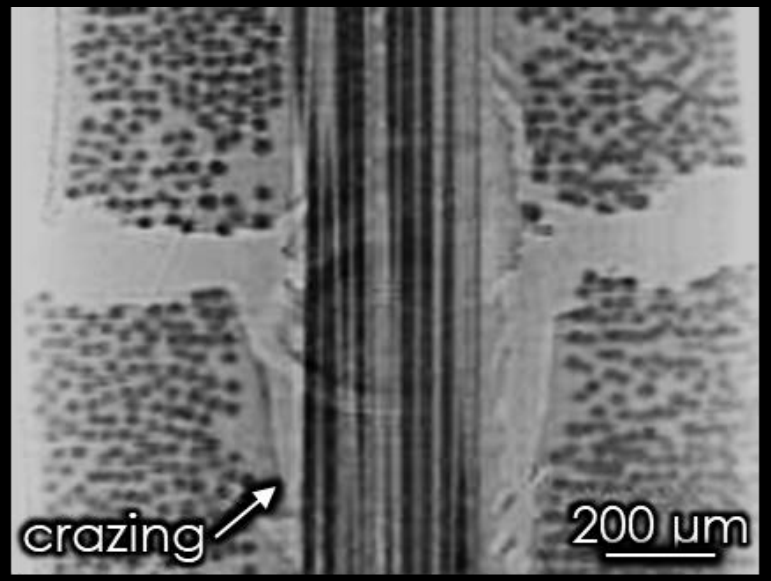

Degradation due to dose rate

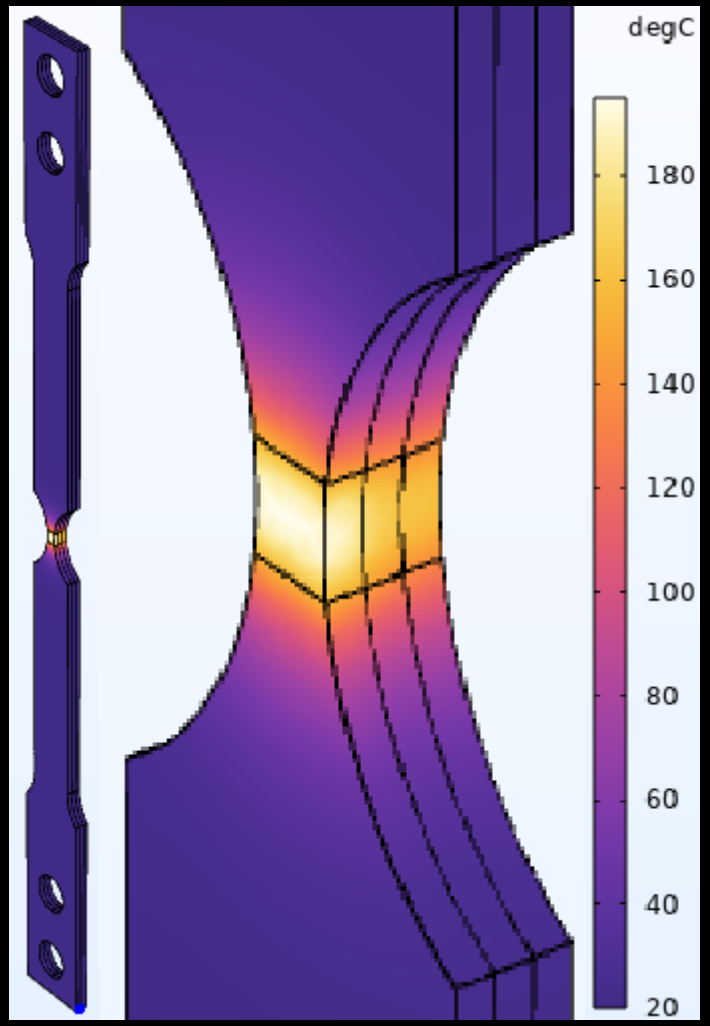

Ultrafast radiography:
Future challenges and opportunities

Challenges:

- High enough flux without degrading specimen
- Triggering

Opportunities

- HPV-X3 just launched
- Slower but more sensitive camera alternatives

Three synchrotron techniques

Continuous acquisition

Ultrafast radiography

Holotomography

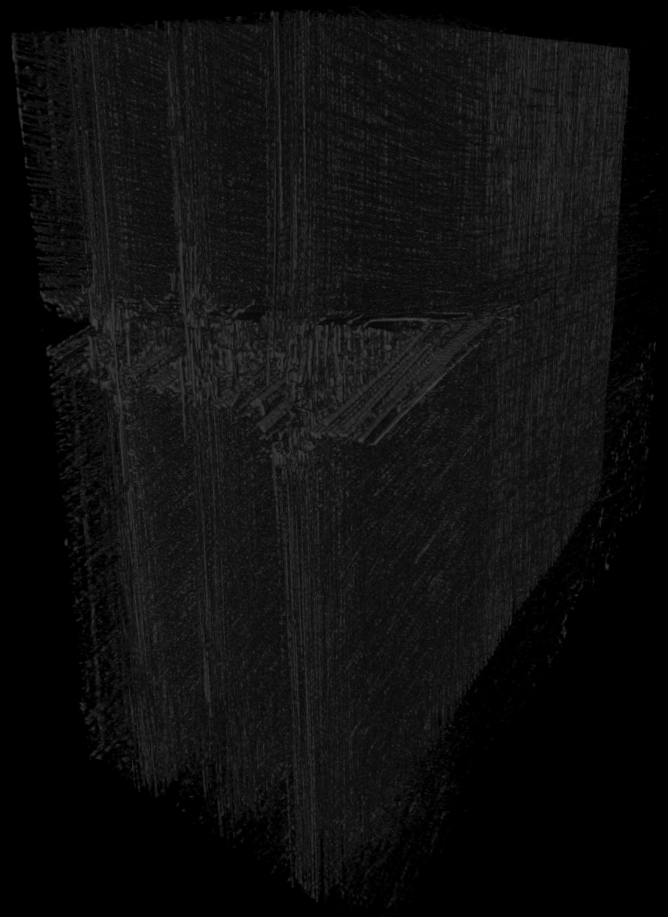

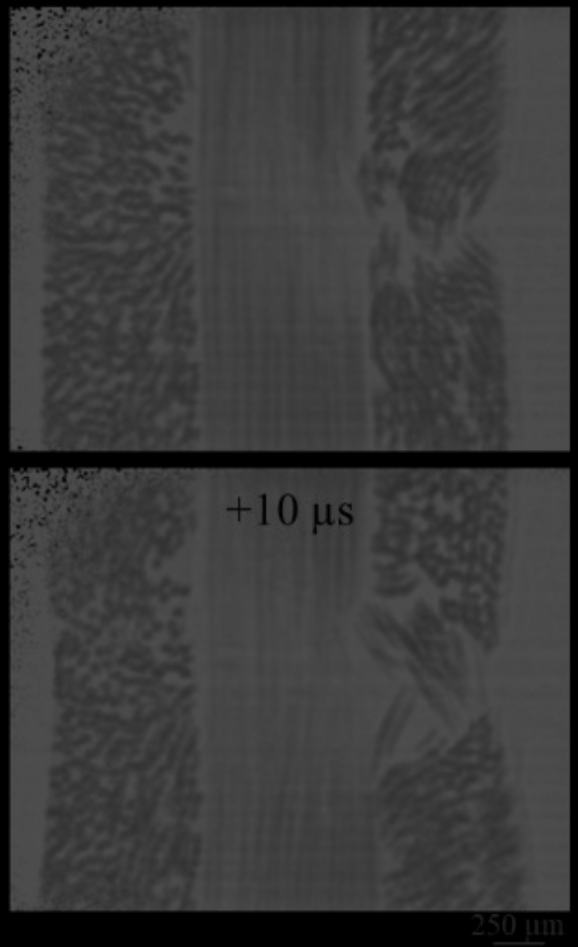

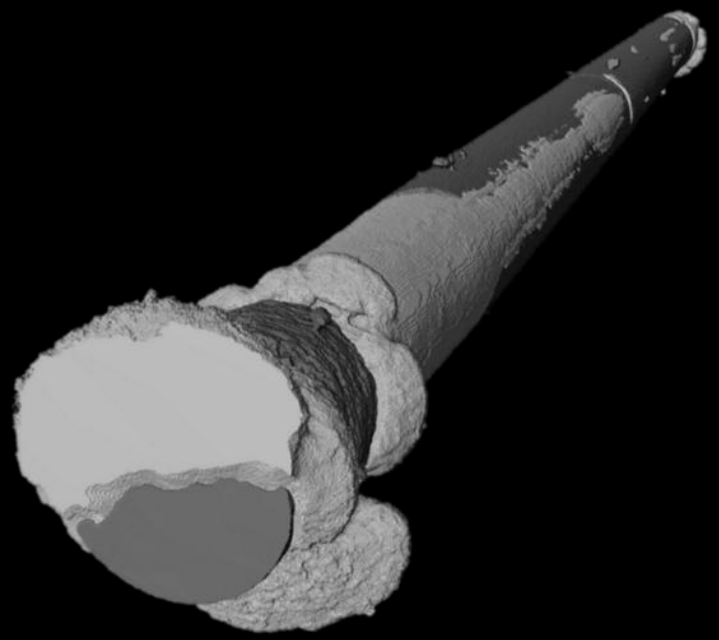

The basics of holotomography

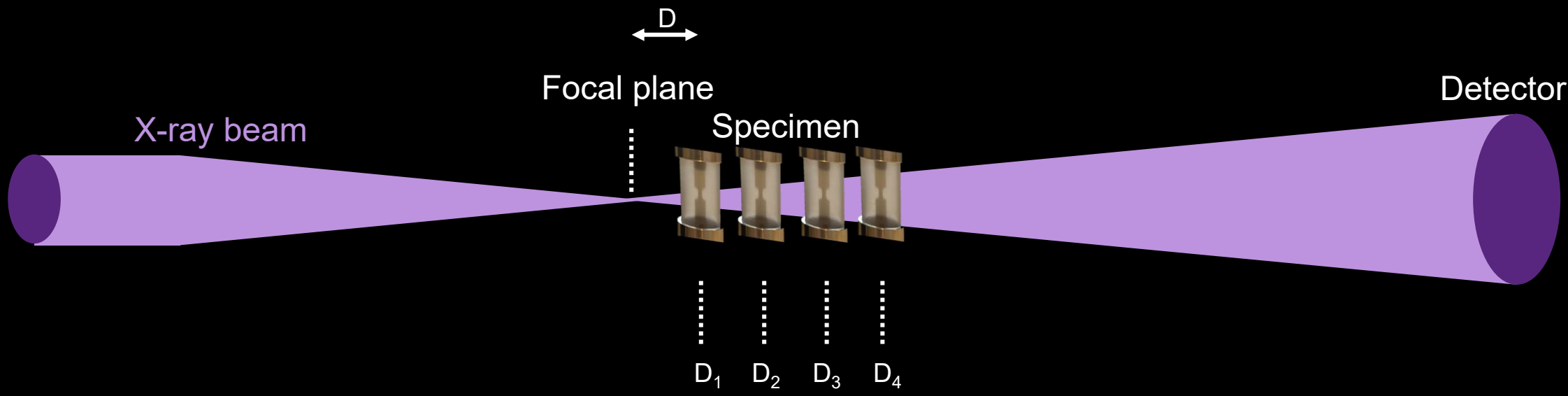

The benefits of full phase contrast retrieval

Attenuation contrast: $I = I_0 e^{-\mu d}$ (Beer-Lambert law)

- μ = attenuation coefficient ~ Z^4
- d = thickness of material

Phase contrast:

- Very sensitive to changes in refractive index
- ➔ Great at matrix-air and air-fibre interface

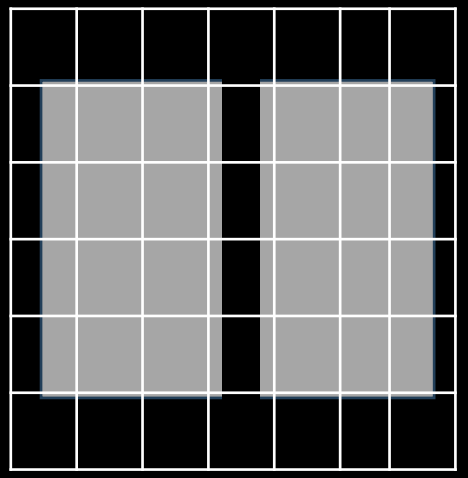

Setup and load rig at ID16B (ESRF)

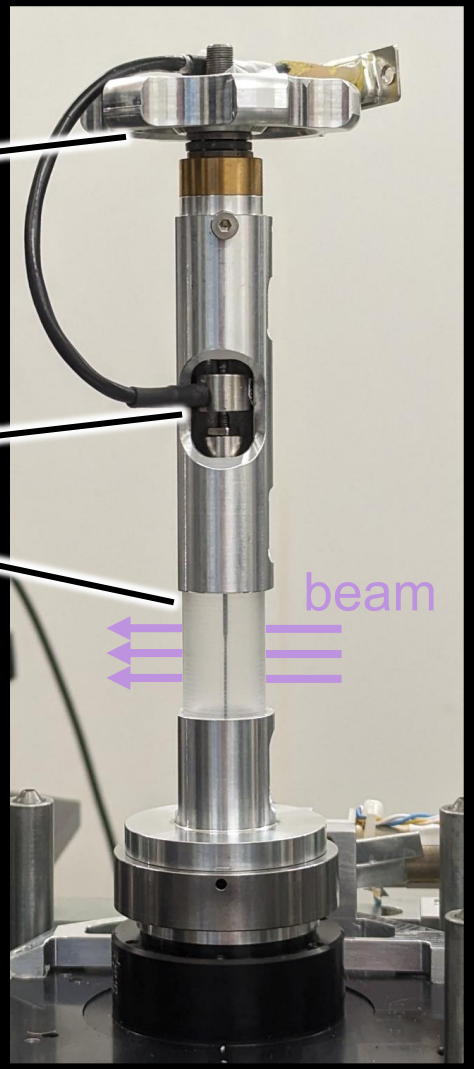

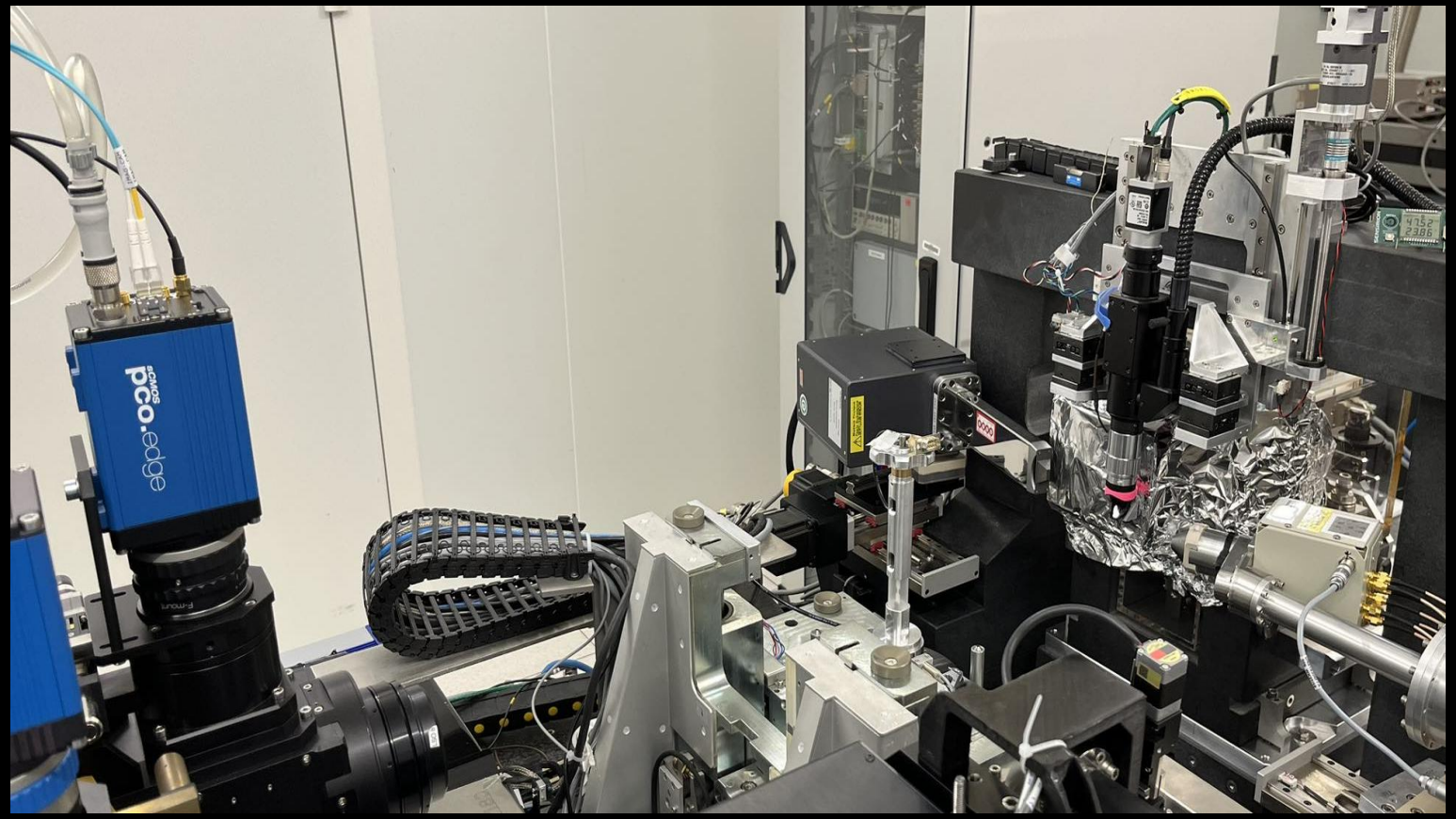

Damage development in single-fibre composites

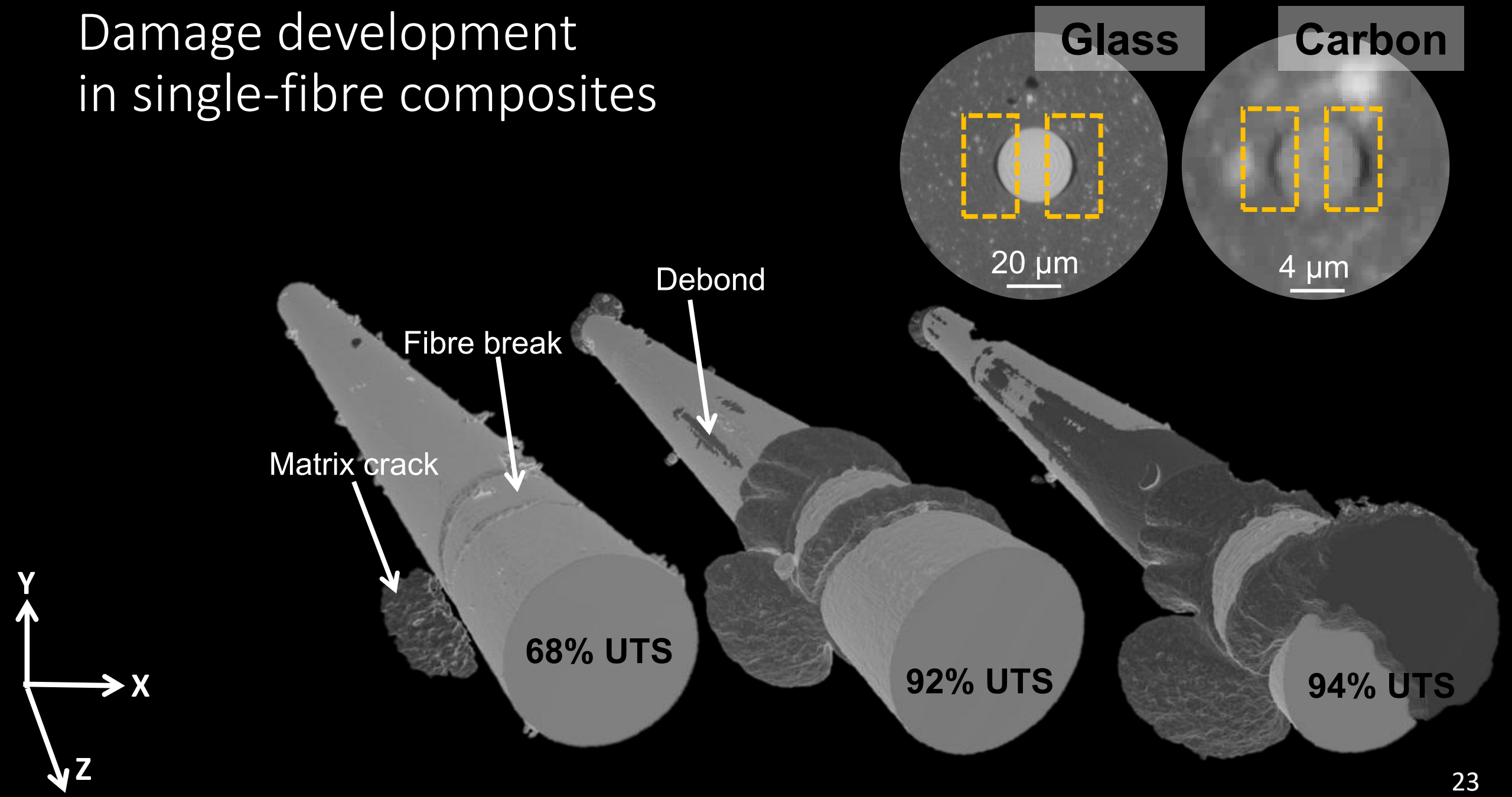

Damage development in glass multi-fibre composites

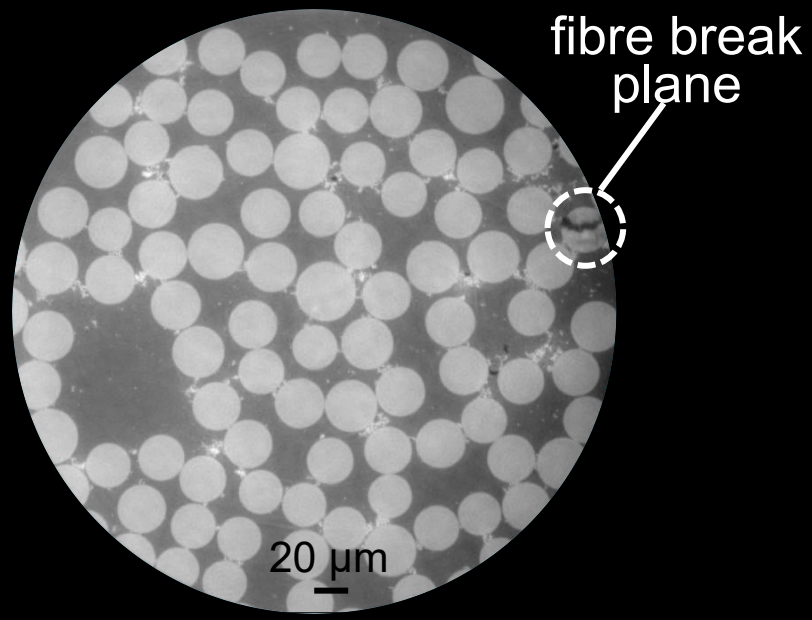

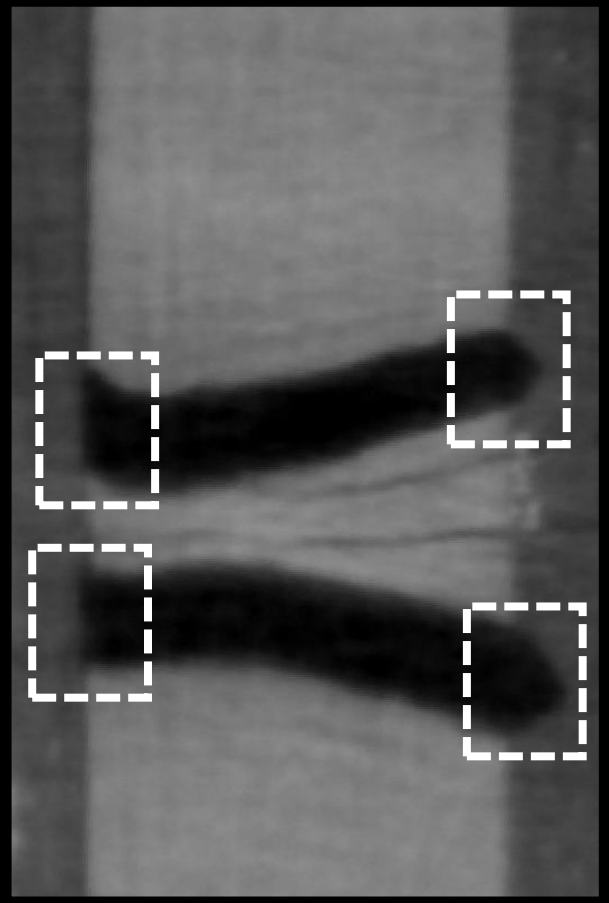

90% UTS

Holotomography
Future challenges and opportunities

Challenges:

- Availability: ESRF ID16B (and potentially PETRA III P05)
- Reconstruction
- Rigs

Opportunities

- Even higher resolutions (50 nm!)
- Ptychography (ID16A)

Conclusion

New technique development
- Multidisciplinary work
- Requires beamline scientists
- Specialised rigs

New capabilities
- Enable new insights
- Challenge models

Software needs
- Ultrafast = lots of data
- Reconstruction algorithms

What's next? - Multiprojection imaging

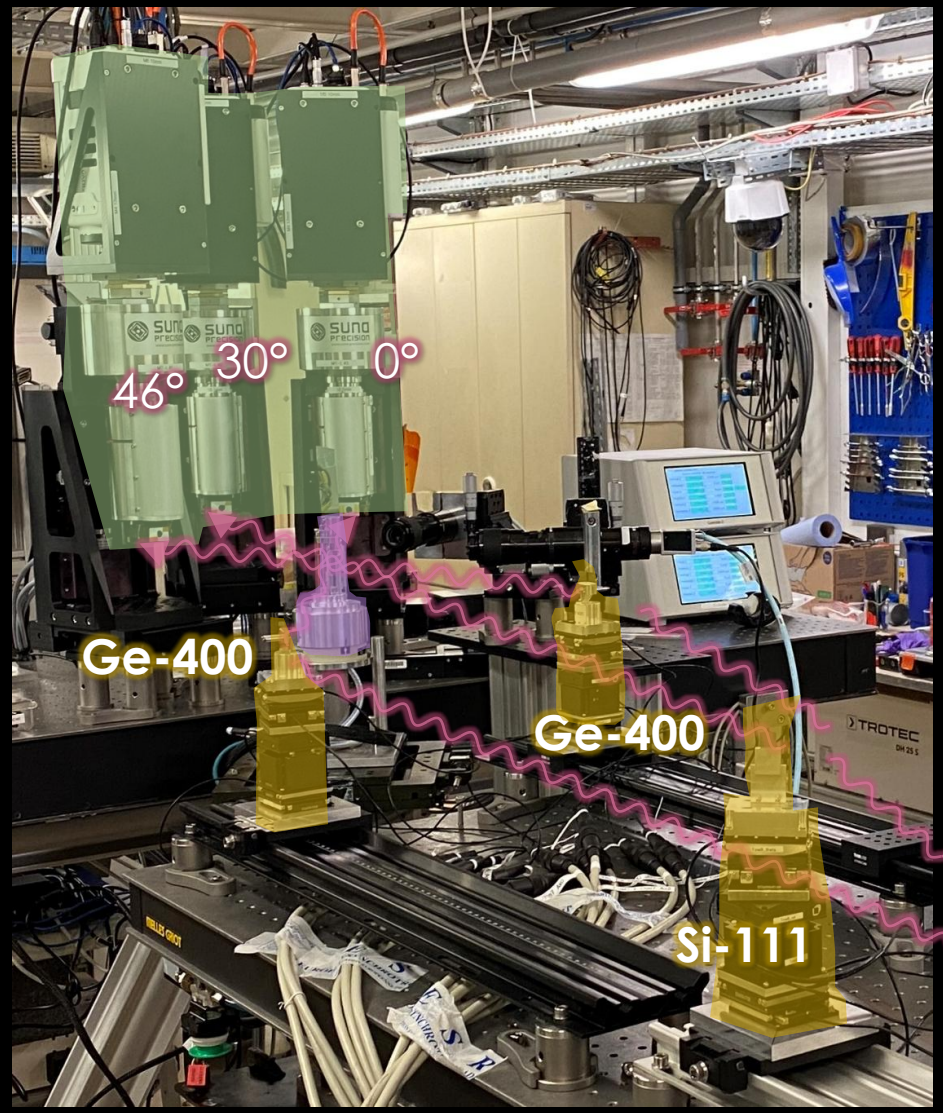

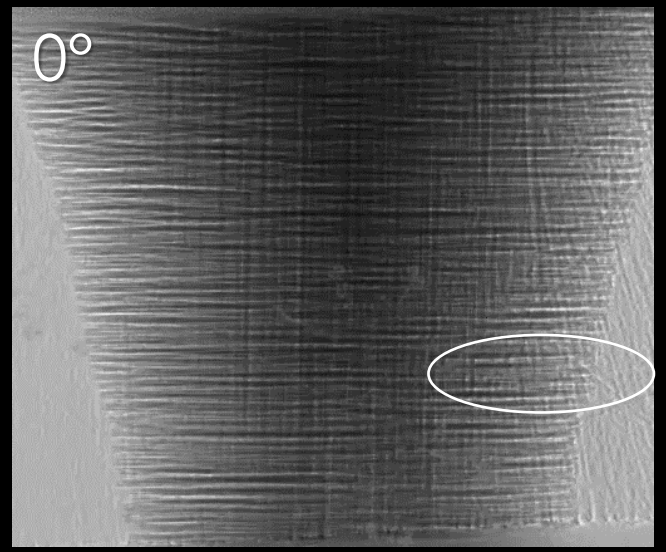

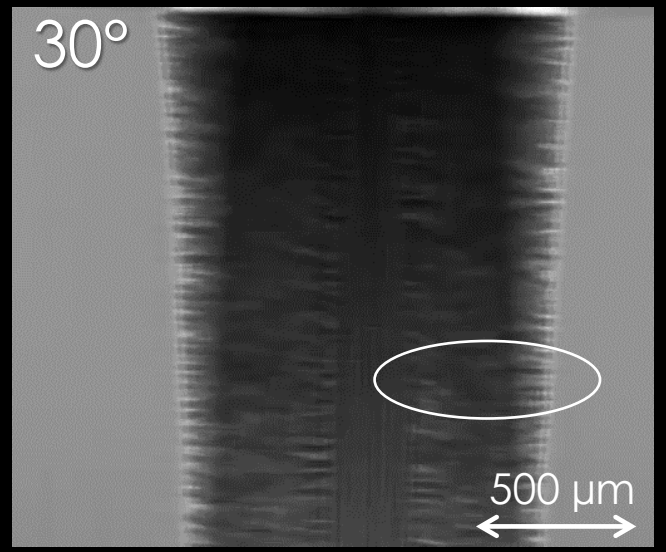

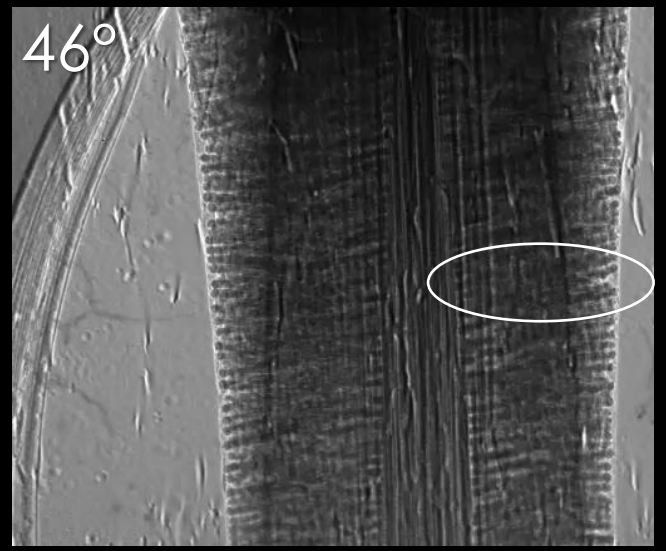

What's next? – X-ray free electron laser (XFEL)

Much brighter than conventional synchrotron light

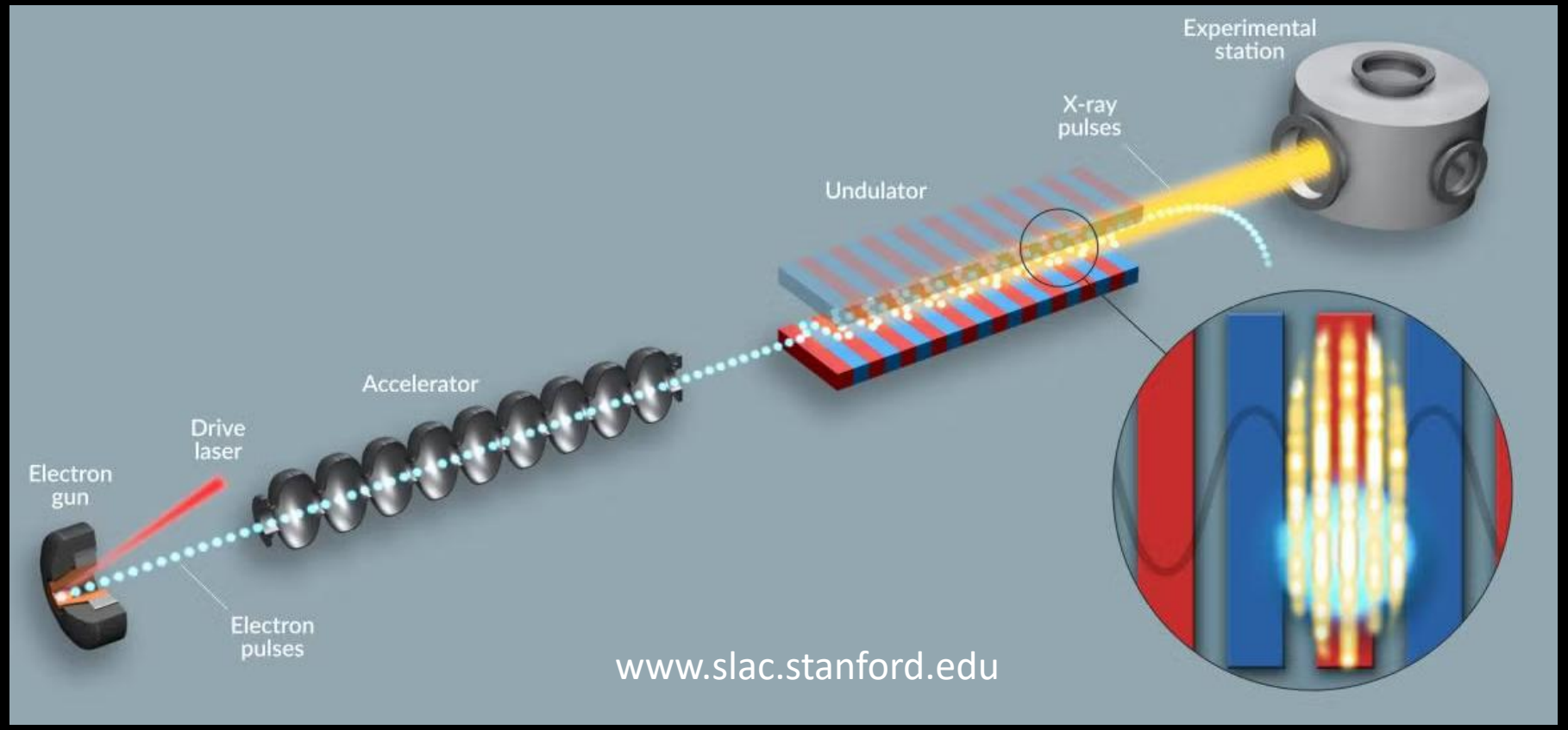

Contributors


Elise Van Vlierberghe


Thanasis Chatziathanasiou


Mahoor Mehdikhani


Sina AhmadvashAghbash


Christian Breite

LUND UNIVERSITY


Pablo Villanueva-Perez

Kelly Prize

Challenges and opportunities in synchrotron computed tomography imaging of composites

Yentl Swolfs
+ Elise Van Vlierberghe, Thanasis Chatziathanasiou,
Sina AhmadvashAghbash, Mahoor Mehdikhani, Christian Breite

05-08-2025

KU LEUVEN

Composite Materials Group

Toward Autonomous Qualification of Aerospace Composites: From AI-Driven Calibration to Digital Estimation of Allowables

Navid Zobeiry, PhD (navidz@uw.edu)
Associate Professor, Materials Science & Engineering Department
Adjunct Associate Professor, Aeronautics and Astronautics Department
University of Washington

http://composites.uw.edu

BE BOUNDLESS

Aerospace Certification Process: Analysis Supported by Testing

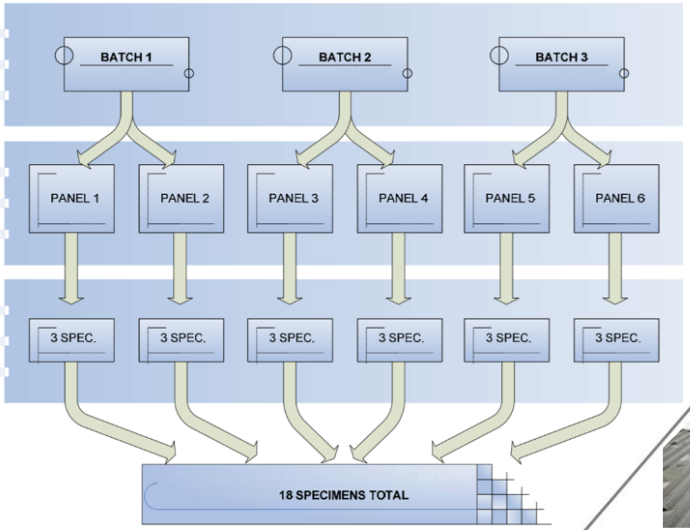

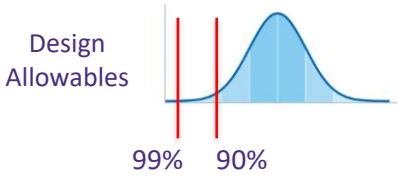

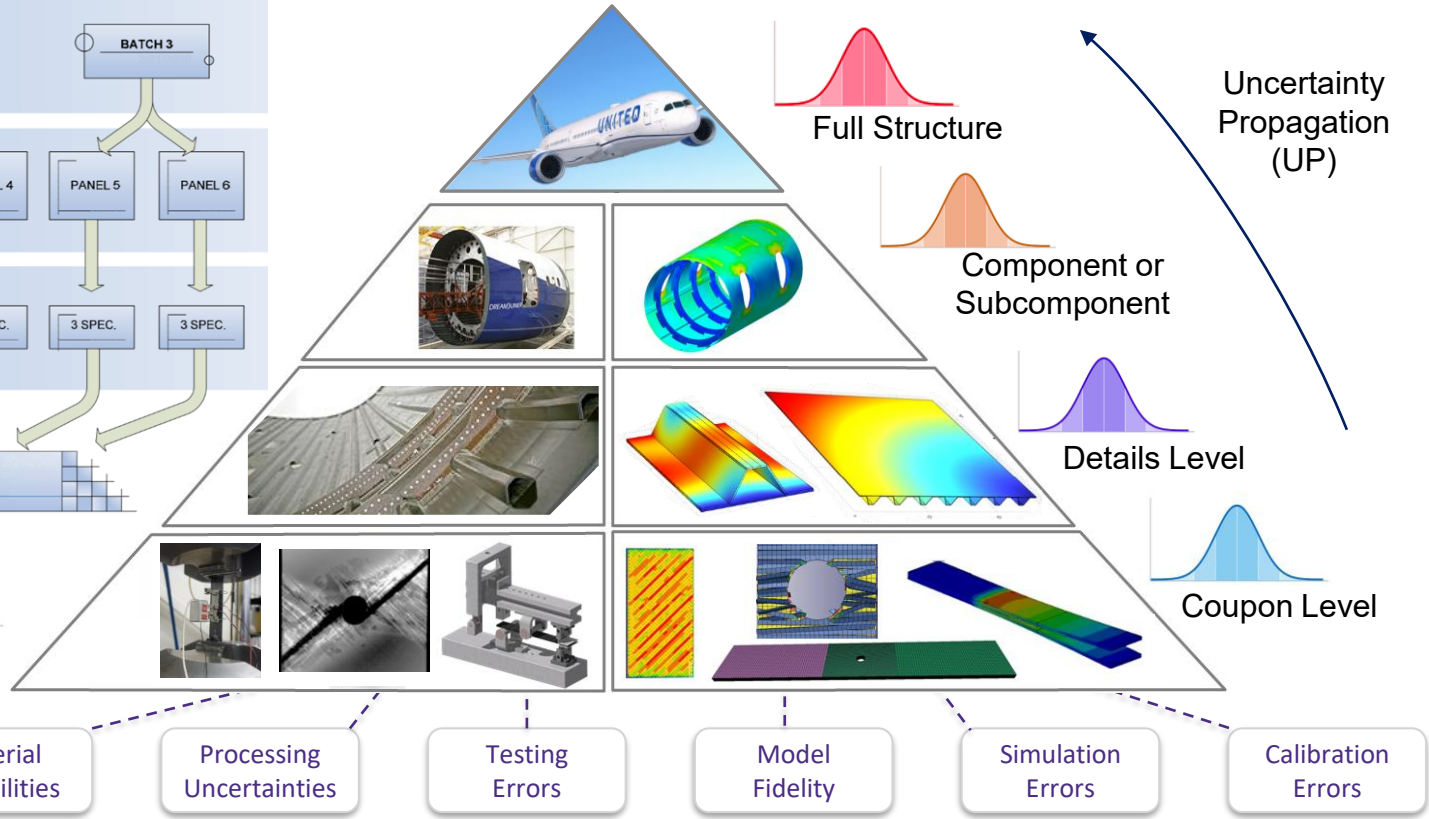

Material Variabilities and Processing Uncertainties

Raw Material



Lay-up



Vacuum Bagging

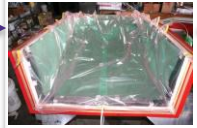

Curing



Sample Prep.

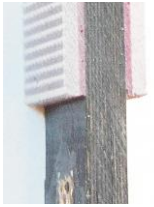

Testing



Matrix Weight%
Fiber Areal W.
Out-time
Humidity
Fiber Diameter
…

Tool Tolerance
AFP Speed
AFP pressure
AFP steering
Temperature
…

Bagging Steps
Bagging Pleats
Bagging Leaks
Vac. Pressure
Debulking cond.
…

Autoclave Load
Tool Nesting
Autoclave airflow
Temperature cycle
Pressure cycle
…

Cutting method
Tabbing
Adhesive thickness
…

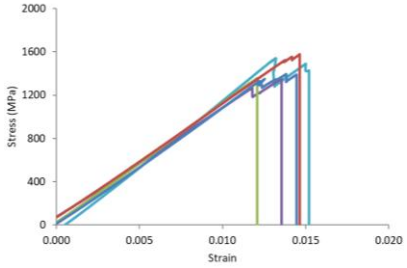

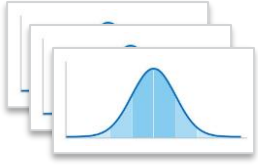

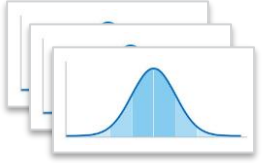

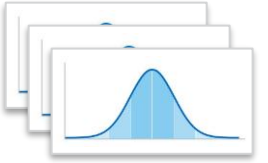

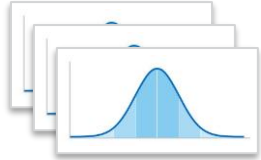

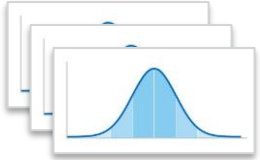

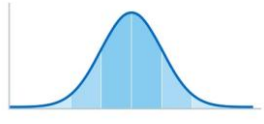

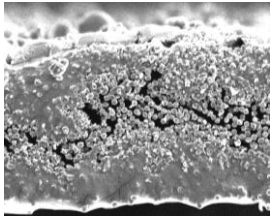



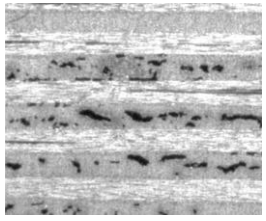

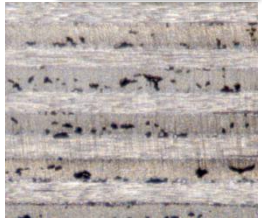

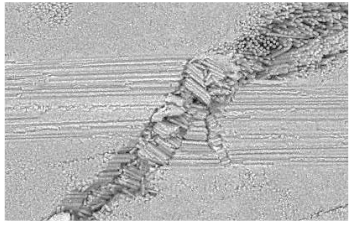

Current Industry Approach

> Current approach, requires engineers to manually set-up problems in a preprocessor, submit the simulation, and analyze the results. They rely on experience and know-how and repeat this process, until the model is calibrated.

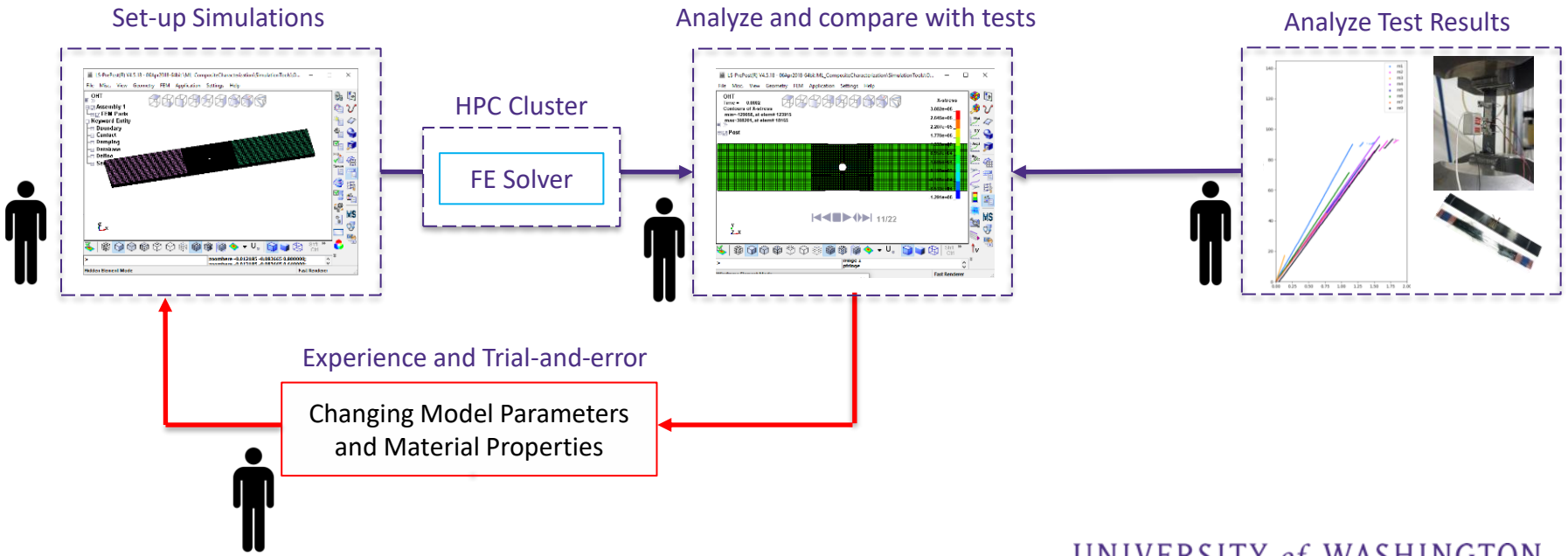

CFACS: an Autonomous Framework to Assist Certification

Automatic Pre- and Post-Processing, and FE submission

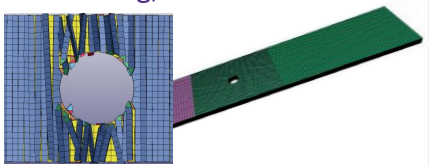

Automatic Calibration and Optimization

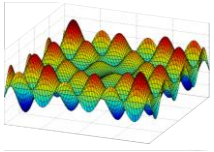

Automatic Test Outlier Detection

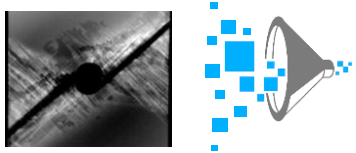

Sensitivity Analysis & Uncertainty Quantification

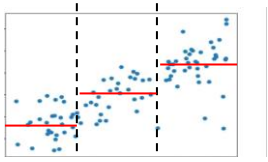

Statistical Analysis, Advanced Analytics & Machine Learning

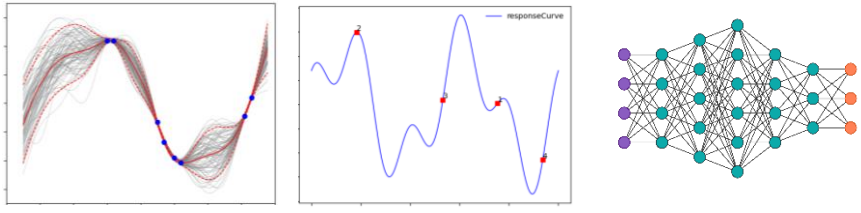

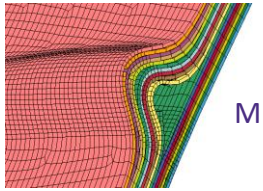

TIEBREAK
Mixed mode delamination

Fiber aligned MAT 261

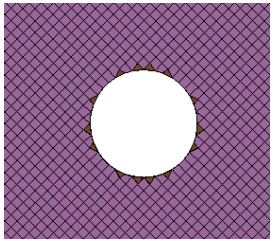

MAT 138 Cohesive

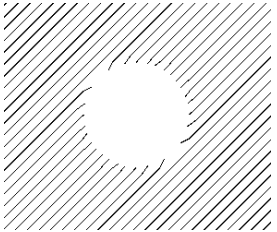

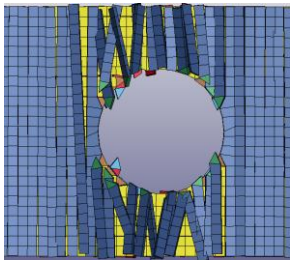



2023 NAFEM World Congress Award

Patent# US20230252206A1
Patent# US12189376B2

Outliers in Small Data

Example:
Open Hole
Tension (OHT) Test

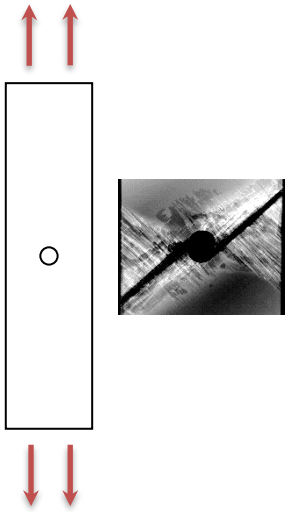

Load-displacement Outlier Types

Type 1: premature failure

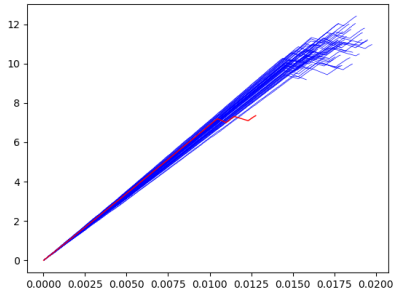

Type 2: stiffness mismatch

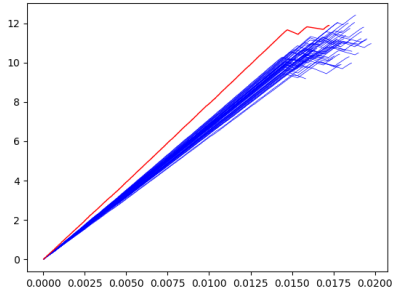

Type 3: stiffness variation

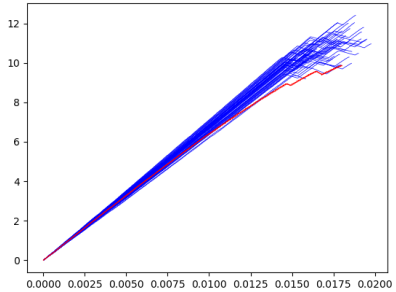

Type 4: mismatch in jumps

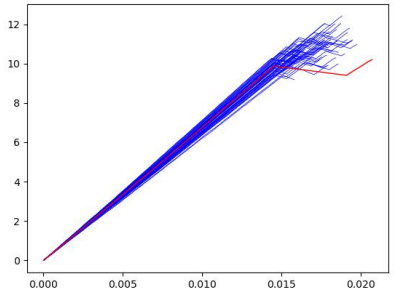

Type 5: noisy data

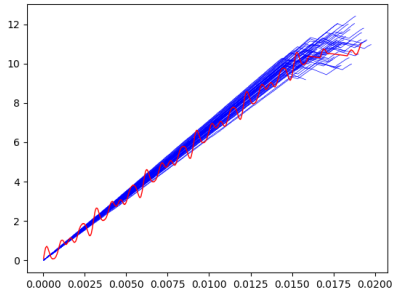

Type 6: premature jumps

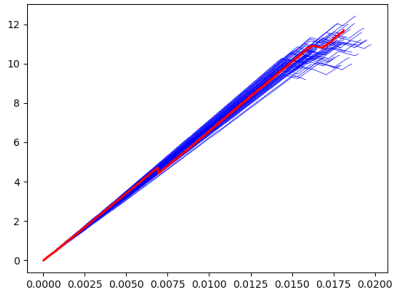

Noise and Outlier Detection

Tests Data

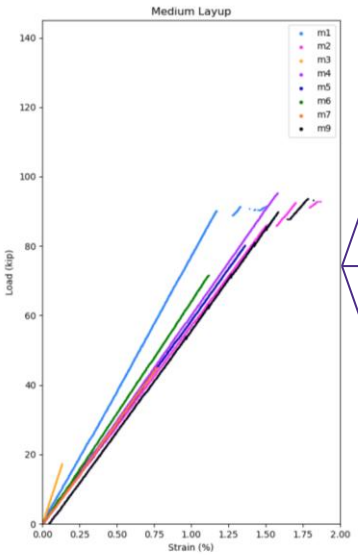

Features

All features
- Force –Displacement
- Failure images
- …

Selected Features
- Peak load
- Load drops
- …

Engineered Features
- Derivative of data (stiffness)
- Integral of data (energy)
- …

Outlier Detection Methods

- SG error
- PCA eigen value
- PCA eigen vector
- RPCA
- …

Results

Matrix of results

	Test 1	…	Test n
Method 1	Outlier		
…			
Method m		Outlier	

Identify Outlier Type and potential Cause

- **Type-1**: Pre-mature failure
- **Type-2**: Distant stiffness variation
- **Type-3**:Stiffness error test fixture influence
- **Type-4**: Nonlinear variation due to MV
- **Type-5**: Sparse & Noisy data
- **Type-6**: Unexpected sharp load drop

Outlier detection and management, Patent# US12189376B2, 2025

Noise and Outlier Detection: RPCA

> RPCA (Robust Principal Component Analysis) learns the underlying low rank data (L) and noise (S), from the observed data (Y), by solving an optimization problem:

$$minimize(\|L\|_* + \lambda\|S\|_1)\ subject\ to\ Y = L + S$$

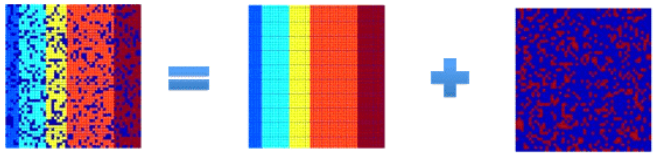

Original Data	$Y = L + S$
Noise	S
Corrected Data	L

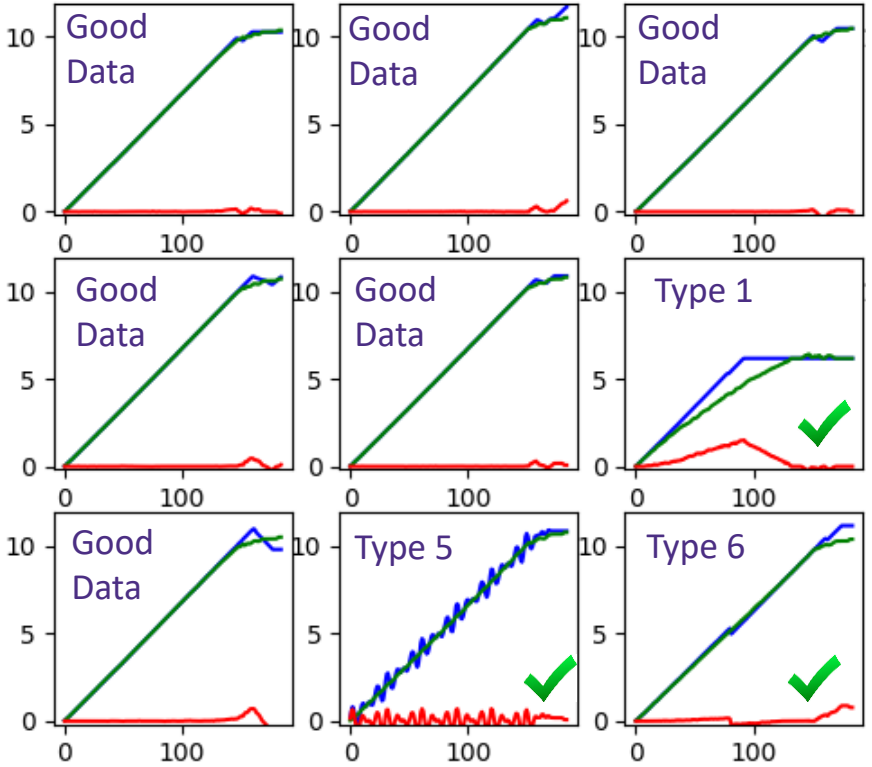

Background: Gaussian Process Regression (GPR)

- Gaussian Process Regression (GPR) models the unknown function using two key assumptions:
  - At each input, the prediction is a Gaussian distribution (mean + uncertainty).
  - Nearby points are correlated using a kernel function (e.g., smoother if inputs are close).

Small experimental data

$Y(X)|D_n$

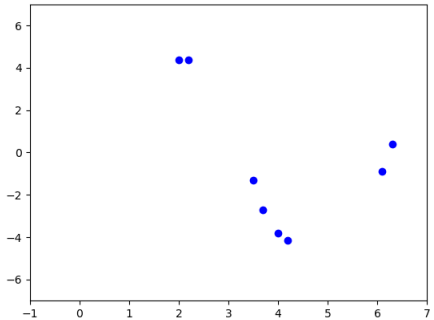

Unknown True response

$Y(X)$

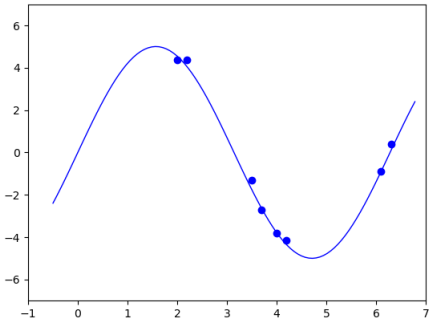

Probabilistic Machine Learning

$D_n \sim N(\mu(x), \sigma^2(x))$

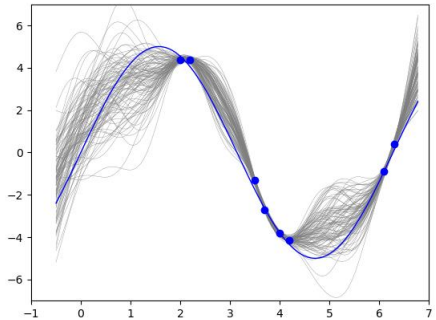

Zone of confidence interval

$\mu(x) \pm Z \times \sigma$

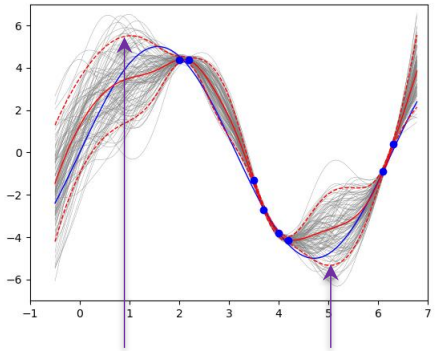

Background: Shape of COV matrix (Kernel)

Dot product

$\Sigma = x.x' + c$

Polynomial

$\Sigma = (x.x' + c)^3$

RBF
(Radial Basis Function)

$\Sigma = e^{-\gamma\|x-x\prime\|^2}$

Mix

$\Sigma = (x.x' + c)^3 + e^{-\gamma\|x-x\prime\|^2}$

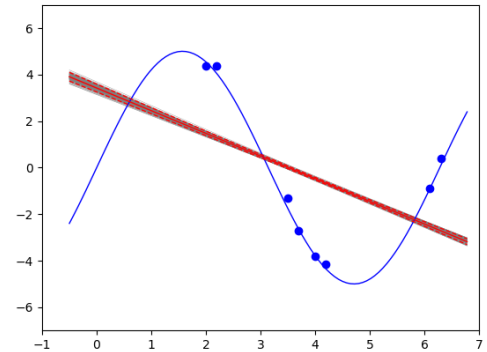
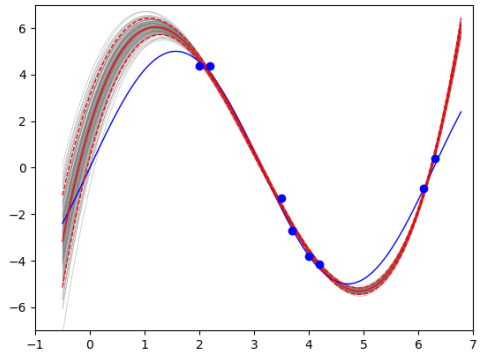
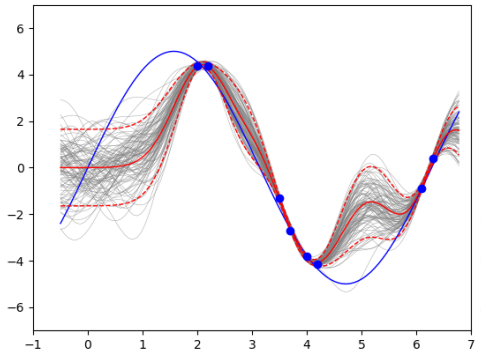
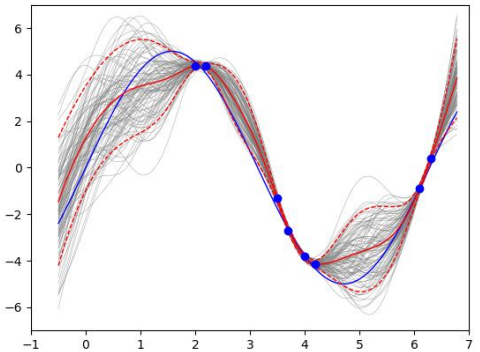

Initial GPR Training

> The initial GPR kernel was trained using prior simulation results. For each new case, it is then fine-tuned using a limited amount of data from that problem.

Example: Compact Compression
(15000 simulations)

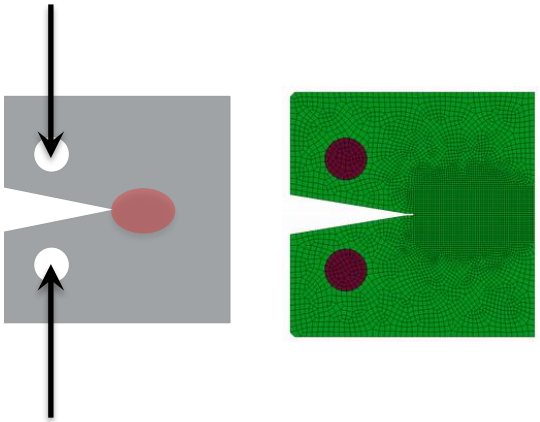

FE Inputs (material models)

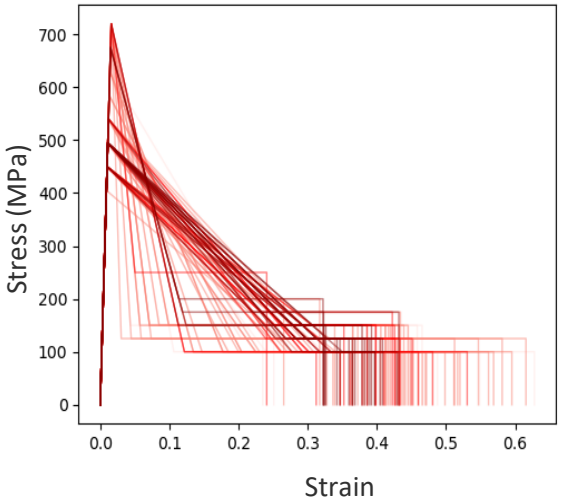

FE Outputs

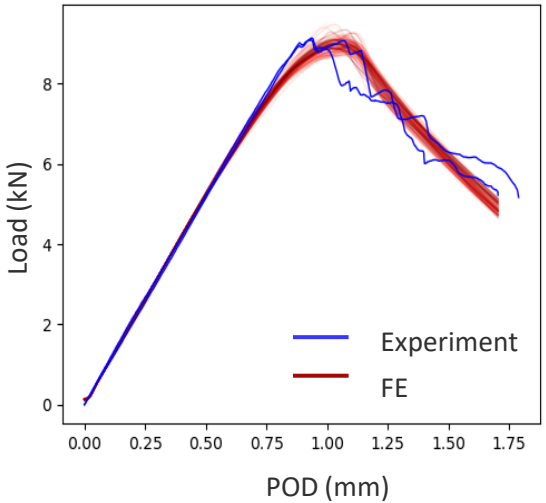

Reiner, J., Vaziri, R., & Zobeiry, N. (2021). Machine learning assisted characterisation and simulation of compressive damage in composite laminates. Composite Structures, 273, 114290.

Automatic FE Calibration using Machine Learning

Experimental Data

Automatic Simulation Data

Iteration

Compare Simulation with Test

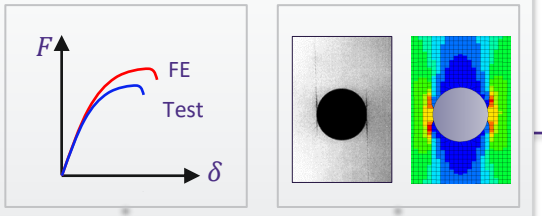

Fine-Tuning GPR

Initial GPR Training

Global Optimization

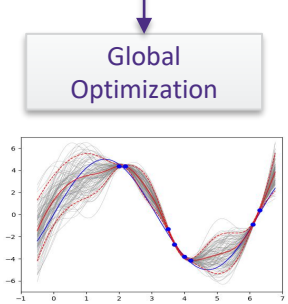

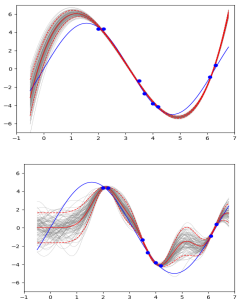

Automatic Selection of FE Inputs

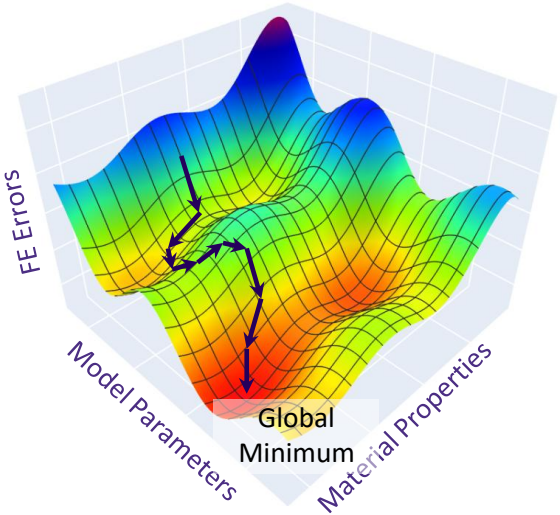

Simulation Model Validation for Structure Material Characterization, Patent# US20230252206A1, 2023

Case Study 1: In-plane Shear

- HEXCEL IM7/8552, Layup – $[\pm 45]_S$
- 0.02” element size, ~12,000 elements
- In-plane MAT261, In-plane cohesive MAT138, Interlayer TIEBREAK
- Calibrated parameters: 2 (MAT138, splitting)
- Calibrated with 10 simulations to <2% peak load error

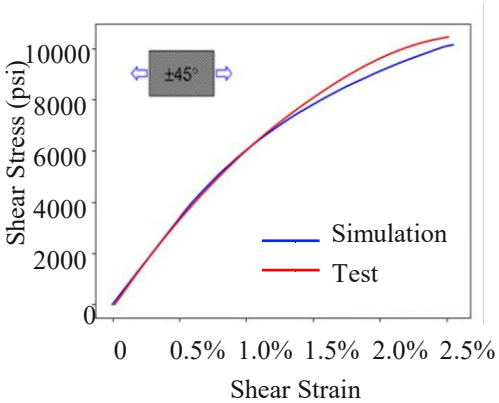

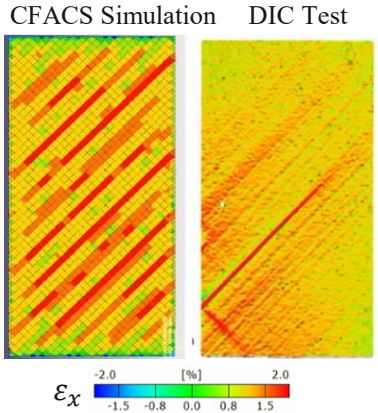

Case Study 2: Double Cantilever Beam (DCB)

- HEXCEL IM7/8552, UD Layup
- In-plane MAT261, Interlayer TIEBREAK
- Calibrated to <2% peak load error
- Calibrated parameters: 2 (delamination)
  - TIEBREAK: mode I fracture toughness
  - TIEBREAK: strength

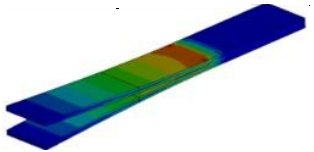

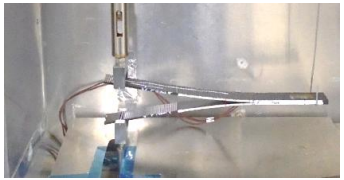

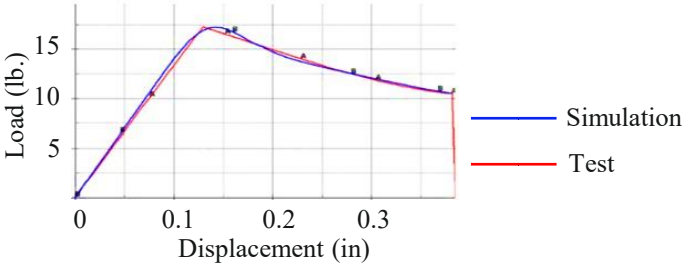

Zobeiry, Navid, Ashith Joseph, Amirali Eskandariyun, Huilong Fu, Steven Brunton, Byar Alan, Mohammed Kabir et al. "Hybrid Physics and Machine Learning Modeling for Material Characterization and Failure Analysis." In AIAA SCITECH 2024 Forum, p. 1526. 2024.

Case Study 3

- HEXCEL IM7/8552
- In-plane MAT261, Interlayer TIEBREAK
- Calibrated with 11 simulations to 1% error
- Calibrated parameters: 6
  - MAT261 : fiber fracture toughness in tension
  - MAT261 : matrix fracture toughness in tension
  - MAT261 : matrix fracture toughness in shear-T
  - MAT261 : matrix fracture toughness in shear-L
  - TIEBREAK : mode I fracture toughness
  - TIEBREAK : mode II fracture toughness

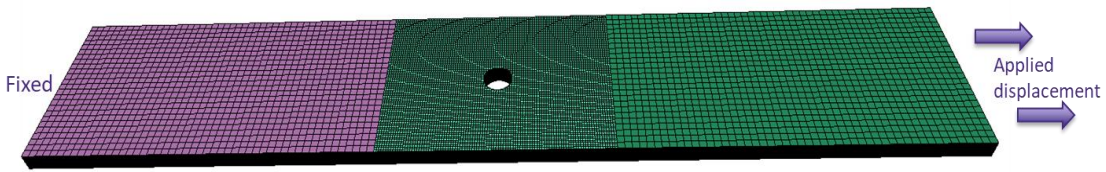

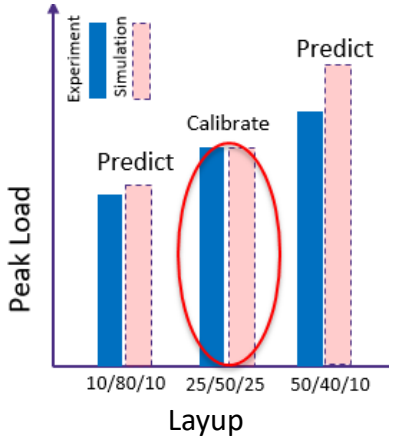

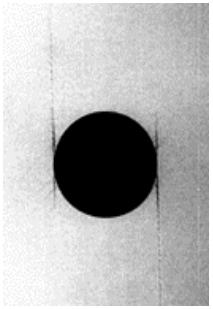
CT Scan

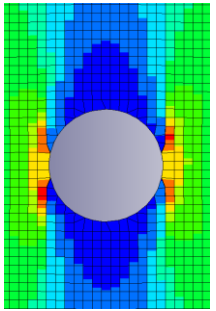
Simulation

Task	Layup	Peak Load Error
Calibration	Medium (25/50/25) Laminate $[45/0/-45/90/45/0/-45/90]_S$	<2%
Validation	Soft (10/80/10) Laminate $[45/-45/0/45/-45/90/45/-45/45/-45]_S$	-3.5%
Validation	Hard (50/40/10) Laminate $[0/45/0/90/0/-45/0/45/0/-45]_S$	4.1%

Zobeiry, Navid, Ashith Joseph, Amirali Eskandariyun, Huilong Fu, Steven Brunton, Byar Alan, Mohammed Kabir et al. "Hybrid Physics and Machine Learning Modeling for Material Characterization and Failure Analysis." In AIAA SCITECH 2024 Forum, p. 1526. 2024.

Digital Estimation of Allowables

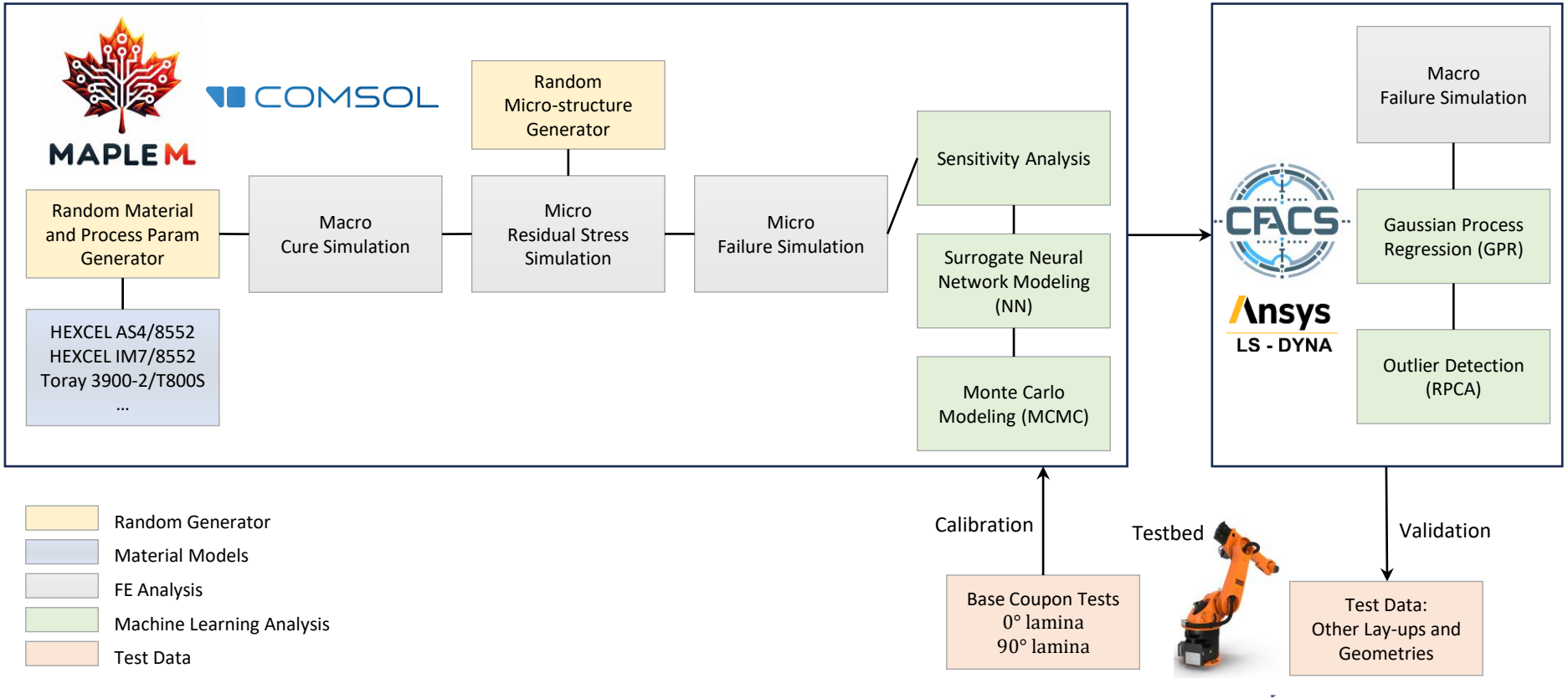

MAPLE/ML: MAterials PLayground for Engineers powered by ML

Stochastic Integrated Process and Failure Analysis

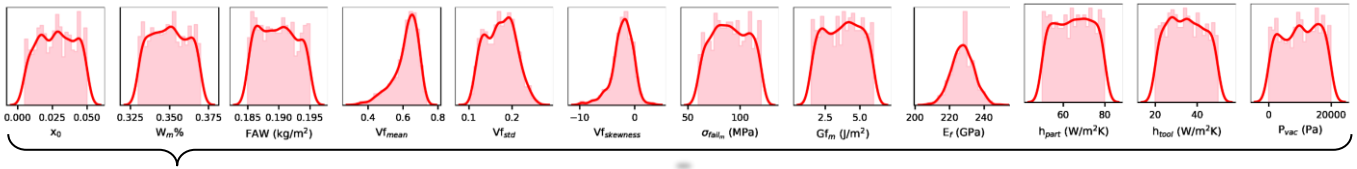

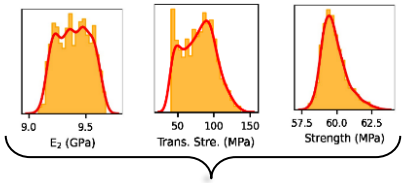

Distributions of Inputs

Resin:
- Initial Degree of Cure
- Strength
- Fracture Energy

Fiber:
- Diameter
- Strength
- Fracture Energy

Prepreg:
- Matrix Weight Fraction
- Fiber Areal Weight
- Lay-up
- Ply thickness

Autoclave:
- Heat Transfer Coefficient
- Tooling Material and thickness
- Temperature Cycle
- Pressure cycle

…

Processing

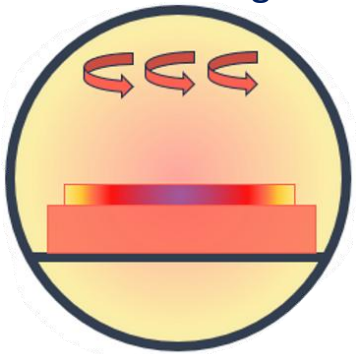

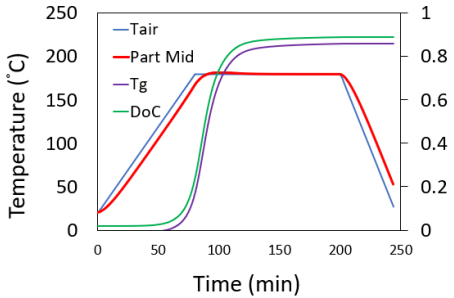

Residual Stresses

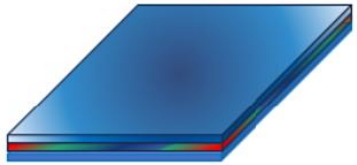

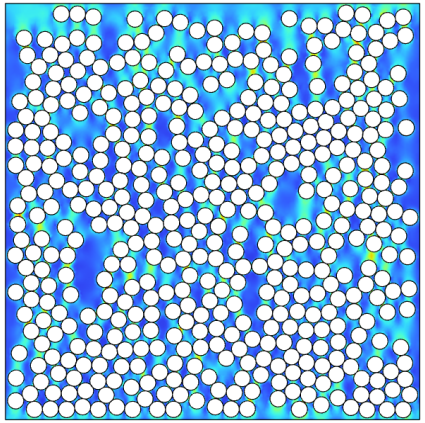

Ply-level Failure



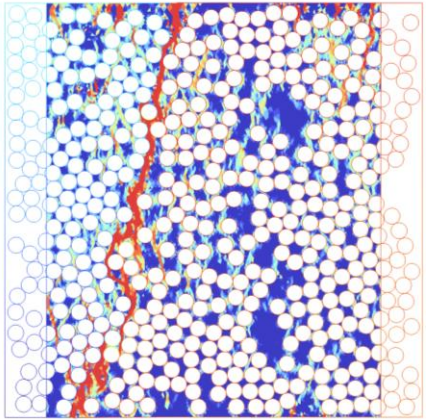

A Multi-Fidelity Approach

COMSOL & Python
Low-fidelity FE
1000 simulations (<2 days)

COMSOL & Python
High-fidelity FE
50 simulations (<1 week)

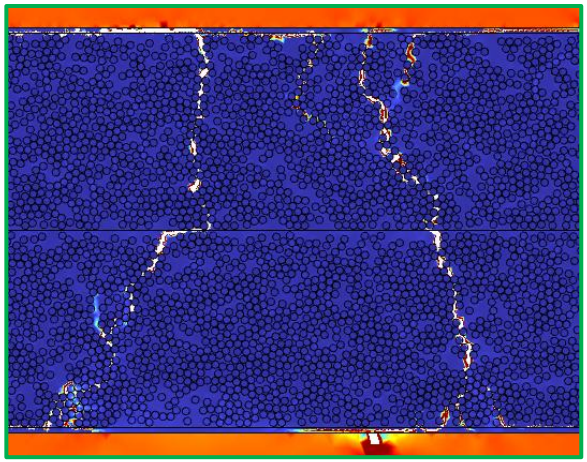

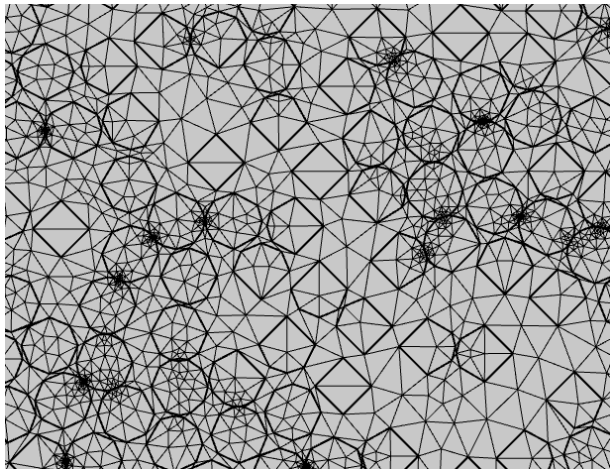

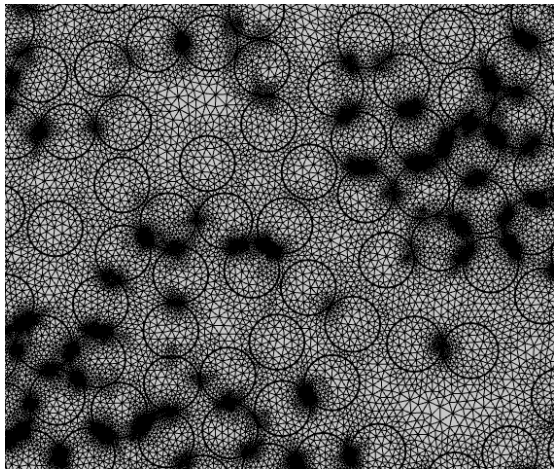

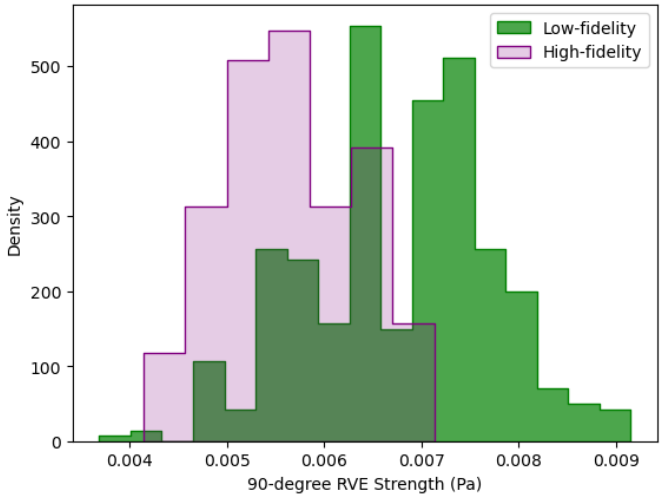

SOBOL Sensitivity Analysis: Transverse Tensile Strength

HEXCEL AS4/8552

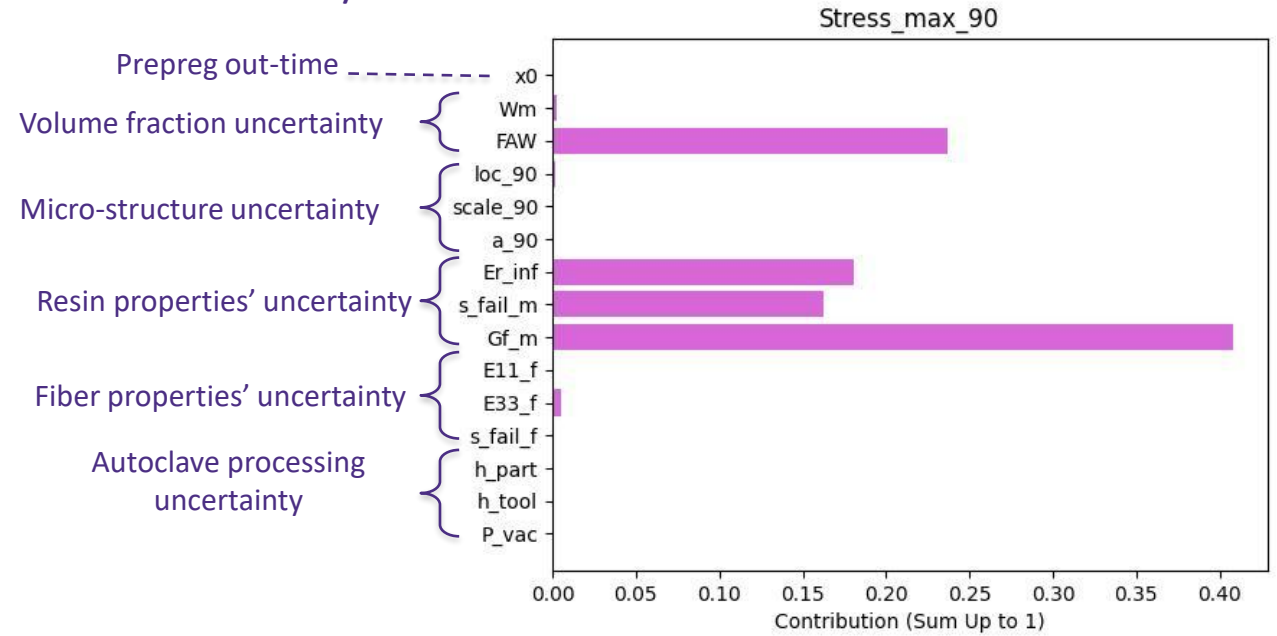

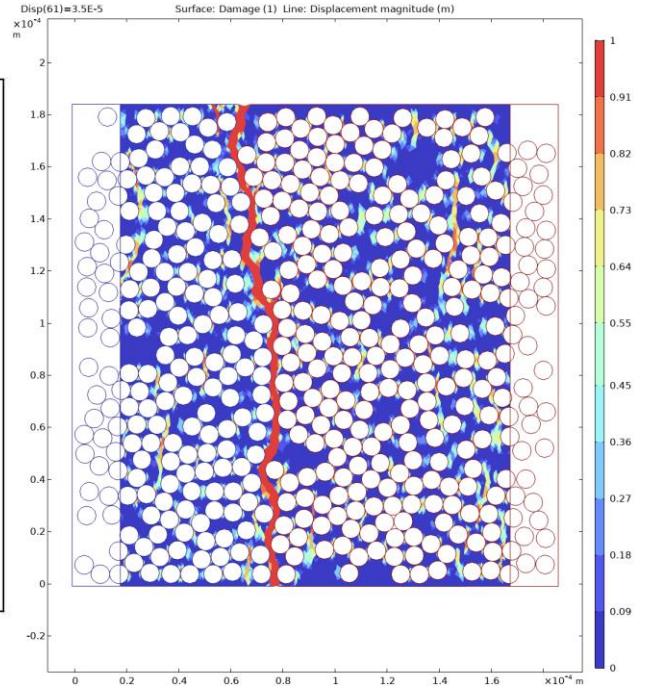

Initial Training and Fine-tuning Surrogate ML models

1000 Low-Fidelity FE Data

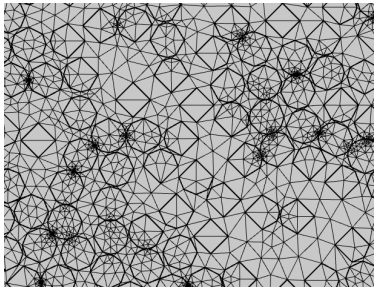

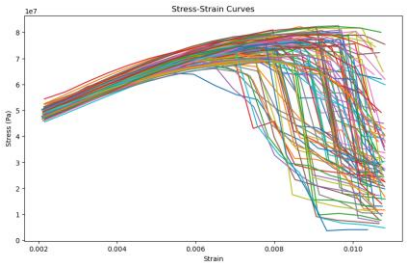

Initial Training

Neural Network

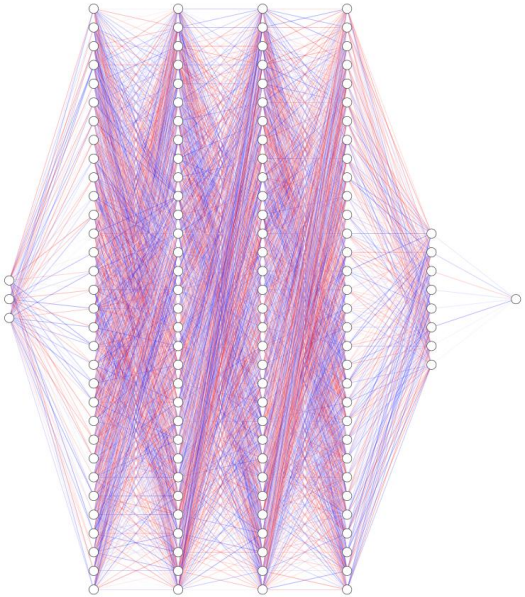

Fine-tuning

50 High-fidelity FE Data

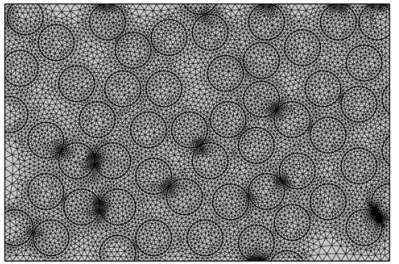

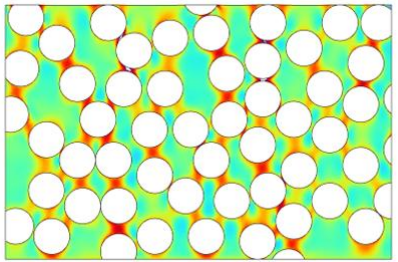

Fine Tuning with High-Fidelity Data

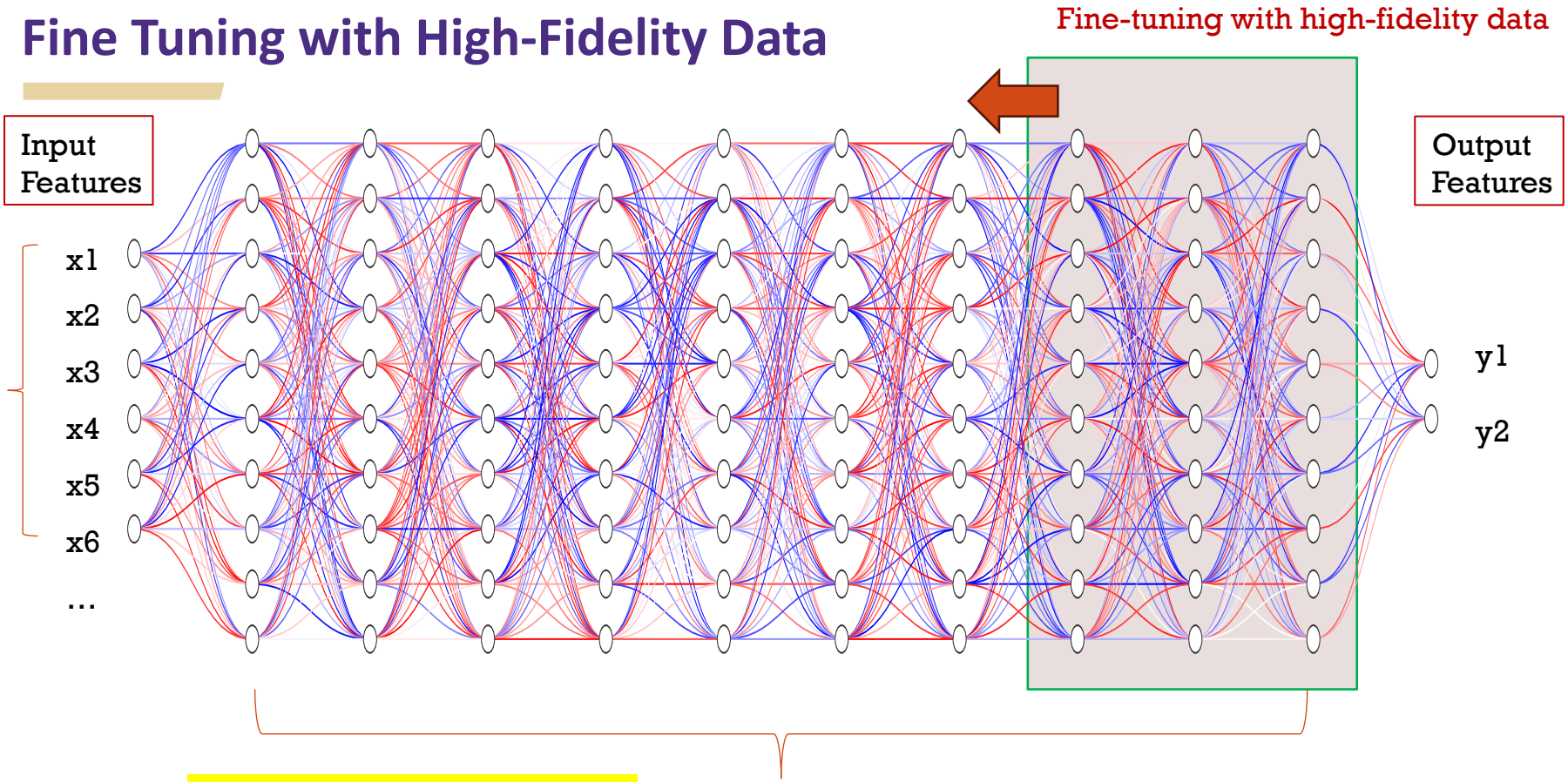

Uncertainty Quantification with Markov Chain Monte Carlo (MCMC)

Test Data: Transverse Strength

HEXCEL AS4/8552 $[90]_{11}$

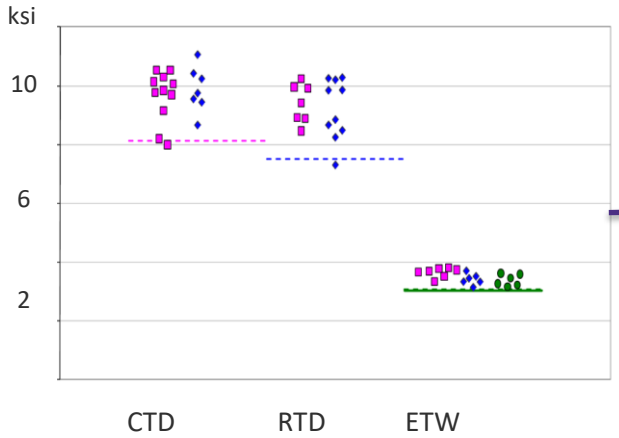

Environmental Conditions

Trained NN + MCMC

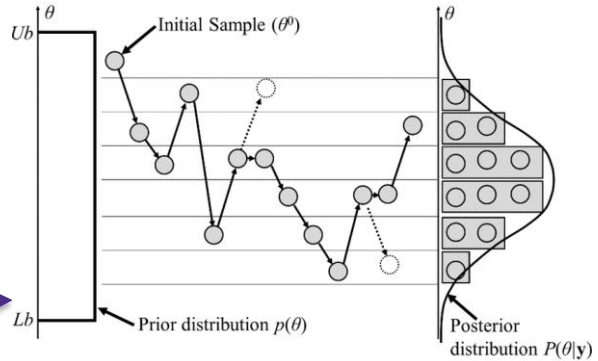

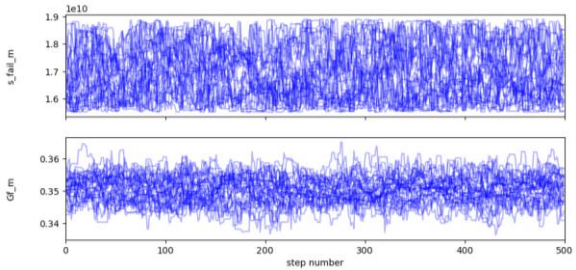

Quantify Uncertainties

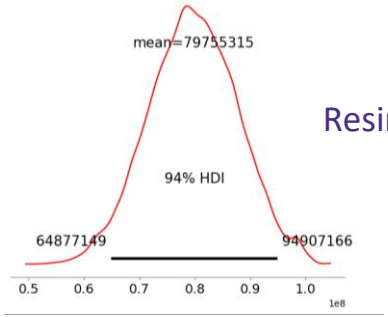

Resin Strength (Pa)

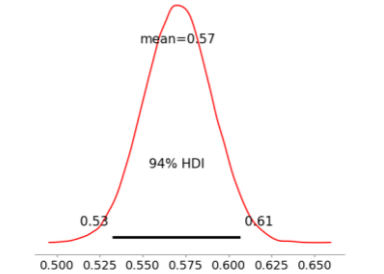

Volume fraction

Clarkson, E. (2011). Hexcel 8552 AS4 unidirectional prepreg qualification statistical analysis report. FAA special project no SP4614WI-Q, Report No NCP-RP-2010-008 Rev D," Wichita State University, USA.

Eskandariyun, Amirali, et al. "A Novel Machine Learning Framework for Digital Estimation of Allowables in Aerospace Composites." ASME Aerospace Structures, Structural Dynamics, and Materials Conference. Vol. 87745. American Society of Mechanical Engineers, 2024.

Lamina Level: Digital Estimation of Allowables

- 50 simulations were conducted using the distributions of inputs from previous step.
- Cross-ply Failure Simulation (LS-DYNA, MAT261)

- Matrix weight fraction
  (normal|0.37|0.003)
- Autoclave Heat Transfer Coefficients
  (normal|70|10) W/m^{2}K (bag side)
- Autoclave Heat Transfer Coefficient
  (normal|35|10) W/m^{2}K (tool side)
- Matrix strength
  (normal|79.7E6|7.97E6) Pa
- Matrix fracture energy
  (normal|2.485|0.24) J/m^2
- Fiber strength
  (normal|3.578E9|0.35E9) Pa
- Fiber modulus
  (normal|227.6E+9|6.5E+9) Pa
- Lamina fracture energy (90)
  (normal|3270|430) J/m^2

Inputs

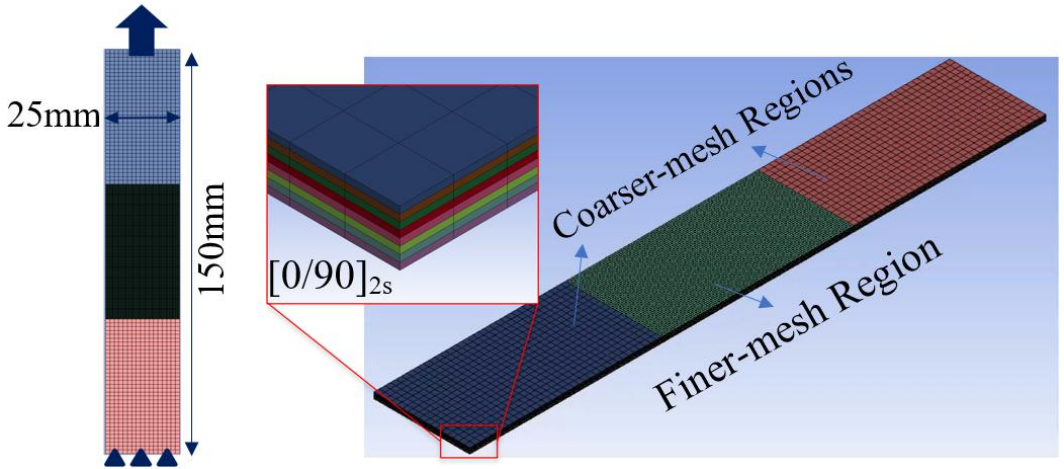

Lamina Level: Digital Estimation of Allowables

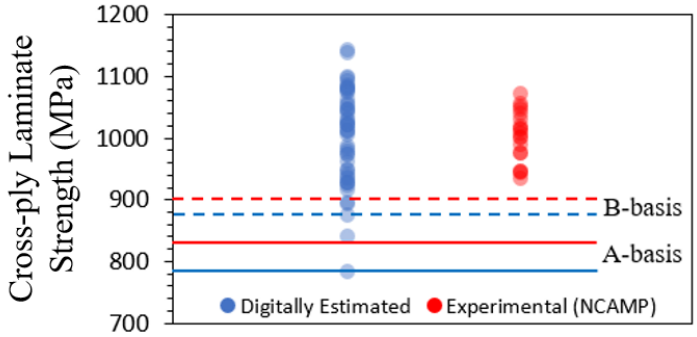

	Estimated (50 Simulations)	Experimental (19 tests)
Mean	1004 (MPa)	1003 (MPa)
C.V.	6.07 %	7.64 %
B-Basis Allowable	878 (MPa) (-2.6%)	901 (MPa)
A-Basis Allowable	785 (MPa) (-5.7%)	833 (MPa)

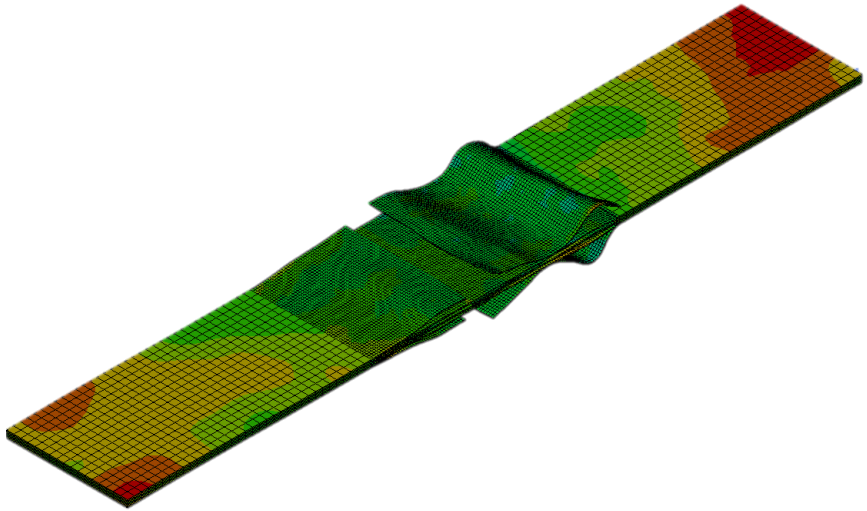

Eskandariyun, Amirali, et al. "A Novel Machine Learning Framework for Digital Estimation of Allowables in Aerospace Composites." ASME Aerospace Structures, Structural Dynamics, and Materials Conference. Vol. 87745. American Society of Mechanical Engineers, 2024.

Conclusions

- We introduced a framework that integrates fast testing, high-fidelity simulations, and machine learning to enable autonomous calibration and digital estimation of allowables.
- Key potential benefits:
  - AI-assisted screening of materials and lay-ups
  - Uncertainty quantification and risk-aware certification
  - Reduced reliance on extensive physical testing
  - Automated, efficient process qualification

- Acknowledgments

BOEING



UNIVERSITY of WASHINGTON

ICCM24 24TH INTERNATIONAL CONFERENCE ON COMPOSITE MATERIALS
AUG 4-8, 2025 • BALTIMORE CONVENTION CENTER • BALTIMORE, MARYLAND

A FAST UNCERTAINTY QUANTIFICATION METHOD FOR FAILURE PREDICTION OF LARGE COMPOSITE STRUCTURAL ELEMENTS

Runze Li[1], Mário Miranda[2] and Silvestre T. Pinho[3]

[1]Department of Aeronautics, Imperial College London,
SW7 2AZ, London, United Kingdom
Email: runze.li@imperial.ac.uk

[2] Department of Aeronautics, Imperial College London,
SW7 2AZ, London, United Kingdom
Email: m.miranda23@imperial.ac.uk

[3] Department of Aeronautics, Imperial College London,
SW7 2AZ, London, United Kingdom
Email: silvestre.pinho@imperial.ac.uk

Keywords: Uncertainty quantification, failure prediction, composite wing, large structure

ABSTRACT

Composite materials are widely adopted in civil aircraft, as they contribute to lightweight, strong structures and offer the possibility of innovative structural concepts. However, traditional and empirical tools are often inadequate for evaluating such novel designs in the early stages of development, limiting the exploration of their full potential. To address this limitation, fast prediction models are needed to efficiently explore the design space. A key challenge in modelling large composite structures is the curse of dimensionality caused by detailed laminate stacking sequences, which greatly increases the demand for training data and computational resources. In this study, we propose a fast uncertainty quantification (UQ) model for predicting failure in composite wing boxes using Bayesian Neural Networks. The model predicts the mean failure response across various wing box geometries while quantifying the influence of different composite layups with stochastic terms. We focus on a novel structural concept, a Z-beam wing box, which is designed to achieve favourable bending–torsion coupling. Unit cells of the Z-beam structure are simulated under periodic boundary conditions. Failure indices are computed using refined local models at stress concentrations, based on the LaRC05 failure criterion. A diverse set of geometries and layups is sampled to train the UQ model. Results show that the proposed approach can accurately and quickly predict the probability distributions of failure indices for different wing box designs under varying load conditions. The predicted bounds of maximum failure indices provide valuable insights for structural assessment and highlight the need for further layup optimization when necessary.

1 INTRODUCTION

Europe's aviation sector has launched the "Destination 2050" initiative, aiming for net-zero emissions in aviation by mid-century [1]. One key strategy is increasing the wing aspect ratio to reduce induced drag [2]. For instance, Boeing's 777-X incorporates folding wingtips to extend wingspan [3]. Similarly, Airbus' ZEROe program [4] and the University of Bristol's Ultra-Green Wing (BUG) project [5], among others, are investigating the opportunities and challenges associated with high-aspect-ratio wings (HARW) [2]. A primary challenge lies in the significant structural weight increase associated with higher aspect ratios [6].

Aeroelastic tailoring has emerged as a promising passive technique to enhance both aerodynamic and structural performance [7]. Stodieck [8 and Airbus 9] introduced a Z-beam structural concept designed to improve aeroelastic tailoring, especially in reducing maneuver and gust loads. This approach shows potential in overcoming the aeroelastic limitations of HARW designs. As illustrated in Figure 1, the black lines represent the wing box spars and ribs, the grey lines indicate stringers, and the red lines highlight the Z-beams.

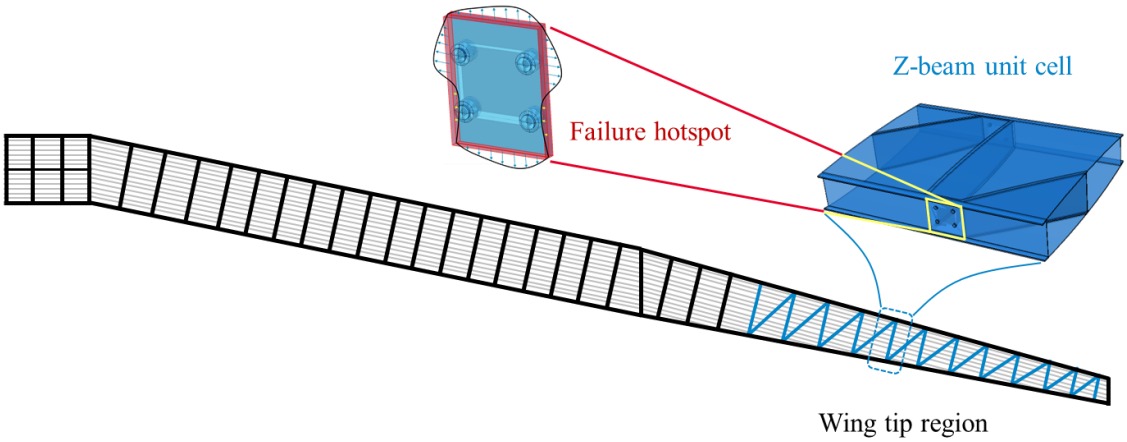

Figure 1: Z-beam structures in the wing tip region of BUG wing, and the hotspot for failure

This paper proposes an uncertainty quantification framework based on Bayesian neural networks for rapid prediction of novel wing structures. The Z-beam concept is selected as a representative case study. To model the behaviour of the Z-beam wing box at the wing tip, the structure is divided into multiple repeating unit cells, as illustrated in Figure 1. Each unit cell is analysed under periodic boundary conditions to capture its response to tension, bending, and torsion. Following this, the primary failure hotspot within the composite structure is identified. A refined local model is then developed for detailed failure analysis at this critical region.

2 PARAMETRIC MODELLING AND COMPUTATIONAL METHODS

2.1 Parameters of the Z-beam Unit Cell

The Z-beam unit cell comprises the upper and lower cover skins, front and rear C-shaped spars, a zigzag I-shaped beam, and titanium bolts. The bolts are made from aerospace-grade Ti-6Al-4V, while all other components use IM7/8551-7 carbon/epoxy composite. For simplicity, the design is parameterized using three independent geometric variables ($\Theta = [t_{\text{spar}}, t_{\text{beam}}, \alpha_{\text{beam}}]$), as illustrated in Figure 2. The definitions and ranges of these parameters are provided in Table 1. It is important to note that the spanwise length (L_z in mm) is a function of the beam angle α_{beam}.

The composite layup configuration of the wing box components is denoted by Γ, which encodes the ply orientation angles for all layers across all structural components. As a result, Γ is a high-dimensional parameter, because there are often hundreds of plies in laminates for large structures. Additionally, its dimensionality varies with laminate thickness, as different components may have different numbers of plies. These characteristics make modeling Γ particularly challenging for fast prediction models.

In this study, the geometric parameters are uniformly sampled within the ranges specified in Table 1 to generate a training dataset. For each wing box geometry, composite layups for the spars and Z-beam are then sampled. To ensure design feasibility, the layups are selected from a predefined set of candidate configurations. The front and rear spars share the same layup, while the cover skin layup is fixed to nominal values throughout this work.

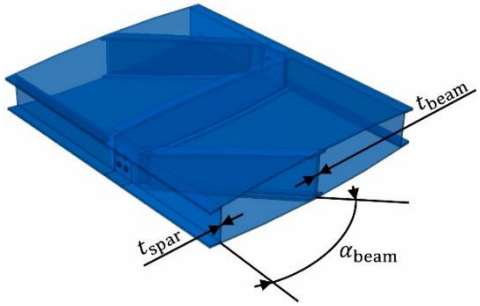

Figure 2: Geometric parameters of the Z-beam unit cell model [10]

Variable	Meaning	Range
t_{spar} (mm)	thickness of spar	[5, 25]
t_{beam} (mm)	thickness of beam	[10, 22]
α_{beam} (°)	angle between diagonal member of the beam and the spar	[20, 60]

Table 1: Independent geometric parameters

2.2 Finite Element Models

The training data for machine learning is obtained from multiscale simulations; the simulation process is shown in Figure 3. Abaqus is used as the numerical solver in this work. The behaviour of the complete zigzag beam in the wing tip region of BUG wing, as shown in Figure 1, is approximated by Z-beam unit cells arranged in a one-dimensional series. The aeroelastic deformation of the full wing box can be simulated by reduced order models [11], which only requires the homogenized stiffness matrix of each unit cell:

$$\begin{bmatrix} F_z \\ M_z \\ M_x \\ M_y \end{bmatrix} = \begin{bmatrix} C_{11} & C_{12} & C_{11} & C_{14} \\ C_{21} & C_{22} & C_{23} & C_{24} \\ C_{31} & C_{32} & C_{33} & C_{34} \\ C_{41} & C_{42} & C_{43} & C_{44} \end{bmatrix} \begin{bmatrix} \epsilon_z \\ \kappa_z \\ \kappa_x \\ \kappa_y \end{bmatrix} \tag{1}$$

At the structural element level, the loads (Δ) applied on the unit cell model include the axial strain in z-axis (ϵ_z), twist rate about z-axis (κ_z, rad/mm), and the curvature about x/y-axis (κ_x, κ_y, 1/mm). The loads are employed using periodic boundary conditions (PBCs), and the displacement boundaries ($\boldsymbol{u}$) around failure hotspots are determined.

At the hotspot level, stress ($\boldsymbol{\sigma}$) and strain ($\boldsymbol{\epsilon}$) fields are assessed on a finer mesh using a global-local approach. Then, failure indices (FIs, $\boldsymbol{v}$) are calculated using the LaRC05 failure criteria [13]. By analysing various strain states, a failure index map is generated by identifying the maximum failure index within the structure. Consequently, the failure envelop can be obtained from the FI map. The details can be found in [10,14] and are therefore not repeated here.

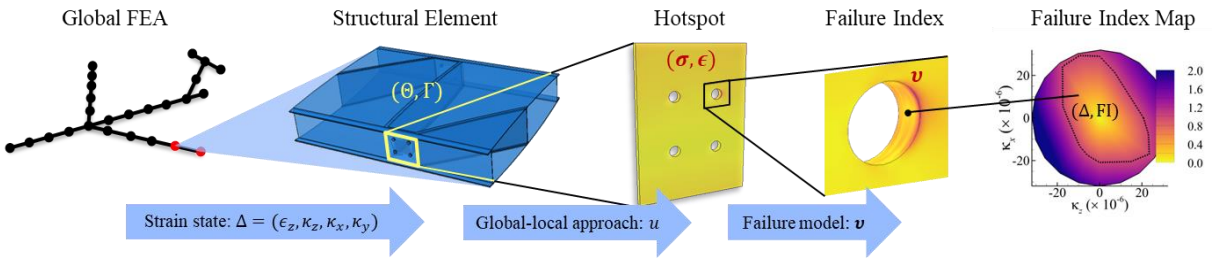

Figure 3: Multiscale simulation of composite Z-beam wing box elements

3 MACHINE LEARNING FOR Z-BEAM WING BOXES

3.1 Database

There are 1400 valid unit cell samples in the database. The homogenized stiffness matrix [C] and mass matrix [M] are extracted. Figure 4 shows the relationship between the stiffness components with geometry parameters, when the composite layup are set to nominal values. It shows that t_{spar} dominates C_{11}, C_{33}, C_{13}; t_{beam} dominates C_{23}; t_{spar} and t_{beam} have same level of influence on C_{22}.

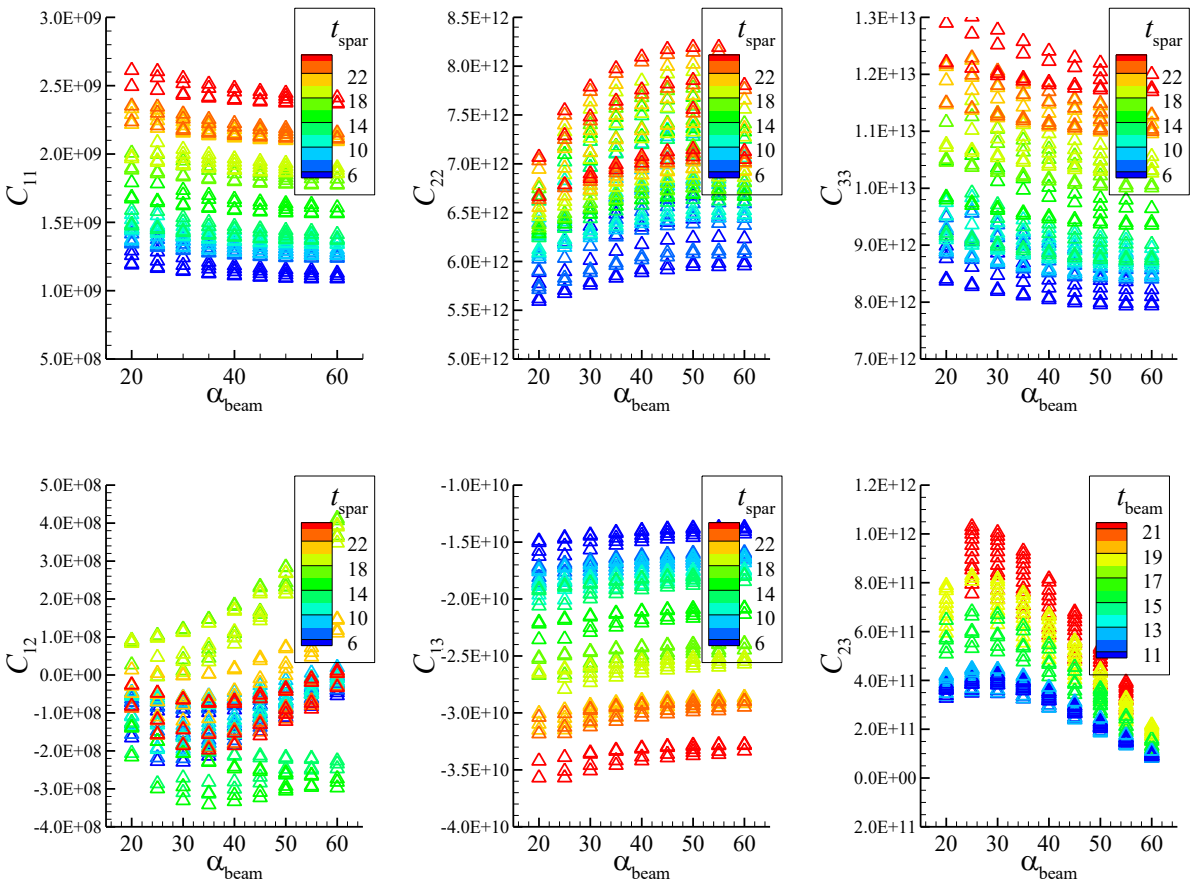

Figure 4: Distribution of stiffness components in the database

3.2 A Machine Learning Model for Z-beam Unit Cell's properties

A machine learning model is used to predict the properties of Z-beam unit cell that are independent of the loads, i.e., the weight and homogenized stiffness matrix. The model input is the geometric parameters Θ and superlayer parameters ($\Omega = [r_{0,\text{beam}}, r_{90,\text{beam}}, r_{0,\text{spar}}, r_{90,\text{spar}}]$), the output is the weight (w) and the homogenised stiffness matrix ($[C]$), as shown in Figure 5. The superlayer parameters, i.e., percentage of plies in the beam and spar are used to predict the homogenised stiffness. It is because the structure dimension (i.e., wing box height) is much larger than the laminate thickness, consequently, the stacking sequence details have insignificant influence on $[C]$.

A simple artificial neural network (ANN) is employed, which contains three hidden layers with 512 neurons. The loss function is the mean square error (MSE) between the predicted values and the real values. The initial learning rate is 0.001 for 500 epochs. Adam optimizer[15] is used for training. 20 samples are randomly selected for testing. Figure 6 shows the prediction error on the training set and testing set during training. It shows that the model can achieve a good prediction accuracy.

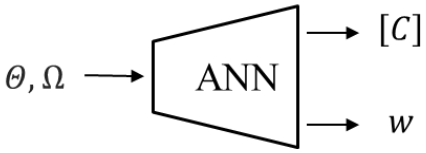

Figure 5: ANN for the prediction of weight and stiffness

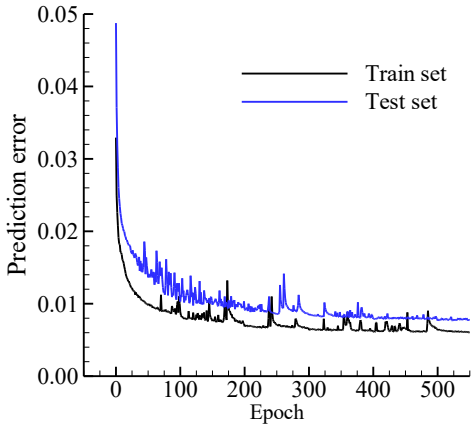

Figure 6: Prediction error on the training set and testing set during training.

3.3 Bayesian Neural Networks for Failure Prediction

Bayesian neural networks are trained on the wing box database. The loss function is the evidence lower bounds (ELBO) on the training set. The initial learning rate is 0.001 for 2,000 epochs. Adam optimizer is again used for training. Figure 7 presents a predicted maximum failure index map of a Z-beam geometry. The details of the proposed uncertainty quantification model and more results will be presented in the conference.

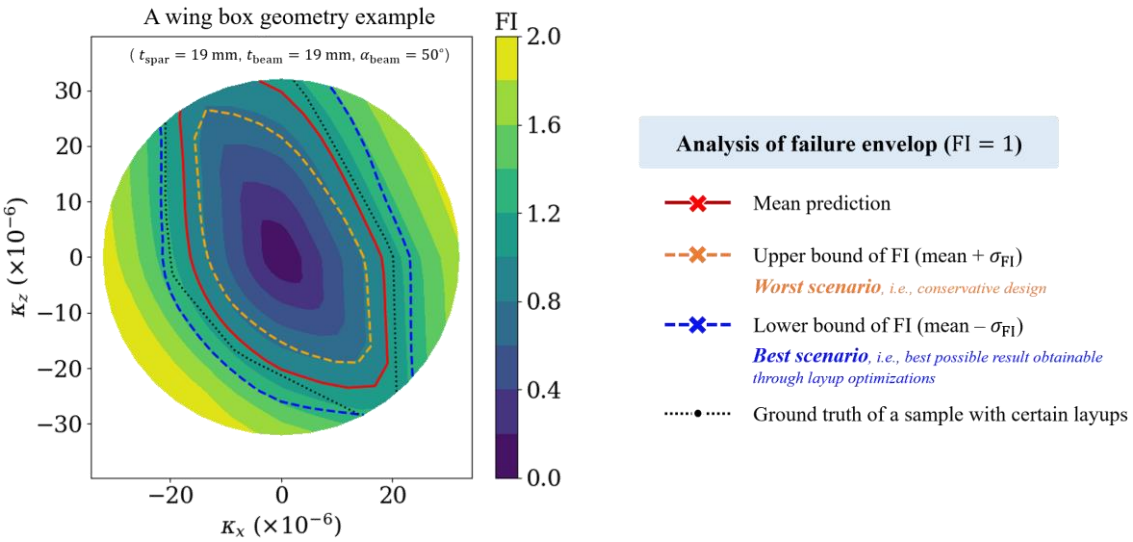

Figure 7: The expected maximum failure index map of a Z-beam wing box geometry. The wing box is under bending strains (κ_x) and torsional strains (κ_z), the geometric parameters are $t_{\text{spar}} = 19, t_{\text{beam}} = 19, \alpha_{\text{beam}} = 50°$. The solid red line shows the expected failure envelop ($\mu(\text{FI}) = 1$), the orange and blue dashed lines show the upper and lower bounds of FI (or 1σ confidence interval). The black dashed lines show the failure envelop of the wing box geometry with the nominal layup.

3 CONCLUSIONS

The Z-beam structure enables tailored bending–torsion coupling through geometric modifications, making it well-suited for high aspect ratio wing applications. A simple neural network is trained to predict the homogenized stiffness of the Z-beam unit cell, enabling fast and accurate evaluations for preliminary design. To assess structural reliability, an uncertainty quantification model is developed and trained to predict failure behavior and capture the influence of composite layup variations. Results demonstrate that the proposed method can efficiently and accurately predict the probability distributions of failure indices across different wing box configurations under varying loading conditions. This

approach is therefore well-suited for early-stage design and evaluation of novel composite wing concepts.

ACKNOWLEDGEMENTS

The authors would like to gratefully acknowledge the funding from Innovate UK under the Next Wing project No. 10002372 (https://gtr.ukri.org/projects?ref=10002372). The authors also thank Nicolae Lucian Iorga from Airbus UK for the support and helpful discussions.

REFERENCES

[1] A route to net zero European aviation, Destination 2050, https://www.destination2050.eu/, last accessed on 02/05/2024.
[2] Y. Ma, A. Elham, Designing high aspect ratio wings: A review of concepts and approaches, *Progress in Aerospace Sciences*, 145: 100983, 2024.
[3] A. Kretov, D. Tiniakov, Evaluation of the Mass and Aerodynamic Efficiency of a High Aspect Ratio Wing for Prospective Passenger Aircraft, *Aerospace*, 9: 497, 2022
[4] ZEROe, towards the world's first hydrogen-powered commercial aircraft, Airbus. https://www.airbus.com/en/innovation/low-carbon-aviation/hydrogen/zeroe, last accessed on 02/05/2024.
[5] O. Stodieck, J. E. Cooper, S. A. Neild, and M. H. Lowenberg, Slender-Wing Beam Reduction Method for Gradient-Based Aeroelastic Design Optimization, *AIAA Journal*, 56(11): 4529-4545, 2018
[6] F. Afonso, J. Vale, E. Oliveira, et al., A review on non-linear aeroelasticity of high aspect-ratio wings, *Progress in Aerospace Sciences*, 89: 40-57, 2017
[7] M. Shirk, T. Hertz and T. Weisshaar, Aeroelastic tailoring - Theory, practice, and promise, *AIAA/ASME/ASCE/AHS 25th Structures, Structral Dynamics and Materials Conference,* Palm Springs, CA, May 14-16, 1984
[8] O. Stodieck, Tech-insight: Aeroelastic tailoring of wings using a z-beam concept, University of Bristal, 2019
[9] L. Iorga. Aerofoil structures with stiffness properties adjustment component. U.S. Patent No. 11,772,780 B2. United States Patent and Trademark Office. 3 Oct. 2023
[10] M. Miranda, R. Li, L. Iorga, and S. T. Pinho, Multiscale modelling strategy for a novel wingbox structure with increased bend-twist coupling. *Composite Structures*, 119291, 2025.
[11] H. Hesse, R. Palacios, Reduced-Order Aeroelastic Models for Dynamics of Maneuvering Flexible Aircraft, *AIAA Journal*, 52(8): 1717-1732, 2014
[12] J. Dizy, R. Palacios, S. Pinho, Homogenisation of slender periodic composite structures, International Journal of Solids and Structures, 50: 1473-1481, 2013
[13] S. Pinho, R. Darvizeh, P. Robinson, et al., Material and structural response of polymer-matrix fibre-reinforced composites, *Journal of Composite Materials*, 46(20):2313–2341, 2012.
[14] M. Miranda, R. Li, S. Pinho, Multiscale modelling of a novel wing box structure with increased bend-twist coupling, 21st European Conference on Composite Materials, Nantes, France, July 2024.
[15] D. Kingma, J. Ba, Adam: A method for stochastic optimization, *arXiv preprint*, 2014, arXiv:1412.6980.

ICCM24
24TH INTERNATIONAL CONFERENCE ON COMPOSITE MATERIALS

24th International Conference on Composites Materials
Baltimore, USA – August 2025

UNIVERSITY OF DELAWARE

AI-driven Method for Predicting Fibre Orientation in Composites

César García-Gascón, *Pablo Castelló-Pedrero, Javier Bas-Bolufer, Juan Antonio García-Manrique, Francisco Chinesta*

Instituto de Diseño y Fabricación (IDF), Universitat Politècnica de València (UPV)

Processes and Engineering in Mechanics (PIMM), École nationale supérieure d'Arts et Métiers (ENSAM)

UNIVERSITAT POLITÈCNICA DE VALÈNCIA

idf INSTITUTO DE DISEÑO Y FABRICACIÓN

Arts Sciences et Technologies et Métiers

Financiado por la Unión Europea
NextGenerationEU

Plan de Recuperación, Transformación y Resiliencia

About us





UNIVERSITAT POLITÈCNICA DE VALÈNCIA

INSTITUTO DE DISEÑO Y FABRICACIÓN

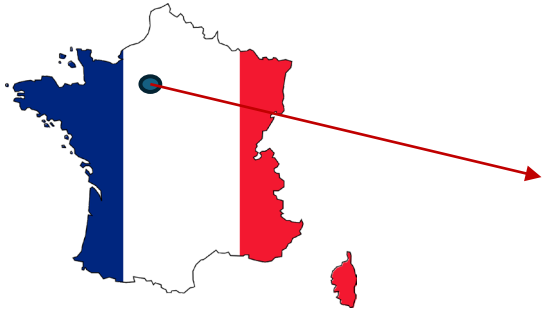

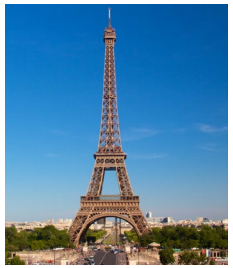

Arts et Métiers Institute of Technology

Procédés et Ingénierie en Mécanique et Matériaux



PhD Student: Pablo Castelló Pedrero



PhD Student: César García Gascón



PhD Student: Javier Bas Bolufer



Professor: Juan A. García Manrique



Professor: Francisco Chinesta Soria

UNIVERSITY OF DELAWARE

UNIVERSITAT POLITÈCNICA DE VALÈNCIA

INSTITUTO DE DISEÑO Y FABRICACIÓN

Arts et Métiers Sciences et Technologies

Motivation

Super Discovery 3D printer



- Regular printing volume: 1300x2500x1000mm

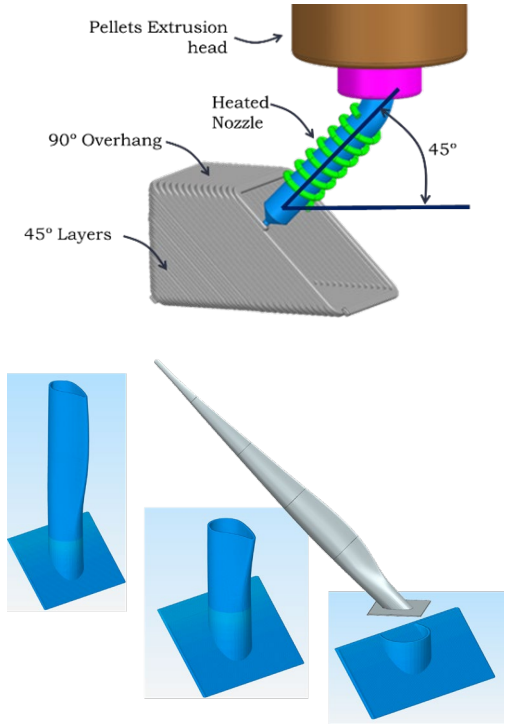

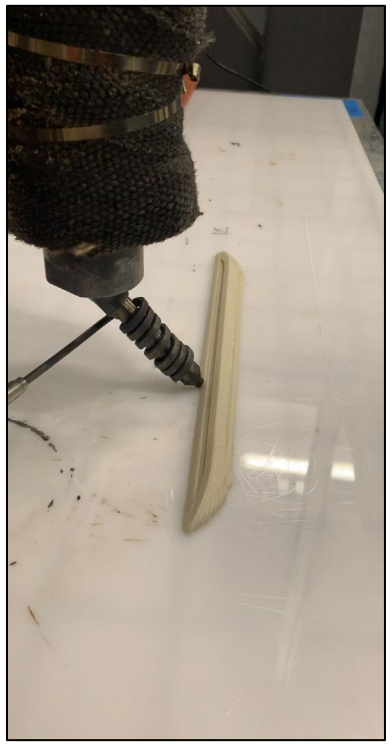

- Capable of printing in out of plane trajectories.

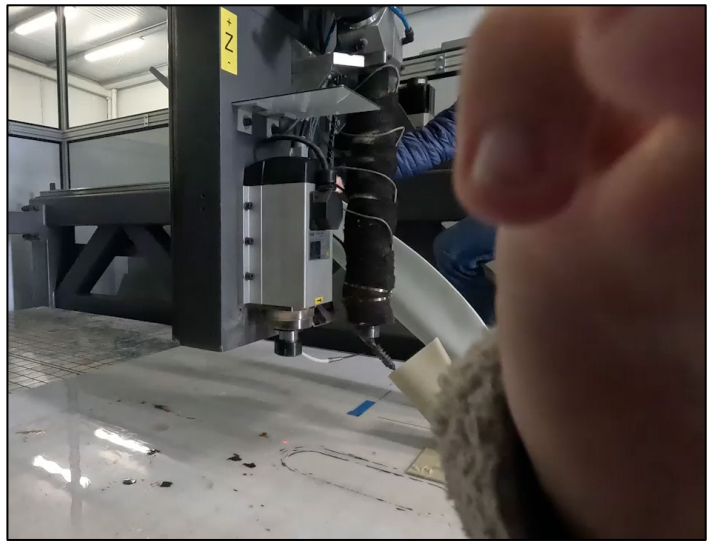

Motivation

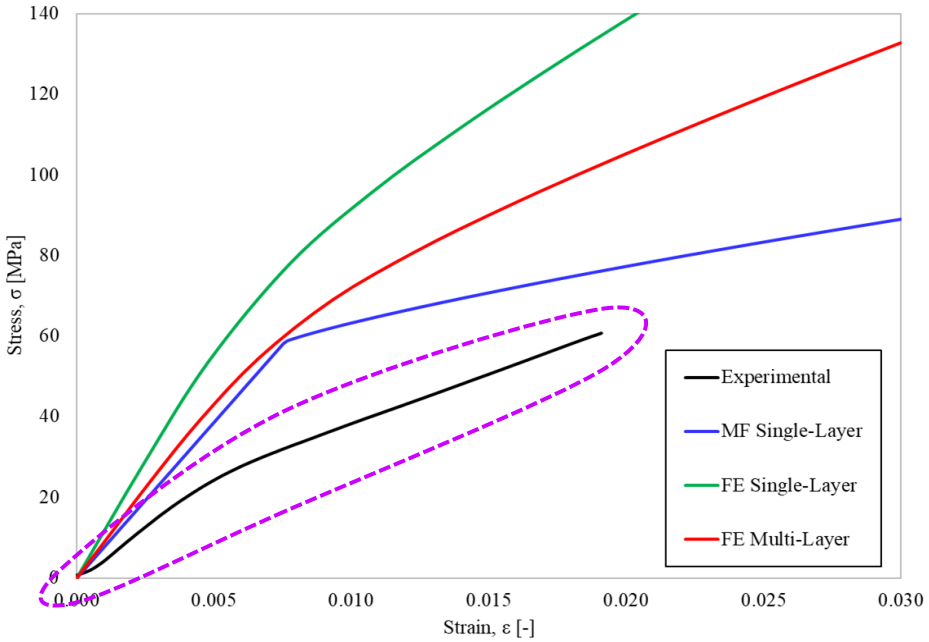
140
120
100
80
60
40
20
0
Stress, σ [MPa]
0.000
0.005
0.010
0.015
0.020
0.025
0.030
Strain, ε [-]
Experimental
MF Single-Layer
FE Single-Layer
FE Multi-Layer

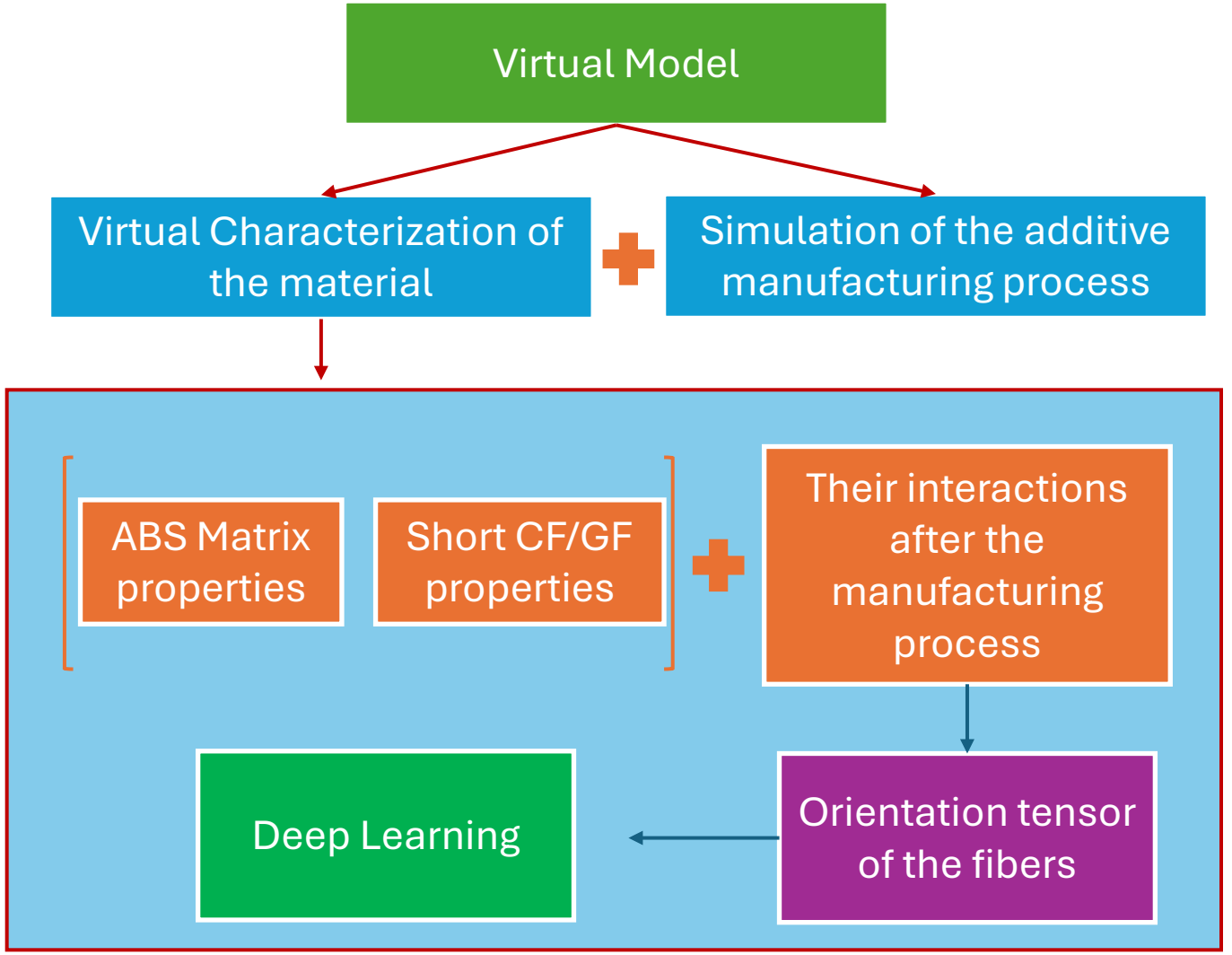
Virtual Model
Virtual Characterization of the material
Simulation of the additive manufacturing process
ABS Matrix properties
Short CF/GF properties
Their interactions after the manufacturing process
Deep Learning
Orientation tensor of the fibers

Materials

Composite material

- Matrix: ABS
- GF short inclusions

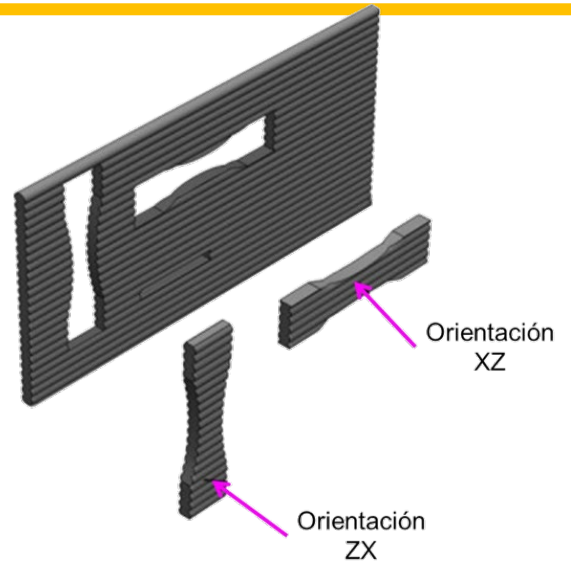



Sanding and polishing
with diamond paste





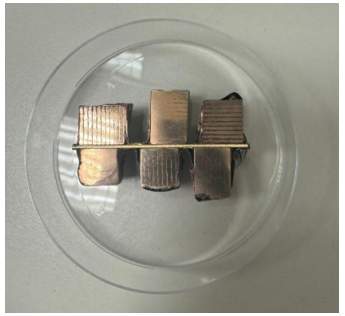



Materials

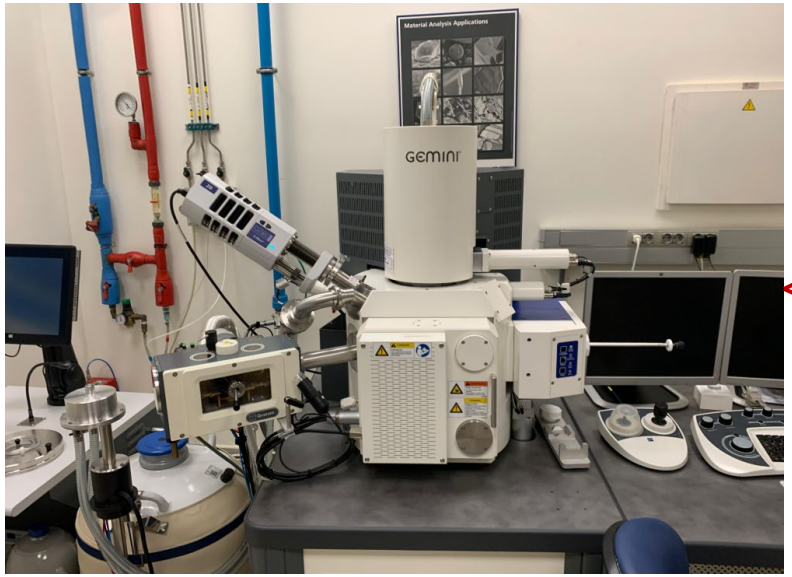

Scanning electron microscope (SEM)

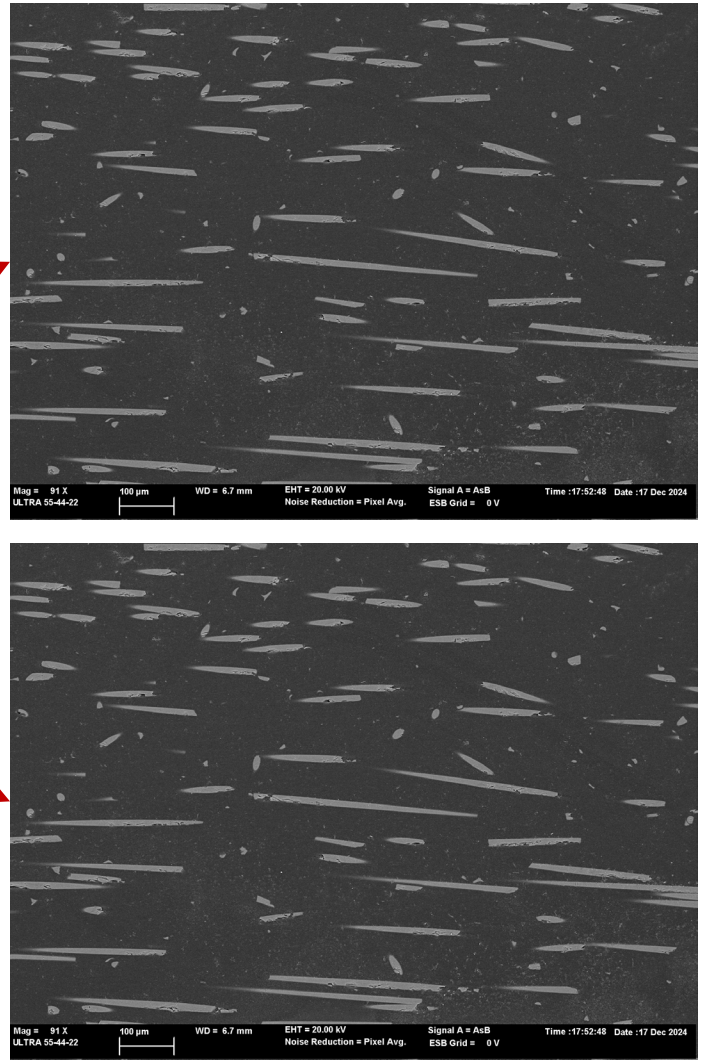

Methods

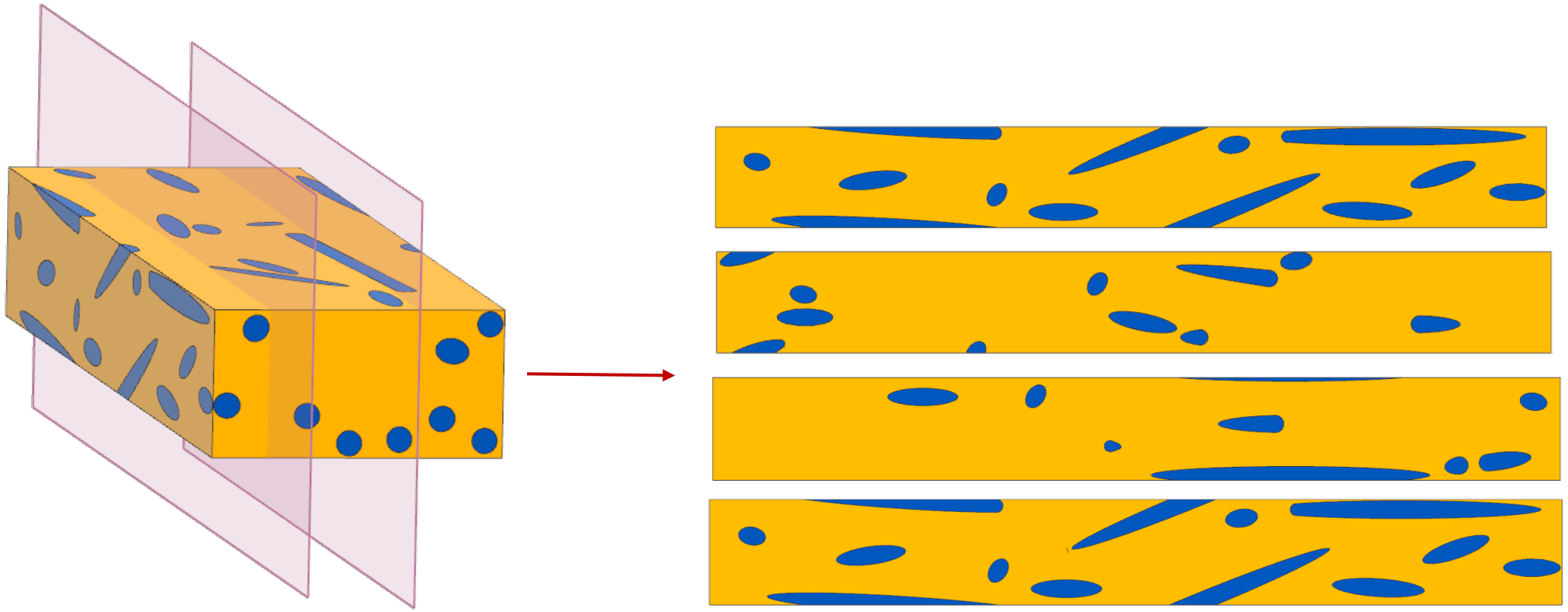

Methods



FIJI/ImageJ:

- Very tedious
- Human errors
- Not very accurate
- Not suitable for measuring a big representative Surface of the material

Binarization

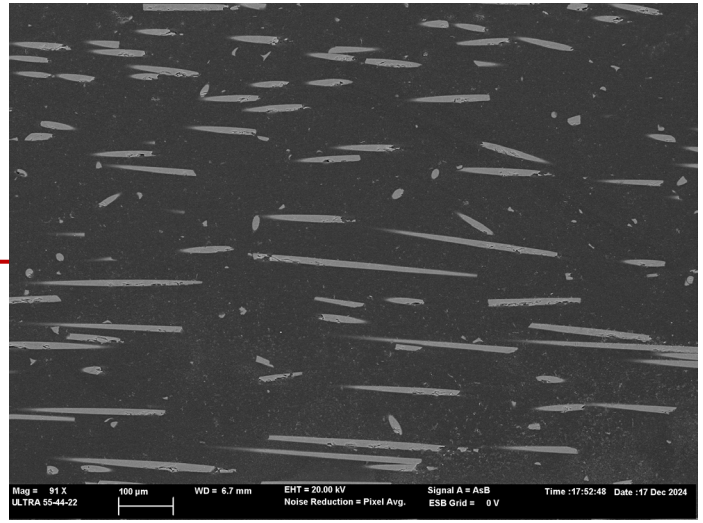



$$a_{ijk\ldots l} = \int p_i\, p_j\, p_k \cdots p_l\, \psi(p)\, \mathrm{d}p$$

$$p_x^2 + p_y^2 + p_z^2 = 1$$

Advani and Tucker, 1987

Methods

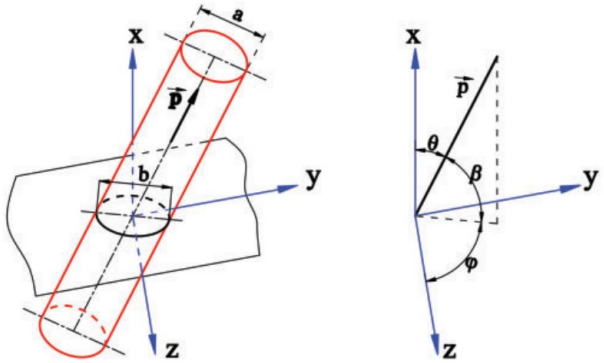

Lila Cai, 2020

$$a_{xx} = a_{11} = \frac{1}{N}\sum_{i=1}^{N} \sin^2(\beta_i)\,,$$

$$a_{yy} = a_{22} = \frac{1}{N}\sum_{i=1}^{N} \cos^2(\beta_i)\,\sin^2(\varphi_i)$$

$$a_{zz} = a_{33} = \frac{1}{N}\sum_{i=1}^{N} \cos^2(\beta_i)\,\cos^2(\varphi_i)$$

$$sin\,\beta = \frac{a}{b}$$

Being:

- a: the diameter of a single glass fiber
- b: length of the long axis of the ellipse
- N: number of glass fibers
- Φ: Orientation angle with respect z and y

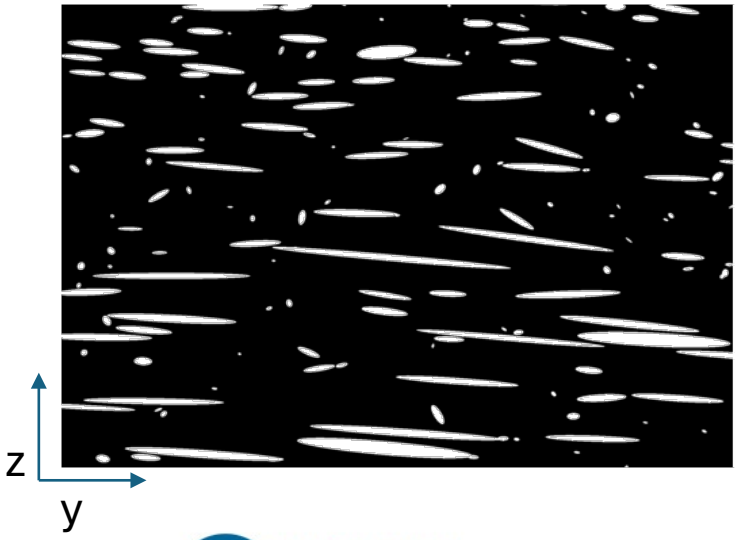

Deep Learning Data Augmentation

Variables:

- a: the diameter of a single glass fiber
- b: length of the long axis of the ellipse
- p: % of area occupied by ellipses
- Φ: Orientation angle with respect z and y.

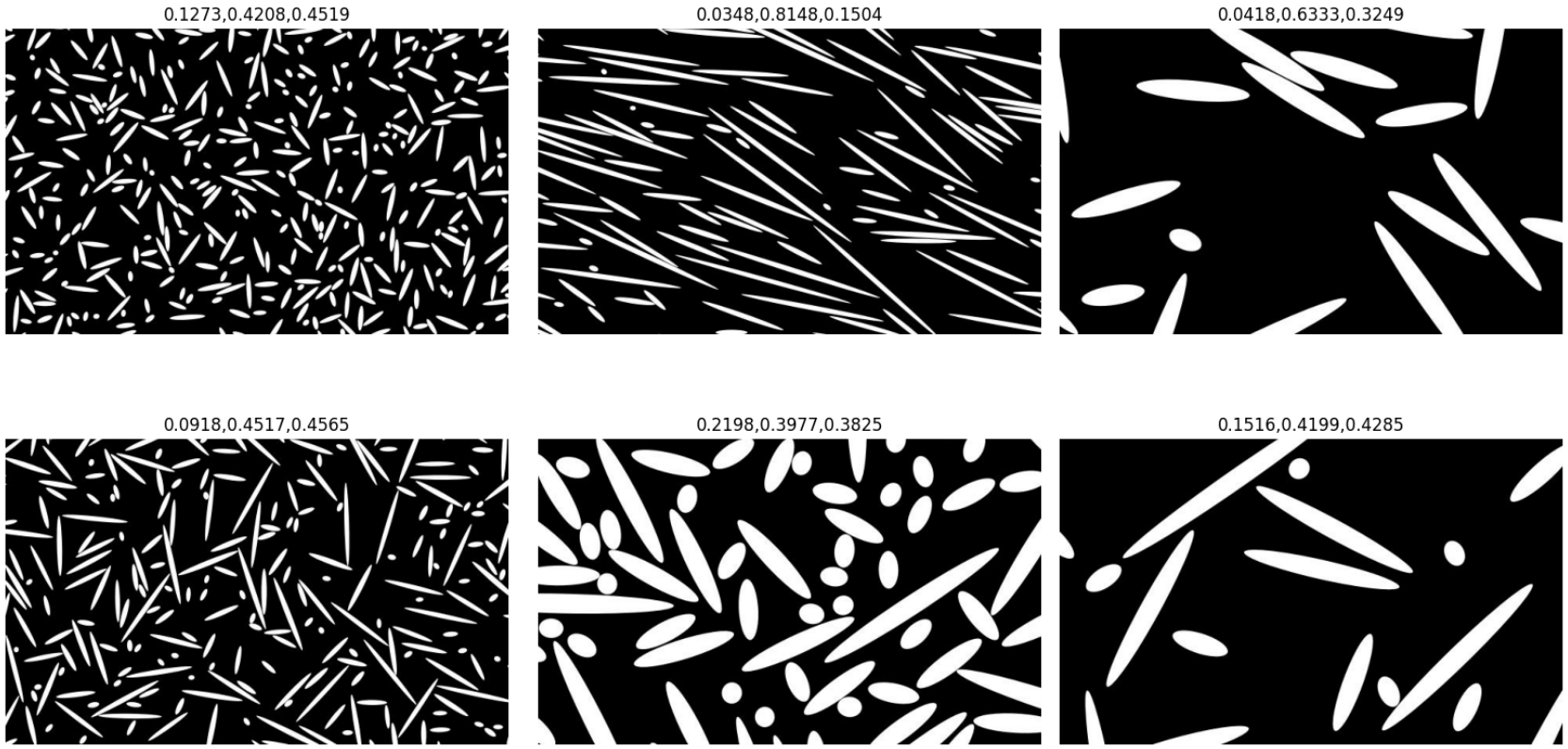

A total of 40000 images generated to train the Neural Network

Parameters adjustement

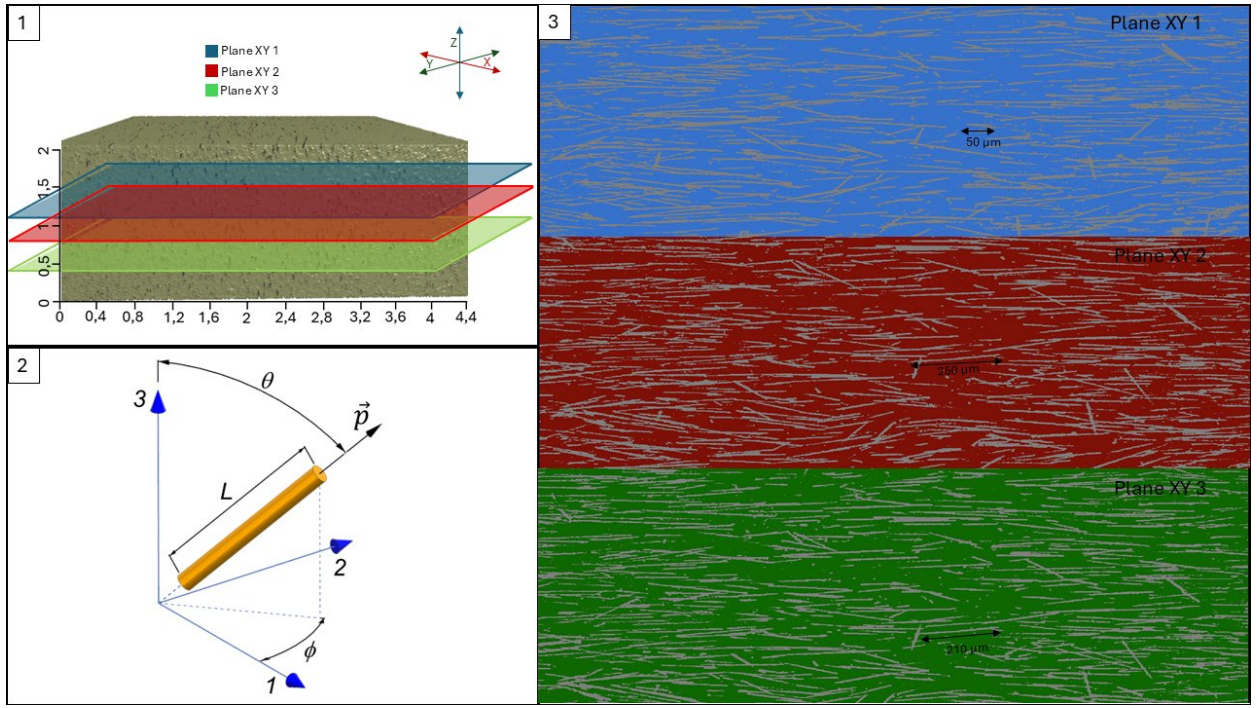





Convolutional Neural Network

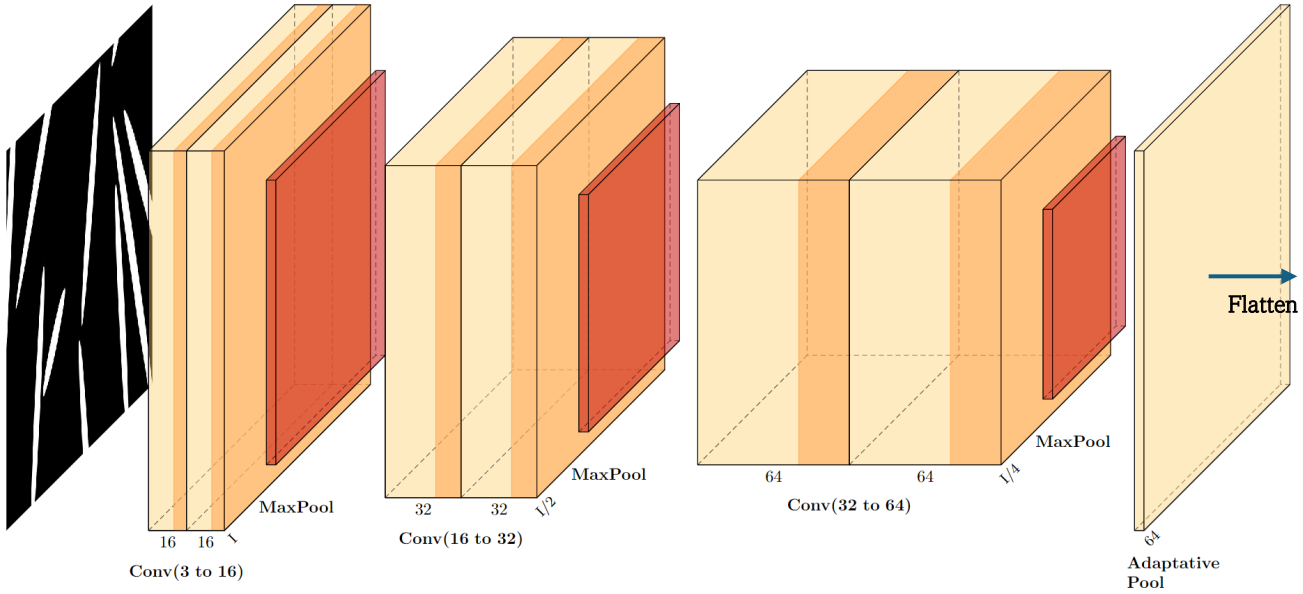

MLP 64x128 → ReLU → Dropout 10% → MLP 128x3 → SoftMax

$[a_{xx}, a_{yy}, a_{zz}]$

Convolutional Neural Network

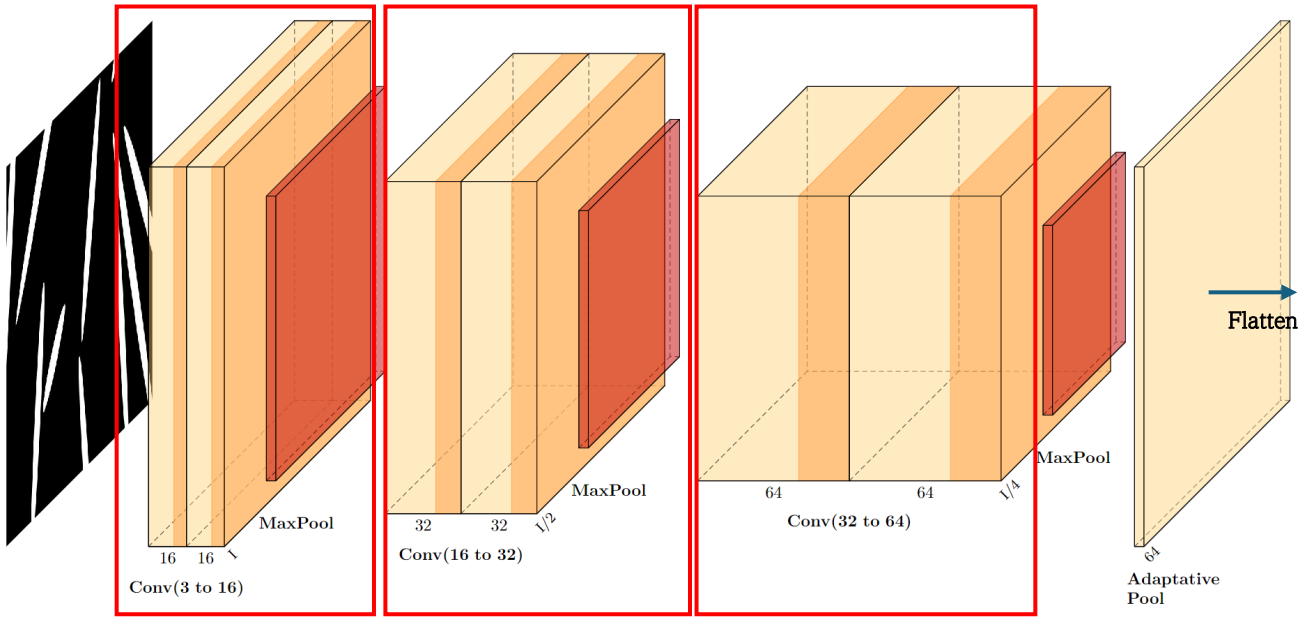

Flatten → MLP 64x128 → ReLU → Dropout 10% → MLP 128x3 → SoftMax → $[a_{xx}, a_{yy}, a_{zz}]$

Convolution + MaxPool

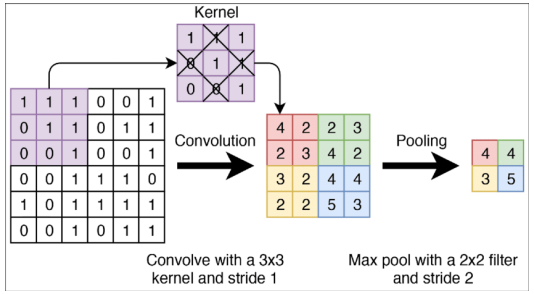

+

Batch Normalization

$$\hat{x}_i = \frac{x_i - \mu_B}{\sqrt{\sigma_B^2 + \epsilon}}$$

Convolutional Neural Network

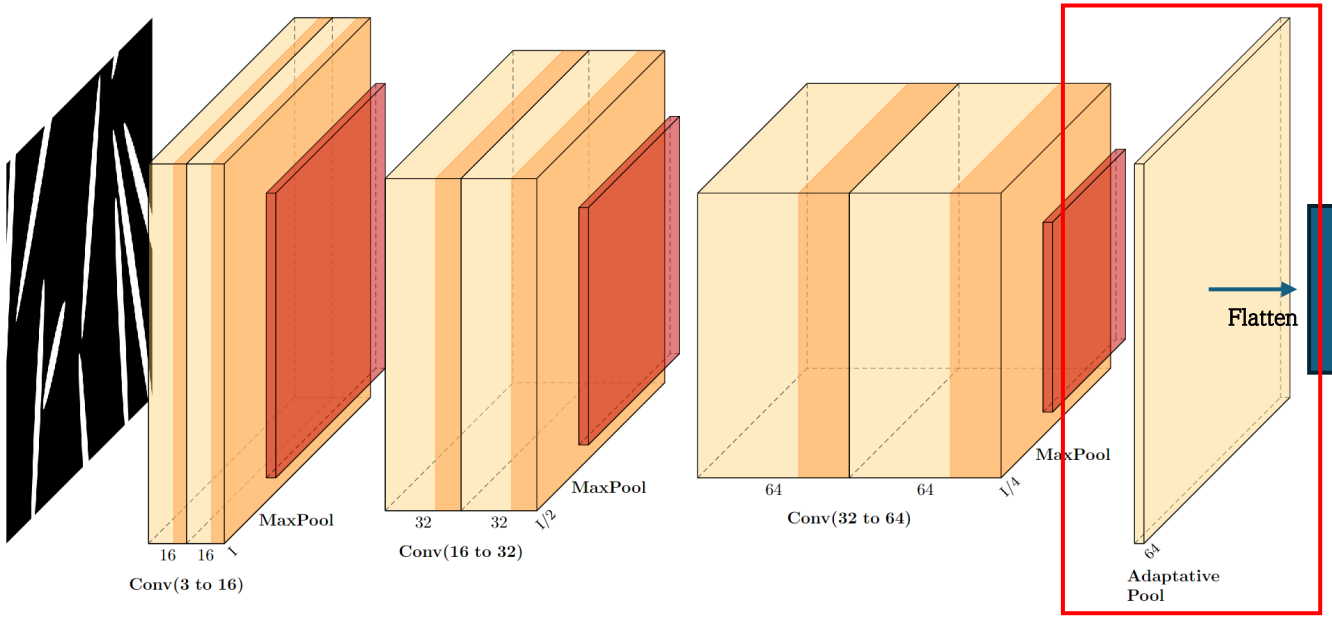

MLP 64x128 → ReLU → Dropout 10% → MLP 128x3 → SoftMax

$$[a_{xx}, a_{yy}, a_{zz}]$$

Adaptative Pooling

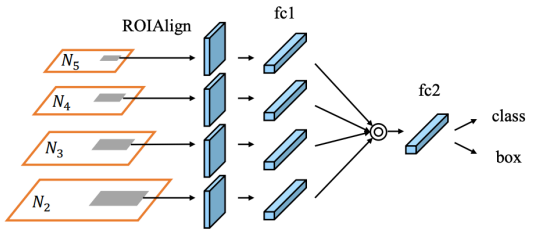

Figure 6. Illustration of adaptive feature pooling on box branch.

$$\text{Output}(c) = \frac{1}{H_{\text{in}} \times W_{\text{in}}} \sum_{h=1}^{H_{\text{in}}} \sum_{w=1}^{W_{\text{in}}} \text{Input}(c, h, w)$$

Flatten to 64 outputs

$$\text{Output} = \sigma(\mathbf{W} \cdot \mathbf{x} + \mathbf{b})$$

Convolutional Neural Network

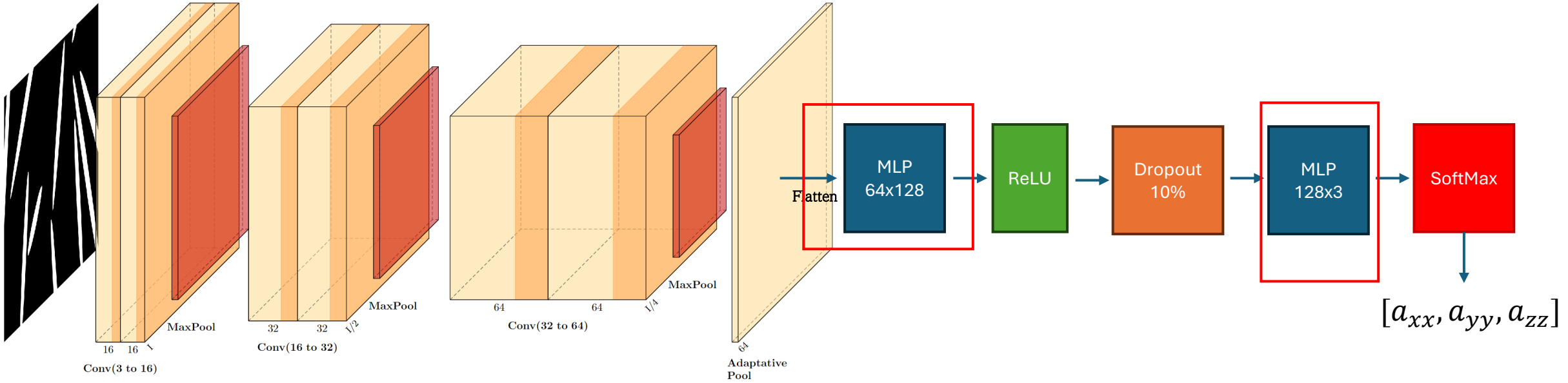

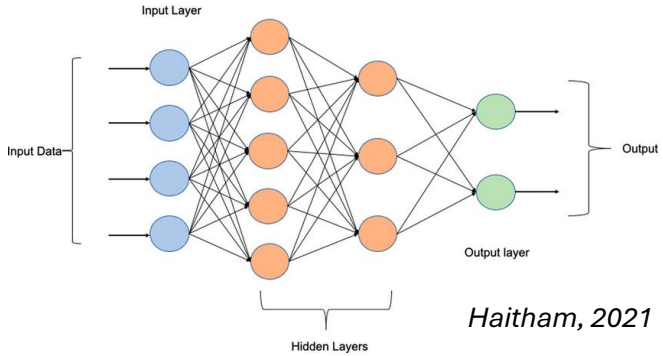

Haitham, 2021

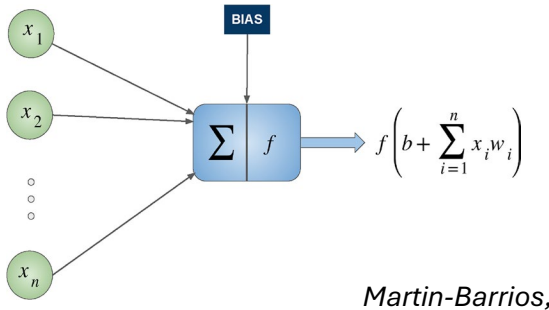

Martin-Barrios, 2024

Convolutional Neural Network

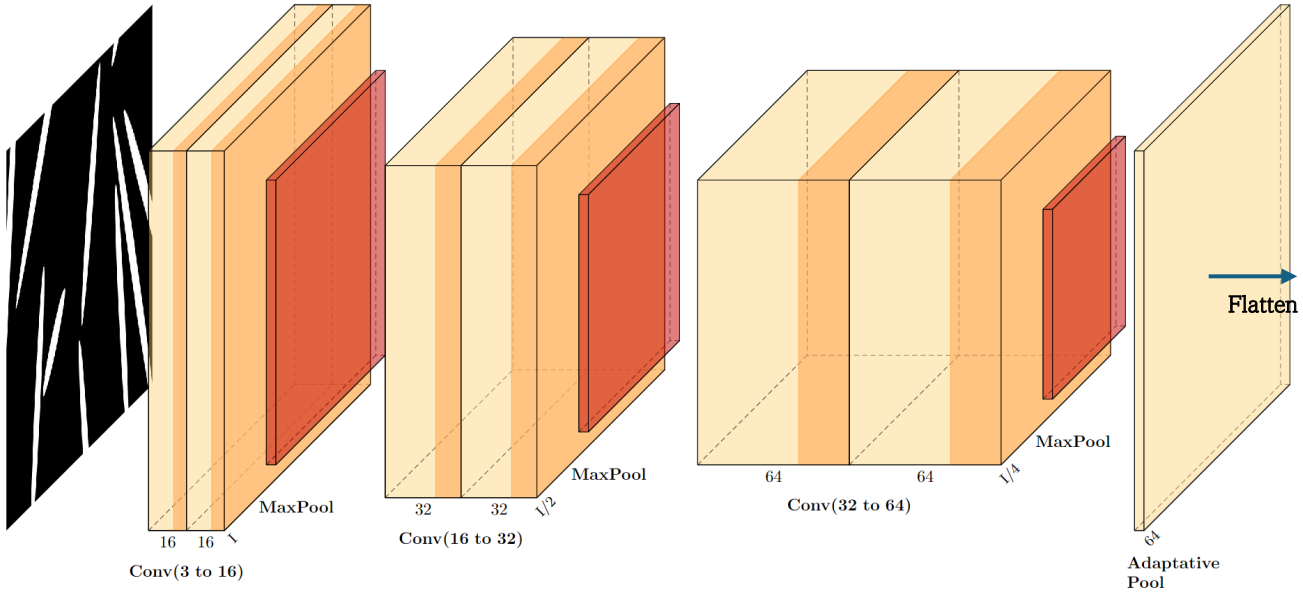

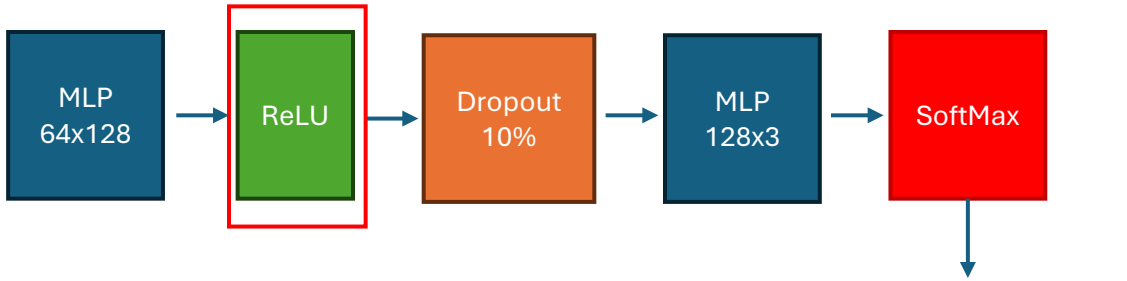

ReLU activation function for no-linearity

$$R(x) = \begin{cases} x & \text{if } x \geq 0 \\ 0 & \text{otherwise} \end{cases}$$

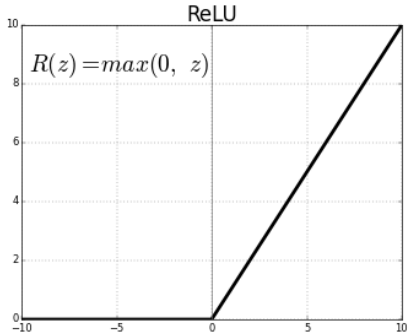

Convolutional Neural Network

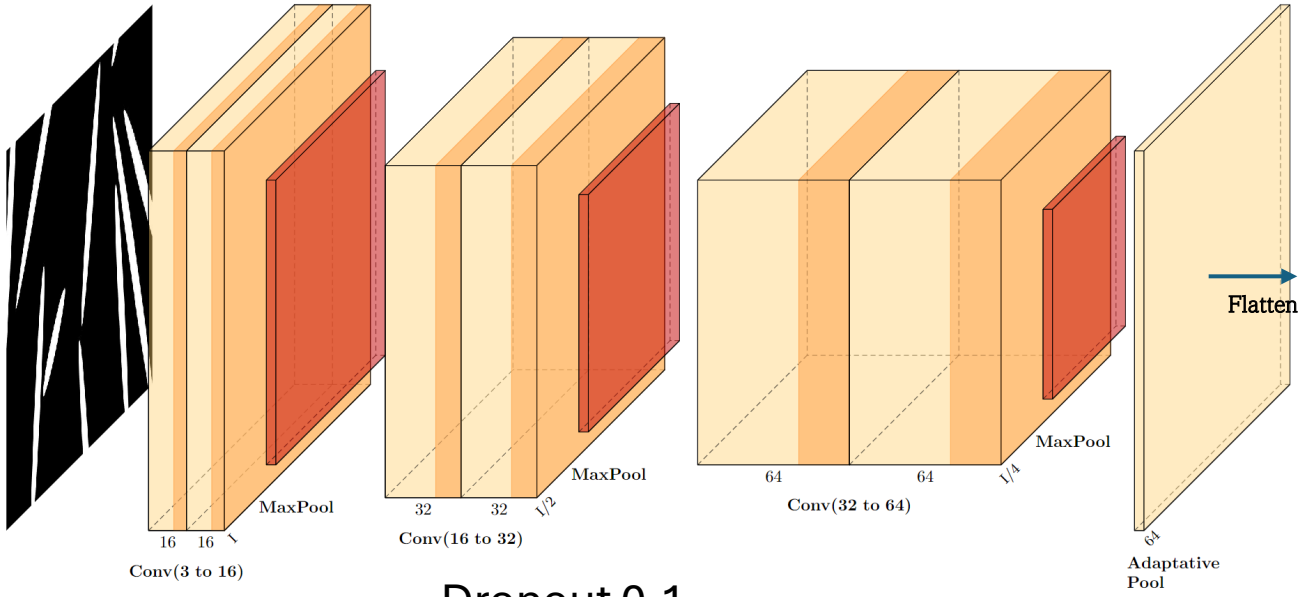

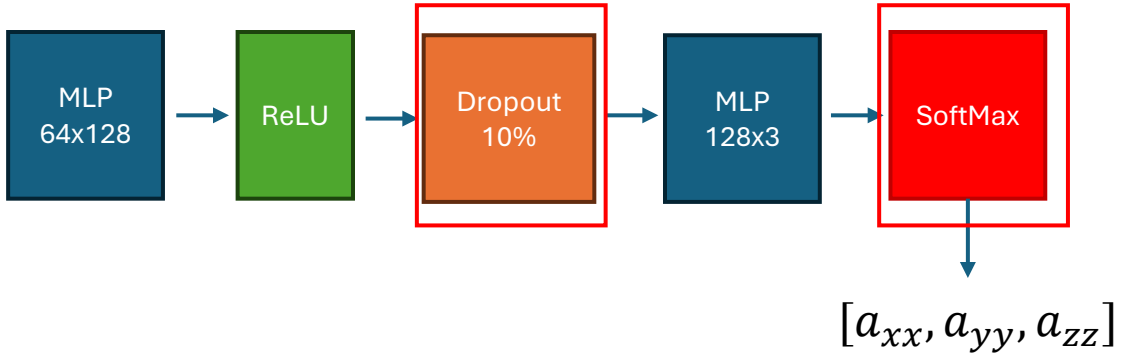

Dropout 0.1

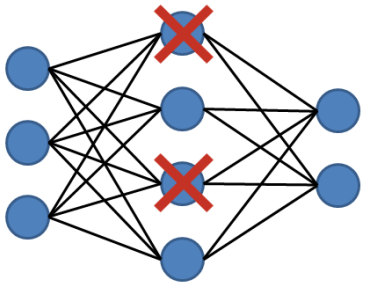

Softmax

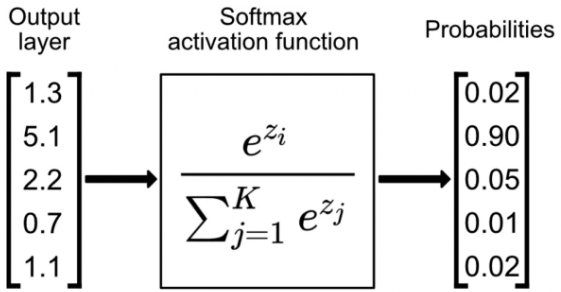

Deep Learning: Training and Results

Configuration	
Training size	0.8
Validation size	0.1
Test size	0.1
Learnign rate	0.001
Epochs	150
Batch size	16
Loss function	MSE
Optimizer	Adam
Scheduler	On
Training time	4 hour

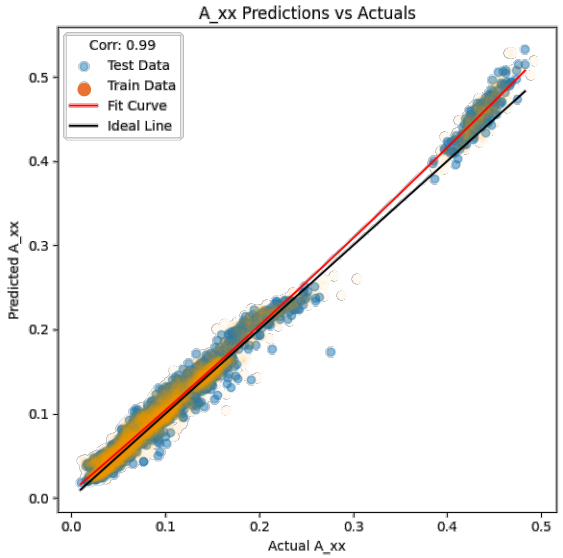

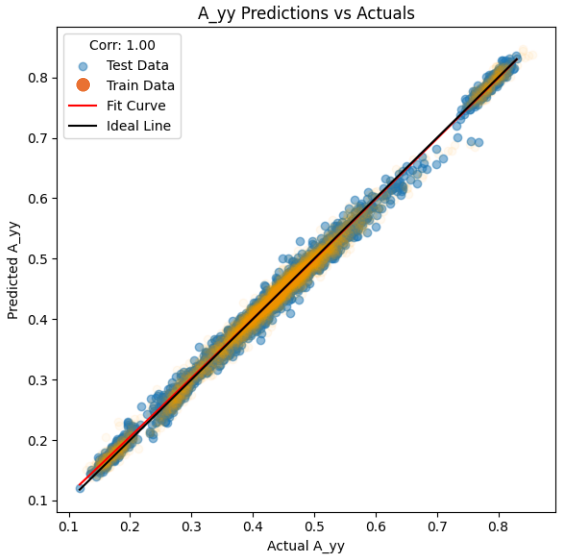

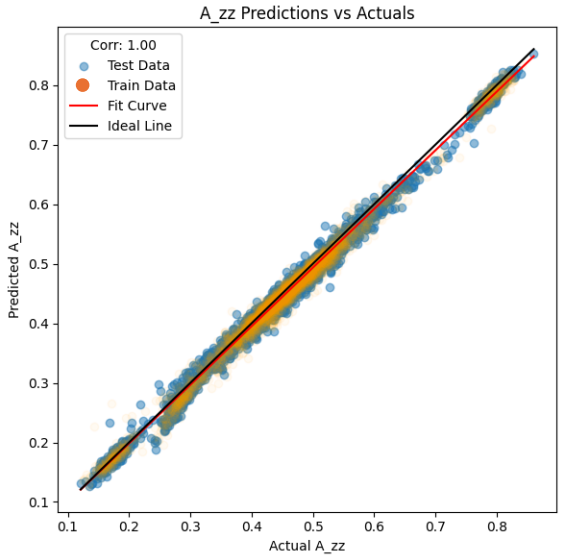

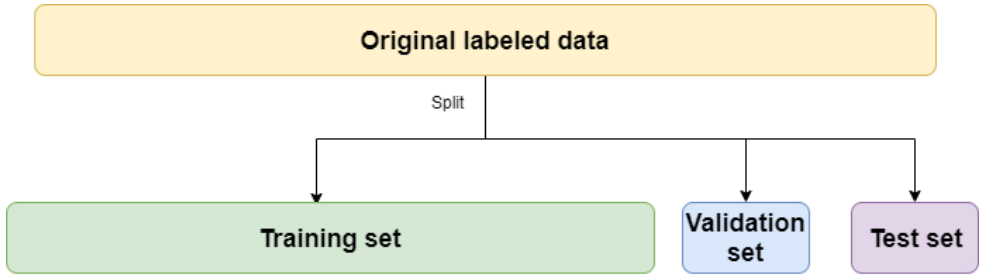

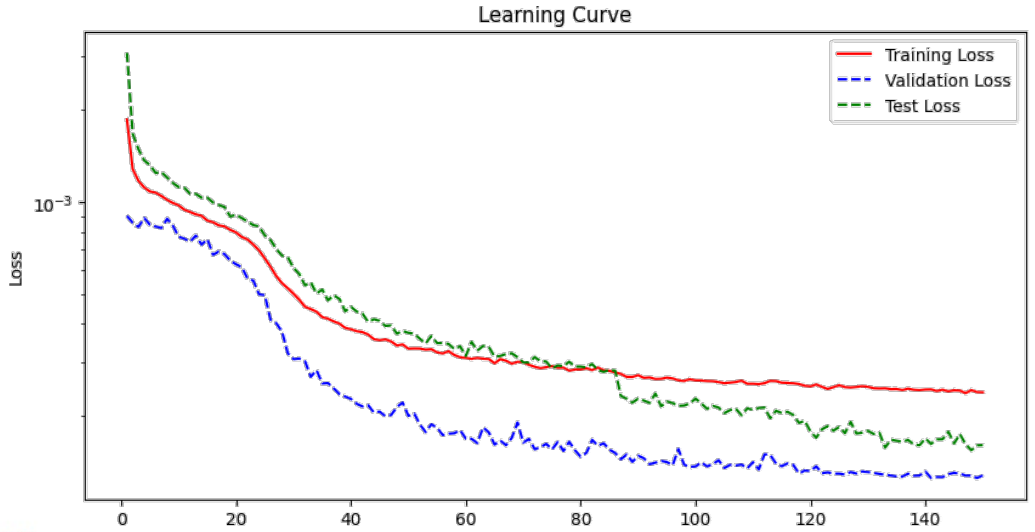

Deep Learning: Results

Category	Metric	Value
Train Data	Mean Cosine Similarity	0.99953
	Mean Angular Error [°]	**1.39502**
	Pearson - a_xx	0.99356
Validation Data	Mean Cosine Similarity	0.99951
	Mean Angular Error [°]	**1.42294**
	Pearson - a_yy	0.99359
Test Data	Mean Cosine Similarity	0.99962
	Mean Angular Error [°]	**1.26876**
	Pearson - a_zz	0.99453

Metric	Value
JSD_global	0.00023
MAE_global	0.00809
MAPE_global	4.78343
MSE_global	0.00012
R^2_global	0.98937
RMSE_global	0.01108

$Real$: $[0.1104, 0.4132, 0.4764]$
$Predicted$: $[0.1062, 0.4122, 0.4816]$
$\boldsymbol{Mean\ angular\ error}$: $\mathbf{0.56°}$

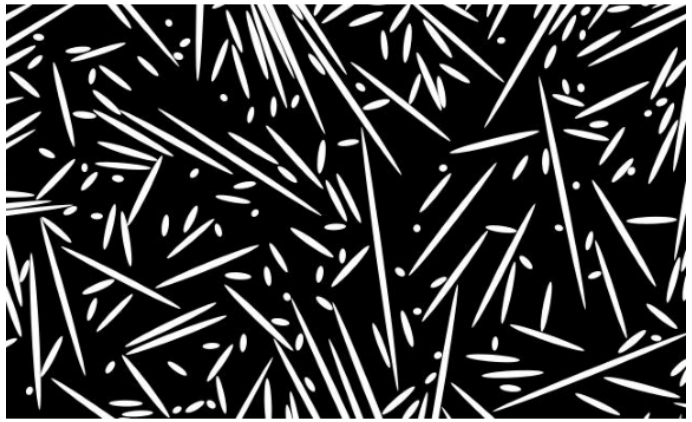

$Real$: $[0.0412, 0.8143, 0.1445]$
$Predicted$: $[0.0471, 0.8032, 0.1496]$
$\boldsymbol{Mean\ angular\ error}$: $\mathbf{0.66°}$



$Real$: $[0.1230, 0.4584, 0.4186]$
$Predicted$: $[0.0900, 0.4633, 0.4467]$
$\boldsymbol{Mean\ angular\ error}$: $\mathbf{3.59°}$



$Real$: $[0.1464, 0.3999, 0.4537]$
$Predicted$: $[0.1388, 0.4012, 0.4600]$
$\boldsymbol{Mean\ angular\ error}$: $\mathbf{0.85°}$

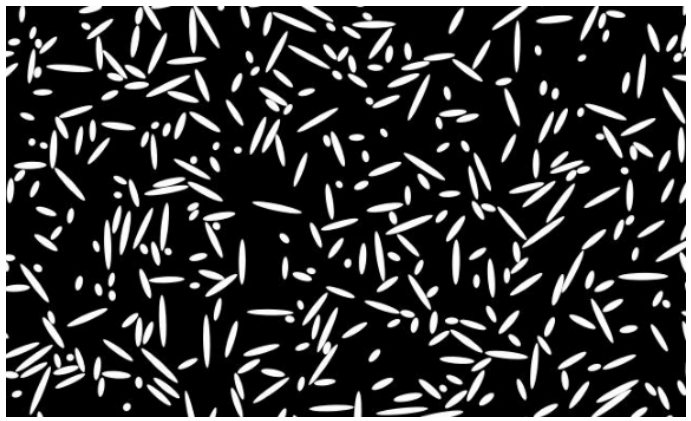

Deep Learning: Crossvalidation

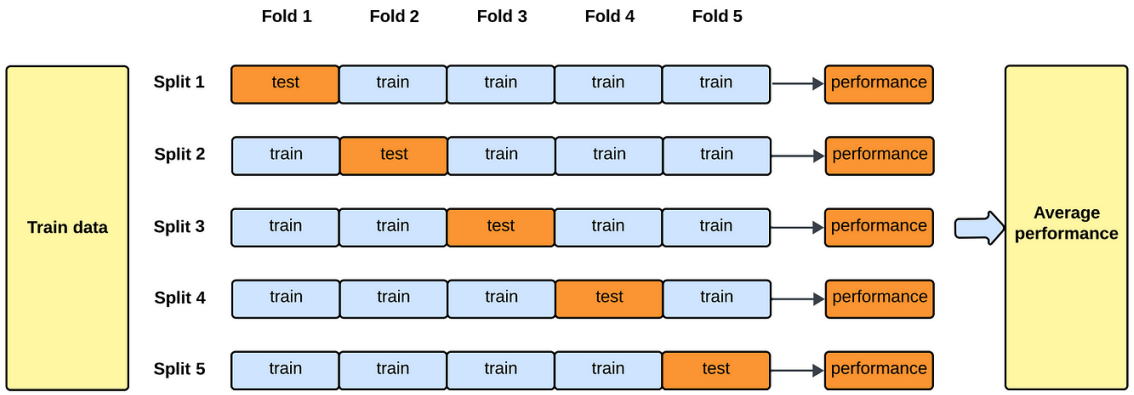

	JSD_global	MAE_global	MAPE_global	MSE_global	R^2_global	RMSE_global
Fold_1	0.000217	0.007402	4.782471	0.000183	0.989594	0.011109
Fold_2	0.000275	0.007206	4.784370	0.000100	0.988649	0.011050
Fold_3	0.000253	0.008822	4.784095	0.000122	0.988954	0.011081
Fold_4	0.000240	0.008292	4.782855	0.000113	0.989103	0.011089
Fold_5	0.000196	0.008506	4.782794	0.000199	0.989282	0.011035
Mean	**0.000236**	**0.008046**	**4.783317**	**0.000144**	**0.989116**	**0.011073**
σ	**0.00003**	**0.00071**	**0.00085**	**0.00004**	**0.00035**	**0.00003**

5 folds cross-validation

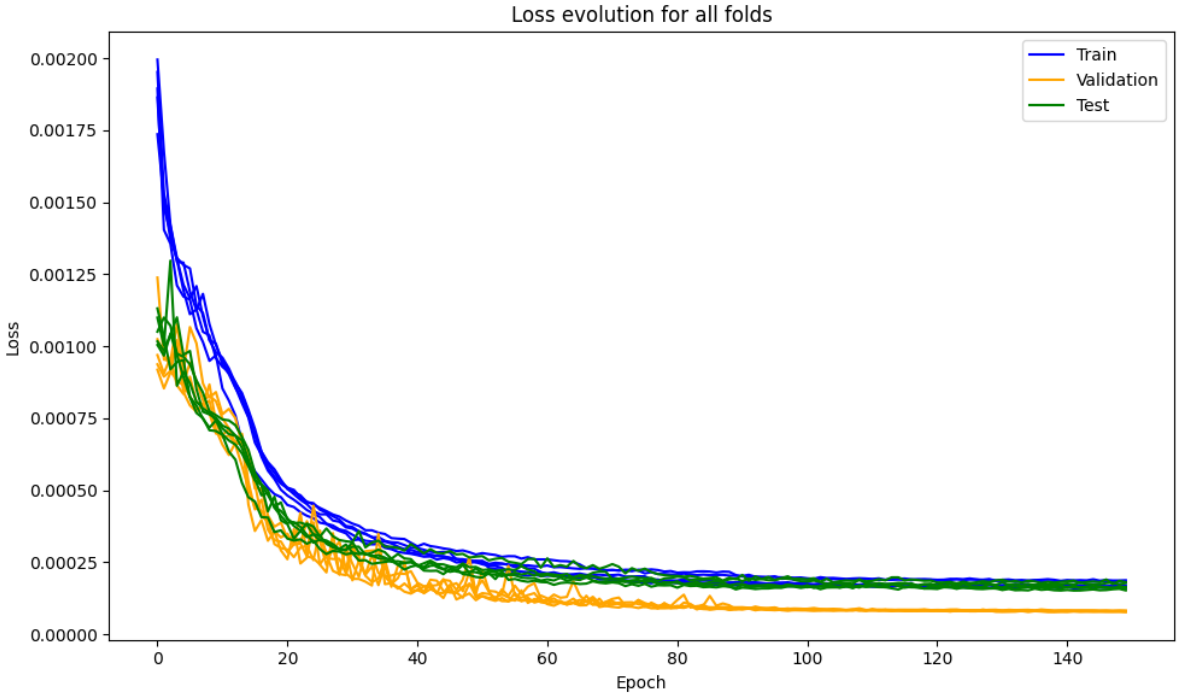

Deep Learning vs Manual Measurement

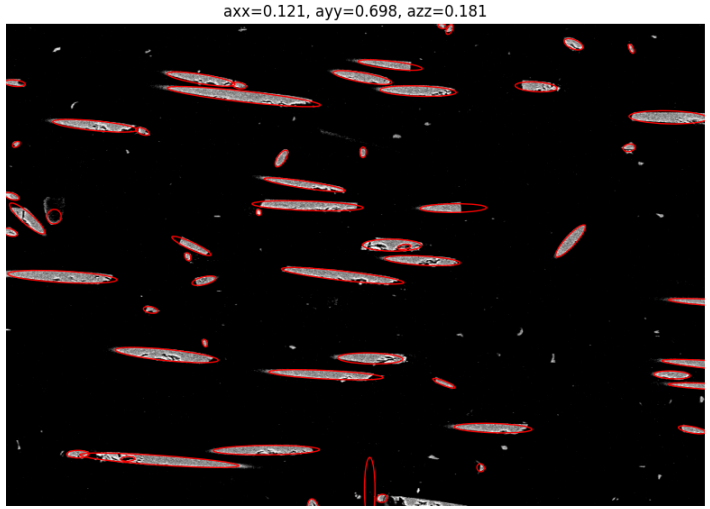

$$a_{xx} = a_{11} = \frac{1}{N}\sum_{i=1}^{N} \sin^2(\beta_i),$$

$$a_{yy} = a_{22} = \frac{1}{N}\sum_{i=1}^{N} \cos^2(\beta_i)\ \sin^2(\varphi_i)$$

$$a_{zz} = a_{33} = \frac{1}{N}\sum_{i=1}^{N} \cos^2(\beta_i)\ \cos^2(\varphi_i)$$

$$sin\,\beta = \frac{a}{b}$$

Manual

Weighted average tensor calculated manually:

$[0.11533, 0.78703, 0.09764]$

Weighted average tensor:

$$\bar{T} = \frac{\sum_{i=1}^{N} \frac{1}{z_i} \cdot T_i}{\sum_{i=1}^{N} \frac{1}{z_i}}$$

Deep Learning

Weighted average tensor calculated with Deep Learning:

$[0.10507, 0.72362, 0.17130]$

$\bar{T}$: Weighted average tensor.

T_i: Tensor corresponding to the i-th image.

z_i: Zoom level of the i-th image.

$\frac{1}{z_i}$: Weight assigned to the i-th image, inversely proportional to the zoom.

N: Total number of images.

$Mean\ Angular\ Error = 6.93º$

Workflow

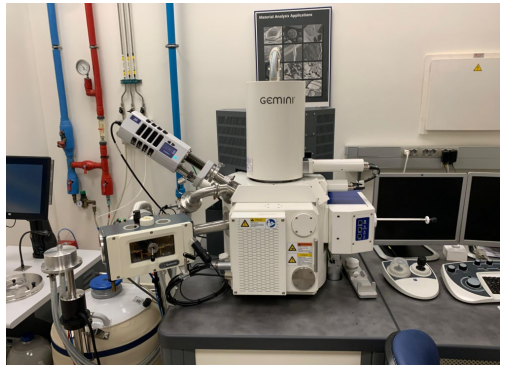

Obtaining Images

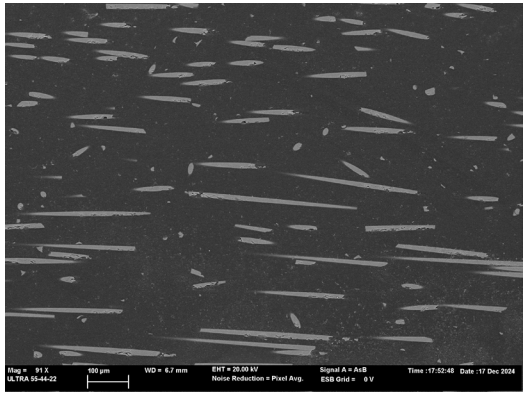



Binarize the images

Neural Network

$[a_{xx}, a_{yy}, a_{zz}]$

This process is repeated for each image

Store tensor and corresponding magnification of the image

$$\bar{T} = \frac{\sum_{i=1}^{N} \frac{1}{z_i} \cdot T_i}{\sum_{i=1}^{N} \frac{1}{z_i}}$$

Weighted Average Orientation Tensor

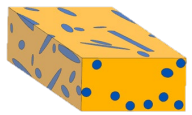

Generate microstructure and create numerical model in DIGIMAT

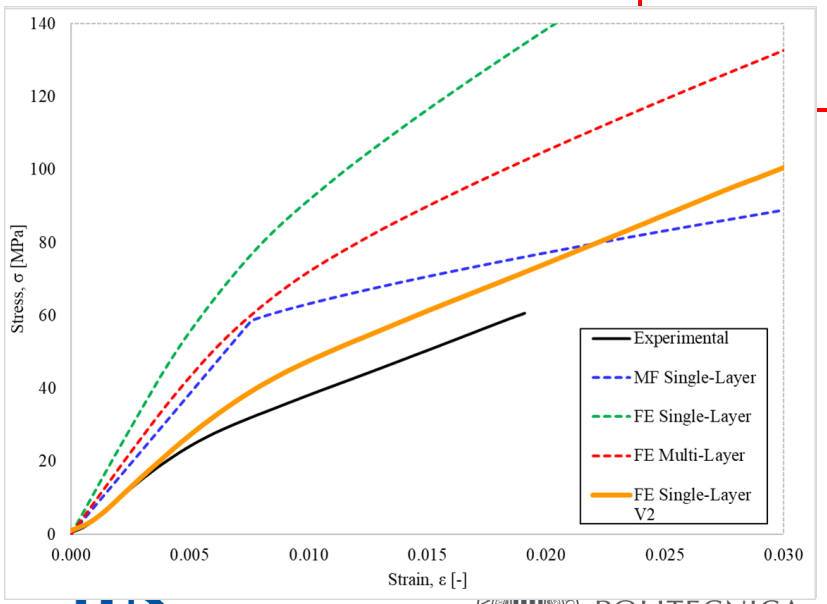

Conclusions

- Data augmentation techniques are a powerful tool to overcome data scarcity: more than 40000 images generated

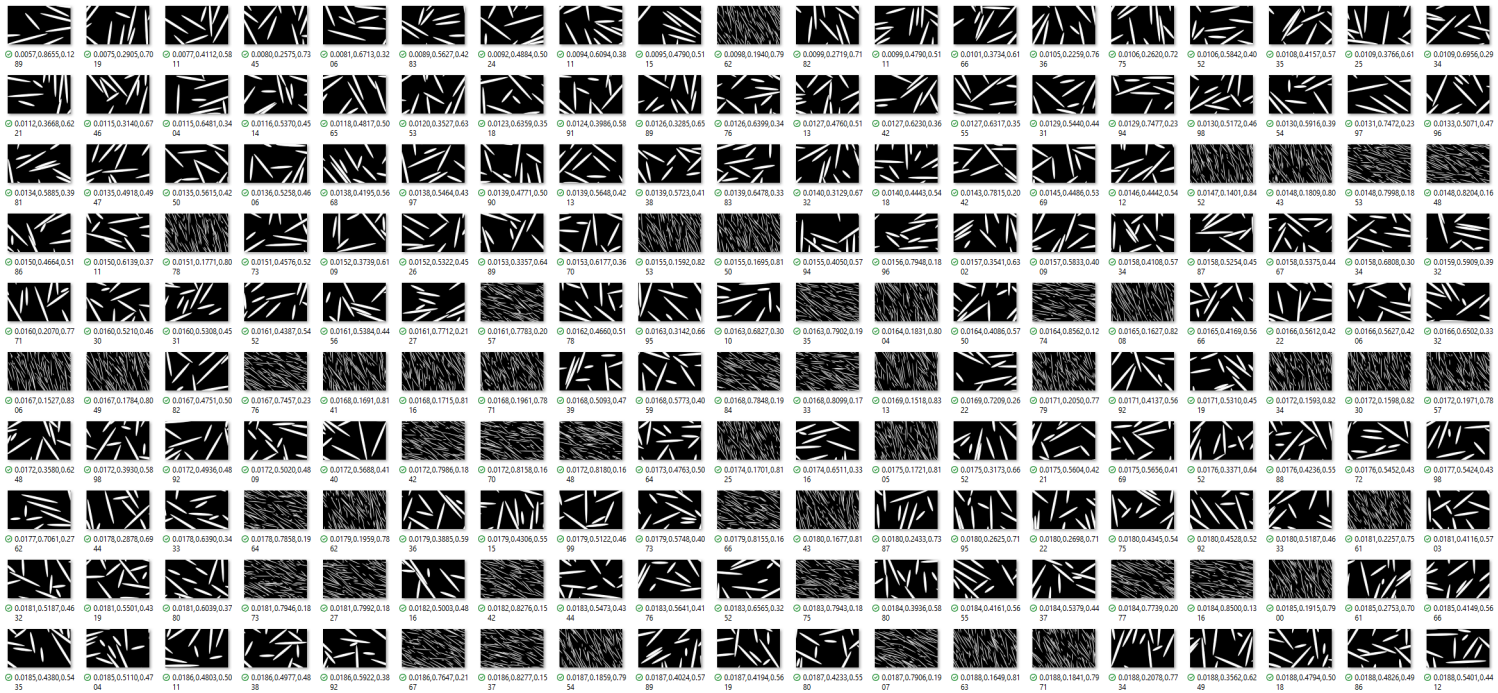

Conclusions

- Data augmentation techniques are a powerful tool to overcome data scarcity: more than 40000 images generated
- Using Deep Learning as a tool to measure the Orientation Tensor allows to process a big amount of images effortless with high accuracy

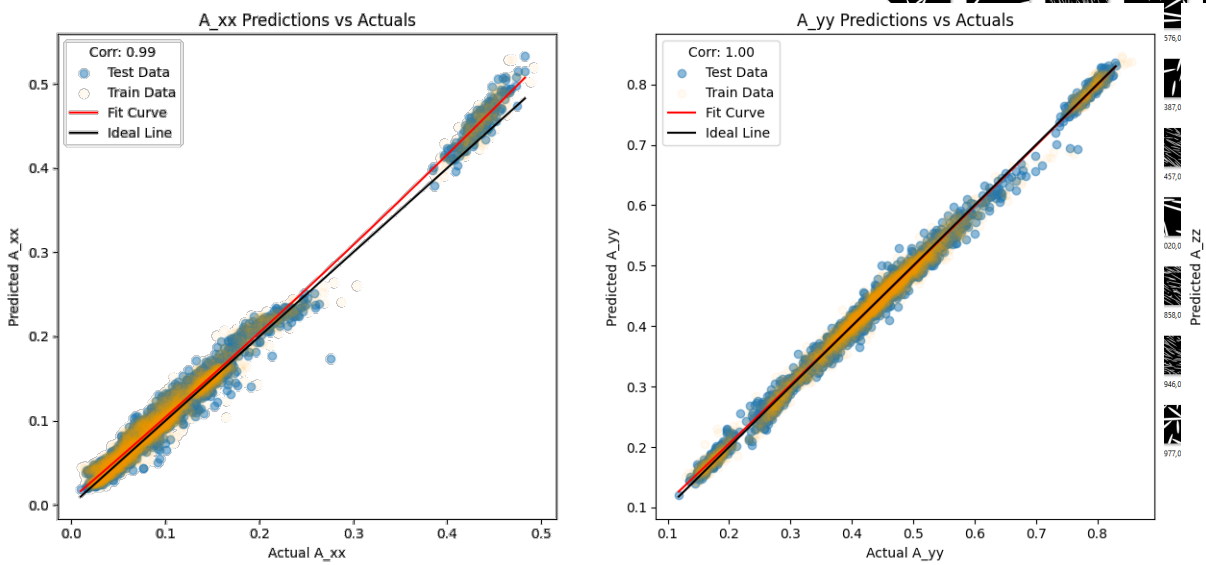

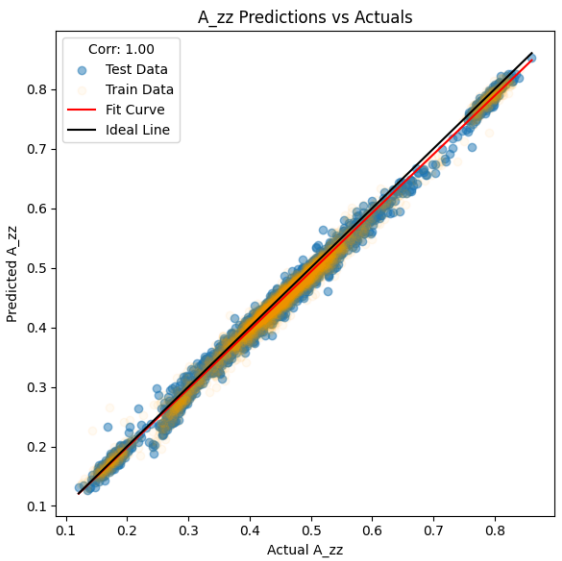





Real: [0.104, 0.132, 0.764]

Mean angular error: 0.56°

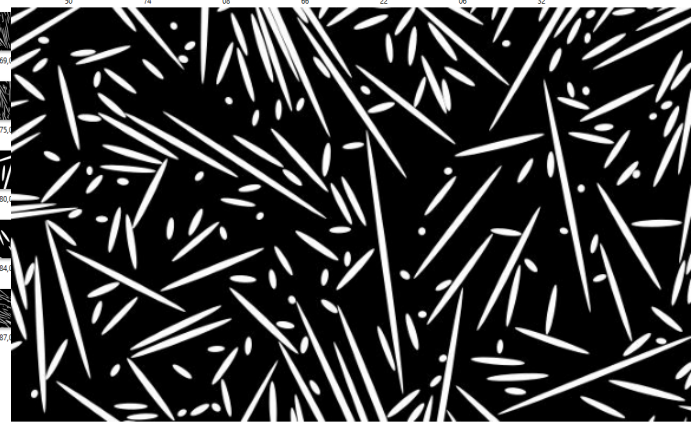

Conclusions

- Using Deep Learning as a tool to measure the Orientation Tensor allows to process a big amount of images effortless with high accuracy
- Finite Elements techniques can be highly improved thanks to Deep Learning techniques allowing to increase the accuracy of digital twins.

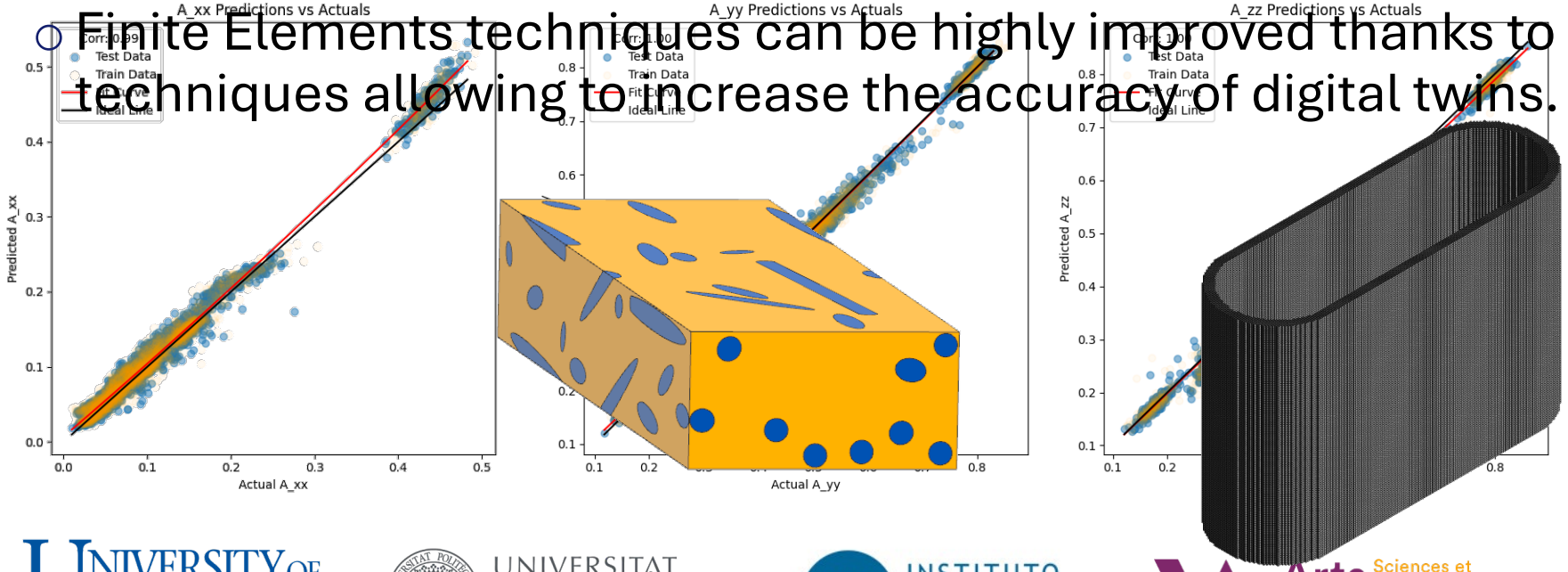



Conclusions

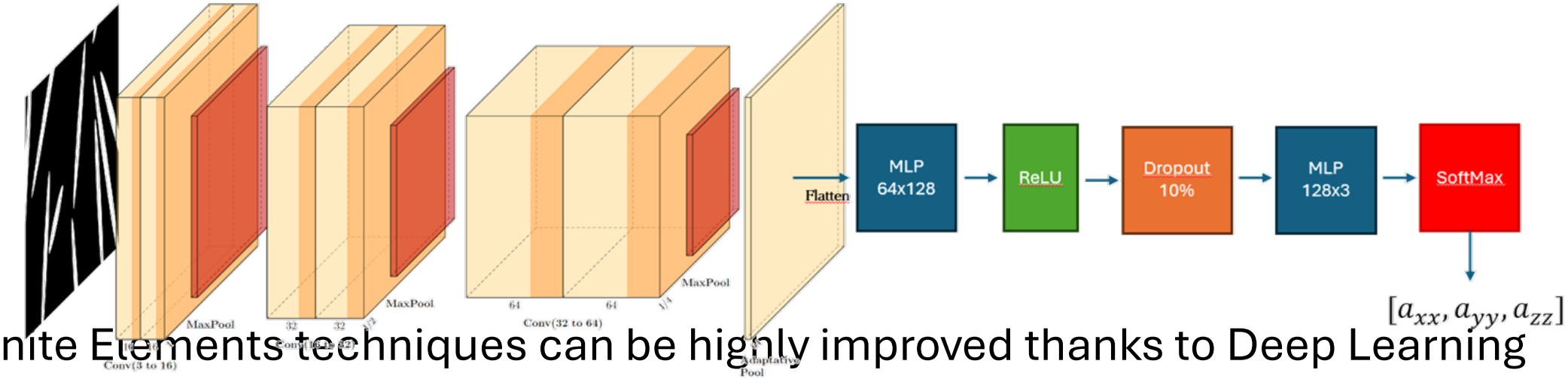

- Finite Elements techniques can be highly improved thanks to Deep Learning techniques allowing to increase the accuracy of digital twins.
- Deep Learning is a super adaptable tool for many ap s, where the main 2 difficulties are: D enough creativit n is the limit.

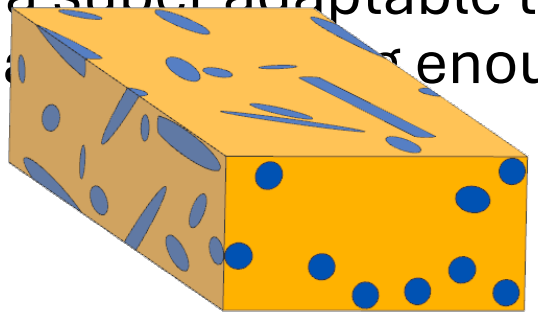

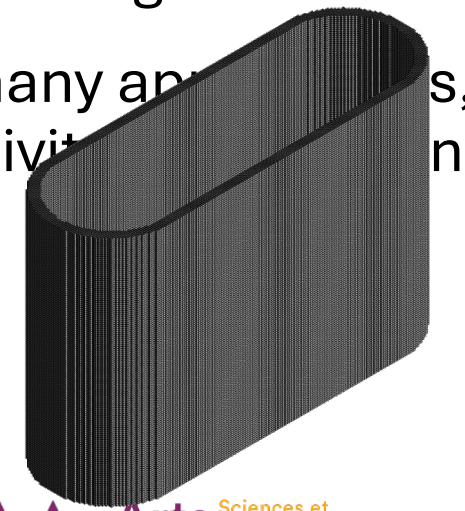

Acknowledgements

GENERALITAT VALENCIANA

INVEST/2022/131,
CIACIF/2021/286,
IDIFEDER/2021/040

GOBIERNO DE ESPAÑA
MINISTERIO DE CIENCIA E INNOVACIÓN

TED2021-130879B-C21
PID2019-108807RB-I00

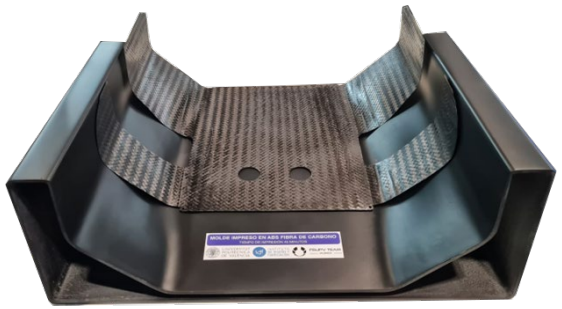



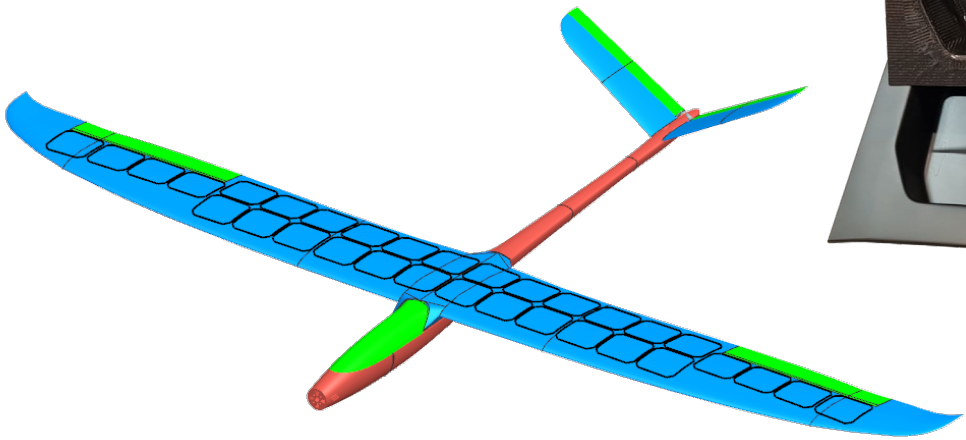

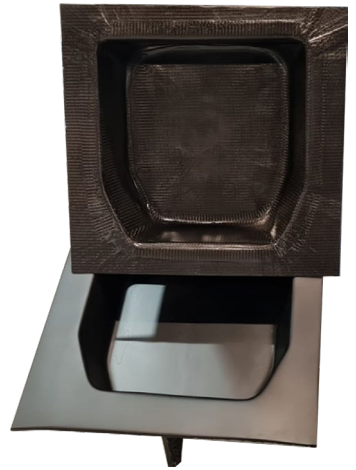

Financiado por la Unión Europea
NextGenerationEU
Plan de Recuperación, Transformación y Resiliencia

UNIVERSITAT POLITÈCNICA DE VALÈNCIA
INSTITUTO DE DISEÑO Y FABRICACIÓN
Arts et Métiers Sciences et Technologies

UNIVERSITY OF LEICESTER

Digital twin using nested machine learning for sintering deformation of ceramic-matrix composites

Jingzhe Pan*, Baber Saleem, Ran He, Peter Polak

School of Engineering, University of Leicester, Leicester, LE1 7RH, UK

UNIVERSITY OF LEICESTER

The problem

UNIVERSITY OF LEICESTER

Computer simulated sintering distortion of a CMC part using ABAQUS

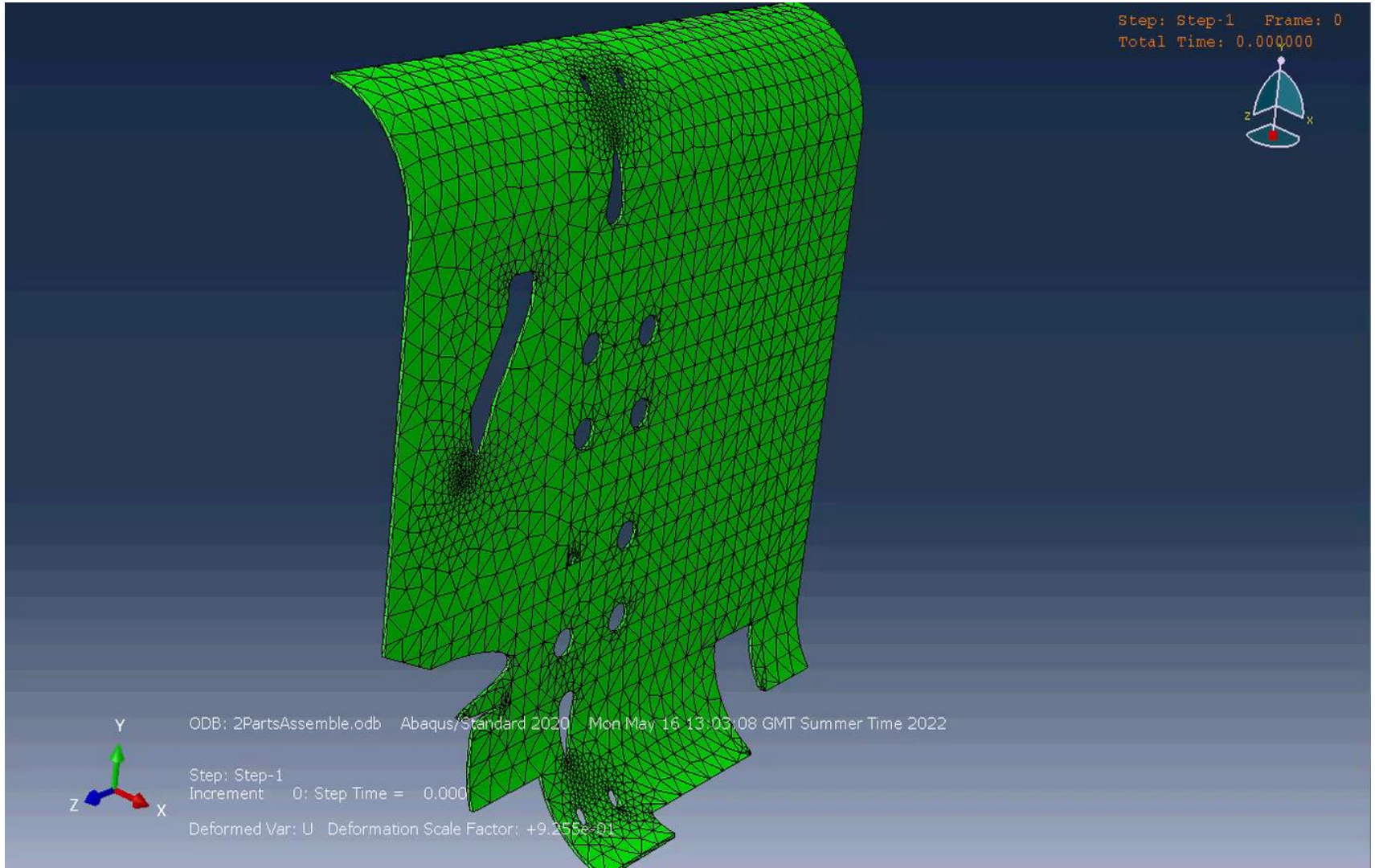

UNIVERSITY OF LEICESTER

A digital twin

UNIVERSITY OF LEICESTER

Physics-based neural network as constitutive law for finite element analysis of sintering
R He, V Ghantasala, P Polak, B Saleem, J Pan - Ceramics International, 2024
https://doi.org/10.1016/j.ceramint.2024.02.333
Machine Learning Nested in Multiphysics Finite Element Analysis: Application to Flash Sintering
R He, M Xia, P Polak, B Saleem, X Yu; J Pan, submitted to Journal of Intelligent Manufacturing

Digital twin of sintering with nested ANN, that enables commercial finite element package to do machine learning

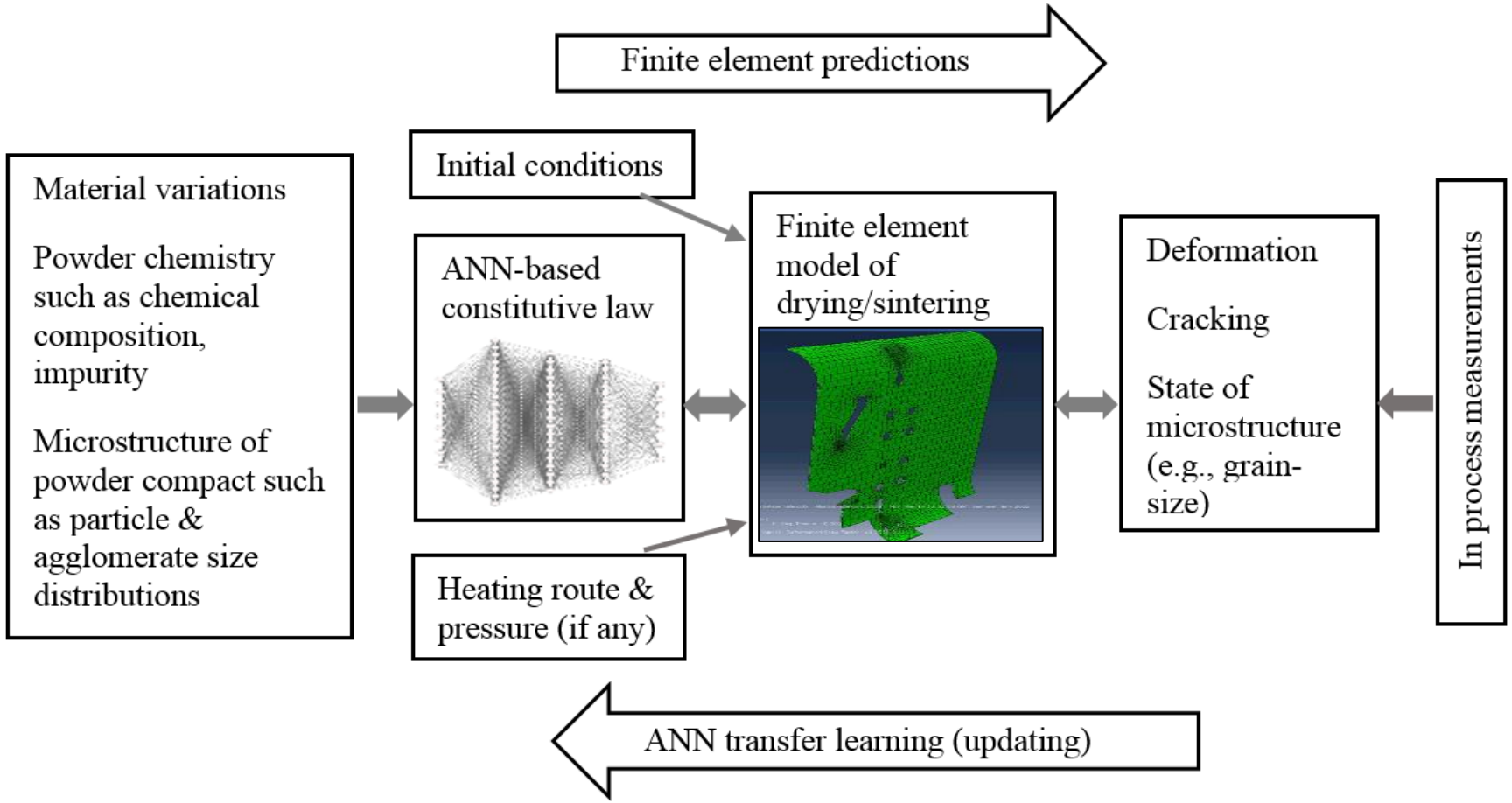

UNIVERSITY OF LEICESTER

Replace constitutive law with an ANN

UNIVERSITY OF LEICESTER

A constitutive law (using Olevsky's model as an example)

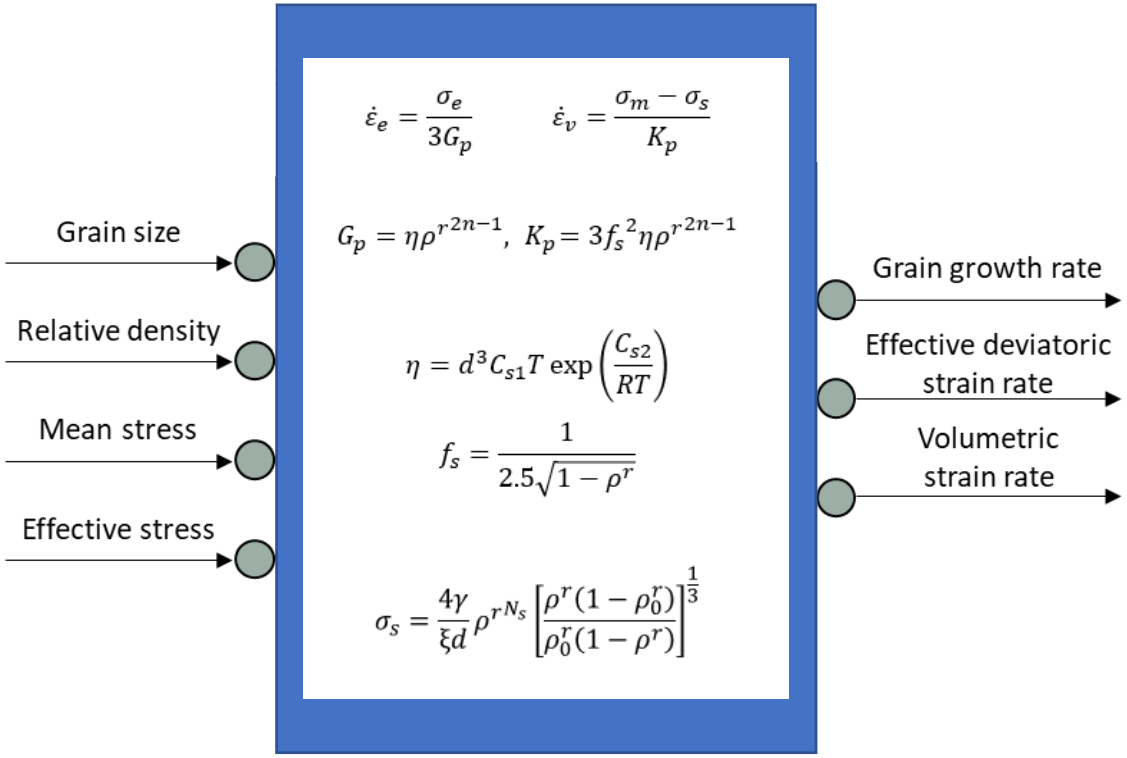

Olevsky E.A. (1998), Theory of sintering: from discrete to continuum. Review, *Mater. Sci. & Eng. R: Reports*, 40-100

UNIVERSITY OF LEICESTER

A constitutive law in the format of an ANN

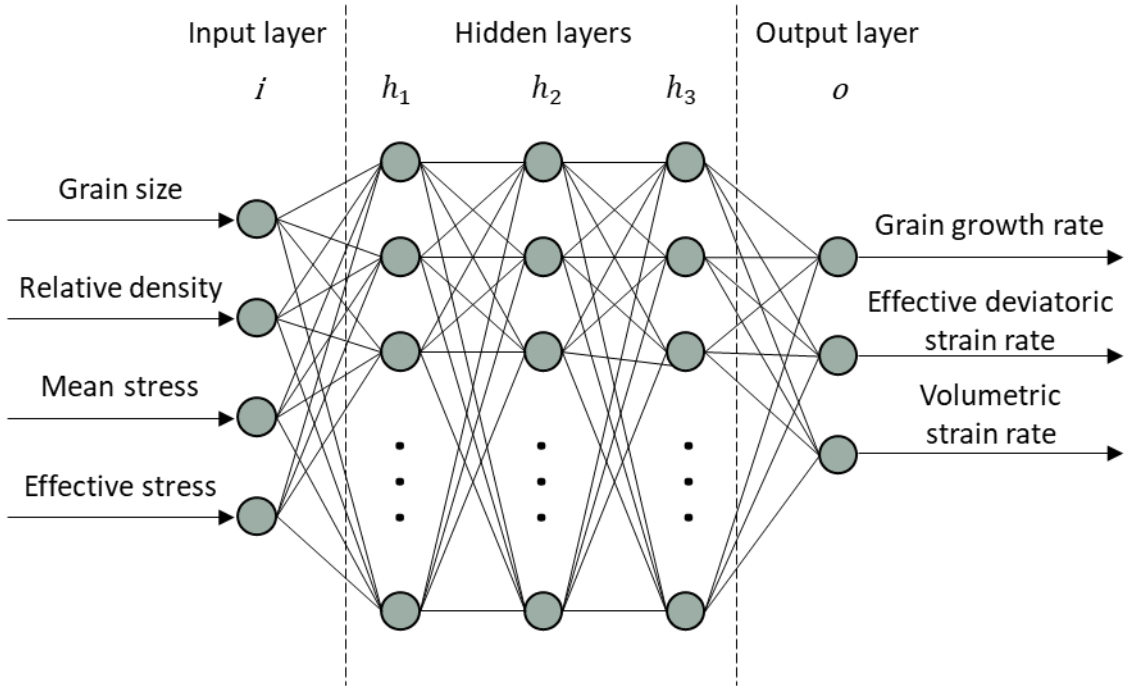

UNIVERSITY OF LEICESTER

Implementation of ANN in Abaqus using CREEP subroutine

```
      SUBROUTINE CREEP(DECRA,DESWA,STATEV,SERD,EC,ESW,P,QTILD,
     1 TEMP,DTEMP,PREDEF,DPRED,TIME,DTIME,CMNAME,LEXIMP,LEND,
     2 COORDS,NSTATV,NOEL,NPT,LAYER,KSPT,KSTEP,KINC)
C
      INCLUDE 'ABA_PARAM.INC'
C
      CHARACTER*80 CMNAME
C
      DIMENSION DECRA(5),DESWA(5),STATEV(*),PREDEF(*),DPRED(*),
     1 TIME(2),EC(2),ESW(2),COORDS(*)

c       user coding t

      RETURN
      END
```

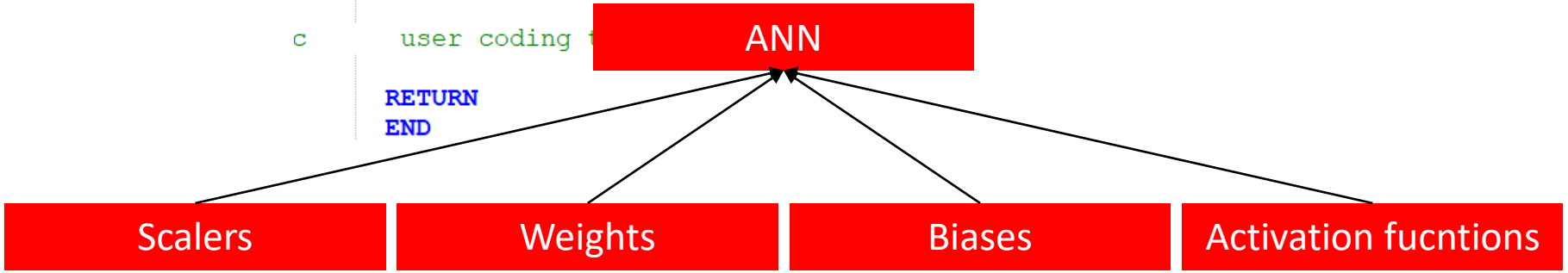



UNIVERSITY OF
LEICESTER

Training the ANN

UNIVERSITY OF LEICESTER

A constitutive law in the format of an ANN

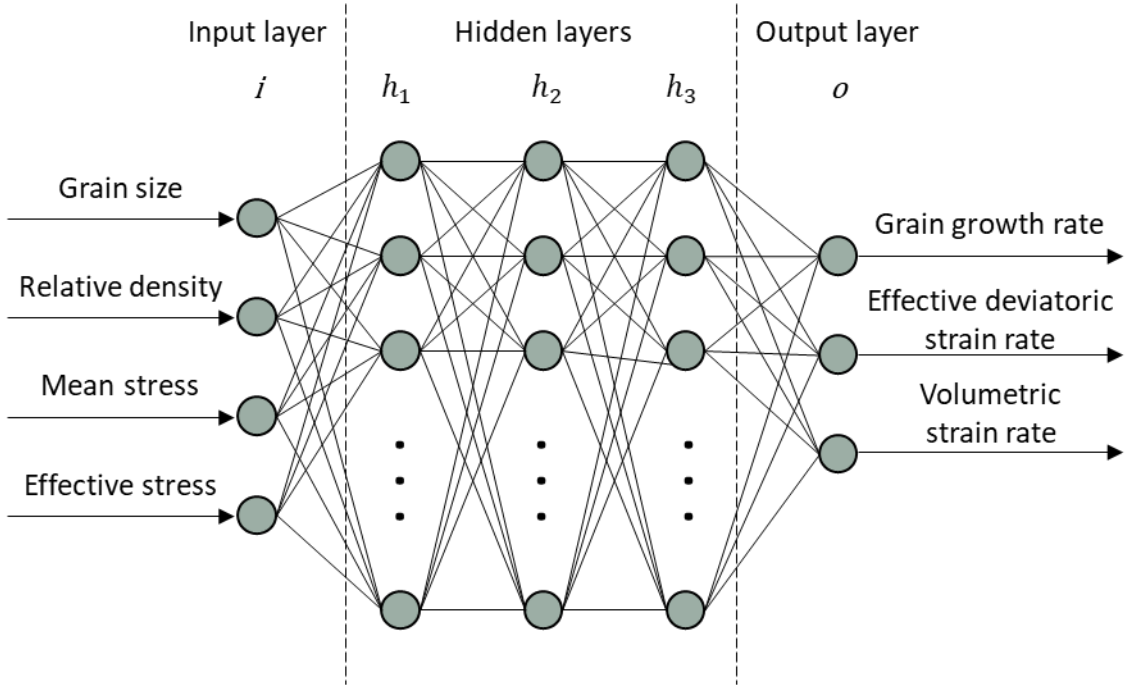

Forward calculation

$$z_j^{lk} = f\left(z0_j^{lk}\right) = f\left(\sum_i \left(w_{ji}^l z_i^{(l-1)k}\right) + b_j^l\right)$$

UNIVERSITY OF LEICESTER

Approach 1 – standalone training

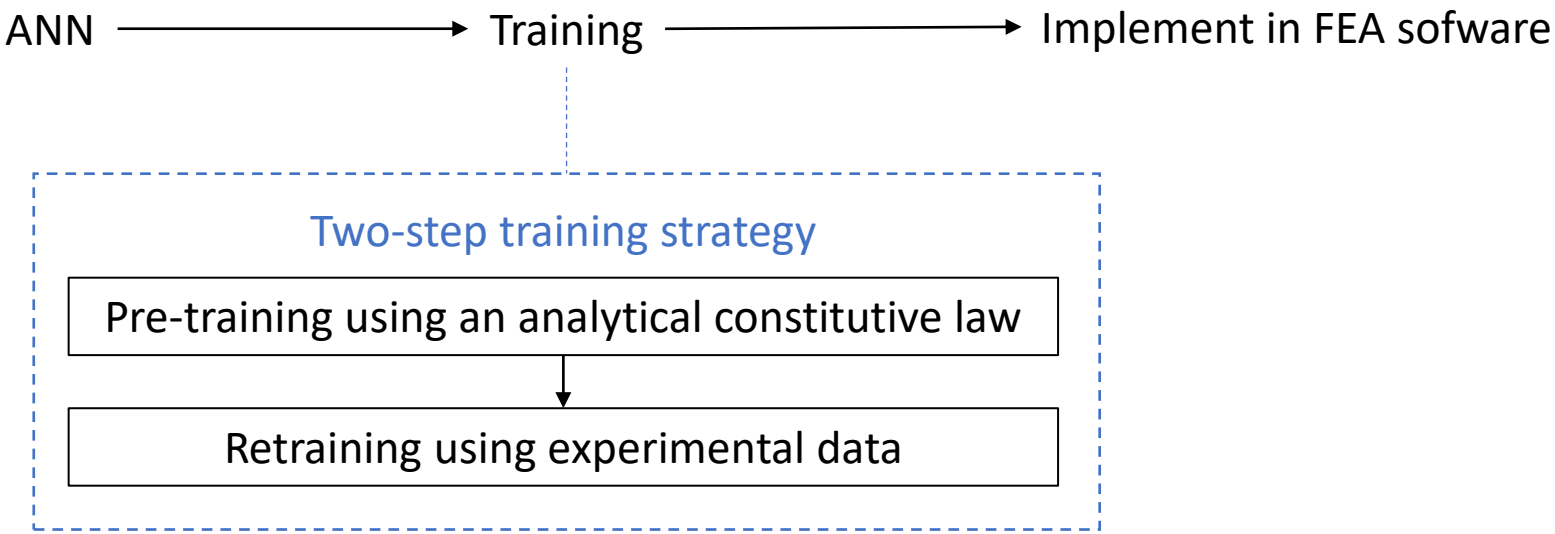

UNIVERSITY OF LEICESTER

Physics-based neural network as constitutive law for finite element analysis of sintering
R He, V Ghantasala, P Polak, B Saleem, J Pan - Ceramics International, 2024
https://doi.org/10.1016/j.ceramint.2024.02.333

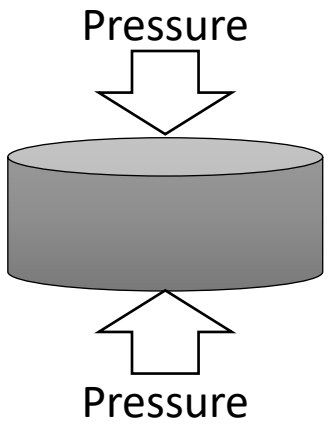



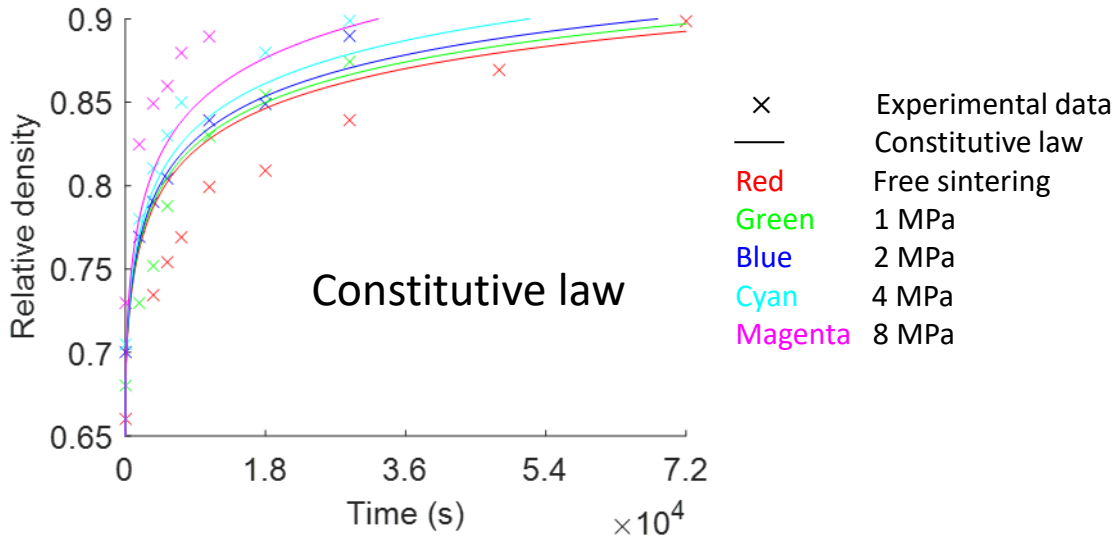

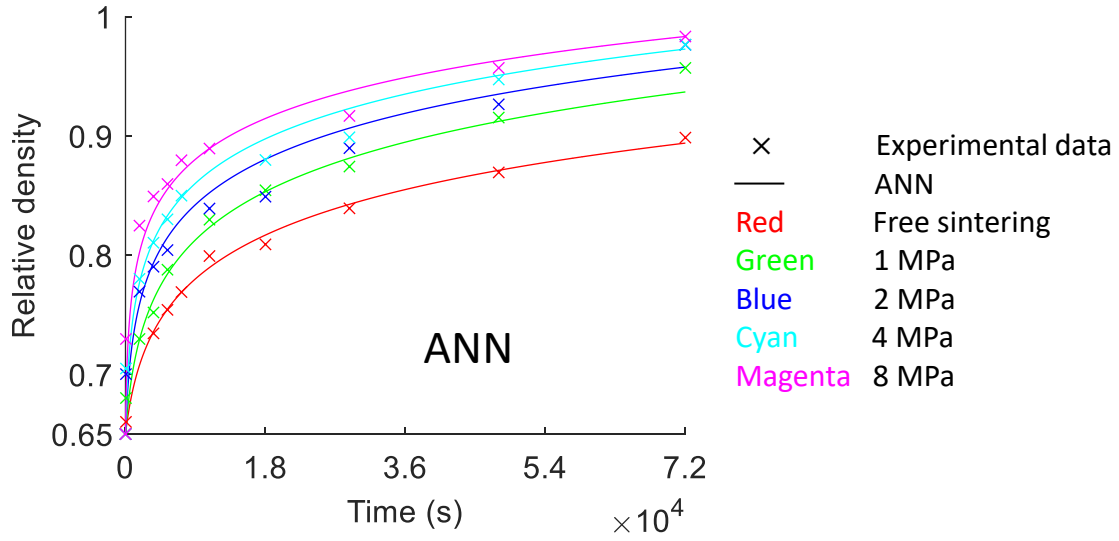

Machine Learning Nested in Multiphysics Finite Element Analysis: Application to Flash Sintering
R He, M Xia, P Polak, B Saleem, X Yu; J Pan, submitted to Journal of Intelligent Manufacturing

Approach 2 – training ANN nested in finite element analysis using a new backpropagation algorithm

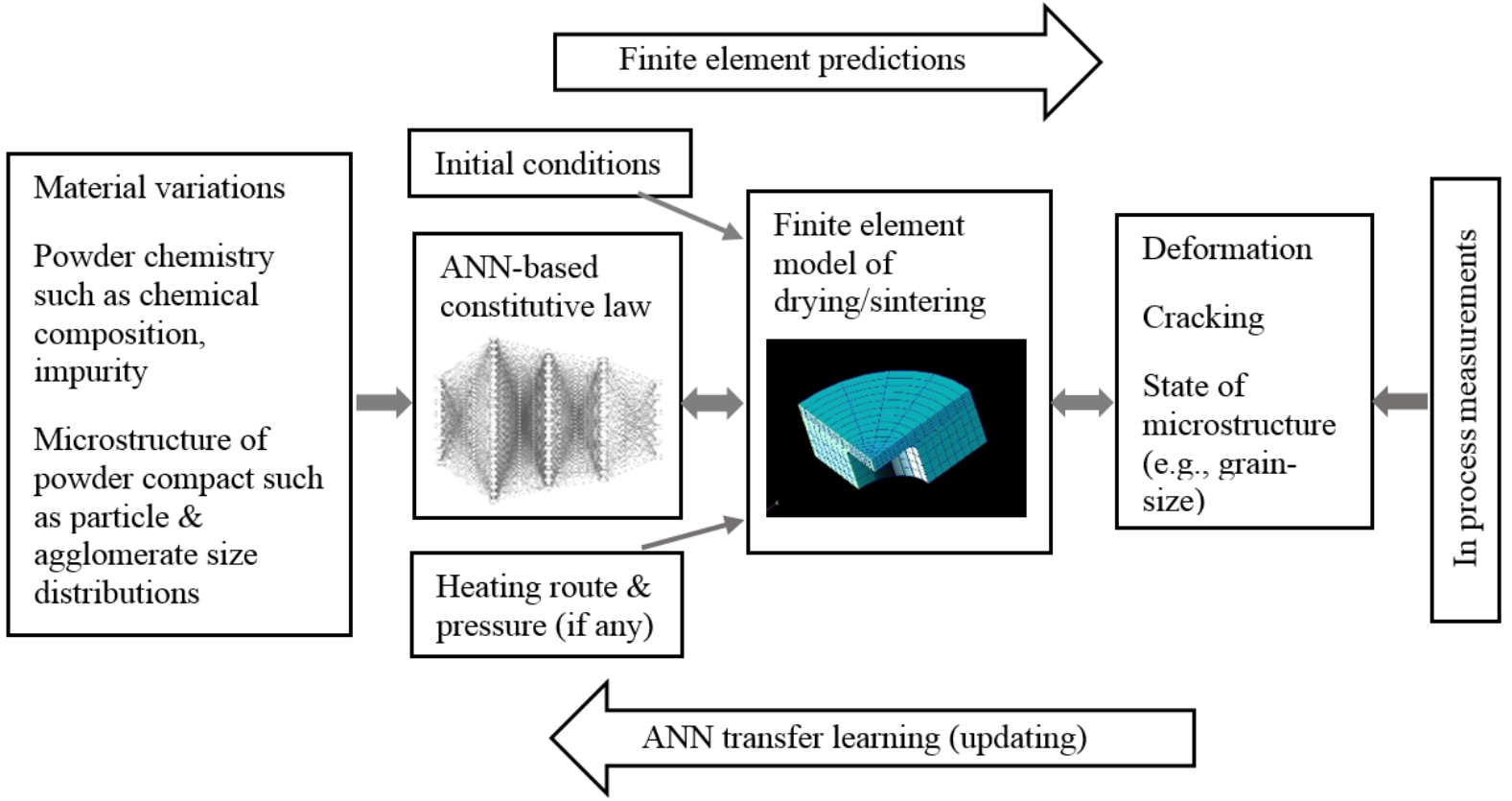

Approach 2 – training ANN nested in finite element analysis using a new backpropagation algorithm

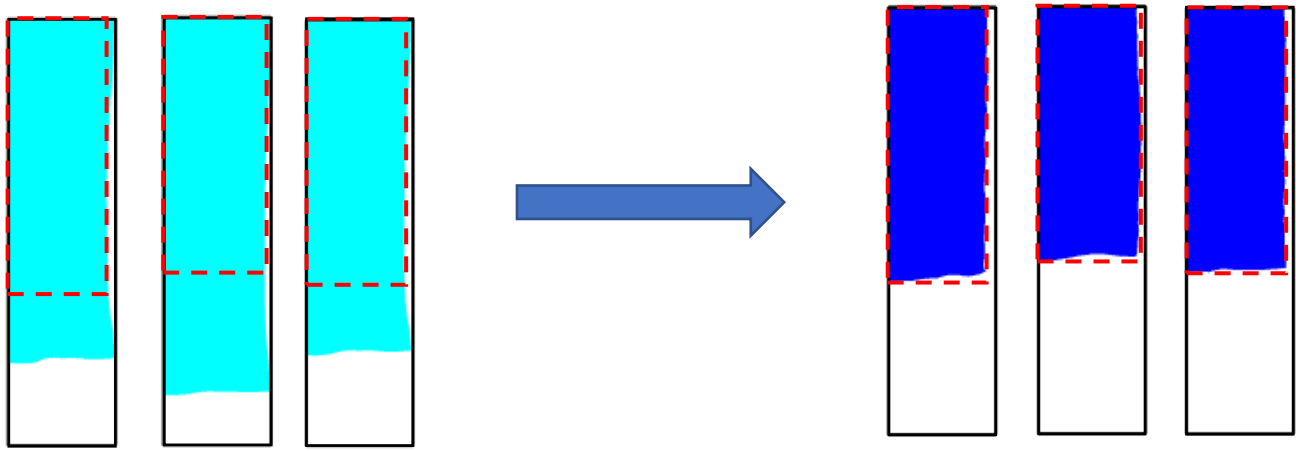

Application of DFEM in Sintering Distortion Analysis of Oxide-Oxide Ceramic Matrix Composite: Digital Twin, Baber Saleem, Ran He, Peter Polak, James Lander, Ian Edmonds, Xiaoxia Yu, Jingzhe Pan, 2025, accepted by International Journal of Ceramic Engineering and Science

Our best effort for a CMC panel so far – ongoing work

UNIVERSITY OF LEICESTER

Application of DFEM in Sintering Distortion Analysis of Oxide-Oxide Ceramic Matrix Composite: Digital Twin, Baber Saleem, Ran He, Peter Polak, James Lander, Ian Edmonds, Xiaoxia Yu, Jingzhe Pan, 2025, accepted by International Journal of Ceramic Engineering and Science

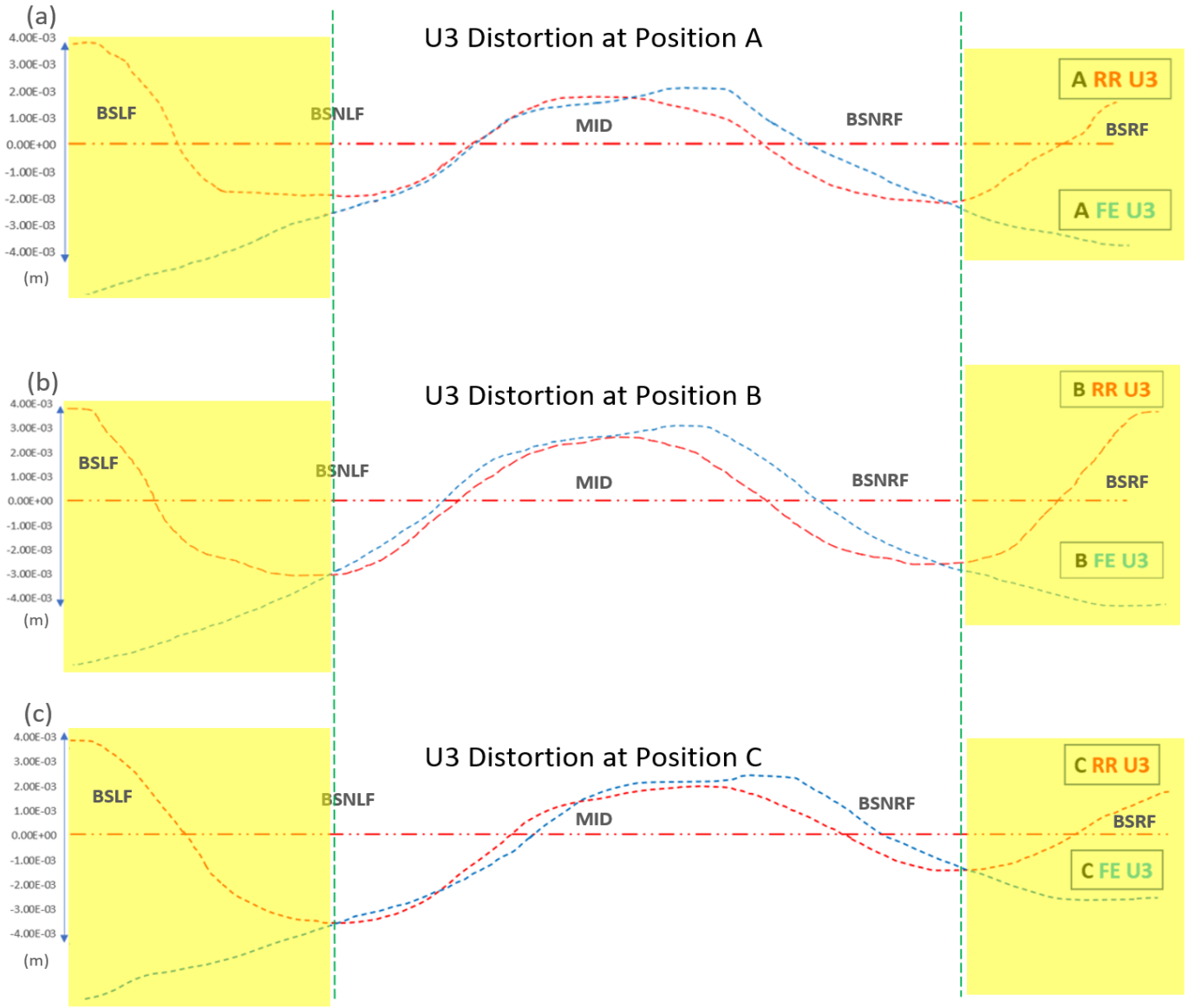

UNIVERSITY OF LEICESTER

Conclusion:

We have developed digital twins with nested ANNs, which enables commercial finite element package to do machine learning.

Acknowledgment



The Midlands

Midlands advanced ceramics for industry 4.0

SIPF investment: £18 million

The Midlands Industrial Ceramics Group (MICG) is a consortium of researchers, manufacturers and end-users. Together, the group will develop streamlined processes for proving and bringing new advanced ceramics technologies to market faster, with less energy usage and lower carbon emissions. This will enable effective problem-solving and faster commercialisation of new products, unlocking improved performance for next generation products including:

- fuel cells and batteries
- 5G communications
- ceramic-matrix composites for aero engines
- medical devices.

It will also boost the competitiveness of manufacturers in the region by developing a robust advanced ceramics supply chain, able to export into one of the fastest growing international industry sub-sectors. Advanced ceramics are vital 'enablers' for many manufacturing sectors





Introducing Midlands Advanced Ceramics for Industry 4.0, the project that will help the Midlands' ceramics industry to innovate more efficiently. Video credit: UKRI. On-screen captions and an auto generated transcript is available on YouTube.

Digital Twin Laboratory

School of Engineering, University of Leicester

Project PI - Prof Jingzhe PAN (jp165@le.ac.uk)

UNIVERSITY OF LEICESTER

Vision

Our vision is to revolutionise ceramic manufacturing by enabling seamless, real-time interactions between computer simulations and real-world processes. We continuously update finite element models (FEM) with real-time data to eliminate uncertainties and enhance precision

Through **Digital Twinning**, we aim to optimise manufacturing efficiency and address critical industrial challenges, such as controlling sintering shrinkage and distortion, ensuring precision in advanced ceramics and other high-value applications.

Leveraging Machine Learning & Artificial Neural Networks (ANNs):
Improving the accuracy of sintering simulations by replacing empirical laws in finite element analysis with nested ANNs trained with experimental data, enhancing industrial processes like flash sintering.

Predictive Accuracy & Custom Subroutines: By developing custom UMAT, CREEP and MATLAB unites for ABAQUS and COMSOL (using Fortran, Python, and MATLAB), we integrate machine learning and physics-based neural networks, optimizing manufacturing processes and advancing predictive accuracy in critical industrial applications.

Industrial Challenge: Controlling Sintering **Shrinkage** and **Distortion**

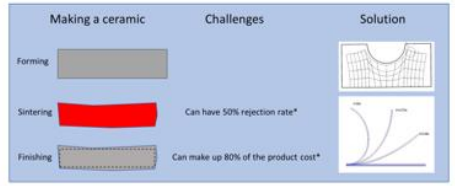

Digital Twin Lab: Shaping Future Ceramic Manufacturing



Funded for £2.1 million by UKRI's Strength in Places Fund

Impact: Transforming Advanced Ceramics Manufacturing through real-time data integration and digital twin models nested with ANNs, we aim to reduce inefficiencies, lower rejection rates, and minimize post-sintering costs. This approach fine-tunes manufacturing conditions, reducing waste and energy consumption, and promoting sustainable practices.

Collaborative Network: UK Industries and Universities (logos displayed) contribute data, research, and testing environments, ensuring effective integration of digital twins into real-world processes.

MICG Midlands Industrial Ceramics Group · University of Birmingham · Loughborough University · LUCIDEON · Morgan Advanced Materials · Rolls-Royce

Research Expertise of Project Team Members



Prof. Jingzhe Pan
Project PI
Digital twins for manufacturing process of advanced ceramics using finite element analysis with deep machine leaning.

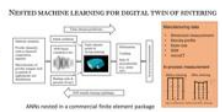



Miss Mingxuan Xia
PhD student
Development of ***nested machine learning algorithm.***
Modelling polymer degradation using nested machine learning.

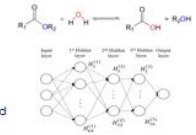



Dr. Ran He
Research fellow
ANNs as constitutive laws in finite element analysis of sintering deformation.
Digital twin of ***flash sintering*** using nested machine learning.

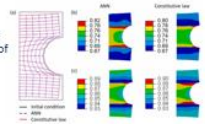

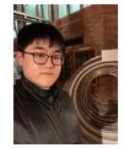

Mr. Michael Yu
PhD student
Finite Element Analysis of ***polyphase flash sintering.***
CFD characterisation of 3D-printed ceramic filters.

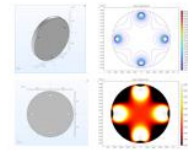



Mr. Peter Polak
Research fellow
ANNs as viscosities in finite element analysis of sintering deformation.
Digital twin for ***industrial sintering*** process using nested machine learning

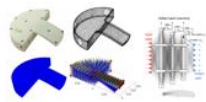



Dr. Xiaoxia Yu
Research fellow
Comparative study and documentation of numerical tools used in digital twins of ceramic manufacturing.

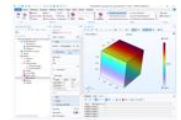



Dr. Baber Saleem
Research fellow
Densification based finite element analysis of sintering deformation.
Master sintering curves.
Digital twin for sintering of ***ceramic matrix composites.***

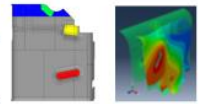

$$\dot{\varepsilon}_{ij} = \frac{s_{ij}}{2\eta_S} + \frac{\sigma_m}{3\eta_B}\delta_{ij} - \frac{\sigma_z}{3\eta_B}\delta_{ij}$$

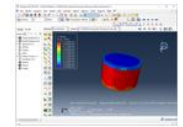

A Simulation-Based Machine Learning Approach for Optimizing Preform Charges in Sheet Molding Compound Manufacturing

Mikhael Tannous[1], Sebastian Rodriguez[1], Chady Ghnatios[2], and Francisco Chinesta[1]

[1]PIMM, ENSAM Institute of Technology, Paris − France
[2]University of North Florida, Jacksonville− USA

August, 2025

This project has received funding from the European Union's **Horizon Europe** Research and Innovation programme under Grant Agreement No. 101091449

Motivation

The Sheet Molding Compound (SMC) process is widely used for producing composite structures in high-volume manufacturing due to its efficiency and scalability.

- **Challenges associated with complex mold geometries**
  - What is the initial charge shape for optimal mold filling and low material overflow ?
  - How to reduce flow bouncing on the boundary since it could perturbate fiber orientation ?

- **State of the art solution**
  - If assumed initial charge shape, simulation can predict final material distribution along with fiber orientation.
  - Requires trial and error to find the initial shape.
  - No scientific approach or adapted simulation tool.
  - **Limitation**:
    - Computationally expensive
    - Non-optimized initial charge shapes

- **Objectives**:
  - Develop a reverse flow simulation tool that can compute the initial charge shape if given final mold geometry.
  - Create a digital twin of the SMC reverse simulation that can predict initial charge shape in real-time.
  - In this research, we first limit our approach for 2D molds.

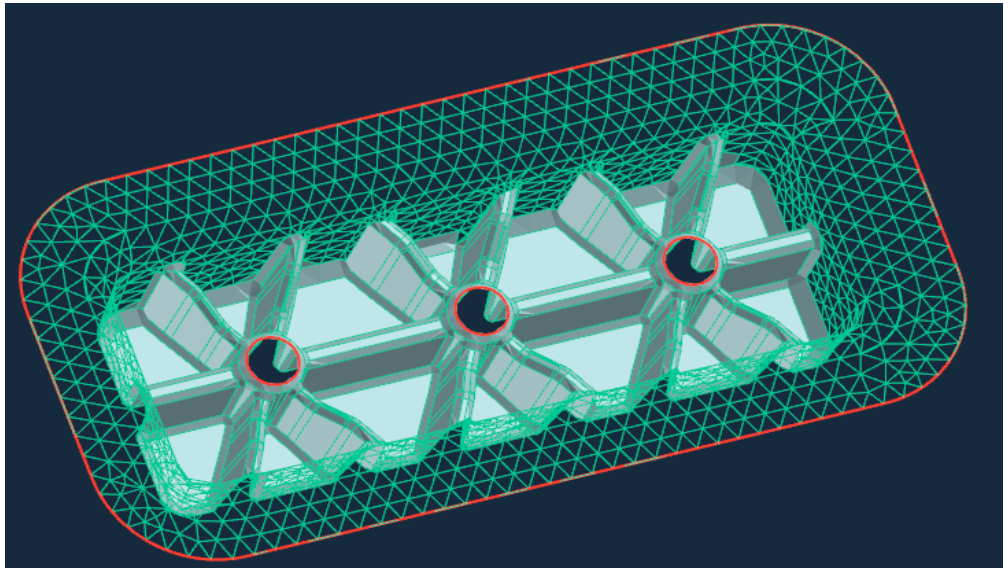

SMC simulation on a part manufactured by MARELLI as a technology demonstrator for the SMC process

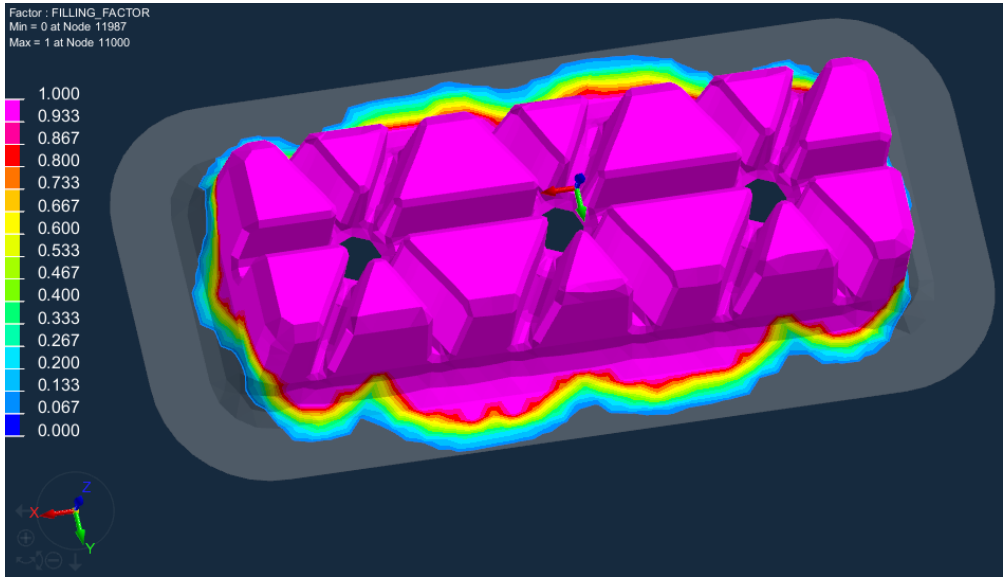

Reversing the SMC flow simulation

SMC flow simulation:

- SMC simulation enabled by solving [1, 2] :
  - Stokes equation simplified for narrow gaps by lubrication theory : $\boxed{\nabla \boldsymbol{P} = \eta \Delta \boldsymbol{v}}$
    - η = dynamic viscosity,
    - $\boldsymbol{P}$ = Pressure field
    - $\boldsymbol{v}$ = velocity field
  - Constant mesh grid

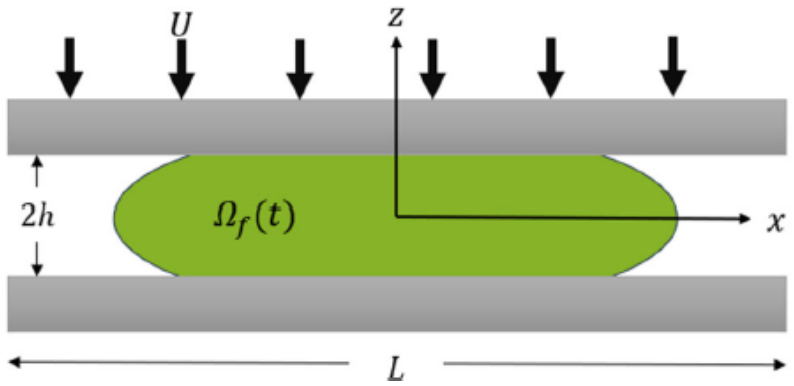

- We distinguish fluid domain $\Omega_f(t)$ where $\boldsymbol{P}$ is to be computed from empty domain $\Omega_e(t)$ where $\boldsymbol{P}$=0
- By setting appropriate BCs, the average velocity field in 2D : $\boxed{\tilde{\boldsymbol{v}}(\boldsymbol{x},\mathrm{y}) = -\frac{h^2}{3\eta}\nabla \boldsymbol{P}}$
- Since the fluid domain is evolving, we need to describe the fluid front by :

$$\boldsymbol{I}(\boldsymbol{x},t) = \begin{cases} 1 \text{ if } & \boldsymbol{x} \in \Omega_f(t) \\ 0 \text{ if } & \boldsymbol{x} \in \Omega_e(t) \end{cases} \text{ with: } \boldsymbol{I}(\boldsymbol{x}, \ t=0) = I_{init}$$

- $\boldsymbol{I}(\boldsymbol{x},t)$ is described by: $\boxed{\frac{\partial \boldsymbol{I}(\boldsymbol{x},t)}{\partial\, t} + \boldsymbol{v}(\boldsymbol{x},t).\nabla \boldsymbol{I}(\boldsymbol{x},t) = 0}$ (1)
- Combining the equations of $\boldsymbol{P}$ and $\boldsymbol{I}$ leads to the weak-formulation:

$$\boxed{\int_\Omega \left(\boldsymbol{I}\nabla\widehat{\boldsymbol{P}}\left(\frac{h^2}{3\eta}\nabla \boldsymbol{P}\right) + (\boldsymbol{1}-\boldsymbol{I})\widehat{\boldsymbol{P}}\boldsymbol{P}\right)d\Omega = \int_\Omega \left(\boldsymbol{I}\widehat{\boldsymbol{P}}\widetilde{\boldsymbol{U}}\right)d\Omega} \quad (2)$$

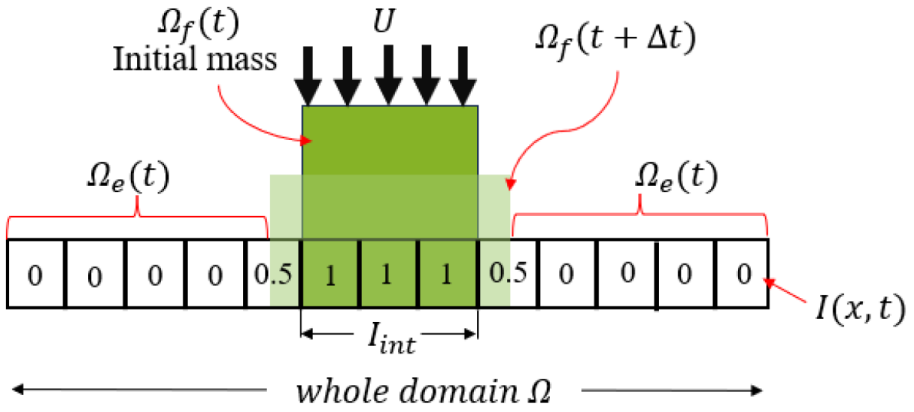

References:

[1] *J. García, L. Gascón and F. Chinesta. A fixed mesh numerical method for modelling the flow in liquid composites moulding processes using a volume of fluid technique.Computer Methods in Applied Mechanics and Engineering, 192(7–8): 877–893, 2003*.

[2] F. Ebrahimian, S. Rodriguez, D. Di Lorenzo and F. Chinesta, Optimization of precharge placement in sheet molding compound process. International Journal of Material Forming. Vol. 17, 2024.

SMC flow simulation:

- Solving eq.(1) and eq.(2) numerically includes using flux limiters for $\boldsymbol{I}$:

$$\frac{\partial \boldsymbol{I}(\boldsymbol{x},t)}{\partial\, t} + \boldsymbol{v}(\boldsymbol{x},t).\nabla \boldsymbol{I}(\boldsymbol{x},t) = 0$$

$$\int_{\Omega} \left(\boldsymbol{I}\nabla\widehat{\boldsymbol{P}}\left(\frac{h^2}{3\eta}\,\nabla \boldsymbol{P}\right) + (\mathbf{1}-\boldsymbol{I})\widehat{\boldsymbol{P}}\boldsymbol{P} \right) d\Omega = \int_{\Omega} \left(\boldsymbol{I}\widehat{\boldsymbol{P}}\widetilde{\boldsymbol{U}}\right) d\Omega$$

- For cell e, field values at time step t_{i+1} are deduced from time step t_i:

$$\boldsymbol{I}_{i+1}^{e} = \boldsymbol{I}_{i}^{e} - \boxed{\frac{\Delta t}{A(e)} \sum_{j=1}^{3} l^{ej} \hat{\boldsymbol{f}}^{ej}.\boldsymbol{n}^{ej}} \rightarrow \boldsymbol{\Phi} = \text{flow flux}$$

$$h(t_{i+1}) = h_0 - \frac{U * t_{i+1}}{2}$$

Reverse SMC flow

$$\boldsymbol{I}_{i+1}^{e} = \boldsymbol{I}_{i}^{e} + \boxed{\frac{\Delta t}{A(e)} \sum_{j=1}^{3} l^{ej} \hat{\boldsymbol{f}}^{ej}.\boldsymbol{n}^{ej}}$$

$$h(t_{i+1}) = h_0 + \frac{U * t_{i+1}}{2}$$

- With:
  - $A(e)$ is the area of the control volume
  - $\boldsymbol{n}^{ej}$ is the outward unit vector on the common edge of control volumes e and j
  - l^{ej} is the length of that edge
  - $\hat{\boldsymbol{f}}^{ej}.\boldsymbol{n}^{ej}$ represents the fluid flux across this edge.

Simulation conditions

- 1000 simulation performed for diverse 2D mold shapes

- Reverse flow simulation starting with a charge thickness of 5mm.
  - Define fluid domain using control points forming a closed curve
  - Use NURBS to avoid sharp corners

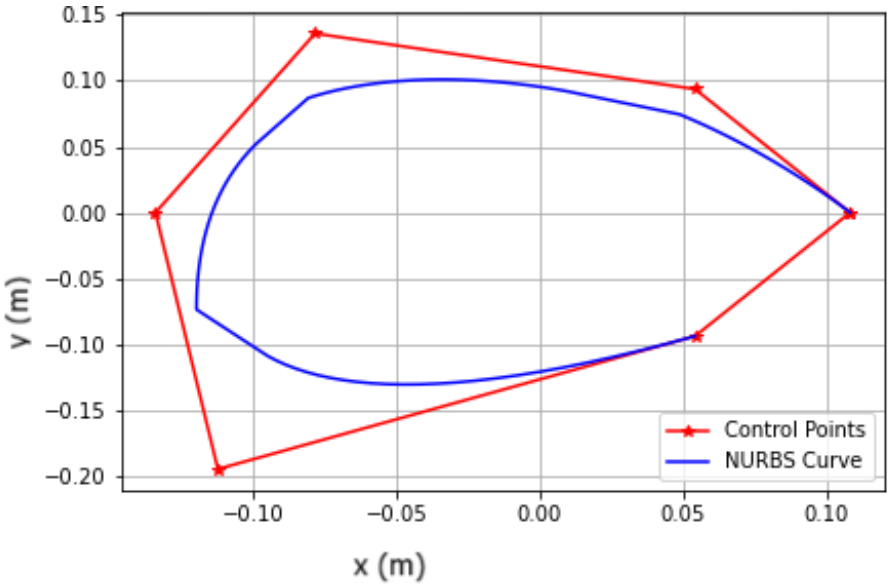

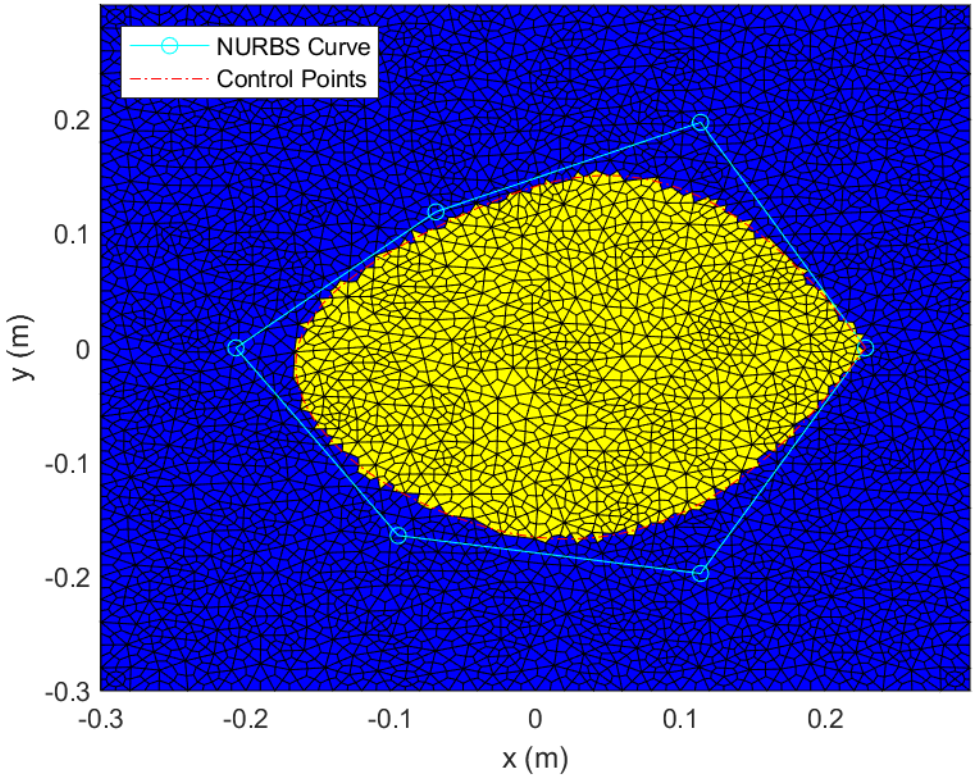

- Mold velocity 1 mm/s for 36s with 12 000 time steps.

- Computational cost: ~12 min on a: 13th Gen Intel Core i9-13950HX CPU clocked at 2.20 GHz and equipped with 32GB of memory.

Simulation applications and results

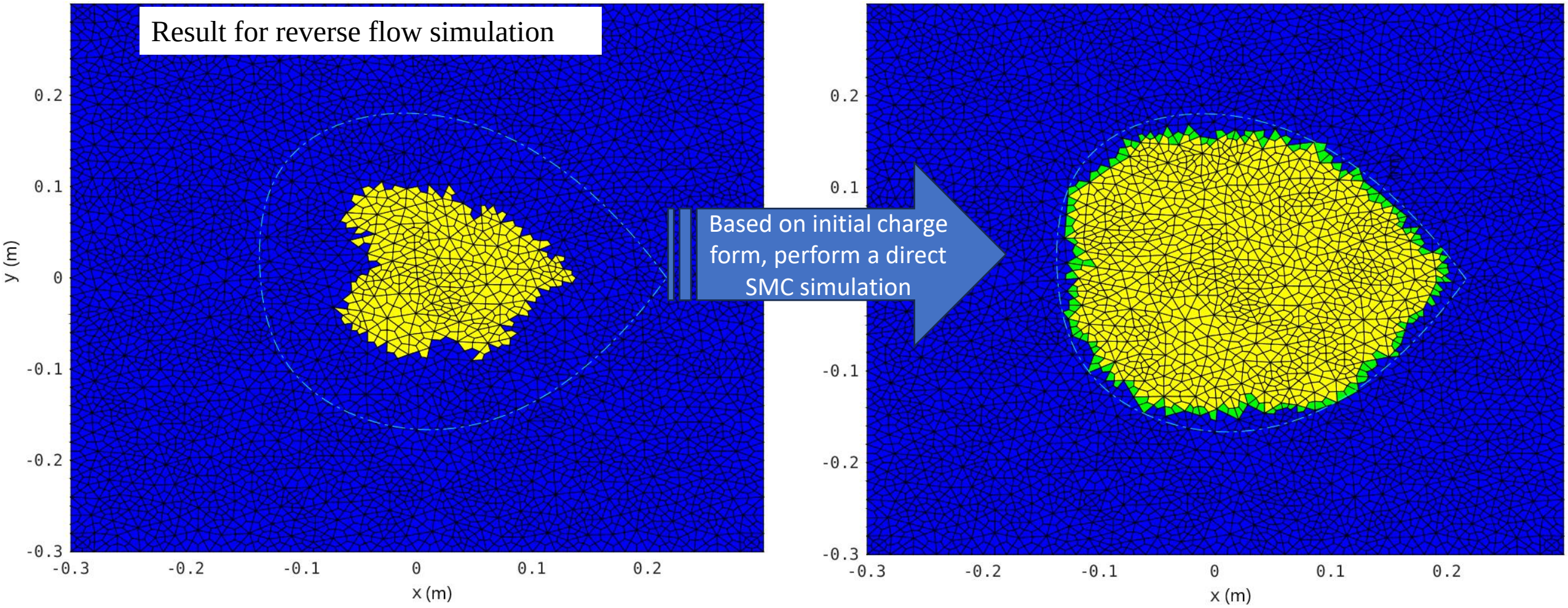

Simulation applications and results

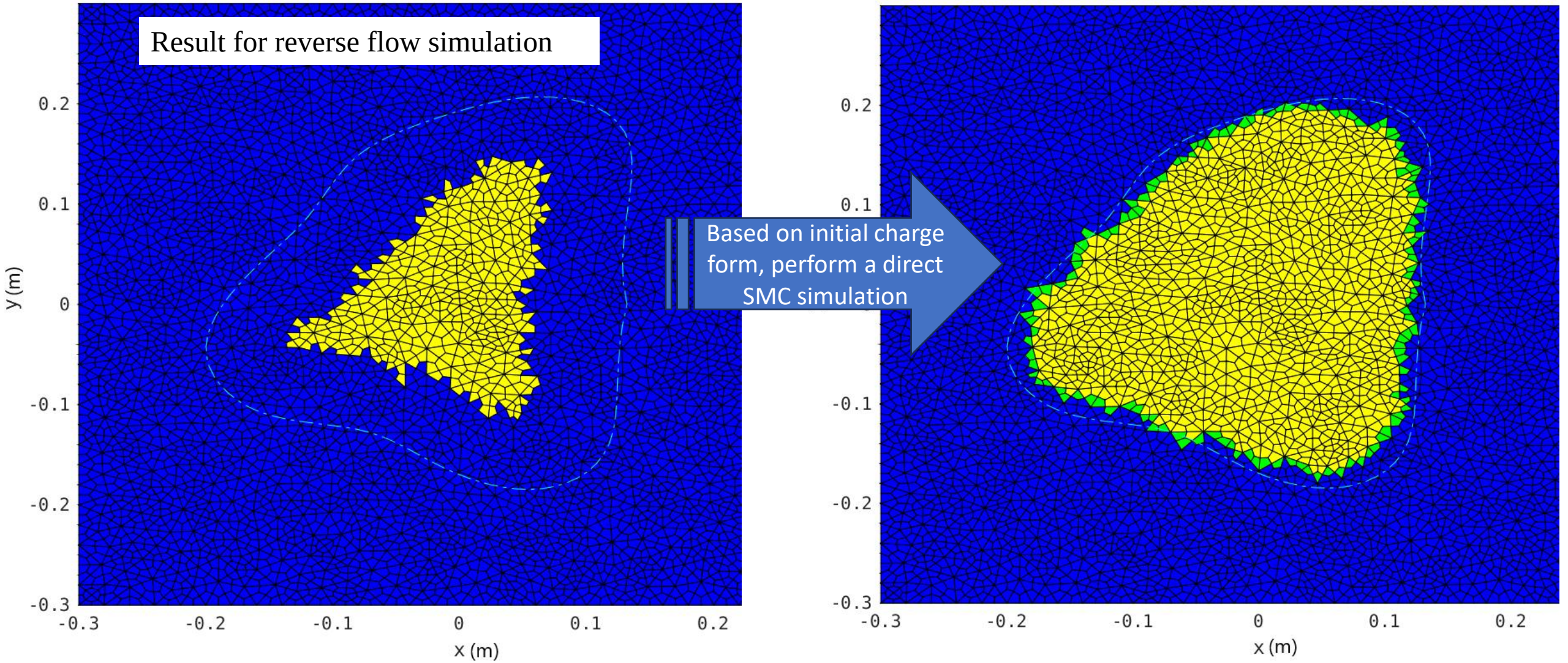

Simulation applications and results

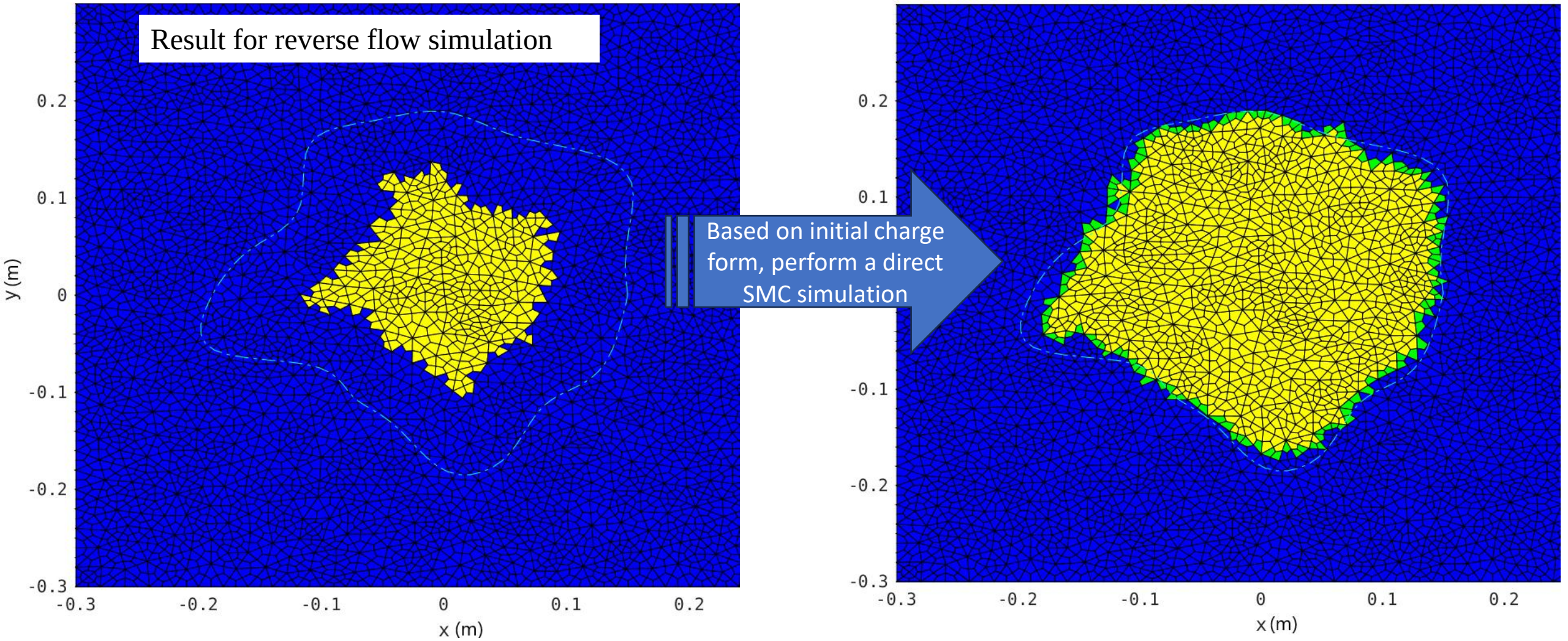

Pushing the method to the extreme

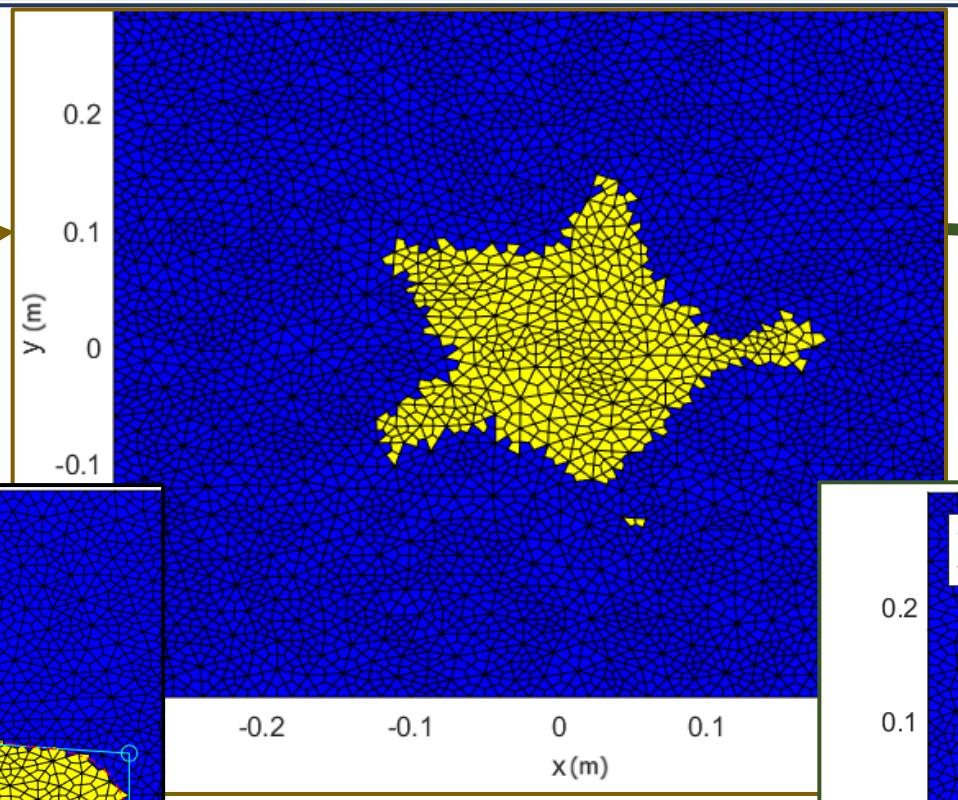

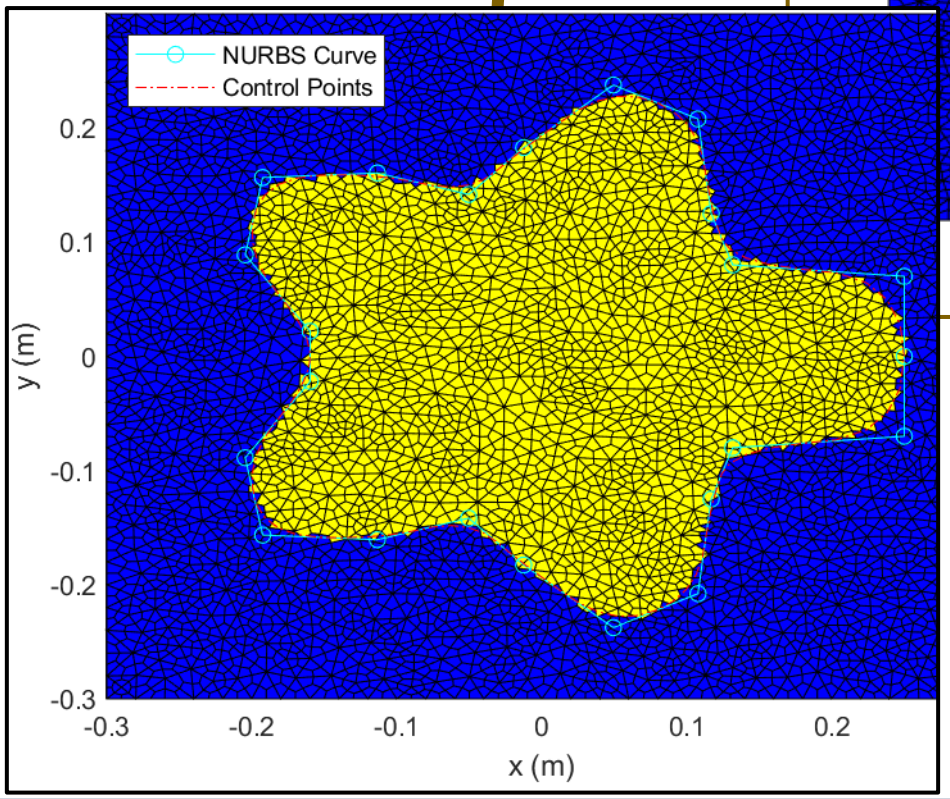

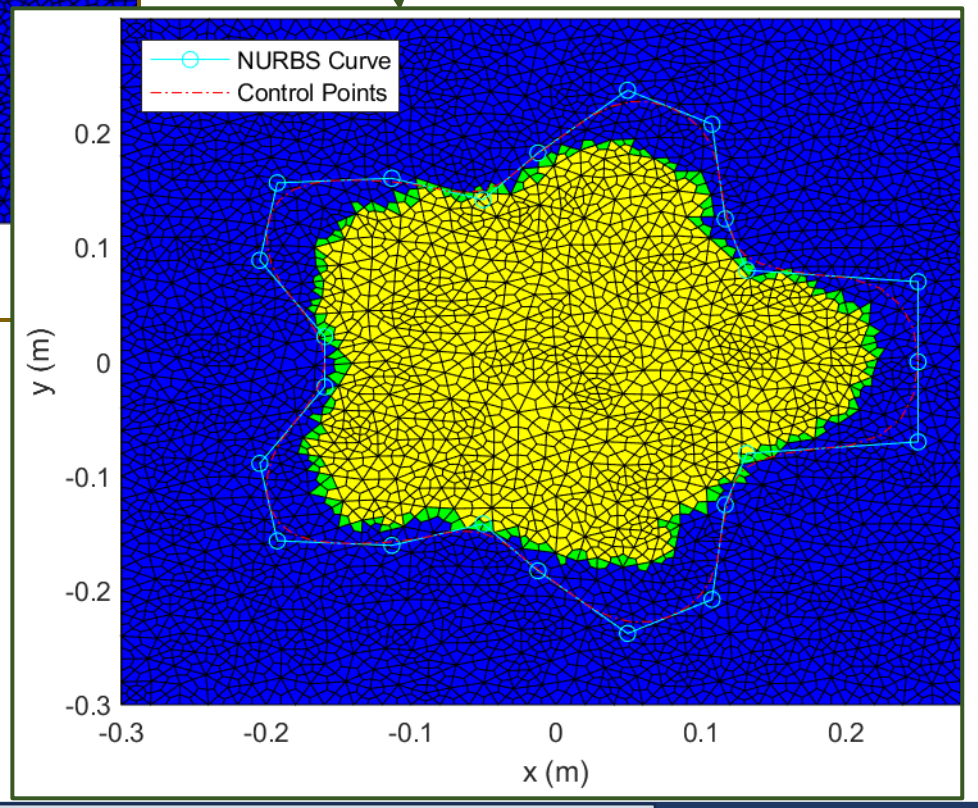

Basic conclusions

- Reverse simulation is a powerful tool to predict initial charge shape for the SMC process
- Computational cost is low when considering 2D flow over a flat 2D mold.
- Computational cost could scale if mold is 3D
- When performing reverse SMC simulation to compute initial charge shapes and then based on the computed initial shape perform a standard SMC simulation, we notice that some elements are lost (mass is not fully conserved).
- Simulation is dependent on mesh size, time steps and other numerical parameters: need to fine tune such parameters for optimized outcome

Motivation for a machine learning based digital twin

- Machine learning :
  - could provide equivalent accuracy with faster computational cost
  - could work in real-time on SMC machines
  - is independent of mesh size and numerical parameters
- Machine learning is to be evaluated as a tool for creating digital twin when SMC simulation is extended to include
  - 3D applications including
  - fiber orientation

} Increased computational cost

Generating a Digital Twin of the SMC Process: choosing a ML architecture

Requirements

- Inputs and outputs are both images and can't be dealt with differently.
- Grey image only considered with 1 indicating SMC material and 0 indicating no material.
- Other important inputs are:
  - charge initial thickness
  - charge final thickness.

  Initial and final thicknesses are different from one use case to the other
- SMC process simulation is not history dependent. GRU, LSTM and similar RNNs are not necessary.

Options

- Convolutional Neural Network should be used to deal with images
- Combining image input with initial and desired thicknesses of charges require an embedding layer
- Possible architectures include :
  - Convolutional Autoencoders
  - GANs (Generative Adversarial Networks) or more specifically Conditional GANs (cGAN)
  - Variational Autoencoders (VAEs) or U-Net Autoencoder
- Best match is a U-Net Autoencoder with skip connections between corresponding layers of the encoder and decoder. This helps propagate fine details from the higher-resolution layers in the encoder directly to the decoder, avoiding loss of spatial information

Generating a Digital Twin of the SMC Process: UNet Auto-Encoder Architecture

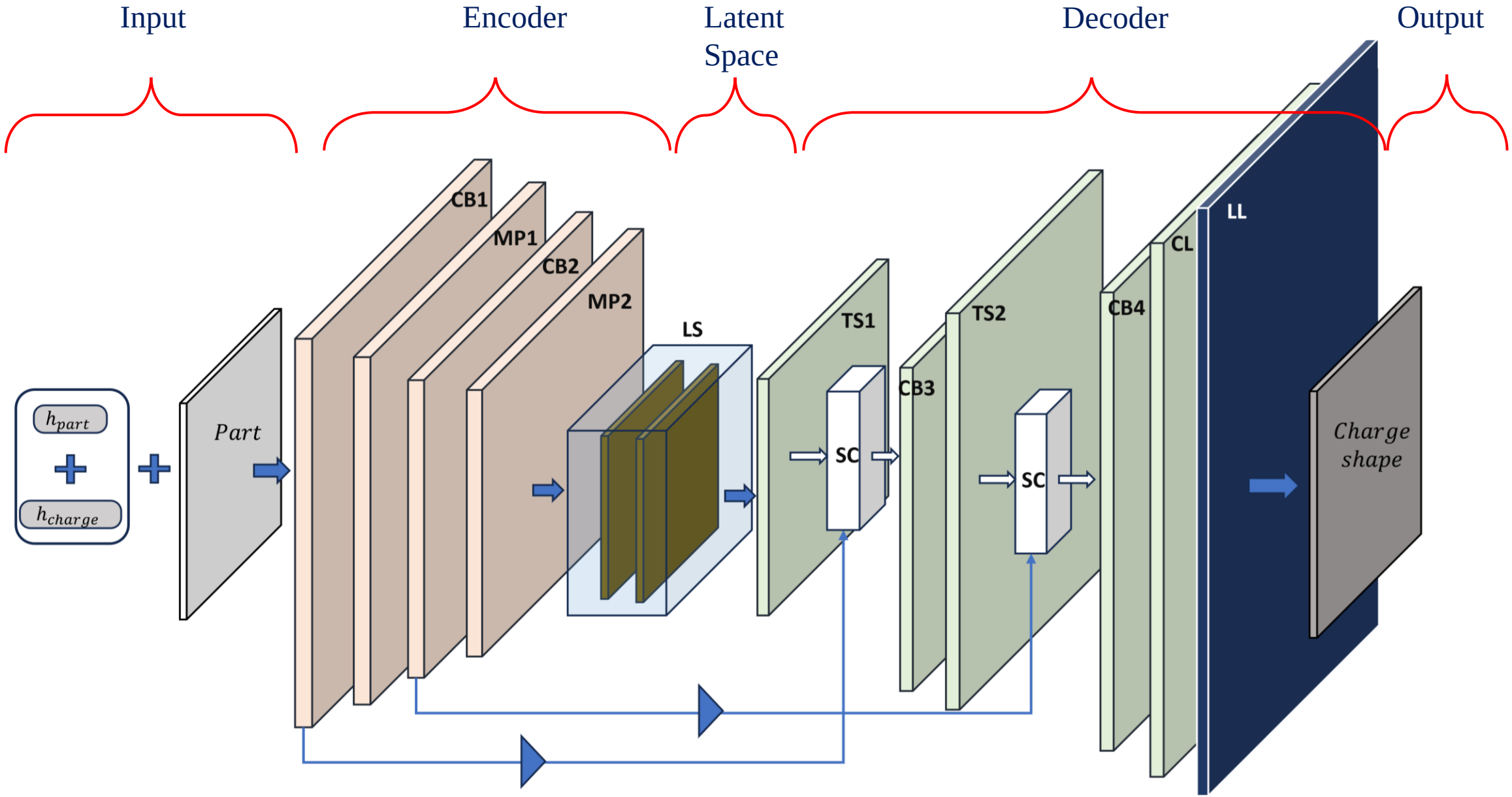

Generating a Digital Twin of the SMC Process: UNet Auto-Encoder Architecture

Block ID	Block Nature	Input Channels	Output Channels	Other Characteristics
CB1	Convolutional Block	1	32	–
MP1	Max Pooling	–	–	max pooling = 2
CB2	Convolutional Block	32	64	–
MP2	Max Pooling	–	–	max pooling = 2
LS	Latent Space Block	64	128	–
TS1	Transpose convolutional layer	128	64	drop out = 30 %
SC	Skip connection	–	–	–
CB3	Convolutional Block	128	64	–
TS2	Transpose convolutional layer	64	32	drop out = 30 %
SC	Skip connection	–	–	–
CB4	Convolutional Block	64	32	–
CL	Convolutional layer	32	1	kernel size = 3, padding = 1
LL	Logical Activation Layer	–	–	–

Details of a convolutional block

ID	Layer Nature	Input Channels	Output Channels	Kernel Size	Padding	Dropout Rate
1	Convolutional layer	x_{in}	x_{out}	3	1	–
2	ReLu activation layer	x_{out}	x_{out}	–	–	–
3	Dropout	x_{out}	x_{out}	–	–	30 %
4	Convolutional layer	x_{in}	x_{out}	3	1	–
5	ReLu activation layer	x_{out}	x_{out}	–	–	–
6	Dropout	x_{out}	x_{out}	–	–	30 %

Important features:

- 466,000 trainable parameters
- 1000 simulation cases
  - 200 kept for testing and never seen by the network during training
  - 100 used for validation during training. Help prevent overfitting
- 2000 training epochs with decreasing learning rate
- Accelerated training using GPUs

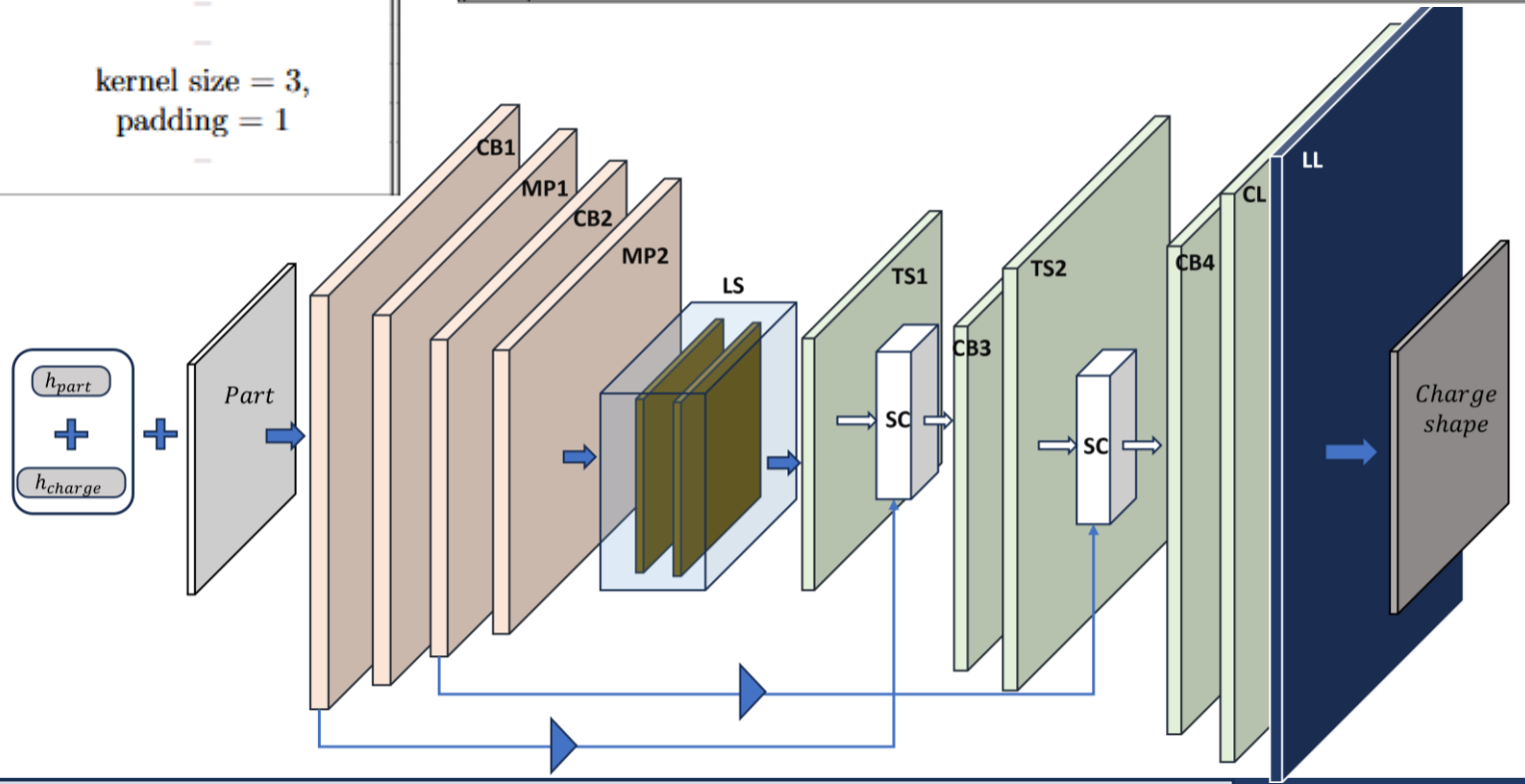

Initial Charge Shapes Generation Results

- Test on a complex mold shape
  - Available charge thickness 41 mm
  - Part thickness 5 mm

Reverse SMC simulation



ML prediction



ML vs Simulation difference

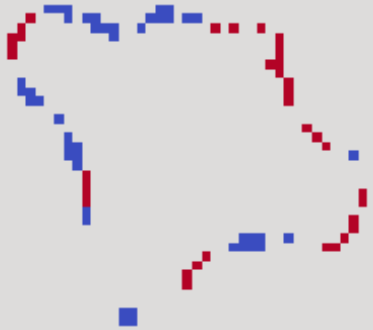

- ML solution is “filtered”:
  - Smooth charge boundary
  - No local material loss
- Predicted charge shape and thickness perfectly aligns with problem physics

Initial Charge Shapes Generation Results

- Test on a complex mold shape
  - Available charge thickness 41 mm
  - Part thickness 5 mm

Reverse SMC simulation



ML prediction



ML vs Simulation difference

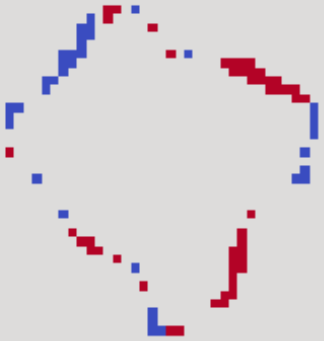

Initial Charge Shapes Generation Results

- Test on a complex mold shape
  - Available charge thickness 41 mm
  - Part thickness 5 mm

Reverse SMC simulation

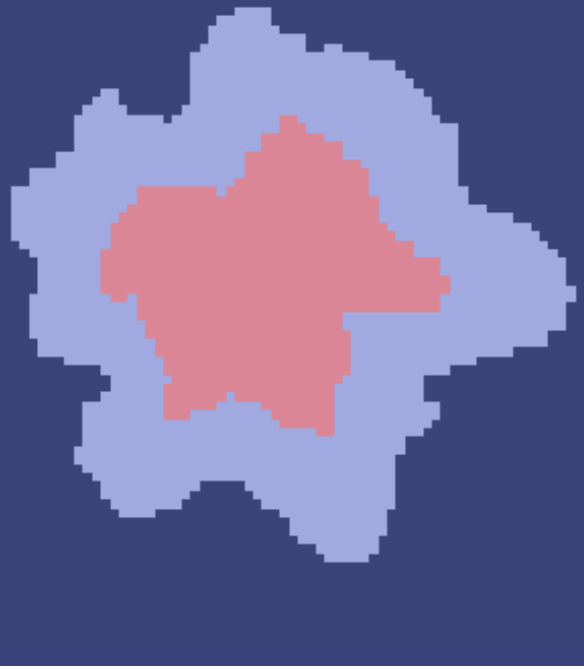

ML prediction

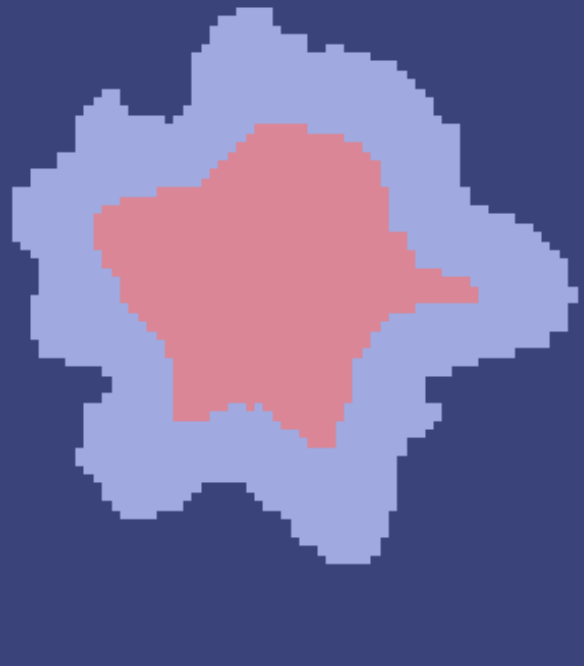

ML vs Simulation difference



Initial Charge Shapes Generation Results

- Test on a complex mold shape
  - Available charge thickness 41 mm
  - Part thickness 5 mm

Reverse SMC simulation

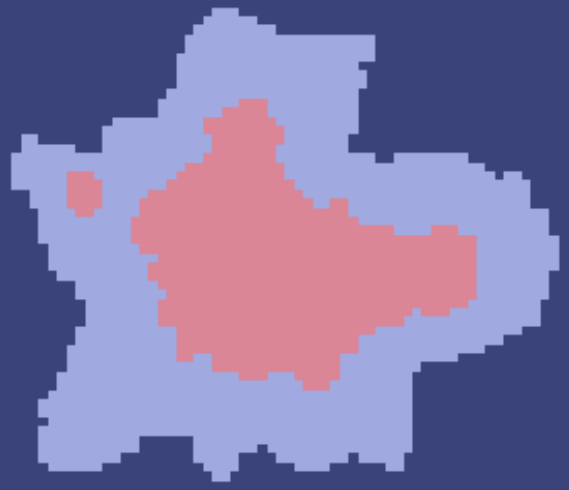

ML prediction

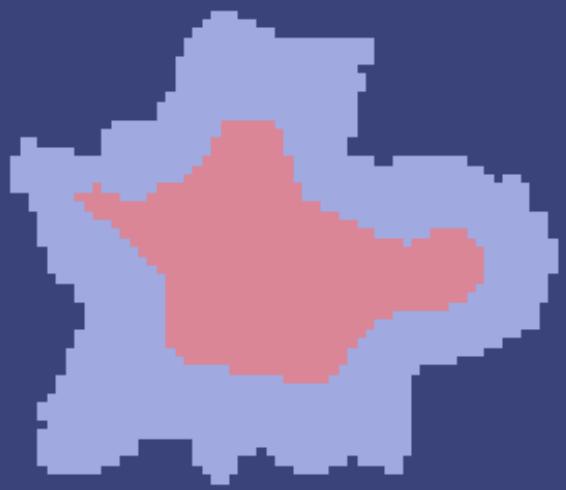

ML vs Simulation difference

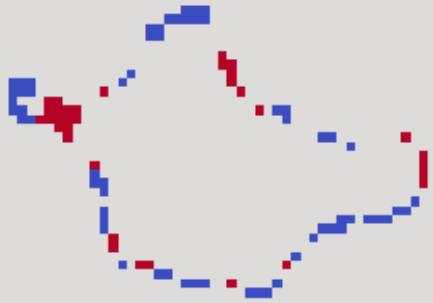

Conclusions and perspectives

- Created a numerical simulation tool that reverses the SMC simulation process and predicts the initial charge shape

- Implemented a digital twin for 2D SMC reverse flow using a UNet Auto-Encoder architecture

  - ML prediction matches simulation precision on unseen data sets.
    - Error is around 5% on unseen data.
    - Max error on few cases could reach 15% and minimum error is lower than 1%.

- **Future Expansion:**

  - Expand to include fiber orientation.
  - Expand to 2D flow over non-flat (3D) molds.

ADVANCED MACHINE LEARNING TECHNIQUES FOR RTM INJECTION SURROGATE MODELING

Sofía Fernández León[1,3], Roberto Valle[1], Luis Baumela[1] and Carlos González[2,3]

[1]Department of Artificial Intelligence, Universidad Politécnica de Madrid, E.T.S. de Ingenieros Informáticos, 28660 Madrid, Spain
Email : sofia.fernandez@imdea.org, roberto.valle@upm.es, lbaumela@fi.upm.es

[2]Department of Materials Science, Universidad Politécnica de Madrid, E.T.S. de Ingenieros de Caminos, 28040 Madrid, Spain
Email: c.gonzalez@upm.es

[3]IMDEA Materials, C/Eric Kandel 2, 28906, Madrid, Spain

Keywords: RTM, PMCs, Computational modelling, Artificial Intelligence

ABSTRACT

Resin Transfer Molding (RTM) is a widely adopted manufacturing technique for polymer matrix composites (PMCs), especially in aerospace and automotive sectors. However, accurate prediction of resin flow during the injection stage is computationally intensive, making real-time optimization unfeasible with conventional numerical solvers. This study proposes advanced deep learning-based surrogate models as a viable alternative to accelerate simulation and facilitate smart manufacturing. Specifically, it emphasizes the importance of architectural choices in surrogate modeling and presents a systematic comparison between two architectures: a fully convolutional encoder-decoder and a MIONet neural operator, both trained on synthetic datasets generated via OpenFOAM simulations.

The encoder-decoder model leverages densely connected convolutional layers to learn spatially structured mappings, while MIONet approximates nonlinear operators via coordinate-wise predictions using a dual-branch and trunk network formulation. Both models are evaluated on their ability to predict temporal evolutions of pressure and impregnation fields given information regarding the permeability field, the inlet pressure and the spatiotemporal coordinates. Two study cases, permeability fields with sharp and smooth permeability variations, are considered to account for different injection process disturbances. Results show that while both architectures demonstrate strong agreement with ground truth simulations, encoder-decoder model achieves higher predictive accuracy, particularly in capturing sharp resin fronts and local pressure gradients, as convolution-based inductive biases improve the fidelity of field reconstructions. Additionally, both models offer significant speedups, up to four orders of magnitude compared to OpenFOAM, highlighting the role of surrogate models as key enabling technologies for Digital Twin systems, which facilitate resilient and adaptive RTM Smart Manufacturing by enhancing the process's responsiveness to real-time disturbances.

1 INTRODUCTION

Resin Transfer Moulding (RTM) is a cost-competitive manufacturing process for Polymer Matrix Composites (PMCs), suitable for large complex parts and large scales, and ideal for structural lightweight applications such as those required in aerospace and automotive industries. Its effectiveness is mainly related to the quality of resin impregnation in the fibers during injection, therefore, resin flow dynamics within the preform are modelled in early design stages to ensure an optimal injection strategy by using numerical filling simulations. However, inherent distortions to the manufacturing process usually arise, such as fiber misalignment, thickness variations and curvatures or mould gaps, being impractical to address real-time process optimization with numerical filling simulations because of their high computational and runtime demand. To overcome these drawbacks, surrogate modelling emerges as an alternative to numerical filling simulations, providing approximate

results in significantly reduced time with low computational cost associated. It allows real-time application, being one of the key enabling technologies for Digital Twins, essential to make the RTM manufacturing process resilient and insensitive to processing distortions towards Smart Manufacturing.

Data-driven surrogate models replicate complex physical processes by learning input–output relationships directly from data, usually collected from physical models or simulations, bypassing the need for explicit physical equations since they are assumed implicitly in data. In this context, Deep Learning (DL) models, a subset of Machine Learning, stand out due to their robustness and efficacy in handling complex, large-scale datasets. Among the various data-driven approaches, fully convolutional encoder-decoders [1] and neural operator-based models such as DeepONets [2], have gained significant popularity. In essence, if the learning task is viewed as a mapping from function-valued inputs, such as initial conditions, boundary conditions, or source terms, to function-valued outputs representing physical fields or system responses, both approaches aim to approximate the same underlying functional relationship, and the distinction, therefore, lies not in the nature of the learning task, but in the architectural choices that govern how data is processed and generalized. The architecture of a deep learning model plays a critical role in determining how effectively it captures patterns within complex datasets. It defines the pathway by which information flows from input to output, influencing both the model's expressive capacity and its ability to generalize beyond the training distribution.

In this work, we conduct a systematic comparison between a fully convolutional encoder-decoder model and a MIONet architecture, a variant of DeepONet which includes two branch nets, employed as surrogate models for the RTM injection stage. The synthetic dataset generation process, including the two-phase fluid flow forward model and the dataset design, is described in Section 2. Section 3 details the architectures of both the convolutional encoder-decoder and the MIONet models, along with the training procedures. Section 4 presents a comparative analysis of the two approaches in terms of performance and inference time and finally, Section 5 outlines the key conclusions and reflects on their relevance for the optimization of the RTM process.

2 SYNTHETIC DATASET GENERATION

2.1 Two-phase fluid flow forward model

The flow of resin through porous media such as fiber preforms can be modeled by Darcy's law, which links the average velocity of the fluid to the pressure gradient via a proportionality involving the material's permeability and the fluid's viscosity (1). Under the assumption of mass conservation, this relation leads to a pressure field equation that, together with proper boundary and initial conditions, allows the transient flow to be determined. As the liquid front progresses through the domain, the problem can be formulated as one with a moving boundary, where classical finite element methods can be used to iteratively resolve the pressure and velocity fields.

$$\boldsymbol{v}(\boldsymbol{x}, t) = -\boldsymbol{K}(\boldsymbol{x}) \cdot \nabla p(\boldsymbol{x}, t)/\mu \tag{1}$$

In the context of resin injection processes, where two immiscible fluids such as resin and air interact, the interface evolution can be modeled using the Volume of Fluid (VOF) technique. This method introduces a variable denoted as α, which takes values between 0 and 1 to distinguish air (α = 0) from resin (α = 1). It is governed by the advection equation (2), allowing the interface to evolve consistently throughout the simulation. In this work, simulations were carried out using OpenFOAM, a widely used open-source platform for computational fluid dynamics. Specifically, the interFoam solver designed to simulate isothermal, incompressible two-phase flow using the VOF method, was employed.

$$d\alpha/dt + \nabla \cdot (\alpha \boldsymbol{v}) = 0 \tag{2}$$

2.2 Dataset design

Simulations were run on a 96×96 structured mesh with a single cell of thickness created with Abaqus, assuming in-plane flow in the mould. The left wall of the domain was defined as an inlet, where a fixed pressure condition (3) was imposed, the right one was treated as a pressure outlet, with a fixed pressure of 0 bar, and the remaining ones were set as slip-free walls. Figure 1a) depicts the computational domain and boundary conditions employed.

$$p_{inlet} = p_0(1\text{-}e^{-\gamma t}) \tag{3}$$

In order to account for process disturbances occurring during the injection stage, which lead to distinctive flow front deformations, two representative scenarios were considered: smooth and strong permeability variations. The first case represents the effects of fiber misalignment or non-uniform compaction, which result in an inhomogeneous flow front. It was modeled by sampling a Gaussian Random Field (GRF). The second case emulates the formation of preferential flow paths along the mould edges due to fiber gaps, where the resin advances faster. These channels, usually known as race-tracking, were modeled as regions of higher permeability compared to the bulk material ($\beta_{RT} = K/K_0$) [3]. Figure 1b) c) shows a permeability field example resulting from each disturbance scenario.

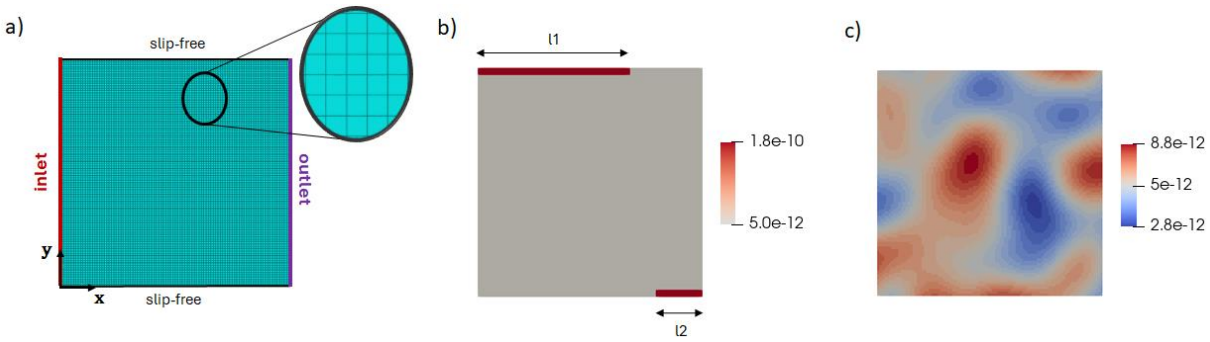

Figure 1: a) Computational domain and boundary conditions: inlet (left), outlet (right), and slip-free walls. A zoomed view of the structured mesh is highlighted. Permeability field with b) strong variations and c) smooth variations.

A diverse dataset of simulations was generated by sampling parameter tuples with Latin hypercube to ensure a uniform coverage of permeability and inlet pressure variations. Table 1 shows the range of the sampled parameters. The entire simulation pipeline, parameter generation, OpenFOAM configuration, execution, and output extraction, was automated via Python scripts and libraries such as PyFoam, Meshio and Gstools. A preprocessing step was carried out to non-dimensionalize the dataset, enabling the surrogate models to generalize to different process conditions, such as changes in resin viscosity, part scale, or maximum injection pressure (p_0), after being trained as long as they remain homothetic. Spatial coordinates were non-dimensionalized by the mold length L_0, pressure values by the maximum applied pressure p_0, and time by a characteristic filling time defined as $t_0 = \mu_0 L_0^2/2 K_0 p_0$ which represents the duration required to fill a mould of length L_0 when the flow occurs under steady conditions with constant viscosity μ_0 and bulk permeability K_0. Data normalization was also applied to improve the training stability and convergence of the surrogate models.

γ (s^{-1})	β_{RT}	l_1 (mm)	l_2 (mm)
[0.002, 0.025]	[10, 100]	[5, 95]	[5, 95]

Table 1: Parameter ranges for synthetic dataset generation

3 ADVANCE DEEP LEARNING TECHNIQUES

3.1 Fully convolutional encoder-decoder

The fully convolutional encoder-decoder architecture employed in this work is the one proposed in [1]. This architecture employs a sequence of densely connected convolutional blocks [4], where each layer obtains inputs not only from the preceding layer but from all previous layers within the block, using k=24 as feature map growth rate. Transition layers follow each dense block to modulate feature map resolution via strided convolutions and deconvolutions in the encoder and decoder, respectively. The entire architecture contains approximately 3.5 M trainable parameters. An schematic overview is shown in Figure 2.

Its purpose is to represent high-dimensional input information by means of the encoder into a latent space of low dimensionality, to then reconstruct high-dimensional predictions via the decoder. Particularizing for the RTM process, the permeability field of the fibre preform (a 96x96 image) is encoded and then concatenated with gamma (γ), a pressure build-up parameter, and a time vector. In this way, the latent space contains all the key process information. After that, from this low dimensional latent space, data is reconstructed to predict fluid field and pressure fields over time (96x96 images) using two separated decoders.

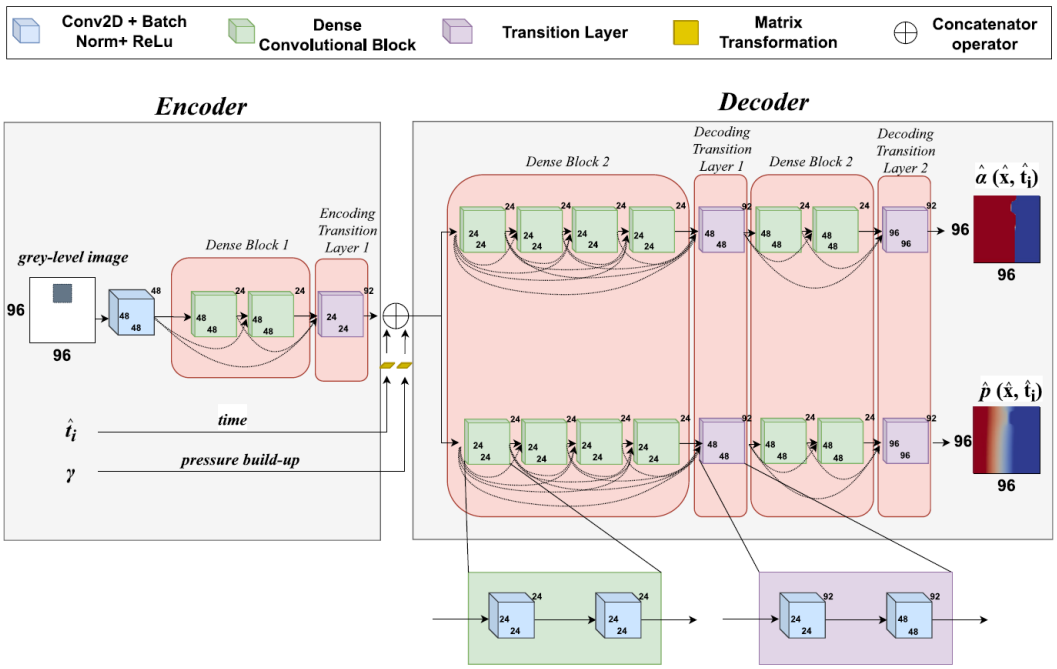

Figure 2: Architectural overview of the fully convolutional encoder-decoder surrogate model [1].

3.2 MIONet

MIONet architecture consists of three interacting subnetworks: two branch networks that encode distinct input functions, and a trunk network that processes the spatial or temporal coordinates where predictions are to be made. The outputs of the branch and trunk networks are subsequently combined through an element-wise product followed by a sum to generate the final output function. Its purpose is to approximate nonlinear operators by learning mappings from function-valued inputs, such as initial conditions, boundary conditions, or source terms, to function-valued outputs corresponding to physical fields or system responses. In the context of the RTM process, the first branch network receives the permeability field as input, while the second branch network takes a discretized representation of the inlet pressure function, sampled at 25 time points. The trunk network, in turn, is provided with the spatial and temporal coordinates corresponding to the target prediction locations.

With respect to the backbone architectures of the branch and trunk networks, this study considers two MIONet configurations that differ in the implementation of the first branch network. The first configuration is the originally proposed in [5], named as Vanilla MIONet, which adopts fully connected neural networks (FNNs) for all three components, both branch networks and the trunk network. The second configuration remains the second branch and trunk networks fully connected, whereas the first branch network is replaced with a densely connected convolutional encoder identical to the one described in the previous section. To optimize the performance of both configurations, a systematic exploration of FNN hyperparameters was carried out by evaluating different combinations of network depth [2,4,6,8,10] and width [128,256,512,800,1024]. An schematic overview of the two proposed MIONet configurations is shown in Figure 3. Vanilla MIONet of width=6 and depth=800, with a total of approximately 17 M trainable parameters, achieved the best performance and is therefore adopted as the reference model for all subsequent comparisons in this study.

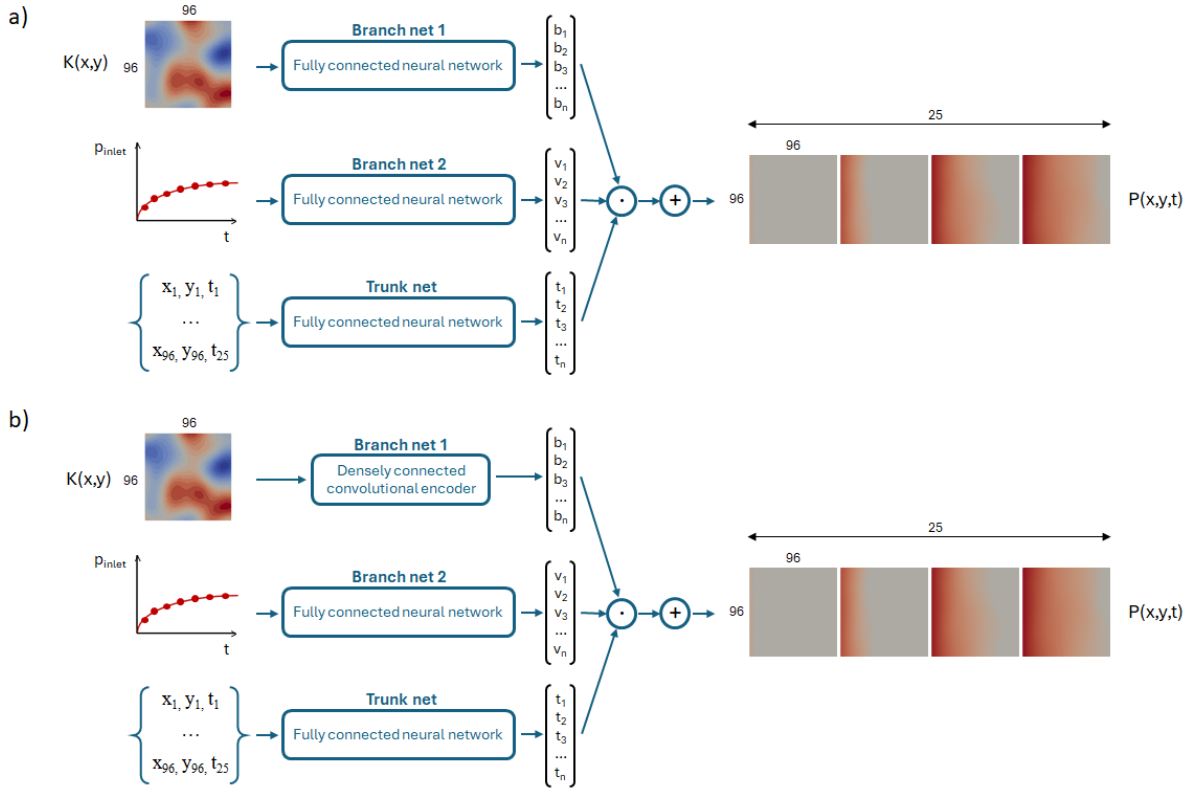

Figure 3: Overview of the MIONet configurations considered in this study. (a) Vanilla MIONet, composed entirely of fully connected networks. (b) MIONet variant incorporating a densely connected convolutional encoder as the first branch network.

3.3 Training

The training process was structured in two distinct phases: the first one focused on learning the pressure field and the second one, the impregnation field. To ensure a fair and rigorous comparison between the encoder-decoder and MIONet architectures, multiple training configurations were systematically evaluated to determine the most effective setup for each model. This included variations in regularization strategies (with or without batch normalization), optimization algorithms (SGD, Adam, L-BFGS, and NNCG), and loss functions (MAE, MSE and $L_{n\text{-}log}$ composite loss).

During the first training stage, a $L_{n\text{-}log}$ composite loss function was employed. This loss function combines power and logarithmic terms in a piecewise manner to enhance convergence in scenarios where residuals exhibit a bimodal distribution, an aspect commonly encountered in dual-phase flow simulations. Additional information regarding this loss function can be found in [1]. Normalization

was applied through batch normalization, weights were initialized using He initialization and ReLU was used as activation function. The Adam optimizer was used in combination with a learning rate scheduling strategy based on the ReduceLROnPlateau scheduler. The initial learning rates were set to 0.01 for the encoder-decoder model and 0.001 for MIONet. Patience values of 20 and 50,000 iterations were configured respectively for learning rate reduction, with a decay factor of 0.1. To prevent undertraining due to time constraints, early stopping was implemented with patience values of 60 and 100,000 iterations, and the maximum number of training epochs was set to 500 and 250.000 for the encoder-decoder and MIONet models, respectively. Overall, training times were approximately 3 hours for the encoder-decoder and 2 days and 7 hours for MIONet.

The second training phase was carried out differently for the encoder–decoder and MIONet architectures. For the encoder-decoder, the prediction of the impregnation field was formulated as a binary classification task, distinguishing resin (1) from air (0), and trained using the binary cross-entropy (BCE) loss function. In contrast, due to the design of DeepONet, in which the outputs of the branch and trunk networks are combined via an inner product, the model cannot guarantee output values constrained to the [0, 1] interval. This structural limitation renders a binary classification approach unsuitable for MIONet. To address this, the impregnation field for MIONet was modeled as a level-set function, a continuous scalar field where the resin–air interface (flow front) is identified by a sharp gradient. This level-set representation was constructed using information from the pressure field, leveraging the physical correlation between pressure gradients and flow front propagation in RTM processes. As such, the task was reformulated as a regression problem, and the $L_{n\text{-}log}$ composite loss function was employed to guide training. After inference, the predicted impregnation field was thresholded to obtain a binary mask, enabling a direct comparison with the encoder–decoder output. All remaining training settings were kept consistent with those described previously. The total training duration was approximately 3 hours for the encoder-decoder and 2 days and 10 hours for MIONet.

4 COMPARATIVE ANALYSIS

Figure 3 and Figure 4 illustrate the predictive performance of both the encoder-decoder and MIONet surrogate models for resin impregnation and pressure field across different time steps, using two representative permeability cases with strong variations and smooth variations, respectively. Both models exhibit high agreement with the target fields, successfully capturing the global behavior of the impregnation and pressure distributions. Among the two models, the encoder–decoder exhibits greater predictive accuracy, particularly in tracking the advancing resin front and capturing the spatial pressure gradients across the domain. MIONet, while successfully reproducing the overall flow behavior, presents slightly larger deviations. This is due to the encoder-decoder processes the entire input field as a structured image, preserving spatial locality through convolutions and hierarchical feature extraction, which enables the model to capture fine-grained spatial patterns, such as sharp interfaces at the resin front and local pressure gradients. In contrast, MIONet operates on coordinate-wise predictions, evaluating the output at individual spatial points without modeling the global structure of the output field, as each prediction is made independently of its neighbors.

From a computational standpoint, Table 2 demonstrates that both surrogate models achieve a substantial reduction in simulation time, decreasing inference time by several orders of magnitude compared to traditional OpenFOAM solvers. While the encoder-decoder achieves predictions in just 12 ms and MIONet in 83 ms, conventional simulations require nearly 4 minutes per case. This drastic improvement in computational efficiency highlights the potential of both approaches for accelerating resin transfer molding simulations. In particular, their speed and responsiveness make them strong candidates for real-time simulation and control applications within manufacturing environments.

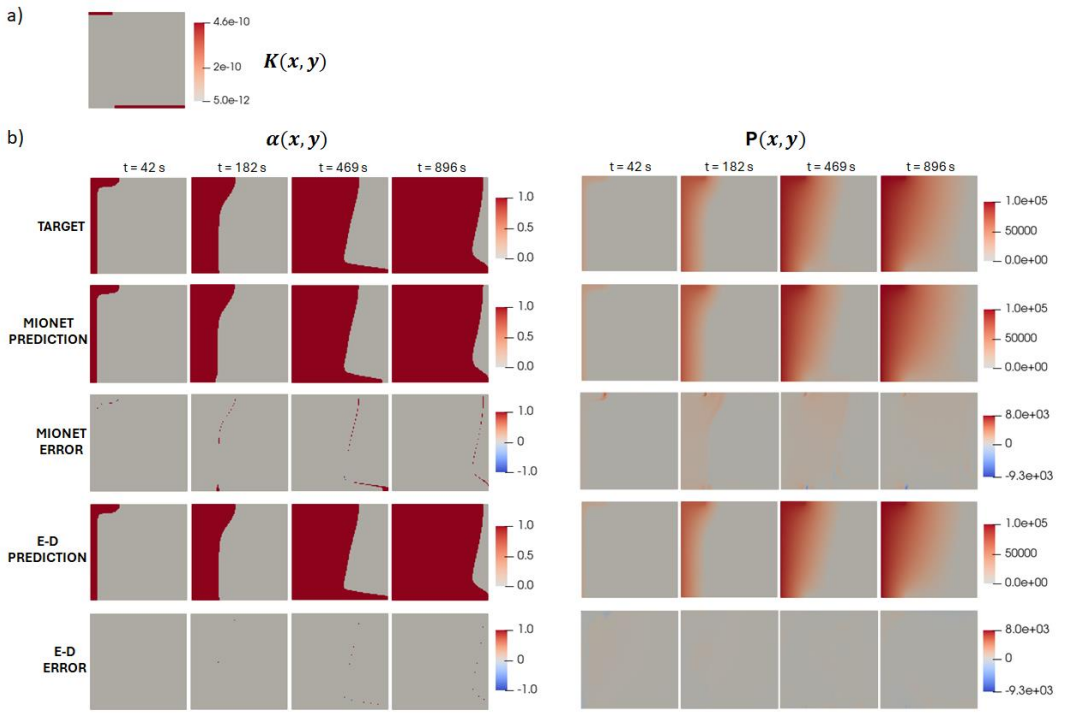

Figure 4: Surrogate models' predictions for a permeability field with strong variations. a) Spatial distribution of the permeability field. b) Temporal evolution of the resin impregnation field (left) and pressure field (right) at selected time steps. Rows correspond to the ground truth (OpenFOAM), predictions from MIONet and encoder–decoder (E–D) models, and their respective error maps.

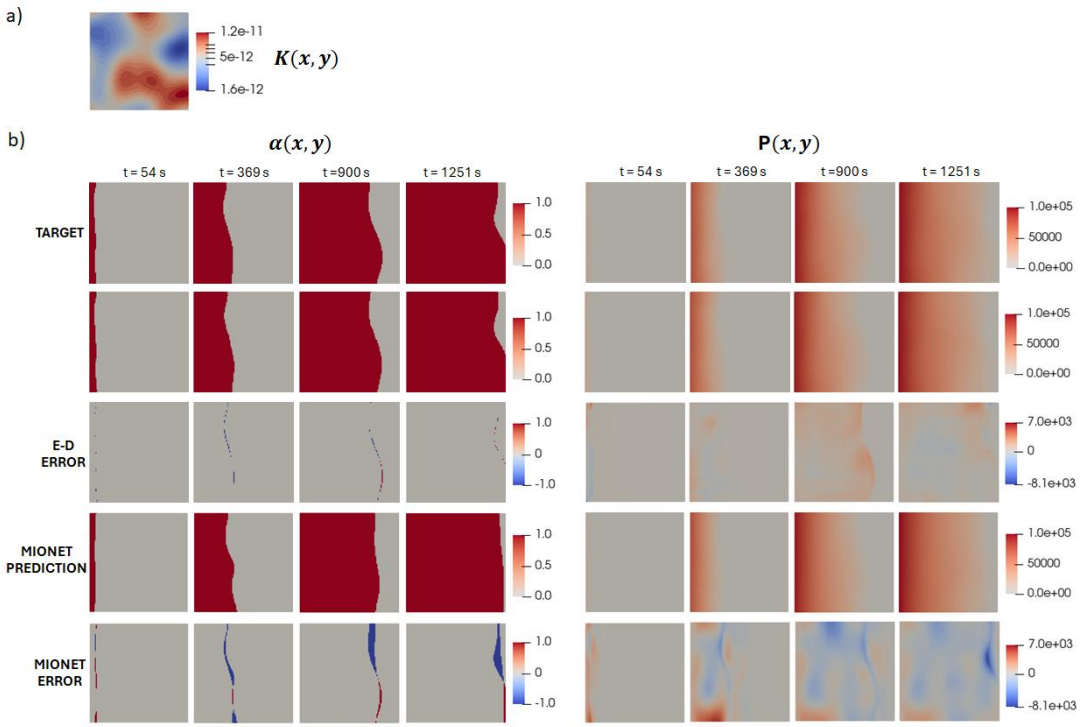

Figure 5: Surrogate models' predictions for a permeability field with smooth variations. a) Spatial distribution of the permeability field. b) Temporal evolution of the resin impregnation field (left) and pressure field (right) at selected time steps. Rows correspond to the ground truth (OpenFOAM), predictions from MIONet and encoder–decoder (E–D) models, and their respective error maps.

	ED	MIONet	OpenFOAM
Inference time	12 ms	83 ms	3.95 min

Table 2: Execution time comparison

5 CONCLUSIONS

This work has investigated and compared the performance of two advanced deep learning architectures, fully convolutional encoder-decoder and MIONet, as surrogate models for the RTM injection stage. Two representative scenarios were addressed to reflect inherent disturbances that appear during the RTM injection: one involving sharp heterogeneities in the permeability field and another representing smooth heterogeneities in the permeability field. By analyzing their predictive performance on the estimation of the impregnation and pressure fields over time, the study provides valuable insights into the trade-offs between spatially structured models and operator-learning frameworks in simulating two-phase flow dynamics during resin injection. While both architectures capture the global flow dynamics and pressure distributions with high fidelity, the encoder–decoder consistently outperforms MIONet in predictive accuracy, particularly for sharp resin fronts and spatial pressure gradients, due to its ability to leverage spatial inductive biases through convolutional processing. These findings underscore the critical importance of architectural design in deep learning-based surrogate modeling. Moreover, both models significantly accelerate simulation time, achieving speedups of several orders of magnitude over conventional solvers. This real-time execution enables their integration into Digital Twin frameworks for Smart Manufacturing, facilitating real-time process monitoring and control to make the manufacturing process more robust and resilient to unexpected disturbances that naturally arise during operation.

REFERENCES

[1] Fernández-León, J., Keramati, K., Miguel, C., González, C., Baumela, L., 2023. A deep encoder-decoder for surrogate modelling of liquid moulding of composites. Engineering Applications of Artificial Intelligence 120, 105945 (doi: 10.1016/j.engappai.2023.105945).

[2] Lu, L., Jin, P., Karniadakis, G.E., 2021. DeepONet: Learning nonlinear operators for identifying differential equations based on the universal approximation theorem of operators. Nat Mach Intell 3, 218–229 (doi: 10.1038/s42256-021-00302-5).

[3] Fernández-León, J., Keramati, K., Garoz, D., Baumela, L., Miguel, C., González, C., 2022. A Machine Learning Strategy for Race-Tracking Detection During Manufacturing of Composites by Liquid Moulding. Integr Mater Manuf Innov 11, 296–311 (doi: 10.1007/s40192-022-00263-6).

[4] Huang, G., Liu, Z., Maaten, L. van der, Weinberger, K.Q., 2018. Densely Connected Convolutional Networks (doi: 10.48550/arXiv.1608.06993).

[5] Jin, P., Meng, S., Lu, L., 2022. MIONet: Learning multiple-input operators via tensor product (doi: 10.48550/arXiv.2202.06137).

A NEURAL NETWORK BASED BAYESIAN METHOD FOR ESTIMATING AND PREDICTING RESIN FLOW IN RESIN TRANSFER MOLDING

Nicholas Wright[1], Oliver Maclaren[1], Piaras Kelly[1], Suresh G. Advani[2] and Ruanui Nicholson[1]

[1]Department of Engineering Science and Biomedical Engineering, University of Auckland, Auckland 1010, New Zealand

[2]Department of Mechanical Engineering and Center for Composite Materials, University of Delaware, Newark, 19716, DE, USA.

Keywords: Computational modelling, Statistical properties, Numerical analysis, Process Monitoring, Resin Transfer Molding

ABSTRACT

Resin transfer molding (RTM) is widely used to manufacture composite materials, where maintaining control over resin flow is crucial to avoid defects such as dry spots and voids that can compromise structural integrity. We introduce a Bayesian framework specifically designed to predict race tracking effects in RTM, which result from unpredictable high-permeability channels formed during the manufacturing process. By integrating Bayesian inference with pressure sensor data collected during resin injection, we estimate race tracking strength with uncertainty, enabling predictions of resin flow behavior under varying race tracking conditions.

Although Bayesian inference offers valuable insights for race-tracking prediction, the computational demands of RTM simulations present a challenge, particularly for real-time applications. To address this, a neural network surrogate model is introduced to approximate the complex, discontinuous behavior of RTM simulations caused by race tracking. This surrogate model accurately captures the resin flow patterns generated by traditional finite element-control volume (FECV) methods, enabling significantly faster computations within the Bayesian framework. We demonstrate that utilizing a neural network surrogate within the Bayesian framework can accurately predict both race tracking strengths and non-homogeneous permeability fields in a preform. This integrated approach enables real-time monitoring and control, supporting adaptive RTM systems that respond dynamically to variations in race tracking and produce higher-quality composite products. The findings contribute to the optimization of the RTM process, offering a pathway to reduce manufacturing defects and increase reliability in composite material production.

1 INTRODUCTION

Resin transfer molding (RTM) is widely used in industrial applications due to its relatively rapid production cycle and straightforward experimental setup, which enables the production of parts with shapes close to their final form. However, the production of complex parts is limited by the resin filling stage. This stage is particularly critical for simulation efforts, as it involves careful planning of the injection and venting layout to ensure complete impregnation of the preform and to avoid air entrapment. Trapped air pockets become voids after curing, compromising the composite's structural integrity. For composite parts with complex geometries, this becomes increasingly difficult.

Although simulation tools can be used to design mold injection sites and exit vents, theoretically ensuring complete resin impregnation, there is variability in resin movement. The permeability of the reinforcement primarily influences these deviations. Permeability is typically measured through experiments or estimated numerically [1] [2], and assumed to be constant through the reinforcement and between different preform samples. In reality, the permeability in the preform will vary due to variations or issues in the manufacturing process or draping. In some cases, the inaccurate lay-up of the fabric can

result in regions of lower fiber density on certain edges of the mold, which can act as high-permeability *race tracks* [3] [4] [5]. Race tracks can also be created at bends within the mold.

This research aims to predict the spatially varying permeability of the preform based on pressure measurements made during fill time. This is an inverse modelling problem, which we choose to tackle using Bayesian inference. Bayesian inference provides a principled approach to inverse problems, such as permeability estimation, by incorporating uncertainty directly into the modeling process. We consider both the prediction of only race tracking strengths, modelling the rest of the preform as a homogeneous field, and the prediction of a more general spatially varying field.

2 BAYESIAN INFERENCE IN RESIN TRANSFER MOULDING

We now briefly describe the mathematical model used to describe the resin impregnation stage of RTM. We then explain how this model can be integrated into the Bayesian framework for estimating permeability.

2.1 Mathematical Model

Darcy's law adequately describes the flow of resin through a porous medium [6] [7] [4] [8] [9] [10] [11]:

$$q(x,t) = -\frac{K(x)}{\mu}\nabla p(x,t), \tag{1}$$

where x is a vector denoting position, q is the resin flux vector, p is the pressure, μ is the fluid viscosity, K is the permeability tensor and t is time. Assuming that the flow is quasi-static, conservation of mass gives:

$$\nabla \cdot q(x,t) = 0. \tag{2}$$

The volume of resin is modelled with a fixed pressure of $p = p_{in}$ at the injection sites, and $p = 0$ at any exit vents, along with the moving flow front. Where the resin reaches the mold walls, impermeable slip boundaries ($q(x,t) \cdot n(x) = 0$) are enforced. The following model applies only to the region of the mold where resin is present. For the remainder of the dry mold, the pressure is fixed at $p = 0$.

2.2 Computational Model

The most common method for simulating this process is the Finite Element-Control Volume (FECV) method [12] [7] [8] [13] [14] [15] [16]. This method employs a typical finite element mesh to solve for the pressure distribution. Offset from those finite elements are control volumes, which monitor the saturation of the preform. After the pressure is solved, the flow between control volumes can be computed, and the saturation of incompletely filled control volumes can be updated.

2.3 Bayesian Inference

The Bayesian approach to inverse problems is widely adopted, as it provides a systematic means of incorporating and quantifying uncertainty. We are considering an inverse problem with an additive error model, where we attempt to estimate parameters x (in this case, a parameterization of the permeability) from measurements y (in this case, pressure measured from discrete sensor locations during fill time). In the Bayesian framework, the solution to the inverse problem is the posterior probability density (or simply *the posterior*) $\pi(x|y)$, i.e. the conditional distribution of x given y. For in-depth discussions on the Bayesian approach, see [17] [18] [19], among many.

Bayes' formula allows us to express the posterior as

$$\pi(x|y) \propto \pi(x)\pi(x|y) \tag{3}$$

where $\pi(y|x)$ is the likelihood function and $\pi(x)$ is the prior distribution on the parameters x. We suppose that the collected data and parameters of interest are linked by a setup of the form

$$y = f(x) + e \tag{4}$$

where f denotes a model relating parameters to outputs of interest and e denotes a measurement error, which signifies noise present in experimental measurements. We assume a Gaussian distribution for this error term $e \sim N(0, \Gamma_e)$. In this case, the likelihood $\pi(y|x)$ can be expressed as

$$\pi(y|x) = \pi_e\big(y - f(x)\big) \propto \exp\left(-\frac{1}{2}\left\|L_e\big(y - f(x)\big)\right\|_2^2\right) \tag{5}$$

where $L_e^T L_e = \Gamma_e^{-1}$. We also postulate a Gaussian distribution for the prior $\pi(x) \sim N(x_0, \Gamma_x)$, which mathematically can be written

$$\pi(x) \propto \exp\left(-\frac{1}{2}\|L_x(x_0 - x)\|_2^2\right) \tag{6}$$

where $L_x^T L_x = \Gamma_x^{-1}$. Based on the above expressions for the prior (Equation (6)) and the likelihood (Equation (5)), the posterior can be expressed through Equation (3) as

$$\pi(x|y) \propto \exp\left(-\frac{1}{2}\left\|L_e\big(y - f(x)\big)\right\|_2^2 - \frac{1}{2}\|L_x(x - x_0)\|_2^2\right) \tag{7}$$

A variety of approaches exist for characterizing the posterior for a given problem. For nonlinear inverse problems involving expensive-to-evaluate forward models (as is the case here), high-dimensional parameters, and/or a need for rapid results, fully characterizing the posterior presents a challenge. Complete characterization using methods such as Markov chain Monte Carlo (MCMC) is generally infeasible. In such cases, one approach would be to take the Laplace approximation [20]. Here, we use optimization methods such as Gauss-Newton to find the value of x that maximizes $\pi(x|y)$. This is termed the maximum a posteriori (MAP) estimate, x_{MAP}. Once this is known, we can linearize $f(x)$ about x_{MAP} with a Taylor series expansion:

$$f(x) \approx f(x_{MAP}) + F_{MAP}(x - x_{MAP}), \qquad F_{MAP} = \frac{\partial f}{\partial x}\Big|_{x = x_{MAP}}. \tag{8}$$

Substituting this expression into Equation (7) gives $\pi(x|y) \approx N(x_{MAP}, \Gamma_{post})$, with $\Gamma_{post} = (F_{MAP}^T \Gamma_e^{-1} F_{MAP} + \Gamma_x^{-1})^{-1}$.

3 NEURAL NETWORK SURROGATES

The use of a surrogate model - one that closely approximates the actual process but runs significantly faster - is driven by two key advantages in our application. First, the FECV model within LIMS is highly computationally intensive: every time the moving flow-front boundary changes, it must re-solve the entire FEM problem. By replacing this with a lightweight approximation of the permeability–pressure relationship, we can evaluate the posterior distribution in a fraction of the time without sacrificing essential fidelity.

Second, choosing a neural network as our surrogate ensures a smooth, continuous mapping between permeability and pressure. In contrast, the FECV model exhibits parameter-induced discontinuities that hinder accurate posterior inference: its permeability–pressure curve is not reliably characterized [21]. A neural network built with smooth activation functions naturally overcomes these discontinuities, yielding a more realistic and stable posterior estimate.

We now discuss how the inputs and outputs of the NN are defined for our problem. In Section 3.4, we then discuss how the NN is structured and trained. In Section 3.5, we discuss how inaccuracies in the NN can be accounted for in the Bayesian framework.

3.1 Model Inputs – Parameterization 1

In this first parameterization, we assume that the permeability of the preform is homogeneous, apart from the race tracking regions. Each race tracking region i is assigned a strength x_i, which is related to the permeability in that region K_i with

$$K_i = \exp(x_i) K_{bulk} \tag{9}$$

where K_{bulk} is the homogeneous permeability outside of the race tracking regions. Upon $x = [x_1, x_2, \dots]$, we postulate an independent Gaussian prior with mean $x_0 = 2.0$, $\sigma_x = 2.0$, i.e. $\Gamma_x = \sigma_x^2 I$.

3.2 Model Inputs – Parameterization 2

In an alternative and more interesting parameterization, we allow the permeability to vary throughout the mold, with increased variation in the race tracking regions. To parameterize this, we consider an element-wise log-permeability parameter k, defined by

$$K_i = \exp(k_i)\, K_{bulk} \tag{10}$$

where i is the element number and K_i is the permeability assigned to that element. On k, we postulate a Gaussian prior that encodes a correlation between the permeabilities of neighboring elements and allows for greater variation in the race tracking regions. We achieve this by firstly neglecting the race tracks, and considering a correlated Gaussian exponential squared covariance of the form

$$\hat{\Gamma}_k[i,j] = \sigma_k^2 \exp\left(-\frac{1}{2l^2}\left\|\mathrm{x}_i - \mathrm{x}_j\right\|_2^2\right) \tag{11}$$

where $\sigma_k^2 = 0.2$, $l = 0.015$m is a scalar characteristic length that controls the extent of the correlation and x_i is the location of the center of element i. We then encode the increased variation in the race tracks by applying the following transformation:

$$\Gamma_k = W \hat{\Gamma}_k W, \tag{12}$$

where W is diagonal, and defined as

$$W[i,i] = \begin{cases} 2, & \text{if element } i \text{ is in a race track} \\ 1, & \text{otherwise.} \end{cases} \tag{13}$$

In addition, we have a non-zero prior mean k_0 on k, which is zero in a race tracking element and zero otherwise. Sampling from $k \sim N(k_0, \Gamma_k)$ produces permeability strength for every element as required.

To reduce the dimensionality of this parameterization, we take a principal component analysis (PCA) of this prior to represent k as a lower-dimensional x. Use of PCA is a standard approach to dimensionality reduction [22] [23], so we omit the mathematical details here. We have the truncated singular value decomposition of $\hat{\Gamma}_k$

$$\hat{\Gamma_k} \approx V_n \Sigma_n V_n^T \tag{14}$$

where Σ_n is a diagonal matrix containing the first n eigenvalues, ordered by magnitude and V_n is the first n eigenvectors. In the numerical experiments discussed in Section 4.2, we choose $n = 100$.

We then consider the following transformation

$$k = W V_n x, \qquad x = V_n^T W^{-1} k. \tag{15}$$

This transformation converts k, which contains the same number of entries as elements in a finite element model, to x - which is only 100-dimensional.

3.3 Model Outputs

Regardless of the choice of model parameterization, we consider the simulated pressures for the model output. To simulate this, we consider fixed pressure sensor locations throughout the mold. We then extract the simulated pressures at those locations, at specific measurement times t. These measurements have an assumed measurement error $e \sim N(0, \Gamma_e)$ associated with them. We postulate the following covariance on e:

$$\Gamma_e = \sigma^2_{measurement} I + \sigma^2_{sensor} \text{diag}(\mathbb{1}, \mathbb{1}, \dots) \tag{16}$$

where $\mathbb{1}$ is a square matrix of ones, with one row/column for each measurement time. This allows for some independent measurement error, along with a systematic sensor error, applied uniformly to every measurement from a single sensor. We choose $\sigma^2_{measurement} = \sigma^2_{sensor} = 2e^{-4}$ for the numerical experiments here.

As with the second permeability parameterization, we have a very high-dimensional output, which presents difficulties for the learning of the NN. As such, we again reduce the dimension of the output using PCA. After generating training and testing data for $f(x)$ using the LIMS model, we consider the fitted Gaussian on those outputs, $f(x) \sim N(f_0, \Gamma_f)$. We then take

$$\Gamma_f = U_m \Sigma_m U_m^T \tag{17}$$

$$f^*(x) = U_m^T (f(x) - f_0) \tag{18}$$

where Σ_m is the first m eigenvalues diagonalized and F_m are the corresponding eigenvectors. $f^*(x)$ now represents a model that produces only m outputs that represent the predicted pressures. For the numerical experiments described here, we choose $m = 100$.

In this reduced data space, we can still create Bayesian posteriors. This is a novel approach we take here, for reasons that we will soon describe. Consider applying a similar PCA transform as in Equation (18) to the data y, starting from Equation (4):

$$U_m^T (y - f_0) = U_m^T (f(x) + e - f_0). \tag{19}$$

We can then define $y^* = U_m^T (y - f_0)$ and $e^* = U_m^T e$, which gives

$$y^* = f^*(x) + e^*. \tag{20}$$

By conducting Bayesian inference with these alternatives to y, $f(x)$ and e, the usual Bayesian equations derived in Section 2.3 still apply, with the respective changes to notation. The significance of approaching the problem in this way is that it allows for the simple integration of the NN into the Bayesian framework, which will only produce outputs in this PCA space, rather than the original data space. In what follows, it will be useful to note

$$\Gamma_{e^*} = U_m^T \Gamma_e U_m \tag{21}$$

3.4 Network Design

The neural network is designed to match the input-output relationship of $f^*(x)$ created by LIMS (and the PCA). While alternative approaches to NN surrogate modelling of a physical process, most notably the physics-informed neural network (or PINN) [24] [25], this approach is chosen for its simplicity. The neural network is minimizing the loss between the NN outputs, which we term $g(x)$ and $f^*(x)$. We generate 100000 samples using LIMS for training, and 10000 each for training and testing.

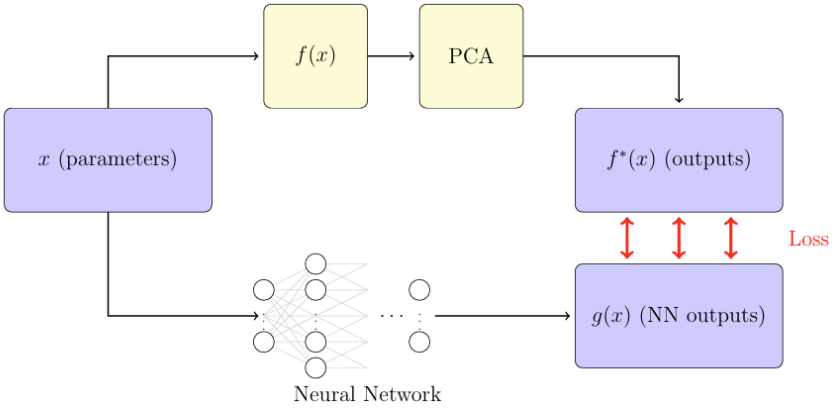

Figure 1: Neural network surrogate framework

3.5 Bayesian Approximation Error

Using a surrogate $g(x)$ instead of the underlying model (in this case, LIMS) $f(x)$ introduces surrogate approximation error. Approaching this inverse problem within the Bayesian framework enables the systematic incorporation of this error by augmenting the error term. This is referred to as the Bayesian approximation error (BAE) approach. Consider the following definition for the approximation error ε:

$$\varepsilon(x) = f^*(x) - g(x). \tag{22}$$

We postulate a Gaussian on ε, conditional upon x, of the form $\varepsilon \sim N(\varepsilon_{0|x}, \Gamma_{\varepsilon|x})$, where

$$\varepsilon_{0|x} = \varepsilon_0 + \Gamma_{\varepsilon x}\Gamma_x^{-1}(x - x_0) \tag{23}$$

$$\Gamma_{\varepsilon|x} = \Gamma_\varepsilon - \Gamma_{\varepsilon x}\Gamma_x^{-1}\Gamma_{x\varepsilon} \tag{24}$$

These matrices can all be determined by considering the joint Gaussian of x and ε. ε can then be simply incorporated into the Bayesian framework by defining a new total error term $\eta = e^* + \varepsilon$. Combining this with Equation (23) gives

$$y^* = g(x) + \eta, \tag{25}$$

where we can define $\eta|x \sim N(\eta_{0|x}, \Gamma_{\eta|x})$

$$\eta_{0|x} = \varepsilon_0 + \Gamma_{\varepsilon x}\Gamma_x^{-1}(x - x_0) \tag{26}$$

$$\Gamma_{\eta|x} = F_m^T\Gamma_e F_m + \Gamma_\varepsilon - \Gamma_{\varepsilon x}\Gamma_x^{-1}\Gamma_{x\varepsilon} \tag{27}$$

Using this augmented total error term, we can accurately account for both measurement and surrogate approximation errors in our results. It will also be useful to define $L_{\eta|x}^T L_{\eta|x} = \Gamma_{\eta|x}$.

In summary, the expression in Equation (7) expresses $\pi(x|y)$, based on the FECV LIMS model. If we substitute the NN surrogate (considering the problem in PCA space), but don't account for the approximation errors, we have

$$\pi_{NN}(x|y) \propto exp\left(-\frac{1}{2}\left\|L_{e^*}\left(y^* - g(x)\right)\right\|_2^2 - \frac{1}{2}\|L_x(x - x_0)\|_2^2\right) \tag{28}$$

where $L_{e^*}^T L_{e^*} = \Gamma_{e^*}$. However, if we incorporate the surrogate approximation error correctly, we have

$$\pi_{BAE}(x|y) \propto exp\left(-\frac{1}{2}\left\|L_{\eta|x}(y^* - g(x) - \varepsilon_0 - \Gamma_{\varepsilon x}\Gamma_x^{-1}(x - x_0))\right\|_2^2 - \frac{1}{2}\|L_x(x - x_0)\|_2^2\right) \quad (29)$$

4 RESULTS

We now present the results of numerical experiments. Here, we create a theoretical truth for the permeability parameterization x_{ref}, generate synthetic data by running LIMS to create $f(x)$ and add error e, sampled from the error distribution $N(0, \Gamma_e)$. Based solely on y, we then construct or attempt to estimate the posterior $\pi(x|y)$ and compare this prediction to x_{ref}. We consider the two parameterizations, although both use the same geometry, shown in Figure 2. We use a rectangular preform sheet, bent at four positions to create a ridge. The edges of the mold and those ridges act as potential regions of race tracking.

There are two injection sites, as indicated in Figure 2. These injection sites both inject with a fixed pressure of 100kPa. We use the bulk permeability of $K_{bulk} = 1e^{-10}\text{m}^2$ a viscosity of 0.2Pa s.

4.1 Race tracking only

When we consider the parameterization of only the race tracking regions, as discussed in Section 3.1, we are estimating only eight parameters. For this relatively low-dimensional parameterization, it is possible to obtain a view of the posterior using LIMS ($\pi(x|y)$). We can then compare this to the posterior produced by the NN surrogate, both with and without the Bayesian approximation error. To do this, we consider the problem marginally. That is, we fix all $x = x_{ref}$ and we then change one component of x between a range of values, evaluating the posterior at each instance. This 'gridding' of the posterior is done to visualize the effects of the NN posterior and this methodology but would not work in practice, as knowledge of x_{ref} is needed. The results of this analysis are shown in Figure 3. Note that these posteriors are exact, without any approximation.

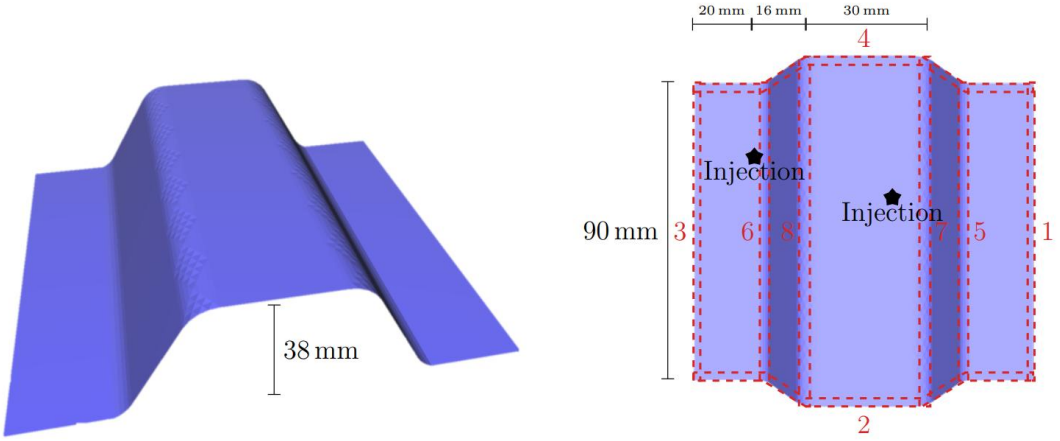

Figure 2: Mold geometry for the numerical experiments in this paper. Injection sites are indicated with black stars, and the race tracking regions are indicated in red.

The Bayesian posterior using LIMS ($\pi(x|y)$) is shown in red. This posterior is narrow and incorporates the truth, indicated by the dashed black line. However, this posterior is very coarse. Posteriors of this shape are difficult to discover in higher-dimensional problems. A Gaussian approximation of this posterior would not be an appropriate fit, and finding the MAP estimate will become infeasible in high dimensions using optimization algorithms.

$\pi_{NN}(x|y)$ has a similar narrow range to $\pi(x|y)$, as they use a very similar error model. However, as we have not incorporated the surrogate approximation error, $\pi_{NN}(x|y)$ often is incorrect in the predictions and confident with the incorrectness. When the approximation error is considered, we have $\pi_{BAE}(x|y)$, which is wider to accommodate the larger error term, but always contains the truth within

the range of predictions. In addition, $\pi_{BAE}(x|y)$ is orders of magnitude faster than $\pi(x|y)$ to generate and use, due to the computational speedup of $g(x)$ over $f(x)$.

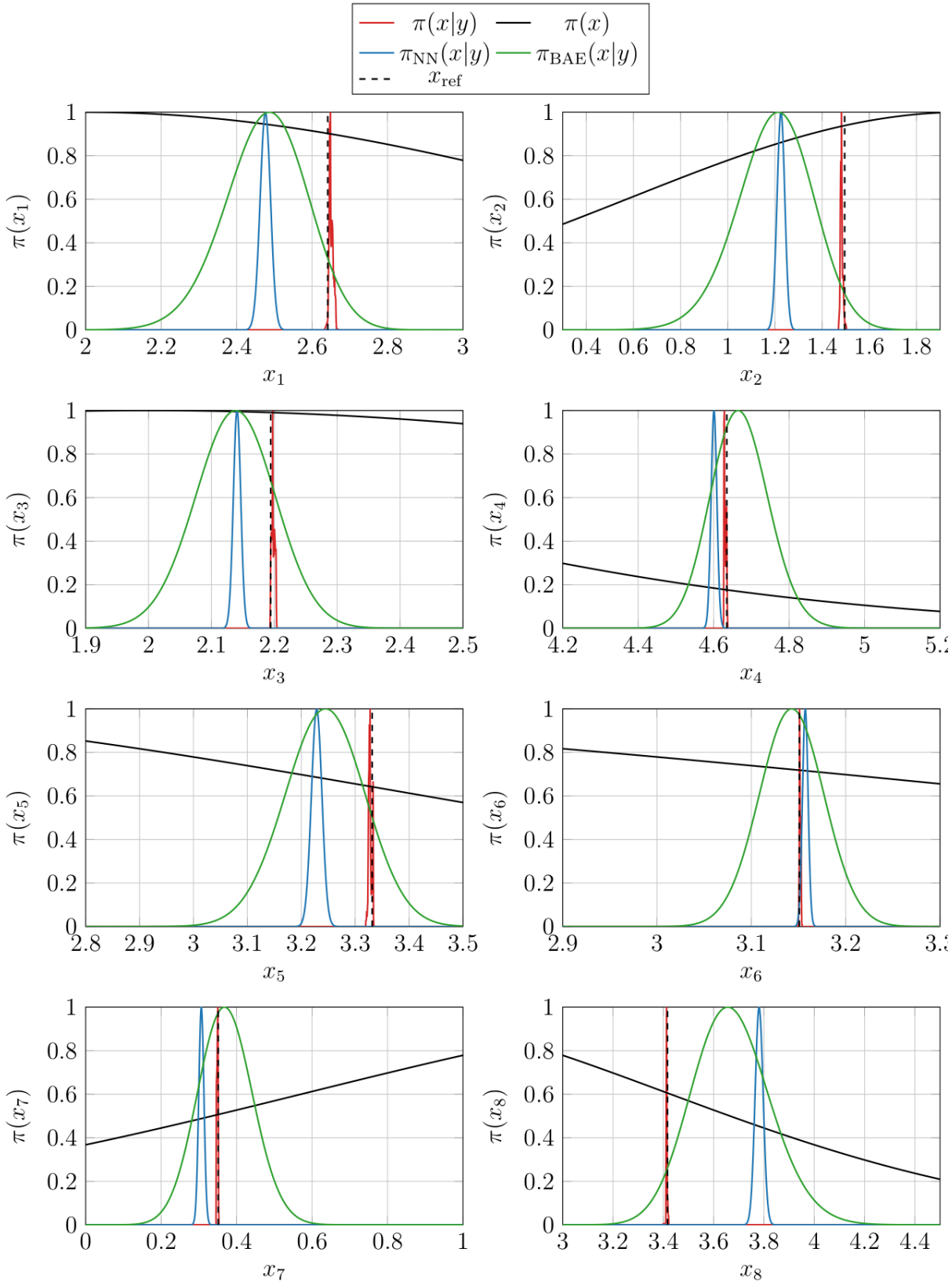

Figure 3: Prior and posteriors, normalized to a height of one. The x axis is zoomed to better show the shape of the posteriors.

General Field

We now consider the higher-dimensional parameterization described in Section 3.2. With the 100-dimensional parameter x, it is no longer possible to use LIMS to generate the posterior $\pi(x|y)$, or even to fully characterize the BAE posterior $\pi_{BAE}(x|y)$. Instead, we take a Laplace approximation, as described in Section 2.3, computing a MAP estimate and posterior covariance matrix about that estimate. Results from this investigation are shown in Figure 4.

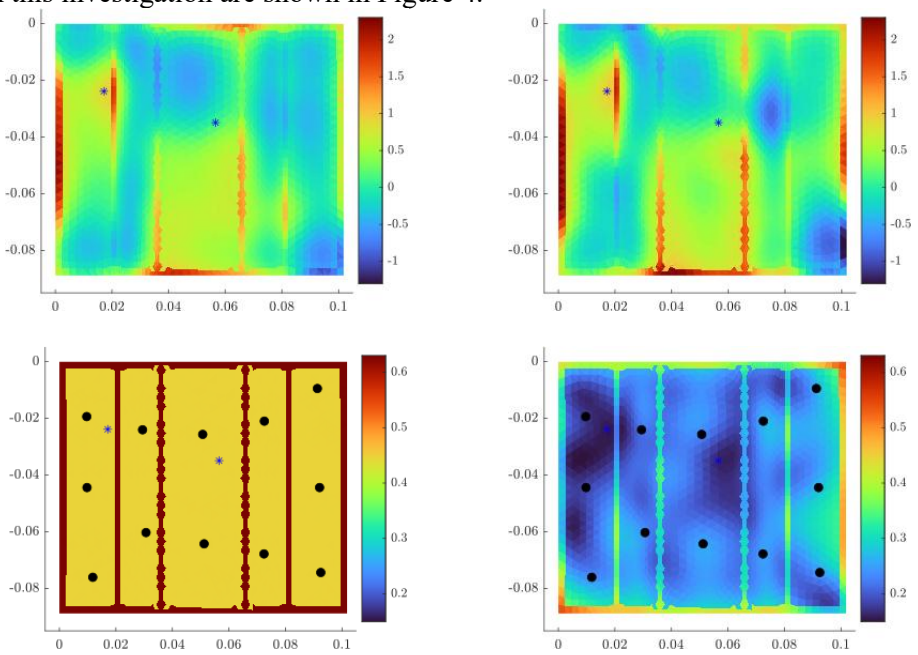

Figure 4: MAP estimate (top left) vs the truth (top right). The prior uncertainty is shown in the bottom left plot, and the posterior in the bottom right. Injection sites are marked with blue stars, while black dots denote sensor locations.

In Figure 4, we reverse the PCA transform on our estimations to visualize k, the permeability strengths or σ_k^2 in the case of the uncertainty plots. Note the similarity between the MAP estimate and the truth – our algorithm correctly identifies a race tracking region in the center of the left mold boundary and accurately estimates the strength of the race track. It also correctly identifies the increased permeability at the bottom-center of the mold.

In this example, we observe a posterior covariance with much lower uncertainty than in the prior, as expected. As with the prior, there is greater uncertainty in the race tracking regions. The uncertainty is greatest in the corners of the mold and on the right boundary. This result is logical because the resin reaches these regions last, and the permeability there has a minimal effect on the pressures and movement of the resin away from them. We observe reduced uncertainty near injection sites; however, interestingly, there is no correlation between the sensor locations and the uncertainty. Measurements at the sensors are affected by permeability throughout the mold, not just in the vicinity.

To further compare our estimations, we can examine the difference in flow front movement when both x_{MAP} and x_{ref} are simulated, as well as when the permeability is homogeneous. These are shown in Figure 5. When the permeability is homogeneous, as is typically modelled, the resin takes over 50 seconds to fill the mold, finishing in the bottom right corner. However, our MAP estimate and the truth match very closely, predicting that the mold filled in roughly 40 seconds. They also both predict that the resin moves quickly to the bottom left corner of the mold, then races along the bottom of the mold, finishing not in the bottom right corner but uniformly along the right edge.

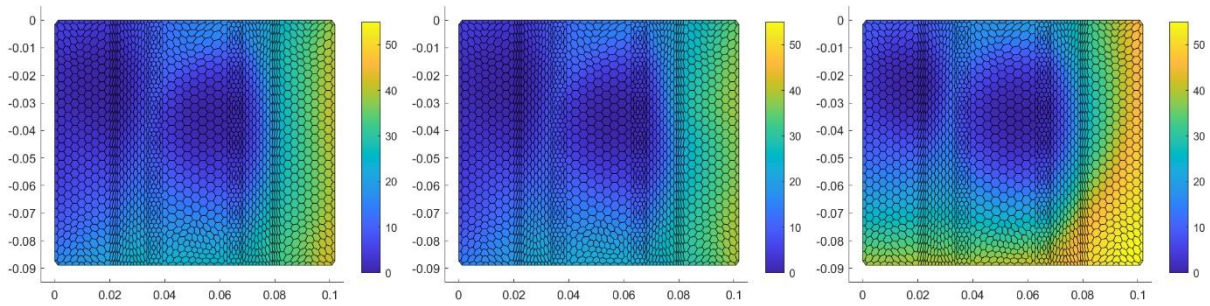

(a) MAP Estimate *(b) Truth* *(c) Homogeneous*

Figure 5: Flow front visualized, for three different permeability scenarios. Each control volume is colored according to the time it takes to fill that control volume (in seconds).

5 CONCLUSIONS AND FUTURE WORK

We proposed a Bayesian framework for predicting preform permeability based on pressure measurements taken during the RTM filling process. To avoid numerical issues caused by the FECV method implemented by LIMS, which is commonly used to model RTM, we use a neural network surrogate and incorporate the approximation error into our Bayesian posteriors. The NN surrogate has the additional advantage of being incredibly fast to run, whereas the FECV method can be very computationally expensive.

We first demonstrated our methodology for a low dimensional parameterization of permeability, considering the estimation of only the race tracking strengths. Our results showed that a posterior that included the surrogate approximation error ($\pi_{BAE}(x|y)$) could correctly encompass the true permeability within its uncertainty. Neglecting these approximation errors when using the surrogate ($\pi_{NN}(x|y)$) creates precise but inaccurate posteriors that are misleading or erroneous. We next demonstrated the same methodology with a larger parameterization, which considers general variations in permeability throughout the preform, with greater variation in the race tracks. Using 12 pressure sensors distributed throughout the mold, we can estimate an unknown permeability field sampled from the prior with high precision. Using our estimate for permeability, we can accurately predict the resin flow pattern.

The following steps in this research involve using real-time permeability estimates for online control of the resin flow. Our research has shown that accurate estimations of the permeability field can be made with a limited number of pressure sensors and almost instantly, using the NN surrogate. Approaches such as an extended Kalman filter [26] [27] are designed to adapt the classical Bayesian approach into a real-time updating posterior. As the mold is filled, we can use the posterior to consider the range of permeability scenarios that may be occurring and take control action (such as adjusting the pressure at one of the two sensors) to minimize the chance of creating voids within the part.

6 REFERENCES

[1] A. Gokce, K.-T. Hsiao and S. G. Advani, "Branch and bound search to optimize injection gate locations in liquid composite molding processes," *Composites Part A: Applied Science and Manufacturing,* vol. 33, pp. 1263-1272, 2002.

[2] P. B. Nedanov and S. G. Advani, "Numerical computation of the fiber preform permeability tensor by the homogenization method," *Polymer Composites,* vol. 23, p. 758, October 2002.

[3] S. Bickerton and S. G. Advani, "Characterization and modeling of race-tracking in liquid composite molding processes," *Composites Science and Technology,* vol. 59, pp. 2215-2229, 1999.

[4] M. Devillard, K.-T. Hsiao, A. Gokce and S. G. Advani, "On-line characterization of bulk permeability and race-tracking during the filling stage in resin transfer molding process," *Journal of Composite Materials,* vol. 37, pp. 1525-1541, 2003.

[5] A. Kumar and M. Shukla, "Race tracking and related issues in liquid composite moulding process," *Journal for Manufacturing Science and Production,* vol. 14, p. 209–217, 2014.

[6] S. G. Advani and E. M. Sozer, Process Modeling in Composites Manufacturing, CRC Press, 2003.

[7] M. Devillard, K.-T. Hsiao and S. G. Advani, "Flow sensing and control strategies to address race-tracking disturbances in resin transfer molding—part II: automation and validation," *Composites Part A: Applied Science and Manufacturing,* vol. 36, pp. 1581-1589, 2005.

[8] K.-T. Hsiao and S. G. Advani, "Flow sensing and control strategies to address race-tracking disturbances in resin transfer molding. Part I: design and algorithm development," *Composites Part A: Applied Science and Manufacturing,* vol. 35, pp. 1149-1159, 2004.

[9] B. Liu, S. Bickerton and S. G. Advani, "Modelling and simulation of resin transfer moulding (RTM)—gate control, venting and dry spot prediction," *Composites Part A: Applied Science and Manufacturing,* vol. 27, pp. 135-141, 1996.

[10] K. M. Pillai and S. G. Advani, "Numerical simulation of unsaturated flow in woven fiber preforms during the resin transfer molding process," *Polymer Composites,* vol. 19, p. 71–80, 1998.

[11] P. Simacek, D. Heider, J. W. Gillespie Jr and S. Advani, "Post-filling flow in vacuum assisted resin transfer molding processes: Theoretical analysis," *Composites Part A: Applied Science and Manufacturing,* vol. 40, p. 913–924, 2009.

[12] M. V. Bruschke and S. G. Advani, "A finite element/control volume approach to mold filling in anisotropic porous media," *Polymer Composites,* vol. 11, pp. 398-405, 1990.

[13] M. Kang, J. Jung and W. I. Lee, "Analysis of resin transfer moulding process with controlled multiple gates resin injection," *Composites Part A: Applied Science and Manufacturing,* vol. 31, pp. 407-422, May 2000.

[14] L. J. Lee, W. B. Young and R. J. Lin, "Mold filling and cure modeling of RTM and SRIM processes," *Composite Structures,* vol. 27, pp. 109-120, 1994.

[15] P. Simacek, S. Advani and C. Binetruy, "Liquid injection molding simulation (LIMS) a comprehensive tool to design, optimize and control the filling process in liquid composite molding," *JEC-Compos,* vol. 8, pp. 58-61, January 2004.

[16] P. Simacek and S. G. Advani, "Desirable features in mold filling simulations for liquid composite molding processes," *Polymer Composites,* vol. 25, p. 355–367, 2004.

[17] D. Calvetti and E. Somersalo, An Introduction to Bayesian Scientific Computing: Ten Lectures on Subjective Computing, vol. 2, Springer Science & Business Media, 2007.

[18] J. Kaipio and E. Somersalo, "Statistical inverse problems: discretization, model reduction and inverse crimes," *Journal of computational and applied mathematics,* vol. 198, p. 493–504, 2007.

[19] A. M. Stuart, "Inverse problems: a Bayesian perspective," *Acta numerica,* vol. 19, p. 451–559, 2010.

[20] A. Erkanli, "Laplace Approximations for Posterior Expectations When the Mode Occurs at the Boundary of the Parameter Space," *Journal of the American Statistical Association,* vol. 89, p. 250–258, 1994.

[21] N. Wright, O. Maclaren, P. Kelly, S. Advani and R. Nicholson, *Addressing Discontinuity in Finite Element – Control Volume Based Liquid Injection Moulding Simulations using Neural Network Surrogates,* 2025.

[22] K. P. F.R.S., "LIII. On lines and planes of closest fit to systems of points in space," *The London, Edinburgh, and Dublin Philosophical Magazine and Journal of Science,* vol. 2, pp. 559-572, 1901.

[23] I. T. Jolliffe, Principal Component Analysis, 2nd (2009) ed., Springer, 2002.

[24] J. Lee, M. Duhovic, D. May, T. Allen and P. Kelly, "Physics-informed neural networks for real-time simulation of transverse Liquid Composite Moulding processes and permeability measurements," *Composites Part A: Applied Science and Manufacturing,* vol. 193, 2025.

[25] Y. Chen, P. Simacek and S. Advani, "Physics-informed neural networks for resin flow prediction in fibre textiles," in *21st European Conference on Composite Materials*, Nantes, 2024.

[26] R. E. Kalman, "A New Approach to Linear Filtering and Prediction Problems," *Transactions of the ASME-Journal of Basic Engineering,* vol. 82, pp. 35-45, 1960.

[27] R. S. Bucy, *Extended Kalman filtering for nonlinear systems via Taylor expansion,* 1969.

ICCM24
AUGUST 4-8, 2025
BALTIMORE CONVENTION CENTER
BALTIMORE, MARYLAND, USA

No Technical Paper Submission for:

Venkatesh Ananchaperumal

INVERSE DESIGN OF MANUFACTURING PROCESSES USING PHYSICS-INFORMED NEURAL OPERATOR LEARNING

Rui Wan[1], Minglei Lu[1], Yidong Xia[2], Gang Li[1], Srikanth Pilla[3] and Zhen Li[1]

[1]Department of Mechanical Engineering, Clemson University
216 S Palmetto Blvd, Clemson, SC 29634, USA
Email: zli7@clemson.edu,

[2]Energy and Environment Science & Technology, Idaho National Laboratory
1955 Fremont Ave, Idaho Fall, ID 83415, USA

[3]Center for Composite Materials, University of Delaware
101 Academy Street, Newark, DE 19716, USA

Keywords: Composites, Machine Learning, Neural Network, Operator Network, Small Data

ABSTRACT

Machine learning-based approaches, especially neural network models, have achieved remarkable success in diverse scientific applications, where the deep neural operator (DNO) enables the learning nonlinear operators between infinite-dimensional function spaces and is able to approximate governing equations of time-dependent engineering processes. This paper presents two novel applications of DNO learning to accelerate the design of composite materials and their manufacturing processes. First, we develop a DNO-based surrogate model for finite element simulations of transient mechanical response of 3D interpenetrating phase composites (IPCs) fabricated via additive manufacturing. These IPCs consist of randomly structured metallic phases with different elastic moduli. DNO is trained using a sequence-to-sequence incremental learning approach based on 5,000 finite element simulations of an IPC beam subject to random strain loads, resulting in a 98% prediction accuracy on transient stress at various cross-sections of the IPC beam under dynamic loading. The trained DNO enables real-time prediction of mechanical properties, significantly reducing the design iterations for composites. Second, we introduce an enhanced physics-informed DNO (PIDNO+) model for predicting the particle size distribution in biomass comminution processes. PIDNO+ integrates a population balance model into a hybrid DNO+ architecture that incorporates both material and processing parameters. This integration enables high accuracy with a limited small dataset while preserving physical consistency. The shared parameter network with the embedded physical model allows for differential operation in parameter space and enables inverse design of manufacturing parameters to meet target outcomes. Both DNO applications demonstrate the potential of operator learning for fast and accurate surrogate modeling in composite material design and accelerated optimization of manufacturing processes.

1 INTRODUCTION

Although deep learning algorithms have been implemented into physical problems by many researchers [1-3], it is still challenging to solve the mapping problem between time-dependent and space-dependent functions using traditional deep neural networks (DNNs). There are, in general, two possible scenarios when we develop a DNN model for composite materials. First, if we have sufficient prior physical knowledge on the composite materials and know their governing equations explicitly, i.e., in the form of partial differential equations (PDEs), it becomes possible to encode the PDEs into the DNN, which leads to the physics-informed neural network (PINN) models [4]. Second, if we lack physical knowledge of the given composites (i.e., with three or more enforcing phases) and do not know the explicit form of its governing equations, we need to learn the implicit governing equations or operators from available observed data. This motivated the development of deep neural operator (DNO) methods [5], which learn nonlinear operators between infinite-dimensional function spaces and can

approximate governing equations of time-dependent engineering processes. Deep Operator Network (DeepONet) [6], as one type of DNO, brings a new solution to find the operators. DeepONet can learn the diverse continuous nonlinear operator between input and output, so that it can be used to solve various explicit and implicit mapping functions. In the present paper, two examples of DNO application will be introduced, including DNO acting as a surrogate of physics-based composites models in time-dependent problems, and DNO enabling inverse design of manufacturing process based on small experimental dataset.

The first example of DNO application introduced in Section 2 is on neural operator learning acting as surrogate of physics-based composite model to offer real-time prediction of transient mechanical response of composites under dynamic loading. The mechanical behavior of composites, especially under dynamic loading, is highly sensitive to their 3D structural design. However, evaluating their dynamic response subject to dynamic loading typically requires time-intensive finite element analysis (FEA) or physical testing, which can take hours to days for each design. To overcome this limitation, a DNO model is developed to learn the transient mechanical response of interpenetrating phase composites (IPCs) under dynamic strain loads. DNO consists of one trunk network to encode the domain of the output functions and one DNN or multiple DNNs to encode the discrete input function space as its branch network [7]. A 3D IPC beam composed of two metals with a Young's modulus ratio of 2.7 is used to generate training data through 5,000 FEA simulations with random strain inputs. Once trained, DNO serves as a fast and reliable surrogate to predict stress fields in seconds, greatly accelerating IPC design and optimization.

The second example of DNO application introduced in Section 3 is on inverse design of manufacturing processes based on a small experimental dataset, where an enhanced Deep Neural Operator (DNO+) model is designed to learn how comminution outcomes are influenced by a parameter space consisting of both manufacturing parameters and material properties. To reduce the reliance of DNO+ on experimental data and enable effective DNO+ training on small experimental datasets, we integrate a transport equation of a population balance model (PBM) into the DNO+ framework, creating a physics-informed enhanced deep learning operator (PIDNO+) model. PIDNO+ integrates physics into the DNO+ model to combine the strengths of deep learning and physics-based modeling, therefore, it can reduce the data requirements and improve physical consistency of the model. This integration endows the PIDNO+ model with robust predictive capabilities across diverse conditions and enables inverse design of manufacturing processes for target product features.

2 A SURROGATE OF PHYSICS-BASED COMPOSITE MODEL

We start with the introduction of the physical problem setup. As shown in Figure 1(a), an IPC beam with a cuboid structure composed of stainless steel and aluminum alloy is considered, with one fixed end and one free end, where an arbitrarily dynamic strain loading is applied to the free end. The typical dynamic strain loads created by a Gaussian random process are shown in Figure 1(b). The mechanical response of interest is the time evolution of the normal stress along the x-direction σ_{xx} inside the IPC beam, where x denotes an arbitrary location in the IPC beam. The IPC beam is set to 500 mm in length with a cross section of 100 mm by 100 mm. The beam structure is divided into 40 identical cubic subdomains, each with a side length of 50 mm. Stainless steel and aluminum alloy are randomly assigned to these cubes to form a composite beam.

When the applied strain exceeds the yield point, both the elastic and plastic responses of the constituent materials (stainless steel and aluminum alloy) with significant different elastic moduli and tensile strengths should be considered. This introduces pronounced nonlinearity into the dynamic behavior of the IPC composite beam. The elasticity of the constituent materials is determined by the Young's modulus and Poisson's ratio, while the plasticity deformation is described using a multilinear isotropic hardening model derived from available stress-strain curves [8]. As shown in Figure 1(c), under a given dynamic strain loading, the IPC beam exhibits coupled deformation modes, including bending, axial stretching/compression, and twisting, due to asymmetrical distribution of material properties within the IPC beam structure.

To simulate the dynamic mechanical response, the IPC beam is discretized using the finite element method and solved numerically using the commercial software ABAQUS. The time-evolution of stress

distribution is analysed under varying dynamic strain loadings. A time-dependent strain function is created by drawing from a random Gaussian process. To ensure smooth strain loading conditions, the strain function is modulated by a sine envelope, $\sin(\pi t)$, so that the strain applied to the free end of the IPC beam always starts from a zero strain at $t = 0$ s and ends with a zero strain at $t = 1$ s, as illustrated in Figure 1(b).

A total of 5,000 FEA simulations are performed, each corresponding to a different realization of the dynamic strain loading, to generate enough data for DNO training. Each simulation runs from $t = 0$ s to $t = 1$ s with a sampling interval $\Delta t = 0.01$ s, and generates one dataset consisting a time sequence t_i with i = (1, 2,…, 101), a time-dependent input $Y_i = \varepsilon(t_i)$, and a time-dependent output $U_i = \sigma(\boldsymbol{x}, t_i)$ with $\boldsymbol{x}$ being an arbitrary location inside the IPC beam. Both the branch net and the trunk net of DNO have one input layer, five hidden layers, and one output layer, with a neural network architecture of 101×200×200×300×200×200×101, in which the integers represent the number of neurons in those layers. The model is trained using the Adam optimizer with a learning rate of 0.001 to minimize the mean squared error (MSE) between the DNO predictions and the FEA results. Of the 5,000 datasets, 4,900 are used for training and the rest for testing. The DNO model is iteratively updated until the desired accuracy is achieved or the predefined maximum number of iterations is reached.

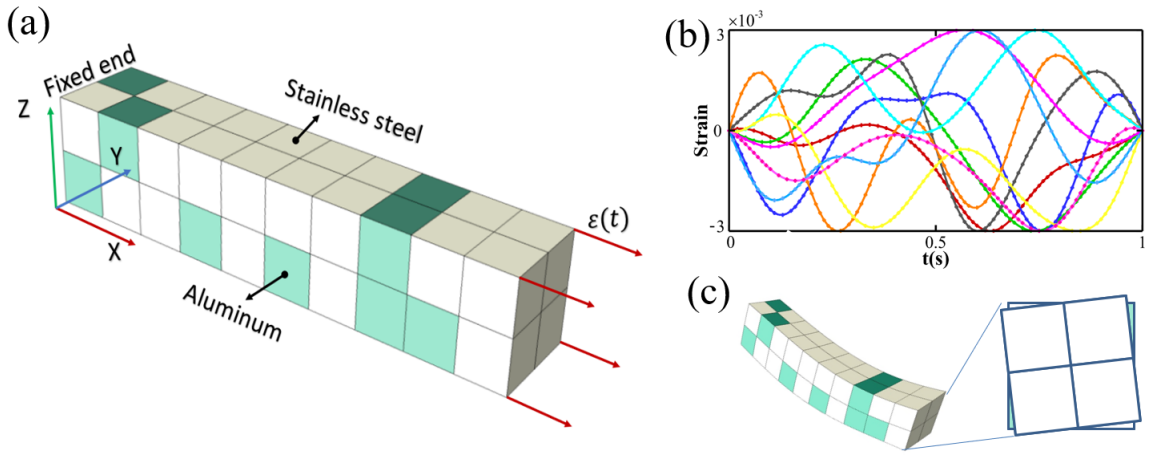

Figure 1: (a) Computational domain and boundary condition of an IPC beam subject to dynamic strain loading. (b) Arbitrary dynamic strain loading is created by drawing a smooth time-dependent function between 0 to 1 seconds from a Gaussian random process. (c) Coupled bending, stretching/compression, and twisting deformation of the IPC beam under strain loading.

Figure 2(a1) and 2(a2) show the stress distribution at the central cross-section (perpendicular to the x-axis) of the IPC beam at $t = 0.5$ s for the FEA simulation and DNO prediction, respectively. The DNO model achieves an average prediction accuracy of 98%. The corresponding error distribution, as shown in Figure 2(a3), reveals that the prediction error is minimal in the central region and increases toward the edges. This pattern of error distribution could be attributed to the higher material uniformity in the central area and increased heterogeneity near the edge of the structure. The maximum error occurs in the upper-right corner, which is consistent with the fact that edge region has high structural complexity and freedom due to the boundary condition - only one end of the IPC beam is fixed. Under compressive loading, this boundary condition allows the structure to bend and twist simultaneously, as observed in Figure 1(c), which makes the stress distribution more complicated.

At the end of the dynamic loading, i.e., $t = 1$ s, although the applied strain at the free end returns to zero, residual stresses remain in the structure, as shown in Figure 2(b1), These residual stresses arise due to irreversible plastic deformation accumulated during the dynamic loading process. Interestingly, even if the applied strain passes through the zero point one or more times, different internal stress states may result each time due to the path-dependent plasticity. This reflects the fact that the process is both time- and space-dependent, making it hard to predict using traditional neural networks. In general, the trained DNO model demonstrates robust prediction capability, achieving stress prediction accuracies ranging from 95% to 99% across various cross-sections when compared to FEA results.

This establishes the DNO as an effective surrogate of physics-based FEA models for real-time prediction of the transient mechanical behavior of composite structures under dynamic loading, which will significantly accelerate computational analysis in composite design and material discovery.

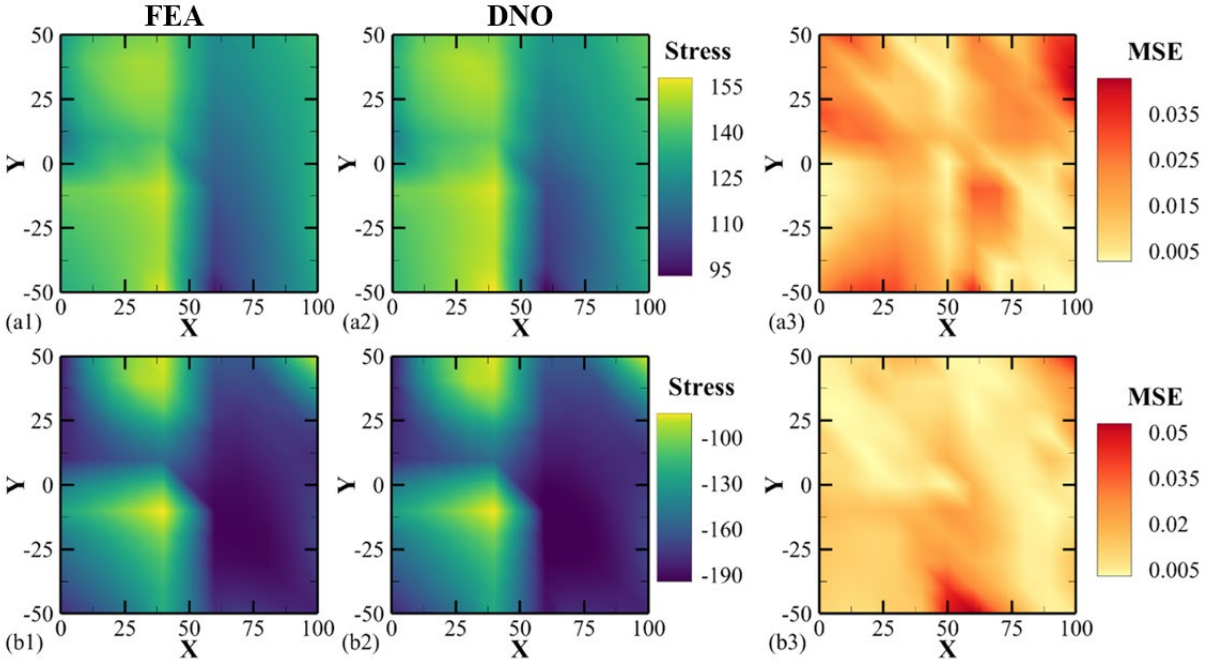

Figure 2: DNO as a surrogate of FEA model to predict the cross-section stress distribution. (a1) and (b1) show the transient stress distribution of a selected cross-section from FEA model at 0.5 s and 1.0 s respectively. (a2) and (b2) illustrate the DNO prediction of stress distribution of the selected cross-section at 0.5 s and 1.0 s respectively. (a3) and (b3) show the prediction error distribution within the cross-section at 0.5 s and 1.0 s respectively.

3 INVERSE DESIGN OF MANUFACTURING PROCESSES

3.1 An Enhanced Physics-informed Deep Neural Operator (PIDNO+) Model

To enable inverse design of a manufacturing process by optimizing adjustable manufacturing parameters, we must enable differential operations in the manufacturing parameter space. To this end, an enhanced deep neural operator (DNO+) model developed by Lu et al. [9] is adopted to map the relationship between the system's input and output while incorporating additional variables that impact the mapping. The DNO+ model consists of a trunk net, a branch net, and a parameter net, as shown in Figure 3. In particular, the branch network takes the cumulative mass distribution with reference to the particle size sequence as input, the trunk net handles the particle size sequence through the entire comminution process, and the parameter network correlates the impact of important feed material properties and manufacturing parameters on the resultant particle size distribution (PSD) of comminuted material.

The primary input of the biomass comminution DNO+ model is the feed-in cumulative mass distribution $\boldsymbol{\Phi}_{\text{in}}$ with reference to a particle size sequence $\boldsymbol{x}$, and the influence parameters $\boldsymbol{p}$. The cumulative mass distribution $\boldsymbol{\Phi}_{\text{out}}$ as output is then expressed as

$$\boldsymbol{\Phi}_{\text{out}} = \mathscr{F}(\boldsymbol{\Phi}_{\text{in}})\cdot\mathscr{R}(\boldsymbol{x}) + \mathscr{L}(\boldsymbol{p})\cdot\mathscr{R}(\boldsymbol{x}), \tag{1}$$

where $\mathscr{F}$, $\mathscr{L}$, and $\mathscr{R}$ represent different operators and are approximated by the neural network. Here, a fully connected neural network is used in the trunk net to process each input feature independently, while convolutional neural networks are used in the branch and parameter networks to extract features from spatially structured data by virtue of their shared-weight architecture. The introduction of additional parameter networks enables the DNO+ model to consider the impact of material or process

parameters on system results and thus more effectively capture the relationship between system input and output.

To address the challenge of training DNO+ on limited experimental data, a physical model is integrated into the DNO+ structure to reduce the data requirements for training the DNO+ model. In this work, a population balance model (PBM) [10] for modeling particle breakage and the evolution of PSD is used to constrain DNO+ training. The core concept of PBM is to track the statistical distribution of a population of particles over time or space, accounting for key phenomena such as breakage and aggregation. PBM describes how larger particles disintegrate into smaller ones under the influence of mechanical stress (e.g., compression, shear, or impact), which is suitable for this biomass comminution DNO+ model.

Let the breakage matrix of PBM be X, and the classification matrix for considering the effects of screen size and passing efficiency be C. The mapping function between the feed PSD (F_{PSD}) and the product PSD of milled materials (P_{PSD}) can be expressed as

$$P_{\mathrm{PSD}} = \sum_{k=1}^{\infty} C\cdot(1-C)^{k-1}\cdot X^{k}\cdot F_{\mathrm{PSD}}. \tag{2}$$

However, Eq. (2) lacks a description of the impact of material properties or manufacturing parameters on the system. To address this limitation, the advantage of high-dimensional expression of neural networks can be used to establish a complex relationship by allowing the matrices X and C to be functions of material properties and manufacturing parameters.

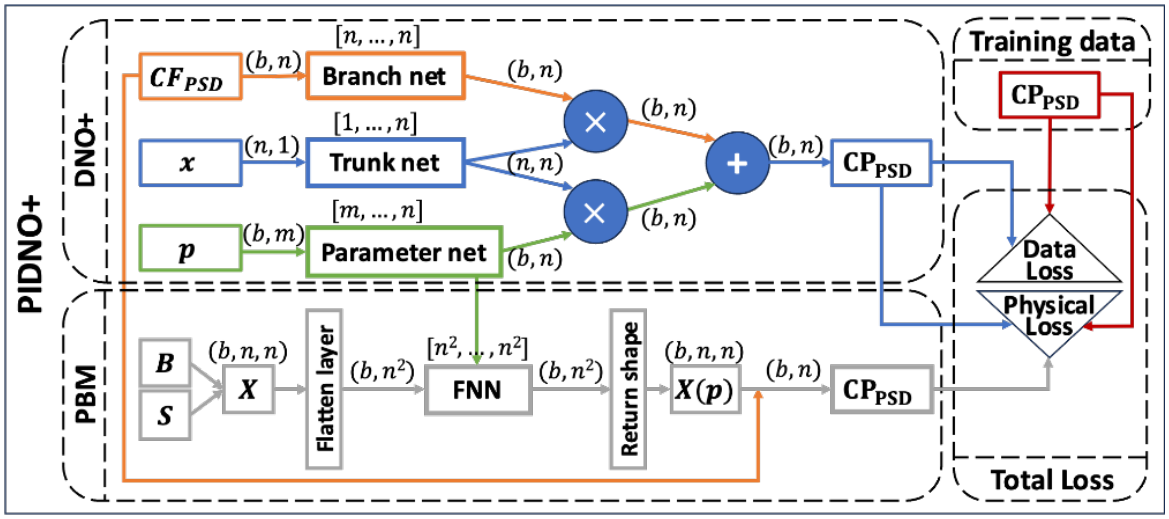

Figure 3: The structure of physics-informed deep neural operator (PIDNO+) model. The PIDNO+ model combines the population balance model (PBM) and DNO+ and establishes the connection between PBM and model parameters through neural networks. The total loss of the PIDNO+ model is the summation of data loss and physical loss. Data loss enables the model to learn from the available data, while physical loss aids the model in learning from the physical-based model.

Figure 3 illustrates the structure of a physics-informed deep neural operator (PIDNO+) model by integrating a PBM into a DNO+ model. The original breakage matrix X in PBM is defined by the breakage function B and the breakage probability S. From Eq. (2), it can be observed that if a connection can be established between matrix X and parameters $\boldsymbol{p}$, which represent feed material properties and manufacturing parameters, the influence of these parameters on the system can be determined. In the PIDNO+ model, X is a matrix with size (b, n, n), where b is the batch size and n the data length. After a flattening process, X changes into X_{flat} with size (b, n^2). The influence of parameter net is introduced in the fully connected neural network, which establishes a relationship between a parameter dependent breakage matrix $X(\boldsymbol{p})$ and X_{flat}. Therefore, the breakage matrix X in Eq. (2) can be replaced by $X(\boldsymbol{p})$, resulting in the milled materials P_{PSD} various with respect to the parameters $\boldsymbol{p}$.

The overall loss function L_{total} in PIDNO+ is formulated by combining three key components: the data-fitting loss between the real data U_{real} and the DNO+ model data $U_{\mathrm{DNO+}}$, the data-fitting loss

between the real data U_{real} and the physical model data U_{phys}, and the consistency loss between the DNO+ model data U_{DNO+} and the physical model data U_{phys},

$$L_{total} = \lambda_1 \cdot MSE(U_{real}, U_{DNO+}) + \lambda_2 \cdot MSE(U_{real}, U_{phys}) + MSE(U_{DNO+}, U_{phys}), \quad (3)$$

where λ_1 and λ_2 serve as weights to determine the significance of different losses. $MSE(U_{real}, U_{DNO+})$ ensures the accuracy of the data-driven part in fitting the data within the entire model. $MSE(U_{real}, U_{phys})$ helps the embedded PBM find suitable built-in parameters. $MSE(U_{DNO+}, U_{phys})$ ensures the auxiliary role of the physical model in the prediction results of the PIDNO+ model.

3.2 Inverse Design of Manufacturing Processes

To validate the PIDNO+ model proposed in this paper, corn stalks were used as an example and experiments were conducted on the comminution process of corn stalks. The material was prepared to have different moisture content levels that represent typical ranges found in corn stover feedstocks in the U.S. Midwest and South. The preparation involved conditioning the corn stalks to achieve the desired moisture levels before comminution. A G1635 Granulator knife mill was configured with a motor capable of operating at different frequencies to adjust the blade tip speed. Different output frequencies were employed from 40 Hz to 60 Hz, corresponding to blade tip speeds ranging from 6.5 $m \cdot s^{-1}$ to 9.8 $m \cdot s^{-1}$. Different discharge screen sizes were chosen to investigate their impact on the particle size distribution of the comminuted material.

To test the feasibility of the model and its data requirements, training and testing datasets need to be prepared. The information contained in one training dataset includes distribution of feed mass versus sieve size, feed moisture content, discharge screen size, and distribution of discharged mass versus sieve size. When the DNO+ model is trained with sufficient data, i.e., 400 datasets, it demonstrates high prediction accuracy for any input within the feasible domain. However, in many cases, sufficient data may not always be available, and the performance of DNO+ without a physical model will be negatively affected. Figure 4(a) shows the prediction results of DNO+ model trained on 100 datasets. It can be observed that although the prediction results generally follow the trend, they deviate a little from the actual values. More extremely, some data points may exceed 100%, rendering the results physically meaningless. In contrast, the PIDNO+ model, trained on a much smaller dataset, achieves an average prediction accuracy of 98% without any values exceeding 100% of cumulative mass, as shown in Figure 4(b). This high accuracy is attributed to the support of the integrated physical model, which not only requires less training data but also conforms to certain physical rules.

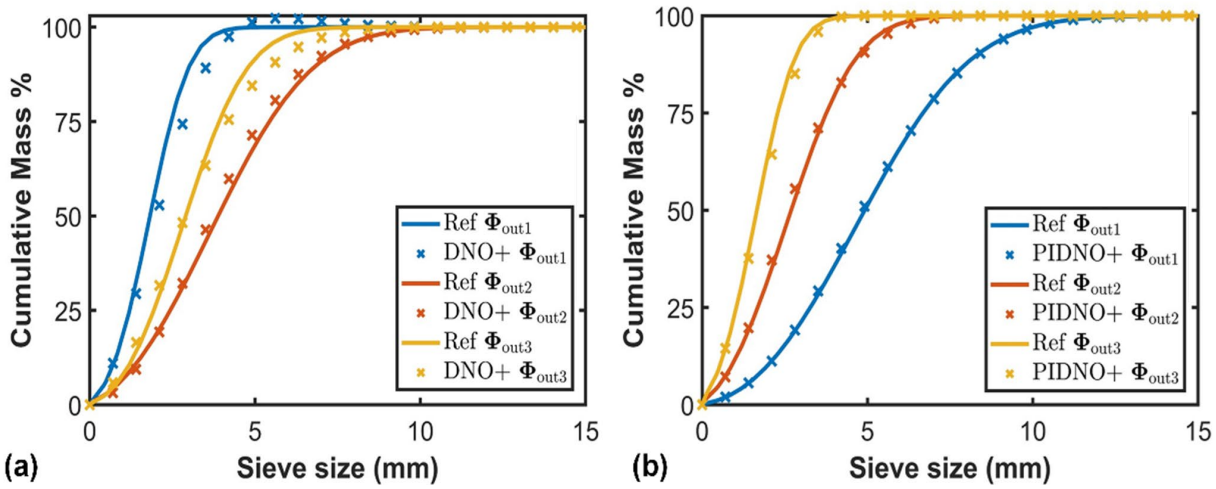

Figure 4: Comparison of the prediction results on the cumulative mass percentage changed with various sizes of sieve: (a) DNO+ with 100 datasets, (b) PIDNO+ with 50 datasets.

The additional parameter network in PIDNO+ enables differential operations in the parameters space, which includes the influence of feed material properties and manufacturing parameters. The trained PIDNO+ model will approximate the nonlinear mapping between the PSD of feed material,

moisture content, screen size, and the resulting PSD of the milled material, which can be optimized to determine the ideal combination of the feed material PSD, moisture levels and screen size to achieve the desired product PSD. Figure 5 demonstrates an inverse design of corn stalks comminution process using PIDNO+. By giving an expected cumulative particle size distribution (PSD) and a feed material PSD, PIDNO+ can determine the moisture content of 30.71% and a screen size of 20.52 mm for the milling machines to produce a cumulative PSD of milled materials consistent with the expected PSD. As a result, the corresponding cumulative PSD outputs are successfully obtained for each case. The real-time prediction of comminution products and inverse design of manufacturing parameters not only enhance manufacturing process control but also reduces energy consumption and operational costs by minimizing trial-and-error experimentation.

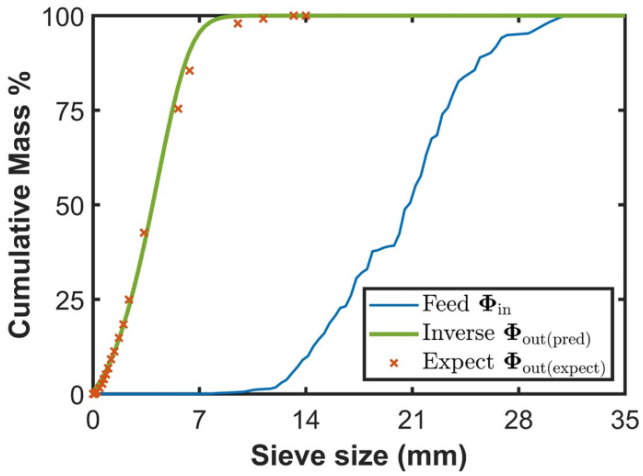

Figure 5: Inverse design of comminution manufacturing parameters. Given an expected cumulative particle size distribution (PSD) with a feed material PSD, PIDNO+ predicts that the moisture content should be adjusted to 30.71% and a screen size of 20.52 mm, which produces a cumulative PSD of milled materials consistent with the expected PSD.

4 CONCLUSIONS

Two significant advancements in modeling and prediction of complex material systems using neural operator learning were presented. First, a Deep Neural Operator (DNO) model was developed to serve as a superfast and accurate surrogate for finite element analysis (FEA) in predicting transient mechanical response of interpenetrating phase composites (IPCs) under dynamic loading. Unlike conventional FEA-based methods that require repeated simulations for different loading conditions, the trained DNO can offer real-time prediction of mechanical responses for arbitrary strain sequences. The use of arbitrary random strain loads in DNO training improves its ability to be generalized for extended temporal inputs. The high accuracy of DNO in predicting stress distributions promises to significantly accelerate composites design and material optimization. Future work may involve integrating Bayesian neural networks [11] for improved uncertainty quantification in noisy data scenarios.

Second, an enhanced Physics-Integrated Deep Neural Operator (PIDNO+) model with an additional parameter network was introduced for predicting particle size distributions (PSD) in a comminution process, offering a flexible and interpretable deep learning framework by integrating a DNO+ model with a physics-based population balance model (PBM). The PIDNO+ model reduces data dependency by embedding physical laws directly into the learning architecture. By incorporating multi-physics relationships and empirical laws from PBM into DNO+, the model captures the influence of material properties and manufacturing parameters on particle breakage with improved generality and adaptability across different regimes, which were validated on experimental comminution data of flexible materials (corn stalks). PIDNO+ offers fast and interpretable predictions of PSD evolution in comminution processes, in which the differentiable parameter network enables the inverse design of manufacturing processes through optimizing feed material properties and manufacturing parameters.

With differentiable parameter network for optimizing manufacturing parameters, this DNO+ inverse design framework will be applied to manufacturing processes of composites, including the inverse design of thermoforming processes for carbon fiber reinforced polymer composites [12], and the inverse design of injection molding parameters for thermoplastic composites [13], based on experimental data generated at the University of Delaware Center for Composite Materials.

ACKNOWLEDGEMENTS

This work was supported as part of the AIM for Composites, an Energy Frontier Research Center funded by the U.S. Department of Energy, Office of Science, Basic Energy Sciences at Clemson University under award #DE-SC0023389.

REFERENCES

[1] M. Agarwal, P. Pasupathy, X. Wu, S.S. Recchia and A.A. Pelegri. Multiscale computational and artificial intelligence models of linear and nonlinear composites: A review, *Small Science*, **4**(5), 2024, pp. 2300185.

[2] C. Lin, Z. Li, L. Lu, S. Cai, M. Maxey and G.E. Karniadakis. Operator learning for predicting multiscale bubble growth dynamics, *The Journal of Chemical Physics*, **154**, 2021, pp. 104118.

[3] M. Yin, E. Zhang, Y. Yu and G.E. Karniadakis. Interfacing finite elements with deep neural operators for fast multiscale modeling of mechanics problems, *Computer Methods in Applied Mechanics and Engineering*, **402**, 2022, pp. 115027.

[4] G.E. Karniadakis, I.G Kevrekidis, L. Lu, P. Perdikaris, S. Wang and L. Yang. Physics-informed machine learning, *Nature Reviews Physics*, **3**(6), 2021, pp. 422-440.

[5] N. Kovachki, Z. Li, B. Liu, K. Azizzadenesheli, K. Bhattacharya, A. Stuart and A. Anandkumar. Neural operator: Learning maps between function spaces with applications to PDEs, *Journal of Machine Learning Research*, **24**, 2023, pp. 1-97.

[6] L. Lu, P. Jin, G. Pang, Z. Zhang and G.E. Karniadakis. Learning nonlinear operators via DeepONet based on the universal approximation theorem of operators, *Nature Machine Intelligence*, **3**(3), 2021, pp. 218–229.

[7] M. Lu, A. Mohammadi, Z. Meng, X. Meng, G. Li and Z. Li. Deep neural operator for learning transient response of interpenetrating-phase composites subject to dynamic loading, *Computational Mechanics*, **72**, 2023, pp. 563–576.

[8] X. Yun, Z. Wang and L. Gardner. Full-range stress-strain curves for aluminum alloys. *Journal of Structural Engineering*, **147**(6), 2021, pp. 04021060.

[9] M. Lu, Y. Xia, T. Bhattacharjee, J. Klinger and Z. Li. Predicting biomass comminution: Physical experiment, population balance model, and deep learning, *Powder Technology*, **441**, 2024, pp. 119830.

[10] M. Capece, Population balance modeling applied to the milling of pharmaceutical extrudate for use in scale-up, *Advanced Powder Technology*, **29**(12), 2018, pp. 3022-3032.

[11] L. Yang, X. Meng and G.E. Karniadakis. B-PINNs: Bayesian physics-informed neural networks for forward and inverse PDE problems with noisy data, *Journal of Computational Physics*, **425**, 2021, pp. 109913.

[12] M. Limaye, D. Morgan, A. Deshpande, S. Pradeep, S. Pilla and G. Li. Use of non-isothermal cure cycles for reducing cure induced deformation in laminated composites, *Manufacturing Letters*, **40**, 2024, pp. 121-124.

[13] S. Pradeep, A. Deshpande, B. Shah, S. Khan, S. Farahani, J. Sternberg, G. Li and S. Pilla. Advancing automotive light-weighting: Material–Process–Microstructure–Performance (MP2) relationships of supercritical foam injection of PP–graphene nanocomposite foams and over-molding, *SAE International Journal of Sustainable Transportation, Energy, Environment, & Policy*, **5**(3), 2024, pp. 249-262.

ICCM24
AUGUST 4-8, 2025
BALTIMORE CONVENTION CENTER
BALTIMORE, MARYLAND, USA

No Technical Paper Submission for:

Taejoon Park

ICCM24
AUGUST 4-8, 2025
BALTIMORE CONVENTION CENTER
BALTIMORE, MARYLAND, USA

No Technical Paper Submission for:

Elham Kianiharchegani

WHITE-ROT FUNGI OXIDATIVE COCKTAIL AS A TOOL FOR MODIFYING KRAFT LIGNIN INTO SUSTAINABLE CARBON FIBER PRECURSORS

Evanildo F. de Souza Junior[1], Leilivan R. Pimentel[1], Beatriz R. Penna[2], Verônica M. A. Calado[1] and Nei Pereira Jr. [1]

[1] Department of Chemical Engineering,
Center of Biofuels, Oil and Derivatives, School of Chemistry,
Federal University of Rio de Janeiro,
Rio de Janeiro 21941909, Brazil
Email: efsjevanildo@eq.ufrj.br; leilivan.pimentel@eq.ufrj.br; calado@eq.ufrj.br; nei@eq.ufrj.br
Web page : http://epqb.eq.ufrj.br

[2] National Center for Structural Biology and Bioimaging,
Federal University of Rio de Janeiro,
Av. Carlos Chagas Filho, 373, bloco K, CENABIO I
Rio de Janeiro 21941902, Brazil
Email: beatriz.penna@bioqmed.ufrj.br, web page: https://cenabio.ufrj.br

Keywords: Biopolymerization; Carbon mat; Lignin fibers.

ABSTRACT

The growing demand for renewable materials has driven interest in lignin as a sustainable precursor for bio-based carbon fibers (CFs). However, its low molecular weight and limited thermal performance restrict its direct applicability. This study explores the enzymatic modification of Kraft lignin (KL) using an oxidative cocktail (LADEBIO-*Pys*) derived from *Pycnoporus sanguineus*, aiming to enhance its structural and processing characteristics for CF production. KL was treated with LADEBIO-*Pys* and *Trametes versicolor* laccase (KL-*Pys* and KL-Tvs, respectively). Both treatments significantly increased molecular weight (by over 150%) and polydispersity (over 110%), indicating efficient polymerization. FT-IR analysis showed intensified bands at 1700 and 1600 cm^{-1}, associated with carbonyl formation, Cα oxidation, and the emergence of conjugated structures. ^{1}H NMR revealed reduced methoxyl protons and increased aliphatic hydroxyls, especially in KL-Tvs, suggesting extensive oxidation, demethylation, and radical coupling reactions (C–C and C–O), leading to a restructured lignin matrix. Thermal analysis indicated higher thermal instability in enzymatically treated lignins, with ~58% mass loss, reflecting side-chain degradation and structural rearrangements involving β-O-4 and β-1 linkages. Despite reduced stability, the treatments resulted in high-molecular-weight, reactive lignin structures with improved processability. Electrospinning experiments confirmed the benefits of enzymatic treatment. While untreated KL yielded brittle, discontinuous fibers, KL-*Pys* produced flexible, homogeneous mats. The addition of 1% polyethylene oxide (PEO) further improved fiber uniformity and mechanical integrity, yielding nanofibers with average diameters of ~ 0.20 µm. The resulting material shows strong potential as a scalable, sustainable precursor for CFs and other high-performance biobased materials.

1 INTRODUCTION

Global demand for carbon fibers (CFs) has grown substantially over the past decade and a half [1–3]. From 42,900 metric tons in 2010, demand rose to 115,000 metric tons by 2023, an increase of approximately 168% [4]. This trend is projected to continue, reaching 280,300 metric tons by 2030, which would represent an additional 144% growth [4]. This expansion reflects CF's increasing relevance across a diverse range of sectors, including wind energy, automotive, pressure vessels, and construction [2,3]. As the market diversifies and scales up, there is a growing imperative to identify sustainable, cost-effective alternatives to petroleum-based precursors [2]. In this context, lignin, a widely available and chronically underutilized byproduct of the pulp and paper industry, has attracted increasing interest as a renewable precursor to produce lignin-based carbon fibers (LCFs) [1,2,5]. It is estimated that nature produces between 0.5 and 3.6 billion tons of lignin annually, with more than 70 million tons commercially generated, largely discarded as industrial waste [5]. Despite its abundance, the industrial application of lignin in CF production remains limited, constrained by its structural complexity and unresolved processing challenges [1,5].

The conversion of lignin into high-performance LCFs faces significant challenges due to its intrinsic structural complexity and the presence of contaminants such as ash, cellulosic residues, and inorganic salts, all of which can compromise fiber quality [6]. Unlike synthetic precursors such as PAN, lignin lacks a standardized conversion pathway [2]. Its transformation into spinnable fibers typically begins with compositional and rheological characterization, followed by targeted purification steps and spinning processes, such as melt, electrospinning, dry, or wet, chosen according to its physicochemical properties[1,5,7].

To improve LCFs' quality and mechanical performance, various strategies have been explored, including chemical, physical, and enzymatic treatments and their combinations. Among these, enzymatic approaches are particularly promising, leveraging oxidative enzymes such as laccases (Lac), lignin peroxidases (LiP), and manganese peroxidases (MnP). These enzymes catalyze the oxidation of phenolic and non-phenolic substructures in lignin, facilitating the cleavage of its resistant aromatic bonds [8]. As a result, they can promote increased molecular linearity, structural homogeneity, and hydroxyl group removal, yielding lignin with higher molecular weight and greater suitability as a PAN alternative in the production of high-performance CFs [9].

Despite these advantages, the industrial application of enzymes remains limited by factors such as low catalytic efficiency, narrow substrate specificity, and incomplete degradation [10,11]. In contrast to cellulose, which is efficiently hydrolyzed by well-optimized cellulolytic cocktails [12–14], lignin requires enzyme blends specifically tailored to address its heterogeneous and highly cross-linked structure. Effective cocktail design must consider the lignin source, pretreatment method, and desired end-products. While the synergistic interactions of cellulolytic enzymes are well-characterized and widely applied to enhance bioethanol yields from lignocellulosic biomass [15], lignin-directed enzymatic systems remain underdeveloped at an industrial scale.

This gap highlights a key biotechnological challenge: the development of enzymatic strategies that are not only effective but also economically and environmentally viable for lignin valorization. Within this framework, ligninolytic enzyme cocktails derived from white-rot fungi have emerged as a compelling solution. The basidiomycete *Pycnoporus sanguineus* has shown promise in producing key oxidative enzymes capable of targeting and cleaving lignin's aromatic framework. This study aimed to enhance Kraft lignin (KL) via enzymatic modification using a customized oxidative enzyme cocktail (LADEBIO-*Pys*) derived from *P. sanguineus*. The objective was to improve KL's polymerization behavior and processing characteristics, thereby reinforcing its potential as a sustainable precursor for CF production.

2 MATERIALS AND METHODS

2.1 Production of the Enzymatic-Oxidative Cocktail from *P. sanguineus*

The oxidative enzymatic cocktail (LADEBIO-*Pys*) was produced by submerged cultivation of *P. sanguineus* (strain 2512, CCIBt/SP) in a bubble column reactor (Biostat B, B. Braun Biotech, USA) under fed-batch conditions for nine days. The culture medium was based on Mandels and Reese's [16]

formulation, optimized with a specific carbon-to-nitrogen ratio and supplemented with enzymatic inducers. The secretome was concentrated by tangential flow filtration (TFF), combining microfiltration (0.2 µm) and ultrafiltration (10 kDa), as previously described in our early study [17]. To evaluate the efficiency of the concentration process, three parameters were determined: the membrane rejection coefficient (ω) (equation 1); the volumetric concentration factor (Fc) (equation 2); and the overall process yield efficiency (R) (equation 3).

$$\omega\ (\%) = \left(1 - \frac{C_{UF}}{C_{PER}}\right) x100 \quad \text{Equation (1)}$$

$$F_c = \frac{V_{Eb}}{V_{UF}} \quad \text{Equation (2)}$$

$$R\ (\%) = \ (F_c)^{(\omega-1)} x100 \quad \text{Equation (3)}$$

Where C_{UF} is the enzymatic concentration in the ultrafiltration retentate (U/L); C_{PER} is the residual enzymatic concentration in the permeate (U/L); V_{Eb} is the initial volume of crude extract (L); V_{UF} is the final volume after 10 kDa ultrafiltration (L).

2.2 Enzymatic Activity Assays and Protein Quantification

Lac, MnP, and LiP activities were measured by the oxidation of ABTS (420 nm), phenol red (610 nm), and veratryl alcohol (310 nm), respectively, following established protocols, Wolfenden and Willson and Tien and Kirk [18–20]. Xylanase (XyL), β-glucosidase (β-G), avicelase (AV), FPase (FP), and CMCase (CMC) were quantified according to Eveleigh et al.[21]. One enzymatic unit (U) corresponds to the oxidation of 1 µmol of substrate per minute. Total protein (PTN) content was determined using the Bradford method with BSA as a standard (595 nm) [22]. The enzymatic cocktail was evaluated by SDS-PAGE to assess its protein diversity, using 12–15% denaturing polyacrylamide gels under standard Laemmli [23] conditions. Protein visualization was performed using Coomassie Brilliant Blue staining, and molecular weight markers (Pierce, Thermo Scientific) were used for reference [24].

2.3 Enzymatic Oxidation of KL

Enzymatic modification was performed in a reaction medium containing 10 g/L of KL, an enzyme load of 30 mg/g (based on total protein), using either the LADEBIO-*Pys* cocktail or a commercial laccase from *Trametes versicolor* (> 0.5 U/mg). The medium also included ABTS (25 mg/g), H_2O_2 (10 mg/g), and $MnSO_4$ (10 mg/g), in 2 mmol/L sodium phosphate buffer (pH 5.0). Reactions were performed in 250 mL bioreactors at 40 °C, 400 rpm for 48 h with continuous air flow (2 L/min). After treatment, the enzymes were thermally inactivated (80 °C, 10 min), washed three times with deionized water, centrifuged (25,000 g, 15 min), and oven-dried at 60 °C for 48 h.

2.4 Physicochemical Characterization of Modified Lignin

Molecular weight distribution was determined by Advanced Polymer Chromatography (APC) using DMSO/LiBr (0.5% w/v) as solvent at 90 °C and a 0.5 mL/min flow rate [25]. Calibration was performed with polystyrene sulfonate standards. Thermal stability was assessed using thermogravimetric analysis (TGA) on a Q500 analyzer under nitrogen (30 mL/min), heating samples from 30 °C to 800 °C at 10 °C/min. Differential scanning calorimetry (DSC) was used to determine glass transition temperature (T_g), employing a heating protocol from 50 °C to 200 °C (20 °C/min), followed by controlled cooling and second heating (10 °C/min), under nitrogen flow (50 mL/min). Structural analysis by FT-IR was performed with KBr pellets (2 mg lignin + 200 mg KBr, pressed at 10 MPa), scanning from 4000 to 400 cm^{-1}. Oxidation degree (Θ) was determined by calculating the absorbance ratio between the characteristic oxidation bands and the reference band at 1510–1513 cm^{1}, which corresponds to aromatic

skeletal vibrations and remains largely unaffected by oxidative reactions, thus serving as an internal standard [26]. ^{1}H NMR spectra were acquired after dissolving 20 mg of dried lignin in 600 µL DMSO-d_6 with 22 µL pentafluorobenzaldehyde (PFB) as internal standard. Analyses were performed at 25 °C, using the *zgpr* pulse sequence with 128 scans and 10 s relaxation delay. Peaks were referenced to PFB (10.28 ppm) and DMSO-d_6 (2.50 ppm) [27].

2.5 Electrospinning and Morphological Analysis

Electrospinning was performed using a custom-built setup with a 30 kV power source, syringe pump, and metallic collector. The voltage was fixed at 16 kV, with a 0.05 mL/min flow rate, 8.0 cm needle-to-collector distance, and stainless-steel 18G 1/2 needle. Two formulations were evaluated: KL enzymatically treated with the LADEBIO-*Pys* cocktail alone and blended with 1% (w/w) polyethylene oxide (PEO). The solutions were prepared at a 2:3 (w/w) solid-to-solvent ratio in DMF: acetone (9:1, w/w) [28,29]. Resulting lignin fibers were characterized by Scanning Electron Microscopy (SEM) using a Hitachi TM3030Plus at 15 kV, with magnifications from 200× to 6000×. Samples were analyzed, and average fiber diameters (θ) were calculated using ImageJ software.

3 RESULTS AND DISCUSSION

3.1 Obtention and Characterization of the LADEBIO-*Pys* Cocktail

Figure 1 presents the enzymatic activities of Lac, LiP, MnP, and PTN following TFF and concentration using a hollow fiber system. As shown, sequential microfiltration and ultrafiltration steps led to the recovery of four enzymatic cocktails highly enriched in ligninolytic enzymes. Lac and MnP activities reached their maximum values in the third batch, while LiP activity peaked in the first. This variation reflects the dynamics of enzyme secretion during cultivation and recovery.

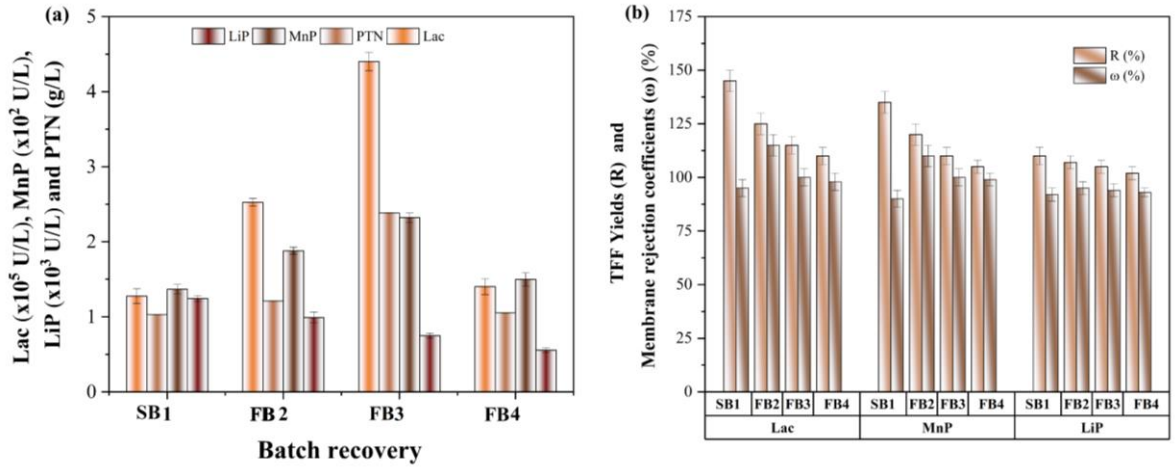

Figure 1: Batch recovery and tangential flow filtration (TFF) performance of the oxidative enzymatic cocktail LADEBIO-Pys from *P. sanguineus*. (a) Enzyme recovery in batch mode for Lac, LiP, MnP, and PTN (b) TFF yield (R) and membrane rejection coefficient (ω) for SB1 and FB2–FB4. SB1: first single batch; FB2–FB4: fed-batch recoveries performed after alimentation on the seventh, eighth, and ninth days, respectively.

Ultrafiltration using a hollow fiber system with a 10 kDa molecular weight cut-off resulted in substantial increases in enzymatic activity (>100%, Fig. 1b), primarily due to the removal of low-molecular-weight compounds and water. This led to volumetric concentration and enrichment of active enzymes. The membrane rejection coefficients (ω) remained consistently high for all enzymes (89.81%–98.78%, Fig. 1b), indicating strong selectivity and process efficiency, with LiP exhibiting the highest retention. These results reinforce the robustness of the TFF system (Fig. 1) in concentrating enzymatic cocktails while minimizing losses and denaturation. Kinetic monitoring revealed an increasing trend in

R and ω values post-filtration, likely due to progressive membrane fouling caused by pigment accumulation, especially cinabarin, a red phenoxazinone compound secreted in large amounts by *P. sanguineus* (Fig. 2b). This fouling may contribute to enhanced enzyme retention by forming a secondary filtration layer, as visually supported by the crude extract's color profile (Fig. 2a-c). These values position *P. sanguineus* as a potent producer of ligninolytic enzymes, corroborated by prior studies [24,30,31].

The enzymatic profile of the LADEBIO-Pys cocktail, produced by *P. sanguineus*, reflects the cumulative outcome of four sequential batches obtained through TFF and reveals a remarkable co-secretion of lignin-modifying enzymes (LMEs) alongside cellulolytic hydrolases, as illustrated in Figure 2. Post-filtration activity levels for Lac, LiP, and MnP reached 6.8×10^5, 3.0×10^4, and 1.5×10^3 U/L, respectively, reflecting the strain's strong oxidative capacity. Concomitantly, substantial activities of β-G, Xyl, AV, FP, and CMC were also detected, with β-G and CMC activities ranging from 4 to 5,000 U/L, indicating a robust polysaccharide-degrading potential (Fig.2e).

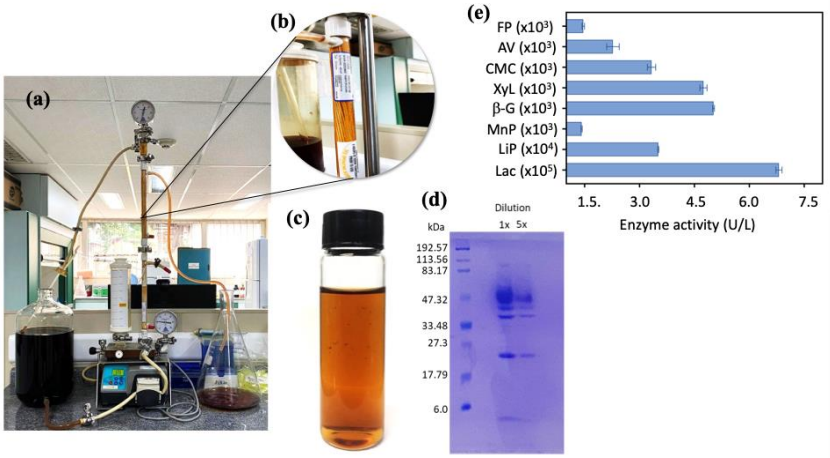

Figure 2: Recovery and partial characterization of the oxidative enzymatic cocktail LADEBIO-*Pys* from *P. sanguineus*. (a) Hollow fiber filtration system used for TFF and concentration; (b) membrane segment showing crude extract pigmentation; (c) LADEBIO-*Pys* after ultrafiltration; (d) protein profile by SDS-PAGE (MW marker, 1x and 5x dilutions); (e) enzymatic activity profile of the lignocellulolytic complex.

The observed enzymatic profile is consistent with prior reports: Pereira Scarpa et al. [32] identified a similar range of enzymes, including LMEs and glycoside hydrolases, during solid-state fermentation; Azmi, Jalil, and Kalil [33] reported elevated FP, CMC, and exoglucanase activities under α-cellulose fermentation; and Sahaid Kalil et al. [34] demonstrated peak cellulase production within 48 h of cultivation. The coexistence of oxidative and hydrolytic activities in a single fungal secretome not only underscores the metabolic flexibility of *P. sanguineus* but also reinforces its biotechnological relevance for integrated biorefinery strategies focused on the enzymatic valorization of lignocellulosic biomass into high-value compounds such as platform chemicals and functional biomaterials.

3.2 Molecular Characterization of Enzymatically Modified KL

Figure 3 shows that the enzymatic treatments of KL using either *T. versicolor* commercial laccase (KL-Tvs) or the LADEBIO-*Pys* cocktail (KL-*Pys*), both in the presence of ABTS mediator, resulted in a significant increase in molecular weight (Mw) and polydispersity index (PDI) after 48 hours of reaction, when compared to the untreated control (KL).

Mw values rose by 157% (Lac-Tv) and 152% (LADEBIO-*Pys*), while PDI increased by 110% and 115%, respectively. These findings align with those reported by Ibarra et al. [35], who observed a 1.8-fold Mw increase with bacterial laccase SiLA (SiLA-KL1) and a 1.7-fold increase with fungal laccase MtL (MtL-KL1), accompanied by similar increases in PDI. According to Areskogh et al. [36], such

outcomes are attributed to the non-selective radical–radical coupling reactions triggered by the oxidation of terminal phenolic groups in lignin, wherein free radicals spontaneously couple without spatial or steric control (Fig. 3b). This leads to broad molecular weight distributions, thereby increasing polydispersity.

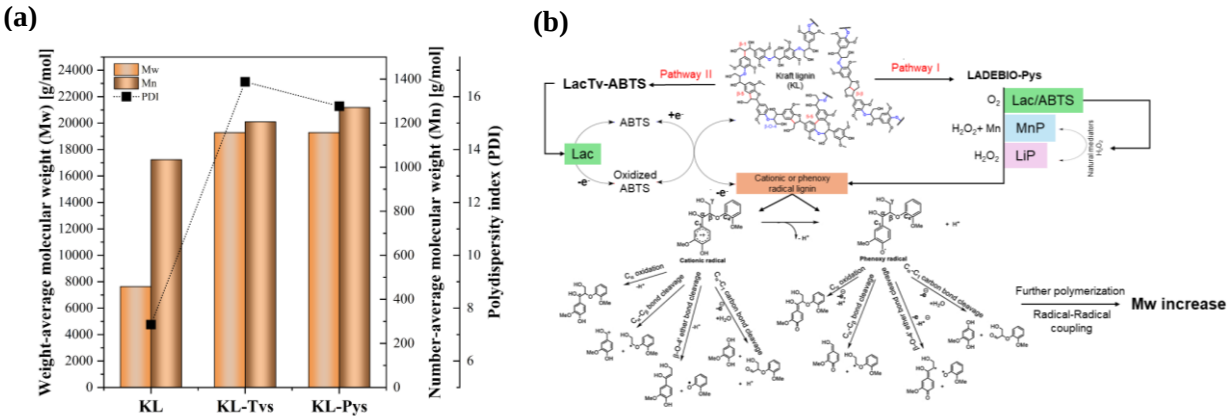

Figure 3: Enzymatic modification of Kraft lignin (KL). (a) GPC analysis and (b) Oxidation pathways: (I) LADEBIO-*Pys* system promotes radical formation and synergistic polymerization; (II) LacTv-ABTS acts via redox cycling.

Despite the longer reaction time applied in our study (48 h), the results suggest that the LADEBIO-*Pys* system efficiently promotes structural remodeling of lignin not only through oxidative polymerization, but also via cleavage of key interunit linkages such as β–O–4, β–5, β–β, 4–O–5, and 5–5, as proposed by Vignali et al. [37] and Zhu et al. [36] (Fig. 3b). Our findings support the literature postulate that polymerization is initiated by single-electron abstraction from the phenylpropanoid moieties of lignin by either LacTv or the LADEBIO-*Pys*/ABTS system, generating phenoxyl radicals that activate the lignin surface [38,39]. Given the extended π-conjugation systems in lignin, the unpaired electron is delocalized to more stable resonance structures. Phenolic units are oxidized to phenoxyl radicals, whereas non-phenolic regions form β-aryl and benzylic radicals. These species act as reactive intermediates that undergo radical–radical coupling, involving either lignin–lignin or lignin–mediator linkages. This process results in covalent polymer growth and an overall increase in Mw, as illustrated in Figure 3, thus demonstrating the dual oxidative and structural modification capabilities of the enzymatic systems evaluated [38,39].

3.3 Structural Modifications Detected by FT-IR and ^{1}H NMR

FT-IR spectroscopic analysis (Figure 4a-b) indicated that, although the aromatic scaffold of KL remained largely conserved following enzymatic oxidation, substantial alterations were observed in specific functional groups, notably in the ν(OH), ν(COOH), ν(C=O), and ν(OCH_3) absorption regions. The broad ν(OH) stretching band (3300–3600 cm^{-1}), present across all spectra, showed a marked attenuation at approximately 3441 cm^{-1} in the KL-Tvs sample.

This reduction suggests a significant depletion of – OH, likely attributable to the pronounced oxidative potential of *T. versicolor* laccase, especially when operating within the ABTS-mediated redox system [40]. Conversely, the KL-*Pys* sample exhibited a comparatively moderate decrease in this band, possibly resulting from simultaneous oxidative cleavage and regeneration of hydroxyl functionalities at the side chains, a phenomenon that may be enhanced by the synergistic action of accessory oxidoreductases present in the LADEBIO-*Pys* enzymatic cocktail. Additionally, both enzymatically treated samples displayed a discernible decline in the ν(C–H) stretching bands (2800–2900 cm^{-1}), corresponding to aliphatic methylene and methyl groups (Fig. 4b) [41]. This behavior is indicative of partial demethylation and demethoxylation processes, in agreement with previously reported depolymerization and structural simplification mechanisms for lignin matrices subjected to oxidative biocatalysis [42].

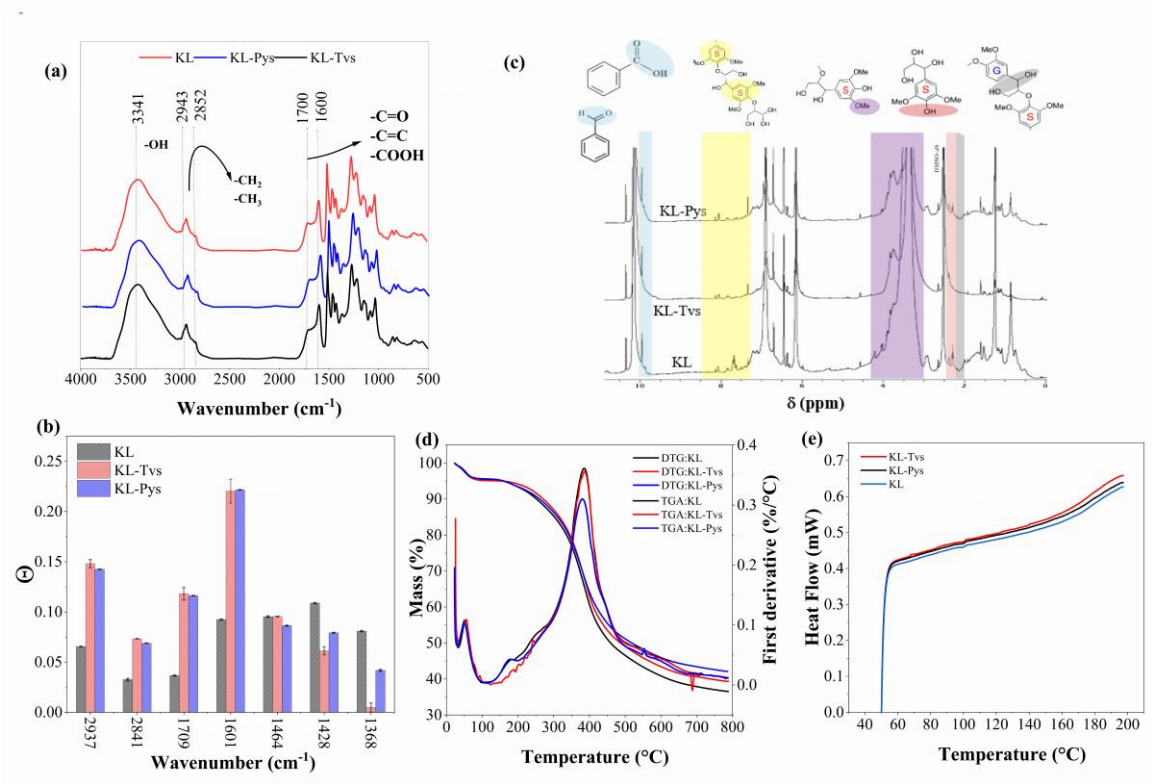

Figure 4: Structural and thermal characterization of Kraft lignin (KL) before and after enzymatic treatment with LADEBIO-*Pys* and *T. versicolor* laccases. (a) FTIR spectra acquired via KBr pellet method; (b) Quantitative comparison of main functional group peaks (Θ); (c) ^{1}H NMR spectra; (d) TGA and DTA thermograms; (e) DSC curves.

More notably, oxidative effects were evident in the carbonyl domain: normalized intensities at ~1600 cm^{-1} (ν(C=O) in conjugated systems) and ~1700 cm^{-1} (non-conjugated ν(C=O)) increased by up to 2.88-fold and 1.71-fold, respectively, in both treatments (Figure 4b). These spectral changes are consistent with oxidative cleavage of Cα–OH groups, quinone formation, and disruption of interunit linkages such as β–O–4, α–O–4, and 4–O–5, as proposed by Gouveia *et al.* [43]. Concurrent reductions at 1464, 1428, and 1368 cm^{-1} support partial loss of –OCH_3 and aliphatic –OH moieties, indicating demethylation reactions [42]. Visual darkening of lignin samples (data not shown) corroborates the formation of extended π-conjugated systems.

^{1}H NMR analysis (Fig. 4c) revealed marked structural changes across KL, KL-*Pys*, and KL-Tvs, particularly in regions assigned to aromatic protons (Ar–H, 8.6–6.28 ppm), methoxyl groups (–OCH_3, 4.2–3.1 ppm), aromatic hydroxyls (Ar–OH, 2.5–2.25 ppm), aliphatic hydroxyls (Al–OH, 2.25–2.0 ppm), and aliphatic acetates (–O–$COCH_3$, ~2.23 ppm). The signal reduction in Ar–OH and Al–OH was more pronounced in KL-Tvs, indicating a greater oxidative impact. A significant decrease in the –OCH_3 region, particularly in KL-Tvs, suggests extensive demethylation, corroborated by FT-IR analysis. Simultaneously, the increase in –O–$COCH_3$ signals indicates the formation of new Al–OH groups through oxidative cleavage and rearrangement. The marked reductions in Ar–H signals support the occurrence of oxidative coupling reactions (C–C and C–O–C), leading to aromatic ring condensation. Collectively, these transformations point to complex biochemical mechanisms, including direct oxidation of phenolic units, demethylation of –OCH_3 groups, formation of quinones and carbonyl functionalities (–CHO, –CO–), and radical-mediated polymerization.

3.4 Thermal Properties and Stability of Modified Lignin

The thermal analysis (TGA-DTA and DSC) of enzymatically treated KL provides critical insights

into the structural transformations as shown in Figure 4d-e and Table 1, both KL-*Pys* and KL-Tvs exhibited a decrease in the onset ($T_{d,onset}$) and maximum degradation temperatures ($T_{d,max}$), accompanied by a higher total mass loss (~58%) compared to the untreated control (KL, 64.1%).

	$T_{d,\ onset}$ (ºC)	$T_{d,\ máx}$ (ºC)	Mass loss (%)	T_g (ºC)	Tc (ºC)
KL	236	389	64.10	154.95	
KL-Tvs	226	374	57.88	164.78	n.d.
KL-Pys	229	379	57.63	163.65	

Table 1: Thermal parameters of native and enzymatically modified KL samples.

This reduction in thermal stability suggests that enzymatic oxidation, despite leading to polymerization and molecular weight increase as evidenced by GPC (Fig. 3), also introduces thermolabile functional groups such as C=O, COOH, and conjugated systems, as confirmed by FT-IR and ^{1}H-NMR (Fig. 4c). These functionalities weaken the internal cohesion of the lignin matrix, facilitating early-stage degradation. The DTG profiles (Fig. 4e) further substantiate this interpretation, indicating a shift in the degradation of propanoid side chains and aryl-ether bonds to lower temperature ranges. This behavior likely stems from the oxidative cleavage of interunit linkages (β-O-4, β-5), followed by cross-linking and radical coupling reactions, as discussed in the mechanistic analysis (Fig. 2b), resulting in a KL structure that is simultaneously more condensed yet more chemically reactive and thermally sensitive.

DSC analysis (Fig. 4e) revealed an approximately 6.5 % increase in T_g for both KL-*Pys* and KL-Tvs, compared to KL, indicating restricted polymer chain mobility due to oxidative crosslinking. Despite the reduced thermal stability observed by TGA, this elevation in T_g suggests the formation of rigid, high-molecular-weight domains (e.g., β–1, β–β), which counterbalance the presence of low-molecular-weight fragments introduced during oxidation. This dual thermal behavior aligns with FT-IR and ^{1}H-NMR evidence of desmethoxylation, C=O incorporation, and radical-induced condensation. Interestingly, KL-*Pys* exhibited a T_g comparable to KL-Tvs, despite showing milder spectroscopic changes, indicating that the multienzymatic nature of the LADEBIO-*Pys* cocktail (rich in Lac, LiP, and MnP) may promote broader oxidative diversification than a single purified laccase.

Notably, no crystallization temperature (T_c) was detected in any sample. Although enzymatic oxidation modifies lignin's macromolecular structure, it does not induce long-range order or crystallinity, consistent with the amorphous nature of lignin. These thermal features, summarized in Table 1, reinforce those enzymatic treatments, particularly with broad-spectrum oxidative cocktails, enhance lignin's rigidity and thermal behavior without altering its fundamental amorphous character, improving its suitability for FC precursor applications.

3.5 Electrospinning Performance and Mat Morphology

Electrospinning assays demonstrated that oxidative enzymatic modification of KL using the LADEBIO-*Pys* cocktail significantly enhanced its ability to form lignin-based FC precursors. As shown in Figure 5a–b, native KL, either with or without the addition of polyethylene oxide (PEO), resulted in electrospraying, producing non-fibrous, brittle mats composed of aggregated lignin droplets. These outcomes underscore the structural limitations of unmodified KL for direct fiber formation via electrospinning, the first step in the CF production chain. In contrast, KL-*Pys* generated continuous lignin fibers (Fig. 5c), indicating that oxidative modifications conferred by the LADEBIO-*Pys* cocktail effectively adjusted the physicochemical properties of KL, enabling filament formation. The inclusion of PEO (Fig. 5d), used here as a rheological aid rather than a structural matrix, further improved the quality and cohesion of the lignin fiber mats. However, SEM analysis revealed bead formation in KL-*Pys*:PEO samples, indicating the need for further optimization of the lignin-to-PEO ratio to minimize defects and promote uniformity.

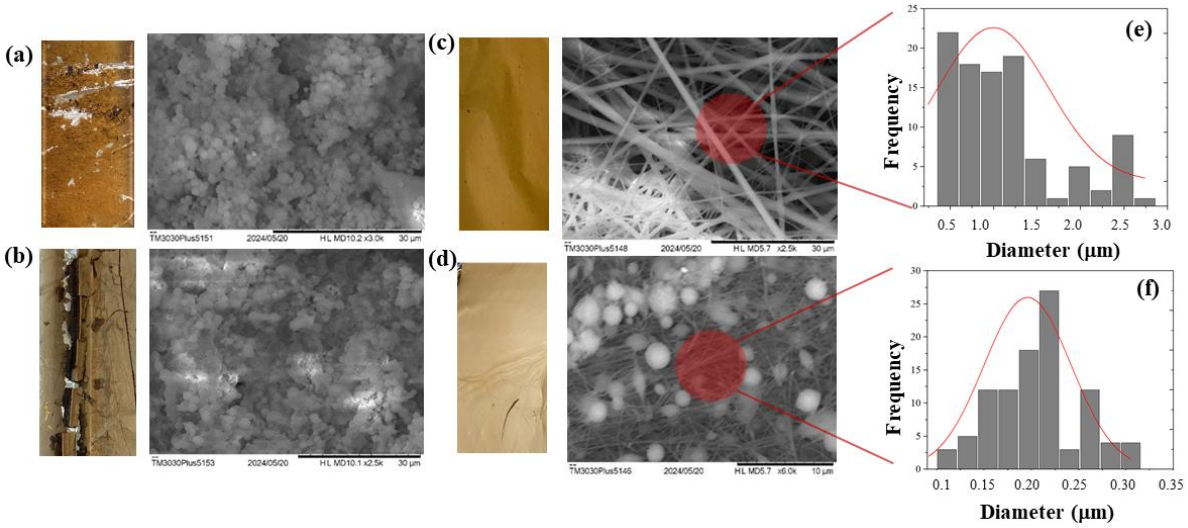

Figure 5: Electrospinning performance of Kraft lignin (KL) samples. (a–b) optical and SEM images of untreated KL with and without PEO (c) 100 % KL-*Pys*; (d) 99% KL-*Pys*:1 % PEO; (e–f) Diameter distribution histograms for KL-Pys and KL-*Pys*:PEO fibers, respectively

Diameter distribution histograms (Fig. 5e–f) confirmed a significant reduction in average fiber diameter from 0.99 µm in KL-*Pys* to 0.20 µm in KL-*Pys*:PEO along with a decrease in the coefficient of variation (6.4% to 4.2%), suggesting improved control over lignin fiber deposition when PEO is used as a processing aid. These findings agree with previous reports that emphasize the importance of polymer additives in modulating solution viscosity and electrospinning behavior, particularly for lignin-rich systems [38].

3.6 Technological Potential of LADEBIO-*Pys*

The oxidative enzymatic cocktail LADEBIO-*Pys*, obtained from *P. sanguineus* via submerged fermentation and concentrated using single TFF, stands out as a low-cost, high-performance biocatalyst for KL modification. With high activities of Lac, LiP, and MnP along with relevant cellulolytic enzymes, this ultrafiltrate enabled effective oxidative depolymerization and repolymerization. Together, the results confirm that the enzymatic oxidative modification of KL promotes the formation of continuous lignin nanofibers. The improvements in spinnability are attributed to structural transformations such as partial depolymerization, oxidative repolymerization, and the introduction of oxygenated functionalities, reflected in increased M_w, higher T_g, and new IR-active groups positioning KL-*Pys* as a promising renewable precursor for FC production.

Notably, the LADEBIO-*Pys* system combines catalytic efficiency with operational simplicity; it circumvents the need for costly and time-consuming downstream purification. Given that downstream processing is often cited as a major economic bottleneck in enzyme production, the ability to obtain a crude yet highly active oxidative cocktail that performs on par with purified enzymes is of considerable industrial relevance. The synergistic interplay among its enzymes enables not only oxidative cleavage but also controlled radical polymerization, yielding structurally reorganized lignin with enhanced thermal behavior and processability. As Perna et al. [38] emphasize, such enzyme synergy is crucial for tailoring polymer architectures, and our results confirm this principle even in non-purified enzyme systems.

Despite its demonstrated potential, oxidative enzymatic cocktails like LADEBIO-*Pys* remain underdeveloped and largely unavailable in the commercial market. This scarcity is especially notable considering increasing interest in lignin valorization and the rise of "Lignin-First" strategies, which prioritize early-stage lignin processing in biorefinery models. The limited availability of such catalytic systems hampers innovation in lignin-derived materials, not only for FC production, but also for high-performance composites, adhesives, supercapacitors, and fine chemicals. Therefore, expanding the development, accessibility, and application of multienzymatic oxidative systems represents a critical

step toward democratizing lignin bioconversion technologies, reducing processing costs, and enabling sustainable pathways for the transformation of lignin into high-value biomaterials.

4 CONCLUSIONS

The findings of this study demonstrate that the oxidative enzymatic cocktail LADEBIO-Pys is a powerful and scalable tool for the structural modification of KL. By promoting efficient polymerization and oxidation, the system significantly enhanced the molecular weight, thermal stability, and chemical reactivity of KL. When combined with PEO, the enzymatically modified lignin yielded electrospun mats with superior morphological and structural integrity. Their nanofibrous architecture and improved uniformity make them strong candidates for FC precursors. Altogether, LADEBIO-*Pys* offers a promising route for lignin valorization within integrated and sustainable biorefinery platforms.

ACKNOWLEDGEMENTS

The present work was supported by the Brazilian Council for Research (CNPq) (Grant numbers 304102/2022-9 and 311254/2018–7), Foundation Carlos Chagas Filho Research Support of the State of Rio de Janeiro (FAPERJ) (Grant number E-26/ 203.005/2017), the Coordination for the Improvement of Higher Education Personnel (CAPES) and the São Paulo Institute of Botany (CCIBt).

REFERENCES

[1] W. Qu, P. Hu, J. Liu, H. Jin and K. Wang, Lignin-based carbon fiber: A renewable and low-cost substitute towards featured fiber-shaped pseudocapacitor electrodes, *Journal of Cleaner Production*, **343**, 2022, 131030 (doi: 10.1016/j.jclepro.2022.131030).

[2] D. Choi, H.S. Kil and S. Lee, Fabrication of low-cost carbon fibers using economical precursors and advanced processing technologies, *Carbon*, **142**, 2019, pp. 610–649 (doi: 10.1016/j.carbon.2018.10.028).

[3] J. Zhang, V.S. Chevali, H. Wang and C.H. Wang, Current status of carbon fibre and carbon fibre composites recycling, *Composites Part B: Engineering*, **193**, 2020, 108053 (doi: 10.1016/j.compositesb.2020.108053).

[4] H. Chen, H.P.H. Liddell, A.A. Ogale, Z.C. Miao, M.W. Ijeoma and M. Carbajales-Dale, A critical review and meta-analysis of energy demand, carbon footprint, and other environmental impacts from carbon fiber manufacturing, *Resources, Conservation & Recycling*, **219**, 2025, 108302 (doi: 10.1016/j.resconrec.2025.108302).

[5] S. Wang, J. Bai, M.T. Innocent, Q. Wang, H. Xiang, J. Tang *et al.*, Lignin-based carbon fibers: Formation, modification and potential applications, *Green Energy & Environment*, **7**, 2022, pp. 578–605 (doi: 10.1016/j.gee.2021.04.006).

[6] F. Souto, V. Calado and N. Pereira, Lignin-based carbon fiber: A current overview, *Materials Research Express*, **5**, 2018, 072001 (doi: 10.1088/2053-1591/aaba00).

[7] R. P. Dumitriu, E. Stoleru, J. T. Rosnes, N. Sharmin, F. Doroftei and M. Brebu, Rheological properties influence on the electrospinning of caseinate for loading with antioxidant rosemary extract, *Food Hydrocolloids*, **151**, 2024, 109883 (doi: 10.1016/j.foodhyd.2024.109883).

[8] L. Munk, A. K. Sitarz, D. C. Kalyani, J. D. Mikkelsen and A. S. Meyer, Can laccases catalyze bond cleavage in lignin?, *Biotechnology Advances*, **33**, 2015, pp. 13–24 (doi: 10.1016/j.biotechadv.2014.12.008).

[9] Q. Li, S. Xie, W. K. Serem, M. T. Naik, L. Liu and J. S. Yuan, Quality carbon fibers from fractionated lignin, *Green Chemistry*, **19**, 2017, pp. 1628–1634 (doi: 10.1039/C6GC03555H).

[10] M. R. Mäkelä, E. L. Bredeweg, J. K. Magnuson, S. E. Baker, R. P. de Vries and K. Hildén, Fungal Ligninolytic Enzymes and Their Applications, *Microbiology Spectrum*, **4**, 2016, pp. 1–13 (doi: 10.1128/microbiolspec.funk-0017-2016).

[11] A. Kumar and R. Chandra, Ligninolytic enzymes and its mechanisms for degradation of lignocellulosic waste in environment, *Heliyon*, **6**, 2020, e03170 (doi: 10.1016/j.heliyon.2020.e03170).

[12] S. Malgas, R. Chandra, J. S. Van Dyk, J. N. Saddler and B. I. Pletschke, Formulation of an optimized synergistic enzyme cocktail, HoloMix, for effective degradation of various pre-treated hardwoods, *Bioresource Technology*, **245**, 2017, pp. 52–65 (doi: 10.1016/j.biortech.2017.08.186).
[13] Q. Zhang, Q. Wang, H. Chen, L. Chen, F. Wang, Z. Gu *et al.*, Lignin-degrading enzyme production was enhanced by the novel transcription factor Ptf6 in synergistic microbial co-culture, *Microbiological Research*, **280**, 2024, 127575 (doi: 10.1016/j.micres.2023.127575).
[14] J. Méndez Arias, L. F. A. Modesto, I. Polikarpov and N. Pereira, Design of an enzyme cocktail consisting of different fungal platforms for efficient hydrolysis of sugarcane bagasse: Optimization and synergism studies, *Biotechnology Progress*, **32**, 2016, pp. 1222–1229 (doi: 10.1002/btpr.2306).
[15] P. Chylenski, Z. Forsberg, J. Ståhlberg, A. Várnai, M. Lersch, O. Bengtsson *et al.*, Development of minimal enzyme cocktails for hydrolysis of sulfite-pulped lignocellulosic biomass, *Journal of Biotechnology*, **246**, 2017, pp. 16–23 (doi: 10.1016/j.jbiotec.2017.02.009).
[16] D. E. Eveleigh, M. Mandels, R. Andreotti and C. Roche, Measurement of saccharifying cellulase, *Biotechnology for Biofuels*, **2**, 2009, 21 (doi: 10.1186/1754-6834-2-21).
[17] E. F. de Souza, I. M. T. S. Santos, F. Souto, V. Calado and N. Pereira, Optimization and Implementation of Fed-Batch Strategy to Produce Ligninolytic Enzyme from the White-Rot Basidiomycete *Pycnoporus sanguineus* in Bubble Column Reactor, *Fermentation*, **8**, 2022, 418 (doi: 10.3390/fermentation8090418).
[18] B. S. Wolfenden and R. L. Willson, Radical-cations as reference chromogens in kinetic studies of one-electron transfer reactions: Pulse radiolysis studies of 2,2′-azinobis-(3-ethylbenzthiazoline-6-sulphonate), *Journal of the Chemical Society, Perkin Transactions 2*, **1982**, pp. 805–812 (doi: 10.1039/p29820000805).
[19] M. Kuwahara, J. K. Glenn, M. A. Morgan and M. H. Gold, Separation and characterization of two extracelluar H_2O_2-dependent oxidases from ligninolytic cultures of *Phanerochaete chrysosporium*, *FEBS Letters*, **169**, 1984, pp. 247–250 (doi: 10.1016/0014-5793(84)80327-0).
[20] M. Tien and T. K. Kirk, Lignin-degrading enzyme from *Phanerochaete chrysosporium*: Purification, characterization, and catalytic properties of a unique H_2O_2-requiring oxygenase, *Proceedings of the National Academy of Sciences*, **81**, 1984, pp. 2280–2284 (doi: 10.1073/pnas.81.8.2280).
[21] M. Mandels, R. Andreotti and C. Roche, Measurement of saccharifying cellulase, *Biotechnology and Bioengineering Symposium*, **2**, 1976, pp. 21–33 (doi: 10.1186/1754-6834-2-21/figures/7).
[22] M. M. Bradford, A rapid and sensitive method for the quantitation of microgram quantities of protein utilizing the principle of protein-dye binding, *Analytical Biochemistry*, **72**, 1976, pp. 248–254 (doi: 10.1016/0003-2697(76)90527-3).
[23] U. K. Laemmli, Cleavage of structural proteins during the assembly of the head of bacteriophage T4, *Nature*, **227**, 1970, pp. 680–685 (doi: 10.1038/227680a0).
[24] D. Quaratino, F. Federici, M. Petruccioli, M. Fenice and A. D'Annibale, Production, purification and partial characterisation of a novel laccase from the white-rot fungus *Panus tigrinus* CBS 577.79, *Antonie van Leeuwenhoek*, **91**, 2007, pp. 57–69 (doi: 10.1007/s10482-006-9096-4).
[25] I. Sulaeva, G. Zinovyev, J. M. Plankeele, I. Sumerskii, T. Rosenau and A. Potthast, Fast track to molar-mass distributions of technical lignins, *ChemSusChem*, **10**, 2017, pp. 629–635 (doi: 10.1002/cssc.201601517).
[26] I. Bykov, Characterization of natural and technical lignins using FTIR spectroscopy, Master's thesis, Luleå University of Technology, Division of Wood Science and Technology, Skellefteå, Sweden, 2008.
[27] P. Buono, A. Duval, P. Verge, L. Averous and Y. Habibi, New insights on the chemical modification of lignin, *ACS Sustainable Chemistry & Engineering*, **4**, 2016, pp. 5212–5222 (doi: 10.1021/acssuschemeng.6b00903).
[28] M. Schreiber, S. Vivekanandhan, A. K. Mohanty and M. Misra, A study on the electrospinning behaviour and nanofibre morphology of anionically charged lignin, *Advanced Materials Letters*, **3**, 2012, pp. 476–480 (doi: 10.5185/amlett.2012.icnano.336).
[29] H. Nie, A. He, J. Zheng, S. Xu, J. Li and C. C. Han, Effects of chain conformation and entanglement on the electrospinning of pure alginate, *Biomacromolecules*, **9**, 2008, pp. 1362–1365 (doi: 10.1021/bm701349j).

[30] J. Liu, Z. Yu, X. Liao, J. Liu, F. Mao and Q. Huang, Scalable production, fast purification, and spray drying of native *Pycnoporus* laccase and circular dichroism characterization, *Journal of Cleaner Production*, **127**, 2016, pp. 600–609 (doi: 10.1016/j.jclepro.2016.03.154).

[31] L. I. Ramírez-Cavazos, C. Junghanns, R. Nair, D. L. Cárdenas-Chávez, C. Hernández-Luna, S. N. Agathos *et al.*, Enhanced production of thermostable laccases from a native strain of *Pycnoporus sanguineus* using central composite design, *Journal of Zhejiang University Science B*, **15**, 2014, pp. 343–352 (doi: 10.1631/jzus.B1300246).

[32] J. de C. Pereira Scarpa, N. Paganini Marques, D. Alves Monteiro, G. M. Martins, A. V. de Paula, M. Boscolo *et al.*, Saccharification of pretreated sugarcane bagasse using enzymes solution from *Pycnoporus sanguineus* MCA 16 and cellulosic ethanol production, *Industrial Crops and Products*, **141**, 2019, 111795 (doi: 10.1016/j.indcrop.2019.111795).

[33] M. A. A. M. Azmi, R. Jalil and M. S. Kalil, Production of cellulase from *Pycnoporus sanguineus*, *Indian Journal of Science and Technology*, **9**, 2016, pp. 1–7 (doi: 10.17485/ijst/2016/v9i21/95230).

[34] R. Jalil, M. S. Kalil, N. A. Rahman, A. A. Hamid and M. F. Ahmad, Seed culture conditions for high yield of cellulolytic enzymes production from *Pycnoporus sanguineus*, *Malaysian Journal of Analytical Sciences*, **21**, 2017, pp. 231–239 (doi: 10.17576/mjas-2017-2101-27).

[35] D. Ibarra, J. Romero, M. J. Martínez, A. T. Martínez and S. Camarero, Exploring the enzymatic parameters for optimal delignification of eucalypt pulp by laccase-mediator, *Enzyme and Microbial Technology*, **39**, 2006, pp. 1319–1327 (doi: 10.1016/j.enzmictec.2006.03.019).

[36] H. Zhu, D. Areskogh, M. Helander and G. Henriksson, *A preliminary investigation on enzymatic oxidative polymerization of lignin*, Proceedings of the 16th International Symposium on Wood, Fiber and Pulping Chemistry ISWFPC 2011, Tianjin, China, June 8–10, 2011, Volume 1, Paper 42, pp. 238–241.

[37] E. Vignali, M. Gigli, S. Cailotto, L. Pollegioni, E. Rosini and C. Crestini, Front Cover: The Laccase-Lig multienzymatic multistep system in lignin valorization (*ChemSusChem* 20/2022), *ChemSusChem*, **15**, 2022, e202201783 (doi: 10.1002/cssc.202201783).

[38] V. Perna, A. S. Meyer, J. Holck, L. D. Eltis, V. G. H. Eijsink and J. Wittrup Agger, Laccase-catalyzed oxidation of lignin induces production of H_2O_2, *ACS Sustainable Chemistry & Engineering*, **8**, 2020, pp. 831–841 (doi: 10.1021/acssuschemeng.9b04912).

[39] Y. Zheng, M. Guo, Q. Zhou and H. Liu, Effect of lignin degradation product sinapyl alcohol on laccase catalysis during lignin degradation, *Industrial Crops and Products*, **139**, 2019, 111544 (doi: 10.1016/j.indcrop.2019.111544).

[40] T. Senthilvelan, J. Kanagaraj and R. C. Panda, Enhanced biodegradation of lignin by laccase through HOBT mediator: Mechanistic studies supported by FTIR and GC–MS studies, *Environmental Processes*, **4**, 2017, pp. 201–217 (doi: 10.1007/s40710-017-0209-z).

[41] O. Faix, D. S. Argyropoulos, D. Robert and V. Neirinck, Determination of hydroxyl groups in lignins: Evaluation of ^{1}H-, ^{13}C-, ^{31}P-NMR, FTIR and wet chemical methods, *Holzforschung*, **48**, 1994, pp. 387–394 (doi: 10.1515/hfsg.1994.48.5.387).

[42] S. Malric-Garajova, F. Fortuna, F. Pion, E. Martin, A. R. Thottathil, A. Guillemain, A. Doan, A. Lomascolo, C. B. Faulds, S. Baumberger, et al., Modification of a marine pine Kraft lignin sample by enzymatic treatment with a *Pycnoporus cinnabarinus* laccase, *Molecules*, 28, 2023, p. 4873 (doi: 10.3390/molecules28124873).

[43] S. Gouveia, C. Fernández-Costas, M. A. Sanromán and D. Moldes, Polymerisation of Kraft lignin from black liquors by laccase from *Myceliophthora thermophila*: Effect of operational conditions and black liquor origin, *Bioresource Technology*, **131**, 2013, pp. 288–294 (doi: 10.1016/j.biortech.2012.12.155).

[44] E. A. Widianto, Q. K. Anjani, H. Sudibyo, B. Sutrisno and M. R. Rohman, Fabrication and characterization of polyethylene oxide/lignin nanofiber by electrospinning for exhaust gas filter application, Proceedings of the 3rd International Conference on Engineering, Technology, and Industrial Application *(*ICETIA*)*, 2019, pp. 1–6.

[45] I. Dallmeyer, L. T. Lin, Y. Li, F. Ko and J. F. Kadla, Preparation and characterization of interconnected, Kraft lignin-based carbon fibrous materials by electrospinning, *Macromolecular Materials and Engineering*, 299, 2014, pp. 540–551 (doi: 10.1002/mame.201300148).

BIOCHAR AS AN ALTERNATIVE FILLER FOR COMPOSITES

G K Lopes[1], J A S Barros[2], J C C da S Pinto[2,3], V Calado[4]

[1]Laboratório de Termoanálise e de Reologia (LabTeR), Departamento de Engenharia Química, Escola de Química, Universidade Federal do Rio de Janeiro, Rua Moniz de Aragão, s/n - Centro de Tecnologia - Bloco K, 3º andar - Cidade Universitária, Rio de Janeiro -R.J., Brazil
Email: gisela.lopes @eq.ufrj.br

[2]Laboratório de Engenharia de Polímeros (EngePol), Programa de Engenharia Química, COPPE, Universidade Federal do Rio de Janeiro, Centro de Tecnologia, Bloco G, sala 115 - Cidade Universitária, Rio de Janeiro – RJ, Brazil
Email: jamilly@peq.coppe.ufrj.br

[3]Laboratório de Engenharia de Polímeros (EngePol), Departamento de Engenharia Química, Escola de Química, Universidade Federal do Rio de Janeiro, R. Moniz de Aragão, s/n - Cidade Universitária, Rio de Janeiro - RJ, Brazil
Email: pinto@peq.coppe.ufrj.br

[4]Laboratório de Termoanálise e de Reologia (LabTeR), Departamento de Engenharia Química, Escola de Química, Universidade Federal do Rio de Janeiro, Rua Moniz de Aragão, s/n - Centro de Tecnologia - Bloco K, 3º andar - Cidade Universitária, Rio de Janeiro -R.J., Brazil
Email: calado@eq.ufrj.br

Keywords: Coconut Fiber, Biochar, Composite

ABSTRACT

The coconut (Cocos nucifera) is a tropical fruit of significant economic importance in Brazil, largely consumed in its immature stage, which contains a high volume of coconut water. However, its widespread consumption results in considerable waste generation. The accumulation of this lignocellulosic biomass contributes to the reduction of landfill lifespan, raising environmental concerns. As an abundant and renewable resource, this biomass represents a promising alternative to fossil-derived materials and a potential feedstock for producing biochar via thermochemical processes such as pyrolysis. Biochar exhibits properties like high hydrophobicity, improved compatibility with polymer matrices, and enhanced thermal stability compared to conventional filler materials. In this context, coconut fiber was investigated for composite applications. Its physicochemical characterization revealed an amount of lignin (insoluble Klason lignin) of approximately 32.0% (w/w). Pyrolysis of the fiber yielded a significant amount of biochar, with CHNSO elemental analysis confirming a high carbon content. Subsequent FTIR spectroscopy verified the successful conversion of biomass into biochar, while TGA/DTG analysis demonstrated its thermal stability. Finally, mechanical testing indicated that coconut-derived biochar holds promise as a sustainable filler for polymer composites.

1 INTRODUCTION

The coconut fruit (*Cocos nucifera*) originates from the coconut palm and is cultivated in over 90 countries, with its primary use in the food industry [1]. According to the latest data from Faostat (2021), the global harvested area of coconuts covers approximately 11.8 million hectares, yielding 62.9 million tons. Three countries - Indonesia, Philippines, and India – account for 73.0% of the cultivated area and 74.1% of the total production. Brazil ranks as

the world's fourth-largest coconut producer, with an estimated output of 2.8 million tons from 257,000 hectares, of which around 15% is destined for the green coconut market [2].

The rising consumption of coconut water (100 to 350 million liters per year), fueled by increasing health-conscious behavior among Brazilians, led to a challenge regarding the disposal of coconut shells, which constitute 80 - 85% of the fruit´s total weight. Commonly discarded in open dumps, landfields and unauthorized areas, these residues not only cause visual pollution and unpleasant odors but also promote disease transmition. Under anaerobic conditions, their decomposition generates methane, a potent greenhouse gas. Although organic in nature, coconut waste is highly resistant to degradation and can take more than 8 years to fully decompose [3].

Extracted from the coconut mesocarp, these fibers are primarily composed of cellulose and hemicellulose and contain a high lignin content (20–48%) [4]. To add value and reduce the environmental impact of this waste, various alternatives have been explored for the utilization of coconut fiber. As a lignocellulosic material, it represents a promising renewable and eco-friendly alternative to fossil resources, especially as a raw material for energy production. Pyrolysis is among the most widely adopted processes for converting biomass into biochar, gas, and bio-oil [5,6]. his process involves the thermal decomposition of the three main components—cellulose, hemicellulose, and lignin—in the absence of oxygen [7,8]. Coconut fiber and its pyrolysis product, biochar, are both promising for various applications. The high lignin content in coconut fibers gives them notable hardness and durability compared to other natural fibers [9] , and their incorporation into composite materials has been widely studied [10,11]. The thermal and acoustic properties of coconut fiber-based materials can vary depending on origin and processing, but they have demonstrated thermal conductivity and sound absorption values comparable to those of conventional synthetic insulation materials such as polyurethane boards, glass wool, and rock wool[11].

Biochar, because of its carbon-rich and porous structure, stands out as a multifunctional material[12]. Beyond its role in carbon sequestration—preventing CO_2 release into the atmosphere [13] —biochar also improves soil fertility, water retention, and microbial activity when applied as a soil amendment [14,15] More recently, its potential as a filler in polymer composites has gained attention. Biochar can enhance the mechanical strength, thermal stability, and even flame-retardant properties of composites [16], making it an attractive material for the development of high-performance, sustainable products.

This study aims to contribute to the development of environmentally friendly materials with enhanced performance. The objective was to produce biochar from coconut fiber, characterize the physical-chemical, structural, and thermal properties of both raw and pyrolyzed materials, and prepare composite materials using coconut fiber and biochar as fillers. Finally, the mechanical properties of the resulting composites were evaluated.

2 MATERIAL AND METHODS

The materials used in this study included coconut fiber supplied by Coco Verde Reciclado, epoxy resin (Epoxy Fiber MC 130) and curing agent (Epoxy Fiber 129), both provided by Epoxyfiber LTDA, and absolute ethanol obtained from Isofar LTDA. The coconut fiber was initially ground using a knife mill (model SL-31, Solab), and the resulting fractions were classified using a set of sieves (Figure 1).

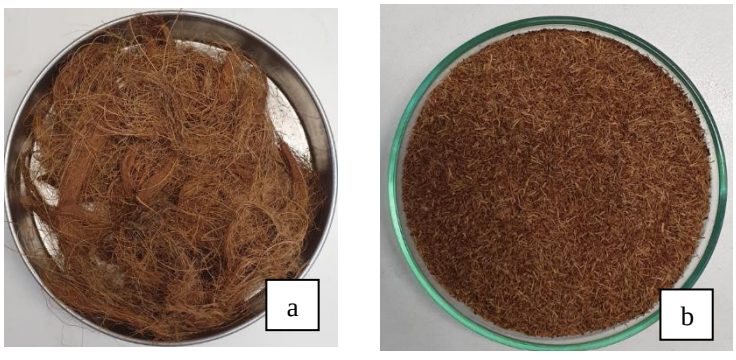

Figure 1: Original coconut fiber (a) and coconut fiber ground (b)

BIOCHAR PRODUCTION

The pyrolysis reaction was performed using coconut fiber to study the reaction conditions. The process was conducted in a bench-scale stainless steel reactor under a continuous nitrogen flow to ensure an inert atmosphere. A total of 5 g of coconut fiber (20 mesh), previously dried to constant weight, was used. The nitrogen (N_2) flow rate was set at 80 mL/min, the reaction temperature was 500 °C, and the total residence time was 30 minutes. Gaseous products were collected during the reaction in Tedlar bags. The mass yields of the condensable fraction and solid residue were determined by direct weighing, while the yield of the gaseous fraction was calculated by difference. The resulting material was referred to as laboratory coconut fiber biochar (LCFB).
A second pyrolysis process was carried out in a semi-pilot stainless steel reactor (6 L capacity) under similar conditions. A total of 1000 g of coconut fiber (60–100 mesh), also dried to constant weight, was used. The nitrogen flow rate was 200 mL/min, the temperature was maintained at 500 °C, and the reaction time was extended to 120 minutes. The condensable fraction and solid residue were quantified by direct weighing of the collection vessels, while the gaseous fraction was obtained by mass balance. The solid product was identified as coconut fiber biochar (CFB) from the pilot unit.

Physical and chemical characterization

Coconut fiber with a particle size of 0.85 mm (20 mesh) was used for physicochemical analysis. Samples were dried at 60 °C until constant weight for the determination of extractives, lignin content, and CHNSO elemental composition.
The analyzed samples included raw coconut fiber and the corresponding biochar. Moisture content, ash content, and pH of both coconut fiber and CFB were determined using standard procedures established by EMBRAPA [17]. The percentages of extractives and lignin in the fiber were also determined. Elemental analysis (CHNSO) was performed using a UNICUBE elemental analyzer (Elementar, Germany).

Structural and thermal analysis

Fourier Transform Infrared Spectroscopy (FTIR) was performed using a PerkinElmer Frontier FT-IR spectrometer. Samples were pelletized with potassium bromide (KBr) at a concentration of 1% (w/w). Spectra were obtained by averaging 32 scans at a resolution of 4 cm^{-1}. Thermogravimetric analysis (TGA) was conducted using a PerkinElmer Pyris One TGA instrument under an inert nitrogen atmosphere, with a flow rate of 25 mL/min and a heating rate of 10 °C/min, from room temperature up to 800 °C.

TENSILE STRENGTH OF COCONUT FIBRE AND COCONUT FIBRE BIOCHAR COMPOSITES

Composite of coir fiber and coconut fiber biochar

To prepare the test specimens, the following materials were used: epoxy resin (Epoxy Fiber MC 130), amine hardener (Epoxy Fiber 129), absolute ethanol, and coconut fiber with a particle size of 0.85 mm (20 mesh). For the composite formulations, coconut fiber biochar (CFB) was used in fine powder form. Both the fiber and biochar materials were dried in an oven at 105 °C prior to use.
The test specimens were prepared using a 100 mm × 100 mm Teflon mold spacer. Fillers (either FC or CFB) were randomly dispersed within the epoxy matrix. The resin-to-filler ratio was set at 60:40 (by weight). For every 10 parts of resin, 1 part of hardener and 1 part of ethanol were added to aid mixing and dispersion, as detailed in Table 1. The curing process involved compression molding: 10 minutes in a cold press, followed by 10 minutes in a hot press, and an additional 10 minutes in a cold press.

.

Materials	Mass (g)	Volume (ml)
Epoxy Resin (Fiber MC 130)	27.0	---
Amine Hardener (Epoxy Fiber 129)	2.7	---
Ethanol	2.7	3.42
FC or CFB	18.0	---

Table 1: Materials and quantities used in the composite

Mechanical properties and standards used

Mechanical testing was conducted using an Instron Electropuls E3000 universal electromechanical testing machine, equipped with a 5 kN Dynacell load cell, an Instron 2630-106 extensometer, and 3 kN-capacity Instron mechanical grips. Thickness measurements were taken using a Digimess digital external micrometer (model 113.054 B). The crosshead speed was set at 2.0 mm/min under ambient conditions of 27 ± 2 °C and 46 ± 5% relative humidity.
The mechanical properties of the epoxy composites containing FC or CFB were evaluated according to ASTM D3039/D3039M standards.

3 RESULTS

Physical and chemical characterization

The physicochemical characteristics of the coconut fiber used in this study are presented in Table 2 and were obtained following rigorous standardized methods. The values obtained slightly differ from those reported in the literature, as such parameters are strongly influenced by the geographic origin and processing conditions of the biomass. Ash content showed the greatest variation, which is likely related to the mineral salts present in the cultivation area. Other parameters exhibited strong agreement with values reported in the literature.

Analisys	Coconuts Fiber	Reference
Moisture (%)	8.79 ± 0,16	6.75 [18]
Ash (%)	1.02 ± 0,01	3.38 [18]
pH	6.06 ± 0,07	6.4[4]
Insoluble lignin[a] (%)	32.07 ± 0,20	20−48[4,19]
Extractives (%)	2.66 ± 0.21	-
C (%)	47.42 ± 0,07	47.6 [20]
H (%)	5.92 ± 0,01	5.7 [20]
N (%)	0.28 ± 0.01	0.2 [20]
S (%)	0.12 0.01	-

a. Ash and protein free; (-): not observed.

Table 2: Physical and chemical characterization of coconut fiber

Biochar production

Pyrolysis reactions were conducted both at the laboratory scale to achieve the best reaction conditions and at the pilot scale to produce sufficient quantities for composite fabrication. Following pyrolysis, three product fractions were obtained: condensable liquids, volatile gases, and solid residue (biochar). Table 3 presents the yields of biochar produced from coconut fiber under identical temperature conditions at the laboratory scale (LCFB) and pilot scale (CFB). It was observed that the yield of solid residue from the laboratory-scale pyrolysis was slightly higher than that obtained from the pilot plant (CFB). This difference is attributed to the higher nitrogen flow rate used in the pilot plant, which favored the formation of volatile products.

Sample	Mass (g)	Condensable (%)	Volatile (%)	Solid residue (%)
LCFB	5	48,2	20,4	31,4
CFB	1000	40,1	36,5	23,4

Table 3: Results of pyrolysis reactions of coconut fiber

Structural and thermal analysis

Figure 6 shows the ATR-FTIR spectra of coconut fiber (CF) samples and biochar obtained from coconut fiber (CFB). In the coconut fiber spectrum, the broad band observed between 3600 and 3200 cm^{-1} corresponds to O–H stretching vibrations associated with the hydroxyl groups present in the biomass macromolecules, namely cellulose, hemicellulose, and lignin. The presence of lignin is confirmed by characteristic signals attributed to aromatic rings (5). The band near 2900 cm^{-1} corresponds to aliphatic C–H stretching linked to the aromatic ring [21]. The intense band at 1747 cm^{-1} (3) indicates the presence of ketone, carbonyl, and ester functional groups [4]. This is followed by peaks at 1607 cm^{-1} and 1506 cm^{-1} (4 and 5), which are assigned to the C=O conjugated and C=C stretching in the aromatic rings of lignin [22]. The peak at 1467 cm^{-1} (6) is attributed to C–H bending vibrations. The peak at 1321 cm^{-1} (7) corresponds to C–H deformation of methyl groups and O–H of phenolic structures [4].

The peak at 1238 cm^{-1} (8) is related to C–C, C–O, and C=O stretching in the guaiacyl units of lignin [22]. Peaks observed between 1160 and 990 cm^{-1} (9) are attributed to β-glycosidic bonds present in cellulose.

In the CFB spectra, a reduction in several characteristic peaks of coconut fiber is observed, notably the absorption band between 1400 and 907 cm^{-1} (10). Furthermore, the peak attributed to the β-glycosidic bond (peak 9) is no longer detected, indicating that pyrolysis effectively decomposed cellulose components.

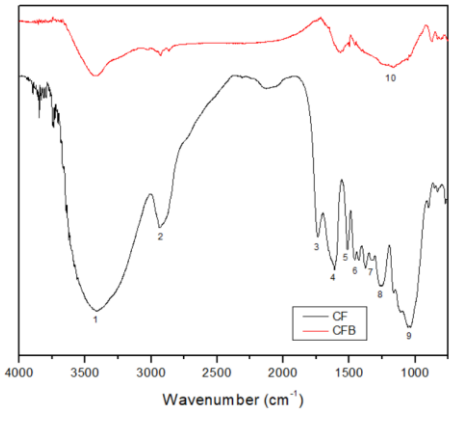

Figure 2: FTIR results for coconut fiber (CF) and coconut fiber biochar (CFB).

The thermal stability of coconut fiber and coconut fiber biochar was evaluated by thermogravimetric analysis (Figure 3). The decomposition of coconut fiber components occurs within characteristic temperature ranges: hemicellulose, because of its amorphous structure, decomposes between 200–260 °C; cellulose between 240–360 °C; and lignin between 280–360 °C [23].

In the thermogram of coconut fiber, two major events were observed. The first, occurring below 100 °C, corresponds to moisture loss. The second event comprises two degradation stages. The first stage, from 203 °C to 315 °C, is associated with the decomposition of hemicellulose and part of the cellulose. The second stage, from 315 °C to 492 °C, corresponds to the degradation of lignin and the remaining cellulose. The maximum rate of mass loss was observed at 301 °C (T_{onset}). Therefore, significant lignin degradation and the formation of biochar only occur above 492 °C, which is the temperature range of interest for this study.

For the coconut fiber biochar, the thermogram indicated enhanced thermal stability, consistent with the thermal behavior observed for lignin-derived pyrolysis products [24]. The DTG curve for the biochar showed two main events. The first was a minor peak associated with residual moisture loss. The second, a single-stage degradation event, occurred between 337 °C and 640 °C, with a maximum degradation rate (T_{onset}) at 446 °C and a peak degradation temperature at 547 °C. These findings are in agreement with values reported in the literature and are attributed to the carbonization of biomass and the formation of stable carbon structures [25].

Tensile strength of coconut fibre and coconut fibre biochar composites

The tensile strength and tensile modulus of epoxy resin-based composites were evaluated to investigate the effect of incorporating coconut fiber and biochar. The addition of biochar significantly influenced the mechanical performance of the composites. Acting as a reinforcing filler, biochar enhanced the load-bearing capacity of the material, likely because of its porous structure and high surface area, which improve interfacial adhesion within the polymer matrix [26].

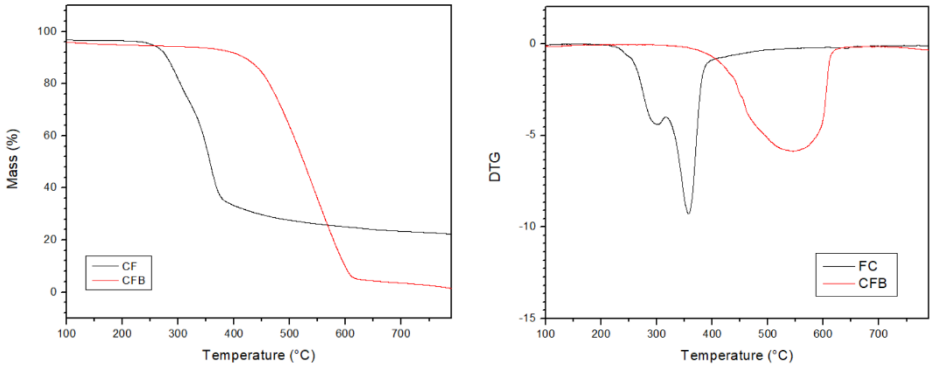

Figure 3: TGA and DTG results for coconut fiber (CF) and coconut fiber biochar (CFB)

In this study, the final composite plates produced with coconut fiber or coconut fiber biochar as fillers and epoxy resin as the matrix exhibited homogeneous structure, smooth surfaces, and moderate gloss (Figure 4). No bubbles or surface roughness were observed. The composite reinforced with coconut fiber showed a tensile modulus of 3.63 GPa, whereas the composite containing biochar (CFB) exhibited a higher modulus of 4.48 GPa. This indicates that incorporating biochar significantly enhances the stiffness of the composite, likely due to improved filler–matrix interfacial interactions. Table 4 presents the tensile test data for both composites, and the corresponding results are graphically represented in Figure 5.

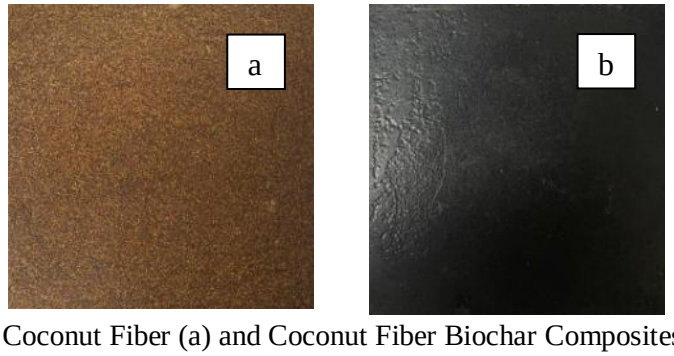

Figure 4: Coconut Fiber (a) and Coconut Fiber Biochar Composites (b)

Sample	Strain (MPa)	Stress (%)	Tensile modulus (GPa)
FC	26.59 ± 0,99	0.79 ± 0.05	3.63 ± 0.18
CFB	20.42 ± 2.21	0.45 ± 0.02	4.48 ± 0.53

Table 4: Mechanical properties of epoxy composites with Coconut Fiber (CF) and Coconut Fiber Biochar (CFB)

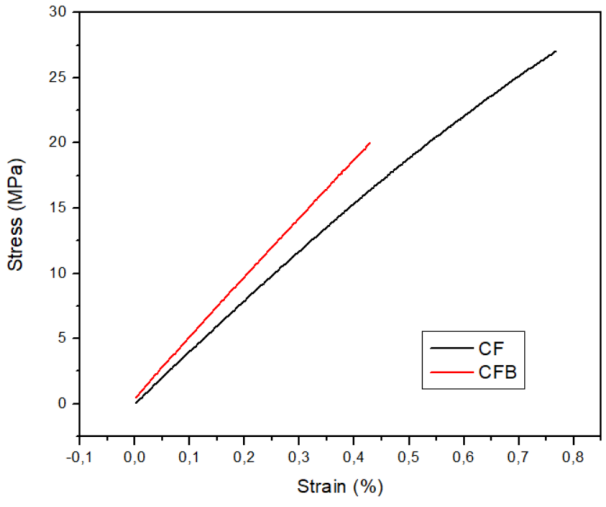

Figure 5: Mechanical properties of epoxy composites with Coconut Fiber (CF) and Coconut Fiber Biochar (CFB)

4 CONCLUSIONS

Coconut fiber is a natural lignocellulosic material with a high lignin content compared to other plant-based fibers, which makes it a promising candidate for applications across various industrial sectors. This study evaluated the use of biochar derived from coconut fiber as a reinforcing filler in epoxy resin composites.

FTIR and TGA analyses confirmed that the pyrolysis conditions were favorable for biochar production, evidencing structural and thermal transformations. Mechanical testing demonstrated the viability and effectiveness of incorporating biochar, with a modest but significant increase in tensile modulus—from 3.6 GPa for the coconut fiber composite to 4.3 GPa for the biochar-reinforced composite.

These findings suggest that both coconut fiber and its biochar can serve as sustainable, environmentally friendly alternatives to conventional fillers in composite materials.

ACKNOWLEDGEMENTS

The authors acknowledge to Coco Verde Reciclado LTDA for donating the coconut fibre material used and to the IMA's Lapin laboratory for the FTIR analyses.

REFERENCES

[1] M.S.C.P. Brainer, Produção de coco: o Nordeste é destaque nacional. *Cad. Setorial ETENE* 3, n.61, 2018.

[2] Faostat - Food and Agriculture Organization of the United Nations. (Organização das Nações Unidas para Alimentação e Agricultura) *Crops and livestock products*. Disponível em: https:// www.fao.org/faostat/en/#data/ Acesso em: 18 out. 2021.

[3] O.A. Carrijo, R.S. Liz and N. Makishima, Fibra da Casca do Coco Verde Como Substrato Agrícola. Horticultura Brasileira, Brasília, 20, 4, pp. 533-535. 2002.

[4] R. Chaudhary and P.L.Dephe, Depolymerization of Lignin Using a Solid Base Catalyst, *Energy Fuels*, **33**, 2019, pp. 4369−4377 (doi: 10.1021/acs.energyfuels.9b00621).

[5] S.R. Wang, G.X. Dai, H.P. Yang and Z.Y. Luo, Lignocellulosic Biomass Pyrolysis Mech-Anism: A State-of-the-Art Review, *Progress in Energy and Combustion Science*, **62**, 2017, pp. 33–86 (doi: https://doi.org/10.1016/j.pecs.2017.05.004).

[6] P. Giudicianni, V. Gargiulo, C.M. Grottola, M. Alfè, A.I. Ferreiro, M.A .A . Mendes, M. Fagnano and R. Ragucci, Inherent metal elements in biomass pyrolysis: a re-view, *Energy Fuels*, **35**, 2021, pp. 5407–5478 (doi: https://doi.org/10.1021/acs.energyfuels.0c04046).

[7] M. Carrier, M. Windt, B. Ziegler, J. Appelt, B. Saake, D. Meier and A. Bridgwater, Quantitative insights into the fast pyrolysis of extracted cellulose, hemicellu-loses, and lignin, *ChemSusChem*, **10,** 2017, pp. 3212–3224 (doi: 10.1002/cssc.201700984).

[8] S.D. Stefanidis, K.G. Kalogiannis, E.F. Iliopoulou, C.M. Michailof, P.A. Pilavachi and A .A . Lappas, A study of lignocellulosic biomass pyrolysis via the pyrolysis of cellulose, hemicellulose and lignin, *Journal of Analytical and Applied Pyrolysis*, **105**, 2014, pp.143–150 (doi: https://doi.org/10.1016/j.jaap.2013.10.013).

[9] R.V. Silva, D. Spinelli, W.W. Bose Filho, S. C. NETO, G. O. CHIERICE and J. R. TARPANI, Fracture toughness of natural fibers/castor oil polyurethane composites, *Composites Science Tecnology*, **66**, 2006, pp.1328-1335 (https://doi.org/10.1016/j.compscitech.2005.10.012).

[10] J. Rout, M. Misra, S.S. Tripathy, S.K. Nayak, A.K. Mohanty, The influence of fibre treatment on the performance of coir-polyester composites, *Composites Science and Technology*, **61**, 2001, pp.1303-1310 (https://doi.org/10.1016/S0266-3538(01)00021-5).

[11] A. Figueiredo, G. Vela, G. Ascensão, E. Vettorazzi, R. Vicente and M Oliveira, Development of an innovative biocomposite using coconut fibres and bio-based binder for thermal and acoustic aplications in buildings, *Journal of Cleaner Production*, **49**, 2025, pp.144834 (https://doi.org/10.1016/j.jclepro.2025.144834).

[12] Q. Zhang, K. Li, Y. Fang, Z. Guo, Y. Wei and K. Sheng, Conversion from bamboo waste derived biochar to cleaner composites: synergistic effects of aramid fiber and silica. *Journal of Cleaner Production*, **347**, 2022, pp.131336 (https://doi.org/10.1016/j.jclepro.2022.131336).

[13] S. Li, Y. Xu, X. Jing, G. Yilmaz, D. Li and L.S. Turng, Effect of carbonization temperature on mechanical properties and biocompatibility of biochar/ultra-high molecular weight polyethylene composites, *Composites Part B: Engineering*, **196**, 2020, pp.108120 (doi:https:// doi.org/10.1016/j.compositesb.2020.108120).

[14] C. Yang, J. Liu and S. Lu, Pyrolysis temperature affects pore characteristics of rice straw and canola stalk biochars and biochar-amended soils. *Geoderma*, **397**, 2021, pp. 115097 (https://doi.org/10.1016/J.GEODERMA.2021.115097).

[15] J. Matuˇstík, T. Hn´atkov´a and V. Koˇcí, Life cycle assessment of biochar-to-soil systems: a review, *Journal of Cleaner Production*, **259**, 2020, pp. 120998 (https://doi.org/10.1016/j.jclepro.2020.120998).

[16] R. Sundarakannan, V. Arumugaprabu, T. Sathish and S.M. Rangappa and S. Siengchin, Mechanical and rosion performance of sugarcane biochar-reinforced polymer composites, *Biomass Conversion and Biorefinery*, **14**, 2024, pp.15453–15468 (https://doi.org/10.1007/s13399-022-03612- 9).

[17] J. P. S. Morais, M. F. Rosa and J. M. Marconcini, *Procedimentos para análise lignocelulósica*, Embrapa Algodão, Campina Grande, 2010. (https://www.infoteca.cnptia.embrapa.br/infoteca/handle/doc/883400, Retrieved July 7, 2025).

[18] K. C. Lima, D M. Souza, G. Kappler, R.C.E. Modolo and C.A.M. Moraes, In natura and carbonized fiber characterization from pyrolysis process, *Mix Sustentável*, **8**, 2022, pp.27-38 (http:// doi.org /10.29183/2447-3073).

[19] C. Asasutjarit, J. Hirunlabh, J. Khedari, S. Charoenvai, B. Zeghmati and U.C. Shin, Development of coconut coir based lightweight cement board, *Construction and Building Materials*, **21**, 2007, pp.277−288 (doi:10.1016/j.conbuildmat.2005.08.028)

[20] V. Dhyani and T. Bhaskar T., A comprehensive review on the pyrolysis of lignocellulosic biomass, *Renewable Energy*, **129**, 2018, 695e716 (http://dx.doi.org/10.1016/j.renene.2017.04.035).

[21] S. R. Albinante, E. B. A. V. Pacheco, L. L. Y. Visconte, M. I. B. Tavares, Caracterização de Fibras de Bananeira e de Coco por Ressonância Magnética Nuclear de Alta Resolução no Estado Sólido, *Polímeros*, **22**, n. 5, 2012, pp. 460-466 (doi:http://dx.doi.org/10.1590/S0104-14282012005000057).

[22] F. Souto and V. Calado, Mystifications and Misconceptions of Lignin: Revisiting Understandings, *Green Chemistry*, **14**, 2012, pp. 8172-8192 (doi: 10.1039/D2GC01914K).

[23] V. Alvarez and A. vázquez, Thermal degradation of cellulose derivatives/starch blends and sisal fibre biocomposites, *Polymer Degradation and Stability*, **84**, 2004, pp.13-21 (doi:10.1016/j.polymdegradstab.2003.09.003).

[24] Z. Yi , C. Li, L. Zhang, S. Zhang, W. Gao, S. Wang, B. Li and X. Hu, Impacts of CO2 atmosphere on property of the biochar from pyrolysis of lignina, *Journal of Analytical and Applied Pyrolysis*, **167**, 2022, pp.105689. (https://doi.org/10.1016/j.jaap.2022.105689)

[25] Y. Wei, C. Shen, J. Xie and Q. Bu, Study on reaction mechanism of superior bamboo biochar catalyst production by molten alkali carbonates pyrolysis and its application for cellulose hydrolysis, *Science of The Total Environment*, **712**, 2020, pp. 136435. (https://doi.org/10.1016/j.scitotenv.2019.136435)

[26] S. Rajendran, G. Palani, A. Veerasimman, V. H. Shanmugam, U. M., K. Korniejenko, H. Trilaksana, A. Majumder, F. Stochino, Enhancing carbon fiber composites with fish scale biochar for superior strength and environmental sustainability, *Cleaner Engineering and Technology*, **27,** 2025, pp.100996 (https://doi.org/10.1016/j.clet.2025.100996).

DEVELOPMENT OF HIGH-PERFORMANCE BIOMASS COMPOSITES USING A PA11/GLYCOL LIGNIN MATRIX

Jonathon Tanks[1], Kenji Tamura[2] , Kimiyoshi Naito[1], Thi Thi Nge[3] and Tatsuhiko Yamada[3]

[1]Research Center for Structural Materials, National Institute for Materials Science, Tsukuba, Japan
Email: tanks.jonathon@nims.go.jp, web page: samurai.nims.go.jp/profiles/tanks_jonathon

[2]Research Center for Electronic and Optical Materials, National Institute for Materials Science, Tsukuba, Japan
Email: tamura.kenji@nims.go.jp, web page: samurai.nims.go.jp/profiles/tamura_kenji

[3]Center for Advanced Materials, Forestry and Forest Products Research Institute, Tsukuba, Japan

Keywords: Polyamide 11, Glycol lignin, Biomass composites, Mechanical properties

ABSTRACT

Polyamides (PA, “nylon”) is a class of thermoplastic polymers characterized by good heat/chemical resistance, mechanical properties, and processability, leading to widespread use in various automotive components. The two most common varieties, PA6 and PA66, are petroleum-based and carry a relatively large carbon footprint. Thus, bio-based alternatives such as PA11 have been introduced in recent decades. However, these polymers tend to have longer alkyl chains and exhibit lower mechanical properties than their traditional counterparts. In this work, glycol-modified lignin (GL) biomass is added to PA11 to create a blended matrix for short-carbon fiber composites in order to improve performance while maintaining a high biomass content. Characterization of the structure and properties of the resulting blends shows that PA11 and GL are highly compatible with uniform dispersion, which is essential for improving mechanical properties without sacrificing processability. Furthermore, the tensile modulus and strength of the short-fiber composites containing lignin exceeds that expected from the rule of mixtures, reaching performance comparable to super engineering plastic compounds like PEEK/GF30. The applicability of these biomass composites for more sustainable automotive components is discussed.

1 INTRODUCTION

The growing demand for sustainable materials has accelerated the development of biomass-based composites, particularly those using bio-derived plastics and additives. These composites offer a compelling alternative to conventional petroleum-based materials, driven by the need for environmentally friendly options that also deliver high performance in demanding applications. Recent advances have focused on incorporating bio-derived thermoplastics, such as polylactic acid (PLA), polyhydroxyalkanoates (PHA), and bio-based polyamides (PA11, PA1010, etc), into composite formulations [1-7]. These bio-based matrices not only address environmental concerns but also provide high mechanical properties, making them viable candidates for industries ranging from automotive to electronics and aerospace.

However, despite these advancements, there remain several challenges in bringing them into high-performance applications. Bio-derived plastics often exhibit limitations in processing, thermal stability, and mechanical properties compared to their petroleum-based counterparts. Issues like brittleness, low-temperature performance, and moisture sensitivity can hinder their widespread adoption, especially in demanding environments where durability and reliability are essential [5,6]. Furthermore, achieving uniformity and consistency in the bio-plastic matrix during composite fabrication, while maintaining environmental sustainability, presents significant technical challenges. In the specific case of PA11, its long alkyl segment and relatively low hydrogen bond (HB) density compared to conventional PA6 gives it low modulus (~1.5 GPa) and strength (~40 MPa). Thus, simply adding reinforcing fibers will not make

it competitive with conventional engineering plastic composites. Overcoming these barriers requires innovative approaches to both material design and manufacturing techniques.

In this context, lignin, a natural polymer obtained as a byproduct of the pulp and paper industry, has gained attention as a promising additive in biomass-based composites [8]. Lignin's complex aromatic structure and high antioxidant properties make it a suitable candidate for enhancing the performance of petroleum- and bio-derived polymers alike [9]. Recent studies have shown that lignin can significantly improve the oxidative stability of polyolefins [10] and PA6 [11], protecting the material from degradation under UV exposure and high temperatures. Additionally, lignin can enhance the mechanical properties of composites by acting as a reinforcing agent [10]. However, the main issue impeding widespread use is the typically poor compatibility with many polymers used in composites. The phenolic and hydroxyl groups in lignin have the potential to interact with functional groups on the host polymer and thus increase tensile strength and modulus. Various approaches to improve lignin's dispersibility such as alkyl, acetyl, and hydroxyl modifications have been met with varying degrees of success [12,13].

This work reports the fabrication of PA11/carbon fiber (CF) composites using a PEG-grafted glycol lignin (GL) in a scalable melt-mixing process. Synergistic interactions between the three constitutents lead to unprecedented improvements in tensile modulus and strength, rivalling conventional super engineering plastics like PPS and PEEK. Material characterization results and implications for future work are discussed.

2 EXPERIMENTS

2.1 Materials and fabrication

The polymer used in this study was an unreinforced, standard-grade PA11 (BML OTLD, Arkema). The glycol lignin (GL) was produced by acid-catalyzed PEG solvolysis of softwood biomass yield lignin derivatives grafted with about 26 wt% PEG400, as described elsewhere [14]. Chopped carbon fibers (PYROFIL™ TR06NLB5K) having length of roughly 6 mm and diameter of about 7 μm were purchased from Mitsubishi Chemical.

PA11 and GL were both dried at 90 °C for 24 hr before blending in a twin-screw extruder (S1KRC, Kurimoto) at 240-250 °C. Blends containing different amounts of GL and CF ranging from 0-30 wt% were then injection molded (Mini JET II, Thermo Scientific) into ISO 527-2 dumbbell specimens at cylinder and mold temperatures of 230 °C and 80 °C, respectively. No other heat treatments were applied before characterization.

2.2 Characterization

Mechanical behavior was evaluated by tensile testing according to ASTM D638 using an electromechanical testing machine (EZ-LX, Shimadzu) equipped with a 5kN load cell and video extensometer, at a crosshead speed of 5 mm/min. FTIR spectra were collected at room temperature over the range 500-4000 cm^{-1} in ATR mode (IR Affinity, Shimadzu).

Differential scanning calorimetry (DSC7020, Hitachi Hi Tech) was performed over the range 20-250 °C at a heating/cooling rate of 10 °C/min, using 2-3 mg of sample. The crystallinity (X_c) was approximated by the equation:

$$X_c = \frac{\Delta H_m}{(1-f)\Delta H_m^0} \quad (1)$$

where f is the mass fraction of filler (e.g., GL), and ΔH_m and ΔH_m^0 are the melting enthalpies of the specimen (taken from the first DSC scan) and a perfect crystal (taken as 220 J/g [15]), respectively.

3 RESULTS

3.1 Composite fabrication and structure

Melt-mixing of the blends and composites was successfully performed in a twin-screw extruder, without significant changes in processibility even up to 20 wt% GL loading, although an increase was noticed for 30 wt% GL loading. Figure 1 depicts the fabrication process along with a schematic of the expected material structure. The abundant hydroxyl groups on lignin, supplemented with grafted PEG chains allows for polar and HB interactions between GL and PA11. Additionally, the aromatic backbone of lignin should exhibit high affinity for the surface of carbon fibers.

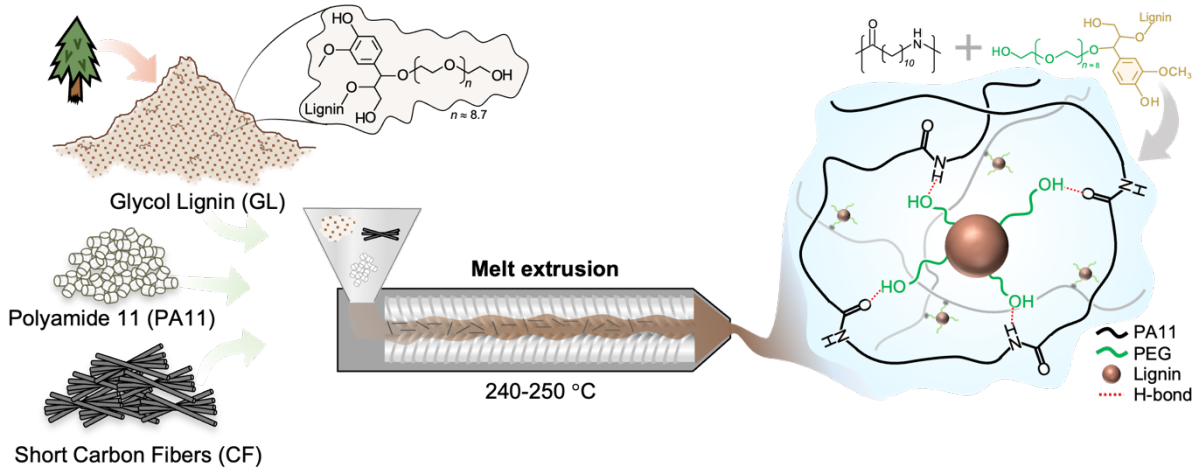

Figure 1: Fabrication of short-carbon fiber composites using PA11/GL blends via melt-mixing, with the proposed polymer/lignin interactions.

FTIR did not show significant presence of GL, despite the substantial loading (0-30 wt), but slight shifts in the carbonyl region of amide II (1640 cm^{-1}) indicated HB interaction. FTIR can be useful for studying HB interactions in polymers, but the changes tend to be small when comparing different forms of H-bonds, rather than the increase or decrease in their number. Recent work has indicated that GL may form H-bonds with polyamide in a disordered configuration, which does not appear the same as so-called “free” carbonyls [11]. The melting temperatures and enthalpies shifted noticeably with increasing GL content (Figure 2), which can be attributed to a change in the crystal phase composition due to the presence of lignin [11]. In addition, the crystallinity increased by several percent while the crystallization temperature decreased by several degrees, which indicates that lignin has a retardation effect that promotes slower crystal growth (Table 1).

Sample	T_m (°C)	T_c (°C)	X_c (%)
PA11	189.7	159.5	28.3
PA11-GL10	187.9	157.8	28.5
PA11-GL20	187.7	154.5	29.5
PA11-GL30	187.4	153.7	30.1

Table 1: Thermal properties of PA11/GL blends.

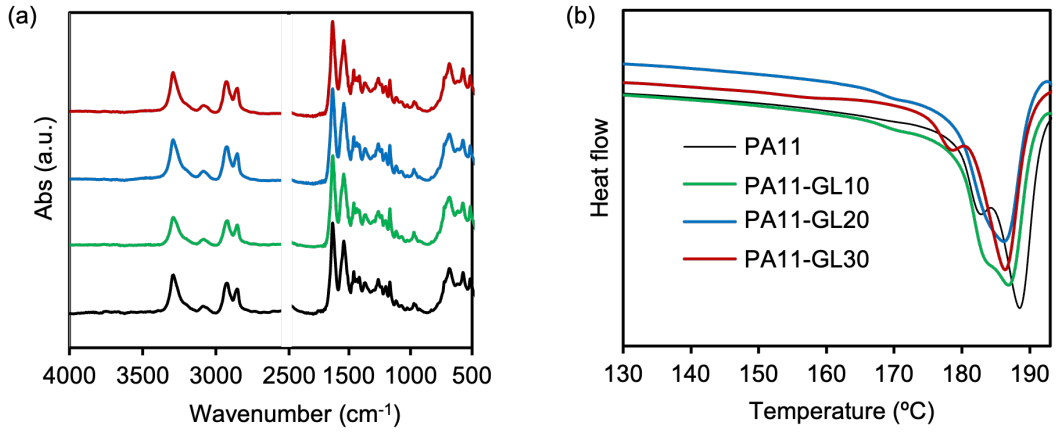

Figure 2: (a) FTIR spectra and (b) DSC thermograms of PA11/GL blends.

3.2 Tensile properties

The addition of GL alone did not significantly increase the tensile strength or modulus of PA11 until 30 wt% loading, as seen in Figure 3(a,b). The failure strain was for 10 wt% GL blends did not change drastically, and although higher GL content resulted in lower failure strains compared to neat PA11, over 100% was still achieved at 30 wt% GL.

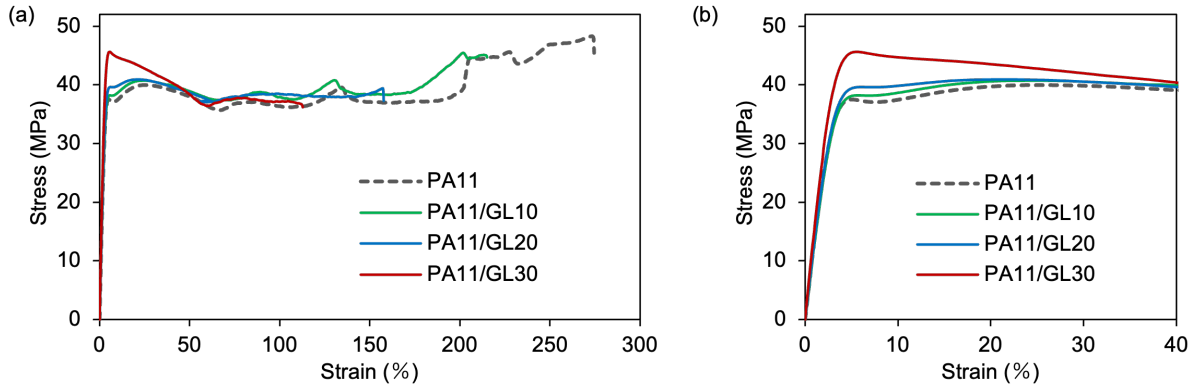

Figure 3: Stress-strain curves for PA11/GL blends for the (a) full and (b) elastic strain regions. (c) Stress-strain curves for PA11/CF composites. Stress-strain curves of biomass composites fixed at (d) 10 wt% CF and (e) 20 wt% CF to highlight the effect of lignin.

Figure 4(a) shows typical tensile behavior of short-fiber composites was observed for PA11/CF. Despite the minimal reinforcing effect of GL on PA11, a drastic improvement in reinforcing efficiency was observed for the biomass-matrix short fiber composites. This is demonstrated in Figure 4(b) by fixing CF at 10 wt% whereby the strength increases by 10% and 40% for GL loadings of 10 wt% and 20 wt%, respectively. The same trend is observed for 20 wt% CF composites in Figure 4(c). Such a drastic synergistic reinforcing effect has never been reported in the literature before, although a similar (but less drastic) effect was reported for PP/GL composites [9]. This suggests that PEG-grafted glycol lignin possesses a unique ability to aid in stress transfer between fibers. The full set of data for all composites in the study is summarized in Figure 4(d,e), with comparison to typical values of PEEK-GL30 for reference. In particular, an exceptionally high modulus of 16 GPa was achieved for the GL30-CF30 composite (70% biomass by weight), which is (to the authors' knowledge) the highest reported for a high-biomass-content composite.

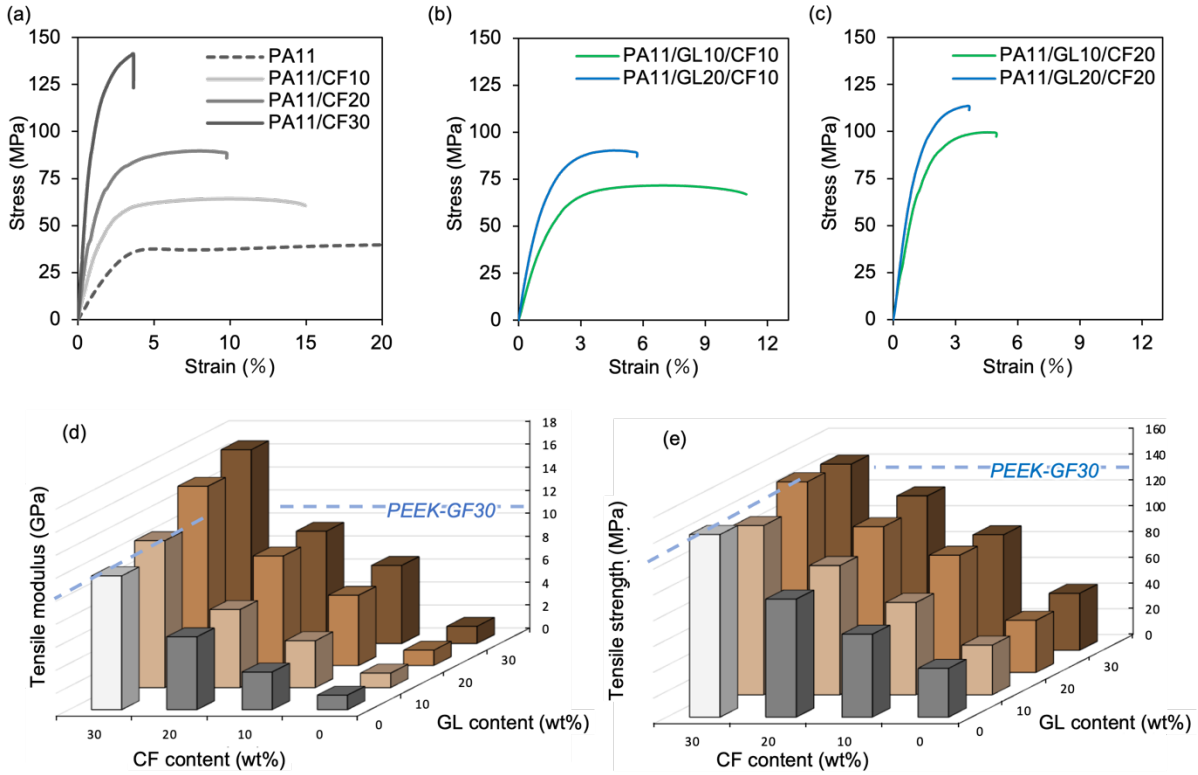

Figure 4: (a) Stress-strain curves for PA11/CF composites. Stress-strain curves of biomass composites fixed at (b) 10 wt% CF and (c) 20 wt% CF to highlight the effect of lignin. Summarized results for (d) tensile modulus and (e) tensile strength for all composites in this study.

9 CONCLUSIONS

In this study, all-biomass matrix materials of PA11 and PEG-grafted glycol lignin were prepared by scalable melt-mixing, then combined with short carbon fibers to create biomass composites. Polar and HB interactions between the GL and PA11 did not significantly increase the tensile properties of the polyamide itself, but the blend exhibited a synergistic reinforcing effect that drastically improved the tensile properties of the short fiber composites. The tensile modulus for some blends reached levels similar to PEEK-GF30. More study is needed to understand the detailed mechanisms of how lignin influences crystallization and deformation behavior of PAs, but this work demonstrates that PA11/GL composites have potential for high-performance applications.

ACKNOWLEDGEMENTS

This work was supported by MAFF (Ministry of Agriculture, Forestry and Fisheries), Japan commissioned project “Development of Glycol Lignin–Based High-Value-Added Materials” (Grant Number J008722). The authors also thank T. Akagawa (Hosei University) and M. Kamon (NIMS) for assistance with sample preparation with mechanical testing.

REFERENCES

[1] A.K. Mohanty, S. Vivekanandhan, J.-M. Pin and M. Misra, Composites from renewable and sustainable resources: challenges and innovations, *Science*, **362**, 2018, pp. 536-542, (doi: 10.1126/science.aat9072).

[2] R. Chen, M.A. Abdelwahab, M. Misra and A.K. Mohanty, Biobased ternary blends of lignin, poly(lactic acid), and poly(butylene adipate-co-terephthalate): The effect of lignin heterogeneity on blend morphology and compatibility, *Journal of Polymers and the Environment*, **22** , 2014, pp. 439-448, (doi: 10.1007/s10924-014-0704-5).

[3] M. Li, Y. Jia, X. Shen, T. Shen, Z. Tan, W. Zhuang, G. Zhao, C. Zhu and H. Ying, Investigation into lignin modified PBAT/thermoplastic starch composites: thermal, mechanical, rheological and water absorption properties, *Industrial Crops and Production*, **171**, 2021, pp. 113916, (doi: 10.1016/j.indcrop.2021.113916).

[4] M.A.S. Anwer, H.E. Naguib, A. Celzard and V. Fierro, Comparison of the thermal, dynamic mechanical and morphological properties of PLA-lignin & PLA-tannin particulate green composites, *Composites Part B*, **82**, 2015, pp. 92-99. (doi: 10.1016/j.compositesb.2015.08.028).

[5] Y.-L. Chung, J.V. Olsson, R.J. Li, C.W. Frank, R.N. Waymouth, S.L. Billington and E.S. Sattely, A renewable lignin-lactide copolymer and application in biobased composites, *ACS Sustainable Chemistry and Engineering*, **1**, 2013, pp. 1231-1238, (doi: 10.1021/sc4000835).

[6] S.-J. Xiong, B. Pang, S.-J. Zhou, M.-K. Li, S. Yang, Y.-Y. Wang, Q. Shi, S.-F. Wang, T.-Q. Yuan, R.-C Sun, Economically competitive biodegradable PBAT/lignin composites: effect of lignin methylation and compatibilizer. *ACS Sustainable Chemistry and Engineering*, **8**, 2020, pp. 5338-5346, (doi: 10.1021/acssuschemeng.0c00789).

[7] M.A. Abdelwahab, S. Taylor, M. Misra and A.K. Mohanty, Thermo-mechanical characterization of bioblends from polylactide and poly(butylene adipate-co-terephthalate) and lignin, *Macromolecular Materials and Engineering*, **300**, 2015, pp. 299-311, (doi: 10.1002/mame.201400241).

[8] Future Markets, Inc., The Global Market for Lignin 2021-2031 (Report 5331648). https://www.futuremarketsinc.com/the-global-market-for-lignin-2021-2031/, 2022 (accessed 5 May 2022).

[9] J. Tanks, K. Tamura, K. Naito, T.T. Nge and T. Yamada, Glycol lignin/MAH-g-PP blends and composits with exceptional mechanical properties for automotive applications, *Composites Science and Technology,* **238**, 2023, pp. 110030 (doi: 10.1016/j.compscitech.2023.110030).

[10] J. Tanks, K. Tamura, K. Naito, T.T. Nge and T. Yamada, Durable and recyclable biomimetic glycol lignin/polyolefin compounds for a circular economy, *Journal of Materials Chemistry A,* **12**, 2023, pp. 3014-3025 (doi: 10.1039/D3TA06230A).

[11] J. Tanks, T. Akagawa, K. Tamura, Y. Nemoto, K. Naito, T.T. Nge, Y. Watanabe and T. Yamada, Enhancing the thermo-oxidative stability of polyamide 6 by scalable melt-blending with PEG-grafted glycol lignin, *Polymer,* **accepted**, 2025.

[12] P. Buono, A. Duval, P. Verge, L. Averous and Y. Habibi, New insights on the chemical modification of lignin: Acetylation versus silylation, *ACS Sustainable Chemistry and Engineering*, **4**, 2016, pp. 5212-5222, (doi: 10.1021/acssuschemeng.6b00903).

[13] H. Sakai, K. Kuroda, S. Muroyama, T. Tsukegi, R. Kakuchi, J. Takada, A. Hata, R. Kojima, T. Ogoshi, M. Omichi, K. Ninomiya, K. Takahashi, Alkylated alkali lignin for compatibilizing agents of carbon fiber-reinforced plastics with polypropylene, *Polymer Journal*, **50**, 2018, pp. 281-284, (doi: 10.1038/s41428-017-0009-3).

[14] T.T. Nge, Y. Tobimatsu, S. Takahashi, E. Takata, M. Yamamura, Y. Miyagawa, T. Ikeda, T. Umezawa and T. Yamada, Isolation and characterization of polyethylene glycol (PEG)-modified glycol lignin via PEG solvolysis of softwood biomass in a large-scale batch reactor, *ACS Sustainable Chemistry and Engineering*, **6**, 2018, pp. 7841-7848, (doi: 10.1021/acssuschemeng.8b00965).

[15] K. Jariyavidyanont, A. Janke and R. Androsch, Crystal self-nucleation in polyamide 11 of different semicrystalline morphology, *Polymer*, **184**, 2019, pp. 121864 (doi: 10.1016/j.polymer.2019.121864).

ICCM24
AUGUST 4-8, 2025
BALTIMORE CONVENTION CENTER
BALTIMORE, MARYLAND, USA

No Technical Paper Submission for:

Ole Thomsen

ICCM24
AUGUST 4-8, 2025
BALTIMORE CONVENTION CENTER
BALTIMORE, MARYLAND, USA

No Technical Paper Submission for:

Richard Butler
Andrew Rhead

ICCM24
AUGUST 4-8, 2025
BALTIMORE CONVENTION CENTER
BALTIMORE, MARYLAND, USA

No Technical Paper Submission for:

Janice Barton
Ole Thomsen

AERO INDUSTRY BUILDING BLOCK CERTIFICATION LOGIC

CERTEST WORKSHOP

ICCM24
BALTIMORE, MD
4 AUGUST 2025

Dr. C. Q. Rousseau
Structures Senior Tech Fellow
Fort Worth, TX

LOCKHEED MARTIN

DISTRIBUTION STATEMENT A: Approved for public release; distribution is unlimited.

©2025 Lockheed Martin Corporation. All Rights Reserved

Airframe Design, Analysis, and Certification Process

Top-Level Technical and Programmatic Issues:

- *Overall scope (non-recurring cost/span, strategic teaming/sub-contracting, recurring-cost, anticipated production quantity/span, mods/sustainment/lifecycle cost-span, etc) is defined by similar legacy programs and current customer requirements.*
  - *New programs must generally stay within the historical norms;*
  - *Airframe structure is a relatively minor part of the overall program scope, and generally targeted to be low-risk and not the biggest cost- or schedule-driver (though it sometimes becomes so).*
- *Different decision-making in various phases of air vehicle lifecycle:*
  - *Pre-design*
  - *Lay-out*
  - *Drawing-release*
  - *Full-Scale-Testing*
  - *Final Strength Summary & Operating Restrictions*
  - *Factory MRB support*
  - *Field support*
  - *Modification, repair, sustainment, life-extension*

2024: Digital tools can potentially automate portions of every phase and reduce span

©2025 Lockheed Martin Corporation. All Rights Reserved

Airframe Design, Analysis, and Certification Process

Top-Level Technical and Programmatic Issues, Roles and Responsibilities:

- *Designers determine form/fit/function and influence manufacturing, assembly, and make/buy sourcing decisions.*
- *Stress Analysts assure static and fatigue structural integrity, organize/lead structural certification process, and influence weight efficiency.*
- *Materials and Process, and Manufacturing Engineers ensure that raw materials and manufacturing/assembly processes are reliable/repeatable and in control.*
- *Integrated Product Teams work together to make optimum collective decisions regarding airframe weight/cost/span;*
  - *Many non-structural constraints drive airframe design decisions, including machining and assembly limitations, fuel/environmental sealing, systems installation, maintenance access, etc.*
  - *Generally, IPT's choose whichever material or manufacturing process works best for each individual part, or as a system.*

Form/fit/function and applied loads generally determine material choice (no bias for or against particular materials or processes)

©2025 Lockheed Martin Corporation. All Rights Reserved

Airframe Design, Analysis, and Certification Process

Building-Block Certification Logic, Composite Stress Methods:

Element/Subcomponent/component tests may be static, durability, and/or residual strength

Applies regardless of material (metallic & hybrid-structure tests often fatigue; composites usually static)

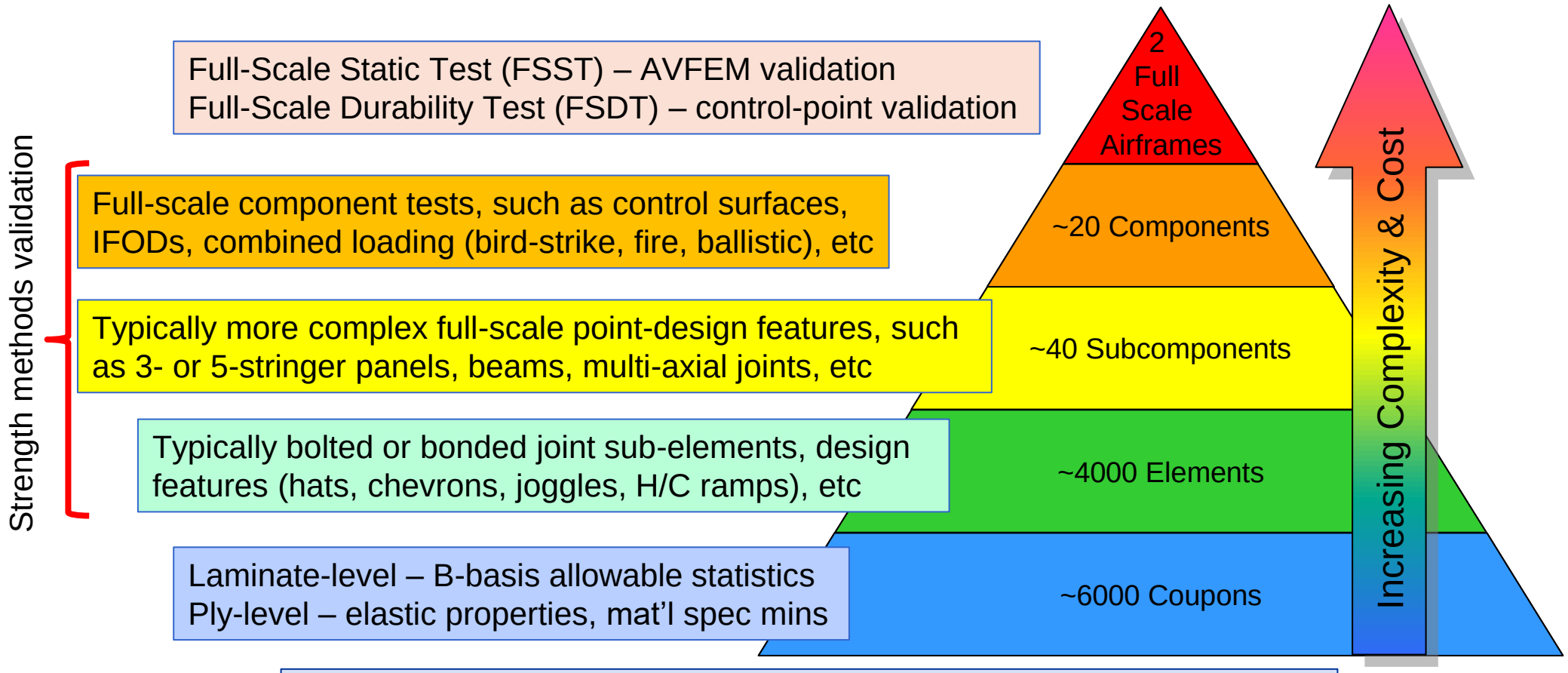

2024: cut all these qty's in half (or more if using legacy data)

©2025 Lockheed Martin Corporation. All Rights Reserved

Airframe Design, Analysis, and Certification Process

Building-Block Certification Logic:

From McSwiggen/Burt ASIP paper (2009)

Structure Design Criteria (SDC)

Define Strength Requirements

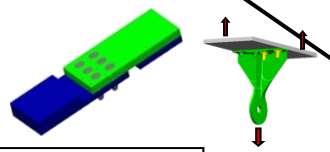

Coupon and Element Tests Generate Allowables for Critical Environments, Failure Modes, Effects of Defects, etc

B-basis allowable statistics

20% metal
40% composite
40% hybrid/other

Flexible span

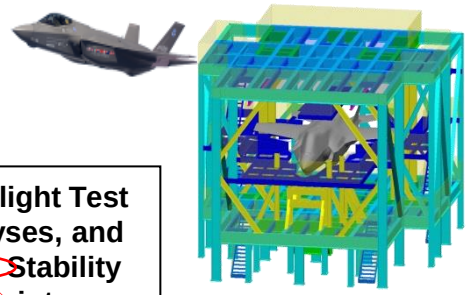

Full Scale Ground and Flight Test Verifies Structural Analyses, and demonstrates Strength, Stability and Loads for critical points on the envelope.

True for civil, less-so for military

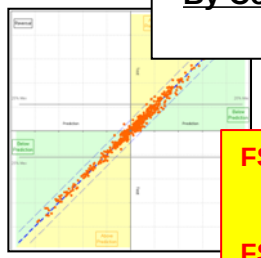

Structural Loads, Models, Methods and Analysis Validated By Comparison to Test Measured Data

FSST = AVFEM internal loads validation

FSDT = DaDT control point validation

Structure Certified for Full Envelope Flight



Airframe Strength is Certified Based on Final Strength Analyses That Incorporates Final Allowable Flight Loads, Validated Internal Loads Models & Stress Analysis Methods

See later chart

Certification by Analysis *(25k load cases)*, ***Supported by Test*** *(a few-100 sub-element configurations to validate strength methods)*

Sub-element data often from legacy programs

©2025 Lockheed Martin Corporation. All Rights Reserved

Airframe Design, Analysis, and Certification Process

Building-Block Certification Logic, Composite Stress Methods:

- **Buckling Ratios-To-Requirements (not failure):**
  - **Linear Eigenvalues**
  - **Snap-Thru (nonlinear)**
- **Typical composite mid-bay MS's:**
  - **FHT/FHC for durability/repairability**
  - **Damage Tolerance MS only if fracture-critical (civil different, see later chart)**
- **Typical land MS's:**
  - **Bearing/by-pass**
  - **Bolt strength**
  - **Pull-thru**
  - **Interlaminar shear (ILS) - beam-shear, pressure, and/or heel-toe induced stress**
- **Edge-of-Part Notch MS's:**
  - **UNT/UNC at characteristic distance**
- **Hat (or similar features, like free flange) MS's:**
  - **Crippling**
  - **ILT/ILS in corners**

Main objective of point stress analysis is to predict the *absence of failure*; not failure.

Thus, accuracy can be traded against simplicity/cost/span.

Examples of conservative deterministic rules which allow reduced cost/span:

- *Top-of-scatter loads, lower-bound strengths;*
- *1.50*DLL static factor of safety;*
- *Assume presence of damage;*
- *Design for 2+ lifetimes;*
- *No detrimental deformation at 1.15*DLL;*
- *No load redistribution;*
- *No damage growth (in composites);*
- *Fibers in (0/45/90) & stacking limited to 3 plies of same orientation*
- *Etc.*

©2025 Lockheed Martin Corporation. All Rights Reserved

Airframe Design, Analysis, and Certification Process

Building-Block Certification Logic, Composite Allowables:

Why Notched-Strength Design Allowables Are Prevalent:

- *Enables much-reduced development cost/span relative to more-complex alternatives*
- *Accounts for typical manufacturing and design realities*
  - *Bag surfaces*
  - *Ply drops*
  - *Slight in-plane and out-of-plane fiber waviness*
  - *Fiber orientation deviation from design*
  - *Small inclusions / resin rich areas*
- *Allows for bolted repair*
- *Covers nuisance durability level damage criteria (“6 ft-lbs”)*
- *Covers fatigue endurance (for fixed-wing airframe structures with modest ILS/ILT stresses)*
- *Usually covers DoD clearly-visible damage criteria*
  - *HW FHC or OHC < (1.5/1.15) x CSAI*
- *Caution – moving away from a notched-strain-controlled design would bring many of these items back into play*

Main objective of point stress analysis is to predict the *absence of failure*; not failure.

©2025 Lockheed Martin Corporation. All Rights Reserved

Airframe Design, Analysis, and Certification Process

Building-Block Certification Logic, Composite Stress Methods:

Element / Sub-Component / Component-Level Testing

Required for Strength-Prediction Methods Verification/Validation

- *Composite Sub-Component-Level Examples:*
  - *CS&E Skin/Spar Joints*
  - *H/C Ramp Termination*
  - *Skin Joggles*
  - *Hat Run-out*
  - *Pi-Preform Joints*
  - *Chevron Notches*
  - *Flange Bending*
  - *Bullnoses/Blade-seals*
  - *Seal-grooves*
  - *Repairs*

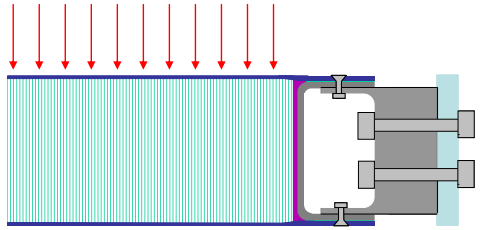

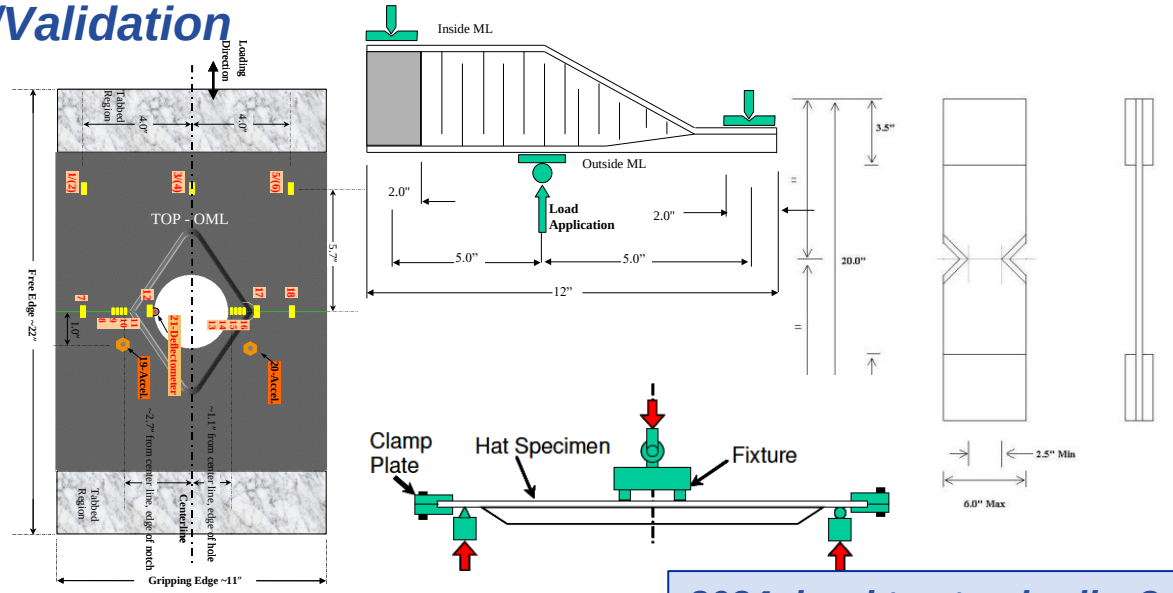

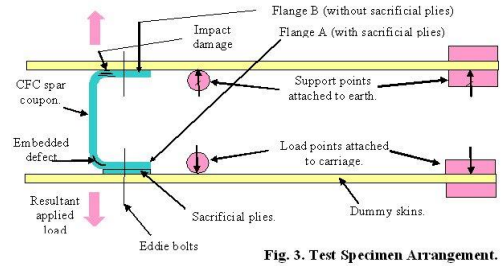

Fig. 3. Test Specimen Arrangement.

2024: hard to standardize?

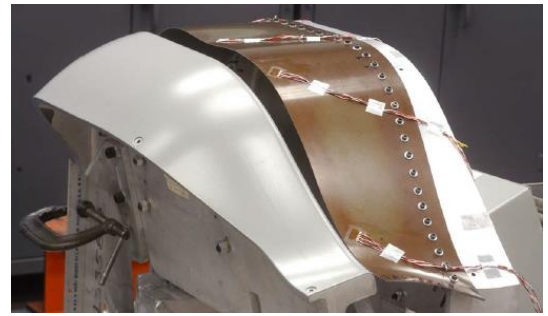

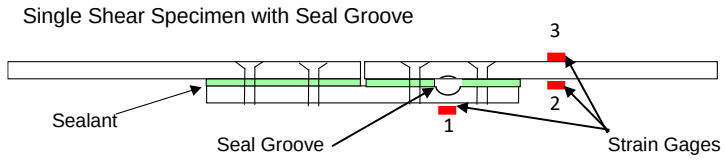

©2025 Lockheed Martin Corporation. All Rights Reserved

LOCKHEED MARTIN

Ramifications for Air System Risk vs. Efficiency

Overall Air System Priorities vs Airframe Cost/Performance:

Global Lessons Learned

- **Large programs must aggressively manage risk**
  - *Overall risk divided into small increments (IPTs)*
  - *Long term benefits of advanced technology may conflict with near term program requirements*
  - *Difficult to capture costs of advanced technology developments in estimation process for new programs*
  - *As cost estimates are refined, design decisions often favor mature technology*
  - *System level cost considerations may over-rule local performance benefits*
- **Recognize that risk management – not technology insertion – is the paramount issue on large programs**
- **Risk adjusted return on investment has to be >> 1**
- **Technology Transition must address:**
  - *Production-friendly methodology gap*
  - *TRL gap*

©2025 Lockheed Martin Corporation. All Rights Reserved

Ramifications for Air System Risk vs. Efficiency

Composites vs. Metals for Various Airframe Components:

Wings

- *Most clean-sheet designs now sport composite wing skins (big, contoured, tailored stiffness).*
- *Spars are also often composite – due to thermal-mismatch for long wings – except for tactical fixed wing aircraft with a ballistic survivability requirement (need metal flanges that yield under hydraulic-ram loading).*
- *Ribs, shear clips, etc often still metal due to small size, min-gauge, and complex shapes.*

Fuselages

- *Design constraints vary widely by application and size … "loads tell you what mat'l part wants to be made from".*
- *Skins most likely to be composite (min-gauge and post-buckling inhibit composite usage).*
- *Frames rarely composite, due to min-gauge and complex shapes (braided RFI 787 frames a notable exception).*
- *Keel beams and fighter carry-thru bkhds almost always metal (most complicated shapes, min-gauge, highly post-buckled)*

Empennages

- *Almost all-composite for weight/CG/dynamic reasons.*
- *H/C control surfaces have given composites bad reputation for poor reliability.*

©2025 Lockheed Martin Corporation. All Rights Reserved

Certification/Qualification of New Materials

- **For successful transition of structural materials**
  - *Must have a good set of generic notched laminate allowables ready when program requests the material*
  - *Recently projects are satisfying this need, and thus new material transition story is getting better*
  - *We don't need new cert/qual guidance*

2024: please stop all the "virtual allowables" nonsense!

- **LM Aero opinion - all ~~multi-functional~~ materials in use today only have non-structural applications**

2024: multi-functional = nano

  - *Since non-structural, then cert/qual not truly an issue*
  - *Thus, no need for special cert/qual plans for these materials*
- **Would we like to speed up the qualification process for new materials?**
  - *Yes, however understand that in the big picture, the material qualification funding is small relative to the large-scale certification tests performed on an SDD aircraft*

2024: still can't beat IM7/977-3 and/or IM7/5250-4 tape… if we ever got better mat'ls, qualifying them and generating design values is no big deal.

©2025 Lockheed Martin Corporation. All Rights Reserved

Back-Up Charts

©2025 Lockheed Martin Corporation. All Rights Reserved

Airframe Design, Analysis, and Certification Process

Building-Block Certification Logic, Internal Loads-Development:

- *Performed by FEM specialists at Air-Vehicle-level and IPT stress analysts at assembly- and component-levels.*

•STOVL aircraft structure is modeled and solved in numerous configurations based on parameters specified for any given load condition:

- **Positions of Control Surfaces**
- **Positions of Doors**
- **Positions of Landing Gear**
- **Engine Types**
- **Weapon Adapter Types**
- **Access Panel Stiffness Assumptions**

Cost/span = approximately 18 man-years over 9 months (industry average)

2024: opportunities for simplification/automation

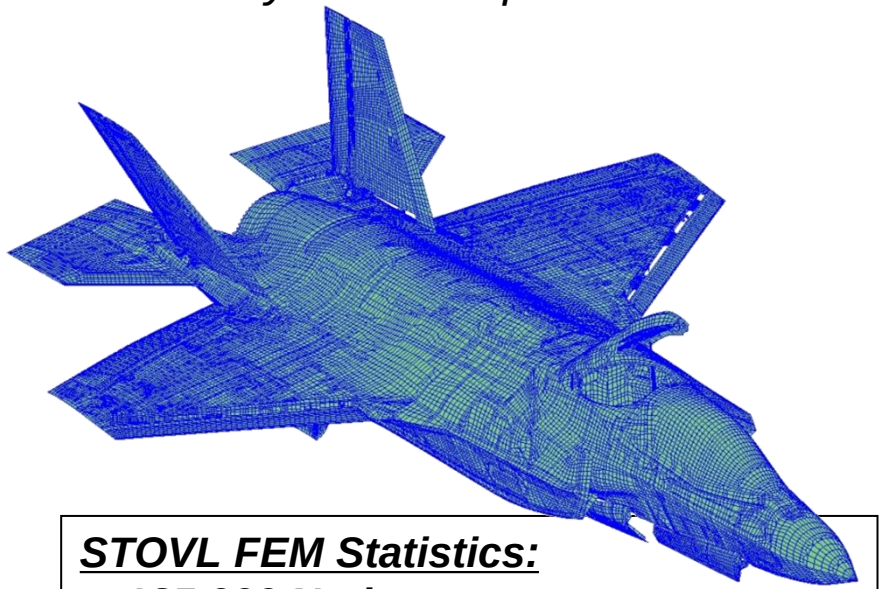

STOVL FEM Statistics:

- **185,000 Nodes**
- **260,000 Elements**
- **1,100,000 Degrees of Freedom**
- **26,194 Load Conditions**
- **2300 Configurations of Control Surface, Door and Gear Positions.**

Element Topology:

- **Skins, floors and webs modeled with SHELL elements.**
- **Stiffeners modeled with shell elements if the cross section is wide compared to its length and the resulting shell aspect ratios are acceptable, otherwise BEAM elements are used.**
- **3D (SOLID) elements are used for core applications and other areas where volume is significant as compared to surface area.**

©2025 Lockheed Martin Corporation. All Rights Reserved

Airframe Design, Analysis, and Certification Process

Building-Block Certification Logic, Internal Loads-Development:

- *IPT stress analysts build/run multiple fine-grid FEMs (fgFEMs) at assembly- and component-levels.*

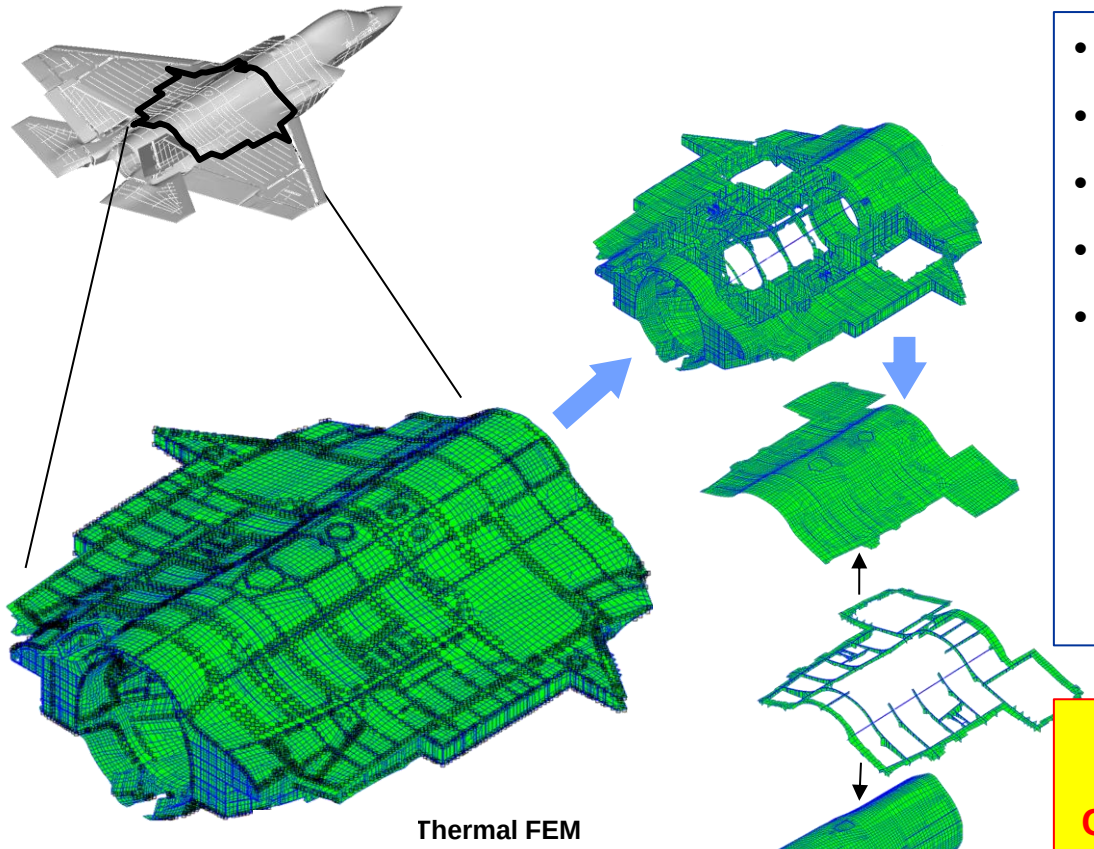

Hybrid metal-composite thermal loads captured by springing skins off sub-structure

- **Refined meshes yield FEMs with as many/more DOF than AVFEM**
- **Linear buckling always checked**
- **Non-linear response often also done (fuel pressure, snap-thru, etc)**
- **Fastener locations modeled with beam elements**
- **Element groups used to define mid-bays, lands, stiffeners, etc**
  - **Composite point stress analyses batch-post-processed for mid-bays, notch features, and each bolt location (not done w/in FEM) – very efficient**
  - **Metallic point stress analyses done in semi-automated manner using spreadsheets**

Generally (not for specific structure shown)

Cost/span (stress ONLY) = approximately 1-3 man-months/part over 12 months

Span = 70% FEM-building, 30% batch-generation of MS's & report-writing

©2025 Lockheed Martin Corporation. All Rights Reserved

Airframe Design, Analysis, and Certification Process

Building-Block Certification Logic, Composite Stress Methods:

Element / Sub-Component / Component-Level Testing

Required for Strength-Prediction Methods Verification/Validation

- *Component-Level Example: Rudder Static and Fatigue Tests*
- *Overall:*
  - *Empirical verification/validation required for all failure criteria, so high-fidelity (e.g., expensive to develop/install/train/use in both cost and span) failure models don't start saving test-costs until at least their second use … but many features are design-specific.*
  - *Best cost/span solution is thus to use simple failure criteria with empirical correction factors.*
  - *These BBT levels also used to demonstrate certification requirements such as "no delamination growth", residual strength-after-damage, fail-safety, etc.*

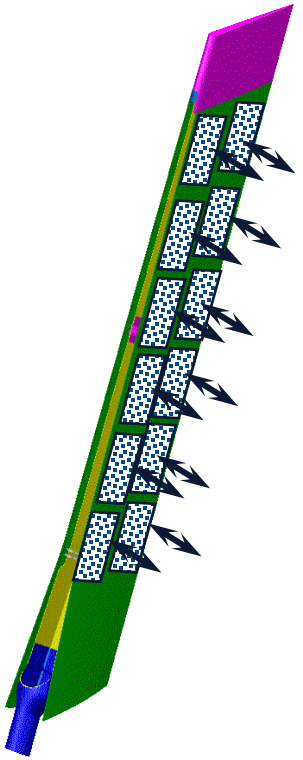

2024: typically, this testing does not impact development span due to time req'd to build full scale test articles

©2025 Lockheed Martin Corporation. All Rights Reserved

Airframe Design, Analysis, and Certification Process

Composite and Metallic Damage Tolerance:

Very Cursory Overview (much has been done/written on this)

- FAA Part 25.571 and JSSG-2006 section 3.12 differ in certain details.
  - Terminology – fatigue vs durability
  - Load levels – 1.50*DLL vs Pxx*DLL (Pxx usually 1.05-1.15)
- General requirement to maintain adequate residual strength in the presence of defects and damage until detected is similar for civil and military, and independent of material.
- Means of *compliance* with this requirement differs significantly between metals and composites.
  - Physics of damage initiation and growth is very different in metals vs composites.
  - Metals exhibit self-similar fatigue crack initiation/growth from intrinsic flaws, but static strength is still adequate (*thus DT compliance demonstrated via FCGR fatigue life prediction and critical crack-length determination*).
  - Composites exhibit diffuse matrix cracking/delamination, and significant/sudden loss of static strength due to in-service delamination damage, but little/no loss of fatigue life (*thus DT compliance demonstrated via residual-static-strength-after-damage strain limit*).

Damage Tolerance requirements are material-independent.
Means of compliance with requirements are not.

©2025 Lockheed Martin Corporation. All Rights Reserved

LOCKHEED MARTIN

Airframe Design, Analysis, and Certification Process

Composite and Metallic Damage Tolerance: *Differences in FAA and DoD*

Similar to JSSG "Durability"

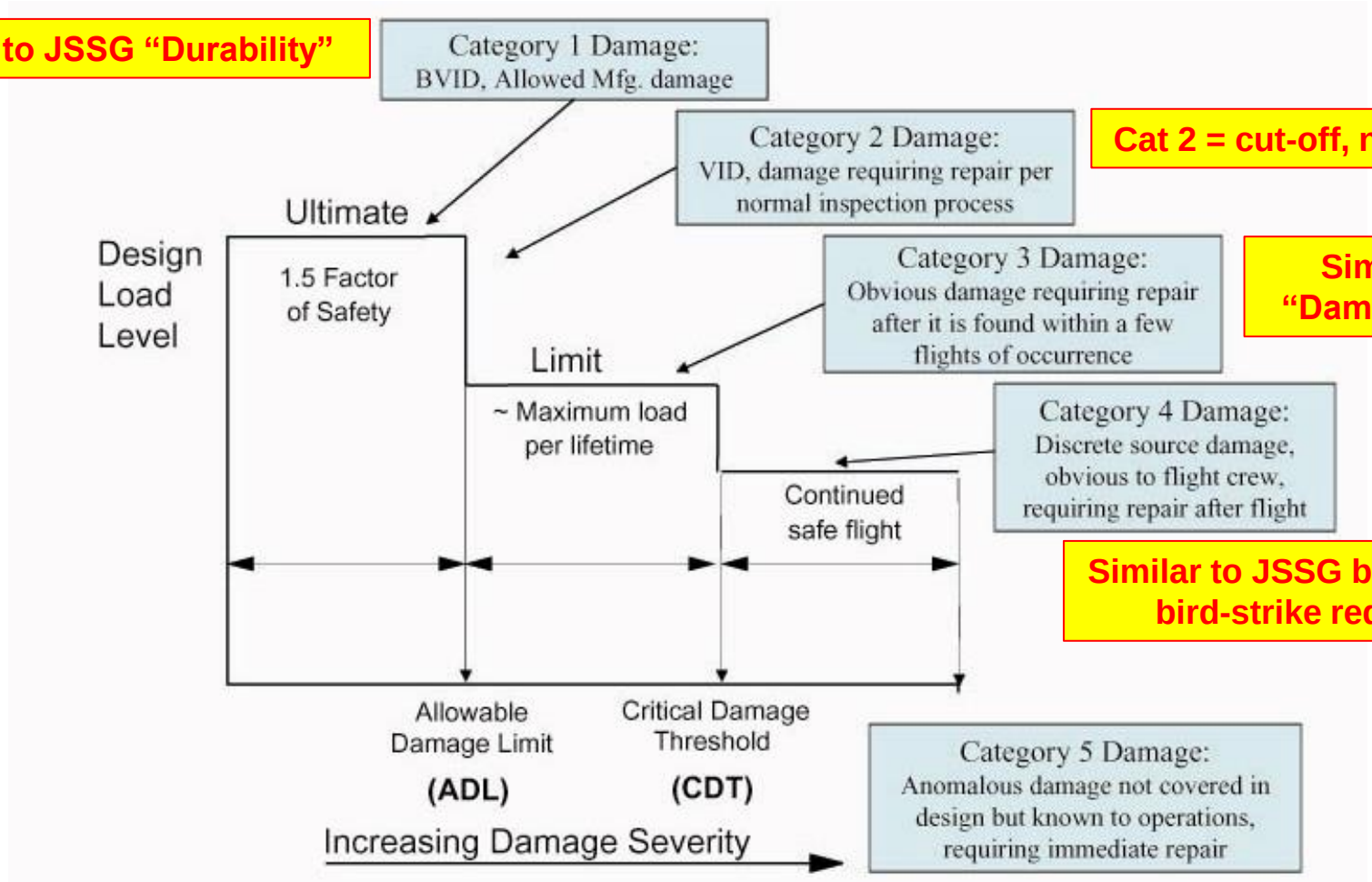

Cat 2 = cut-off, not range

Similar to JSSG "Damage Tolerance"

Similar to JSSG ballistic & bird-strike reqmts

Schematic diagram showing design load levels versus categories of damage severity

©2025 Lockheed Martin Corporation. All Rights Reserved

Ramifications for Air System Risk vs. Efficiency

Overall Air System Priorities vs Airframe Cost/Performance:

Air System vs. Airframe

- *Air System includes Air Vehicle (Airframe, Vehicle Systems, Mission Systems, Software), Production Operations, Logistics/Support, Supply Chain Mgmt (at least).*
- *Airframe is often the least-costly (and thus least-important) of the broad management areas noted above, so Program managers are often dis-inclined to accrue risk on the airframe.*
- *Of all the above-noted areas, airframe is also often the most mature technology.*
- *Airframe Cost vs Weight*
  - *Weight-savings can generally only be realized during development when big bones are designed/sized (research only helps new programs).*
  - *Non-recurring cost savings in certification and tooling also only accrue in the development phase.*
  - *Recurring cost-savings, however, can be implemented throughout the lifecycle of existing Programs, and positively influence Prod Ops, Logistics, and SCM.*

Airframe is not biggest driver in Air System cost/performance

Significant R&D has been directed at Airframe recurring cost savings in recent time, but little toward weight-saving performance improvements

Airframe technology must be better, faster, AND cheaper (not just 2 of 3)

©2025 Lockheed Martin Corporation. All Rights Reserved

Ramifications for Air System Risk vs. Efficiency

Composites vs. Metals for Various Airframe Components:

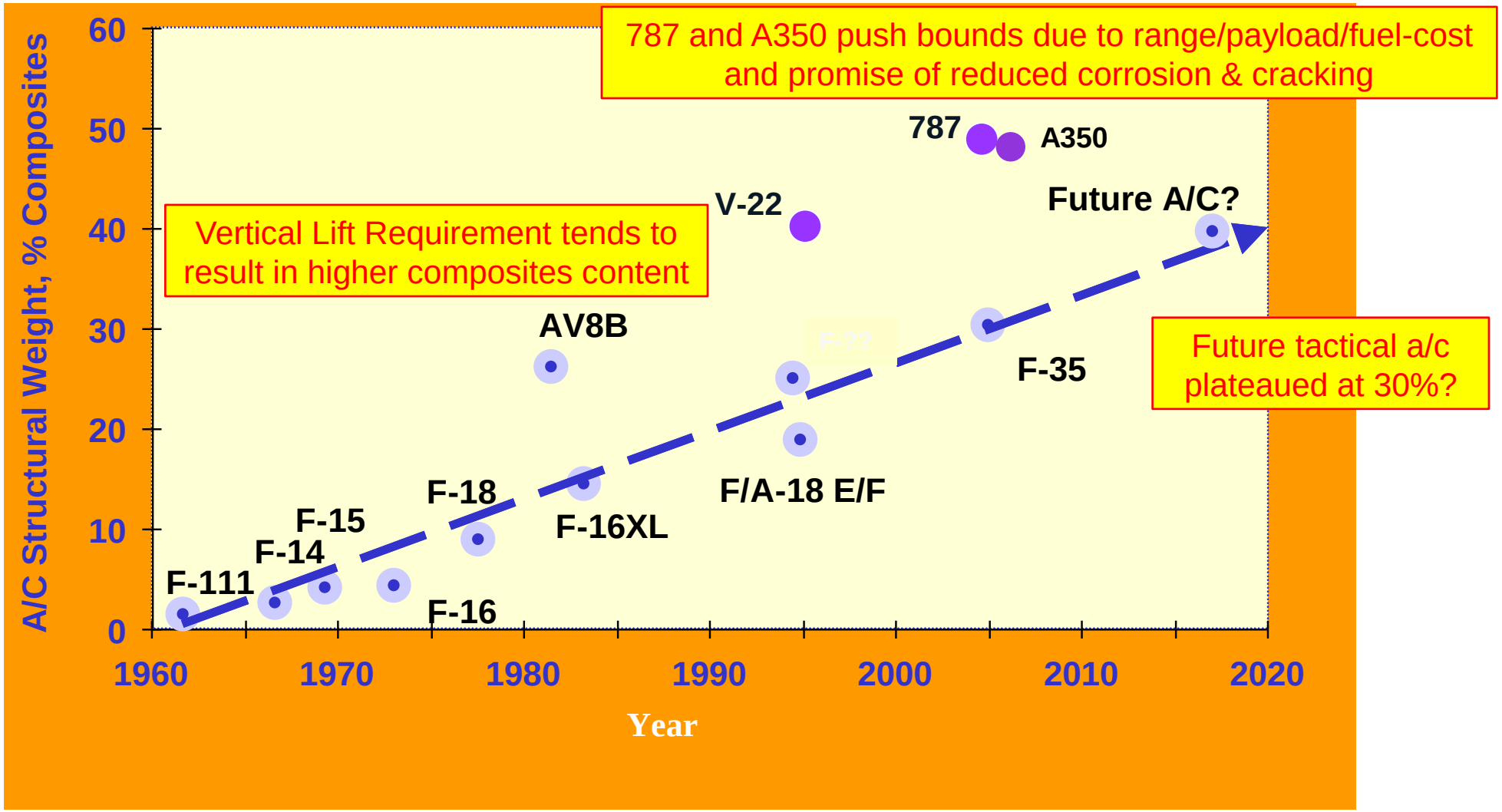

©2025 Lockheed Martin Corporation. All Rights Reserved

LOCKHEED MARTIN

Ramifications for Air System Risk vs. Efficiency

Composites vs. Metals for Various Airframe Components:

Metals

- *Despite forgings being the longest-lead item of all, and DaDT-based design allowables strain-limiting the composite skins, Ti-6V-4Al and 7050 are still preferred for most complex parts.*
- *Metal parts are easier to "tweak" after initial design release (add stiffeners, change radii, etc).*
- *Steeper ramps, far better flange-bending capability, and thinner min-gauge make metal sub-structure parts lighter than the same part designed/built with composites (plus they are cheaper/faster to design/build).*

Composites

- *In-plane fatigue endurance limit above 0.67*F_{UNC}, so generally considered to have infinite fatigue life.*
- *More sub-element strength validation required for composites, than for metals (despite uncertainty in decades-old metallic empirical factors and MIL-HDBK-5 allowables).*

2024: some structure is just hard to make stiffer and stronger out of anything but Al or Ti.

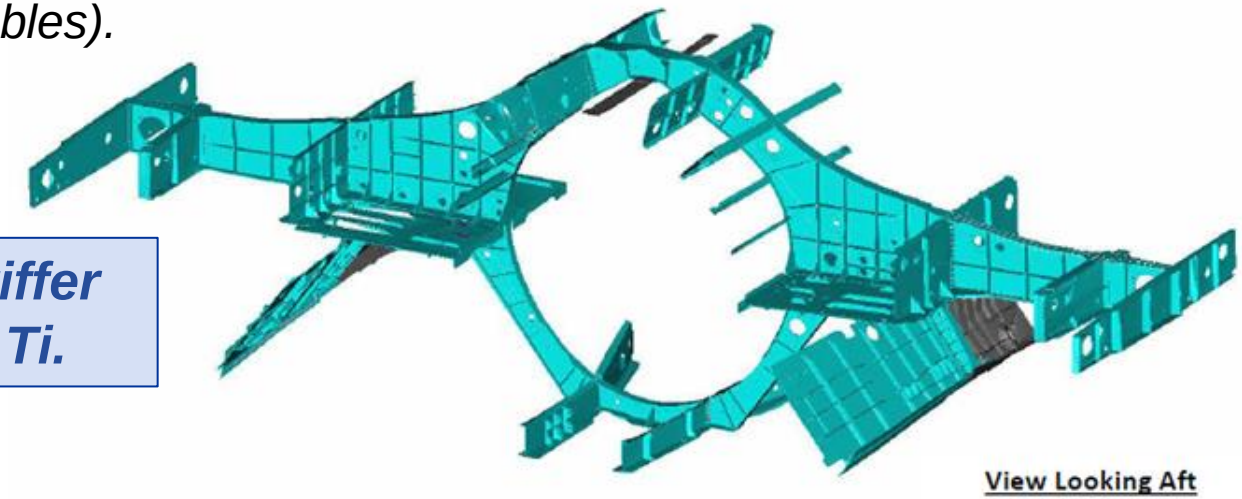

©2025 Lockheed Martin Corporation. All Rights Reserved

Ramifications for Air System Risk vs. Efficiency

Composites vs. Metals for Various Airframe Components:

Improved Materials?

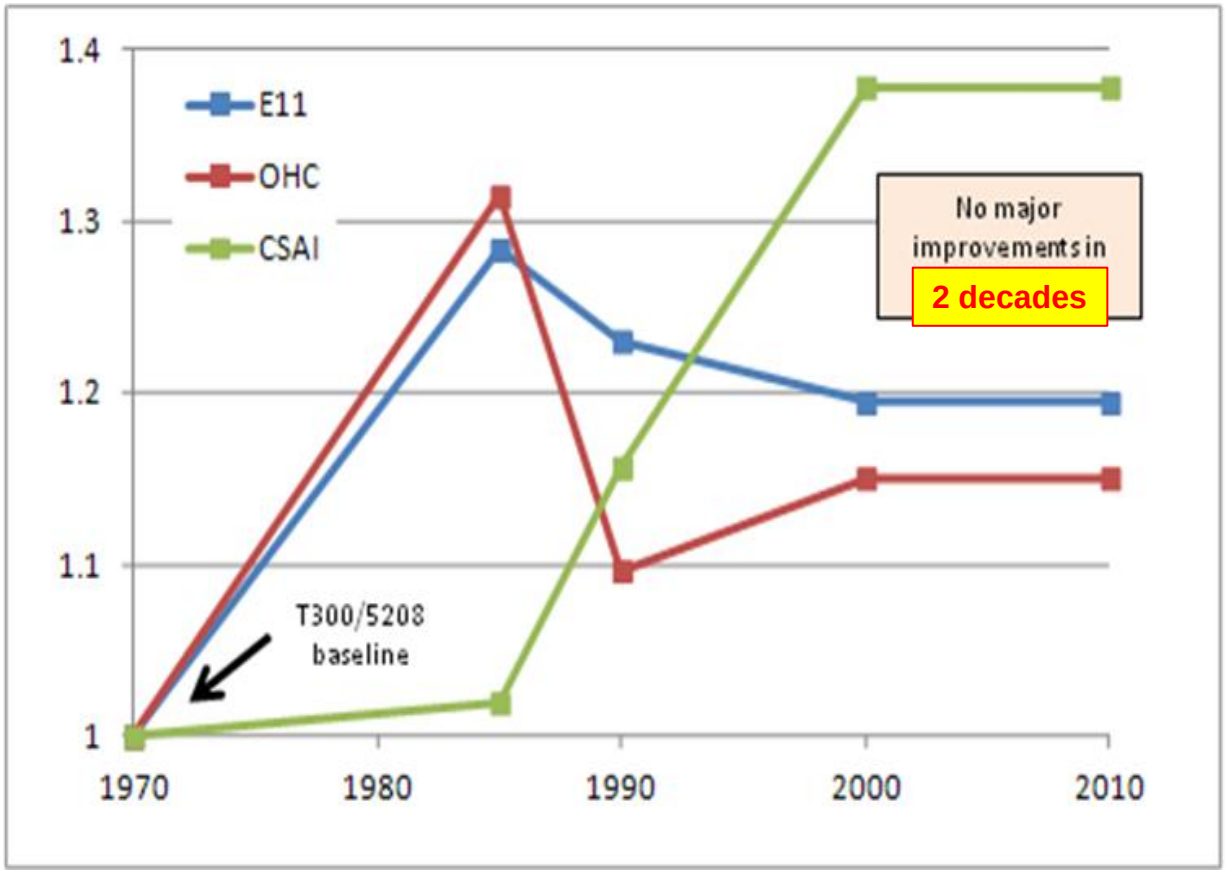

Normalized Carbon/Epoxy Stiffness and Strength vs. Time

- **Aerospace grade carbon/epoxy has seen one 20 – 30% improvement in stiffness (the change from standard- to intermediate-modulus fiber) over 30 years ago**
- **Steady, dramatic improvement in Compression Strength After Impact (CSAI) (at a given impact energy level) since the mid-1980's**
  - *CSAI (damage tolerance) improvement came at the expense of Open Hole Compression (OHC) strength and axial modulus (E11)*
  - *OHC strength decrease is due to tougher resins not allowing as much beneficial matrix cracking to blunt the stress concentration due to the hole*
  - *E11 decreased as resin content was increased in order to improve processability and impact damage resistance*

2024: will there ever be any breakthrough to increase CFRP tape F11cu (kink band)?

©2025 Lockheed Martin Corporation. All Rights Reserved

Ramifications for Air System Risk vs. Efficiency

Composites vs. Metals for Various Airframe Components:

Improved Materials?

- **Perhaps the toughest challenge for industry and academia is how to simultaneously improve both fiber-direction stiffness and compressive strength**
  - **Reduction in compression strength with increased fiber modulus is due to a change in failure mode from**
    - *Microbuckling in PAN-based intermediate-modulus (IM) fibers to*
    - *Fiber compression and/or interface failure in PAN-based high modulus (HM) fiber and*
    - *Transverse splitting in pitch-based ultra-high modulus (UHM) fiber*
- **Thus, it is obvious that research into increasing HM fiber compressive strength is necessary if significant gains in practical weight efficiency of composite structure are to be realized**

2024: can Boron fiber and/or HyBor hybrid mat'l be cost-competitive?

©2025 Lockheed Martin Corporation. All Rights Reserved

Ramifications for Air System Risk vs. Efficiency

Composites vs. Metals for Various Airframe Components:

Improved Materials?

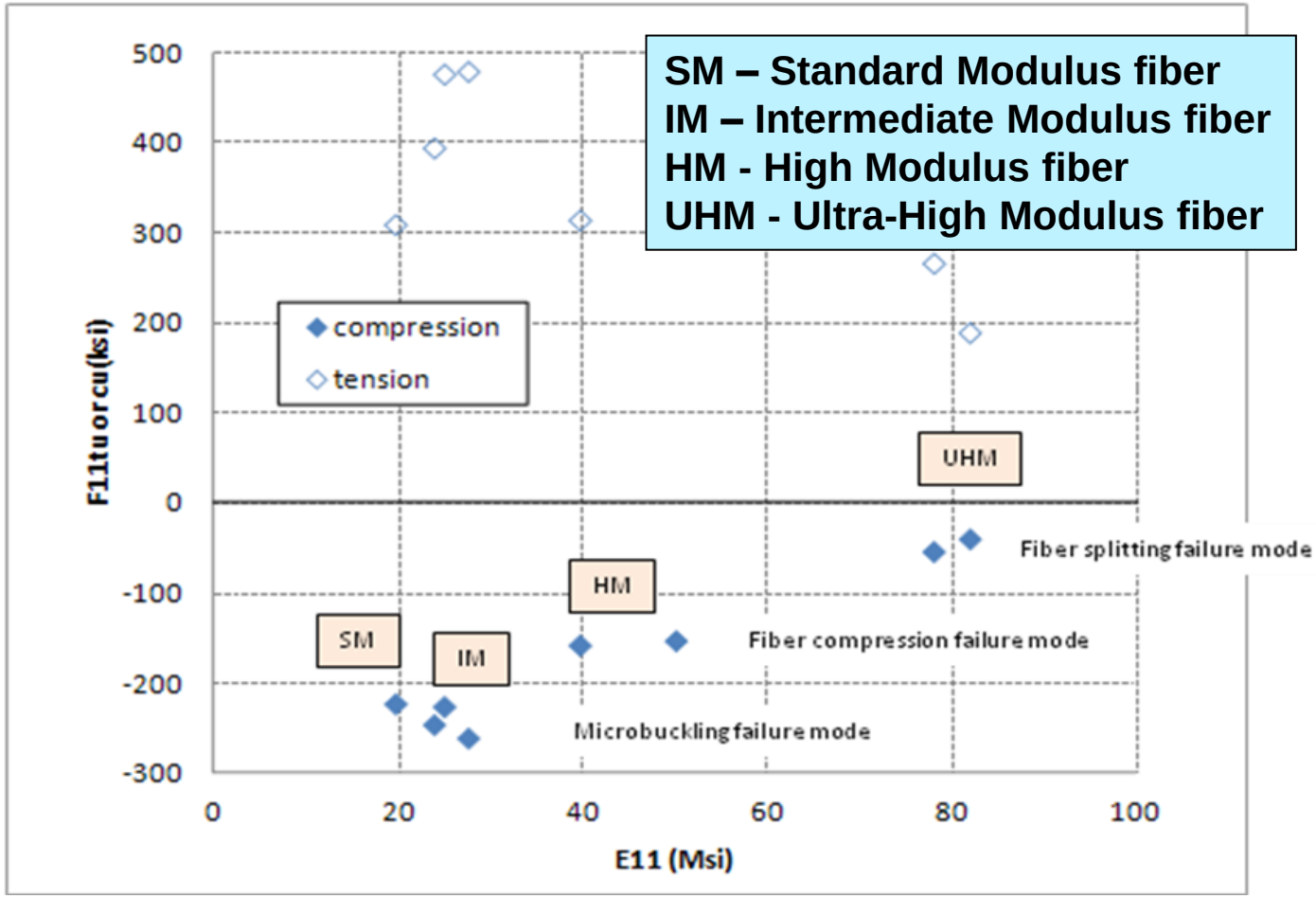

Fiber-Direction Carbon/Graphite Tape

Compression/Tension Strength vs. Modulus

- *Carbon/graphite fiber technology development has yielded no practical improvement in intermediate-modulus fiber for the past 20+ years*
- *For today's HM fibers, tensile strength is reduced and, most importantly to airframe designs, compression strength goes down drastically*
- *OEM's have generally failed to devise ways to take advantage of high-stiffness/low-strength carbon fibers in local applications (e.g., spar caps, panel breakers, etc)*
- *"low cost" low performing carbon fibers offer very little benefit for aircraft primary structure*

©2025 Lockheed Martin Corporation. All Rights Reserved

LOCKHEED MARTIN

Ramifications for Air System Risk vs. Efficiency

Composites vs. Metals for Various Airframe Components:
Improved Materials?

- **CSAI increase may or may not increase damage tolerance (BVID or CVID) allowable strength, depending on the certification criteria being imposed**
  - **Dents are more visible in certain brittle resin systems, and thus can lead to lower impact energies and higher effective CSAI strengths than for "tough" resins**
  - **Differences in civil and military damage tolerance requirements (1.5*DLL vs Pxx*DLL) have led to**
    - *Use of very tough resin systems in recent civil aircraft designs (at the expense of hot/wet OHC strength)*
    - *Military applications continue to use older less-tough resin systems since CSAI does not size as much structure as does bolted joint strength, which is related most closely to OHC strength*

2024: is there a better damage tolerance criteria than BVID/CVID/dent-depth?

©2025 Lockheed Martin Corporation. All Rights Reserved

Ramifications for Air System Risk vs. Efficiency

Overall Air System Priorities vs Airframe Cost/Performance:

Global Lessons Learned Resulting from Legacy Composite R&D Efforts

- **Industry Conservatism Manifests Itself in:**
  - *Flight certification process/requirements*
  - *Problem resolution at the technology level*

- **Developmental Gap Between Technology and Program Communities**
  - *Program-critical factors not always realistically captured or accounted for during tech transition (design details, certification cost, design flexibility, subsystem integration)*
  - *Technology community often does not have the funding and/or expertise to develop Production-friendly stress analysis methods (e.g., simple, robust, highly-automated)*
    - *SDD BTP stress analysis must be done at a very fast pace and be performed concurrently by a large number of stress analysts, all of whom cannot be composites experts or 20-year veterans*
  - *Development lead times are long and SDD programs are schedule driven*

    …so program specific developmental work needs to start prior to the SDD funding availability (for both lead time and "buy-in" time)

©2025 Lockheed Martin Corporation. All Rights Reserved

Composite Aircraft Design Drivers

- **Aircraft Skins typically sized by stiffness, strength, buckling, damage tolerance, and repair allowables**
  - *Compression after impact, Open Hole Compression/Tension, Filled Hole Compression/Tension*
- **Joints sized by bearing/bypass, adhesive strength, subelement tests, damage tolerance**
- **Shear webs sized by shear strength, damage tolerance, repair allowables, and buckling**
- **Manufacturing, tooling, processing, QA, and manufacturing-scale-up issues greatly drive composite designs**

2024: determinate ass'y of metallic parts is changing the span and recurring cost metrics for future programs and challenging the continued use of composites

©2025 Lockheed Martin Corporation. All Rights Reserved

Aircraft Structural Integrity Program

Five Factors for Technology Transition

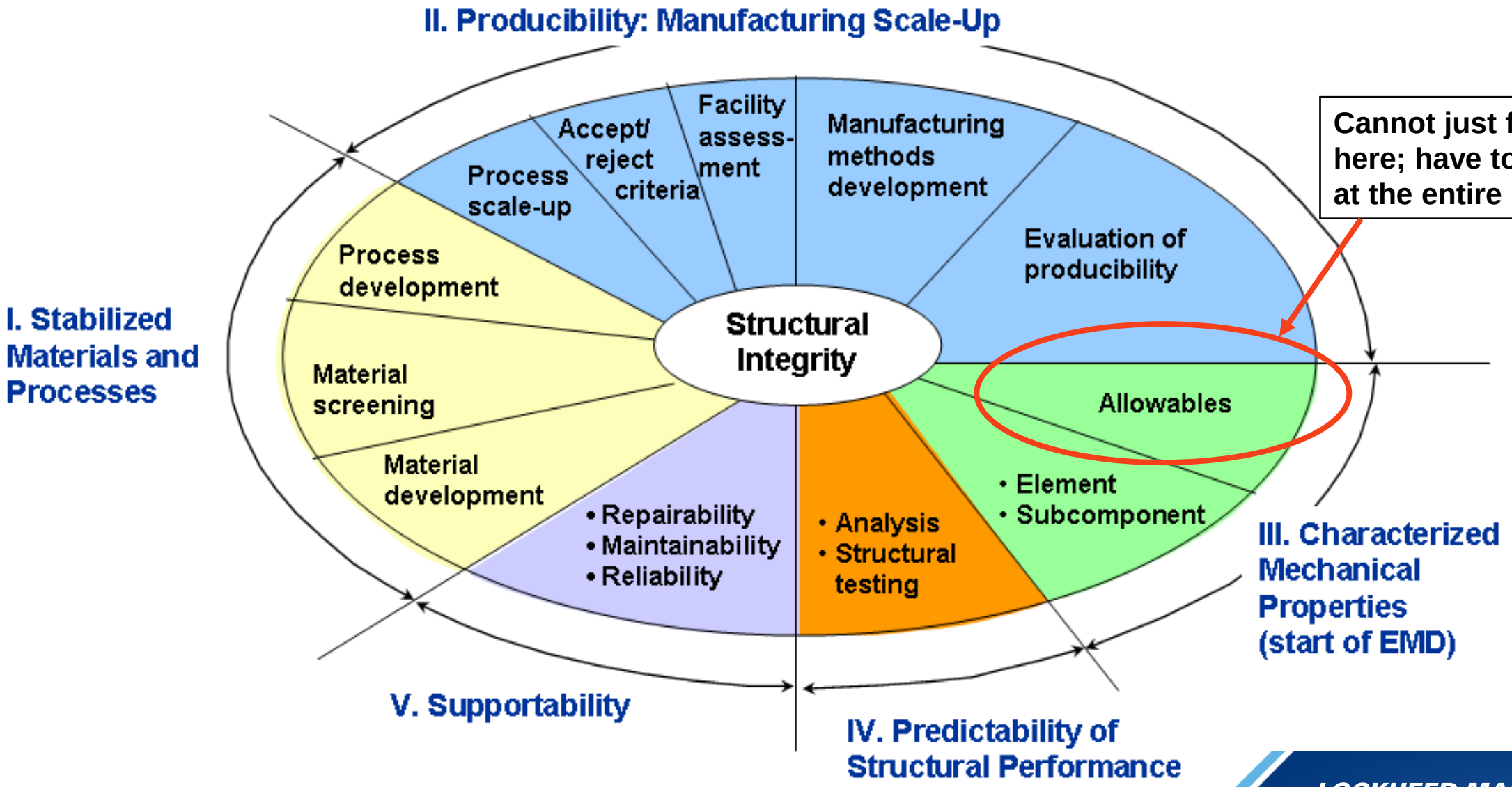

©2025 Lockheed Martin Corporation. All Rights Reserved


LOCKHEED MARTIN

ICCM24
AUGUST 4-8, 2025
BALTIMORE CONVENTION CENTER
BALTIMORE, MARYLAND, USA

No Technical Paper Submission for:

Adam Sawicki

ICCM24
AUGUST 4-8, 2025
BALTIMORE CONVENTION CENTER
BALTIMORE, MARYLAND, USA

No Technical Paper Submission for:

Kyle Wetzel

ICCM24
AUGUST 4-8, 2025
BALTIMORE CONVENTION CENTER
BALTIMORE, MARYLAND, USA

No Technical Paper Submission for:

Cindy Ashforth

ICCM24
AUGUST 4-8, 2025
BALTIMORE CONVENTION CENTER
BALTIMORE, MARYLAND, USA

No Technical Paper Submission for:

Mike Hinton

ICCM24
AUGUST 4-8, 2025
BALTIMORE CONVENTION CENTER
BALTIMORE, MARYLAND, USA

No Technical Paper Submission for:

Sayata Ghose
Isabelle Paris

ICCM24
AUGUST 4-8, 2025
BALTIMORE CONVENTION CENTER
BALTIMORE, MARYLAND, USA

No Technical Paper Submission for:

Ole Thomsen

ICCM24
AUGUST 4-8, 2025
BALTIMORE CONVENTION CENTER
BALTIMORE, MARYLAND, USA

No Technical Paper Submission for:

Takumi Sekino

EXPERIMENTAL AND NUMERICAL STUDY ON THE BENDING BEHAVIOR OF GLASS-FABRIC RUBBER COMPOSITES

Oguz Kagan GENC[1,2*], Fabrice Schmidt[1], Steven Marguet[1], Gilles Dusserre[1], Pablo Navarro[1], Alice Courtois[2], Amina H. Brahami[3], Nathan Selles[3]

[1]Institut Clément Ader (ICA), Université de Toulouse, CNRS, IMT Mines Albi, INSA, ISAE SUPAERO, UT, 3 Rue Caroline Aigle d'Aigle, 31400 Toulouse, France
Web page : https://ica.cnrs.fr

[2]Airbus Operations SAS, 316 route de Bayonne, 31060 Toulouse, France
Web page : https://www.airbus.com/en

[3]Elanova Laboratory, 60 rue Auber, 94408 Vitry-sur-Seine, France
Web page : https://elanova.fr/

Keywords: Elastomer matrix composites, Fabrics, Anisotropic hyperelasticity, Identification, Properties, Computational modelling, Finite element modelling

ABSTRACT

The study mainly focuses on the instantaneous mechanical behavior of glass-fabric rubber composites. Aside from principal-invariant-driven isotropic hyperelasticity, the strain energy contribution of fabric layer to the overall constitutive behavior of the composite can be defined by pseudo-invariant-driven anisotropic hyperelasticity. The approach accounts for the anisotropy of the silicone rubber matrix reinforced by plain-wave glass fabric using pseudo-invariants defined by vectors aligned with the warp and weft directions. Subsequently, the composite specimens with 0- and 45-degree fabric orientations were considered for the uniaxial tensile tests on top of the tests on pure rubber under different modes. The parameters of the analytical models with the above-mentioned approach were then identified from the test results. Moreover, different anisotropic hyperelastic material models were scripted and subsequently implemented into Abaqus using the UANISOHYPER_INV material subroutine. After checking the developed material subroutines with the coupon tests, this paper constructively paves a path to delve deeper into bending behavior of fabric rubber composites with the developed methodology accompanied with 3-point bending tests.

1 INTRODUCTION

Fabric rubber composites have been prominently utilized in industries such as space [1], aerospace [2-4], and automotive [5] due to their great sealing capacity and durability under harsh environmental conditions. In particular to aero-engine seals, the sealing performance is directly correlated to engine performance since they reduce leakage and optimize clearances [6,7]. Sealing of the cooling systems in aero-engines also greatly contributes to the performance by controlling clearances, as seen in Fig. 1 from the Turbine Case Cooling (TCC) seal improvement on High-Pressure Turbine (HPT) tip clearance [7]. An example of TCC seal is also provided in Fig. 2 [8].

On top of the performance contributions of seals, aero-structure seal malfunctioning would result in serious consequences, as highlighted by Shabbir [9]. In the same study, it was noted that a design defect in the knife edge seal of Pratt&Whitney's (P&W) GTF (geared turbofan engine) on Airbus A320neo caused sudden shutdowns during flight or take-off, resulting in a call back of these engines. Similarly, the failure of the Auxiliary Power Unit compressor carbon seal caused oil leakage and subsequent heavy smoke, resulting in the urgent evacuation of the Airbus A330-323 P&W turbofan engine in 2016 at London Heathrow Airport [10]. Besides the substantial benefits of seals on aero-engine performance, seal malfunctioning issues have highlighted how seals play an important role in aircraft. Thus, this study aims to shed light on the macro mechanical properties of fabric rubber composite seals of interest under different deformation modes, providing reliable numerical models to support composite seal design.

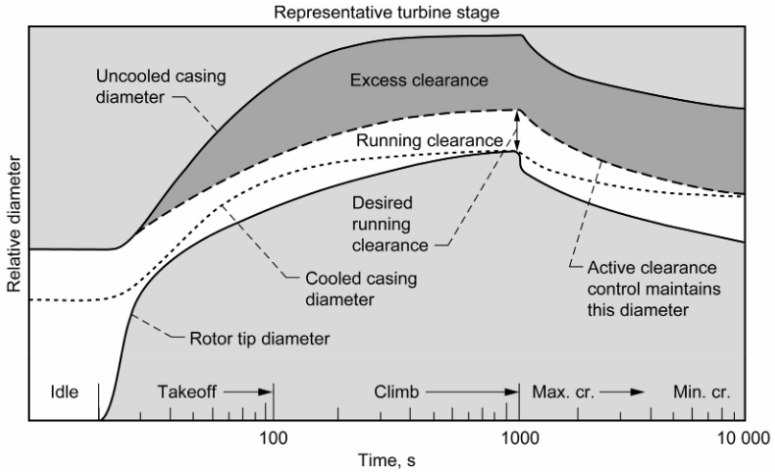

Figure 1: TCC effect on HPT blade tip clearance [7]

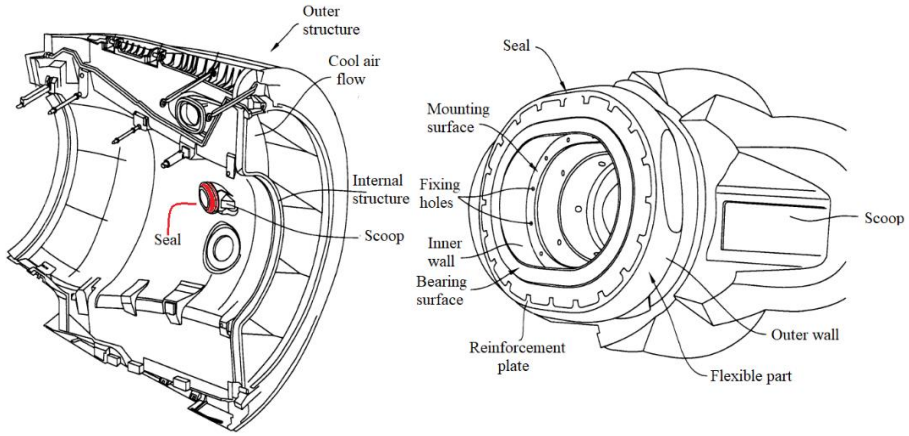

Figure 2: Turbine case cooling seal (left) and zoom on the seal (right) [11]

Fabric rubber composite seals usually include several layers of fabric reinforcement to provide stiffness, fireproofing, and abrasion resistance, as seen from a "P" seal drawing in Fig. 3. Thus, the composite exhibits anisotropic properties on top of hyperelastic, viscoelastic, and Mullins effects [12]. In this study, a set of coupon tests has been performed on pure rubber and plain-wave glass-fabric-rubber composites, accounting for different fabric orientations to characterize anisotropy. In particular, the campaign included uniaxial and equibiaxial tensile tests and uniaxial and planar compression tests for pure rubber and uniaxial tensile tests for composites. Then, the test results of pure rubber are used to identify invariant-based isotropic hyperelastic material models' parameters such as Neo-Hookean [13], Mooney [14]-Rivlin [15], and Ogden [16]. Furthermore, Spencer's theory [17] proposes some pseudo-invariants, based on the principal invariants defined with vectors, to account for anisotropy introduced by fabric reinforcement, analytically estimating the contribution of fabric layer in terms of strain energy. One of the most used anisotropic hyperelastic material models based on Spencer's theory is the Holzapfel-Gasser-Ogden (HGO) [18] model whose strain energy density function is given in Table 1 with other similar models. The material parameters of the anisotropic hyperelastic constitutive models are then identified from the coupon test results of fabric rubber composites. Finally, the anisotropic material models presented in Table 1 are scripted and implemented into Abaqus using UANISOHYPER_INV subroutine. It should be noted that the first parts of the strain energy potentials, i.e., defined by principal invariants, presented in Table 1 belong to isotropic hyperelasticity and the rest of the potential terms to account for fabric contributions.

Since most seals undergo bending deformation to provide sufficient sealing between the counterparts as seen in Fig. 2 from the TCC seal, pointing out that the bending behavior of fabric rubber composites is a crucial validation step in providing reliable numerical models for the composite seals. Hence, an in-

plane driven material identification methodology is developed to account for anisotropy and then implemented into Abaqus. Having preliminary results of bending tests reported, this study paves a path on the future bending behavior studies of fabric rubber composites with the developed methodology.

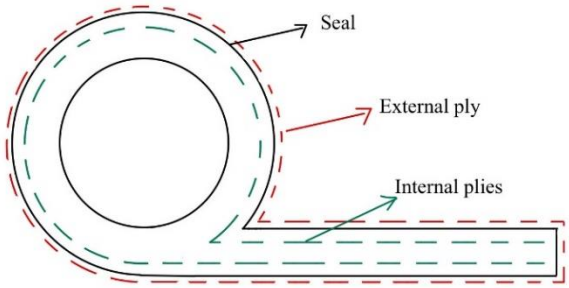

Figure 3: Conventional P-section seal cross-section view

Reference	Strain energy functions
HGO [18]	$W = C_{10}(\bar{I}_1 - 3) + \frac{k_1}{2k_2}\sum_{i=4,6}^{W(I_1,I_4,I_6)} \{\exp[k_2(\bar{I}_i - 1)^2] - 1\}$
Dong et al. [19]	$W = C_{10}(\bar{I}_1 - 3) + C_{01}(\bar{I}_2 - 3) + \frac{k_1}{2k_2}\sum_{i=4,6}^{W(I_1,I_4,I_6)} \left[e^{k_2(\bar{I}_i-1)^2} + \frac{k_2}{4}(\bar{I}_i - 1)^2 - 1\right]$
Gong et al. [20]	$W = C_{10}(\bar{I}_1 - 3) + C_{01}(\bar{I}_2 - 3) + \frac{k_1}{2k_2}\sum_{i=4,6}^{W(I_1,I_4,I_6,I_8)} \left[e^{k_2(\bar{I}_i-1)^2} + \frac{k_2}{4}(\bar{I}_i - 1)^2 - 1\right] + k_3(\bar{I}_8)^2$

Table 1: Constitutive models for fabric rubber composites

2 EXPERIMENTAL CAMPAIGNS

In this section, an experimental campaign is performed to characterize the mechanical behavior of pure rubber and fabric reinforced rubber composite under various loading conditions. In a first step, coupon tests enable to access materials response whereas in a second step, structural behavior is investigated through three points bending tests.

The vulcanized rubber and plain-wave glass fabric was processed at Elanova Laboratory in Paris. A set of moving-die-rheometer (MDR) tests was carried out for the vulcanized rubber subjected to different temperatures as per ISO3417, optimizing the manufacturing process parameters such as vulcanization temperature and duration. The test has revealed that the 100% vulcanization is secured after 20 min under 150°C. Accordingly, 2 mm silicone rubber sheets were vulcanized with a compression moulding setup under 150°C for 20 min while the 3 mm thick composites with one layer of composite sheets were kept 30 min under the same temperature. In addition, a 15 mm thick composite plate with 3 layers of 0.2 mm-thick glass fabric evenly placed through the thickness, keeping the fabric orientations identical for all layers, was also processed within the same setup for 45 min under 150°C. In addition, a different die was utilized to process pure rubber cylindrical specimens to be tested under compression. Lastly, the average density of pure rubber was measured as 1.289 g/cm3, while that of composite was found to be 1.333 g/cm3. Consequently, the processed materials were cut by die whose precision is regularly validated at Elanova laboratory.

2.1 Coupon tests

In order to check that the material model applies to any deformation modes, four different deformation modes in Table 2, i.e., uniaxial tensile (UT) and compression (UC), planar compression (CPL), and equibiaxial tensile (ET), were considered for pure rubber testing campaigns. VMQ represents silicone rubber while CVMQ represents composite silicone. The results of the above-mentioned tests on

pure rubber are plotted in Figure 4. As expected, the responses of the equibiaxial tensile and planar compression are stiffer than that of uniaxial tensile and uniaxial compression, respectively. A small dispersion of the uniaxial tensile test results would be caused by the unidirectional manual mixing procedure of unvulcanized rubber. Overall, the repeatability of the tests, with a small dispersion margin, shows the reliability of the tests.

Initial state	Dimensions and Material	Boundary conditions	Final state
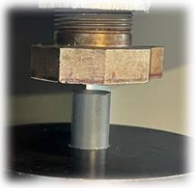	Diameter 18 mm Height 25 mm Pure rubber VMQ	Uniaxial compression (UC) 8 N pre-load 0.25 mm/min loading pace	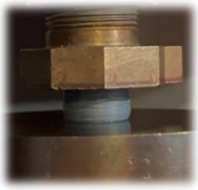
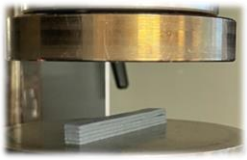	Size 10x10x100 mm Pure rubber VMQ	Planar compression (CPL) 8 N pre-load 0.10 mm/min loading pace	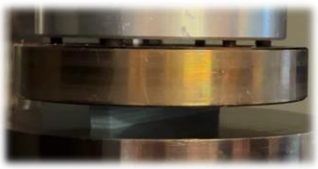
	Size 2x10x60 mm Pure rubber VMQ	Uniaxial tensile (UT) 0.6 N pre-load 0.6 mm/min loading pace	
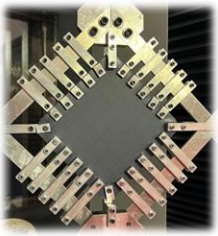	Size 2x110x110 mm Pure rubber VMQ	Equibiaxial tensile (ET) 2 N pre-load 1.10 mm/min	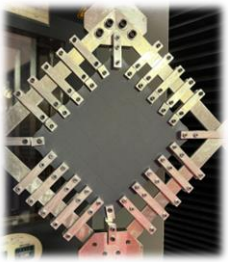
	Size 3x30x180 mm Composite 1 layer of glass fabric (CVMQ) 0 and 45 degree fabric orientations	Uniaxial tensile (UT) 8 N pre-load 1.8 mm/min	

Table 2: Coupon test matrix for pure rubber and composite

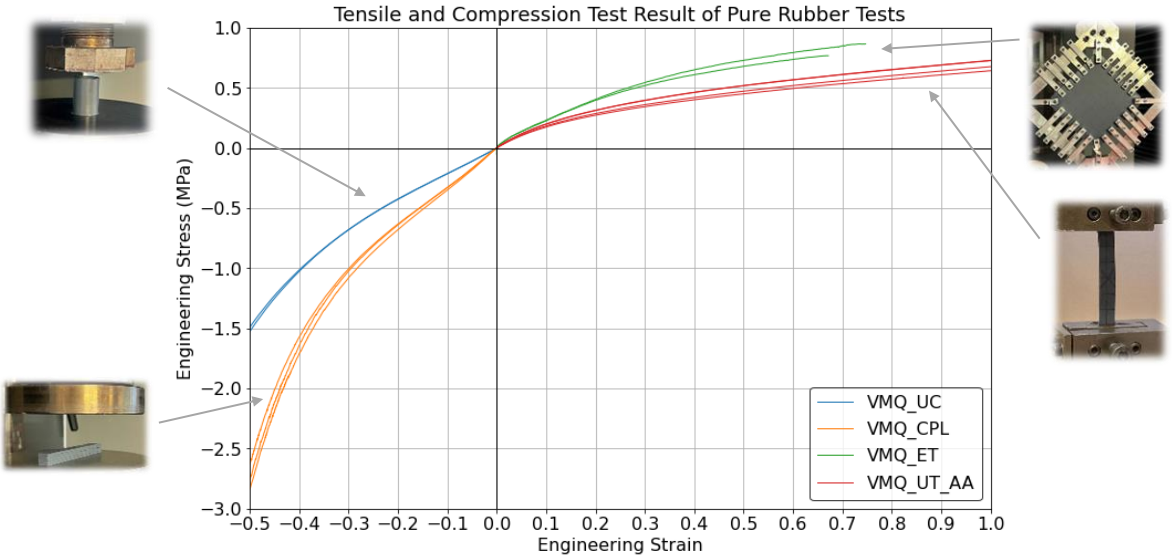

Figure 4: Tests results of pure rubber specimens under various loading conditions

On the other hand, the composite specimens were tested under 2 different fabric orientations, i.e., 0 and 45 degrees, to account for the anisotropy. The initial and final states of the tests as well as boundary conditions and dimensions were shared in Table 2. The test results of the composite with 2 different fabric orientations were plotted in Figure 5 where CVMQ_UT_0 indicates a 0-degree fabric-orientated composite while CVMQ_UT _45 is for 45-degree fabric-oriented composites. It can be clearly seen in Figure 5 that the material is highly anisotropic and non-linear, especially in the 45-degree case where the fabric is free to shear.

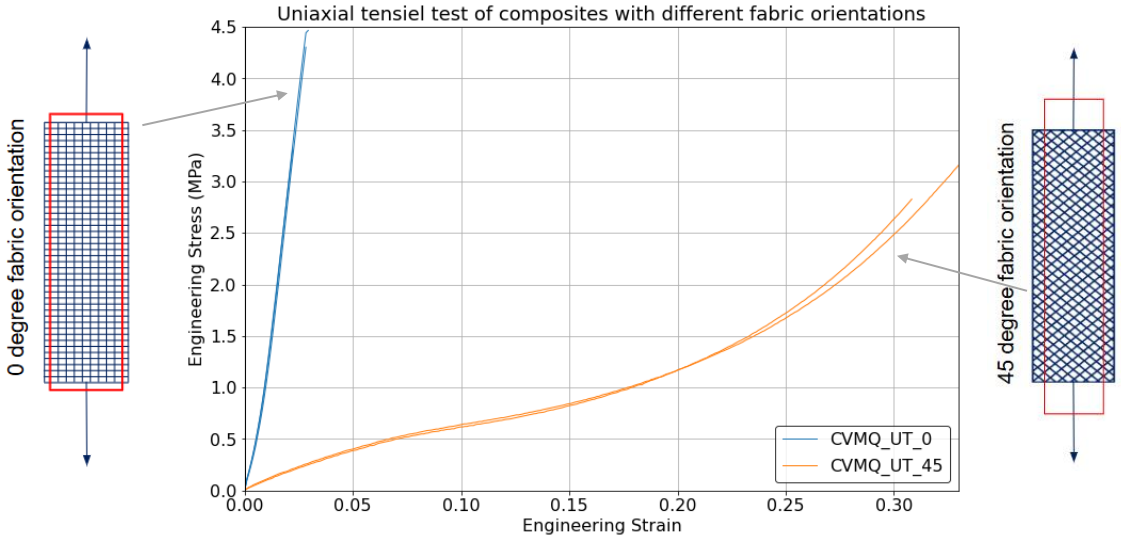

Figure 5: Tests results of composite specimens with one layer of glass fabric

Finally, a set of tests on pure rubber and composite with one layer of glass fabric has been conducted to initiate material modeling process that is going to be detailed in the following sections.

2.2 Three points bending campaign

Three-point bending tests have been carried out on composite specimens that include 3 layers of plain-wave glass fabric whose warp and weft directions are identical in all 3 layers. The experiments consider two different fabric orientations, i.e., 0- and 45-degree fabric orientations according to the axis along the length of specimens. The specimens with the dimensions of 15×15×70 mm were subjected to

0.5 mm/min displacement at the middle of the 50 mm middle span, as illustrated in Figure 6. The specimens were loaded till 6 mm middle displacement and the force output was recorded for each sample. The three point bending test results re plotted in Fig. 7. There is a clear difference between the results with the change of fabric orientation. The maximum load measure at 6 mm mid-span displacement is 37.22 N for the composite with 0-degree fabric orientation while it is 28.37 N for the composite with 45-degree orientation, indicating 30% increased force from 0 to 45 degree orientations.

.

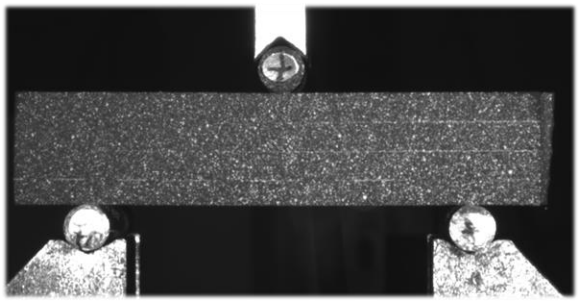

Figure 6: Initial state of 3-point bending test setup of a composite with 3 layers glass fabric

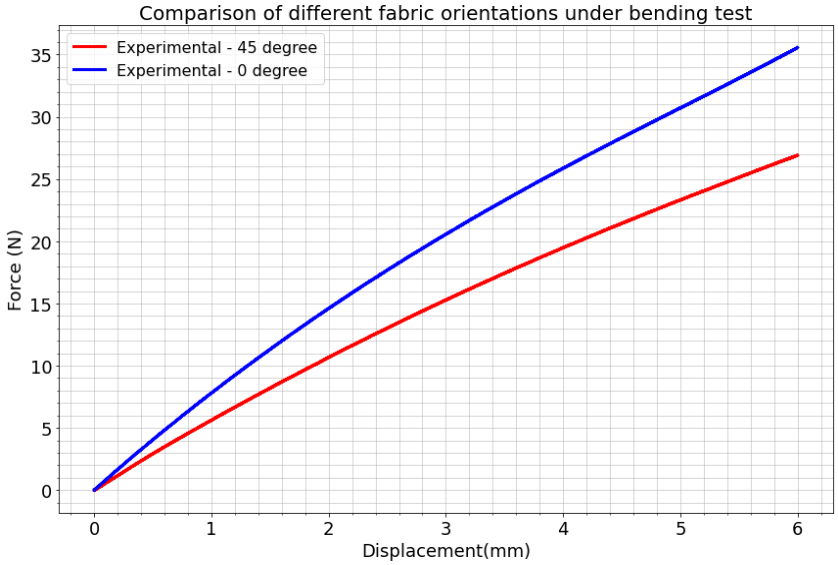

Figure 7: Three point bending test setup of composite specimens with 3 layers glass fabric

3 MODELING STRATEGY AND MATERIAL PARAMETER IDENTIFICATION

3.1 Constitutive model

Cauchy stress tensor can be defined in terms of strain energy as follows

$$\sigma = \frac{2}{J}\boldsymbol{F}\cdot\frac{\partial W}{\partial \boldsymbol{C}}\cdot\boldsymbol{F}^{T} - p\boldsymbol{I} \tag{1}$$

where W is strain energy function, $\boldsymbol{F} = \partial \boldsymbol{x}/\partial \boldsymbol{X}$ is deformation gradient, $\mathbf{C} = \boldsymbol{F}^{T}\cdot\boldsymbol{F}$ is right Cauchy-Green deformation tensor, $J = \det(\boldsymbol{C})$ is compressibility term, p is arbitrary pressure, and $\boldsymbol{I}$ is an identity tensor. The strain energy function W is defined as a function of the principal strain invariants for isotropic hyperelasticity and also as a function of pseudo-invariants to account for anisotropy as follows

$$W = W(I_1, I_2, I_3, I_4, I_6, I_8, I_i) \tag{2}$$

The first three invariants are the principal invariants and are defined as follows

$$I_1 = \mathrm{tr}\mathbf{C}$$
$$I_2 = \frac{1}{2}[(\mathrm{tr}\mathbf{C})^2 - \mathrm{tr}(\mathbf{C}^2)] \quad (3)$$
$$I_3 = \det(\mathbf{C})$$

I_4 and I_6 are the pseudo-invariants that account for fiber stretches in the two fiber directions. Moreover, I_8 is an interaction term that characterizes the interaction between rubber and fabric accounting shearing behavior between materials. The pseudo-invariants are derived from the vector definitions, N and M, aligned with the warp and weft directions of the fabric, on top of Cauchy-Green deformation tensor C. Having two vectors in the directions of two perpendicular fiber families, N and M vector expressions with respect to the Cartesian axes X and Y, are

$$\mathrm{N} = \begin{bmatrix} \sin\alpha \\ -\cos\alpha \\ 0 \end{bmatrix}, \mathrm{M} = \begin{bmatrix} \cos\alpha \\ \sin\alpha \\ 0 \end{bmatrix} \quad (4)$$

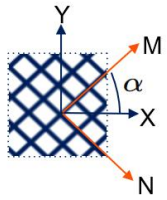

Figure 8: (N, M) vectors used to define the warp and weft directions of the fabric

Finally, based on the above-described vectors and the deformation tensor, the pseudo-invariants are derived with double-dot (:) and dyadic product ($\otimes$) as follows

$$I_4(\mathrm{M}) = \mathbf{C}:\mathrm{M}\otimes\mathrm{M},\ \ I_6(\mathrm{N}) = \mathbf{C}:\mathrm{N}\otimes\mathrm{N},\ \ I_8(\mathrm{M},\mathrm{N}) = \mathbf{C}:\mathrm{M}\otimes\mathrm{N} \quad (5)$$

Furthermore, considering the loading modes, e.g., uniaxial tensile and planar compression, one can easily define the deformation gradient for incompressible isotropic materials. In a specific case of uniaxial loading conditions and incompressible isotropic material, the deformation gradient is written as $F = \boldsymbol{diag}[\lambda, \lambda^{-\frac{1}{2}}, \lambda^{-\frac{1}{2}}]$. It should be noted that the second and third components of the deformation gradient become equal due to isotropy and incompressibility assumption. However, in the case of the anisotropic materials, obtaining deformation gradient is not a straight-forward step and requires an update of the deformation gradient at every load step. This paper will delve deeper into this topic in the following identification process.

In addition to the anisotropic strain energy functions provided in the introduction, the isotropic incompressible strain energy functions used in this study are listed in Table 3. It should be noted that the incompressibility assumption makes the third principal invariant zero ($I_3 = 0$).

Model Name	Strain energy potentials
Neo-Hookean [13]	$W = C_{10}(\bar{I}_1 - 3)$
Mooney [14]-*Rivlin* [15]	$W = C_{10}(\bar{I}_1 - 3) + C_{01}(\bar{I}_2 - 3)$
Ogden [16]	$W = \sum_{p=1}^{N} \frac{\mu_p}{\alpha_p}(\lambda_1^{\alpha_p} + \lambda_2^{\alpha_p} + \lambda_3^{\alpha_p} - 3)$

Table 3: Constitutive models for isotropic materials such as pure rubber

Consequently, the Cauchy stress tensors are derived substituting these potentials into Equation 1. Applying simple deformation modes, this method allows identification of the material parameters of the constitutive models for the material of interest.

3.2 Identification of material parameters

The identification process of the material parameters was achieved by minimizing, in the sense of least squares, the difference between the stress and strain curves between experimental results on uniaxial tensile loading mode and the analytical formulations of the models. Pure rubber models were identified prior to composites. For that purpose, a Python program, relying on the trust region optimization algorithm available in SciPy library [21] was developed. To have a complete stress equation, upon substituting all the components into Equation 1, one can calculate the arbitrary pressure p knowing that stress in the thickness direction is zero ($\sigma_{33}=0$) for all the loading conditions used in this study. Having p substituted back in Equation 1, the equation now is ready for the optimization process for isotropic hyperelastic models. On contrary, obtaining deformation gradient F is not straightforward for anisotropic hyperelasticity due to anisotropy. For example, considering incompressibility, the deformation gradient for the uniaxial loading case is now a function of first and second principal stretches due to possible inequality of second and third principal stretches because of anisotropy, seen below. Thus, at every step of imposed λ_{11}, λ_{22} was estimated by solving high order non-linear equation for $\sigma_{22}=0$. This equation is numerically solved at every λ_{11} step since there is no direct analytical solution for such complex equations.

$$\mathbf{F}_{\text{uniaxial}} = \begin{bmatrix} \lambda_{11} & 0 & 0 \\ 0 & \lambda_{22} & 0 \\ 0 & 0 & (\lambda_{11}\lambda_{22})^{-1} \end{bmatrix} \tag{6}$$

Based on the identification procedure explained above, one can obtain all stress equations for all above-mentioned material models with each given loading condition. As examples, only the stress equations of isotropic Mooney [14]-Rivlin [15] and anisotropic model by Gong et al. [20] under uniaxial boundary conditions are derived, in Equation 7 and 8, respectively. It is not possible here to state the stress equation for the Gong et al. [20] model explicitly for every updated deformation gradient. Thus, more general definitions are made in Equation 8.

$$\sigma_{11} = 2\left(C_{10} + \frac{C_{01}}{\lambda_{11}}\right)\left({\lambda_{11}}^2 - \frac{1}{\lambda_{11}}\right) \tag{7}$$

$$\boldsymbol{\sigma} = 2[W_1\mathbf{C} - W_2\mathbf{C}^{-1} + I_4W_4\mathbf{M}\otimes\mathbf{M} + I_6W_6\mathbf{N}\otimes\mathbf{N} + \frac{W_8(\mathbf{M}\otimes\mathbf{N}+\mathbf{N}\otimes\mathbf{M})}{2}] \tag{8}$$

where **M** and **N** are now tensors in which the above defined vectors multiplied with deformation gradient and its transpose as described in Equation 1 and W_i is the derivation of strain energy potential with respect to i^{th} strain invariant. Based on the identification performed on pure rubber, one can now identify the material constants associated with anisotropy (k_1, k_2, k_3 in Table 1). Remembering that I_4 and I_6 pseudo-invariants account for fiber extensions in fiber directions, associated k_1 and k_2 parameters can be then identified based on the uniaxial tensile test of the composite with 0-degree fabric orientation. The parameter k_3 associated with I_8 is optimized based on the uniaxial tensile test of the composite with 45-degree fabric orientation.

Furthermore, the above described and derived constitutive equations were scripted in Fortran and implemented into Abaqus using the UANISOHYPER_INV material subroutine. The developed material subroutines were then used to simulate composite tests with the same conditions, checking the subroutines. It must be noted that all the simulations employed implicit solution scheme and 0.5 mm hybrid brick elements considering geometric non-linearity assumption.

The material parameter identification process has resulted in material parameters presented in Table 4. Simulating the same coupon test conditions, the results were evaluated comparatively with experimental and analytical results. The numerical results with identified k_1 and k_2 parameters for the HGO [18] model are plotted in Fig. 9. Even if the numerical and analytical curves are in satisfactory agreement in this case of composite with 0 degree fabric orientation under tensile, it can be clearly seen that the model underestimates the material response for the 45-degree fabric orientation case. A very

similar observation was made for the model of Dong et al. [19] where no improvement in 45-degree case was observed, seen in Fig. 10 despite the new terms added into both isotropic and anisotropic parts of the strain energy function. Moreover, the parameter k_3 was identified to account for the shearing behavior between fabric and rubber. As seen in Fig. 11, the inclusion of I_8 resulted in improved results, which indicates the importance of modelling the shearing behavior of the composite with the additional pseudo-invariant. The identified material constants and the error metrics of the optimization studies were also shared in Table 4. In Table 5, one can easily notice the similar outcomes in the stress distribution results of the simulations at two different stretch values for Dong et al. [19] and Gong et al. [20] models with 45 degree fabric orientation, resulting in higher stress in Gong et al. [20] model around the transition zone as a result of the inclusion of shearing parameter.

Model Name	Strain energy functions
HGO [18]	$C_{10}(MPa) = 0.201\,,\quad k_1(MPa) = 28.72,\quad k_2 = 79.34,\quad ,\ R^2 = 0.639$
Dong et al. [19]	$C_{10}(MPa) = 0.166\,,\quad C_{01}(MPa) = 0.0352$ $k_1(MPa) = 23.02\,,\quad k_2 = 96.16,\quad R^2 = 0.705$
Gong et al. [20]	$C_{10}(MPa) = 0.166,\quad C_{01}(MPa) = 0.0352$ $k_1(MPa) = 23.02\,,\quad k_2 = 96.16,\quad k_3 = 0.279,\quad R^2 = 0.974$

Table 4: The identified material parameters for each material model

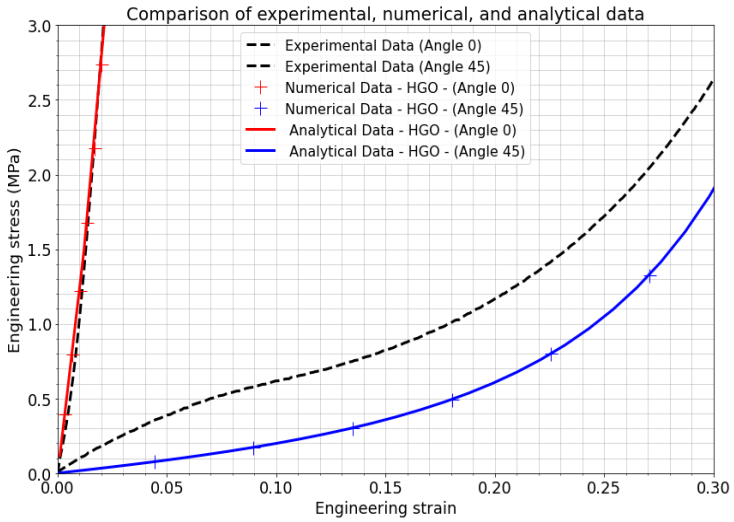

Figure 9: Analytical and simulation results of the HGO [18] model with experimental results

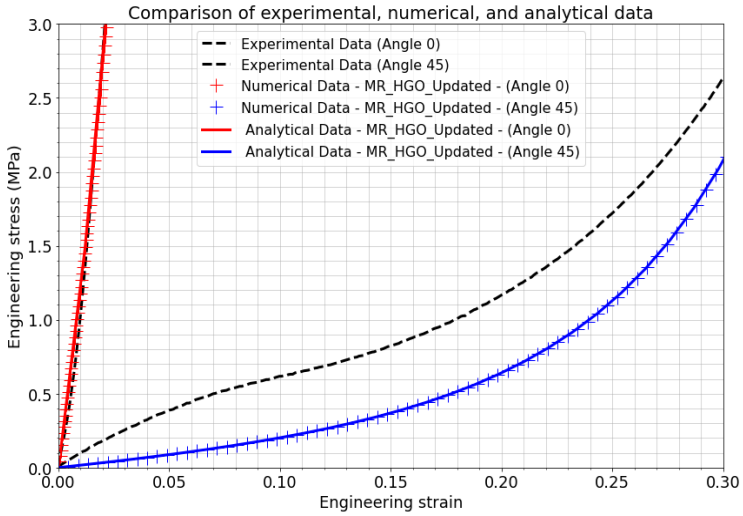

Figure 10: Analytical and simulation results of the *Dong et al.* [19] model with experimental results

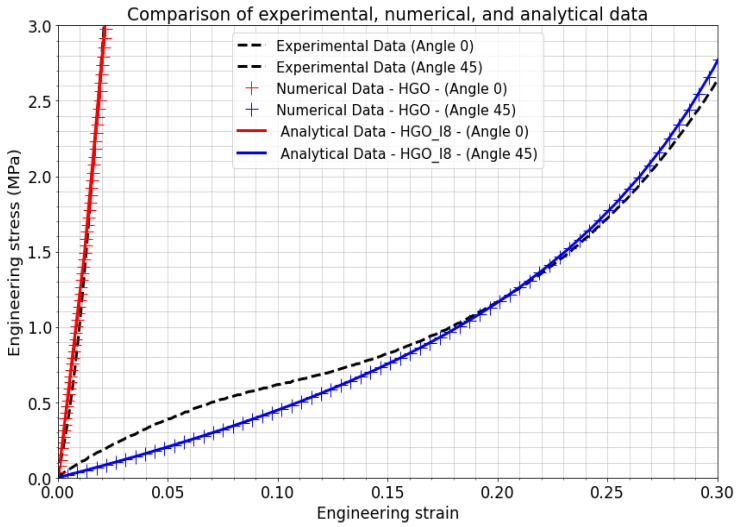

Figure 11: Analytical and simulation results of the *Gong et al.* [20] model with experimental results

S11(MPa)	Stress distributions
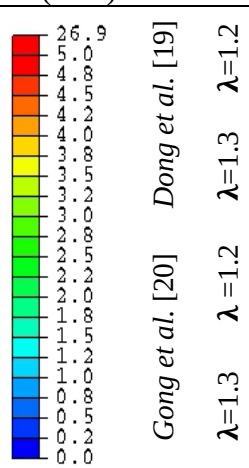	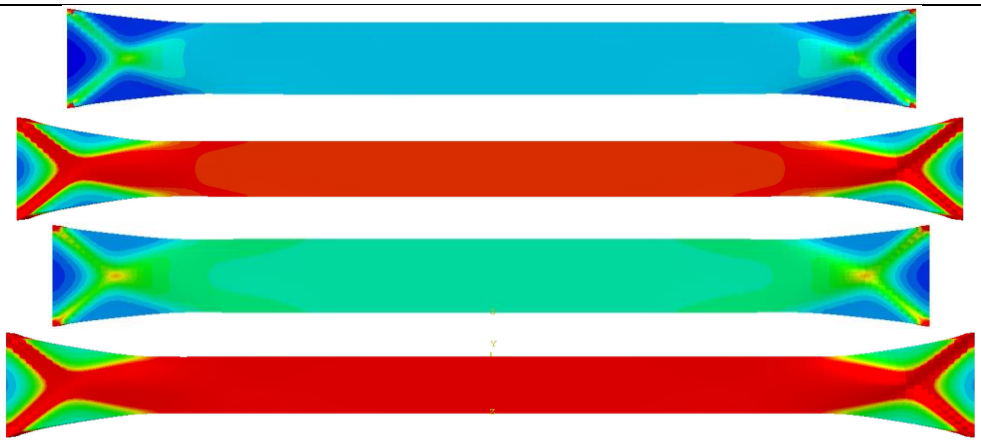

Table 5: Stress distribution of composites with 45-degree fabric-oriented under uniaxial tensile loading

4 CONCLUSIONS

In this paper several hyperelastic models, dedicated to pure rubber and fiber reinforced rubber, have been studied. In a first step, the model has been described, and the stress equations have been derived on specific loading cases of interest for identification purposes. Secondly, an identification process of pure rubber and composite materials has been conducted to obtain material parameters. Compared with the experimental results, the capabilities of different anisotropic material models, for composite modeling, were highlighted. The material models that do not include pseudo-invariant I_8 to account for shearing behavior between rubber and fabric are clearly seen incapable of reproducing material response especially for 45-degree fabric-oriented composite specimens. Moreover, the material model with I_8 defined resulted in satisfactory results in terms of the reproduction of material response. In the third step, the models with the identified material parameters were implemented in a finite element implicit framework using material subroutines. The composite simulations carried out with the developed subroutines under uniaxial loading conditions have resulted in a satisfactory mechanical response in comparison with experimental and analytical data. To conclude, this numerical modeling methodology provided and the 3-point bending tests pave the path for modeling bending behavior of fabric rubber composites for further studies.

REFERENCES

[1] P. H. Dunlap, « An Overview of Advanced Elastomeric Seal Development and Testing Capabilities at NASA Glenn Research Center », in *50th AIAA/ASME/SAE/ASEE Joint Propulsion Conference*, Cleveland, OH: American Institute of Aeronautics and Astronautics, juill. 2014. doi: 10.2514/6.2014-3599.

[2] Y. Fu et Y. Dong, « Evaluation of Key Performance of Aircraft Fabric Rubber Seal During Flight », *J. Aircr.*, vol. 58, nº 5, p. 1154-1167, sept. 2021, doi: 10.2514/1.C036331.

[3] M. F. Aksit, R. E. Chupp, O. S. Dinc, et M. Demiroglu, « Advanced Seals for Industrial Turbine Applications: Design Approach and Static Seal Development », *J. Propuls. Power*, vol. 18, nº 6, p. 1254-1259, nov. 2002, doi: 10.2514/2.6060.

[4] R. C. Bill, « Wear of Seal Materials Used in Aircraft Propulsion Systems », *Wear 59*, p. 165-189, 1980.

[5] H. Nishina, « Trends in Automotive Sealing Materials Technology », *Int. Polym. Sci. Technol.*, vol. 35, nº 3, p. 51-60, mars 2008, doi: 10.1177/0307174X0803500315.

[6] S. Lattime et B. Steinetz, « Turbine Engine Clearance Control Systems: Current Practices and Future Directions », in *38th AIAA/ASME/SAE/ASEE Joint Propulsion Conference & Exhibit*, Indianapolis, Indiana: American Institute of Aeronautics and Astronautics, juill. 2002. doi: 10.2514/6.2002-3790.

[7] R. E. Chupp, R. C. Hendricks, S. B. Lattime, et B. M. Steinetz, « Sealing in Turbomachinery », *J. Propuls. Power*, vol. 22, nº 2, p. 313-349, mars 2006, doi: 10.2514/1.17778.

[8] D. L. MORRILL, « TURBINE CASE COOLING SYSTEM », US 2016/0003151A1

[9] S. Shabbir, « Aerospace Sealing Technology for Maintenance, Repair and Overhaul of engines: a review », 2019.

[10] A. P. S. U. Govt., « Aircraft Incident Report 12/2017 N276AY EW/C2016/06/02 », 2017.

[11] B. Serge, « Joint d'étanchéité à appui intégré », FR2920218A1, 27 février 2009 [En ligne]. Disponible sur: https://patents.google.com/patent/FR2920218A1/fr

[12] L. Mullins, « Effect of Stretching on the Properties of Rubber », *Rubber Chemistry and Technology*, p. 281-300, 1948.

[13] L. R. G. Treloar, « The elasticity of a network of long-chain molecules—II », *Trans Faraday Soc*, vol. 39, nº 0, p. 241-246, 1943, doi: 10.1039/TF9433900241.

[14] M. Mooney, « A Theory of Large Elastic Deformation », *J. Appl. Phys.*, vol. 11, nº 9, p. 582-592, sept. 1940, doi: 10.1063/1.1712836.

[15] R. S. Rivlin, « Large elastic deformations of isotropic materials IV. further developments of the general theory », *Philos. Trans. R. Soc. Lond. Ser. Math. Phys. Sci.*, vol. 241, nº 835, p. 379-397, oct. 1948, doi: 10.1098/rsta.1948.0024.

[16] R. W. Ogden, « Large deformation isotropic elasticity – on the correlation of theory and experiment for incompressible rubberlike solids », *Proc. R. Soc. Lond. Math. Phys. Sci.*, vol. 326, nº 1567, p. 565-584, févr. 1972, doi: 10.1098/rspa.1972.0026.

[17] A. J. M. Spencer, *Continuum Theory of the Mechanics of Fibre-Reinforced Composites*. Vienna: Springer Wien, 2014.

[18] G. A. Holzapfel, T. C. Gasser, et R. W. Ogden, « A new Constitutive Framework for Arterial Wall Mechanics and a Comparative Study of Material Models », in *Cardiovascular Soft Tissue Mechanics*, S. C. Cowin et J. D. Humphrey, Éd., Dordrecht: Kluwer Academic Publishers, 2004, p. 1-48. Consulté le: 16 juillet 2024. [En ligne]. Disponible sur: http://link.springer.com/10.1007/0-306-48389-0_1

[19] Y. Dong, X. Yao, H. Yan, L. Yuan, et H. Yang, « Macro- and mesoscopic mechanical properties of complex fabric rubber composite under different temperatures », *Compos. Struct.*, vol. 230, p. 111510, déc. 2019, doi: 10.1016/j.compstruct.2019.111510.

[20] Y. Gong, X. Peng, Y. Yao, et Z. Guo, « An anisotropic hyperelastic constitutive model for thermoplastic woven composite prepregs », *Compos. Sci. Technol.*, vol. 128, p. 17-24, mai 2016, doi: 10.1016/j.compscitech.2016.03.005.

[21] P. Virtanen *et al.*, « SciPy 1.0: fundamental algorithms for scientific computing in Python », *Nat. Methods*, vol. 17, nº 3, p. 261-272, mars 2020, doi: 10.1038/s41592-019-0686-2.

Modeling High Temperature Cross-linking Between Graphitic Surfaces and Glassy Carbon

Jacob R. Gissinger
Stevens Institute of Technology
Chemical Engineering and Materials Science

jgissing@stevens.edu
ICCM24
8/05/25

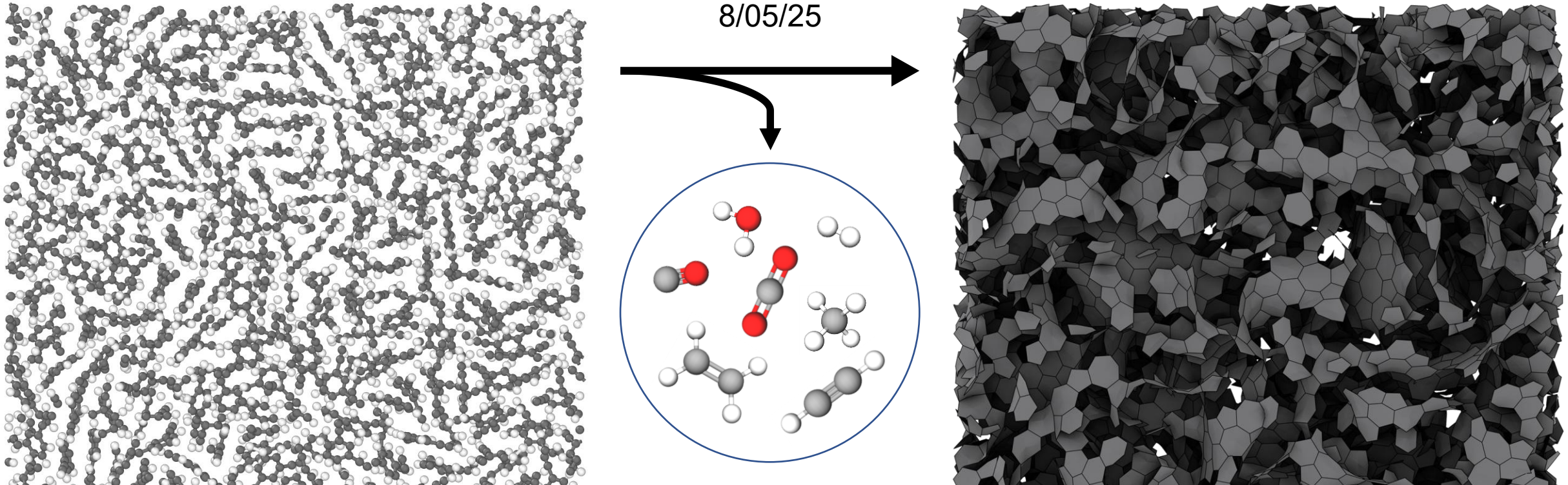

Molecular Dynamics (MD) for Nanoscale Insight

- Molecular dynamics (MD) is a computer simulation technique for modeling the motion and interaction of atoms and molecules
- Atomic positions are updated using a small timestep and Newtonian mechanics, $a = F/m$
- In traditional MD, bonded connections are defined once at beginning of simulation and not changed during the simulation
- Mechanical properties can be predicted at the nanoscale (ultimate strength, elastic modulus, interfacial shear strength)

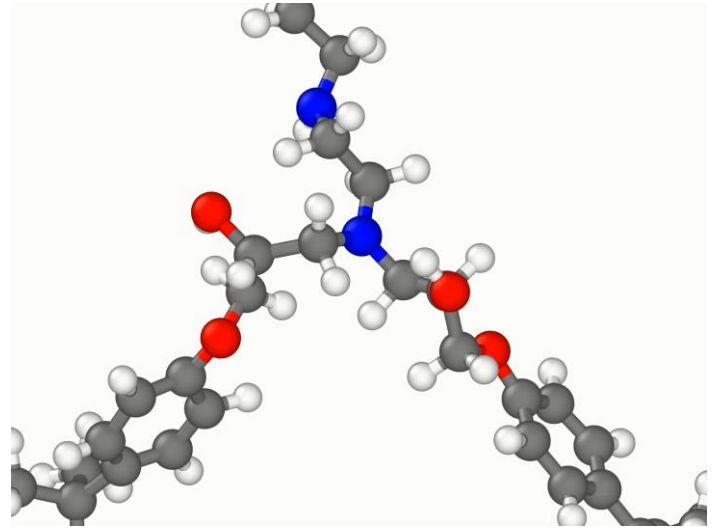

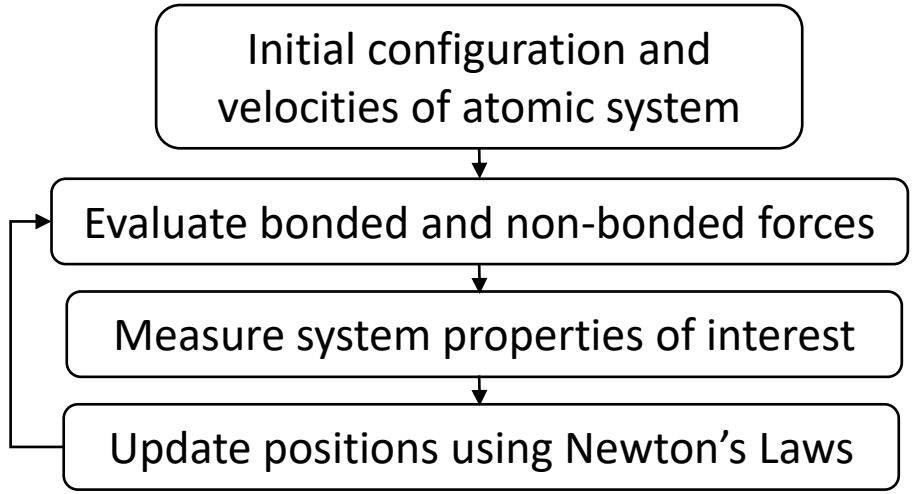

Nanocomposites have Advanced Properties

- Composites have replaced many components of aircraft, cars, sports equipment and other technologies such as energy storage
- Interfaces and defects are nucleation sites for mechanical failure
- Failure mechanisms of composite materials are complex, and difficult to relate back to processing conditions
- Molecular dynamics (MD) models can help us understand the origin and propagation of material failure
- **<u>Grand Challenge:</u> Developing Materials that can Serve Both as Temperature-Resistant and High-Strength Structural Components**



Aerospace



Automotive



NASA’s Orion spacecraft recovered after Artemis I test flight

Interfacial Interactions are Critical

- The properties of composite materials remain well below their theoretical values
- Interfacial interactions and defects often determine the material's ultimate properties!
- Embedded interfaces are difficult to probe using experimental techniques
- Atomistic MD can predict the properties and dynamic response of complex multicomponent systems

Tensile tests of CNT fiber reinforced polymer composites.

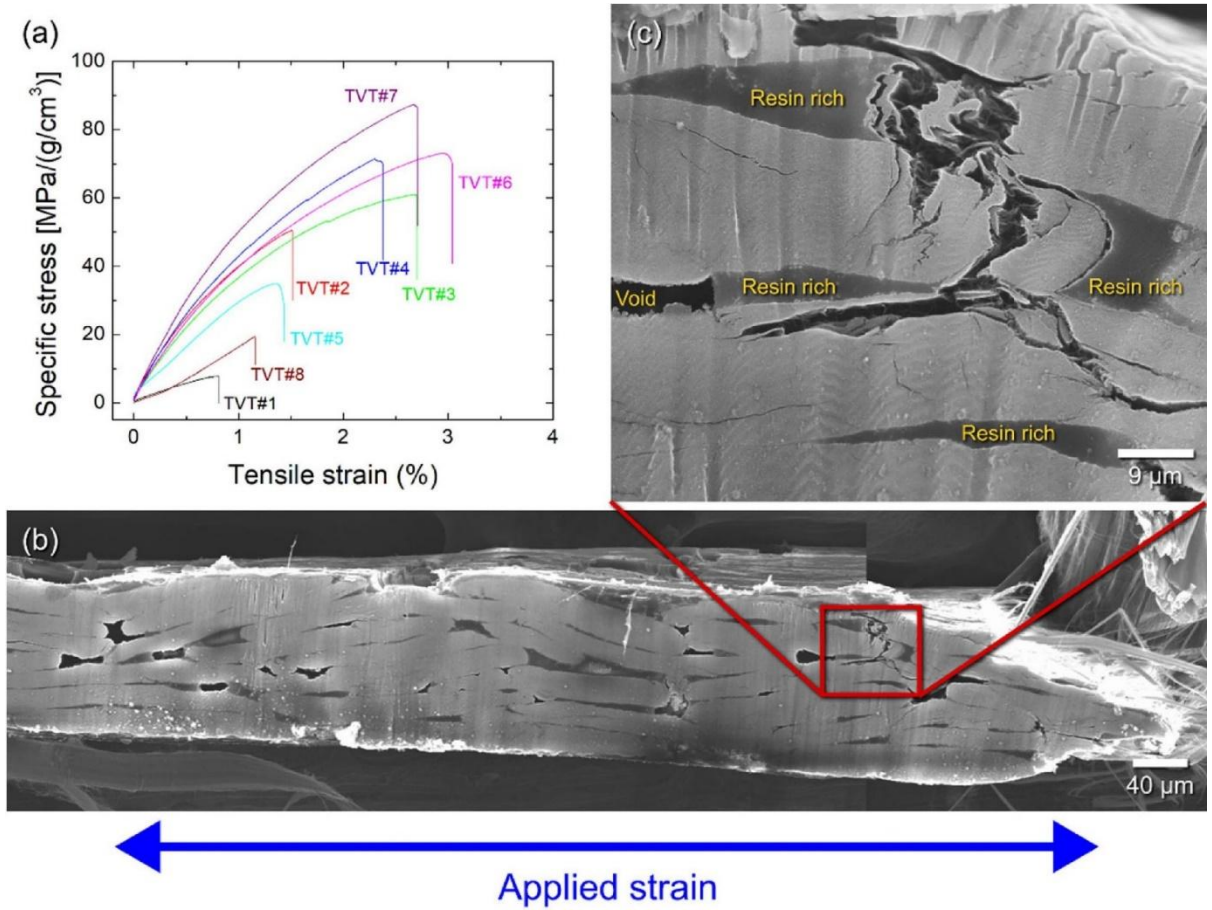

Kim et al. *Composites Part A: Applied Science and Manufacturing* (2023): 107449.

Why is Char Yield Important?

- Char yield is the amount of material left over after subjecting it to high temperature pyrolysis
  - Thermogravimetric analysis (TGA) is used to obtain plots of mass vs time and/or temperature (typically ramped up to 800°C -1000°C)
- High char materials require fewer cycles of carbonization and resin infiltration to achieve desired properties

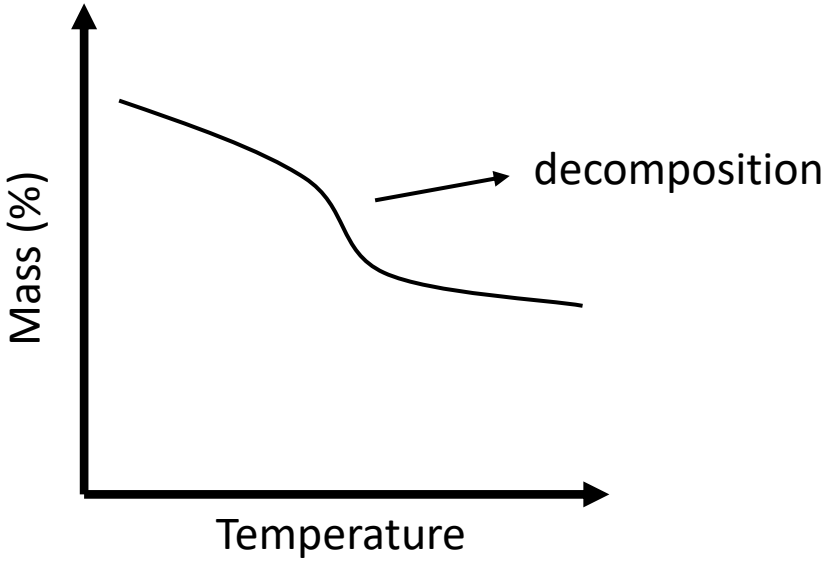

Typical TGA plot

Prior Efforts to Predict Char Yield

- Correlate existing literature data with empirical formulas
  - Element ratios, molecular group analysis, quantitative structure-property relationships (QSPR)
  - Achieves reasonable correlations with low-char yield resins
- Not enough chemical intuition to predict outlier behavior

Molar group contribution values.

Chemical group[a]	Type[b]	Molar group contributions			Ψ_i/M_i J/g K
		Ω_i MJ/mol	X_i g/mol	Ψ_i kJ/mol K	
$-C(CH_3)_2-$	B	2.63	0	85.5	2036
$-CH_3$	S	0.50	0	18.5	1233
$-CH_2-$	B	0.51	0	14.4	1029
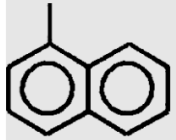	S	4.84	0	108.6	855
–O–	B	0.12	0	11.1	694

Lyon, Richard E., et al. "A Molecular Basis for Polymer Flammability." *Polymer* 50, no. 12, 2608–17 (2009).

Large-Scale Reactive MD is Challenging

- Quantum mechanics can model reactions from first principles
- Levels of abstraction come with a tradeoff: accuracy *vs.* speed
- Reactive force fields can achieve near-DFT accuracy
  - Much faster than DFT, much slower than classical molecular dynamics (MD)

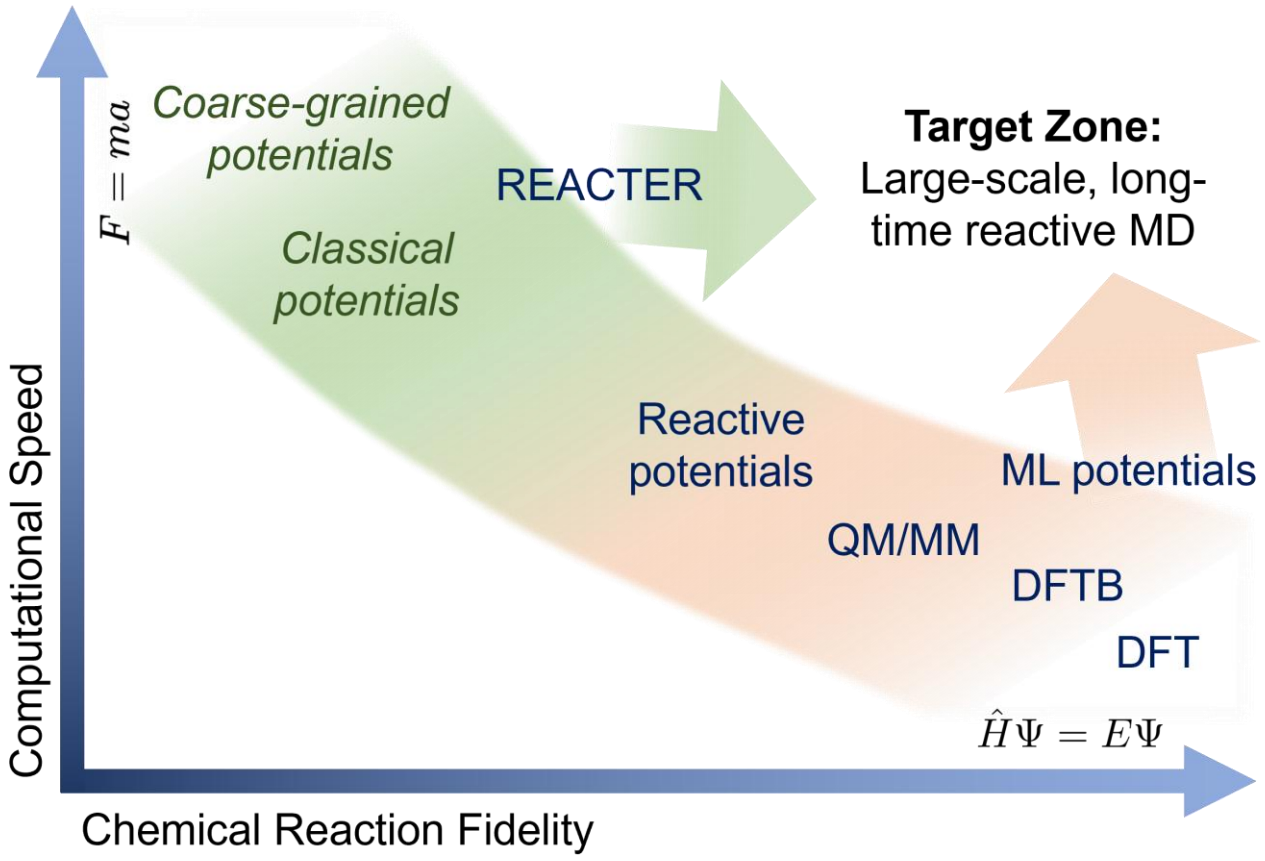

Gissinger et al. "Modeling chemical reactions in classical molecular dynamics simulations." *Polymer* 128 (2017): 211-217.

Case Study: Carbonization Reactions

- Starting point: diethynylbenzene polymerized via linear and cyclotrimerization reactions
- Define carbonization moves from polymerized polyarylacetylene (PAA) motifs, as well as ring-closing and Diels-Alder reaction
- End goal: Approximate model of the carbonization and/or graphitization process

polyarylacetylene (PAA)

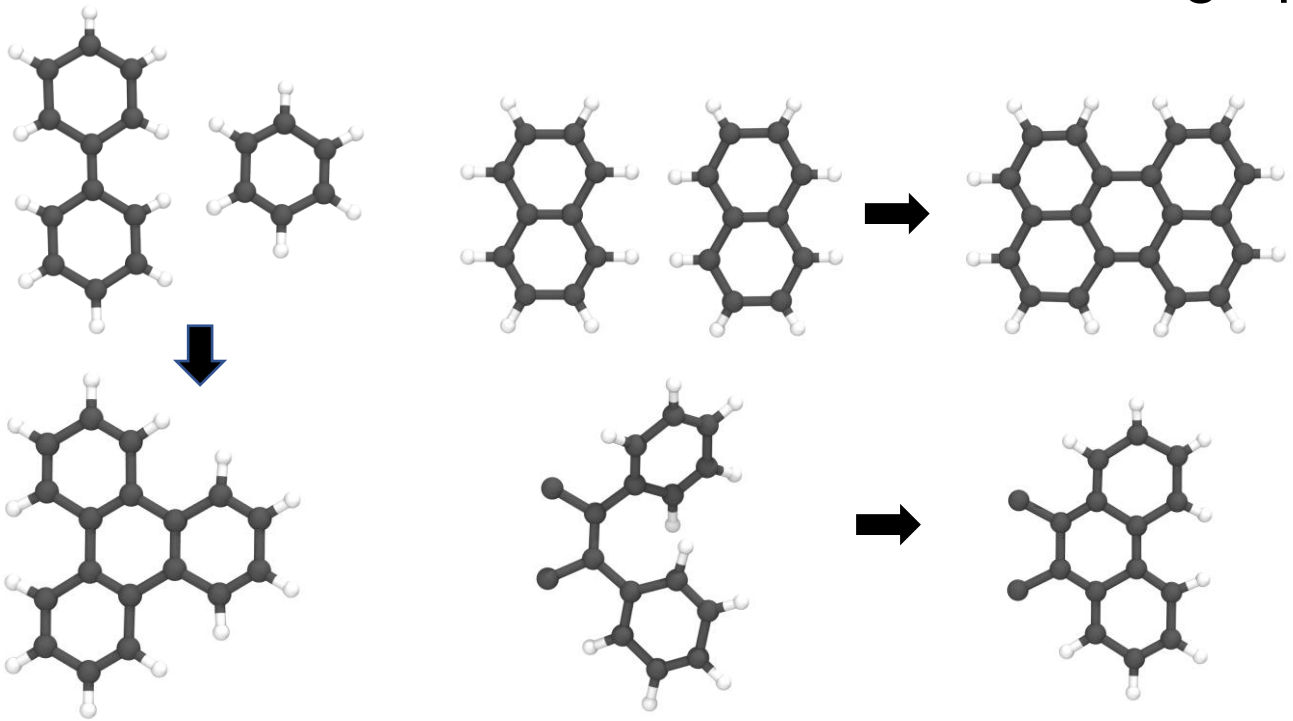

Case Study: Nanoribbon Formation

Slice is 7 Å thick; only rings shown

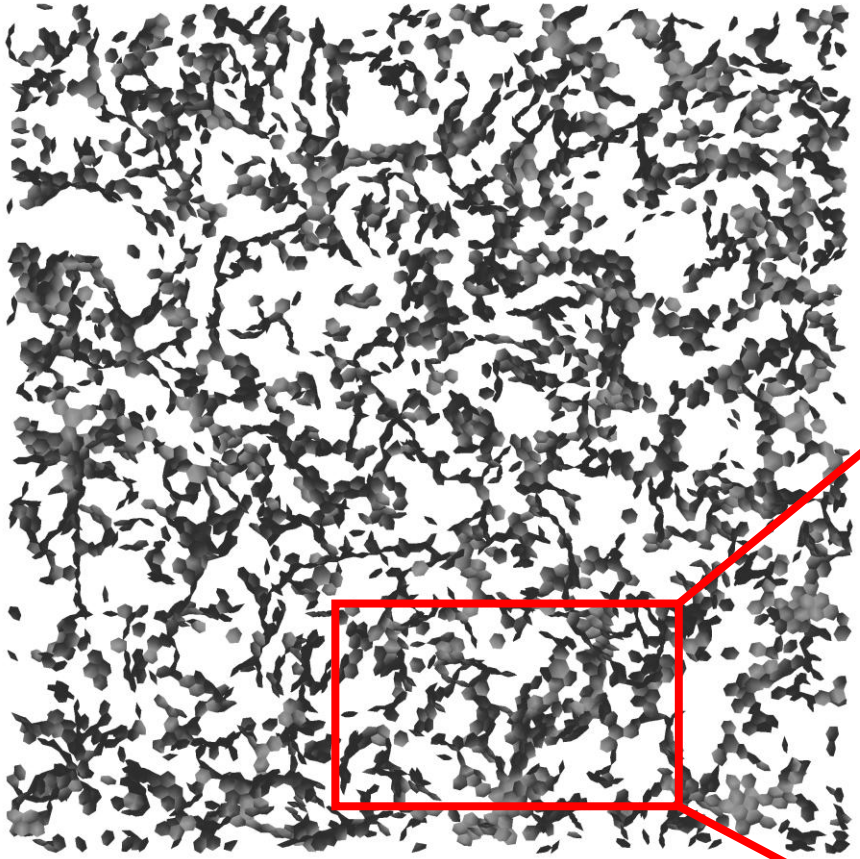

Density: 1.0 g/cm^3

Box Size: 13.8 nm

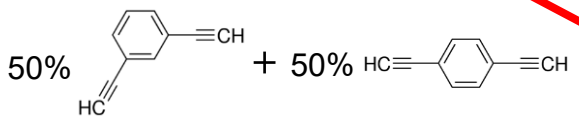

After ~99% polymerization and ~14.5K carbonization reactions

Expedient large-scale model for early-stage pyrolysis of polyarylacetylene (200K atoms)

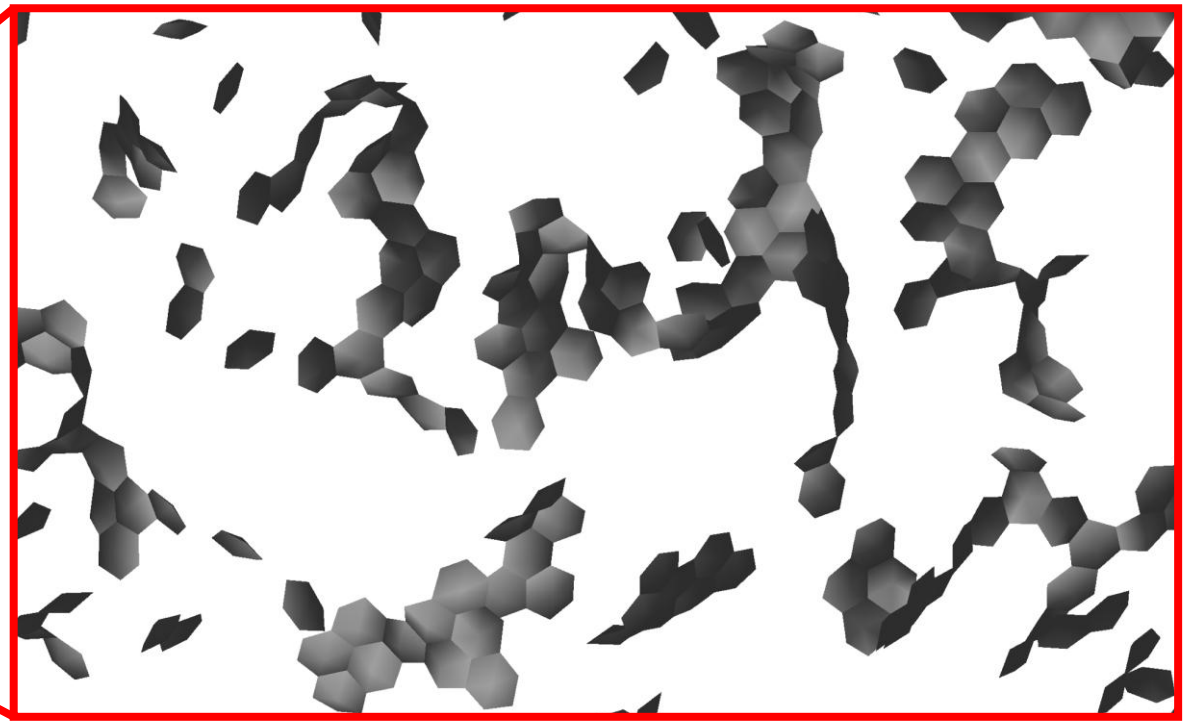

ReaxFF: Inherently Reactive Model

- Reactive force field that does require explicit input of reaction mechanisms
  - Based on bond order formulation (see definition below)
- Trained on DFT data: small molecules for reactions and graphitic structures for mechanical properties
- Effective method for smaller-scale simulations that involve complex chemical transformations

$$E_{\text{system}} = E_{\text{bond}} + E_{\text{over}} + E_{\text{under}} + E_{\text{val}} + E_{\text{pen}} + E_{\text{tors}} + E_{\text{conj}} + E_{\text{vdWaals}} + E_{\text{Coulomb}}$$

van Duin et al. "ReaxFF: A Reactive Force Field for Hydrocarbons." The Journal of Physical Chemistry A 105, no. 41, 9396–9409 (2001).

Char Yield Simulation Protocol

- Temperature ramp cycle
  - 300 K - 3000 K at 10 K/ps
  - High temperatures/rates to accelerate reactions
- Anneal at high pressure (1 GPa) to achieve final densities of 1.8 g/cm^3 - 2.0 g/cm^3
- ReaxFF with periodic removal of outgassing products to allow for carbonization and densification
- Initial system size: 36000 atoms

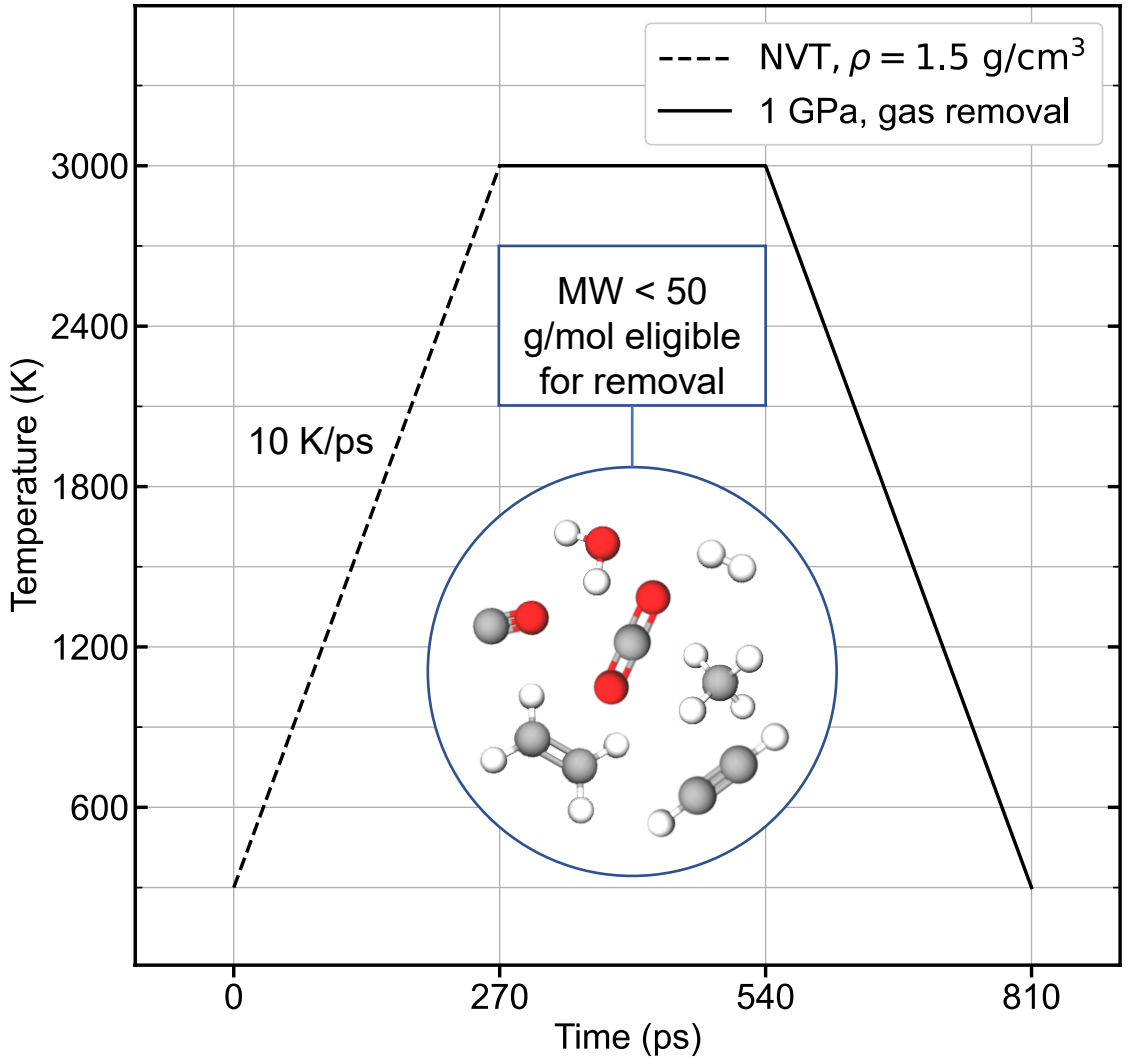

Char Yield Results for Various Chemistries

- Simulation protocol able to accurately predict char yield trends across a wide range of functional groups, heteroatom content and char yield values
- Chemically specific method
- No assumptions or fitting of experimental results

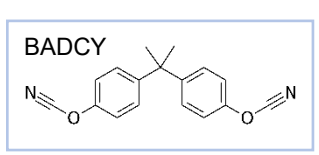

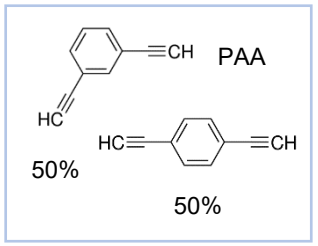

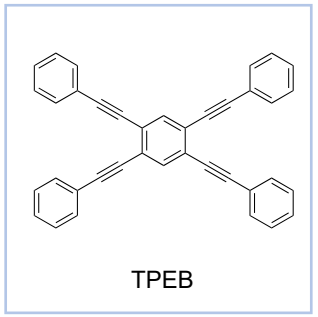



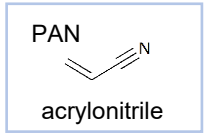

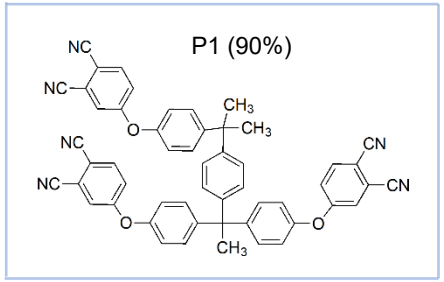

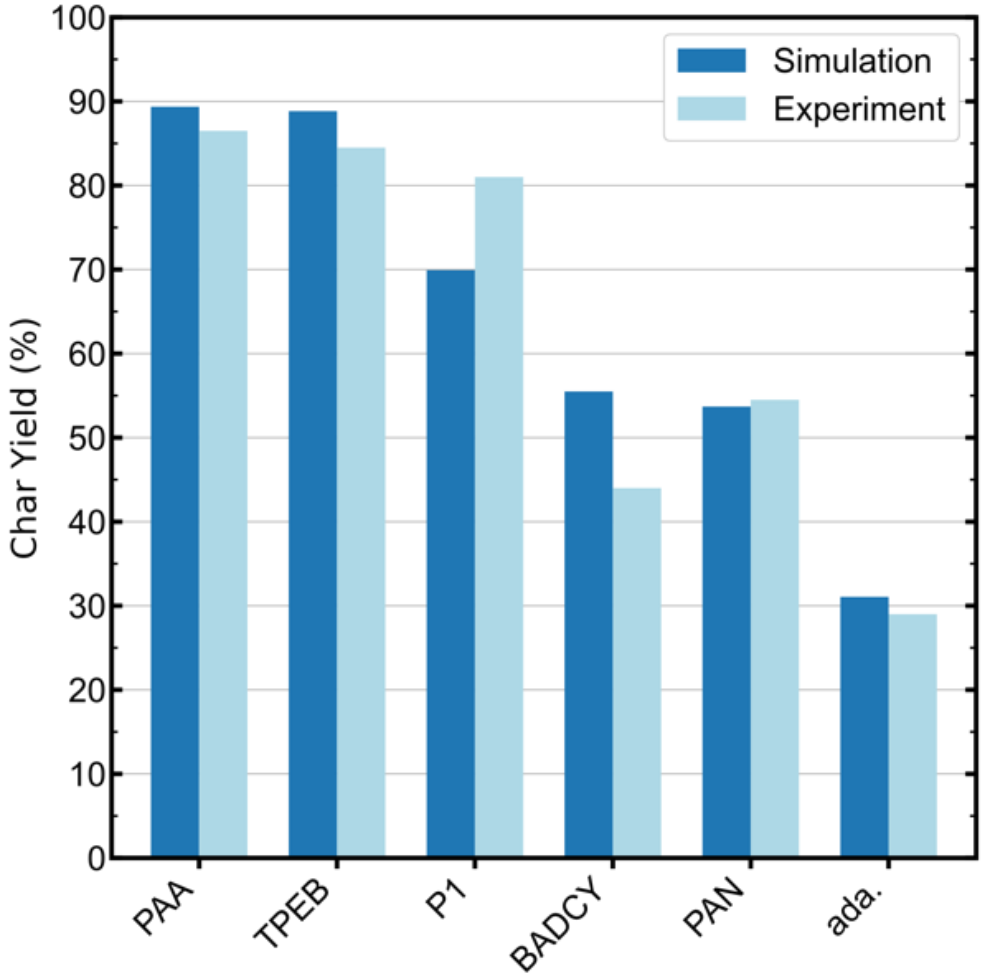

Gissinger et al. "Predicting char yield of high-temperature resins." *Carbon* 202 (2023): 336-347.

Mechanical Properties of Glassy Carbon

- Nonporous char morphology results in high predicted elastic moduli
- Predicted values in expected range for glassy carbon (~30 GPa @ 1.5 g/cm^3), but far lower than high modulus carbon fibers
- Highlights importance of achieving structures with high density and low defects, porosity

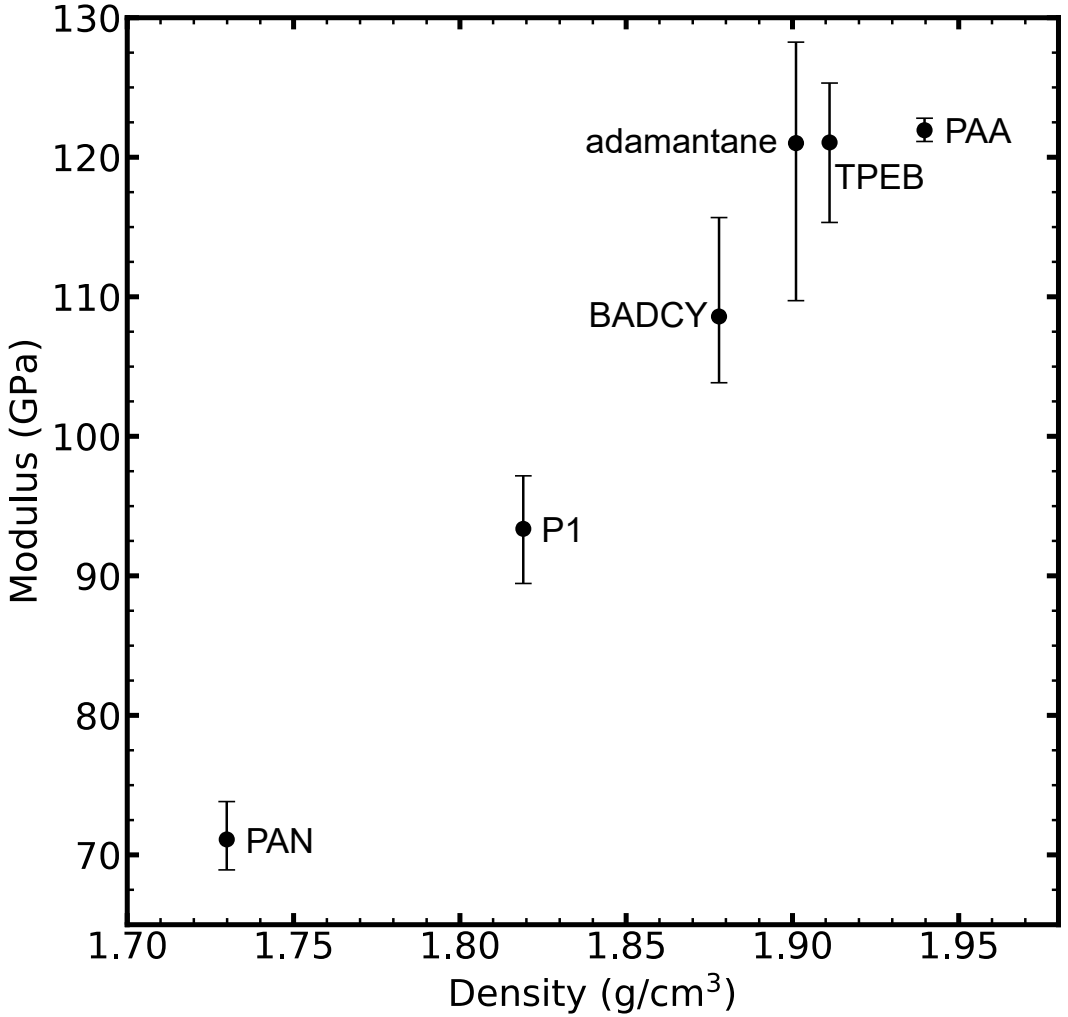

Strain to Failure

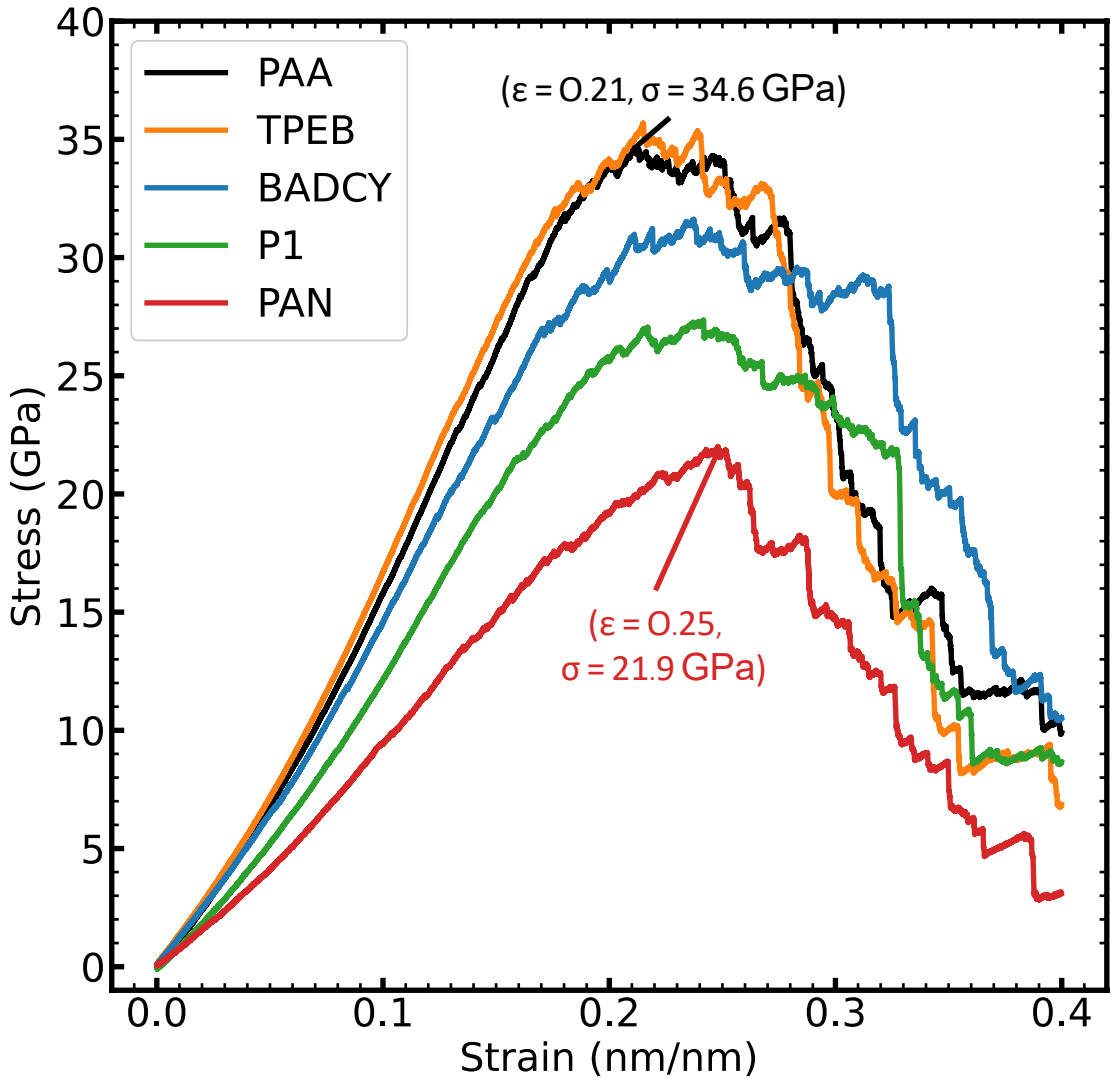

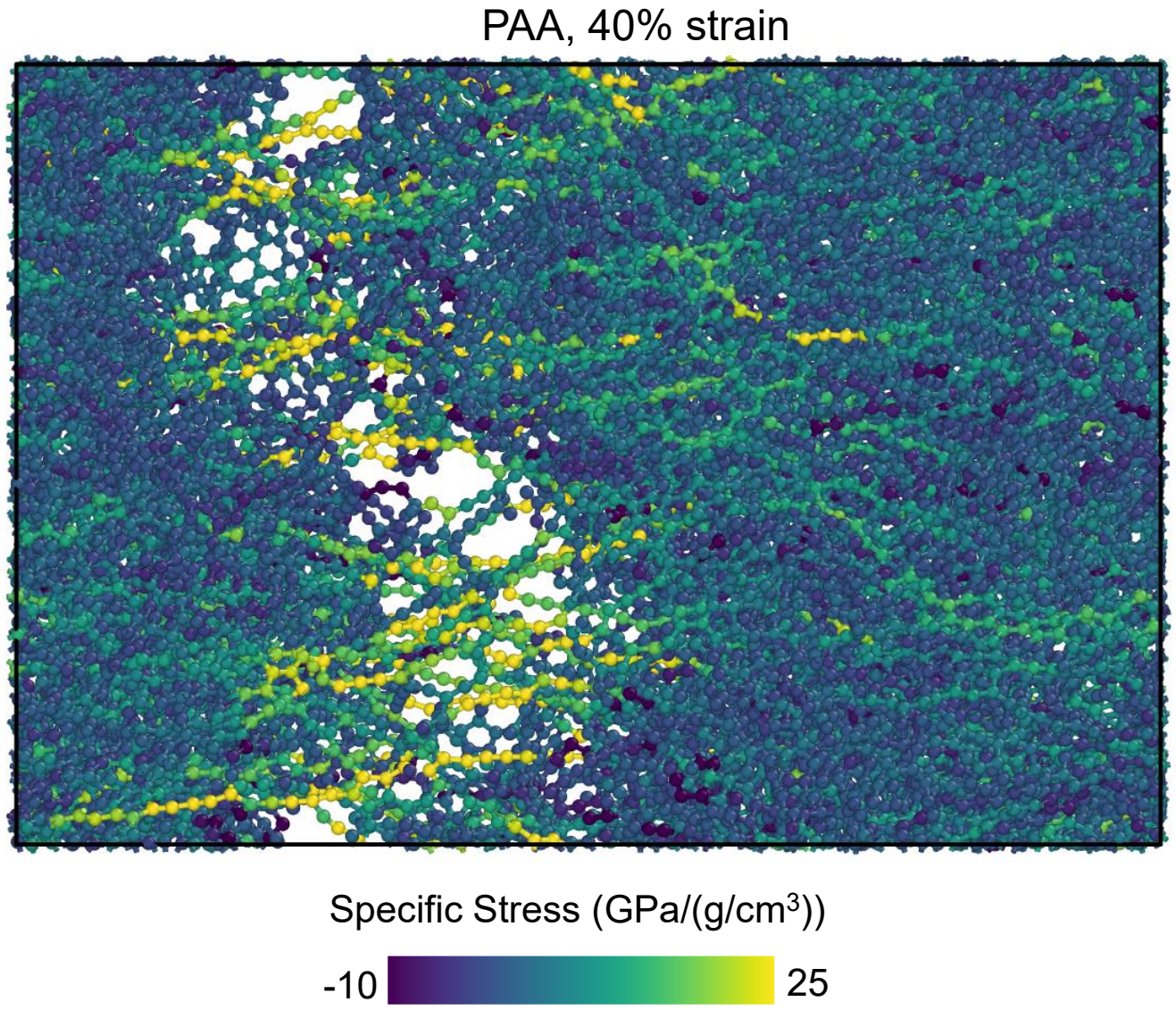

Carbon Hybridization/Heteroatoms Evolution

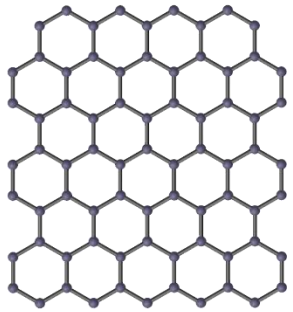

All precursor resins converge to glassy sp^2 carbon as heteroatoms are removed and the system densifies

Ternary 'glassy carbon' phase diagram. Axes = fractional number of atoms

Final Morphology: Ring Distribution

- Final carbonized structure consists primarily of fused five-, six- and seven-membered carbon rings
- Twice as many six-membered rings as other sizes, but rings are well distributed with respect to ring size
- Similar final morphology obtained for lower char yield resins

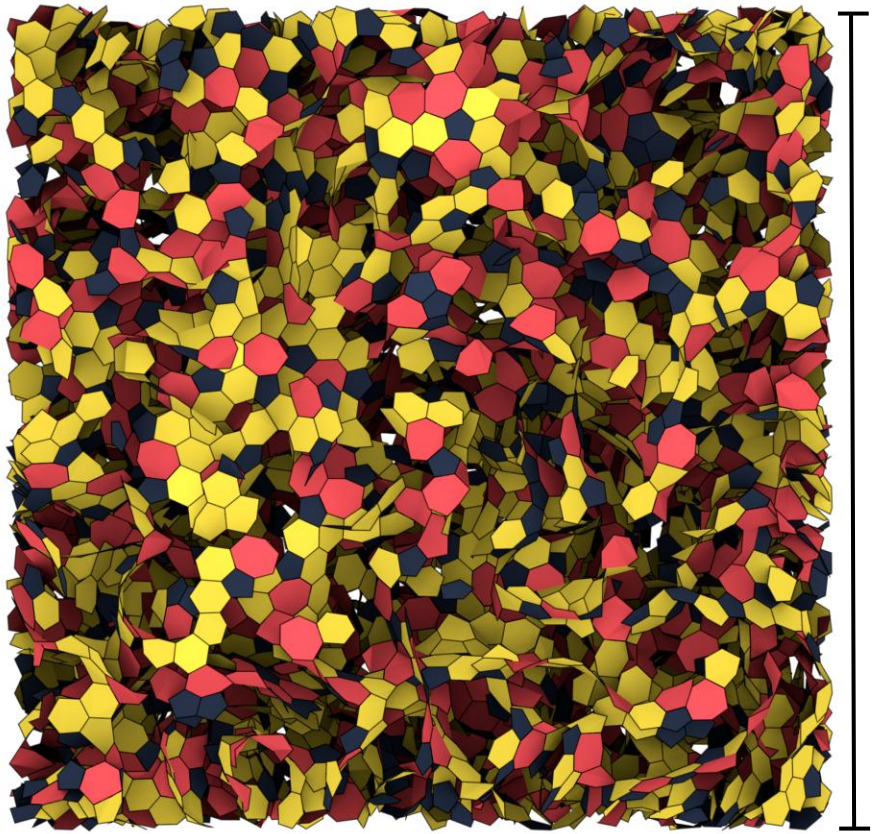

Polyarylacetylene (PAA)

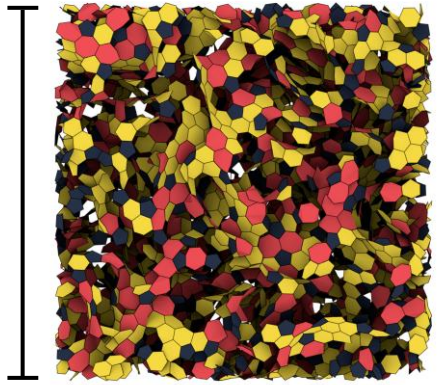

Cyanate ester (BADCY)

Gissinger et al. *Carbon* 202 (2023): 336-347.

Five-membered ring Six-membered ring Seven-membered ring

Topological Analysis: Cluster Definition

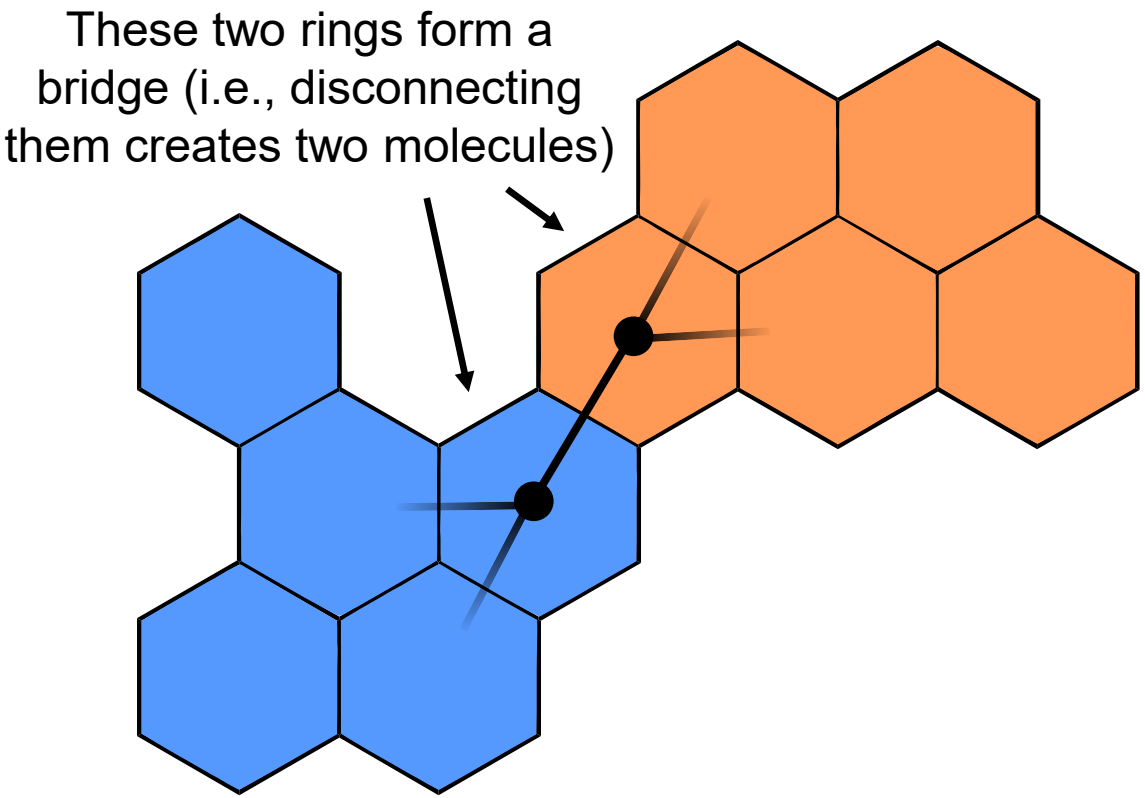

Two clusters

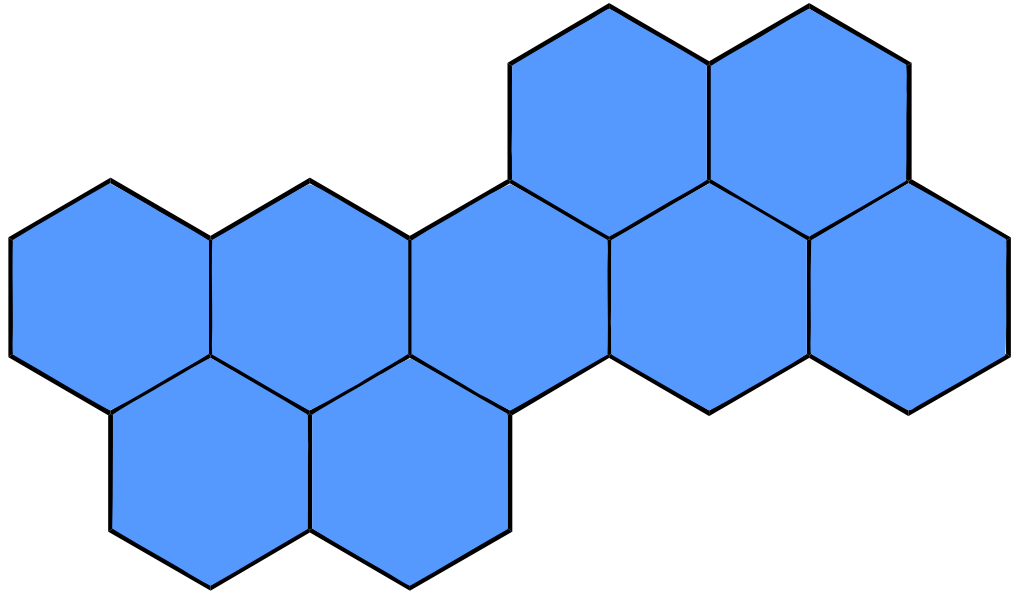

One cluster (no bridges, i.e. each fused ring pair shares at least one other ring)

Final Morphology: Cluster Distribution

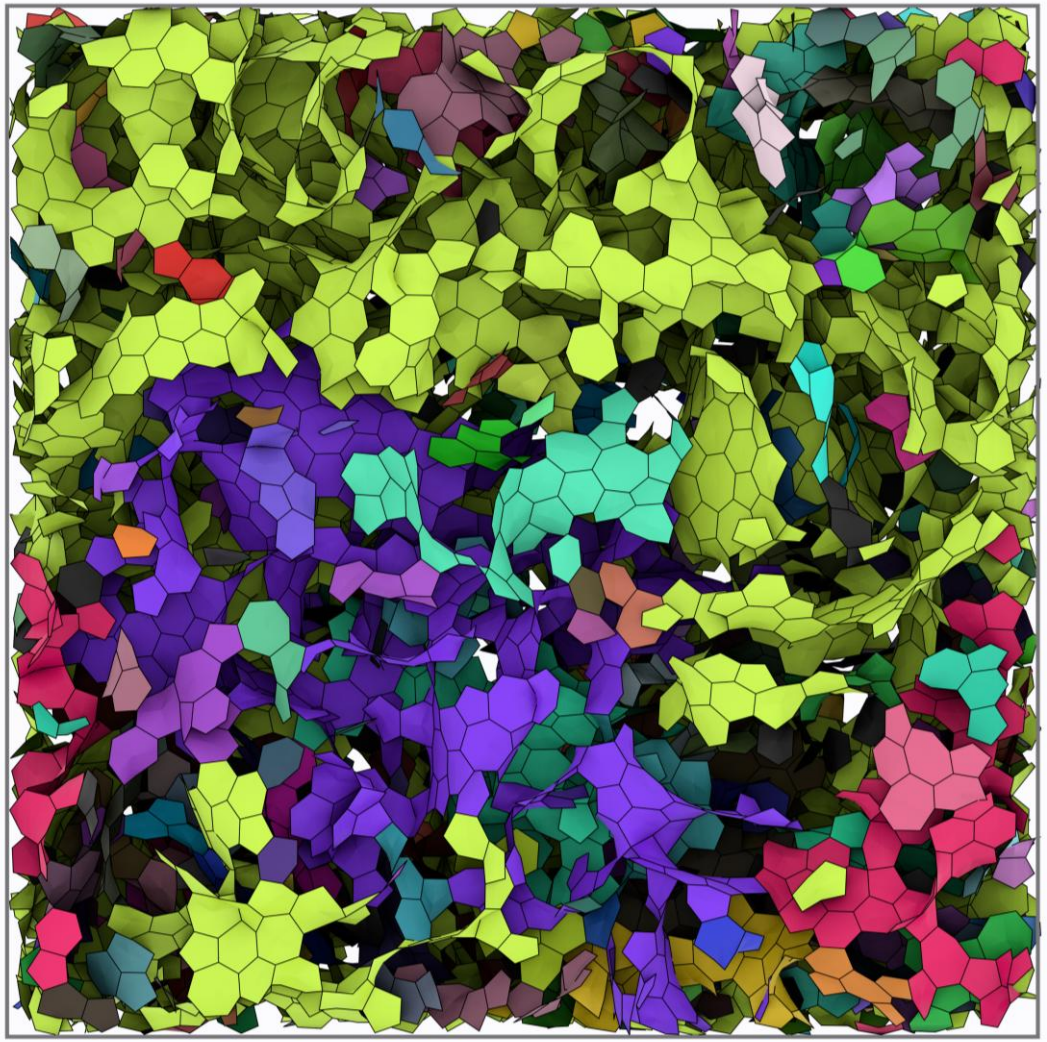

PAA

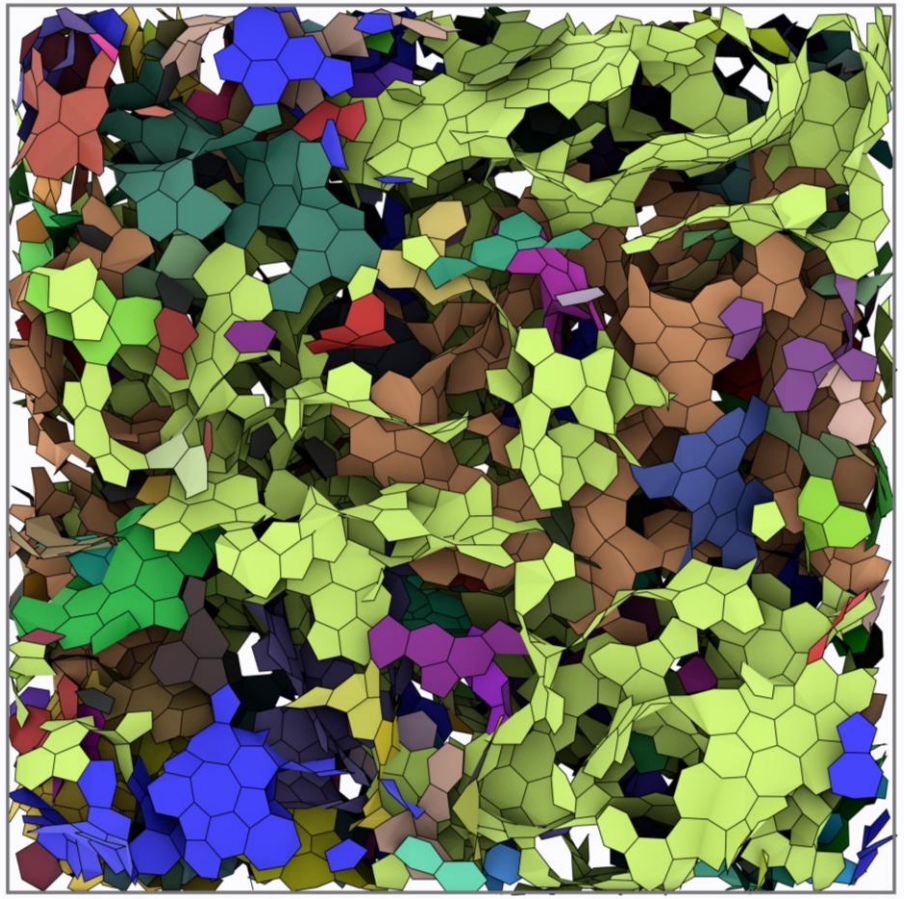

BADCY

Final Morphology: Cluster Distribution

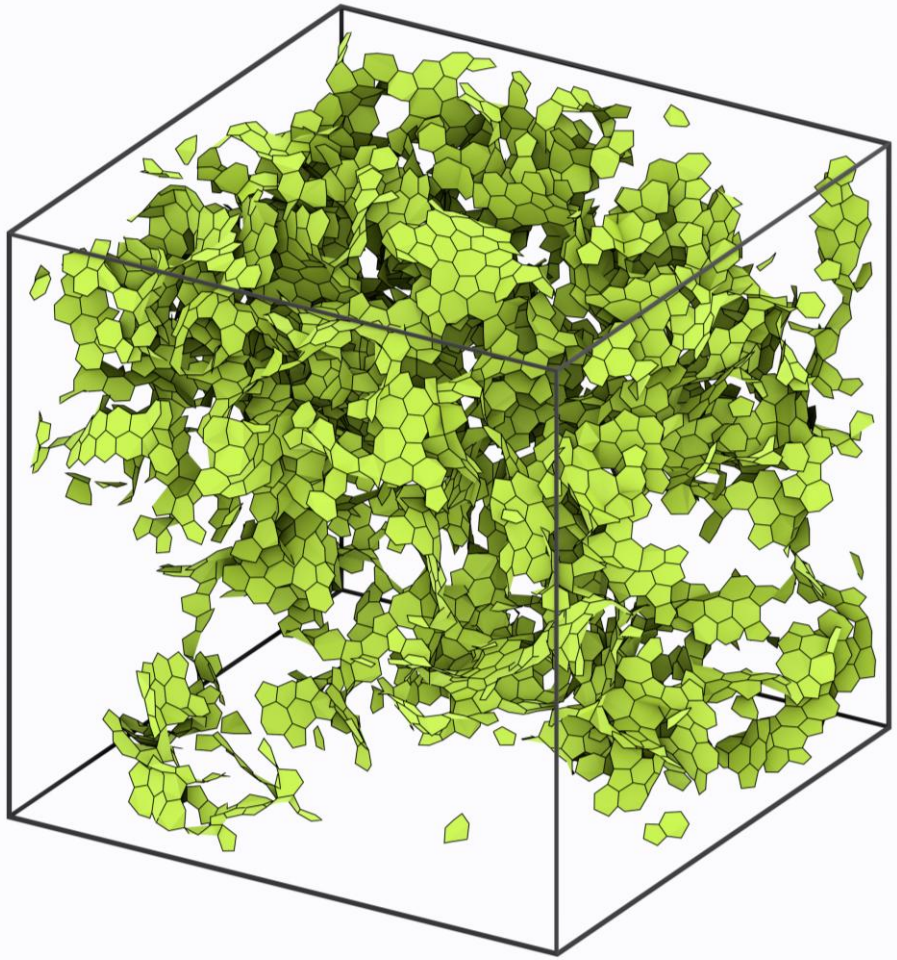

PAA, largest cluster

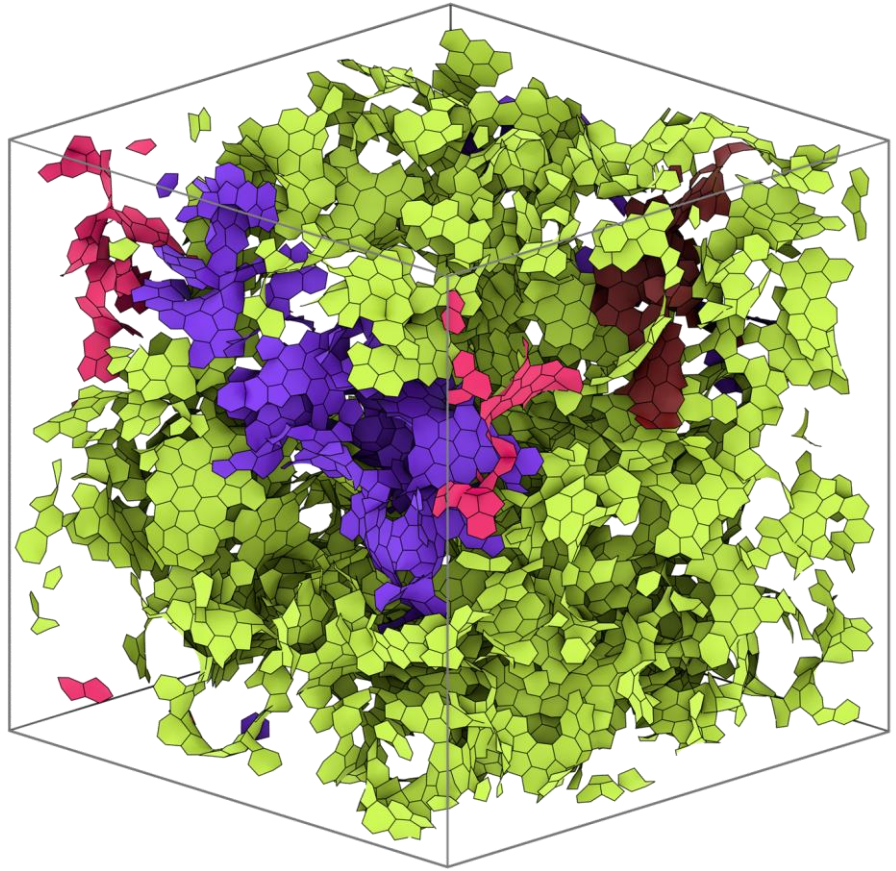

PAA, top four largest clusters

Outgassing Products

- Protocol keeps track of molecules removed from the system to mimic outgassing
- Primarily CO for oxygen-containing resins (highly stable bond)
- Useful metric to compare to experimental techniques such as TGA-mass spectrometry to confirm the chemistry is being captured accurately

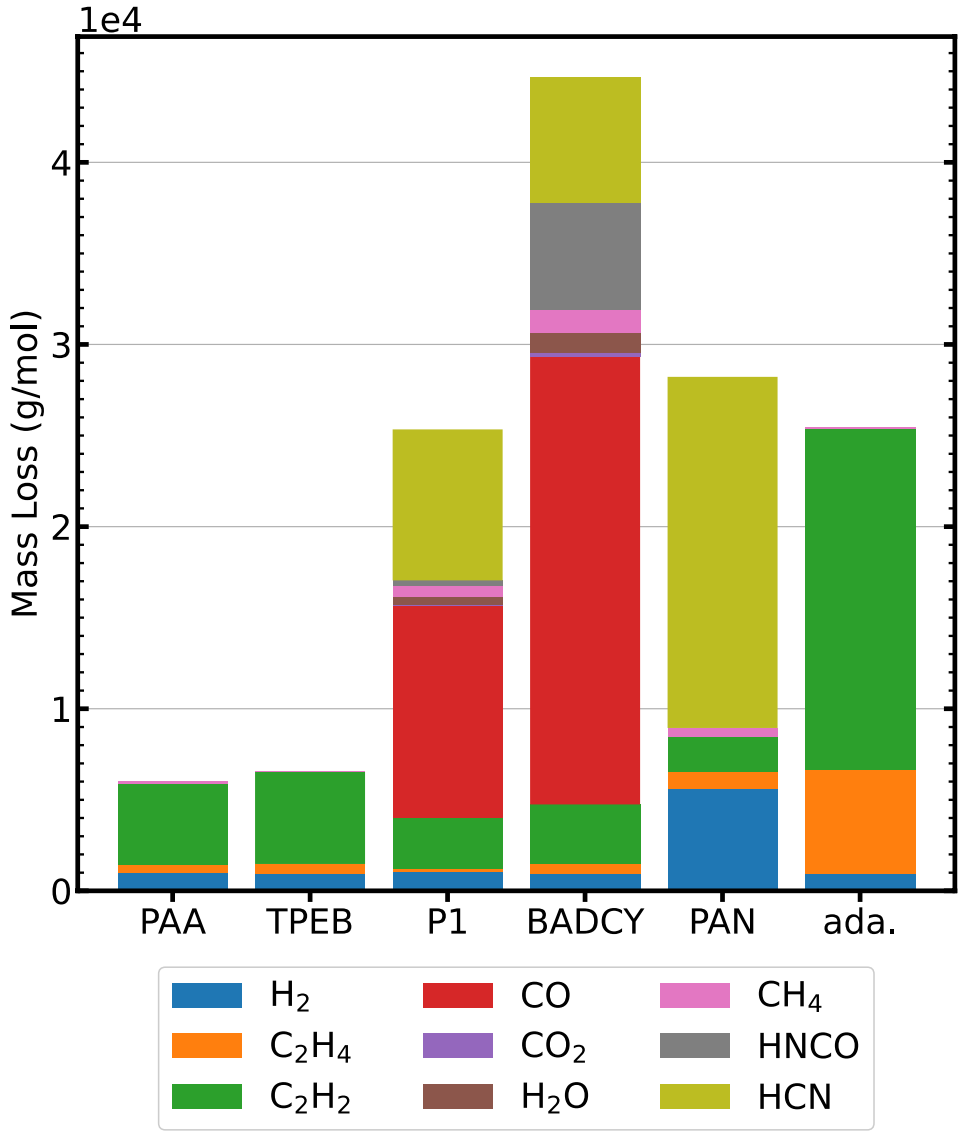

TGA: Thermal Gravimetric Analysis

Tools for Direct Experimental Comparison

- Simulated XRD pattern allows for direct comparison with experimental morphologies
- Curve is typical of non-graphitized glassy carbon at lower carbonization temperatures
- The 002 peak, which indicates graphitic structure, notably sharpens after increasing the annealing time

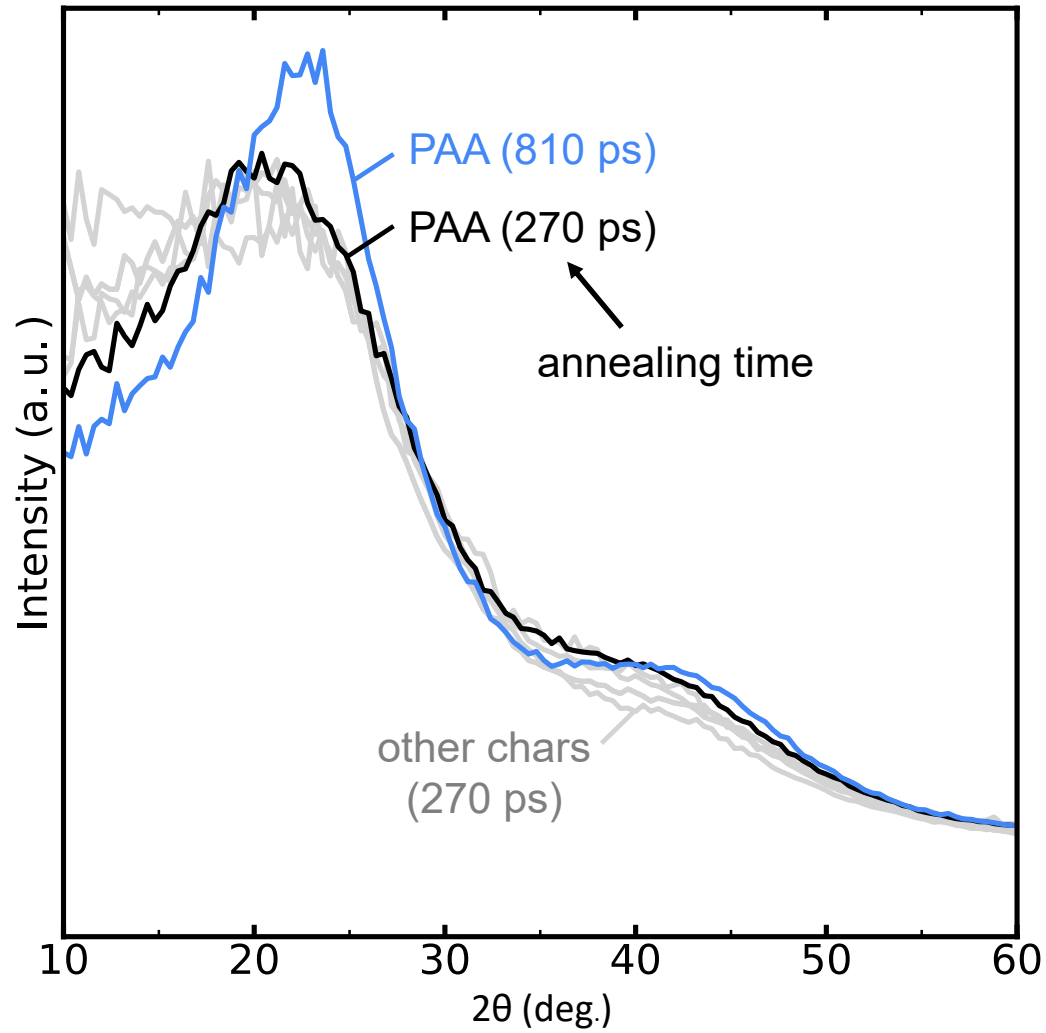

Simulating High-Resolution Microscopy

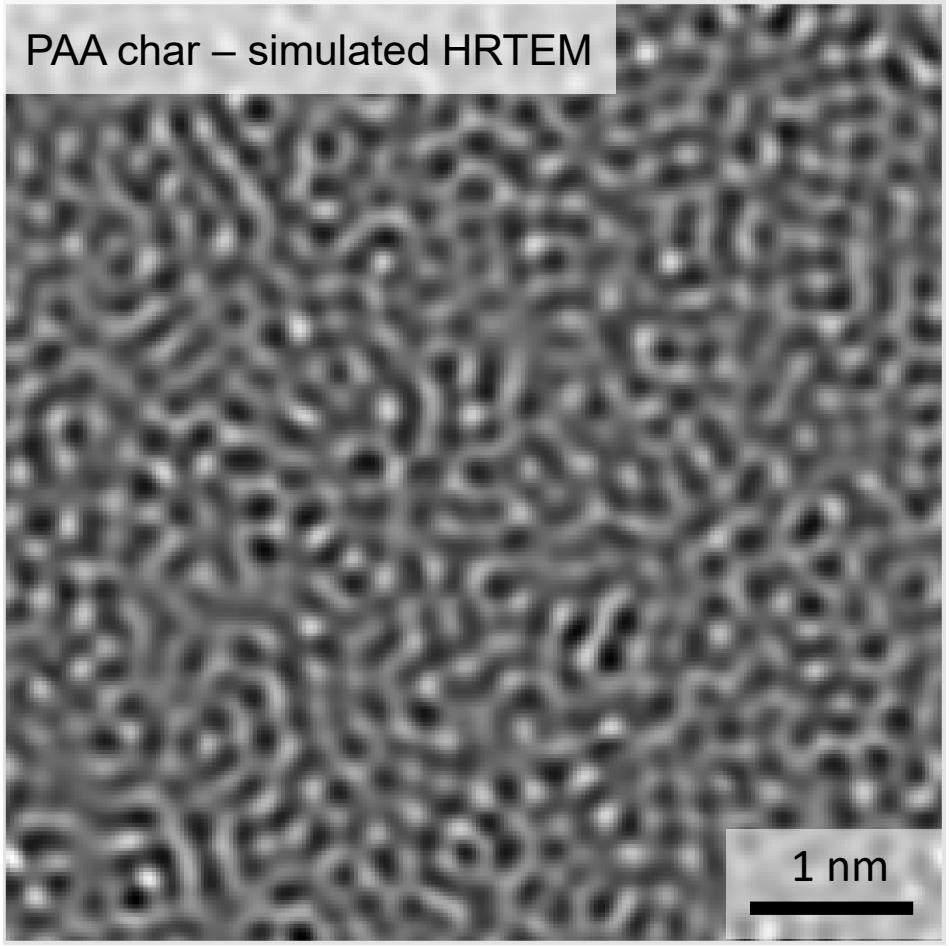

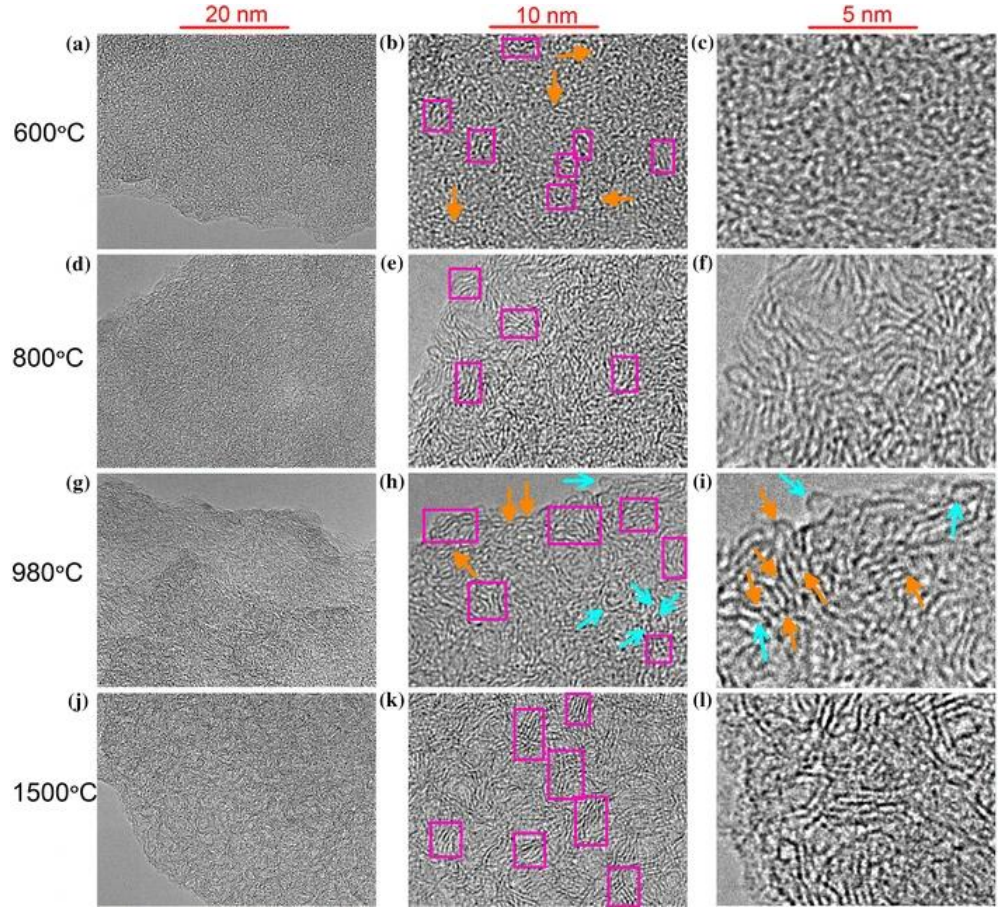

Experimental HRTEM vs. carbonization temperature

Jurkiewicz, Karolina, et al. "Evolution of glassy carbon under heat treatment: correlation structure–mechanical properties." *Journal of materials science* 53.5 (2018): 3509-3523.

Simulated microscopy consistent with non-graphitized glassy carbon at lower temperatures

Adding Interfaces to the Model

- Triple-layer graphene inserted into initial monomer configuration for composite model
- Bulk PAN char: 54 wt%, 1.76 g/cm^3
- Confined PAN: 42 wt%, 1.96 g/cm^3
- Significantly larger regions of fused six-membered rings observed at interface due to templating effect of graphene

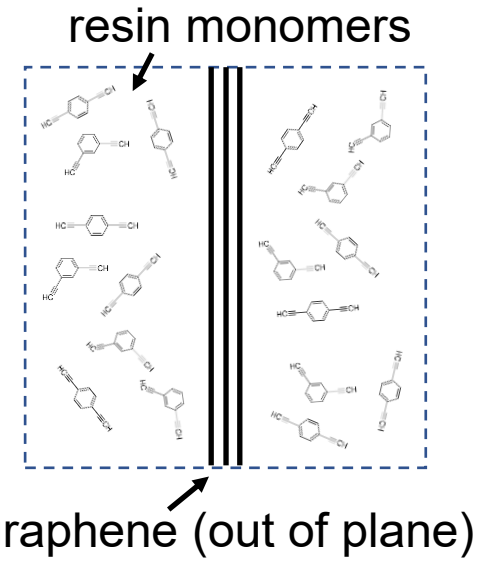

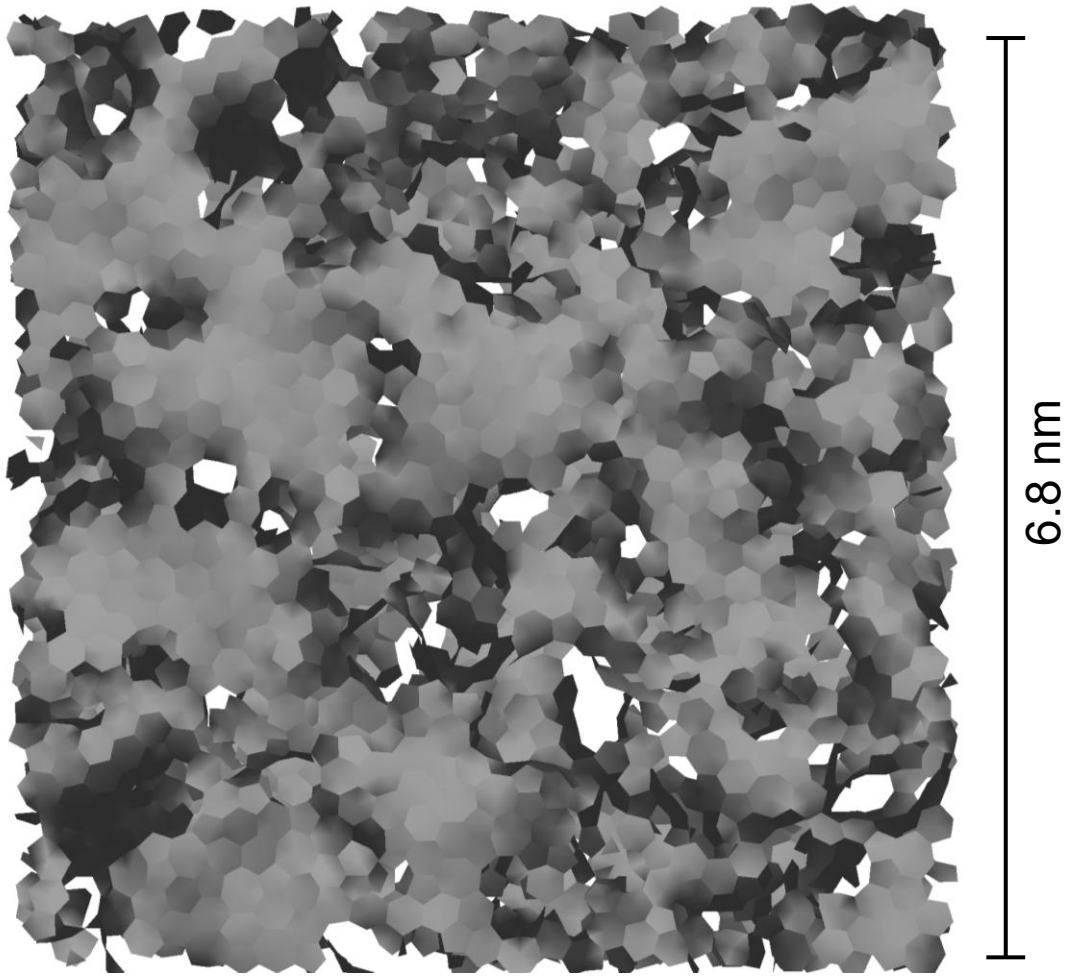

PAN char (graphene hidden)

Neat vs Confined Resin Char Yields

- Char yields for confined resins in composite systems matched those recorded for neat resin
- Implies that prediction of char yield is mostly independent of degree of confinement for this modeling protocol
- Technical Note: Graphene sheets should remain mobile to obtain realistic results

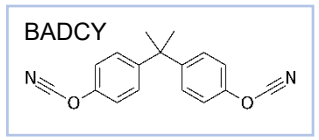

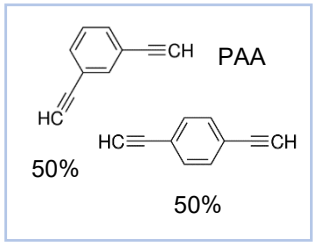

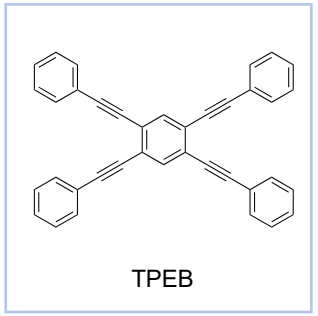



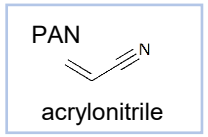

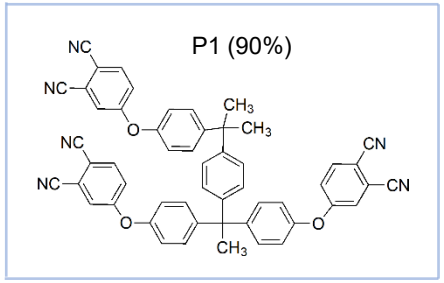

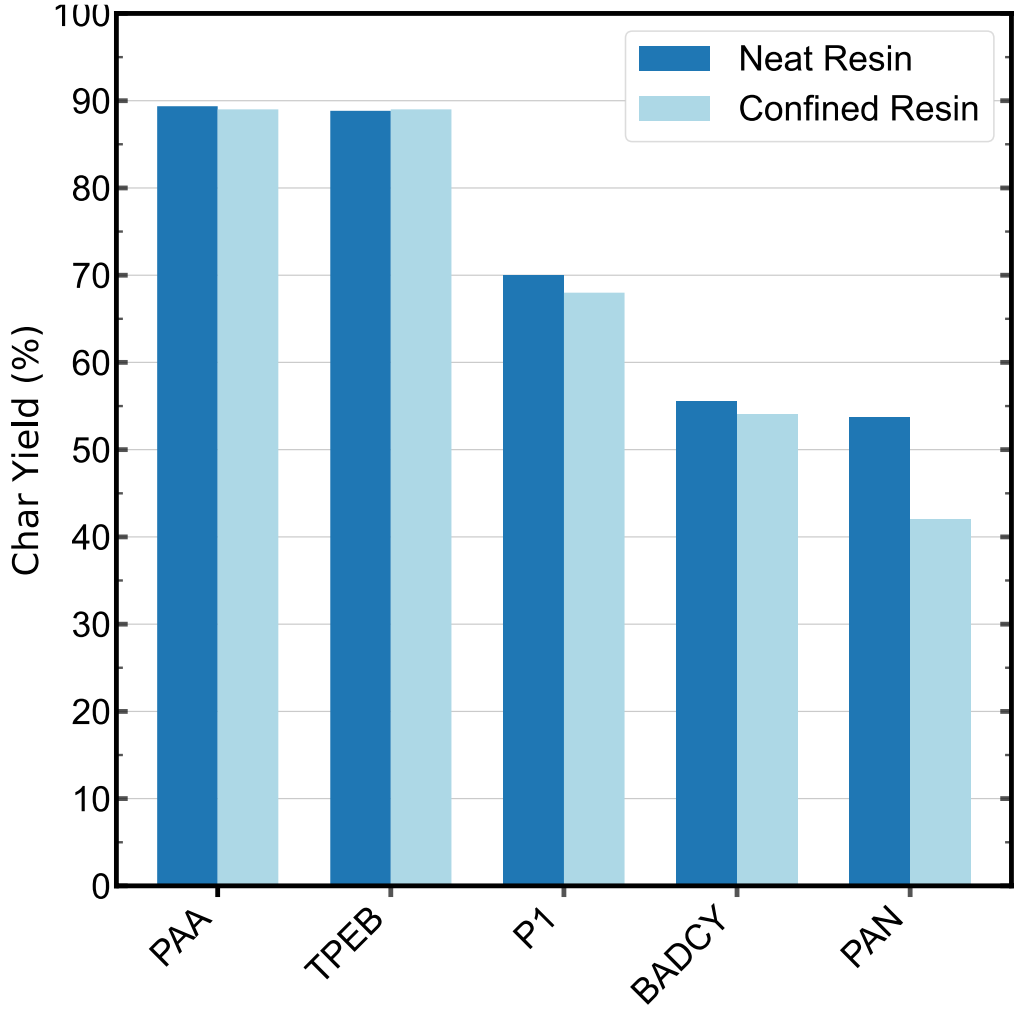

Reactivity at the Graphene Sheet Interface

- It was critical to keep graphene surface mobile to achieve charring behavior
- At each graphene-resin interface (~46 nm^2), crosslinking occurred at ~7 sites, often involving two or more adjacent crosslinks that distort the surface

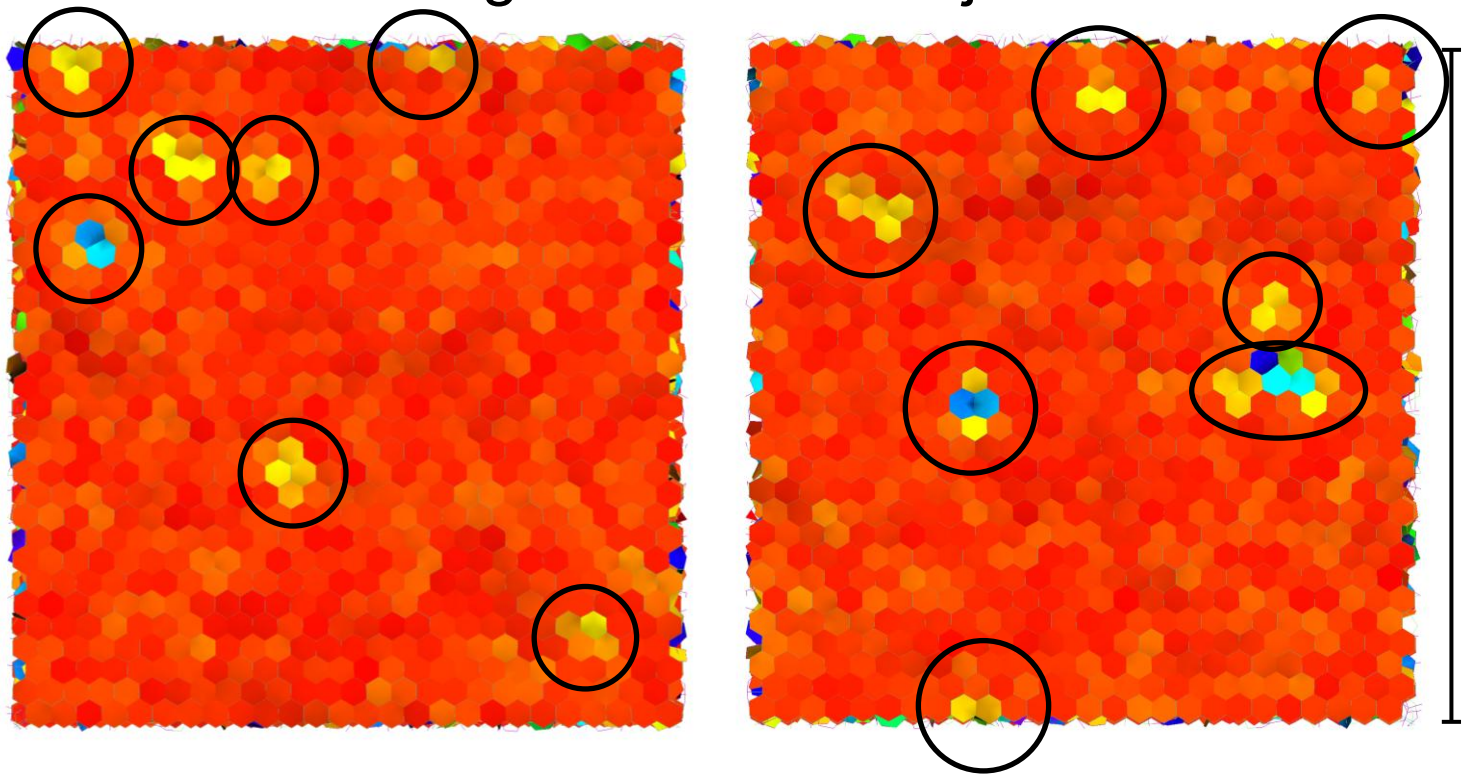

Non-resin-facing side of graphene sheets with crosslinks indicated

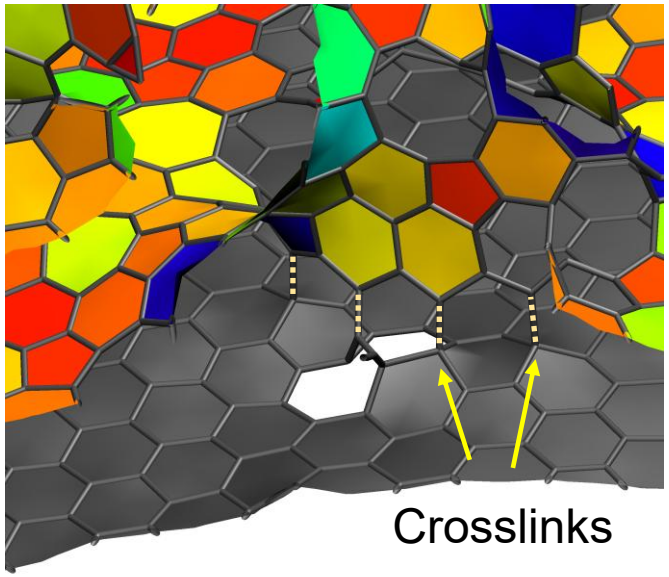

Above, graphene sheets in gray and resin char in color

Promising Method for Predicting Char Yield

- A chemically specific protocol was developed to predict char yield for high temperature resins
  - No prior knowledge of high-temperature behavior required
- Validated for low, medium and high char yield resins with various chemical structures and number of heteroatoms
- Additional outputs include atomistic structure, composition, morphology, mechanical properties, chemical pathways, outgassing products
- Currently being used to investigate and screen new chemistries

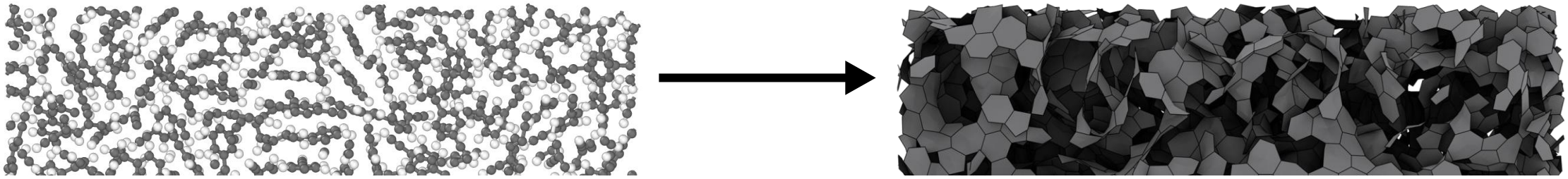

Thank You!

Acknowledgements

Vikas Varshney, AFRL
Benjamin D. Jensen, NASA Langley
CMMR Lab, the Odegard Group at Mich. Tech.
Kristopher E. Wise, NASA Langley
Emilie (Mia) J. Siochi, NASA Langley









Email (Jake Gissinger): jgissing@stevens.edu

References (experimental char yield values):

PAA (polyarylacetylene): Katzman, H. A. et al. DTIC Accession Number ADA302053, 1995.

TPEB (1,2,4,5-tetraphenylethynylbenzene): Jones, K. M. et al. Polymer, 36, 187, 1995.

P1 (phthalonitrile): Hu, Y. et al. RSC Advances, 8, 32899, 2018.

BADCY (bisphenol A dicyanate ester): Wang, Y. et al. Polymer, 77, 354, 2015.

PAN (polyacrylonitrile): Song, C. et al. J Porous Materials, 16, 197, 2009.

Adamantane: Kazanskii, B. A. et al. Russian Chemical Bulletin, 17, 2506, 1968.

MESOSTRUCTURE-INFORMED NUMERICAL MODELLING OF POST-CONSOLIDATION ARCHITECTURE IN ADVANCED PLACED PLY LAMINATES

Saral Mittal[1] and B. Gangadhara Prusty[1]

[1] ARC Training Centre for Automated Manufacture of Advanced Composites (AMAC), School of Mechanical & Manufacturing Engineering, UNSW Sydney, NSW 2052, Australia
Email: s.mittal@unsw.edu.au, g.prusty@unsw.edu.au
Web page: https://www.unsw.edu.au/research/amac/our-people,
https://www.unsw.edu.au/staff/gangadhara-prusty

Keywords: Automated Fibre Placement, Architected Materials, X-ray Computed Tomography, Finite Element Modelling

ABSTRACT

With the advent of advanced composite additive manufacturing techniques such as Automated Fibre Placement, enhanced control over the layup architectures of composite laminates has become feasible. One notable design opportunity arising from this advancement is the Advanced Placed Ply (AP-Ply) strategy which offers a promising possibility to substantially enhance delamination resistance and damage tolerance in composite laminates. As these architectures involve tows traversing across different laminate plies, conventional ply-wise modelling strategies are insufficient for accurately predicting their mechanical behaviour. A comprehensive understanding of their internal architecture, along with the effective translation of these structural characteristics into numerical models, is therefore imperative. To this end, the present work focuses on the detailed morphological characterisation of AP-Ply laminates and the subsequent development of morphology-informed numerical models. By overcoming the limitations of existing characterisation studies, this approach advances the mechanistic insight into AP-Ply architectures and simultaneously lays the groundwork for rapid and scalable performance prediction of numerous such configurations made possible through tow-level layup customisation.

1 INTRODUCTION

With the growing sophistication in composites manufacturing, there has been a search for novel design strategies that can enhance the critical mechanical properties of composite laminates. Such novel design strategies should be adaptable with advanced manufacturing methods, like Automated Fibre Placement (AFP), to enable their effective integration into current manufacturing practices and support scalable adoption. Among these, Advanced Placed Ply (AP-Ply) architectures present a promising approach to significantly improve delamination resistance and damage tolerance in composite laminates [1,2]. Numerous studies have explored the damage tolerance of these architectures through compression-after-impact (CAI) tests, reporting configuration-dependent enhancements of 5–26% relative to conventional unidirectional composites [2–6]. This is achieved by the strategic modification of the tow placement sequence, to create architectures akin to the textile laminates. The tow drop features formed by interweaving the tows from one ply to adjacent plies act as effective crack arrestors to resist delamination propagation.

The AP-Ply layup strategy strategically skips a defined number of adjacent tows during the initial deposition passes along a specific fibre orientation. Subsequent passes, executed in alternate fibre directions, are then used to populate these intentionally left gaps, resulting in a laminate with consistent overall thickness. An example of AP-Ply architecture employing a single tow skipping is presented in Figure 1.



Figure 1: Buildup of the most straightforward AP-Ply Pattern [0,90].

Altering the sequence of tow placement in AP-Ply laminates facilitates the creation of varied meso-architectures, each with distinct mechanical characteristics. However, determining the optimal configuration for a specific application through trial-and-error methods is resource-intensive and time-consuming. This highlights the necessity for a robust computational framework capable of accurately predicting both mechanical responses and failure mechanisms in such complex architectures.

Conventional ply-level modelling approaches are inadequate for representing AP-Ply laminates, as these architectures feature inter-ply tow transversal. To address this, several modelling strategies have emerged. Li et al. [7] developed a tow-wise modelling (TWM) methodology, which showed good agreement in predicting short beam strength [8], though it underperformed in simulating damage propagation under low-velocity impact [5]. Alternatively, Kok et al. [9] proposed a unit-cell-based model that homogenised undulation zones into simplified box-like elements. While this approach produced satisfactory results for quasi-static and dynamic tensile simulations [9,10], it also fell short in accurately predicting impact-induced damage [6].

These inconsistencies stem from oversimplifications in the representation of meso-scale features. Existing models often approximate tow cross-sections as idealised rectangles and address tow junctions using separation-based contact interactions or homogenisation techniques [7,9], rather than explicitly modelling the tapering of tows near the edges. Realistic simulation of deformation and damage progression at the tow level requires a detailed geometrical description of the mesoscale architecture, particularly the "tow drops", which are distinct geometric features formed where tows shift between plies.

Two principal domains have addressed meso-structural characterisation of tow drops. The first focuses on fibre waviness induced by defects such as gaps or overlaps during the layup process, which can degrade in-plane performance by up to 45% [11–13]. Here, parameters like undulation amplitude, wavelength, and angle are commonly extracted from optical micrographs, with sinusoidal representations often used to approximate tow trajectories [14–17]. However, these investigations primarily deal with isolated features and do not reflect the periodicity and complexity of patterned AP-Ply designs.

The second area relates to textile composites, where post-consolidation fibre geometry has been extensively studied using various characterisation techniques, particularly X-ray computed tomography (CT) [18–20]. Various segmentation strategies have been introduced to identify individual tow morphology, including automated approaches based on structure tensor analysis of greyscale intensity gradients [21,22]. However, challenges persist in resolving tow structures at lower voxel resolutions, that are required to capture large-scale architectural patterns, due to low phase contrast in carbon fibre-reinforced polymers (CFRPs). Even advanced techniques such as structure tensor filtering or contour stitching struggle to delineate tow boundaries when in-plane intensity gradients are weak.

This work presents the first comprehensive attempt to parametrically evaluate the post-consolidation tow morphology in AP-ply laminates using a combination of multiple characterisation techniques. High-resolution microscopic imaging is employed to capture out-of-plane undulation characteristics, while low-resolution CT scans with large scanning windows enable 3D visualisation of the periodic tow structure. A novel through-thickness morphological gradient based approach is introduced which leverages directional differences in X-ray attenuation caused by fibre orientation to enhance the visibility of low-contrast features, enabling more effective interpretation of internal geometry in CFRPs. The extracted morphological parameters are then incorporated into finite element simulations of tensile behaviour, with the numerical predictions validated against experimental results from corresponding AFP-fabricated specimens.

2 EXPERIMENTAL PROGRAM

2.1 Manufacturing

Three distinct AP-Ply laminate configurations with [0/90] design were fabricated (as shown in Figure 1), each differing in the spacing between adjacent tows. The first configuration followed the standard AP-Ply layup, incorporating a single tow gap that was subsequently filled during later passes in the same orientation. In contrast, the second and third configurations introduced additional inter-tow gaps measuring 40% and 80% of the tow width respectively, which resulted in final inter-tow gaps of 20% and 40% of the tow width after all passes were completed.

Carbon fibre epoxy prepreg tapes (HTS45E23/E−752-LT) by Park Aerospace, were used for the layup. Each tape measured 6.35 mm in width and 0.19 mm in thickness. The layup process was carried out using an AFP machine developed by Trelleborg Sealing Solutions® located at the University of New South Wales. For each configuration, ten AP-Ply style plies were deposited to form square panels measuring 300 mm × 300 mm. Curing was performed in an ASC autoclave at 177°C and 6.2 bar, following the supplier's recommended protocol.

Prior to consolidation, surface irregularities were evident across all panels. These were caused either by out-of-plane waviness in the no-gap configuration or by the presence of inter-tow gaps in the gapped variants. However, post-consolidation, all laminates exhibited smooth and uniform surfaces. This can be attributed to tow spreading, which not only filled the gaps but also led to a reduction in overall thickness for the gapped panels. Final thicknesses were measured at 2.55 mm and 2.2 mm for the 20% and 40% gap configurations, respectively. In contrast, the baseline and 0% gap panels retained a thickness of 3 mm, consistent with the material's standard specification. Figure 2 illustrates the layup progression for the 40% gap configuration.

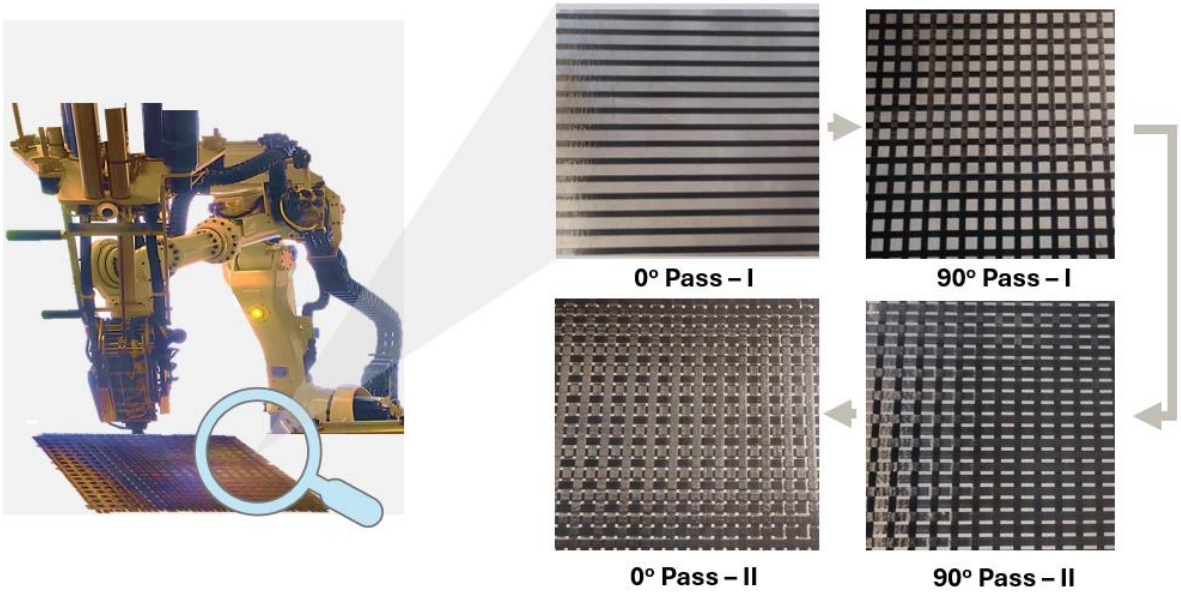

Figure 2: Hot gas torch-based AFP machine at UNSW Sydney. The right side of the figure presents a robot layup sequence during the fabrication of 40% gap AP-Ply configuration.

2.2 Optical Microscopy

The undulation patterns were analysed using optical microscopy to examine the internal structure of the laminates. For each configuration, small specimens were extracted along the midline of the undulating tows. Microscopic imaging was performed using a DSX510 optical microscope operating at 10× magnification. The boundaries of the undulating tows were extracted through digital image processing of the obtained high-resolution optical micrographs. A sine wave-like curve emerged when the manually traced coordinates were plotted on the X-Y axis. This curve was then fitted to a sine

function to characterise the undulation. By calculating the maximum slope of the fitted curve, the out-of-plane undulation angle was estimated. Figure 3 graphically illustrates the methodology described above.

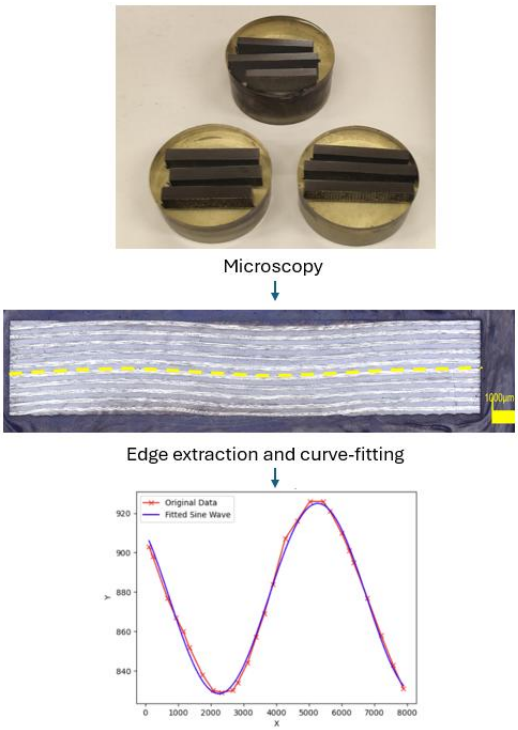

Figure 3: Characterisation methodology for optical microscopy method.

2.3 X-Ray CT scanning

To complement the 2D insights from optical microscopy, a three-dimensional understanding of the laminate morphology was obtained through X-ray computed tomography (CT). Using a HeliScan™ micro-CT system (Mark I), samples from each configuration measuring 44 mm x 35 mm were scanned. A voxel resolution of 29.44 µm was selected, balancing the need to capture at least twice the representative unit cell (RUC) size with sufficient detail to resolve the sinusoidal tow undulations.

Scans were conducted along a circular trajectory at 60 kV and 105 µA, with a 1 mm aluminium filter, and the rotation axis aligned parallel to the warp (1st pass) tows. This setup ensured that the warp fibres remained perpendicular to the X-ray beam throughout the scan, while the weft fibres rotated from perpendicular to parallel orientations. Due to their alignment with the X-ray beam during scanning, the weft fibres experienced increased attenuation, primarily caused by small-angle scattering. This resulted in slightly higher intensity values for such voxels. To verify that this contrast was directionally dependent, the laminate (20% gap configuration) was rotated so that the weft fibres remained perpendicular to the beam throughout the scan. Under this new orientation, the warp fibres exhibited increased intensity, confirming the influence of fibre orientation on X-ray attenuation.

Because the inter-ply spacing was much smaller than the voxel resolution and no universal threshold could reliably distinguish warp from weft tows, conventional segmentation techniques proved ineffective. To overcome these limitations, signal processing-based algorithms were developed to identify individual tows within the bulk laminate structure.

Prominent intensity peaks, attributed to the asymmetrical scanning setup, were observed in the through-thickness intensity profiles and corresponded to the weft tows. These peaks were used to precisely map the geometry of the weft tows. As demonstrated in the 20% gap configuration, rotating the CT scan setup proves to be an effective approach for characterising the geometry of warp tows.

To detect the most prominent peaks in the intensity data, the find_peaks function in Python was applied, using a minimum spacing parameter based on ply thickness. However, due to sub-peak

detection or missing prominent peaks, the number of detected peaks sometimes differed from the actual number of weft plies. To correct these inconsistencies, a sequence correction algorithm was introduced. This method replaced inaccurate peak sets, those with incorrect lengths, with corrected ones inferred from adjacent regions where the peak count matched the expected ply number. Figure 4 presents the flow chart for the above-described characterisation methodology.

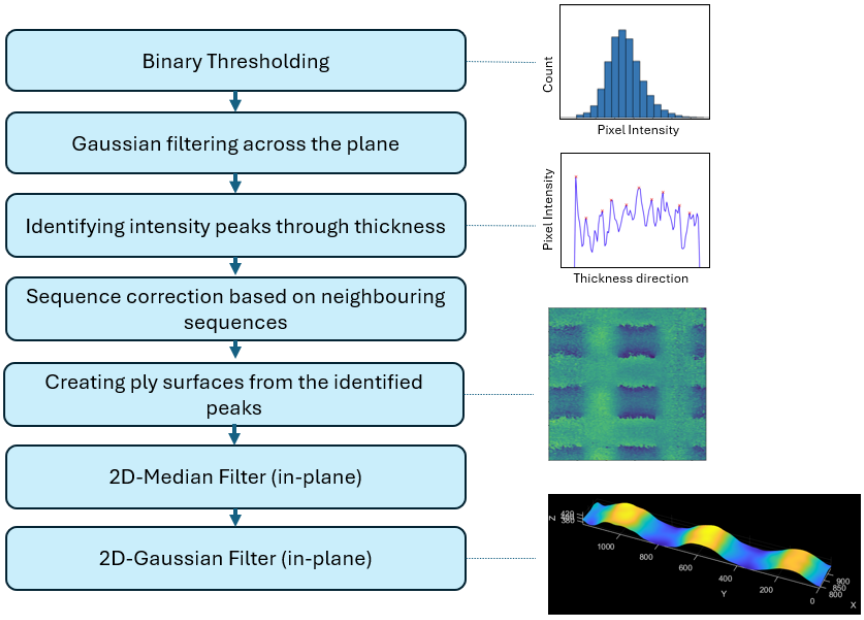

Figure 4: Characterisation methodology for individual tow segmentation using CT-scan data.

2.4 Tensile testing

Following ASTM D3039, tensile tests were conducted to evaluate the static mechanical performance of the fabricated laminates. Using a water-cooled diamond saw, five specimens per configuration were sectioned to 35.56 mm × 254 mm, with their length aligned along the warp direction. To mitigate fibre damage at the grips, 82 mm-long glass fibre tabs were bonded to both ends using epoxy resin. Testing was performed on an Instron 3369 machine, equipped with hydraulic grips to maintain secure clamping. A constant displacement rate of 2 mm/min was applied throughout the test. Strain measurement was achieved using unidirectional linear gauges placed on the underside of each specimen, directly above a non-undulating warp tow.

3 FINITE ELEMENT MODELLING

To preserve key architectural features while maintaining computational efficiency, several geometric simplifications were introduced in the AP-Ply laminate models:

1. Instead of manually modelling the unique undulation angle for each tow, the average undulation angle derived from microscopy data, was applied uniformly across all tows in both directions.
2. The sinusoidal out-of-plane tow paths were idealised as trapezoidal trajectories. This assumption, commonly adopted in textile composite modelling improves mesh conformity and eliminates voids, thereby enhancing computational performance.
3. A trapezoidal cross-section was assigned to each tow, to capture the tapering at tow edges. This choice complements the trapezoidal undulation profile and further facilitates the generation of a conformal mesh.

Figure 5 illustrates the representative geometric models constructed using these assumptions.

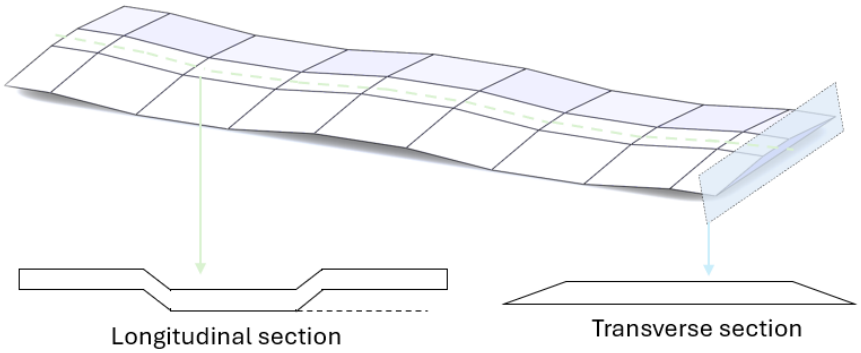

Figure 5: Representative geometry of the undulating tow along with longitudinal and transverse cross sections views.

To predict failure initiation in composite laminates, 3D Hashin criterion is employed due to its ability to differentiate between fibre and matrix damage under both tensile and compressive loads [23]. This extended formulation consists of four distinct sub-criteria, each addressing a specific failure mode.

Fibre tension failure:

$$F_{ft} = \left(\frac{\sigma_{11}}{X_t}\right)^2 + \left(\frac{\sigma_{12}}{S_{12}}\right)^2 + \left(\frac{\sigma_{13}}{S_{13}}\right)^2 \geq 1 \tag{1}$$

Fibre compression failure:

$$F_{fc} = \left(\frac{\sigma_{11}}{X_c}\right)^2 \geq 1 \tag{2}$$

Matrix tension failure:

$$F_{mt} = \left(\frac{\sigma_{22}+\sigma_{33}}{Y_t}\right)^2 + \left(\frac{\sigma_{23}^2-\sigma_{22}\sigma_{23}}{S_{23}^2}\right) + \left(\frac{\sigma_{13}}{S_{13}}\right)^2 + \left(\frac{\sigma_{12}}{S_{12}}\right)^2 \geq 1 \tag{3}$$

Matrix compression failure:

$$F_{mc} = \left(\frac{\sigma_{22}+\sigma_{33}}{2S_{23}}\right)^2 + \frac{\sigma_{22}+\sigma_{33}}{Y_c}\left[\left(\frac{Y_c}{2S_{23}}\right)^2 - 1\right] + \left(\frac{\sigma_{23}^2-\sigma_{22}\sigma_{23}}{S_{23}^2}\right) + \left(\frac{\sigma_{12}}{S_{12}}\right)^2 + \left(\frac{\sigma_{13}}{S_{13}}\right)^2 \geq 1 \tag{4}$$

Post-failure behaviour in composite laminates is heavily influenced by how damage evolves across different failure modes. Although various softening laws, like linear, exponential, or sigmoidal, have been proposed [9,24], the bilinear softening model offers the most accurate representation of tensile stress-strain response along the fibre direction [24,25] and hence been used to simulate fibre tensile damage evolution in this work. Damage evolution for the remaining failure modes is modelled through linear softening model.

To simulate inter-tow interactions, built-in contact algorithms in ABAQUS were used. Cohesive surfaces governed by a linear traction-separation law captured interlaminar behaviour, with delamination strength defining the peak traction. Normal and tangential contact forces were handled using ABAQUS' general contact algorithm, where a hard contact condition was applied to prevent ply interpenetration. The material parameters for the prepreg tapes (HTS45E23/E−752-LT) were utilised according to the specifications outlined in previous studies [8,26,27].

Displacement-controlled boundary conditions were imposed at one end of the laminate, while the opposite end was fully constrained in ABAQUS Explicit. A smooth ramp function was used to gradually increase displacement to reduce dynamic effects from sudden loading.

Mesh sensitivity analysis guided the selection of a 0.5 mm mesh size, ensuring reliable results without excessive computational cost. Given the trapezoidal tow geometry, wedge elements (C3D6) were employed to maintain uniform meshing. Element deletion was triggered when the fibre damage factor exceeded 1, indicating complete stiffness degradation in the fibre direction.

4 RESULTS

4.1 Optical Microscopy

To quantify tow undulation, edge coordinates from the fifth ply were extracted and fitted to a sine function, enabling derivation of undulation parameters for each laminate configuration. While the 0% gap configuration exhibited a near-perfect sinusoidal trajectory, and the 20% gap case followed a similar pattern, the 40% gap configuration deviated significantly. This disruption was caused by ply slippage, which introduced irregular overlaps and gaps at tow junctions, resulting in alternating steep and shallow undulation slopes.

Figure 6 reports the undulation angles along with associated uncertainties. In both the 0% and 20% gap cases, the weft direction exhibited higher undulation angles than the warp. However, the 20% gap configuration showed reduced undulation angles overall, attributed to thinner tows and increased spacing between them.

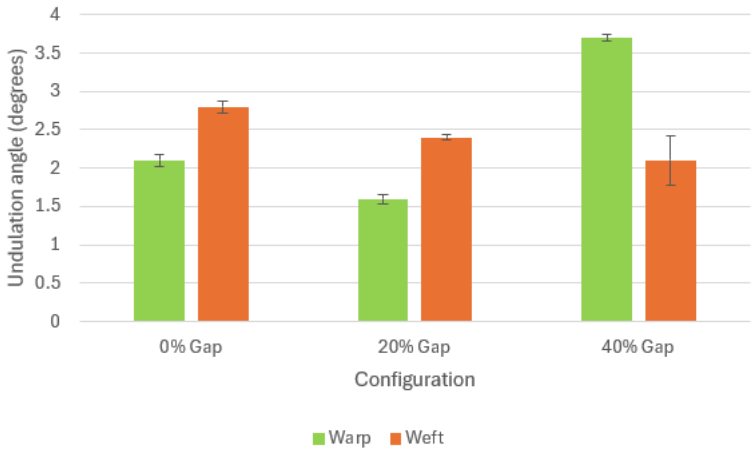

Figure 6: Microscopy derived undulation angle for each AP-Ply configuration in both warp ad weft direction. Error bars represent standard deviation.

4.2 X-Ray CT scanning

To locate the mid-planes of warp and weft tows, morphological gradients along the thickness direction were analysed. After filtering, the 3D geometry and mid-line trajectory of the same ply are visualised in Figure 7. The undulating tows in the 0% case closely follow sinusoidal path, where 20% gap case showed considerable deviation. This regularity breaks down further in the 40% gap configuration, where the trajectory shows altering pattern mirroring microscopy observations.

Doubly curved mid-planes of the weft tows at the crest zones were a unique morphology characteristic observed in 3D analysis. These curvatures are due to their location directly beneath the undulations of the warp tows. In contrast, peak regions above straight tows show no such curvature. However, CT scan analysis consistently reported angles 15–20% lower than microscopic observations for various directions and configurations. This discrepancy stems from the limited resolution of CT scans, where undulation heights are only 4–5 times the voxel size.

Still, CT-based measurements correctly captured key trends such as higher weft undulation angles in the 0% gap case than the warp angles and a general reduction in angle for the 20% gap configuration. While CT offers valuable 3D visualisation, its quantitative accuracy remains resolution-dependent.

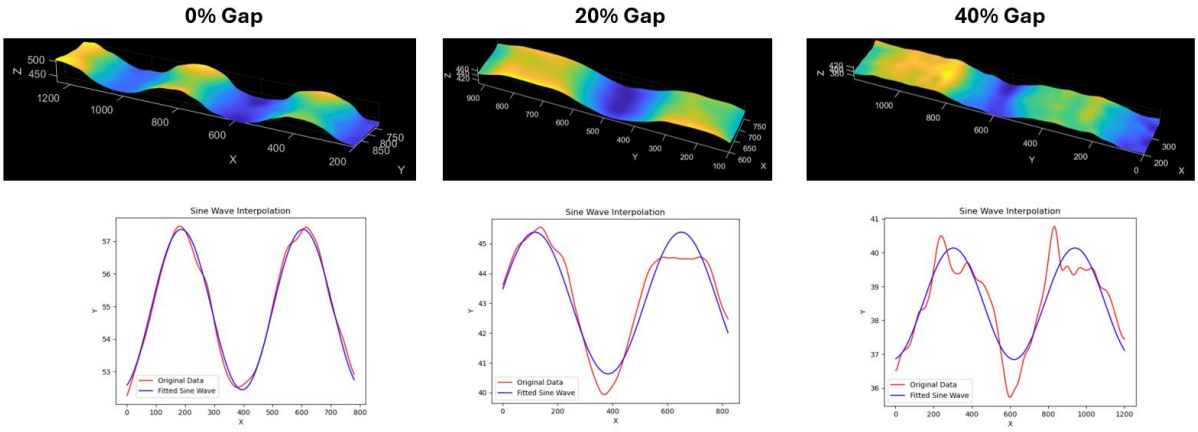

Figure 7: Visualisation of the undulating tows in each AP-ply configuration and their corresponding out-of-plane trajectory (with fitted sine-curve).

4.3 Tensile performance

The tensile response of AP-Ply laminates was simulated using the morphologically-informed model described in Section 3. Figure 8 compares the simulated tensile behaviour for each configuration with the experimentally observed response. Given the high degree of manufacturing inconsistencies observed in 40% gap laminate, this configuration was excluded from the FEA analysis. Table 1 presents a summarized comparison of the numerical and experimental strength values. Compared to conventional models [8,9], this approach significantly improves predictive accuracy.

Minor under-prediction of strength was observed across simulations, specifically for 0% gap configuration. This can be attributed to the to the sharp geometric transitions in the modelled laminate, which differ from the smoother contours found in actual specimens. Despite experimental results showing nearly identical strength, the simulation predicted slightly higher values for the 20% gap configuration than the 0% gap case. This discrepancy stems from minor defects found during characterisation of the 20% gap samples, which were not included in the model.

The numerical model effectively captured both the onset and evolution of tensile failure mechanisms. Owing to the lower strain-to-failure threshold in the matrix compared to the fibres, matrix tensile damage initiated early in the transverse tows. This damage mode progressively intensified, ultimately leading to complete matrix failure and a significant reduction in transverse stiffness within the failed tows much before fibre failure occurred.

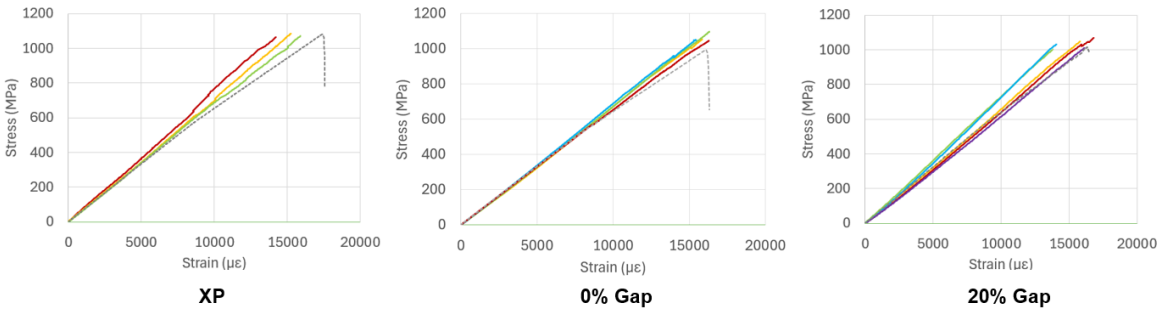

Figure 8: Stress-strain response obtained through simulation for each configuration.

Configuration	Strength, MPa (CV%)	Simulated Strength, MPa	Error (%)
XP	1087.92 (2.00%)	1082.08	-0.54%
0% Gap	1055.09 (2.60%)	997.38	-5.47%
20% Gap	1032.75 (2.70%)	1012.67	-1.94%

Table 1: Comparison of experimental and simulated tensile strength.

Figure 9 shows the stress field maps which identifies the stress concentration sites in longitudinal tows, particularly near nodes where transverse tows taper. These regions are formed by the intersection of flat and sloped surfaces which creates sharp edges that triggered fibre failure. Once initiated, failure propagated rapidly due to low fracture toughness in the fibre direction. Crack fronts in longitudinal tows develop in transverse direction, which is coherent with post-failure inspection of the tested samples.

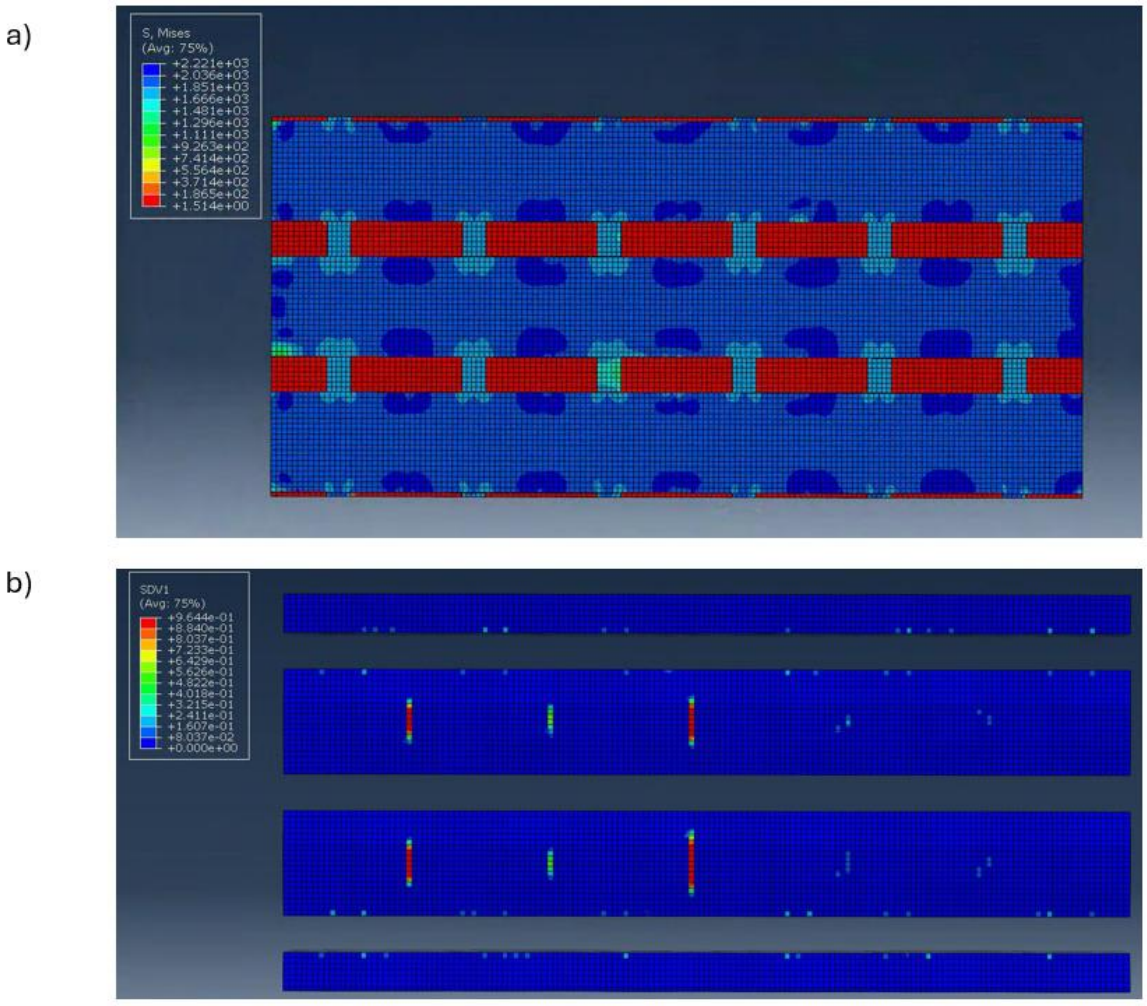

Figure 9: a) Stress distribution field showing principal stress in fibre direction when the fibre failure initiates; b) Fibre tensile damage initiation sites in longitudinal tow.

9 CONCLUSIONS

This study utilises detailed morphological characterisation of AP-Ply laminates to develop a high-fidelity finite element model capable of accurately predicting their tensile behaviour. Three distinct AP-

Ply architectures were fabricated using a hot-gas torch-based Automated Fibre Placement (AFP) system. While the layup process initially produced highly uneven surfaces, the developed protrusions or gaps were eliminated post-curing, primarily due to tow spreading. Internal geometries for these laminates were characterised using optical microscopy and X-ray computed tomography (CT), and the extracted meso-structural data were parameterised to construct representative geometries for numerical modelling.

Given the minimal inter-ply spacing after consolidation and the limited resolution of CT scans, conventional segmentation techniques proved inadequate. To address this, novel segmentation algorithms were developed to reliably isolate individual tows.

Notably, AP-Ply laminates maintained strength and stiffness performance close to baseline laminates, despite the presence of fibre undulations. This reinforces their suitability as replacements for conventional non-woven architectures, with the added benefit of enhanced toughness.

The morphologically informed numerical framework developed in this work demonstrated strong predictive capability, estimating tensile strength within a 6% margin of experimental results. Furthermore, the model successfully captured the initiation and evolution of distinct damage modes within individual tows. Overall, this research establishes a foundation for meso-scale modelling strategies that can accurately predict both mechanical behaviour and failure mechanisms in meso-architectured laminates, an essential step toward the design of next-generation composite structures.

ACKNOWLEDGEMENTS

The authors would like to acknowledge the following funding:
ARC LIEF: Australasian facility for the automated fabrication of high-performance bespoke components (LE140100082).
ARC ITTC: ARC Training Centre for Automated Manufacture of Advanced Composites (IC160100040).
ACM CRC: Australian Composites Manufacturing Cooperative Research Centre (ACM CRC) (CRCXXIIIA000003).
The authors further acknowledge the Tyree X-ray CT Facility, X-ray Analysis Facility, Mark Wainwright Analytical Centre, UNSW Sydney, for the acquisition of the 3D μXCT images.

REFERENCES

[1] M. Nagelsmit, C. Kassapoglou, Z. Gürdal, Nationaal Lucht-en Ruimtevaartlaboratorium National Aerospace Laboratory NLR NLR-TP-2010-626 A New Fibre Placement Architecture for Improved Damage Tolerance, in: 2011. https://www.semanticscholar.org/paper/Nationaal-Lucht-en-Ruimtevaartlaboratorium-National-Nagelsmit-Kassapoglou/b61a6df932bed39c5c4e23afa5bae054edae36eb (accessed April 7, 2024).

[2] M.H. Nagelsmit, Fibre Placement Architectures for Improved Damage Tolerance, [object Object], 2013. https://doi.org/10.4233/UUID:F8C8AD4E-5D52-4BFD-8449-2748BAD26673.

[3] K. Kodagali, C. Vakili Rad, S. Sockalingam, Z. Gurdal, E. Miller, Low velocity impact and compression-after-impact response of hybrid pseudo-woven meso-architectured carbon/epoxy composite laminates manufactured via automated fiber placement, Composites Part B: Engineering 271 (2024) 111154. https://doi.org/10.1016/j.compositesb.2023.111154.

[4] C. Vakili Rad, K. Kodagali, J. Roark, D. Revilock, C. Ruggeri, R. Harik, S. Sockalingam, High velocity impact response of hybridized pseudo-woven carbon fiber composite architectures, Composites Part B: Engineering 203 (2020) 108478. https://doi.org/10.1016/j.compositesb.2020.108478.

[5] X. Li, Mesoscale Numerical Modelling and Failure Prediction of Automated Fibre Placement Composites, PhD Thesis (2022).

[6] R. Kok, R. Cuvillo, V. Rodríguez-García, J. Pernas, J.A. Artero-Guerrero, R. Guzmán de Villoria, F. Martínez-Hergueta, Low velocity impact response of Automated Fiber Placement Advanced Placed Ply composites, Composites Science and Technology 253 (2024) 110636. https://doi.org/10.1016/j.compscitech.2024.110636.

[7] X. Li, J. Dufty, G.M. Pearce, Automation of tow wise modelling for automated fibre placement and filament wound composites, Composites Part A: Applied Science and Manufacturing 147 (2021) 106449. https://doi.org/10.1016/j.compositesa.2021.106449.
[8] X. Li, S.A. Brown, M.W. Joosten, G.M. Pearce, Tow wise modelling of non-conventional automated fibre placement composites: short beam shear study, Composites Part A: Applied Science and Manufacturing 154 (2022) 106767. https://doi.org/10.1016/j.compositesa.2021.106767.
[9] R. Kok, F. Martinez-Hergueta, F. Teixeira-Dias, Tensile response of AP-PLY composites: A multiscale experimental and numerical study, Composites Part A: Applied Science and Manufacturing 159 (2022) 106989. https://doi.org/10.1016/j.compositesa.2022.106989.
[10] R. Kok, M. Peroni, F. Martinez-Hergueta, A. Pellegrino, Dynamic response of Advanced Placed Ply composites, Composites Part B: Engineering 248 (2023) 110347. https://doi.org/10.1016/j.compositesb.2022.110347.
[11] X. Ju, J. Xiao, D. Wang, C. Zhao, T. Gao, X. Wang, Effect of gaps/overlaps induced waviness on the mechanical properties of automated fiber placement (AFP)-manufactured composite laminate, Mater. Res. Express 9 (2022) 045305. https://doi.org/10.1088/2053-1591/ac6858.
[12] H.M. Hsiao, I.M. Daniel, Elastic properties of composites with fiber waviness, Composites Part A: Applied Science and Manufacturing 27 (1996) 931–941. https://doi.org/10.1016/1359-835X(96)00034-6.
[13] M.H. Nguyen, A.A. Vijayachandran, P. Davidson, D. Call, D. Lee, A.M. Waas, Effect of automated fiber placement (AFP) manufacturing signature on mechanical performance of composite structures, Composite Structures 228 (2019) 111335. https://doi.org/10.1016/j.compstruct.2019.111335.
[14] B. Böckl, A. Wedel, A. Misik, K. Drechsler, Effects of defects in automated fiber placement laminates and its correlation to automated optical inspection results, Journal of Reinforced Plastics and Composites 42 (2023) 3–16. https://doi.org/10.1177/07316844221093273.
[15] Z. Zhang, C. Chen, S. Zhang, C. Guo, M. Ni, X. Liu, K. Yang, Q. Chen, H. Wang, Effect of AFP induced triangular gaps on manufacturing quality and stress distribution of composite panels, Composites Science and Technology 243 (2023) 110222. https://doi.org/10.1016/j.compscitech.2023.110222.
[16] M.H. Nguyen, P. Davidson, A.M. Waas, Experimental and numerical study on the tensile failure behavior of toughened-interlayer composite laminates with automated fiber placement (AFP) induced gap and overlap defects, Int J Mater Form 14 (2021) 105–119. https://doi.org/10.1007/s12289-020-01581-w.
[17] J. Wang, K. Potter, K. Hazra, M. Wisnom, Experimental fabrication and characterization of out-of-plane fiber waviness in continuous fiber-reinforced composites, Journal of Composite Materials 46 (2012) 2041–2053. https://doi.org/10.1177/0021998311429877.
[18] R.D.B. Sevenois, D. Garoz, F.A. Gilabert, S.W.F. Spronk, S. Fonteyn, M. Heyndrickx, L. Pyl, D. Van Hemelrijck, J. Degrieck, W. Van Paepegem, Avoiding interpenetrations and the importance of nesting in analytic geometry construction for Representative Unit Cells of woven composite laminates, Composites Science and Technology 136 (2016) 119–132. https://doi.org/10.1016/j.compscitech.2016.10.010.
[19] J. Holmes, S. Sommacal, R. Das, Z. Stachurski, P. Compston, Characterisation of off-axis tensile behaviour and mesoscale deformation of woven carbon-fibre/PEEK using digital image correlation and X-ray computed tomography, Composites Part B: Engineering 229 (2022) 109448. https://doi.org/10.1016/j.compositesb.2021.109448.
[20] A. Madra, P. Breitkopf, A. Rassineux, F. Trochu, Image-based model reconstruction and meshing of woven reinforcements in composites, International Journal for Numerical Methods in Engineering 112 (2017) 1235–1252. https://doi.org/10.1002/nme.5555.
[21] I. Straumit, S.V. Lomov, M. Wevers, Quantification of the internal structure and automatic generation of voxel models of textile composites from X-ray computed tomography data, Composites Part A: Applied Science and Manufacturing 69 (2015) 150–158. https://doi.org/10.1016/j.compositesa.2014.11.016.

[22] M. Krause, J.M. Hausherr, B. Burgeth, C. Herrmann, W. Krenkel, Determination of the fibre orientation in composites using the structure tensor and local X-ray transform, J Mater Sci 45 (2010) 888–896. https://doi.org/10.1007/s10853-009-4016-4.
[23] Z. Hashin, Failure Criteria for Unidirectional Fiber Composites, Journal of Applied Mechanics 47 (1980) 329–334. https://doi.org/10.1115/1.3153664.
[24] J. Xue, K. Kirane, Effect of the shape of the softening damage law on the predicted tensile fracturing and energy dissipation in textile composites, International Journal of Damage Mechanics 30 (2021) 786–822. https://doi.org/10.1177/1056789520986849.
[25] N. Zobeiry, R. Vaziri, A. Poursartip, Characterization of strain-softening behavior and failure mechanisms of composites under tension and compression, Composites Part A: Applied Science and Manufacturing 68 (2015) 29–41. https://doi.org/10.1016/j.compositesa.2014.09.009.
[26] A. Air, B. Gangadhara Prusty, Manufacturing feasibility of a bend free ellipsoidal composite pressure vessel using automated fibre placement, Composites Part A: Applied Science and Manufacturing 177 (2024) 107968. https://doi.org/10.1016/j.compositesa.2023.107968.
[27] C. Furtado, G. Catalanotti, A. Arteiro, P.J. Gray, B.L. Wardle, P.P. Camanho, Simulation of failure in laminated polymer composites: Building-block validation, Composite Structures 226 (2019) 111168. https://doi.org/10.1016/j.compstruct.2019.111168.

SIMULATING ADDITIVELY MANUFACTURED COMPOSITE STRUCTURAL JOINTS USING FASTDM4C

Antonio A. Deleo[1], Sean E. Phenisee[1], Derek Shelley[1], Mark Flores[1], Daniele Pelessone[1] and Marco Salviato[2]

[1]ES3
600 B Street, 19th floor, San Diego, CA 92101, USA
Email: antonio.deleo@es3inc.com, web page: https://www.es3inc.com

[2]Department of Aeronautics & Astronautics, University of Washington
3940 Benton Lane NE, Seattle, WA 98195, USA
Email: salviato@uw.edu, web page: https://www.aa.uw.edu

Keywords: Discrete Modeling, Additive Manufacturing, Fracture

ABSTRACT

Additive manufacturing (AM) of composite materials offers unmatched flexibility and tailored properties for aerospace structures. However, accurately predicting structural performance and fracturing behavior in additively manufactured composite joints remains complex due to intricate micro and mesoscale damage mechanisms. This work uses FastDM4C, an advanced discrete computational model specifically developed to simulate and optimize composite structural joints fabricated using Electroimpact's Scalable Composite Robotic Additive Manufacturing (SCRAM) system and Anisoprint PROM 500. SCRAM uniquely integrates Automated Fiber Placement (AFP) and Fused Filament Fabrication (FFF), enabling rapid production of aerospace-grade continuous fiber-reinforced thermoplastic composites with exceptional mechanical performance. While traditional continuum models effectively characterize the elastic response, they inadequately represent complex fracture behaviors at finer scales. FastDM4C addresses these shortcomings by utilizing a discrete, sub-lamina approach that captures microdamage initiation and propagation in a computationally efficient manner. This model enhances the original DM4C framework by employing edge-based constitutive laws, significantly improving accuracy and efficiency. In the current study, digital twins of composite structural joints are created directly from machine codes, providing exact virtual replicas of physical specimens. Integrating detailed experimental data and material properties, these digital twins enable comprehensive simulations using FastDM4C to predict mechanical responses under various conditions. Furthermore, a multi-stage optimization algorithm calibrates elastic and fracture parameters at multiple scales based on manufacturing parameters. By merging cutting-edge discrete modeling techniques, digital twin technologies, and advanced additive manufacturing processes, this study offers a powerful tool for optimizing composite structural joints, substantially accelerating the development and validation of aerospace structures.

1 INTRODUCTION

Additive manufacturing (AM) has significantly advanced the capability to produce complex structural components, especially within the field of composite materials [1, 2]. Despite these advancements, accurately ensuring the structural integrity of additively manufactured composite joints remains a substantial challenge due to intricate damage mechanisms at the micro and mesostructural levels. Composite materials typically exhibit complex behaviors such as fiber micro-buckling, fiber kinking under compression, fiber shearing, and matrix microcracking under shear, complicating accurate prediction and simulation [3-5]. Traditional continuum-based computational models attempt to characterize these damage mechanisms but often become mathematically cumbersome, limiting general

applicability and requiring extensive experimental calibration. These homogenized continuum models substitute the explicit fiber and matrix details with numerous complicated equations and parameters that lack clear physical interpretations. Consequently, their predictive capabilities are limited, and model calibration becomes labor-intensive.

This study introduces an advanced discrete computational model, the Fast Discrete Model for Composites (FastDM4C), designed to effectively overcome these limitations [6-10]. Unlike continuum models, FastDM4C explicitly represents fiber-matrix interactions through discrete, edge-based constitutive laws, significantly improving the accuracy of damage initiation and propagation simulations at reduced computational cost. Additionally, this research utilizes the Electroimpact Scalable Composite Robotic Additive Manufacturing (SCRAM) system integrating Automated Fiber Placement (AFP) and Fused Filament Fabrication (FFF) to manufacture composite structural joints. Digital twins are created directly from manufacturing machine codes, ensuring perfect virtual replicas of physical specimens. By incorporating detailed experimental data and specific material properties into these digital twins, FastDM4C simulations yield reliable predictions of mechanical behavior and structural performance. The enhanced computational efficiency and scalability of FastDM4C facilitate rapid iterations, sensitivity analyses, and optimization procedures, significantly accelerating design iteration cycles. The insights provided through virtual testing enhance reliability, safety, and performance, driving innovation in structural design for critical applications in aerospace, automotive, robotics, and beyond.

2 MODEL DESCRIPTION

The first iteration of FastDM4C was developed to model classical composite laminates using a Representative Unit Cell (RUC), whose dimensions are selected to match the average distance between splitting cracks observed in experimental results [11-13]. Within the RUC, fibers are discretized using the newly developed Discrete Fiber Model (DFM), while the matrix and shear behavior is captured using a second novel Discrete Matrix Model (DM2), combined with a new finite element called the FacetElement (FE). This methodology was later adapted to model composites manufactured by additive techniques, such as extrusion or tape deposition as discussed in this article but all the basic elements are the same.

The Discrete Fiber Model resembles a Timoshenko beam element but allows further monitoring of the energy dissipated by each integration point, which is critical during fracturing behavior. Each beam element in DFM has full six degrees of freedom (DOF) per node, so it is capable of handling axial, shear, bending, and torque forces. The major assumption of the fiber model is that the fracture localizes at the mid-section of an element. The mid-section is discretized as another generalized Finite Element mesh, so that many different shapes are possible. In Figure 1, a circular cross section is used even though any generalized cross section can be used. In the case of tape deposition as in the SCRAM, a rectangular cross section is generally used. Moreover, each beam is split into two segments of equal length. The two segments are separately tied to each of the nodes that define the beam and two segments from adjacent beams that share the same node form a rigid cell that is tied to the 6 DOF of the shared node. Using this methodology, there is no need of using element deletion or element erosion as once the fracture criterion is reached, the rigid cell is split into two segments each with a copy of the node. This is easily seen in Figure 2. Moreover, this implementation allows further control of the dissipation of energy of each integration point which is not possible to achieve by using a classical Timoshenko beam. The constitutive equation of the beam is a simple linear softening formulation [14]. Further detail is discussed in the next section.

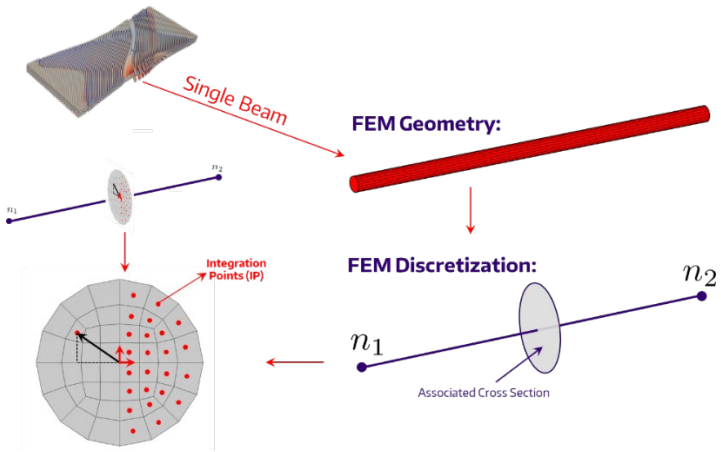

Figure 1: Visual representation of the Discrete Fiber Model (DFM). Each beam element is characterized by two nodes and it is assumed to fracture in the middle. The cross section in the middle is as well a generalized finite element mesh.

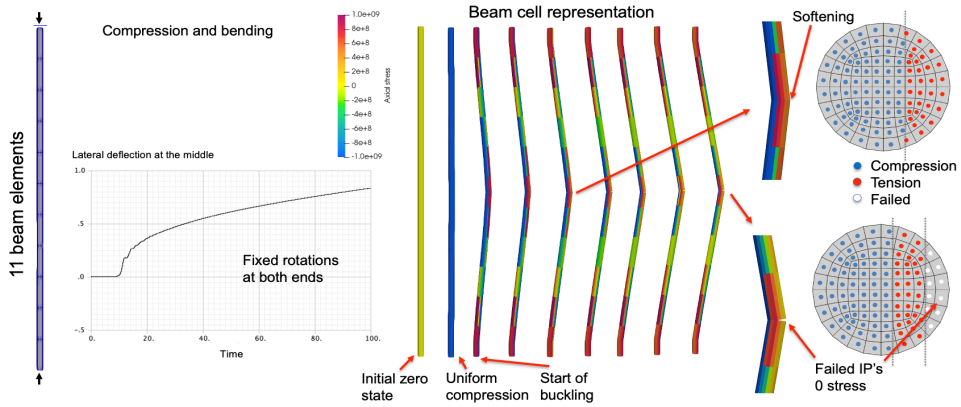

Figure 2: Practical considerations for the Discrete Fiber Model. While behaving similarly to Timoshenko Beam Elements, the DFM allows for further control of each integration point during failure, properly dissipating the right amount of energy needed for the element to fail.

The Discrete Matrix Model (DM2) and the associated new element called FacetElement (FE) are now presented. In DM4C, the matrix is represented by an embedded tetrahedral mesh where each element is further discretized into FacetElements oriented on multiple planes. In FastDM4C, the facet element is created upon a single edge element that is taken from the RUC or the deposited filament or tow. At the mid-point of the edge element, a polygonal facet is used to describe the damaging and fracturing behavior (equations discussed in the next section). In Figure 3, a graphical interpretation of a FacetElement is given together with plots of the constitutive response.

Once the additively manufactured layers are generated using the methods outlined above, the interlaminar connection between nodes from each layer needs to established. From node pairs of two plies, a 3D constrained Delaunay Triangulation is carried out to generate a temporary set of tetrahedral elements. However, non-co-planar edge elements are only retained. With these edge elements, all the mid-points are found and used to generate either a (i) Voronoi tessellation for standard laminates or (ii) mid-planar projection and tetrahedral intersection for printed complicated 3D parts. This process allows for a very robust generation of facets which are parallel to the printed layers and almost independent of the complexity of each layer.

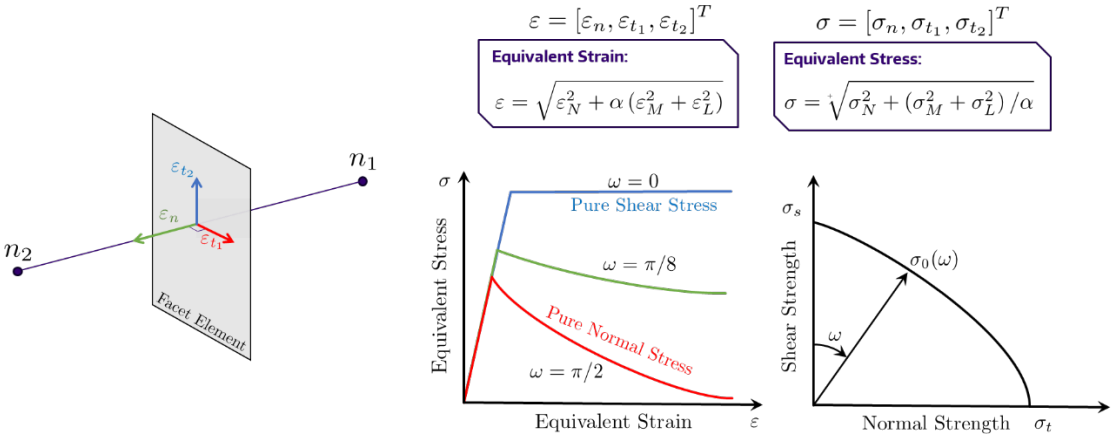

Figure 3: Discrete Matrix Model (DM2) and FacetElement (FE) graphical interpretation.

The final step involves model calibration and validation through carefully designed laboratory-scale specimens matching the geometrical and material characteristics of the composite and manufacturing system. Calibration tests include longitudinal tension/compression, transverse tension/compression, shear, and fracture energy-driven assessments such as Mode I (DCB) and Mode II (ENF) fracture toughness. To efficiently calibrate the model, an automated parallel computational procedure using the Message Passing Interface (MPI) framework is employed. In this parallel approach, a manager rank supervises parameter selection, while multiple worker ranks run concurrent simulations. Parameters are iteratively swept and adjusted until convergence with experimental data is achieved. After calibration, the validated model parameters reliably predict the behavior of other composite structures manufactured using the same equipment, materials, and processing conditions, greatly improving modeling accuracy and confidence.

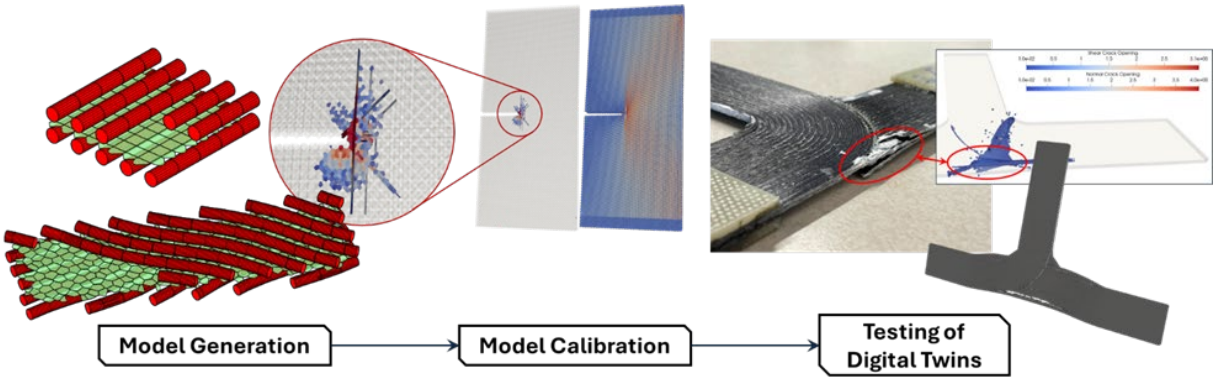

Figure 4: General steps for model generation, calibration and testing of the proposed framework.

3 THEORETICAL FRAMEWORK

3.1 Constitutive Law for Fiber Beams

Fiber tows are explicitly modeled as Timoshenko beam elements in the FastDM4C framework. The constitutive law for beam elements is defined in the integration points of each beam element. The elastic behavior of the beam elements resembles the Hooke's law in one dimension. The axial stress, σ_f, is linearly proportional to the elastic strain, ε_f, as presented in Equation 1:

$$\sigma_f = E_f \varepsilon_f \tag{1}$$

where E_f represents the modulus of fiber beams and is a calibration parameter which dominantly determines the modulus of a composite material in longitudinal direction, E_1.

Fiber beams exhibit a linear softening behavior when the axial stress goes over the strength limit, σ_c, under a tensile loading condition. The linear softening boundary is a function of the elongation of a beam element, δ, as shown in Equation 2:

$$\sigma_f(\delta) = \max\left[0, \sigma_c\left(1 - \frac{\delta - \delta_c}{\delta_f - \delta_c}\right)\right] \quad (2)$$

where the elongation limit, $\delta_c = \sigma_c L_0 / E_f$, indicates the initiation of the linear softening. L_0 is the length of a beam element. Once the elongation reaches the failure length, $\delta_f = (2G_f)/\sigma_c$ where G_f is the fracture energy of a fiber, the axial stress becomes zero.

3.2 Constitutive Law for Matrix Elements

The vectorial stress-strain relationship computed at each facet describes the constitutive behavior of a matrix. In this section, the elastic and the inelastic behavior for a matrix are introduced.

3.2.1 Elastic Behavior

The elastic relation between each vectorial stress component and each vectorial strain component resembles the Hooke's law in one dimension as shown in Equations 3 – 5:

$$\sigma_N = E_0 \varepsilon_N \quad (3)$$
$$\sigma_M = \alpha E_0 \varepsilon_M \quad (4)$$
$$\sigma_L = \alpha E_0 \varepsilon_L \quad (5)$$

where E_0 represents the modulus in the normal direction of a facet, and α is a parameter which indicates the shear-normal coupling. These two parameters are defined in the facet level and represent meso-scale properties. The calibration procedure determines their value such that the FastDM4C model will match the macroscopic elastic properties in transverse direction such as major Poisson's ratio, ν_{12}, and transverse modulus, E_2.

3.2.2 Fracturing Behavior in Tension

A facet with a positive normal strain ($\varepsilon_N > 0$) exhibits the fracturing behavior when the critical condition is met. This behavior is described with the relation between the effective strain, ε, and the effective stress, σ, following the Lattice Discrete Particle Model formulation introduced by Cusatis et al. [ref]. Two effective variables are defined in Equation 6 and 7.

$$\varepsilon = \sqrt{\varepsilon_N^2 + \alpha(\varepsilon_M^2 + \varepsilon_L^2)} \quad (6)$$
$$\sigma = \sqrt{\sigma_N^2 + (\sigma_M^2 + \sigma_L^2)/\alpha} \quad (7)$$

The effective stress has the incrementally elastic relation with the effective strain ($\Delta\sigma = E_0\Delta$). The tensile boundary $\sigma_{bt}(\varepsilon, \omega)$, which is a function of the normal-shear ratio variable, ω, and the history-dependent maximum effective strain ε_{max}, sets the exponential softening law.

$$\sigma_{bt}(\varepsilon, \omega) = \sigma_0(\omega) \exp\left(-H_0(\omega)\frac{\langle \varepsilon_{max} - \varepsilon_0(\omega) \rangle}{\sigma_0(\omega)}\right) \quad (8)$$

In Equation 8, Macaulay's bracket follows the notion: $\langle x \rangle = max(x, 0)$, and the normal-shear ratio variable, ω, is defined as

$$\tan\omega = \frac{\varepsilon_N}{\sqrt{\alpha}\varepsilon_T} \quad (9)$$

where the effective shear stress $\varepsilon_T = \sqrt{\varepsilon_M^2 + \varepsilon_L^2}$ is used. In a facet, ω can be used to evaluate the degree of interaction between normal and shear loads. For the tensile boundary, the strength limit, $\sigma_0(\omega)$, depends on the normal-shear ratio variable and is computed as shown in Equation 10:

$$\sigma_0(\omega) = \sigma_t \frac{-\sin(\omega) + \sqrt{\sin^2(\omega) + 4\alpha\cos^2(\omega)/r_{st}^2}}{2\alpha\cos^2(\omega)/r_{st}^2} \tag{10}$$

where $r_{st} = \sigma_s/\sigma_t$ represents the ratio between the shear strength, σ_s, and the tensile strength, σ_t. In Equation 8, the elastic limit, $\varepsilon_0(\omega)$, is computed using the strength limit following the expression: $\varepsilon_0(\omega) = \sigma_0(\omega)/E_0$. The rate of decay for the tensile boundary, $H_0(\omega)$, is a function of ω as expressed in Equation 20:

$$H_0(\omega) = H_t \left(\frac{2\omega}{\pi}\right)^{n_t} \tag{11}$$

where $H_t = 2E_0/(\ell_t/\ell - 1)$, and ℓ is the length of the edge on the tetrahedral element containing the facet in evaluation. The tensile characteristic length, ℓ_t is proportional to the fracture energy of the matrix, G_t, and is computed as $\ell_t = 2E_0G_t/\sigma_t^2$. In summary, four meso-scale parameters $(\sigma_s, \sigma_t, \ell_t, n_t)$ characterize the tensile failure of facets with positive normal strain; therefore, the calibration of these parameters allows to match the tensile strength and the fracture energy of a matrix.

3.2.3 Hardening Behavior in Compression

When a facet experiences the compression ($\varepsilon_N < 0$), the normal stress component exhibits the hardening behavior after it passes the elastic regime. The hardening behavior implemented in FastDM4C follows the formulation proposed in the LDPM formulation, which describes the hardening boundary dependent on both the volumetric strain, ε_V, and the deviatoric strain, $\varepsilon_D = \varepsilon_N - \varepsilon_V$ as expressed in Equation 12:

$$\sigma_{bc}(\varepsilon_D, \varepsilon_V) = \begin{cases} \sigma_{c0} \quad \text{for} \quad -\varepsilon_{DV} \le 0 \\ \sigma_{c0} + < -\varepsilon_{DV} - \varepsilon_{c0} > H_c(r_{DV}) \quad \text{for} \quad 0 \le -\varepsilon_{DV} \le \varepsilon_{c1} \\ \sigma_{c1}(r_{DV}) \exp\left((-\varepsilon_{DV} - \varepsilon_{c1})\frac{H_c(r_{DV})}{\sigma_{c1}(r_{DV})}\right) \quad otherwise \end{cases} \tag{12}$$

where σ_{c0} represents the compressive yielding strength of a facet. In the hardening boundary, $\varepsilon_{DV} = \varepsilon_V + \beta\varepsilon_D$ and $\varepsilon_{c0} = \sigma_{c0}/E_0$. The Macaulay bracket in the second line of Equation 12 follows the same notion used for the tensile boundary. In this study, β is set to be zero. The rehardening initiates when $|\varepsilon_{DV}| > \varepsilon_{c1}$ where $\varepsilon_{c1} = \kappa_{c0}\varepsilon_{c0}$. The rehardening stress is defined as $\sigma_{c1}(r_{DV}) = \sigma_{c0} + (\varepsilon_{c1} - \varepsilon_{c0})H_c(r_{DV})$. The initial hardening modulus, $H_c(r_{DV})$, is computed as defined in Equation 13:

$$H_c(r_{DV}) = \frac{H_{c0} - H_{c1}}{1 + \kappa_{c2} < r_{DV} - \kappa_{c1} >} + H_{c1} \tag{13}$$

where H_{c0}, κ_{c1}, and κ_{c2} are meso-scale parameters defined in facet level associated to the properties of a matrix and $H_{c1} = \kappa_{c3}E_0$ where κ_{c3} is set to be 0.1 in this study. The values of both σ_{c1} and H_c change based on the variable, r_{DV} which is computed following Equation 14:

$$r_{DV} = \begin{cases} -\frac{|\varepsilon_D|}{\varepsilon_V - \varepsilon_{V0}} \quad \text{for} \quad \varepsilon_V \le 0 \\ \frac{|\varepsilon_D|}{\varepsilon_{V0}} \quad \text{for} \quad \varepsilon_V > 0 \end{cases} \tag{14}$$

where $\varepsilon_{V0} = \kappa_{c3}\varepsilon_{c0}$. In summary, five meso-scale parameters $(\sigma_{c0}, H_{c0}, \varepsilon_{c1}, \kappa_{c1}, \kappa_{c2})$ characterize the hardening behavior of normal strain component in facets under compression.

3.2.4 Frictional Behavior in Compression

The shear components of the stress vector in a facet under compression experience the frictional behavior which can increase the shear strength depending on the magnitude of compressive normal stress. The effective stress, σ_T, expressed in Equation 15 behaves incrementally elastic until it reaches the frictional boundary, σ_{bs}, defined in Equation 16:

$$\sigma_T = \sqrt{\sigma_M^2 + \sigma_L^2} \tag{15}$$

$$\sigma_{bs} = \sigma_s + \alpha(\mu_0 - \mu_\infty)\sigma_{N0} - \alpha\mu_\infty\sigma_N - \alpha(\mu_0 - \mu_\infty)\sigma_{N0}\exp\left(\frac{\sigma_N}{\sigma_{N0}}\right) \tag{16}$$

where σ_s represents the shear strength of a facet without any compressive normal stress. σ_{N0} governs the transition between the initial friction coefficient, μ_0, and the asymptotic friction coefficient, μ_∞. In summary, four meso-scale parameters $(\sigma_s, \sigma_{N0}, \mu_0, \mu_\infty)$ characterize the frictional behavior of facets under compressive stress.

4 CALIBRATION AND COMPARISON TO EXPERIMENTAL DATA

Figure 5 presents the discretization workflow and resulting models for specimens manufactured by two additive processes: tape deposition with the SCRAM system and fused filament fabrication with the PROM system. Although the calibration values differ for each process, the workflow used to obtain them is identical. The machine's G-code is parsed into a sequence of 3D line segments that represent the toolpath, then resampled to create fiber segments of uniform length. For machines that follow complex 3D trajectories, the local nozzle orientation is also captured so that, when the segments are converted to beam elements, the accompanying normal reference frame is preserved. This orientation data is optional for circular cross sections, but it is essential for the SCRAM process because its rectangular cross section must be aligned correctly along the path to reproduce the actual extrusion geometry. Once the beam network is established, a constrained tetrahedral mesh is generated around it. The edges of this mesh define the facet elements that represent the matrix response. Many geometries have been printed and validated with this methodology with both systems; in this non confidential study, a representative T joint specimen printed with the PROM is used to demonstrate the approach.

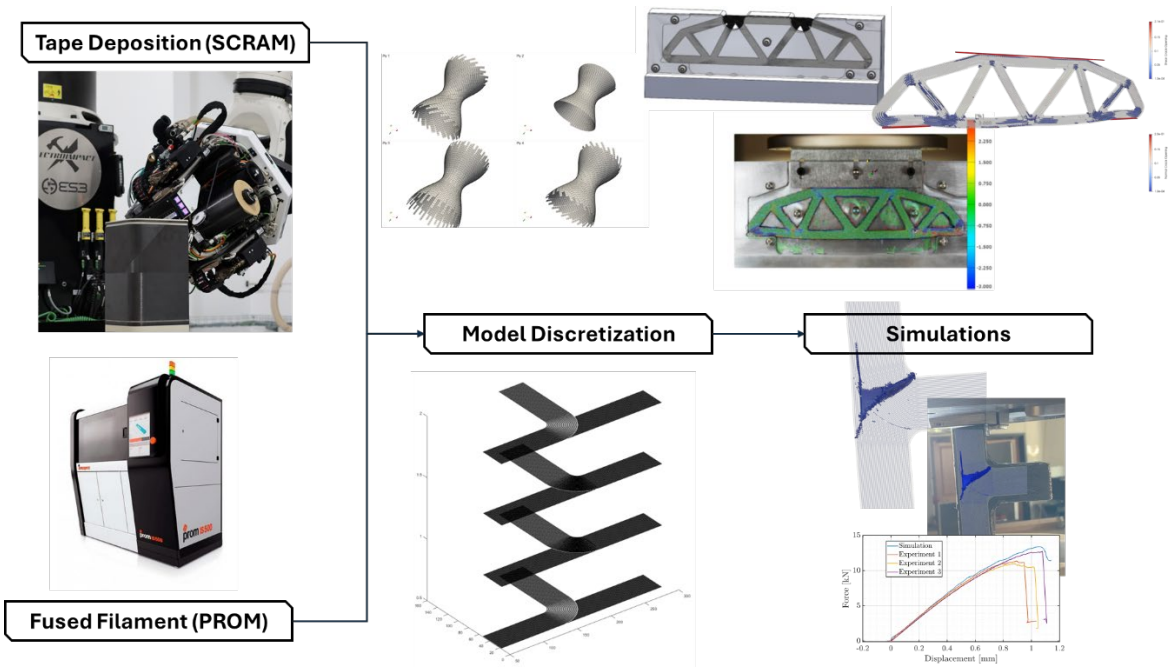

Figure 5: Both Tape Deposition (SCRAM) and Fused Filament (PROM) technologies can be used together with FastDM4C to generate Finite Element Models.

All the T-joint specimens were manufactured at ES3 using the PROM 500 and tested at the University of Washington in Seattle. Three specimens were produced for each configuration and loaded in tension on a 306 Bia West (formerly Shore Western) frame. One flange of the T-joint was gripped, the opposite flange was pulled along the joint's major axis, and the remaining flange was left free. All Joint A specimens completed testing without issue, while one Joint B specimen was misaligned during setup and its data were excluded. The finite element models were built with the FastDM4C framework as explained above. For each type of joints, a unidirectional laminate coupon model is extracted from a straight section to perform the calibration on FastDM4C parameters. After calibration, full-scale simulations were run and compared with the experimental curves. Figure 6 presents the comparison results for both types of structural joint.

Joint B delivered significantly higher stiffness and strength because its printing strategy avoided fiber interruptions along the loading direction. Joint A displayed a slight nonlinear response, typical of discontinuous fiber reinforcement, yet the DM4C model reproduced this behavior accurately. The formulation also captured the onset and progression of damage and fracture, as illustrated in Figure 6.

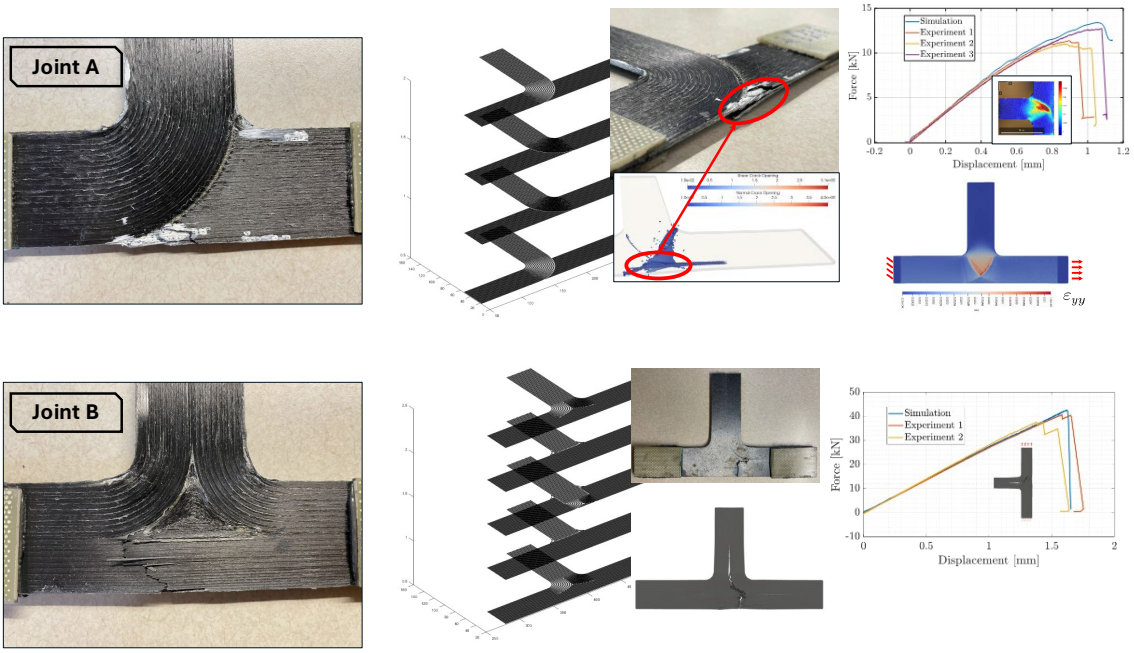

Figure 6: Comparisons between the experimental and computational results for both T-Joints.

5 CONCLUSIONS

This study introduces FastDM4C, an integrated and automated modeling framework for predicting the mechanical performance of additively manufactured composite joints produced using both the SCRAM tape deposition system and the PROM fused filament system. The methodology directly converts manufacturing G-code into a digital twin, discretizing continuous fiber paths into beam elements while embedding a tetrahedral mesh whose edges form facet elements to capture the matrix behavior. A parallel calibration process based on the Message Passing Interface (MPI) enables rapid tuning of both elastic and fracture parameters. Once calibrated, the model can be applied to full-scale specimens without further adjustments.

The validation shown in this article is based on experimental tests of T-joint specimens, and they showed strong agreement between simulation and measured data. In both cases, FastDM4C accurately predicts not only the global load-displacement response but also the onset and propagation of damage and fracture, as observed during physical testing.

The results of this study demonstrate that FastDM4C provides a robust and process-agnostic modeling pipeline that can accommodate different deposition technologies and geometries. Its edge-based constitutive formulation ensures that material parameters retain clear physical meaning, making the calibration transferable across machines and material systems. The computational efficiency of the MPI-based parameter sweep significantly accelerates convergence, allowing for practical integration into design workflows. Furthermore, the findings highlight the importance of continuous fiber paths in achieving optimal structural performance, reinforcing the need to reduce fiber interruptions during the printing process. This modeling framework enables more accurate simulations, informed design decisions, and faster validation of complex composite structures for aerospace and other demanding applications.

ACKNOWLEDGEMENTS

The authors gratefully acknowledge the Air Force Research Laboratory (AFRL) for their generous support, the Department of Defense High Performance Computing (DOD HPC) program for providing the computational resources used in this work, and the University of Washington for access to their advanced testing facilities.

REFERENCES

[1] I. Gibson, D. W. Rosen, B. Stucker, M. Khorasani, D. Rosen, B. Stucker, M. Khorasani, Additive manufacturing technologies, Vol. 17, Springer, 2021.

[2] P. Parandoush, D. Lin, A review on additive manufacturing of polymer-fiber composites, Composite Structures 182 (2017) 36–53.

[3] E. J. Barbero, Introduction to composite materials design, CRC press, 2010.

[4] A. M. Waas, C. R. Schultheisz, Compressive failure of composites, part ii: experimental studies, Progress in Aerospace Sciences 32 (1) (1996) 43–78.

[5] W. H. Ng, A. G. Salvi, A. M. Waas, Characterization of the in-situ non-linear shear response of laminated fiber-reinforced composites, Composites Science and Technology 70 (7) (2010) 1126–1134.

[6] M. Salviato, S. Phenisee, A. Deleo, D. Pelessone, M. Flores, A novel discrete, mesoscale modeling framework for the simulation of the damaging and fracturing behavior of composites, in: ASME International Mechanical Engineering Congress and Exposition, Vol. 86717, American Society of Mechanical Engineers, 2022, p. V009T12A015.

[7] A. A. Deleo, S. E. Phenisee, D. Pelessone, J. Furmanski, M. Flores, M. Salviato, Analysis of additive manufactured structural joints using discrete model for composites (dm4c), in: SAMPE, SAMPE, 2023.

[8] M. Salviato, S. E. Phenisee, A. A. Deleo, D. Pelessone, M. Flores, To the mesoscale and beyond! capturing complex damage mechanisms in composites via simple, physics-based, discrete mathematical models of fibers and matrix, in: Proceedings of The American Society for Composites-Thirty-Eighth Technical Conference, 2023.

[9] S. E. Phenisee, A. A. Deleo, D. Pelessone, M. Flores, M. Salviato, Discrete, meso-scale modeling of fiber-reinforced composites (dm4c): Application to additive manufacturing of continuous fiber composites, in: Proceedings Of The American Society For Composites-Thirty-Seventh Technical Conference, 2022.

[10] A. A. Deleo, S. E. Phenisee, D. Pelessone, J. Furmanski, M. Flores, M. Salviato, Discrete modeling and machine learning assisted calibration of 3d printed carbon fiber reinforced plastics (cfrp) structural joints, in: Proceedings Of The American Society For Composites-Thirty-Seventh Technical Conference, 2022.

[11] Qiao, Yao, Antonio Alessandro Deleo, and Marco Salviato. "A study on the multi-axial fatigue failure behavior of notched composite laminates." Composites Part A: Applied Science and Manufacturing 127 (2019): 105640.

[12] Greenhalgh, Emile. Failure analysis and fractography of polymer composites. Elsevier, 2009.

[13] De Carvalho, N. V., S. T. Pinho, and P. Robinson. "An experimental study of failure initiation and propagation in 2D woven composites under compression." Composites Science and Technology 71.10 (2011): 1316-1325.

[14] Belytschko, Ted, et al. "Strain-softening materials and finite-element solutions." Computers & Structures 23.2 (1986): 163-180.

ICCM24
AUGUST 4-8, 2025
BALTIMORE CONVENTION CENTER
BALTIMORE, MARYLAND, USA

No Technical Paper Submission for:

Amirali Amirian

Iby and Aladar Fleischman Faculty of Engineering Tel Aviv University
הפקולטה להנדסה ע"ש איבי ואלדר פליישמן אוניברסיטת תל-אביב

ICCM24
24TH INTERNATIONAL CONFERENCE ON COMPOSITE MATERIALS

TEL AVIV UNIVERSITY אוניברסיטת תל אביב

Attack Angle Influence on Growth Efficiency of Vertically Aligned Carbon Nanotubes

Lev Rovinsky*, Yarden Frenkel, Noa Lachman

PhD Student

CSI Group

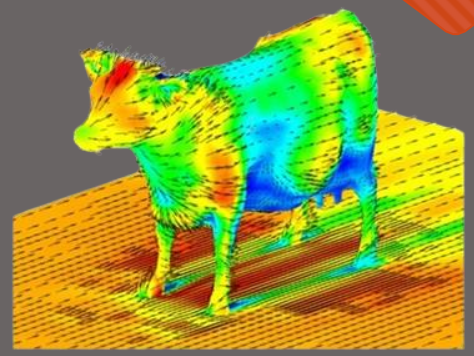

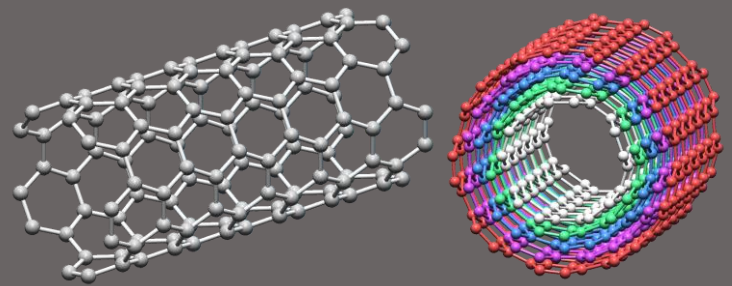

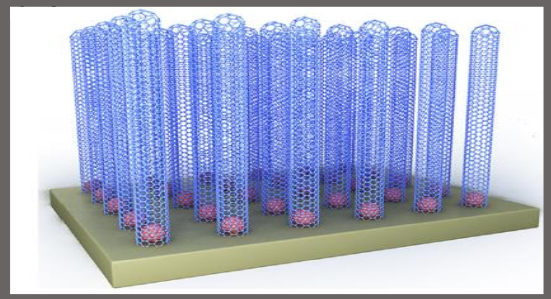



Vertically Aligned Carbon Nanotubes: Highly useful for Composite Materials

- Carbon nanotubes (CNT) have exceptional properties.
- Vertically aligned CNT (VACNT) retain anisotropic transport properties.
- Due to VACNT high porosity, immense surface is available for applications.

Property	Single-walled carbon nanotube	Double-walled carbon nanotube	Multiwalled carbon nanotube
Tensile strength (GPa)	50–100	23–63	10–60
Elastic modulus (TPa)	1	–	0.3–1
Elongation at break (%)	5.8	28	–
Density (g/cm^3)	1.3–1.5	1.5	1.8–2.0
Electric conductivity (S/m)	10^6	10^6	10^6
Thermal conductivity at room temperature (W/m K)	6000	3000	2000

https://doi.org/10.1016/j.compositesb.2017.08.020

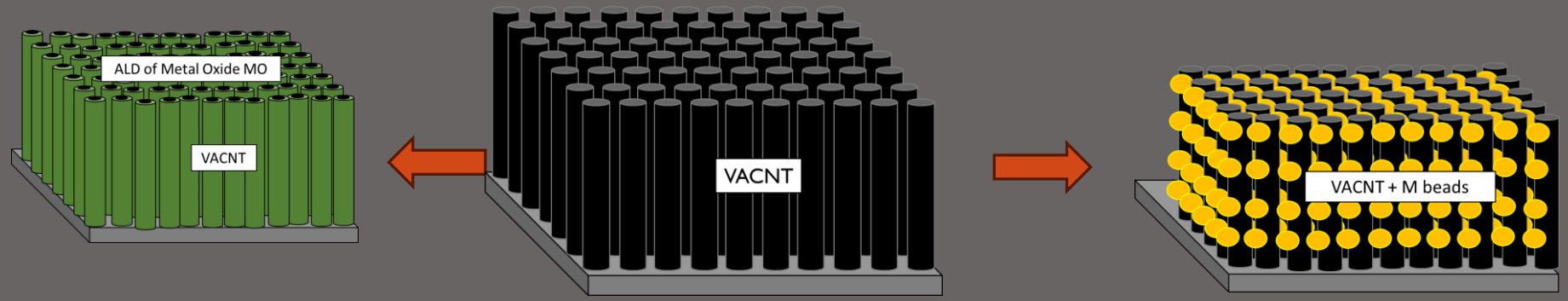

VACNT Synthesis: Chemical Vapor Deposition

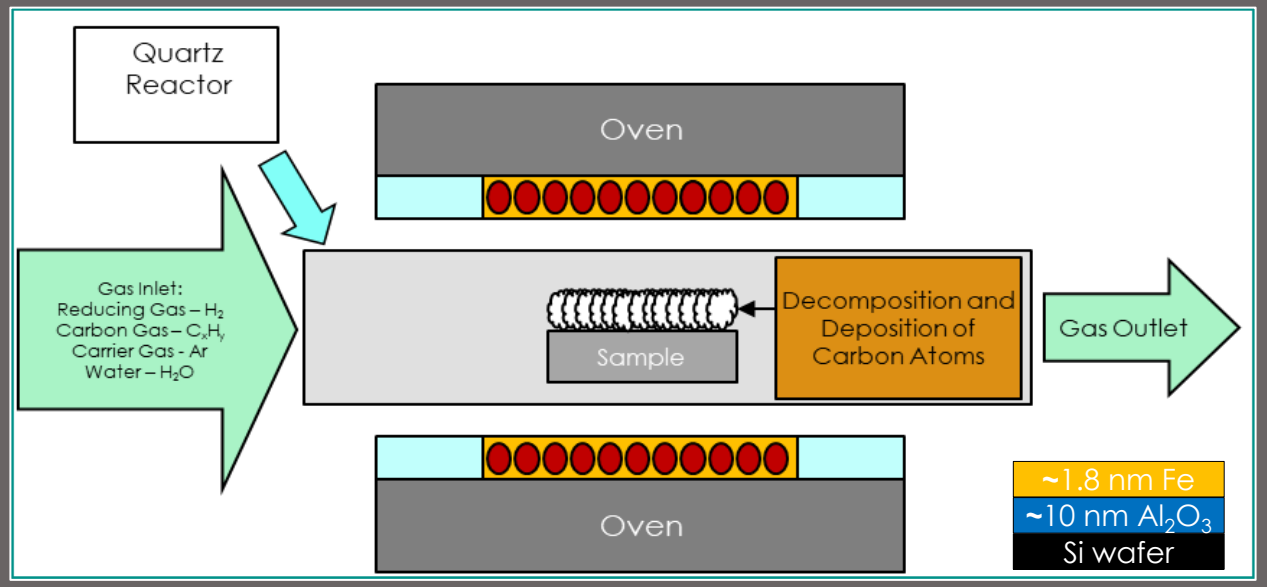

Rovinsky *et al.* - 10.1021/acsanm.0c02681

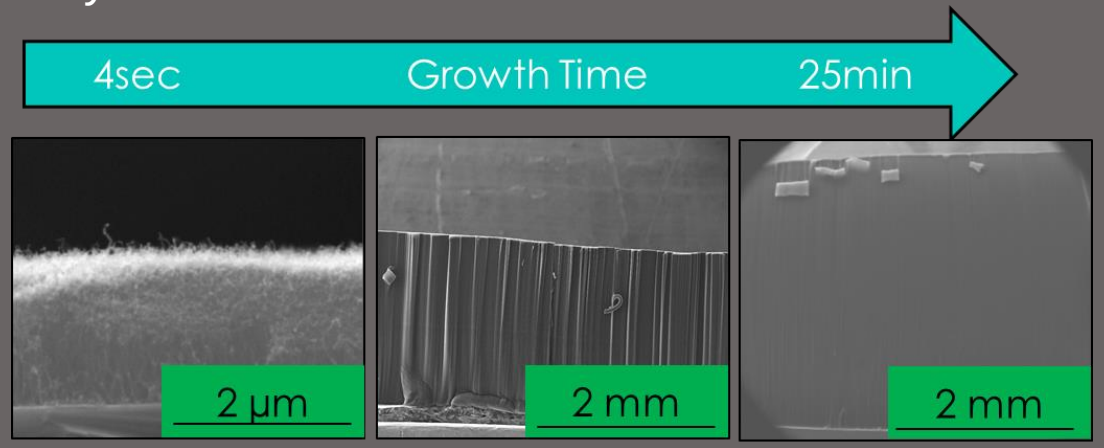



Taller VACNT reduces prominence of CNT-CNT contacts, weak links, both mechanical and electrically.

VACNT Synthesis and Challenges: Carbon Feeding Difference

- Different regions on the sample grow at different rates.
- Above certain heights, this becomes apparent and causes sinking.
- Extreme sinking results in the collapse of the sample centers.
- We started looking for an explanation.
- Can you help us?

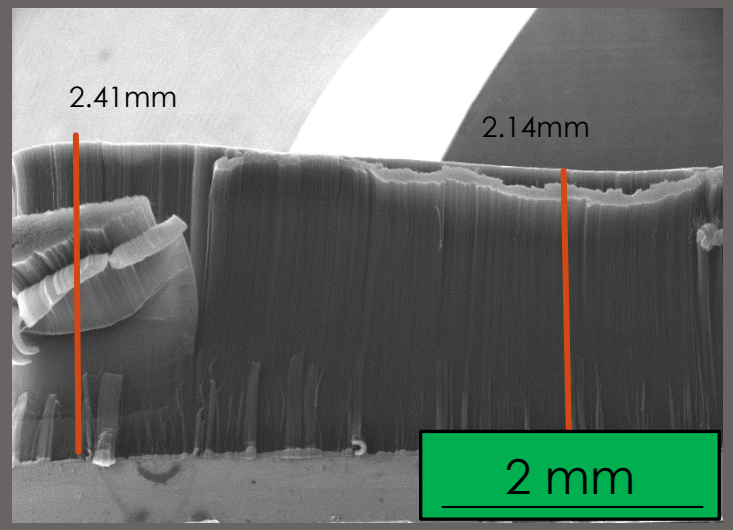

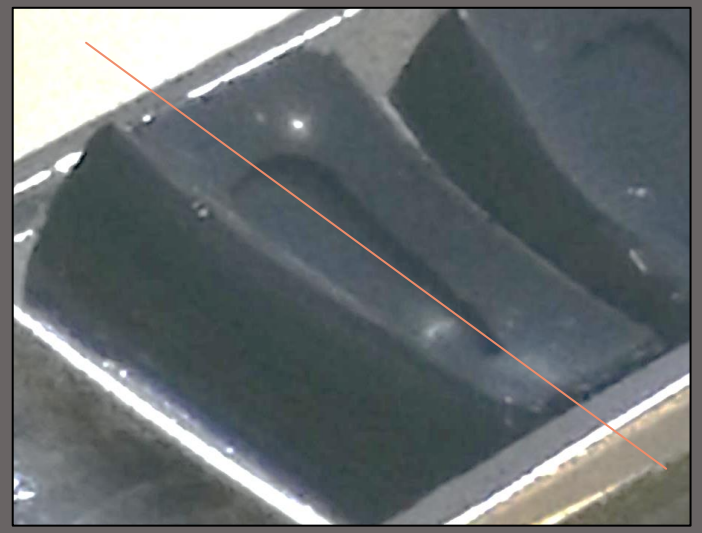

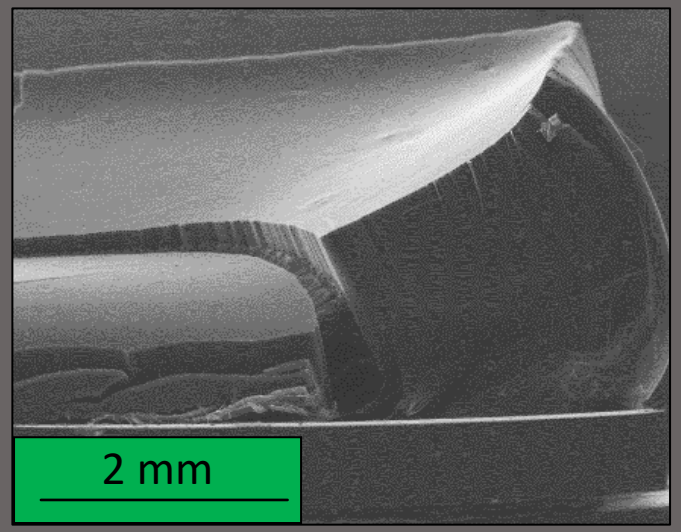

Computational Fluid Dynamics

- A branch of finite-element analysis (FEA) deals with the movement and interaction of fluids. Gases are considered fluids.
- The fluid velocity during VACNT CVD was simulated in several times along the growth process.
- My assumptions (first-order approximation):
  - Inert (physical) flow, disregard heat and mass transfer.
  - Rigid sample, disregard porous structure.
  - Fluid properties are C_2H_4.

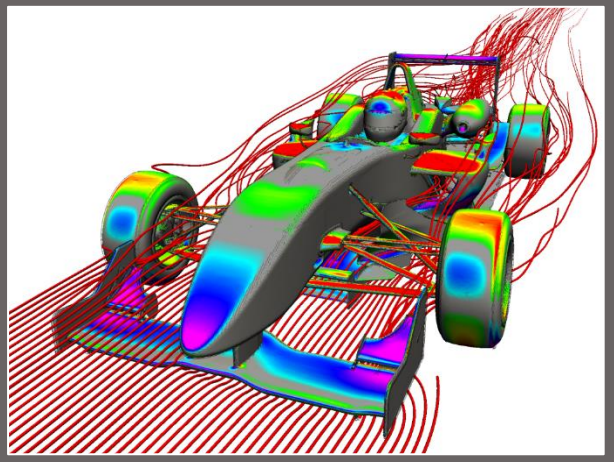

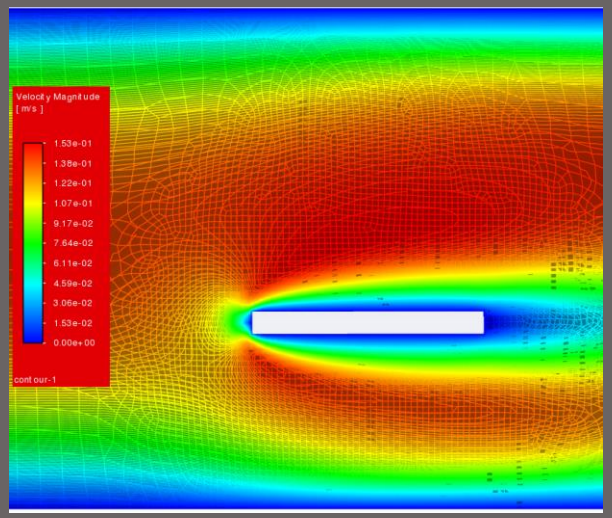

Methodology:
CFD/Real-life CVD Hybrid

CVD → CFD → CFD2 → Tool → CVD2

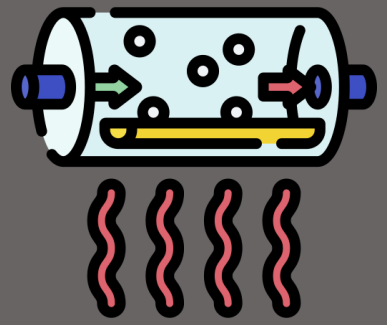







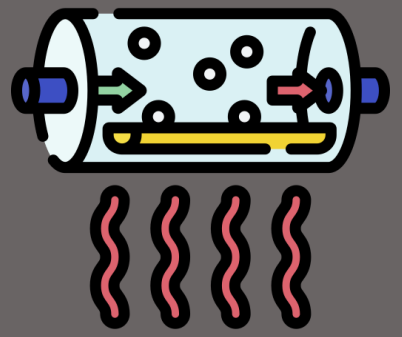







CFD Results

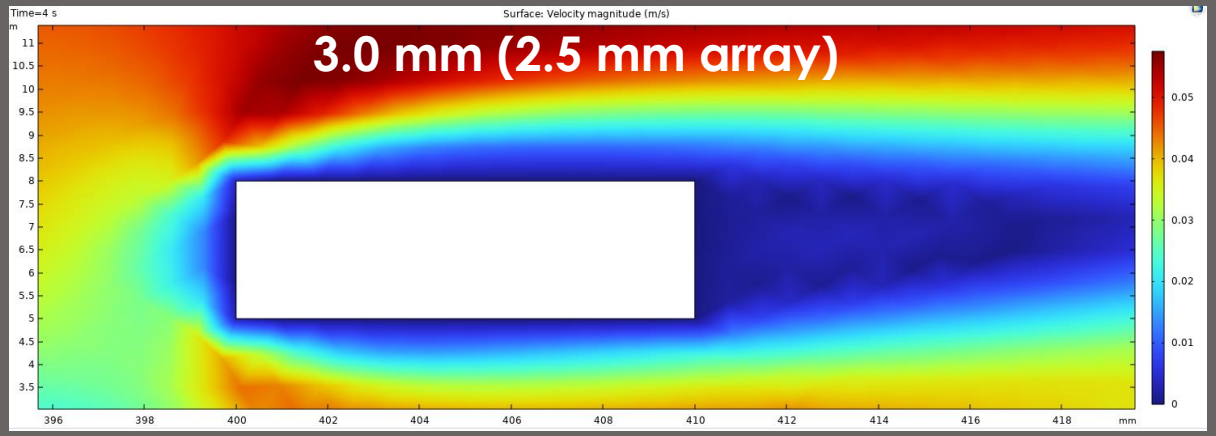

$$\delta = 99\% \cdot U\infty$$

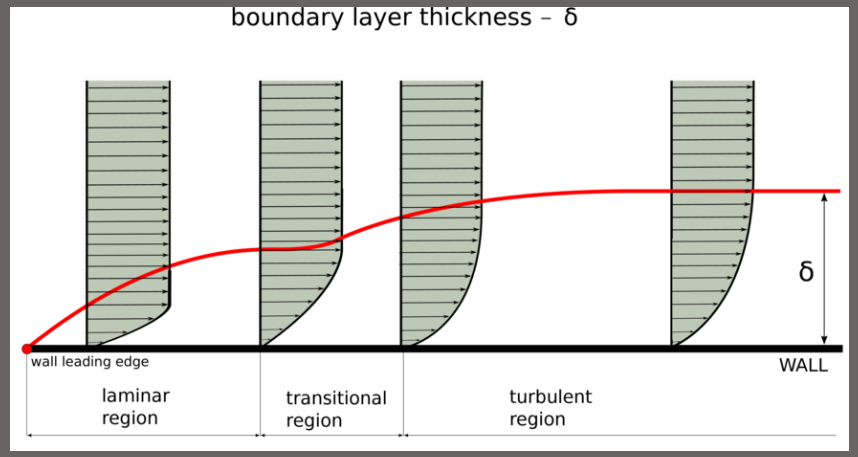

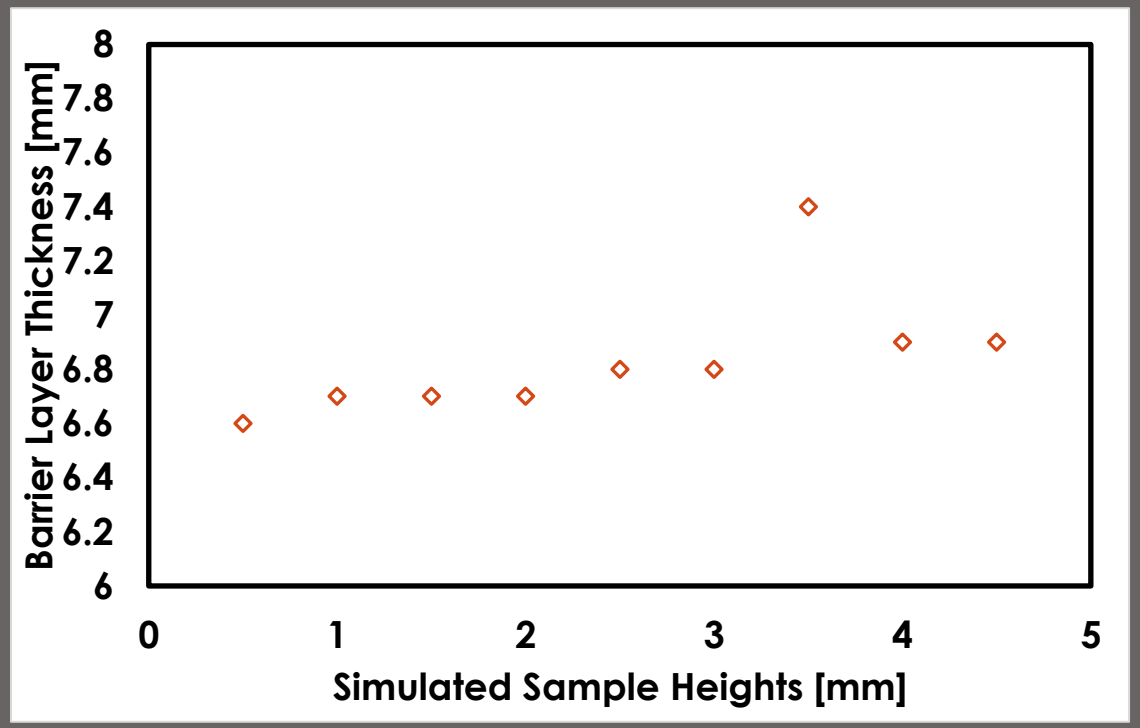

Assumed Phenomenon: Separation bubble

- The inbound flow traps a vortex on the surface, which decreases the growth rate in the middle of the sample.
- Higher step – larger trapped vortex.
- The angle decreases the dimensions of the trapped vortex.

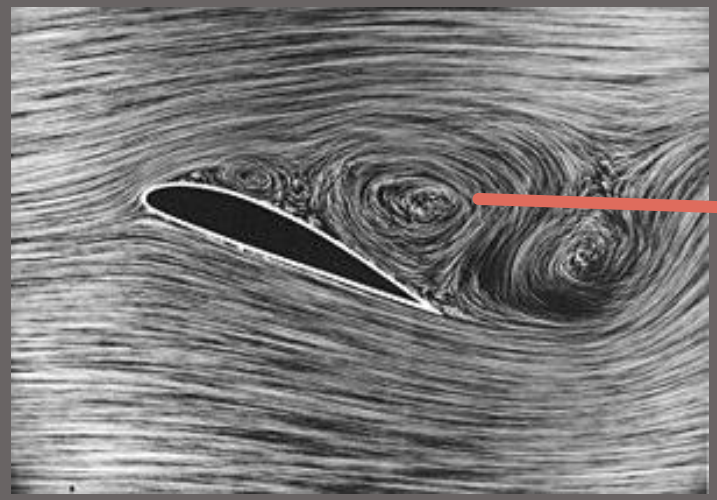

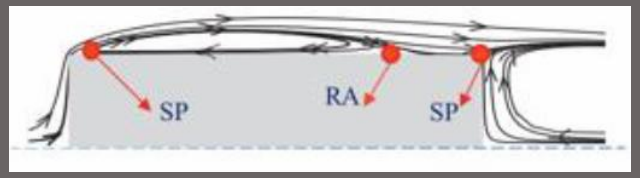

In VACNT case:

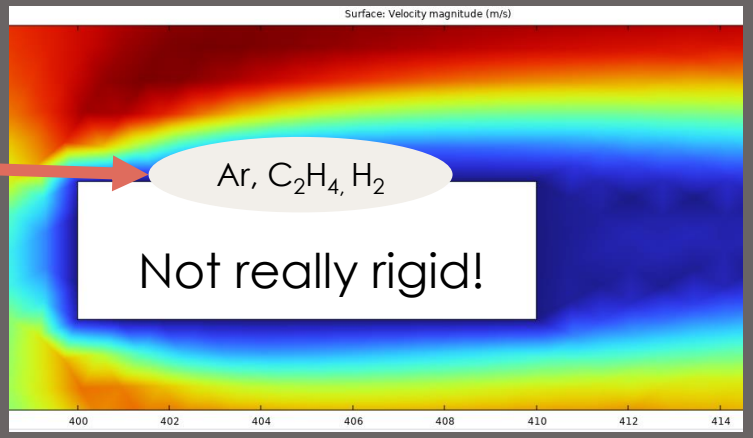

CFD Results – Attack Angle

- In an effort to reduce boundary layer thickness, the concept of attack angles was introduced.

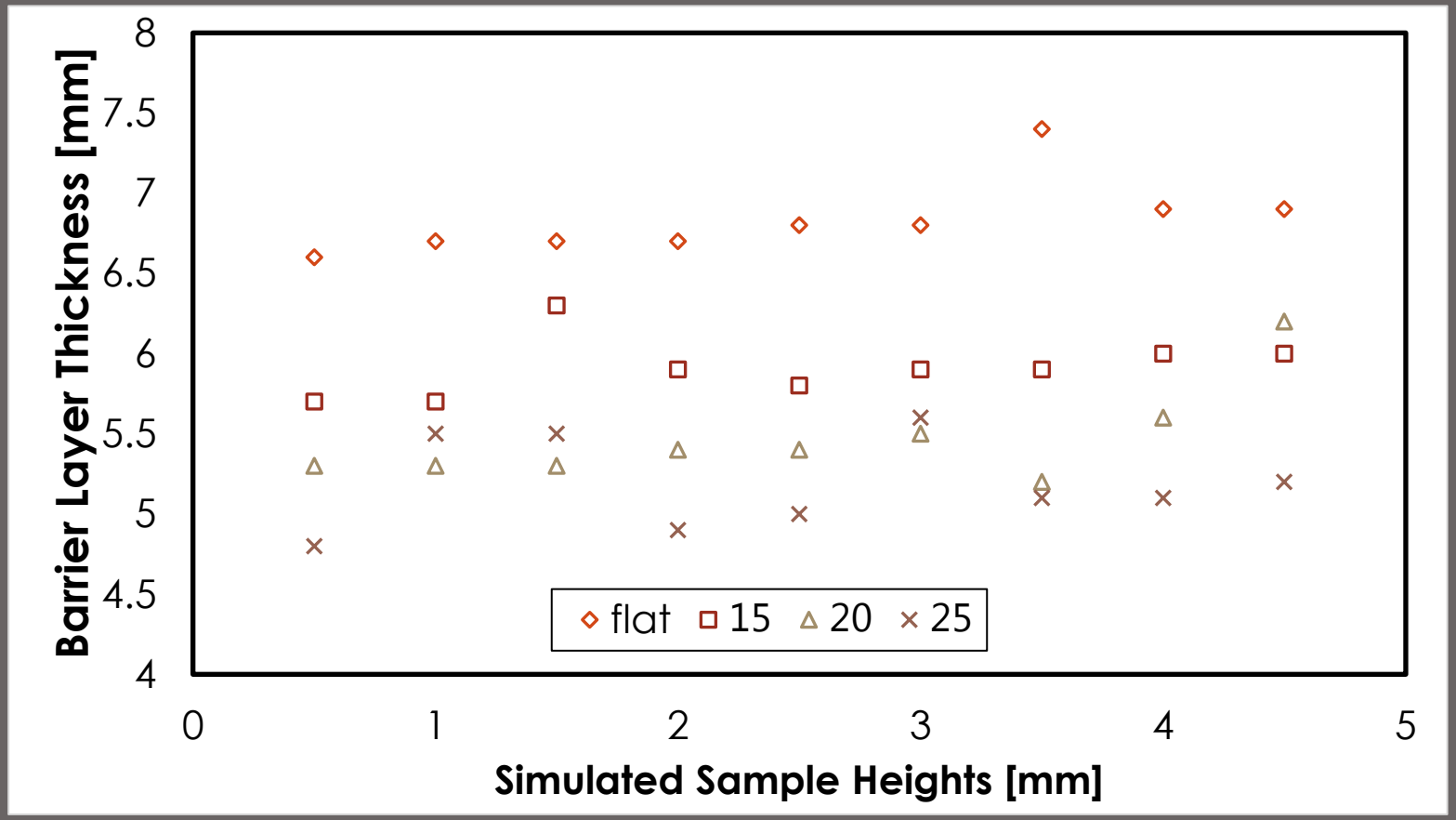

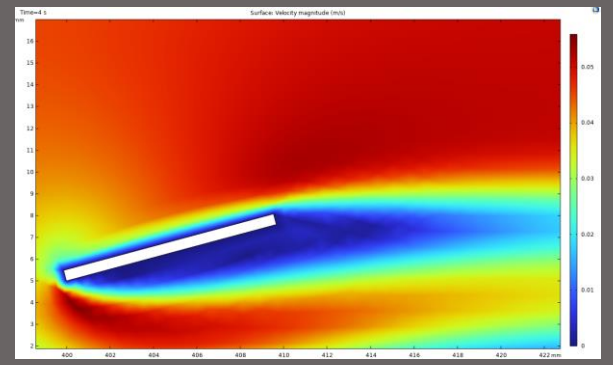

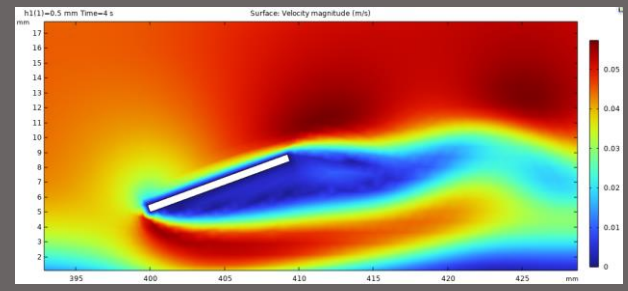

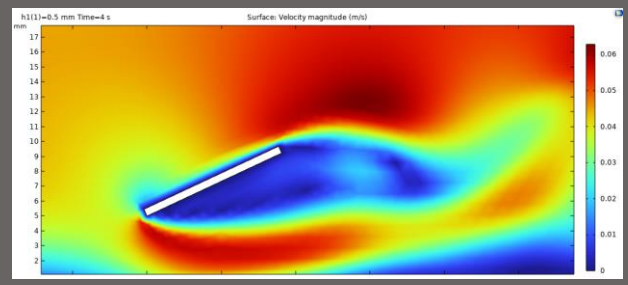

Quartz Substrate Jigs:

- Designed dedicated jigs with attack angles, so that the substrate would be at an angle.

Gig Generation 1

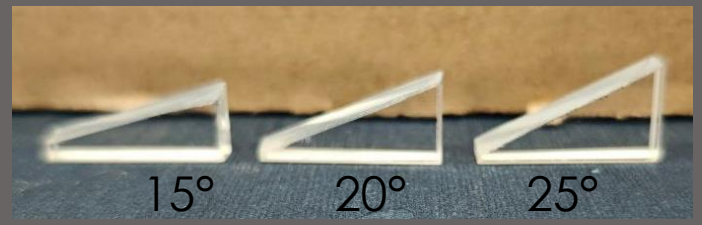

Gig Generation 2

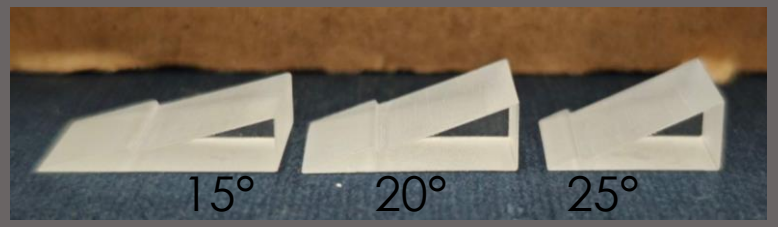

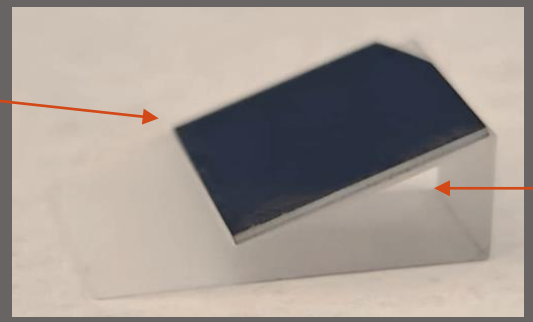

Height of VACNT as f(θ), as f(growth t)

- Clear correlation between attack θ and sample height.
- Interestingly, best results are 25°, while in the simulations its 20°.

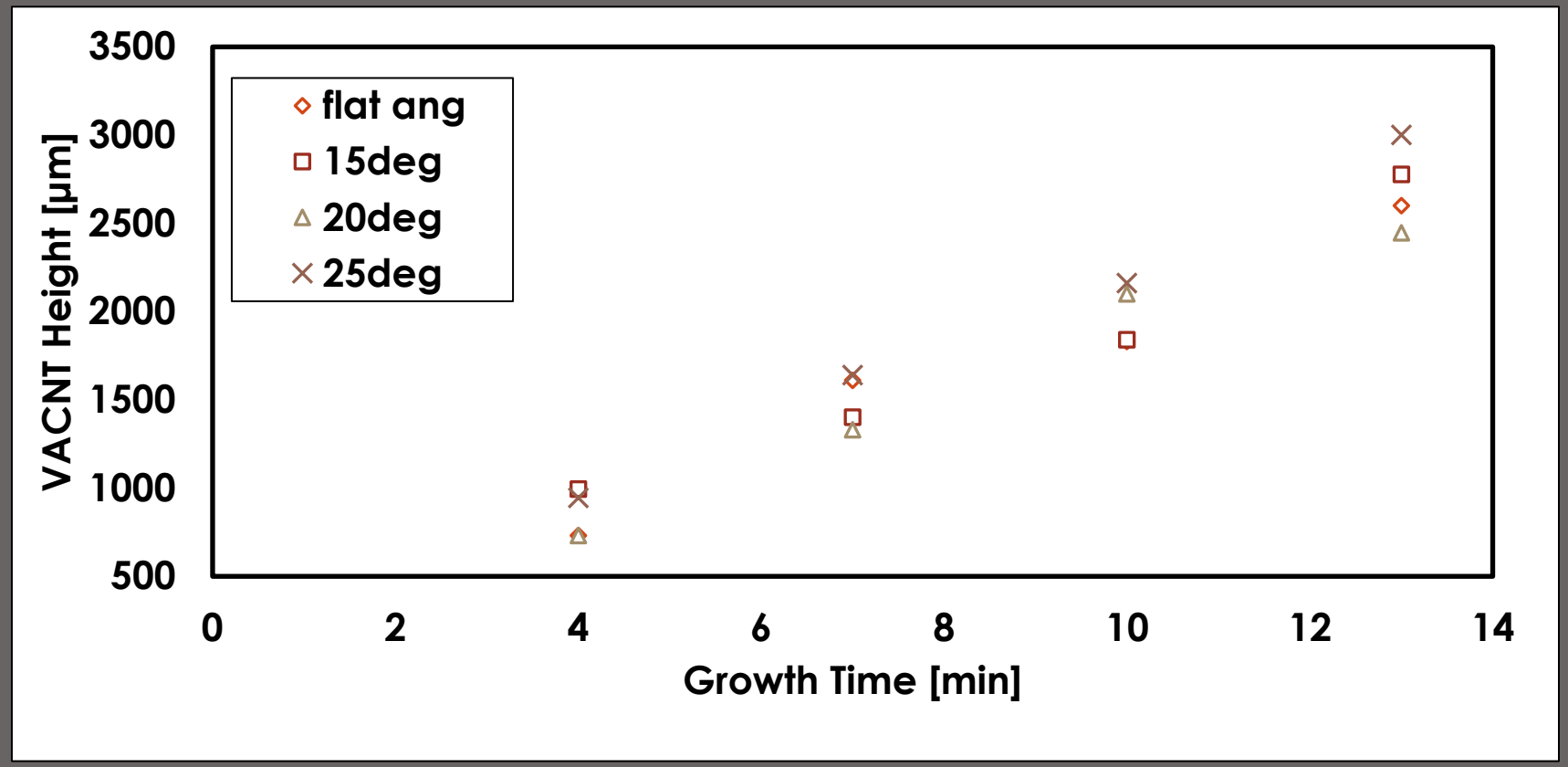

Conclusions

- The effectiveness of fluid dynamics becomes noticeable when ‘pushing the envelope’ of nanofabrication.
- VACNT samples’ centers sink, and even collapse during fabrication.
- CFD show barrier layer thickness increases as function of sample height.
- Some attack angles show decrease in the barrier layer thickness.
- VACNT sample height enhanced with attack angle.

ALTERNATIVE RECONSTRUCTION AND ACQUISITION TECHNIQUES FOR IMAGING LARGE CFRP SAMPLES

Ford Collins, Evelien Zwanenburg, Mark Williams and Jay Warnett
Centre for Imaging, Metrology, and Additive Technologies, WMG, University of Warwick, Coventry, CV4 7AL, UK
Email: Ford.Collins@warwick.ac.uk, web page: https://warwick.ac.uk/fac/sci/wmg

Keywords: Non-destructive testing, Carbon fibre, Defects

ABSTRACT

X-ray Computed Tomography (CT) is a powerful tool for non-destructive imaging of materials but is ill-suited for scanning the high aspect ratio geometries typical of standard test pieces and industrial composite panels. Computed Laminography (CL) offers a solution to overcome the current limitations of CT by using a tilted axis of rotation. This work demonstrates how a CL trajectory may be implemented on a conventional laboratory-based CT system with source and detector offsets. The performance of the technique was compared to a standard CT scan for region-of-interest imaging of a large carbon-fibre laminate plate. A low tilt angle of 20° was found to produce superior image quality to CT in slices through the face of the sample whilst mitigating the associated laminographic artefacts across horizontal views. The resulting fibre orientation analysis demonstrated CL to be an effective technique to accurately characterise the fibre architecture of large composite structures.

1 INTRODUCTION

X-ray computed tomography (CT) is becoming an increasingly important non-destructive imaging technique for the internal microstructural characterisation of fibre-reinforced polymers, both during manufacturing and under in-service conditions [1]. Despite recent advancements in the capabilities of laboratory-based CT systems, the constituent material properties of carbon-fibre reinforced polymers (CFRP) coupled with the typically high aspect ratio geometries of industrial components provide fundamental challenges to high-resolution X-ray imaging. One of the main concerns for CFRP and an important factor for feature detection is image contrast. The small difference in attenuation coefficient results in low contrast between the fibres and polymer resin within the greyscale image, for which a low tube voltage is likely required but at the expense of penetration depth through the sample [2]. Consequently making it more difficult to distinguish fibres for orientation analysis and/or defects such as narrow matrix cracks. Also, with individual fibre diameters between 5-7μm, the physical dimensions of real industrial components often impede on the geometric magnification necessary to resolve small bundles or strands giving a trade-off between sample size and spatial resolution. Further, flat plate-like geometries characteristic of industrial composite panels and specific standard test pieces are ill-suited conventional CT imaging. The high aspect ratio means that X-ray energies which optimise the dynamic range face-on are likely insufficient for imaging the plate edge-on. As such, the large difference in absorption through different projection angles result in pronounced reconstruction artefacts [3]. For region-of-interest (ROI) scanning of flat plate carbon-fibre sheet moulded compound, this constitutes sample sizes greater than 75% excess material experiencing a significant decline of in image quality [4].

A potential solution to overcome these challenges is computed laminography (CL). Rotary CL is the simplest trajectory, and like CT it consists of the acquisition of projection datasets, but the axis of rotation is inclined by an angle (<90°) instead of being perpendicular to the X-ray beam [5]. By tilting the axis of rotation planar samples can be positioned closer to the X-ray source and achieve a similar x-ray transmission through all projection angles to provide improvements in noise level and resolution. This technique has been successfully implemented using synchrotron radiation to provide

high-resolution, in-situ, three-dimensional analysis of structure failure in polymer composites, otherwise unattainable via CT [6]. It is possible to implement CL trajectories using commercial laboratory X-ray CT systems; however, its application so far has been dependant on sample manipulator arms which are not readily available at most facilities [7,8]. Although CL provides an efficient method to image flat samples its reconstruction is an ill-posed problem. Due to the tilted scanning trajectory, sampling of the object in the Fourier domain is incomplete, therefore, CL reconstruction inherently suffers from tail artefacts and inter-slice aliasing. The severity of which is proportional to the extent of laminographic tilt angle. Traditionally, this angle has been fixed to either 30° or 45° to reduce the X-ray path length through sufficiently dense samples such as printed circuit boards. Hence, it can be inferred that better quality laminography results are obtained with lower tilt angles (≤ 30°) and for more homogeneous samples [9]. It has been shown that suppression of laminography artefacts can be achieved using iterative reconstruction with total variation (TV) regularization [9,10] but this involves careful selection of the regularization parameter. A commonly observed drawback of TV-regularisation is the loss of fine details, as such, it is often advisable to search for a balance between artefact suppression and over-smoothing especially in cases that include important small features such as polymer composites.

This paper demonstrates how a CL trajectory can be accomplished using a conventional laboratory CT system, without the need for specialist equipment, through source and detector offsets. The performance of the method is compared to a standard CT scan for a large CFRP plate and is assessed in terms of image quality and its application for fibre orientation analysis. As this trajectory limits the maximum laminographic tilt angle, the achievable image quality for a low tilt angle across both vertical and side views are evaluated to explore if iterative reconstruction methods are necessary to perform characterization tasks for polymer composites.

2 EXPERIMENTAL METHODOLOGIES

2.1 Composite specimen

In this work, the composite material studied is a quasi-isotropic CFRP plate, as shown in Figure 1, obtained from Easy Composite (product code: CFS-RI-1-0056) with dimensions 250 mm × 230 mm × 4 mm. The layup schedule for the specimen consists of eight layers arranged symmetrically as follows: 210g 2/2 twill, 300g ±45° biaxial, four consecutive layers of 650g 2/2 twill, 300g ±45° biaxial, and 210g 2/2 twill layer.

2.2 CL Trajectory

The acquisition process is similar for both imaging techniques with projections obtained as the object rotates 360° around the rotation axis. For CL, the source and detector are positioned to different heights on opposite sides of the object stage. Specifically, the source is lowered, and the detector is raised to tilt the optical axis of the CT system and achieve a rotary CL trajectory (Figure 2). The extent of vertical translation for the detector permits a maximum laminographic tilt angle of 20° which was used in this study. A key benefit of this CL trajectory appears at magnifications corresponding to a ≥15μm voxel size, where the displacement is sufficient for larger samples to rotate freely above the source without risk of collision to enable higher resolutions otherwise unattainable with CT.

2.3 X-ray Acquisition

Both scan trajectories were performed on the TESCAN UniTom XL (TESCAN, Czech Republic) XCT system using a detector cropped to 2000-pixel square, 2005mm from the source, which with magnification of the sample, resulted in a 14μm voxel size. For fair comparison, the acquisition parameters remained constant between the CT and CL scans with the exception of exposure time. A voltage of 40kV was used to provide adequate penetration and contrast for both trajectories. The power was selected such that the spot size was approximately equal to pixel size, and exposure chosen

to maximise the dynamic range as described in the standardised setup process [2]. To minimise the X-ray path length for each scan the sample was mounted vertically in CT and horizontally in CL. Using the CT trajectory projections viewing the flat plate edge-on experienced propagation-based phase effects causing over-saturation, therefore, resulting in the difference between exposure times of 2.4s and 3.5s for CT and CL, respectively. A total of 3000 projections were collected using step-and-shoot mode and three averages. Both datasets were then reconstructed using the Feldkamp, Davis, and Kress (FDK) algorithm within Panthera.

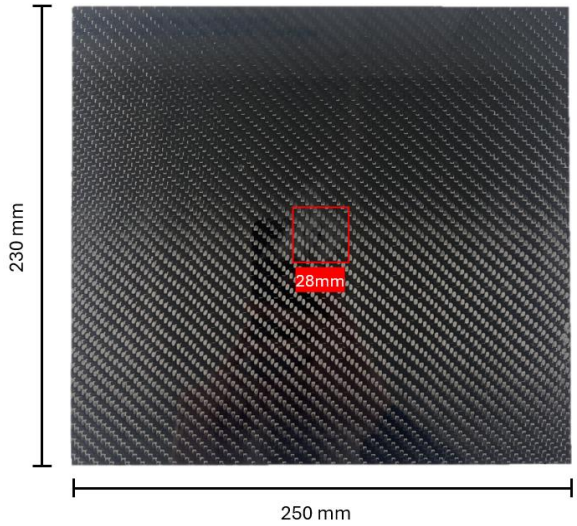

Figure 1: Flat plate geometry with 250mm width and 4mm thickness. The red box indicated the 28mm field-of-view achieved at 14µm voxel size.

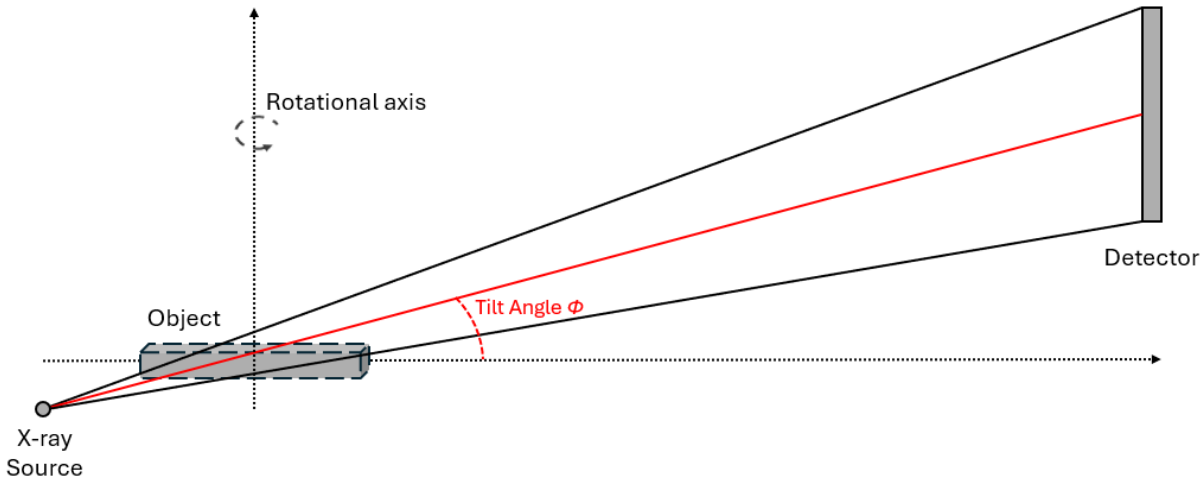

Figure 2: Schematic representation illustrating the CL acquisition geometry.

3 RESULTS AND DISCUSSION

The centre slice reconstructions are displayed in Figures 3 and 4 for CT and CL, respectively. Visually, the CT reconstruction does provide adequate image quality to observe the fibre architecture; however, the high aspect ratio geometry of the specimen contributed to several artefacts across each view. The view through the face of the specimen (3a) contains a pronounced ring artefact, characteristic of anisotropic attenuation, and due to its appearance it can obscure small defects and/or be mistaken for fibres during computational analysis. Additionally, horizontal fibres orientated parallel to the axis of rotation encounter a noticeable drop in sharpness. With CT, this issue presents another trade-off for flat plate laminates with 0°/90°/±45° ply orientations since any alternative positioning of the specimen to avoid this would further increase x-ray path lengths. When observing the plate edge-on (3b), the extent of image noise across the volume makes it difficult to distinguish the lay-up scheme or identify any defects. Alternatively, the CL reconstruction (Figure 4) produces superior image quality in terms of noise and suppression of attenuation-based artefacts especially in views through the thickness of the specimen. As shown in (4a), the ring artefact is effectively removed and fibres appear brighter, owing to the increased x-ray exposure time, and maintain sharpness of the fibre bundles in both the vertical and horizontal direction. In addition, the reduction of noise due to consistent absorption through projection angles can be quantified by CL having nearly double the signal-to-noise (SNR) ratio to that of CT with SNR values of 11.82 and 5.99, accordingly. It can therefore be inferred that thicker composites are likely to experience greater improvements in image quality from CL as they exhibit a higher proportion of projection angles associated with longer X-ray path lengths in CT. Due to the relatively low 20° tilt angle, the horizontal view (4b) does not extensively suffer from laminography artefacts which in this case consist of a cone beam artefact above the specimen proportional to the tilt angle and a slight inter-slice aliasing for plies orientated in the x-direction. With the significant reduction in noise and retention of spatial resolution of horizontal plies, the side view through CL is preferable to CT for visual observation of the specimen's lay-up scheme.

To evaluate the task-based effectiveness of each imaging technique fibre orientation analysis was performed for each volume using VGSTUDIO MAX 2024.1. The corresponding space orientation for each slice is shown in Figures 3(c-e) for CT and Figure 4(c-e) for CL. As illustrated in Figures 3(c) and 4(c), the analyses well replicate the 0°/90° weave pattern through the specimen's thickness and well match what can be observed from image slice. In both cases, some individual voxels within a bundle are subject to misorientation of 45° despite the improvement in image noise for CL. Since the investigation is on fibre bundles the small fluctuations can be resolved by increasing the integration area radius to up to half the bundle height, as shown in Figures 3(e) and 4(e) for the perpendicular view when this parameter is set to two voxels. The main difference between analyses of the weave fibre slices lies with the ring artefact in the CT reconstruction being incorrectly identified as horizontal fibres as seen by the blue strip through the centre of the image (3c). For side views facing the plate edge-on, the outer unidirectional and horizontal weave plies are more faithfully represented with CL (4d) than CT (3d) due to the significant decrease in image noise along this plane. The consequence of the slight inter-slice aliasing artefacts in CL is demonstrated within low depth areas of weave fibres orientated in the horizontal-x direction where voxels are misoriented to 45°. Although, increasing the area parameter to two voxels (4e) produces a more accurate portrayal of vertical fibres that reflect the results of CT (3d&e). Since for practical applications this parameter is optimised in accordance with the specimen's bundle size, the CL trajectory can be deemed an effective imaging technique to accurately characterise the fibre architecture of high aspect ratio structures. A 20° tilt angle effectively mitigated the expected tail artefacts associated with CL reconstruction using the normative FDK algorithm, as such, TV regularisation methods are likely unnecessary for fibre-based tasks at low laminography tilt angles. However, laboratory-based CL imaging of low-density materials may benefit from standard iterative reconstruction methods to aid high-throughput acquisition whereby the increased scan duration attained by additional exposure time could be offset by reducing the number of projections collected.

.

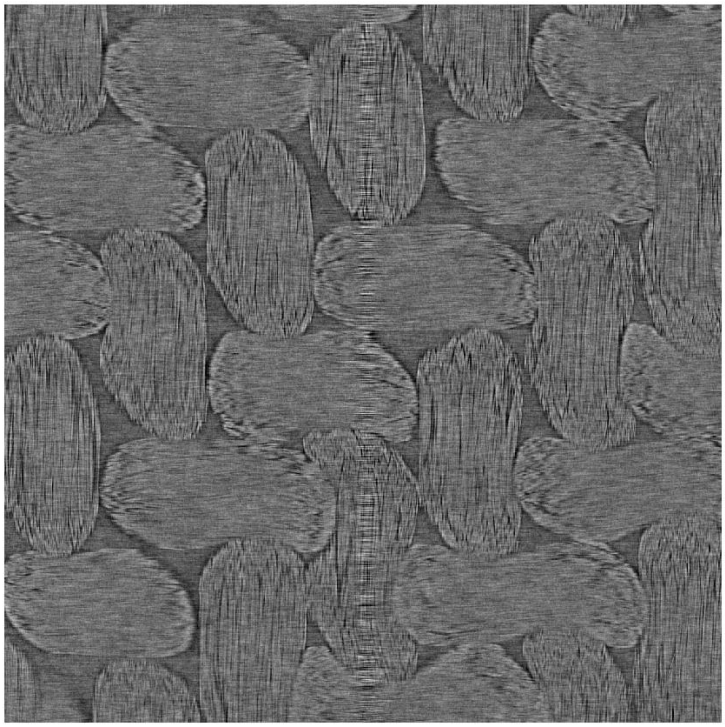

(3a)

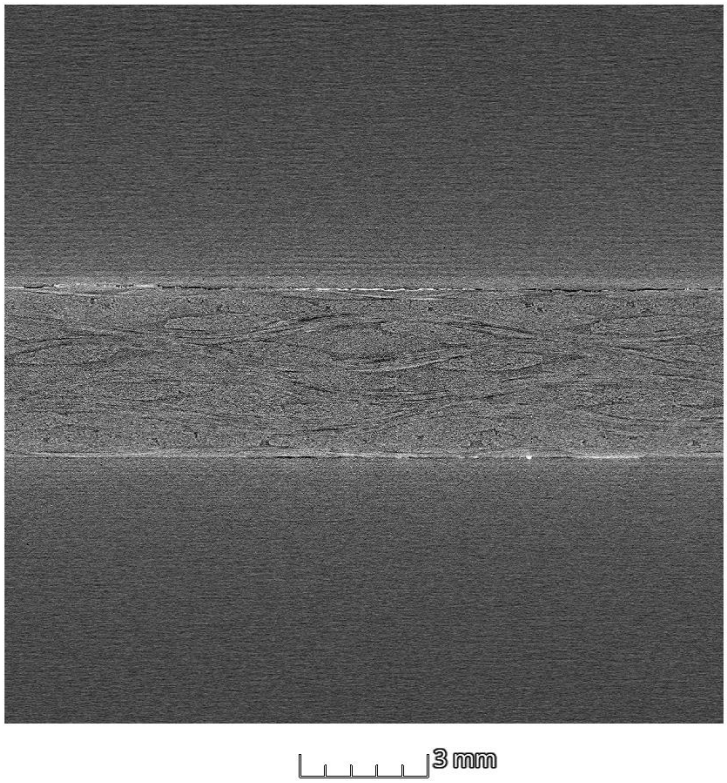

(3b)

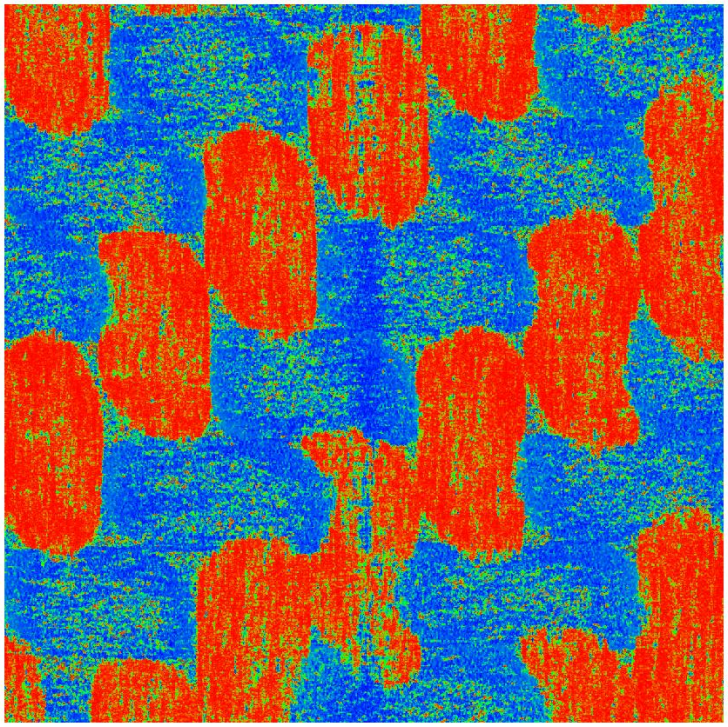

(3c)

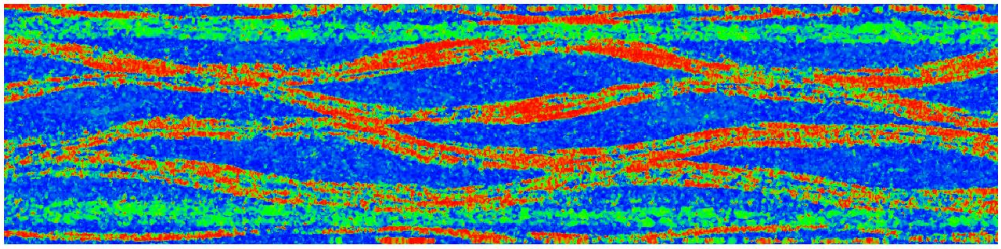

(3d)

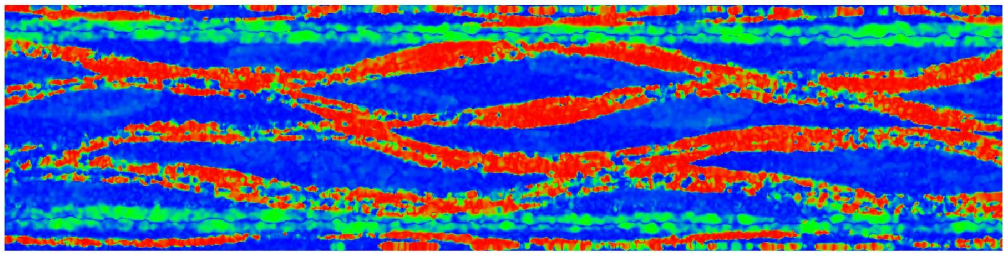

(3e)

Figure 3: (a) Central CT slice through the face of the specimen; (b) Central CT slice through the edge of the specimen; (c) Space Orientation of the CT slice presented in (a); (d) Space Orientation of the CT slice presented in (b); (e) Space orientation with an integration area radius of 2.

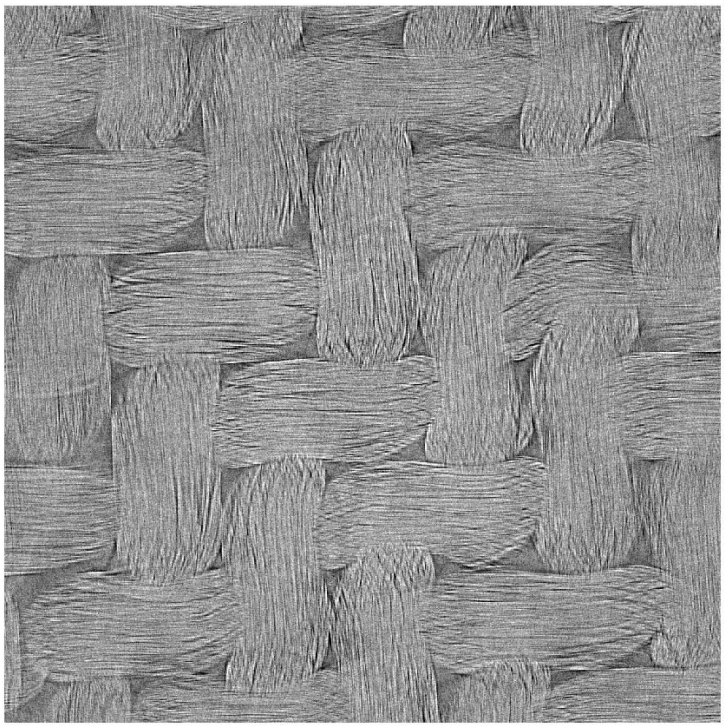

(4a)

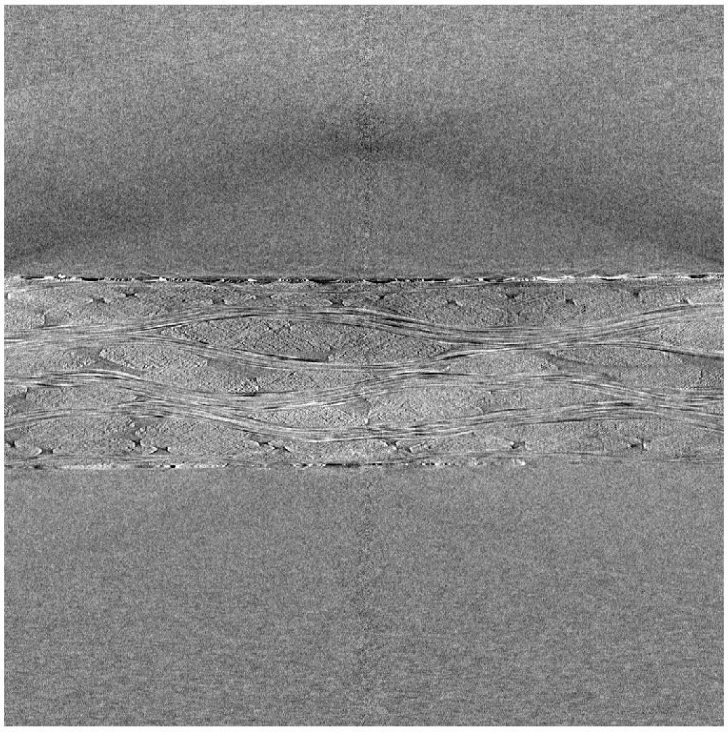

(4b)

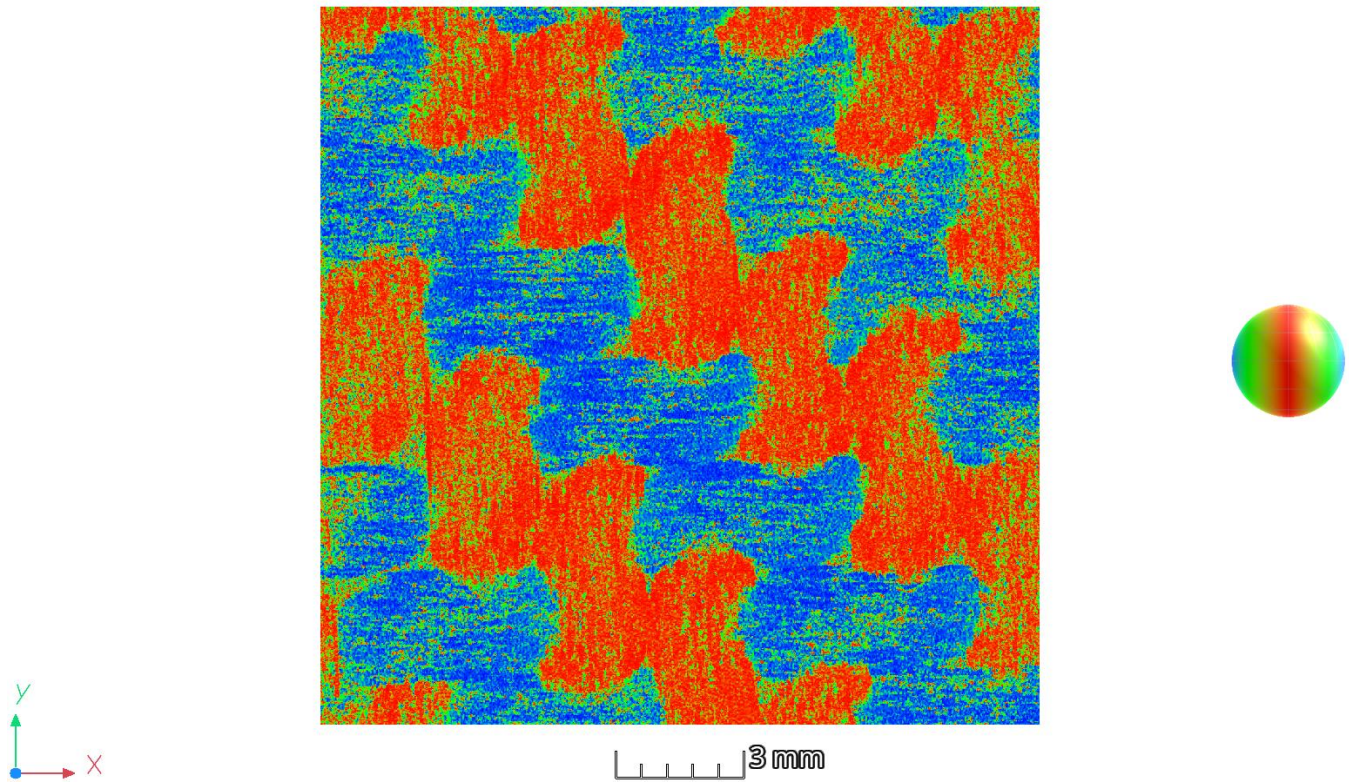

(4c)

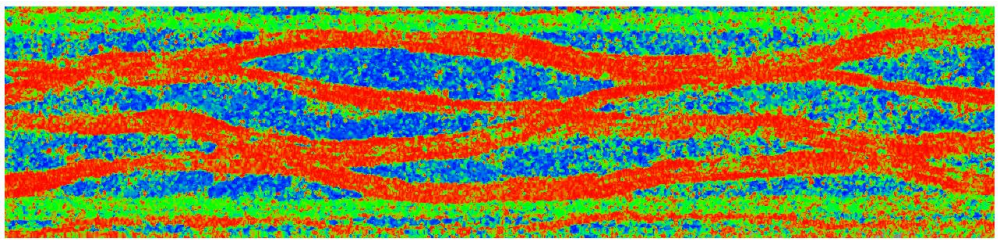

(4d)

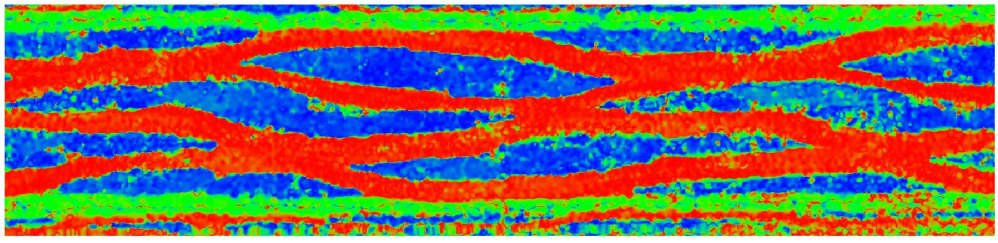

(4e)

Figure 4: (a) Central CL slice through the face of the specimen; (b) Central CL slice through the edge of the specimen; (c) Space Orientation of the CL slice presented in (a); (d) Space Orientation of the CL slice presented in (b); (e) Space orientation with an integration area radius of 2.

4 CONCLUSIONS

In this study, an alternative laminography trajectory was implemented to characterise the fibre architecture of a large high-aspect ratio carbon-fibre laminate. The CL reconstruction was found to produce superior image quality in the plane parallel to the plate's face compared to CT as quantified by an improvement in SNR of 11.89 from 5.99 for the central slice. CL also avoids the consequences of anisotropic attenuation as shown by the suppression of artefacts and preservation of image sharpness for horizontally aligned fibres. Notably, the main difference in computational analysis between the parallel slices was the pronounced ring artefact in the CT reconstruction being misidentified as horizontal fibres. In the side view, a low tilt angle of 20° alleviates the characteristic laminographic artefacts, at which, standard FDK reconstruction is sufficient for CL reconstruction when imaging composite materials. In fact, due to the significant reduction in image noise in this plane, CL provides more visual information of the specimen's lay-up scheme. Further, the results of orientation analysis demonstrate CL as an effective technique for the accurate calculation of fibre direction in laterally extended samples. Overall, the implementation of the CL trajectory is likely to facilitate the greatest benefit for thicker composites and/or structures larger than 400mm where the specimen is free to rotate over the source to achieve a higher resolution otherwise unattainable with CT. Future work will focus on the application of standard iterative reconstruction methods to CL to reduce acquisition times and facilitate high-throughput inspection.

ACKNOWLEDGEMENTS

This work was supported by PhD funding from TESCAN and the National Facility of X-Ray CT (EP/T02593X/1).

REFERENCES

[1] Garcea, S. C., Wang, Y., & Withers, P. J. (2018). X-ray computed tomography of polymer composites. *Composites Science and Technology*, *156*, 305-319. https://doi.org/10.1016/j.compscitech.2017.10.023
[2] Zwanenburg, E. A., Williams, M. A., & Warnett, J. M. (2022). Review of high-speed imaging with lab-based x-ray computed tomography. *Measurement Science and Technology*, *33*(1), 012003. https://doi.org/10.1088/1361-6501/ac354a
[3] Titarenko, S., Titarenko, V., Kyrieleis, A., Withers, P. J., & De Carlo, F. (2011). Suppression of ring artefacts when tomographing anisotropically attenuating samples. *J Synchrotron Radiat*, *18*(Pt 3), 427-435. https://doi.org/10.1107/s0909049511006005
[4] Zwanenburg, E. A., Norman, D. G., Qian, C., Kendall, K. N., Williams, M. A., & Warnett, J. M. (2023). Effective X-ray micro computed tomography imaging of carbon fibre composites. *Composites Part B: Engineering*, *258*, 110707. https://doi.org/10.1016/j.compositesb.2023.110707
[5] Helfen, L., Myagotin, A., Mikulík, P., Pernot, P., Voropaev, A., Elyyan, M., Di Michiel, M., Baruchel, J., & Baumbach, T. (2011). On the implementation of computed laminography using synchrotron radiation. *Rev Sci Instrum*, *82*(6), 063702. https://doi.org/10.1063/1.3596566
[6] Xu, F., Helfen, L., Moffat, A. J., Johnson, G., Sinclair, I., & Baumbach, T. (2010). Synchrotron radiation computed laminography for polymer composite failure studies. *J Synchrotron Radiat*, *17*(2), 222-226. https://doi.org/10.1107/s0909049510001512
[7] Wood, C. E., O'Brien, N., Denysov, A., & Blumensath, T. (2019). Computed Laminography of CFRP Using an X-Ray Cone-Beam and Robotic Sample Manipulator Systems. *IEEE Transactions on Nuclear Science*, *66*(3), 655-663. https://doi.org/10.1109/TNS.2019.2895910
[8] Fisher, S. L., Holmes, D. J., Jørgensen, J. S., Gajjar, P., Behnsen, J., Lionheart, W. R. B., & Withers, P. J. (2019). Laminography in the lab: imaging planar objects using a conventional x-ray CT

scanner. *Measurement Science and Technology*, *30*(3), 035401. https://doi.org/10.1088/1361-6501/aafcae
[9] Jørgensen, J. S., Ametova, E., Burca, G., Fardell, G., Papoutsellis, E., Pasca, E., Thielemans, K., Turner, M., Warr, R., Lionheart, W. R. B., & Withers, P. J. (2021). Core Imaging Library - Part I: a versatile Python framework for tomographic imaging. *Philosophical Transactions of the Royal Society A Mathematical Physical and Engineering Sciences*, *379*(2204), 20200192. https://doi.org/10.1098/rsta.2020.0192
[10] Nikitin, V., Wildenberg, G., Mittone, A., Shevchenko, P., Deriy, A., & De Carlo, F. (2024). Laminography as a tool for imaging large-size samples with high resolution. *J Synchrotron Radiat*, *31*(Pt 4), 851-866. https://doi.org/10.1107/s1600577524002923

ICCM24
AUGUST 4-8, 2025
BALTIMORE CONVENTION CENTER
BALTIMORE, MARYLAND, USA

No Technical Paper Submission for:

Israr Uddin

ICCM24
AUGUST 4-8, 2025
BALTIMORE CONVENTION CENTER
BALTIMORE, MARYLAND, USA

No Technical Paper Submission for:

Abderrahmane Ayadi

IMT Mines Alès
École Mines-Télécom

RÉPUBLIQUE FRANÇAISE
Liberté
Égalité
Fraternité

ICCM24
24TH INTERNATIONAL CONFERENCE ON COMPOSITE MATERIALS

Manufacturing fiber reinforced recycled Polyethylene terephthalate (PET) TAPES: a capillarity-based approach

Elise Mathouillot[1], Monica Francesca Pucci[2] and Pierre-Jacques Liotier[1]

[1] Polymers Composites and Hybrids (PCH), IMT Mines Ales, Ales, France
[2] LMGC, IMT Mines Ales, Université Montpellier, CNRS, Ales, France

CONTEXT



Major environmental issues :

- One of the most widely used polymers [1] → **413 Mt of plastic produced in 2023** [2] → **6,2 %** of PET waste [2]
- Efficient, sustainable, circular and low-energy impact recycling method are **essential**



Current recycling method :

- Most plastics are **shredded**: mechanical recycling process → **degradation of mechanical properties** [3]
- New recycling method: impregnation of fibers to make thermoplastic tapes → **Capillarity characterization**

1 : A. K. Singh et. al, *Compos. Part B Eng.*, vol. 219, p. 108928, Aug. 2021 – 2 : V. D. Neelalochana et. al, *J. Environ. Chem. Eng.*, vol. 13, no. 3, p. 116823 – 3 : A. Ruvolo-Filho and P. S. Curti, *J. Mater. Sci.*, vol. 43, no. 4, pp. 1406–1420, Feb. 2008

GOALS

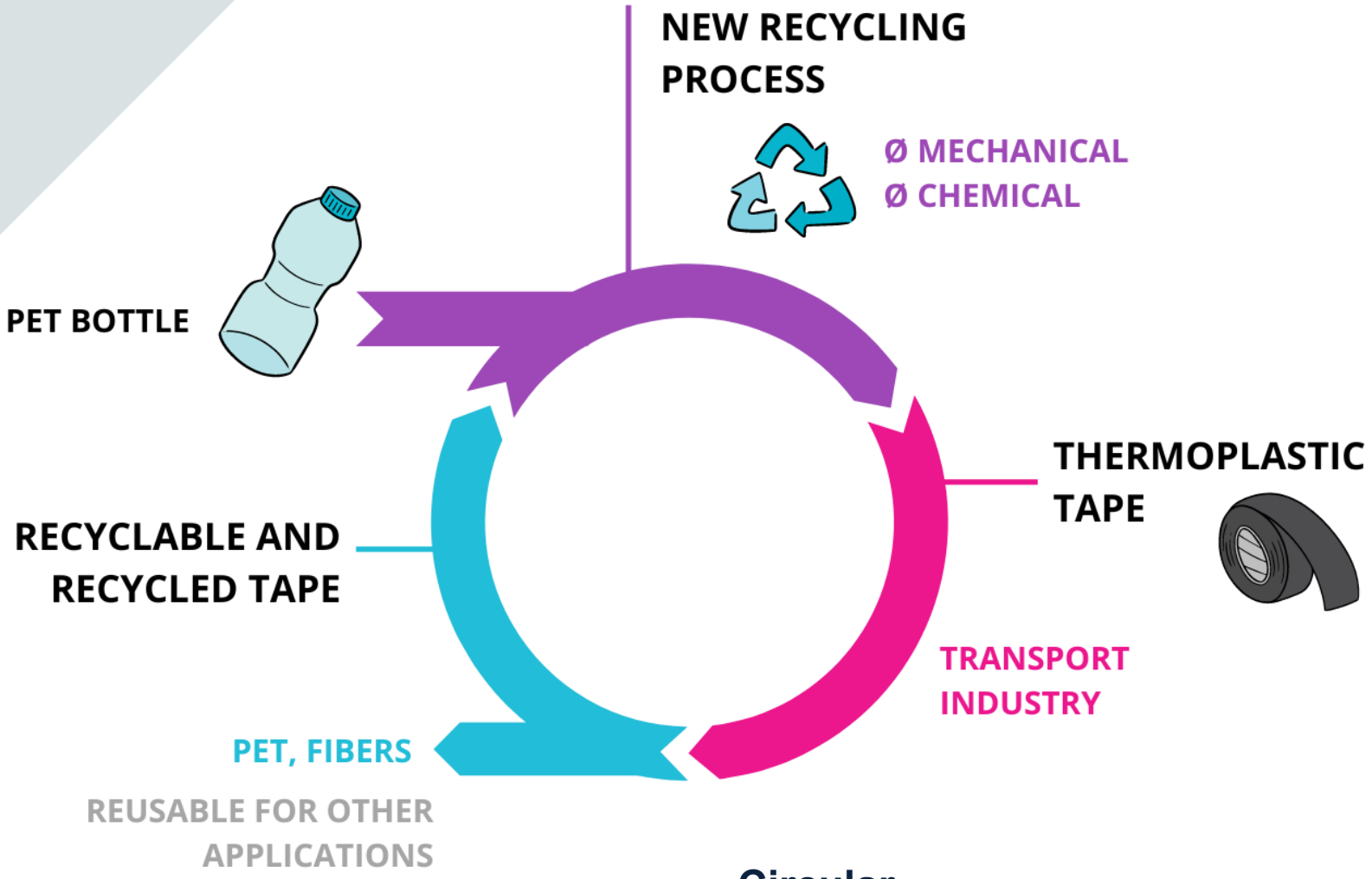

- Circular
- Sustainable
- Low energy impact

METHODOLOGY

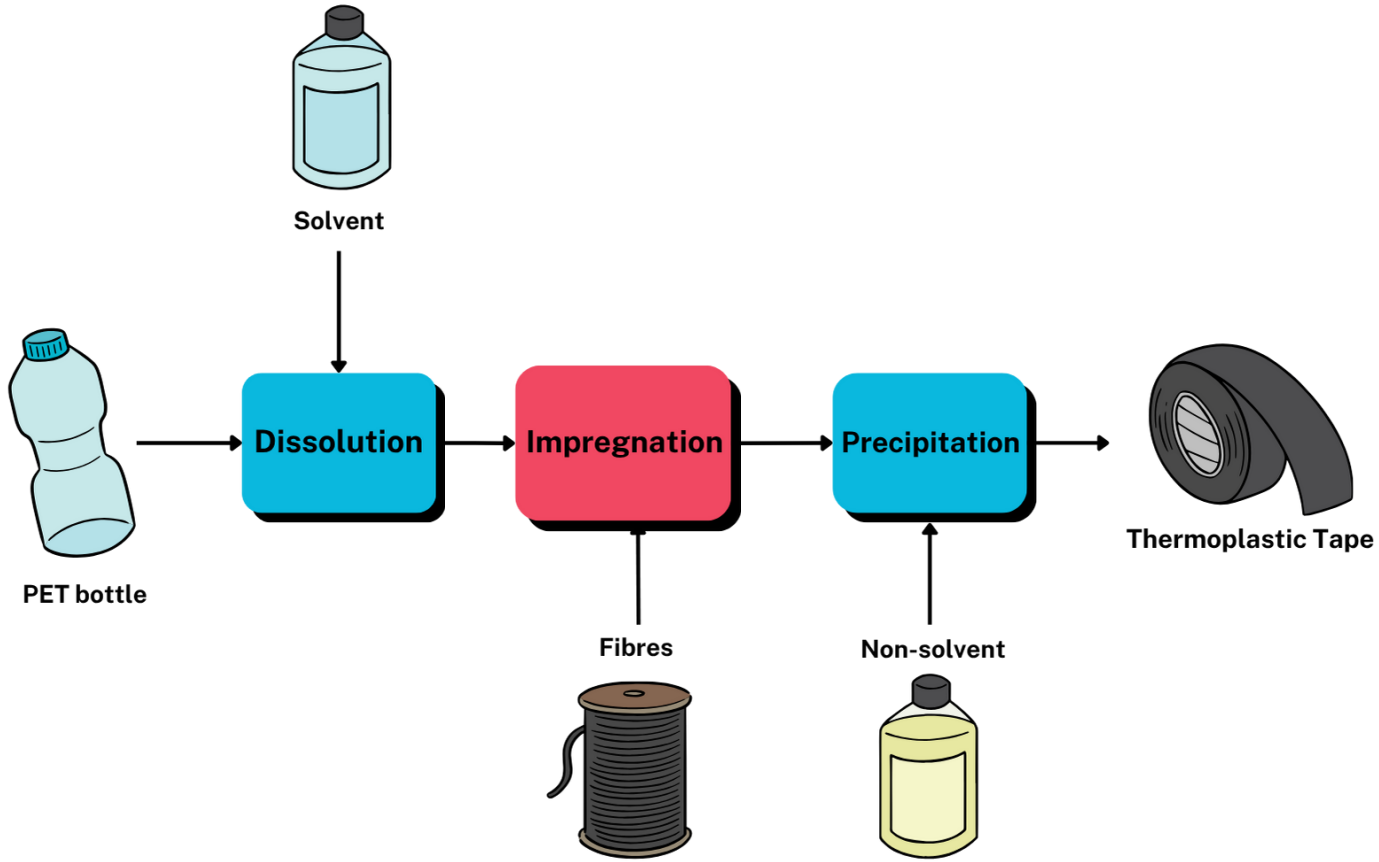

3 important steps :

- **Dissolution** of PET with a suitable solvent
- **Impregnation** of the solution on/ in the fibers
- **Precipitation** of the polymer on/in the fibers thank to a non-solvent

METHODOLOGY - DISSOLUTION

Théorème de solubilité de Hansen [4]

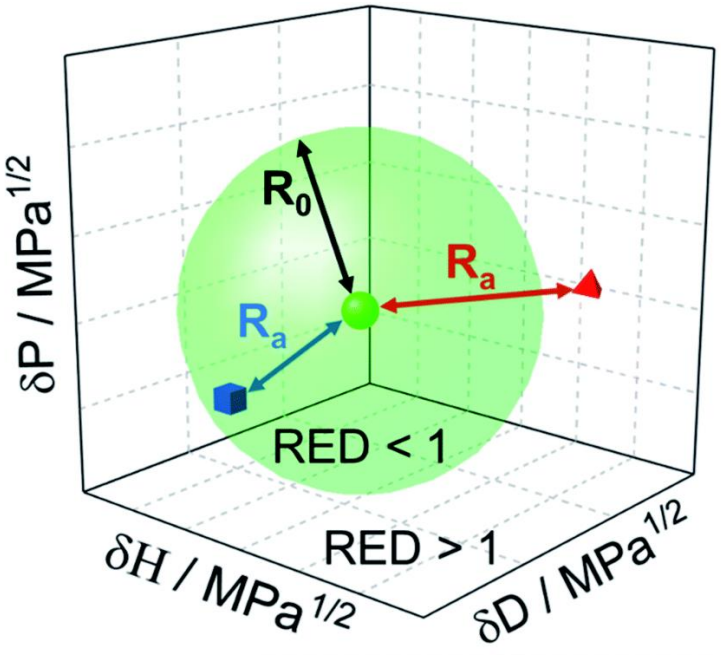

$$\delta = \sqrt{\delta_d^2 + \delta_p^2 + \delta_h^2}$$

→ **Hexafluoroisopropanol (HFIP)**



PET flakes
1-2 cm²



HFIP, 25°C, without agitating



HFIP/PET solution
Limit : 30 wt.%

4 : C. M. Hansen, *Hansen Solubility Parameters: A User's Handbook, Second Edition*, 2e éd. Boca Raton: CRC Press, 2007. doi: 10.1201/9781420006834.

METHODOLOGY - PRECIPITATION

NIPS : Non-solvent Induced Phase Separation [5]

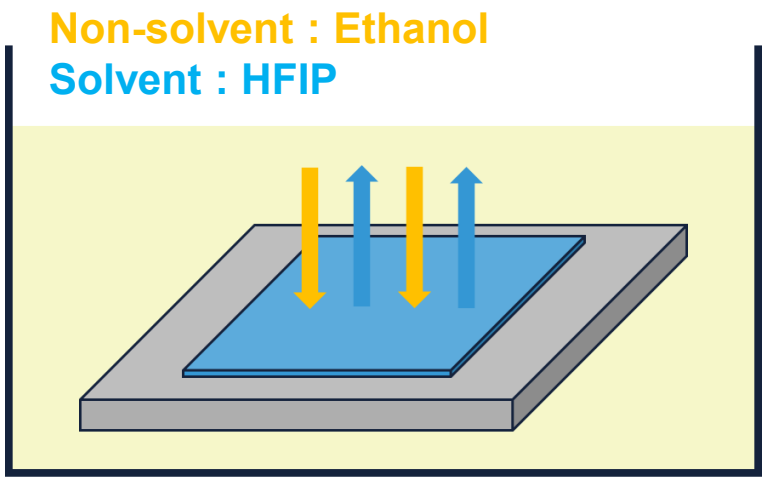

- Methods from **membranes fabrication principles**
- **Ethanol** as a **non-solvent**
- **Diffusion** of the solvent in the non-solvent and of the non-solvent on the solvent

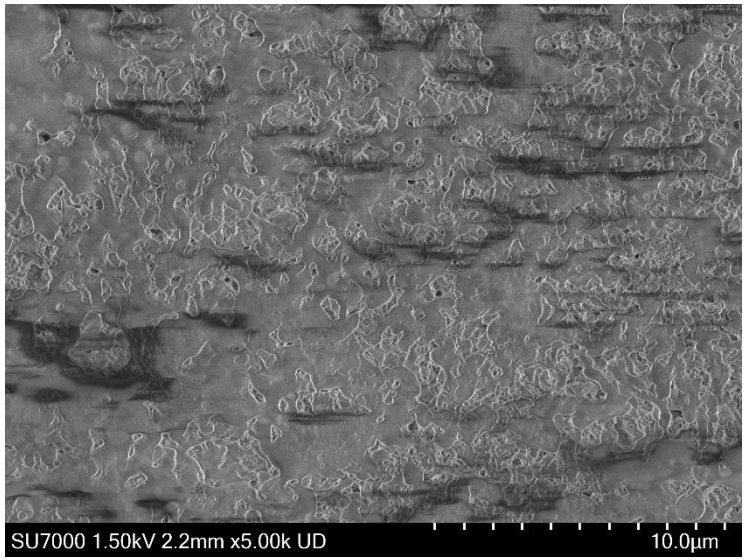

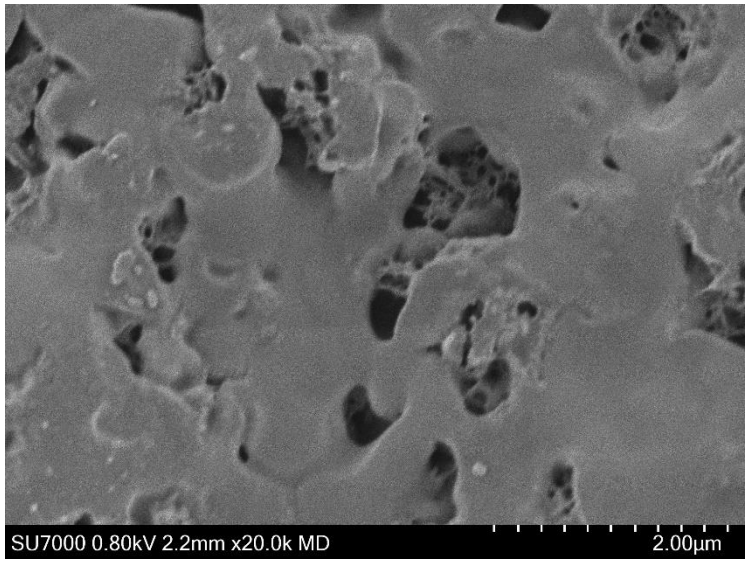

5 : M. Mulder, *Basic Principles of Membrane Technology*. Springer Science & Business Media, 2012.

CHARACTERIZATION - PET

Several analyses shows that PET properties are conserved [6]

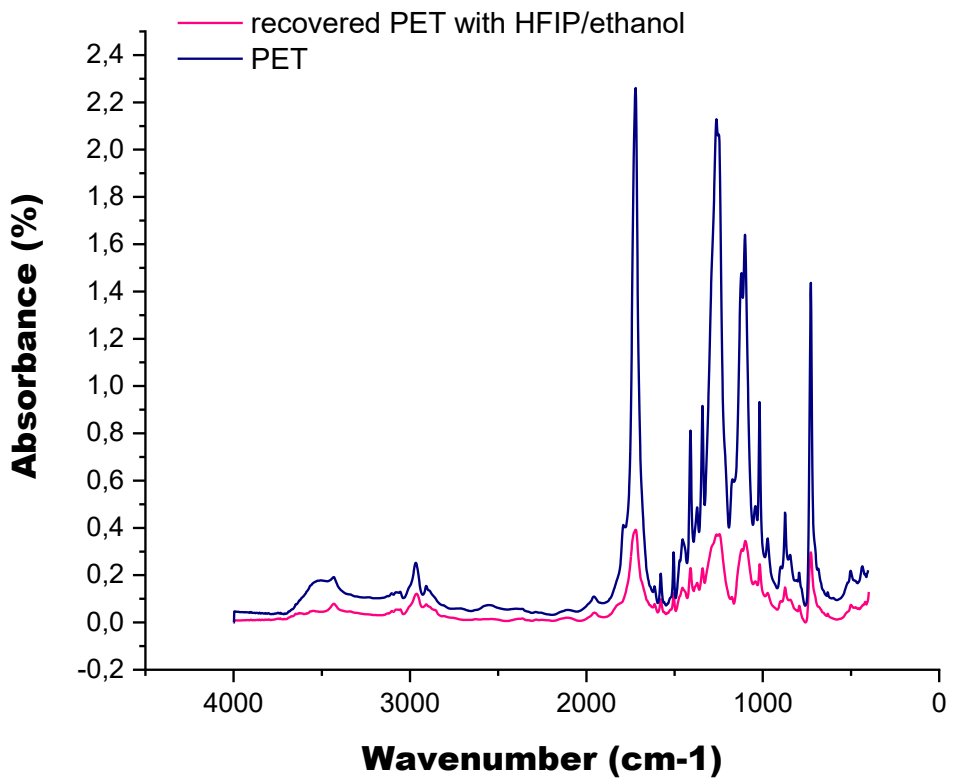

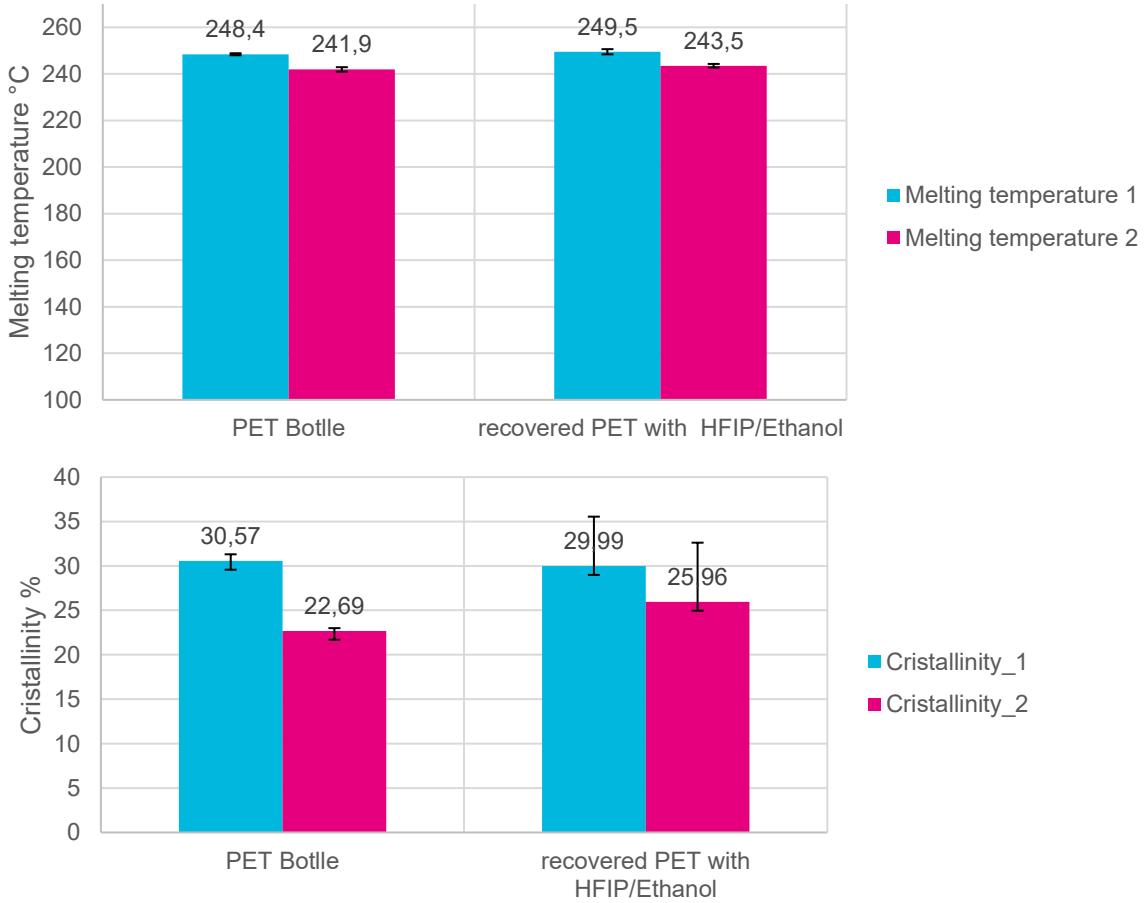

6 : E. Mathouillot, M. F. Pucci, et P.-J. Liotier, « New pet recycling method : manufacture of thermoplastic tape », 21st European Conference on Composites Materials, juill. 2024.

IMPREGNATION - CHARACTERIZATION

Characterization of impregnation kinetics

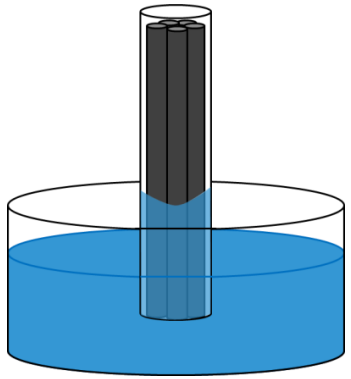

Capillary wicking [7]

$$m^2(t) = C \times \frac{\rho^2 \gamma_L \cos\theta_a}{\eta} t$$

- Density
- Viscosity
- Surface Tension



HFIP pur | 5 wt.% PET | 10 wt.% PET | 15 wt.% PET

7 : M. F. Pucci, P.-J. Liotier, and S. Drapier, 'Capillary wicking in flax fabrics – Effects of swelling in water', *Colloids and Surfaces A: Physicochemical and Engineering Aspects*, vol. 498, pp. 176–184, Jun. 2016, doi: 10.1016/j.colsurfa.2016.03.050.

IMPREGNATION - CHARACTERIZATION

Density determination

$$\rho = V \times m$$



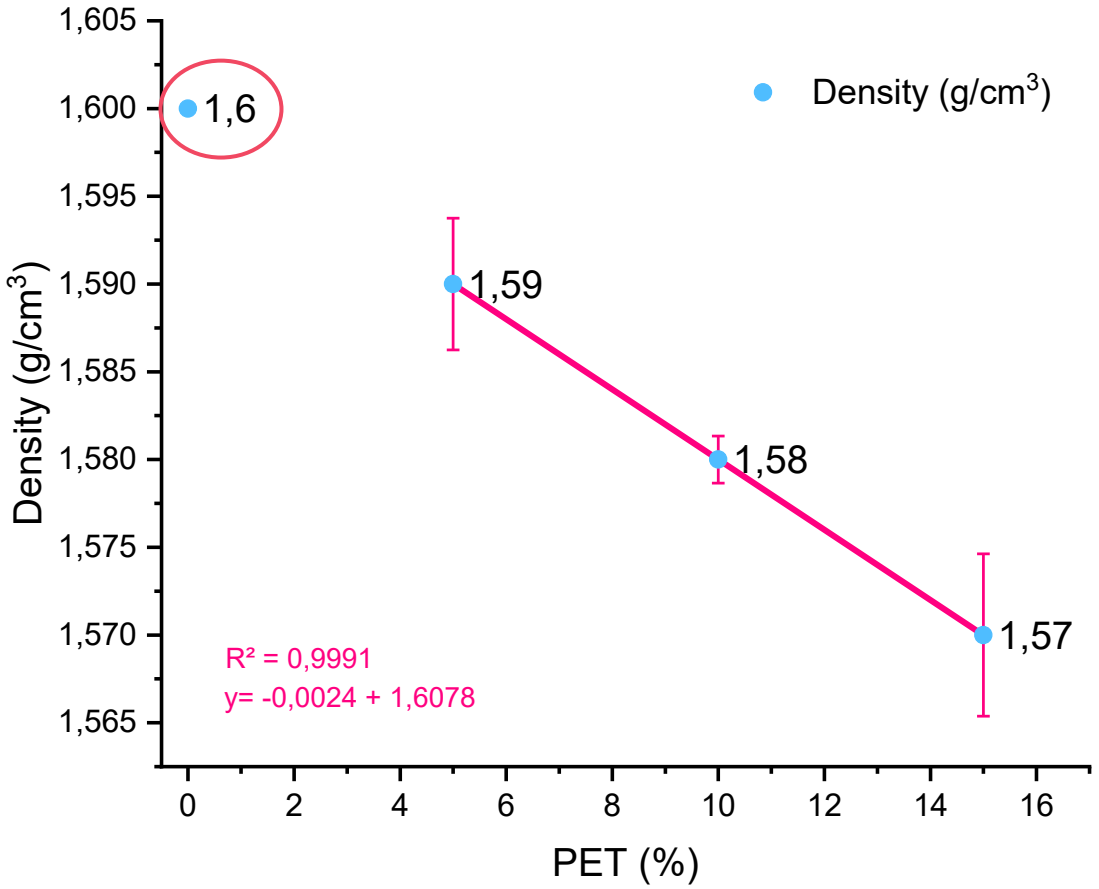

7 : M. F. Pucci, P.-J. Liotier, and S. Drapier, 'Capillary wicking in flax fabrics – Effects of swelling in water', *Colloids and Surfaces A: Physicochemical and Engineering Aspects*, vol. 498, pp. 176–184, Jun. 2016, doi: 10.1016/j.colsurfa.2016.03.050.

IMPREGNATION - CHARACTERIZATION

Viscosity determination [8]



$$\eta = \frac{M}{2\pi R^3 \Omega}$$

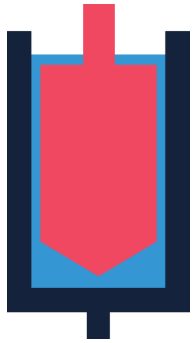

$$\eta = \frac{M}{2\pi H R^2 \Omega}$$

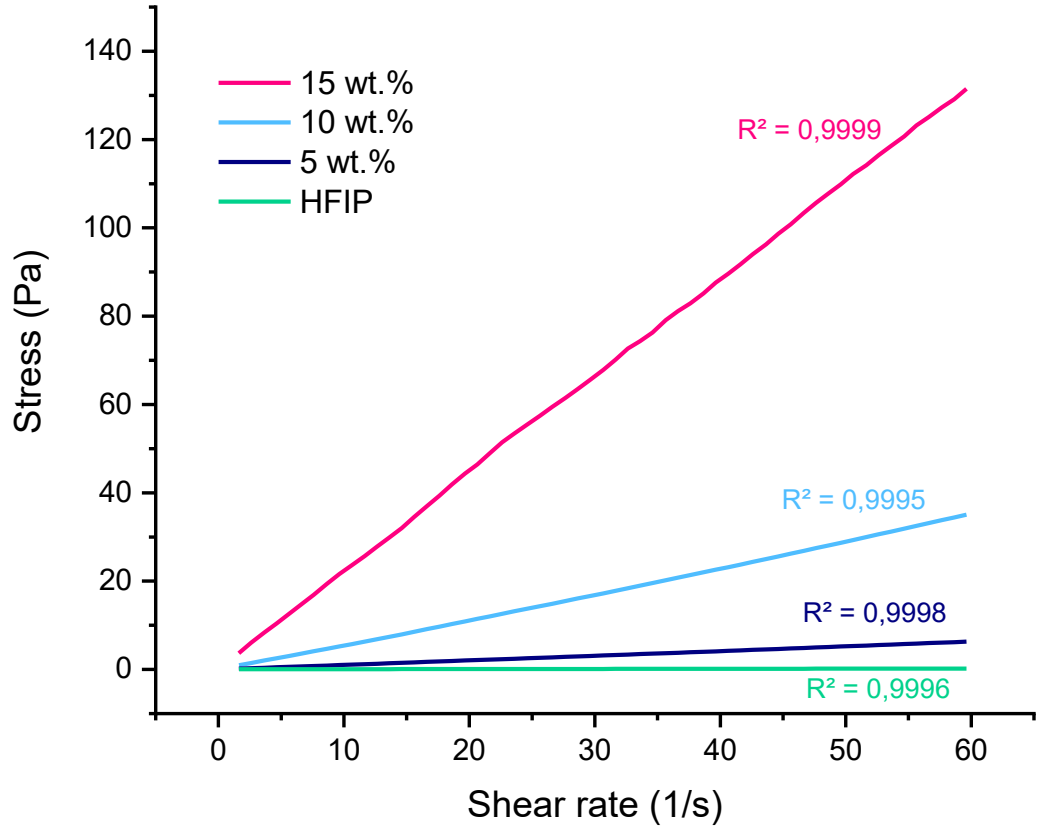

8 : C. J. May and K. O. Henderson, 'Rheological Measurement Methods and Equipment. doi: 10.1007/978-0-387-92897-5_969.

IMPREGNATION - CHARACTERIZATION

Viscosity determination [8]



$$\eta = \frac{M}{2\pi R^3 \Omega}$$

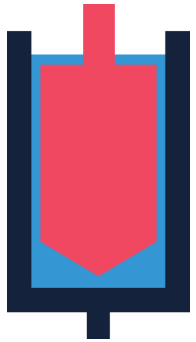

$$\eta = \frac{M}{2\pi H R^2 \Omega}$$

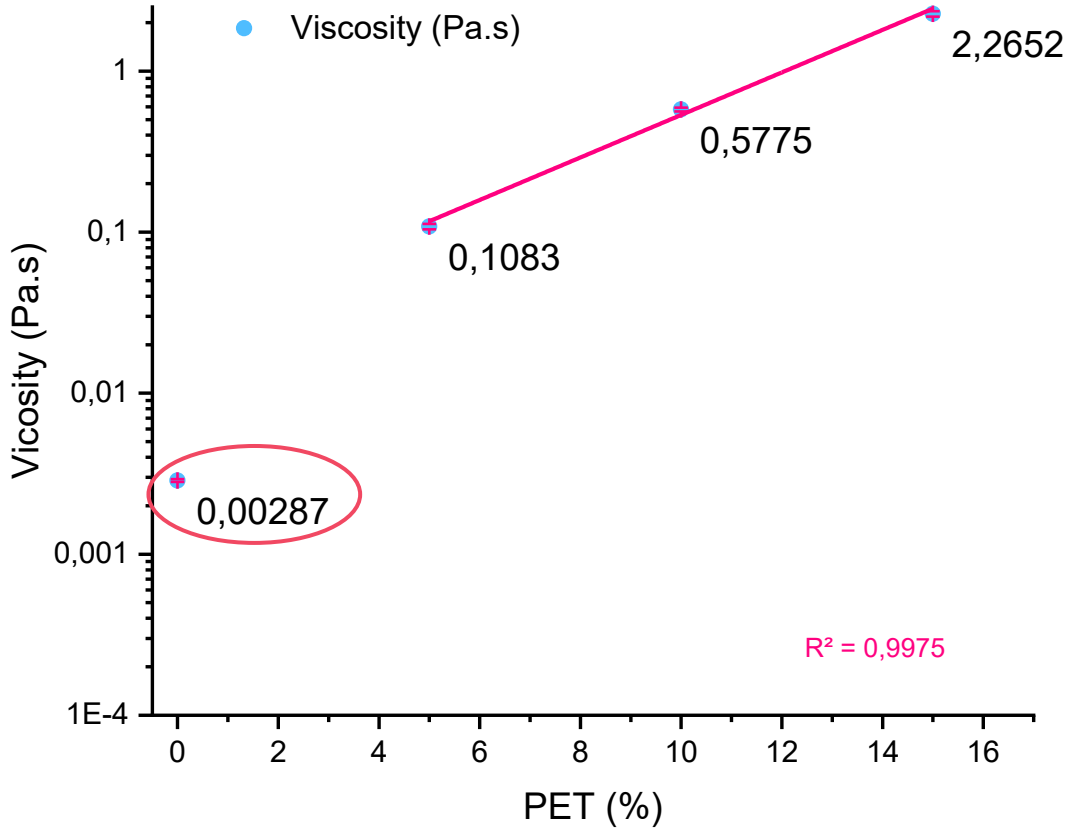

8 : C. J. May and K. O. Henderson, 'Rheological Measurement Methods and Equipment. doi: 10.1007/978-0-387-92897-5_969.

IMPREGNATION - CHARACTERIZATION

Surface tension determination [9]

$$F_c = mg = \gamma_{LV}\, p\, cos\theta$$

$$\gamma_{LV} = \frac{mg}{p}$$

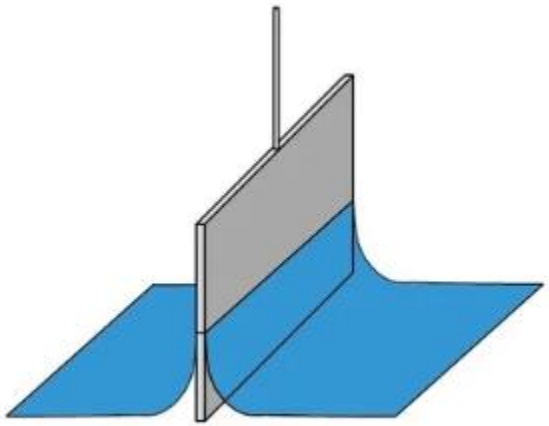

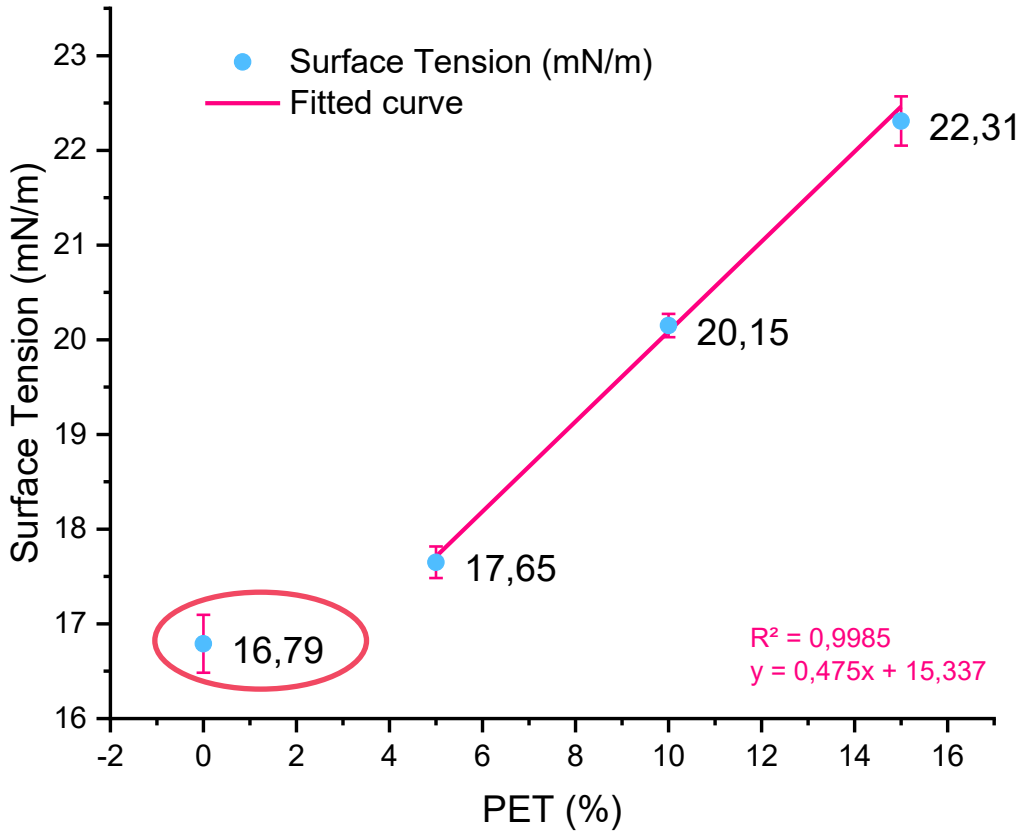

9 : M. F. Pucci, P.-J. Liotier, and S. Drapier, 'Capillary effects on flax fibers – Modification and characterization of the wetting dynamics', *Composites Part A: Applied Science and Manufacturing*, vol. 77, pp. 257–265, Oct. 2015, doi: 10.1016/j.compositesa.2015.03.010.

IMPREGNATION – WICKING TESTS

Determination of impregnation kinetics as a function of concentration of PET

$$m^2(t) = \left[\frac{(c\bar{r})\epsilon^2(\pi R^2)^2}{2}\right] \times \frac{\rho^2 \gamma_L cos\theta_a}{\eta}\ t$$

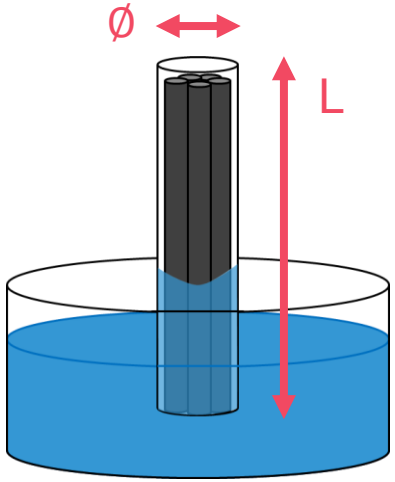

$$\boldsymbol{L} = 20\ mm$$

$$\boldsymbol{R} = Ø/2 = 1{,}75\ mm$$

$$\boldsymbol{c\bar{r}} = 6{,}44.10^{-3}\ mm$$

$$\boldsymbol{V_f} = 51{,}51\ \%$$

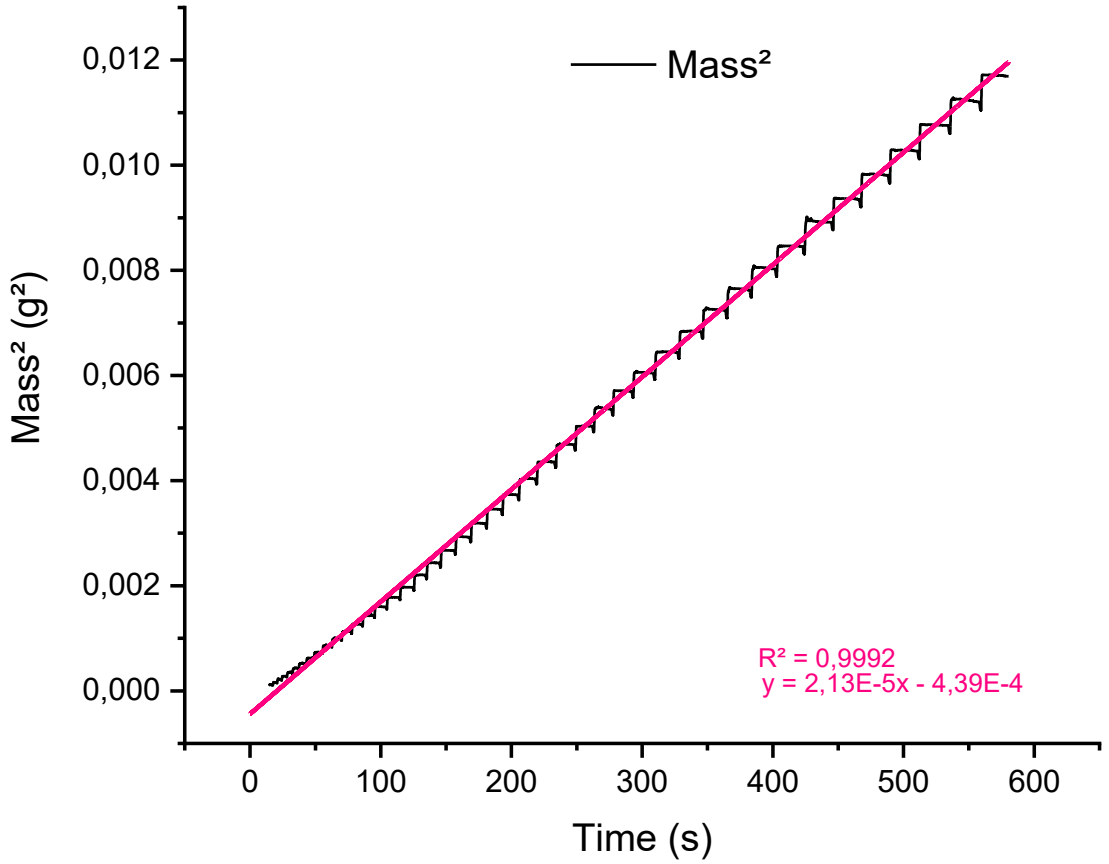

7 : M. F. Pucci, P.-J. Liotier, and S. Drapier, 'Capillary wicking in flax fabrics – Effects of swelling in water', *Colloids and Surfaces A: Physicochemical and Engineering Aspects*, vol. 498, pp. 176–184, Jun. 2016, doi: 10.1016/j.colsurfa.2016.03.050.

IMPREGNATION – WICKING TESTS

Determination of impregnation kinetics as a function of concentration of PET

$$m^2(t) = \left[\frac{(c\bar{r})\epsilon^2(\pi R^2)^2}{2}\right] \times \frac{\rho^2 \gamma_L cos\theta_a}{\eta}\ t$$

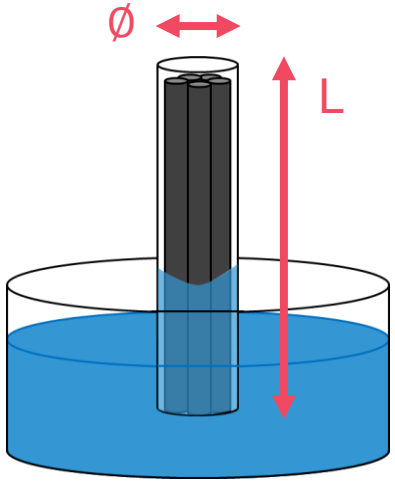

$$\boldsymbol{L} = 20\ mm$$

$$\boldsymbol{R} = Ø/2 = 1{,}75\ mm$$

$$\boldsymbol{c\bar{r}} = 6{,}44.10^{-3}\ mm$$

$$\boldsymbol{V_f} = 51{,}51\ \%$$

PET	m²/t (g²/s)	R²	θa (°)
5 wt%	1,554E-05	0,991	88,1
10 wt%	1,471E-05	0,993	81,6
15 wt%	4,217E-06	0,993	81,3

7 : M. F. Pucci, P.-J. Liotier, and S. Drapier, 'Capillary wicking in flax fabrics – Effects of swelling in water', *Colloids and Surfaces A: Physicochemical and Engineering Aspects*, vol. 498, pp. 176–184, Jun. 2016, doi: 10.1016/j.colsurfa.2016.03.050.

IMPREGNATION LINE – METHODOLOGY

MODULES OF IMPREGNATION LINE

- Impregnation bath : polymer solution
- Precipitation bath : non-solvent
- Guide rollers
- Steamrollers
- Motorised winding coil

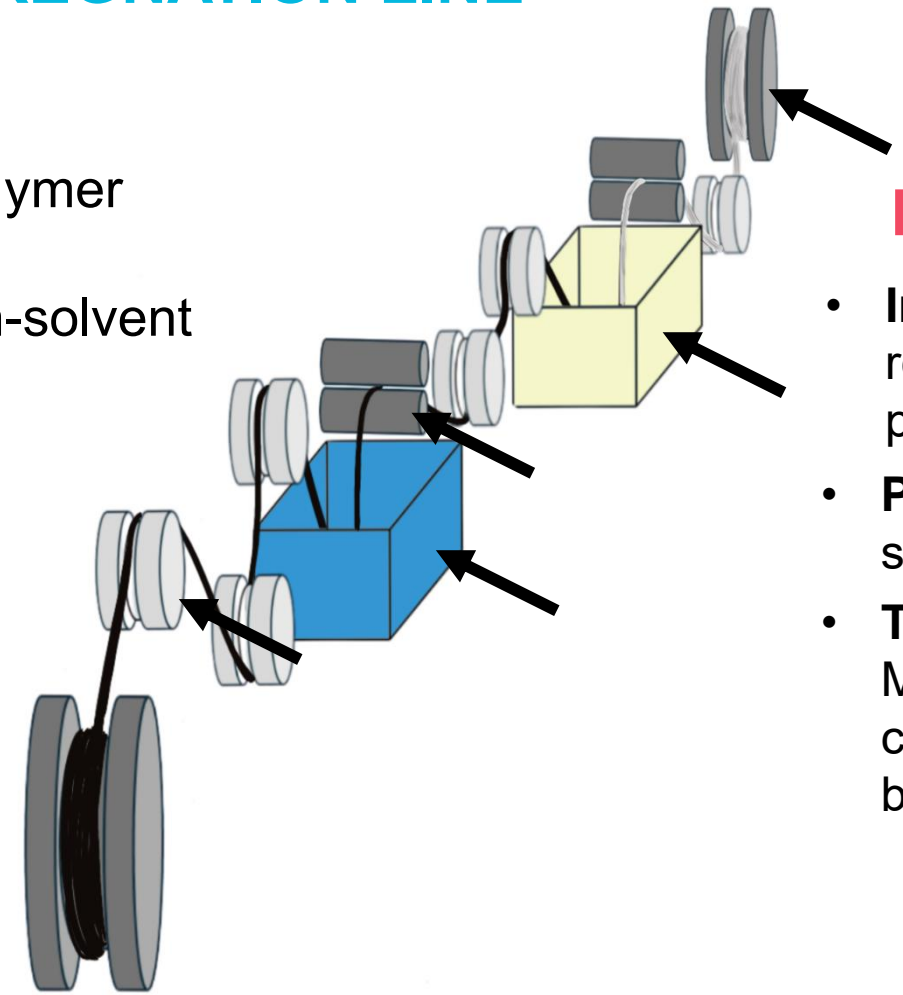

Parameters optimization

- **Impregnation** : impregnation speed, rollers tension, concentration of polymer
- **Precipitation** : precipitation speed, solvent recovery
- **Tapes characterization** : Morphology and porosity characterization, mecanical behaviour, fibres volumic fraction

IMPREGNATION LINE – METHODOLOGY

MODULES OF IMPREGNATION LINE

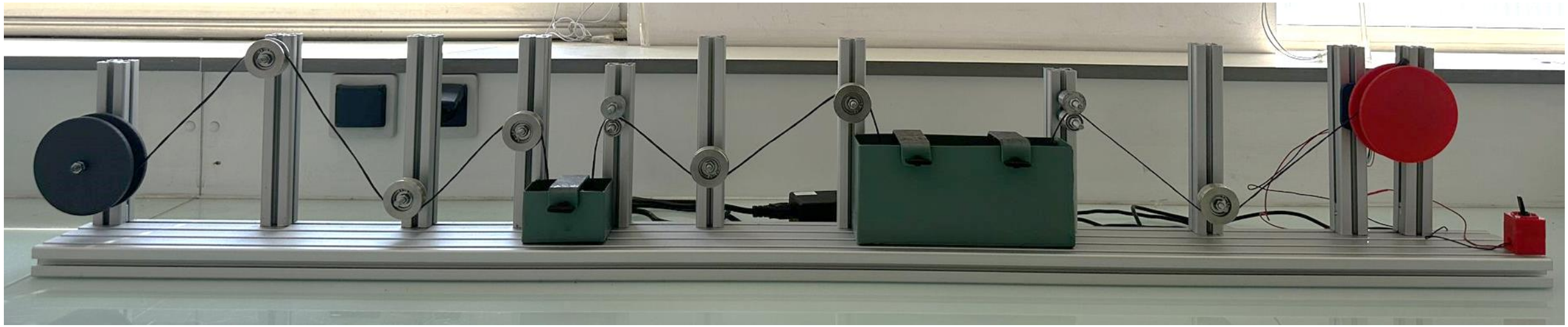

IMPREGNATION LINE – CHARACTERIZATION

SEM analyses – Morphology of the thermoplastic tapes

- Carbon fibers **IM7 12k** - Hexcel
- $V = 6mm/s$

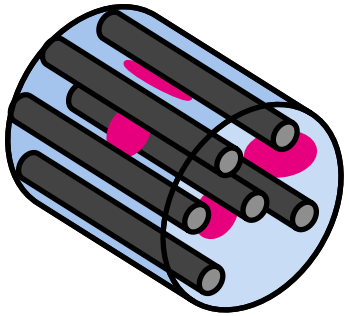

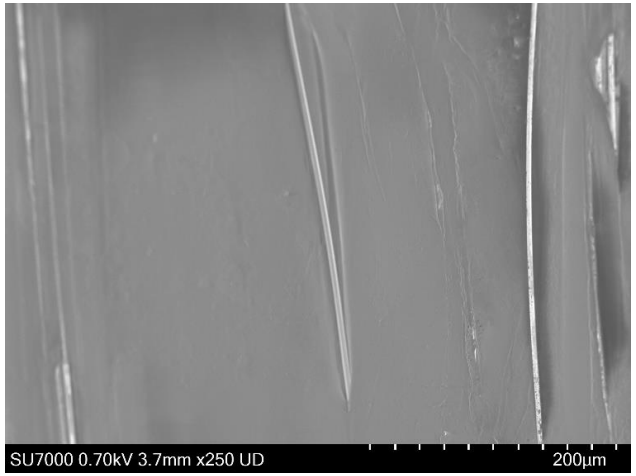

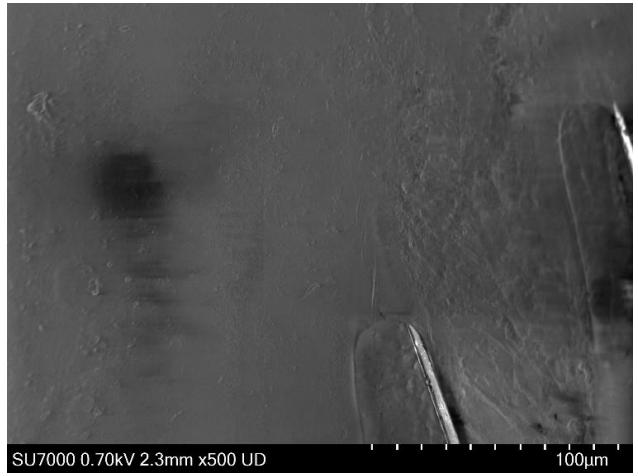

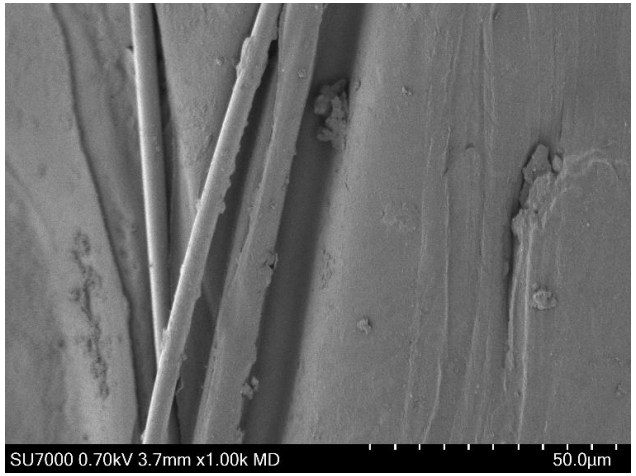

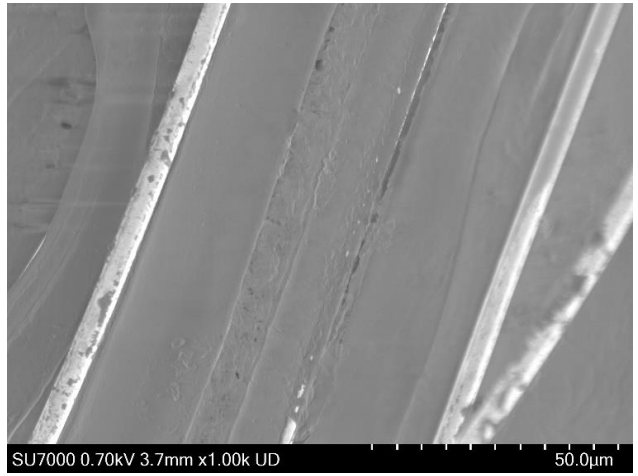

CONCLUSIONS PROSPECTS

CONCLUSIONS

- **Dissolution / Precipitation method** has been selected and validated.
- **Innnovative and efficient method for recycling PET has been developped.**
- **Production of tapes** has started and is running successfully

PROSPECTS

- **Optimise** production parameters : speed, tension, concentration
- **Characterization** of the produced tapes
- Test with a **robotised draping process**

IMT Mines Alès
École Mines-Télécom

RÉPUBLIQUE FRANÇAISE
Liberté
Égalité
Fraternité

Thank you
for your attention

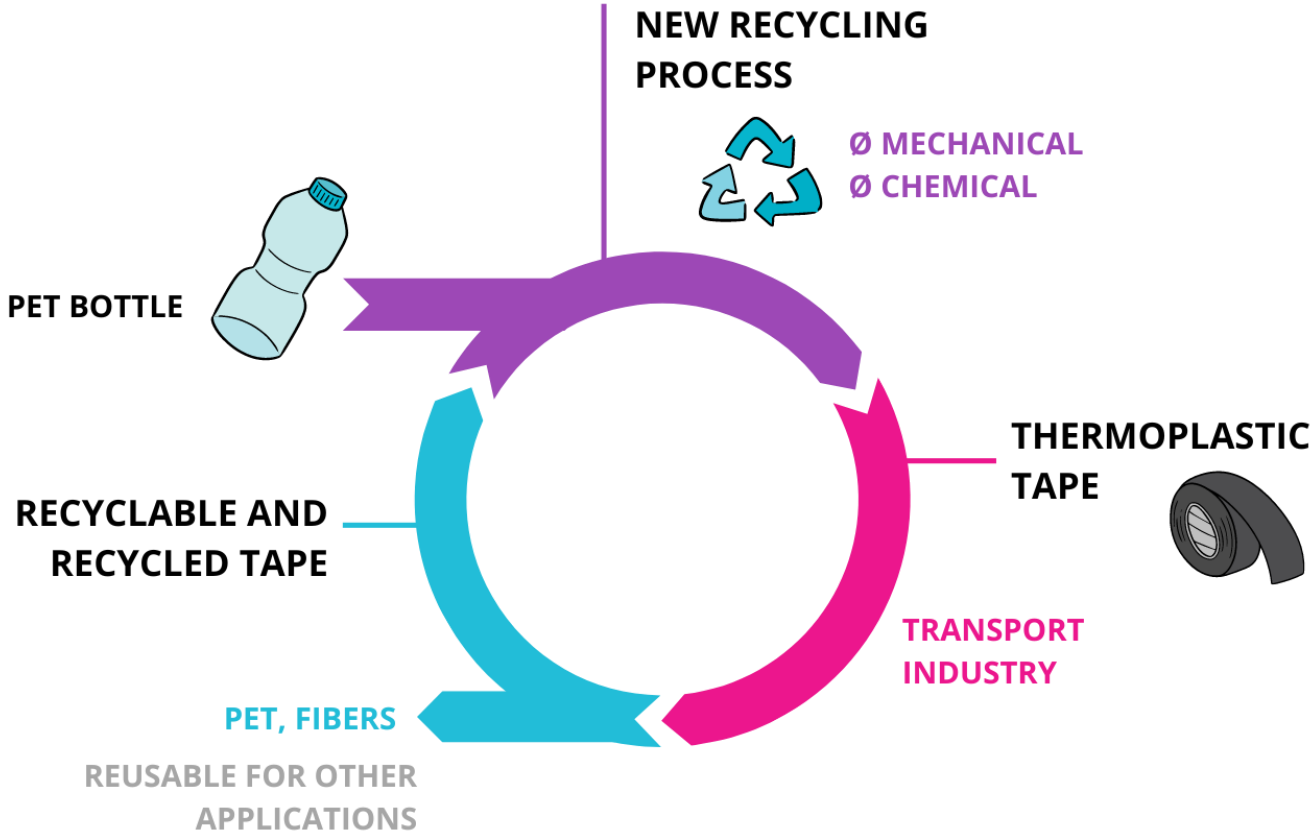

Elise.mathouillot@mines-ales.fr

Singapore Institute of Manufacturing Technology
A*STAR SIMTech

Reprocessing Thermoplastic Composite Trim Waste with High-Temperature Compression Moulding

A. Haris[1], S. Logesh[1], M.A. Debowski[1], C. Wang[1], B.F. Ng[2], W.S. Teo[1]*

[1]Singapore Institute of Manufacturing Technology (SIMTech), Agency for Science, Technology and Research (A*STAR), 5 CleanTech Loop #01-01, CleanTech Two Block B, Singapore 636732, Republic of Singapore

[2]Nanyang Technological University

* wsteo@simtech.a-star.edu.sg

ICCM24
24TH INTERNATIONAL CONFERENCE ON COMPOSITE MATERIALS
August 4-8, 2025 Baltimore Convention Center - Baltimore, MD

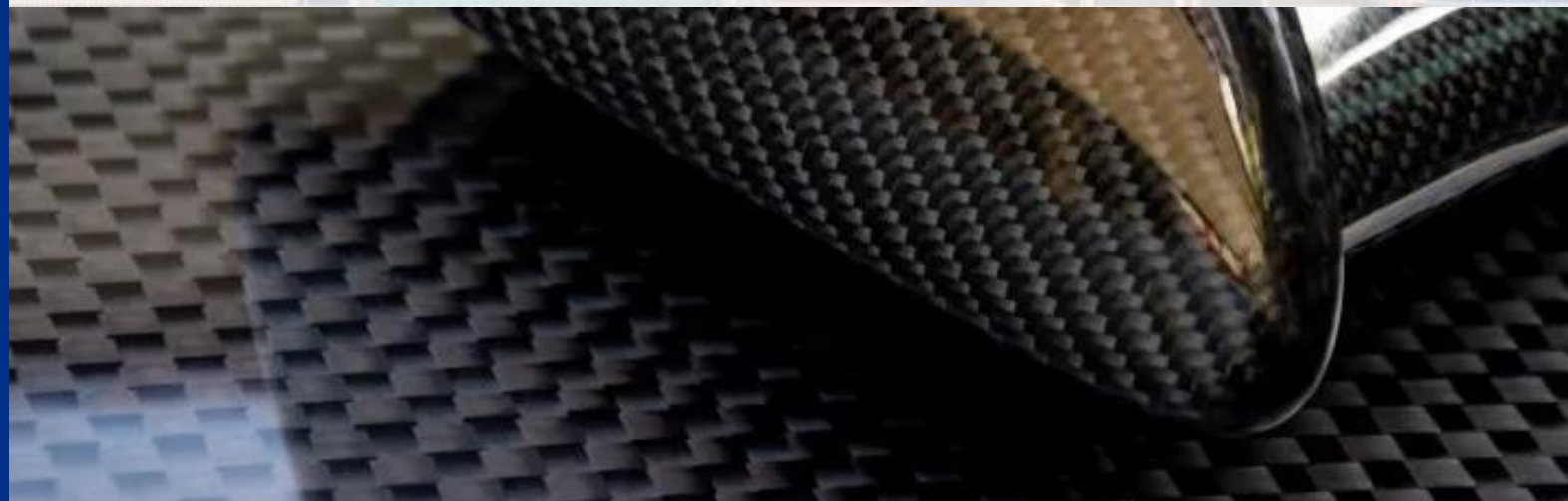

Singapore Institute of manufacturing Technology (SIMTech), A*STAR



Almost the furthest flight to ICCM



Singapore Institute of Manufacturing Technology

(5 Cleantech Loop, #01-01, CleanTech Two Block B, Singapore 63673)

MTI MINISTRY OF TRADE AND INDUSTRY SINGAPORE

Agency for Science, Technology and Research SINGAPORE

Singapore Institute of Manufacturing Technology SIMTech

A world-class innovation partner in advanced manufacturing technologies, systems and capabilities

- Founded in 1993
- SIMTech have 400+ staff, ~90 students

Manufacturing will be Smarter, Greener and More Connected in the Future

Next-Gen Manufacturing Processes

- 4D Additive Manufacturing
- Adaptive Machining & Surface Engineering
- Hybrid & Multi-Materials Forming
- MedTech Manufacturing
- Extreme Manufacturing
- ***Advanced Polymer and Composite processing***

Industry 5.0

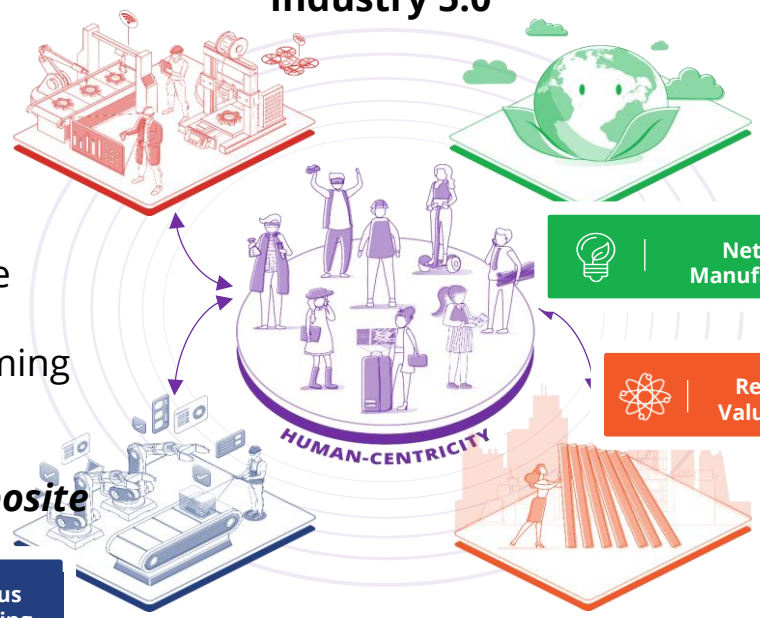

Enabling Data-Driven and Knowledge-Based Manufacturing with Workforce Augmentation Technologies

Polymer and Composite Processing Group @ SIMTech

- 01. Injection Moulding Process
- 02. Sheet Compression Moulding & Thermoforming
- 03. Extrusion and Additive Manufacturing
- 04. Lightweight Design and Process Simulation


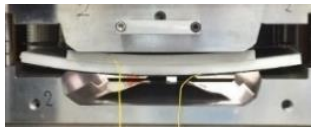

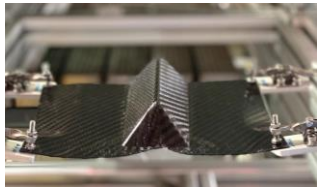

- Vacuum Forming
- 2IR Composite Thermoforming
- Compression Moulding
- In-situ consolidation
- In-situ polymerization



❑ Polymer Injection Moulding (Auburg Allrounder 570H, 200T, 2500bar, 450°C)



❑ Injection Compression Moulding (Witmann Ecopower 110, 110T, 2100bar, 350°C)



❑ High Temperature Extruder (Leistritz ZSE 27 MAXX, L/D ratio: 48, screw Diameter: 27mm, 450°C, melt pressure: 220 bar)



❑ Integrated Composite Thermoforming (320T-1.2x1.2m 125kW 2IR)



❑ Hot Press Sheet Consolidator (60T-40x40cm platen - 450°C, equipped with a water chiller)



❑ Vacuum Thermoforming (Formech HD1500, 1.5x1m,x10mm, 55kW quartz heater)



❑ Vacuum Thermoforming (CMS eidos se 1.5x1mx10mm, 75kW halogen heater)



❑ Microinjection Moulding (Babyplast, 6T, 1850bar, 75x75x70mm mould)



❑ Drying oven (Gen lab, 1.6x1.1m sheet size, 50 sheets 250°C)



❑ Portable Hot Bonder (Aerofom Composites AHB-380-s, 16 Amp or 32 Amp and 10 thermocouples



❑ Composites Curing Oven (OV301 - 1070x440x500mm - 200°C)

Background

- **Forged composite molding (FMC)**, originally developed for compression molding of chopped carbon fiber-reinforced thermosets, is widely used in the automotive sector.
- With growing focus on sustainability and circularity, **thermoplastic molding compounds** are gaining traction.
- **Thermoplastic BMCs/SMCs** also offer benefits better fracture toughness and faster cycle times, though they require higher processing temperatures than thermosets.
- This study investigates the use of a **high-temperature compression moulding** unit for **reprocessing thermoplastic waste** via bulk moulding.



Mitsubishi CF thermoset SMC
[https://www.m-chemical.co.jp/carbon-fiber/en/product/fmc/]



GF thermoset SMC used to produce battery box
[https://teijin-mobility.com/en/new_tech/gf-smc/]



Toray chopped fiber thermoplastic BMCs
[https://www.toraytac.com/products/thermoplastic/bulk-molding-compounds]

What is LCF?

- Trim waste, known as **Loose Chip Forms (LCF)**, is generated during prepreg cutting and is repurposed into **uniform rectangular chips** for recycling.
- A **die cutter** is used to shape the chips into consistent sizes.
- The uniform chips are then **recycled using a compression moulding process**.
- This approach gives **a second life to the trim waste**, turning it into useful material.



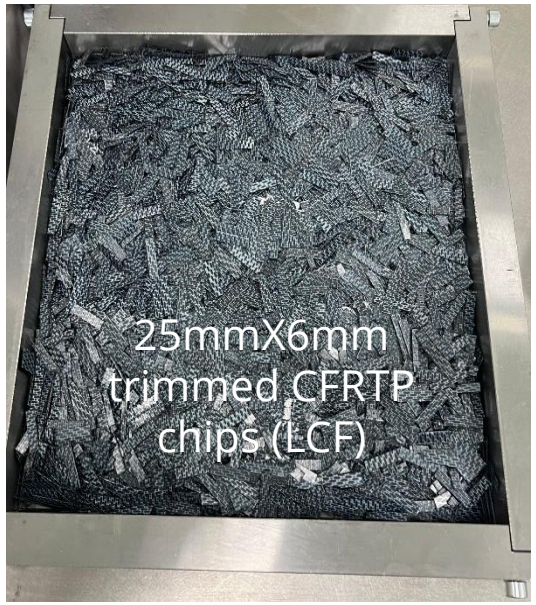



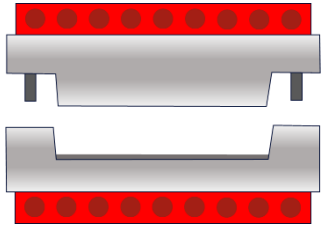

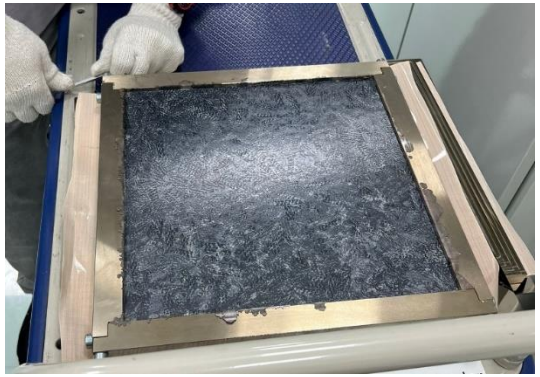

Fabricated LCF composite panel

LCFs of 5HS CF-PPS (Polyphenylene Sulfide)



Excess, waste material

Die Cutter

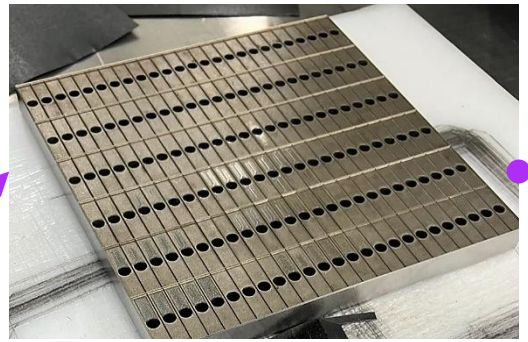

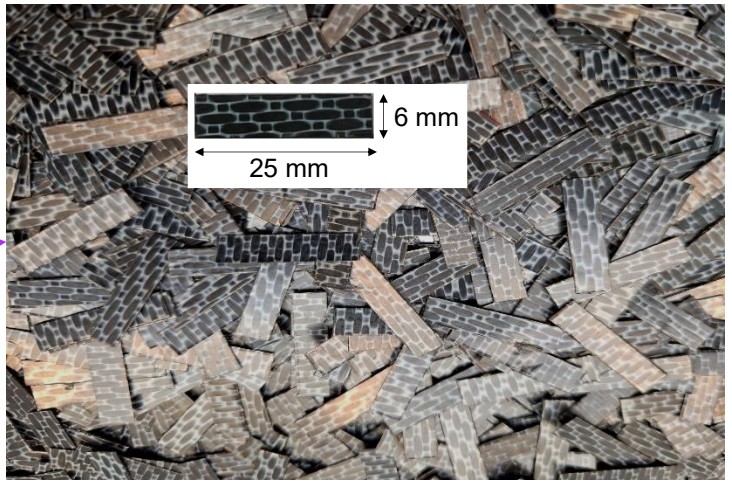

Uniform LCF



Shredder/Grinder



Non-uniform LCF

Thermal Characterization

- **Melting, crystallization** (from DSC) and **degradation temperature** (from TGA) data shows **processing window** whereby PPS can flow and allow forming of the prepreg without degradation onset.
- Higher % crystallinity: polymer crystals are hard and strong, which affects **mechanical properties**.

DSC

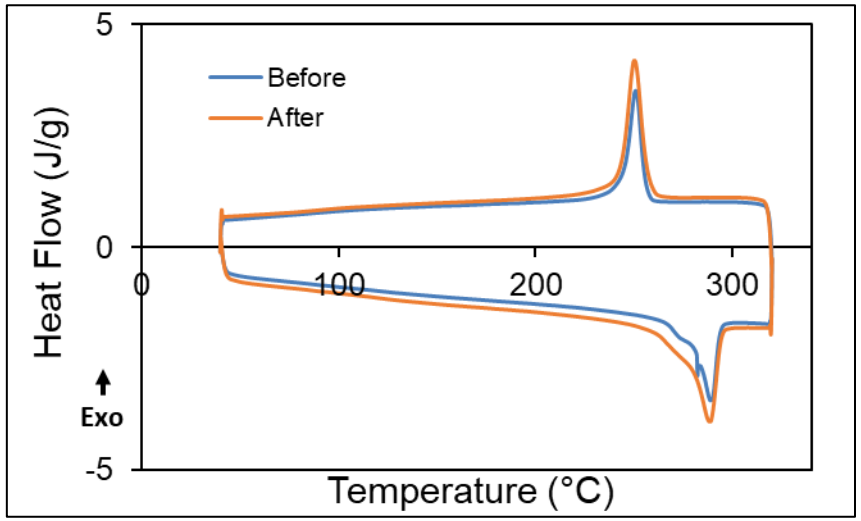

- Melting point: **289°C**; Crystallisation point: **251°C**; Crystallinity: 45.3 (as received), 43.9 (after processing)

TGA

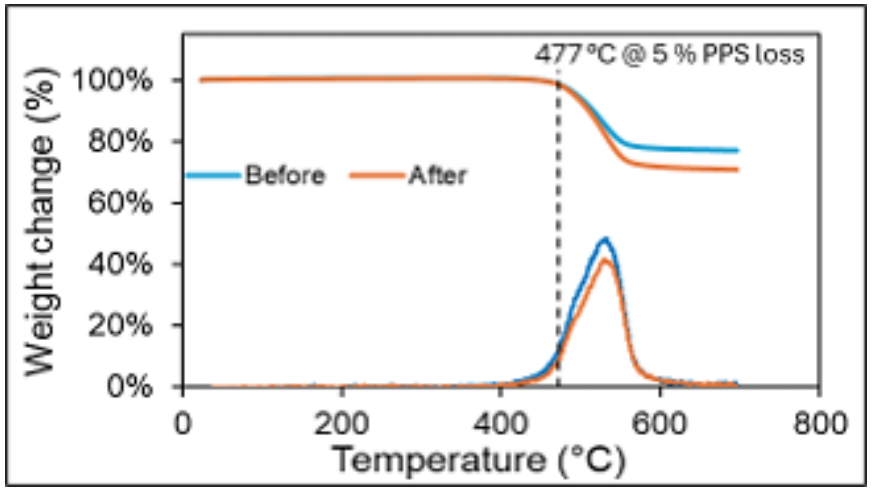

- Onset degradation temperature: **477°C** at 5% PPS loss; PPS content: 35.7 wt%.

Processing parameters	
Heating temperature	320°C – 330°C
Cooling rate	10°C/min (quench)
Pressure	12.5 bar – 15 bar

Tensile performance: Uniform vs Non-uniform LCF

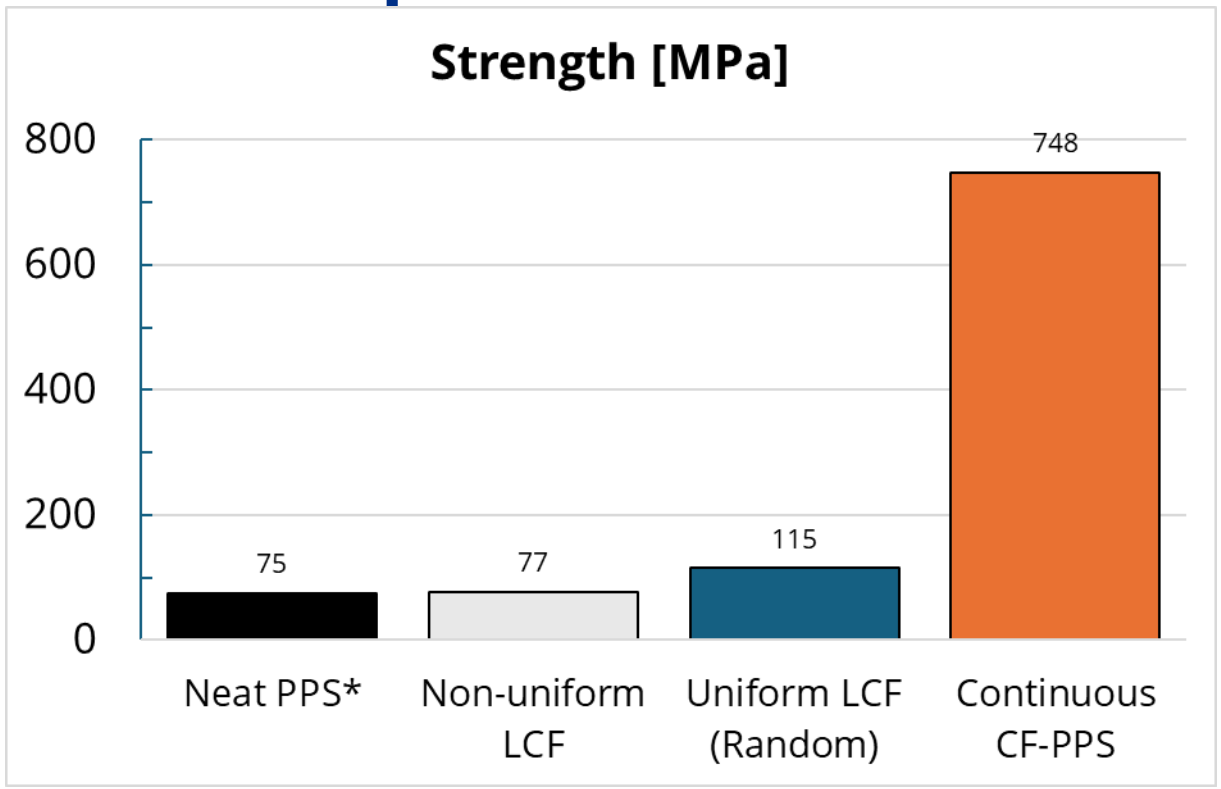

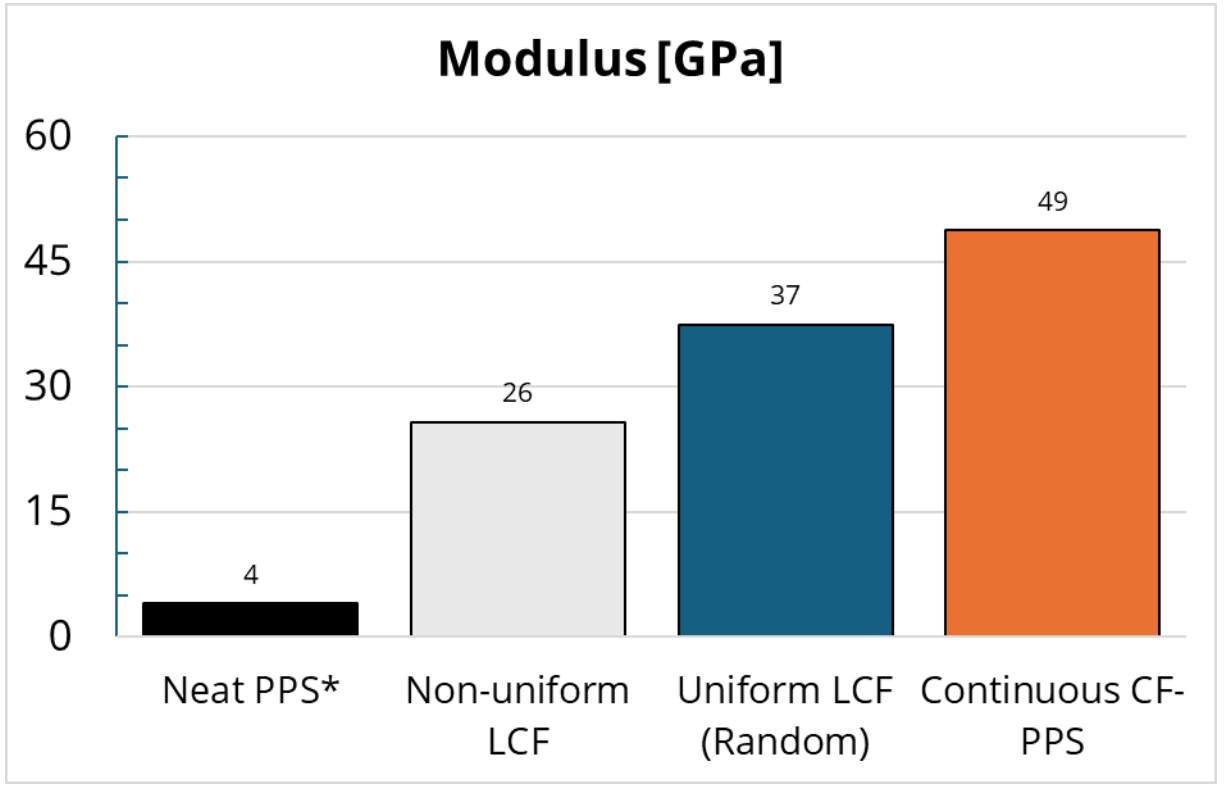

- Uniform LCF (random) outperforms non-uniform LCF by 49% in tensile strength.
- Non-uniform LCF shows no meaningful improvement over neat PPS in tensile strength.
- Uniform LCF achieves 15%, and non-uniform LCF only 10%, of the tensile strength of continuous CF-PPS.

- Non-uniform LCF shows a 6.5x improvement in tensile modulus over neat PPS, but is:
  - 30% lower than Uniform LCF
  - 47% lower than Continuous CF-PPS
- The lower tensile strength and modulus of **non-uniform LCF** is likely due to **more fiber fractures during the shredding process**, resulting in **shorter, damaged fibers** that reduce reinforcement efficiency.

- [https://omnexus.specialchem.com/selection-guide/polyphenylene-sulfide-pps-plastic-guide] ; [https://www.mcam.com/en/products/pps]

Failure of Uniform and Non-uniform LCF

Uniform LCF

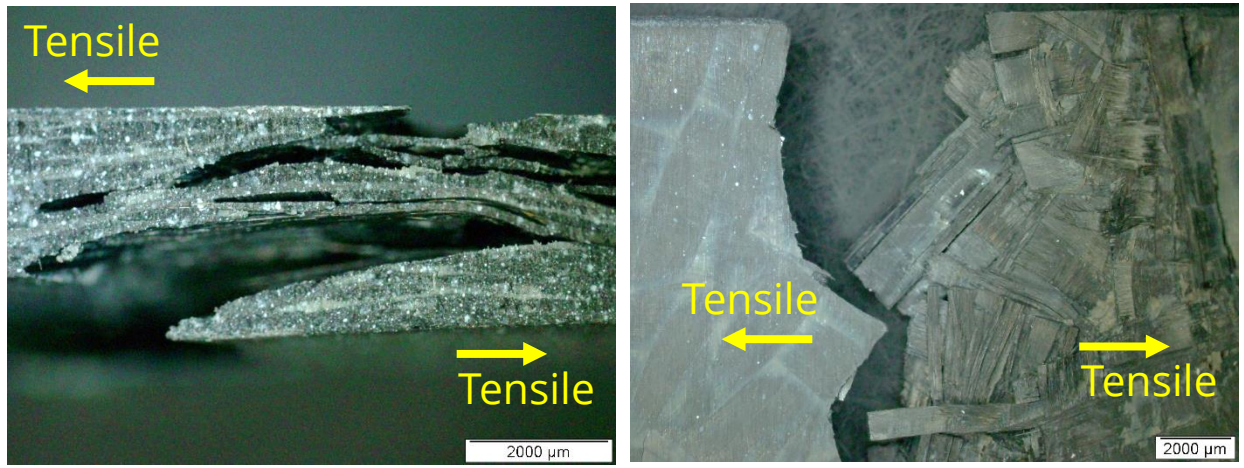

Non-uniform LCF

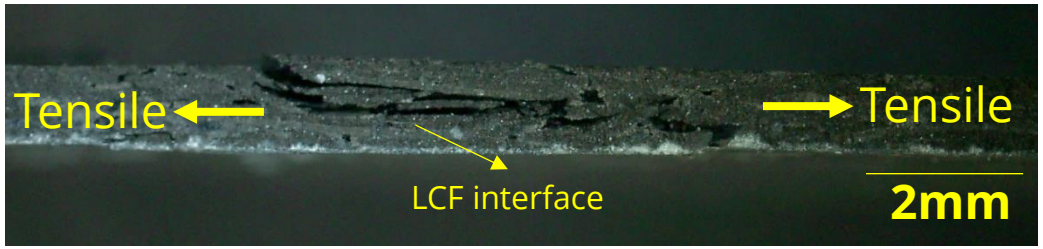

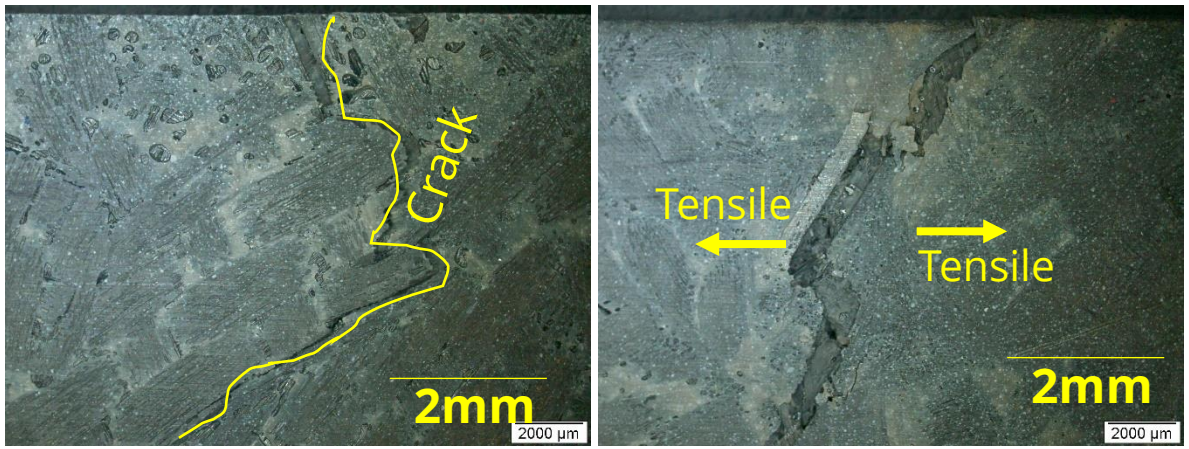

- **Both uniform and non-uniform LCF composites** primarily failed at **the fiber–matrix interface,** indicating **matrix-dominated failure mechanisms**.
- This is supported by cross-sectional fracture images, which show poor debonding rather than fiber breakage.
- As a result, the overall tensile strength of these composites remains relatively close to that of neat PPS.

Efforts to Improve Mechanical Performance

1. **Material Blending**
   - Added uniform LCF to PPS pellets with 30% short fibers.
   - Aimed at increasing matrix-fiber interaction and strength.
2. **Chip Arrangement (Ordered)**
   - Used overlapping and stacked configurations of LCF.
   - Improved load transfer paths and reduced weak inter-chip interfaces.
3. **Processing Parameter Enhancement**
   - Applied isothermal crystallization at 270°C during compression moulding.
   - Targeted improved crystallinity and interfacial bonding for better mechanical integrity.

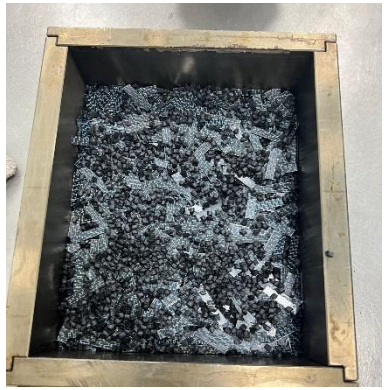

5HS CF-PPS (100g) + short fiber CF-PPS pellets (50g)

1. Blended with short fiber reinf. PPS pellets

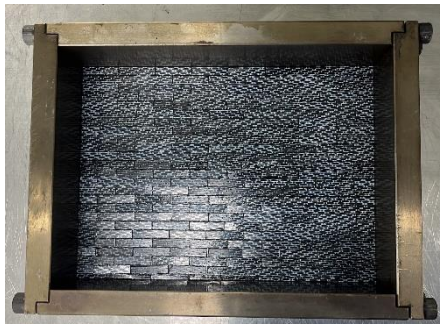

2. Ordered

3. Processing parameters	Standard	Optimized
Heating temperature	320°C – 330°C	320°C – 330°C
Isothermal crystallization	-	**270°C for 30 mins**
Cooling rate	10°C/min	10°C/min
Pressure	12.5 bar – 15 bar	12.5 bar – 15 bar

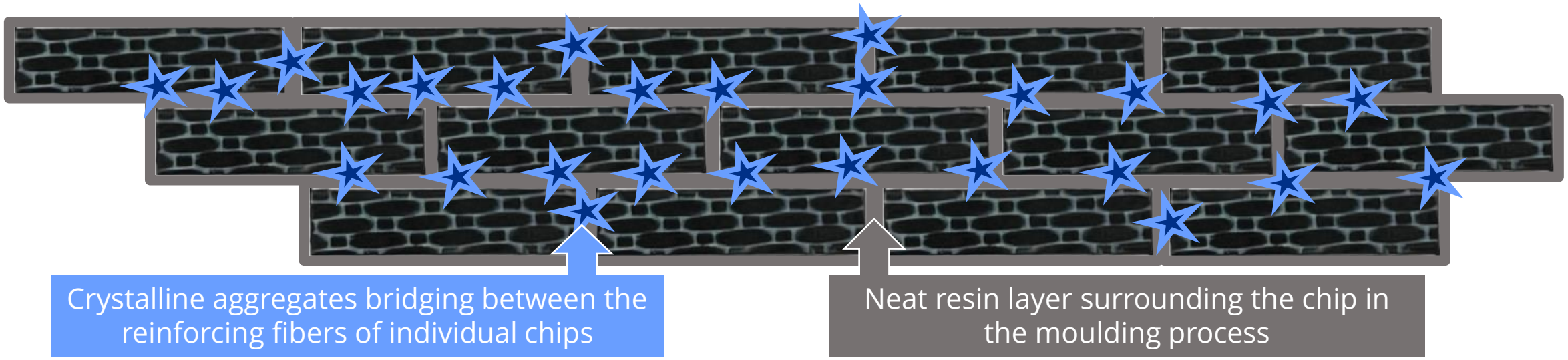

- Manipulate crystallization process to promote larger crystal aggregates bridging between individual chips.
- This should allow for mechanically interconnected or interlocked the individual chips => stronger connection between the chips.
- Unlike method 2 (chip arrangement / ordered LCF), isothermal crystallization does not require additional time or automation for chip alignment.

Improvement on Tensile Properties

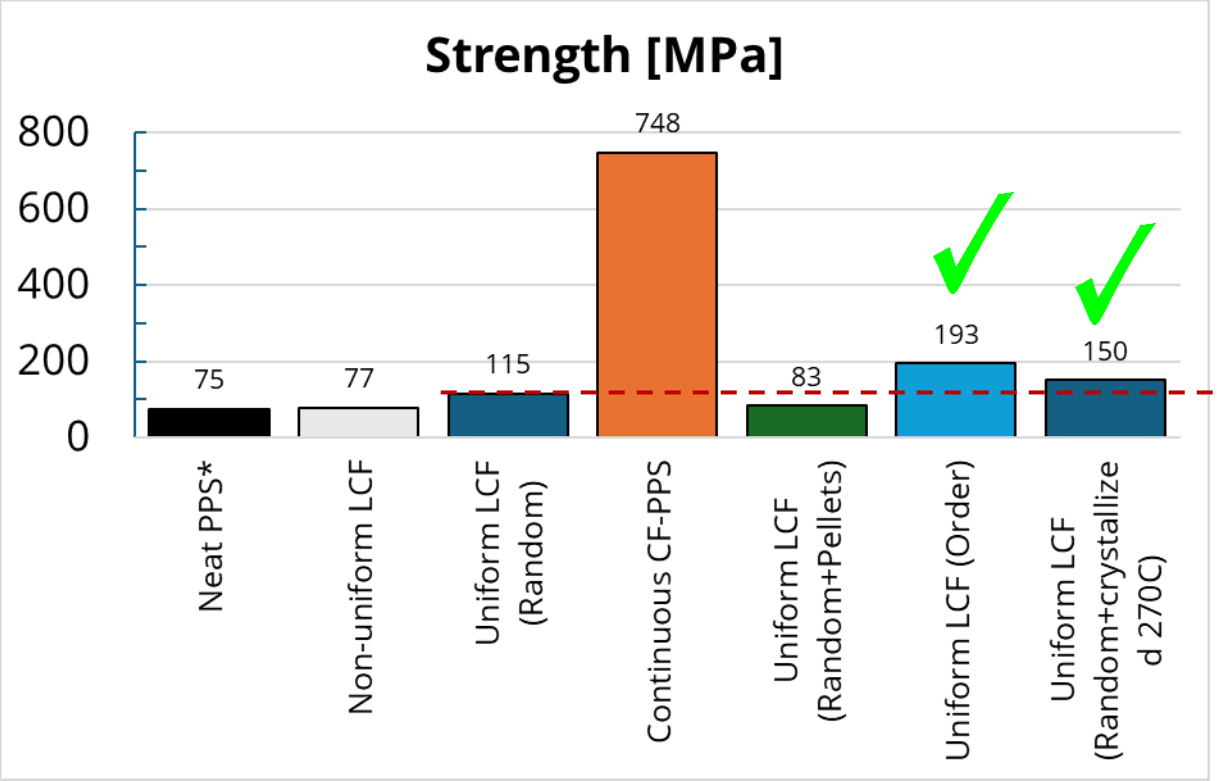

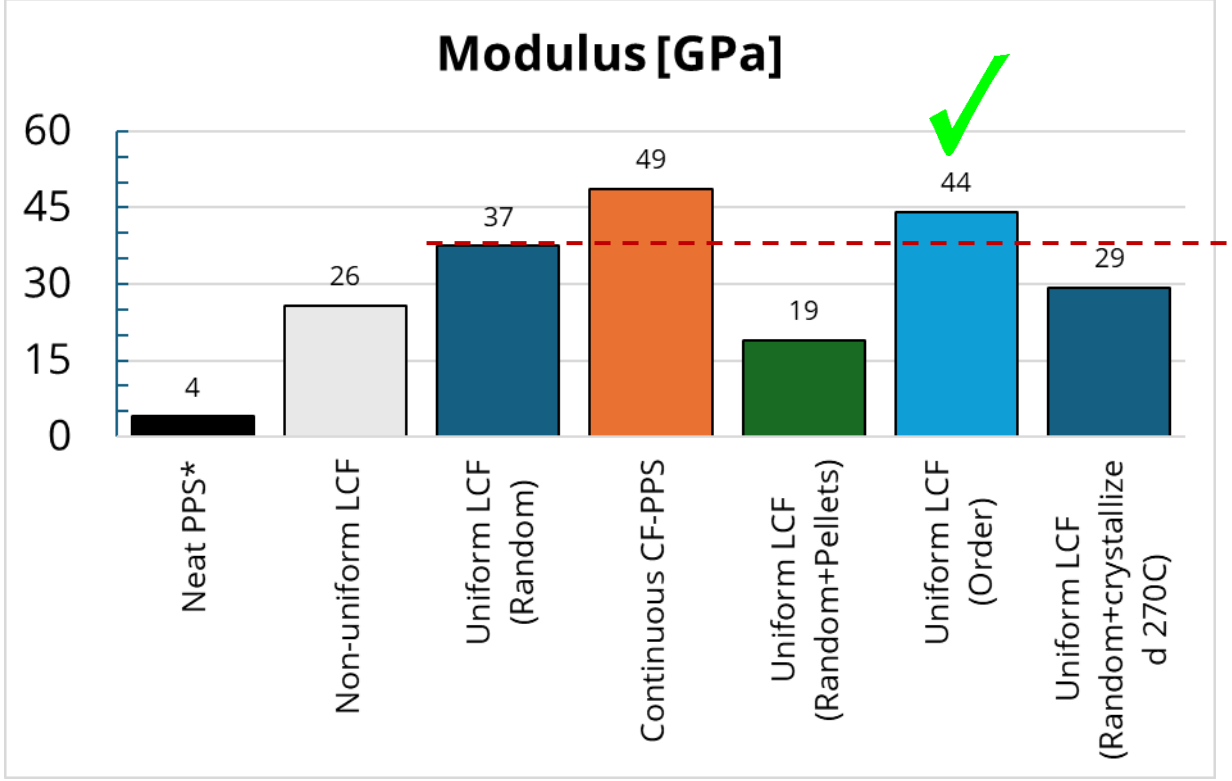

Compared to the Uniform LCF (Random):

- **Blending with short-fiber PPS pellets reduced both tensile strength and modulus**, reflecting limited fiber-matrix reinforcement and a more matrix-dominated structure due to reduced fiber content.
- **Aligning and stacking LCF chips enhanced tensile strength by 68% and modulus by 19%,** attributed to improved load transfer through better chip-to-chip connectivity.
- **Isothermal crystallization led to a moderate strength gain**, likely resulting from increased crystallinity.

Benchmarking against a Commercial Thermoset SMC

- SMC is commonly used for interior panels and cabin linings, including window surrounds, wall panels, galley modules, lavatory shells, and floor liners.



Aviation-certified glass-filled SMC from Polynt composites (HUP 27/25 RN-9010)

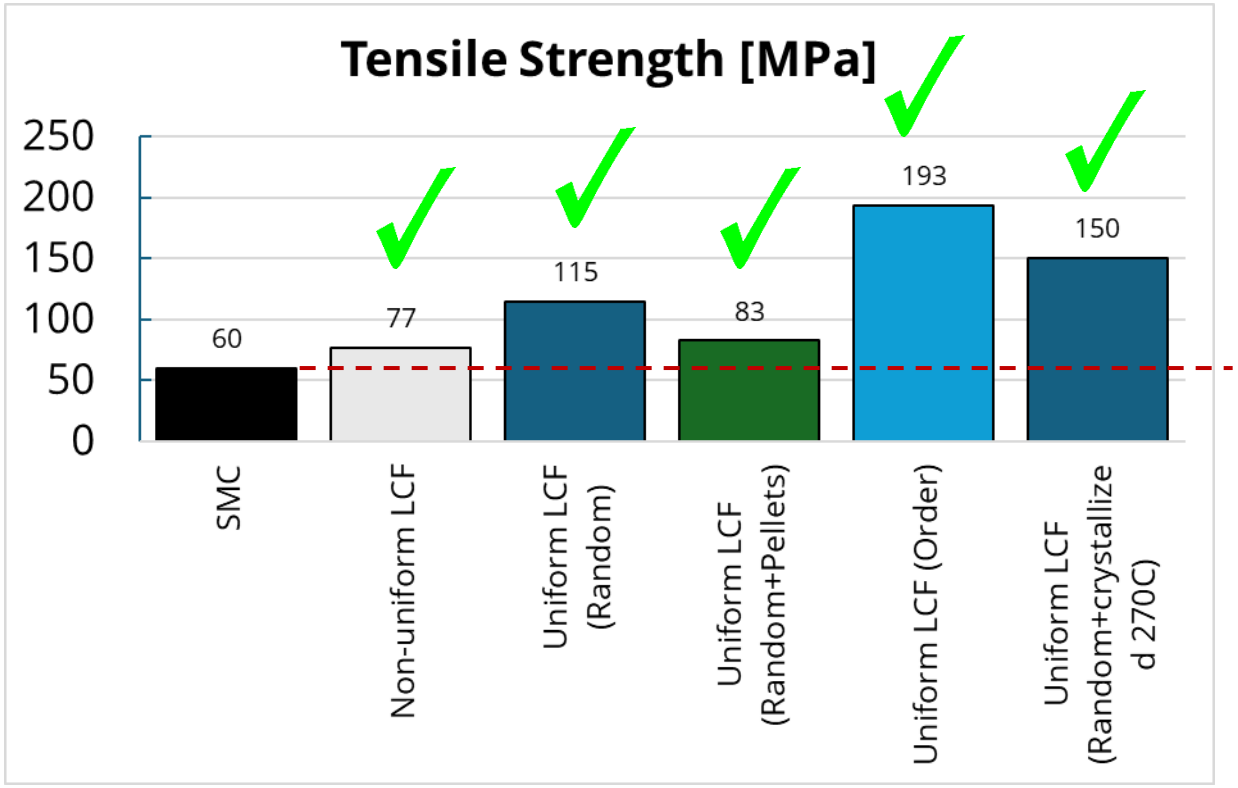

- All reprocessed LCF composites outperformed the commercial aviation-grade glass-filled SMC (60 MPa) in tensile strength demonstrating that even in their various forms, **reprocessed LCFs** offer superior mechanical performance and are **viable candidates for interior cabin applications**.

Conclusion

- **Non-uniform (shredded) LCF underperformed** compared to uniform LCF, with 30% lower tensile strength and modulus, likely due to fiber damage and shortened lengths.
- **Ordered LCF arrangement yielded the best mechanical enhancement**, achieving 2.6x higher tensile strength and 11x higher modulus than neat PPS, and reaching 26% of the tensile strength and 90% of the modulus of continuous CF-PPS.
- **The thermal processing (Isothermal crystallization)** approach also **showed a positive effect on the mechanical properties,** delivering 1.3x higher tensile strength than randomly aligned uniform LCF.
- **Material blending with short-fiber reinforced PPS pellets** showed **negligible improvement** in tensile properties.
- **The ability of reprocessed LCFs to meet or exceed the tensile strength of thermoset SMC highlights their potential for lightweight, recyclable thermoplastic alternatives** in aerospace interior applications, offering additional benefits in sustainability.

Future work

- Investigate the **effect of LCF size and aspect ratio** on mechanical performance.
- Evaluate **notch sensitivity** through open-hole tension (OHT) and open-hole compression (OHC) testing, benchmarking the results against neat PPS and continuous CF-PPS to assess damage tolerance and structural applicability.

ICCM25 – welcome to SG



https://en.wikipedia.org/wiki/Marina_Bay_Sands#/media/File:Marina_Bay_Sands_in_the_evening_-_20101120.jpg



https://en.wikipedia.org/wiki/Gardens_by_the_Bay#/media/File:Supertree_Grove,_Gardens_by_the_Bay,_Singapore_-_20120712-02.jpg



https://www.tripadvisor.co.id/Attraction_Review-g294265-d644919-Reviews-Merlion_Park-Singapore.html



https://www.visitsingapore.com/neighbourhood/featured-neighbourhood/marina-bay/singapore-flyer/

Singapore Institute of Manufacturing Technology

A*STAR SIMTech



PCP members

THANK YOU

ASTARSG ASTAR-SG

Acknowledgement

The authors would like to acknowledge the funding support from the Agency for Science, Technology for the Manufacturing, Trade and Connectivity (MTC) IAF-PP Project WP3.4 Material Circularity under Grant No. M23L5a0002.

Transforming Thermoplastic Waste through Manufacturing into Engineering Products

Shristi Ghosh [1]

Kyriaki Kalaitzidou [1,2]

[1]School of Materials Science & Engineering, Georgia Institute of Technology

[2]George W. Woodruff School of Mechanical Engineering, Georgia Institute of Technology

Georgia Tech

Acknowledgement

Dr. CAROLYN SEEPERSAD
Woodruff Professor, Georgia Tech

CHARLOTTE CRAFF
Project Manager, Re:3D

SAMANTHA SNABES
Founder, Re:3D

Outline

- Current landscape of thermoplastic recycling
- Experimental approach
- Implications of the main results to date
- Moving forward

Why focus on PC and PP?

Properties	PC	PP
Chemical structure	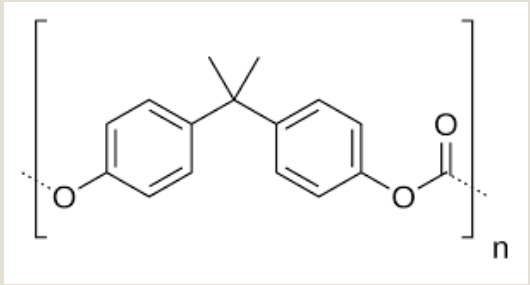	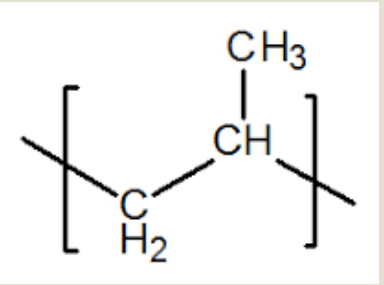
Production volume % out of total thermoplastics [1,2]	2 - 4	16 – 20
% recycled [3]	<10%	<2-5%
Global market size projection [4,5]	$24.01B in 2025 to $38.44B by 2030	$99.3-169.7B in 2025 to $118.7-219.7B by 2030
Environmental Impact	BPA leaching Low recyclability	GHG emission Landfill toxicity
Degradation time (years)	500 – 1000 in landfills	20 – 30 in landfills

NOTE: About 80% of all consumed plastics are thermoplastics

1. Plastic Polymers & Resins, Report ID: FBI101583, June 16, 2025
2. Bulk Chemicals, A01555, August, 2025
3. Houssini, K., Li, J. & Tan, Q. Complexities of the global plastics supply chain revealed in a trade-linked material flow analysis. *Commun Earth Environ* **6**, 257 (2025)
4. Global Polycarbonate Market Size, Share, and COVID-19 Impact Analysis, SI1451, January 2023
5. Polypropylene Market Insights - Size, Share & Industry Forecast 2025 to 2035, June 13, 2025

Georgia Tech

Major roadblock to recyclability: Quality of feedstock

Polycarbonate Applications [1]

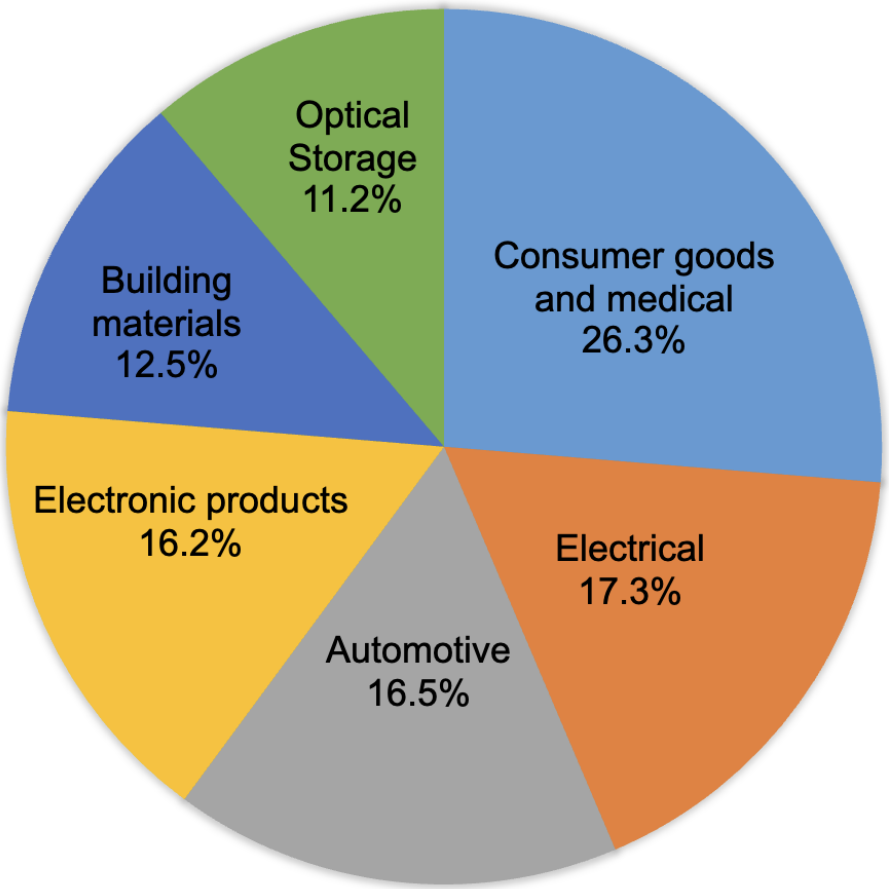

Polypropylene Applications [2]

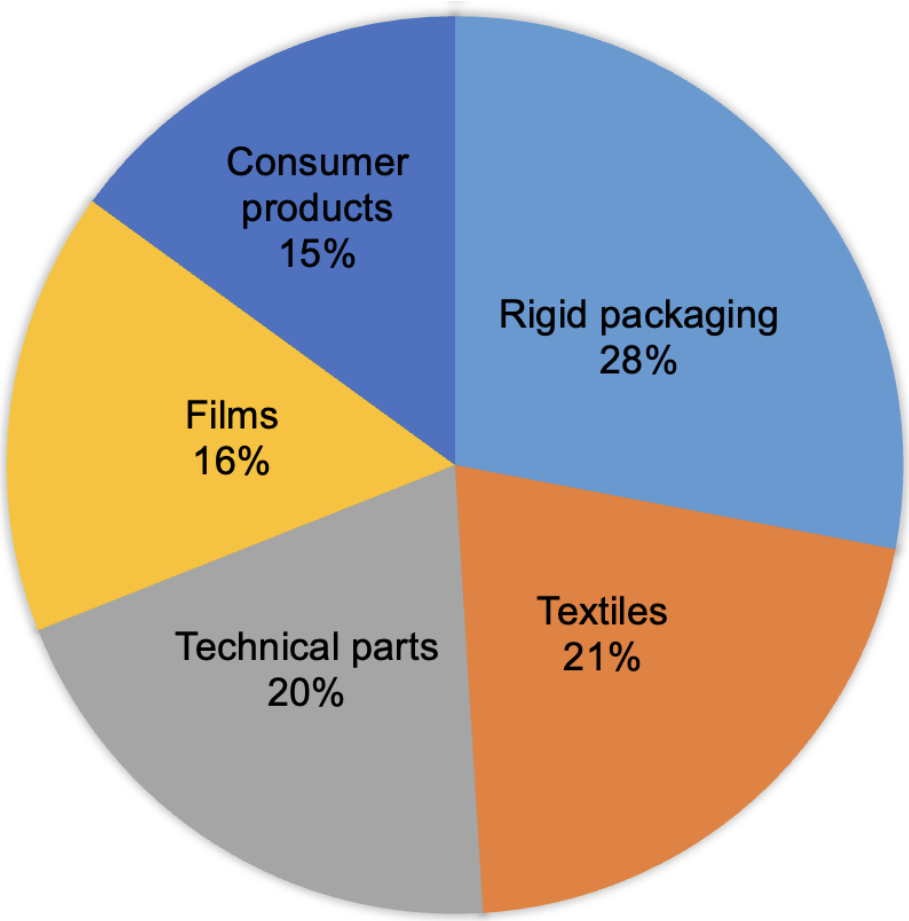

1. Polycarbonate market trend
2. The essential chemistry industry

Georgia Tech

What recycling methods are being used for PC and PP

- Mechanical recycling
- Chemical recycling

Our project focus:

- In-depth materials research for tailored material compositions for additive manufacturing

Broader aim:

- Increase community access to 3D printing.
- Drive localized and on-demand production.

1. Plastic recycling facts, 2024 American Chemistry Council, 2024

Questions this research will address

We aim to salvage both PC and PP, regardless of their feedstock or source.

- Is reprocessing affecting the performance of recycled PC and PP?
  - If yes, is degradation occurring and why?
  - Can additives combat this degradation?

Fabrication of test coupons



Pellets



Control Panel

Extruder

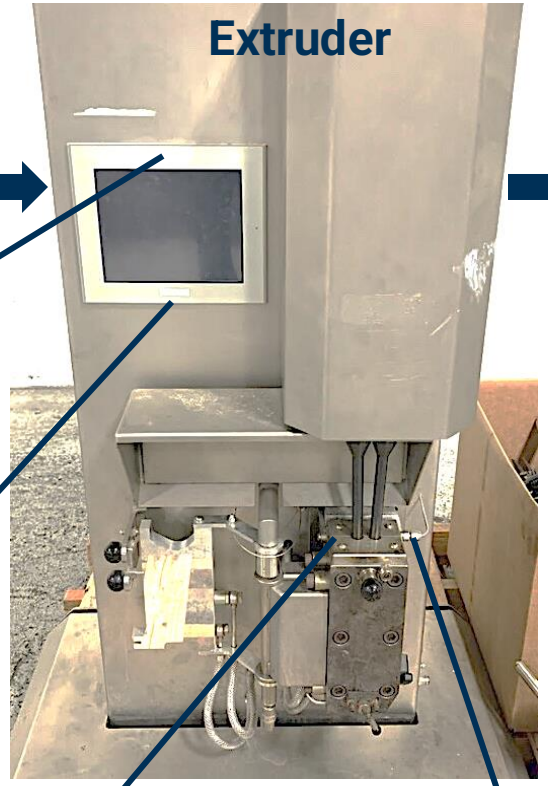



Barrel (open state) and screws



Extrudates

Injection mold unit

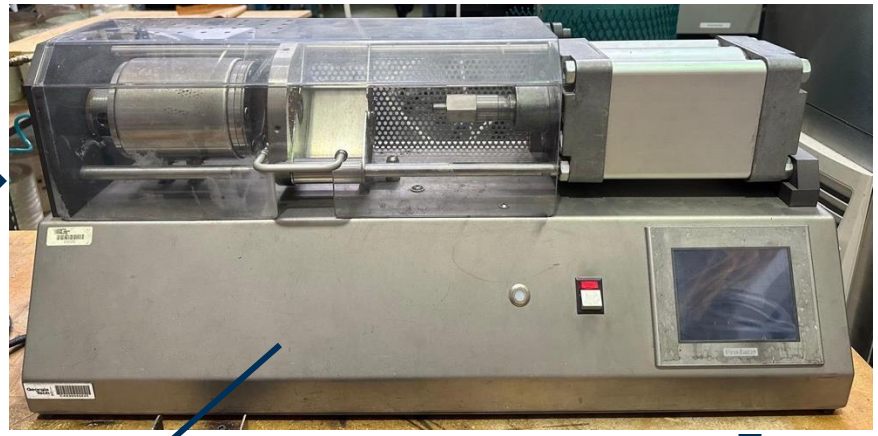



- Transfer mold (moves melt from barrel to mold)
- Mold (inserted into heater jacket)

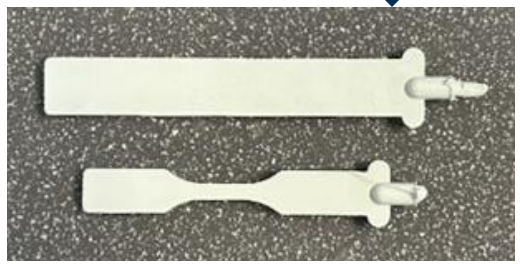

Test coupons

Georgia Tech

Naming Scheme

Parts	
1st	• r: recycled; or, • v: virgin
	• PC: polycarbonate; or, • PP: polypropylene
2nd	• EX: Extrusion
	• 1 (or, 10): Number of melt cycles
3rd	• C: Compatibilizer, Polypropylene-graft-maleic anhydride, PP-g-MA; or, • IM: Impact modifier, Poly(ethylene-co-methyl acrylate-co-glycidyl methacrylate)), EMAG; or, • WF: Wood flour mechanical reinforcement
	• 3(or, 5, 10): Weight% of additive in composite

➢ Examples: rPP-EX1-WF10, rPC-EX1-C3-WF10

Georgia Tech

Tensile behavior of rPC formulations

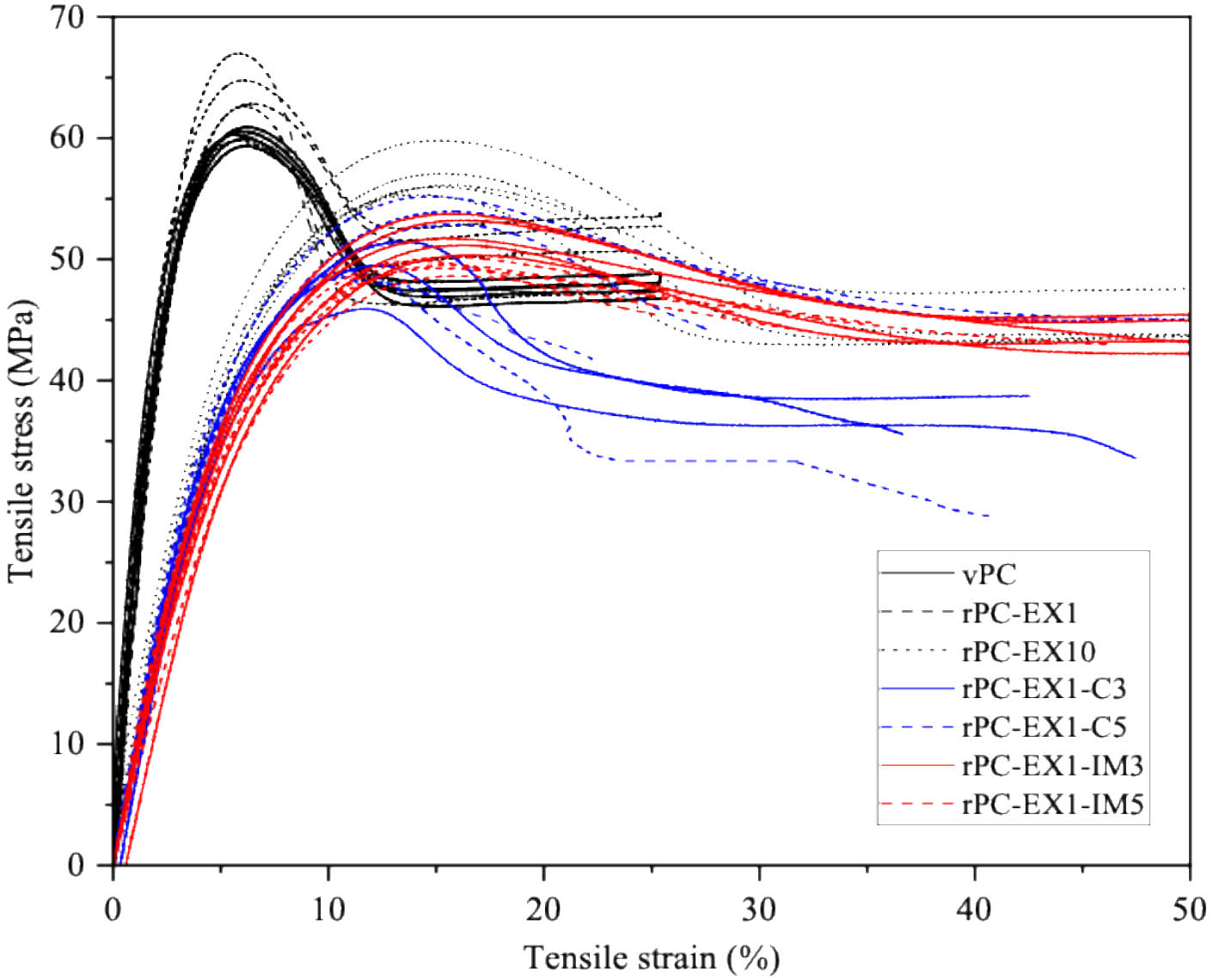

Georgia Tech

Tensile behavior of rPC formulations

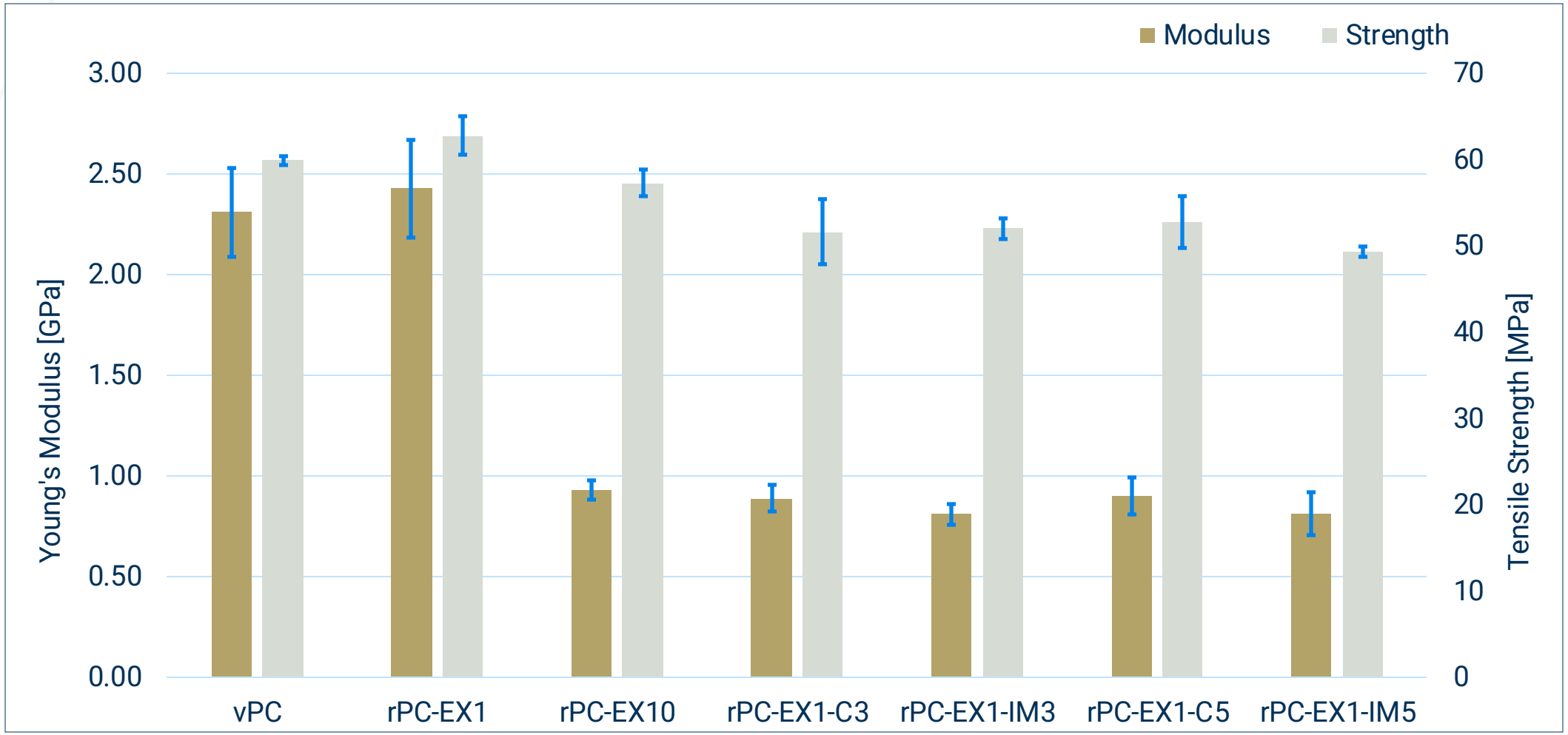

Theoretical tensile properties of PC: (a) Tensile modulus: 2.2 – 2.5 GPa; (b) Tensile strength: 55 -77 MPa

Georgia Tech

Flexural behavior of rPC formulations

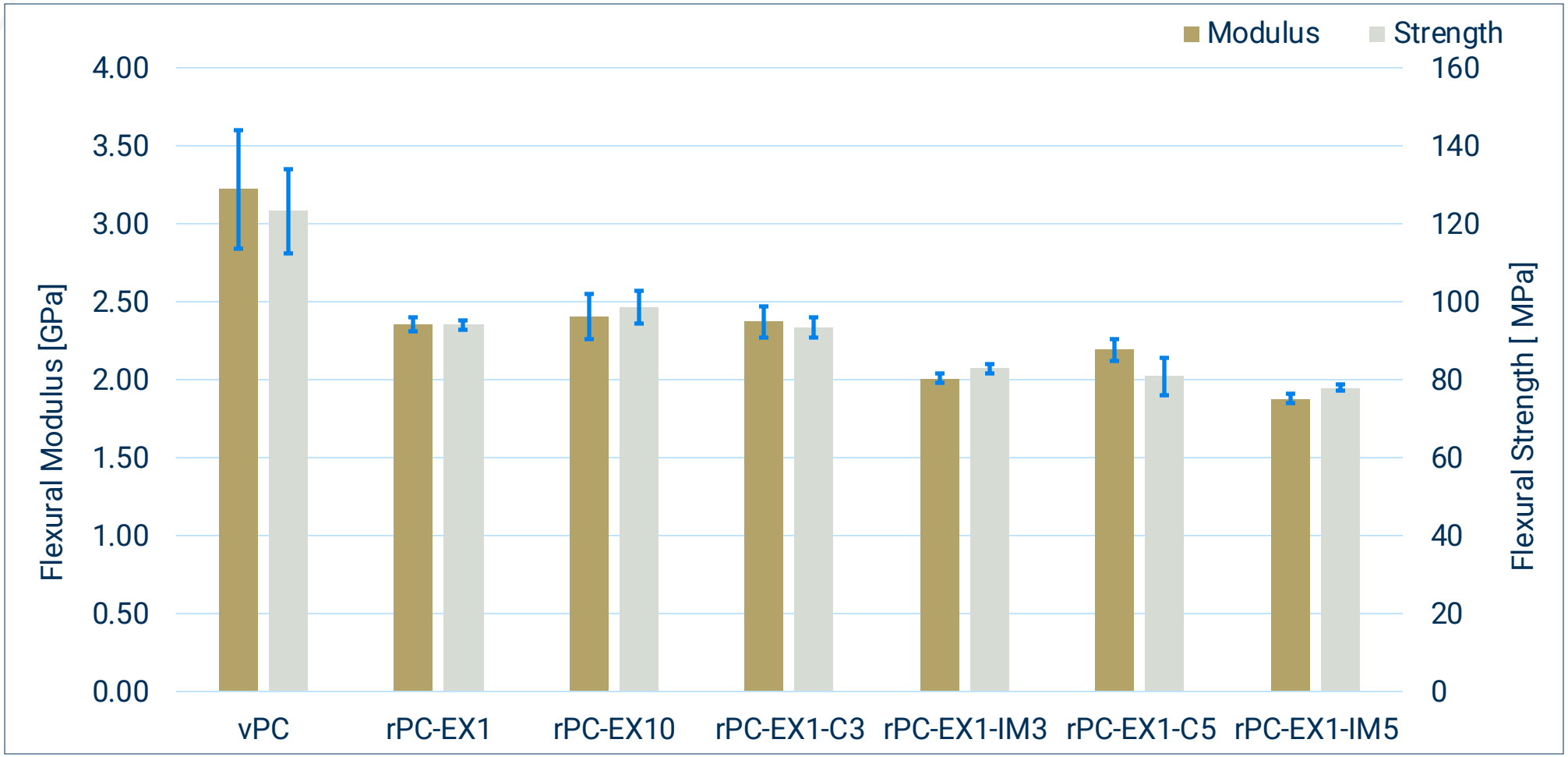

Theoretical flexural properties of PC: (a) Flexural modulus: 1.8 – 4.1 GPa; (b) Flexural strength: 75 - 110 MPa

Georgia Tech

Density of rPC composites

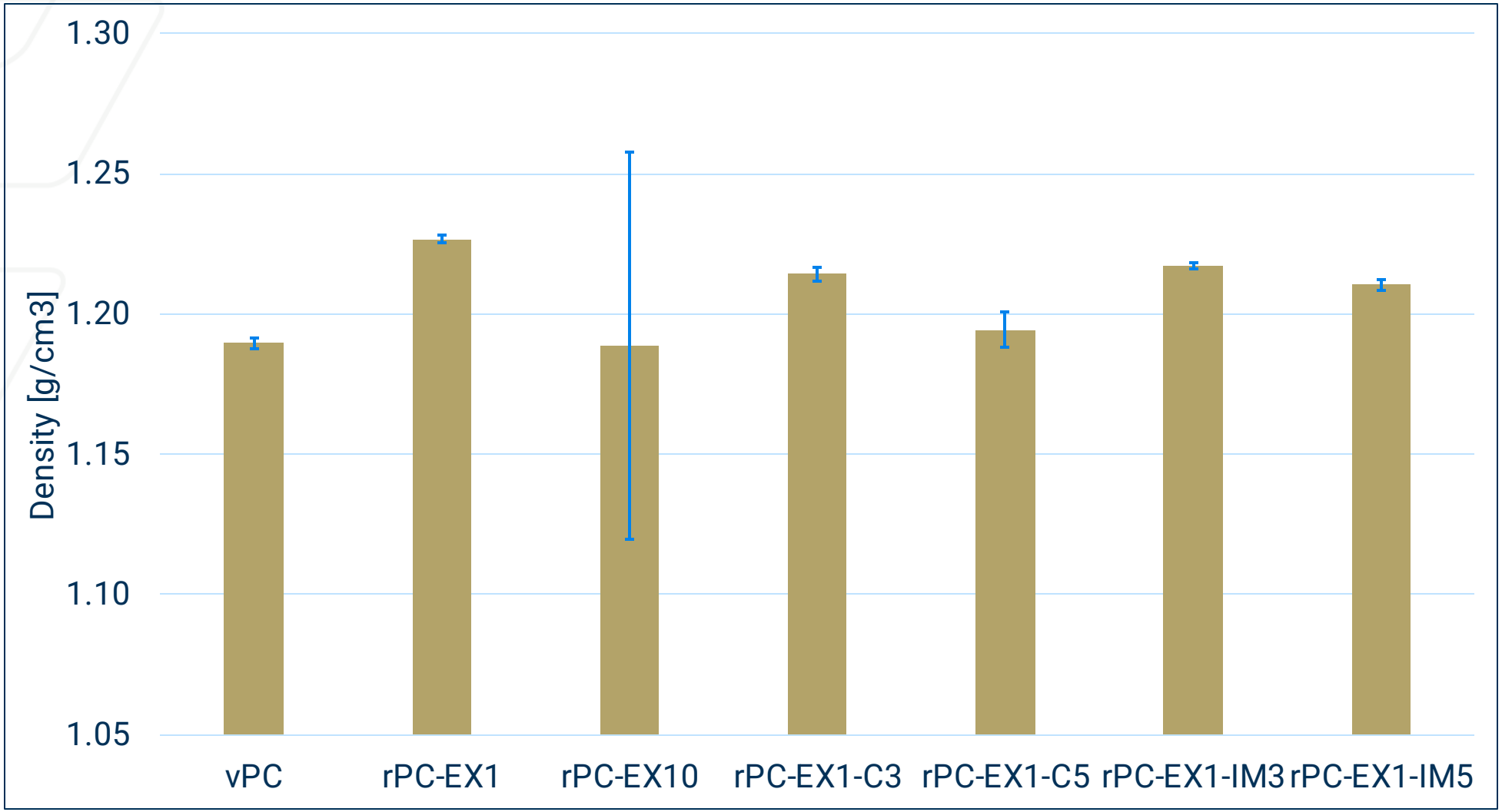

Feedstock material:
rPC

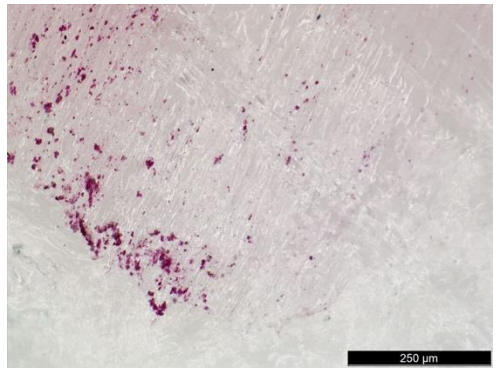

Theoretical densities:

- PC: 1.2 g/cm^3 [1]
- C: 0.934 g/cm^3 [2]
- IM: 0.94 g/cm^3 [3]

1. Polycarbonate, British Plastics Federation, 2025
2. Polypropylene-graft-maleic anhydride, Millipore Sigma
3. Poly(ethylene-co-methyl acrylate-co-glycidyl methacrylate), Millipore Sigma

Georgia Tech

Thermal transitions of rPC formulations

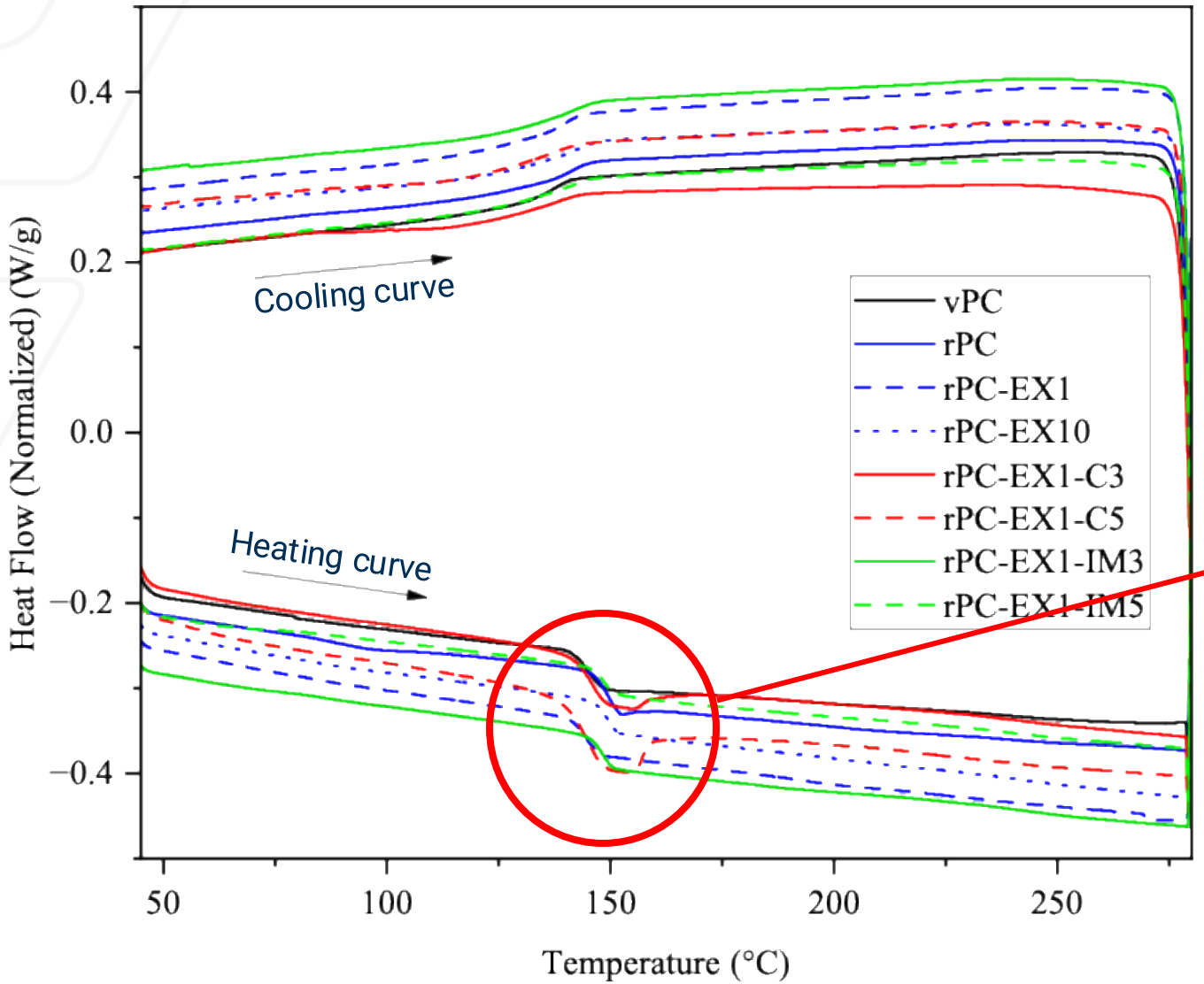

T_g at 10°C/min

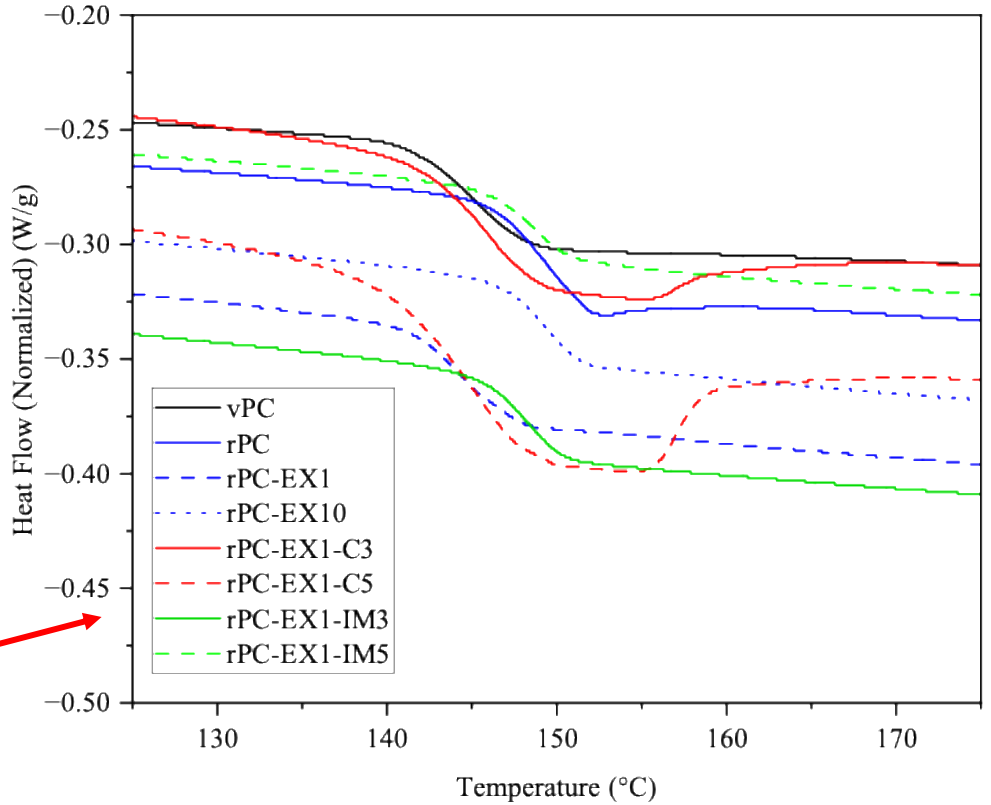

Thermal transition temperatures from literature [1]:

- T_g: 145 – 150 °C
- T_c: 120 – 190 °C
- T_m: 220 – 315 °C

1. Overview of materials for Polycarbonate, Extruded

FTIR of rPC

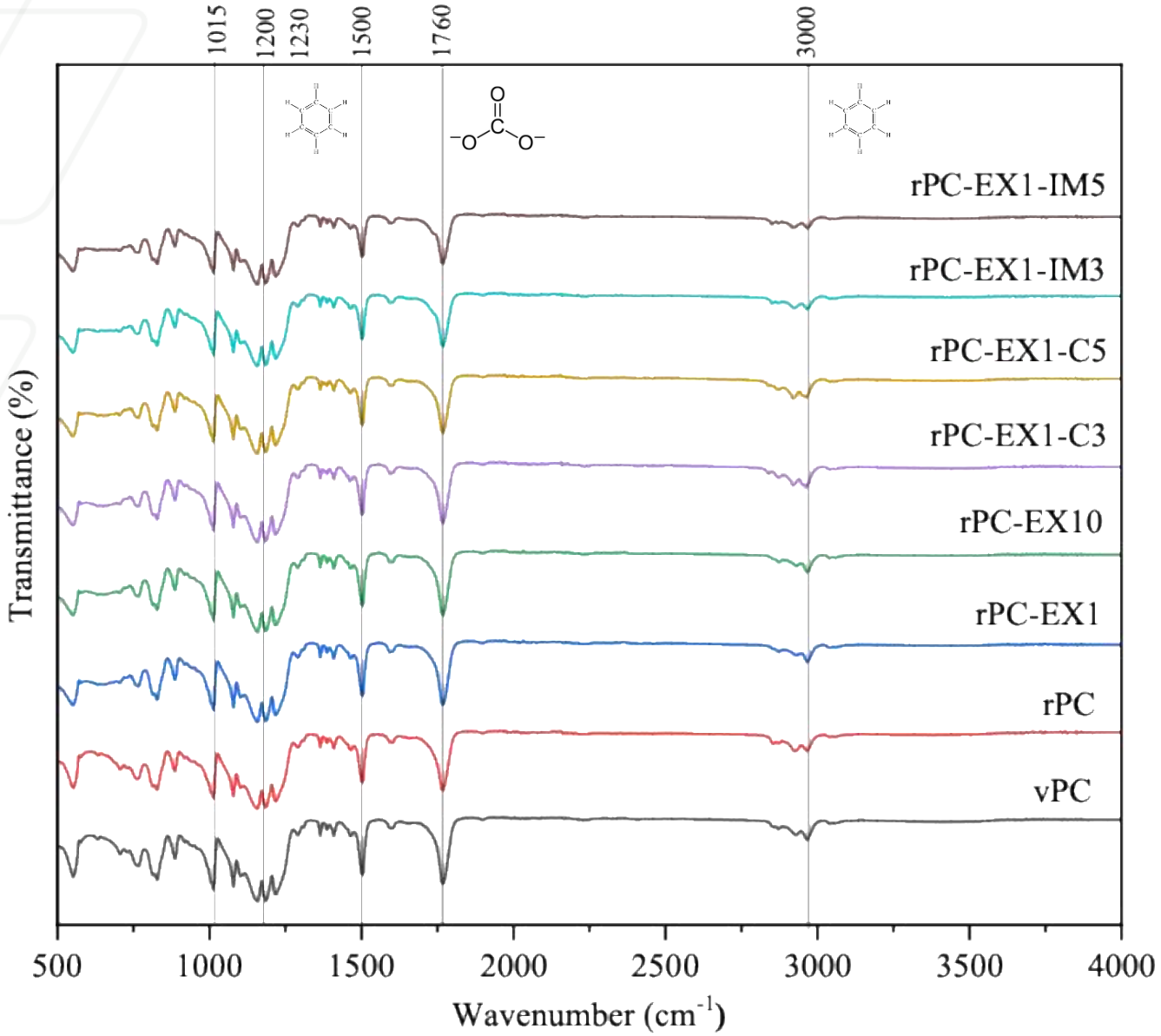

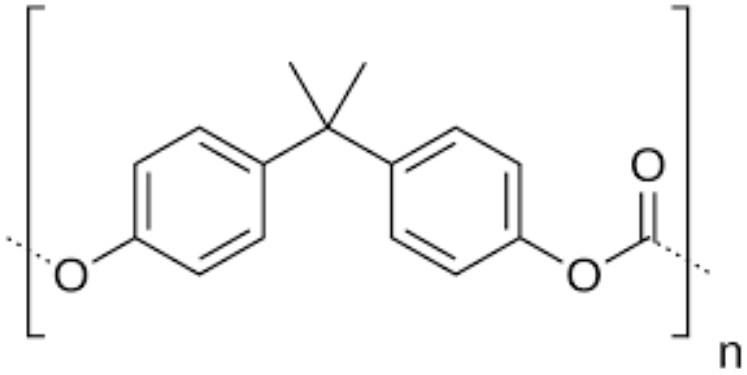

Principal peaks observed in PC:

- 2996 cm-1: C-H single bond stretching, aromatic ring
- 1760 cm^{-1}: C=O carbonate group deformation
- 1500 cm^{-1}: C=C stretching vibration, aromatic ring
- 1200 - 1230 cm^{-1}: O-C-O asymmetric stretching vibration
- 1015 cm^{-1}: O-C-C stretching vibration

Georgia Tech

FTIR of PC

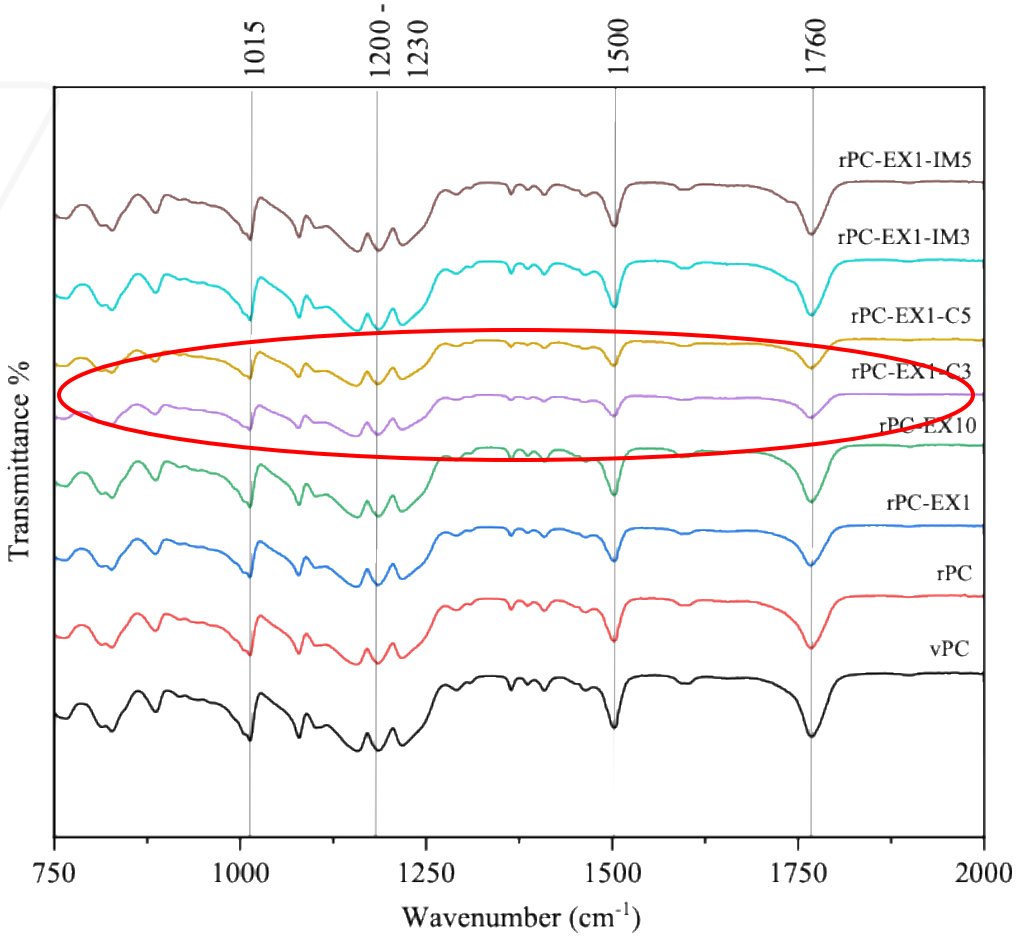

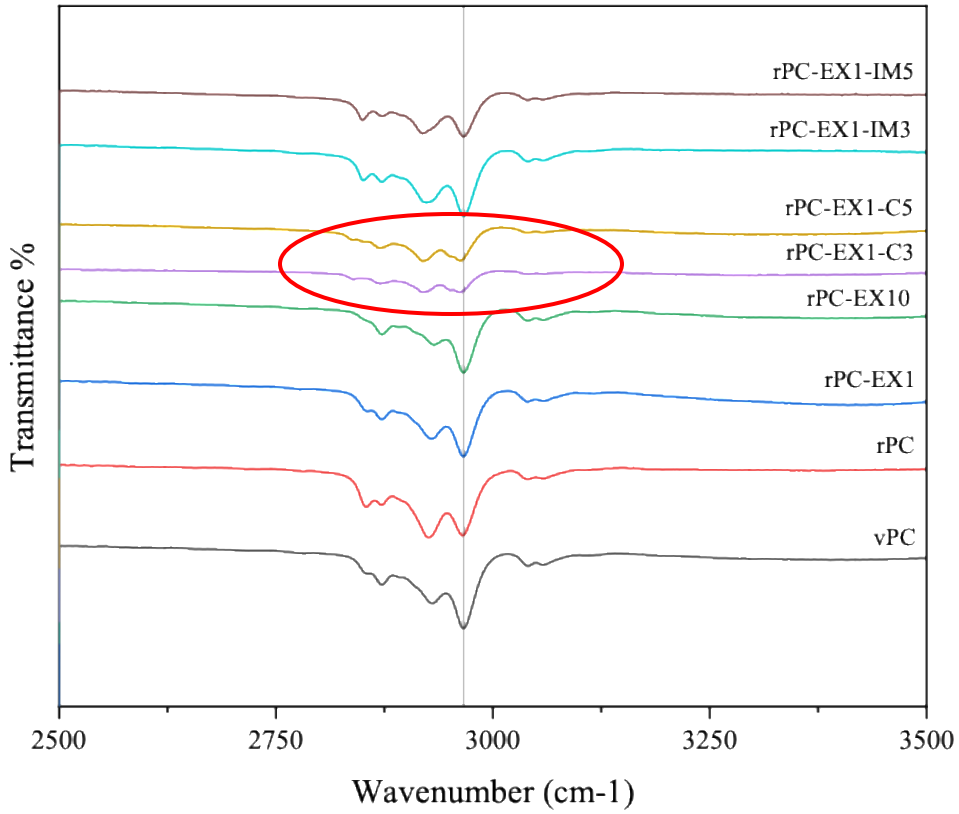

EMAG

Methyl acrylate

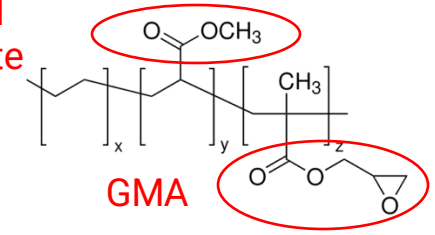

GMA

PP-g-MA

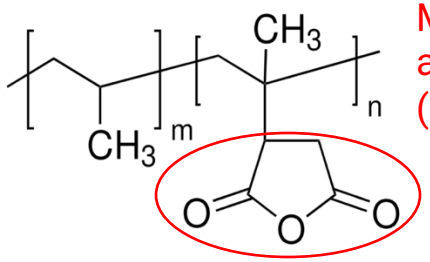

Maleic anhydride (MAH)

Georgia Tech

Tensile behavior of rPP formulations

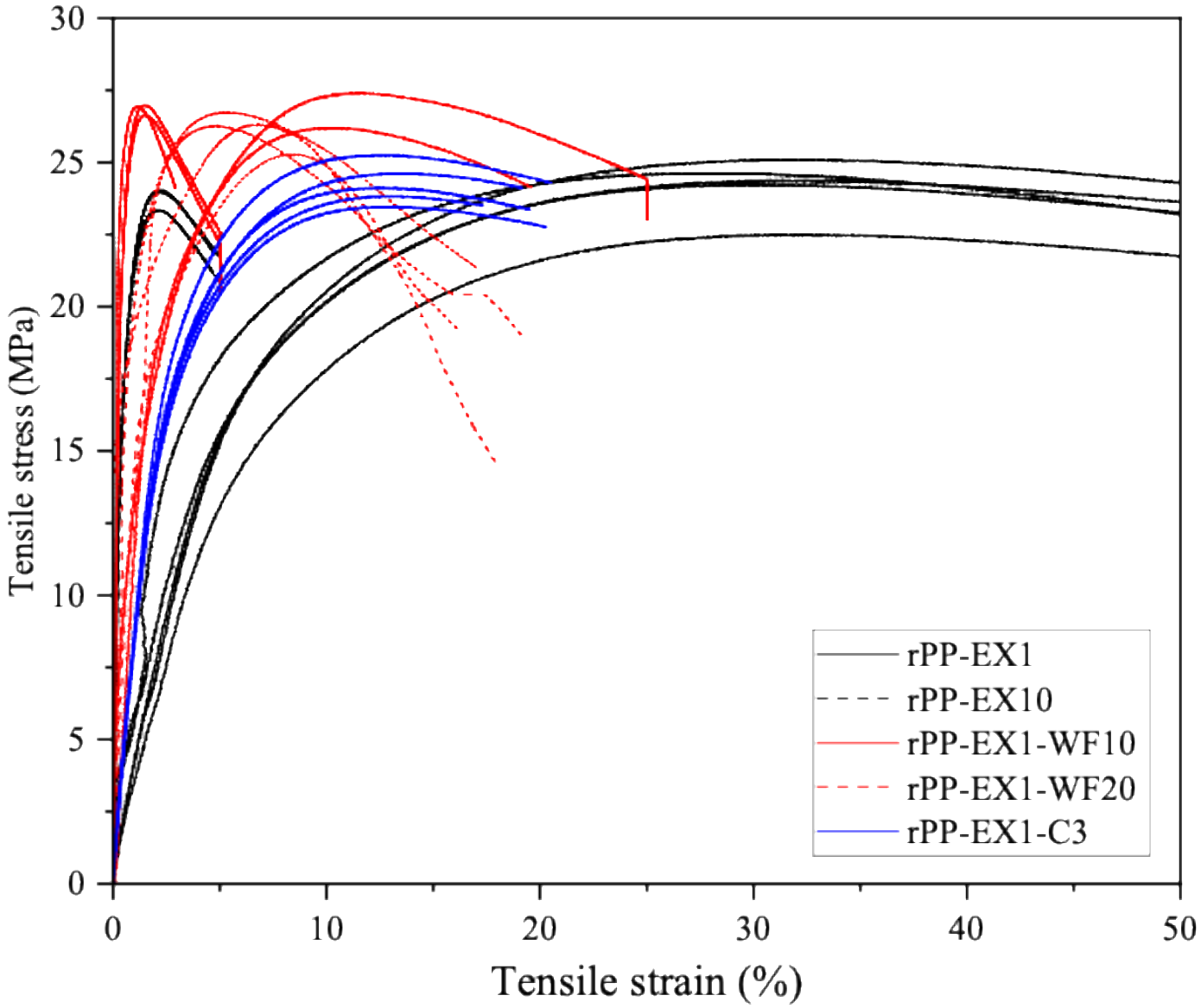

Georgia Tech

Tensile behavior of rPP formulations

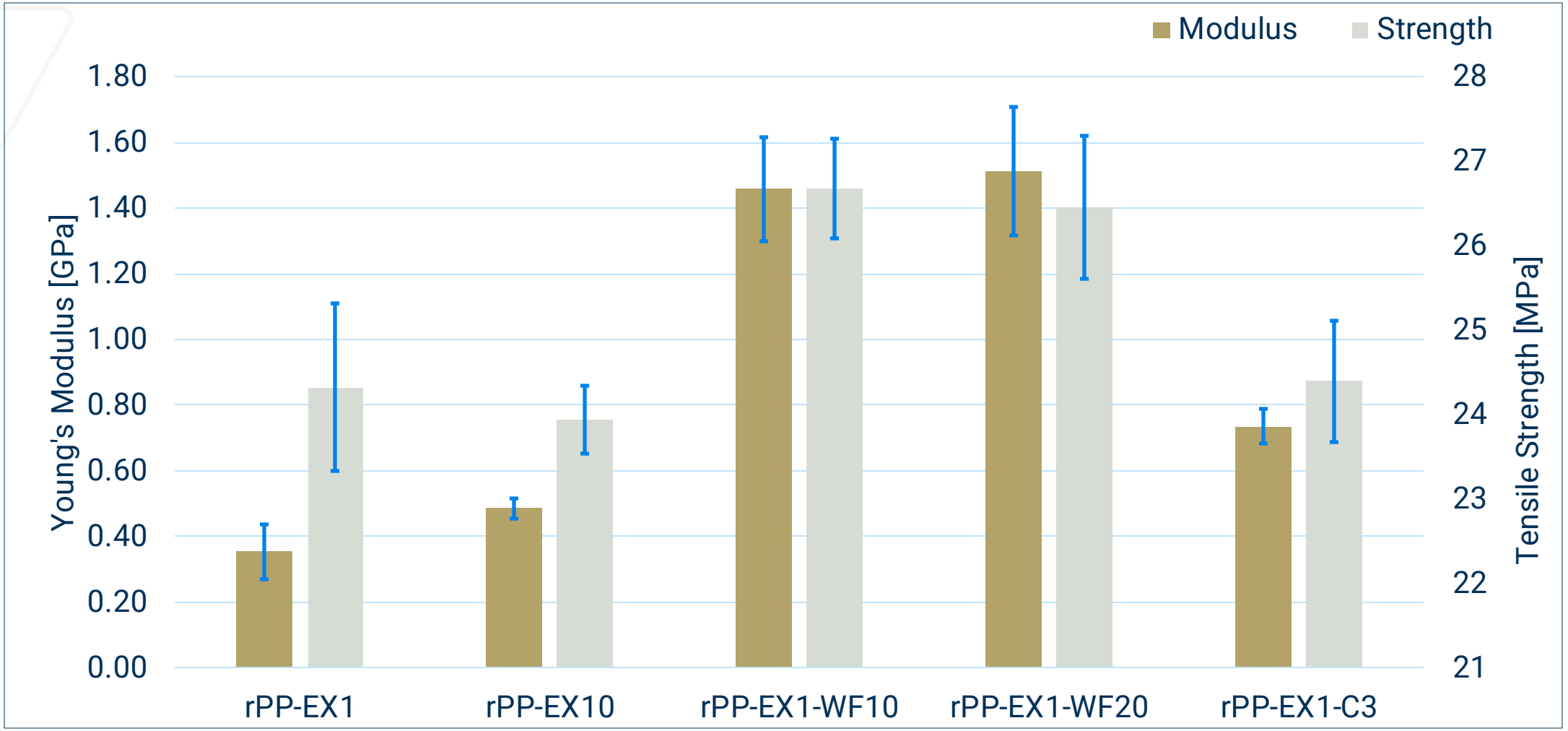

Theoretical tensile properties of PP: (a) Tensile modulus: 1.1 – 1.6 GPa; (b) Tensile strength: 27 – 48 MPa

1. Polypropylene – PP Homopolymer, Plascams
2. Polypropylene (PP): Understanding the key benefits and applications, Protolabs - Manufacturing Accelerated

Georgia Tech

Flexural behavior of rPP formulations

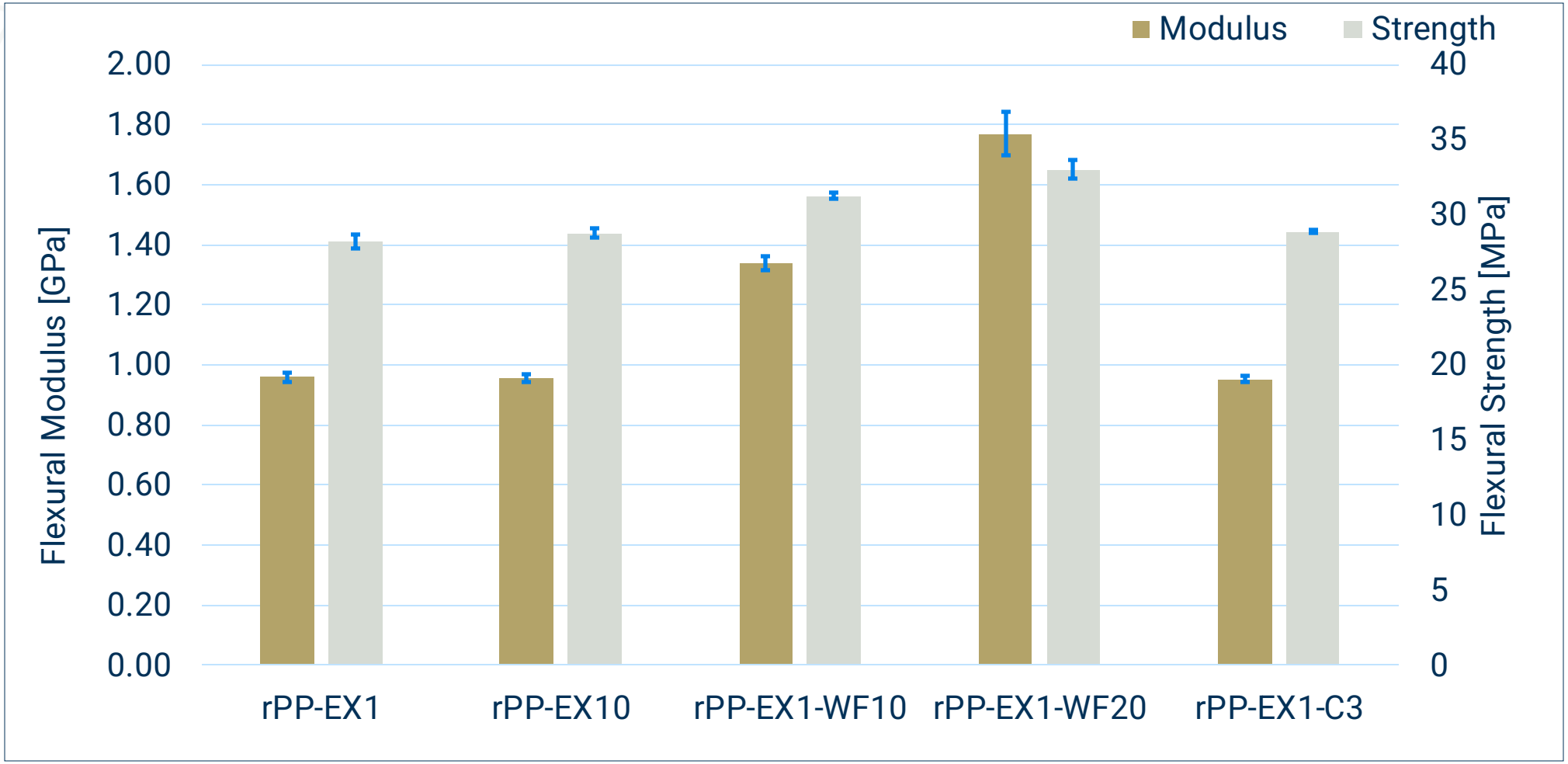

Theoretical flexural properties of PP: (a) Flexural modulus: 0.8 – 1.7 GPa; (b) Flexural strength: 40 - 70 MPa

1. Polypropylene – PP Homopolymer, Plascams
2. Polypropylene (PP): Understanding the key benefits and applications, Protolabs - Manufacturing Accelerated

Impact Behavior

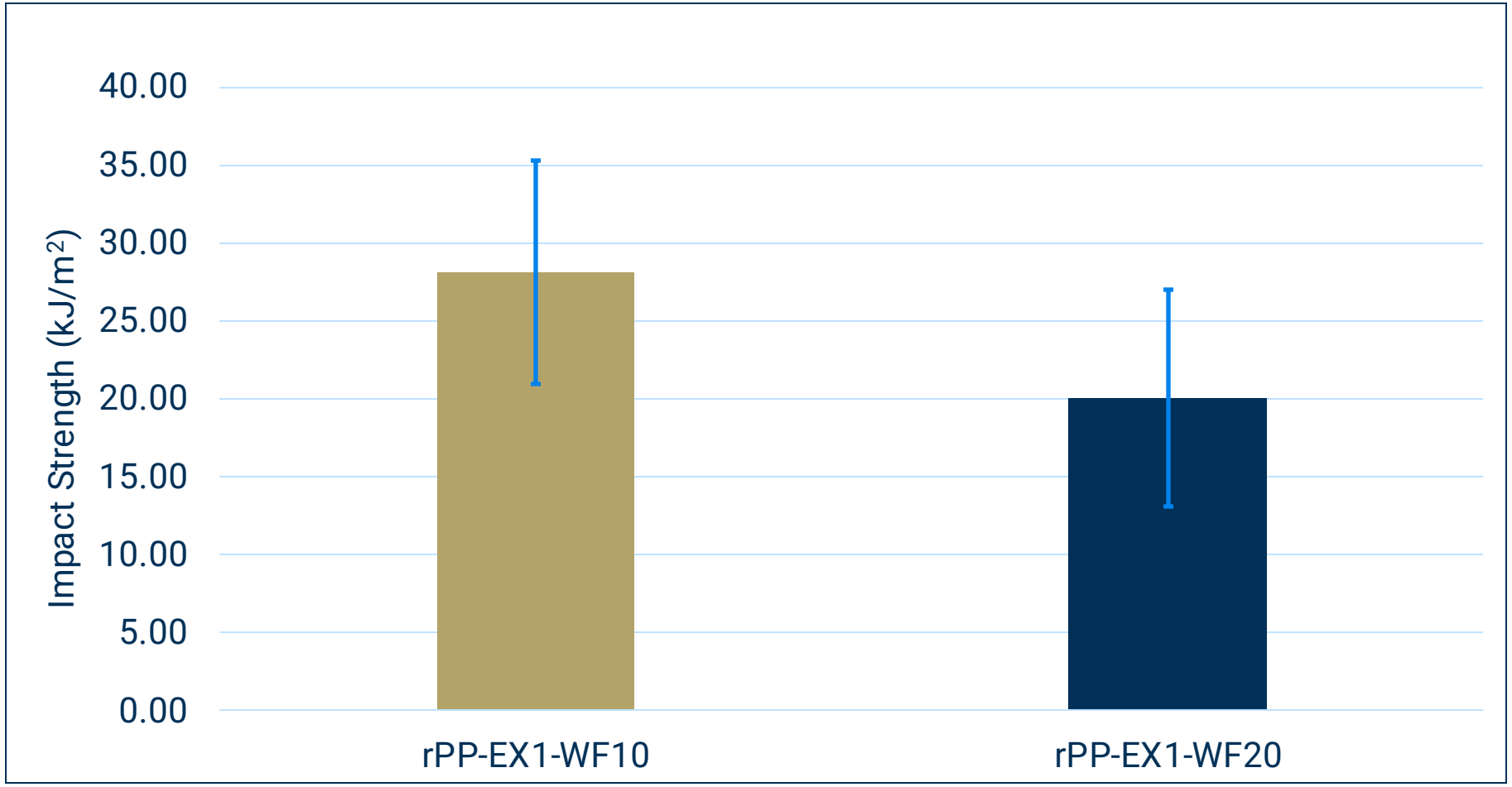

Theoretical impact properties of PC and PP: (a) PP Impact strength: 3 – 30 kJ/m^2 [1]; (b) PC Impact strength: 10 – 90 kJ/m^2 [2]

1. Polypropylene, British plastics federation
2. Overview of materials for Polycarbonate, extruded, MatWeb material property data

Georgia Tech

Density of rPP composites



Feedstock material: rPP

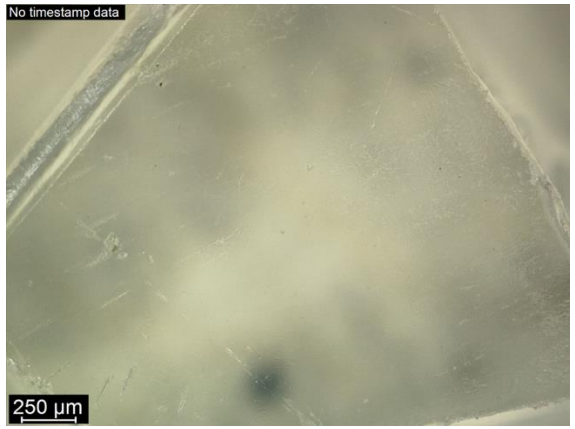

Theoretical densities:

- PP: 0.895 – 0.92 g/cm^3 [1]
- C: 0.934 g/cm^3 [2]

1. Polyolefin properties, Plastics Europe – Enabling a sustainable future
2. Polypropylene-graft-maleic anhydride, Sigma aldrich

Thermal transitions of rPP formulations

T_m at 10°C/min

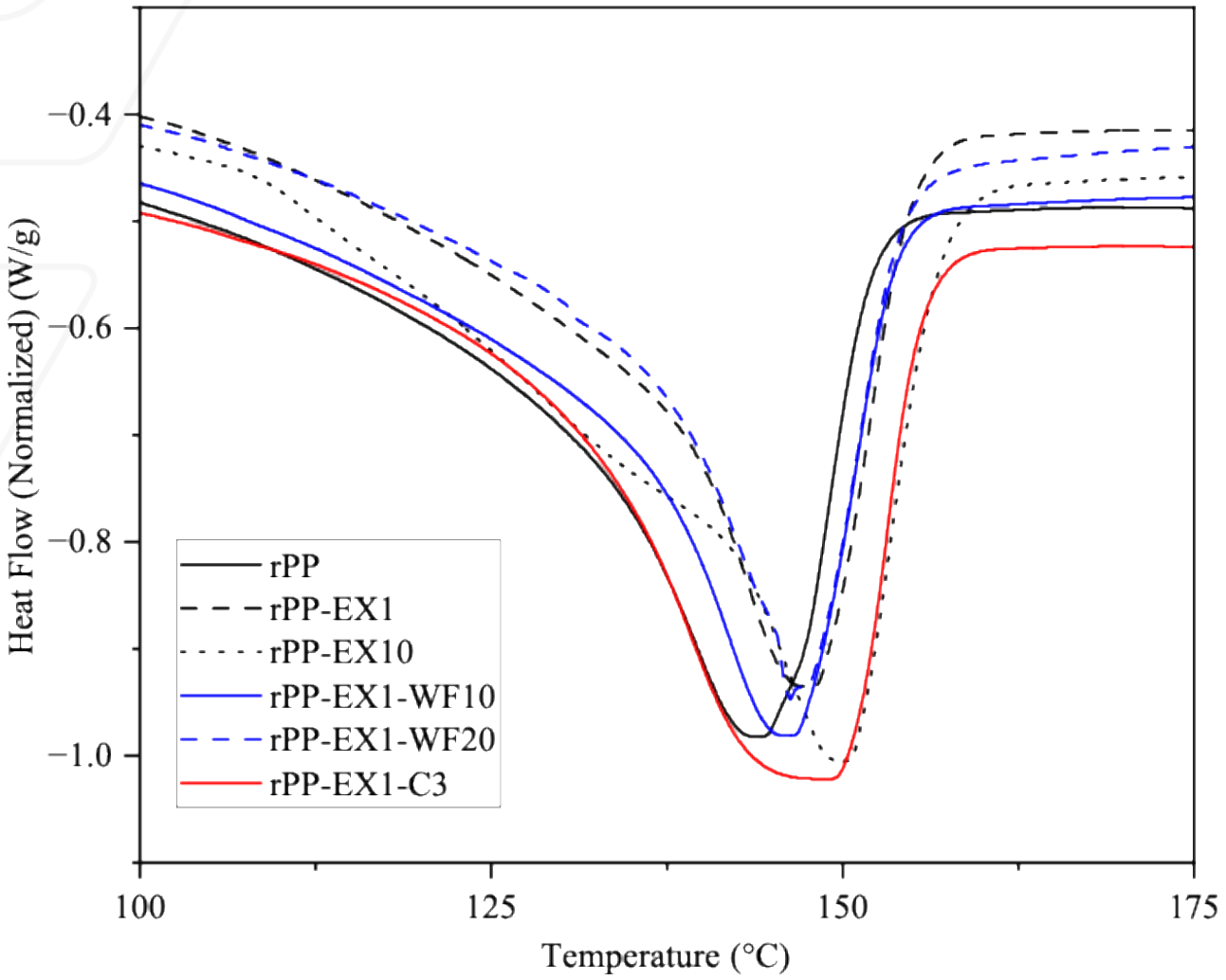

T_c at 10°C/min

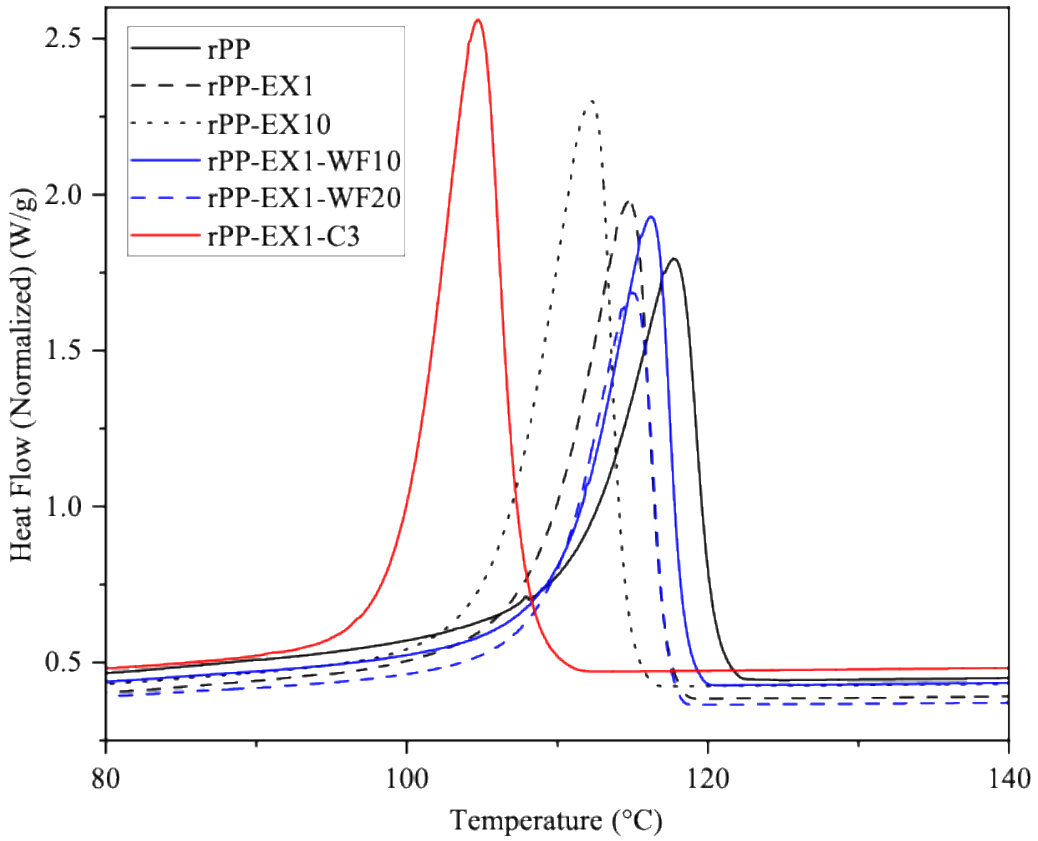

Theoretical thermal transition temperatures of PP [1,2]:

- T_m: 130 - 170 °C
- T_c: 100 – 120 °C
- T_g: 0 – -20 °C

1. Materials guide, Polypropylene (PP) melting point, August 8, 2024
2. Glass transition temperature of polypropylene, April 19, 2025

FTIR of rPP

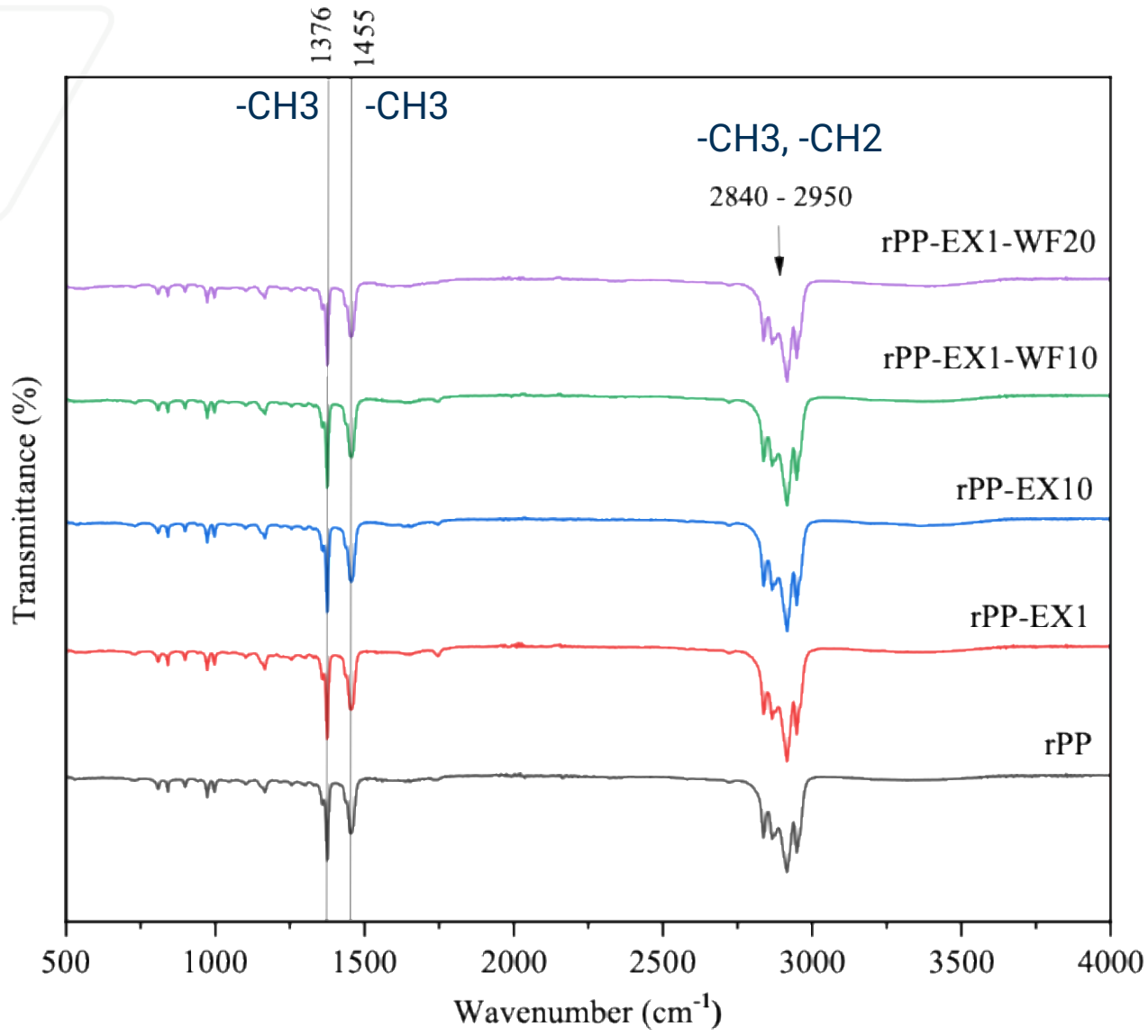

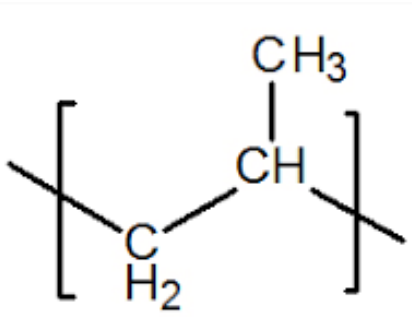

Principal peaks of Polypropylene

- 2840 – 2950 cm^{-1}: C-H stretching vibration in methyl and methylene groups
- 1455 cm^{-1}: Asymmetric C-H bending in -CH3
- 1376 cm^{-1}: Symmetric C-H bending in –CH3

Georgia Tech

Conclusions and going forward

Is reprocessing affecting the performance of recycled PC and PP?	Is degradation occurring, and why?	Can additives combat this degradation
Both PC and PP formulations withstand 10 melt cycles.	Extensive degradation not observed.	Additives didn't significantly affect our properties, except: 1. Enhanced performance in PP/WF-based formulations 2. Reduction in the tensile modulus of PC.

Moving forward:

- Study PC/PP blends across extrusion temperature, residence time, and reprocessing cycles.
- Conduct detailed rheology analysis of all formulations.
- Introduce reclaimed glass fiber into PP and PC (to combat the tensile modulus reduction).

Georgia Tech

ARTIFICIAL NEURAL NETWORK-BASED SEQUENTIAL APPROXIMATE OPTIMIZATION FOR FREE FIBER PATH DESIGN IN VARIABLE-AXIAL COMPOSITES

Xin Wang[1], Shinya Honda[2], Katsuhiko Sasaki[3] and Ryo Takeda[4]

[1] Human Mechanical Systems and Design, Hokkaido University
Kita 13, Nishi 8, Kita-ku, Sapporo, Hokkaido 060-8628, Japan
Email: xin.wang.t0@elms.hokudai.ac.jp, web page: https://ldc.eng.hokudai.ac.jp

[2] Division of Mechanical and Aerospace Engineering, Hokkaido University
Kita 13, Nishi 8, Kita-ku, Sapporo, Hokkaido 060-8628, Japan
Email: honda@eng.hokudai.ac.jp, web page: https://ldc.eng.hokudai.ac.jp

[3] Division of Mechanical and Aerospace Engineering, Hokkaido University
Kita 13, Nishi 8, Kita-ku, Sapporo, Hokkaido 060-8628, Japan
Email: katsu@eng.hokudai.ac.jp, web page: https://ldc.eng.hokudai.ac.jp

[4] Division of Mechanical and Aerospace Engineering, Hokkaido University
Kita 13, Nishi 8, Kita-ku, Sapporo, Hokkaido 060-8628, Japan
Email: r.takeda@eng.hokudai.ac.jp, web page: https://ldc.eng.hokudai.ac.jp

Keywords: Composite materials, Curvilinear fiber paths, Artificial neural network, Vibration, Finite elements

ABSTRACT

This study presents an Artificial Neural Network–based Sequential Approximate Optimization (ANN-SAO) framework for the multi-dimensional design of curvilinear fiber paths in variable-axial composite laminates to maximize their fundamental natural frequencies. In each iteration, a feedforward neural network with four hidden layers, each composed of a linear transformation, layer normalization, SiLU activation, and dropout is trained on the current database of high-fidelity simulations. Early-stopping, weight decay, and adaptive learning-rate scheduling ensure both accuracy and generalization while keeping computational cost tractable. Covariance Matrix Adaptation Evolution Strategy (CMA-ES) is then applied to the ANN response surface to identify an exploitation point, whereas a companion Radial Basis Function based density function searches the sparsest region of the design space for exploration. The two candidates are evaluated with full Finite Element Analysis (FEA), their responses are appended to the training set, and the ANN surrogate is retrained. This cycle repeats until the maximum number of iterations is reached. Using this strategy, the number of expensive simulations is reduced while maintaining a global search capability. Numerical results for composite laminate plates show that the optimized curvilinear fiber architectures achieved by ANN-SAO yield substantial increases in the first natural frequency and favorable tailoring of the mode shape, thereby mitigating resonance risk and enhancing dynamic reliability. The proposed ANN-SAO framework thus provides an efficient, scalable, and accurate tool for vibration-driven design of advanced composite structures with free fiber trajectories.

1 INTRODUCTION

Carbon Fiber Reinforced Plastics (CFRP) are composite materials consisting of carbon fibers embedded within a resin matrix. These materials exhibit high strength and high stiffness [1], making them increasingly favored in industries such as aerospace and automotive [2]. The anisotropic nature of CFRPs enables the tailoring of fiber orientations to meet specific mechanical requirements, offering design advantages over isotropic materials, albeit with increased complexity. Recent advancements in fiber placement technologies have further expanded this design space. Automated Fiber Placement (AFP)

enables high-throughput deposition of steered tows along non-straight trajectories, yielding complex, load-adapted laminates [3], while Tailored Fiber Placement (TFP) stitches continuous fiber tows directly onto a substrate, realizing variable-axial paths with minimal waste [4]. Recent advancements in continuous fiber-reinforced polymer additive manufacturing techniques now enable the fabrication of continuous fiber-reinforced polymer composites with complex geometries and tailored fiber orientations, enhancing mechanical performance and expanding design possibilities for composite structures [5]. Previous studies have presented analytical methods for determining the natural frequencies and vibration modes of laminated plates with curvilinear reinforcing fibers. The results demonstrate that curvilinear fiber paths can significantly influence the dynamic behavior of composite structures [6-8]. To exploit this potential, researchers have applied a variety of optimization strategies. Early work focused on stacking-sequence or lay-up optimization of straight fiber laminates, using meta-heuristics such as particle swarm optimization (PSO) to maximize fundamental frequencies [6] and nonlinear lay-up optimization of variable stiffness composite cylindrical panels in free vibration using gradient-based methods, demonstrating enhanced fundamental frequencies through tailored fiber orientations [9]. While effective, these direct-search approaches require thousands of high-fidelity finite element evaluations and therefore become expensive when the design space expands to free (curvilinear) fiber paths.

The classical Sequential Approximate Optimization (SAO) framework encompasses various surrogate modeling techniques, such as Kriging, Radial Basis Function (RBF) networks, and Support Vector Regression (SVR). These methods are extensively applied in engineering optimization, particularly when dealing with computationally expensive numerical simulations, as they effectively reduce the number of function evaluations required [10]. More recently, artificial-neural-network (ANN) surrogates have exhibited higher approximation accuracy and better generalization than linear regression (LR), decision tree (DT) and random forest regression (RF) when learning highly non-linear composite behaviors, particularly for buckling and strength prediction [11]. Building on these advances, this study proposes an Artificial Neural Network-based Sequential Approximate Optimization (ANN-SAO) framework to optimize curvilinear fiber paths in variable-axial composite laminates. In each iteration of the ANN-SAO, an ANN surrogate model (response surface) is constructed, and its predicted optimum is taken as a new sample point for local refinement. To maintain global search coverage, a radial-basis-function-based density metric identifies sparsely sampled regions and guides the addition of exploratory sample points. Through these exploitation and exploration steps, the surrogate model's accuracy is progressively improved, facilitating the discovery of fiber path configurations that significantly enhance the structure's dynamic performance.

2 EXPRESSIONS OF CURVILINEAR FIBER PATHS BY RADIAL BASIS FUNCTIONS

As a first step, we describe how curvilinear fiber paths are parametrically represented using radial basis functions, which will serve as the design variables for optimization. To represent high-degree curvilinear fiber paths on a plane, a surface generated by radial basis functions (RBFs) is employed. This approach involves generating a surface using RBFs, through a linear combination of three Gaussian functions, as shown in Eq. (1).

$$f(x,y)_{surface} = \sum_{i=1}^{3} w_i \, exp\left(-\frac{\left(x-x_{c,i}\right)^2+\left(y-y_{c,i}\right)^2}{r_i^2}\right) \tag{1}$$

This approach can capture the shape of a surface with a a high degree of flexibility. Here $(x_{c,i}, y_{c,i})$ represents the center point, and the parameter r_i influences the surface smoothness: larger r_i values yield flatter shapes, whereas smaller r_i values produce sharper peaks. Each Gaussian component is multiplied by a weight factor w_i and summed to form the surface, which means the fiber path can be controlled by adjusting the parameters $x_{c,i}, y_{c,i}, r_i$ and w_i (where $i = 1, 2, 3$), the fiber path can be flexibly controlled (Fig. 1a). The contour lines of this RBF-generated surface define the nominal fiber paths. To ensure the path is manufacturable via the TFP process, the tool's vertical (z-axis) movement is modulated according to the fiber tow overlap rate α (Eq. 2), as illustrated in Fig. 1b.

$$\alpha = \frac{w_f - d}{w_f} \tag{2}$$

Where w_f is the width of a single fiber and d is the spacing of the centerline of the fiber tow. These contour lines are then discretized into segments using the curve's gradient from Eq. (3) to determine each segment's slope relative to the element centroid. This discretization facilitates their expression in a finite element model, as shown in Fig. 1c.

$$\theta_e = Tan^{-1}\left(\frac{\partial f/\partial y}{\partial f/\partial x}\right)\Big|_{x=x_e, y=y_e} \tag{3}$$

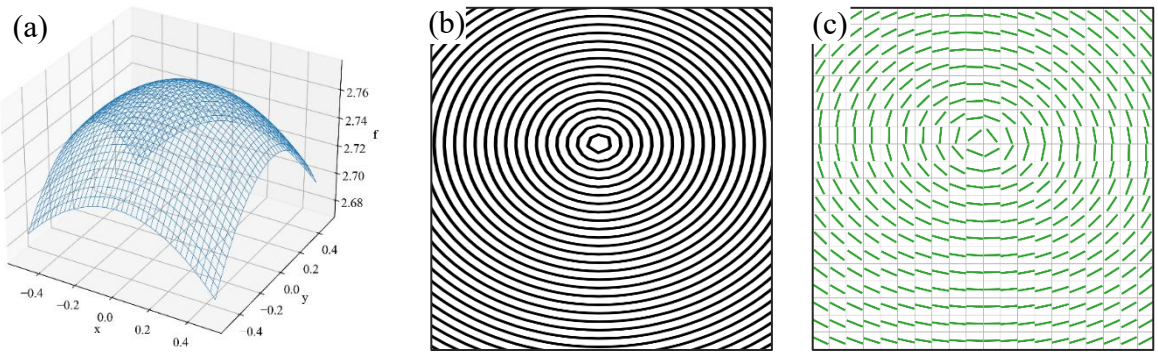

Figure 1: (a) Surface defined by three Gaussian functions; (b) adjusted fiber path considering fiber wots overlap; (c) discretized contour lines on a 20×20 FE mesh.

The natural frequencies of the composite laminate were determined through a structured computational workflow. Initially, ANSYS software was utilized to design the structural geometry, providing essential model parameters such as element count, nodal coordinates, and node numbering. Subsequently, Python scripts integrated the fiber orientation angles for each element into ANSYS Mechanical APDL to perform modal analysis. For visualization, the Matplotlib library was employed to graphically represent the fiber paths. This Python-based automation facilitated the execution of the aforementioned steps, streamlining the optimization process.

In the modal analysis, SHELL281 elements from ANSYS were employed. Each element comprises eight nodes with six degrees of freedom, suitable for analyzing thin to moderately thick shell structures. A 100 mm × 100 mm square plate was discretized into a 20 × 20 mesh, resulting in 400 elements. The laminate configuration, as depicted in Figure 2, consists of a symmetric eight-layer stack: [(TFP)$_2$/PW 45°/PW 0°]s. This arrangement includes layers of Plain Weave (PW) and TFP, designed to be compatible with future fiber stitching machinery. The base material comprises two PW layers oriented at 0° and 45°, forming the foundational structure. Two TFP layers with identical fiber paths are then superimposed, exhibiting contoured patterns that reflect their customized fiber orientations, stitched onto the outer surfaces of the base layers. This alternating configuration results in a symmetrically arranged laminate, aimed at enhancing frequency characteristics through variable fiber orientations within the TFP layers.

Material properties are summarized in Table 1. The thickness of the Plain Weave (PW) layer is defined as 0.191 mm. For the TFP layer, the local thickness is computed as a function of the fiber distribution determined by the overlap rate $\alpha(x, y)$. Assuming the fiber tow has a thickness of t_f when there is no overlap, the thickness at a point $(x,\ y)$ where the overlap rate is $\alpha(x, y)$ can be expressed as:

$$t(x, y) = \frac{t_f}{1 - \alpha(x, y)} \tag{4}$$

The spacing $d(x, y)$ between fiber tow at a point (x, y) is determined by the following relationship (Eq. 5):

$$\alpha(x, y) = 1 - \frac{|\nabla f(x, y)|}{|\nabla f|_{max}}(1 - \alpha_{max}) \tag{5}$$

Where$|\ \nabla f(x, y)\ |$represents the local gradient magnitude of the fiber orientation function at position (x, y), which is inversely proportional to the fiber spacing at that point. The quantity $|\ \nabla f\ |_{max}$

corresponds to the maximum gradient within the domain, occurring where the fiber tows are most densely packed, i.e., where the fiber spacing reaches its minimum. The maximum overlap rate α_{max} is set to 0.6. Substituting this into the thickness expression gives:

$$t(x,y) = \frac{|\nabla f|_{max}}{|\nabla f(x,y)|} t_{max} \tag{6}$$

Where $t_{max} = t_f/1 - \alpha_{max}$ represents the maximum thickness corresponding to the maximum overlap condition. This formulation ensures that the TFP thickness varies spatially in response to fiber curvature and distribution, approaching the actual fiber stacking behavior. In Table 1, "L" denotes the longitudinal fiber direction, and "T" signifies the transverse direction relative to the fibers.

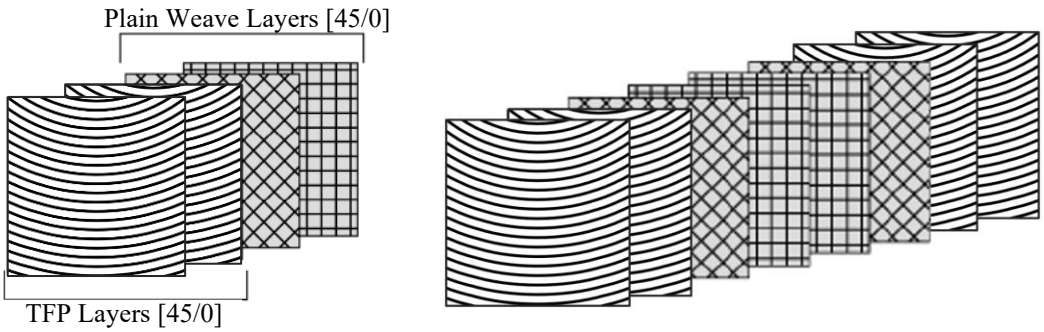

Figure 2: Cross-sectional view of the composite laminate showing the arrangement of TFP and plain weave layers.

Engineering constant		Plain Weave Layer	TFP Layer
E_L	[GPa]	37.7	103
E_T	[GPa]	37.7	9.04
ν_{LT}	–	0.3	0.3
G_{LT}	[GPa]	3.26	5.05
ρ	[kg/m^3]	1442	1295

Table 1: Material constants for Plain Weave layer and TFP fiber tow.

3 SEQUENTIAL APPROXIMATE OPTIMIZATION USING ARTIFICIAL NEURAL NETWORKS

3.1 Sequential Approximate Optimization

Sequential Approximate Optimization (SAO) is particularly effective for addressing complex optimization problems characterized by nonlinearity, multidimensionality, and computationally intensive evaluations. Unlike conventional metaheuristic methods such as PSO and GA, which operate by directly moving design variables and require many costly evaluations, SAO adopts a model based strategy. It begins by constructing a surrogate model or response surface, that approximates the objective function based on a set of strategically selected sample points within the design space.

The optimization process proceeds by identifying candidate optima on the surrogate surface. These points are then evaluated using the high-fidelity objective function, and the results are used to iteratively update and refine the surrogate model. This cycle continues, with each iteration improving the model's accuracy and predictive power. To ensure adequate coverage of the design space and prevent premature convergence to local optima, a density function is introduced. This function identifies sparsely sampled regions, guiding the addition of exploratory points to improve the global search effectiveness of the algorithm.

One of SAO's key strengths lies in its capacity to generate accurate surrogate models that effectively

approximate complex physical phenomena. This makes it especially suitable for applications where direct evaluations are expensive, such as finite element analyses or experimental testing. By leveraging surrogate modelling, SAO significantly reduces the number of high-cost simulations required to identify optimal solutions [10]. A typical SAO framework follows a structured sequence of steps, as outlined in Fig. 3.

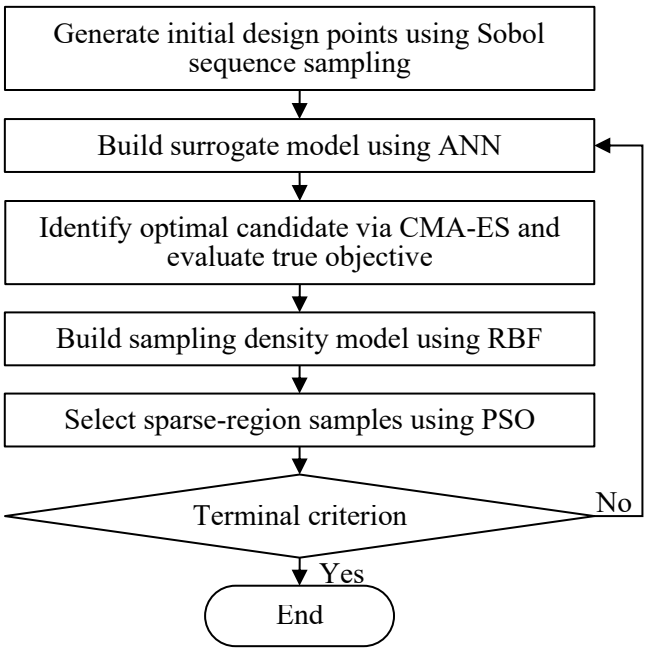

Figure 3: Workflow of the proposed Sequential Approximate Optimization framework.

In this study, a Sequential Approximate Optimization (SAO) framework is proposed using ANN as surrogate models. Initial sampling points are generated via Sobol sequences to ensure a well-distributed and space-filling design. An ANN-based response surface is then constructed to capture the nonlinear relationship between design variables and the objective function. To explore promising regions, the surrogate is optimized using the Covariance Matrix Adaptation Evolution Strategy (CMA-ES), and the obtained optimum is evaluated with the high-fidelity model. Simultaneously, a sampling density function is modeled using a RBF network, and PSO is employed to identify sparse regions in the design space, from which additional sampling points are selected. These new samples are incorporated into the dataset to refine both the surrogate and the density model. This iterative process continues until a predefined convergence criterion is met.

3.2 Artificial Neural Network

In this study, a feedforward Artificial Neural Network (ANN) with four hidden layers, each containing 126 neurons, is employed as the surrogate model to approximate the nonlinear relationship between the design variables and the objective function. The ANN architecture, training procedures, and implementation were adapted based on guidelines presented by Subramanian [12].

Specifically, for each hidden layer l, the pre-activation output is computed as:

$$\boldsymbol{z}^{(l)} = \boldsymbol{W}^{(l)}\boldsymbol{h}^{(l-1)} + \boldsymbol{b}^{(l)}, \quad l = 1, 2, \dots, L-1, \quad \boldsymbol{h}^{(0)} = \boldsymbol{x} \tag{7}$$

Each hidden layer applies the SiLU activation function defined as:

$$\phi(\boldsymbol{s}) = \boldsymbol{s}\sigma(\boldsymbol{s}), \quad \delta(\boldsymbol{s}) = \frac{1}{1+e^{-\boldsymbol{s}}} \Rightarrow h^{(l)} = \phi\left(z^{(l)}\right) \tag{8}$$

Layer normalization and dropout (rate = 0.1) are applied after each activation to enhance generalization and prevent overfitting. The final output of the network is given by:

$$\hat{y}(\boldsymbol{x}; \boldsymbol{w}) = \boldsymbol{W}^{(L)}\boldsymbol{h}^{(L-1)} + \boldsymbol{b}^{(L)} \tag{9}$$

where $w = \{\boldsymbol{W}^{(l)}, \boldsymbol{b}^{(l)}{}_{l=1}^{L}\}$ denotes all weights and biases in the model. The ANN is trained to minimize the regularized mean-squared error:

$$E(\boldsymbol{w}) = \sum_{i=1}^{m} (y_i - \hat{y}(\boldsymbol{x_i}; \boldsymbol{w}))^2 + \lambda \sum_{j} w_i^2 \tag{10}$$

An Adam optimizer is employed, along with an adaptive learning-rate scheduler and early stopping. After each iteration of the Sequential Approximate Optimization (SAO) process, the ANN surrogate model is retrained using the expanded dataset, thereby maintaining its accuracy and currency with newly sampled data points.

3.3 Density Function

To evaluate the distribution of sampling points across the design space, a sampling density function $D(\boldsymbol{x})$ is constructed using the same RBF structure defined in Eq. (1), where each existing sample point is assigned a nominal value of 1:

$$\boldsymbol{y}_D = (1, 1, \cdots, 1)^T \tag{11}$$

The normalized inputs $\boldsymbol{x}_D$ are obtained using the same scaling strategy as in the fiber path representation, with an expansion factor $\alpha = 1.2$ applied if necessary to ensure full basis coverage. The corresponding RBF weight vector $\boldsymbol{w}_D$ is solved via regularized least squares:

$$\boldsymbol{w}_D = (\boldsymbol{H}^T \boldsymbol{H} + \lambda \boldsymbol{I})^{-1} \boldsymbol{H}^T \boldsymbol{y}_D \tag{12}$$

The density function is then given by:

$$D(\boldsymbol{x}) = \sum_{i=1}^{m} w_i^D h_i(\boldsymbol{x}) \tag{13}$$

By minimizing $D(\boldsymbol{x})$ using PSO, the sparsest region of the current design space is located, enabling exploration beyond already-sampled areas and supporting global optimization.

4 FIBER PATH OPTIMIZATION

With the ANN surrogate and sampling strategies defined above, we next set up the specific fiber path optimization problem including design variables and objective function. The design variables for the curvilinear fiber path are defined by the RBF parameters (Eq. 14), while those for the straight fiber path consist of a single fiber orientation angle (Eq. 15). The objective function in both cases aims to maximize the fundamental frequency, reformulated as a minimization task by negating its value (Eqs. 16 and 17).

The ANN-based response surface is optimized using the CMA-ES, configured with an initial standard deviation (σ_0) of 0.15 and a maximum of 300 iterations. For the density function surrogate, PSO is employed with a swarm of 500 particles, inertia weight $w = 0.7$, and acceleration coefficients $c1 = c2 = 2.0$, with 60 iterations. The ANN-SAO algorithm is configured to perform a total of 600 evaluations of the objective function, regardless of whether the fiber path is curvilinear or straight. The number of initial sampling points N_{init} is determined by:

$$N_{init} = 2 \times (\mathrm{n} + 1) \tag{14}$$

where n is the number of design variables. The entire optimization process, including surrogate modeling and iterative updates, can typically be completed within approximately 100 minutes. The design variables and objective formulation are summarized in Table 2.

	Design variables	Objective function
Curvilinear fiber path	$x_{c,i}, y_{c,i}, r_i, w_i\ (i = 1,2,3)$ $-2 \le x_{c,i} \le 2$ $-2 \le y_{c,i} \le 2$ $0.5 \le r_i \le 4$ $-2 \le w_i \le 2$	$f(x_{c,i}, y_{c,i}, r_i, w_i) = -(f^{1st\ ferquency}) \rightarrow min$
Straight fiber path	$-89.9° \le \theta_{Fiber\ Angle} \le 90°$	$f(\theta) = -(f^{1st\ frequency}) \rightarrow min$

Table 2: Design variables and objective function formulations for the curvilinear vs. straight fiber path optimization.

The objective of this study is to optimize the fiber orientation of four TFP layers located at the outermost part of a symmetric eight-layer laminate using ANN-SAO. To ensure consistent material properties, the same TFP configuration is applied to both curvilinear and straight fiber paths. Boundary conditions are defined using 'F' for free edges. Fiber path optimization is carried out under all free boundary conditions to evaluate the effectiveness of the ANN-SAO framework.

5 NUMERICAL RESULTS

Under the FFFF boundary condition, the optimized straight fiber path exhibits a uniform orientation of −45°, achieving a fundamental frequency of 1038.42 Hz. Its mode shape reveals deformation primarily aligned parallel to the fiber orientation, with maximum displacement concentrated at the corners along the shortest fiber segments. In contrast, the optimized curvilinear fiber path forms concentric circular patterns centered at the midpoint of the plate, as shown in Fig. 3. This configuration enhances dynamic performance significantly, yielding a 24.41% increase in the fundamental frequency relative to the optimal straight fiber design. The mode shape exhibits that deflections are primarily confined to the four corners.

The detailed element wise distribution of fiber orientation and thickness resulting from the ANN-SAO optimization is depicted in Fig. 3. Although the thickness distribution under the curvilinear design exhibits slight spatial variation, the colorbar indicates that these fluctuations are minor. Notably, both designs share the same average thickness of 4.76 mm, confirming that the observed performance gains are attributed to fiber orientation tailoring rather than increased material usage. These results validate that the ANN-SAO framework effectively exploits smooth spatial variation in both fiber angles and layer thickness to optimize the fundamental frequency.

	Straight Fiber	Curvilinear Fiber	Difference
Fiber Orientation	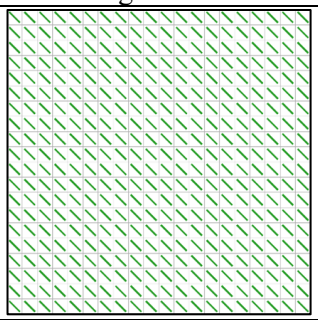	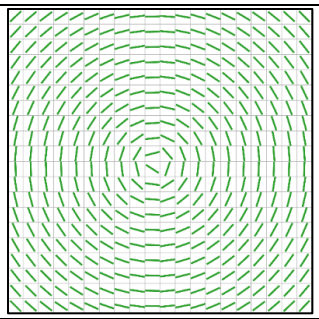	—
Natural Frequency	1038.42	1291.87	+24.41%
Mode Shape	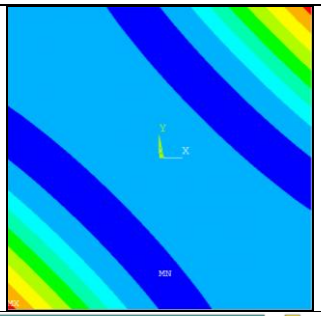	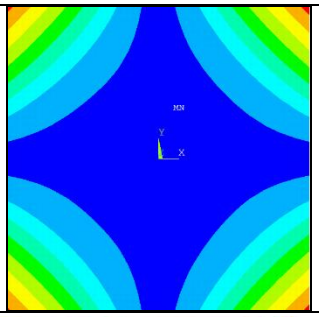	—
Thickness Distribution	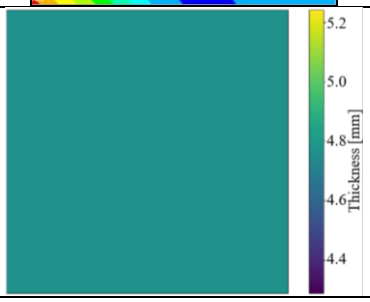	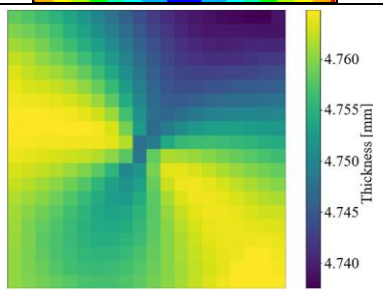	—
Average Thickness	4.76	4.76	0%

Figure 3: Comparison between the optimized straight-fiber baseline and the optimized curvilinear fiber orientation (green segments) under FFFF boundary conditions. Insets illustrate the corresponding mode shapes and thickness distributions.

6 CONCLUSIONS

This study proposed an Artificial Neural Network-based Sequential Approximate Optimization (ANN-SAO) framework to optimize curvilinear fiber paths in symmetric laminated composites. By employing ANN to construct the surrogate model and integrating density-based sampling strategies, the method efficiently captured nonlinear relationships and improved optimization convergence. Compared with straight fiber configurations, the ANN-SAO optimized curvilinear paths significantly increased the first natural frequency under the tested boundary condition, indicating the effectiveness of tailored fiber steering for vibration performance.

Future work will focus on experimental validation of the optimized designs and extending the ANN-SAO framework to more complex composite structures and loading scenarios, further assessing its robustness and practical applicability in advanced manufacturing environments.

ACKNOWLEDGEMENTS

This research was supported by JSPS KAKENHI Grant Number 24K07369 and JST SPRING, Grant Number JPMJSP2119.

REFERENCES

[1] F. Ning, W. Cong, J. Qiu, J. Wei and S. Wang, Additive manufacturing of carbon fiber reinforced thermoplastic composites using fused deposition modeling, *Composites Part B: Engineering*, **80**, 2015, pp. 369–378 (doi: 10.1016/j.compositesb.2015.06.013).

[2] H. Zheng, W. Zhang, B. Li, J. Zhu, C. Wang, G. Song, G. Wu, X. Yang, Y. Huang and L. Ma, Recent advances of interphases in carbon fiber-reinforced polymer composites: A review, *Composites Part B: Engineering*, **233**, 2022, 109639 (doi: 10.1016/j.compositesb.2022.109639).

[3] E. Oromiehie, B.G. Prusty, P. Compston and G. Rajan, Automated fibre placement based composite structures: Review on the defects, impacts and inspections techniques, *Composite Structures*, **224**, 2019, 110987 (doi: 10.1016/j.compstruct.2019.110987).

[4] A. Spickenheuer, C. Scheffler, L. Bittrich, R. Haase, D. Garray, G. Heinrich and D. Weise, Tailored Fiber Placement in Thermoplastic Composites, *Technologies for Lightweight Structures*, **1(2)**, 2017, pp. 116–127 (doi: 10.21935/tls.v1i2.95).

[5] D. Zhao, X. Zha, L. Zhou and Y. Xiong, Additive manufacturing of continuous fiber reinforced polymer composites: Process planning and intelligent control, *Journal of Manufacturing Processes*, **144**, 2025, pp. 170–189 (doi: 10.1016/j.jmapro.2025.04.015).

[6] S. Honda and Y. Narita, Natural frequencies and vibration modes of laminated composite plates reinforced with arbitrary curvilinear fiber shape paths, *Journal of Sound and Vibration*, **331(1)**, 2012, pp. 180–191 (doi: 10.1016/j.jsv.2011.08.019).

[7] D.A. Pereira, T.A.M. Guimarães, H.B. Resende and D.A. Rade, Numerical and experimental analyses of modal frequency and damping in tow-steered CFRP laminates, *Composite Structures*, **244**, 2020, 112190 (doi: 10.1016/j.compstruct.2020.112190).

[8] S. Honda, H. Takisawa, R. Takeda, K. Sasaki and K. Katagiri, Estimation of damping characteristics and optimization of curvilinear fiber shapes for composites fabricated by electrodeposition resin molding, *Mechanics of Advanced Materials and Structures*, **30(21)**, 2022, pp. 4407–4418 (doi: 10.1080/15376494.2022.2095063).

[9] T. Farsadi, M. Rahmanian and H. Kurtaran, Nonlinear lay-up optimization of variable stiffness composite skew and taper cylindrical panels in free vibration, *Composite Structures*, **262**, 2021, 113629 (doi: 10.1016/j.compstruct.2021.113629).

[10] S. Kitayama, M. Arakawa and K. Yamazaki, Sequential Approximate Optimization using Radial Basis Function network for engineering optimization, *Optimization and Engineering*, **12(4)**, 2011, pp. 535–557 (doi: 10.1007/s11081-010-9118-y).

[11] X. Liu, J. Qin, K. Zhao, C.A. Featherston, D. Kennedy, Y. Jing and G. Yang, Design optimization of laminated composite structures using artificial neural network and genetic algorithm, *Composite Structures*, **305**, 2023, 116500 (doi: 10.1016/j.compstruct.2022.116500).

[12] V. Subramanian, *Deep learning with PyTorch: A practical approach to building neural network models using PyTorch*, Packt Publishing Ltd, 2018.

Optimal Design of Seamless C/SiC Combustor with Multi-Cooling Channels for Rocket Engines Based on a Data-Driven Model

2025. 08. 05

Kyeong Mo Kang, Jihoon Yang, Woong-Ryeol Yu*

Department of Materials Science and Engineering, Seoul National University,
599 Gwanak-ro, Gwanak-gu, Seoul 151-742, Republic of Korea

Contents

I. Introduction

II. Methodology

III. Results and Discussions

Contents

I. Introduction

II. Methodology

III. Results and Discussions

The rise of hypersonic technology: a global strategic priority

US hypersonic programmes to receive almost $7 billion in 2025

2nd April 2024 - 10:23 GMT | by Flavia Camargos Pereira in Kansas City RSS

Rocket Lab Onramped To Multi-Billion Dollar U.S. and U.K. Defense Contracts To Expand Hypersonic Technology Development with HASTE

Provided by Business Wire • Apr 15, 2025 6:00am

Europe Hypersonic Missiles Market to Surpass USD 2 Billion by 2032 with Strong Growth

Report Ocean Mar. 11, 2025 12:01







[Hypersonic weapons and alternatives]

(Source: Congressional Budget Office, https://www.cbo.gov/publication/58924)

Combustor: key element in hypersonic engines

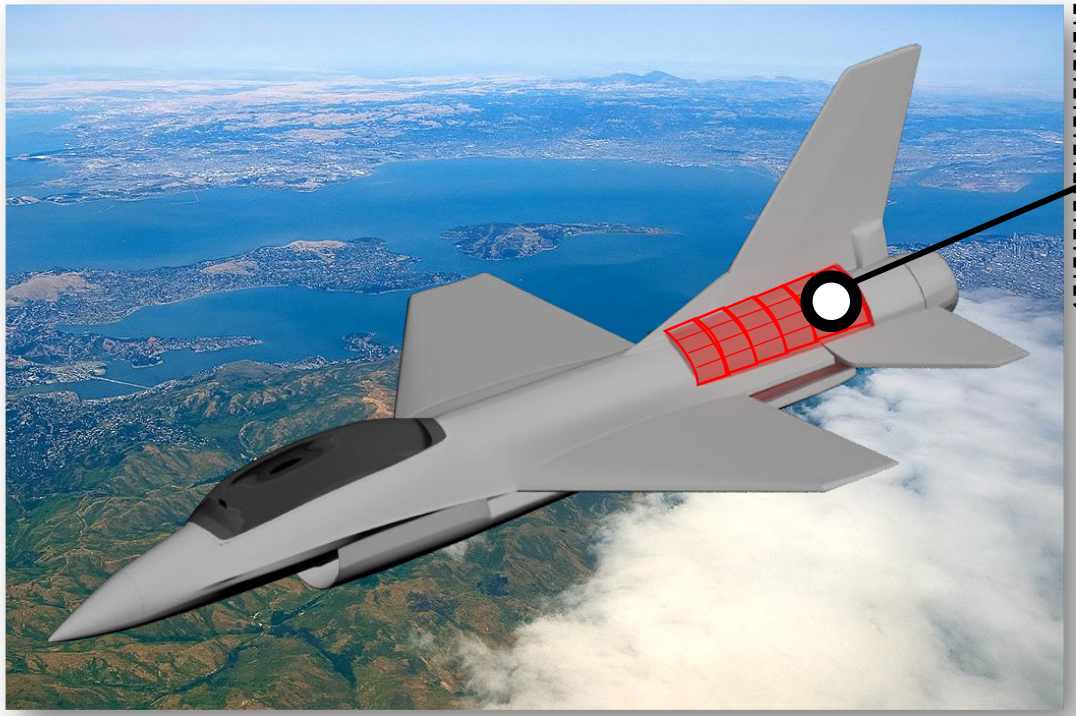

[Hypersonic vehicle and combustor schematic]

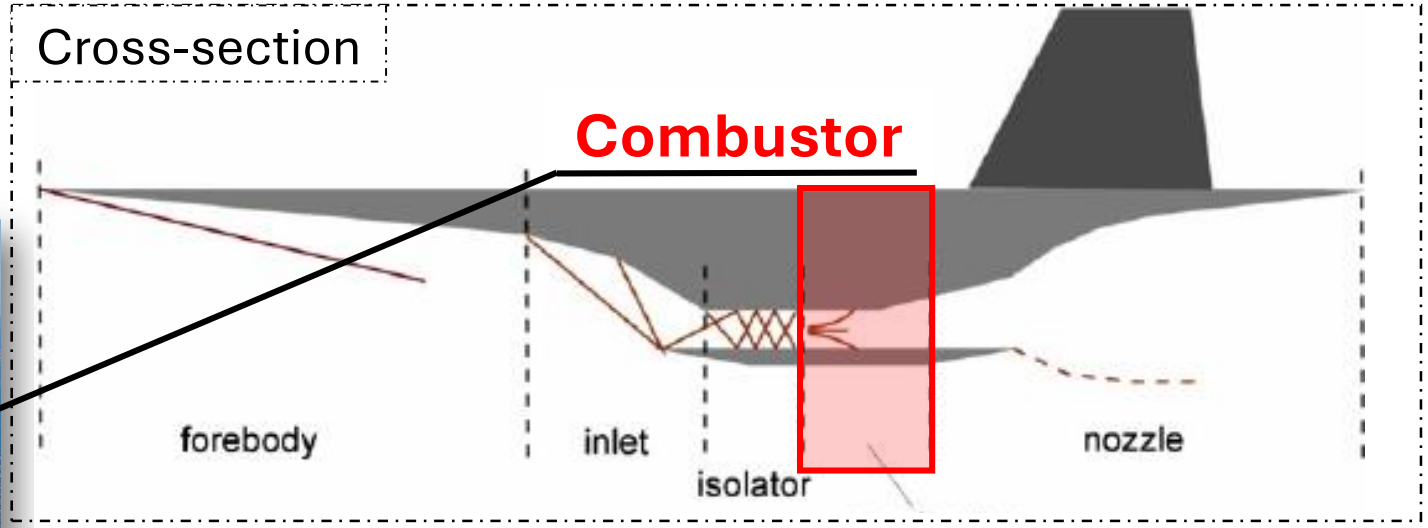

High Performance Computing in Science and Engineering 2011, 429–441

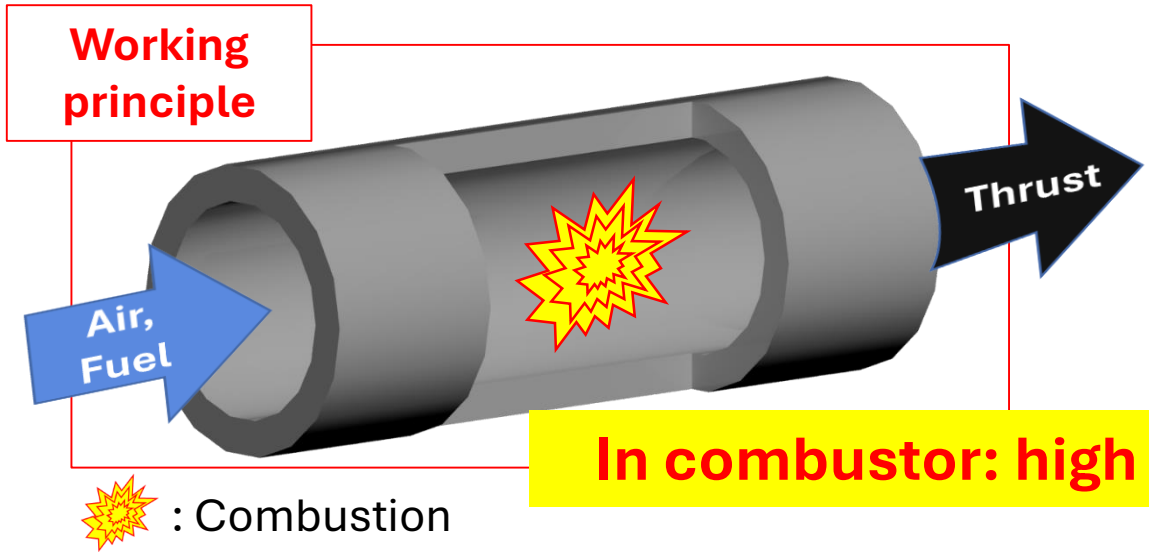

Materials and cooling strategies for extreme conditions

- **Ceramic matrix composites (CMCs)**

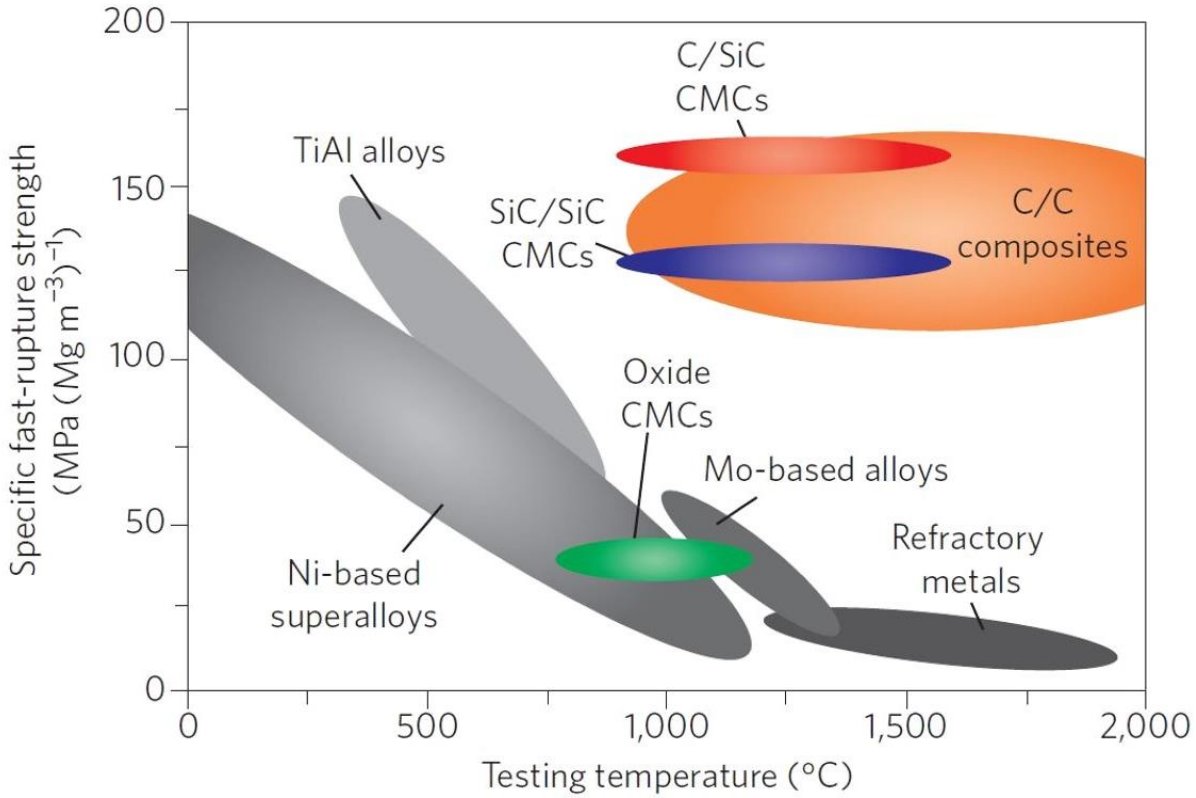

Trans Indian Inst Met (2019) 72(8):2043–2059

[Specific fast-rupture strength of different materials]

- **Regenerative cooling**

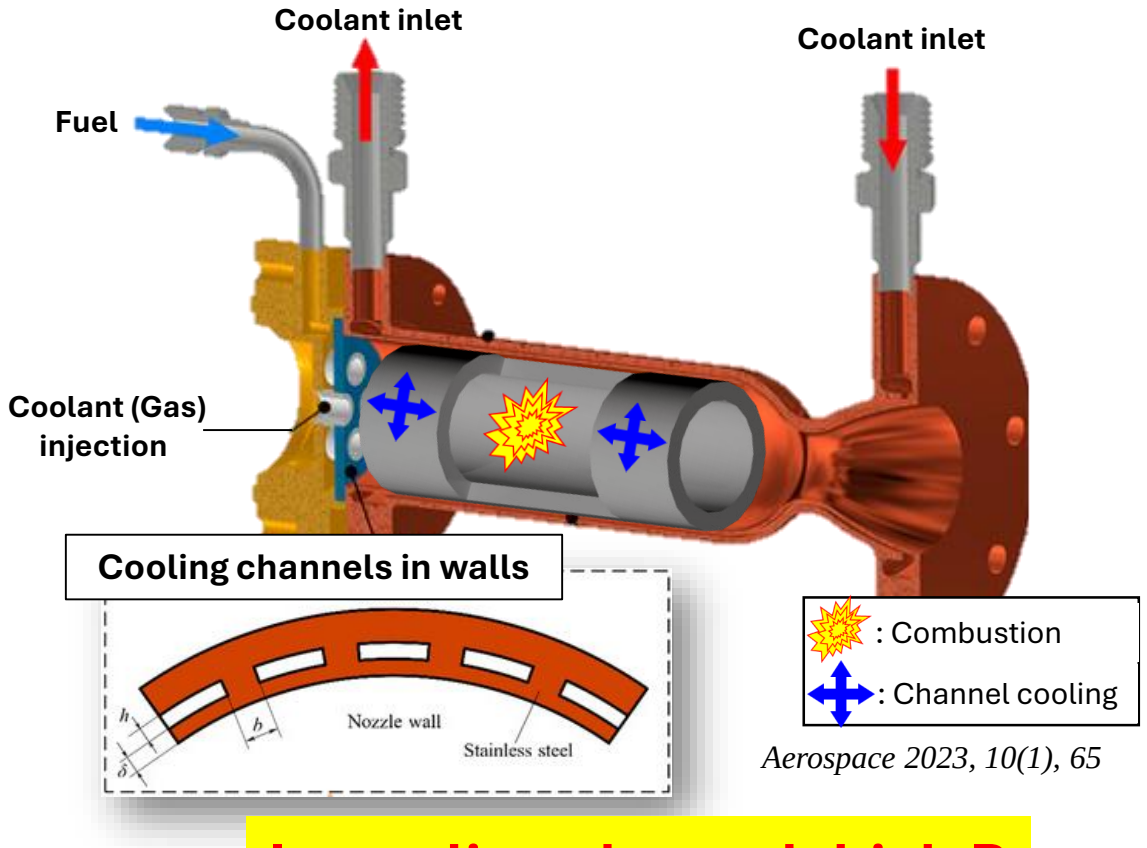

Aerospace 2023, 10(1), 65

In cooling channel: high P

[Schematic of regenerative cooling]

PTAH-SOCAR: leading technique, but

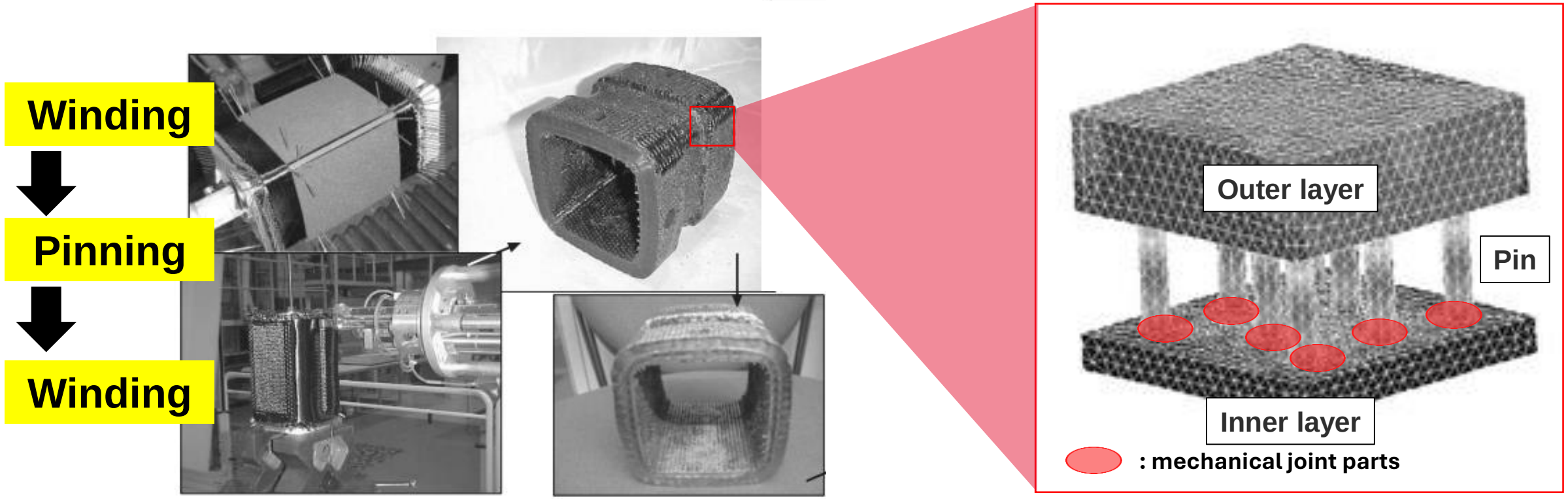

[PTAH-SOCAR process]

Progress in Propulsion Physics 1 (2009) 627-644

- ✓ Complex-shaped combustor composites are manufactured through a combined winding and pinning process.
- ✓ However, **mechanical joints interrupt the continuity of cooling channels,** causing stress concentration and reducing structural strength. → need of seamless structures

Advanced weaving technology for seamless structures

- **Double-tubular composites**

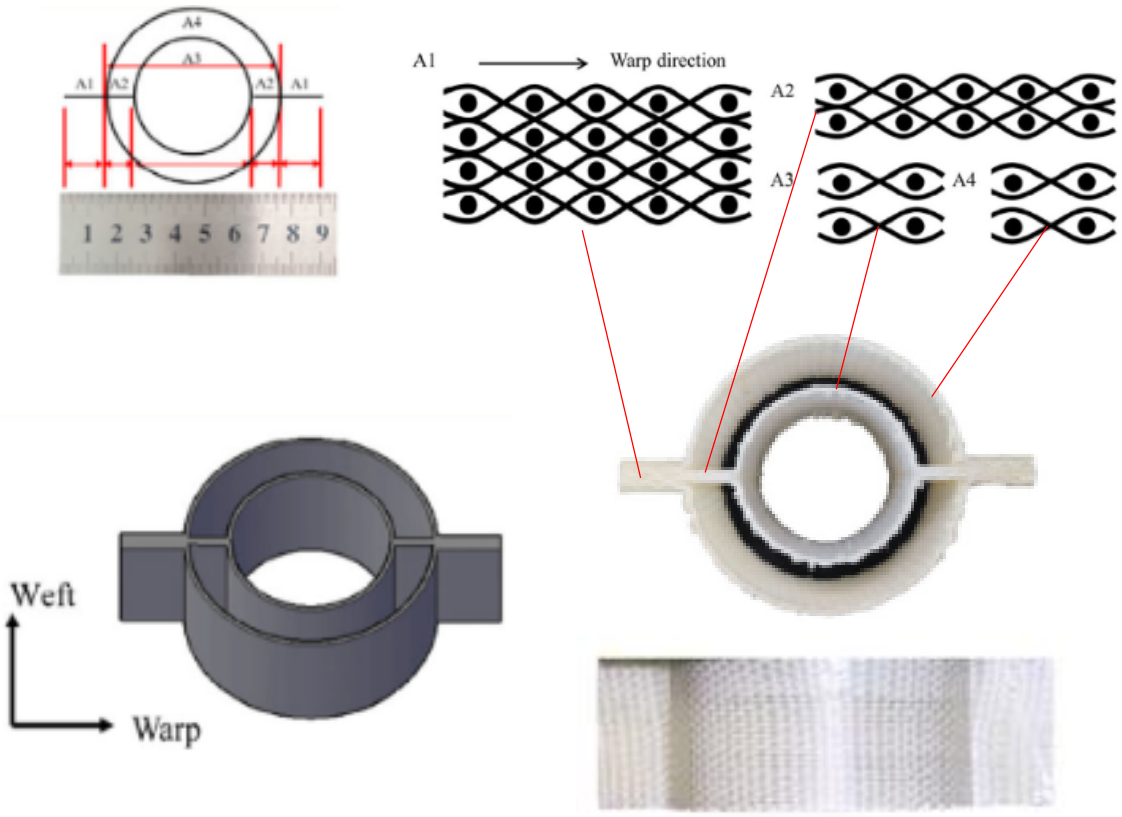

Polymer Composites. 2024;45:8282–8295

[Double-tubular composites with woven architecture]

- **Box-shaped composites**

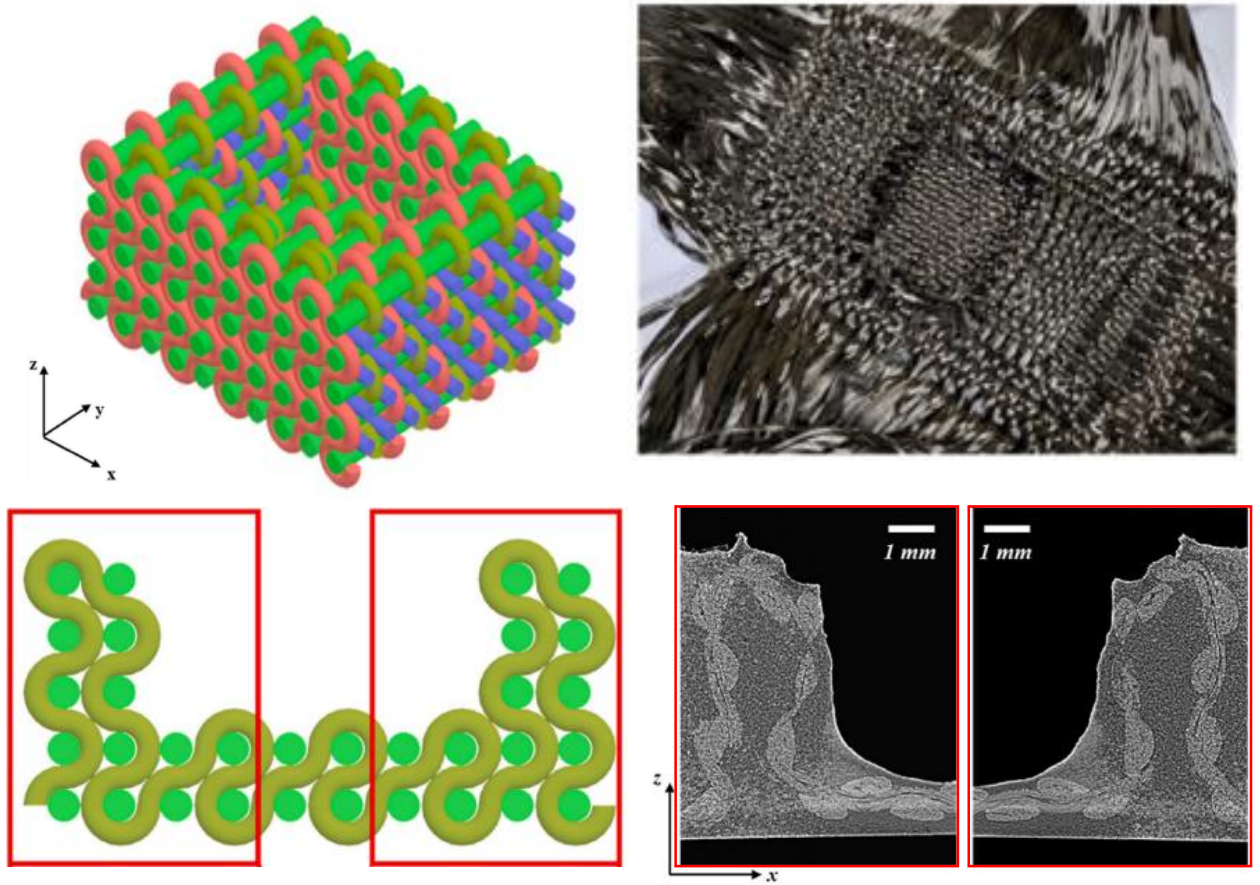

Heliyon 10 (2024) e2412

[Box-shaped composites with woven architecture]

Need of structural optimization

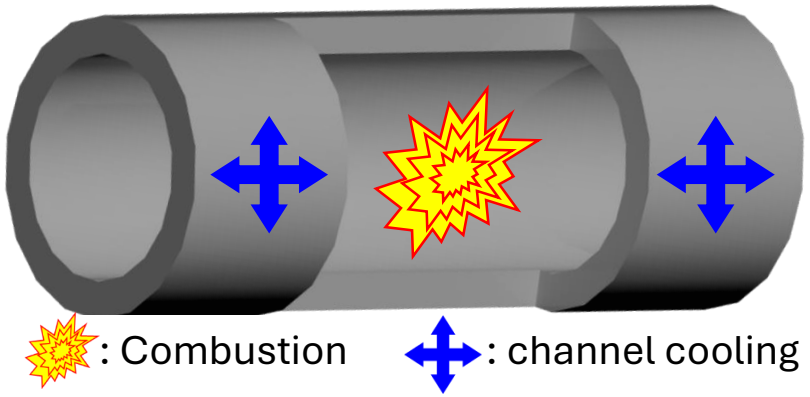

In combustor: high T, P

In cooling channel: high P

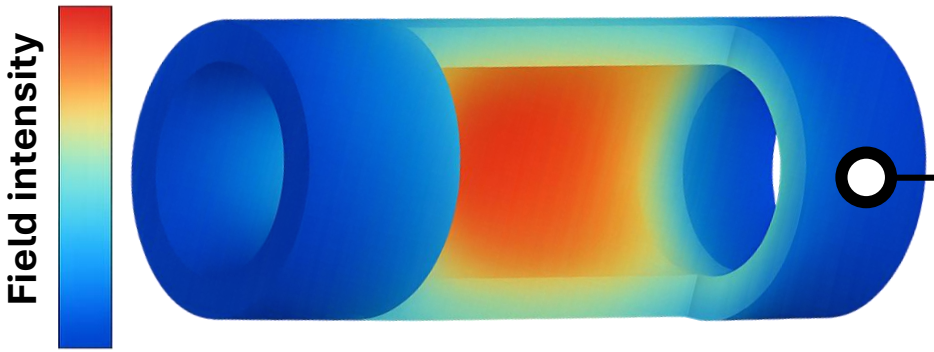

Performances

Burst resistance — ? — Weight

Pressure drop — Cooling

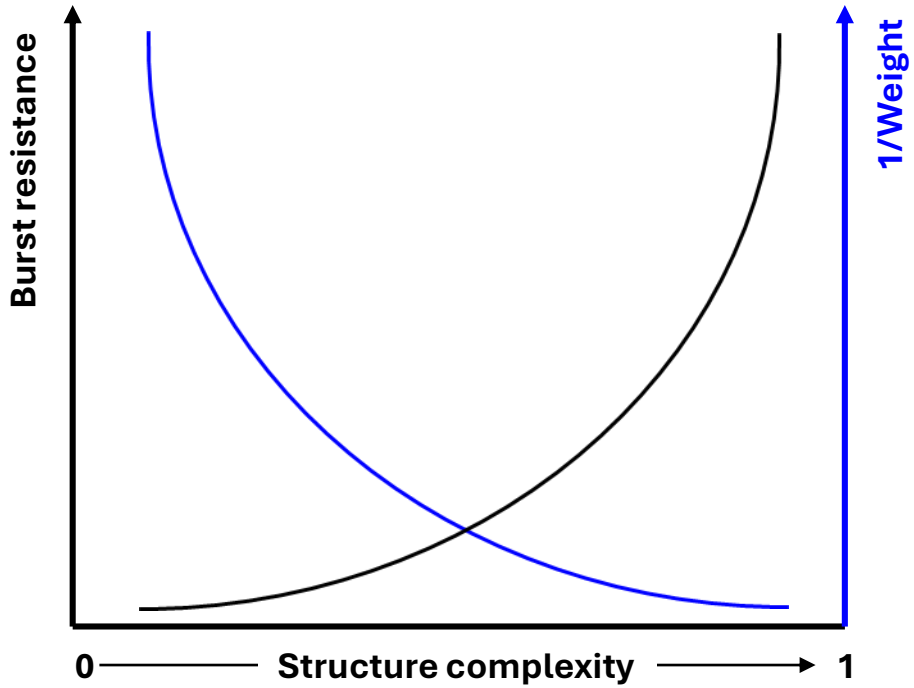

[4 types of performance and example of trade off]

Research goal

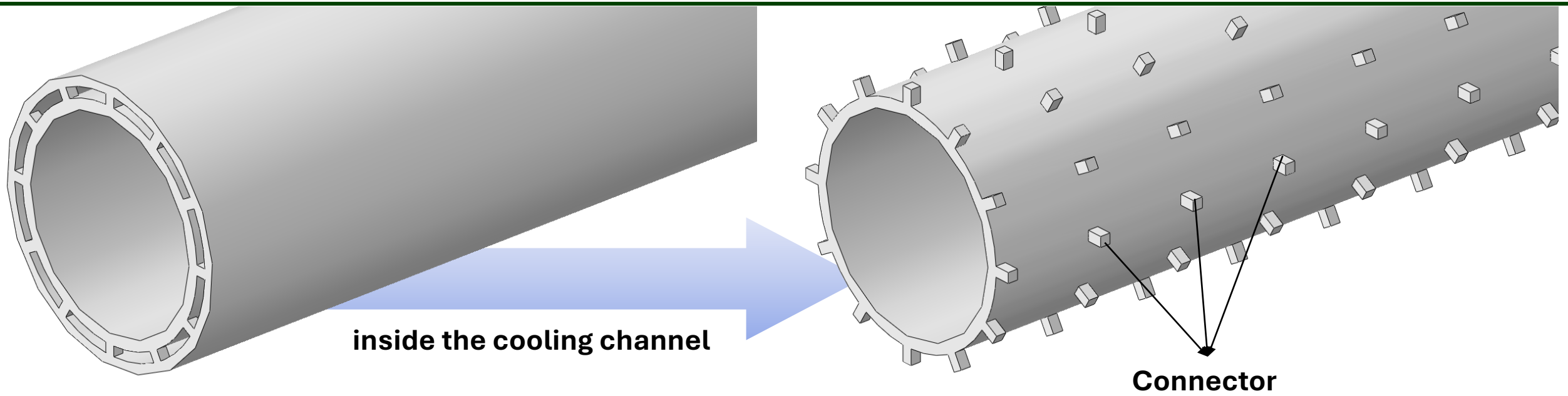

[CMC combustors with cooling channels]

Goal: fabrication of seamless combustors with multi-cooling channels

1. Optimization of cooling channels considering

(1) Burst resistance, (2) Weight, (3) Pressure drop of coolant, (4) Cooling performance

2. Development of fabrication method for seamless combustors with cooling channels

Research outline

1. Optimization of cooling channels considering

(1) Burst resistance, (2) Weight, (3) Pressure drop of coolant, (4) Cooling performance

[1] Design parameters → **[2] Objective functions** → **[3] Optimization (NSGA-II algorithm)**

$$\begin{bmatrix} n_{AC} \\ n_{TC} \\ L_a \\ L_t \\ t_i \\ t_o \\ h \end{bmatrix}$$

(1) Burst resistance (f_1)
: AI model

(2) Weight (f_2)
: # of used connectors

(3) Pressure drop (f_3)
: analogy model

(4) Cooling (f_4)
: contact area of coolant

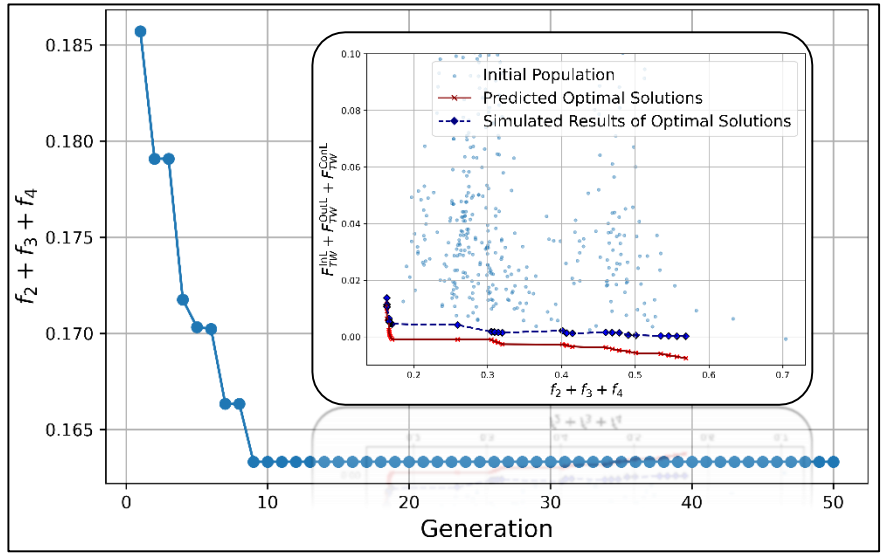

Contents

I. Introduction

II. Methodology

III. Results and Discussions

Numerical models for burst simulation

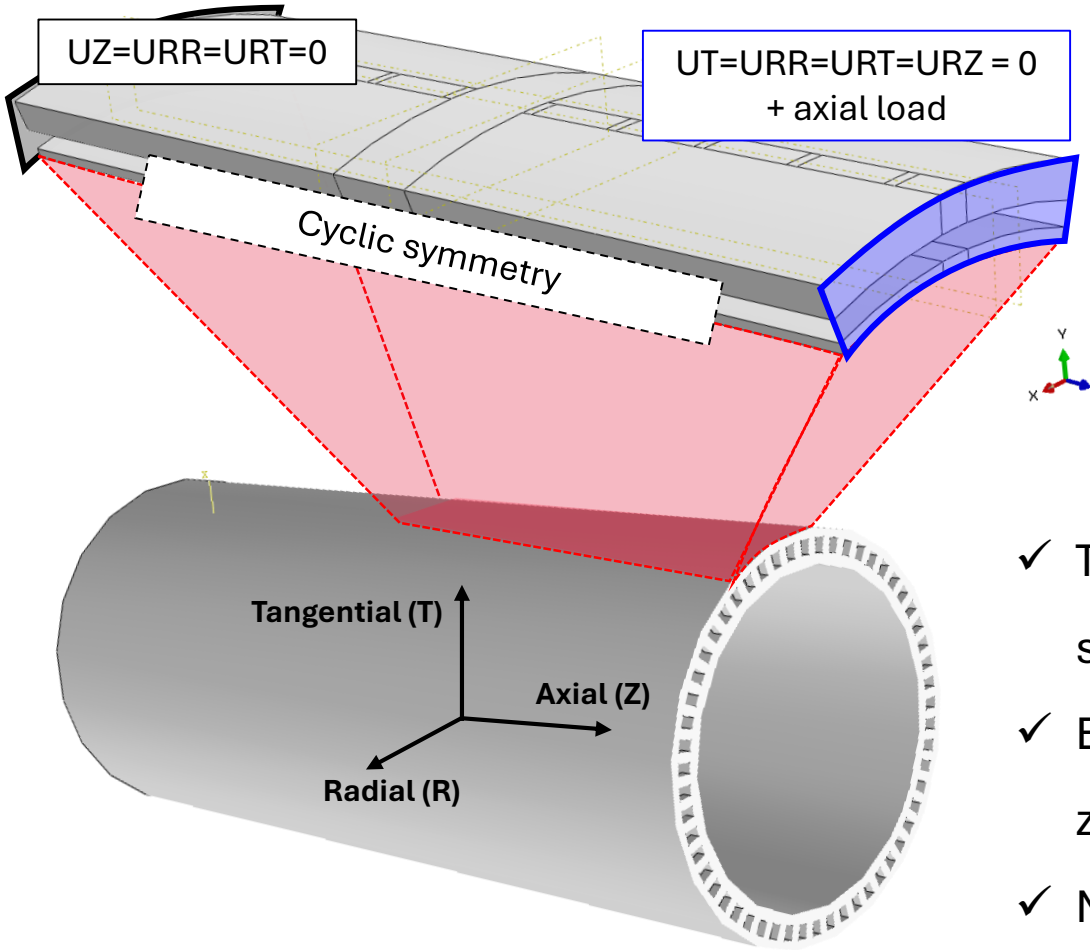

[Full model and half model of the combustors]

Mesh

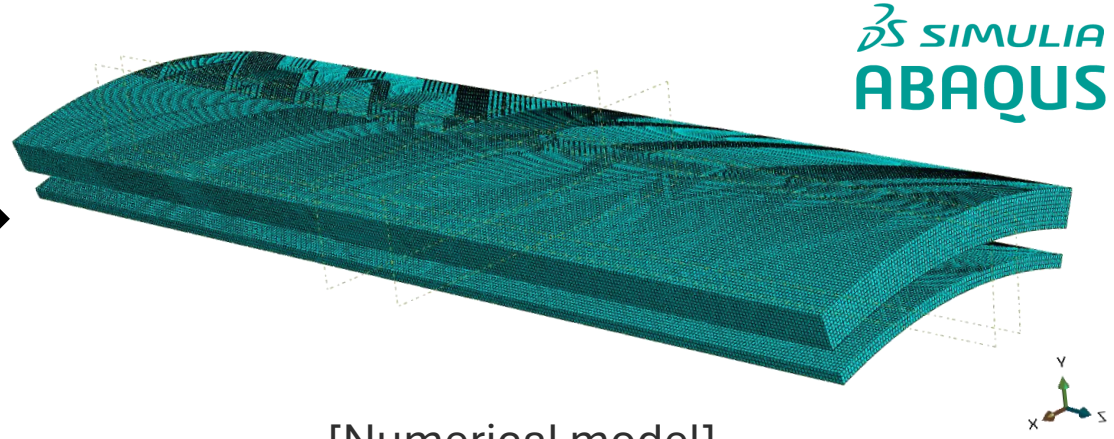

[Numerical model]

- ✓ To reduce the computing time for simulation of bursting, a cyclic half-section (i.e., half model) of the combustor was selected for analysis.
- ✓ Boundary conditions:

  z-symmetry and radial/axial free + axial load
- ✓ Mesh and element:

  0.3 mesh size / Hex-dominated (structured) / C3D8R

Simulation conditions

Trans Indian Inst Met (2019) 72(8):2043–2059

Handbook of ceramic composites. Vol. 165., 2005.

- **Loading conditions**

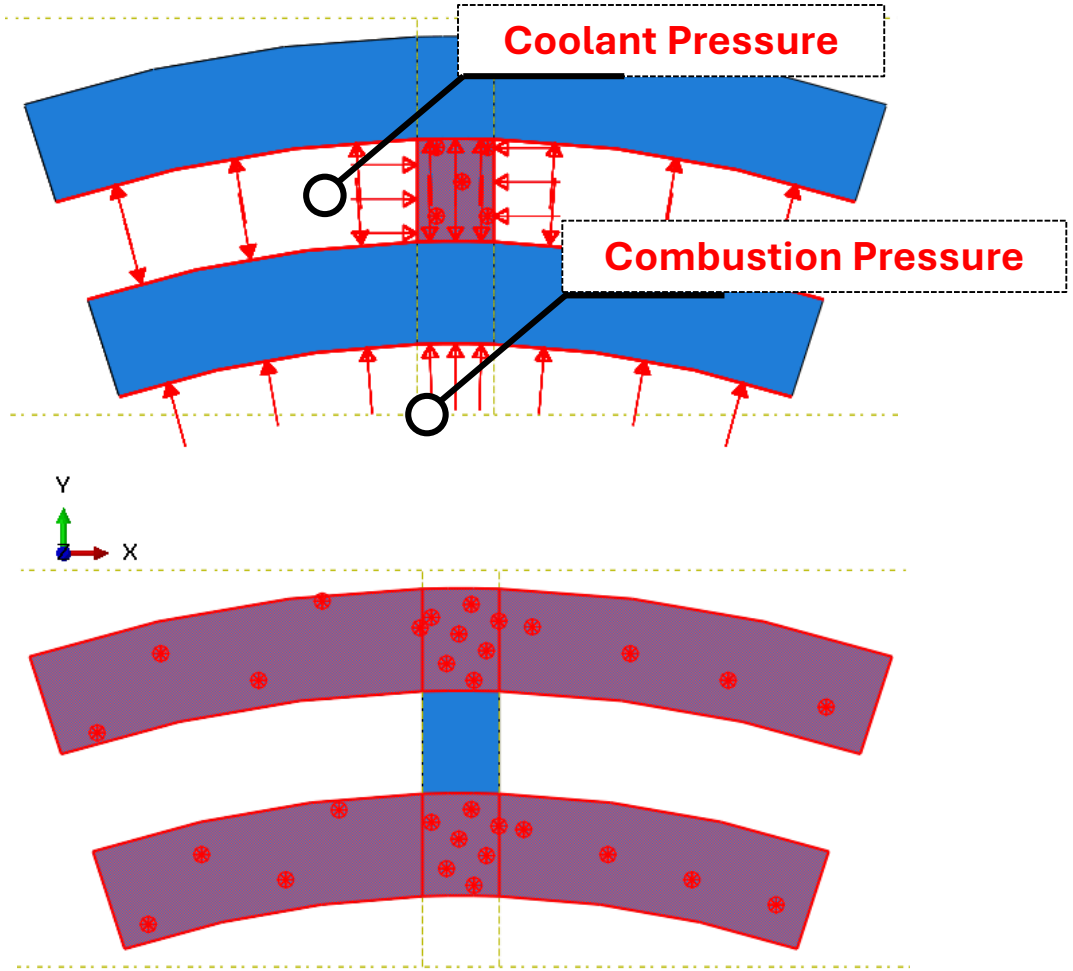

[Cross-sectional view of internal pressure and axial force]

- **Materials: 2D C/SiC composites**

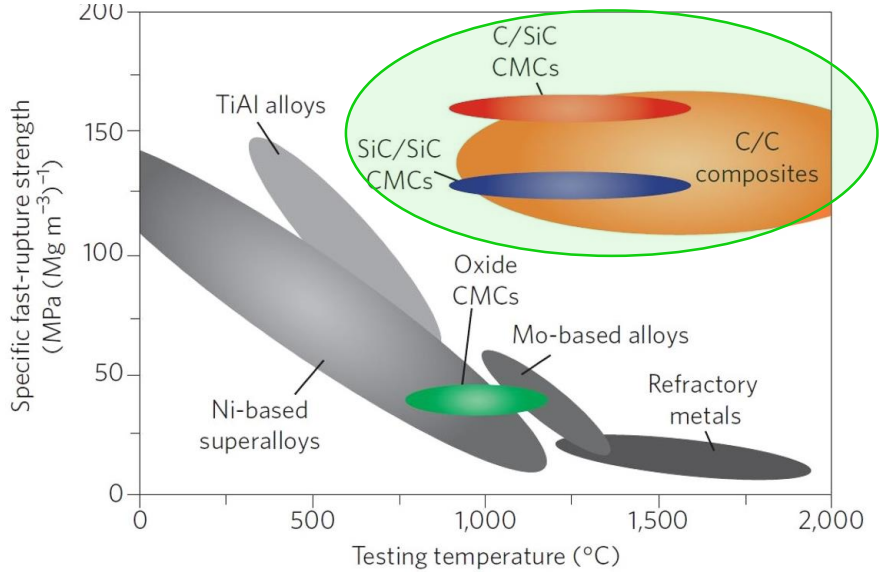

[High thermal performance of C/SiC composites]

E_1	E_2	E_3	v_{12}	v_{13}	v_{23}	G_{12}	G_{13}	G_{23}
	$[MPa]$			-			$[MPa]$	
60100	60100	48400	0.1	0.05	0.05	25000	20000	20000

X_T	Y_T	Z_T	X_C	Y_C	Z_C	S_{12}	S_{13}	S_{23}
				$[MPa]$				
98.9	98.9	11.4	265	265	62	57.5	35.3	35.3

[Material properties of 2D C/SiC composites]

Parameters for burst resistance

- ✓ The most commonly used criteria, Tsai-Wu ($\boldsymbol{F_{TW}}$), is chosen as failure factor: *Composite Structures 337 (2024) 118099*

$$F_1\sigma_1 + F_2\sigma_2 + F_3\sigma_3 + F_4\sigma_4 + F_5\sigma_5 + F_6\sigma_6$$
$$+F_{11}\sigma_1^2 + F_{22}\sigma_2^2 + F_{33}\sigma_3^2 + F_{44}\sigma_4^2 + F_{55}\sigma_5^2 + F_{66}\sigma_6^2$$
$$+2F_{12}\sigma_1\sigma_2 + 2F_{13}\sigma_1\sigma_3 + 2F_{23}\sigma_2\sigma_3 < 1.0$$

$$where\ F_i = \frac{1}{\sigma_{it}} - \frac{1}{\sigma_{ic}}\ for\ i = 1,2,3, F_4 = F_5 = F_6 = 0,$$
$$F_{ii} = \frac{1}{\sigma_{it}\sigma_{ic}}\ for\ i = 1,2,3,$$
$$F_{jj} = \frac{1}{\tau_{jk}^2}\ for\ shear\ (j = 4,5,6, jk = 12,23,31)$$
$$F_{ij} = -\frac{1}{2}\sqrt{F_{ii}F_{jj}}\ for\ ij = 12,23,31$$

Composites Part C:Open Access 4 (2021) 100122

- ✓ 3 individual, maximum index values are extracted by the part:

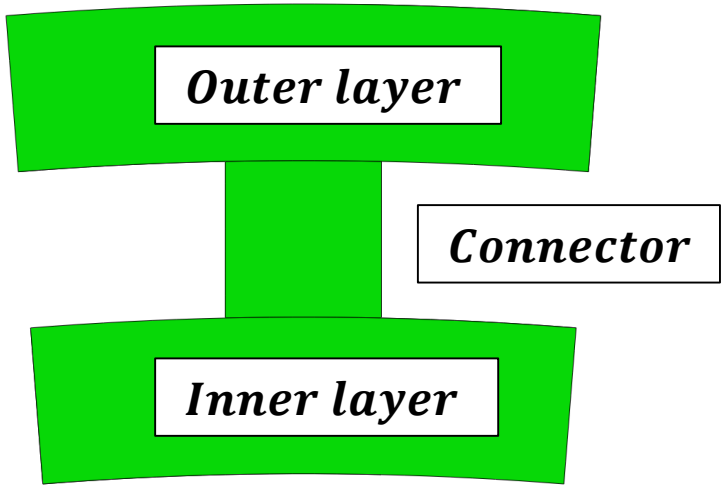

I. $\boldsymbol{F_{TW}^{InL}}$ *in inner layer*

II. $\boldsymbol{F_{TW}^{OutL}}$ *in outer layer*

III. $\boldsymbol{F_{TW}^{Con}}$ *in connector*

Design parameters $(n_{AC}, n_{TC}, L_a, L_t, t_i, t_o, h)$

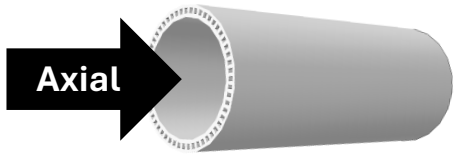

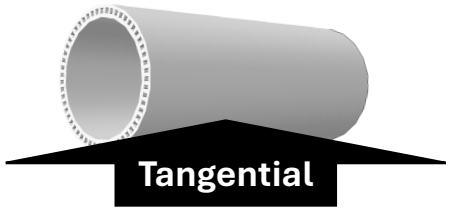

Circumferential (C)

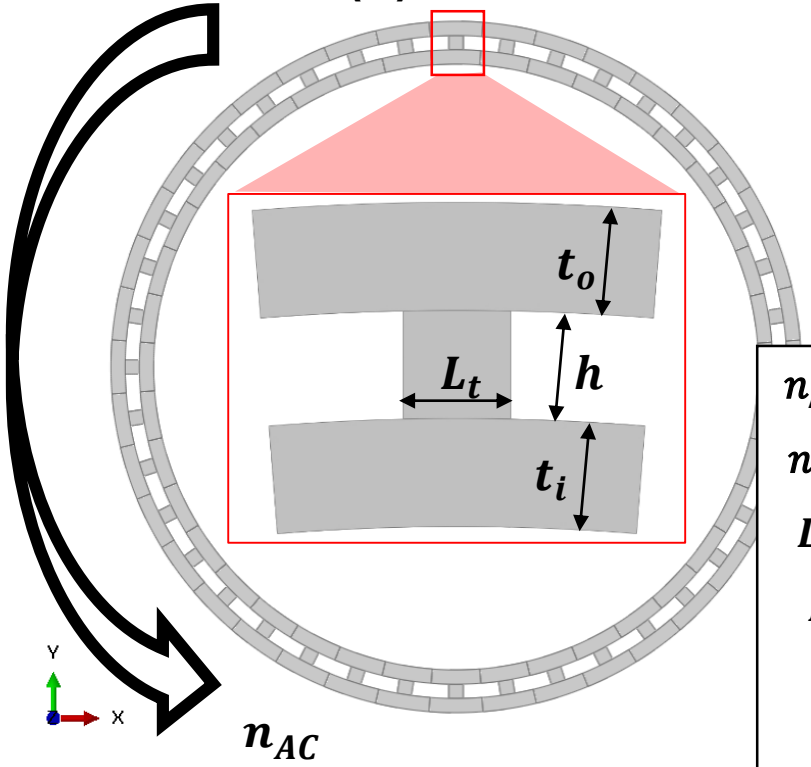

[Axial view of combustors]

Longitudinal (L)

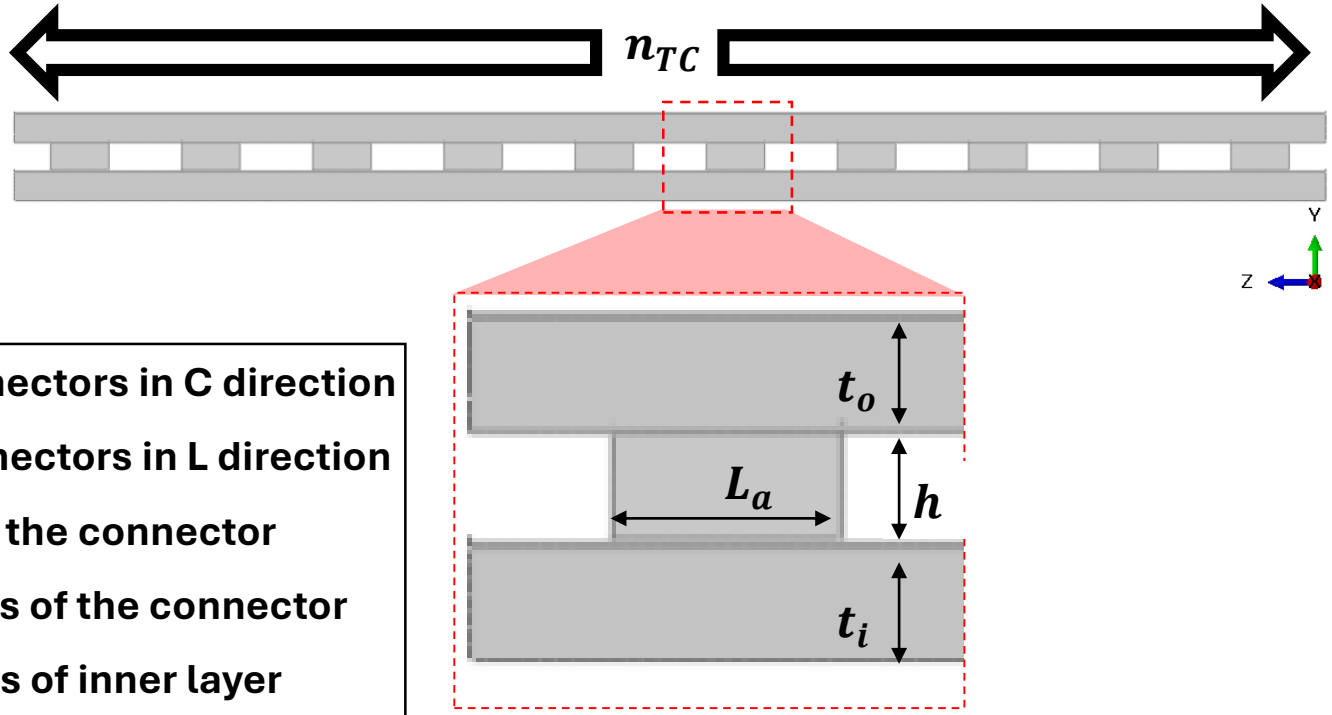

[Tangential view of combustors]

n_{AC}: # of connectors in C direction

n_{TC}: # of connectors in L direction

L_a: length of the connector

L_t: thickness of the connector

t_i: thickness of inner layer

t_o: thickness of outer layer

h: height of the channel

Pressure drop in cooling channels

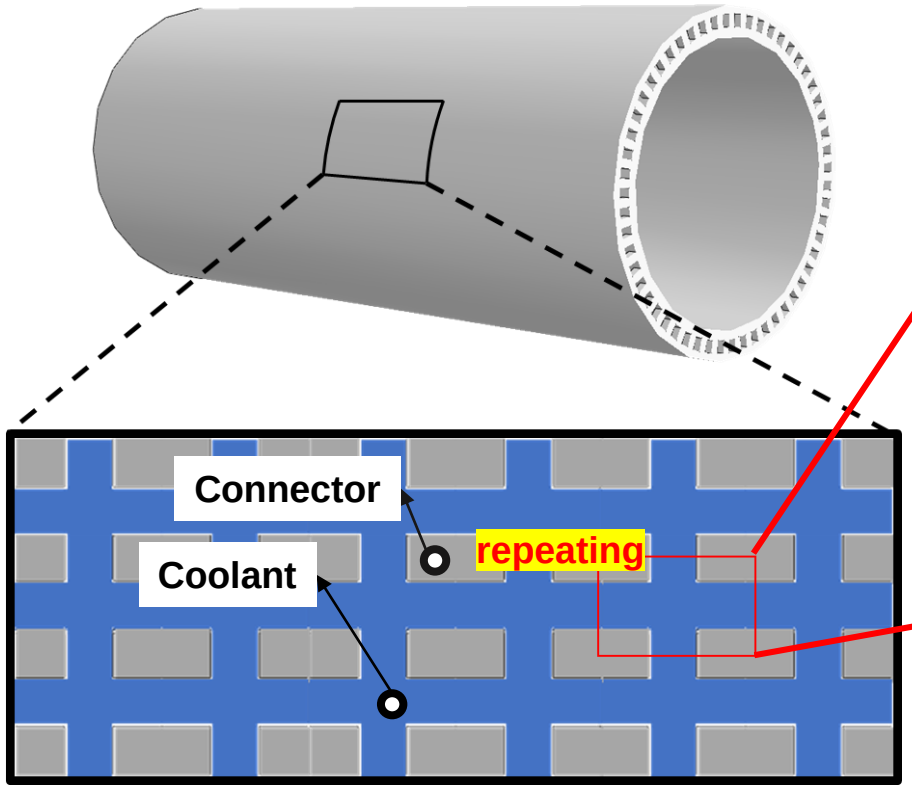

[Repeating structure of cooling channels]

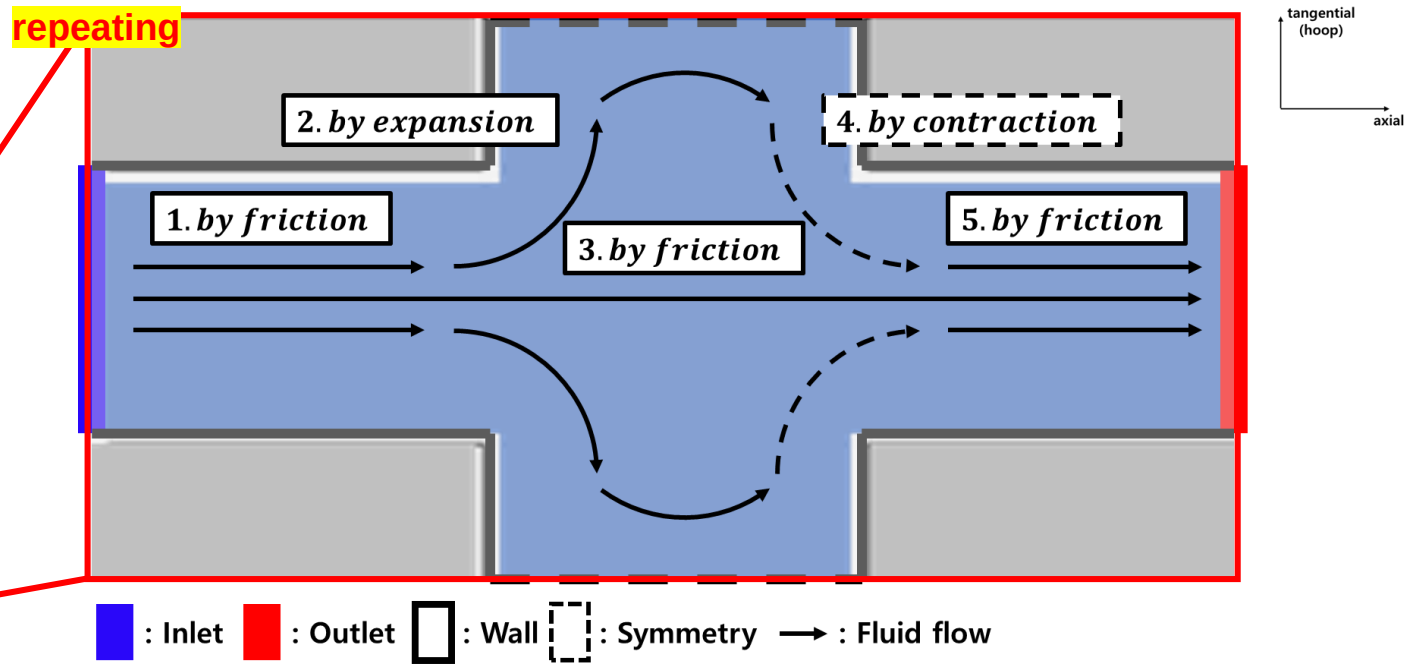

[5 steps of pressure drop behavior]

- ✓ A representative repeating unit is defined.
- ✓ It is assumed that the pressure drop behavior within the repeating unit occurs in 5 steps.

1. by friction + 5. by friction → Friction loss by 4 walls

3. by friction → Friction loss by 2 walls

2. by expansion + 4. by contraction → Form loss

Analogy model for pressure drop

Crane Technical Paper No. 410, "Fluid Mechanics" by Frank M. White

Spurk, Joseph et al. _Fluid Mechanics / by Joseph Spurk, Nuri Aksel._ 2nd ed. 2008.. Berlin, Heidelberg: Springer-Verlag, 2008.

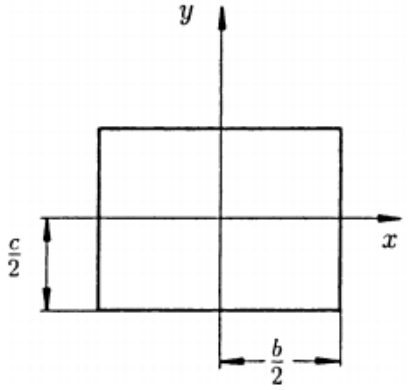

[*Hagen-Poiseuille equation*]

Assumptions

- ✓ *Incompressible fluid*
- ✓ *Laminar flow*
- ✓ *Steady state*

Boundary conditions

(1) by 4 walls

$$u\left(\pm\frac{b}{2}, y\right) = 0$$

$$u\left(x, \pm\frac{c}{2}\right) = 0$$

(2) by 2 walls

$$u(\pm\infty, y) = 0$$

$$u\left(x, \pm\frac{c}{2}\right) = 0$$

Friction loss by 4 walls

$$\Delta P_1 = \frac{12\mu QL}{bc^3}\left\{1 - \frac{c}{b}\frac{192}{\pi^5}\sum_{n=1}^{\infty}\tanh\left(\frac{c}{b}\frac{(2n-1)\pi}{(2n-1)^5}\right)\right\}^{-1}$$

Friction loss by 2 walls

$$\Delta P_2 = \frac{12\mu QL}{bc^3}$$

Form loss

$$\Delta P_3 = K\frac{\rho u_m^2}{2}$$

$$\therefore \boldsymbol{\Delta P_{out} = 2 \cdot \Delta P_1 + \Delta P_2 + \Delta P_3 + \Delta P_4}$$

b: *width* (mm)
c : *height* (mm)
Q: *volumetric flow rate* (m^3/s)
μ: *dynamic viscosity* $(Pa \cdot s)$
L: *length* (mm)
ρ: *density* (kg/m^3)
u_m: *mean flow rate* (m^2/s)
K: *form loss coefficient*

- ✓ Assuming steady-state laminar coolant flow: pressure drop in a rectangular channel is calculated. → establishment of **pressure drop analogy model** for objective function

Contents

I. Introduction

II. Methodology

III. Results and Discussions

Burst simulation results: F_{TW}(>1) distribution

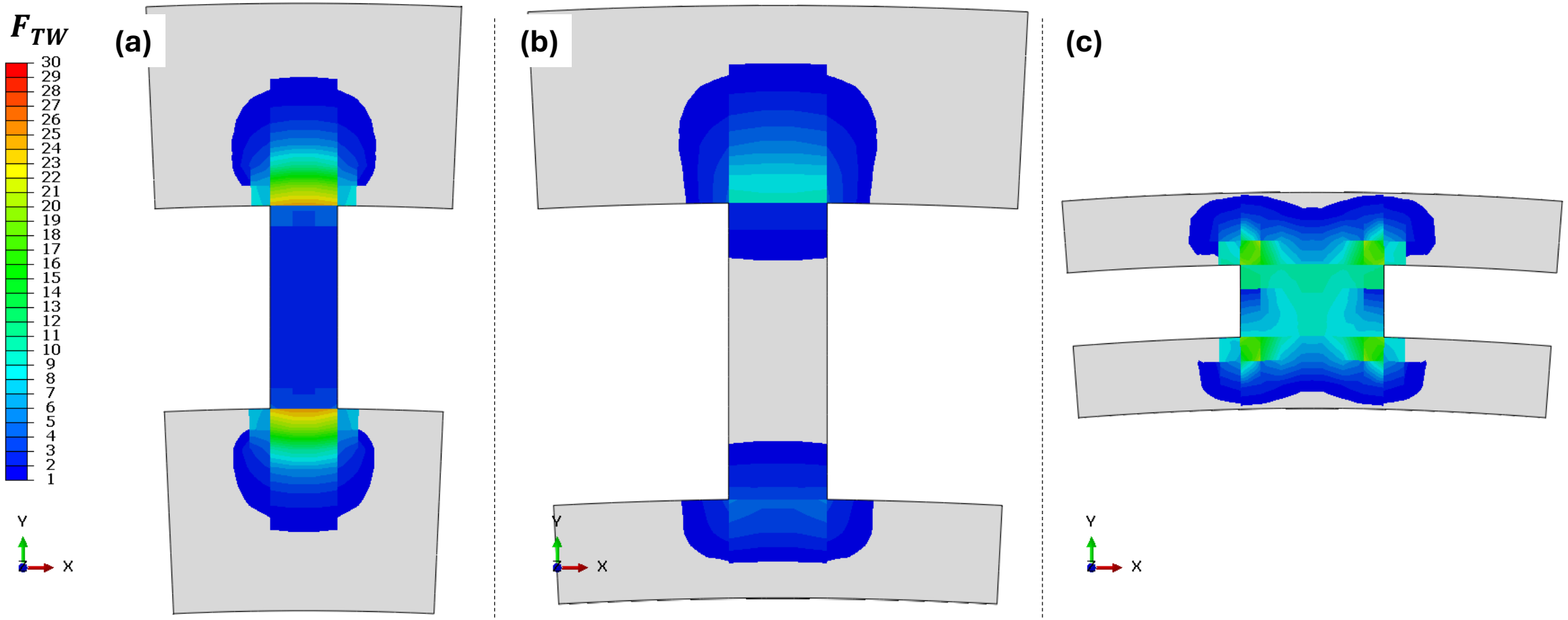

[Axial cross-sectional view of half models]

$(n_{AC}, n_{TC}, L_a, L_t, t_i, t_o, h)$

(a) combustor 1: $(\mathbf{69}, \mathbf{28}, \mathbf{1}, \mathbf{1}, \mathbf{3}, \mathbf{3}, \mathbf{3})$

(b) combustor 2: $(\mathbf{57}, \mathbf{30}, \mathbf{2}, \mathbf{3}, \mathbf{2}, \mathbf{3}, \mathbf{1})$

(c) combustor 3: $(\mathbf{44}, \mathbf{36}, \mathbf{1}, \mathbf{1}, \mathbf{1}, \mathbf{2}, \mathbf{2})$

: safe zone

Training and performance of AI models

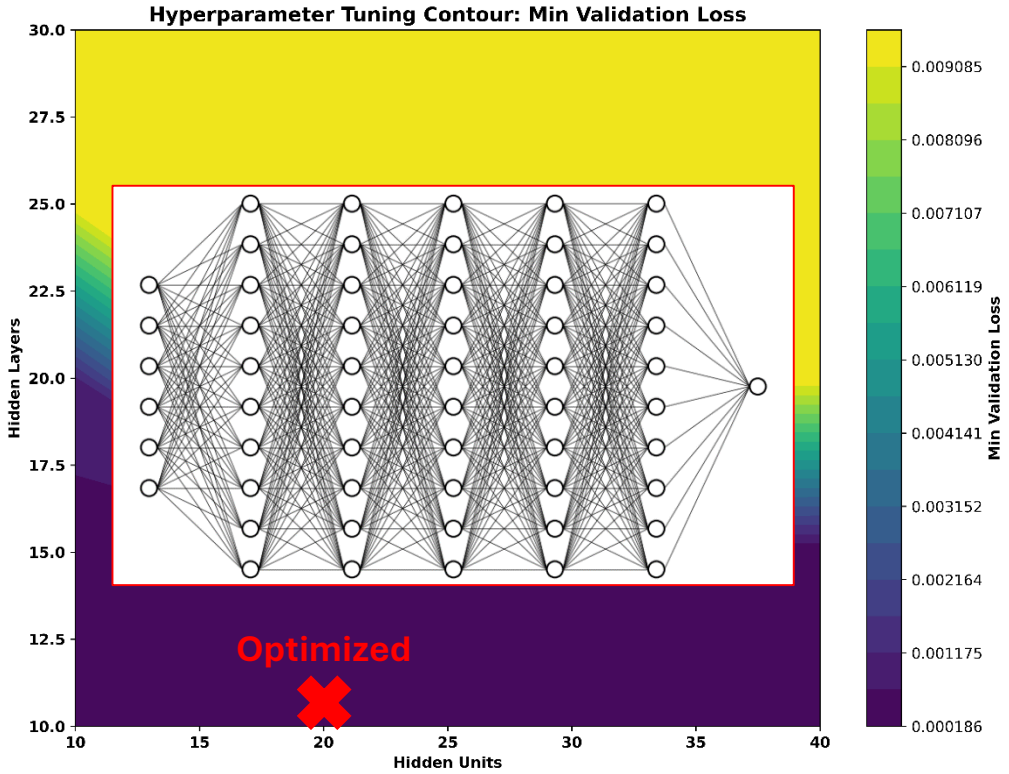

[Results of hyper parameter tuning]

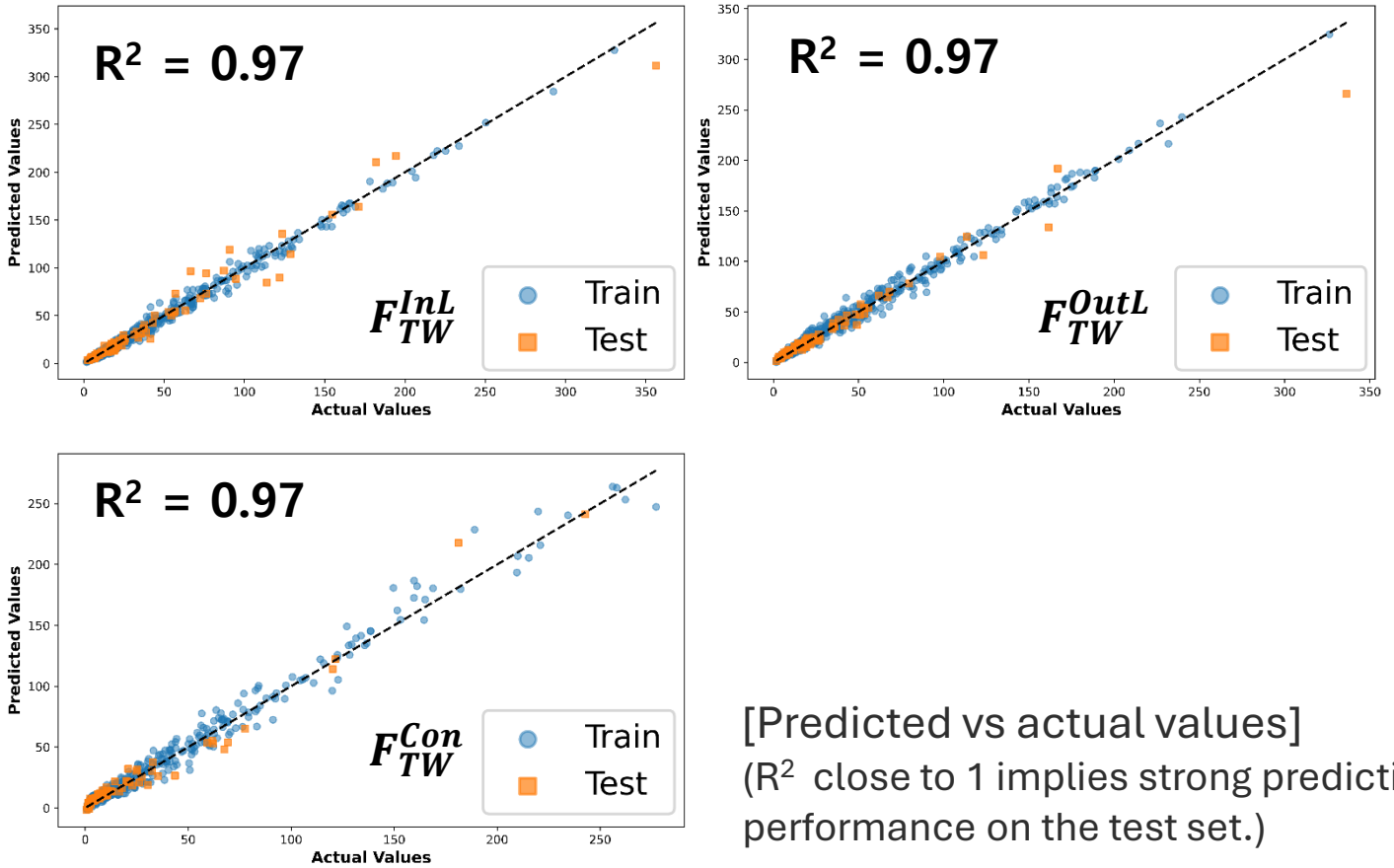

[Predicted vs actual values]
(R^2 close to 1 implies strong predictive performance on the test set.)

- ✓ **800 datasets** were obtained.
  - → Hyperparameter tuning for building a high-performance AI model architecture
- ✓ Adam optimizer, ReLU activation function, max 100-iteration learning condition

Validation of pressure drop analogy model

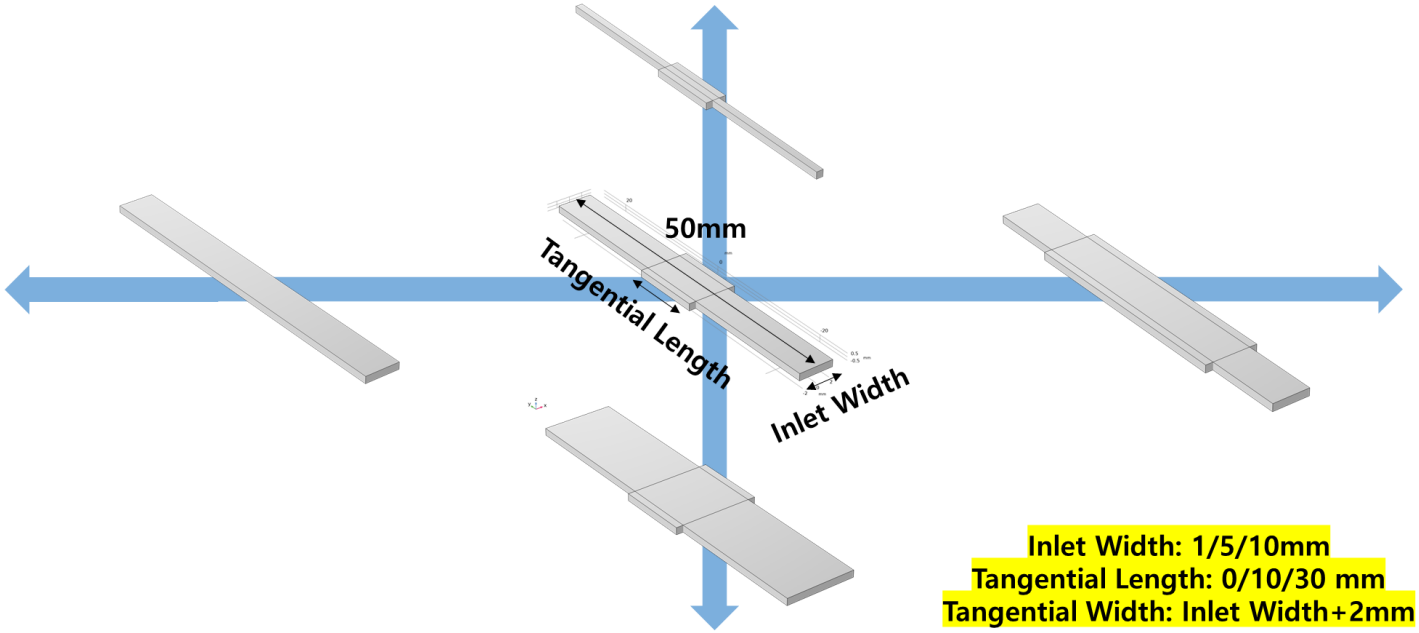

Inlet Width: 1/5/10mm
Tangential Length: 0/10/30 mm
Tangential Width: Inlet Width+2mm

[Geometric conditions of the repeating units for comparison simulations]

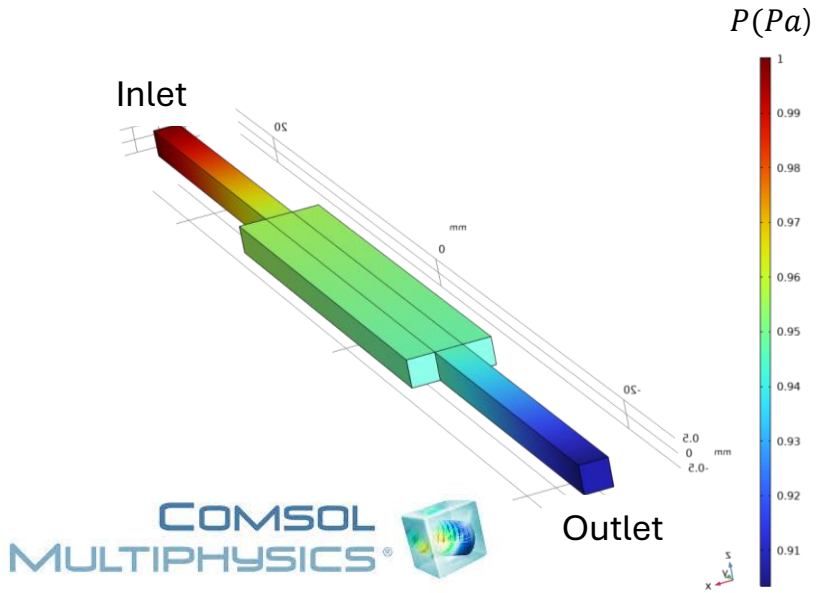

[Example of pressure drop simulation]

- ✓ The validity of the analogy model was demonstrated by comparing its results with those obtained from COMSOL.
  : water is used as coolant

		Tangential Length (mm)		
	(%)	0	10	30
Inlet Width (mm)	1	0.9	2.6	3.8
	5	1.4	3.05	3.3
	10	1.8	3.0	3.0

[Error rate of pressure drop]

Definition of optimization problem

- **Burst resistance** $f_1 = \frac{1}{3}(F_{TW}^{InL} + F_{TW}^{OutL} + F_{TW}^{Con})$

- **Weight** $f_2 = \frac{W_{connector}}{W_{connector}^{Max}}$

- **Pressure loss** $f_3 = \frac{\Delta P_{out}}{\Delta P_{Max}}$

- **Cooling** $f_4 = 1 - \frac{ConArea}{ConArea_{Max}}$

$$\begin{cases} minimize & f_1 \\ & f_2 + f_3 + f_4 \\ where, X = [n_{AC}, n_{TC}, L_a, L_t, t_i, t_o, h] \end{cases}$$

✓ Definition of 4 objective functions

f_1: AI model, f_3: analogy model

f_2: total weight of connectors, f_4: contact area

✓ Definition of a two-objective optimization problem

Exploration for $W_{connector}^{Max}$, ΔP_{Max}, $ConArea_{Max}$

***Boundary conditions**

$$10 \le n_{AC} \le 70 \qquad 1 \le L_t \le 3$$
$$20 \le n_{TC} \le 36 \qquad 1 \le t_i \le 3$$
$$1 \le L_a \le 5 \qquad 1 \le t_o \le 3$$
$$1 \le h \le 3$$

- ✓ To normalize the performance objective functions (f_2, f_3, f_4), reference values were investigated.
- ✓ Tsai–Wu-based f_1 was normalized between 0 and 1.

Region where the channel width < 4 mm

Weight

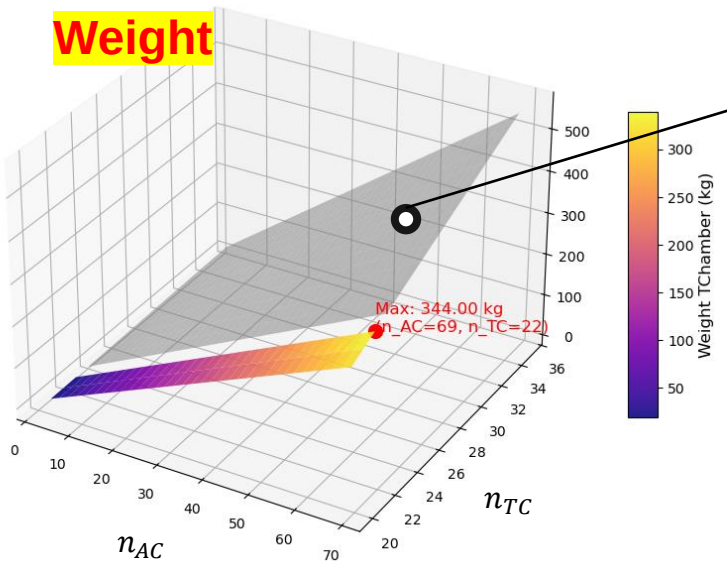

$(70, 20, 5, 3, 3, 3, 3)$

Pressure drop

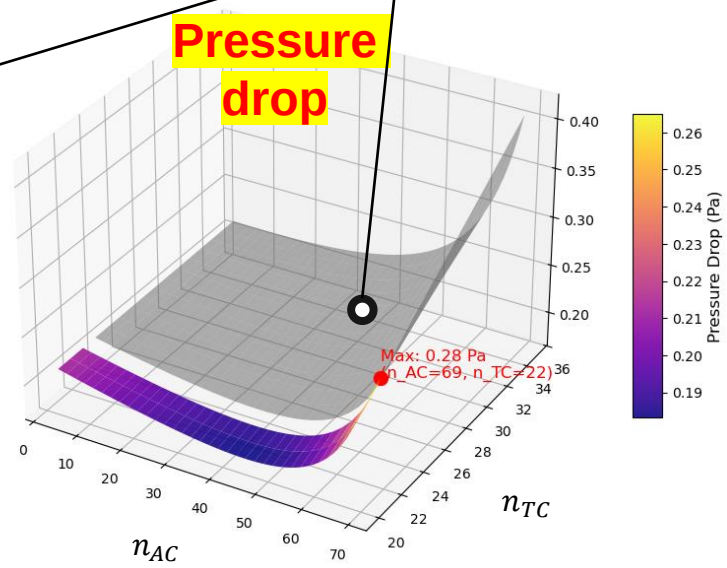

$(70, 22, 4, 3, 1, 1, 1)$

Cooling

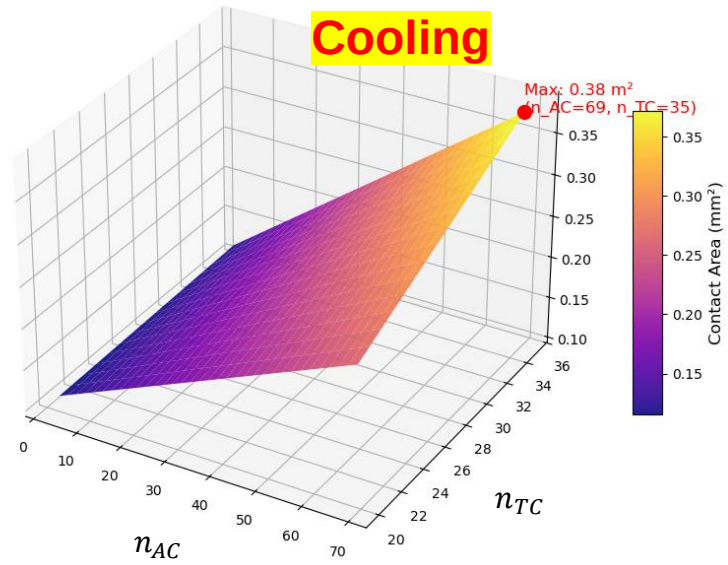

$(70, 36, 1, 3, 3, 1, 3)$

[Results of exploration]

Optimization algorithm for multi-objective problem

✓ Application of **Non-Dominated Sorting Genetic Algorithm II (NSGA-II)** via Python programming
*__NSGA-II__: a genetic algorithm-based multi-objective optimization method for deriving a single Pareto front

*Pareto front: group of optimized solutions

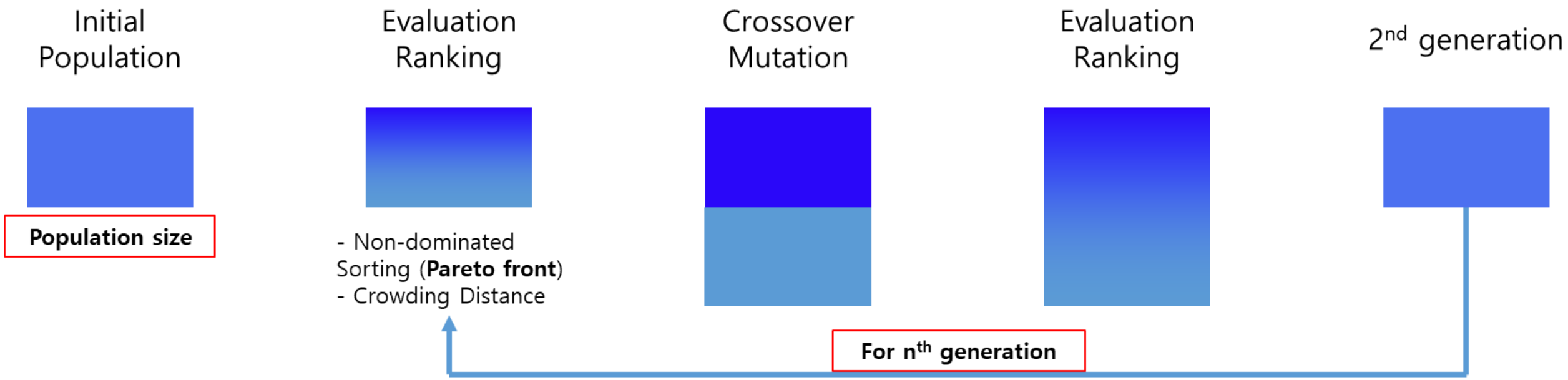

[Schematic of the working principle of NSGA-II]

✓ Conditions for optimization process: **population size = 500, the number of generation = 50**

Verma, Shanu, Millie Pant, and Vaclav Snasel. IEEE access 9 (2021): 57757-57791.

Optimization results

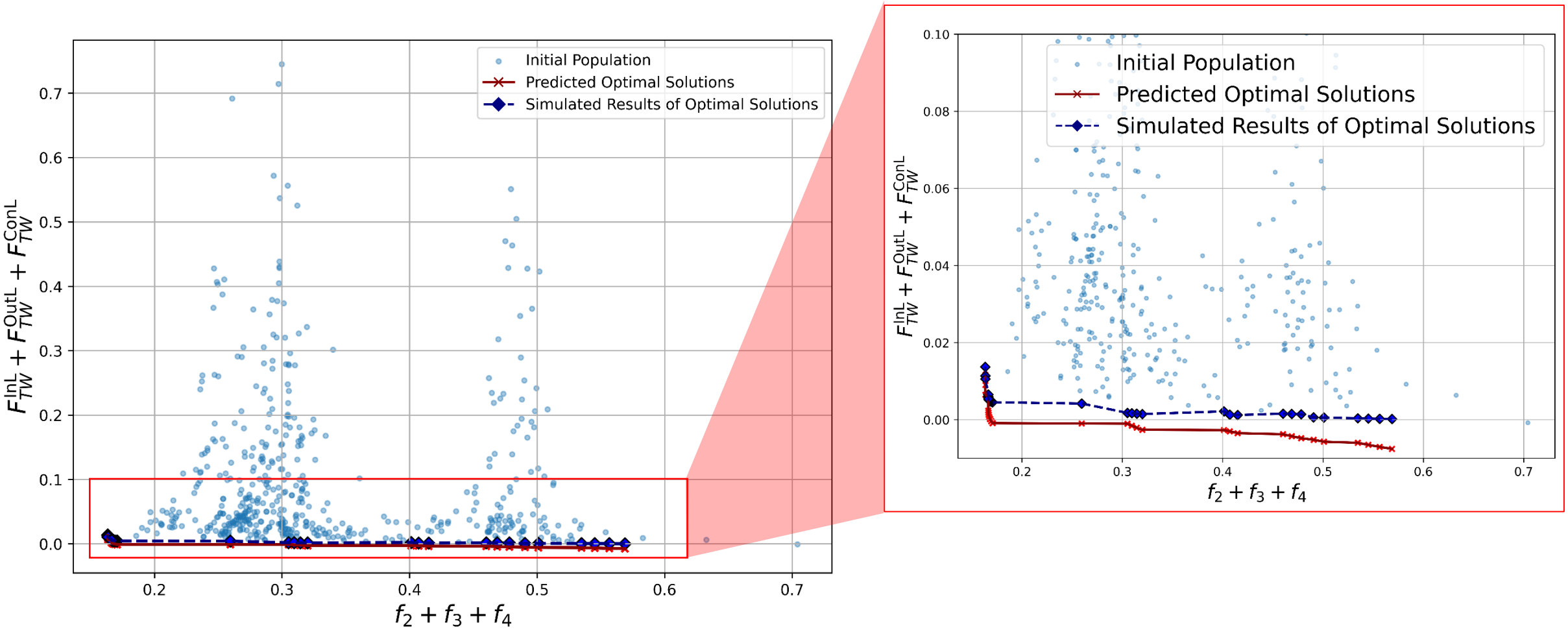

[Initial population and optimal solutions with corresponding simulation results]

Optimized combustor designs within the design space

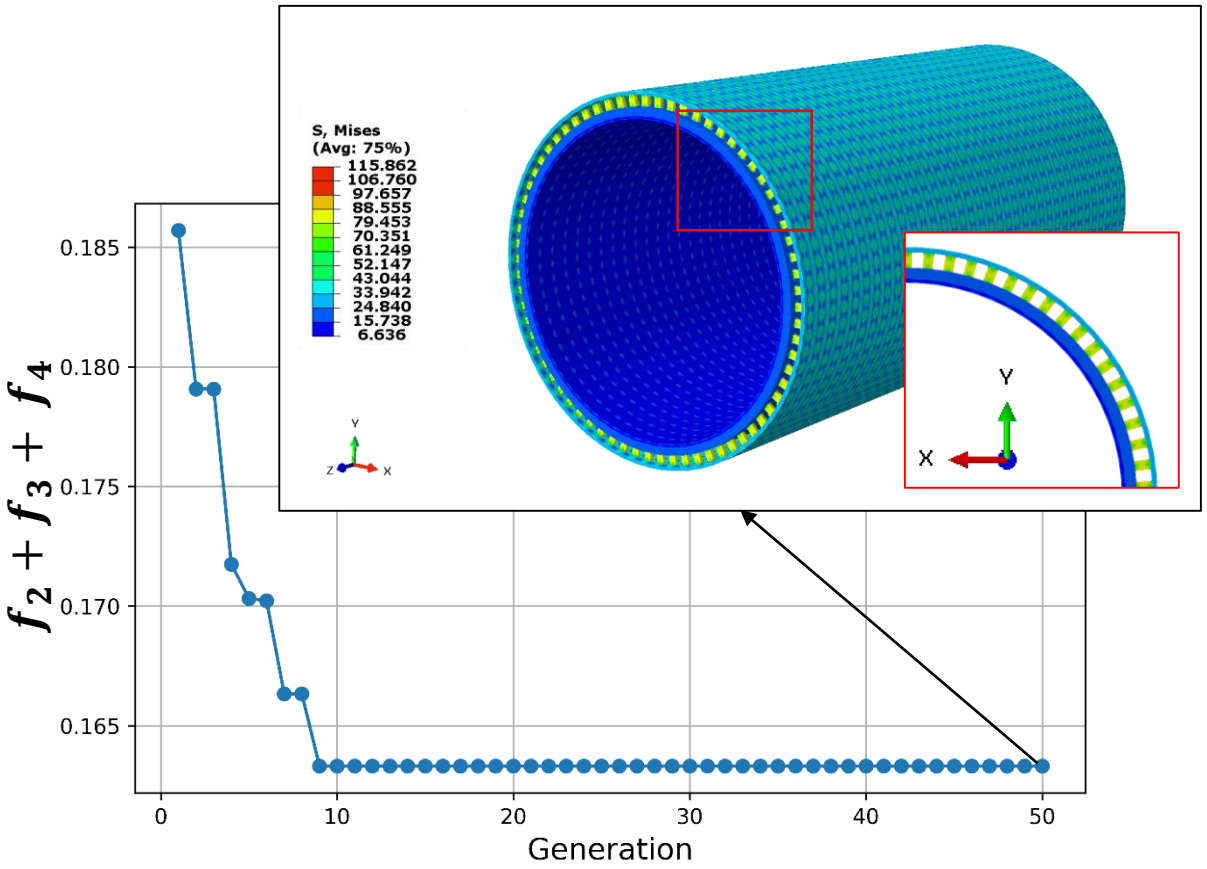

[Convergence of $f_2 + f_3 + f_4$ during optimization]

Best $f_2 + f_3 + f_4$ value in given datasets: **0.525**

	F_{TW}^{InL}	F_{TW}^{OutL}	F_{TW}^{Con}	w	ΔP	S
		-		[Kg]	[Pa]	[m^2]
Conv.	**6.37**	**6.50**	**2.69**	**87.5**	**0.024**	**0.31**

$$(n_{AC}, n_{TC}, L_a, L_t, t_i, t_o, h) = (64, 36, 1, 2, 1, 3, 3)$$

Optimization

Optimal $f_2 + f_3 + f_4$ value in given design space: **0.490**

	F_{TW}^{InL}	F_{TW}^{OutL}	F_{TW}^{Con}	w	ΔP	S
		-		[Kg]	[Pa]	[m^2]
Opt.	**4.65**	**6.60**	**4.70**	**95.2**	**0.026**	**0.33**
	$(n_{AC}, n_{TC}, L_a, L_t, t_i, t_o, h) = (70, 36, 1, 2, 3, 1, 3)$					
Sim.	**6.81**	**7.16**	**3.47**		-	

Conclusions

I. Four quantitative metrics and objective functions were established.

II. **Burst performance was predicted using AI models** and applied to structural optimization.

III. Further studies will explore **design constraints and target-based optimization**.

IV. The final composite combustor will be **seamlessly fabricated** and tested for validation.

Thank you / Q&A

Contact
woongryu@snu.ac.kr *
bbambirra@snu.ac.kr

This work was supported by Korea Research Institute for defense Technology planning and advancement (KRIT) grant funded by the Korea government(DAPA(Defense Acquisition Program Administration)) (No. KRIT-CT-23-039, Development of Hypersonic Heat Shielding Light weight Combustion Chamber Structure).

Appendix. Full model vs Half model

Full

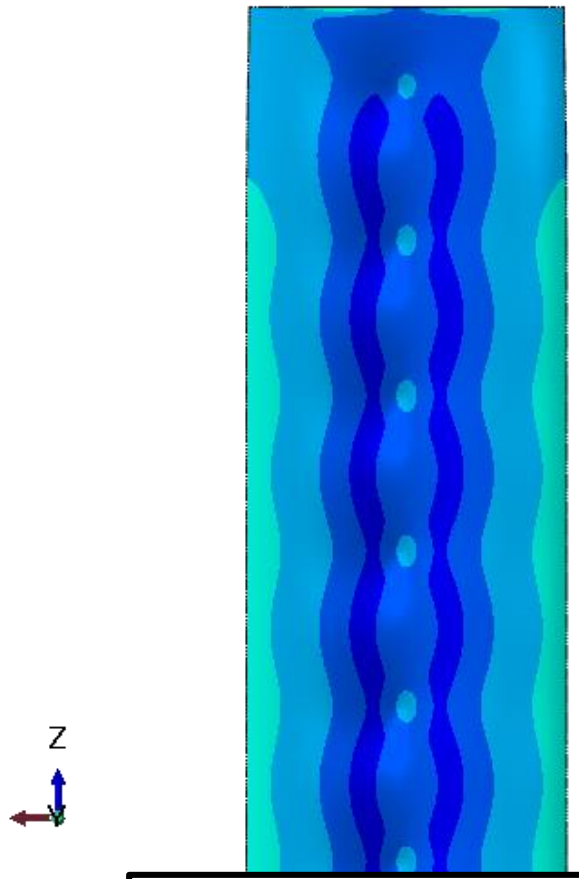

40 mins per 1 model

Half

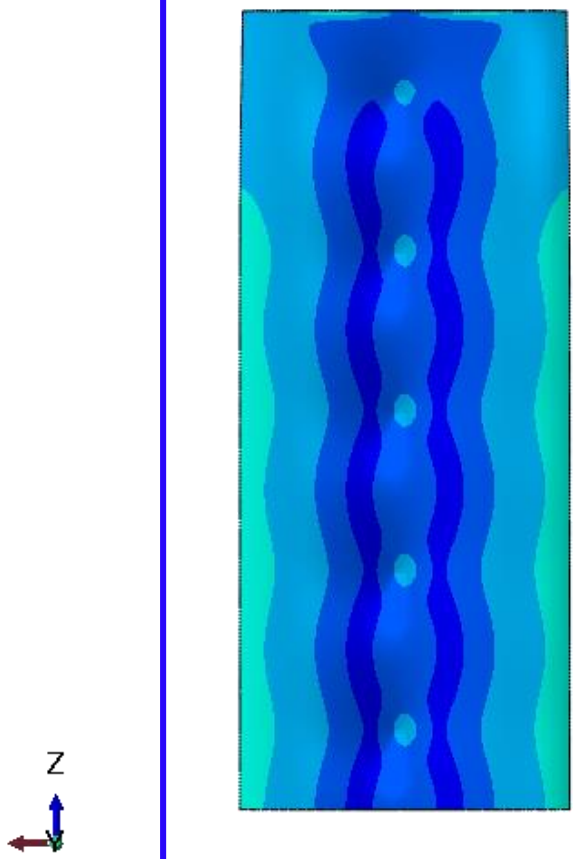

5 mins per 1 model

Appendix. Material orientation (1)

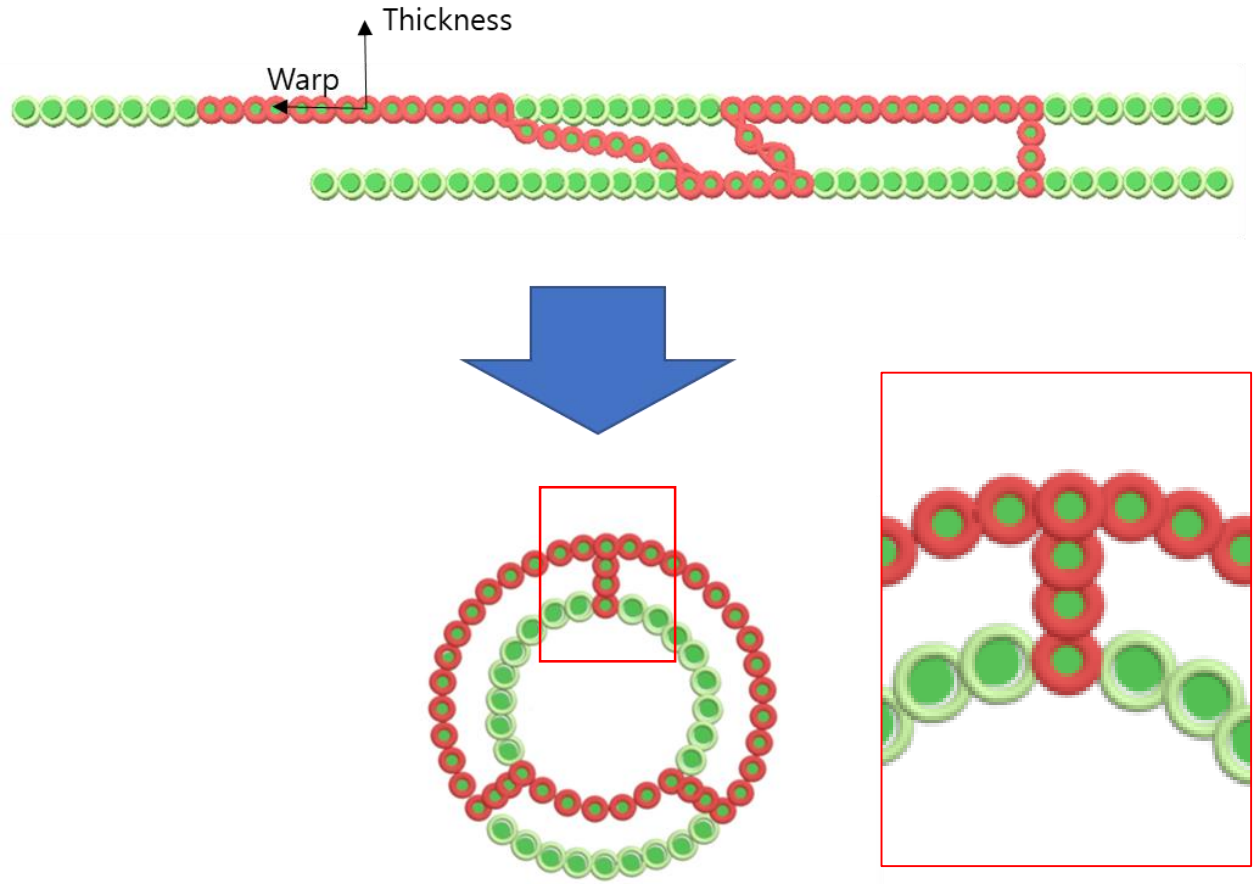

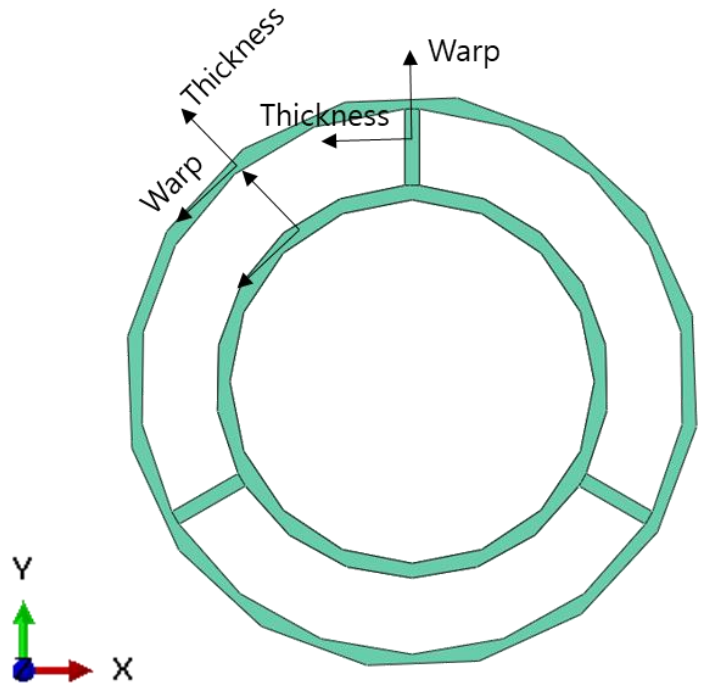

Appendix. Material orientation (2)

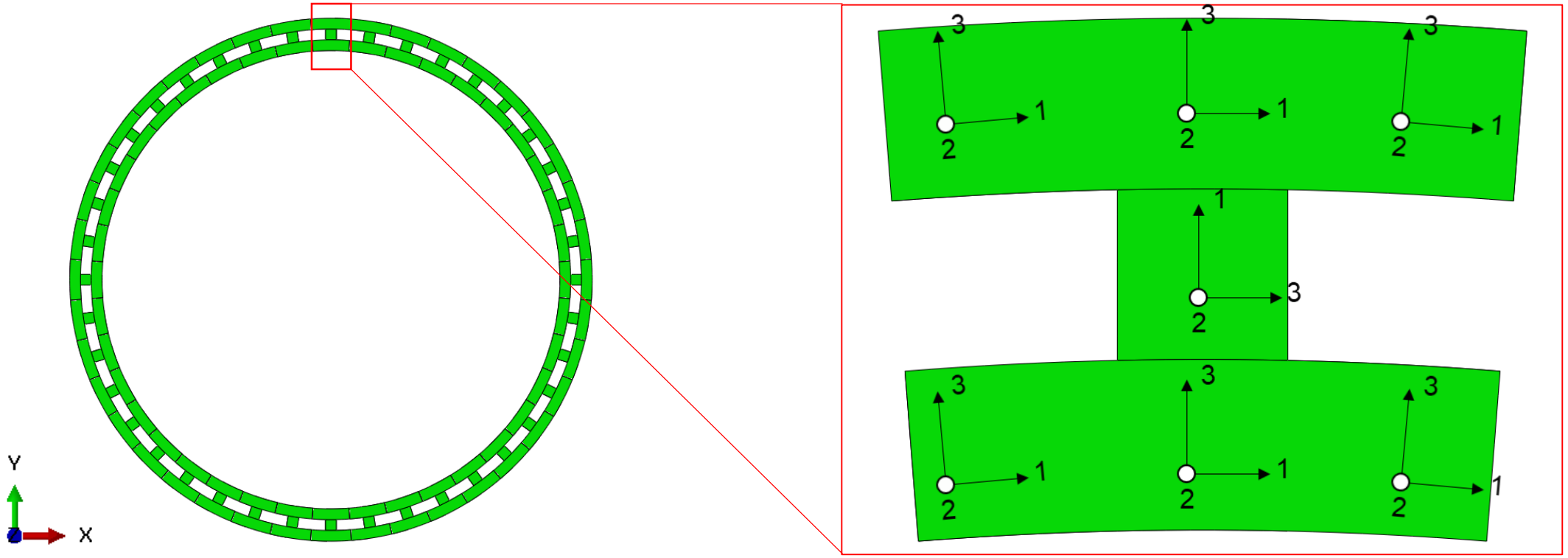

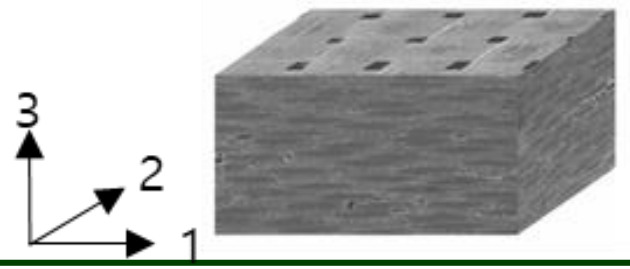

Appendix. Friction loss model

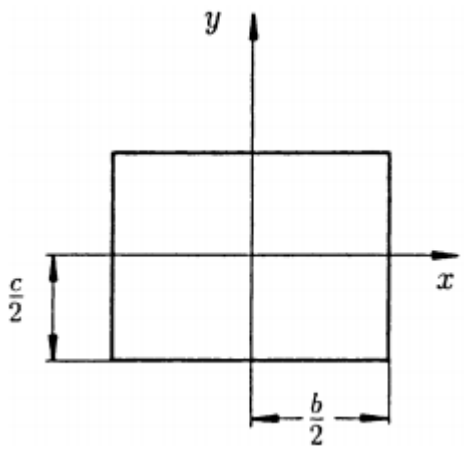

- ✓ *Incompressible fluid*
- ✓ *Laminar flow*
- ✓ *Steady state*

Friction loss by 4 walls

$$(1)\quad u\left(\pm\frac{b}{2},y\right)=0,\qquad u\left(x,\pm\frac{c}{2}\right)=0$$

$$Q=\frac{Kbc^3}{12\mu}\left\{1-\frac{c}{b}\frac{192}{\pi^5}\sum_{n=1}^{\infty}\tanh\left(\frac{c}{b}\frac{(2n-1)\pi}{(2n-1)^5}\right)\right\}$$

Friction loss by 2 walls

$$(2)\quad u(\pm\infty,y)=0,\qquad u\left(x,\pm\frac{c}{2}\right)=0$$

$$u=\frac{K}{2\mu}\left[\frac{1}{4}c^2-y^2\right]$$

$$Q=\frac{Kbc^3}{12\mu}$$

K: *the pressure gradient* (ΔP)
b: *width* (mm)
c : *height* (mm)
Q: *volumetric flow rate* (m^3/s)
μ: *dynamic viscosity* $(Pa\cdot s)$
L: *length* (mm)

Appendix. Form loss model

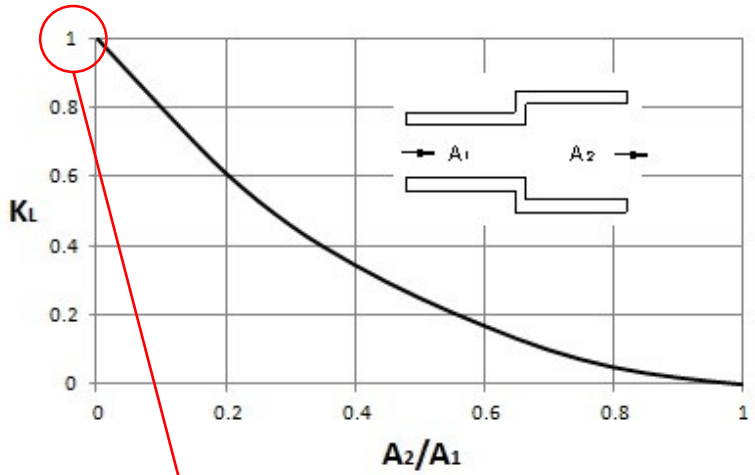

그림. form loss coefficient (Expansion)

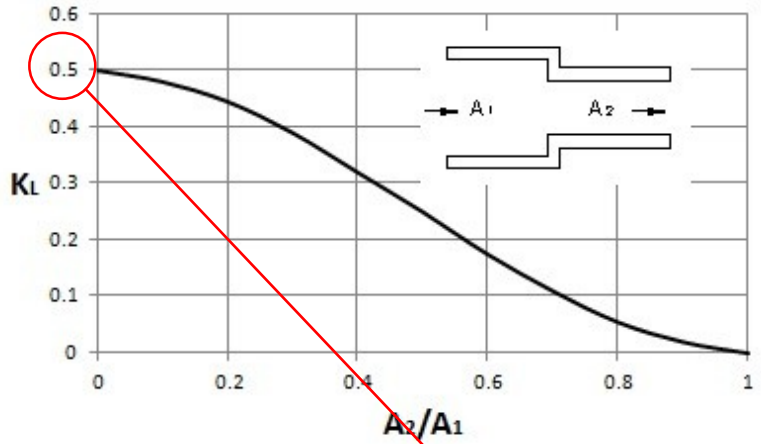

그림. form loss coefficient (Contraction)

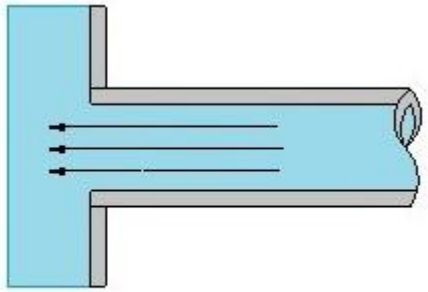

Sharp-Edged K_L=1.0

$$\Delta p = K \frac{\rho u_m^2}{2}$$

ρ: $density$ (kg/m^3)
u_m: $mean\ flow\ rate$ (m^2/s)
K: $form\ loss\ coefficient$
$K_E = (1-\sigma)^2$
$K_C = 0.5(1-\sigma)^2$
σ: $area\ ratio$

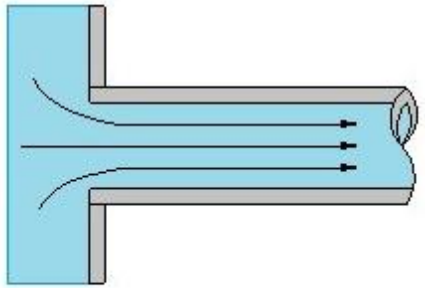

Sharp-Edged K_L=0.5

https://sbainvent.com/fluid-mechanics/minor-head-loss/

Appendix. CFD simulation conditions

Pipe	**Rectangular (3D)**	
Type	Height	Length
[-]	[h, m]	[L, m]
smooth	0.001	0.05

Fluid		**water**	
Inlet Pressure	Outlet Velocity	Density	Dynamic viscosity
[Pa]	[m/s]	[ρ, kg/m^3]	[μ, Pa·s]
1	0.0001	1000	0.001

Appendix. Equation for f_2, f_4

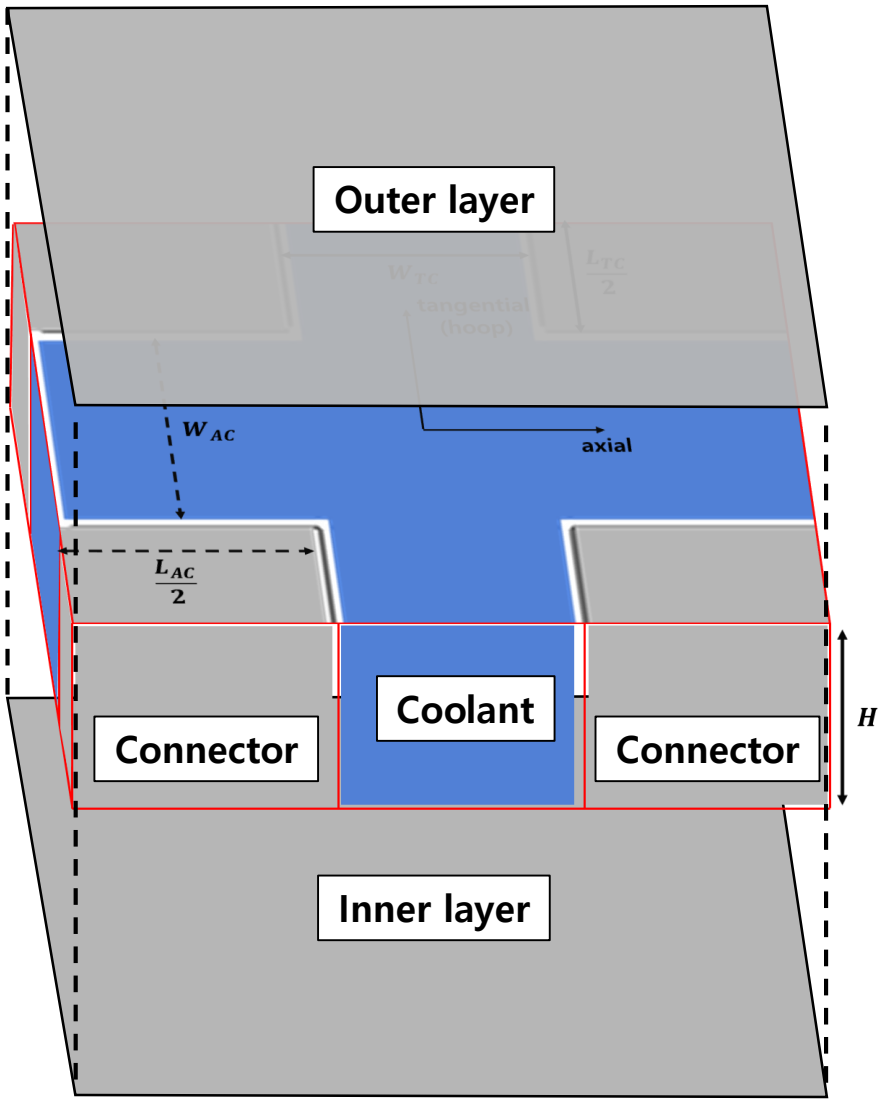

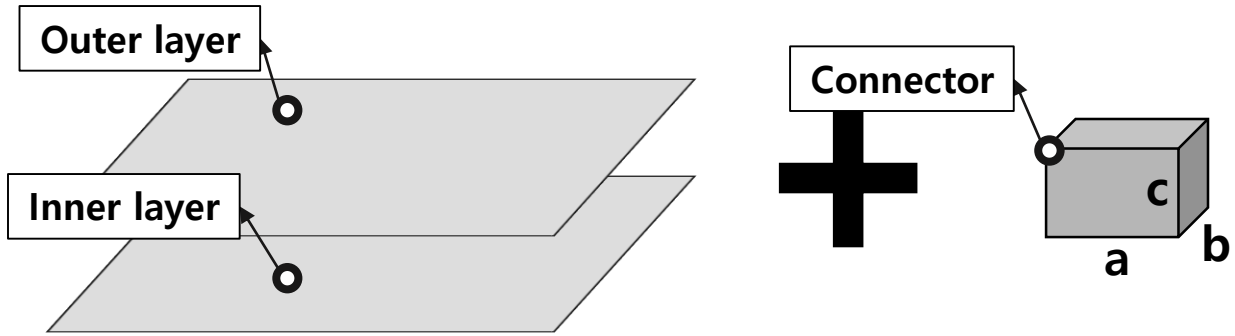

$$\therefore for\ f_2, Weight$$
$$= density\ of\ CMC\ * n_{AC}(n_{TC} - 1)\ * abc$$

$$\therefore for\ f_4, Total\ Contact\ Area\ (ConArea)$$
$$= Area\ of\ Inner\ layer + Area\ of\ Outer\ Area$$
$$+ n_{AC}(n_{TC} - 1)(2(ac + bc) - 2ab)$$



Deep-learning-guided Particle Filter for Remaining Useful Life Estimation of Composite Materials

So Young Oh[a†] · Björn Beck[b] · Frank Henning[b] · In Yong Lee[c] · Young-Bin Park[a*]

[a] Department of Mechanical Engineering, UNIST

[b] Fraunhofer Institute for Chemical Technology

[c] Department of Mechanical Engineering, Dong-A University



FIMLab
Functional Intelligent Materials Lab

UNIST

Research Motivation

*CFRP: Carbon-fiber-reinforced plastic
*PdM: Predictive maintenance

+ Material properties
+ Industrial application

– High material cost
– Low repairability

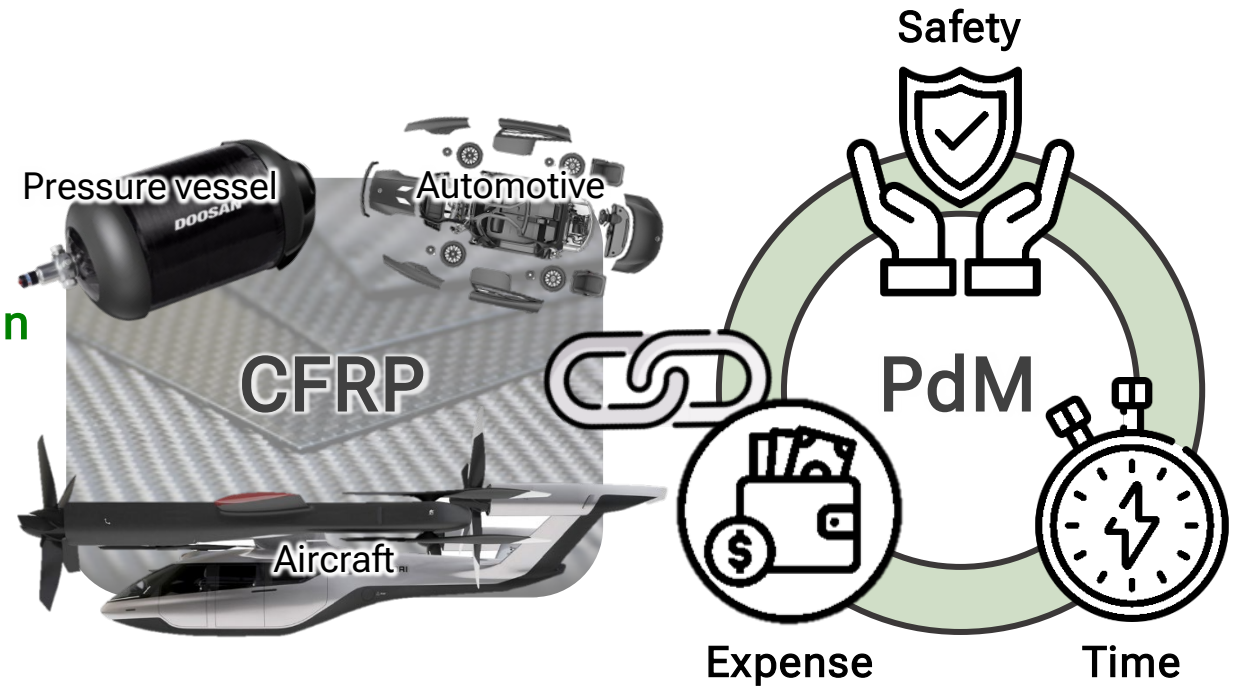

+ Prevents unexpected failures
+ Reduces operational cost
+ Efficient repair scheduling

➢ Remaining Useful Life

- CFRPs have abundant potential industrial applications owing to their various advantages.
- PdM denotes a real-time analysis to predict potential damages which may lead to failure.
- **Application of PdM into CFRPs** is highly required for their longevity and efficiency.

Research Motivation: Existing CFRP SHM Studies

*CFRP: Carbon-fiber-reinforced plastic
*SHM: Structural health monitoring

	Self-sensing	Fiber Bragg grating	C-scan
Installation	Built-in sensor network (CFs serve as self-integrated sensors) Cost ↓	Expensive and laborious	Scanning pool and a scanner are required
Monitoring	In-situ real-time	Real-time with extra sensing devices	Schedule-based
Adaptability	No limitations	Brittle sensing device with limited to geometric shape	Frequency setting is required
Geometry	No limitations	Limited to geometric shape (sensor installment)	Plate-shaped
Sensor arrangement	Array or periphery (beneficial for large structures)	Array with numerous data channels	Limited to the scanning pool size

- **Self-sensing** is advantageous for real-time health status monitoring over other SHM/NDT technologies.

Research Motivation: Self-sensing

*CFRP: Carbon-fiber-reinforced plastic

Microscopic view

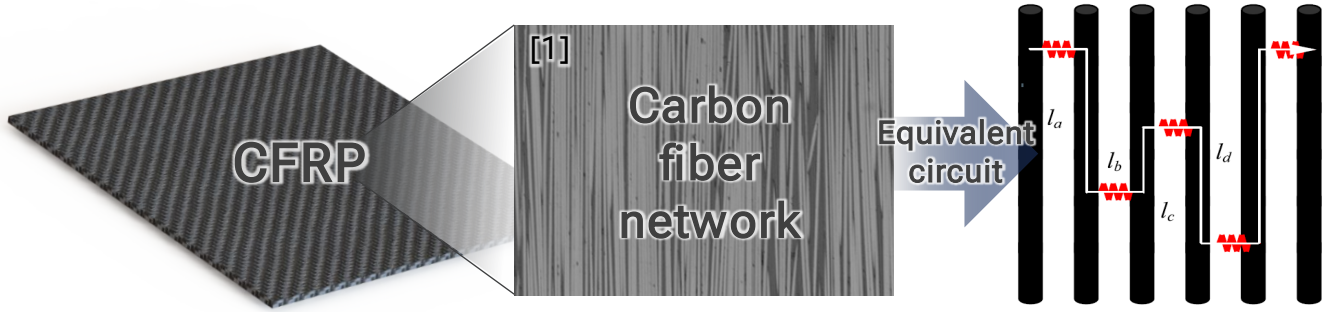

Macroscopic view

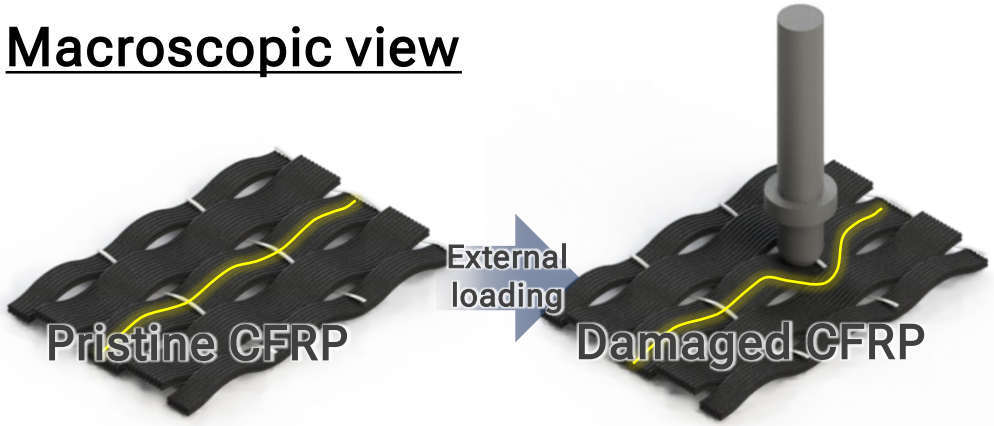

Self-sensing

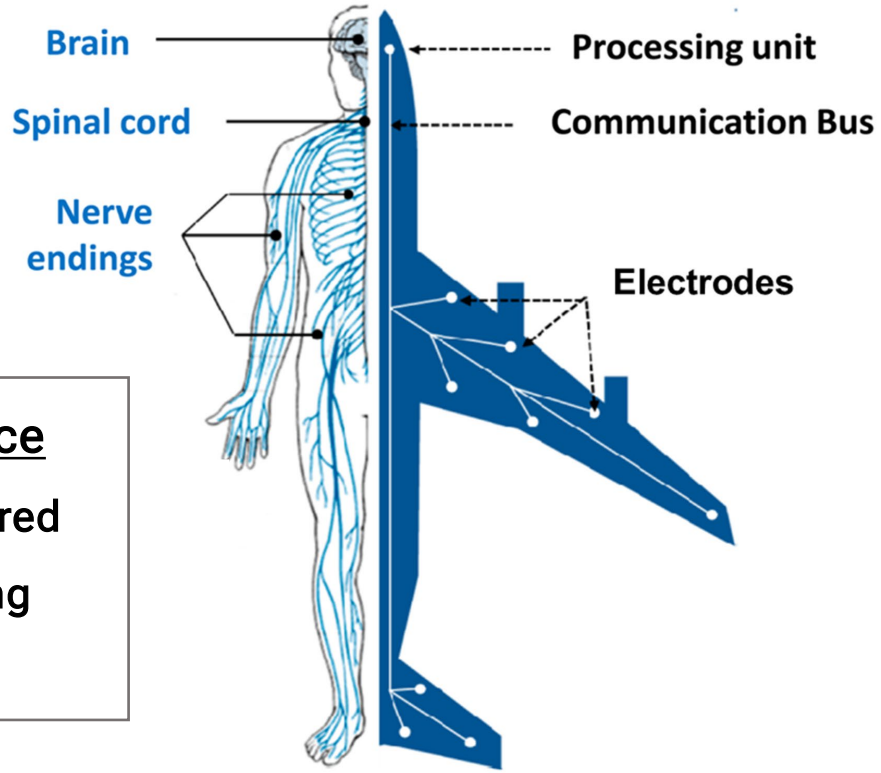

Electrical resistance

- Real-time measured
- Simple processing
- Fewer sensors

- **Self-sensing** employs the inherent electrical network consisted of carbon fibers.
- Damages in CFRPs can be electromechanically characterized by **electrical resistance**.

[1] Park, J. B., et al. (2006). *Smart Mater. Struct.*, *16*(1), 57.

Experimental Details: CFRP Fatigue Test

*CFRP: Carbon-fiber-reinforced plastic

CFRP specimen

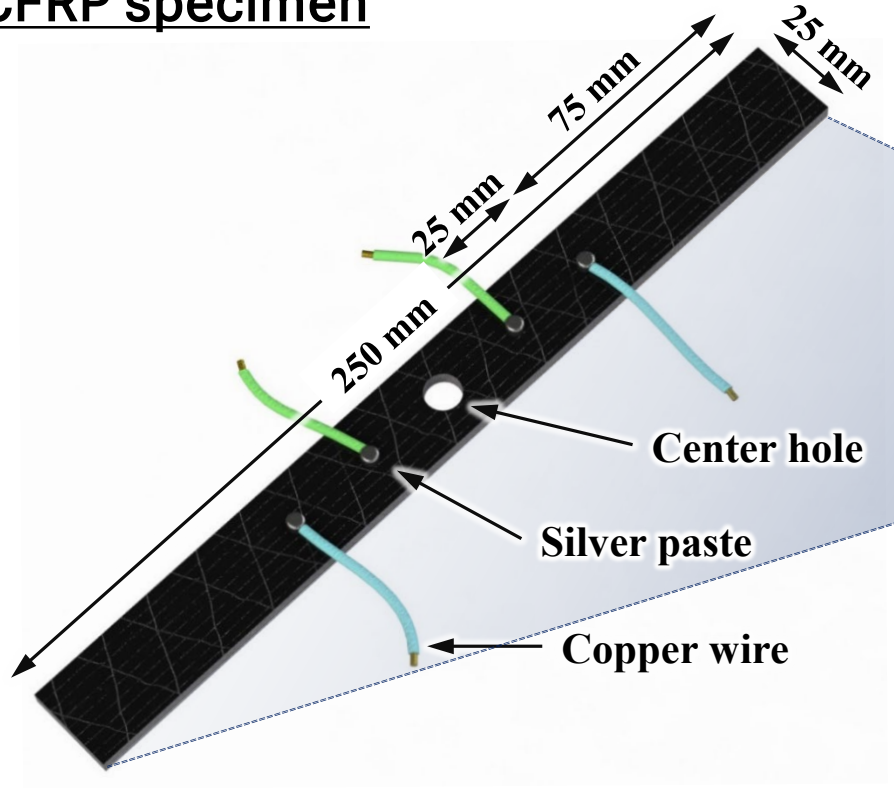

Fatigue test

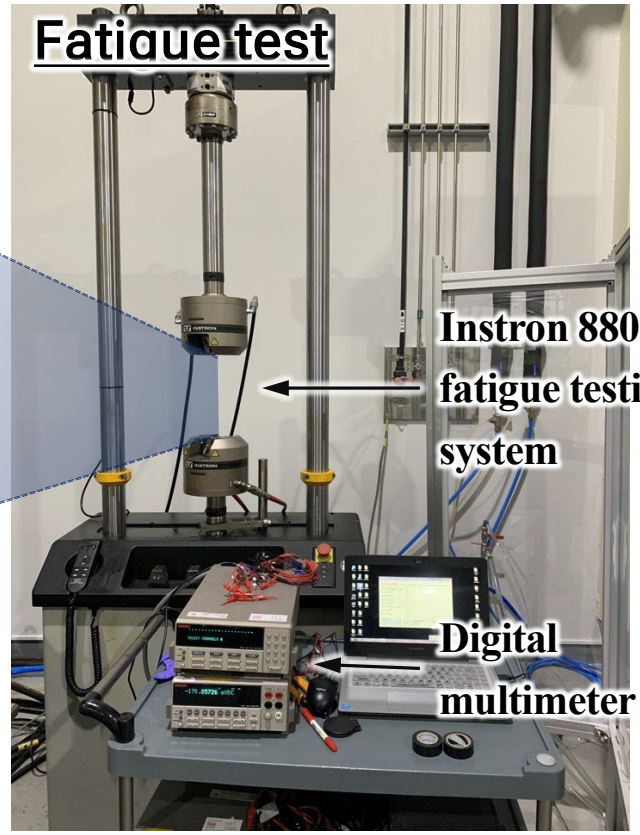

Sample specification

- $[0_2/45_2/-45_2/90_2]$
- $[0/\pm45/90]_s$

Test specification

- $S_{max} = 0.6 * UTS$
- $S_{min} = 0.1 * S_{max}$
- Loading frequency = 3 Hz

Measurement specification

- 4-probe measurement

- Repetitive operation of a system significantly influences its lifespan. → **Fatigue test**
- **Electrical resistance signal** was simultaneously measured with the test.

Results: Electromechanical Analysis

*CFRP: Carbon-fiber-reinforced plastic

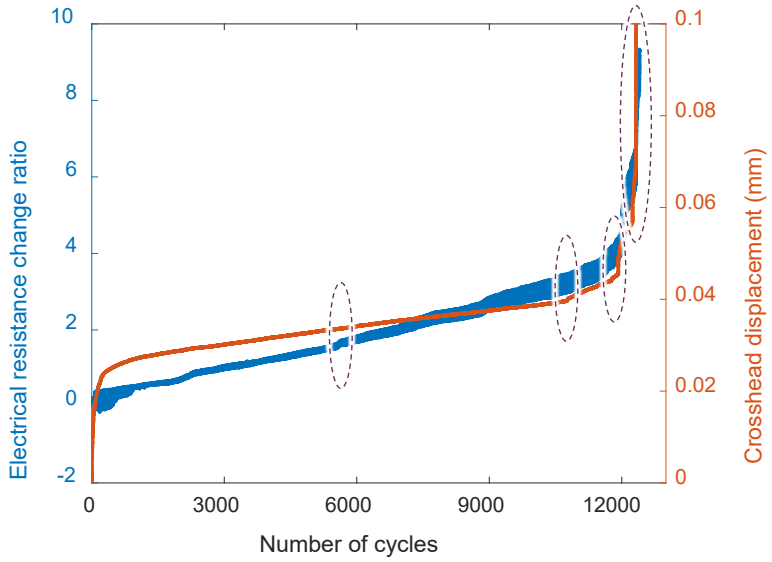

$[0_2/45_2/-45_2/90_2]$

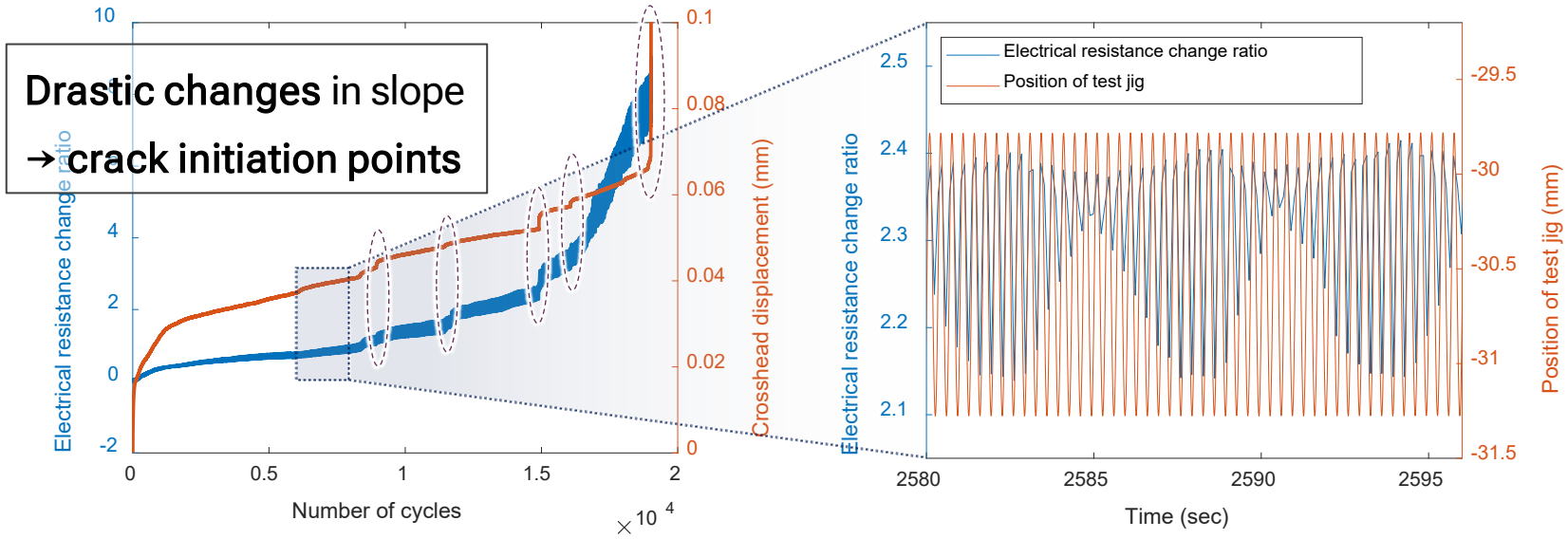

$[0/\pm45/90]_s$

Loading & unloading detection

- Overall electrical resistance increased with a decrease in number of fiber contact points and load-bearing capacity of CFRPs.

→ **The electrical resistance signal can be considered as health indicator of composites.**

RUL Prediction Strategies

Physics-based model	Data-driven model
+ Solid foundation of system + Easy to generalize + Interpretable	+ No priori understanding required + Can be improved with more data + Extensible to new observations
– Sensitive to numerical instability – Requires deep domain experts – Vulnerable to new data	– Black boxy – Requires large dataset
➢ **Knowledge-dependent**	➢ **Data-dependent**

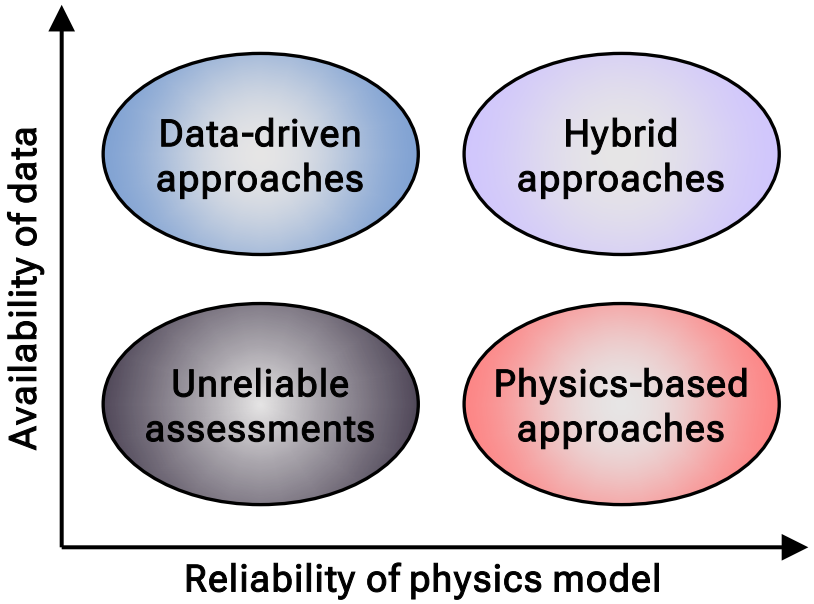

1. Feedforward neural network (FFNN) ➔ Data-driven
2. Long short-term memory (LSTM) ➔ Data-driven
3. Physics-informed neural network (PINN) ➔ Hybrid
4. Deep-learning-guided particle filter (DLG-PF) ➔ Hybrid *Newly proposed!

Performance comparison

Comparative Study: FFNN

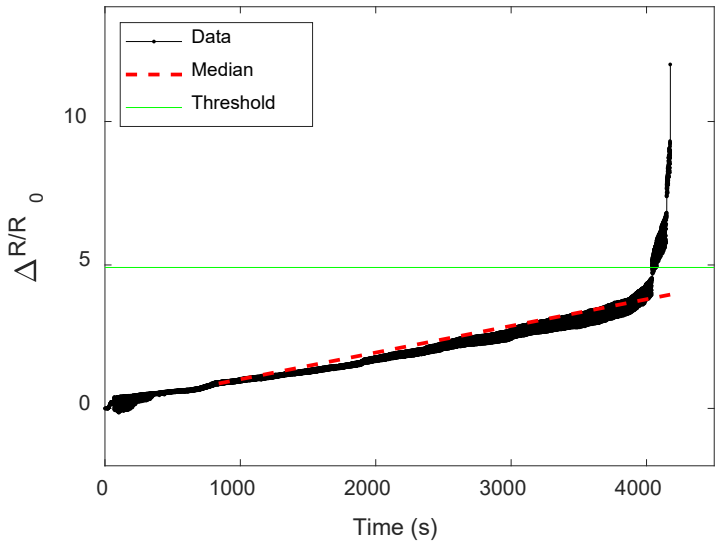

$[0_2/45_2/-45_2/90_2]$

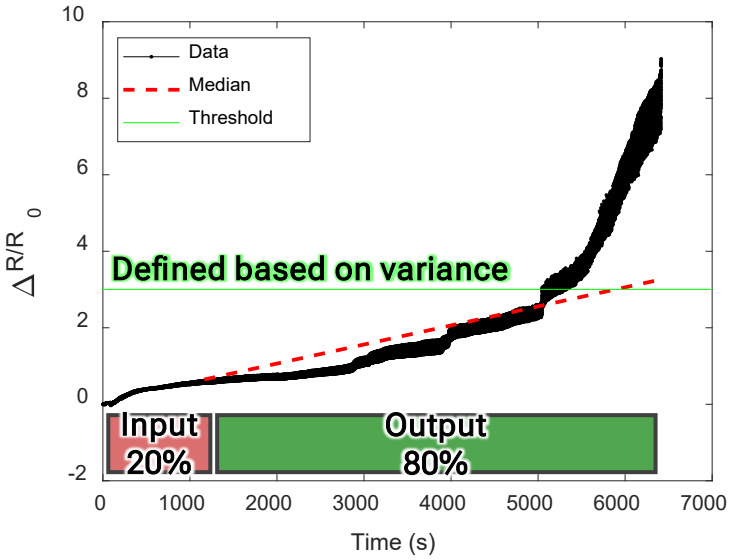

$[0/\pm45/90]_s$

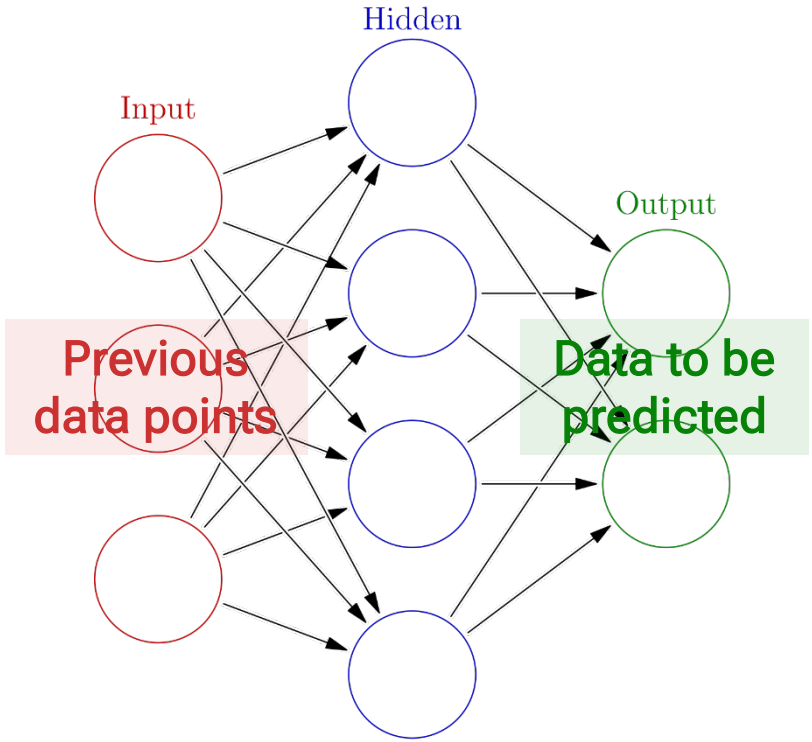

- FFNN performed **3-point extrapolation** using early 20% of observation.
- The result showed **linear propagation** due to the electromechanical behavior in elastic regime.
- Results from data-driven approach **highly depend on the input training data.**

Comparative Study: LSTM

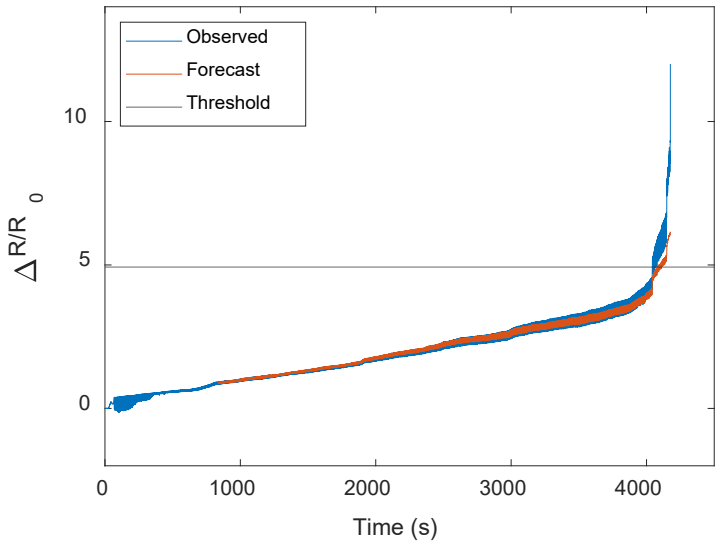

$[0_2/45_2/\text{-}45_2/90_2]$

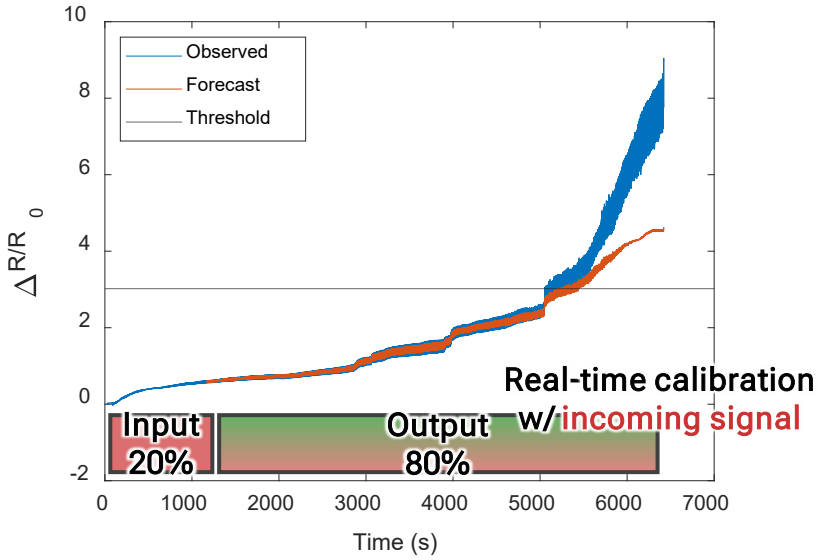

$[0/\pm45/90]_s$

Data to be predicted

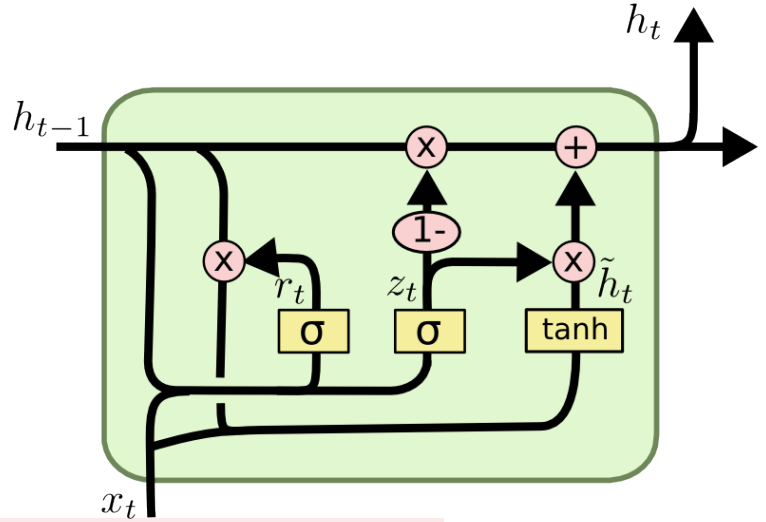

Previous data points

- LSTM performed **3-point extrapolation** using early 20% of observed data.
- LSTM was firstly trained with the early data, then **re-trained** with simultaneously incoming data.
- **Long training time and high computational cost** are required.

Comparative Study: PINN

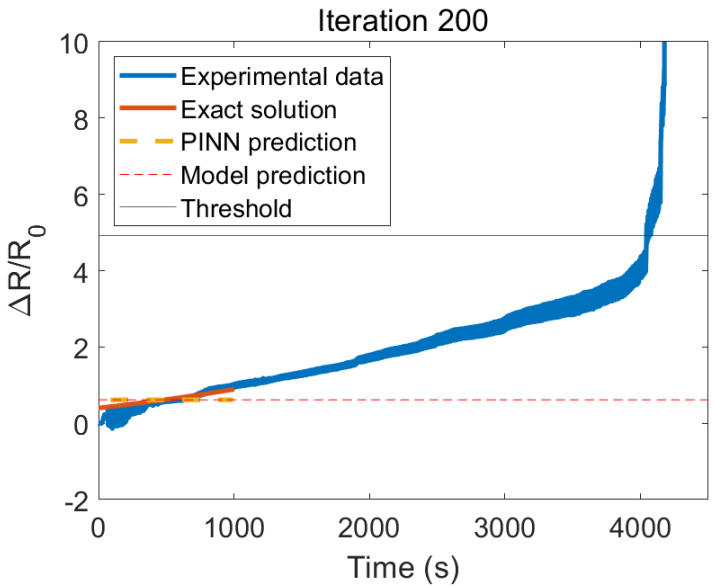

$[0_2/45_2/\text{-}45_2/90_2]$

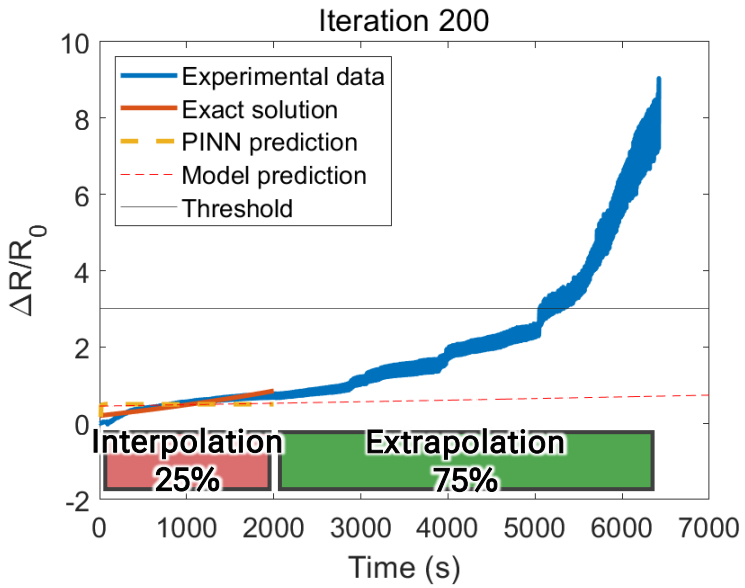

$[0/\pm45/90]_s$

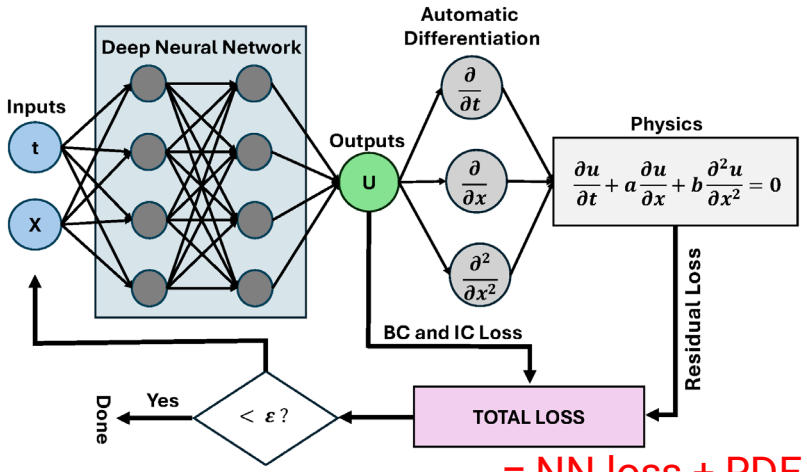

= NN loss + PDE loss

Degradation model $R_k = e^{bx} \times R_{k-1}$

$$\frac{\partial R}{\partial t} = \lambda \cdot R(t) \qquad {}^*\lambda(t) = \frac{e^{b(t)} - 1}{\Delta t}$$

- PINN **interpolates** the early data by optimizing the pre-defined loss function and predicts the signal propagation using **extrapolation** adopting the exponential degradation model.
- The whole process requires multiple parameter input, which are highly **operator-dependent**.

Hybrid Approach: Deep-learning-guided Particle Filter

*LSTM: Long short-term memory

How to handle knowledge-dependent characteristic of physics-based approaches?

→ 'What if machine learning sets the boundaries?'

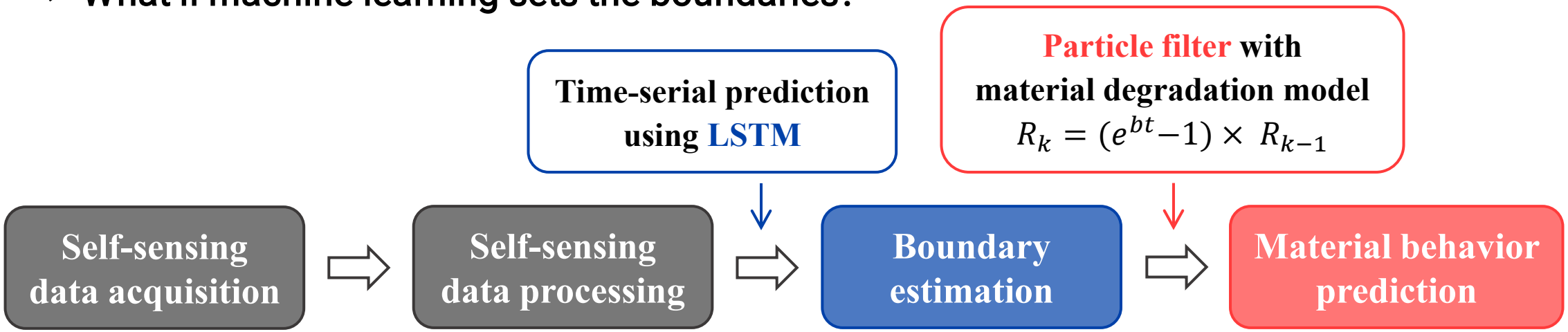

- **LSTM** *Data-driven
  - stores information over long series
  - robust to gradient vanishing problems

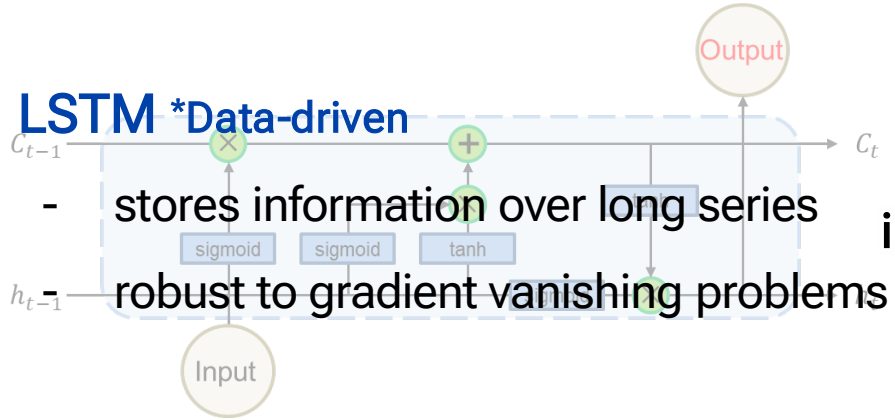

Define initial condition

- **Particle filter** *Physics-based
  - is suitable for non-linear models.
  - employs an exponential function as a physical model.

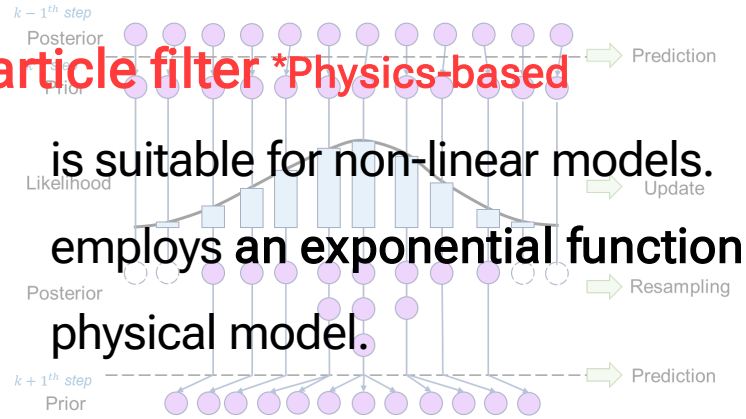

Hybrid Approach: Deep-learning-guided Particle Filter

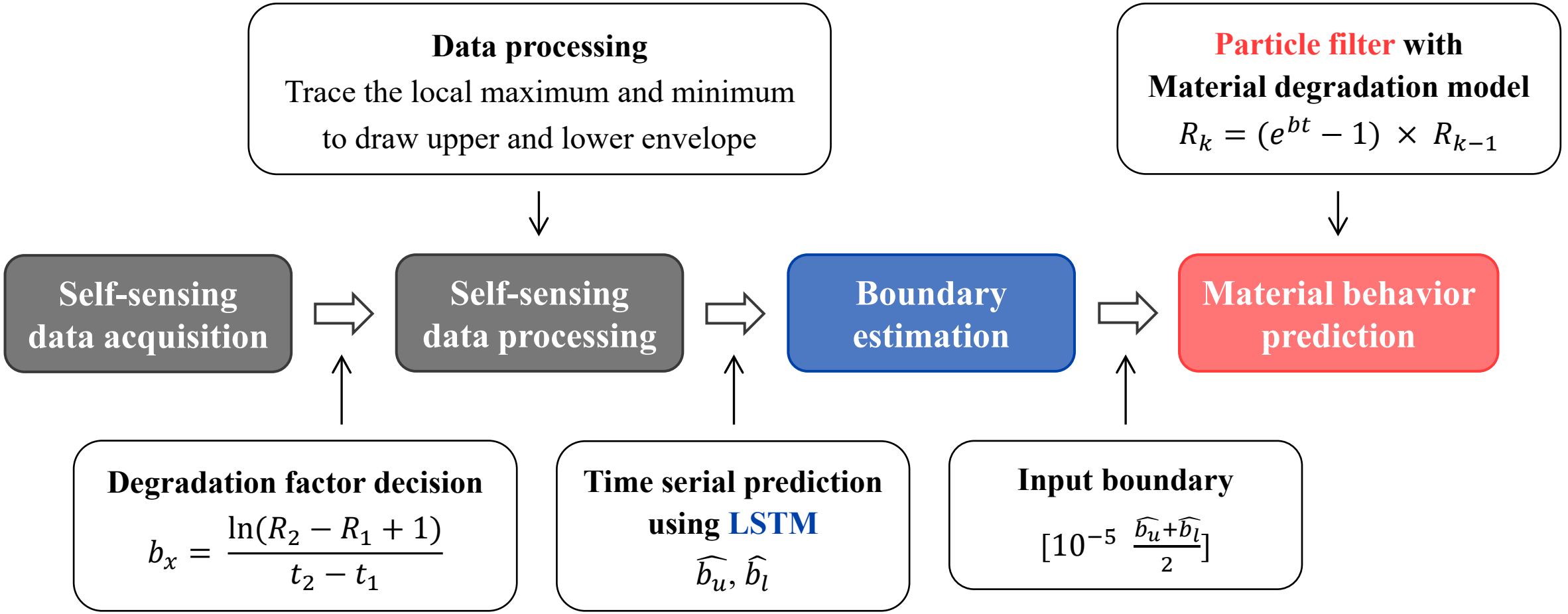

Know-how: Electrical resistance increases under tensile load

Hybrid Approach: Deep-learning-guided Particle Filter

*RUL: Remaining useful life

Material degradation model $z_k = e^{bx} \times z_{k-1}$

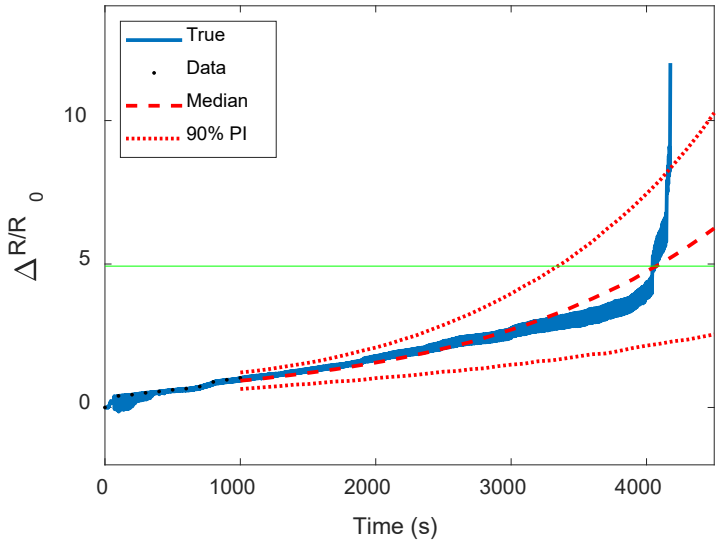

$[0_2/45_2/\text{-}45_2/90_2]$

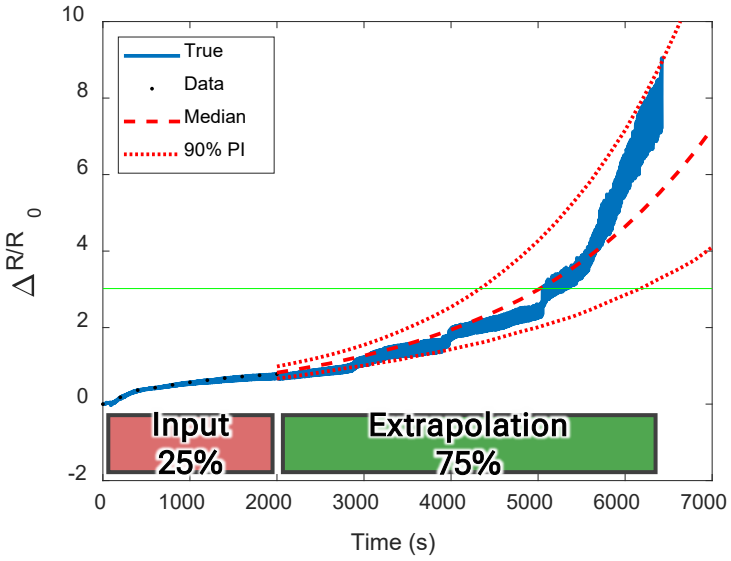

$[0/\pm45/90]_s$

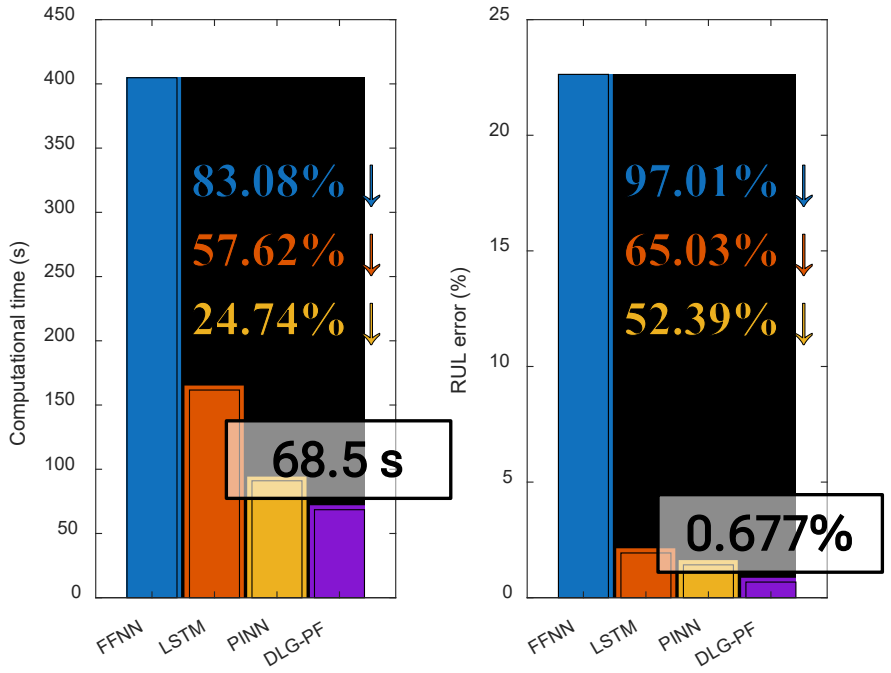

- Particle filter estimates the propagation of the electrical resistance signal and predicts RUL using the LSTM-defined initial condition.
- **DLG-PF significantly reduced computational time and RUL error** compared to conventional RUL prediction approaches.

Suggestions on Degradation Model: Global Load Sharing

*CFRP: Carbon-fiber-reinforced polymer
*DC: Direct current

Assumptions

1. Load lost by fiber breakage will be transferred equally to all intact fibers.
2. Each fiber can be considered as a resistor; CFRPs can be approximated into DC circuit.

Stress-strain relation

$$\sigma = \underbrace{fE_f\varepsilon\left(1-\frac{1}{2}\left(\frac{E_f\varepsilon}{\sigma_c}\right)^{m+1}\right)}_{\text{fiber}} + \underbrace{(1-f)\sigma_y}_{\text{matrix}} \qquad (1)$$

Apply (1) to circuit model

$$\frac{\Delta R}{R_0} = \frac{(1+\alpha\varepsilon)}{1-N_f/N} - 1 = \frac{(1+\alpha\varepsilon)}{exp\left[-\left(\frac{\delta_{ec}}{L_0}\right)\left(\frac{E_f\varepsilon}{\sigma_0}\right)^m\right]} - 1$$

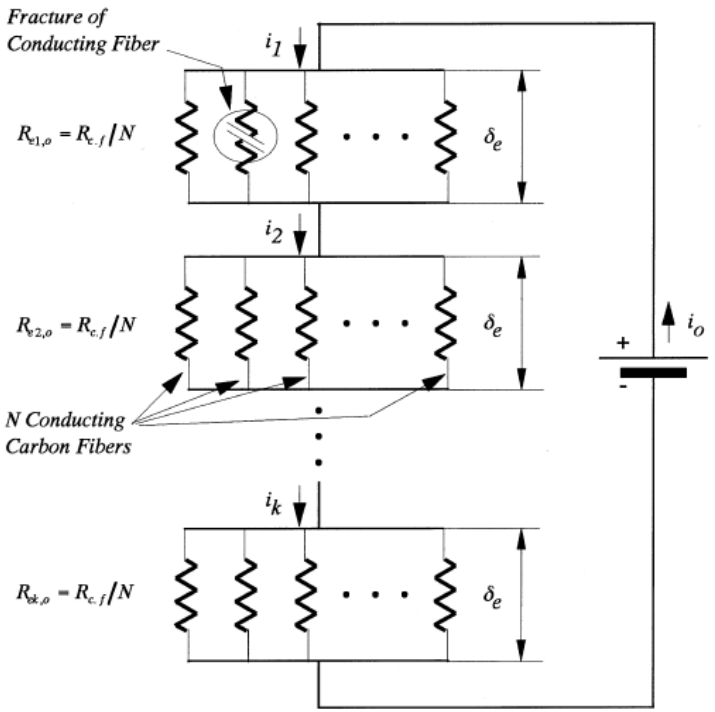

$$i_o = i_1 = i_2 = \cdots = i_k$$

$$R_{e1} > R_{e2} = R_{e3} = \cdots = R_{ek}$$

DC series circuit with equally spaced discrete parallel cells

[2] Park, J. B., et al. (2002). Compos Part A, 33(2), 267-275.

Suggestions on Degradation Model

*GLS: Global load sharing
*CFRP: Carbon-fiber-reinforced plastic

Case I. Employ GLS model

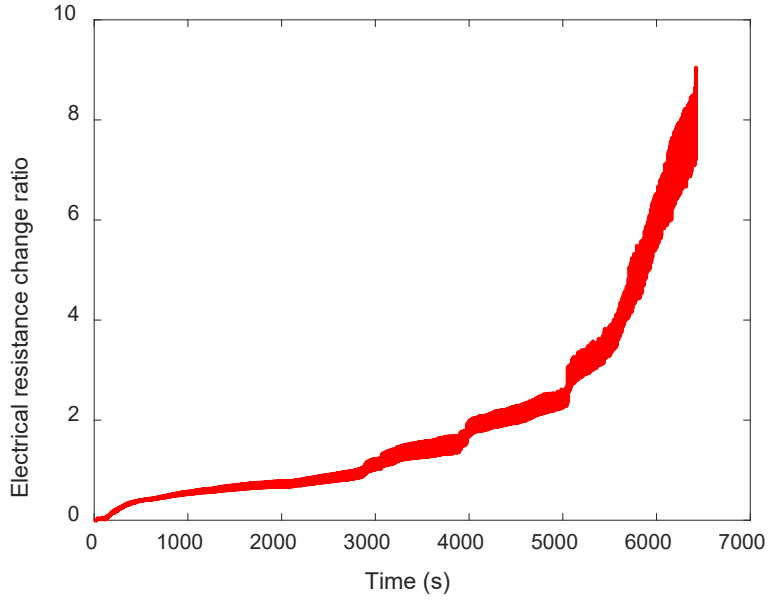

Self-sensing signal during fatigue test

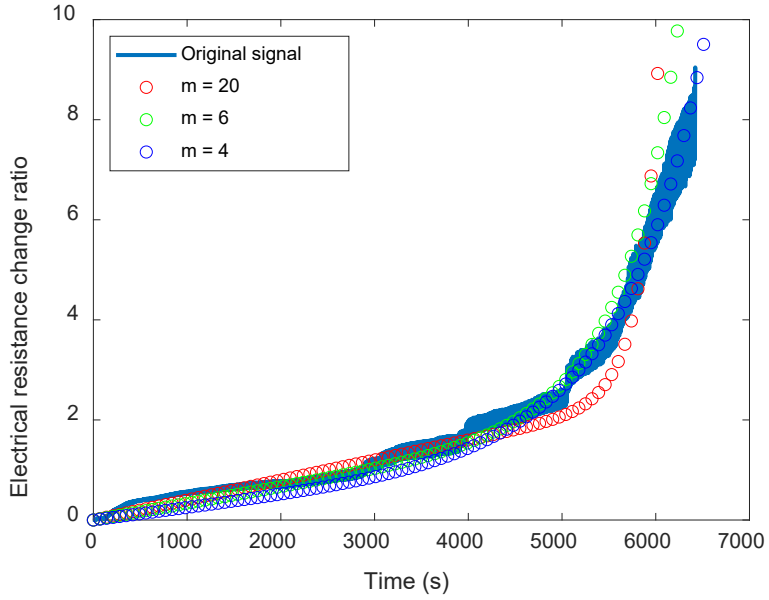

Suggested model

$$\frac{\Delta R}{R_0} = \frac{(1+\alpha\varepsilon)}{exp\left[-\left(\frac{\delta_{ec}}{L_0}\right)\left(\frac{E_f\varepsilon}{\sigma_0}\right)^m\right]} - 1$$

Simplify

$$\frac{\Delta R}{R_0} = \frac{(1+\alpha t)}{exp[-(\beta t)^m]} - 1$$

- Simplified GLS model can approximate the CFRP electromechanical behavior under fatigue.
- The exponent m and coefficients α and β can be adjusted based on observation.

Suggestions on Degradation Model

Case II. Apply different equations section-by-section

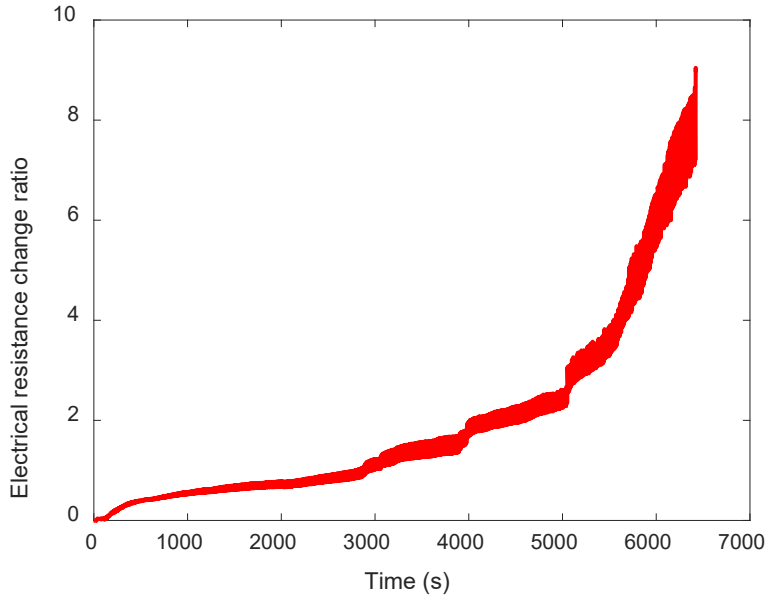

Self-sensing signal during fatigue test

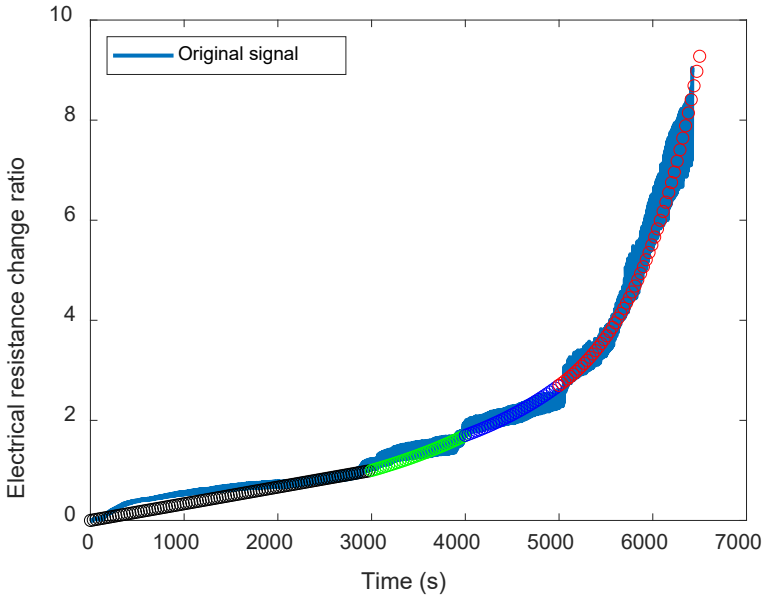

Suggested model

$$\frac{\Delta R}{R} = \begin{cases} a * x \\ (0 \le x < 3000) \\ \exp\left(b_1 * (x - 3000)\right) + b_2 \\ (3000 \le x < 4000) \\ \exp\left(c_1 * (x - 4000)\right) + c_2 \\ (4000 \le x < 5000) \\ \exp\left(d_1 * (x - 5000)\right) + d_2 \\ (5000 \le x < 6500) \end{cases}$$

- Data points that exhibit abrupt increases indicates severe damage occurrence.
- Based on those points, different exponential equations can be applied section-by-section.

Suggestions on Degradation Model

Case III. Adopt linear threshold function

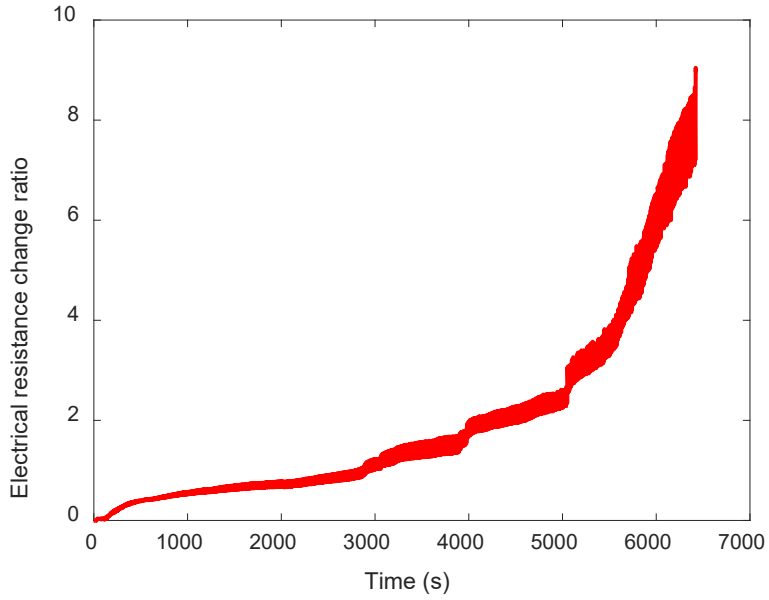

Self-sensing signal during fatigue test

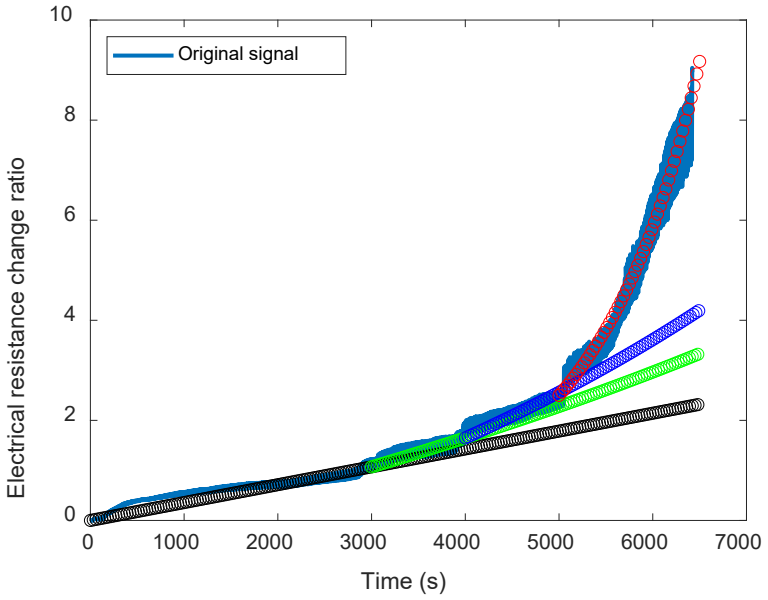

Suggested model

Linear threshold function

$$u(t) = \begin{cases} 0, & t < 0 \\ t, & t \geq 0 \end{cases}$$

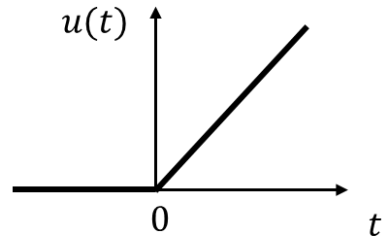

$$\frac{\Delta R}{R} = a * x + \exp\left(b * u(x - 3000)\right) + \exp\left(c * u(x - 4000)\right) + \exp\left(d * u(x - 6500)\right) + e$$

- Linear threshold function can be applied to reduce values to be predicted.
- Each term in the model will be activated after abrupt increase by real-time monitoring.

Concluding Remarks

*RUL: Remaining useful life

Conclusions

- **Self-sensing electrical resistance signal** can act as a health indicator of composite materials.
- **DLG-PF hybrid approach** significantly reduced the computational cost and error compared to conventional RUL prediction tools.
- **Electromechanical material degradation models** were suggested.

Future Work

- **Apply DLG-PF algorithm into the suggested models** to precisely predict the future behavior of electrical resistance signal

ICCM24 24TH INTERNATIONAL CONFERENCE ON COMPOSITE MATERIALS
AUG 4-8, 2025 • BALTIMORE CONVENTION CENTER • BALTIMORE, MARYLAND

GENERATIVE MODEL-DRIVEN DESIGN OF LONG DISCONTINUOUS CARBON FIBER COMPOSITES FOR TARGETED MECHANICAL PROPERTIES

Hyunsu Lee[1], Akshay Zaveri[1], Mark W. D. Nielsen, Keith D. Humfeld, Sung-Hoon Ahn[2] and Ji Ho Jeon[1*]

[1]School of Mechanical, Aerospace, and Manufacturing Engineering, University of Connecticut, Storrs, Connecticut, 06269, USA
[2]Department of Mechanical Engineering, Seoul National University, Seoul, 08826, Republic of Korea
[*]*Corresponding author (jiho.jeon@uconn.edu)*

Keywords: Carbon fiber, Discontinuous reinforcement, Finite element analysis (FEA), Microstructure, Numerical analysis, Mechanical properties, Computational modelling

ABSTRACT

This study presents a two-stage inverse-design framework for discontinuous carbon-fiber composites that generates variable-stiffness structures by linking macro-scale structural requirements with region-specific microstructural design. A genetic algorithm (GA) was used to determine macro-scale region-specific stiffness targets for a quarter-cornerhole geometry, reducing maximum local longitudinal S_{11} stress by 25% relative to a uniform stiffness baseline in which all fibers are aligned parallel to the applied load, while maintaining a longitudinal specimen stiffness above 30 GPa. Next, an Abaqus FEA pipeline generated a dataset of two-dimensional representative volume elements (RVEs) varying fiber volume fraction, length, width, orientation, and gap to characterize microstructural stiffness responses. Finally, a conditional GAN (cGAN), trained on this RVE dataset, inversely mapped the GA-derived stiffness targets to manufacturable microstructural parameters. FEA validation confirmed that the cGAN generated microstructures met the stiffness targets within 1 GPa and enabled a 13% reduction in average fiber volume fraction without compromising performance. This GA and cGAN workflow enable region-by-region generation of fiber microstructures that achieve target stiffness distributions and provides a scalable method for extending inverse design to three dimensional composite architectures and physical validation.

1 INTRODUCTION

Designing composite materials that simultaneously meet requirements for stiffness, strength, and geometry remains a critical challenge in aerospace and automotive applications. In such domains, precise control over material properties is essential to ensure structural performance under spatial and loading constraints [1]. Traditional composite design approaches have largely relied on empirically derived design rules from extensive experimental coupon testing regimes [2]. Due to their robust and conservative nature, such methods create initial designs where further optimization is constrained. Forward design using finite element analysis (FEA) simulations is limited due to computational cost, which increases significantly for nonlinear materials or complex geometries, making repeated simulation over large design spaces impractical [3]. Thus, FEA is generally used at later design stages to produce accurate assessments of mechanical behavior for predefined configurations of fibers and matrix systems [4]. To improve initial design, simple physics-based analytical models such as the rule of mixtures and Halpin–Tsai equations have been employed to estimate effective properties [5,6], however the models inherently break down for more complex design scenarios. While these different design methods have proven valuable, they are either too restrictive, too computationally expensive, or too inaccurate for the full complex inverse design problem of determining optimal material configurations that satisfy specific performance targets for realistic design parts [7].

To address these limitations, machine learning-based inverse design strategies have been introduced providing scope for improved accuracy and speed of computation [8]. Among them, generative modeling approaches offer a promising direction by directly constructing material configurations conditioned on target mechanical properties. Unlike regression-based surrogate models or traditional optimization, which improve existing designs within fixed spaces, generative models synthesize new designs that reflect desired physical behaviors. Generative adversarial networks (GANs) and other deep generative architectures such as variational autoencoders and conditional U-Nets have been applied in materials science to accelerate design workflows and reduce reliance on high-resolution simulations [9,10]. When trained on representative volume element (RVE) FEA datasets paired with mechanical response labels, these models can generate material structures aligned with specified performance metrics [3].

This study proposes a generative modeling framework for the inverse design of discontinuous fiber reinforced composites (DFRCs). Leveraging a FEA dataset of systematically varied RVE configurations and their corresponding stiffness values for training [11], the proposed approach aims to generate composite designs that satisfy user-defined mechanical targets [12]. This framework offers a scalable and efficient alternative to conventional FEA-based methods and supports performance-driven composite design.

2 RELATED WORKS

2.1 Surrogate modeling approaches in composite design

To mitigate the computational cost associated with simulation-based composite design, surrogate models trained on numerical results have been extensively employed. Techniques such as linear regression, polynomial response surfaces, and Gaussian process (GP) regression have been used to approximate mechanical responses within a reduced design space using a limited set of simulation samples [13]. These models enable rapid evaluation and are effective in capturing low-order design trends. However, their predictive accuracy diminishes significantly in high-dimensional or strongly nonlinear design spaces characteristic of complex composite systems. In response to these limitations, physics-informed machine learning (PIML) methods have been proposed to enhance the extrapolation and generalization capability of surrogate models [14]. These methods incorporate governing physical laws either as soft constraints in the loss function or via hybrid inputs combining simulation results and domain knowledge. While promising, PIML approaches often demand substantial training data and still struggle when operating beyond the distribution of the original training set [15]. Moreover, most surrogate modeling techniques are inherently constructed for forward prediction. As such, they are not directly suited for inverse design tasks, where the goal is to generate material configurations that achieve specified property targets or satisfy performance criteria under design constraints.

2.2 Deep generative modeling for inverse material design

Generative approaches have recently emerged as effective tools for inverse design, particularly in materials science domains characterized by high-dimensional, nonlinear, and non-convex design spaces. While generative adversarial networks (GANs) are widely studied, other frameworks such as variational autoencoders (VAEs), conditional U-Nets, and diffusion models have also demonstrated promising results in structural and microstructural synthesis [16, 17]. VAEs enable latent encoding of geometric and material features, facilitating efficient sampling and interpolation across the design space. Such models have been used to generate microstructure configurations aligned with target properties through structure–property mapping in the latent space [18]. Similarly, U-Net–based generative models have proven effective in pixel-wise or voxel-wise material structure prediction when conditioned on optimization results or segmentation masks [19]. More recently, diffusion models have been explored for the generation of high-resolution material topologies under physics-guided constraints. These models can produce diverse and stable outputs and can be conditioned on properties such as stiffness, porosity, or thermal conductivity during the iterative denoising process [20]. Despite their efficiency, generative models often require additional post-processing or constraints to ensure physical validity and manufacturability of the generated designs.

2.3 Inverse design in composite materials

Due to the inherent anisotropy and microstructural complexity of composite materials, inverse design requires handling diverse factors such as fiber orientation, stacking sequences, and matrix behavior. Several studies have adapted generative approaches specifically for composites by incorporating structure–property datasets based on RVEs [8]. These models learn latent design spaces where interpolation or sampling can yield new configurations aligned with mechanical targets. Such data-driven frameworks have shown particular promise for discontinuous fiber-reinforced composites, extending inverse design capability to discontinuous fiber reinforced composites (DFRCs) [19].

3 METHODOLGY

A two-stage framework integrating macro-scale structural optimization with micro-scale inverse material design is presented. First, a Genetic Algorithm (GA) identifies the optimal distribution of target mechanical properties for distinct regions within a structure to meet specified global performance criteria, such as stiffness and stress constraints. Second, the optimized regional properties are used to inversely generate manufacturable microstructural parameters. This inverse design process utilizes a conditional Generative Adversarial Network (cGAN) trained on a dataset of Representative Volume Elements (RVEs) obtained via finite element simulations. This integrated approach ensures that macro-scale structural requirements are practically translated into micro-scale design parameters, enabling efficient material usage with targeted performance.

3.1 Macro-scale structural optimization using GA

In this study, a GA was employed to optimize the discrete fiber composite material distribution of a quarter-cornerhole specimen loaded in uniaxial tension, see Figure 1. The objective of the GA optimization was twofold: (a) minimize the maximum local longitudinal stress, $S_{11,MAX}$, while (b) maintaining a minimum effective specimen longitudinal Young's modulus, $E_{11,SP}$, of 30 GPa. The structural domain was discretized into four distinct regions, and each region was assigned a set of orthotropic material properties as design variables. Specifically, directional Young's moduli (E_{11}, E_{22}), in-plane Poisson's ratio (v_{12}), and shear modulus (G_{12}) were allowed to vary in accordance with the range of material configurations in the RVE dataset, as detailed in Section 3.3 and summarized in Table 1. The GA optimization procedure, as illustrated in Figure 1, began with an initial population comprising 16 randomly generated sets of these material properties within the ranges [10, 30] GPa (E_{11}) and [1, 20] GPa (E_{22}, G_{12}). Each candidate solution (individual) within the population was evaluated through FEA using Abaqus, providing fitness scores based on the primary structural optimization goal of minimizing $S_{11,MAX}$ while only being accepted for further generations if they achieve the minimum effective specimen stiffness target, $E_{11,SP}^{T}$. Subsequently, genetic operators including selection, crossover, and mutation were applied iteratively to generate improved populations. The optimization loop continued until satisfaction of convergence criteria by either (i) change of the lowest found minimum of maximum local stress, $\Delta S_{11,MAX}^{min}(G) \leq$ minimum improvement value, MIV , of 1x10^{-3} (ii) number of iterations, G, reaches the maximum value, N, of 30. The outcome of the GA optimization was a set of optimal target mechanical properties defined for each region, reducing maximum stress concentrations and maintaining structural integrity. These optimized regional properties served as inputs for the subsequent micro-scale inverse design step, explained in Section 3.3, using the pre-trained cGAN model, explained in Section 3.2.

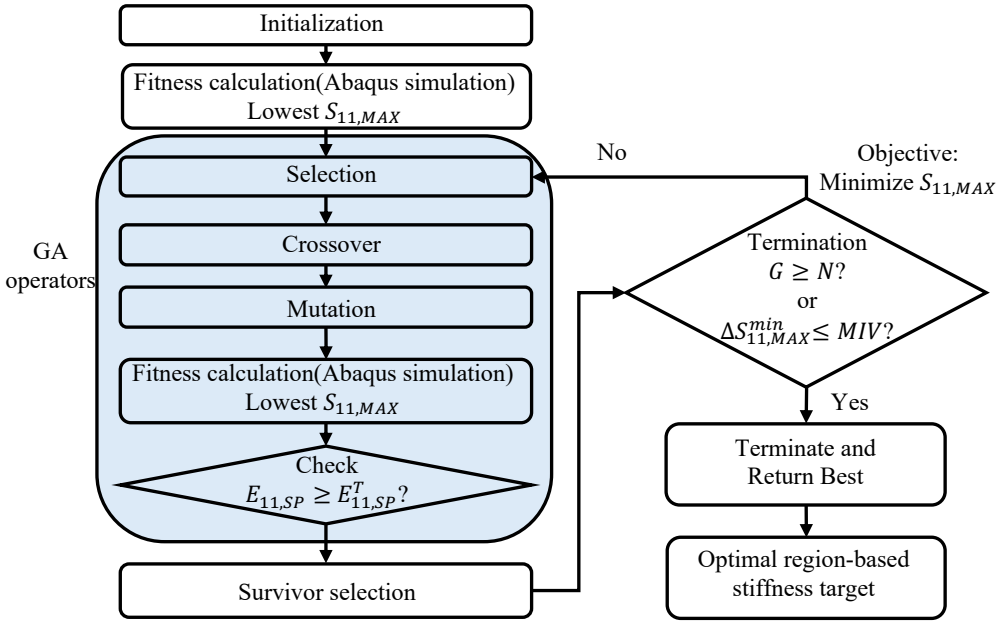

Figure 1: Architecture of genetic algorithm operators within each generation.

3.2 RVE dataset for cGAN model

To train the proposed conditional generative model for inverse design, a dataset was constructed using FEA of DFRC structures. Each data sample corresponds to a two-dimensional RVE, modeled as a square domain containing same direction fibers embedded in a continuous matrix. The geometrical and material configurations of the fibers were systematically varied to produce a wide range of mechanical responses under in-plane loading. The key design parameters considered during RVE generation include fiber gap, volume fraction, fiber length and width, orientation angle, and the elastic moduli of the fiber and matrix materials. These parameters were selected based on their known influence on in-plane stiffness characteristics of unidirectional composite plies. A subset of 200 RVE configurations was sampled from the full-factorial parameter space to ensure representative coverage across all key design variables. The parameter definitions and their corresponding ranges are summarized in Table 1.

Parameter		Range
Fiber gap (f_g)	$[mm]$	0.1-3.0
Volume fraction (V_f)	–	0.1-0.6
Fiber length (f_l)	$[mm]$	5-25
Fiber width (f_w)	$[\mu m]$	0.5-5
Fiber orientation (θ_f)	[°]	0-90
Fiber Young's modulus (E_{11})	$[GPa]$	231
Fiber Young's modulus (E_{22})	$[GPa]$	10
Fiber Young's modulus (G_{12})	$[GPa]$	5
Fiber Poisson's ratio (v_{12})	–	0.3
Matrix Young's modulus (E_m)	$[GPa]$	5
Fiber Poisson's ratio (v_m)	–	0.3

Table 1: Parameter ranges and increments used for generating the RVE dataset

For each configuration, static finite element simulations were conducted using Abaqus to evaluate the homogenized in-plane elastic properties, including directional Young's moduli and Poisson's ratios. The geometry generation, meshing, simulation, and data extraction were implemented in a unified workflow to ensure consistency across all samples. The RVE microstructures were generated as 2D

images with fiber regions shown in yellow and matrix regions in teal. Figure 2 (a) highlights the key geometric parameters: fiber width, fiber gap, and fiber orientation. The final dataset consists of approximately 200 samples, each comprising a paired input–output tuple: a binary microstructure image and the corresponding scalar stiffness value. This dataset serves as the training foundation for the cGAN. Figure 2 (b) presents representative the statistical distributions of the dataset parameters and mechanical responses obtained by randomly sampling values within the ranges specified in Table 1.

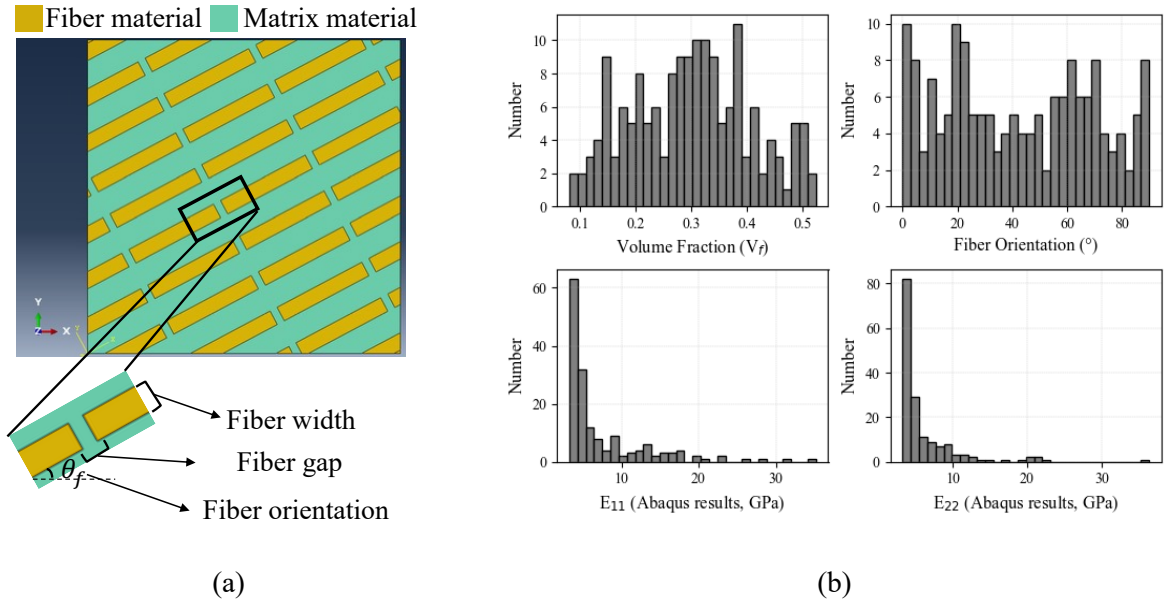

(a) (b)

Figure 2: (a) Samples RVE structure with fiber width, gap and orientation (b) Distributions of dataset variables: volume fraction, fiber orientation, and the corresponding stiffness values E_{11} and E_{22}

3.3 Micro-scale inverse design via cGAN

A cGAN was synthesized to predict the microstructural parameters of DFRC structures that satisfy user-defined stiffness targets. The model is based on the standard cGAN formulation, where both the generator G and discriminator D receive a condition vector c to guide the generation process. In this implementation, the condition vector consisted of the raw stiffness target and the desired loading direction. This structure allows the model to generate designs tailored to specific mechanical responses along the specified axis. The generator takes as input a concatenated vector $[z, c]$, where z is a latent noise vector sampled from a standard Gaussian distribution. The output is a vector of RVE design parameters, including fiber volume fraction, fiber orientation, fiber length, fiber width and fiber gap. These parameters define a composite structure that is expected to achieve the desired stiffness when evaluated under the given loading condition.

The discriminator is trained to distinguish between real (dataset-derived) and fake (generated) RVE configurations, conditioned on the same stiffness and direction input c. This enforces conditional realism in the generated structures. The training process employs adversarial loss, feature matching regularization, and label smoothing to stabilize convergence and improve the fidelity of the generated samples. An overview of the proposed generative design pipeline is illustrated in Figure 3. After training the generator G and discriminator D together, the generator G is used to predict parameters that are likely to result in the real vector c.

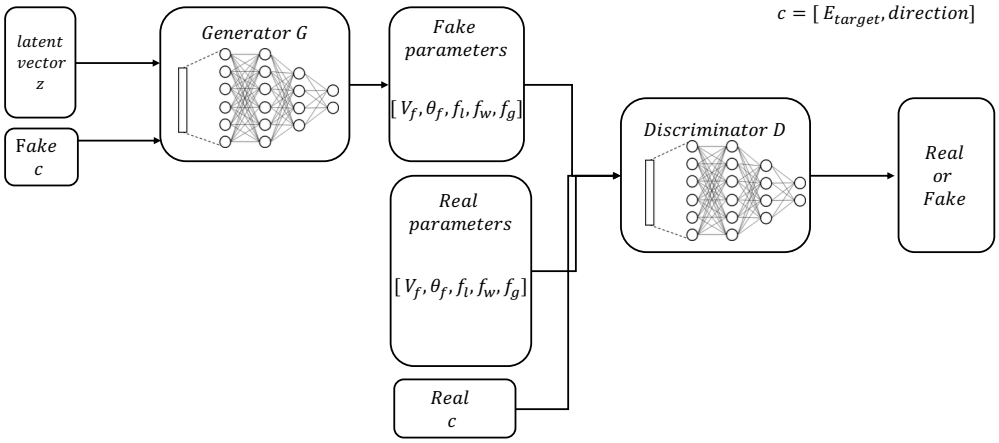

Figure 3: Architecture of the cGAN for inverse design of composite microstructures.

To quantitatively validate the generator output, a separate property prediction model is incorporated into the framework. Predictor is a fully connected neural network trained on the simulation-based dataset. It takes the generated RVE design parameters as input and estimates the corresponding equivalent stiffness. The predicted value is compared with the original target to assess inverse design accuracy and guide model refinement.

4 RESULTS AND DISCUSSIONS

4.1 Macro-scale optimization results

Macro-scale optimization was evaluated on a quarter-cornerhole specimen results using the GA-based method outlined in Section 3.1. A quarter-cornerhole specimen with four distinct stiffness regions was chosen as the representative geometry (Figure 4). The objective of the GA optimization was twofold: (a) maintain a minimum global Young′s modulus of 30 GPa, and (b) minimize the maximum S_{11} stress under uniaxial tension. The GA optimization began from randomly generated initial stiffness values within the ranges of [10, 30] GPa (E_{11}) and [1, 20] GPa (E_{22}, G_{12}), running for 30 generations with a population size of 16. Fitness evaluation involved running Abaqus finite element analyses to calculate effective stiffness and maximum S_{11} stress for each candidate. Results from the optimization demonstrate that region-wise tailored stiffness values significantly reduce local stress concentrations compared to a baseline uniform stiffness distribution. Specifically, the optimized design achieved a maximum stress reduction of approximately 25%, lowering the peak stress from 391 MPa to 289 MPa.

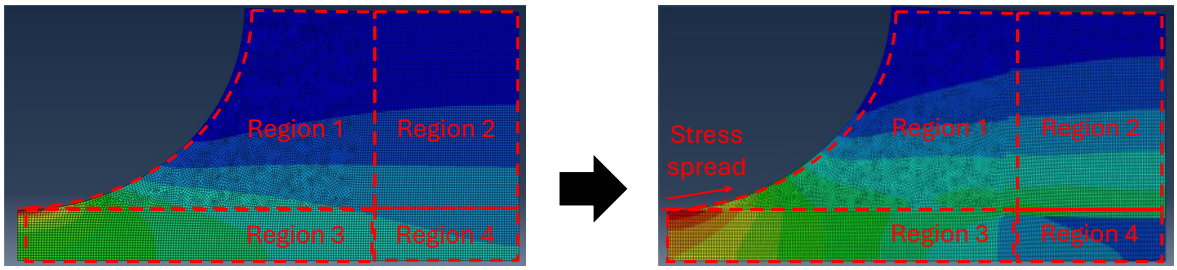

Stiffness (E_{11}): 30.02 GPa
Max Stress: 391.43 MPa

	Region 1	Region 2	Region 3	Region 4
E_{11} (GPa)	30.00	30.00	30.00	30.00
V_f	0.39	0.39	0.39	0.39

Stiffness (E_{11}): 30.46 GPa
Max Stress: 289.27 MPa

	Region 1	Region 2	Region 3	Region 4
E_{11} (GPa)	29.22	35.20	36.59	10.58
V_f	0.36	0.46	0.47	0.10

Figure 4: Von Mises stress contours for the quarter-cornerhole specimen under uniaxial tension: (a)

Baseline design with a uniform Young's modulus of 30 GPa (b) GA–optimized stiffness distribution reduces the maximum S_{11}

Furthermore, Figure 4 compares baseline and optimized designs. With fiber length fixed at 25 mm, the optimized design showed a reduction in the average fiber volume fraction from 0.39 (baseline) to 0.34, representing about a 12.8% material saving while still satisfying stiffness constraints. This result highlights the effectiveness of the proposed GA optimization in achieving both structural performance and material efficiency, which is beneficial for manufacturing.

4.2 Micro-scale inverse design results

Performance of the cGAN-based inverse design method described in Section 3.2 was evaluated. Experiments were conducted on simplified square-shaped RVEs. The trained cGAN model generated RVE design parameters fiber volume fraction (V_f), orientation angle (θ_f), fiber gap (f_g), fiber width (f_w), and fiber length (f_l) based on user-defined stiffness targets and loading directions (either E_{11} or E_{22}). Representative RVE designs obtained from the cGAN model and corresponding stiffness results computed via Abaqus simulations are summarized in Table 2.

	Sample 1	Sample 2	Sample 3	Sample4
Target	10 Gpa (E_{11})		4 Gpa (E_{22})	
Design parameters	V_f= 0.17, θ_f = 0 °, f_l = 19.79 mm, f_g = 2.5 mm, f_w = 2.06 μm	V_f= 0.24, θ_f = 15 °, f_l = 21.71 mm, f_g = 0.83 mm, f_w = 3.0 μm	V_f= 0.44, θ_f = 37 °, f_l = 10.00 mm, f_g = 0.79 mm, f_w = 1.51 μm	V_f= 0.38, θ_f = 28 °, f_l = 8.29 mm, f_g = 0.69 mm, f_w = 1.38 μm
Abaqus results (GPa)	9.86	9.96	4.47	4.04

Table 2: Representative RVE designs for target stiffness values, showing design parameters and the corresponding effective modulus obtained from Abaqus FEA.

For a 10 GPa E_{11} target, generated designs exhibited V_f values of 0.17, 0.24, and 0.44, producing moduli of 9.86 GPa, 9.96 GPa, and 10.04 GPa, respectively. For a 4 GPa E_{22} target, designs with V_f of 0.38 and 0.44 yielded 4.04 GPa and 4.47 GPa. The results illustrate that multiple distinct RVE configurations can satisfy the same stiffness target. Figure 5 further compares target stiffness values, Abaqus-computed stiffness, and predicted stiffness from the trained neural network predictor. The cGAN-generated designs accurately matched the target stiffness values, with a mean absolute error (MAE) of 0.78 GPa for E_{11} and 0.62 GPa for E_{22}..

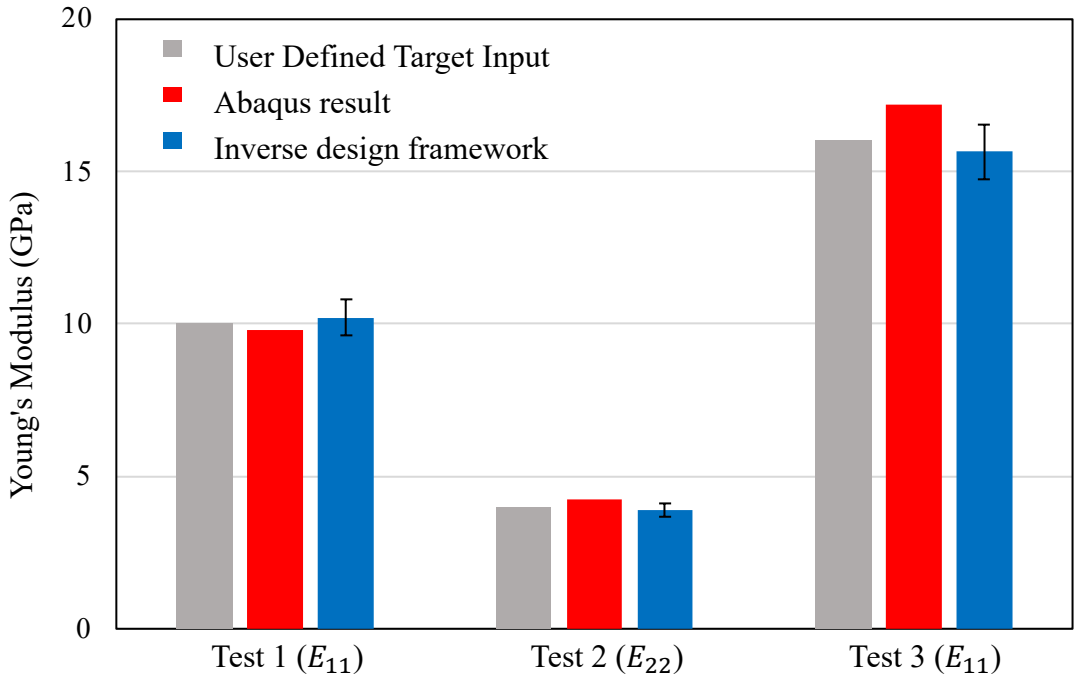

Figure 5: Comparison of target stiffness inputs, Abaqus-computed results, and cGAN-based inverse design predictions for three test cases

4.3 Discussions

This study presented a two-stage inverse-design framework integrating macro-scale structural optimization using a GA and micro-scale inverse design using a cGAN. The results indicate that this combined approach effectively achieves region-specific stiffness targets while significantly reducing maximum stress concentrations compared to baseline uniform stiffness distributions. Specifically, the two-stage optimization process resulted in a reduction of approximately 25% in maximum stress and approximately 13% material savings through optimized fiber configurations. By automating the workflow between region-wise property optimization (GA) and microstructure generation (cGAN).

However, the current approach has several limitations that should be addressed in future research. The present RVE dataset was limited to two-dimensional microstructures; extending the data set and inverse-design space to 3D laminated regions is necessary for laminated composite part design. Practical considerations such as fiber misalignment, resin flow during manufacturing, and thermal residual stresses introduced during additive manufacturing, must be systematically investigated, as these factors critically affect the mechanical performance of composite structures. Extending the dataset to three-dimensional RVEs for a single lamina accounting for these manufacturing effects, and including experimental validation data, would enhance the model's predictive capability and broaden its practical application. This study was conducted on a simplified quarter-cornerhole geometry under uniaxial loading conditions; real-world structural components typically involve more complex geometries, curved surfaces and multi-axial loading conditions. Future research should focus on adapting and validating this inverse-design framework for complex three-dimensional geometries under realistic operational loading scenarios. Lastly, for practical deployment in additive manufacturing processes, key challenges such as printer resolution limitations, accuracy in fiber placement, and void formation must be addressed. Incorporating these manufacturing constraints into the inverse-design process will be critical to ensuring that optimized designs can be reliably and efficiently realized in practice.

5 CONCLUSIONS

This research introduced a two-stage inverse-design framework combining macro-scale structural optimization using a GA and micro-scale material design through a conditional Generative Adversarial Network cGAN. The proposed GA-cGAN framework successfully prescribed manufacturable fiber microstructure parameters that satisfied region-specific stiffness requirements while achieving up to 25% reduction in maximum stress compared to uniform-stiffness baselines. Additionally, optimized fiber configurations enabled approximately 13% material savings without compromising mechanical performance. Future studies will focus on extending the framework to fully three-dimensional microstructures, performing experimental validation of optimized designs.

ACKNOWLEDGEMENTS

This research was supported by Korea Institute for Advancement of Technology (KIAT) grant funded by the Korea Government (MOTIE) (RS-2024-00436124, Human Resource Development Program for Industrial Innovation (Global))

REFERENCES

[1] M.F. Ashby and D. Cebon, Materials selection in mechanical design, Le Journal de Physique IV, 03(C7), 1993, pp. C7-1–C7-9 (doi: 10.1051/jp4:1993701).

[2] Department of Defense. (2002). Composite Materials Handbook, Volume 3: Polymer Matrix Composites Materials Usage, Design and Analysis (MIL-HDBK-17-3F). Chapter 5: Design and Analysis (Rev F). U.S. Department of Defense.

[3] C. Qian, R.K. Tan and W. Ye, Design of architectured composite materials with an efficient, adaptive artificial neural network-based generative design method, Acta Materialia, 225, 2022, Article 117548 (doi: 10.1016/j.actamat.2021.117548).

[4] O.O. Ochoa and J.N. Reddy, Finite element analysis of composite laminates, Solid Mechanics and its Applications, Vol. 7, Kluwer Academic Publishers, Dordrecht, 1992.

[5] R.M. Christensen, Mechanics of Composite Materials, Wiley-Interscience, 1979.

[6] J.C. Halpin and J.L. Kardos, The Halpin–Tsai equations: A review, Polymer Engineering & Science, 16(5), 1976, pp. 344–352.

[7] M. Raissi, P. Perdikaris and G.E. Karniadakis, Physics-informed neural networks: A deep learning framework for solving forward and inverse problems involving nonlinear partial differential equations, Journal of Computational Physics, 378, 2019, pp. 686–707 (doi: 10.1016/j.jcp.2018.10.045).

[8] Hwang, H. Y. (2025). A review of generative AI applications for composite materials and composite structure design. JMST Advances, 1-8. (doi: 10.1007/s42791-025-00095-3).

[9] Y. Chen, J. Zhang, Z. Li, H. Zhang, J. Chen, W. Yang, T. Yu, W. Liu and Y. Li, Intelligent methods for optimization design of lightweight fiber-reinforced composite structures: A review and the-state-of-the-art, Frontiers in Materials, 10, 2023, Article 1125328 (doi: 10.3389/fmats.2023.1125328).

[10] C. Gurbuz, F. Kronowetter, C. Dietz, M. Eser, J. Schmid and S. Marburg, Generative adversarial networks for the design of acoustic metamaterials, The Journal of the Acoustical Society of America, 149(2), 2021, pp. 1162–1174 (doi: 10.1121/10.0003501).

[11] R. Cang, Y. Xu, S. Chen, Y. Liu, Y. Jiao and M.Y. Ren, Microstructure representation and reconstruction of heterogeneous materials via deep belief network for computational material design, arXiv preprint, 2017 (doi: 10.48550/arXiv.1612.07401).

[12] T. Xie and J.C. Grossman, Crystal graph convolutional neural networks for an accurate and interpretable prediction of material properties, Physical Review Letters, 120(14), 2018, Article 145301 (doi: 10.1103/PhysRevLett.120.145301).

[13] A. Forrester, A. Sobester and A. Keane, Engineering design via surrogate modelling: a practical guide, Wiley, 2008.

[14] G.E. Karniadakis, I.G. Kevrekidis, L. Lu, P. Perdikaris, S. Wang and L. Yang, Physics-informed machine learning, Nature Reviews Physics, 3(6), 2021, pp. 422–440 (doi: 10.1038/s42254-021-00314-5).

[15] Z. Zhang and G.X. Gu, Physics-informed deep learning for digital materials, Theoretical and Applied Mechanics Letters, 11(1), 2021, Article 100220 (doi: 10.1016/j.taml.2020.100220).

[16] G.X. Gu, C.T. Chen, D.J. Richmond and M.J. Buehler, Bioinspired hierarchical composite design using machine learning: simulation, additive manufacturing, and experiment, Materials Horizons, 5(5), 2018, pp. 939–945 (doi: 10.1039/C8MH00505H).

[17] M. Habibi and M. Fuge, Inverse design with conditional cascaded diffusion models, Proceedings of the ASME 2024 International Design Engineering Technical Conferences, IDETC-CIE, Vol. 88360, 2024, V03AT03A020 (https://doi.org/10.1115/DETC2024-143607).

[18] J. Wang, Y. Wang and Y. Chen, Inverse design of materials by machine learning, Materials, 15(5), 2022, Article 1811 (doi: 10.3390/ma15051811).

[19] S. Oh, Y. Jung, S. Kim, I. Lee and N. Kang, Deep generative design: integration of topology optimization and generative models, Journal of Mechanical Design, 141(11), 2019, Article 111405 (doi: 10.1115/1.4044329).

[20] C. Düreth, P. Seibert, D. Rücker, S. Handford, M. Kästner and M. Gude, Conditional diffusion-based microstructure reconstruction, Materials Today Communications, 35, 2023, Article 105608 (doi: 10.1016/j.mtcomm.2023.105608).

FABRICATION OF DEPLOYABLE COMPOSITE STRUCTURE WITH MULTI-MATRIX DOSING PROCESS FOR ROBOTICS APPLICATIONS

Seung Mo Son[1], SeungWoo Jung[1] and Dong Gi Seong[1,2]

[1]School of Chemical Engineering, Pusan National University
Busandaehak-ro 63beon-gil 2, Geumjeong-gu, Busan 46241, Republic of Korea
Email: ssm6568@pusan.ac.kr (S. M. Son), re99ulus@pusan.ac.kr (S. W. Jung),
dgseong@pusan.ac.kr (D. G. Seong), web page: http://www.composite.pusan.ac.kr

[2]Department of Polymer Science and Engineering, Pusan National University
Busandaehak-ro 63beon-gil 2, Geumjeong-gu, Busan 46241, Republic of Korea
web page: http://www.composite.pusan.ac.kr

Keywords: Polymer-matrix composites (PMCs), Impact behaviour

ABSTRACT

Origami-inspired deployable structures require materials that balance mechanical stiffness with foldability, yet most composites cannot localize these properties without compromising integrity. In this study, we propose a dual-matrix fiber-reinforced composite laminate featuring spatially tailored stiffness, fabricated through a novel dual-resin dosing and wet compression molding process. By selectively impregnating para-aramid and carbon fibers with compliant and stiff epoxy systems, we created monolithic laminates with both foldable and load-bearing regions. Thermal and rheological analyses guided the simultaneous curing of the two resins, ensuring phase compatibility and clean interface formation. Mechanical testing confirmed high contrast in flexural strength—707.7 MPa in stiff regions, 23.9 MPa in compliant zones—while Izod impact tests revealed over twofold improvement in toughness with the compliant epoxy. DMA and cyclic folding tests demonstrated excellent durability under extreme deformation, retaining over 90% of the initial modulus after 1,000 cycles. The fabricated laminates enabled the construction of Kresling origami tubes and other morphing geometries with minimal hysteresis and high mechanical repeatability. This dual-matrix system offers a scalable solution for integrating spatially programmable stiffness and flexibility in next-generation deployable systems across robotics, protective structures, and aerospace applications.

1 INTRODUCTION

Deployable and compliant materials have become increasingly vital in modern robotic systems, particularly for applications involving complex morphing, spatial constraints, and cyclic actuation [1]. As robotics evolves towards more adaptive, human-interactive, and miniaturized systems, the demand for materials that combine mechanical robustness with structural adaptability has grown substantially. These materials must withstand repetitive mechanical stresses and accommodate varying geometries without compromising structural integrity, making them indispensable in fields such as aerospace deployables, soft robotic manipulators, and foldable sensing devices [2, 3].

Conventional polymeric materials commonly used in soft robotic applications—such as silicone, thermoplastic elastomers, and polyurethane-based elastomers—provide adequate compliance but often lack the necessary tensile and flexural strength, load-bearing capacity, and durability under repeated mechanical loading. These limitations significantly restrict their use in load-bearing or mission-critical scenarios [4, 5]. Typically, such materials require additional mechanical components such as hinges and joints to facilitate motion, complicating system designs and potentially compromising structural performance.

Origami-inspired structures have emerged as promising platforms for achieving reconfigurable, lightweight, and compact systems by transforming two-dimensional sheets into three-dimensional deployable forms through strategic creases and folding patterns [6, 7]. These fold-based expandable designs enable compact storage, lightweight construction, and programmable deformation pathways. However, typical origami structures made from homogeneous monolithic materials, such as paper or polymer films, struggle to fulfill the simultaneous demands of mechanical strength and flexural compliance. Furthermore, their fatigue performance under cyclic deformation remains insufficient, primarily due to a lack of structural segmentation that allows localized property tuning.

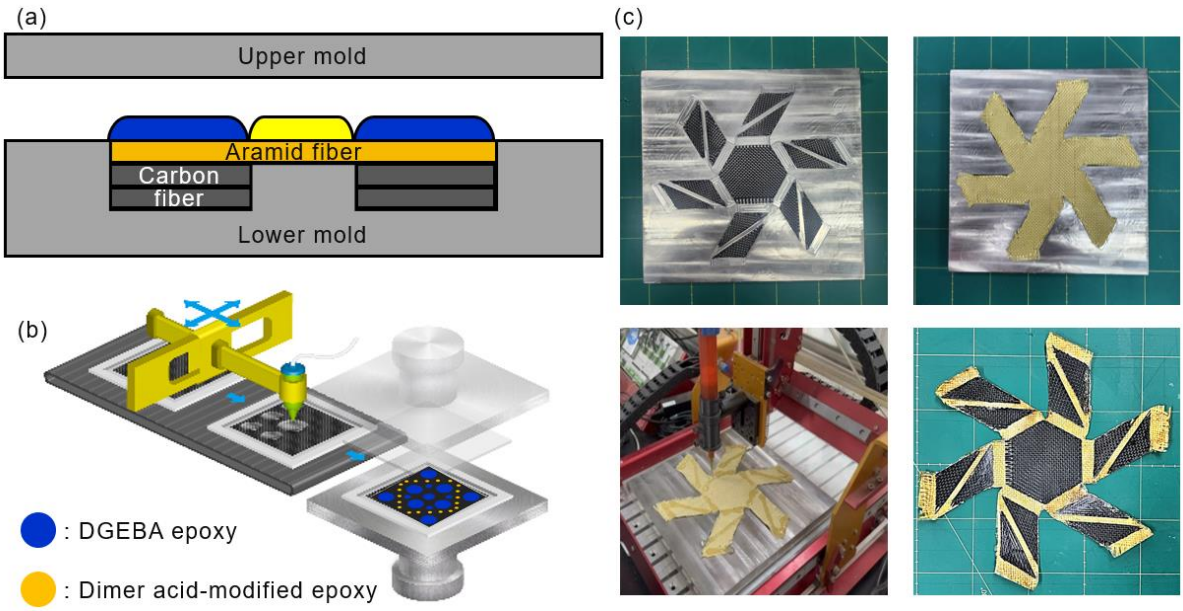

Figure 1: (a), (b) Schematic images and (c) images of the dual-matrix dosing process based on wet compression molding.

To overcome these challenges, this study introduces an advanced integrated composite laminate approach that combines stiff and compliant epoxy matrices through a novel dual-matrix dosing method coupled with wet compression molding. This hybrid laminate architecture allows for precise spatial control of stiffness and compliance, creating structures that integrate stiff load-bearing regions with compliant flexible zones [8, 9]. By controlling resin deposition patterns onto fiber preforms, we introduce tailored stiffness variations that are beneficial for structures requiring localized flexibility and directional deformation capability.

Unlike traditional composite systems that rely predominantly on fiber orientation for property differentiation, our strategy incorporates mechanical anisotropy through dual-matrix resin differentiation. Additionally, this approach circumvents the complexities associated with post-process adhesives or mechanical joints commonly required in segmented composite systems. Crucially, the compliant matrix—an aliphatic epoxy synthesized from dimeric fatty acids—features significantly reduced viscosity and a controlled curing profile compared to conventional urethane-modified epoxies, which enables precise resin dosing, clear interfaces, and thorough fiber impregnation [10].

The development of this dual-matrix laminate requires careful control over epoxide ring-opening reaction kinetics, viscosity evolution, and interfacial bonding strength. Accordingly, thermodynamic and rheological analyses were performed to optimize resin formulations and process parameters. These analyses ensured complete curing and minimal intermixing between resin phases, yielding integrated composite laminates capable of enduring extensive cyclic deformation without structural degradation.

To demonstrate the practical viability of this laminate concept, we fabricated and characterized deployable Kresling origami tubes utilizing the proposed dual-matrix composite system. Kresling tubes were selected due to their multi-degree-of-freedom deformation capabilities, including axial compression-extension, bending, and twisting motions, which are essential for advanced robotic actuators and deployable structural components [11]. Mechanical testing and cyclic deployment evaluations confirmed that the fabricated composite laminates maintained structural integrity, demonstrated highly repeatable actuation performance, and exhibited excellent durability under repeated mechanical loading cycles, highlighting their strong potential for next-generation deployable robotic and aerospace applications [12, 13].

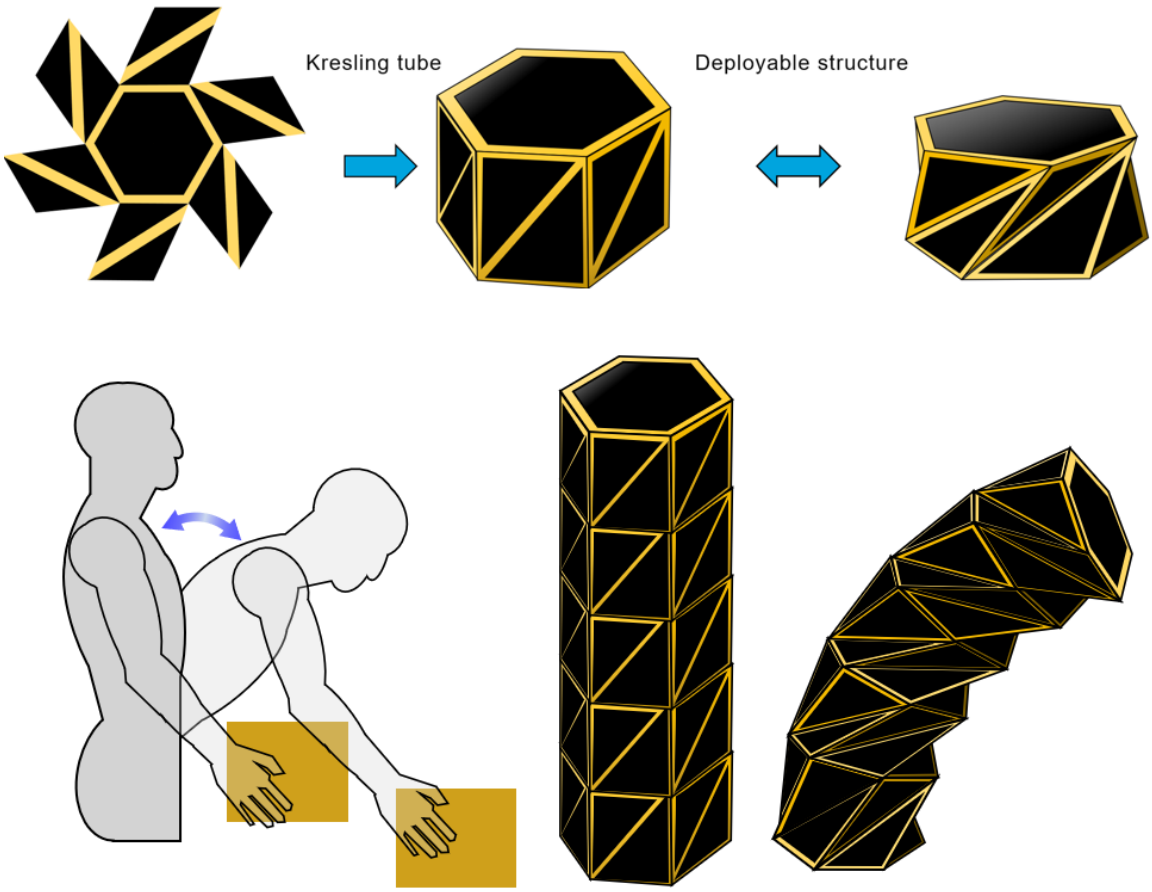

Figure 2: Kresling origami tube demonstrating reversible transformation between compact and expanded states. Stacked configurations enable multi-degree-of-freedom deformation, including axial, bending, and twisting motion, suitable for robotic articulation.

2 MATERIALS AND METHODS

2.1 Materials

Stiff epoxy consisted of Bisphenol A diglycidyl ether (DGEBA)-based epoxy (KFR-120V) with an epoxide equivalent weight (E.E.W.) of 200 g/eq and amine hardener (KFH-163) with an amine hydrogen equivalent weight (A.H.E.W.) of 58.1g/eq. Compliant epoxy was synthesized from dimeric fatty acid-based aliphatic epoxy with an E.E.W. of 430 g/eq and G640 hardener with an A.H.E.W. of 110 g/eq (Kukdo Chemical, Korea). Fiber reinforcements included plain-weave carbon (208 g/m², Hyundai Fiber) and para-aramid fabrics (180 g/m², Taekwang).

2.2 Resin characterization

To optimize the molding conditions for the dual epoxy resin system consisting of DGEBA and

aliphatic epoxy matrices, rheological and thermodynamic analyses were conducted using a rotational rheometer and differential scanning calorimetry (DSC), respectively. A rotational rheometer (MCR 702e, Anton Paar, Austria) equipped with a 25 mm parallel plate geometry was used to characterize the temperature-dependent viscosity of each resin system. A temperature sweep was conducted from 30 to 200 °C at a heating rate of 5 °C/min, 1 Hz frequency, and 0.1% strain. The curing behavior of each resin was investigated using a DSC (Q20, TA Instruments, USA) under a nitrogen atmosphere. Dynamic scans were performed from 30 to 220 °C at 5 °C/min to determine the total heat of epoxide ring-opening reaction and curing onset temperature. Isothermal scans were conducted to calculate the degree of cure, confirming that both resins achieved over 90% conversion within 30 min.

2.3 Composite fabrication

Composite laminates were fabricated using a dual-matrix dosing process combined with wet compression molding. Plain weave fiber reinforcements were precisely cut and arranged into designed laminate architectures, consisting of compliant and stiff regions. The compliant sections were composed of a single ply of plain-weave *p*-aramid fabric. The stiff sections were constructed by stacking two plies of plain-weave carbon fabric over one ply of *p*-aramid fabric in a [0/90] cross-ply configuration.

Each resin system was degassed under vacuum at 60 °C for 20 min to remove entrapped air. Resin dosing was performed by a programmable pneumatic dosing system (WINC V1, Nordson EFD, USA) equipped with a 55 mL syringe and a 0.063'' inner diameter tip. The dosing head traversed at a constant speed of 0.6 mm/s with a discharge pressure of 0.5 psi. The distance between the tip and the fiber surfaces was maintained at 0.5 mm, and the resin temperature was held at 60 °C during dosing to ensure stable viscosity and precise flow control.

Following deposition, the preforms were consolidated via wet compression molding at 160 °C under a pressure of 5 MPa for 30 min. This process ensured full curing of both resin systems, sharp interfacial boundaries between regions, and uniform fiber wet-out, resulting in a monolithic laminate with embedded spatially graded compliance suitable for deployable applications. The thicknesses of the obtained laminate's compliant section and stiff section were 0.25 mm and 0.70 mm, respectively.

2.4 Mechanical testing

To evaluate the mechanical performance of the dual-matrix composite system, separate specimens were fabricated using either the stiff or the compliant epoxy formulation. Compliant FRP specimens were prepared using four plies of plain-weave *p*-aramid fabrics while maintaining the same overall fiber volume fraction as the single ply of *p*-aramid fabric counterparts to ensure direct comparability.

Flexural properties were measured based on ASTM D790 using 60 mm × 25 mm rectangular specimens in a three-point bending configuration with a universal testing machine (RB301, Unitech, R&B, Korea). The span length was set to 32 mm, and the crosshead speed was 0.85 mm/min. The upper loading nose and lower support rollers had diameters of 9 mm and 3 mm, respectively.

Dynamic mechanical analysis (DMA, MCR 702e, Anton Paar, Austria) was conducted to evaluate the viscoelastic properties of stiff and compliant sections. Rectangular specimens measuring 60 mm × 10 mm were analyzed using a dual-cantilever bending configuration. Measurements were performed at a frequency of 1 Hz, a strain amplitude of 0.1%, and temperatures ranging from 50 to 200 °C at a heating rate of 5 °C/min. Additionally, cyclic bending durability tests were conducted on a 1 mm-thick compliant composite laminate (4-ply *p*-aramid), applying 1,000 bending cycles at a frequency of 1 Hz and a cyclic amplitude of 1,000% in single-cantilever mode.

Izod impact tests were performed according to ASTM D256 using an Izod pendulum impact tester (CEAST 9050, Instron, equipped with a 22 J hammer). Four different composite laminates—carbon/DGEBA epoxy, carbon/compliant epoxy, *p*-aramid/DGEBA epoxy, and *p*-aramid/compliant epoxy—were tested to systematically investigate the effects of fiber type and matrix stiffness on impact

resistance.

The compressive deployment behavior of the fabricated Kresling origami tubes was evaluated under cyclic strain conditions. The tubes were repeatedly compressed and re-expanded between 30% and 80% axial strain for 10 cycles. Load–displacement behavior and shape recovery were monitored to assess mechanical integrity, actuation repeatability, and fatigue resistance during transformation.

3 RESULTS AND DISCUSSION

3.1 Resin optimization for dual-matrix injection

To enable simultaneous impregnation and curing of the stiff and compliant epoxy systems, comprehensive thermal and rheological analyses were conducted to determine the optimal processing window.

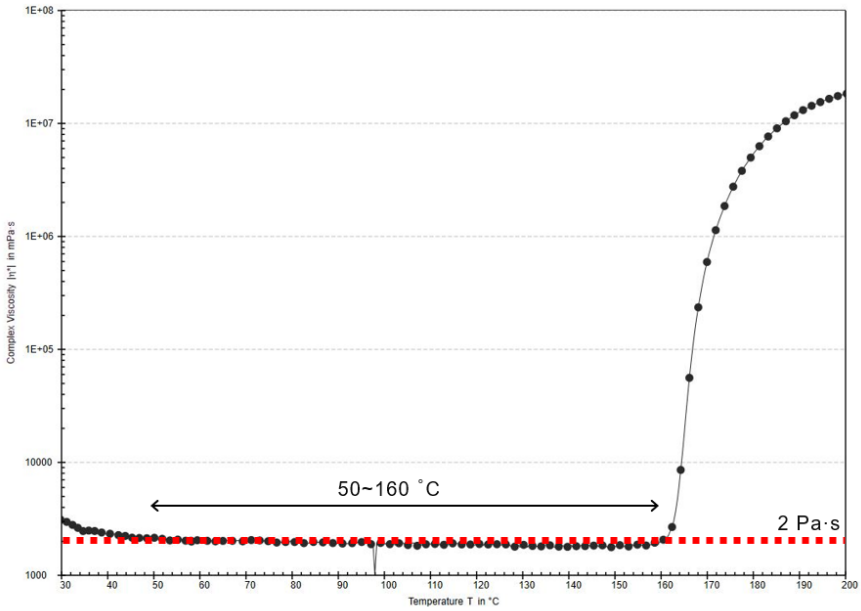

Figure 3: Temperature-dependent viscosity of the compliant epoxy measured by rheometer dynamic scan.

Rheological analysis was conducted to determine a suitable processing window for the compliant epoxy system. As shown in Figure 3, the complex viscosity remained relatively constant around 2 Pa·s across a broad temperature range from 50 °C to 160 °C, indicating excellent flow stability suitable for liquid molding. A sharp increase in viscosity was observed beyond 160 °C, corresponding to the onset of epoxide ring-opening and gelation reactions, marking the transition to rapid crosslinking and network formation.

Based on this behavior, the molding temperature was set to 60 °C to maintain low viscosity and ensure uniform resin distribution during dispensing. The curing temperature was set to 160 °C to initiate and complete crosslinking within a practical processing time. This temperature regime provided sufficient flowability during impregnation while ensuring rapid gelation and full curing during compression molding.

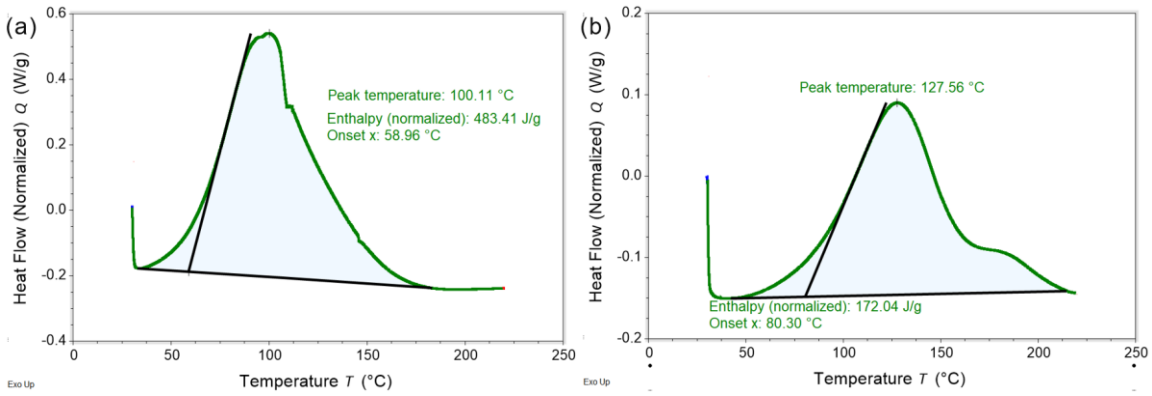

Figure 4: Dynamic DSC curves of (a) DGEBA epoxy and (b) compliant epoxy

As shown in Figure 4, dynamic DSC measurements revealed that the DGEBA-based stiff epoxy exhibited a reaction enthalpy of 483.41 J/g, indicating rapid crosslinking and high reactivity. In contrast, the compliant epoxy exhibited a lower enthalpy of 172.04 J/g, suggesting slower and more gradual curing behavior suitable for spatially controlled processing. To further assess curing kinetics, isothermal DSC scans were performed, and the degree of cure was calculated. The resulting conversion profiles confirmed that both epoxy systems reached over 90% cure within 30 min at 160 °C, demonstrating compatibility for concurrent curing in a dual-matrix system.

Based on these analyses, the processing conditions for the dual-resin system were established as follows: dispensing at 60 °C for low-viscosity flow and mold wet-out, followed by compression molding and curing at 160 °C, enabling complete crosslinking without premature gelation. These conditions ensured sharp interface formation, uniform fiber impregnation, and full structural integration between stiff and compliant regions.

3.2 Resin-fiber and resin-resin interface

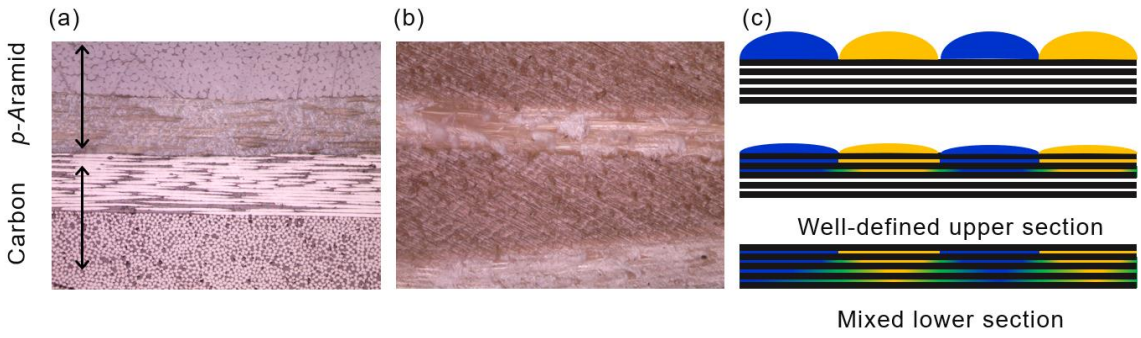

Figure 5: Resin intermixing behavior and interfacial compatibility in dual-matrix laminate structures. Cross-sectional optical microscopy images of (a) the stiff epoxy region and (b) the compliant epoxy region. (c) Schematic illustrating slight resin intermixing during impregnation.

Since both stiff and compliant matrices are epoxy-based thermoset processed via the liquid molding process, significant phase separation or poor interfacial adhesion was not observed. Due to resin impregnation dynamics, the lower side reveals some penetration of the DGEBA epoxy (~100 mPa·s, yellow) into the compliant epoxy region (~2 Pa·s, blue), resulting in indistinct boundaries and molecular-level mixing without notable phase separation. In Figure 5(a), Cross-sectional micrographs show carbon and *p*-aramid fiber layers within the stiff epoxy section, with a low void content. Similarly, Figure 5(b) indicates through impregnation of compliant epoxy within the *p*-aramid fiber region, it also exhibits low void content and confirms excellent resin-fiber compatibility.

3.3 Mechanical behavior of stiff and compliant sections

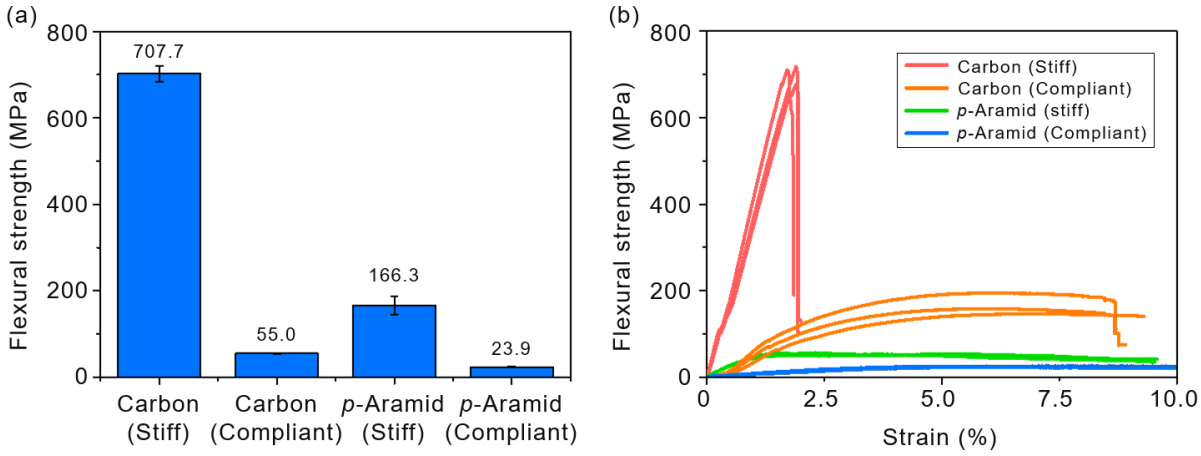

Figure 6: (a) Flexural strength of laminates with different fiber-resin combinations. (b) Corresponding flexural stress-strain curves.

To investigate the effect of the compliant epoxy matrix on flexural properties, four composite laminates were tested with different combinations of fiber type and matrix stiffness, as shown in Figure 6. The stiff section, composed of two plies of carbon fabric and one ply of *p*-aramid fabric impregnated with DGEBA epoxy, exhibited the highest flexural strength (707.7 MPa). This superior rigidity ensures that the stiff regions maintain their planar geometry during deployment, enabling well-defined crease lines in the origami structure. The DGEBA–*p*-aramid specimen also showed a relatively high flexural strength (166.3 MPa), although the lower fiber modulus compared to carbon led to more compliance. This confirms that structural rigidity in origami systems is primarily governed by the carbon fiber–DGEBA combination.

In contrast, the compliant section, composed of *p*-aramid fabric impregnated with the compliant epoxy, showed a significantly lower flexural strength (23.9 MPa), allowing for easy and localized bending. The laminate remained unbroken even when bent until the jigs made contact, indicating excellent ductility. Interestingly, the carbon–compliant epoxy laminate exhibited a flexural strength of 55.0 MPa, significantly lower than its DGEBA counterpart, confirming that matrix stiffness has a dominant influence on bending resistance. Moreover, the high strain-to-failure observed in both compliant laminates indicates their suitability for foldable zones within deployable structures.

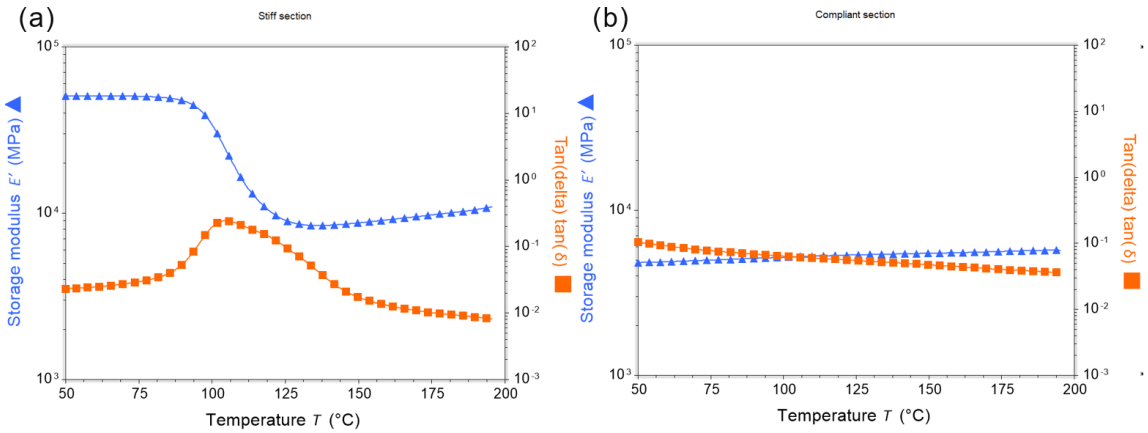

Figure 7: Temperature ramp DMA results of the (a) stiff and (b) compliant section

Dynamic mechanical analysis (DMA) results for the stiff and compliant composite sections are presented in Figure 7. Figure 7(a) shows the temperature-dependent viscoelastic behavior of the stiff section during a temperature ramp test. The storage modulus remains high up to approximately 100 °C, indicating that the stiff section effectively maintains its structural rigidity under typical use conditions. However, the sharp drop in modulus beyond 108 °C, coinciding with the tan δ peak (Tg), suggests that the material may lose its load-bearing capacity at elevated temperatures, becoming susceptible to folding or deformation. In contrast, Figure 7(b) demonstrates that the compliant section exhibits a relatively low but stable storage modulus across the entire temperature range. The nearly constant storage modulus and tan δ indicate thermally stable softness, making the compliant section highly suitable for applications requiring repeated bending. While the soft epoxy ensures excellent flexibility at room temperature, its Tg was separately confirmed to be below –20 °C, implying that the material becomes stiff under sub-zero conditions and may not be suitable for cryogenic or arctic applications. At room temperature, the storage modulus of the stiff section is nearly two orders of magnitude higher than that of the compliant section, establishing a clear mechanical contrast essential for origami-inspired deployment designs. Thus, the effective operating range for the dual-matrix laminate is approximately –20 °C to 100 °C, beyond which folding performance or rigidity may be compromised depending on the material region.

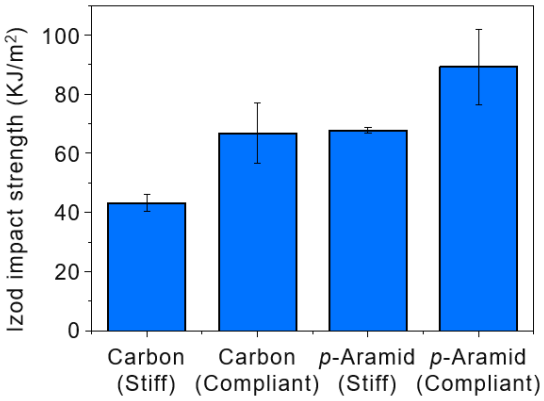

Figure 8: Izod impact strength of composite laminates with different fiber-matrix combinations.

Figure 8 presents the Izod impact strength of composite laminates with different fiber and matrix combinations. The conventional carbon fiber–DGEBA epoxy configuration exhibited the lowest impact resistance at 43.2 kJ/m², consistent with the known brittle nature of stiff epoxy systems. In contrast, the *p*-aramid–compliant epoxy system achieved the highest impact resistance at 89.2 kJ/m², more than doubling that of the carbon fiber–DGEBA epoxy. This significant enhancement is attributed to the high elongation and energy-absorbing nature of both the compliant epoxy and *p*-aramid fibers.

Interestingly, the carbon–compliant configuration also demonstrated markedly improved impact performance (66.8 kJ/m²), comparable to or exceeding that of the *p*-Aramid–Stiff system (67.8 kJ/m²), which is widely used in protective composite applications. These results suggest that the compliant matrix plays a dominant role in enhancing impact toughness, even when paired with inherently brittle fibers, such as carbon.

The combination of compliant matrix and high-ductility fibers not only enhances the material's ability to withstand direct impact but also holds promise for use in deployable origami structures. In such structures, deformation-based energy dissipation can further amplify impact resistance through mechanical motion, such as controlled folding, buckling, or twisting. Therefore, the *p*-Aramid–Compliant laminate emerges as a highly promising candidate for applications requiring both impact tolerance and deployability, such as protective soft robotics, aerospace shielding, or wearable armor systems.

3.4 Performance validation of the Kresling origami tube and other structure

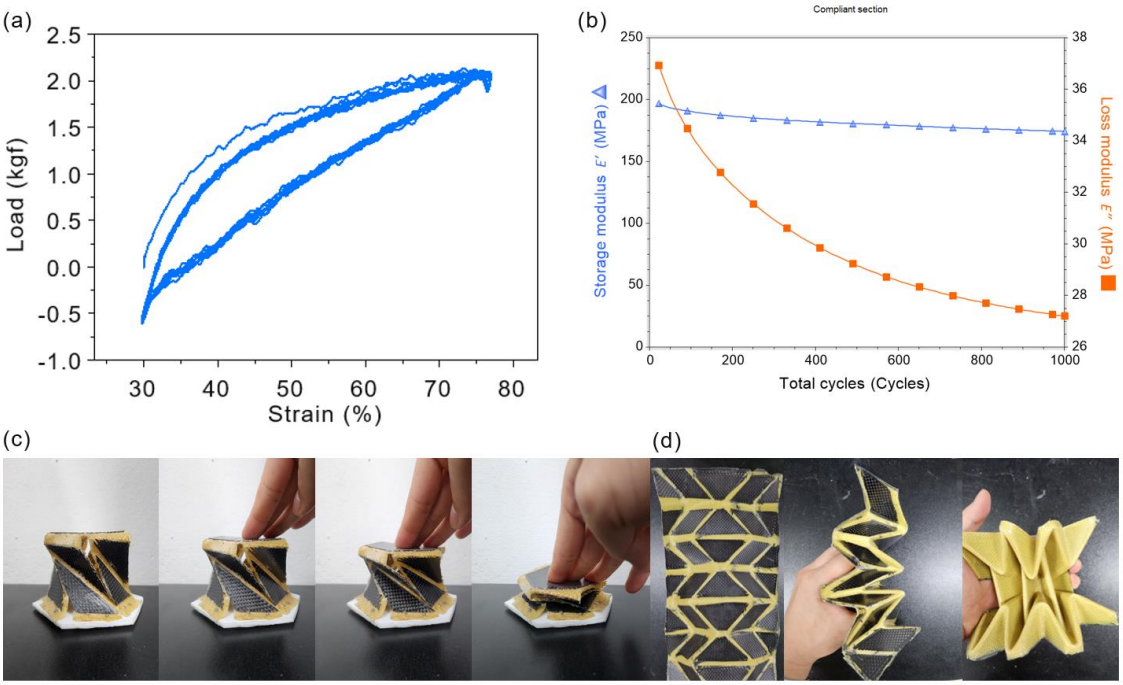

Figure 9: (a) Cyclic load–strain response of a Kresling tube under 30–80% axial strain. (b) DMA single-cantilever test results of the compliant section over 1,000 cycles at 1,000% strain. (c) Sequential compression and expansion images of the fabricated Kresling tube. (d) Tachi–Miura polyhedron structure fabricated via dual-resin dosing process.

Figure 9 presents the cyclic performance and structural versatility of the dual-matrix composite system. Figure 9(a) shows the cyclic deployment test of a Kresling tube under axial strain ranging from 30% to 80%. After initial cycle conditioning, the load–strain curves demonstrated minimal hysteresis over 10 cycles, confirming outstanding mechanical repeatability and resilience of the integrated composite structure.

To further evaluate durability under extreme deformation, DMA single-cantilever mode tests were performed on the compliant composite section under 1,000 cycles at 1,000% strain. As shown in Figure 9(b), the storage modulus retained over 90% of its initial value, while a gradual decrease in loss modulus was observed, indicating viscoelastic stabilization and sustained energy-dissipation capability of the compliant matrix during repeated folding cycles, validating its suitability for repeated folding and actuation.

Figure 9(c) displays sequential images of the fabricated Kresling tube undergoing manual compression and expansion, visually demonstrating its reversible deformation and structural robustness. In addition, Figure 9(d) showcases a Tachi–Miura polyhedron structure manufactured using the same dual-resin dosing process, highlighting the fabrication speed and geometric versatility of the method. The ability to produce complex foldable geometries such as Tachi–Miura patterns extends the applicability of this technique to broader categories of deployable and morphing structures in soft robotics and aerospace systems.

4 CONCLUSIONS

This work introduces a dual-resin composite approach that integrates stiff and compliant epoxy matrices to engineer spatially tunable mechanical properties within a single laminate architecture. Through detailed thermal and rheological characterization, we optimized a processing window that

supports simultaneous impregnation and curing of both matrix systems. The successful application of a programmable resin-dosing process allowed for precise deposition of low-viscosity, selectively cured epoxies into designed fiber regions without interfacial delamination or phase separation. Mechanical testing demonstrated that the stiff regions provide structural rigidity suitable for maintaining defined creases during deployment, while compliant regions support reversible folding and recoverable deformation. Notably, the compliant epoxy significantly enhanced impact toughness, even when combined with brittle carbon fibers, highlighting the dominant role of matrix properties in energy absorption. Temperature-dependent DMA and long-cycle durability tests confirmed excellent thermo-mechanical stability of both regions under realistic operating conditions. Furthermore, this architecture enabled the fabrication of advanced deployable structures such as Kresling tubes and Tachi–Miura polyhedra, which exhibited robust actuation over repeated deformation. The combined advantages of low processing complexity, mechanical programmability, and long-term durability position this dual-resin strategy as a promising platform for next-generation soft robotics, deployable aerospace components, and impact-resilient morphing systems.

ACKNOWLEDGEMENTS

This research was supported by the Nano & Material Technology Development Program through the National Research Foundation of Korea (NRF), funded by the Ministry of Science and ICT (2022M3H4A1A04076372, RS-2024-00412289).

REFERENCES

[1] A. A. Deleo, J. O'Neil, H. Yasuda, M. Salviato, and J. Yang, Origami-based deployable structures made of carbon fiber reinforced polymer composites, *Composites Science and Technology*, **191**, 2020, pp. 108060 (doi: 10.1016/j.compscitech.2020.108060).

[2] Q. Chen, F. Feng, P. Lv and H. Duan, Origami spring-inspired shape morphing for flexible robotics, *Soft Robotics*, **9(4)**, 2022, pp. 798–806 (doi: 10.1089/soro.2021.0030).

[3] D. Li, D. Fan, R. Zhu, Q. Lei, Y. Liao, X. Yang, Y. Pan, Z. Wang, Y. Wu, S. Liu and H. Wang, Origami-inspired soft twisting actuator, *Soft Robotics*, **10(2)**, 2023, pp. 395–409 (doi: 10.1089/soro.2021.0185).

[4] C.M. Stafford, B. D. Vogt, C. Harrison, D. Julthongpiput, R. Huang, Elastic moduli of ultrathin amorphous polymer films, *Macromolecules*, **39(15)**, 2006, pp. 5095-5099 (doi: 10.1021/ma060790i).

[5] H. Sugimoto, Y. Aoki, Preparation and physical properties of transparent foldable poly(methyl methacrylate) based materials using reactive poly(vinyl butyral), *Journal of Polymer Research*, **28**, 2021, pp. 121 (doi: 10.1007/s10965-021-02469-2).

[6] M. Cozmei, T. Hasseler, E. Kinyon, R. Wallace, A. A. Deleo, M. Salviato, Aerogami: Composite origami structures as active aerodynamic Ccontrol, *Composite Part B: Engineering*, **184**, 2020, pp. 107719 (doi: 10.1016/j.compositesb.2019.107719).

[7] M. Moshtaghzadeh, A. Bakhtiari, E. Izadpanahi, P. Mardanpour, Artificial neural network for the prediction of fatigue life of a flexible foldable origami antenna with Kresling pattern, *Thin-Walled Structures*, **174**, 2022, pp. 109160 (doi: 10.1016/j.tws.2022.109160).

[8] S. I. Kang, J. J. Yoo, M. G. Kim, D. G. Seong, A new variant of liquid composite molding process based on multi-drop resin filling, *Materials Today Communication*, **31**, 2022, pp. 103363 (doi: 10.1016/j.mtcomm.2022.1033363).

[9] S. I. Kang, M. G. Kim, D. G. Seong, Fabrication of functional hybrid carbon fiber-reinforced plastics with imparted surface concentrated electrical conductivity via multi-drop filling, *Korea-Australia Rheology Journal*, **Jun 4**, 2024, pp. 1-1 (doi: 10.1007/s13367-024-00094-1).

[10] H. J. Kim, M. Yoon, B. Seo, C. S. Lim, Effects of fatty acid modified epoxy resin on long-chain epoxy and its physical properties, *Journal of Polymer Science*, **61(18)**, 2023, pp. 2194-2202 (doi:10.1002/pol.20230242).

[11] C. Jiang, D. Wang, P. Cheng, L. Qiu, C. Li, Desing and optimization of a novel multi-layer conical Kresling origami mechanism (MCKOM) for linear actuation, *Mechanisms and Machine Theory*, **203**, 2024, pp. 105796 (doi: 10.1016/j.mechmachtheory.2024.105796).

[12] H. Yasuda, T. Yein, T. Tachi, K. Miura, M. Taya, Folding behavior of Tachi―Miura polyhedron bellows, *Proceedings of the Royal Society A: Mathematical, Physical and Engineering Sciences*, **469(2159)**, 2013, pp. 20130351 (doi: 10.1098/rspa.2013.0351).

[12] K. Yamaguchi, Y. Miyazawa. H. Yasuda, Y. Song, S. Shimokawa, U. Gandhi, J. Yang, Post-fabrication tuning of origami-inspired mechanical metamaterials based on Tachi―Miura polyhedron, *Materials & Design*, **233**, 2023, pp. 112170 (doi: 10.1016/j.matdes.2023.112170).

COLLIER AEROSPACE

Framework for Optimization of AFP Composite Structures

ICCM24

24TH INTERNATIONAL CONFERENCE ON COMPOSITE MATERIALS

AUG 4-8, 2025 • BALTIMORE CONVENTION CENTER • BALTIMORE, MARYLAND

August Noevere, Von Jamora – Collier Aerospace

Matt Godbold, Brian Tatting – Clemson

Design, Repair and Lifecycle

Tuesday, August 5, 2025 From 3:05 PM to 3:25 PM

Contact us: www.collieraerospace.com

© Copyright 2024 Collier Aerospace Corporation. Confidential Information.

Motivation/Introduction

Methodology

Example Application

Conclusions

© Copyright 2024 Collier Aerospace Corporation. Confidential Information.

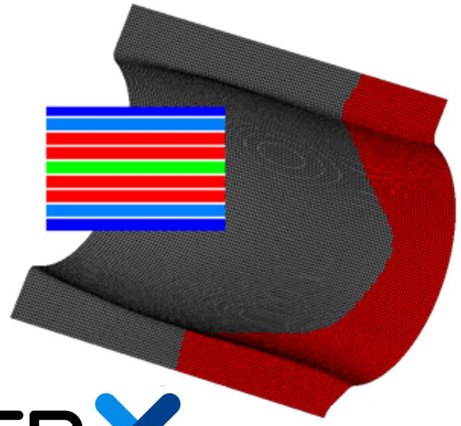

HYPERX

Stress analysis and laminate optimization for thousands of load cases

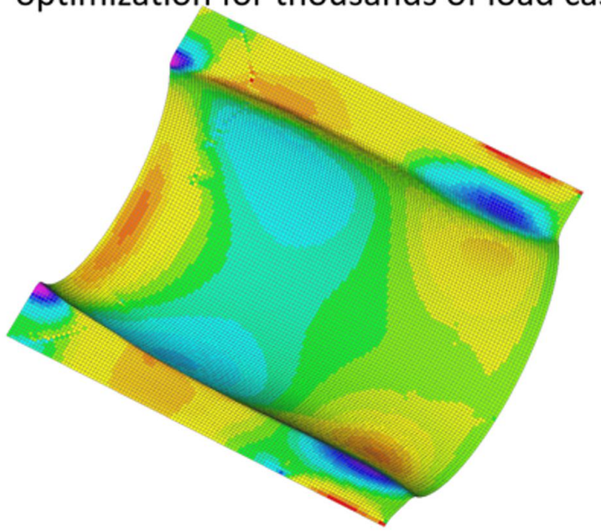

Optimized ply shapes, counts, and orientations

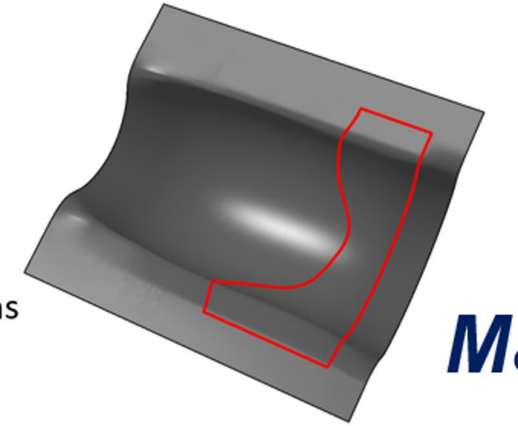

Mapped AFP data

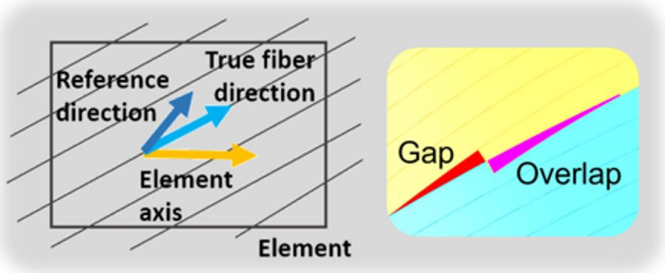

AFP Manufacturing Simulation

Tow path generation, lap/gap identification, steering violations

CAPP

VCP

VERICUT® Composite Applications

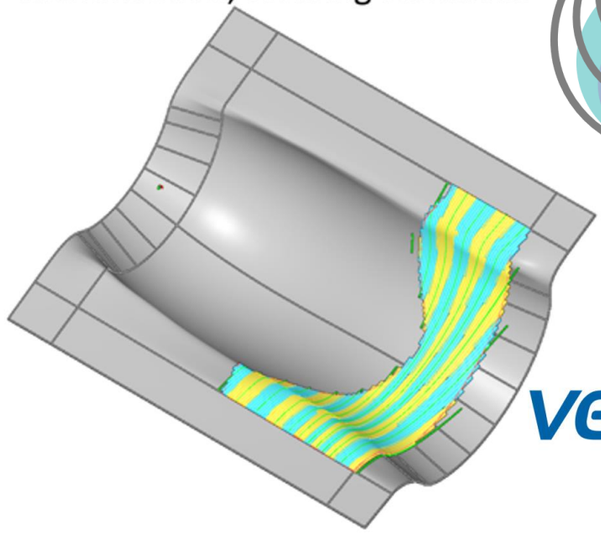

© Copyright 2024 Collier Aerospace Corporation. Confidential Information.

Summary of Software Integration

- Completed workflow shown on previous slide
- Developed standardized file formats/approaches to exchange model data between HyperX, CAPP, and VCP
- Created & enhanced software APIs (Application Programming Interfaces) to facilitate automated data exchange between software
- Created & enhanced software GUIs (Graphical User Interfaces) to facilitate execution of DFM processes
- Developed new algorithms to simultaneously optimize for structural integrity and manufacturing

HYPERX

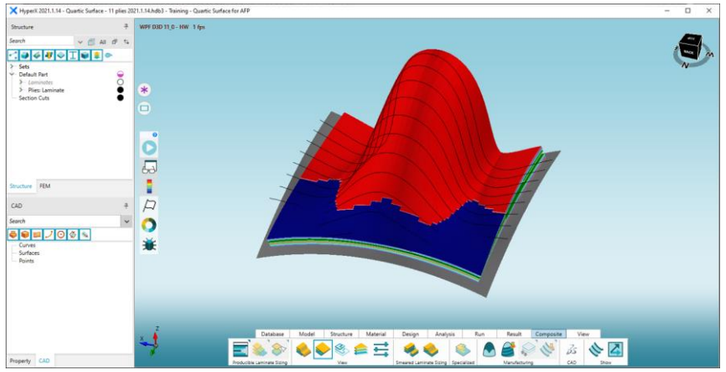

CAPP

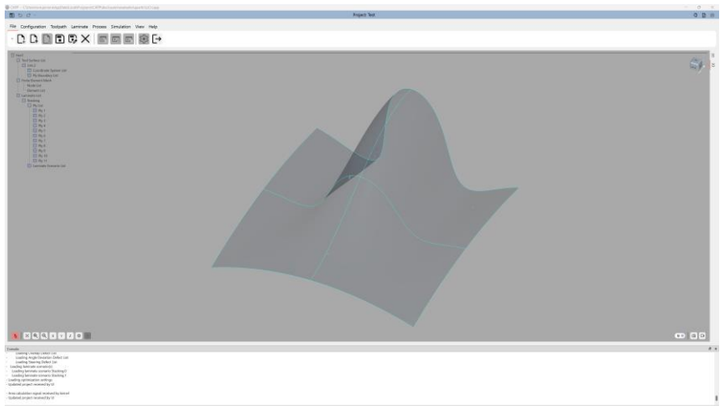

VCP
VERICUT® Composite Applications

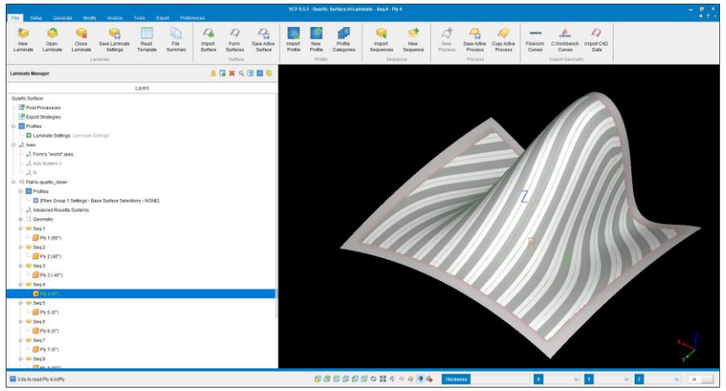

© Copyright 2024 Collier Aerospace Corporation. Confidential Information.

Motivation/Introduction

Methodology

Example Application

Conclusions

© Copyright 2024 Collier Aerospace Corporation. Confidential Information.

- Objective: develop laminate design that satisfies both stress and manufacturing requirements
- Bi-level strategy selected due to complexity and runtime of software involved
  - Lower level: HyperX and CAPP iterate with VCP to optimize for stress and manufacturing respectively
  - Upper level: global iterations to converge the solution

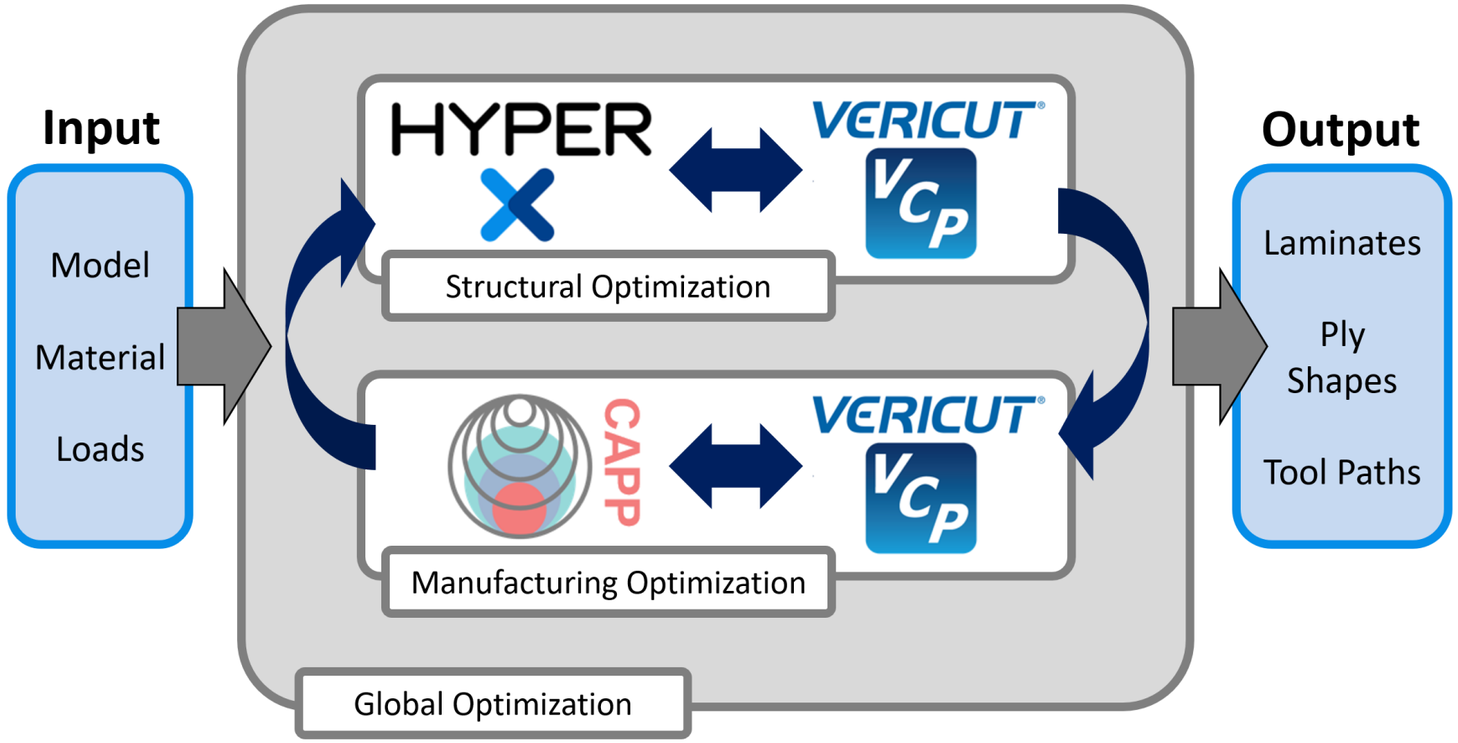

© Copyright 2024 Collier Aerospace Corporation. Confidential Information.

Initial Plies

-45°
45°
0°
90°

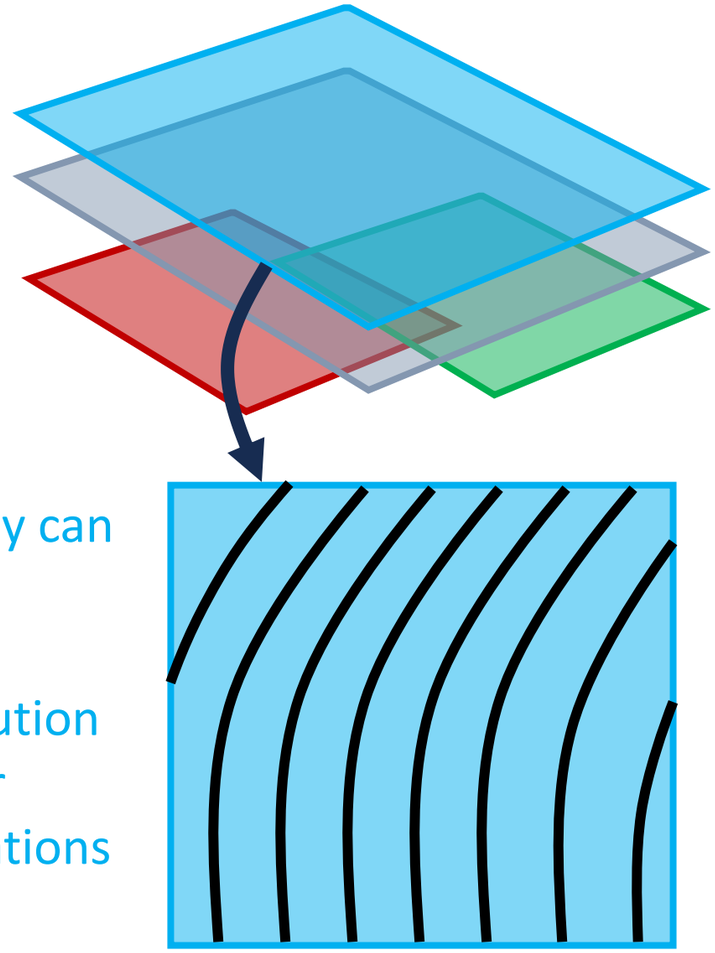

Each ply can have a unique distribution of fiber orientations

“Reference” Ply Setup

Each initial ply having one or more unique features listed below becomes a “reference ply”

- Coverage
- Orientation (0/45/90/etc)
- Fiber directions

Ref Ply 1

Ref Ply 2

Ref Ply 3

Ref Ply 4

© Copyright 2024 Collier Aerospace Corporation. Confidential Information.

Stacking Optimization

Explore inserting reference plies into the stack

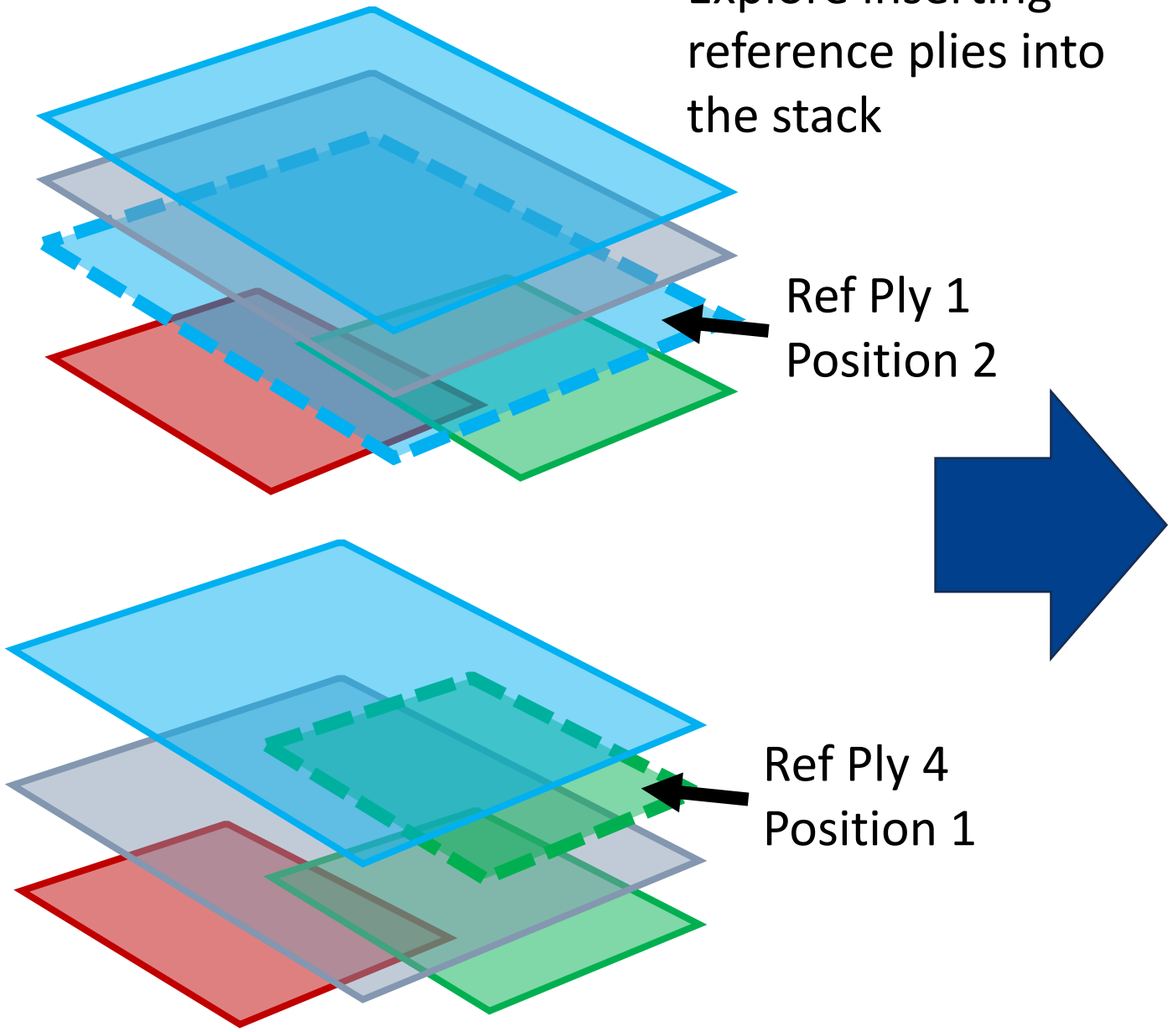

Final Result

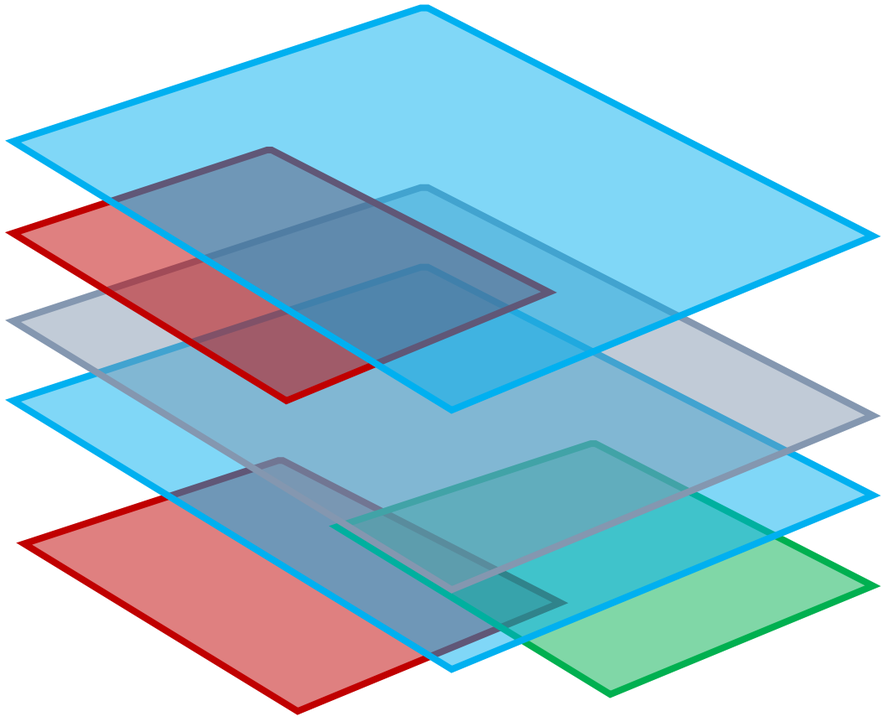

© Copyright 2024 Collier Aerospace Corporation. Confidential Information.

HyperX AFP Defect/Feature Handling

- Effect of defect testing/simulation is best left up to the manufacturer due to considerations specific to their material, manufacturing, etc
- Instead of implementing a specific analysis approach, create a framework to allow defects/features of any type from any source to be mapped to the user's FEM and analyzed with user-specific criteria

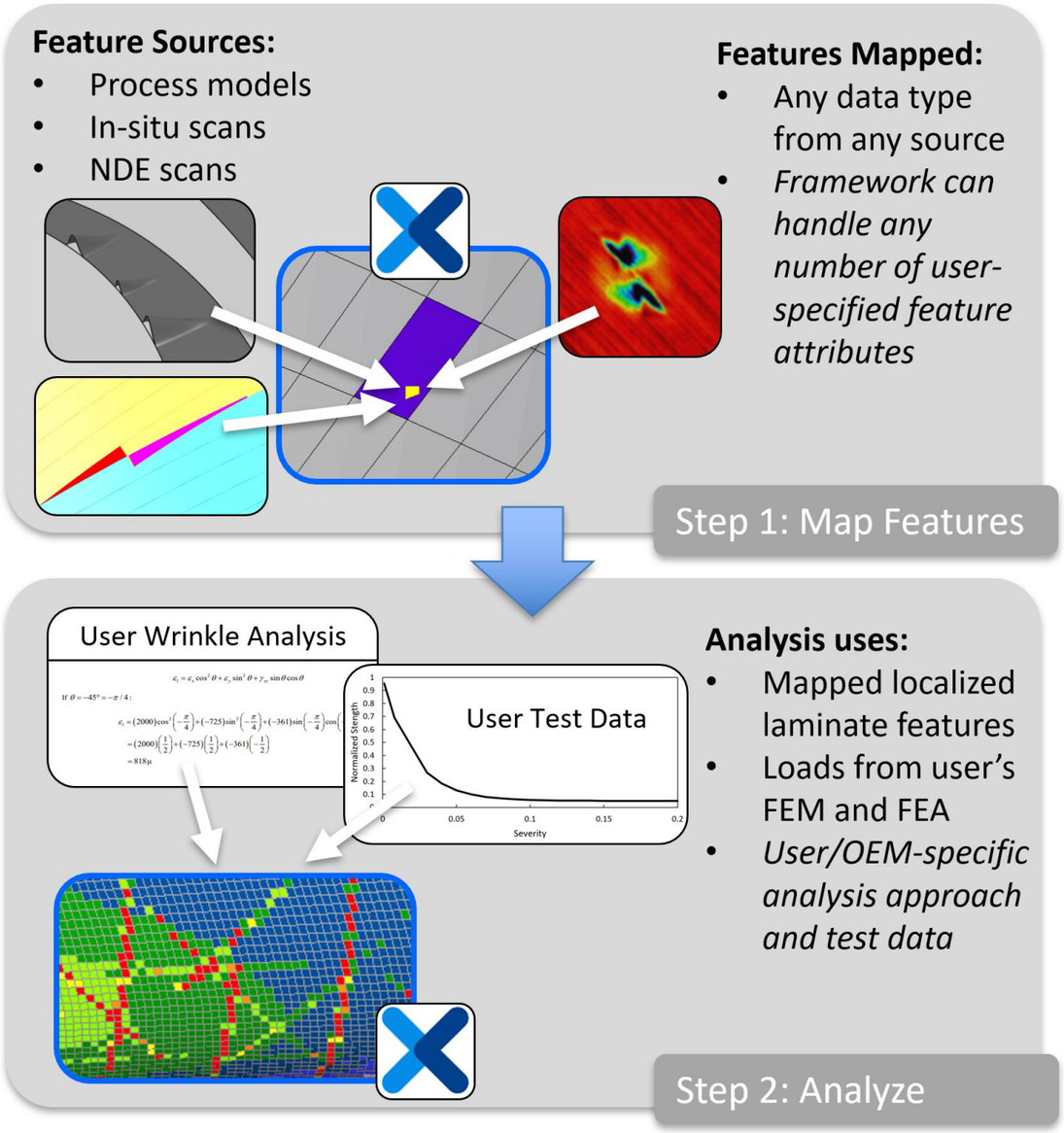

© Copyright 2024 Collier Aerospace Corporation. Confidential Information.

- Developed a command-line user interface (CLUI) for headless communication with DFM partner software applications
- Established stable protocol and optimized data handling for HyperX-CAPP-VCP communication
- Implemented customizable settings and an expanded GUI with enhanced capabilities
- Integrated margin-of-safety data within optimization process

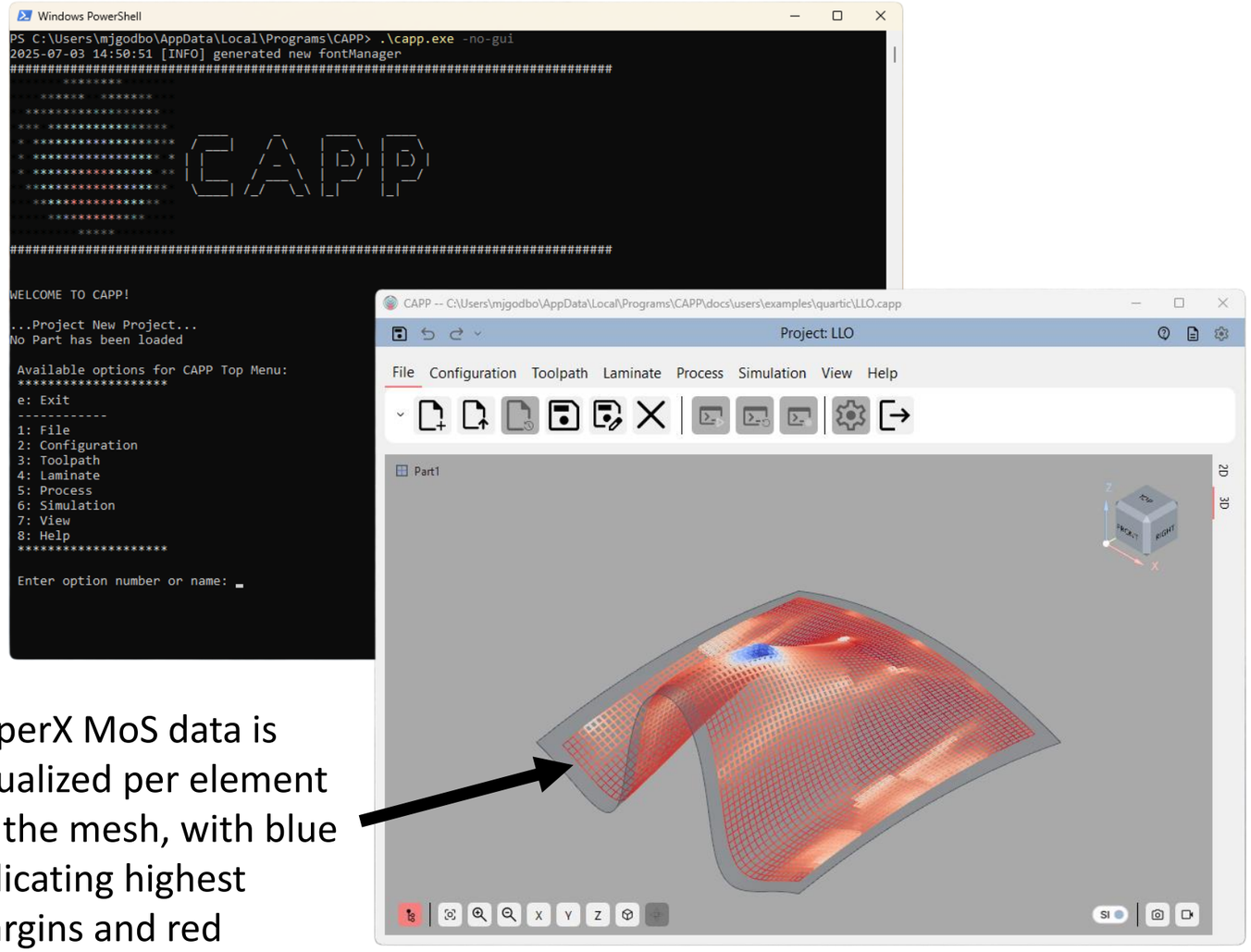

HyperX MoS data is visualized per element on the mesh, with blue indicating highest margins and red indicating lowest margins

CAPP 1.0.0 Screenshots (CLUI/GUI)

© Copyright 2024 Collier Aerospace Corporation. Confidential Information.

- CAPP optimizes manufacturability by assessing features such as tow overlap/gaps and excess steering radius
- Optimization at two levels
  - Ply level: maximize manufacturability per individual ply
  - Laminate level: minimize stacking of defects through the laminate thickness
- Both approaches move defects away from areas of critical margin of safety

Un-optimized

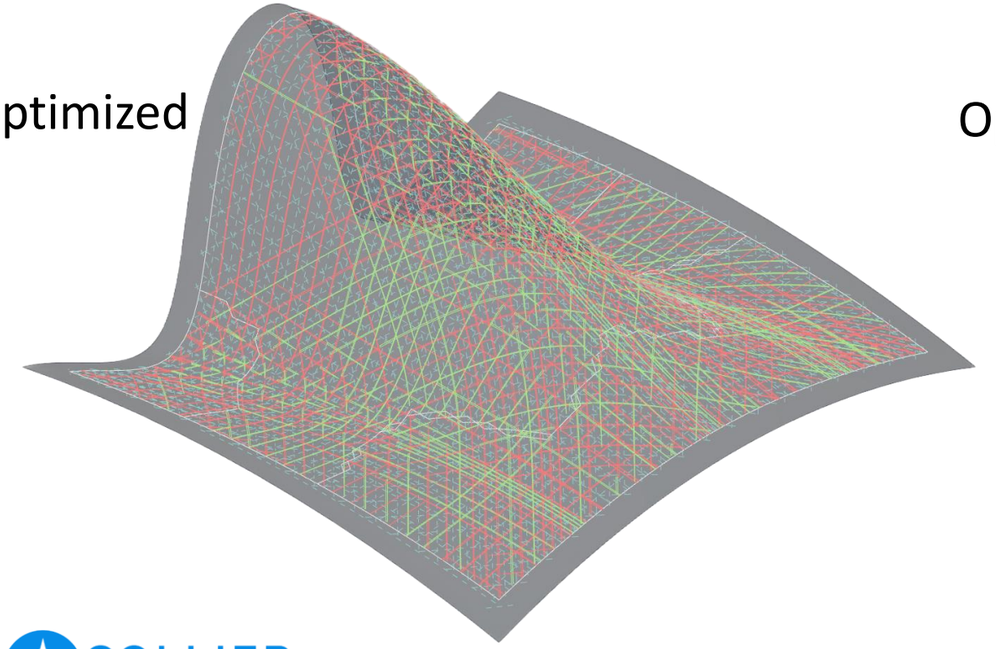

Optimized

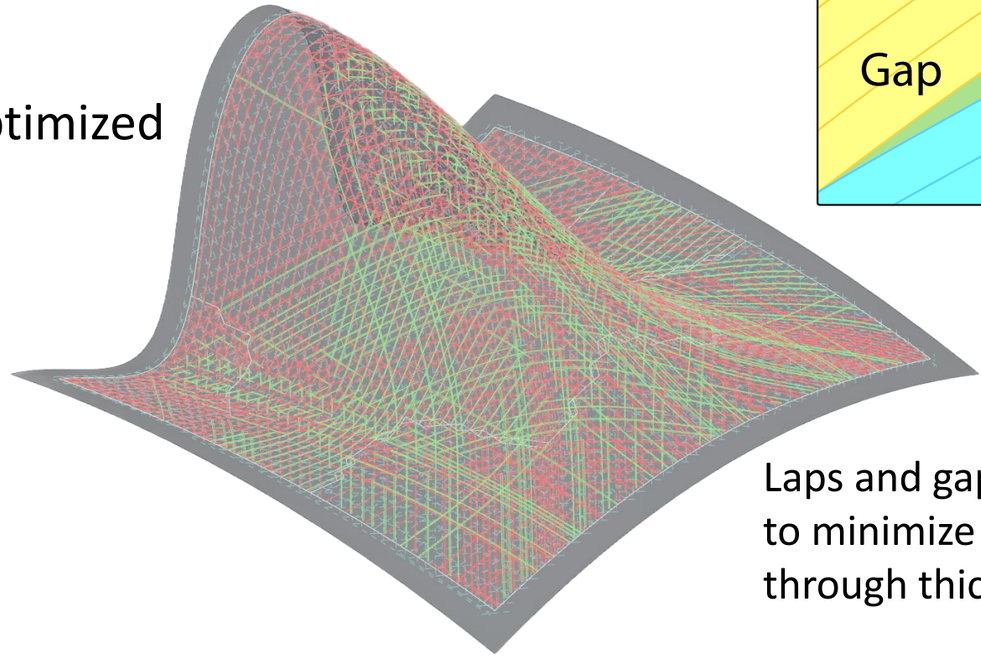

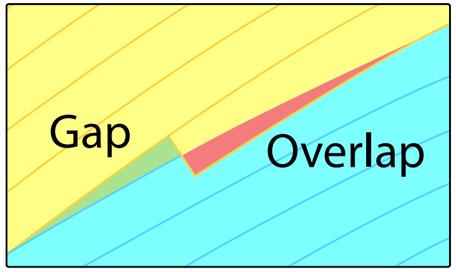

Laps and gaps spread out to minimize stacking-through thickness

© Copyright 2024 Collier Aerospace Corporation. Confidential Information.

Motivation/Introduction

Methodology

Example Application

Conclusions

© Copyright 2024 Collier Aerospace Corporation.

Example Application (Video)

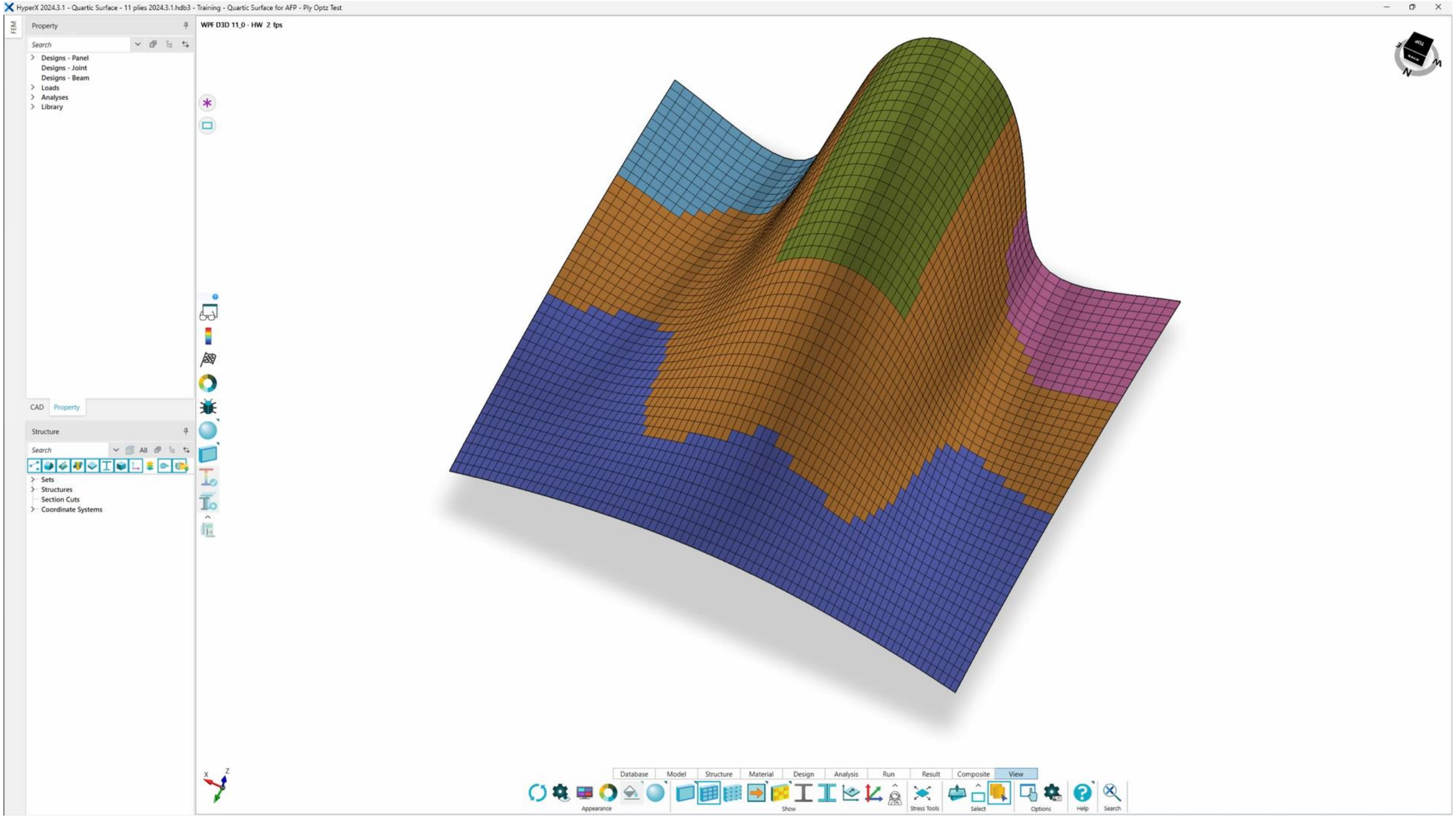

© Copyright 2024 Collier Aerospace Corporation. Confidential Information.

Motivation/Introduction

Methodology

Example Application

Conclusions

© Copyright 2024 Coll orporation. Confidential Information.

- Framework has been completed to enable simultaneous optimization of structural performance and manufacturability of composite AFP structures
- Developed framework performs automated iterations between commercial stress analysis tools and AFP manufacturing tools
- Functionality demonstrated on a variety of test models and real parts under the NASA HiCAM program

© Copyright 2024 Collier Aerospace Corporation. Confidential Information.

Acknowledgements

The material contained in this paper is based upon work supported by NASA under award No. 80NSSC22M0157.

Any opinions, findings, and conclusions or recommendations expressed in this material are those of the author(s) and do not necessarily reflect the views of the National Aeronautics and Space Administration.

© Copyright 2024 Collier Aerospace Corporation. Confidential Information.

Questions?

Contact us: www.collieraerospace.com

© Copyright 2024 Collier Aerospace Corporation. Confidential Information.

Next Generation Wind Turbine Blade Repair Residual Stress and Void Analysis in UV-cured Scarf Patches

Prof. Puneet Mahajan
Professor

Collaborators

Ayush Varshney, PhD Student (IIT, Delhi)
Dr. Daniel Paul, Research Fellow (Brunel University London)
Dr. Leon Mishnaevsky Jr., Senior Scientist (DTU, Denmark)

Applied Mechanics Department,
Indian Institute of Technology Delhi, India

Wind turbine blade: Damages

Types of Wind Turbine Blade Damage:
Surface Damage:

- Leading edge erosion due to rain, hail, and debris impact.
- Microcracks in the surface and coatings.
- Lightning strike damage.

Structural Damage:

- Cracks and splits in the blade structure.
- Physical impact such as bird.
- Delamination (separation of layers).
- Bonding failures between different blade components.
- Broken or kinked fibers within the blade.

Average downtime per repair varies based on the type of repair and location.

- Minor damage, typical downtimes range from 2 to 7 days,
- Major structural repairs can cause 10 to 30 days



A wind turbine blade that has undergone leading edge erosion [*]



Structural damage in wind turbine blade [cotech]

[*] Mishnaevsky Jr, L., 2019. Repair of wind turbine blades: Review of methods and related computational mechanics problems. Renewable energy, 140, pp.828-839

Introduction to the problem

If damaged wind turbine blades are not repaired catastrophic failure may occur.

Surface and sub-surface structural damage → scarf repair technique

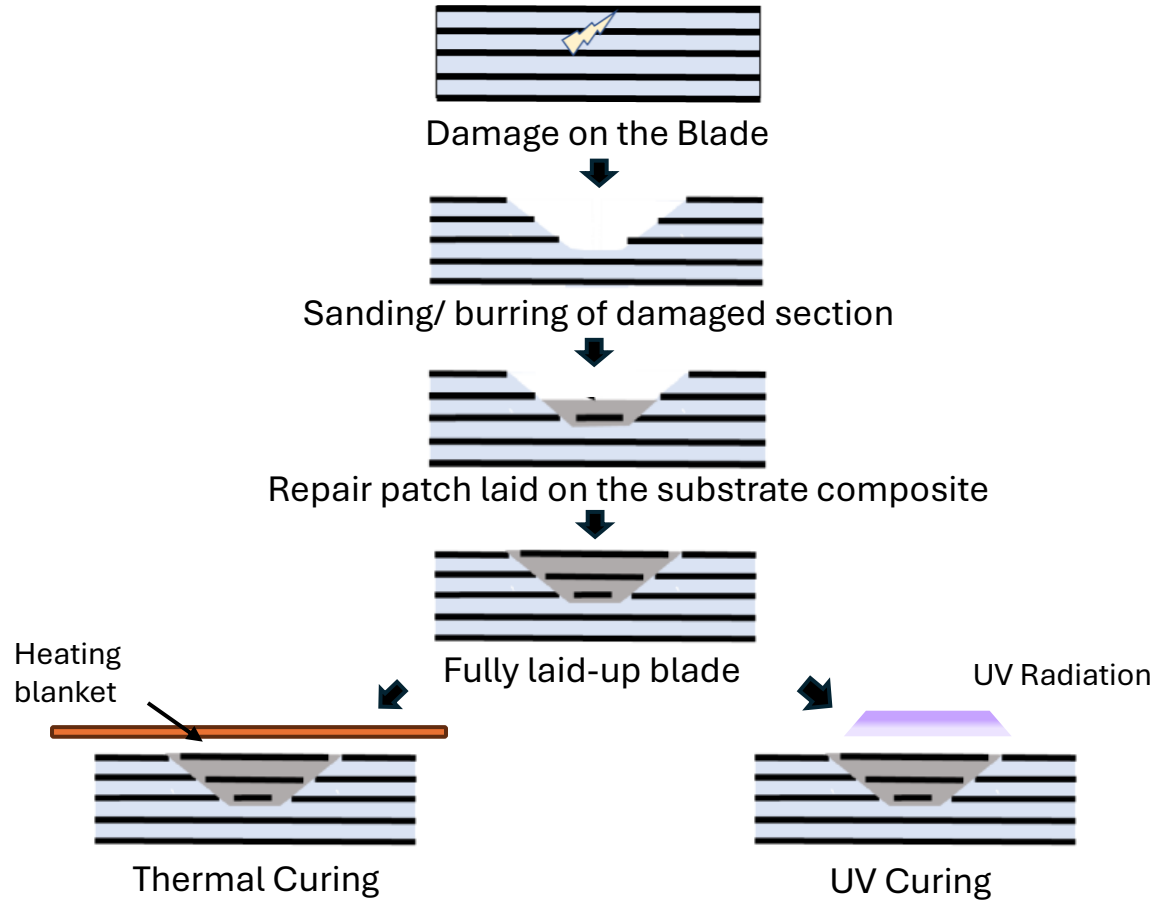

Fig: Schematic depicting scarf patch repair techniques



Fig: Repair on actual wind turbine blade *

[*] Cotech blade repair group and Gurit wind energy group

Curing

Curing is a chemical process that produces the toughening or hardening of a polymer material by cross-linking of polymer chains.

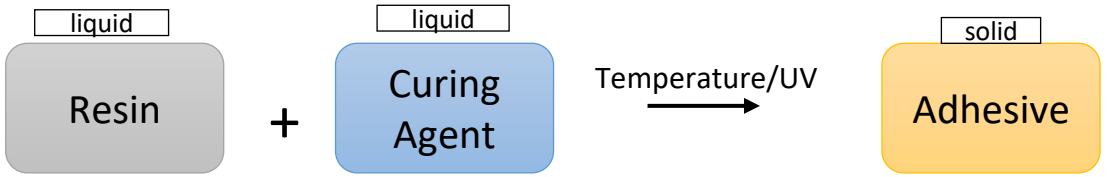

- Chemical Shrinkage due to the curing process.
- Thermal strain due to change in temperature.
- Void Size Evolution

→ Residual Stresses

UV Curing

- UV curing completes in minutes vs hours for thermal curing.
- Uses photoinitiators activated by UV light.
- Safer and eliminates need for heating blankets.
- Reduces blade downtime and labor costs.

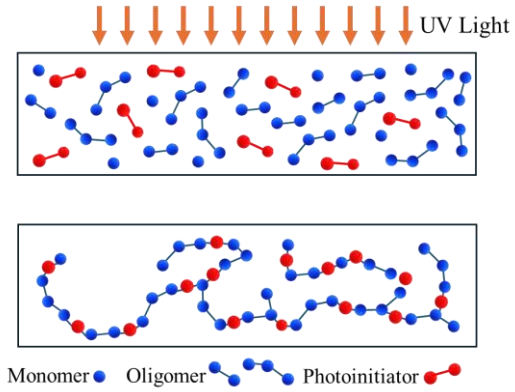

Fig: Cross-linking of the UV cured resin

Cure Kinetics model

The cure process is modelled using an autocatalytic model according to Kamal and Sourour [*]

$$\frac{d\alpha}{dt} = (k_1 + k_2\alpha^m)(1-\alpha)^n$$

$$k_i = k_{0_i} exp\left(-\frac{E_{a_i}}{RT}\right)$$

α is the degree of cure,
$d\alpha/dt$ is the rate of cure,
m and n are model coefficients
E_{ai} are the activation energies (i = 1,2)
R is the universal gas constant
T is the absolute temperature.

Gel Point: The point at which the system stops flowing – rapid and sudden increase in viscosity

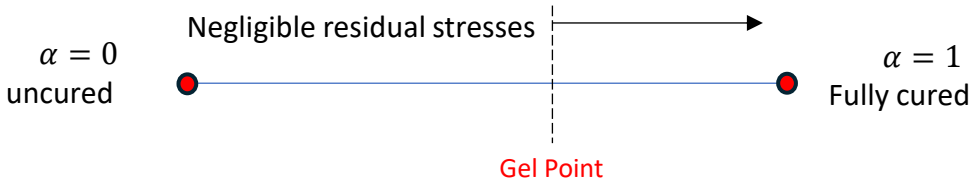

Equilibrium equation

$$\nabla . \boldsymbol{\sigma} + \boldsymbol{b} = 0$$

Heat transfer equation

$$\nabla \cdot \left(k\, \nabla T(v,t)\right) + \dot{q} + \varphi = \rho C \frac{\partial T(v,t)}{\partial t}$$

$$\dot{q} = v_r \rho_r \Delta H_r \frac{d\alpha}{dt}$$

$k\ is$ the thermal conductivities,
ρ is the density

C is the specific heat of the adhesive.
φ Mechanical energy dissipation

v_r is the resin volume fraction,
ρ_r is the density of the resin
ΔH_r is the polymerization enthalpy of resin

Stresses

$$\boldsymbol{\sigma} = \boldsymbol{Q}\,(\boldsymbol{\epsilon}_{total} - \boldsymbol{\epsilon}_{thermal} - \boldsymbol{\epsilon}_{chemical})$$

Q is the stiffness matrix

Thermal and chemical strain

$$\Delta\epsilon_{thermal} = (CTE)\Delta T \qquad \Delta\epsilon_{chemical} = (CCS)\Delta\alpha$$

$(CTE)_i$ coefficient of thermal expansion
$(CCS)_i$ coefficient of chemical shrinkage

[*] Mortensen, U.A., Andersen, T.L. and Mikkelsen, L.P., 2018, July. Pragmatic approach to cure profile enhancement for improved fatigue performance of thermoset matrix composites. In IOP Conference Series: Materials Science and Engineering (Vol. 388, No. 1, p. 012014). IOP Publishing

Material model: Viscoelastic with cure and temperature dependency

The stresses in an orthotropic composite are given as:

$$\boldsymbol{\sigma_{ij}(t)} = \left(\boldsymbol{Q_{ij}}\right)_{\infty} \boldsymbol{\epsilon} + \sum_{\boldsymbol{p=1}}^{\boldsymbol{N}} \left(\boldsymbol{Q_{ij}}\right)_{\boldsymbol{p}} \exp\left(-\frac{\boldsymbol{t}}{\boldsymbol{\tau_p}}\right) \boldsymbol{\epsilon_j}$$

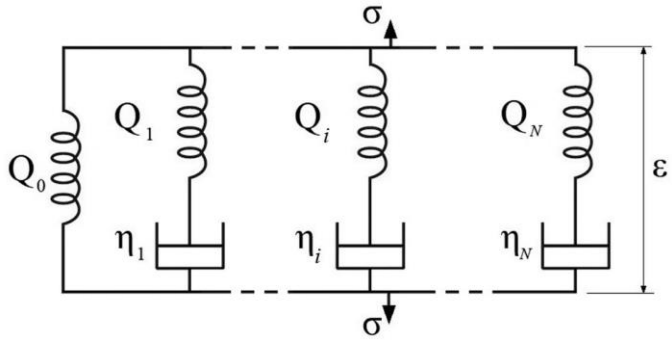

$\boldsymbol{Q}_{\infty}$ is the long-term (orthotropic) stiffness matrix, $\boldsymbol{Q_p} = w_p \boldsymbol{Q}_{\infty}$ is the stiffness matrix associated with the pth prony element, w_p and τ_p are the prony constants.

Degree of cure dependency

$$\tau_p(\alpha) = 10^{\left[\log\left(\tau_p(\alpha_r)\right) + (f(\alpha) - (\alpha - \alpha_r)\log(\lambda_p))\right]}$$

$$f(\alpha) = 9.1347\alpha^2 + 0.6089\alpha + 9.3694$$

$$\lambda_p = \frac{\tau_{peak}}{\tau_p(\alpha_r)}$$

Temperature dependency

$$a_T = 10^{\left[-a_1 \exp\left(\frac{1}{\alpha - 1}\right) - a_2\right][T - T_r]}$$

$$\xi^t = \int_0^t \frac{ds}{a_T(\alpha, T)} \;;\; \xi^s = \int_0^s \frac{ds}{a_T(\alpha, T)} \;;\; \xi^{\Delta t} = \int_t^{t+\Delta t} \frac{ds}{a_T(\alpha, T)}$$

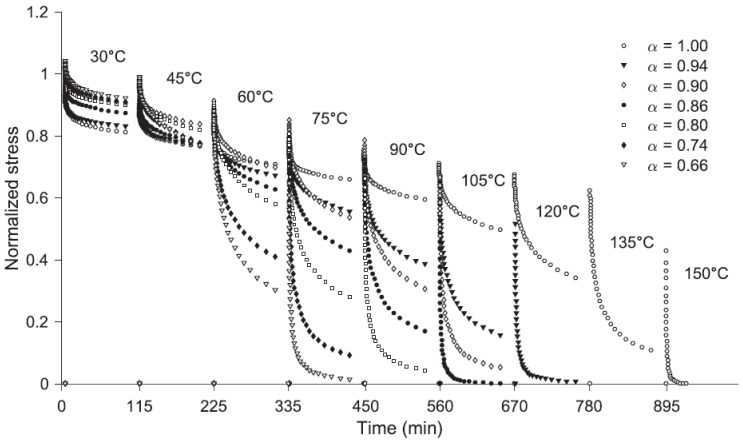

[*] Sebastian Blanco, Hangil You, Tomas Webbe Kerekes, and Gun Jin Yun. Cure-induced residual stress buildup and distortions of cfrp laminates with stochastic thermo-chemical and viscoelastic models: Experimental verifications. Mechanics of Advanced Materials and Structures, 29(19):2740–2756, 2022

Objective

- To model the entire repair process numerically.
- To estimate the residual stresses at the end of the repair process UV curing using hybrid analytical-numerical modeling.
- To compare the results with the conventional technique (i.e. Thermal curing) different temperature cycles.
- Influence of void defects on the development of residual stresses.
- Investigate the post-repair mechanical behavior of UV-cured tensile coupon samples through both numerical simulations and experimental testing.

Residual stress analysis

The numerical analysis of the scarf model is executed on ABAQUS standard. A coupled temperature-displacement problem is solved to predict the residual stresses developed during the curing process.

Geometry configuration

Patch: 100 *100 mm ; 6 plies (each of thick 0.5 mm); 3° scarf angle

Adhesive layer: 0.1mm thickness

Substrate composite: 16 plies (each of thick 0.5 mm)

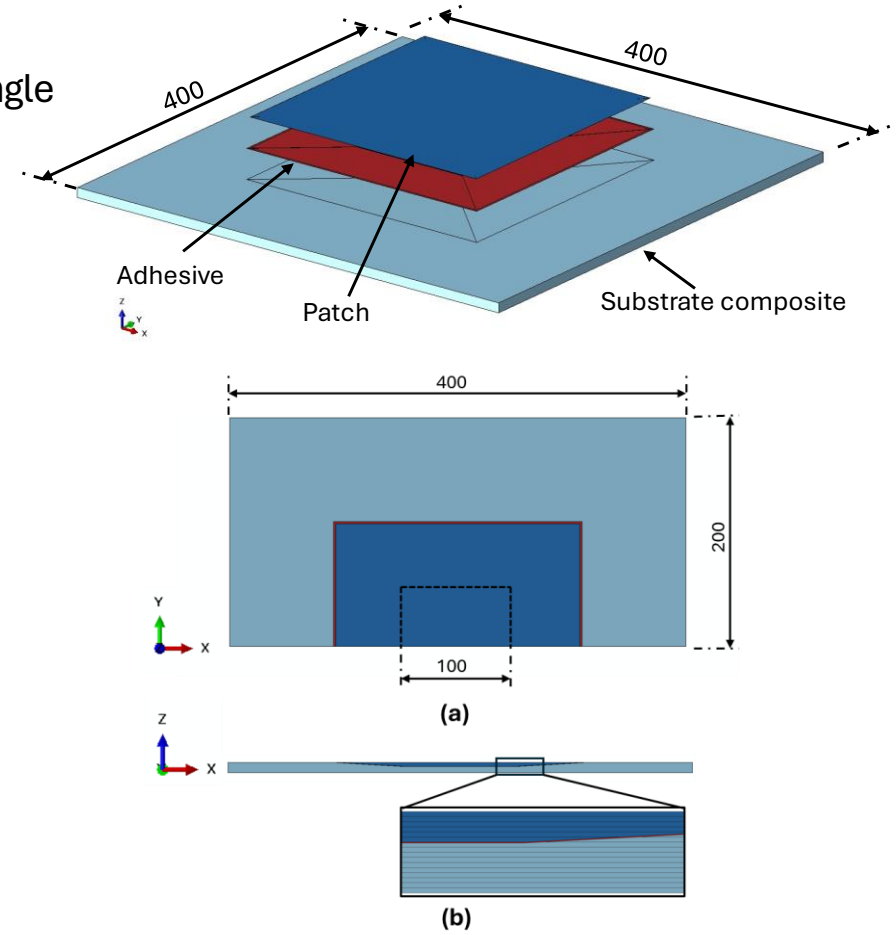

Fig: (a) The geometry of the half model.
(b) A cross-sectional view of the model.

Model :

- Heat generation during curing
- Cure and temperature dependent viscoelastic model:
  - Resin (epoxy) exhibits viscoelastic behavior
  - Pronounced at low degree of cure and high temperature

To reduce the computational time, half model is used

Subroutines used:

Material model → UMAT

Thermal + chemical strains → UEXPAN

Heat generation due to the curing process → HETVAL

UV light field → USFLD

Thermal Curing

- **Magnitude**: Residual stresses typically range between 15–25 MPa.
- **Location of Maximum Stress**: Near the interface between the substrate composite and the repair patch.
- **Repair Integrity**: These stresses worsen debonding at the interface during post-repair loading, potentially reducing long-term durability of the repair.

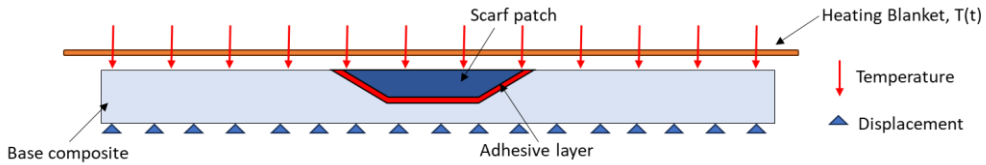

Fig: Schematic of the boundary conditions applied

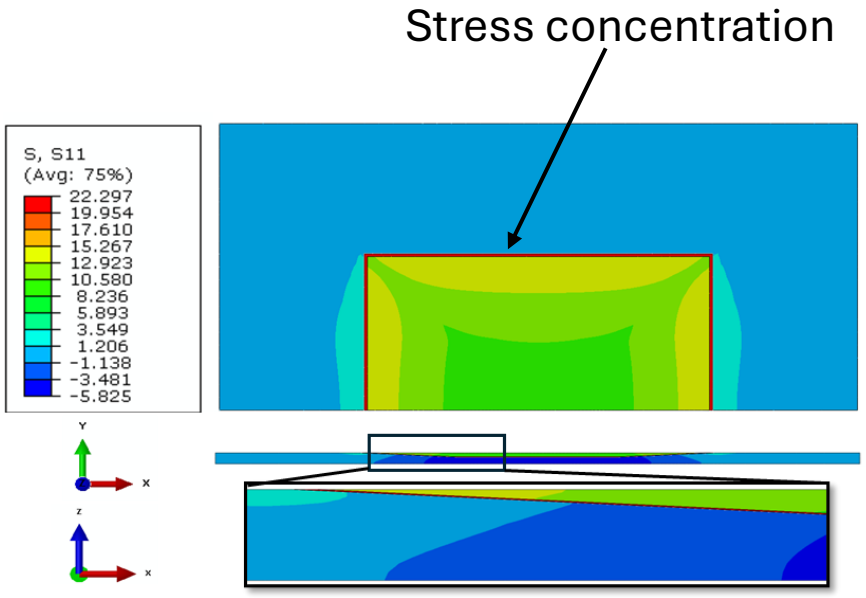

Fig: In-plane stress contours for single ramp 100°C

UV Cure Kinetics model

UV cure kinetics model *

$$\frac{d\alpha(v,t)}{dt} = \varphi I^{p}(v,t)\beta^{q}\exp\left(\frac{-E}{RT_{\text{abs}}(v,t)}\right)\alpha^{m}(v,t)\left(1-\alpha(v,t)\right)^{n}$$

ϕ pre-exponential factor of rate constant
α is the degree of cure at any time
β is the photoinitiator concentration
m and n are the reaction order
k is the rate constant
I light Intensity

Light intensity values at the laminate surface
(assuming Gaussian intensity distribution)

$$I_s(\nu,t) = I_{max}\exp\left[-2\left(\frac{s(\nu,t)}{w_0}\right)^2\right]$$

I_{max} is peak light intensity,
w_0 is light beam radius
s is the position in time of a point

Light intensity along the thickness
(Beer-Lambert law)

$$I(\nu,t) = I_s(\nu,t)\exp[-\lambda z]$$

λ is the attenuation constant
z is the depth.

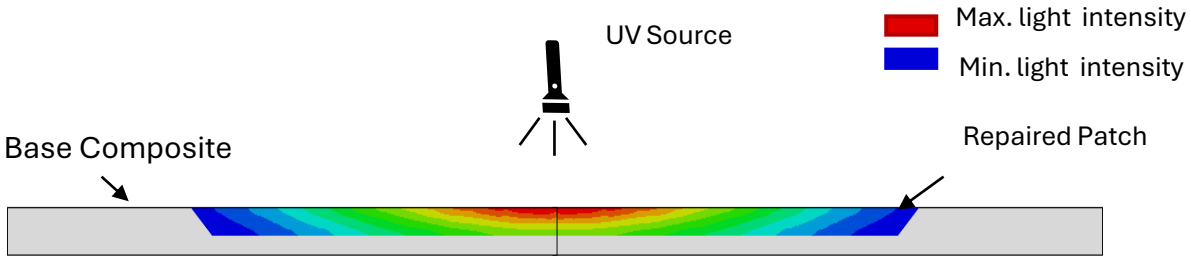

Fig: Light intensity variation along the thickness

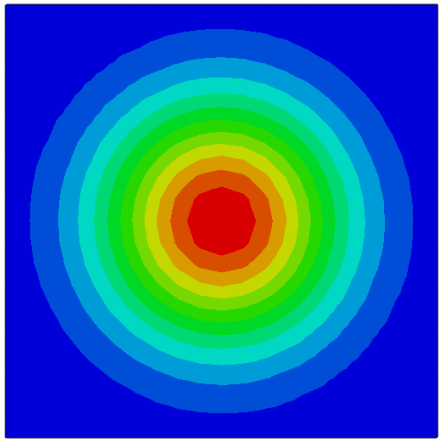

Fig: Light intensity variation at the laminate surface

[*] Yebi, A., & Ayalew, B. (2015). Optimal layering time control for stepped-concurrent radiative curing process. *Journal of Manufacturing Science and Engineering*, *137*(1), 011020.

- UV lamp consists of a series of UV LEDs arranged linearly,
- Adhesive (Gurit Renuvo MPS) is applied between substrate and patch.
- UV Light Source: Wavelength 395 nm (UV-A).
- UV lamp travels at a maximum of 20 mm/sec – for 20 passes and 300 mm/sec for the next 20 passes.
- Maximum light intensity of 300 mW/cm^2

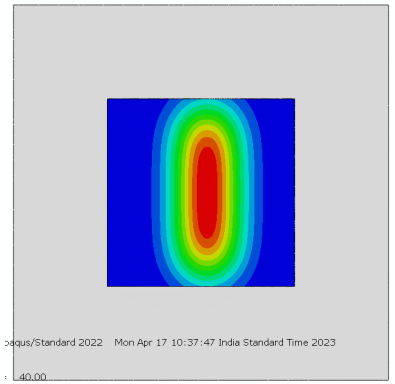



Fig: UV curing on wind turbine blade. [Gurit]

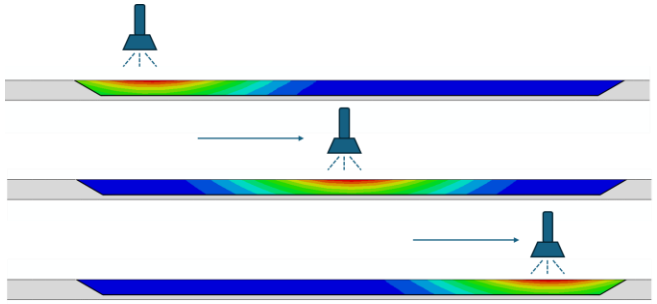

Fig: Movement of UV lamp.

Property	Patch (UV-cured Prepreg)	Adhesive (UV-cured resin)
E_{11}	41 MPa	4 MPa
$E_{22} = E_{33}$	13 MPa	4 MPa
ρ	1800 Kg/m^3	1200 Kg/m^3

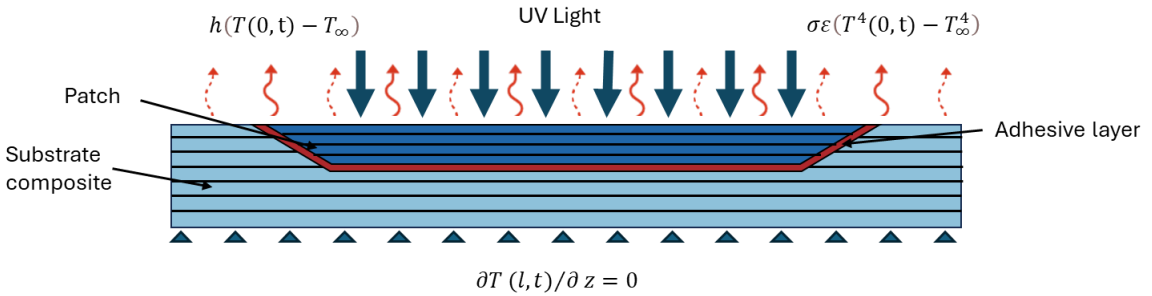

Fig: Boundary conditions applied to the scarf patch repair model.

Results

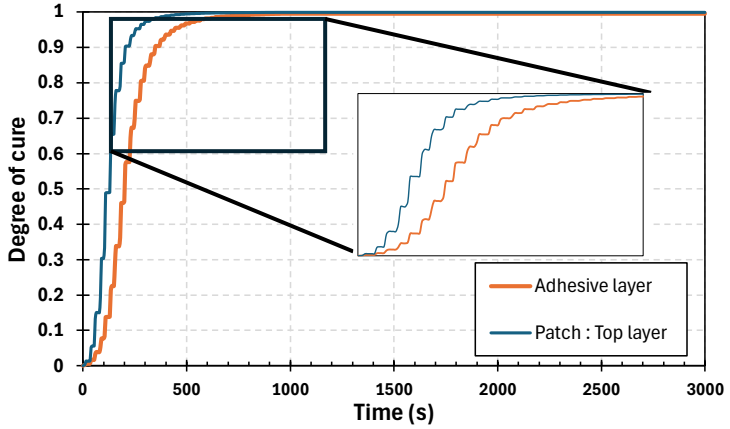

Fig: Degree of cure

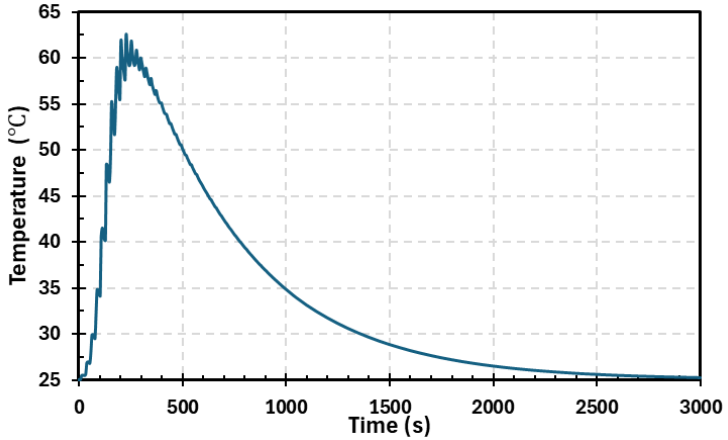

Fig: Temperature rise at a node in top layer of patch

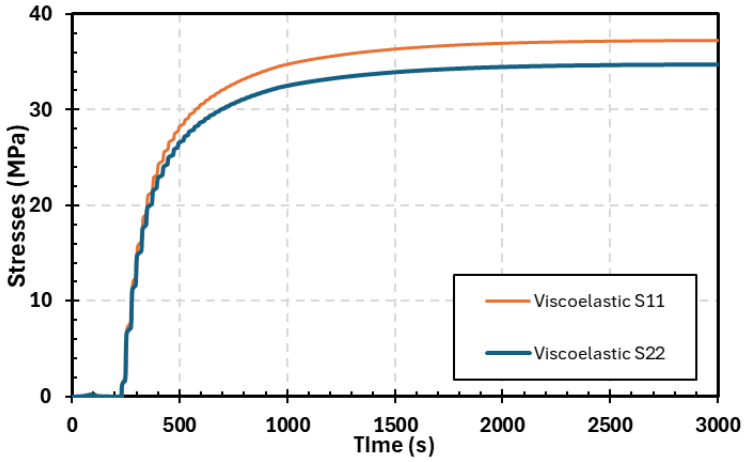

Fig: Stress at the center in the adhesive layer

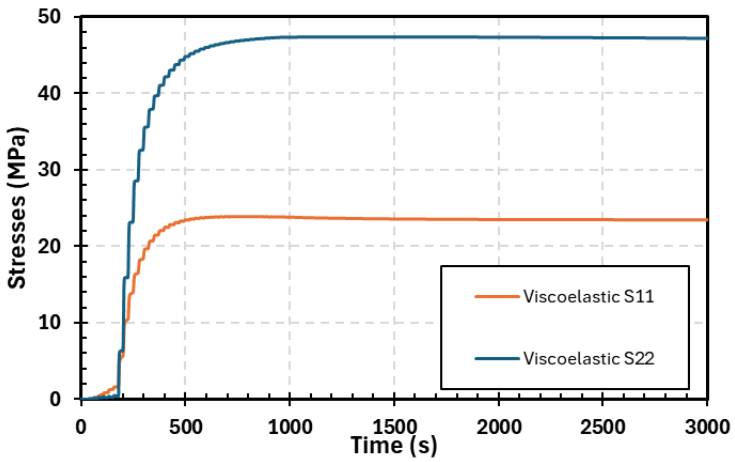

Fig: Stress at the center in the patch

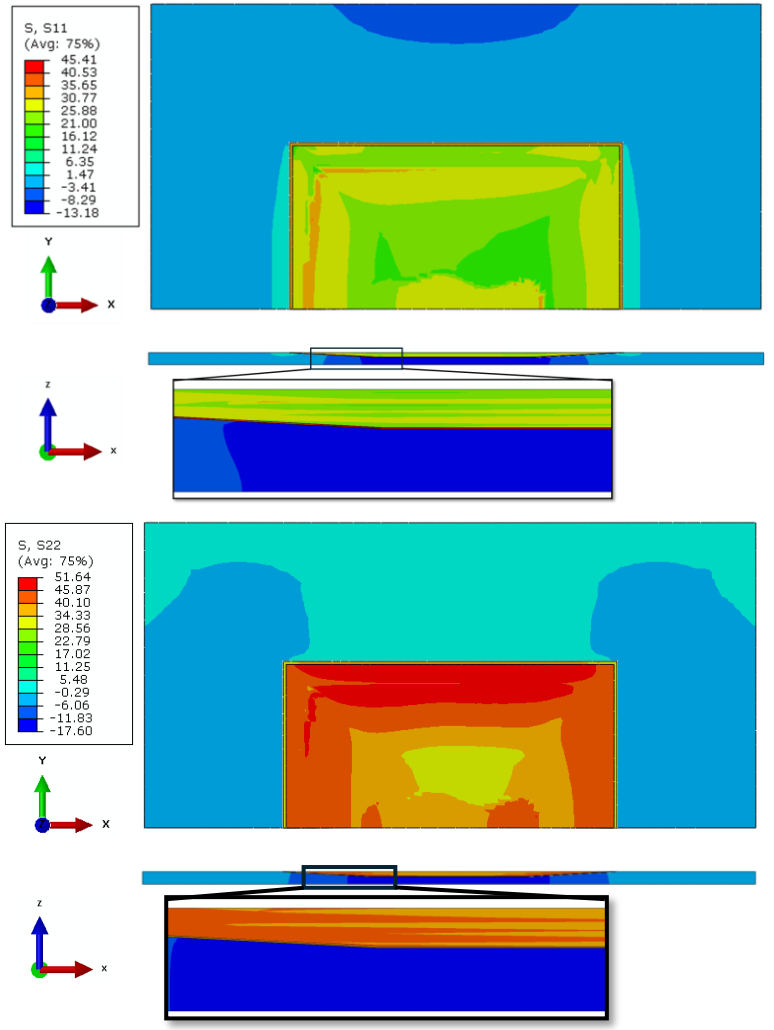

Fig: In-plane stress contours

Results

- Unlike thermal curing, UV curing produces non-uniform residual stress fields.
- Residual stresses range from 45–55 MPa, nearly double that of thermal curing. (due to high chemical shrinkage coefficient)
- Stresses are concentrated at the interface between the substrate and patch, increasing the risk of debonding.

Limitation:

Can be used only for thin laminates because of limited light penetration

Multi-Stage Repair of Thick Laminates

Thick laminate can be cured in a number of stages.

Model 1: First Layer Curing

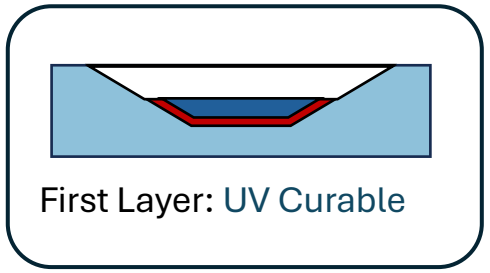

Model 2: Second Layer Curing

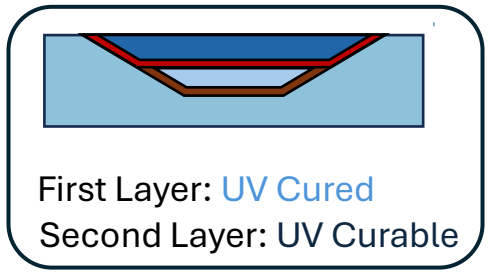

To repair thick laminates, multi-stage repair is investigated, which shows a 13% reduction in residual stresses compared to single-stage repair.

Compare simulation results with experimental measurements

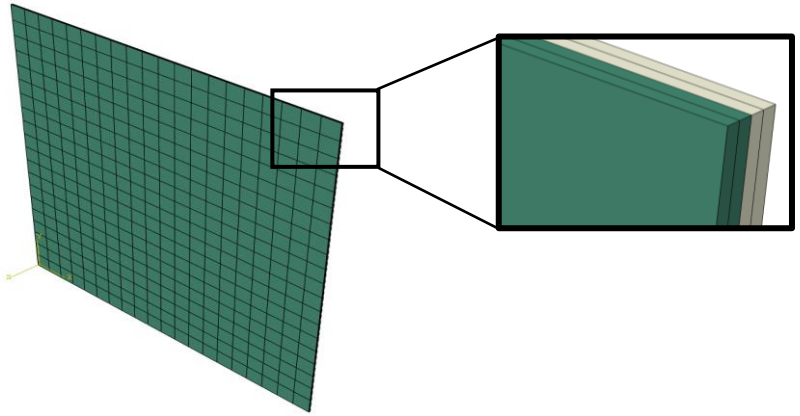

- Laminate modeled in ABAQUS (150 mm × 150 mm)
- Stacking sequence: $[0_2/90_2]$
- Material: Gurit RENUVO UV-cured prepreg

Results:

Numerical Warpage:

Saddle-shaped profile

Max deflections: 4.11 mm and 3.21 mm

Experimental Warpage:

Laminate fabricated using RENUVO UV-cured prepreg

Measured via dial gauge

Max deflections: 4.3 mm and 3.1 mm

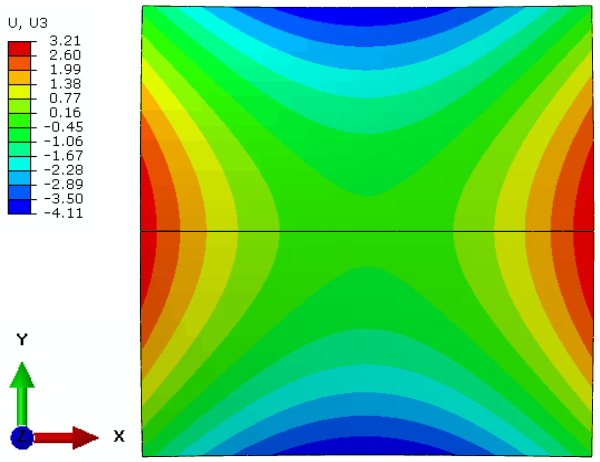

Fig.: Maximum out-of-plane displacement (z-direction) predicted by the numerical model

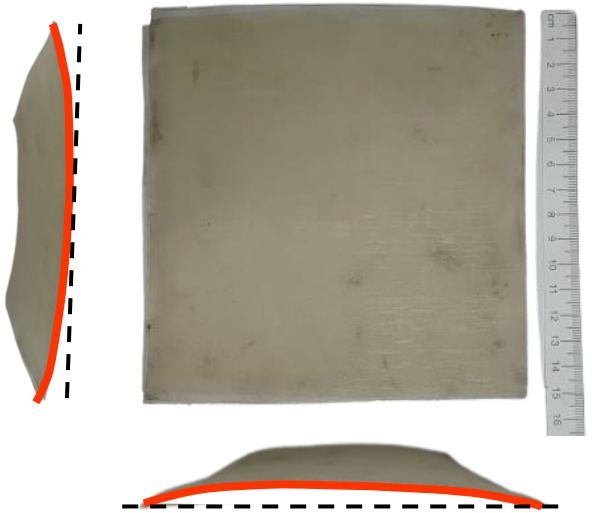

Fig.: Experimentally observed warpage in the UV-cured laminate

Voids and Effects

Causes

- Air entrapment during resin flow (primary cause)
- Gas is created due to chemical reactions during curing
- Nucleation of dissolved gases in the resin.

Effects

- Voids reduce mechanical properties, especially strength and fatigue resistance
- Voids at the interface can lead to:
  - Reduced strength
  - Premature debonding under mechanical loads

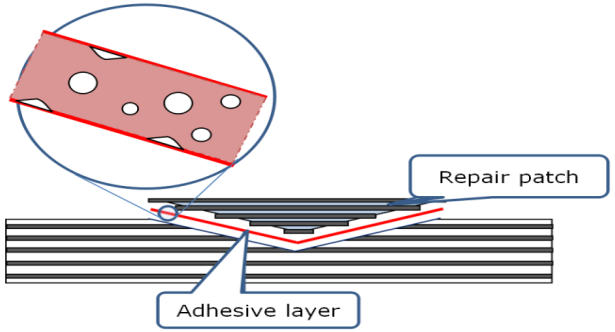

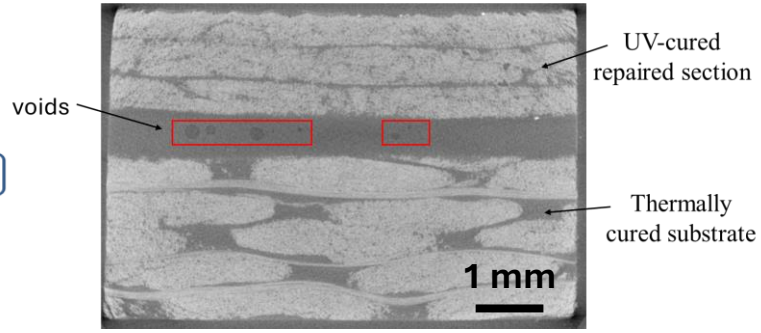

Fig: Micro-CT scan of the repaired sample

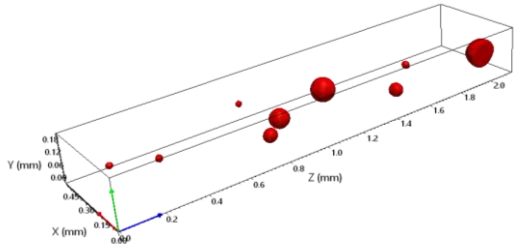

Void distribution

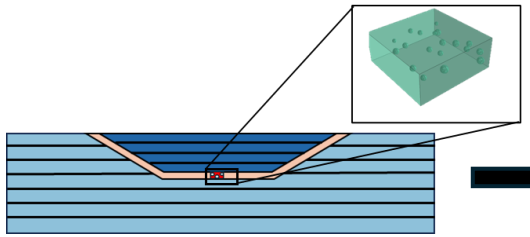

Sub modelling Technique

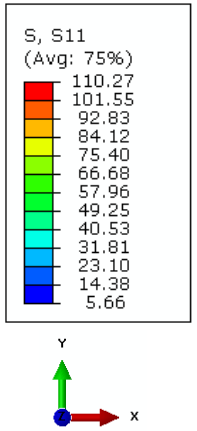

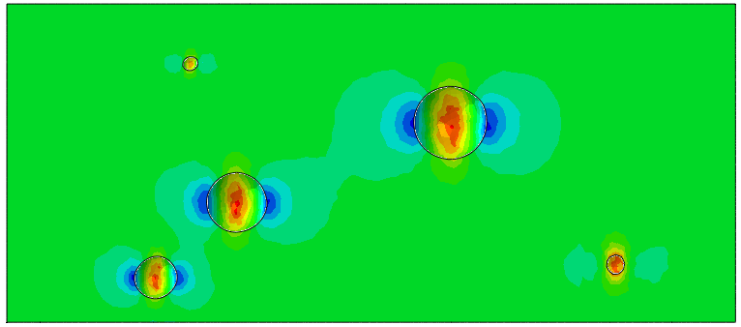

Stresses concentration near the voids.

Paul, D., Varshney, A., Mahajan, P., & Mishnaevsky Jr, L. (2023). Post-repair residual stresses and microstructural defects in wind turbine blades: Computational modelling. *International Journal of Adhesion and Adhesives*, *123*, 103356.

Post-repair mechanical behaviour of the repaired samples

Experimental

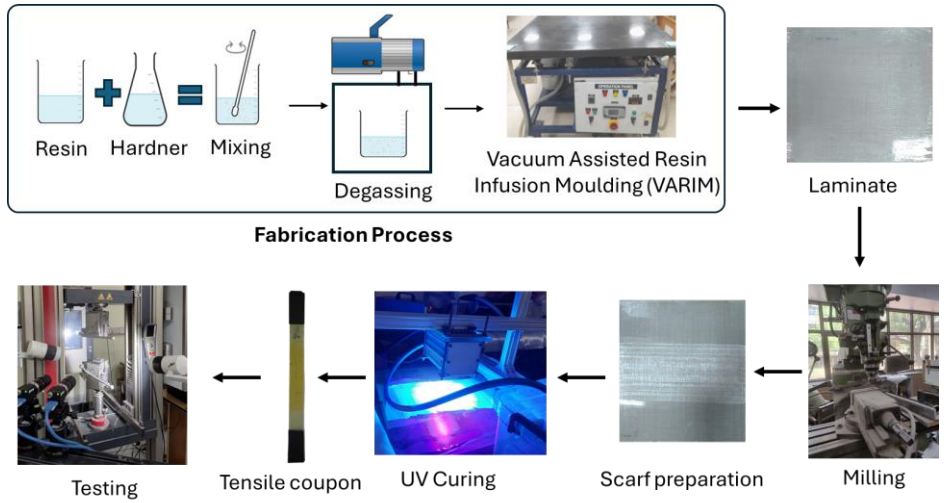

Initial Damage: Debonding at the interface

Damage Propagation: This leads to the separation of the patch from the substrate.

Final Failure: The substrate composite fails in the region with reduced cross-sectional area due to load redistribution.

Numerical

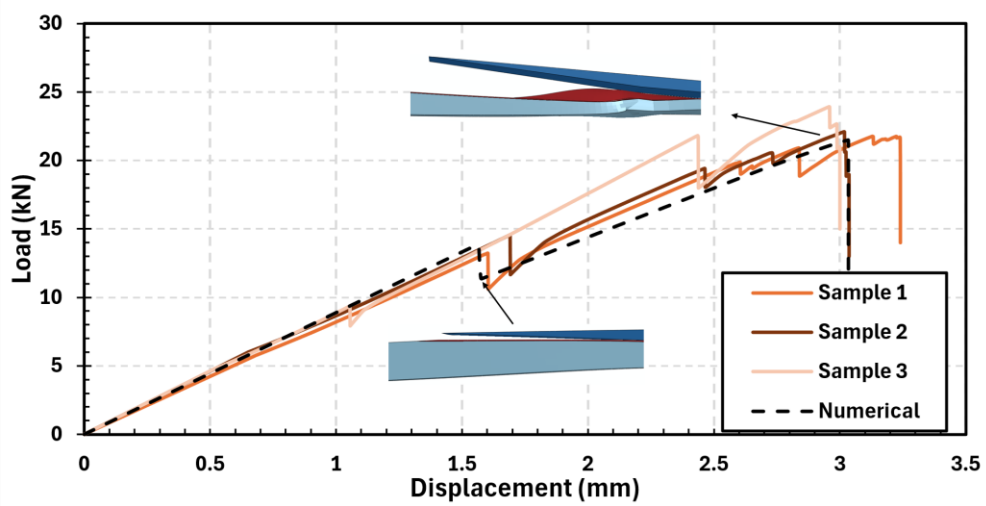

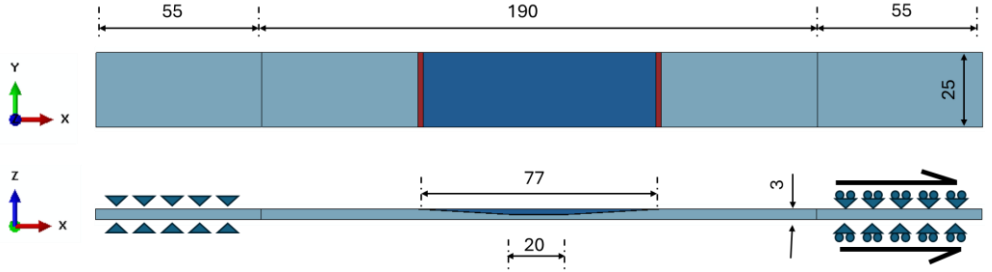

Thermally repaired composite samples exhibit **higher strength** compared to **UV-cured repairs.**

Conclusion

- A hybrid analytical-numerical model is proposed to estimate residual stresses for a given set of cure parameters and repair patch geometry.
- The numerical analysis is performed in ABAQUS using user subroutines (UMAT, UEXPAN, HETVAL, and USDFLD).
- Analysis findings:

  -Residual stresses heavily depend on the temperature cycle used (single-ramp vs. two-ramp)

  -Voids within the adhesive cause stress concentrations up to 2 to 2.5 times the average stresses.

  -Maximum stresses occur at the interface between the repair patch and the base composite.

  -Residual stresses induced by UV curing are higher compared to thermal curing.


Thank You!

The 24th International Conference on Composite Materials (ICCM24)
Fatigue and Damage Mechanics of Composites
Tuesday, August 5, 2025

Effect of Cooling Rate on Mode II Fatigue Crack Growth Behavior in Carbon Fiber Reinforced Polyphenylene Sulfide

Yu Zusho[1], Sota Oshima[1,2], Ryo Higuchi[1],
Tomohiro Yokozeki[1], Takahira Aoki[1]

1. The University of Tokyo
2. Tokyo University of Agriculture and Technology

BACKGROUND

Carbon fiber reinforced thermoplastics (CFRTP)

Attention given to cycle time, material storage, toughness, recyclability, etc.

Aerospace applications → PPS, PAEK family (PEEK, PEKK, etc.)

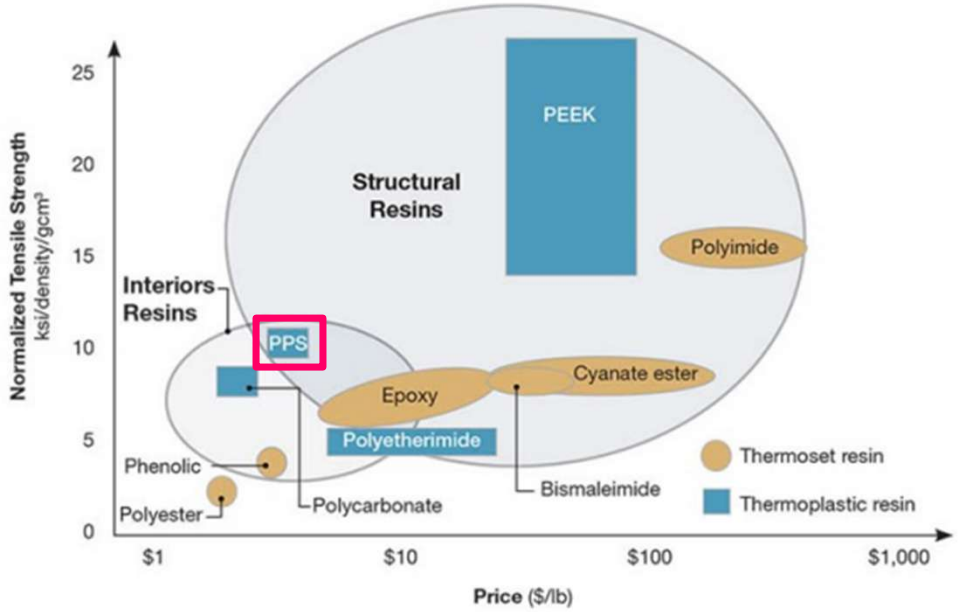

[1] Tenney et al. NASA/CR–2011-217076 (2011)

Polyphenylene Sulfide (PPS)

-Crystalline

-High specific strength and toughness

-Relatively inexpensive

-Excellent thermal stability

-Excellent moisture and chemical resistance

BACKGROUND

CF/PPS application in aircraft

Excerpt from [2] Table A-II Flying structural parts made of thermoplastic composites (TPC).

Description	Manufacturer	Manufacturing Process	Date	Notes
Airbus 340 wing leading edge access panels	GKN Fokker	Co-consolidated.	2002	
Airbus A350 brackets	GKN Fokker	Stamp formed clips and cleats bolted to skins and frames.	2002	The Airbus 350-XWB has **over 8,000** TPC brackets.
Boeing 787 brackets	Dahar		2014	Over 10,000 per aircraft.
Fokker 50 main landing gear doors	GKN Fokker	Assembled with Resistive welding.		
Leonardo (AgustaWestland) AW169 helicopter horizontal tail leading edge	GKN Fokker	Two omega sections butted between flat skins to produce a full span torsion box.	2018	JEC 2013 innovation award. 15% lighter than previous design.
Airbus 340-600 ribs and angle brackets	GKN Fokker			Used on keel beam and ailerons.

CF/PPS has **high demand** in terms of high-rate production and weight reduction.

[2] Krueger et al. NASA/TM–20240005376 (2024)

BACKGROUND

CFRTP manufacturing: Hot press molding

Material placed in mold → Heating & Pressing → Cooling (Consolidation)

- High molding temperature

Crystallinity changes depending on **cooling rate**

→ Large mismatch in thermal expansion between the base material and the fibers

- In the case of crystalline resin: Thermal shrinkage + Volumetric shrinkage due to crystallization

→ Large thermal residual stress

Cooling rate → **Crystallinity** → **Mechanical Properties, Fracture Behavior**

Purpose Elucidation of cooling rate dependence of basic properties in CF/PPS composite materials

Our Previous study: Evaluation of Thermal, Mechanical, and Fracture Properties of PPS and CF/PPS

Today's Content

Mode II Fatigue Fracture Characterization of CF/PPS

(ENF Fatigue Test, Fracture Surface Observation)

EXPERIMENTAL METHOD

- CFRTP Specimen

  CF/PPS unidirectional prepreg sheet (TenCate Cetex® TC1100, Toray)

  (Carbon fiber; AS4, Vf = 59 vol%)

  → CF/PPS laminate $[0_{12}//0_{12}]$

  - Hot press molding: 325 ºC, 20 min
  - Cooling rate during consolidation: **1, 5, 10 ºC/min**

- Characterization of mode II fatigue crack propagation

  → End-notched flexure (ENF) fatigue test



EXPERIMENTAL METHOD

- Preliminary experiments for parameter setting

  Static loading while changing initial crack position a

  → Calculation compliance C at each crack position a

  → Relationship between crack length a - compliance C

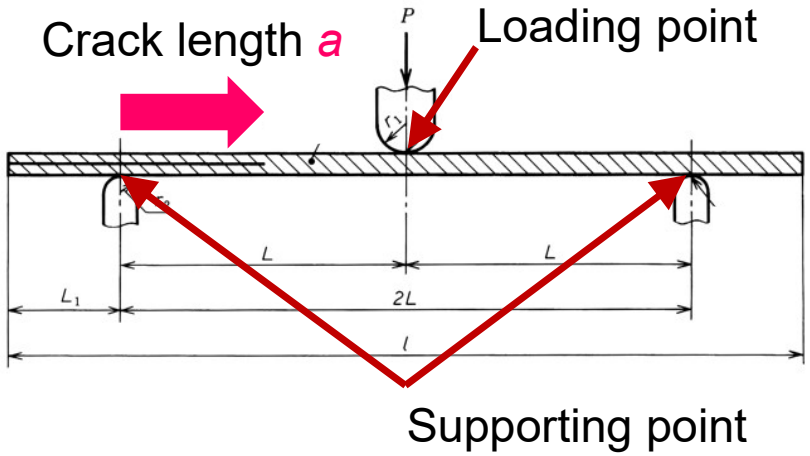

$$(2h)^3 B C = \beta_0 + a^3 \beta_1$$ (h: thickness, B: width β0, β1: constant)

For fatigue test, setting crack length a and energy release rate G_{max} and determine P_{max}

$$G_{max} = \frac{P^2}{2B}\frac{\partial C}{\partial a} = \frac{P_{max}^{\ 2}}{2B^2}\frac{3a^2}{(2h)^3}\beta_1$$ (Modified Compliance Calibration Method)

EXPERIMENTAL METHOD

- Fatigue test
  - Fatigue testing machine: Electropuls E10000 (Instron)
  - Load ratio: R = 0.1 (P_{max} / P_{min})
  - Frequency: 10 Hz
  - Sampling interval: 5 ms (20 points / wave)
  - Load gradation test method (× 0.99, 5 to 10 times / test)

Calculation of compliance C for each cycle, and crack length a corresponding to C

→ Calculation of G_{max} for each cycle

→ Setting ΔN at which the average R^2 value of G_{max} is greater than 0.90

→ Ploting fatigue crack propagation characteristics ($da/dN - G_{max}$ diagram)

$$G_{max} = \frac{P^2}{2B}\frac{\partial C}{\partial a} = \frac{P_{max}^{\ 2}}{2B^2}\frac{3a^2}{(2h)^3}\beta_1$$ (Modified Compliance Calibration Method)

RESULTS AND DISCUSSION

Fatigue crack propagation characteristics (da/dN − G_{max} diagram)

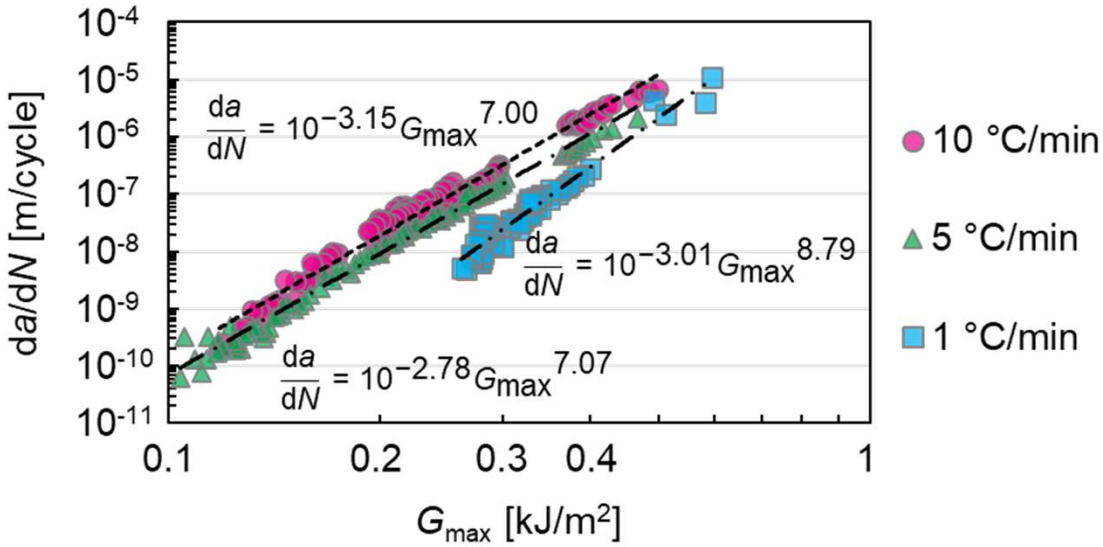

- Cooling rate 10, 5 ºC/min (G_{max} = 0.1～0.5 kJ/m^2)

  Proportional relationship between da/dN and G_{max} on both logarithmic graphs (Paris law)

  → Behavior following the Paris law until around da/dN = **10^{-10}** m/cycle

  → Fatigue crack growth threshold is not clear.

RESULTS AND DISCUSSION

Fatigue crack propagation characteristics (da/dN − G_{max} diagram)

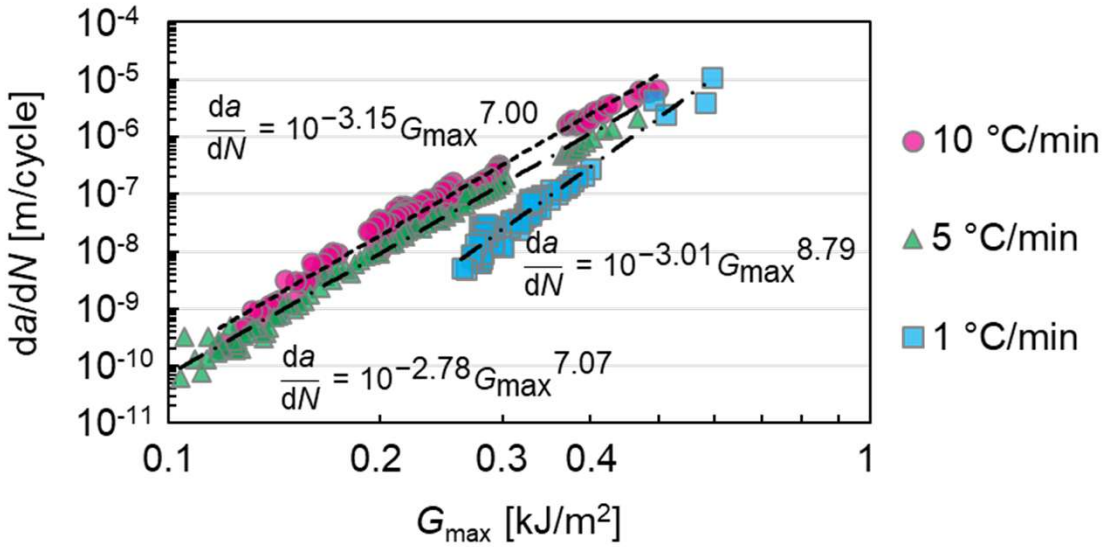

- Cooling rate 1 ºC/min (G_{max} = 0.3～0.6 kJ/m^2)

  Proportional relationship between da/dN and G_{max} on both logarithmic graphs (Paris law)

  Fatigue crack growth stops at around G_{max} = 0.26 kJ/m^2 → Fatigue crack growth threshold

  1 ºC/min is particularly variable (Large crystal size → Fracture might dominate local properties)

RESULTS AND DISCUSSION

(Crystallinity, Static fracture toughness test) Oshima et al. *Composites Part A* 164 (2023)

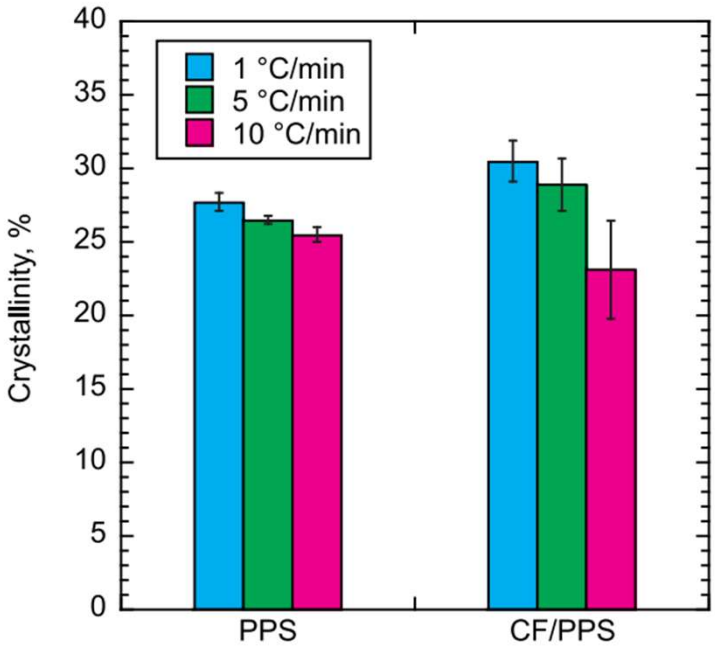

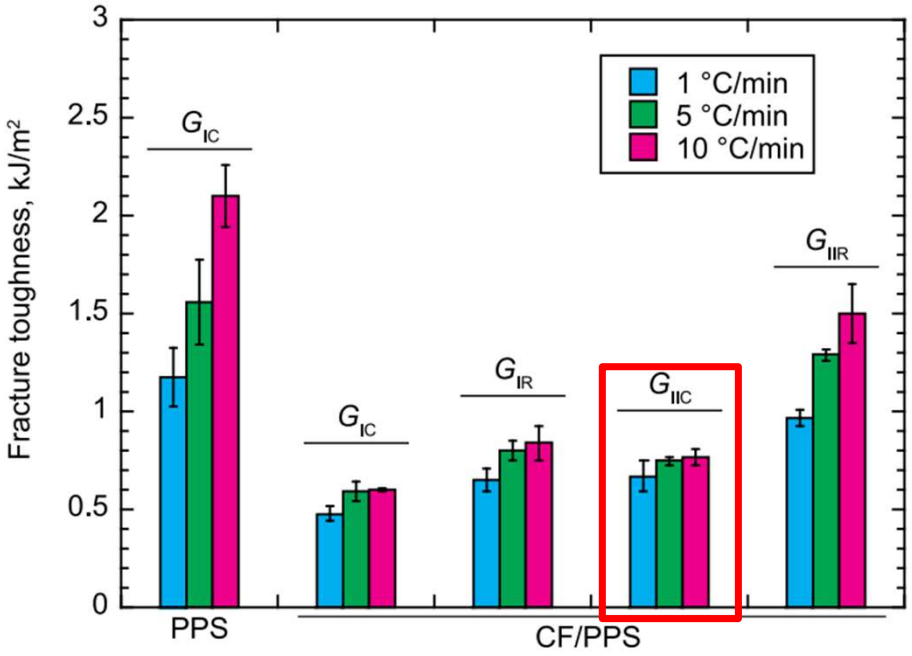

- Lower cooling rate → **Higher crystallinity** and **lower fracture toughness**

  (Reasonable results considering the properties of thermoplastic resins)

- G_{IIC}: **Equivalent at 5 and 10 ºC/min**, lower and more variable at 1 ºC/min

RESULTS AND DISCUSSION

Fatigue crack propagation characteristics (da/dN − G_{max} diagram)

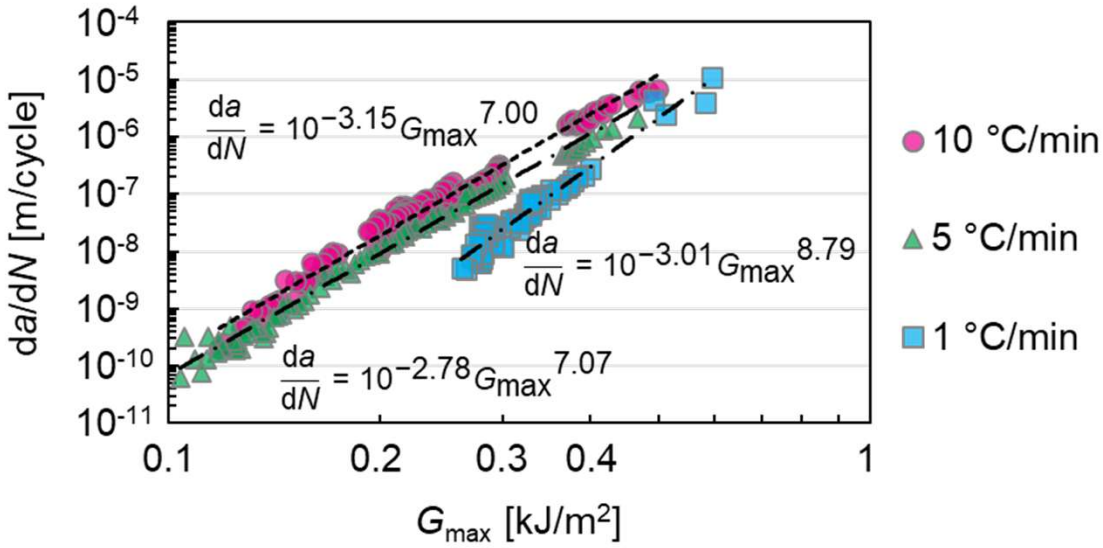

- Plot value and slope: **Equivalent at 5 and 10 ºC/min**, lower and more variable at 1 ºC/min

  → **Trends consistent with static test results**

- **Lower cooling rate → Crack propagation rate (da/dN) decreased**

(**The large slope at 1 ºC/min** corresponds to the **low toughness** in the static test region (higer G_{max}))

RESULTS AND DISCUSSION

Fatigue crack propagation characteristics (da/dN − G_{max} diagram)

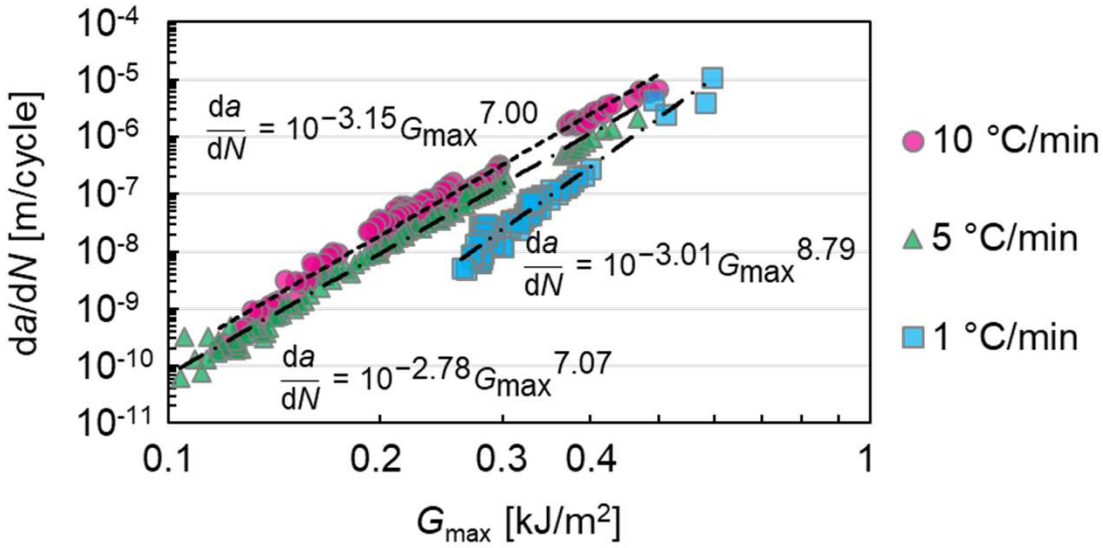

This suggests a possible transition in fracture mode between 5 ºC/min and 1 ºC/min.

→ The region of **significant change in crystallization behavior**

(→ Discussed later in fracture surface observation)

RESULTS AND DISCUSSION

Fracture Surface (SEM Image)

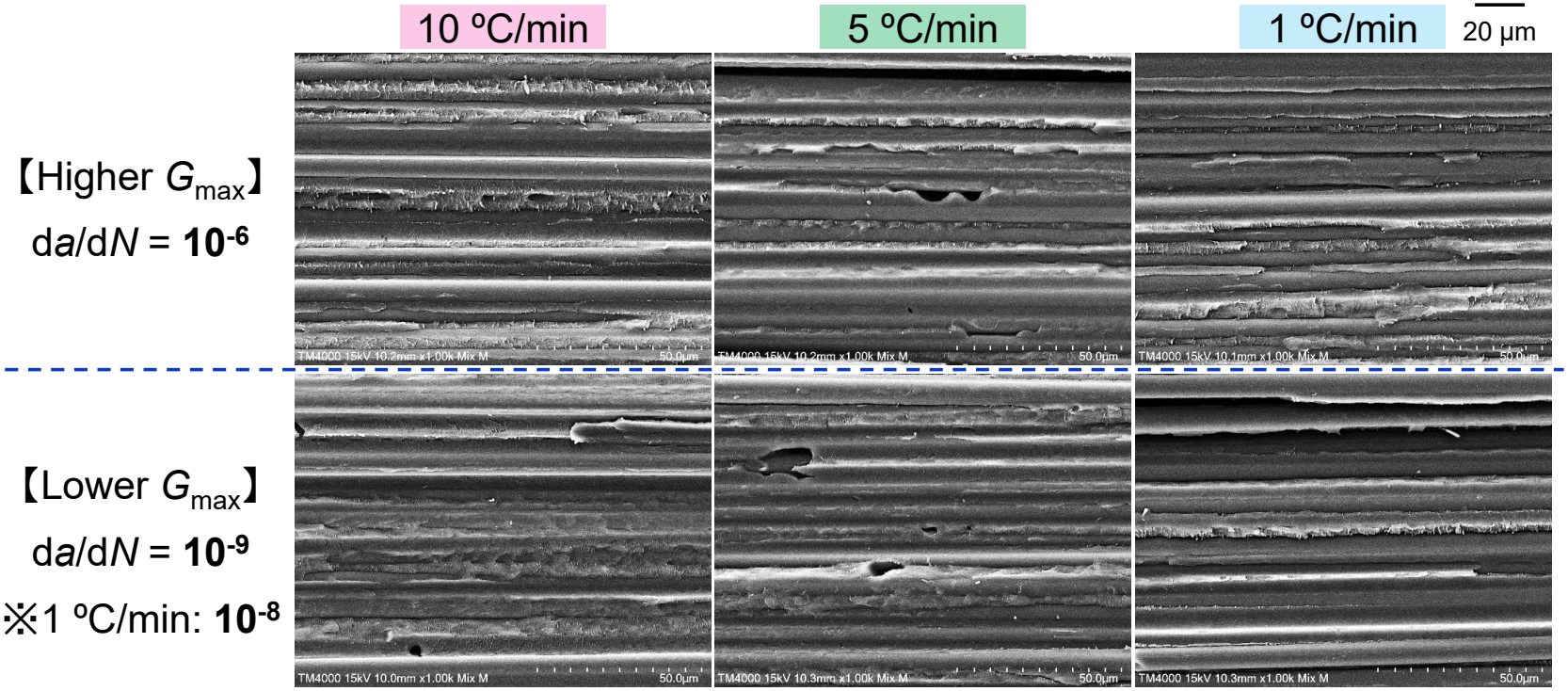

CF/Epoxy [3]

da/dN = **10^{-7}**

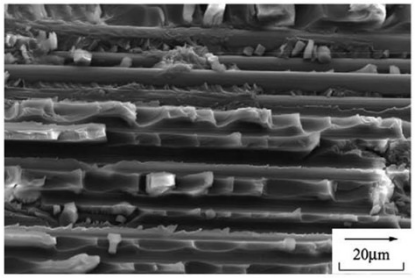

- **Ductile fracture of PPS matrix** observed throughout
  (Brittle fracture of epoxy: hackle pattern)
- Small effect of cooling rate on fracture morphology

[3] Hojo et al. *Int J Fatigue* 28 (2006)

RESULTS AND DISCUSSION

Fracture Surface (SEM Image)

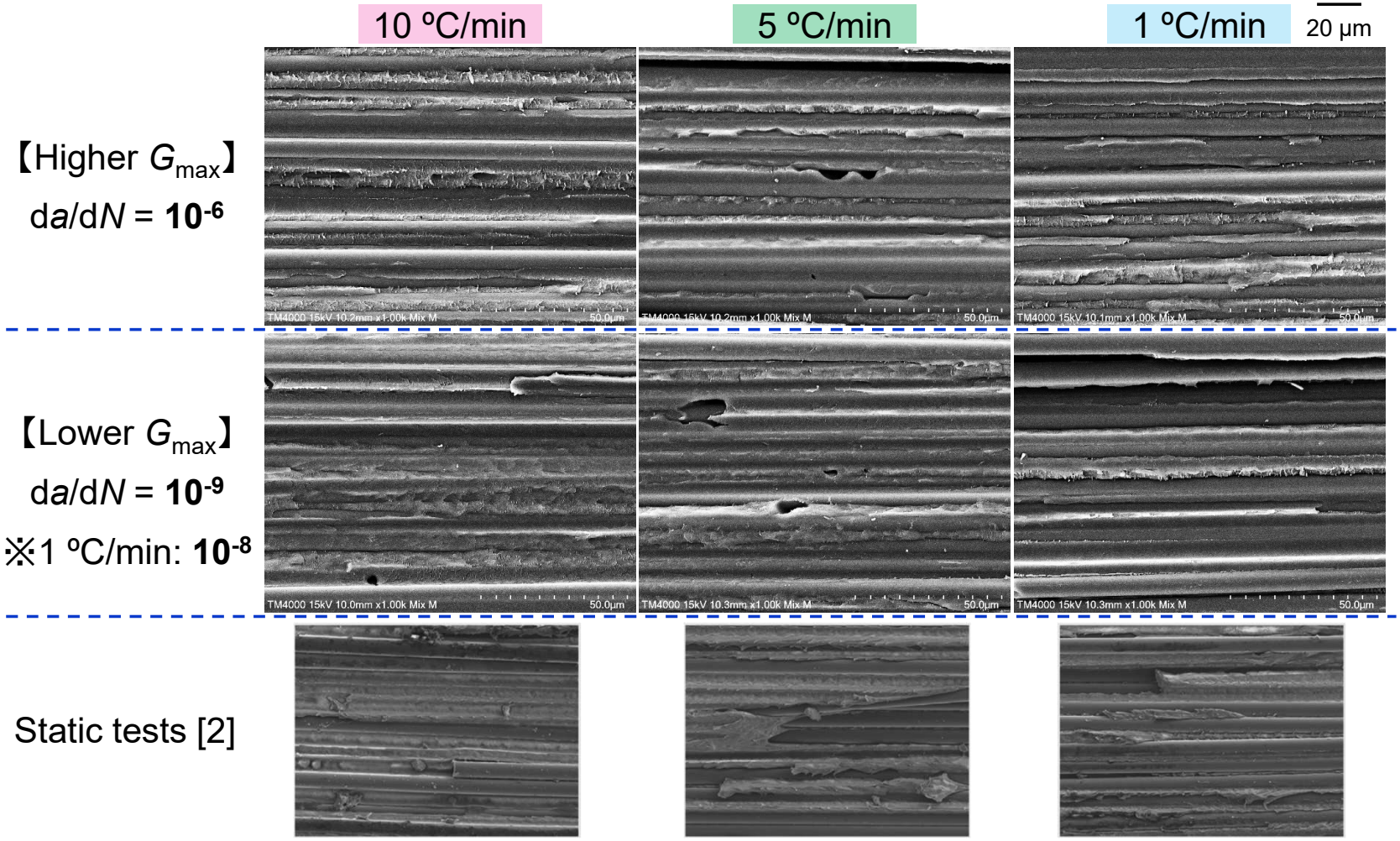

[2] Oshima et al. (2023)

RESULTS AND DISCUSSION

Fracture Surface (SEM Image)_Enlarged View

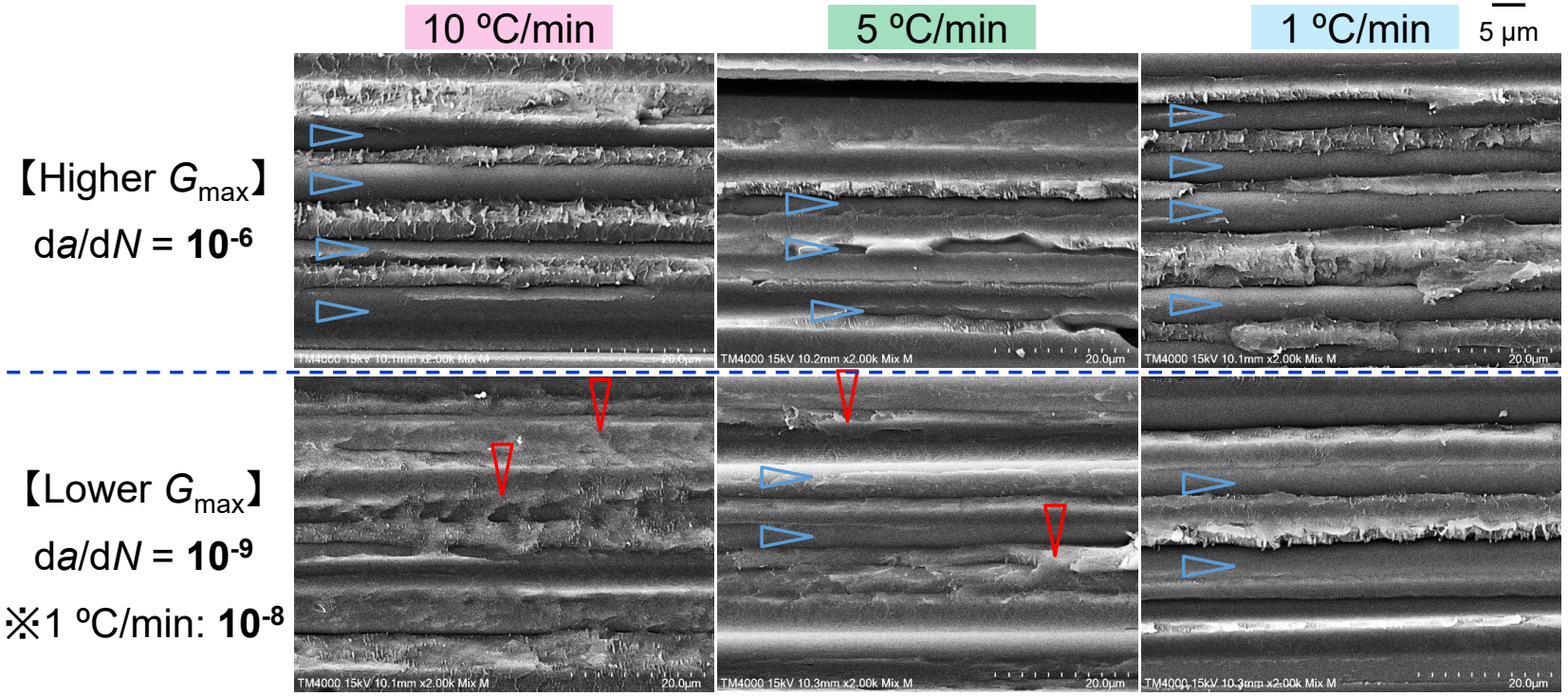

CF/Epoxy [3]

da/dN = **10^{-7}**

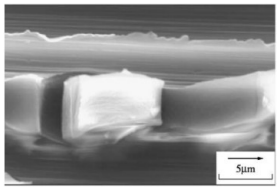

- Higher G_{max} Exposed carbon fiber ▷ (low interface strength)
- Lower G_{max} Resin elongated significantly ▽ in 10, 5 ºC/min

Influence of cooling rate appears at lower G_{max}

[3] Hojo et al. *Int J Fatigue* 28 (2006)

RESULTS AND DISCUSSION

Comparison with another polymer matrix

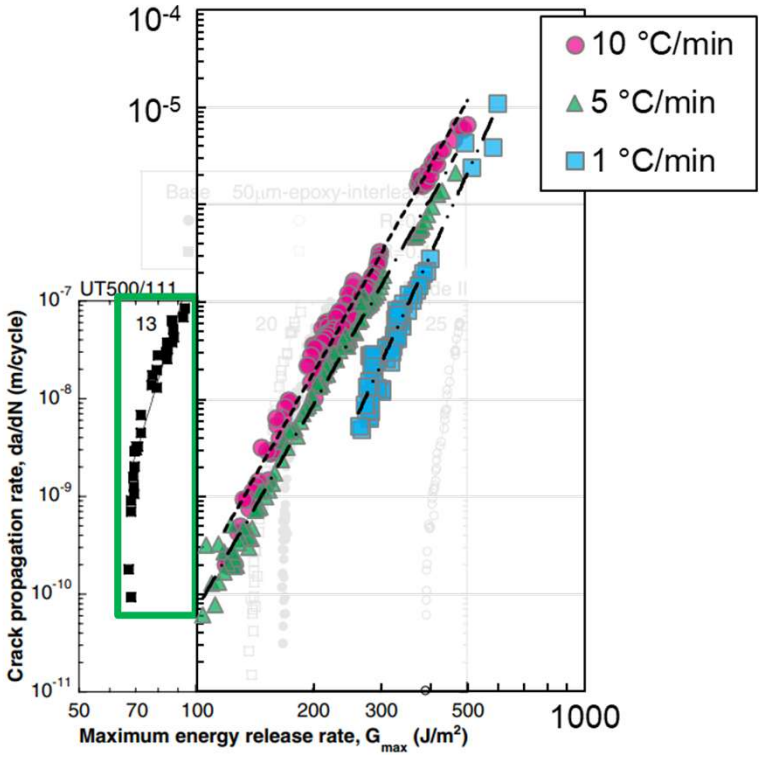

Fig. 14. Relation between crack propagation rate and maximum energy release rate under mode II loading for base and 50 μm-epoxy-interleaved laminates.

[3] Hojo et al. *Int J Fatigue* 28 (2006)

Compare with conventional **CF/Epoxy [3]** ...

- CF/PPS: Lower d*a*/d*N* and Higher G_{max}

→ CF/PPS has higher resistance to fatigue crack propagation than CF/Epoxy

RESULTS AND DISCUSSION

Comparison with another polymer matrix

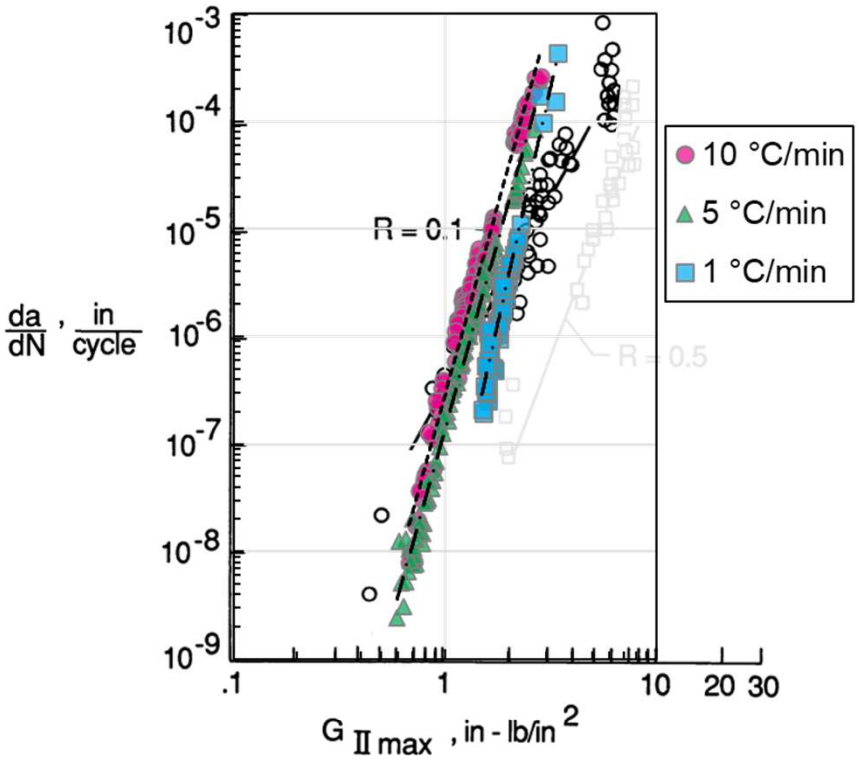

[4] Martin et al. *NASA TECHNICAL MEMORANDUM* 100577 (1988)

Compare with **CF/PEEK [4]** …

- Value: Close to CF/PEEK
- Slope: CF/PEEK < CF/PPS (easier crack propagation)

→ **CF/PPS is inferior to CF/PEEK fatigue resistance**

∵ Interface properties, trans-crystal formation

Prospects of CF/PPS

Improvement of performance

by modifying fiber-base material interface

e.g. resin modification, CF surface treatment, molding process improvement, etc.

CONCLUSION

Influence of Cooling Rate on Fatigue Damage Mechanisms in CF/PPS Composites

- ✓ **Lower cooling rate → Lower crack growth rate**

  Cooling rate 10, 5 ºC/min → No clear fatigue crack growth threshold

  Cooling rate 1 ºC/min → Fatigue crack growth threshold around G_{max} = 0.26 kJ/m^2

- ✓ Fracture surface → Ductile fracture of PPS matrix

  Influence of cooling rate on fracture morphology appears at lower G_{max}

- ✓ Resistance to fatigue crack propagation

  CF/Epoxy << CF/PPS < CF/PEEK

Leibniz-Institut für Verbundwerkstoffe

Modified Curing Cycles and Accompanying Polymer and Adhesion Changes in Fiber Metal Laminates

A. Baumann[1], S. Mrzljak[2], F. Walther[2], J. Hausmann[1]
[1]Leibniz Institut für Verbundwerkstoffe GmbH, Kaiserslautern
[2]Chair of Materials Test Engineering (WPT), TU Dortmund University

Chapter

1. Motivation
2. State of the art
3. Materials and methods
4. Modified curing cycle results
5. Adhesion between epoxy and metal sheets
6. Alternative approach
7. Conclusion & outlook

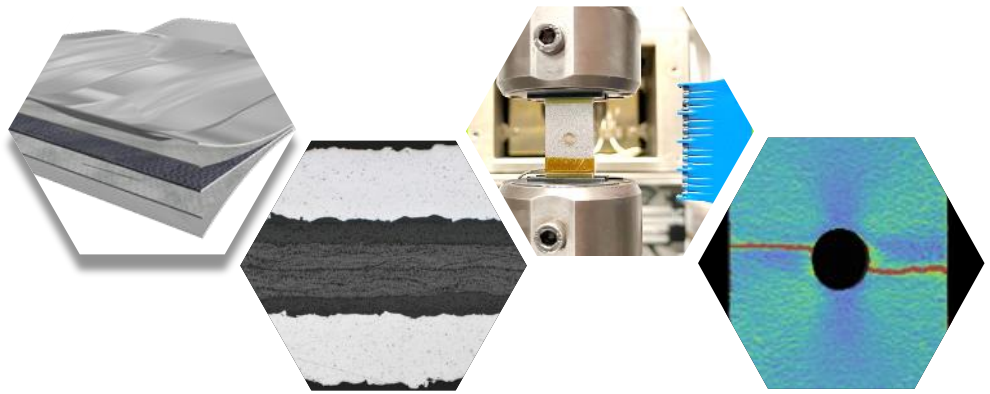

Fiber-metal laminates (FML) can improve:

- Damage tolerance
- Fatigue performance
  - Especially if carbon fibers are used
- Bearing strength
  - Especially if steel sheets are used

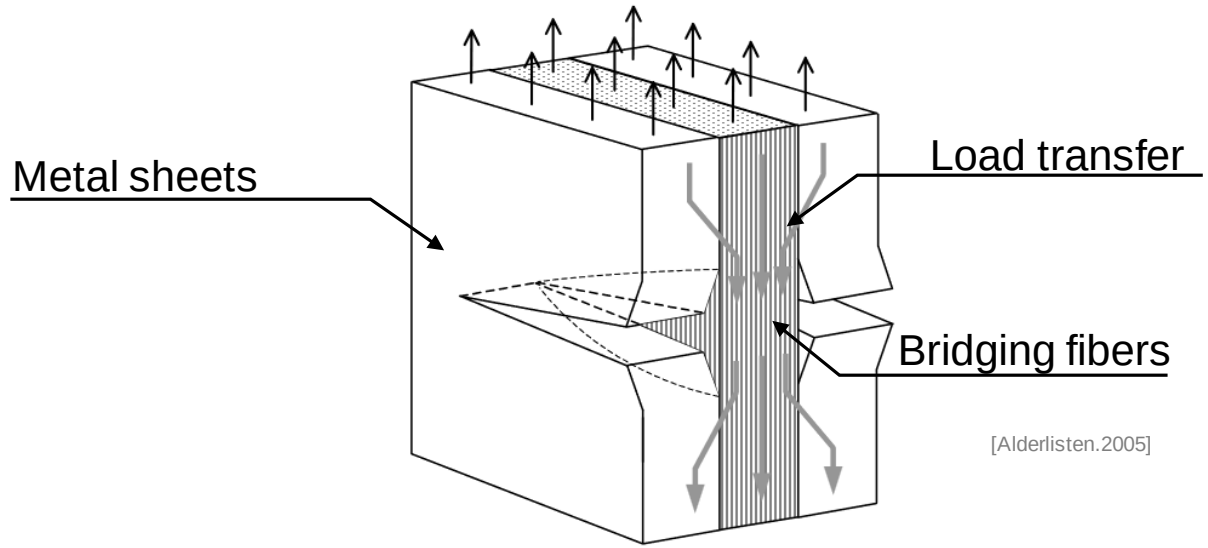

[Alderlisten.2005]

Problems associated with FML:

- Corrosion
- Surface treatment and adhesion
- Thermal residual stresses induced during the thermal cycle of polymer cure or melting



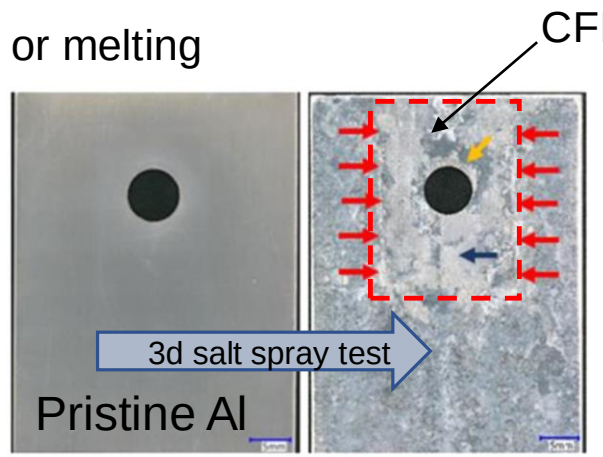

[Dammulla.2023]

Conventional curing cycle:

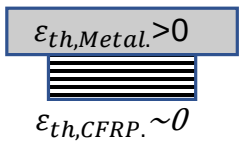

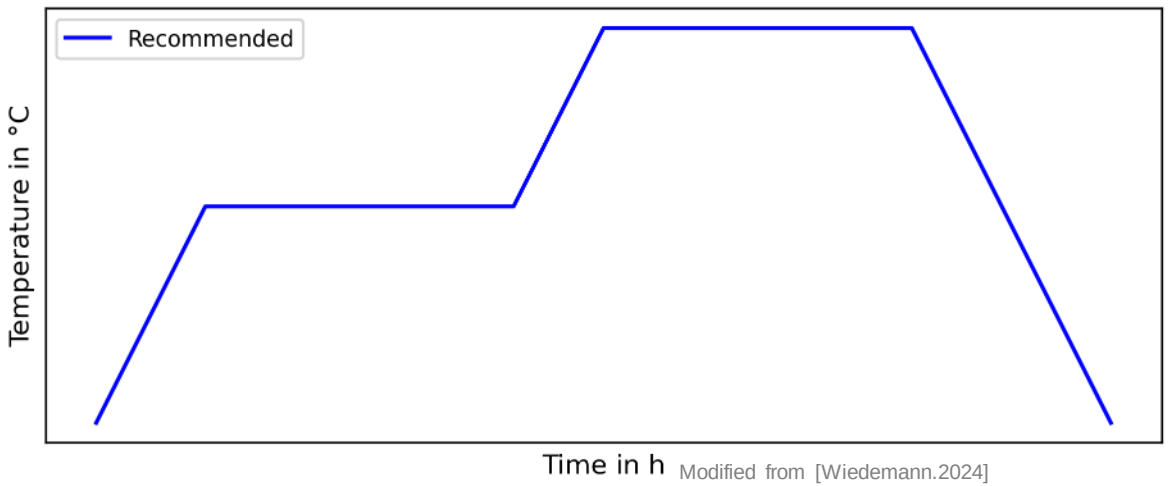

Modified from [Wiedemann.2024]





Replace

The modified curing cycle → lower Δϑ between curing and operation :

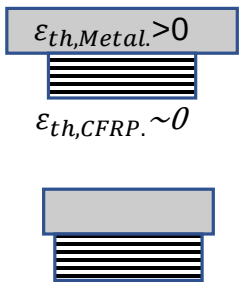

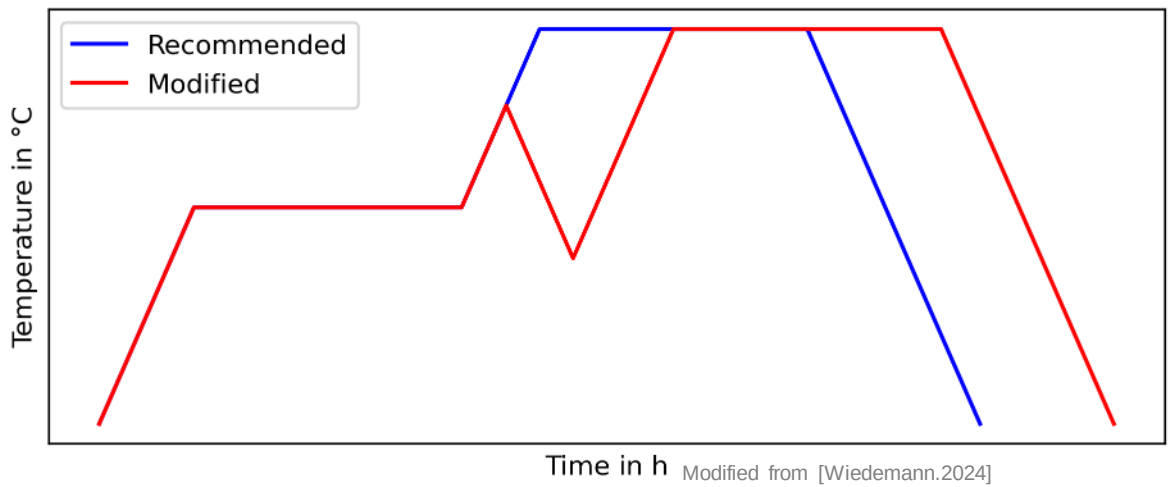

Modified from [Wiedemann.2024]

Increased fatigue life

→Solidification at a lower temperature

Replace

The modified curing cycle → lower Δϑ between curing and operation :





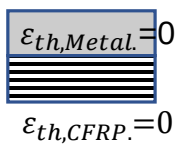

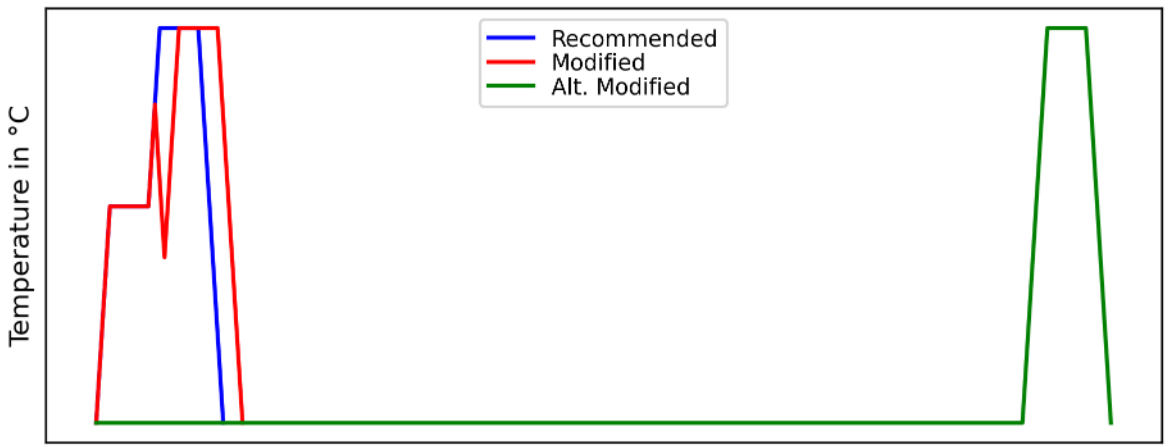

Modified from [Wiedemann.2024]

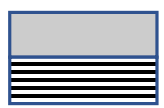

Further increase in fatigue life?

→Solidification at the lowest temperature possible.

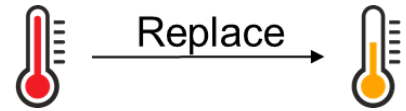

Effect of cure on fatigue crack resistance

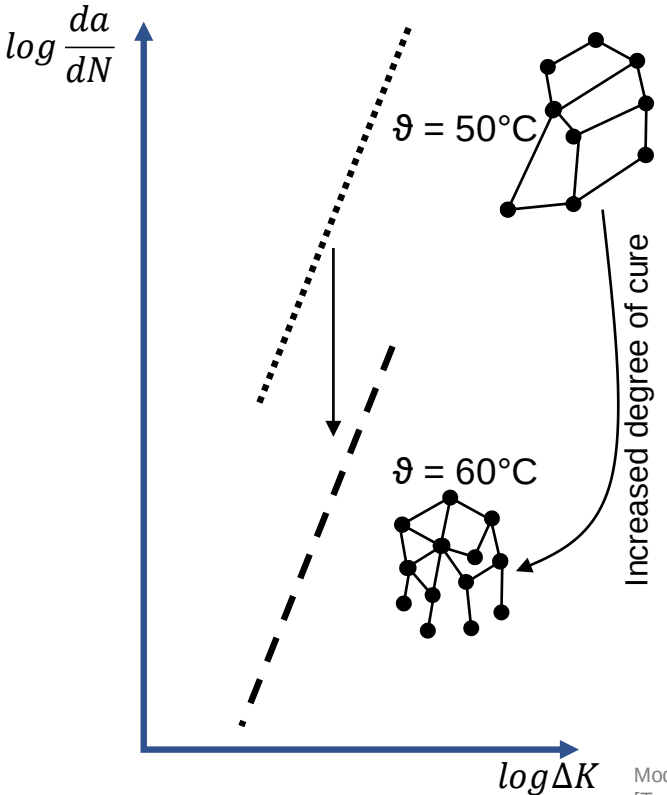

Modified from [Trappe.2012]

→Decreased fatigue crack propagation rate by increased curing temperature (identical curing time)

Effect of cure on adhesion (lap shear strength)

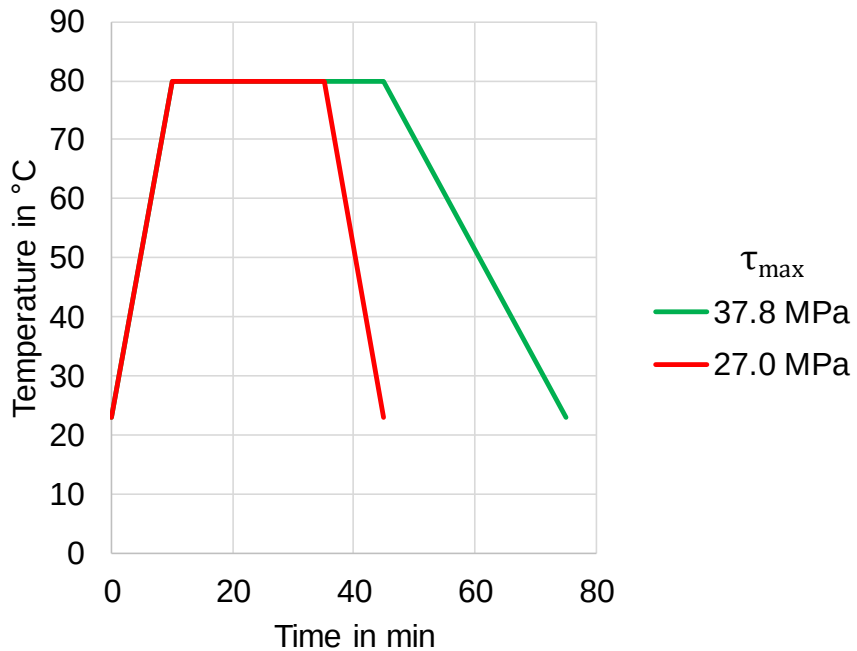

[Kotynia.2017]

→Curing cycle affects the resulting lap shear strength

Replace

Polymer
SR 1660 / SD 7820

Carbon fiber non-crimp fabric

Stainless spring steel
1.4310 t ~ 0.1-0.3 mm

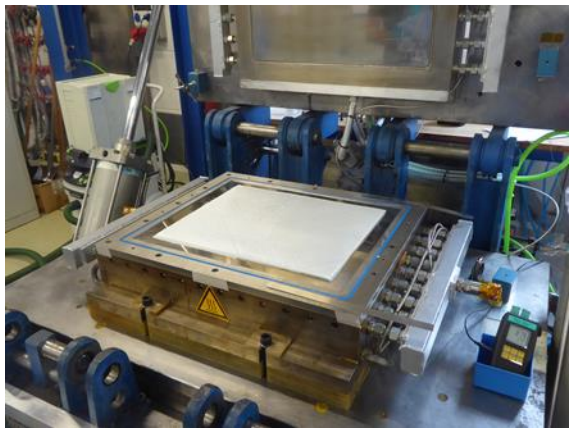

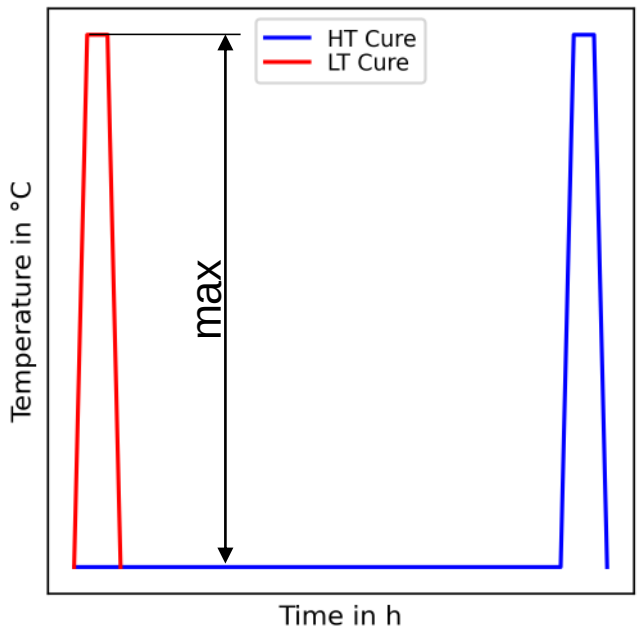

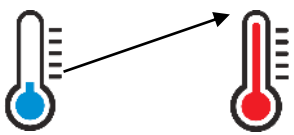

RTM process choices:

A. Non-stationary

Cold tooling and heating ramp → good impregnation but maximum heating rate will define curing temperature, i.e. residual stresses

B. Isothermal

Preheated tooling and slightly heated resin → resin takes on tooling temperature immediately

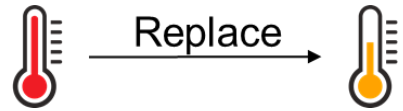

Imperfect impregnation, due to maximized curing temperature for isothermal process (B)

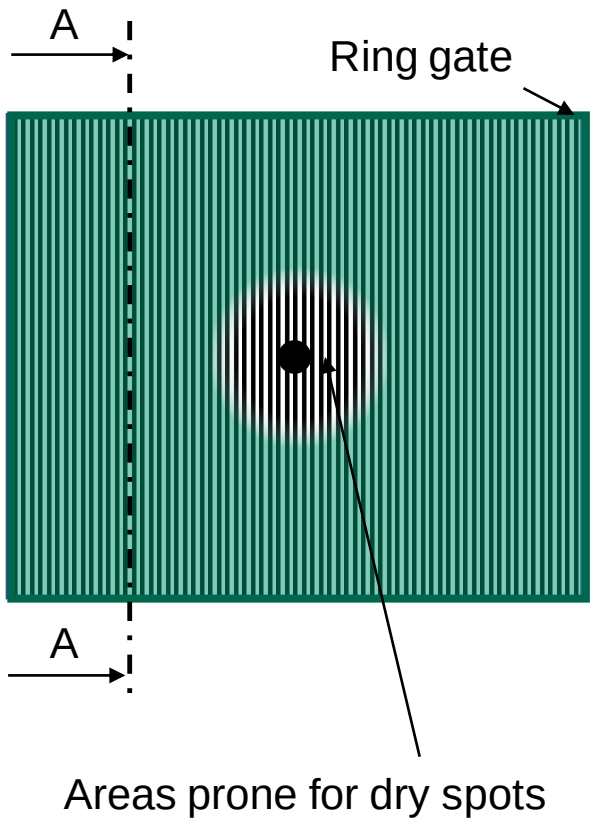

Race tracking around the metal sheets

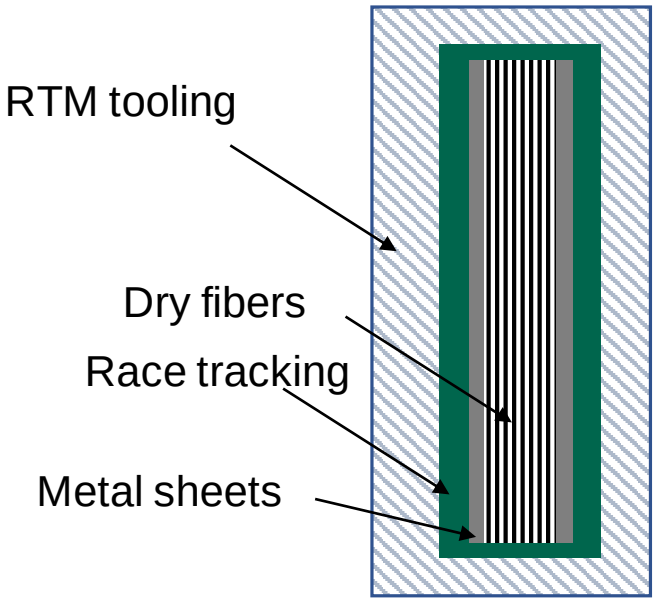

A-A

Replace

B. Isothermal process

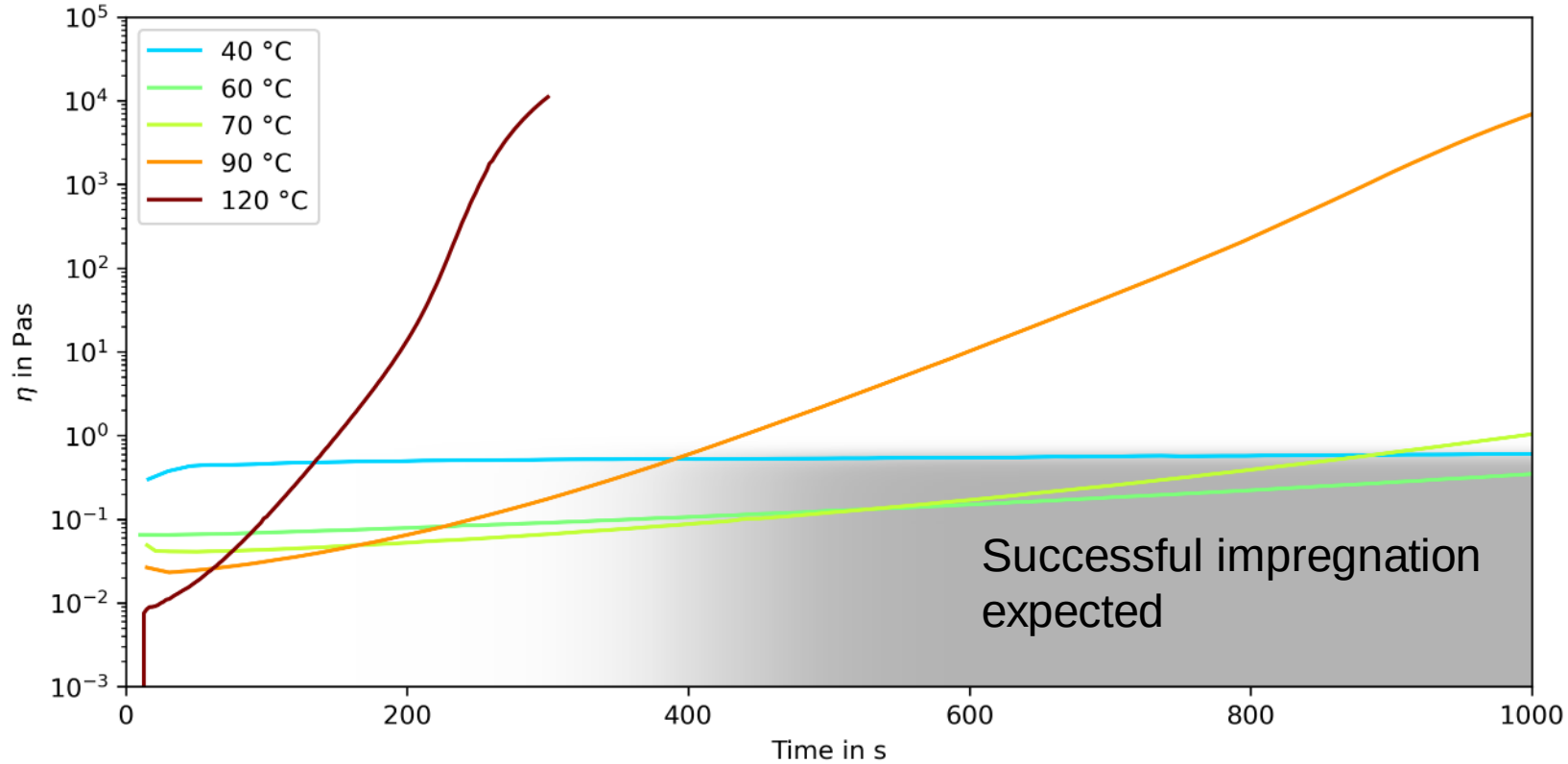

Definition:

- Low temperature cure: 48h@35°C + Post-cure
- High temperature cure: 3h@90°C

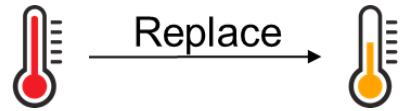

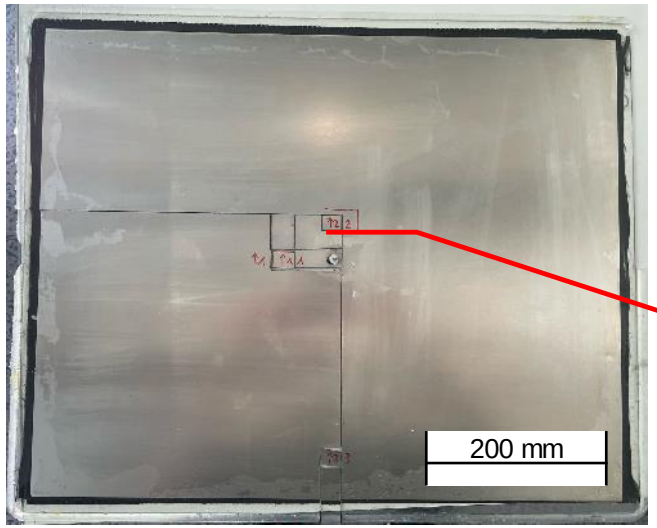

QC of manufactured plates

- No race tracking evident
- Fully impregnated at 90°C

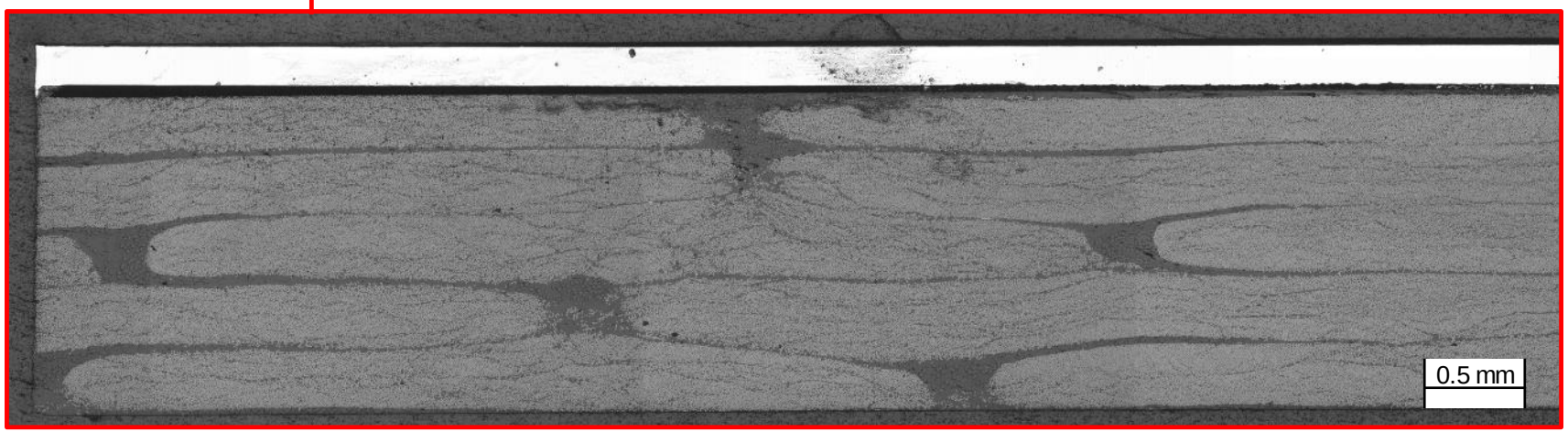

Replace

Seemingly no adhesion possible with various surface treatments



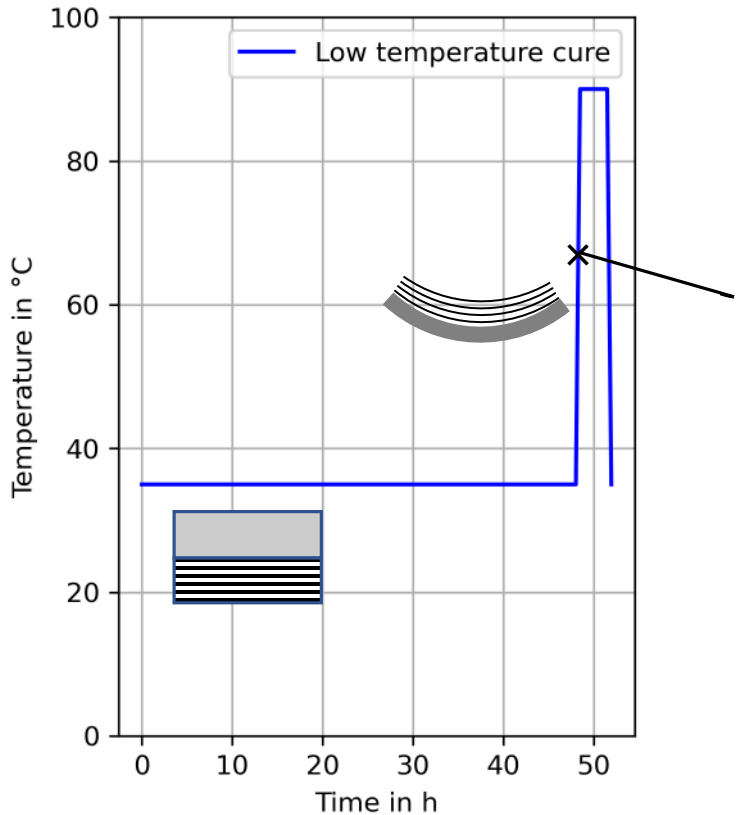

Potential adhesive failure during post-cure

5 Adhesion between epoxy and metal sheets
A function of cure and post-cure

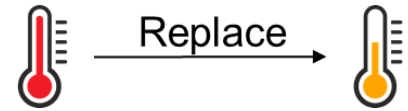

Lap shear specimens produced by adhesively connecting metal to metal possible, however lap shear strength depends on the curing and post-curing cycle



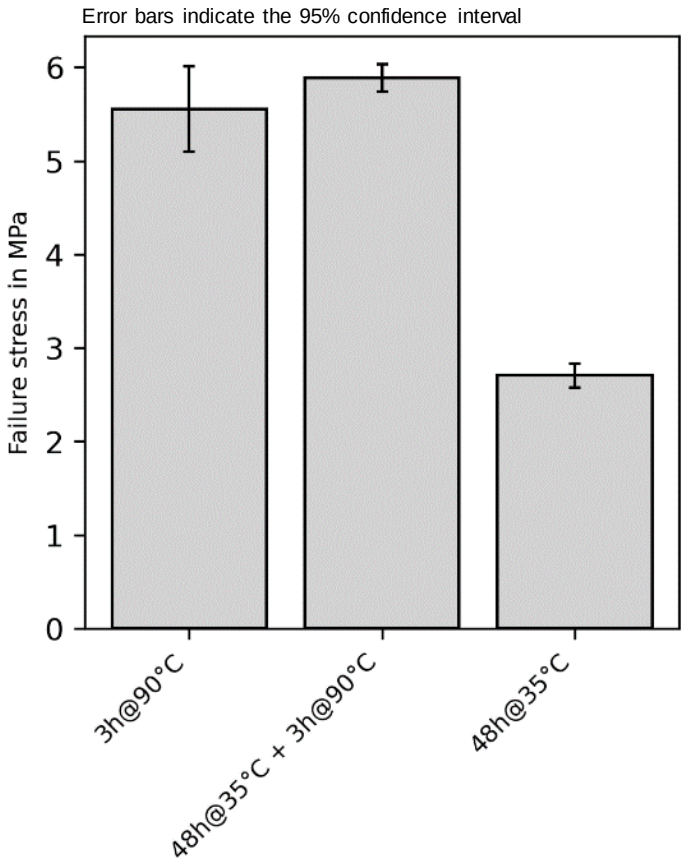

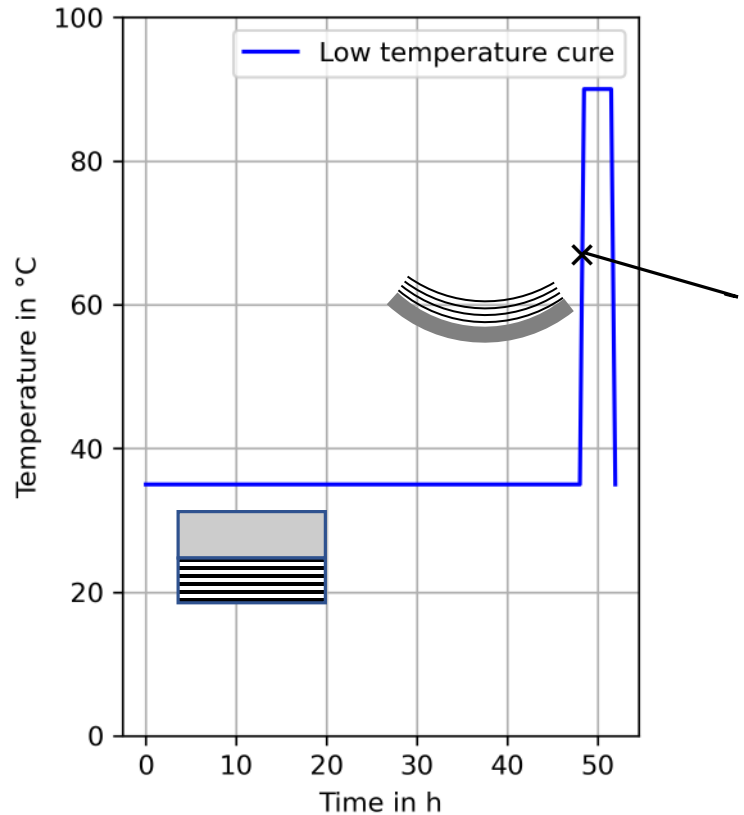

Potential adhesive failure during post-cure

Conclusion: Thermal stresses during the post-cure treatment might exceed the bond strength.

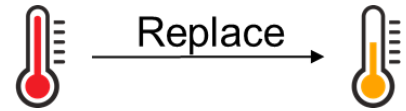

Countermeasures:

- Reduced thickness of the metal sheets (0.3 mm → 0.12 mm)
- Suitable surface treatment (DLR Braunschweig / Germany)
- Slow heating rate during post-cure ramp

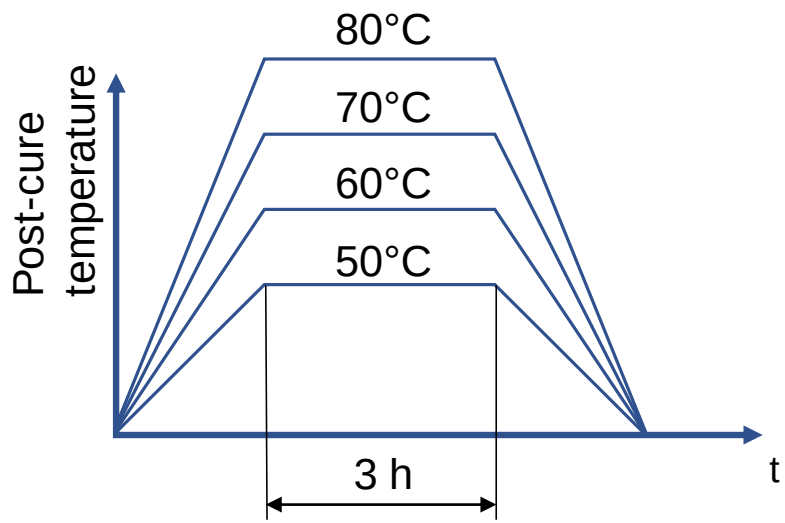

Investigation of adhesive strength in a conventional lap shear setting so far unsuccessful from a testing point of view but sufficient adhesive strength was achieved across at all post-curing stages

Result: Yielding of the metal sheets before bond failure for a sufficiently large overlap

Effect of cure on fatigue crack resistance and fracture toughness

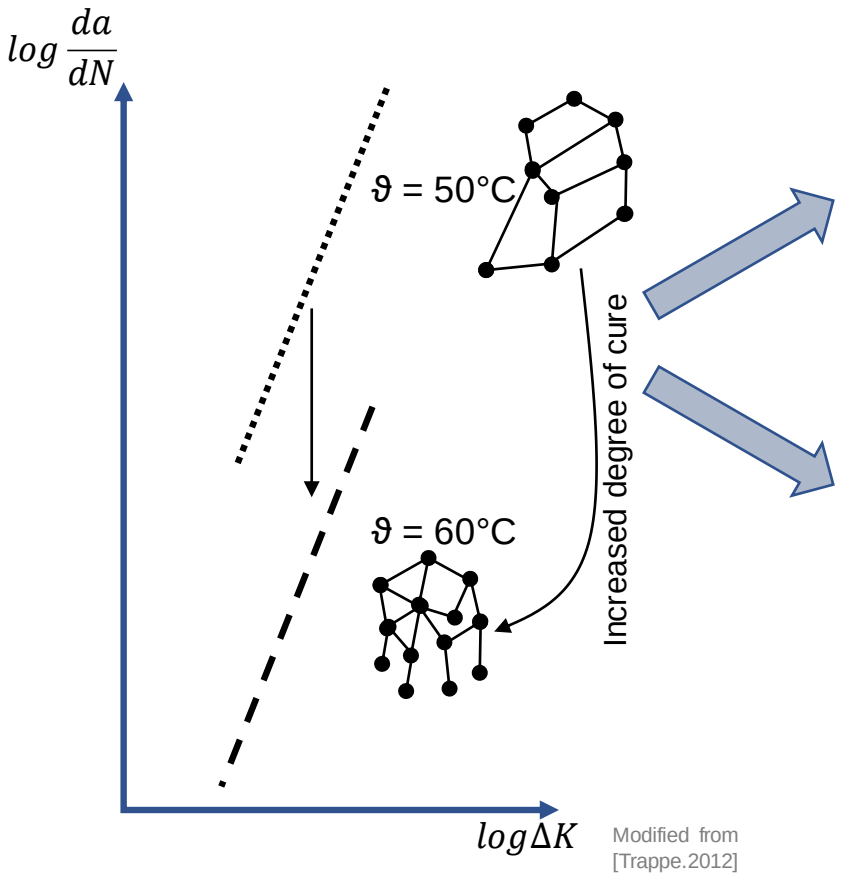

Modified from [Trappe.2012]

Neat polymer characterization

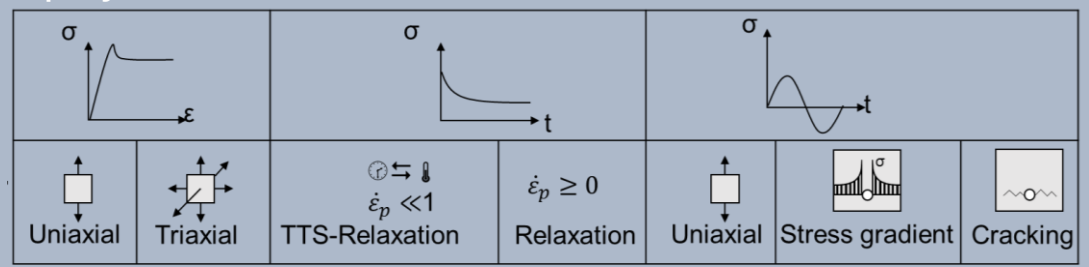

[Baumann.2025]

Change of residual stresses in FML without alterations in the curing cycle

$$\Delta\varepsilon_{th}(\theta)+\Delta\varepsilon_{el} = \frac{\sigma_{res}}{E} = \min_{\theta} \Delta\varepsilon_{th}(\theta)$$

High-temperature cure

Low-temperature cure

Mechanical pre-strain $\Delta\varepsilon_{th}(\theta)+\Delta\varepsilon_{el}$

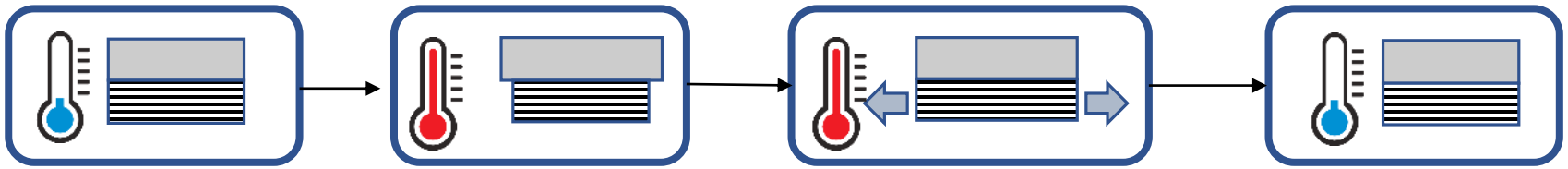

Strategy:

What if we could adjust the elongation of the carbon fibers to the thermal expansion of the metal sheets by applying a mechanical strain before and during cure?

Mechanical pre-strain of the carbon fibers will be released during cool down of the high temperature cured laminate

Impregnation

CF pre-stressed

Cured with elongated CF

Ends were impregnated and cured in preliminary step







Compensation

Thermal residual stresses

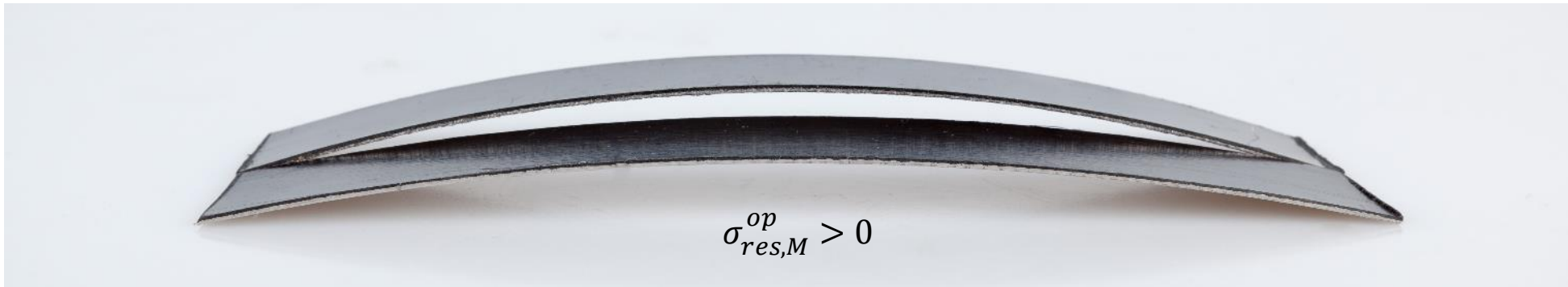

High temperature cure with mechanically strained CFRP during cure

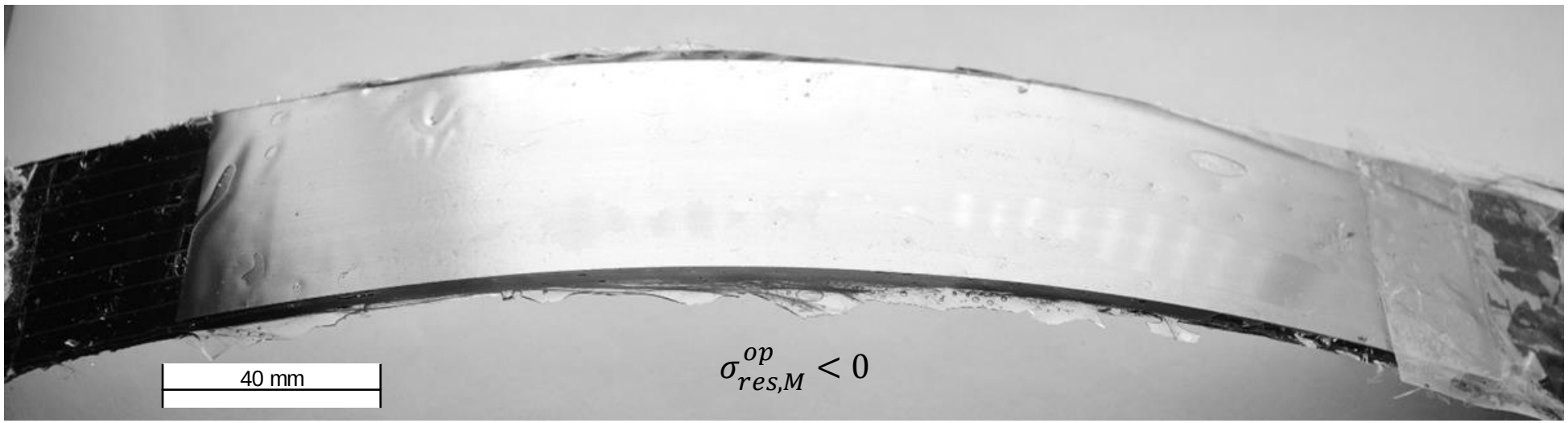

6 Alternative Approach
New Manufacturing Set-up for Larger Plates

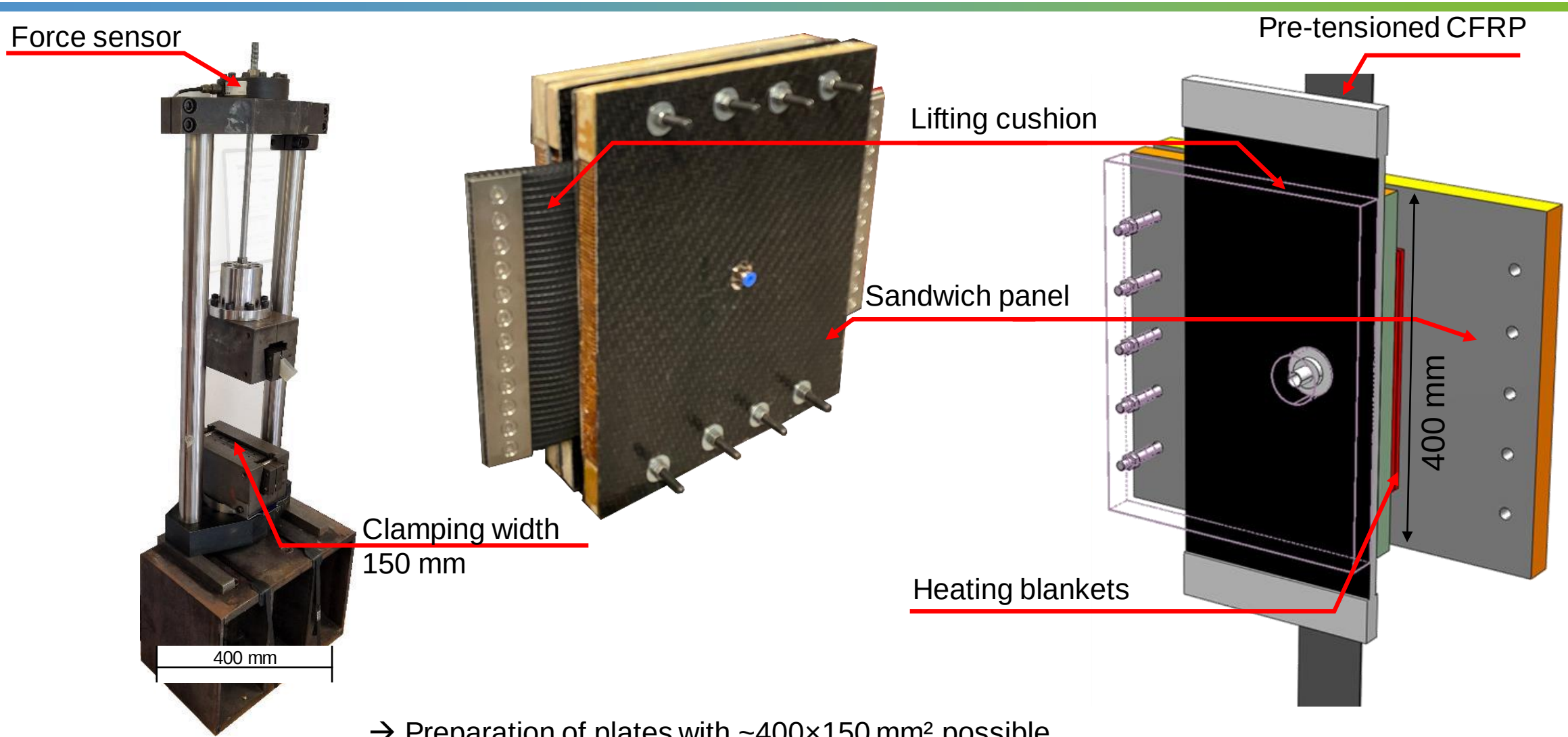

→ Preparation of plates with ~400×150 mm² possible

Current working hypothesis:

Adhesion of the metal sheets develops as a function of post curing treatment and can become critical if:

- The interface needs to transfer high shear loads, e.g. as a result of thermal stresses during post-curing
- Can be different as a result of the used surface treatment

→ More understanding and additional shear or peel tests are needed to fully understand the active mechanisms

Strategy to identify changes in the polymer or adhesive properties:

Comparison of modified curing cycle with mechanically modified residual stresses can c.p. show if any of the relevant parameters (adhesion, polymer toughness etc.) is affected by changes in the curing cycle

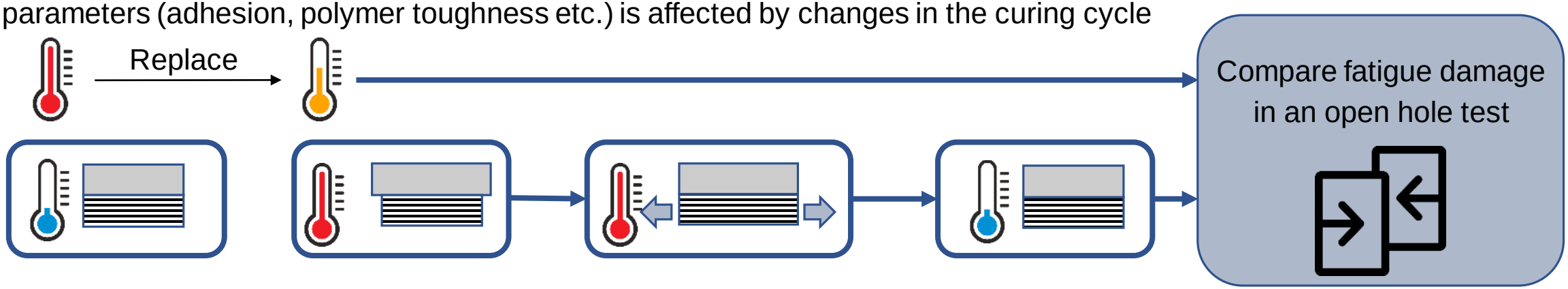

In addition to post-cure straining to induce residual stresses as result of plastically deformed metal sheets

- J. Wiedemann, S. Mrzljak, J. Koord, C. Hühne, F. Walther: Modified cure cycles for increased fatigue performance of fiber metal laminates. **Composite Structures**, vol. 351, 118631, **2025**, doi: 10.1016/j.compstruct.2024.118631
- S. Mrzljak, M. Trautmann, G. Wagner, F. Walther: Very high cycle fatigue assessment of thermoplastic-based hybrid fiber metal laminate by using a high-frequency resonant testing. **International Journal of Fatigue**, 108361, **2024**. doi: 10.1016/j.ijfatigue.2024.108361
- A. Baumann, J. Hausmann: Effect of high-energy radiation on the relaxation of residual stresses in Polycarbonate and Epoxy resin by stress optics. **Radiation Physics and Chemistry**, 112236, **2024**, doi: 10.1016/j.radphyschem.2024.112236
- S. Mrzljak, S. Schmidt, A. Kohl, D. Hülsbusch, J. Hausmann, F. Walther: Testing procedure for fatigue characterization of steel-CFRP hybrid laminate considering material dependent self-heating. **Materials** 14 (12), 3394, **2021**. doi: 10.3390/ma14123394

References

- [Alderliesten .2005] Alderliesten RC. Fatigue crack propagation and delamination growth in GLARE [dissertation]. Delft, the Netherlands: Delft University of Technology; 2005.
- [Wiedemann.2024] J. Wiedemann, S. Mrzljak, J. Koord, C. Hühne, F. Walther: Modified cure cycles for increased fatigue performance of fiber metal laminates. Composite Structures, vol. 351, 118631, 2025, doi: 10.1016/j.compstruct.2024.118631
- [Trappe.2012] V. Trappe, S. Günzel, M. Jaunich: Correlation between crack propagation rate and cure process of epoxy resins. Polymer Testing, vol. 31, no. 5, 654–659, 2012, doi: 10.1016/j.polymertesting.2012.03.007
- [Kotynia.2017] R. Kotynia, K. Adamczewska, A. Strąkowska, M. Masłowski, K. Strzelec: Effect of accelerated curing conditions on shear strength and glass transition temperature of epoxy adhesives. Procedia Engineering, vol. 193, 423–430, 2017, doi: 10.1016/j.proeng.2017.06.233
- [Baumann.2024] A. Baumann, J. Hausmann: Effect of high-energy radiation on the relaxation of residual stresses in Polycarbonate and Epoxy resin by stress optics. Radiation Physics and Chemistry, 112236, 2024, doi: 10.1016/j.radphyschem.2024.112236
- [Wächter.2017] M. Wächter, A. Esderts, C. Müller, Angewandter Festigkeitsnachweis nach FKM-Richtlinie: Kurz und bündig. in SpringerLink Bücher. Wiesbaden: Springer Vieweg, 2017. doi: 10.1007/978-3-658-17459-0
- [Kawai.2007] M. Kawai, M. Koizumi. Nonlinear constant fatigue life diagrams for carbon/epoxy laminates at room temperature. Composites Part A: Applied Science and Manufacturing, vol. 38, no. 11, 2342–2353, 2007, doi: 10.1016/j.compositesa.2007.01.016
- [Dammulla.2023] Dammulla, I. N., & Swain, G. M. (2023). Inhibiting metal galvanic and carbon corrosion in aluminum Alloy-Carbon fiber reinforced composite joints by spontaneous deposition of diazonium adlayers on exposed carbon fibers. Journal of the Electrochemical Society, 170(9), 091503. https://doi.org/10.1149/1945-7111/acf889
- [Baumann.2025] A. Baumann, “Factors controlling damage initiation in fatigue loaded unidirectional composites under the influence of different matrix properties,” doctoralthesis, Rheinland-Pfälzische Technische Universität Kaiserslautern-Landau, 2025. doi: 10.26204/KLUEDO/8619.



Acknowledgement

Funded by

DFG Deutsche Forschungsgemeinschaft
German Research Foundation

Project number: 541803764

DLR

Support with treated steel sheets



Dr.-Ing. Andreas Baumann
Phone: +49 631 2017 320
E-Mail: andreas.baumann@leibniz-ivw.de

Prof. Dr.-Ing. Joachim Hausmann

M.Sc. Selim Mrzljak
Phone: +49 231 755 8494
E-Mail: selim.mrzljak@tu-dortmund.de

Prof. Dr.-Ing. Frank Walther

Open for discussion

Conductive-hydrophobic coating on gas diffusion layer for enhanced proton exchange membrane fuel cell performance

Myungjin Hong, Seung-cheol Shin, Taesik Eom, Sang Eui Lee+

Multifunctional Composite and Structural Integration Lab

Mechanical Engineering Department, Inha University

+ E-mail: selee@inha.ac.kr

2025.08.05

Contents

01. Introduction

1. Background of PEMFC and GDL
2. Challenges in Balancing Conductivity and Hydrophobicity in GDLs
3. Research objectives

02. Materials and Experiment

1. CNT/PTFE-coated GDBs (CP-GDBs)

03. Results and Discussion

1. Characterization of CP-GDBs
- morphology, wettability, electrical conductivity, mechanical properties

2. Characterization of CP-GDLs
- contact resistance between CP-GDBs and MPL

3. PEMFC unit cell performance

04. Conclusion

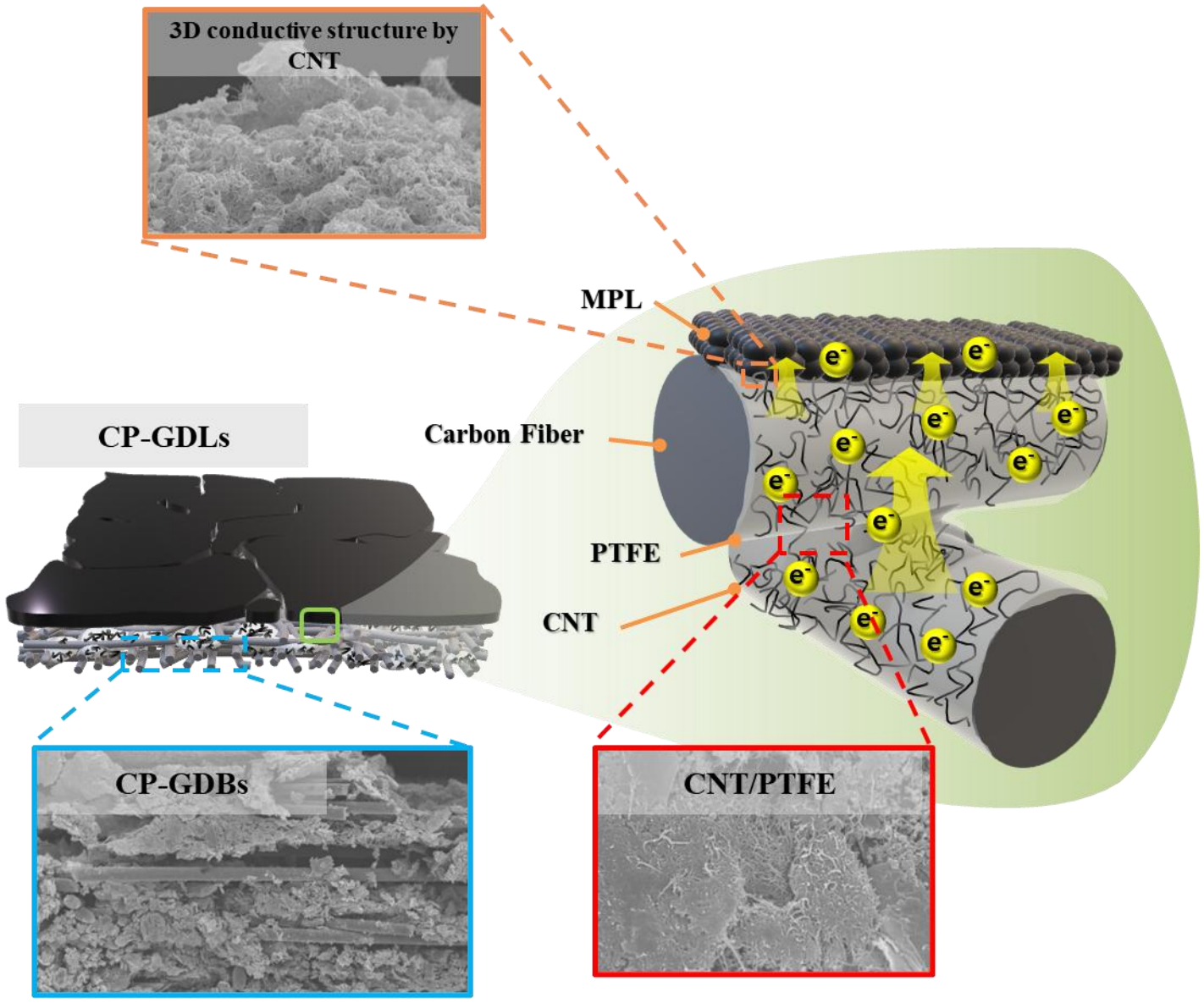

01. Introduction

1. Background of PEMFC and GDL
2. Challenges in Balancing Conductivity and Hydrophobicity in GDLs
3. Research objectives

Background of PEMFC and GDL

❖ PEMFC (Proton Exchange Membrane Fuel Cell)

- **Electric energy and water (H_2O)** are generated via the **electrochemical reaction** between hydrogen (H_2) and oxygen (O_2).
- Due to **fast startup** and **low operating temperature (80–120 °C)**, PEMFCs are gaining attention in mobility applications.
- A PEMFC unit cell consists of (1) **B**ipolar **P**lates, (2) **G**as **D**iffusion **L**ayers, (3) Membrane, and (4) **C**atalyst **L**ayers.

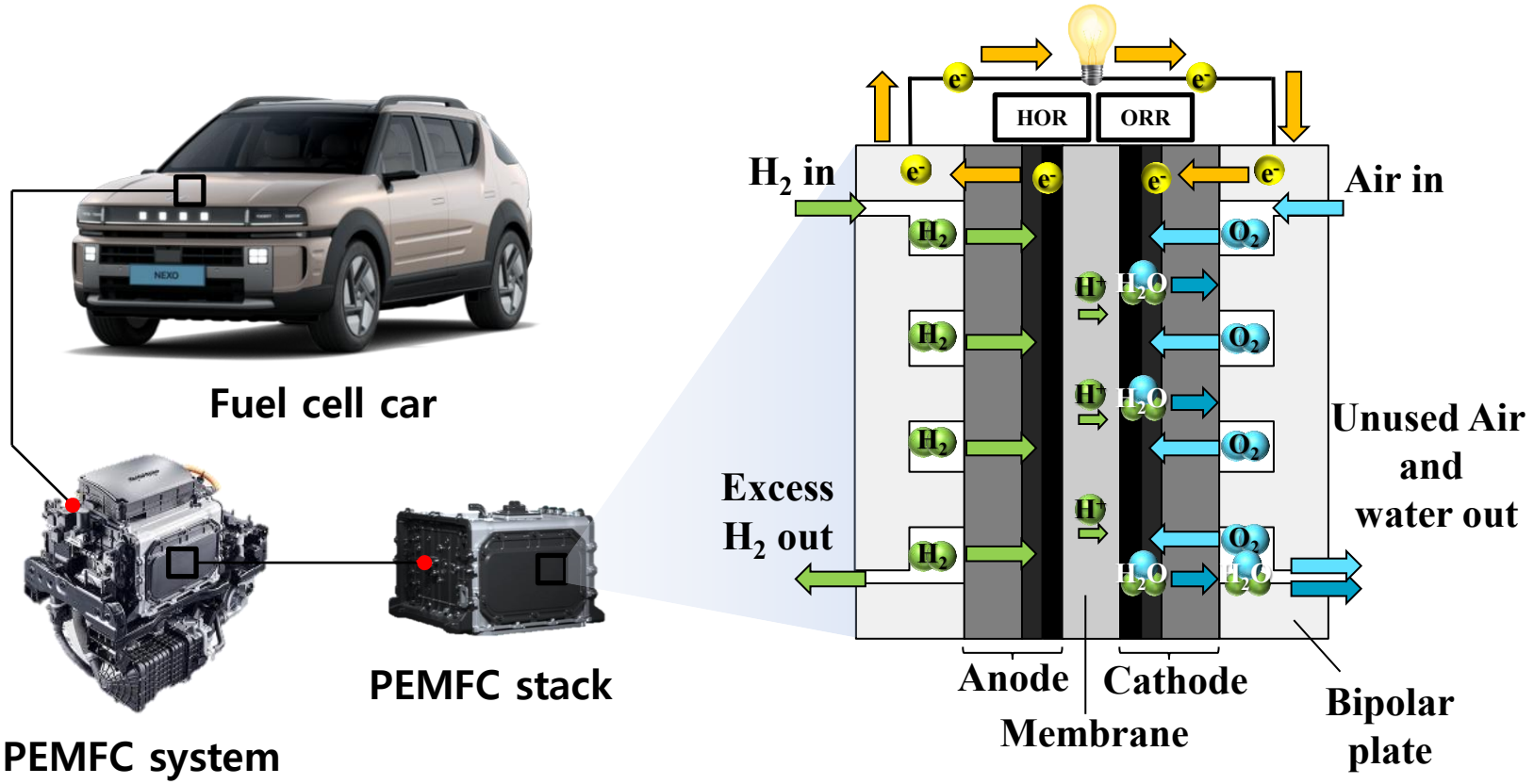

Figure. Schematic image of PEMFC unit cell

Electrochemical Reactions in PEMFC

Hydrogen oxidation reaction in Anode :

$$H_2 \rightarrow 2H^+ + 2e^-$$

Oxygen reduction reaction in Cathode :

$$0.5O_2 + 2H^+ + 2e^- \rightarrow H_2O$$

Overall Cell Reaction :

$$H_2 + 0.5O_2 \rightarrow H_2O$$

Background of PEMFC and GDL

❖ GDL (Gas Diffusion Layer)

- **GDL** consists of **GDB** (Gas Diffusion Backing layer) coated with **MPL** (Micro Porous Layer).
  - ✓ GDL serves **1) uniform diffusion of reactant gases, 2) conduction of generated electrons and heat, 3) removal pathway for produced water**.
- **GDB** : **Carbon paper composed of carbon fiber layers is typically used**, providing structural support to GDL
- **MPL** : Mainly composed of carbon black-based slurry; **it reduces contact resistance with catalyst layer and prevents catalyst loss.**

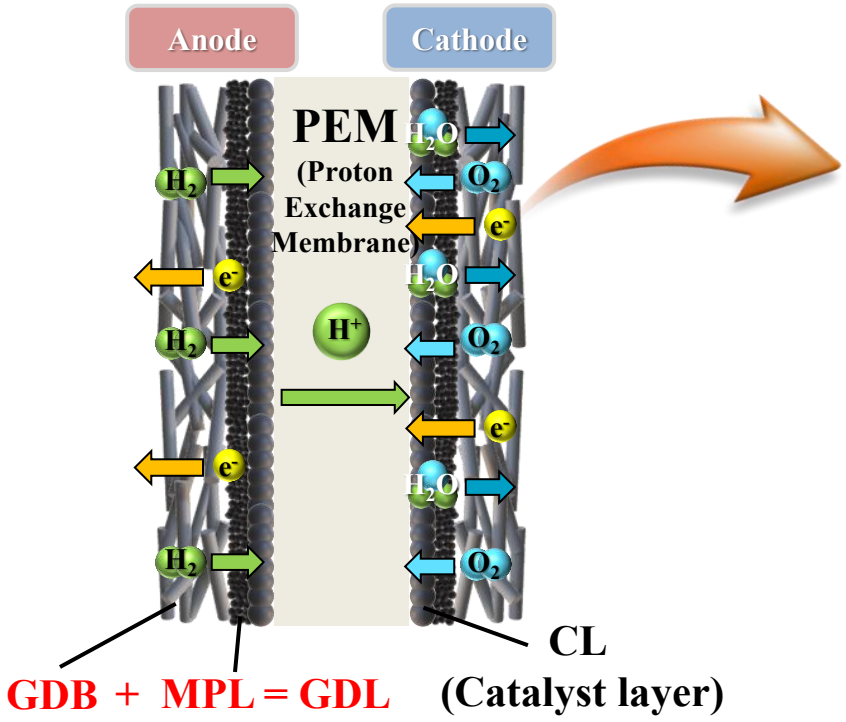

Figure. Illustration of gas diffusion layer

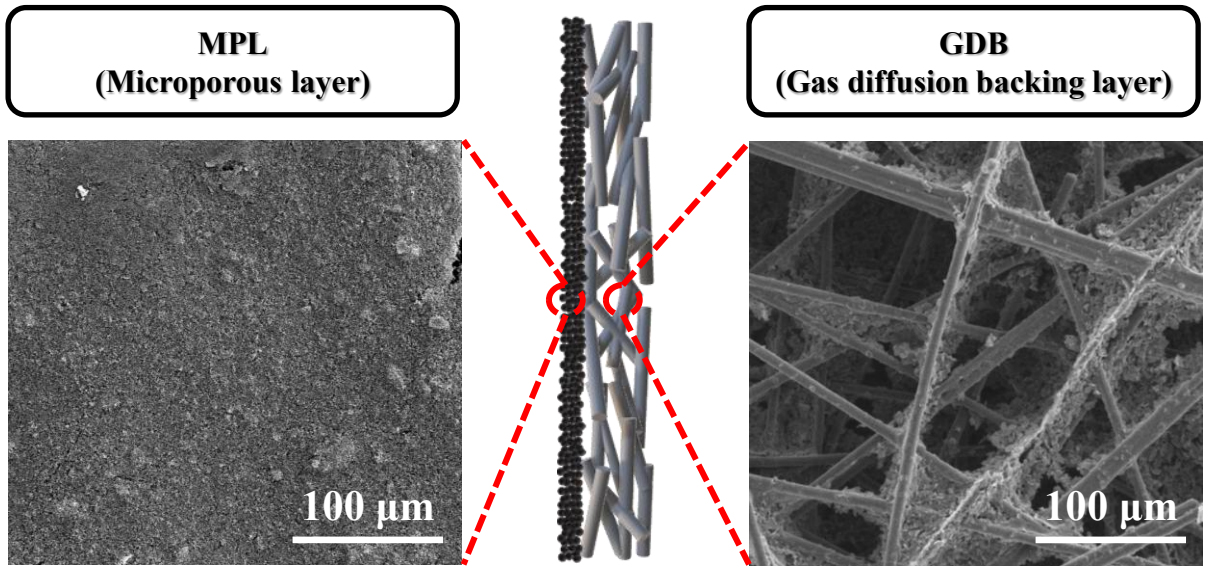

Figure. Images of GDB and MPL

Background of PEMFC and GDL

❖ Voltage losses in PEMFC

- During operation, PEMFCs exhibit **lower voltages than the theoretical value due to various losses.**
- These losses are typically categorized by the current density regions in which they have the greatest impact.
- Minimizing these losses requires **improving the material properties and performance of individual cell components.**

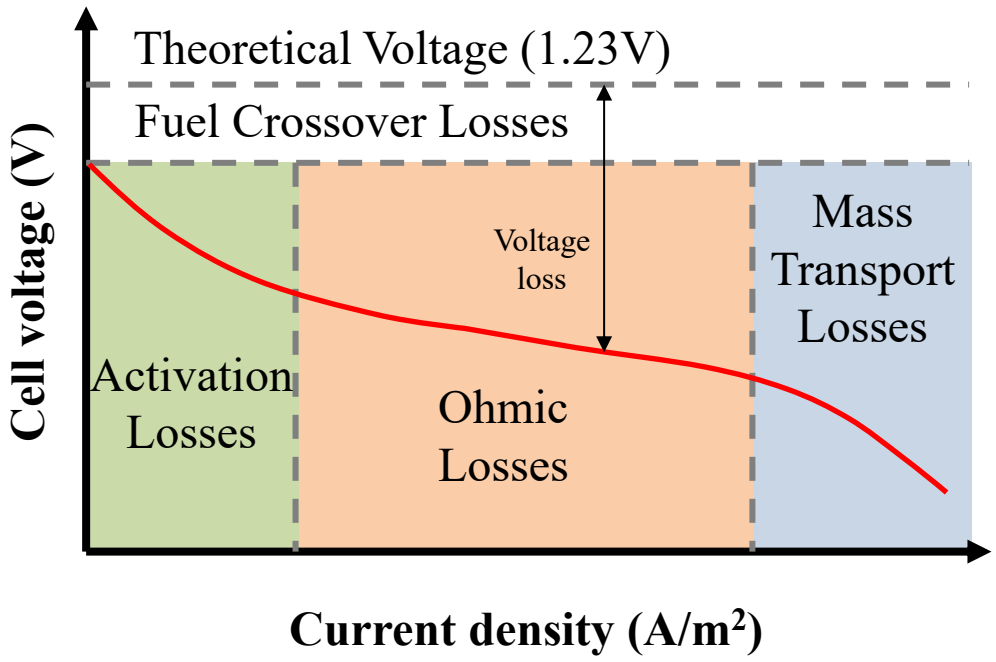

Figure. Various types of losses that occur during PEMFC operation

Table. Classification of major losses in PEMFC

Loss type	Loss mechanism
Fuel crossover loss	Losses caused by hydrogen diffusing through the membrane without reacting, reducing efficiency and open circuit voltage.
Activation loss	Losses caused by the activation energy barrier of the electrochemical reactions,particularly due to the slow kinetics of the oxygen reduction reaction (ORR).
Ohmic loss	Losses caused by resistance to ion flow in the membrane and electron flow in cell components, reducing cell voltage.
Mass transport loss	Losses caused by insufficient gas supply or water accumulation that blocks the pores of the gas diffusion layer, limiting reactant transport at high current densities.

Background of PEMFC and GDL

❖ Hydrophobic coating on GDB (Gas Diffusion Backing layer)

- Commercial carbon paper based GDBs are coated with **hydrophobic** agents such as **fluoropolymers, primarily PTFE.**
- This treatment prevents **water condensation and pore blockage**, thereby reducing **mass transport loss** in PEMFC.

✓ However, **fluoropolymers** are **electrically insulating** and significantly reduce the **through-plane electrical conductivity** of the GDB.

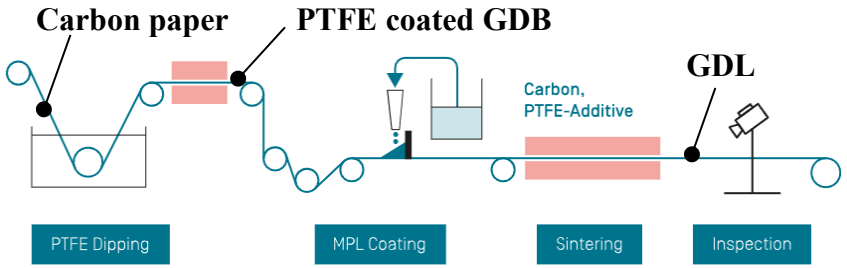

[1]SIGRACET® SGL Carbon's Gas diffusion layers(GDL)

Figure. PTFE coating process of commercial GDB

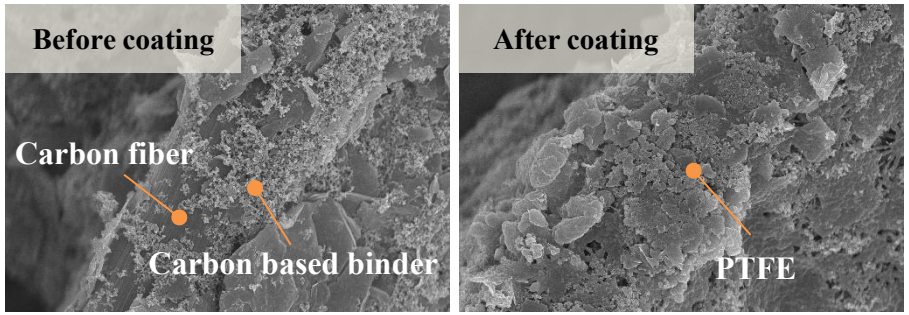

Figure. Surface morphology of carbon paper before and after PTFE coating

PTFE content ↑ → Through-plane conductivity ↓

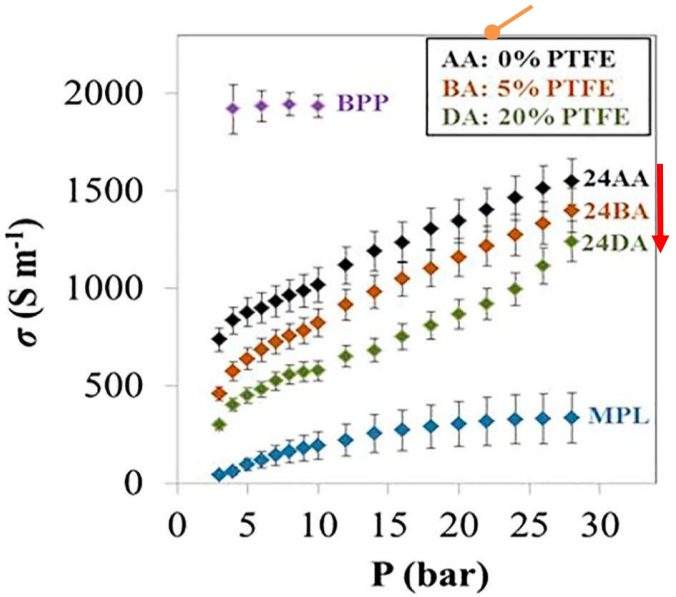

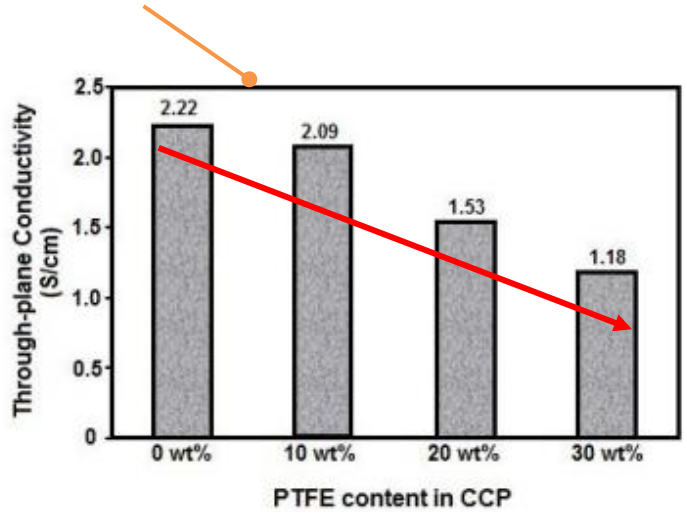

[2]Energy Convers. Manag. 2017, 154, 191-202

[3]IOP Conf. Ser.: Mater. Sci. Eng. 2017, 154, 191-202

Figure. Reduction in through-plane electrical conductivity of GDL due to PTFE coating

Challenges in Balancing Conductivity and Hydrophobicity in GDLs

❖ Studies on enhancing electrical conductivity of GDBs

- Various approaches have been used to enhance GDB conductivity via **structure, materials, and coatings.**
- **Metal-based GDBs and conductive coatings** still require **hydrophobic coatings for water management**, which **offset conductivity gains.**

✓ Therefore, it is essential to address the **fundamental issue of conductivity loss caused by hydrophobic coatings** themselves.

a)



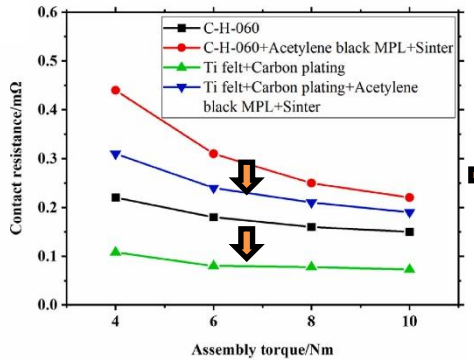

Reduced resistance compared to carbon paper-based GDL

[4] *Int. J. Hydrogen Energy. 2024, 83, 604-613*

b)

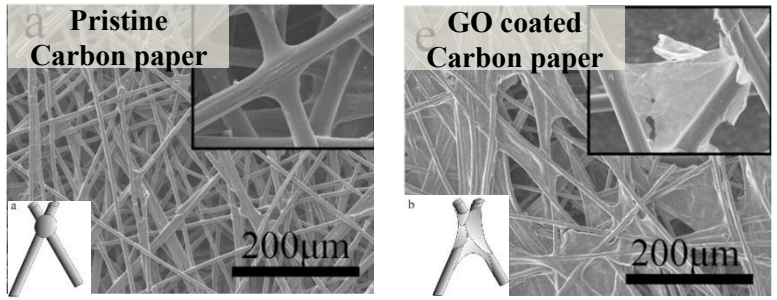

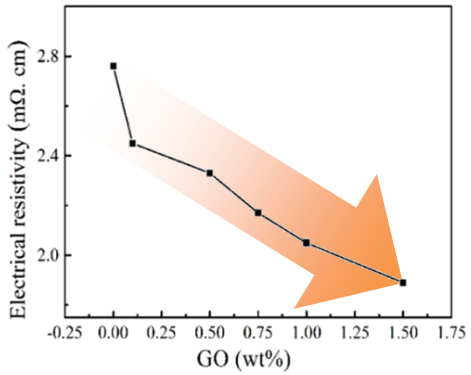

[5] *J. Electrochem. Soc. 2019, 167(1), 013520*

c)

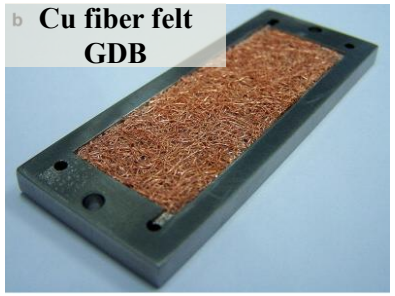

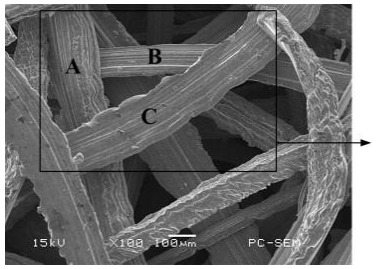

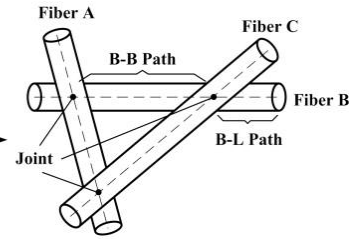

[6] *Int. J. Hydrogen Energy. 2010, 35(18), 9661-9677*

Figure. (a) Metal-based GDB, (b) Graphene-oxide coated GDB, (c) Cu fiber felt GDB

Research objectives

❖ Conductive and highly-hydrophobic coating on GDB for enhanced PEMFC performance

- **CNT/PTFE conductive-hydrophobic nanocomposite coating** on carbon paper (CP-GDBs)
  - Enhanced electrical conductivity, lower contact resistance, PTFE coating-level hydrophobicity, and improved PEMFC performance
- Analysis of **GDB and GDL property variations according to CNT/PTFE ratio** in the coating
  - Characterization: SEM, contact angle, conductivity, compressibility, and cell performance testing

➢ **New coating improves conductivity over PTFE, contributing to PEMFC performance enhancement**

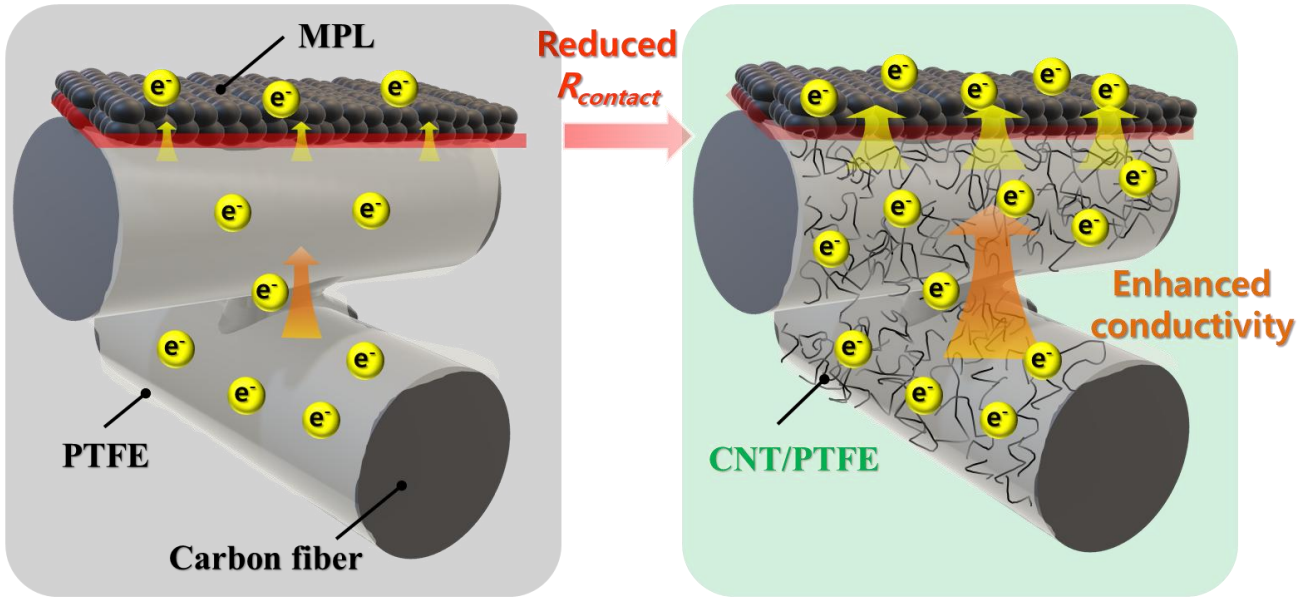

PTFE-coated GDL　　CNT/PTFE-coated GDL

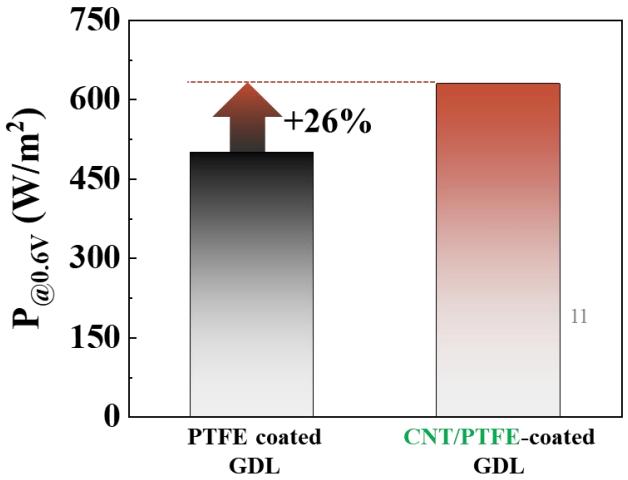

Enhanced PEMFC power (at RH 50%)

02. Materials and Experiments

1. CNT/PTFE coated GDBs (CP-GDBs) and MPL coated CP-GDBs (CP-GDLs)

CNT/PTFE-coated GDBs (CP-GDBs)

❖ **Fabrication process of CNT/PTFE-coated GDBs (CP-GDBs)**

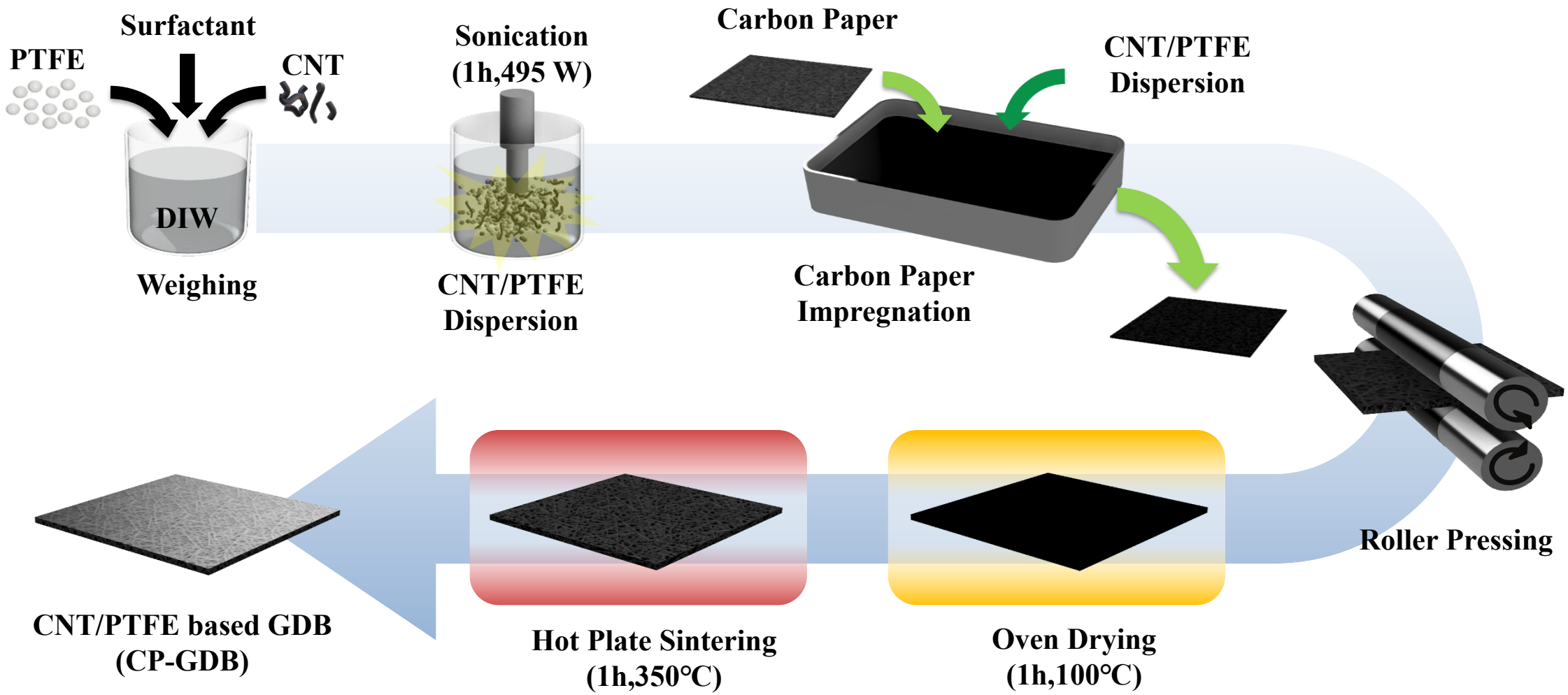

Figure. Schematic illustration of fabrication of CP-GDBs

CNT/PTFE-coated GDLs (CP-GDLs)

❖ MPL coated CP-GDBs (CP-GDLs)

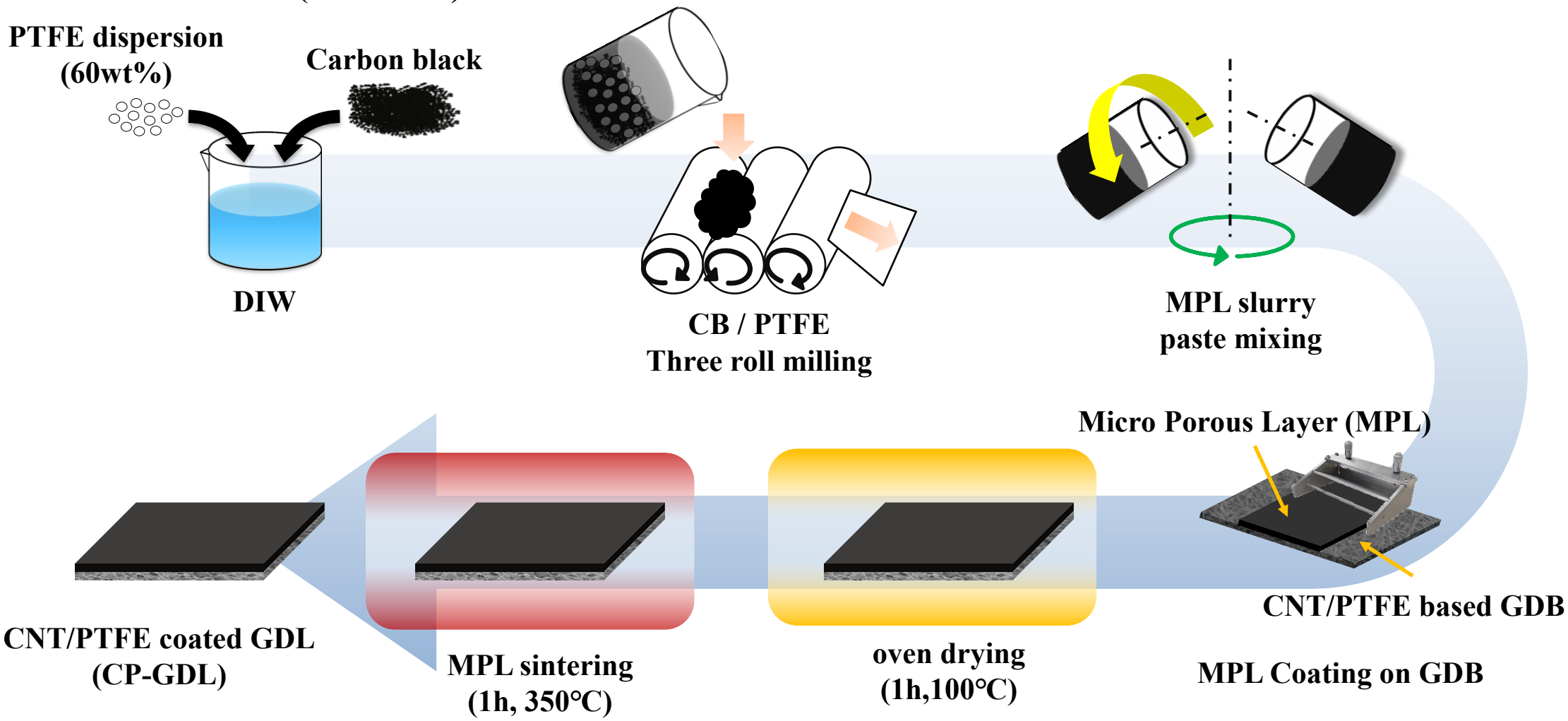

Figure. Schematic illustration of fabrication of CP-GDLs

03. Results and discussion

1. Characterization of CNT/PTFE nanocomposite
2. Characterization of CP-GDBs
3. Characterization of CP-GDLs
4. PEMFC unit cell performance

Characterization of CNT/PTFE nanocomposite

❖ Dispersion of CNT/PTFE Nanocomposite (CxxPyy)

- To evaluate the dispersion of the CNT/PTFE nanocomposite, a film was formed by removing the water from the dispersion.
- **No noticeable agglomeration of CNT or PTFE** was observed at the microscale.
- **The small variation in electrical conductivity of the film** also indicated **uniform dispersion** of the nanocomposite.

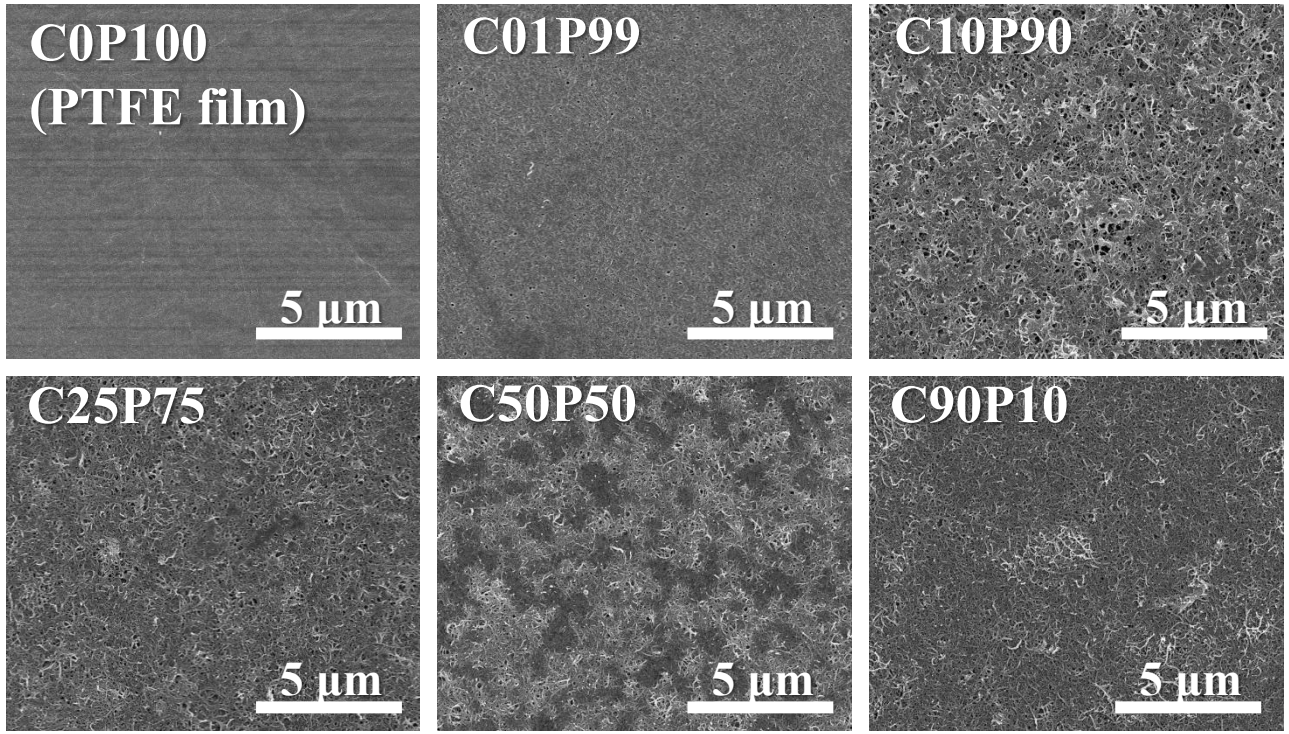

Figure. Microstructure images by CNT/PTFE nanocomposite

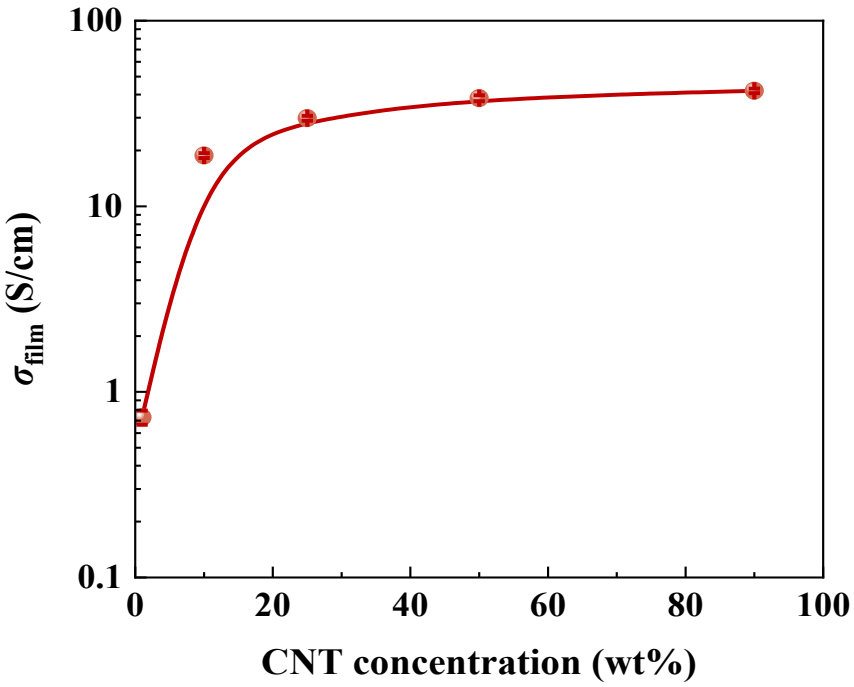

Figure. Electrical conductivity of CNT/PTFE nanocomposite film

Characterization of CP-GDBs

❖ Surface morphology of CP-GDBs (CxxPyyB)

- SEM images reveal **CNT/PTFE nanocomposite microstructures** forming **film-like layers between carbon fibers**.
- As **CNT ratio in the nanocomposite increases, denser CNT networks** are formed while **PTFE content decreases.**
- **No CNT agglomeration** observed at the microscale, indicating **uniform dispersion of the nanocomposite.**

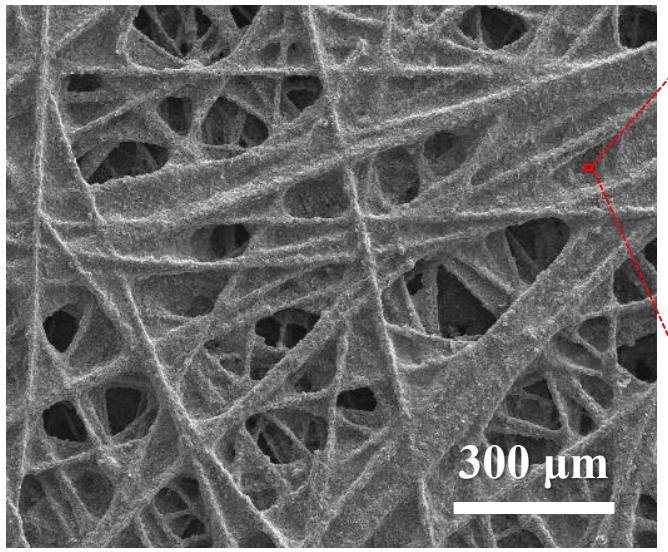

Figure. Magnified region (example)

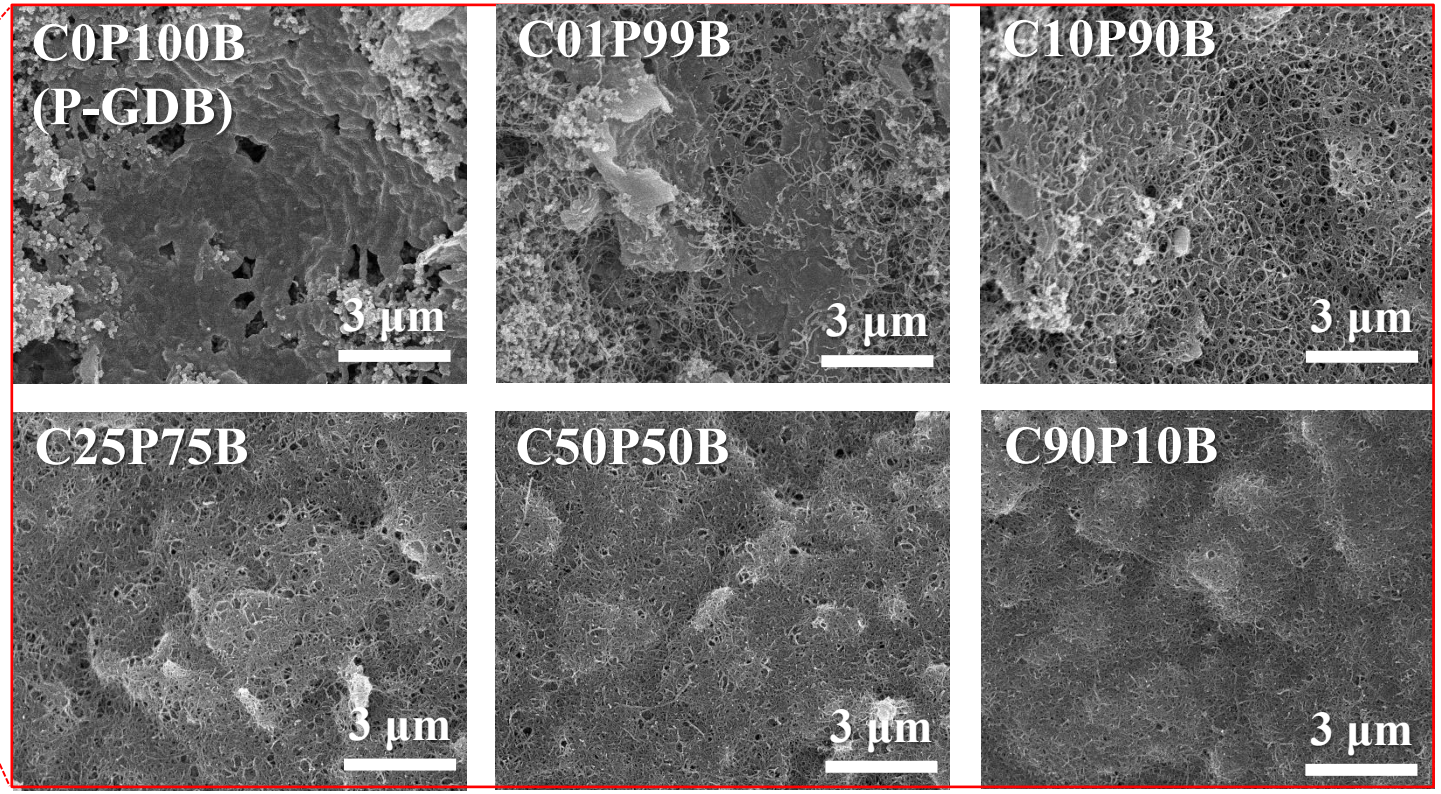

Figure. Microstructure images by CNT/PTFE composition in nanocomposite

Characterization of CP-GDBs

❖ Hydrophobicity of CP-GDBs (CxxPyyB)

- **CNT/PTFE coating** imparted hydrophobicity **comparable to that of conventional PTFE-coated GDB (C0P100B, P-GDB),** with a contact angle around 140º.
- **C90P10B exhibited hydrophobicity similar to pristine carbon paper** due to the **low PTFE content in the coating.**

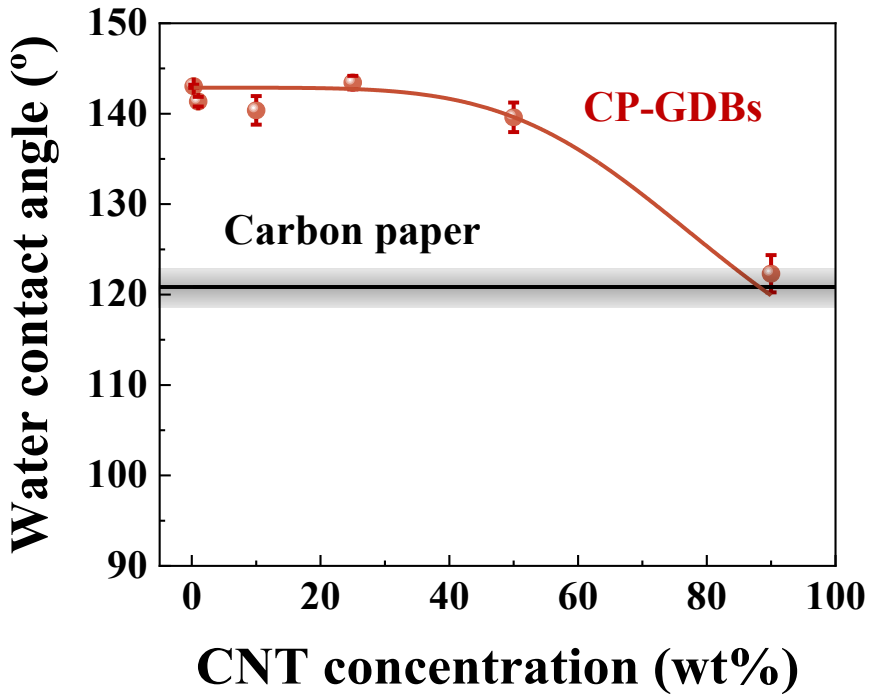

Figure. Contact angle of CP-GDBs according to CNT-to-PTFE ratio in the nanocomposite

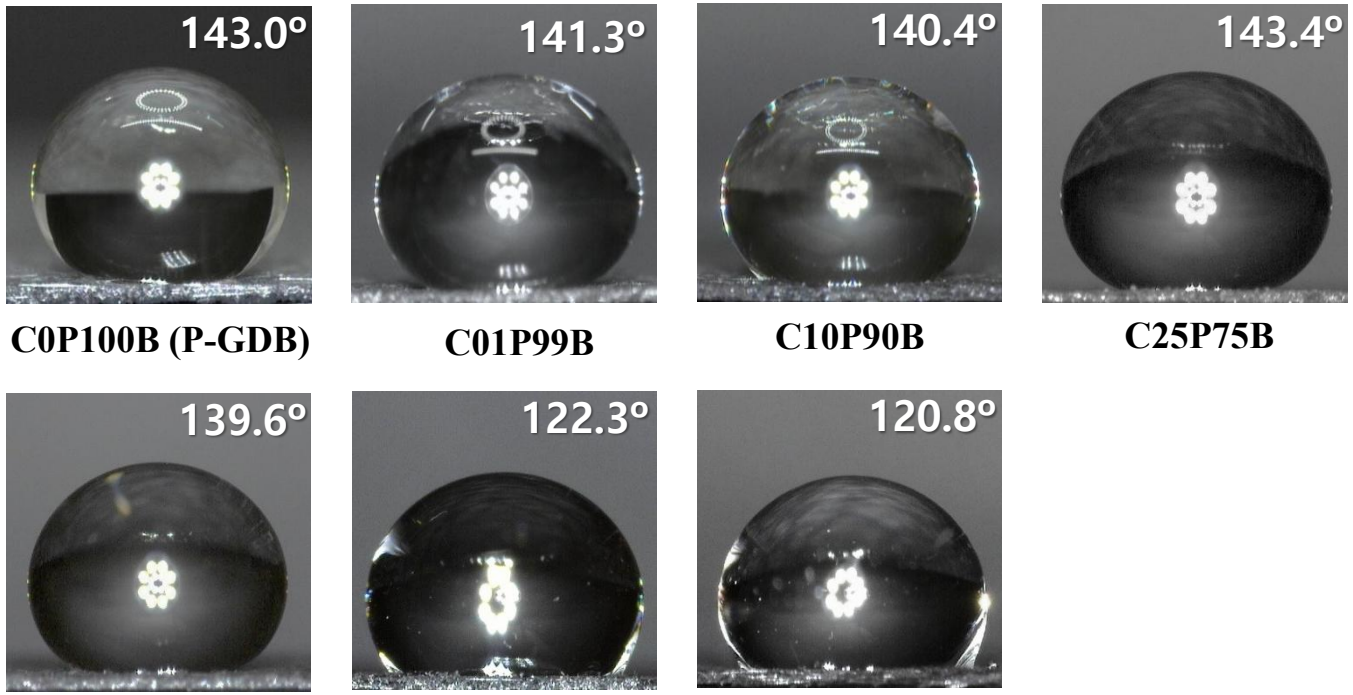

Figure. Water droplet images during contact angle measurement

Characterization of CP-GDBs

❖ Electrical conductivity of CP-GDBs (CxxPyyB) in TP* and IP** directions

- **TP electrical conductivity** was significantly **improved by CNT/PTFE coating compared to conventional PTFE-coated GDB (P-GDB).**
  - ➢ Increased from **4.85 S/cm (P-GDB) to 6.98 S/cm (C90P10B)**, representing a **44% enhancement.**
- **IP electrical conductivity remained nearly constant**, regardless of the coating composition.

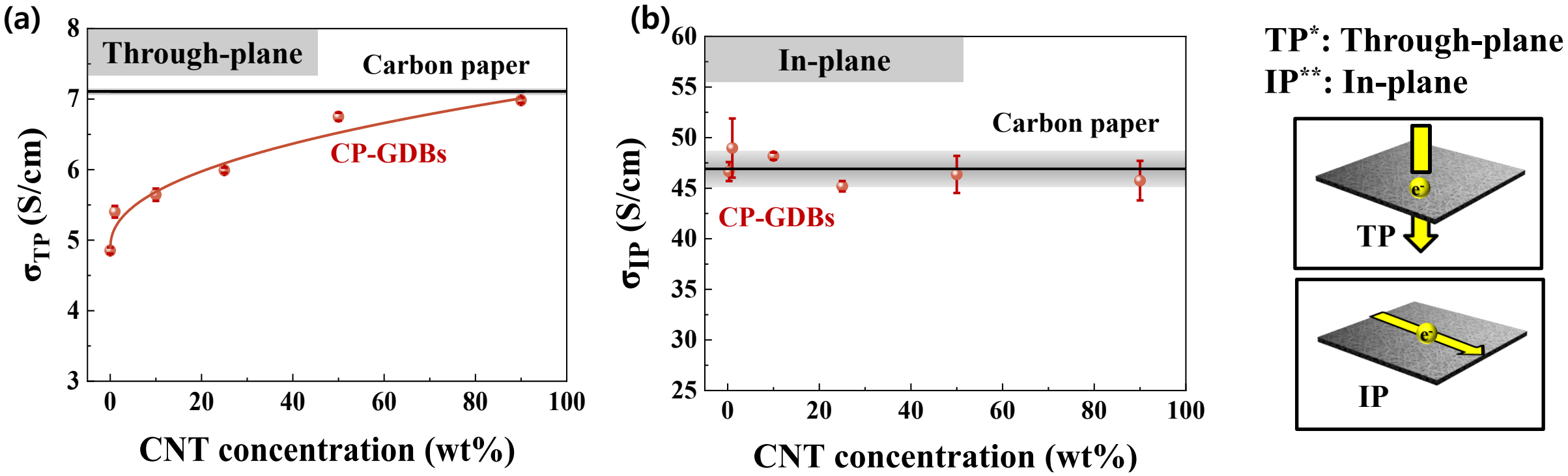

Figure. (a) TP and (b) IP electrical conductivity according to CNT-to-PTFE ratio of the coating

Characterization of CP-GDBs

IP*: In-plane
TP**: Through-plane

❖ Cause of electrical conductivity trends in CP-GDBs (CxxPyyB) in TP* and IP** directions

- **TP direction** : **In P-GDB (C0P100B), insulating PTFE blocks point contacts** between carbon fiber layers, **while CNT/PTFE coatings form additional inter-fiber conductive paths**, enhancing TP electrical conductivity.
- **IP direction : IP electrical conductivity** is **governed by continuous carbon fibers**, so coating has minimal effect.

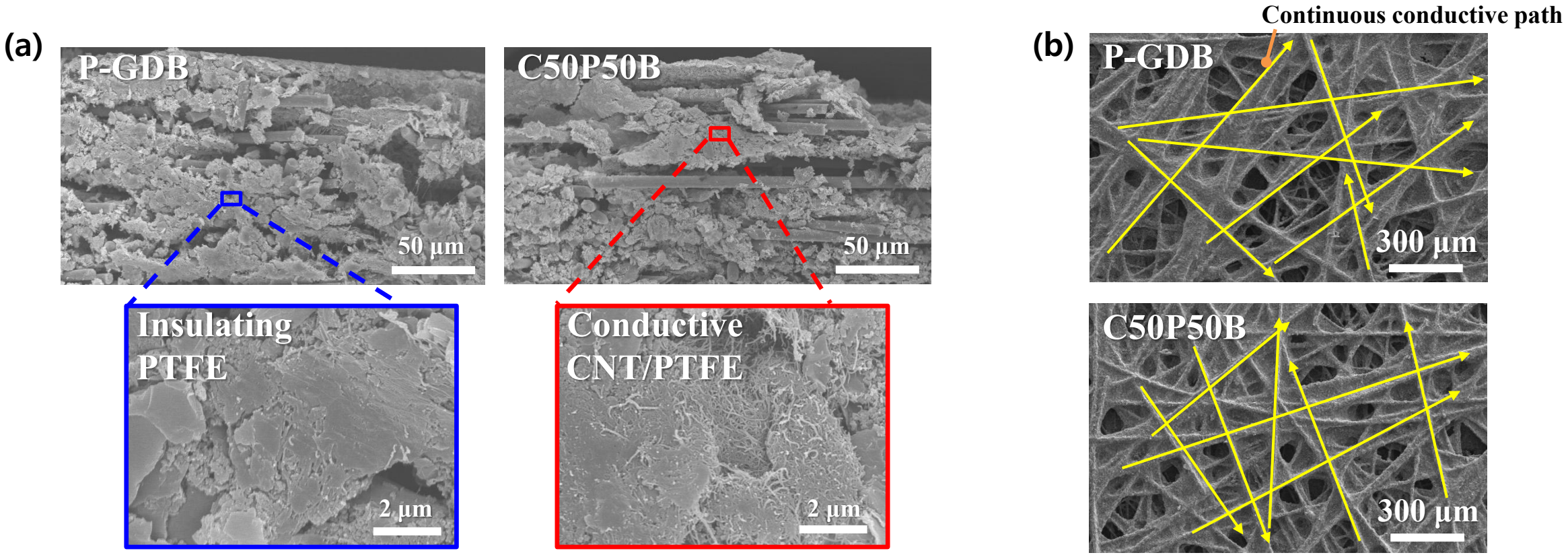

Figure. (a) Cross-sectional SEM images of P-GDB and CP-GDBs, (b) surface SEM images of P-GDB and CP-GDBs

Characterization of CP-GDBs

❖ Mechanical properties of CP-GDBs (CxxPyyB)

- Compressive properties were evaluated for various CNT-to-PTFE ratios in the coating.
- As the proportion of PTFE (serving as a binder of GDB) decreased, **compressibility increased** and **stiffness decreased.**
- Mechanical property trend: **P-GDB > C01P99B ≒ C10P90B ≒ C25P75B ≒ C50P50B > C90P10B**

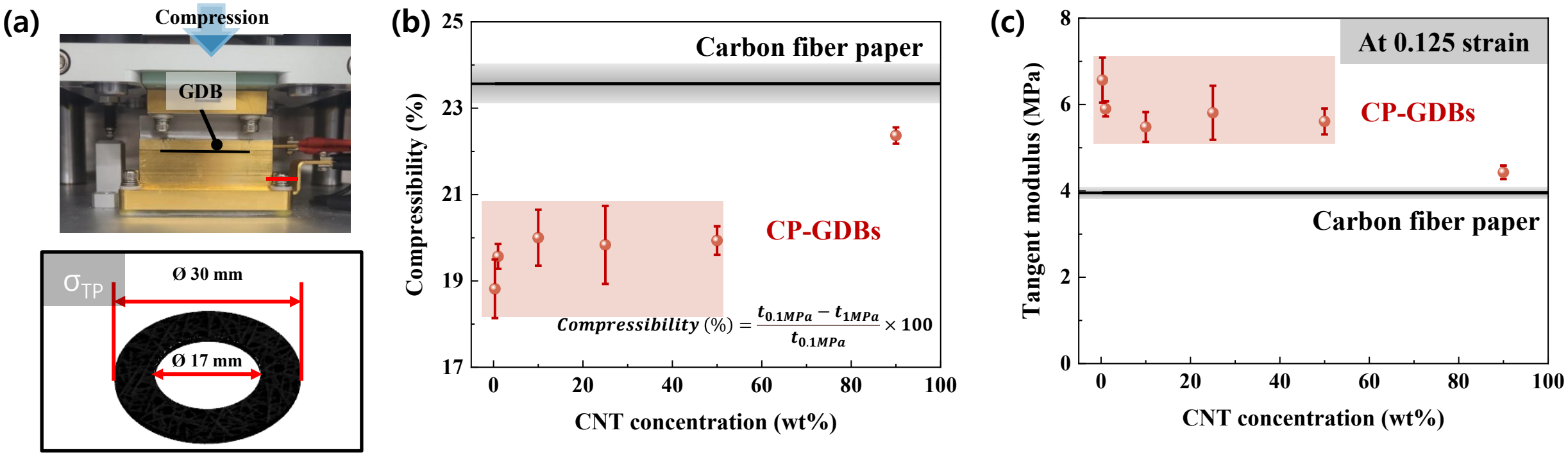

Figure. (a) Compression test setup and specimen dimensions, (b) compressibility by CNT-to-PTFE ratio in the coating, and (c) tangent modulus at 0.125 strain

Characterization of CP-GDLs

❖ Reduced contact resistance between CP-GDBs and MPL (in CP-GDLs, CxxPyyL)

- CP-GDBs exhibited **more than 50% lower contact resistance with MPL** compared to P-GDB.

✓ The **3D conductive CNT network** in the CNT/PTFE coating of CP-GDBs **entangles with the MPL**, increasing the conductive interface.

- **Contact resistance (R_{cont}) between CP-GDBs and MPL** was indirectly **estimated as R_{GDL}-R_{GDB}=R_{cont}+R_{MPL}.**
  - ➢ Since MPL was coated with the same composition and thickness, R_{MPL} was assumed to be constant.

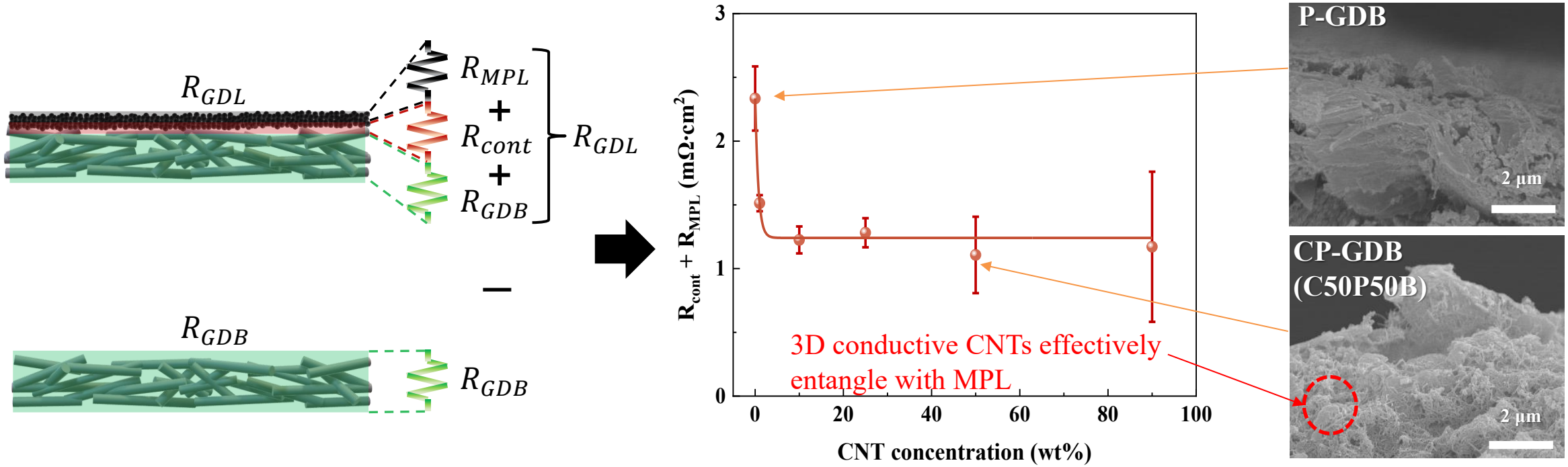

Figure. Contact resistance between CP-GDBs and MPL in CP-GDLs

PEMFC unit cell performance

❖ Fuel cell performance (I-V, I-P curve) evaluation: relative humidity(RH) 50% and 100% conditions

- Under both low and high humidity conditions, **CP-GDLs showed superior performance compared to P-GDL (C0P100L).**
- **Performance increased with higher CNT-to-PTFE ratio in the coating**, reaching up to a 26% improvement.
  - ➢ **CNT/PTFE coating enhanced the electrical conductivity** of the GDB, leading to **reduced cell ohmic loss.**
- Despite higher conductivity, **C90P10L exhibited lower performance to C50P50L** due to its **relatively lower hydrophobicity.**

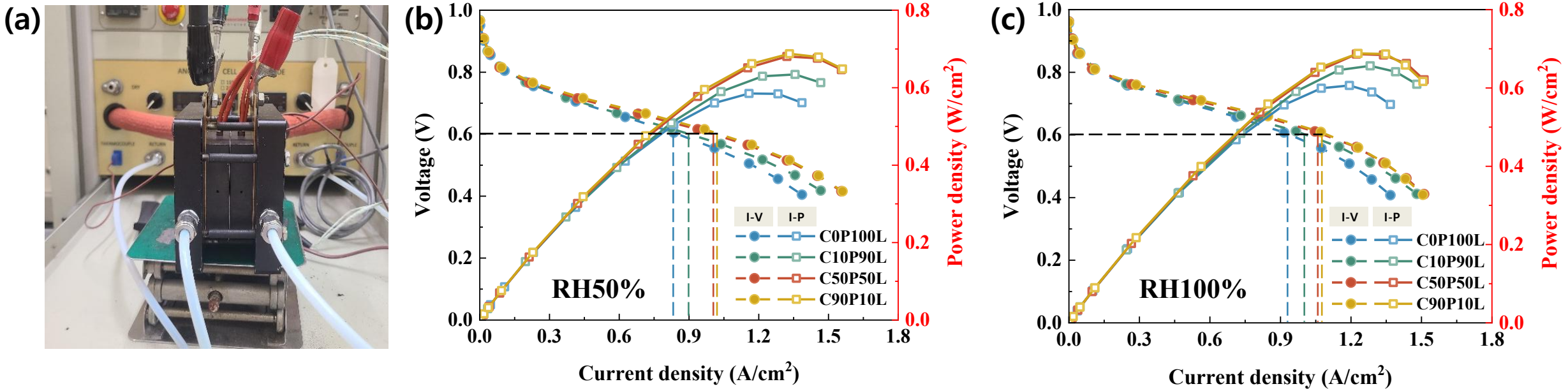

Figure. (a) Device setup for fuel cell performance test; I-V and I-P curves with CP-GDLs applied as cathode GDL, (b) Performance curves at RH 50%, and (c) performance curves at RH 100%. (I-V curve: dotted line, I-P curve: solid line

04. Conclusion

Conclusion

❖ Conductive-hydrophobic coating of GDB via CNT/PTFE

- Conclusion

- CNT/PTFE conductive-hydrophobic coating on GDB:
  - ✓ **Enhanced electrical conductivity**
  - ✓ **Improved unit cell performance (reduced ohmic loss)**
  - ✓ **Provided hydrophobicity**
  - ✓ **Maintained compressive stiffness**

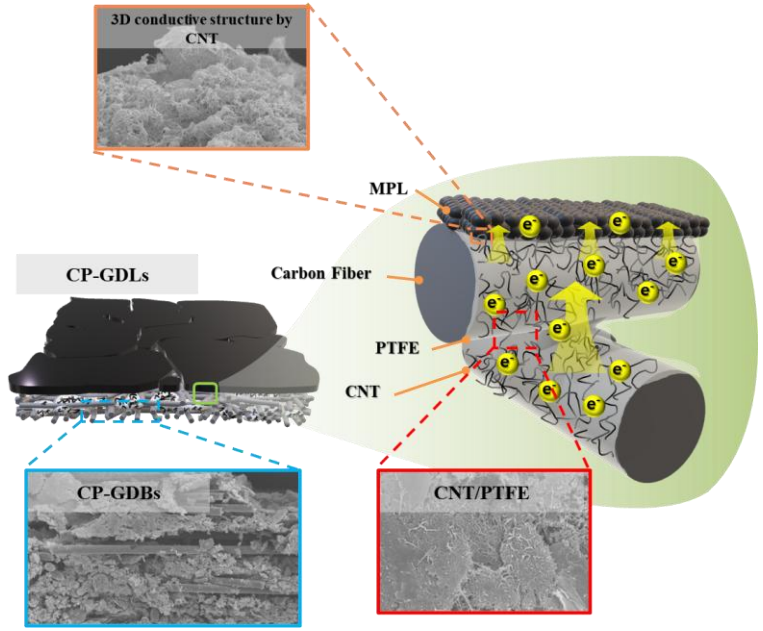

- Property variation by CNT/PTFE ratio
  - ✓ GDB properties are tunable according to the CNT-to-PTFE ratio in the coating.

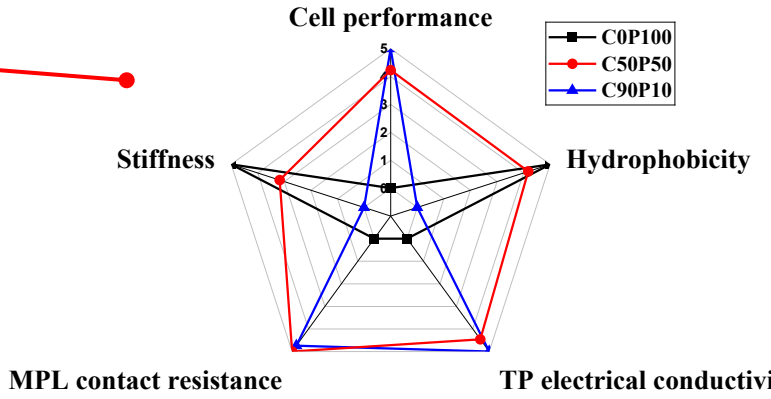

- Optimal composition by condition
  - ✓ Under general operating conditions, C50P50 is optimal (balanced properties).
  - ✓ Under low-humidity conditions, C90P10 is optimal due to maximized conductivity.



Myungjin Hong
(2nd year)
M.S candidate
E-mail : bc120m@inha.edu

Thank you

MCSI Lab (http://mcsi.inha.ac.kr/)
Multifunctional Composites & Structural Integration Lab

인하대학교 INHA UNIVERSITY

❖ Acknowledgement

This work was supported by the National Research Foundation of Korea (NRF) grant funded by the Korea government (MSIT) (No. NRF2022R1A2C1006020)

References and Q&A

❖ References

1) SIGRACET® SGL Carbon's Gas diffusion layers(GDL),https://www.sglcarbon.com/en/markets-solutions/material/sigracet-fuel-cell-components/

2) F. Destyorini, Indriyati, N. Indayaningsih, B. Prihandoko, A. Z. Syahirial, Properties of carbon composite paper derived from coconut coir as a function of polytetrafluoroethylene content, IOP Conference Series: Materials Science and Engineering 316 012054

3) H. Sadeghifar, In-plane and through-plane electrical conductivities and contact resistances of a Mercedes-Benz catalyst-coated membrane, gas diffusion and micro-porous layers and a Ballard graphite bipolar plate: Impact of humidity, compressive load and polytetrafluoroethylene, Energy Conversion and Management 154 (2017) 191-202.

4) T.C. Ma, H.J. Guo, Z.H. Gu, W.K. Lin, J.X. Qi, C.F. Yu, J.H. Li, Performance analysis and experimental study of titanium GDL in proton exchange membrane fuel cell, International Journal of Hydrogen Energy 83 (2024) 604-613.

5) P. Yang, Z. Xie, H. Li, P. Wang, Q. Huang, Graphene oxide reinforced ultra-thin carbon paper used for fuel cells and the mechanisms of reinforcement, International Journal of Hydrogen Energy 42(16) (2017) 11699-11709.

6) Y. Tang, W. Yuan, M. Pan, Z. Wan, Feasibility study of porous copper fiber sintered felt: A novel porous flow field in proton exchange membrane fuel cells, International Journal of Hydrogen Energy 35(18) (2010) 9661-9677.

❖ Acknowledgement

This work was supported by the National Research Foundation of Korea (NRF) grant funded by the Korea government (MSIT) (No. NRF2022R1A2C1006020)

Development of a Height-Tapered Double Cantilever Beam Test Method for Mode I Interlaminar Fatigue Testing

Shagata Das
PhD Candidate
Department of Civil and Environmental Engineering | Center for Composite Materials

ICCM24

University of Delaware

Motivation

Importance of Delamination and Mode I Failure in Composite Laminates

- Delamination is one of the most critical failure modes in laminated composite structures.
- It is often visually undetectable, making it highly dangerous and difficult to monitor.
- Leads to a significant reduction in both stiffness and strength.
- Fatigue-induced delamination is: Hard to detect; Irreversible; performance degradation or even catastrophic failure
- Design Philosophies in Practice:
  - No-Delamination Growth Principle (Conservative approach)
  - **Damage Tolerance Philosophy** (widely recommended): Emphasizes understanding failure mechanisms; Requires accurate prediction and monitoring tools
- In 2009, the Federal Aviation Administration (FAA) introduced **'slow growth' approach** to the certification of composites
- Among delamination modes, Mode I (opening mode) is often most critical.
- Dominates early-stage crack initiation in fatigue

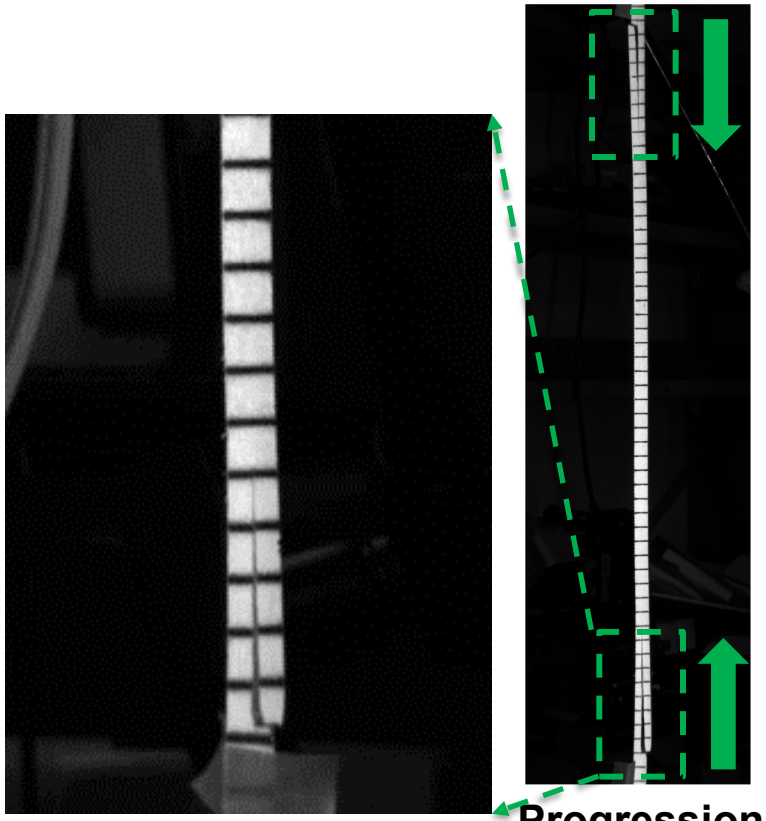

Single Step Lap Joint Failure: Combination of Mode-I and Mode-II Loading

Challenges in Traditional Mode-I Fatigue Testing Methods

- Traditional Mode-I fatigue testing methods - based on constant load range (ΔP) or displacement range (Δd) - fail to maintain constant ΔG
- Under load control, ΔG increases with crack growth, leading to instability (da/dN → ∞)

$$\Delta G = \frac{(P_{max}^2 - P_{min}^2)a^2}{bEI}$$

- Conversely, under displacement control, ΔG decreases with increasing crack length, resulting in crack arrest (da/dN → 0)

$$\Delta G = \frac{9EI}{4ba^4}(\delta_{max}^2 - \delta_{min}^2)$$



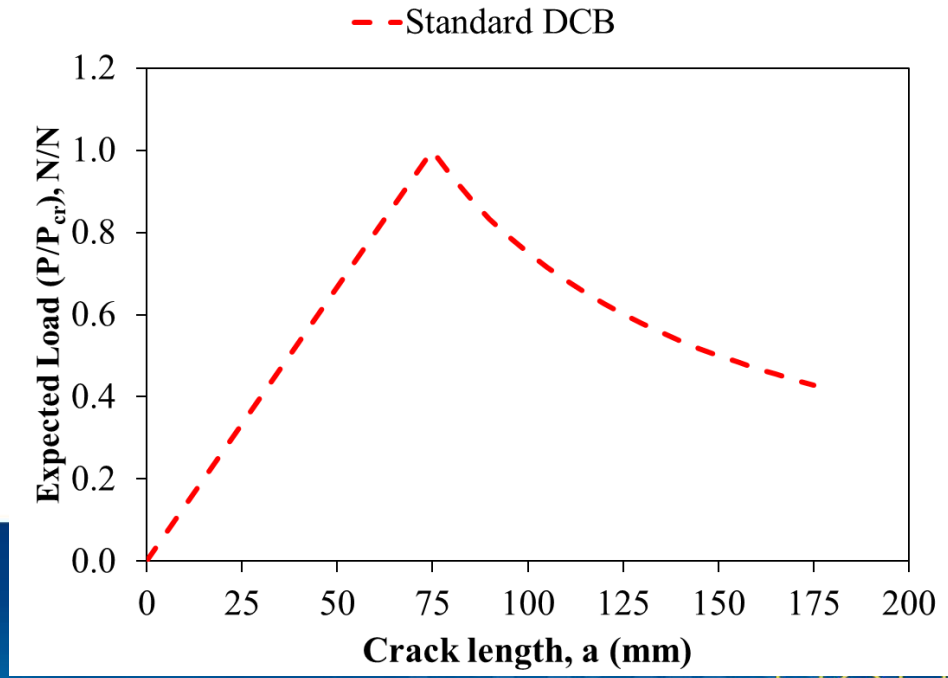

G-controlled Mode I Fatigue Testing

Russell & Street, 1988: *A Constant ΔG Test for Measuring Mode I Interlaminar Fatigue Crack Growth Rates*

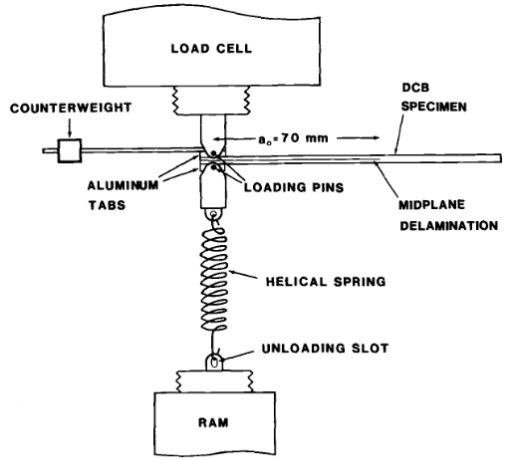

FIG. 1—*Experimental arrangement for constant ΔG interlaminar fatigue.*

- Double Cantilever Beam (DCB) specimen loaded in series with a linear elastic spring.
- Spring mechanism provides optimum control of energy release rate (ΔG) during fatigue crack propagation.
- Displacement-controlled cyclic loading.

Manca et al., 2015: *G-control fatigue testing for cyclic crack propagation in composite structures*

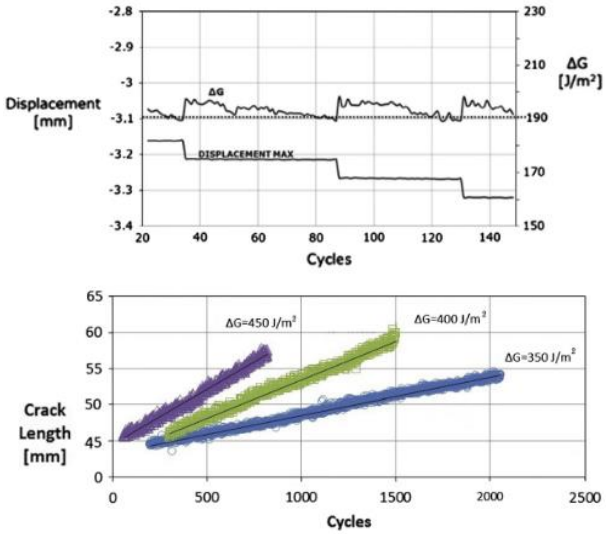

- **Computer-controlled G-control testing** methodology
- Displacement-controlled fatigue

$$\Delta G = \frac{9EI}{4ba^4}\delta_{max}^2(1-R^2)$$

Arhant et al., 2021: *Fatigue crack growth properties of carbon-polyamide 6 thermoplastic composites using a multi-ΔG control method*

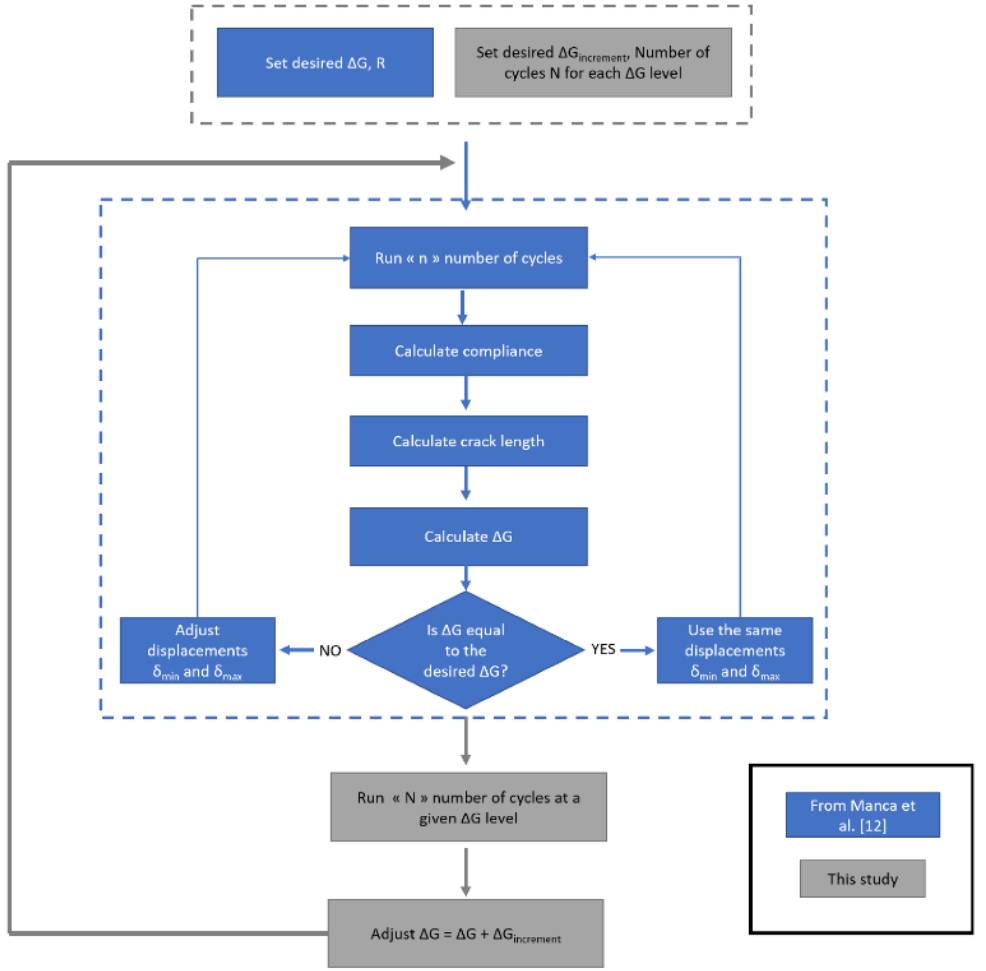

G-controlled Mode I Fatigue Testing

Research Gaps

1. *Frequent adjustment of displacement in the standard DCB fatigue testing to keep ΔG constant*
2. *Even small increments in crack length can cause significant changes in ΔG*
3. *Lack of Consideration for R-Curve Effects; difficult to understand the R-curve effect with standard DCB*
4. *The influence of R-curve behavior on the accuracy and reliability of Paris law fitting remains poorly understood.*

Geometry-Based G-controlled Mode I Quasi-Static Testing

- Achieve constant ΔG during crack growth by altering the geometry of standard DCB
- ASTM Standard Available for HTDCB of Adhesively Bonded Metal Joints
- No standard available to perform ***fatigue HTDCB testing***
- **No comprehensive guidance exists** for designing HTDCB specimens specifically for fatigue testing of composite materials
- Prior studies focused exclusively on **Quasi-static behavior of adhesively bonded metal–metal or Wood**, with no application to composite laminates.

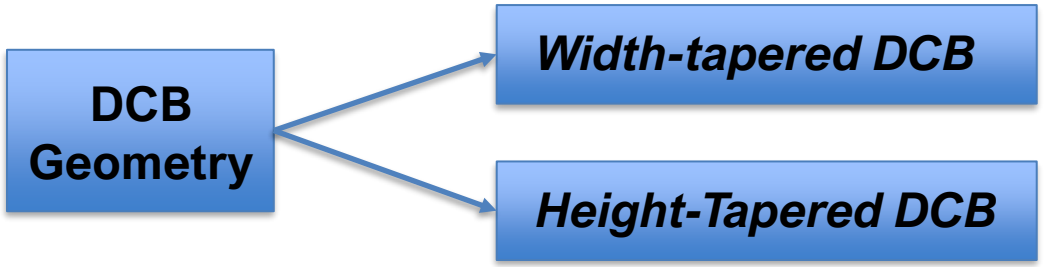

ASTM D3433: Standard Test Method for Fracture Strength in Cleavage of Adhesives in Bonded Metal Joints

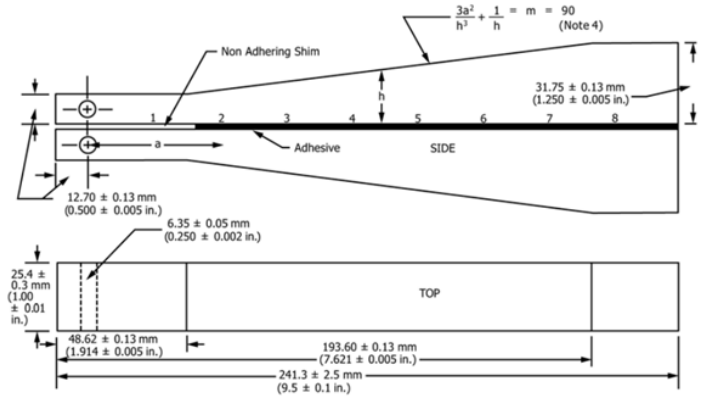

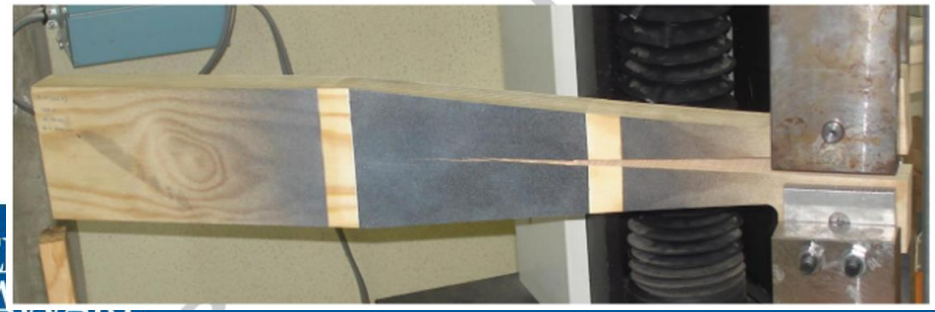

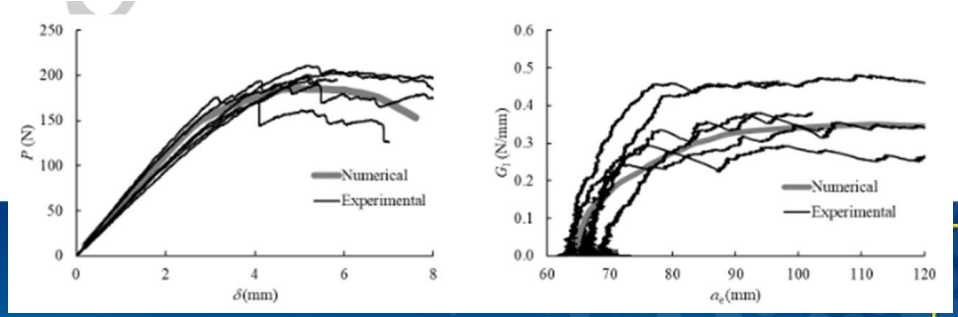

Objective of This Study

- Designing Height-Tapered DCB (HTDCB) specimen to **maintain a constant energy release rate (G) and load (P)** during **quasi-static** delamination testing
- HTDCB configuration effectively maintains a **constant G during fatigue loading** conditions
- Ensure **stable crack growth** throughout fatigue testing
- Obtain **sufficient crack length** to accurately calculate fatigue crack growth rate (da/dN)

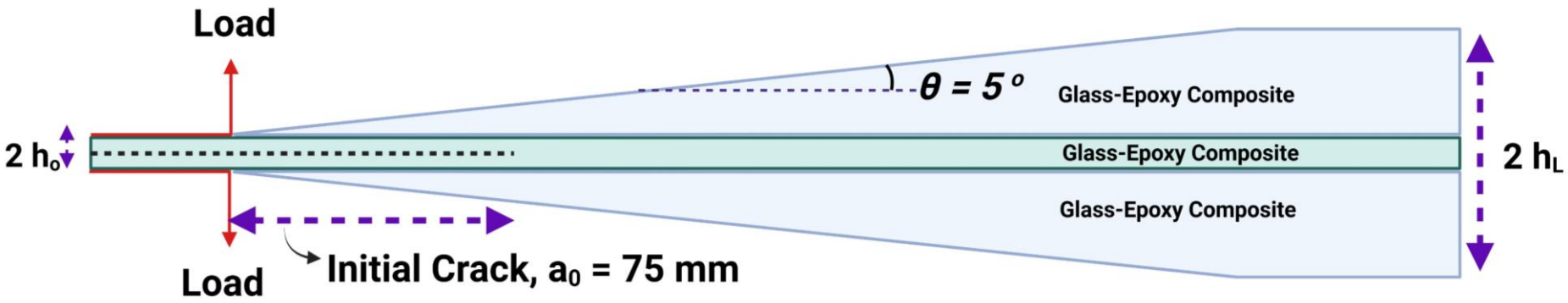

Design of HTDCB for Mode I Fatigue Testing of Composites

- **Shear flexible Timoshenko beam** is described through the following two differential equations:

$$Moment, \mathrm{M}(x) = \mathrm{EI}\frac{d\emptyset_z(x)}{dx} = Px$$

$$Shear\ force, \mathrm{V}(x) = k_s AG\ (\frac{dy}{dx} - \emptyset_z(x)) = -P$$

For classical Euler–Bernoulli formulation, $k_s AG = \infty$; shear-rigid beam

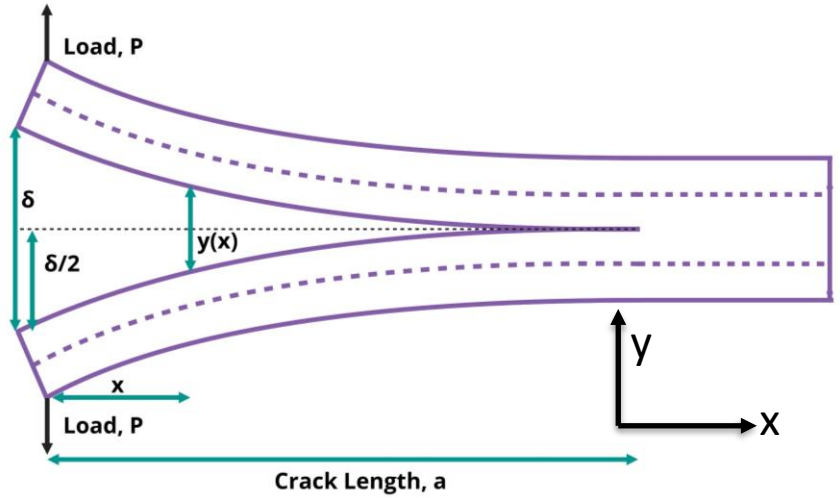

Here, P = Load, E = Flexural modulus, I = Moment of inertia, k_s = Shear correction factor, A = cross-sectional area, $\emptyset_z(x) = cross - sectional\ rotation$, y = deflection

$$\frac{d\emptyset_z(x)}{dx} = \frac{Px}{EI}$$

$$\frac{dy}{dx} = -\frac{P}{k_s AG} + \emptyset_z(x)$$

Deflection equation, y(x), was obtained by solving the two equations with the applied boundary conditions, $\emptyset_z(a) = 0\ and\ y(a) = 0$

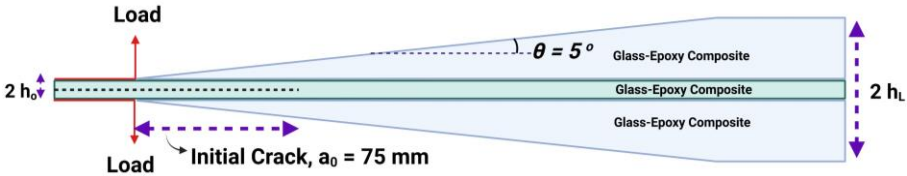

$$h_L = h_o + \alpha a$$

$$\tan\theta = \frac{h_L - h_o}{a} = \alpha$$

$$k = \frac{\alpha}{h_o}$$

Design of HTDCB for Mode I Fatigue Testing of Composites

- **Timoshenko Beam Theory**, deflection, and compliance equations were analytically derived, accounting for both **flexural and shear effects**
- **Linear elastic fracture mechanics**-based strain energy release rate (**SERR**) equation (G) was derived
- **Validated** against **ASTM D3433-99** for metal joints (Poisson's ratio = 1/3)

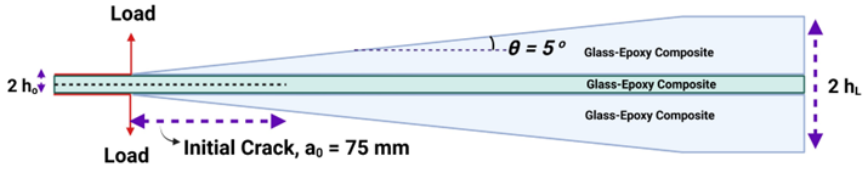

$$h_L = h_o + \alpha a \qquad k = \frac{\alpha}{h_o}$$

$$\tan\theta = \frac{h_L - h_o}{a} = \alpha$$

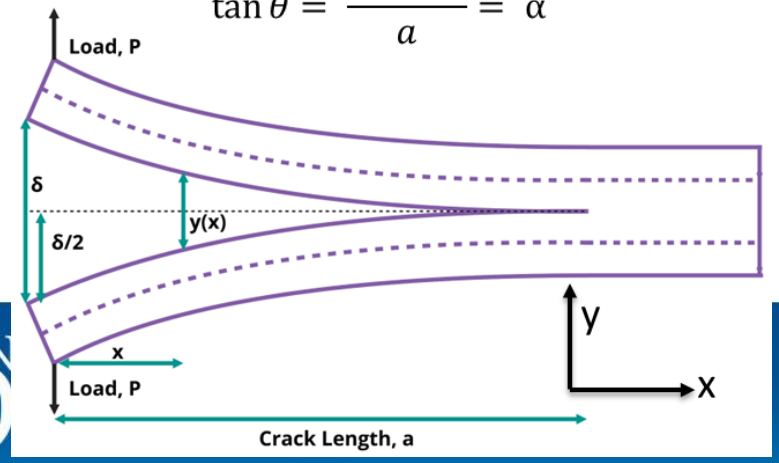

- $\boldsymbol{Deflection\ at\ loading\ point, y(x=0) = \delta}$

$$Deflection, \delta = \frac{Pa(-2-3ka)}{EI_o k^2(1+ka)^2} + \frac{2P\log(1+ka)}{EI_o k^3} + \frac{2P}{A_o G}\frac{log(1+ka)}{k}$$

$$C = \frac{\delta}{P}$$

$$Compliance, C = \frac{a(-2-3ka)}{EI_o k^2(1+ka)^2} + \frac{2\log(1+ka)}{EI_o k^3} + \frac{2}{A_o G}\frac{log(1+ka)}{k}$$

$$G_I = \frac{P^2}{2b}\frac{dC}{da}$$

$$SERR, G_I = \frac{12P^2a^2}{Eb^2{h_o}^3(1+ka)^3} + \frac{P^2}{k_s G b^2 h_o (1+ka)}$$

Rearranging Equation

$$G_I = \frac{4P^2}{Eb^2}\left[\frac{3a^2}{{h_L}^3} + \frac{3E}{8Gh_L}\right]; \textit{Equation similar to ASTM D3433}$$

$$G_I = \frac{4P^2}{Eb^2}\left[\frac{3a^2}{{h_L}^3} + \frac{1}{h_L}\right]; \textit{ASTM D3433 Equation}$$

Geometry-Based Approaches to Maintain Constant ΔG During Mode-I Fatigue Testing

- Three approaches available to achieve constant ΔG during crack growth by altering the geometry of standard DCB

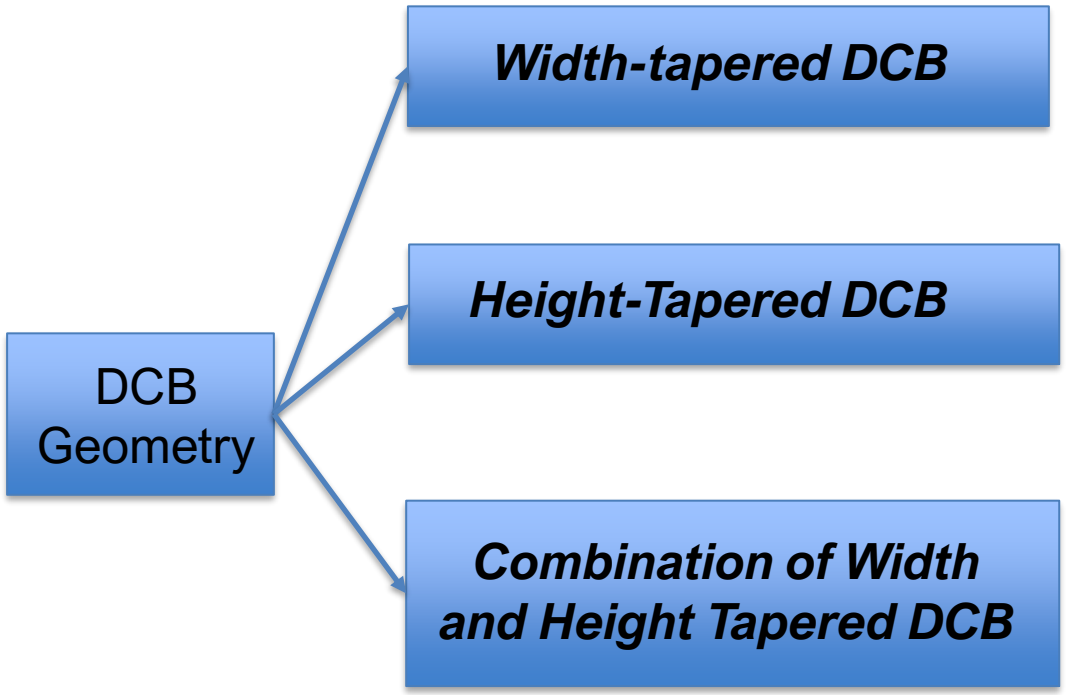

$$SERR, G_I = \frac{12P^2a^2}{Eb^2(1+k_2a)^2{h_o}^3} + \frac{P^2}{k_sGb^2(1+k_2a)^2h_o}$$

$$SERR, G_I = \frac{12P^2a^2}{Eb^2{h_o}^3(1+k_1a)^3} + \frac{P^2}{k_sGb^2h_o\,(1+k_1a)}$$

$$SERR, G_I = \frac{12P^2a^2}{Eb^2(1+k_2a)^2{h_o}^3(1+k_1a)^3} + \frac{P^2}{k_sGb^2(1+k_2a)^2h_o\,(1+k_1a)}$$

Parametric Study Varying Tapered Angle of HTDCB

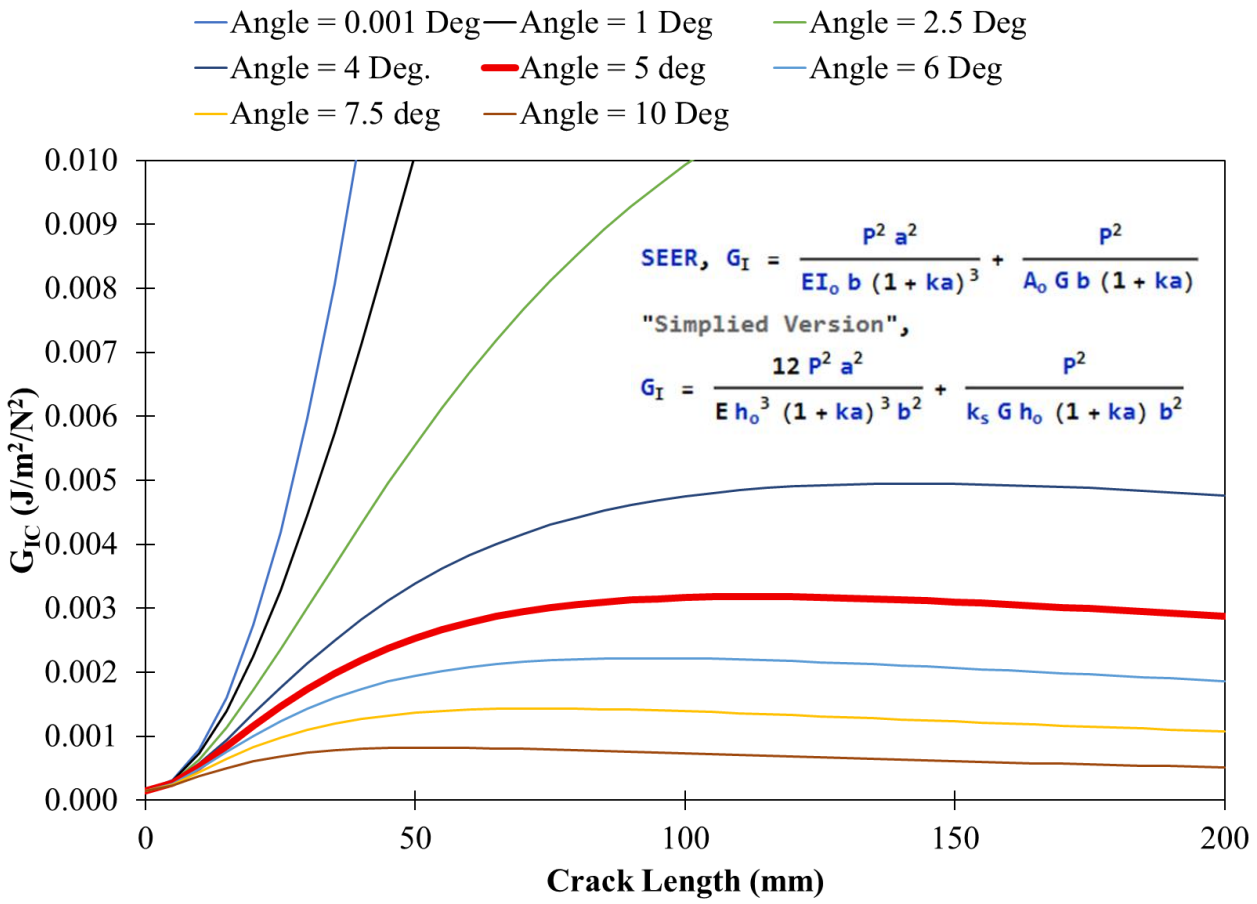

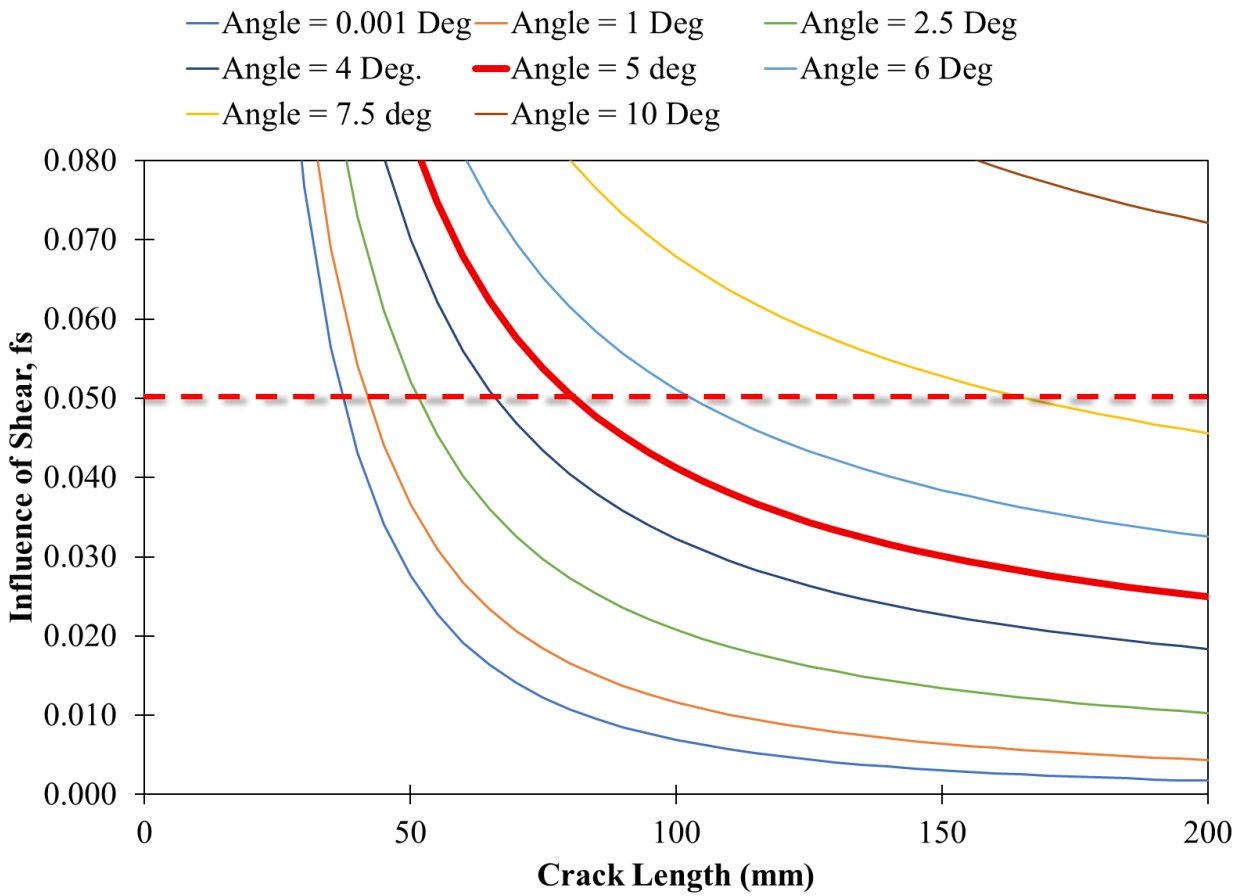

- **Parametric analysis** varying the tapered angle (α) from 0° to 10° identified a **5° taper with an initial crack length of 75 mm**

Parametric Study Varying Tapered Angle of WTDCB

- Performed parametric analysis on Width-Tapered DCB (WTDCB) specimens by varying the taper angle from 0° to 45°
- Found that a taper angle of **at least 45°** is necessary to maintain a constant G with an initial crack length of **~80 mm**
- Such large taper angles lead to a **beam-to-plate transition**, complicating specimen geometry and testing
- Consequently, the **HTDCB configuration** was selected for further investigation

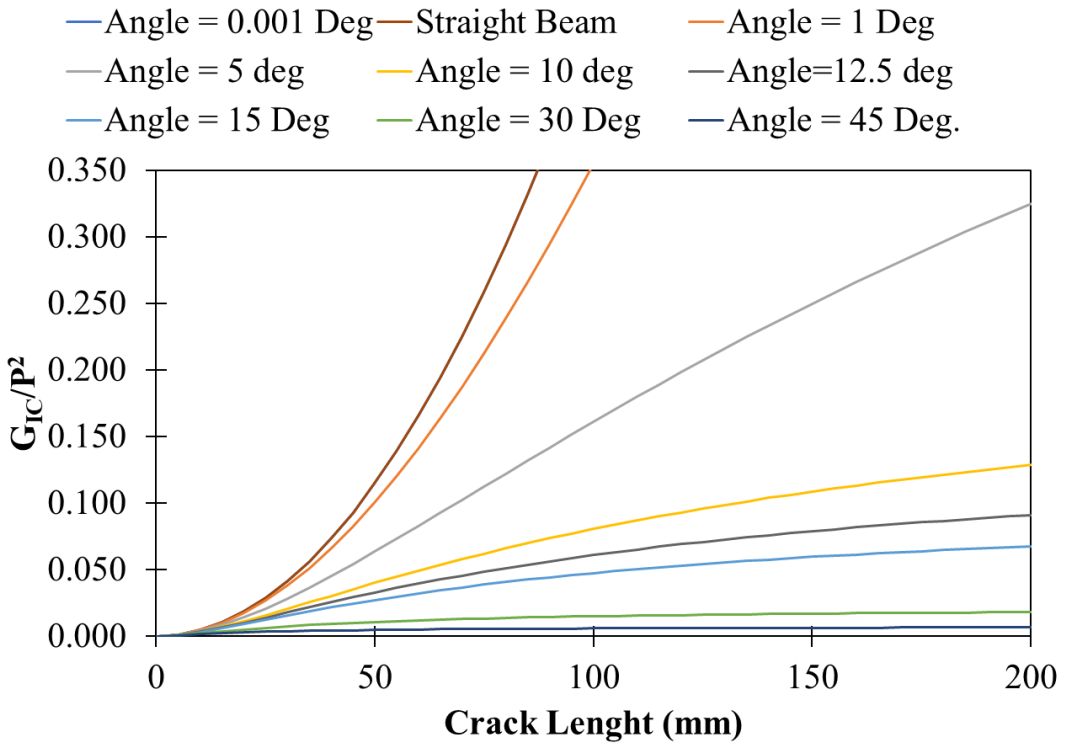

HTDCB Geometry to Maintain Constant ΔG During Mode-I Fatigue Testing

Analytical equation indicates ΔG remains independent of crack growth during fatigue testing

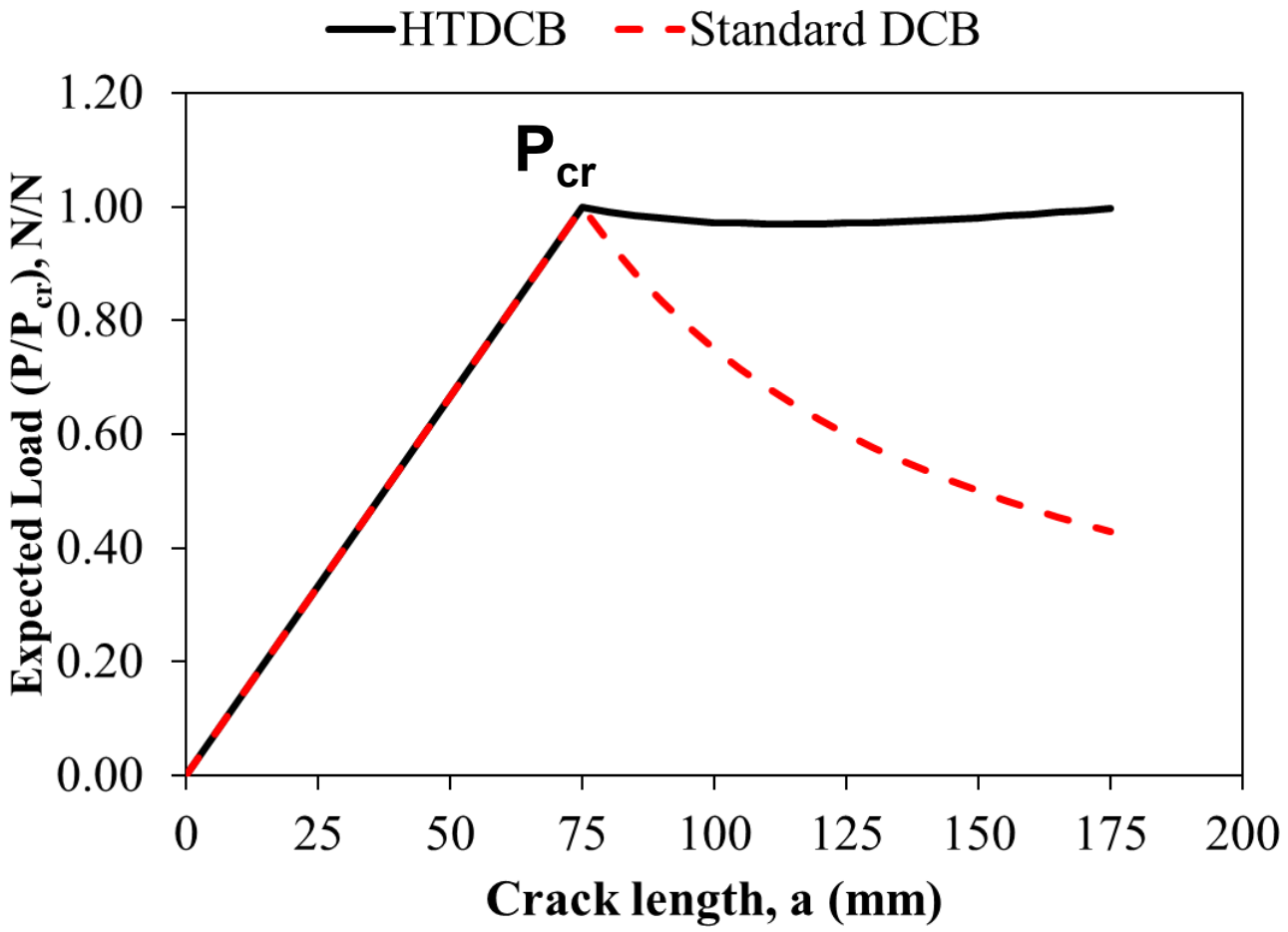

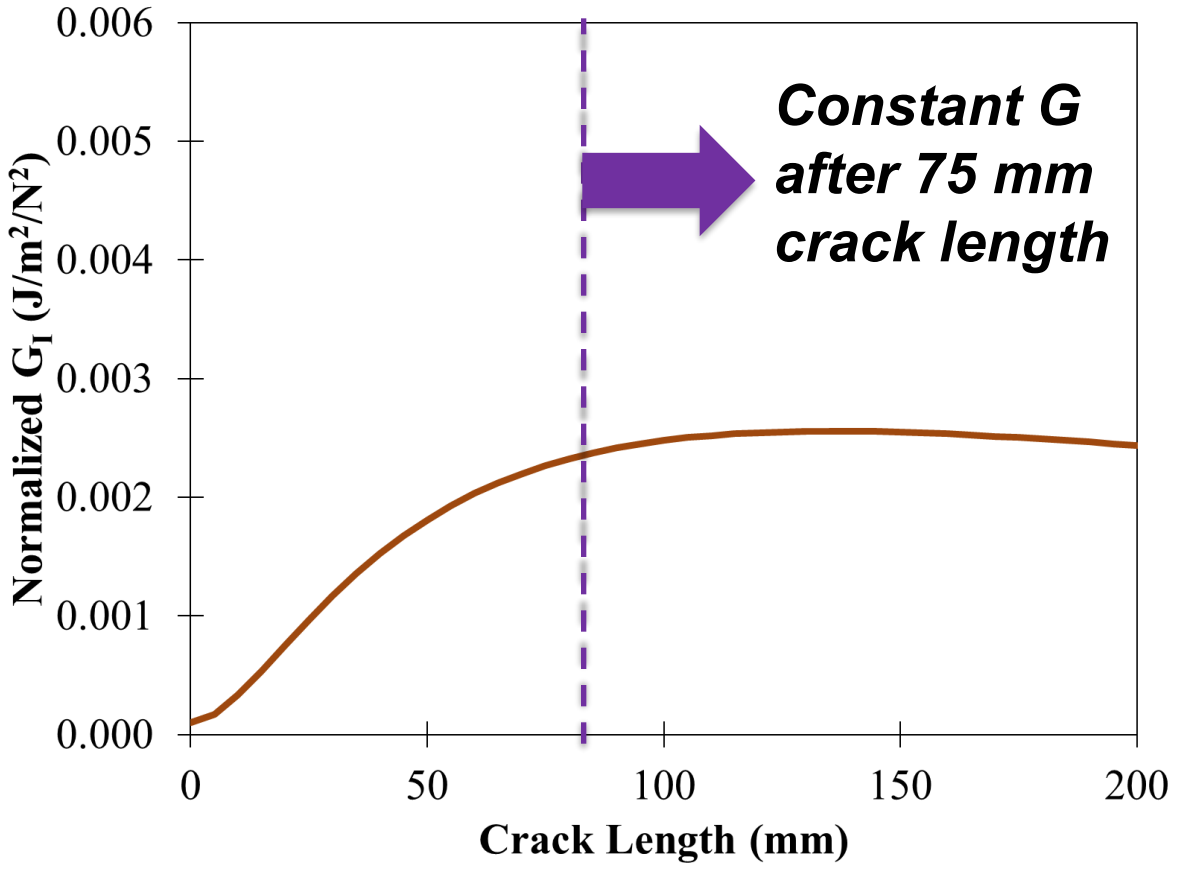

Materials and Methodology

- 463 S-glass Plain Weave Fabric
- RDL-RDC-Epoxy Resin
- Vacuum Assisted Resin Transfer Molding (VARTM) at 60 ℃
- Curing: 80℃ for 2.5 hrs and 121℃ for 4 hrs
- Flexural Modulus: ~ 20 GPa
- Shear Modulus: ~ 2.5 Gpa
- **16-layer PW-RDL-RDC composite** with a pre-crack length of 100 mm at the mid-plane using a Teflon film

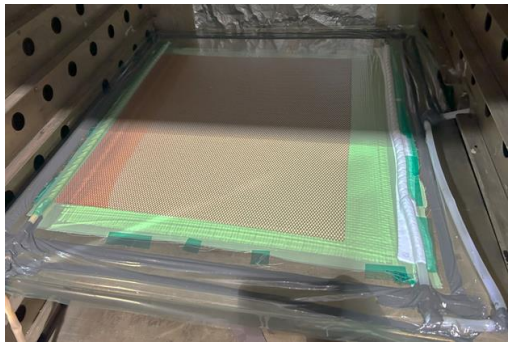

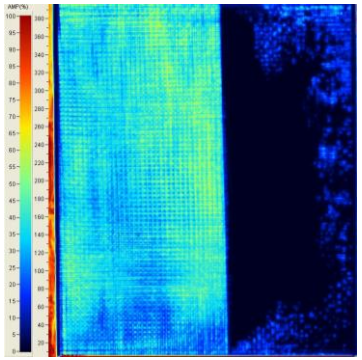

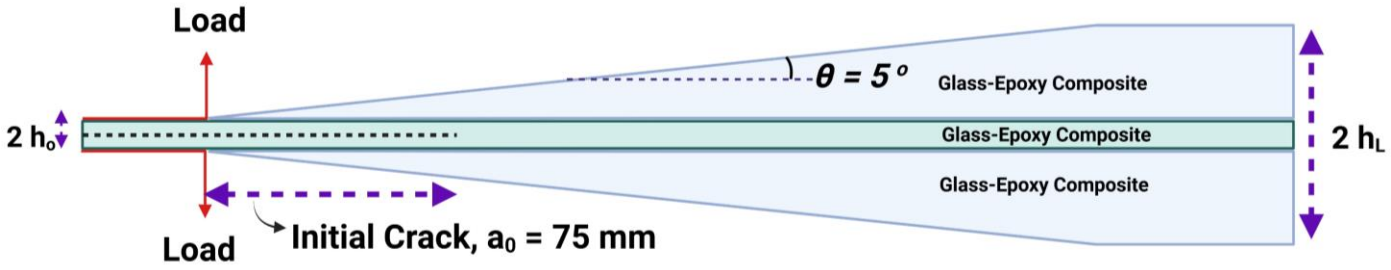

$2h_0 = 10\ mm$ **(Thickness of 16-layer PW-RDL-RDC composite)**

Materials and Methodology

- **24-layer PW-RDL-RDC** composite used to fabricate the tapered geometry
- Tapered section machined from a 19 mm-thick panel using CNC milling or waterjet cutting
- Bonded to the pre-cracked composite panel using LOCTITE EA 9309.3NA AERO epoxy adhesive
- Final cure performed at 80 ℃ for 2 hours

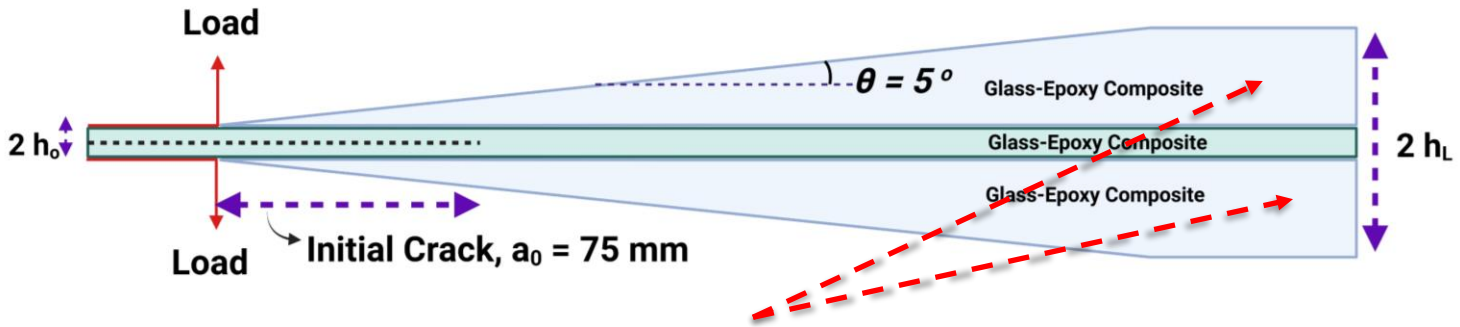

Tapered sections bonded symmetrically on top and bottom of the pre-cracked panel

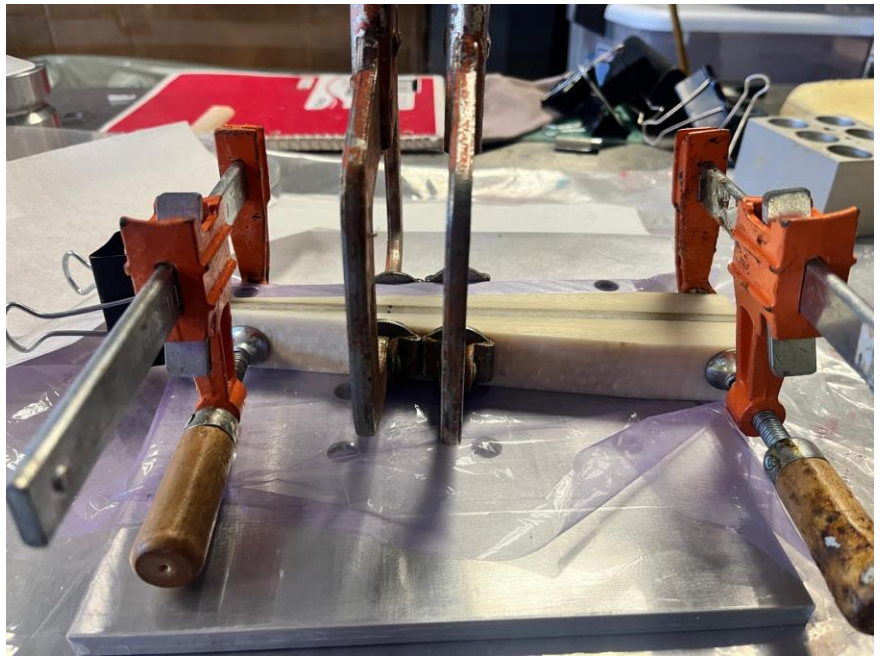

Fixture used for bonding the tapered section to the composite panel

HTDCB Quasi-Static Testing

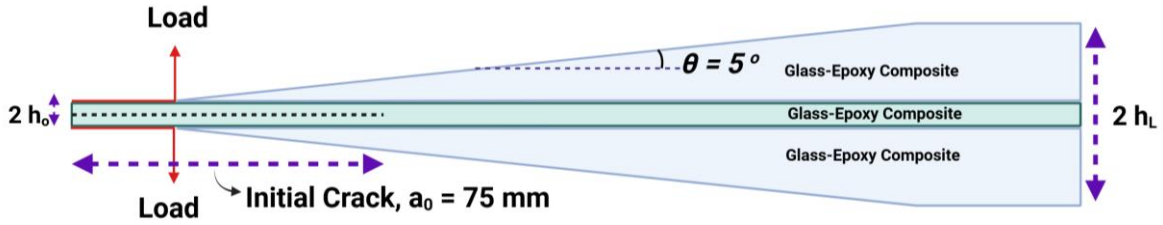

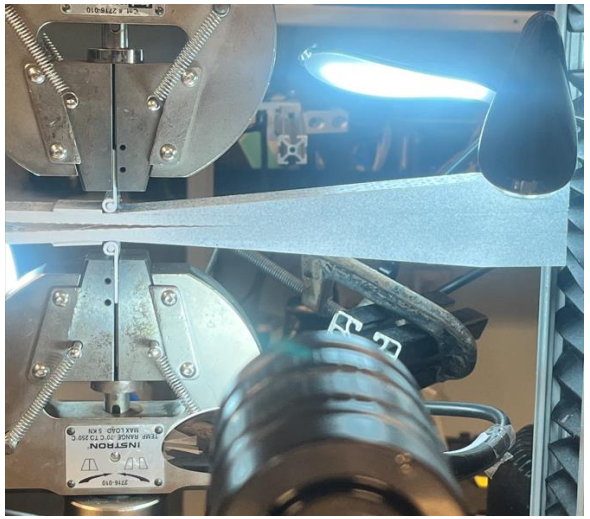

HTDCB Test Setup

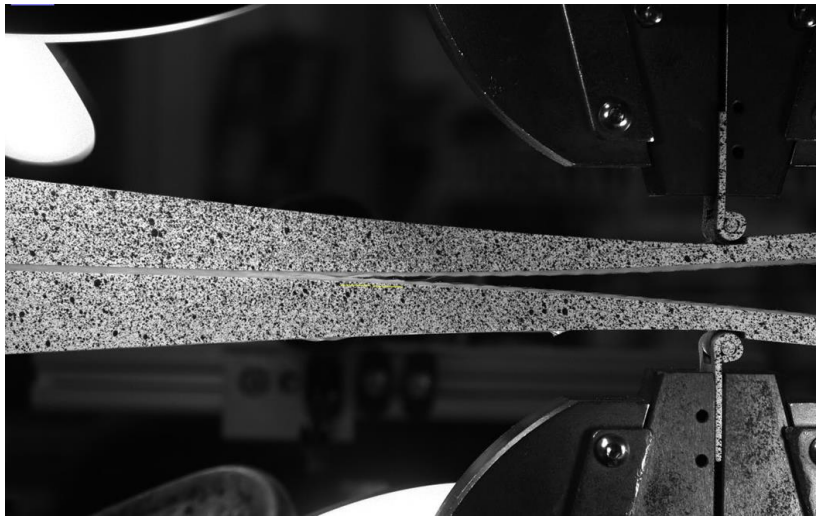

Image processing software, Fiji ImageJ, used to measure the crack propagation distance

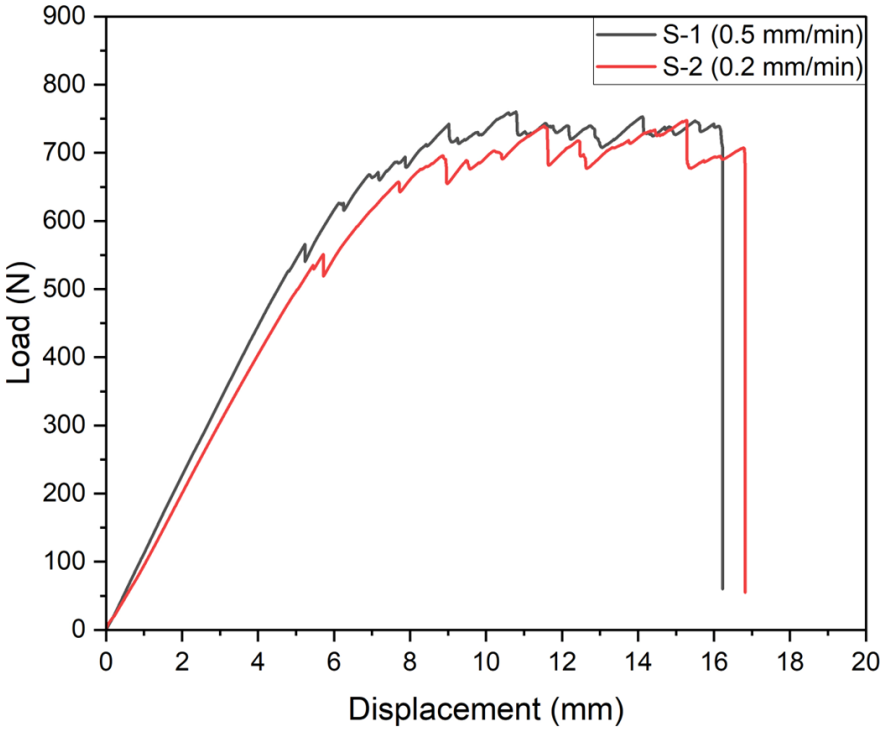

- Quasi-static tests were conducted at two displacement rates (**0.2 mm/min and 0.5 mm/min**) to assess rate effects.
- No rate dependence was observed within this range.

HTDCB Quasi-Static Test Result

- **Load increases** during the **initial ~20 mm** of crack growth, indicating **R-curve behavior**.
- **Load stabilizes** once fracture toughness reaches the **plateau region**.
- Design equation was developed assuming **constant fracture toughness**.
- R-curve behavior attributed to mechanisms such as **fiber bridging, tow-to-tow delamination, and secondary cracking**.

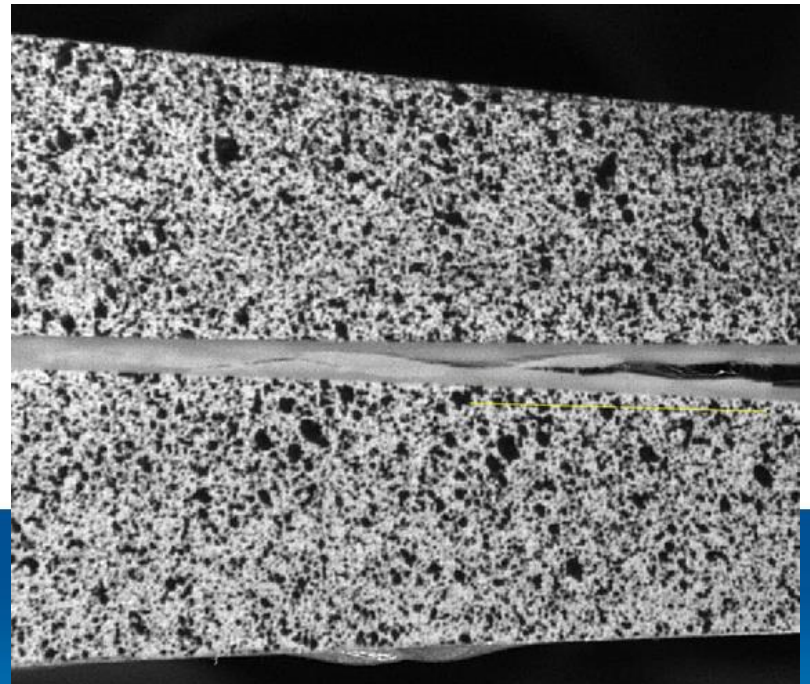

Experimental Results

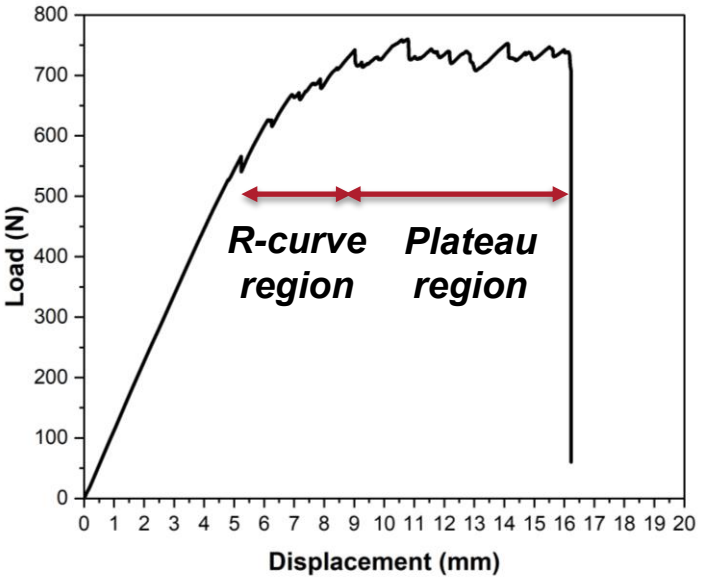

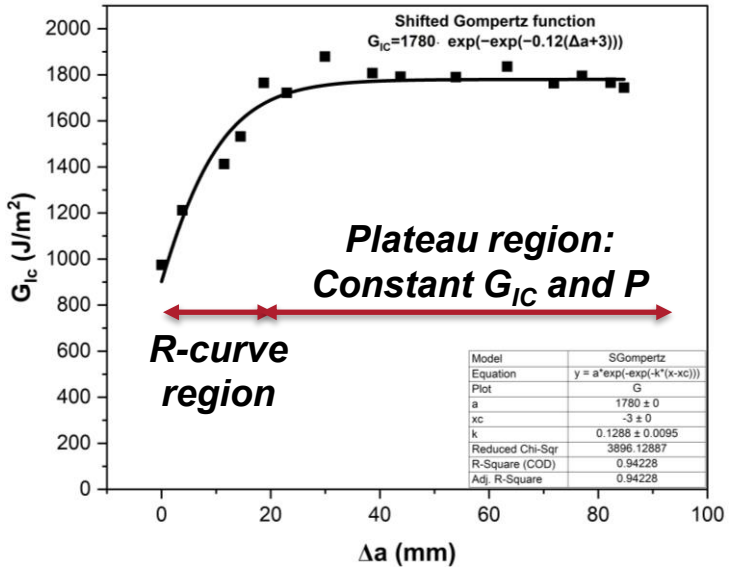

Analytical Prediction

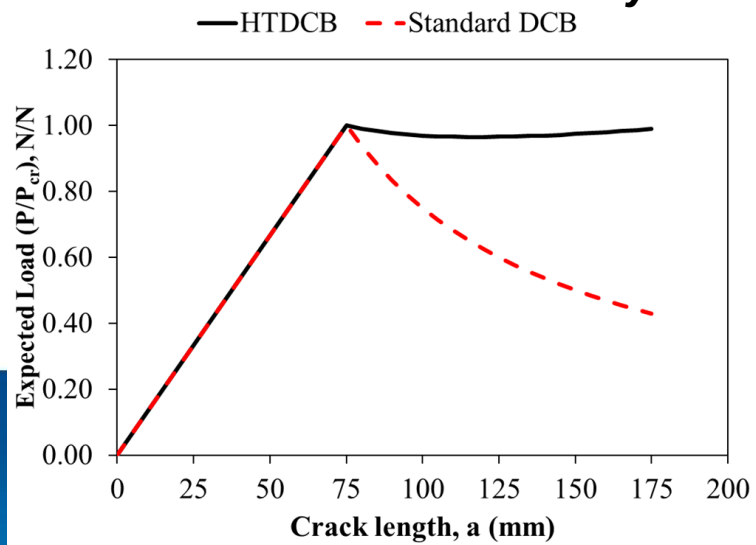

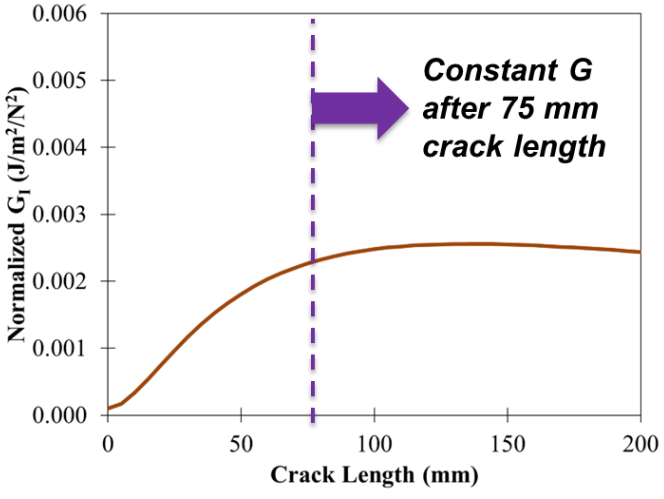

HTDCB vs Standard DCB Quasi-Static Test Result

- Fracture toughness (G_{IC}) vs crack growth (Δa) compared
- HTDCB demonstrated **R-curve behavior comparable** to Standard DCB tests for the PW-RDL-RDC composites
- Welch's t-test on **$G_{Plateau}$ values**
- p-value: 0.57
- p-value > 0.05, **no statistically significant difference** in the mean fracture toughness at the 95% confidence level

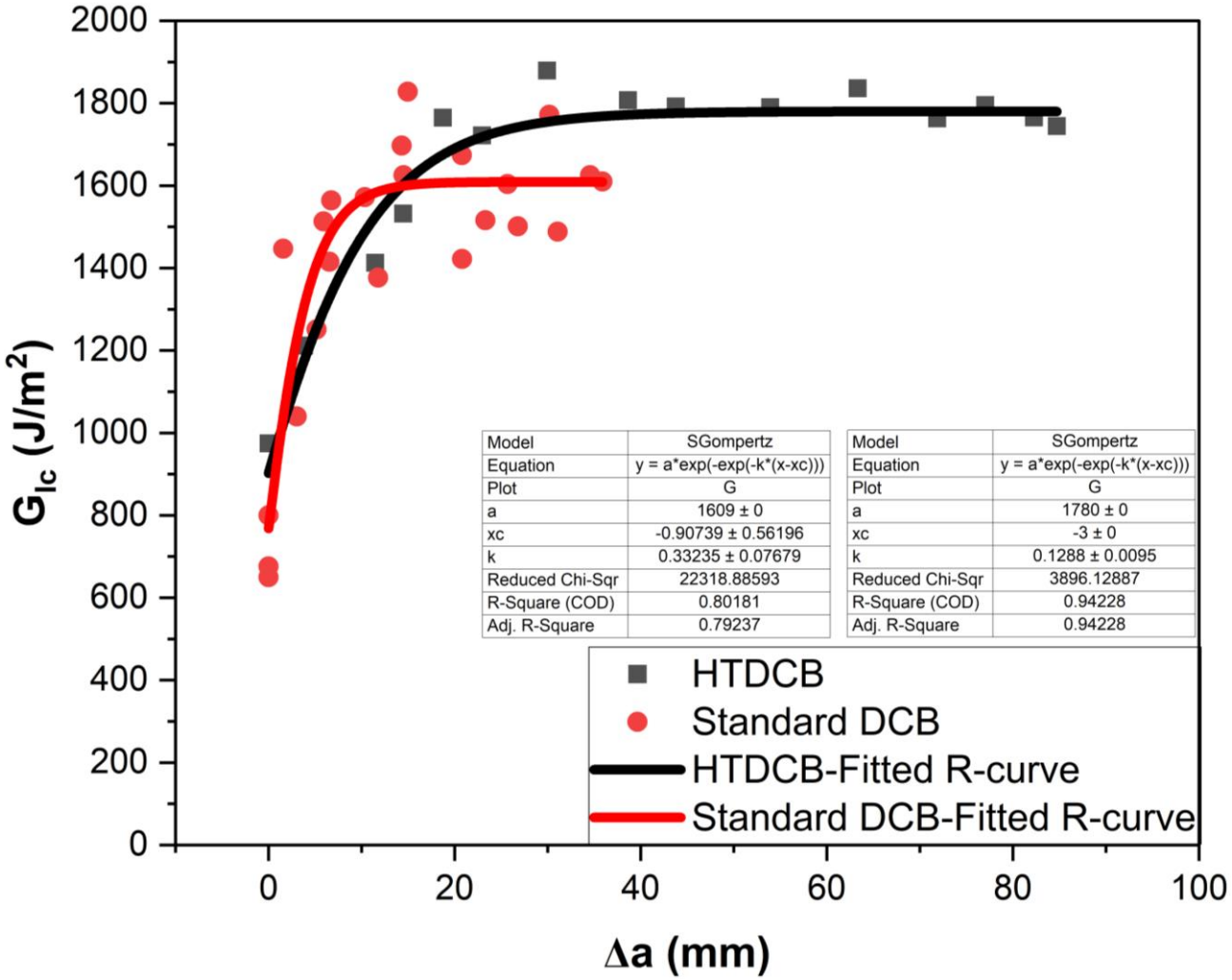

Model	SGompertz
Equation	y = a*exp(-exp(-k*(x-xc)))
Plot	G
a	1609 ± 0
xc	-0.90739 ± 0.56196
k	0.33235 ± 0.07679
Reduced Chi-Sqr	22318.88593
R-Square (COD)	0.80181
Adj. R-Square	0.79237

Model	SGompertz
Equation	y = a*exp(-exp(-k*(x-xc)))
Plot	G
a	1780 ± 0
xc	-3 ± 0
k	0.1288 ± 0.0095
Reduced Chi-Sqr	3896.12887
R-Square (COD)	0.94228
Adj. R-Square	0.94228

Fatigue Testing of HTDCB

Loading-controlled vs Displacement-controlled Fatigue

Fracture toughness equation for HTDCB

"Simplied Version",

Load-controlled fatigue ⇒ $$G_I = \frac{12\,P^2\,a^2}{E\,h_o^3\,(1+ka)^3\,b^2} + \frac{P^2}{k_s\,G\,h_o\,(1+ka)\,b^2}$$

Compliance, $C = \frac{\delta}{P}$

Displacement-controlled fatigue ⇒ $$G_I = \frac{12\left(\frac{\delta}{C}\right)^2 a^2}{E\,h_o^3\,(1+ka)^3\,b^2} + \frac{\left(\frac{\delta}{C}\right)^2}{k_s\,G\,h_o\,(1+ka)\,b^2}$$

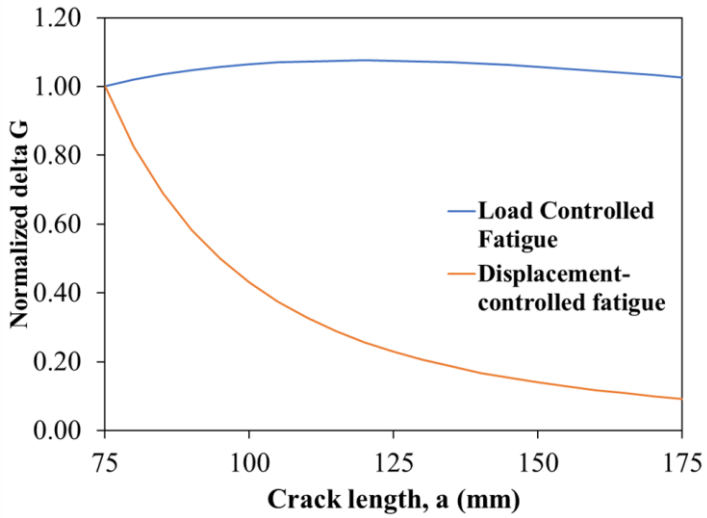

1. To be conservative, **90% $G_{plateau}$**
2. **A-basis allowable** = Mean of plateau load – 3 * Standard deviation = **720 N**

P_{max}	720 N	δ_{max}	8.0 mm
P_{min}	72 N	δ_{min}	0.8 mm

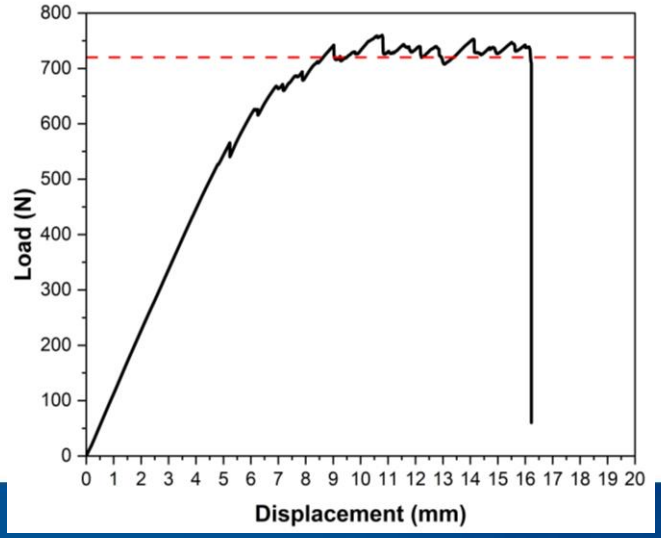

- **ΔG remains constant** under **load-controlled fatigue**, whereas it **decreases** progressively under **displacement-controlled fatigue**.
- HTDCB **fatigue testing** should be conducted under **force control** to maintain a constant ΔG during crack growth.

HTDCB Fatigue Testing: Proof of Concept

- Load-controlled fatigue
- Load ranges: 55 N to 550 N
- Fatigue frequency = 1 Hz
- delta $G/G_{plateau}$ = 65%
- *65% of $G_{plateau}$ (A basis allowable) = 1080 J/m^2*
- Crack was propagated quasi-statically until the crack tip reached the plateau region

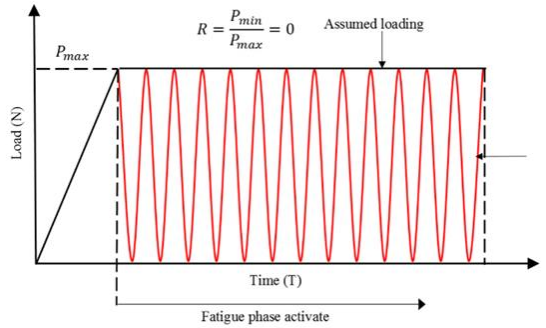

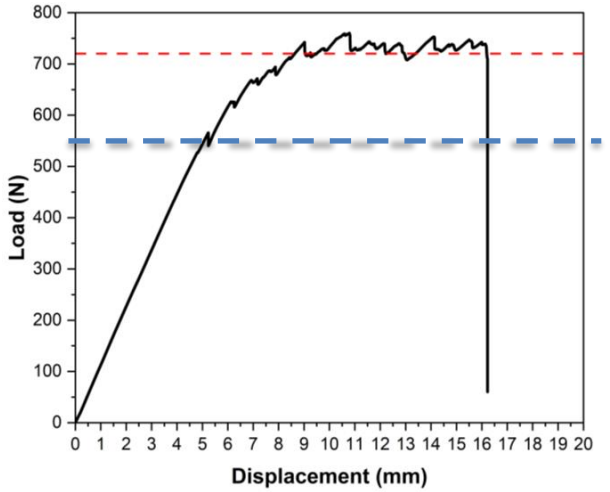

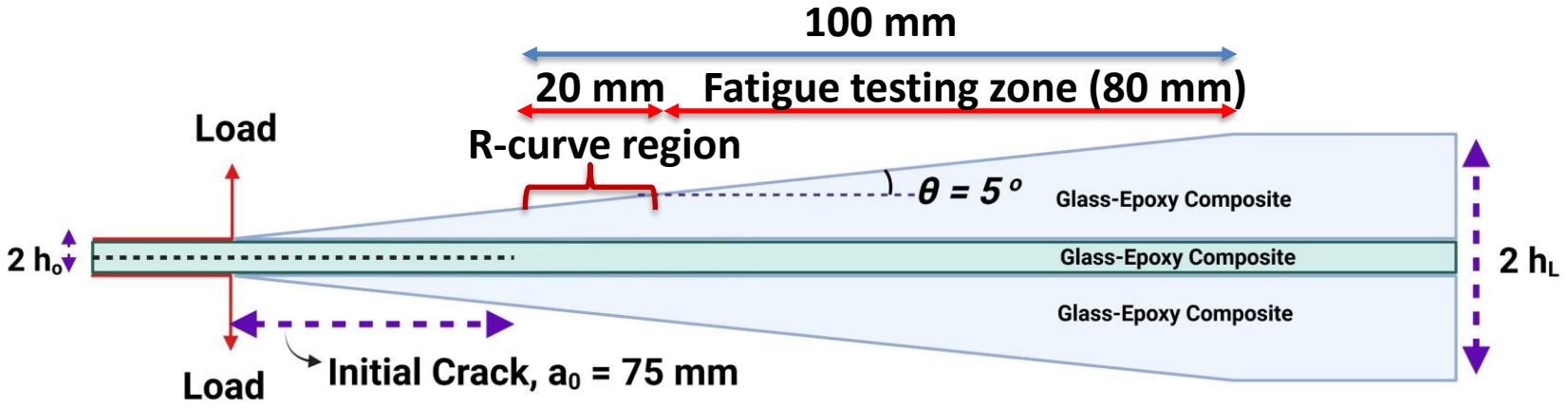

HTDCB Fatigue Testing: Proof of Concept

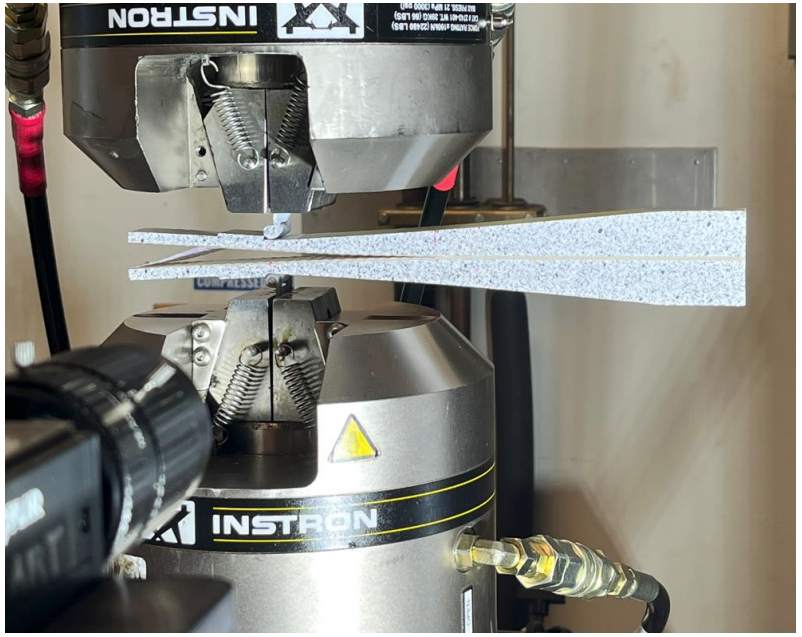

Mode-I Fatigue Test Instrumentation

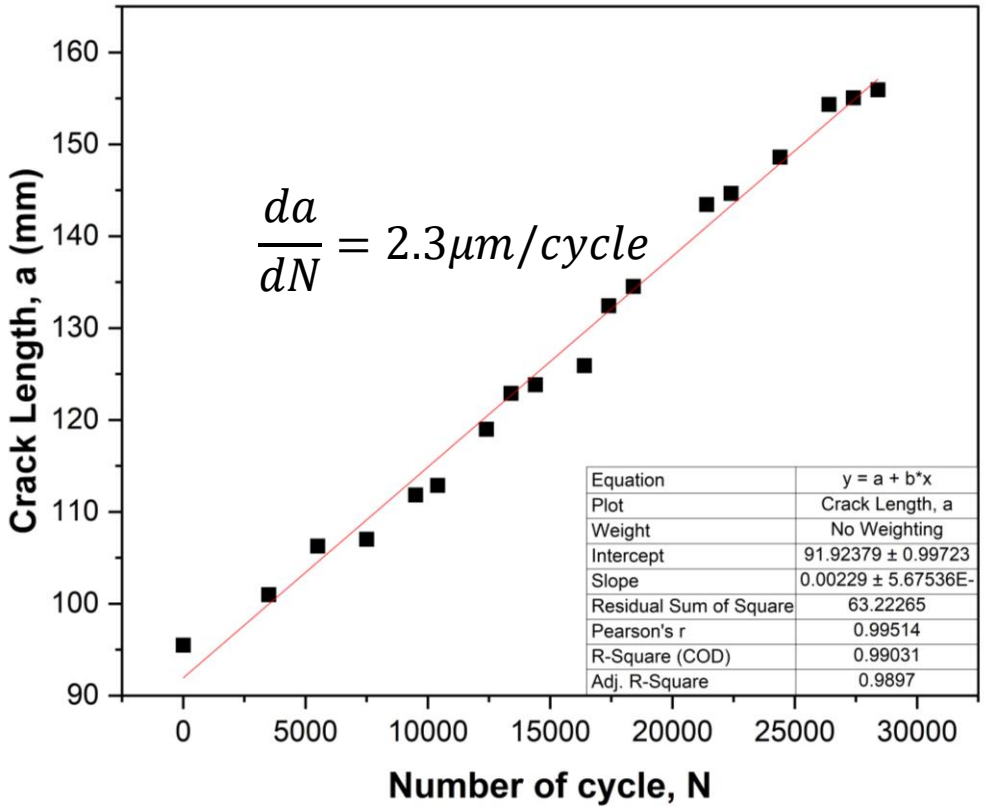

- Stable fatigue crack growth

Conclusion

- **Deflection and compliance equations** were derived using **Timoshenko Beam Theory**, incorporating both **flexural and shear effects**.
- **LEFM-based SERR equation (G)** was derived and validated against ASTM D3433-99 for metal joints.
- **Parametric analysis** identified a **5° taper angle with a 75 mm** initial crack length as optimal among the 0°–10° range.
- Quasi-static testing of HTDCB showed **R-curve behavior** comparable to Standard DCB for PW-RDL-RDC composites.
- **Load increased** during the **R-curve region** and **plateaued** after reaching **stable fracture toughness**.
- R-curve behavior resulted from mechanisms including **fiber bridging, tow-to-tow delamination, and secondary cracking**.
- **Stable fatigue crack growth** was achieved at 65% of G_{IC}
- HTDCB configuration ensured **ΔG remains independent of crack growth** during fatigue testing.

Ongoing Work

- Establish a Fatigue Delamination Model for Mode I Fatigue of Plain Weave S-glass Epoxy
- Growth of delamination damage in composite laminates is conventionally described by a Paris-law type of relation given below:

$$\frac{da}{dN} = C\left(\frac{\Delta G}{G_C(a)}\right)^m$$

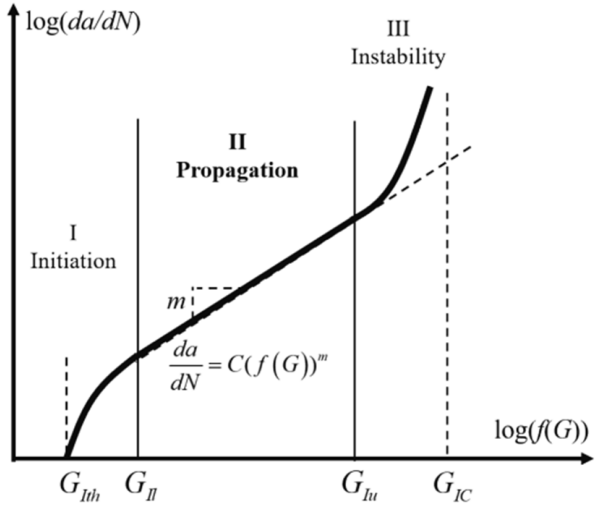

- Validation of Fatigue Delamination Model using Standard DCB Specimen
- Establish a Cohesive Zone Model (CZM) based on Fatigue Delamination Model (or Paris Law) for Mode I Fatigue of Plain Weave S-glass Epoxy Composite
- This approach can potentially be applied for characterizing Mode II and mixed-mode (I/II) fatigue delamination behavior

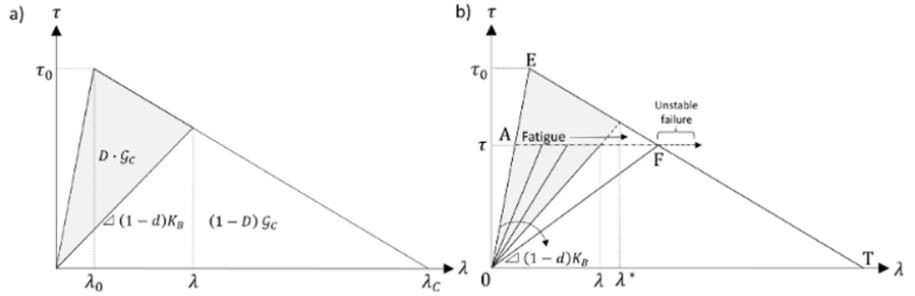

Acknowledgement



Prof. John W. Gillespie Jr.



Prof. Jovan Tatar



Prof. Harry W. Shenton III



Sagar Doshi



Art Yiournas



Johnny Thiravong



Alex Vanarelli

Thanks to the iCREATE team-Ankita Bisht, Munetaka Kubota, Paul Samuel

Acknowledgement

Research was sponsored by the Army Research Laboratory and was accomplished under Cooperative Agreement Number W911NF-24-2-0127. The views and conclusions contained in this document are those of the authors and should not be interpreted as representing the official policies, either expressed or implied, of the Army Research Laboratory or the U.S. Government. The U.S. Government is authorized to reproduce and distribute reprints for Government purposes notwithstanding any copyright notation herein.

Questions?

Influence of Fabric Architecture and Sizing on ILFT/LVI Property for Improving Durability and Damage Tolerance of GFRP Composites

M. Kubota, P. D. Samuel, A. Yiournas, S. Das, A. Bisht,

S. M. Doshi, J. W. Gillespie Jr.

University of Delaware, Newark, DE, USA

Center for Composite Materials

Department of Materials Science and Engineering

24th International Conference on Composite Materials

August 4th-8th, 2025

UNIVERSITY OF DELAWARE

Composites in Protective Applications



Vehicle primary protective structure
Source: AGY 2009



Spall Liner
Source: AGY 2009

Composites in Protective Applications

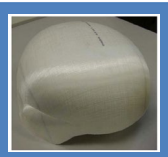

Helmets and body armor
Source: Crouch 2017

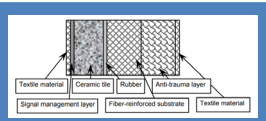

Components of multi-material armor systems
Source: Ma 2006

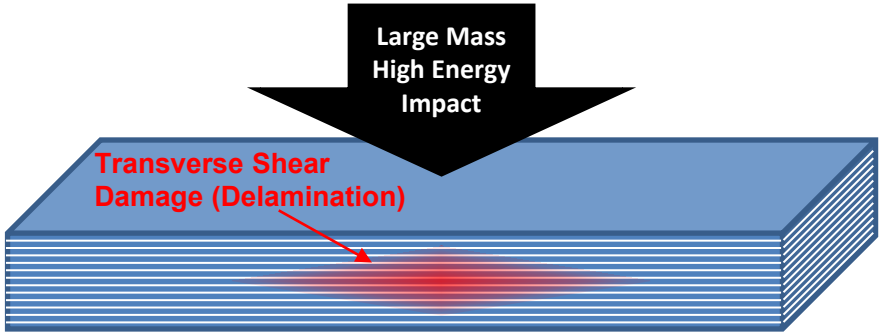

Design Goal	Attribute	Design Outcome
Durability	Resistance to Damage	High Delamination Resistance
Damage Tolerance	Retention of Functional Performance after Damage	High Retention of Original Stiffness after Impact Damage

Impact Damage Energy Absorption

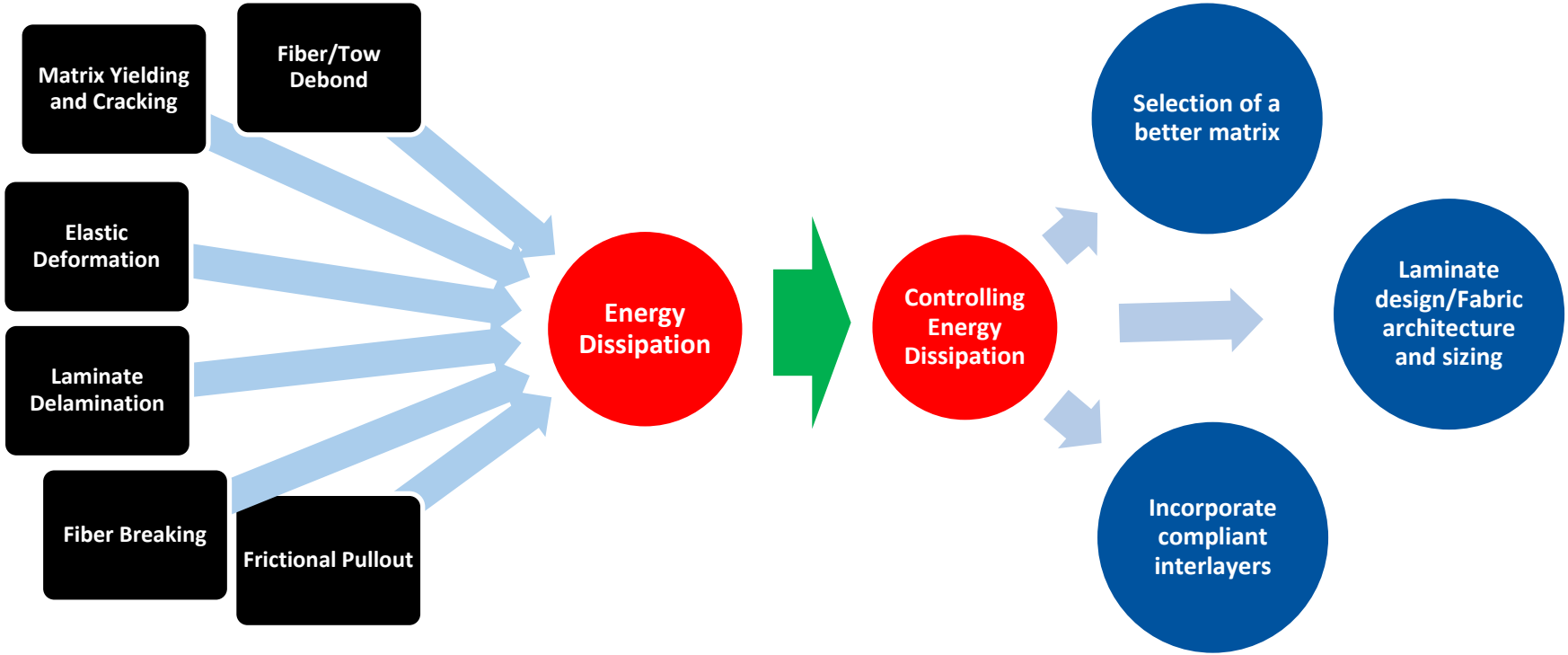

Improving Energy Dissipation

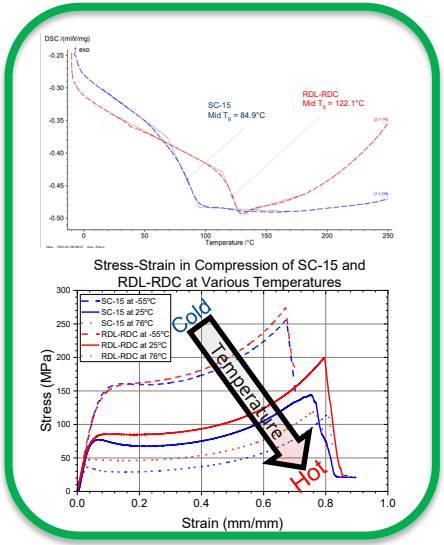

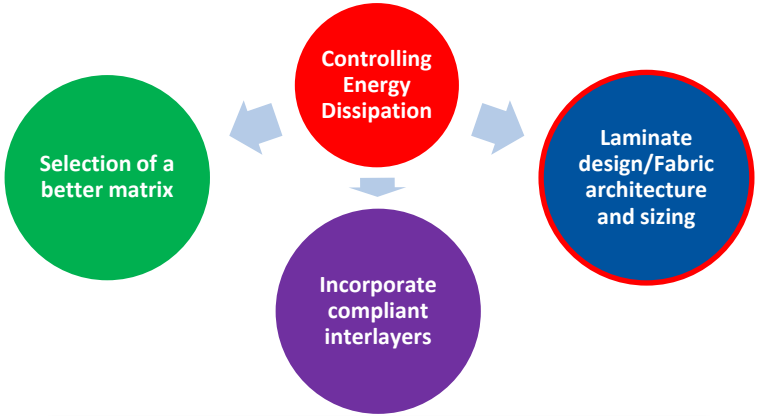

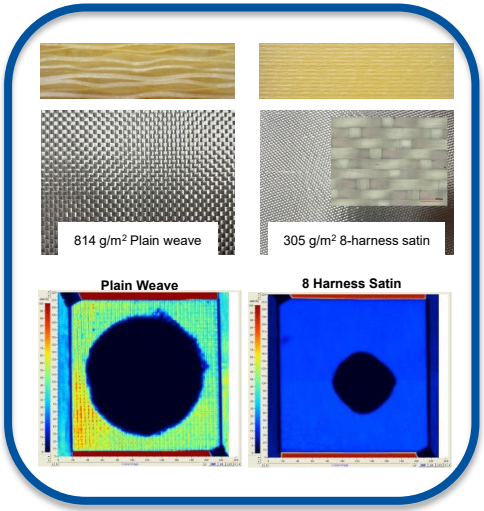

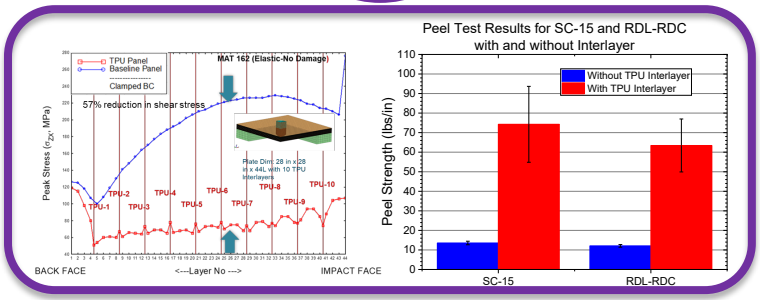

Objective

Improve durability and damage tolerance GFRP

Improve durability and damage tolerance protective-structural parts against low velocity impact (LVI)

Role of fracture toughness

Understand the role of fracture toughness on the LVI performance

Role of fabric architecture

Understand the role of fabric architecture and nesting on fracture toughness and impact performance

Role of sizing and fiber/matrix interface

Understand the role of fiber/matrix interface on fracture toughness and impact performance

Material Systems: Resin Systems

SC-15 Epoxy (Baseline)

- Long standing baseline, being replaced due to issues with high temperature performance (T_g = 85°C)
- Two part infusible toughened epoxy resin system

RDL-RDC Epoxy

- SC-15 replacement by Huntsman with superior high temperature performance (T_g = 122°C)
- Similar to SC-15, an infusible two part toughened
- Similar or better mechanical strengths with S-2 Glass

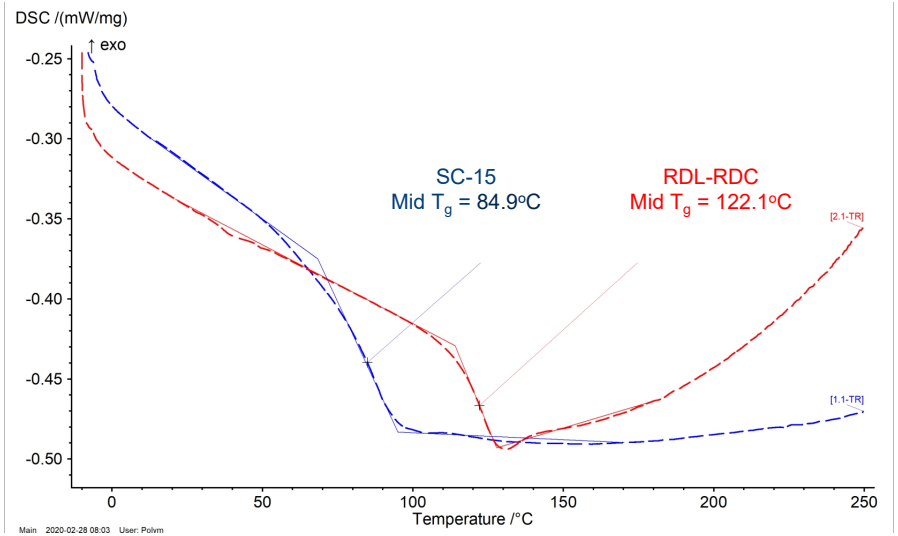

The Army's wet T_g requirement requires a change in the matrix system

Material System: Fabric Architecture

S-2 Glass

- High strength aluminosilicate glass used for protective-structural applications in the US Army vehicles

Fabric Weave Architecture

- Coarse plain weave historically used for protective-structural
- A light weight 8-harness satin weave, approximately 37% areal weight of the plain weave

Sizing

- 463 sizing system historically used for this application
- 933 sizing marketed as a damage tolerant sizing system

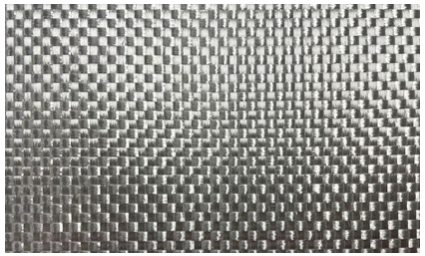

814 g/m^2 Plain weave
8 plies for a 5 mm thick sample

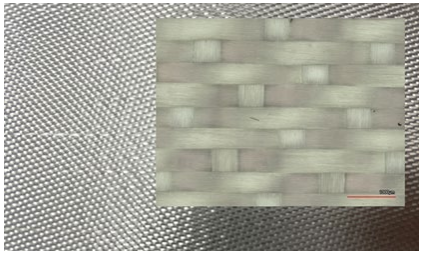

305 g/m^2 8-harness satin
20 plies for a 5 mm thick sample





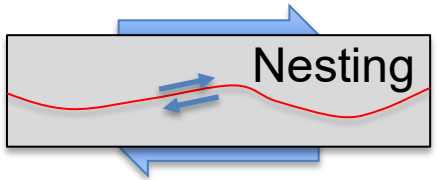

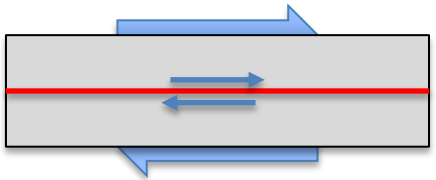

Material System Combinations Evaluated

Sample Fabrication

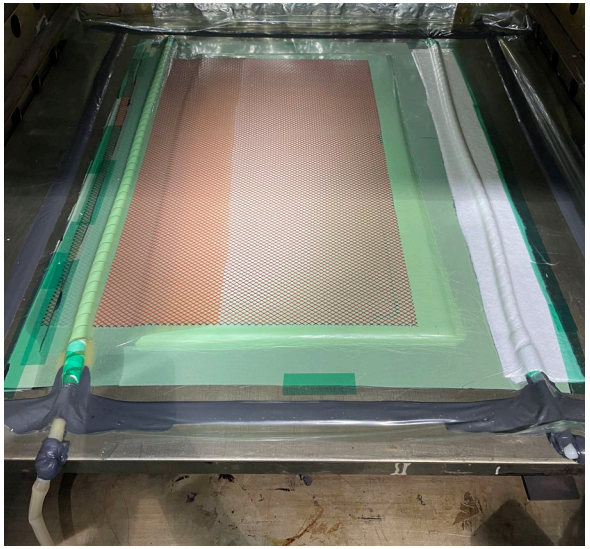

System Combinations

	Plain Weave (24 oz/yd^2)	8-Harness Satin (9 oz/yd^2)
AGY 463 Sizing	SC-15 and RDL-RDC	N/A
AGY 933 Sizing	SC-15 and RDL-RDC	SC-15 and RDL-RDC

Evaluating Mode II Fracture Toughness

End Notched Flexure (ENF) Test

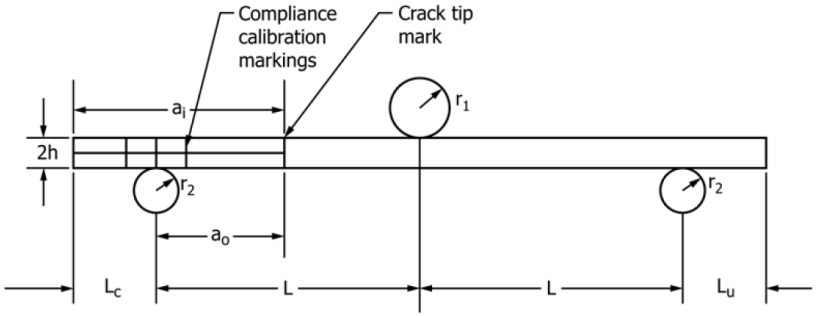

FIG. 2 ENF Specimen, Fixture, and Dimensions

$$G_{IIC}^{SH} = \frac{9P^2a^2}{16E_f w^2 h^3}\left(1 + 0.2\left(\frac{E_f}{G_{13}}\right)\left(\frac{h}{a}\right)^2\right)$$

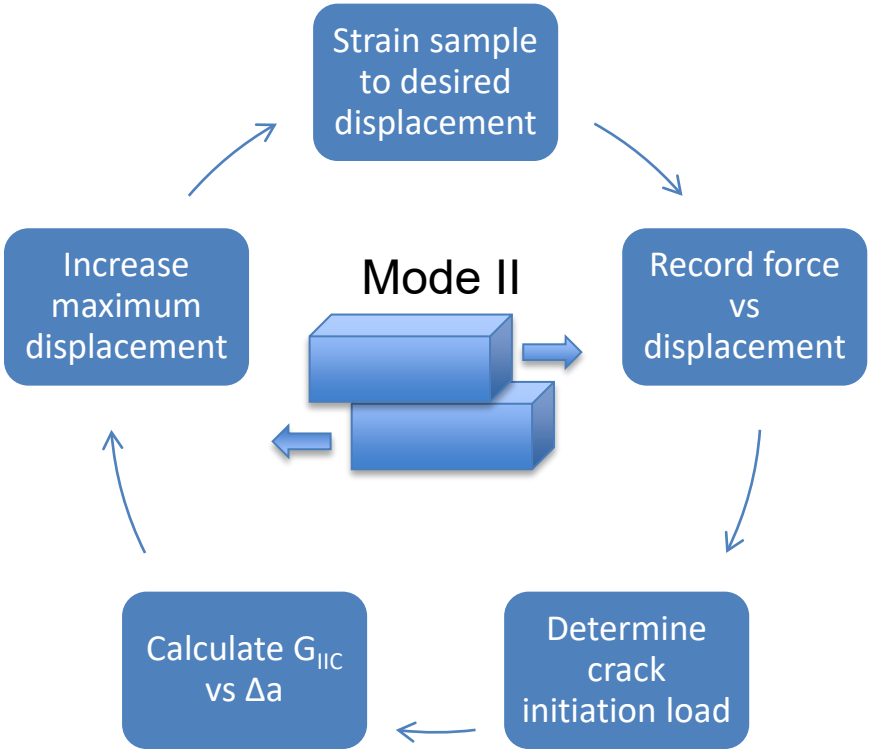

ENF Testing

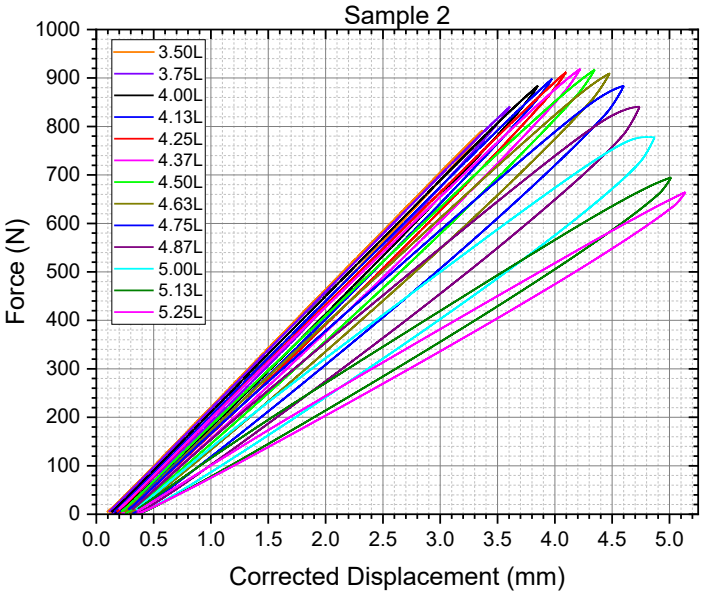

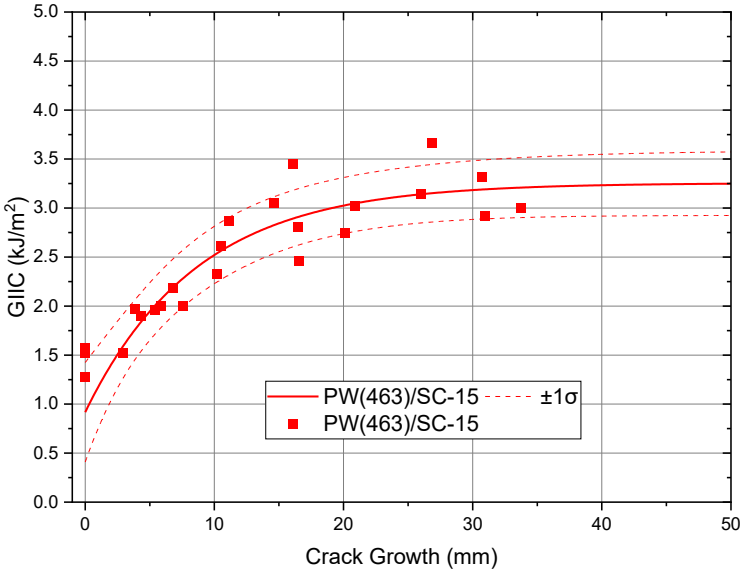

$$G_{IIC}^{SH} = \frac{9P^2a^2}{16E_f w^2 h^3}\left(1 + 0.2\left(\frac{E_f}{G_{13}}\right)\left(\frac{h}{a}\right)^2\right)$$

Effect of the Resin

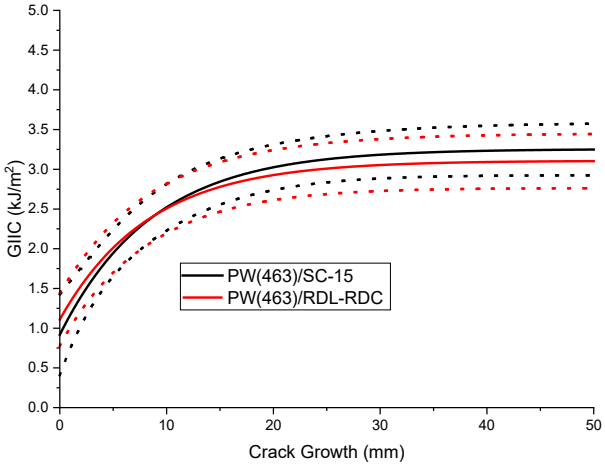

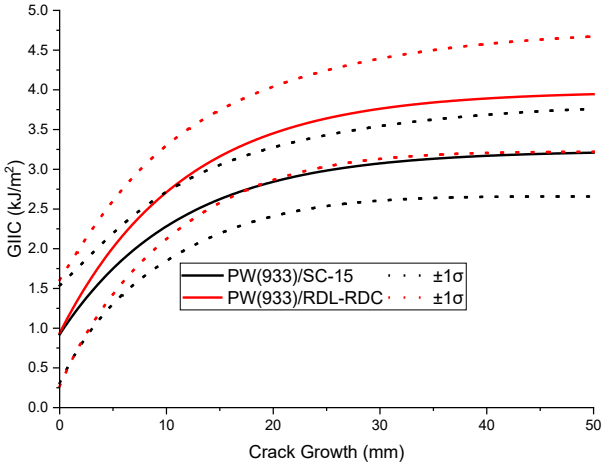

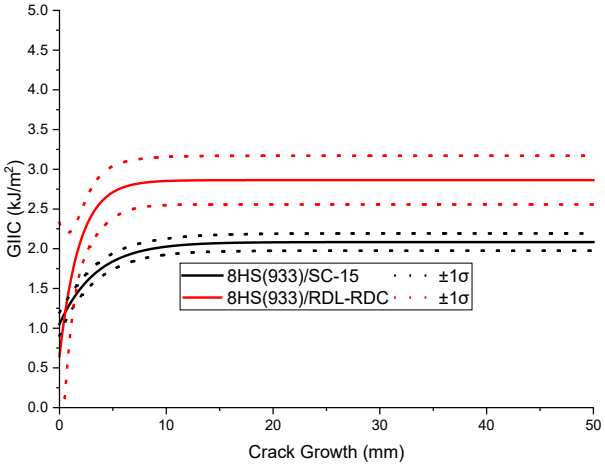

PW(463) shows resin insensitivity, while RDL-RDC shows improved fracture toughness over SC-15 with 933 sizing; however, the plain weave architecture seems to be creating a larger spread in the data

Effect of the Fiber Sizing

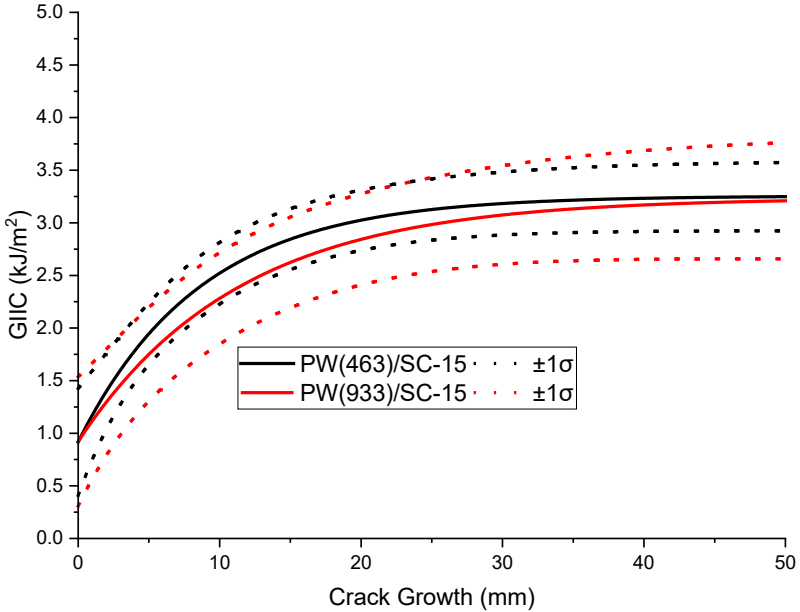

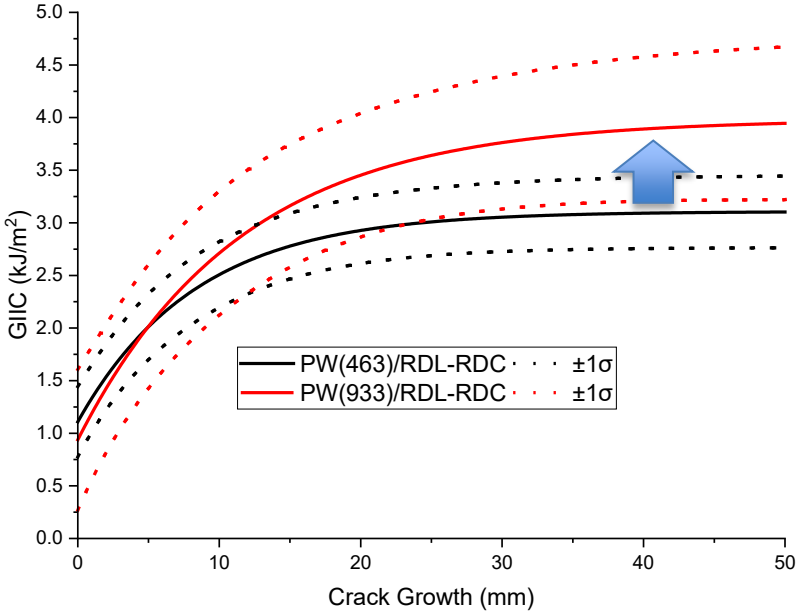

SC-15 shows sizing insensitivity while RDL-RDC seems to show a modest increase in fracture toughness due to the sizing

Effect of the Fabric Architecture

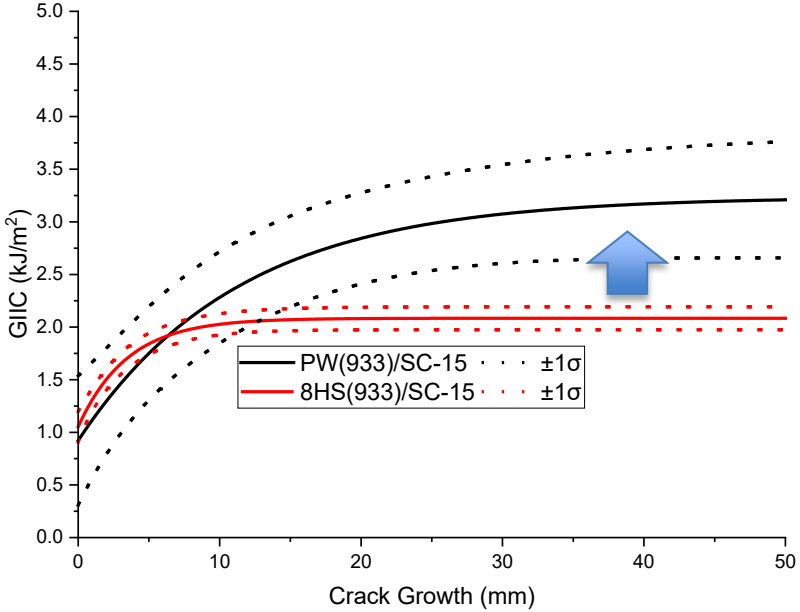

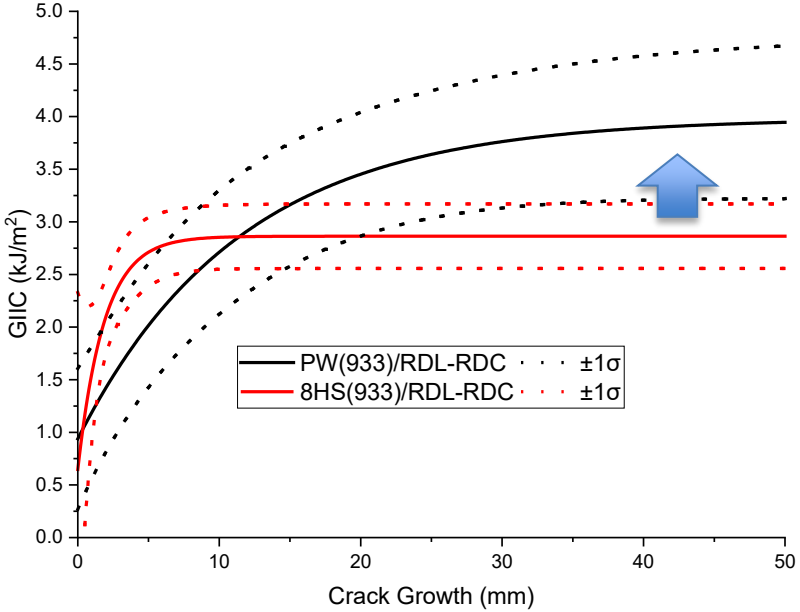

The fabric architecture shows an increase in fracture toughness due to the nesting, requiring more energy to fracture

Higher Fracture Toughness vs Increasing Interfaces

24 oz/yd^2 PW

- Higher fracture toughness at larger crack lengths
- Mechanical interlocking of tows for increased energy absorption through

9 oz/yd^2 8HS

- x2.7 more interlaminar interfaces to potentially fracture

24 oz/yd^2 Plain Weave (8 plies/5 mm)



9 oz/yd2 8-HS (20 plies/5 mm)

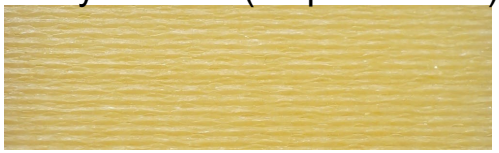

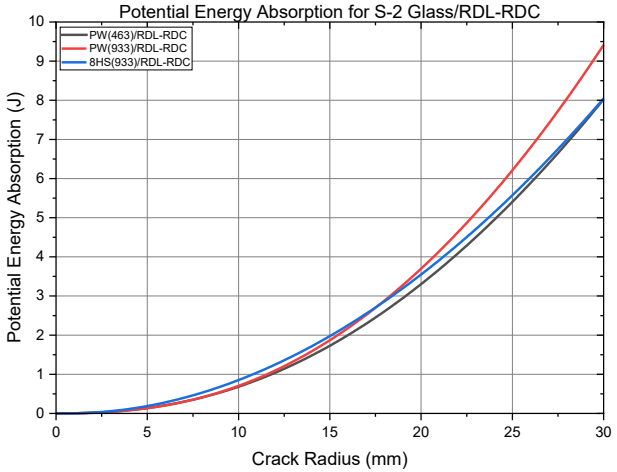

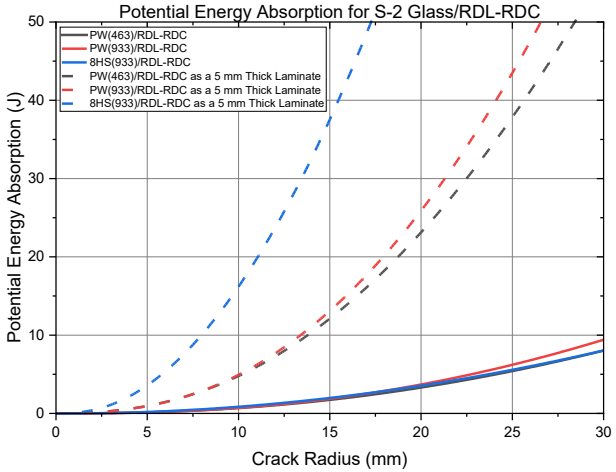

Low Velocity Impact Test



Initial Stiffness

- Bolts tighten to 75 lbf-in
- Loaded to 0.8 mm
- Subtract machine compliance

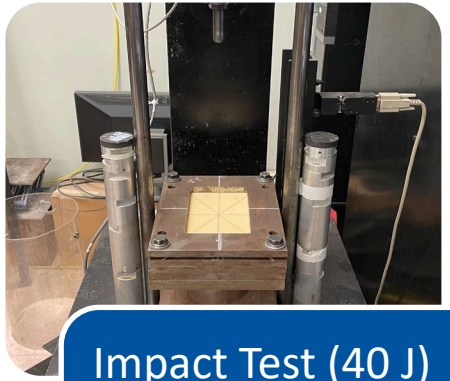

Impact Test (40 J)

- Mass: 13.7 kg
- Height: 0.3 m
- Velocity: 2.4 m/s
- Impactor Geometry: 12 mm hemispherical tup

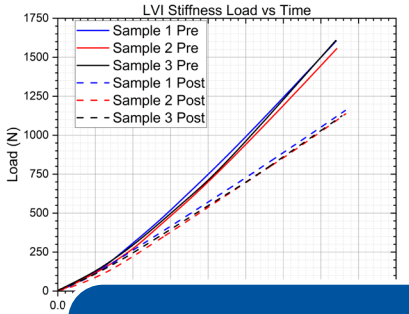

Post Impact Stiffness

- Bolts tighten to 75 lbf-in
- Loaded to 0.8 mm
- Subtract machine compliance

LVI Impact Energy

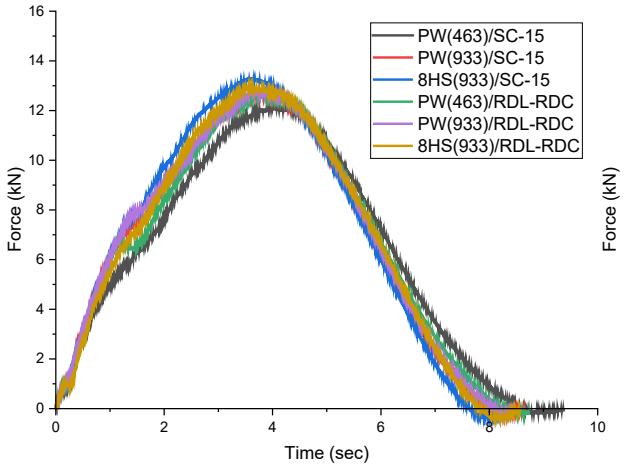

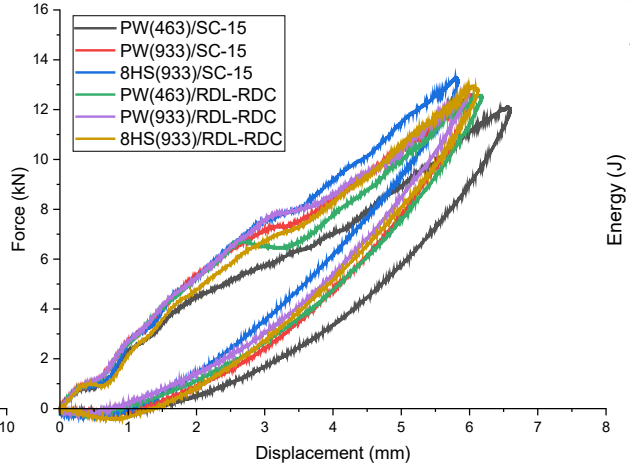

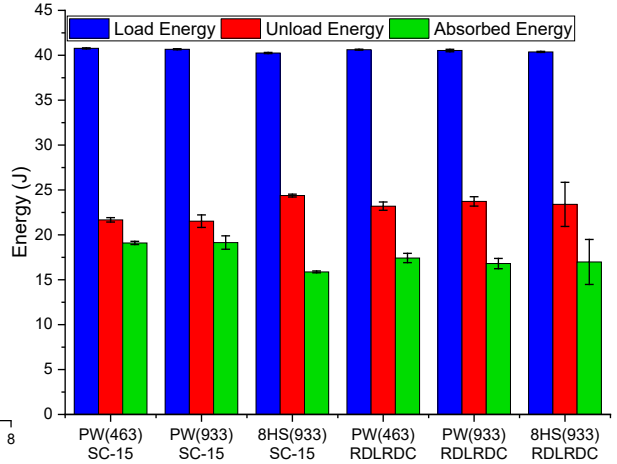

- The force vs time and displacement show similar responses
- The absorbed energy shows RDL-RDC generally absorbs less energy, thus less damage is expected

LVI Damage and Property Retention

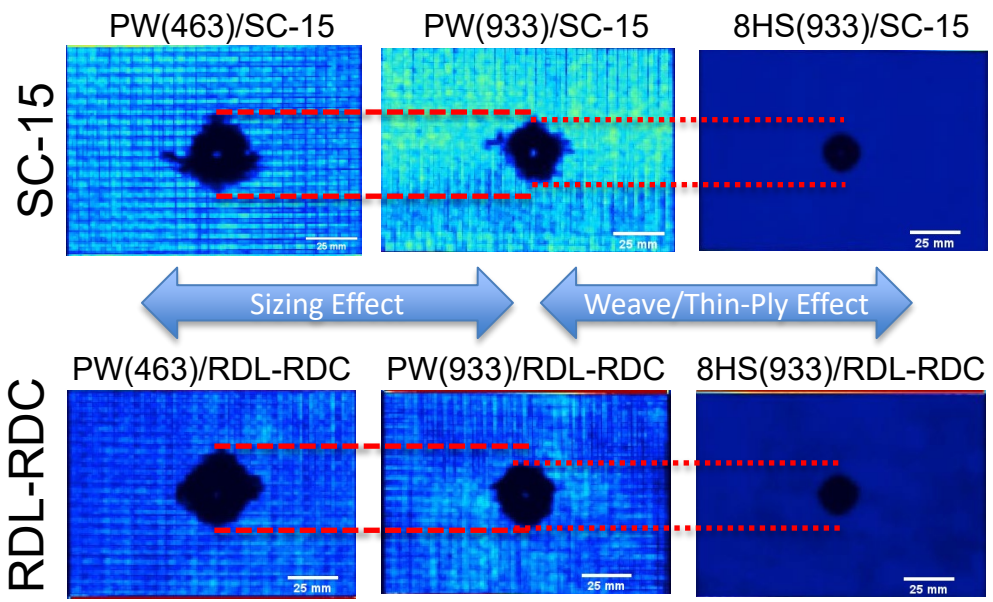

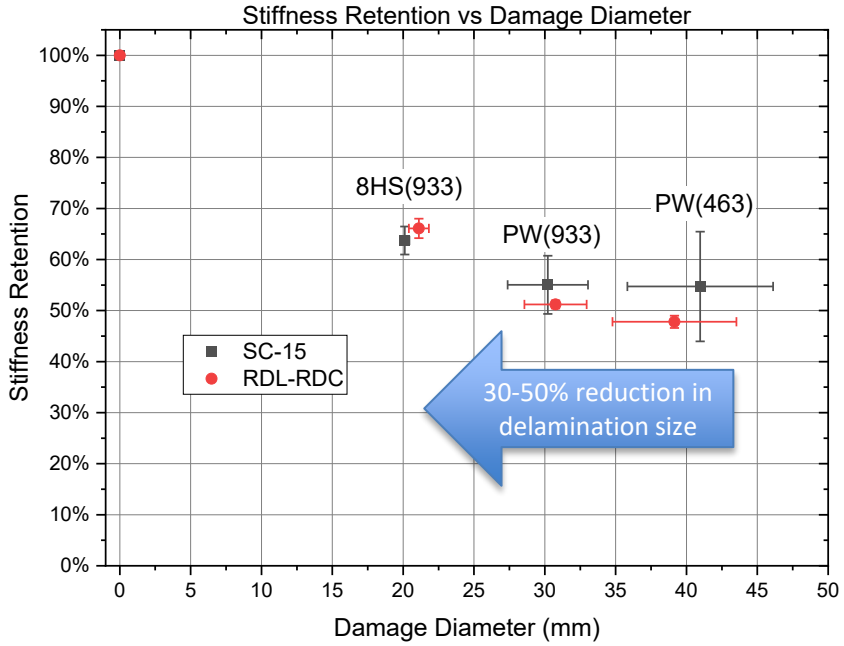

S-2 Glass/SC-15 LVI Samples Sectioned

- PW shows ~7 primary cracks
- Crack branching and tow cracking observed
- 8HS shows only nine interlaminar interface fractures (19 interfaces are present) and some back face damage due to tension failure

PW(463)/SC-15

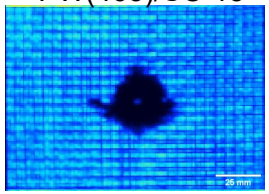

PW(933)/SC-15

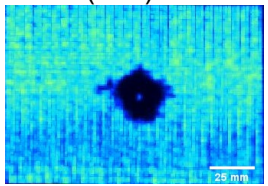

8HS(933)/SC-15

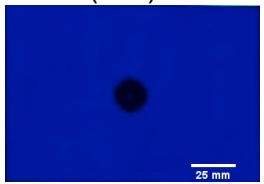

PW(463)/SC-15

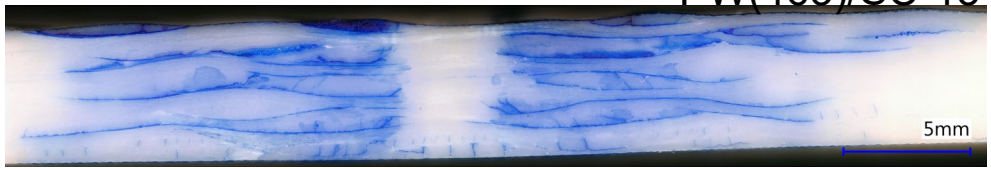

PW(933)/ SC-15

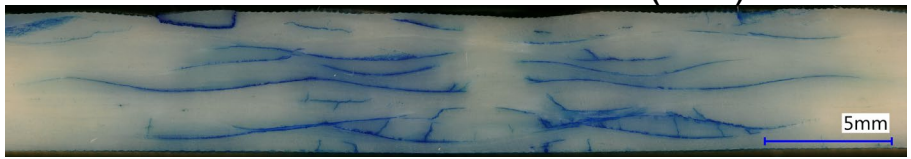

8HS(933)/ SC-15

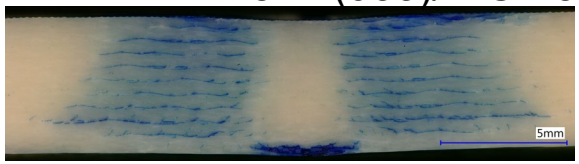

S-2 Glass/RDL-RDC LVI Samples Sectioned

PW(463)/RDL-RDC

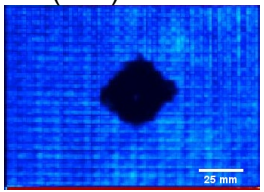

PW(933)/RDL-RDC

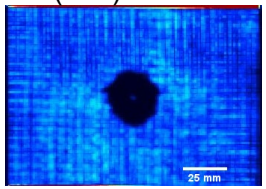

8HS(933)/RDL-RDC

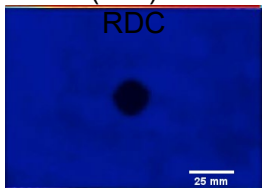

PW(463)/RDL-RDC

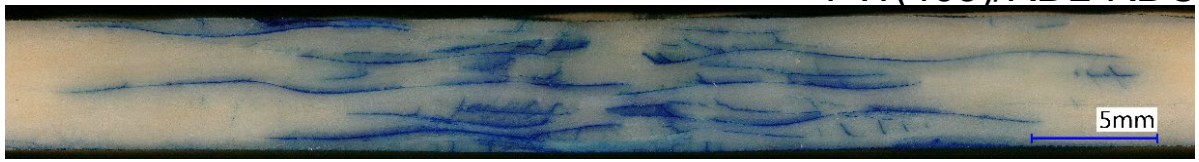

PW(933)/RDL-RDC

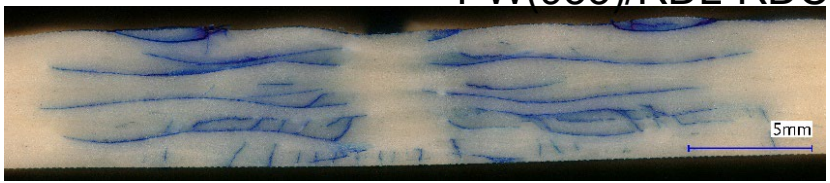

8HS(933)/RDL-RDC

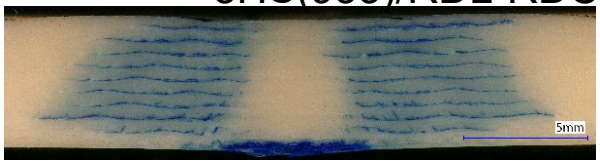

Main Crack Measurements and Analysis

- Energy absorption from the primary crack only captures <50% of the absorbed energy
- The effects of tow cracking, crack branching, fiber breaking, strain rate effects, and other damage modes are unaccounted for

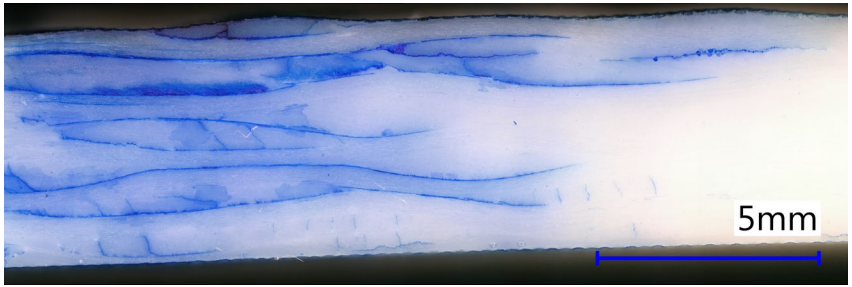

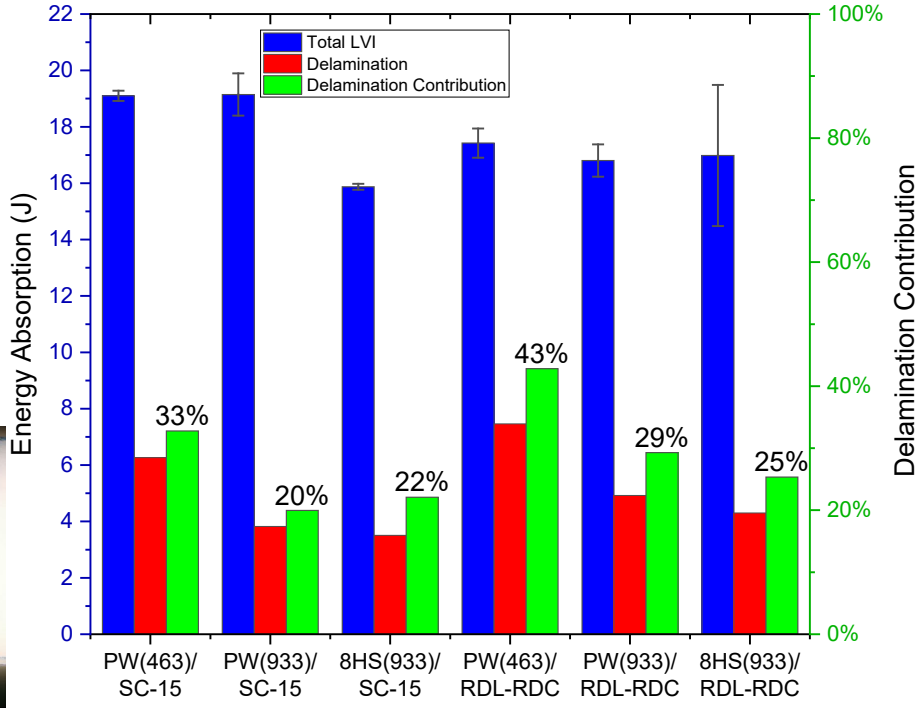

Key Findings on

Fracture Toughness

- Sizing alone shows a slight improvement in mode II fracture toughness for one of the epoxy systems
- The fabric architecture and mechanical interlocking due to fabric nesting show significant contributions to fracture toughness

Damage Tolerance and Durability

- Modest increases in fracture toughness show a reduction in damage
- Increasing interlaminar interfaces reduces the damage area more significantly than the increase in fracture toughness

Key Findings on

- Evaluation of the sectioned laminates shows that the main interlaminar cracks account for less than half of the energy absorbed; further evaluation is necessary to determine other sources of energy absorption
  - Tow cracking, crack branching, fiber breaking, etc
- 8HS(933)/RDL-RDC showed a 50% reduction in delamination diameter, indicating improvement in durability and more than 33% improvement in damage tolerance while meeting the wet T_g requirements previously not met by the PW(463)/SC-15 system

Path Forward

- Improved fracture area analysis needs to be developed for a better understanding of the damage extent
- The strain-rate effect on the fracture toughness of these systems needs to be understood to capture the fracture energy release rates better for an LVI event
- Fracture surface analysis to understand the damage mode and compare to the ENF testing to gain insights into some key differences in damage evolution and identify potential mechanisms not captured in ENF present in LVI experiments
- Incorporation of a compliant thermoplastic interlayer may be able to absorb and allow for the flexture during impact, preventing or restricting delamination and retaining higher property retention

References

- AGY. (2009). *Technical Product Guide*.
- Crouch, I. G., Sandlin, J., & Thomas, S. (2017). Polymers and fibre-reinforced plastics. In *The Science of Armour Materials* (pp. 203–268). Elsevier. https://doi.org/10.1016/b978-0-08-100704-4.00005-0
- Ma, Z.-D., Wang, H., Cui, Y., Rose, D., Socks, A., & Ostberg, D. (2006). *Designing an Innovative Composite Armor System for Affordable Ballistic Protection*. https://www.researchgate.net/publication/235192106
- ASTM Standard D7905/D7905M - 19 “Standard Test Method for Determination of the Mode II Interlaminar Fracture Toughness of Unidirectional Fiber-Reinforced Polymer Matrix Composites.” (2019). In *ASTM International*. ASTM International. https://doi.org/10.1520/D7905_D7905M-19E01

Acknowledgements

Thank you to Kushal Mehta for helping prepare the various samples and Dr. Nick Shevchenko for C-scanning samples

This Research was sponsored by the Army Research Laboratory and was accomplished under Cooperative Agreement Number W911NF-24-2-0127. The views and conclusions contained in this document are those of the authors and should not be interpreted as representing the official policies, either expressed or implied, of the Army Research Laboratory or the U.S. Government. The U.S. Government is authorized to reproduce and distribute reprints for Government purposes notwithstanding any copyright notation herein.

ICCM24
AUGUST 4-8, 2025
BALTIMORE CONVENTION CENTER
BALTIMORE, MARYLAND, USA

No Technical Paper Submission for:

Suhasini Gururaja

MECHANICAL PROPERTIES AND DAMAGE ANALYSIS OF BRAIDED CFRP COMPOSITE REBAR

University of Southern Queensland

Mazhar Peerzada, Xuesen Zeng, Ali Mirzaghorbanali, Hadi Nourizadeh, Behshad Jodeiri Shokri, David John, Karsten Hoehn and Scott Barnes

Centre For Future Materials, University of Southern Queensland, Australia

CSIRO, Australia

Mining3, Australia

ICCM24

24TH INTERNATIONAL CONFERENCE ON COMPOSITE MATERIALS

AUG 4-8, 2025 • BALTIMORE CONVENTION CENTER • BALTIMORE, MARYLAND

Contents

- Rebars
- FRP Rebars
- Methodology
- Results
- Summary

Rebars

- ✓ Used as reinforcement in concrete.
- ✓ Improve the tensile strength
- ✓ Resist forces like bending, stretching, and cracking.



Concrete

Excellent: Compression strength

Poor: Tensile strength, prone to cracking



Concrete + Rebar

- ✓ **Significantly Stronger**
- ✓ **Prevent cracks from forming and spreading**
- ✓ **Increased Durability**



Residential



Work Offices





Industrial



Industrial



Bridges

Rebars used in Mining tunnels

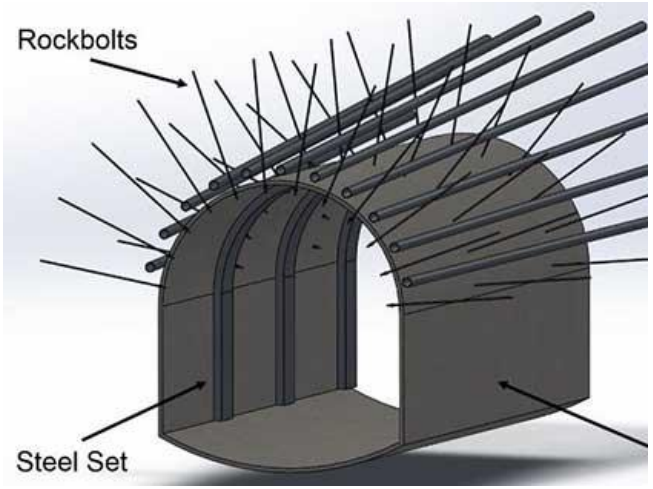

- The conventional standard choice is Steel Rebar.
- High Ductility
- Low initial cost
- Can be bent and cut on-site

Drawbacks

- Low corrosive protection and compromise properties over a period of time.
- Heavy

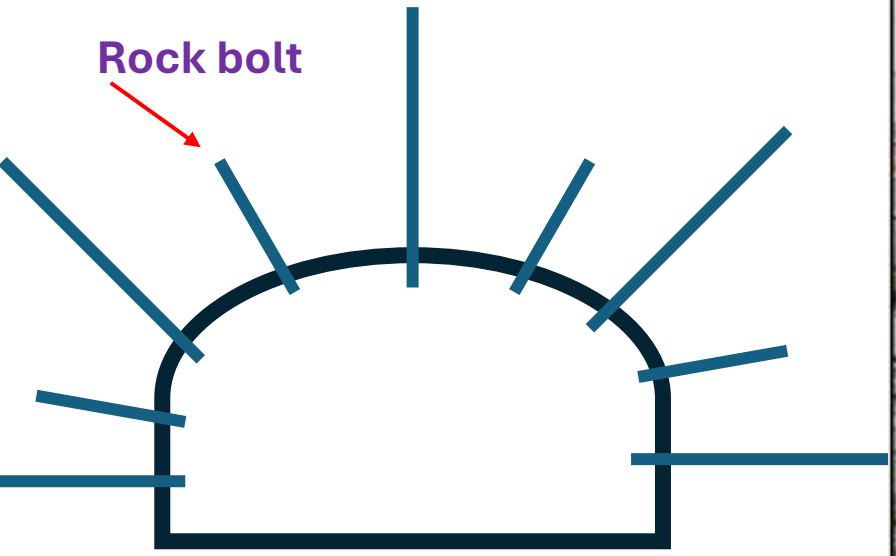









FRP composites rods

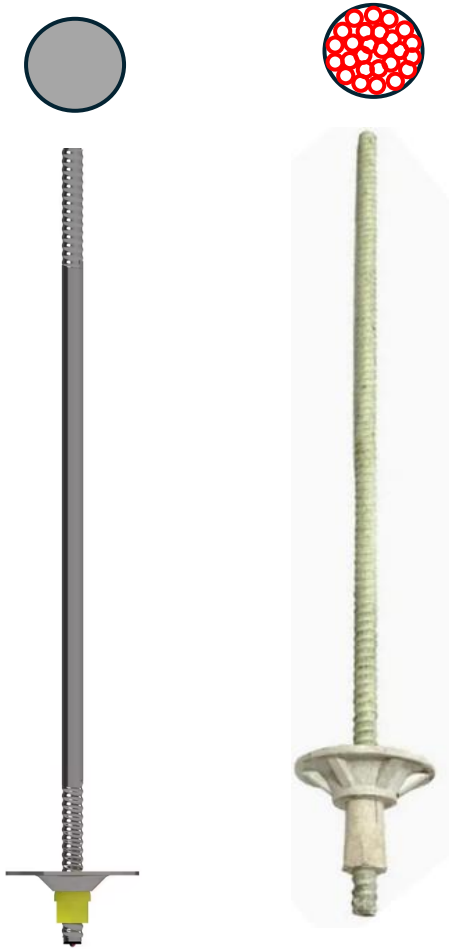

Steel Rockbolt

GFR Rockbolt

- Light-weight
- No corrosion
- No fatigue
- Optimum strength in fibre direction

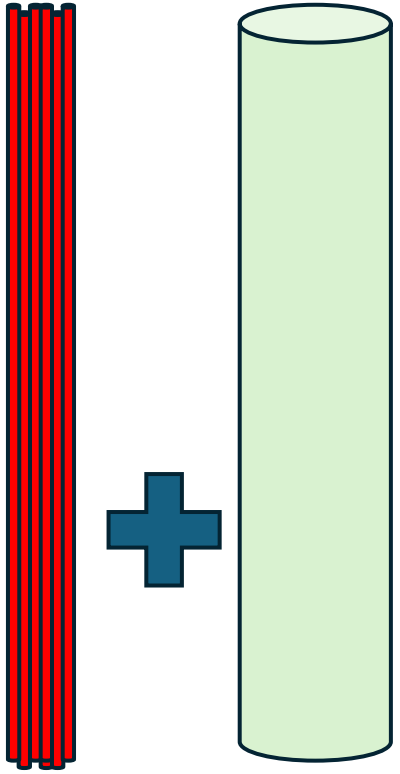

Glass Fibre Filaments

Resin System

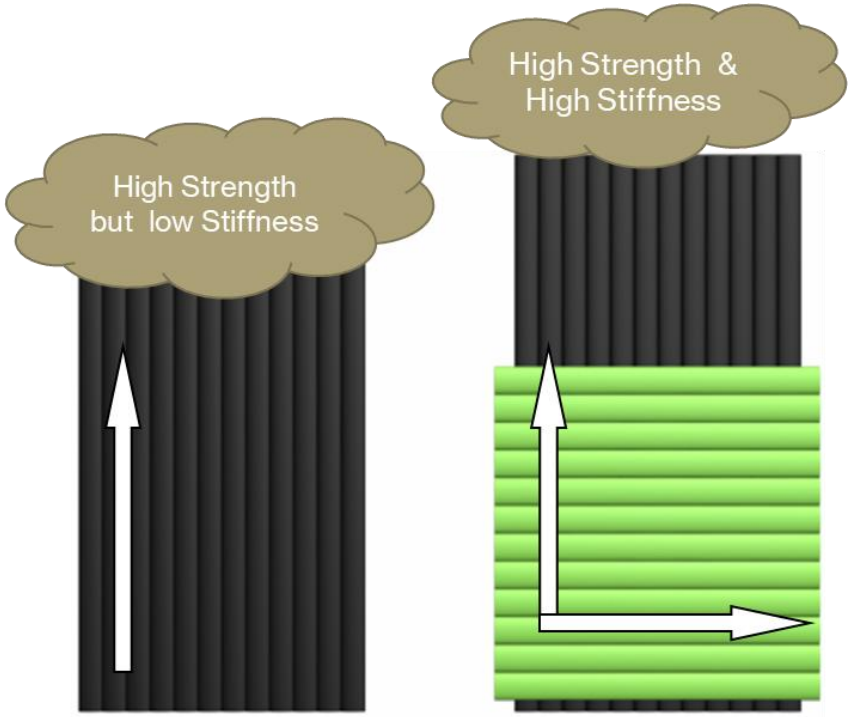

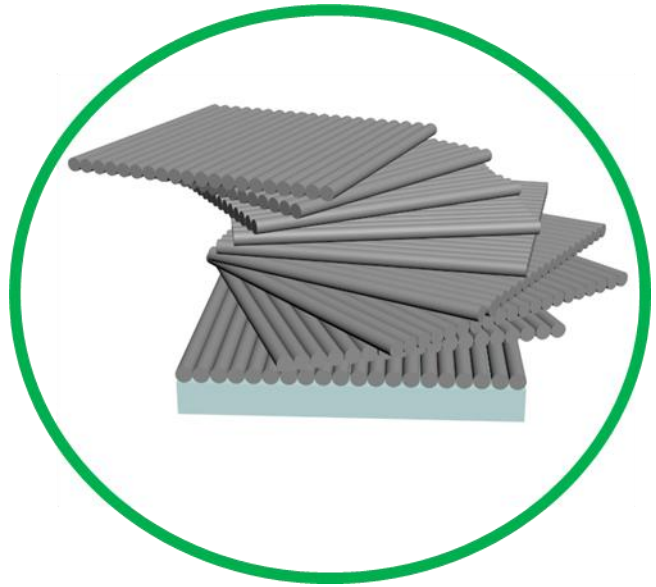

Quasi-isotropic Material

Methodology

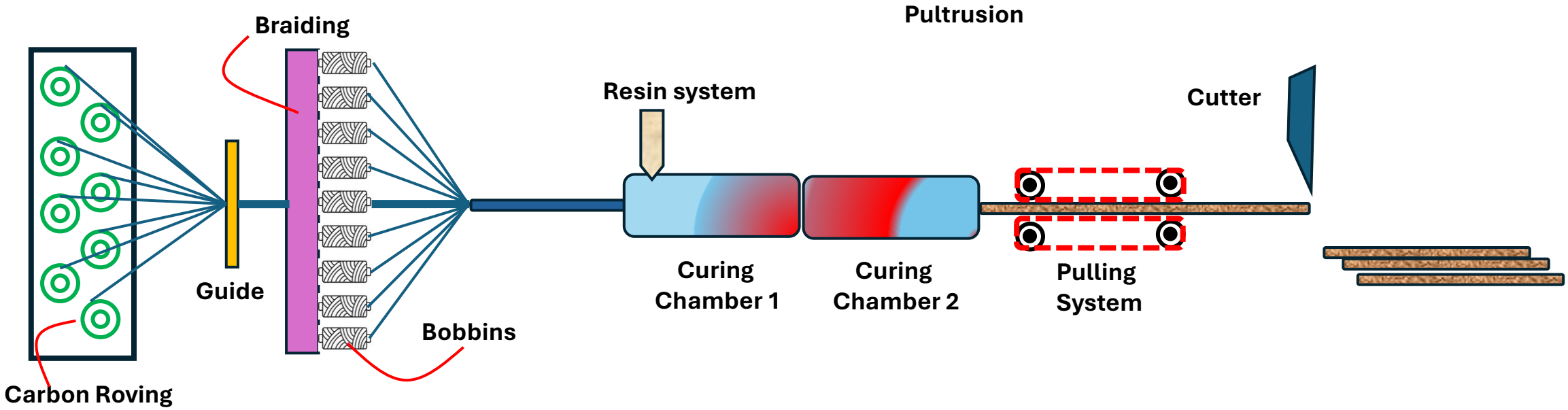

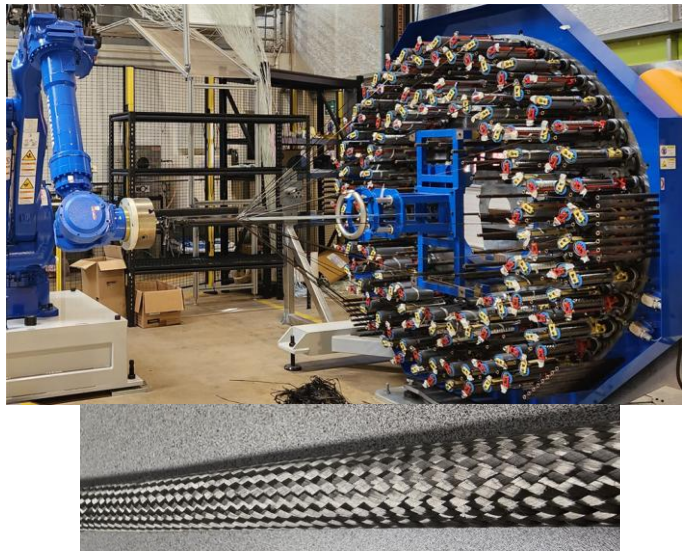

Carbon Braided Rope



Braided CFRP Composite Rebar

Carbon Fibre Braiding

- ✓ Braiding Machine – 84/**60** carriers
- ✓ Carbon Filament – 24k
- ✓ Wound 60 bobbins for braiding
- ✓ Carbon braided rope dia – 22 mm

Bobbin Winding Unit

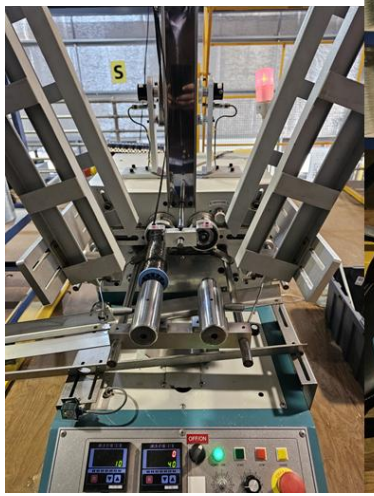

Front View

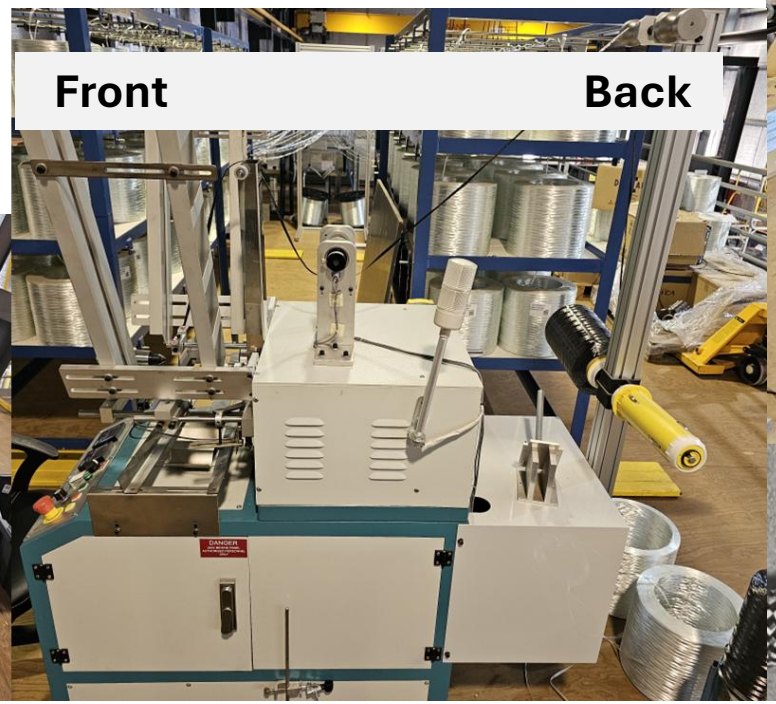

Side View

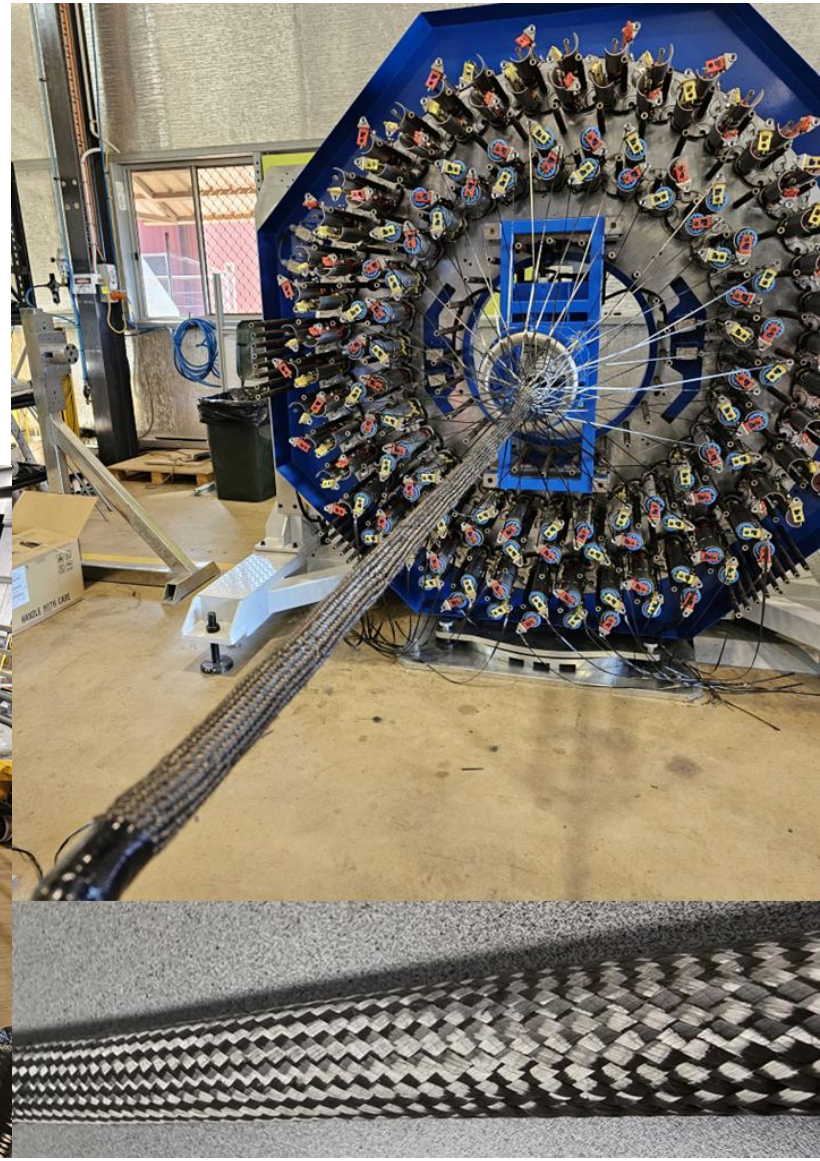

Fixed Length CFRP Composites Rebar

- ✓ Material: Carbon Braided rope
- ✓ Resin/Hardener: Epoxy resin system
- ✓ Mix ratio and Curing time: Provided by supplier

- ✓ Carbon Fibre Rebar successfully made with and without Ribs:
  - 24 mm diameter with Ribs
  - 22 mm diameter without Ribs.

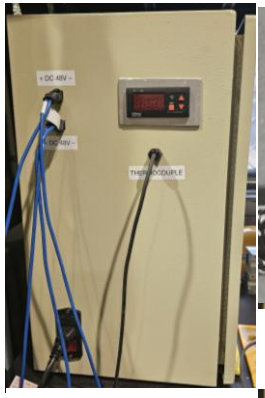

Interface



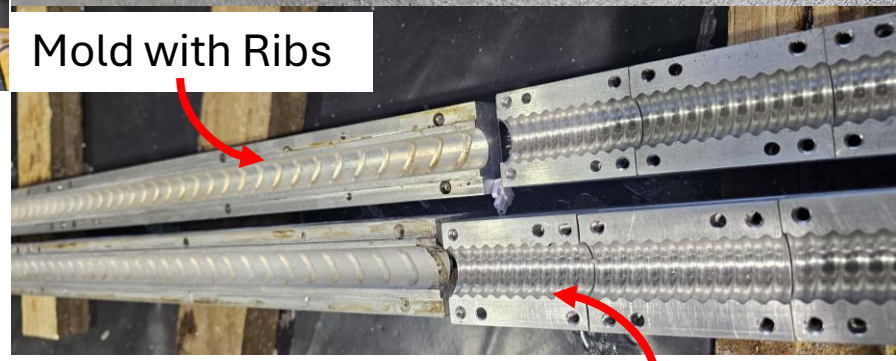

Rein + hardener

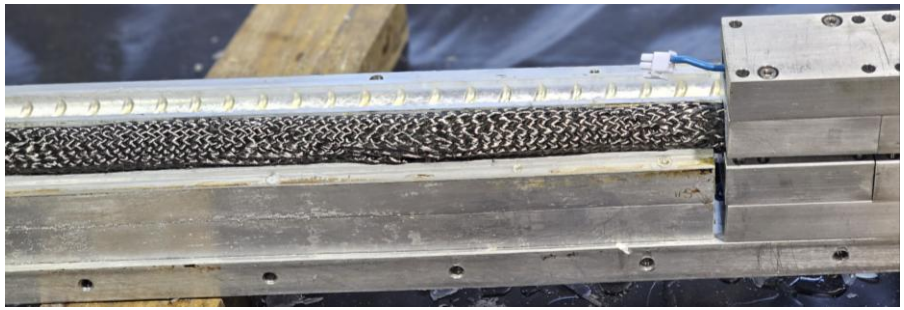



Comparison of Tensile Capacity

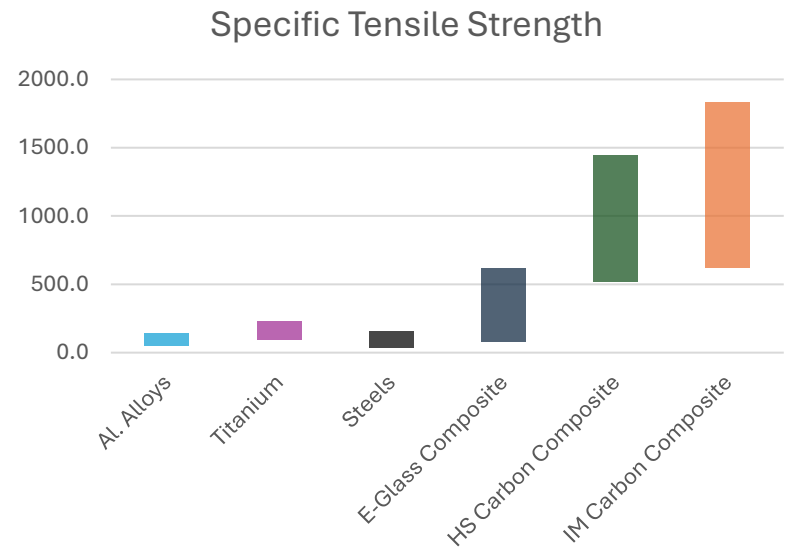

Sample	Rebar Material	XS area (mm^2)	Ultimate Tensile Peak Load (kN)	Normalised Specific Tensile peak load (kN/mm^2 XS area relative M24)	Displacement at Peak load (mm)	Mass per metre (g/m)
M24 Steel Rock Rebar	**Steel**	378	325	325	56.35	2900
20-tonne fibreglass Rebar*	**Glass Fibre**	310	200	244	14.86	645
Braided CRFP Rebar	**Carbon Fibre**	285	236	313	29.2	465

* P. Gregor, A. Mirzaghorbanali, K. McDougall, N. Aziz, and B. Jodeiri Shokri, "Shear Behaviour of Fibreglass Rock Bolts for Various Pretension Loads," Rock Mech. Rock Eng., vol. 56, no. 11, pp. 8083–8113, Nov. 2023

Comparison of Single Shear Capacity of 20-tonne Glass Fibre and Braided Carbon Composites Rebar

Sample	Rebar Material	XS area (mm^2)	Average Shear Peak Load (kN)	Displacement at Peak load (mm)	Normalised Shear peak load (kN)
20-tonne fibreglass Rebar *	Glass Fibre	310	39.3	7.11	48
Braided CRFP Rebar	Carbon Fibre	285	75.03	13.56	100

* P. Gregor, A. Mirzaghorbanali, K. McDougall, N. Aziz, and B. Jodeiri Shokri, "Shear Behaviour of Fibreglass Rock Bolts for Various Pretension Loads," Rock Mech. Rock Eng., vol. 56, no. 11, pp. 8083–8113, Nov. 2023

Guillotine Double Shear Testing

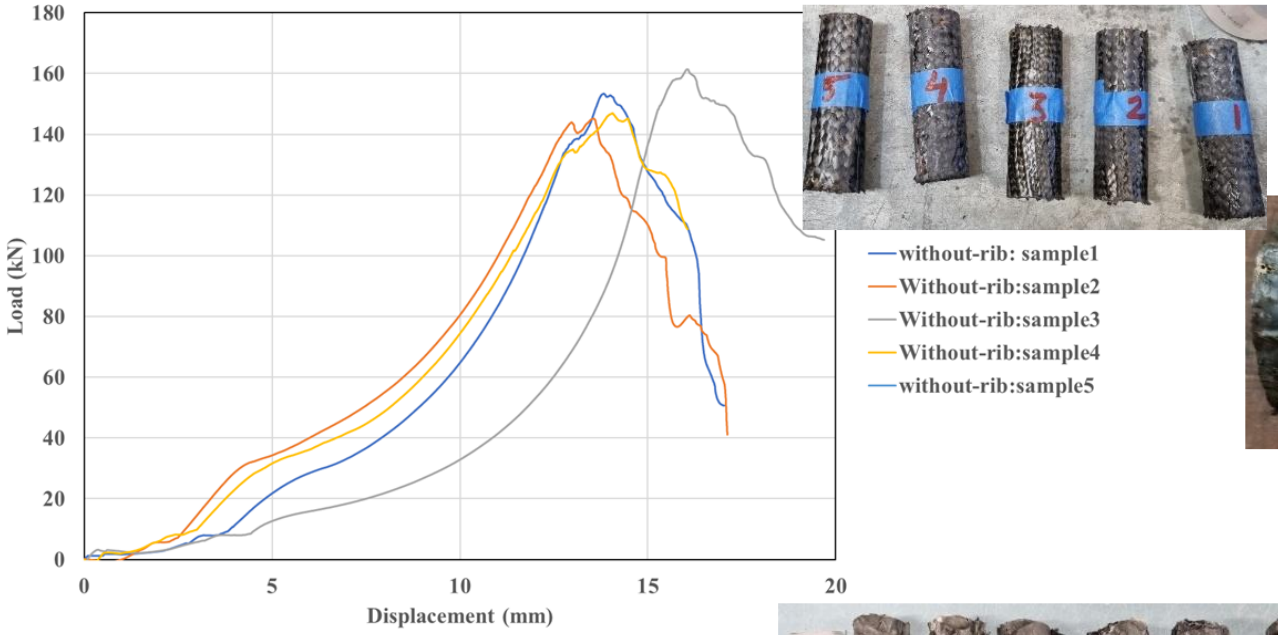



Sample 5 – Without Rib



Guillotine Double Shear Apparatus

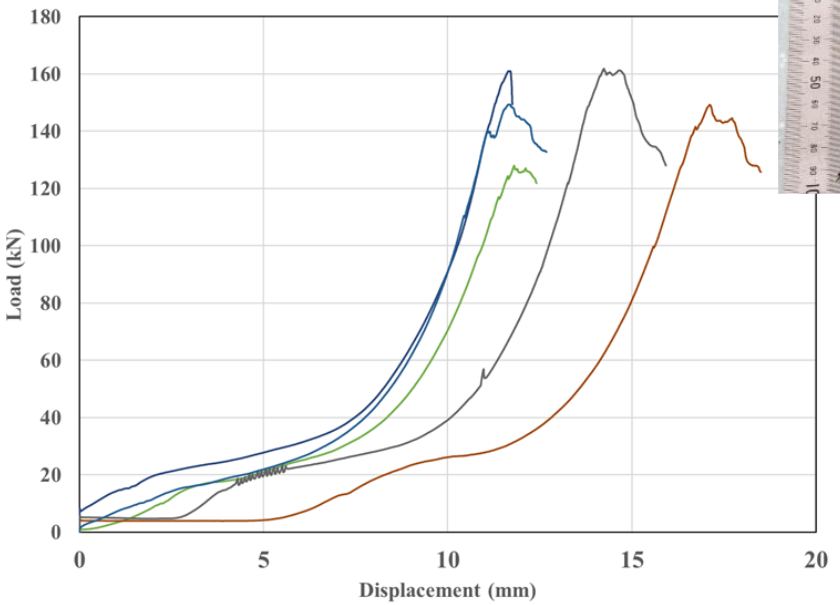





Sample 5 – With Rib

Guillotine Double Shear results

Sample No.		Displacement at Maximum Load (mm)	Maximum Double Shear Load (kN)	F Shear Plane (kN)	Carbolt Diameter (mm)	τ (ratio between shear force and cross-section area) (Mpa)
Without Rib	Sample1	13.833	153.4	76.7	29.49	112.29
	Sample2	13.562	145.5	72.75	29.16	108.67
	Sample3	16.048	161.4	80.7	28.73	124.48
	Sample4	14.072	146.9	73.45	27.34	125.11
	Sample5	12.98	146.7	73.35	28.1	118.28
With Rib	Sample1	11.8	128	64	24.12	140.1
	Sample2	11.7	161	80.5	23.97	178.5
	Sample3	17.1	149.2	74.6	24.29	160.9
	Sample4	14.2	161.8	80.9	24.19	176.2
	Sample5	15.4	151.1	75.55	24.31	162.9
	Sample6	11.2	149.3	74.65	23.95	165.8

Tensile Strength Testing

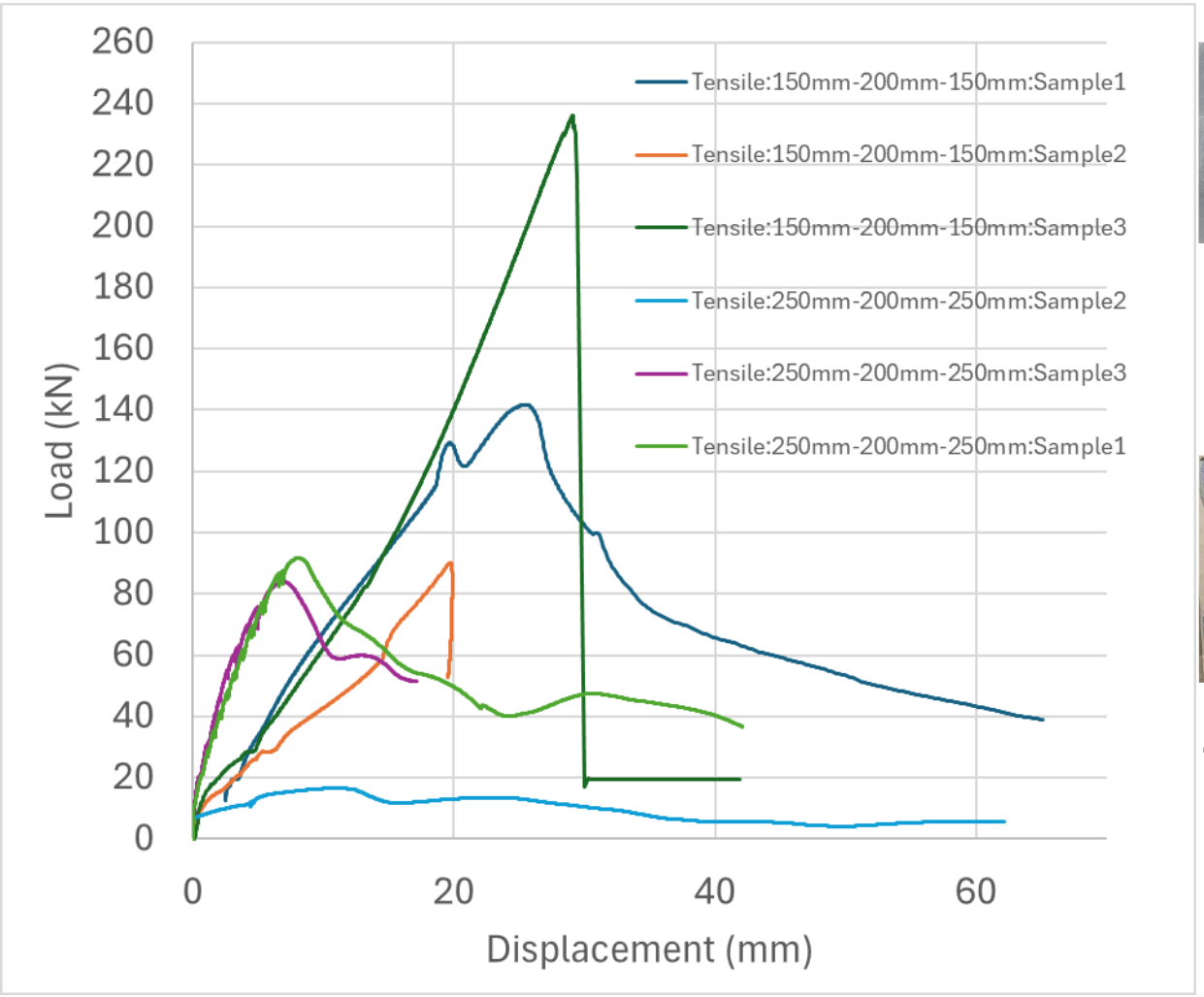



Before casting



Tensile samples after grouting



Pull-out Testing

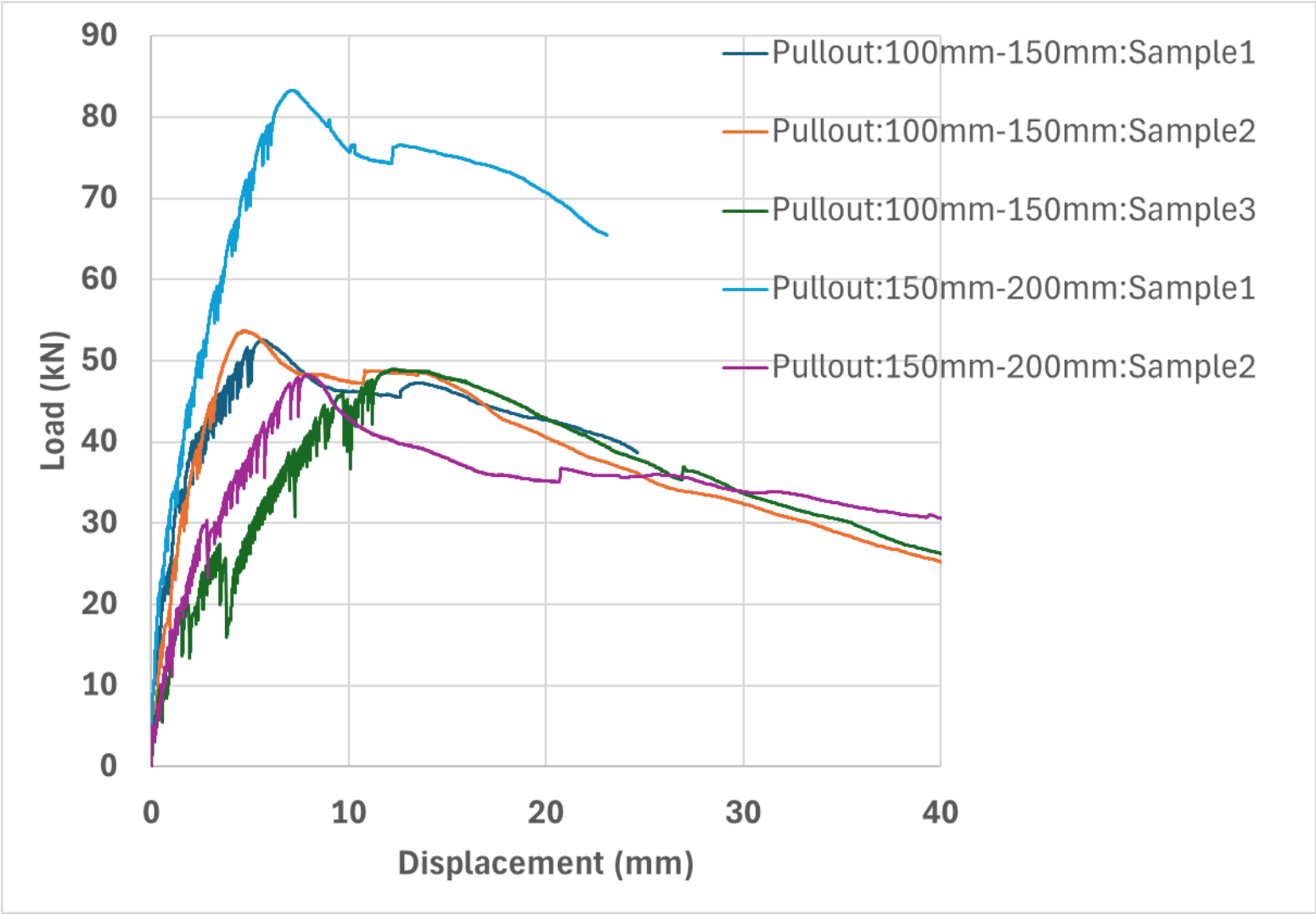



150mm-200mm
pull-out specimen



100-150mm
pull-out specimen

Damage Analysis during Pull-out testing

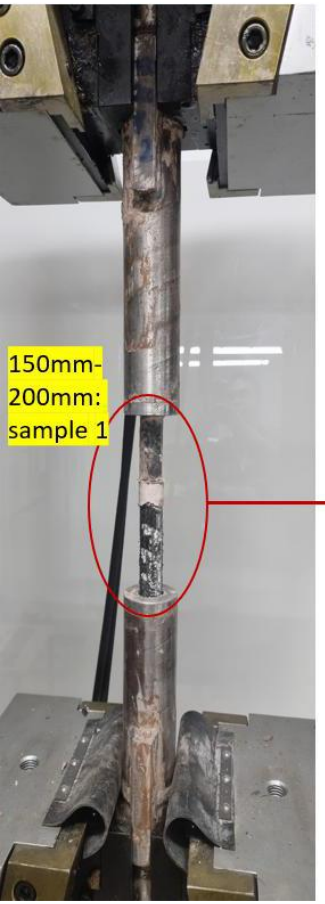





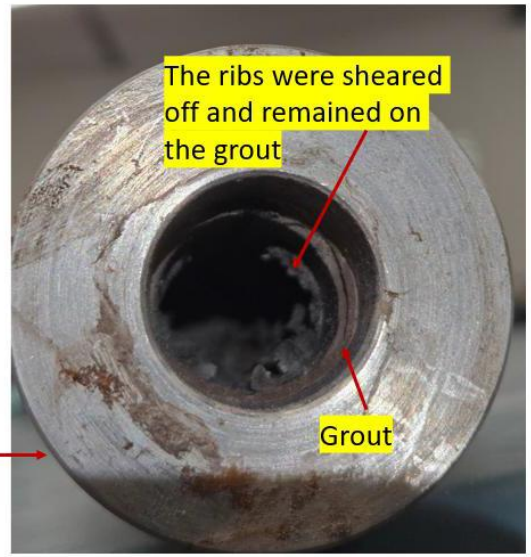

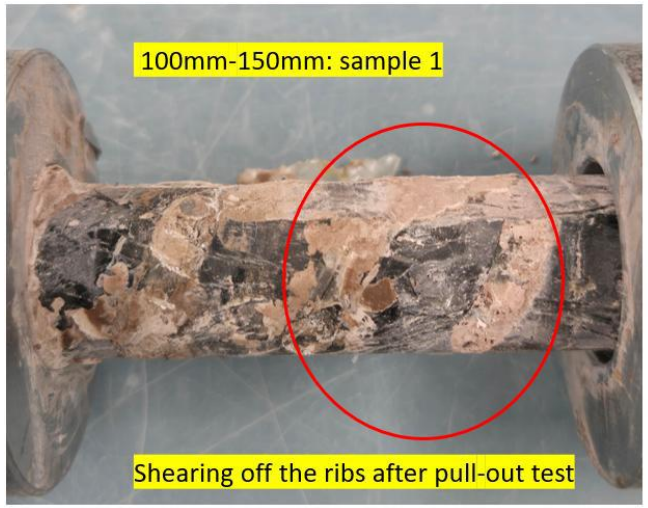

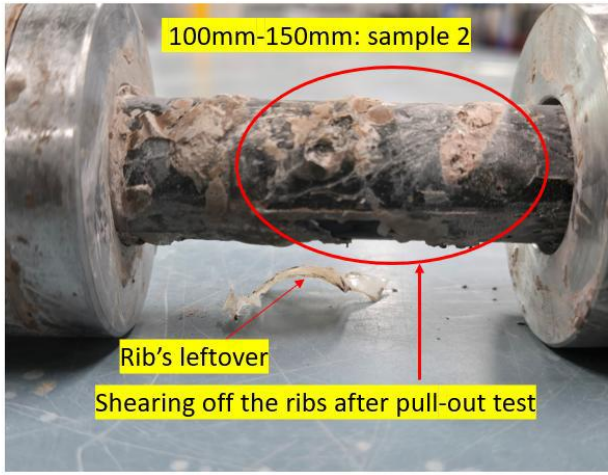

Summary

- ✓ The testing results shows that Braided Carbon FRP composites Rebar (Carbolt) as viable alternative or complement to the traditional Steel rock bolts.
- ✓ Although, prototype demonstrated strengths, yet there are further refinement to achieve full commercial viability.
- ✓ In terms of single shear strength, the braided CFRP composite Rebar was lower than M24 Steel rock bolt but remained superior to that of glass fibre rebar. The use of braided carbon fibre contributed to the higher normalized single shear strength, improving load bearing capacity, and energy absorption.
- ✓ The braided CFRP composite rebar performed well in tensile strength when its specific strength was normalized for cross-sectional area. The results suggests that with further optimization of the carbon fibre content, the braided CFRP composite rebar could match or exceed the tensile strength of steel rockbolt.
- ✓ Overall the results suggest that the braided CFRP composite rebar has significant potential as a corrosion-resistant, light weight, alternative to steel rock bolts.

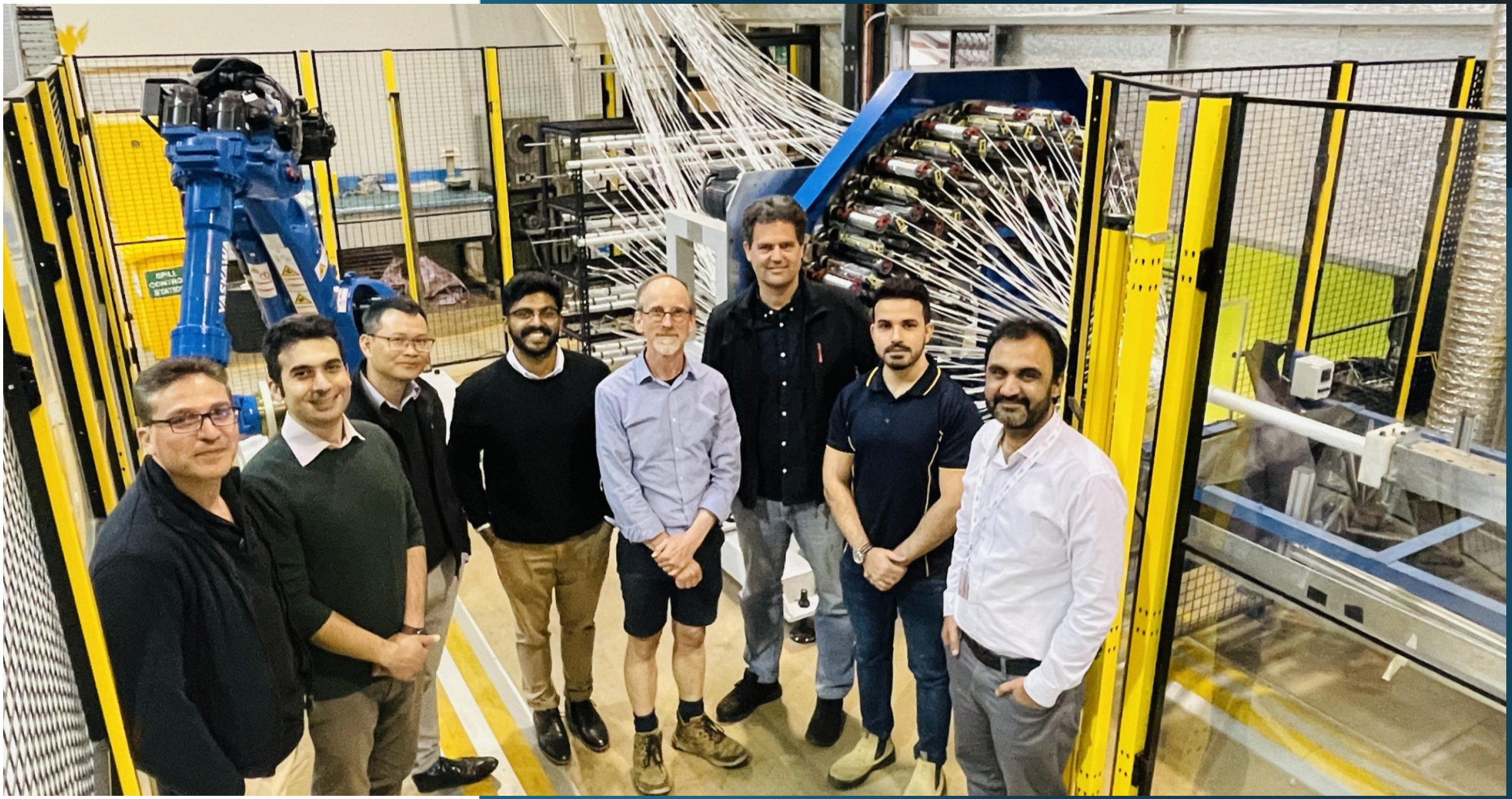
YASKAWA

Acknowledgements

I would like to express my sincere gratitude to the following organizations for their invaluable support and contributions to this research:

- **Centre for Future Materials** (CFM), University of Southern Queensland – for providing the state-of-the-art facilities, technical guidance, and a collaborative research environment throughout the project.
- **Mining3** – for their industry partnership, strategic direction, and ongoing encouragement that made this applied research impactful and relevant to real-world challenges.
- **CSIRO** – for their scientific collaboration, expertise, and support in advancing the technical scope of the research.

Their collective contributions have been instrumental in the successful completion and presentation of this work. I am truly grateful for the opportunity to be part of this collaboration.

Thank You!

Any questions?





Optimization of Cationic Frontal Polymerization Experiments: An Analysis of Compositions, Reproducibility, and Materials

Brecklyn Groce

VUB SUME SUSTAINABLE MATERIALS ENGINEERING RESEARCH GROUP

ICCM24
24TH INTERNATIONAL CONFERENCE ON COMPOSITE MATERIALS

OVERVIEW OF THIS TALK

- Frontal polymerization

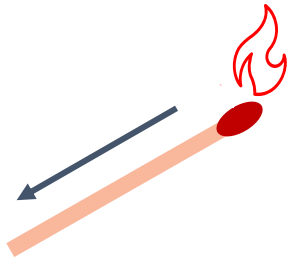

- Radical-induced cationic frontal polymerization

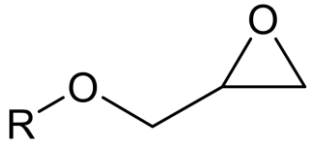

- Motivation, experimental design/optimization
  - Data collection, formulation chemistry, mold design

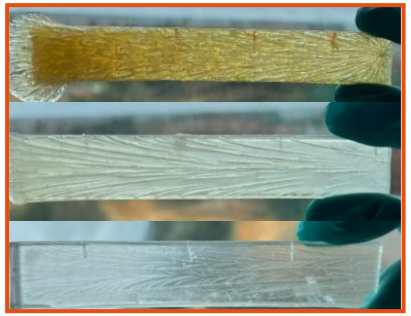

WHAT IS FRONTAL POLYMERIZATION?

- Propagating localized reaction zone
- Vital: greater rate of heat production than heat loss
- One-pot formulations
- Cure on-demand
- Long pot lives
- Fast curing



Acrylate (free-radical) FP initiated via UV light

Pojman, J. A. Frontal Polymerization, In: *Polymer Science: A Comprehensive Reference*, K. Matyjaszewski, M.Möller, Eds., Elsevier BV, Amsterdam, **2012**, *4*, 957 - 980.
Suslick B. A. et al. *Chemical Reviews* **2023,** *123*(6), 3237-3298.

RADICAL-INDUCED CATIONIC FRONTAL POLYMERIZATION

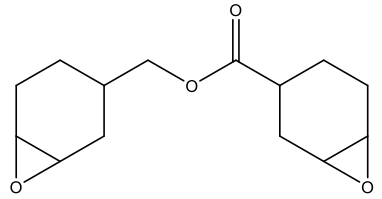

3,4-epoxycyclohexylmethyl 3,4-epoxycyclohexane carboxylate (CE)

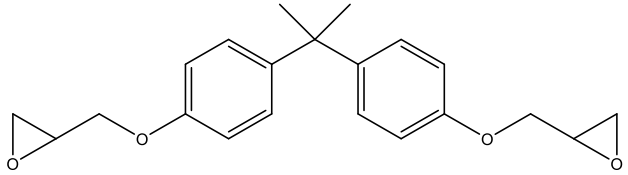

Bisphenol A diglycidyl ether (BADGE)

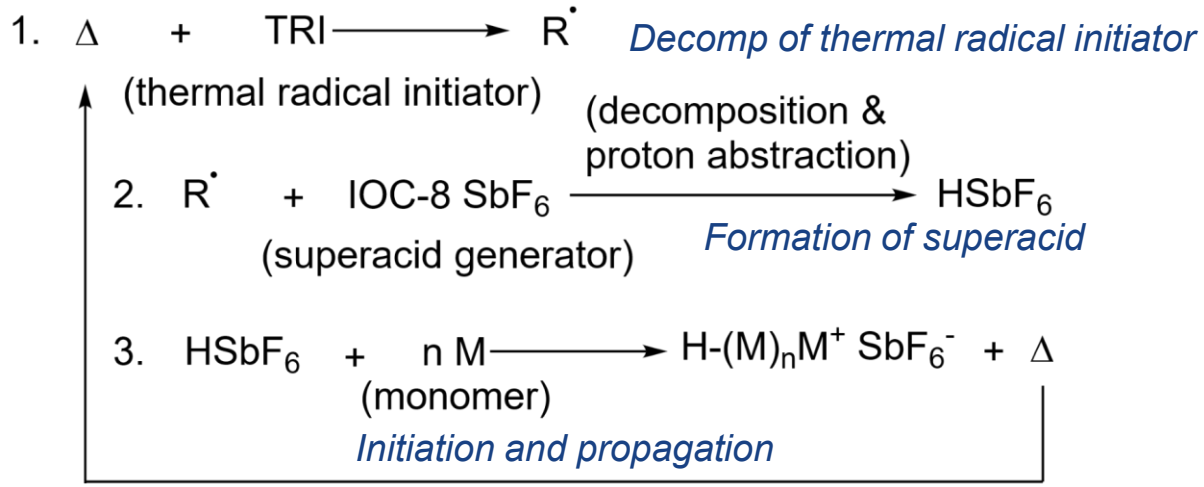

- First described by Mariani et al. of an epoxy resin
- Onium salts (photoacid generators) + thermal frontal polymerization (FP)
- Counterion properties affect kinetics

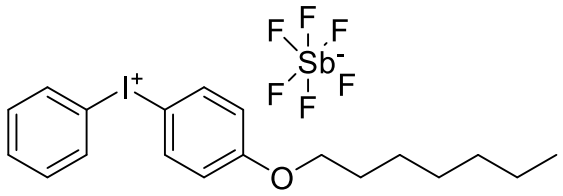

p-(octyloxyphenyl)phenyliodonium hexafluoroantimonate (IOC-8)

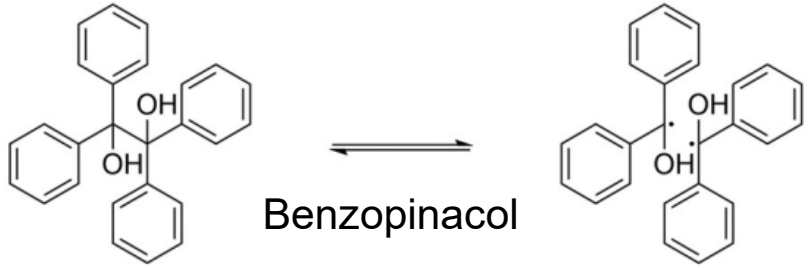

Benzopinacol

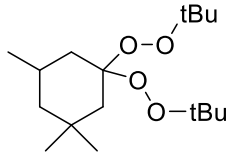

1,1-Bis(tert-butylperoxy)-3,3,5-trimethylcyclohexane (Luperox® 231)

Gachet, B. et al. *RSC Adv*. **2020**, *10*, 41915.
Bomze, D.; Knaack, P.; Liska, R. *Polym. Chem* **2015**, *6*, 8161 - 8167.
Mariani, A. et al. *J. Poly. Sci. Part A. Polym. Chem.* **2004**, *42*, 2066-2072.

RICFP: LITERATURE APPLICATIONS

Carbon fiber composite RICFP from Sangermano et al.

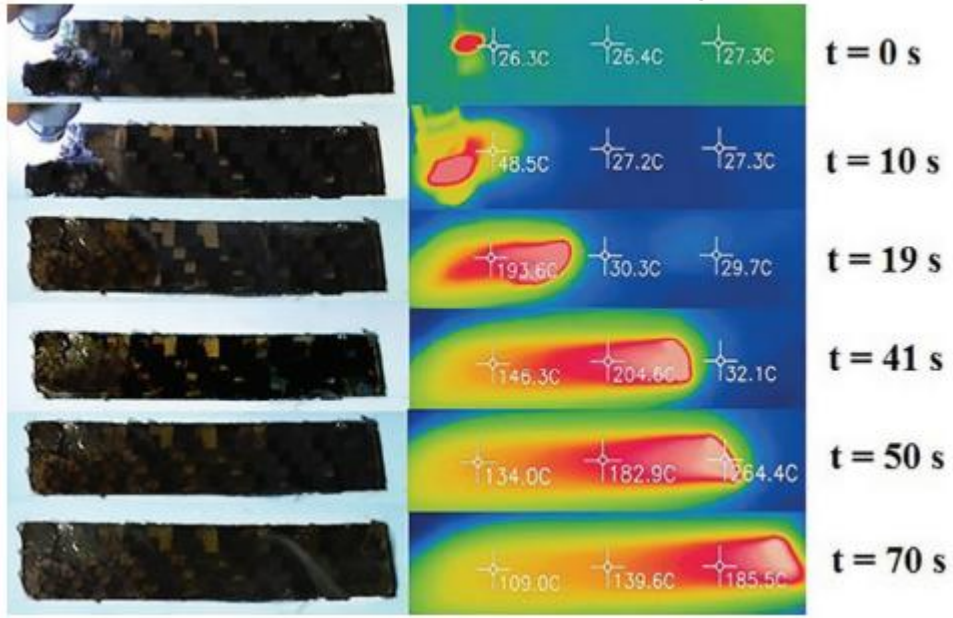

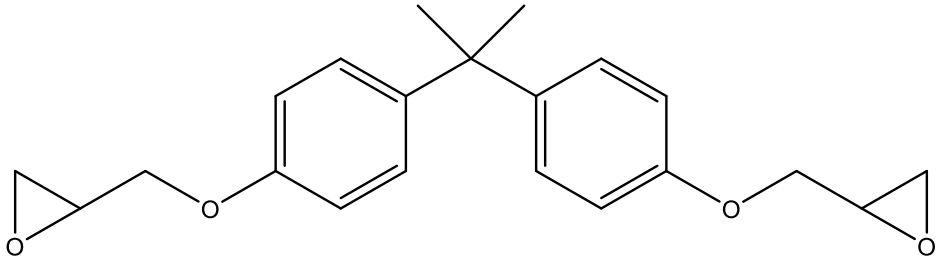

Bisphenol A diglycidyl ether (BADGE)

Effect of different fillers o
Tran et al.

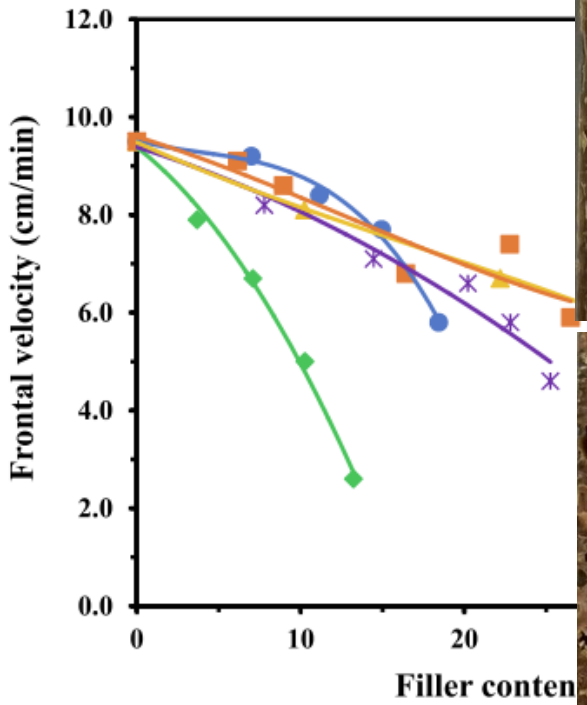

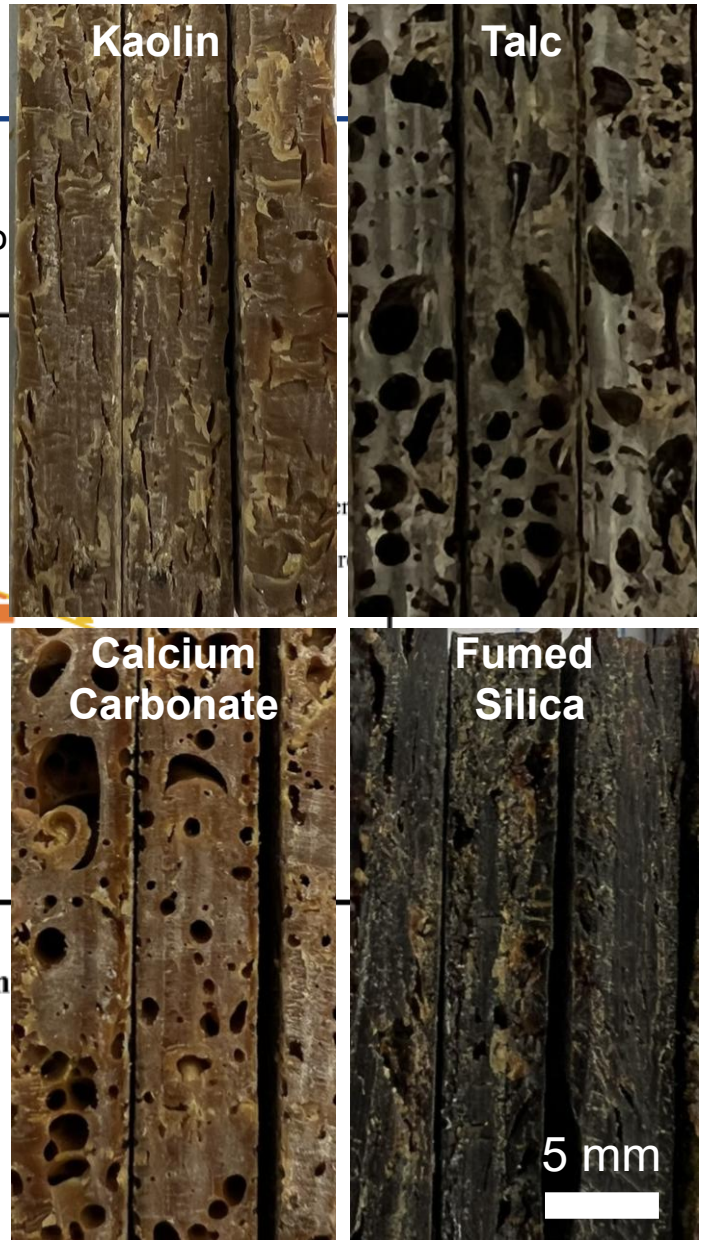

Tran, A. D. et al. *Composites Part A: Applied Science and Manufacturing* **2020,** *132*, 105855.
Sangermano, M. et al. *Polym Int.* **2020,** *68*(10), 1662-1665.
Groce, B. R. et al. *ACS Appl. Mater. Interfaces* **2023**, 15, 15, 19403–19413
Groce et al. *ACS Appl. Polym. Mater.* **2024**, 6, 1, 572−582

MOTIVATION

- Mechanistic model of radical-induced cationic frontal polymerization
- Use kinetic data from experiments

RICFP mechanism →

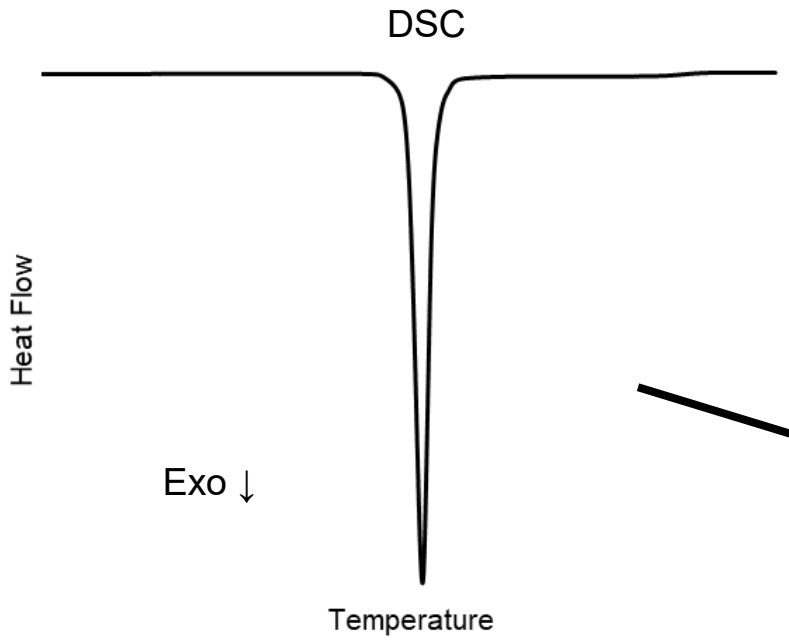

Experimental FP setups and data ↓

Predict viability of FP under varying conditions and different systems

FORMULATION PREPARATION: MONOMER & INITIATOR

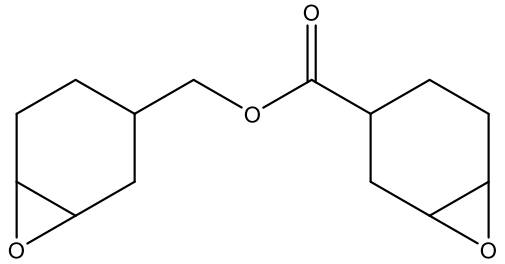

3,4-epoxycyclohexylmethyl 3,4-epoxycyclohexane carboxylate (CE)

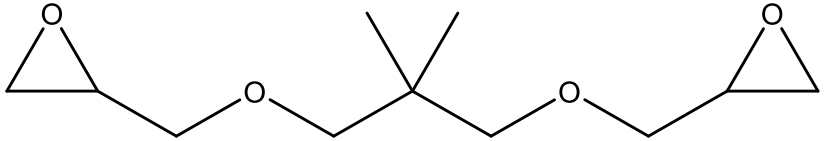

Neopentyl gylcol diglycidyl ether (NPDGE)

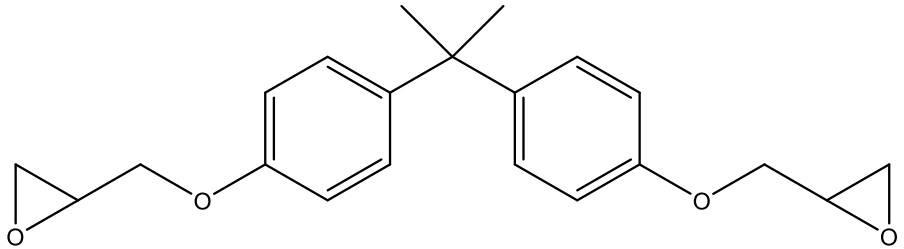

Bisphenol A diglycidyl ether (BADGE)

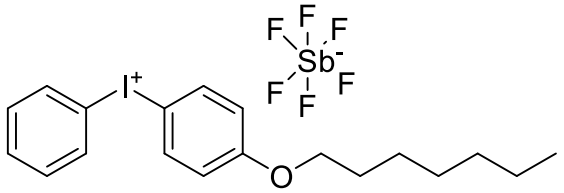

p-(octyloxyphenyl)phenyliodonium hexafluoroantimonate (IOC-8)

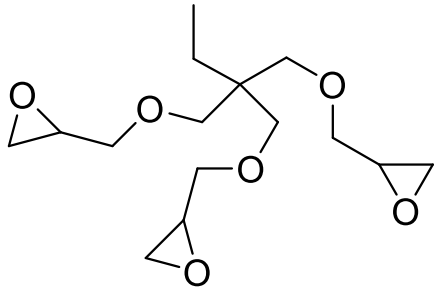

trimethylolpropane triglycidyl ether (TMPTE)

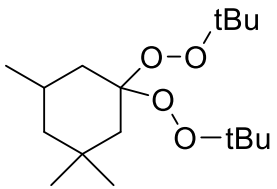

1,1-Bis(tert-butylperoxy)-3,3,5-trimethylcyclohexane (Luperox® 231)

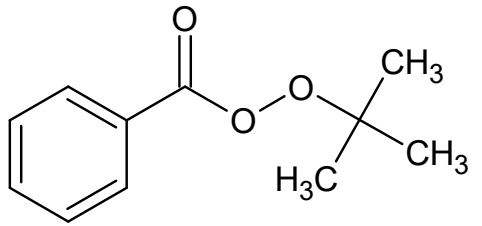

Luperox® P (tert-butyl peroxybenzoate)

FORMULATION PREPARATION: FIRST FRONTS

Increasing IOC concentration

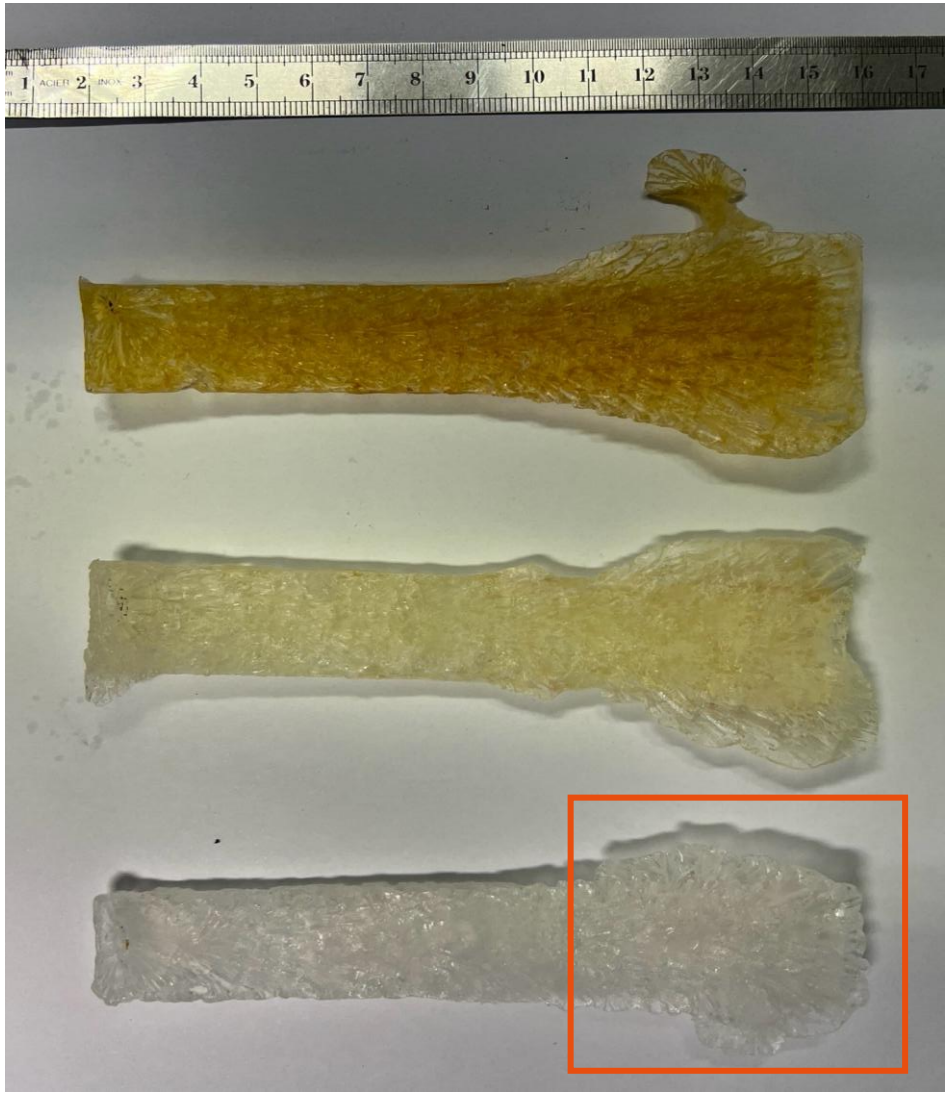



Large amount of bubbles

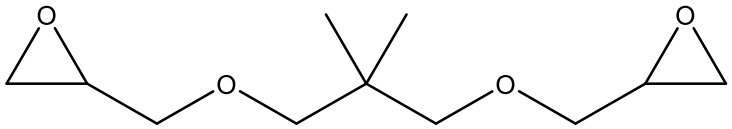

Neopentyl gylcol diglycidyl ether (NPDGE)

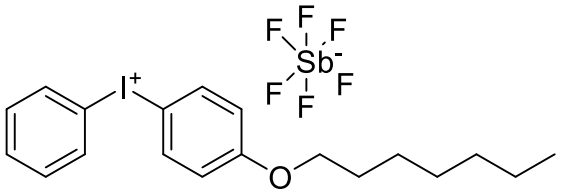

p-(octyloxyphenyl)phenyliodonium hexafluoroantimonate (IOC-8)

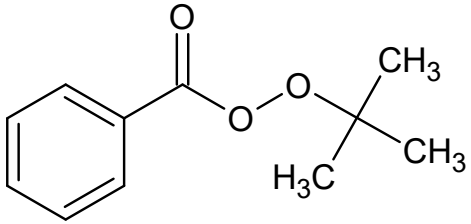

Luperox® P (tert-butyl peroxybenzoate)

FORMULATION PREPARATION: FIRST FRONTS

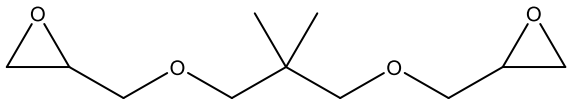

Neopentyl gylcol diglycidyl ether (NPDGE)

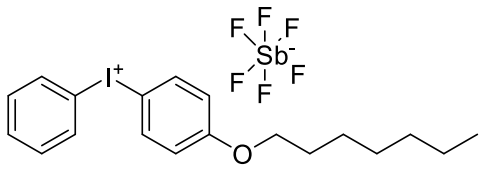

p-(octyloxyphenyl)phenyliodonium hexafluoroantimonate (IOC-8)

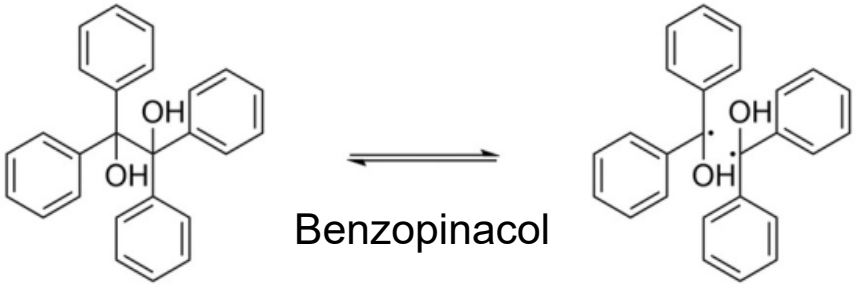

Benzopinacol



Luperox P



TPED

FORMULATION PREPARATION: IOC OPTIMIZATION

- Previous literature: pyrolysis of IOC → generation of benzene-based volatiles



Decreasing IOC Concentration



Front

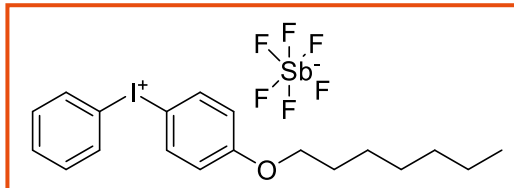

p-(octyloxyphenyl)phenyliodonium hexafluoroantimonate (IOC-8)

Previous Luperox P sample



VUB SUME SUSTAINABLE MATERIALS ENGINEERING RESEARCH GROUP

W. E. McEwen and J. W. DeMassa. *Heteroatom Chemistry* **1996**, 7(5), 349-354

DESIGN OF MOLDS

- Silicone mold (heat resistant up to 294 °C)
  - Can adapt to many different needs
  - Rapidly generate molds for studies of boundary conditions



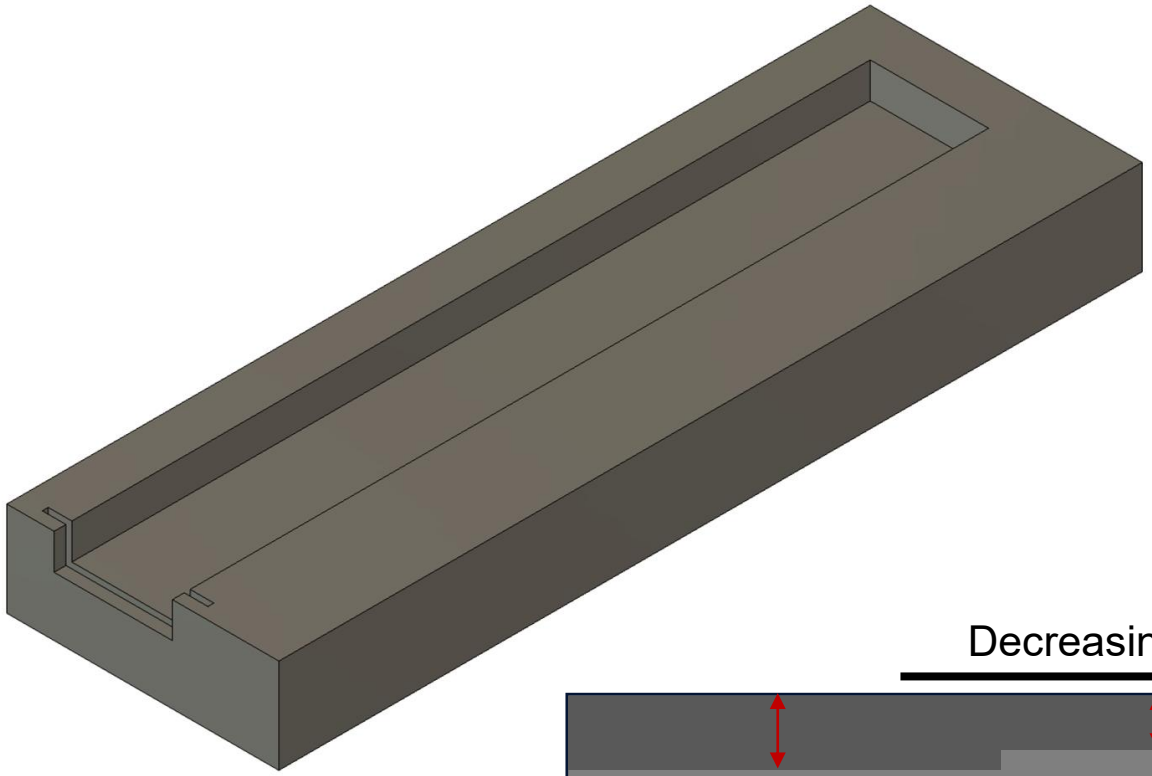

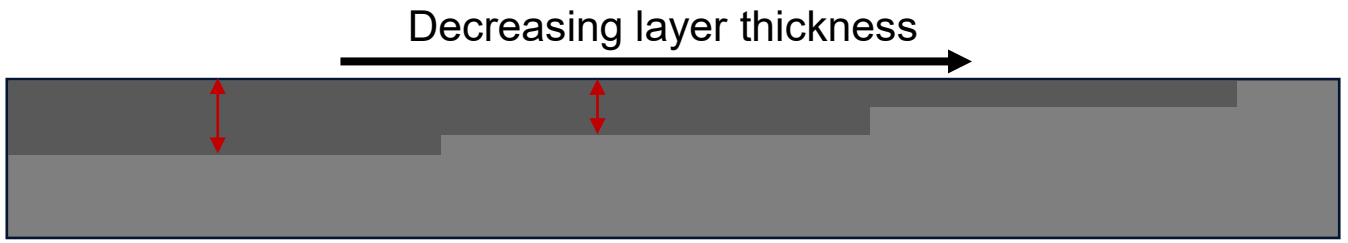

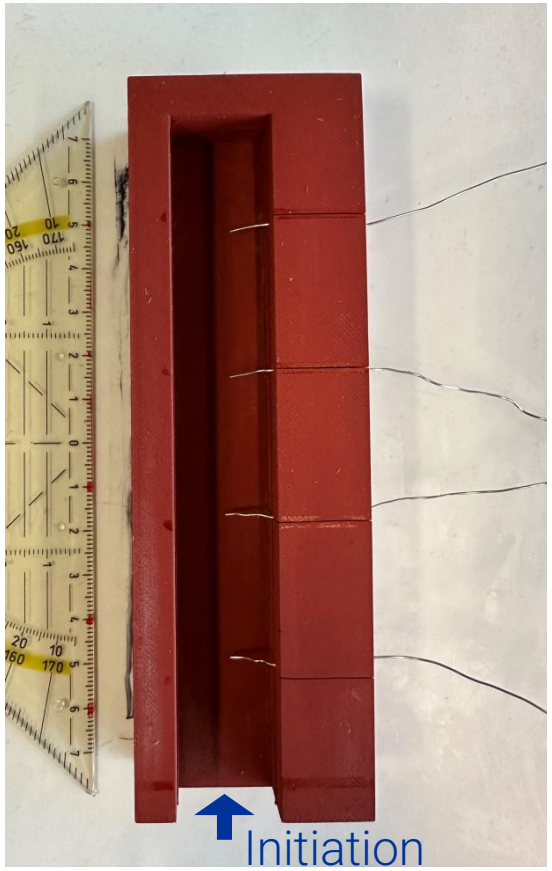

DESIGN OF MOLDS

- Also possible: creation of wooden mold
  - Adaptable as well
  - Basswood, as shown here
  - Differences in thermal properties





Propagating front in wooden mold

DESIGN OF MOLDS: EFFECT ON FP

- Wooden mold: little uncured material left
- Silicone mold: much more uncured material remaining

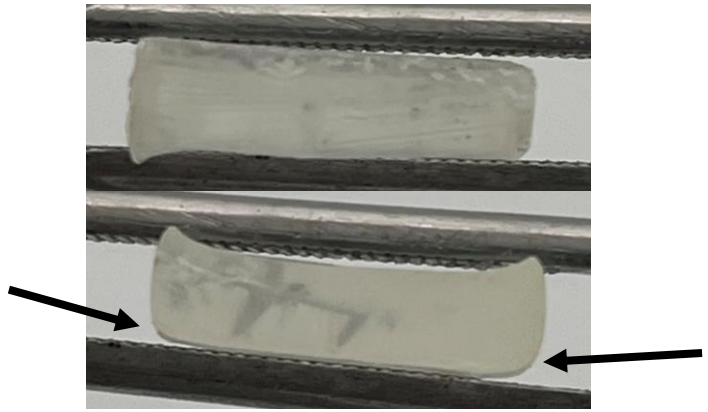

Top: polymer after FP in wooden mold
Bottom: polymer after FP in silicone mold





After FP polymer removed

INITIATION OF FRONTS

- RICFP initiated with heat for our case
  - Decompose radical initiator → acid generation from IOC decomposition
  - w/ direct contact → found that initiation temp has little effect on velocity
    - Also results in longer time to stable front

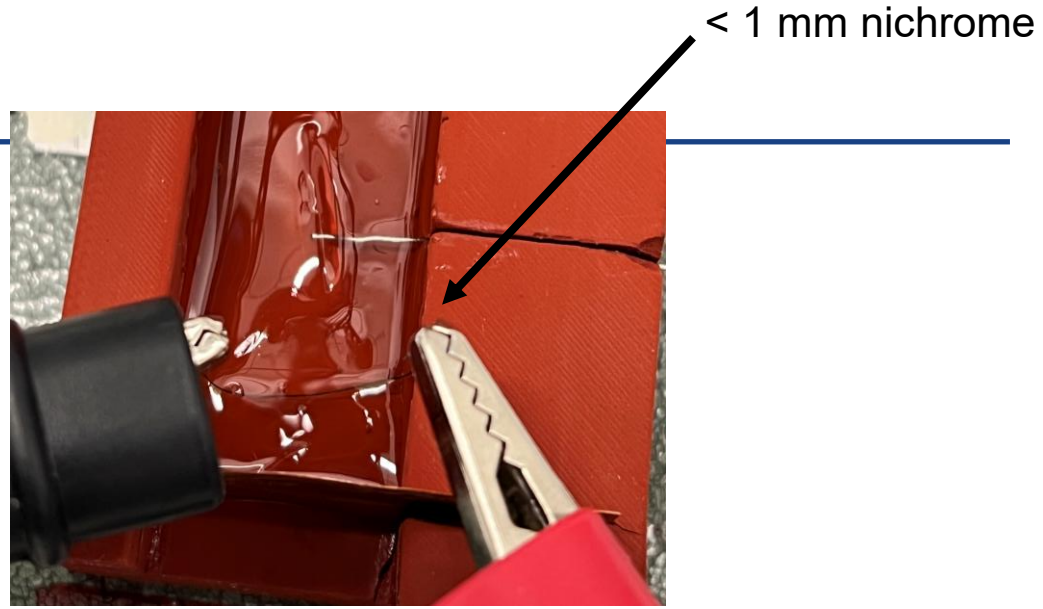

Insert metal plate to initiate the front from side

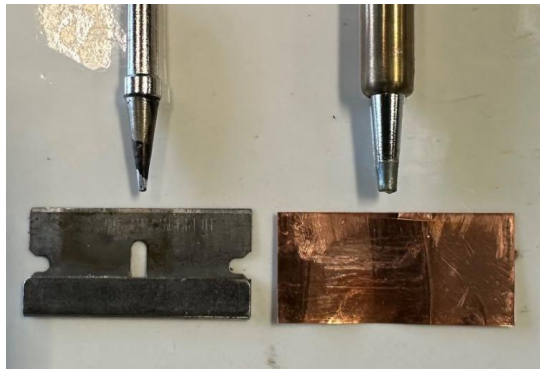

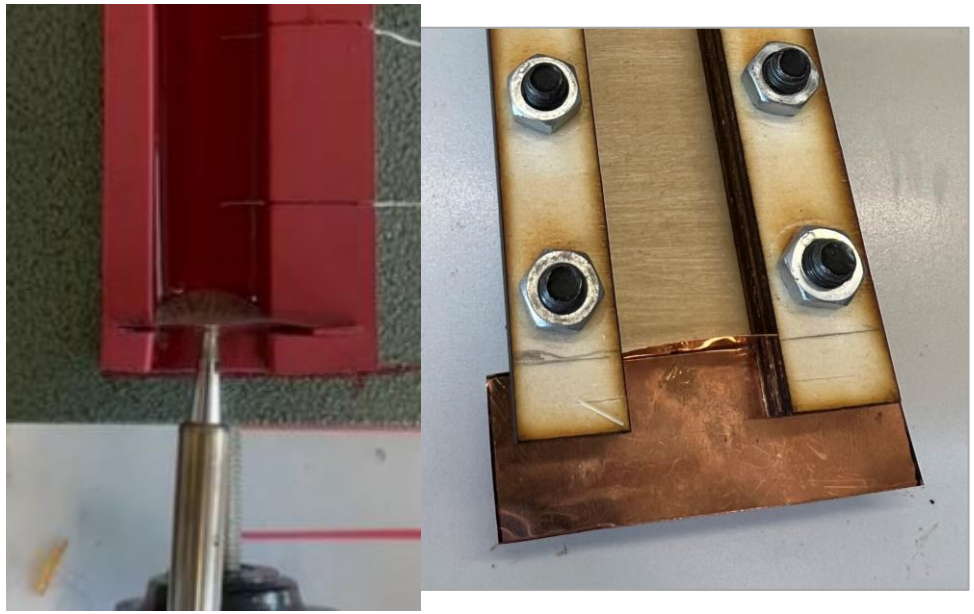



Resistive nichrome wire w/ direct current

OBSERVATION OF FRONTS: THERMOCOUPLES

- Insert thermocouples into resin
- Calculate velocity based on max dT/dt

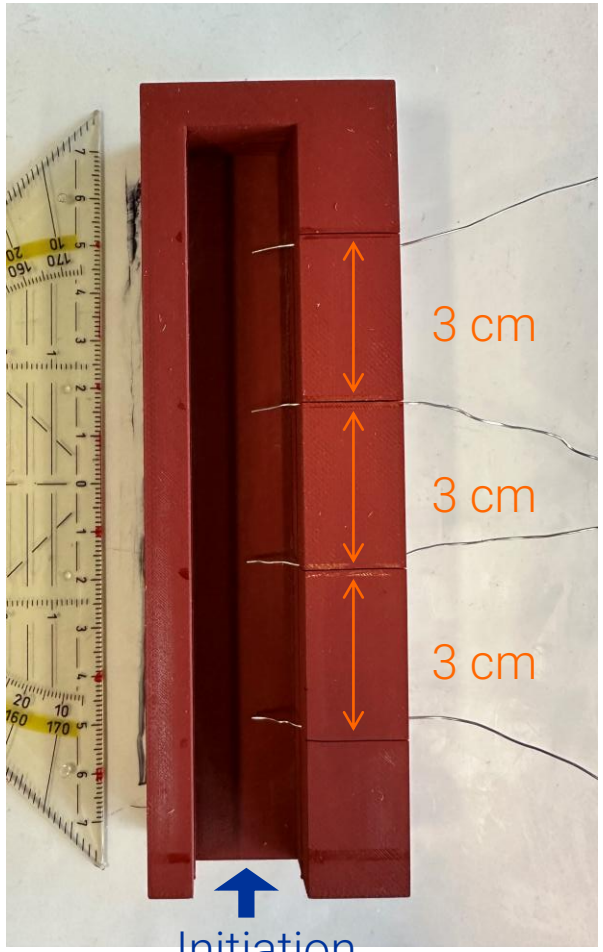

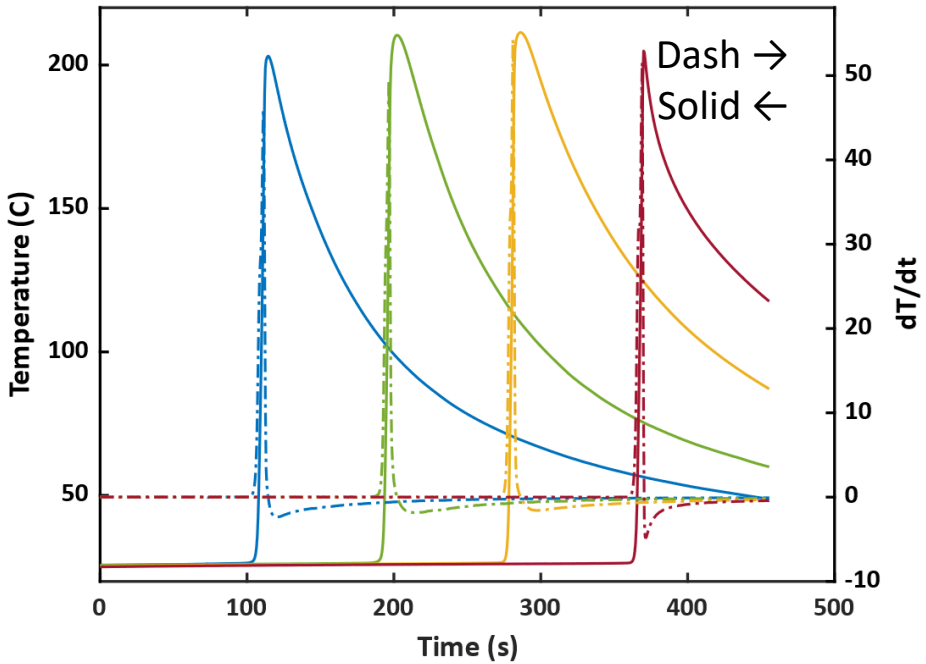

Example plot temperature extracted by thermocouples

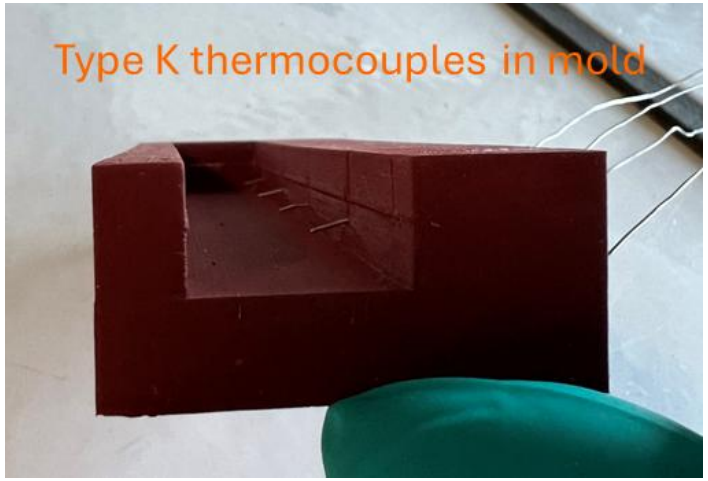

OBSERVATION OF FRONTS: IR CAMERAS

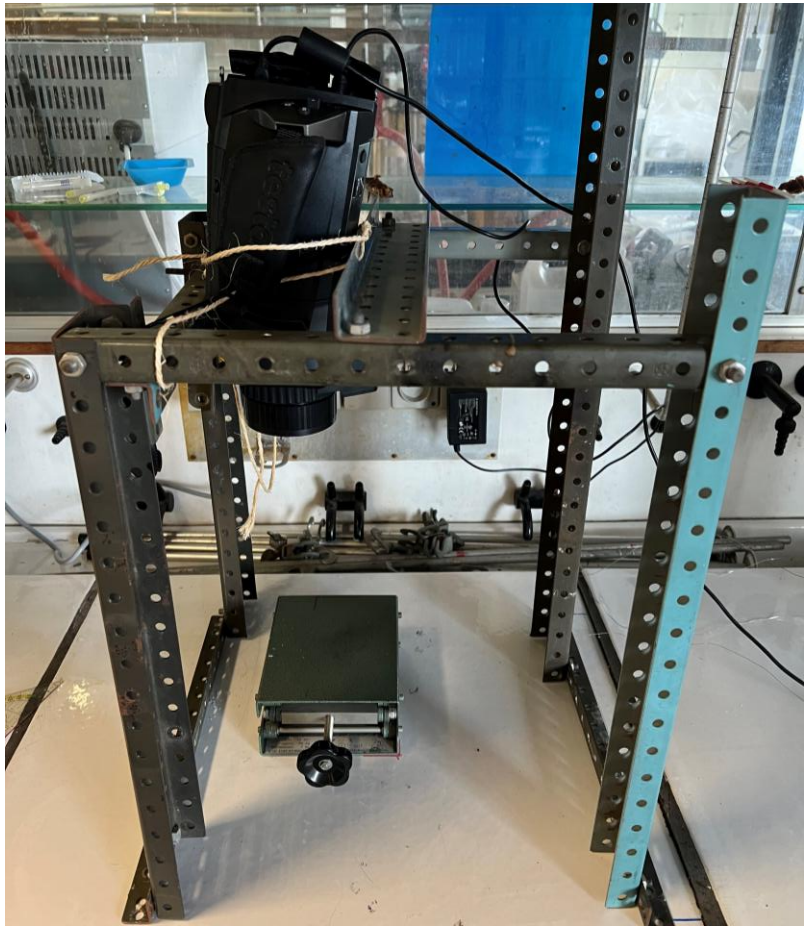



Left: Testo IR camera
Right: FLIR mobile IR camera
Equivalent formulations

OBSERVATION OF FRONTS: THERMOCOUPLE EFFECTS

- 8 thermocouples max (all type K)
  - 3 different brands:
    - 0.5 mm diameter, exposed wire type
    - 0.7 mm diameter, soldered tip
    - 0.35 mm diameter, twisted wire

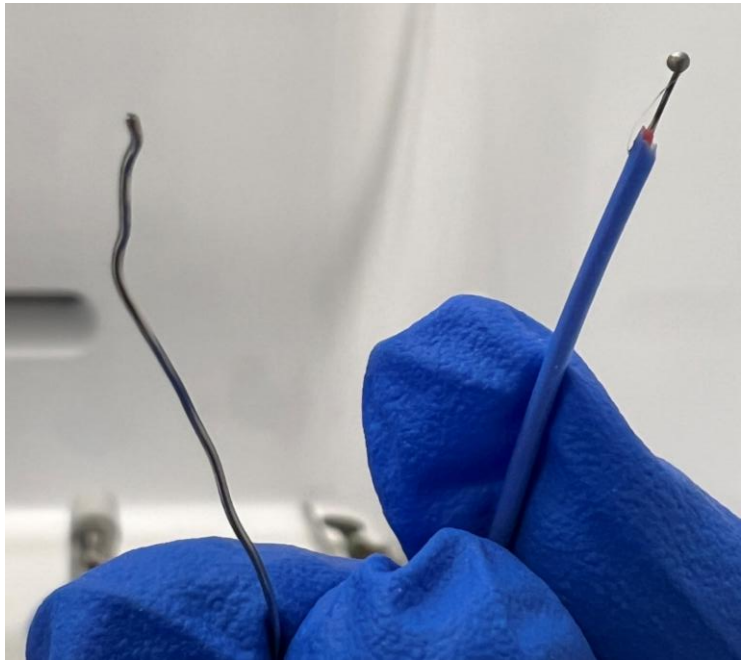

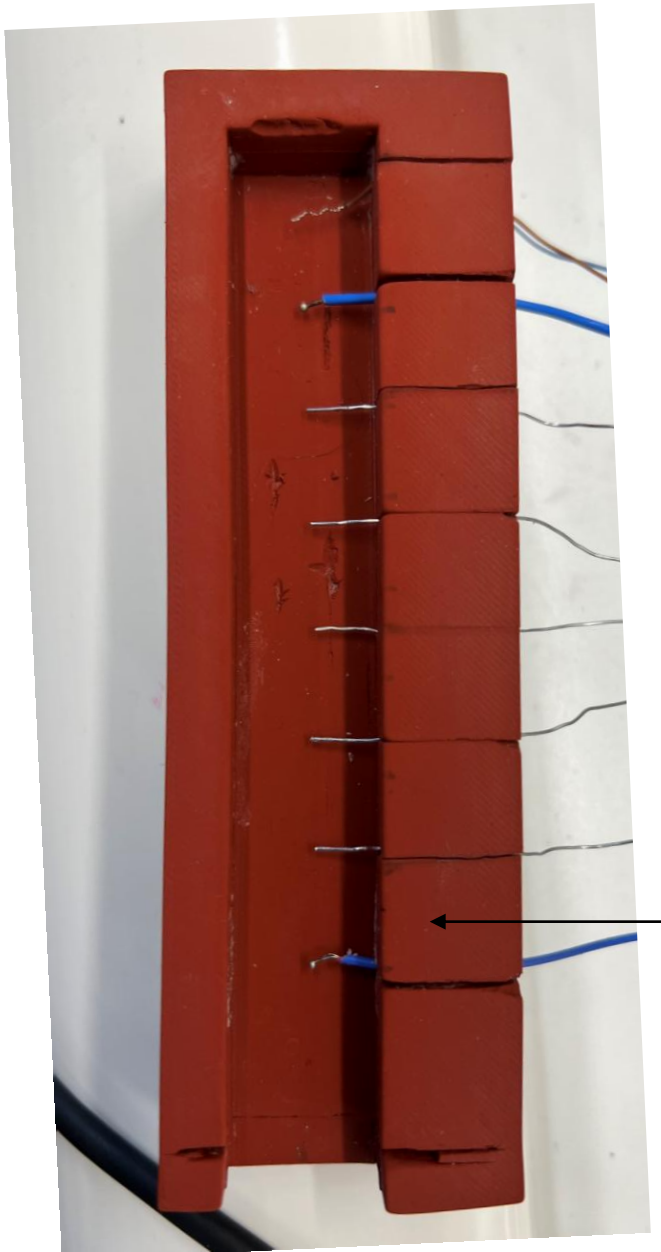

THERMOCOUPLE EFFECTS



(approx. position of TCs)

- No significant difference in front stability

THERMOCOUPLE EFFECTS: FRONT TEMPERATURE

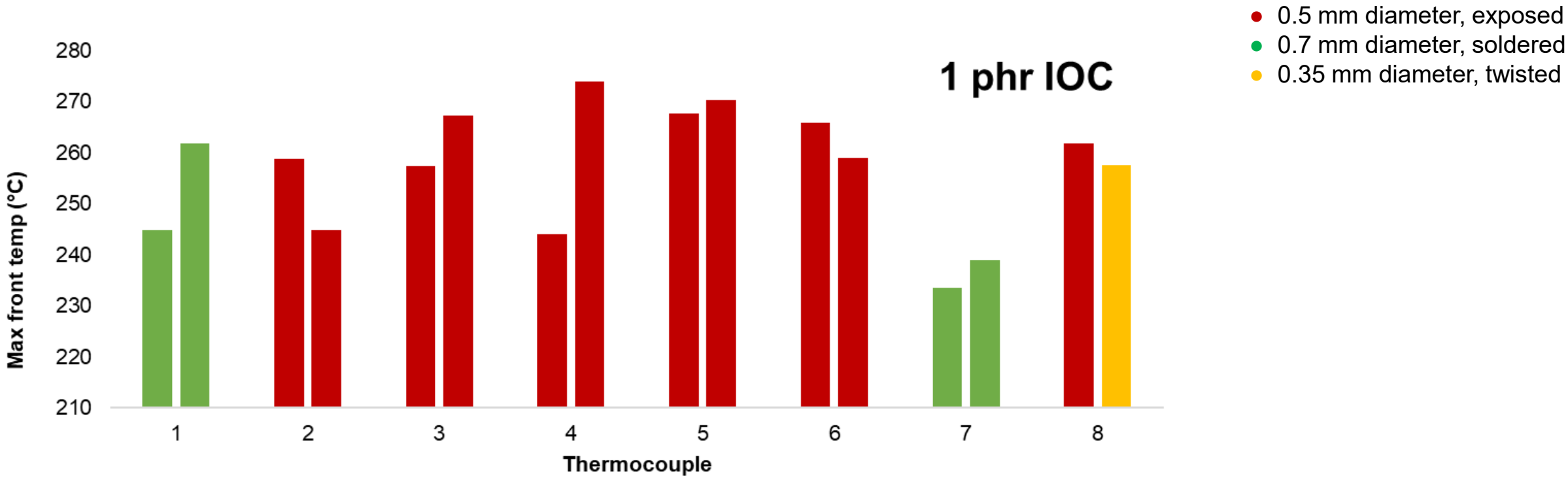

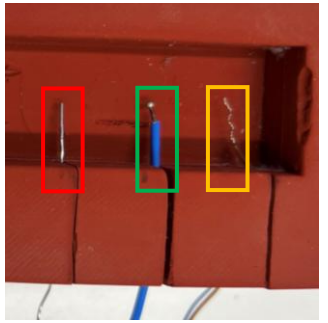



THERMOCOUPLE EFFECTS: NUMBER OF THERMOCOUPLES

1 phr IOC, 1 phr TPED, NPDGE			
# thermocouples	TCs used	Front velocity (cm/min)	Front temperature (C)
8	12345678	5.40 ± 0.08	256.7 ± 2.5
7	1234567	5.36 ± 0.12	256.3 ± 3.1
	2345678	5.43 ± 0.03	257.2 ± 1.6
6	123456	5.31 ± 0.08	259.6 ± 3.2
	234567	5.39 ± 0.07	256.8 ± 2.3
	345678	5.50 ± 0.08	258.1 ± 3.1
5	23456	5.32 ± 0.00	260.9 ± 2.2
	12345	5.40 ± 0.05	259.0 ± 4.5
	45678	5.51 ± 0.14	257.3 ± 2.7

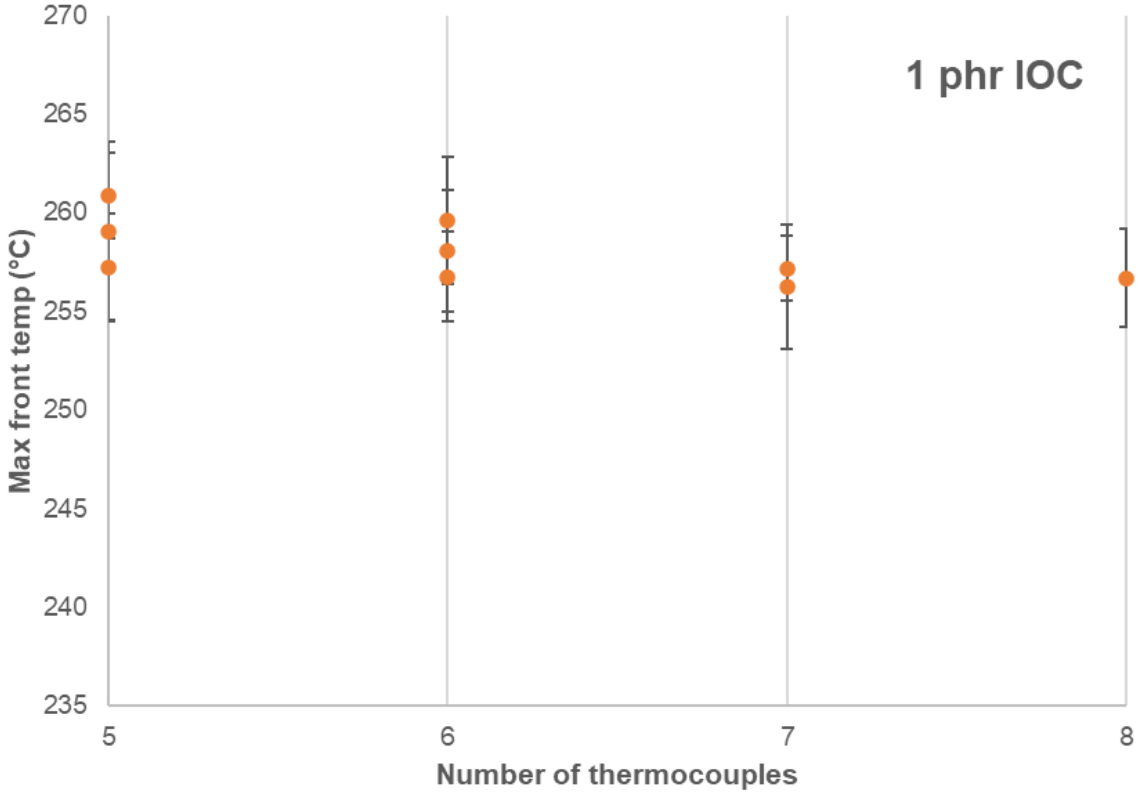

- After 4, within same range for velocities

OBSERVATION OF FRONTS: IR CAMERA

- Problem with IR camera: no length scale
  - Cannot calculate velocity based on observed position of the front
- Heat up using heat gun, polyester tape heats faster than copper

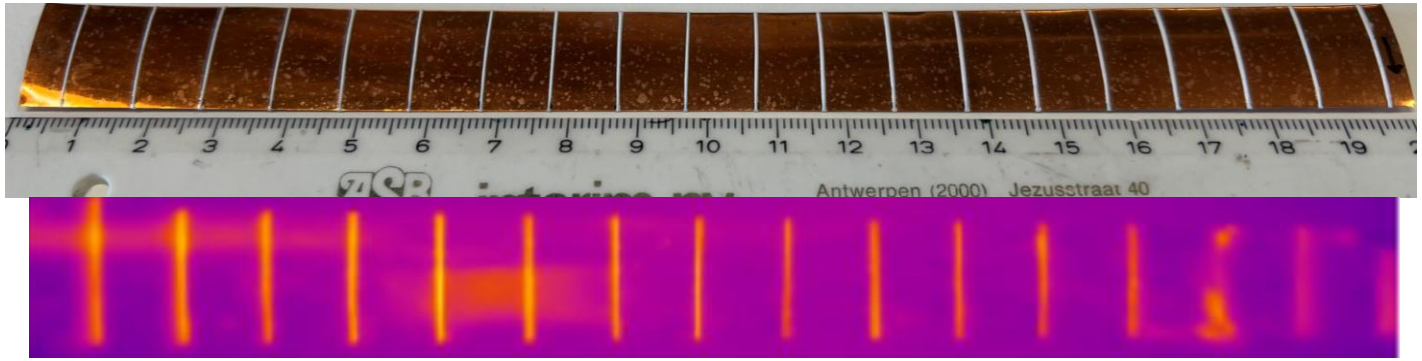

- Larger difference higher concentration IOC samples
- Provides data for front velocity at the boundary

FUTURE WORKS AND CHALLENGES: PURIFICATION

- Another issue with front reproducibility: monomer purity
- 4 bottles of NPDGE

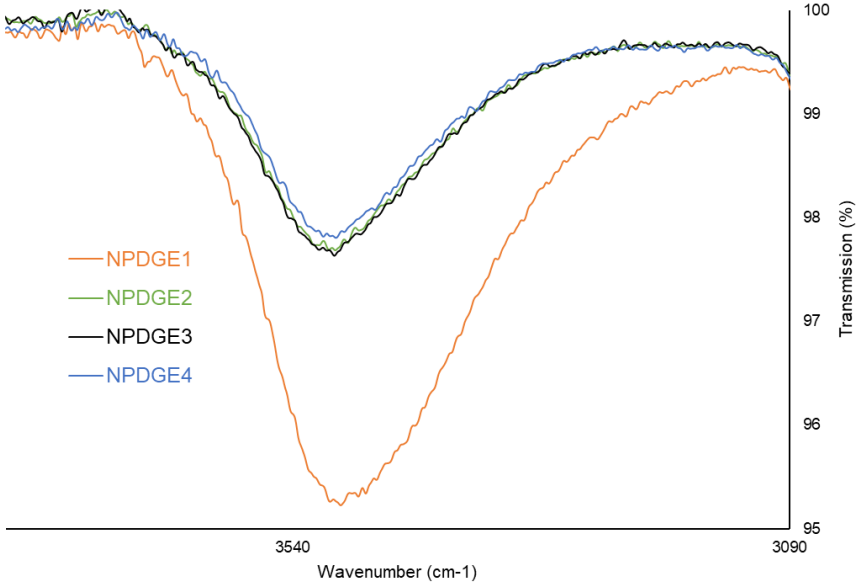

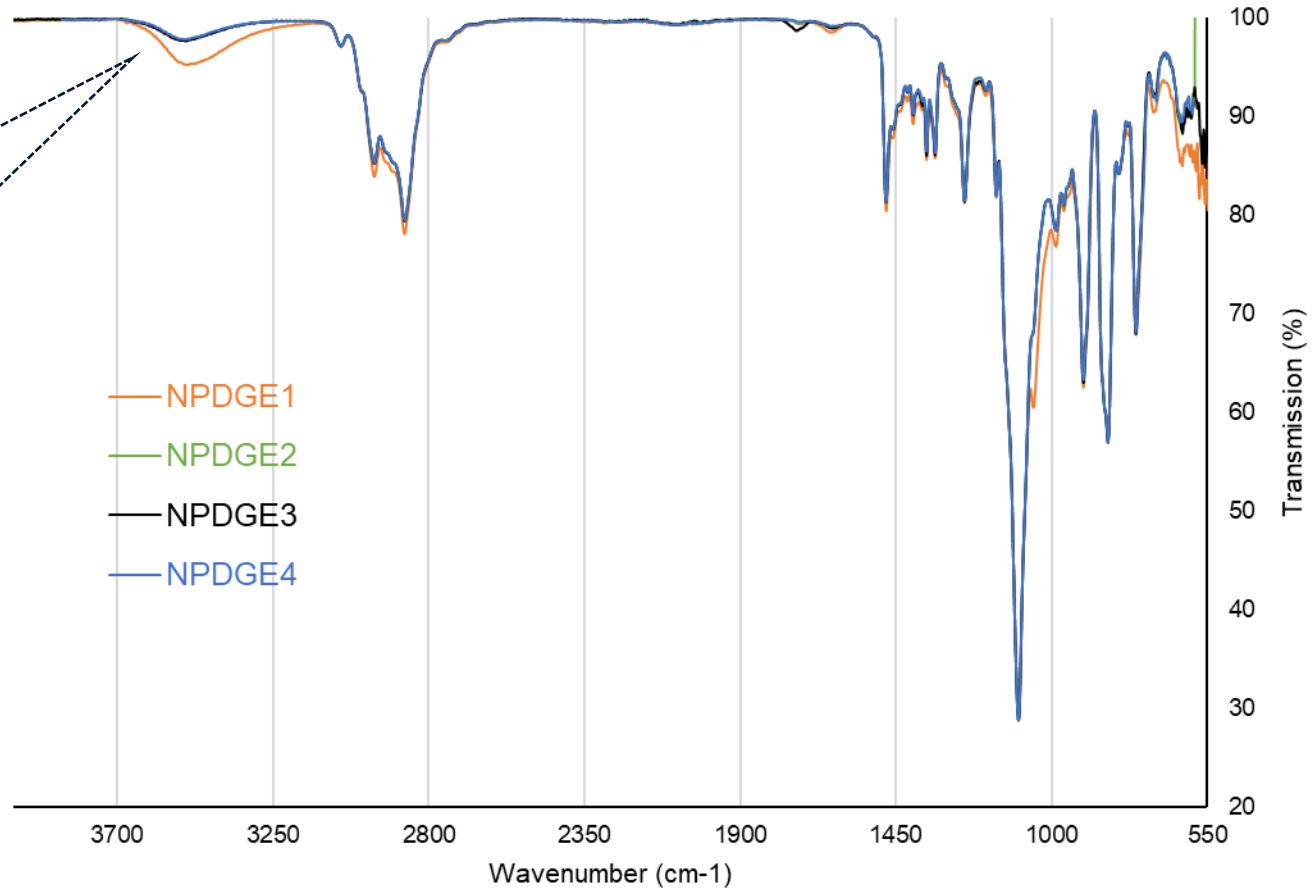

ACKNOWLEDGEMENTS

- Dr. Laurence Rongy (ULB),

  Dr. Miltiadis Papalexandris (UCL)

VUB SUME SUSTAINABLE MATERIALS ENGINEERING RESEARCH GROUP

UCLouvain

ULB UNIVERSITÉ LIBRE DE BRUXELLES

fwo

weave Research funding without borders

fnrs LA LIBERTÉ DE CHERCHER

Photothermal Initiation of Frontal Polymerization in Additive Manufacturing of Discontinuous Fiber-reinforced Thermoset Composites

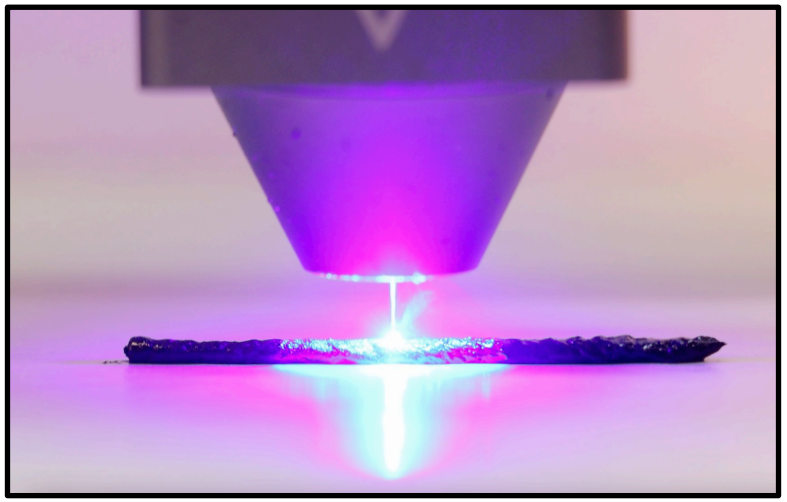

Mostafa Yourdkhani, Alireza Masoumipour, Morteza Ziaee, Carter Dojan

School of Manufacturing Systems and Networks

Arizona State University

August 5th, 2025

Arizona State University

ICCM24
24TH INTERNATIONAL CONFERENCE ON COMPOSITE MATERIALS

Challenges in Composite Manufacturing

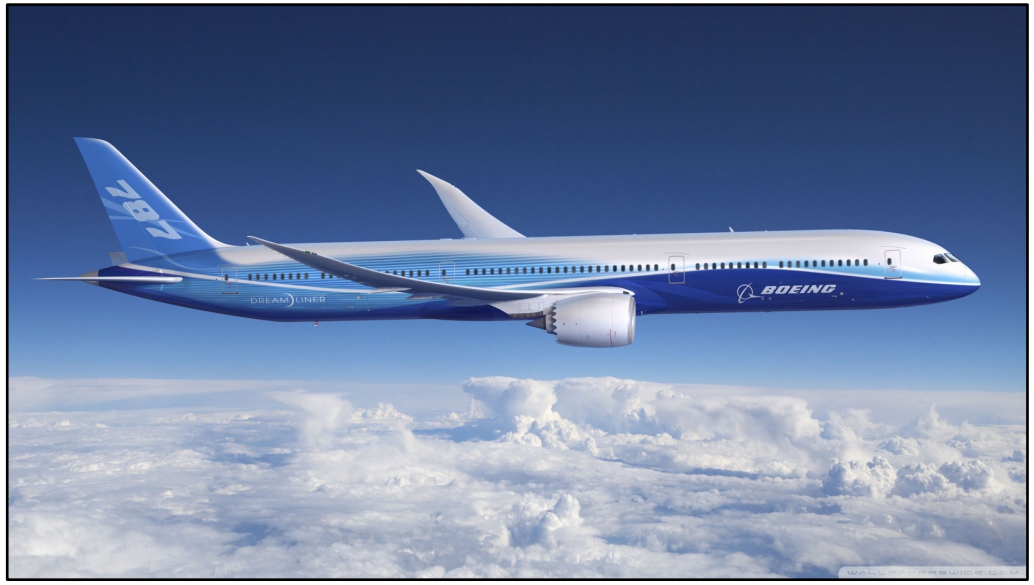





Boeing autoclave



Heated mold for manufacturing a wind blade

Frontal Polymerization (FP)

Self-propagative exothermic reaction wave driven by heat of polymerization

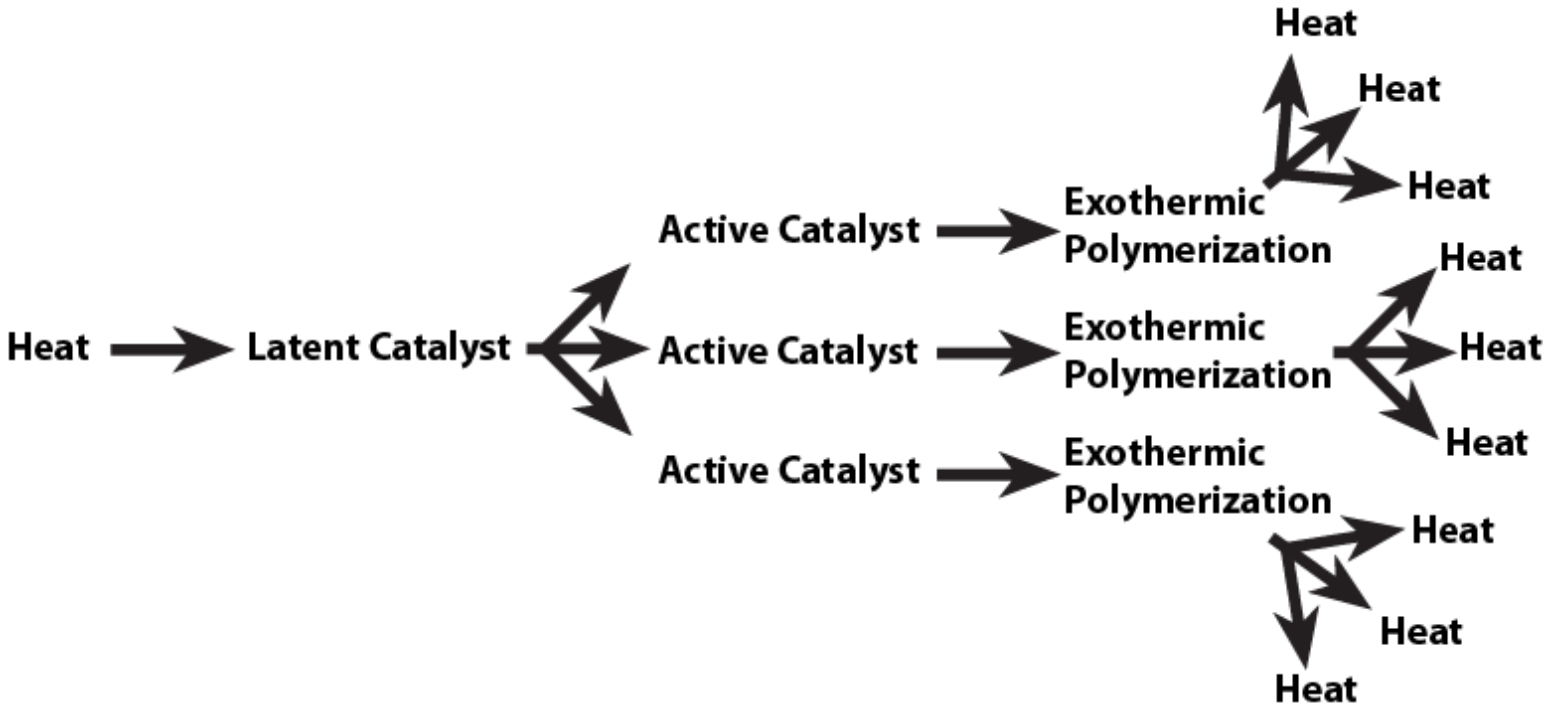



Robertson, Yourdkhani et al., *Nature*, 2018

3D Printing via Frontal Polymerization

- Rapid curing of thermoset composites during 3D printing processes
- Freeform and layer-by-layer printing enabled by synchronized and asynchronized frontal curing

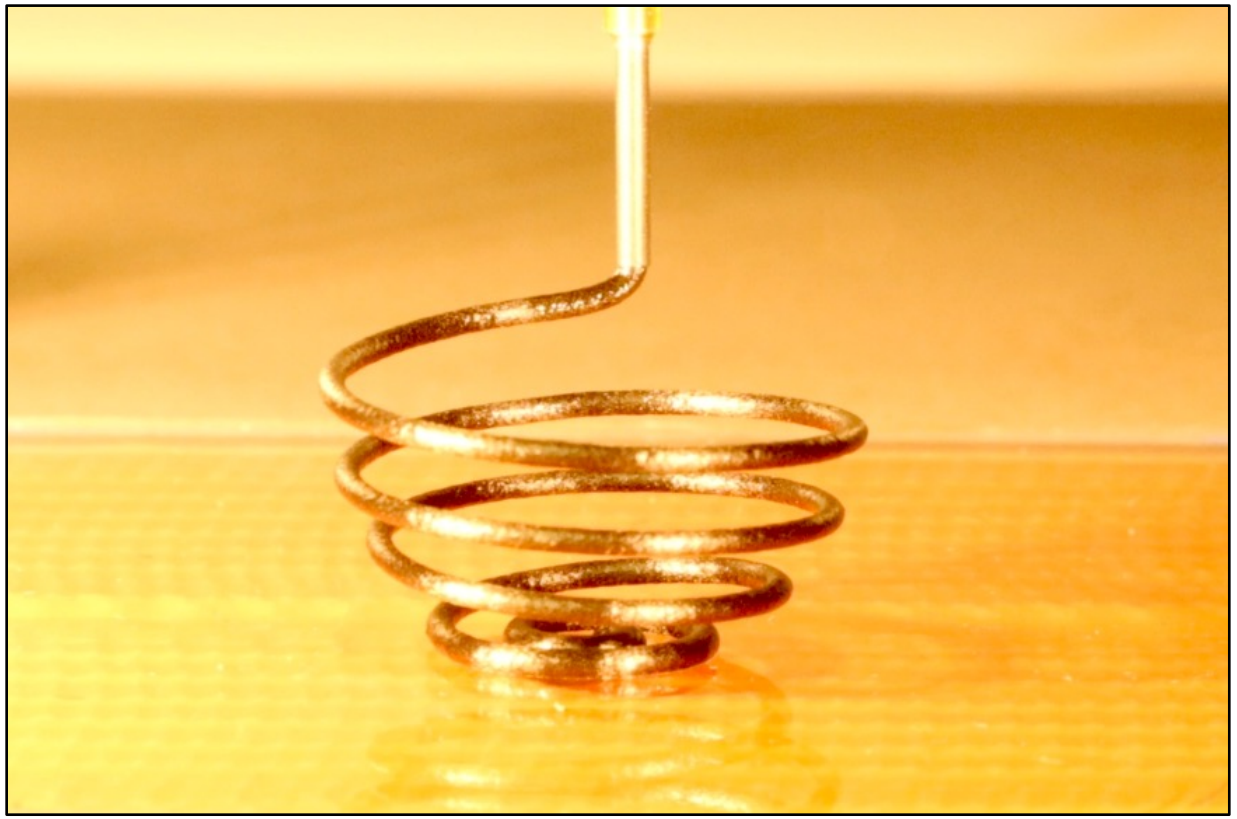

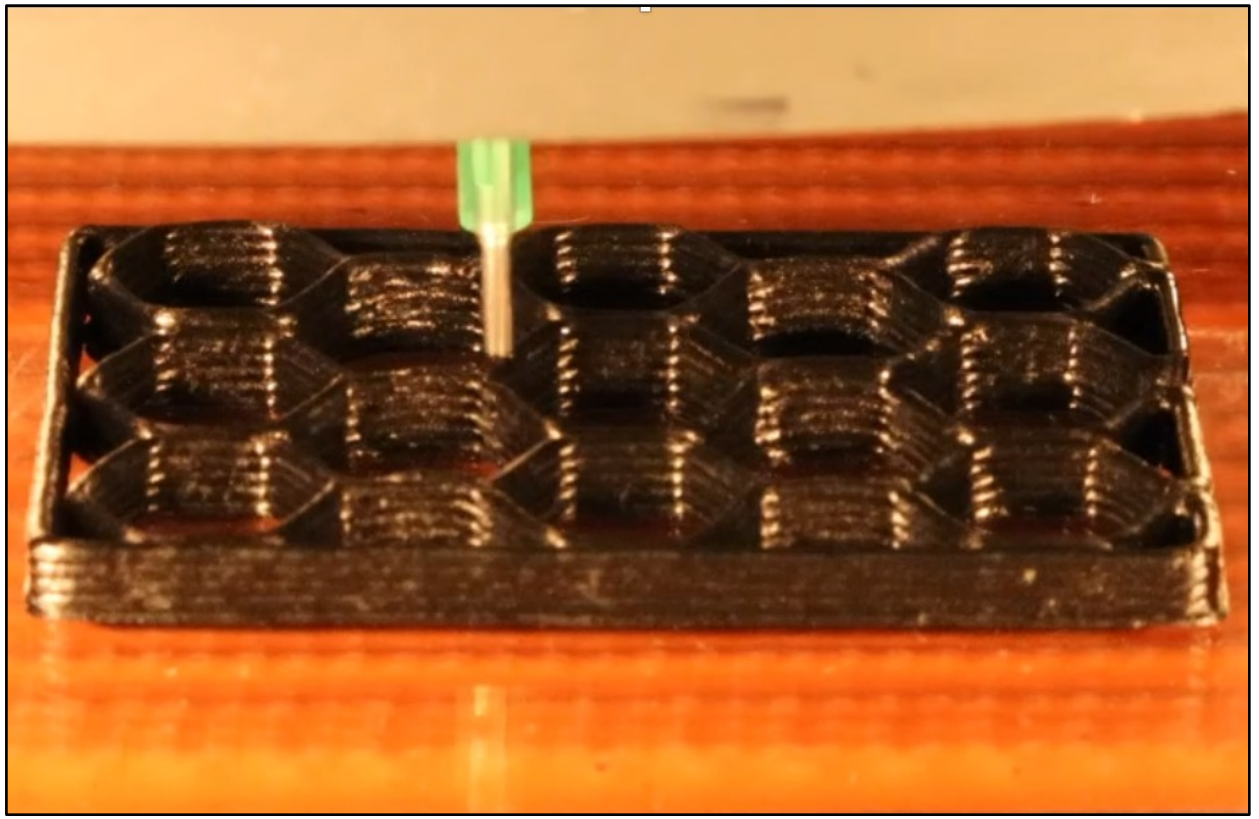

Ziaee et al., *ACS Applied Materials & Interfaces*, 2022

Activation of Frontal Reaction

Frontal polymerization is typically activated using thermal contact methods

- Long activation times (few seconds to minutes)
- Local variation in material properties or damage to material







Activate frontal polymerization remotely

Photothermal Activation

- Photothermal activation offers
  - Remote initiation
  - Precise control of energy input

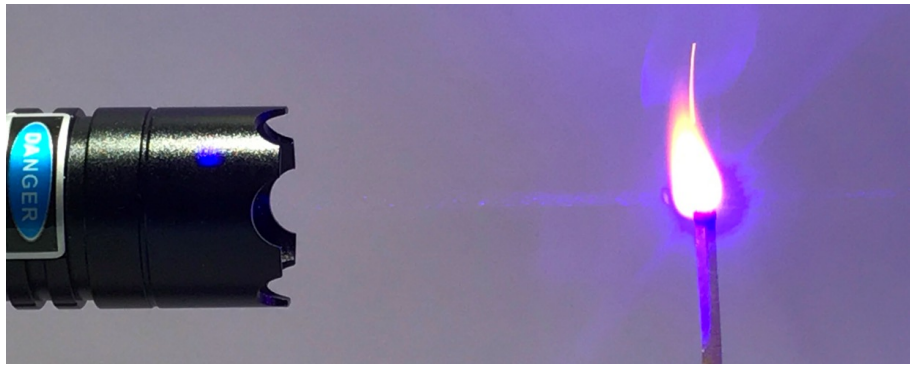

- Exploit high absorptivity of carbon fibers
  - Blue laser light source (wavelength = 450 nm)

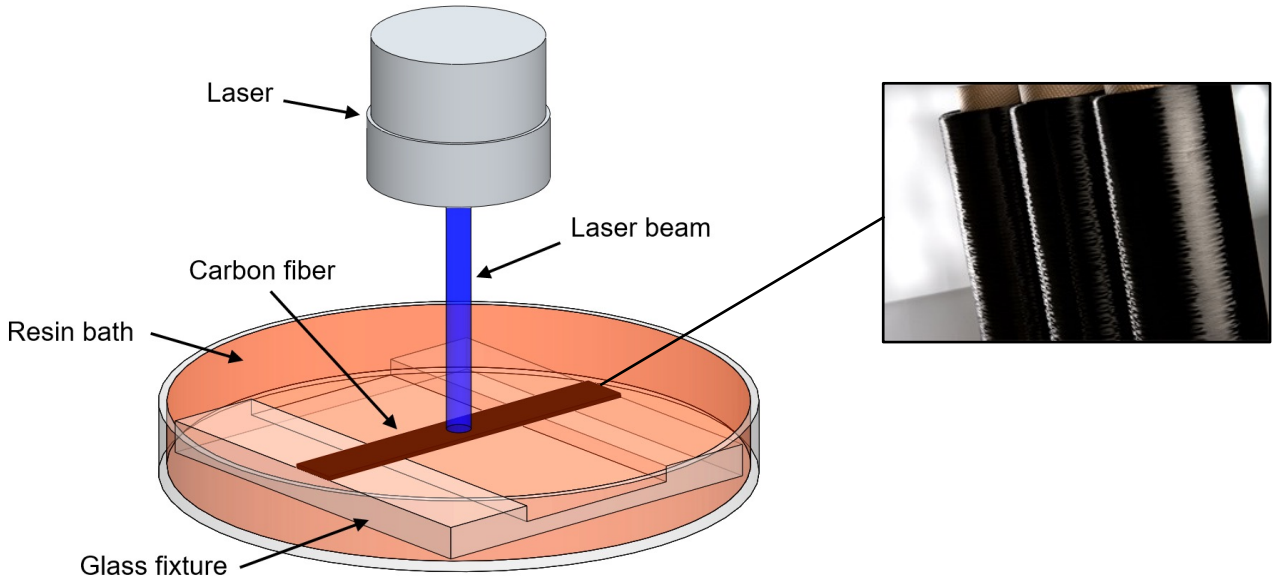

Rapid Initiation of Frontal Reaction

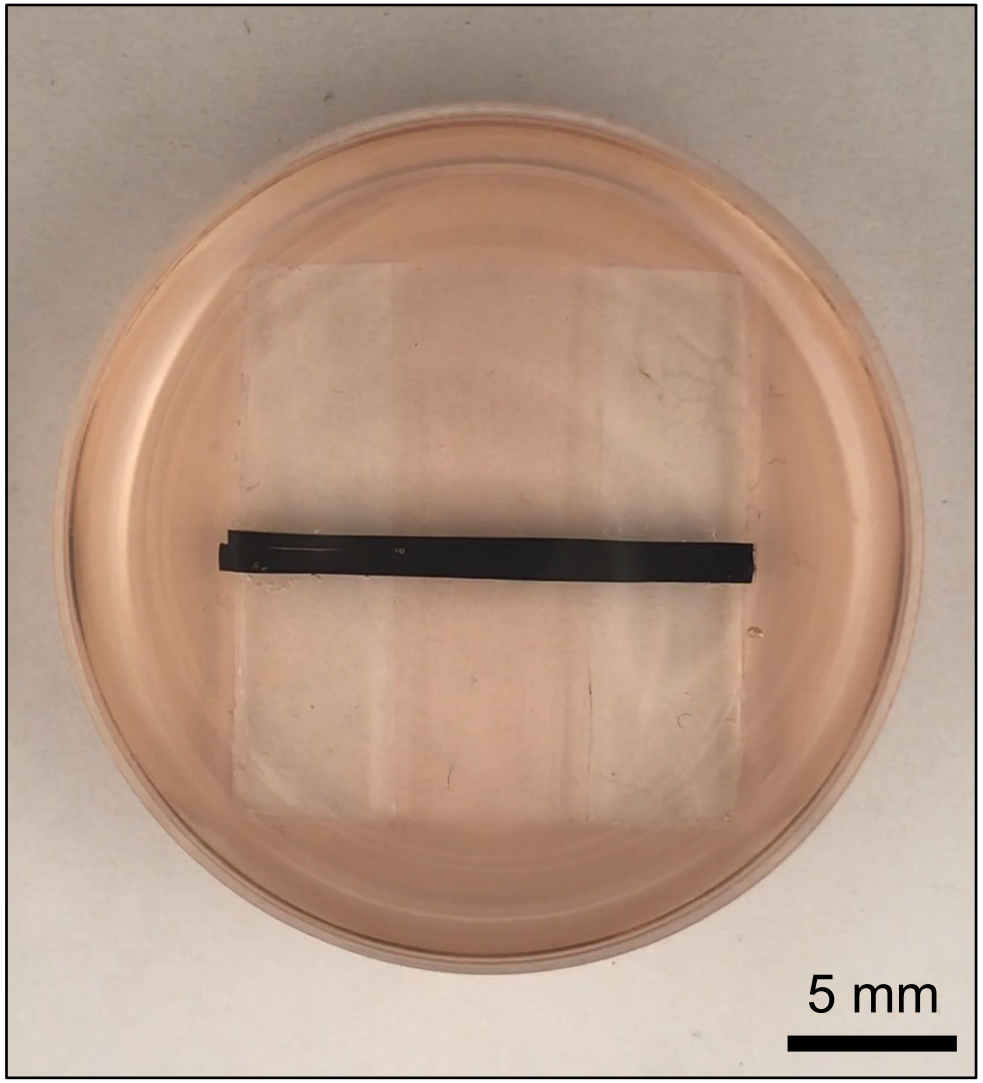

- Frontal activation within 200 ms

FP Initiation During Composite Printing

Rapid, remote initiation of frontal polymerization during direct ink writing (DIW) of carbon fiber composites

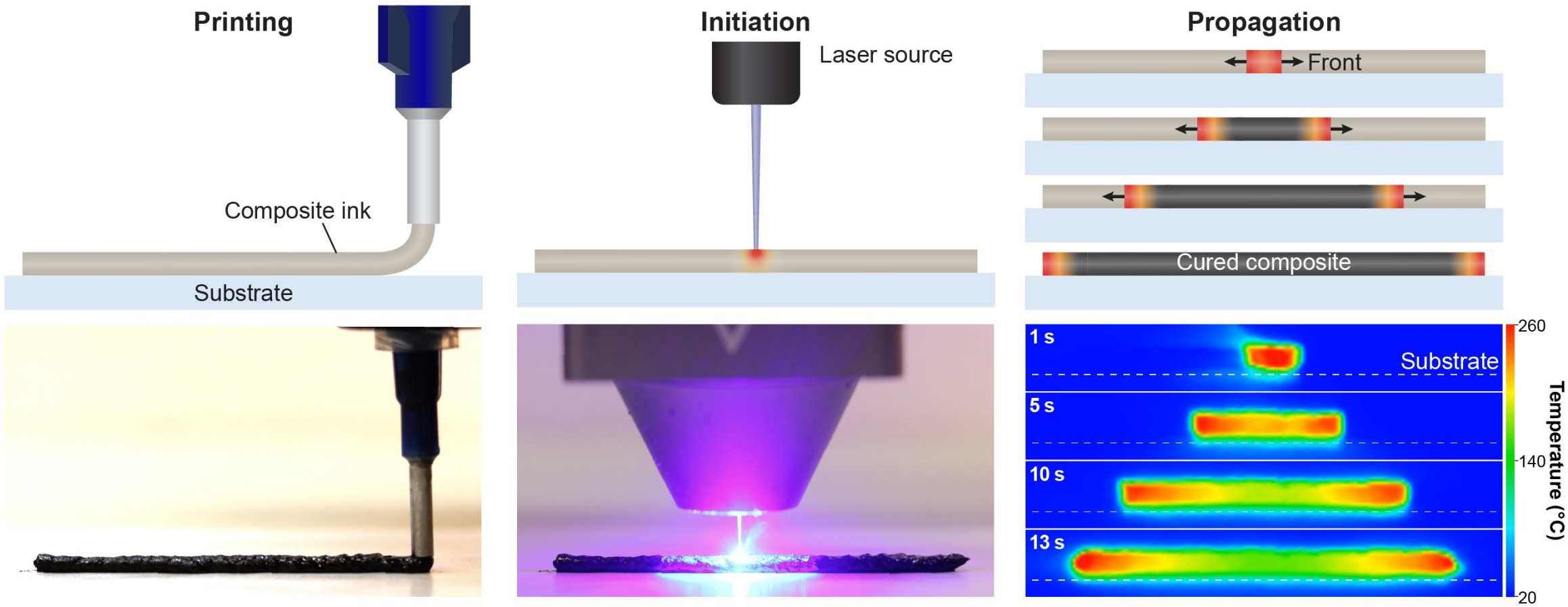

Effect of Material and Processing Parameters

Initiation time of FP can be tuned by varying the material and processing parameters

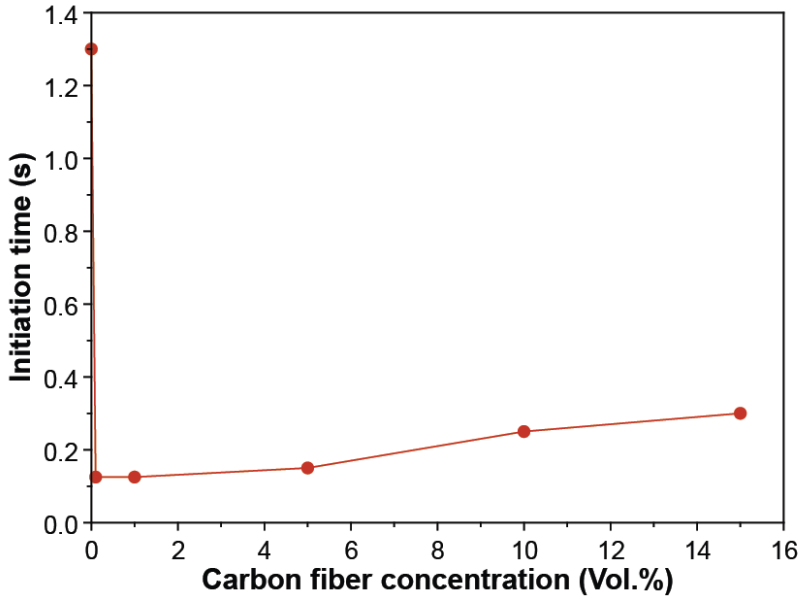

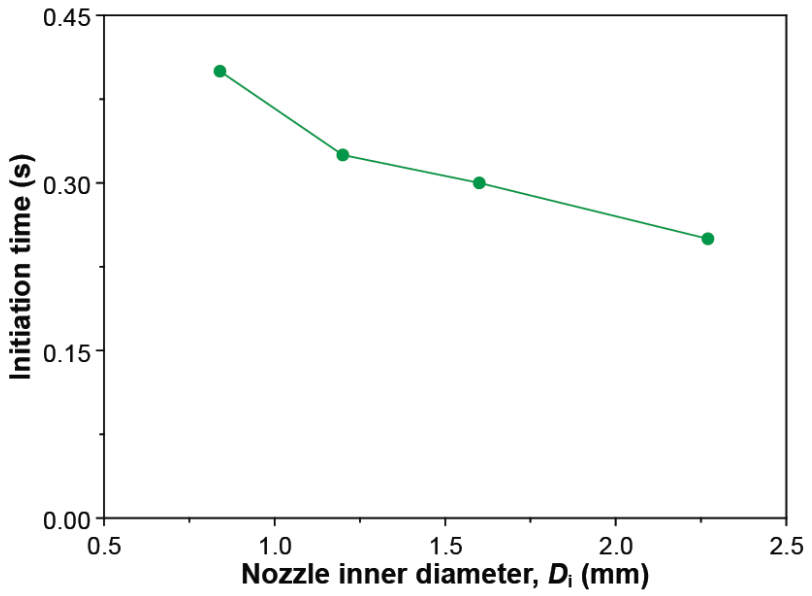

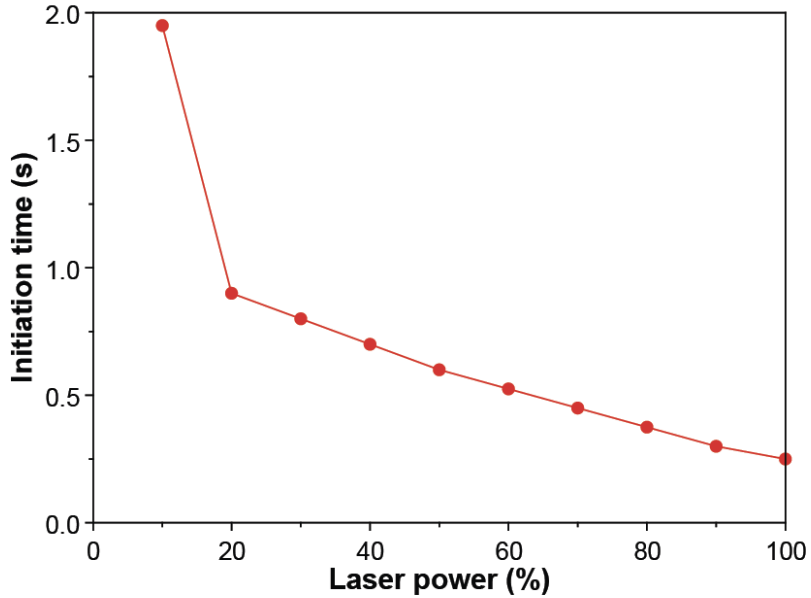

FP initiation in < 1s using various concentrations of milled carbon fibers

Multipoint Initiation

Overall cure time can be reduced by applying multiple laser pulses

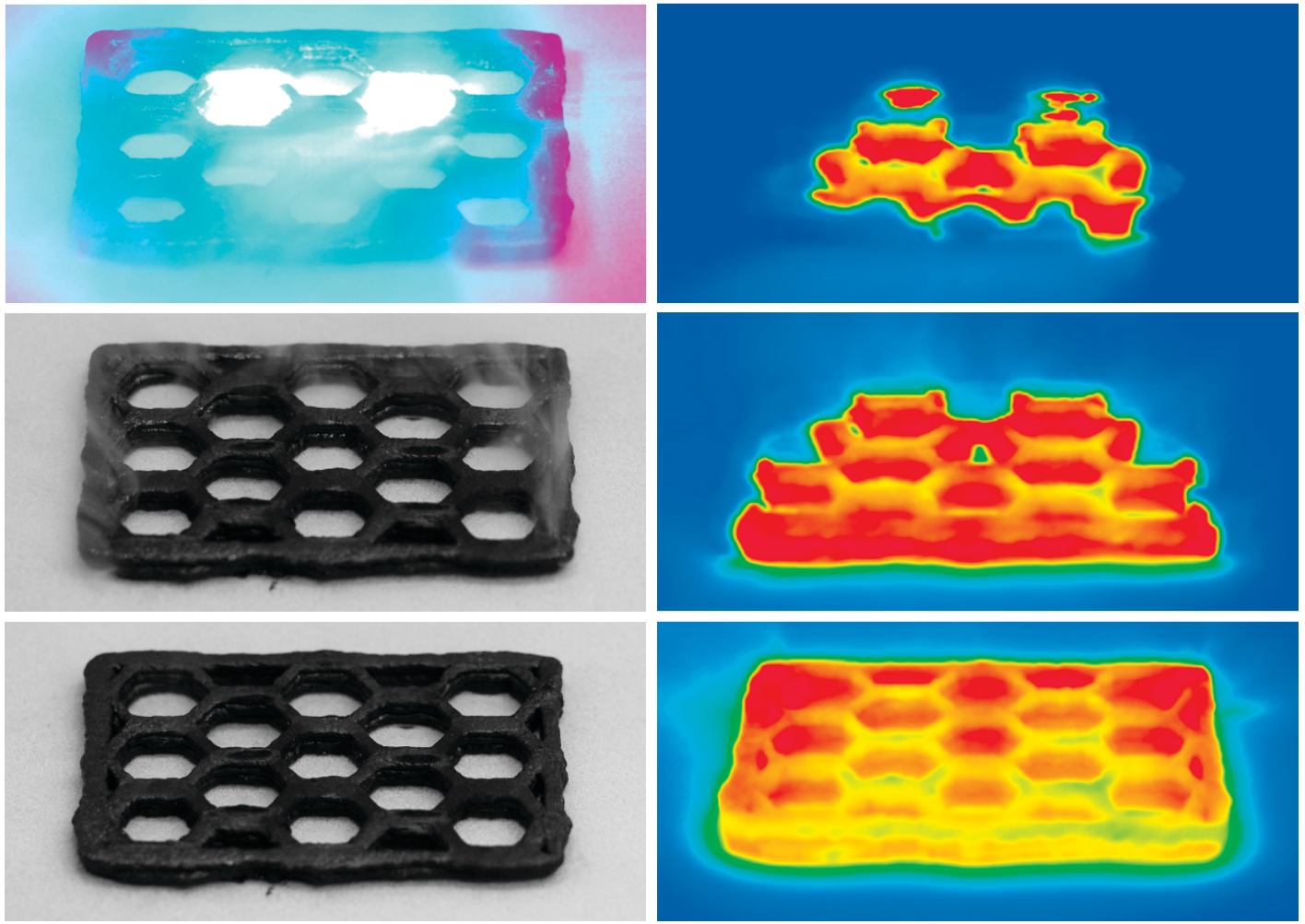

Conclusions

- Low-power laser enables rapid, remote initiation of FP during DIW of thermoset composites
- Reliable initiation achieved with as little as 0.1 vol% carbon fiber for photothermal conversion
- Automated laser integration allows multipoint initiation, significantly reducing layer cure times
- Compatible with diverse FP resin systems and fiber reinforcements
- Supports spatially controlled, on-demand curing for manufacturing freeform, unsupported, and complex multi-layer structures

ICCM24
AUGUST 4-8, 2025
BALTIMORE CONVENTION CENTER
BALTIMORE, MARYLAND, USA

No Technical Paper Submission for:

Christopher York

Double-Double Laminates: Homogenisation, Mechanical Performance and Compression After Impact

ICCM24
24TH INTERNATIONAL CONFERENCE ON COMPOSITE MATERIALS

Aidan Hawkins MEng | Ph.D. Researcher

Supervisors: Dr Ali Aravand, Dr Scott Millen, Prof Stephen W. Tsai

QUEEN'S UNIVERSITY BELFAST | SCHOOL OF MECHANICAL AND AEROSPACE ENGINEERING

SPIRIT AEROSYSTEMS

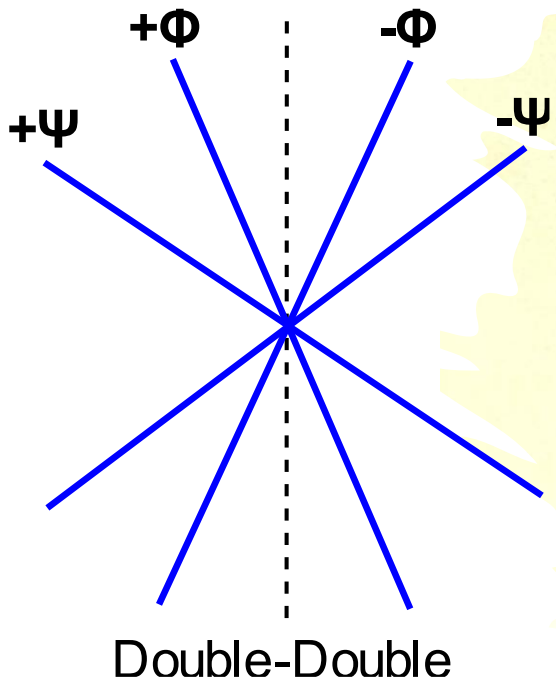



Prof. Stephen Tsai and Aidan Hawkins (Hawaii, 2023)

5th August 2024

Introduction

QUEEN'S UNIVERSITY BELFAST
SCHOOL OF MECHANICAL AND AEROSPACE ENGINEERING
SPIRIT AEROSYSTEMS

Traditional Quad Laminates

Collection of 0°, ±45° & 90° plies

Same principle since the 1960s

- Large number of stacking sequence permutations

(>1 Million for a 32 ply laminate)

- Layup constrained by 30+ legacy rules [3]

……

→ Stacking sequence optimisation is virtually impossible

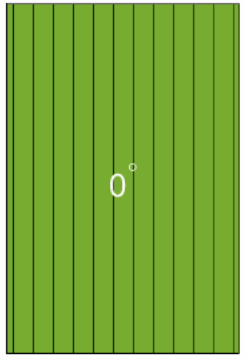

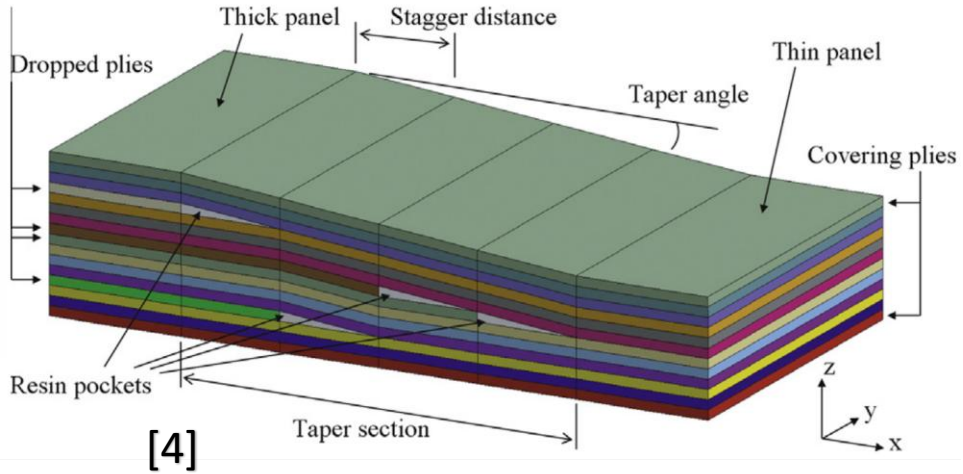

[4]

→ Internal discontinuities

→ Resin pockets

→ Ply wrinkles

→ More difficult to detect defects

[3] J. A. Bailie, R. P. Ley, and A. Pasricha. A Summary of Composite Laminate Guidelines. 1997.
[4] Irisarri, F.-X. *et al.* (2014) 'Optimal design of laminated composite structures with ply drops using stacking sequence tables'

Double-Double Laminates

QUEEN'S UNIVERSITY BELFAST

Proposed by Prof. Stephen Tsai in 2017 [5].

Removes the design limitations imposed by quad laminates

Simplify the design and manufacturing of composite laminates

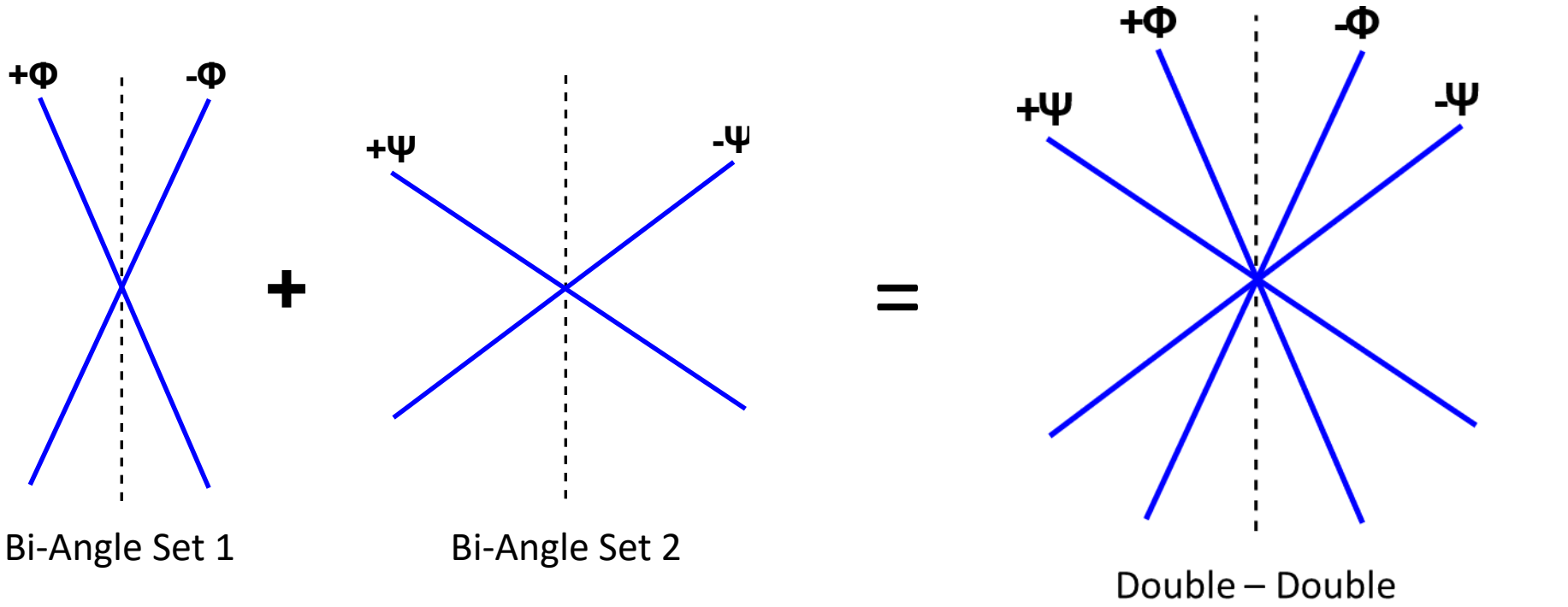

Bi-Angle Set 1

Bi-Angle Set 2

Double – Double

[5] Tsai, Stephen W., José Daniel D. Melo, Sangwook Sihn, Albertino Arteiro, and Robert Rainsberger. Composite Laminates: Theory and Practice of Analysis, Design and Automated Layup. Stanford Aeronautics & Astronautics, 2017

Double-Double Laminates

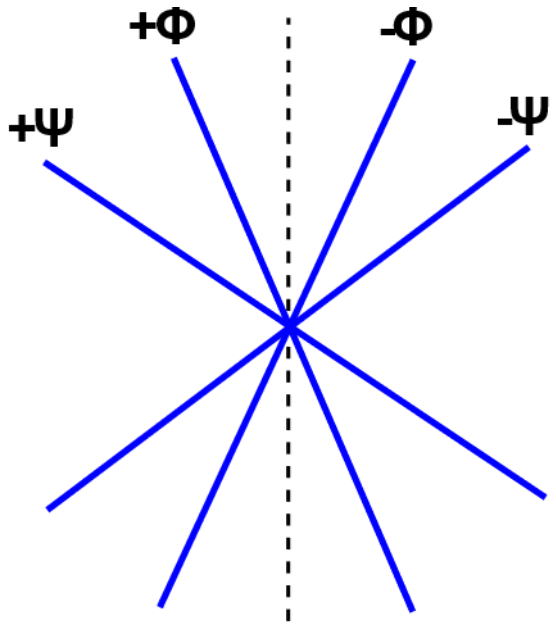

Double – Double

Sub-laminate

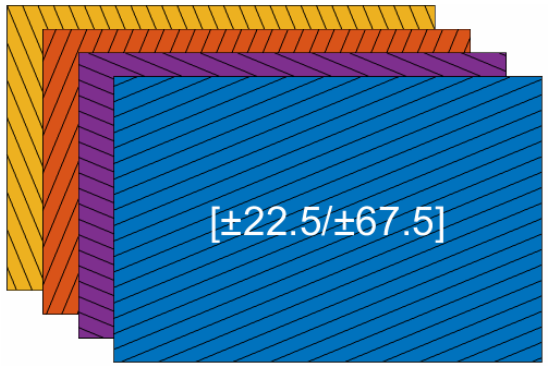

Homogenised laminate

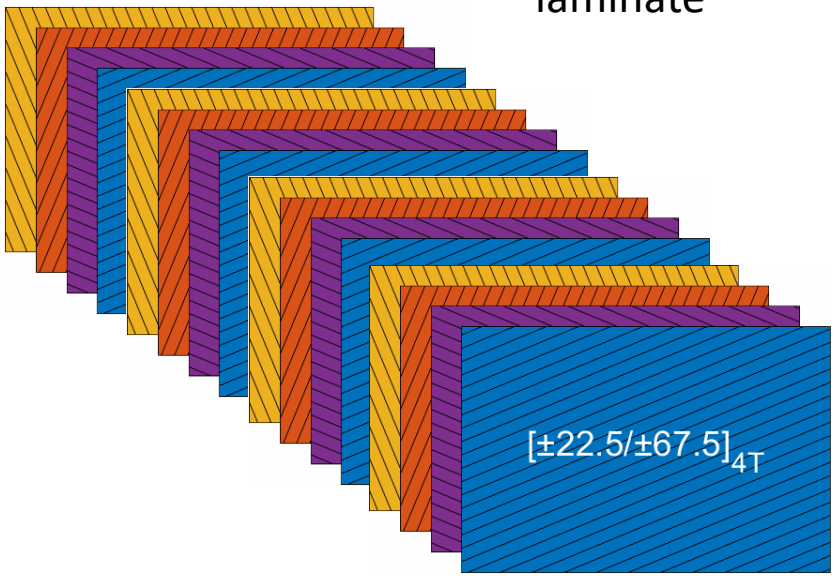

Homogenisation of Double-Double Laminates

QUEEN'S UNIVERSITY BELFAST
SCHOOL OF MECHANICAL AND AEROSPACE ENGINEERING
SPIRIT AEROSYSTEMS

Homogenisation of DD Laminates

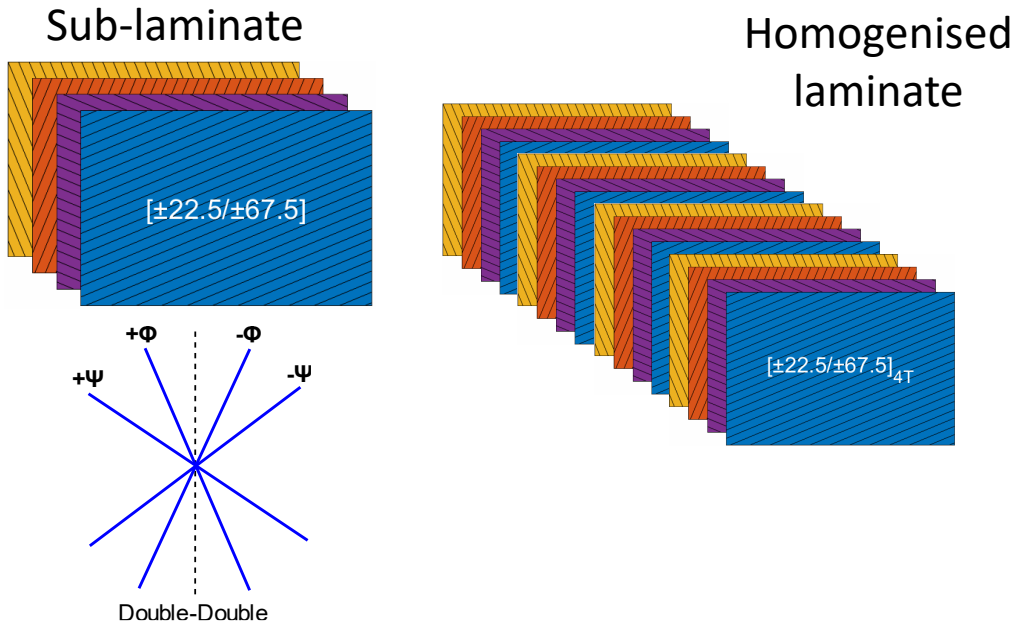

How many sub-laminate repeats are needed to meet the homogenisation criteria [8]?

$$|D^{Tr*} - A^{Tr*}| < 0.02 \quad \& \quad B^{Tr*} < 0.02$$

Thickness normalised terms based on Master Ply values

What sequence of angles within the sub-laminate minimises the required repeats?

[±Φ/±Ψ], [+Φ/-Ψ/-Φ/+Ψ], [+Φ/-Ψ /+Ψ /-Φ]……

[8] Vermes, B. *et al.* (2021) 'Application of the Tsai's modulus and double-double concepts to the definition of a new affordable design approach for composite laminates', *Composite Structures*, 259, p. 113246.

Homogenisation of DD Laminates

Sub-laminate

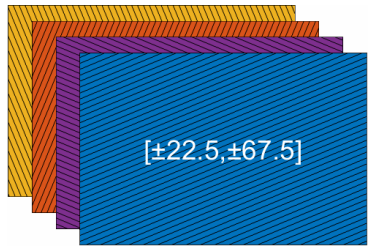

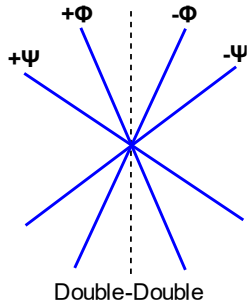

Homogenised laminate

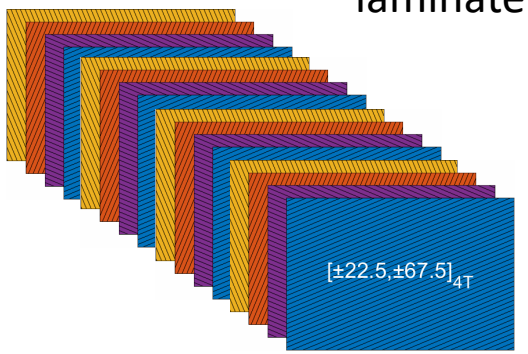

Sub-laminate repeats to satisfy original homogenisation criteria [8]

$$|D^{Tr*} - A^{Tr*}| < 0.02 \quad \& \quad B^{Tr*} < 0.02$$

Sequence of angles minimising the required repeats?

[±Φ/±Ψ], [+Φ/-Ψ/-Φ/+Ψ], [+Φ/-Ψ /+Ψ /-Φ]……

Aim is to prevent laminate warpage

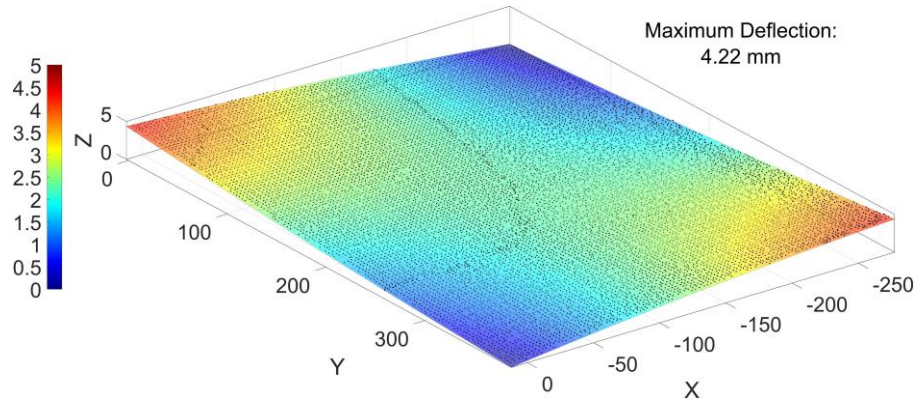

[8] Vermes, B. *et al.* (2021) 'Application of the Tsai's modulus and double-double concepts to the definition of a new affordable design approach for composite laminates', *Composite Structures*, 259, p. 113246.

Homogenisation of DD Laminates

DD Homogenisation Grid

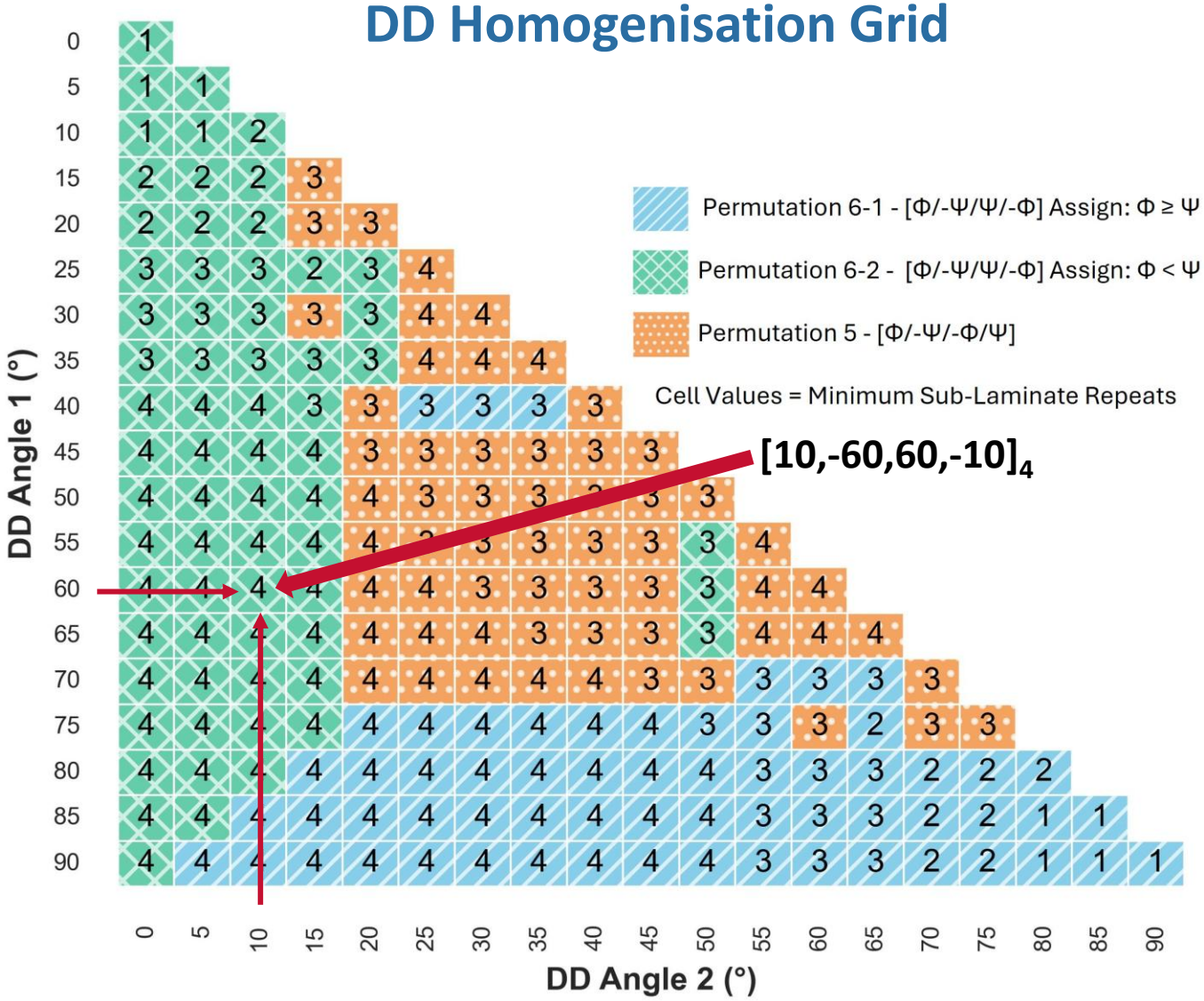

Sub-laminate repeats to satisfy original homogenisation criteria [8]

$$|D^{Tr*} - A^{Tr*}| < 0.02 \quad \& \quad B^{Tr*} < 0.02$$

Sequence of angles minimising the required repeats?

[±Φ/±Ψ], [+Φ/-Ψ/-Φ/+Ψ], [+Φ/-Ψ /+Ψ /-Φ]……

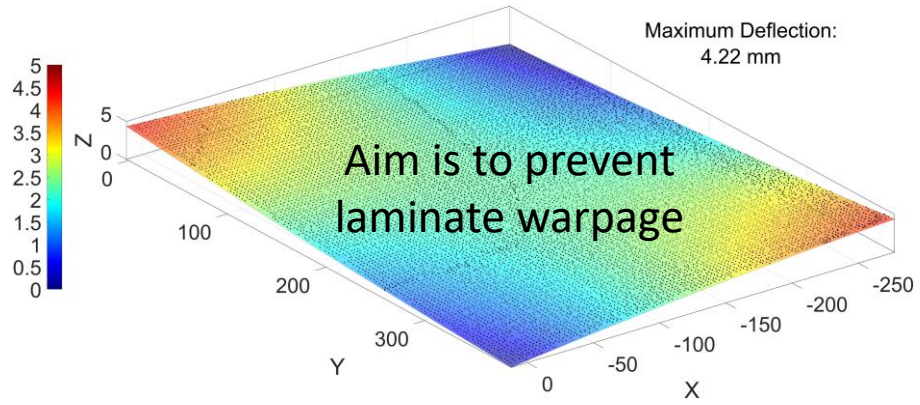

[8] Vermes, B. *et al.* (2021) 'Application of the Tsai's modulus and double-double concepts to the definition of a new affordable design approach for composite laminates', *Composite Structures*, 259, p. 113246.

Experimental Homogenisation Results

QUEEN'S UNIVERSITY BELFAST

Original homogenisation criteria [8]

$$|D^{Tr*} - A^{Tr*}| < 0.02 \quad \& \quad B^{Tr*} < 0.02$$

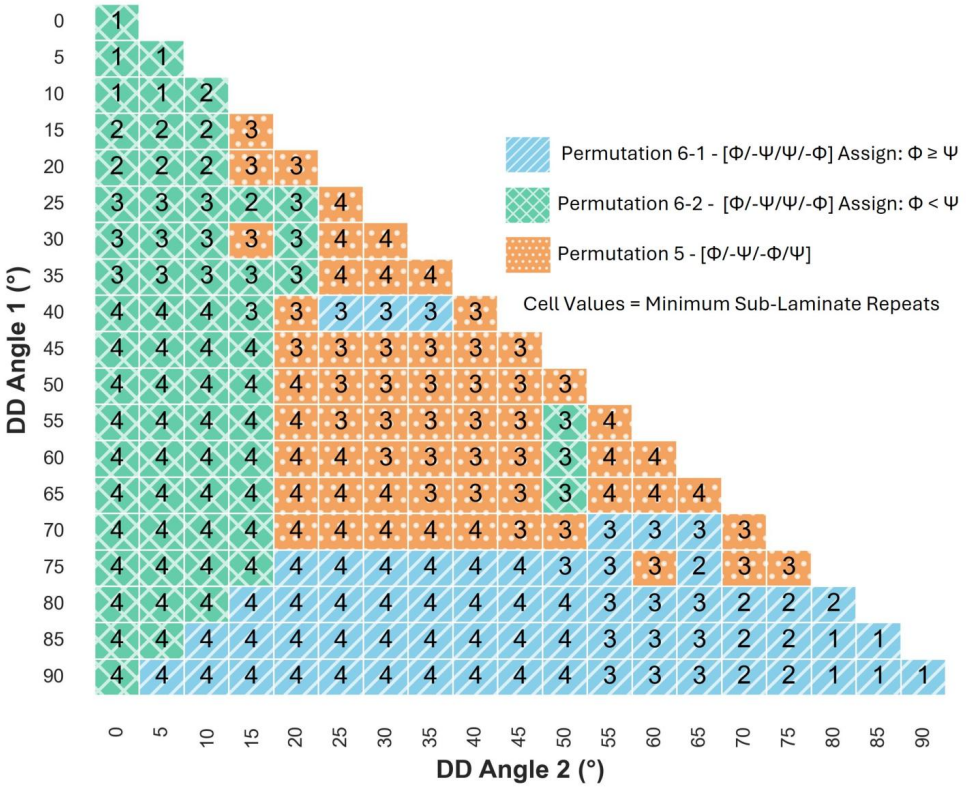

Manufactured Panels IM7 977-2 Prepreg



$[22.5/-67.5/-22.5/67.5]_4$



$[22.5/-67.5/67.5/-22.5]_4$



$[9, -47, -9, 47]_5$

[8] Vermes, B. *et al.* (2021) 'Application of the Tsai's modulus and double-double concepts to the definition of a new affordable design approach for composite laminates', *Composite Structures*, 259, p. 113246.

Experimental Homogenisation Results

QUEEN'S UNIVERSITY BELFAST

Original homogenisation criteria [8]

$$|D^{Tr*} - A^{Tr*}| < 0.02 \quad \& \quad B^{Tr*} < 0.02$$

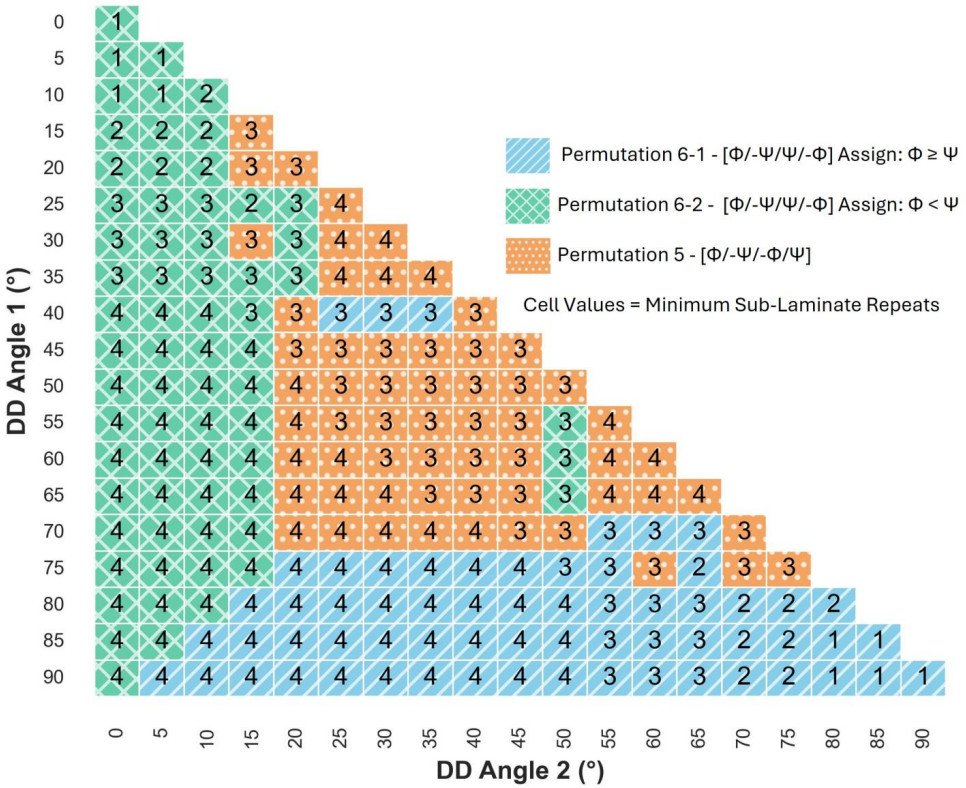

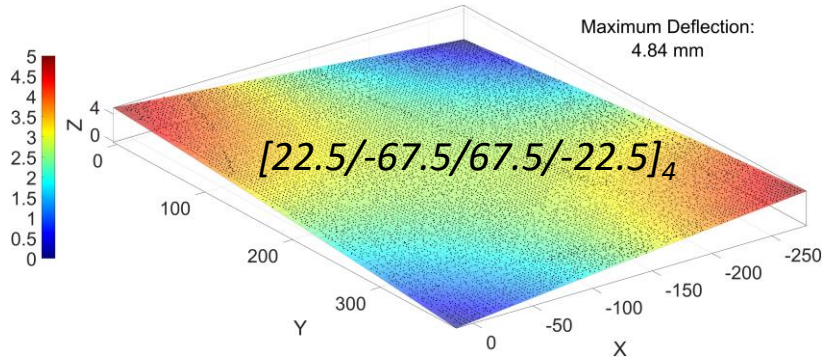

Point cloud data from surface scanning

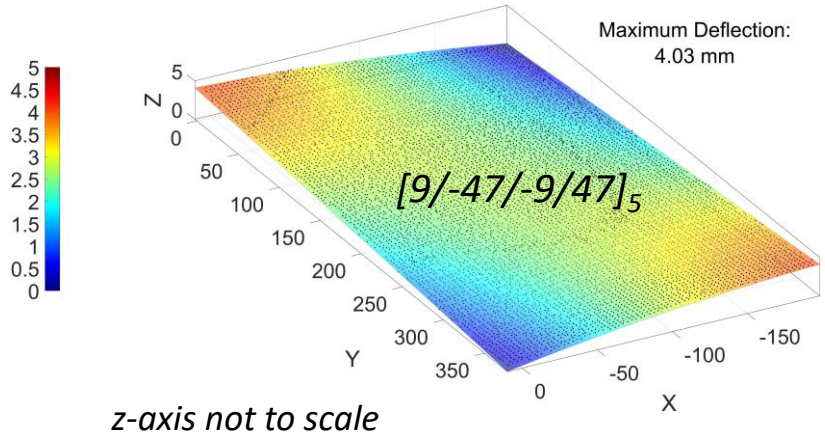

z-axis not to scale

Panels exhibited warpage

Conclusion:

The "arbitrary" 2% homogenisation criteria [8] is not sufficient to prevent warpage

[8] Vermes, B. *et al.* (2021) 'Application of the Tsai's modulus and double-double concepts to the definition of a new affordable design approach for composite laminates', *Composite Structures*, 259, p. 113246.

Updated Homogenisation Criteria

Proposing updated homogenisation criteria:

$$|D^{Tr*} - A^{Tr*}| < 0.02 \quad \& \quad B^{Tr*} < 0.01$$

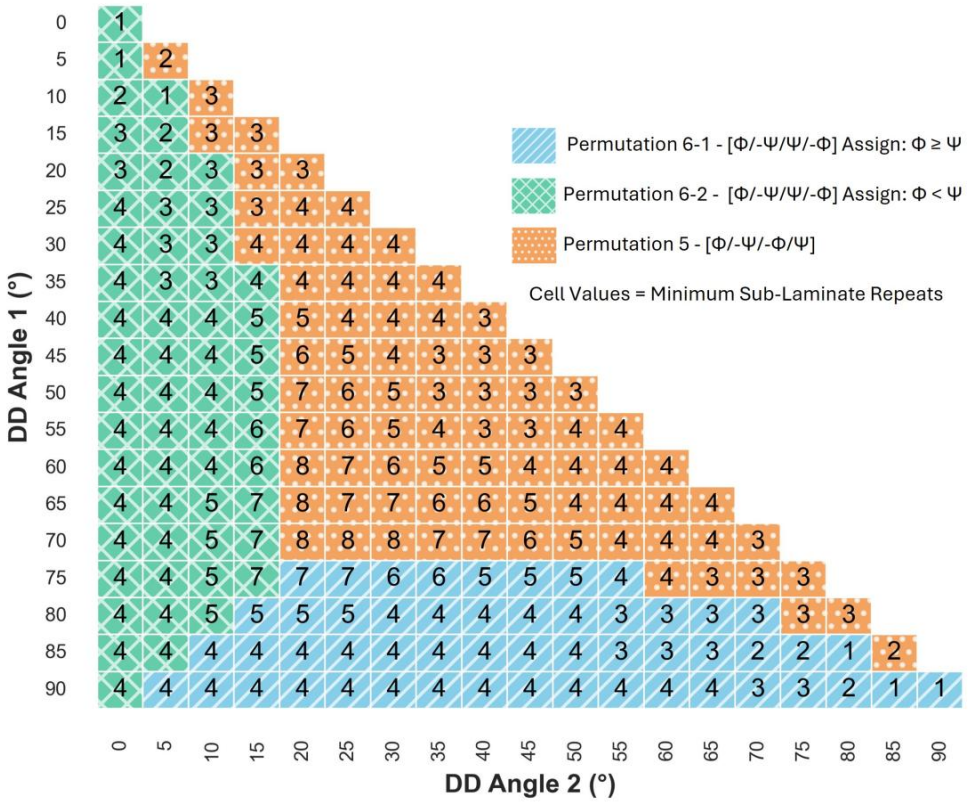

Updated Homogenisation Criteria

QUEEN'S UNIVERSITY BELFAST

Proposing updated homogenisation criteria:

$$|D^{Tr*} - A^{Tr*}| < 0.02 \quad \& \quad B^{Tr*} < 0.01$$

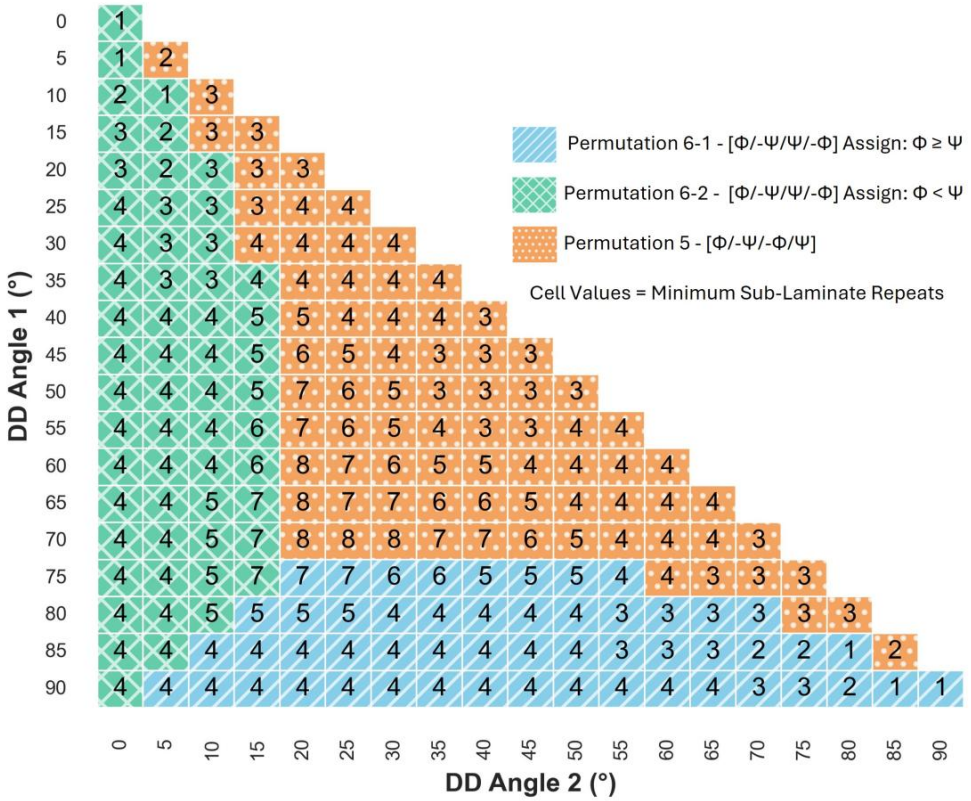

Laminates manufactured meeting these criteria, have shown very minimal to negligible warpage

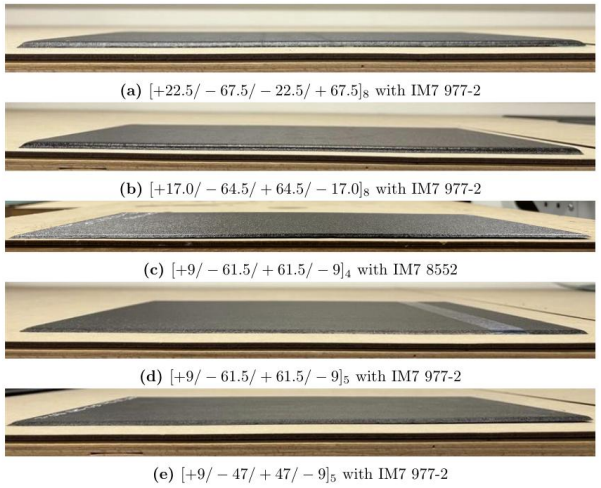

(a) $[+22.5/-67.5/-22.5/+67.5]_8$ with IM7 977-2

(b) $[+17.0/-64.5/+64.5/-17.0]_8$ with IM7 977-2

(c) $[+9/-61.5/+61.5/-9]_4$ with IM7 8552

(d) $[+9/-61.5/+61.5/-9]_5$ with IM7 977-2

(e) $[+9/-47/+47/-9]_5$ with IM7 977-2

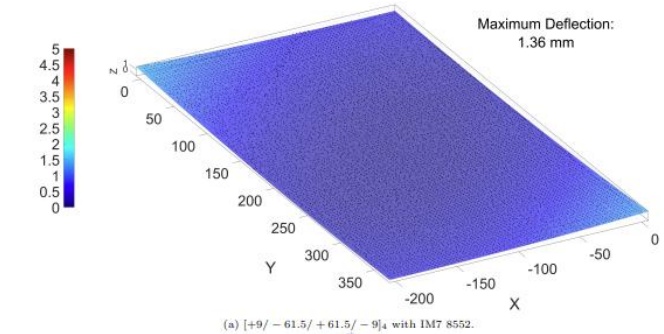

(a) $[+9/-61.5/+61.5/-9]_4$ with IM7 8552.

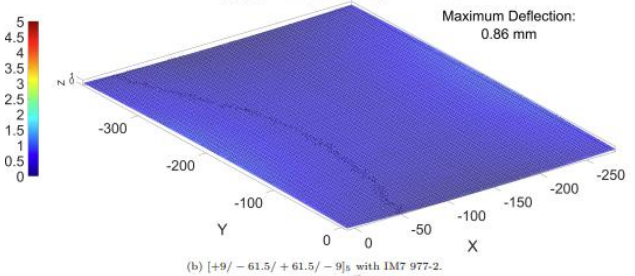

(b) $[+9/-61.5/+61.5/-9]_5$ with IM7 977-2.

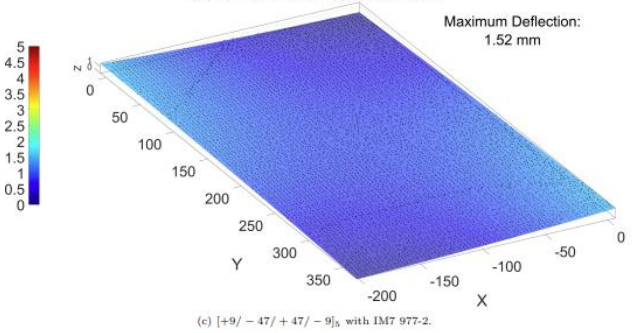

(c) $[+9/-47/+47/-9]_5$ with IM7 977-2.

Updated Homogenisation Criteria

Proposing updated homogenisation criteria:

$$|D^{Tr*} - A^{Tr*}| < 0.02 \quad \& \quad B^{Tr*} < 0.01$$

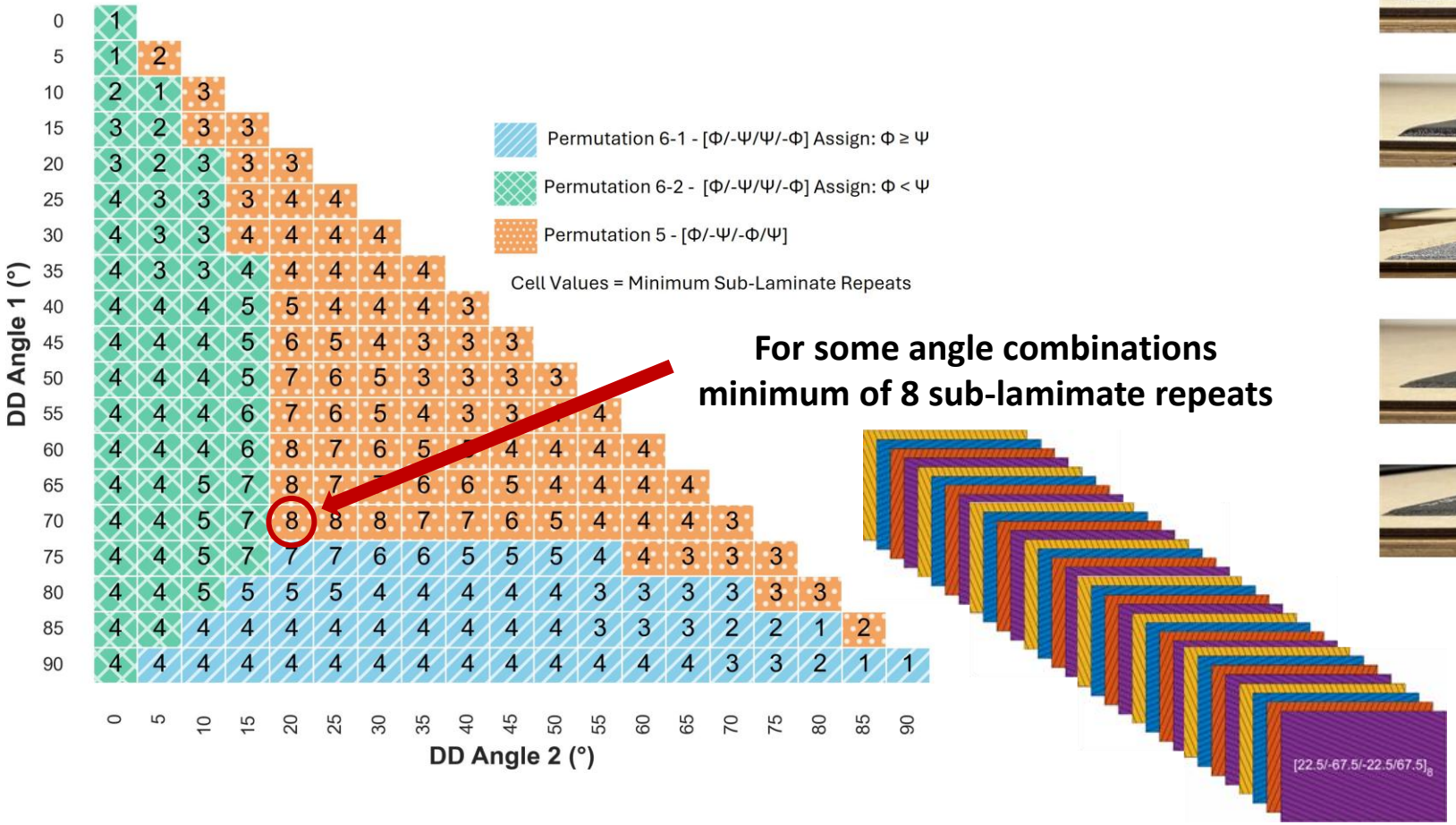

For some angle combinations minimum of 8 sub-lamimate repeats

Minimal to zero warpage

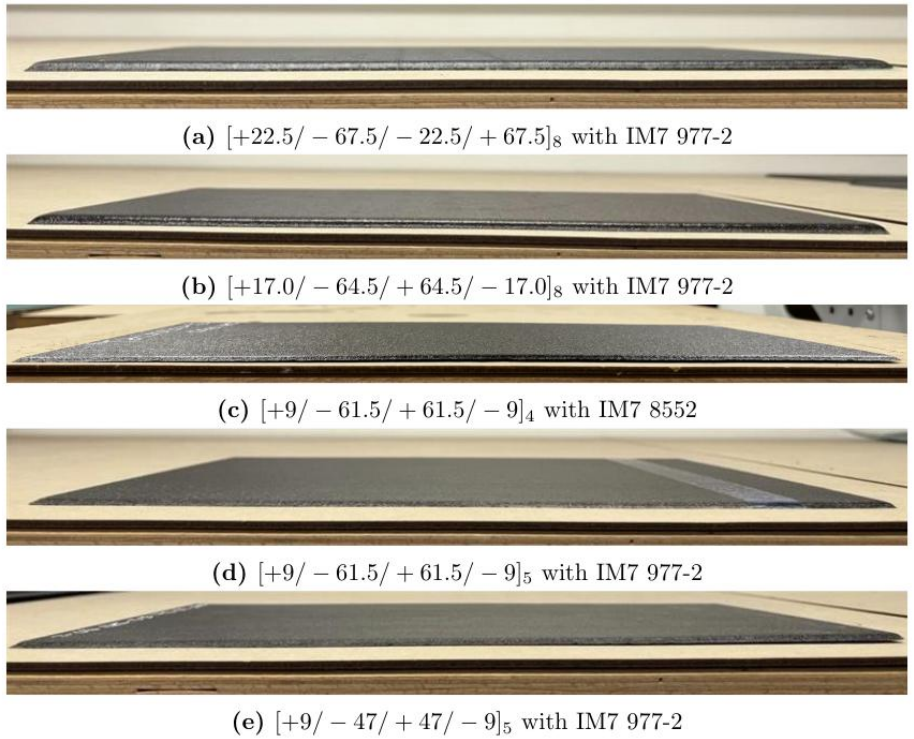

(a) $[+22.5/-67.5/-22.5/+67.5]_8$ with IM7 977-2

(b) $[+17.0/-64.5/+64.5/-17.0]_8$ with IM7 977-2

(c) $[+9/-61.5/+61.5/-9]_4$ with IM7 8552

(d) $[+9/-61.5/+61.5/-9]_5$ with IM7 977-2

(e) $[+9/-47/+47/-9]_5$ with IM7 977-2

Updated Homogenisation Criteria

Proposing updated homogenisation criteria:

$$|D^{Tr*} - A^{Tr*}| < 0.02 \quad \& \quad B^{Tr*} < 0.01$$

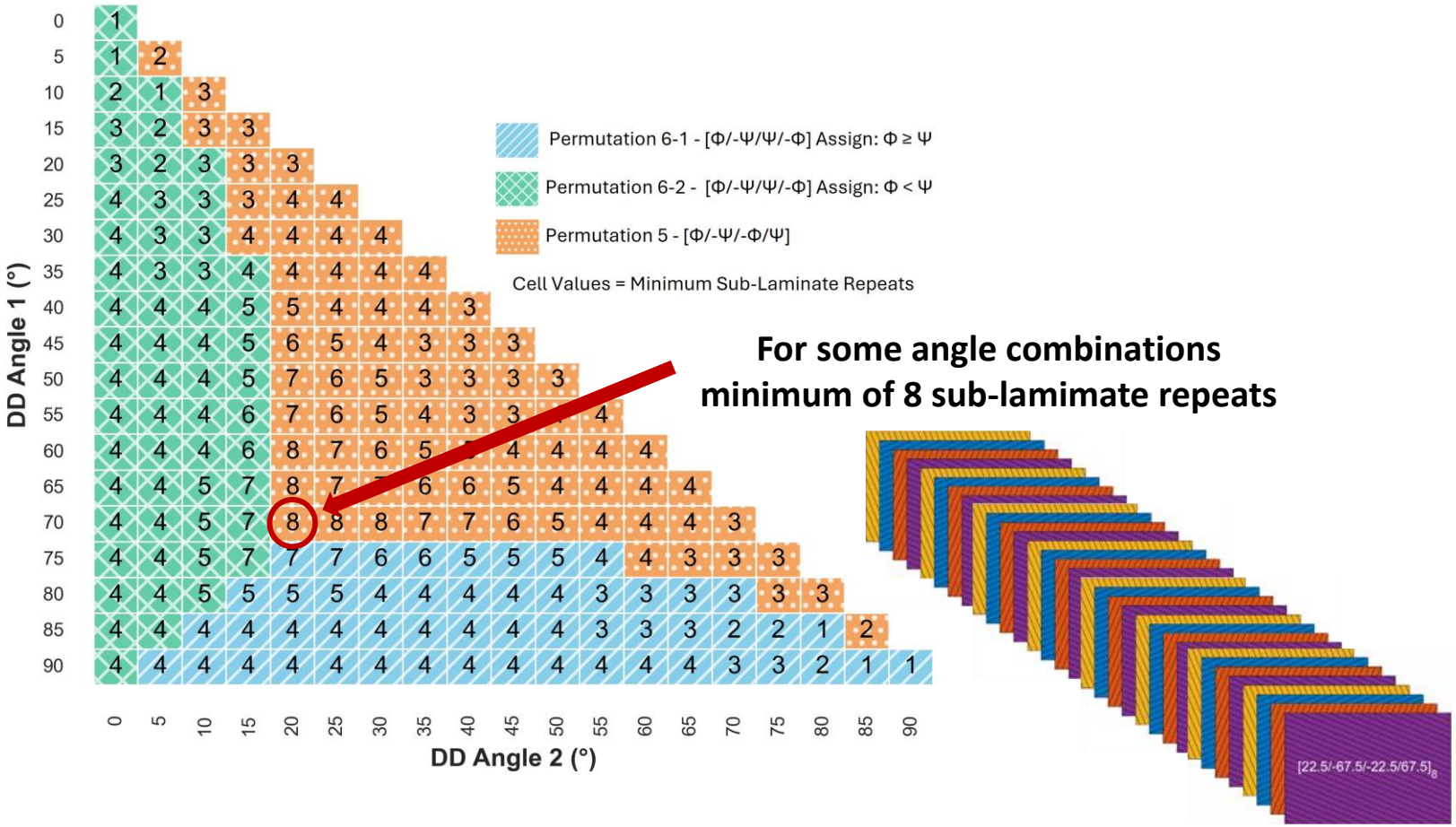

For some angle combinations minimum of 8 sub-lamimate repeats

One Step Further

?

Symmetry-Enhanced Double-Double (SEDD) Laminates

Symmetry-Enhanced Double-Double (SEDD) Laminates

SEDD-1

$[(BB)_s/(BB)_r]_T$

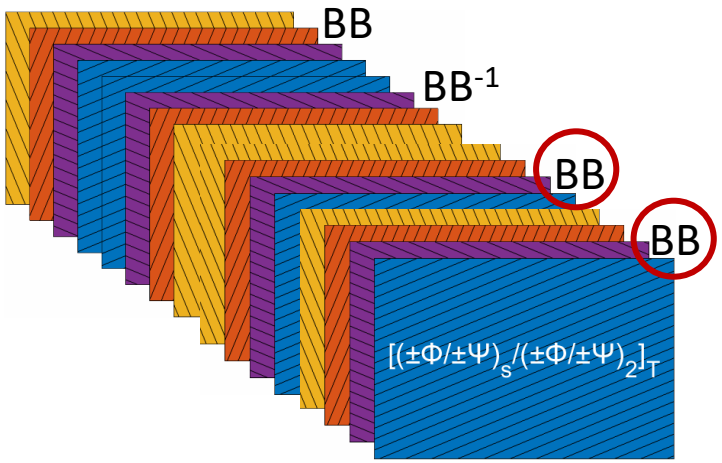

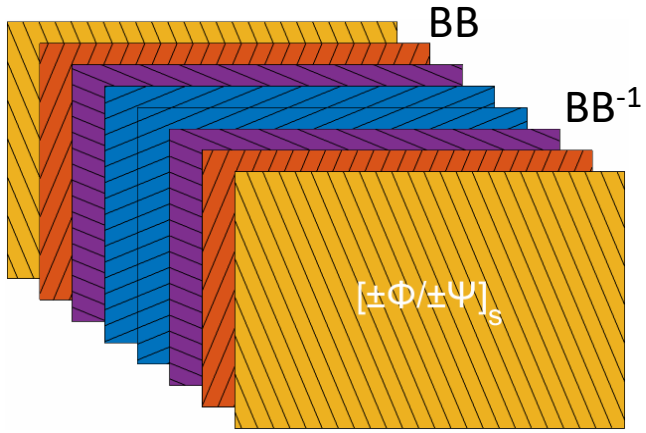

Symmetric DD sub-laminate as foundation

Advantage?

Homogenisation criteria satisfied with a lower number of sub-laminate repeats

SEDD-2

$[(BB)_{s.r}/(BB)_n]_T$

Where r ≥ 1 and n = 0 or 1

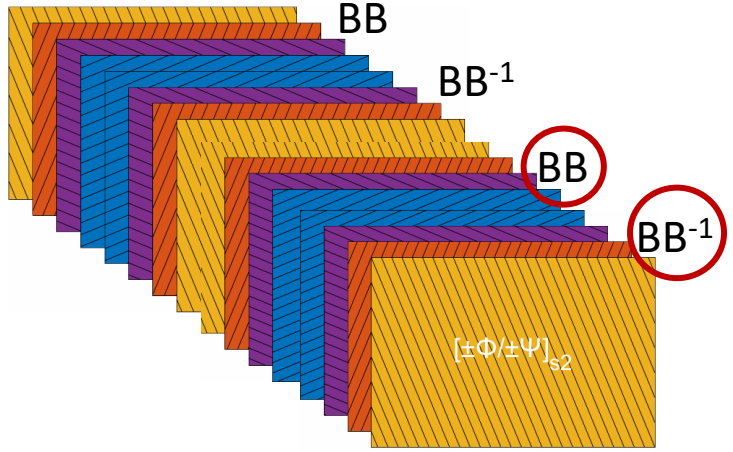

BB = Building Block (sub-laminate)

Symmetry-Enhanced Double-Double (SEDD) Laminates

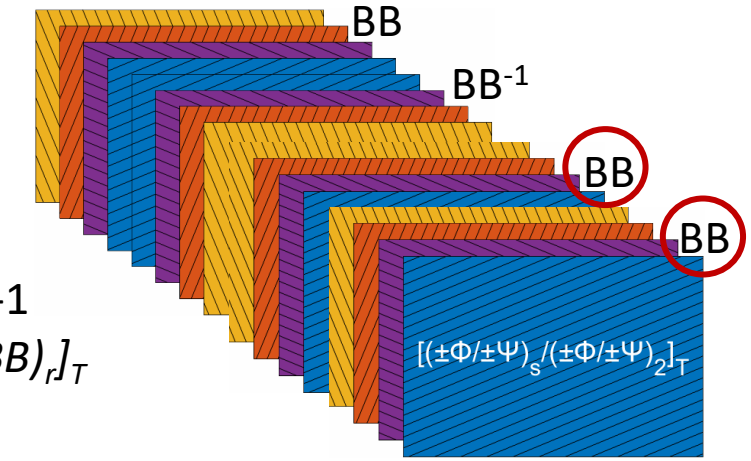

SEDD-1

$[(BB)_s/(BB)_r]_T$

Symmetric DD sub-laminate as foundation

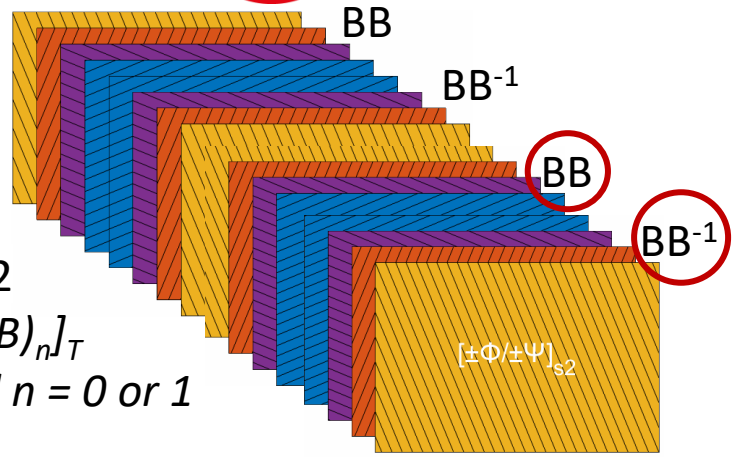

SEDD-2

$[(BB)_{s.r}/(BB)_n]_T$

Where r ≥ 1 and n = 0 or 1

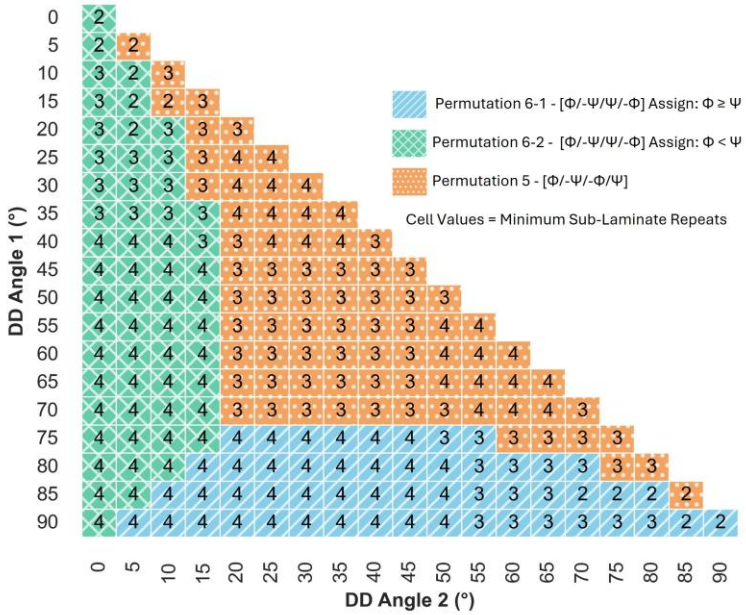

Advantage?

Homogenisation criteria satisfied with a lower number of sub-laminate repeats

Updated homogenisation criteria:

$$|D^{Tr*} - A^{Tr*}| < 0.02 \quad \& \quad B^{Tr*} < 0.01$$

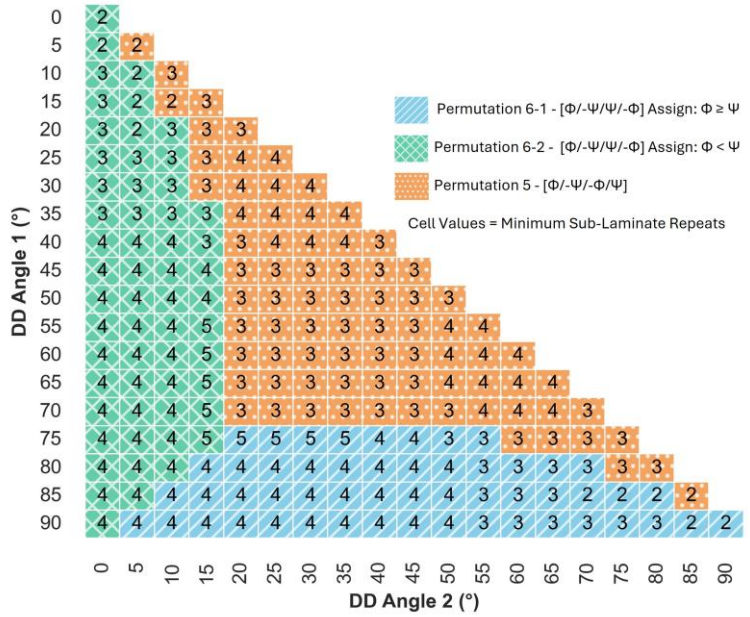

BB = Building Block (sub-laminate)

Symmetry-Enhanced Double-Double (SEDD) Laminates

Maximum B^{Tr*} Term for $[22.5/-67.5/-22.5/67.5]_r$

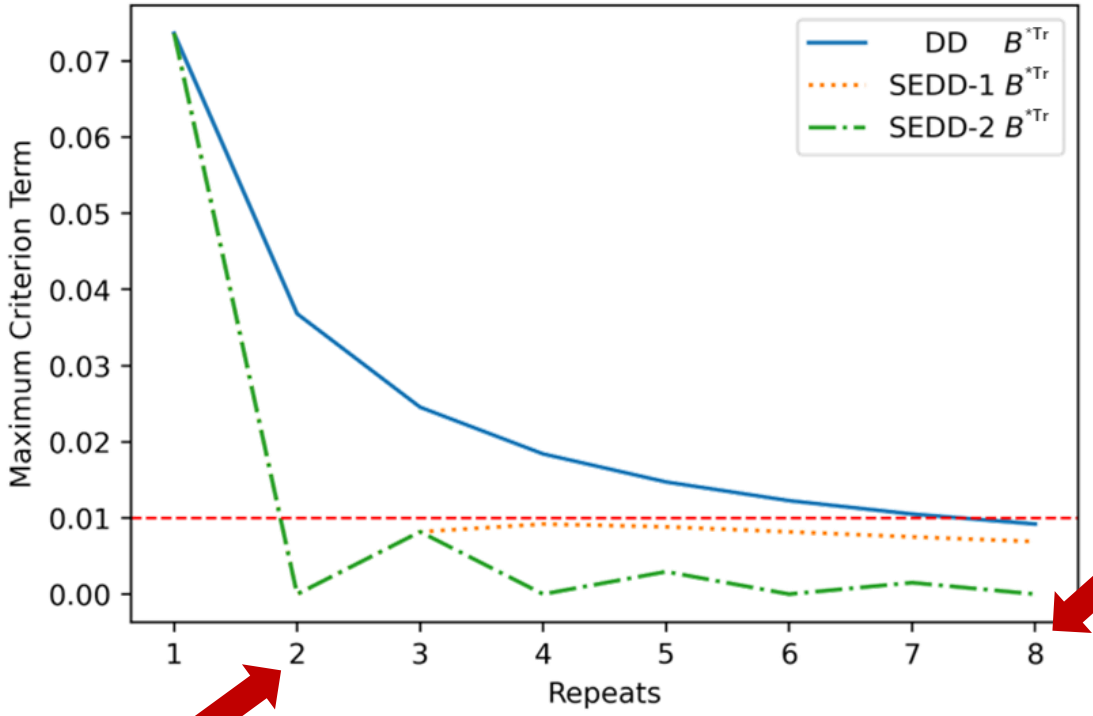

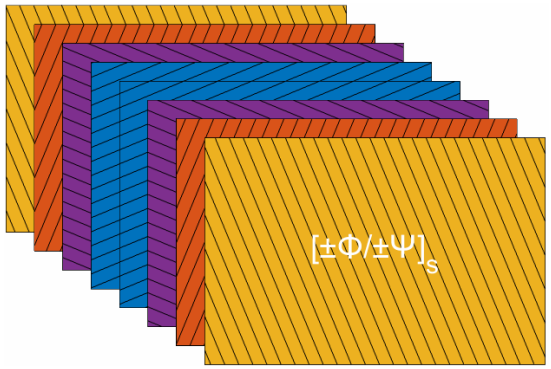

Symmetry-Enhanced Double-Double (SEDD) Laminates

Original DD Stacking Sequence: **$[BB]_{rT}$**

For some angle combinations minimum 8 BB's

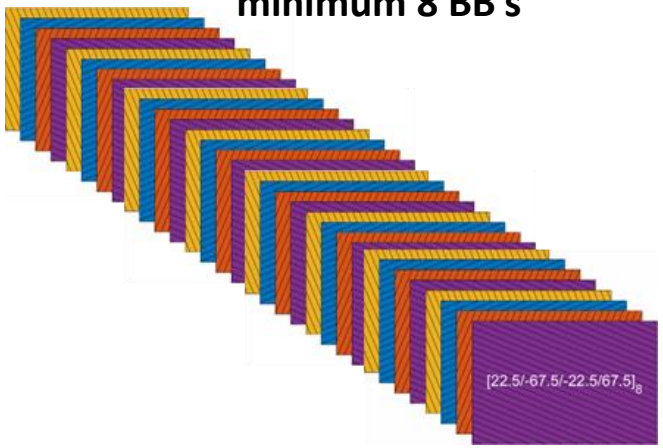

B^{Tr*} < 0.01 criterion met with ≥ 2 BB's

for any angle combination

Symmetry-Enhanced Double-Double (SEDD) Laminates

Maintain the ability to taper with ply drops on the external faces



Can taper to a much thinner laminate

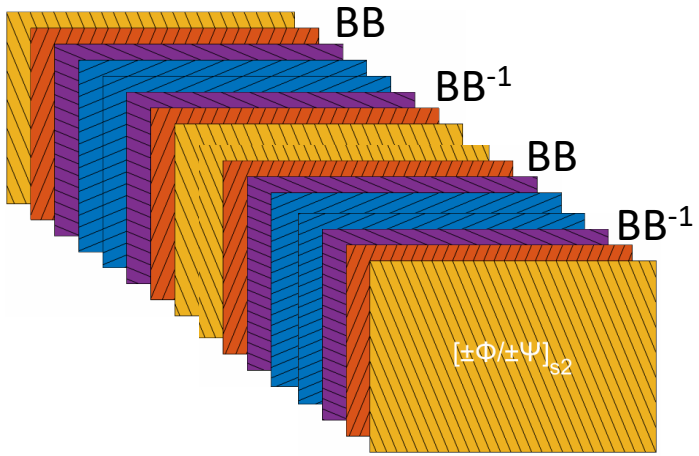

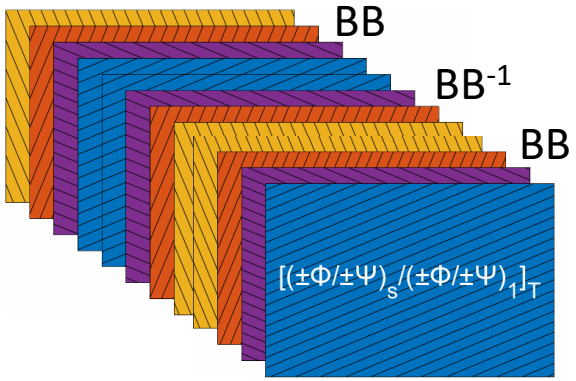

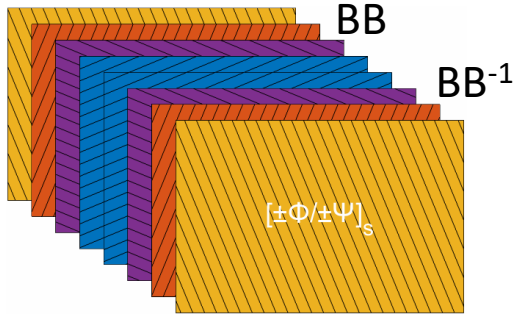

Mechanical Performance of Double-Double Laminates

QUEEN'S UNIVERSITY BELFAST
SCHOOL OF MECHANICAL AND AEROSPACE ENGINEERING
SPIRIT AEROSYSTEMS

Lamination Parameters

Lamination parameters describe the stiffness properties of a laminate independent of the ply material

Lamination Parameters

$$\begin{bmatrix} A_{11}^* \\ A_{22}^* \\ A_{12}^* \\ A_{66}^* \\ A_{16}^* \\ A_{26}^* \end{bmatrix} = \begin{bmatrix} 1 & V_1 & V_2 & 0 & 0 \\ 1 & -V_1 & V_2 & 0 & 0 \\ 0 & 0 & -V_2 & 1 & 0 \\ 0 & 0 & -V_2 & 0 & 1 \\ 0 & V_3/2 & V_4 & 0 & 0 \\ 0 & V_3/2 & -V_4 & 0 & 0 \end{bmatrix} \begin{bmatrix} U_1 \\ U_2 \\ U_3 \\ U_4 \\ U_5 \end{bmatrix}$$

Material Invariants

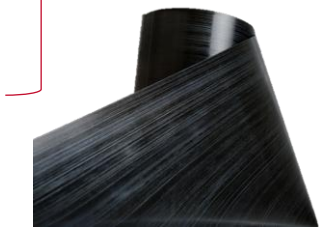

Thickness normalised in-plane matrix terms

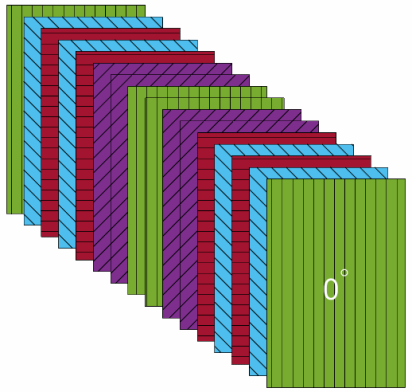

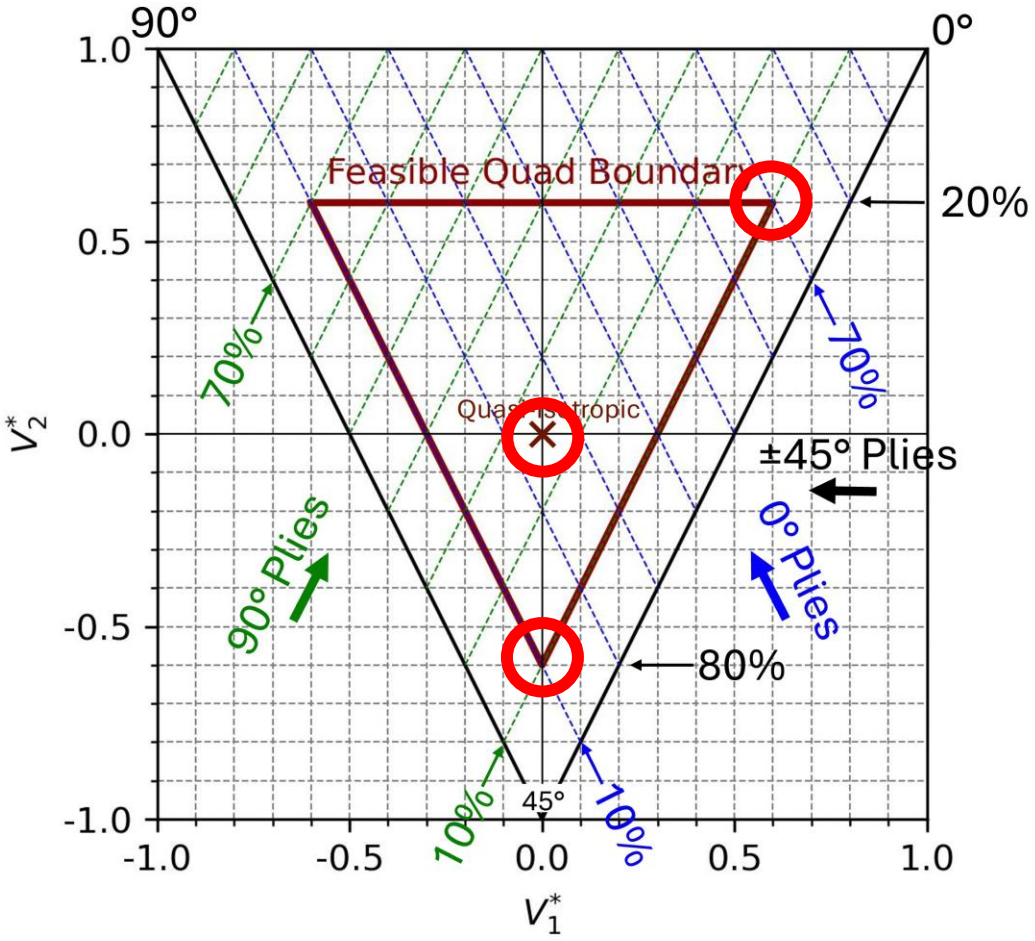

Lamination Parameters

Lamination parameters describe the stiffness properties of a laminate independent of the ply material

Lamination Parameters

$$\begin{bmatrix} A_{11}^* \\ A_{22}^* \\ A_{12}^* \\ A_{66}^* \\ A_{16}^* \\ A_{26}^* \end{bmatrix} = \begin{bmatrix} 1 & V_1 & V_2 & 0 & 0 \\ 1 & -V_1 & V_2 & 0 & 0 \\ 0 & 0 & -V_2 & 1 & 0 \\ 0 & 0 & -V_2 & 0 & 1 \\ 0 & V_3/2 & V_4 & 0 & 0 \\ 0 & V_3/2 & -V_4 & 0 & 0 \end{bmatrix} \begin{bmatrix} U_1 \\ U_2 \\ U_3 \\ U_4 \\ U_5 \end{bmatrix}$$

Material Invariants

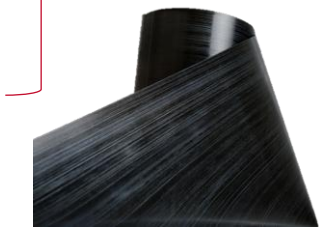

Thickness normalised in-plane matrix terms

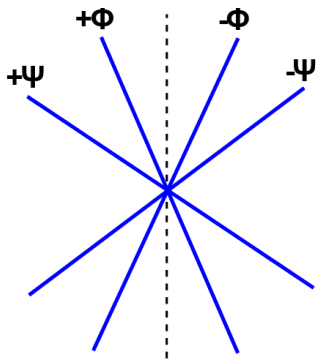

Double – Double

Lamination Parameter Plot
Standard DD (±φ,±ψ)

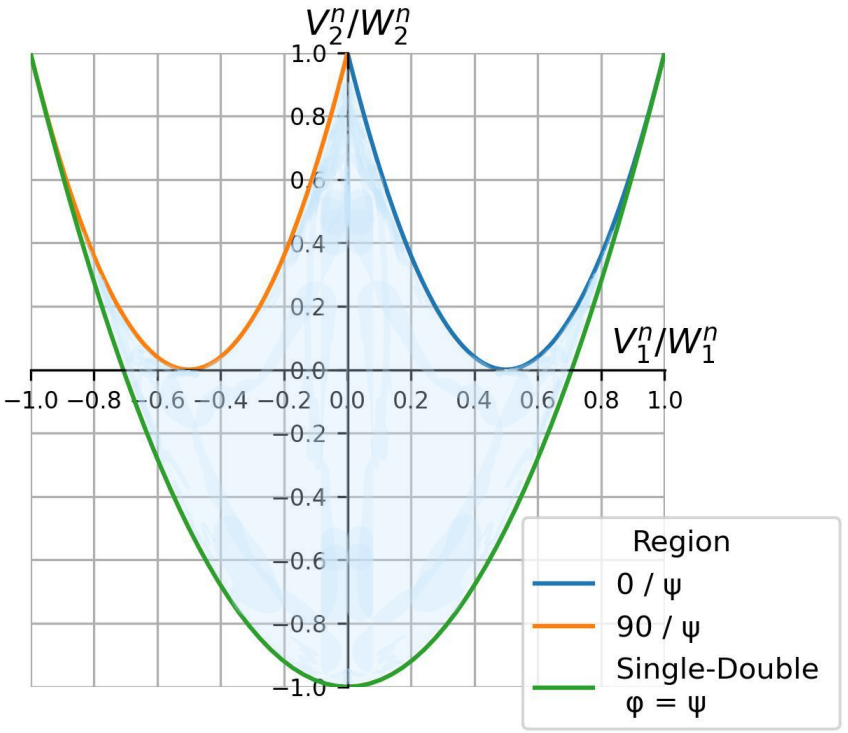

Conversion to DD Sub-Laminates

A framework has been established to convert any CFRP laminate to DD sub-laminate

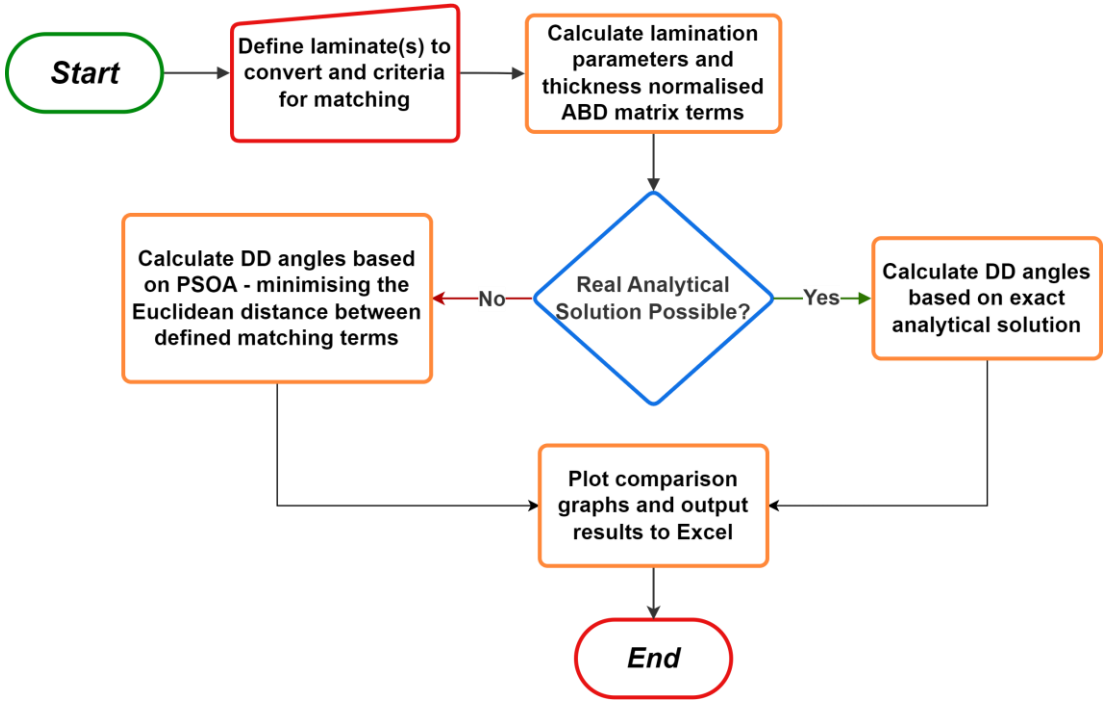

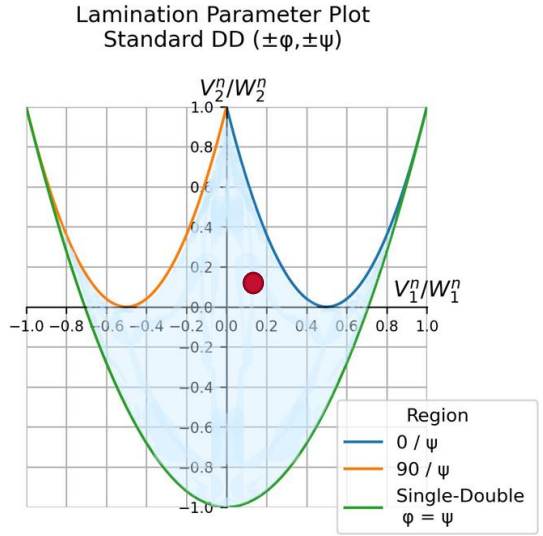

$$\cos(2\psi) = V_1 + \sqrt{-V_1^2 + \frac{V_2}{2} + \frac{1}{2}}$$

$$\cos(2\phi) = 2V_1 - \cos(2\psi)$$

V_1, V_2 = Lamination Parameters

Conversion to DD Sub-Laminates

A framework has been established to convert any CFRP laminate to DD sub-laminate

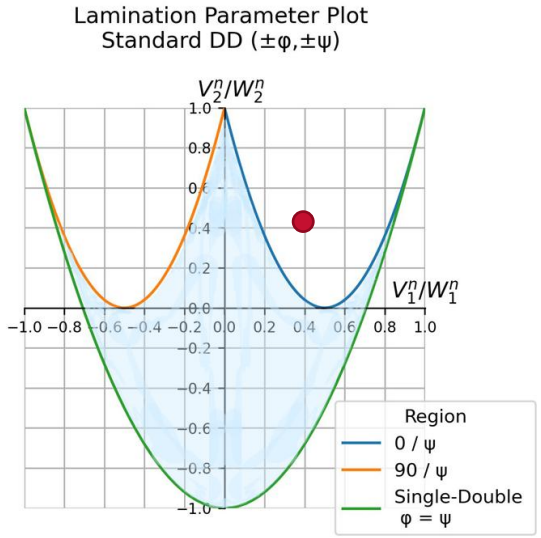

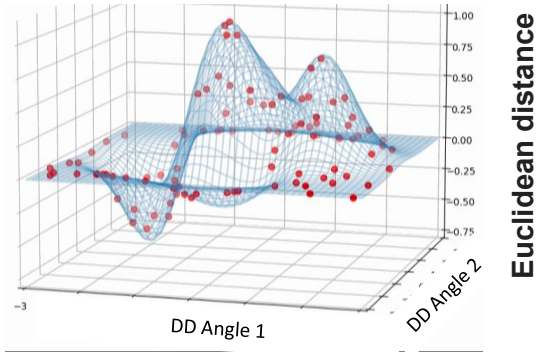

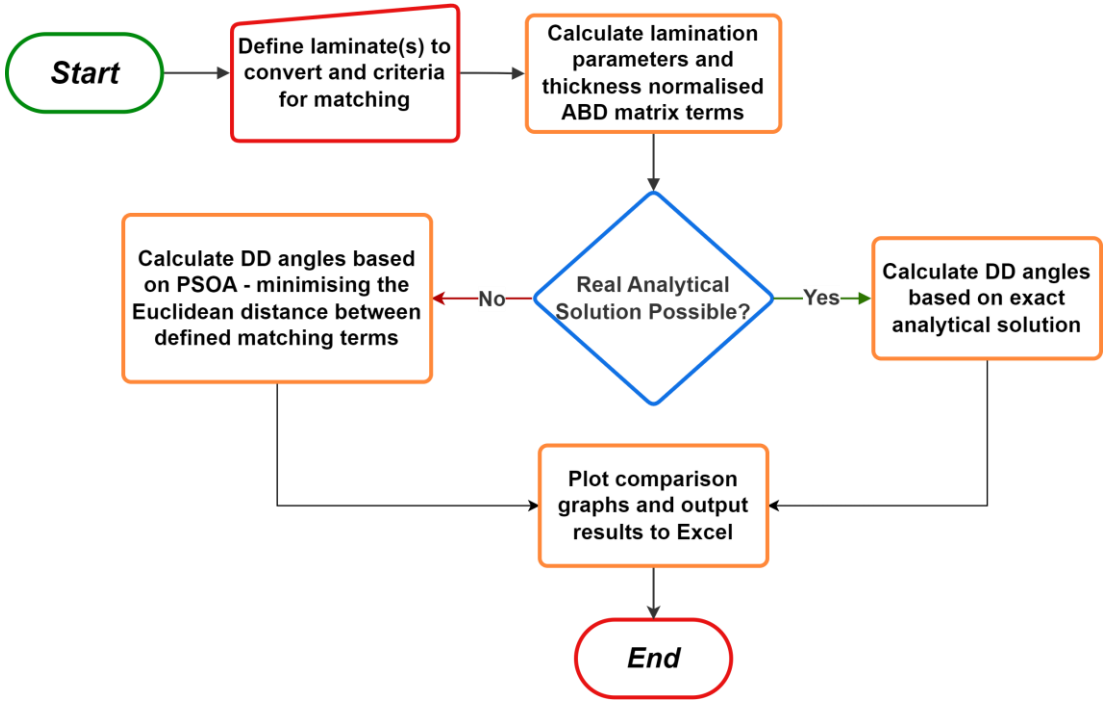

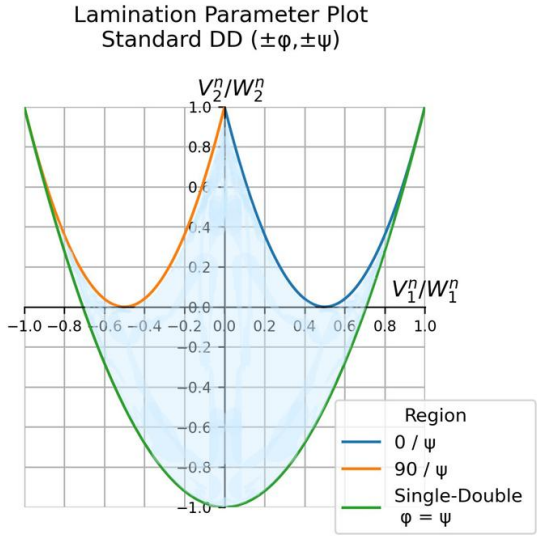

$$\cos(2\psi) = V_1 + \sqrt{-V_1^2 + \frac{V_2}{2} + \frac{1}{2}}$$

$$\cos(2\phi) = 2V_1 - \cos(2\psi)$$

Test Laminates

Laminate	Quad Layup	In-Plane (**DD-A**) Match	Out-of-Plane (**DD-D**) Match
Soft	$[\pm 45/0/\pm 45/90/\pm 45_2]_s$	$[(31.5/-58.5/-31.5/58.5)_{s2}/(31.5/-58.5/-31.5/58.5)]_T$	$[(27.5/-55.5/-27.5/55.5)_{s2}/(27.5/-55.5/-27.5/55.5)]_T$
Quasi	$[0/45/90/-45]_{2s}$	$[22.5/-67.5/67.5/-22.5]_4$	$[9/-61/61/-9]_4$
Hard1	$[45_2/0_4/-45_2/90_2]_s$	$[9/-61.5/61.5/-9]_5$	$[9/-47/47/-9]_5$
Hard2	$[45/0_2/-45/90_2/-45/0_2/45]_s$		$[(7.5/-58/58/-7.5)_{s2}/(7.5/-58/58/-7.5)_1]_T$

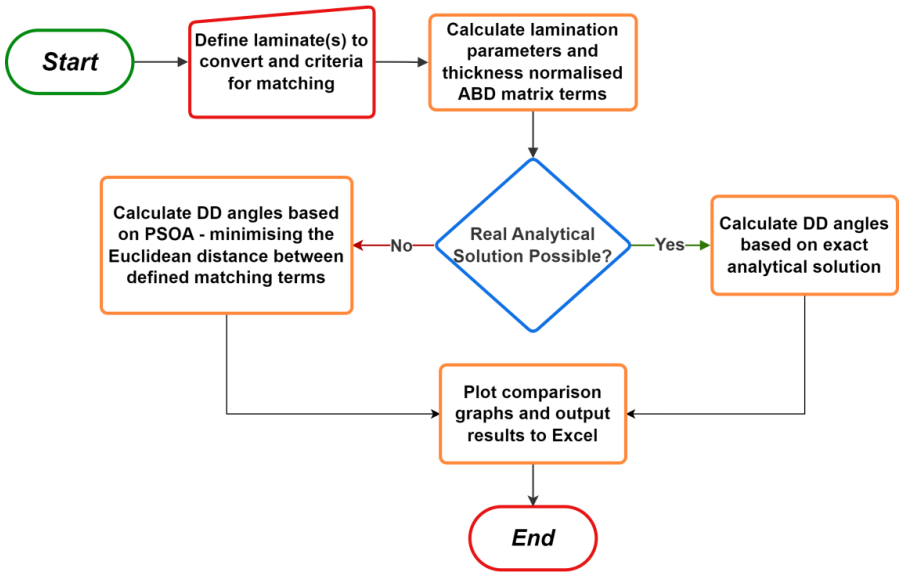

Test Laminates

Laminate	Quad Layup	In-Plane (**DD-A**) Match	Out-of-Plane (**DD-D**) Match
Soft	$[\pm45/0/\pm45/90/\pm45_2]_s$	$[(31.5/-58.5/-31.5/58.5)_{s2}/(31.5/-58.5/-31.5/58.5)]_T$	$[(27.5/-55.5/-27.5/55.5)_{s2}/(27.5/-55.5/-27.5/55.5)]_T$
Quasi	$[0/45/90/-45]_{2s}$	$[22.5/-67.5/67.5/-22.5]_4$	$[9/-61/61/-9]_4$
Hard1	$[45_2/0_4/-45_2/90_2]_s$	$[9/-61.5/61.5/-9]_5$	$[9/-47/47/-9]_5$
Hard2	$[45/0_2/-45/90_2/-45/0_2/45]_s$		$[(7.5/-58/58/-7.5)_{s2}/(7.5/-58/58/-7.5)_1]_T$

In-Plane LPP

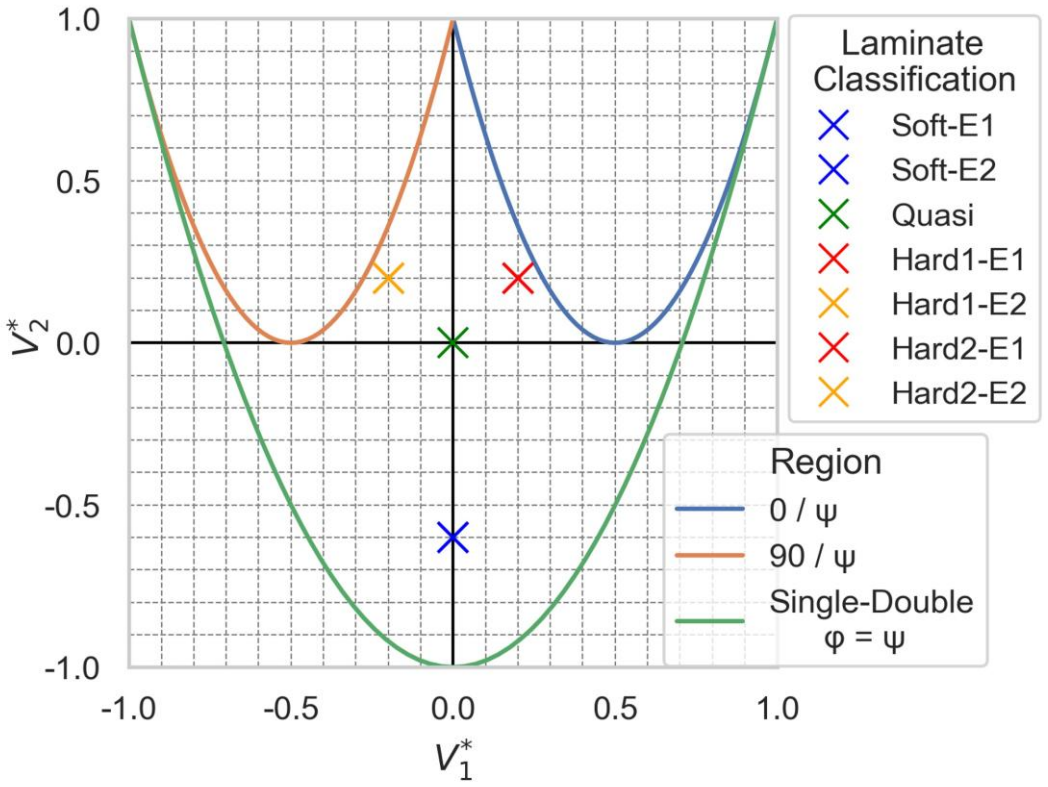

Out-Of-Plane LPP

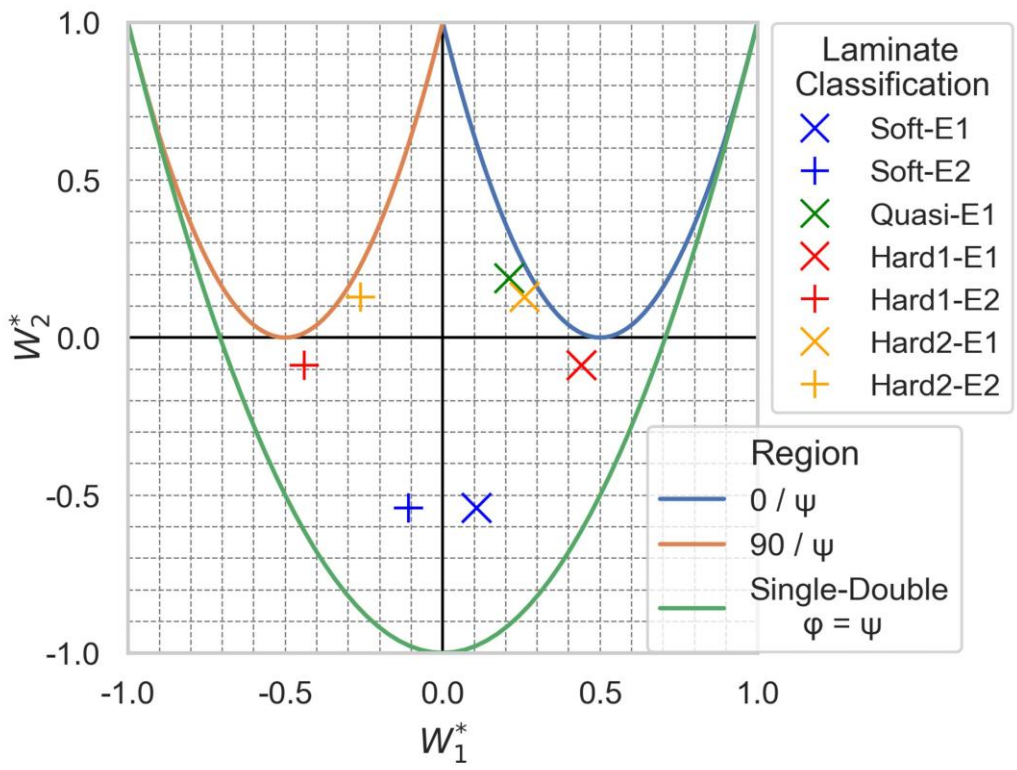

Test Laminates

Laminate	Quad Layup	In-Plane (**DD-A**) Match	Out-of-Plane (**DD-D**) Match
Soft	$[\pm 45/0/\pm 45/90/\pm 45_2]_s$	$[(31.5/-58.5/-31.5/58.5)_{s2}/(31.5/-58.5/-31.5/58.5)]_T$	$[(27.5/-55.5/-27.5/55.5)_{s2}/(27.5/-55.5/-27.5/55.5)]_T$
Quasi	$[0/45/90/-45]_{2s}$	$[22.5/-67.5/67.5/-22.5]_4$	$[9/-61/61/-9]_4$
Hard1	$[45_2/0_4/-45_2/90_2]_s$	$[9/-61.5/61.5/-9]_5$	$[9/-47/47/-9]_5$
Hard2	$[45/0_2/-45/90_2/-45/0_2/45]_s$		$[(7.5/-58/58/-7.5)_{s2}/(7.5/-58/58/-7.5)_1]_T$

Unnotched Tension



Unnotched Compression

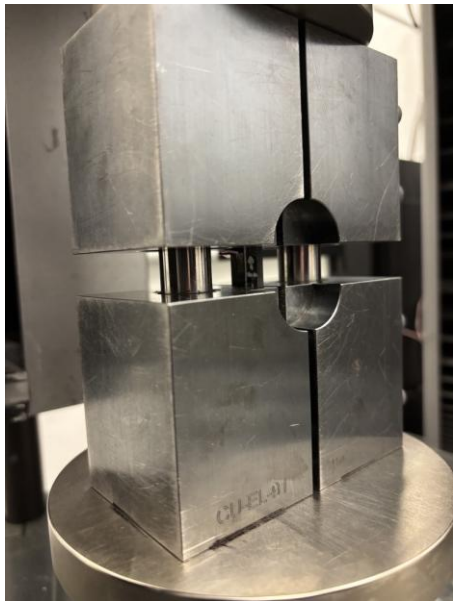

Open-Hole Tension

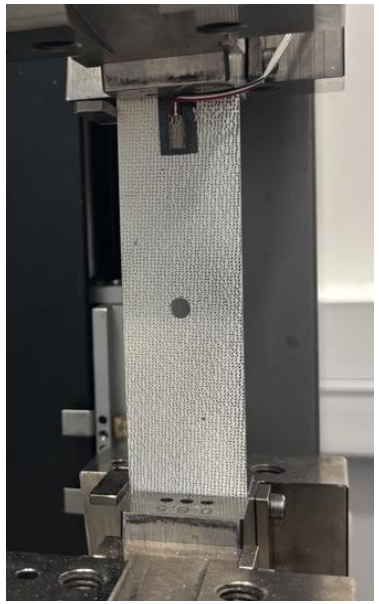

Open-Hole Compression

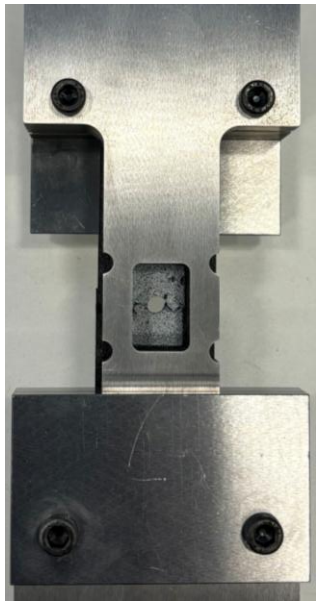

Flexural 3-Point-Bend

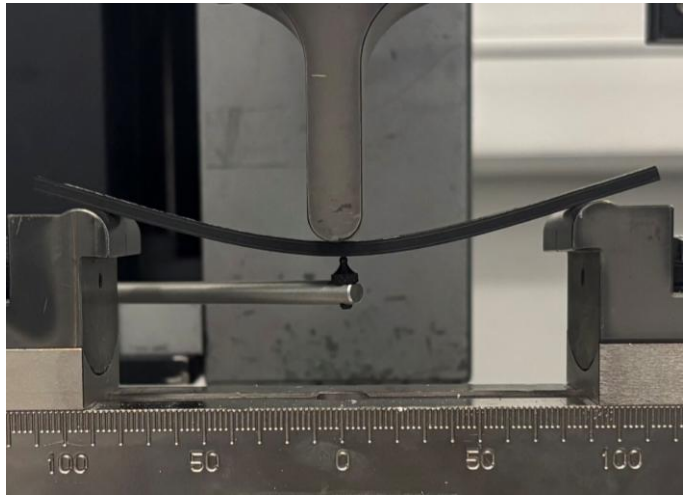

Conversion Framework Validation: In-plane

A framework has been established to convert any CFRP laminate to DD sub-laminate

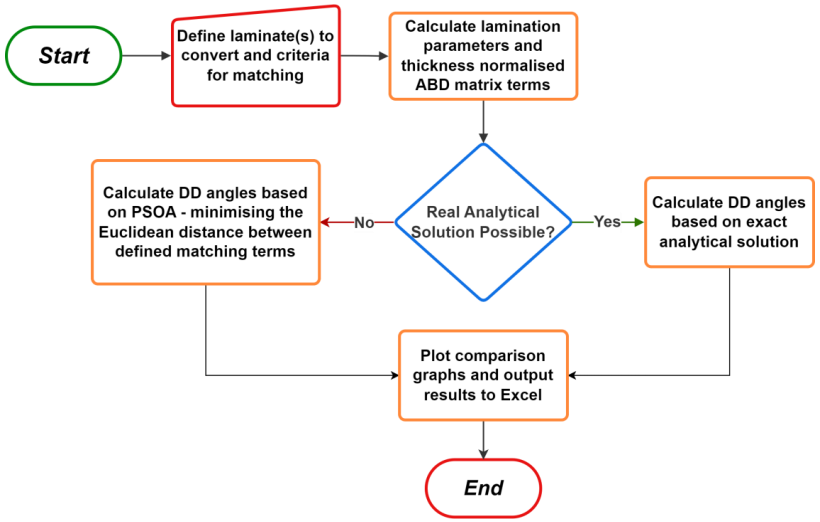

Laminate	Quad Layup	In-Plane (**DD-A**) Match
Soft	$[\pm 45/0/\pm 45/90/\pm 45_2]_s$	$[(31.5/-58.5/-31.5/58.5)_{s2}/(31.5/-58.5/-31.5/58.5)]_T$
Quasi	$[0/45/90/-45]_{2s}$	$[22.5/-67.5/67.5/-22.5]_4$
Hard1	$[45_2/0_4/-45_2/90_2]_s$	$[9/-61.5/61.5/-9]_5$
Hard2	$[45/0_2/-45/90_2/-45/0_2/45]_s$	

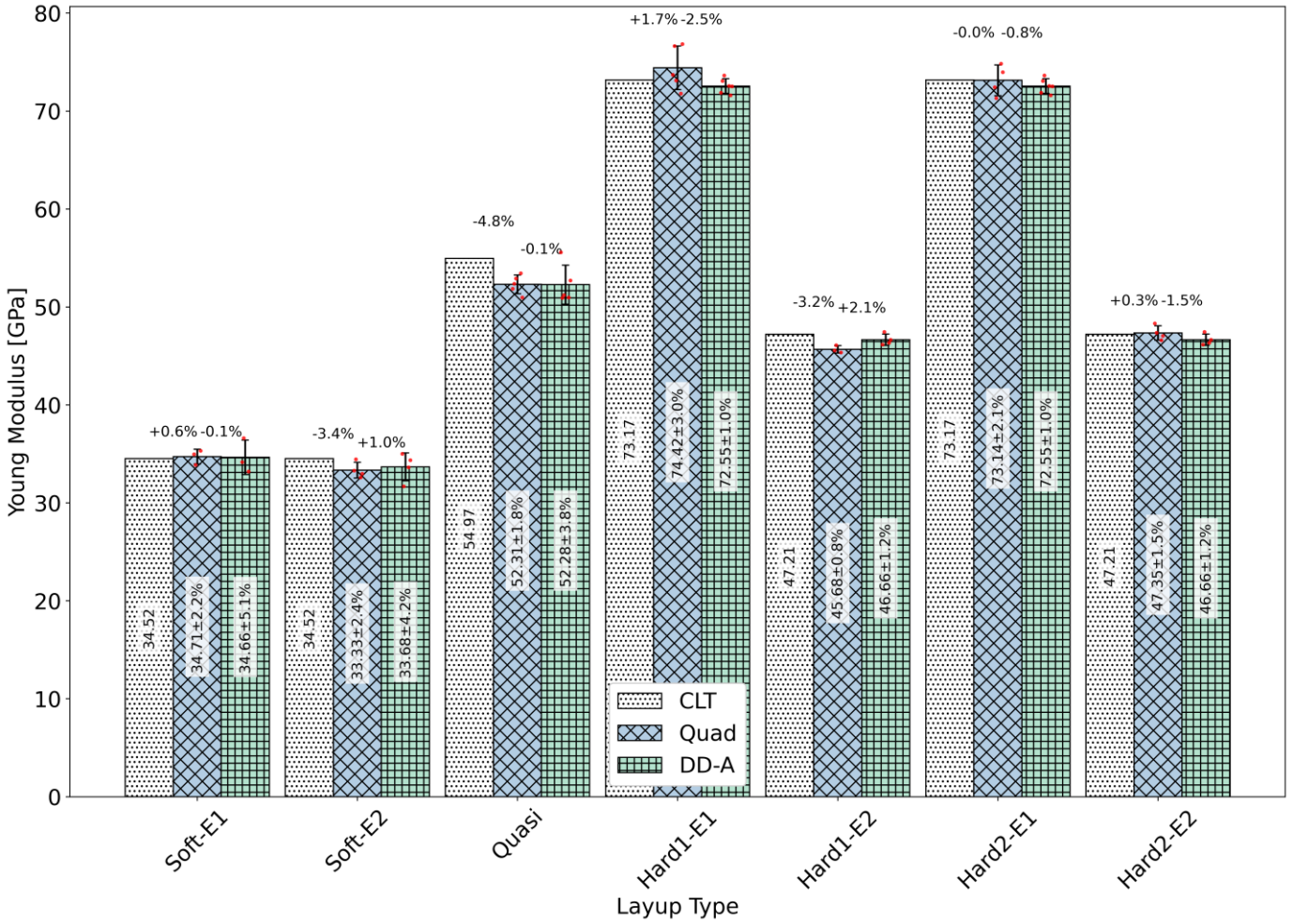

Young's modulus comparison CLT vs Quad vs DD for a range of laminates

Unnotched Tensile Strength - First Ply Failure

Average increase of 7.49% for the DD in FPF strength

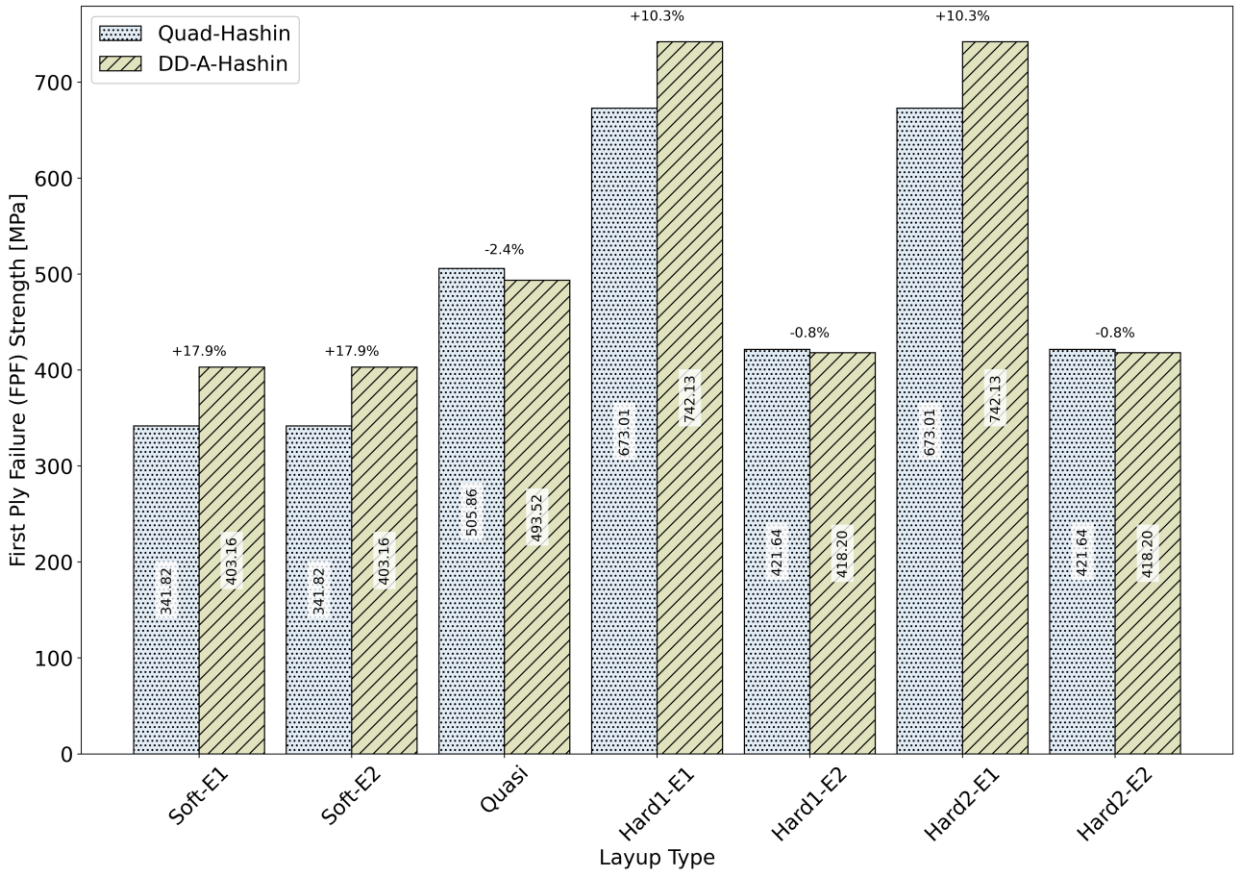

First Ply Failure (FPF) comparison Quad vs DD for a range of laminates

Laminate	Quad Layup	In-Plane (**DD-A**) Match
Soft	$[\pm 45/0/\pm 45/90/\pm 45_2]_s$	$[(31.5/-58.5/-31.5/58.5)_{s2}/(31.5/-58.5/-31.5/58.5)]_T$
Quasi	$[0/45/90/-45]_{2s}$	$[22.5/-67.5/67.5/-22.5]_4$
Hard1	$[45_2/0_4/-45_2/90_2]_s$	$[9/-61.5/61.5/-9]_5$
Hard2	$[45/0_2/-45/90_2/-45/0_2/45]_s$	

Unnotched Tensile Strength – Ultimate Strength

Average decrease of 5.64% in experimental ultimate strength for the DD laminate

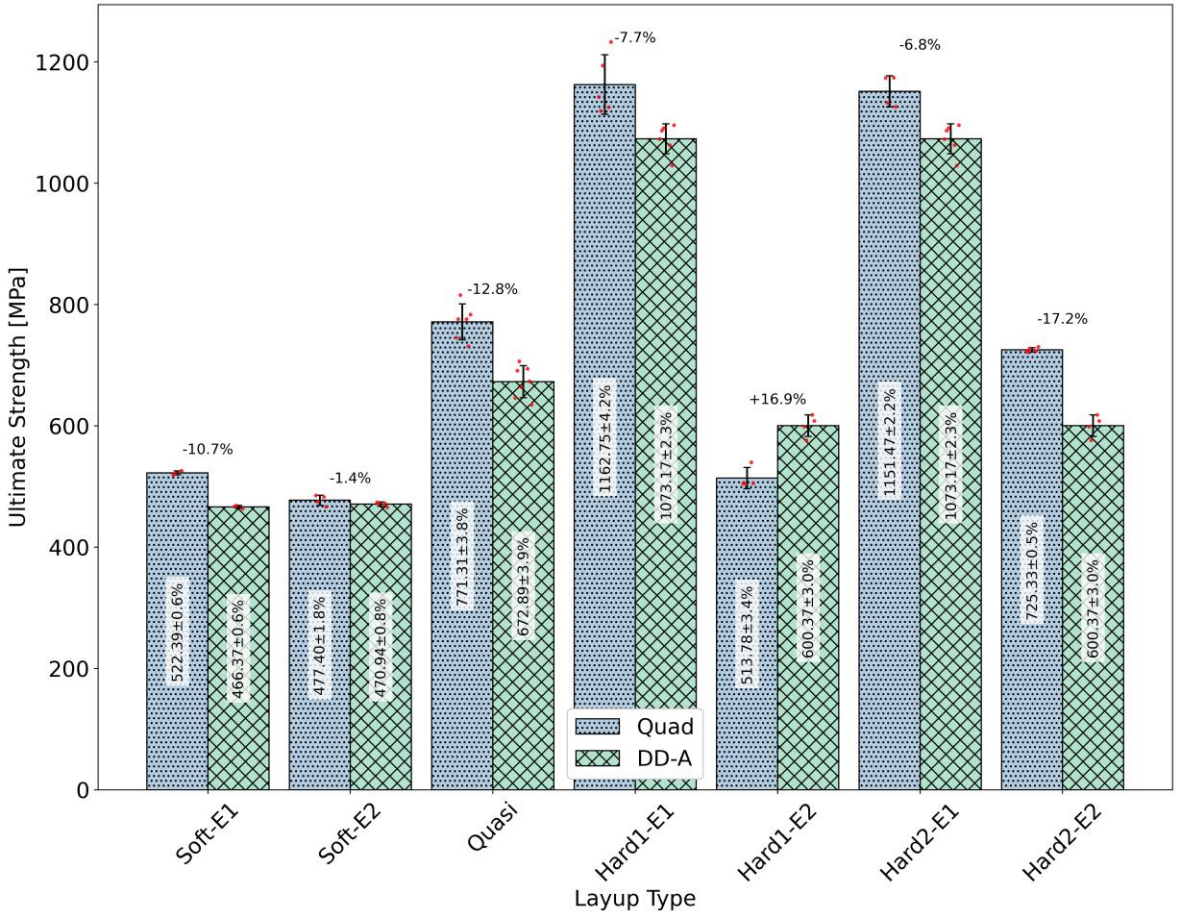

Unnotched tensile experimental ultimate strength comparison Quad vs DD for a range of laminates

Laminate	Quad Layup	In-Plane (**DD-A**) Match
Soft	$[\pm45/0/\pm45/90/\pm45_2]_s$	$[(31.5/-58.5/-31.5/58.5)_{s2}/(31.5/-58.5/-31.5/58.5)]_T$
Quasi	$[0/45/90/-45]_{2s}$	$[22.5/-67.5/67.5/-22.5]_4$
Hard1	$[45_2/0_4/-45_2/90_2]_s$	$[9/-61.5/61.5/-9]_5$
Hard2	$[45/0_2/-45/90_2/-45/0_2/45]_s$	

Why are these laminates of equivalent stiffness failing at different stresses?

Unnotched Tensile Strength – Ultimate Strength

Why are these laminates of equivalent stiffness failing at different stresses?

Conduct progressive failure analysis:

→ Determine ply failure modes

→ Predict Last Ply Failure (LPF) strengths

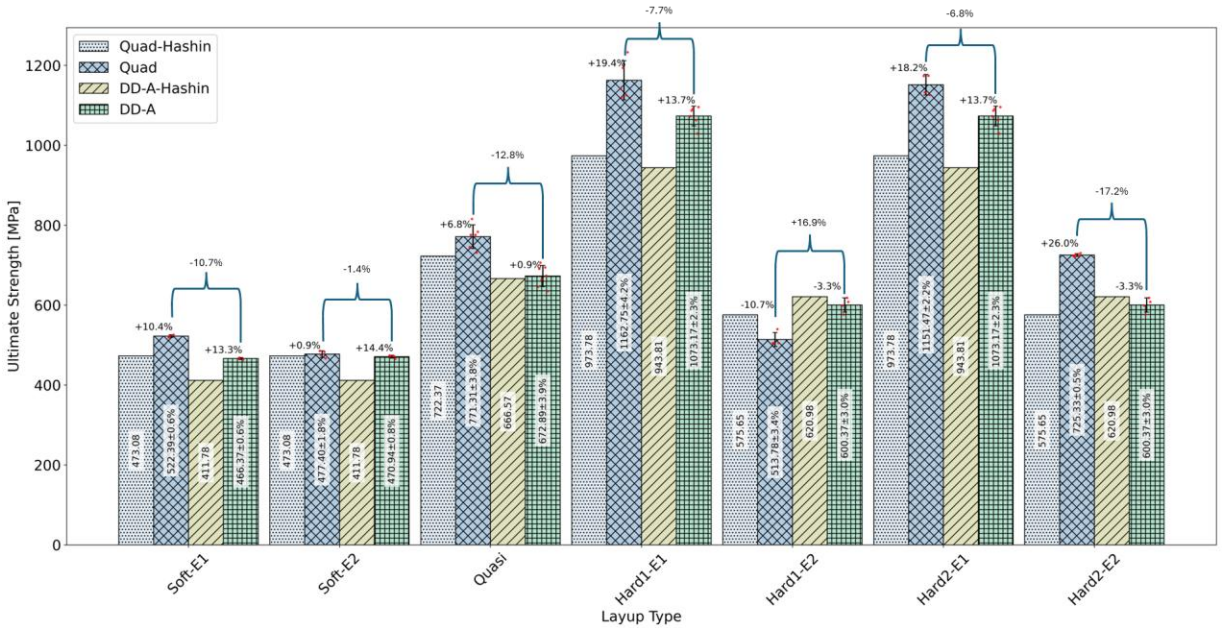

Unnotched tensile LPF and experimental ultimate strength comparison Quad vs DD for a range of laminates

Quasi Quad

Ply No.	Angle (°)	Final Failure
1	0	FT
2	45	MT
3	90	FC
4	-45	FT
5	0	FT
6	45	MT
7	90	FC
8	-45	FT
9	-45	FT
10	90	FC
11	45	MT
12	0	FT
13	-45	FT
14	90	FC
15	45	MT
16	0	FT

Laminate failure dominated by fibre failure

Quasi DD-A

Ply No.	Angle (°)	Final Failure
1	22.5	FT
2	-67.5	MT
3	67.5	MT
4	-22.5	FT
5	22.5	FT
6	-67.5	MT
7	67.5	MT
8	-22.5	FT
9	22.2	FT
10	-67.5	MT
11	67.5	MT
12	-22.5	FT
13	22.5	FT
14	-67.5	MT
15	67.5	MT
16	-22.5	FT

Laminate failure dominated by matrix failure

Unnotched Tensile Strength – Ultimate Strength

QUEEN'S UNIVERSITY BELFAST

Why are these laminates of equivalent stiffness failing at different stresses?

Conduct progressive failure analysis:

→ Determine ply failure modes

→ Predict Last Ply Failure (LPF) strengths

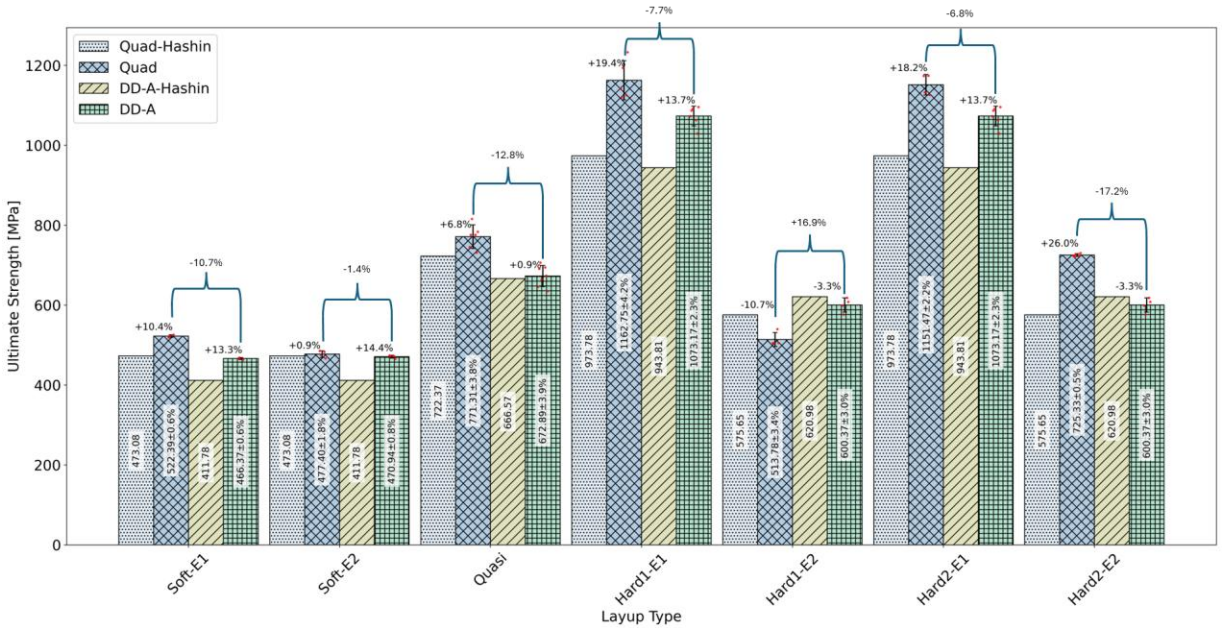

Unnotched tensile LPF and experimental ultimate strength comparison Quad vs DD for a range of laminates

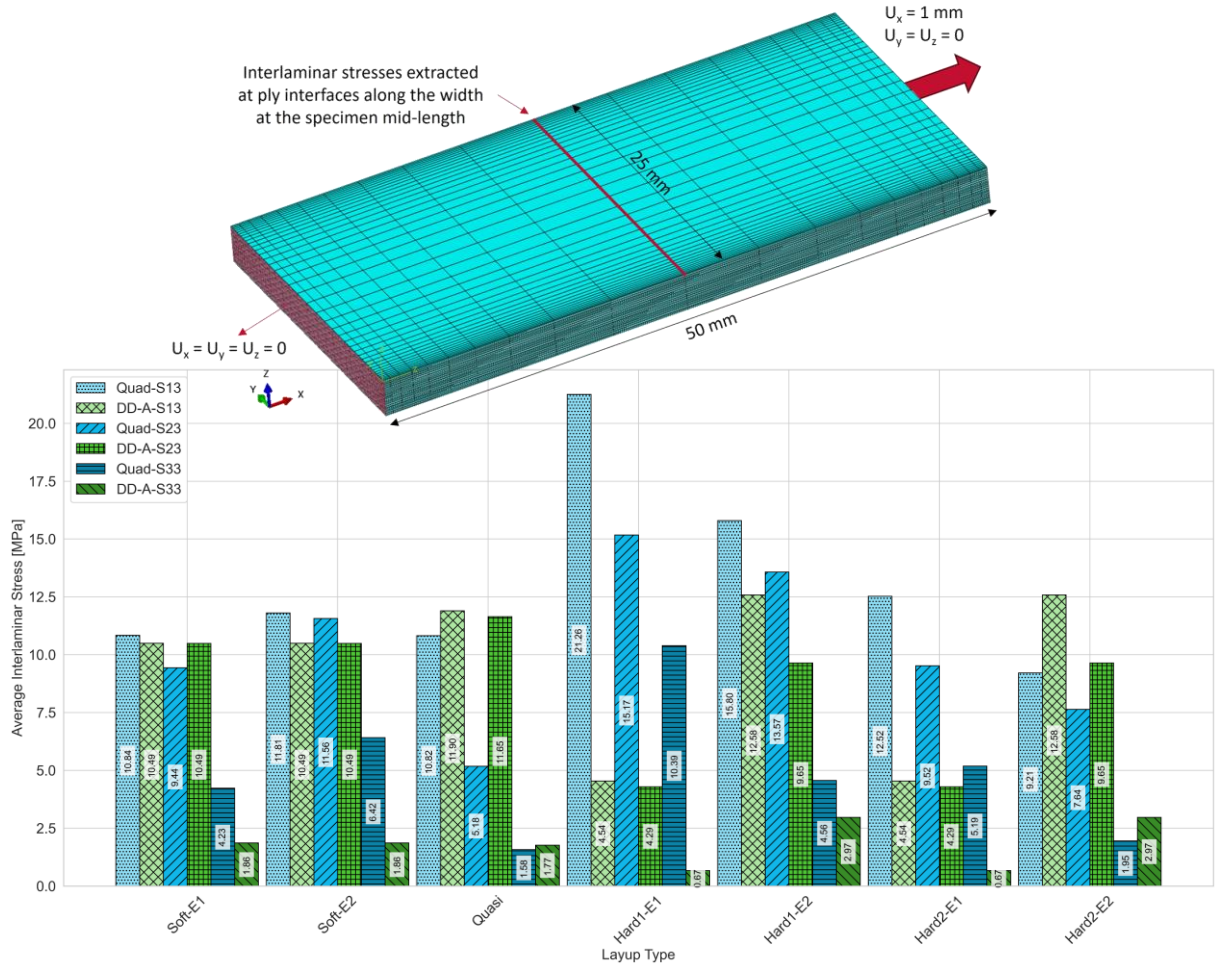

Interlaminar stress comparison of Quad and DD laminates.

Unnotched Compressive Strength

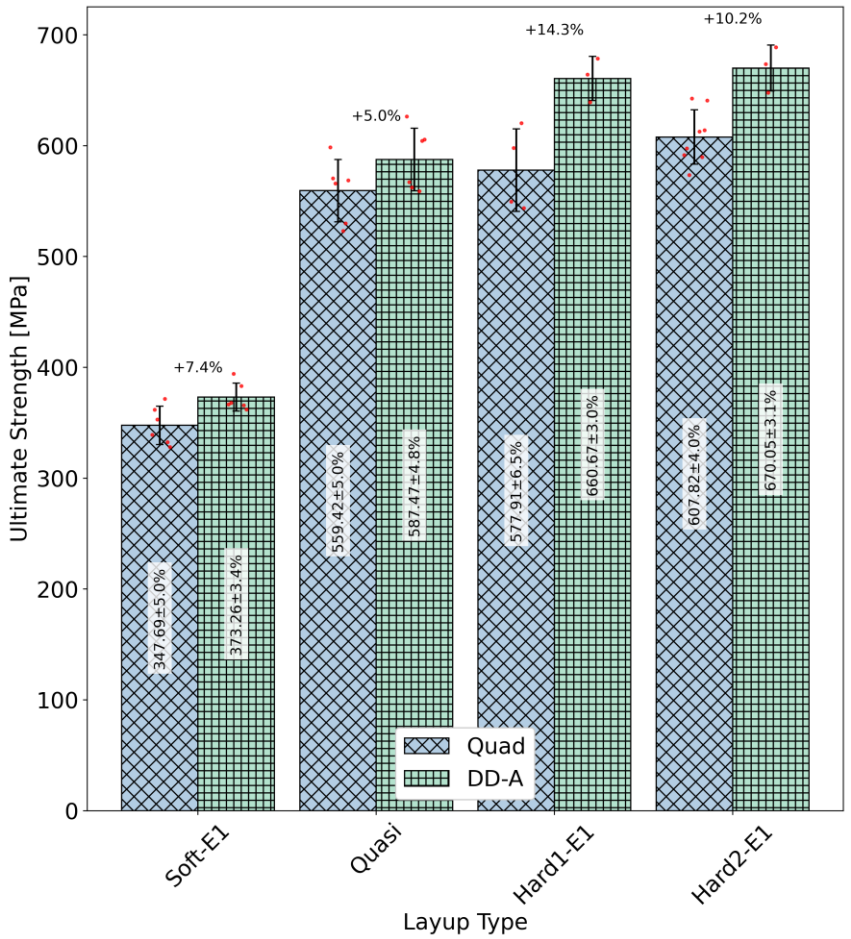

Unnotched compression experimental ultimate strength comparison Quad vs DD for a range of laminates

Laminate	Quad Layup	In-Plane (**DD-A**) Match
Soft	$[\pm45/0/\ \pm45/90/\pm45_2]_s$	$[(31.5/-58.5/-31.5/58.5)_{s2}/(31.5/-58.5/-31.5/58.5)]_T$
Quasi	$[0/45/90/-45]_{2s}$	$[22.5/-67.5/67.5/-22.5]_4$
Hard1	$[45_2/0_4/-45_2/90_2]_s$	$[9/-61.5/61.5/-9]_5$
Hard2	$[45/0_2/-45/90_2/-45/0_2/45]_s$	

→ Average 9.22% increase in unnotched compressive strength for the DD laminate.

→ Analysis of the compressive failure modes from the specimens is being used to explain the failure trends observed

Hard1 Quad E1



Hard1 DD-A E1



Open-Hole Tensile Results

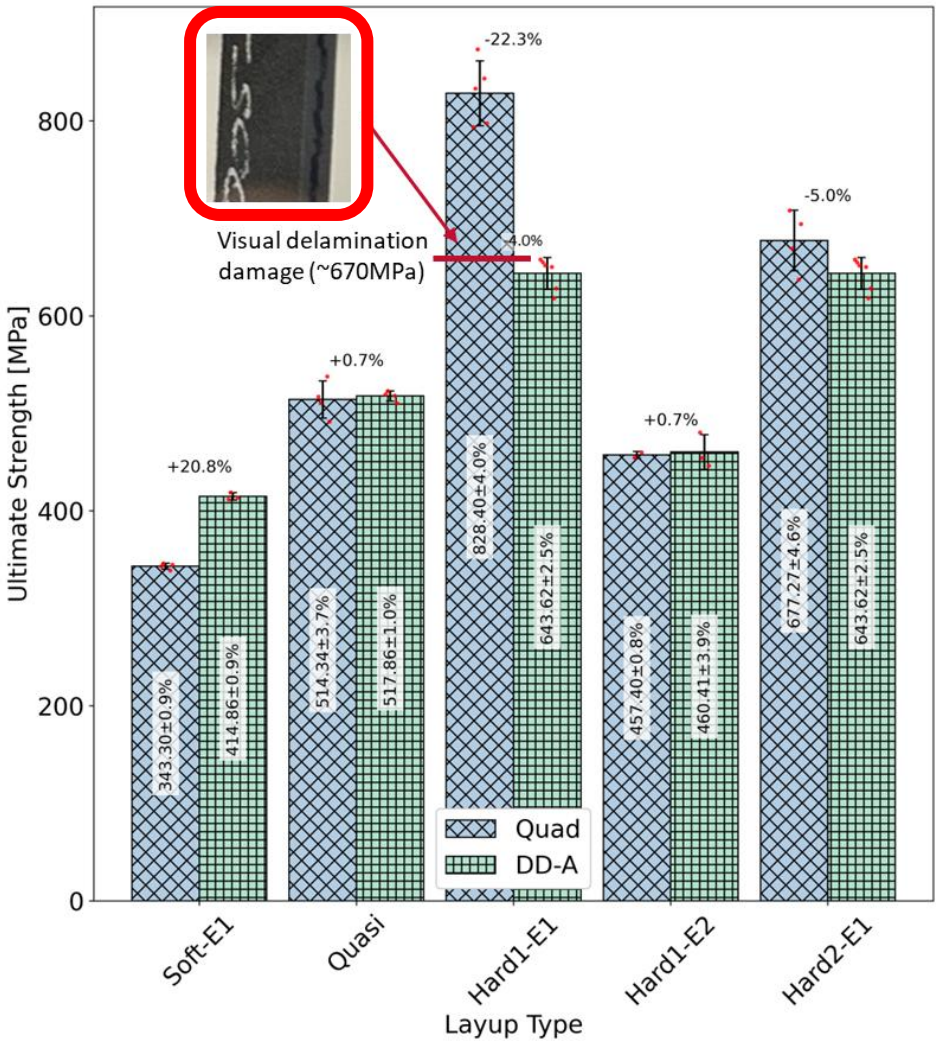

Open-hole tensile strength comparison Quad vs DD for a range of laminates

- Average 1.02% decrease in strength with the DD-A laminate.
- However, for Hard1 E1 Quad the delamination due to blocked plies distributed the stress concentration leading to an artificially increased OHT strength.
- Taking the severe visual delamination point as failure of the Hard1 E1 Quad laminate, an average increase of 2.64% is seen for the DD-A laminates.

Laminate	Quad Layup	In-Plane (**DD-A**) Match
Soft	$[\pm45/0/\pm45/90/\pm45_2]_s$	$[(31.5/-58.5/-31.5/58.5)_{s2}/(31.5/-58.5/-31.5/58.5)]_T$
Quasi	$[0/45/90/-45]_{2s}$	$[22.5/-67.5/67.5/-22.5]_4$
Hard1	$[45_2/0_4/-45_2/90_2]_s$	$[9/-61.5/61.5/-9]_5$
Hard2	$[45/0_2/-45/90_2/-45/0_2/45]_s$	

Open-Hole Tension

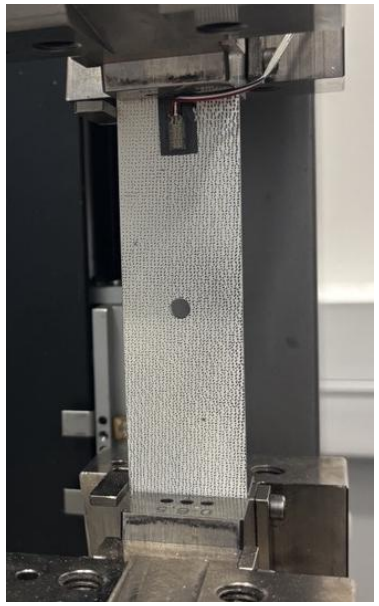

Open-Hole Compression Results

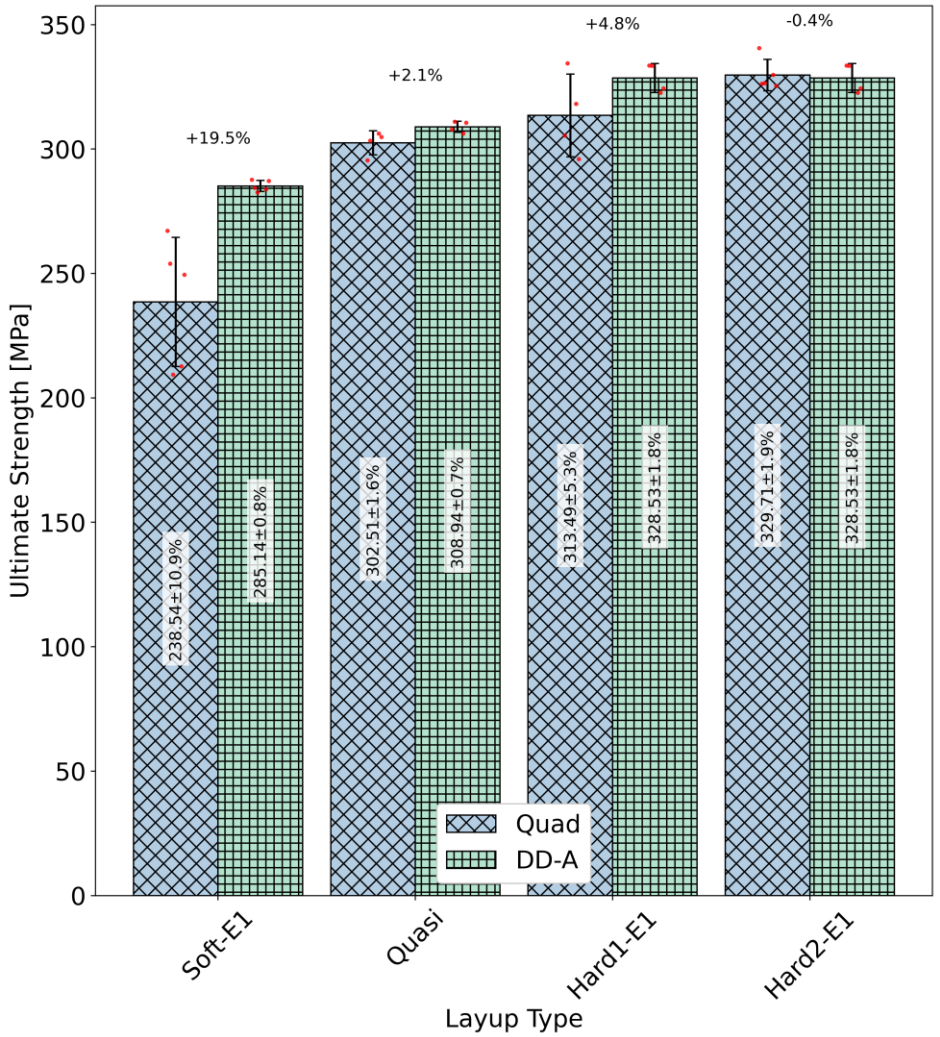

Open-hole compression strength comparison Quad vs DD for a range of laminates

→ Average increase of 6.5% in open-hole compressive strength for the DD-A laminates

Laminate	Quad Layup	In-Plane (**DD-A**) Match
Soft	$[\pm45/0/\pm45/90/\pm45_2]_s$	$[(31.5/-58.5/-31.5/58.5)_{s2}/(31.5/-58.5/-31.5/58.5)]_T$
Quasi	$[0/45/90/-45]_{2s}$	$[22.5/-67.5/67.5/-22.5]_4$
Hard1	$[45_2/0_4/-45_2/90_2]_s$	$[9/-61.5/61.5/-9]_5$
Hard2	$[45/0_2/-45/90_2/-45/0_2/45]_s$	

Open-Hole Compression

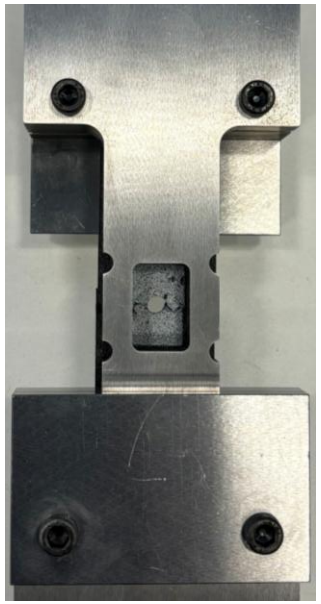

OHT DIC Results Example – Soft Laminates 325 MPa

QUEEN'S UNIVERSITY BELFAST

Soft OHT Quad
$[\pm45/0/\pm45/90/\pm45_2]_s$

Soft OHT DD-A
$[(31.5/-58.5/31.5/58.5)_{s2}/(31.5/-58.5/-31.5/58.5)]_T$

Calculation of average strain on a concentric circle (strain at distance from hole)

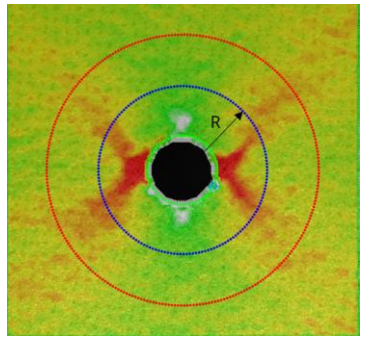

Axial Strain (ε_y)

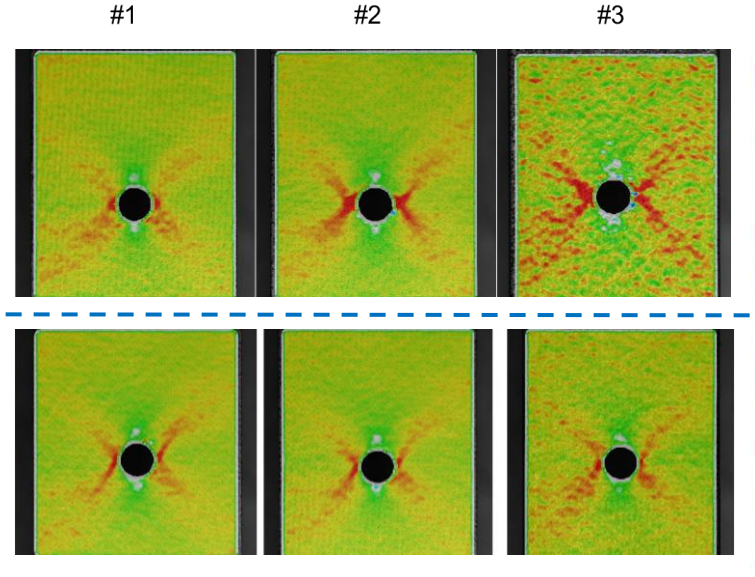

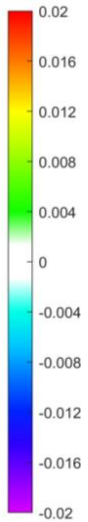

Shear Strain (ε_{xy})

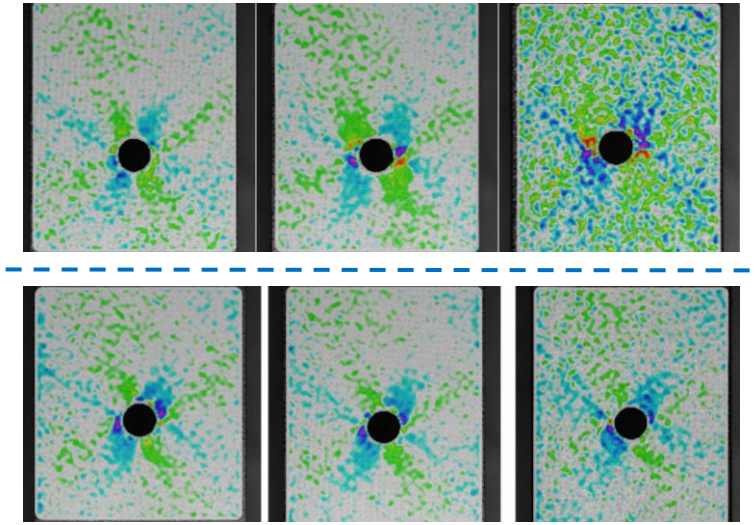

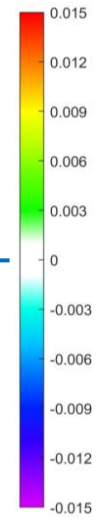

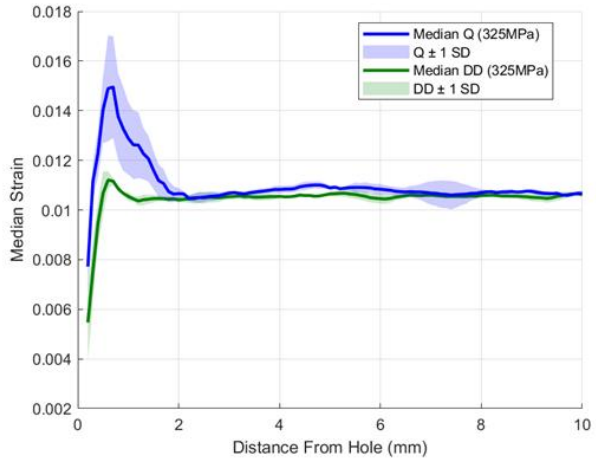

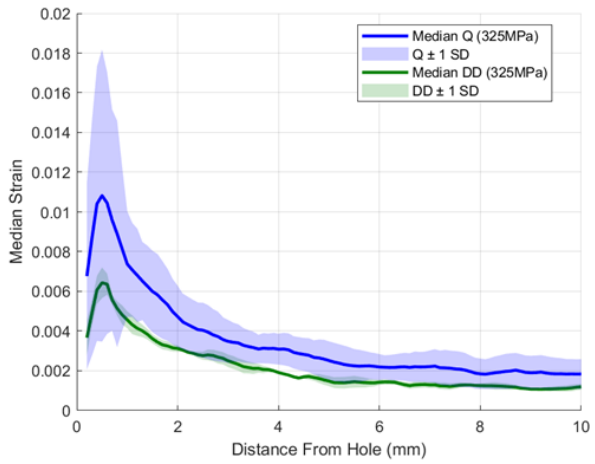

Conversion Framework Validation: Out-of-Plane

A framework has been established to convert any CFRP laminate to DD sub-laminate

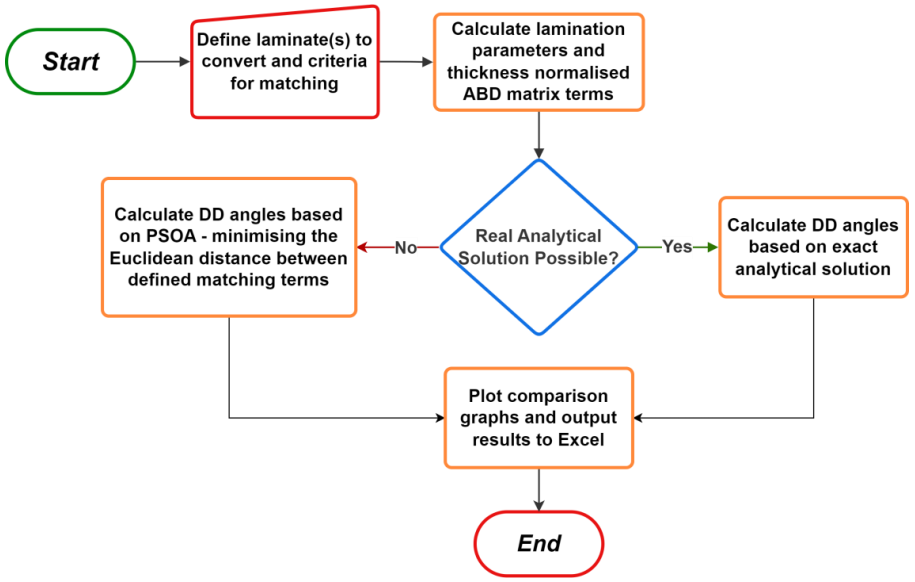

Laminate	Quad Layup	Out-of-Plane (**DD-D**) Match
Soft	$[\pm 45/0/\pm 45/90/\pm 45_2]_s$	$[(27.5/-55.5/-27.5/55.5)_{s2}/(27.5/-55.5/-27.5/55.5)]_T$
Quasi	$[0/45/90/-45]_{2s}$	$[9/-61/61/-9]_4$
Hard1	$[45_2/0_4/-45_2/90_2]_s$	$[9/-47/47/-9]_5$
Hard2	$[45/0_2/-45/90_2/-45/0_2/45]_s$	$[(7.5/-58/58/-7.5)_{s2}/(7.5/-58/58/-7.5)_1]_T$

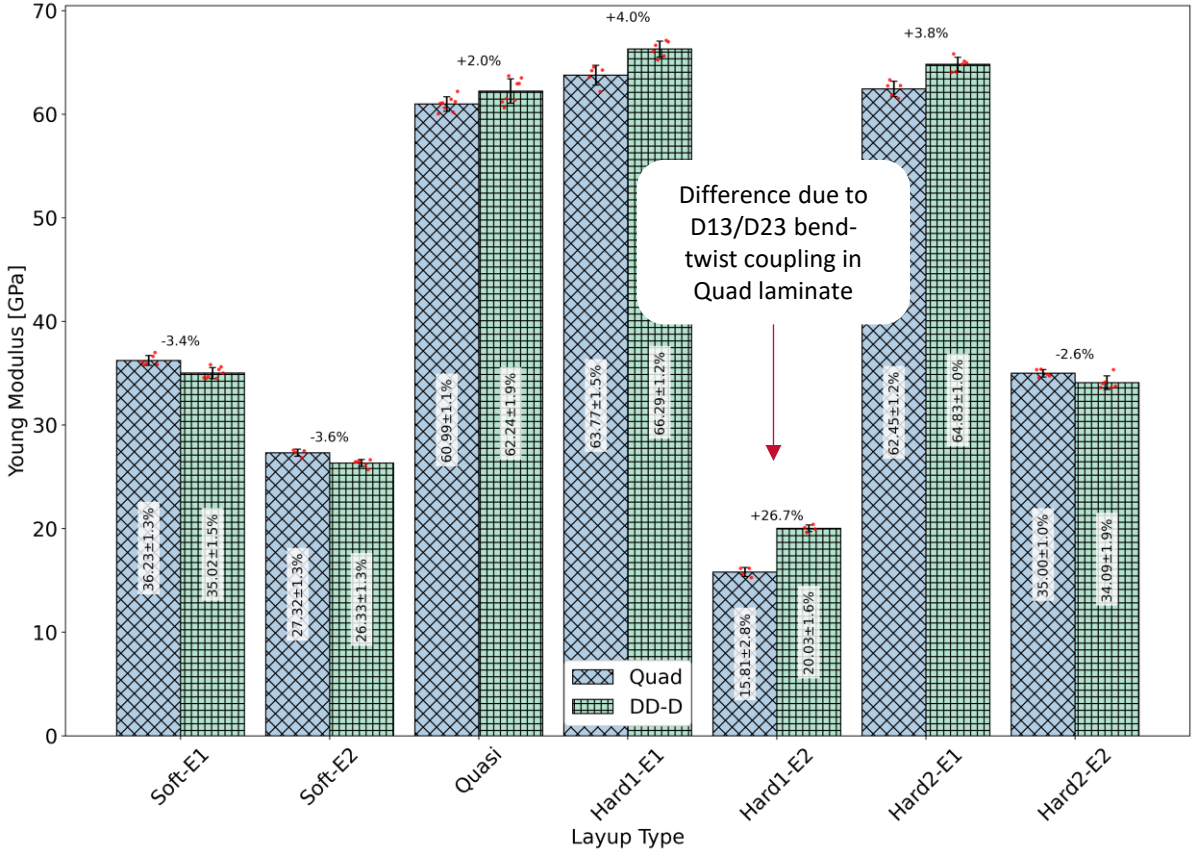

Flexural modulus comparison Quad vs DD for a range of laminates

Flexural Strength Results

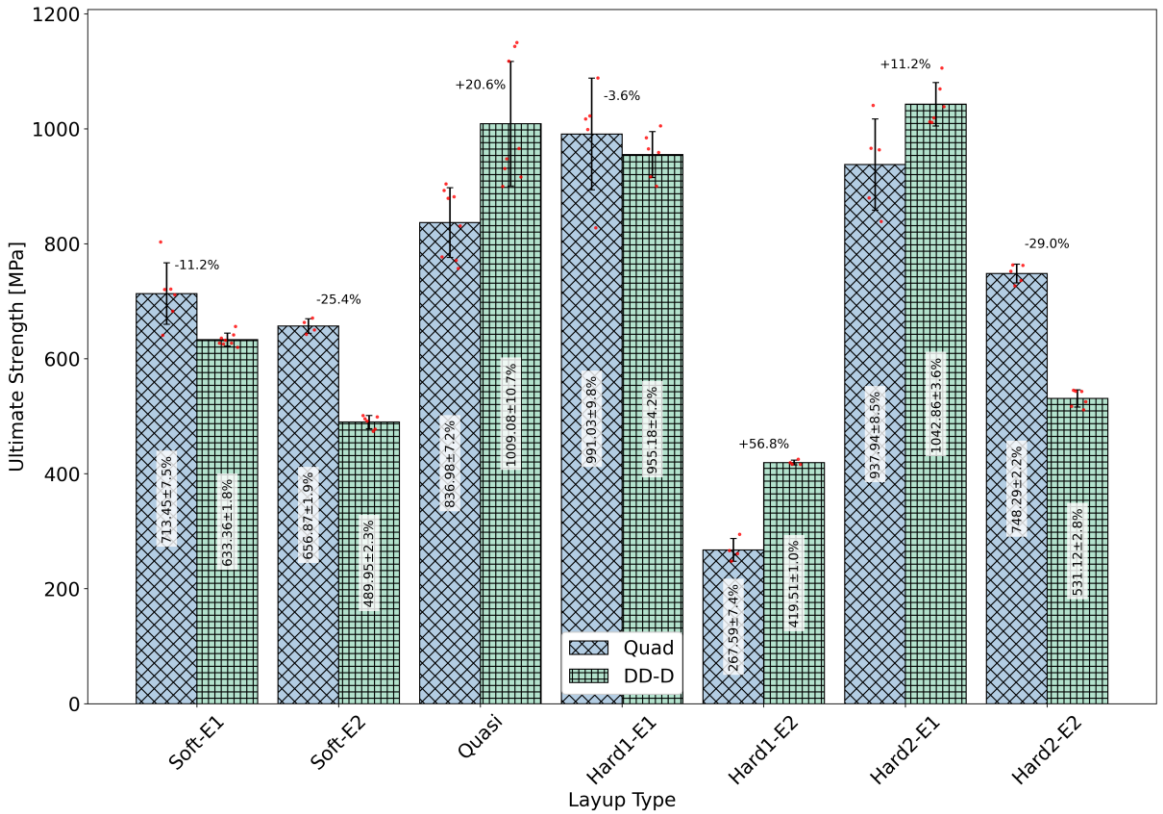

Flexural strength comparison Quad vs DD for a range of laminates

→ Average 2.8% increase in strength using DD-D laminates.

→ No clear trend to determine if Quad or DD laminates are superior in certain flexural scenarios.

Laminate	Quad Layup	Out-of-Plane (**DD-D**) Match
Soft	$[\pm 45/0/\pm 45/90/\pm 45_2]_s$	$[(27.5/-55.5/-27.5/55.5)_{s2}/(27.5/-55.5/-27.5/55.5)]_T$
Quasi	$[0/45/90/-45]_{2s}$	$[9/-61/61/-9]_4$
Hard1	$[45_2/0_4/-45_2/90_2]_s$	$[9/-47/47/-9]_5$
Hard2	$[45/0_2/-45/90_2/-45/0_2/45]_s$	$[(7.5/-58/58/-7.5)_{s2}/(7.5/-58/58/-7.5)_1]_T$

LVI and CAI Performance of DD Laminates

QUEEN'S UNIVERSITY BELFAST
SCHOOL OF MECHANICAL AND AEROSPACE ENGINEERING
SPIRIT AEROSYSTEMS

LVI / CAI: Laminates

Thinner Laminates: 2.9mm using SEDD layup

Laminate	Quad Layup	In-Plane (**SEDD-A**) Match	Out-of-Plane (**SEDD-D**) Match
Thin-Soft	$[\pm45/0/\pm45/90/\pm45_2]_s$	$[(31.5/-58.5/-31.5/58.5)_{s2}/(31.5/-58.5/-31.5/58.5)]_T$	$[(27.5/-55.5/-27.5/55.5)_{s2}/(27.5/-55.5/-27.5/55.5)]_T$
Thin-Hard1	$[45/0_2/-45/\ 90_2/-45/0_2/45]_s$	$[(9/-61.5/61.5/-9)_{s2}/(9/-61.5/61.5/-9)_1]_T$	$[(7.5/-58/58/-7.5)_{s2}/(7.5/-58/58/-7.5)_1]_T$
		In-Plane (**ExSEDD-A**) Match	Out-of-Plane (**ExSEDD-D**) Match
Thin-Hard2	$[45/0_2/-45/0_2/45/0/-45/90]_s$	$[12/-57/0/57/-12]_{s2}$	$[9.5/-46.5/0/46.5/-9.5]_{s2}$

Thicker Laminates: 5.8 - 4.35 mm using conventional DD layup

Laminate	Quad Layup	In-Plane (**DD-A**) Match	Out-of-Plane (**DD-D**) Match
Thick-Quasi	$[0/45/90/-45]_{4s}$	$[22.5/-67.5/-22.5/67.5]_8$	$[17/-64.5/64.5/-17]_8$
Thin-Hard1	$[45/0_2/-45/90_2/-45/0_2/45]_{2s}$	$[9/-61.5/61.5/-9]_{10}$	
Thin-Hard2	$[0_2/45/-45/0_2/45/0_2/-45/90_2/45/0_2/-45]_s$	$[0/-53.5/53.5/0]_8$	$[0/-40/40/0]_8$
		In-Plane (**ExDD-A**) Match	Out-of-Plane (**ExDD-D**) Match
		$[12/-59/0/59/-12]_6$	$[7\ /-51.5/\ 7/\ -7/\ 51.5/\ -7]_5$

→ 19 different laminates spanning a wide range of stiffness.

→ In-plane and out-of-plane matched laminates compared.

→ Both conventional DD and symmetry-enhanced (SEDD) laminates assessed.

In-plane LPP for all laminates

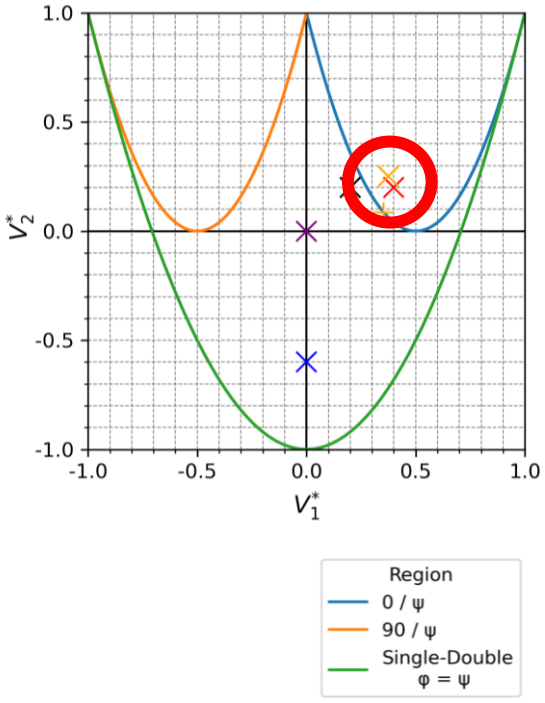

Out-of-plane LPP for all laminates

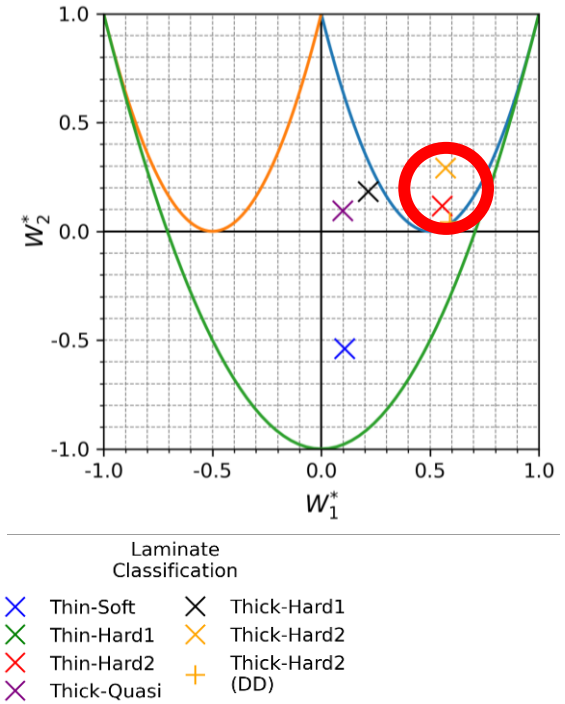

LVI Results

→ LVI conducted in accordance with ASTM D7136.

→ Post impact – NDT inspection – C-scan images.

→ Delamination area computed used custom Python script.

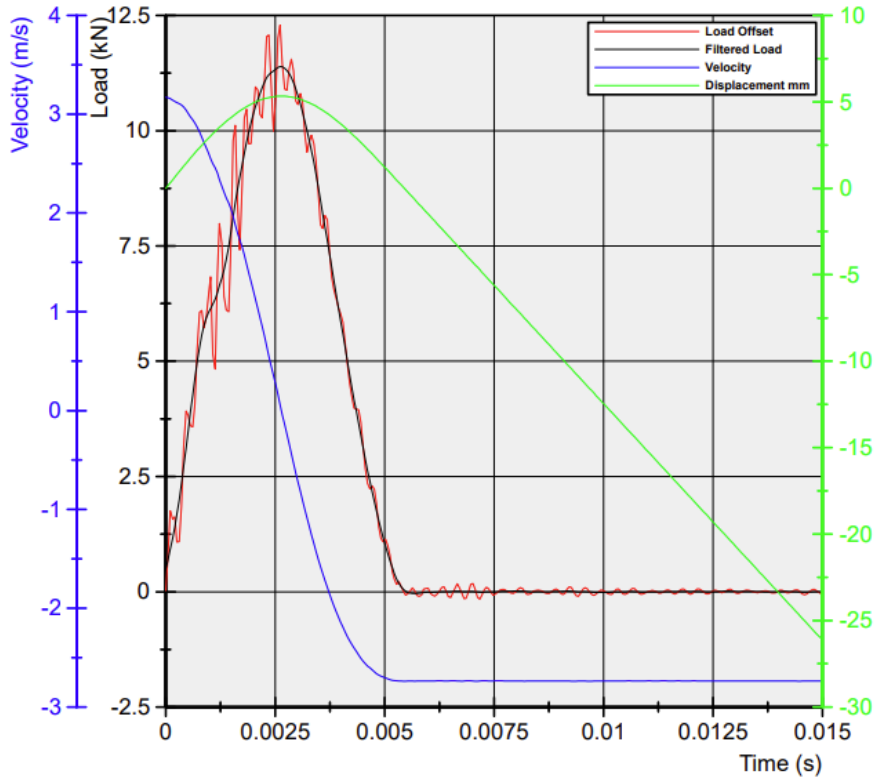

Raw C-Scan

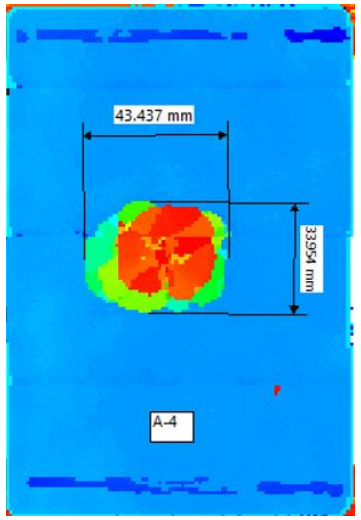

Area identified

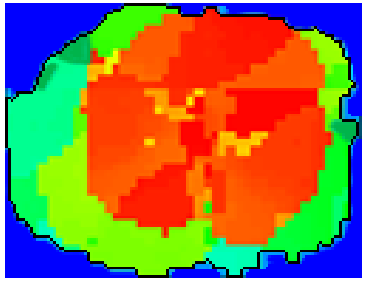

Calibration applied and area computed

1158.7 mm^2

LVI Results

- → LVI conducted in accordance with ASTM D7136.
- → Post impact – NDT inspection – C-scan images.
- → Delamination area computed used custom Python script.

Raw C-Scan

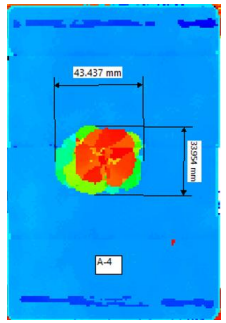

Area identified

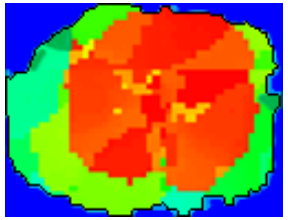

Calibration applied and area computed

1158.7 mm^2

Thinner Laminates

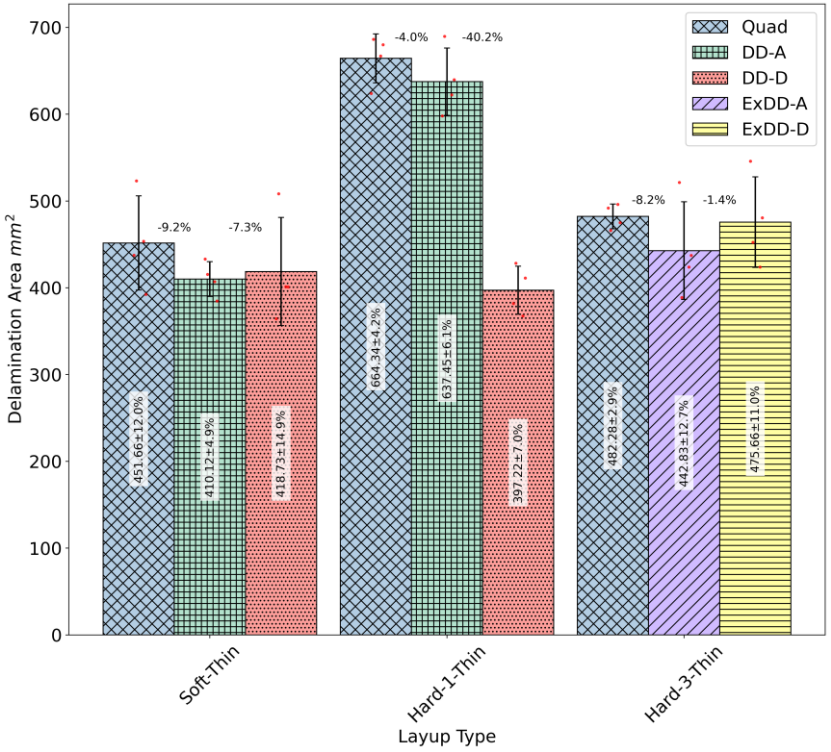

Thicker Laminates

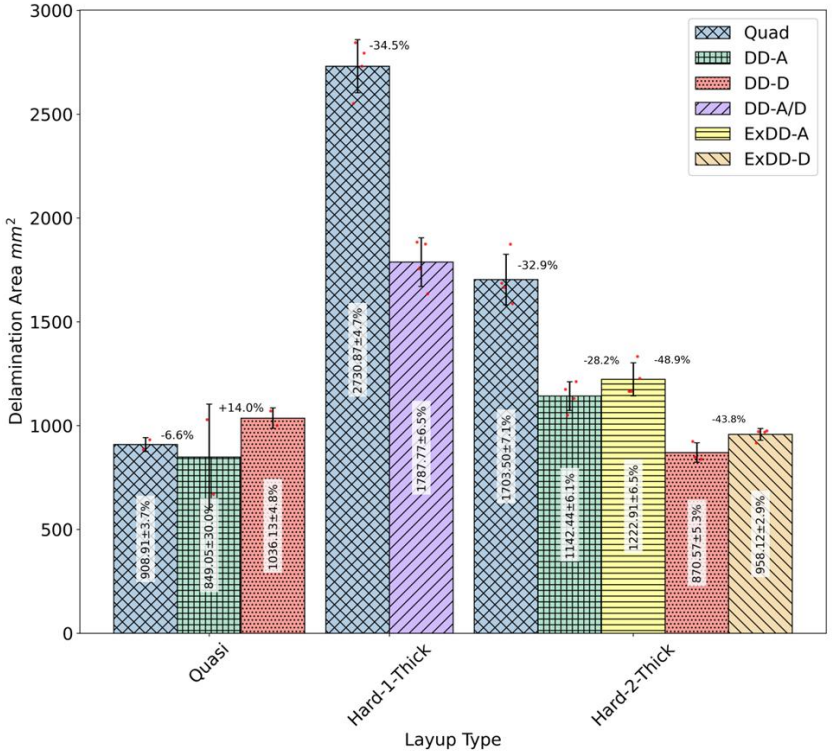

- → Average 17.7% decrease in delamination area using DD-A laminates.
- → Average 23.2% decrease in delamination area using DD-D laminates.

CAI Results

→ CAI testing in accordance with ASTM D7137.

→ 3D DIC carried out for thinner laminates.

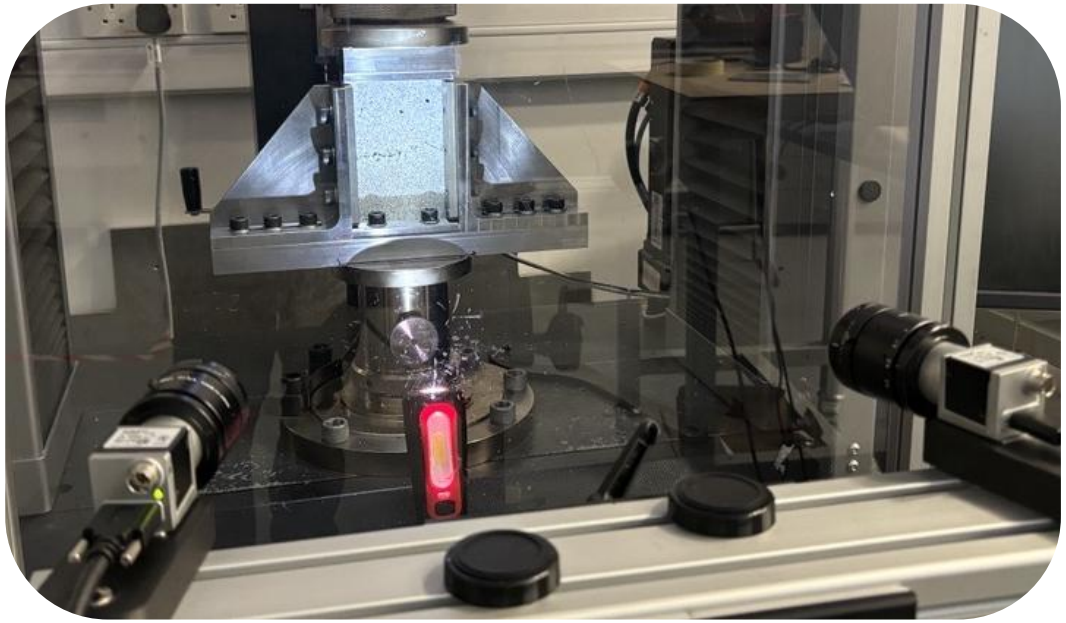

CAI test with 3D DIC setup

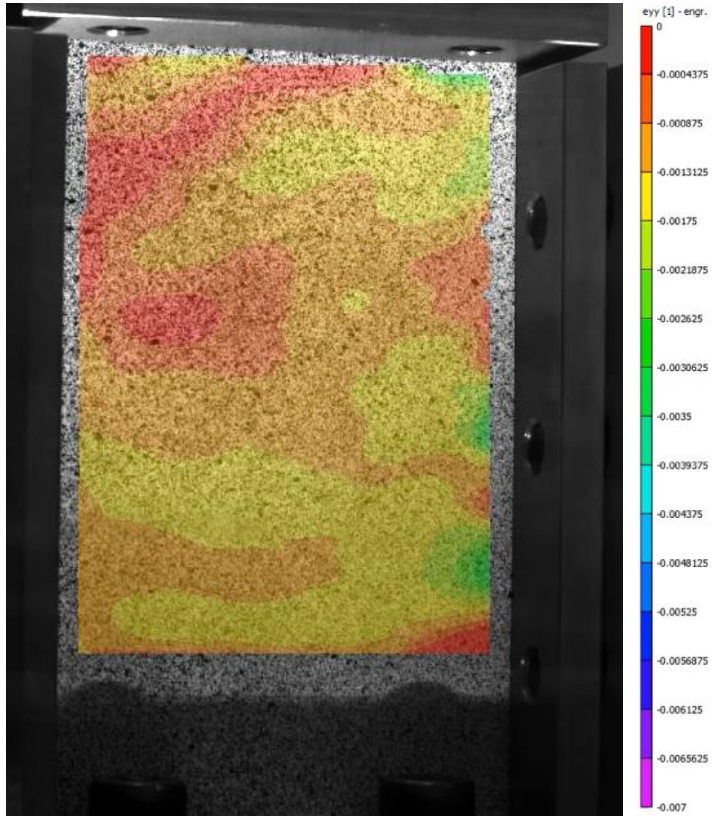

Axial strain during CAI test

CAI Results

→ CAI testing in accordance with ASTM D7137.

→ 3D DIC carried out for thinner laminates.

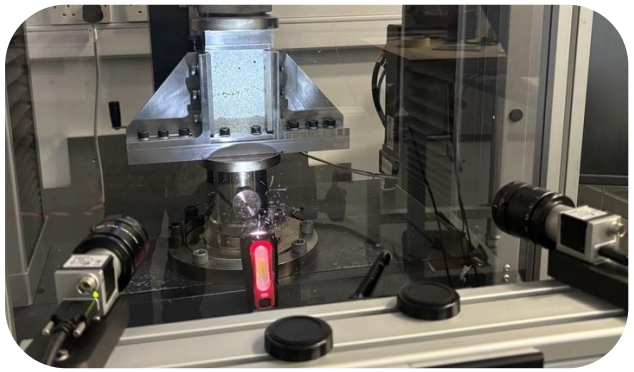

CAI test with 3D DIC setup

Thinner Laminates

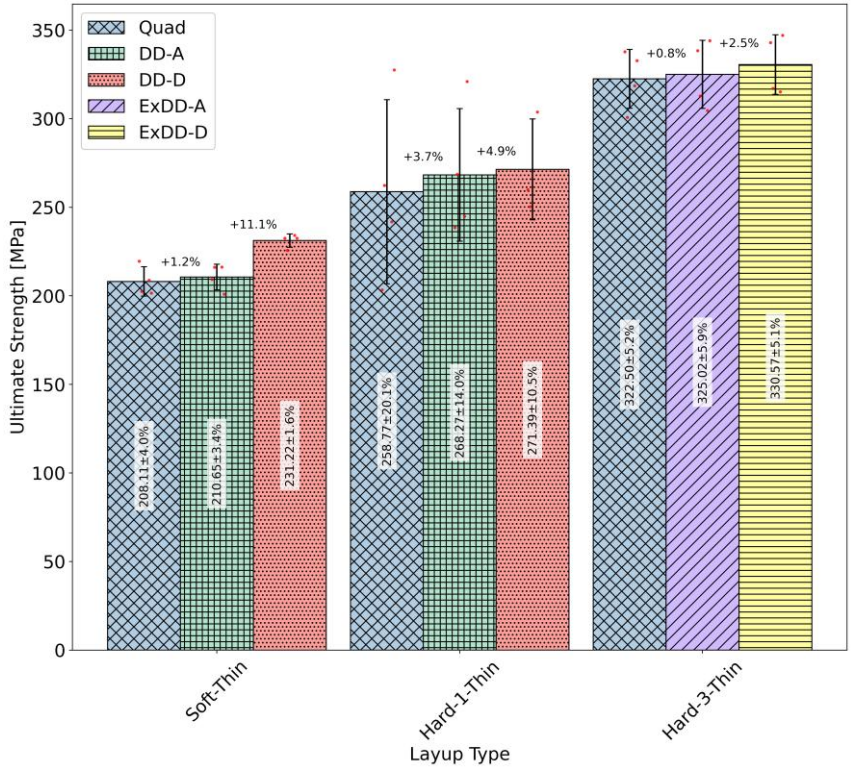

Thicker Laminates

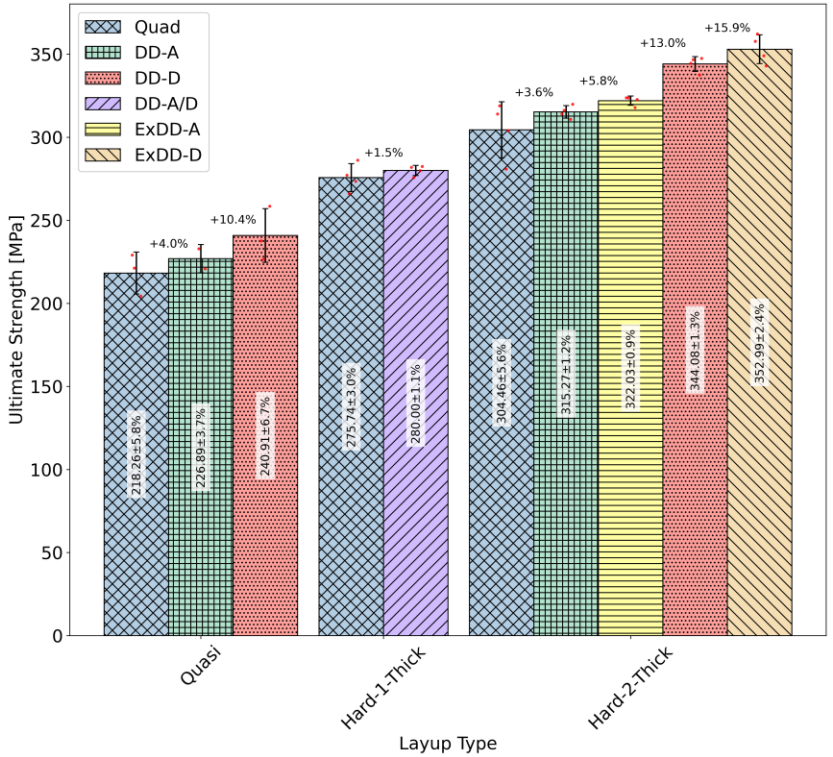

→ Similar CAI strength between Quad and DD-A laminates with average difference of 2.9%.

→ Average 8.5% increase in CAI strength using DD-D laminates.

→ Large variation in Hard thin CAI strength values due to buckling of the specimens – verified through DIC.

Summary

1. Proposed and validated robust homogenisation criteria & introduced Symmetry-Enhanced Double-Double (SEDD) Laminates

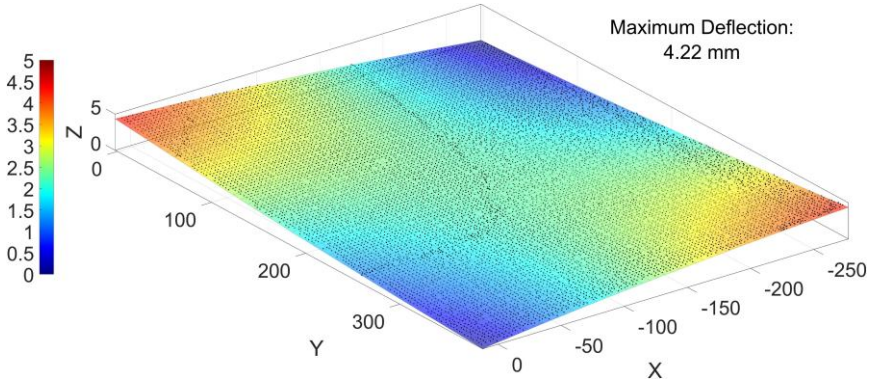

$B^{Tr*} < 0.02$

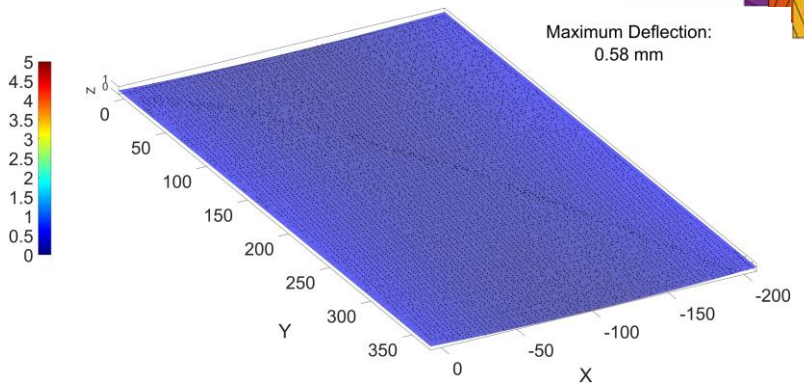

$B^{Tr*} < 0.01$

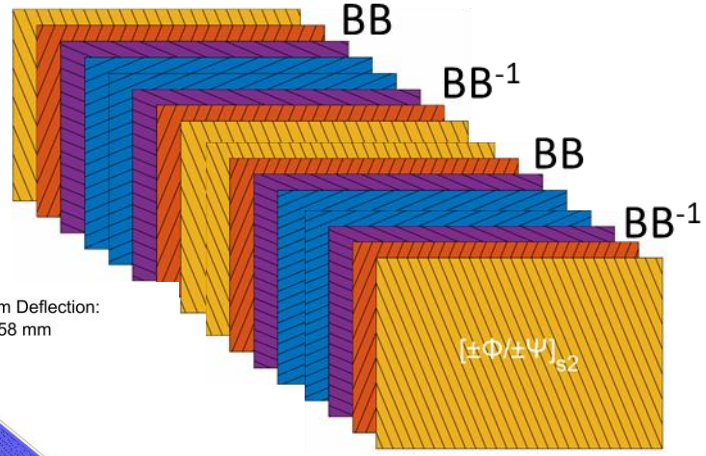

Summary

1. Proposed and validated robust homogenisation criteria & introduced Symmetry-Enhanced Double-Double (SEDD) Laminates.

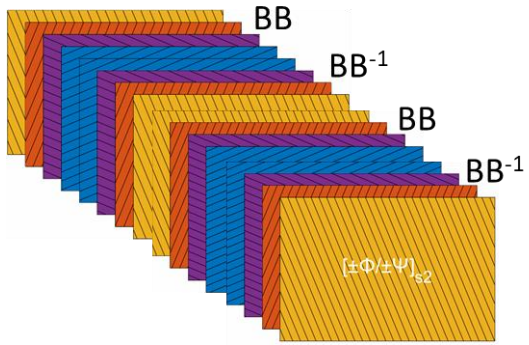

2. Developed a framework to convert any laminate to DD laminate & assessed strength through various mechanical tests.

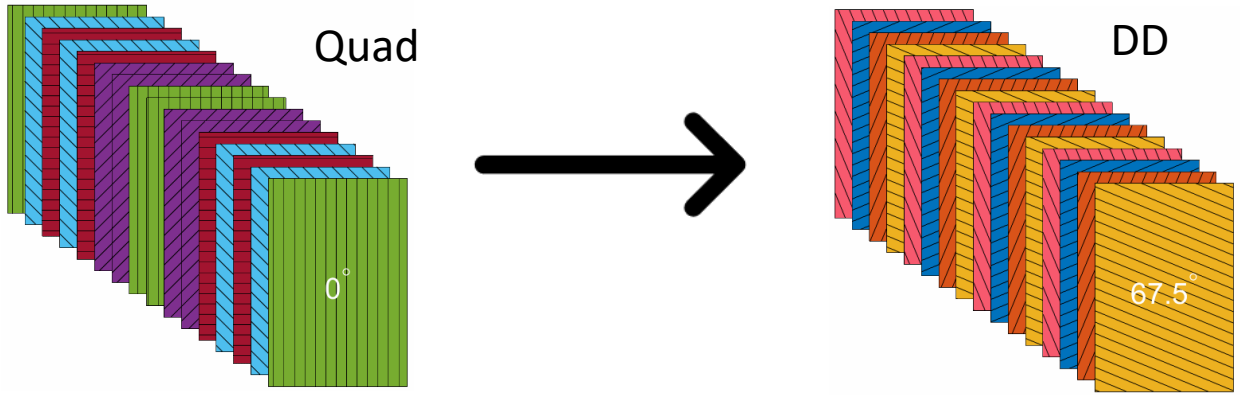

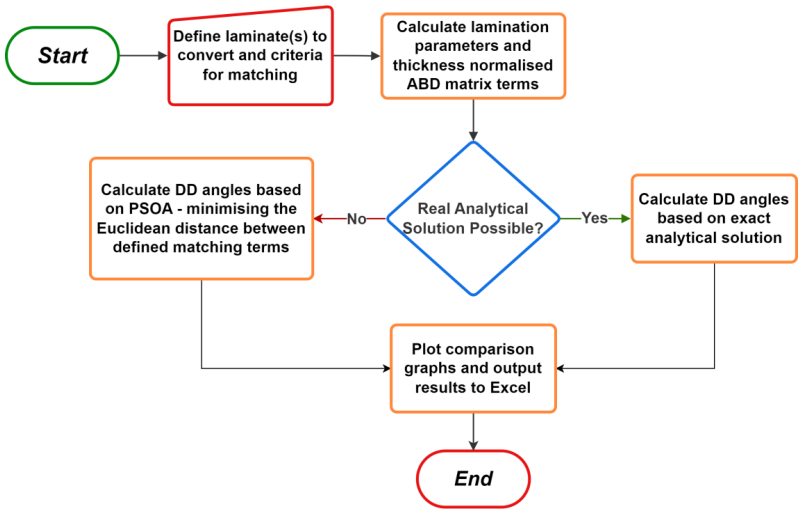

Summary

1. Proposed and validated robust homogenisation criteria & introduced Symmetry-Enhanced Double-Double (SEDD) Laminates.

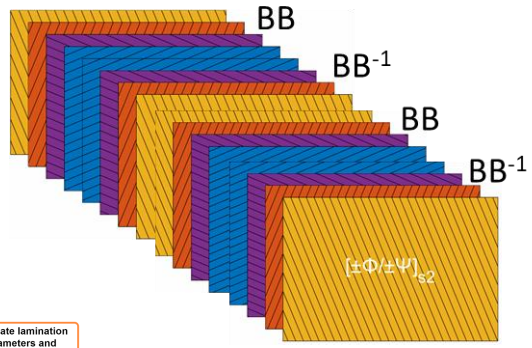

2. Developed a framework to convert any laminate to DD laminate & assessed strength through various mechanical tests.

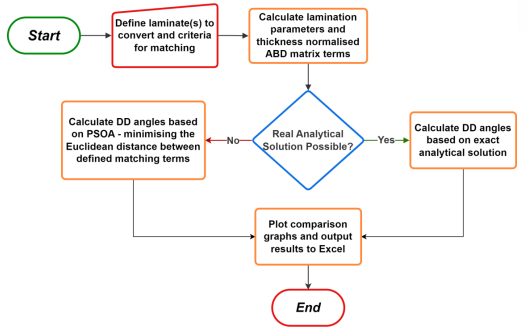

3. LVI and CAI testing assessing the performance of DD laminates and their comparison to Quad laminates.

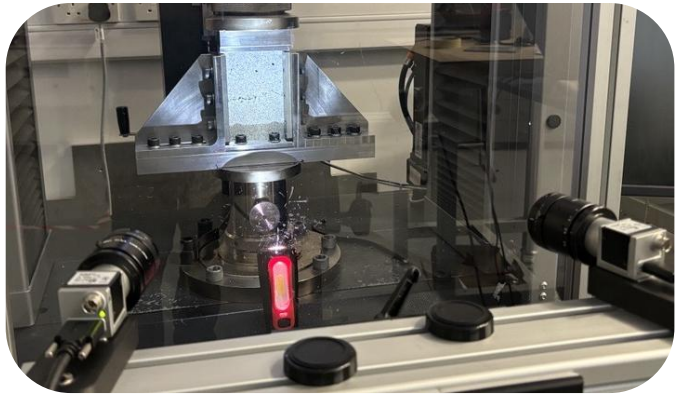

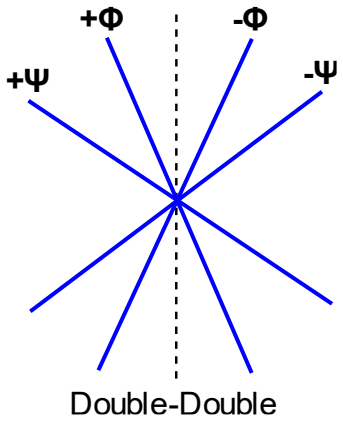

Questions?

Homogenisation Paper

Aidan Hawkins MEng | Ph.D. Researcher
ahawkins05@qub.ac.uk

LinkedIn

QUEEN'S UNIVERSITY BELFAST
SCHOOL OF MECHANICAL AND AEROSPACE ENGINEERING

Acknowledgements:
Dr Ali Aravand
Dr Scott Millen
Prof Stephen Tsai

SPIRIT AEROSYSTEMS

Study of the Impact and Compression After Impact behavior of Double-Double Laminate

Geoffrey Gisclon[1,2], Pablo Navarro[1], Olivier Dorival[1], Steven Marguet[1], Jean François Ferrero[1], Leonard Serrano[2]

1 : Université de Toulouse, Institut Clément Ader, UMR CNRS 5312, INSA/ISAE/Mines Albi/UPS, 3 Rue Caroline Aigle, 31400, Toulouse, France
geoffrey.gisclon@univ-tlse3.fr

2 : Alten Labs, Toulouse, France

Abstract

This study deals with the low velocity impact and post-impact behavior of Double-Double laminates. Impact on composite structures is one of the most common and critical sources of damage. The brittleness of composite materials makes them more vulnerable to such type of loading (matrix cracking, fibre breakage, delamination). The recent Double-Double method developed by S.Tsai [1] offers new perspectives for design optimization and manufacturing. Double-Double method seems to allow a better freedom and a possible better optimization in a laminate choice. The work presented aims to understand and quantify the key damage mechanisms in these structures, as well as to compare impact and post impact response to traditional laminates, with a view to a potential replacement and weight saving. For this, drop-weight impact tests and compression after impact tests have been carried out.

Keywords: Low velocity impact, Compression after impact, Double-Double laminates, damage tolerance

1. Introduction

Impact is one of the most common and most penalizing sources of damage for composite structures. Indeed, the brittleness, heterogeneity and lamination make them more vulnerable to this effect. Impact have to be studied for laminate structures especially in the field of aeronautics as it can be critical: bird collision, hail, tool falls during maintenance [2].

The impact damages commonly observed are intralaminar matrix cracks, delaminations and fibers breakage [3,4]. The mechanisms that control the initiation and propagation of theses damages are strongly influenced by the architecture of the composites. The first damage that appears is matrix cracking, then delamination is initiated which are very penalizing for the compressive strength of the laminates [5,6].

As failure mechanisms are difficult to represent with simple models, in industry, conservative empirical models and charts have been implemented.

The Double-Double method developed by Stephen W. Tsai [1] & al. is an innovative concept of lamination. It consists of a stack of structures called “building blocks” comprising 4 angles $[\pm\varphi/\pm\psi]$ [1], [7], [8]. These angles are defined according to the desired mechanical properties and can be between 0° and 90°.

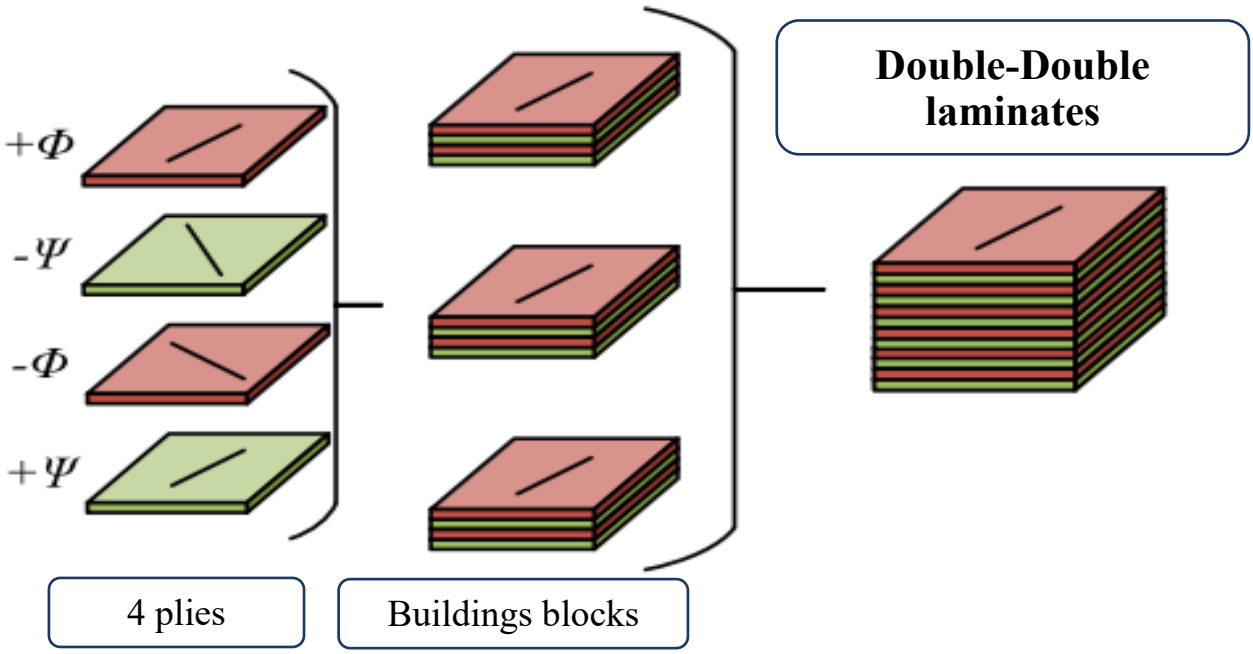

Figure 1 General principle of double-double method [12]

This method was developed to provide more freedom in the sizing and to bypass the restrictive lamination rules for manufacturers. Better optimization for composite seems possible.

Double-Double laminates are different than traditional ones (interface numbers, mismatch angle, homogenization…). Because of these properties, impact and compression after impact behavior may be different from traditional laminate behavior and challenge the principles of impact sizing.

There are a few studies that focus on the impact tolerance of Double-Double composites [9],[10],[11].

The research is still in its early stages, and no study has reached a definitive conclusion. A deeper understanding of the damage mechanisms in this type of laminate is needed.

The objective of this paper is to compare the response to low-velocity impact and post-impact of a Double-Double laminate and a traditional laminate. To do so, a traditional oriented laminate was chosen as the basis of the study named QUAD in this paper, the chosen Double-Double laminate has the same elastic properties in the plane and similar flexural properties as the reference laminate. So, the differences in stratification of the Double-Double method (angle between 0 and 90, homogenization, inter-ply angle, numbers of interface, etc...) compared to the traditional method are really studied. These two configurations were tested under low-speed impact for energies of 9J, 16J and 25J. Some specimens were analyzed using Tomography. Finally, these two configurations were tested under compression (Compression After Impact) in order to fully evaluate the impact tolerances of these two configurations. The tests were carried out according to ASTM D7136/D7136M and ASTM D7137/7137M standards.

2. Material and Methodology

2.1. Material and Stacking sequence design.

In this work, the material used was Toray 2510 Prepreg, P707AG-15 Fiber T700G. The

unidirectional propriety are summarized in Table 1. The base line Quad laminate was selected not according to the ASTM D7136. The QUAD stacking sequence is $\mathbf{[45/0_2/-45/90_2/45/0_3/-45/90]_s}$ resulting of a total thickness of 3.65 mm.

The configuration of the Double-Double laminate was made so that the in plane and flexion elastic properties are nearly the same as the QUAD laminate properties. For the comparison study it is important to have the same membrane stiffness for in plane load, whereas in impact test bending stiffness is more relevant.

The classic laminate theory (CLT) describes the behavior of laminate with the matrix $[\boldsymbol{A}, \boldsymbol{B}, \boldsymbol{D}]$:

$$\begin{bmatrix} \boldsymbol{A} & \boldsymbol{B} \\ \boldsymbol{B} & \boldsymbol{D} \end{bmatrix}$$

With;

A: in-plane stiffness matrix

B: membrane-bending coupling matrix

D: Bending stiffness matrix

It was arbitrary decided to have a perfect match for the in-plan properties and nearly the same for bending properties.

A way to achieve that is to use the laminates parameters. Tsai and Pagano [13] demonstrate that matrix A, B and D are a combination of materials parameters and laminates parameters. These lamination parameters depend only on the stacking sequence of the laminate (orientation and positioning of the plies)

In-plane laminates parameters $\boldsymbol{\xi^1_{A,Quad}, \xi^2_{A,Quad}}$ were evaluated for the QUAD laminate and the angles of Double-Double were calculated with this:

Quad stacking sequence $\longrightarrow (\boldsymbol{\xi^1_{A,Quad}, \xi^2_{A,Quad}})$

$(\boldsymbol{\xi^1_{A,Quad}, \xi^2_{A,Quad}}) \longrightarrow (\boldsymbol{\xi^1_{A,DD}, \xi^2_{A,DD}})$

$(\boldsymbol{\xi^1_{A,DD}, \xi^2_{A,DD}}) \longrightarrow \boldsymbol{\varphi \; and \; \psi}$

The Double-Double laminate for this specimen based on the extensional stiffness matrix was $\mathbf{[7/-64/64/-7]_{6T}}$. For these specimens, a perfect match was achieved with the [A] matrix and [D] matrix were quite similar. The A, B and D matrix are summarized in table 2.

Concerning the bending stiffness, the difference between the maximum of the matrix coefficient $\boldsymbol{D_{11}}$ is less than $\mathbf{2}\%$. Moreover, according to Christoforou [14] the response of FRP under low velocity impact is a function of the equivalent bending stiffness $\mathbf{D_{eq}} = \sqrt{\frac{\mathbf{A+1}}{\mathbf{2}}\mathbf{D_{11}D_{22}}}$, where $\mathbf{A} = \frac{\mathbf{D_{12}+2D_{16}}}{\sqrt{\mathbf{D_{11}D_{22}}}}$. The difference in equivalent bending stiffness between the laminates is less than 3%. It can be considered that Double-Double and Quad specimen have nearly the same elastics properties.

Engineering constant		Identification
E_1	[GPa]	125
E_2	[GPa]	8.41
ν_{12}	–	0.31
G_{12}	[GPa]	4.23
ρ	[kg.m^{-3}]	1 517
Ply thick-ness	[mm]	0.152

Table 1 Materials properties

The absence of mirror symmetry does not allow to obtain a zero-coupling matrix B. Mechanical couplings and thermal warping may exist. Homogenization makes it possible to overcome these problems. The repetition of building block makes it possible to obtain a "homogeneous" distribution of plies in the thickness of the laminate. Homogenization allows Double-Double laminates to behave like a homogeneous orthotropic material — meaning no mechanical coupling, no thermal

Matrix A, B and D for the Quad laminate:

$$A = \begin{bmatrix} 247 & 43.7 & 0 \\ 43.7 & 175 & 0 \\ 0 & 0 & 49{,}5 \end{bmatrix} \times 10^6 \quad D = \begin{bmatrix} 283 & 57.3 & 18.1 \\ 57.3 & 167 & 18.1 \\ 18.1 & 18.1 & 63.8 \end{bmatrix} \quad and \; B = [0]_{3,3}$$

Matrix A, B and D for the Double-Double laminate:

$$A = \begin{bmatrix} 247 & 43.7 & 0 \\ 43.7 & 175 & 0 \\ 0 & 0 & 49.5 \end{bmatrix} \times 10^6 \quad D = \begin{bmatrix} 278 & 47.8 & 0 \\ 47.8 & 191 & 0 \\ 0 & 0 & 54.3 \end{bmatrix} \quad and \; B = \begin{bmatrix} 0 & 0 & -4820 \\ 0 & 0 & 4820 \\ -4820 & 4810 & 0 \end{bmatrix}$$

Table 2 Matrix A $(Pa.m)$,B $(Pa.m^2)$ and D $(Pa.m^3)$

warping. While perfect homogenization is never truly achieved, increasing the repetition of building block brings the laminate closer to this ideal behavior. For this reason, a homogenization criterion has been defined [1]. When this criterion is met, the laminate is generally expected to exhibit no warping during curing, no excessive residual stresses, and no membrane-flexural coupling.

Homogenization criterion [1]:

$$|A^* - D^*| < 2\% \; Tsai$$
$$and$$
$$|B^*| < 2\% \; Tsai$$

With $A^* = \frac{A}{h}$; $B^* = \frac{2B}{h^2}$; $D^* = \frac{12D}{h^3}$ and

h the laminate thickness

The criterion is validated by the Double-Double laminate.

The two laminates therefore exhibit similar macroscopic elastic behavior in theory. However, from a mesoscopic perspective, the ply orientations differ between them, leading to a different distribution of both in-plane and out-of-plane stresses. Additionally, the number of interfaces and the inter-ply angles vary between the two stacking sequences.

Specimen	Quad	Double-Double
Number of interface	14	23
Inter-angle ply	Always 45°	Variable 72°, 53° *et* 14°

Table 3 Laminates configurations

2.2. Drop-weight and compression after impacts test

2.2.1. Drop-weight

Specimen were tested for low-velocity impact using a drop-weight device with a mass of 2 kg and an hemispheric impactor with a diameter of 16 mm for impact speeds between 3 and 5 m/s. The specimen dimensions are 150 x 100 mm. These low-velocity impacts are characteristic of so-called "classic" incidents in the workshop, such as tools falling onto parts or collisions during transport. The specimens were placed over a flat support fixture base with a 125 x 75 mm rectangular frame, which allowed the impactor to contact through the specimen without interferences.

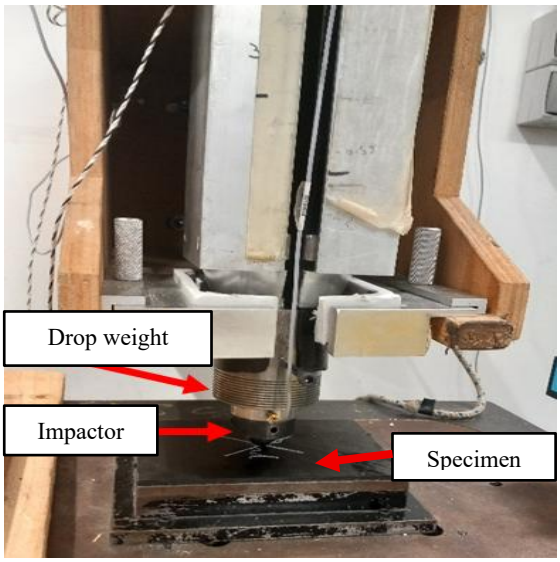

Figure 2 Impact test setup

Impact energies of 9 J, 16 J, and 25 J were applied, corresponding respectively to impact velocities of 3 m/s, 4 m/s, and 5 m/s. For each energy level, two specimens per configuration were tested.

2.2.2. Compression after impact test

The Compression After Impact (CAI) tests were performed using a Hydraulic test machine (Schenk PCS 450 kN) and a 250 kN load cell. To prevent global buckling, anti-buckling devices were implemented. Digital image correlation was employed to identify the buckling mode and monitor strain evolution.

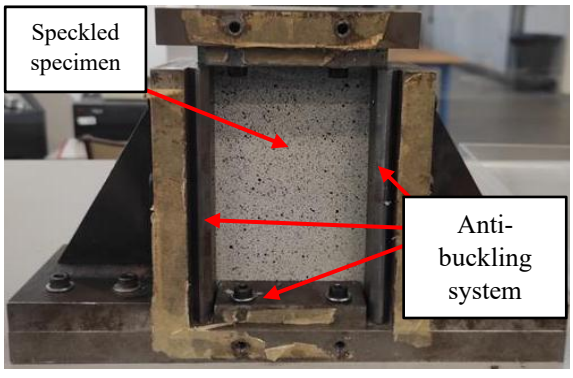

Figure 3 CAI test apparatus

3. Results

At 3 m/s, the damage induced is not significant enough to observe clear differences in either the impact response or the compression after impact performance. For the highest speed (5m/s), the samples are fully perforated so the difference in behavior between QUAD and Double-Double laminate is not relevant.

Fig 4 shows a comparison between the response of the two stacking sequences at $4\,m.s^{-1}$ $(E = 16J)$. It can first be observed that both laminates exhibit similar elastic behavior, which confirms the relevance of the selected stacking sequence. However, the energy dissipated by the Quad laminates is significantly higher than that dissipated by the Double-Double laminates. The first noticeable drop in stiffness — indicative of the onset of severe damage — does not occur at the same load level. The Quad laminates show a gradual reduction in stiffness starting around 3 kN, whereas the Double-Double laminates experience a more abrupt drop later, at approximately 3.8 kN, suggesting a delayed but more sudden damage initiation.

To complete this study, X-ray computed tomography (CT) scans were performed. Figure 5 shows the total delaminated area for both stacking configurations. The Quad laminates exhibit approximately twice the delaminated area ($\mathbf{15\,400\ mm^2}$) compared to the Double-Double laminates ($\mathbf{8000\ mm^2}$), suggesting that the Quad laminates sustained more severe damage during impact.

The delamination shape in the Quad laminates corresponds to the typical patterns observed in this type of test. In contrast, the Double-Double laminates display more circular delamination zones, likely due to their distinct ±45° inter-ply angles. Interestingly, while the Double-Double laminates present a greater number of delaminated interfaces, these are smaller in size. Conversely, the Quad laminates exhibit fewer delaminated interfaces, but the damage is more severe at each one.

This suggests that the Double-Double stacking sequence may distribute impact energy more effectively across multiple interfaces, leading to smaller, more controlled delaminations.

Figure 6 presents the results of the compression-after-impact (CAI) tests. As expected, both laminates exhibit similar elastic behavior. However, the failure load is significantly higher for the Double-Double laminates, reaching 50 kN compared to 33 kN for the Quad laminates. This corresponds to failure stresses of 137 MPa and 90 MPa, respectively. This difference in residual strength can be attributed to the extensive delamination observed in the Quad laminates. The large delaminated areas result in the formation of several thinner sub-laminates, which are more prone to local buckling and thus offer lower post-impact compressive resistance.

Additionally, the failure modes differ notably: the Double-Double laminates exhibit a more abrupt, brittle failure, whereas the Quad laminates show a more progressive failure behavior.

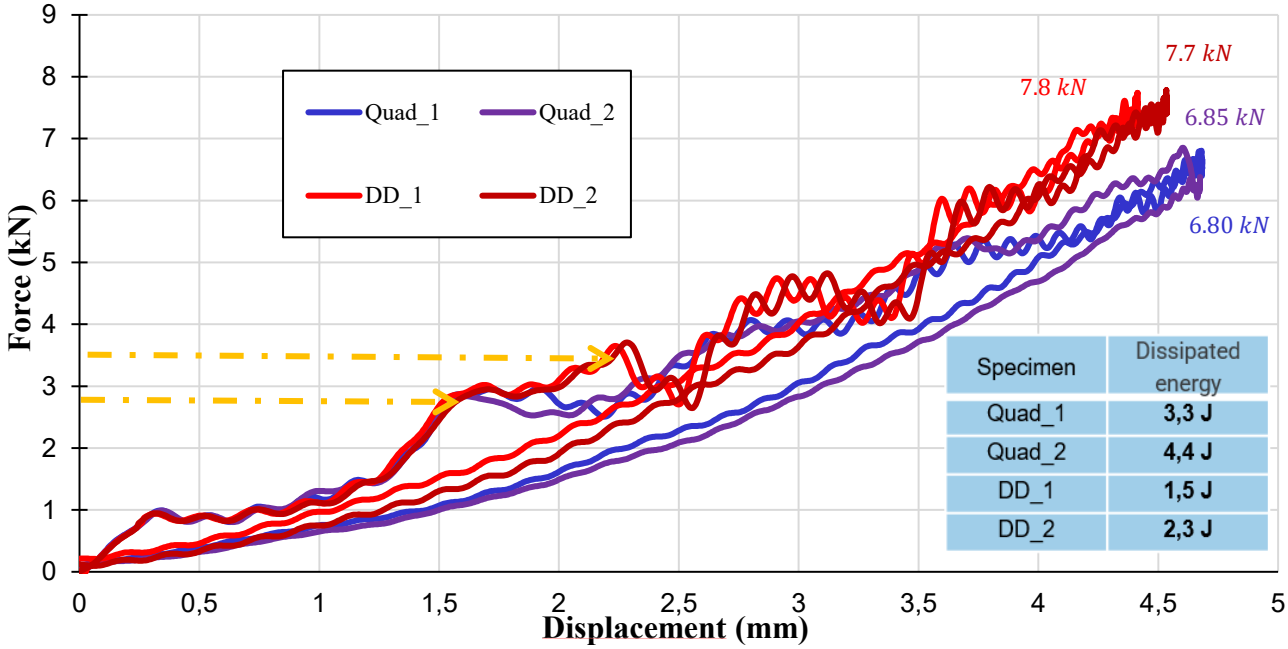

Figure 4 Impact results at 4 m/s for Quad & Double-Double laminates

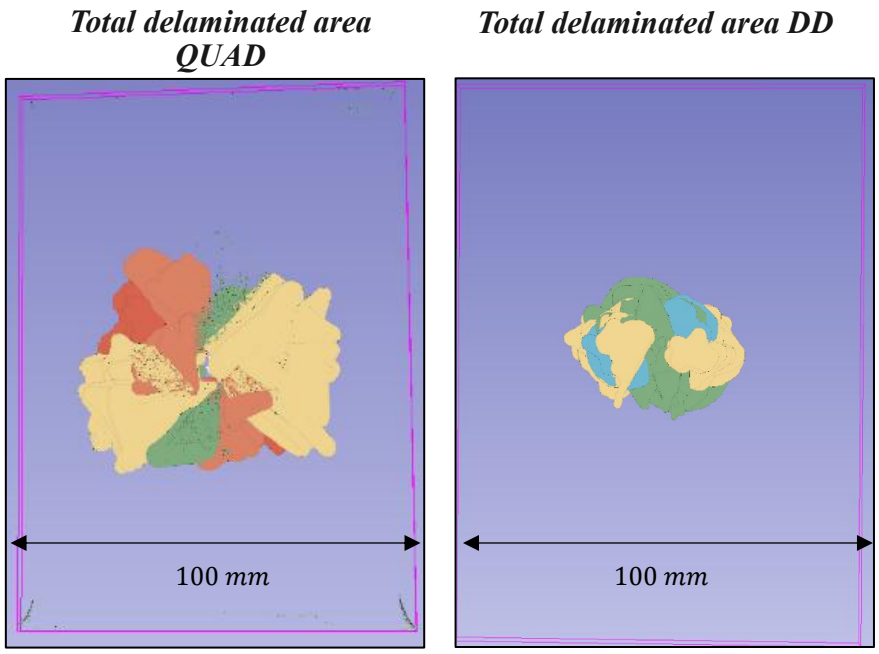

Figure 5 Delaminated surfaces after impact at 4 m/s on a Double-Double laminate (left) & Quad (right)

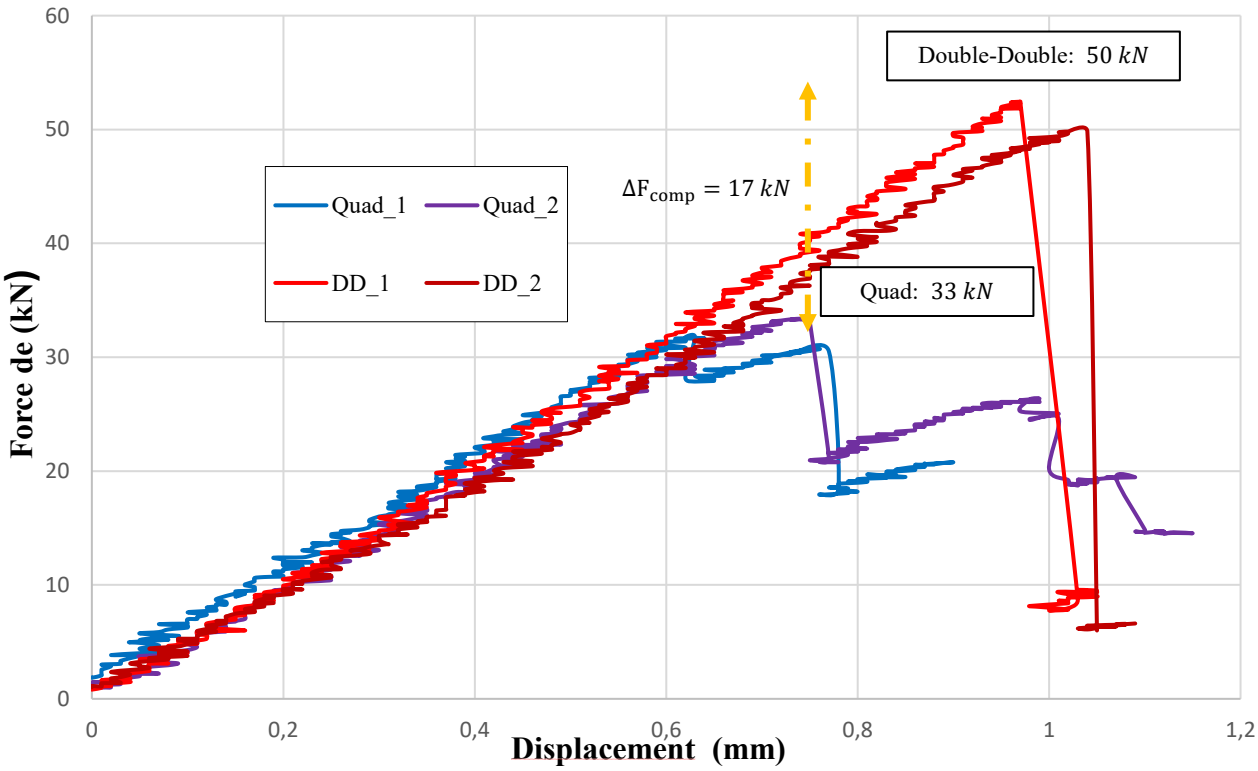

Figure 6 CAI results with LVI at 4 m/s for Quad & Double-Double laminate

4. Conclusion & perspectives

In this study, the response of a Double-Double laminate was analyzed and compared to that of a traditional Quad laminate with equivalent elastic properties. The selected Double-Double configuration appears to exhibit better damage tolerance than its Quad counterpart. However, caution is warranted: only one Double-Double configuration was studied, and the Quad laminate used for comparison may not have had the most optimized ply dispersion, as the primary objective was to comply with all the traditional design constraints.

Beyond the number of interfaces, other factors may contribute to the improved performance of the Double-Double laminate—such as a more favorable distribution of transverse shear stresses, the absence of bending-twisting coupling, or differing interfacial properties. Further investigation is necessary to better understand the damage mechanisms involved. Digital image correlation will be used to analyze both global and local buckling behavior of the specimens.

Since Double-Double laminates represent a broad class of layups, no general conclusions can be drawn based on the study of a single configuration. Future work will involve exploring other Double-Double configurations with varied angles and stacking sequences.

In addition to impact and compression-after-impact tests, quasi-static tests will be conducted to further understand the damage evolution in this type of laminate. To complement the experimental work, a numerical campaign will be carried out using the semi-continuous model developed at the Clément Ader Institute of Toulouse [15].

References

[1] S. W. Tsai, B. G. Falzon, and A. Aravand "*Double-double: Simplifying the Design and Manufacture of Composite Laminates"*, 2nd ed. Stanford University, Department of Aeronautics & Astronautics, 2023.

[2] N. Hongkarnjanakul, "Modélisation numérique pour la tolérance aux dommages d'impact sur stratifié composite: de l'impact à la résistance résiduelle en compression" , Ph.D. dissertation, ISAE, Toulouse, France, 2013

[3] S. Abrate "Impact on laminated composites: recent advances" *Applied Mechanical Review*, 47 (11), pp. 517-544, 1994.

[4] J. Aboissière "Propagation de dommages d'impact dans un matériau composite stratifié à fibres de carbone et résine époxyde" , Ph.D. thesis, Université de Toulouse, 2003.

[5] H. Choi, F. Chang "A model for predicting damage in graphite/epoxy laminated composites resulting from low-velocity point impact" *J Compos Mater*, 26, pp. 2134-2169, 1992.

[6] P. Hu, "An experimental study on the influence of intralaminar damage on interlaminar delamination properties of laminated composites", *Composites Part A: Applied Science and Manufacturing* 131 (105783)

[7] S. W. Tsai, "Double–Double: New Family of Composite Laminates", AIAA Journal, vol. 59, issue 11, Nov. 2021, doi : 10.2514/1.J060659

[8] T. Massard, "Opening the frontiers between manufacturing, materials and optimum design of composite structures", Stanford University,

[9] R. D. da Cunha, T. G. Targino, C. Cardoso, E. P. da Costa Ferreira, R. C. S. Freire Júnior, and J. D. D. Melo, "Low velocity impact response of non-traditional double-double laminates," *Journal of Composite Materials*, vol. 57, pp. 1807–1817, 2023

[10] S. L. J. Millen, M. A. Aravand, Z. Ullah, and B. Falzon, "Studies on the impact and compression-after-impact response of 'Double-Double' carbon-fiber reinforced composite laminates," *Double-Double: Simplifying the Design and Manufacture of Composite Laminates*, pp. 161–180, 2023.

[11] P. Shabani, L. Li, and J. Laliberte, "Low-velocity impact (LVI) and compression after impact (CAI) of Double-Double composite laminates," *Composite Structures*, 2024.

[12] P. Fang, « Uniform multiple laminates interpolation model and design method for double–double laminates based on multi-material topology optimization », *Computer Methods in Applied Mechanics and Engineering*, 2025.

[13] S. W. Tsai et N. J. Pagano, *Invariant properties of composite materials*. Technomic Publishing Company Lancaster, 1968. Consulté le: 8 juillet 2025.

[14] A. P. Christoforou, A. S. Yigit, « Scaling of low-velocity impact response in composite structures », *Composite Structures*, vol. 91, nº 3, p. 358-365, 2009.

[15] L. Manseri, P. Navarro, O. Dorival, S. Marguet, B. Mahmoud, et J.-F. Ferrero, « Development of a hybrid element to model intralaminar damage in thick

composite plates under impact loading », *Composites Part B: Engineering*, vol. 222, p. 109024, 2021.

ICCM24
AUGUST 4-8, 2025
BALTIMORE CONVENTION CENTER
BALTIMORE, MARYLAND, USA

No Technical Paper Submission for:

Carlos Cimini

INVESTIGATION OF THE MECHANISMS OF FUZZBALL FORMATION AND GROWTH IN AUTOMATED FIBER PLACEMENT (AFP) OF THERMOSET COMPOSITES

Genki Matsubara[1,2], Kameron Harmon[2], Samuel F. Pedigo[2] and Marco Salviato[2,3]

[1]William E. Boeing Department of Aeronautics and Astronautics, University of Washington
3940 Benton Lane NE, UWAA Box 352400, Seattle, WA 98195, USA
Email: genki55@uw.edu, web page: www.linkedin.com/in/genki-matsubara-2a7b391bb

[2]Advanced Composites Center, University of Washington, Seattle, WA 98195, USA
Web page: https://www.uwacc.uw.edu/

[3]William E. Boeing Department of Aeronautics and Astronautics, University of Washington
3940 Benton Lane NE, UWAA Box 352400, Seattle, WA 98195, USA

Keywords: Fuzzball, Composite Manufacturing, AFP, Prepreg, Mechanical Defects

ABSTRACT

In this work we investigated the fundamental mechanisms behind fuzzball formation in Automated Fiber Placement (AFP), leveraging an Electroimpact AFP 4.0 cell. The goal was to develop a deeper understanding of the sources of imperfections that degrade the mechanical performance of composite components fabricated via AFP. To this end, we achieved direct observation of fuzzball formation by integrating an optical microscope into the AFP end effector. These observations revealed that most fuzz accumulation occurs in the feeding channel section. To further study the phenomenon, we developed a dedicated AFP workbench that allows for controlled material feeding under variable prepreg tension. Using this setup, we examined fuzzball formation under different prepreg tensions and feed rates in a static environment with constant temperature and humidity. These tests enabled real-time visualization of the fuzzball growth process. We then performed a quantitative analysis of the initiation and steady state growth phases. Our measurements showed that fuzzball growth rate scales with a power-law function of growth duration, feed rate, and prepreg tension. Additionally, we extended our investigation to full AFP operations, focusing on the effects of path curvature. By applying the same quantitative evaluation method, we found that fuzzballs grow more rapidly as the radius of curvature decreases. This curvature effect was further characterized in terms of the contact angle between the feeding channel and a prepreg tape, revealing a strong correlation with fuzzball formation.

1 INTRODUCTION

In modern aircrafts such as the Boeing 787 and Airbus A350, carbon fiber composite materials are integral to critical structural components, comprising approximately 50% of the total weight of the aircraft [1]. For manufacturing, initially hand layup was the predominant fabrication method, however, to address the limitations, automated processes such as Automated Tape Laying (ATL) and Automated Fiber Placement (AFP) were soon introduced.

A 2008 Airbus report [2, 3], based on data from Spirit AeroSystems [4], indicated that the actual laydown rate for the Boeing 787 was only 8.6 kg per hour—just 20% of Boeing's original estimate of 45.4 kg per hour [3, 5]. This discrepancy arises because composite layup involves more than just material deposition; it also requires extensive rework to correct imperfections. Boeing's analysis of the 787 fuselage barrel production at its South Carolina facility [6, 7] revealed that machine layup accounted for only 24% of the total floor-to-floor cycle time, whereas inspection and rework contributed to 63% (Figure 1a). Similarly, a 2014 report from Electroimpact [8, 9], a world-leader in AFP technology development, showed that, during part fabrication, 32% of time was dedicated to inspection and repair, 14% to process errors, and only 30% to machine layup (Figure 1b). Additionally, at the Defense Manufacturing Conference 2014, USA, Maass reported 55% of floor-to-floor time is consumed for 37%

inspection and 18% rework (Figure 1c). Consequently, more than half of AFP build time is spent on imperfection repair. This issue strongly motivates research into defect reduction and its impact on mechanical properties.

Harik et al. [11] classified AFP imperfections into 14 categories, with tow gaps/overlaps and wrinkles identified as common defects. Among these defect types, Foreign Object Debris (FOD) represents a unique anomaly [11]. FOD refers to unintended objects that become embedded in a part during layup, such as glove fragments, washers, backing films [12], or foil [10, 13]. These contaminants can degrade component performance by inducing wrinkles and other structural defects [14]. One of the specific FOD, i.e. fuzzball (Figure 2), consists of accumulated composite material—either carbon fiber or resin—that collects on the AFP machine head and is dropped on the part under fabrication, introducing excessive material volume into laminates [11]. Benson and Arnold [15] investigated fuzzball formation during the tape slitting process for AFP using Bismaleimide (BMI) prepregs. Their findings revealed that fiber fragments accumulate on machine components when fibers rub against surfaces in the material path process. The study examined five different BMI materials, all of which produced unacceptable amounts of fuzz despite considerable efforts by material vendors to reduce fuzz generation.

Although several studies on fuzzball formation have been published, quantitative investigations remain limited. This is likely due to the difficulty of evaluating fuzzball formation under standardized conditions, given variations in AFP machines, material properties, layup path designs, material feed rates, prepreg tension, and environmental factors such as temperature and humidity. To enhance AFP composite manufacturing efficiency and ensure component reliability, this research aims to establish a quantitative evaluation framework for fuzzball formation. Specifically, this study focuses on developing a controlled workbench for fuzzball formation analysis, conducting in-situ observations of fuzzball growth during AFP operations, and assessing the dependence of fuzzball growth rates on manufacturing conditions.

2 MATERIALS AND METHODS

2.1 Materials and AFP system

For this study, we used a 1/4” unidirectional prepreg slit tape (P2362W-19L:T800S-24K/3900-2C) supplied by Toray Industries Inc. [16]. The prepreg material, featuring a fiber areal weight of 192 g/m2 and a resin content of 35.5 wt%, was stored in a freezer at a temperature of -18.6 ◦C (-1.4 ◦F) before use. Before each test, the bobbins were allowed to reach room temperature inside a vacuum bag for 24 h. For all tests performed in this study, room temperature and humidity ranged between 17.9 and 24.5◦C and 20 and 53% respectively. The experimental work presented in this report was carried out on an Electroimpact AFP 4.0 cell installed at the Advanced Composites Center (ACC) [17], at the University of Washington (Figure 3).

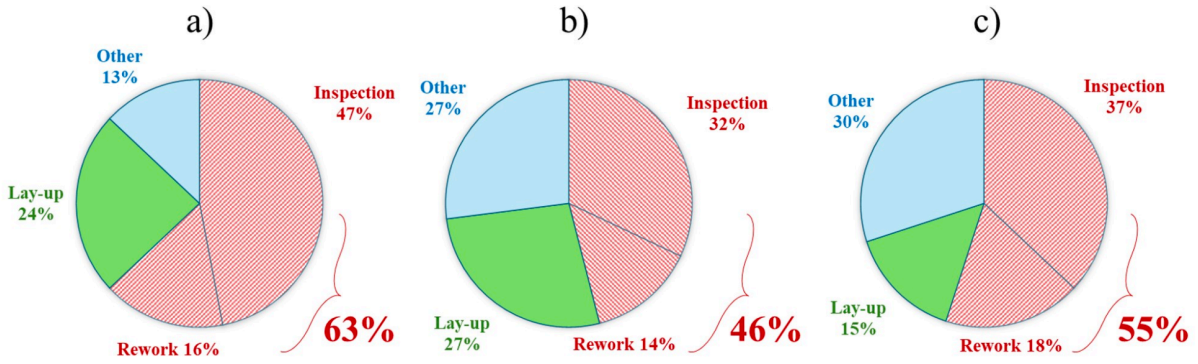

Figure 1: Study on floor-to-floor time distribution for fuselage barrels [10]. a) 787 fuselage barrel AFP performance by Boeing (2012) [6, 7] b) Electroimpact report (2014) [9] c) Estimate at the Defense Manufacturing Conference (2014) [10].

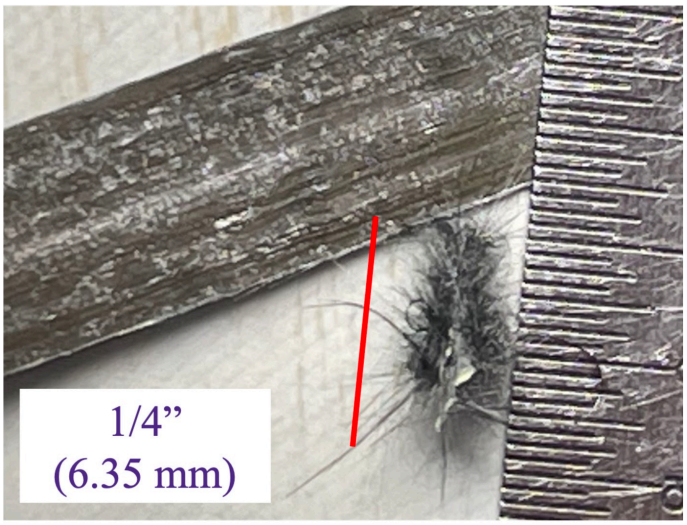

Figure 2: A fuzzball formed on a curved path operation. The scale bar corresponds to 1/4” (6.35 mm).

2.2 Workbench study

The end-effector is composed of multiple components (Figure 4). Through a series of test runs, we determined that the majority of fuzz accumulation occurs at the feeding channel of the AFP end effector module components (Figure 4h, Figure 5). To investigate the fundamental effects of prepreg tension and feed rates, we employed an external module – referred to as the AFP workbench (Figure 6a) to feed prepregs out of the AFP head.

A USB digital microscope (AF7915MZTL by Dino-Lite [18]) was mounted to observe the feeding channel directly. Since fuzz formation is driven by contact between material and fixtures, we intentionally introduced lateral contact between the prepreg tape and the edge of the feeding channel module outlet. In all experiments, the prepreg ran parallel to the outlet edge while being fed straight through the system, as shown in Figure 4f. Feed rate and prepreg tension were varied independently. Feed rates ranged between 2.52 and 10.1 in/s; 8.4 in/s representing our standard feed rate for qualified flat straight layups. Prepreg tension was maintained between 0 and 3.42 lbs, of the upper limit for our AFP system. Notably, no thermal input was applied during workbench tests, as heating typically occurs only during material deposition onto the tool surface (Figure 6d). Our analysis focused on the following observable operation parameters: (1) material feed rate, (2) prepreg tension, (3) layup path radius.

2.3 AFP operation study

We investigated whether the fuzzball formation model on the workbench study can be applied to realistic AFP operation in the same manner. To compare the results, we laid prepregs up on a flat coupon table in the AFP cell. For this case we used the laser heating system because otherwise the laid prepregs frequently get peeled off the tool table, although the fuzzball formation spot on the feeding channel is not exposed directly to the laser. We fed prepregs at the feed rates close to the workbench cases. We also fed at 1.67 in/s, but it showed no apparent fuzzball. To be consistent with regular AFP operations, we followed the basic operation program, at which condition the prepreg tension is linearly decided by the material feed rate (Figure 6c). We also changed the layup path radius to several values: 51.5”, 62.0”, 70.0”, 80.0”, and 89.7” (Figure 7). This range was tested because with radii less than 51.5” path radius, we frequently see out-of-plane prepreg deformation on the flat table. On the other hand, if it exceeds 89.7”, we hardly see fuzzballs. Due to the difficulty of microscope mounting, we instead used a short focal lens camera mounted on the laser heating module (Figure 6b).

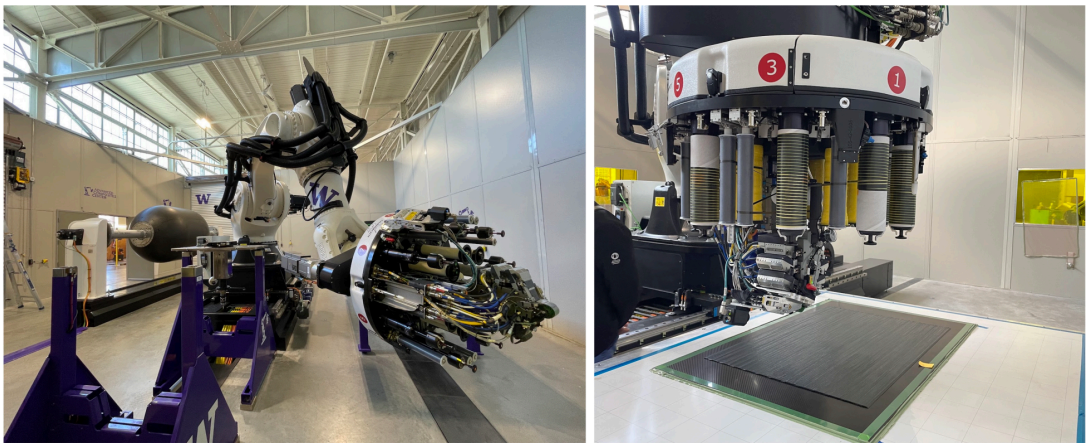

Figure 3: AFP cell at Advanced Composites Center (ACC), University of Washington. (Left) Front overview. (Right) The closeup of the end-effector equipped with 8 bobbins shown while manufacturing a 91 cm × 127 cm (36” × 50”) composite plate.

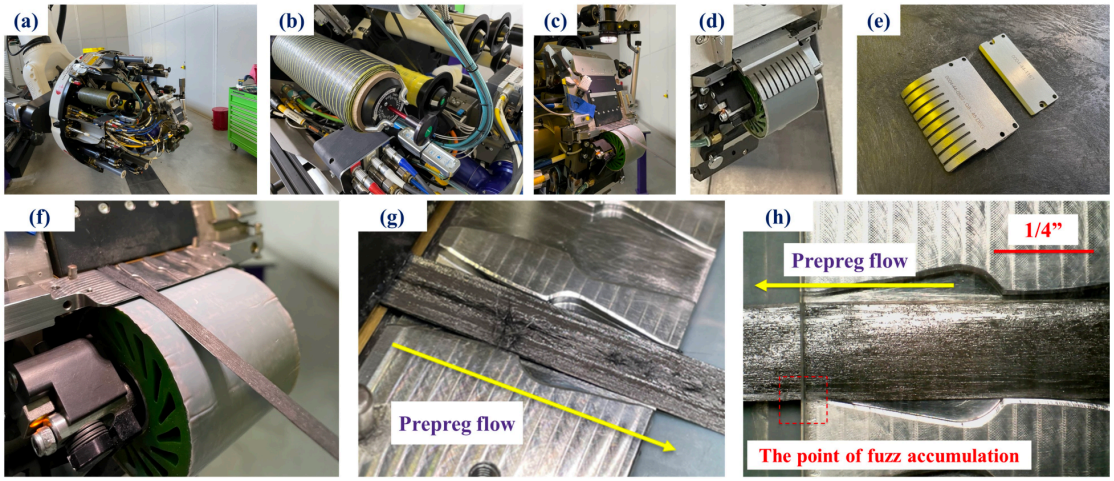

Figure 4: AFP robot end-effector and prepreg-fixture contact configuration for the tests presented in this work: end-effector (a) featuring one prepreg roll spool (b), from which the prepreg thread is fed on to the feeding module (c). The thread goes onto the compaction roller (d) through the feeding channel (e), at which the prepreg contacts the feeding channel edge (g,h).

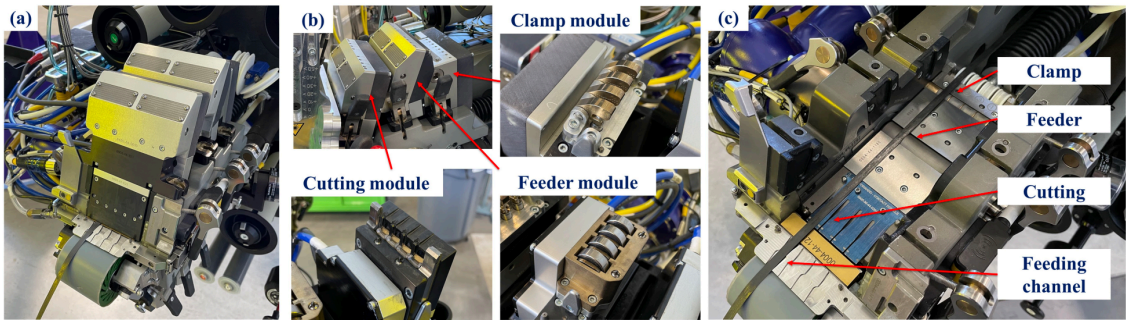

Figure 5: AFP Robot Module Components. (a) The end-effector feeder front view. (b) The feeder components: cutting module, feeder module, and clamp module. (c) The material path in the feeder.

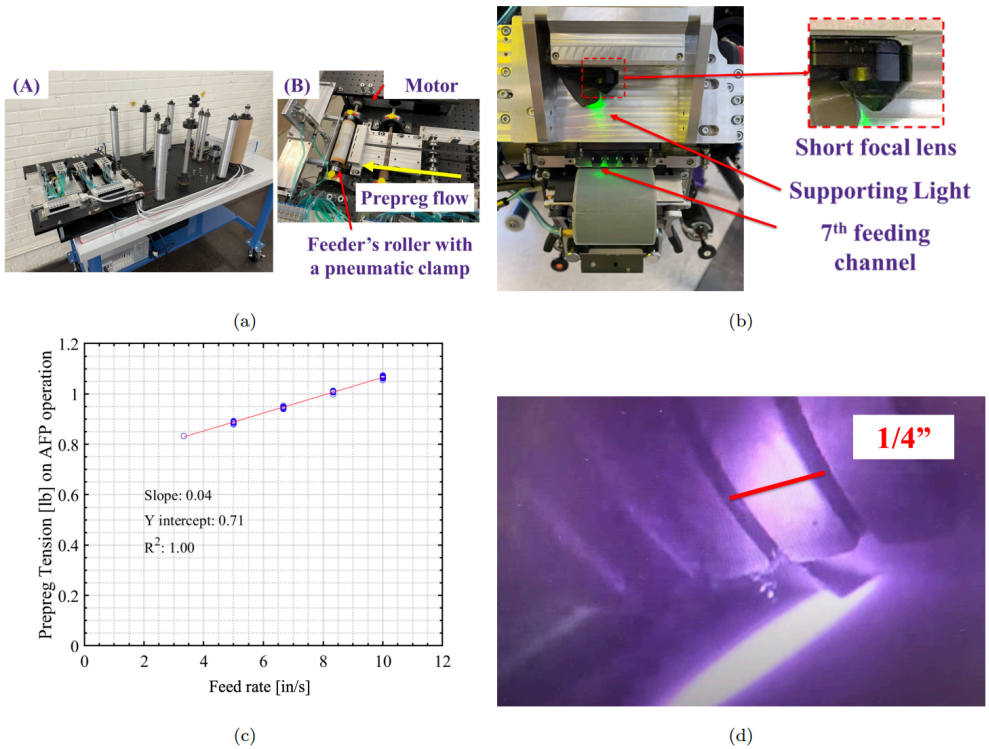

Figure 6: AFP cell's adjacent components and specifications. (a) AFP Workbench scheme: (A) Overview of the workbench module (B) The workbench feeder module. With an external motor, it pulls a prepreg thread out of the end-effector in the park zone 2. (b) The short focal lens for the fuzzball observation in AFP operation. (c) The relationship between the feed rate and prepreg tension in AFP operation. (All prepreg roll results are plotted.) (d) The prepreg local heating on the 7th channel thread. The bright area is exposed to the laser. It occurs locally in between the prepreg out of the feeder on the compaction roller and the tool table/fixture.

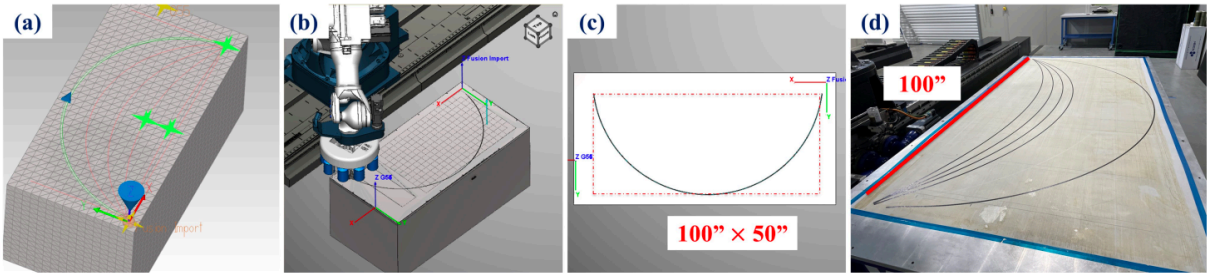

Figure 7: AFP operation path making. (a) Curved path design with VCP [19]. (b) Layup simulation onto the tool table. (c) Top view of simulation result. (d) The prepreg threads laid onto the tool table by the designed operation.

3 RESULT AND DISCUSSION

3.1 Fuzzball formation observation

In the workbench study, we captured the fuzzball formation process and examined its structural evolution (Figure 8). A fuzzball formation begins with the appearance of a white accumulation composed of prepreg matrix material that has been ground or scattered due to mechanical feeding. Shortly thereafter, chopped black fibers become embedded in the resin and are twisted together by the motion of the advancing prepreg tape. This interaction forms a spheroidal mass of resin and fibers that elongate over time. As growth continues, the spheroid begins to twist into a tangled, thread-like structure – commonly referred to as a fuzzball. The fuzzball grows in size and complexity by continuously

absorbing additional resin and chopped fibers. Eventually, it becomes large enough to be caught by the material flow and is pulled away, detaching from the feeding channel. Based on these observations, we categorized the fuzzball growth process into four distinct phases: 1) Initiation: rapid formation and growth of a spheroidal structure, 2) Stable Growth: semi-constant growth while retaining a spheroidal shape, 3) Unstable Growth: transition to an irregular, non-spheroidal morphology, and finally 4) Detachment: separation of the fuzzball from the material flow. In the following sections, we focus primarily on the behavior observed during Stages 1 and 2 (Initiation and Stable Growth), which precede the onset of morphological instability.

In the workbench study, we captured the fuzzball formation process and observed its structure (Figure 8). A fuzzball starts to form with white accumulation. This white part is made of prepreg matrix ground/scattered by the feeding. Then, black chopped fibers are involved in the initial resin, being twisted by the flowing prepreg thread. It forms a spheroidal object of resin and fibers, and that quickly begins to elongate. Next it starts to be twisted again into a tangled thread ball, or a fuzzball. As it keeps growing, the object gets longer and bigger absorbing more resin and chopped fibers, and finally that fuzzball is hooked by material flow and then detached.

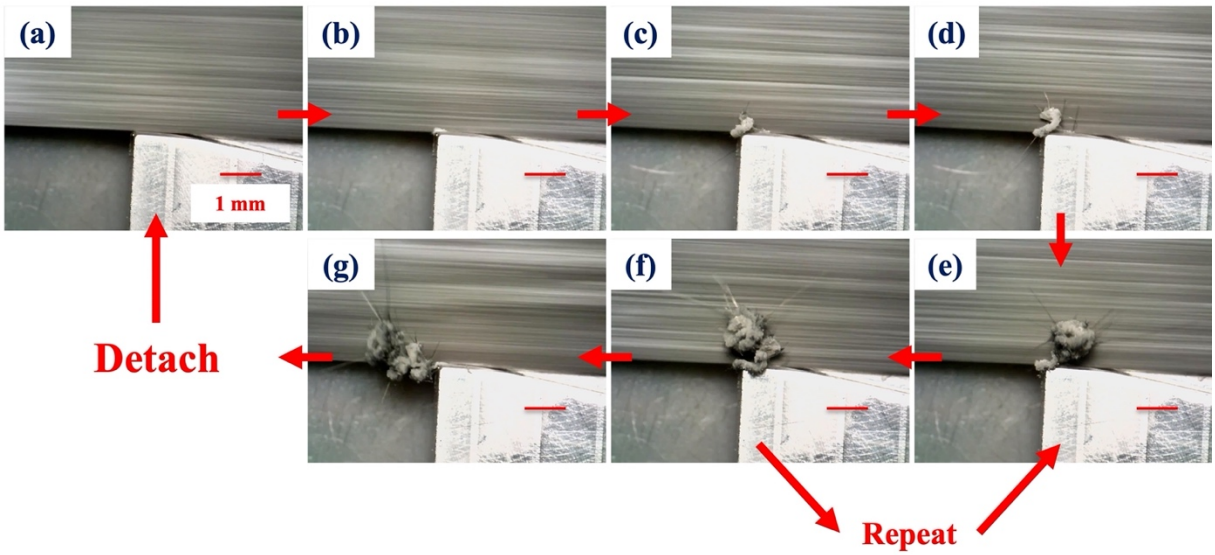

Figure 8: Fuzzball growth cycle. (a) Feeding starts. (b) Initiation (A fuzzball seed is formed.) (c) Stable growth in a spheroid form. (d) Starting to be twisted. (Unstable growth starts in a non−spheroidal form.) (e) Keep growing unstably. (f) Twisted again and grow until (g) it gets large enough to be hooked by the prepreg, and then detached.

3.2 Workbench study result

To quantitatively analyze the fuzzball growth process, we plotted the fuzzball major and minor axis lengths against the corresponding amount of fed prepreg material (Figure 9). The results suggest that the amount of material fed is not the primary factor determining fuzzball size. In contrast, Figure 10b shows the aspect ratio between the major and minor axes remains nearly constant throughout growth. This ratio follows a normal distribution with a mean value of approximately 5. Assuming the fuzzball can be approximated as a prolate spheroid with a constant aspect ratio s, the minor axis length l_{minor} is constantly proportional to the major axis length l_{major}, as expressed in Equation (1). Consequently, the fuzzball volume can be approximated using the standard formula for the volume of a prolate spheroid, as shown in Equation (2).

$$l_{major} = s\, l_{minor} \tag{1}$$

$$Fuzzball\ Volume = \frac{4\,\pi l_{major}^3}{3\,s^2} \tag{2}$$

The underlying assumption of our analysis is that the rate of fuzzball volume growth is proportional to Q, the volume of material removed per unit time as Equation (3):

$$\frac{d}{dt}\left(\frac{4\,\pi l_{major}^3}{3\,s^2}\right) = C_{Env.Mat.}\,Q \tag{3}$$

This relationship includes a proportionality coefficient, $C_{Env.Mat.}$, which accounts for environmental conditions (e.g. temperature and humidity). In this study, $C_{Env.Mat.}$ is assumed to be constant under the controlled test conditions. To quantify growth, we measured the fuzzball size starting from the point of initiation—defined as the moment when the fuzzball length first begins to increase from zero as (4):

$$l_{major} = \left(\frac{C_{Env.Mat.}\,Q}{\frac{4}{3}\pi s^{-2}}\right)^{\frac{1}{3}} t^{\frac{1}{3}} \tag{4}$$

$$\because\ l_{major}(t=0) = 0$$

To normalize the effect of prepreg tension on fuzzball growth, we draw upon principles from Metal Cutting Theory. This theory suggests that the depth of cut a is proportional to the product of powers of cutting speed and cutting force [20]. In the context of our study, these variables correspond to the feed rate and prepreg tension, respectively (Figure 11) This relationship is expressed as follows:

$$\frac{d}{dt}l_{major} = \left(\frac{C_{Env.Mat.}\,Q}{\frac{4}{3}\pi s^{-2}}\right)^{\frac{1}{3}} \frac{1}{3}\,t^{-\frac{2}{3}} \tag{5}$$

$$a = C_{CT}\,V^{a_V}\left(\frac{P}{b}\right)^{a_P}(1-\sin(\alpha))^{a_\alpha} \tag{6}$$

where b represents the width of cut—equivalent to the thickness of the prepreg tape in our setup—and C_{CT} is a proportionality constant. Additionally, α denotes the rake angle (i.e. the angle between the material and the cutting surface), and a_α is its associated exponent. In the workbench tests, α is assumed to be constant.

Following this framework, the material removal rate per unit time (Q) can be expressed as the product of cutting speed, width of cut, and depth of cut as in (7):

$$Q = V\,b\,a \tag{7}$$

By substituting Equations (6) and (7) into the earlier expression for fuzzball growth rate, Eq. (5), the following growth model can be derived as (8):

$$\begin{aligned}\frac{d}{dt}l_{major} &= C_{L.M.}P^{(\frac{a_P}{3})}V^{\frac{(a_V+1)}{3}}t^{a_t}\,(1-\sin(\alpha))^{(\frac{a_\alpha}{3})}\\ &\equiv C_{L.M.}\,P^{A_P}V^{A_V}t^{a_t}\,(1-\sin(\alpha))^{A_\alpha}\\ \because\ C_{L.M.} &= \frac{1}{3}\left(\frac{C_{Env.Mat.}\,b^{(1-a_P)}C_{CT}}{\frac{4}{3}\pi s^{-2}}\right)^{\frac{1}{3}}\end{aligned} \tag{8}$$

According to this equation model, $a_t = -\frac{2}{3}$, $A_V = 1$ and $A_P = 0.59$ are determined. We plot the growth rate/$V^{A_V}P^{A_P}$ to t^{a_t} (Figure 12). It organizes the manufacturing condition effects of material feed rate and prepreg tension normalized with the growth duration in fuzzball stable growth.

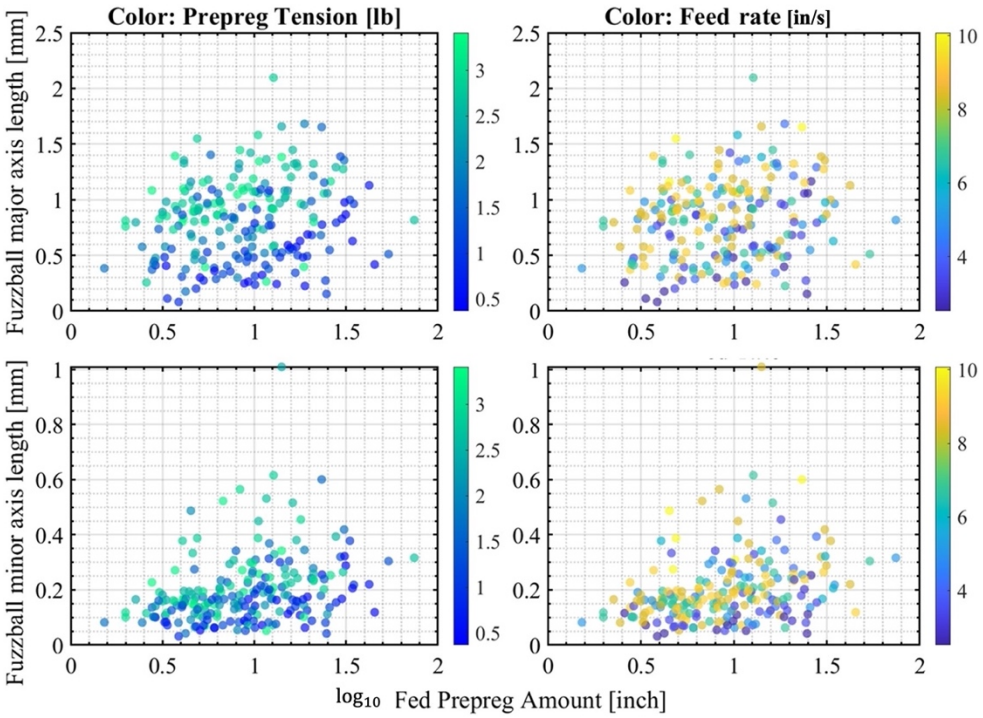

Figure 9: Fuzzball major/minor axis length to log the fed prepreg amount.

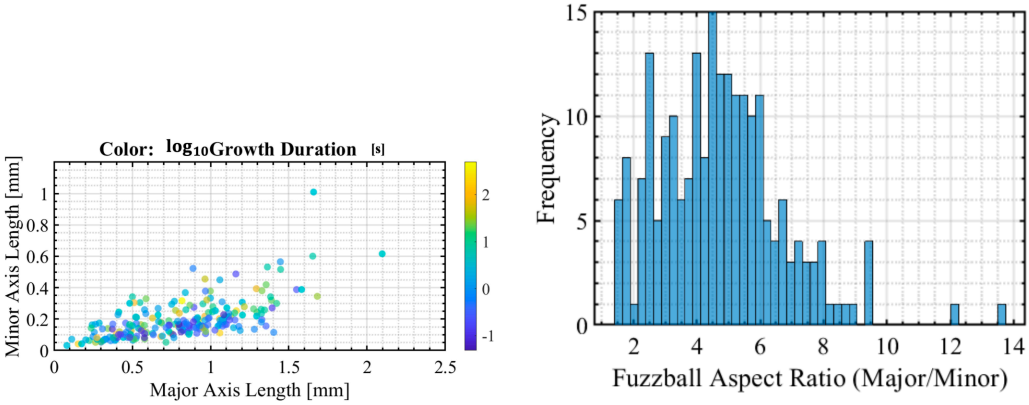

Figure 10: Aspect ratio behavior to growth duration. Aspect ratio refers to the division of the major axis length by the minor axis length. (a) The relationship between the major and minor axis length. (b) Fuzzball aspect ratio histogram.

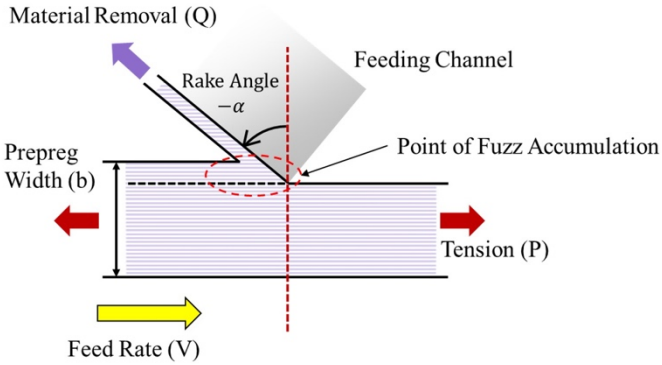

Figure 11: Schematic geometry of fuzzball formation in accordance with Cutting Theory [20]. The rake angle is positive in the clockwise direction.

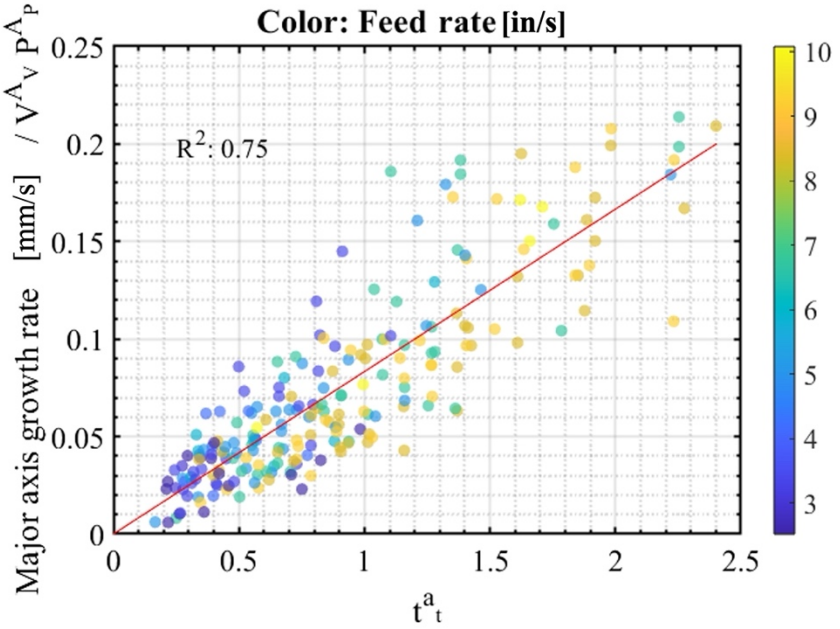

Figure 12: Major axis growth rate/$V^{A_V}P^{A_P}$V to t^{a_t}.

3.3 AFP Operation Study Result

We investigated fuzzball growth behavior during AFP operations along curved paths with constant radii of curvature. The major axis growth rate was normalized using the same parameters defined in the workbench study specifically A_V, A_P and a_t. We plot the normalized growth rate to that in Figure 13 and measured the slopes of each subplot. The slope comparison to path radius is in Figure 14 (Left). The workbench experiments correspond to straight-path feeding, which translates to a path radius greater than 89.7". Notably, we did not observe any fuzzball formation when the path radius exceeded this value. To incorporate curvature effects into the cutting model, we attempted to relate the rake angle α and its exponent A_α to the path radius, as path curvature influences the prepreg's position within the feeding channel and thus alters the effective rake angle. However, due to the small range of observed α, it was not possible to obtain direct quantitative measurements. To address this, we defined the rake angle α parametrically as a function of path radius R, using a characteristic length l_{sp}:

$$\alpha = \frac{\pi}{2} - \arctan\left(\frac{l_{sp}}{R}\right) \tag{9}$$

This formulation satisfies two key constraints: (1) the variation in rake angle is minimal and visually negligible across cases, and (2) following the definition of rake angle [20], $\alpha = \frac{\pi}{2}$ corresponds to zero depth of cut, as the blade becomes parallel to the material surface. The parameter l_{sp} was determined in Figure 14 (Right), however, we found that any value less than approximately 0.3" yielded a good fit to the experimental data. Therefore, we selected the prepreg width of 1/4" as a representative length for l_{sp}. Additionally, we enforced the boundary condition that no fuzzball growth occurs in straight path layups (i.e. as $R \to \infty$). Based on these considerations, we determined the rake angle exponent to be $A_\alpha = 0.25$.

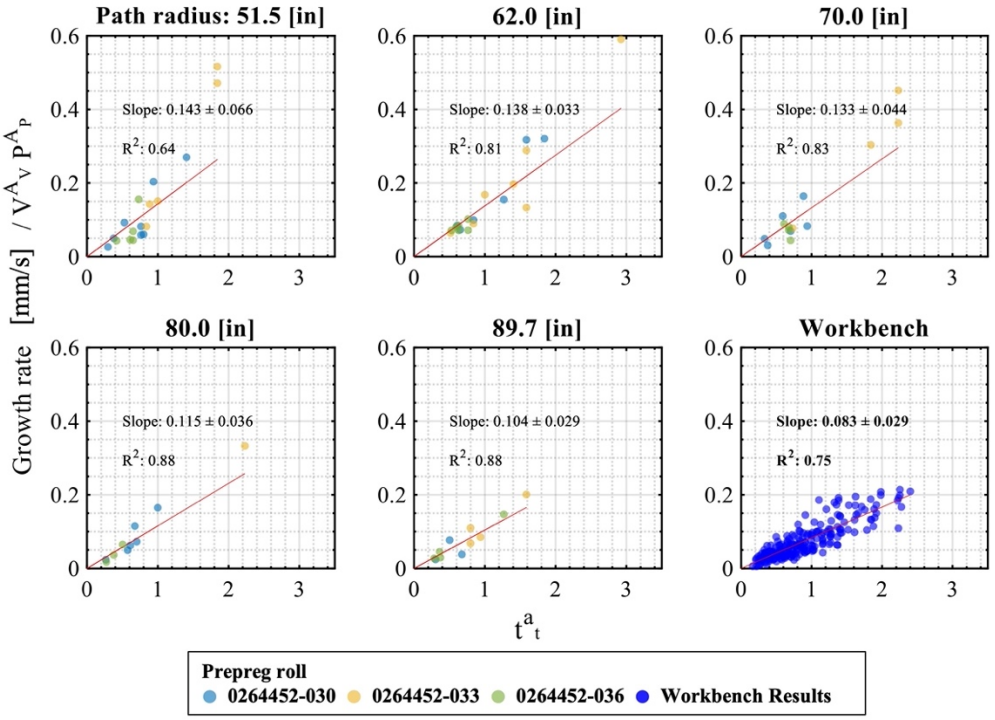

Figure 13: Major axis growth rate/$V^{A_V} P^{A_P}$ to t^{a_t} for curved-path AFP operations and workbench comparison. The workbench plot represents its data for all prepregs.

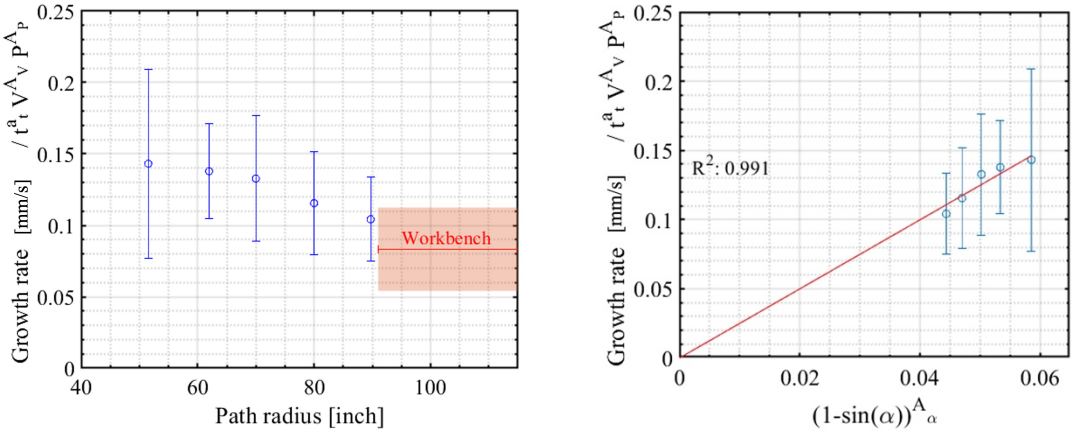

Figure 14: (Left) Path curvature effect to growth rate. (Right) Evaluation of the rake angle effect to the growth rate. For this case, α is parametrically defined in Equation (9).

4 CONCLUSIONS

This study investigated the fundamental mechanisms of fuzzball formation during Automated Fiber Placement (AFP) operations. Using a microscope, we directly observed fuzzball formation both in controlled workbench experiments and during actual AFP operation. In the workbench study, we quantified the fuzzball size and growth duration under various feed rates and prepreg tension levels. The results, interpreted through the framework of Metal Cutting Theory, revealed that the fuzzball growth rate is proportional to the product of power functions of growth duration, feed rate, and prepreg tension. In the AFP operation study, we extended this evaluation method to examine the influence of path curvature. The results quantitatively demonstrated that increased curvature (i.e. smaller path radius) leads to faster fuzzball growth. Through this combined analysis, we evaluated how key manufacturing parameters—prepreg tension, feed rate, and path curvature affect fuzzball growth rate. This framework

offers a basis for quantitatively predicting fuzzball formation behavior, and it can be extended to incorporate material-specific and environmental effects. Such predictive capabilities are critical for improving the producibility and reliability of composite components fabricated in AFP. Future work will focus on extending this study to the effects of temperature and humidity leveraging the new upgraded AFP cell at the UW Advanced Composites Center (ACC). Furthermore, computational work leveraging quasibrittle fracture mechanisms [21] frameworks such as the microplane model [22, 23] and the Discrete Model for Composites (DM4C) [24, 25, 26] is ongoing to be able to predict some of the constants identified in this work.

ACKNOWLEDGEMENTS

The authors gratefully acknowledge the generous support from ES3 Inc. and the University of Washington Advanced Composites Center (ACC), which made the experimental work presented in this study possible. We also extend our sincere thanks to Toray Industries for providing the prepreg material used in this research, through the UW ACC–Toray technical partnership.

REFERENCES

[1] Victor Giurgiutiu. Stress, vibration, and wave analysis in aerospace composites: SHM and NDE applications. Academic Press, 2022. ISBN: 978-012-813308-8.

[2] Airbus SE. Airbus SE. Accessed: January 18, 2025. URL: https://www.airbus.com/en.

[3] Airbus SAS. Boeing 787: Lessons Learnt. Accessed: January 16, 2025. 2008. URL: http://wpage.unina.it/fabrnico/DIDATTICA/PGV_2012/MAT_DID_CORSO/Design_Cases/Boeing_787_Lessons_learnt.pdf.

[4] Inc. Spirit AeroSystems Holdings. Spirit AeroSystems Holdings, Inc. Accessed: January 18, 2025. 2025. URL: https://www.spiritaero.com/.

[5] Dirk H.-J.A. Lukaszewicz, Carwyn Ward, and Kevin D. Potter. "The engineering aspects of automated prepreg layup: History, present and future". In: Composites Part B: Engineering 43.3 (2012), pp. 997–1009. ISSN: 1359-8368. DOI: https://doi.org/10.1016/j.compositesb.2011.12.003. URL: https://www.sciencedirect.com/science/article/pii/S1359836811005452.

[6] Allen Halbritter and Robert Harper. "Big parts demand big changes to the fiber placement status quo". In: SME composites manufacturing 2012 (2012).

[7] Alex Brasington et al. "Automated fiber placement: A review of history, current technologies, and future paths forward". In: Composites Part C: Open Access 6 (2021), p. 100182. ISSN: 2666-6820. DOI: https://doi.org/10.1016/j.jcomc.2021.100182. URL: https://www.sciencedirect.com/science/article/ pii/S2666682021000773.

[8] Electroimpact Inc. 2025. URL: https://www.electroimpact.com/ (visited on 01/04/2025).

[9] Todd Rudberg et al. "Improving AFP cell performance". In: SAE International Journal of Aerospace 7.2014-01-2272 (2014), pp. 317–321. URL: https://www.electroimpact.com/WhitePapers/2014-01-2272.pdf.

[10] Katharina Schlegel. "A literature review of quality control for automated lay-up processes". In: Zeitschrift Kunststofftechnik (2019). URL: https: //api.semanticscholar.org/CorpusID:209101443.

[11] Ramy Harik et al. Automated fiber placement defect identity cards: cause, anticipation, existence, significance, and progression. Tech. rep. 2018. URL: https://ntrs.nasa.gov/api/citations/20200002536/downloads/20200002536.pdf.

[12] Carsten Schmidt et al. "Thermal Image-based Monitoring for the Automated Fiber Placement Process". In: Procedia CIRP 62 (2017). 10th CIRP Conference on Intelligent Computation in Manufacturing Engineering - CIRP ICME '16. [Edited by: Roberto Teti, Manager Editor: Doriana M. D'Addona], pp. 27–32. ISSN: 2212-8271. DOI:

https://doi.org/10.1016/j.procir.2016.06.058. URL: https://www.sciencedirect.com/science/article/pii/S221282711630676X.

[13] Carsten Schmidt et al. “Evaluation of eddy current testing for quality assurance and process monitoring of automated fiber placement”. In: Composites Part B-engineering 56 (2014), pp. 109–116. URL: https://api.semanticscholar.org/CorpusID:108984122.

[14] Shashidhar Krishnappa and Suhasini Gururaja. “Compressive failure mechanisms in unidirectional fiber reinforced polymer composites with embedded wrinkles”. In: Composites Part B: Engineering (2024). URL: https://api.semanticscholar.org/CorpusID:271101315.

[15] Vernon M. Benson and Jonahira Arnold. “Automated Fiber Placement of Advanced Materials (Preprint)”. In: 2006. URL: https : / / api . semanticscholar.org/CorpusID:135932497.

[16] Toray Composite Materials America Inc. 3900 Prepreg System Data Sheet. 2024. URL: https : / / www . toraycma . com / wp - content / uploads / 3900 - Prepreg-System.pdf (visited on 01/04/2025).

[17] University of Washington. Advanced Composites Center. 2025. URL: https://www.uwacc.uw.edu/ (visited on 02/02/2025).

[18] Dino-Lite. USB Microscope AF7915MZTL. 2024. URL: https: // www.dinolite.us /products /usb- microscopes /usb - edge/ af7915mztl/ (visited on 07/10/2024).

[19] CGTech. VERICUT Composites Programming. 2024. URL: https://cgtech.com/products/vcp.html (visited on 07/10/2024).

[20] John S. Agapiou David A. Stephenson. “Metal Cutting Theory and Practice”. In: CRC Press, 2016, p. 28.

[21] Zdeněk P Bažant, Jia-Liang Le, Marco Salviato, et al. Quasibrittle fracture mechanics and size effect: A first course. Oxford University Press, 2021.

[22] Kedar Kirane, Marco Salviato, and Zdeněk P Bažant. “Microplane triad model for simple and accurate prediction of orthotropic elastic constants of woven fabric composites”. In: Journal of Composite Materials 50.9 (2016), pp. 1247–1260.

[23] Marco Salviato, Shiva Esna Ashari, and Gianluca Cusatis. “Spectral stiffness microplane model for damage and fracture of textile composites”. In: Composite Structures 137 (2016), pp. 170–184.

[24] Marco Salviato et al. “A novel discrete, mesoscale modeling framework for the simulation of the damaging and fracturing behavior of composites”. In: ASME International Mechanical Engineering Congress and Exposition. Vol. 86717. American Society of Mechanical Engineers. 2022, V009T12A015.

[25] Sean E Phenisee et al. “Discrete, Meso-Scale Modeling of Fiber-Reinforced Composites (DM4C): Application to Additive Manufacturing of Continuous Fiber Composites”. In: Proceedings Of The American Society For Composites-Thirty-Seventh Technical Conference. 2022.

[26] MARCO SALVIATO et al. “To the mesoscale and beyond! capturing complex damage mechanisms in composites via simple, physics-based, discrete mathematical models of fibers and matrix”. In: PROCEEDINGS OF THE AMERICAN SOCIETY FOR COMPOSITES-THIRTY-EIGHTH TECHNICAL CONFERENCE.

NRC·CNRC

NRC.CANADA.CA

Enhancing Quality And Productivity In Automated Fiber Placement: Strategies For AFP Programming, In-process Inspection and Process Optimization

Jihua Chen, Marc Palardy-Sim and Ali Yousefpour
Aerospace Manufacturing Technology Center
Aerospace Research Center
National Research Council Canada (NRC)

24th International Conference on Composite Materials

August 4-8, 2025, Baltimore, MD, USA

Outline

- Introduction
  - Why Automated Fiber Placement (AFP)?
- AFP Activities at NRC Aerospace
- Key Stages in AFP Process Development
- Our Approaches to Optimize AFP Manufacturing Process
- Case Study
- Summary

Introduction

What is AFP?:

- Automated Fiber Placement (AFP) is a manufacturing process that uses computer controlled AFP machines to make composite structures by laying down composite slit tape layer by layer precisely.

Why AFP?:

- Large structures with complex shapes
- Consistent quality
- Faster and efficient
- Less waste and cost
- High precision and quality



Manufacturing fuselage panels for the A350 XWB (Picture © Premium Aerotec GmbH.)

Composites Research at NRC Aerospace

- Composites manufacturing
  - Automated fibre placement
  - Liquid composite moulding
  - Thermoplastic composite joining and manufacturing
  - Autoclave processing
  - Compression moulding
  - Low-cost tooling
- Process modeling and simulation
- Composites joining and repair
- Structure design and stress analysis
- Material characterization and mechanical testing

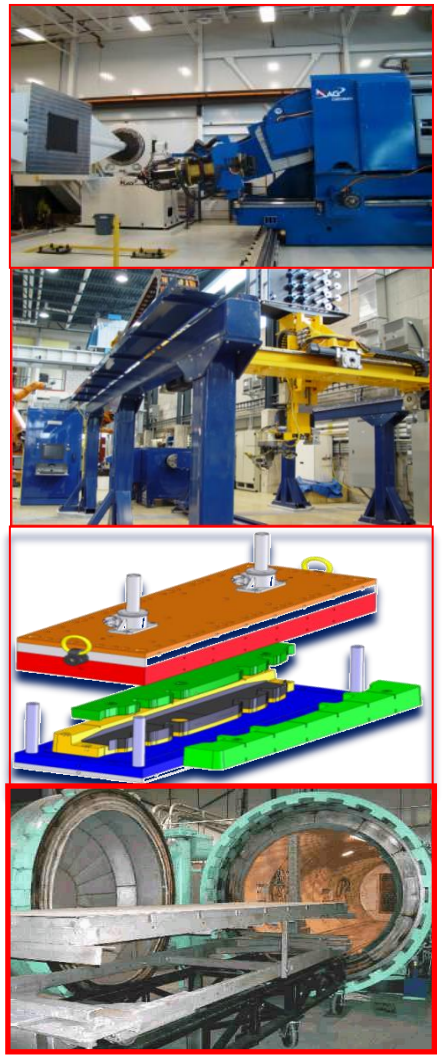

Automated Fiber Placement Activities at NRC Aerospace


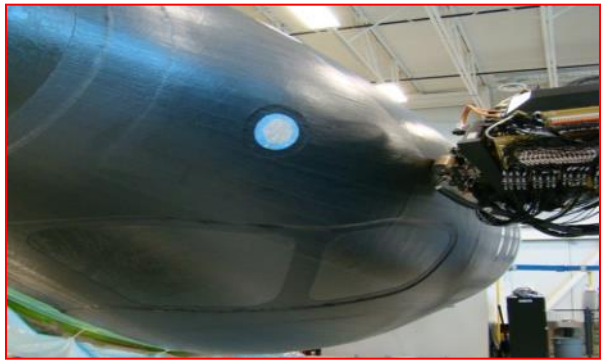
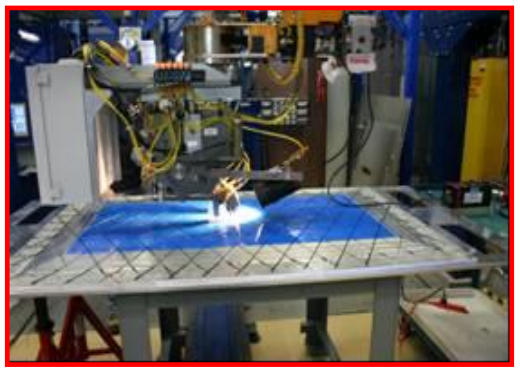


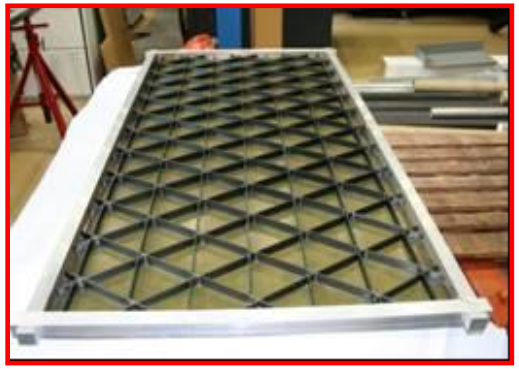

Tail boom

Front Fuselage

Isogrid Panel

Bell Helicopter
A Textron Company

BOMBARDIER

COMPOSITES ATLANTIC LIMITED
GROUP EADS SOGERMA

IsoGrid Composites Canada Inc (ICCI)

Automated Fiber Placement Activities at NRC Aerospace





Helicopter skid

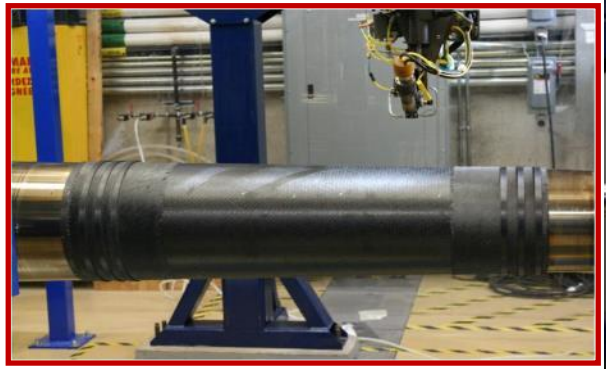



Thermoplastic tailboom



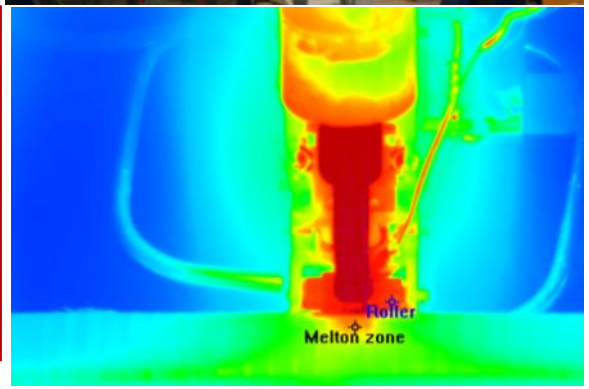

Process modelling and simulation

Key Stages in Automated Fiber Placement Process

- Part Design
- AFP Simulation and Programming
- AFP Manufacturing
- Inspection and Quality Control
- Part Curing
- Testing and Evaluation

Our strategy: Optimize the AFP process by optimizing each individual stage

The challenge: Each stage is linked to the others. Optimizing any stage depends on iterative data transfer and feedback within a closed-loop workflow

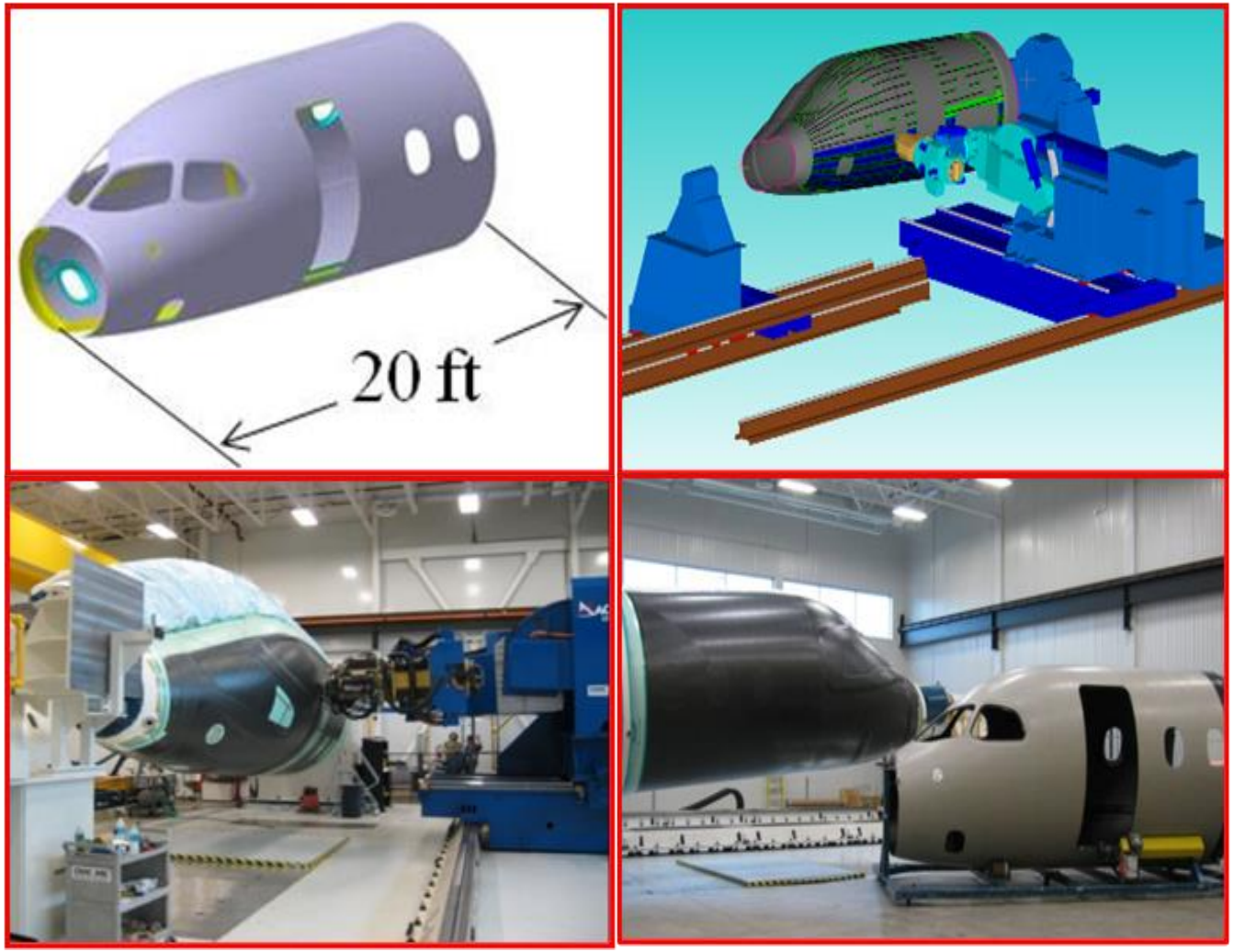

Closed-Loop Workflow of Automated Fibre Placement Process

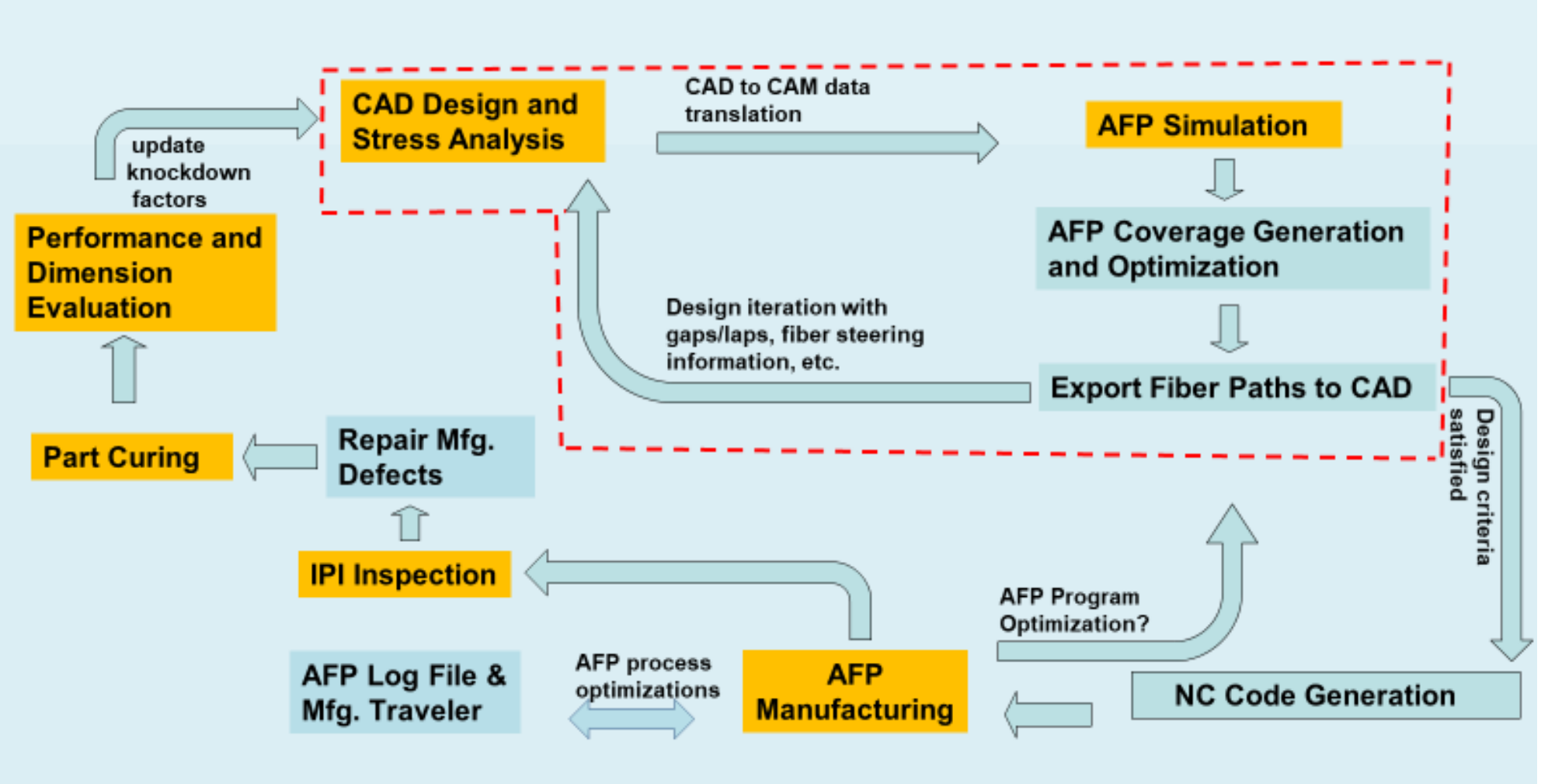

AFP Simulation

Main Tasks of AFP Simulation

- Tooling validation and process feasibility study
- Ply coverage generation and optimization
- Defects prediction, e.g. gaps/laps and fiber steering, etc.
- AFP programming and virtual commissioning
- Productivity and cost analysis

Important Parameters for AFP Simulation

- Mesh size
- Surface update
- Tow count and tow thickness
- Coverage method, start point and layup directions
- Fiber orientation
- Stagger offset
- Gap/overlap ratios
- ……

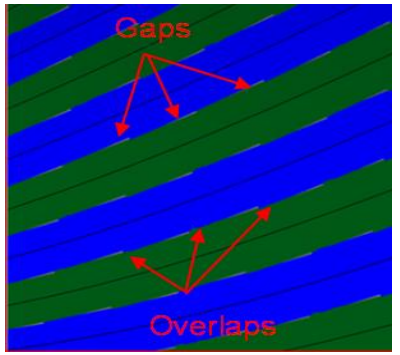

0%·Overlap → → 100%·Overlap¶



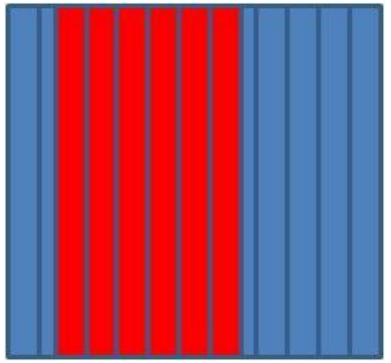

Fiber stagger

Case Study: Fiber Placement of A Curved Composite Panel

Part Info:

- Panel size: 15.5 x 27 inches
- Material: Carbon fiber/epoxy
- Layup sequence: [45/0/-45/0]s



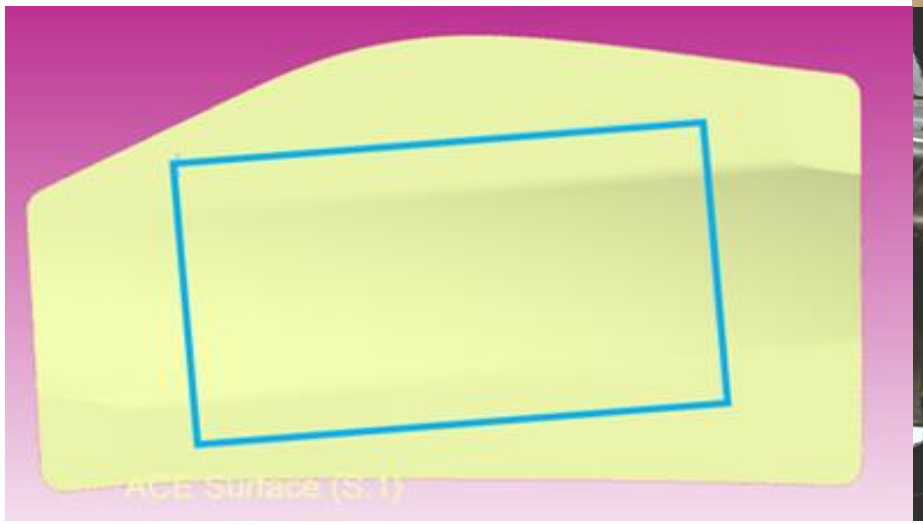



AFP Simulation: Surface Meshing

Common question:
Is the mesh size good enough for this part?

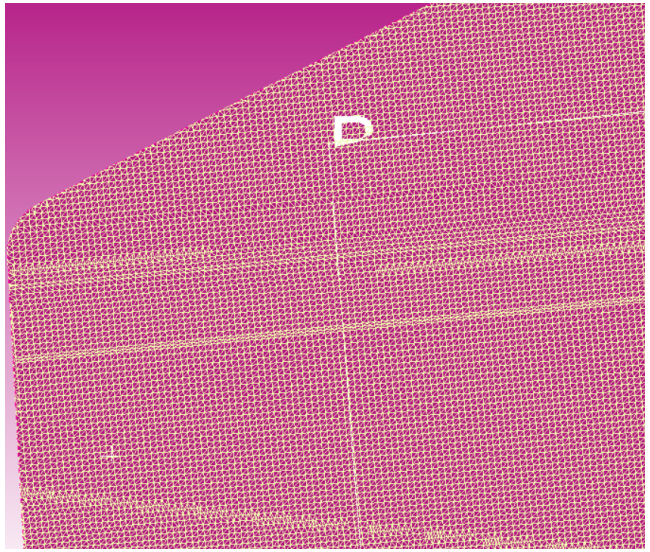

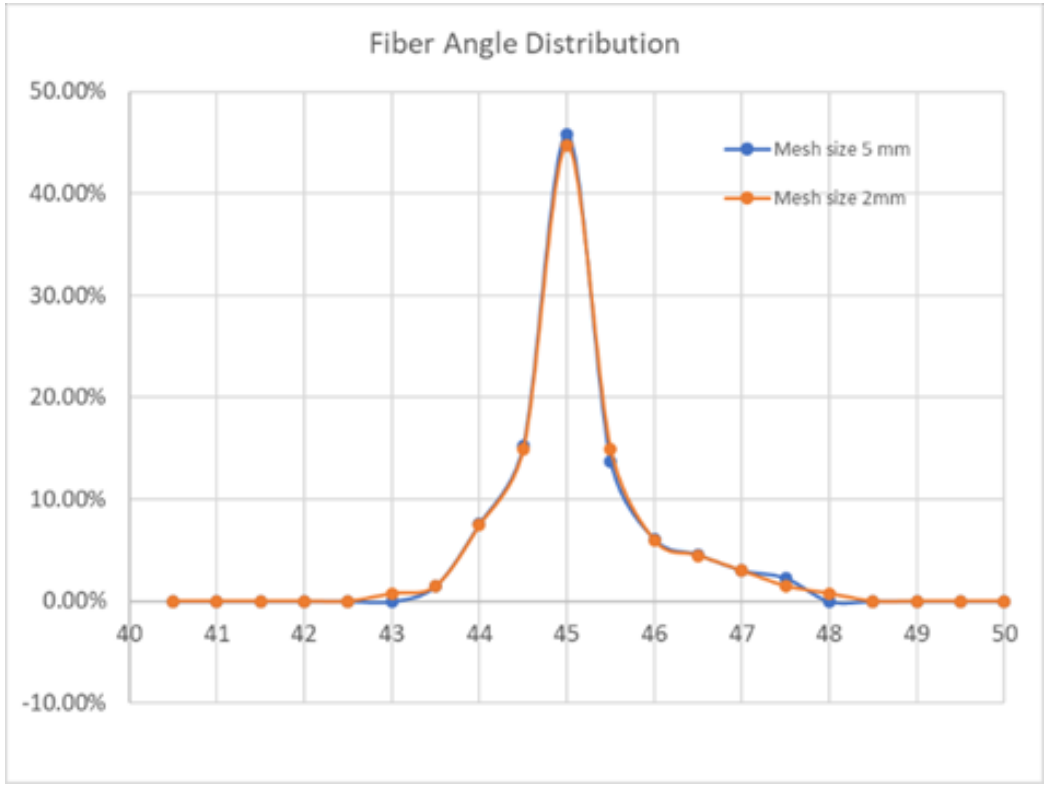

- Finer mesh improves path accuracy on complex surface
- Mesh size depends on geometry, part size, and computer capability
- For example, for this curved panel, reducing mesh from 5 mm to 2 mm increased ply time by 2.5×

Mesh Strategy: Balancing simulation accuracy and computational time is key

AFP Simulation: Tooling Validation and Process Feasibility Study

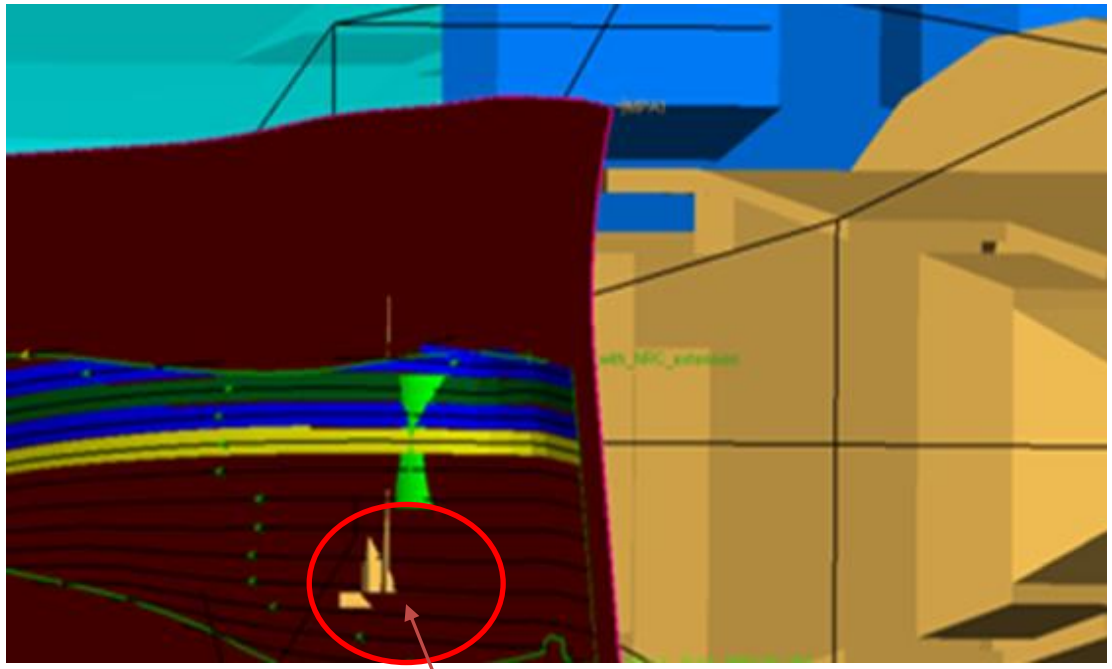

Collision in 0° ply

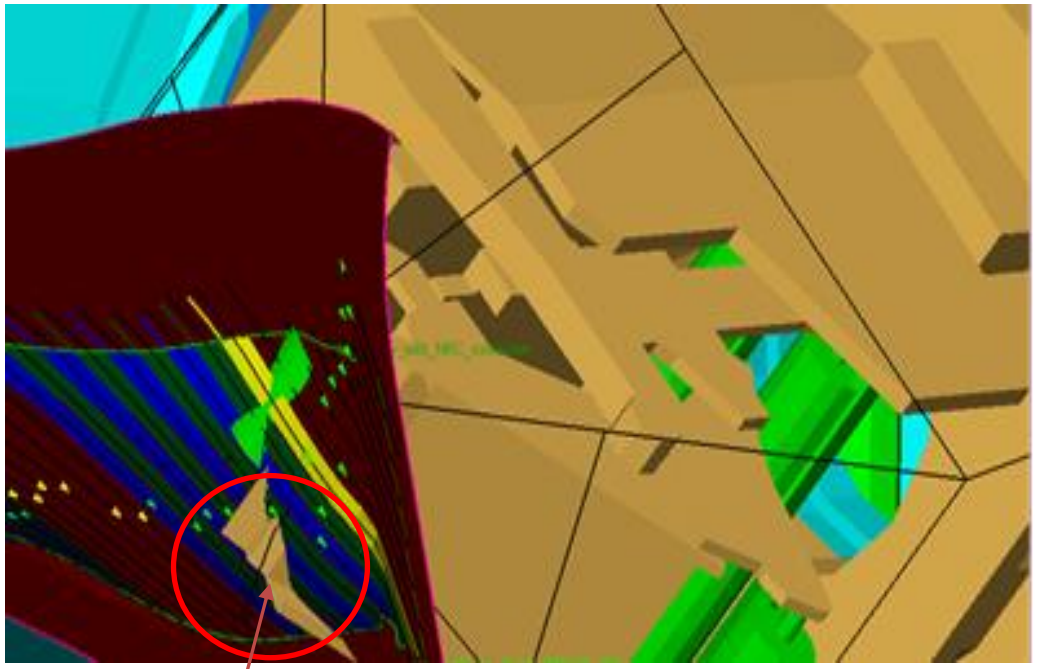

Collision in 45° ply

AFP Simulation: Identifying potential collisions (*illustrative example, not from this project*)

AFP Simulation: Coverage Method Selection

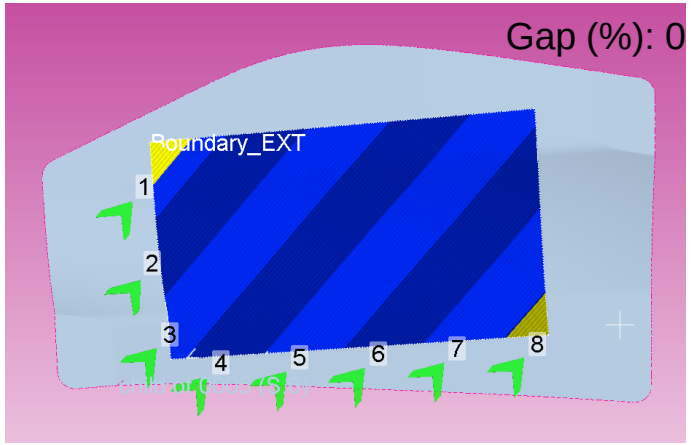

Parallel Limited (3° dev. allowed)

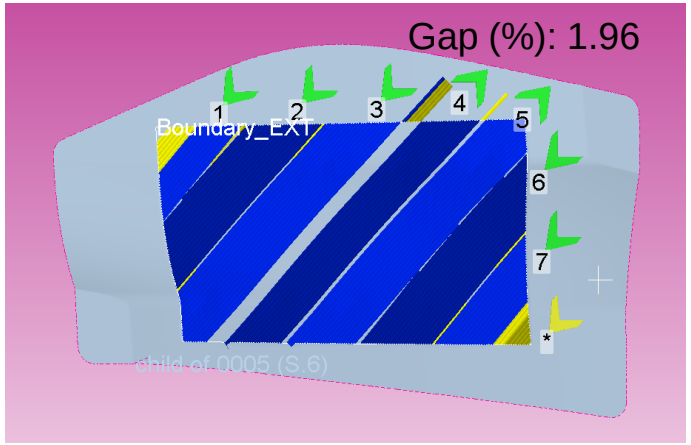

Natural Path

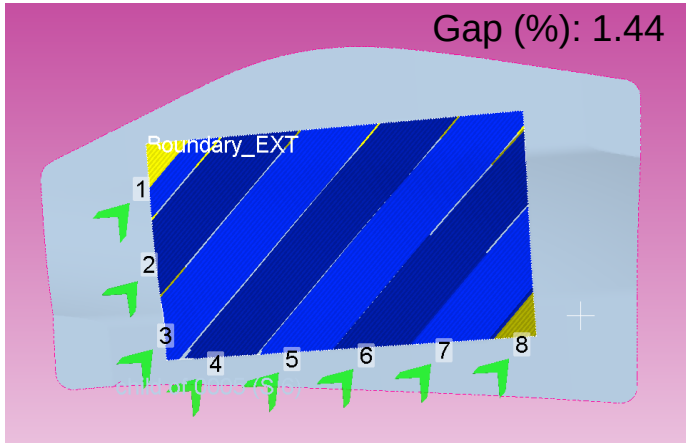

Fixed Angle

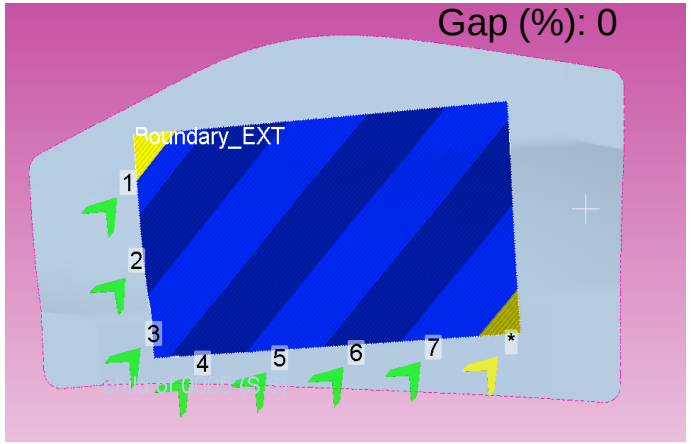

Fixed Parallel

Coverage Method Selection Strategies:

- Design requirements
- Part geometry
- Part application

AFP Simulation: Influence of Start Point Location

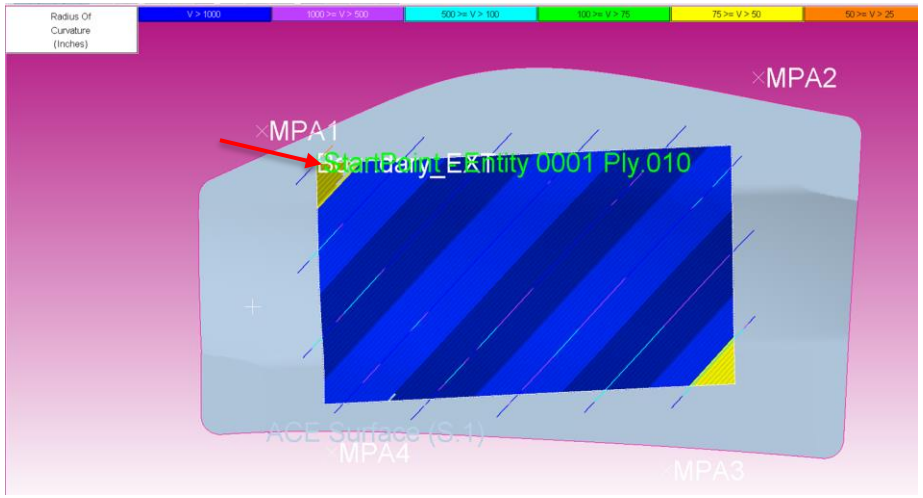

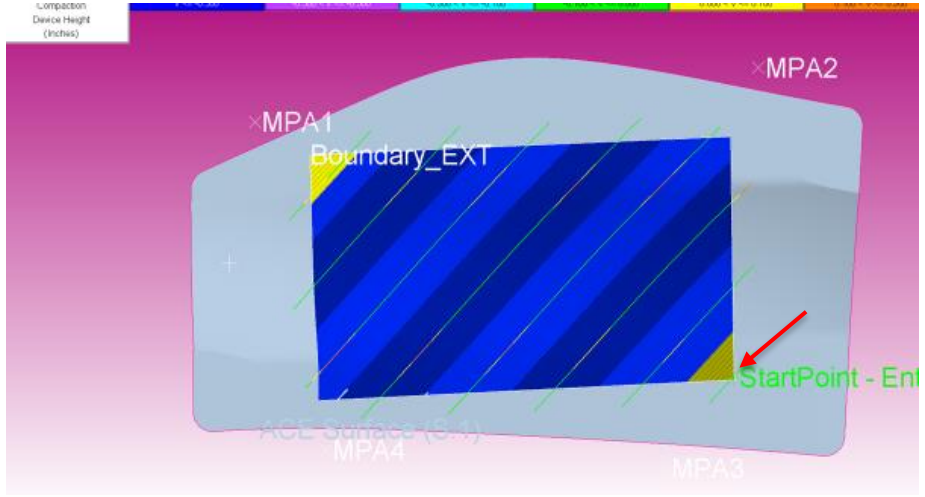

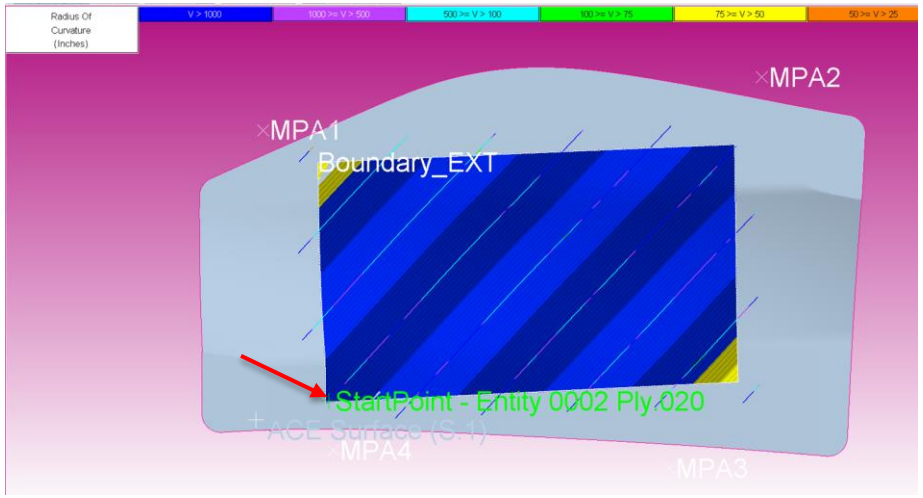

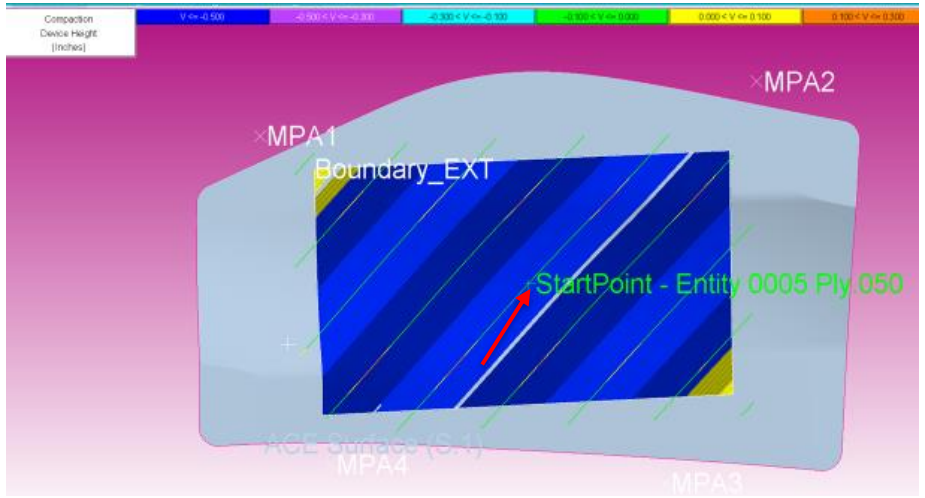

Start Point:

- The start point acts as the origin for coverage generation
- It is one of the most critical parameters in AFP simulation

AFP Simulation: Influence of Start Point Location

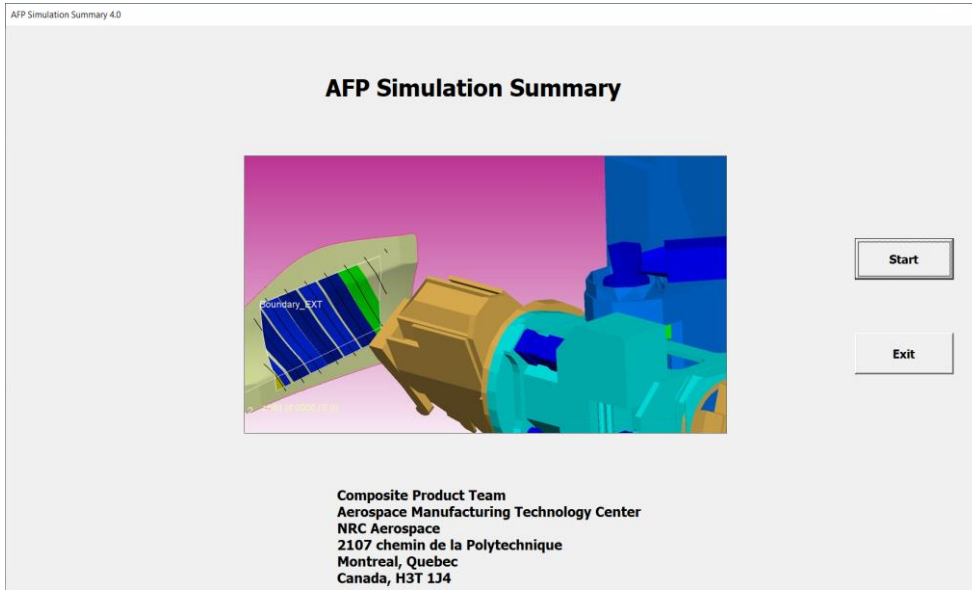

A proprietary program developed at NRC, *AFP Simulation Summary,* was used to analyze AFP simulation data

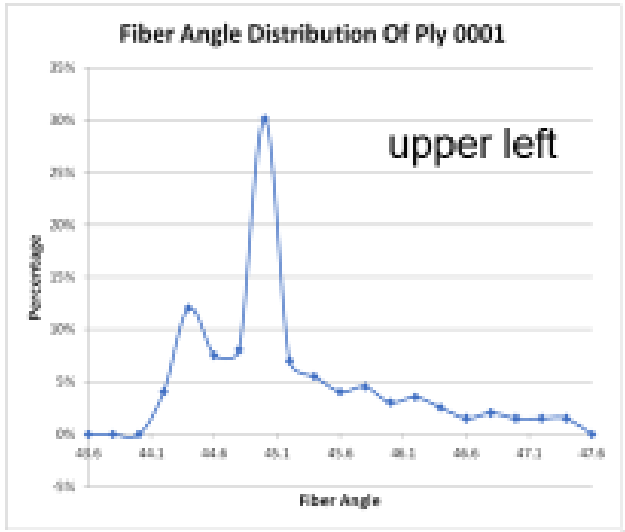

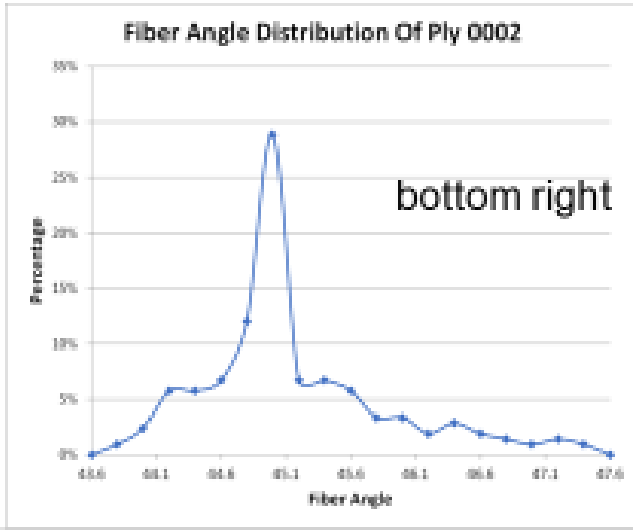

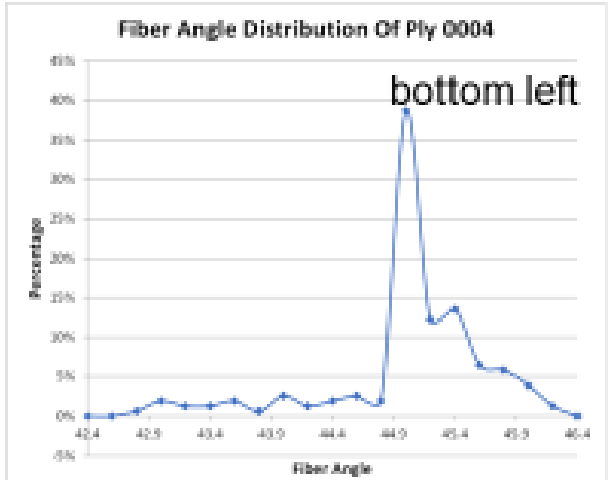

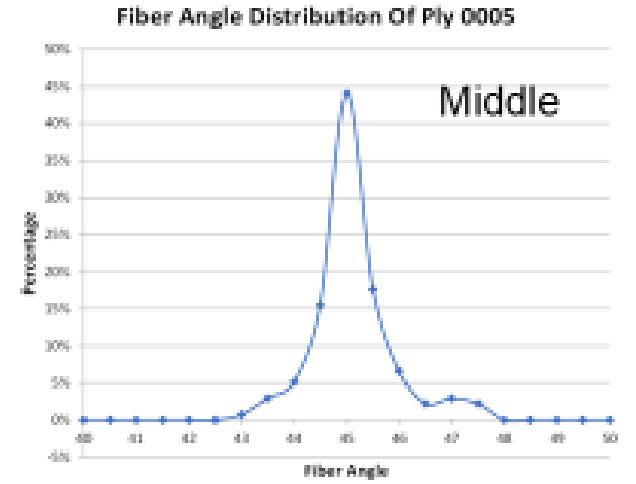

AFP Simulation Summary

AFP Programming Parameters	Summaries	Notes
ACE V2 Version	V2.R2.72n (Coverage); V2.R2.72o (Program)	
Project Description	Influence of start point	Project #: TBD
Date of Documentation (Y/M/D)	2025-06-25	
AFP Part Name	StartPoint: Middle	
ACE Program Name	CurvedTool_Fiber Path Analysis	
Ply Number #	Ply 0005	BDY Name: Boundary_EXT
Path Orientation (ACE Axis System)	45	FAD <= 3°: 100.00 (%); FAD <= 5°: 100.00 (%)
Average Tool Misalignment (in)	0.03386	Tool misalignment is moderate
Ply Layup on Surface #	5	
Tow Count	32	
Course Count in this Ply	9	
Coverage Method	Fixed Parallel	
Coverage Start Point (Design Coordinate)	X=3.491, Y=1.19, Z=4.445	
Coverage Step Size (in)	0.25	
Gap in the Ply %	0	
Overlap in the Ply %	0	
Min Ply Roller Sag (in)	-0.028	
Max Ply Roller Crown (in)	0.257	No compaction issues expected
Minimum Tow Length Used for the Ply Coverage (in)	0.00	Warning: Patches are needed for short fiber paths
The Ply's Minimum Radius of Curvature (in)	27.37	Warning: Medium risk of fiber wrinkles
Head Clearance DiatanceX (in)	40.00	
Collision Avoidance Enable	TRUE	
Predicted Material Usage of the Ply (lb)	0.132	
Predicted Ply Cycle Time (h:m:s) [On Surface]	00:01:59 [00:00:48]	
Predicted Material Yield (lbs/hour)	3.979	AFP down time is not included in the caculation

*** The warnings in this table are based on AFP simulation results. The final results of AFP process will be also influenced by various other manufacturing parameters**

This Table is generated by the *AFP Simulation Summary* program

AFP Manufacturing: Parameters and Strategies

Important Parameters for AFP Manufacturing

- Compaction force
- Fiber tension
- Heating temperature
- Humidity level
- Layup speed
- Material tackiness
- Substrate temperature
- …..

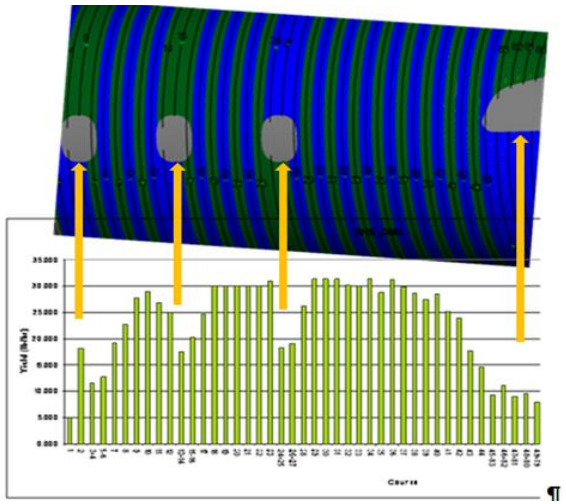

Strategies to Improve AFP Productivity and Quality

- Establish standard work instructions for AFP setup and operation
- Use virtual simulation to pre-validate layup strategy
- Perform dry-run of the AFP program - fully or only in critical areas for large parts
- Maximize layup speed
- Use large material spools to reduce load time
- Enable automated in-line inspection to reduce downtime
- Adjust parameters based on material & environment conditions
- Avoid small cutouts, tight radii, and complex geometries in design
- Favor long continuous fiber courses during path planning
- Optimize layup sequence and fiber direction
- Minimize off-surface movements of the AFP head
- Schedule regular head maintenance — don’t wait for failure

AFP Manufacturing: Data Tracking and Analysis

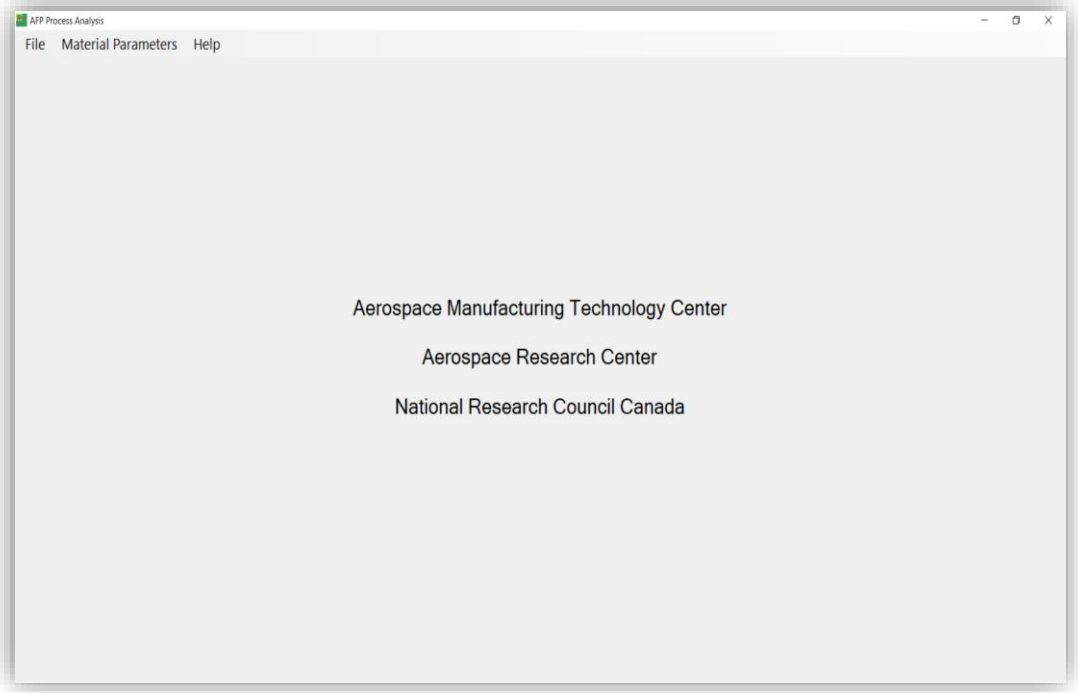

A proprietary program developed at NRC, *AFP Process Analysis,* was used to analyse AFP manufacturing process

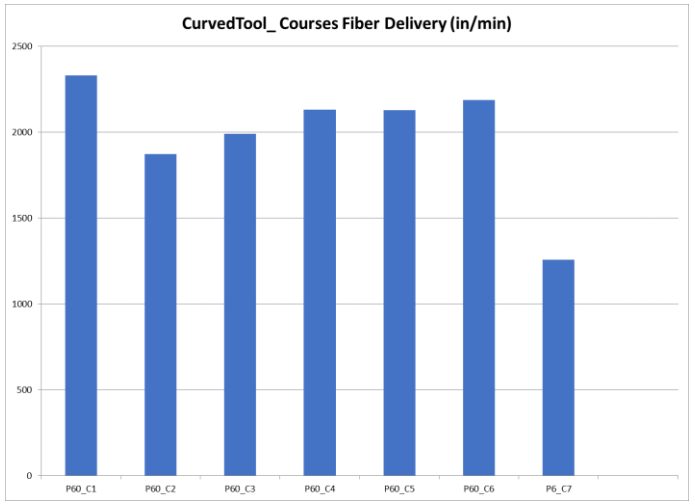

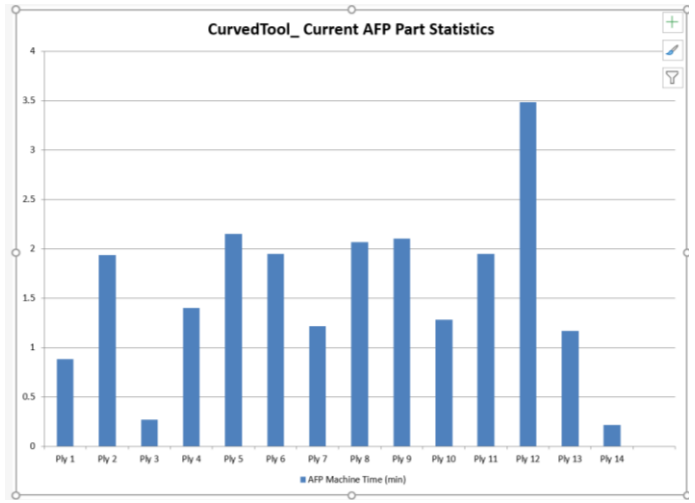

AFP·Layup·Information¶

Total·number·of·plies·for·this·part:·14·plies¶

AFP·Machine·Time·(min):·22.07¶

Down·Time·(min):·173.00¶

Total·Time·(min):·195.07¶

Machine·Occupation·Time·(min):·3·hours·and·16.48·minutes¶

Fibers·Length·(in):·33943.41¶

Fiber·Delivery·(in/min):·1424.85¶

Weight·(lbs):·1.35¶

Wasted·Material·(lbs):·0.17¶

Layup·Rate·(lbs/hr):·3.41¶

Error·Messages¶

Tensioner·Fault:·4¶

Problem·While·Restarting:·3¶

Problem·While·Feeding:·2¶

Zp·Axis·Fault:·0¶

Pressure·Fault:·0¶

Bladder·failure:·0¶

Other·Errors:·0¶

Total·Errors:·9¶

Quality Assurance

Typical AFP Manufacturing Defects

- Gaps/overlaps
- Fiber bridging
- Wrinkles
- Fiber fuzz
- Missing tow
- Twisted tow
- Foreign Object/debris (FOD)







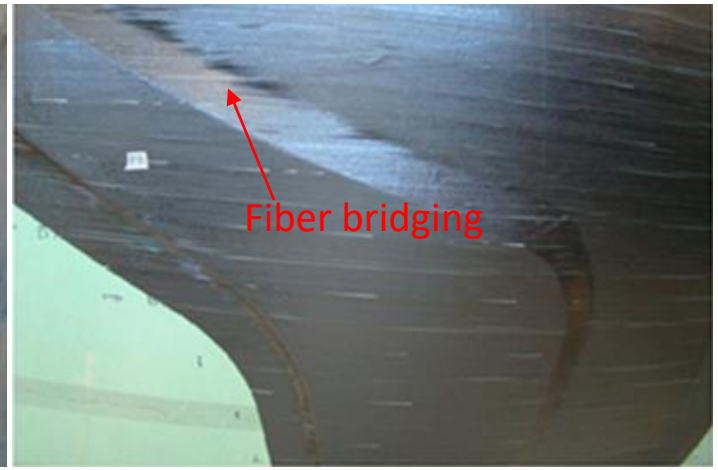



In-Process Inspection

- Conducts real-time inspection
- Operates without interfering with the AFP process
- Identifies the type, dimensions and location of the defects
- Provides warnings for the oversized defects that need rework
- Documents the inspection results automatically
- Creates digital data tracking and travelers
- Largely increases the efficiency of the AFP process

NRC's Viper 4000:

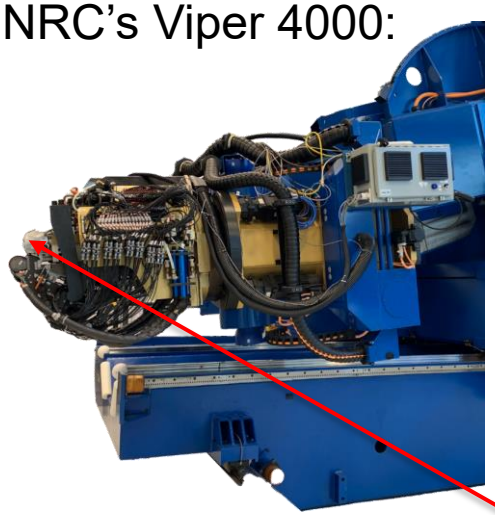

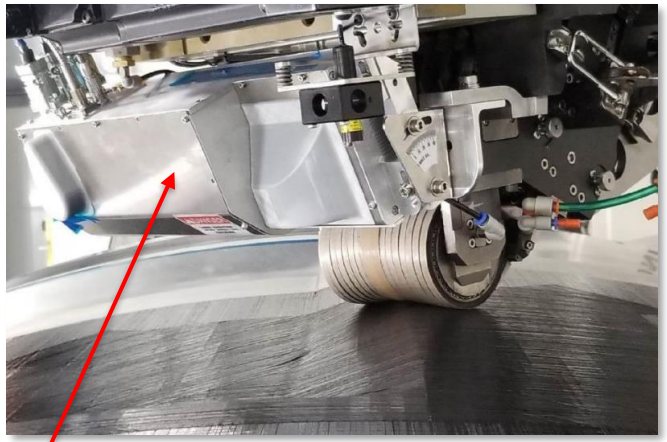

NRC prototype sensor

Fives Robotic Viper:

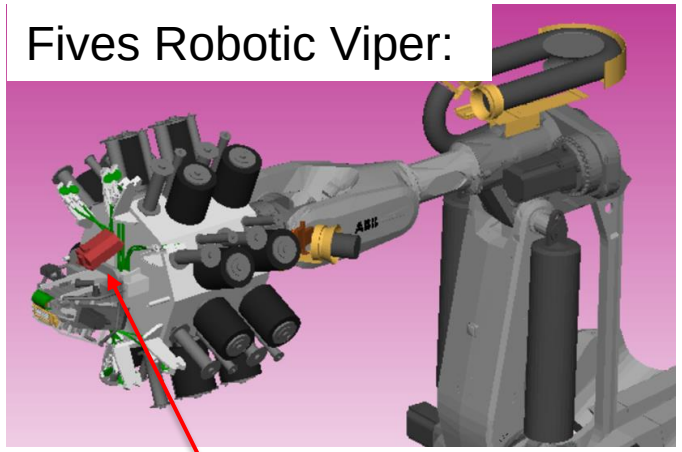

Fives COAST system

- Patented technology based on **Optical Coherence Tomography technology**—a mature laser-based, volumetric imaging technique
- Process driven custom sensor system designed and integrated with various AFP machines in partnership with Fives Group

fives ultimate machines ultimate factory

In-Process Inspection

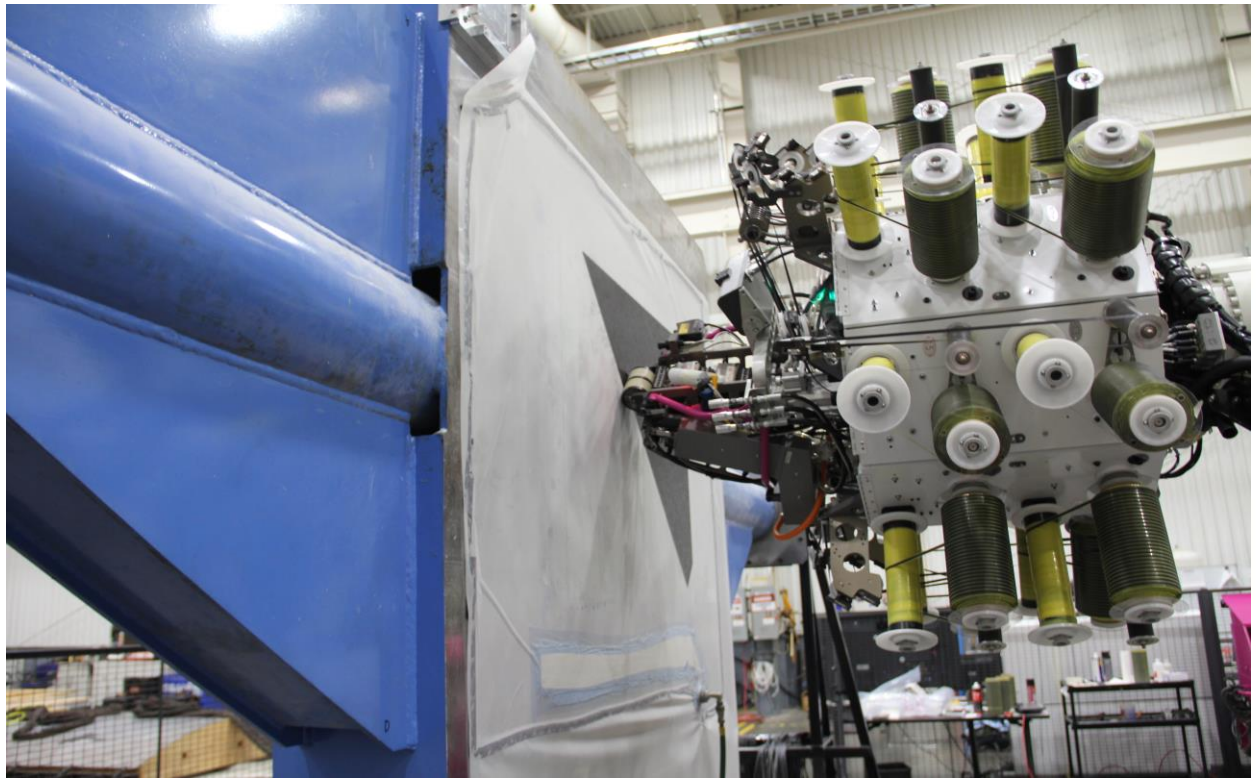

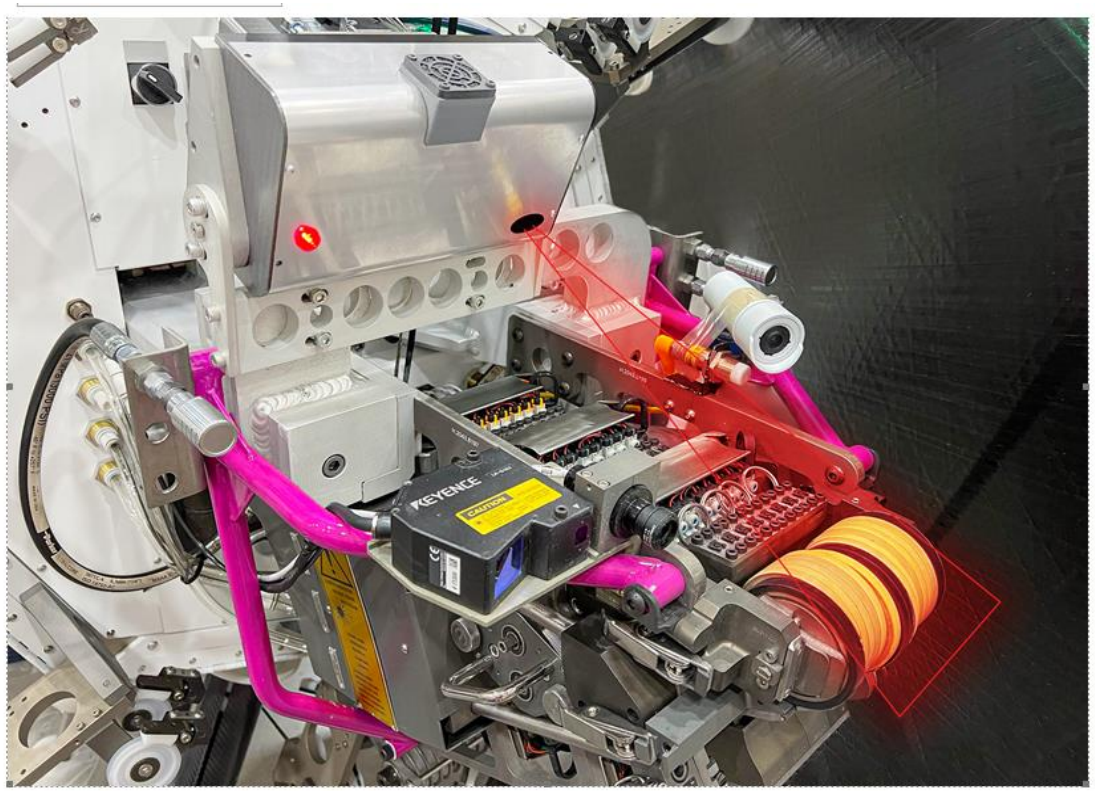

More info about Fives COAST system: https://youtu.be/L2Q9SvEcAfc?si=NhkV8qsMtZ6iQv69

fives ultimate machines ultimate factory

NRC·CNRC

In-Line Inspection System: Examples of Defect Detection

In-process measurements:

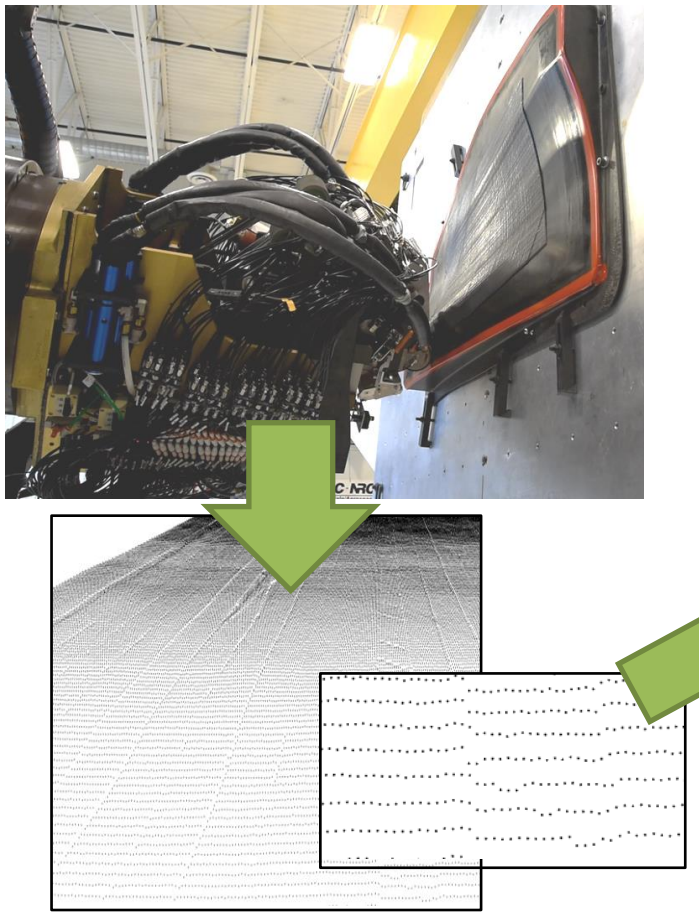

High resolution 3D located point cloud

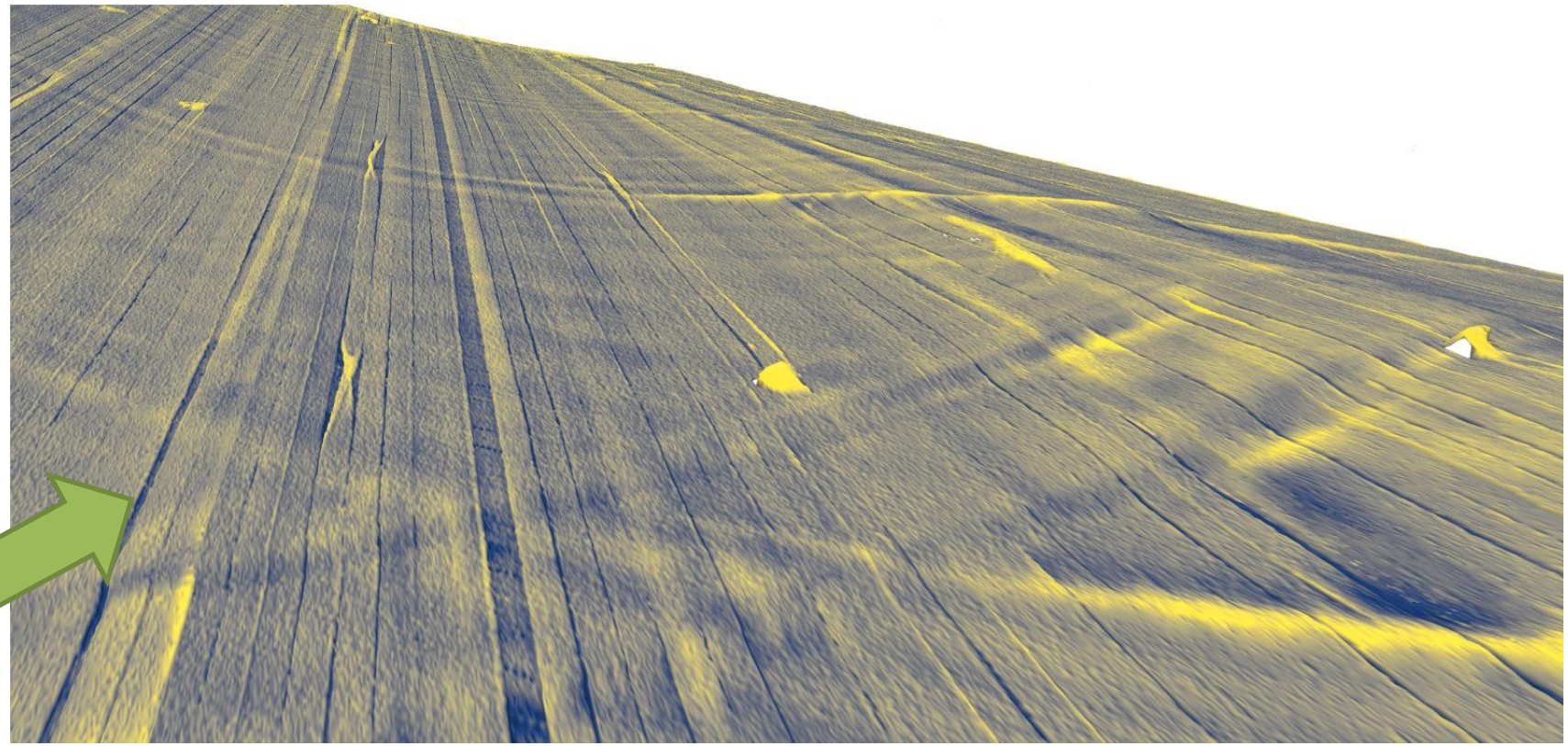

Ply 60, approx. 9.7 mm thick ply stack

In-Line Inspection System: Examples of Defect Detection

In-process measurements:



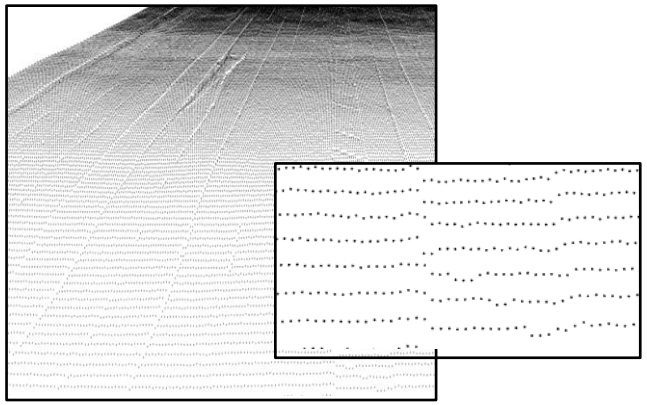

High resolution 3D located point cloud

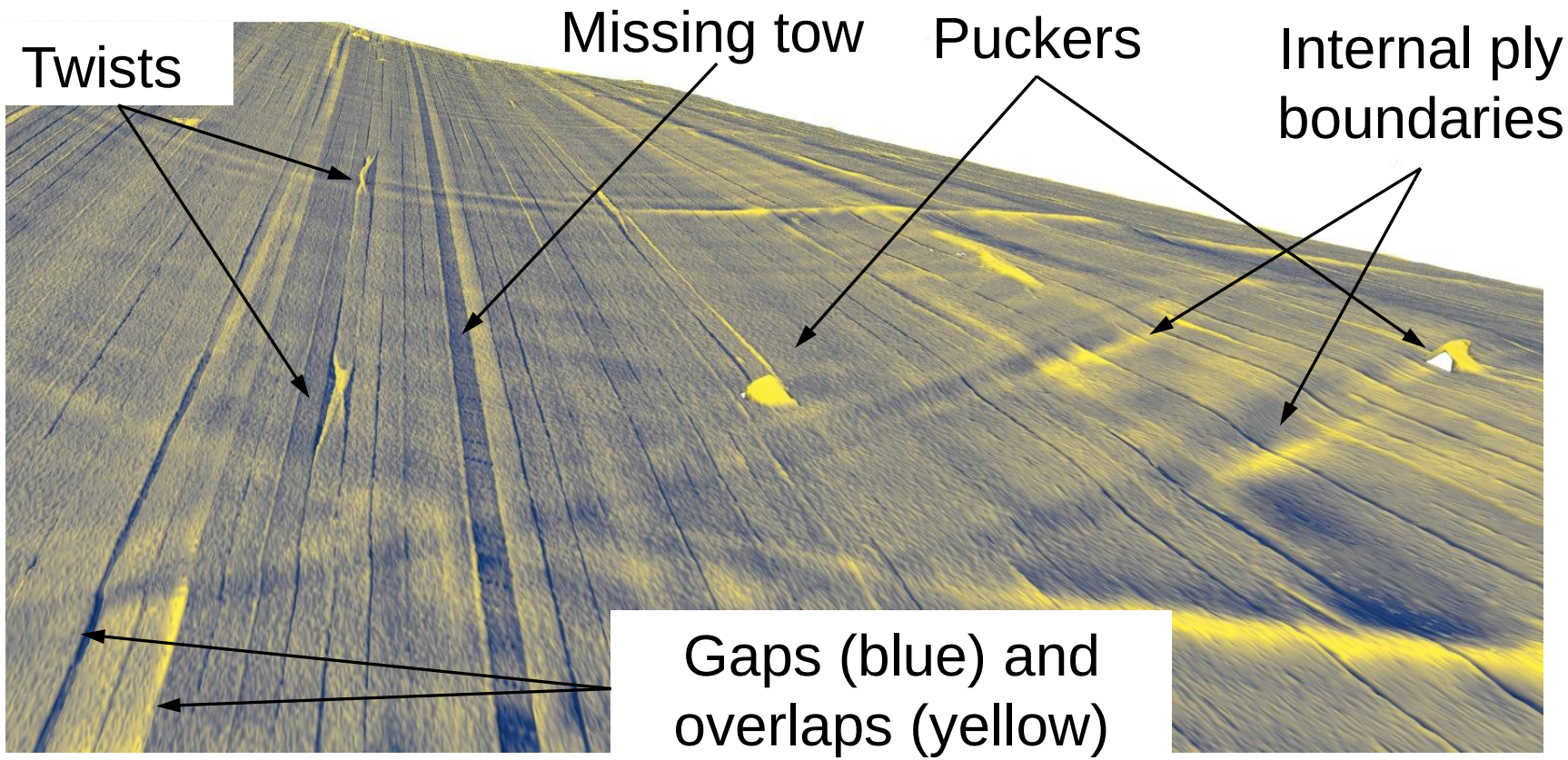

Ply 60, approx. 9.7 mm thick ply stack

Summary

- AFP process can be categorized into six key stages: CAD design, AFP simulation and programming, AFP manufacturing, inspection and quality control, part curing, testing and evaluation
- Closed-loop data flow is essential in AFP process — each AFP stage influences and depends on the others
- AFP process optimization relies on continuous feedback between stages to ensure better outcome
- NRC is actively developing software tools and sensors to collect, track, and analyze AFP simulation and process data
- These capabilities have enabled NRC to successfully develop hundreds of composite structures with partners across sectors
- We will continue refining this approach — using ply-by-ply AFP simulation studies to guide design decisions and ensure consistent, high-quality outcomes

Thank You

Contact:

Jihua Chen , Dr. –Ing.
Senior Research Officer
Aerospace Manufacturing Technology Center
Aerospace Research Center
National Research Council Canada
Phone: (514) 283-9052
Courriel / Email : Jihua.Chen@nrc-cnrc.gc.ca.ca

SMART ROLLER: AN ESSENTIAL TOOL FOR AUTOMATED FIBER PLACEMENT

C. Picciotto*, X. Yin, A. Poursartip, J. Madden, and A. Clare

Composites Research Network, Department of Materials Engineering, The University of British Columbia, Vancouver, Canada

Keywords: Lay-up (automated), prepreg

Background: In-situ measurements at the nipping point of an Automated Fiber Placement (AFP) process

- In AFP, measuring and controlling the local compaction pressure (as opposed to globally applied compaction force) is crucial to understanding the process at the nip point
- Various examples with a significant pressure gradient at the nip point:

Complex tool geometry



Tow steering

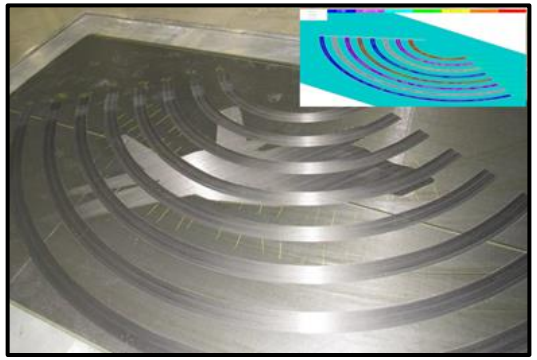

- In-situ measurements provide insight into the local conditions that control the process

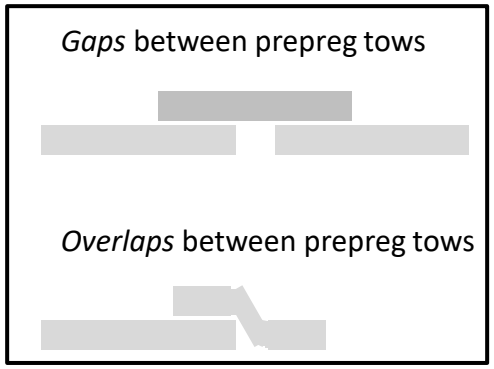

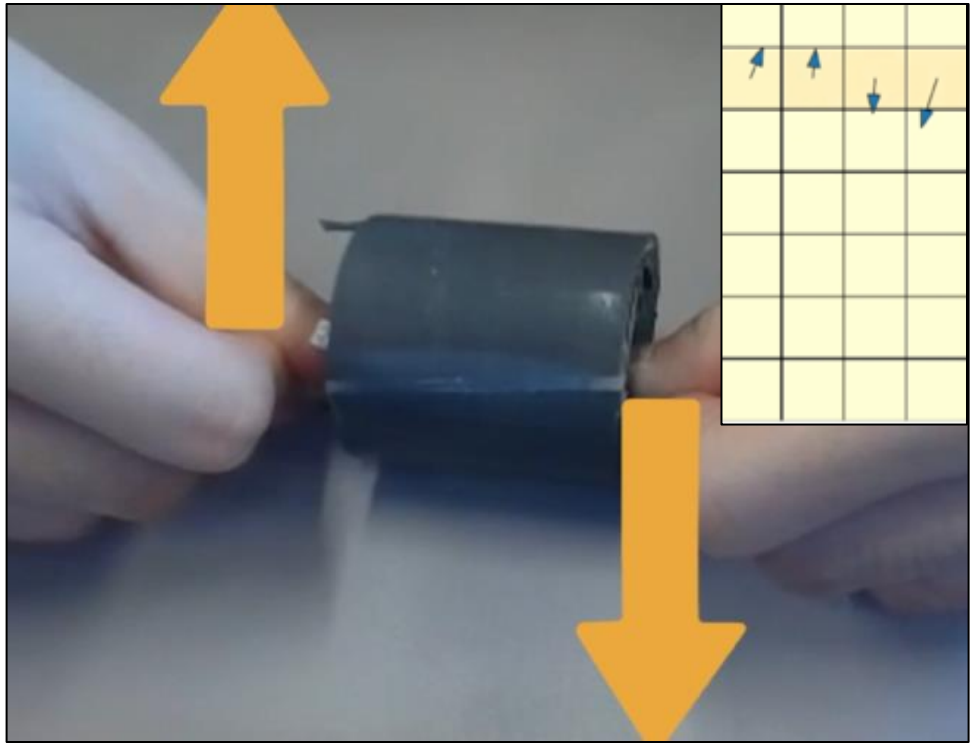

Smart Roller measuring shear and local pressure at the contact surface, giving AFP machines tactility at the nip point of the process.

© CRN UBC (2025) -- DO NOT REPRODUCE WITHOUT WRITTEN PERMISSION

Outline

1. Fabrication and custom Smart Rollers

- Parametric 3D-printed molds
- Match performance to that of standard compaction rollers
- Custom sensor layout



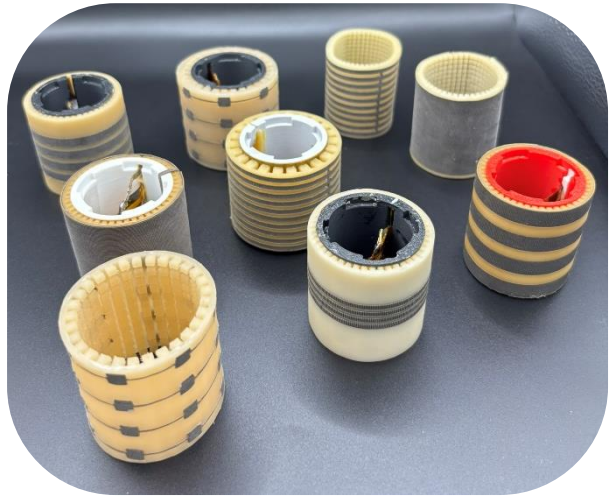

2. Sensor Calibration

Tailor sensitivity for an expected pressure range.

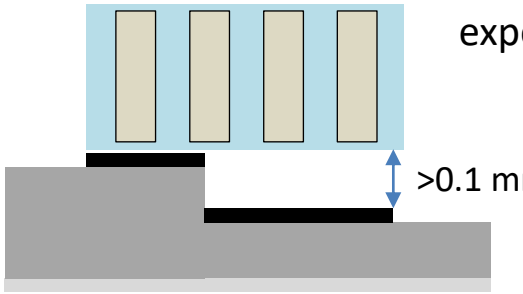

3. In-line process control

- Feature detection
- Wrinkle prediction

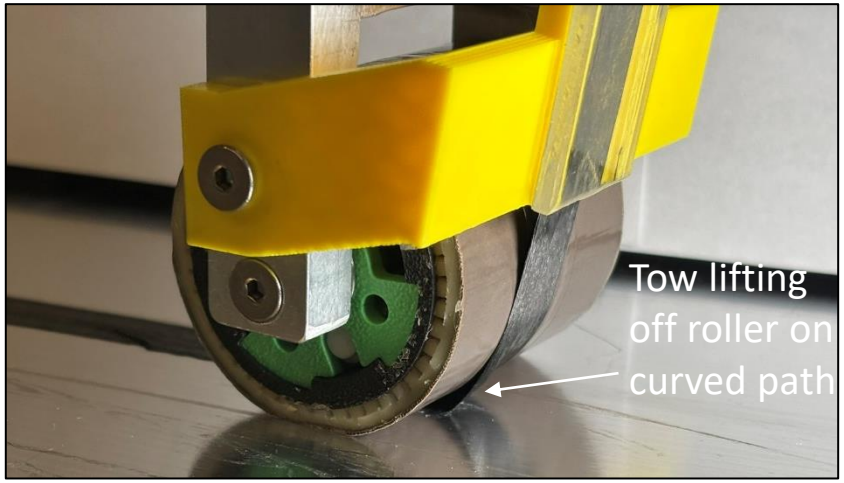

CRN Composites Research Network

© CRN UBC (2025) -- DO NOT REPRODUCE WITHOUT WRITTEN PERMISSION

Fabrication

Fabricated Smart Roller with cross-section showing makeup of sensors



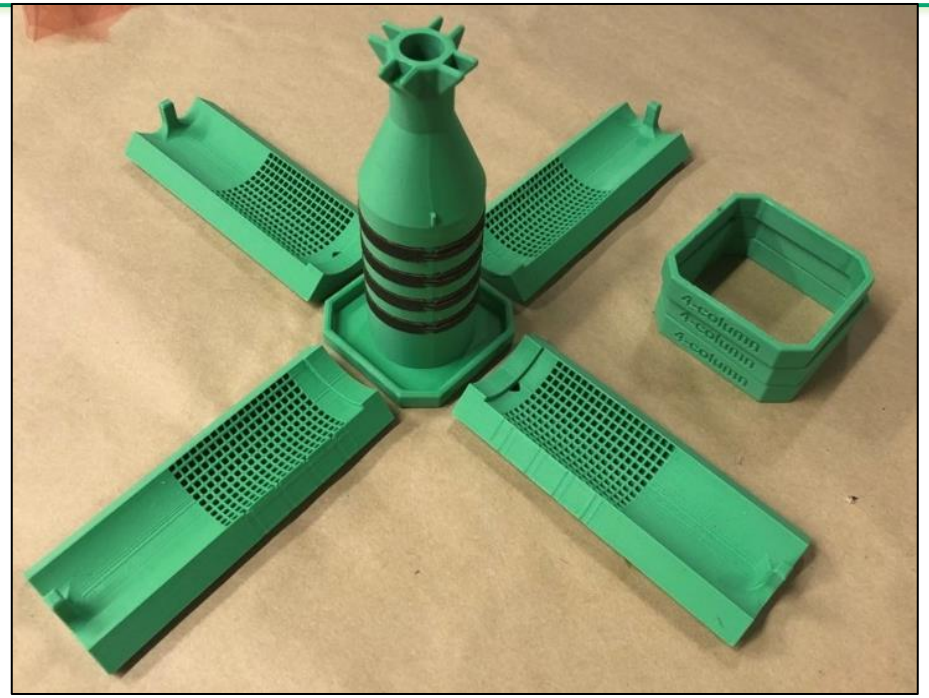



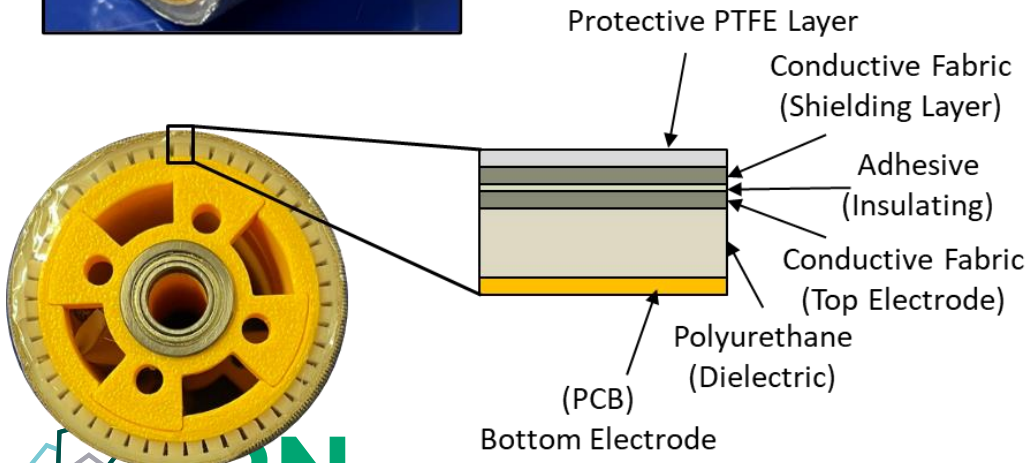

Parametrically designed 3D printed mold with conductive fabric electrodes on core. Urethane is injected into the mold to make tire.

This closed-mold fabrication method is used to make Smart Rollers with a seamless tire and embedded electrode.

Composites Research Network

© CRN UBC (2025) -- DO NOT REPRODUCE WITHOUT WRITTEN PERMISSION

Custom Smart Rollers



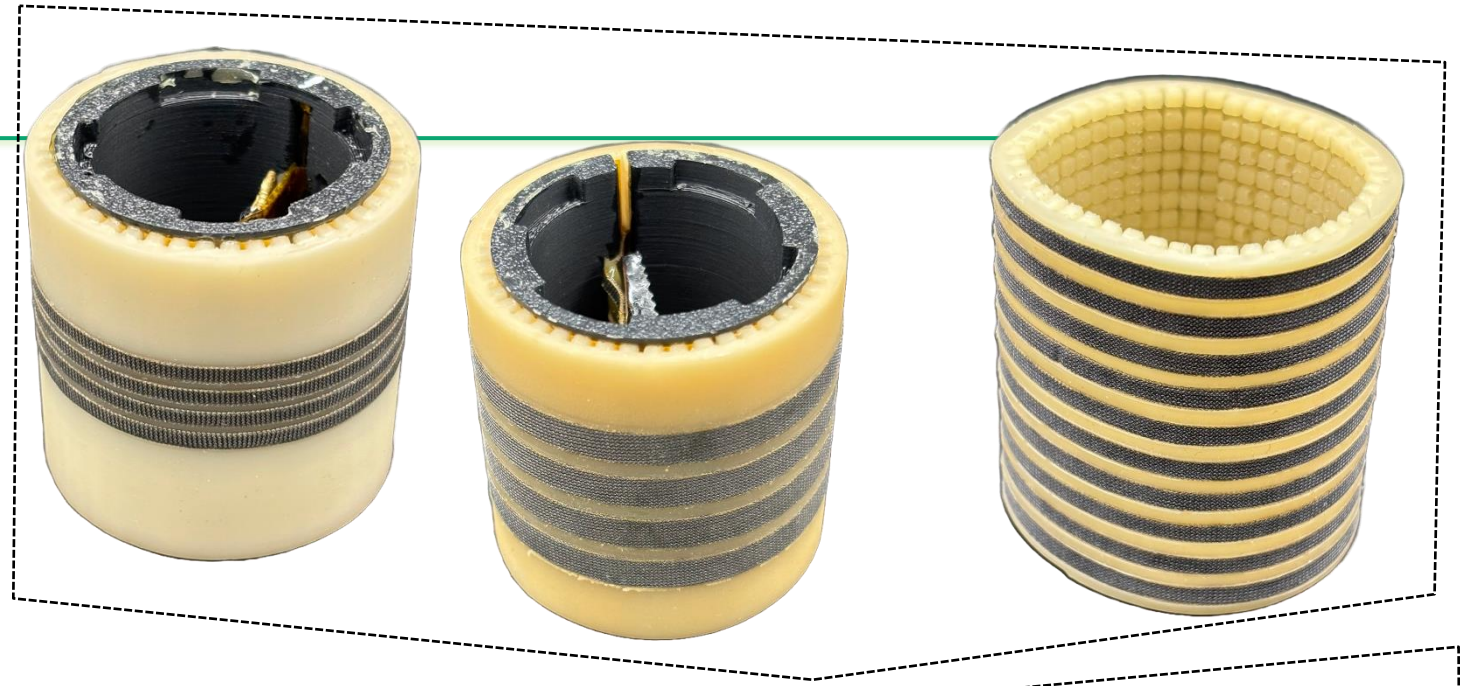



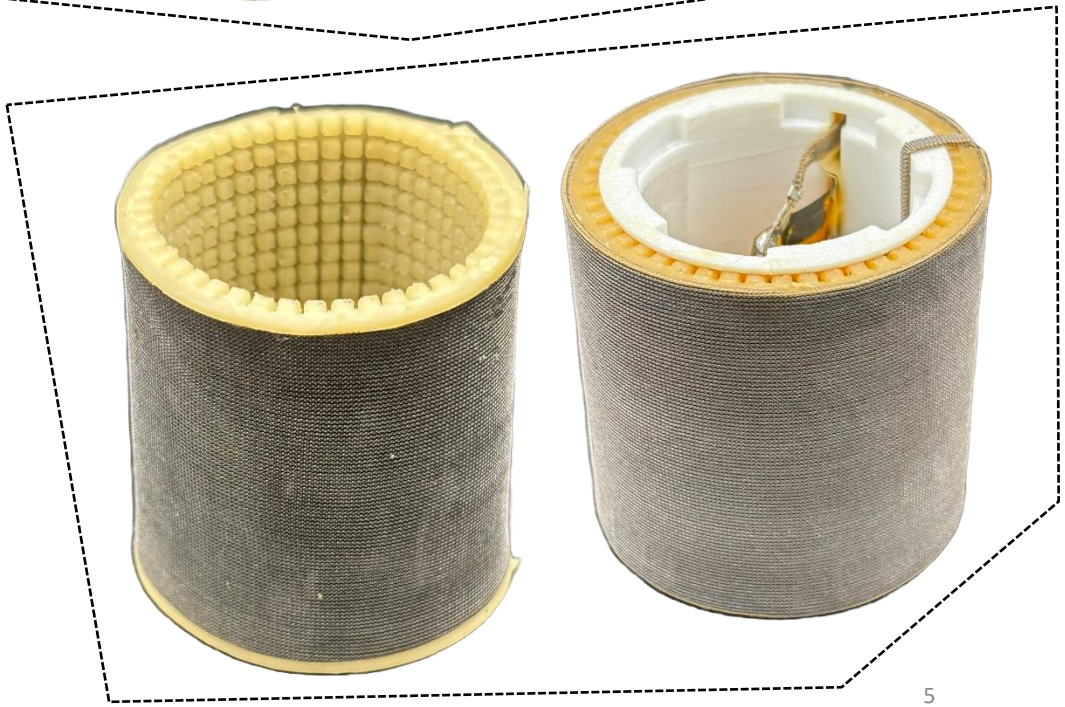

Composites Research Network

© CRN UBC (2025) -- DO NOT REPRODUCE WITHOUT WRITTEN PERMISSION

Custom Compliance

Simple compliance model outputs:

- Material (shore hardness)
- Pillar length (tire thickness)

Other customizations:

- Roller diameter
- Pillar geometry
  - Shape/size
  - Spacing

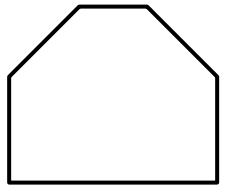

These parameters feed into the parametric mold to fabricate custom smart rollers

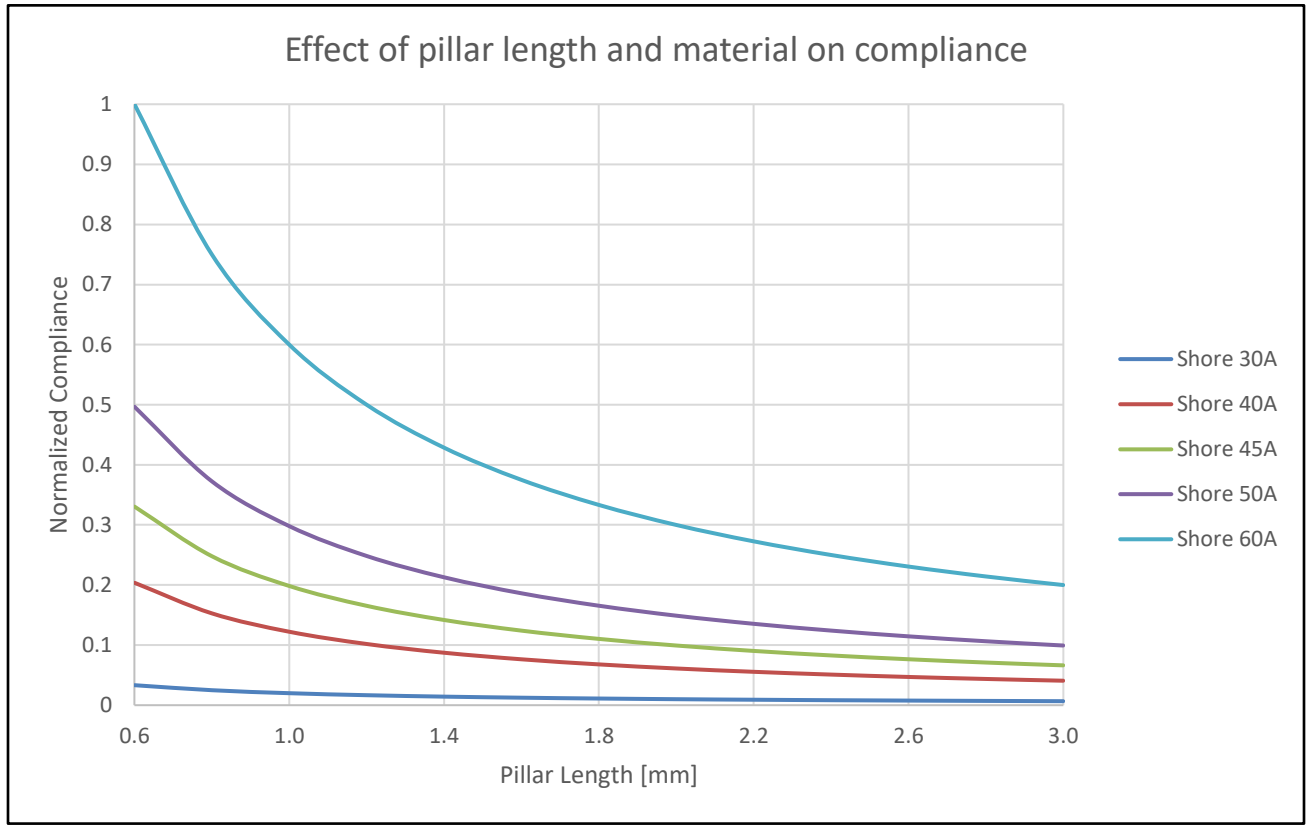

Composites Research Network

© CRN UBC (2025) -- DO NOT REPRODUCE WITHOUT WRITTEN PERMISSION

Sensor Overview

Pressure Sensing:

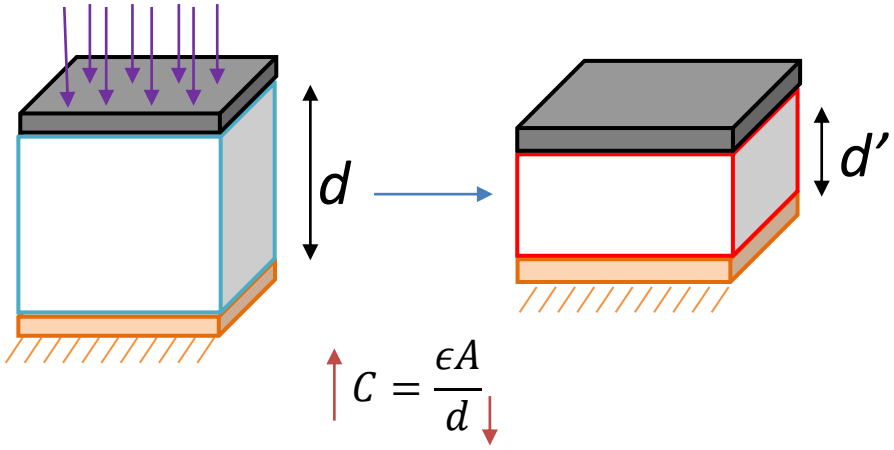

Shear Sensing:

Mutual Capacitance:

Increases
Decreases
No change

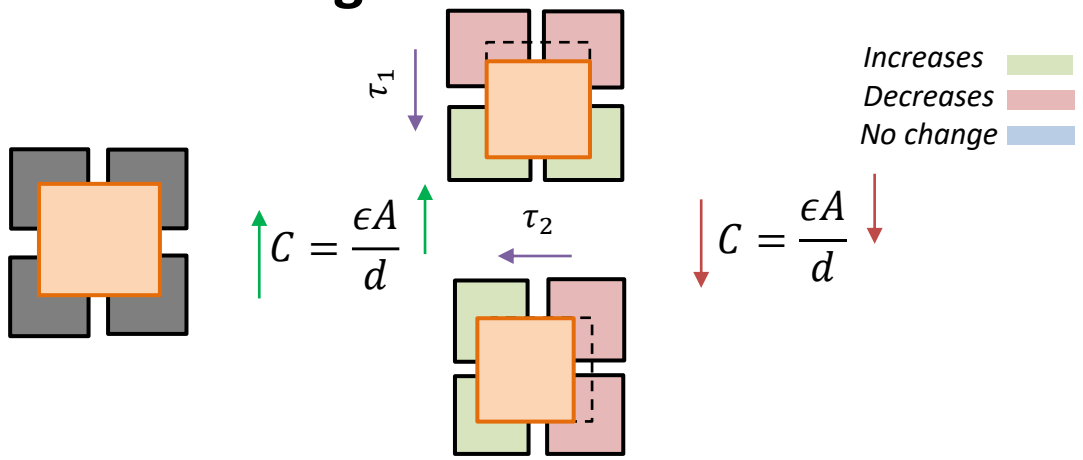

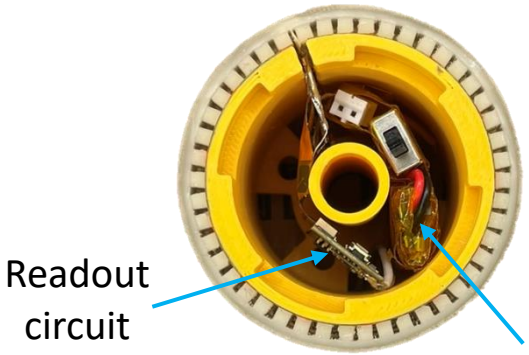

Bluetooth Low-Energy (BLE)



BLE Receiver

Windows 11 (Python 3.10)

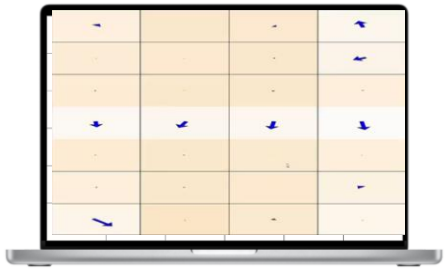

Visualization/Recording Data

Patents:
US20230139916A1 (pending)
US10401241B2

© CRN UBC (2025) -- DO NOT REPRODUC

Yin, X., Chen, Z., Bakhshi, N., Tong, O., Xiong, X., Chen, Y., Li, Y., Gao, J., Sarwar, M. S., Poursartip, A., & Madden, J. D. W. (2023). Smart roller: Soft sensor array for automated fiber placement. *Advanced Sensor Research, 2*(9), 2200074. https://doi.org/10.1002/adsr.202200074 (connectedpapers.com, doaj.org)

Sensor Calibration

Automated Characterization using Instron Machine

- Characterizes the smart roller
- **Basic calibration**: Indent in the center of each sensor
- **Advanced calibration**: Indent around the circumference every 5 degrees

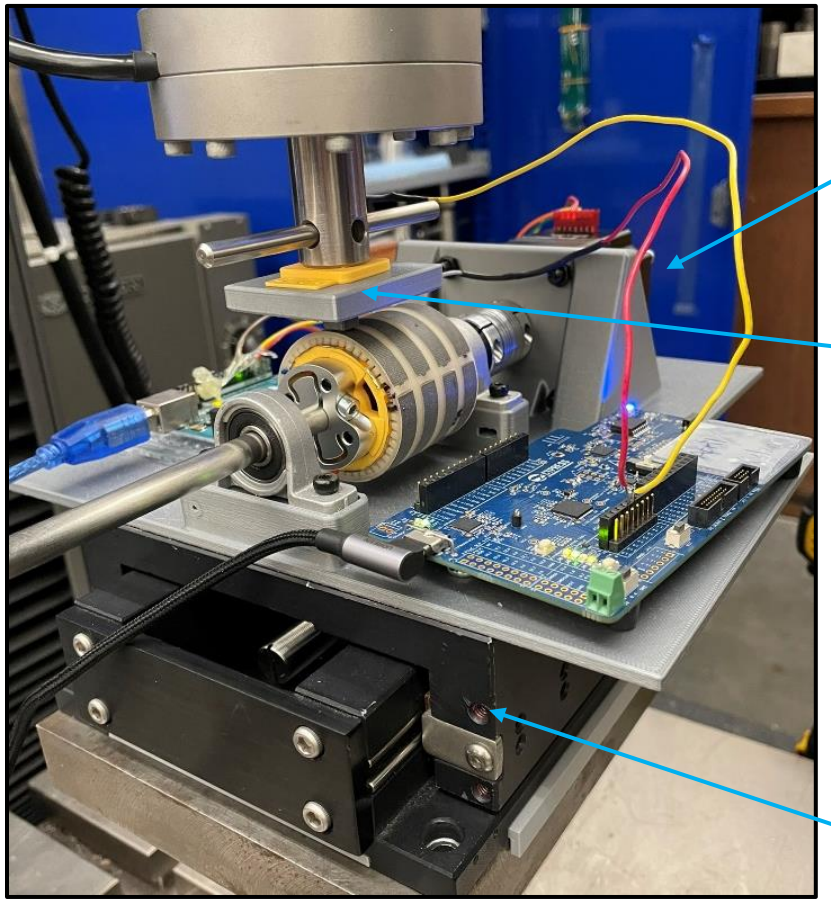

Stepper motor actuated by Instron signal

Custom indenter

Linear stage actuated by Instron signal

CRN
Composites Research Network

© CRN UBC (2025) -- DO NOT REPRODUCE WITHOUT WRITTEN PERMISSION

Identifying faulty sensors

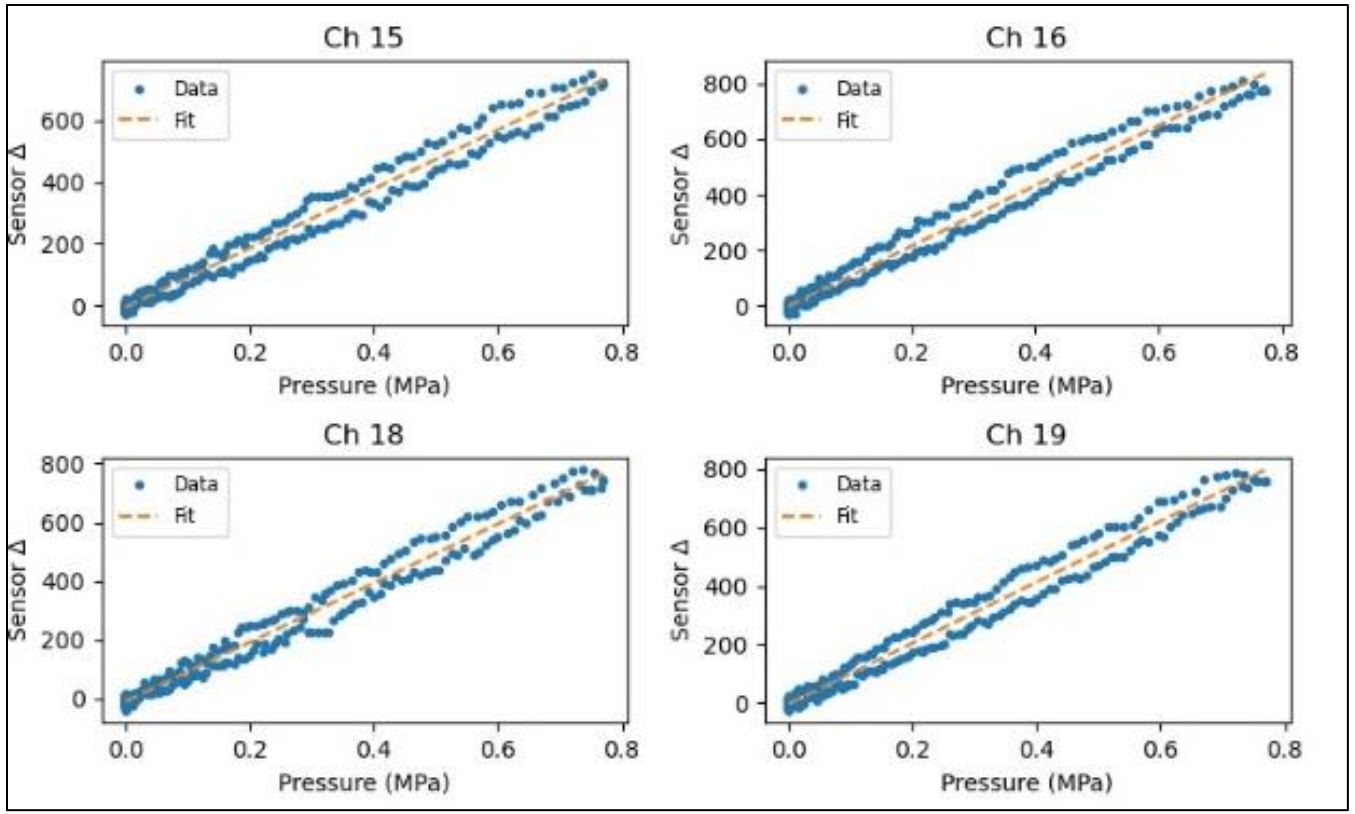

Normal sensor calibration

Electronics need to be re-tuned

Broken sensor

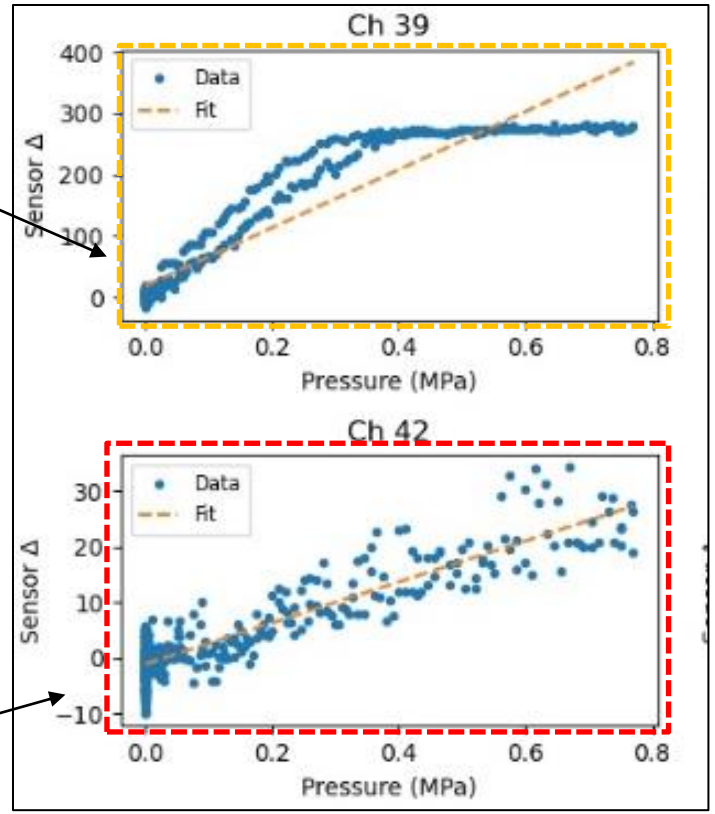

Abnormal sensor calibration

© CRN UBC (2025) -- DO NOT REPRODUCE WITHOUT WRITTEN PERMISSION

CRN
Composites Research Network

THE UNIVERSITY OF BRITISH COLUMBIA

In-line Process Control

Test Setup

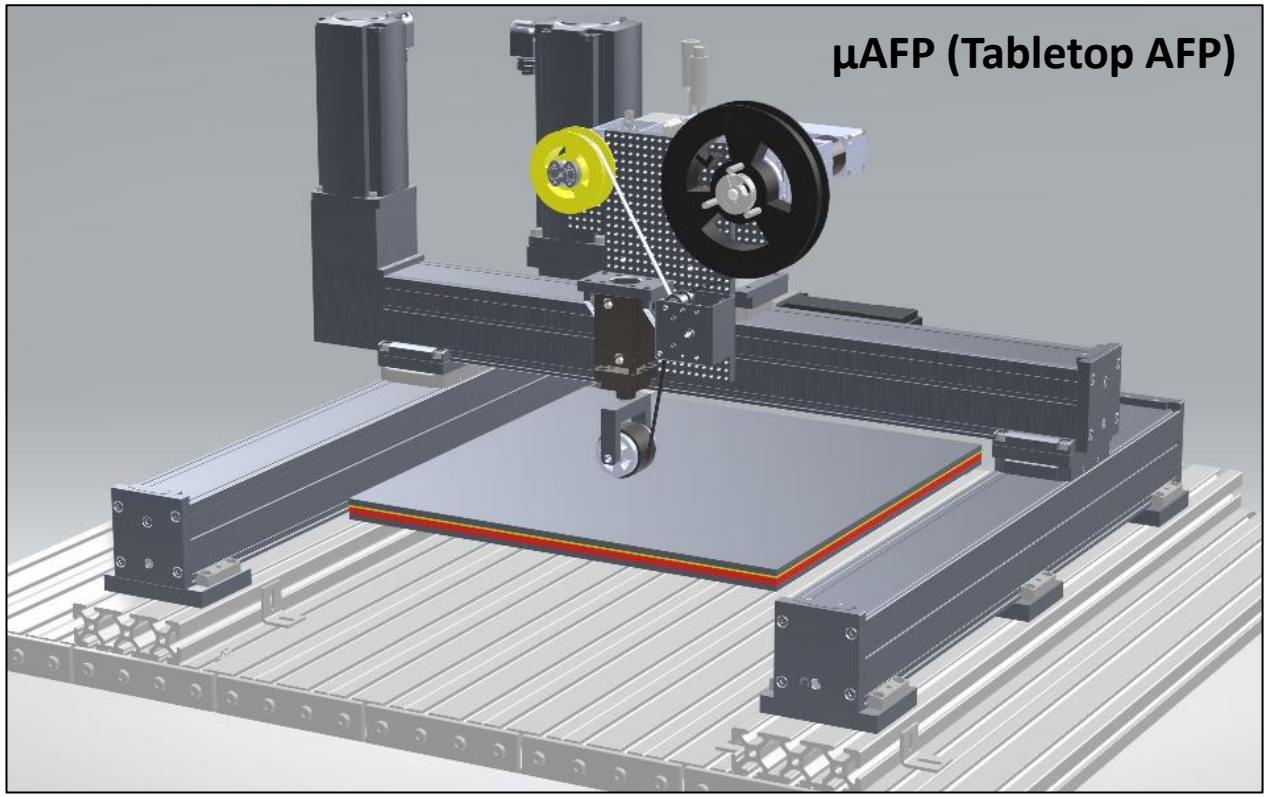

The following experiments are done using a tabletop Automated Fibre Palcement machine. This machine can deposit short paths of prepreg under controlled conditions, as well as perform tack tests.

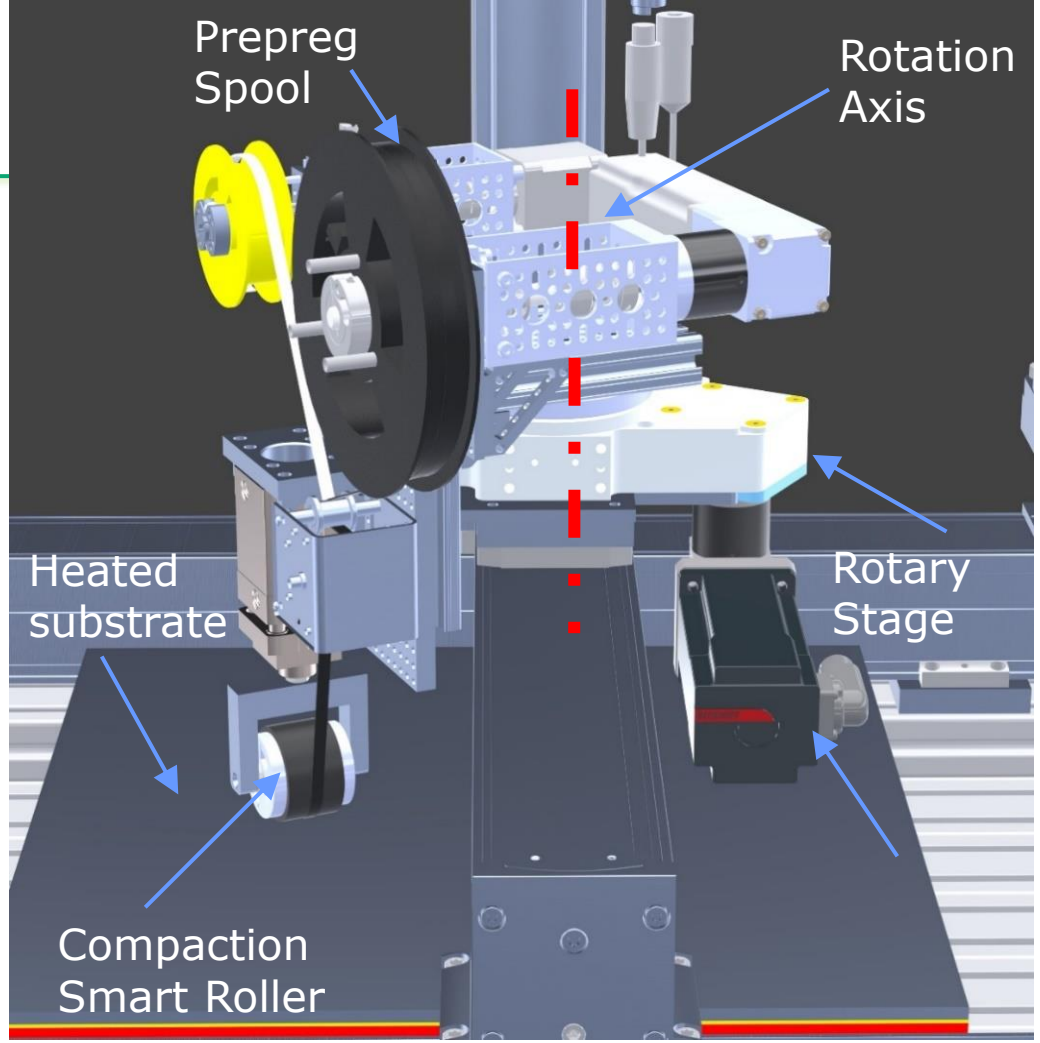

Compaction system

Bakhshi, N. (2023). *Investigation of prepreg tack through development of an AFP simulator using in-situ sensing and physics-based simulation* (Doctoral dissertation). University of British Columbia. https://doi.org/10.14288/1.0438302 (open.library.ubc.ca)

CRN Composites Research Network

© CRN UBC (2025) -- DO NOT REPRODUCE WITHOUT WRITTEN PERMISSION

Low-tack detection

Test Conditions

Compaction Force	100 N
Deposition/Peel Speed	0.025 m/s
Gap depth	1 mm
Gap width	8 mm

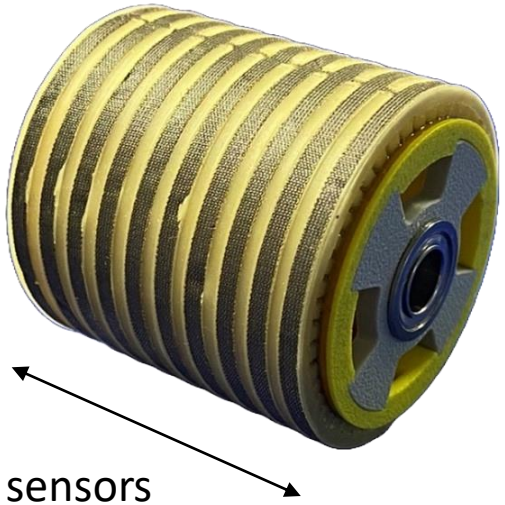

8 sensors
across width

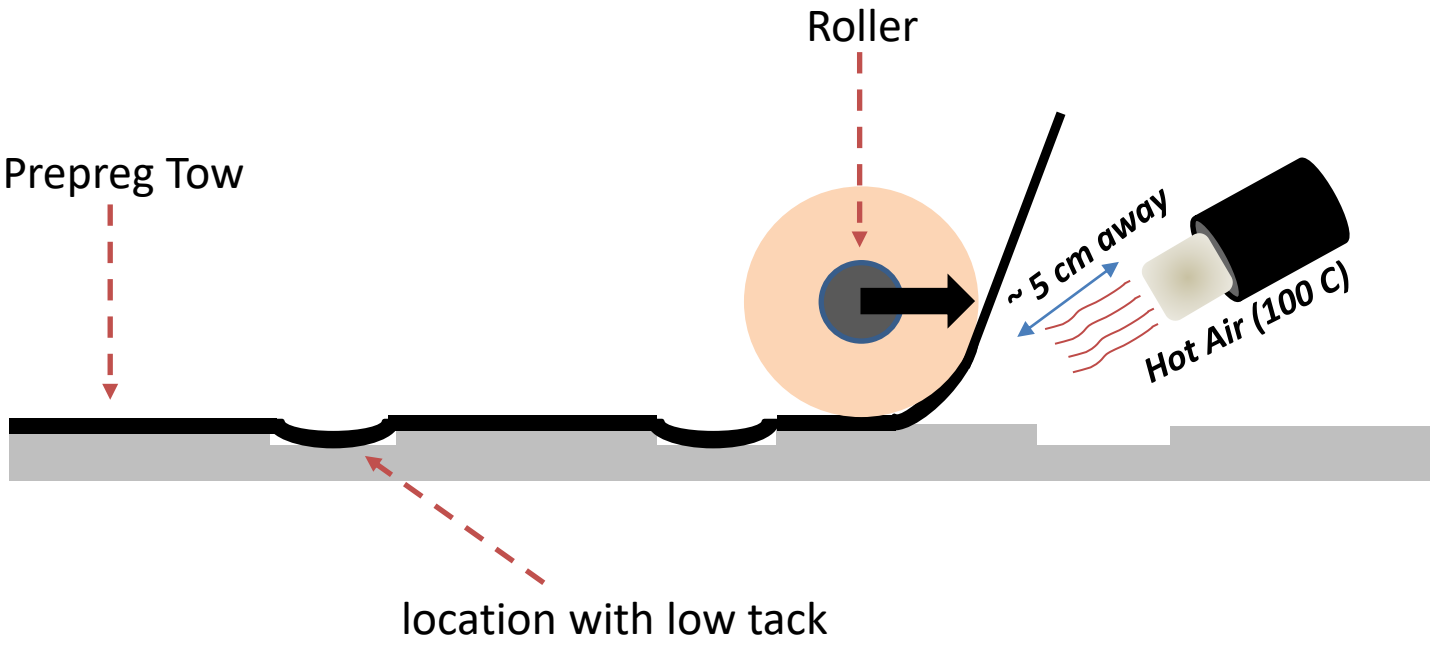

Substrate after deposition, before peeling off

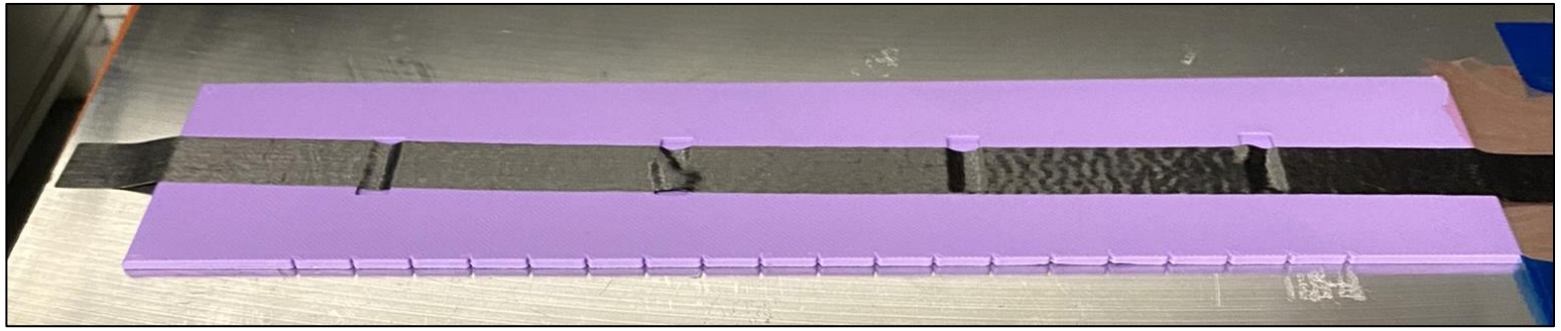

© CRN UBC (2025) -- DO NOT REPRODUCE WITHOUT WRITTEN PERMISSION

Aligning Smart Roller data in deposition with tow tension during peel

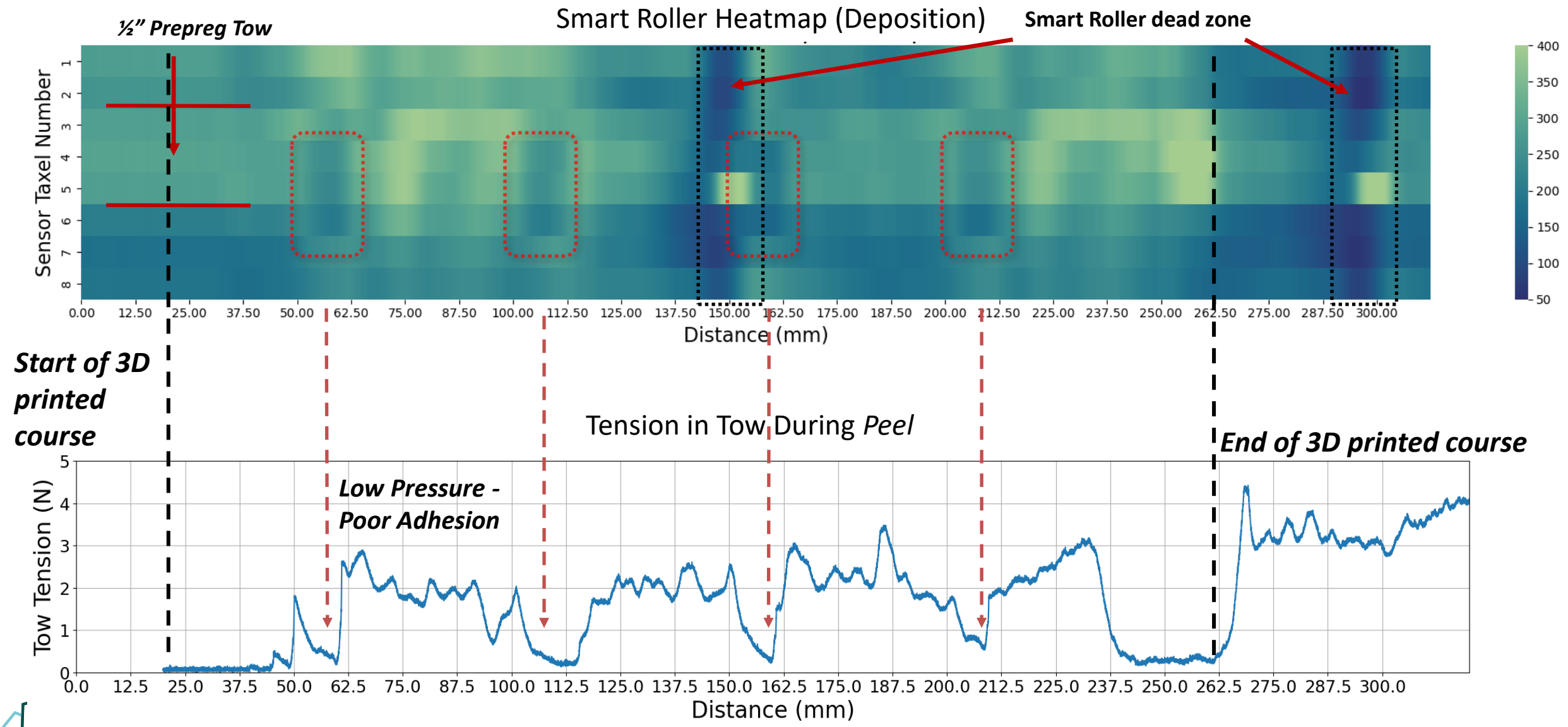

© CRN UBC (2025) -- DO NOT REPRODUCE WITHOUT WRITTEN PERMISSION

Depositing a curve and measuring the twist in the tow

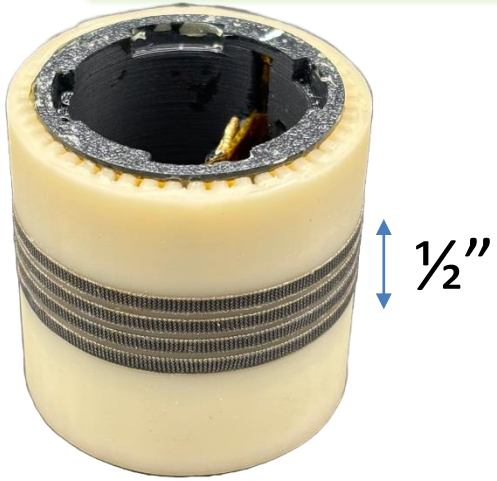

400 mm radius



750 Mm radius

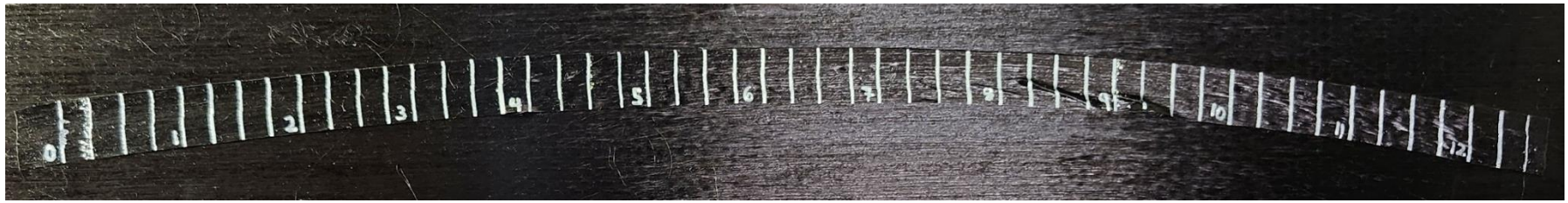

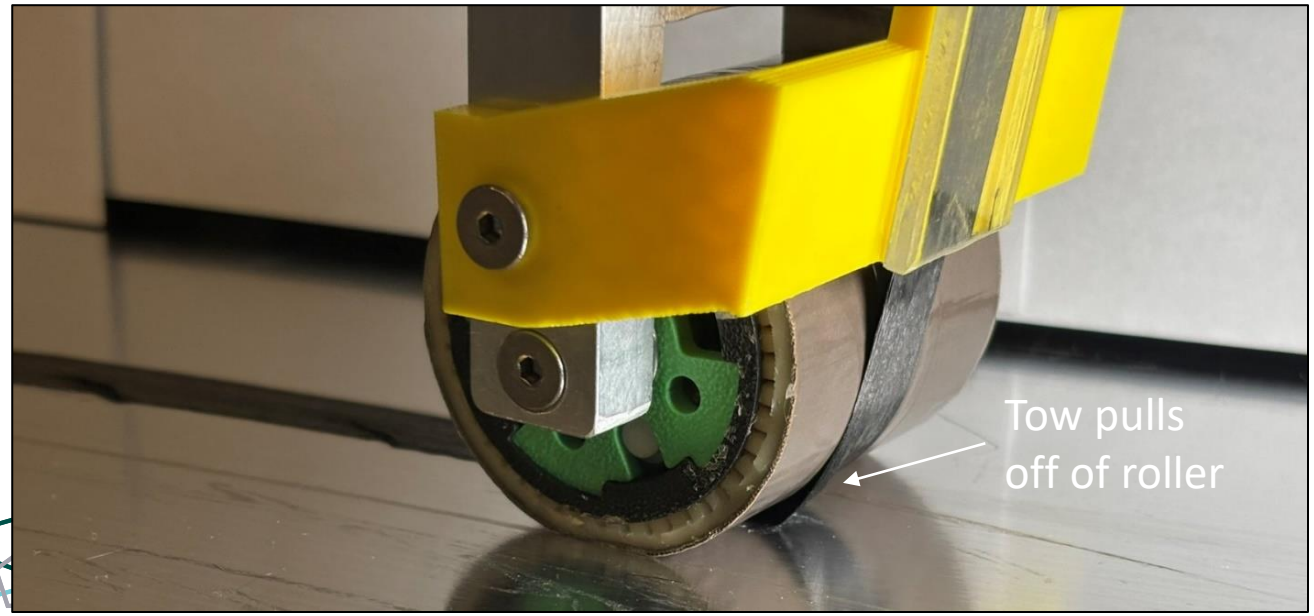

Deposit curves of various radii to measure the twist in the tow before deposition. A tighter radius leads to more wrinkle formation, and the Smart Roller can predict wrinkle formation by measuring the pressure gradient across a twisted tow.

© CRN UBC (2025) -- DO NOT REPRODUCE WITHOUT WRITTEN PERMISSION

Interpreting Smart Roller data

Smart Roller on µAFP

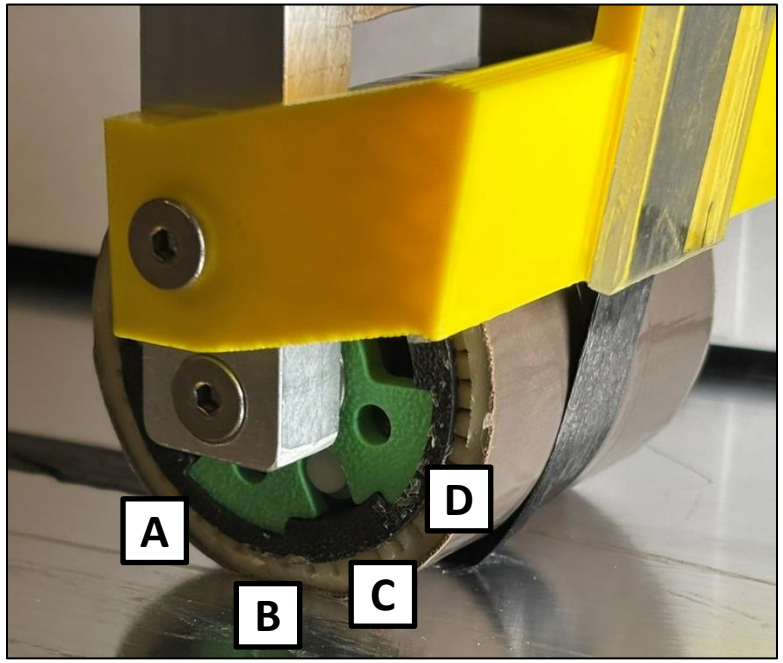

Each square represents one local pressure-sensing “taxel”. There are 4 taxels across the width of one ½” tow, and 13 rows of taxels around the circumference.

Each spoke in the visualization is one row of taxels across the width of the tow, with the taxels on the outer radius of the heatmap corresponding to the outer radius of the deposited path.

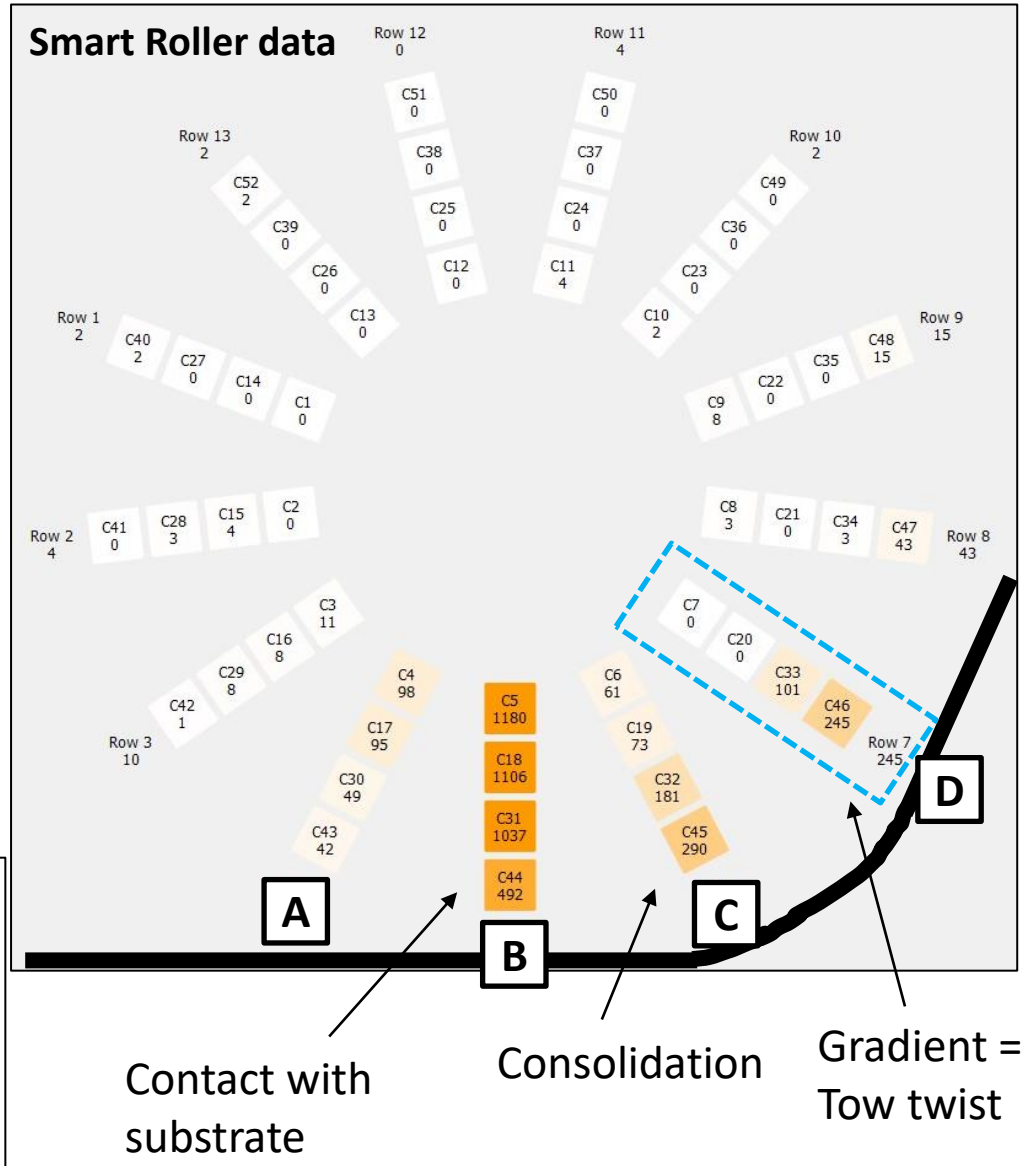

Location D on the heatmap corresponds to the location on the compaction roller where the carbon tow twists before consolidation. The twist can be measured by looking at the gradient in pressure from the taxels on the outer radius to the ones on the inner radius, at this location.

Composites Research Network

© CRN UBC (2025) -- DO NOT REPRODUCE WITHOUT WRITTEN PERMISSION

Comparing tow twist for 400mm curve and 750mm curve

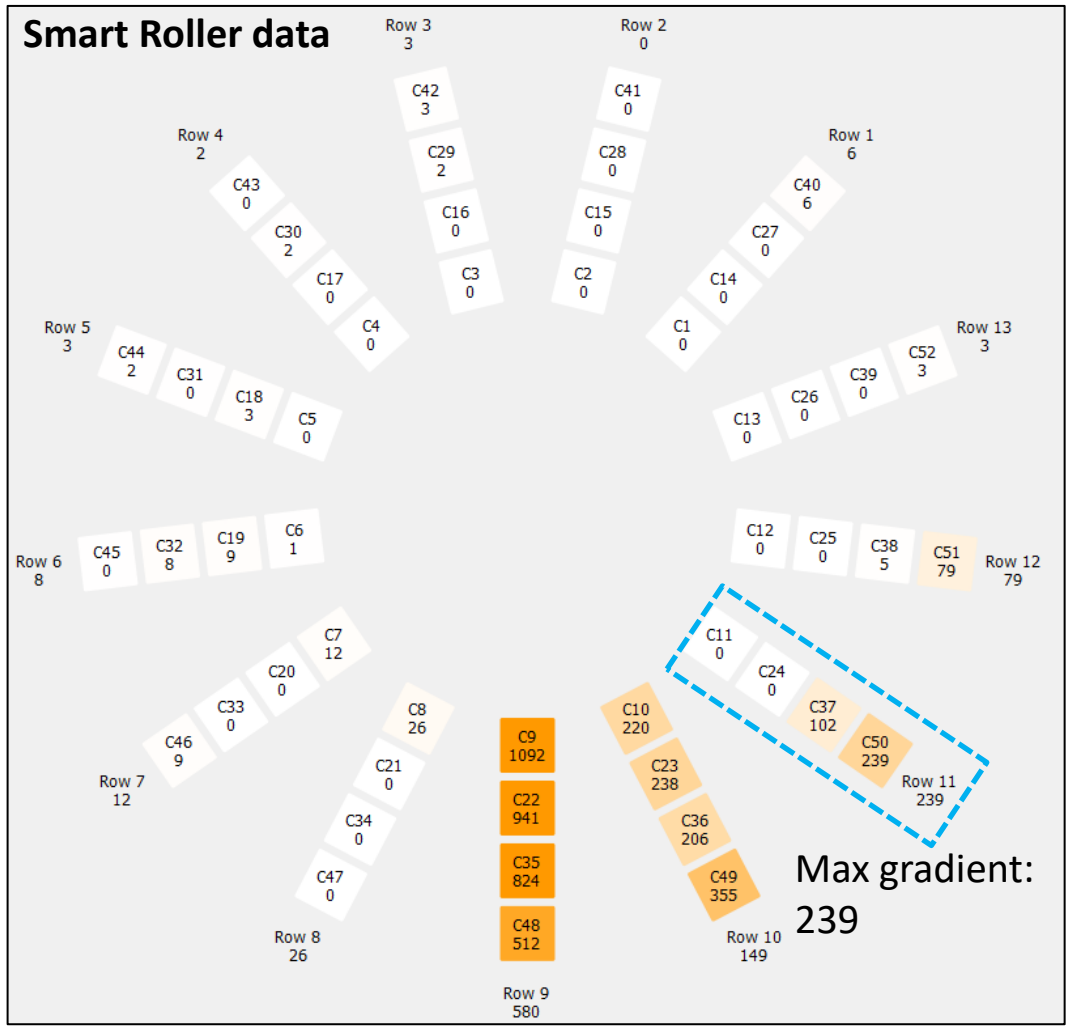

400mm radius curve

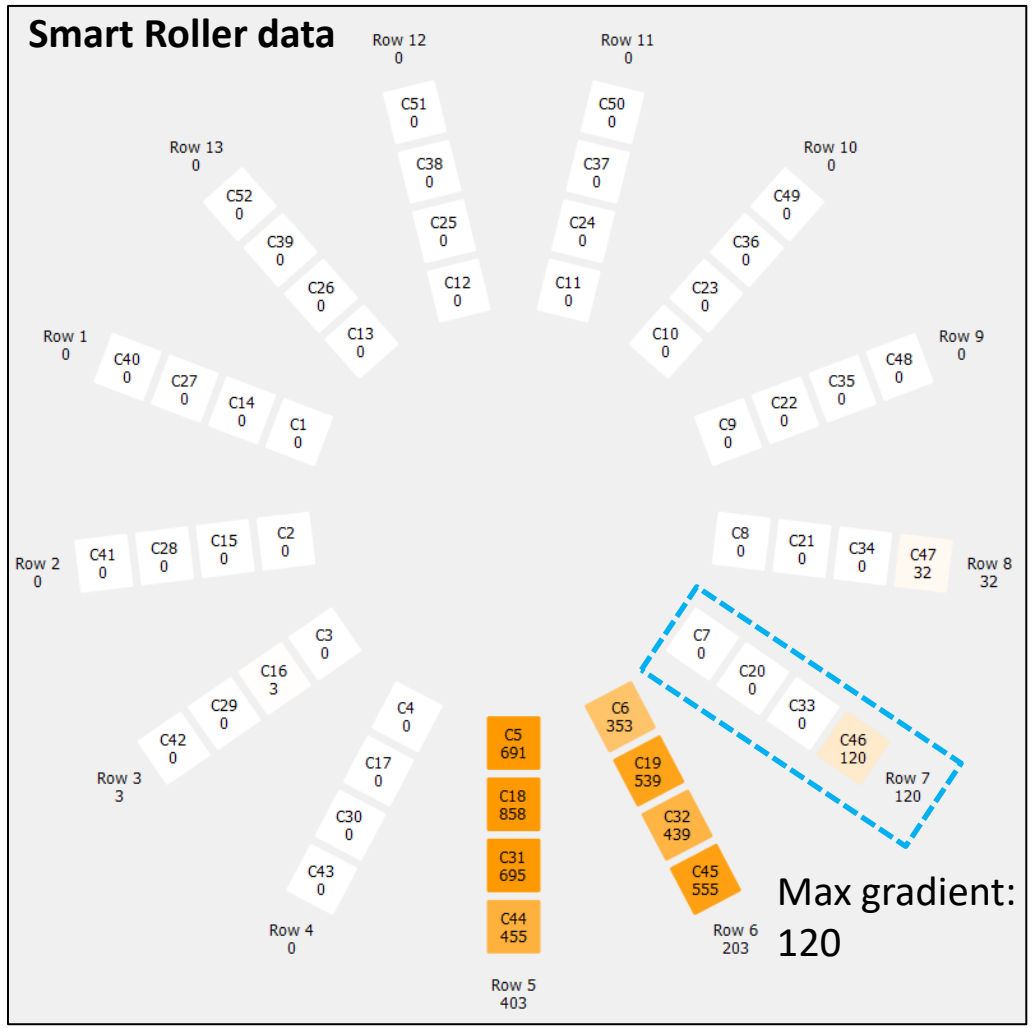

750mm radius curve

© CRN UBC (2025) -- DO NOT REPRODUCE WITHOUT WRITTEN PERMISSION

Smart Roller Data for straight path

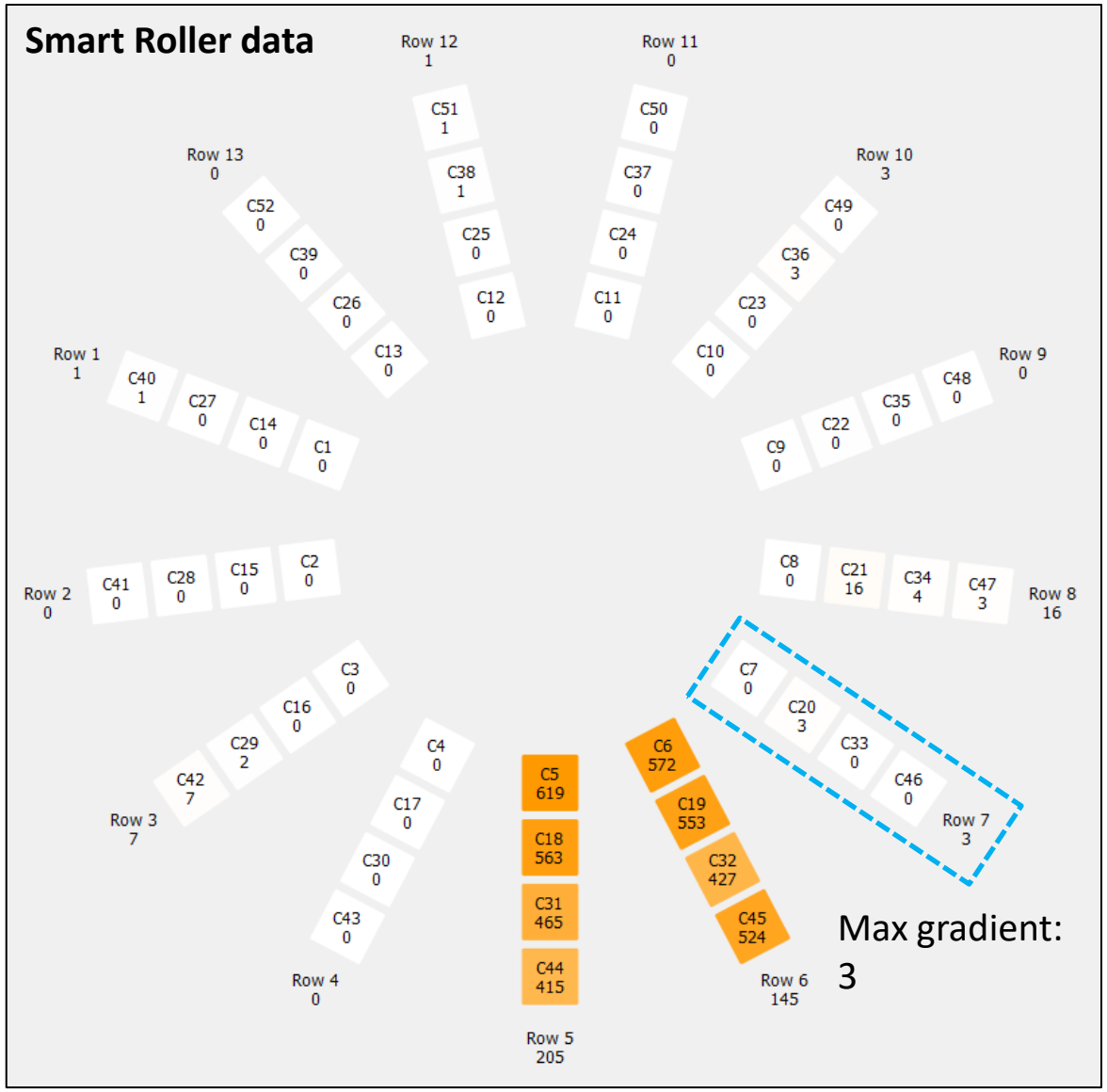

The next step for this experiment is to threshold the Smart Roller data so it can trigger an alert when it detects an abnormality (i.e. torsion in the tow, gaps/laps, or low tack).

Composites Research Network

© CRN UBC (2025) -- DO NOT REPRODUCE WITHOUT WRITTEN PERMISSION

Summary and Future Work

1. The Smart Roller is made with custom dimensions, compliance, and sensor arrangement to match the mechanical performance of a standard compaction roller and add pressure/shear force sensing capability.
2. The sensors on the Smart Roller are characterized to convert a displacement measurement to an accurate local pressure/shear value.
3. The Smart Roller can detect certain gaps, overlaps, low tack regions, and tow torsion before consolidation.

Next…

- Use the Smart Roller as a real-time alert system by creating models that interpret the data and predict potential defects.
- Install the Smart Roller on a full-sized AFP machine to validate on a machine other than our in-house tabletop AFP.
- Make a Smart Roller version for higher temperatures (AFP with thermoplastics).

© CRN UBC (2025) -- DO NOT REPRODUCE WITHOUT WRITTEN PERMISSION

Acknowledgments

- Dr. Anoush Poursartip
- Dr. Adam Clare
- Dr. John Madden
- Mr. Xiulun Yin
- All CRN colleagues

Composites Research Network

© CRN UBC (2025) -- DO NOT REPRODUCE WITHOUT WRITTEN PERMISSION

August 05, 2025
24th International Conference on Composite Materials (ICCM24)
Baltimore Convention Center, Baltimore, MD

High-Fidelity Digital Twin Autoclave Tool for Quality Informed Composite Fabrication

Jim Lua, Kalyan Shrestha, Anand Karuppiah
Global Engineering and Materials, Inc., Princeton, NJ

Mark Walthers
National Institute for Aviation Research (NIAR), Wichita, KS

Jinhui Yan
University of Illinois at Urbana-Champaign , Urbana-Champaign, IL

Dianyun Zhang
Purdue University, West Lafayette, IN

NAVAIR Public Release SPR# 2025-0404. Statement A - Approved for public release; Distribution is unlimited.

Acknowledgement

This work is funded by Naval Air Warfare Center (NAVAIR), Aircraft Division under the Contract of N68335-23-C-0116.

Motivation





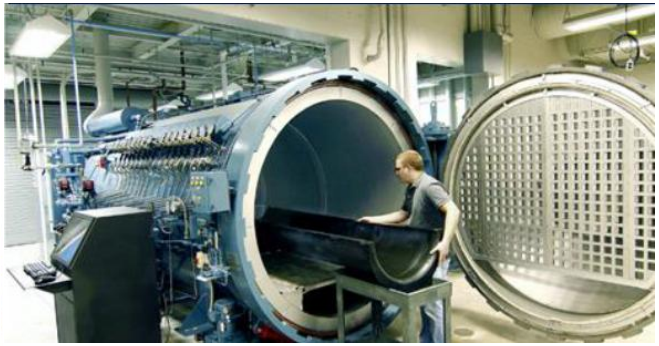

- Autoclave time is the bottleneck in manufacturing lines increasing overall production time and cost
- Optimization of the autoclave process by simultaneously curing multiple parts without deviating from the recommended cure cycle can significantly reduce scrap rate and also the overall production time and cost
- GEM and the team propose to deliver a high-fidelity multi-physics predictive simulation toolkit (SMARTCLAVE) that can optimize the autoclave process condition to balance the throughput and quality of cured-composite parts

NAVAIR Public Release SPR# 2025-0404. Distribution Statement A - Approved for public release; Distribution is unlimited.

Overview of Technical Approach

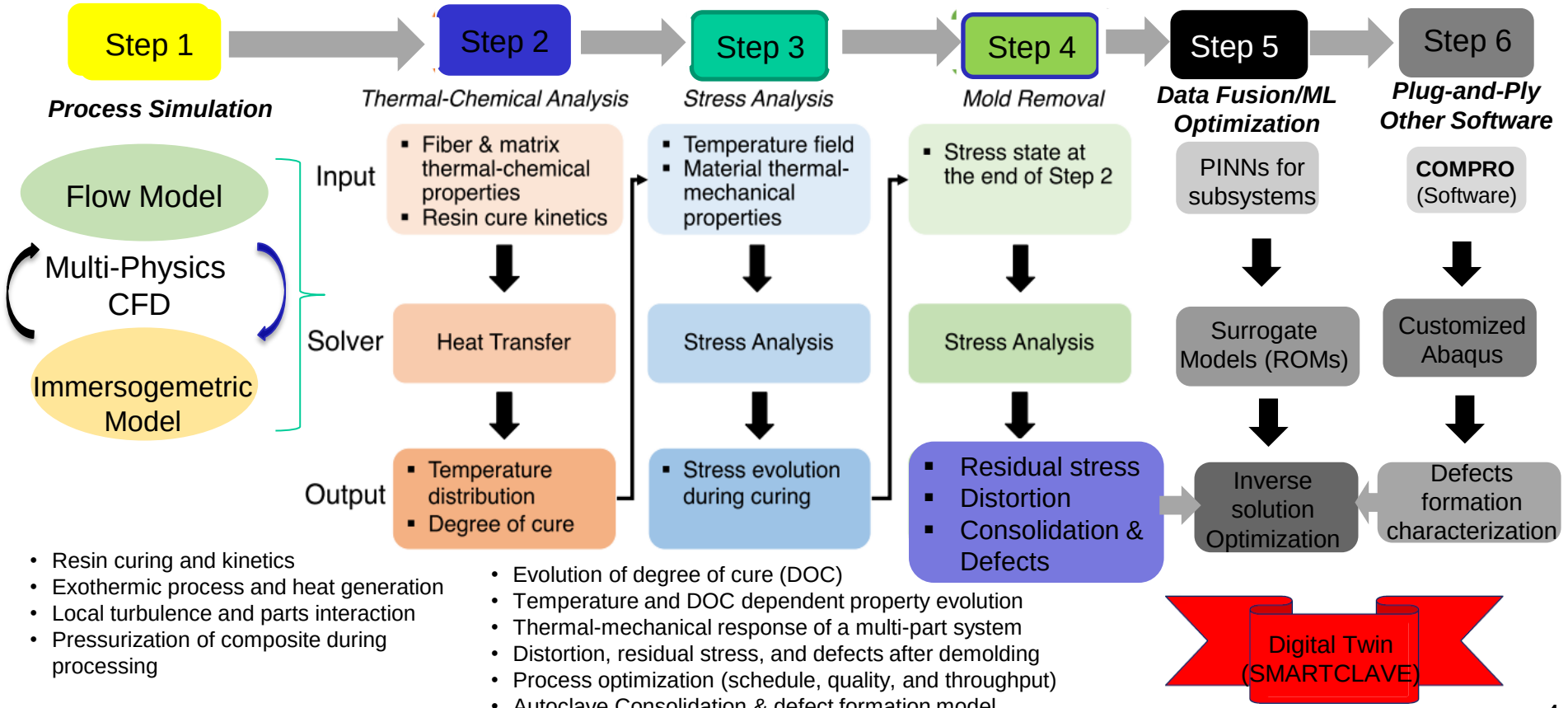

- Resin curing and kinetics
- Exothermic process and heat generation
- Local turbulence and parts interaction
- Pressurization of composite during processing

- Evolution of degree of cure (DOC)
- Temperature and DOC dependent property evolution
- Thermal-mechanical response of a multi-part system
- Distortion, residual stress, and defects after demolding
- Process optimization (schedule, quality, and throughput)
- Autoclave Consolidation & defect formation model

Digital Twin (SMARTCLAVE)

NAVAIR Public Release SPR# 2025-0404. Distribution Statement A - Approved for public release; Distribution is unlimited.

Summary of SMARTCLAVE Capability

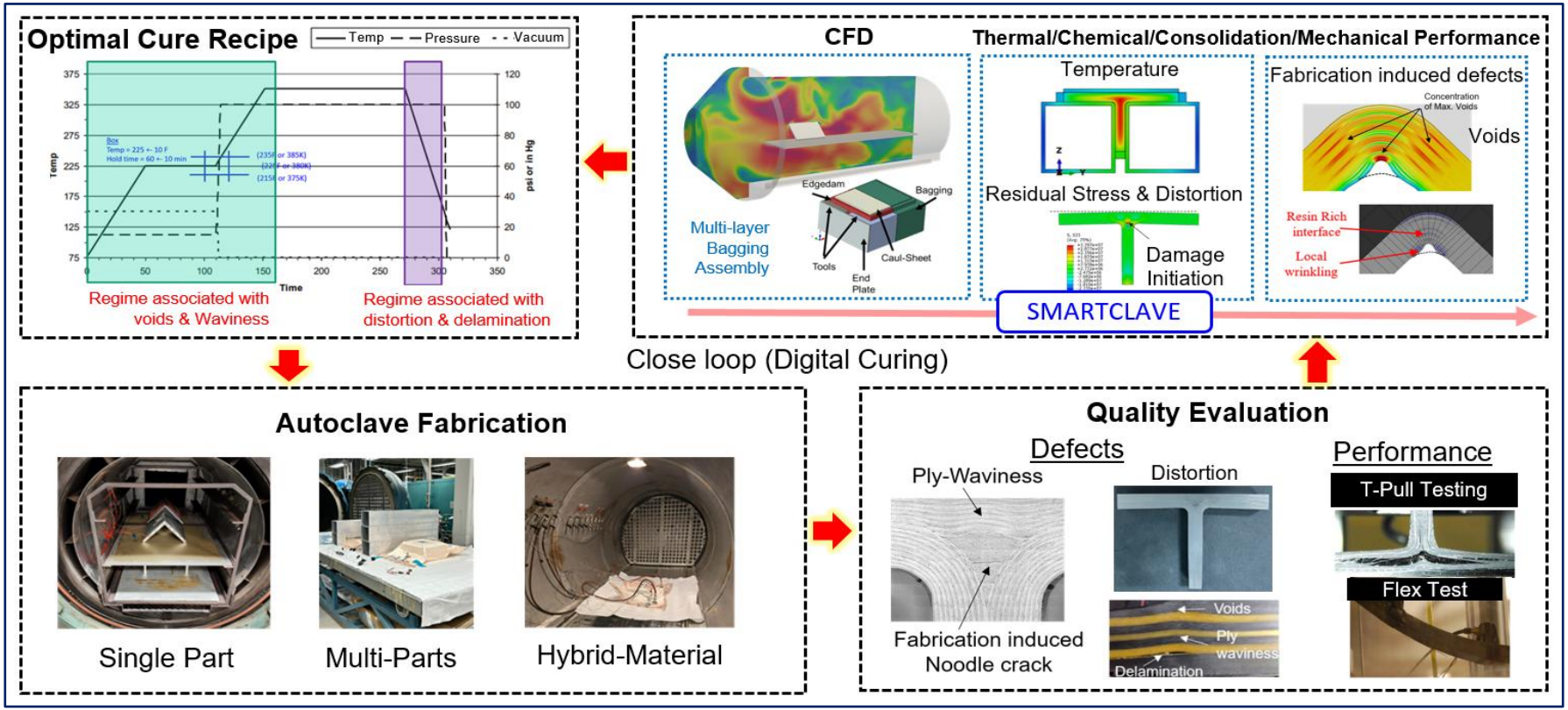

GEM's SMARTCLAVE GUI

Step 1: Autoclave setup

User Inputs:

- CAD model
- Autoclave Parts (i.e., bagging assembly & table)
- Material system
- Part placement

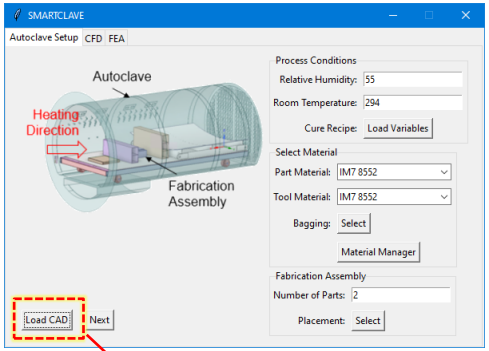

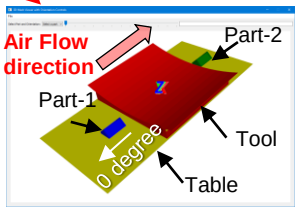

3D interactive interface
(load CAD & adjust placement)

Step 2: Heat Transfer Coefficient

User Inputs:

- Model file with Mesh & BCs
- Time step

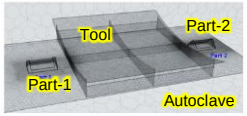

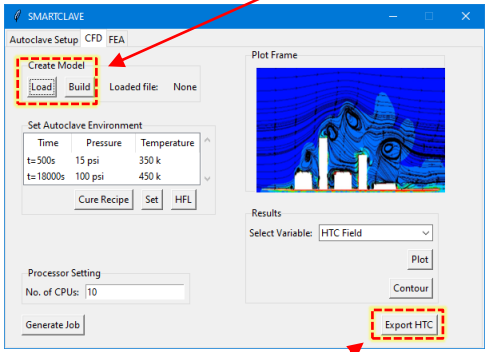

Outputs:

- Flow Field
- HTC Field

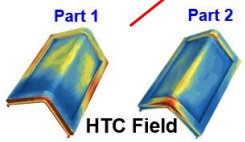

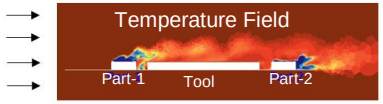

Step 3: Temperature, Consolidation & Residual stress

User Inputs:

- Model file with Mesh, layup & BCs
- Time step

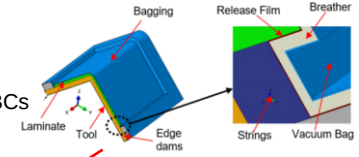

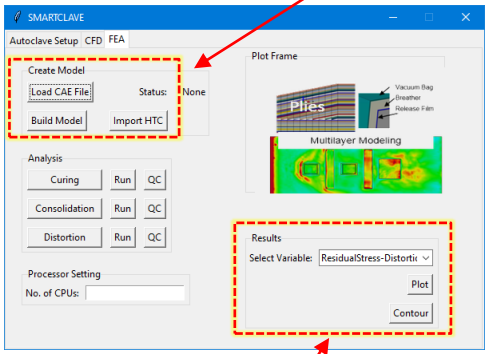

Outputs:

- Temperature
- Degree of Cure
- Residual stress & Distortion
- Consolidation (thickness change + fiber volume fraction)
- Fabrication induced defects such as ply-waviness, voids & delamination zone

Degree of Cure

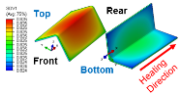

History plot

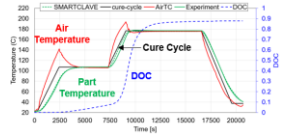

Residual Stress & Distortion

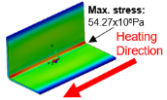



NAVAIR Public Release SPR# 2025-0404. Distribution Statement A - Approved for public release; Distribution is unlimited.

NIAR's Autoclave Experiment on an L-beam

L-Beam Fabrication

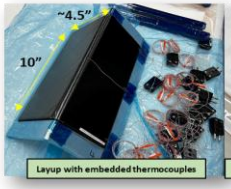



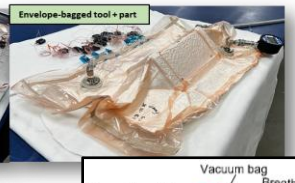

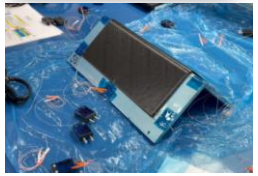



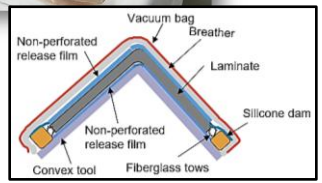

Material: IM7/8552
Layup: [45/0/-45/90]3s
Tool: Al 6061 (Convex)

Thermal Survey Data

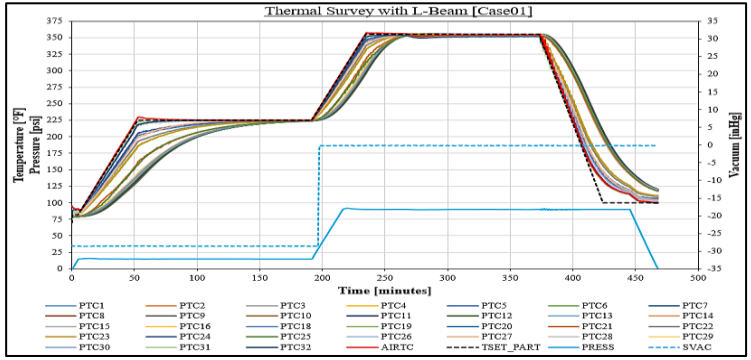

Autoclave Setup

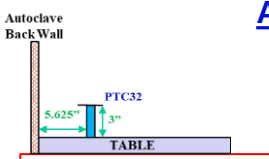

Air temperature measurements close to autoclave back wall.

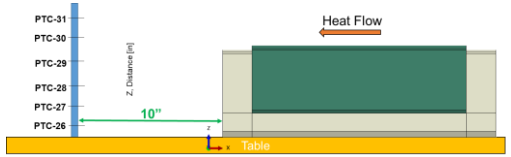

Air temperature measurements behind part assembly

PTC26- 0.425"
PTC27- 1.488"
PTC28- 2.550"
PTC29- 3.613"
PTC30- 4.675"
PTC31- 5.378"

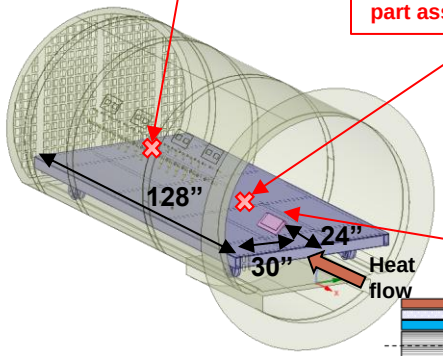

L-Beam Part & Tool Assembly

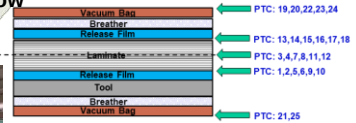



NAVAIR Public Release SPR# 2025-0404. Distribution Statement A - Approved for public release; Distribution is unlimited.

Thermal CFD Model

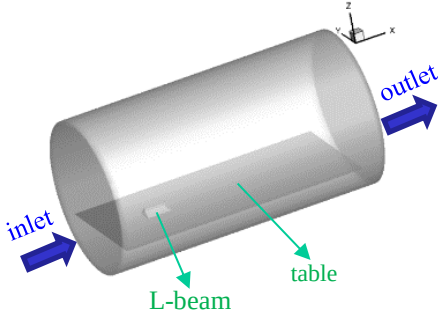

~1.4 million cells

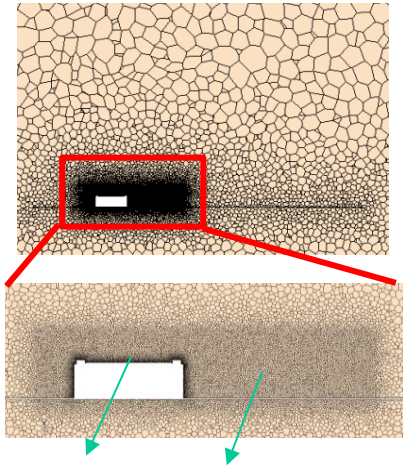

Temperature contours with velocity streamlines

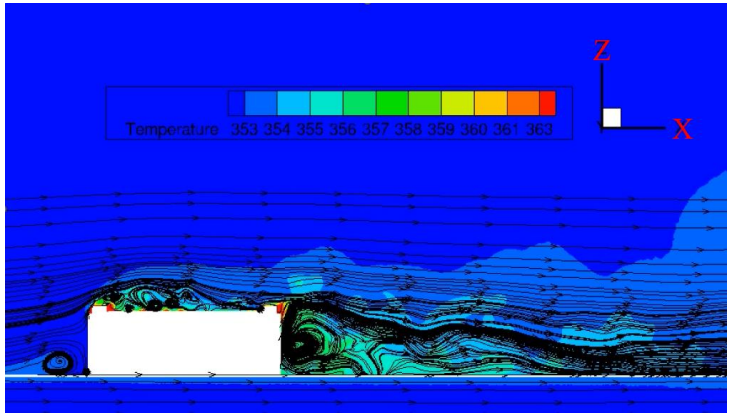

Front Section

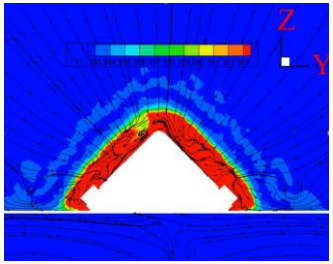

Rear Section

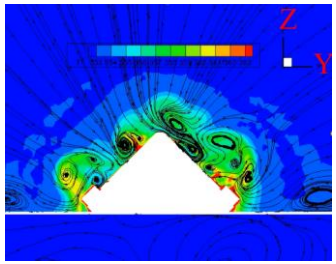

Q-criterion

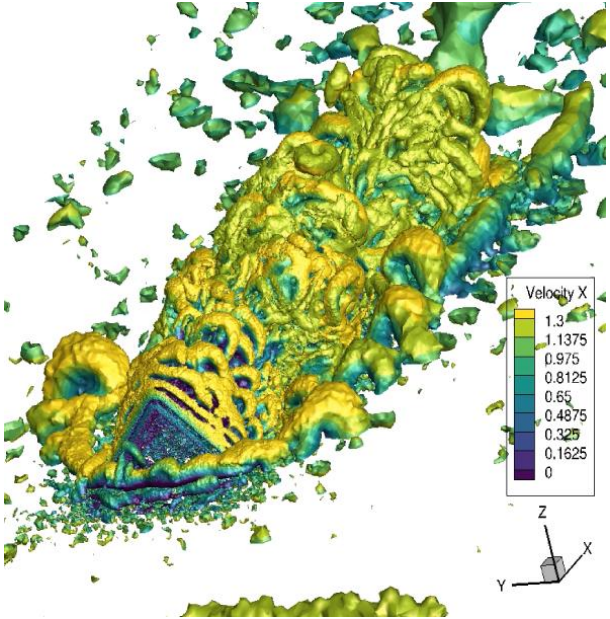

NAVAIR Public Release SPR# 2025-0404.
Distribution Statement A - Approved for public release; Distribution is unlimited.

User-Defined Multilayer Abaqus Model

NIAR's Autoclave

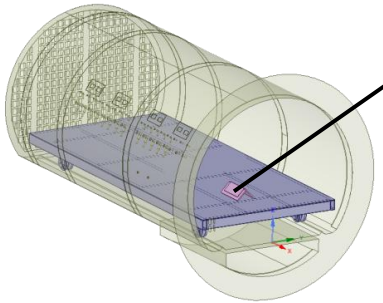

Experiment



LBeam Bagging Assembly

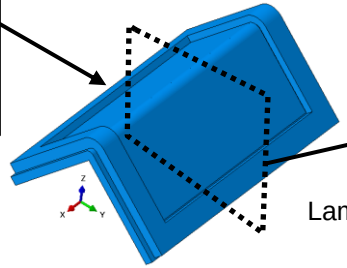

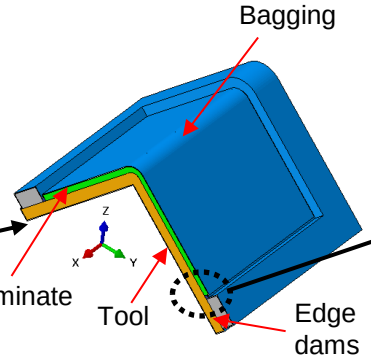

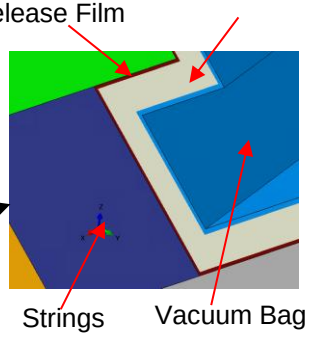

Boundary Conditions

Heat Transfer Analysis

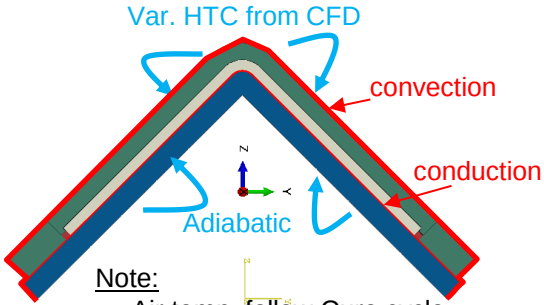

Note:
- Air temp. follow Cure cycle
- Spatially Varying HTC from CFD

Stress Analysis Model

During Curing

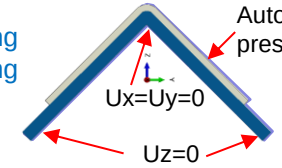

After Demold

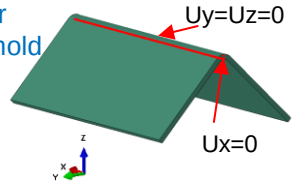

Bagging

- Vacuum Bag
- Breather
- Release Film

$$K_{eff} = \frac{K_b K_{air}}{K_b + K_{air}}$$

assumed as a thermal circuit in a series connection

K_b = 0.43 W/m/K
K_{air} = 0.015 W/m/K
K_{eff} = 0.0117 W/m/K

NAVAIR Public Release SPR# 2025-0404. Distribution Statement A - Approved for public release; Distribution is unlimited.

Validation of the Thermal History

Temperature

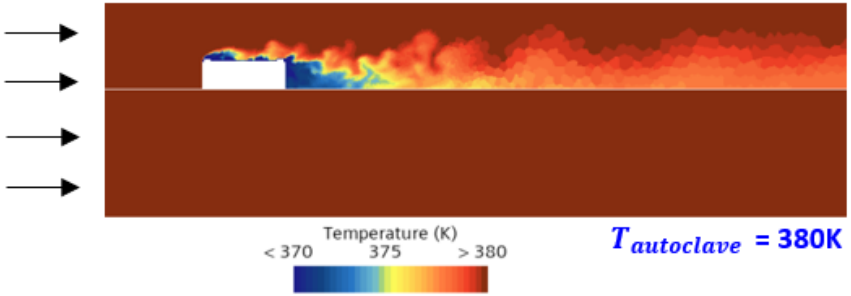

$T_{autoclave}$ = 380K

9in X 10in composite part
Material: IM7/8552
Layup: [45/0/-45/90]3s; 24 plies
Tool: Al 6061 (Convex); 0.25” corner radius

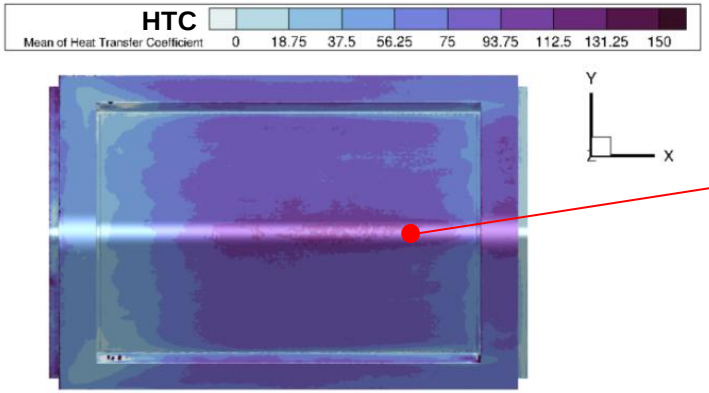

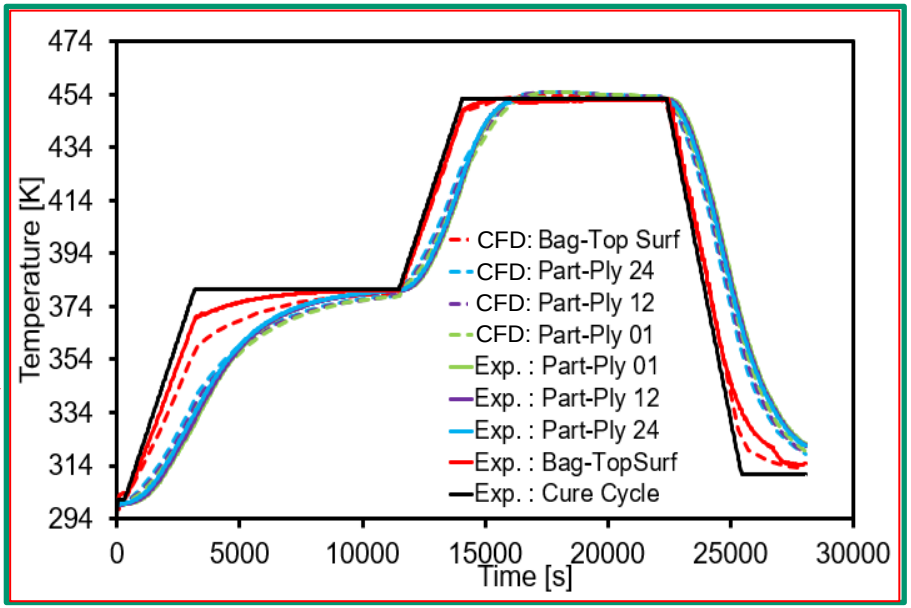

NAVAIR Public Release SPR# 2025-0404. Distribution Statement A - Approved for public release; Distribution is unlimited.

Residual Stress and Distortion Validation

	During Cure (at t=20,548s)	After fully Cured	After Demold
Von Mises Stress	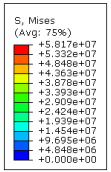 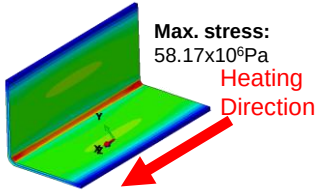 Max. stress: 58.17x10^{6}Pa Unit is Pa	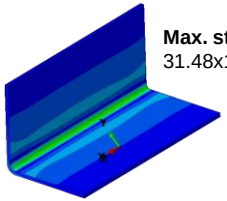 Max. stress: 31.48x10^{6}Pa	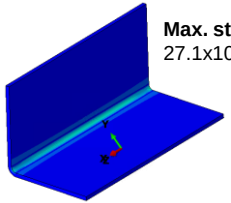 Max. stress: 27.1x10^{6}Pa
Component 33 of Strain	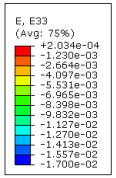 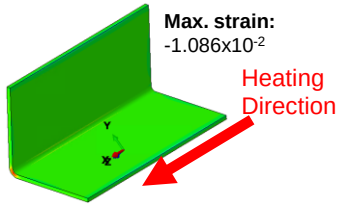 Max. strain: -1.086x10^{-2}	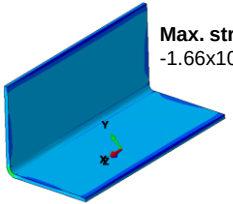 Max. strain: -1.66x10^{-2}	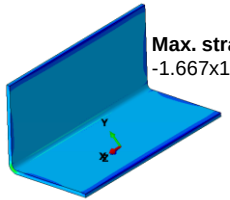 Max. strain: -1.667x10^{-2}
Spring-in Deformation	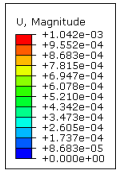 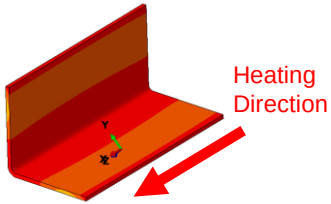 Unit is meter Max. Displacement: 1.042x10^{-3}	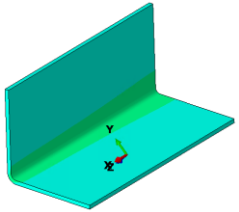 Max. Displacement: 4.13x10^{-4}	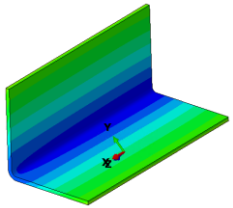 Max. Displacement: 6.522x10^{-4}

Experiment **Simulation**

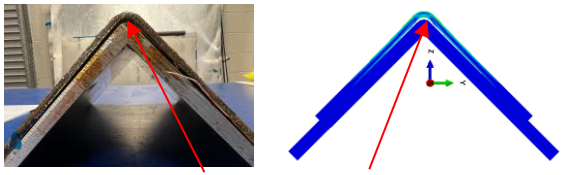

Tool-Part separation

Distortion after demolding



Front Rear

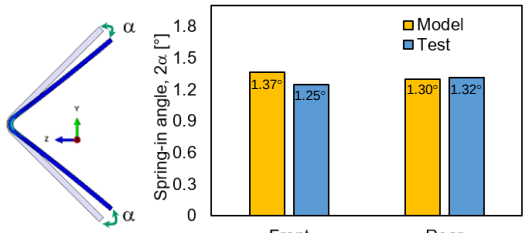

NAVAIR Public Release SPR# 2025-0404. Distribution Statement A - Approved for public release; Distribution is unlimited.

Conclusions

- Developed a multiphysics CFD modeling approach to capture flow, temperature, and multiple parts interaction in an autoclave
- Developed the customized Abaqus model for thermo-chemo-mechanical prediction using local CFD-driven boundary condition
- Efficient generation of HTC field from CFD results without using exhaustive calibration autoclave runs
- Validated the performance prediction using the measured spring-in angles
- Established a digital twin autoclave for the rational selection of the processing parameters to balance the parts load out and the quality

NAVAIR Public Release SPR# 2025-0404. Distribution Statement A - Approved for public release; Distribution is unlimited.

SMART COMPOSITE PRODUCTION LINE PLANNING USING AI BASED DIGITAL TWIN TO OPTIMIZE THE PRODUCTION PLANNING UNDER UNCERTAINTY

M. Malaibari[1], S. Abdoli[1], M. Siddiqui[1], G. Pearce[1], and L. Djukie[2]

[1]School of Mechanical and Manufacturing Engineering University of New South Wales, Sydney, Australia
Email : s.abdoli@unsw.edu.au

[2]Omni Tanker

Keywords: Digital Twin, Machine learning, Production planning, Scenario based optimization, Uncertainty

ABSTRACT

Various composite material production systems are inherently complex and labour-intensive, relying heavily on skilled human workers for critical tasks. This human dependency introduces significant uncertainty into production planning, with fluctuations in worker availability, process durations, and quality-related rework impacting system stability and efficiency. Traditional planning methods often fail to adapt to these dynamic conditions, highlighting the need for a more flexible and predictive approach. This study presents a novel framework that integrates Digital Twin (DT) and Machine Learning (ML) to optimize workforce allocation and production planning in composite manufacturing environments. A discrete-event simulation-based DT was developed to replicate system behaviour under varying operational conditions. An ML algorithm was used to forecast key performance indicators (KPIs), while a Reinforcement Learning (RL) algorithm was employed to optimize resource allocation across multiple uncertainty scenarios. The framework was applied to a real composite production line, yielding a 34% reduction in worker cost and a 16% decrease in time in system, without compromising throughput. The results demonstrate the effectiveness of the proposed approach in supporting resilient, data-driven decision-making for human-centric composite manufacturing systems.

1 INTRODUCTION

Global competition and increasing customer demands compel modern production, assembly, and logistics systems to become more efficient, responsive, and adaptive. These complex systems involve dynamic interactions between numerous components, making their behaviour difficult to predict using traditional analytical methods alone. To evaluate potential improvements and validate operational strategies, simulation-based approaches are often required to capture the evolving behaviour of such systems [1,2].

In parallel, the rise of Industry 4.0—driven by the integration of digital technologies such as the Internet of Things (IoT), Artificial Intelligence (AI), Machine Learning (ML), and cloud computing—has transformed how industrial systems are designed and managed. One of the most prominent concepts emerging from this digital transformation is the Digital Twin (DT) [3].

A Digital Twin is a virtual representation of a physical asset, process, or system that enables real-time monitoring, predictive analysis, and informed decision-making. DTs have found widespread application in manufacturing, where they support functions such as production control, asset management, and predictive maintenance. Recent studies have explored various aspects of DT development, including their architecture, lifecycle integration, software platforms, and industrial impact [4].

This study focuses on the development and application of a Digital Twin framework within a composite manufacturing system (CMS)—a production environment known for its high complexity, process variability, and dependence on human labour. In such systems, production planning is especially

challenging due to uncertainties in worker availability, process durations, and output quality. These uncertainties can lead to shifting bottlenecks, reduced throughput, and inefficient resource utilization—limitations that are often not addressed adequately by static or one-off optimization methods.

1.1 Objective

This research investigates the integration of AI-driven Digital Twin technologies into composite production systems, with a particular focus on proactive production planning (PP) under uncertainty. The objective is to enable scenario-based optimization through RL, allowing the system to simulate and evaluate a wide range of possible future states and operational conditions. By incorporating these insights, the production plan can be dynamically adjusted to improve system-level Key Performance Indicators (KPIs).

The key contributions of this study are:

Assessment of Digital Twin modeling approaches and software platforms for CMS, including evaluation of features such as real-time connectivity, 3D visualization, and implementation cost.

Proposal of a reinforcement learning-based scenario analysis framework to address planning uncertainties related to human resource variability and production quality.

Application of the proposed framework to a real-world composite production case study, demonstrating its effectiveness in generating optimized and resilient production plans.

This work contributes to the growing body of knowledge on AI-enhanced Digital Twin systems and their potential to improve decision-making in complex, uncertainty-prone manufacturing environments.

2 DIGITAL TWIN

DT technology has garnered significant interest across academia and industry for its ability to support smart manufacturing within the broader Industry 4.0 paradigm. A DT is a dynamic virtual representation of a physical asset or system, enabling real-time monitoring, simulation, and optimization through the integration of physical and digital environments.

The concept of the DT was initially proposed by Dr. Michael Grieves in 2003, comprising three key elements: the physical product, the virtual product, and the data connections between them. NASA's implementation of a DT for the International Space Station in 2012 marked a major milestone, demonstrating the potential of DTs to improve system design, monitoring, and maintenance. Their definition emphasized high-fidelity, multi-physics simulations informed by real-time data and predictive models [5].

Advances in AI, IoT, and cloud computing have accelerated DT adoption, enabling applications in real-time control, predictive analytics, and lifecycle management [3].

2.1 Digital Twin Architecture

Early DT architectures were limited to three elements—physical, virtual, and connection—but Tao et al. expanded this to a more comprehensive five-dimensional model including data and service layers [6]. These components collectively support the DT ecosystem:

- Physical Part: The real-world asset or system
- Virtual Part: The digital counterpart
- Connection: Real-time communication between the two
- Data: Collected via IoT and manufacturing systems
- Service: The computational intelligence for decision-making
- Modern manufacturing generates massive volumes of heterogeneous data from sensors, supply chains, and user interactions. Managing and integrating these datasets is foundational to effective DT implementation.

2.2 Modeling Approaches for Digital Twin

Modeling is critical for DT development as it determines the system’s semantics, structure, and behavior. A variety of modeling approaches have been proposed [7-11]:

- UML and SysML: Useful for system-level design and stakeholder communication but limited in execution semantics.
- Object-Oriented Modeling: Widely used in DTs for encapsulating state and behavior but requires additional tools for simulation.
- Petri Nets and Colored Petri Nets (CPN): Effective for modeling discrete event systems and concurrency, though limited in visualization.
- Functional Mock-up Units (FMUs): Promote interoperability between simulation tools via standard interfaces.
- Ontologies: Structure heterogeneous data and improve semantic integration in DTs across lifecycles.
- Knowledge Graphs: Enhance data connectivity and inferencing capabilities by organizing relationships and attributes.
- AutomationML: Supports data exchange between manufacturing tools and preserves engineering semantics.

Despite this variety, a lack of standardized, reusable, and holistic DT development methodologies remains a key limitation. Current implementations often omit key parameters (e.g., input/output configurations) and offer little support for integration across the full system lifecycle.

2.3 Digital Twin Applications in Manufacturing

DT applications are most prevalent in manufacturing, covering multiple stages of the product lifecycle—from design to retirement. Applications include [3]:

- Design: Virtual prototyping, simulation, and optimization
- Manufacturing: Production control, resource allocation, workpiece quality prediction, and real-time monitoring
- Service: Predictive maintenance, diagnostics, and system health monitoring
- End-of-life: Dismantling, reuse, and recycling planning

In the manufacturing stage, DTs enable real-time data collection from machines and human operators, which can be used to compute and optimize Key Performance Indicators (KPIs). These KPIs serve as the basis for evaluating system performance and guiding continuous improvement initiatives.

The benefits of DT adoption include improved production efficiency, fault prediction, optimized scheduling, and enhanced decision-making.

2.4 Software Platforms for Digital Twin Implementation

Various software platforms support DT development, each with strengths tailored to different use cases. These platforms fall into four categories [11-16]:

- Discrete Event Simulation (DES) Tools: General-purpose simulation platforms (e.g., Arena, AnyLogic) using historical data and system logic modeling.
- Manufacturing Simulation Software: Tools with domain-specific capabilities, real-time data integration, and enhanced visualization (e.g., Siemens Plant Simulation, FlexSim).
- IoT Platforms: Focused on live system monitoring with cloud integration and real-time dashboards (e.g., Azure Digital Twins, AWS IoT TwinMaker).
- Other Tools: Specialized software not fitting above categories, often including AR/VR or 3D modeling (e.g., Unity, Dassault 3DEXPERIENCE).
-

Software capabilities are often compared across features such as:

- Real-time data integration (API/IoT) [17]
- Cloud deployment
- AI/ML support
- Customizability
- 3D visualization
- Licensing and cost

Selection of the appropriate platform depends on the system's complexity, real-time requirements, and long-term integration goals. Table 1 demonstrates the available software with their modelling approaches and their pros and cons in the context of developing DT for manufacturing systems.

Table 1 Comparison of Available software's

Software	Category	Modelling Scope	Pros	Cons
Simio MathWorks(MATLAB ,Simulink) Anylogic Flexsim Simul8	Discrete Event Simulation (DES)	Mainly behaviour modelling, and basic physical modelling	Well-suited for design and experimentation. Focus on system level and general flow. Abstract level of detail. In most cases, based on historical data. Easier to develop and implement. In most cases, cheaper than other types.	Limited support for real-time data. Limited level of detail Limited features for modelling complex systems
Ansys Twin Builder Siemens Tecnomatix Dassault DELMIA	Manufacturing Simulation	Behaviour, physical, and geometric Simulation based	Can be used to simulate running factories or design new ones. High level of detail. A wider range of features related to the manufacturing industry. Ability to simulate real-world conditions. Support real-time data and historical data.	More complex to develop. In most cases, more expensive than DES.
AWS IoT TwinMaker Azure Digital Twins Siemens Mindsphere PTC ThingWorx	IoT Platform	Data Driven	Best suited for running factories that do not require simulation. Real-time data from sensors and IoT devices. Cloud-based. Usually for monitoring and control.	More complex to develop and use. Limited simulation features
Unity	Animation	Physical, and geometric. Simulation-Based	An interactive environment. - Cross-platform support (a wide range of platforms including Augmented Reality/Virtual Reality devices).	More complex to develop. Not focused on simulation.

3. MODELING AND MANAGING UNCERTAINTY IN DIGITAL TWIN SYSTEMS

Composite material manufacturing systems are inherently uncertain, due in part to their dependence on human labor and variable curing or quality conditions [17]. DTs, while powerful, must be integrated with robust uncertainty modeling techniques to remain effective under real-world conditions.

- Uncertainty in DT systems can be broadly categorized as:

- Stochastic Uncertainty [18]: Inherent randomness in system parameters such as worker arrival times and task durations. Modelled using probabilistic distributions.
- Epistemic Uncertainty [19]: Incomplete knowledge of system behaviour or input conditions. Addressed using Bayesian inference methods.

Aleatory Uncertainty: Intrinsic variability that is irreducible [20] (e.g., raw material inconsistencies).

4. FRAMEWORK

This study presents an integrated framework that combines DT and RL to optimize production planning (PP) in a composite manufacturing system (CMS). The framework is designed to handle uncertainties—particularly in human resource availability—through scenario-based learning and optimization.

The approach consists of the following key steps:

Development of a DT using Discrete Event Simulation (DES) to simulate CMS operations.

Integration of RL to model and predict uncertain parameters, such as workforce availability and task durations.

Scenario generation using ML/RL based on historical and predicted uncertainties.

Simulation of production outcomes under different scenarios to assess their impact on key performance indicators (KPIs).

Optimization of production plans and worker allocation policies using RL, aiming to improve KPIs such as throughput, cycle time, and resource utilization.

The framework was implemented and validated on a real-world composite production line. KPIs such as production output, bottleneck reduction, and worker utilization were prioritized. All DT and RL components were developed in MathWorks and cross-validated using a Simio-based DT model to ensure robustness and accuracy.

4.1 Digital Twin Development

The DT serves as a virtual replica of the production line, enabling real-time simulation and analysis [21]. It provides insight into several KPIs, including Production throughput, Bottleneck identification, Cycle time and Worker utilization.

The DT was modeled using Discrete Event Simulation (DES) to capture dynamic system behavior and task sequences. Each production station, task duration, and resource dependency were modelled with high granularity, enabling assessment of operational performance under various conditions.

A significant innovation in this research was the dual-platform validation of the DT. While the main model was developed in MathWorks, it was independently validated using a Simio-based DT. This addresses a known challenge in DT research—lack of standard validation methods—and strengthens confidence in the simulation accuracy and results.

4.2 Scenario Analysis

Scenario analysis was used to evaluate how uncertainty in parameters related to human resource affects system-wide KPIs. The DT enabled dynamic simulation of task sequences, human-machine interaction, and queue formation between stations. The key KPIs analyzed include:

Resource utilization

Queue length minimization

Production volume maximization

The scenario analysis methodology included the following components:

Historical data integration: Real production and workforce data can be used to model variability in task durations and attendance patterns.

ML-based forecasting: An ML model can be trained on historical data to predict future workforce availability and its downstream effects on production.

Scenario generation and simulation:

A range of scenarios can be created based on predicted workforce variability. These scenarios can be simulated within the DT to assess their effects on system KPIs.

This process enabled the system to evaluate not only likely but also unseen edge-case scenarios, facilitating resilient production planning.

4.3 Optimization Using Reinforcement Learning

To optimize production planning, particularly worker allocation across stations, the framework employed a Reinforcement Learning (RL) algorithm. This model was trained in the DT environment, which allowed it to:

- Learn from simulated feedback in a risk-free setting
- Adaptively adjust policies to meet changing operational conditions
- Optimize KPIs under uncertainty
- The RL model's objective function is targeted: Maximizing throughput, minimizing total worker cost, and Reducing time in system for each product on average.

By leveraging DT for safe experimentation and RL for adaptive decision-making, the framework supports data-driven, scenario-aware, and resilient production planning.

5. CASE STUDY

To validate the proposed framework, a real-world composite manufacturing system (CMS) was modeled. Due to confidentiality agreements, the name of the partner company is withheld. The production system consists of seven interconnected stations, each historically staffed with dedicated operators using a static, manually scheduled workforce assignment.

The developed Digital twin in MathWorks and Simio are shown in Fig. 1 and Fig. 2 respectively.

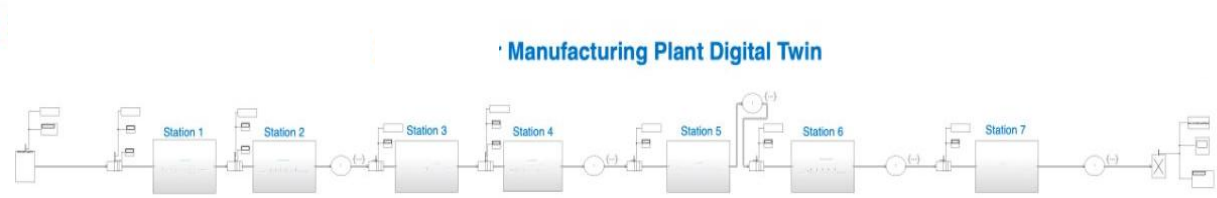

Figure 1. Developed Digital twin in MathWorks

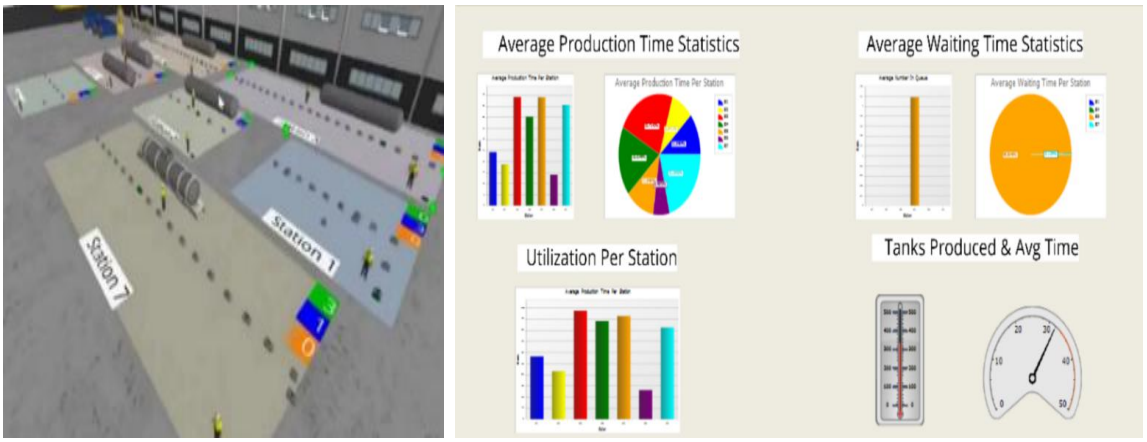

Figure 1. a) Developed Digital twin in Simio b) Developed Dashboard in Simio for Digital Twin

A new category of flexible, multi-skilled shop-floor workers was introduced. These workers are capable of operating across multiple stations, albeit at a higher wage. The key objective was to determine an optimal workforce allocation strategy that balances throughput (T), total worker cost (C), and time in system (TIS). These KPIs were prioritized based on the factory's operational strategy: throughput (60%), worker cost (30%), and TIS (10%).

5.1 Human Resource Uncertainty and Modelling Enhancements

The subjected CMS faces operational uncertainty primarily due to two factors:

- Variability in human resource availability (e.g., sick leave, absenteeism)
- Quality-induced rework which reintroduces components back into the production flow

These uncertainties significantly impact production schedules and system stability. To address this, the Digital Twin (DT) was enhanced with features that simulate the effects of rework and human resource fluctuations. This new version extended the previously developed model by adding:

- Dynamic modeling of worker types and availability
- Simulation of 81 interdependent processes, both sequential and parallel
- Time variability per task and resource-based processing times
- Movement and behavior of workers and products
- Modeling of station capacity constraints
- Automatic dynamic allocation of workers
- Full 3D visual animation
- A live KPI dashboard and WIP (work-in-progress) metrics

These enhancements allowed for robust scenario generation and simulation across a broad range of operational conditions.

5.2 Scenario Analysis Using Machine Learning

A data-driven scenario analysis was conducted to quantify the impact of human resource uncertainty on system performance and identify optimal worker allocation strategies.

Applied Methodology:

- Historical data on worker attendance and production variability in ERP was used to train the ML model.
- An ML model was developed to predict system performance under varying worker availability and process durations.
- The Digital Twin simulated hundreds of production scenarios incorporating predicted variations.
- Scenario results informed the reinforcement learning optimization process.

This enabled a nuanced understanding of how shifts in workforce capacity influenced production bottlenecks, queue lengths, and throughput.

5.3 Reinforcement Learning-Based Optimization

The optimization process used a Reinforcement Learning (RL) framework. The framework included:

- Simulation Dataset Generation: A year's worth of possible worker availability combinations (~11,250 scenarios) was generated using the DT.
- ML-Based Performance Prediction: The ML model forecasted KPIs based on simulated outcomes.
- RL Agent Optimization: The RL agent iteratively adjusted worker allocations.

Rewards were calculated using the weighted objective function based on throughput, worker cost and time in the system for each product.

Through multiple training episodes, the agent learned to maximize throughput while minimizing costs and delays.

5.4 Key Outcomes and Impact

The integration of DT with RL enabled a robust, data-driven framework for resilient workforce planning in a high-variability environment. Compared to baseline operations:

- Worker costs were reduced by 34%
- System time was reduced by 16%
- No negative impact on throughput, despite labor constraints

These findings demonstrate the potential of combining simulation, predictive modeling, and reinforcement learning to achieve adaptive, cost-effective, and scalable production strategies in human-intensive manufacturing systems.

The case study also confirmed the feasibility of conducting advanced optimization in a risk-free virtual environment, with actionable insights ready to be applied to real operations. Future work will extend this framework to include additional constraints (e.g., maintenance schedules, product customization) and explore real-time decision-making integrations.

6. CONCLUSION

This paper presented a scenario-driven optimization framework that integrates Digital Twin (DT), Machine Learning (ML), and Reinforcement Learning (RL) to enhance production planning in a human-intensive composite manufacturing system. The proposed approach addressed key uncertainties related to human resource availability and process variability, which are common challenges in such manufacturing environments.

A DT model, developed and validated across two platforms, was used to simulate dynamic operations and generate realistic production scenarios. A ML model predicted performance metrics under varying conditions, enabling the RL agent to explore and optimize worker allocation strategies efficiently.

The framework was validated through a real-world case study, demonstrating significant reductions in total worker cost (34%) and time in system (16%), while maintaining maximum achievable throughput under existing capacity constraints. These results highlight the value of integrating data-driven decision-making tools within virtual environments for resilient and efficient production planning.

Future work will focus on extending this framework to real-time decision support and incorporating additional production constraints, further improving its applicability in dynamic and complex manufacturing settings.

ACKNOWLEDGEMENTS

This paper acknowledges the support of ACM CRC in funding this research.

REFERENCES

[1] S. Abdoli and S. Kara, A modelling framework to design executable logical architecture of engineering systems, 2017, 75.

[2] S. Abdoli and S. Kara, A modelling framework to support design of complex engineering systems in early design stages, Research in Engineering Design, 31, 2020, : 25-52.

[3] X. Ji and S. Abdoli, Challenges and opportunities in product life cycle management in the context of industry 4.0. Procedia CIRP 119 (2023): 29-34.

[4] M. Malaibari, M. Siddiqui, S. Xie, B. Bahramimianrood, S. Abdoli, and L. Djukic, Digital Twin as A New Approach to Data Management: A Review, Procedia CIRP 128, 2024, 375-380..

[5] M. Grieves, Digital twin: manufacturing excellence through virtual factory replication, White paper, vol. 1, no. 2014, pp. 1-7, 2014.

[6] F. Tao, J. Cheng, Q. Qi, M. Zhang, H. Zhang, and F. Sui, Digital twin-driven product design, manufacturing and service with big data, The International Journal of Advanced Manufacturing Technology, 2018, vol. 94, no. 9-12, pp. 3563-3576.

[3] L. Sorensen, T. Gmür and J. Botsis, Delamination propagation measurement using long gauge-length FBG sensors, *Proceedings of the 3rd International Conference on Composites Testing and Model Identification CompTest 2006 (Eds. P. Camanho, F. Pierron, M. Wisnom), Porto, Portugal, April 10-12, 2006,* University Press, Porto, Paper 41, 2006, pp. 174-175.

[7] Q. Bao, G. Zhao, Y. Yu, S. Dai, and W. Wang, The ontology-based modeling and evolution of digital twin for assembly workshop, *The International Journal of Advanced Manufacturing Technology,* vol. 117, no. 1-2, pp. 395-411, 2021, doi: 10.1007/s00170-021-07773-1

[8] F. Tao, Q. Qi, A. Liu, and A. Kusiak, Data-driven smart manufacturing, Journal of Manufacturing Systems, 2018, vol. 48, pp. 157-169.

[9] Abdoli, Shiva. Experimentable digital twin for virtual validation of manufacturing systems. In Proceedings of the 2023 10th international conference on industrial engineering and applications, 2023, pp. 91-97.

[10] F. Tao and M. Zhang, Digital Twin Shop-Floor: A New Shop-Floor Paradigm Towards Smart Manufacturing, 2017, *IEEE Access,* vol. 5, pp. 20418-20427.

[11] J. Akroyd, S. Mosbach, A. Bhave, and M. Kraft, "Universal Digital Twin - A Dynamic Knowledge Graph," *Data-Centric Engineering,2021,* vol. 2.

[12] Anylogic. "AnyLogic simulation software." https://www.anylogic.com/ (accessed 29-9-2023, 2023).

[13] Flexsim. "3D Simulation Modeling and Analysis Software." https://www.flexsim.com/ (accessed 29-9-2023, 2023).

[14] Simul8. "Simulation software so intuitive, fast and effective you'll use it every day." https://www.simul8.com/ (accessed 29-9-2023, 2023).

[15] Simio. "Simulation, production planning and Scheduling Software. https://www.simio.com/ (accessed 29-9-2023, 2023).

[16] D.Ye and S.Abdoli, "An Investigation on Available Technologies and Approaches for Integration of Control Systems with the Digital twin in Cyber-Physical Production Systems." In Proceedings of the 2023 10th International Conference on Industrial Engineering and Applications, 2023, pp. 128-134.

[17] T. S. Mesogitis, A. A. Skordos, and A. C. Long, "Uncertainty in the manufacturing of fibrous thermosetting composites: A review," *Composites Part A: Applied Science and Manufacturing,* , 2014, vol. 57, pp. 67-75.

[18] R.-q. Zhang, "Research on Capacity Planning under Stochastic Production and Uncertain Demand," *Systems Engineering - Theory & Practice,* , 2007, vol. 27, no. 1, pp. 51-59.

[19] F. Hoti *et al.*, "Knowing the unknowns: Uncertainties during radiological emergencies," *International Journal of Disaster Risk Reduction,* , 2021vol. 59, p. 102240.

[20] Z. Li and F. Montomoli, "Aleatory uncertainty quantification based on multi-fidelity deep neural networks," *Reliability Engineering & System Safety,* 2024, vol. 245, p. 109975.

[21] M. Siddiqui, G. Kahandawa, and H. S. Hewawasam, "Artificial Intelligence Enabled Digital Twin For Predictive Maintenance in Industrial Automation System: A Novel Framework and Case Study," in *2023 IEEE International Conference on Mechatronics (ICM)*, 2023, pp. 1-6.

[22] L. Nishii and P. Wright, "Variability Within Organizations: Implications for Strategic Human Resource Management," *CAHRS Working Paper Series,* 2008.

[23] P. Kohlmann and F. Sahling, "A flexible planning approach for integrated lot sizing and rework planning with random proportion of defective products," *International Journal of Production Research, 2024,* vol. 62, no. 19, pp. 6961-6978.

[24] E. Flores-García, J. Bruch, M. Wiktorsson, and M. Jackson, *Towards a Reduction of Uncertainty in Production System Design Decisions*. 2016.

ICCM24
24TH INTERNATIONAL CONFERENCE ON COMPOSITE MATERIALS

Enhancing Cure Kinetics Estimation for Thermosetting Carbon Fiber-Epoxy Prepregs Through Chemistry-Informed Machine Learning

Geun Young Kim, Shreyes N. Melkote, Jonathan S. Colton
Georgia Institute of Technology

Georgia Tech

Contents

- Introduction
  - Exothermic reactions in composite manufacturing
  - Challenges in deriving cure kinetics
- Methodology
  - Data preprocessing
  - Model architecture
- Results
  - Validation testing
  - Robustness testing
- Conclusion and Future Plan

Georgia Tech

Manufacturer's Recommended Cure Cycle (MRCC)

- Each resin system has its own cure cycle for best performance

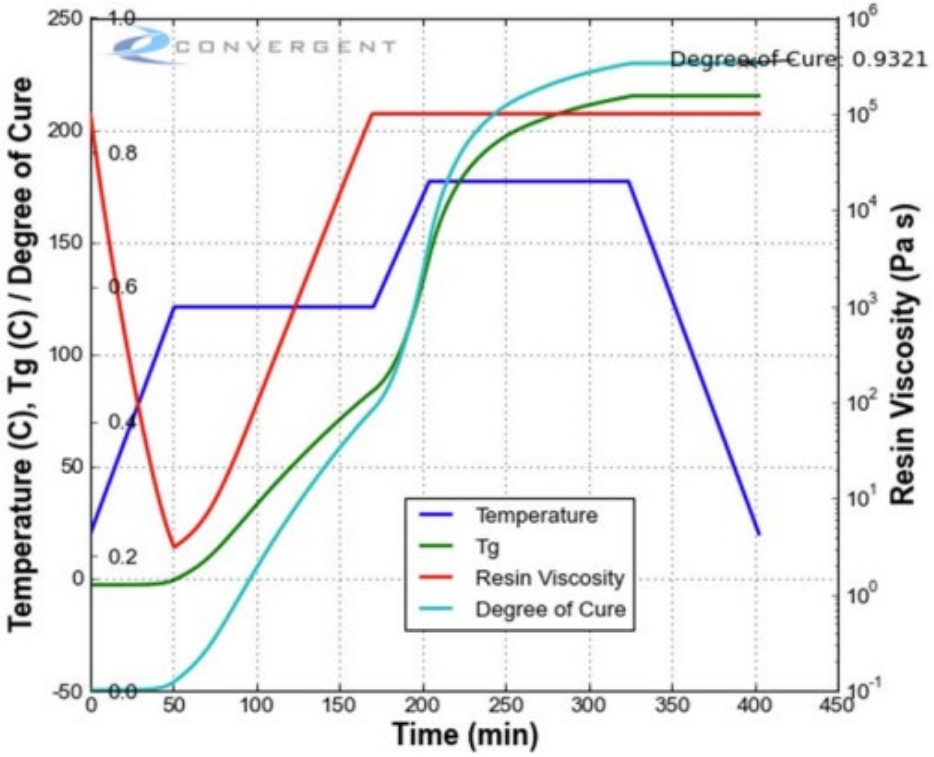

Cycom 5320-1

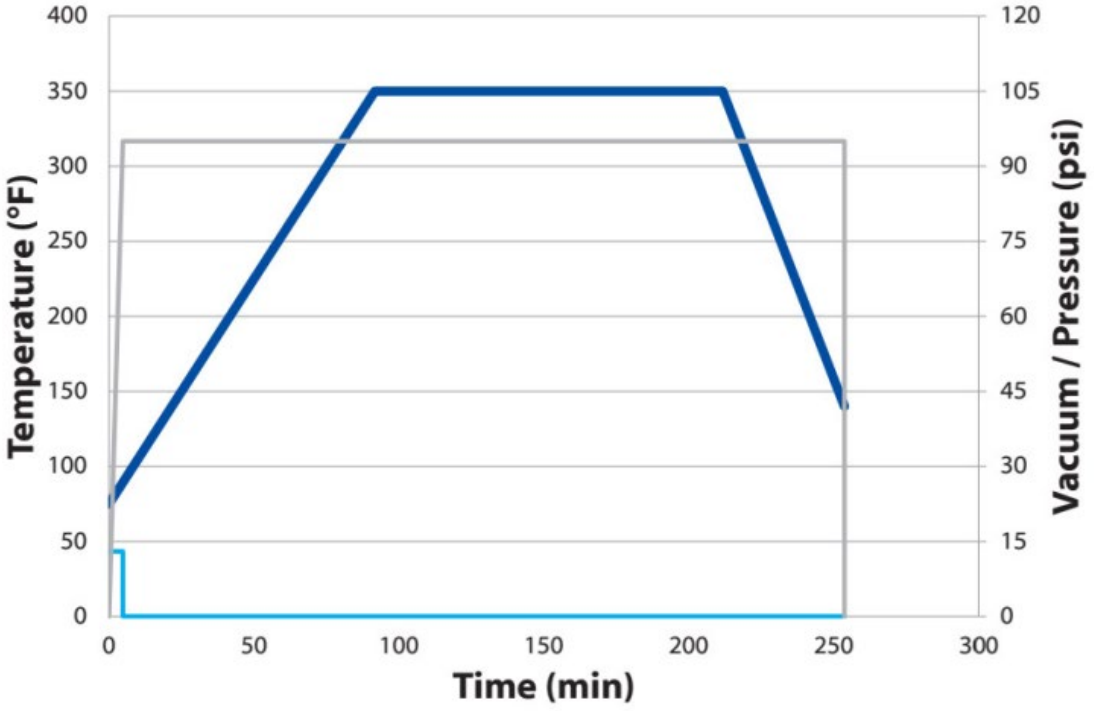

Toray 3900

Georgia Tech

Exothermic Reactions in Composite

- Produce significant temperature gradient along the part, leading to defects

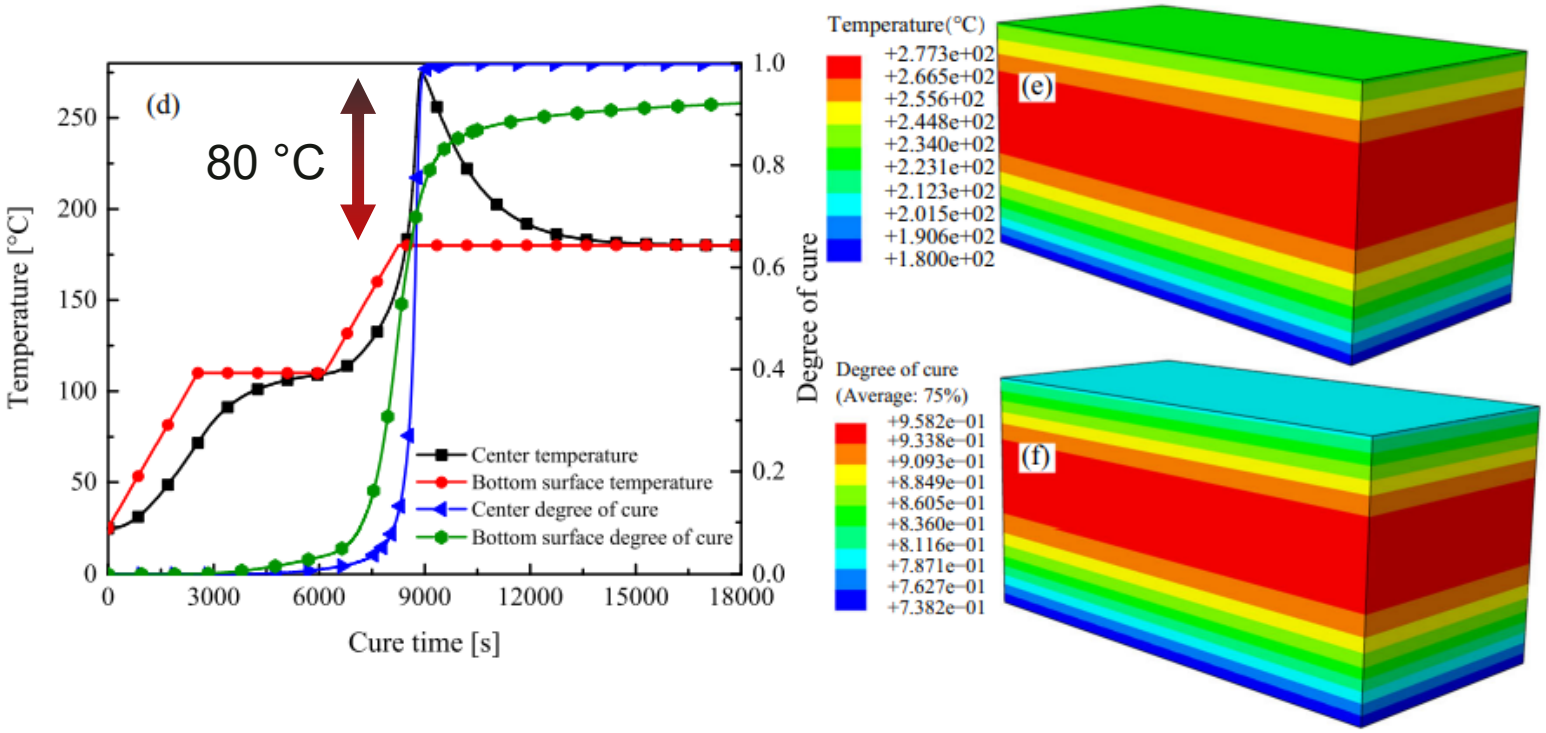

Hexcel 8552 resin system, Zhang et.al (2021)

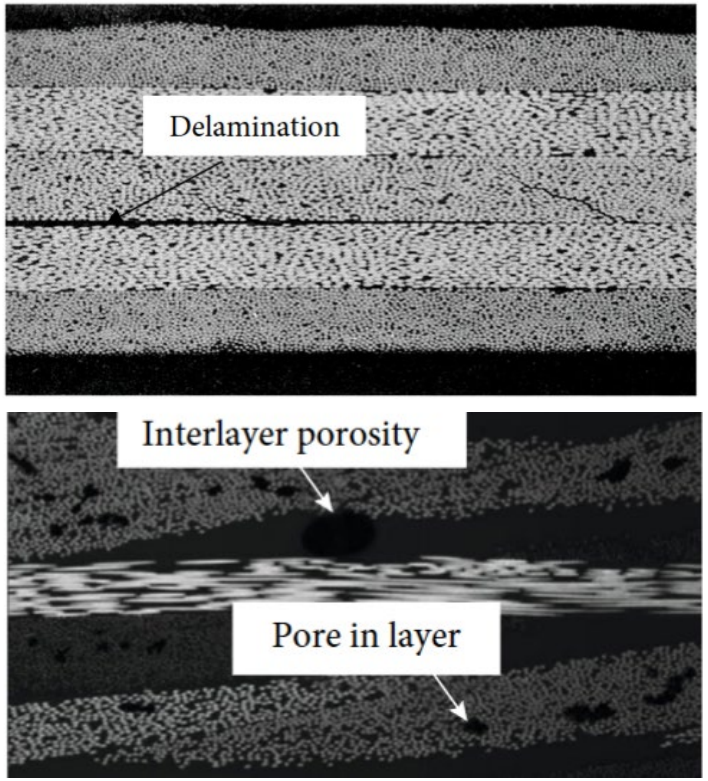

Cure defects, Wang et.al (2022)

→ *Consider cure kinetics to predict how much heat will be generated*

Georgia Tech

Modeling Methods of Cure Kinetics

Fundamental

Table 1
Monomer structure, characteristics and nomenclature

Monomer	Formula	Molar mass (g mol^{-1})	Melting point (°C)
Diglycidyl ether of bisphenol A	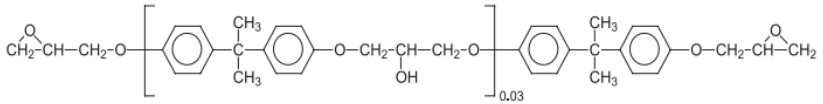	349	45
p-Toluidine		107	43
4,4′-Diamino diphenyl methane	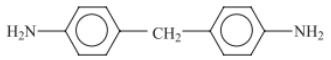	198	80

$$E + OH \underset{k'}{\overset{k}{\rightleftharpoons}} E\text{–}OH$$

$$E + A_1 \xrightarrow{k_1} A_2 + OH$$

$$E + A_2 \xrightarrow{k_2} A_3 + OH$$

$$E\text{–}OH + A_1 \xrightarrow{k_1'} A_2 + 2OH$$

$$E\text{–}OH + A_2 \xrightarrow{k_2'} A_3 + 2OH$$

Polymerization of Diglycidyl Ether of Bisphenol A (DGEBA), Blanco, et. al (2022)

Phenomenological

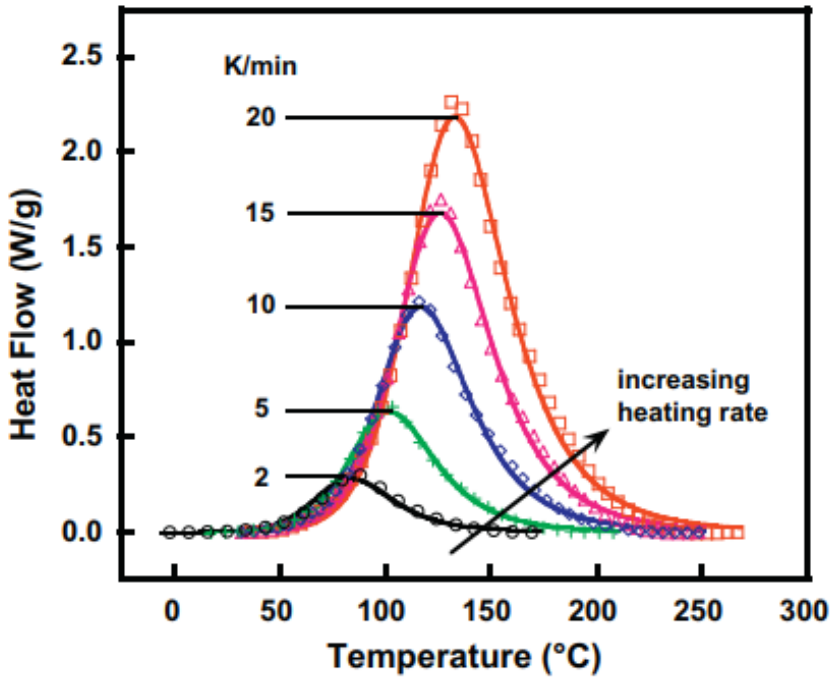

Differential Scanning Calorimetry, Hardis, et. al (2013)

Georgia Tech

Modeling Methods of Cure Kinetics

Fundamental

Table 1
Monomer structure, characteristics and nomenclature

Monomer	Formula	Molar mass (g mol^{-1})	Melting point (°C)
Diglycidyl ether of bisphenol A	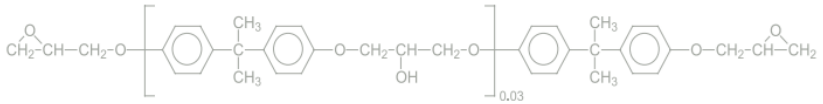	349	45
p-Toluidine		107	43
4,4′-Diamino diphenyl methane	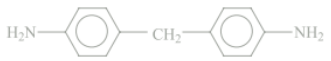	198	80

$$E + OH \underset{k'}{\overset{k}{\rightleftharpoons}} E\text{–}OH$$

$$E\text{–}OH + A_1 \xrightarrow{k_1'} A_2 + 2OH$$

$$E + A_1 \xrightarrow{k_1} A_2 + OH$$

$$E\text{–}OH + A_2 \xrightarrow{k_2'} A_3 + 2OH$$

$$E + A_2 \xrightarrow{k_2} A_3 + OH$$

Polymerization of Diglycidyl Ether of Bisphenol A (DGEBA), Blanco, et. al (2005)

Phenomenological

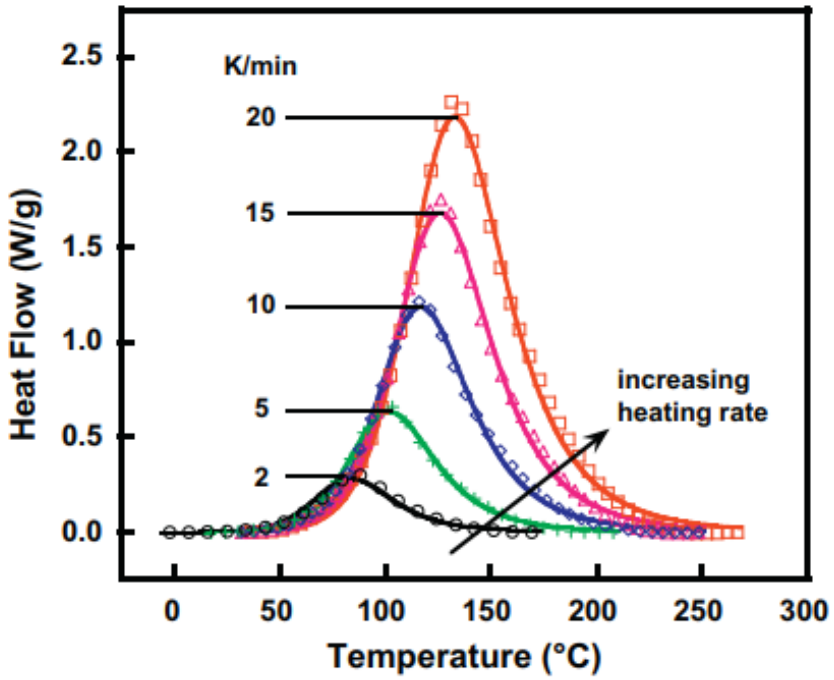

Differential Scanning Calorimetry, Hardis, et. al (2013)

Phenomenological approach is often selected due to proprietary restrictions

Georgia Tech

Phenomenological Approach

Model free kinetics (MFK)

$$\frac{d\alpha_i}{dt} = K_{\alpha_i} f(\alpha_i),$$

$$where\ K_{\alpha_i} = A_{\alpha_i} exp\left(-\frac{E_{\alpha_i}}{RT}\right)$$

Pros

Coefficients

Model-independent

Cons

Implementation

Isoconversional method

Applicability

Only for single-step reaction

Multivariate regression

$$\frac{d\alpha}{dt} = K_1(1-\alpha)^{n_1} + K_2\alpha^{m_2}(1-\alpha)^{n_2} + \cdots$$

$$where\ K_i = A_i exp\left(-\frac{E_i}{RT}\right)$$

Pros

Implementation

Least square method

Applicability

Represent multi-step reaction

Cons

Coefficients

Rely on initial guess & model

Georgia Tech

Research Objectives

To build a neural network-based cure kinetics model that captures cure kinetics efficiently, with the following characteristics:

- Model architecture handles:
  - ✓ **Numerical stability**

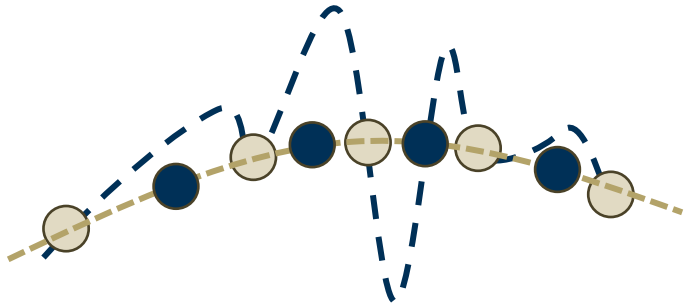

: Trained

: Untrained

: Ground truth

: Prediction

  - ✓ **Chemical validity**

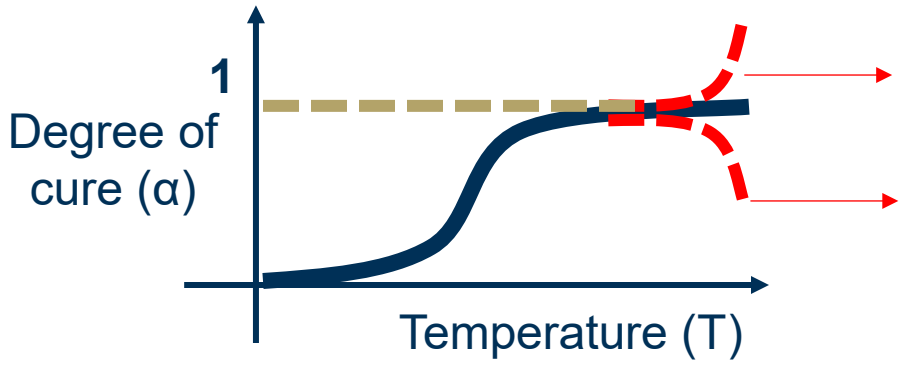

α ∈ [0,1]

Irreversible reaction

($\frac{d\alpha}{dt}$ ≥ 0)

Georgia Tech

Model Selection Strategy

Scenario based model selection

Traditional NN validation accuracy
→ Constant heating rate cycle

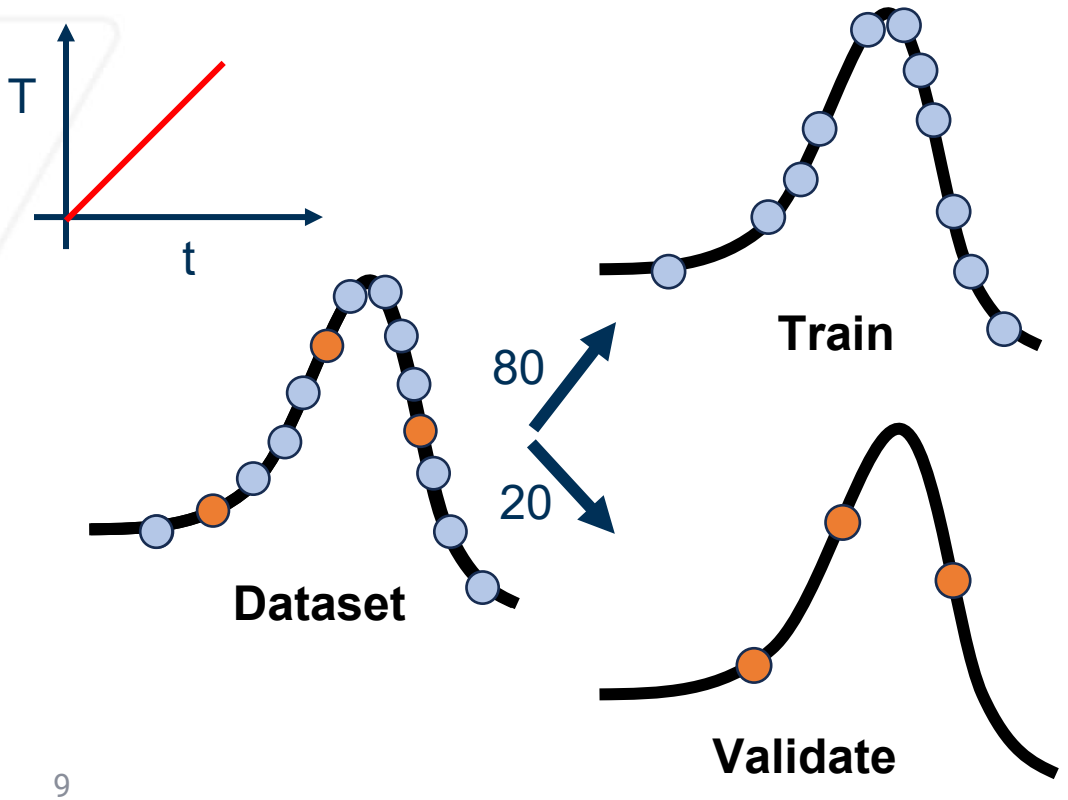

Proposed method
→ Manufacturer's recommended cure cycle

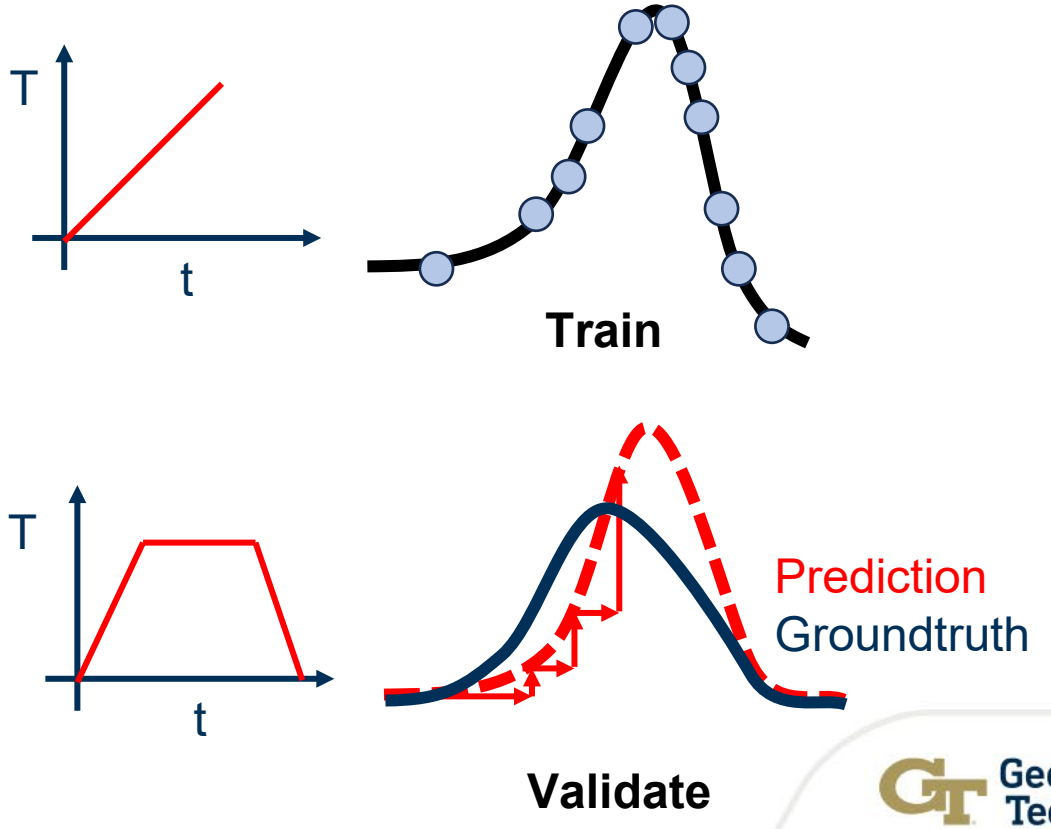

Georgia Tech

Model Architecture

Previous work on NN based approach (Hui, 2022)

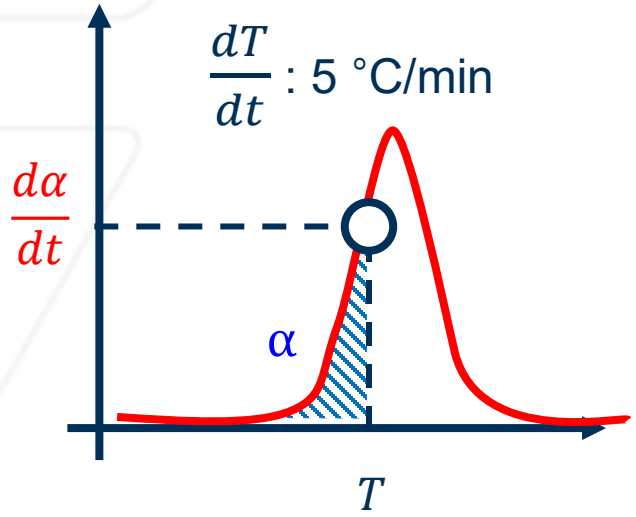

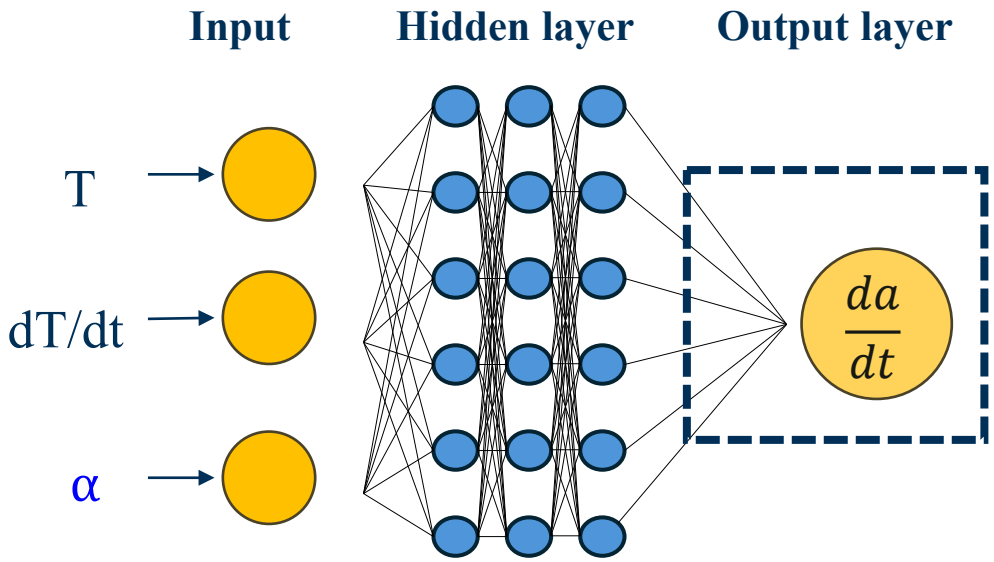

$$Loss = MSE\ (\hat{y} - y_{measured})$$

$$\hat{y} = \frac{da}{dt}\left(T, a, \frac{dT}{dt}\right)$$

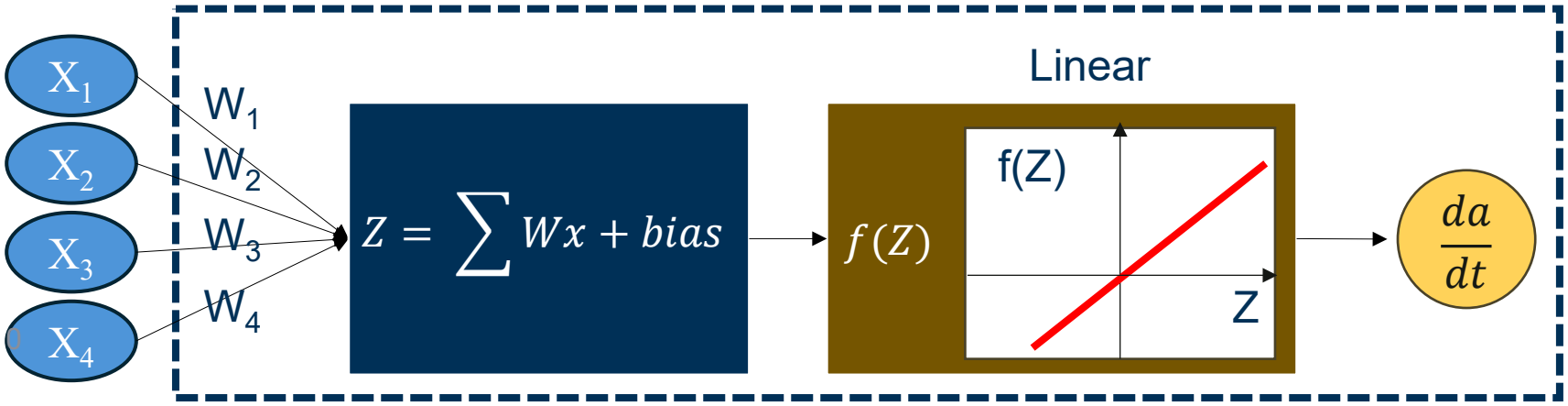

$$\frac{da}{dt} = f(Z) \in [-\infty, +\infty]$$

Georgia Tech

Model Architecture

Chemistry-informed Neural Network (CINN)

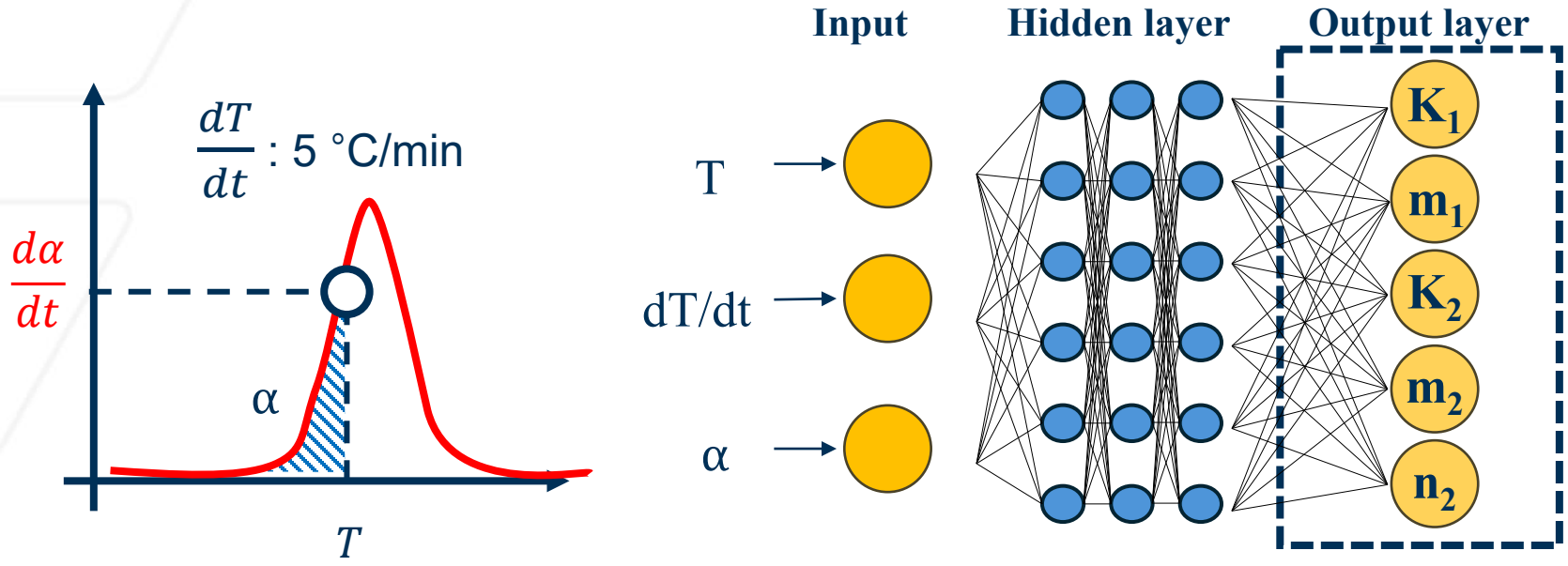

$$Loss = MSE\ (\hat{y} - y_{measured})$$

$$\hat{y} = K_1(1-\alpha)^{n_1} + K_2 * \alpha^{m_2}(1-\alpha)^{n_2}$$

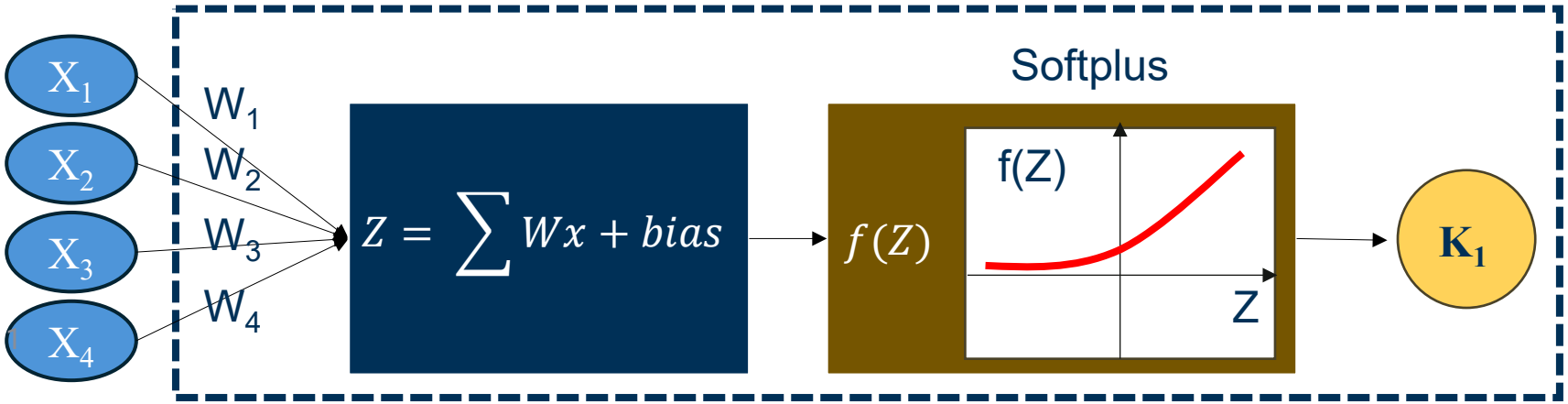

$$K_i, m_i, n_i = f(Z) \in [0, +\infty]$$

Georgia Tech

Dataset

- (1 °C/min ~ 10°C/min) X (80°C ~ 300 °C, 1°C increment) = 2210 data points
- Assumption: Initial degree of cure of uncured prepreg = 0

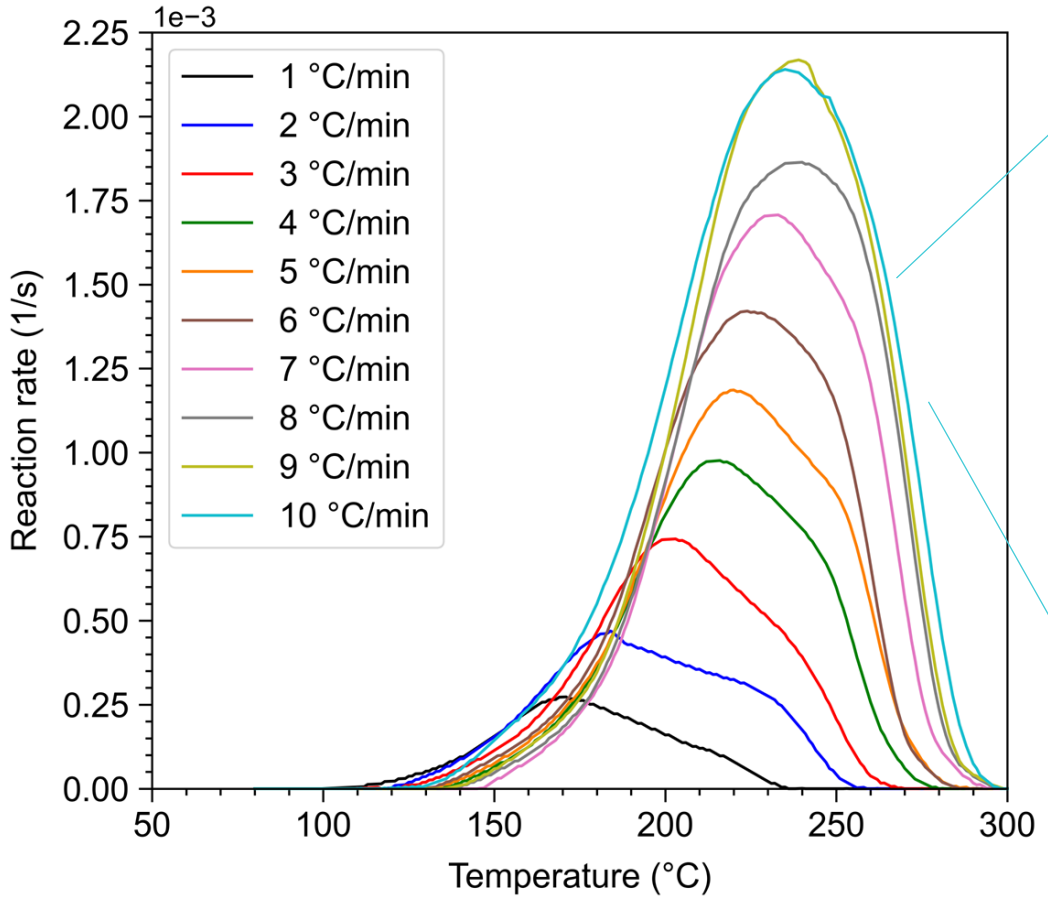

A	B	C	D	E
	Temperature (C)	Reaction Rate	Ramp rate (C/min)	Degree of Cure
40	120	3.20E-06	10	3.45E-05
41	121	8.07E-07	10	4.66E-05
42	122	4.31E-06	10	6.19E-05
43	123	1.92E-06	10	8.06E-05
44	124	5.43E-06	10	0.000102696
45	125	3.04E-06	10	0.000128114
46	126	6.55E-06	10	0.000156884
47	127	4.16E-06	10	0.000189006
48	128	7.67E-06	10	0.00022448
49	129	5.28E-06	10	0.000263305
50	130	8.78E-06	10	0.000305482
51	131	1.23E-05	10	0.000368701
52	132	1.58E-05	10	0.000452962
53	133	1.93E-05	10	0.000558266
54	134	2.28E-05	10	0.000684611
55	135	2.63E-05	10	0.000831999
56	136	2.98E-05	10	0.001000429
57	137	3.92E-05	10	0.001207592
58	138	4.27E-05	10	0.001453488
59	139	5.21E-05	10	0.001738116
60	140	5.56E-05	10	0.002061476

Georgia Tech

Experimental Setup

- Material: Toray T830H 6K/3900-2D carbon fiber prepreg
- Sample mass: 11 ~ 15 mg
- Pan & lid: T-zero Hermetic

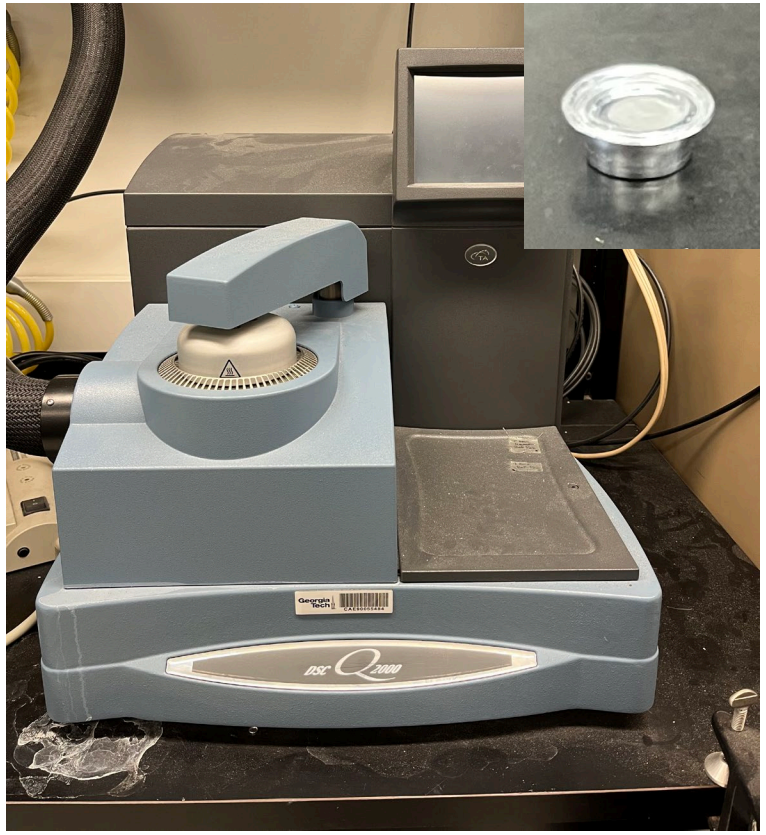

DSC: Q2000 (TA Instruments)



Oven: HAFO 1602

Georgia Tech

Training Accuracy

Goodness of the fit to the trained curve

- Closely matches DSC curve, but Hui's model shows a negative reaction rate

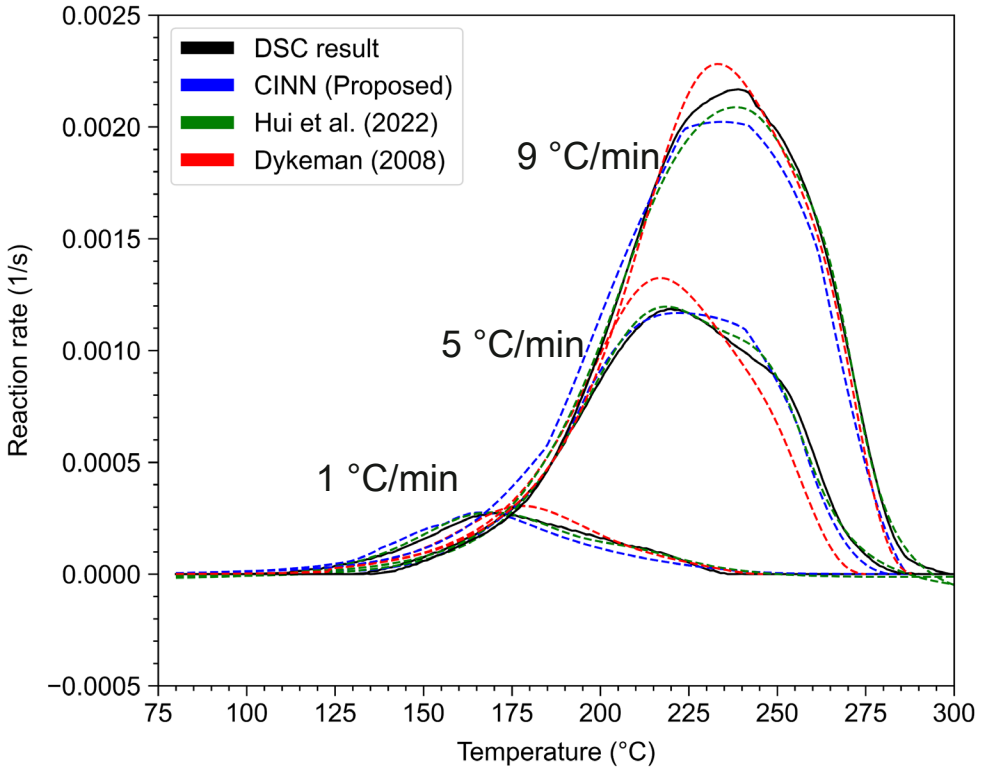

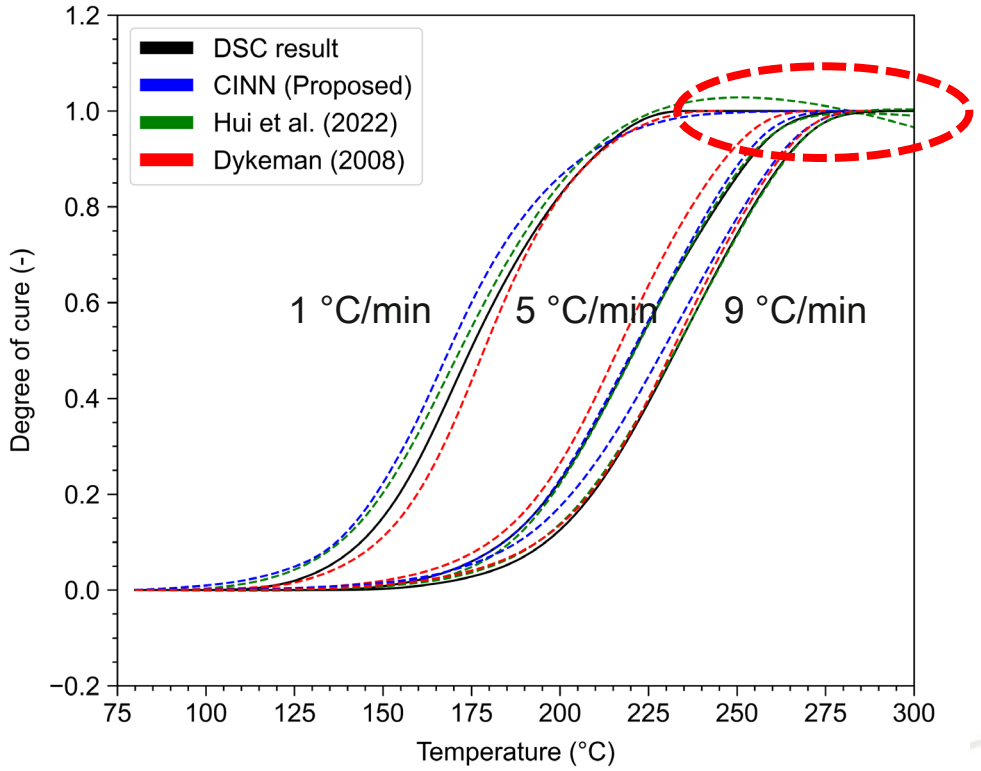

Validation Accuracy

Both models show minimum error at 1500 epochs

- 60-minute hold : 4.9% relative error (CINN)
- 120-minute hold: 0.9% relative error (CINN)

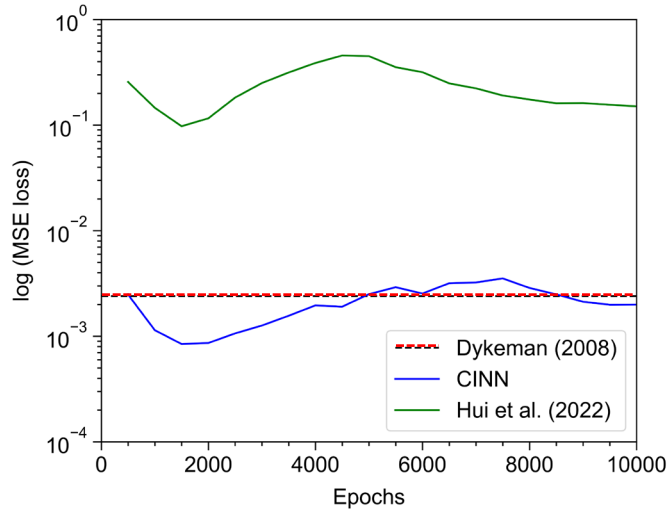

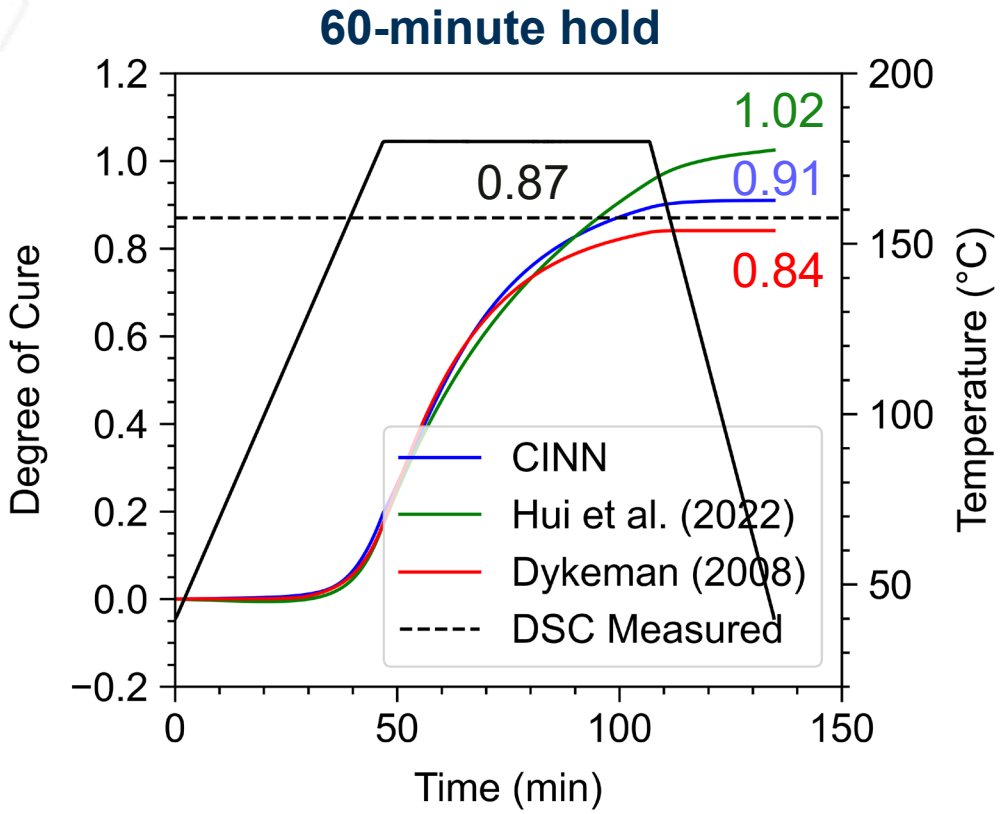

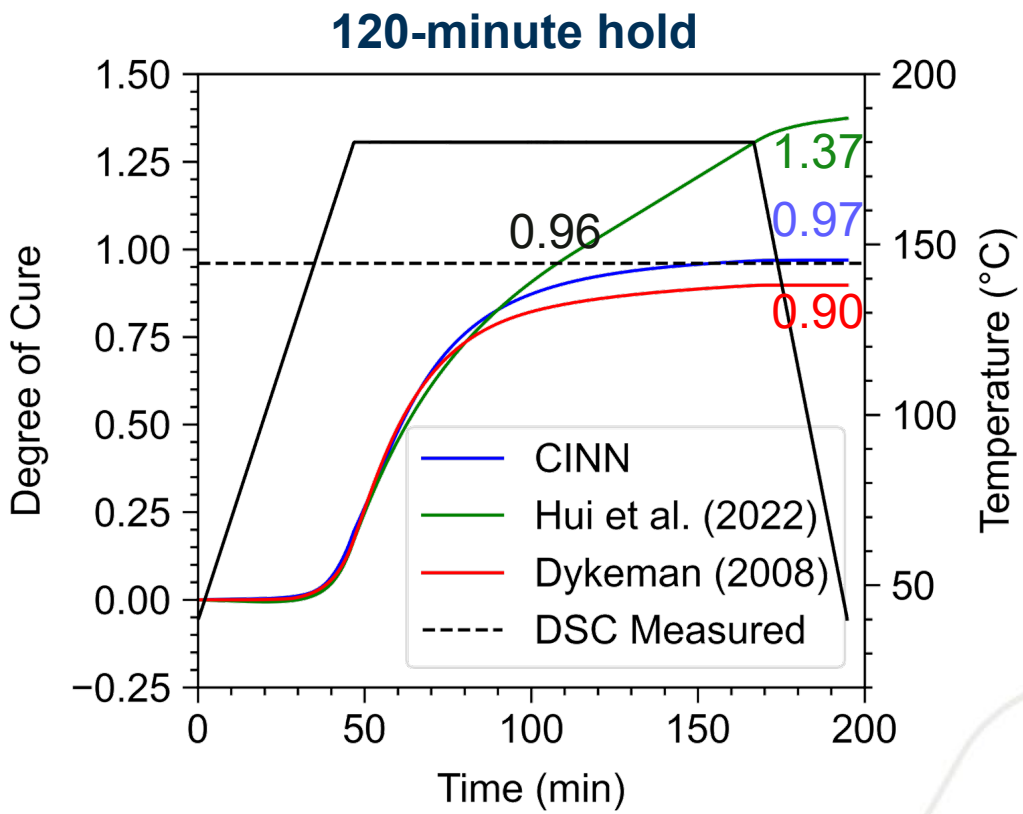

Robustness Tests

Thermal disturbance

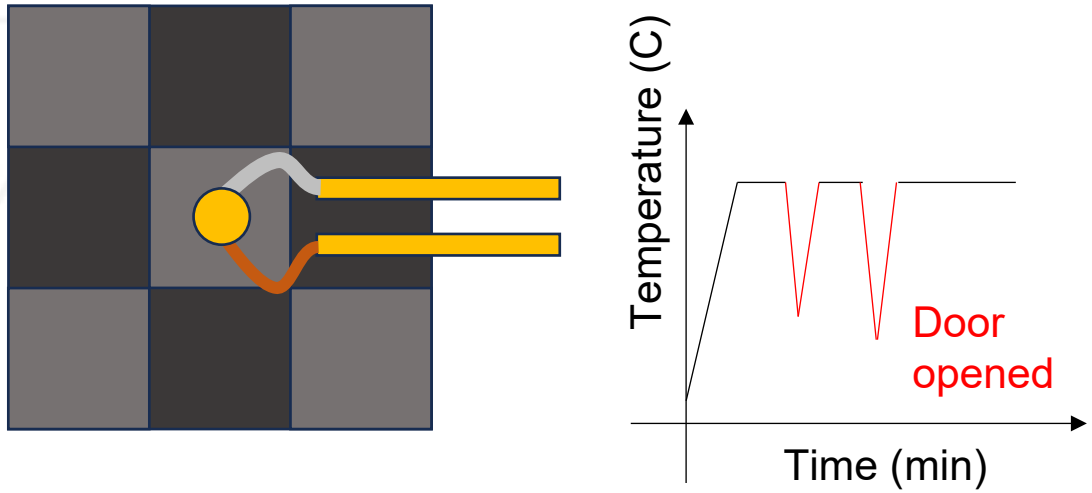

- 4 Samples
- Each of a part size: 12 mm x 12 mm x 0.25 mm
- Cure cycle: Varies

Fabrication

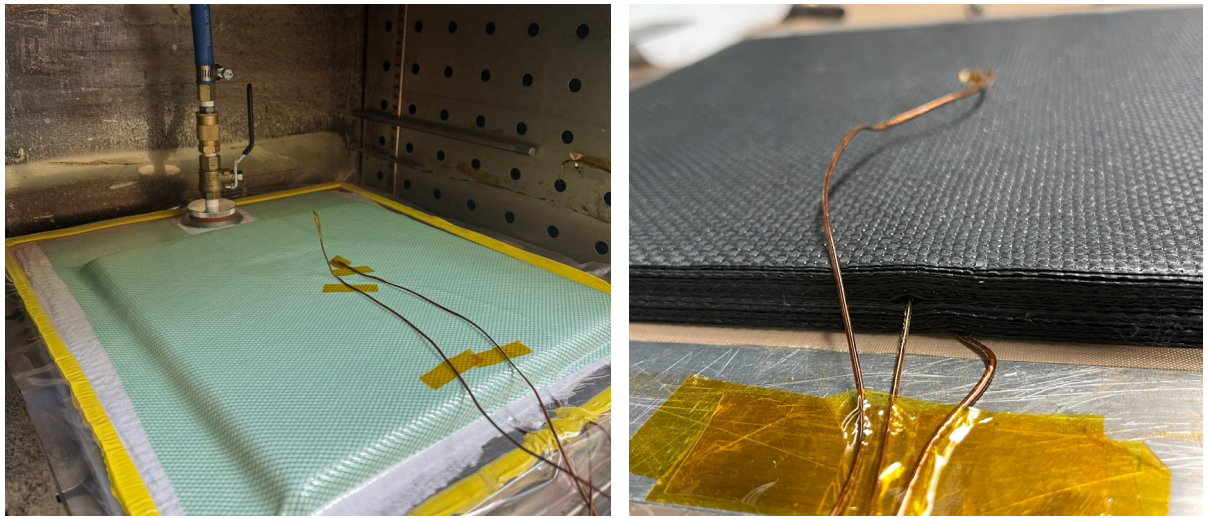

- Part size: 300 mm x 300 mm x 12.5 mm
- Cure cycle: MRCC (3 hours hold)

Georgia Tech

Thermal Disturbance Test

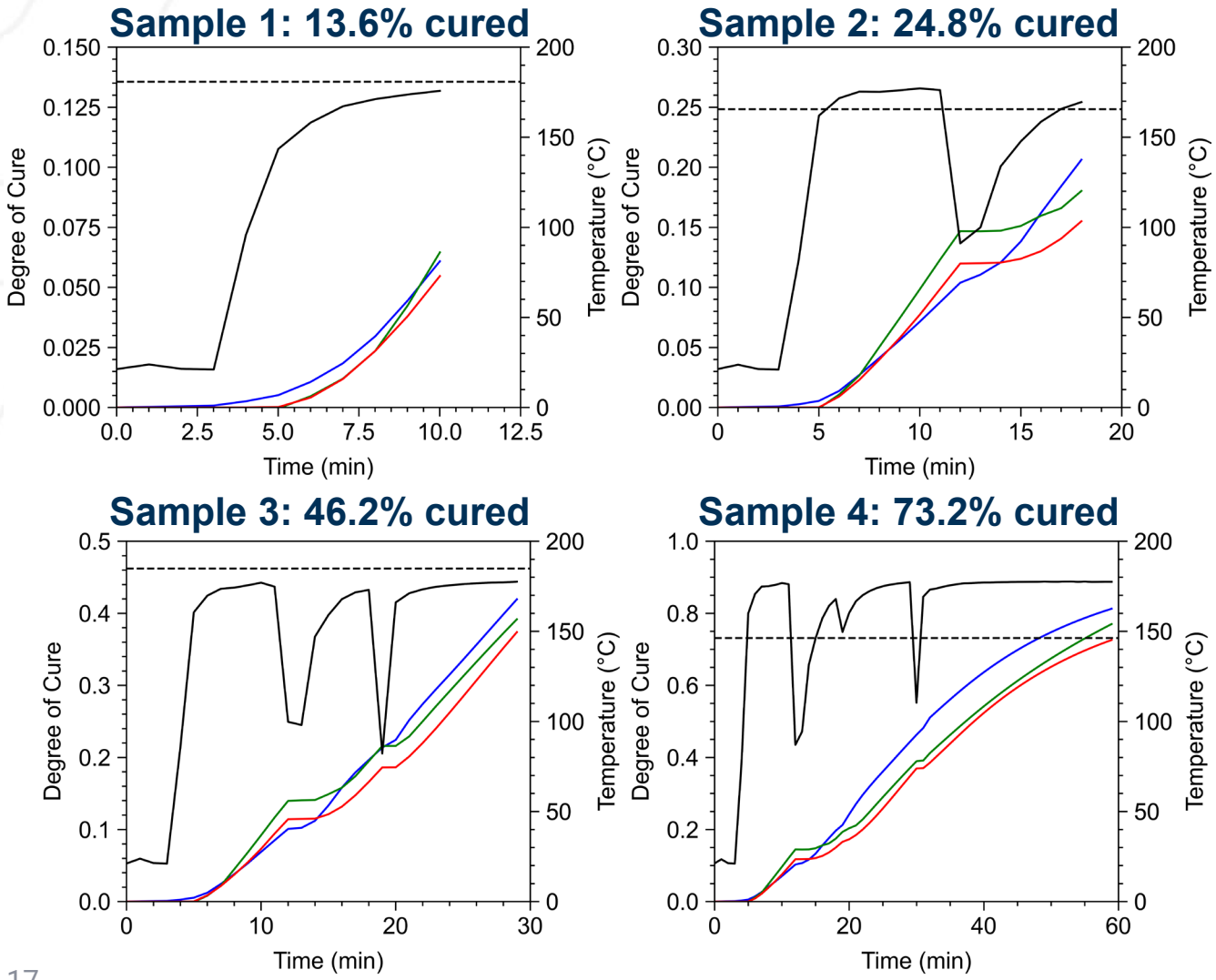

Measured

CINN

Dykeman (2008)

Hui et al. (2022)

All models match well

Georgia Tech

Fabrication Test

- CINN showed similar trend, even outperforming the Dykeman's model
- Hui's model starts to deviate as temperature reaches peak and hold
  → Overestimates heating rate

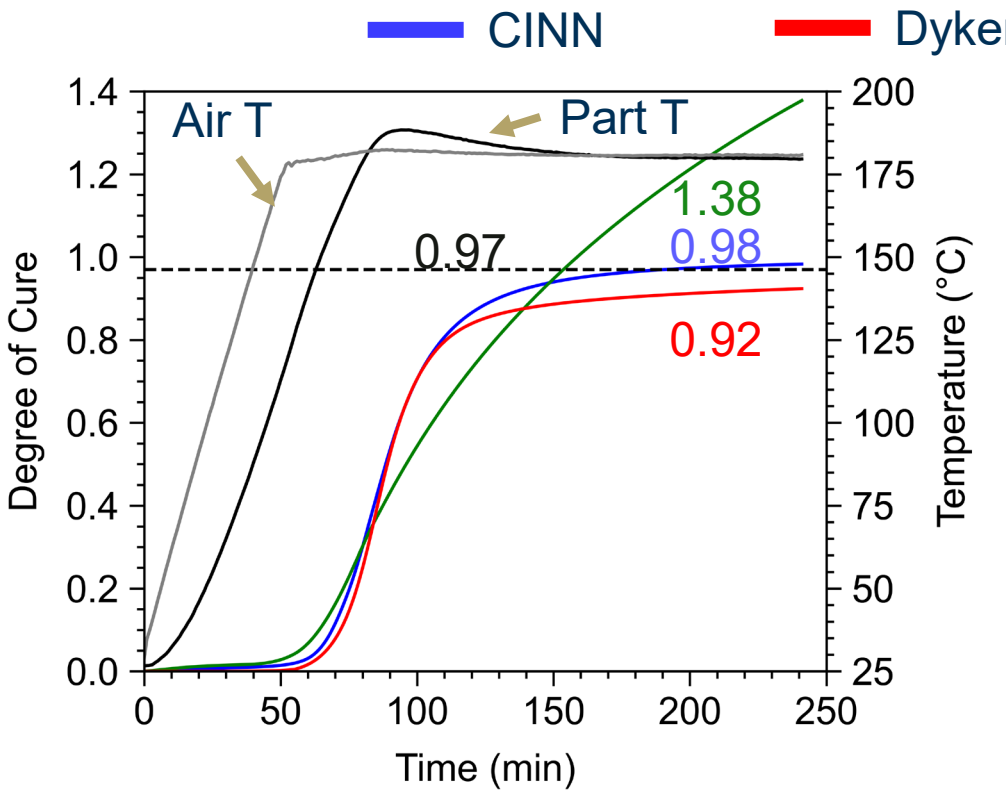

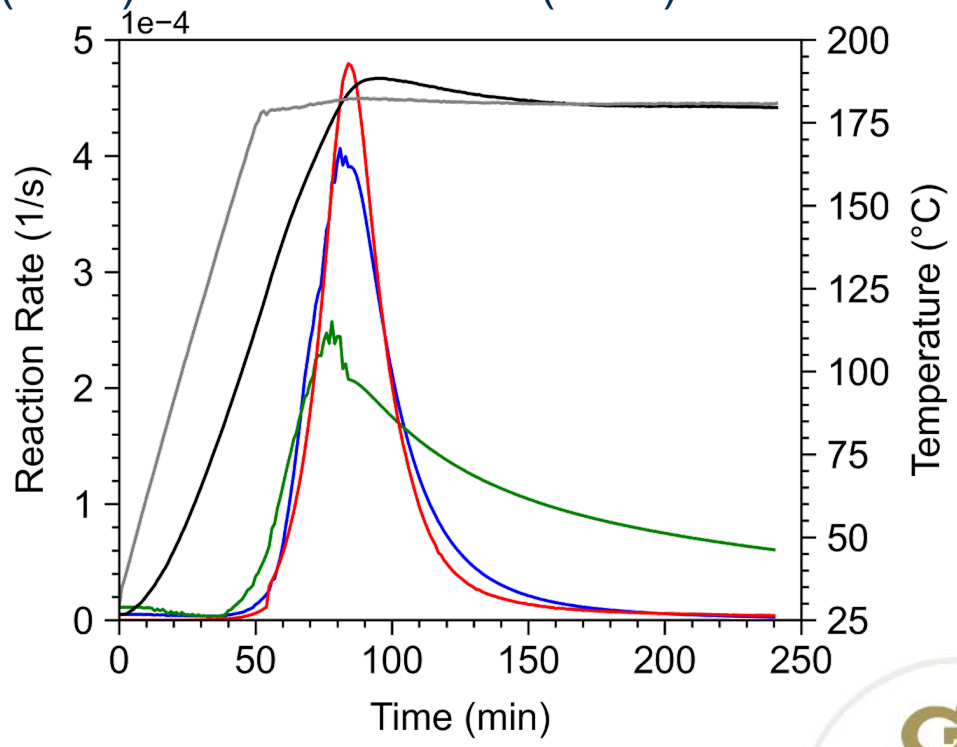

Georgia Tech

Conclusion

- Chemistry-induced neural network model (CINN) showed not only high accuracy but also numerical stability and chemical validity.
- Scenario based selected model showed consistent performance.

Future Plans

- Test using different resin systems for generalizability
- Elaborate model selection method

Georgia Tech

Thank you for your kind attention

Ph.D. Student, Geun Young Kim
George W. Woodruff School of Mechanical engineering
Georgia Institute of Technology
✉ gkim439@gatech.edu

Acknowledgment

This paper was funded by the U.S. Department of Energy's Office of Energy Efficiency & Renewable Energy Grant DE-EE0011030.
The content is solely the responsibility of the authors and does not necessarily reflect the official views of the U.S. Department of Energy.

Georgia Tech

Appendix: Dykeman's Model (Dykeman, 2008)

Total Model:

$$\dot{\alpha} = K_{1eff}(1-\alpha)^{n_1} + K_{2eff}\alpha^{m_2}(1-\alpha)^{n_2} + K_{3eff}\alpha^{m_3}(1-\alpha)^{n_3} \qquad 5.19$$

Chemical Reaction:

$$\dot{\alpha} = K_1(1-\alpha)^{n_1} + K_2\alpha^{m_2}(1-\alpha)^{n_2} + K_3\alpha^{m_3}(1-\alpha)^{n_3}$$

Primary-Amine and Epoxy:

If $T < 124^{o}C$ and $\alpha < 0.035$, Then $A_1 = 34378*\mathrm{Ln}(\alpha) + 229563$ /sec and $E_1 = 73300$ J/mol;

If $A_1 < 50000$ /sec, Then $A_1 = 50000$ /sec.

End If.

Else, If $T < 124^{o}C$ and $\alpha > 0.035$, Then $A_1 = 113881$ /sec and $E_1 = 73300$ J/mol;

Else, If $T > 124^{o}C$, Then $A_1 = 14240$ /sec and $E_1 = 66435$ J/mol.

End If.

Secondary-Amine and Epoxy: $A_2 = 473684$ /sec, $E_2 = 73063$ J/mol

Etherification: $A_3 = 1.5E9$ /sec, $E_3 = 115624$ J/mol

Reaction Orders:

$m_1 = 0$, $n_1 = 1$

$m_2 = 1$, $n_2 = 2.5$

$m_3 = 2.91$, $n_3 = 0.83$

Georgia Tech

Appendix: Dykeman's Model (cont.)

Tg-α:

$$Tg = \frac{\lambda\alpha(Tg_\infty - Tg_0)}{1-(1-\lambda)\alpha} + Tg_0 + \frac{D}{1+\exp[-F(\alpha-\alpha_{critical})]}$$

λ (copolymer) = 0.8, Tg_0 = 8.8°C, Tg_∞ (copolymer) = 200°C, D = 35, F = 25

Tg_∞ (epoxy) ≥ 222°C

$\alpha_{critical}$:

If dT/dt < 0.0001 K/sec, Then $\alpha_{critical} = (0.0025/K)*T - 0.3329$;

Else, $\alpha_{critical} = (0.0025/K)*T - (0.00017K/\sec)/\dot{T} - 0.3329$.

End If.

If $\alpha_{critical} < 0.675$, Then $\alpha_{critical} = 0.675$.

End If.

If $\alpha_{critical} > 1$, Then $\alpha_{critical} = 1$.

End If.

Diffusion:

Primary and secondary amine reactions with epoxide:

$$k_{d1,2} = A_{d1,2}\exp\left(-\frac{E_{d1,2}}{RT} - \frac{b_{1,2}}{f_v}\right)$$

$A_{d1,2}$ = 4E12 /sec, $E_{d1,2}$ = 60 kJ/mol, $b_{1,2}$ = 0.52, and $f_v = a_f$(T-Tg) + f_g, a_f = 0.00008 /°C, f_g = 0.025

If T-Tg <-50 K, Then $K_{d1,2}$ = 1E-99 /sec

End If.

Etherification:

$$k_{d3} = A_{d3}\exp\left(-\frac{b_3}{f_v}\right)$$

A_{d3} = 1.5E9 /sec, b_3 = 0.7, and $f_v = a_f$(T-Tg) + f_g, a_f = 0.00008 /°C, f_g = 0.025

If T-Tg <-50 K, Then K_{d3} = 1E-99 /sec

End If.

$k_{d,1-2}$ and $k_{d,3}$ are added to k_1 , k_2 and k_3 chemical by the Rabinowitch equation:

$$\frac{1}{K_e} = \frac{1}{K_c} + \frac{1}{K_d}$$

Georgia Tech

Appendix: Validation Loss

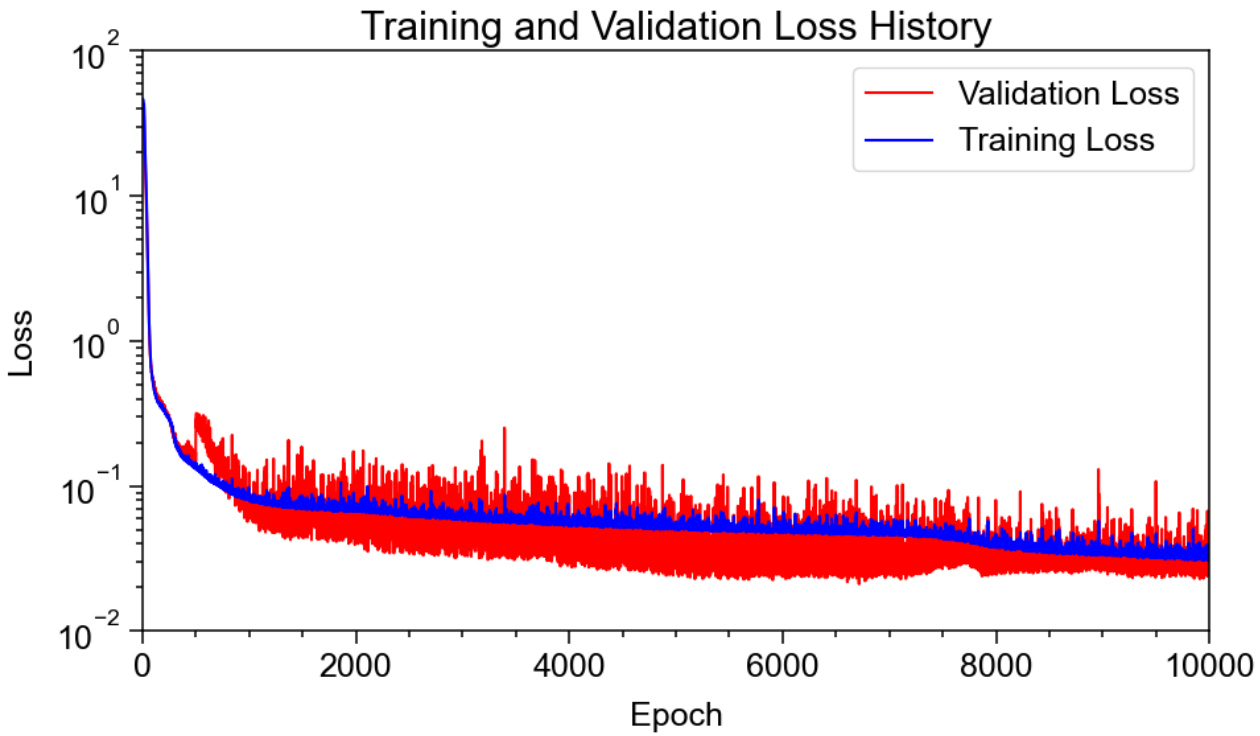

Traditional training – validation loss

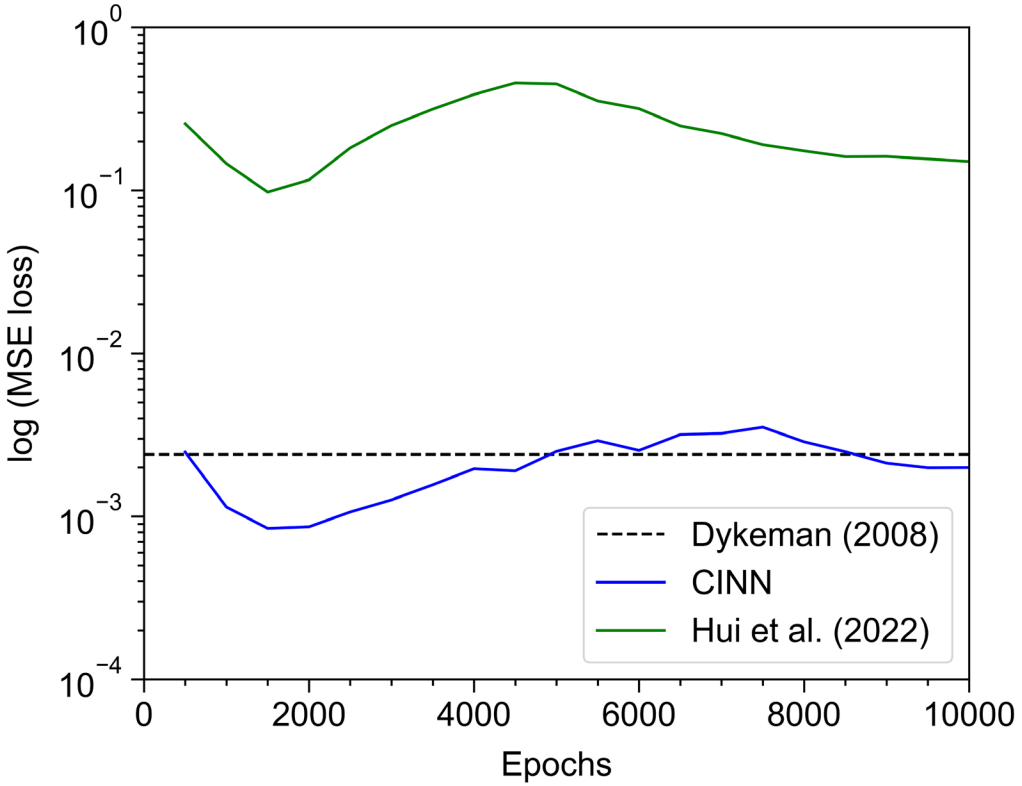

Scenario-based validation loss

Georgia Tech

Appendix: Surface Response Plot of the Reaction Rate

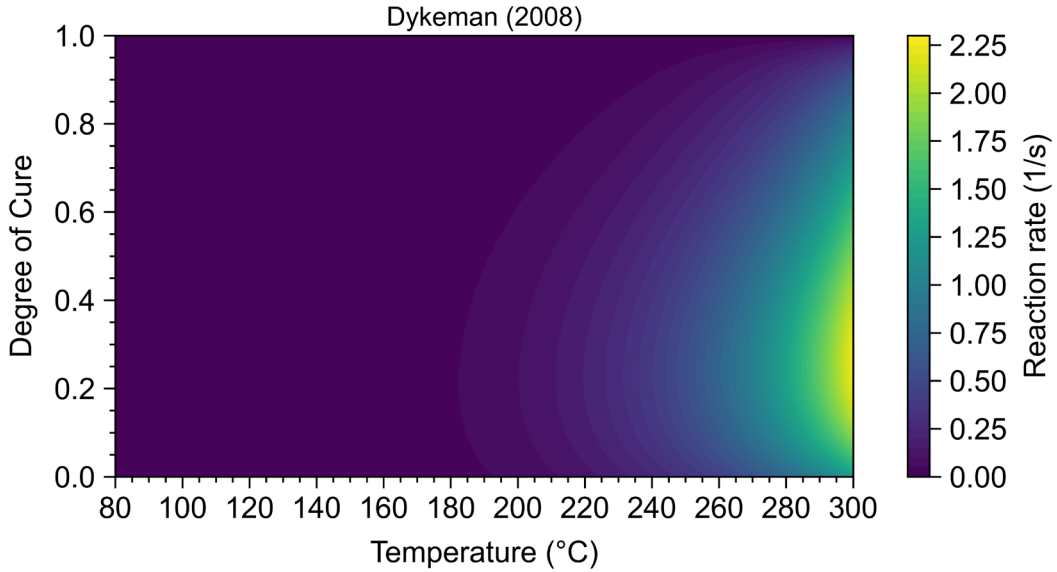

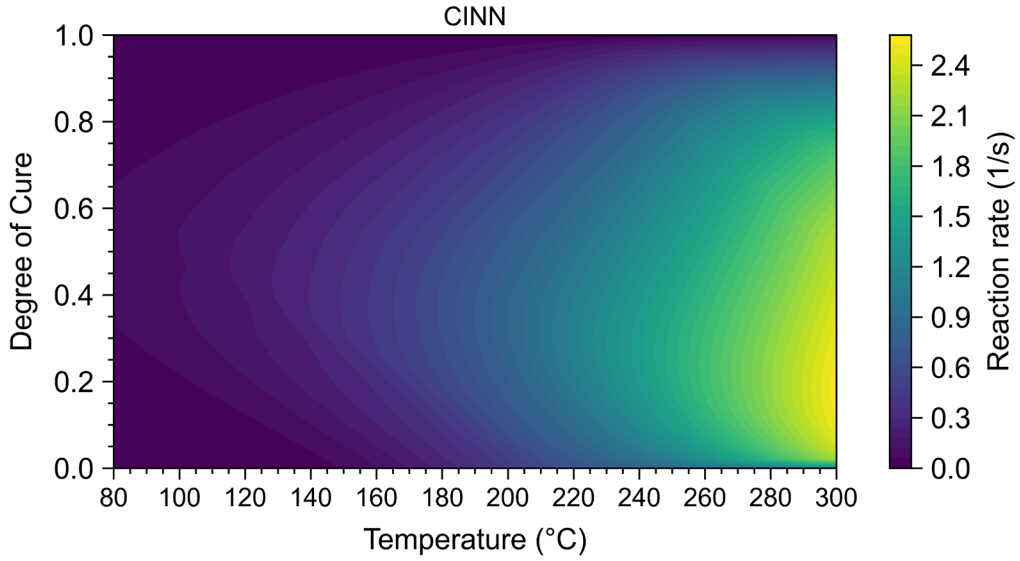

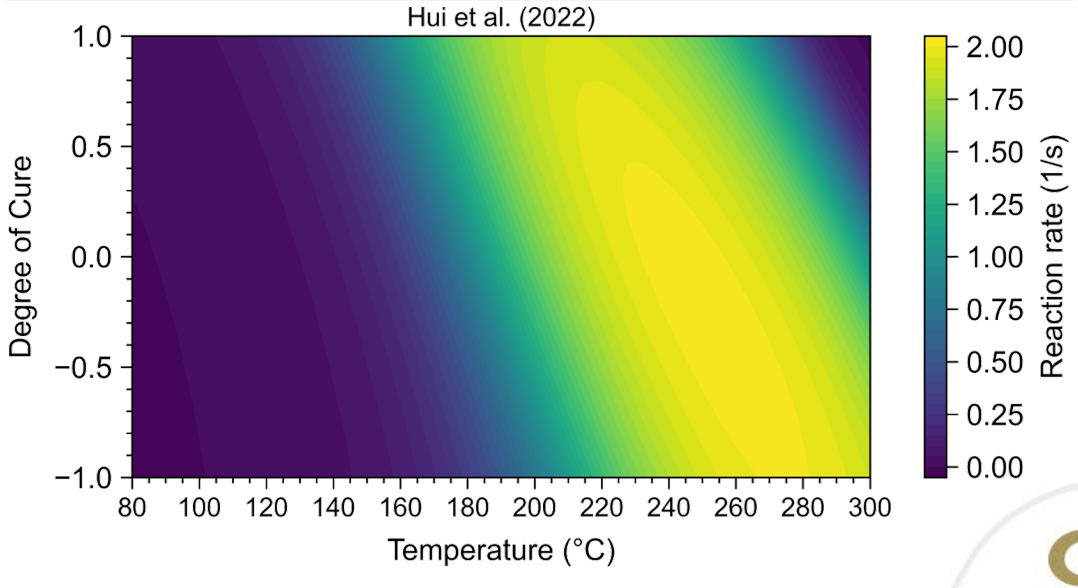

Georgia Tech

Appendix: Reference

[1] Zhang, W., et al. (2021). "A multi-dwell temperature profile design for the cure of thick CFRP composite laminates." *The International Journal of Advanced Manufacturing Technology* **117**(3): 1133-1146.

[2] Wang, B., et al. (2022). "Ultrasonic Testing of Carbon Fiber-Reinforced Polymer Composites." *Journal of Sensors* **2022**(1): 5462237.

[3] Blanco, M., et al. (2005). "Mechanistic kinetic model of an epoxy resin cured with a mixture of amines of different functionalities." *Polymer* **46**(19): 7989-8000.

[4] Hardis, R., et al. (2013). "Cure kinetics characterization and monitoring of an epoxy resin using DSC, Raman spectroscopy, and DEA." *Composites Part A: Applied Science and Manufacturing* **49**: 100-108.

[5] Hui, X., et al. (2022). "Cure process evaluation of CFRP composites via neural network: From cure kinetics to thermochemical coupling." *Composite Structures* **288**: 115341.

[6] Dykeman, D. (2008). Minimizing uncertainty in cure modeling for composites manufacturing. *University of British Columbia*. Retrieved from https://open.library.ubc.ca/collections/ubctheses/24/items/1.0066334

Georgia Tech

The First European Benchmark Exercise on Squeeze Flow Testing of High-performance Carbon Fibre Sheet Moulding Compounds

Connie Qian, Miro Duhovic, Dominic Schommer, Florian Gortner, Andreas Gebhard, Thomas Neumeyer, Marcel Olma, Louis Schreyer, Luise Kärger, Martin Hohberg, Hao Yuan, Anna Julia Imbsweiler, Sepehr Simaafrookhteh, Jan Ivens, Stepan V. Lomov, Gerben Bieleman, Wouter Grouve, Francois Mahé, Christophe Binetruy, Andreas Kapshammer, Zoltan Major, Dmitry S. Ivanov, Jonathan P.-H. Belnoue, Anatoly Koptelov, Jakub Jakimow, Dimitra Ramantani, Yvonne Aitomaki, Steven Nothhelfer, Nicole Stoess

Content

- Background and motivation
- Participants and facilities
- Experimental methodology
- Data collection
- Conclusions

High-performance SMC

- Long fibres (length>10mm, typically 25mm)
- High fibre content (volume fraction >30%)
  - ➢ Formation of “fibre network”
  - ➢ Suspension theory no longer applies
- Rapid cure resin system
- High-rate compression moulding processes
- High compression forces and pressures (>100 bar)
- High variabilities caused by the manufacturing (compounding) process



CT image of a compression moulded CF-SMC sample
(25mm fibre length, 47% wt, scanned area approximately 35mm x 25mm)

The squeeze flow test

- Squeeze flows – flows in which a material is compressed between two parallel plates
- Increasing popularity for SMC flow characterization
  - ➢ Similar to compression moulding
  - ➢ Easy to setup with existing load frames/presses
  - ➢ Wide range of strain rates
  - ➢ Internal material deformation is ensured
  - ➢ High variabilities, inhomogeneous (and anisotropic) flow due to the nature of the material
  - ➢ Lacking standarised test setup and procedure

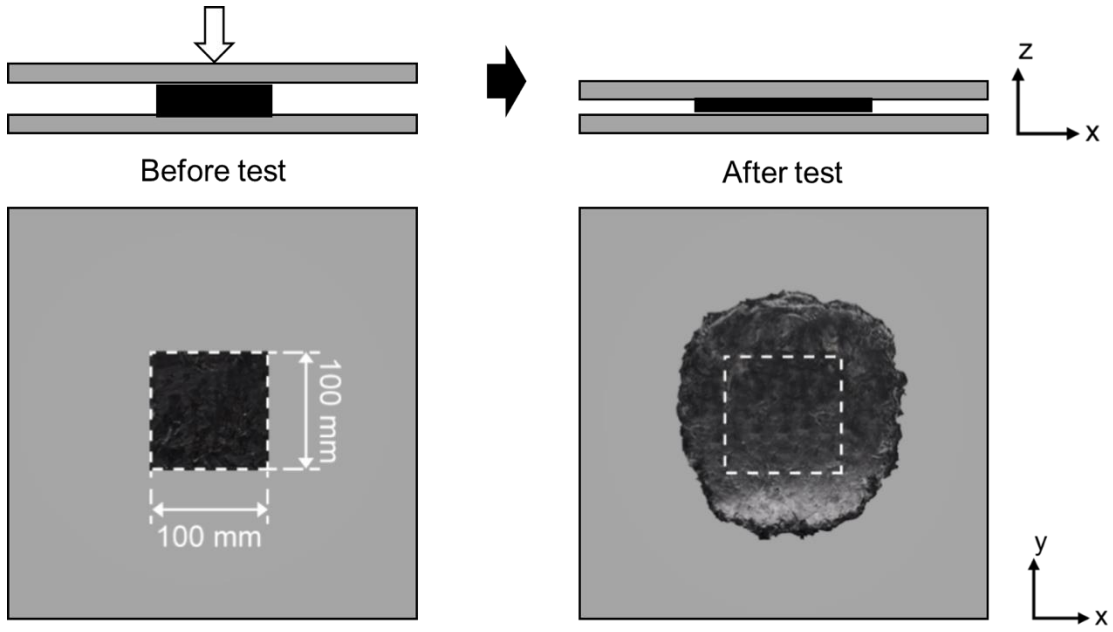

Schematic illustration of the SMC squeeze flow test

Scope of the benchmark

Anticipated outcomes:

- Understanding the sources of variabilities -> improve the reliability and repeatability
- Moving towards the development of a testing standard

Anticipated impact:

For academia

- Robust and reliable experimental approach
- Downstream research e.g. process simulation development

For industry

- Quality assurance testing
- Improved process robustness
- Material selection

Benchmark Overview



- 14 research institutes, 10 testing facilities, 7 countries
- 500kg material donation from Polynt Composites
- 5-day testing campaign, up to 120 samples total per participant
- 3 months from material manufacturing to the completion of testing campaign





Total materials donated by Polynt Composites

Facilities overview

Institute	Platen size [mm]	Testing machine	Heating method	Force limit [kN]
ECN & HESAM	220	Static frame	Heated platens	100
IVW	345	Hydraulic press	Heated platens	6500
JKU	Ø200	Hydraulic frame	Heated platens	50
KIT & SIM	300	Static frame	Heated platens	500
KUL	Ø280	Static frame	Thermal chamber	250
RISE	Ø100	Static frame	Heated platens	100
TUM	250	Static frame	Thermal chamber	250
UOB	Ø200	Static frame	Heated platens	100
UTW & TPRC	Ø246	Static frame	Heated platens	40
WMG & UOS	350	Hydraulic frame	Heated platens	250

Example testing setup



Hydraulic press
Heater platen



Static frame
Thermal chamber

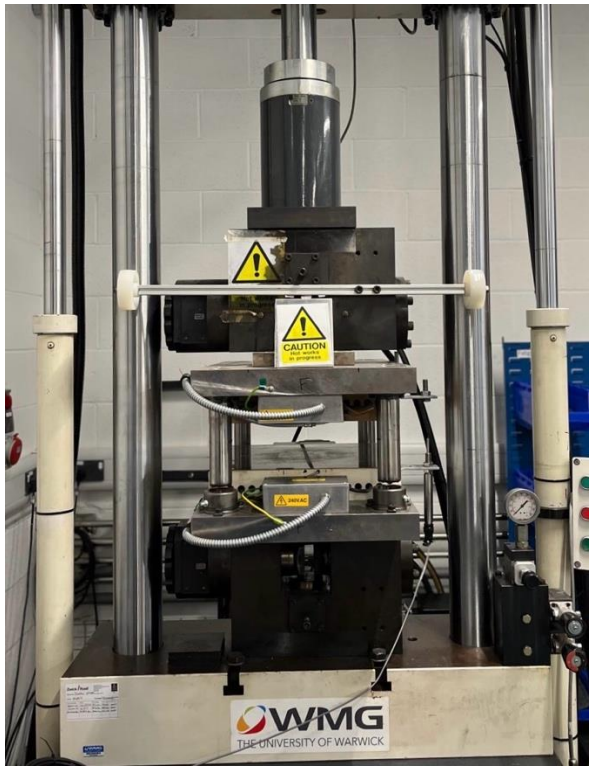

Hydraulic frame
Heated platen
(square)

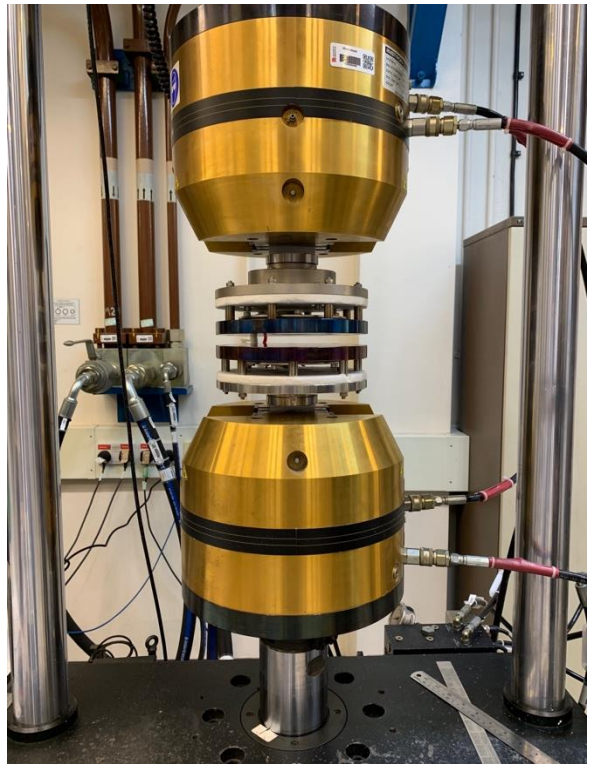

Static frame
Heated platen
(circular)

Materials

- Carbon fibre SMCs (C-SMC), **5** different specifications
- Identical vinylester resin system
- Recommended processing temperature **125-140°C**
- Recommended cure time **35s / mm part thickness**
- Shelf life **3 months** at room temperature or 6 months frozen
- Materials received by IVW and redistributed to all testing facilities

Product code	**Fibre tow size**	**Fibre length [mm]**	**Fibre weight fraction [%]**	**Target areal weight [g/m²]**
24 CF50-50K*	50K	25.4	50	1800
24 CF50-12K**,***	12K	25.4	50	1800
24 CF50-3K**	3K	25.4	50	1800
24 CF40-12K***	12K	25.4	40	1800
24 CF60-12K***	12K	25.4	60	1800

*Baseline material – Polynt's best selling C-SMC
** Effects of fibre tow size
*** Effects of fibre content

Sample preparation

- Square samples of 100mm and 50mm edge length
- Platen size ≥ 220mm -> both sample sizes
- Platen size < 220mm -> 50mm sample only
- 6 plies
- Fixed cutting plan and stacking sequence
  - ➢ Material tracing through UUIDs
- Strictly controlled sample preparation time (minimise exposure to air)

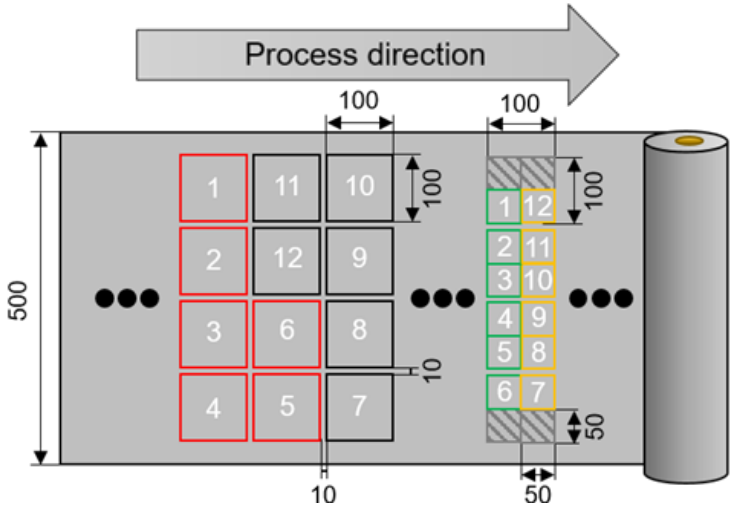

Cutting plan

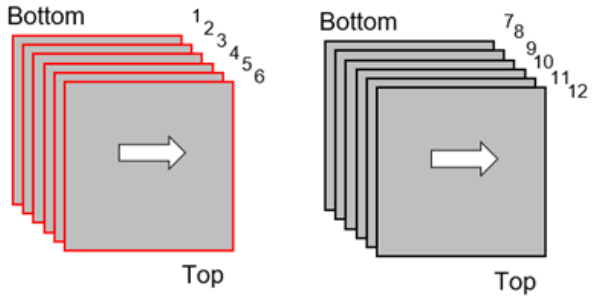

Stacking sequence

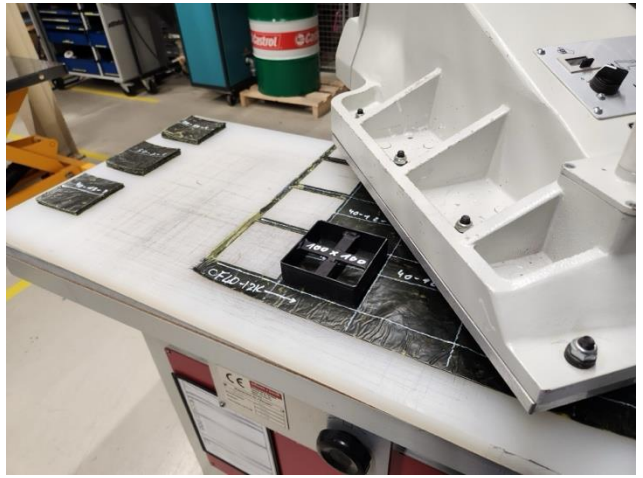

Clicker press



Manual cutting

Testing procedure

- Mould temperature 140°C
- Closing speed 0.5 mm/s
- Initial cavity height 11mm
- Final cavity heights 7, 5, and 3mm
- 10s sample loading time
- 210s minimum cure time
- Platens lined with Kapton films coated with release agent
- 6 repeats per testing configuration
- Fully randomised testing plan
  - ➢ Testing parameters alternated in blocks
  - ➢ Randomised material order within blocks

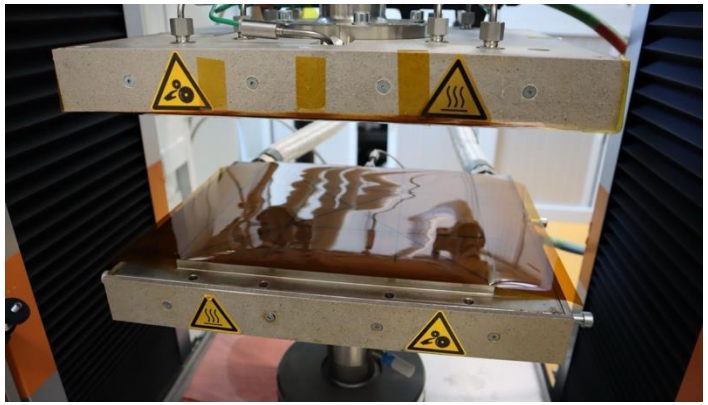

Kapton film lining

Test number	UUID	Material	Side length	Tool closing distance
WMG-	-		mm	mm
CF6012K-1	07b01c13-6900-4c35-b42c-813b04a6aa8b	CF6012K	100	8
CF4012K-1	3e316e3e-7f55-42c6-9624-f28c96c4ecad	CF4012K	100	8
CF5050K-1	71e2becf-0bab-47d1-b55b-04133c5ad9f2	CF5050K	100	8
CF5012K-1	9beafb3f-1e9c-4054-bd0d-4d3b47d6ae6e	CF5012K	100	8
CF503K-1	263ca7bc-4ab3-4220-9e4a-0b795052f233	CF503K	100	8
CF4012K-2	5c673b68-75d4-4fb8-a68b-75585dbda238	CF4012K	100	5
CF5012K-2	8df05cb9-20e8-4912-b48e-6a8ecbfbd167	CF5012K	100	5
CF503K-2	04bcd4af-fec2-4867-8ae5-91a69fefef64	CF503K	100	5
CF6012K-2	d4a025e2-9959-4b9c-9270-0f9bafeb6979	CF6012K	100	5
CF5050K-2	b6f6057a-ddd8-4053-a5d9-8fe28d0e396d	CF5050K	100	5
CF6012K-3	34a0d166-6a16-4ee8-9778-63c3555cb9d3	CF6012K	100	3
CF5012K-3	de68f8b9-ddde-436c-97b6-31004b1deacd	CF5012K	100	3
CF5050K-3	56a6021e-91cd-4e7d-828c-805b7aa3735f	CF5050K	100	3
CF503K-3	2b8ae493-b9a5-4609-b988-d567eea89d8c	CF503K	100	3
CF4012K-3	1063fad3-b708-41a0-a750-b4bc96619add	CF4012K	100	3
CF5050K-4	10041741-c945-4953-b891-645258e1f4b5	CF5050K	50	3
CF6012K-4	7f8fbef5-77ff-4a73-8661-05ccf4e1cd8f	CF6012K	50	3
CF4012K-4	1435f9fa-5ed1-4eb0-99b5-73a3caa7939f	CF4012K	50	3
CF503K-4	8713abc0-f029-4703-8372-e7f31bef9ba9	CF503K	50	3
CF5012K-4	15bc05da-66a5-436e-86cf-f39e6a43ad3b	CF5012K	50	3

Example testing plan

Data collection



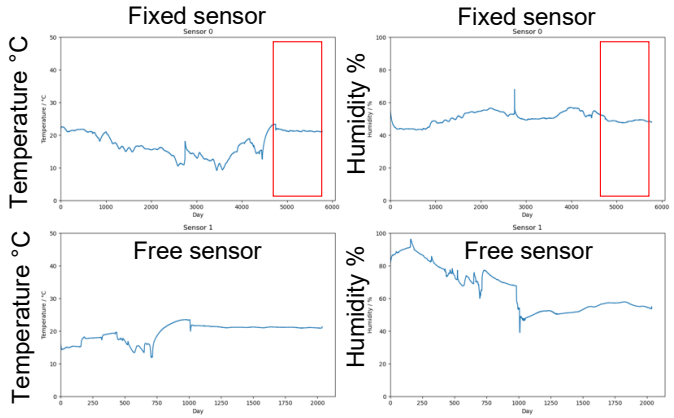

Temperature and humidity history

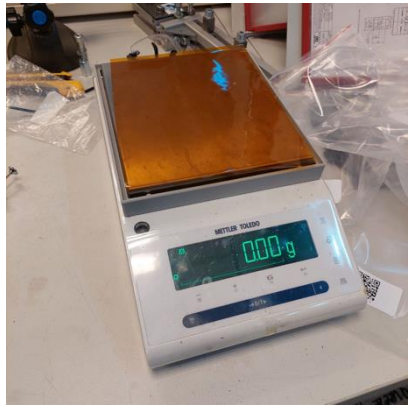

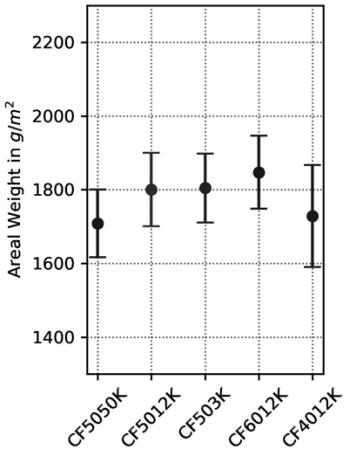

Areal mass variations

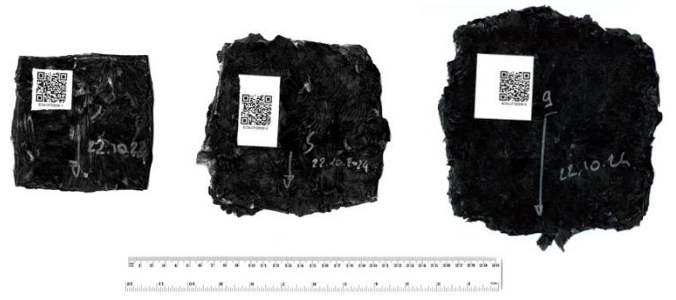

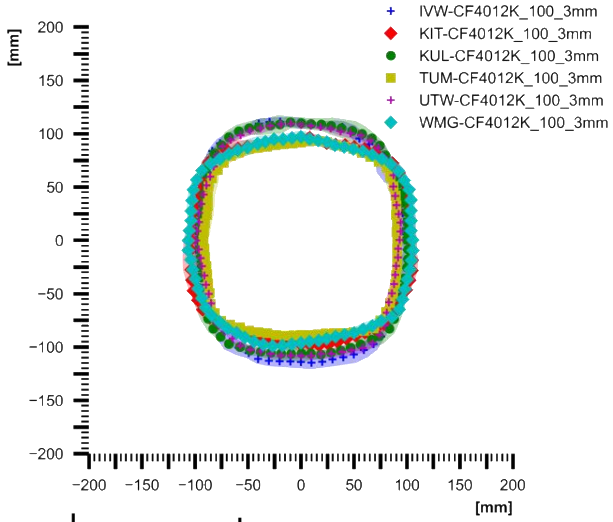

Flow front development

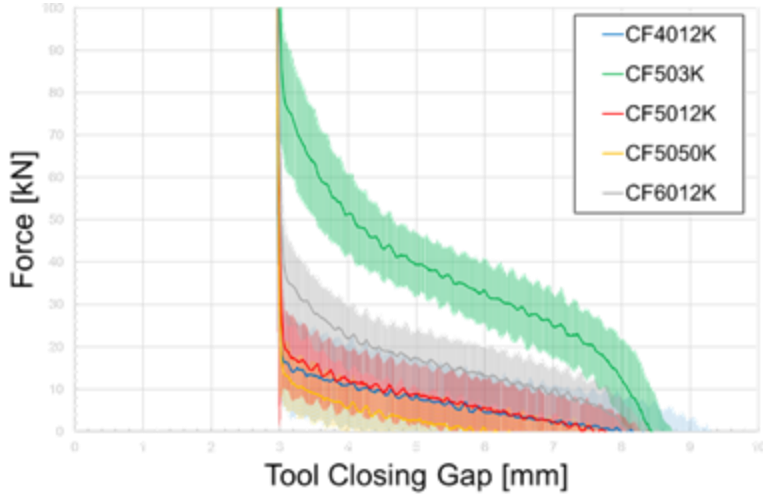

Force-displacement curves

Conclusions

Summary of the benchmark

- C-SMCs of 5 different specifications have been tested at 10 research facilities
- A well-defined testing procedure has been implemented to minimise the variabilities caused by testing conditions
- A comprehensive range of testing data and information has been collected
- Data analysis is being conducted to assess the variabilities in the testing results, and their potential causes

Potential next steps

- Follow-on benchmark exercise on squeeze flow modelling
- Development of an ATSM standard for high-performance SMC squeeze flow testing
- Collaborate projects on developing further SMC flow characterisation and flow simulation techniques
- Collaborate projects on improving quality controls of existing C-SMC products

Thanks for listening!

University of Sheffield

Connie Qian

Leibniz-Institut für Verbundwerkstoffe

Miro Duhovic

Dominic Schommer

Florian Gortner

Andreas Gebhard

Thomas Neumeyer

Karlsruhe Institute of Technology

Marcel Olma

Louis Schreyer

Luise Kärger

SIMUTENCE GmbH

Martin Hohberg

University of Warwick

Hao Yuan

Technical University of Munich

Anna Julia Imbsweiler

KU Leuven

Sepehr Simaafrookhteh

Jan Ivens

Stepan V. Lomov

TPRC & University of Twente

Gerben Bieleman

Wouter Grouve

HESAM Université

Francois Mahé

Ecolé Centrale de Nantes

Christophe Binetruy

Johannes Kepler University Linz

Andreas Kapshammer

Zoltan Major

University of Bristol

Dmitry S. Ivanov

Jonathan P.-H Belnoue

Anatoly Koptelov,

Jakub Jakimow

Research Institutes of Sweden

Dimitra Ramantani

Yvonne Aitomaki

Polynt Composites

Steven Nothhelfer

Nicole Stoess

Rapid Curing of Composites by Filament Winding Technique



Soroush Dashtizad, Mahdi Baniasadi, Walter Jordan, Carter Dojan, Mostafa Yourdkhani

School of Manufacturing Systems and Networks

Arizona State University

August 5th, 2025

Arizona State University

ICCM24

Outline

- Challenges with current filament winding approaches
- Frontal polymerization
- Frontal curing of composites during filament winding
- Experimental methods
- Understanding the underlying processing science
- Conclusions

Pressure Vessel

Composites are increasingly replacing metals in pressure vessel applications due to their superior strength-to-weight ratio and corrosion resistance

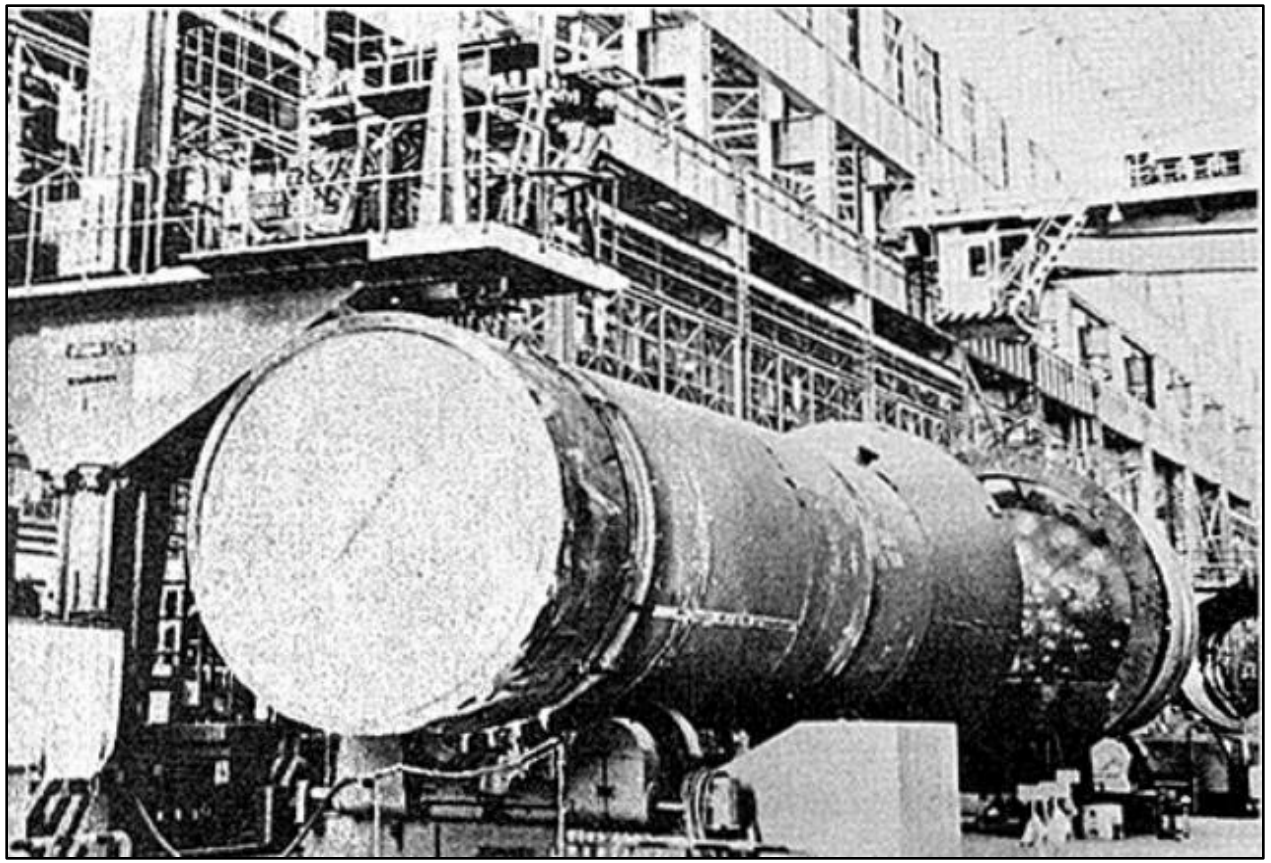

Ando et al., *Journal of Pressure Vessel Technology*, 1974



Blachut et al., *Composite Structures*, 2023

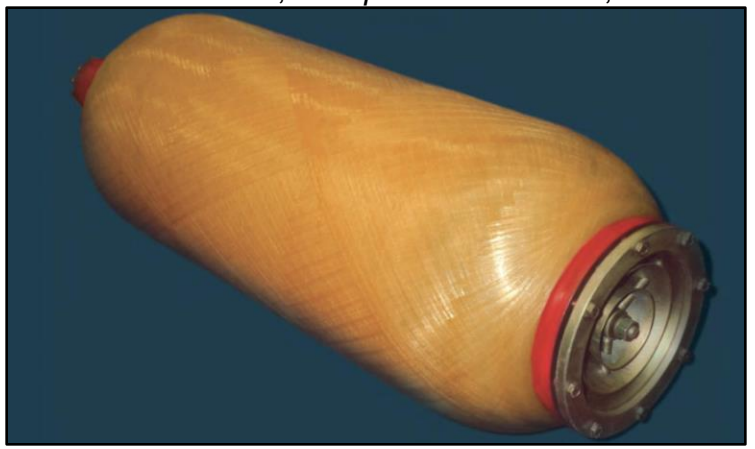

Vasiliev et al., *Composite Pressure Vessels*, 2009

Filament Winding

Filament winding is widely used for manufacturing composite pressure vessels

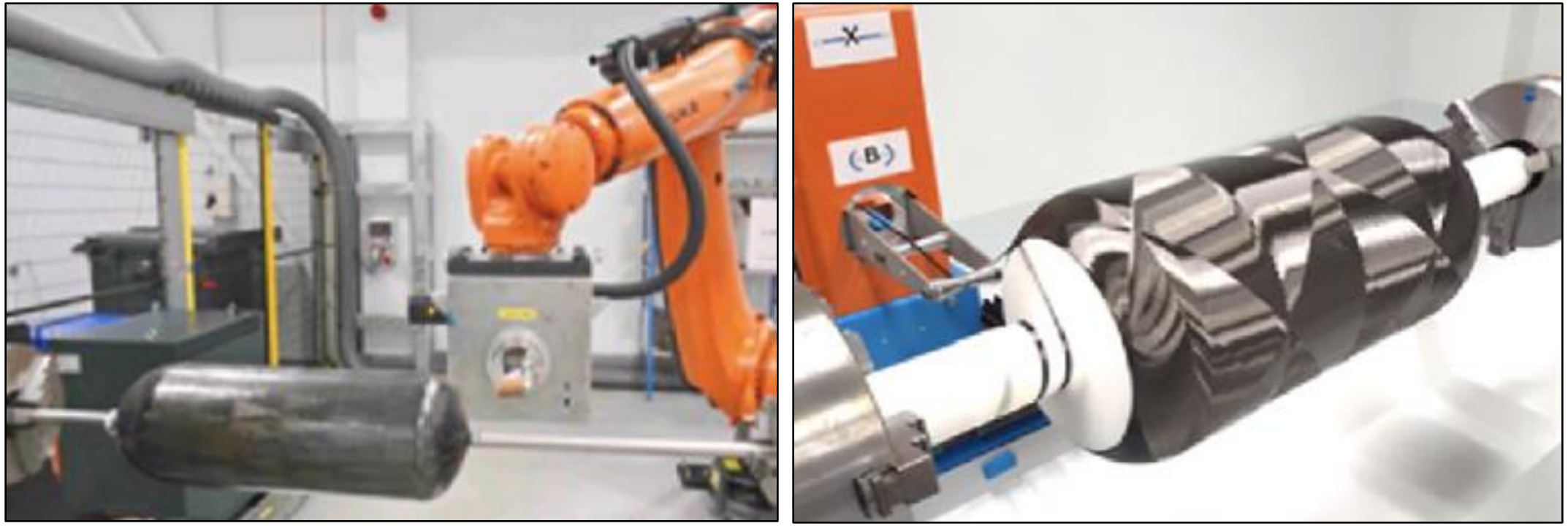

Ma et al., *International Journal of Hydrogen Energy* , 2024

- Fibers are wound on a mandrel using wet or prepreg techniques to tailor mechanical properties
- Conventional curing remains slow and energy-intensive, requiring hours of heating even with optimized processes

Filament Winding with *In-Situ* Curing

Rapid, one-step composite manufacturing enabled by in-situ frontal curing during filament winding

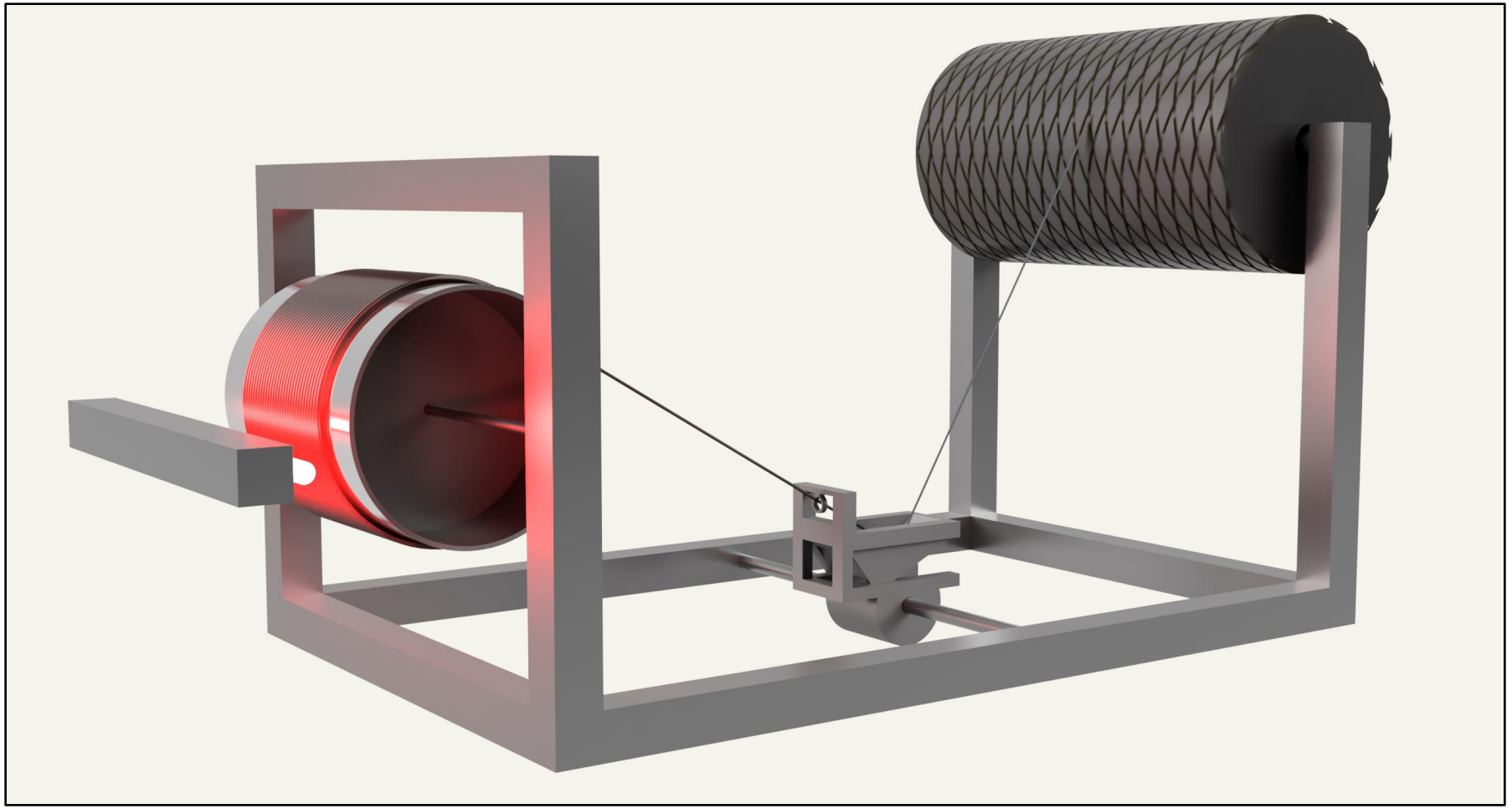

Materials

- Carbon fiber tow
- Dicyclopentadiene (DCPD)
- Second generation grubbs' (GC2)
- Tributyl phosphate (TBP)
- Phenyl cyclohexane (PCH)

Thermal Profile Measurement Setup

- Outer surface temperature measured using a thermal camera
- Inner surface temperature measured using a thermocouple

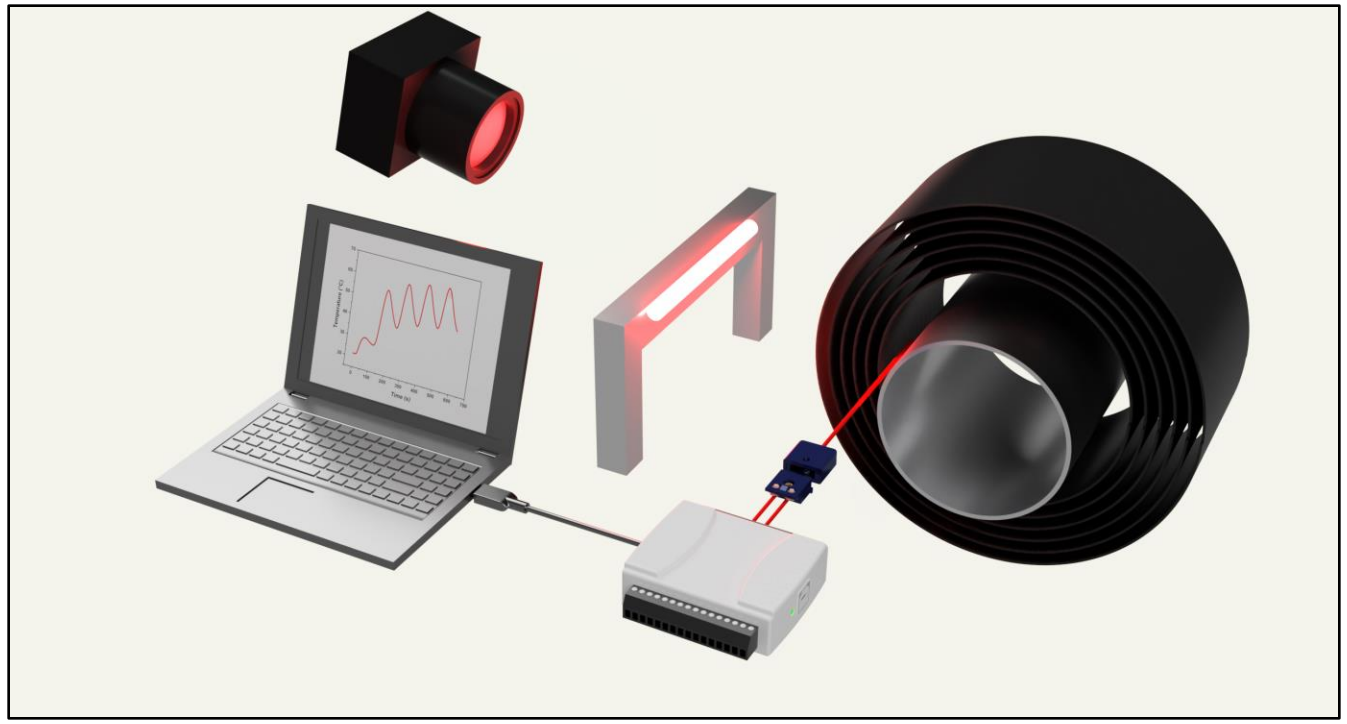

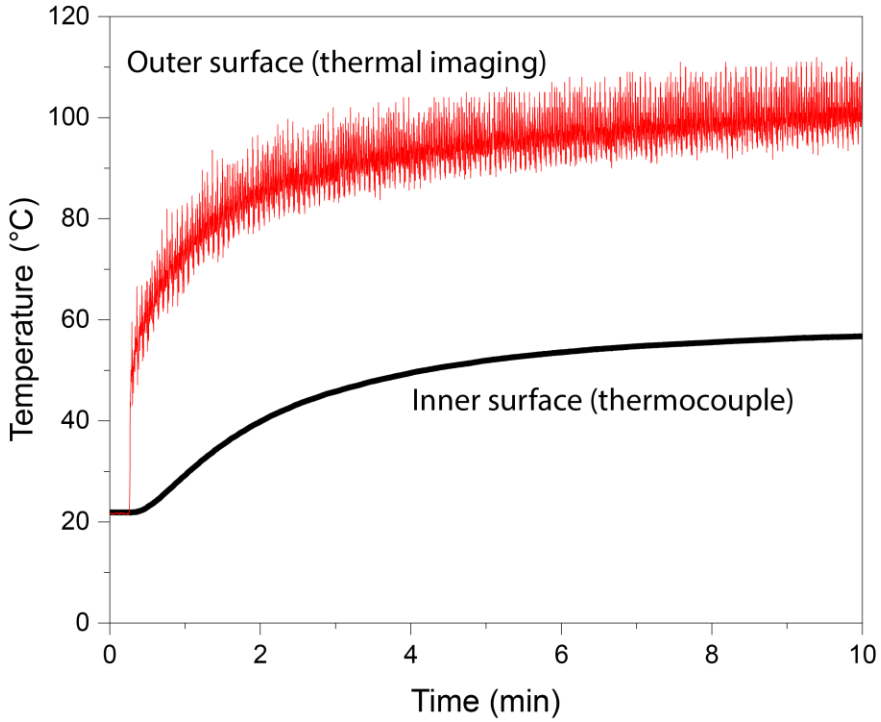

Dry Fiber Winding

Dry fiber winding is used to study the effect of input power and mandrel rotation on photothermal performance of carbon fiber tows

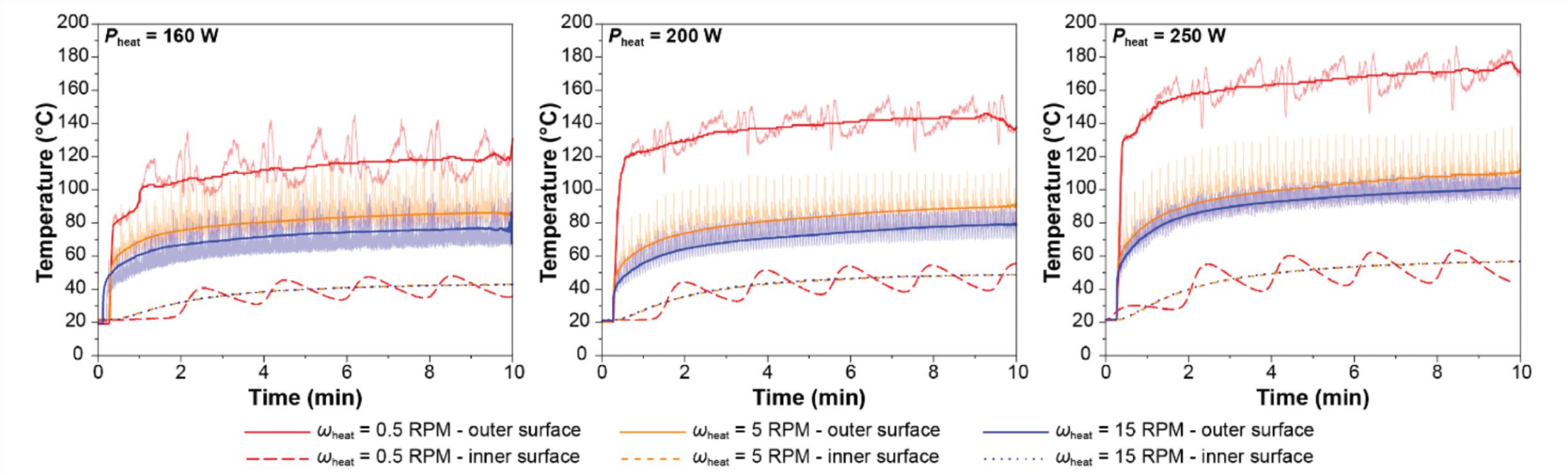

Higher mandrel speeds improve uniformity but lower the average temperature

Wet Winding

Based on the results of dry fiber winding, two processing conditions are selected for wet winding studies

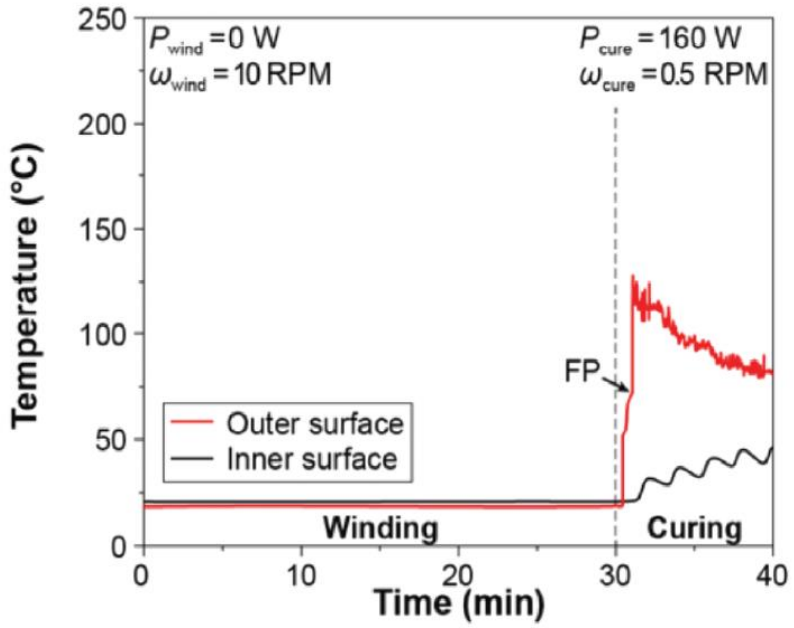

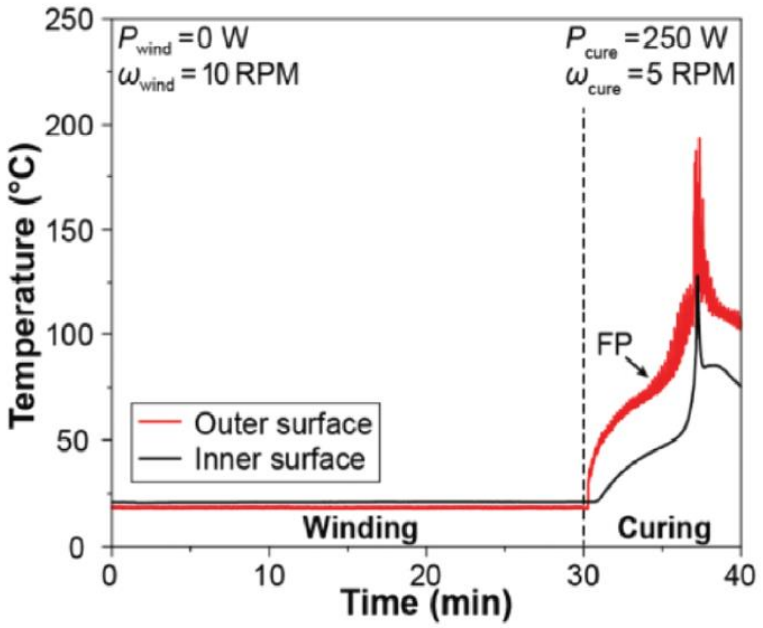

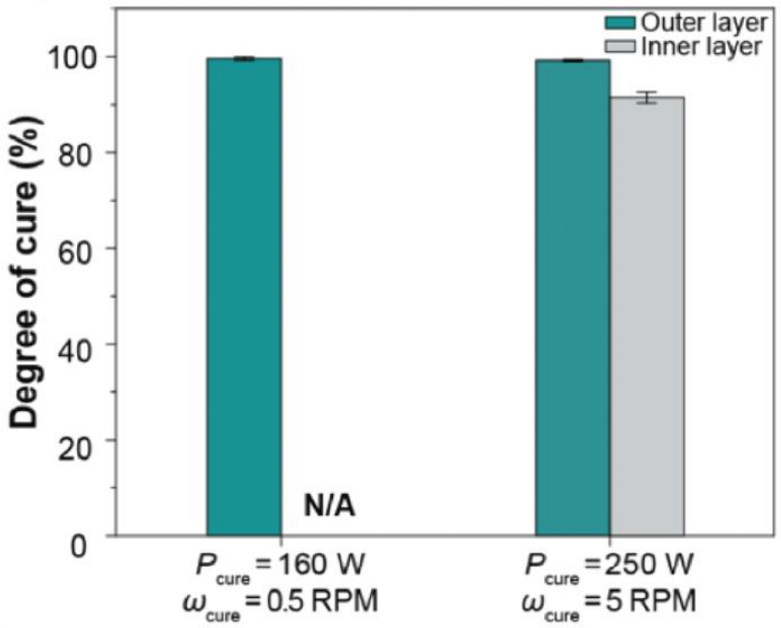

- Low-power curing starts FP but leaves inner layers uncured
- High-power curing enables full cure but causes uneven through-thickness curing

Wet Winding with Preheating

Preheating during the winding step to increase the initial temperature of the material and its reactivity

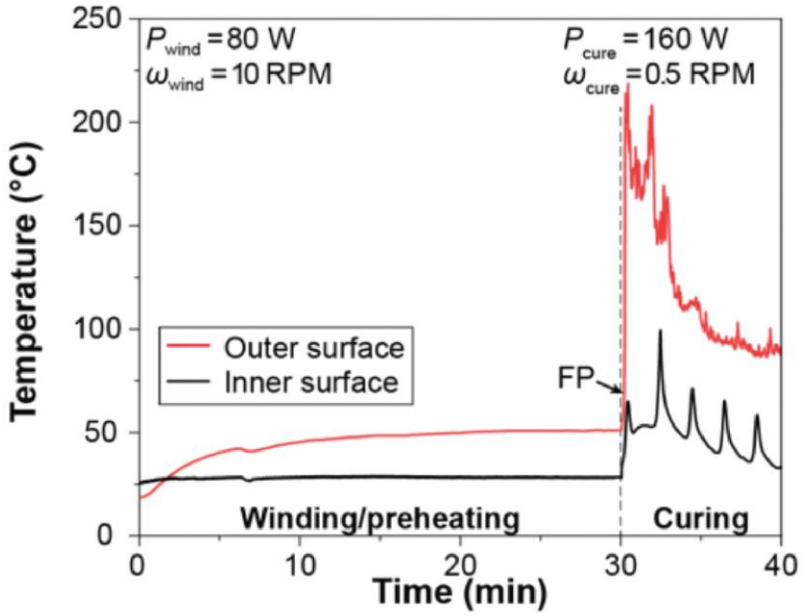

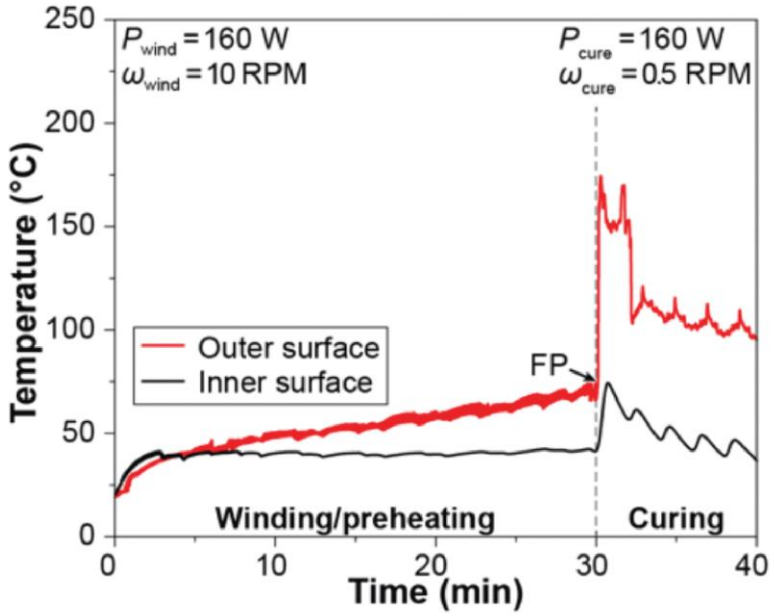

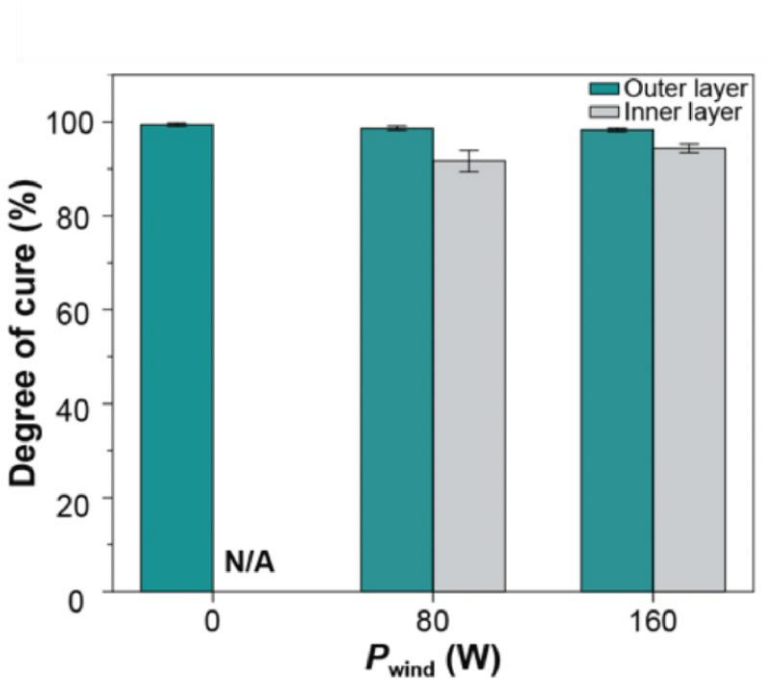

Preheating enables more uniform curing and faster initiation of frontal polymerization

Conclusions

- A new approach is developed for rapid, energy-efficient, *in-situ* curing of composites during filament winding using IR-assisted frontal polymerization
- Photothermal-assisted frontal polymerization enables on-mandrel curing of composite parts within minutes
- Varying IR power and mandrel rotation speed affects front propagation dynamics and cure quality
- Preheating during winding enhances front initiation and sustained propagation throughout the composite
- Controlled IR input results in uniform curing, while excessive heating leads to surface defects

Acknowledgements

COLORADO

Office of Economic Development & International Trade



School of Manufacturing Systems and Networks
Arizona State University

Fabrication of SiC Fiber-Reinforced 3D Woven Composites Using Tow Sizing and Optimized Preform Structures

2025.08.05

Yoon Min Oh, Min Seok Ahn, and Woong-Ryeol Yu*

Department of Materials Science and Engineering (MSE) and Research Institute of Advanced Materials (RIAM), Seoul National University, Seoul, 08826, Republic of Korea

Index

I. Introduction

II. Methodology

III. Results & Discussion

IV. Conclusions

Index

I. Introduction

II. Methodology

III. Results & Discussion

IV. Conclusions

Expansion of application fields of ceramic matrix composite (CMC)

CMC exhaust nozzles in F135 aero engine



Materials Science and Engineering 678 (2019) 012043

SiC/SiC CMC combustor liner by SNECMA



Materials Science and Engineering 678 (2019) 012043

SiC/SiC turbine guide vane before and after hot test

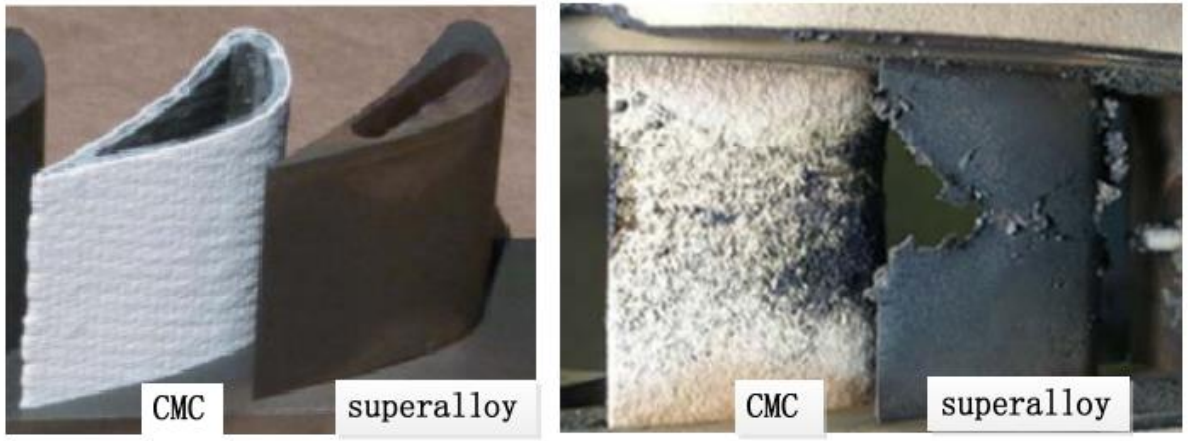

Materials Science and Engineering 678 (2019) 012043

Strength and temperature data for ceramics and metal alloys

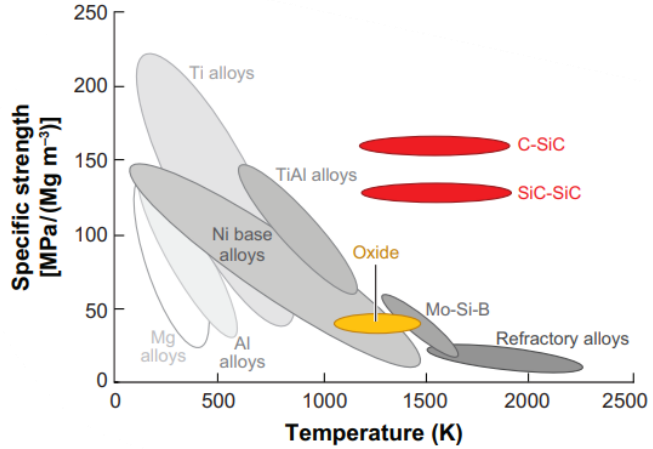

Annu Rev Mater Res, 38 (1) (2008), pp. 425-443

Need for 3-Dimensional SiC_f/SiC composite

SiC/SiC complex three-dimensional structure

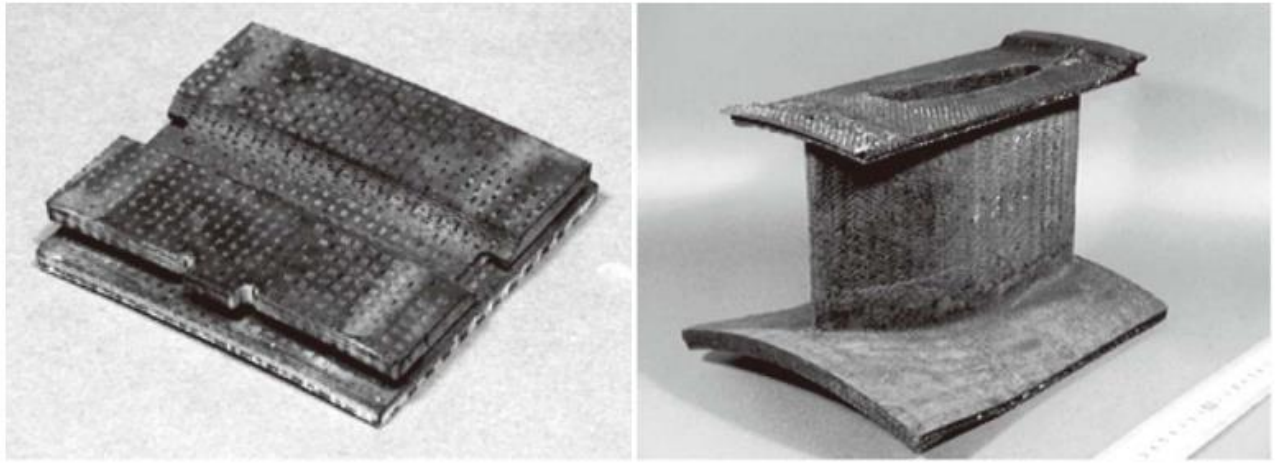

Materials Science and Engineering 678 (2019) 012043

Examples of three-dimensional woven structures

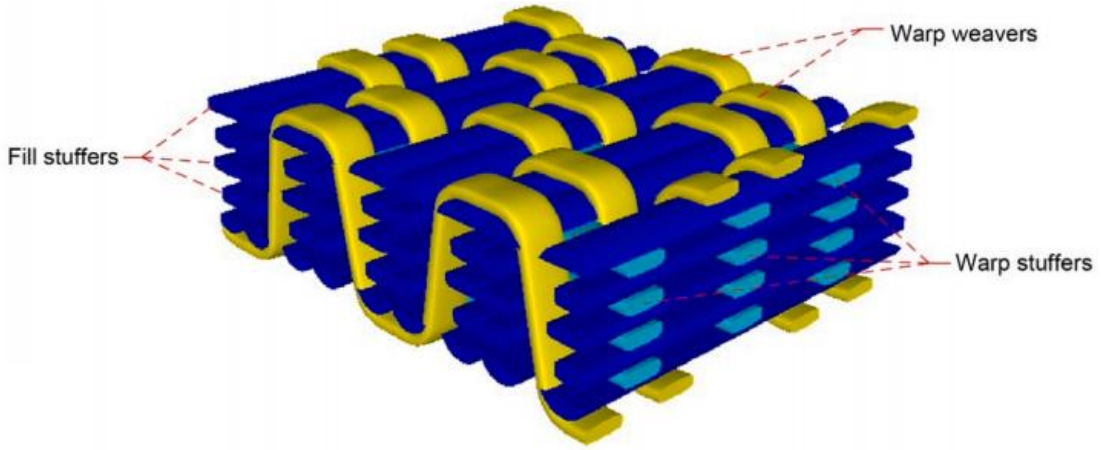

Journal of the European Ceramic Society 44 (2024) 116739

- SiC_f/SiC composites are prized in aerospace for their superior oxidation resistance
- Although **3D weaving** is essential for fabricating **complex structures**, process challenges mean composites are implemented in 2D or 2.5D architectures

High-Temperature stability of Tyranno SA fiber

Tensile strength and creep resistance at high T

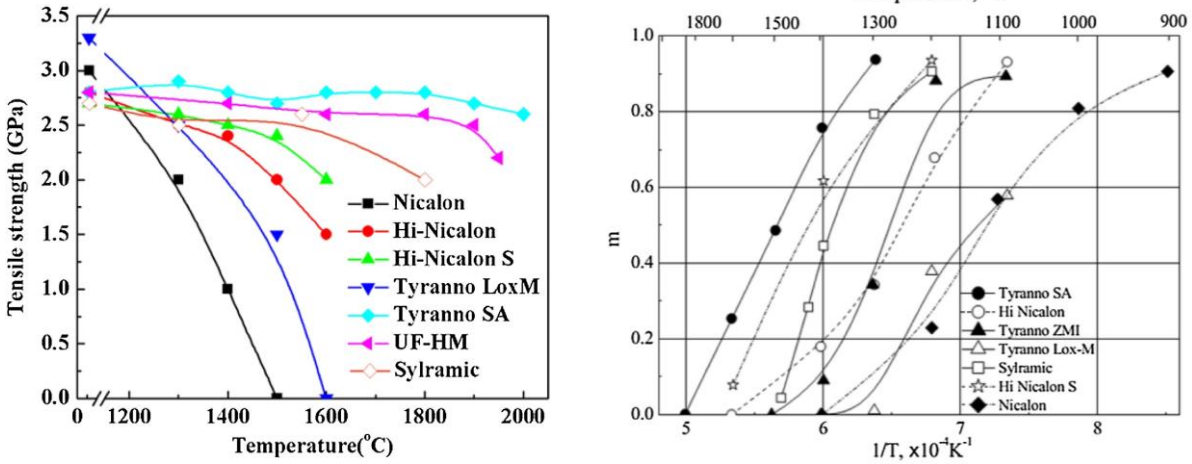

Journal of Materials Science & Technology 35 (2019) 2743–2750

- Tyranno SA fiber maintains higher tensile strength and creep stability at high temperatures compared to other fibers
- Its thermal conductivity is higher than other fibers, making it advantageous in fields like nuclear energy where thermal diffusion is crucial

Change in composite thermal conductivity at high T

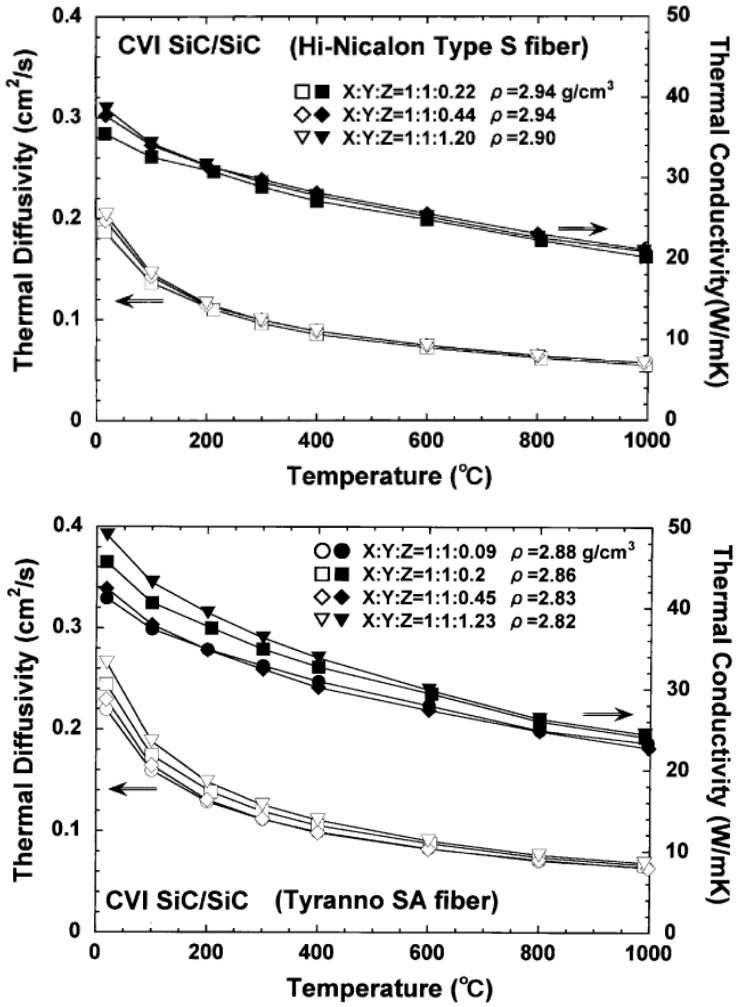

Journal of Nuclear Materials 329–333 (2004) 497–501

SiC fibers susceptible to friction

Comparison of Scanning Electron Microscopy (SEM) images of SiC fibers

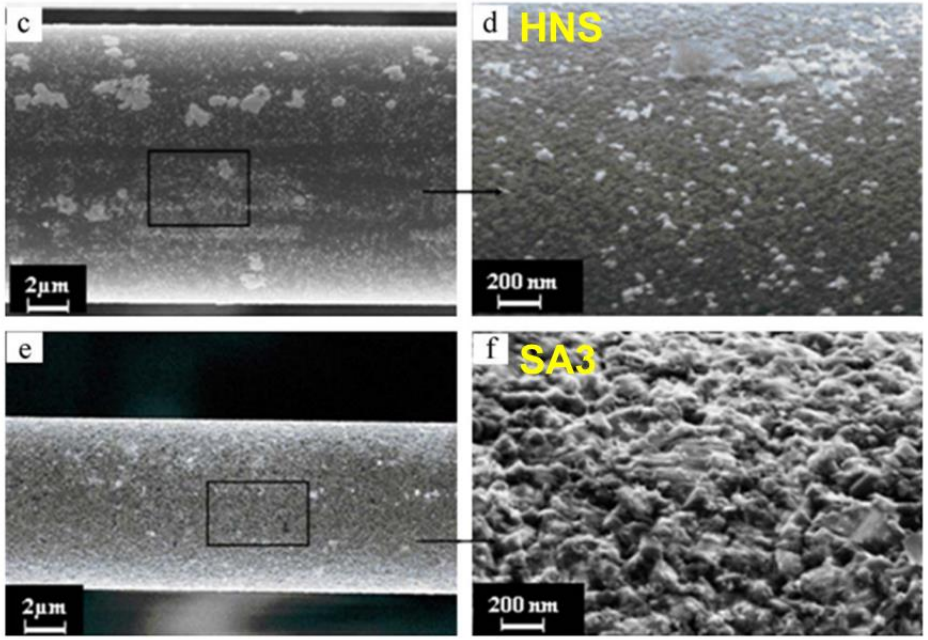

Journal of the European Ceramic Society 32 (2012) 547–557

Comparison of Atomic Force Microscopy (AFM) images of SiC fibers

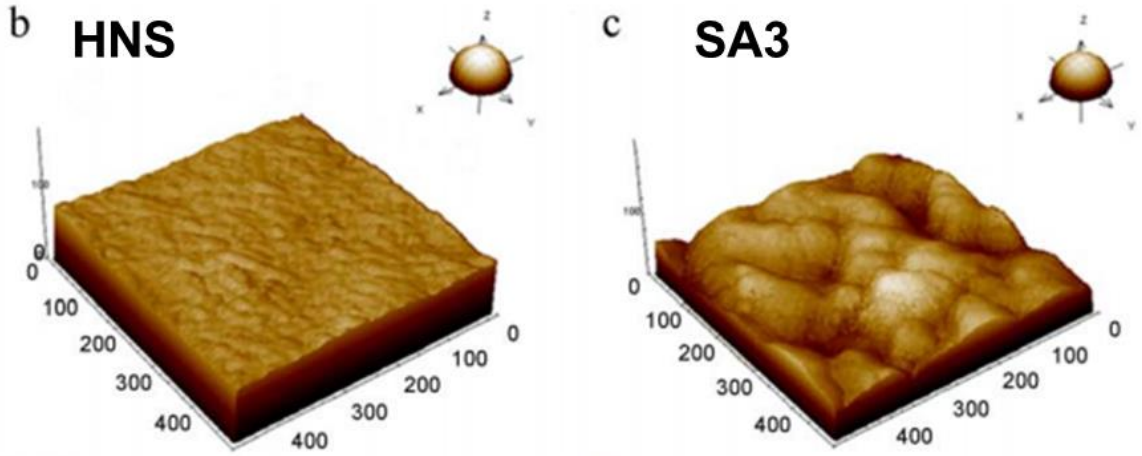

Journal of the European Ceramic Society 32 (2012) 547–557

- Tyranno fibers are produced at higher temperatures than other fibers, resulting in **greater crystallinity** and thus **superior thermal properties**
- However, this causes the fiber surface to be extremely **rough**, resulting in severe **abrasion damage** and increased fiber brittleness

Low flexibility of SiC fibers

Low flexibility of SiC fibers (UBE-SA3)

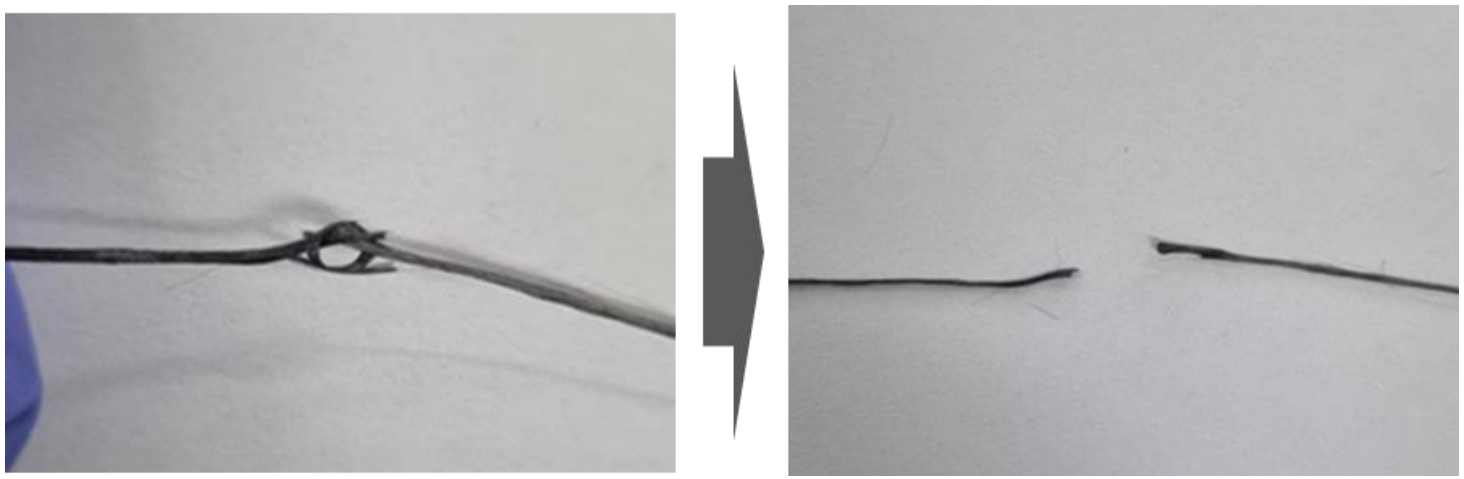

- SiC fibers have **high brittleness**, resulting in much **lower fracture strain** compared to carbon fibers, which are commonly used in weaving

UBE TYRANNO-SA Grade 3	
	Nominal properties
Atomic composition	SiC O,Al < 0.008
Tensile strength (GPa)[a]	2.8
Tensile mudulus (GPa)[a]	420
Elongation (%)	0.7
Density (g/cm³)	3.02
Fibre diameter (μm)	10
Thermal conductivity (W/m K)	64.6 (at 25 °C)

Materials Science & Engineering A 638 (2015) 305–313

FIBER PROPERTIES **Toray T700**

PROPERTY	ENGLISH	METRIC	METHOD
Tensile Strength	711 ksi	4,900 MPa	TY-030B-01
Tensile Modulus	34.8 Msi	240 GPa	TY-030B-01
Strain at Failure		2.0%	TY-030B-01
Density		1.80 g/cm³	TY-030B-02
Filament Diameter		7 μm	
Yield	12K	800 g/1000m	TY-030B-03

T700G Rev. 5: Updated April 13, 2018

Research strategy - Covering

3D depiction of covering tow

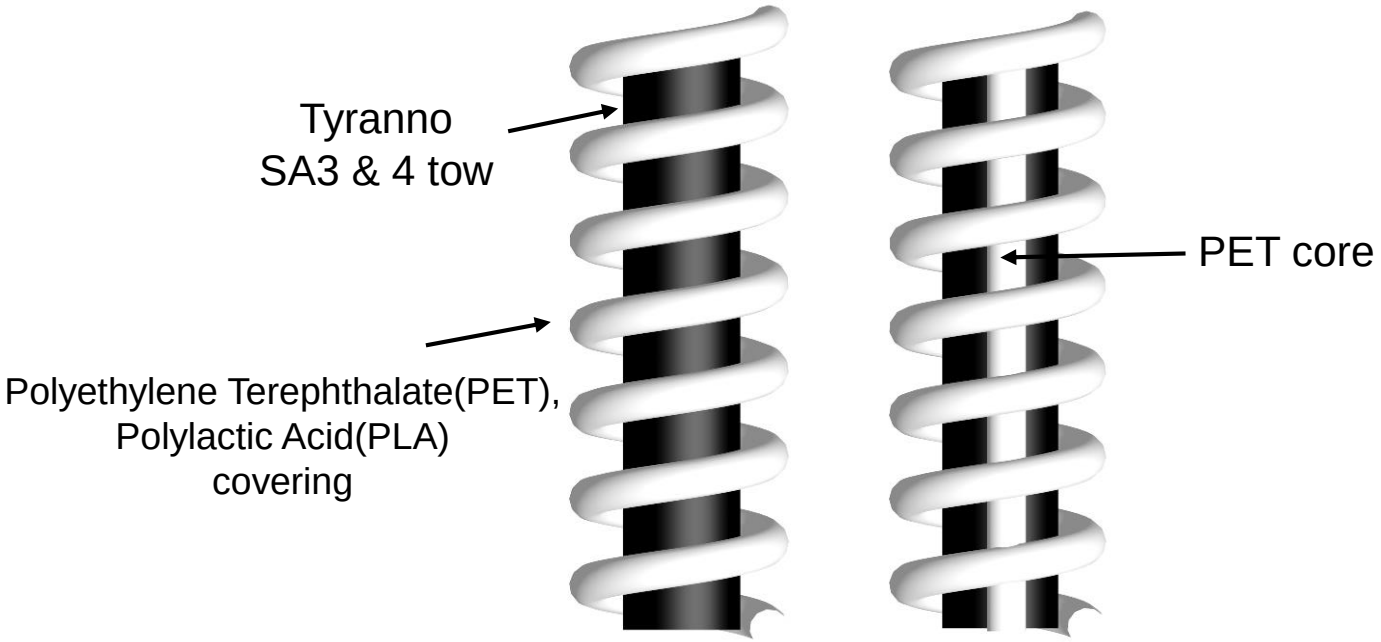

Covering process method

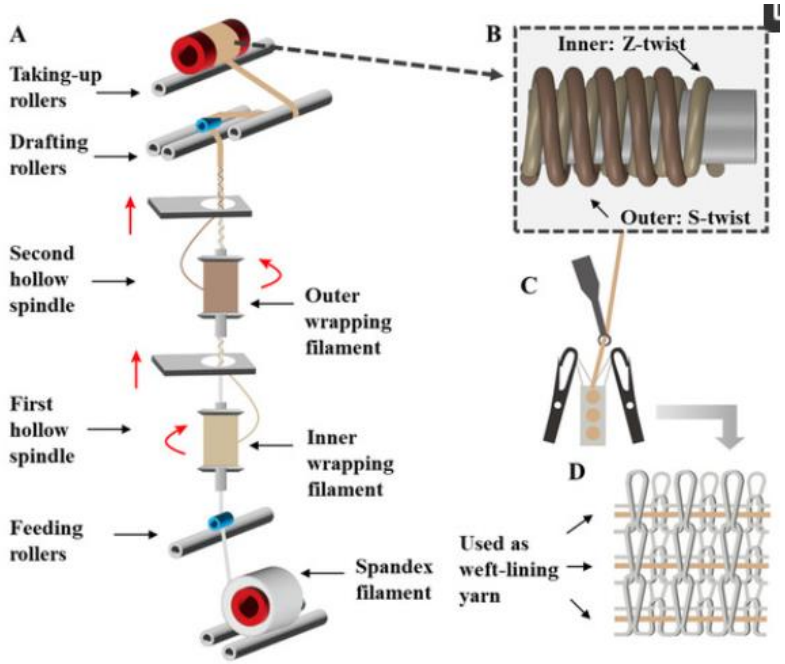

Polymers 2024, 16(17), 2476

- Goal of the covering process is to enhance the mechanical properties of the tow, including bending strength, and increase friction resistance
- SA3 tow was covered with PET, and SA4 tow was covered with PLA. In the case of SA3, an inner core was added beneath the covering, and both were compared together

Research objective

- To examine the strengthening effect at the tow level when covering is applied
- To assess the effect of covering in the weaving process and understand its impact on the material properties at the composite level

Index

I. Introduction

II. Methodology

III. Results & Discussion

IV. Conclusions

Experiment – Tow level property

Ceramic tow tensile test (ISO 22459)

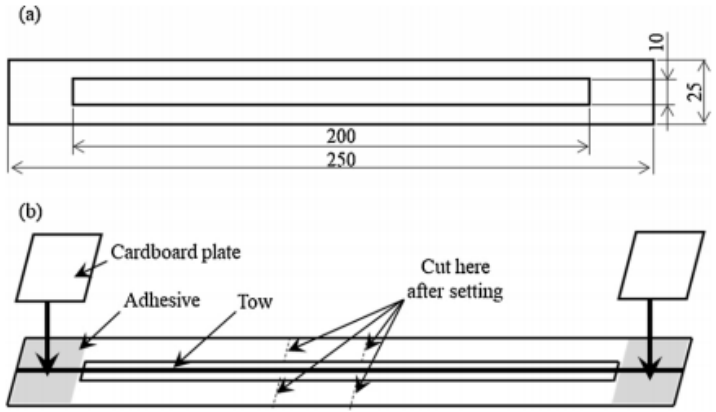

Journal of the European Ceramic Society 42 (2022) 1928–1937



Kawabata bending test

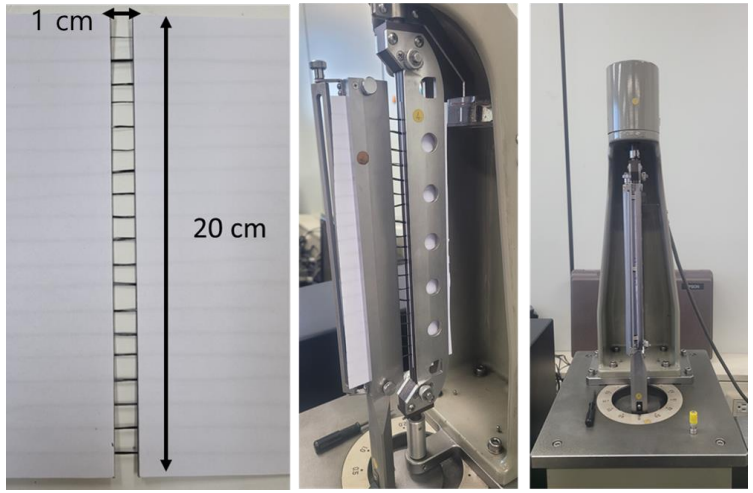

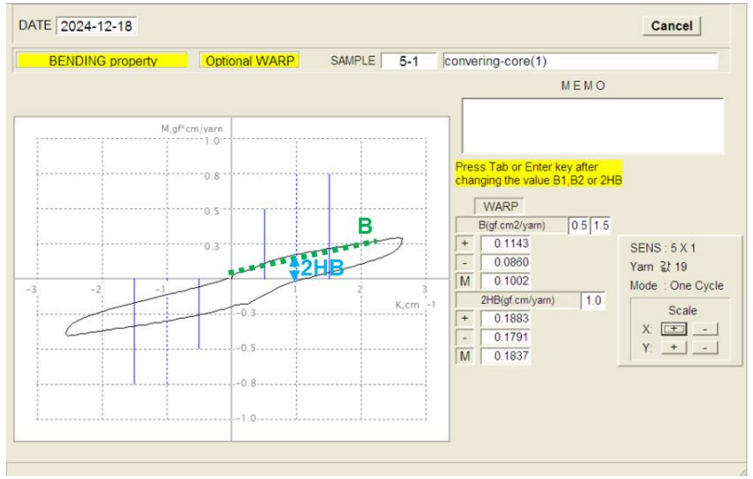

Sinclair loop test (Maximum curvature)

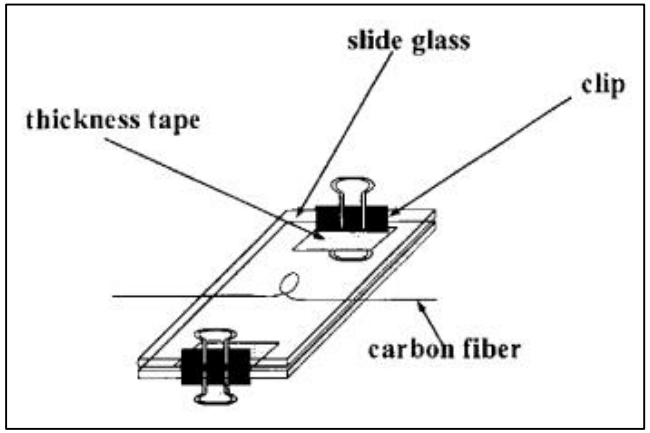

Advanced Composite Materials, 8:3, 281-291

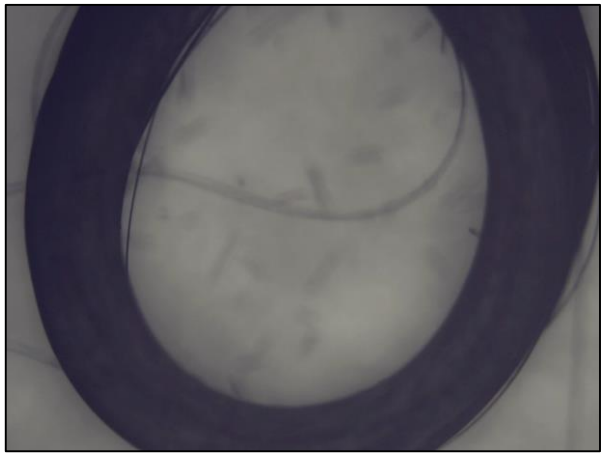

3D Weaving machine

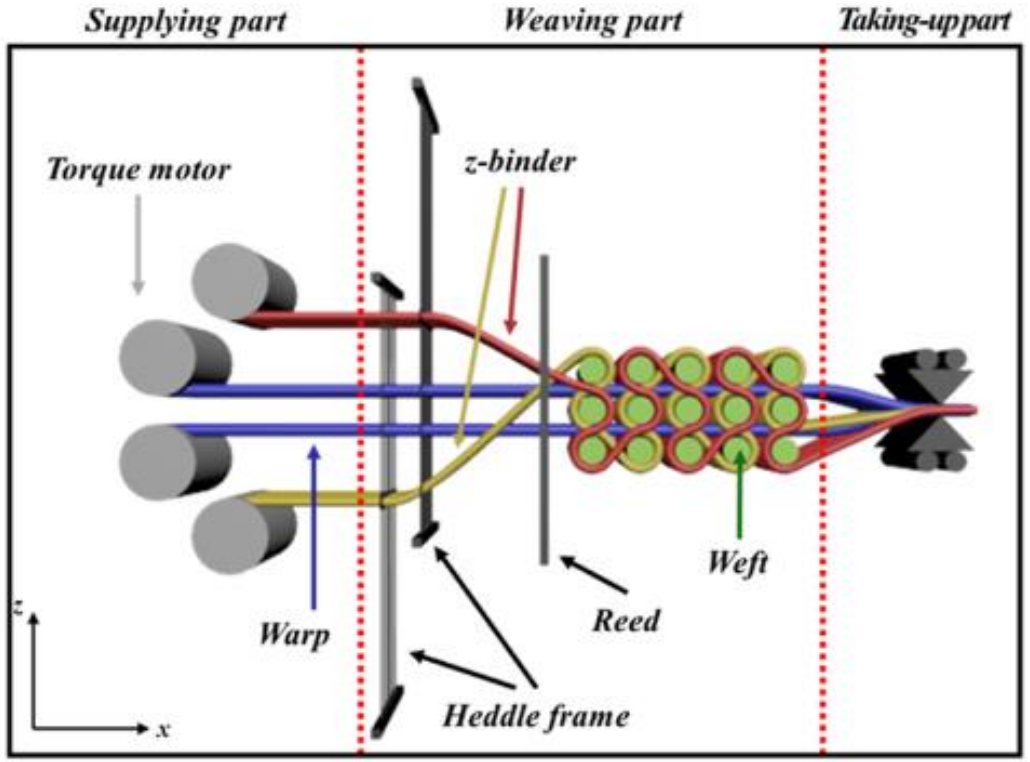

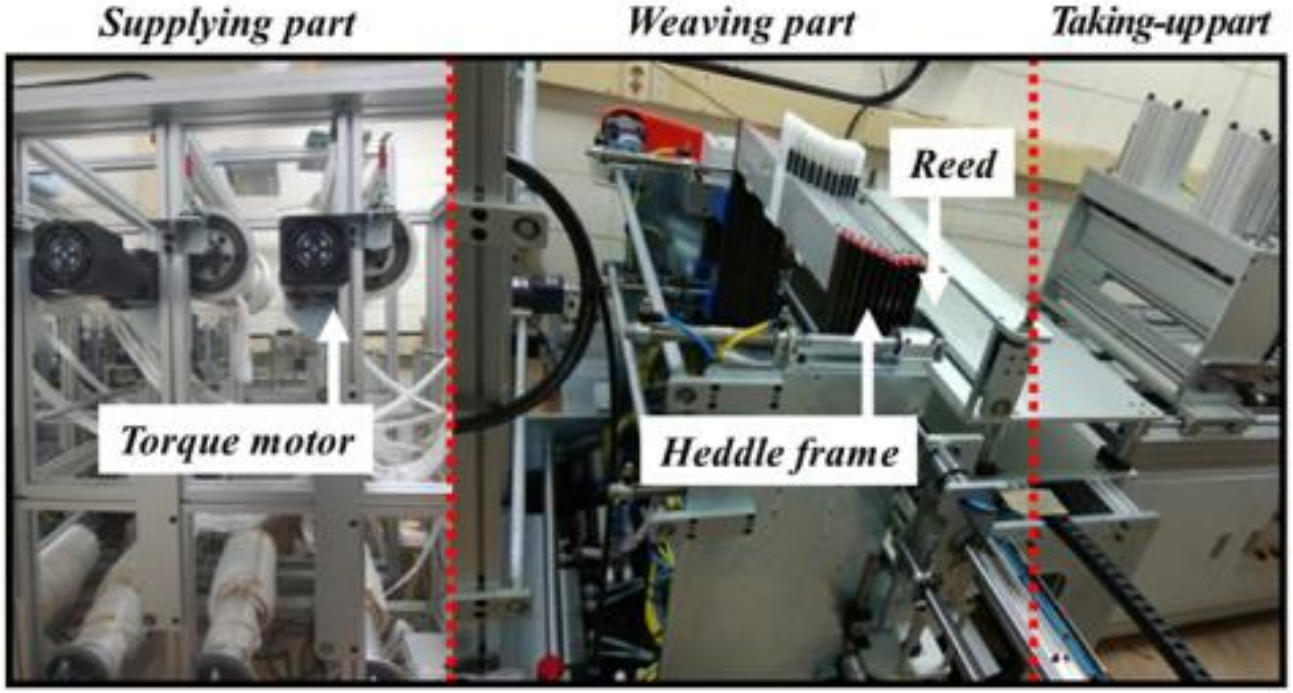

Index

I. Introduction

II. Methodology

III. Results & Discussion

IV. Conclusions

Morphological analysis of covered SiC tow

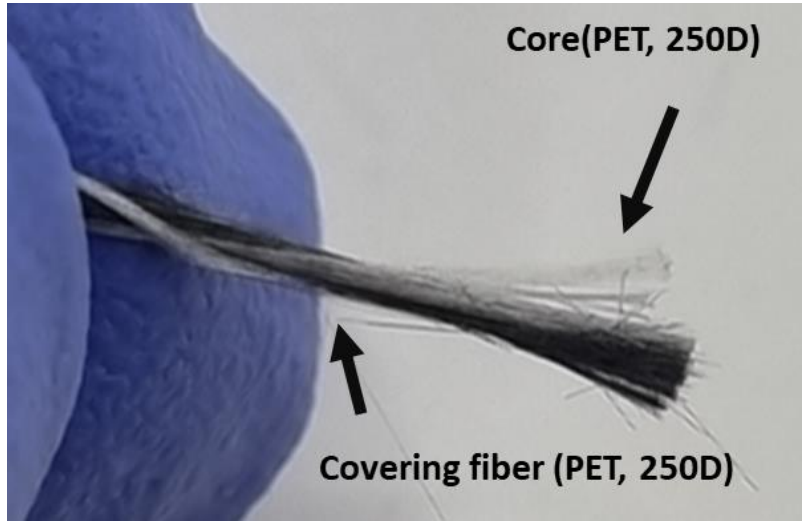

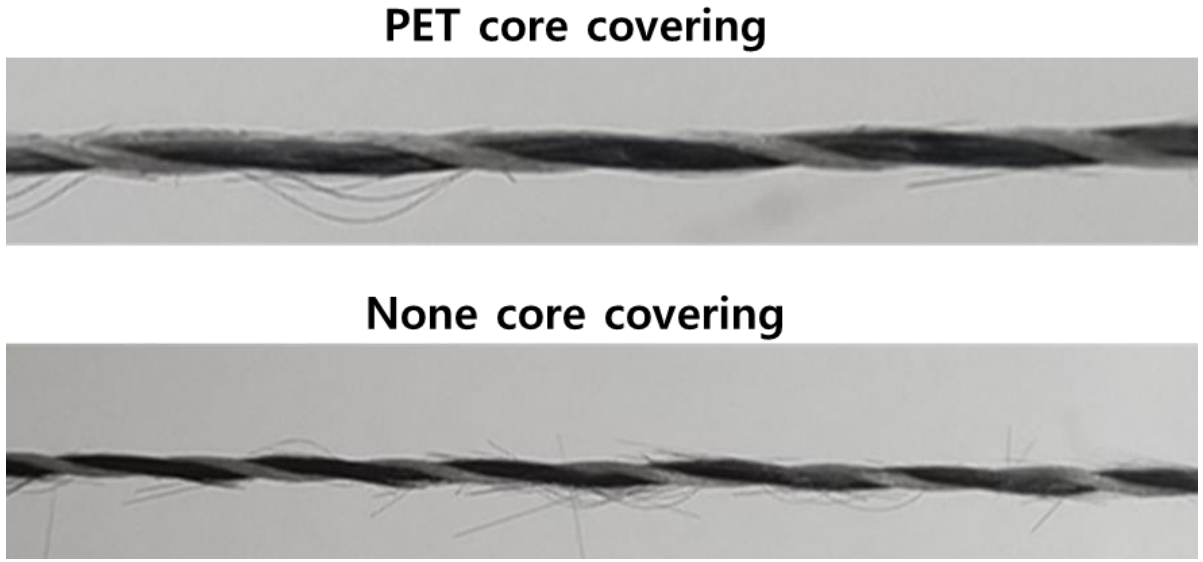

- Both covered samples were processed successfully with minimal damage
- Friction during the process caused slight fly debris
- The sample without a core showed more damage due to increased frictional impact

Tensile test results – SA3

Pure Tyranno SA3

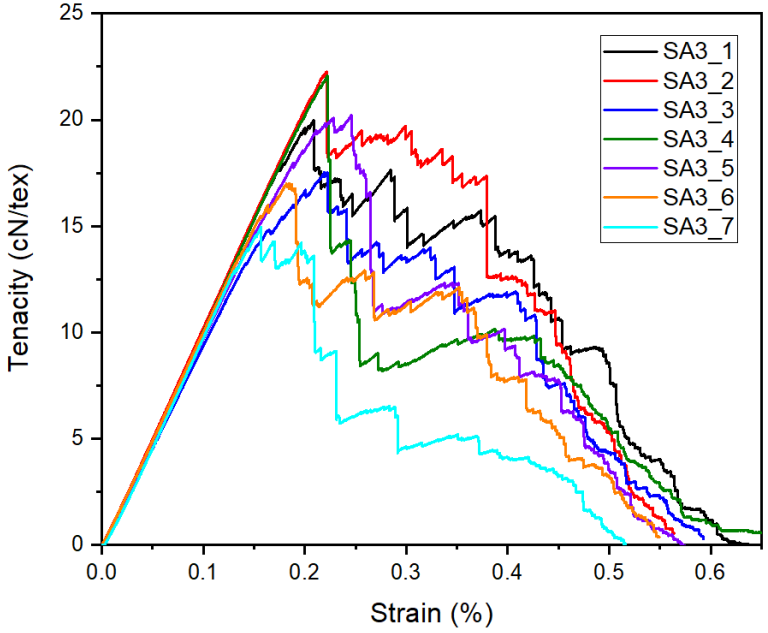

PET core and PET covering

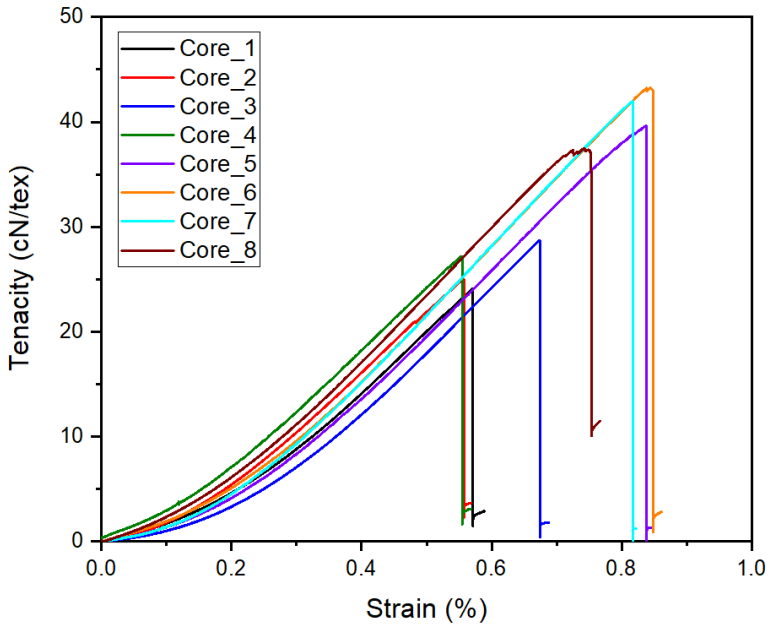

Noncore and PET covering

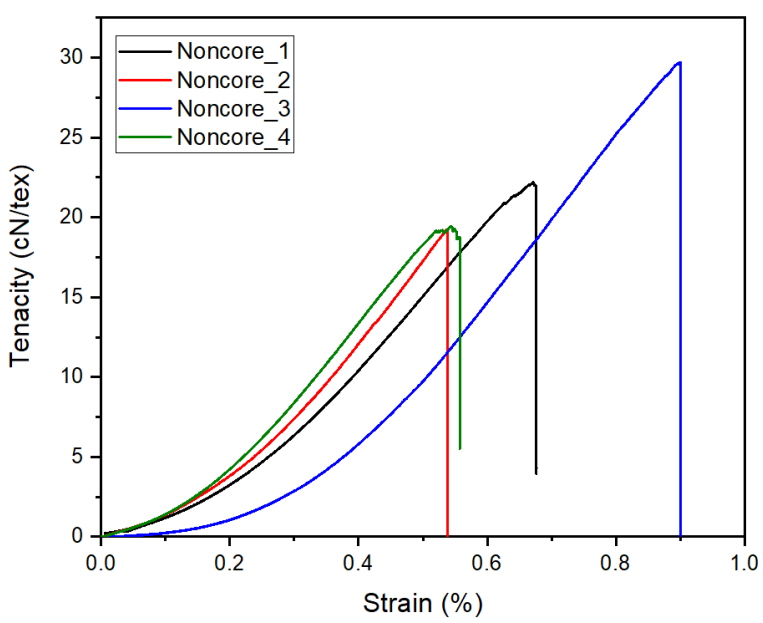

- After covering, both tensile strength and strain significantly increased
- Failure morphology changed from irregular stress reduction to sudden failure

Mechanism of property enhancement through covering

Slip failure of SiC ceramic tow

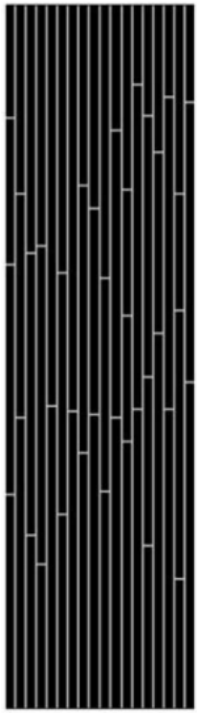

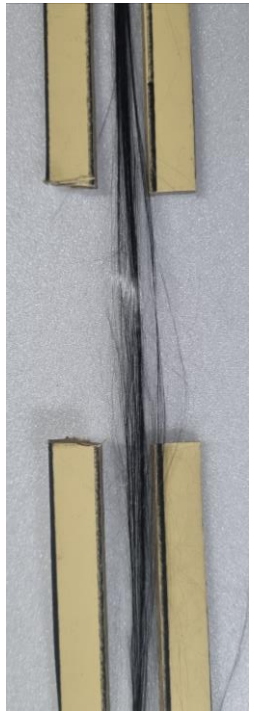

Composites Part A 146 (2021) 106426)

Transverse compressive stress due to covering and simultaneously failure after covering

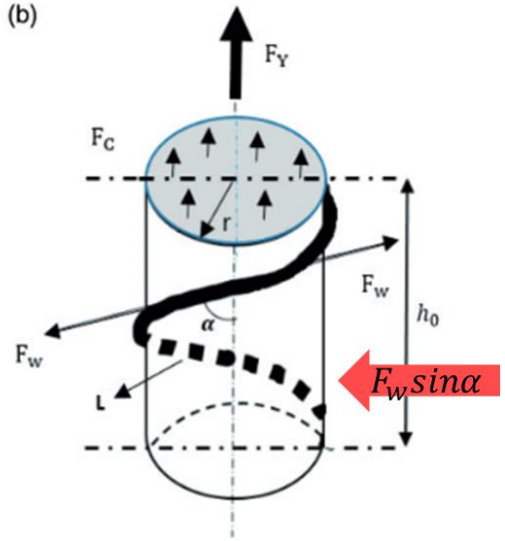

Journal of Industrial Textiles 47(8)



- In the uncovered tow, the fibers are held together only by weak physical bonds, so slip dominates the failure behavior
- Once a covering is applied, however, transverse compressive stresses promote efficient stress transfer between fibers, making fiber fracture the primary failure mode

Tensile test results – SA4

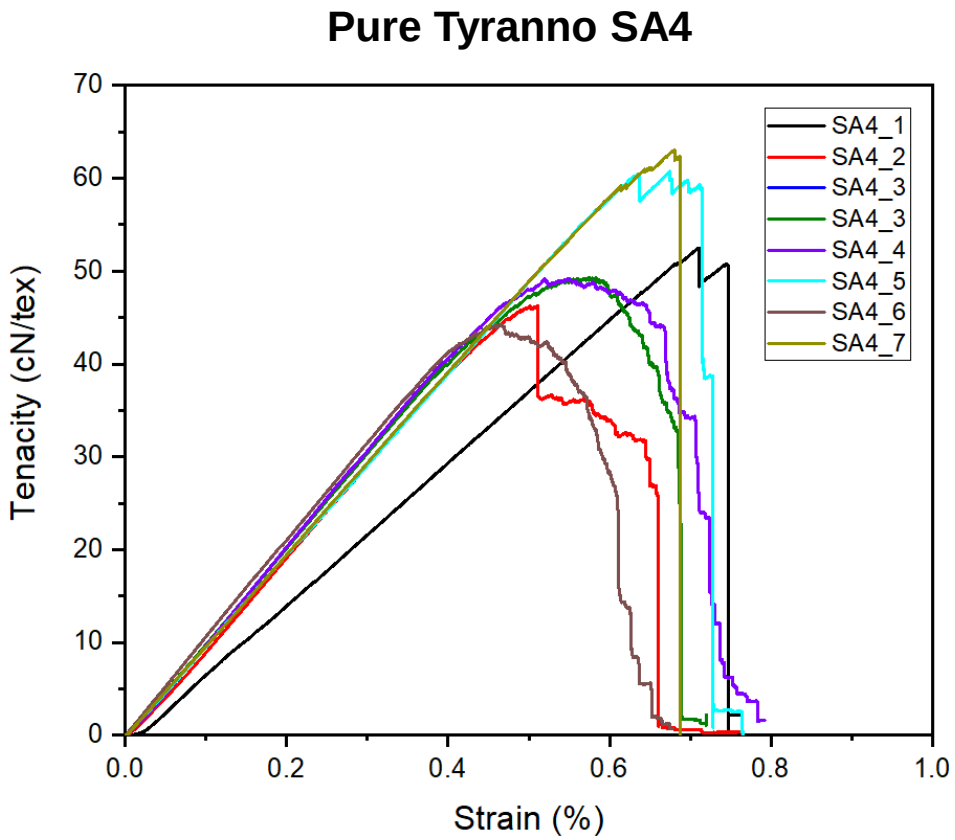

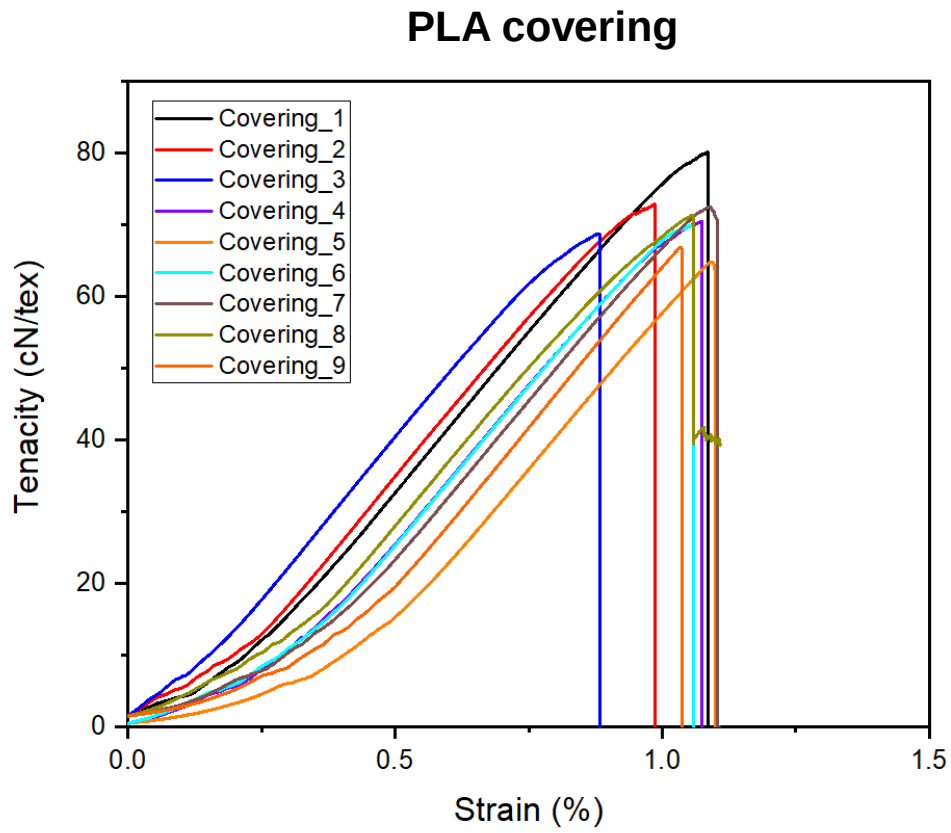

- SA4 exhibits more **uniform fiber properties** and superior sizing compared to SA3, resulting in significantly **less tow slip**
- Nevertheless, when **covered**, it demonstrates a **strengthening effect**, with both stress and strain increasing by approximately 25%

Increase in bending resistance

Tyranno SA3 and PET covering

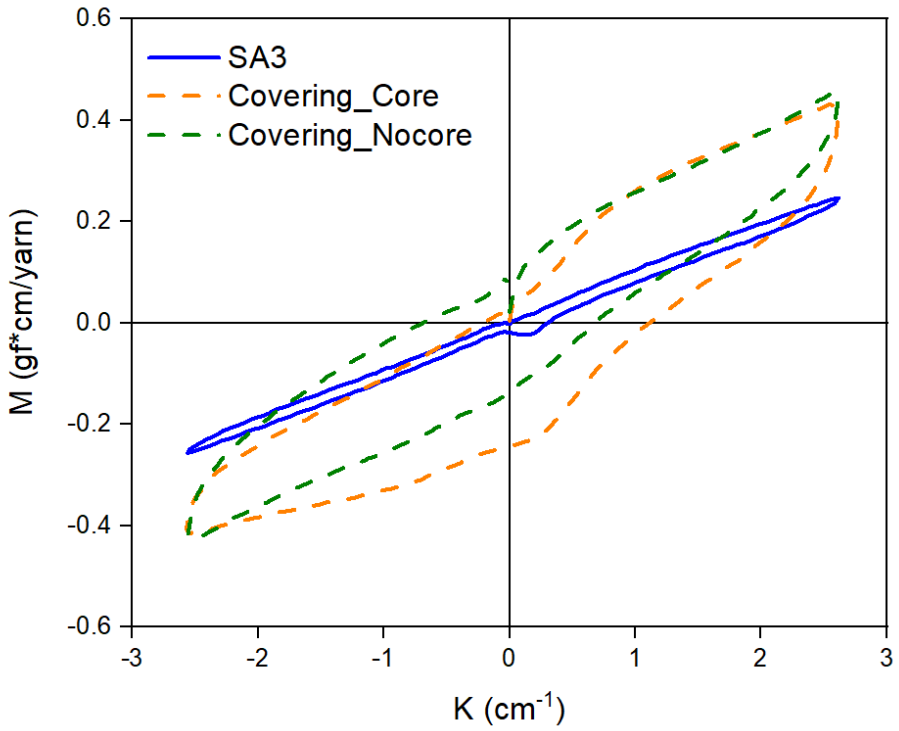

Tyranno SA4 and PLA covering

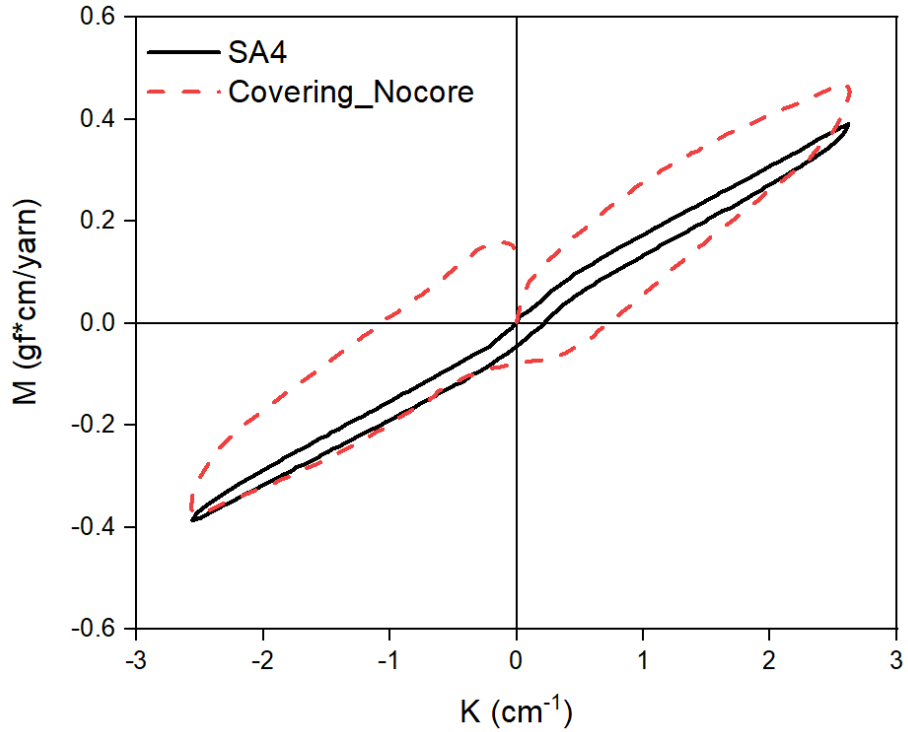

- Following covering, the added thickness of the covering yarn enhances bending resistance
- And the inclusion of low-elasticity polymer fibers leads to greater energy dissipation, thereby increasing hysteresis

Increase in maximum curvature

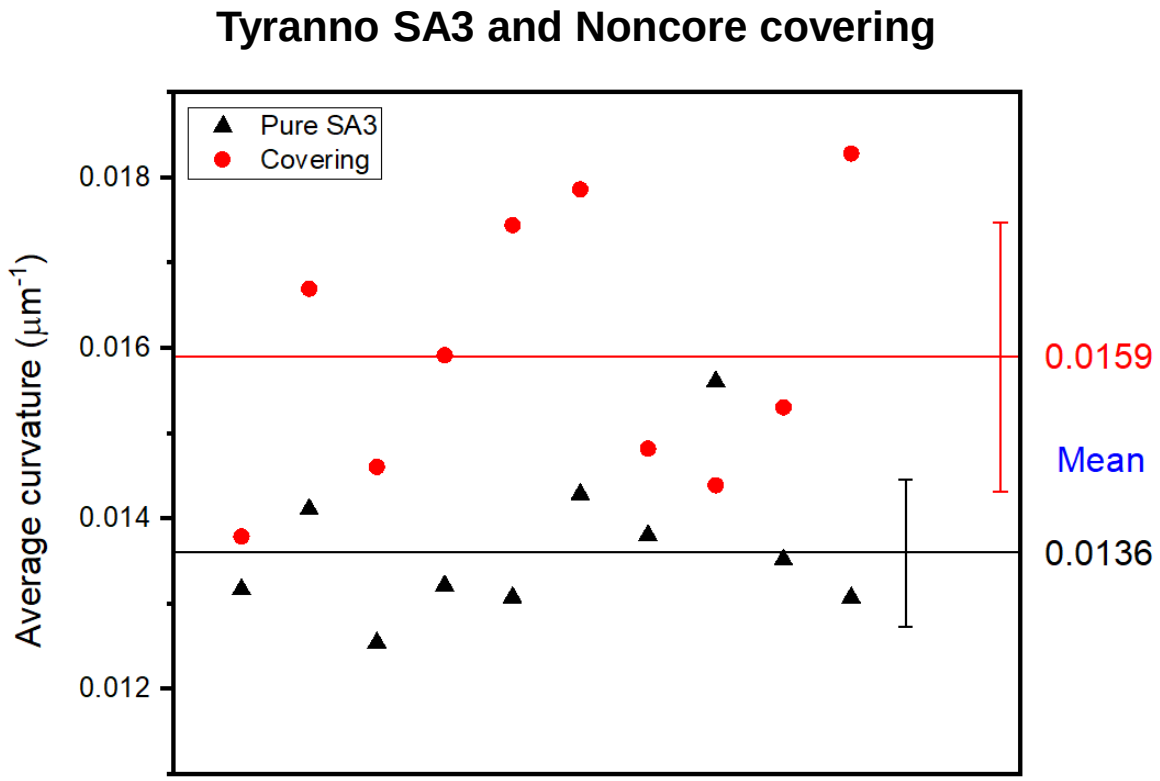

- By facilitating the redistribution of stresses that occur during bending and thereby delaying failure, the maximum curvature increases
- A high maximum curvature enables the fabrication of complex structures in 3D weaving

Enhanced weavability resulting from covering

Tyranno SA3 woven

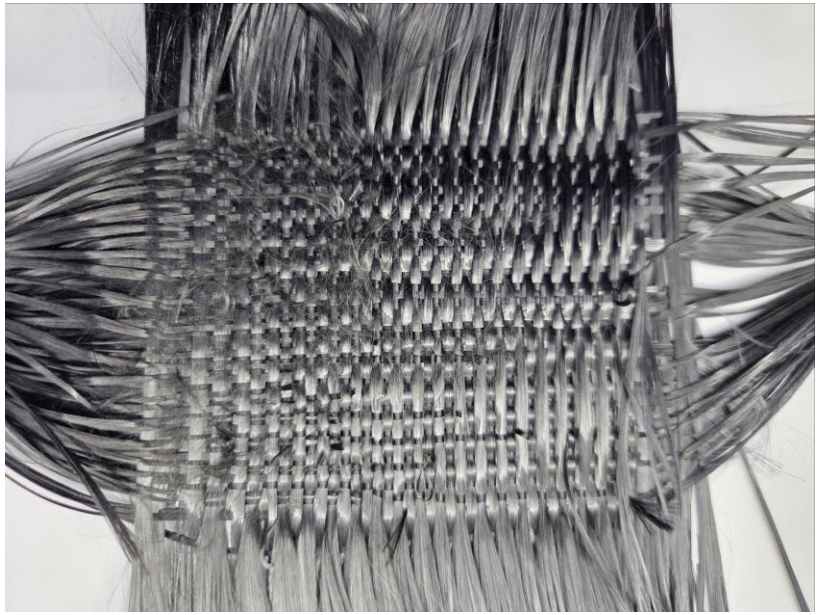

SA3	Held 1 Z-binder	Held 2 Fixed warp	Held 3 Fixed warp	Held 4 Z-binder	Held 5 Fixed warp	Held 6 Fixed warp	Held 7 Fixed warp	Held 8 Z-binder
Remaining tows	5/15	0/15	12/15	0/15	14/15	11/15	13/15	9/15

Tyranno SA3 and covering woven

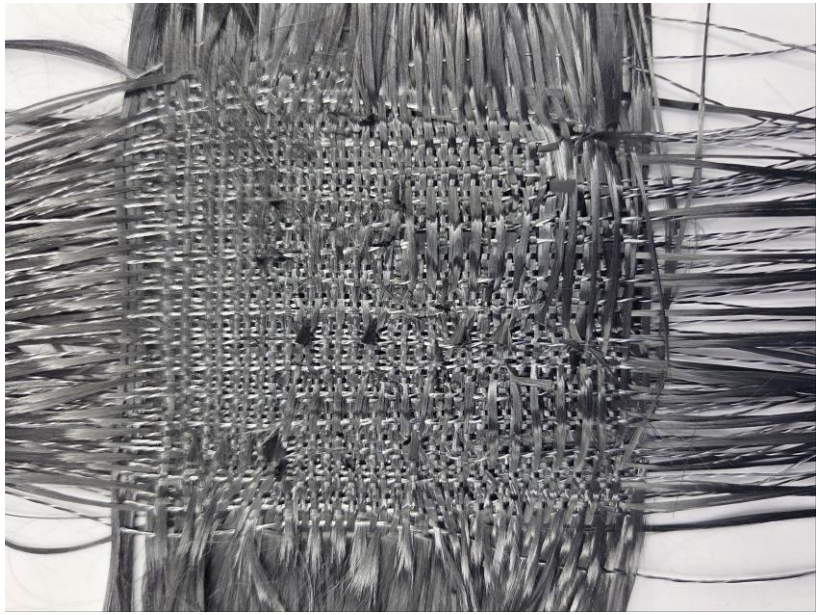

PET cover	Held 1 Fixed warp	Held 2 Z-binder	Held 3 Fixed warp	Held 4 Z-binder	Held 5 Fixed warp	Held 6 Z-binder	Held 7 Fixed warp	Held 8 Z-binder
Remaining tows	15/15	9/15	15/15	0/15	15/15	9/15	15/15	3/15

- Pure SA3 suffered significant friction-induced damage over roughly 10 cm of weaving, whereas the covering tow used as the fixed warp incurred zero losses

Index

I. Introduction

II. Research object and strategy

III. Methodology

IV. Conclusions

Conclusions

I. As aerospace activities intensify, research into SiC 3D-woven ceramic composites capable of fabricating complex structures is essential

II. However, because SiC fibers are inherently brittle and have poor weavability, fiber reinforcement processes are required

III. Applying a polymer-fiber covering to the SiC tow resulted in increases in various tow-scale properties

IV. Friction-induced damage and failure during the weaving process were greatly reduced, and composite-scale property changes will be measured subsequently

Thank you

Contact

woongryu@snu.ac.kr *

ryan0728kr@snu.ac.kr

This work was supported by Nano Material Technology Development Program through the National Research Foundation of Korea(NRF) funded by Ministry of Science and ICT(RS-2024-00455314)

ICCM24
AUGUST 4-8, 2025
BALTIMORE CONVENTION CENTER
BALTIMORE, MARYLAND, USA

No Technical Paper Submission for:

Mosiur Rahaman

Biobased composite fibers and films with keratin from chicken feathers as matrix and calcium carbonate as nanoreinforcement materials

Yuanyi Shao, Bingnan Mu, Lan Xu, and Yiqi Yang*

Department of Textiles, Merchandising, and Fashion Design

Department of Agronomy and Horticulture

Department of Biological Systems Engineering

University of Nebraska-Lincoln



Acknowledgements

- USDA National Institute of Food and Agriculture (A1531)
- Nebraska Environmental Trust
- Agricultural Research Division at the University of Nebraska-Lincoln

Problems with petro-based fibers and composites

- Sustainability
- Environmental and health problems
  - Particles found in rainfall and in snow
  - Accumulated in human body
- Alternatives
  - Sustainable
  - Responsible
  - Profitable

Keratinous wastes

- Safe and abundant
  - At least 5 millions tons of chicken feather/year globally
    - 2.5 times higher than the current annual production of both wool and silk
  - Protein content: > 90%
- Good property
  - High degrees of crosslinkages
    - Good tensile property
    - Good water stability

Preparation of keratin fiber and keratin films



Feathers

Extraction



Keratin extracts

Dissolution

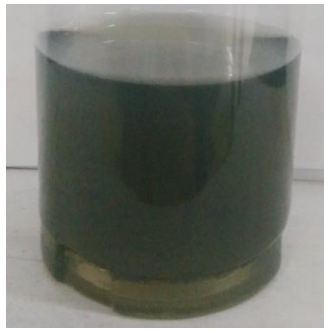

Keratin aqueous solutions



Keratin film

Wet-spinning





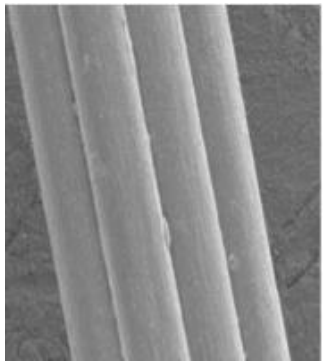

Wet spun keratin fibers

Green Chemistry. **22**(5), 1726-1734 (2020).

Morphological structure of films and fibers

- Keratin films
  - Thickness: around 0.12 mm
- Fine fibers produced
  - 15-20 μm in diameter
- Good recovery of crystallinity
  - Fine alignment of molecules
- High concentration of beta-sheet
  - High drawing ratio

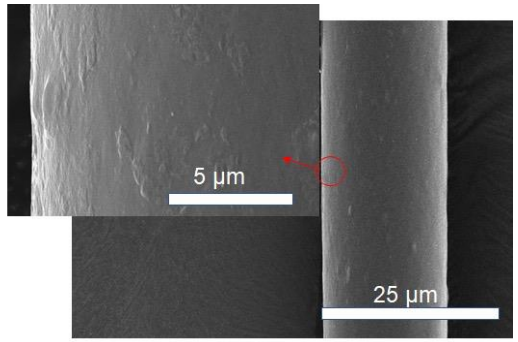

Materials	Degree of crystallinity		
	Total crystallinity	**Portion of α-helix**	**Portion of β-sheet**
Chicken feather	31%	11%	20%
Regenerated fibers	24%	5%	19%

Green Chemistry. **22**(5), 1726-1734 (2020).

Problems of keratinous materials and solutions

- Problems
  - Poor mechanical properties and wet stability
- Solution
  - Reinforcement
- Concerns
  - Compatibility between matrix and reinforcement
  - Decreased strain
- Approach
  - $CaCO_3$ nanoparticles with excellent compatibility via coordination
  - No plasticizers, therefore, good wet stability

Interactions between $CaCO_3$ nanoparticles and keratin matrix

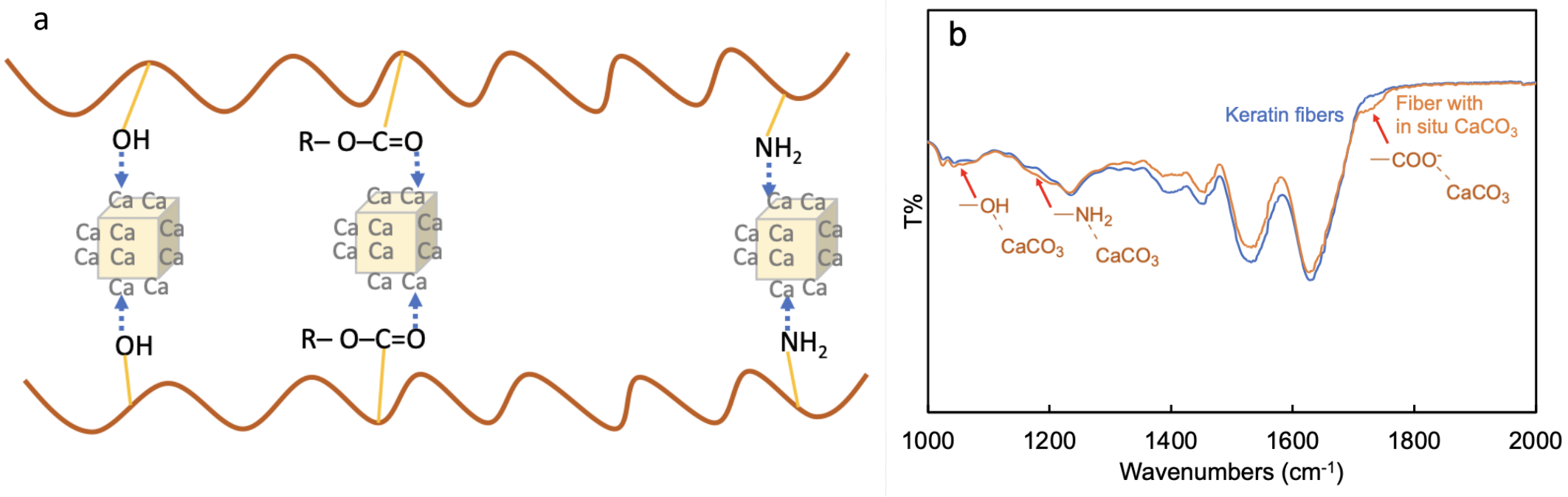

Mechnical properties and SEM of $CaCO_3$/keratin composites

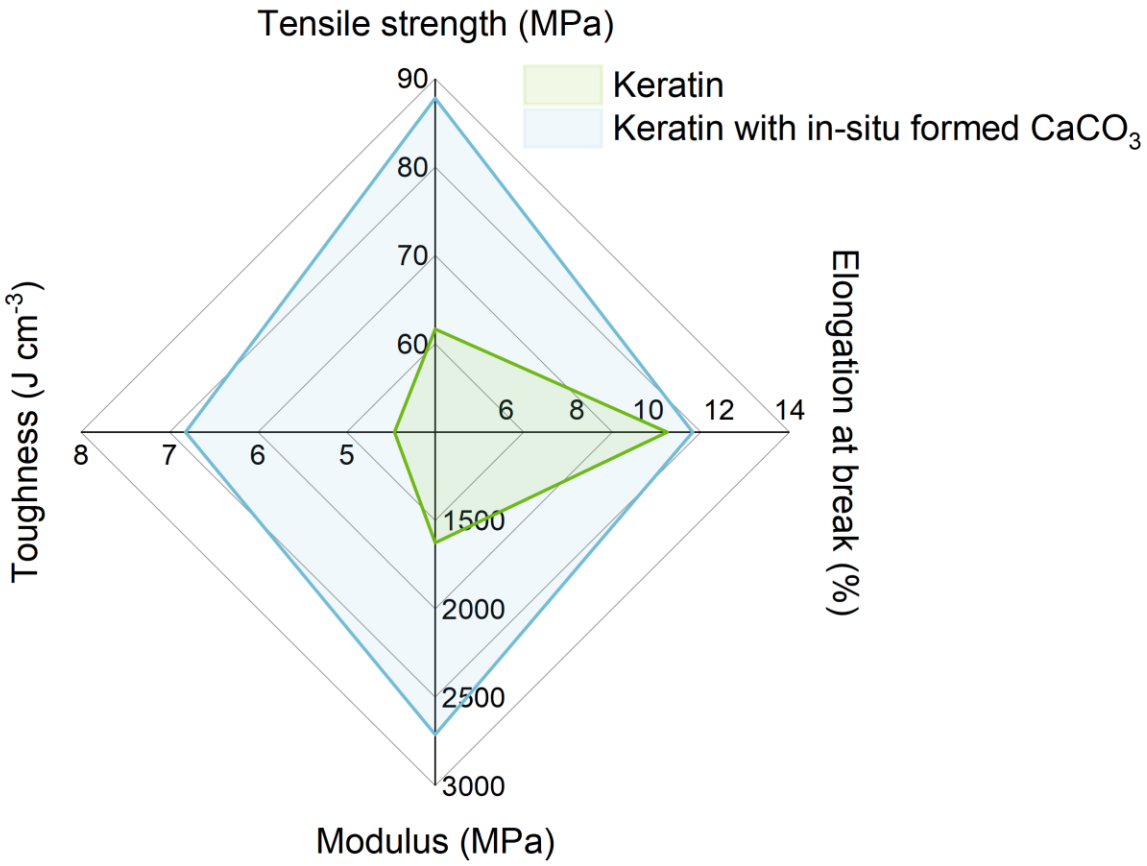

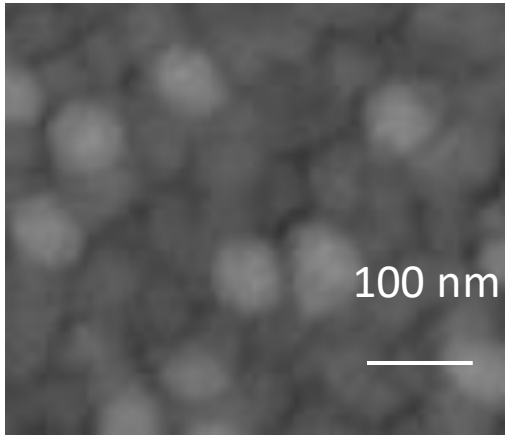

Property improvements for keratin/$CaCO_3$ films

Keratin resources	Reinforcement	Tensile Strength (MPa)	Breaking Elongation	Ref
Wool	Chitosan	34±10	7±2%	a
Duck feather	cysteine particles	47-68 6 (wet)	4-5% 30% (wet)	b
Chicken feather	chitin nanoparticles	20–35	20–40%	c
Chicken feather	Nanoclay	~4.1	16.5%	d
Chicken feather	**$CaCO_3$ nanoparticle**	**66-87** **3.6-6.1(wet)**	**10-11%** **82-99% (wet)**	**This work**

a. Biomaterials 23(3) (2002) 817-825.
b. Colloids and Surfaces B: Biointerfaces 177 (2019) 33-40.
c. Composites Science and Technology 200 (2020) 108462.
d. Food Hydrocolloids 31(2) (2013) 340-345.

Property improvements for keratin/$CaCO_3$ fibers

	Dry properties		Wet properties		ref
Fiber source	Tensile strength/MPa	Elongation at break/%	Tensile strength/MPa	Elongation at break/%	
Chicken feathers	140-180	6-12	100-140	15-21	1
Wool	120-174	25-35	120-160	42-50	2
Keratin fibers	138±30.5	11±2.8	50-90	25-35	3
Keratin fibers crosslinked with sugar-aldehydes	205±10.5	19±4	120-140	27-35	4
Keratin fibers reinforced with chitin NP	240-260	17-22	150-170	33-38	5
Keratin fibers reinforced with $CaCO_3$ NP	208±13	15±2	132±9	60±9	This work

1. J. Polym. Environ., 15 (2) (2007), pp. 81-87
2. Heidelberg (2015)
3. Green Chem., 22 (5) (2020), pp. 1726-1734
4. Sustain. Mater. Technol., 31 (2022), p. e00367
5. Chem. Eng. J., 482(2024), 148850

Summary

- Keratinous fibers and films successfully reinforced by $CaCO_3$ nanoparticles
- Improved tensile strength, elongation and wet stability without plasticizers
- Better than other protein materials
- Potential for textile, agricultural and packaging applications

Protein based biocomposites from cottonseed meals reinforced with chitin nanoparticles

Yuanyi Shao, Lan Xu, and Yiqi Yang

Department of Textiles, Merchandising, and Fashion Design

Department of Agronomy and Horticulture

Department of Biological Systems Engineering

University of Nebraska-Lincoln



Acknowledgements

- Cotton Inc. (Project number 23-886)

Demand for bio-based materials

- Petro-based materials
  - Non-renewable
  - Environmental persistence
- Natural biodegradable polymers
  - Natural polysaccharides
  - Natural proteins

Cottonseed Protein as matrix

- Cost-effective
  - price 20%-50% lower than soybean meals
- Protein-rich
  - Containing 40% proteins
- Containing gossypol
  - Not suitable to serve as food or feed
  - Natural antimicrobial agent
- Suitable protein structure for spinning
  - High molecular weight
  - High degree of disulfide crosslinkages
- Value Addition to cotton industry
  - Producing 1 kg of cottonseed protein fibers could add $6 values

Previous efforts and challenges

Extraction and dissolution process

- Damage to protein backbones

  High alkalinity

- Failure to break all intra- and inter-molecular interactions

  Disulfide bonds, hydrophobic interactions

Film development

- Insufficient extension of protein molecules
- Poor recovery of disulfide cross-linkages

Low extratcion yield (24-67%)

Low mechanical properties: brittleness, poor wet stability

Reinforcement

- Problems
  - Poor interfacial bonding
  - Brittleness
- Partially deacetylated chitin nanoparticles
  - Free amine groups
  - Interaction

Cost-effective extraction of cottonseed proteins

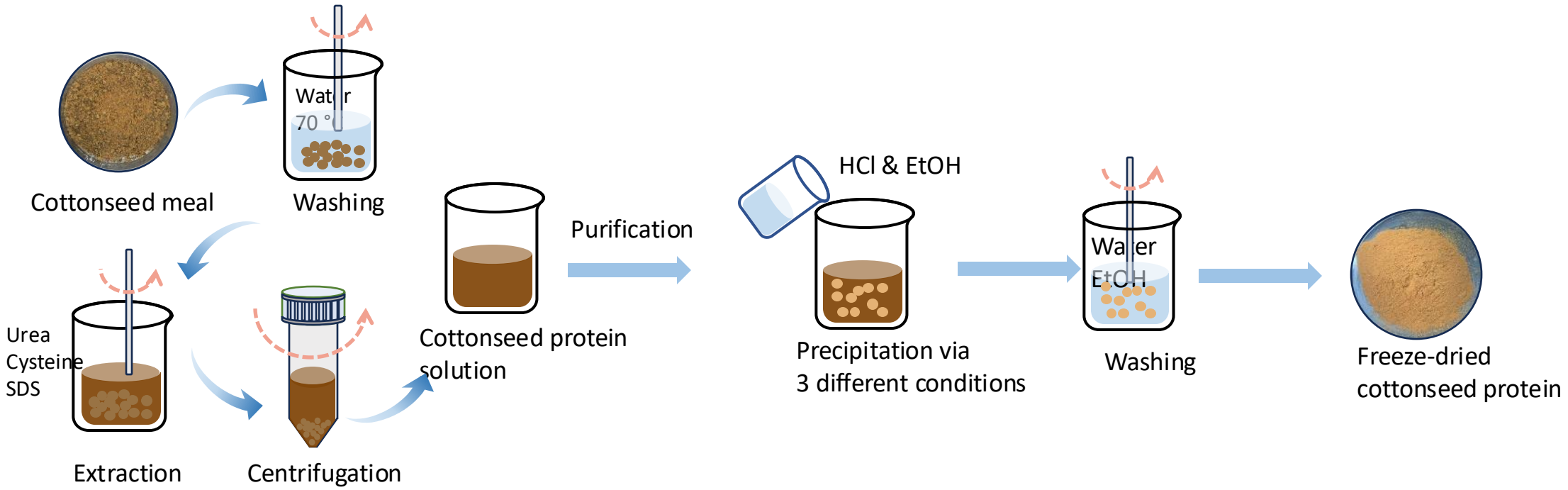

International Journal of Biological Macromolecules, *282*, 137251.

Partially deacetylated chitin nanoparticles





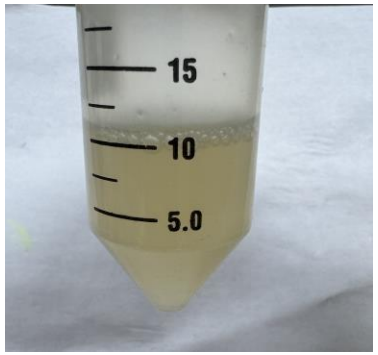

Characterization of chitin nanoparticles

Degrees of deacetylation

$$DD\ (\%) = \left(1 - \frac{\frac{I_{Ac}}{3}}{\frac{I_{H2-6}}{6}}\right) * 100$$

Where I_{Ac} is the integral intensity of acetyl group and I_{H2-6} is the summation integral intensities of H2, H3,H1,H5,H6.



Mechanical properties of biocomposites

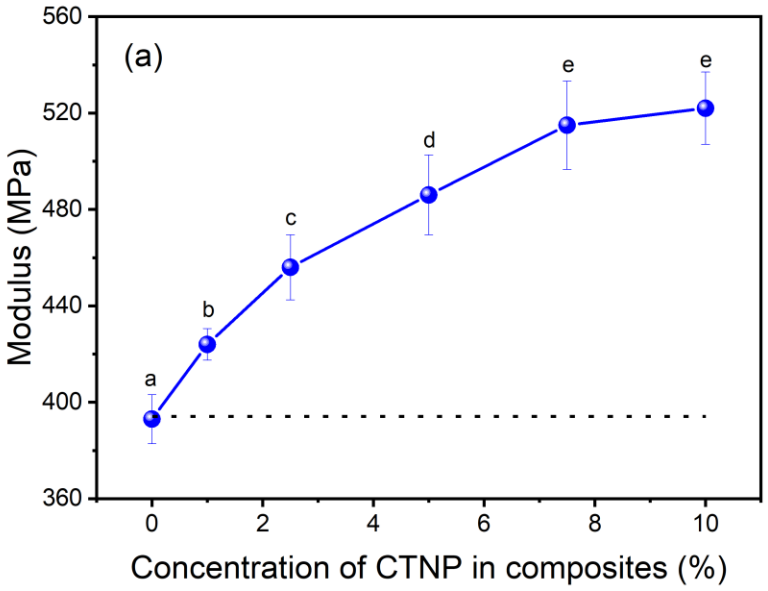

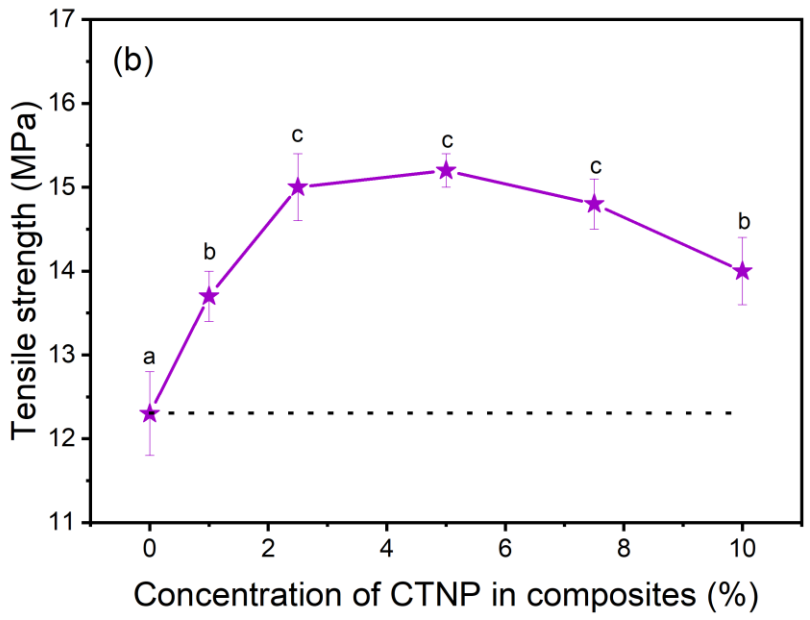

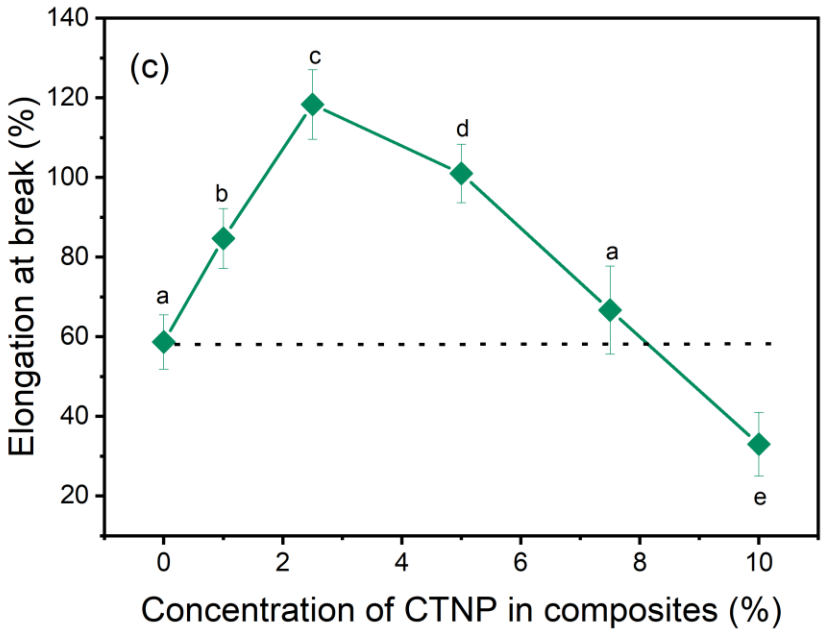

Summary

- Ductile and wet-durable protein biocomposites from cottonseed meals reinforced by chitin-nanoparticles with controlled deacetylation have been developed.
- The resulting biocomposites demonstrated exceptional mechanical properties and moisture stability.
- A sustainable and high-performance solution for applications requiring ductility, toughness, and moisture resistance.

ICCM24
AUGUST 4-8, 2025
BALTIMORE CONVENTION CENTER
BALTIMORE, MARYLAND, USA

No Technical Paper Submission for:

Heather LaFrance

ICCM24 24TH INTERNATIONAL CONFERENCE ON COMPOSITE MATERIALS
AUG 4-8, 2025 • BALTIMORE CONVENTION CENTER • BALTIMORE, MARYLAND

RHEOLOGY AS A RAPID METHOD FOR SIMPLE AND PRECISE DETERMINATION OF THE PERCOLATION THRESHOLD IN SHORT-FIBER POLYMERIC BIOCOMPOSITES: INSIGHTS INTO SUSTAINABLE MATERIAL DESIGN

Giovanni Filippone[1], Lucia Gioiella[1] and Libera Vitiello[1]

[1]Dipartimento di Ingegneria Chimica, dei Materiali e della Produzione Industriale, Università di Napoli Federico II
Piazzale Tecchio 80, 80125 Napoli, Italy
Email: gfilippo@unina.it

[1]Dipartimento di Ingegneria Chimica, dei Materiali e della Produzione Industriale, Università di Napoli Federico II
Piazzale Tecchio 80, 80125 Napoli, Italy
Email: lucia.gioiella@unina.it

[1]Dipartimento di Ingegneria Chimica, dei Materiali e della Produzione Industriale, Università di Napoli Federico II
Piazzale Tecchio 80, 80125 Napoli, Italy
Email: libera.vitiello@unina.it

Keywords: Polymer-matrix composites; Thermoplastic resins; Discontinuous reinforcement; Rheological properties; Environmental degradation

ABSTRACT

The determination of the percolation threshold (Φ_c) in particulate and short-fiber composites is essential for understanding mechanical behavior, transport properties, and degradation, especially in biocomposites with hydrolysable matrices. In such systems, percolating fiber networks promote water and degradation agent penetration, potentially accelerating biodegradation. Conventional methods to determine Φ_c (e.g. theoretical models or conductivity-based techniques) are unsuitable for biocomposites containing non-conductive, variable natural fibers. Here we summarize the results of two studies in which (i) a simple rheological protocol is proposed to accurately determine Φ_c in poly(lactic acid) biocomposites reinforced with short hemp or kenaf fibers, and (ii) the relevance of Φ_c for biodegradation purposes is thoroughly examined for the hemp-based composites.

Regarding the first point, the proposed method for the assessment of Φ_c relies on the linear viscoelastic "two-phase model" originally developed for nanocomposites but general enough to be extended to microcomposites despite the non-Brownian nature of microfibers. Rheological estimates of Φ_c were compared with values obtained via dielectric spectroscopy, which is a more complex and time-consuming method requiring water equilibration of the samples over several weeks. Regarding the second point, changes in molecular weight under two environmental conditions (water and mature compost) were studied in hemp-based composites below and above Φ_c. The results highlighted non-linear behavior in relation to filler content and showed contrasting degradation patterns between aqueous and soil-like media due to the effect of the crystallinity forming during degradation.

Overall, besides providing valuable guidance for the development of environmentally sustainable PLA-based materials with improved end-of-life performance, this study demonstrates that rheological analysis is a fast, accurate, and effective method to determine Φ_c, even in highly inhomogeneous and anisotropic materials like natural fiber biocomposites. Compared to other experimental techniques (e.g. dielectric spectroscopy), rheology offers shorter testing times and easier sample preparation, making it a promising standard method for characterizing percolation behavior in sustainable, fiber-reinforced biocomposites.

1 INTRODUCTION

Biodegradable polymer composites reinforced with natural fibers have attracted growing interest due to their eco-friendly nature and potential to replace conventional plastics. Among them, polylactic acid (PLA) is a widely used bio-based polyester derived from renewable sources such as corn starch or sugarcane. However, PLA biodegradation in natural environments can be unacceptably slow. This process involves abiotic hydrolysis of ester bonds followed by microbial assimilation of the resulting low-molecular-weight fragments. Since only chains with a molecular weight below 10–20 kDa can be mineralized by microorganisms, the rate-limiting step is the initial hydrolytic cleavage.

One strategy to accelerate PLA degradation is incorporating lignocellulosic fillers, which promote water diffusion through their hygroscopic hemicellulose content. Their swelling in moist environments can also induce matrix-filler debonding, creating capillaries that enhance water ingress. However, the overall impact of natural fibers on PLA degradation is complex and influenced by filler properties such as chemical composition, geometry, and content. In particular, the fiber volume fraction plays a crucial role, especially when it exceeds the percolation threshold (Φ_c). The latter is the critical point at which fibers form a continuous network that facilitates the transport of water and pro-degradative agents into the composite's core.

Beyond biodegradation, the identification of Φ_c is fundamental due to the abrupt changes it causes in key material properties, such as mechanical strength, rheological behavior, and diffusivity. Nevertheless, accurately determining Φ_c in green composites is challenging. Theoretical models often rely on unrealistic assumptions, while many experimental techniques are unsuitable due to the non-conductive and variable nature of natural fibers.

In this context, we present the results of two studies [1, 2] carried out on PLA-based composites filled with short fibers from hemp and kenaf, focusing on how fiber content and morphology affect degradation and percolation behavior. Two complementary experimental techniques—dielectric spectroscopy and rheological analysis—were used to identify Φ_c. While dielectric spectroscopy requires lengthy water equilibration, rheology offers a faster, simpler, and equally accurate alternative. By applying a linear viscoelastic two-phase model originally developed for nanocomposites, we isolated the fiber contribution and precisely determined Φ_c, which was around 10% for hemp and 20% for kenaf. Moreover, degradation kinetics in water and compost environments were monitored for the hemp-based composites to highlight the relevance of Φ_c for biodegradation purposes. Our results indicate that filler content has non-monotonic effects, with significant differences between conditions. These findings underline the importance of understanding the interplay between percolation, crystallinity, and filler structure to design more sustainable PLA-based materials with controlled end-of-life behavior.

2 EXPERIMENTAL

2.1. Materials

PLA pellets (Luminy® LX175, density: 1.24 g cm^{-3}, MFI: 6 g/10 min at 210 °C/2.16 kg) were obtained from Corbion. Hemp shives and kenaf bast fibers were sourced from Equilibrium S.r.l. (Nibionno, Italy) and Kenaf Eco Fibers Italia (Guastalla, Italy), respectively. Prior to compounding, fibers were ground using a Retsch cutting mill with a 0.25 mm sieve. Images of the fibers before and after milling (Fig. 1) show a mix of micrometer-scale fibers and finer debris, likely generated during grinding. The ground fibers used in our composites can be assimilated to short, capped cylinders. The hemp fibers are slightly shorter than the kenaf ones (volume average length: 376±181 μm for hemp, 461±213 μm for kenaf) [1]. The distribution of the aspect ratio (length-to-diameter ratio) of the fibers after milling is also shown in Fig. 1.

2.2. Melt Compounding and Sample Preparation

PLA and fibers were compounded using a Brabender Pantograph EC batch mixer. Samples were prepared at fiber volume fractions (Φ) of 5, 10, 15, 20, 25, 30, and 35%. Prior to mixing, PLA pellets were vacuum-dried at 85 °C overnight, and fibers were conditioned at 25°C and 80% relative humidity. Compounding was carried out at 180 °C and 60 rpm for 6 min. The mixture was then dried again at 85°C under vacuum and compression molded into 100×100×3 mm^3 plates using a Lab Tech Engineering hydraulic press. Molding involved a preheating phase at 180°C without pressure (5 min), compression at ~150 bar (4 min), and cooling under pressure to room temperature. The molded plates were then cut

into 30×30×3 mm^3 specimens for rheological tests. Regarding the samples for the degradation tests in water and soil, the material, sandwiched between two Teflon sheets, was placed in the mold preheated at 180°C and softened for 5 minutes without pressure. Then the pressure was increased to ~15 MPa and kept constant for 4 min. Finally, the mold was cooled to ~40°C under constant pressure. The resulting plates were cut into rectangular specimens (30×10×3 mm^3) using a circular saw.

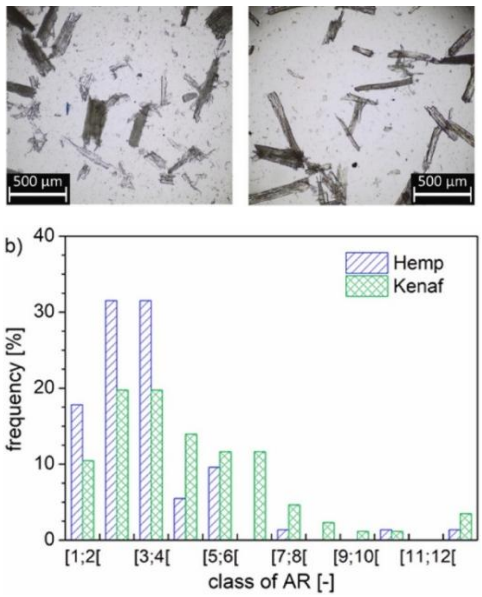

Figure 1: Upper row: hemp (a–c) and kenaf (a′–c′) fibers before (a, a′) and after (b, b′, c, c′) grinding. Lower row: distribution of the aspect ratio (AR; length-to-diameter ratio) of the fibers. Images taken from [1].

2.3. Characterization Techniques

Fiber size and aspect ratio were determined via image analysis from optical micrographs obtained with an Olympus BX53M microscope. Approximately 100 particles were analyzed per fiber type. For improved visualization, fibers were suspended in diluted poly(vinyl alcohol) (PVA) solution before deposition on glass slides.

Sample microstructure was examined using scanning electron microscopy (SEM, Leica 420, Wetzlar, Germany). Samples were cryo-fractured at ca. -80°C and gold-coated before imaging.

Rheological measurements were conducted on a TA Instruments AR-G2 rheometer with parallel plate geometry (25 mm diameter). Specimens were dried at 80 °C under vacuum before testing. All tests were performed using a 2 mm plate gap, with samples taken from consistent positions on the plates to minimize orientation effects from compression molding. Small-amplitude oscillatory shear (SAOS) tests were conducted at 180 °C in nitrogen. The elastic (G′) and viscous (G″) moduli were collected in a frequency range between ω=0.06 and ω=600 rad/s. Strain amplitudes were set between 0.2% and 2%, ensuring linear viscoelastic behavior and reliable stress measurements.

For the degradation tests in water, the specimens were immersed in test tubes containing 50 mL of water (pH≈7.5) and kept at 45°C with gentle stirring in a shaking incubator (Bormarc Shaker SKI 4). Before subsequent characterization, the samples were collected at fixed time intervals and carefully dried until reaching a constant weight. The specimens for the degradation tests in soil were buried in mature green compost (water holding capacity 80%, moisture content 55%, pH=6.6) and kept in an incubator (Bormarc Shaker SKI 4) at 55°C and 20% RH. The samples were collected at fixed times and subjected to the following analyses.

Size exclusion chromatography (SEC) was performed with a Waters 590 chromatographic system equipped with HSPgel HR3 and HR4 columns and a refractive index detector. Tetrahydrofuran (THF) was used as the mobile phase at a flow rate of 0.3 mL/min. The weight-average molecular weight (Mw) and the polydispersity index (M_w/M_n) were determined based on a calibration curve generated with polystyrene standards ranging from 0.370 to 100 kg/mol.

3 RESULTS

3.1. Assessment of the percolation threshold – The two-phase model

Unlike nanoparticles, which undergo Brownian motion even in highly viscous polymer melts and tend to form fractal aggregates that percolate at very low filler loadings (Φ_c~1%), the fibers employed in this study are too big do exhibit Brownian behavior In similar cases, percolation theory can be applied to estimate Φ_c by using the concept of excluded volume, V_{ex}, defined as the region around a filler particle within which the center of another particle cannot enter [3]. However, theoretical calculations suffer from the wideness of the aspect ratio distribution, which reflects in wide ranges of possible Φ_c. Further uncertainty stems from the variability of the orientation of the fibers, which affects V_{ex}. As a result, the Φ_c for the hemp fibers was estimated to range between 5.2 vol.% (perpendicular orientation) and 20.8 vol.% (parallel orientation). The range of Φ_c for the kenaf fibers was 4.3-17.2 vol.% (parallel).

To assess the values of Φ_c with much higher accuracy, experimental methods must be used. Unfortunately, when dealing with very flexible and non-conductive natural fibers dispersed in viscoelastic polymer matrices, the experimental detection of Φ_c is anything but simple. Here we propose to resort to rheology, which is a well-established characterization technique in the field of polymeric materials. In particular, we exploit the prediction ability of a simple two-phase model that we derived to describe the linear viscoelasticity of polymer nanocomposites [4, 5, 6]. Since the two-phase model only works for samples at $\Phi>\Phi_c$, and being the $G'(\omega)$ curves of these samples scalable on a single master curve by means of only two shift factors with a precise physical meaning, the Φ_c can be easily computed. In brief, the vertical shift factors for the building of the master curve represent the precise values of the elasticity of the networks of nanoparticles, G'_0. The percolation theory predicts that the latter scale with the volume fraction as $G'_0 \sim (\Phi-\Phi_c)^\nu$, where ν is a critical exponent that depends on the stress bearing mechanism. Fitting this law to the experimental values of the vertical shift factors for the building of the master curve eventually returns the Φ_c of the system. This simple procedure is made robust because of the deterministic feature of the shift factors, which makes the scaling of a G' curve of a sample at $\Phi<\Phi_c$ not possible.

When trying to extend such an approach to natural fibers, many differences emerge (see Figure 2).

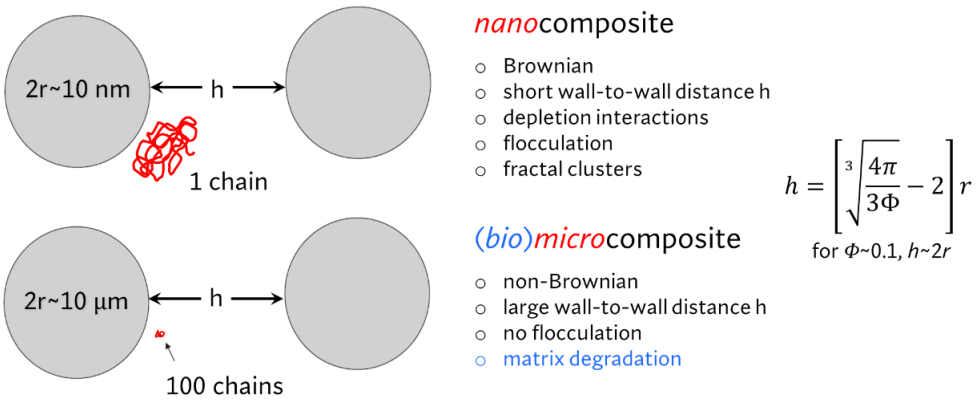

Figure 2: differences between nano- and microcomposites. The relationship between wall-to-wall interparticle distance h and particle volume fraction Φ is shown on the left-hand side.

The non-Brownian feature of micron-sized particles prevents them from moving and rearranging in the host medium due to thermal energy, eventually flocculating in the host matrix at very low particle volume fractions. Percolation at low Φ is also disfavored by the relatively long wall-to-wall distance (h) between contiguous particles. Nonetheless, the basic principle underlying the two-phase model, i.e. the coexistence of two well-distinct populations of dynamical species (the particle network and the host polymer matrix) remain valid. As a result, we expect that the previous procedure to compute Φ_c can be used also for the biocomposites under investigation.

The master curves built for the hemp- and kenaf-based composites are shown in Figure 3.a and b. The critical scaling of the network elasticity with $\Phi-\Phi_c$ is reported in Figure 3.c.

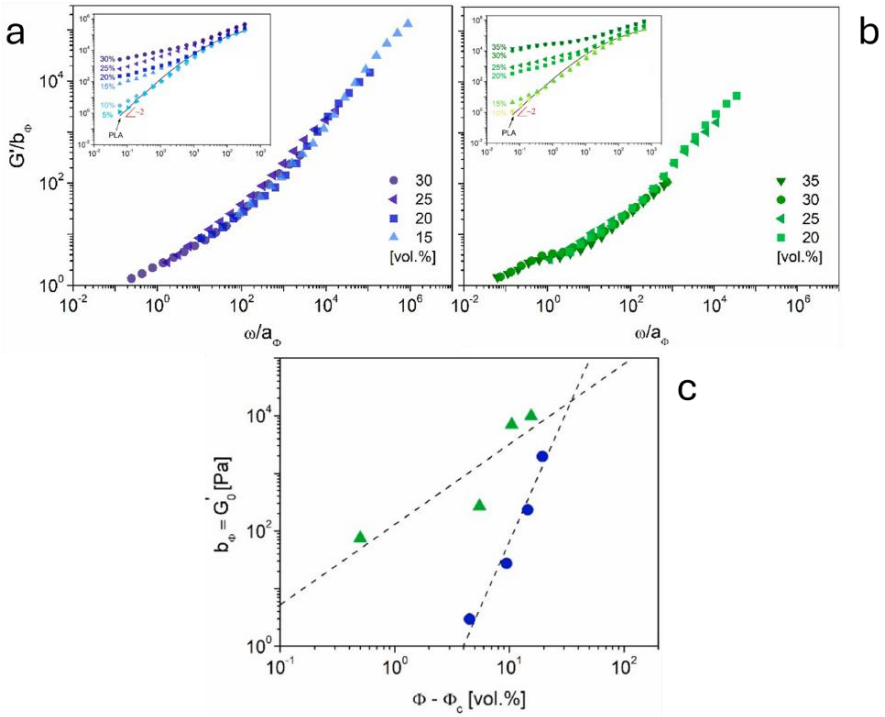

Figure 3: a and b) Master curves of G′ for hemp- (a) and kenaf-based composites (b) at Φ≥15 vol% and Φ≥20 vol%, respectively. The inserts show the G′ curves of samples at different Φ before the scaling. c) Critical scaling of the network elasticity for hemp- (circles) and kenaf-based (triangles) composites. The dashed lines are the best fitting curves. R^2=0.9780 (hemp) and 0.9311 (kenaf). Images readapted from [1].

The above procedure led to Φ_c=10.1 and 19.5 vol% for the hemp- and kenaf-based composite, respectively. These values were confirmed by means of broadband dielectric spectroscopy, which was carried out by using an ARES rheometer equipped with a dielectric analysis tool connected to an Agilent E4980A LCR meter. This method exploits the high sensitivity of the complex permittivity (ε*) to the water contained in the fibers, which makes it possible to correlate Φ_c to a discontinuity in the (di)electric response [7, 8, 9]. In this way we obtained Φ_c=10.1 and 18.5 vol% for the hemp- and kenaf-based composite, in excellent agreement with the linear viscoelasticity results. It is worth mentioning that a much more laborious and time-consuming procedure was needed in the case of dielectric tests because of the need of a very long (ca. 1 month) conditioning step before the measurements [1].

3.2. Effect of the percolation threshold of the degradation kinetics of PLA-hemp biocomposites

Once the percolation threshold has been estimated with accuracy, its role in dictating the degradation kinetics of hydrolysable matrices was investigated. The results of degradation tests in freshwater and mature compost are summarized in Table 1, where the evolution of M_w and M_n assessed by SEC is reported as a function of time for samples at different Φ.

After 50 days of immersion in freshwater, a clear inverse relationship emerges between fiber content and molecular weight: as the fiber loading increases, M_w decreases. This means that the formulation with the highest fiber fraction shows the most pronounced reduction in molecular weight (over 40%). Interestingly, even though the fiber network becomes more interconnected beyond the percolation threshold (Φ_c=10.1%), no abrupt changes in the degradation trend are observed.

The PLA exhibits a significantly faster degradation rate in soil, which is expected due to the elevated temperature and microbial activity typical of composting conditions. Regarding the influence of fibers, an acceleration in the degradation kinetics is observed after 10 days. An effect of the percolation threshold is noticed, even if a substantial acceleration is only observed from Φ=15vol%, that is well above Φ_c. What is more interesting is that the trend reverses at longer burial times, when the fibers surprisingly appear to inhibit degradation.

	Φ [vol.%]	0	5	10	15	20	25	30
as prepared samples (reference)	M_w [kDa]	113.9		110.3		100.8		113.6
	M_w/M_n	1.6		1.4		1.6		1.5
after 50 days in freshwater	M_w [kDa]	85.8	84.8	80.6	79.5	79.1	76.5	69.4
	M_w/M_n	1.6	1.6	1.6	1.6	1.6	1.6	1.6
after 10 days in soil	M_w [kDa]	83.2	89.4	84.3	78.7	73.1	67.4	65.6
	M_w/M_n	1.7	1.7	1.7	1.7	1.7	1.8	1.8
after 20 days in soil	M_w [kDa]	24.8	41	53.6	56.3	71.8	63.4	70.3
	M_w/M_n	1.8	1.8	1.7	1.7	1.5	1.7	1.6

Table 1: Average molecular weight and polydispersity indices of PLA composites in different environments.

The reduction in molecular weight is known to be autocatalytic, with the degradation process accelerating once the molecular weight drops below a critical threshold (M_c), beyond which oligomeric chains begin to solubilize into the surrounding medium [10]. According to Stloukal *et al.*, this threshold is approximately 20 kDa for PLA in soil [11]. As shown in Table 1, pure PLA reaches this value within around 20 days, whereas composites with increasing fiber content require more time. Nonetheless, degradation remains relatively fast, with composites approaching M_c between 20 and 40 days. After 40 days, size exclusion chromatography (SEC) reveals the presence of three distinct chain populations: low (~2 kDa), intermediate (~5 kDa), and high (>10 kDa) molecular weights. It is important to note that SEC measurements at extended burial times may underestimate degradation due to the loss of water-soluble oligomers, which are no longer present in the solid phase. Despite this limitation, the data indicate that fiber incorporation slows degradation, particularly at higher loadings. To understand this behavior, which contrasts with observations in freshwater, one must consider the relationship between molecular weight evolution and the crystallinity of the samples during composting. A thorough DSC characterization (DSC Q2000, TA Instruments) demonstrated that the reduced degradation rate observed in composites with high Φ can be attributed to the protective influence of fiber-induced crystallinity, which hinders water penetration and shields the amorphous regions from hydrolytic attack [2]. In essence, within mature compost, the fibers initially facilitate water uptake during the early stages of burial. This effect, which seems to be favored at fiber contents well above Φ_c, vanishes over time. As burial progresses, the crystallinity promoted by the fibers becomes dominant, ultimately slowing down the overall degradation process.

4 CONCLUSIONS

The percolation threshold of PLA-based composites reinforced with short hemp shives or kenaf bast fibers (average length <500 μm) was evaluated by applying and validating a model originally conceived to depict the linear viscoelasticity of polymer nanocomposites. Despite the substantial differences with biocomposites, the physics underlying the two-phase model keeps working, the only difference being the higher filler contents needed for percolation in this class of composites based on micron-sized reinforcing fibers. The two-phase model led to Φ_c values of ~10.1 vol% for hemp and 19.5 vol% for kenaf composites. Dielectric spectroscopy supported these findings, though it required more complex sample preparation. Regarding the relevance of the percolation threshold on the degradation kinetics, the impact of short hemp fibers on PLA degradation in freshwater and mature compost was evaluated using SEC analyses, with fiber content ranging from 5 to 30 vol%, surpassing the percolation threshold. A contrasting behavior was observed: in freshwater, fibers accelerated degradation by promoting hydrolysis and enabling water infiltration, even affecting crystalline regions. In compost, degradation

was generally faster due to the biotic environment and higher temperature (~55 °C). While fibers initially enhanced hydrolysis and surface erosion, over time, the fiber-induced crystallinity slowed PLA degradation compared to the neat polymer. Additionally, the fibers slightly improved the flexural modulus of the composites, potentially enabling material savings and enhancing sustainability throughout their life cycle.

ACKNOWLEDGEMENTS

G.F. acknowledges financial support under the National Recovery and Resilience Plan (NRRP), Mission 4, Component 2, Investment 1.1, Call for tender No. 104 published on 02.02.2022 by the Italian Ministry of University and Research (MUR), funded by the European Union - NextGenerationEU- Project Title "Untapping the potential of GREEN COmposites by combining performance and environmental sustainability - GREENCO", grant number 20223LWKTC, grant assignment decree No. 966 adopted on 30/06/2023 by MUR.

REFERENCES

[1] L. Vitiello, M. Salzano de Luna, V. Ambrogi and G. Filippone, A simple rheological method for the experimental assessment of the fiber percolation threshold in short fiber biocomposites, *Composites Science and Technology*, **245**, 2024, p. 110345 (doi: 10.1016/j.compscitech.2023.110345)

[2] L. Vitiello, S. C. Carroccio, V. Ambrogi, E. Podda, G. Filippone and M. Salzano de Luna, Degradation kinetics of PLA/hemp biocomposites: Tradeoff between nucleating action and pro-hydrolytic effect of natural fibers, *Composites Science and Technology*, **257**, 2024, p. 110345 (doi: 10.1016/j.compscitech.2024.110806)

[3] I. Balberg, C. H. Anderson, S. Alexander and N. Wagner, Excluded volume and its relation to the onset of percolation. *Physical review B*, **30**, 1984, p. 3933 (doi: 10.1103/PhysRevB.30.3933).

[4] G. Filippone, G. Romeo and D. Acierno, Viscoelasticity and structure of polystyrene/fumed silica nanocomposites: filler network and hydrodynamic contributions. *Langmuir*, **26**, 2010, pp. 2714-2720. (doi: 10.1021/la902755r)

[5] G. Filippone, M. Salzano de Luna, D. Acierno and P. Russo, Elasticity and structure of weak graphite nanoplatelet (GNP) networks in polymer matrices through viscoelastic analyses, *Polymer*, **53**, 2012, pp. 2699-2704. (doi: 10.1016/j.polymer.2012.04.037)

[6] G. Capuano, G. Filippone, G. Romeo and D. Acierno, Universal Features of the Melt Elasticity of Interacting Polymer Nanocomposites, *Langmuir*, **28**, 2012, pp. 5458-5463. (doi: 10.1021/la205105m)

[7] A. N. Fraga, E. Frullloni, O. De la Osa, J. M. Kenny and A. Vázquez, Relationship between water absorption and dielectric behaviour of natural fibre composite materials. *Polymer testing*, **25(2)**, 2006, pp. 181-187 (doi: 10.1016/j.polymertesting.2005.11.002)

[8] E. Jayamani, S. Hamdan, M.R. Rahman and M. K. B. Bakri, Comparative study of dielectric properties of hybrid natural fiber composites. *Procedia Engineering*, **97**, 2014, pp. 536-544 (doi: 10.1016/j.proeng.2014.12.280)

[9] W. Wang, M. Sainand P. A. Cooper, Study of moisture absorption in natural fiber plastic composites. *Composites science and technology*, **66**, 2006, pp. 379-386 (doi: 10.1016/j.compscitech.2005.07.027)

[10] M. Karamanlioglu, R. Preziosi and G. D. Robson, Abiotic and biotic environmental degradation of the bioplastic polymer poly (lactic acid): A review. *Polymer Degradation and stability*, **137**, 2017, pp. 122-130 (doi: 10.1016/j.polymdegradstab.2017.01.0)

[11] P. Stloukal, S. Pekařová, A. Kalendova, H. Mattausch, S. Laske, C. Holzer, L. Chitu, S. Bodner, G. Maier, M. Slouf and M. Koutny, Kinetics and mechanism of the biodegradation of PLA/clay nanocomposites during thermophilic phase of composting process. *Waste Management*, **42**, 2015, pp. 31-40 (doi: 10.1016/j.wasman.2015.04.006)

ICCM24
AUGUST 4-8, 2025
BALTIMORE CONVENTION CENTER
BALTIMORE, MARYLAND, USA

No Technical Paper Submission for:

Sung Kang

SUSTAINABLE POLYMER MATERIALS: EFFECT OF AGRICULTURAL WASTE REINFORCEMENT ON THE PERFORMANCE OF PBS AND PBAT COMPOSITES

I. Bavasso[1], A. Marinelli[2], M. Sambucci[1], E. Palazzi[1], E. Bruno[1], A. Pantaleoni[1], L. Paterlini[2], B. Del Curto[2], F. Sarasini[1] and J. Tirillò[1]

[1]Department of Chemical Engineering Materials Environment, University of Rome. UdR INSTM, Via Eudossiana 18, 00184 Rome, Italy
Email: irene.bavasso@uniroma1.it, matteo.sambucci@uniroma1.it, erika.palazzi@uniroma1.it, bruno.1788045@studenti.uniroma1.it, alessia.pantaleoni@uniroma1.it, fabrizio.sarasini@uniroma1.it, jacopo.tirillo@uniroma1.it web page: http://www.uniroma1.it

[2]Department of Chemical, Materials and Chemical Engineering "Giulio Natta", Politecnico di Milano, Piazza Leonardo Da Vinci 32, 20133 Milan, Italy
Email: andrea.marinelli@polimi.it, luca.paterlini@polimi.it, barbara.delcurto@polimi.it
web page: http://www.polimi.it

Keywords: Agricultural wastes, Biodegradable polymers, Green Composites, Mechanical Properties, Thermal Properties

ABSTRACT

The increasing accumulation of post-consumer plastic waste, particularly from single-use packaging, has intensified global concerns regarding environmental sustainability. Currently, plastic packaging constitutes nearly half of all plastic waste generated worldwide, highlighting the urgent need for sustainable alternatives. In response, the plastics industry is undergoing a transition from petroleum-based polymers to biodegradable, compostable, and biobased materials. However, the adoption of biodegradable polymers remains limited by their lower mechanical strength, durability, and processing performance compared to conventional plastics. To address these limitations, the use of green composites represents a promising solution, offering not only materials with enhanced performance but also cost-effective. This study explores the use of natural fillers to improve the properties of biodegradable polymers such as polybutylene succinate (PBS) and polybutylene adipate terephthalate (PBAT). Agricultural by-products such as rice straw and wheat straw were used as reinforcement at loadings up to 30 wt.%. Mechanical (tensile, flexural) tests and thermal (TGA, DSC) analyses were conducted on both neat polymers and composite formulations to evaluate performance improvements. Results show that incorporating 30 wt.% wheat straw significantly promoted the mechanical properties of both polymers. For PBS-based composites, tensile strength increased by approximately 16.5%, with >400% rise in tensile modulus. PBAT-based composites demonstrated even greater enhancements, including a 42.9% increase in tensile strength and a significant improvement in Young's modulus compared to pure PBAT.

1 INTRODUCTION

The extensive use of petroleum-based polymers, such as polyethylene (PE), polypropylene (PP), and polyvinyl chloride (PVC), has resulted in their accumulation in the environment. These materials are adopted in different sectors from packaging and automotive components to medical devices and construction. However, their environmental persistence has emerged as one of the most pressing challenges of our century [1]. Due to their chemical inertness, high hydrophobicity, and mechanical durability, these polymers resist degradation in natural environments, leading to their long-term accumulation in terrestrial and marine ecosystems. This buildup, often termed "white pollution," results not only in visual alteration but also in profound ecological consequences, including harm to wildlife, soil fertility degradation, and microplastic contamination of food chains [2].

To address this environmental issue, researchers and industries have turned to biodegradable polymers as more sustainable alternatives. Biodegradable plastics such as poly(lactic acid) (PLA), polyhydroxyalkanoates (PHAs) like polyhydroxybutyrate-co-valerate (PHBV), poly(butylene adipate-co-terephthalate) (PBAT), and poly(butylene succinate) (PBS) offer the potential to reduce long-term environmental impact by breaking down into non-toxic by-products (CO_2 and H_2O) under biodegradation or composting conditions. These materials, derived from renewable or partially renewable sources, have gained attention not only for their ecological compatibility but also for their potential to support circular economy models and reduce dependence on fossil resources [3].

PBS and PBAT are examples of biodegradable aliphatic polyesters: PBS is synthesized through the polycondensation of succinic acid and 1,4-butanediol and is known for its high thermal resistance, good ductility and compatibility with conventional polymer processing techniques, including injection molding and extrusion [4]. These properties make PBS a suitable candidate for various applications, especially in food packaging, mulching films, and disposable items. PBAT, an aliphatic-aromatic copolyester composed of 1,4-butanediol, adipic acid, and terephthalic acid, possesses high ductility and impact resistance. It is often used in films, bags, and packaging applications that require high elongation at break. However, PBAT is derived from fossil-fuel sources and suffers from relatively low mechanical strength, which can limit its adoption [5].

Despite the intrinsic ecological benefits of PBS and PBAT, their widespread commercial adoption faces several obstacles. These include the relatively high production costs and low durability [6].

To address these shortcomings, in particular performance and cost, one promising strategy is the incorporation of fillers into biodegradable polymer matrices to enhance tensile strength, thermal stability, stiffness, and impact resistance. Natural fillers derived from renewable agricultural by-products represent an interesting solution due to their low cost, availability, renewability, and intrinsic biodegradability. Among these there are lignocellulosic residues, such as straw, husks and plant fibers. These materials are rich in cellulose and lignin, making them suitable for reinforcement purposes when properly processed and introduced into polymer matrices [7]. These wastes are often discarded, underutilized, or burned contributing to environmental degradation and greenhouse gas emissions. Their addition into biodegradable polymers not only provides an effective waste management strategy but also adds value to agricultural by-products by transforming them into functional eco-friendly materials. This dual benefit aligns with global sustainability goals and supports rural economies [8]. In this context, wheat and rice straws represent examples of lignocellulosic agricultural residues that can serve as reinforcing materials: their potential has been mainly explored in polylactic acid (PLA)-based composites, especially when used as fibers. Results in literature have demonstrated that the addition of these fibers can significantly enhance the tensile and flexural properties of PLA matrix when fibers are adequately processed. Common strategies to improve fiber-matrix adhesion include chemical modifications such as alkaline treatment, silane modification, and grafting with compatibilizers. These treatments alter the fiber surface by removing impurities, increasing surface roughness, and introducing reactive functional groups that promote interfacial bonding with the polymer matrix.

Feng et al. [9] demonstrated that the addition of 30 wt.% of NaOH and silane-treated rice straw fibers into a PLA/PBAT blend enhanced its mechanical properties, resulting in a tensile strength of 12 MPa and a flexural strength of 18 MPa. Similarly, Beniwal et al. [10] used PLA-grafted rice straw fibers to improve dispersion and adhesion within PLA matrix, leading to enhanced mechanical performance and biodegradability. In the case of wheat straw, Liao et al. [2] introduced the 30 wt.% of fibers treated with alkaline and hydrogen peroxide into PLA and observed improved tensile strength and modulus. They also explored the effects of adding PBS to the formulation. Berthet et al. [11] investigated the role of fiber size and surface characteristics by adding wheat straw fibers into PHBV matrix, observing changes in thermal stability and mechanical behavior depending on fiber content and processing conditions.

The biodegradability attitude of the polymer is maintained in the presence of such natural fillers. Pradhan et al. [12] observed that PLA filled with 30 wt.% of wheat straw maintains its compostable nature. Furthermore, these bio-based fillers can impart tunable properties to composites, such as improved water vapor permeability due to their inherent hydrophilicity [11] and contribute to economic sustainability with potential cost reductions of up to 30%.

While most of the works previously summarized focused on PLA-based systems and waste fibers, this study examines the effect of as-received wheat and rice straw incorporated into PBS and PBAT

matrices, without specific particle size selection or chemical modification, to assess their intrinsic reinforcement capabilities, aiming for more environmentally and economically sustainable manufacturing operations. The mechanical properties of the materials were evaluated under quasi-static conditions through tensile and flexural tests. In addition, the thermal characteristics of the composites were analyzed by thermogravimetric analysis (TGA) and differential scanning calorimetry (DSC), while morphological analysis by scanning electron microscopy (SEM) was useful to point out the interfacial features that influence composite performance.

2 MATERIALS AND METHODS

Rice straw (RS) was provided by Azienda Riso Milano (Italy) and wheat straw (WS) by Agriturismo Cascina Scanna (Italy). Both straws were washed with tap water and oven-dried at 80 °C for 24 hours. As a final step, the materials were ground using a knife mill and sieved through a 1 mm mesh sieve.

PBS and PBAT maleic anhydride (MA) grafted granules were purchased from Auser Polimeri (Italy). The polymers have a density equal to 1.26 g/cm³ (ISO 1183) and melt mass flow rate of 8 g/10 min and 4 g/10 min, respectively (measured at 190 °C and 2.16 kg, ISO 1133). The MA content is ≤0.1%.

The composite materials were prepared using a two-stage process involving extrusion (co-rotating twin-screw extruder, Thermo Scientific Process 11, Thermo Fisher Scientific) and injection molding (Haake MiniJet IIPro, Thermo Fisher Scientific). During melt compounding, the following temperature profile from feeder to die was adopted: 145 °C—155 °C—155 °C—160 °C—170 °C—170 °C—165 °C—165 °C. The screw speed was set at 150 rpm. During the injection, a pressure of 450 bar was maintained for 10 s and a post-injection was operated at 150 bar for 10 s. The mold was maintained at 50 °C while the loading cylinder was kept at 165 °C. Prior to extrusion, the pellets and fillers were dried at 80 °C overnight.

The particle size distribution (PSD) of WS and RS was analyzed using a Microtrac Sync laser diffraction particle size analyzer (Verder Scientific S.r.l., Bergamo, Italy). Measurements were conducted in dry mode, applying a dispersion pressure of 100 kPa and a suction pressure of 70 kPa. The PSD of the fillers is reported as percentile values: D10, D50, and D90. D10 represents the particle diameter below which 10% of the sample (by mass or volume) is finer; D50 corresponds to the median particle size, where 50% of the sample is finer; and D90 denotes the diameter below which 90% of the particles are finer.

Tensile and flexural properties of both neat polymers and composite samples were evaluated using a Zwick/Roell Z010 universal testing machine. Tensile tests were performed under displacement control at a crosshead speed of 10 mm/min and ambient temperature, following the ISO 527-2 standard (specimen type 1BA, gauge length $l_0 = 30$ mm). Three-point bending tests were conducted in accordance with ISO 178, using specimens with dimensions of 80 × 10 × 4 mm, a crosshead speed of 5 mm/min, and a span-to-thickness ratio of 16:1. Each test was carried out with a minimum of five replications.

Thermogravimetric (TGA) analysis was carried out according to ISO 11358 by heating the samples (around 20 mg) from room temperature to 800 °C under nitrogen atmosphere (50 mL/min) and with a heating rate of 10 °C/min (TG209 F1 Libra instrument by Netzsch). Differential scanning calorimetry (DSC) analysis was performed according to ISO 11357 with a nitrogen flow of 60 mL/min (DSC 214 Polyma by Netzsch). Specimens (around 10 mg) were analyzed with a temperature program from −100 °C to 200 °C with a heating/cooling/heating rate of 10 °C/min. Results for melting and crystallization temperatures, as well as the degree of crystallinity (X_c, Equation 1), are reported as the mean values of three repetitions:

$$X_c\ (\%) = \Delta H_m / [\Delta H_m^{\,0} \cdot w_c] \cdot 100 \quad (1)$$

where the subscript "c" specifies the polymer (PBS or PBAT), ΔH_m is its measured enthalpy of melting in J/g, $\Delta H_m^{\,0}$ the enthalpy of melting of fully crystalline polymer equal to 110.3 J/g for PBS [13] and 114.0 J/g for PBAT [14]. w is the polymer mass fraction in the composite.

3 RESULTS

From a thermal perspective, the addition of both fillers into the polymer matrices, in agreement with

findings reported in the literature [15,16], affects the thermal stability of the final composites. This is primarily attributed to the degradation of the hemicellulose components present in the straw-based fillers, which typically decompose at lower temperatures compared to the degradation temperatures of the neat polymer matrices. TGA data supports this observation: the onset of thermal degradation, defined as the temperature at which 5% weight loss occurs ($T_{5\%}$), decreased by 17.0% and 20.0% for PBS matrix composites reinforced with WS and RS, respectively. While for PBAT matrix composites, both fillers induced a comparable reduction of approximately 27.0%. Such values are calculated with respect to the $T_{5\%}$ of the neat polymers, observed at 341.1 °C for PBS and 362.2 °C for PBAT.

From DSC analyses no significant variations in the characteristic thermal transition temperatures such as glass transition, melting and crystallization were observed with the addition of both fillers. However, differences were in the degree of crystallinity of the polymer matrices (calculated according to Equation 1). Neat PBS exhibited a superior degree of crystallinity (61.5%) compared to PBAT (10.0%) while, in presence of WS and RS, the crystallinity of PBS decreased by 14.7% and 2.0% with WS and RS, respectively. For PBAT, the reduction was 5.4% and 4.4% for WS and RS, respectively. These findings indicate that no nucleating effect occurs for either type of filler [17].

Formulations	Tensile strength [MPa]	Flexural strength [MPa]	Young's Modulus [GPa]	Flexural Modulus [GPa]
PBS	33.8 (±1.0)	44.1 (±1.4)	0.7 (±0.1)	0.9 (±0.1)
PBS_30WS	40.5 (±1.5)	64.3 (±1.2)	3.7 (±0.6)	2.9 (±0.2)
PBS_30RS	38.1 (±1.3)	60.3 (±2.3)	2.7 (±0.4)	1.9 (±0.3)
PBAT	11.0 (±3.6)	5.8 (±0.2)	0.1 (±0.1)	0.1 (±0.1)
PBAT_30WS	15.7 (±0.3)	27.2 (±1.0)	1.0 (±0.1)	1.0 (±0.2)
PBAT_30RS	14.5 (±0.4)	24.1 (±0.6)	0.9 (±0.2)	0.7 (±0.1)

Table 1: Quasi-static mechanical properties of polymers and composites.

Table 1 summarizes the results of mechanical characterization, including strength and modulus values under both tensile and flexural loading conditions. Although the materials investigated are grafted polymer formulations, the overall mechanical performances of the neat polymers are consistent with values reported in the literature for both PBS [18] and PBAT [19], also in agreement with their degrees of crystallinity [20], as previously discussed in the DSC results.

The introduction of rigid lignocellulosic fillers led to a significant increase in stiffness, both in tension and in bending. This behavior is typical of composites reinforced with natural fillers [21,22] and, as comparison, the enhancement observed with the addition of 30 wt.% of WS was greater than that recorded for composites with 30 wt.% of RS, in both polymer matrices.

Percentile values	WS Size [µm]	RS Size [µm]
D10	29.4	69.6
D50	181.5	286.8
D90	256.4	464.7

Table 2: Particle size distribution of WS and RS.

This difference can reasonably be attributed to heterogeneities in particle morphology (shape and size) between the two fillers. This is demonstrated by SEM micrographs (Figure 1a–b), where it is possible to notice in both fillers a high morphological heterogeneity, and from results in Table 2 where are summarized the particle size distributions by their cumulative percentiles. WS exhibits a finer

dimension compared to RS, which likely facilitates better distribution of the filler into the matrix and promotes a better load transmission at the interface due to a larger surface area. This interpretation is supported by findings from Berthet et al. [12], who reported that stiffness enhancements are more pronounced when the specific surface area of the filler increases, even in the presence of limited interfacial adhesion. Although the fracture surface micrographs (Figure 1c–f) display signs of fiber pull-out and visible gaps between the matrix and the filler, typically associated with limited interfacial adhesion between the hydrophobic polymer matrices and the hydrophilic lignocellulosic reinforcements [23,24], the overall interfacial bonding is not significantly compromised (Figure 1c), owing to the MA-grafted nature of both polymers.

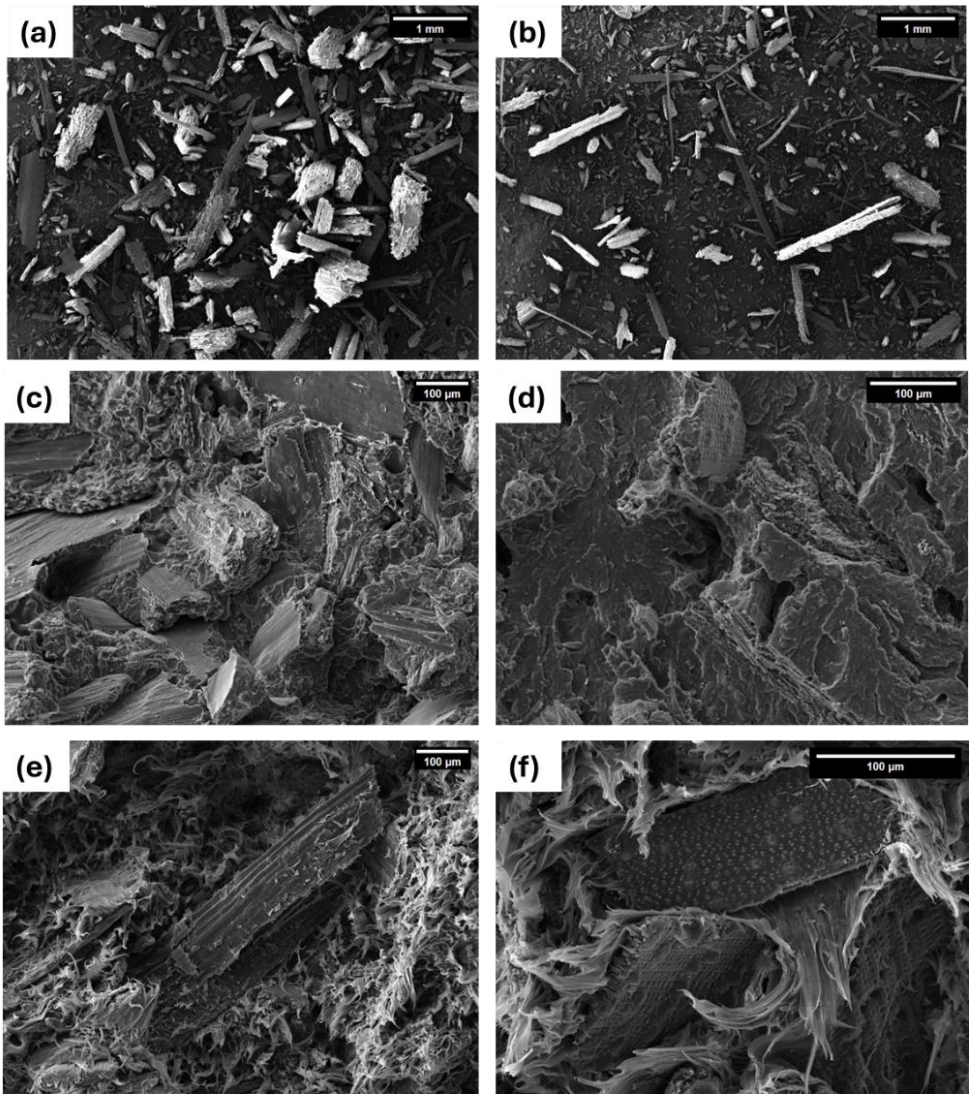

Figure 1: SEM micrographs of (a) WS and (b) RS fillers, and fracture surfaces of composites: (c) PBS_30WS, (d) PBS_30RS, (e) PBAT_30WS and (f) PBAT_30RS.

Interestingly, for both types of fillers, the tensile and flexural strengths also increased, albeit to a lesser extent than the moduli. This trend is consistent with observations by Kumar et al. [16] who measured a superior tensile strength in PBS with 30 wt.% of untreated sisal fibers composites than the neat polymer of about 15.8%. In general, a possible explanation for this behavior lies in the combined effect of chemical anchoring (promoted by the presence of MA) and mechanical interlocking effect, wherein the surface roughness of the lignocellulosic particles acts as anchoring points within the matrix,

thereby improving load transfer at the interface [25]. The enhancements observed in tensile and flexural strengths were superior in the PBAT based formulations compared to those with PBS matrix and this is because of the higher ductility of PBAT than PBS (with the highest deformation at maximum tensile strength of 86.1% ± 5.2% compared to 16.6% ± 1.5%), which allows for a more effective mechanical interlocking.

4 CONCLUSIONS

This study investigated the thermal and mechanical behavior of biodegradable polymer composites based on PBS and PBAT matrices reinforced with lignocellulosic by-products, specifically wheat straw (WS) and rice straw (RS). TGA results demonstrated a reduction in the onset degradation temperature upon filler addition, primarily due to the early decomposition of hemicellulose components present in both straws. DSC analysis revealed no significant changes in the characteristic thermal transitions; however, a reduction in crystallinity was observed for both matrices, with PBS showing a more substantial decrease. This suggests the absence of a nucleating effect. The addition of straw fillers significantly improved the stiffness of both polymers under tensile and flexural conditions, with WS proving more effective than RS. This enhancement is attributed to the finer morphology and higher surface area of WS, which facilitates more efficient stress transfer. Despite the limited interfacial adhesion between the hydrophilic fillers and the hydrophobic matrices, the mechanical interlocking effect contributed to strength improvements, particularly in the PBAT based composites.

Overall, the results confirm the potential of such agricultural by-products such as cost-effective and sustainable reinforcing agents in biodegradable polymer systems. However, further optimization, especially at the interface level, is essential to fully exploit their reinforcing capabilities.

ACKNOWLEDGEMENTS

The research was partially funded by the European Union – NextGenerationEU, Mission 4, Component 1, within the BOOMERANG project (Bio-cOmpOsite Material dEsign foR pAckagiNG, CUP B53D23006530006) and partially within the MUSA – Multilayered Urban Sustainability Action – project, funded by the European Union – NextGenerationEU, under the National Recovery and Resilience Plan (NRRP) Mission 4 Component 2 Investment Line 1.5: Strenghtening of research structures and creation of R&D “innovation ecosystems”, set up of “territorial leaders in R&D”.

REFERENCES

[1] A. Phelan, K. Meissner, J. Humphrey and H. Ross, Plastic pollution and packaging: Corporate commitments and actions from the food and beverage sector, *Journal of Cleaner Production*, **331**, 2022, pp. na, (doi: 10.1016/j.jclepro.2021.129827).

[2] C. Liao, Y. Xiao, K. Chen, P. Li, Y. Wu, X. Li and Y. Zuo, Synergistic modification of polylactic acid by oxidized straw fibers and degradable elastomers: A green composite with good strength and toughness, *International Journal of Biological Macromolecules*, **221**, 2022, pp. 773-783, (doi: 10.1016/j.ijbiomac.2022.09.023).

[3] J. Ludwiczak, A. Dmitruk, M. Skwarski, P. Kaczyński and P. Makuła, UV resistance and biodegradation of PLA-based polymeric blends doped with PBS, PBAT, TPS, *International Journal of Polymer Analysis and Characterization*, **28**, 2023, pp. 366-382, (doi: 10.1080/1023666X.2023.2218696).

[4] O. Platnieks, S. Gaidukovs, V. K. Thakur, A. Barkane and S. Beluns, Bio-based poly (butylene succinate): Recent progress, challenges and future opportunities, *European Polymer Journal*, **161**, 2021, pp. na, (doi: 10.1016/j.eurpolymj.2021.110855).

[5] F. V. Ferreira, L. S. Cividanes, R. F. Gouveia and L. M.F. Lona, An Overview on Properties and Applications of Poly(butylene adipate-co-terephthalate)–PBAT Based Composites, *Polymer Engineering and Science,* **59**, 2019, pp. E7-E15, (doi: 10.1002/pen.24770).

[6] D. Nath, M. Misra, F. Al-Daoudc and A. K. Mohanty, Studies on poly(butylene succinate) and poly(butylene succinate-co-adipate)-based biodegradable plastics for sustainable flexible packaging and

agricultural applications: a comprehensive review, *RSC Sustainability*, **3**, 2025, pp. 1267–1302, (doi: 10.1039/d4su00193a).
[7] B. Kitaw Dejene and T. M. Geletaw, Development of fully green composites utilizing thermoplastic starch and cellulosic fibers from agro-waste: a critical review, *Polymer-Plastics Technology and Materials*, **63**, pp. 540-569, (doi:10.1080/25740881.2023.2296649).
[8] A. Sholokhova, V. Varžinskas and R. Rutkaitė, Valorization of Agro-waste in Bio-based and Biodegradable Polymer Composites: A Comprehensive Review with Emphasis on Europe Perspective, *Waste and Biomass Valorization*, **16**, 2025, pp. 1537–1571, (doi: 10.1007/s12649-024-02856-y).
[9] J. Feng, W. Zhang, L. Wang and C. He, Performance Comparison of Four Kinds of Straw/PLA/PBAT Wood Plastic Composites, BioResources, **15**, 2020, 2596-2604, (doi: na).
[10] P. Beniwal and A. P. Toor, Advancement in tensile properties of polylactic acid composites reinforced with rice straw fibers, *Industrial Crops & Products*, **192**, 2023, pp. na, (doi: 10.1016/j.indcrop.2022.116098).
[11] M.A. Berthet, H. A. Coussy, V. Chea, V. Guillard, E. Gastaldi and N. Gontard, Sustainable food packaging: Valorising wheat straw fibres for tuning PHBV-based composites properties, *Composites: Part A*, **72**, 2015, pp. 139–147, (doi: 10.1016/j.compositesa.2015.02.006).
[12] R. Pradhan, M. Misra, L. Erickson and A. Mohanty, Compostability and biodegradation study of PLA–wheat straw and PLA–soy straw based green composites in simulated composting bioreactor, *Bioresource technology*, **101**, 2010, pp. 8489–8491, (doi: 10.1016/j.biortech.2010.06.053).
[13] T. Messin, S. Marais, N. Follain, A. Guinault, V. Gaucher, N. Delpouve and C. Sollogoub, Biodegradable PLA/PBS multinanolayer membrane with enhanced barrier performances, *Journal of Membrane Science*, **598**, 2020, pp. na, (doi: 10.1016/j.memsci.2019.117777).
[14] M. H. López, Z. N. C. Pacheco, S. B. Baños, L. Z. Avejar, J. J. B. Jiménez, M. A. S. Gutiérrez and P. O. Gudiño, Bio-based composite fibers from pine essential oil and PLA/PBAT polymer blend. Morphological, physicochemical, thermal and mechanical characterization, *Materials Chemistry and Physics*, **234**, 2019, pp. 345–353, (doi: 10.1016/j.matchemphys.2019.01.034).
[15] S. Sahoo, M. Misra and A. K. Mohanty, Biocomposites From Switchgrass and Lignin Hybrid and Poly(butylene succinate) Bioplastic: Studies on Reactive Compatibilization and Performance Evaluation, *Marcomolecular Materials and Engineering*, **299**, 2014, pp. 178–189, (doi: 10.1002/mame.201300038).
[16] K. S. Kumar and I. Singh, Sustainable oxalic acid treatment of lignocellulosic fibers for ensuring improved performance of treated fibers based bio PBS composites, International Journal of Biological *Macromolecules,* **294**, 2025, pp. na, (doi: 0.1016/j.ijbiomac.2025.139507).
[17] A.W. Cindradewi, R. Bandi, C.W. Park, J.S. Park, E.A. Lee, J.K. Kim, G.J. Kwon, S. Y. Han and S. H. Lee, Preparation and Characterization of Polybutylene Succinate Reinforced with Pure Cellulose Nanofibril and Lignocellulose Nanofibril Using Two-Step Process, *Polymers*, **13**, 2021, pp. na, (doi: 10.3390/polym13223945).
[18] T. Zhao, J. Yu, X. Zhang, W. Han, S. Zhang, H. Pan, Q. Zhang, X. Yu, J. Bian and H. Zhang, *Polymer Bulletin*, **81**, 2024, pp.2481–2504, (doi: 10.1007/s00289-023-04848-9).
[19] H. Moustafa, C. Guizani, C. Dupont, V. Martin, M. Jeguirim and A. Dufresne; Utilization of Torrefied Coffee Grounds as Reinforcing Agent To Produce High-Quality Biodegradable PBAT Composites for Food Packaging Applications, *ACS Sustainable Chemical Engineering*, **5**, 2017, pp. 1906−1916, (doi: 10.1021/acssuschemeng.6b02633).
[20] A. R. de Matos Costa, A. Crocitti, L. H. de Carvalho, S. C. Carroccio, P. Cerruti and G. Santagata, Properties of Biodegradable Films Based on Poly(butylene Succinate) (PBS) and Poly(butylene Adipate-co-Terephthalate) (PBAT) Blends, *Polymers*, **12**, 2020, pp. na, (doi: 10.3390/polym12102317).
[21] N. Ewurum and A. G. McDonald, Lignin Reinforcement in Polybutylene Succinate Copolymers, *Polymers,* 17, 2025, pp. na, (doi: 10.3390/ polym17020194).
[22] F. Le Digabel, N. Boquillon, P. Dole, B. Monties and L. Averous, Properties of Thermoplastic Composites Based on Wheat-Straw Lignocellulosic Fillers, *Journal of Applied Polymer Science*, **93**, 2004, pp. 428–436, (doi: 10.1002/app.20426).
[23] X. Chena, J. Yuc, Z. Zhangd and C. Lub, Study on structure and thermal stability properties of cellulose fibers from rice straw, *Carbohydrate Polymers*, **85**, 2011, pp. 245–250, (doi: 10.1016/j.carbpol.2011.02.022).

[24] H. Li, H. Zhang, L. Xiong, X. Chen, C. Wang, C. Huang and X. Chen, Isolation of Cellulose from Wheat Straw and Its Utilization for the Preparation of Carboxymethyl Cellulose, *Fibers and Polymers*, **20**, 2019, pp. 975-981, (doi: 10.1007/s12221-019-7717-6).
[25] J. Y. Boey, S. B. Yusoff and G. S. Tay, A review on the enhancement of composite's interface properties through biological treatment of natural fibre/lignocellulosic material, *Polymers and Polymer Composites*, **30**, 2022, pp. 1-11, (doi: 10.1177/09673911221103600).

ICCM24
AUGUST 4-8, 2025
BALTIMORE CONVENTION CENTER
BALTIMORE, MARYLAND, USA

No Technical Paper Submission for:

Jianqun Hao

ICCM24 24TH INTERNATIONAL CONFERENCE ON COMPOSITE MATERIALS
AUG 4-8, 2025 • BALTIMORE CONVENTION CENTER • BALTIMORE, MARYLAND

MACHINE LEARNING-BASED PYROLYSIS CHARACTERIZATION IN CERAMIC-MATRIX COMPOSITES

Paulina Portales Picazo[1], Navid Zobeiry[1].

[1]Materials Science & Engineering Department, University of Washington
Box 352120. 302 Roberts Hall, Seattle, WA, 98195-2120, U.S.A.
Email: ppicazo@uw.edu

Keywords: Machine Learning, Kinetics, Pyrolysis, Characterization

ABSTRACT

Thermoset polymers such as phenolic resins are commonly used as precursors for the ceramic matrix in carbon fiber-reinforced composites due to their high carbon yield in pyrolysis, and desirable thermal properties. Although the initial carbon content is inherent to the polymer, factors such as volatile release and pore structure evolution depend on reaction rates and phase transformations, both of which are strongly influenced by processing conditions. To better understand these complex correlations, it is essential to investigate and characterize the underlying kinetics of transformation, and their impact on property evolution during processing. Experimental data is typically used to establish these governing kinetics; however, accurate characterization remains challenging due to noisy and limited data, as well as the complexity and multiplicity of the reactions involved.

This paper presents a framework that combines machine learning and sparse regression with traditional model-based kinetic analysis to extract governing equations for the pyrolysis of a phenolic thermoset composite. The proposed approach follows three main steps: (1) estimation of activation energies and pre-exponential factors for a multistage process using traditional model-free analysis of thermogravimetric data; (2) prediction of reaction kinetics using a neural network with customized activation functions; and (3) model optimization using LASSO regularization to enforce sparsity, select key features, and reduce overfitting. This combined method improves interpretability and results in a simplified kinetic model that highlights dominant reaction mechanisms.

Applied to dynamic TGA data, the framework achieved strong predictive performance and produced interpretable kinetic expressions. Preliminary results from the in-house Python implementation demonstrate its potential as a promising alternative to traditional kinetic analysis, accurately capturing the kinetics of complex, multistage reactions, with reduced testing. By combining machine learning with sparse regression, this method enhances parameter estimation while offering a scalable and interpretable approach applicable across a range of thermal decomposition processes.

1 INTRODUCTION

Over the past decades, fiber-reinforced composite materials have become increasingly popular across various industries due to their exceptional properties, including high specific strength and stiffness, and resistance to corrosion [1,2]. In particular, ceramic matrix composites are increasingly used in aerospace applications due to their unique combination of high thermal resistance, high strength, and low weight. Thermoset polymers like phenolic resins, for example, form three-dimensional networks through covalent bonding during curing. These crosslinked structures not only provide high thermo-mechanical properties but also exhibit desirable char-forming behavior during thermal decomposition, making them particularly well-suited for applications involving high-temperature exposure, such as ceramic-matrix composite manufacturing, where pyrolysis kinetics plays a critical role in determining the final material properties [3–6]. As a result, considerable effort has been devoted to understanding how processing conditions affect the underlying chemical reactions and, in turn, the resulting material behavior.

In recent years, advanced machine learning models, have emerged as valuable tools for studying high dimensional datasets to uncover underlying patterns, including the effect of processing conditions on material properties [7–9]. These data-driven methods are increasingly employed to uncover complex patterns in material behavior that are difficult to capture through traditional approaches. While conventional physics-based methods remain central to materials science, they often rely on simplifying assumptions, limiting their predictive capabilities in nonlinear, multistage processes [10]. As a result, there is growing interest in hybrid frameworks that integrate physical principles with machine learning to address these challenges, as well as improve generalization and enhance interpretability in complex systems [10].

Despite these advancements, significant challenges remain. For instance, qualification and certification of fiber-reinforced composite structures for aerospace applications still relies on extensive testing campaigns [8]. In the context of reaction kinetics, where understanding the rate and mechanism of chemical reactions under varying conditions is essential, this task is further hindered by the complexity and multiplicity of the reactions involved [5,11]. These limitations underscore the need for efficient, interpretable modeling approaches that can reduce experimental demands while still capturing the essential features of material behavior.

This work introduces a novel, theory-guided machine learning framework for analyzing the high-temperature pyrolysis stage in phenolic-based ceramic-matrix composites manufacturing. The proposed approach, NN-LASSO, integrates sparse regression, neural networks, and established kinetic theories to derive physics-based kinetic expressions from experimental data. The approach builds on the foundation of the Sparse Identification of Nonlinear Dynamics (SINDy) method, extending its applicability to thermo-kinetic systems where overlapping mechanisms and limited data can hinder traditional modeling strategies [10,12]. Experimental data from thermogravimetric analysis (TGA) is used to estimate kinetic parameters through the Friedman isoconversional analysis. These parameters, along with the extent of conversion, are used as inputs to train a neural network with custom activation functions representing candidate reaction mechanisms. Lasso regularization is then applied to enforce sparsity and improve model interpretability.

Preliminary results demonstrate the proposed framework's potential as a scalable alternative to traditional kinetic analysis. By integrating machine learning with sparse regression, the method enables improved parameter estimation while maintaining physical interpretability across multistage, nonlinear reaction systems.

2 MATERIALS AND METHODS

2.1 Data Collection & Transformation

Experimental data used in this study was obtained from TGA tests conducted on cured carbon/phenolic composite samples. The composite was fabricated using a proprietary prepreg and processed into panels with a thickness of 0.64 cm (¼"), and a quasi-isotropic layup of $[(0/90)/(\pm 45)]_{8S}$. Lay-up and bagging were carried out according to the manufacturer's recommended procedures, and the laminates were cured in an autoclave following the manufacturer's recommended pressure and temperature cycles. Microstructural evaluation and density measurements showed results consistent with literature data for similar systems [5]. Samples were sectioned from the cured laminates and used for pyrolysis analysis via TGA. The test specimens had nominal dimensions of 0.2 × 0.1 × 0.64 cm and weighed between 8–10 mg. All samples were obtained from the same composite batches and stored under consistent conditions to minimize variability [11].

TGA tests were performed using a TA Instruments TGA 550 under a nitrogen flow rate of 20 mL/min. Samples were placed in open platinum pans within a sealed chamber. Weight loss and weight loss rate were recorded throughout the pyrolysis process to assess thermal stability and extract kinetic information. Each run was conducted from room temperature up to 1000°C, followed by a 20-minute

isothermal hold before cooling. This temperature range was selected based on prior work establishing that the pyrolysis process in phenolic resins is typically complete by 800°C [13].

For data analysis, the extent of conversion, or degree of pyrolysis (α), was calculated from TGA results using normalized weight loss:

$$\alpha = (m_i - m_t)/(m_i - m_f) \tag{1}$$

where m_i is the initial mass, m_t is the mass at time t, and m_f is the final residual mass for each test [11,14,15].

For solid-state degradation reactions, the reaction rate is typically expressed as a function of the extent of conversion (α), rather than concentration. The general form of the rate equation:

$$\frac{d\alpha}{dt} = k(T)f(\alpha) \tag{2}$$

here $f(\alpha)$ describes the reaction mechanism and $k(T)$is the temperature-dependent rate constant. According to the general form of the Arrhenius equation, the temperature dependency is commonly expressed as:

$$k(T) = Aexp\left(-\frac{R}{RT}\right) \tag{3}$$

where A and E represent the pre-exponential factor and the activation energy, respectively [10,19]. The substitution of Eq. 3 in Eq. 2 gives:

$$\frac{d\alpha}{dt} = Aexp\left(-\frac{E}{RT}\right)f(\alpha) \tag{4}$$

This rate expression is widely used in model-free and model-fitting approaches in thermal analysis [16]. In this study, the Friedman method was used to extract activation energies and pre-exponential factors from the TGA data [16,17]. These parameters, along with the calculated conversions, were used as inputs for the NN-LASSO framework.

2.2 NN-LASSO Framework for Kinetic Modeling

The NN-LASSO framework was developed to identify kinetic models from experimental data by combining neural networks, Lasso-based feature selection, and established pyrolysis kinetic theories. It builds upon the principles of the Sparse Identification of Nonlinear Dynamics (SINDy) method, which assumes that the temporal evolution of dynamic physical systems can be approximated by a sparce summation of nonlinear basis functions [10,12]. In this work, the governing reaction rate is expressed in the form:

$$\frac{d\alpha}{dt} = \sum_{i=1}^{n} \omega_i f_i(\alpha) \tag{5}$$

where $f_i(\alpha)$ are functions representing potential reaction mechanisms, and ω_i are trainable weights. The goal is to select a minimal subset of physics-based features that balances physical interpretability with sufficient accuracy in capturing the observed kinetics.

The experimental TGA data was first segmented into distinct temperature regions based on the observed weight-loss trends, with each segment corresponding to a different pyrolysis stage [11]. Activation energies and pre-exponential factors for each stage were calculated using the Friedman method and used as inputs to the model. A feature library was built from kinetic expressions commonly used to describe solid-state reactions, including functions of the form:

$$f(\alpha) = \alpha^m(1-\alpha)^n \tag{6}$$

$$f(\alpha) = \alpha^m \tag{7}$$

$$f(\alpha) = (1-\alpha)^n \tag{8}$$

$$f(\alpha) = ((1+\alpha)^n - 1)^p \tag{9}$$

Each function was implemented as a custom activation layer within the neural network, parameterized by $m, n,$ and $p,$ and constrained to remain within realistic kinetic ranges during training. Lasso regularization was then applied to the output layer to enforce sparsity by minimizing the L1 norm of the weights, driving non-essential terms to zero [18]. This promotes interpretability and reduces overfitting, resulting in a simplified expression composed of the most relevant kinetic mechanism. The Lasso penalty term is defined by:

$$\phi(\boldsymbol{w}) = \|\boldsymbol{w}\|_1 \tag{10}$$

where $\boldsymbol{w} = (\omega_1, \omega_2, \dots, \omega_n)^n$ is the vector of trainable weights assigned to each feature in the output layer [18].

To optimize performance, a hyperparameter search was performed across regularization strengths, learning rates, batch sizes, and feature combinations. Multiple models were trained using randomly selected subsets of candidate functions. The final model was chosen based on its ability to match experimental trends while maintaining a minimal, interpretable form. **Fig. 1** presents a schematic of the three main steps of the framework.

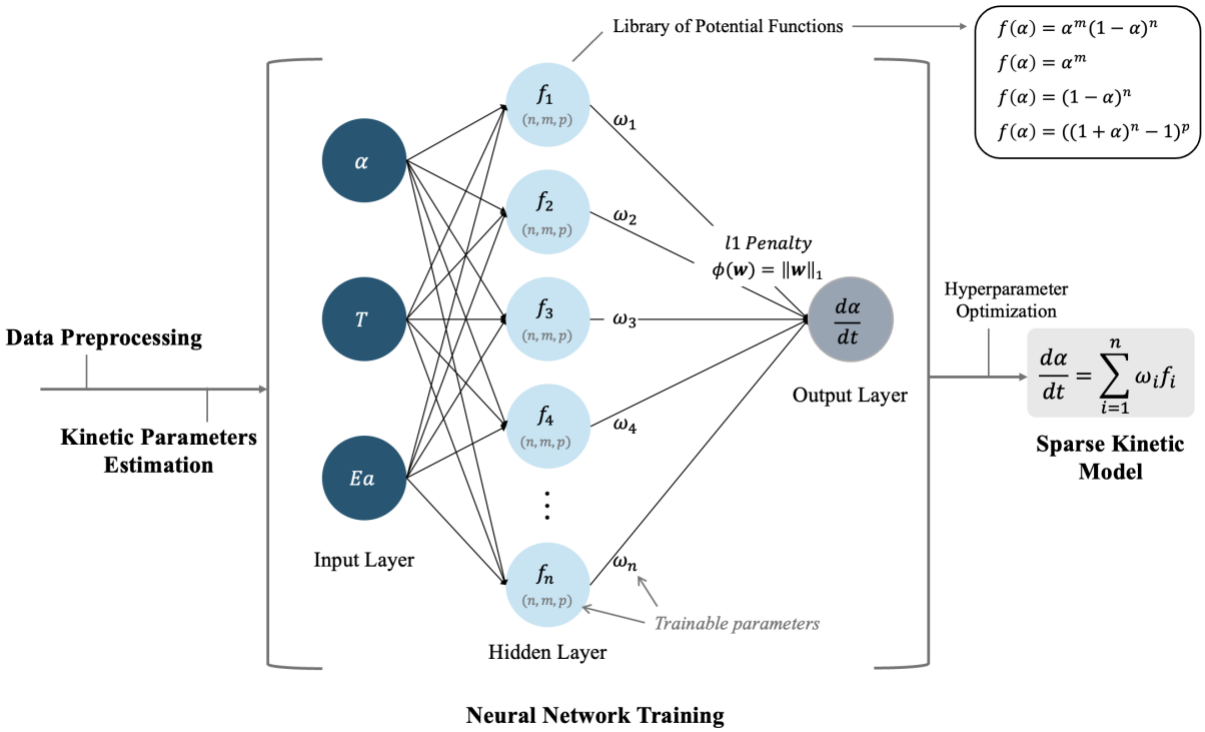

Figure 1: Schematic of the proposed approach for kinetics modeling from experimental data using the NN-Lasso framework.

The framework was validated by comparing predicted reaction rates against experimental TGA results across dynamic and complex temperature cycles.

3 RESULTS

Based on TGA test data and reported results in the literature, three distinct temperature regions with peak degradation rates near 350°C, 550°C, and 600°C were identified for the studied material (**Fig.2**a) [11]. These correspond to crosslinking and chain scission reactions (300-440°C), followed by char formation and oxidation reactions (400-800°C) [13,15]. To focus on thermal degradation behavior, weigth loss below 225°C, associated with polymerization and dewatering during curing, was excluded

from the analysis [19]. As summarized in **Table 1**, average activation energies of 195.5, 104.8, and 136.4 kJ/mol were calculated for these stages using Friedman's isoconversional method (**Fig.2**b) [11,20].

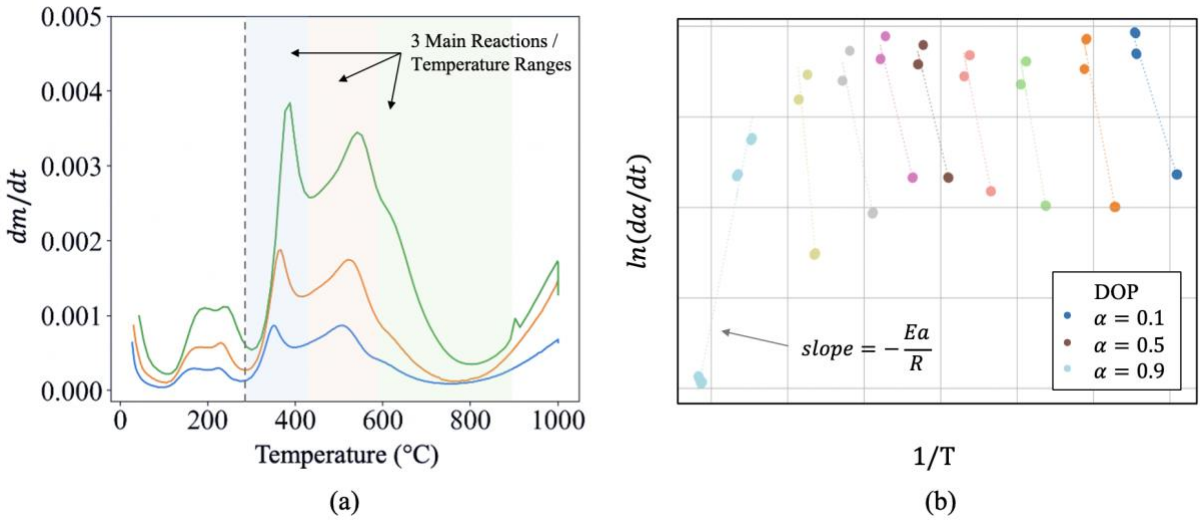

Figure 2: TGA derivative weight loss curves showing main degradation regions (a), and activation energy estimation using Friedman's analysis at various degrees of conversion (b).

Stage	Temperature Range (°C)	$\boldsymbol{Ea}$ $\boldsymbol{(k/mol)}$
1	300-430	195.5
2	430-600	104.8
3	600-900	136.4

Table 1: Kinetic parameters using Friedman analysis for different temperature ranges.

Following previous studies [21,22], the pyrolysis was modeled as a three-stage mechanism, with the rate expressions defined as:

$$\frac{d\alpha_1}{dt} = A_1\, exp\left(-\frac{E_{a,1}}{RT}\right) f(1-\alpha_1)^{n_1} \tag{11}$$

$$\frac{d\alpha_2}{dt} = A_2\, exp\left(-\frac{E_{a,2}}{RT}\right) f(\alpha_1-\alpha_2)^{n_2} \tag{12}$$

$$\frac{d\alpha_3}{dt} = A_3\, exp\left(-\frac{E_{a,3}}{RT}\right) f(\alpha_2-\alpha_3)^{n_3} \tag{13}$$

The overall conversion is expressed as:

$$\alpha(t) = w_1\alpha_1(t) + w_2\alpha_2(t) + w_3\alpha_3(t) \tag{14}$$

with $w_1 + w_2 + w_3 = 1$ and $0 < \alpha(t) < 1$.

To evaluate the NN-LASSO framework under different conditions, two models were trained using TGA data collected at heating rates of 2°C/min and 5°C/min. Training was performed over dynamic temperature cycles ranging from 225°C to 900°C. The mathematical expressions for the resulting kinetic models derived from the training process are presented in Eq. 28 and 29, respectively.

$$\frac{d\alpha}{dt} = 0.0016 * \exp\left(-\frac{E}{RT}\right) x^{0.84} + 0.7 * \exp\left(-\frac{E}{RT}\right) x^4(1-x)^2 + 0.13 * \exp\left(-\frac{E}{RT}\right) x^{0.7}(1-x)^4 \tag{15}$$

$$\frac{d\alpha}{dt} = 0.0223 * \exp\left(-\frac{E}{RT}\right) x^{0.62}(1-x)^5 + 1.32 * \exp\left(-\frac{E}{RT}\right) x^5(1-x)^{3.7} + 0.24 * \exp\left(-\frac{E}{RT}\right) ((1+x)^4 - 1))^5 \tag{16}$$

As shown in **Fig. 3** the predicted conversion rate curves closely matched experimental TGA results. The model trained on 2°C/min data achieved a R^2 value of 0.9703, while the 5°C/min model achieved R^2 = 0.9634. Although both models accurately captured the underlying kinetics, the differences in selected mechanisms and reaction orders across heating rates highlight the sensitivity of pyrolysis behavior to thermal conditions. These variations highlight the complexity of the pyrolysis process and the need for adaptable kinetic modeling approaches to accurately describe thermal degradation under different processing conditions.

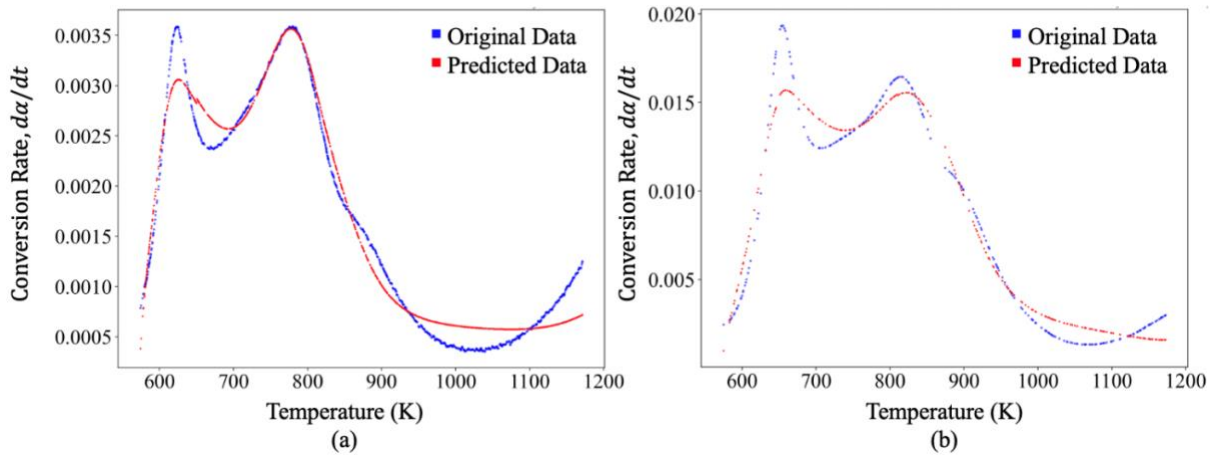

Figure 3: Comparison of the conversion rate (dα/dt) curve predicted for a 2°C/min (a) and a 5 °C/min (b) dynamic cycle with that obtained from experimental results.

To further evaluate model performance under complex processing conditions, the NN-LASSO framework was trained on TGA data collected from a multi-step cycle, which included multiple heating ramps and isothermal holds (5°C/min to 550°C, followed by a 1-hour isothermal hold, and then 2°C/min to 1000°C). The model achieved an R^2 value of 0.9433. However, results shown in **Fig 4**.b reveal that the model struggled to accurately follow material behavior during the isothermal hold, suggesting that the current framework may benefit from incorporating additional variables or modifying the base equations.

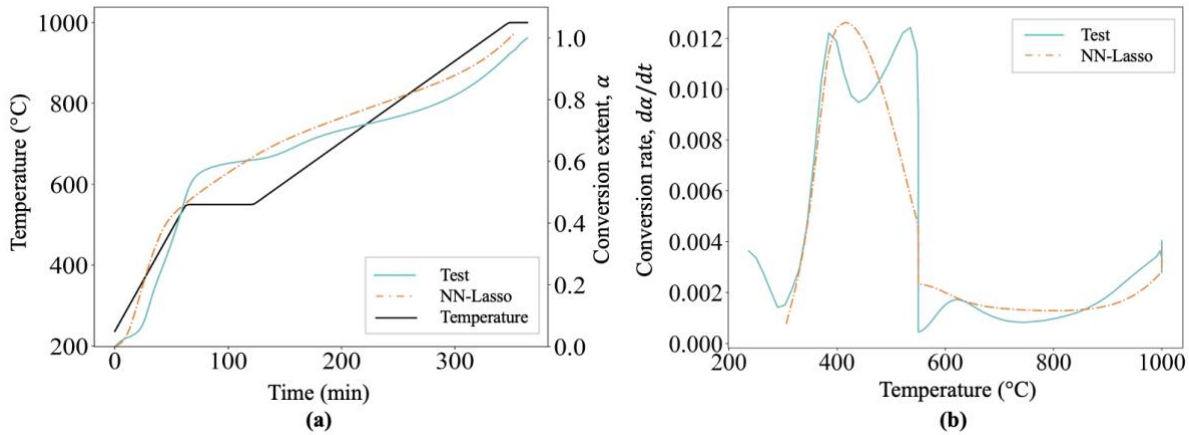

Figure 4: Comparison of the (a) conversion extent (α), and (b) conversion rate (dα/dt) curve predicted for a complex temperature cycle with that obtained from experimental results.

4 CONCLUSIONS

Accurate kinetic modeling of ceramic-matrix composites manufacturing remains a significant challenge, particularly during high-temperature processes like the pyrolysis stage. Predicting material behavior requires understanding the rate and mechanism of chemical reactions under varying thermal conditions, but this is often hindered by the complexity of multistage reactions and the limited, noisy nature of experimental data. These challenges highlight the need for efficient, interpretable modeling approaches that can capture the underlying kinetics while reducing experimental efforts.

Applied to the pyrolysis stage of ceramic-matrix composite manufacturing, the proposed machine learning-based framework demonstrated reliable performance in capturing overall reaction behavior using limited experimental data. By enforcing sparsity, the approach identified physics-based kinetic expressions, that are adaptable across different processing conditions.

While the balance between predictive accuracy and physical interpretability makes the NN-LASSO framework a promising tool for kinetic modeling, developing a single model that generalizes across all manufacturing scenarios remains a challenge. Incorporating physics-based constraints, could be a potential direction to address this challenge and support the development of a more robust machine learning framework. Future work will also focus on extending the application of this framework to other reaction kinetics and various thermally driven material transformations.

REFERENCES

[1] Rajak DK, Pagar DD, Menezes PL, Linul E. Fiber-reinforced polymer composites: Manufacturing, properties, and applications. Polymers (Basel) 2019;11. https://doi.org/10.3390/polym11101667.

[2] Rajak DK, Wagh PH, Linul E. Manufacturing technologies of carbon/glass fiber-reinforced polymer composites and their properties: A review. Polymers (Basel) 2021;13. https://doi.org/10.3390/polym13213721.

[3] Kausar A. Role of Thermosetting Polymer in Structural Composite. Issue 1 Kausar A American Journal of Polymer Science & Engineering 2017;5:1–12.

[4] Sykes GF. NASA Technical Note: Decomposition Characteristics of a Char-Forming phenolic Polymer Used for Ablative Composites. Washington, D. C.: 1967.

[5] Ko T-H. The Effect of Pyrolysis on the Mechanical Properties and Microstructure of Carbon Fiber-Reinforced and Stabilized Fiber-Reinforced Phenolic Resins for Carbon/ Carbon Composites. Polym Compos 1993;14.

[6] Pulci G, Tirillò J, Marra F, Fossati F, Bartuli C, Valente T. Carbon-phenolic ablative materials for re-entry space vehicles: Manufacturing and properties. Compos Part A Appl Sci Manuf 2010;41:1483–90. https://doi.org/10.1016/j.compositesa.2010.06.010.

[7] Wagner N, Rondinelli JM. Theory-guided machine learning in materials science. Front Mater 2016;3. https://doi.org/10.3389/fmats.2016.00028.

[8] Zobeiry N, Reiner J, Vaziri R. Theory-guided machine learning for damage characterization of composites. Compos Struct 2020;246. https://doi.org/10.1016/j.compstruct.2020.112407.

[9] Pawar S, San O, Aksoylu B, Rasheed A, Kvamsdal T. Physics guided machine learning using simplified theories. Physics of Fluids 2021;33. https://doi.org/10.1063/5.0038929.

[10] Bhadriraju B, Narasingam A, Kwon JS Il. Machine learning-based adaptive model identification of systems: Application to a chemical process. Chemical Engineering Research and Design 2019;152:372–83. https://doi.org/10.1016/j.cherd.2019.09.009.

[11] Portales Picazo P, Gray A, Zobeiry N. Efficient characterization and optimization of pyrolysis in carbon-carbon composites through machine learning. Compos Part A Appl Sci Manuf 2025;190. https://doi.org/10.1016/j.compositesa.2024.108664.

[12] Brunton SL, Proctor JL, Kutz JN. Discovering governing equations from data by sparse identification of nonlinear dynamical systems. Proc Natl Acad Sci U S A 2016;113:3932–7. https://doi.org/10.1073/pnas.1517384113.

[13] Nam J-D, Seferis JC. Volatile Evolution in Thermoset Composites from Processing to Degradation. Science and Engineering of Composite Materials 1993;2. https://doi.org/10.1515/SECM.1993.2.3.211.

[14] Trick KA, Saliba TE, Sandhu SS. A Kinetic Model of the Pyrolysis of Phenolic Resin in a Carbon/Phenolic Composite. Carbon N Y 1997;35:393–401.

[15] Jiang H, Wang J, Wu S, Wang B, Wang Z. Pyrolysis kinetics of phenol-formaldehyde resin by non-isothermal thermogravimetry. Carbon N Y 2010;48:352–8. https://doi.org/10.1016/j.carbon.2009.09.036.

[16] Aghili A, Shabani AH. A modification to the Friedman and Ortega isoconversional methods for evaluation of the activation energy as a function of conversion and temperature. Thermochim Acta 2024;736. https://doi.org/10.1016/j.tca.2024.179748.

[17] Gong J, Gu Y, Zhai C, Wang Z. A hybrid pyrolysis mechanism of phenol formaldehyde and kinetics evaluation using isoconversional methods and genetic algorithm. Thermochim Acta 2020;690. https://doi.org/10.1016/j.tca.2020.178708.

[18] Zhang H, Wang J, Sun Z, Zurada JM, Pal NR. Feature Selection for Neural Networks Using Group Lasso Regularization. IEEE Trans Knowl Data Eng 2020;32:659–73. https://doi.org/10.1109/TKDE.2019.2893266.

[19] Portales PP, Gray A, Zobeiry N. A Novel Framework for Accelerated Characterization of Pyrolysis Kinetics of High-Temperature Composites Using Theory-Guided Probabilistic Machine Learning. *Proceedings of the ASME 2023 Aerospace Structures, Structural Dynamics, and Materials Conference, 2023,* San Diego, CA.

[20] Muhammed F, Moretti L, Lavaggi T, Lam C, Tao T, Advani S, et al. Influence of pyrolytic decomposition on the microstructure evolution of benzoxazine-derived carbon–carbon composites. J Mater Sci 2022;57:21915–34. https://doi.org/10.1007/s10853-022-08007-9.

[21] Li C, Strachan A. Molecular scale simulations on thermoset polymers: A review. J Polym Sci B Polym Phys 2015;53:103–22. https://doi.org/10.1002/polb.23489.

[22] Zobeiry N, Humfeld KD. A physics-informed machine learning approach for solving heat transfer equation in advanced manufacturing and engineering applications. Eng Appl Artif Intell 2021;101. https://doi.org/10.1016/j.engappai.2021.104232.

ICCM24
AUGUST 4-8, 2025
BALTIMORE CONVENTION CENTER
BALTIMORE, MARYLAND, USA

No Technical Paper Submission for:

Kim Anh Pham

ICCM24 24TH INTERNATIONAL CONFERENCE ON COMPOSITE MATERIALS
AUG 4-8, 2025 • BALTIMORE CONVENTION CENTER • BALTIMORE, MARYLAND

SHAPE MEMORY BEHAVIOUR OF RE-ENTRANT UNIT CELL STRUCTURE BASED ON 3D PRINTED POLYURETHANE NANOCOMPOSITES

W.T. Nugroho[1], Y. Dong[2] and A. Pramanik[3]

[1]Department of Mechanical Engineering, Politeknik Negeri Jember
P.O. Box 164, Mastrip, 68121, Jember, East Java, Indonesia
Email: wendy@polije.ac.id, web page: http://www.https://teknik.polije.ac.id/

[2]School of Civil and Mechanical Engineering, Curtin University
Kent St, Bentley, Western Australia 6102, Australia
Email: y.dong@curtin.edu.au, web page: http://www.curtin.edu.au/

[3]School of Civil and Mechanical Engineering, Curtin University
Kent St, Bentley, Western Australia 6102, Australia
Email: alokesh.pramanik@curtin.edu.au, web page: http://www.curtin.edu.au/

Keywords: Shape memory behaviour, Re-entrant structure, 3D printing, Polyurethane, Nanocomposites

ABSTRACT

This paper investigates shape memory characteristics, negative Poisson's ratio (NPR) and thermal stability of re-entrant (RE) structures made from polyurethane (PU)/halloysite nanotube (HNT) nanocomposites via fused deposition modelling (FDM). The addition of 10 wt% HNTs within PU matrices enhanced shape fixity ratio of PU/HNT nanocomposites by 12% despite a slight drop in both shape recovery ratio (9%) and NPR (60%), along with prolonged recovery time up to 45%. This result clearly indicated their promising commercial potential as a shape-memory shock absorber in the future. Furthermore, the incorporation of HNTs improved thermal stability of PU/HNT nanocomposites, which was shown by their relatively high thermal decomposition temperatures. It could be associated with barrier effect of HNTs to postpone the degradation of PU hard segments. Additionally, an entrapping mechanism of HNT lumens made a significant contribution in thermal stability improvement of 3D printed nanocomposite structures. Finally, the presence of HNTs also elevated glass transition temperature T_g, melting temperature T_m, crystallisation temperature T_c and the degree of crystallinity χ_c due to much better covalent bonding, microphase separation and nucleating effect of such nanoparticles in addition to mobility restriction of PU molecules.

1 INTRODUCTION

Re-entrant (RE) structures have drawn great attention due to their light-weight and high-strength characteristics, resulting in a high stiffness/strength to mass ratio. Besides, such desired structures also possess unique material behaviour, namely negative Poisson's ratio (NPR), which allows them to exhibit transverse expansion under uniaxial tension and transverse contraction when subjected to uniaxial compression [1]. Lakes [2] mentioned that RE structures with remarkable shear stiffness for the first time, motivated many researchers to create and develop various auxetic structures over many decades.

It is tedious work to manufacture RE structures using conventional manufacturing methods such as injection moulding and melt extrusion owing to their typical lattice structures constructed from simple unit cells with significantly high porosity [3]. This critical issue can be overcome with the aid of 3D printing technology to achieve free-form fabrication. When RE structures are made from shape-memory polyurethane (PU), resulting structures reveal great potential as shock absorbers in possession of shape memory behaviour, enabling them to recover after deformation by using external stimuli such as heat, light, electrical and magnetic fields. Nevertheless, PU possesses typical drawbacks associated with its

mechanical strength [4]. Therefore, such a material requires the reinforcements like fibres and nanoparticles. Among nanoparticles like carbon nanotubes (CNTs), montmorillonites (MMTs) and halloysite nanotubes (HNTs), HNTs have typical advantages since they are classified as a non-toxic material and become abundantly available in nature as low-cost additives to improve mechanical properties [5].

This study presents a comprehensive investigation with respect to the effect of different HNT content (i.e. 0, 2, 4, 6, 8 and 10 wt%) on shape memory behaviour of PU/HNT nanocomposites via fused deposition modelling (FDM). Besides, thermal stability of 3D printed RE structures was also evaluated. Initial nanocomposite samples were prepared via mixing and solution casting processes. They were then examined in compression and shape memory tests, thermogravimetric analysis (TGA) and differential scanning calorimetry (DSC) to determine corresponding Poisson's ratio (PR), shape memory behaviour and thermal stability of 3D printed nanocomposites.

2 MATERIAL AND METHODS

Polyurethane (PU) MM 4520 [6] manufactured by SMP Technologies, Tokyo, Japan, was used as primary polymeric material in this study. Meanwhile, HNT particles were supplied by Imerys Ceramics Kaeo, New Zealand [7]. Dimethylformamide (DMF) [8] was employed as a chemical solvent to dissolve PU pellets for better HNT dispersion. DMF was supplied by Chem-Supply Pty Ltd., SA, Australia. The properties of PU and HNTs are listed in Tables 1 and 2 respectively.

Physical properties		Mechanical properties		Thermal properties	
Melt viscosity (Pa·s at 215°C)	3310	Young's modulus (MPa)	729	Glass transition temperature (˚C)	45
		Tensile strength at break (MPa)	41.4		
		Ultimate elongation (%)	600		
		Shore D hardness	72		

Table 1: PU MM-4520 properties [6].

Property	Value
Moisture content (%)	3.0
Specific gravity	2.55
pH (aqueous slurry at 20% solids)	3.5 – 4.5
Surface area [Brunauer-Emmett-Teller (BET)] (m^2/g)	25
Linear shrinkage (dried at 110°C) (%)	3.8
Modulus of rupture (dried at 110°C) (MPa)	2.9

Table 2: HNT properties [7].

To prepare nanocomposite samples, PU pellets and HNT particles were dried in a vacuum oven at 80°C for 4 and 8 h accordingly [6,9] in order to minimise adverse moisture effect, as depicted in Fig. 1. HNT particles were then dispersed in DMF with a mix ratio of 1:30 [10] using an ultrasonicating bath at the frequency of 25 kHz, power intensity of 90% and sonication time of 1 h [11]. Meanwhile, PU pellets were dissolved in DMF (mix ratio: 1:8) [10]. Before mixing with PU pellets, DMF was heated in a magnetic stirrer at 300°C with the rotor speed of 700 rpm. At this temperature, PU pellets were gradually added into the beaker until such materials were fully dissolved to prevent sedimentation issue.

Afterwards, HNT/DMF mixture was added into PU/DMF under stirring and heating processes for approximately 30 min. PU/HNT/DMF mixture was then cast onto a glass container, and then heated again in an oven at 100°C for 24 h to remove the solvent. Finally, prepared nanocomposite films were stored in a desiccator containing silicon gels before further material testing and characterisation. It is worth mentioning that nanocomposite film preparation in this study followed the same procedure previously mentioned elsewhere [13, 14].

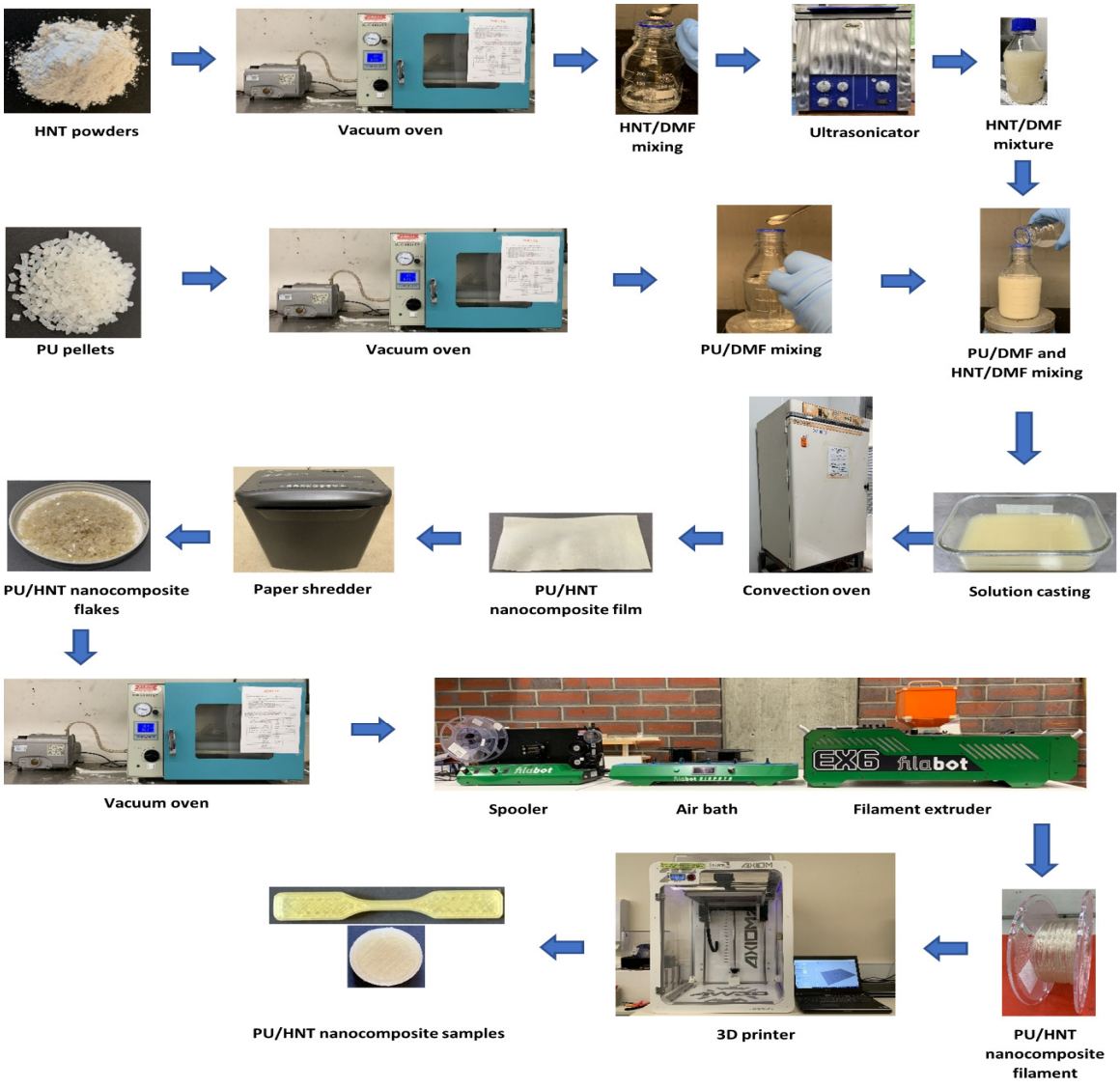

Figure 1: Flow chart of manufacturing PU/HNT nanocomposite films, filaments and samples [12].

The extrusion process was carried out using a single screw filament extruder, Filabot EX6 (Screw diameter: 16 mm and L/D ratio: 24) , supplied by Filabot company, VT, USA. Such an extruder has four temperature chambers consisting of feed, back, middle and front zones with specific temperatures controlled at 45, 165, 165 and 165˚C respectively. On the other hand, screw speed of filament extruder was set to 50 rpm to produce nanocomposite filaments.

Prior to an extrusion process, PU/HNT nanocomposite films were shredded and further chopped into small flakes with the thickness of 0.45 ± 0.1 mm, the width of 3.00 ± 0.1 mm and the length of 4.30 ± 0.5 mm. Processed flakes were then dried using a vacuum oven at a controlled temperature of 80°C for 4 h to reduce moisture content. After the extrusion process, nanocomposite filaments were spooled and further stored in airtight containers with silica gels in order to dry prepared filaments. Filament fabrication from virgin PU pellets also followed this procedure with the exception of no shredding and chopping. Processing parameters for filament extrusion are presented in Table 3.

Finally, nanocomposite samples were manufactured by employing a FDM printer Axiom 20 integrated with a built-in software APEX supplied by Airwolf 3D company, USA. The samples were created at various HNT contents according to Table 4. Meanwhile, the settings of selected 3D printing parameters and other fixed 3D printing parameters are listed in Tables 5 and 6.

Parameter	Setting
Front temperature (T_{front}) (°C)	165
Middle temperature (T_{mid}) (°C)	165
Back temperature (T_{back}) (°C)	165
Feed temperature (T_{feed}) (°C)	45
Extrusion speed (rpm)	50

Table 3: Settings of filament extrusion parameters.

Factor	Level					
HNT content (wt%)	0	2	4	6	8	10
Nozzle temperature (˚C)	210		220		230	
Print speed (mm/s)	10		20		30	
Infill density (%)	40		70		100	
Layer height (mm)	0.2		0.3		0.4	

Table 4: Summary of different HNT contents and 3D printing parameters in this study.

Parameter	Setting
Nozzle temperature (°C)	210
Print speed (mm/s)	10
Infill density (%)	100
Layer height (mm)	0.4

Table 5: 3D printing parameter settings.

Parameter	Specific parameter	Setting
Quality	Shell thickness (mm)	1.6
	Initial layer thickness (mm)	0.5
	Initial layer line width (%)	120
	Top surface quality	precise
Fill	Bottom/top thickness (mm)	1.2
	Infill interface density	dense
	Infill type	triangle
	Infill overlap (%)	15
Temperature	Bed temperature (°C)	55
Speed	Travel speed (mm/s)	150
	Bottom layer speed (mm/s)	15
	Infill speed (mm/s)	30
Filament	Flow (%)	115
Retraction	Speed (mm/s)	30
	Distance (mm)	5
	Minimum travel (mm)	1.5
	Minimal extrusion before retracting (mm)	0.005

Table 6: Fixed 3D printing parameters for PU/HNT nanocomposites.

Compression tests at the first step were carried out to assess the influence of HNT content on Poisson's ratio (PR) of 3D printed samples. Re-entrant (RE) structures were employed in this study for compression tests, which were made from both neat PU and PU/HNT nanocomposites. RE structures, as illustrated in Fig 2(a), have the length of vertical strut (l) of 20 mm, the length of inclined strut (s) of 12 mm and the height (h) of 20 mm. On the other hand, the width (w), the cell thickness (t) and the angle of inclined strut (θ) of this structure are 20 mm, 2 mm and 40º accordingly. Compression tests were

performed with the load-cell capacity of 10 kN to conduct uniaxial quasi-static tests at room temperature in the in-plane *y* direction depicted in Fig. 2(b). Under the tests, RE structures were set on the fixed platen on the universal testing machine, and three structure samples were assessed for test reproducibility at each HNT content.

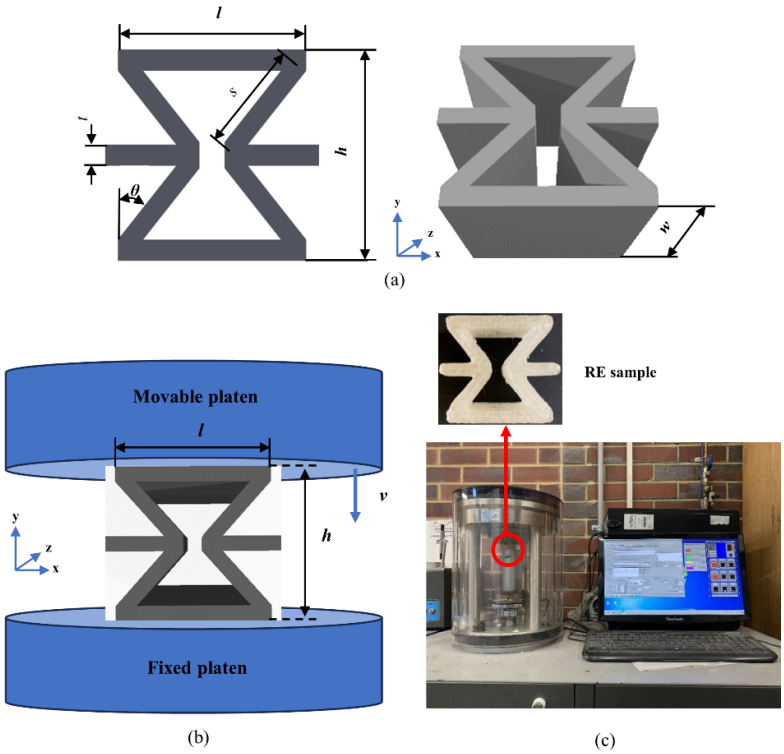

Figure 2: (a) A RE structure and its dimensions (in mm), (b) a schematic diagram of typical compression test for RE structure and (c) compression test for the investigation of shape memory behaviour of RE structure.

The crosshead speed of movable platen travelling downwards was set to 0.5 mm/min according to ASTM C365 standard. The test ended when a densification phenomenon was reached. Nominal stress σ and normal strain ε were determined based on equations (1) and (2) as follows

$$\sigma = \frac{F}{l \times w} \tag{1}$$

$$\varepsilon = \frac{\Delta h}{h} \tag{2}$$

where F and Δh are the applied load and the change of displacement between movable and fixed platens. The built-in software of the universal testing machine was used to automatically record such displacement along with time and force throughout compression tests.

PR in this study can be defined as the negative ratio of lateral strain to axial strain. The axial strain was calculated based on the platen displacement in the *y*-axis. On the other hand, a digital camera Fujifilm X-T3 manufactured by Fujifilm Corporation, Tokyo, Japan, was used to capture RE structure displacement in the *x*-axis. The resulting data were employed to determine the lateral displacement in the *x*-axis with the aid of DaVinci Resolve 18 and ImageJ 153 software. The values of axial strain ε and lateral strain ε_L were determined using equations (2) and (3). In addition, l and Δl denote initial length and the change of the length. Meanwhile, PR was calculated using equation (4) [15].

$$\varepsilon_L = \frac{\Delta l}{l} \tag{3}$$

$$PR = -\frac{\varepsilon_L}{\varepsilon} \quad (4)$$

Compression tests at the second test step to evaluate shape memory behaviour of RE structures were conducted at 50˚C using an asphalt mixture performance tester (AMPT) with the load cell of 15 kN depicted in Fig. 2(c). This device is equipped with an oven, enabling it to perform compression at elevated temperatures. The compression process was ended immediately after Δh reached 8 mm where Δh of 5 mm was considered as the onset densification of RE structures. The oven employed at the first test step was also applied to evaluate shape memory behaviour of RE nanocomposite structures at the second test step. The oven heating temperature was set to 80˚C for fast recovery and twisting effect.

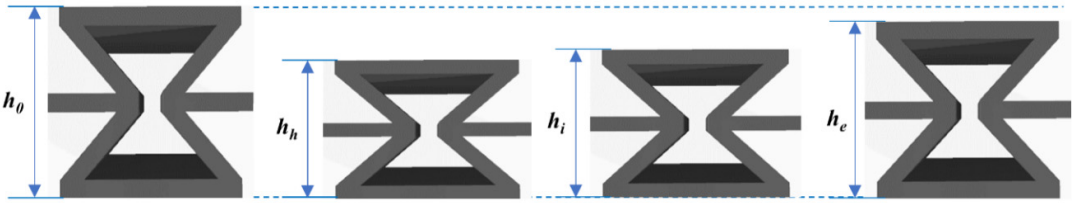

Figure 3: Compression tests for shape memory behaviour of RE structures

Fig. 3 exhibits different heights of RE unit-cell samples, namely the height before compression h_o, the height after compression h_h, the height after load removal h_i and the height after recovery h_e. Equations (5)-(9) can be applied to determine shape fixity ratio R_f, shape recovery ratio R_r, the amount of deformation after load removal ε_u, maximum strain ε_m and the amount of reversible strain ε_p.

$$R_f = \frac{\varepsilon_u}{\varepsilon_m} \times 100\% \quad (5)$$

$$R_r = \frac{\varepsilon_m - \varepsilon_p}{\varepsilon_m} \times 100\% \quad (6)$$

$$\varepsilon_m = \frac{h_o - h_h}{h_o} \quad (7)$$

$$\varepsilon_u = \frac{h_o - h_i}{h_o} \quad (8)$$

$$\varepsilon_p = \frac{h_o - h_e}{h_o} \quad (9)$$

A thermogravimetric analyser (TGA) SDT 2960, supplied by TA Instruments, USA, was used to investigate thermal stability of neat PU and PU/HNT nanocomposites based on sample weight-loss method. A cooling system with cryofill liquid nitrogen was utilised to determine the weight loss of material samples. About 20 mg TGA samples were heated from 25 to 900°C with the heating rate of 10°C/min [13]. Conversely, a differential scanning calorimeter Discovery DSC 25, supplied by Texas Instruments, USA, was in operation to evaluate glass transition temperature (T_g), crystallisation temperature (T_c) and melting temperature (T_m) of neat PU and PU/HNT nanocomposites. About 4 mg DSC samples were placed in aluminium pans, then heated from -50 ˚C to 240˚C with the heating rate of 20˚C/min. To eradicate thermal history, an isothermal condition was kept at 240˚C for 5 min. DSC samples were then cooled from 240˚C to –50˚C with the same cooling rate of 20˚C/min again. Heating-cooling processes were replicated for the second time. T_g and T_m were then detected from the first heating while T_c was determined from the second heating.

3 RESULTS AND DISCUSSION

3.1 Effect of HNT Content on NPR

The addition of HNTs within PU matrices tended to restrict the mobility of polymeric chains, thus resulting in much higher stiffness. The presence of siloxane and aluminol groups on HNT surfaces

induced hydrogen bonding with PU molecular chains, which further reduced their mobility. Moreover, when HNT content was increased up to 10 wt%, it could reduce engineering strain specifically with respect to lateral strain. This is attributed to the limited effect on the movement of polymeric chains, thereby resulting in a decrease in NPR by approximately 60% (Fig. 4). RE structures made from PU/HNT nanocomposites had an auxetic behaviour due to their unique forms, which allowed them to encounter transverse contraction under uniaxial compression [16]. Once compression strain reached 10%, the curve section of the strut in the middle region of RE structure touched each other, which was followed by a decrease in lateral strain. It was evidently observed that all curves had a consistent trend from initial sharp rise to nearly the plateaus, which was in good agreement with Park et al. [17] to investigate the efficacy of chondrocyte proliferation for PU auxetic scaffolds in compressive tests, which was especially applicable to articular cartilage in tissue engineering. Overall, PR versus compressive strain curves of PU/HNT nanocomposites appeared to be in good accordance with Alomarah et al. [18] where PR values were calculated based on lateral engineering strain and axial engineering strain for RE structures under compressive loading in the *x*-direction.

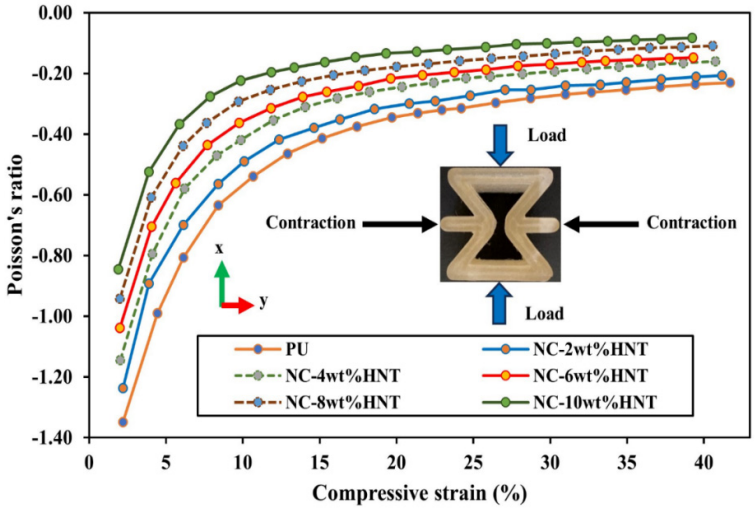

Figure 4: Effect of HNT content on NPRs of PU and PU/HNT nanocomposite samples.

3.2 Effect of HNT content on shape memory behaviour

In relation to shape memory behaviour, the presence of HNTs induced three different effects on 3D printed nanocomposite samples. The first effect was associated with the improved ability of PU/HNT nanocomposite samples to be programmed, which enhanced their shape fixity ratio. The inclusion of 10 wt% HNTs could enhance the shape fixity ratio of nanocomposite samples up to 12%, as opposed to that of virgin PU according to Fig. 5(a). This phenomenon might be related to strain-induced crystallisation effect [17]. The incorporation of rigid nanofillers such as HNTs increased soft-segment crystallinity. Furthermore, the strain distribution in PU matrices in the vicinity of HNTs became greater under deformation. It could be induced by significant modulus difference between the matrices and the fillers [19]. Strain localisation promoted strain-induced crystallisation caused by higher crystallisation to limit the relaxation process of deformed polymeric chains. The increase of HNT content was detected to further enhance strain-induced crystallisation, as indicated by shorter h_i along with higher R_f.

The second effect was related to HNTs to prevent PU matrices from regaining their original form, leading to the reduction of shape recovery ratio. In particular, when PU was incorporated with 10 wt% HNTs, shape recovery ratio of resulting nanocomposite samples slightly declined to 9%. Final effect could be associated with the contribution of existing HNTs to hinder PU molecules from shape recovery, and further prolong the recovery time by 45% with the addition of 10 wt% HNTs in their nanocomposites according to Fig. 5(b).

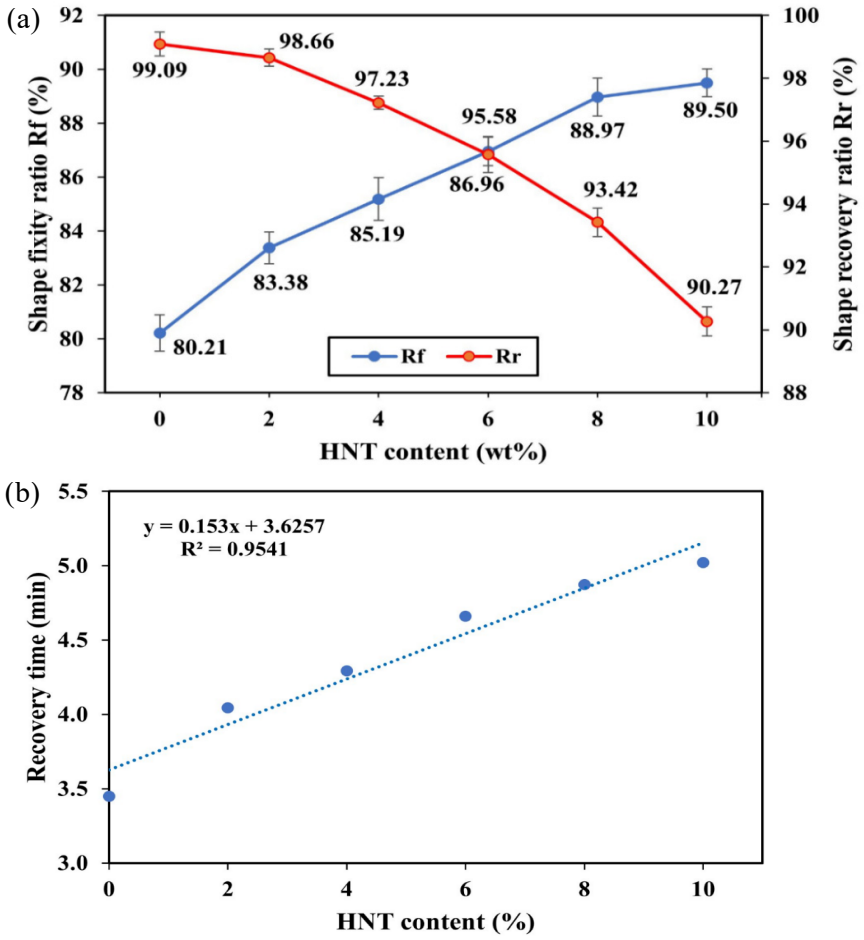

Figure 5: (a) Shape fixity and shape recovery ratios and (b) recovery time of PU/HNT nanocomposites

3.3 Effect of HNT content on thermal stability

Thermal stability for PU/HNT nanocomposites was shown in their TGA thermograms in Fig. 6(a). Four decomposition temperatures, represented by T_{d1}, T_{d2}, T_{d3} and T_{d4}, were associated with hard segment degradation of PU matrices into isocyanate and alcohol along with a clear sign of process complexity [20]. As for T_{d1} and T_{d2}, they were related not only to hard-segment dissociation of PU/HNT nanocomposites [21], but also to a bond disentangle of water molecules in empty tubular lumens of HNTs [22]. T_{d3} and T_{d4} were referred to as the thermal decomposition of PU soft segments [23] and carbon degradation accordingly.

Four TGA peaks appeared for neat PU at the temperature ranges of 41-348˚C, 348-387°C, 387-460°C and 663-788°C. Conversely, four temperature ranges were also identified at 28-358˚C, 358-391˚C, 391-465˚C and 664-782˚C with respect to four corresponding TGA peaks of PU/HNT nanocomposites reinforced with 2 wt% HNTs. The addition of HNTs to PU matrices increased T_{d1}, T_{d2}, T_{d3} and T_{d4} to higher temperature levels when compared with those of neat PU, as indicated in Fig. 6(b). This tendency could be caused by barrier effect of HNTs to postpone the dissociation of PU hard segments, resulting in the increase of T_d [23]. Moreover, an entrapping mechanism of HNT lumens for degradation products of polymers increased thermal stability and significantly delayed mass transport [24]. When HNT content was beyond 2 wt%, the decomposition temperatures of nanocomposite samples slightly decreased, in particular for T_{d3} and T_{d4} of PU/HNT nanocomposites at HNT contents of 4, 6, 8 and 10 wt% shown in Table 7. It might be ascribed to inhibited hydrogen bonding between hard segment domains of PU matrices and embedded HNTs to hinder the retention of thermal stability for polymer

nanocomposites [21]. Generally speaking, T_{d1}, T_{d2}, T_{d3} and T_{d4} of nanocomposite samples were higher than those of neat PU. It implied that the presence of HNTs within PU matrices tended to improve thermal stability of resulting PU/HNT nanocomposites.

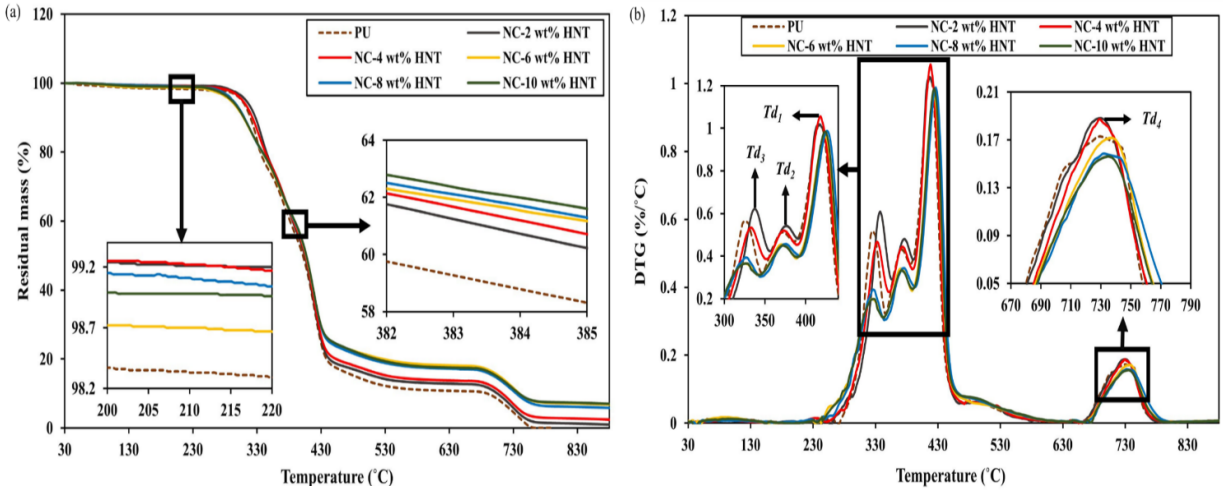

Figure 6**:** TGA thermograms for PU and PU/HNT nanocomposites: (a) TGA curves and (b) DTG curves. Note T_d refers to the decomposition temperature.

Material type	Sample batch	T_{d1} (°C)	DTG (%/°C)	T_{d2} (°C)	DTG (%/°C)	T_{d3} (°C)	DTG (%/°C)	T_{d4} (°C)	DTG (%/°C)
Neat PU	PU	325.31	0.5661	371.19	0.5118	416.85	1.021	730.08	0.1732
2 wt% HNTs	NC-2 wt% HNT	337.59	0.6223	376.4	0.5418	417.49	1.017	730.15	0.1882
4 wt% HNTs	NC-4 wt% HNT	333.04	0.5336	373.41	0.5196	418.13	1.056	729.12	0.1873
6 wt% HNTs	NC-6 wt% HNT	327.52	0.3655	372.4	0.4496	424.3	0.9843	734.81	0.1563
8 wt% HNTs	NC-8 wt% HNT	326.49	0.393	375.97	0.4568	426.36	0.9878	730.2	0.163
10 wt% HNTs	NC-10 wt% HNT	325.82	0.3656	370.47	0.455	423.82	0.9619	737.3	0.1718

DTG stands for derivative thermogravimetry, which is a technique that plots the derivative of the TGA curve and represents the rate of mass change with respect to temperature or time.

Table 7: TGA data summary of PU and PU/HNT nanocomposite samples.

3.4 DSC thermal analysis

DSC thermograms for nanocomposite samples at various HNT contents were displayed in Fig. 7, while their thermal parameters were presented in Table 8. As mentioned earlier, PU molecules comprise hard and soft segments. T_g is connected to hard segments because of covalent bonding of NCO and OH groups to influence the mobility of polymeric chains [25]. The presence of HNTs may promote covalent bonding despite the limitation to chain mobility of PU molecules, resulting in the increase of T_g [26]. The addition of HNT content up to 4 wt% within PU matrices increased T_g to be 42.56°C, as opposed to 40.96°C for neat PU according to Fig. 7(a) and Table 8. When HNT content was increased, urethane stability was disturbed, inducing a further drop in T_g [21]. The incorporation of HNTs within PU matrices generated microphase separation due to specific transformation into hard segments by embedding such nanoparticles [26]. The addition of small amounts of HNTs at approximately 2 wt% in nanocomposites enhanced melting temperature up to 166.16°C when compared with that of neat PU at 161.32°C. Beyond this content level, the purification of soft segments prevailed, which was followed by the extraction of hard segments from the mixture. Accordingly, T_m shifted to the lower temperature level shown in Table 8, which was supported by previous work carried out by Razzaq et al. [27].

The inclusion of HNTs in nanocomposites yielded a higher χ_c owing to typical nucleating effect of HNTs [26]. When HNT content was increased to 6 wt%, χ_c of nanocomposite samples was improved by 55% relative to that of neat PU, as shown in Table 8. A further increase in HNT content from 6 to 10 wt% yielded a reduction in the growth rate of nuclei in the crystallisation process. It was evidenced by approximately 10% increase in χ_c. Additionally, the incorporation of HNTs also shifted DSC peaks with respect to the crystallisation temperatures of hard and soft segments, which were represented by $T_{c,HS}$ and $T_{c,SS}$, as demonstrated in Fig. 8(b) and Table 8. A higher T_c was proven to increase microphase separation, thus leading to pure soft segments and better shape fixity [26, 28].

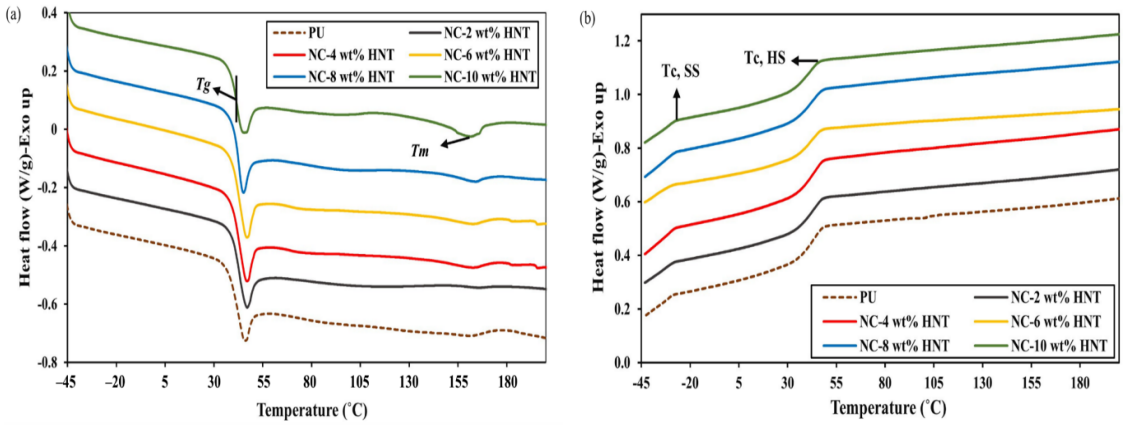

Figure 7: DSC thermograms of nanocomposite samples at various HNT contents: (a) heating process and (b) cooling process.

Material type	Sample batch	T_g (°C)	$T_{c,SS}$ (°C)	$T_{c,HS}$ (°C)	T_m (°C)	ΔH_m (J/g)	ΔH_c (J/g)	χ_c (%)
Neat PU	PU	40.96	–31.05	47.66	161.32	4.34	0.37	2.84
2 wt% HNT	NC-2 wt% HNT	42.44	–30.12	48.44	166.16	4.26	0.34	2.85
4 wt% HNT	NC-4 wt% HNT	42.56	–29.88	49.36	163.32	5.18	0.64	3.38
6 wt% HNT	NC-6 wt% HNT	42.35	–28.56	49.43	163.04	6.23	0.43	4.41
8 wt% HNT	NC-8 wt% HNT	41.57	–28.07	48.42	164.03	6.43	0.49	4.61
10 wt% HNT	NC-10 wt% HNT	41.28	–27.24	48.04	161.78	6.68	0.53	4.89

ΔH_m and ΔH_c denote the heat of fusion and heat of crystallization of neat PU and PU/HNT nanocomposites respectively.

Table 8: DSC thermal properties for neat PU and PU/HNT nanocomposites.

4 CONCLUSIONS

This study presented holistic evaluation of HNT addition on NPR, shape memory behaviour and thermal stability of 3D printed PU/HNT nanocomposites. In general, the presence of HNTs in PU matrices could promote shape fixity ratio of PU/HNT nanocomposites despite slight drop in both shape recovery ratio and NPR, along with prolonged recovery time. The presence of 10 wt% HNTs within PU matrices improved shape fixity ratio of PU/HNT nanocomposites up to 12% though a slight decrease occurred in shape recovery ratio (9%) and NPR (60%), along with prolonged recovery time by 45%. They might have great commercial potential as a shape-memory shock absorber in the future.

The inclusion of HNTs enhanced thermal stability of PU/HNT nanocomposites, which was indicative of their relatively high decomposition temperatures. It could be associated with thermal barrier effect of HNTs to postpone the degradation of PU hard segments. Furthermore, an entrapping mechanism of HNT lumens played a significant role in increasing thermal stability of nanocomposite samples. Finally, the incorporation of HNTs also elevated T_g, T_m, T_c and χ_c due to much better covalent bonding, microphase separation and nucleating effect of HNTs in addition to evident mobility restriction of PU molecules.

ACKNOWLEDGEMENTS

The first author acknowledged the award of a PhD scholarship supported by the Ministry of Finance of the Republic of Indonesia, Secretariat General of Indonesia Endowment Fund for Education, known as Lembaga Pengelola Dana Pendidikan (LPDP) (Grant number S-992/ LPDP.3/2018).

REFERENCES

[1] M. Ozturk, T. Baran and T. Mehmet, Experimental and numerical investigation of conventional and stiffened re-entrant cell structures under compression, *Journal of The Brazilian Society of Mechanical Science and Engineering,* **44**, 2022, pp. 593 (doi: 10.1007/s40430-022-03889-x).

[2] R. S. Lakes, Design considerations for materials with negative Poisson's ratios, *Journal of Mechanical Design*, **115**, 1993, pp. 696–700 (doi: 10.1115/1.2919256).

[3] W. T. Nugroho, Y. Dong and A. Pramanik, Mechanical and Shape Memory Properties of Additively Manufactured Polyurethane (PU)/Halloysite Nanotube (HNT) Nanocomposites, *Nanomaterials*, **14**, 2024, pp. 1373. (doi: 10.3390/nano14161373.

[4] Z. S. Petrovic and J. Ferguson, Polyurethane elastomers, *Progress in Polymer Science*, **16**, 1991, pp. 695–836, (doi: 10.1016/0079-6700(91)90011-9).

[5] G. Biddeci, G. Spinelli, P. Colomba and F. Di Blasi, Nanomaterials: a review about halloysite nanotubes, properties, and application in the biological field, *International Journal of Molecular Sciences*, **23**, 2022, pp. 11518, (doi: 10.3390/ijms231911518).

[6] SMP Technologies, Shape memory polymer. SMP Technologies, 2021. Accessed March 5, 2022, (http://www2.smptechno.com/en/smp/).

[7] Imerys, Halloysite, 2021, Accessed November 2021, (https://www.imerys.com/minerals/halloysite).

[8] Scientific, CSA, Dimethylformamide, CSA Scientific, 2021, Accessed November 4, 2021, (https://shop.chemsupply.com.au/search?ProductSearch=DMF).

[9] R. Bouaziz, K. Prashantha and R. Roger, Thermomechanical modeling of halloysite nanotube-filled shape memory polymer nanocomposites, *Mechanics of Advanced Materials and Structures,* **26** (14), 2019, pp. 1209-1217, (doi: 10.1080/15376494.2018.1432793).

[10] C. Rosales, M. Duarte, H. Kim, L. Chavez, D. Hodges, P. Mandal, Y. Lin and T. Tseng, 3D printing of Shape Memory Polymer (SMP)/Carbon Black (CB) nanocomposites with electro-responsive toughness enhancement, *Material Research Express, 5*, 2018, 1-14, (doi: 10.1088/2053-1591/aacd53).

[11] H. Salam, Synthesis and characterisation of bio-based epoxy/clay nanocomposites. PhD thesis, Curtin University, 2017.

[12] W. T. Nugroho, Y. Dong, A. Pramanik, Z. Zhang and S Ramakrishna, Co-influence of nanofiller content and 3D printing parameters on mechanical properties of thermoplastic polyurethane (TPU)/halloysite nanotube (HNT) nanocomposites, *Nanomaterials*, **13**, 2023, pp. 1975, (doi: 10.3390/nano13131975).

[13] B. Adak, B. Butola and M. Joshi, Effect of organoclay-type and clay-polyurethane interaction chemistry for tuning the morphology, gas barrier and mechanical properties of clay/polyurethane nanocomposites, *Applied Clay Science,* **161**, 2018, pp. 343-353, (doi: 10.1016/j.clay.2018.04.030).

[14] M. Massaro, S. Piana, C. Colletti, R. Noto, S. Riela, C. Baiamonte, C. Giordano, G. Pizzolanti, G. Cavallaro, S. Milioto and G. Lazzara, Multicavity halloysite–amphiphilic cyclodextrin hybrids for co-delivery of natural drugs into thyroid cancer cells, *Journal of Materials Chemistry B,* **3**, 2015, pp. 4074-4081, (doi: 10.1039/C5TB00564G).

[15] L. Chow, K. Yick, K. Wong, M. Leung, Y. Sun, M. Kwan, K. Ning, A. Yu, J. Yip, Y. Chan and Z. Ng, 3D printing auxetic architectures for hypertrophic scar, *Macromolecular Materials and Engineering,* **307**, 2022, pp. 2100866, (doi: 10.1002/mame.202100866).

[16] M. Ozturk, T. Baran and T. Mehmet, Experimental and numerical investigation of conventional and stiffened re-entrant cell structures under compression, *Journal of The Brazilian Society of Mechanical Science and Engineering,* **44**, 2022, pp. 593, (doi: 10.1007/s40430-022-03889-x).

[17] Y. J. Park and J. K. Kim, The Effect of negative Poisson's ratio polyurethane scaffolds for articular cartilage tissue engineering applications, *Advances in Material Sciences and Engineering*, 2023, pp. 853289, (doi: 10.1155/2013/853289).

[18] A. Alomarah, S. H. Masood, I. Sbarski, B. Faisal, Z. Gao, and D. Ruan, Compressive properties of 3D printed auxetic structures: Experimental and numerical studies, *Virtual and Physical Prototyping,* **15**, 2019, pp. 1–21, (doi: 10.1080/17452759.2019.1644184).

[19] H. Koerner, G. Price, N. Pearce, M. Alexander and R. Vaia, Remotely actuated polymer nanocomposites--stress-recovery of carbon-nanotube-filled thermoplastic elastomers, *Nature Materials,* **3**, 2004, pp. 115–120, (doi: 10.1038/nmat1059).

[20] Z. Petrovic, Z Zavargo, J. Flyn and W. Macknight, Thermal degradation of segmental polyurethanes, *Journal of Applied Polymer Science, 51*, 1994, pp. 1087-1095, (doi: 10.1002/APP.1994.070510615).

[21] A. Maamoun, A. Elkhateeb and S. Zulfiqar, (2022) Halloysite-decorated mechanically robust polyurethane nanocomposite foams for acoustic relevance, *Industrial & Engineering Chemistry Research,* **61**, pp. 17937-17949, (doi: 10.1021/acs.iecr.2c03535).

[22] M. Mahunaki, V. Asl, H. Mamaqani, M. Koosha and M. Yazdi, Halloysite-reinforced thermoplastic polyurethane nanocomposites: Physico-mechanical, rheological, and thermal investigations, *Polymer Composites,* **41**, 2020, pp. 3260-3270, (doi: 10.1002/pc.25617).

[23] W. Wu, W. Zhao, X. Gong, Q. Sun, X. Cao, Y. Su, B. Yu, R. Li and R. Vellaisamy, Surface decoration of halloysite nanotubes with POSS for fire-safe thermoplastic polyurethane nanocomposites, *Journal of Materials Science & Technology,* **101**, 2022, pp. 107−117, (doi: 10.1016/j.jmst.2021.05.060).

[24] M. Du, B. Guo and D. Jia, Thermal stability and flame retardant effects of halloysite nanotubes on poly (propylene), *European Polymer Journal,* **42**, 2006, pp. 1362−1369, (doi: 10.1016/j.eurpolymj.2005.12.006).

[25] I. S. Jouibari, V. H. Asl, H. Ahmadi and M. M. Mirhosseini, Micro-phase separation kinetics of polyurethane nanocomposites with neural network, *Polymer Composite,* **40**, 2019, pp. 3904-3913, (doi: 10.1002/pc.25250).

[26] F. Mohammadzadeh, V. Asl, Z. Balzade and I. Jouibari, (2020) Switch segment and halloysite nanotube role in the phase separation behavior of shape-memory thermoplastic polyurethane, *Polymer Composites,* **41**, 2020, pp. 1-9, (doi: 10.1002/pc.25561).

[27] M. Razzaq, M. Anhalt, L. Frormann and B. Weidenfeller, Mechanical spectroscopy of magnetite fillet polyurethane shape memory polymers, *Material Science & Engineering A,* **471**, 2007, pp. 57-62, (doi: 10.1016/j.msea.2007.03.059).

[28] H. Mamaqani, V. Asl and M. Kalajahi, In situ controlled radical polymerization: A review on synthesis of well-defied nanocomposites. *Polymer Review,* **52**, 2012, pp. 142-188, (doi: 10.1080/15583724.2012.668153).

Direct Ink Writing antenna radiator for Conformal Load-bearing Antenna Structure

Jae-An Jeon[1*], Jae-Yeon Cho[1*], Woo-sung Chung[2], Ill-Kyung Park[3], Jae-Won Chang[3], Sang-Eui Lee[1+]

[1]Mechanical Engineering Department, Inha University, [2]DANAM systems, [3]Korea Aerospace Research Institute

[+] E-mail: selee@inha.ac.kr

([*]Equally contributed to this work)

2025.08.05

Contents

01. Introduction
1. Research background
2. Research purpose

02. DIW antenna radiator fabrication and evaluation
1. Development of Materials and Process
2. Fabrication and evaluation of DIW antenna

03. Integration into CLAS
1. Fabrication and Evaluation of MAS
2. Integration of DIW antenna into CLAS

04. Conclusion

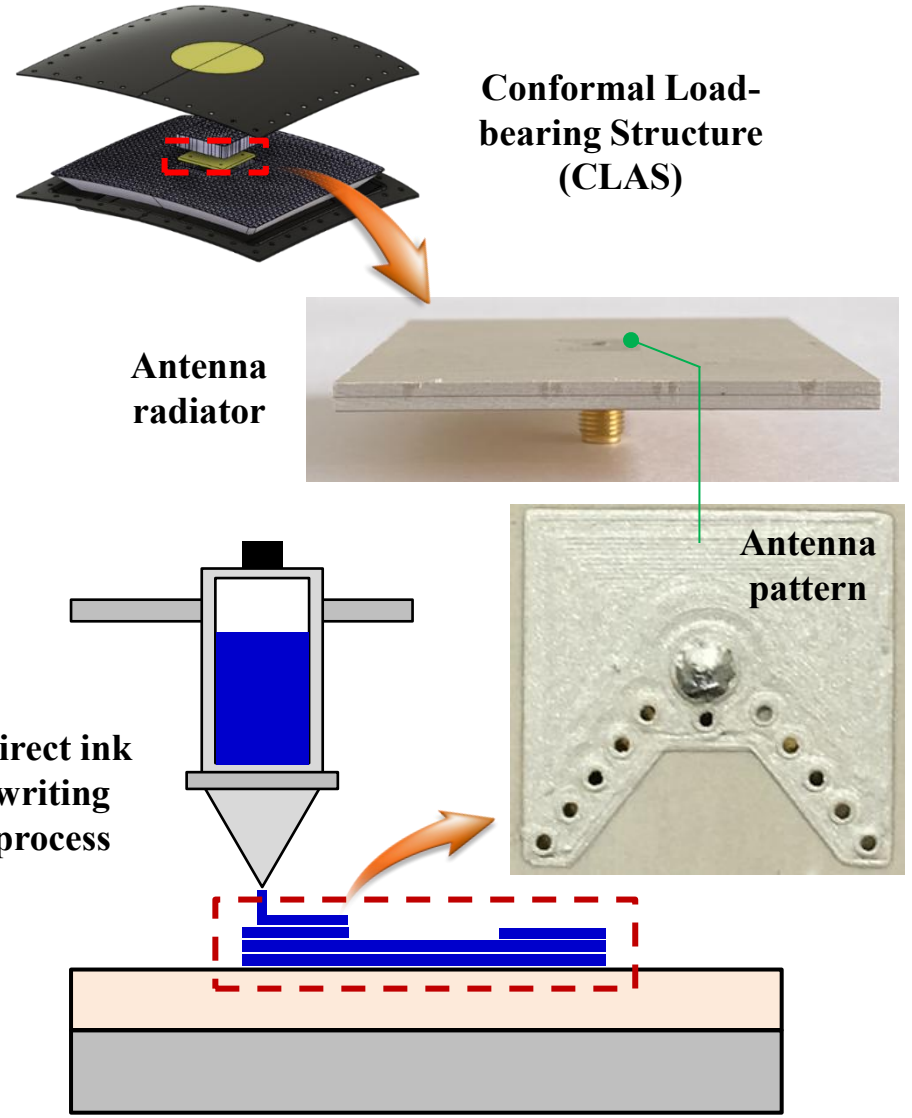

01. Introduction

1. Research background
2. Research purpose

Research background

❖ CLAS (Conformal Load-bearing Antenna Structure)

- **What is Conformal Load-bearing Antenna Structure (CLAS) ?**
  - Next-generation antenna integrated into the aircraft's Outer Mold Line (OML)
  - Replaces protruding antennas for improved aerodynamics
- Composed of multiple parts, including an antenna radiator for signal transmission and reception

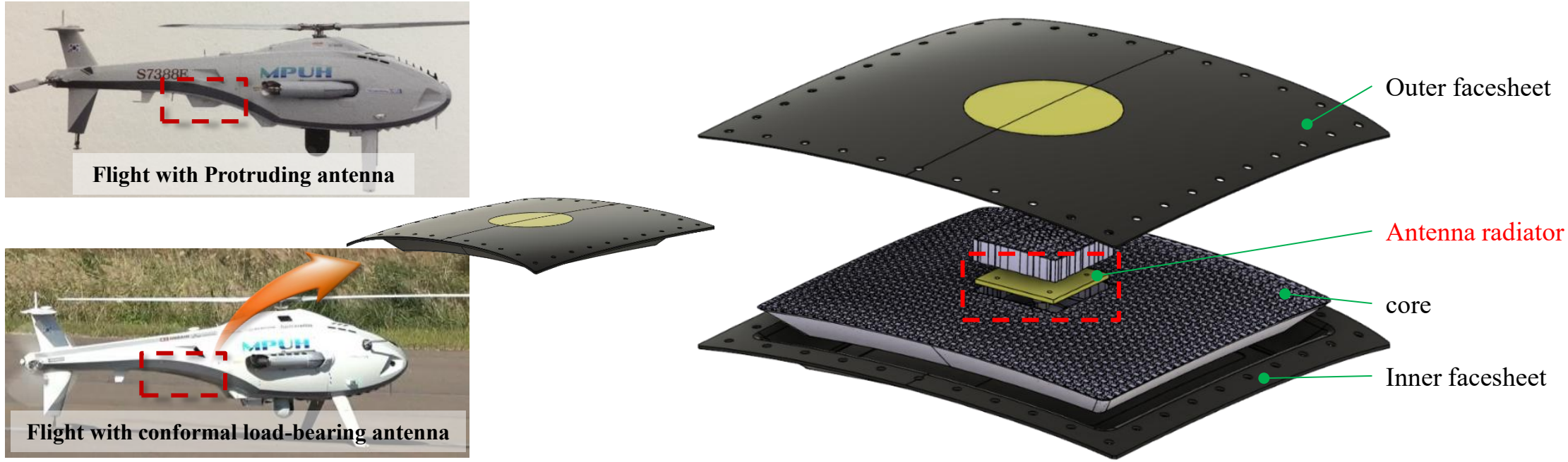

Fig. 1. Schematic of Conformal load bearing antenna structure (CLAS).

Research background

❖ Antenna radiator and limitations of conventional antenna fabrication

- Traditional antenna fabrication is limited by substrate type and shape
- **CLAS often follows curved aircraft surfaces (OML), requiring non-flat substrates**

  → Growing need for antennas on curved or complex geometries
- Direct Ink Writing (DIW) offers a flexible solution for conformal antenna fabrication

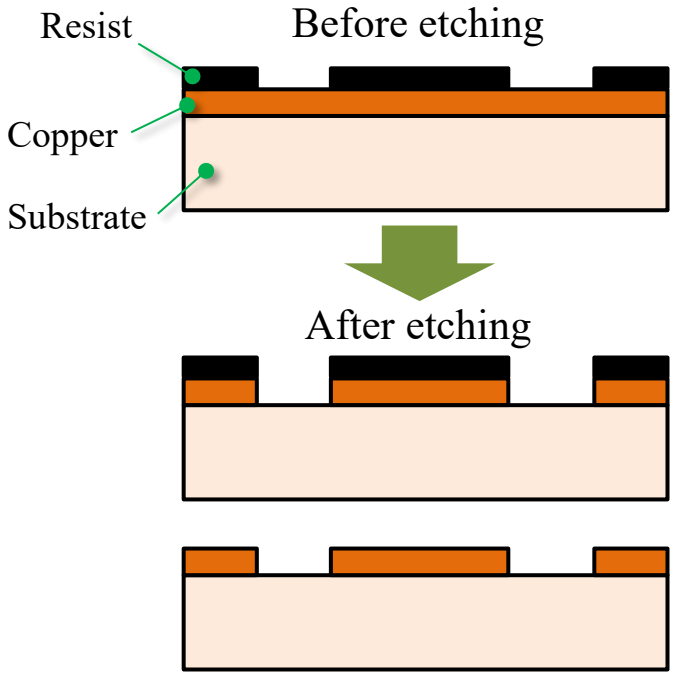

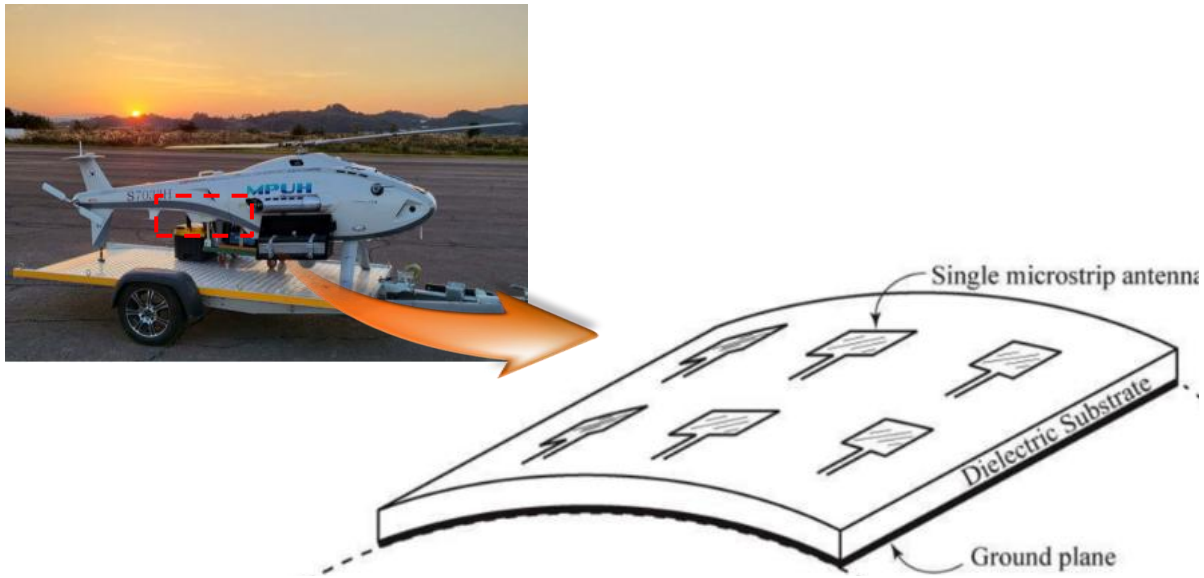

Fig. 2. Copper etching microstrip antenna.

Research background

❖ DIW (Direct Ink Writing) Process [1-7]

- **What is Direct Ink Writing (DIW)?**
  - A type of 3D printing that directly deposits ink onto a substrate
- Enables multifunctional structures using application-specific materials
- Compatible with various substrate shapes, including flat and curved surfaces

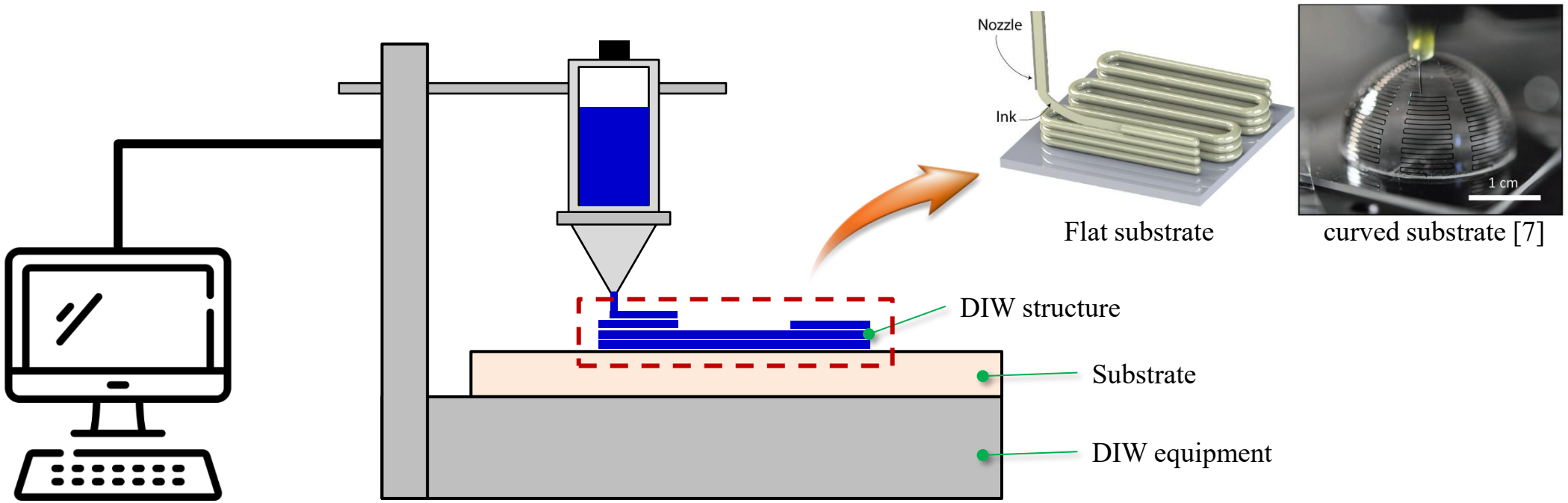

Fig. 3. Schematic of Direct ink writing (DIW) fabrication process.

Research background

❖ Research trends in DIW process

➢ Skylar-Scott et al., PNAS, 2016

- Demonstrated laser-assisted DIW
- Using Silver nanoparticle ink
- Enabled 3D printing without separate sintering

➢ Asrar Alam et al., J. Energy Storage, 2022

- Developed Ag/TiO_2 nanoparticle composite ink
- Electrode material for high-performance supercapacitors
- Cured at 60 °C for 24 hours without sintering

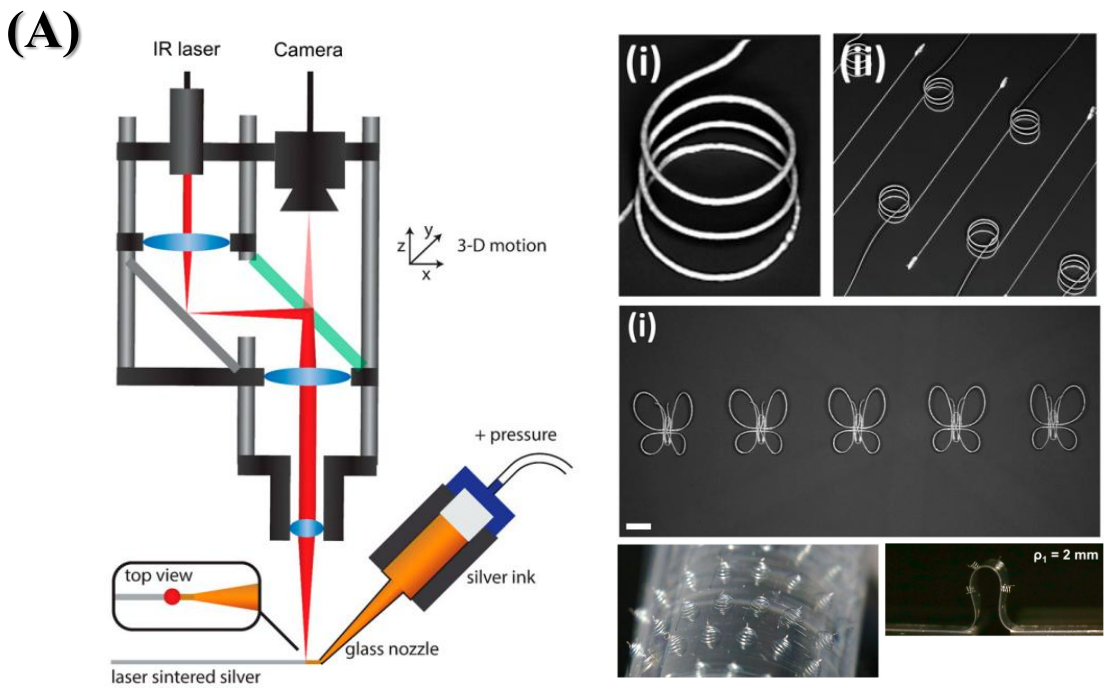

Fig. 4. DIW fabrication process research trends: (A) 2016, PNAS, (B) 2022, J Energy storage.

Research purpose

❖ Study on CLAS with DIW antenna radiator

- **Design requirements for printed antenna radiator patterns**
  - Targeting resonant frequency and bandwidth suitable for structural reliability and operational conditions
- Development and performance evaluation of DIW-based antennas for integration
- Investigation of printed antenna implementation in conformal load-bearing structures

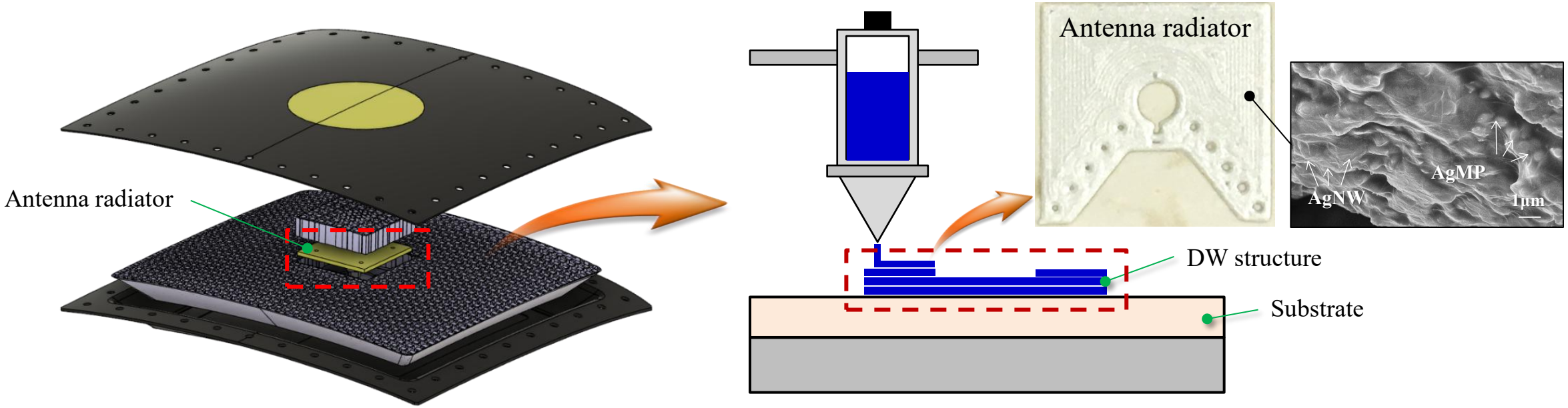

Fig. 5. Research purpsose.

02. DIW antenna radiator fabrication and evaluation

1. Development of Materials and Process
2. Fabrication and evaluation of DIW antenna

Development of DIW Materials and Process

❖ Selection of materials for DIW antenna radiator

- Silver Microparticle Paste (AgMP, ACH35001LV, Protavic Korea)

  → Ensures strong adhesion to substrate

- Silver Nanowires (AgNW, C3NW02, C3nano, USA)

  → Enhances electrical conductivity of printed patterns

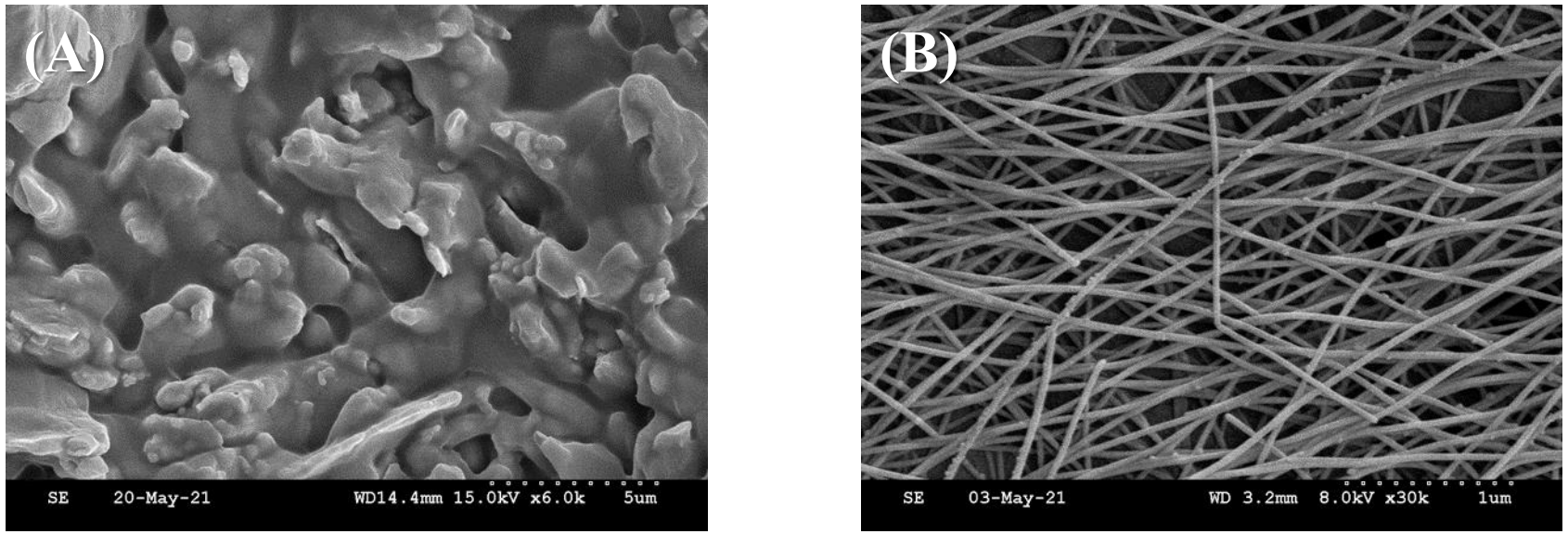

Fig. 6. SEM image of DIW composition materials: (A) AgMP, (B) AgNW.

Development of Materials and Process

❖ Development of DIW antenna radiator material

- **Development and Application of DIW Material Fabrication Method Based on IPA Content Control**
  - AgNP paste and AgNW solution were mixed for 45 minutes
  - IPA was evaporated using a vacuum oven
  - After vacuum processing, a paste mixer was used to uniformly disperse AgMP and AgNW
- The material containing **1.2 wt%$_{AgNW}$ (σ_{elec}= 4.16 (±0.38)×10^{5}S/m)** was used.

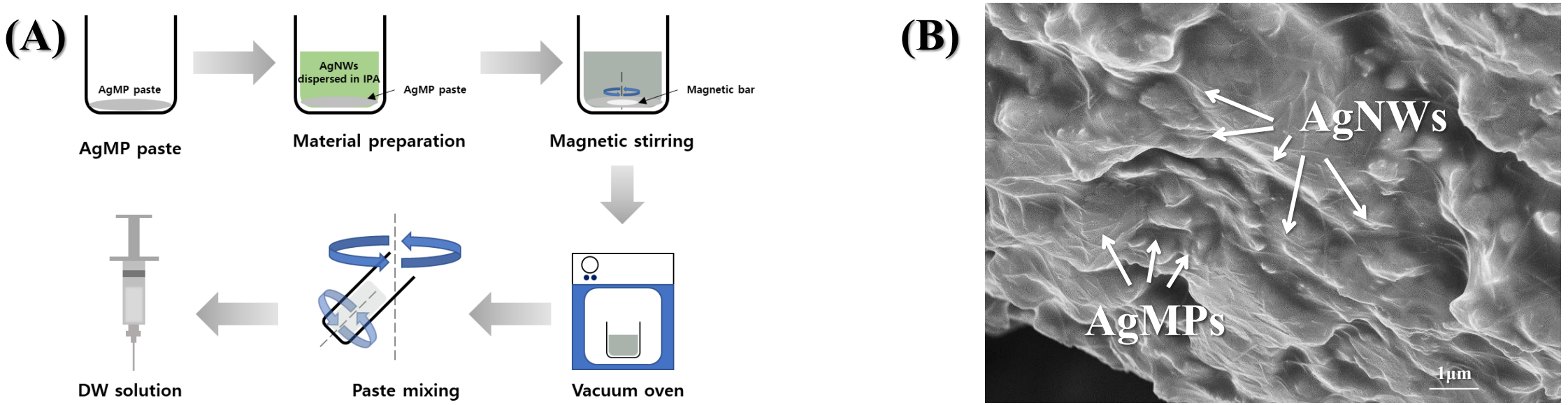

Fig. 7. (A) DIW material manufacturing technique based on IPA content control method, (B) SEM image of DIW material.

Development of Materials and Process

❖ Development of DIW antenna radiator manufacturing process

- Viscosity of DIW paste was tested using a trial extrusion setup
- Extruder mounted on Ender-3 Pro (Creality, China) for 3-axis DIW printing (Fig. A)
- Controlled via display panel and G-code
- Verified stable and consistent print quality (Fig. B)

(A)

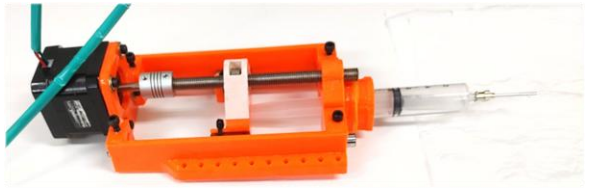

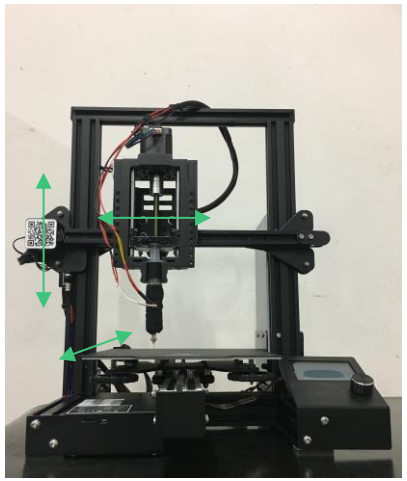

(B)

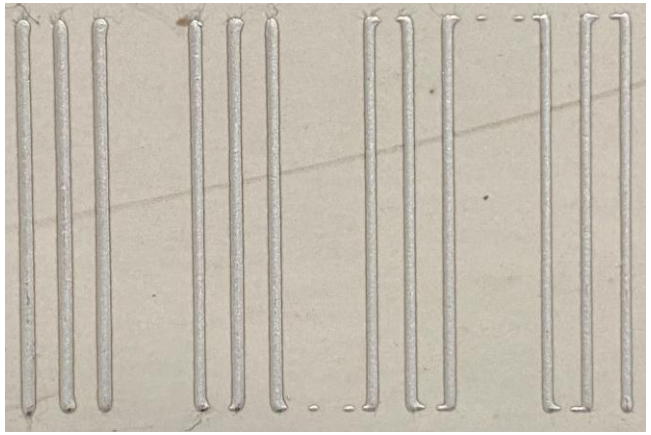

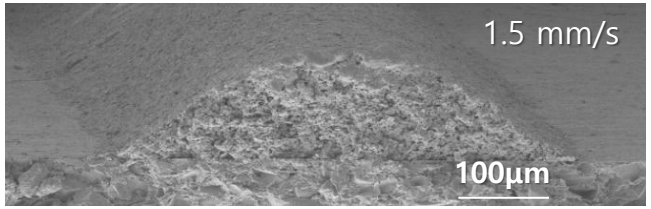

Fig. 8. (A) Extruder for testing and DIW equipment, (B) image of DIW line.

Fabrication and evaluation of DIW antenna

❖ DIW Antenna Pattern Design and Fabrication

- Designed for resonance frequency (f_R) of 5.03 GHz based on copper conductivity
- **DIW antenna pattern fabrication procedure**
  - Antenna pattern fabricated using DIW equipment and cured in an oven
  - Feed line soldered and antenna connector attached

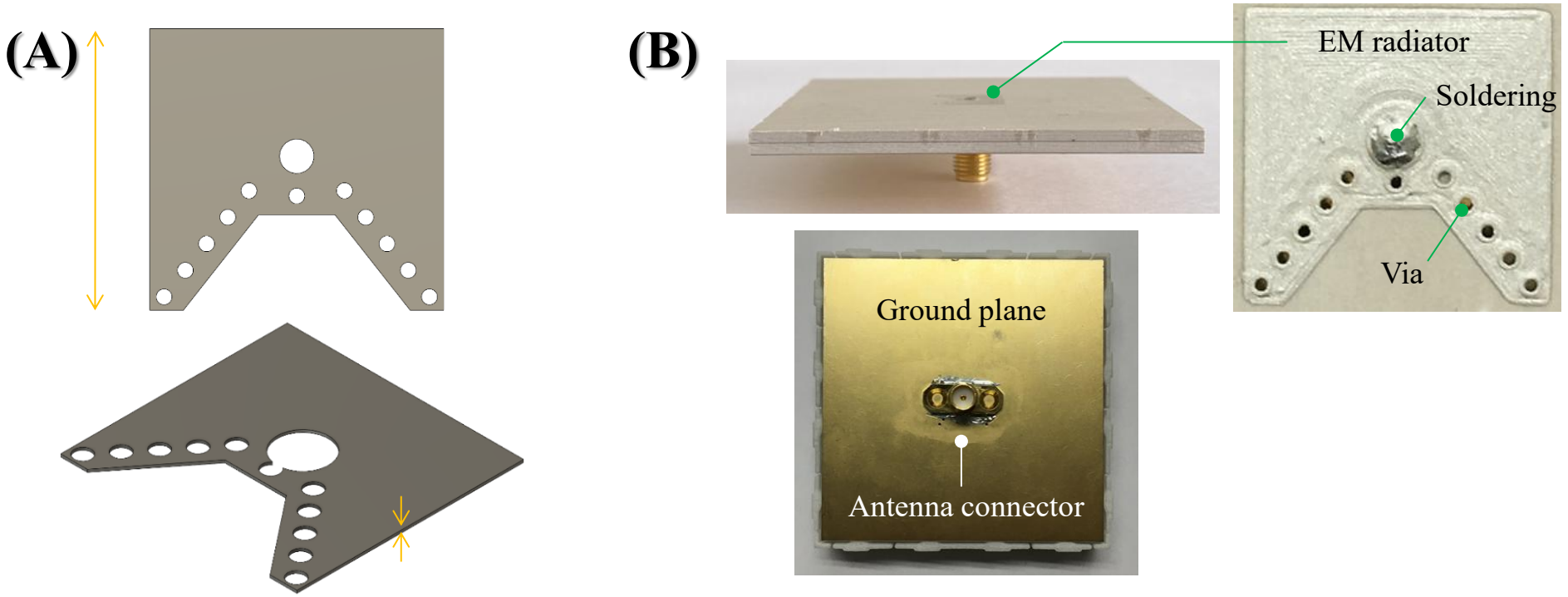

Fig. 9. (A) CAD Modeling of EM radiator, (B) manufactured DIW antenna pattern.

Fabrication and evaluation of DIW antenna

❖ Performance evaluation of DIW antenna radiator

- Antennas were fabricated using both copper etching and direct ink writing (DIW)
- Performance was evaluated in an anechoic chamber



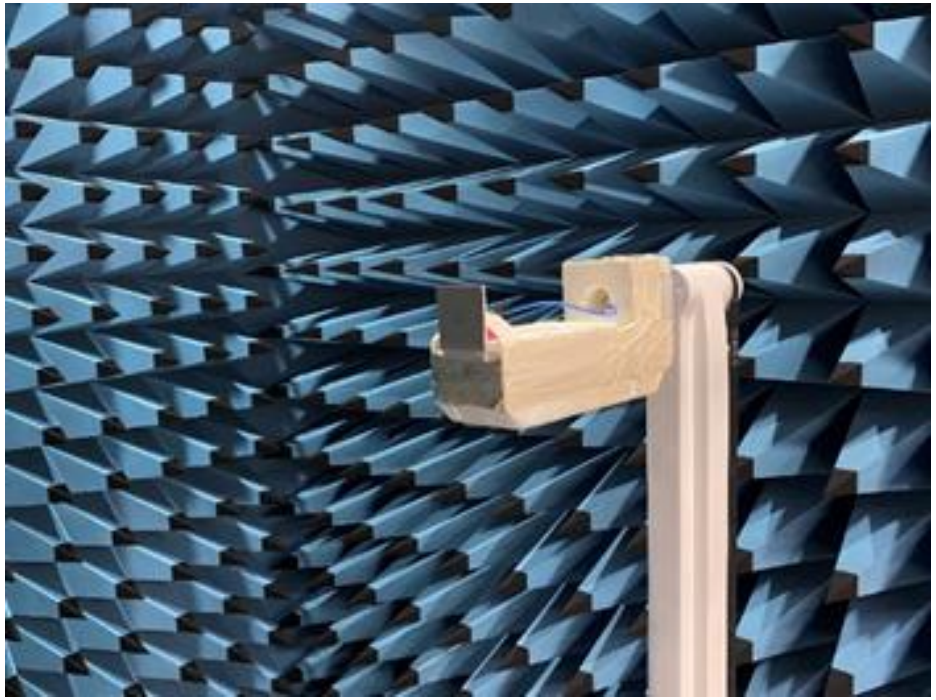

Fig. 10. Performance test of antenna fabricated DIW process on anechoic chamber.

Fabrication and evaluation of DIW antenna

❖ Comparison of Antenna Return Loss Performance

	Resonance frequency(f_R)	Reflection loss (RL)	Bandwidth (BW)
Copper etching antenna	5.04 GHz	-35.304 dB	248 MHz
DIW antenna	**4.925 GHz**	**-33.023 dB**	**241 MHz**

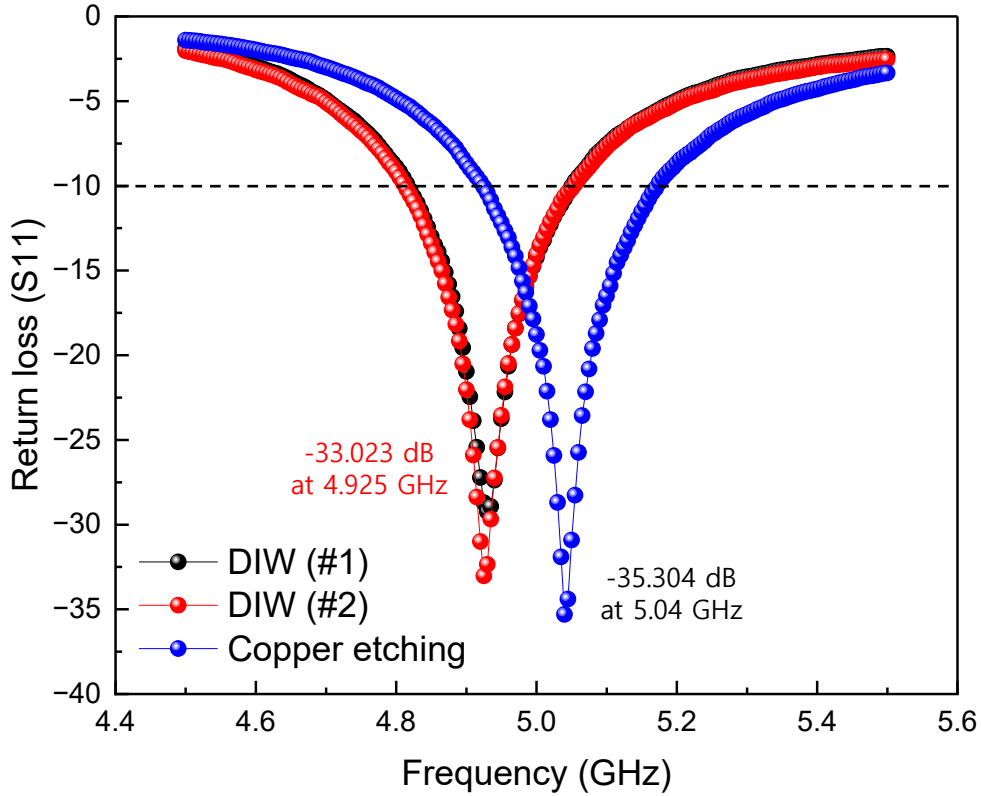

Except for the resonant frequency shift,

the DIW and copper-etched antennas show nearly identical performance across the frequency band

Fig. 11. Return loss of EM radiator fabricated by copper etching and DIW.

Fabrication and evaluation of DIW antenna

❖ Comparison of antenna gain patterns

- Copper-etched and DIW antennas showed no significant difference in radiation pattern and peak gain.

→ **The DIW method demonstrated both structural flexibility and stable electrical performance.**

(A)

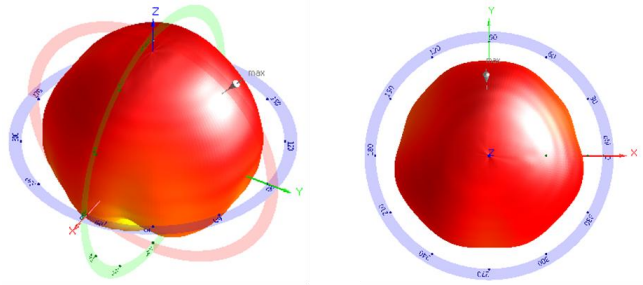

3D gain pattern

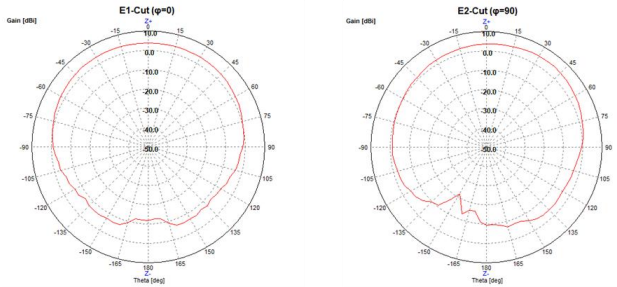

2D gain pattern

Gain (dBi)			Half power (3dB) beam width	
Maximum	φ = 0° Elevation Plane	φ = 90° Elevation Plane	φ = 0° Elevation Plane	φ = 90° Elevation Plane
+4.65	+3.79	+4.65	144.3°	111.8°

(B)

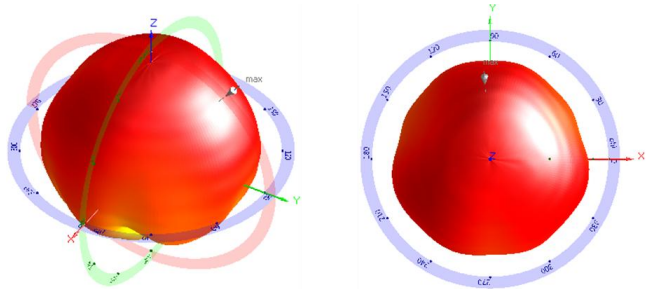

3D gain pattern

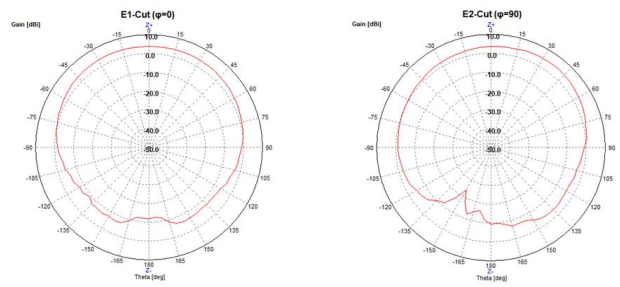

2D gain pattern

Gain (dBi)			Half power (3dB) beam width	
Maximum	φ = 0° Elevation Plane	φ = 90° Elevation Plane	φ = 0° Elevation Plane	φ = 90° Elevation Plane
+4.68	+3.80	+4.68	145.5°	111.2°

Fig. 12. 2D and 3D gain patterns of EM radiator: (A) copper etching antenna, (B) DIW antenna

03. Integration into CLAS

1. Fabrication and Evaluation of MAS
2. Integration of DIW antenna into CLAS

Fabrication and Evaluation of MAS

❖ Design of MAS (Multifunctional Antenna Structure)

- Designed and fabricated a Multifunctional Antenna Structure (MAS)
- Structure composed of facesheet, core, and DIW antenna radiator
- Investigated effects of dielectric loading

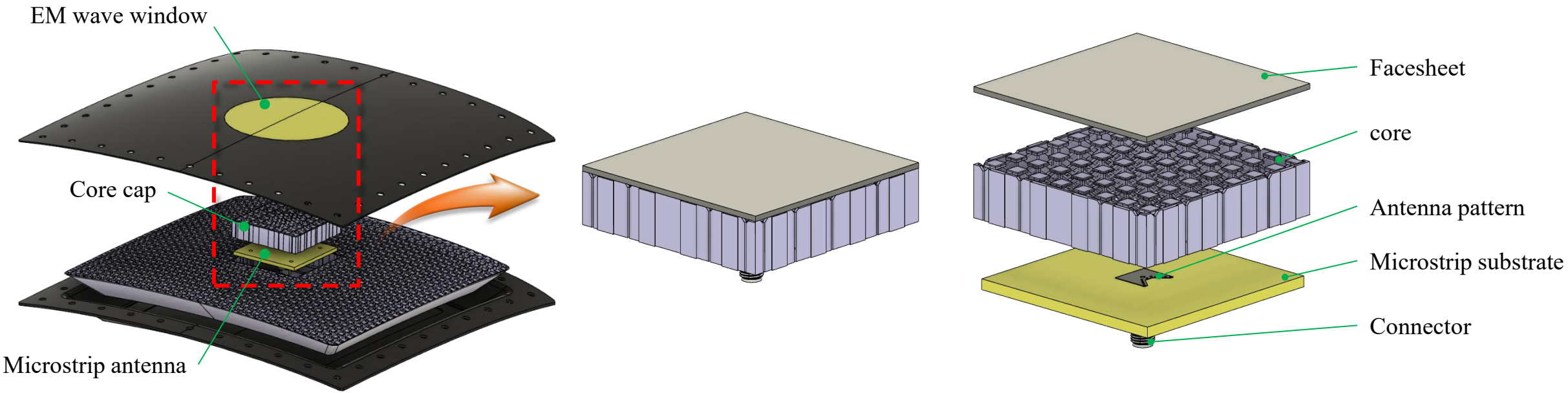

Fig. 13. Schematic of multifunctional antenna structure (MAS).

Fabrication and Evaluation of MAS

❖ Components and fabrication of MAS

- Facesheet : RT/duroid®6002 (Rogers corporation, USA)
- Sandwich core : Duraform ProX PA (3D system, USA) (Selective laser sintering, SLS)
- Adhesive film : AF 163-2K (3MTM, Scotch-WeldTM, USA)

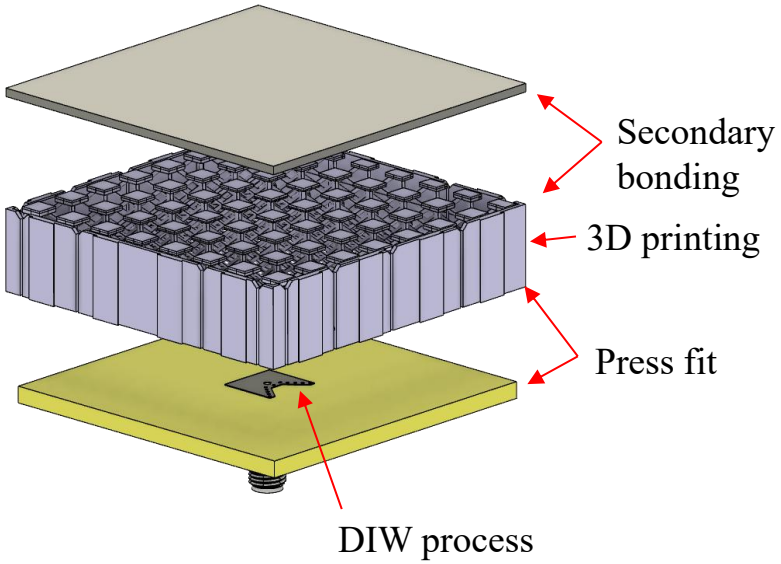




- Top view -


- Side view -


- Bottom view -


- core (Top) -

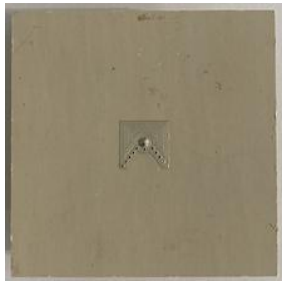
- Microstrip antenna -

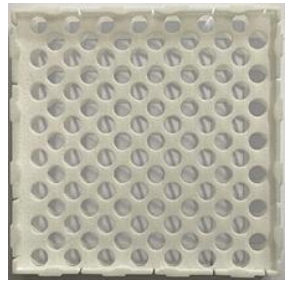
- core (Bottom) -




- Microstrip antenna (Side view) -

Fig. 14. Components and fabrication of multifunctional antenna structure (MAS).

Fabrication and Evaluation of MAS

❖ Comparison of antenna performance evaluation

	Resonance frequency(f_R)	Reflection loss (RL)	Bandwidth (BW)
DIW	4.925 GHz	-33.02 dB	241 MHz
MAS	4.840 GHz	-20.51 dB	232 MHz

DIW → MAS
f_R = 4.925 GHz → 4.840 GHz
※ Effect of Dielectric loading

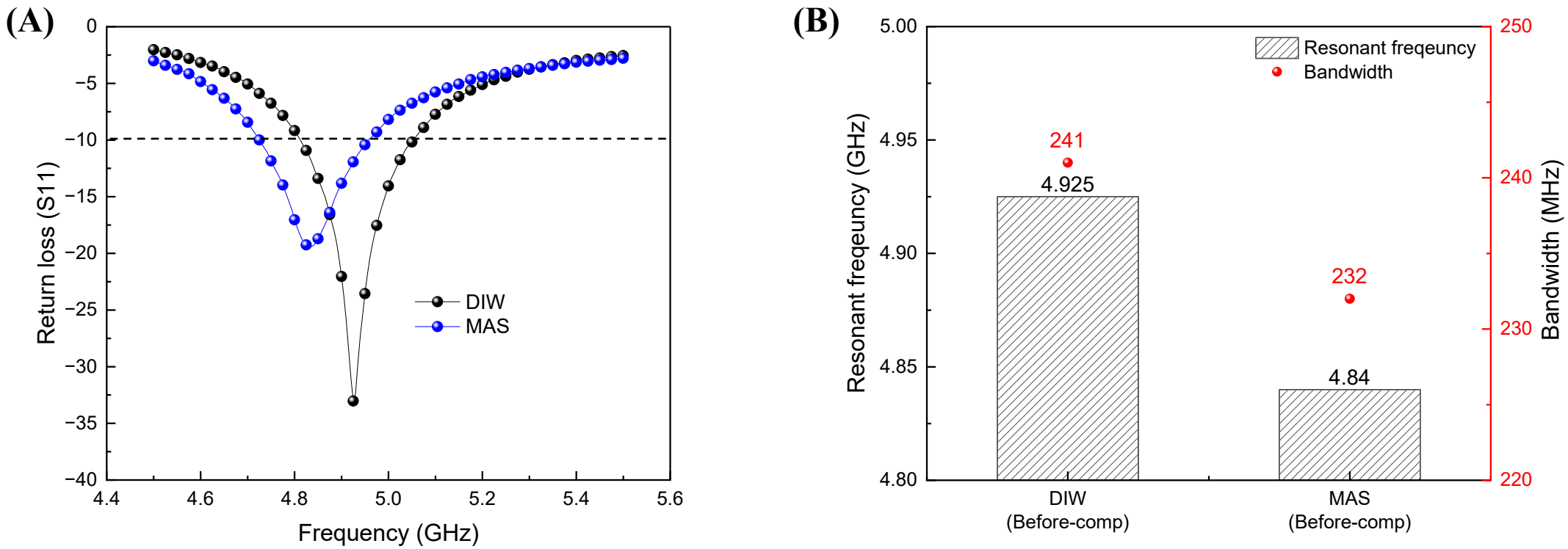

Fig. 15. Antenna performance results: (A) return loss, (B) resonant frequency and bandwidth.

Fabrication and Evaluation of MAS

❖ Comparison of antenna performance evaluation

- Gain pattern and beamwidth remained similar with and without MAS integration
- A shift in resonant frequency was observed due to dielectric loading
- With frequency adjustment, the antenna can be used in CLAS with comparable performance

(A)

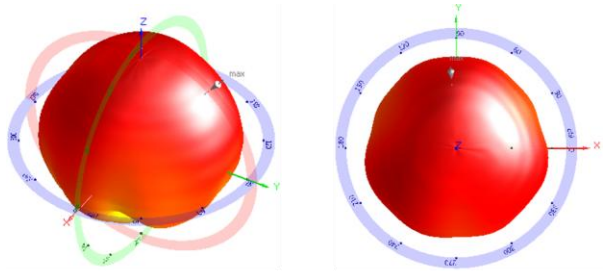

3D gain pattern

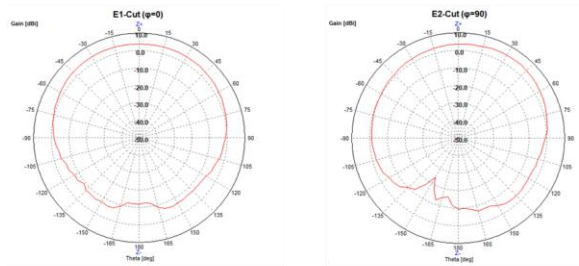

2D gain pattern

Gain (dBi)			Half power (3dB) beam width	
Maximum	φ = 0° Elevation Plane	φ = 90° Elevation Plane	φ = 0° Elevation Plane	φ = 90° Elevation Plane
+4.68	+3.80	+4.68	145.5°	111.2°

(B)

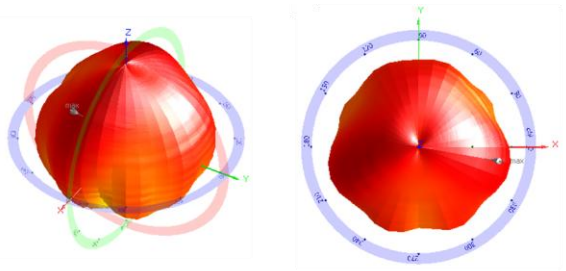

3D gain pattern

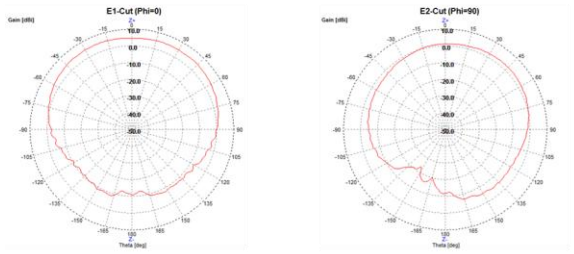

2D gain pattern

Gain (dBi)			Half power (3dB) beam width	
Maximum	φ = 0° Elevation Plane	φ = 90° Elevation Plane	φ = 0° Elevation Plane	φ = 90° Elevation Plane
+4.95	+4.95	+2.38	145.1°	107.1°

Fig. 16. 2D and 3D gain patterns of EM radiator (A) DIW antenna, (B) MAS.

Integration of DIW antenna into CLAS

❖ Fabrication of CLAS with DIW antenna radiator

- Antenna-integrated structure fabricated using a directly printed radiator
- Structure composed of Outer facesheet, Core, Antenna radiator, Inner facesheet
- Verified feasibility of applying the printed radiator to the integrated structure

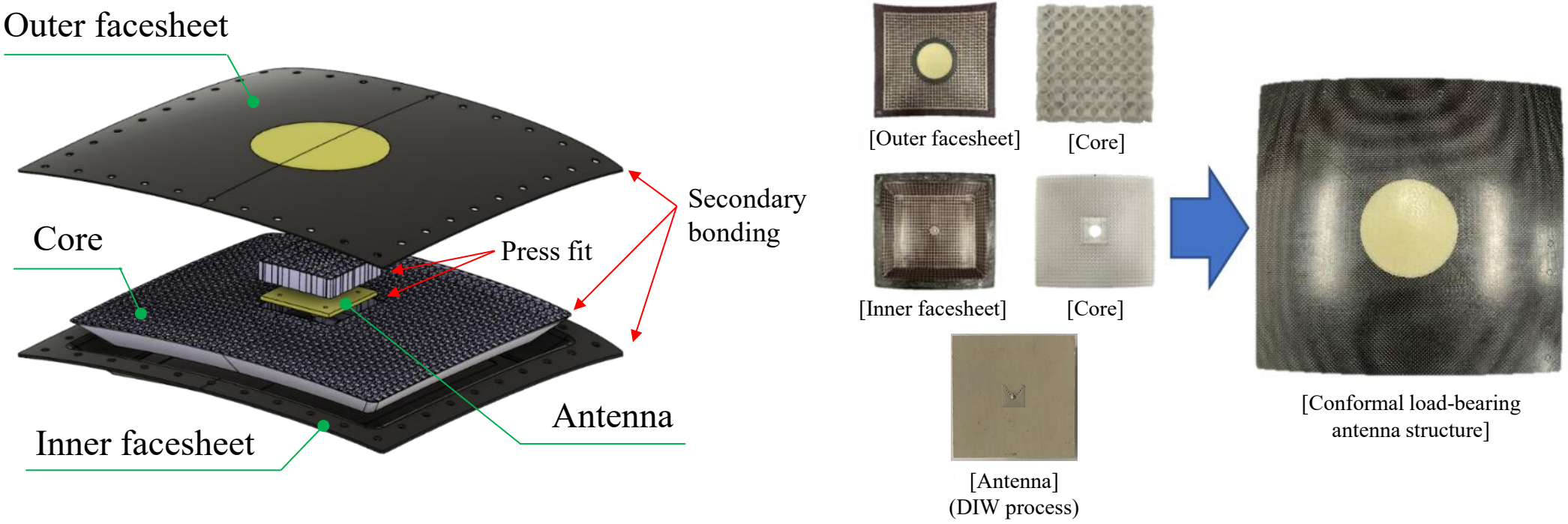

Fig. 17. Fabricated DIW process antenna applied CLAS.

Integration of DIW antenna into CLAS

❖ Fabrication of CLAS with DIW antenna radiator

5.3 GHz	f_R	RL	BW
DIW	5.035 GHz	-44.58 dB	250 MHz
CLAS	4.83 GHz	-29.01 dB	315 MHz

5.4 GHz	f_R	RL	BW
DIW	5.275 GHz	-35.42 dB	290 MHz
CLAS	5.1 GHz	-16.31 dB	290 MHz

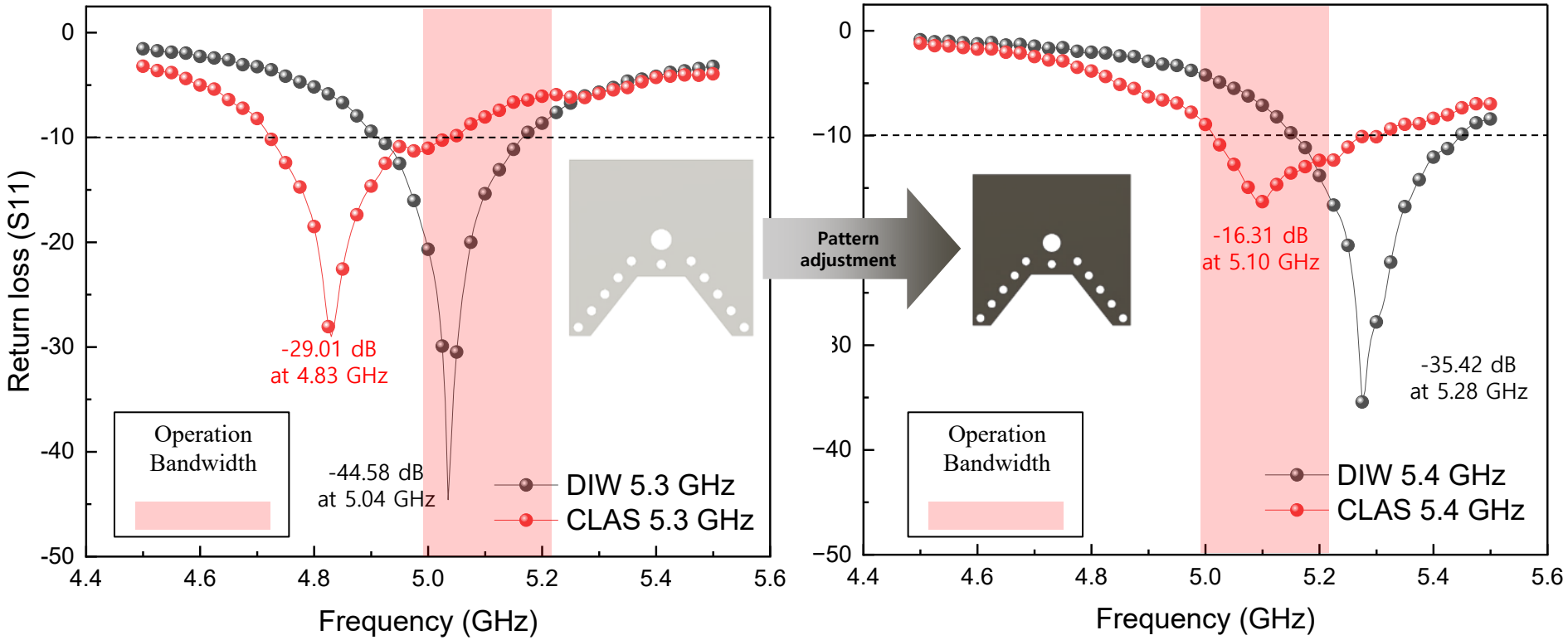

Fig. 18. Antenna performance results according to DIW antenna pattern adjustment

04. Conclusion

Conclusion

❖ Direct Ink Writing antenna radiator for Conformal Load-bearing Antenna Structure

- **DIW Antenna Fabrication and Application to CLAS**
  - ✓ Developed a high-conductivity nanocomposite material for DIW antennas
  - ✓ Established a DIW fabrication process for antenna patterning
  - ✓ Verified the effect of dielectric loading (resonant frequency shift)
  - ✓ Achieved CLAS performance within the target frequency band
  - ✓ Confirmed the feasibility of applying DIW antennas to CLAS

➢ **This approach enables lightweight, conformal, and multifunctional antenna integration for future aerospace systems**

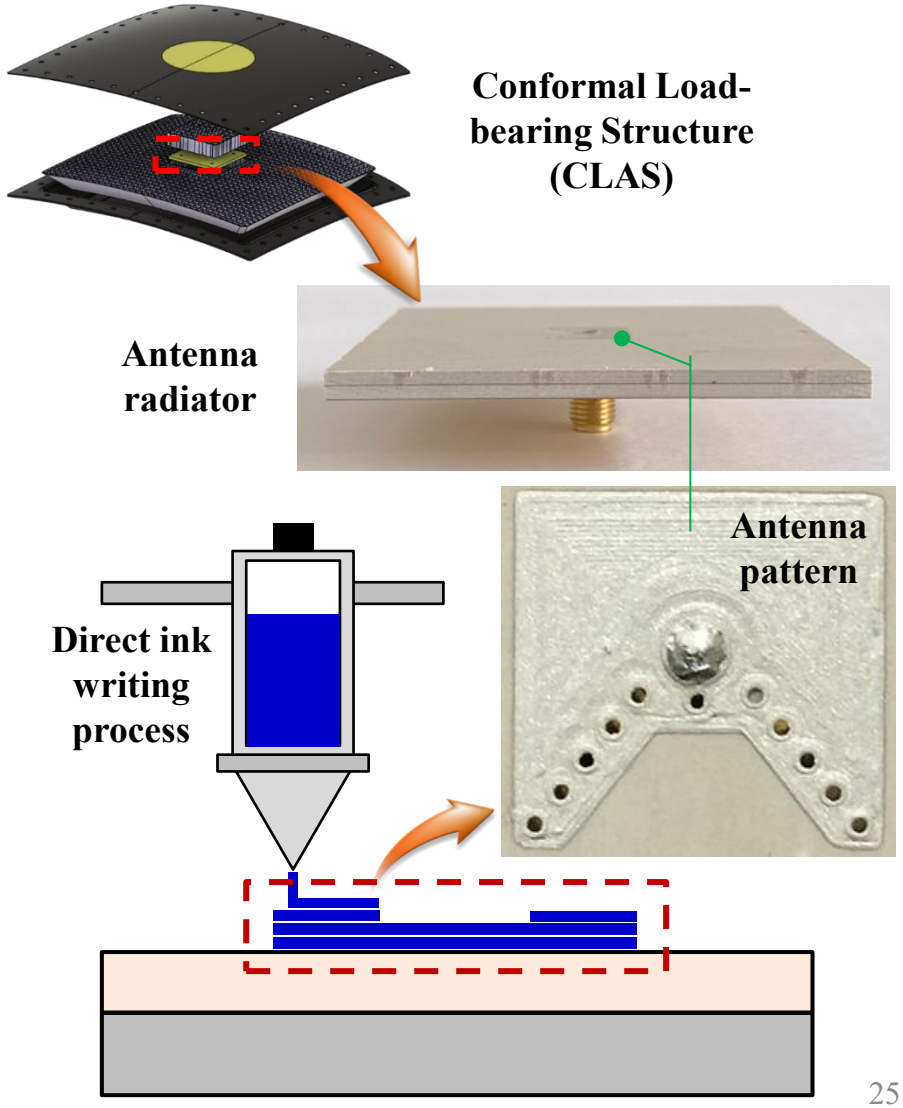



Jae-An Jeon
(4th year)
Ph.D candidate
E-mail : spma2@inha.edu
Homepage : http://mcsi.inha.ac.kr/

Thank you

인하대학교 INHA UNIVERSITY
MCSI Lab
Multifunctional Composites & Structural Integration Lab
DANAM SYSTEMS
KARI 한국항공우주연구원 Korea Aerospace Research Institute

❖ Acknowledgement

This study was conducted as a part of "Design and fabrication techniques of multifunctional electromagnetic structures for unmanned vehicles (2020M3C1C1A01084756)" and was supported by the Ministry of Science and ICT.

Appendices

References

❖ References

1) Jo, Y., J. Y. Kim, S. Y. Kim, Y. H. Seo, K. S. Jang, S. Y. Lee, S. Jung, B. H. Ryu, H. S. Kim, J. U. Park, Y. Choi and S. Jeong (2017). "3D-printable, highly conductive hybrid composites employing chemically-reinforced, complex dimensional fillers and thermoplastic triblock copolymers." Nanoscale 9(16): 5072-5084.

2) Ahn, B. Y., E. B. Duoss, M. J. Motala, X. Y. Guo, S. I. Park, Y. J. Xiong, J. Yoon, R. G. Nuzzo, J. A. Rogers and J. A. Lewis (2009). "Omnidirectional printing of flexible, stretchable, and spanning silver microelectrodes." Science 323(5921): 1590-1593.

3) Anagnostou, D. E., A. A. Gheethan, A. K. Amert and K. W. Whites (2010). "A direct-write printed antenna on paper-based organic substrate for flexible displays and WLAN applications." Journal of Display Technology 6(11): 558-564.

4) Yao, Y. G., K. K. Fu, C. Y. Yan, J. Q. Dai, Y. N. Chen, Y. B. Wang, B. L. Zhang, E. Hitz and L. B. Hu (2016). "Three-dimensional printable high-temperature and high-rate heaters." ACS Nano 10(5): 5272-5279.

5) Muth, J. T., D. M. Vogt, R. L. Truby, Y. Menguc, D. B. Kolesky, R. J. Wood and J. A. Lewis (2014). "Embedded 3D printing of strain sensors within highly stretchable elastomers." Advanced Materials 26(36): 6307-6312.

6) Kim, J. Y., S. Ji, S. Jung, B. H. Ryu, H. S. Kim, S. S. Lee, Y. Choi and S. Jeong (2017). "3D printable composite dough for stretchable, ultrasensitive and body-patchable strain sensors." Nanoscale 9(31): 11035-11046.

7) Bok Yeop Ahn, Steven B. Walker, Scott C. Slimmer, Analisa Russo, Ashley Gupta, Steve Kranz, Eric B. Duoss, Thomas F. Malkowski, and Jennifer A. Lewis (2011) "Planar and Three-Dimensional Printing of Conductive Inks." J Vis Exp. 2011; (58): 3189.

4D-printed composite structures for space applications : towards modular multi-axis structural shape-changing

ICCM24

24TH INTERNATIONAL CONFERENCE ON COMPOSITE MATERIALS

05/08/2025

Julien DESCHAMPS (Presenter)[1,2], Mickaël CASTRO[1,2], Christelle COMBESCURE[1,2,3], Ugo LAFONT[4], Nadia AMEZIANE[5], Antoine LE DUIGOU[1,2,6]

[1]Université de Bretagne Sud- IRDL UMR CNRS 6027, [2]BIONICS Group, [3]CREC Saint-Cyr Coëtquidan,

[4]ESA-ESTEC, [5]Muséum National d'Histoire Naturelle, [6]Institut Universitaire de France

Context : autonomy

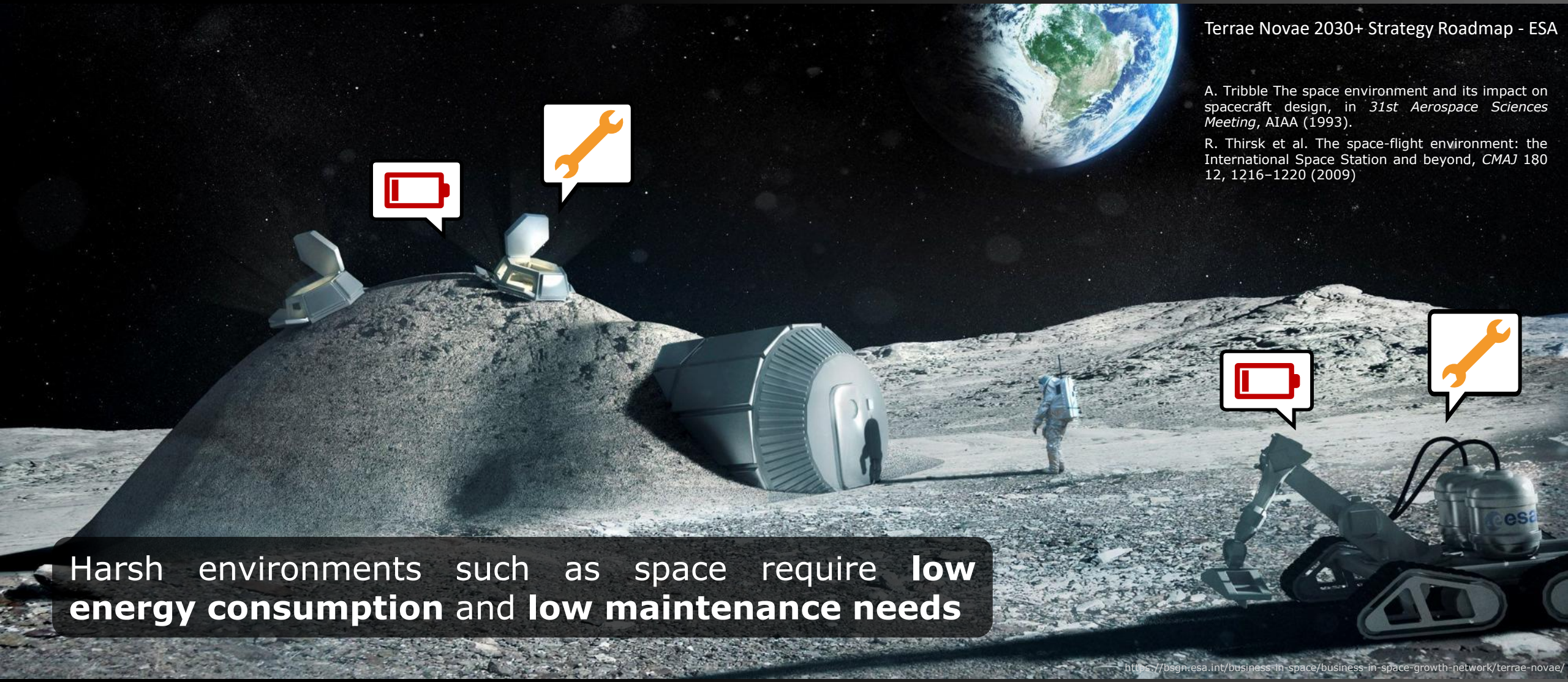

Terrae Novae 2030+ Strategy Roadmap - ESA

A. Tribble The space environment and its impact on spacecraft design, in *31st Aerospace Sciences Meeting*, AIAA (1993).

R. Thirsk et al. The space-flight environment: the International Space Station and beyond, *CMAJ* 180 12, 1216–1220 (2009)

Harsh environments such as space require **low energy consumption** and **low maintenance needs**

https://bsgn.esa.int/business-in-space/business-in-space-growth-network/terrae-novae/

Julien DESCHAMPS
julien.deschamps@univ-ubs.fr

Context : thermal stress

Space technologies are submitted to **large thermal fluctuations**



~ temperature range : **300°C**

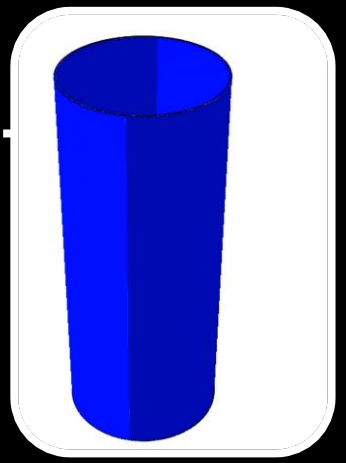

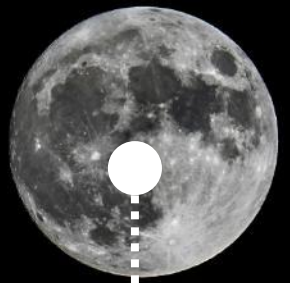



Racca, G. D. Moon surface thermal characteristics for moon orbiting spacecraft thermal analysis. *Planetary and Space Science* 43, 835–842 (1995).

Donohue, J. H. & Frisch, H. P. Thermoelastic Instability of Open-Section Booms, NASA (1969).

Foster, C. et al. Solar-array-induced disturbance of the Hubble Space Telescope pointing system. Journal of Spacecraft and Rockets 32, 634–644 (1995).

Julien DESCHAMPS
julien.deschamps@univ-ubs.fr

Project motivation

Autonomous and passive motion generation

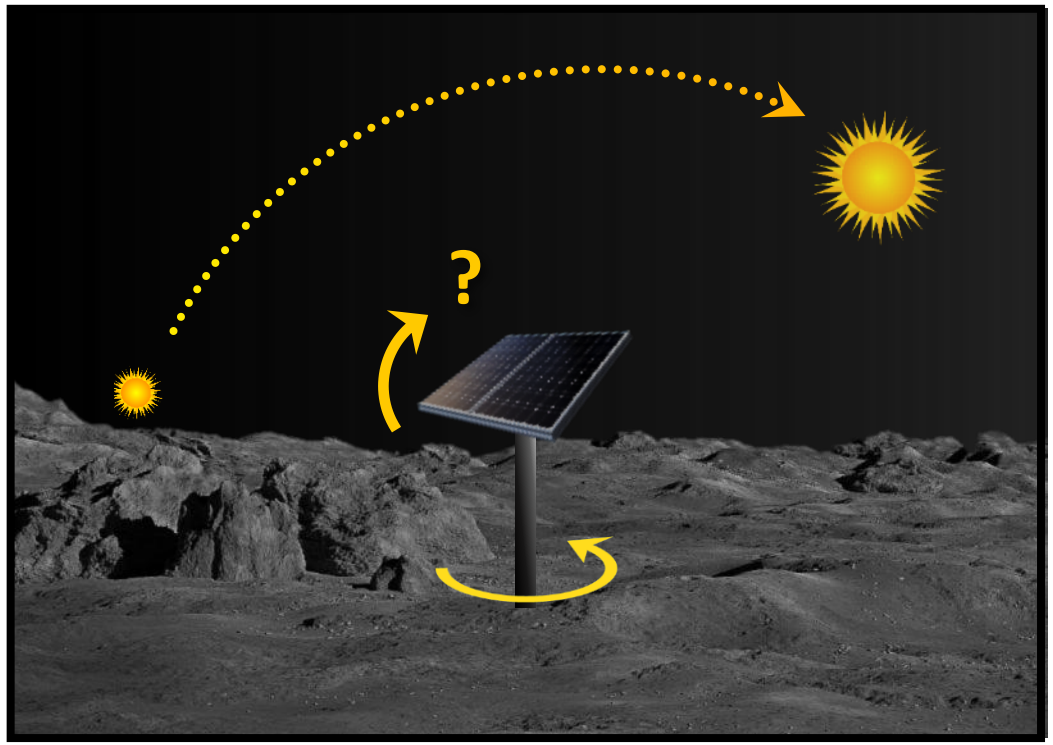

Twisting module

Le Duigou, A. et al. Bioinspired 4D Printed Tubular/Helicoidal Shape Changing Metacomposites for Programmable Structural Morphing. *Advanced Materials Technologies* **10**, 2400237 (2024).





ESA/UBS patent

Bending module

Assembly

Julien DESCHAMPS
julien.deschamps@univ-ubs.fr

Biomimetics : top-down approach

Technical Problem

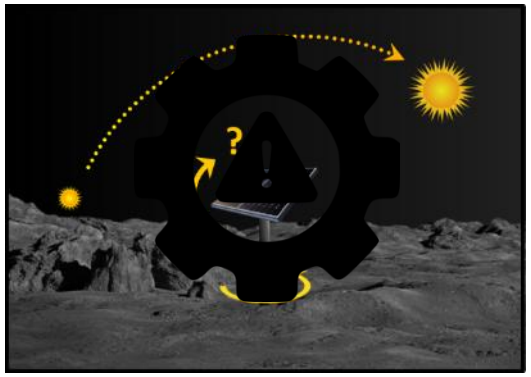

Biological model



Functions identification



Abstraction

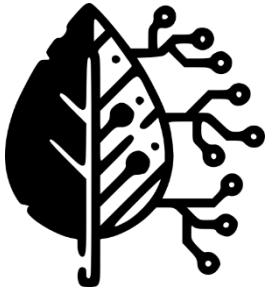

Manufacturing

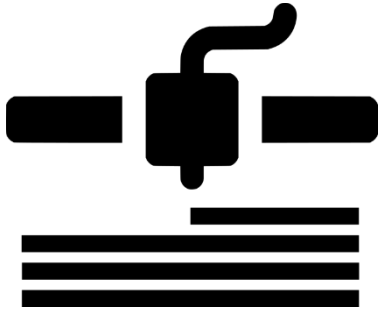

Potential application



Julien DESCHAMPS
julien.deschamps@univ-ubs.fr

Biological model : crinoids

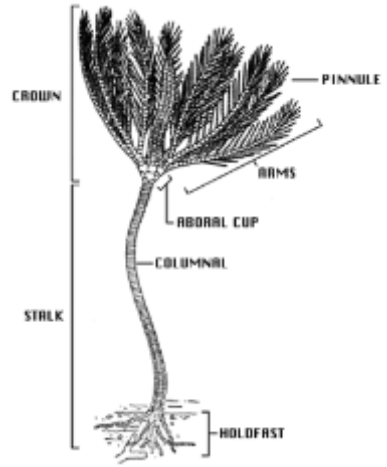

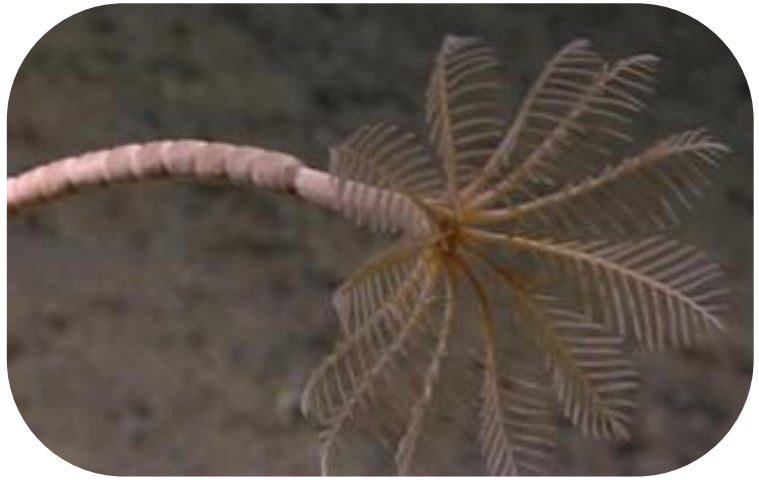



Pictures credits : N. Améziane



Crinoids : deep-sea invertebrates

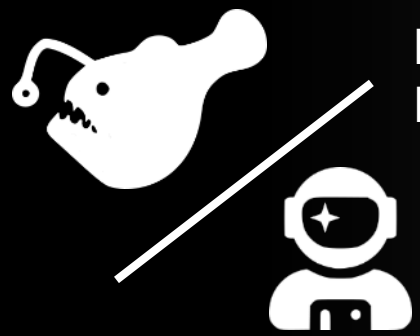

Deep-sea & **space** :
Harsh environments

Ability to **move passively,** in response to the environment



Credits : N. Améziane

Julien DESCHAMPS
julien.deschamps@univ-ubs.fr

05/08/2025

Biomimetics : top-down approach

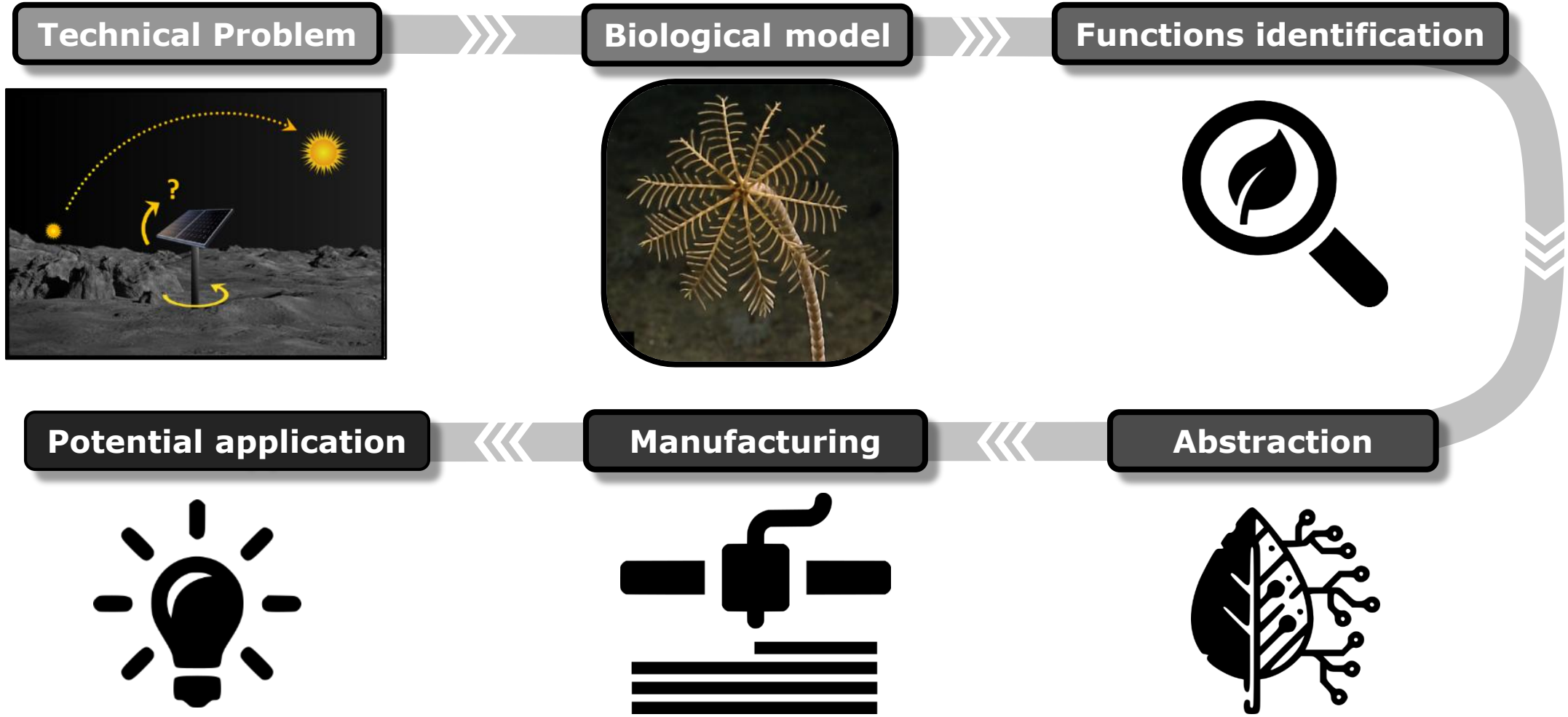

Julien DESCHAMPS
julien.deschamps@univ-ubs.fr

Functions identification : MCTs

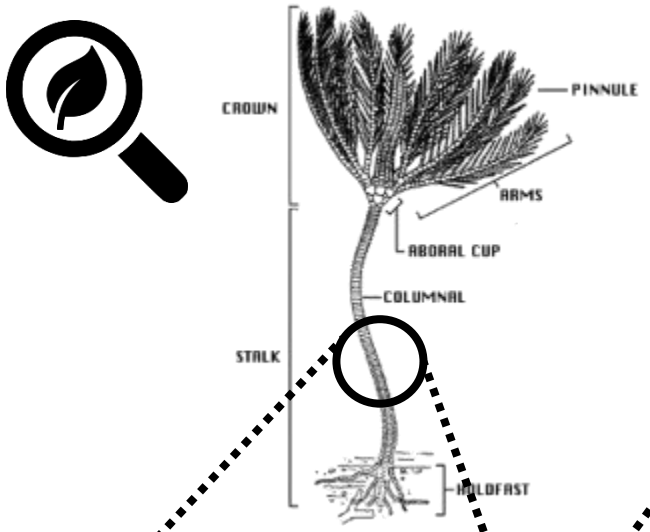

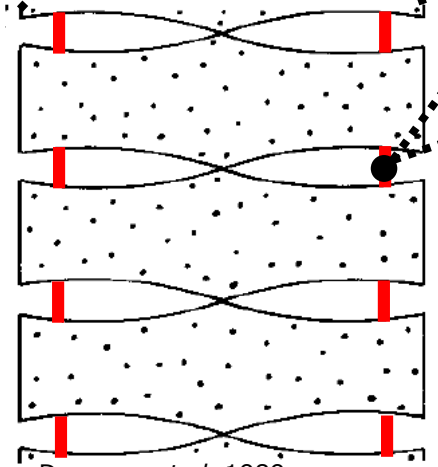

Donovan *et al.* 1989

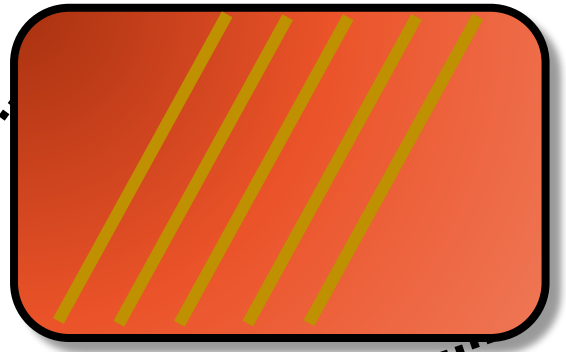

MCTs : Mutable Collagenous Tissues

- Non-contractile collagenous ligaments
- Extracellular martix with contractile properties upon activation by chemicals

Passive flexibility, in response to environment variations

Variable stiffness

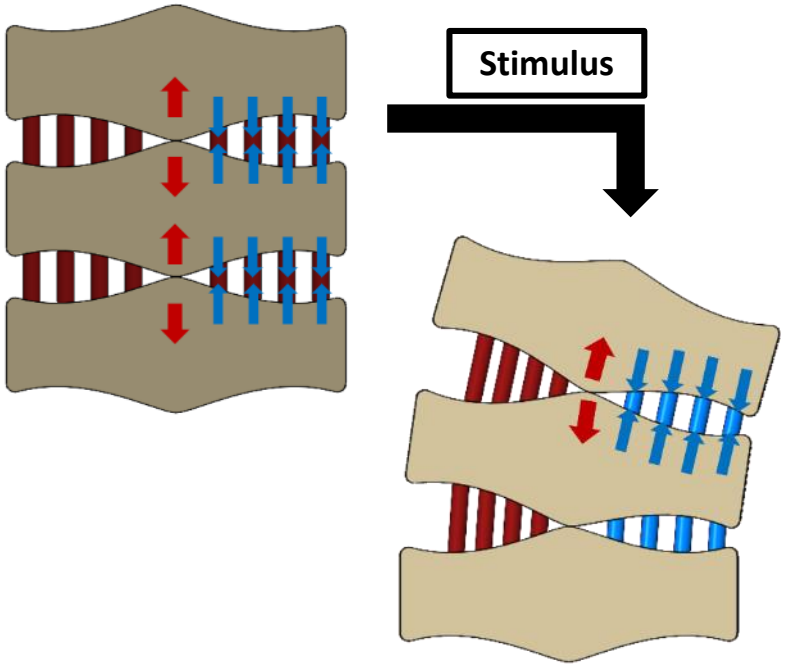

Julien DESCHAMPS
julien.deschamps@univ-ubs.fr

Biomimetics : top-down approach

Technical Problem

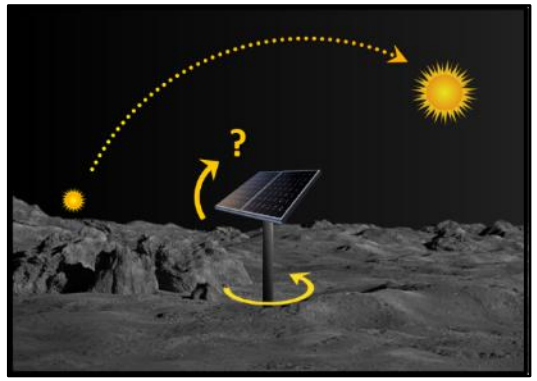

Biological model



Functions identification

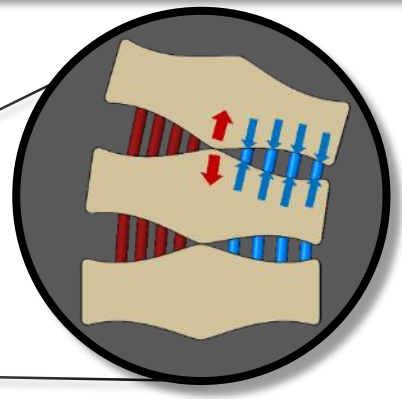

Abstraction

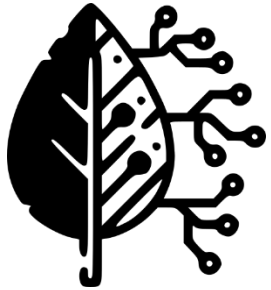

Manufacturing

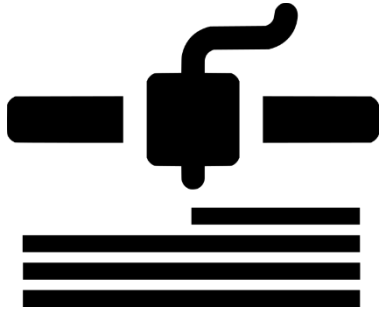

Potential application



Julien DESCHAMPS
julien.deschamps@univ-ubs.fr

Abstraction : translation in materials science terms

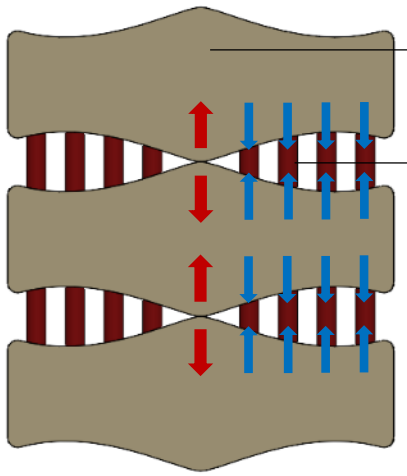

MCT contraction

Contact between ossicles

Stimulus ON

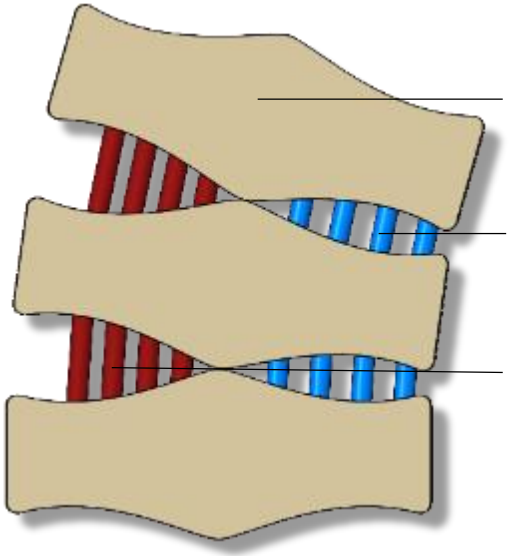

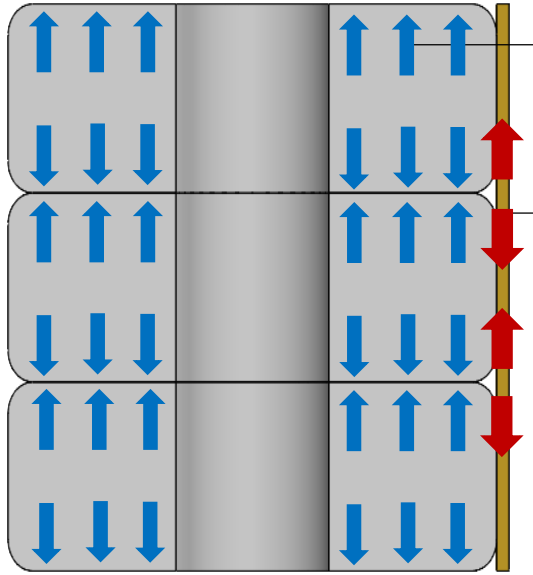

Polymer expansion

Fiber inextensibility = contact between ossicles

Stimulus ON

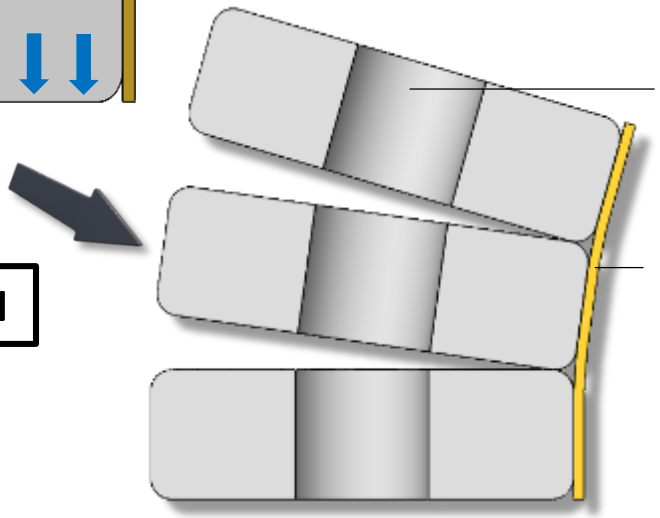

Julien DESCHAMPS
julien.deschamps@univ-ubs.fr

Abstraction : 4D-printing

3D-printing

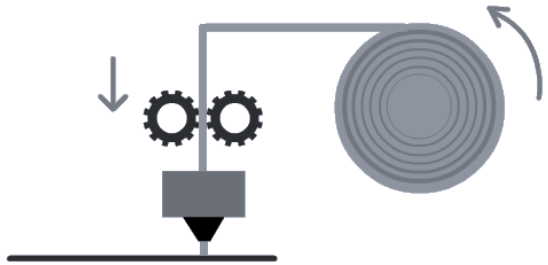

Shape-morphing materials

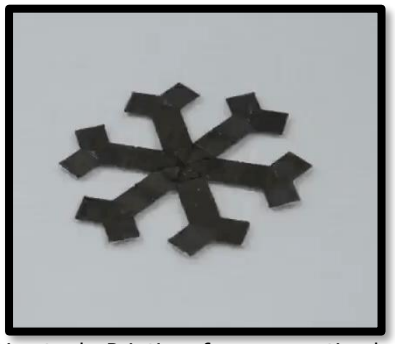

Kim, Y. et al. Printing ferromagnetic domains for untethered fast-transforming soft materials. *Nature* **558**, 274–279 (2018)

Continous fibres deposition

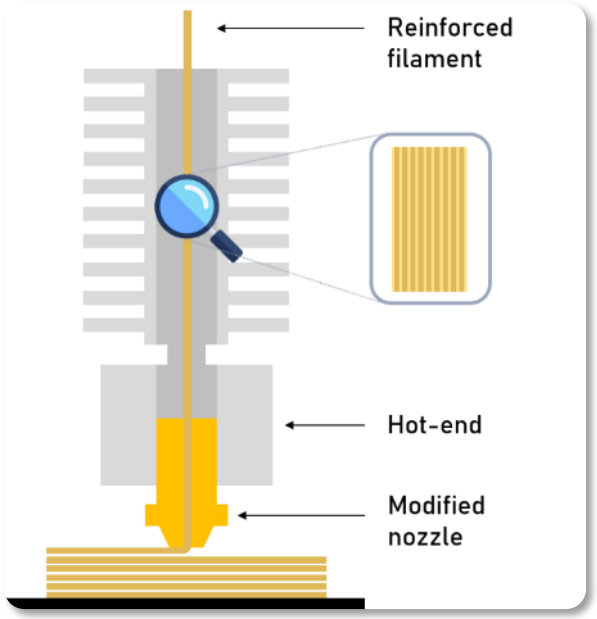

Pichard, P.L. et al. Efficient energy-dissipative bioinspired architectured composite materials with high mechanical properties. *Additive Manufacturing* (2025).

4D-printing

Use of the **environment** as a **source of energy** to induce movement

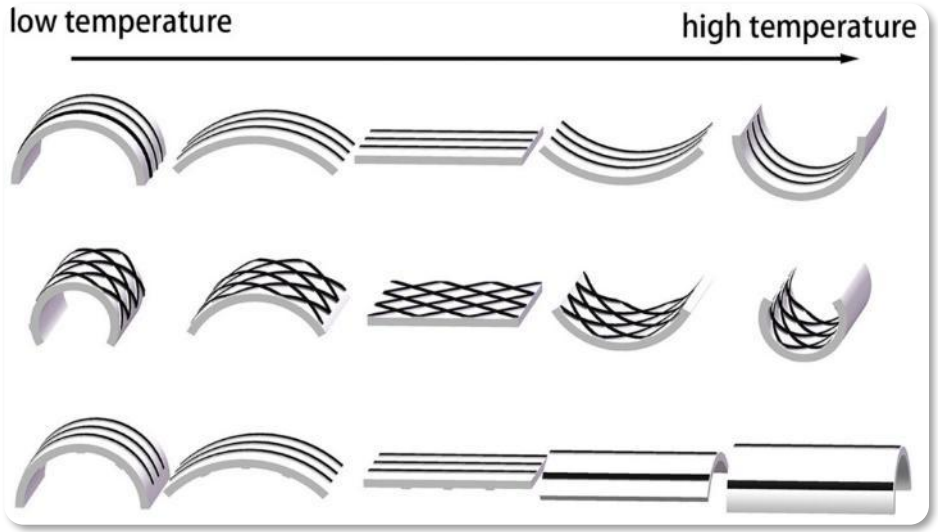

Wang, Q. et al. Programmable morphing composites with embedded continuous fibres by 4D printing. *Materials & Design* **155**, 404–413 (2018).

Biomimetics : top-down approach

Technical Problem

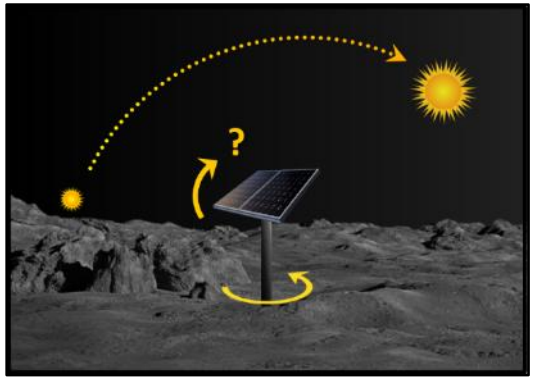

Biological model



Functions identification

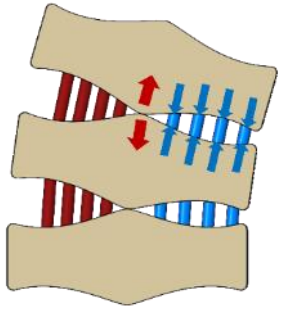

Abstraction

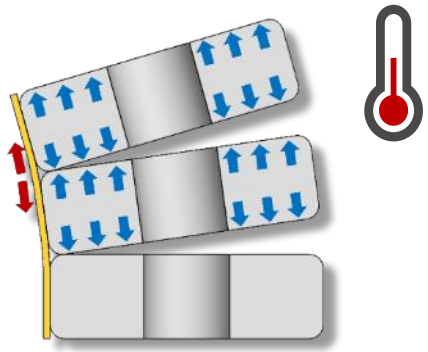

Manufacturing

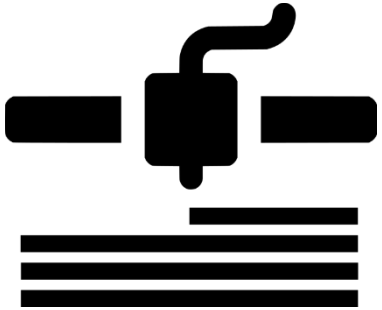

Potential application



Julien DESCHAMPS
julien.deschamps@univ-ubs.fr

Manufacturing : 4D-printing process

3D-printing enables the manufacturing of an infinite number of ossicle topologies



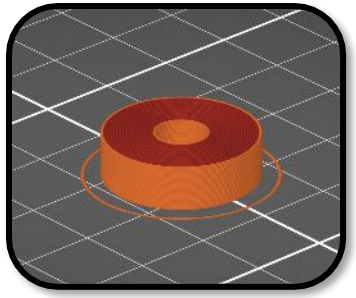

Basalt fibers embedded in a PA12 matrix

Column formed by stacked ossicles

Original device allowing for continuous fibre deposition on curved surfaces

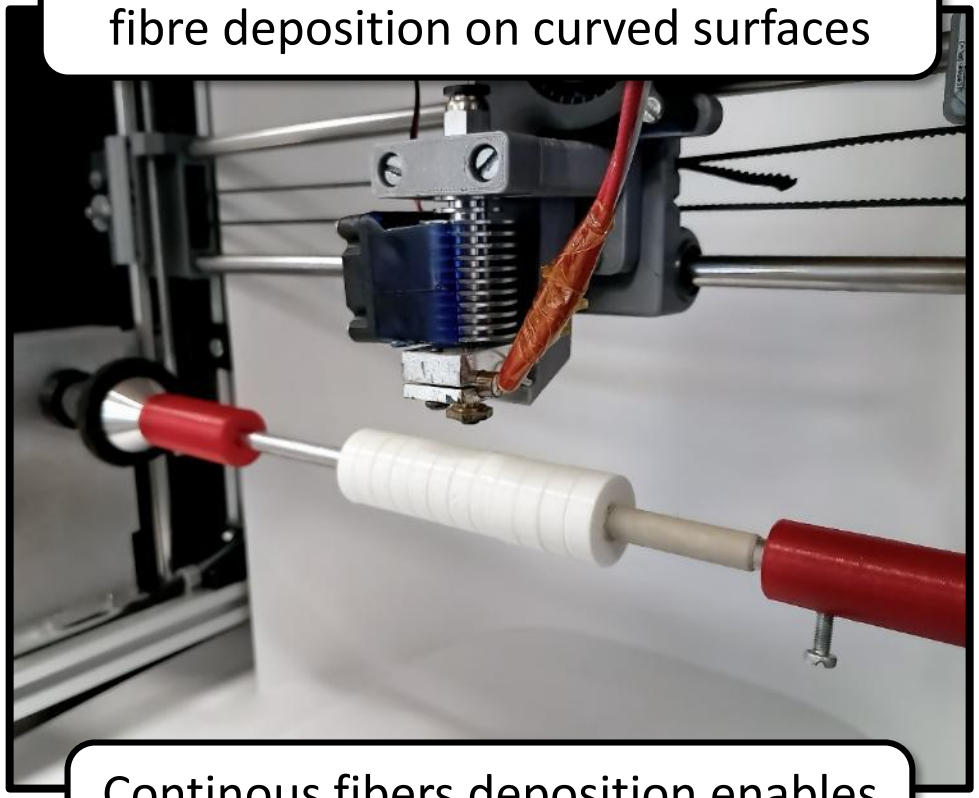

Continous fibers deposition enables perfect control of the anisotropy

Julien DESCHAMPS
julien.deschamps@univ-ubs.fr

Biomimetics : top-down approach

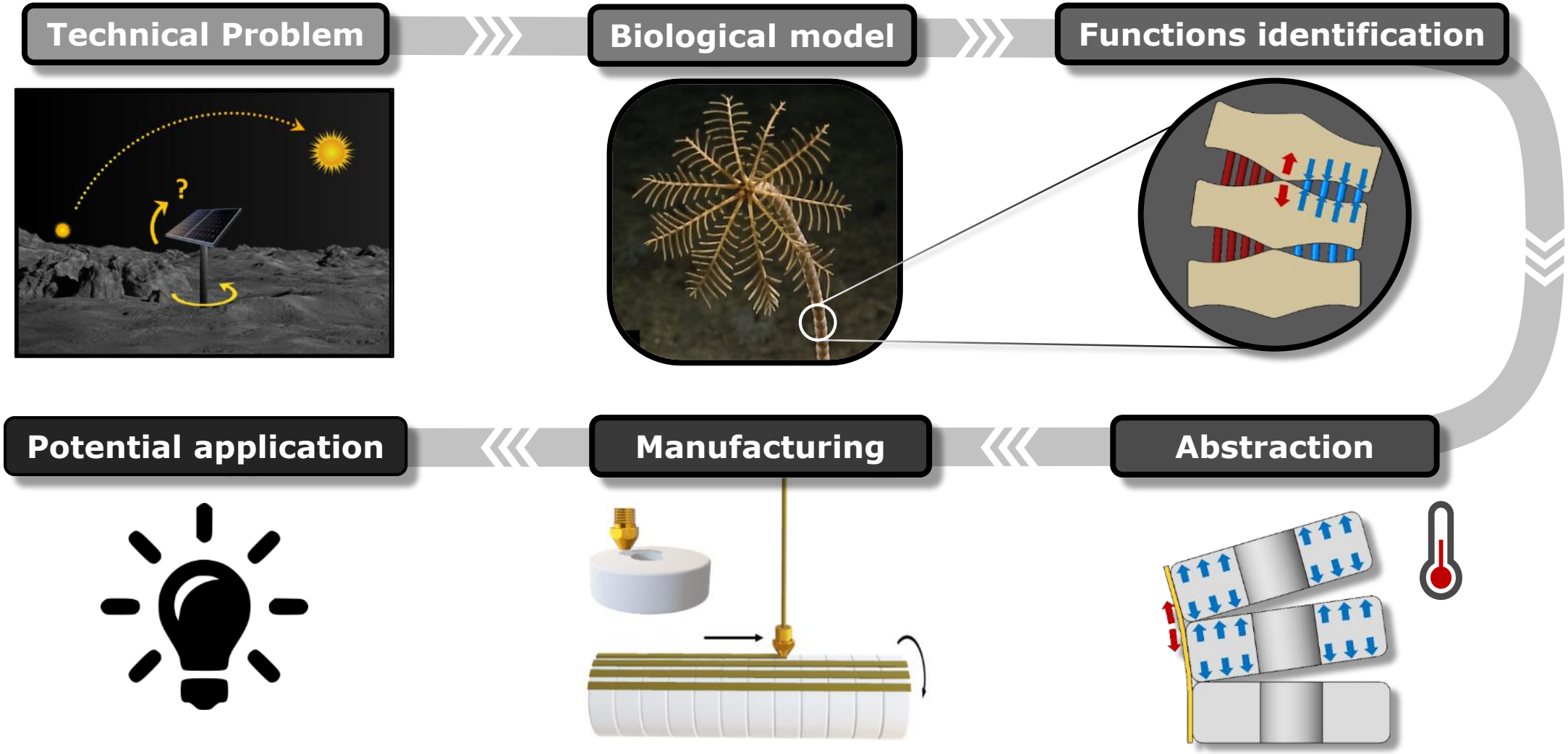

Julien DESCHAMPS
julien.deschamps@univ-ubs.fr

Crinoid-inspired actuator concept



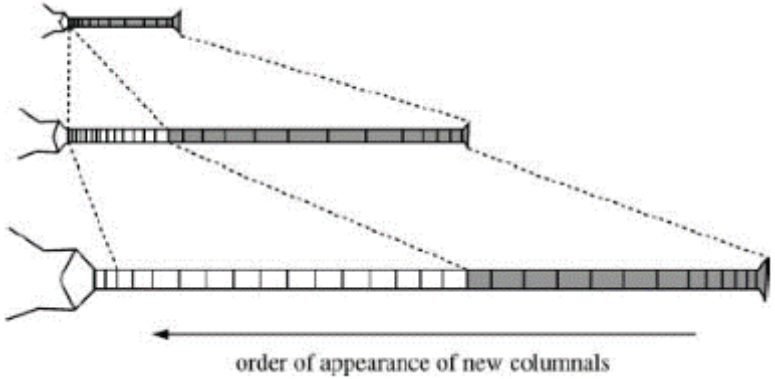

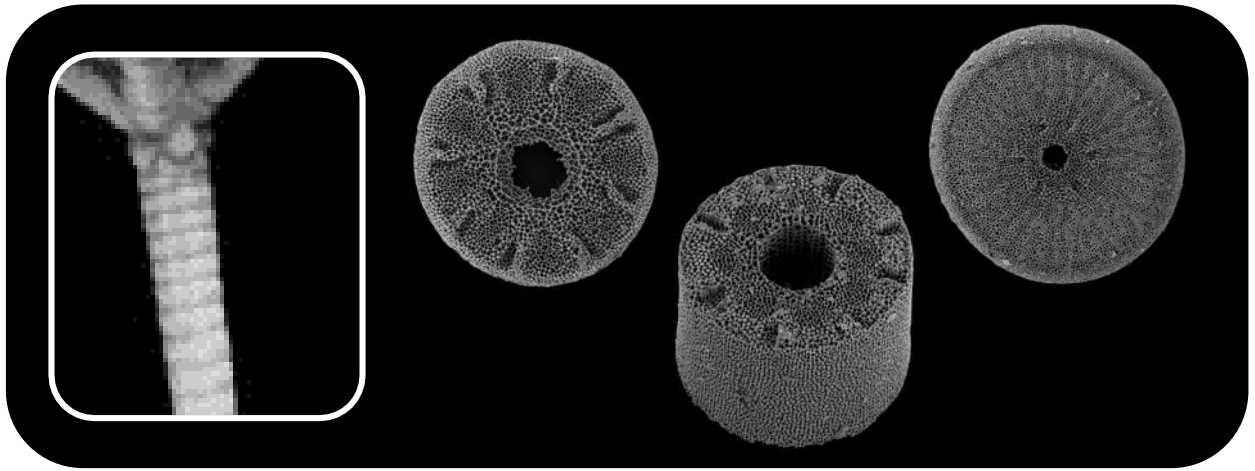

Améziane, N. & Roux, M. Environmental control versus phylogenic fingerprint in ontogeny: The example of the development of the stalk in the genus Guillecrinus (stalked crinoids, Echinodermata). *Journal of Natural History* **39**, 2815–2860 (2005).

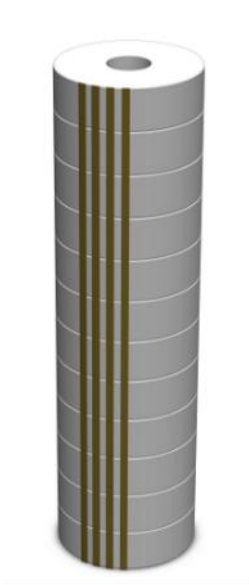

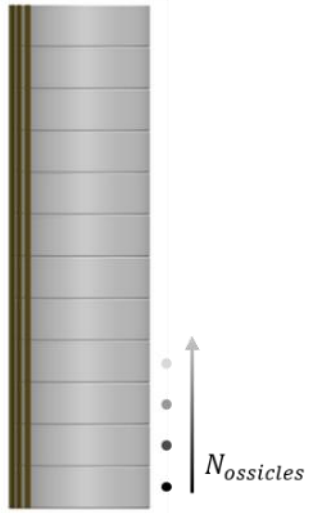

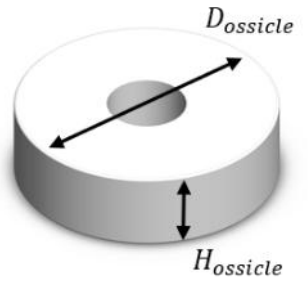

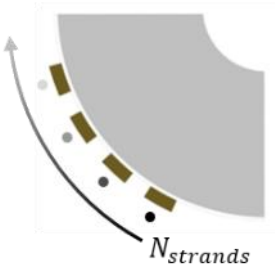

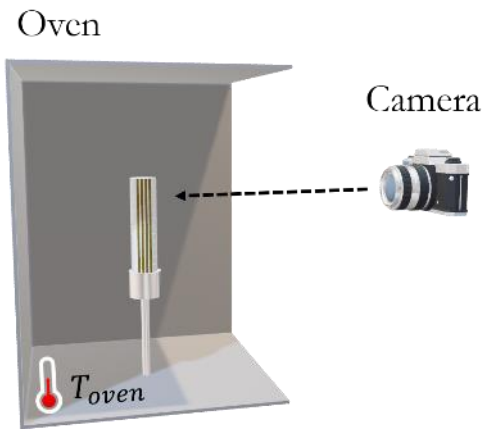

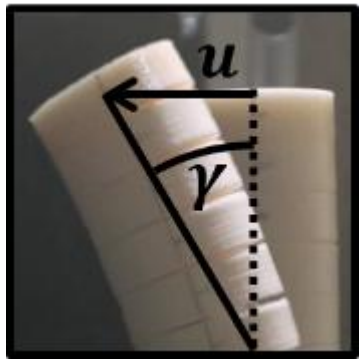

Crinoid-inspired actuator concept

Parametric study

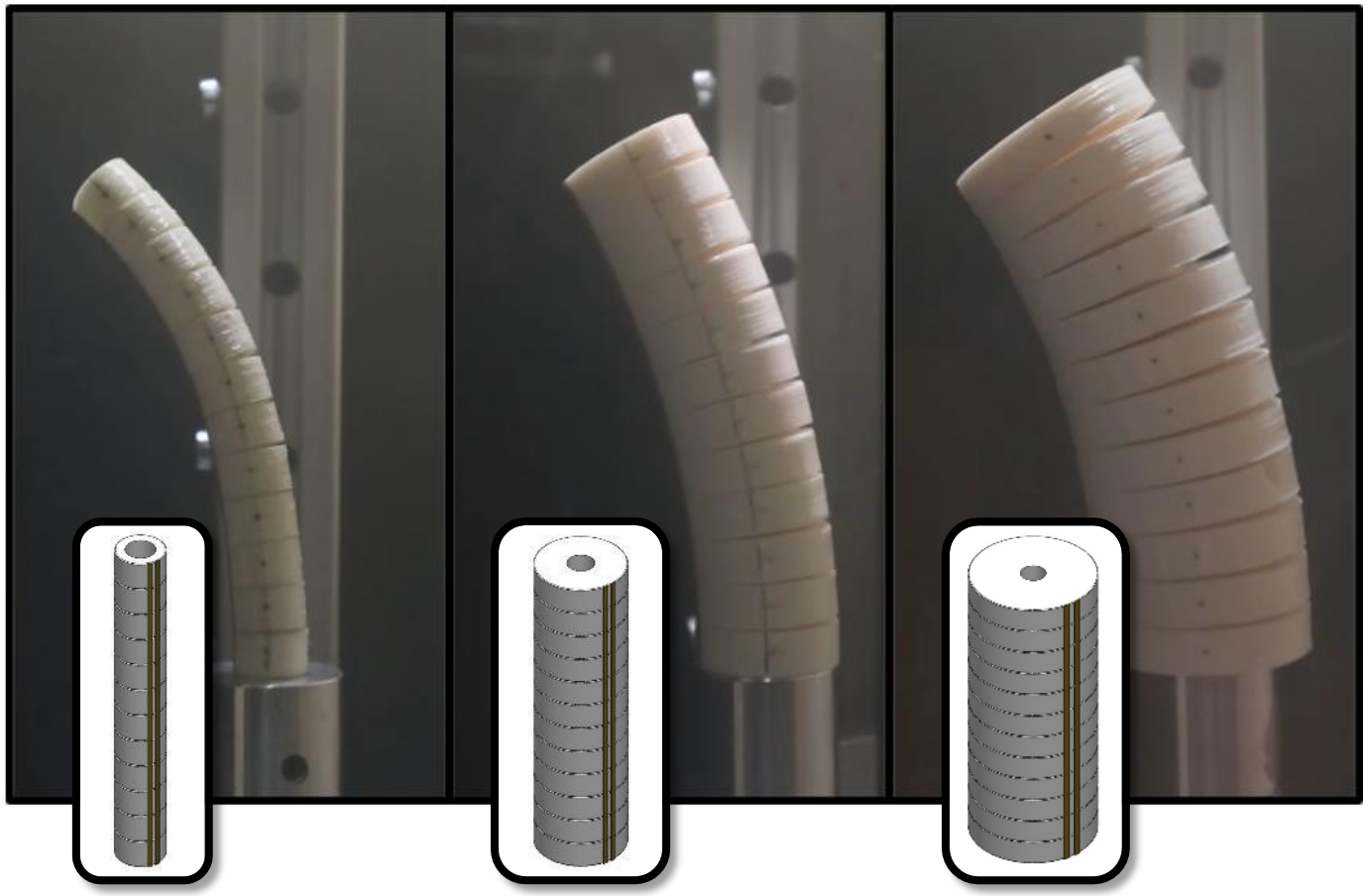

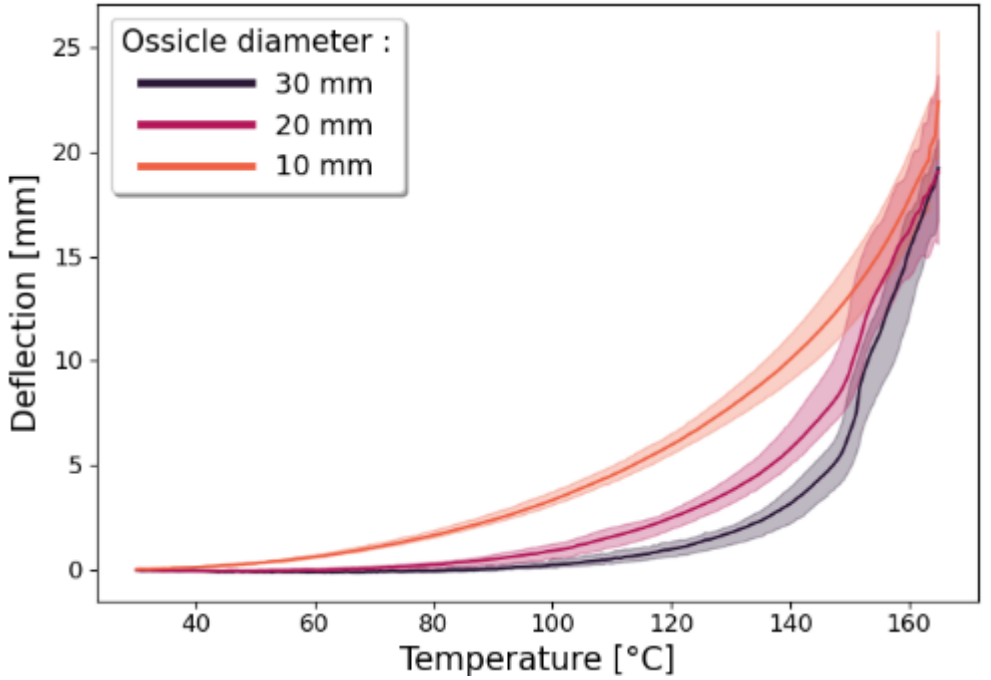

- Nonlinear relation between the ossicles diameter and the bending ability of the column
- Importance of thermal inertia and of the resisting moment resulting from ossicle weight
- Influence of the diameter variation limited to the transient regime

Julien DESCHAMPS
julien.deschamps@univ-ubs.fr

Modular assembly concept



Rotation actuator

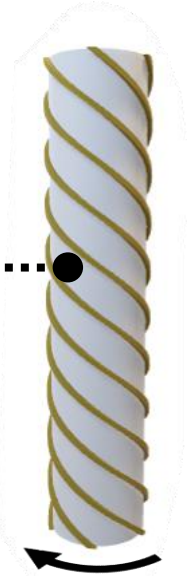

Tuning parameters :

- Active/passive matter ratios
- Aspect ratio
- Fiber angle

Bending actuator



Tuning parameters :

- Ossicle number
- Ossicle geometry
- Fiber quantity

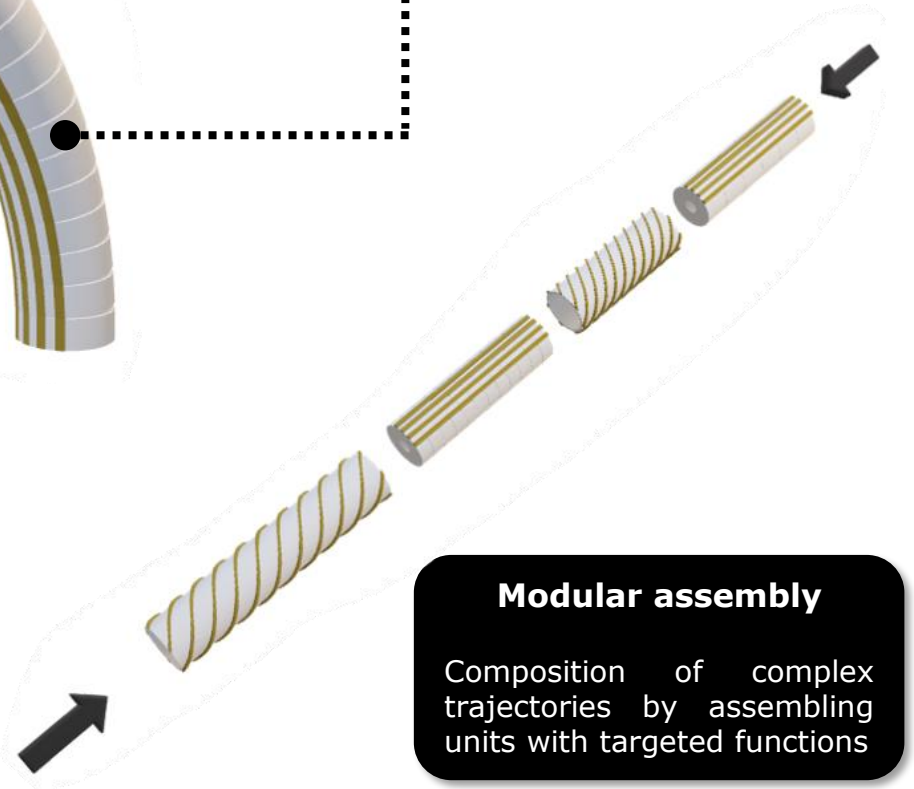

Modular assembly

Composition of complex trajectories by assembling units with targeted functions

Julien DESCHAMPS
julien.deschamps@univ-ubs.fr

Biomimetics : top-down approach

Technical Problem

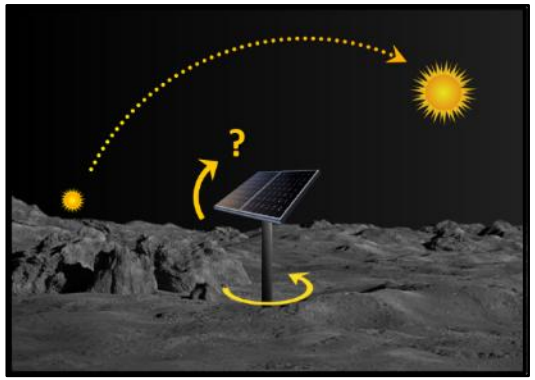

Biological model



Functions identification

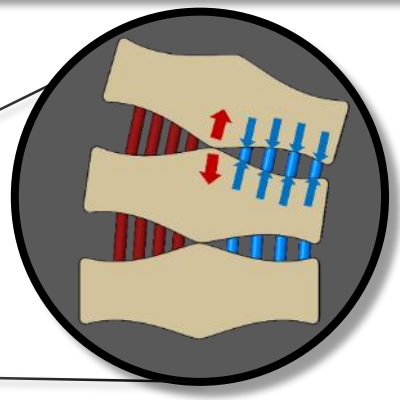

Abstraction

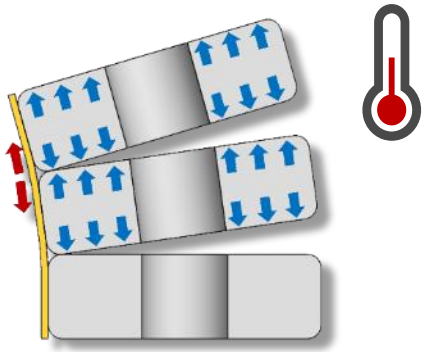

Manufacturing

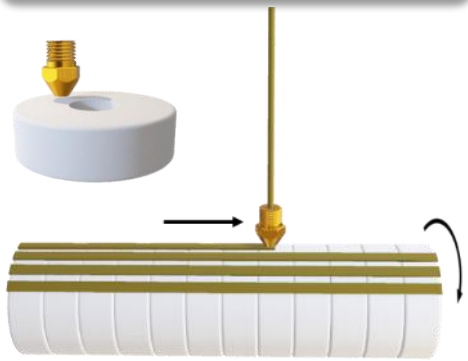

Potential application



Julien DESCHAMPS
julien.deschamps@univ-ubs.fr

4D-printed composite structures for space applications : towards multi-axis structural shape-changing







Thank you for your attention

Julien DESCHAMPS[1,2], Antoine LE DUIGOU[1,2,4], Mickaël CASTRO[1,2], Christelle COMBESCURE[1,2,3]

[1]Institut de Recherche Dupuy de Lôme - Université de Bretagne Sud, [2]BIONICS Group, [3]CREC Saint-Cyr Coëtquidan, [4]Institut Universitaire de France





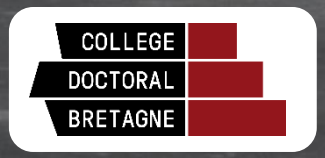

julien.deschamps@univ-ubs.fr

https://www.linkedin.com/in/julien-deschamps-a43873213/

U.S. AIR FORCE

USSF

AFRL

PEEK-Based Polymer Electrolyte with Tailored Morphology for Structural Battery Composites

Mia Carrola, Amir Asadi, Ahmad Amiri, Zhenning Yu, Hilmar Koerner

24th International Conference on Composite Materials

Baltimore, Maryland August 2025

Introduction to Structural Battery Composites

- 1915: First all-metal aircraft
- 1930s: Transition from steel to aluminum
- 1950s: Integration of exotic metals
- 1970s–80s: Fiberglass takes off
- 1990s - Present: Carbon fiber increases in popularity

Parveez, Bisma, et al. "Scientific advancements in composite materials for aircraft applications: a review." *Polymers* 14.22 (2022): 5007.

Introduction to Structural Battery Composites

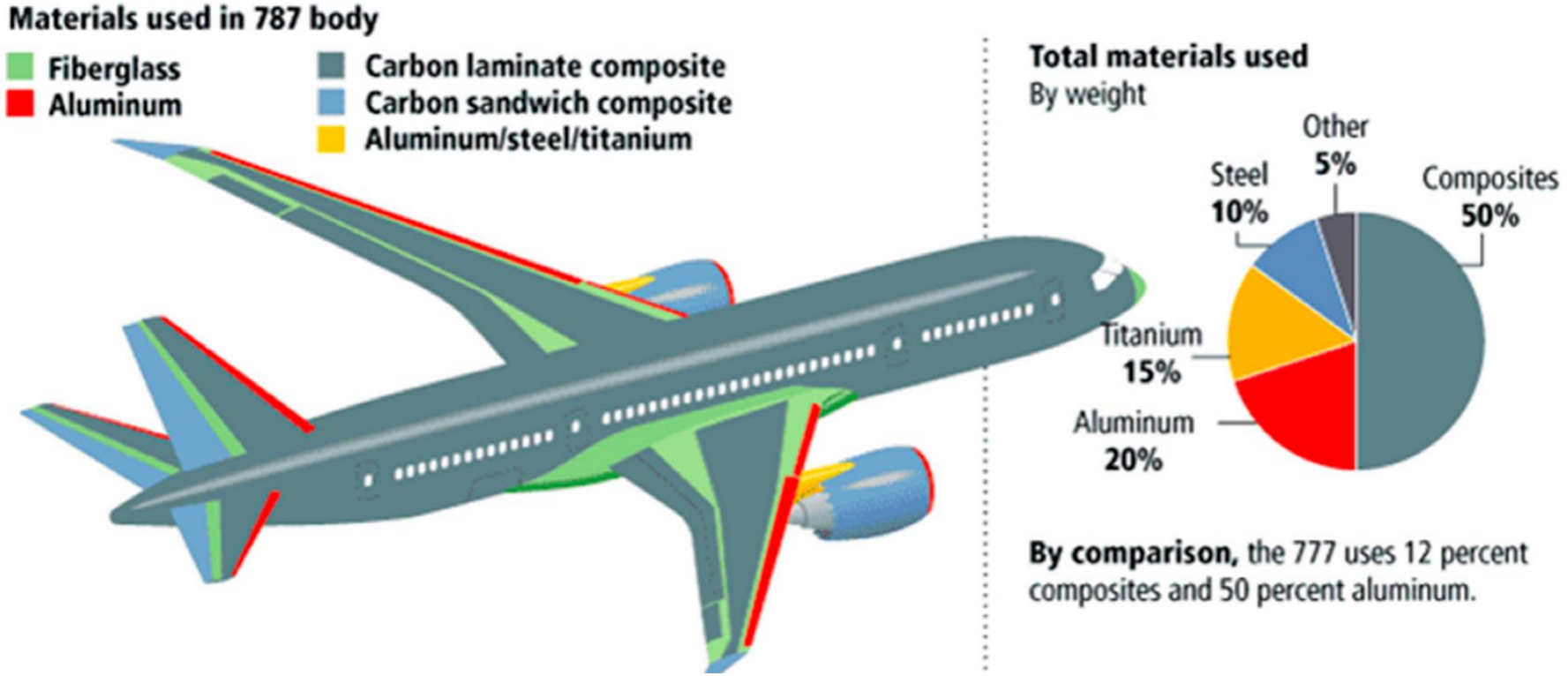

How can we enable the future of composites?

Airbus, Aviation's material evolution, 2017

Introduction to Structural Battery Composites

- Carbon Fiber:
  - Stiffness and Strength
  - Electrode
  - Current Collector
- Polymer Matrix:
  - Binder and Load Transfer
  - Solid Electrolyte

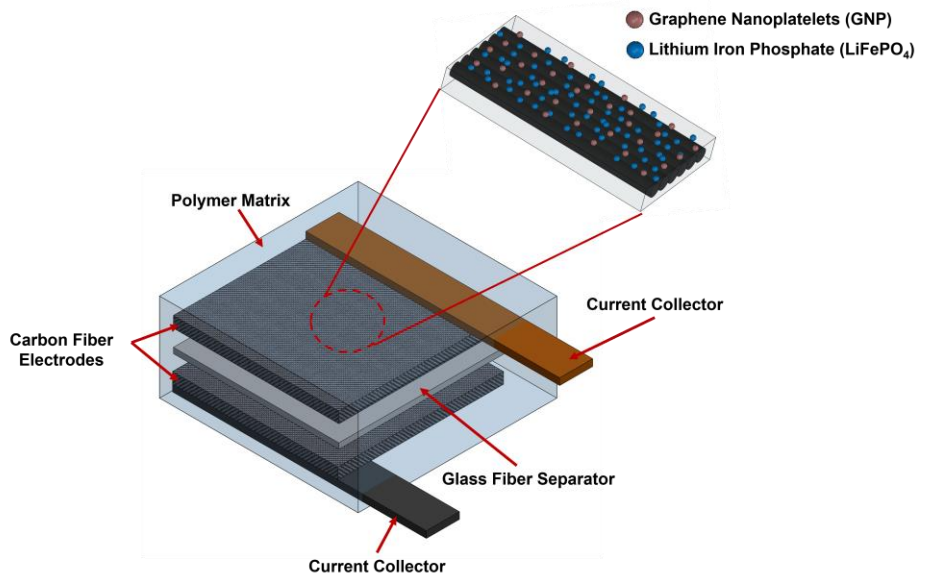

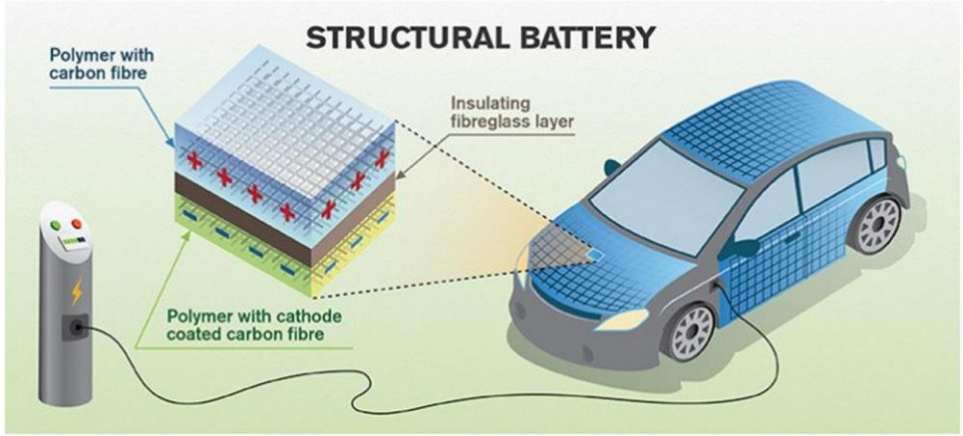

Leif E Asp *et al* 2019 *Funct. Compos. Struct.* **1** 042001

Current State of Electrolytes

Liquid Electrolyte:

- Ionic Conductivity: 10^{-2} S/cm
- Lithium salt solubility
- Ideal wettability & viscosity
- Wide electrochemical stability window

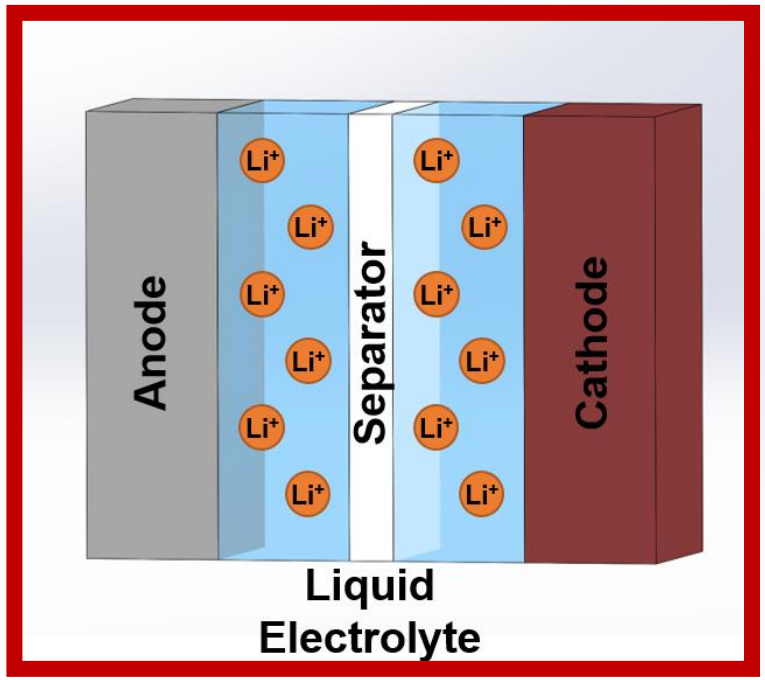

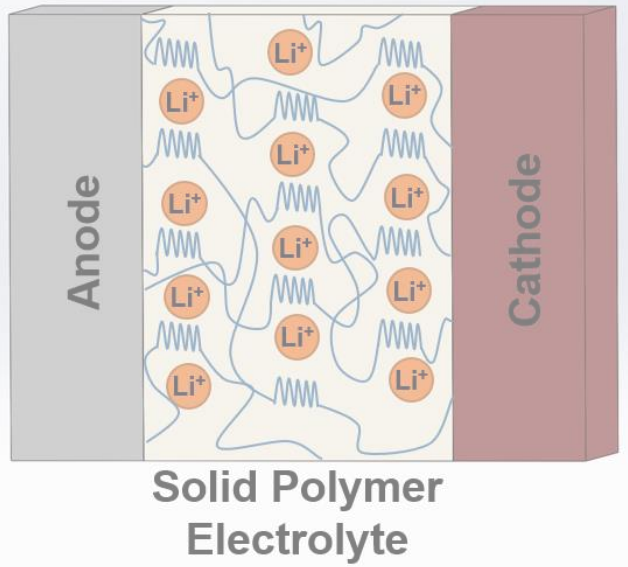

Xu, Kang. "Nonaqueous liquid electrolytes for lithium-based rechargeable batteries." *Chemical reviews* 104.10 (2004): 4303-4418.

Current State of Electrolytes

Solid Polymer Electrolyte (SPE):

- Ionic Conductivity: 10^{-6} S/cm
- No leakage
- Superior thermal stability
- Preventative for lithium dendrite growth

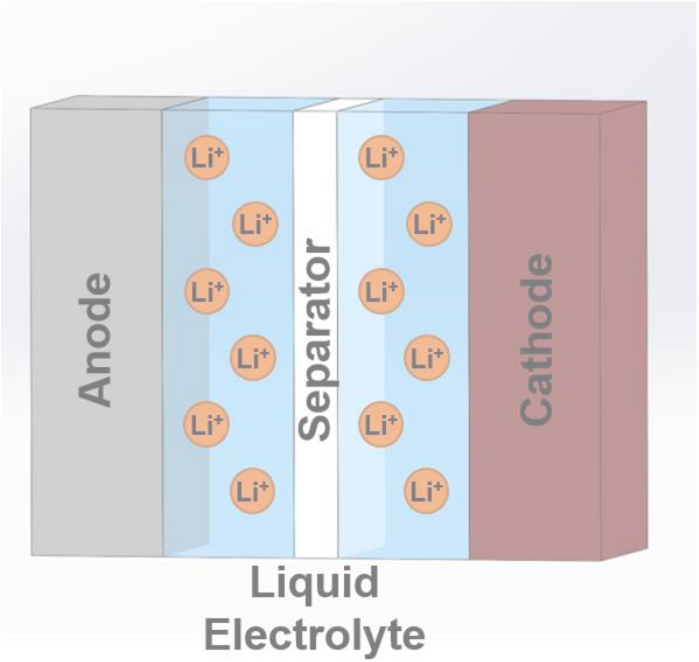

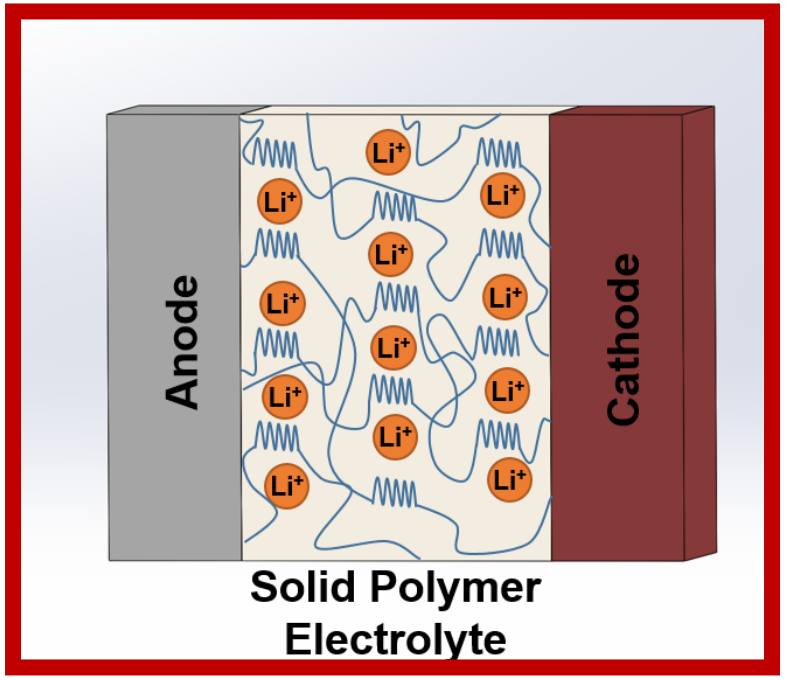

Yue, Liping, et al. "All solid-state polymer electrolytes for high-performance lithium ion batteries." *Energy Storage Materials* 5 (2016): 139-164.

Solid Polymer Electrolyte Morphology Dependence

- Structure-Properties relationship
- Crystallites act as a barrier for lithium-ion transport
  - Inverse relationship with ionic conductivity

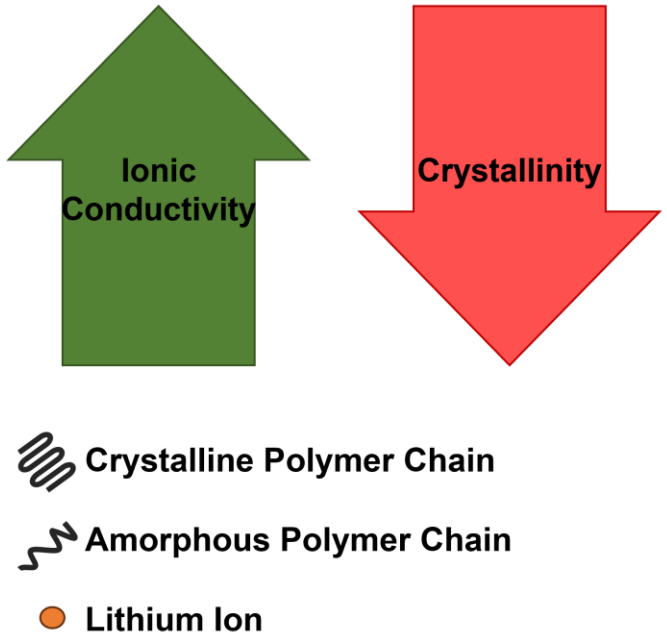

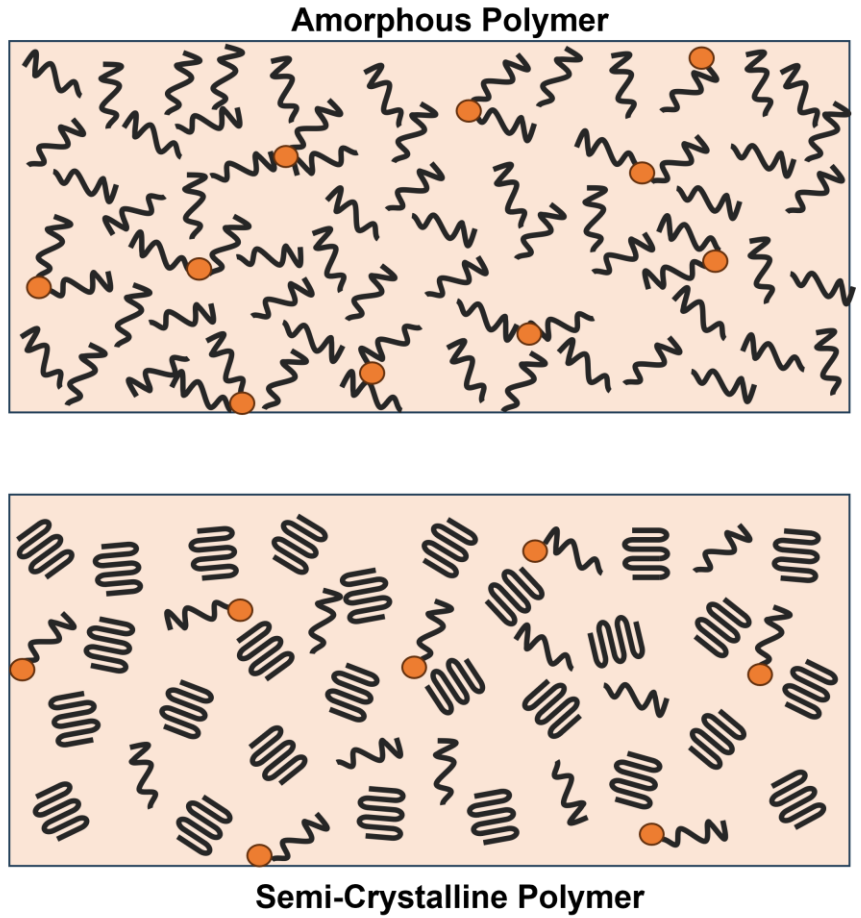

Functionalization of PEEK

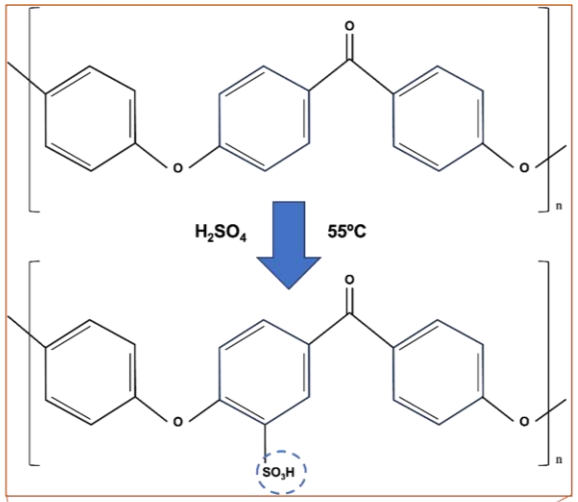

- Sulfonic acid groups on the PEEK backbone enables morphological changes
  - Can be further functionalized with lithiation treatment

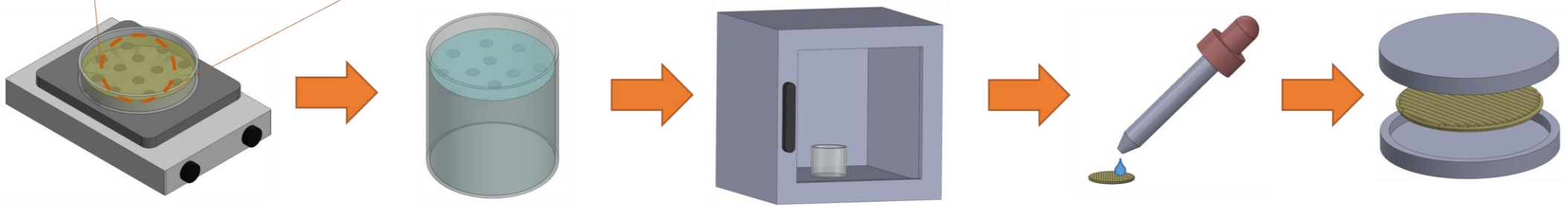

Sulfonate Polymer in H_2SO_4 → Rinse in DI Water → Dry in Vacuum Oven → Add Lithium Salt Solution → Assemble into Coin Cell Battery

Thermal Stability of Functionalized PEEK

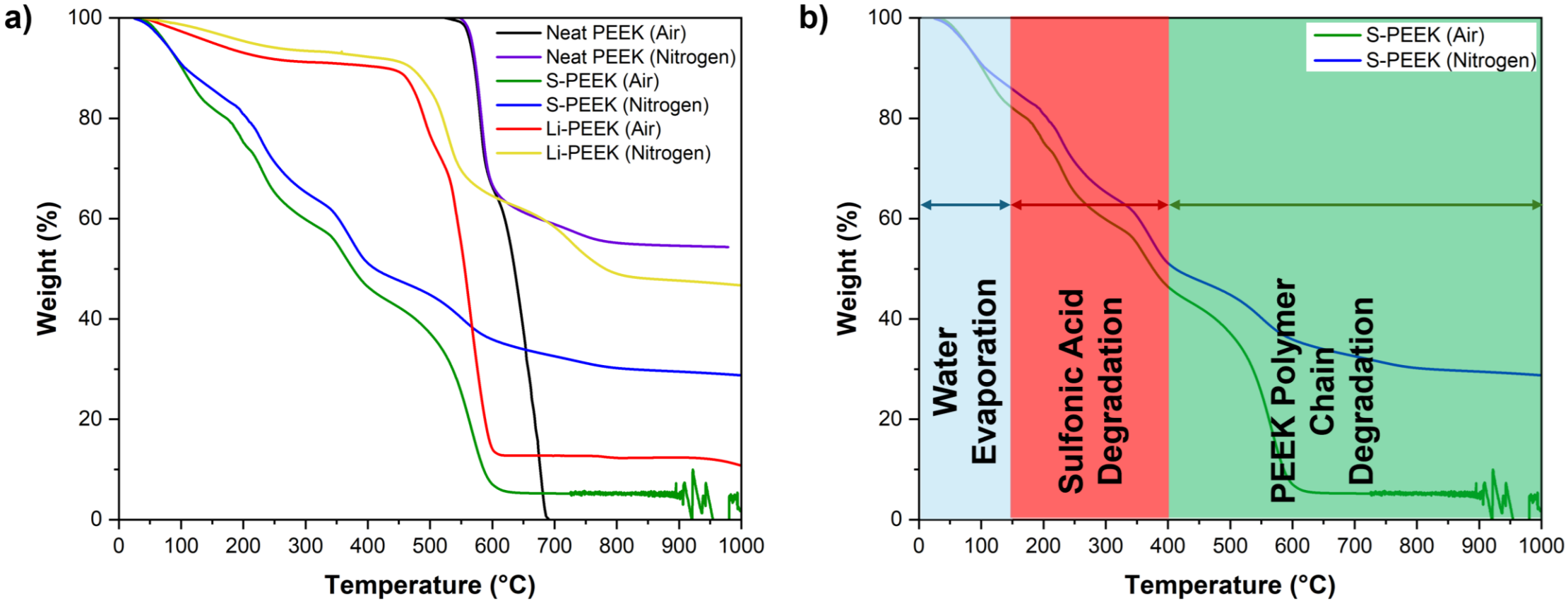

Morphology of Functionalized PEEK

- Lithiated PEEK displays ionomer peak, suggesting ionic conductivity
  - Sulfonated PEEK shows similar behavior

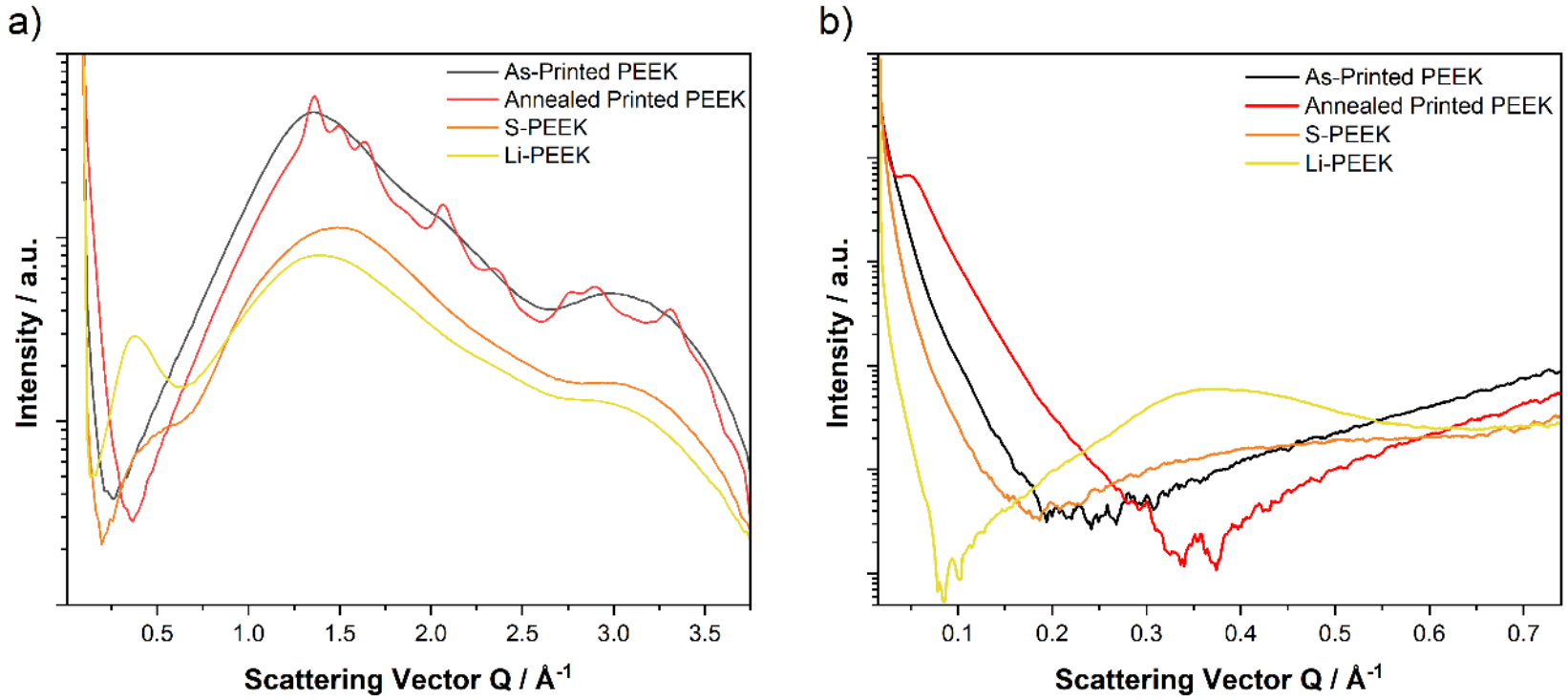

Thermomechanical Properties

- Sulfonated PEEK has highest storage modulus at ambient temperatures
- Lithiated PEEK has lowest storage modulus
  - Consistent at elevated temperatures

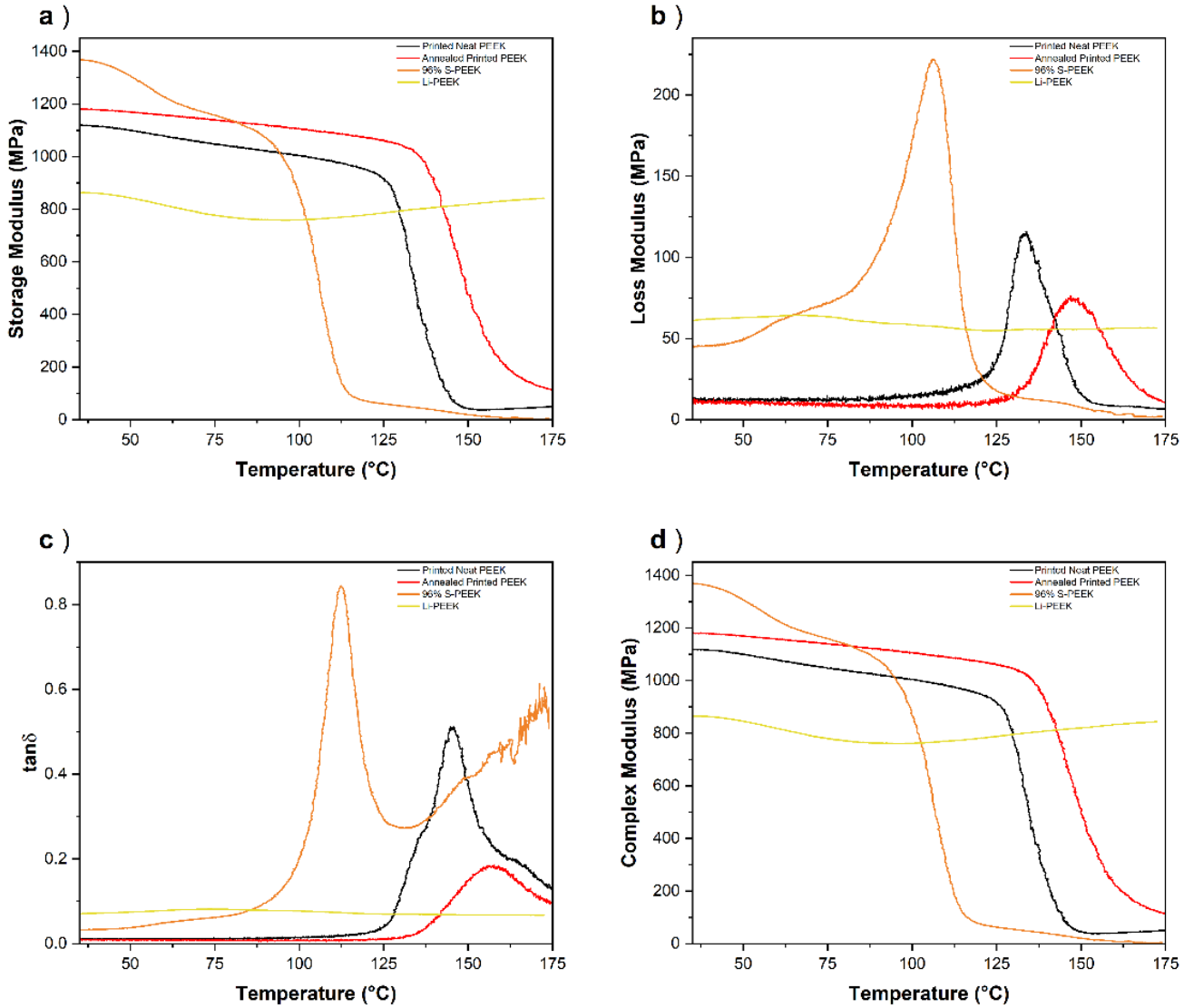

Thermomechanical Properties

How can we optimize the mechanical properties at temperature without compromising ionic conductivity?

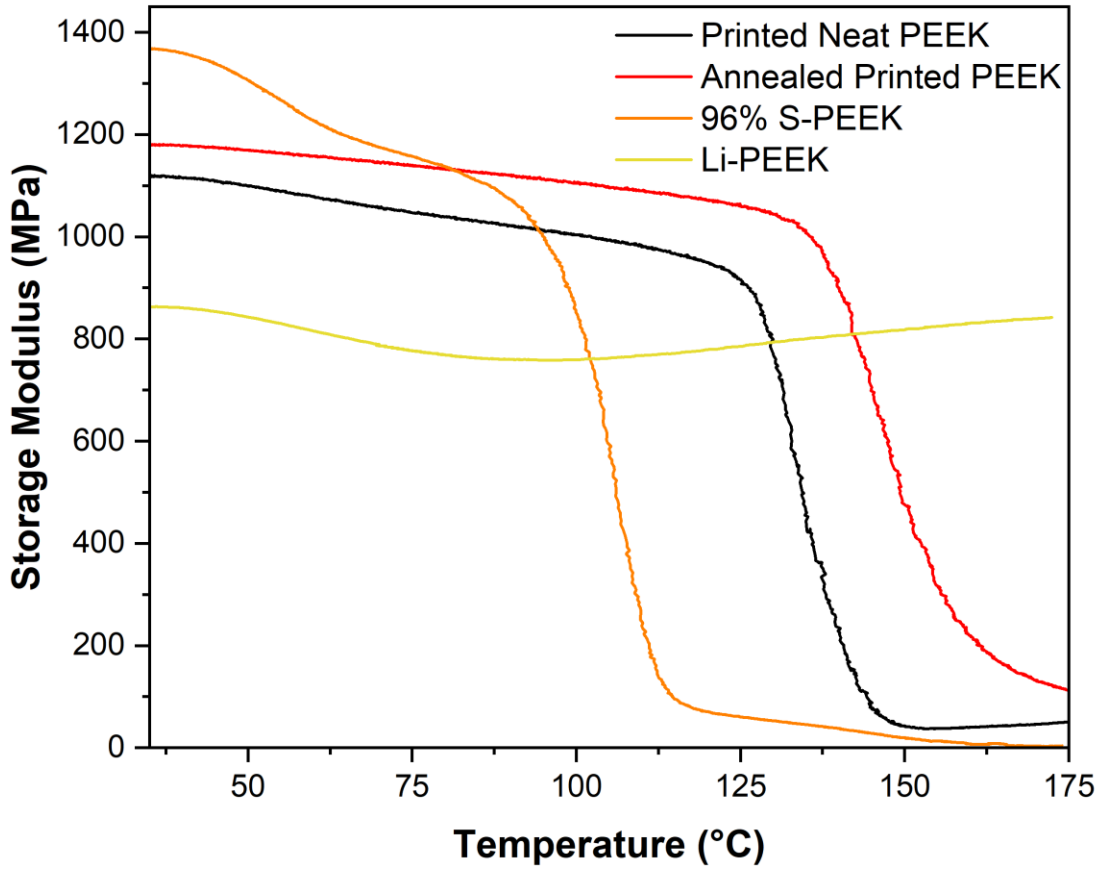

Tailoring Morphological Properties

- Instead of fully functionalizing PEEK, selectively sulfonating the surfaces can allow for amorphous exterior and semi-crystalline interior
  - Balances the mechanical properties and ionic conductivity

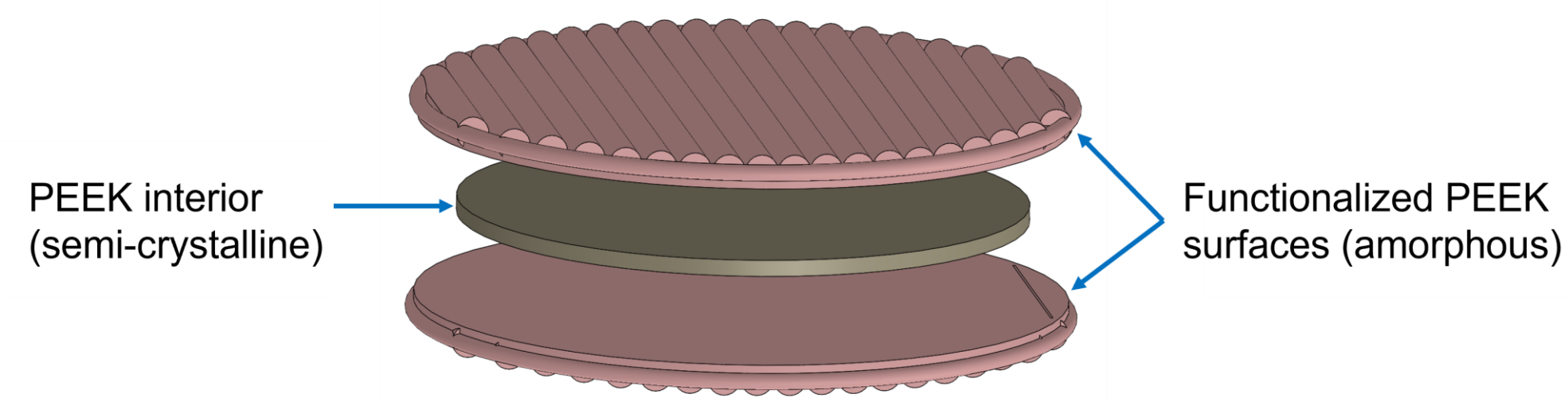

Evaluating Dual Phase Functionalized Structure

- Surface sulfonation provides both amorphous and semi-crystalline structure simultaneously
- Confirms the balancing of properties of ionic conductivity and structure

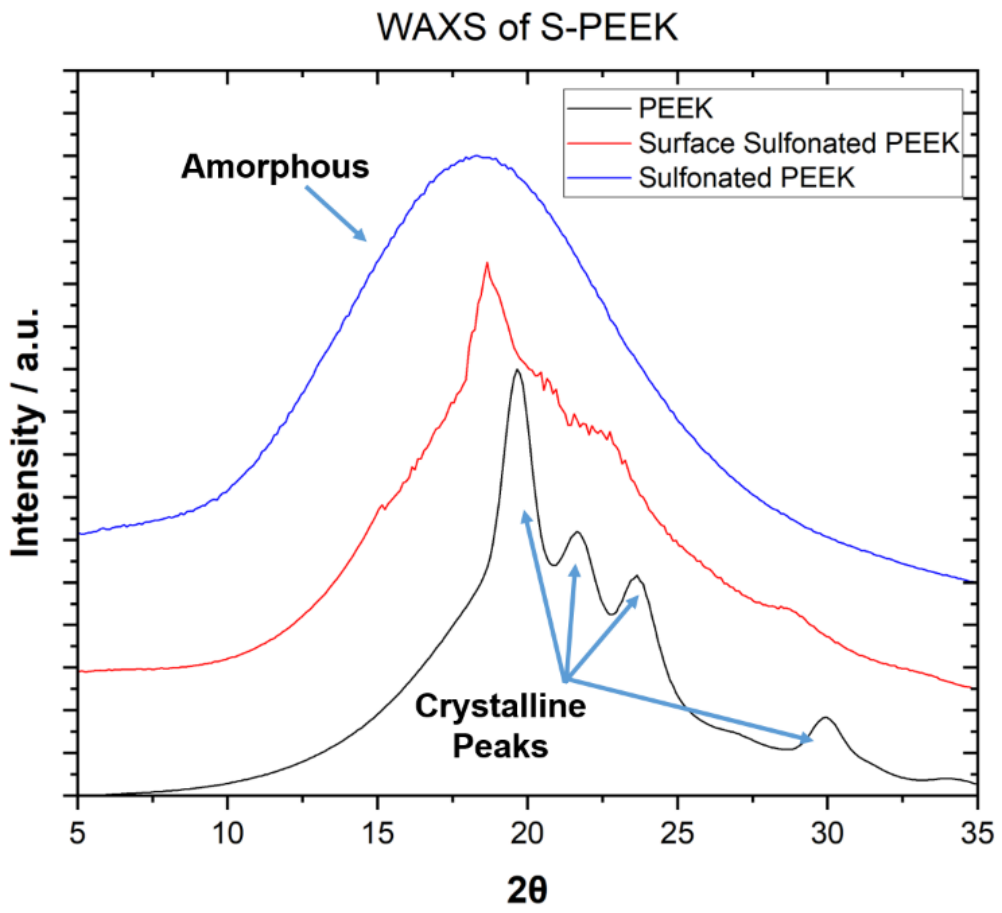

Mapping PEEK Morphology

Crystallinity Behavior of Printed PEEK

- Highest crystallinity is found closest to the print bed
- Crystallinity decreases with increased thermal gradient from supercooling
- No sulfur present in the material

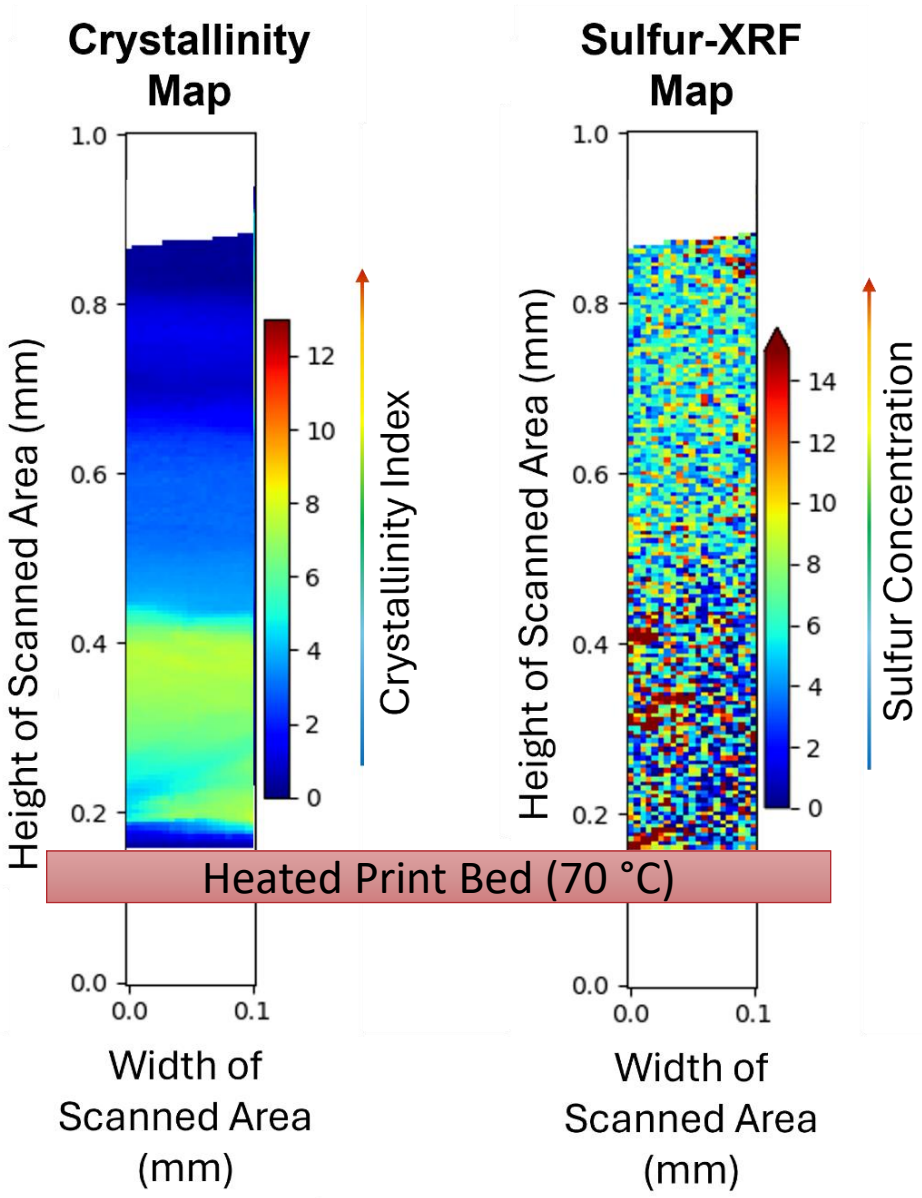

Mapping PEEK Morphology

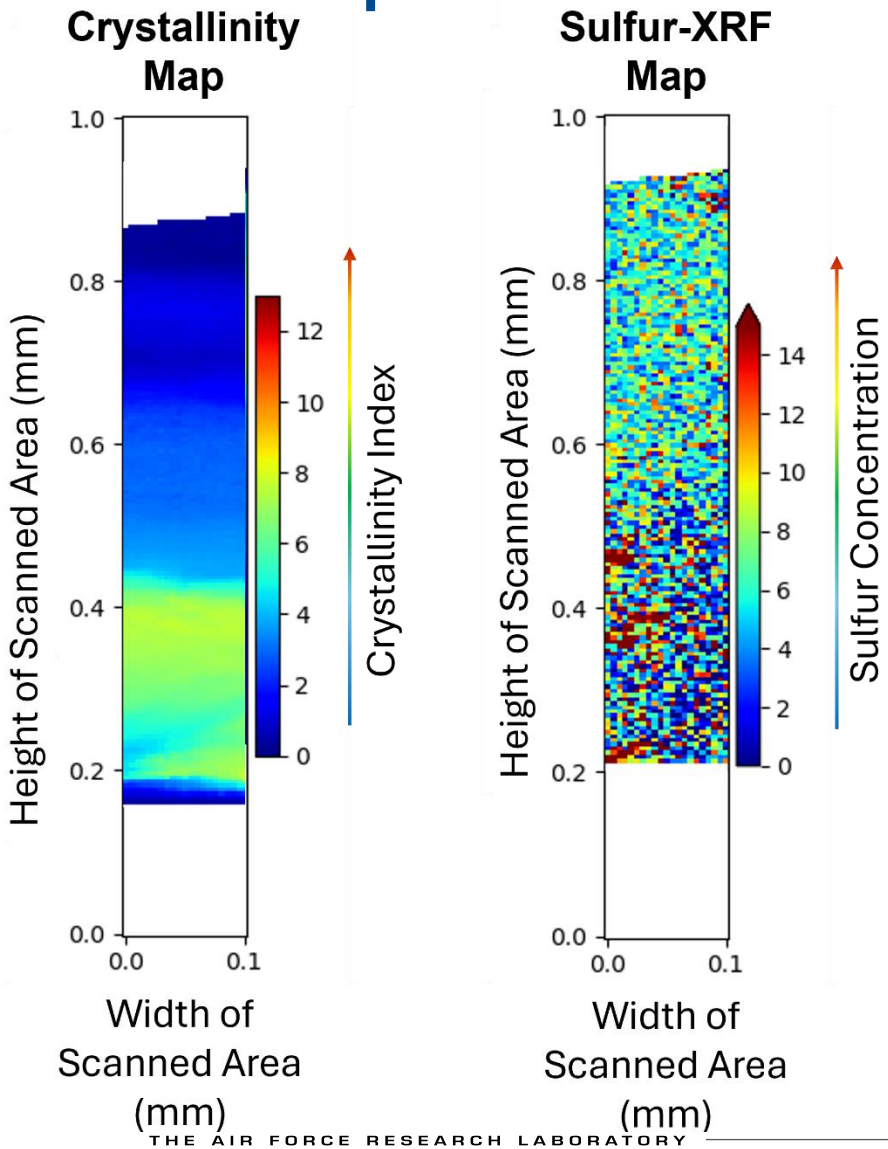

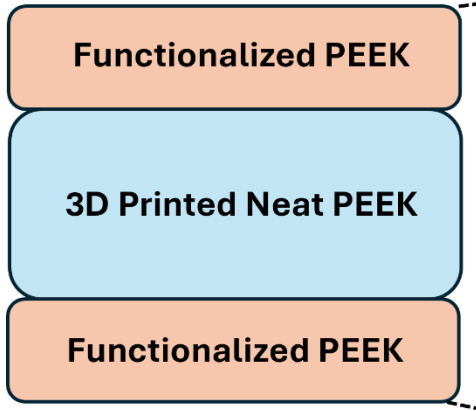

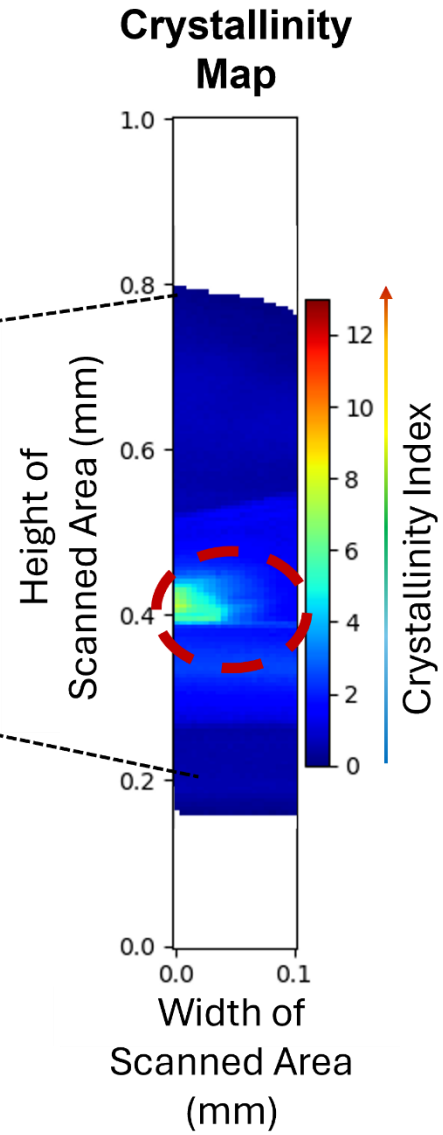

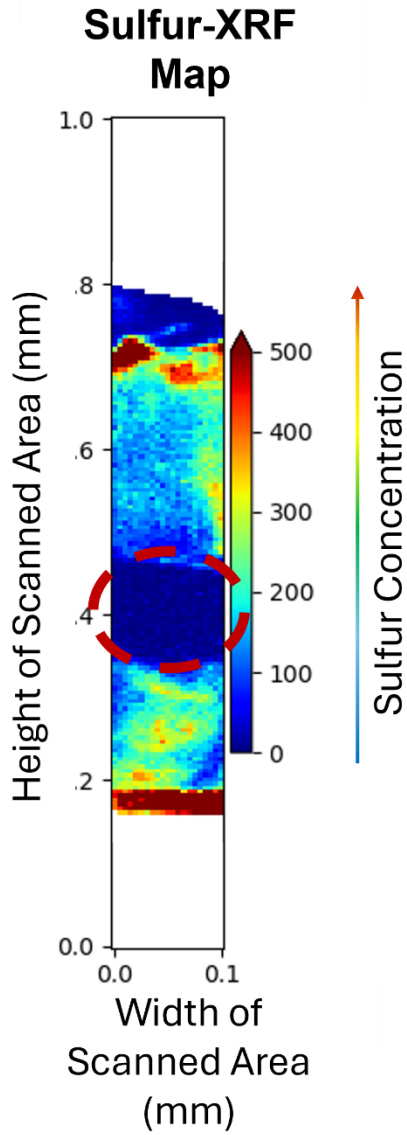

Enabling Additive Manufacturing

- Printed PEEK mesh to maintain mechanical properties
- Functionalized PEEK infill to provide ionic conductivity

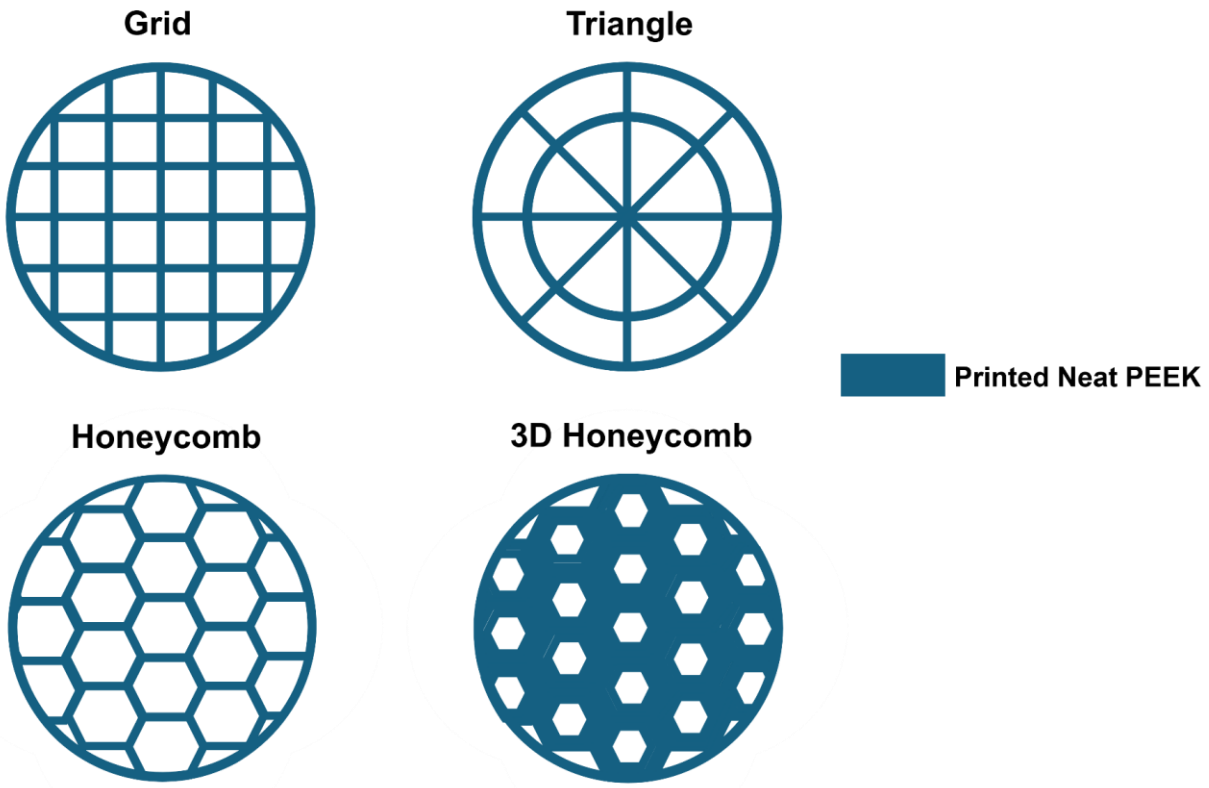

Conclusions & Future Work

- Functionalization of PEEK can provide ionic conductivity to enable its use as a solid polymer electrolyte
- Additive manufacturing allows for selective enabling of crystalline and amorphous morphologies for optimized solid polymer electrolyte

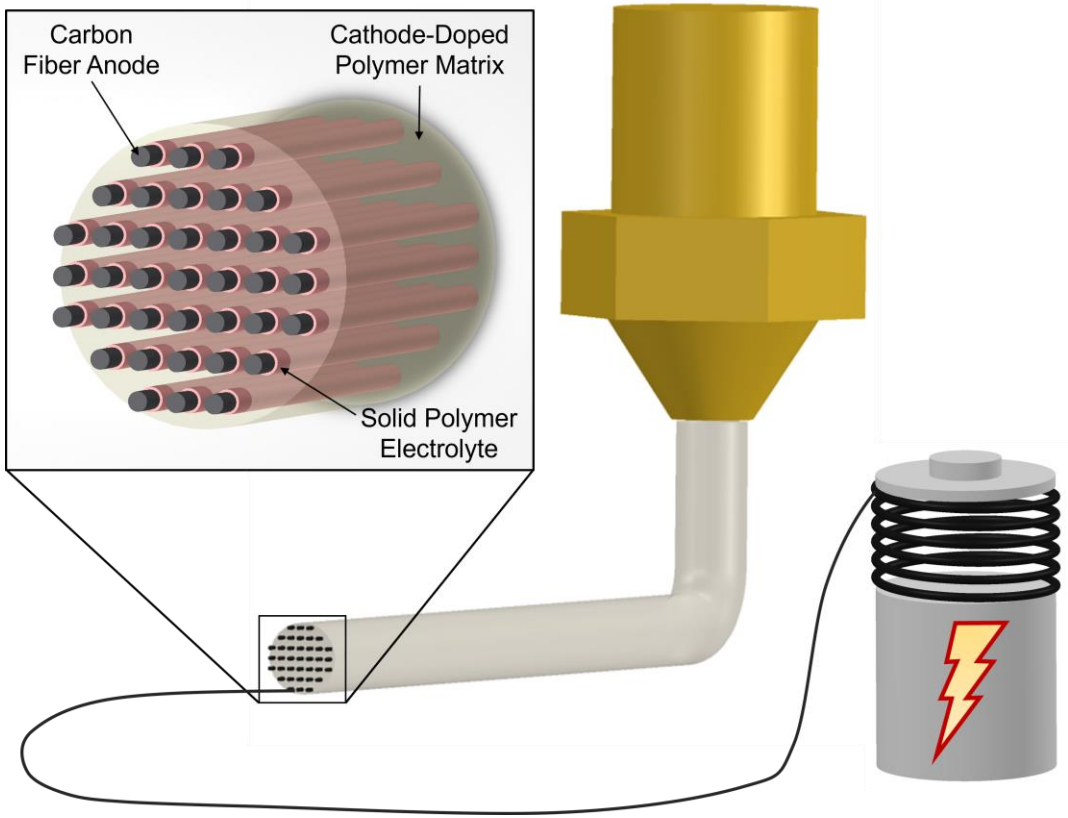

Center for Science of Heterogeneous Additive Printing of 3D Materials

SHAP3D

NSF



Center Director:
Joey Mead, Ph.D.
UMass Lowell

uml.edu/shap3d

University of Massachusetts Lowell



Site Director:
Chris Hansen, Ph.D.

- Polymer, composites processing
- Process-property modeling
- Nano/micro/reactive additives
- Ceramic-/colloidal-based inks

Georgia Tech



Site Director:
Jerry Qi, Ph.D.

- Modeling and simulations
- Functional polymers
- Hybrid 3D printing
- Functional devices & sensors

ASU Arizona State University



Site Director:
Timothy Long, Ph.D.

- Processes (Macromolecular structure & polymerization)
- Sustainable production
- Biodesign
- Green Chemistry

University of Connecticut



Site Director:
Anson Ma, Ph.D.

- Machine learning
- Multi-material printing
- Metal printing
- Food and drug printing

80+ Faculty Involved

54+ Students have participated in and supported Center Projects

Cumulative Center Investment: $5,580,113
(Phase I (5 years) - NSF, Members and Universities)

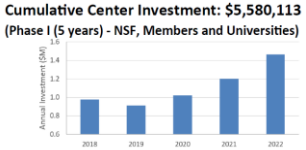

Current Full Member Leveraging: 28:1



Fused Deposition Manufacturing of Multiple Materials

Industry Membership

Compounding Solutions

Akita Innovations

hp

K&C Karagozian & Case

Greene Tweed

"SHAP3D brings together the best brains in the universities and industries to **develop technologies and convert** them into product developments for the benefits of society." – *Greene Tweed*

Integrity Industrial Ink Jet Integration

"SHAP3D has active and engaged industrial members and **provides interaction** with multiple companies in the AM supply chain." – *Integrity Integration*

U.S. ARMY DEVCOM ARMAMENTS CENTER

"Our Partnership with SHAP3D helps to connect **fundamental** research with **applied research** requirements in an Additive Manufacturing design space." – *DEVCOM Armaments Center*

Sandia National Laboratories

Markforged

Raytheon Technologies

stratasys

BARNES

U.S. ARMY DEVCOM SOLDIER CENTER

AFRL THE AIR FORCE RESEARCH LABORATORY

9T LABS

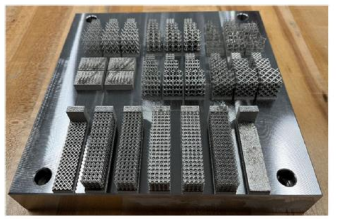

Mesoarchitectures in Topology Optimization



Thermoset Elastomer Printing using ARME Ram Printer Head



SHAP3DLP Printer

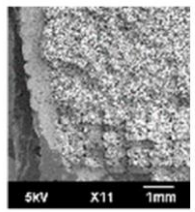

Graded Foams

Australian Government
Department of Defence
Defence Science and Technology Group

Discrete damage modelling of compressively loaded structural supercapacitors

Alex Harman, Benjamin J. Mapleback, Vu Dao, Lachlan Bodsworth, Patrick Frezza and Andrew N. Rider

Platforms Division

Defence Science and Technology Group

PUBLIC RELEASE

Contents

- Background
- Experimental testing
- Discrete damage modelling using BSAM™
- Conclusions
- Further work …..

PUBLIC RELEASE

Background

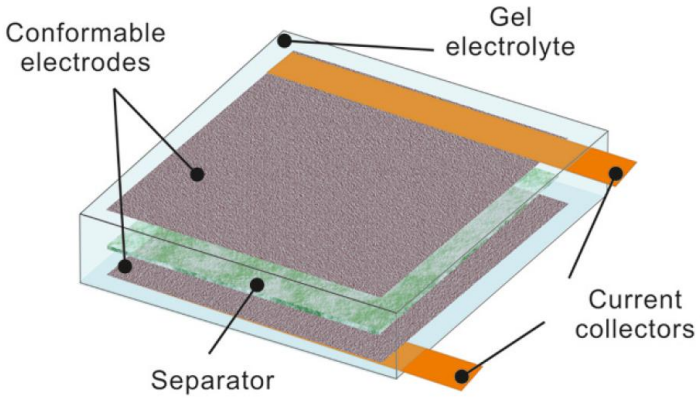

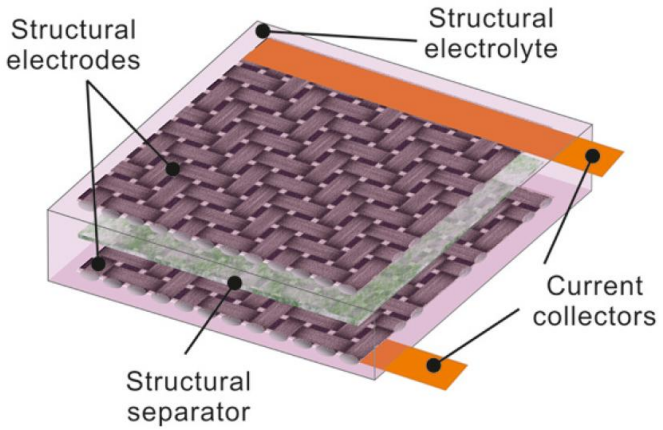

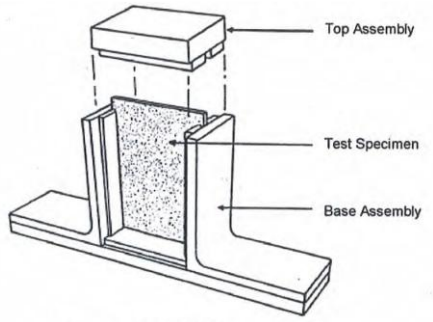

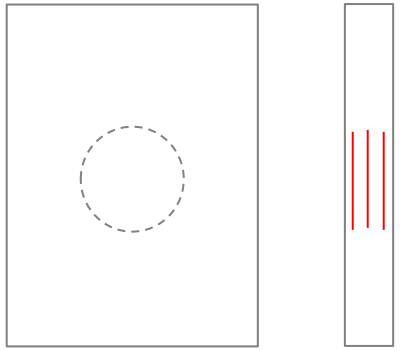

Greenhalgh, E., et.al., Critical review of structural supercapacitors, CS&T, 2023.

- Structural SuperCapacitors (SSC) are being developed for integration into carbon-epoxy composite aircraft structures – Designed for minimal impact on structural integrity

- 26 ply IM7/977-3 laminates prepared with three 50 mm diameter "semi-structural" SC's and PTFE inserts integrated through the thickness

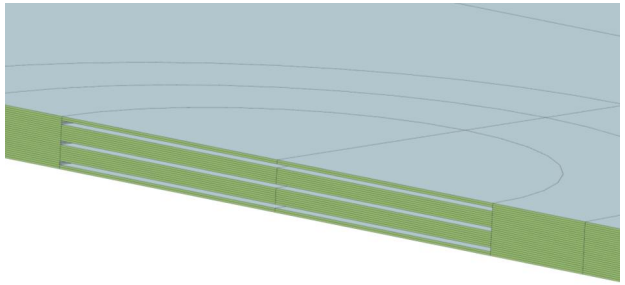

- Test method based on ASTM D7137 used for compression after impact (100 x 150 mm)

PUBLIC RELEASE

Background - configurations

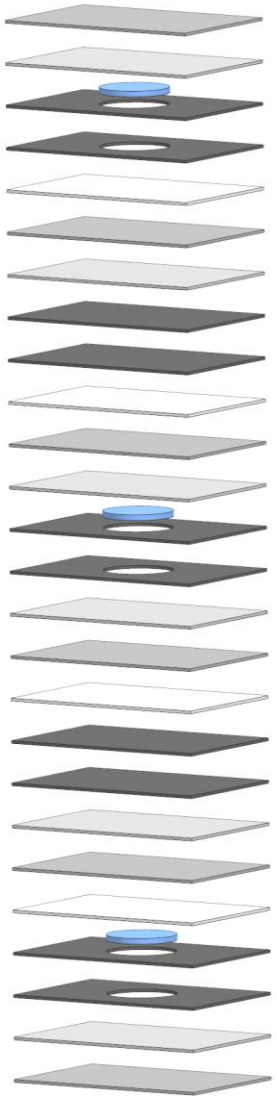

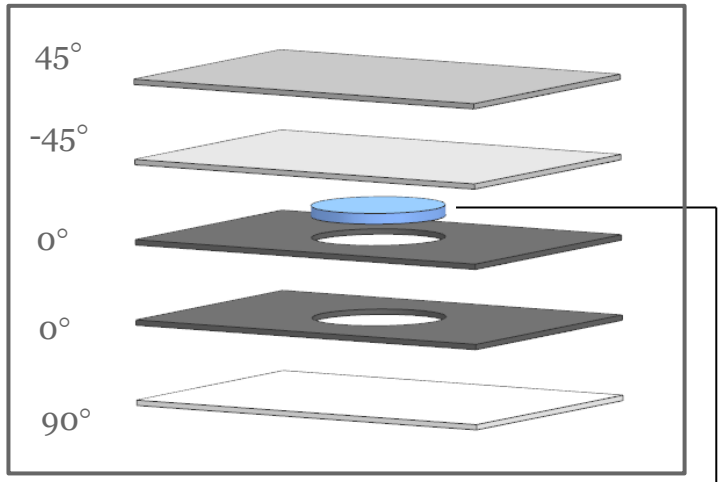

50mm diameter/ SSC

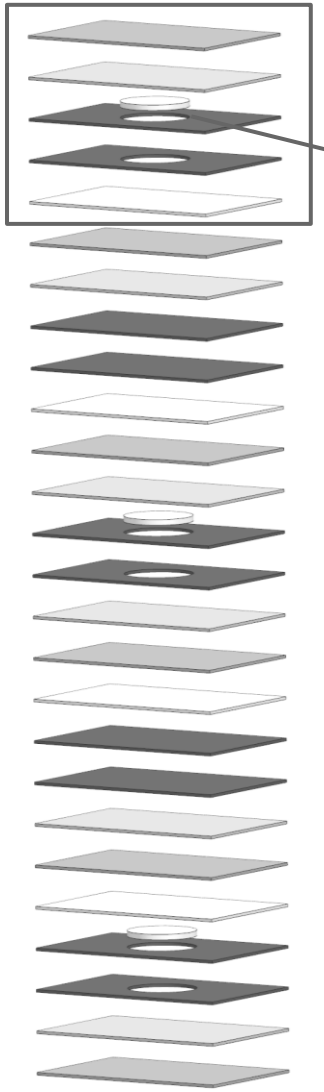

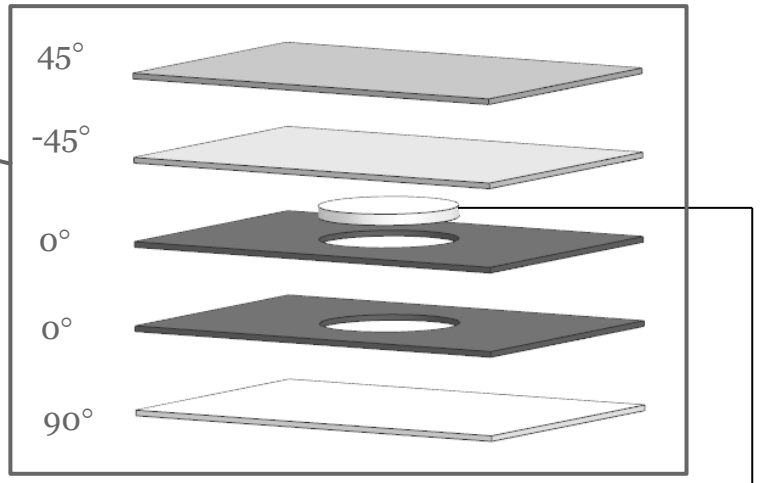

50mm diameter/
0.25mm PTFE insert

Configuration A: SSC

Base laminate:26 ply IM7/977-3

$[(45/-45/0_2/90)_2(45/-45/0)]_S$

Configuration B: 0.25 mm PTFE

Base laminate:26 ply IM7/977-3

$[(45/-45/0_2/90)_2(45/-45/0)]_S$

PUBLIC RELEASE

Experimental testing – Pre-test NDE

Pulse-echo UT

Through transmission UT

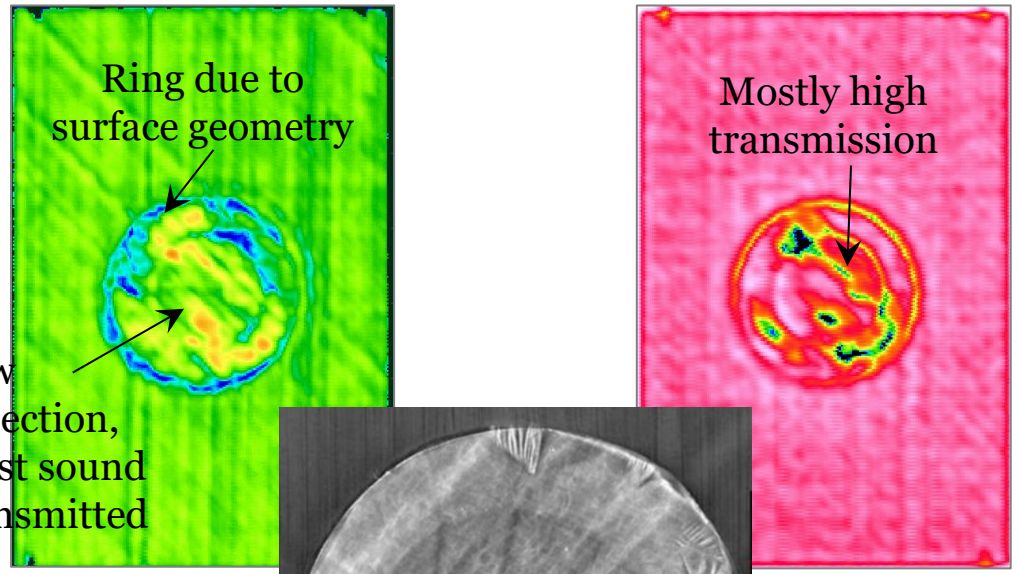



Configuration A: SSC

Base laminate:26 ply IM7/977-3

$[(45/-45/0_2/90)_2(45/-45/0)]_S$

Pulse-echo UT

Through transmission UT

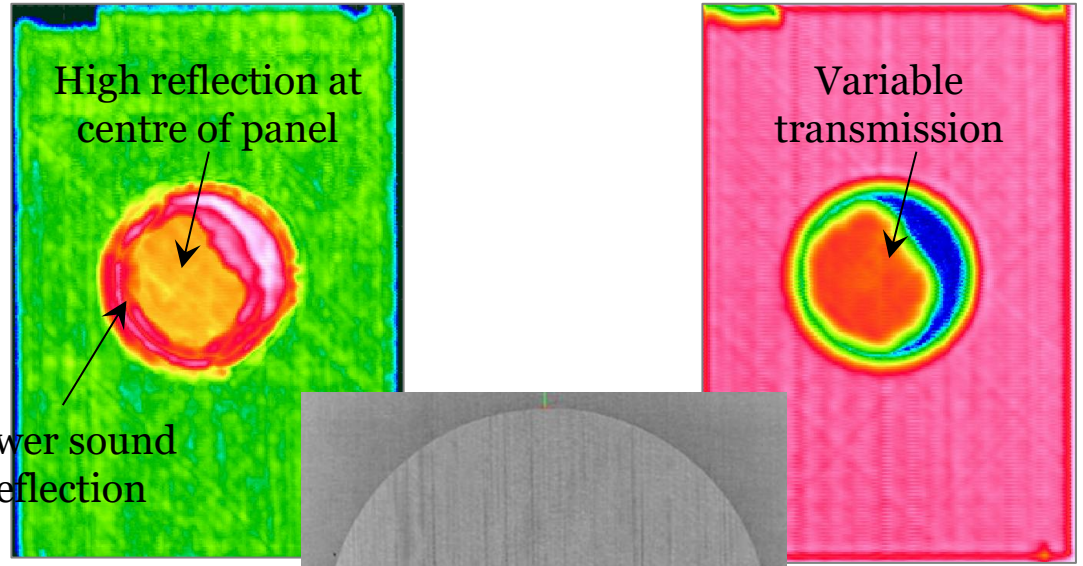

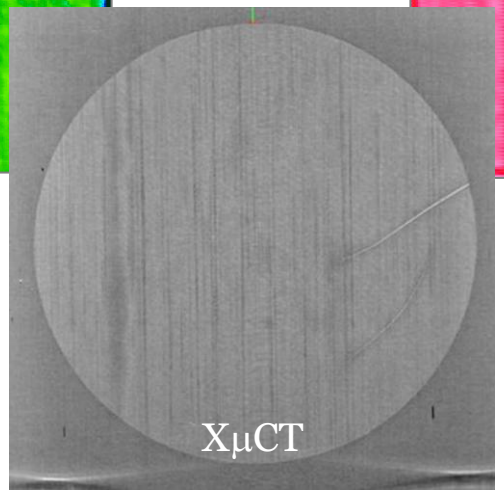

Configuration B: 0.25 mm PTFE

Base laminate:26 ply IM7/977-3

$[(45/-45/0_2/90)_2(45/-45/0)]_S$

PUBLIC RELEASE

Experimental testing – Mechanical response

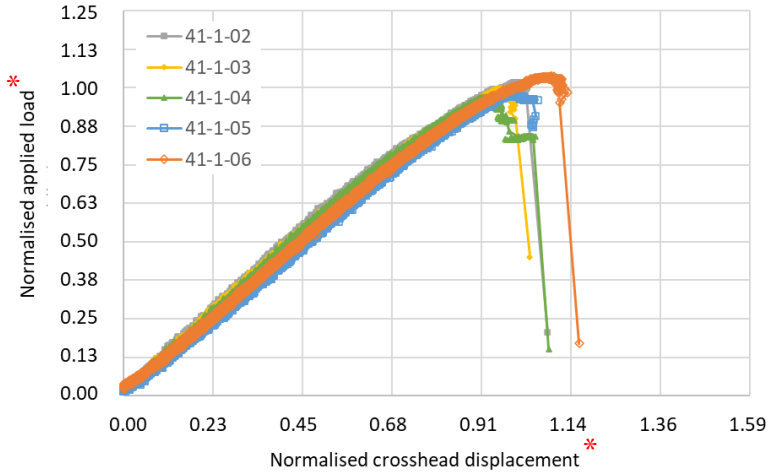

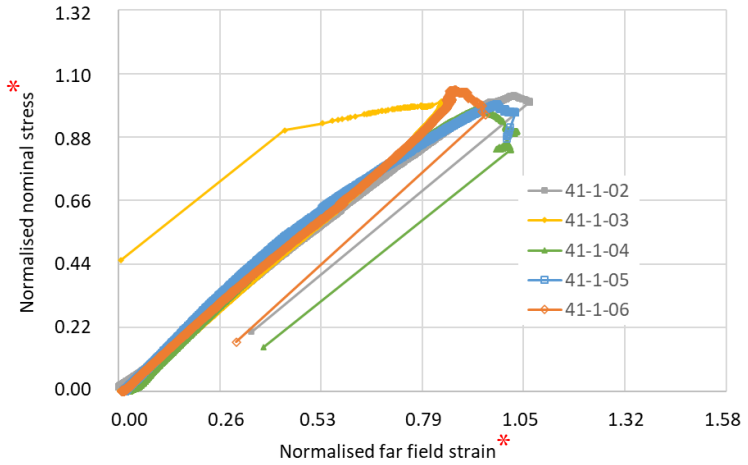

CV = 1.84%

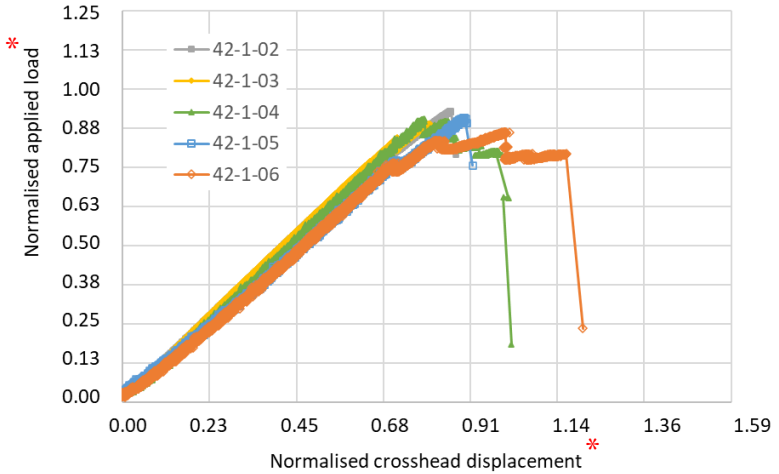

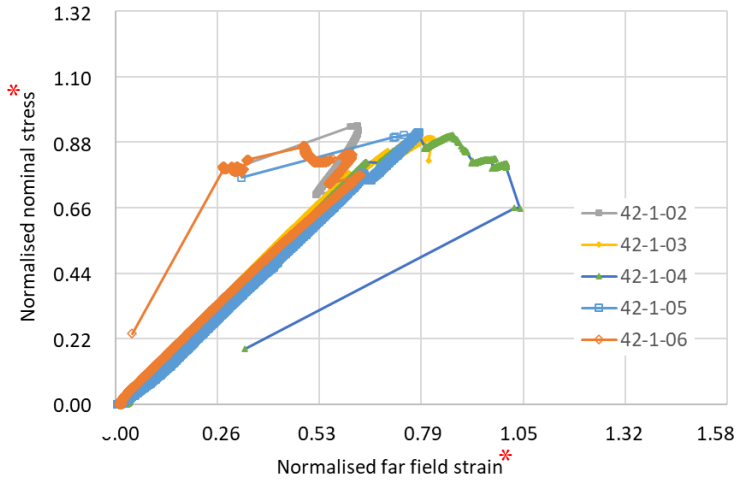

CV = 2.64%

* Average strength and max CH for **configuration A SSC** used for normalisation

Configuration A: SSC

Base laminate:26 ply IM7/977-3

$[(45/-45/0_2/90)_2(45/-45/0)]_S$

* Average strength and max CH for **configuration A SSC** used for normalisation

Configuration B: 0.25 mm PTFE

Base laminate:26 ply IM7/977-3

$[(45/-45/0_2/90)_2(45/-45/0)]_S$

PUBLIC RELEASE

Experimental testing – Configuration A SSC DIC

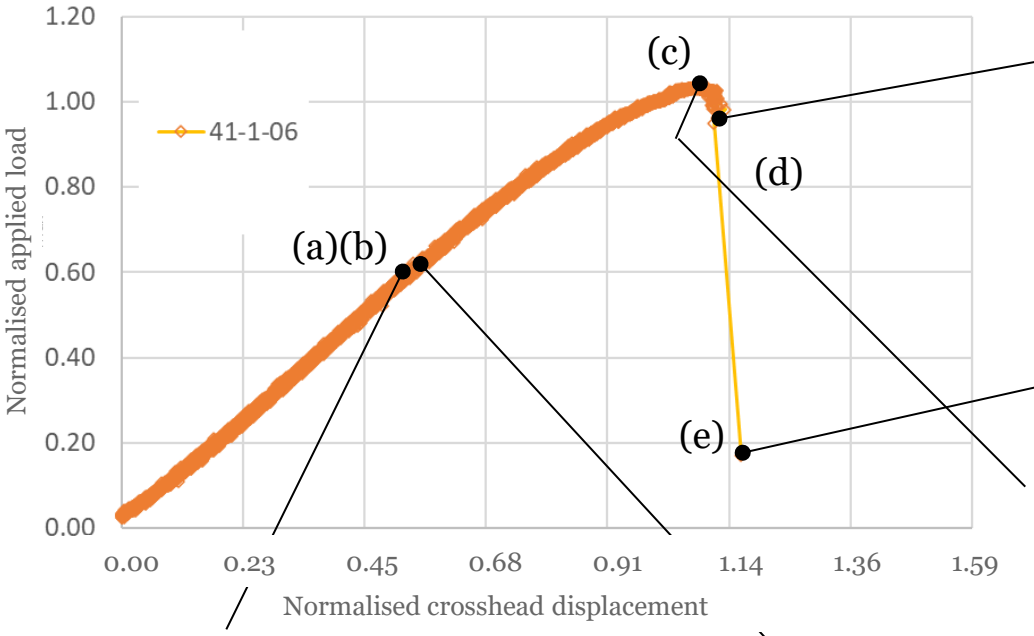

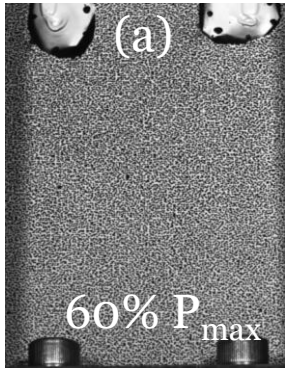

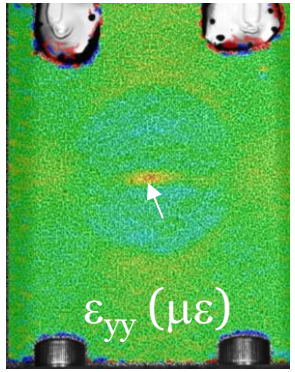

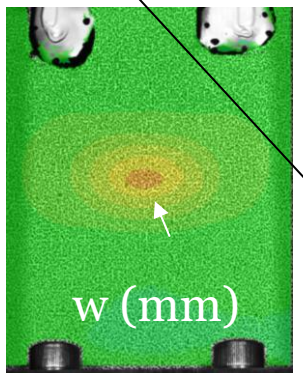

Configuration A: SSC

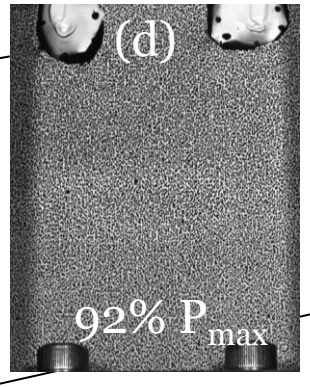

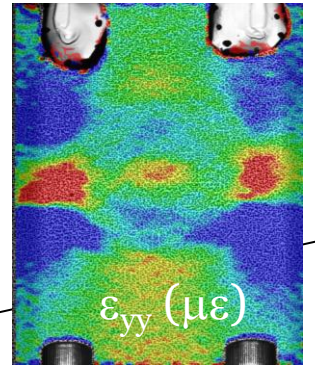

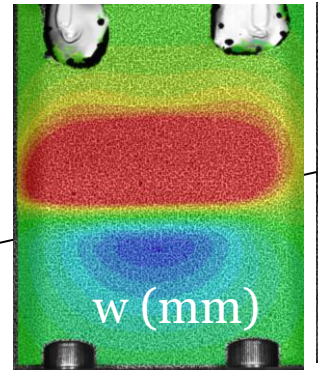

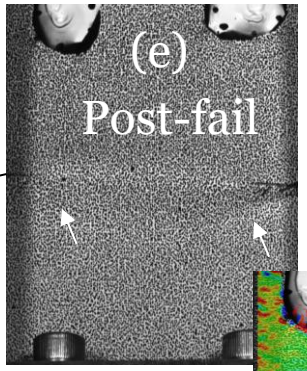

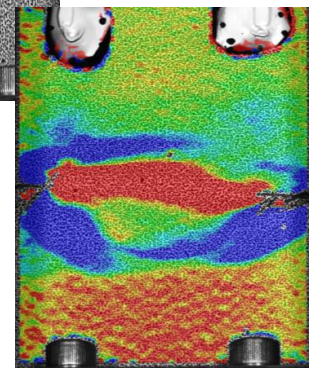

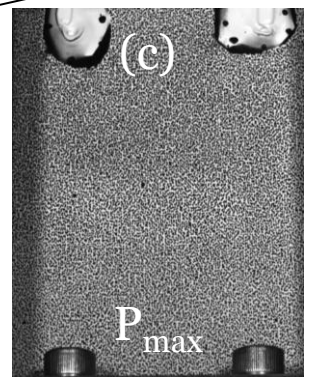

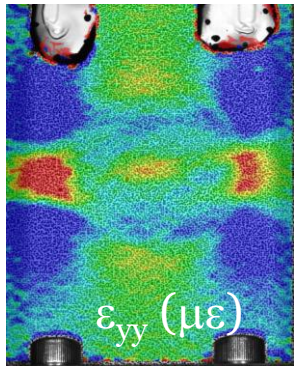

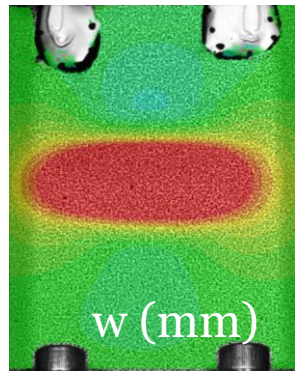



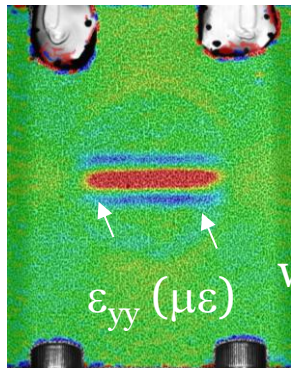

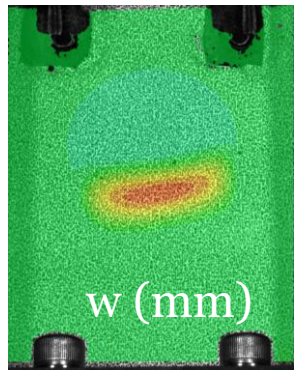

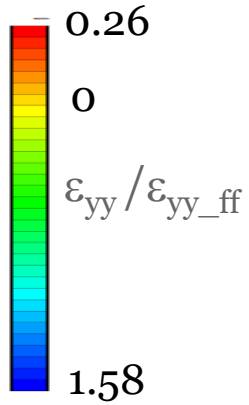

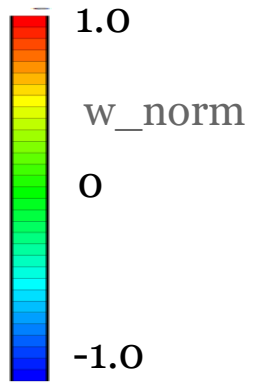

PUBLIC RELEASE

Experimental testing – Configuration B 0.25 mm PTFE DIC

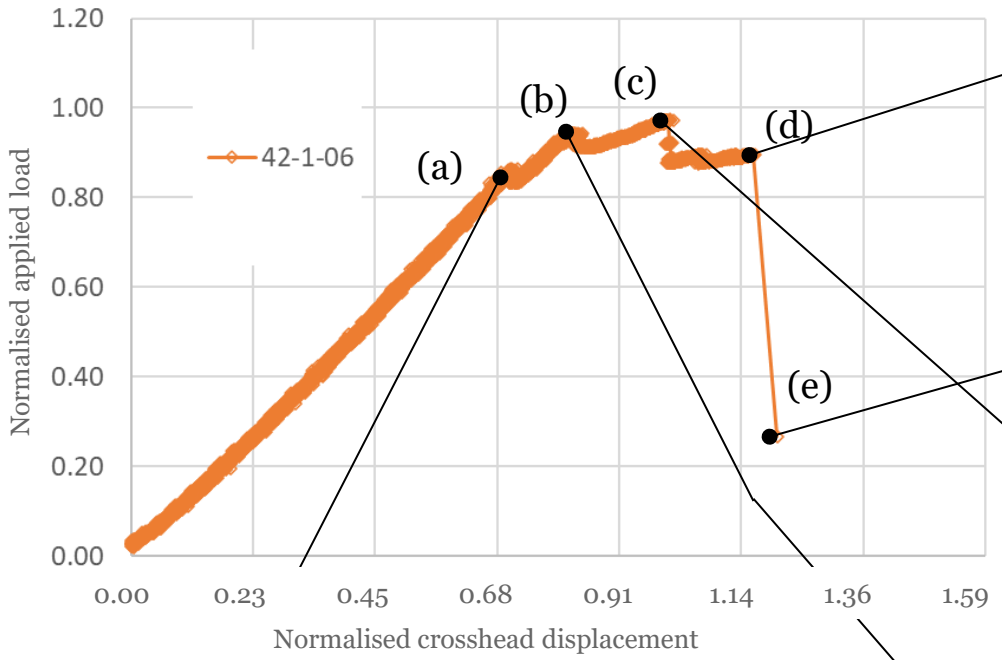

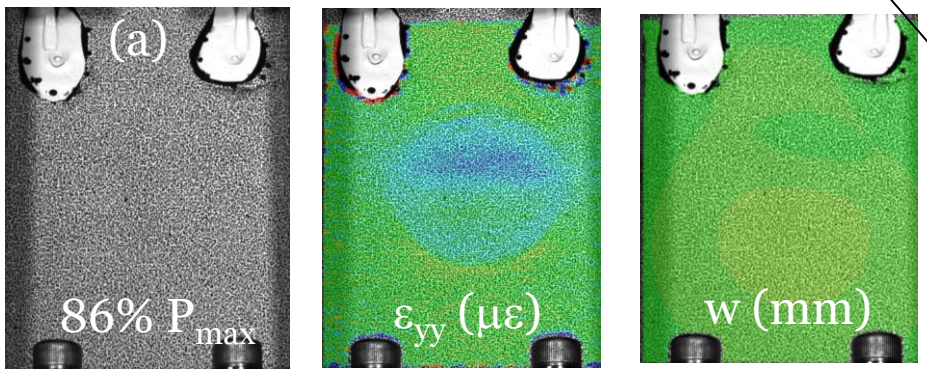

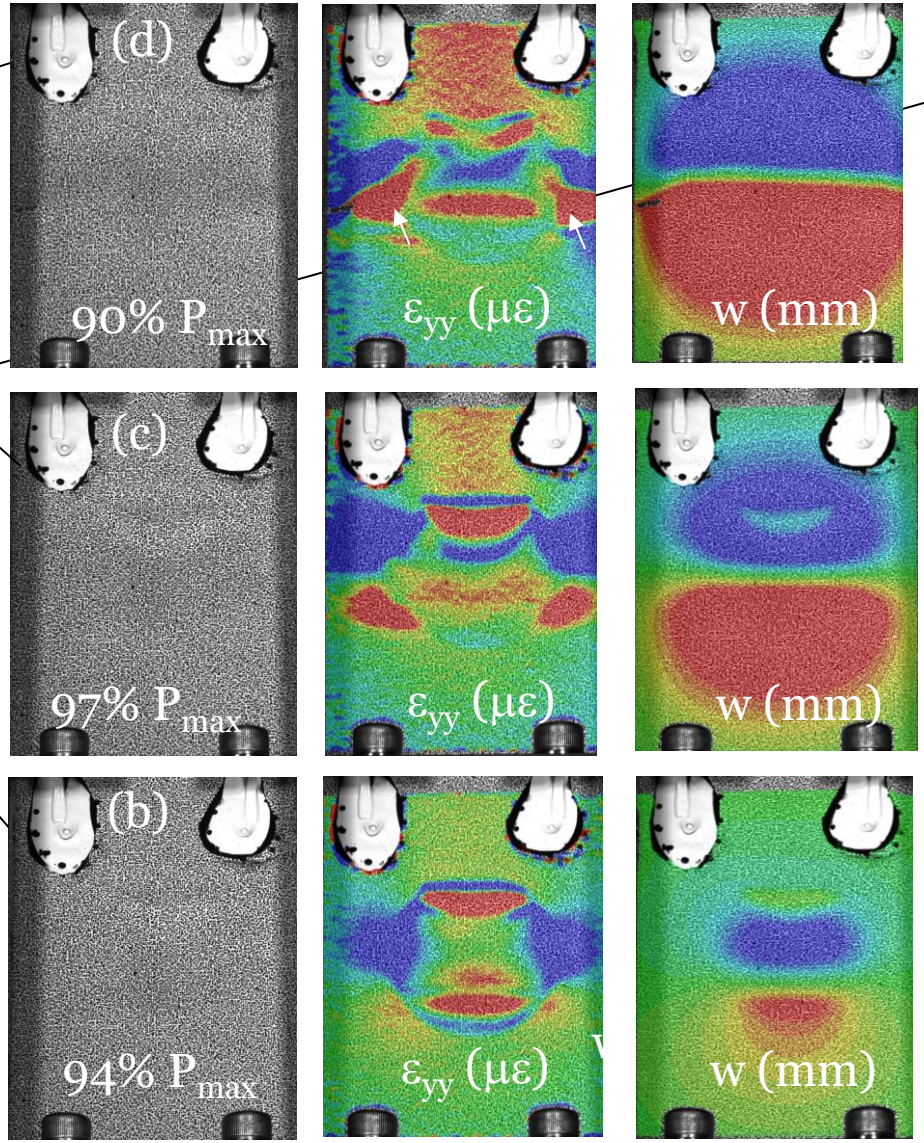

Configuration B: 0.25 mm PTFE

Experimental testing – Post-test examination

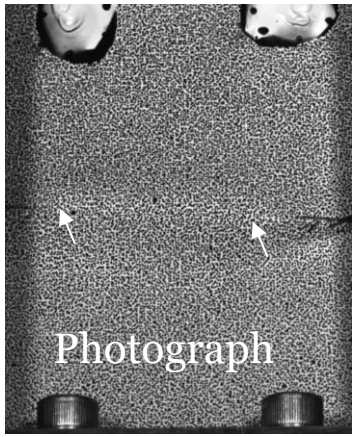

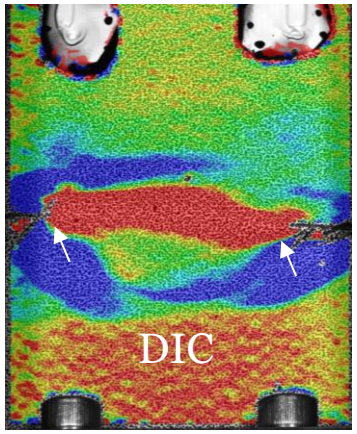

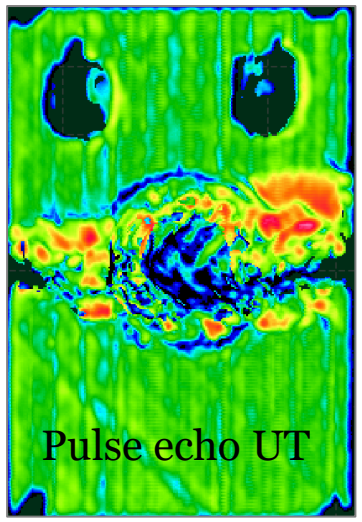

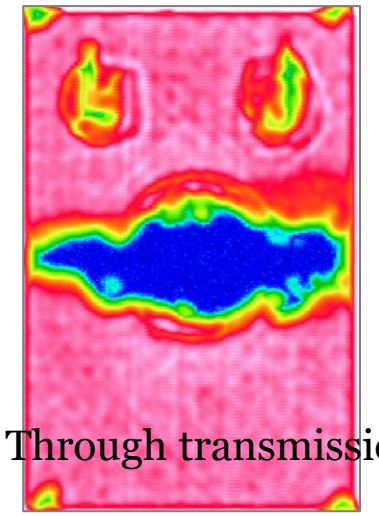

Configuration A: SSC

Base laminate:26 ply IM7/977-3

$[(45/-45/0_2/90)_2(45/-45/0)]_S$

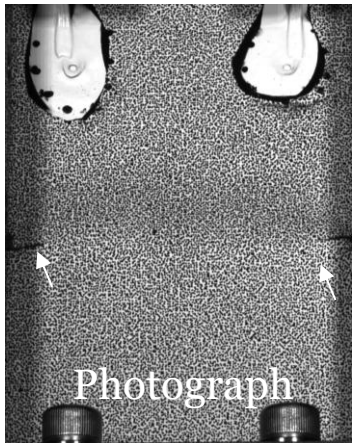

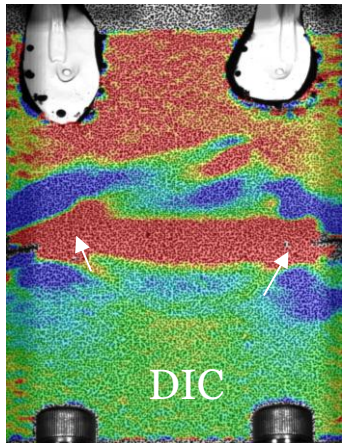

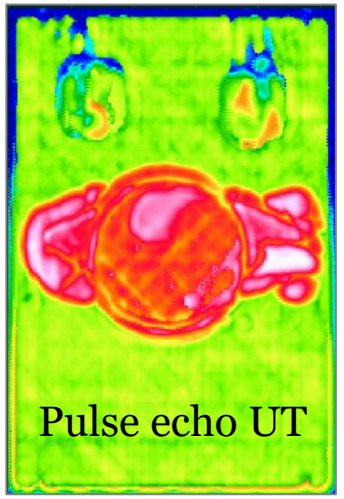

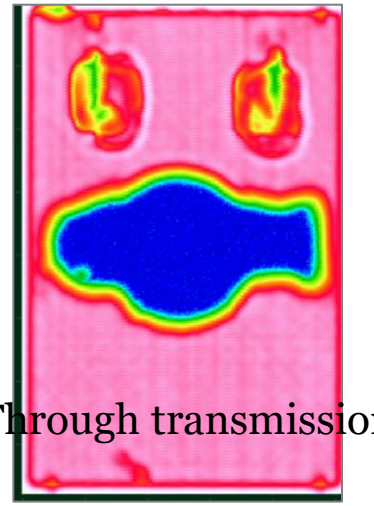

Configuration B: 0.25 mm PTFE

Base laminate:26 ply IM7/977-3

$[(45/-45/0_2/90)_2(45/-45/0)]_S$

PUBLIC RELEASE

Discrete damage modelling using BSAM™

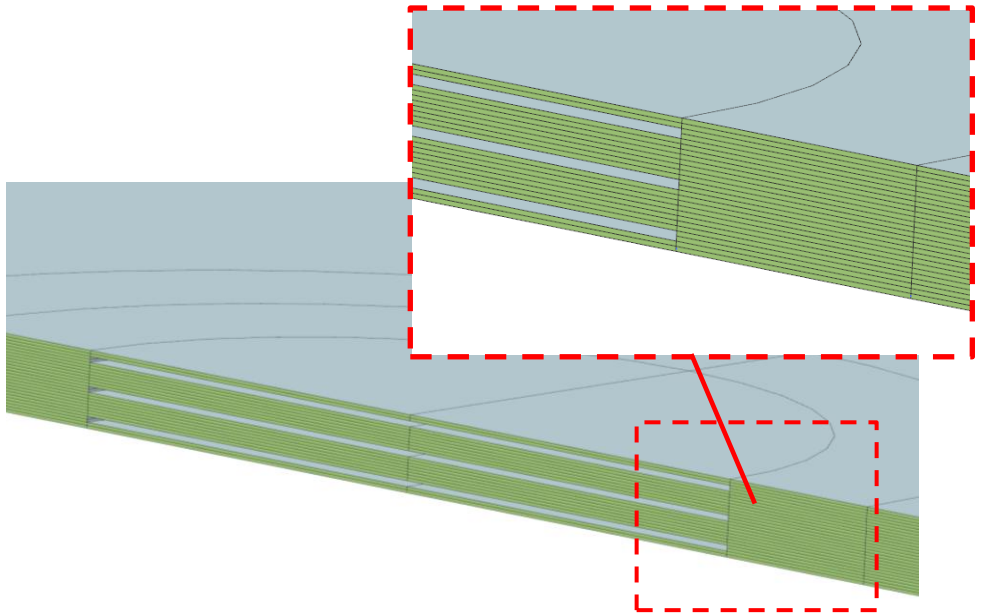

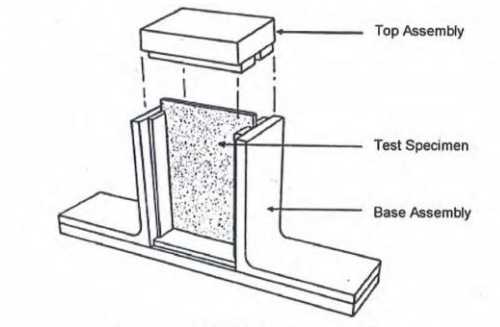

- “Insert region” represented as “filled cavities” that entailed two circular 0° ply “cut-outs”

- Modelling considerations included ……
  - G-control adjusted to “slow down” energy release for MIC/delam near failure for numerical stability
  - CDM enabled to model progressive compression failure of 0° fibres
  - Geometric linear and non-linear formulations were tried

PUBLIC RELEASE

Discrete damage modelling using BSAM™

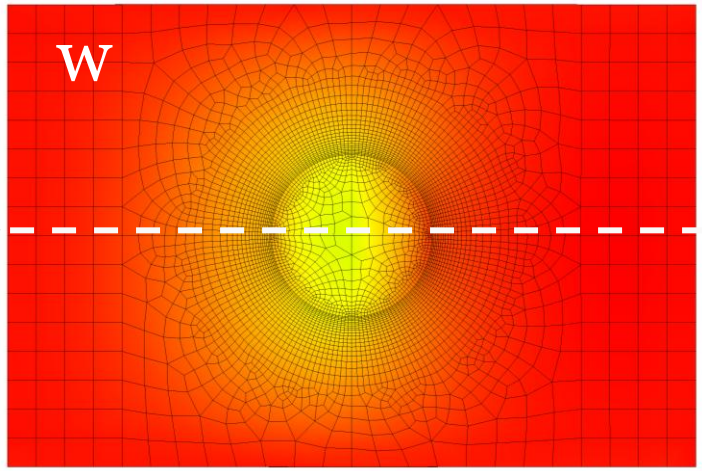

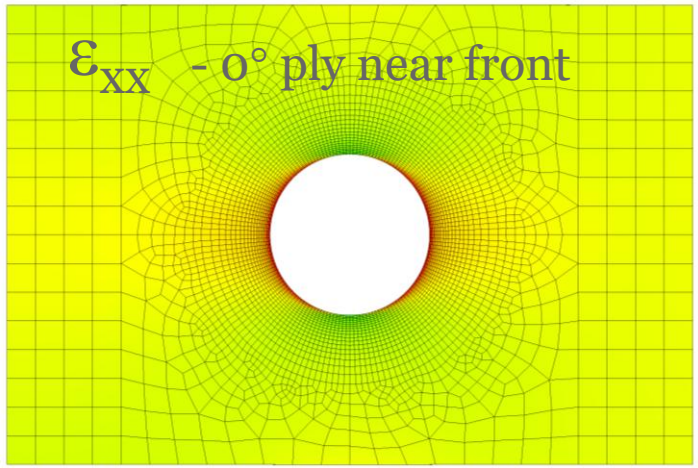

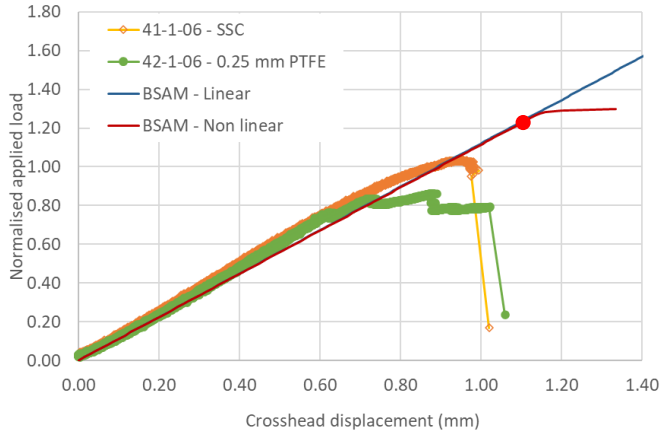

- "Insert region" represented as "filled cavities" that entailed two circular 0° ply "cut-outs"

- Modelling considerations included ……
  - G-control adjusted to "slow down" energy release for MIC/delam near failure for numerical stability
  - CDM enabled model progressive compression failure of 0° fibres
  - Geometric linear and non-linear formulations were tried

PUBLIC RELEASE

Discrete damage modelling using BSAM™

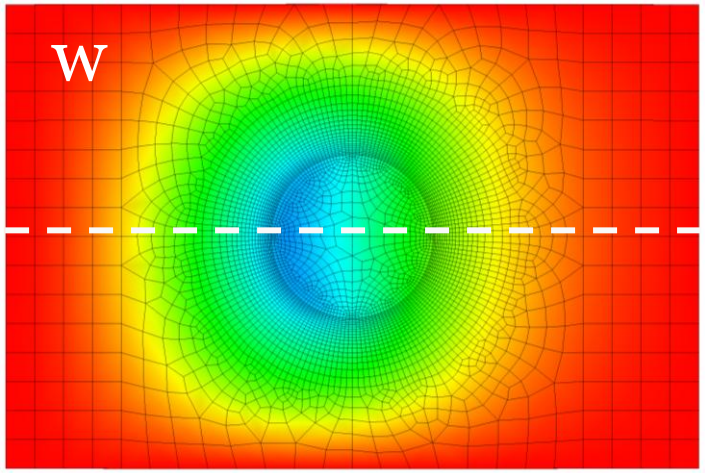

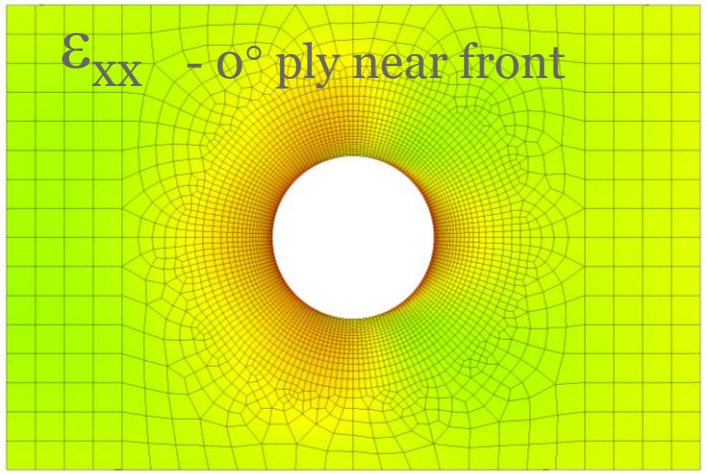

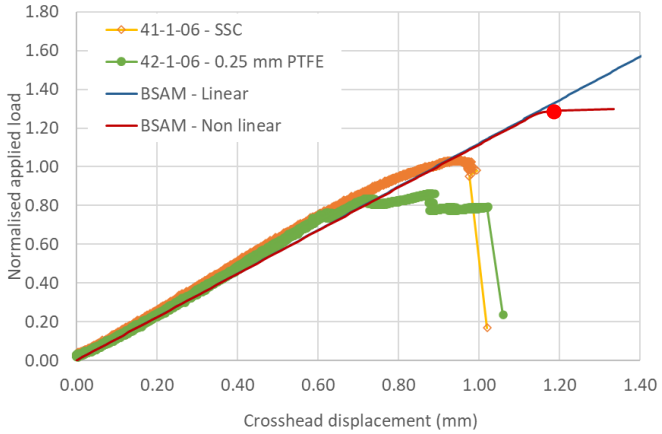

- "Insert region" represented as "filled cavities" that entailed two circular 0° ply "cut-outs"

- Modelling considerations included ……
  - G-control adjusted to "slow down" energy release for MIC/delam near failure for numerical stability
  - CDM enabled model progressive compression failure of 0° fibres
  - Geometric linear and non-linear formulations were tried

PUBLIC RELEASE

Discrete damage modelling using BSAM™

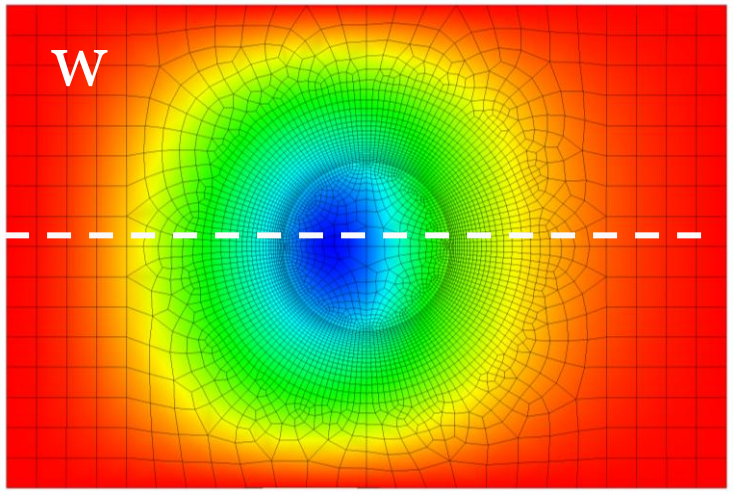

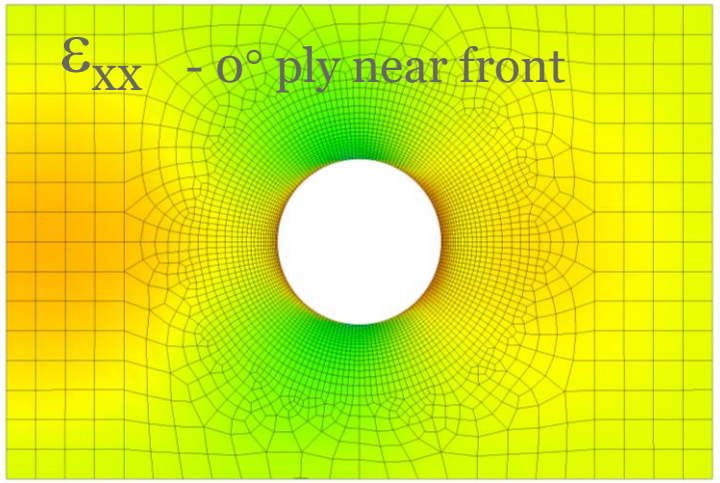

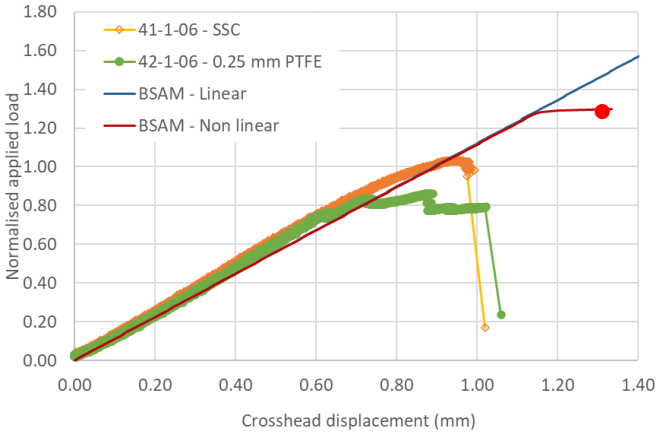

- "Insert region" represented as "filled cavities" that entailed two circular 0° ply "cut-outs"

- Modelling considerations included ……
  - G-control adjusted to "slow down" energy release for MIC/delam near failure for numerical stability
  - CDM enabled model progressive compression failure of 0° fibres
  - Geometric linear and non-linear formulations were tried

PUBLIC RELEASE

Conclusions

- Composite laminates with embedded SSC and PTFE defects were tested under compression with high repeatability (CV 1.84–2.64%).
- SSC specimens were ~10% stronger than PTFE, indicating a structural contribution from the SSC materials.
- Ultrasonic testing showed better sound transmission through SSC regions, confirming improved integrity.
- Sub-critical damage initiated earlier in SSC (60% failure load) than PTFE (85%), involving delamination and local instability.
- Final failure mode included translaminar fracture in both configurations.
- Non-linear BSAM analysis aligned better with experiments than linear analysis but still overpredicted failure by >25%.

PUBLIC RELEASE

Further work .....

- Apply newer versions of analysis software to improve prediction accuracy.
- Conduct more in-depth post-test examinations using X-ray micro-computed tomography (XmCT).
- Perform synchrotron experiments to observe SSC failure modes in greater detail.
- Investigate the structural contribution of SSC materials through high-resolution imaging and in situ testing.
- Refine modelling techniques based on insights from experimental characterisation

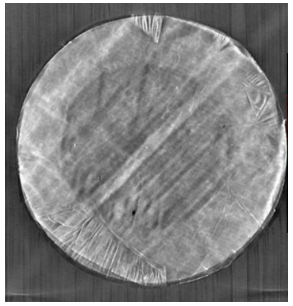

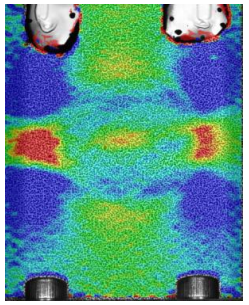

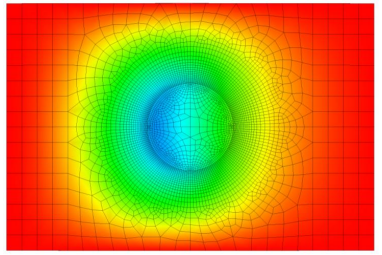

PUBLIC RELEASE

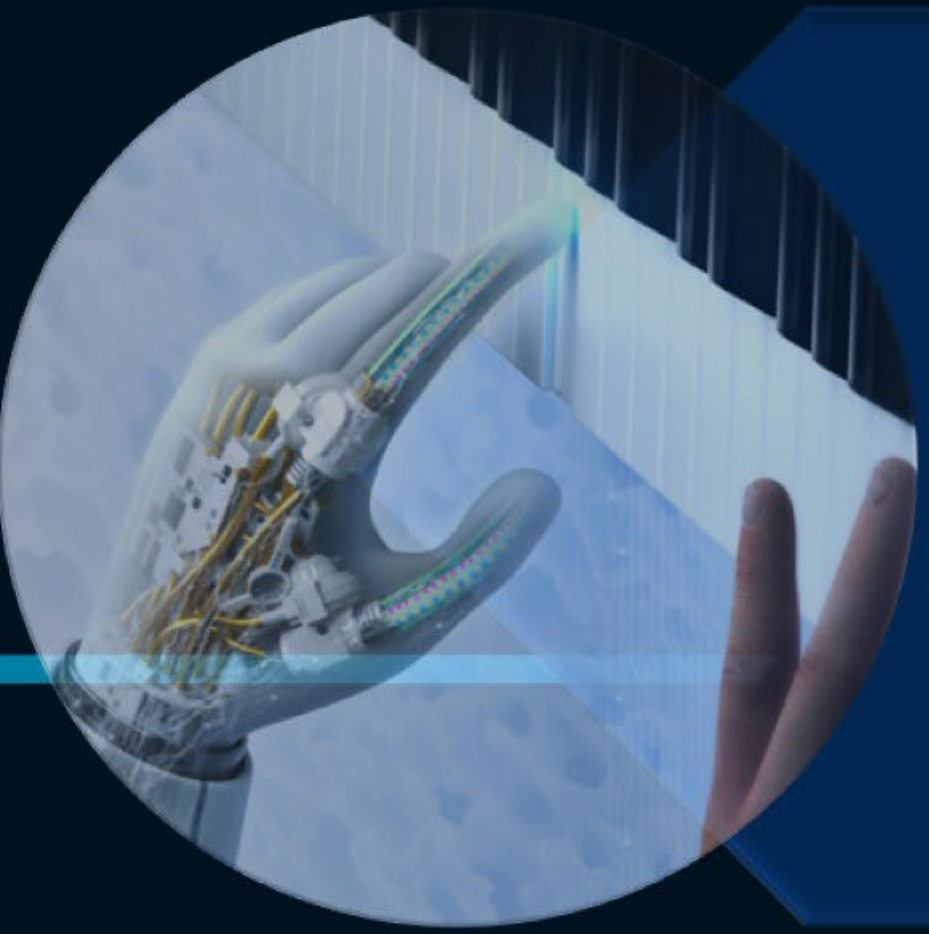

Ultralow–Voltage High–Performance Soft Actuators Using Polysulfonated Covalent–Organic Frameworks as Common Electrolyte–Electrode Hosts

Korea Advanced Institute of Science and Technology (KAIST), Republic of Korea

KAIST

Manmatha Mahato
and
Il-Kwon Oh

ICCM24
24TH INTERNATIONAL CONFERENCE ON COMPOSITE MATERIALS
HOSTED BY: UNIVERSITY OF DELAWARE CENTER FOR COMPOSITE MATERIALS Celebrating 50 Years
AUG 4-8, 2025 BALTIMORE CONVENTION CENTER - BALTIMORE, MARYLAND, USA

About Our Lab at KAIST





SRIM
Soft Robotics
Intelligent Materials

https://srim.kaist.ac.kr/

Soft Robotics and Intelligent Materials Lab

[Total Lab Members : 25]

Il-Kwon Oh (Director)



01. Artificial Muscle and Soft Robotics

02. Energy Storage and Structural Batteries

03. Energy Harvesting and Wearable Sensors

04. Mechanical Metamaterial and Smart Structures

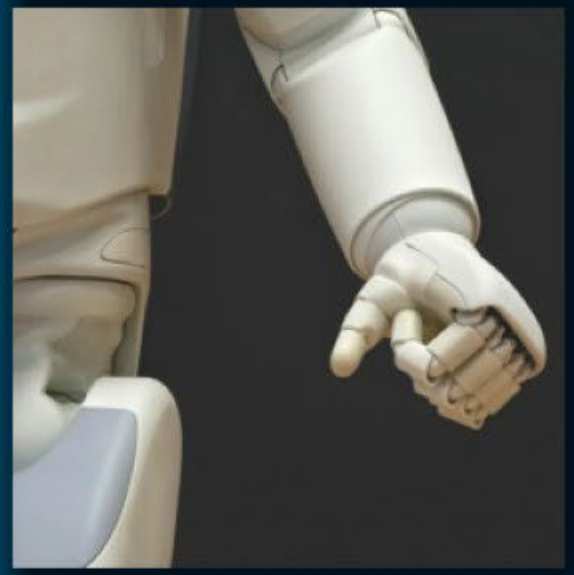

Soft Actuators/Artificial Muscles

CONTENT

[Actuators: Powering the Pulse of Soft Robotics]

1 **Research Importance**

2 **Progress of Research**

3 **Concluding Remarks**

Importance and necessity

- AI Biomedical Revolution.
- Enhanced Patient Care.

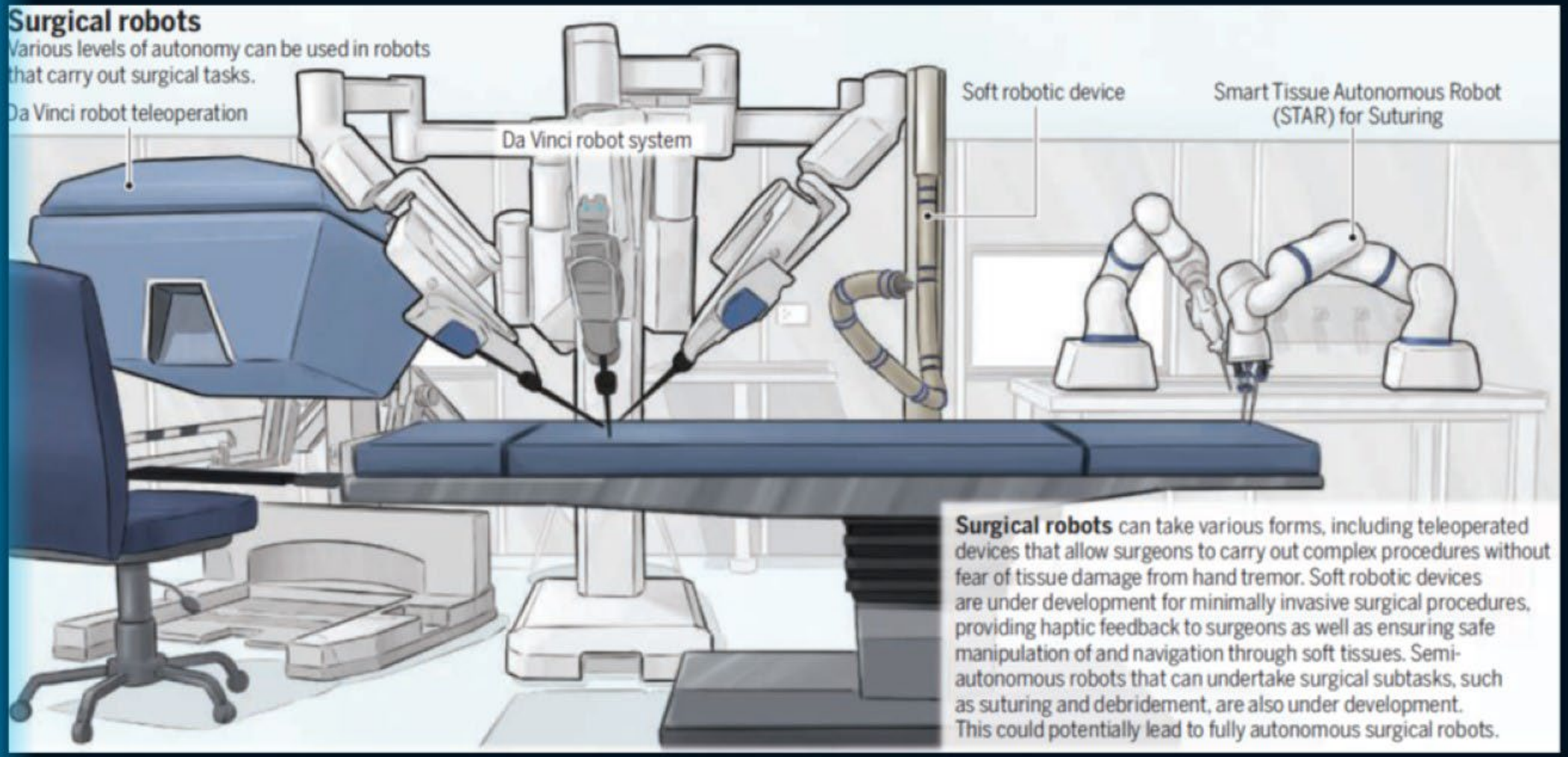

Autonomous era of 5G and AI, electroactive artificial muscles are most appropriate for medical robots

YIP et al. Artificial intelligence meets medical robotics, *Science* **2023**, *381*, 141-146

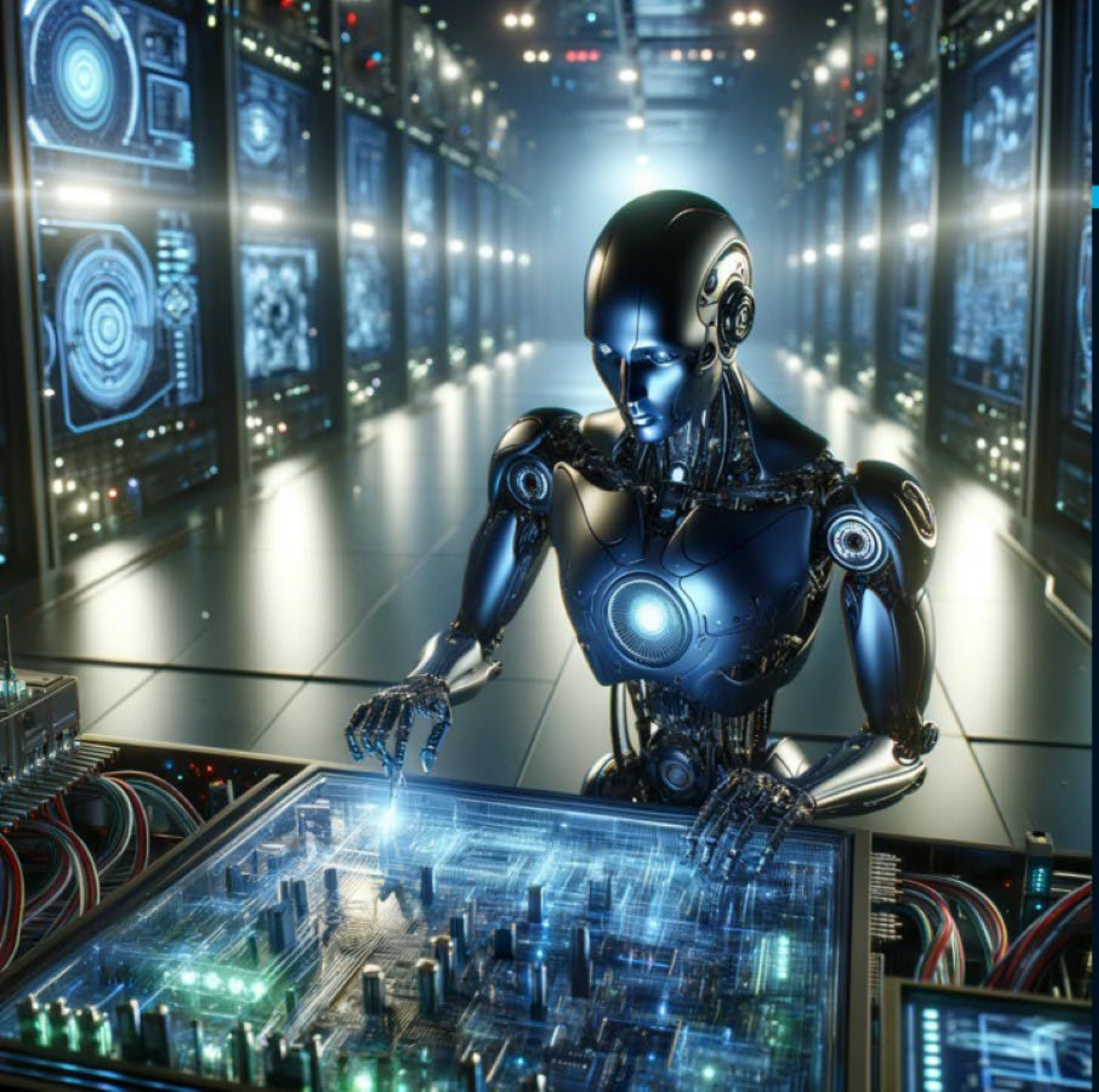

Importance and necessity

"Soft touch is crucial to protect the smart devices from damage"

- A futuristic and technical scene featuring advanced robotics and intricate machinery

Soft artificial muscles and challenges

Mirvakili et al. Artificial Muscles: Mechanisms, Applications, and Challenges, *Advanced Materials* **2018**, *30*, 1704407



❑ Hydraulic

- Large volume
- Complexity

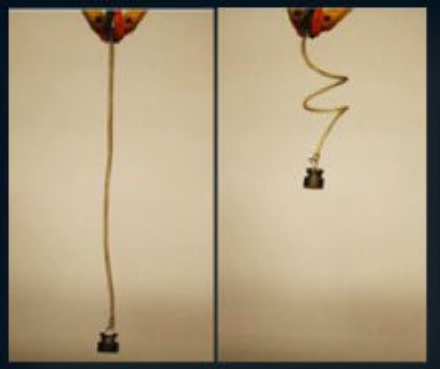

❑ SMA actuator

- Irregular response
- Low cycle life
- High cost



❑ Pneumatic

- Nonlinear actuation
- Complexity

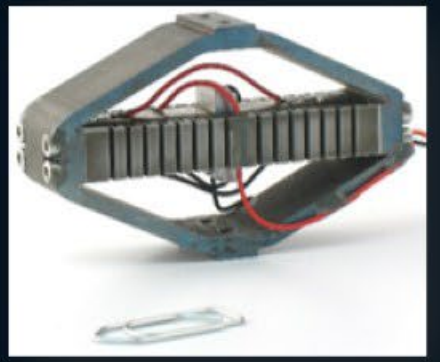

❑ Piezoelectric

- Small strain
- Large excitation field



❑ Thermal

- Heat transfer rate
- Small bandwidth

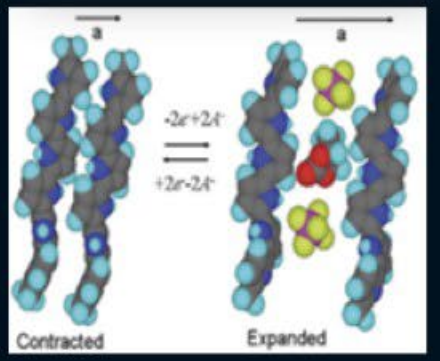

❑ Conducting polymer

- Small force
- Delamination

Electroionic artificial muscles

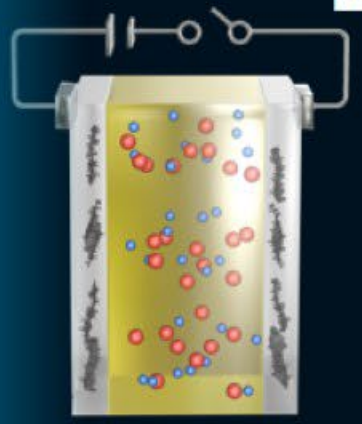

Key challenges up to 2019

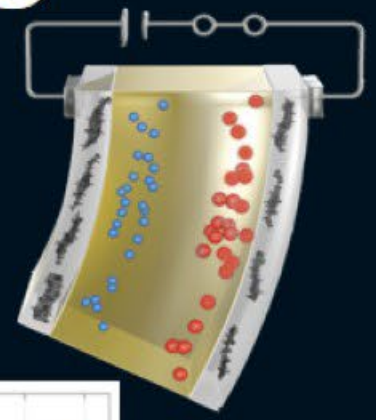

- **Important issues**

1. Low bending
2. Back relaxation
3. Irregular responses
4. Low mechanical force

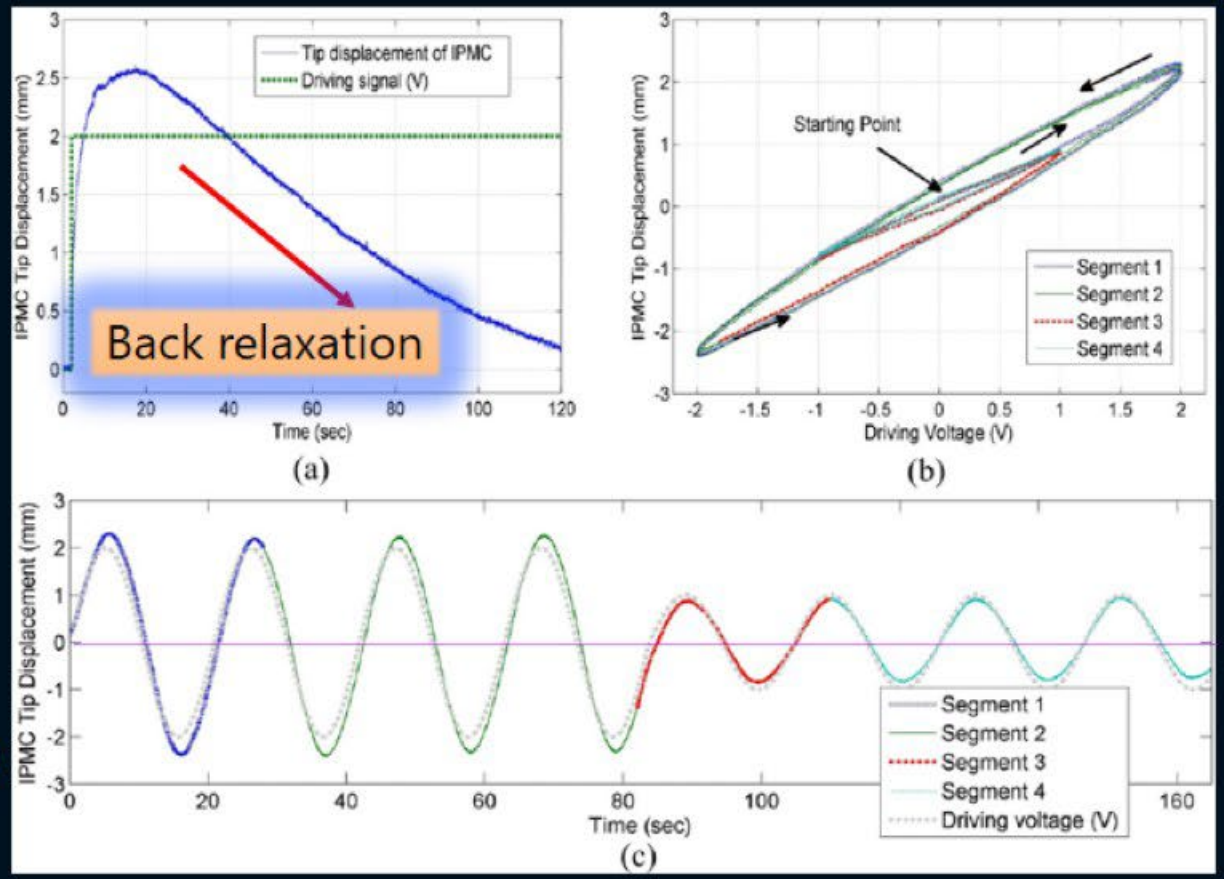

Working principle of soft actuators

❑ EDLC

ⓐ Supercapacitor

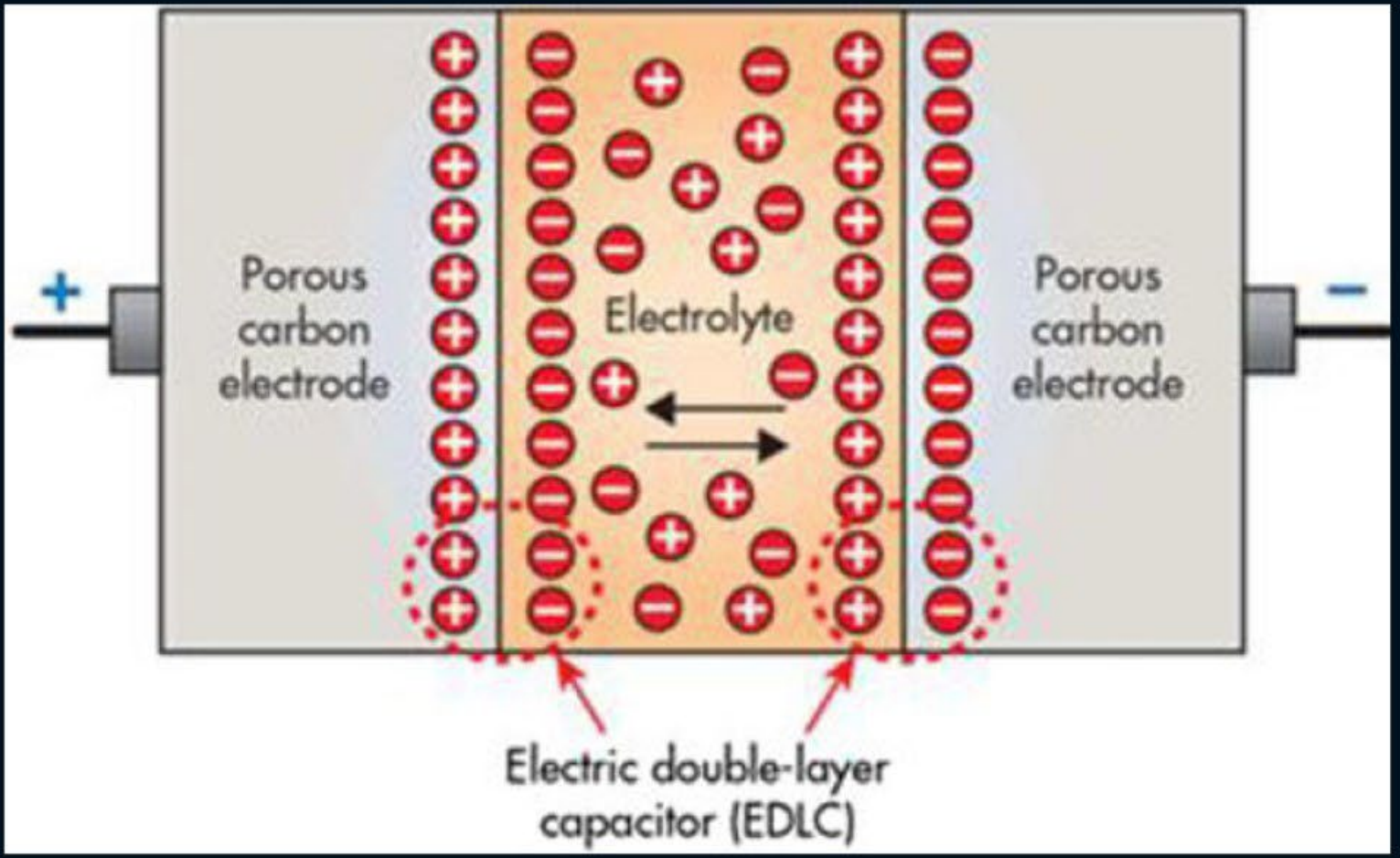

ⓑ Soft actuators

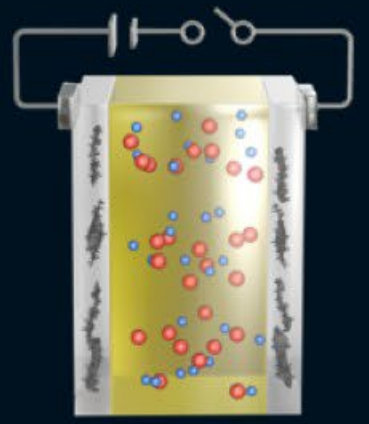

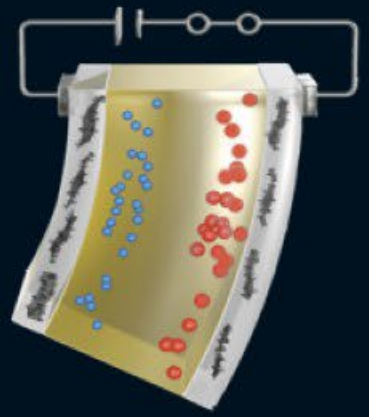

Working principle

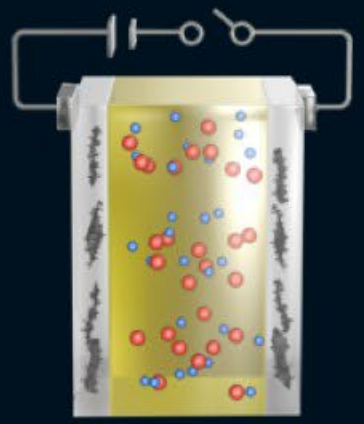

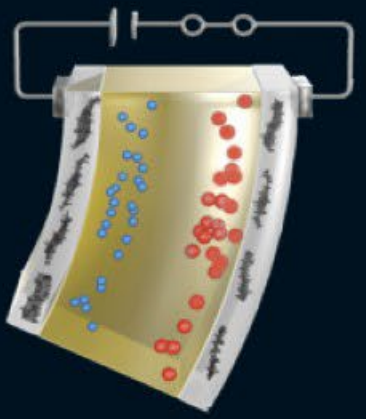

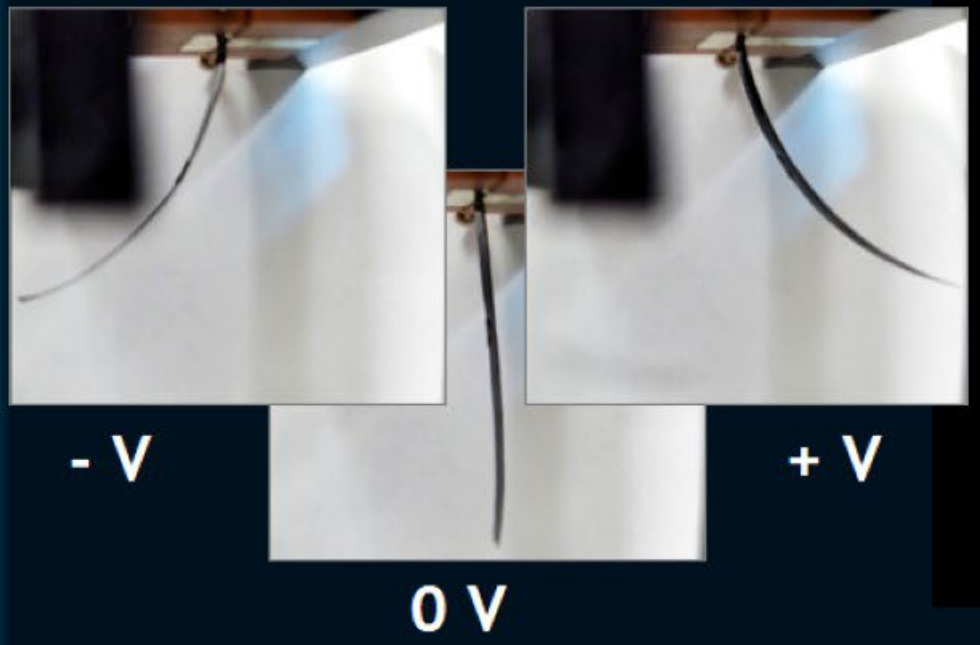



Electrode materials

Fundamental

Key requirements

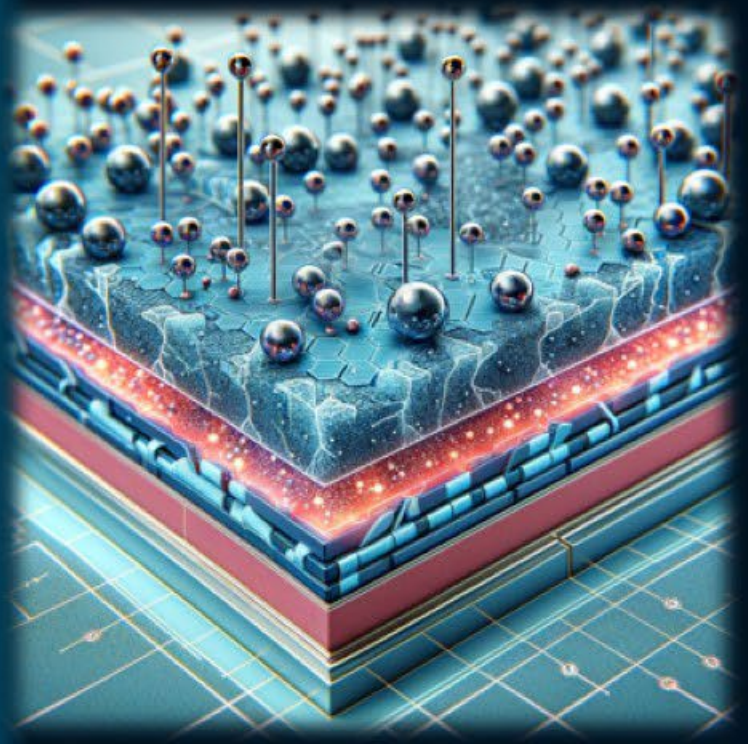

- Stability
- Conductivity
- Porosity
- Surface area
- Host-guest interaction

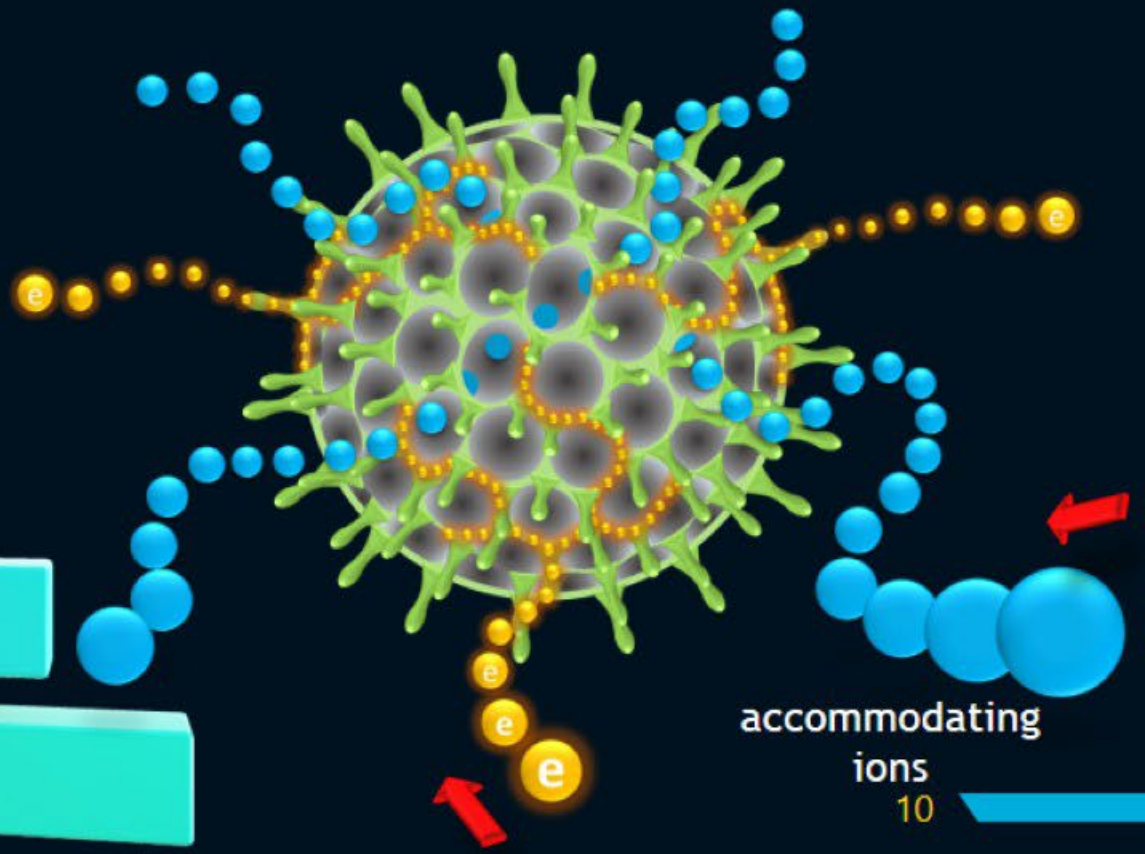

Electroionic artificial muscles

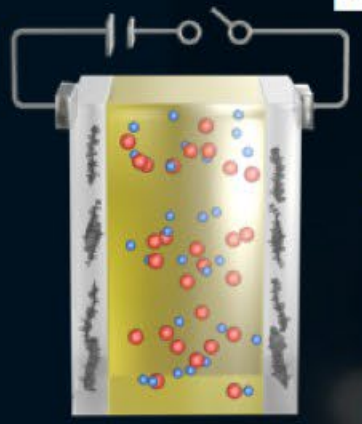

SRIM Lab excels in refining active materials to optimize actuation in soft robots for real-world applications.



Graphene & CNT

- Flexibility
- High chemical stability
- High electrical conductivity



..Until 2017

MXene

- Low chemical stability
- High electrical conductivity
- High specific capacitance



..Until 2019

COFs & MOFs

- High surface area
- High specific capacitance
- High electrical conductivity



From 2019..

Covalent-organic frameworks (COFs) as active materials for Ultralow–Voltage High–Performance

2019 → 2025

Why COFs ?

- Industrial-Scale Manufacturability
- Biocompatibility for biomedical integration
- Ambient Air Operational Stability
- Cost-Effective Material Platform
- Structurally Tunable Properties for Functional Optimization
- Metal-Free Composition for Lightweight and Sustainable Design

Why Polysulfonated Covalent–Organic Frameworks ?

COFs artificial muscles

Initial design to maximize the actuation performances: A total overview

Unit-cell design: **(2018- 2019)** → **(2019-2020)** → **(2021-)**

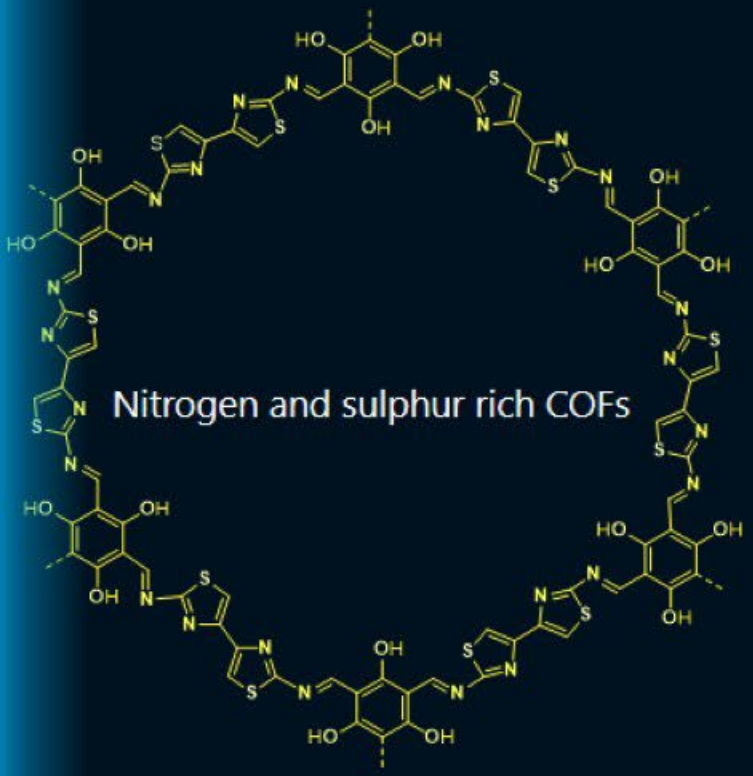

Nitrogen and sulphur rich COFs

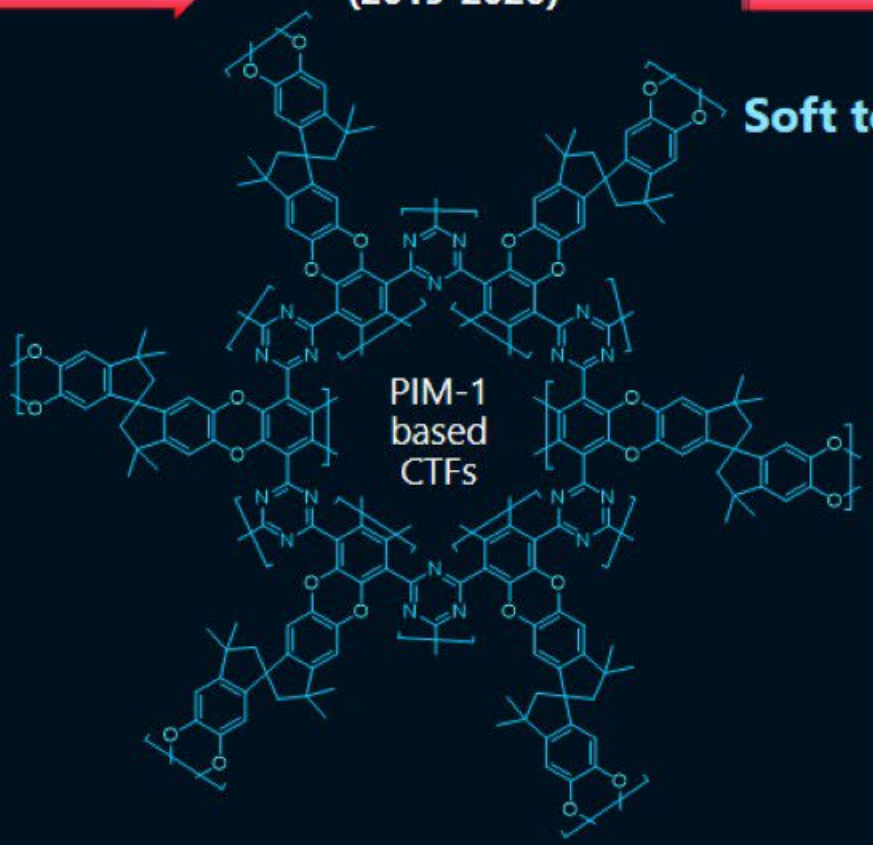

PIM-1 based CTFs

Soft touch finger



Polysulfonated COFs

Mahato and Oh et al. *Adv. Funct. Mater.* **2020**, *30*, 2003863

Mahato and Oh et al. *Nat. Commun.* **2020**, *11*, 5358

Mahato and Oh et al. *Sci. Adv.* **2023**, *9*, eadk9752

NSCOFs artificial muscles

Unit-cell: (2018- 2019)

Rich in hetero-atoms: Nitrogen (N); Sulfur (S); Oxygen (O)

Electronically conjugated conductive frameworks

Nanoporous channel for ions accommodation

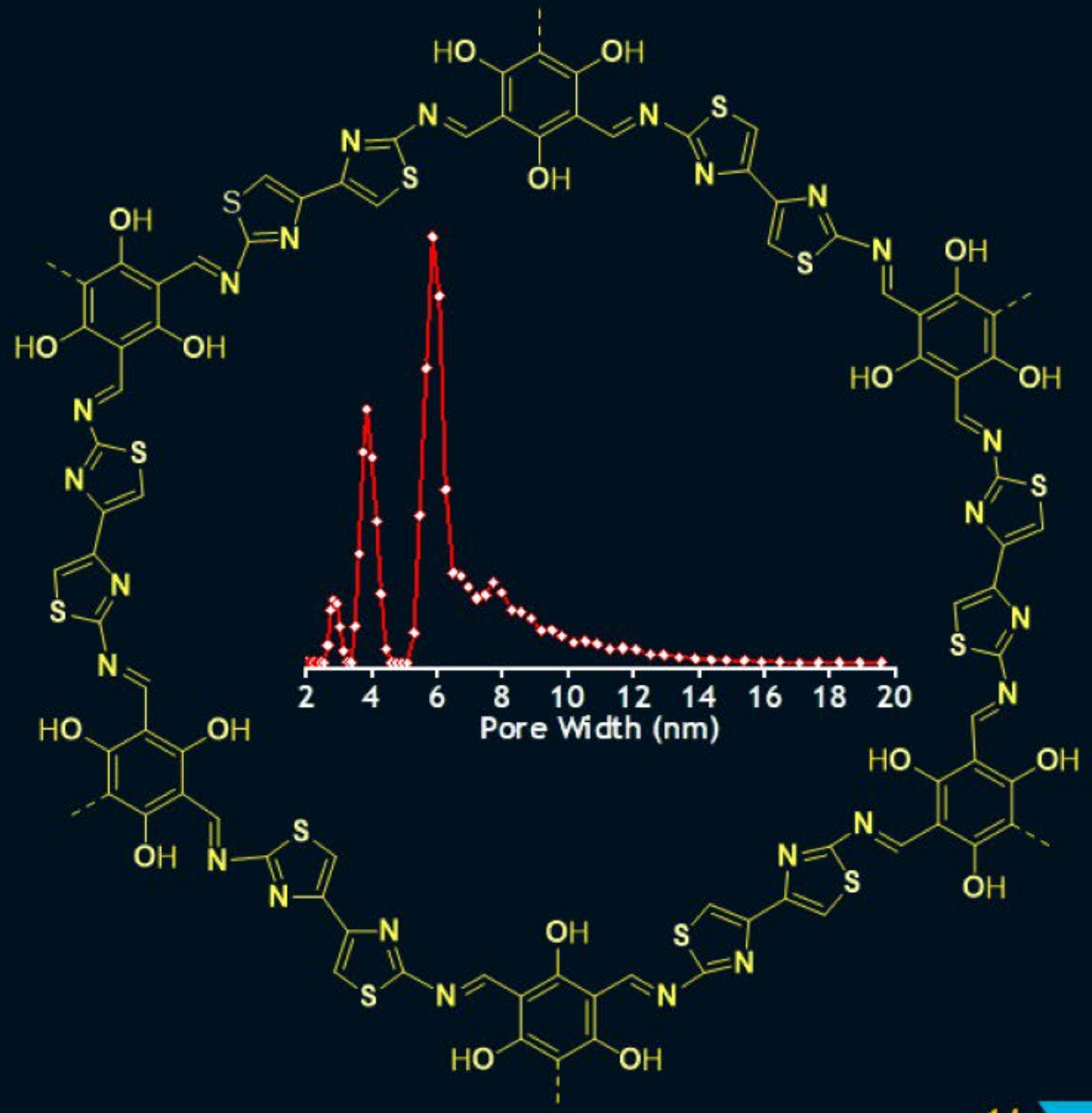

Nitrogen and sulphur rich COFs

Nitrogen and sulphur rich COFs (NSCOFs)artificial muscles

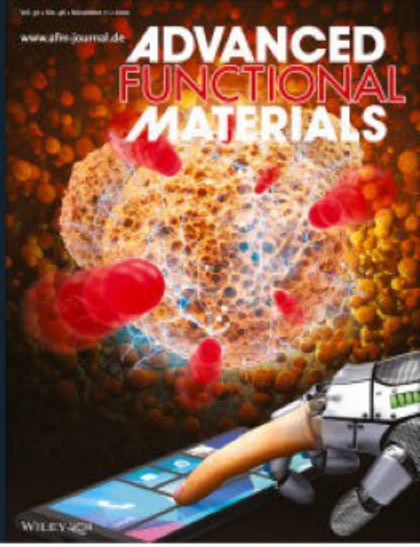

Removes

✓Back relaxation

✓Irregular responses

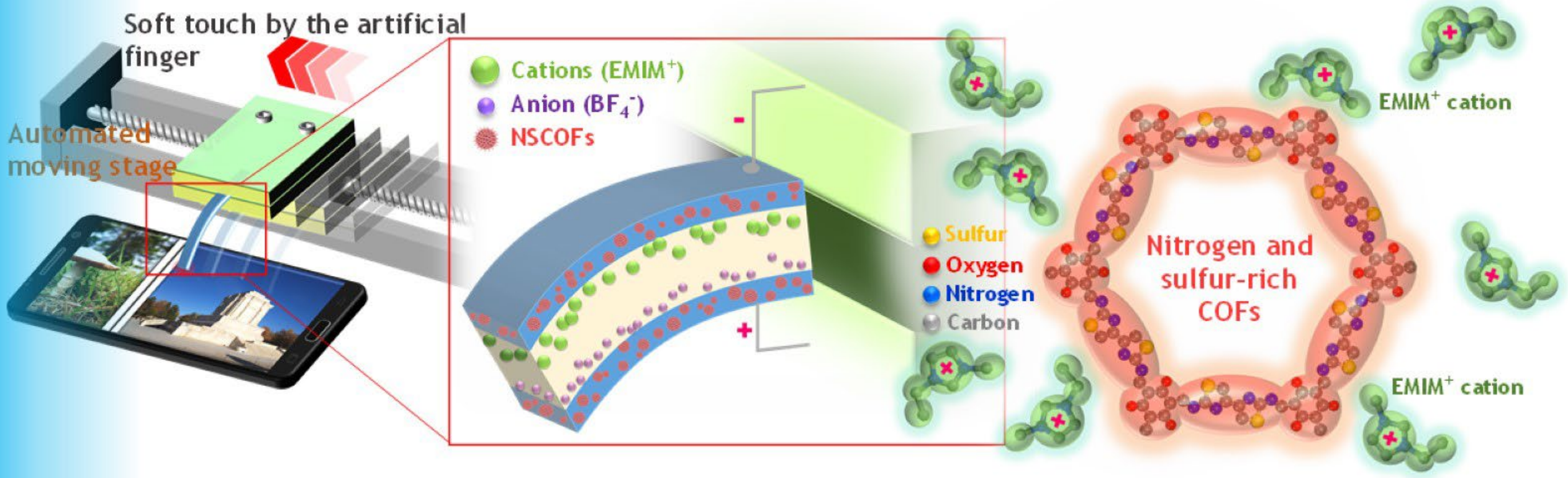

Nitrogen and sulphur rich COFs (NSCOFs)artificial muscles



Page swiping task

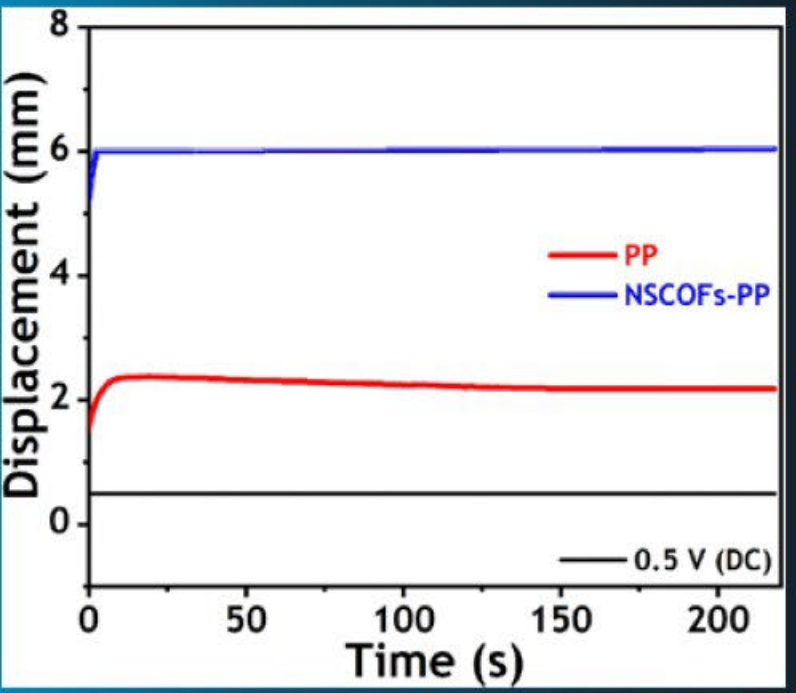

No back relaxation

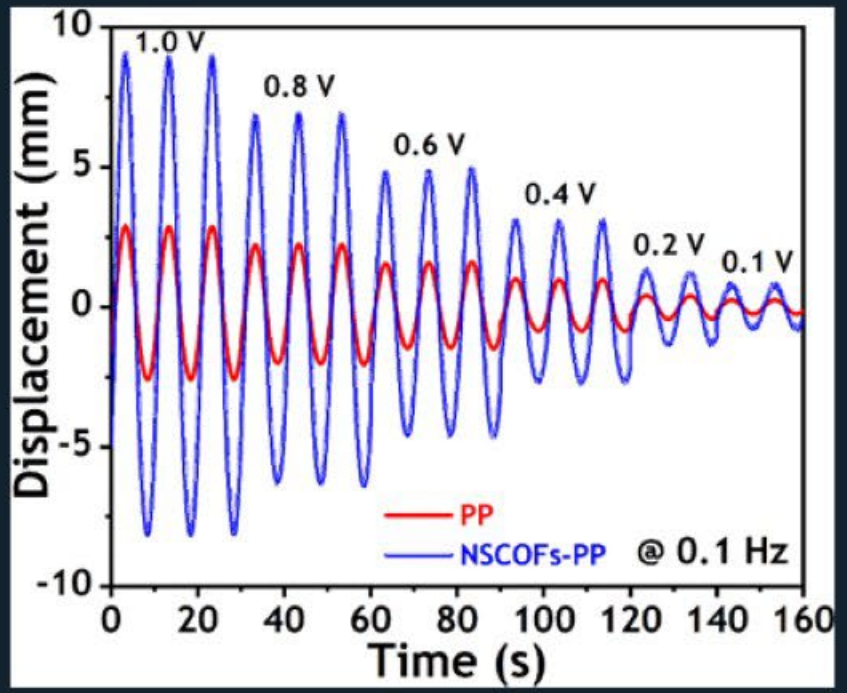

Controllable mechanical bending

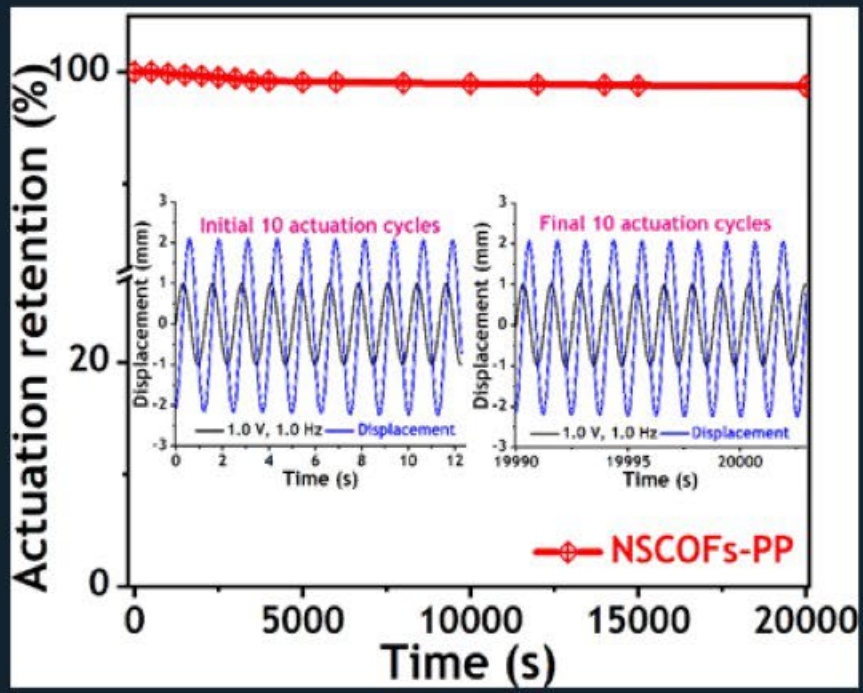

Stability

Nitrogen and sulphur rich COFs (NSCOFs)artificial muscles

Swiping the Touch Screen
by
Soft Robot Finger

Page swiping task

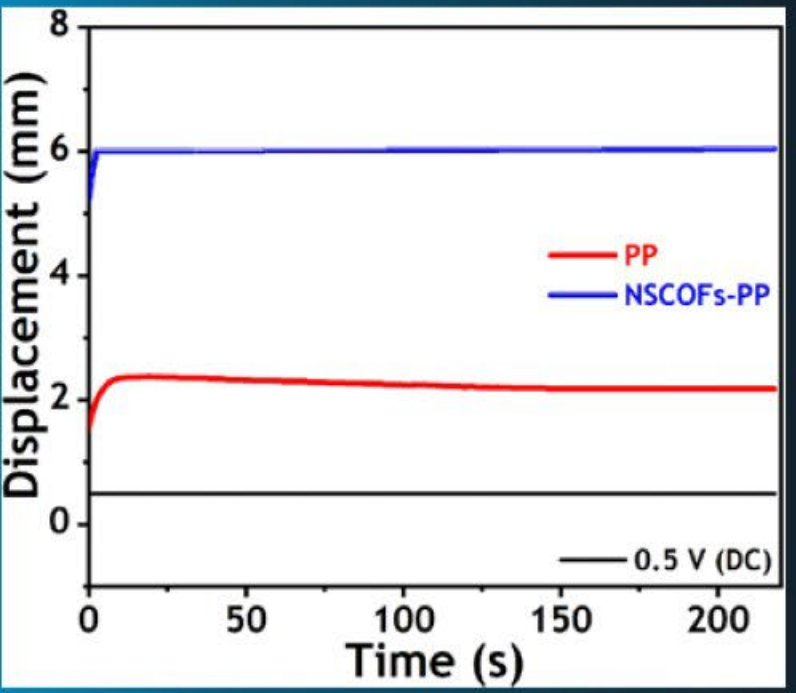

No back relaxation

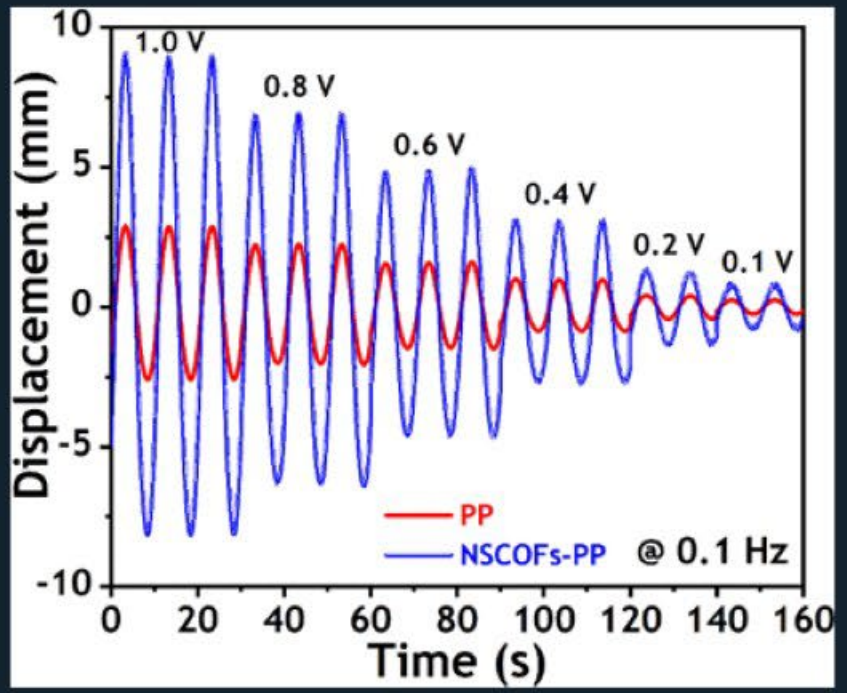

Controllable mechanical bending

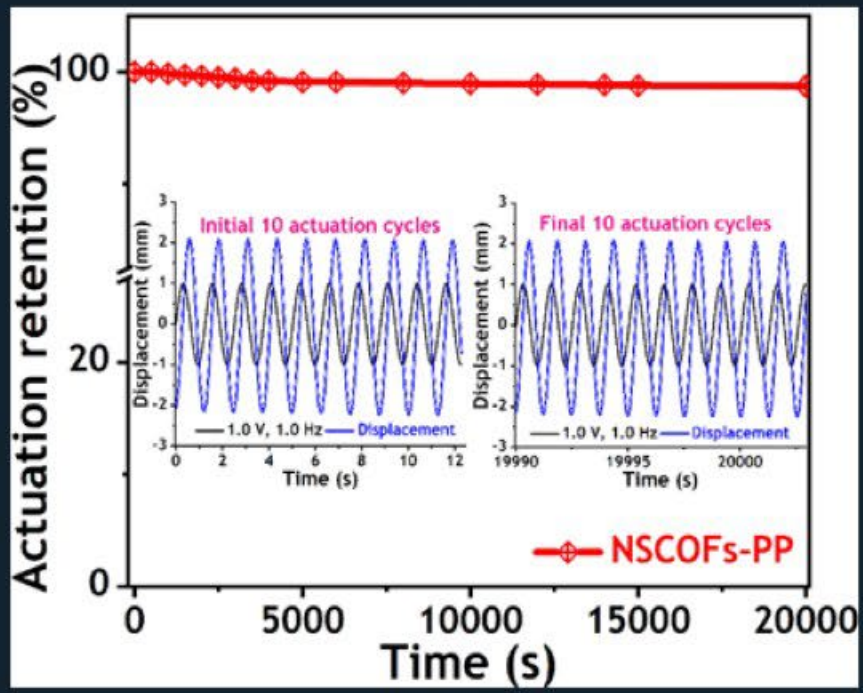

Stability

Nitrogen and sulphur rich COFs (NSCOFs)artificial muscles



Folder opening task



Real-image

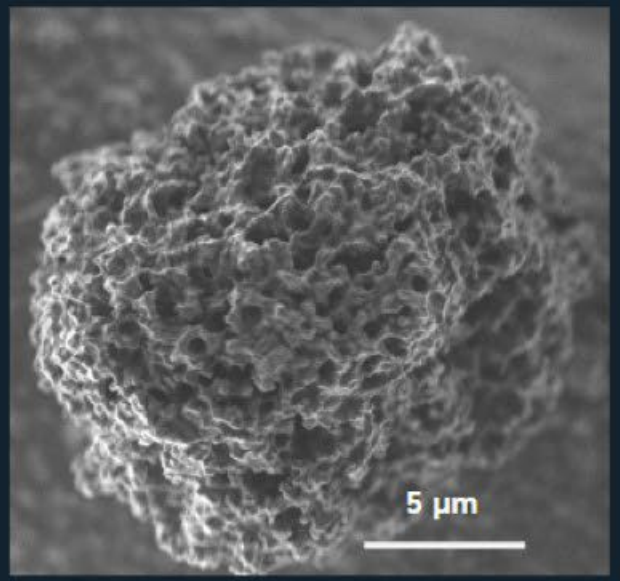

SEM morphology

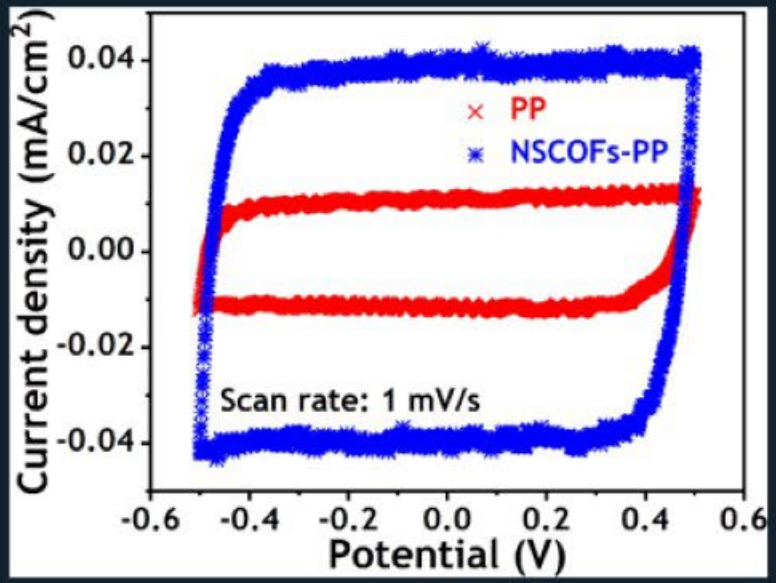

Ions storage

Issues exist

✓Low force

✓Low bending

Nitrogen and sulphur rich COFs (NSCOFs)artificial muscles

Soft Robotic Touch
on a
Touch screan

Folder opening task



Real-image

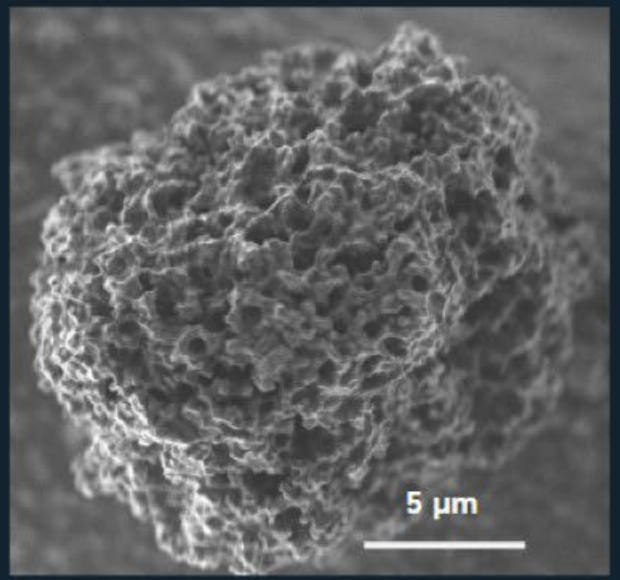

SEM morphology

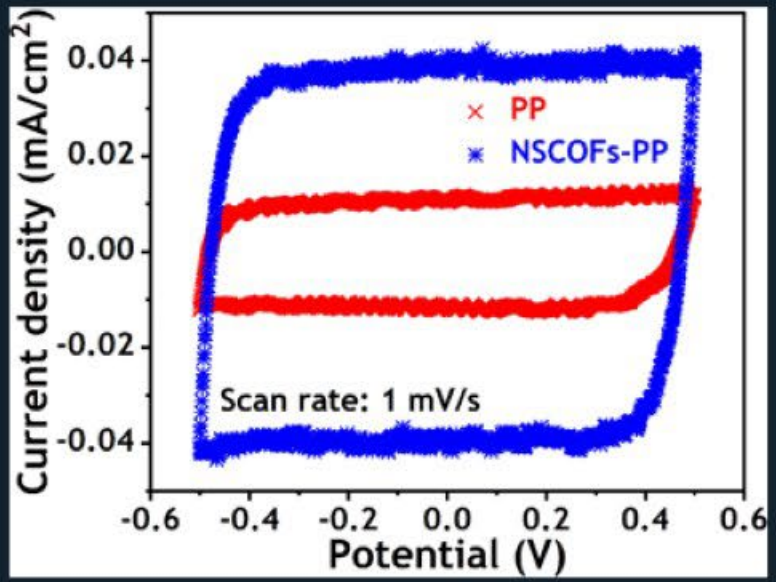

Ions storage

Issues exist

✓Low force

✓Low bending

PIM-1 based CTFs artificial muscles

Unit-cell: (2019-2020)

②

dibenzo-*p*-dioxine moieties help to store the charges during electrochemical cycles

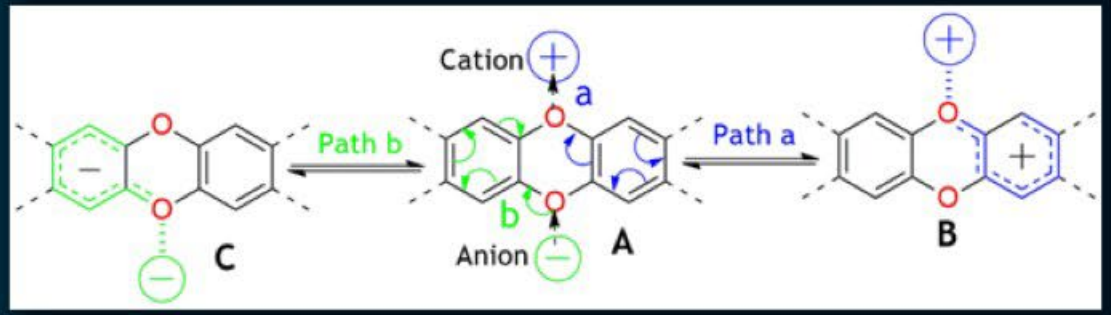

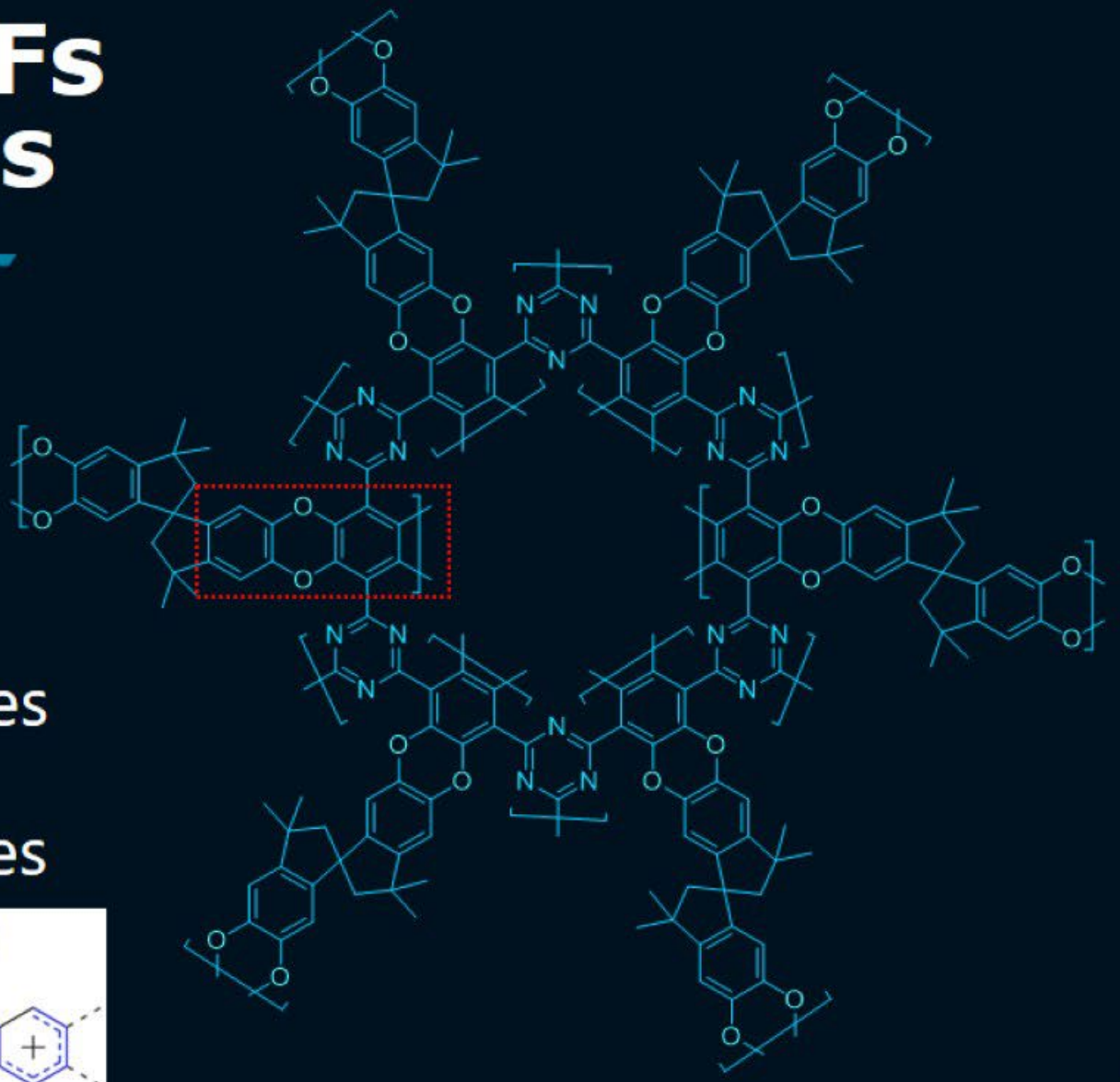

PIM-1 based CTFs

PIM-1 based CTFs artificial muscles

Removes

- ✓ Back relaxation
- ✓ Irregular responses
- ✓ Low bending





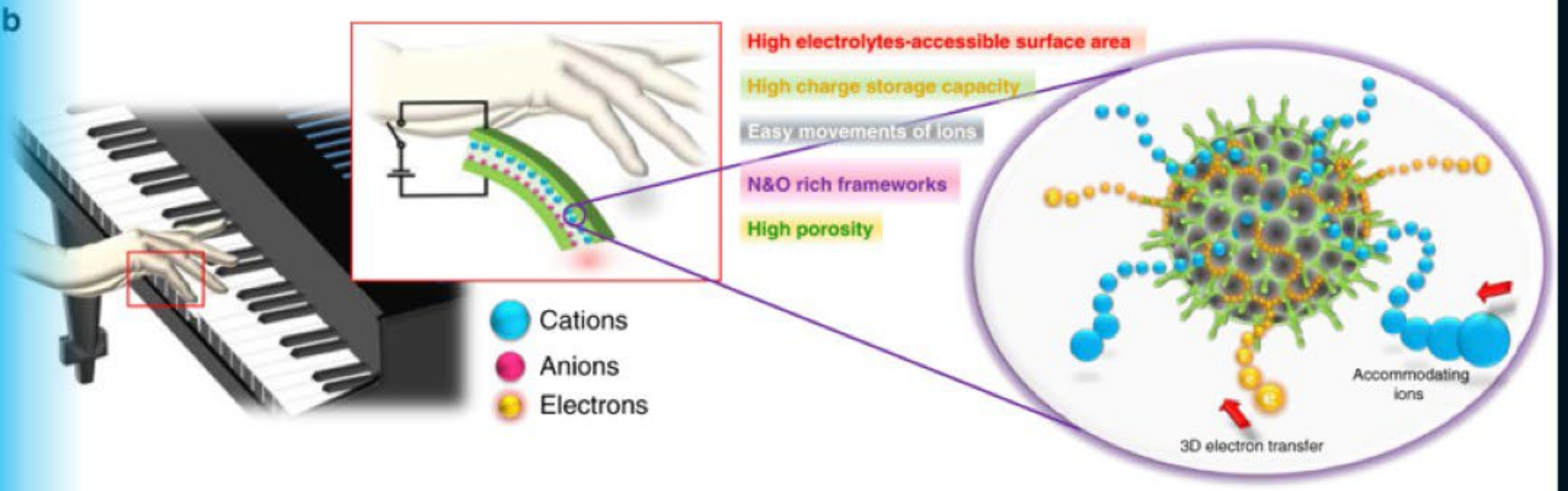

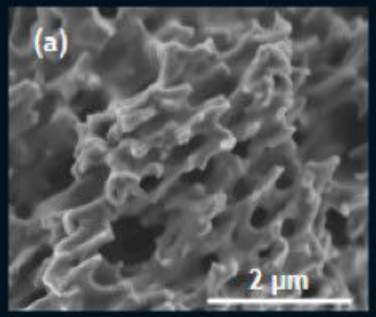

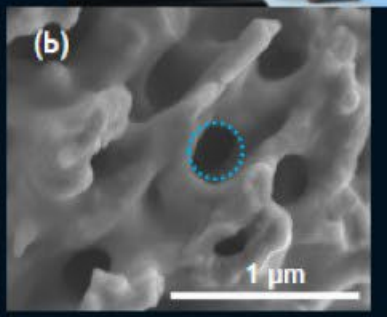

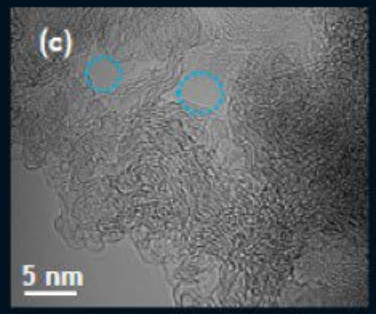

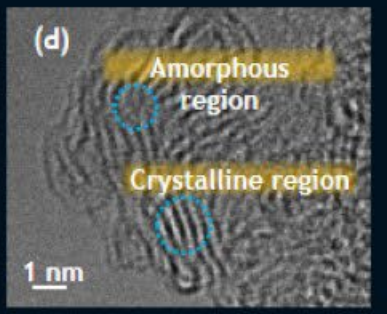

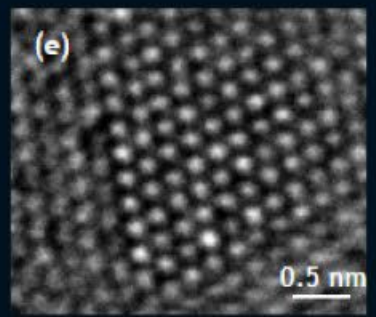

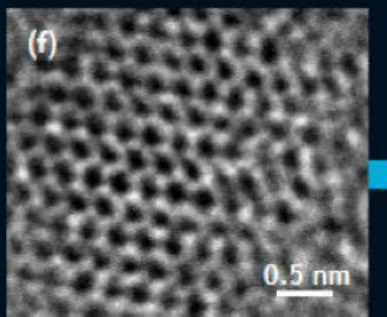

PIM-1 based CTFs artificial muscles

Removes

- ✓Back relaxation
- ✓Irregular responses
- ✓Low bending



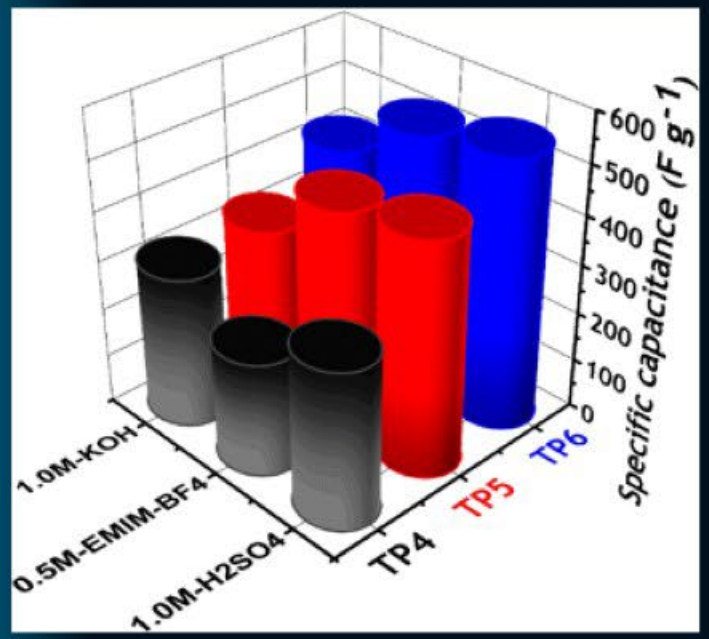

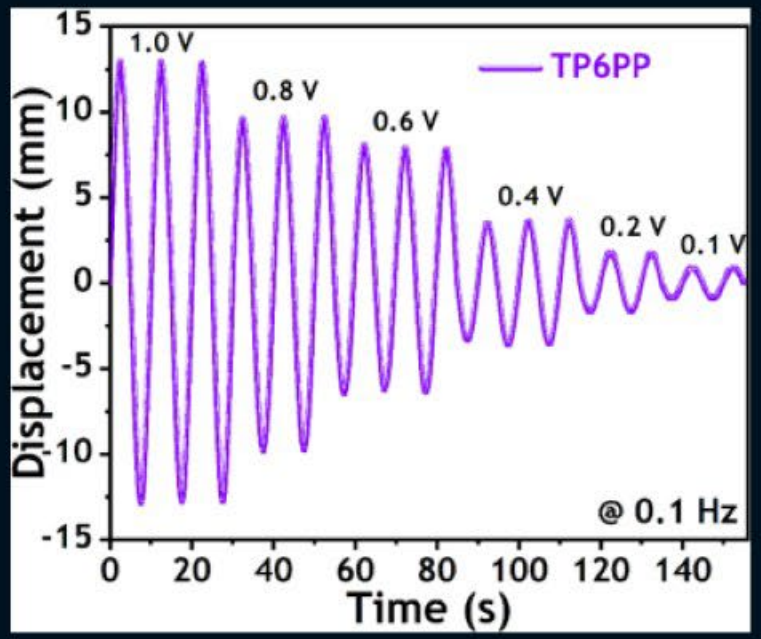

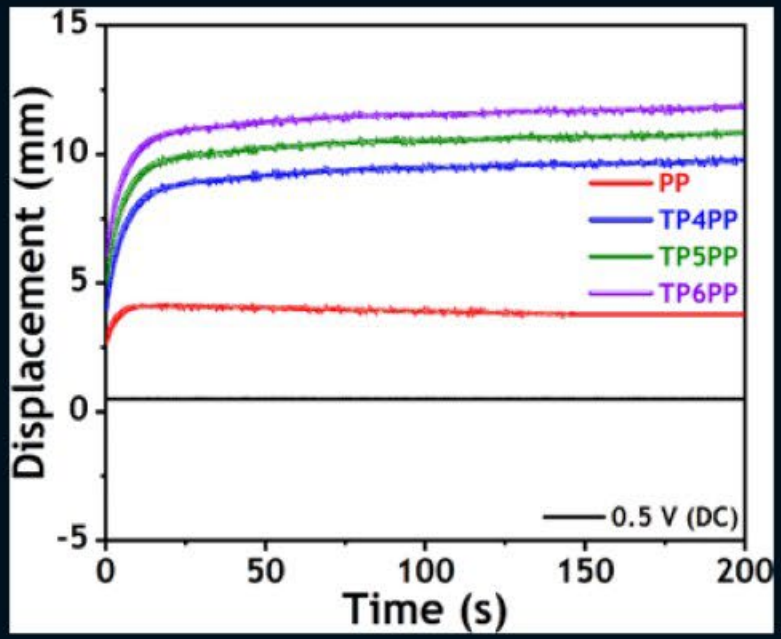

Issues exist: ✓Moderate force — 28-time of its own weight ✓Moderate response — Rising time 4-5 seconds

PIM-1 based CTFs artificial muscles

Removes

- ✓Back relaxation
- ✓Irregular responses
- ✓Low bending



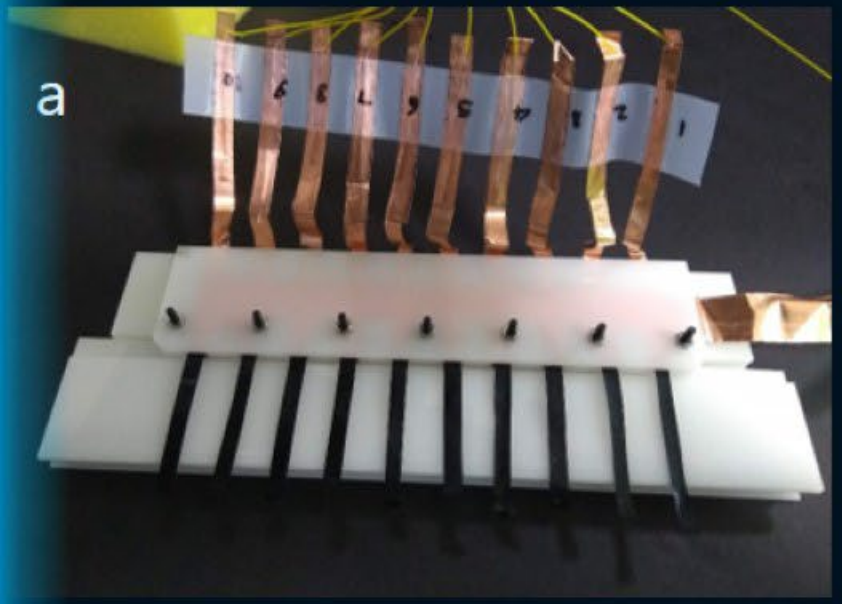

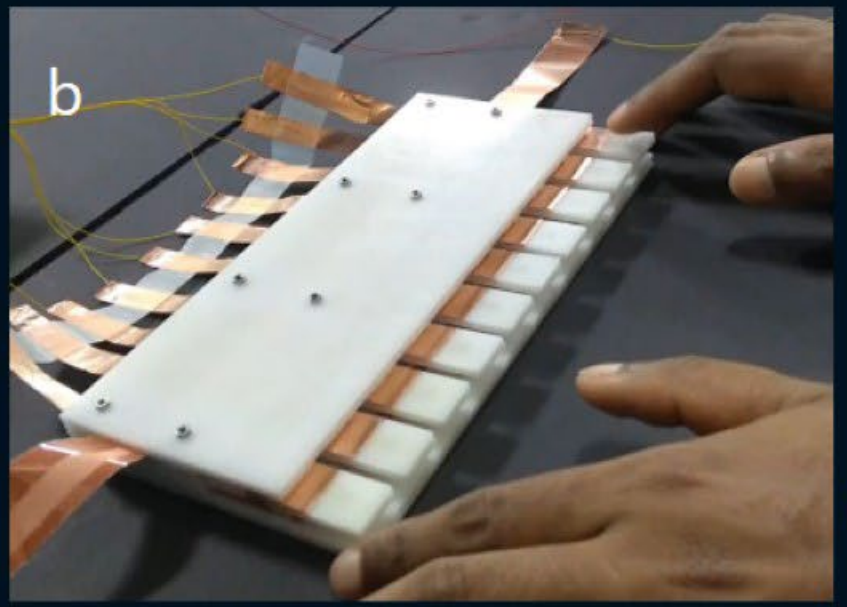



Issues exist: ✓Moderate force 28-time of its own weight ✓Moderate response Rising time 4-5 seconds

PIM-1 based CTFs artificial muscles

Removes

- ✓Back relaxation
- ✓Irregular responses
- ✓Low bending



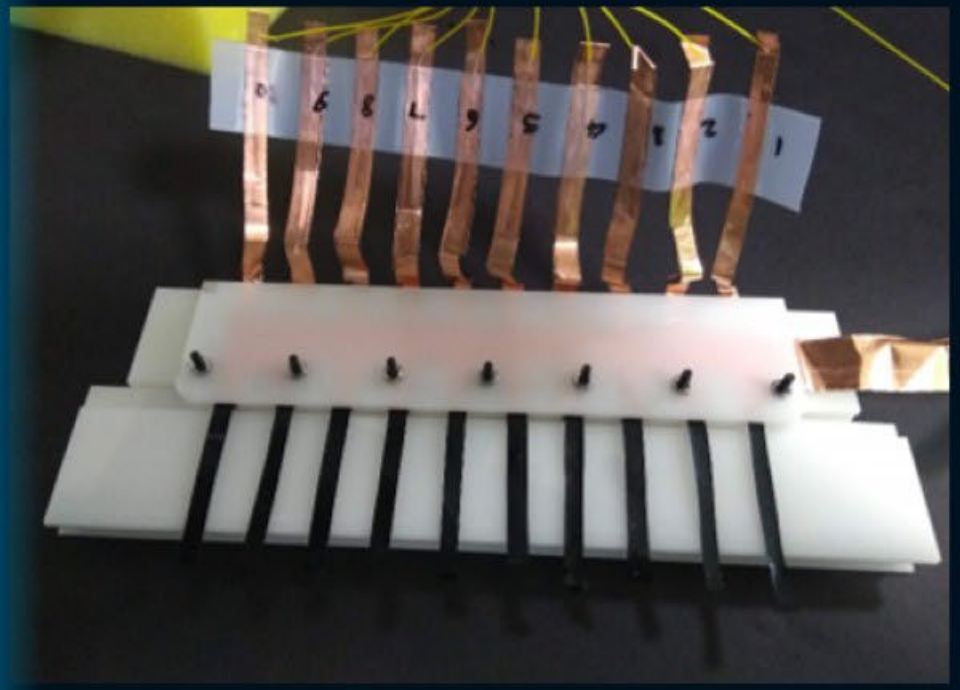

ARTIFICIAL ROBOTIC HAND

Keyboard Test

Issues exist:

- ✓Moderate force — 28-time of its own weight
- ✓Moderate response — Rising time 4-5 seconds

PIM-1 based CTFs artificial muscles

Removes

✓Back relaxation

✓Irregular responses

✓Low bending



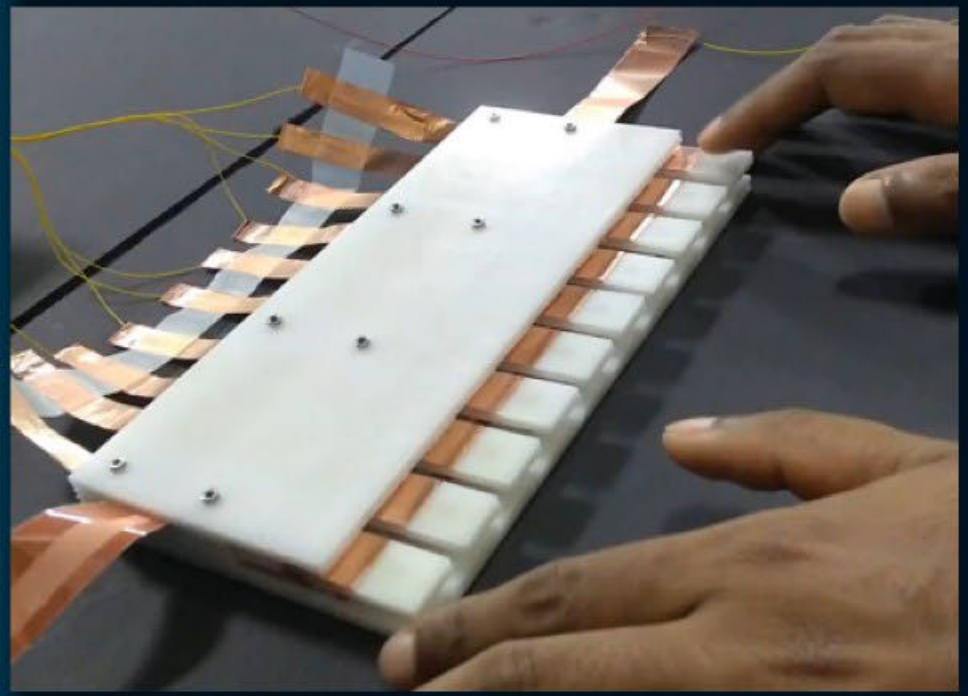

Playing Piano

by artificial finger array

Issues exist: ✓Moderate force 28-time of its own weight ✓Moderate response Rising time 4-5 seconds

COFs artificial muscles

Unit-cell: (2021-2023)

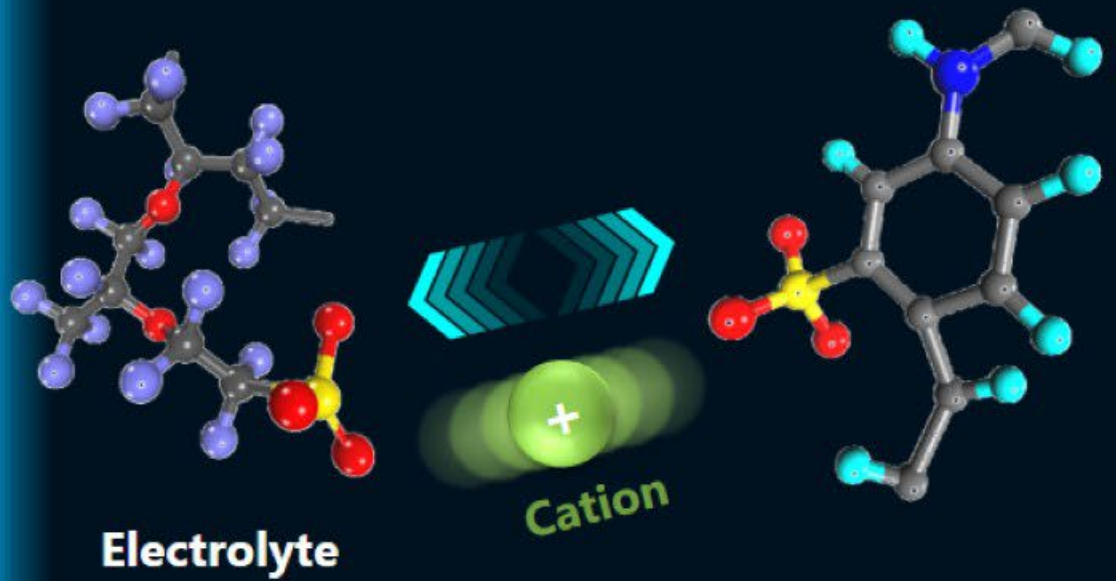

Common Sulfonate Host

Actuation at near zero voltage (~0.01V)

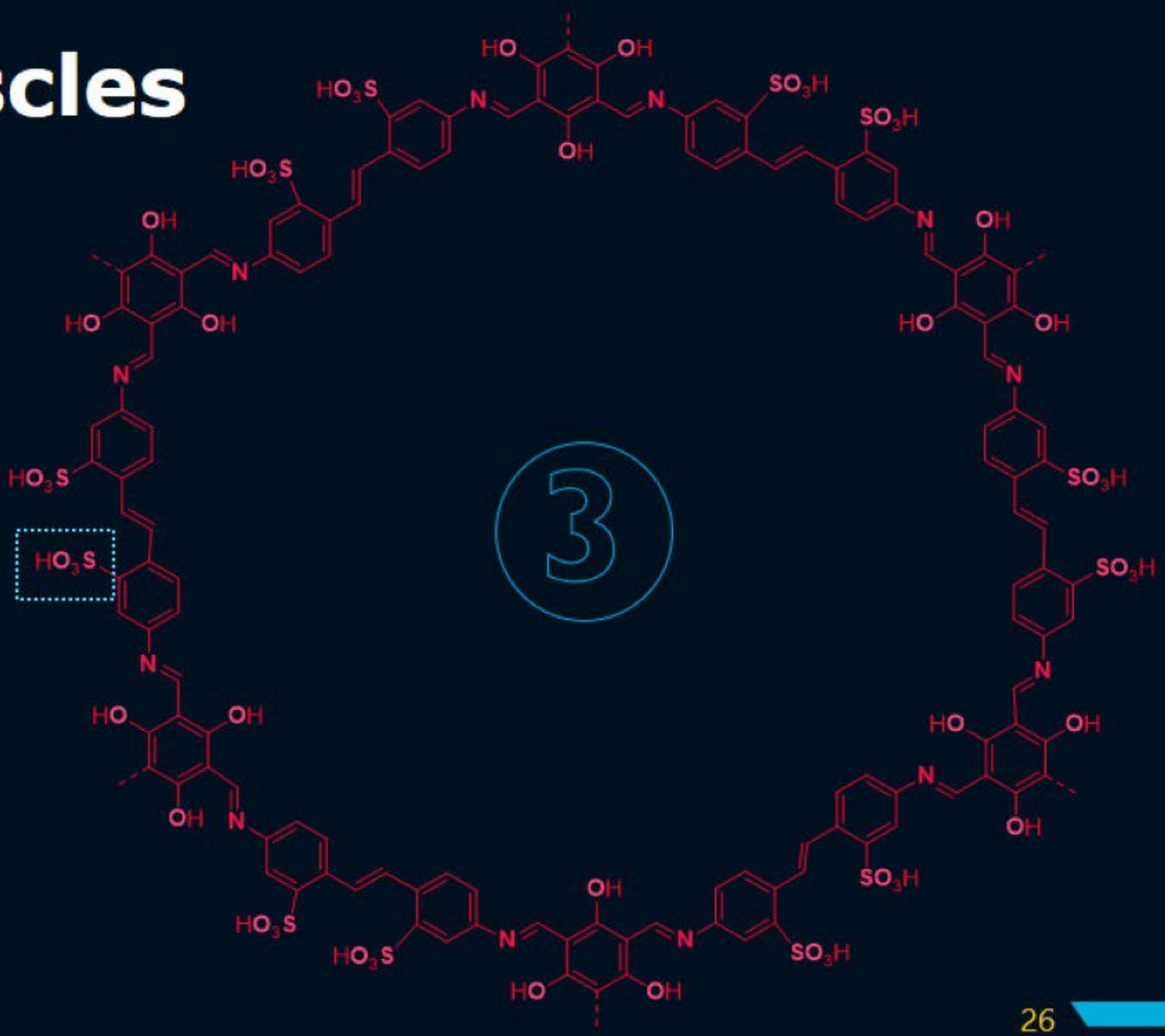

Polysulfonated COFs

Polysulfonated COFs (*p*S-COF) artificial muscles

Removes:

- ✓Back relaxation
- ✓Low bending
- ✓Low response
- ✓Low force
- ✓Irregular responses

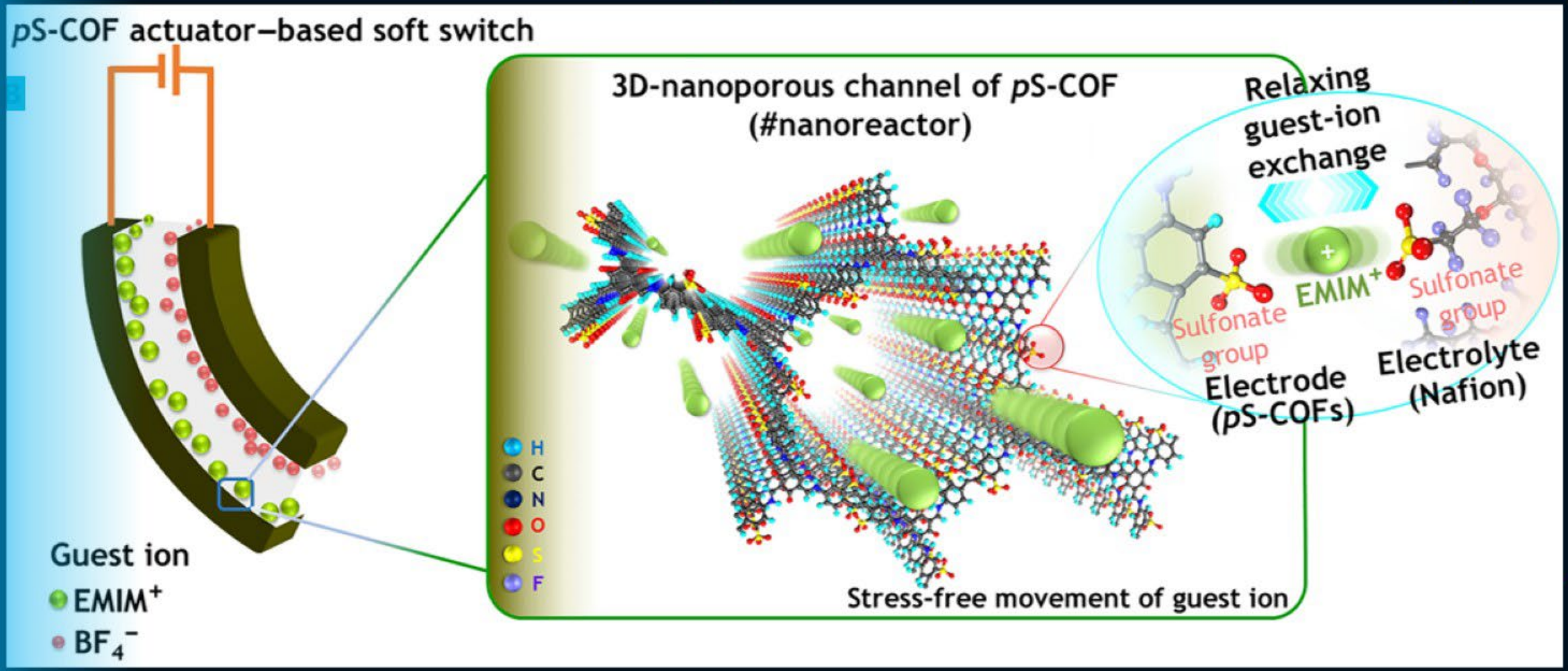

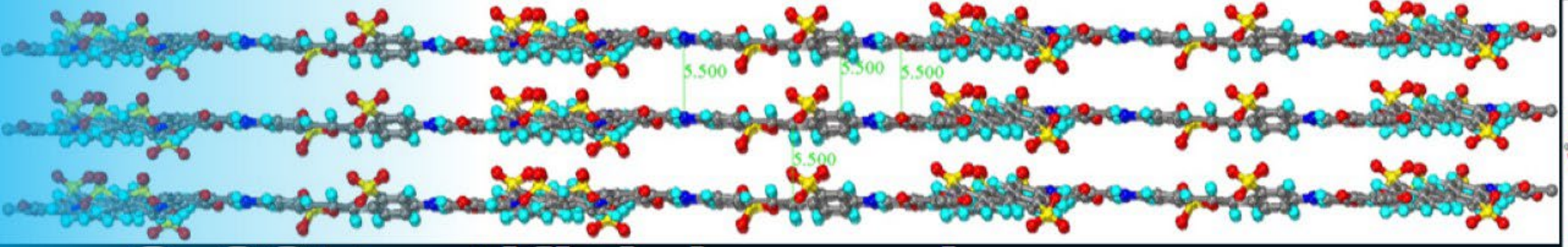

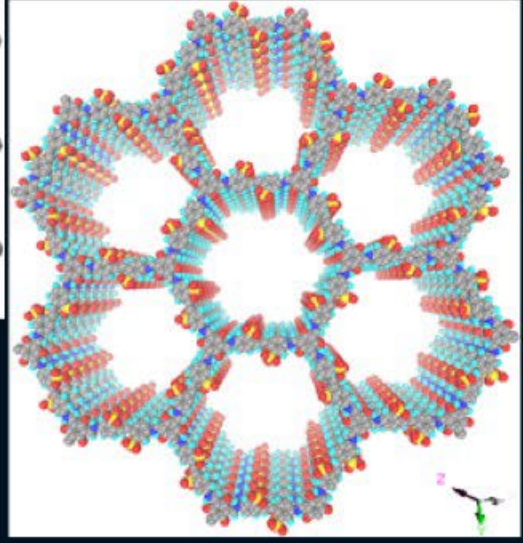

*p*S-COF artificial muscles

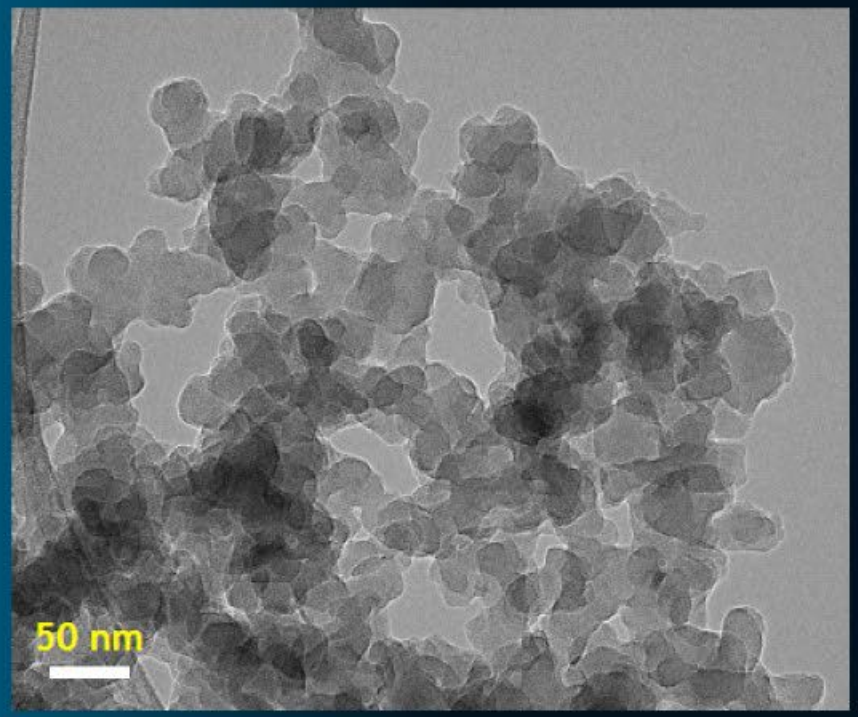

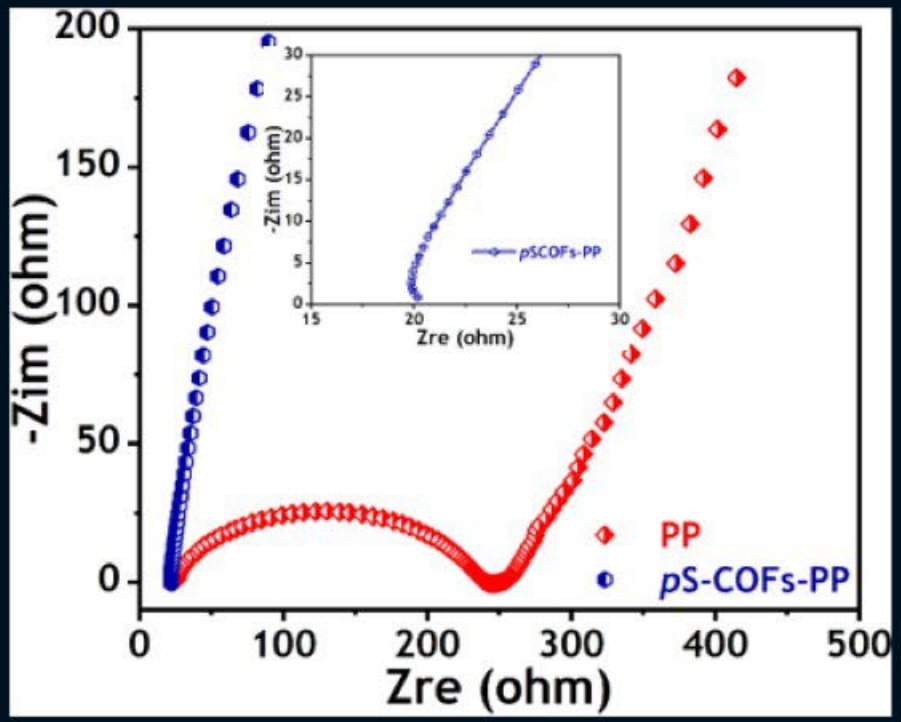

Eclipsed

Rp = 6.56%

SEM: nanoporous ionic channel

EIS: enhanced diffusion of ions

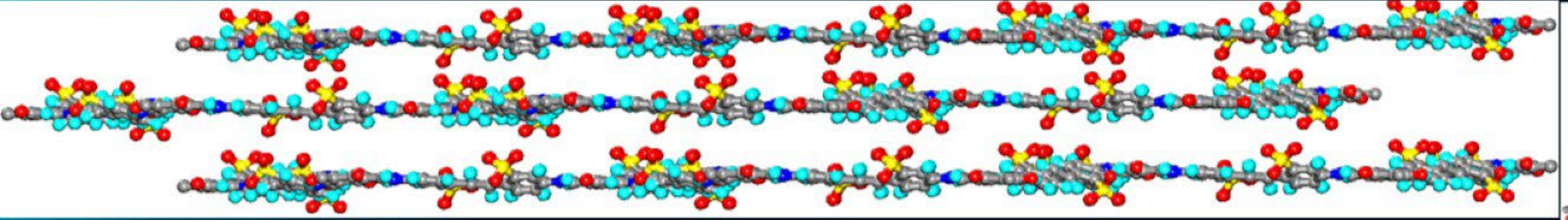

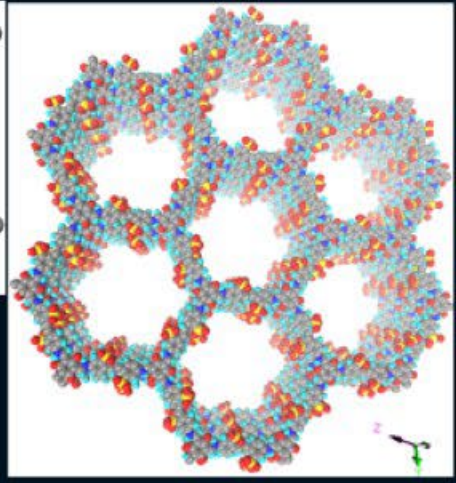

*p*S-COF artificial muscles

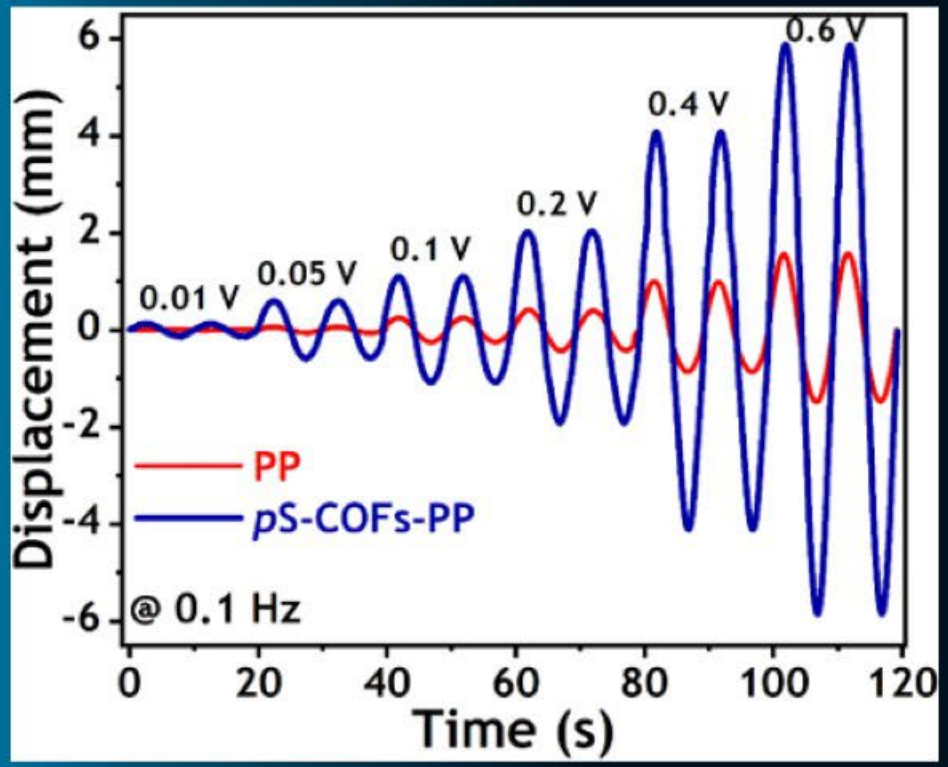

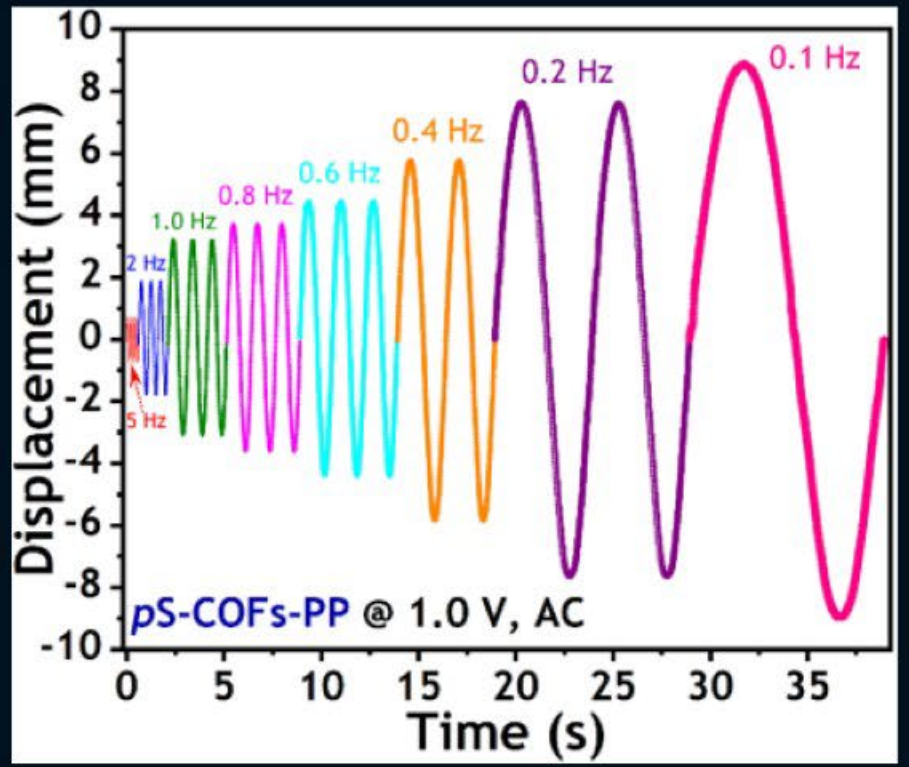

Staggered

Rp = 7.64%

Regular responses at ultralow voltage

High frequency responses

*p*S-COF artificial muscles

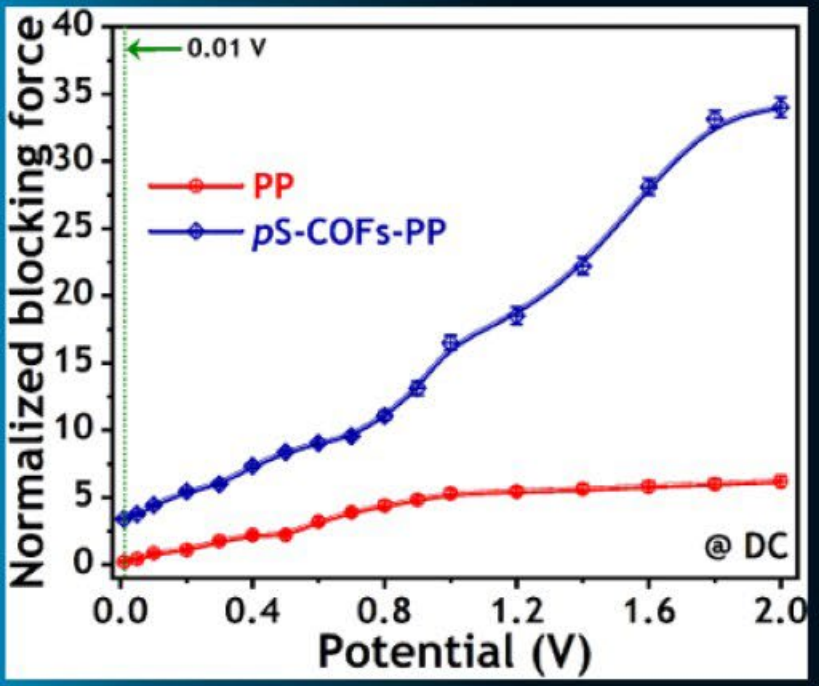

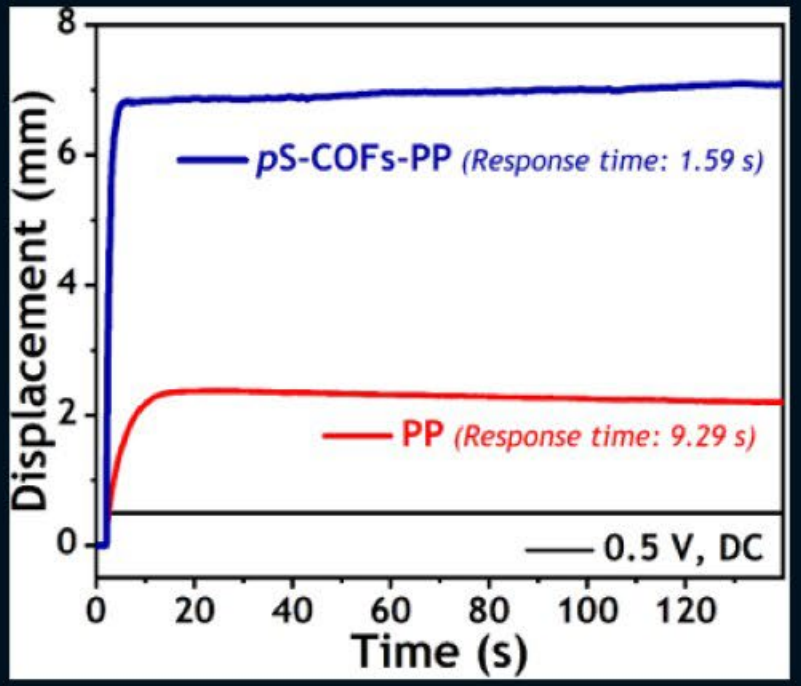

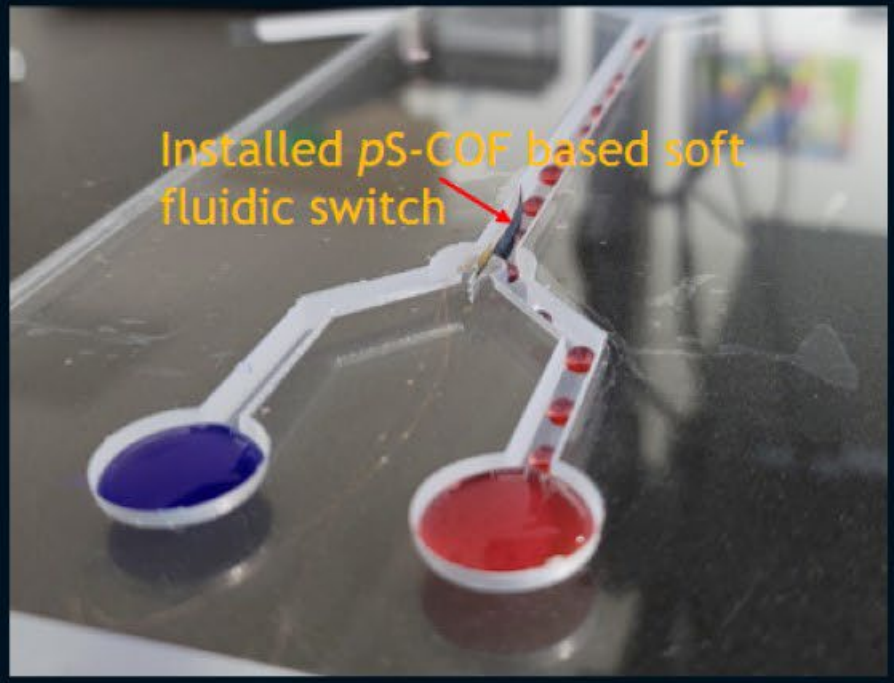

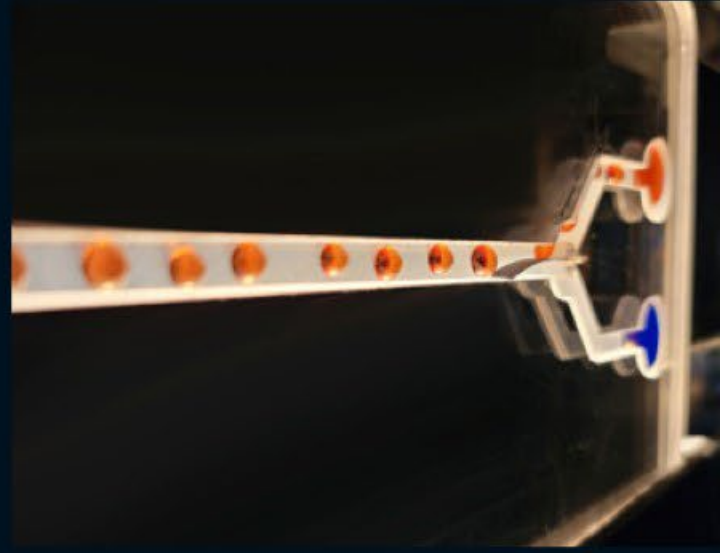

High forces: 34-time of its weight

Fast response: 1.5 seconds

Soft fluidic switch

*p*S-COF artificial muscles

SEM cross section of electroionic artificial muscle

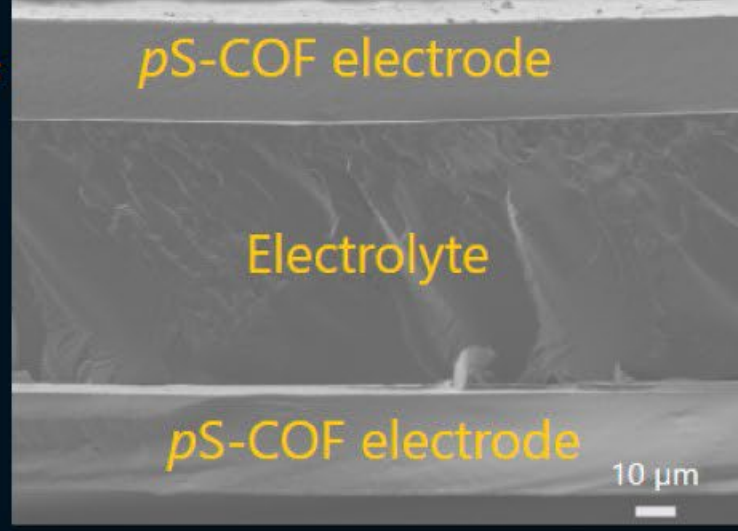

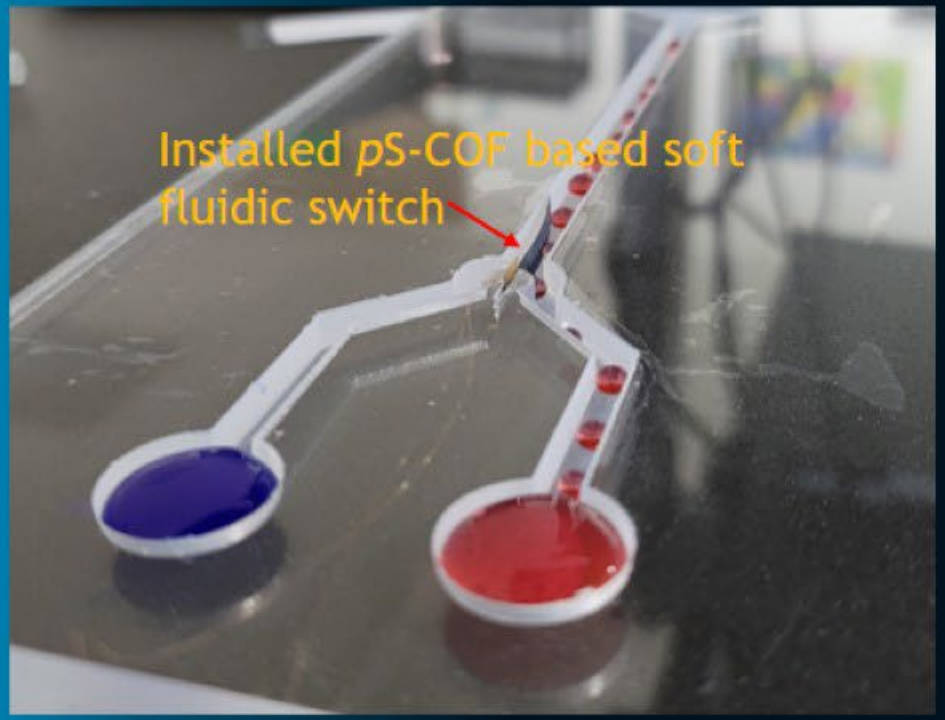

Soft fluidic switch

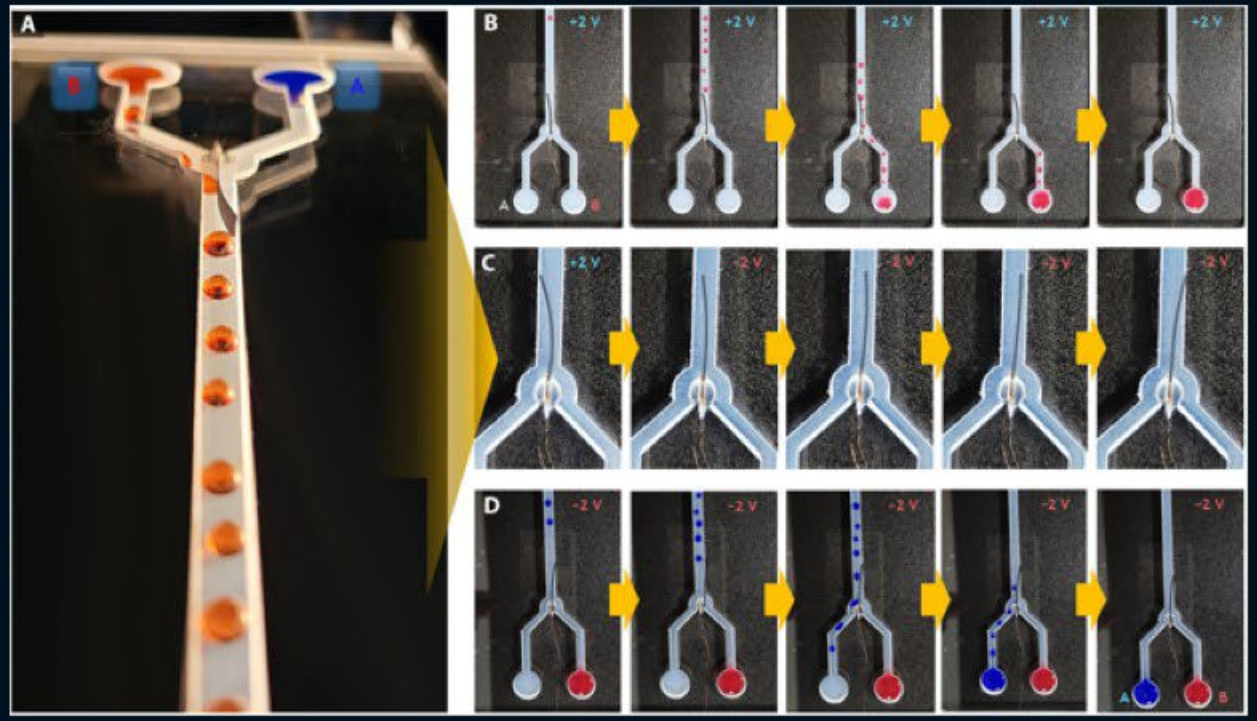

Control of fluid flow

*p*S-COF artificial muscles

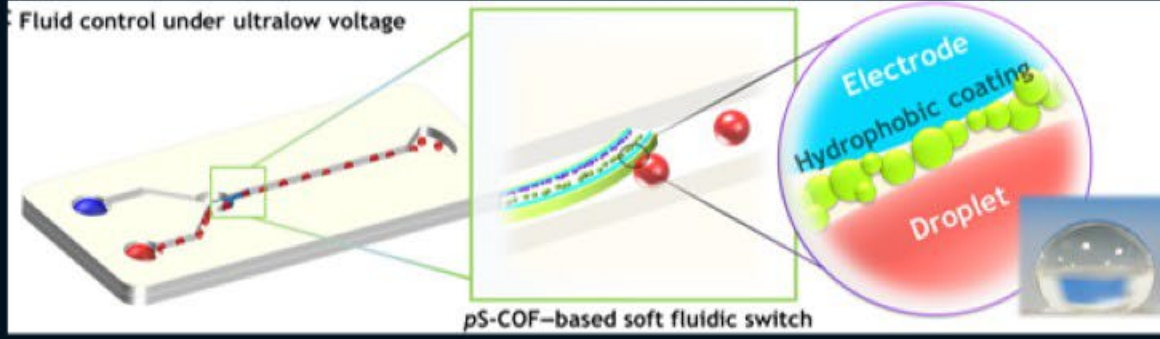

Schematic for the use of artificial muscle as soft fluidic switch

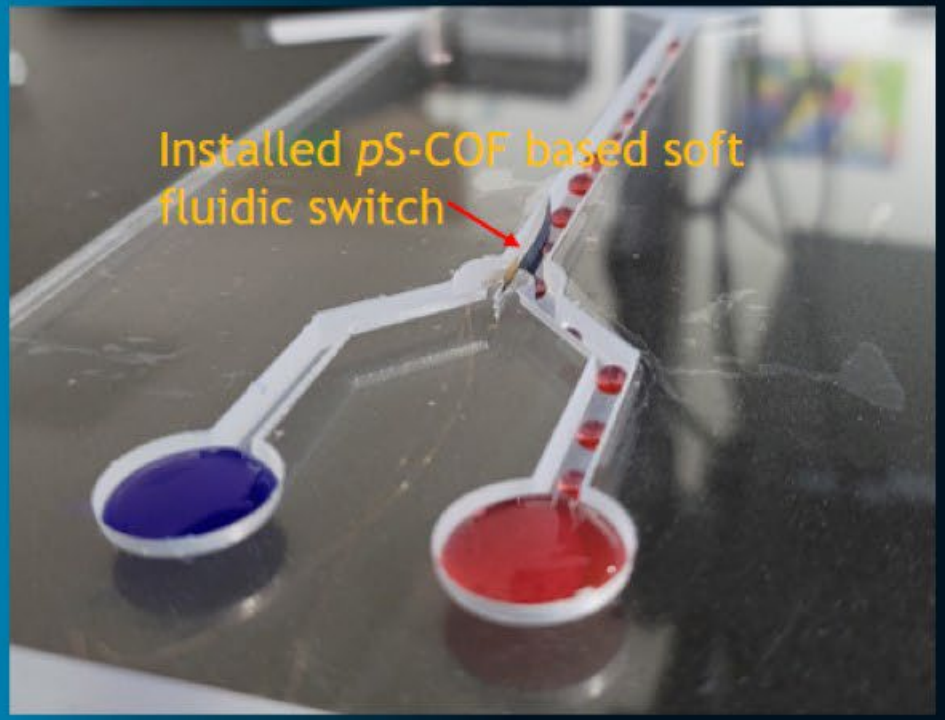

Soft fluidic switch

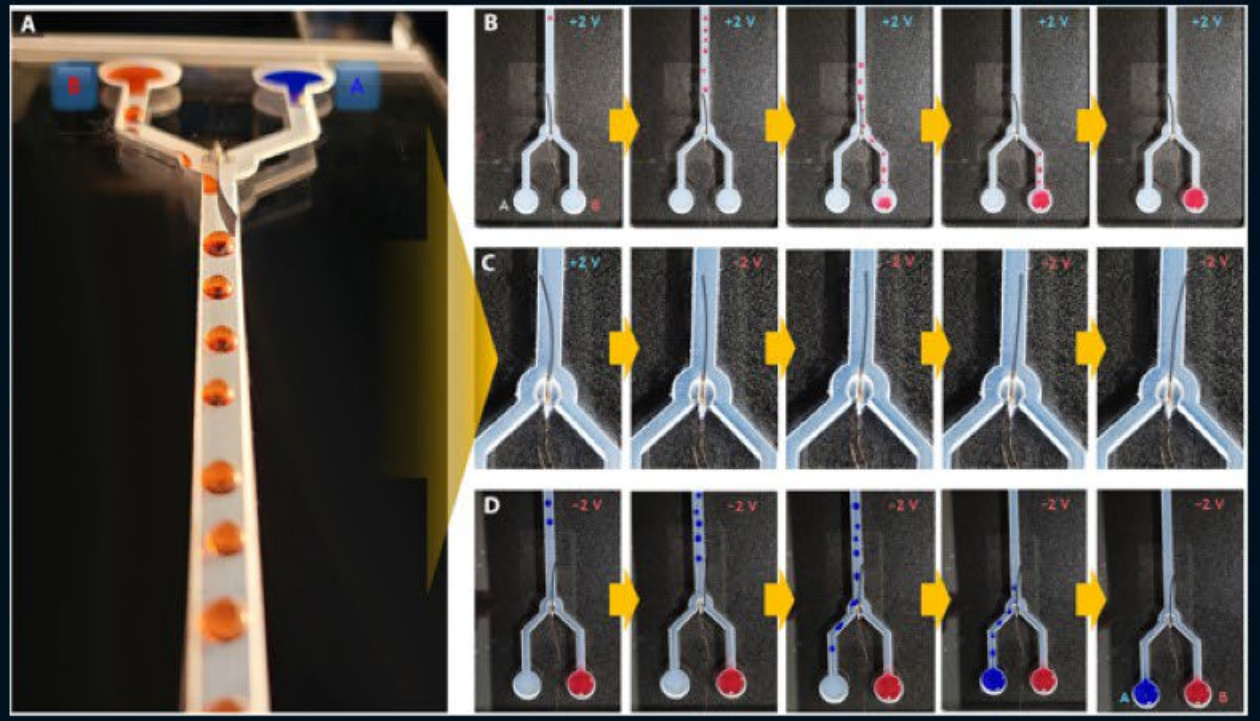

Control of fluid flow

*p*S-COF artificial muscles

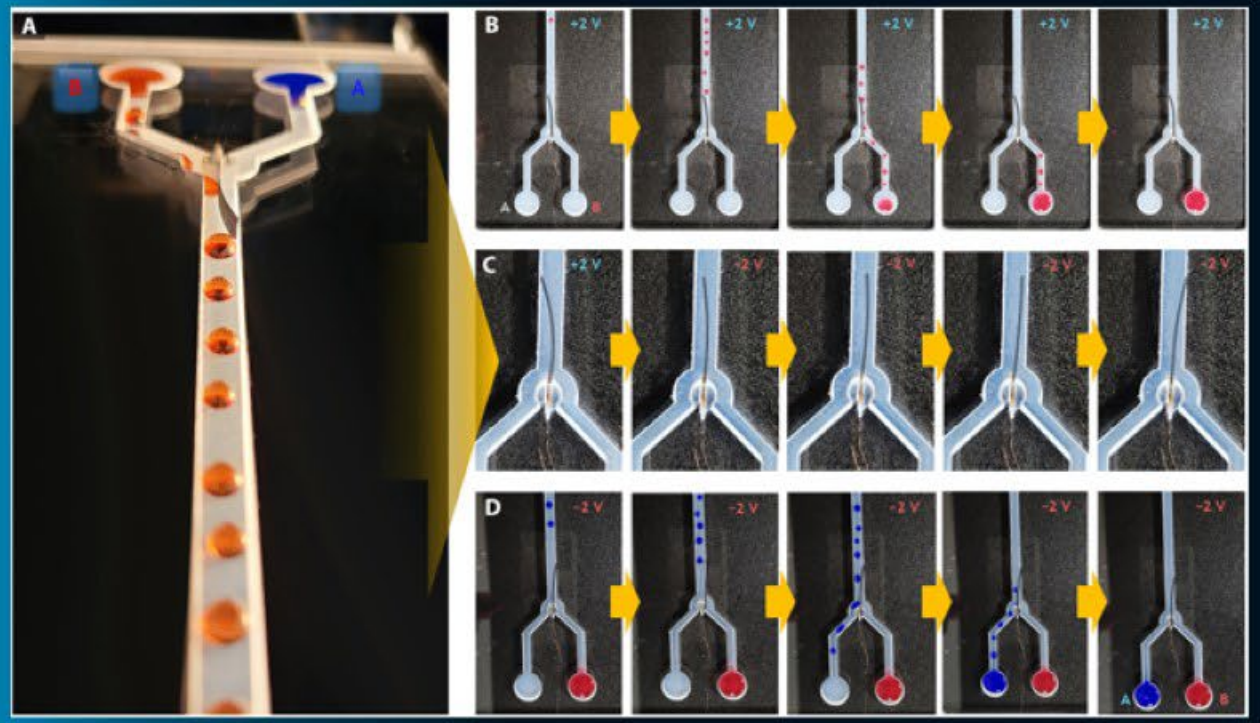

Control of fluid flow

Demonstration

Conclusions

- ✓Ionic artificial muscle with 34x its weight force
- ✓Applicable to use in limited space
- ✓Operated at ultra-low power (< 1.0 V) and broad-band frequencies (~5 Hz).



34배의 큰 힘을 내는 인공근육 소자 개발

소프트 일렉트로닉스 등 다양한 산업현장에 응용될 것이다.

https://news.kaist.ac.kr





https://news.heraldcorp.com

THANK YOU!

Manmatha Mahato

Ph.D.

Phone
+82 10 4263 0223

Email
manmatha@kaist.ac.kr

Iby and Aladar Fleischman Faculty of Engineering Tel Aviv University
הפקולטה להנדסה ע"ש איבי ואלדר פליישמן אוניברסיטת תל-אביב

ICCM24

24TH INTERNATIONAL CONFERENCE ON COMPOSITE MATERIALS

TEL AVIV UNIVERSITY אוניברסיטת תל אביב

Tailoring the Chemistry and Morphology of Vertically Aligned Carbon Nanotubes Forests, Implications for Smart Electrodes

Lev Rovinsky
PhD Student
CSI Group

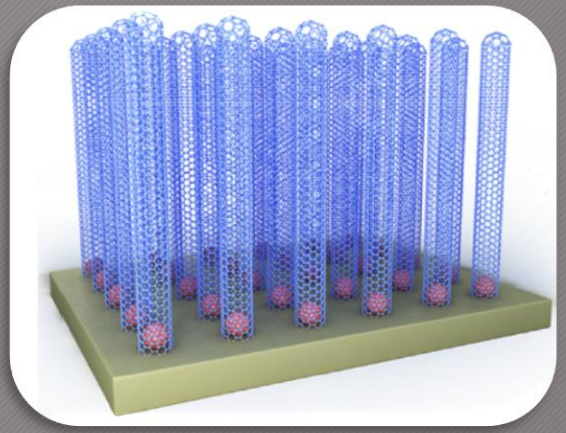





Vertically Aligned Carbon Nanotubes (VA-CNT)

- Showcasing the outstanding properties of CNT has been cumbersome.
- VACNT architecture bypasses 2/3 ‘typical’ CNT challenges.
- Key challenge: The delicate structure complicates solving the third

Property	Single-walled carbon nanotube	Double-walled carbon nanotube	Multiwalled carbon nanotube
Tensile strength (GPa)	50–100	23–63	10–60
Elastic modulus (TPa)	1	–	0.3–1
Elongation at break (%)	5.8	28	–
Density (g/cm^3)	1.3–1.5	1.5	1.8–2.0
Electric conductivity (S/m)	10^6	10^6	10^6
Thermal conductivity at room temperature (W/m K)	6000	3000	2000

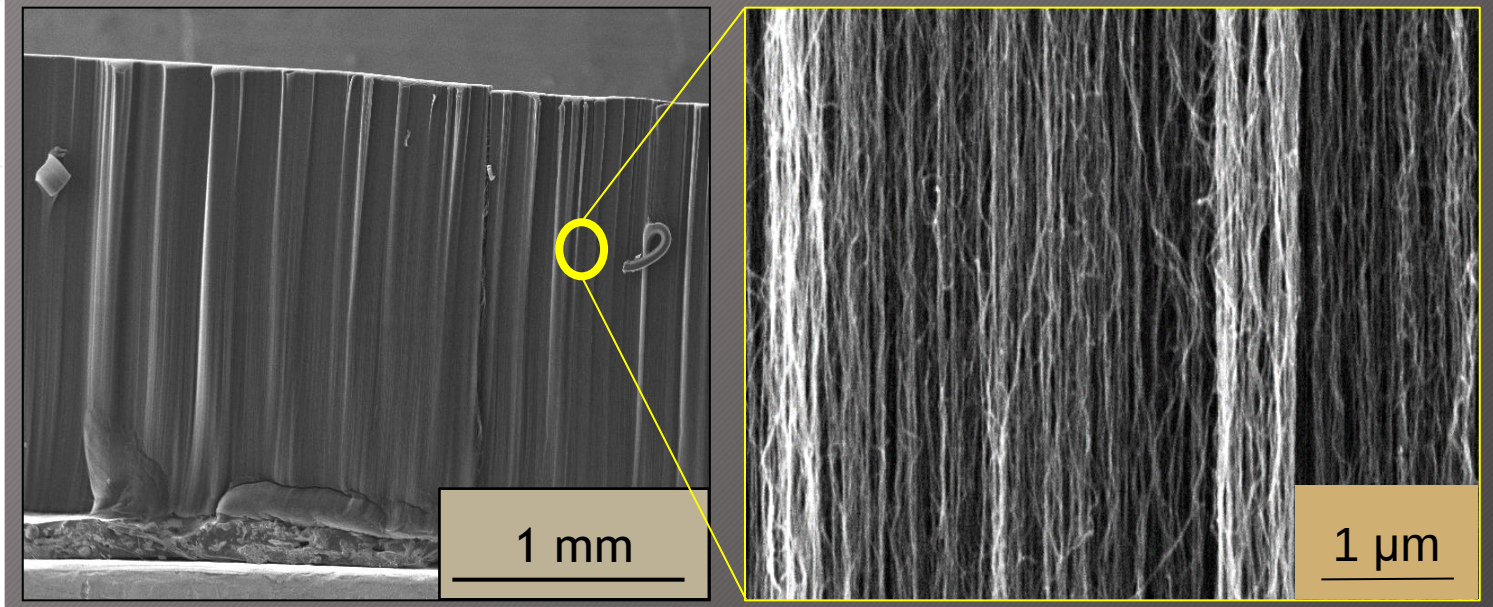

https://doi.org/10.1016/j.compositesb.2017.08.020

Motivation: VACNT-Hybrids

- VACNT are very porous architectures (99vol% air), with immense surface-to-volume ratio
- For example: If a carbon nanotube has 10nm diameter and 2 mm length, aspect ratio will be ~10^6. In typical VACNT (1 cm^2 Si-die) there are **~10^9 CNT**.
- Such conditions are 'prime real-estate' for secondary phases!

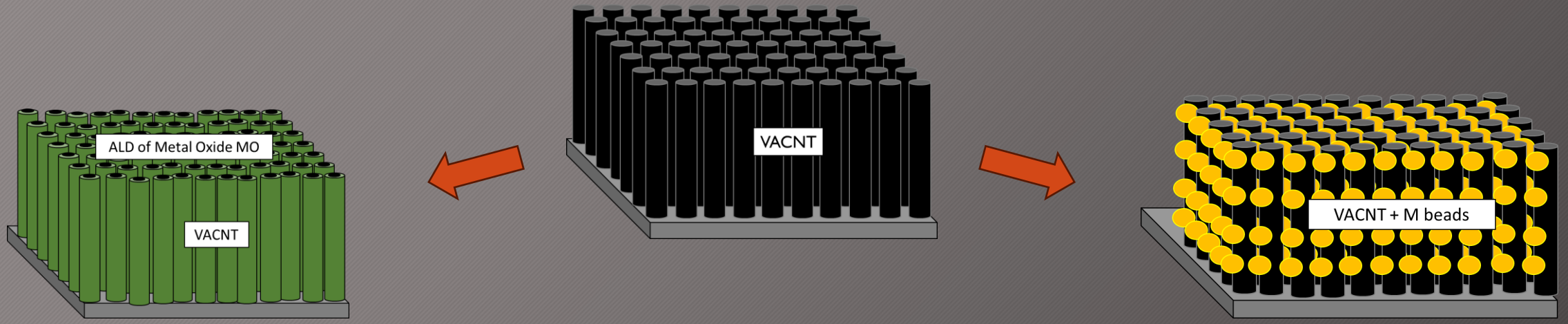

Strategy

1. Protection of CNT Chemistry.
   - Introduction of novel ‘chemical’ success criteria (proof: XPS).
   - On top of existing ‘structural’ criteria (proof: Raman).

2. Retention of VACNT Architecture
   - Morphological analysis (proof: SEM)'
   - Avoiding ‘capillary forces’ of wet methods.

3. Fabrication of VACNT-Hybrid
   - Dry methods, such as sputtering and atomic layer deposition (ALD)

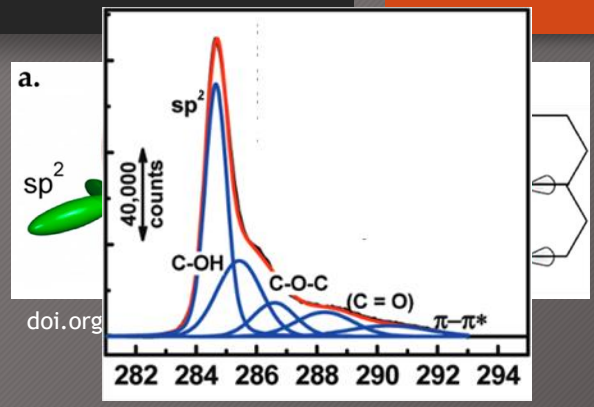



Air

Argon

O_2/Ar Plasma



Controlled Metal Melting



Metal Oxide Coating

Methodology

Scaffold Preparation

Water-assisted Chemical Vapor Deposition of VACNT

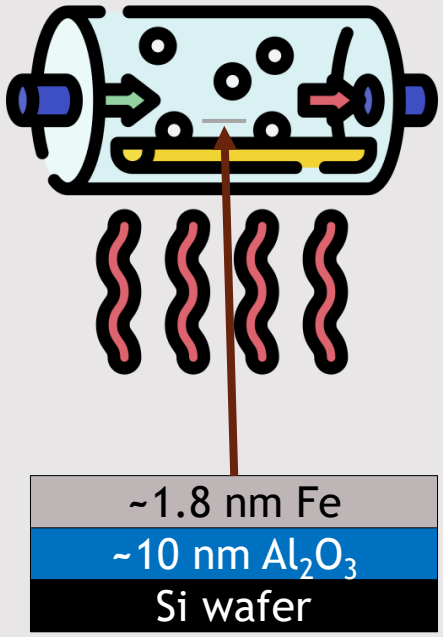

Interphase Engineering

Annealing at atmosphere of choice

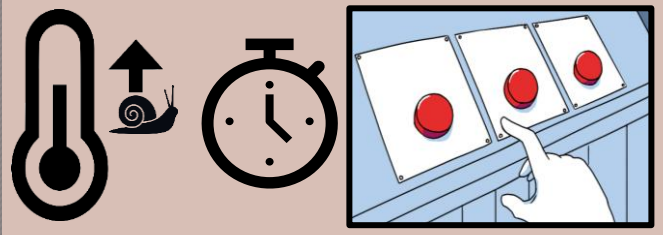

Plasma treatment

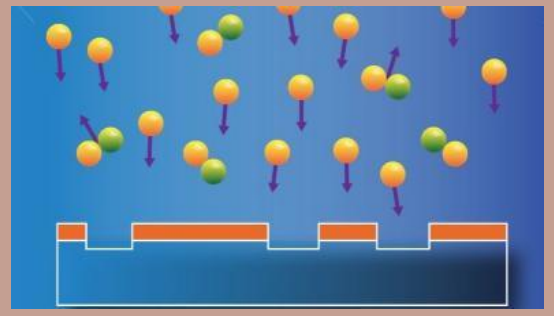

https://sinvacon.be/

VACNT-Hybrid Composite Fabrication

(ALD) of Oxides

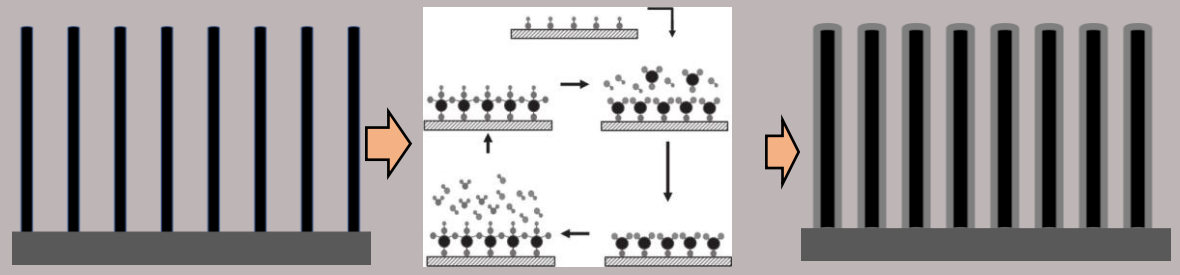

doi.org/10.1071/CH14172

Ostwald Ripening of Metals

Sputtering of gold

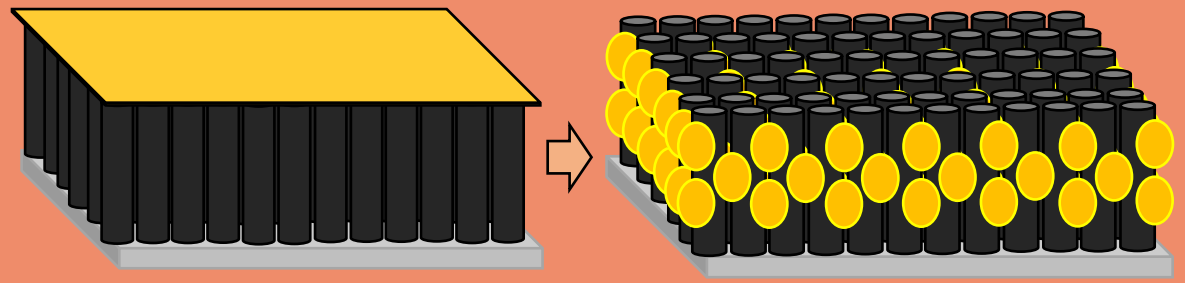

Characterization Techniques

Basic "Toolkit" for the Surface Treating Engineer

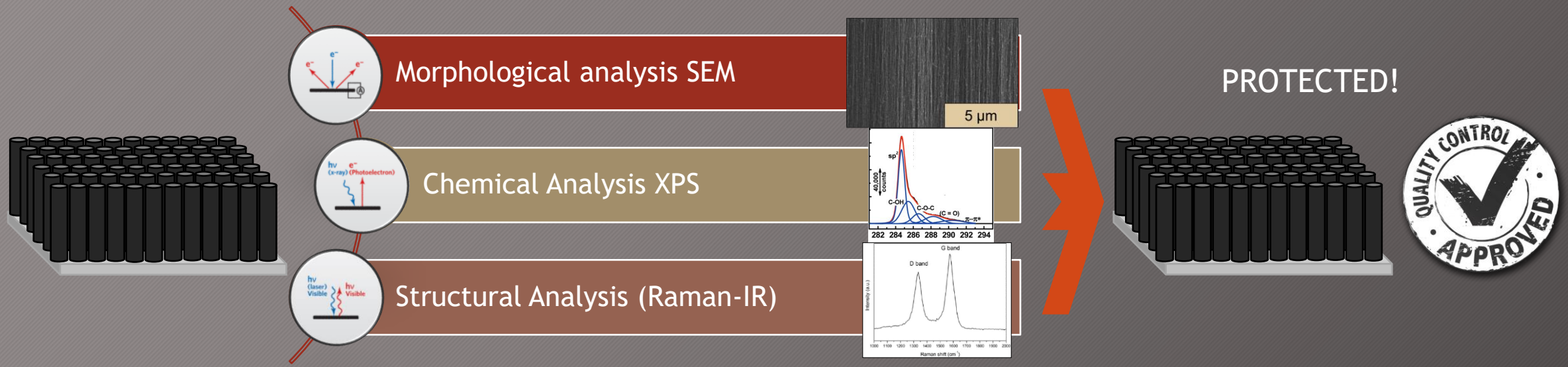

Results - AuNP-beaded VACNT

- Higher temperatures create more spherical nanoparticles.

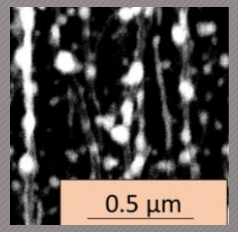

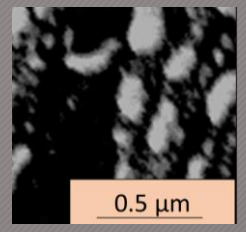

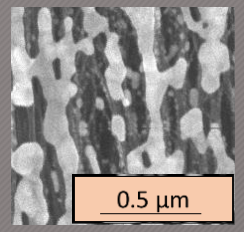

- At low temperature, we need time!

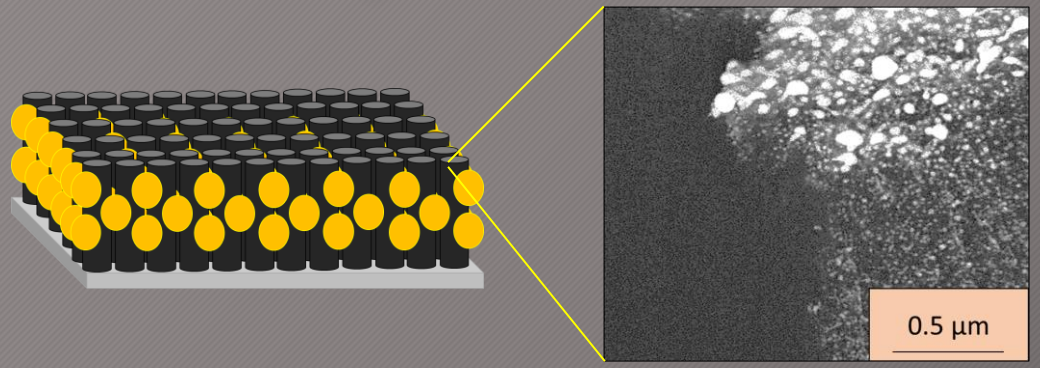

MorphoJ sphericity = $\frac{V^2}{S^3} \cdot \frac{36}{\pi}$

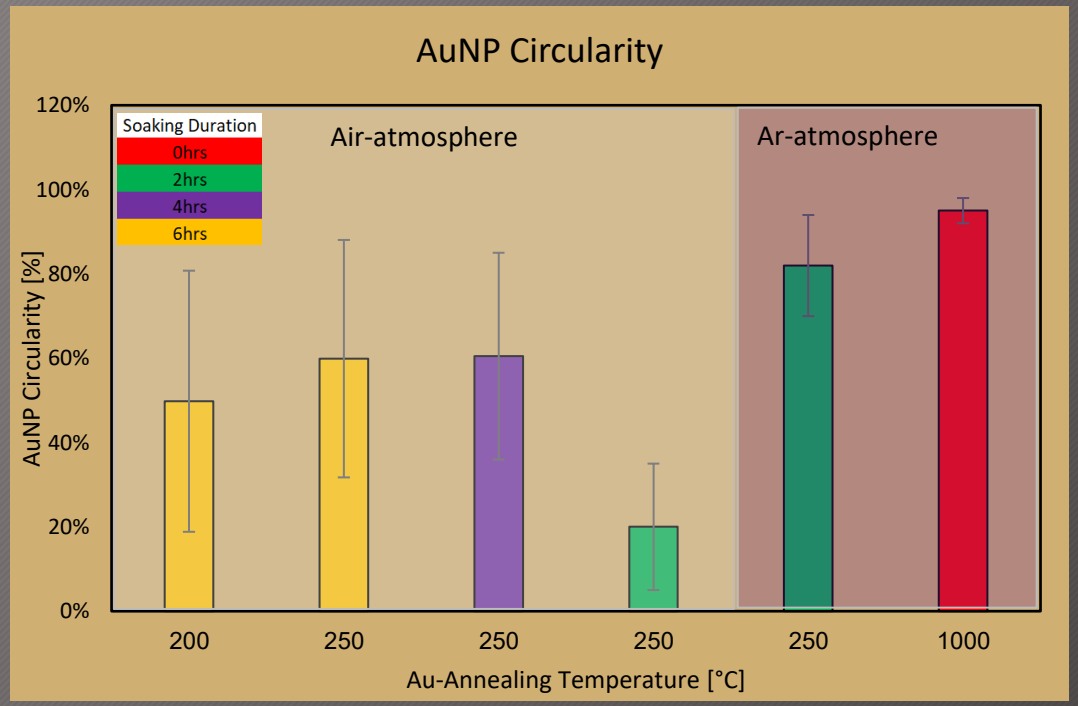

Results – Al_2O_3 coated nanotubes in VACNT

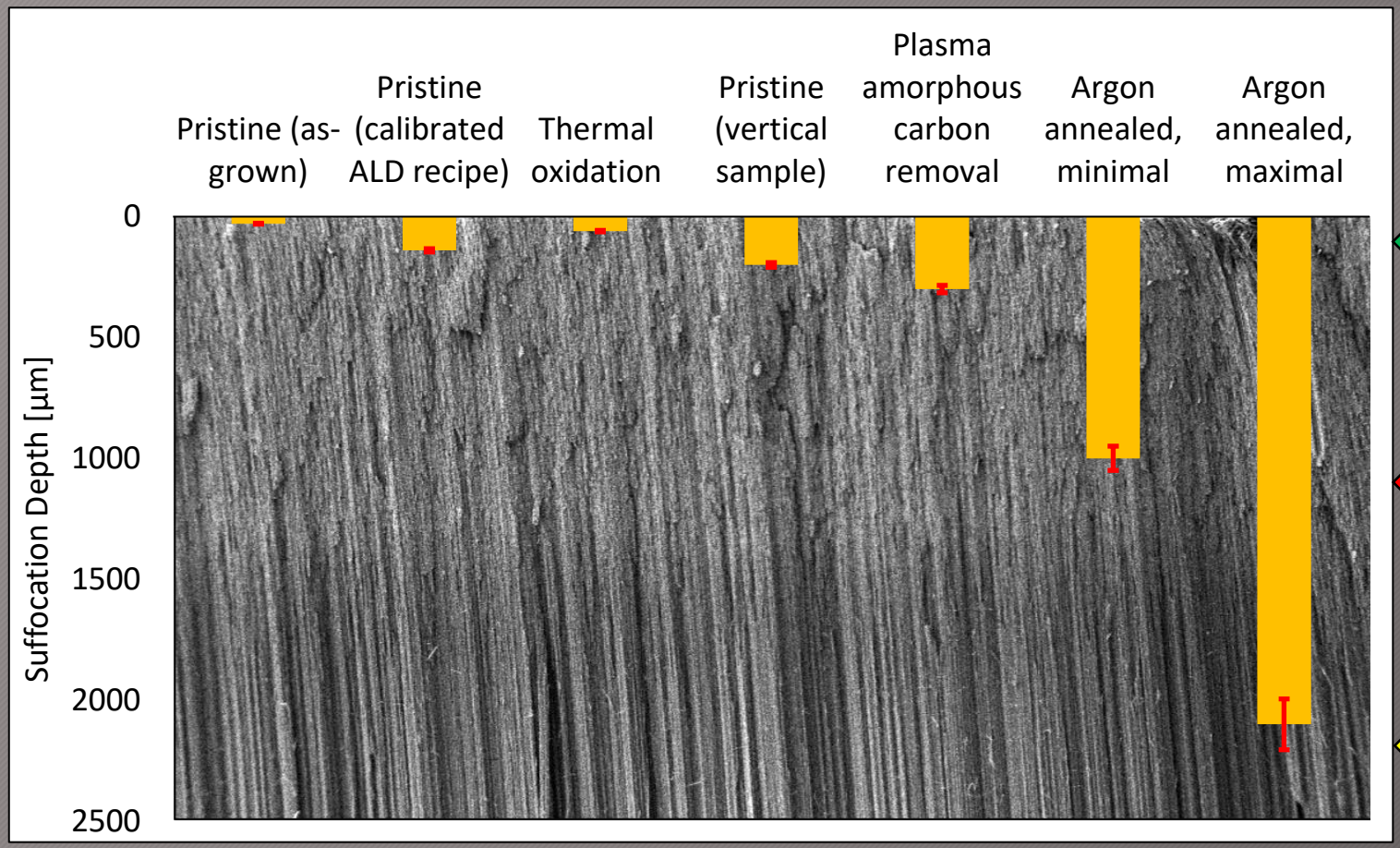

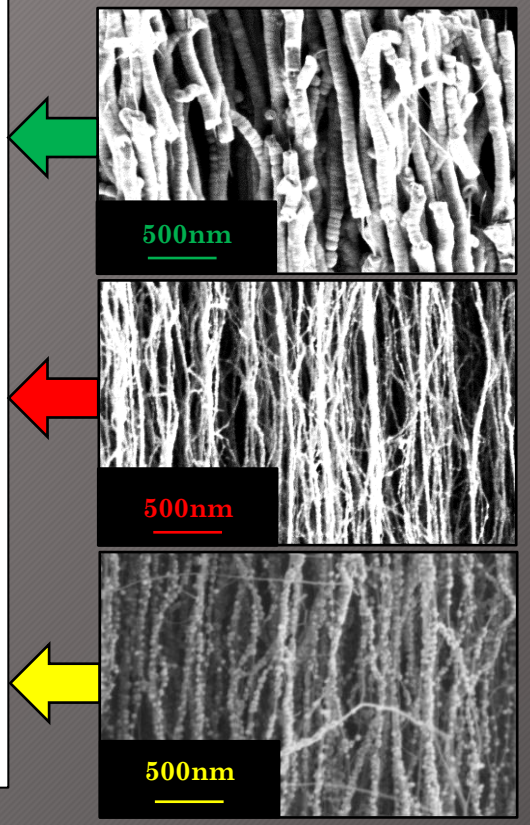

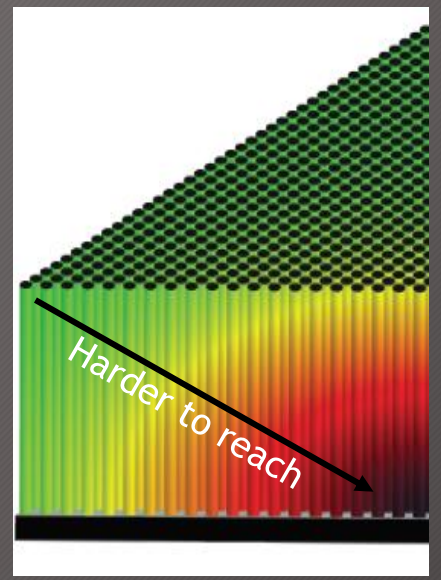

Rovinsky et al. ACS Appl. Nano Mater. 2021, 4, 322−330

Amorphous carbon plasma removal

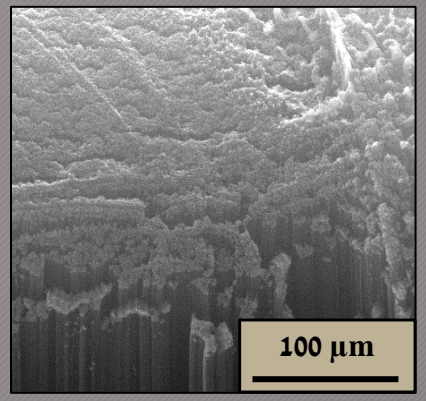

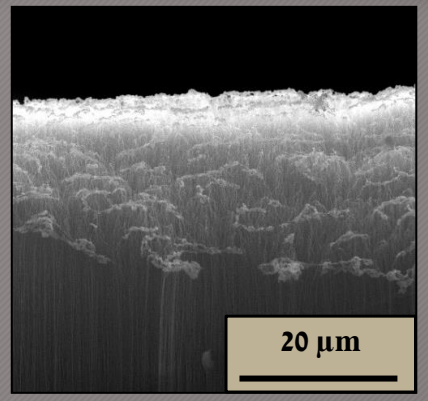

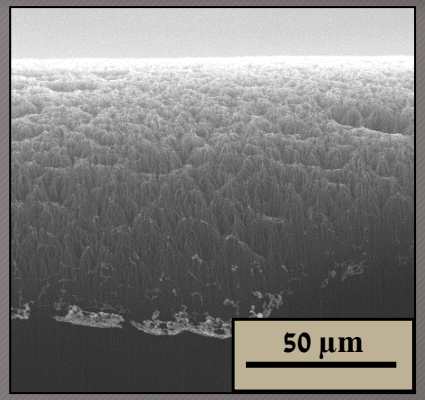

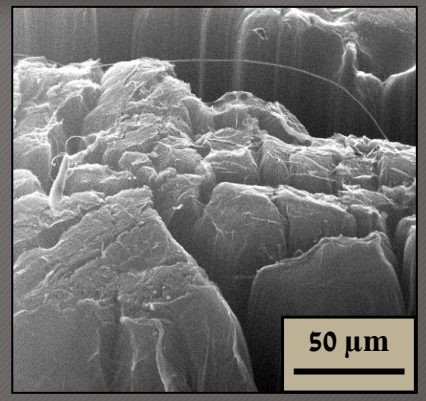

Table 5. - Oxygen content and "π-π*" for VACNT arrays, for pristine and plasma-treated samples, at two different gas ratios, after 2.5 minutes of treatment.

	Pristine	O_2/Ar (3:3)	O_2/Ar (4:2)
Oxygen Center	0.50 (±.05)	8.47 (± 0.8)	1.66 (± 0.16)
Oxygen Periphery	2.85 (± 0.3)	15.55 (± 1.5)	19.93 (± 2)
"π-π*" Center	0.98 (± 0.1)	0.71 (± 0.07)	0.98 (± 0.1)
"π-π*" Periphery	0.91 (± 09)	0.59 (± 0.06)	0.47 (± 0.05)

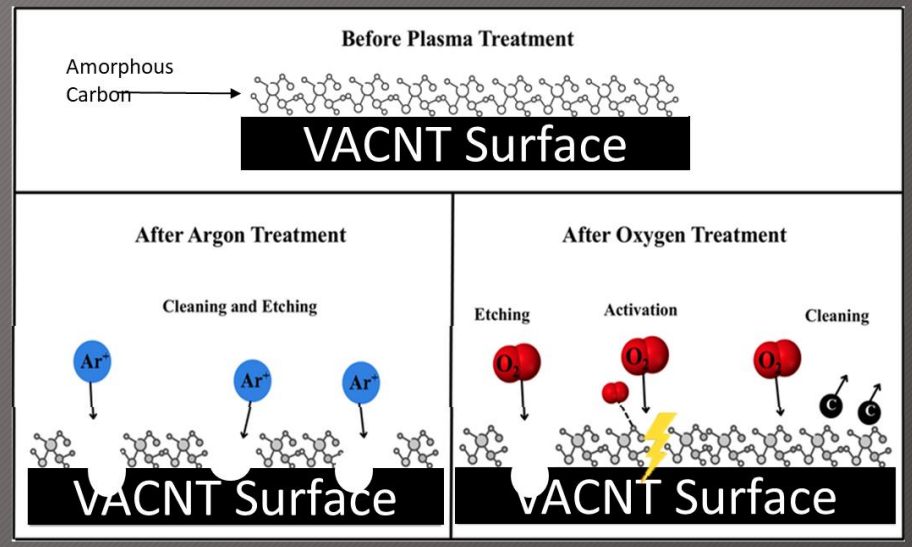

Annealing atmosphere, choice 1 - Air

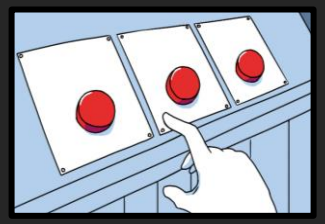

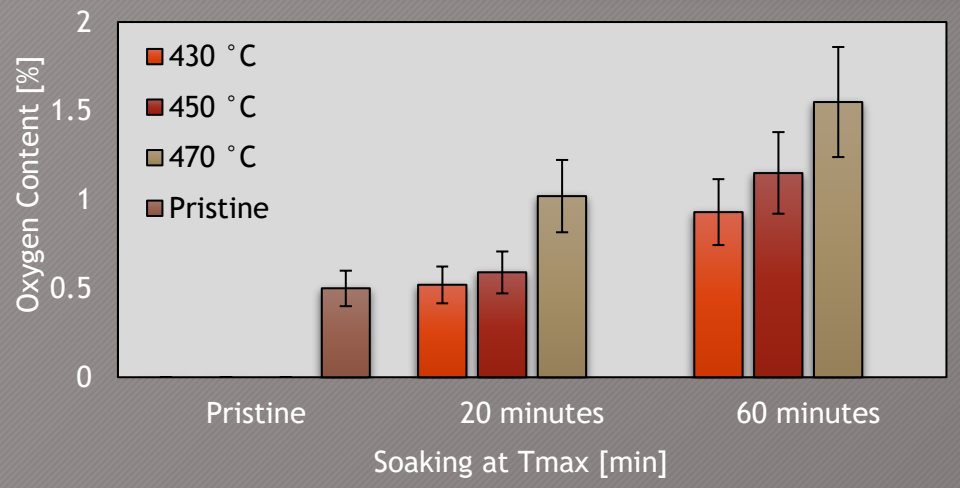

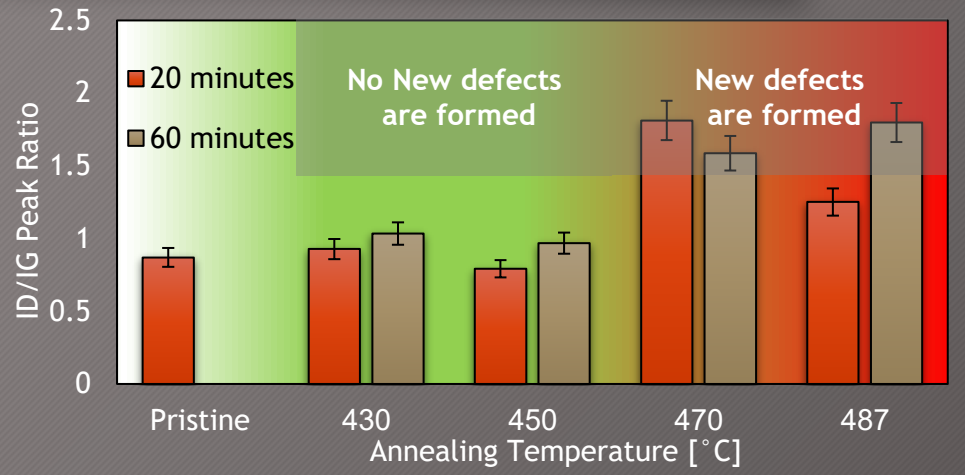

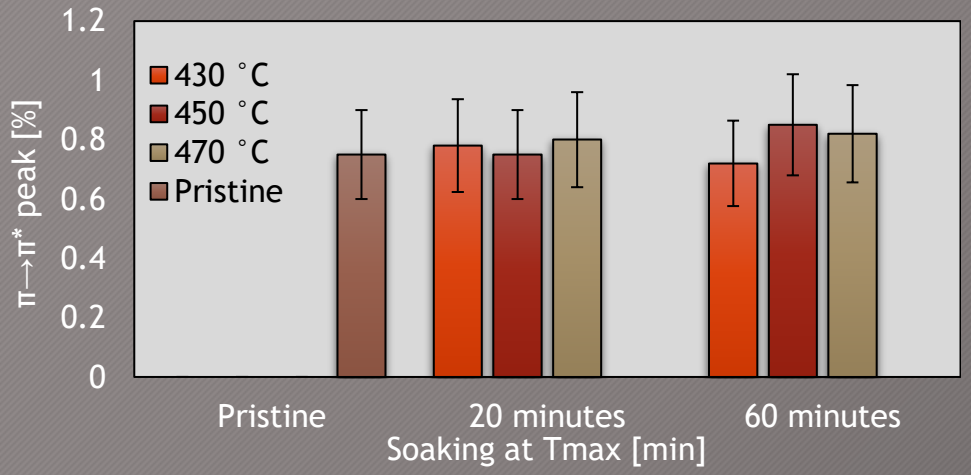

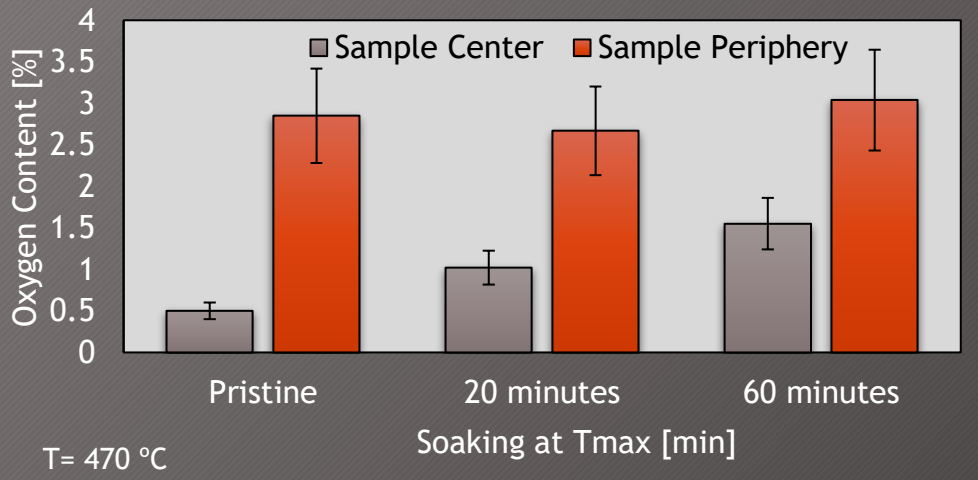

T= 470 °C

Annealing atmosphere, choice 2 – Ar (Shir's and Ella's BSc project)

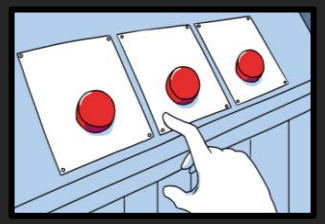

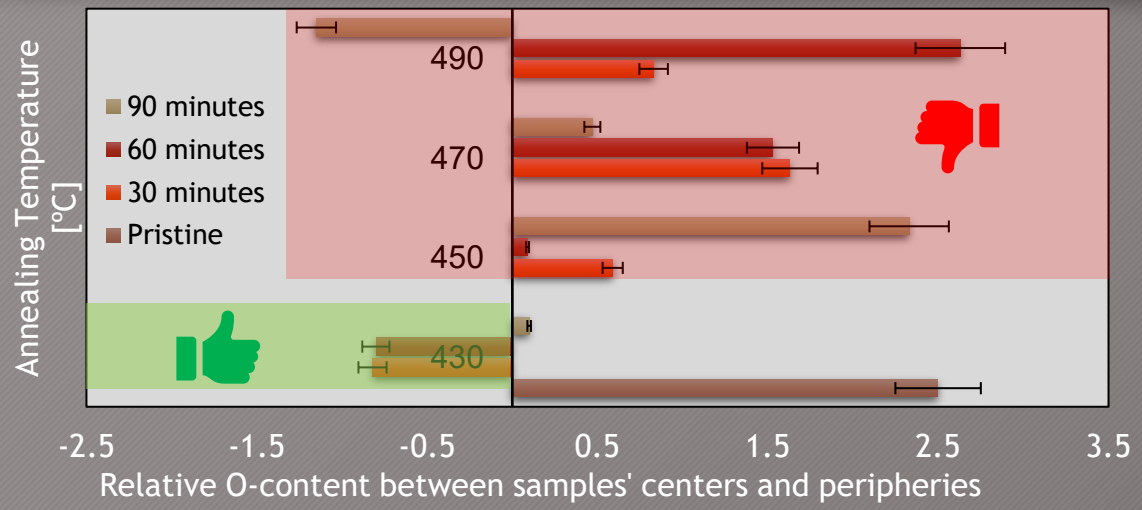

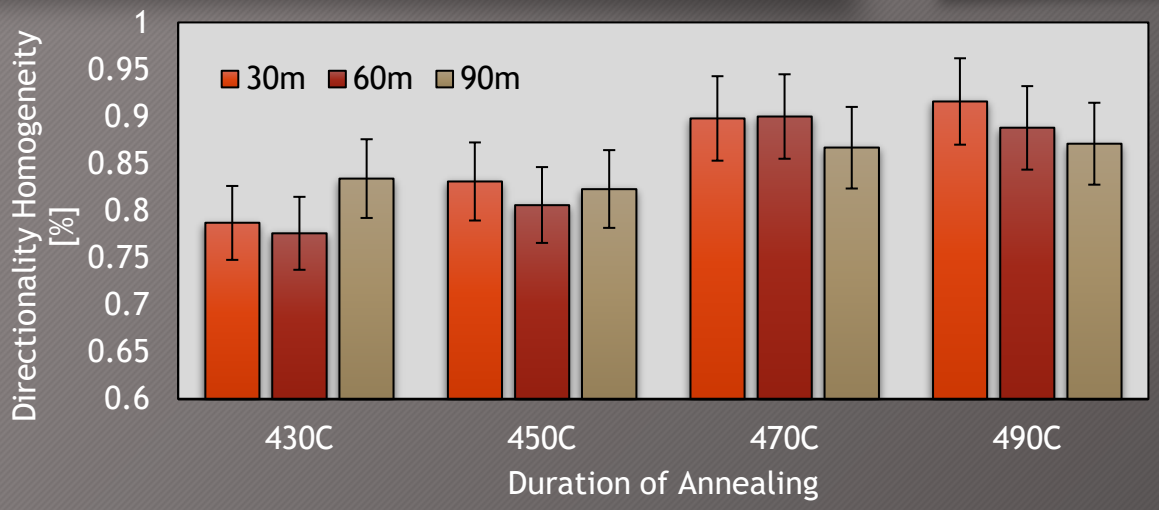

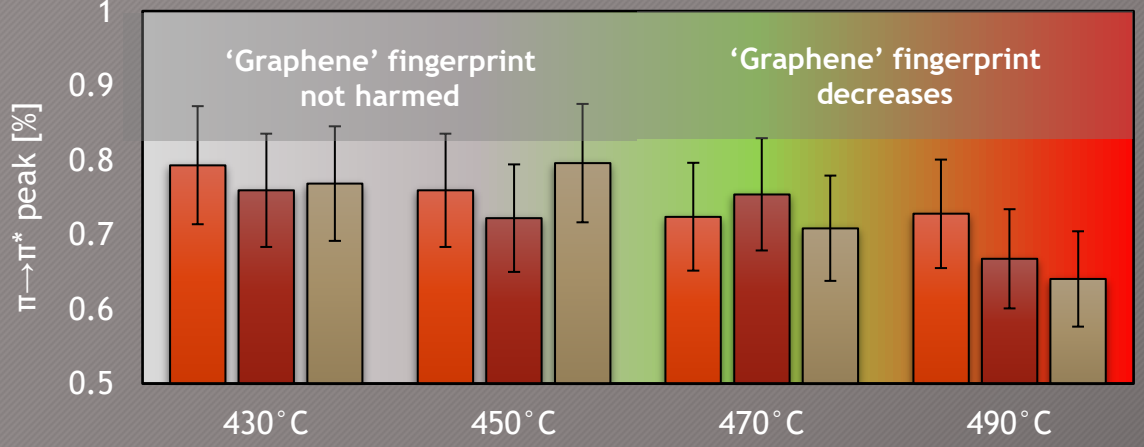

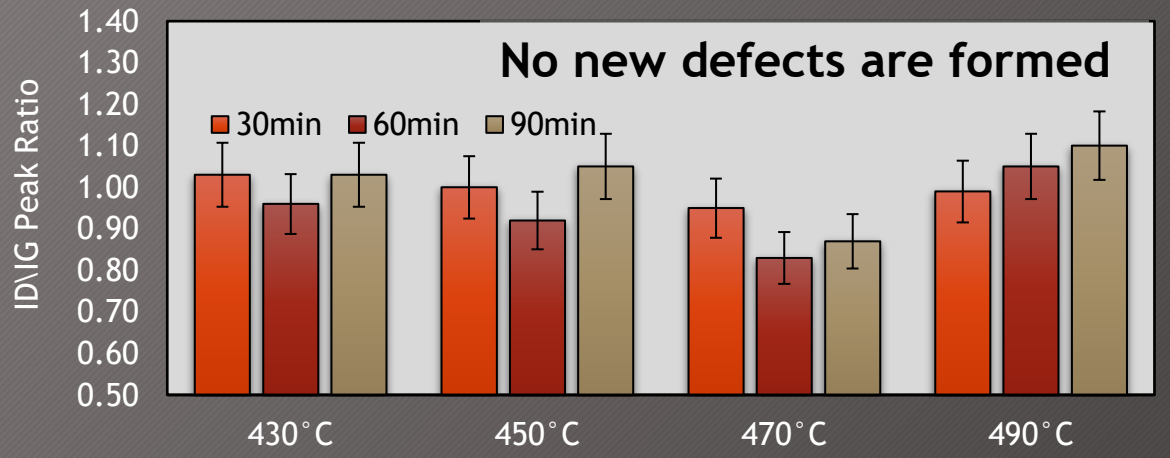

Summary (To take home)

- The electronic structure of MWCNT is conserved in post-treated VACNT, with clear validation criteria.
- VACNT high-interface hybrid structures are naturally inhomogeneous, and require a tailored surface treatment to ensure homogeneity.
- Lowering the fabrication temperature of VACNT-metal hybrids makes them more approachable for various applications (e.g. energy harvesting or bio-medical)

QUASI-DISTRIBUTED PRESSURE SENSORS EMBEDDED INTO SURFACE MATERIALS ON COMPOSITE LAMINATES

Per Hallander[1,6], Nazila Safari Yazd[2], Joao M. B. Pereira[2], Carola Sterner[2], Kenny Hey Tow[2], Åsa Claesson[3], Erik Kullgren[4], Mathias Johansson[5], Tobias Karlsson[6], Malin Åkermo[6]

1: Saab AB, Bröderna Ugglas gata, SE-581 88 Linköping, Sweden
per.hallander@saabgroup.com
2: RISE AB, Fiber Optics, Isafjordsgatan 22, SE-164 40 Stockholm, Sweden
carola.sterner@ri.se
3: RISE AB, Fiberlab, Fibervägen 2-6, SE-824 50 Hudiksvall, Sweden
asa.claesson@ri.se
4: Elitkomposit AB, Kärranäsvägen 9, 451 76 Uddevalla, Sweden
erik.kullgren@elitkomposit.se
5: Saab Surveillance, FCC, Stensholmsvägen 20, SE-561 39, Huskvarna, Sweden
mathias.johansson1@saabgroup.com
6: Department of Engineering Mechanics, KTH Royal Institute of Technology, Teknikringen 8, SE-100 44 Stockholm, Sweden
akermo@kth.se

Keywords: Smart Materials Optical properties techniques Physical properties

ABSTRACT

In this study, upcoated and buffered optical fibres with Fibre Bragg Gratings (FBGs) have been used as quasi-distributed pressure sensors that can be embedded into surface materials for composite structures. The main goal has been to develop compact and robust sensors/sensor materials that measure pressures from 10 to 200 kPa.
The sensor used for this experiment was FBGs inscribed in 125µm optical fiber having either Polyimide (PI) or Acrylate (Ac) as original coating. The wavelength shift of an FBG can be related to strain, and its sensitivity is approximately 1.2 pm/µstrain. To make the FBG sensitive to pressure, the optical fibers with FBGs were coated with a soft up-coating layer of silicone and a stiffer buffer material. The total outer diameter was 1 mm. Four buffered fibre cables were manufactured with combinations of the two original coating materials and two different buffer materials that were either Polyamide (PA) or Polyetheretherketone (PEEK).
The buffered optical fibres were embedded into a couple of different types of surface materials on top of pre-cured 4 mm carbon fibre /epoxy (CFRP) laminates. The surface material was either a syntactic foam material with a 0.1 mm glass fibre/epoxy cover layer or 10 epoxy film layers (36 gsm Hexel 6376 resin) with a 0.1 mm glass fibre/epoxy cover layer. The pressure response of the inbuilt optical fibres was tested in an Instron Machine in the load range of 10 to 200 kPa.
The best combination for pressure sensitivity was either to use an optical fibre with PI coating and PEEK buffer or an optical fibre with Ac coating and PA buffer combined with the syntactic foam surface cover material.

1 INTRODUCTION

Fibre Bragg Gratings (FBGs) are sensitive to external parameters, such as strain and temperature. Their high multiplexing capabilities allows the manufacturing of extremely dense sensing arrays in a single optical fibre, enabling highly localized measurements over a distributed area and making them attractive for structural health monitoring.
Extensive research and development have been performed using FBGs as pressure sensors in a variety of harsh environment applications such as thermoelectric power plant combustion chamber [1] (Rosolem et al) and filament wound pressure tanks [2] (Kang et al). Since FBG-based solutions are intrinsically poorly sensitive to external pressure, it is necessary to convert external pressure to

fibre elongation, more conveniently measured with FBGs and thus increasing the pressure sensitivity of these devices. Thus, the performance analysis of pressure sensors using different types of fibre Rodriguez et al [3] and packaging designs such as flexible diaphragm [4] (Liang et al), polymers [5] (Zhang et al) and bourdon tubes [6] (Huang et al) was addressed in several studies, achieving pressure sensitivities up to 280 nm⁄MPa Sebastian et al [7].
In the aeronautics scenario, Chehura et al [8], demonstrated FBG-based pressure sensors effectively applied to measure pressure on aircraft wings. When compared to traditional pressure sensors, FBG-based technique enables a much higher density of measurement points, thus providing a higher level of details of the wing model under load. The research summarized above shows that FBG sensors can meet the requirements on distributed pressure sensors. However, the FBGs used have a diameter ≥2mm which is too large to effectively be built into composite wing structures. Commercially are also Fabry-Perot sensors available, which measure the pressure in the end of the fibre. However, this type of sensor only allows point measurements. The FBGs presented in earlier studies are added to the surface of the component, thereby vulnerable to surface loads. Older types of sensors integrated into composites have in some cases reduced the mechanical performance of the material since having large radie, around 3 mm or larger.

Wing surface pressure monitoring on an aircraft with traditional technology will employ hundreds of electrically connected sensors on the wing. This is a bulky, complex and costly solution and, therefore, only used in on ground wind tunnel tests today. For measurements during service, there is no existing pressure monitoring system today. In this scenario, optical fibre solutions based on Fibre-Bragg Gratings (FBGs) [3,7,8] are advantageous due to their capability to be seamlessly embedded into lightweight aircraft composite parts, multipoint sensing possibility and immunity to electromagnetic interferences.

In this study optical fibres with FBGs have been used for creating quasi-distributed pressure sensors that can be embedded into surface materials for composite structures.
To enhance the pressure sensitivity, FEM (Finite Element Method) was used to identify the best combination of materials for the coating, upcoating and buffer.
The main goal has been to develop compact and robust sensors/sensor materials that measure pressures from 10 to 200 kPa.

2 EXPERIMENTAL

The FEM study showed that the highest sensitivity could be achieved with a thicker layer of a soft material between the fiber optics diameter (125μm) and the external buffer diameter (limited to 1mm in this study). Several materials were studied for the fiber coating, upcoating and buffering. The combination of the different materials and dimensions were evaluated and the most promising combinations were fabricated for tests.
The sensor used for this experiment was FBGs inscribed in 125μm optical fiber having either Polyimide (PI) or Acrylate (Ac) as original coating. The wavelength shift of an FBG can be related to strain, and its sensitivity is approximately 1.2 pm/μstrain. To make the FBG sensitive for pressure the optical fibers were coated with a soft up-coating layer of Silicone and a stiffer buffer material (see figure 1). The total outer diameter was 1 mm. Four different types of fibres were manufactured with combinations of the two original coating materials and two different buffer materials that were either Polyamide (PA) or Polyetheretherketone (PEEK) (see table 1). The Central Wave length (CW) for each FBG is presented in table 1.

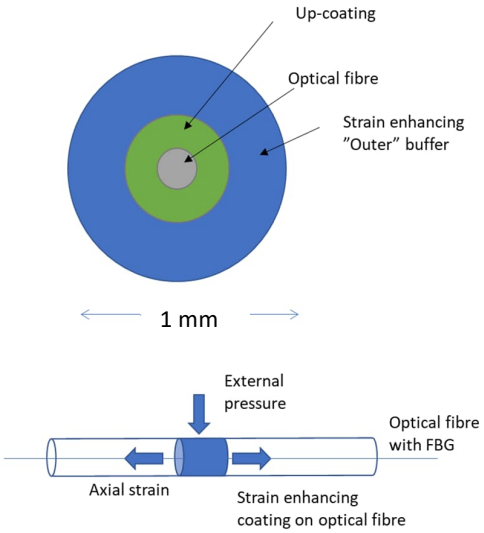

Figure 1: Principle of the pressure-sensitive fibre-optic sensor: the combination of upcoating the fibre and a buffer material changes external pressure to an axial strain. , enhancing the sensitivity to pressure.

Identification	Original Coating	Up-Coating	Buffer	Surface material	Central wave length (CW) [nm]
AC-SI-PEEK-1	Acrylate	Silicone	PEEK	Amspand	1534.79
AC-SI-Nylon-1	Acrylate	Silicone	Polyamide	Amspand	1554.4
PI-SI-PEEK-1	Polyimide	Silicone	PEEK	Amspand	1544.4
PI-SI-Nylon-1	Polyimide	Silicone	Polyamide	Amspand	1539.596
AC-SI-PEEK-2	Acrylate	Silicone	PEEK	Epoxy	1539.5
AC-SI-Nylon-2	Acrylate	Silicone	Polyamide	Epoxy	1549.315
PI-SI-PEEK-2	Polyimide	Silicone	PEEK	Only tested alone	1549.058
PI-SI-Nylon-2	Polyimide	Silicone	Polyamide	Epoxy	1534.38

Table 1: Test samples configuration coating, buffer and composite surface material.

The pressure sensitivity of the coated optical fibres was first measured for the fibres alone in a pressure chamber. In the next test step, the coated optical fibres were built into a couple of different types of surface materials on top of pre-cured 4 mm carbon fibre /epoxy (CFRP) laminates. The CFRP was built up of 7 layers of Hexcel prepreg M49/HS/600 gsm. The surface material was either a syntactic foam material (Amspand) with a 0.1 mm glass fibre/epoxy cover layer (Delta DT120/823) or 10 epoxy film layers (36 gsm Hexcel 6376 resin) with a 0.1 mm glass fibre/epoxy cover layer (see figure 2).

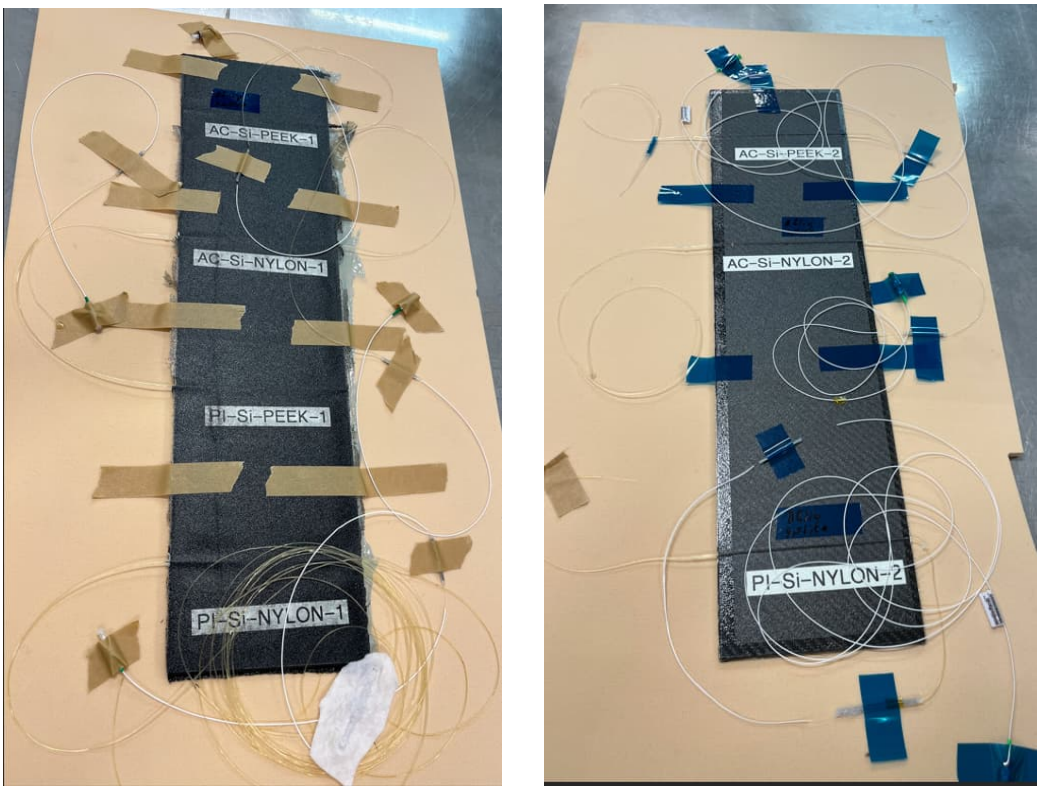

Figure 2: Fibre optics build into a) Amspand surface material b) Epoxy surface material.

The pressure response of the inbuilt optical fibres was tested in an Instron Machine (see figure 3) in load steps of 20, 40, 60, 80, 100, 200 kPa. Each load step contained a one minute hold. The pressure was calculated from the machine compression force and the pressure area.

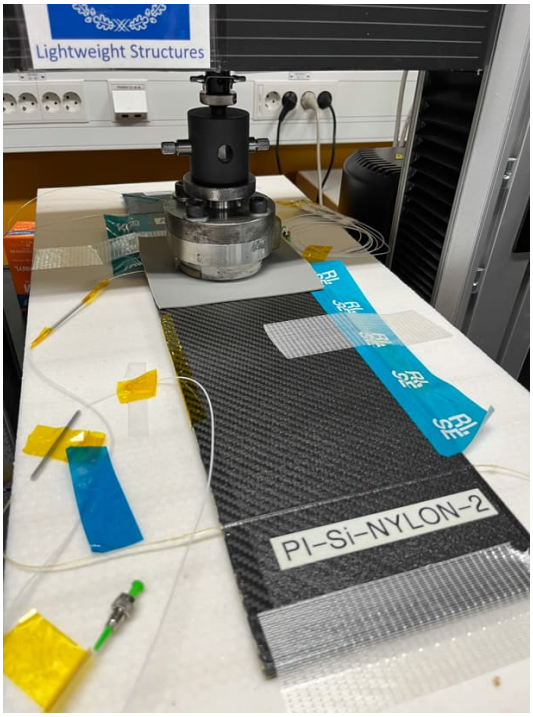

Figure 3: Test set-up in the Instron Machine.

3 RESULTS

The test in the pressure chamber of the single FBG fibres showed hysteresis during the measurements. However, the best results were obtained with the PI coated fiber with PEEK buffer. When the fibres were built into surface material on the top of CFRP laminates, and tested in the Instron Machine, the effect of the hysteresis was less pronounced. The best combination for pressure sensitivity was either to use an optical fibre with PI coating and PEEK buffer or an optical fibre with Ac coating and PA buffer, combined with the syntactic foam (Amspand) surface cover material (see figure 4).

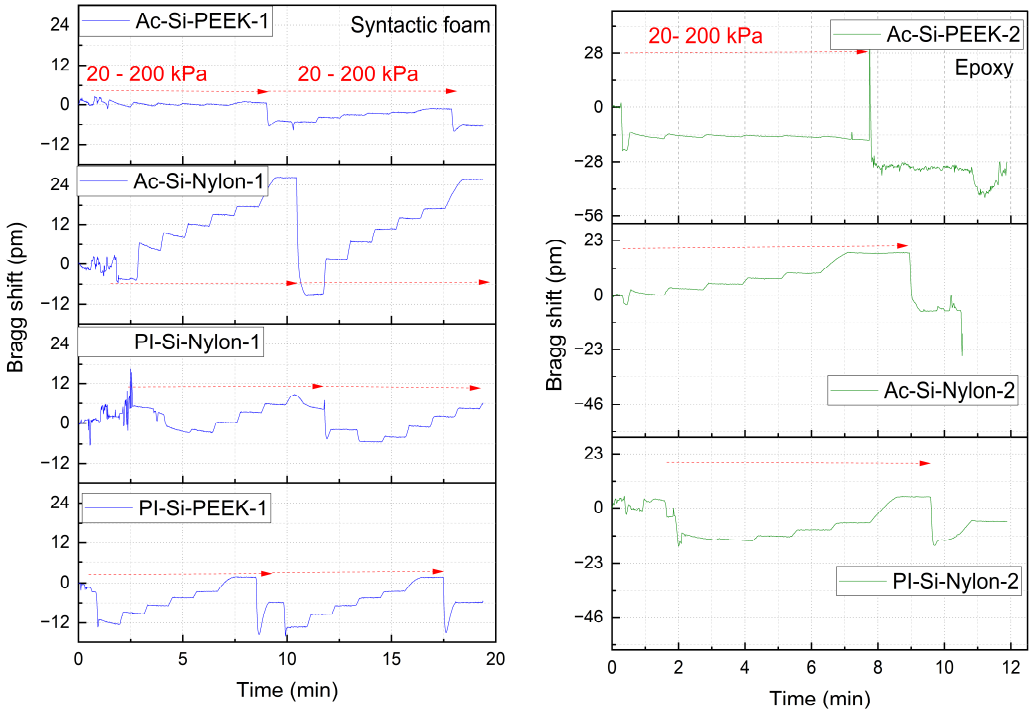

Figure 4: Results from pressure test. 1 was built into Amspand surface material and 2 was built into epoxy surface material.

3 DISCUSSIONS

the test results with the unembedded up-coated and buffered optical fibres did show hysteresis, while the laminates with embedded up-coated and buffered optical fibres, in the syntactic foam (Amspand) did not. This is not in line with a previous study that showed hysteresis when using the Amspand as a buffer material instead of PEEK or Polyamide (PA) in stand-alone measurements with the fibres. However, in the laminate configuration with optical fibres embedded into the surface material on CFRP laminate a 0.1 mm glass fibre/epoxy cover layer was also used on top of the surface material. This glass layer might have a faster recovery due to its stiffness and that might have helped the hysteresis effect to be less pronounced. The measurements of the laminates with the epoxy surface material did show less pressure response compared to the laminates with the Amspand surface material. This is not a surprise

since the epoxy material is much stiffer than the Amspand material.

9 CONCLUSIONS

The aim of this study was to use optical fibres with FBGs for quasi-distributed pressure sensors that could be embedded into surface materials for composite structures. The main goal was to develop compact and robust sensors/sensor materials that measure pressures from 10 to 200 kPa. The study showed that the best combination for pressure sensitivity was either to use an optical fibre with Polyimide coating and Polyetheretherketone buffer or an optical fibre with Acrylate coating and Polyamide buffer, combined with the syntactic foam (Amspand) surface cover material topped with a 0.1 mm glass fibre/epoxy cover layer. The study also showed that the embedded sensors was sensitive for pressure in the required pressure range.

ACKNOWLEDGEMENTS

The authors would like to thank Swedish Governmental Agency for Innovation Systems (Vinnova) through the Vinnova Lighter Strategic Innovation Program Project 2021-04042. Special thanks to Fredrik Fisk and Anna-Karin Holmér for their excellent help with discussing ideas for the fibre optical sensor solution.

REFERENCES

[1] J. B. Rosolem et al., “Electroless nickel-plating sealing in FBG pressure sensor for thermoelectric power plant engines applications,” J. Lightwave Technol. 37(18), 4791–4798 (2019).

[2] D. Kang et al., “In-situ Health Monitoring of Filament Wound Pressure Tanks using Embedded FBG Sensors,” ACCM-4, 963-968 (2004).

[3] G. Rodriguez et al., “Embedded Fiber Bragg Grating Pressure Measurement during Thermal 2 Ignition of a High Explosive,” Appl. Phys. Lett. 109, 164101 (2016).

[4] M. Liang et al., “Temperature compensation fiber Bragg grating pressure sensor based on plane diaphragm,” Photonic Sens. 8(2), 157–167 (2018).

[5] W. T. Zhang et al., “Ultrathin FBG pressure sensor with enhanced responsitivity,” IEEE Photonics Technol. Lett. 19(19), 1553–1555 (2007).

[6] J. Huang et al., “A fiber Bragg grating pressure sensor and its application to pipeline leakage detection,” Adv. Mech. Eng. 5, 1–6 (2013).

[7] S. Sebastian et al., “Highly sensitive fiber Bragg grating-based pressure sensor using side-hole packaging,” Applied Optics Vol. 58(1), 115-121 (2019).

[8] E. Chehura et al., “Pressure measurements on aircraft wing using phase-shifted fibre Bragg grating sensors,” 20th OFS 7503, 750334-1 (2009).

ICCM24 24TH INTERNATIONAL CONFERENCE ON COMPOSITE MATERIALS
AUG 4-8, 2025 • BALTIMORE CONVENTION CENTER • BALTIMORE, MARYLAND

COMPARATIVE STUDY OF GRAPHENE COATED GLASS FIBERS AND CARBON NANOTUBE FORESTS AS EMBEDDED STRUCTURAL HEALTH MONITORING SYSTEMS

Tobias Karlsson[1], Mykhailo Zhybak[2], Per Hallander[1,3] and Malin Åkermo[1]

[1] Material and Structural Mechanics, Department of Engineering Mechanics, KTH Royal Institute of Technology
Teknikringen 8, SE-100 44 Stockholm, Sweden
Email: tobiask2@kth.se, perhalla@kth.se, akermo@kth.se, web page: http://www.kth.se

[2] Grafren AB
Industrigatan 9, SE-582 77 Linköping, Sweden
Email: cto@grafren.se, web page: http://www.grafren.se

[3] SAAB AB
Bröderna Ugglas gata, SE-581 88, Linköping, Sweden
Email: per.hallander@saabgroup.com, web page: http://www.saab.com

Keywords: Graphene, Carbon Nanotube, Multifunctionality, Resistive Sensor, Embedded

ABSTRACT

In this paper, a graphene-coating on glass fiber weave has been evaluated as a multifunctional sensing material based on previous work performed by the authors on embedded vertically aligned carbon nanotube forests. First, the graphene-coating has been assessed as a resistive cure-monitoring sensor when embedded in thermosetting glass fiber/epoxy laminate to monitor its production. The graphene-coating showed similar results to the resistive cure monitoring of carbon nanotubes. However, the graphene-coating diverges in its resistive signature upon reaching cure temperature, showing a continuous resistance decrease in this phase, suggesting a sensitivity to cure-induced shrinkage of the epoxy, not seen in the carbon nanotube sensor. Later, in the cured state, the embedded graphene-coating functions as an excellent temperature sensor, possessing a negative thermoresistive effect. However, as a strain sensor, the graphene-coating does not perform as well as the embedded carbon nanotube sensor, possessing an initial drift in resistance upon its first load cycle and additional drift during constant strain conditions, and when unloaded.

1. INTRODUCTION

Fiber-reinforced composites (FRPCs) have seen increased use within the aerospace, automotive and wind turbine sectors due to their high specific modulus and strength. Together with their increased implementation, the interest in monitoring FRPC structures has increased. This includes monitoring the production of the components, performing cure monitoring, and later structural health monitoring (SHM) during their operational lifetime. To perform SHM, the possibility of monitoring strain, temperature, pressure, and more, experienced by the component is of interest.

FRPCs have the possibility to embed sensors in their structure, obtaining multifunctionality. However, when embedding a sensor into the composite structure, the sensor's size is critical to not interfere with, or deteriorate, the mechanical structure. Preferably, the embedded sensor should be mechanically non-intrusive and possess the ability to perform in-situ online cure monitoring during production of the component for quality and process control. Thereafter, in the cured state, the sensor should be used for other types of sensing, i.e. for structural health monitoring (SHM).

In parallel, new sensitive resistive sensors have been envisioned using carbon nanotubes (CNTs) and graphene-based sensors. Research using CNT-based sensors for strain [1–4] and temperature [3,5] sensing, and cure monitoring [4,6,7] has been published. Similarly, graphene-based sensors have been

studied for strain [8–13] and temperature [8,13–15] sensing and cure monitoring [6,13,16]. In these papers, using CNTs and/or graphene, the sensors have been achieved through modification of the matrix with fillers [1,5,8], fiber-coatings [4,6,13,16], vertically aligned CNT (VACNT) forests [3,7], CNT buckypapers [2], and graphene films [10–12,14,15]. Although much work has been done on graphene-based sensors, limited work exists where graphene-based sensors have been embedded into FRPCs for sensing [6,9,13,16].

In this paper, a graphene-based sensor is embedded into glass fiber/epoxy laminate and evaluated as a resistive sensor. The sensor is compared to previous work conducted by our group studying VACNT forests as embedded resistive sensors. This paper presents initial results on the sensing capabilities of the graphene-based as a 1) cure-monitoring, 2) temperature and 3) strain sensor.

2. Method

2.1 Material

In this work, the glass fiber/epoxy prepreg used was HexPly6376-G-120 from Hexcel. The HexPly6376-G-120 has a fiber volume fraction of 42 %, the weave being a 4-harness satin weave, HexForce 120. In addition, the HexPly 6376 (36g/m^2) epoxy adhesive film was used.

Two materials were used for resistive sensing. First, VACNT forests were used, grown on stainless steel substrate provided by N12 Technologies and used as received. The VACNT forest has been studied in previous work, determining the individual CNTs to contain 7±2 walls and an outer diameter of 8±2 nm. In the same work, the volume fraction of CNTs in the VACNT forest was determined to be 0.4 %; please see [3] for more details. Secondly, a graphene-coated glass fiber weave, delivered by Grafren AB, was used. See section 2.3 for more details on the graphene-coated glass fiber weave.

A copper-nickel-coated non-woven carbon fiber veil from Technical Fibre Products Ltd (Carbon 20444A, 8g/m^2) was used to establish contact with the resistive sensors.

2.2 Deposition of VACNT Forests

To embed the VACNT forest into laminates they were deposited on a prepreg surface. A vacuum bag and a heating plate were used to perform the deposition of the VACNT forest. The substrates with the VACNT forest were placed on the prepreg surface with the VACNT forest facing the prepreg surface. The prepreg was placed inside a vacuum bag, on top of a heating plate, and heated to 55°C. Upon reaching 55°C, vacuum was applied, pressing the substrate and VACNT forest into the prepreg's surface. Vacuum was held for a few seconds. Thereafter, the vacuum bag was opened and the substrates removed, leaving behind the VACNT forest deposited on the prepreg surface.

2.3 Graphene-Coated Glass Fiber Weave

Electrically conductive inks with functionalized graphene (fG) were prepared according to Grafren's patented method [17]. Graphene fG ink was a graphene containing water dispersion with high electrical conductivity (up to 10 Ω/m^2 for 1 µm thick coating). As the dispersion was water-based and free of adhesives, it could be applied to most surfaces. E-glass mats (Hexcel 7781 glass fiber weave) were tested and verified for application with this type of fG ink. The prepared ink was applied to the surface of the glass fiber using Grafren's method [18]. Each individual fiber was covered with nano-flakes of conductive graphene. After several successive surface treatment steps, a complete electrically conductive skin of flexible fG sheets was created. The flake had a nano-sized thickness and a surface spread of 1–3 µm. These overlapped with each other and developed strong bonds between the functional groups in the adjacent flakes. The surface layer thickness achieved allowed high heat and electrical conductivity in the plane and out of the plane. This surface layer will from now on be referred to as the graphene-coating.

2.4 Sample Preparation

Samples with VACNT forests and graphene-coated glass fiber were prepared. The dimensions of all samples were 30x200 in-plane. The VACNT forest samples were 20 plies in thickness, with the VACNT forest being deposited on both prepreg surfaces facing each other in the midplane. During the lay-up, contacts of Carbon 20444A veil were placed in each, exiting the sample, to permit connectivity. In a similar way, the graphene-coated glass fiber weave was placed in the midplane, with 10 plies of HexPly6376-G-120 prepregs on each side. An extra layer of HexPly6376 epoxy adhesive film was added to one of the 10-ply stacks to aid with the wetting of the graphene-coated glass fiber weave. Contacts of Carbon 20444A veil were added and then subsequently cured, see 2.5. Three samples of each type were manufactured and studied in this work.

2.5 Cure Monitoring

The curing of the samples was performed using a vacuum-bag-only method inside an oven. The used cure cycle consisted of the following steps: 30 min at 30°C, followed by a temperature increase to 180°C, using a 2°C/min heat-up. Thereafter, the temperature was kept at 180°C for 2 hours and thereafter cooling down in the oven to room temperature. Full vacuum was applied during the whole curing cycle. A SP-50 Biologic Potentiostat, applying 10 V voltage, recording the current at 1 Hz, was used to monitor the resistive behavior of the embedded VACNT forests. Metallic interconnects were used to bridge the tacky tape and vacuum bag to connect the sample to the potentiostat. Two K-type thermocouples together with a NI9212 module from National Instruments via LabVIEW were used to register the temperature during the curing. The first thermocouple was placed in the oven, monitoring its temperature, the second was embedded in the mid-plane of a separate laminate of equal material and thickness as the samples, to measure the temperature at the placement of the resistive sensors.

2.6 Temperature Sensing

After curing, the samples were exposed to a temperature cycle to study their thermoresistive response. The test was performed using a ACS FM340C climate chamber. The climate chamber was programmed to decrease from 30°C to -70°C at 2°C/min and maintain -70°C during 15 min. Thereafter, the temperature increased 2°C/min to 150°C and was then maintained for 15 min. Lastly, the temperature decreased 2°C/min to 0°C. The resistance and temperature data were recorded as described in section 2.5.

2.7 Strain Sensing

The manufactured samples' piezoresistive response was evaluated performing quasi-static tensile testing together with continuous measurement of the sample's resistance. An Instron 4505 electromechanical tensile test machine was used for tensile testing together with a surface-mounted extensiometer to measure the sample-strain. The samples were loaded 100 N/s, up until 0.5 % strain was reached, staying in the elastic region of the sample. The 0.5 % strain was maintained for 30 seconds, then unloaded with the same speed. This cycle was repeated for each sample 5 times. To perform resistive measurements, the SP-50 Biologic Potentiostat was used to record the current at a constant 10 V voltage using a sampling rate of 10 Hz.

3. Results and Discussion

In this work, the focus is evaluating the performance of the graphene-coating as a multifunctional sensor. This evaluation is based on previous work performed by the authors on VACNT forests for the same applications, namely, cure monitoring [7], and strain and temperature sensor [3].

3.1 Curing

To evaluate the cure monitoring capability of the graphene-coating, a previously established procedure for assessing the VACNT forest's capability has been used. The cure cycle has been divided into phases, based on the cure cycle's temperature. First, phase I is the initial 30 minutes under vacuum at 30°C. Phase II is the heat-up to curing temperature, which has been divided into two parts in [7] due to the significant resistive shift. The third phase corresponds to the time spent at the curing temperature.

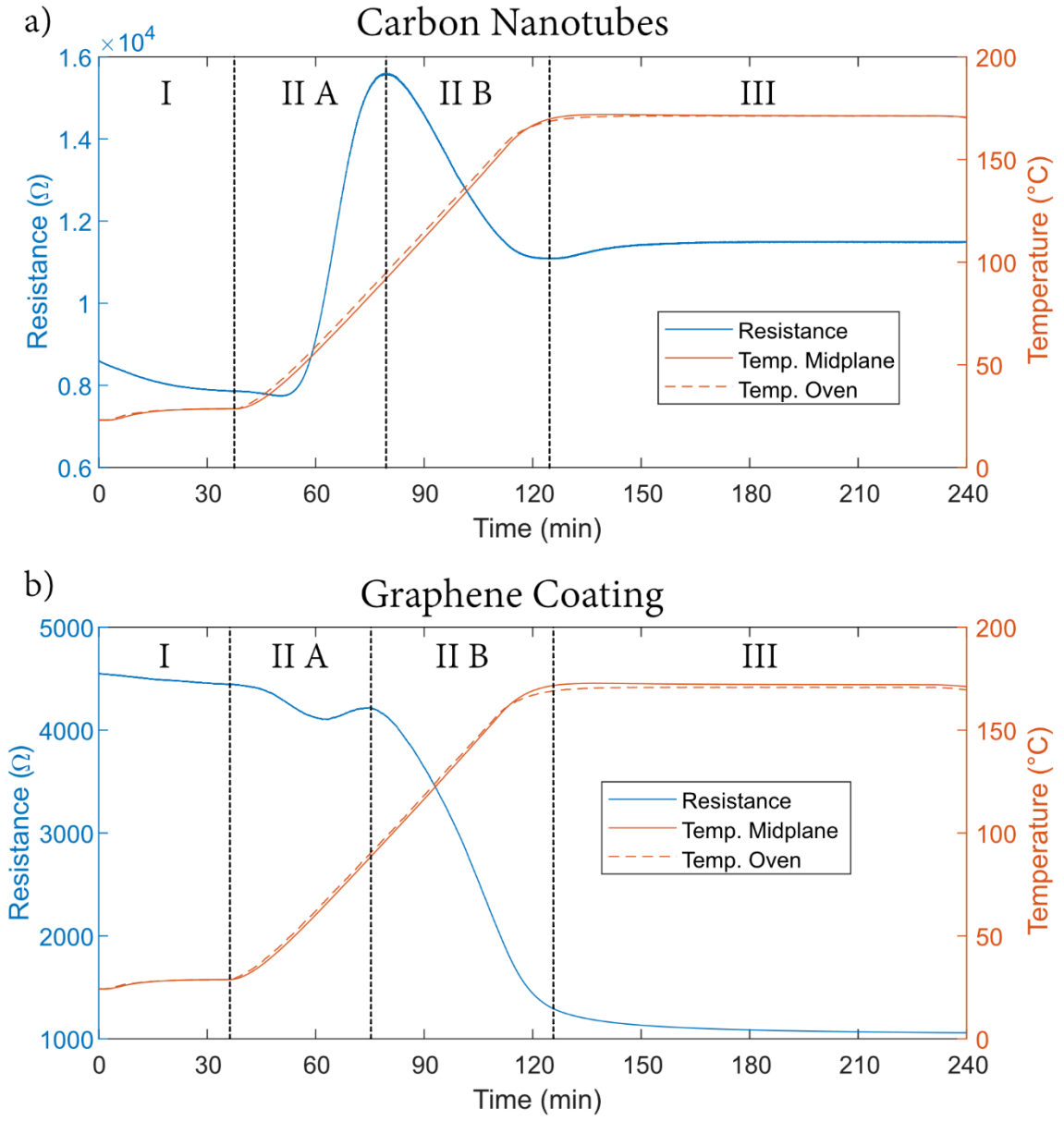

Figure 1: Resisitive cure monitoring of a) embedded CNTs b) graphene-coated glass fibers.

The decreasing resistance in phase I in Fig. 1a is caused by the consolidation of the laminate, the two VACNT forests in the midplane getting into better contact with each other, in addition to the slight increase of temperature to 30°C, both contributing to a lower resistance. In Fig. 1b, a small resistance decrease is also observed. Here, no significant impact of the consolidation is expected on the graphene coated on the glass fiber weave. Rather the slight resistance decrease is believed to be caused by the slight temperature increase, graphene having a negative thermoresisitive effect [13]. In phase II A, Fig 1a, as the heat-up commences, there is first a slight decrease in resistance. This is, again, caused by the

temperature increase, before the viscosity of the prepreg's epoxy is lowered enough to fill the interspace between the embedded CNTs, causing the dramatic resistance increase seen later in phase IIA in Fig. 1a. In Fig. 1b, there is also an initial resistance decrease, which is also reasonably caused by the temperature increase. However, the resistance decrease is lasting into higher temperatures using the graphene-coating than the embedded CNTs. At around 62 min, the resistance turns around and increase slightly until reaching 90°C. We believe this is also caused by the partial infiltration of the epoxy into the graphene-coating. However, the graphene structure's epoxy infiltration is not expected to be as significant as for CNTs, only achieving partial infiltration as presented in [6], explaining the relatively low resistance increase observed in Fig. 1b compared to in Fig. 1a. Later, in phase II B, the resistance decrease in Fig. 1a was determined to be caused by the thermoresisitve effect, decreasing as the temperature increased. The cure-induced shrinkage measured in [7] was concluded not to affect the resistive behavior directly. This is due to the resistive behavior observed in phase III, where the resistance increases, rather than decreases. A resistance decrease would have been expected if the embedded CNTs were significantly affected by the cure-induced shrinkage, resulting in a shorter inter-CNT distance. However, in Fig. 1b, the resistance decreases continuously. Initially, this is reasonably caused also by the thermoresistive effect, until approaching the cure temperature and phase III. Observing the resistance evolution over phase III for the graphene-coating, we observe a continuous resistance decrease over the whole phase, even though the temperature is stable. This may indicate a sensitivity to cure-induced shrinkage, which becomes more pronounced from 160° C, up until ca 15 minutes into the curing temperature, after that, it continues over its whole duration, but at a slower rate. Even though the epoxy infiltration is expected to be less significant in the graphene-coating than the embedded CNTs, the shrinkage of this epoxy is believed to still affect the resistive behavior. Similar observations have been made in [6].

3.2 Temperature Sensing

The thermoresistive response of representative samples of a) embedded CNTs and b) graphene-coated glass fiber weave is presented in Fig. 2 below.

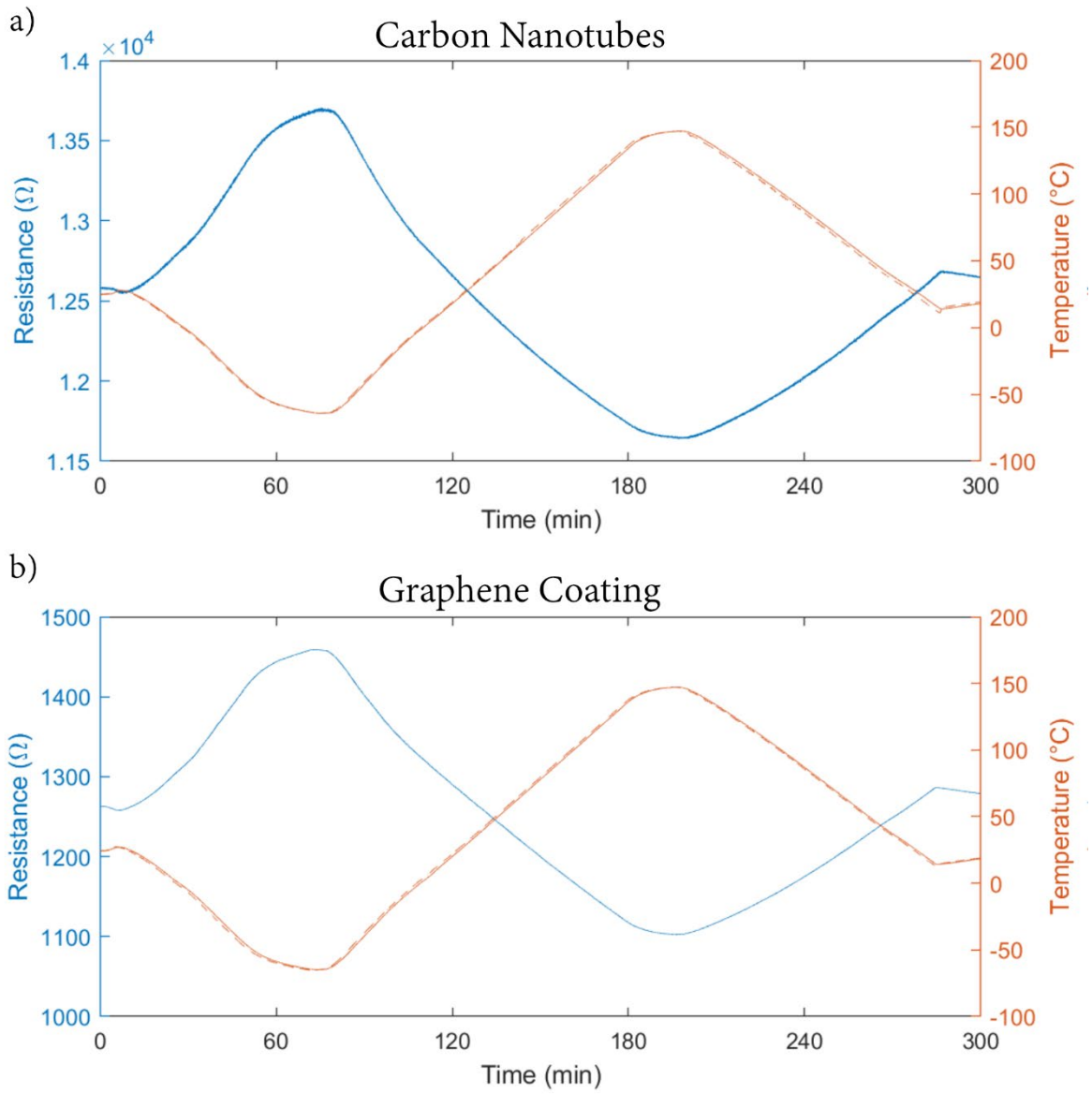

Figure 2: Thermoresisitve response between -70°C and 150°C for a) embedded CNTs and b) graphene-coating.

In both figures, it is obvious that the studied sensors have a significant resistive sensitivity to changes in temperature. The resistive signatures of the two sensors are close to identical, both having a negative thermoresistive effect, i.e. resistance decreasing as a response to a temperature increase.

3.3 Strain Sensing

The piezoresistive response of the two studied sensors is presented in Fig. 3. Fig. 3a presents the resistive changes observed for an embedded VACNT sensor, and Fig. 3b the resistive changes for the graphene-coated glass fiber weave.

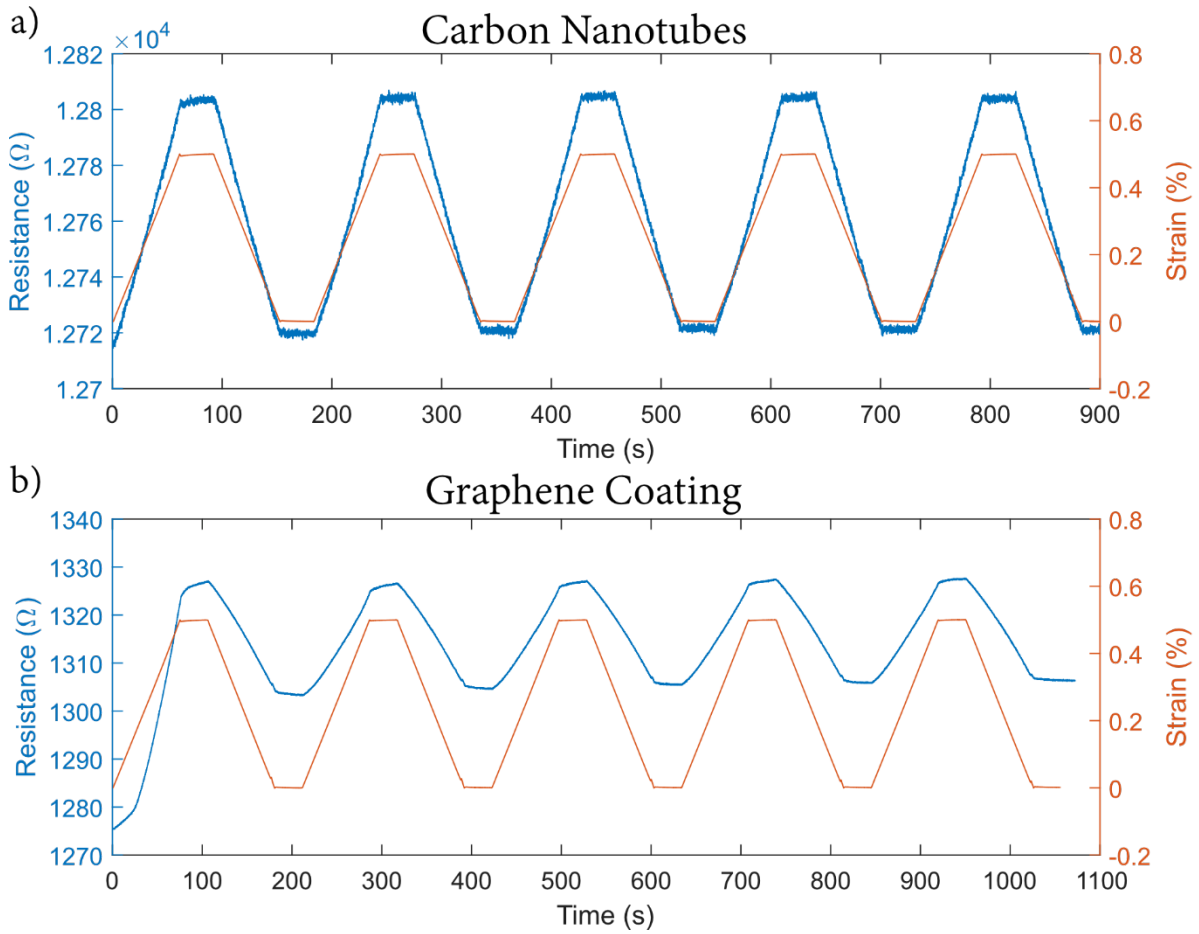

Figure 3: Resistive strain sensing of a) embedded CNTs and b) graphene coating.

First studying Fig. 3a, a linear piezoresistive response to the strain is observed. The resistance is stable during the holds at 0.5 % strain, and when off-loaded, no resistance drifting is observed. This pattern is repeated over the five repetitions. Our previous work [3], showed that the piezoresistive effect of individual CNTs collectively produce the observed piezoresistive response seen here. Looking at the piezoresistive response of the graphene-coated glass fiber weave, Fig. 3b, a large resistance shift is observed in the first load-cycle, the sample's resistance not returning to its original value once off-loaded. However, the following load-cycles are repetitive, indicating the initial behavior to be a one-time occurrence, at least for this specific load-cycle. No explanation for this resistive behavior of the graphene-coating samples is presented in this work, requiring further studies. During the 0.5 % strain holds, the graphene-coating shows a resistance drift, the resistance increasing over time. This is similarly observed when off-loaded, the resistance decreasing slightly. Again, to determine why this resistive behavior is present more work is required. However, the authors suspect the nature of the epoxy infiltration into the graphene-coating on the glass fiber weave to be a cause of this, and plan to investigate this further in future work, and also the adherence of the graphene-coating to the individual glass fibers.

5. Conclusions

In this paper, the suitability of a graphene-coating on glass fiber weave as a multifunctional sensor is evaluated and compared to previous work performed by the authors on embedded VACNT forests. The graphene-coating has been evaluated as a cure-monitoring sensor when embedded in thermosetting glass fiber/epoxy laminate to monitor its production. The graphene-coating showed similar results to the cure monitoring of CNTs, the resistance being sensitive to its surrounding temperature and also believed to respond to partial epoxy infiltration of its structure. However, the graphene-coating diverges from the CNT sensor when kept at cure temperature, showing a continuous resistance decrease in this phase. This

possibly indicates a sensitivity to cure-induced shrinkage of the epoxy, which infiltrated the graphene structure earlier in the cure cycle. Later, in the cured state, the embedded graphene-coating functions as an excellent temperature sensor, possessing a negative thermoresistive effect. However, as a strain sensor, the graphene-coating does not perform as well as the compared-to embedded CNT sensor, possessing an initial drift in resistance upon its first load cycle and additional drift during constant strain conditions at 0.5 % strain, and when unloaded.

ACKNOWLEDGEMENTS

The authors would like to express their gratitude to Erik Khranovskyy and Mykhailo Zhybak at Grafren AB for developing and delivering the studied graphene-coating within the 2DTech project, and also the Swedish Governmental Agency for Innovation Systems, Vinnova, funding the 2DTech project.

REFERENCES

[1] Sanli A, Benchirouf A, Müller C, Kanoun O. Piezoresistive performance characterization of strain sensitive multi-walled carbon nanotube-epoxy nanocomposites. Sens Actuators A Phys. 2017;254:61–8.

[2] Rein MD, Breuer O, Wagner HD. Sensors and sensitivity: Carbon nanotube buckypaper films as strain sensing devices. Compos Sci Techno. 2011;71(3):373–81.

[3] Karlsson T, Hallander P, Liu F, Poot T, Åkermo M. Sensing abilities of embedded vertically aligned carbon nanotube forests in structural composites: From nanoscale properties to mesoscale functionalities. Compos B Eng. 2023;255:110587.

[4] Luo S, Obitayo W, Liu T. SWCNT-thin-film-enabled fiber sensors for lifelong structural health monitoring of polymeric composites - From manufacturing to utilization to failure. Carbon N Y. 2014;76:321–9.

[5] Lasater KL, Thostenson ET. In situ thermoresistive characterization of multifunctional composites of carbon nanotubes. Polymer. 2012;53(23):5367–74.

[6] Wang G, Wang Y, Luo Y, Luo S. Carbon nanomaterials based smart fabrics with selectable characteristics for in-line monitoring of high-performance composites. Materials. 2018;11(9):1677.

[7] Karlsson T, Dutta A, Hallander P, Åkermo M. In-situ cure monitoring of structural composite by embedment of vertically aligned carbon nanotube forests. Compos B Eng. 2025 Mar;293:112105.

[8] Han S, Chand A, Araby S, Cai R, Chen S, Kang H, et al. Thermally and electrically conductive multifunctional sensor based on epoxy/graphene composite. Nanotechnology. 2020;31(7).

[9] Groo LA, Nasser J, Zhang L, Steinke K, Inman D, Sodano H. Laser induced graphene in fiberglass-reinforced composites for strain and damage sensing. Compos Sci Technol. 2020;199(March):108367.

[10] Chun S, Choi Y, Park W. All-graphene strain sensor on soft substrate. Carbon N Y. 2017 May 1;116:753–9.

[11] Yokaribas V, Wagner S, Schneider DS, Friebertshäuser P, Lemme MC, Fritzen CP. Strain gauges based on CVD graphene layers and exfoliated graphene nanoplatelets with enhanced reproducibility and scalability for large quantities. Sensors (Switzerland). 2017;17(12):1–17.

[12] Liu Q, Chen J, Li Y, Shi G. High-Performance Strain Sensors with Fish-Scale-Like Graphene-Sensing Layers for Full-Range Detection of Human Motions. ACS Nano. 2016;10(8):7901–6.

[13] Luo S, Liu T. Graphite nanoplatelet enabled embeddable fiber sensor for in situ curing monitoring and structural health monitoring of polymeric composites. ACS Appl Mater Interfaces. 2014 Jun 25;6(12):9314–20.

[14] Sehrawat P, Abid, Islam SS, Mishra P. Reduced graphene oxide based temperature sensor: Extraordinary performance governed by lattice dynamics assisted carrier transport. Sens Actuators B Chem. 2018;258:424–35.

[15] Liu G, Tan Q, Kou H, Zhang L, Wang J, Lv W, et al. A flexible temperature sensor based on reduced graphene oxide for robot skin used in internet of things. Sensors (Switzerland). 2018;18(5).

[16] Ali MA, Umer R, Khan KA, Samad YA, Liao K, Cantwell W. Graphene coated piezo-resistive fabrics for liquid composite molding process monitoring. Compos Sci Technol. 2017;148:106–14.

[17] Khranovskyy E., Zhybak M., inventors; Grafren AB, assignee. Method for redistributing a flake material into at least two flake size fractions. Swedish Patent SE 543430C2. 2021-02-16.

[18] Khranovskyy E., Zhybak M., inventors; Grafren AB, assignee. Method for inserting 2D flakes of a two-dimensional material into pores of a porous substrate and a porous composite material. Swedish Patent SE 544448C2. 2022-05-31.

REAL TIME MONITORING OF COMPOSITE LAMINATED STRUCTURES WITH EMBEDDABLE SENSING LAYERS

J.Correia[1], H.Rocha[2], R.Alves[2], B.Sousa[2], J.P.Nunes[1] , J.C. Viana[1]

[1]IPC/LASI, Instituto de Polímeros e Compósitos/Laboratório Associado em Sistemas Inteligentes, Universidade do Minho, Campus de Azurém, 4800-058 Guimarães, Portugal – joao.manuel1234@outlook.pt, https://www.ipc.uminho.pt/pt-pt
[2]PIEP, Polo de Inovação em Engenharia de Polímeros, Universidade do Minho, Campus de Azurém, 4800-058 Guimarães, Portugal, https://www.piep.pt

Keywords: Composite materials, Structural Health Monitoring, Embeddable monitoring layer, Strain gages

ABSTRACT

Fiber reinforced composite materials are currently essential for several engineering applications that need to combine high mechanical properties with very low structural weight. However, due to their heterogeneous composition, the failure mechanisms in composites are still very unpredictable, unlike that happens with steel or aluminum [1]. This leads to the need of applying real-time monitoring techniques in composites, through the incorporations of appropriated sensors into them, in order to ensure their safely work in service. This work presents a new layer concept to be embedded within carbon fiber reinforced polymer (CFRP) composite laminated structures, capable of real-time monitoring of their strain status. It contains strain gauges (SG) that can measure the evolution of strains in the internal laminae of structural composites and an electric circuit directly printed on its surface to transmit the data obtained to an acquisition system for further processing and analysis. Bulk CFRP/epoxy samples and equivalent ones containing embedded sensing film and regular polyimide films are submitted to interlaminar shear strength and tensile testing. With the former, it was possible to assess eventual effects on the adhesion between the layers of the composite, while the latter were used to evaluate the influence of the embedded film on the mechanical properties. Moreover, by placing an equivalent surface mounted SG, it was possible to directly compare strain data from the surface and the interior of the composite, thereby serving as validation method for the sensing circuit. The experiments carried out demonstrated that the proposed embedded sensing film allowed indeed accurately monitoring the internal strains developed within composites. Additionally, it was observed that the inserted embedded monitoring layers did not affect significantly the adhesion and mechanical properties of the CFRP composites, unlike what happened with the embedded polyimide layers.

1 INTRODUCTION

The application of composite materials has seen a significant increase in recent decades in several engineering fields, continuously replacing traditional metals such as steel or aluminum. Due to their high strength-to-weight ratio, achieved by combining high mechanical properties fibers with matrices capable of ensuring an efficient stress distribution, the production of parts and structures with high mechanical properties at low structural weights is achieved by multiple manufacturing techniques. In comparison to metals, this means that the mechanical performance is either equal or improved at more reduced fuel consumption and CO_2 emissions as well [2].

One of the issues of composites is the difficulty in predicting their mechanical performance and failure mechanisms at the loading conditions they need withstand by design, because of their inherent heterogenic and anisotropic nature. In addition, polymer matrix composites are sometimes brittle, which makes even more difficult predicting their in-service failure due to the high number of mechanisms involved in this process. It is of particular concern in aeronautic and aerospace applications that composites are also prone to barely visible impact damage (BVID), in which certain low-velocity

impacts caused by relatively small masses, can lead to delamination, fissures or even cracks in the composite laminate [1].
An increasing number of research has been carried out concerning these issues using structural health monitoring (SHM) solutions. Among them, the most auspicious monitoring concepts use built-in structural diagnostic systems containing a sensing network, integrated hardware and software to read and analyze the collected data in real-time during the service life of the composite structure. This is the main idea behind the use of "Embeddable monitoring layers" (EML), which are essentially thin flexible layers with sensing networks for being embedded, as additional layer between structural composite laminae, which are capable of monitoring and transmitting in real-time data regarding the current state of the host structure. When working with composites it is advisable to have such sensors embedded within their inner structure, as it is closer to internal damage sources, which are easier to detect due to the enhanced sensitivity caused from the stronger coupling with the structure [1, 3, 4]. Other advantages include the shielding from environmental factors [5], monitoring throughout the entire lifespan of the structure [6], noise reduction [7], less complexity due to the removal of wiring [8] and surface profile integrity preservation, which is extremely important in aeronautic applications, as aerodynamic efficiency is one of the critical design constrains [9].
It is also worth noting that embedding monitoring devices or sensing films increase the overall complexity of the manufacturing process of composites, mostly regarding difficulties in adhesion and incompatibility between the materials that are being embedded and the surrounding structural layers of the composite. When not properly addressed, the final part or structure could be more susceptible to the occurrence of geometrical defects, namely delamination or increased number of voids in the composite, which affect negatively the overall mechanical performance of the composite structure [10, 11].
This paper presents the development and validation of a new concept for EML to be inserted within CRFP laminated structures, for strain monitoring purposes. The novelty lies in the substrate of the film itself, which is a cured thin strip of epoxy resin, equal to that of the matrix of the composite, to prevent issues with delamination [12] in the interface between the EML and the adjacent structural layers. The experimental work was focused on the development of the EML by using vacuum bag infusion (VBI). Tensile tests are then carried out on bulk CFRP samples and the equivalent ones containing embedded EMLs and regular polyimide (PI) films, in order to verify the performance of the sensing circuit and to evaluate the influence of the inserted sensing films on the mechanical performance of composites. Another group of samples was submitted to ILSS tests to assess the overall adhesion properties. Comparisons are traced out between EML and PI films, as the latter is a very popular substrate used in the design of flexible sensing circuits, and has been embedded in composite materials for monitoring purposes [6, 13, 14].

2 EXPERIMENTAL PROCEDURE

2.1 Materials and methods used for manufacturing the embeddable monitoring layers (EML)

The development of a new EML for internal strain monitoring to apply in polymer reinforced composite materials is presented. Its substrate is meant to be equal to that of the matrix of the composite laminate in which it is going to be inserted into, to achieve compatibility between the matrix of the composite and the EML itself. In this experimental work, the following epoxy resin is used for both of the aforementioned ends:

- Sicomin SR Infugreen 810 resin mixed, at mass fraction of 29%, with the SD4771 hardener.

The EML substrate is obtained by VBI, under the following procedure:

- After mixing the resin with the hardener, it should be impregnated, under vacuum, to the interior of a sealed bag that contains the mold of the film, as shown in Figure 1;
- The mold is composed of two glass plates, with Teflon layers to facilitate demolding, that are vacuum sealed inside a bag, with no observable air leaks. The resin flows between the two glasses, due to the prior application of layers of thin tape on one of the glasses. This ensures that

there is a cavity between the glasses from which the resin can slowly flow and form the film with the desired thickness. For this set of experiments, two layers of 50 µm non-absorbent tape were placed on the edges of a single glass in order to later obtain thin epoxy resin films with 100 µm of thickness;

- The resin fully cures after two days at room temperature. However, at this point, the epoxy resin is very brittle, and there is a serious risk of shattering the film when separating glass. Thus, the separation process needs to take place before the resin is completely cured. Multiple tests with the resin demonstrated that the glasses should be separated approximately 30 hours after resin impregnation. These values are of course completely dependent on the type of resin or matrix that is being utilized to fabricate the films;
- Upon separation, the thin epoxy film is sticked on the glass that contains the reference tape.



Figure 1 - VBI arrangement to manufacture the thin epoxy resin

The sensing circuit used in this work was designed for strain monitoring. It consists on a single bi-directional SG (Omega, model SGT-4/350-XY41 – with 350 Ω base resistance, 2.09 gauge factor and 30000 µm maximum strain), 4 manually screen printed silver ink (Dyoctec, model DM-SIP-2004) conductive tracks used to transmit strain data and 4 soldering terminals (HBM, model 1-LS4-G), from which it is possible to relay the strain data to an acquisition system capable for post-processing and analysis. The circuits can be directly mounted in the epoxy substrate, and since the Ag ink needs to undergo curing at temperatures between 80 and 150 °C, the latter must still be attached to the glass, otherwise, the thin epoxy structure deforms irreversibly. Finally, the film can be detached from the glass plate, thus finalizing the manufacturing of the EML, as shown in Figure 2 a). The main characteristics of the film are its transparency, its low thickness, which was set at 100 µm, and its high flexibility, as can be seen in Figure 2 b).

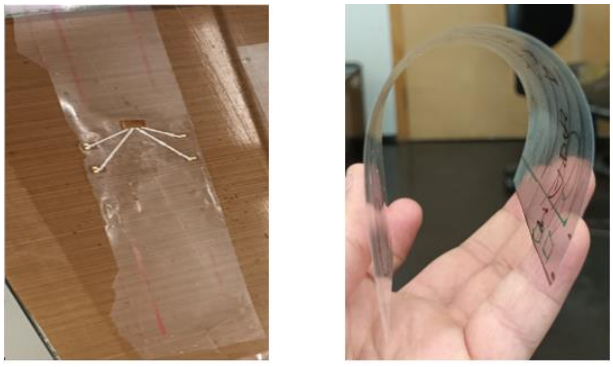

a) b)

Figure 2 - Epoxy substrate EML: a) view with SG sensing circuit; b) EML flexibility

2.2 Manufacture of CFRP samples

The EML was embedded in composite laminates and the manufactured samples were submitted to tensile and ILSS tests. In both experiments three groups of CFRP samples were compared: G1 containing

bulk CFRP samples with no embedded films, G2 including CFPR with embedded EML and G3 having CFRP samples with embedded a PI sensing films.
For both tests, the following sequences for each group of samples were adopted:

- G1 Tensile test (G1-T) sample configuration – $[0]_{3s}$
- G2 Tensile test (G2-T) sample configuration – [0/0/0/EML/ISO/0/0/0/]
- G3 Tensile test (G3-T) sample configuration – [0/0/0/PI/ISO/0/0/0]
- G1-ILSS sample configuration – $[0]_{4s}$
- G2-ILSS sample configuration – [0/0/0/0/EML/ISO/0/0/0/0]
- G3-ILSS sample configuration – [0/0/0/0/PI/ISO/0/0/0/0]

The CFRP laminates were manufactured through VBI, in which each individual layer is stacked on a mold that is subsequently vacuum sealed, and then impregnated with epoxy resin and left to cure for approximately two days at room temperature. The structural layers were obtained from unidirectional carbon fiber fabric 350 UT from Rebelco, with areal weight of 350 g/m^2, and for the specimens that contain PI sensing films, Kapton variant model 300 MT from DuPont, with 0.075 mm of thickness is used. To safeguard the electric circuit from adjacent conductive carbon layers, an additional thin strip of epoxy resin (reference ISO), obtained from the same procedure that is described in section 2.1, is placed on top of the circuit.

The tensile test samples were prepared accordingly ASTM D3039/D3039M standard, while the ones for ILSS ones followed the procedure of ISO 14130:1997 standard. However, to ensure that the internal strain data is being collected from the samples with EML and PI sensing films that are submitted to tensile testing, it was necessary to slightly increase their width. To avoid deformation on these films during the manufacturing process, the width of the structural layers that are placed beneath should likewise be the same. Figure 3 presents a manufactured stacked laminate prior to the addition of the sensing system. As ILSS testing is only conducted to verify the adhesion properties of the laminates, even if these contain embedded sensing films, the data will not be recorded, and all layers, both structural and sensitive, will have the same dimensions. Overall, 60 test specimens were manufactured, belonging 10 to each of the six groups. The dimensions of all manufactured samples are presented in Table 1.



Figure 3 - Stacking sequence used for manufacture of CFRP tensile test specimens with EML

Table 1 - Dimensions for ILSS and tensile test subjects

Sample group	Length (mm)	Width (mm)	Thickness (mm)
G1-T	250	25	2.44 ± 0.0583
G2-T			2.49 ± 0.0772
G3-T			2.46 ± 0.0756
G1-ILSS	27.5 ± 0.5	13.75 ± 0.25	2.75 ± 0.05
G2-ILSS	30.5 ± 0.5	15.25 ± 0.25	3.05 ± 0.05
G3-ILSS	28.2 ± 0.4	14.4 ± 0.2	2.82 ± 0.04

All the samples submitted to tensile tests will contain a single conventional SG (equal to the ones present in EML and PI sensing films) mounted on their surfaces. By comparing the obtained strain data between G1-T, G2-T and G3-T it is possible to assess the effect of the embedded resin layers and PI layers,

present in G2-T and G3-T respectively, on the tensile properties of the CFRP samples. On the other hand, the comparison between internal strains and external strains can be used to validate the sensing performance of EML. Representative ILSS and tensile test specimens are shown in Figure 4.



a) b) c) d)

Figure 4 – Examples of final test samples: a) CFRP specimen with EML for tensile test; b) CFRP specimen with embedded PI film for tensile test; c) Bulk CFRP samples for ILSS tests; d) CFRP samples with EML for ILSS testing

3 RESULTS AND DISCUSSION

3.1 Results and discussion

Composite specimens belonging to groups G1-T, G2-T and G3-T, each representative of a specific condition, were submitted to tensile testing in a MTS Criterion model 45 universal testing machine at a crosshead velocity of 2 mm/min, using a load cell of 250 kN, and 180 mm as initial distance between grips. The SGs used in this work contain two grids, allowing the simultaneous measurement of both longitudinal and transversal displacements and the determination of the Poisson´s ratio (ν_{12}), alongside the Young´s modulus of the composite in the longitudinal (E1) and transverse directions of the fibers, depending on the orientation of the fabric layers of the samples used in the tensile tests.

3.1.1 EML internal circuit validation

To validate the EML strain monitoring mechanism, the respective internal data was compared with the corresponding one obtained from surface SG. Figure 5, for sample reference G2-T3, shows the stress/strain curves (Figure 5 a)), derived from longitudinal strain data, and transversal strains (Figure 5 b)), respectively.

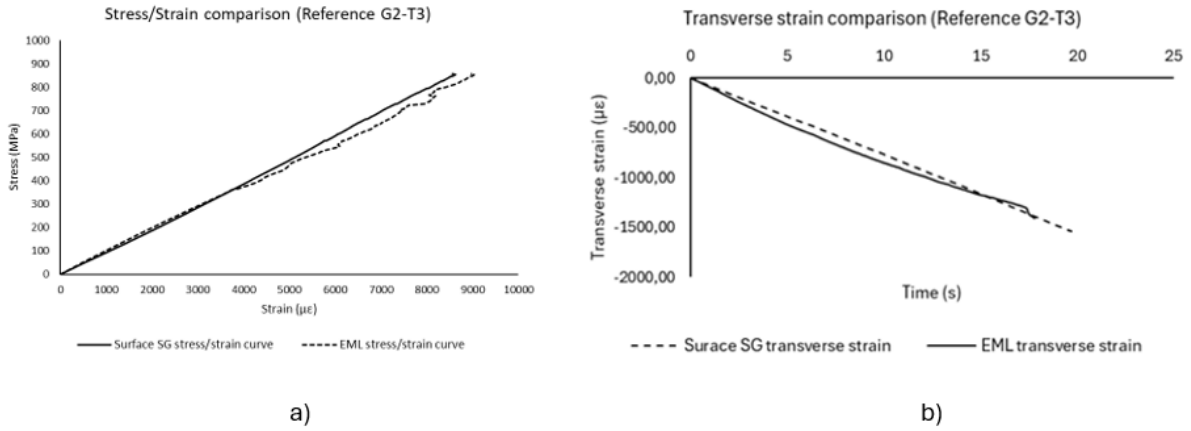

Figure 5 - Comparison between EML mechanism and conventional surface SG during tensile test on sample referenced G2-T3: a) Stress/Strain curve; b) Transversal strain

As can be observed in Figure 5 a), the evolution of stress during the tensile tests is extremely alike considering strain data of both EL and conventional SG sensing methods. The slight differences that are observed starting from 4000 με can be attributed to the fact that both SGs are measuring strains in different surfaces, with the internal SG from the EML measuring the deformation of the embedded epoxy substrate, while the external one is monitoring directly on the carbon surface. Other factors, such as the different location of the sensors in the laminate, potential contamination of the internal tracks with the impregnated epoxy, eventual deformations imposed on the printed ink during the tensile test and the different conductors that are used (metal cables for the conventional surface SG and conductive silver ink for the embedded SG), which may have different associated electrical resistivity, can potentially contribute to the small observed deviations between both sensors. When comparing the linearity of both data sets with the Pearson correlation coefficient, a matching of ≈ 99.83% is obtained indicating very good match. E_1 was calculated in accordance with ASTM D3039/D3039M in which its value corresponds to the slope of the stress/strain curve between strains of 1000 με and 3000 με. For the G2-T3, the measured E_1 from the surface was 96.72 GPa, while the one calculated with data from EML was 95.43, amounting to a final error of 1.3% between the two sensing mechanisms. Overall, considering all the CFRP samples, the average longitudinal moduli measured with EML was 97.6 GPa ± 4,74, while in the surface a mean value of 100 GPa ± 0.105 was determined, with a very small corresponding error of 4.21 ± 2.66, attesting for rather satisfactory performance of the internal strain monitoring mechanism.
Likewise, transverse strains could also be measured with a certain degree of precision with EML, as can be observed in Figure 5 b). These values are negative, since the samples under tensile test tend to shrink, alongside the respective internal and external mounted SGs. Using transverse strains between 1000 με and 3000 με it is possible to calculate ν_{12} with the data from the EML and the surface mounted SG, obtaining, respectively, 0.34 ± 0.0396 and 0.29 ± 0.0425, which translates to an error of approximately 14.7%. This larger error is expected since strain in the transverse direction is more dependent on the behavior of the matrix, which is more susceptible to variability due to matrix cracking or fiber-matrix. Furthermore, considering that the SGs are placed in different locations and measuring strains in different surfaces, with the one from EML being mounted on a flexible epoxy layer, a higher deviation between the external and internal transverse strain may not be fully unexpected and could explain the slight higher deviation of ν_{12} in relation with E_1.

3.1.2 Tensile properties of CFRP laminates with EML

Upon verifying the performance of embedded SG sensing circuits in CFRP composites laminates, it was necessary to verify just how does EML affects the mechanical behavior of the host structural composite. This comparison was made by studying thirty CFRP laminated samples, distributed equally across three different conditions (G1-T, G2-T and G3-T), with all of them containing a surface mounted bi-axial SG for the determination of E_1 and ν_{12}. The results from the tensile tests are presented in Table 2.

Table 2 - Final values of E_1, ν_{12} and ultimate tensile strength for different CFRP tensile test sampling groups.

CFRP sample group	E_1 (GPa)	ν_{12}	Ultimate tensile strength (MPa)
G1-T	105 ± 3.98	0.301 ± 0.0398	925 ± 60.4
G2-T	99.1 ± 4.83	0.311 ± 0.0525	875 ± 8.85
G3-T	96.8 ± 3.08	0.312 ± 0.0650	808 ± 54.5

The insertion of both EML and monitoring PI films has seemingly minimal effect on E_1 and ν_{12} values. When comparing the average E_1 obtained from samples belonging to G2-T and G3-T groups with the control group G1-T, the modulus decreases, respectively, 5.62% and 7.81%. Comparing G1-T with G2-T and G3-T regarding the obtained average values for ν_{12}, it can be attested that the latter increases 3.32% and 3.65%, respectively. The differences between the analyzed groups of CFRP laminates seem to be more noticeable when analyzing the ultimate tensile strength, where, in comparison with the control group G1-T, samples from G2-T showed a reduction in this parameter of approximately 5.41%, whereas the ones belonging to G3-T exhibited a decrease around 12.65%. Since the substrate of the monitoring technique is the only testing parameter that is different across the three types of samples, it can seemingly be attested that while the monitoring technique itself may exert reduction of the mechanical properties of CFRP composites, these effects may be dampened with the application of the epoxy layer substrate corresponding to the material used as the matrix.

The results demonstrated in Table 2 can be better understood through the visualization of representative stress/strain curves in Figure 6, where, once again, it seems that the introduction of the embedded monitoring layer in CFRP laminates does not significantly affect E_1 and ν_{12}, as the slopes for all three curves, calculated for strains between 1000 με and 3000 με, is nearly coincident.

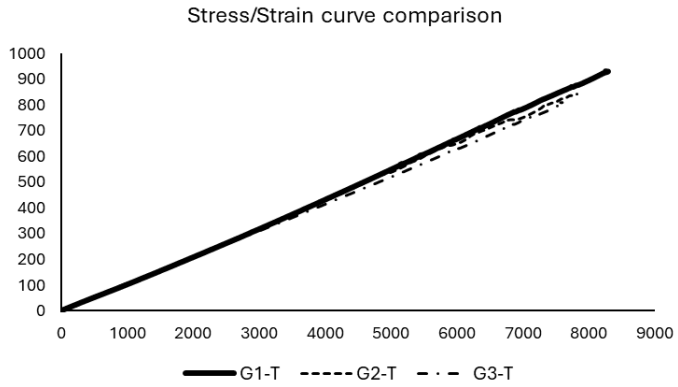

Figure 6 - Comparison of Stress/Strain curves obtained for the different CFRP sampling groups

Slightly higher differences are observed as the tensile samples approach their respective ultimate tensile strength, where it is possible that the inclusion of the SG monitoring circuits could be the main factor in the reduction of this parameter in CFRP laminates belonging to both groups G2-T and G3-T. The advantage in using the proposed epoxy substrate for the EML, regarding the mechanical properties, could be the usage of the thin epoxy film itself, where the latter can sustain slightly higher tensile stress, with the average maximum stress obtained for G2-T being approximately 7.65% higher than the one observed in G3-T CFRP samples.

3.2 Interlaminar shear strength test

One important aspect that must be assessed when inserting the EML inside CFRP laminates, is the effect it may have on the adhesion with the remaining structural plies of the host composite. To that end, ILSS tests were also conducted on CFRP laminated specimens, split between G1-ILSS, G2-ILSS and G3-ILSS, in agreement with ISO 14130:1997 standard. Adhesion can be evaluated with this test, as specimens with small support span lengths are submitted to three-point bending. The apparent interlaminar shear strength (τ) is calculated using (1), where *F* is the failure load in N, *b* the width of the composite in mm and *h* is the thickness of the composite in mm.

$$\tau = \frac{3}{4} \times \frac{F}{bh} \quad (1)$$

The samples are submitted to three point bending at a testing velocity of 1 mm/min, with pre-load of 10 kN, in the universal testing machine Shimadzu Autograph AGX.
Before calculating τ, it is necessary to evaluate the failure mode of the samples. To properly assess the adhesion, the samples have to fail either from single shear or multiple shear, which represent the occurrence of delamination (Figure 7). Four samples of the G1-ILSS group, however, exhibited compression failure, thus rendering their respective results unusable, according to IS0 14130:1997 standard. As all specimens from G2-ILSS and G3-ILSS, which contain respectively the EML and the PI sensing film, presented either single shear or multiple instances of shear, a potential indicator that the embedded monitoring devices could affect adhesion. The calculated results for τ are shown, for each of the tested conditions, in Table 3.

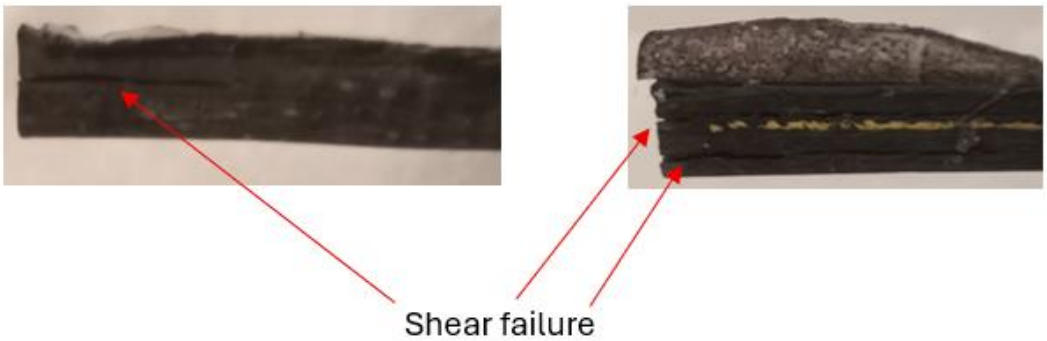

Figure 7 - Single shear and multiple shear failure observed in CFRP samples after ILSS test

Table 3 – Calculated values for τ

CFRP sample group	T (MPa)
G1-ILSS	38.2 ± 2.64
G2-ILSS	37.9 ± 1.12
G3-ILSS	19.5 ± 1.75

From the values obtained for τ, it can be attested that the adhesion properties of composites with embedded monitoring mechanisms are heavily reliant on the substrate of the embedded film. This is due to the fact that the G1-ILSS and G2-ILSS have extremely similar values for τ, with the insertion of EML reducing this value, in average, by approximately 0.785%, whereas the embedment of PI sensing films decreased τ nearly in half by 48.9%. The near coincidence in the results observed for G1-ILSS and G2-ILSS in addition to the extremely large reduction of τ calculated for G3-ILSS seem to indicate that the circuit itself might not affect the adhesion of the overall adhesion of the composite, since it is presented only in G2-ILSS. As such, the main factor that can alter τ could most likely be the substrate used for the

embedded sensing devices, where the PI is vastly outperformed by the thin epoxy film. This is explained by the high mechanical and chemical compatibility of the epoxy that was utilized in the production of EML, which is equal to the resin used for the matrix of the composite.

For a better evaluation of the results shown in Table 3, τ was plotted in relation to the displacement as shown in Figure 8, considering representative ILSS samples from each of the conditions that were studied. There seems to be a good agreement with the values calculated for τ, as the curve for the G3-ILSS is well below the ones from G1-ILSS and G2-ILSS, once more alluding that the PI film could severely affect the interlaminar adhesion of the composite. While this issue with PI can be potentially solved or mitigated with surface treatments, in accordance with the results obtained from the ILSS tests, the epoxy substrate of the EML has seemingly residual effect on the adhesion properties of the host composite, without needing surface treatment.

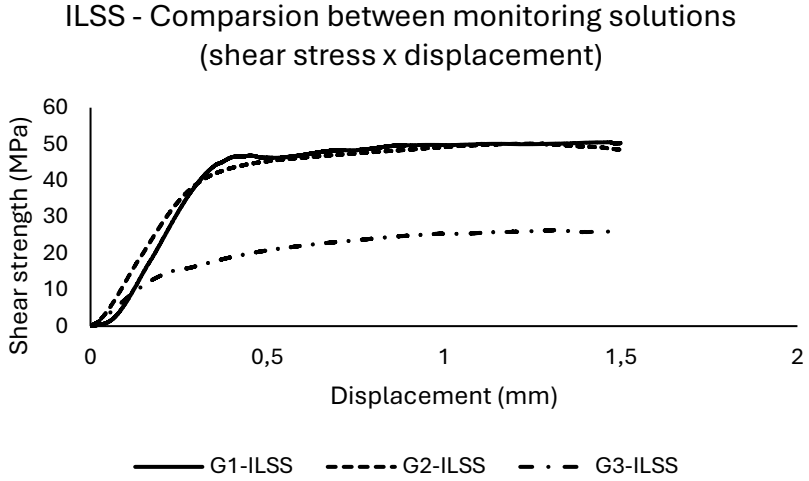

Figure 8 - Plot of τ in relation to the displacement for representative samples.

4 CONCLUSIONS

In this paper, the design, validation and effects of a new proposed EML for real-time monitoring of composite laminated structures was presented. The sensing mechanism was obtained by developing a reliable and repeatable variant of the typical VBI technique that is commonly applied for the production of high-end composite materials. Using that same process, it is possible to create multifunctional composites with EML. Regarding the performance of the internal sensors in measuring strains, it could be observed, from the conduction of tensile tests, that the EML sensing approach was able to precisely measure both transversal and longitudinal strains. Moreover, from the same tests, it was possible to determine that EML and the more common PI sensing films have low effect on the mechanical properties of the CFPR composites, with E_1 decreasing 5.62% in G2-T specimens and 7.81% in G3-T specimens.
The main differences were observed when assessing the influence of the embedded mechanisms in the adhesion of the composite, where it was possible to observe, even before analyzing the data from the tests, that the insertion of the layers could prompt the occurrence of delamination. However, from the analysis of τ, it was possible to verify that the EML outperformed the PI sensing film in preservation of the adhesion properties, where samples from G2-ILSS presented reduction in τ inferior to 1%, whereas in samples from G3-ILSS, this increase was almost 50%.
More studies are still needed to evaluate the effect that the developed EMLs can have on composite materials under bending and impact testing. Additionally, the EML concept needs to be studied with other sensors, such as piezoelectric ones for real-time monitoring of vibrations or impact events, to ensure it can be applied in a wide range of scenarios.

ACKNOWLEDGEMENTS

The research reported in this paper was carried out at the Institute of Polymers and Composites of the Engineering School of Minho University and in PIEP (Pólo de Inovação em Engenharia de Polímeros), which is a research and development company that works closely with the university. The funds for the investigation were supported by the European Union through European Social Fund and FCT (Fundação para a Ciência e Tecnologia), under the scholarship referenced as UI/BD/150795/2020, and from the following two projects referenced as: UIDB/05256/2020 and UIDP/05256/2020.

REFERENCES

1. Giurgiutiu, V., *Structural health monitoring of aerospace composites*. 2015: Academic Press.
2. Soutis, C., *Fibre reinforced composites in aircraft construction.* Progress in Aerospace Sciences, 2005. **41**(2): p. 143-151.
3. Janeliukstis, R. and D. Mironovs, *Smart composite structures with embedded sensors for load and damage monitoring–a review.* Mechanics of Composite Materials, 2021. **57**(2): p. 131-152.
4. Carani, L.B., et al., *Advances in Embedded Sensor Technologies for Impact Monitoring in Composite Structures.* Journal of Composites Science, 2024. **8**(6).
5. Lampani, L., et al., *Analysis of damage in composite laminates with embedded piezoelectric patches subjected to bending action.* Composite Structures, 2018. **202**: p. 935-942.
6. Qing, X.P., et al., *Built-in sensor network for structural health monitoring of composite structure.* Journal of Intelligent Material Systems and Structures, 2007. **18**(1): p. 39-49.
7. Wiedemann, M. and M. Sinapius, *Adaptive, tolerant and efficient composite structures*. 2012: Springer Science & Business Media.
8. Su, Z., et al., *A built-in active sensor network for health monitoring of composite structures.* Smart Materials and Structures, 2006. **15**(6): p. 1939.
9. Tuloup, C., et al., *On the use of in-situ piezoelectric sensors for the manufacturing and structural health monitoring of polymer-matrix composites: A literature review.* Composite Structures, 2019. **215**: p. 127-149.
10. Huang, Y. and S. Nemat-Nasser. *Structural integrity of composite laminates with embedded micro-sensors*. in *Sensor Systems and Networks: Phenomena, Technology, and Applications for NDE and Health Monitoring 2007*. 2007. SPIE.
11. Xiao, Y., et al., *The effect of embedded devices on structural integrity of composite laminates.* Composite Structures, 2016. **153**: p. 21-29.
12. Pappa, E.J., et al., *Experimental study on the interlaminar fracture properties of carbon fibre reinforced polymer composites with a single embedded toughened film.* Polymers, 2021. **13**(23).
13. Annunziato, A., et al., *Design of Polarization-Maintaining FBGs Using Polyimide Films to Improve Strain-Temperature Sensing in CFRP Laminates.* IEEE Photonics Journal, 2021. **13**(2).
14. Hornig, A., et al., *Embedded sensing and actuating in CFRP composite structures - Concept and technology demonstration for tailored embeddable sensor-actuator layers(TEmSAL).* Smart Materials and Structures, 2022. **31**(9).

KU LEUVEN

Simulation approaches for delamination propagation in composite panels subjected to out-of-plane bending

Alice Pagnanini[12], Wenjie Tu[3], John Alan Pascoe[3], Christian Breite[2], Yentl Swolfs[2], Andrea Bernasconi[1], Luca Michele Martulli[1]

[1]Department of Mechanical Engineering, Politecnico di Milano, Italy, [2]Department of Materials Engineering, KU Leuven, Belgium, [3]Department of Aerospace Structures and Materials, Faculty of Aerospace Engineering, Delft University of Technology, The Netherlands

alice.pagnanini@kuleuven.be

Aim of the project

- Benchmark of simulations of delamination propagation modelling techniques

Non-standard tests

Circular delamination front

Out-of-plane loading

Case study

How to model delamination?

LEFM

- **Strain Energy Release Rate (SERR)**
- **Fracture toughness G_C**

↓

Delamination starts:
SERR > G_C

COHESIVE MODELLING

- **Damage status**
- **Traction-separation law**
  Describes how the two surfaces in contact detach from each other
- **Simulation of the debonding of the structure**

Experimental setup

To validate the results obtained from the simulations, this study replicates an experimental test on carbon fiber reinforced polymer (CFRP) panels under quasi-static out-of-plane bending [1].

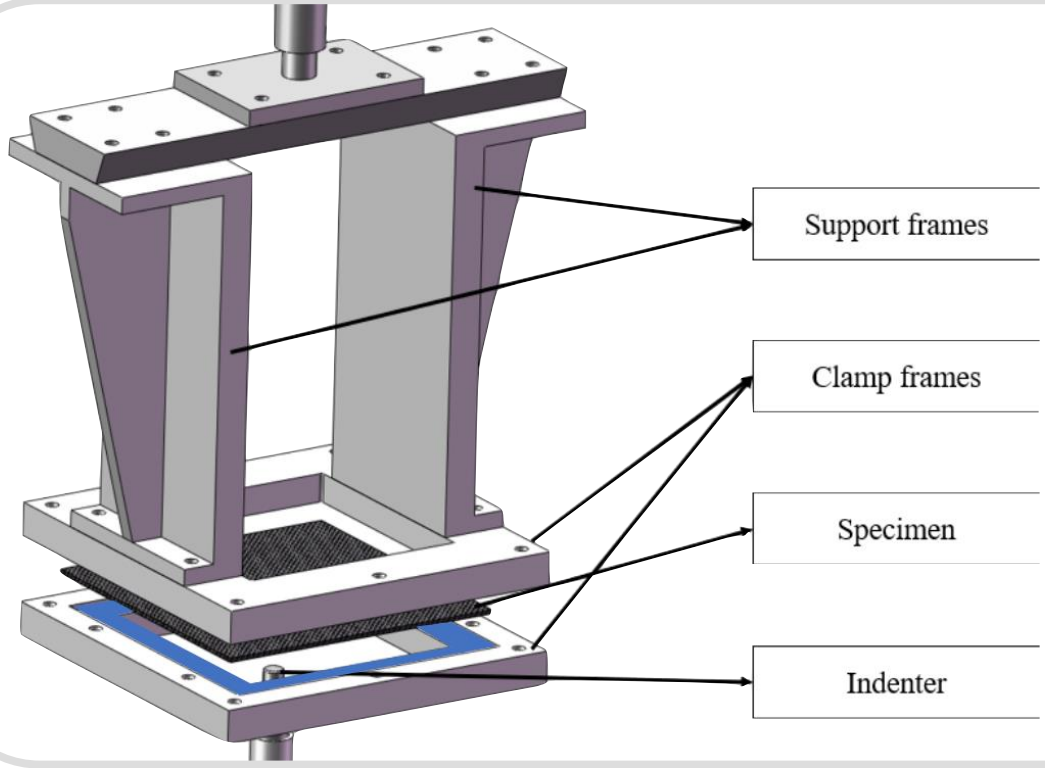

TU Delft Delft University of Technology

Source: Composite Structures, 2024.
“Planar delamination behavior of CFRP panels under quasi-static out-of-plane loading”

[1] W. Tu et al. (2024)

Experimental setup

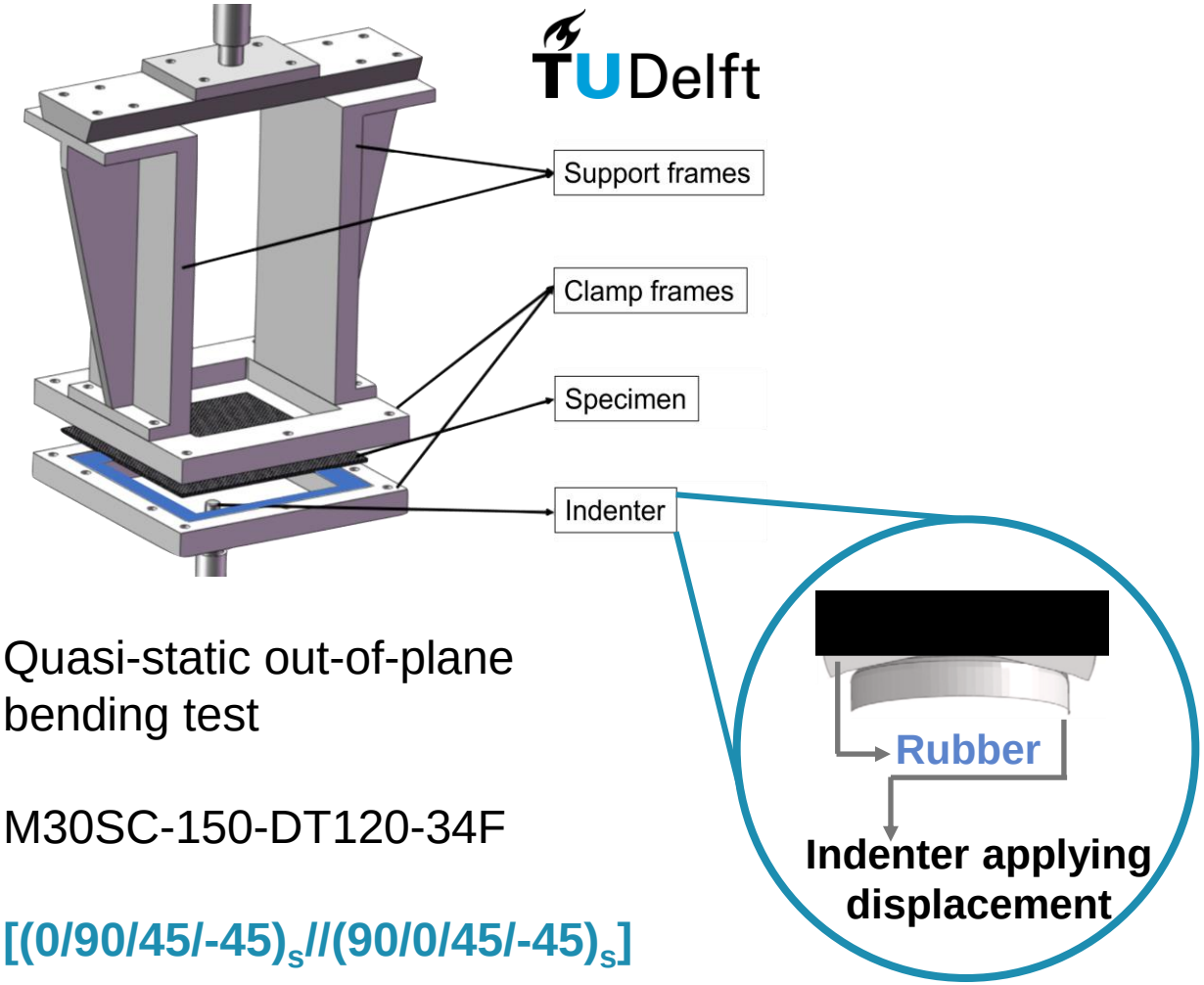

- Quasi-static out-of-plane bending test
- M30SC-150-DT120-34F
- **$[(0/90/45/-45)_s//(90/0/45/-45)_s]$**
- Fully clamped panels

Experimental results

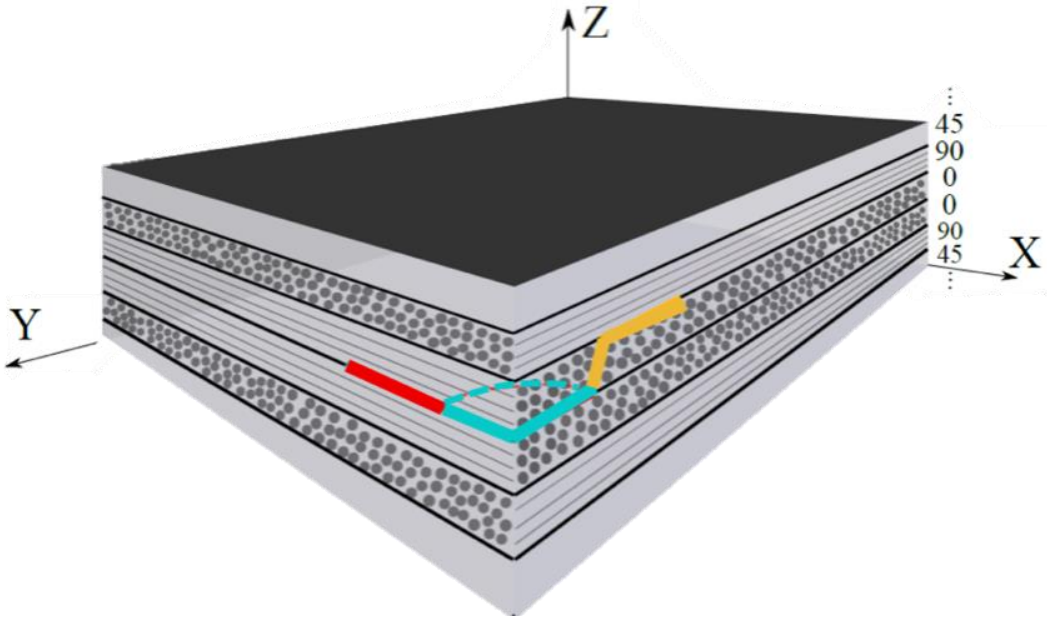

- Teflon insert
- Delamination in middle interface between two panels
- Delamination migrated in the upper ply

Modelling – Design and BCs

PANEL DESIGN

- 140x140 mm
- 2,5 mm thickness
- Partitions to tailor mesh
- Encastre in the purple region

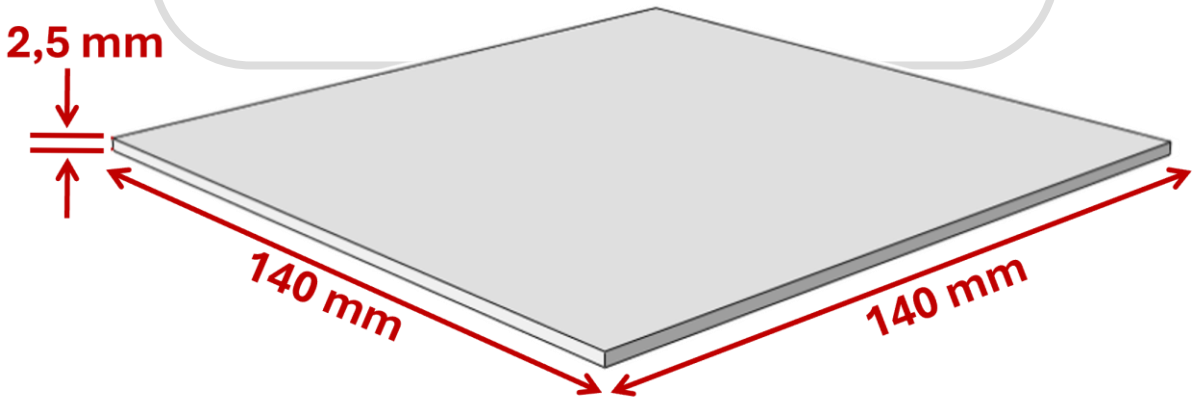

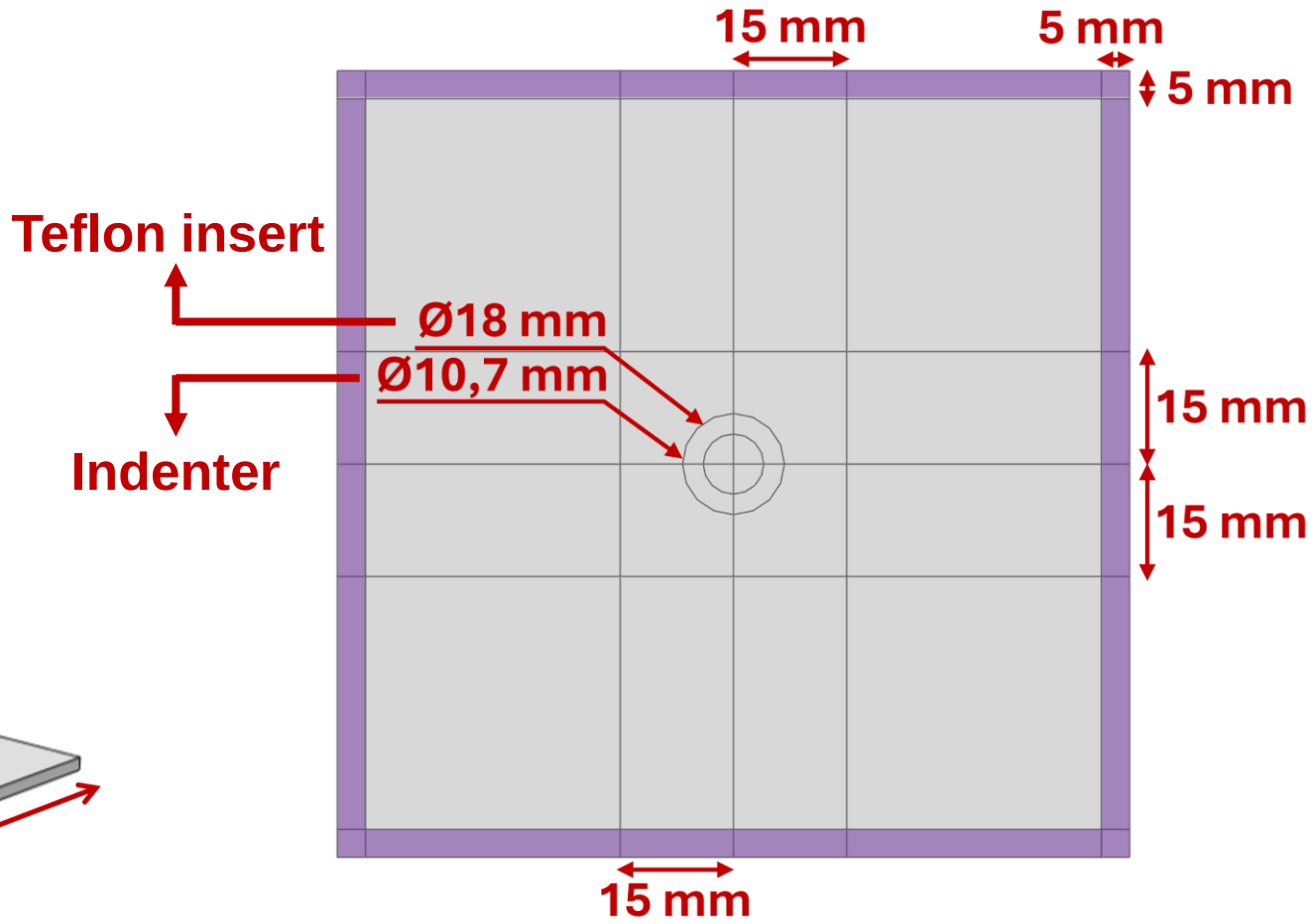

Modelling - Design

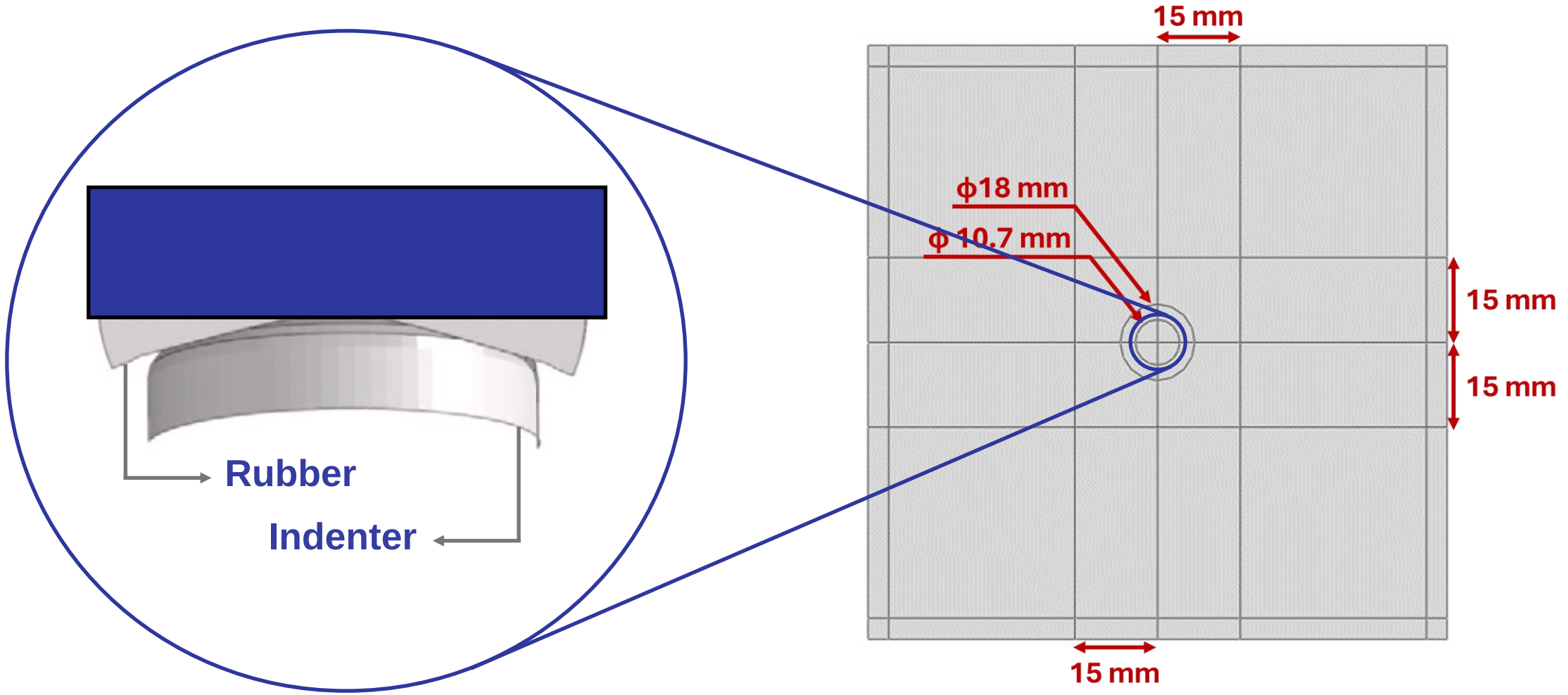

Modelling - Design

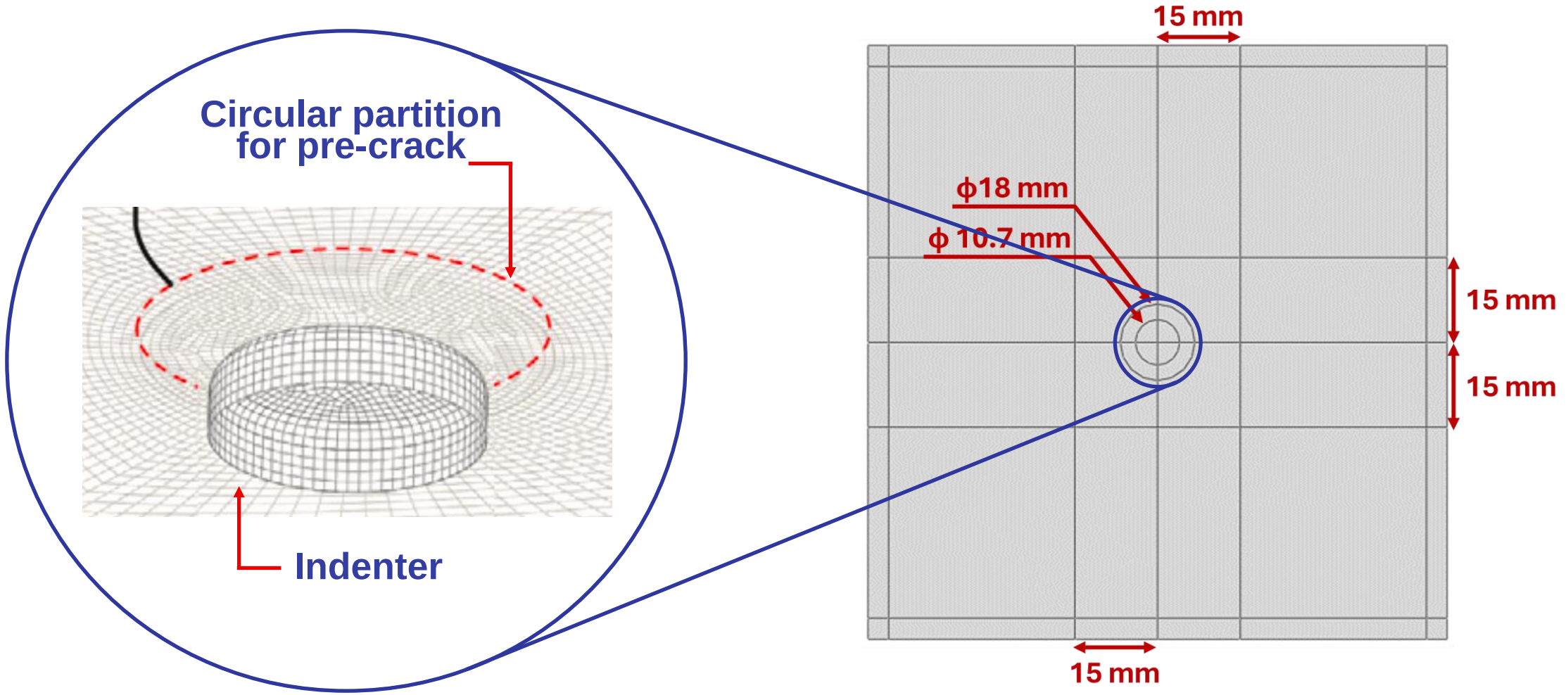

Modelling - Material

MATERIAL

M30SC-150-DT120-34F

Stacking sequence

$[(0/90/45/-45)_s//(90/0/45/-45)_s]$

Mechanical properties

E_1	145 GPa	G_{12}	3.8 GPa
E_2	6.4 GPa	G_{13}	3.8 GPa
E_3	6.4 GPa	G_{23}	2.232 GPa

Fracture toughness

G_{IC} $[kJ/m^2]$	G_{IIC} $[kJ/m^2]$	G_{IIIC} $[kJ/m^2]$
0.611	1.02	1.02

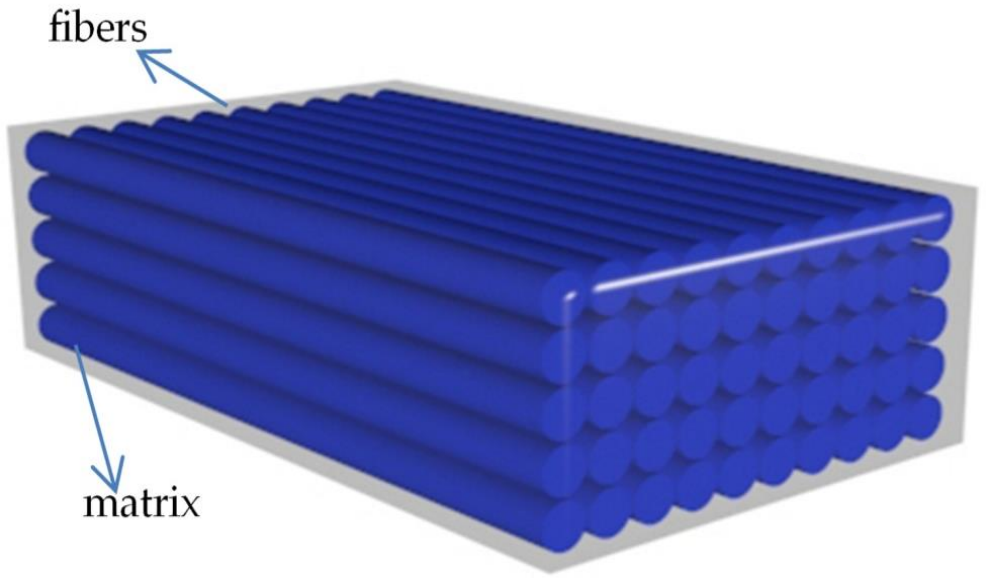

Modelling - Mesh

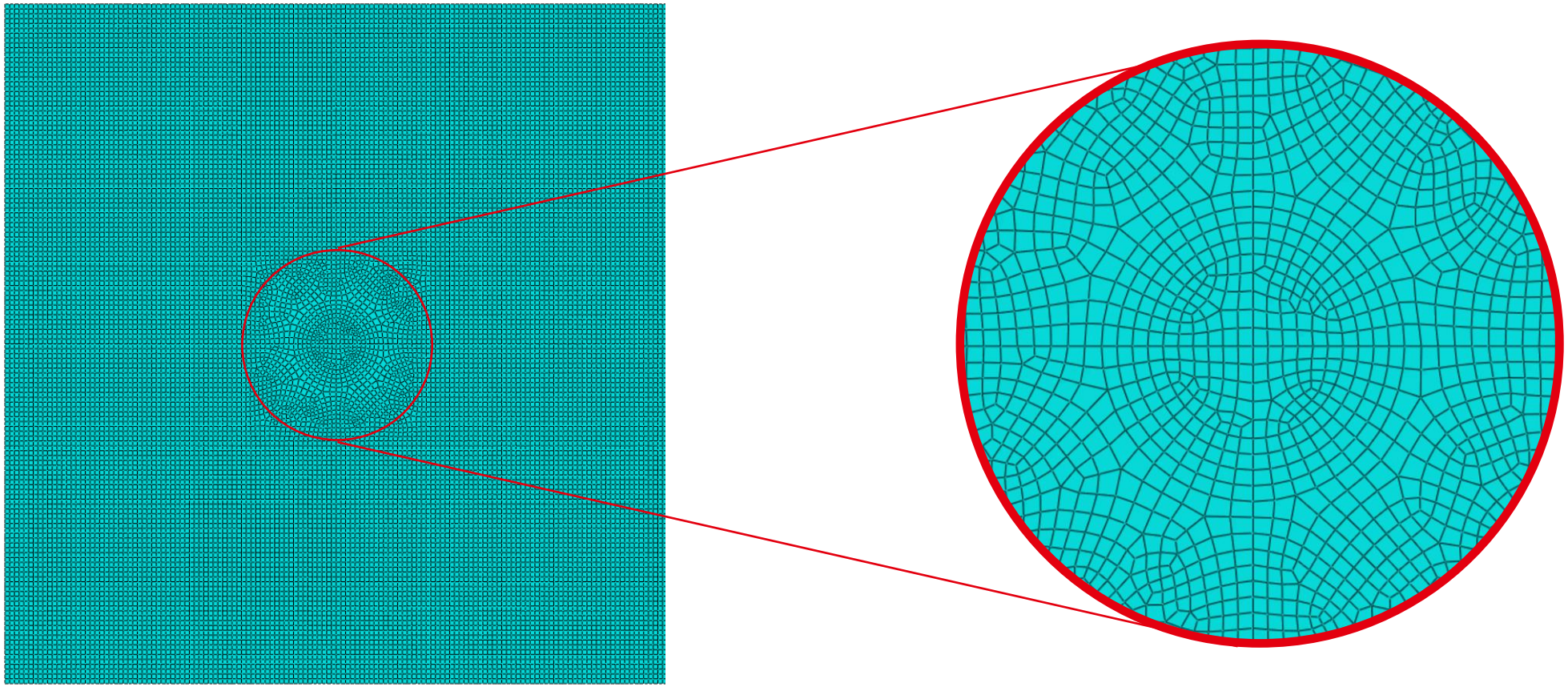

Modelling - Mesh

MESH CHARACTERISTICS

- Continuum shell elements
- Global seed: 1 mm
- Local seed:
  one-element thickness
- Pre-crack

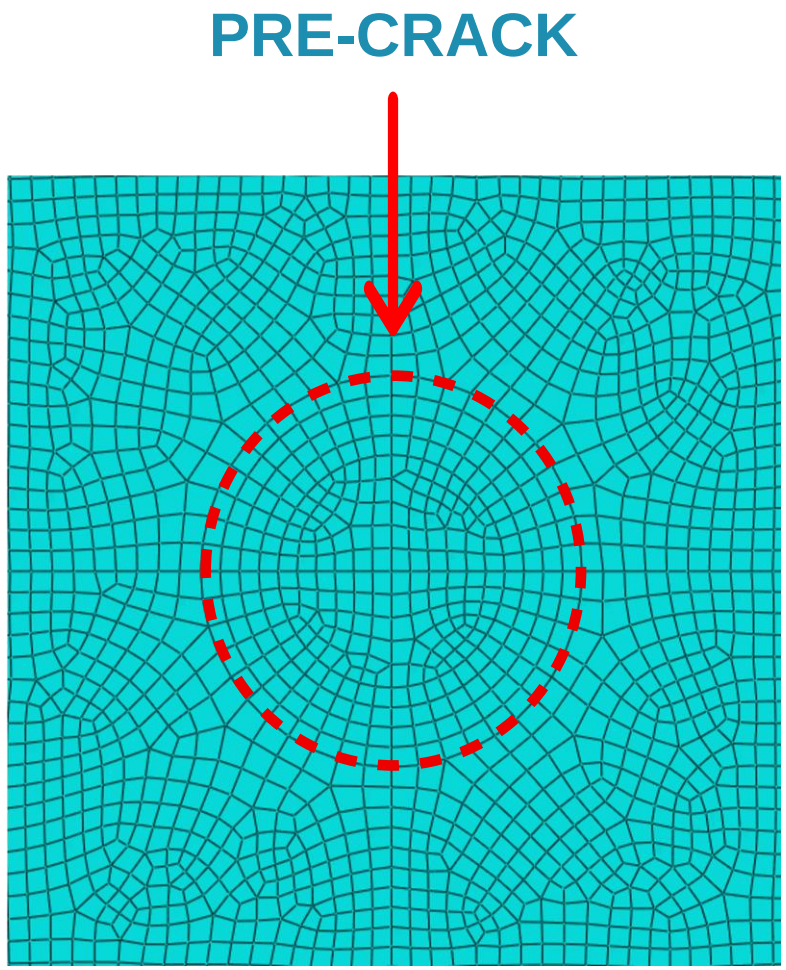

Delamination modelling

Two main approaches for delamination propagation modelling: VCCT and CZM.

VCCT

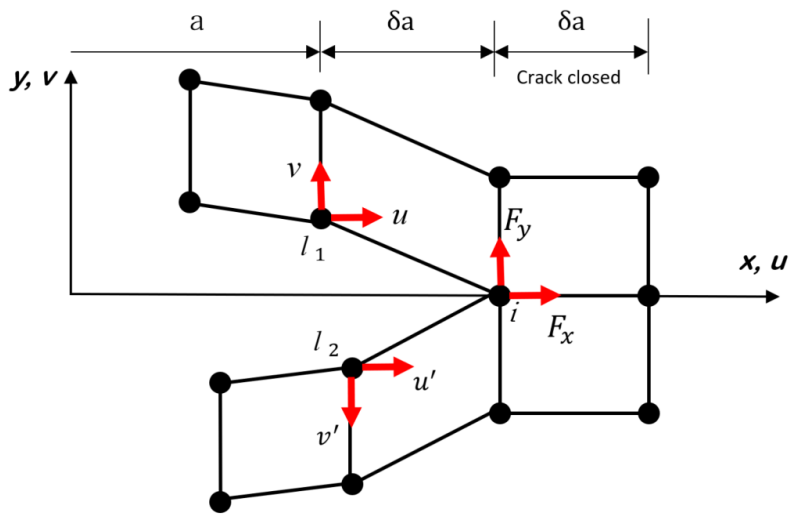

✓ Computation of SERR

✗ Mesh dependence

COHESIVE CONTACT

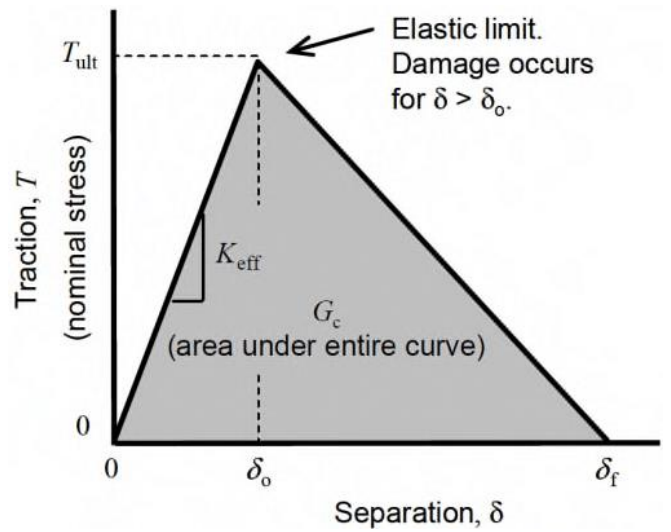

✓ Less mesh dependence

✗ No SERR computation

[1] A. Pirondi et al. (2014), [2] D. Zhang et al. (2016)

Simulation variations

1 Application of VCCT with almost infinite fracture toughness values

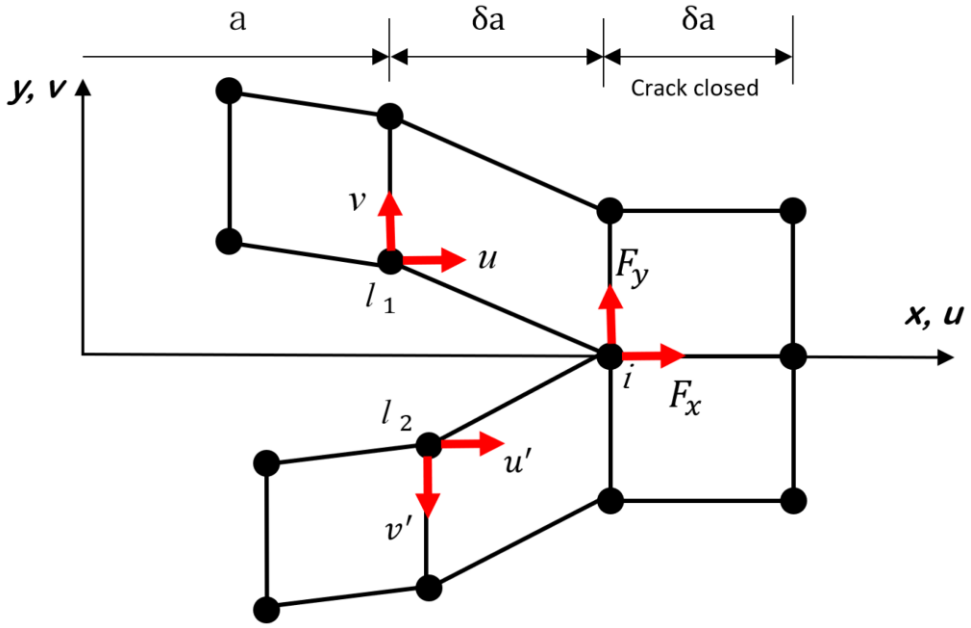

$G_C \rightarrow \infty$

LAYUP

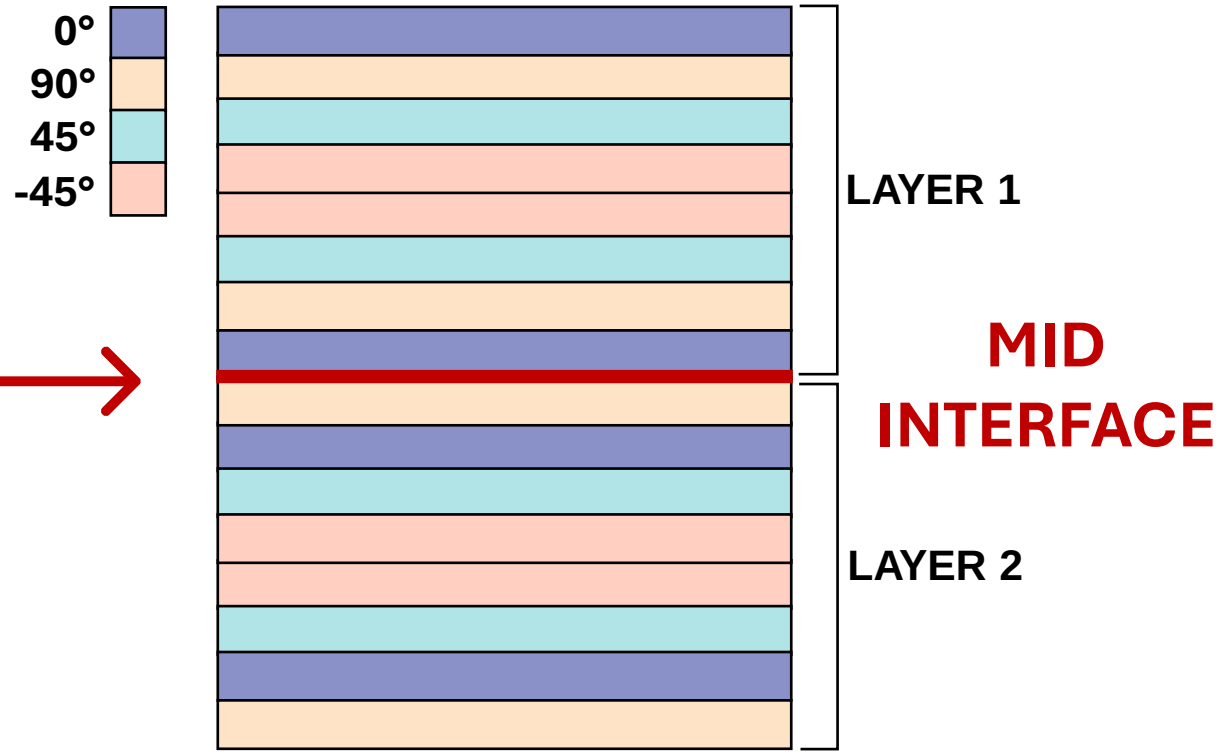

Simulation variations

2 Application of VCCT with real fracture toughness values

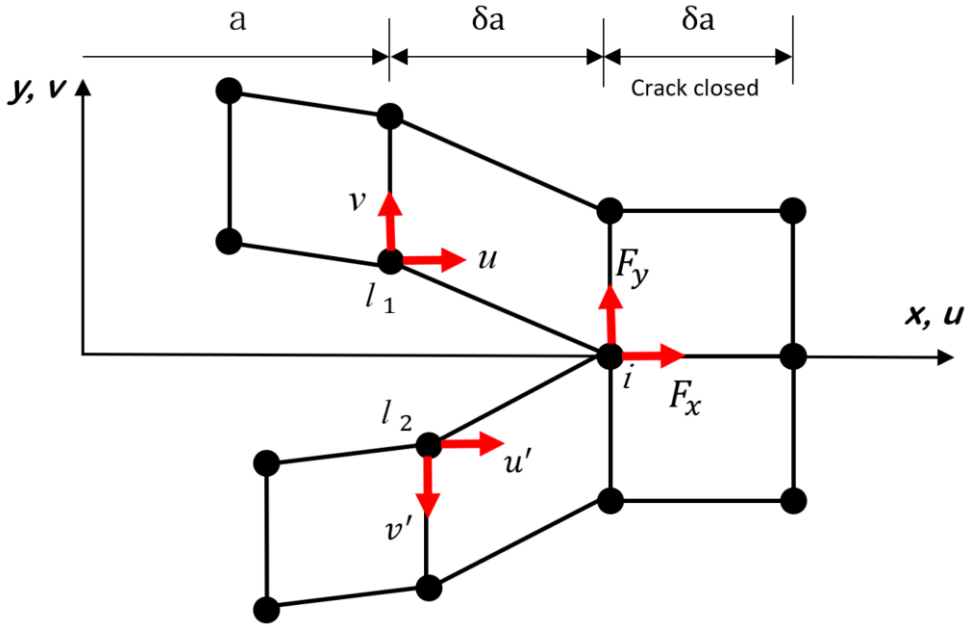

G_I $[kJ/m^2]$	G_{II} $[kJ/m^2]$	G_{III} $[kJ/m^2]$
0.611	1.02	1.02

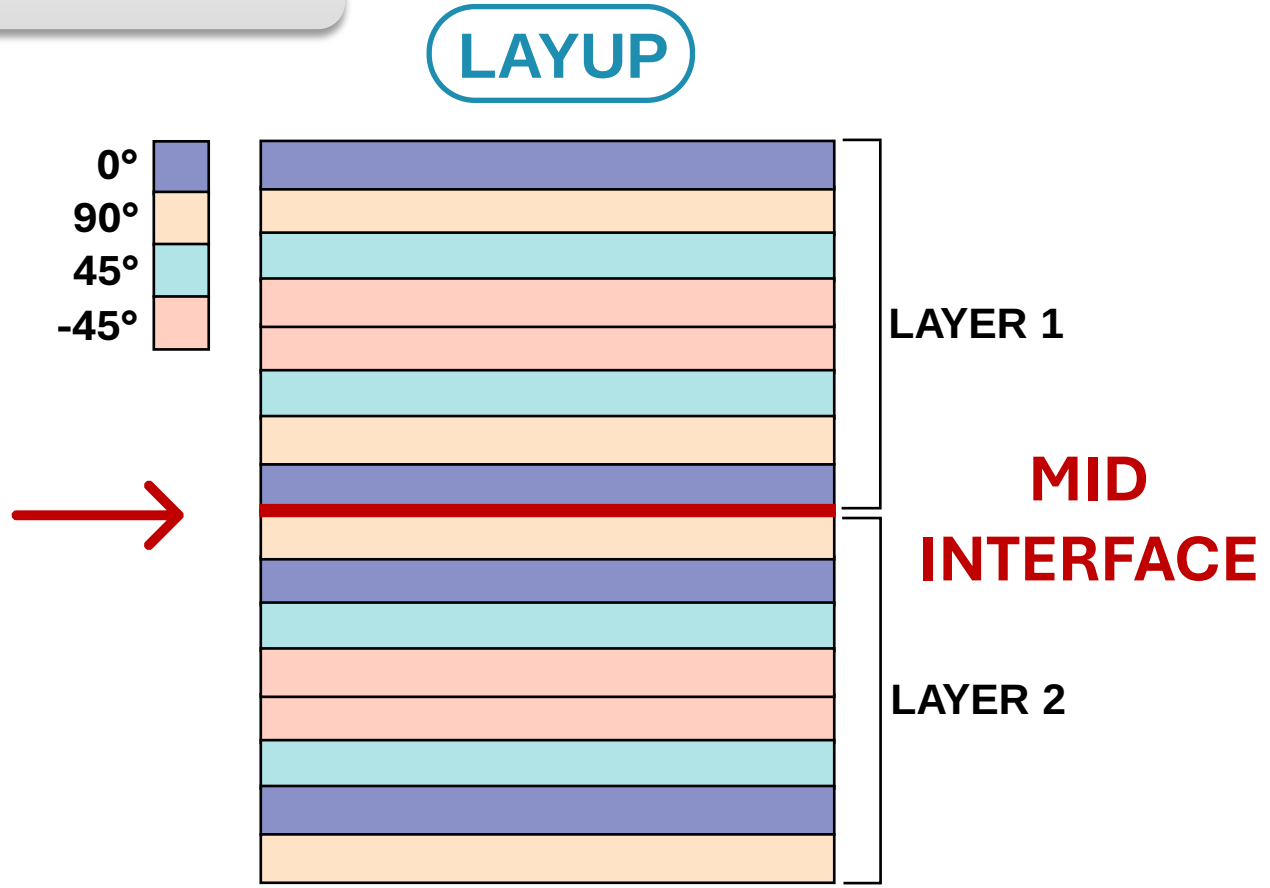

Simulation variations

3 Application of cohesive contact in the middle interface

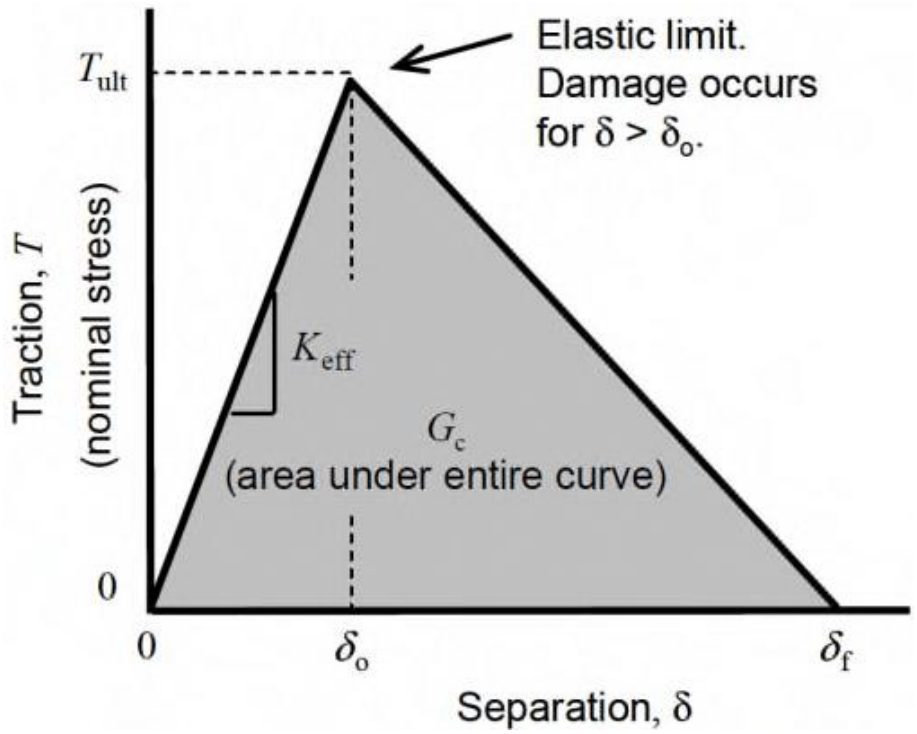

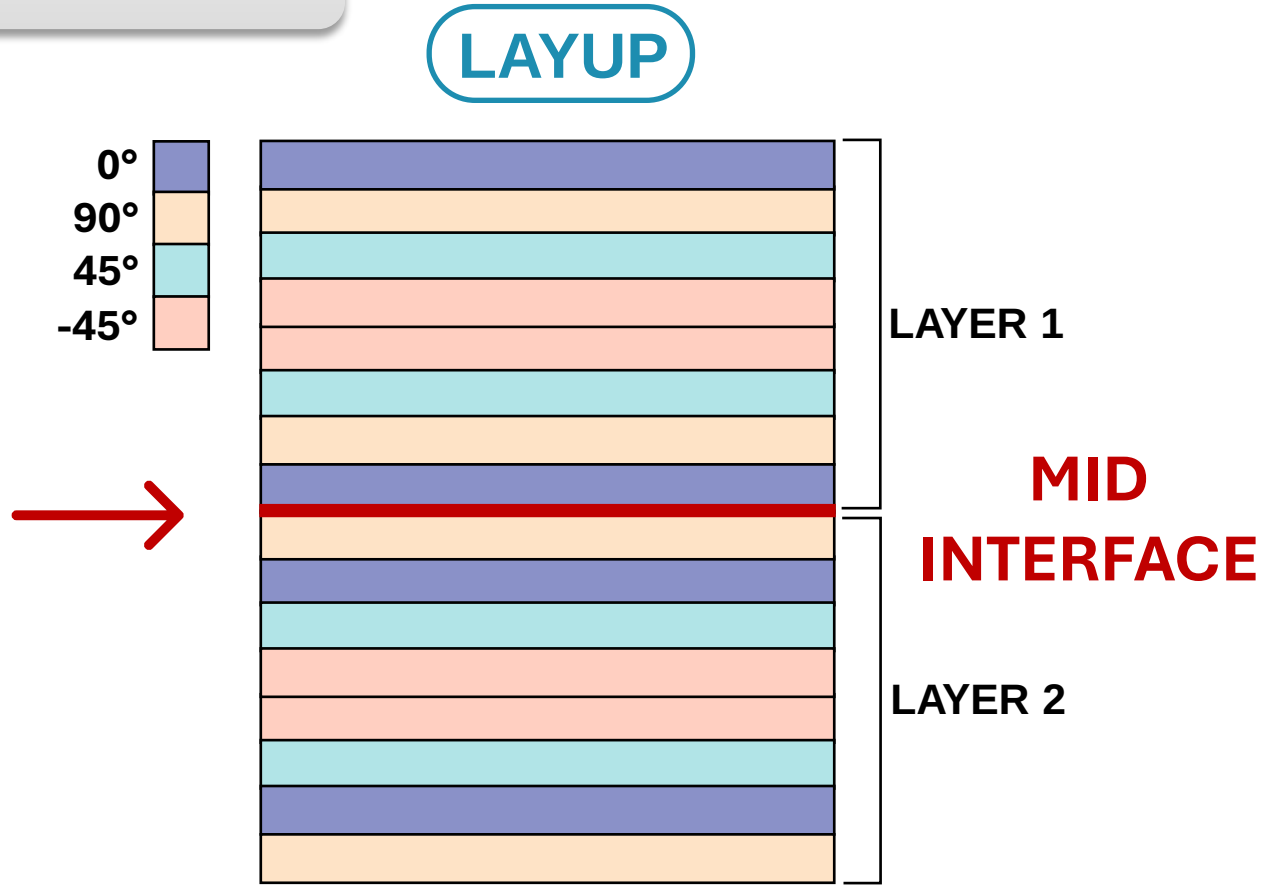

Simulation variations

4 Application of a combination of VCCT and cohesive contact

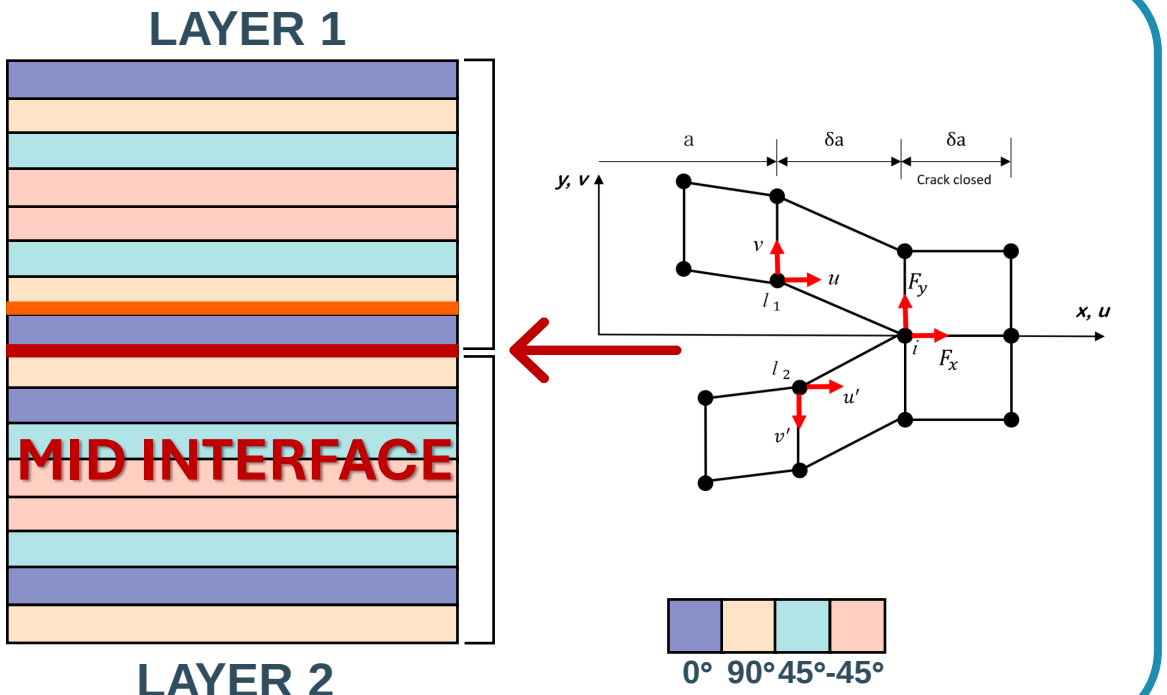

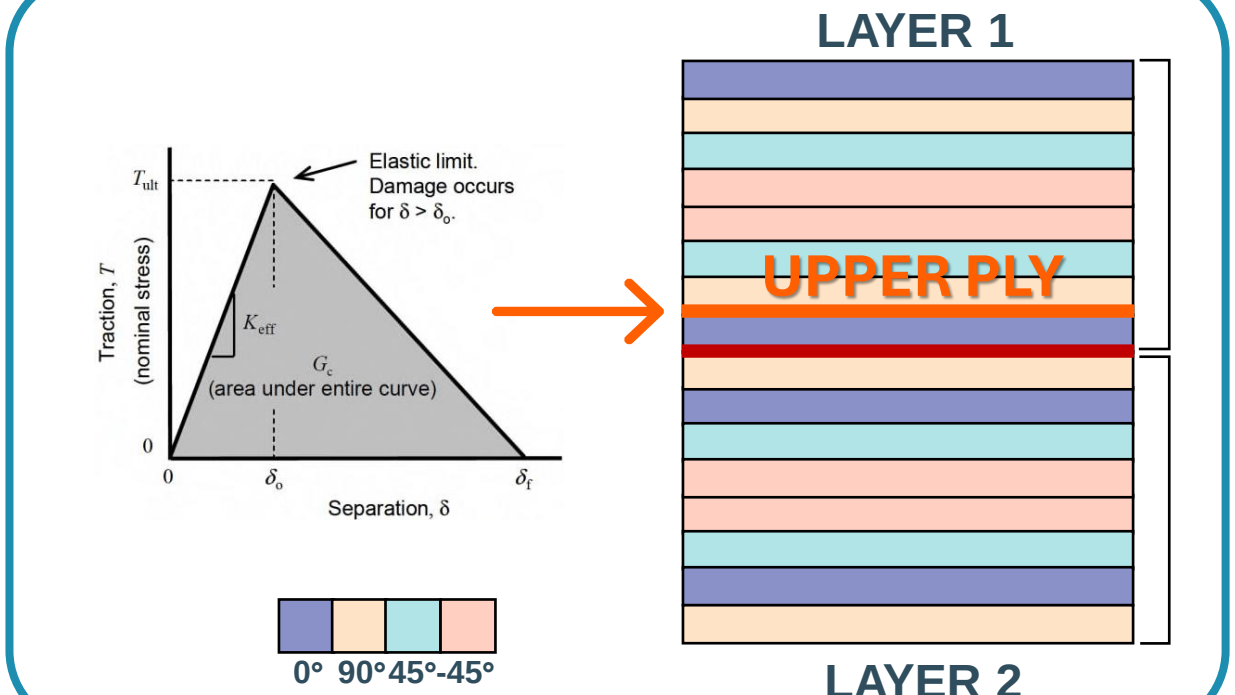

Load application: Spring

➢ Experimental

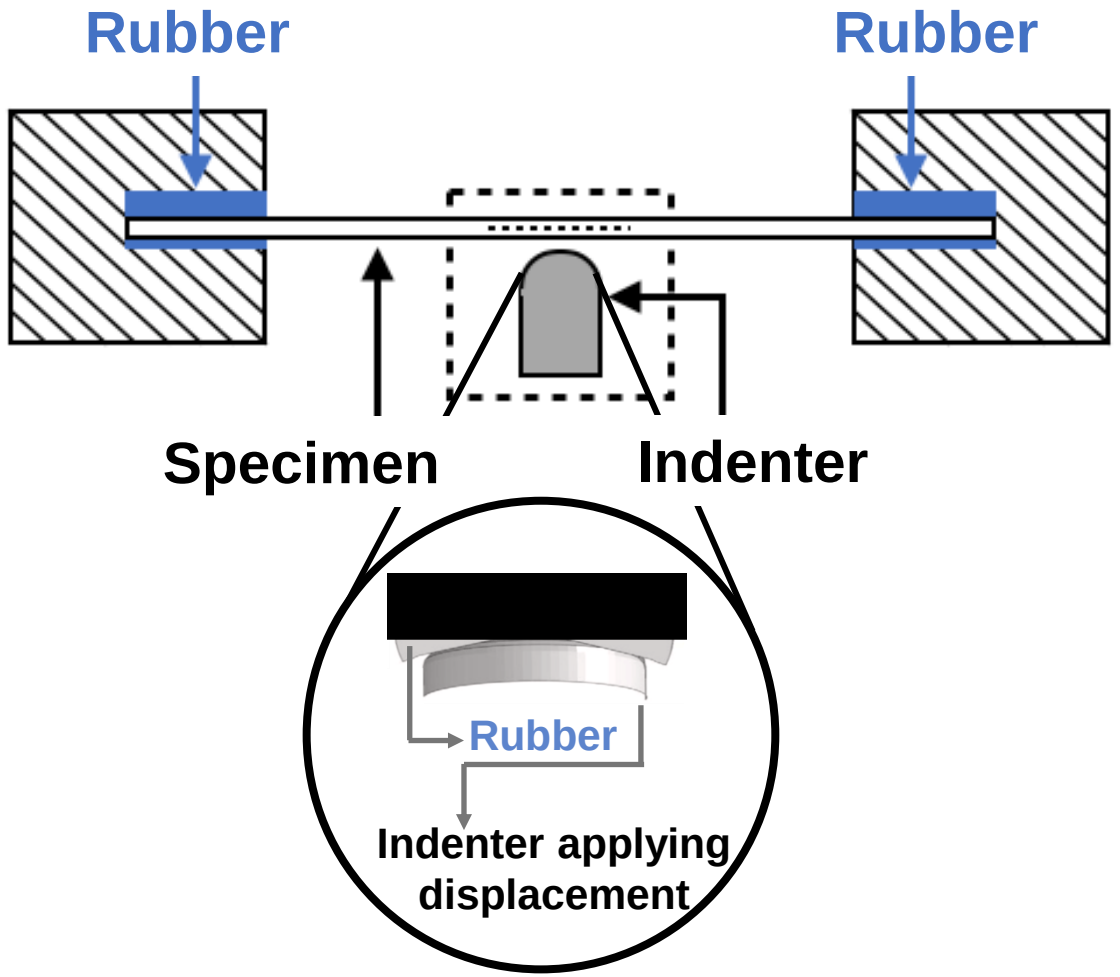

➢ Numerical

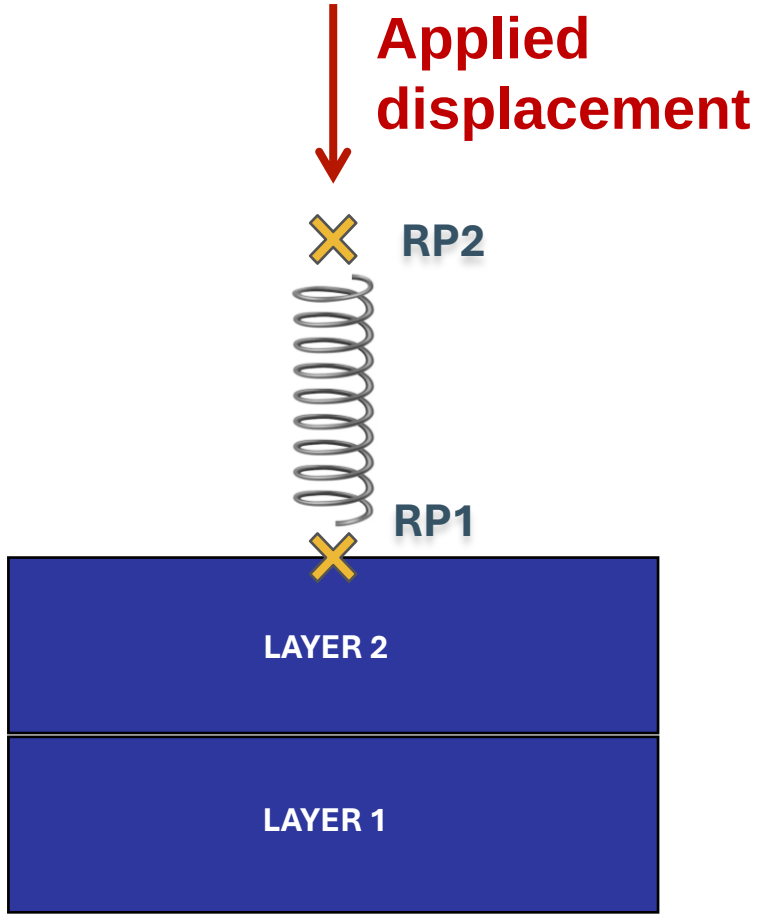

Load application: Spring

PROBLEM

STIFFNESS VALUE that MATCHES the LOAD-DISPLACEMENT CURVE does NOT MATCH the ACTUAL DISPLACEMENT

Problem in the numerical model



Problem in the experimental model

Load application: Spring



Problem in the experimental model

SPRING-DEFINED MODELS

STANDARD LOAD APPLICATION

No spring introduction

STIFFNESS matching LOAD-DISPLACEMENT curve

STIFFNESS matching ACTUAL DISPLACEMENT

Results: No propagation simulations

Strain Energy Release Rate

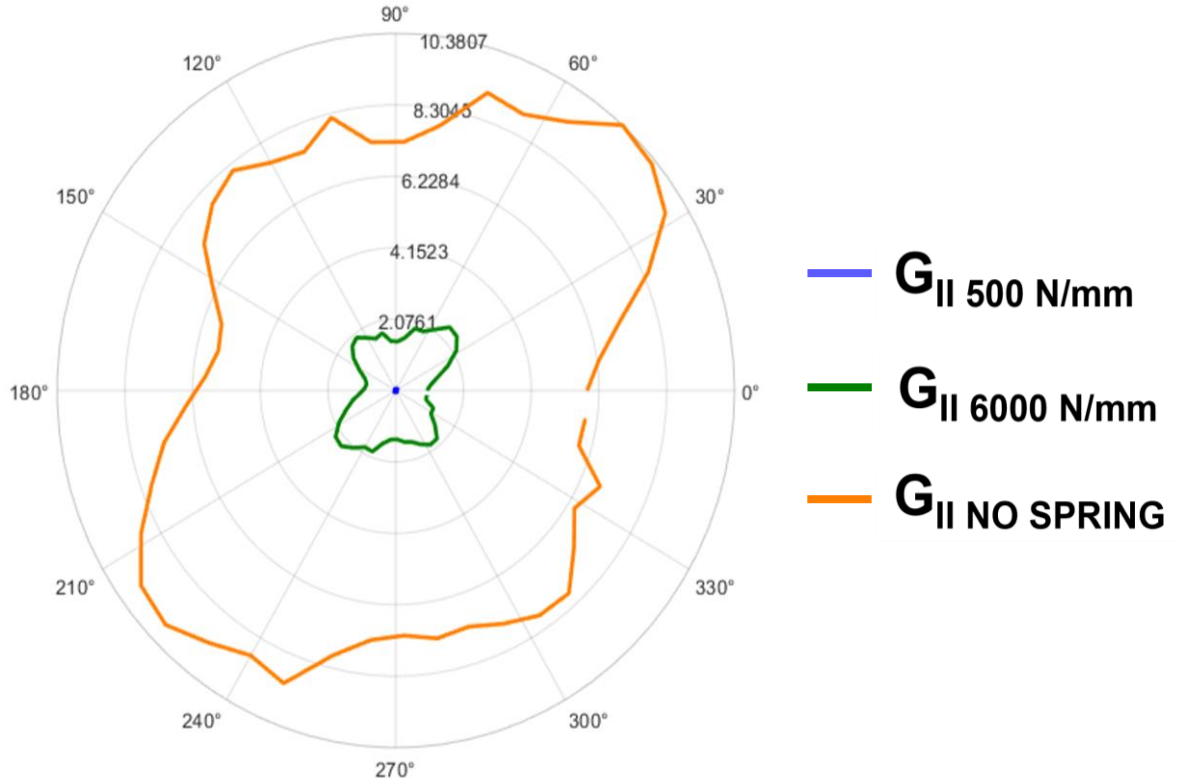

✘ K=500 N/mm G_{II} does not reach GC threshold → **NO propagation**

MESH DEPENDENCE

✘ G_{II} symmetric at 180°, NOT at 90°

✘ GI and GIII presence

Results: Propagation simulations

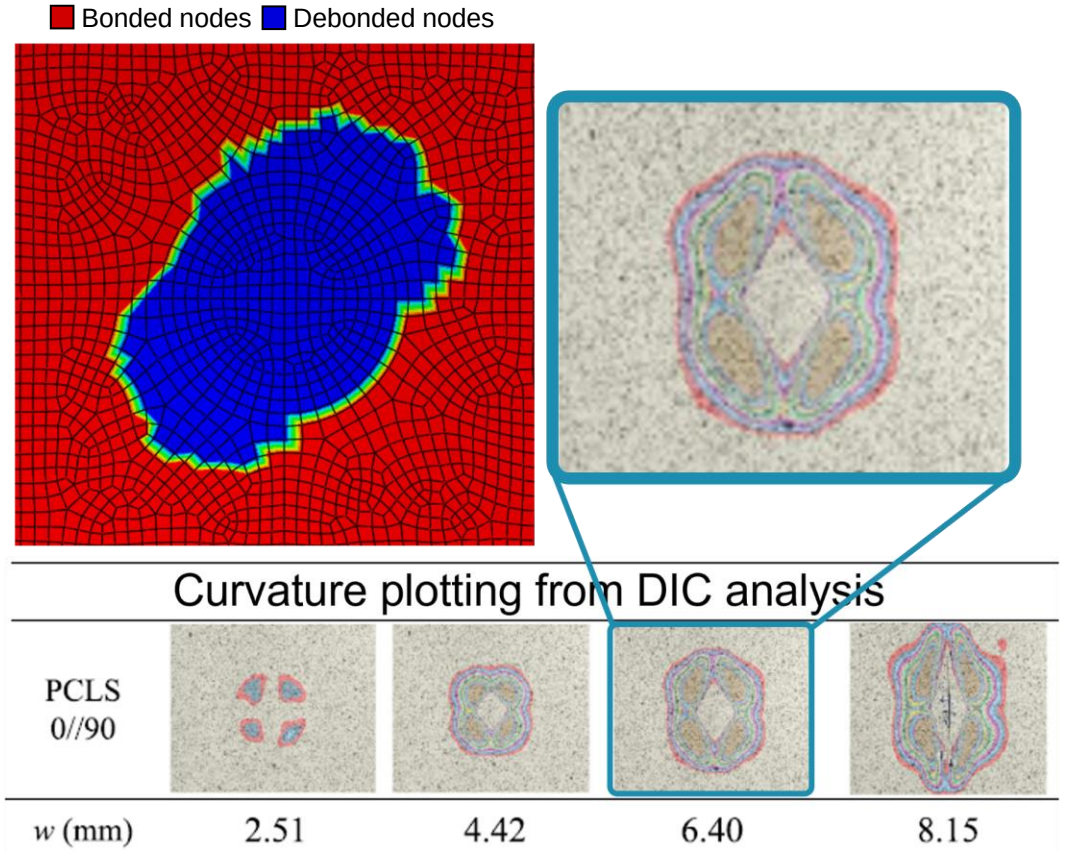

✔ **Propagation shape: 45°**

✘ **Propagation orientation ≠ experimental**

MESH DEPENDENCE

✘ **More mesh-dependent due to mesh discontinuities since propagation is permitted**

Results: Cohesive contact simulations

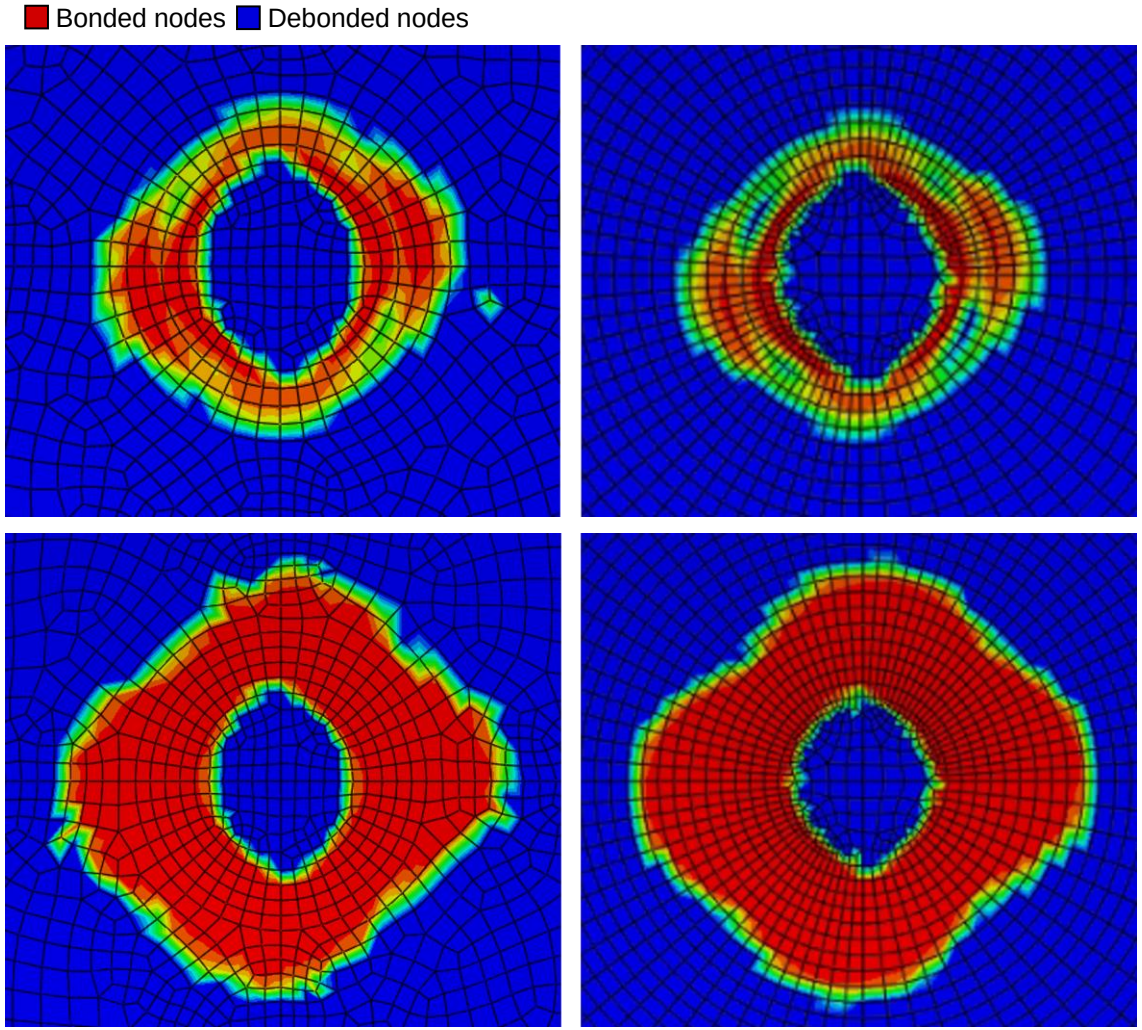

FINER MESH

↓

MESH DEPENDENCE

✓ **LESS mesh dependent**

Results do NOT vary with mesh density or quality

Results: Cohesive contact simulations

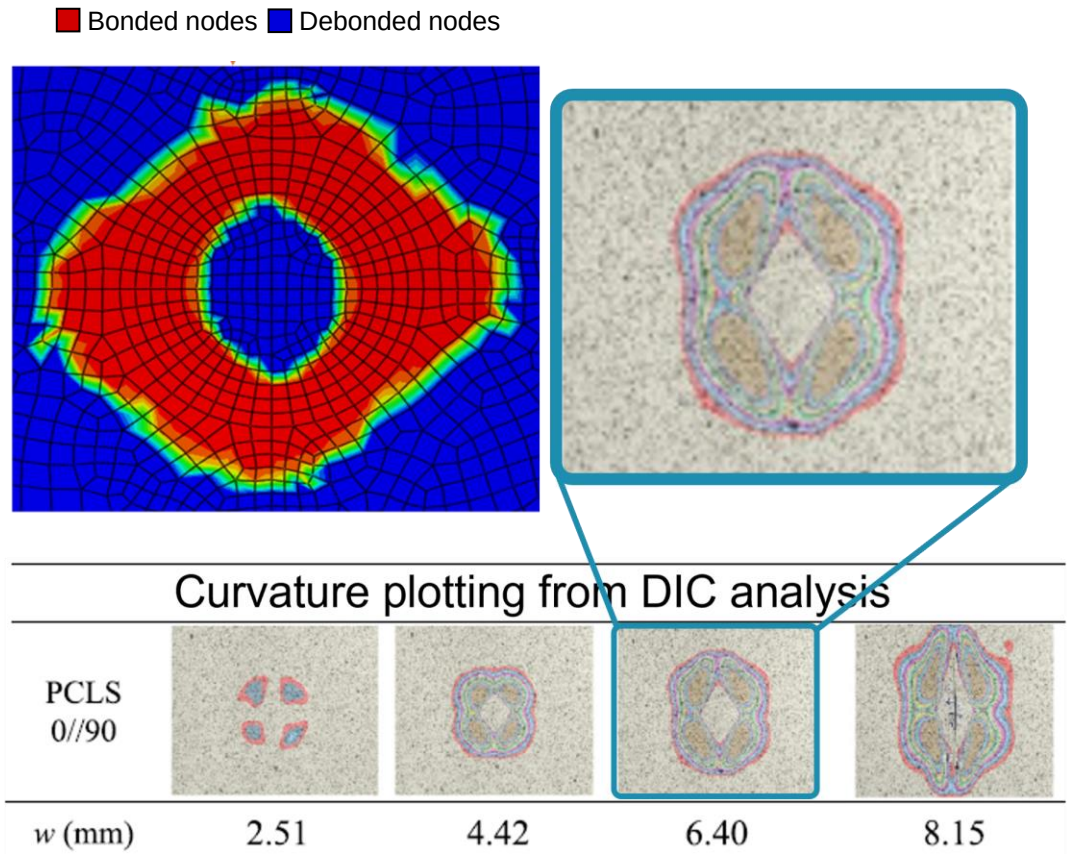

✔ Propagation shape

✘ Propagation orientation: 90°

MESH DEPENDENCE

✔ LESS mesh dependent

Results: Double-approach simulations

UPPER PLY

✔ Cohesive contact captures delamination **MIGRATION**

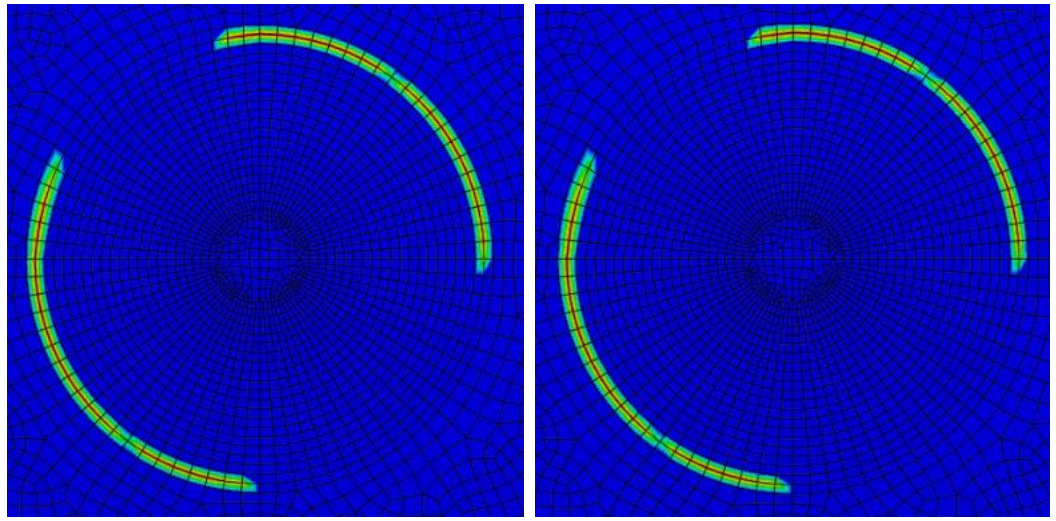

Damage status STD loading simulation

Damage status K=6000 N/mm simulation

✔ **DELAMINATION MIGRATION was reproduced**

↓

- Delamination migration is faster
- Relaxation of VCCT

- Migration interface is weaker
- As enough energy is stored delamination migrates

Results: Double cohesive contact simulation

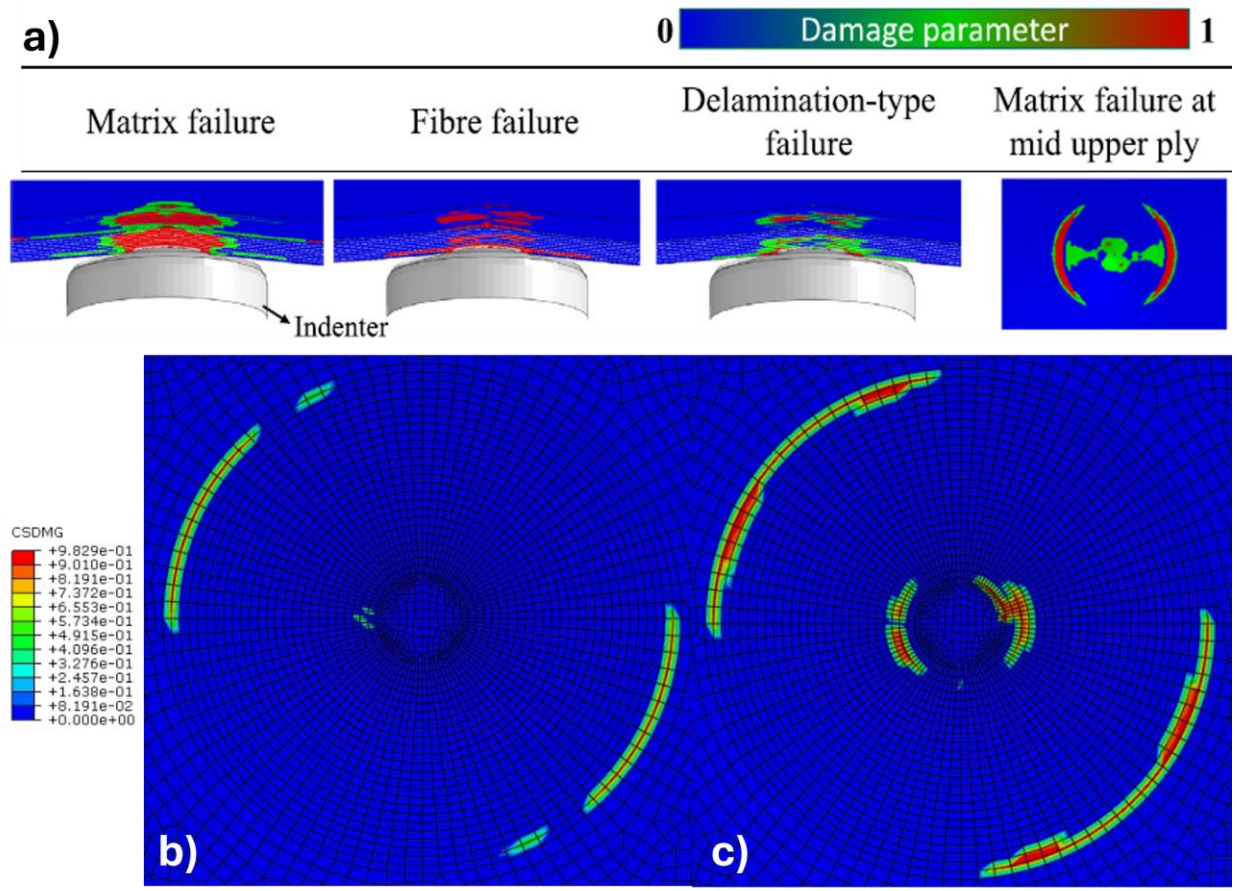

a) Experimental results
b) Damage status in **mid interface**
c) Damage status in **upper ply**

✓ Cohesive contact captures both delamination in **mid interface** and migration in **upper ply**

✓ Propagation shape
✗ Propagation orientation: 90°

Conclusions

- Good performance of VCCT, but high mesh dependence

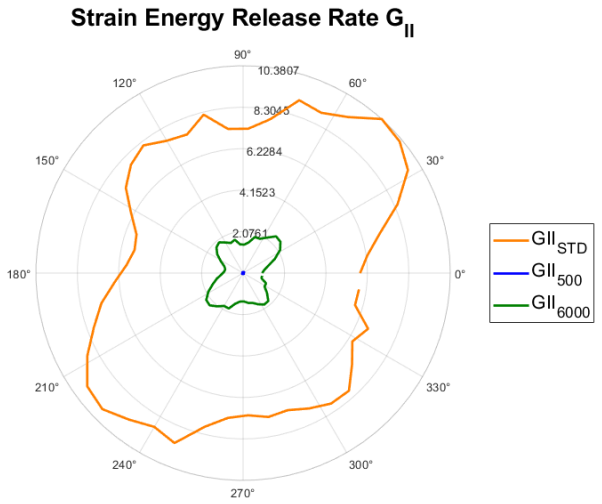

- Cohesive contact:
  - Good performance
  - No mesh dependence

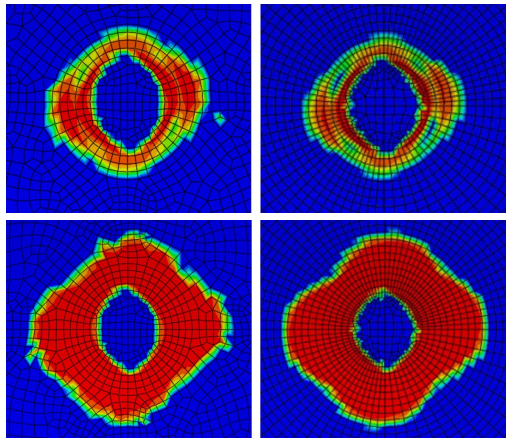

- Double cohesive contact approach:
  - Good performance on both interfaces
  - Reproduction of delamination migration in the upper ply, as in the experiment

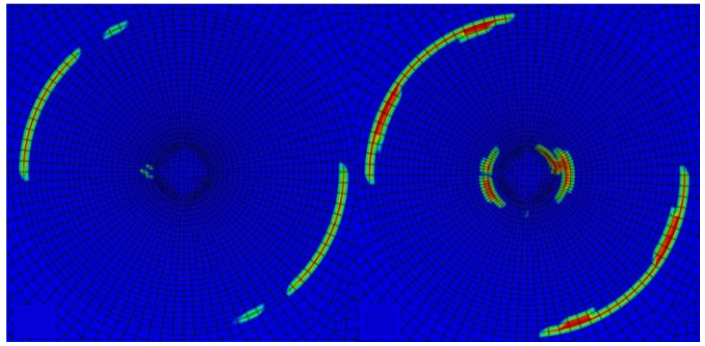

KU LEUVEN

Simulation approaches for delamination propagation in composite panels subjected to out-of-plane bending

Alice Pagnanini[12], Wenjie Tu[3], John Alan Pascoe[3], Christian Breite[2], Yentl Swolfs[2], Andrea Bernasconi[1], Luca Michele Martulli[1]

[1]Department of Mechanical Engineering, Politecnico di Milano, Italy, [2]Department of Materials Engineering, KU Leuven, Belgium, [3]Department of Aerospace Structures and Materials, Faculty of Aerospace Engineering, Delft University of Technology, The Netherlands

alice.pagnanini@kuleuven.be

ICCM24
AUGUST 4-8, 2025
BALTIMORE CONVENTION CENTER
BALTIMORE, MARYLAND, USA

No Technical Paper Submission for:

Neha Chandarana

ICCM24
AUGUST 4-8, 2025
BALTIMORE CONVENTION CENTER
BALTIMORE, MARYLAND, USA

No Technical Paper Submission for:

Jun Koyanagi

ICCM24
AUGUST 4-8, 2025
BALTIMORE CONVENTION CENTER
BALTIMORE, MARYLAND, USA

No Technical Paper Submission for:

Sagar Doshi

INFLUENCE OF LAMINATE SURFACE RESIN DEPTH ON THE INTERFACE STRENGTH OF OVERMOULDED COMPOSITES

Ruaraidh MacLennan[1], Thomas Bach[1], Paul Hanna[2], and Ali Aravand[1]

[1]School of Mechanical and Aerospace Engineering, Queen's University Belfast
Ashby Building, Stranmillis, Belfast, United Kingdom
Email: r.maclennan@qub.ac.uk

[2]Advanced Manufacturing Innovation Centre (AMIC), Queen's University Belfast
Ashby Building, Stranmillis, Belfast, United Kingdom

Keywords: Composite overmoulding, Thermoplastic resin, Thin films, Adhesion, Interface, Computational modelling, Mechanical testing

ABSTRACT

A systematic study was performed to investigate the influence of surface resin depth on the interfacial strength of overmoulded composites using both experimental and simulation methods. Discontinuous fibre reinforced polyetheretherketone (PEEK) was injected over a unidirectional (UD) laminate to manufacture lap-shear specimens, varying both the surface resin depth present on the laminate insert and the weight fraction of discontinuous fibres filling the injected polymer. The surface resin depth was modified from a standard quasi-isotropic laminate with limited surface resin content with inclusion of a film of two different polymers. This included both polyaryletherketone (LMPAEK) and polyetherimide (PEI) film of thickness 40µm. In both cases the films were added to the laminate surface during the consolidation of the laminate. Mechanical tests showed an increase in lap-shear strength when a thin film was present on the specimen surface. A similar improvement in bond strength was achieved for both LMPAEK and PEI surface film layers. A counterpart numerical modelling process was developed to understand the heat transfer process occurring during overmoulding. The primary finding of the simulation was that a reduction in local thermal diffusivity at the interface (such as achieved through a resin-rich layer at the interface) can be used to increase the interface temperature. The results of this study are important for the manufacture of overmoulded composites as both the technical findings and the simulation process presented can be used in the design process to improve interface strength.

1 INTRODUCTION

Composite injection overmoulding is performed by combining injection moulding with the use of continuous fibre reinforced thermoplastic composites (also referred to as the insert or substrate throughout this text) by placement within a mould tool prior to the injection stage. As the molten polymer is injected into the mould, contact with the surface of the insert allows a bond to form and consolidate under pressure, heat, and time. Composite injection overmoulding can reduce the costs associated with the manufacture of complex composite structures. This is the case, as incorporating injection moulding for features can significantly reduce processing times and increase automation. The superior strength of continuous fibre reinforcement can be attained for load-bearing components by incorporation of a composite insert [1]. However, achieving a desired interface strength may be an issue as the formation of a strong bond at the interface is required for maintaining structural integrity in load-bearing applications. The interface strength is dependent on the material and processing conditions which include (but are not limited to) interface temperature, crystallinity, thermodynamic compatibility, and local flow velocity [2-5].

2 METHODOLOGY

During this study a systematic approach was undertaken to understand the relationship between the resin present on the surface of a composite laminate and the interface strength of overmoulded composites. This involved the manufacture and testing of overmoulded single lap-shear specimens alongside the development of a complimentary overmoulding process simulation to understand the heat transfer process (Fig. 1).

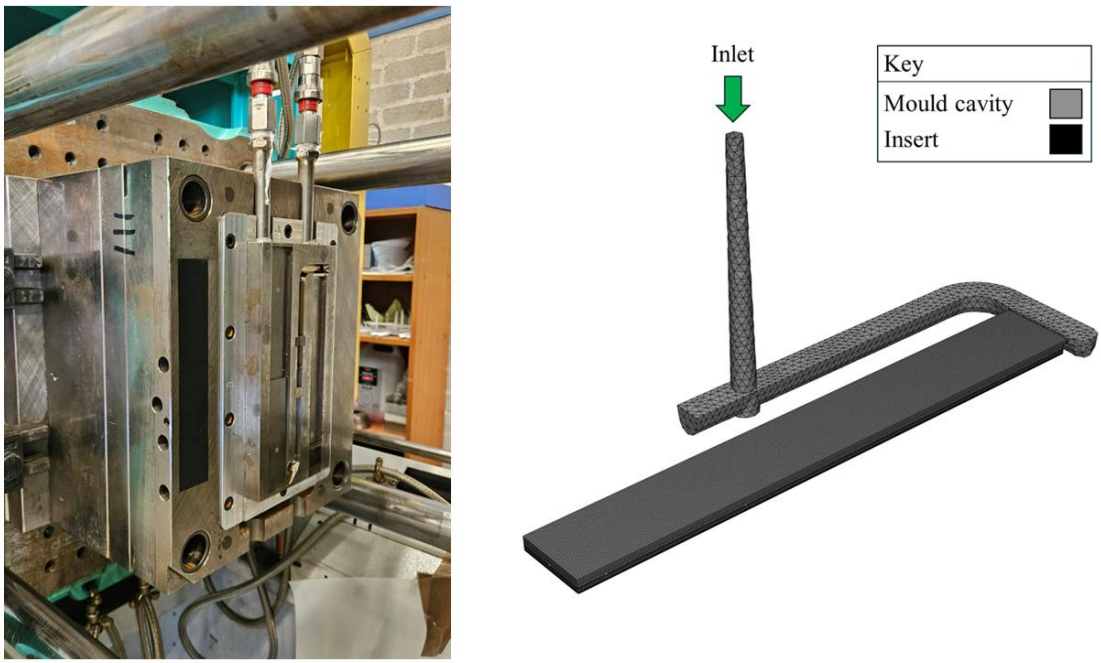

Figure 1: Overmoulding mould used for the manufacture of overmoulded coupons (left) and simulation grid of counterpart process simulation.

2.1 Overmoulding single lap-shear specimens

Rectangular coupons were prepared using quasi-isotropic Toray Cetex TC1225 composite reinforced with T300 carbon fibres. The matrix of the TC1225 composite is a proprietary blend of thermoplastic polymers from the polyaryletherketone (PAEK) family which are selected to reduce its melting point in order to improve processing, particularly for thermal bonding scenarios and is referred to by its suppliers as low-melt PAEK (LMPAEK). To make a comparison between the bond properties of laminates which had a higher surface resin fraction, additional LMPAEK laminates were obtained from Toray which included an additional preconsolidated film on the surface. One side of the surface-resin modified LMPAEK composite was consolidate with an additional LMPAEK film while the other side had a polyethylenimine (PEI) film. This allowed inserts to be flipped to vary whether insert/injected melt interface was on the LMPAEK or PEI side of the laminate. Two different grades of injected material were used to manufacture overmoulded lap-shear specimens. These were two different grades of polyetheretherketone (PEEK) which contained different concentrations of discontinuous reinforced carbon fibres. The two grades of material were Evonik's Vestakeep 2000 CF30 (30wt% carbon) and Vestakeep 4000 CF10 (10wt% carbon) and are abbreviated as V2000 CF30, and V4000 CF10 throughout this work. These two grades of material contain PEEK of a different range of molecular

weights, with V2000 being lower than V4000. PEEK is a polymer within the greater PAEK family and as such highly compatible with both PEI and LMPAEK.

Overmoulding was performed using an Arburg Allrounder 520 S injection moulding machine. The mould block was cooled by pressurised water and produced rectangular coupons of dimensions 144 x 20 mm. Lap-shear specimens were manufactured from the overmoulded bi-material specimens by milling a channel on either side of the specimen, allowing a one-inch overlap about its centre.

2.1 Simulation of the overmoulding process

The overmoulding process was simulated using the Volume of Fluid (VoF) method in the simulation package Ansys Fluent. The following continuity equation is solved for each phase of index i. The continuous phase is denoted by the subscript 1 [6]:

$$\frac{1}{\rho_1}\left[\frac{\delta}{\delta t}(\alpha_i\rho_i) + \nabla\cdot(\alpha_i\rho_i\vec{u})\right] = S_{\rho,i} \tag{1}$$

where ρ is density, t is time in seconds, α is the volume fraction, $\vec{u}$ is the velocity vector. $S_{\rho,i}$ is a density sink term used to return the air pressure to ambient within an enclosed mould. The momentum conservation equation is calculated for a shared velocity field with volume-averaged properties [6]:

$$\frac{\delta}{\delta t}(\rho\vec{u}) + \nabla\cdot(\rho\vec{u}\vec{u}) = -\nabla p + \nabla\cdot\bar{\bar{\tau}} + S_{mo,i} \tag{2}$$

where p is pressure, $\bar{\bar{\tau}}$ is the stress vector and $S_{mo,i}$ is the component i of the momentum source term to balance the momentum equation based on the extracted air. The energy equation is calculated for a shared field:

$$\frac{\delta}{\delta t}(\rho E) + \nabla\cdot\left(\vec{u}(\rho E + p)\right) = \nabla\cdot\left(k\nabla T + (\bar{\bar{\tau}}\cdot\vec{u})\right) + S_E \tag{3}$$

E is the energy contained within a cell, k is thermal conductivity, T is temperature. S_E balances the energy equation for the extracted continuous phase for the shared energy field, similar way to S_{mo}.

Separate material properties are implemented for the composite substrate and the polymer film layer at the insert surface, allowing their relative influence on the heat transfer process to be captured. Figure 2 shows the layers of material used in the insert region of the simulation of heat transfer during the overmoulding process.

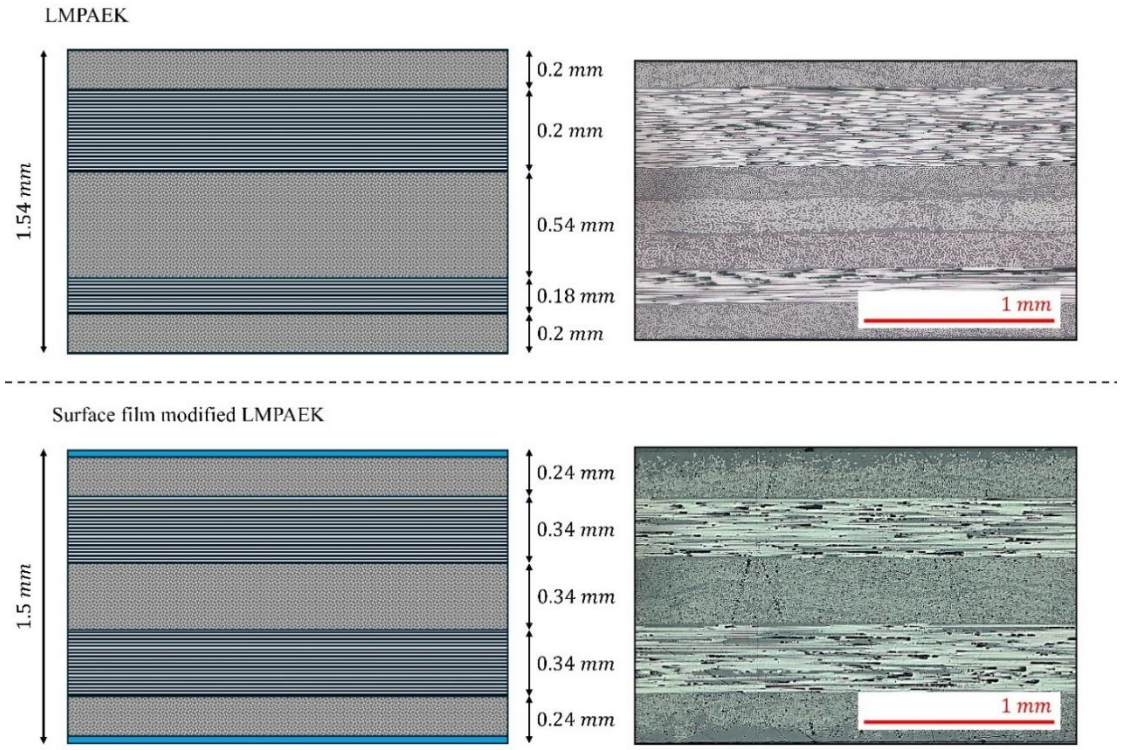

Figure 2: Diagram of the composite thermal domain (left) are shown next to micrographs (right) used to determine dimensions. Images are extracted such that the flow direction is normal to the plane of observation.

For solid composite regions an estimation of specific heat capacity, density, and thermal conductivity was required to compute the heat flux. The rule of mixtures in either the series (Voigt Model) or parallel form (Reuss Model) were used in each of the layers of the composite insert, considering their orientation. As there is a continuous path of fibres to transfer heat, the thermal conductivity in the fibre direction was calculated through the Voigt model (Eq. 4) in addition to all scalar material properties. In the transverse directions, the fibre material is discontinuous and insulated by the matrix material. In this case, the homogenised thermal conductivity is typically closer to its theoretical minimum and the Reuss Model (Eq. 5) offers a better estimation [7].

The Voigt model was implemented for thermal conductivity in the longitudinal direction of the fibres as well as for all scalar properties:

$$P_c = P_f V_f + P_m(1 - V_f) \tag{4}$$

where P represents a generic material property. The subscript c denotes the property relating to the composite whereas f and m relate to its fibre and matrix constituents, respectively. V_f is the fibre volume fraction. The rule of mixtures was applied in the parallel form (Reuss model) to model thermal conductivity in the transverse and vertical directions relative to fibre alignment:

$$\frac{1}{P_C} = \frac{1}{P_f} V_f + \frac{1}{P_m}(1 - V_f) \tag{5}$$

The thermal properties of carbon fibre were extracted from the Toray T300 datasheet. Polymer thermal properties were sourced from the Moldflow database.

3 RESULTS & DISCUSSION

The results of the single lap-shear tests are displayed in Table 1 where they are referred to by their injected material and, where applicable, the presence of a surface film layer is denoted by the brackets. For both injected PEEK grades, the lap-shear strength is improved considerably with the consolidated surface film when compared to the unmodified laminate. Generally, the mean values of lap-shear strength are higher for the 30% carbon fibre loaded injected PEEK overall. However, considerable variation in results are noted for some material configurations, notably the V2000 CF30 (unmodified) and V4000 CF10 with LMPAEK film. However, the material configurations with a PEI film interface generally defies this rule as the lap-shear strength is marginally higher at the lower injected melt fibre concentration. The PEI film also performs marginally better than the LMPAEK surface film, with both higher lap-shear strength and low standard deviation for both injected melt configurations.

Specimen	Lap-shear strength (MPa)
V2000 CF30	9.7 ∓ 4.5
V2000 CF30 (PEI)	16.8 ∓ 0.9
V2000 CF30 (LMPAEK)	15.2 ∓ 0.2
V4000 CF10	7.9 ∓ 1.4
V4000 CF10 (PEI)	18.6 ∓ 0.7
V4000 CF10 (LMPAEK)	14.4 ∓ 2.4

Table 1: Interface strength as measured by single lap-shear tests for all specimen configurations.

The strength of thermally bonded thermoplastic interfaces is known to be closely related to the temperature of the interface and welding time. A spatial dependence on temperature is observed in Figure 3 which occurs due to the variation in time of contact of the injected melt flow with the substrate. In all configurations a significantly higher interface temperature is observed in a localised region near the injection gate due to longer contact time.

The interface temperature after the pressure/velocity switch-over is substantially higher for all configurations when comparing the those with an applied surface film to those which have no film present on the surface. The primary mechanism responsible for this is the increase in the ability of the PEEK melt to transfer heat to the interface (thermal effusivity) at higher carbon fibre concentrations due to an increase in thermal conductivity. Since the time for bonding of thermoplastic polymers through ‘interdiffusion’ is closely related to temperature and time, and is the primary mechanism responsible for interface formation, an increase in interface temperature is likely to be the primary cause of the increase in lap-shear strength in all film configurations results when compared to the unmodified laminate with low surface resin depth present. A higher CF concentration within the injected polymer also results in a comparably higher interface temperature due to an increased thermal effusivity of the phase which allows heat to be exchanged more easily from the injected melt to the interface.

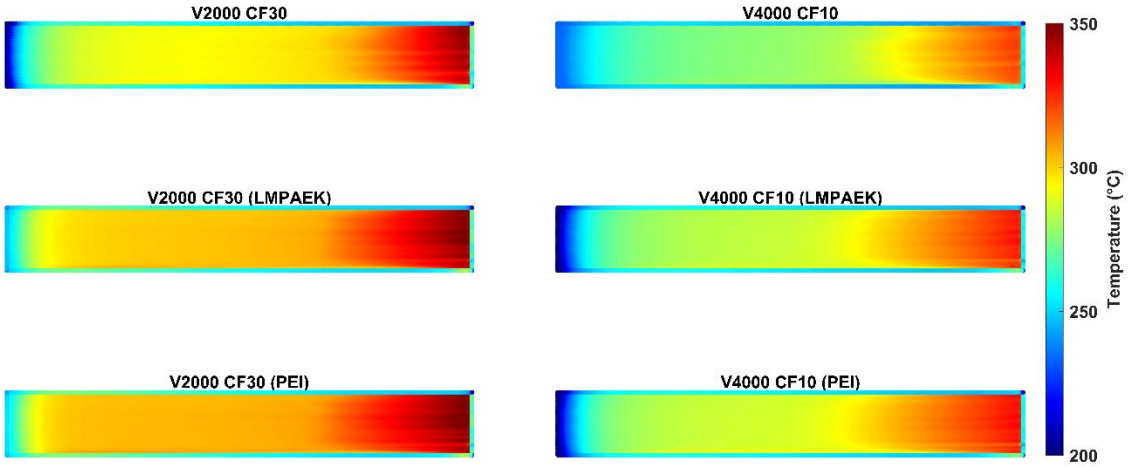

Figure 3: Contours of interface temperature during simulation of the overmoulding process, recorded at the pressure-velocity switch-over.

4 CONCLUSIONS

Overall, it was demonstrated that the interface strength can be improved through the modification of the local thermal diffusivity in the vicinity of the interface. In the case of unidirectional fibre reinforcement, a high volume fraction of carbon fibres may provide useful mechanical properties but at the cost of a high thermal diffusivity. A high thermal diffusivity can prevent the development of a strong interface by increasing the energy flux through the insert and away from the interface where a high temperature promotes the formation of a strong bond. Through a relatively minor surface modification, the local diffusivity at the interface is improved, resulting in the development of a strong bond. Modification of the surface resin depth in this case improves the interfacial bond strength without altering the laminate reinforcement. The results of this study are useful for the design of overmoulded structures. This is especially the case for those which require a high volume fraction of carbon fibres such as in load-bearing structures. The simulation process developed is also useful for this purpose and could be used to optimise the surface resin depth of the composite for both insert composite strength and interface strength of the overmoulded composite.

ACKNOWLEDGEMENTS

The authors gratefully acknowledge the contributions of the following industry and institutional partners: Collins Aerospace UK, and the Polymer Processing Research Centre (PPRC) at Queen's University Belfast (currently part of Advanced Manufacturing Innovation Centre (AMIC)) for their expertise in the design and manufacture of overmoulded composite components. This work was supported by funding from the Department for the Economy (DfE), and the Engineering and Physical Sciences Research Council (EPSRC) under the OVERCOMP project (EP/X041360/1).

REFERENCES

[1] M. A. Aravand, "Composite Injection Overmoulding," in *Design and Manufacture of Structural Composites*, L. Harper and C. M. Eds.: Woodhead Publishing, 2022.

[2] A. Islam, H. N. Hansen, and M. Bondo, "Experimental investigation of the factors influencing the polymer–polymer bond strength during two-component injection moulding," *The International Journal of Advanced Manufacturing Technology,* vol. 50, no. 1-4, pp. 101-111, 2010.

[3] M. A. Aravand and B. G. Falzon, "Characterisation of the interfacial bonding at solid/melt interfaces in multiphase carbon fibre reinforced thermoplastic composites," in *International Conference on Composite Materials (ICCM21)*, 2017.

[4] R. MacLennan and M. A. Aravand, "Crystallinity-based rheological modeling for interface prediction in PEEK overmoulded composites," in *21st European Conference on Composite Materials (ECCM21)*, Nantes, France, July 2nd-5th 2024.

[5] R. MacLennan and M. A. Aravand, "Influence of fibre reinforcement on the development of interface morphology during composite injection overmoulding," in *23rd International Conference on Composite Materials (ICCM23)*, Belfast, Northern Ireland, July 30th - August 4th 2023.

[6] ANSYS, *Inc., ANSYS Fluent User's Guide, Release 2020 R2*. 2020.

[7] N. Burger, A. Laachachi, M. Ferriol, M. Lutz, V. Toniazzo, and D. Ruch, "Review of thermal conductivity in composites: Mechanisms, parameters and theory," *Progress in Polymer Science,* vol. 61, pp. 1-28, 2016/10/01/ 2016, doi: https://doi.org/10.1016/j.progpolymsci.2016.05.001.

ICCM24
AUGUST 4-8, 2025
BALTIMORE CONVENTION CENTER
BALTIMORE, MARYLAND, USA

No Technical Paper Submission for:

Keiichi Shirasu

Uncertainty Quantification of a Ductile Damage Evolution Model in an Adhesively Bonded Single Lap Shear Joint

ICCM24

August 5, 2025

Marcus Stanfield[1], Marcias Martinez[2], and John Erdman[2]

[1]*Southwest Research Institute*

[2]*Clarkson University*

Copyright © Southwest Research Institute.

NOTICE

This work relates to Department of Navy award N00014-21-1-2057 issued by the Office of Naval Research. The United States Government has a royalty-free license throughout the world in all copyrightable material contained herein.

Any opinions, findings, and conclusions or recommendations expressed in this material are those of the author(s) and do not necessarily reflect the views of the Office of Naval Research.

Outline

I. Background
II. Previous Research
III. VVUQ Approach
    I. PIRT
    II. Deterministic Sensitivity Study
    III. Surrogate Model
    IV. Global Sensitivity Analysis
    V. Bayesian Calibration
IV. Validation Testing
V. Summary & Conclusions
VI. Future Work

SwRI Overview

- Founded in 1947
- Nonprofit organization
- More than 3,100 employees
- More than 1,500 acres / 6.1 km2 facility in San Antonio, TX
- More than 2.5 million ft^2 / 232,000 m^2 of laboratories, workshops & offices
- More than 1,500 patents
- 52 R&D 100 awards
- Deep sea to deep space



Motivation

- **Bonded composite** structures are increasingly favored for their potential to reduce weight and improve structural efficiency
- Complex behavior of adhesive joints under varying load conditions necessitates **predictive modeling** approaches that can accurately simulate failure mechanisms
- This study applies the **Ductile Damage Evolution Material** (DDEM) model to single lap shear joints to predict strength and time to failure under shear loading

Previous Research: Simulation

- Single Lap Shear Joint (SLSJ)

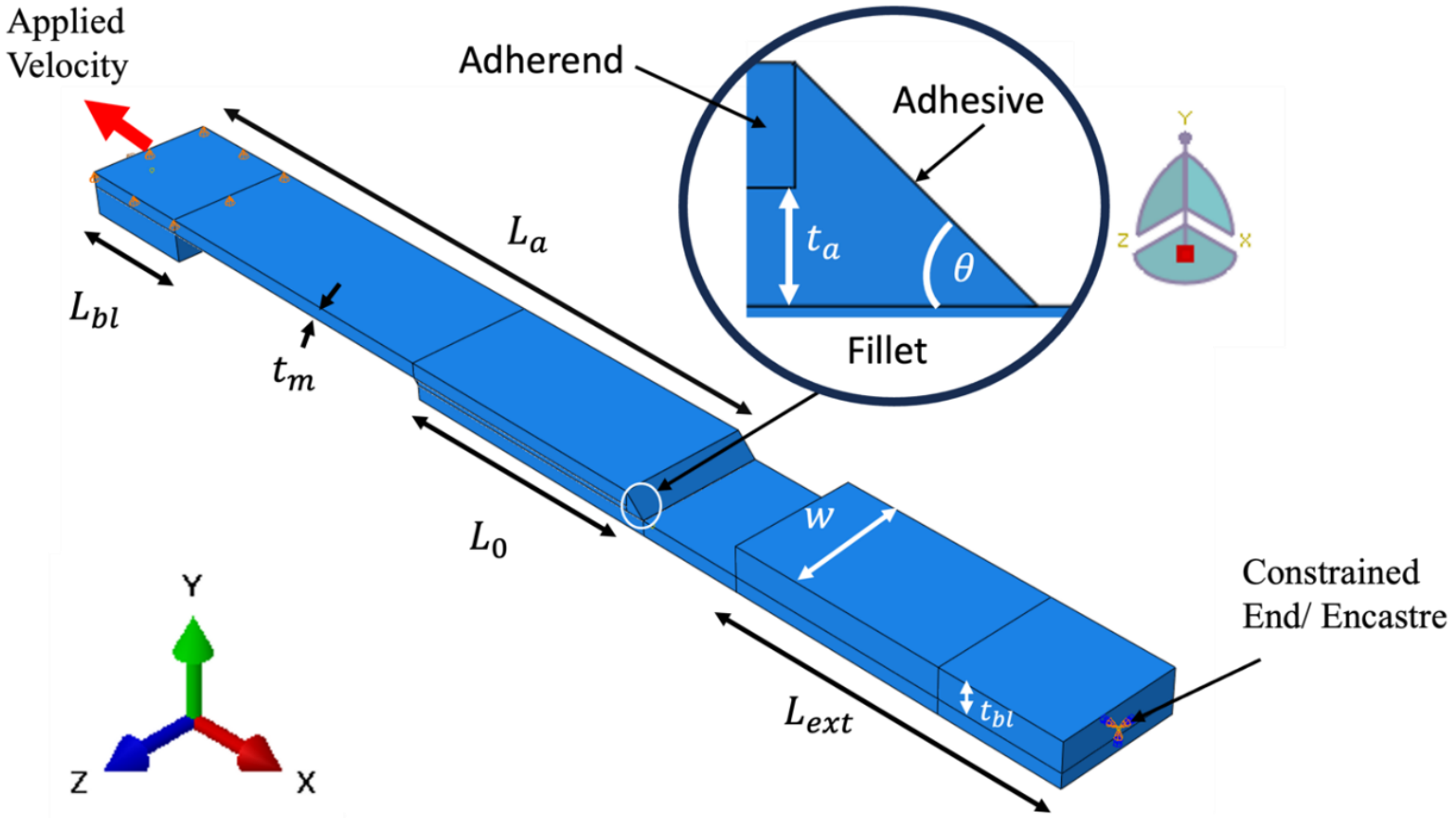

Single Lap Shear Joint Dimensions	
Parameter	**Value (mm)**
t_m	3.18
t_a	1.00
t_b	4.18
L_O	61.10
L_a	150.00
L_{bl}	25.40
L_{ext}	60.00
w	25.40
θ	45°

Previous Research: Material Characterization

- Adherend and adhesive tensile tests

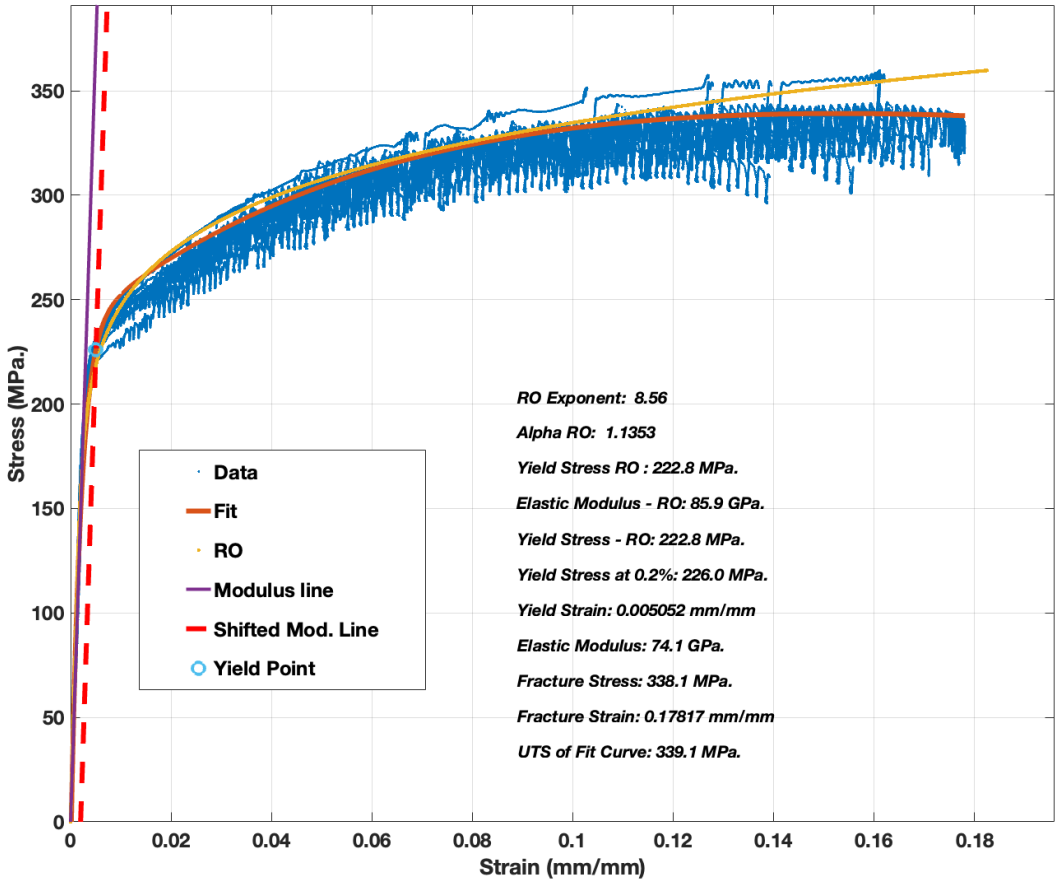

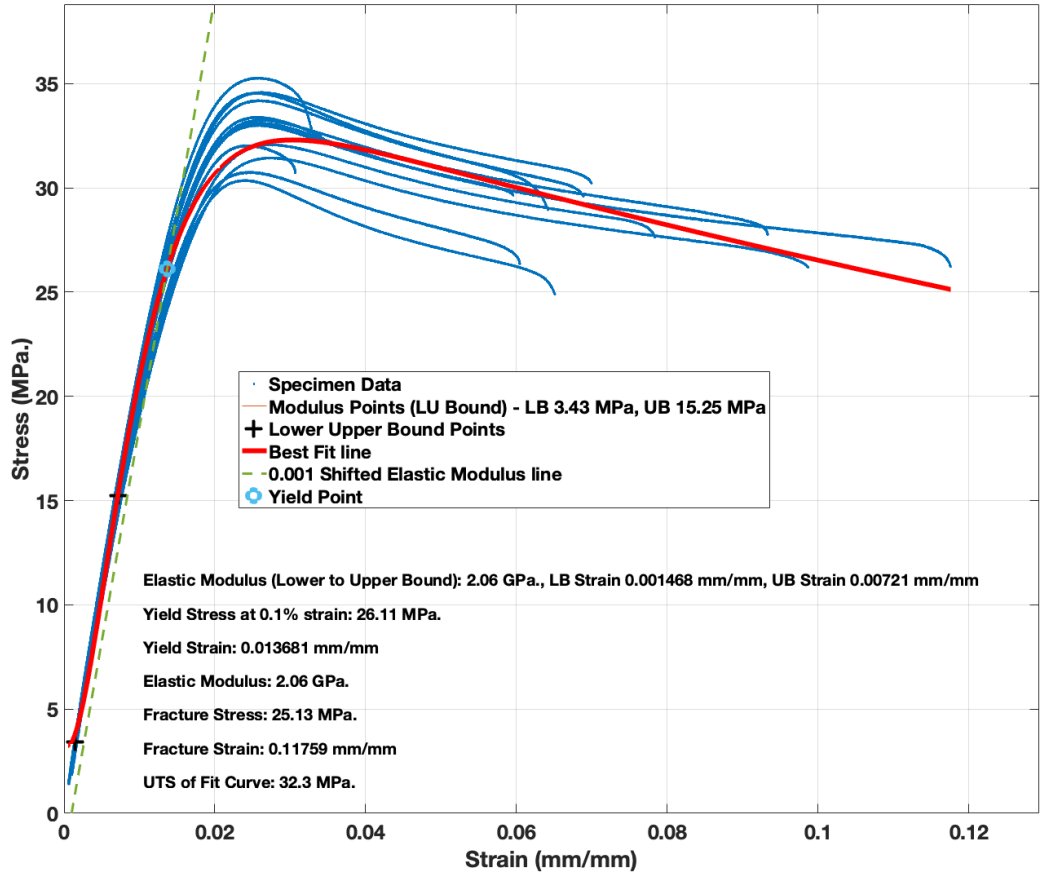

Previous Research: Experimental Results

- SLSJ Strength
- Time-to-failure
- Simulation prediction
  - Pretty good strength
  - Terrible time-to-failure
- Initial conclusion was to investigate the effect of the adherend response

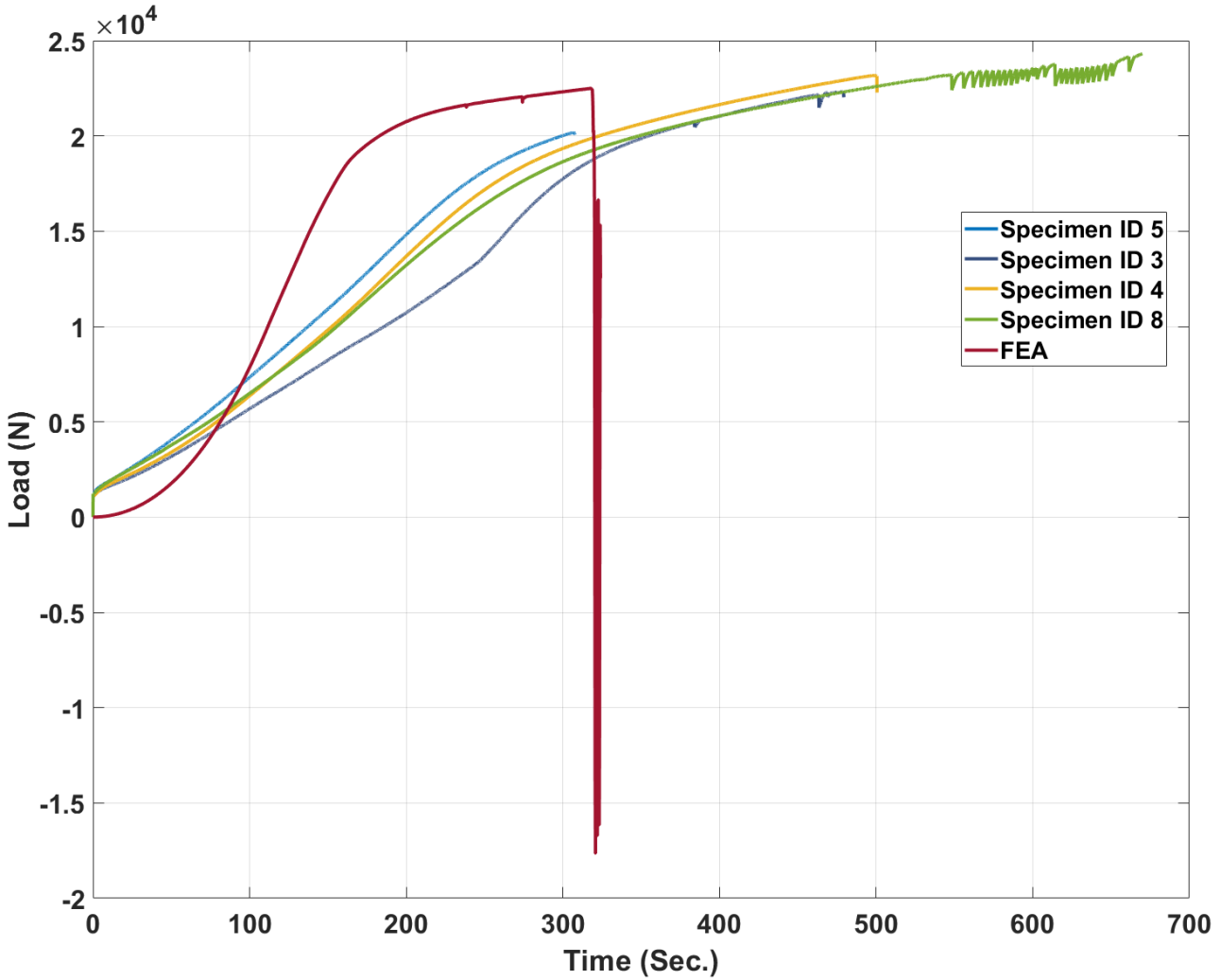

VVUQ Approach

- Parameterize model
- Establish PIRT
- Identify sensitive parameters
- Build surrogate model
- Global Sensitivity Analysis
- Bayesian Model Calibration

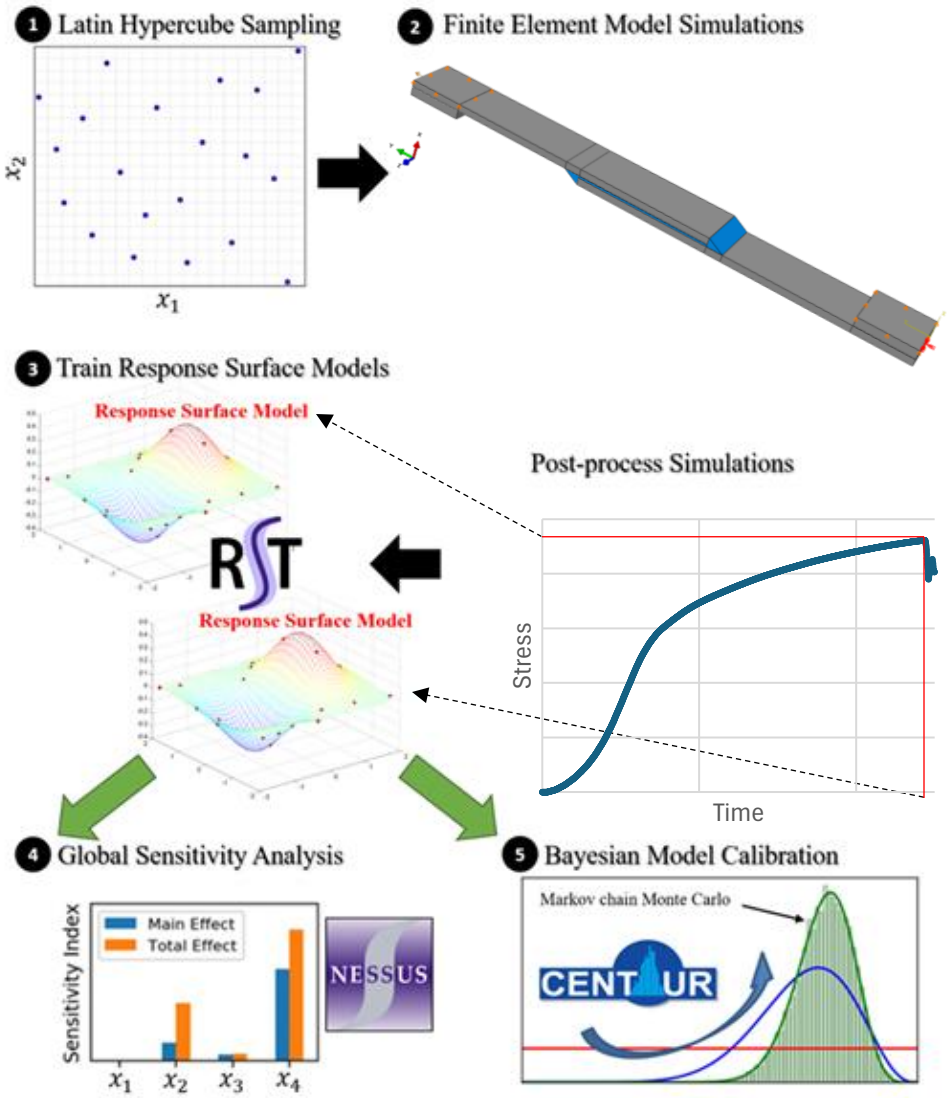

PIRT

- Phenomena (Parameter) Identification Ranking Table
- Engineering judgement
- Quantify parameter uncertainties

Parameter	Symbol	Nominal Value	Variance	Deviation	Distribution	Low	High	Importance	Confidence
Geometry									
Specimen Width	W	0.02540	5%	0.00127	Triangular				
Overlap Length (Adhesive Length)	L_a	0.05000	50%	0.02500	Uniform	0.025	0.075		
Adhesive Thickness	t_a	0.00100	20%	0.00020	Triangular	0.00080	0.00120		
Adhesive Flash Angle	theta	60.0	10%	6.00000	Normal	42	78		
Fixed Adherend Length	L_ae	0.15000	5%	0.00750	Triangular				
Fixed Adherend Thickness	t_ae	0.003175	5%	0.00016	Triangular				
Load Adherend Length	L_al	0.15000	5%	0.00750	Triangular				
Load Adherend Thickness	t_al	0.003175	5%	0.00016	Triangular				
Fixed Block Length	L_be	0.02540	5%	0.00127	Triangular				
Fixed Block Thickness	t_be	t_al + t_a							
Load Block Length	L_bl	0.02540	5%	0.00127	Triangular				
Load Block Thickness	t_bl	t_ae + t_a							
Adherend Material Properties									
Modulus of Elasticity	E_b	7.104E+10	8%	5.918E+09	Normal	53287104000	88792896000		
Poisson's Ratio	nu_b	0.31	5%	0.0155	Normal				
Density	rho_b	2650.0	5%	132.5	Normal				
Yield Strength	Sy_b	186000000	4%	7626000	Normal	163122000	208878000		
Mod Ram. Osg. Power Term	n_b	5.7	3%	0.14	Normal	5.310	6.171		
Adhesive Material Properties									
Modulus of Elasticity	E_a	2.060E+09	4%	7.828E+07	Normal	1825160000	2294840000		
Poisson's Ratio	nu_a	0.40	5%	0.02	Normal				
Density	rho_a	1218.0	5%	60.9	Normal				
Yield Strength	Sy_a	28300000.0	5%	1386700	Normal	24139900	32460100		
Ram. Osg. Power Term	n_a	11.6	7%	0.85	Normal	9.035	14.165		
Fracture Strain	fs_a	0.03169	9%	0.00273	Normal				
Stress Triaxiality	st_a	-0.130	10%	-0.013	Normal				
Strain Rate	sr_a	4.33E-04	10%	4.33E-05	Normal				
Damage Reduction	dr_a	1.29E-03	17%	2.19E-04	Normal				
Damage Displacement	dd_a	1.63E-05	36%	5.87E-06	Normal	0.00000456	0.00002804		
Loading									
Crosshead Rate	velocity	2.167E-05	1%	2.17E-07	Normal				
Load Ramp		Tabular			Deterministic				
Solver Parameters									
Time Period		1050			Deterministic				
Time Points		Tabular			Deterministic				
Mass Scaling		0.01			Deterministic				
Adherend Mesh Density	mesh_adherends	0.001			Deterministic				
Adhesive Mesh Density	mesh_adhesive	0.0001			Deterministic				

Deterministic Sensitivity Study

- Central differencing of nominal parameters with a standard deviation of 1*σ
- Used to identify highest sensitivities
- Down select parameters for next steps
- Adhesive angle identified

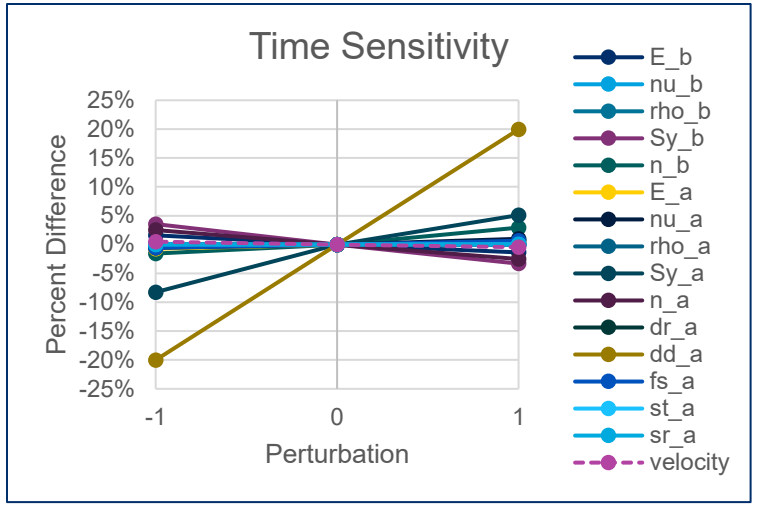

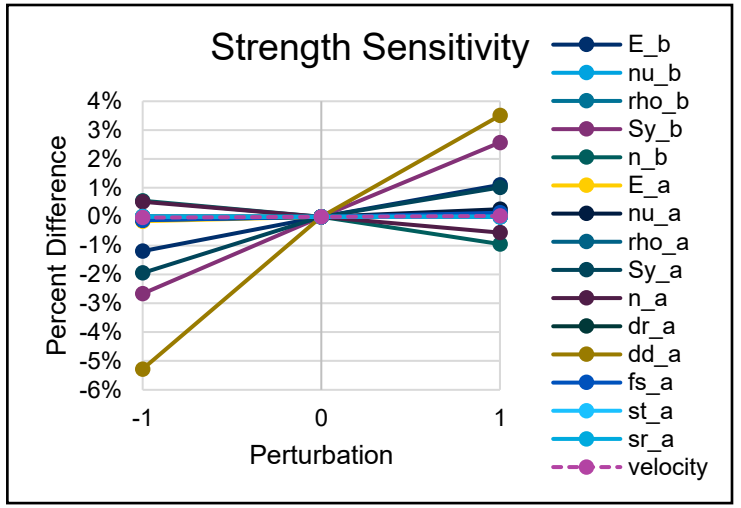

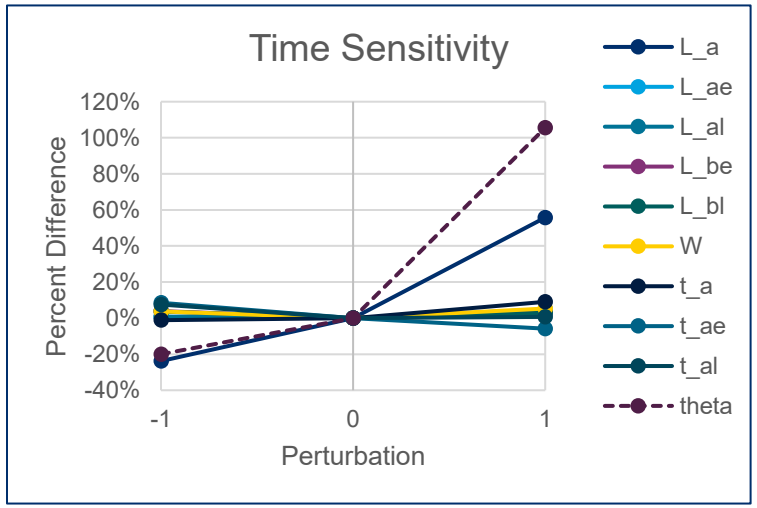

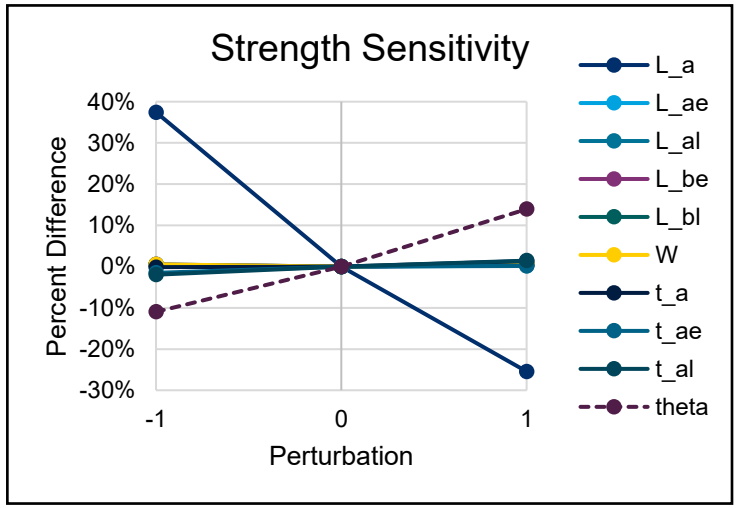

Adhesive Angle Measurement

- Using an optical microscope, the adhesive fillet angles were measured
- Previous assumption was 45 degrees
- Angle was measured closer to 30 degrees

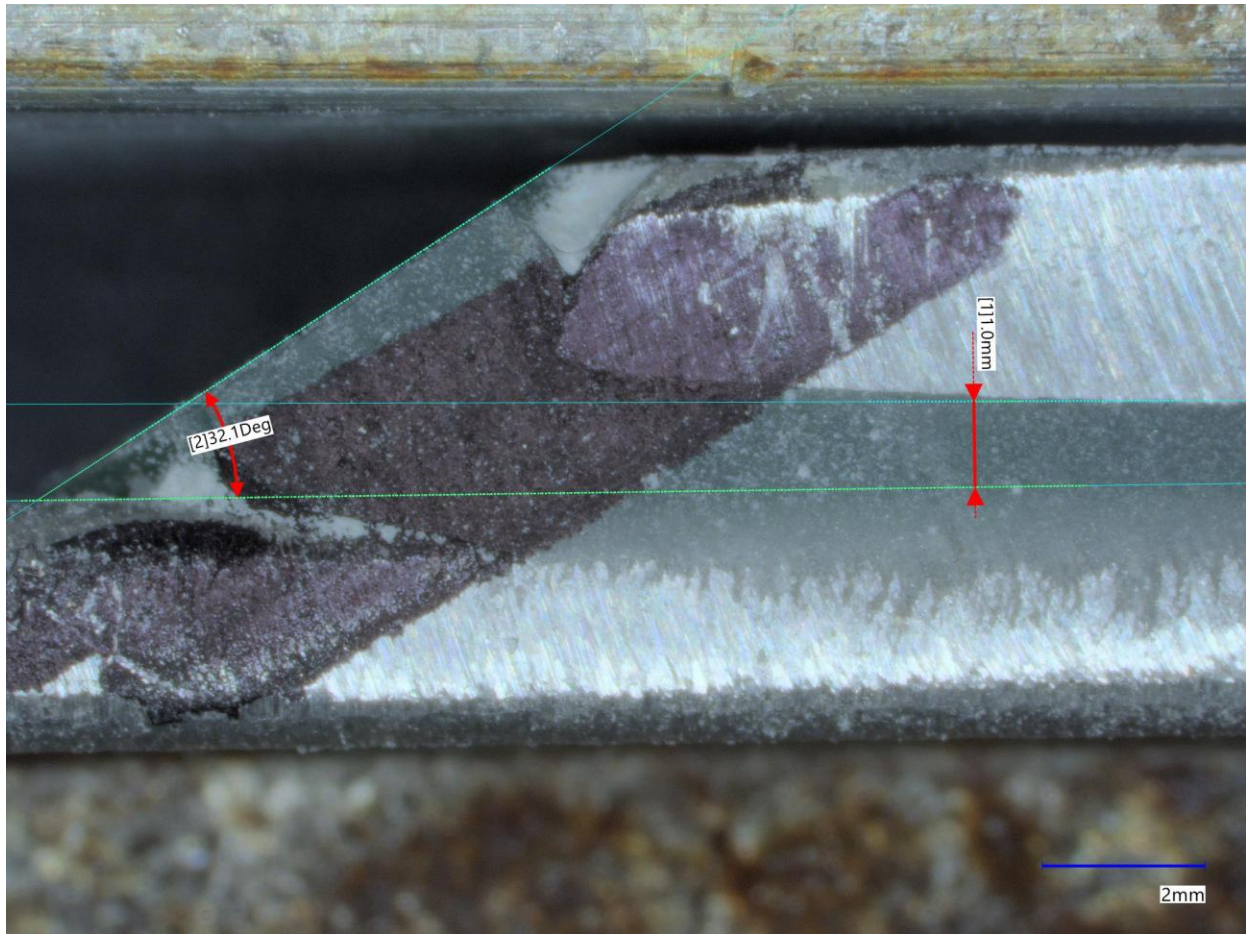

Surrogate Model

- Response Surface created using NESSUS RST
- Latin Hypercube Sampling (LHS) used to generate domain of inputs
- Uniform distribution +/- 3σ
- Typically use 10*variables simulations
- 5% of simulations failed in the adherend, removed from training data
- Gaussian Process Model
- LOO cross-validation

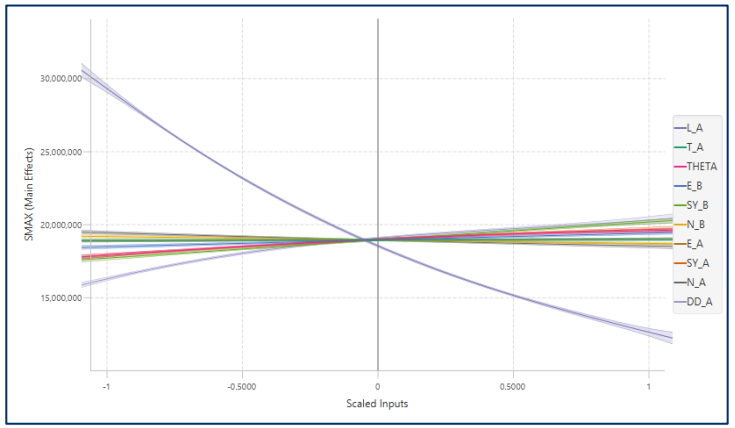

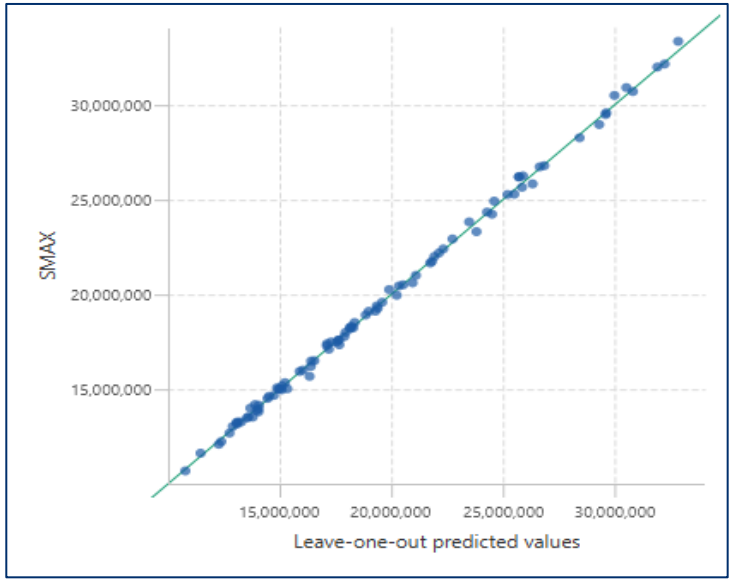

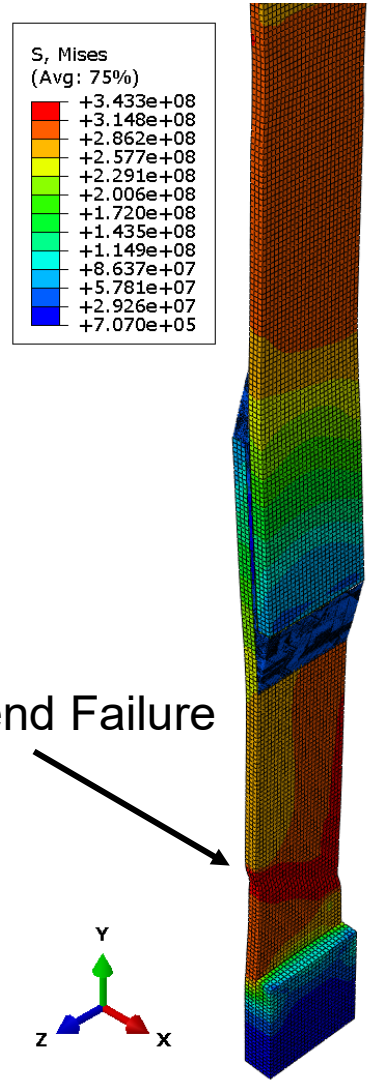

Global Sensitivity Analysis

- Monte Carlo: 100,000 samples
- Sobol indices
- Time-to-failure effects
  - Damage Evolution
  - Adhesive Angle
  - Adhesive Yield Stress
- SLSJ Strength
  - Damage Evolution
  - Overlap Length
  - Adherend Yield Stress

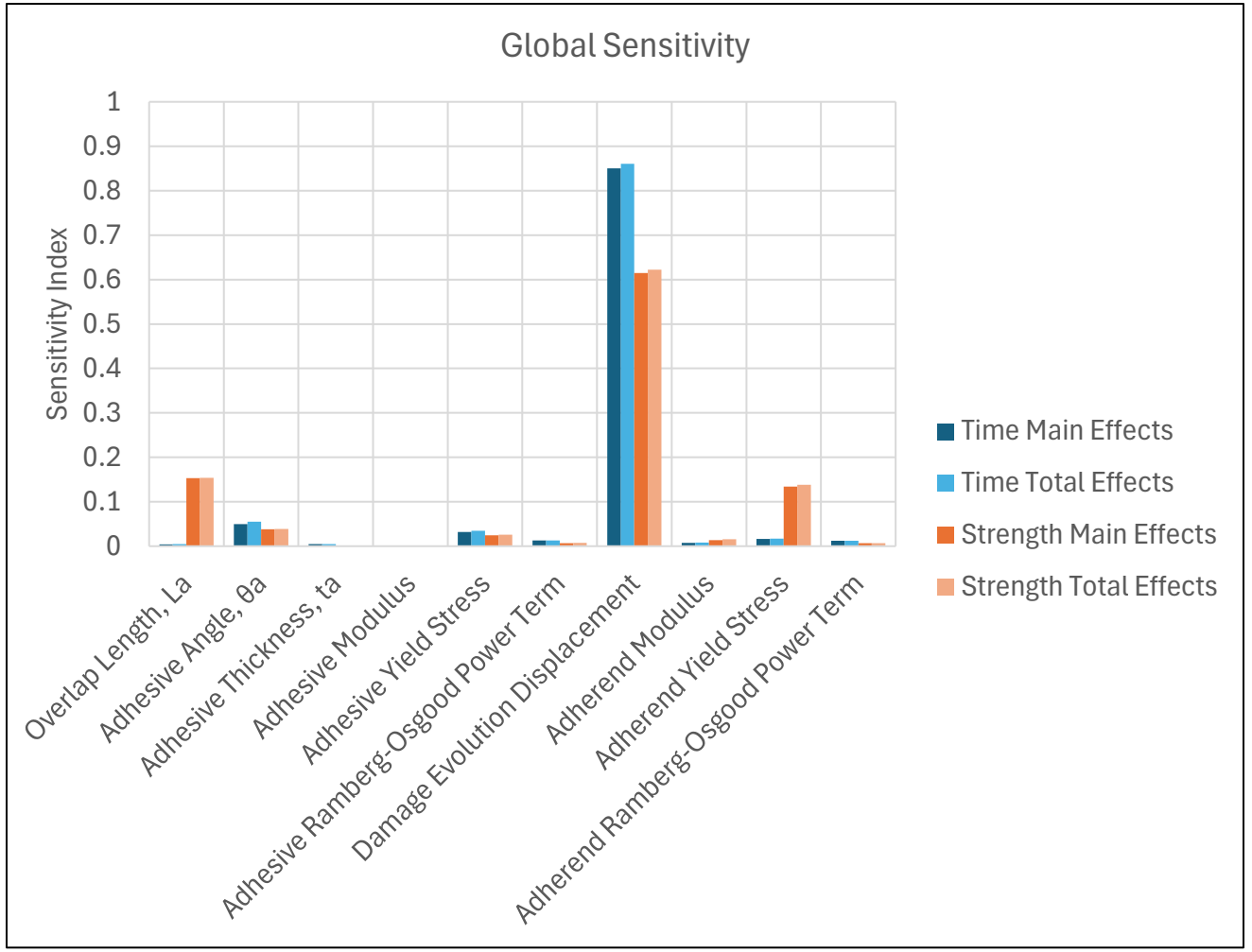

Bayesian Calibration

- Goals
  - Obtain a set of likely model parameters that predicts the two responses of the SLSJ model
  - Capture uncertainty in calibration parameters due to limited data
- Down-selected calibration parameters based on sensitivity analysis
- Used uniform prior distributions
- Likelihood function:

$$L(\theta) = L_{SLSJ,S_{max}}(\theta) \cdot L_{SLSJ,T_{failure}}(\theta)$$

$$L_{SLSJ,S_{max}}(\theta) = \prod NormPDF(GP_{SLSJ,Smax}(\theta) - SLSJ_{S_{max},i}, \sigma_{SLSJ,Smax})$$

- Strength & time-to-failure within 5% of the test data

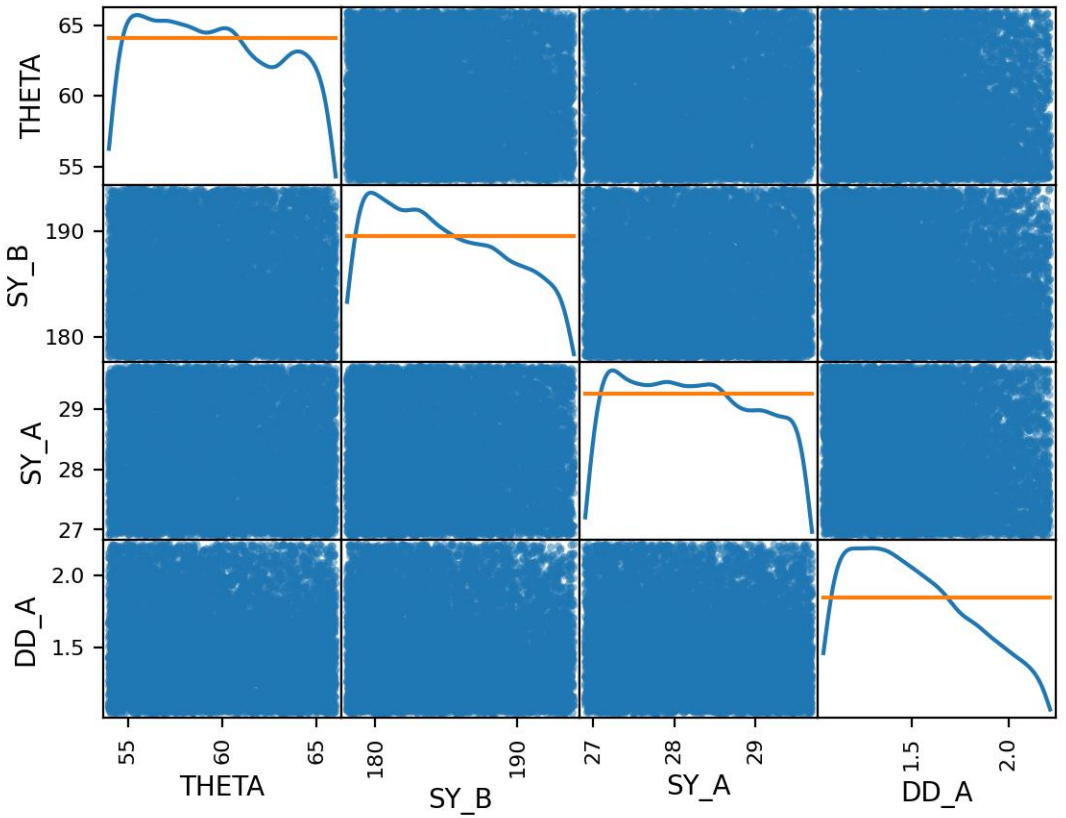

Validation Testing

- Overlap length (30, 60, 75)
- Fillet angle (30, 45, 60)
- FEM accuracy:
  - 7% for strength
  - 17% for time
- NESSUS surrogate model
  - 12% for strength
  - 19% for time

	Specimen Geometry		NESSUS RST		FEA		Test Results		Strength Error (%)		Time Error (%)	
Serial Number	Overlap Length	Fillet Angle	Load	Time	Load	Time	Load	Time	FEA	NESSUS	FEA	NESSUS
SLSJ-25-30-001	0.02881	33.0	21211	264.7	18855	309.6	15200	253.0	24.0	39.5	22.4	4.6
SLSJ-25-30-002	0.02778	37.6	20036	238.2	18010	279.2	15214	226.0	18.4	31.7	23.5	5.4
SLSJ-25-30-003	0.02408	32.0	17801	270.7	16741	248.2	14752	220.0	13.5	20.7	12.8	23.0
SLSJ-25-45-001	0.02731	36.5	19800	244.4	17915	275.8	16822	244.0	6.5	17.7	13.0	0.2
SLSJ-25-45-002	0.02507	37.2	18119	240.5	16898	246.8	15353	273.0	10.1	18.0	9.6	11.9
SLSJ-25-45-003	0.02663	42.6	18761	211.5	17085	250.0	15862	210.0	7.7	18.3	19.0	0.7
SLSJ-25-60-001	0.03153	45.9	21842	195.3	18775	305.0	17398	302.0	7.9	25.5	1.0	35.3
SLSJ-25-60-002	0.03001	49.4	20412	179.5	17727	269.2	18024	252.0	1.6	13.3	6.8	28.8
SLSJ-25-60-003	0.02783	46.2	19251	193.9	17456	254.8	17676	296.0	1.2	8.9	13.9	34.5
SLSJ-60-30-001	0.06533	34.8	25626	497.5	23959	567.4	21669	345.6	10.6	18.3	64.2	44.0
SLSJ-60-30-002	0.07306	31.0	28950	513.8	23956	519.4	20711	438.9	15.7	39.8	18.3	17.1
SLSJ-60-30-003	0.05975	34.5	23467	498.9	23599	557.8	22195	475.0	6.3	5.7	17.4	5.0
SLSJ-60-30-004	0.06100	42.9	24187	543.3	23208	525.0	21153	409.5	9.7	14.3	28.2	32.7
SLSJ-60-45-001	0.06264	42.4	23333	457.6	22900	481.0	23593	500.0	2.9	1.1	3.8	8.5
SLSJ-60-45-002	0.05943	31.5	23519	511.8	23847	587.6	22589	450.0	5.6	4.1	30.6	13.7
SLSJ-60-45-003	0.07387	38.6	26099	480.9	23104	441.4	24405	682.0	5.3	6.9	35.3	29.5
SLSJ-60-60-001	0.06156	51.6	22762	409.9	22136	456.2	24521	518.0	9.7	7.2	11.9	20.9
SLSJ-60-60-002	0.05868	39.0	22739	477.5	23154	515.2	24756	750.0	6.5	8.1	31.3	36.3
SLSJ-60-60-003	0.06352	55.9	23042	385.9	22046	437.0	23400	480.0	5.8	1.5	9.0	19.6
SLSJ-75-30-001	0.07482	28.6	23718	456.4	24233	536.0	24889	585.0	2.6	4.7	8.4	22.0
SLSJ-75-30-002	0.07354	30.6	23275	450.7	23802	499.0	22319	441.0	6.6	4.3	13.2	2.2
SLSJ-75-30-003	0.07295	32.1	23070	446.5	23244	454.0	22668	606.0	2.5	1.8	25.1	26.3
SLSJ-75-45-001	0.06936	44.2	21675	412.9	23172	471.8	23215	508.0	0.2	6.6	7.1	18.7
SLSJ-75-45-002	0.07246	38.4	22789	428.9	23264	461.0	24422	474.0	4.7	6.7	2.7	9.5
SLSJ-75-45-003	0.07546	32.9	23845	444.3	23533	463.0	23190	526.0	1.5	2.8	12.0	15.5
SLSJ-75-60-001	0.07311	53.8	22554	386.9	22116	423.0	24232	511.0	8.7	6.9	17.2	24.3
SLSJ-75-60-002	0.07476	42.9	23400	416.5	23326	458.0	25342	597.0	8.0	7.7	23.3	30.2
SLSJ-75-60-003	0.07325	50.4	22708	396.0	22582	418.0	23731	458.0	4.8	4.3	8.7	13.5
								Avg	7%	12%	17%	19%

Adherend Failure

- Failure observed during validation testing in the adherend, close to the finite element model prediction



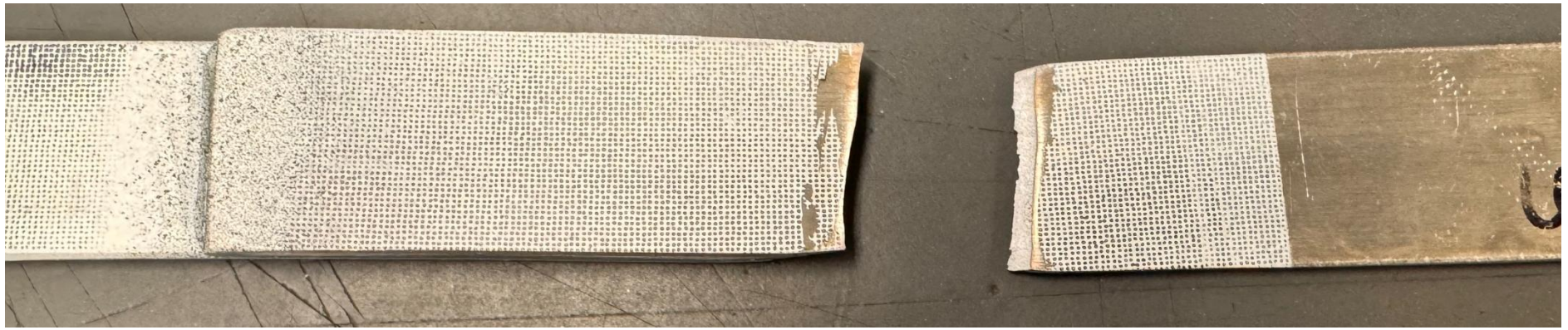

Adhesive Failure

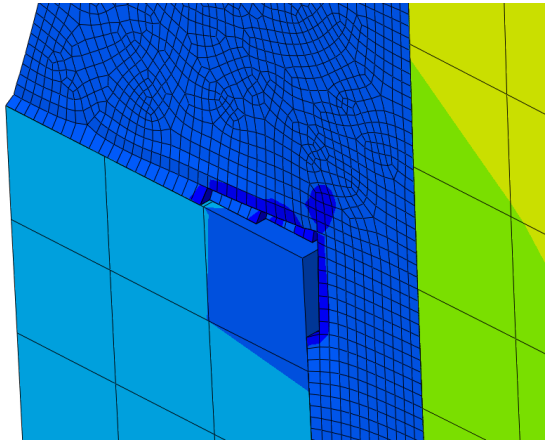

Adherend Failure

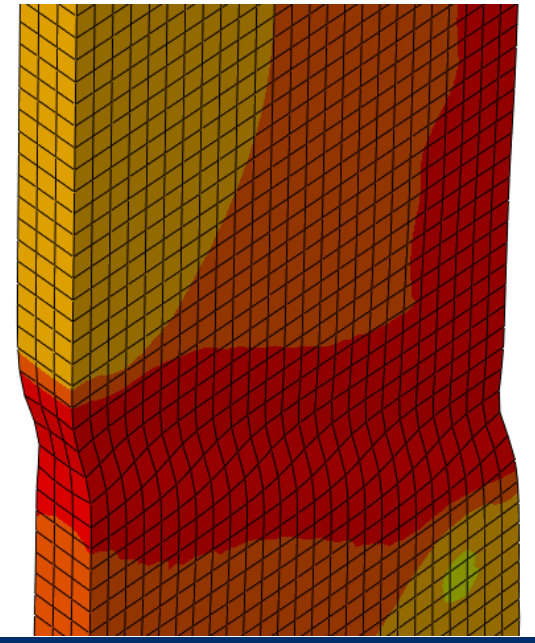

Summary & Conclusions

- VVUQ approach provided a framework to assess major sources of variability in the test and finite element models
- Variability in the fillet angle was major source of error in the initial models
- Discrete Damage Evolution Model remains highest source of uncertainty
- The surrogate model provided similar accuracy as compared to the finite element model
- Model captured adherend failure, which was then observed during validation testing

Future Work

- Double Lap Shear Joint (DLSJ) – currently running LHS to create surrogate models (4x longer simulation time than SLSJ)
- Investigate SLSJ validation testing DIC to obtain velocity ramp rate for simulation
- Deep dive sub model / coupon testing of Discrete Damage Evolution Model inputs
- Investigate adherend failure

Questions?

Budapest University of Technology and Economics (BME)

ICCM24
24TH INTERNATIONAL CONFERENCE ON COMPOSITE MATERIALS

DEPARTMENT OF POLYMER ENGINEERING

PRECISE MODE II FRACTURE TOUGHNESS CONTROL IN HIGH-PERFORMANCE COMPOSITES BY PERFORATED RELEASE FILM INTERLEAVES

Gergely CZÉL (czel.gergely@gpk.bme.hu)
Budapest University of Technology and Economics (BME)
Faculty of Mechanical Engineering
Department of Polymer Engineering

ICCM 24 – 24th International Conference on Composite Materials,
Baltimore, USA, 4-8 August 2025

Stiff, strong, lightweight!



Catastrophic failure





Delamination is a frequent failure mode in static and impact load scenarios

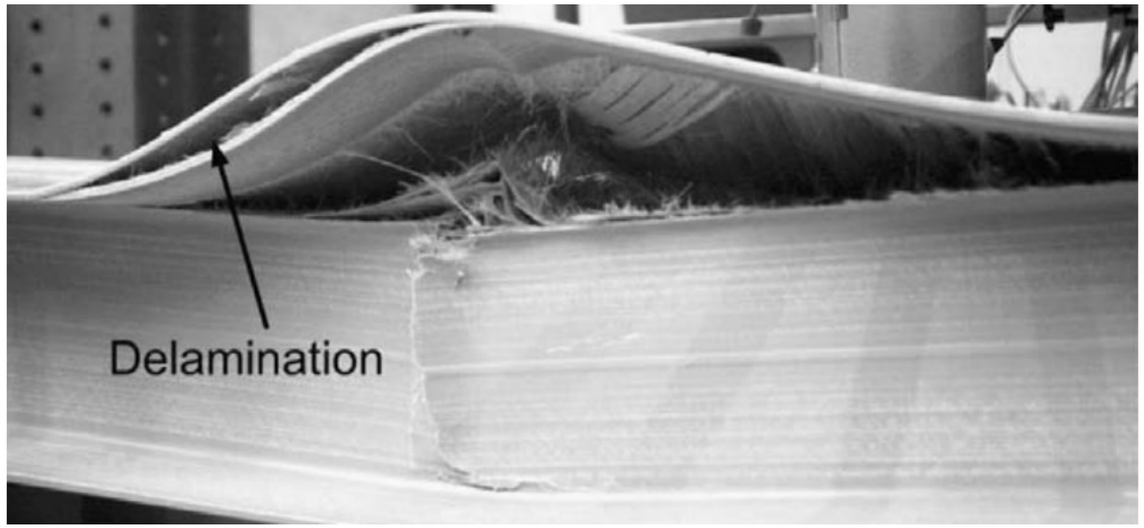



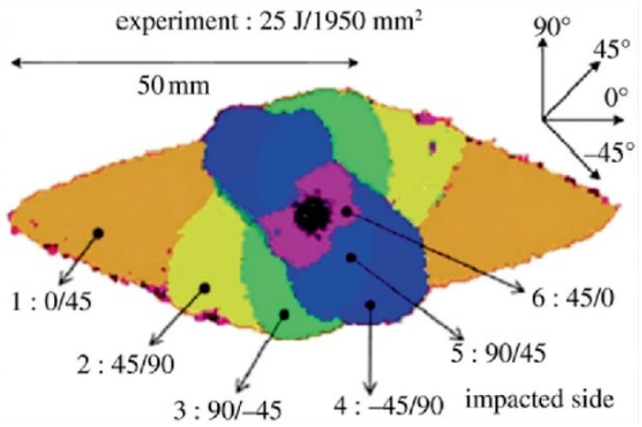

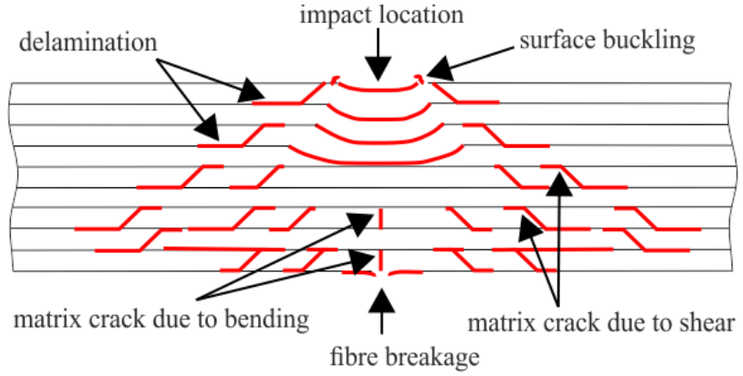

Yu Bai, Till Vallée, Thomas Keller, Delamination of pultruded glass fiber-reinforced polymer composites subjected to axial compression, Composite Structures, Volume 91, Issue 1, 2009, Pages 66-73, https://doi.org/10.1016/j.compstruct.2009.04.030.

Gębura, Andrzej. "Application of Electric Capacity Measurements to Detecting Delamination in Blades of Helicopter's Lifting and Auxiliary Rotors" Polish Maritime Research, vol. 24, no. 2, Sciendo, 2017, pp. 105-112. https://doi.org/10.1515/pomr-2017-0056

Syed Abdullah, S.I.B. (2021). Low Velocity Impact Testing on Laminated Composites. In: Hameed Sultan, M.T., Shah, A.U.M., Saba, N. (eds) Impact Studies of Composite Materials. Composites Science and Technology . Springer, Singapore. https://doi.org/10.1007/978-981-16-1323-4_1

Wronkowicz-Katunin, Angelika, and Krzysztof Dragan. "Evaluation of Impact Damage in Composite Structures Using Ultrasonic Testing" Fatigue of Aircraft Structures, vol. 2018, no. 10, Sciendo, 2018, pp. 82-92. https://doi.org/10.2478/fas-2018-0008

Introduction

- Laminated composite materials are prone to delamination, which plays a key role in their design
- Film interleaving with tough materials that bond well to the composite plies is an established approach to improve delamination resistance
- Precisely controlled reduction of the fracture toughness is useful to direct delamination damage accumulation to a chosen interface within a laminate
- Perforation patterns for release film interleaves were designed, and their geometry was analysed optically
- Tensile tests on novel central cut layer coupons were executed to obtain the mode II fracture toughness (G_{IIC}) of the interfaces

Materials

Fibre type	Manufacturer	Diameter	Elastic modulus	Strain to failure	Tensile strength	Density
		[μm]	[GPa]	[%]	[GPa]	[kg/m³]
Flite Strand S-glass	Owens Corning	9	92	3.6-4.4	3.3-4.1	2450

Prepreg type	Manufacturer	Nominal fibre areal density	Fibre volume fraction	Nominal cured ply thickness	Predicted elastic modulus	Failure strain
		[g/m²]	[%]	[mm]	[GPa]	[%]
S-glass fibre/913 epoxy (GF/EP)	Hexcel	305	49	0.25	47.1	3.9[c]

Release film type	Manufacturer	Material	Nominal thickness	Tensile strength (both directions)	Failure strain (machine direction)	Failure strain (cross direction)
			[μm]	[MPa]	[%]	[%]
Vabatec RF7	Vabatec	ETFE	15	>40	>170	>300

Perforation pattern design

Quadratic pattern

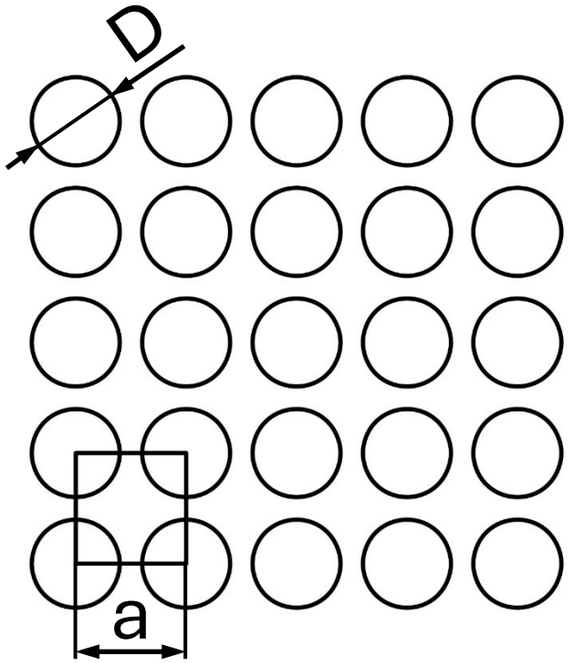

Quadratic pattern rotated by 45°

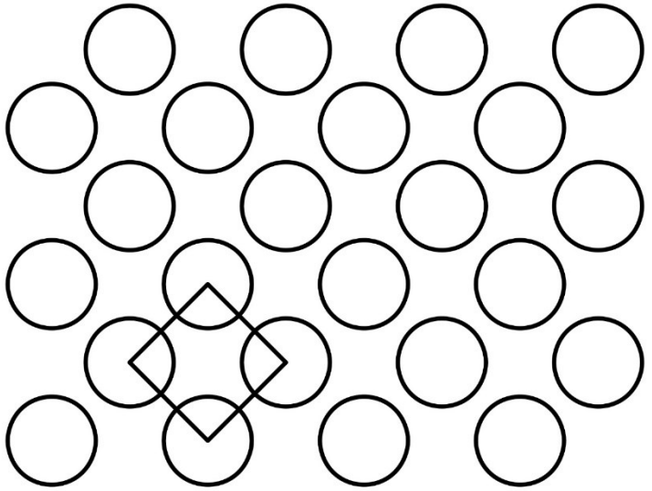

Hexagonal pattern

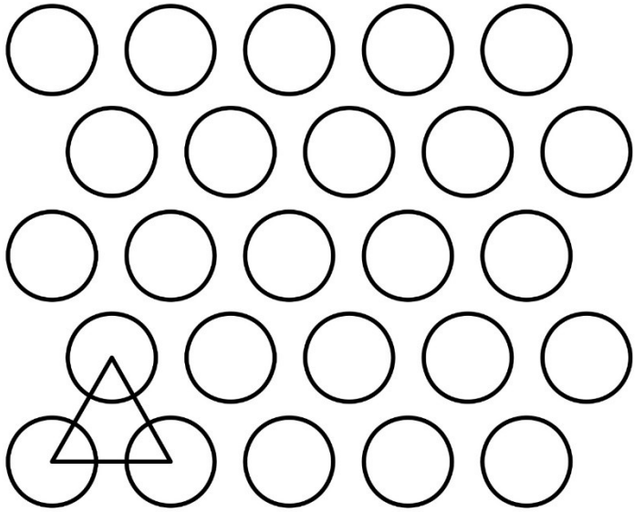

Definition of interlaminar contact area ratio:

$$ICAR = \frac{A_{PERF}}{A_{TOT}} = \frac{D^2\pi}{4a^2}$$

Centre offset for quadratic pattern:

$$a = \sqrt{\frac{\frac{D^2\pi}{4}}{ICAR}} = \sqrt{\frac{D^2\pi}{4(ICAR)}}$$

Coupon design

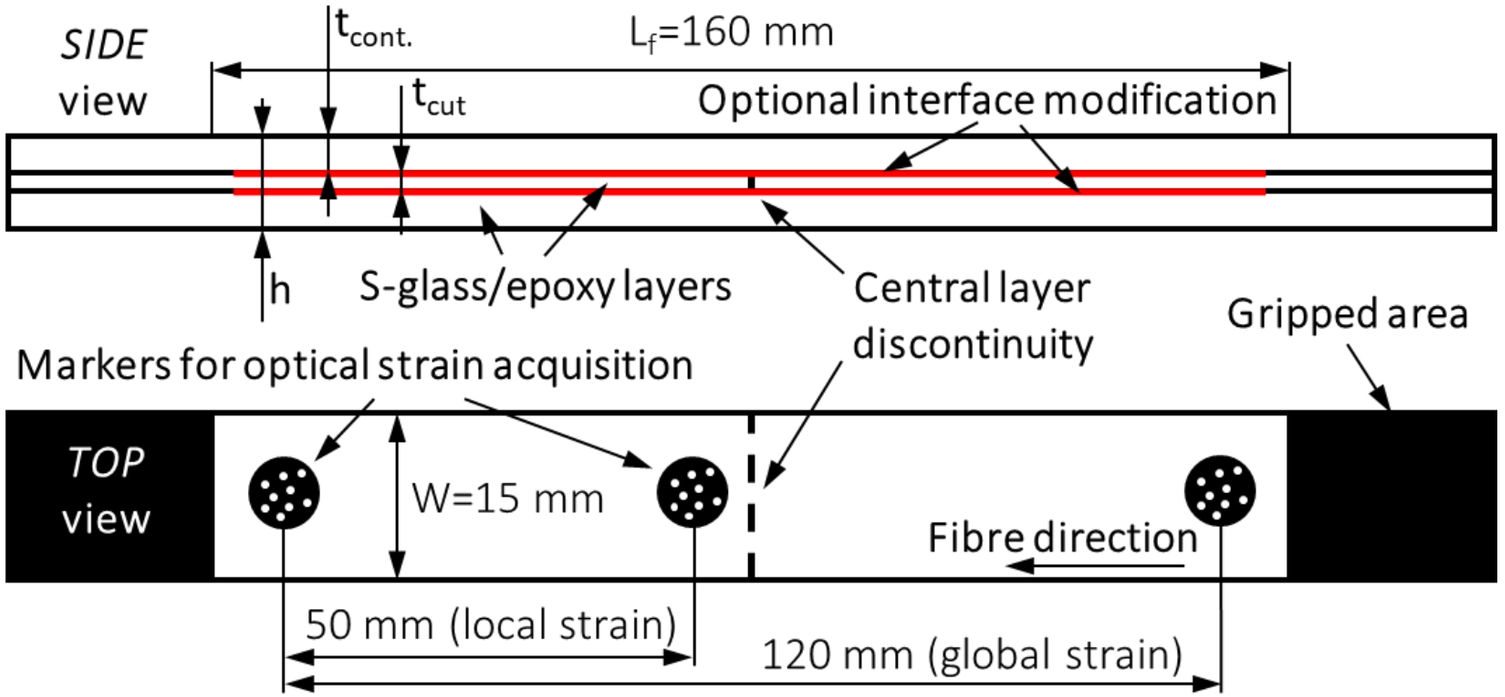

Design criteria for delamination:

$$G_{II} = \frac{E\varepsilon^2 h t_{cut}}{4(h - t_{cut})}$$

$$t_{cont} > \frac{\varepsilon_{del} E t_{cut}}{2E\left(\varepsilon_{b\,GF/EP} - \varepsilon_{del}\right)}$$

Laminate assembly, interleaf positioning

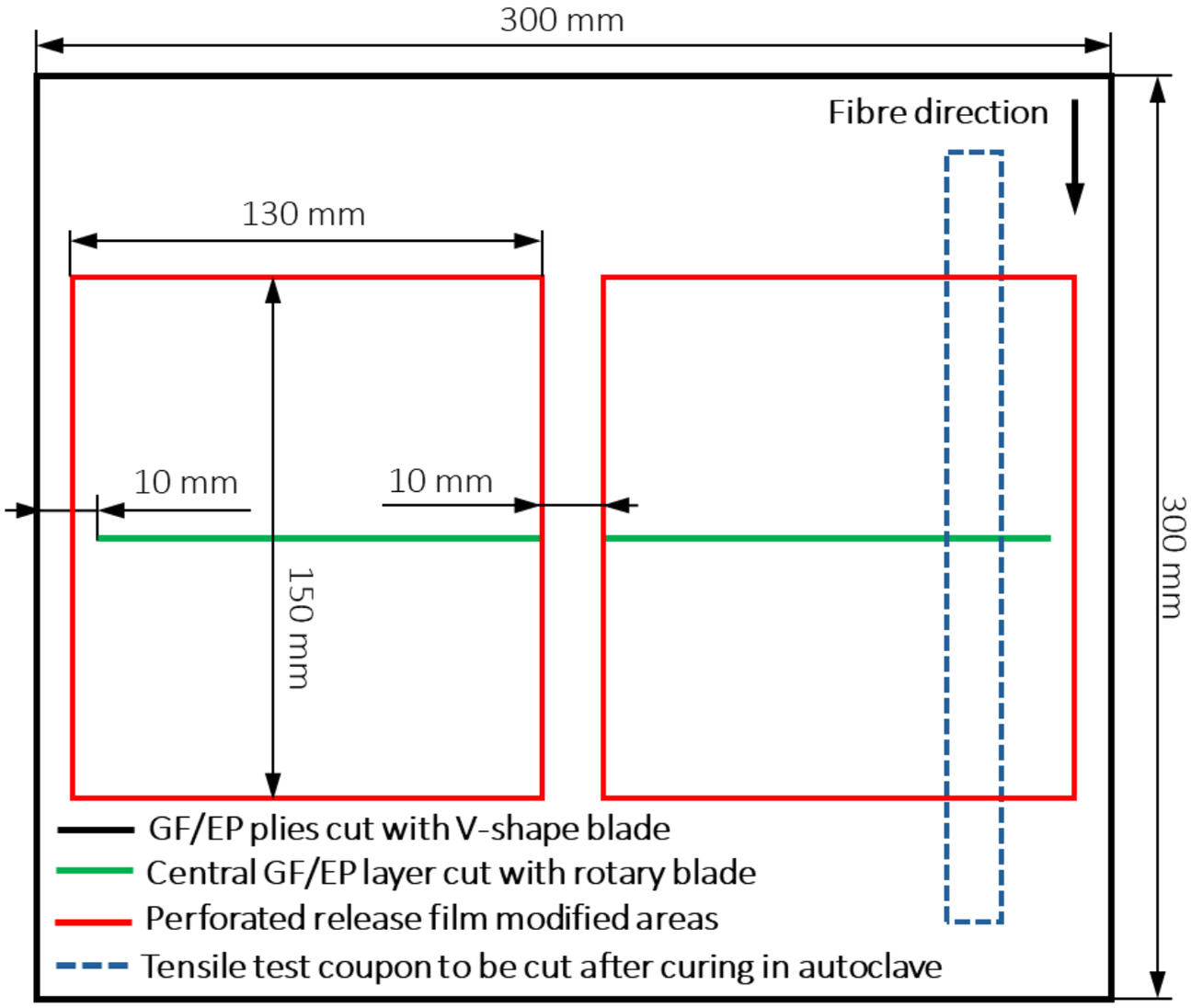

- Patterns were cut with a Versa Laser VLS2.30 type cutting/engraving CO_2 laser with a 10.6 µm wavelength and 30 W maximum power
- Perforated release films were interleaved between prepreg layers manually
- The central ply blocks of the laminates were cut manually with a rotary blade

Pattern designation	Nominal perforation diameter (D_n)	Nominal interlaminar contact area ratio (ICAR)
	[mm]	[-]
D1.5mmICAR0.2	1.5	0.2
D1.5mmICAR0.3	1.5	0.3
D1.5mmICAR0.4	1.5	0.4
D1.5mmICAR0.5	1.5	0.5
D1.0mmICAR0.2	1	0.2
D1.0mmICAR0.3	1	0.3

Perforation pattern geometry assessment

With a **Keyence IM-7020** type image dimension measurement system featuring a 1-inch, 6.6-megapixel monochrome CMOS sensor

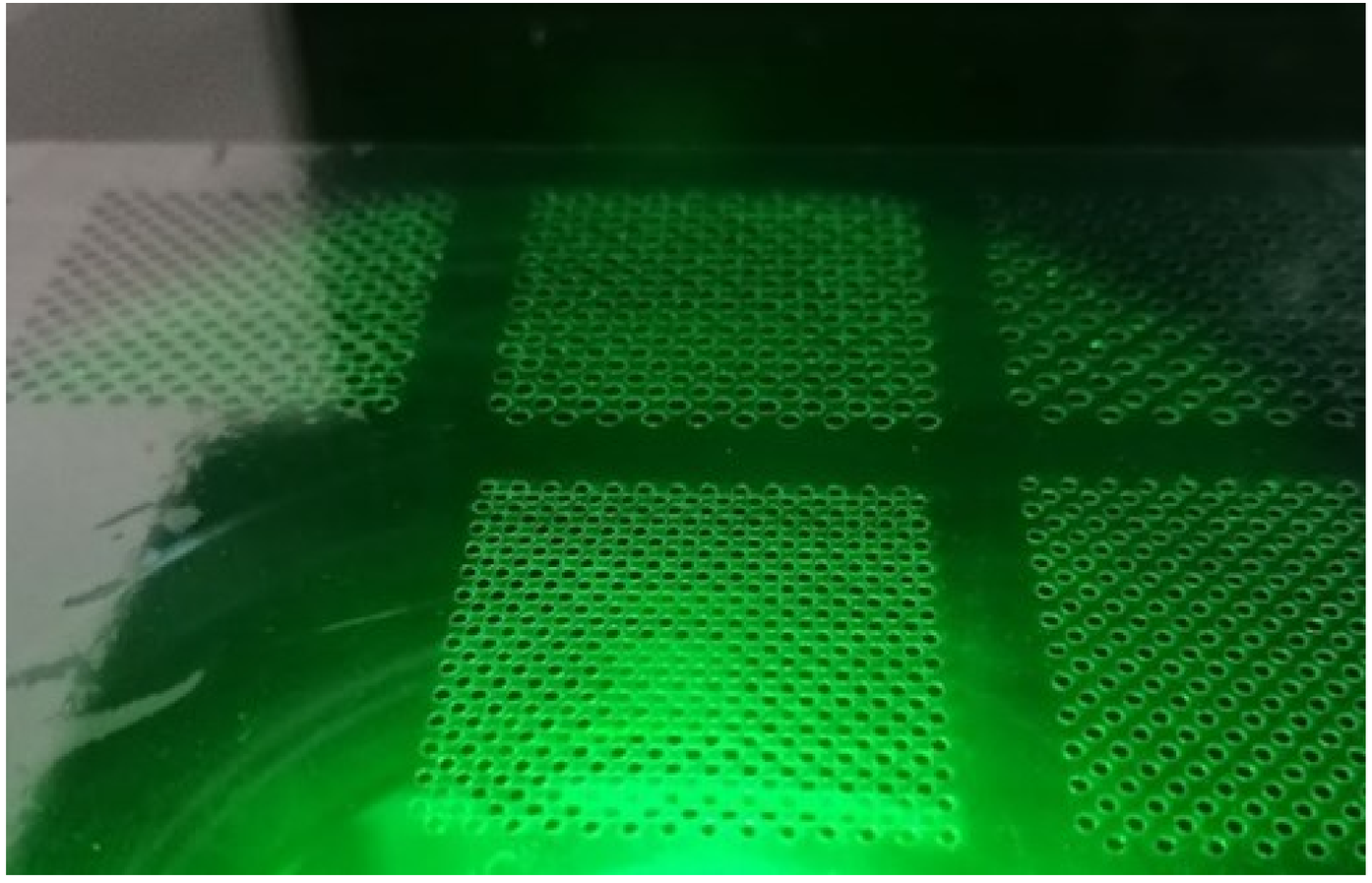

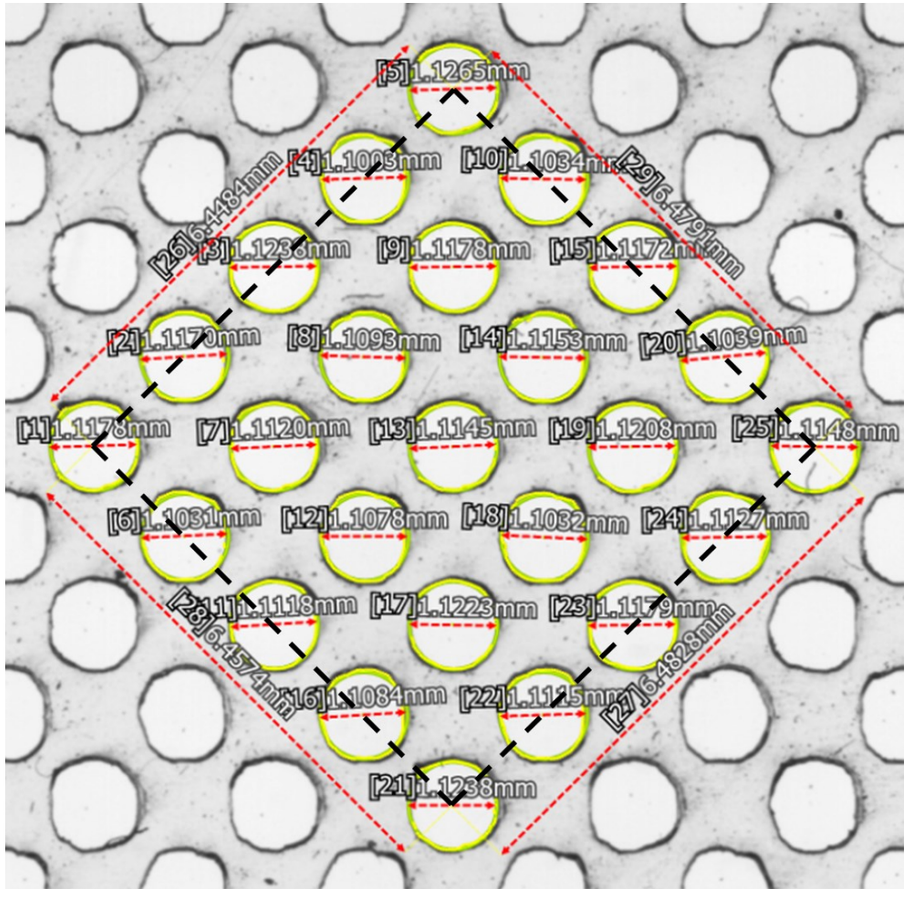

Results of optical pattern geometry assessment

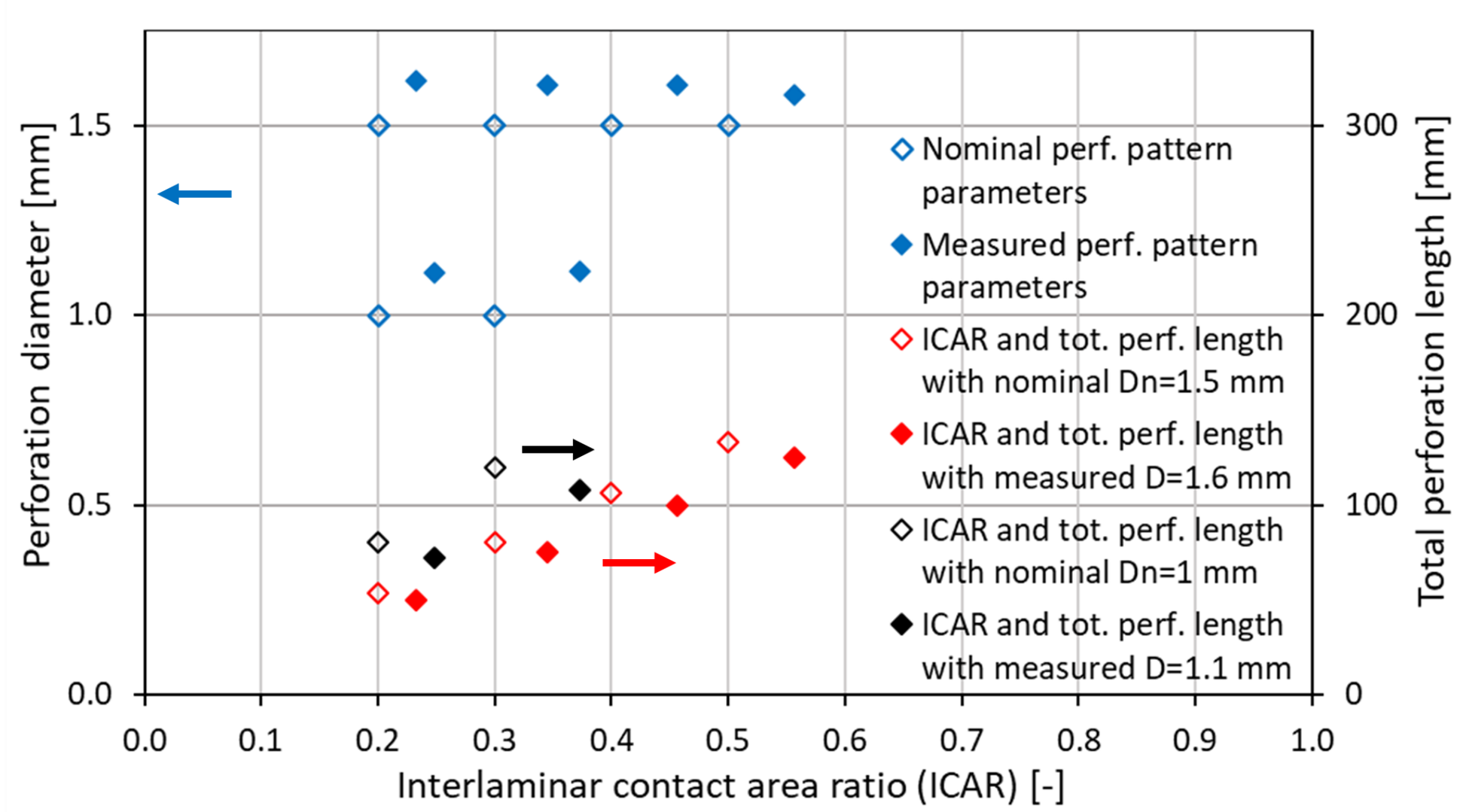

Results of optical pattern geometry assessment

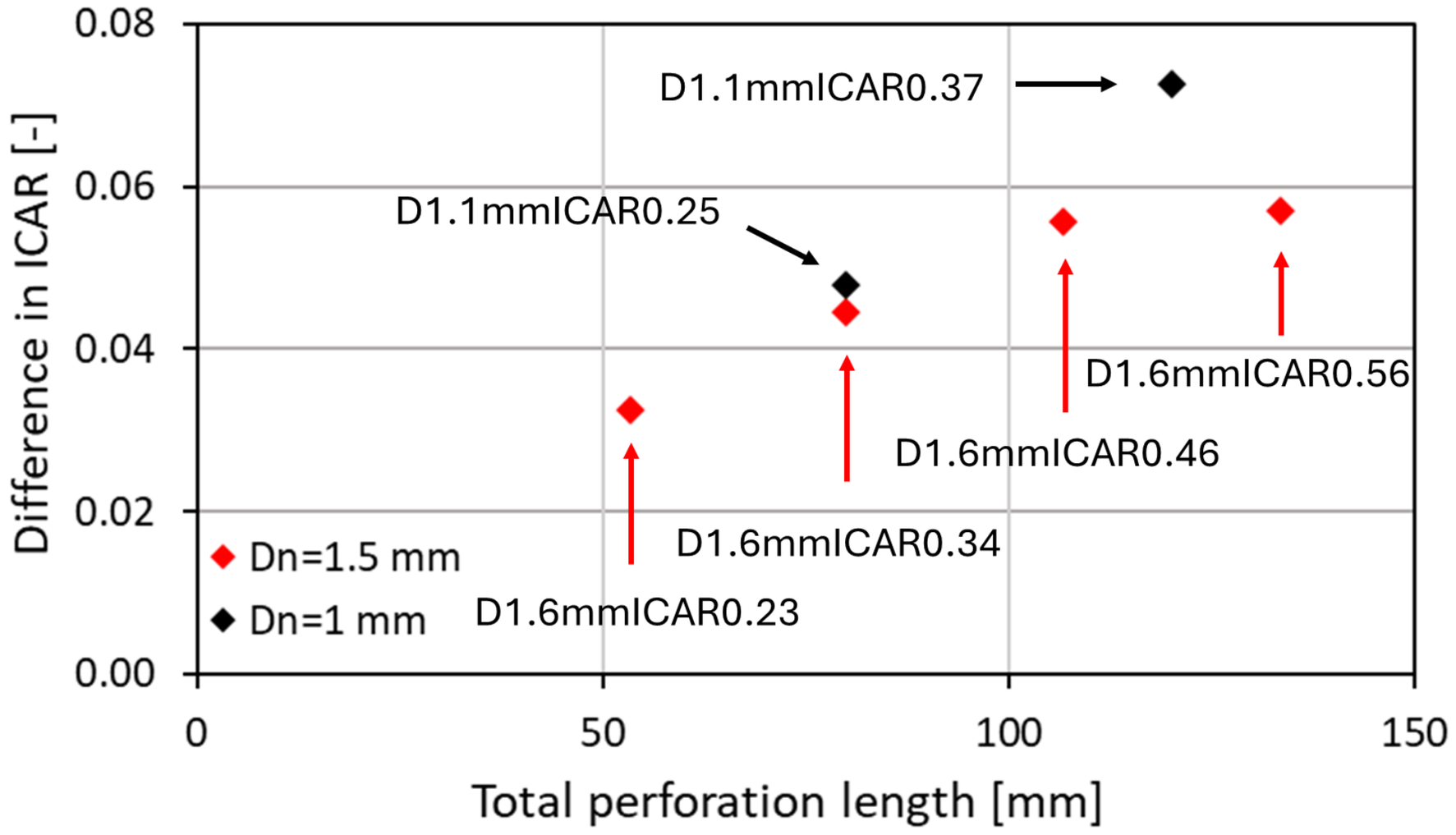

Results of optical pattern geometry assessment

	Nominal diameter (D_n)	Measured average diameter (D)	Absolute/ relative difference in diameter	Nominal ICAR	Average ICAR calculated from measured data	Difference in ICAR	Total perforation length to cover 100 mm²
	[mm]	[mm]	[mm]/[%]	[-]	[-]	[-]	[mm]
D1.5mmICAR0.2	1.5	1.617 (0.62)	**0.117**/ 7.819	0.2	0.233	0.033	53.3
D1.5mmICAR0.3	1.5	1.607 (0.69)	**0.107**/ 7.140	0.3	0.344	0.044	80.0
D1.5mmICAR0.4	1.5	1.607 (0.72)	**0.107**/ 7.159	0.4	0.456	0.056	106.7
D1.5mmICAR0.5	1.5	1.581 (0.79)	**0.081**/ 5.405	0.5	0.557	0.057	133.3
D1mmICAR0.2	1	1.113 (0.97)	**0.113**/ 11.25	0.2	0.248	0.048	80.0
D1mmICAR0.3	1	1.114 (0.67)	**0.114**/ 11.38	0.3	0.373	0.073	120.0

Results of G_{IIC} measurements

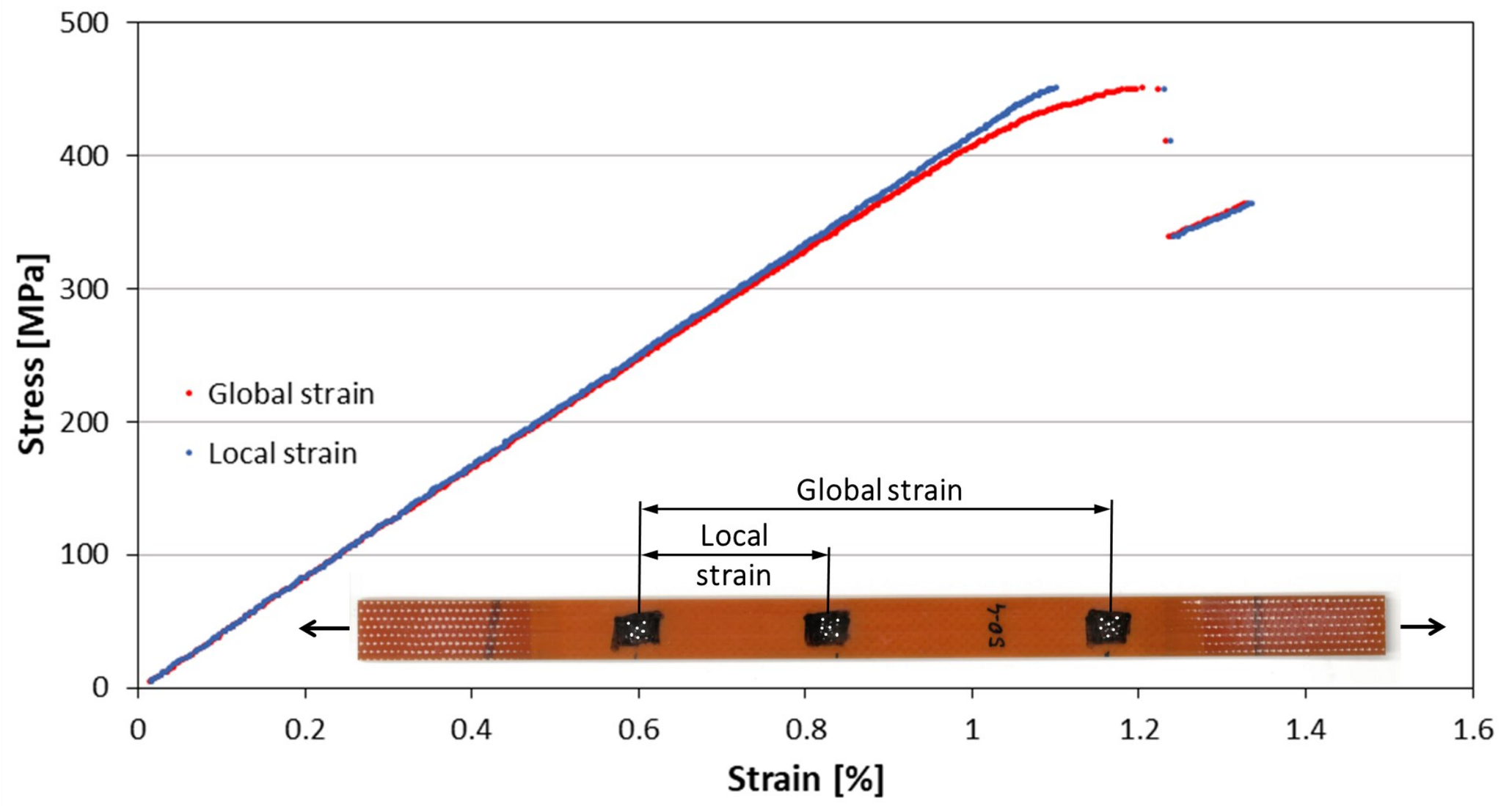

Results of G_{IIC} measurements

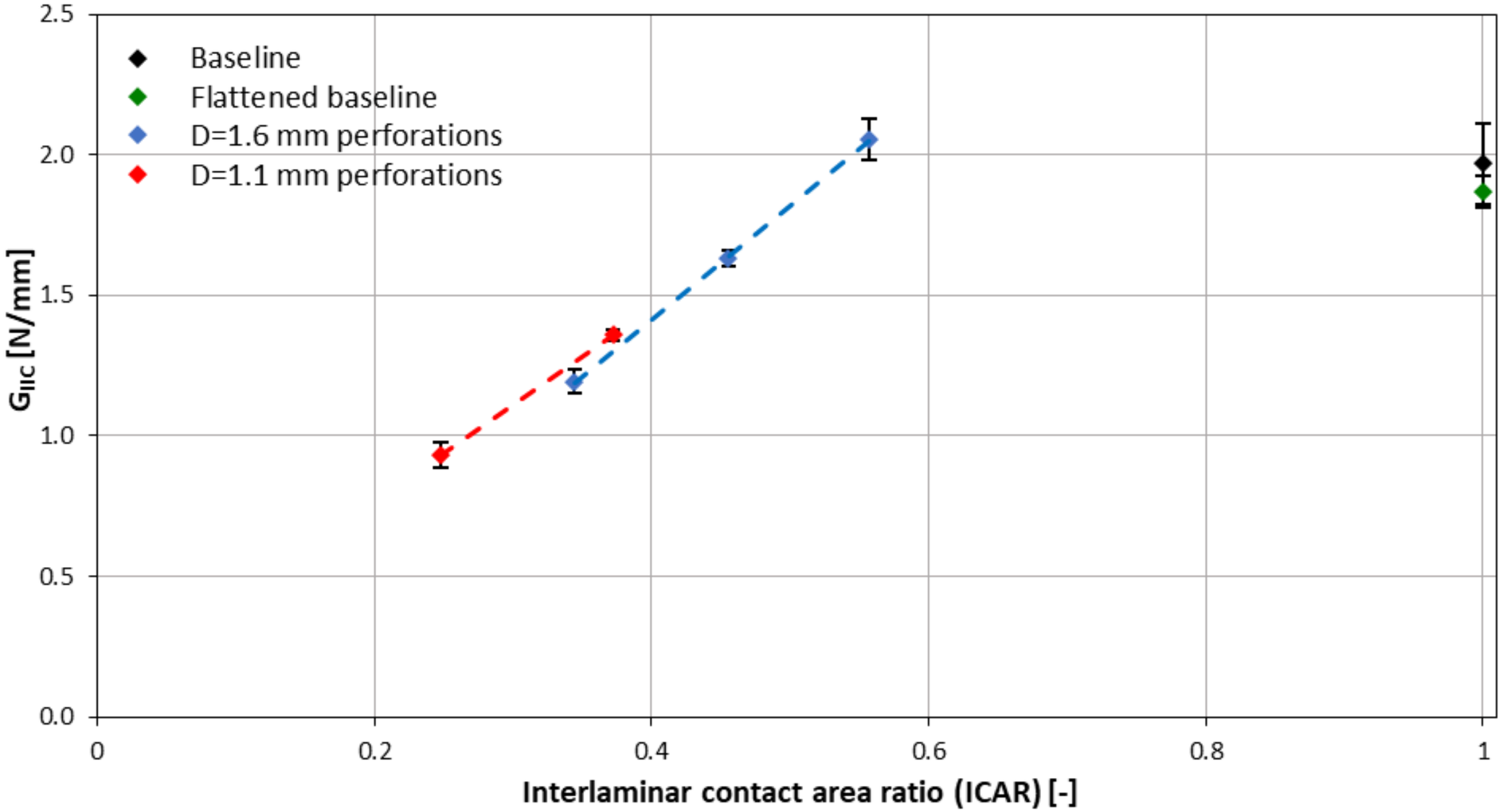

Results of G_{IIC} measurements

	Measured width (W)	Total measured thickness (h)	Estimated cut layer thickness (t_{cut})	Elastic modulus (E)	Delam-ination stress	Delam-ination strain	G_{IIC} from stress	Relative difference in G_{IIC}*
	[mm]	[mm]	[mm]	[GPa]	[MPa]	[%]	[N/mm]	[%]
Baseline	15.02 (0.14)	1.51 (0.70)	0.503	43.53 (1.34)	673.3 (3.00)	1.564 (4.04)	1.968 (7.24)	**5.37**
Flattened baseline	15.03 (0.07)	1.47 (1.67)	0.491	43.74 (1.53)	665.9 (1.72)	1.542 (1.42)	1.868 (2.96)	-
D1.6mmICAR0.34	15.04 (0.08)	1.49 (3.40)	0.497	42.54 (1.55)	522.2 (1.94)	1.237 (2.81)	1.194 (3.39)	-36.08
D1.6mmICAR0.46	15.04 (0.08)	1.54 (0.81)	0.512	42.98 (0.93)	605.0 (1.16)	1.424 (1.38)	1.634 (1.74)	-12.52
D1.6mmICAR0.56	15.04 (0.05)	1.52 (0.95)	0.507	43.38 (0.93)	684.9 (1.90)	1.598 (1.66)	2.056 (3.60)	**10.07**
D1.1mmICAR0.25	15.06 (0.11)	1.52 (1.40)	0.506	42.49 (1.15)	456.8 (2.67)	1.087 (3.57)	0.932 (4.73)	**-50.11**
D1.1mmICAR0.37	15.07 (0.10)	1.52 (1.14)	0.507	42.30 (1.70)	549.8 (1.57)	1.315 (0.81)	1.359 (1.61)	-27.26

*Compared to the average G_{IIC} of the flattened baseline series.

Conclusions

- Perforation patterns were systematically designed for geometrical characterisation and interface modification.
- **Six** laser-cut perforation **patterns** were **analysed** optically, the **actual perforation diameters were larger** than the nominal values regardless of the nominal diameter.
- The laser-cutting-induced increase in the perforation diameters resulted in a **difference between** the **nominal and actual interlaminar contact area ratios (ICAR)**. The differences in the ICAR values showed a monotonic increase with the total perforation length.
- Unidirectional composite tensile test coupons having one-third of their plies cut in the central layer were suitable for G_{IIC} assessment.
- The $\boldsymbol{G_{IIC}}$ of the modified laminates **showed a strong linear trend with increasing ICAR**, which enables the control of composite layer interface properties.
- The **maximum reduction of $\boldsymbol{G_{IIC}}$ was up to 50%** with the applied perforation patterns, but the test campaign results indicate that the full range may be covered.
- Baseline laminates with flattened interfaces showed slightly lower G_{IIC} values than the pristine ones.
- The **perforation pattern with the highest ICAR (0.56) increased the $\boldsymbol{G_{IIC}}$ of the laminate by 10%**. This offers scope for limited, but well-controlled increase of G_{IIC}.

Acknowledgement

NATIONAL RESEARCH, DEVELOPMENT AND INNOVATION OFFICE



Hungarian Academy of Sciences

1825

The research was supported by the National Research, Development and Innovation Office (NRDI, Hungary) through grant OTKA FK 131882. The author acknowledges the Ministry of Culture and Innovation of Hungary for support from the National Research, Development and Innovation Fund through grant no. NKKP ADVANCED 149578. The research was supported by the Ministry of Culture and Innovation of Hungary from the National Research, Development and Innovation Fund, under the TKP2021-NVA funding scheme through grant no. TKP-6-6/PALY-2021 and from the Complex Development funding scheme through grant no. 2022-2.1.1-NL-2022-00012 Creation of National Laboratories. The author is grateful for support through the János Bolyai Research Scholarship of the Hungarian Academy of Sciences. Special thanks to Ádám Stocker for his help with the experiments.

Thank you for your attention!

Budapest University of Technology and Economics (BME)

ICCM24
24TH INTERNATIONAL CONFERENCE ON COMPOSITE MATERIALS

DEPARTMENT OF POLYMER ENGINEERING

PRECISE MODE II FRACTURE TOUGHNESS CONTROL IN HIGH-PERFORMANCE COMPOSITES BY PERFORATED RELEASE FILM INTERLEAVES

Gergely CZÉL (czel.gergely@gpk.bme.hu)
Budapest University of Technology and Economics (BME)
Faculty of Mechanical Engineering
Department of Polymer Engineering

ICCM 24 – 24th International Conference on Composite Materials,
Baltimore, USA, 4-8 August 2025

ICCM24 24TH INTERNATIONAL CONFERENCE ON COMPOSITE MATERIALS
AUG 4-8, 2025 • BALTIMORE CONVENTION CENTER • BALTIMORE, MARYLAND

ASSESSMENT OF NUMERICAL APPROACHES FOR QUASI-STATIC, FATIGUE, AND DYNAMIC PROPAGATION OF DELAMINATION IN CURVED LAMINATES

Maikel Khella[1], Pietro Ballarin[1], Carlos G. Dávila[2], Alessandro Airoldi[1]

[1]Dept. of Aerospace Science and Technology, Politecnico di Milano, Via La Masa, 34, 20156 Milano, Italy

[2]Durability, Damage Tolerance, and Reliability Branch, NASA Langley Research Center, Hampton, VA 23601, USA

Keywords: Composites; Carbon fibre; Delamination; Fatigue; Numerical analysis

ABSTRACT

The accurate prediction of fatigue delamination growth and critical damage size remains an open challenge in enabling the Slow-Growth design and damage-tolerance substantiation in composite aircraft structures. Delamination is especially important due to difficult detectability and the high sensitivity of laminated composites to this failure mode. This work presents a preliminary experimental characterization of the fatigue-driven delamination in a thick, pre-damaged L-shaped composite specimen. To support and interpret these results, a cohesive zone-based finite element (FE) fatigue modelling framework was first verified on standard Mode I (DCB), Mode II (ENF), and Mixed-Mode (MMB) specimens, using experimental data from the literature. The framework was then applied to simulate the fatigue behaviour of the L-shaped specimen. Finally, the variation of energy release rate with crack-growth was investigated to explain the observed failure modes, highlighting the strong sensitivity of delamination growth to initial loading conditions.

1 INTRODUCTION

Laminated composite structures are inherently susceptible to out-of-plane loading, with delamination initiating at stress levels significantly lower than those required for in-plane failure. Low-velocity impacts frequently induce internal delaminations that may not be externally visible but compromise structural performance. Delamination disrupts interlaminar stress transfer, inhibiting load redistribution mechanisms between plies and reduces sustainable load in compression. The FAA Advisory Circular AC 20-107A [1] addresses damage tolerance in composite structures, particularly for Category 2 barely visible impact damages, which may reduce residual strength below the Ultimate Load (UL) but never below Limit Load (LL). Three substantiation approaches are identified: (i) no-growth, where damage is stable over inspection intervals; (ii) arrested-growth, where propagation halts before reaching a critical size; and (iii) slow-growth, allowing controlled propagation, which is monitored via scheduled inspections. Slow-growth design leads to greater structural efficiency than no-growth but requires predictive models for both residual strength and fatigue crack growth [2]. Consequently, finite element (FE) models used for a slow-growth design of composite structures must reliably predict (i) residual static strength in the presence of damage, and (ii) delamination growth under cyclic loading.

Existing models for static delamination strength are well-established while, in contrast, fatigue modelling remains an active research area. Traditional FE-based fatigue models [3], [4], [5], [6], [7], [8], typically rely on Paris-law parameters and fracture mechanics inputs, which pose significant experimental and computational demands. Recently, a simplified S-N-based framework for the FE simulation of fatigue loading of structures has been proposed [9], [10], [11], using a two-step Simple Cyclic Loading (SCL) method based on a monotonic preload followed by a constant-amplitude fatigue step that activates the fatigue damage accumulation. Different versions of such functions have been proposed. The most recent version of fatigue damage accumulation function, presented in [10], is empirical in nature, and it is calibrated via Paris rate data and two fitting parameters for each

delamination mode, I and II. While initial calibrations in the literature are manual (trial and error), an automated procedure is also possible [12].

The studies presented in the literature are typically focused on the development and validation of fatigue damage accumulation functions at the coupon levels, considering different propagation modes and levels of severity. This work investigates the crack growth in thick L-shaped laminates containing a pre-existing delamination (at a critical interface) under fatigue loading. Specimens were tested under a tensile opening configuration, which induces an interlaminar tensile stress state in the curved zone of the specimens that promotes crack growth. Despite the large amount of research work on the inelastic quasi-static response of L-shaped and curved structural elements, studies on their fatigue behavior are rare. An accurate analysis and comparison between quasi-static and fatigue failure modes is presented in [14,15] for unidirectional and cross-ply L-shaped laminates without pre-damage. In the present research activity, attention is focused on the analysis of crack growth regimes and rate. Moreover, the predictive capabilities of a modelling approach based on fatigue damage accumulation laws are presented, outlining the potential and the challenges for the application of these methods to the prediction of growth rates in structural elements.

2 EXPERIMENTS ON L-SHAPED COMPOSITE LAMINATES

Fatigue tests were conducted on pre-delaminated, L-shaped, thick-laminate specimens with a width of 20 mm, promoting an interlaminar mode I crack propagation by applying loads at the ends of the arms. The geometry, shown in Figure 1-(a), is representative of curved laminates that are typically prone to delamination in aeronautical composite structures. In particular, the experimental activity aims to support broader efforts in characterizing slow-growth fatigue behaviour in thick curved composite elements of rotorcraft structures. In Figure 1-(b), the experimental setup is presented. Loads were applied through hinged grips clamping the first 30 mm of each leg. Fatigue tests were conducted in displacement control with a displacement ratio $R = 0.1$ and a frequency of 5 Hz. Maximum and minimum forces and the cycle count were recorded throughout the test.

All specimens were manufactured from AS4/8552 unidirectional (UD) prepreg, with the layup $[0]_{48}$ using the manufacturer-recommended cure cycle. The nominal cured ply thickness is 0.13 mm [13], resulting in a total nominal laminate thickness of 6.24 mm. The material elastic properties and the most significant interlaminar properties for the presented activity are reported in Table 1, where G_{Ic} is the critical energy release rate for mode I, and $\sigma_{c0\ is}$ the interlaminar tensile strength.

E_{11T} [MPa]	E_{11C} [MPa]	$E_{22}=E_{33}$ [MPa]	$G_{12}=G_{13}$ [MPa]	G_{23} [MPa]	$\nu_{12}=\nu_{13}$ [-]	ν_{23} [-]	G_{Ic} [kJ/m^2]	σ_{c0} [MPa]	G_{IIc} [kJ/m^2]	τ_{c0} [MPa]
127,277	111,488	9239	4826	3553	0.302	0.3	0.26	105	0.87	128

Table 1: AS4/8552 elastic and interlaminar properties [13] and [14]

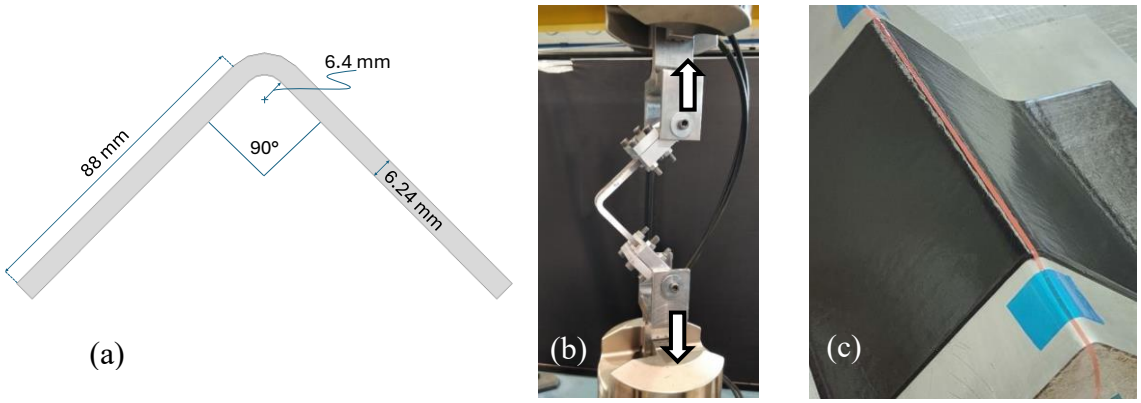

Figure 1: Specimen dimensions (a), test set-up (b), and pre-delamination placement (c)

All the specimens were manufactured with a 2-mm long artificial delamination induced with a Teflon film placed at the centre of the curved region, at one-third through the thickness (between the 16th and 17th plies). This location corresponds to the region of maximum interlaminar tensile stress for the considered load condition [15]. (Figure 1-(c)).

Before fatigue testing, two static tests were conducted to evaluate the way in which damage progresses (Figure 2). In both tests, the initial linear-elastic phase in which the defect did not propagate was followed by a sudden load drop (Figure 2-(a)). The drop corresponds to an unstable growth from the pre-delamination through the whole curved region (Figure 2-(c)). Further loading extended the crack into the specimen legs (Figure 2-(d)), which is reflected in the reduction of the secant stiffness in the force–displacement curves.

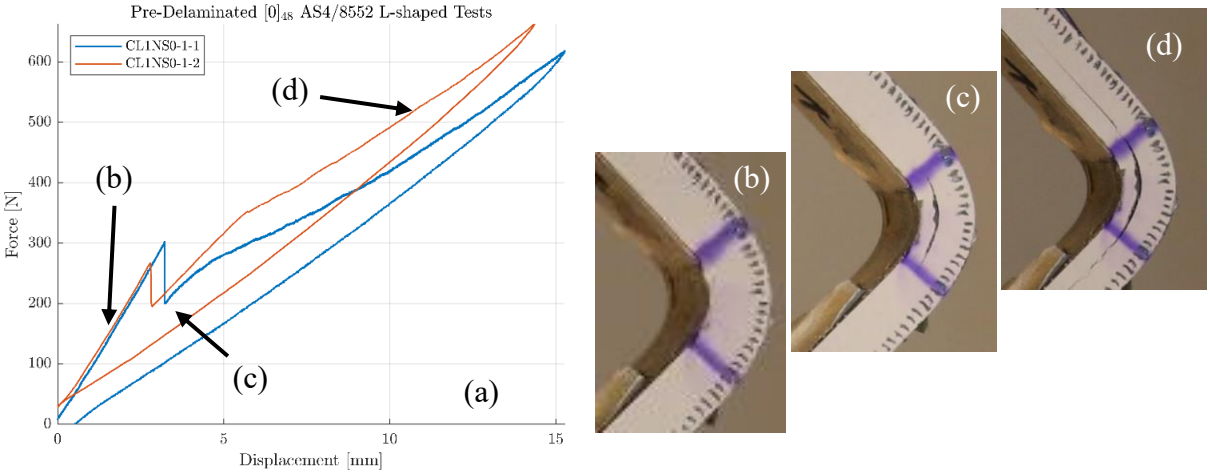

Figure 2: Static tests on L-shaped specimens

Fatigue tests were performed on five specimens in displacement control. Initial test severities were derived from the static tests (Figure 2), as a function of the displacement at the onset of unstable delamination propagation. Assuming an initial linear elastic response, fatigue loading levels were selected to correspond to a target load severity (defined in terms of strain energy release rate), scaled from the critical propagation value δ_{crit} (at delamination onset under static loading), using the relation:

$$\frac{G_{max}}{G_{crit}} = Severity = \frac{\delta^2_{max}}{\delta^2_{crit}} \quad (1)$$

where δ_{max} is the maximum applied displacement in fatigue. The Irwin-Kies equation, $G = \frac{P^2}{2B}\frac{dC}{da}$, was used, where P is the applied load, C the specimen compliance, B the specimen width, and a the crack length. Table 2 summarizes the nominal load-levels decided for the fatigue test, the corresponding maximum displacements, and the corresponding G-severities (all with a displacement ratio R=0.1). Two specimens were tested at high severity levels (0.90 and 0.75) and three specimens were tested with a nominal severity of about 0.60. The effective displacement and force levels were adjusted considering the response of each specimen and the discrepancies with the nominal levels are also due the presence of mechanical plays and contact tolerances in the test setup. Regarding the codes used to identify specimens, the first number indicates the specific production batch they were cut from, and the second is a number specific to each.

Specimen name	CL1NF0-1-4	CL1NF0-1-5	CL1NF0-2-3	CL1NF0-2-1	CL1NF0-2-4
F_{max} (nominal)	270 N	220 N	160 N	160 N	160 N
δ_{max}	2.688 mm	2.272 mm	1.870 mm	1.670 mm	1.700 mm
G-severity	0.90	0.75	0.62	0.55	0.57
F_{max} (effective)	269 N	222 N	165 N	159 N	160 N

Table 2: Specimens tested under fatigue loading, the initial test severity and the test maximum displacement (R = 0.1)

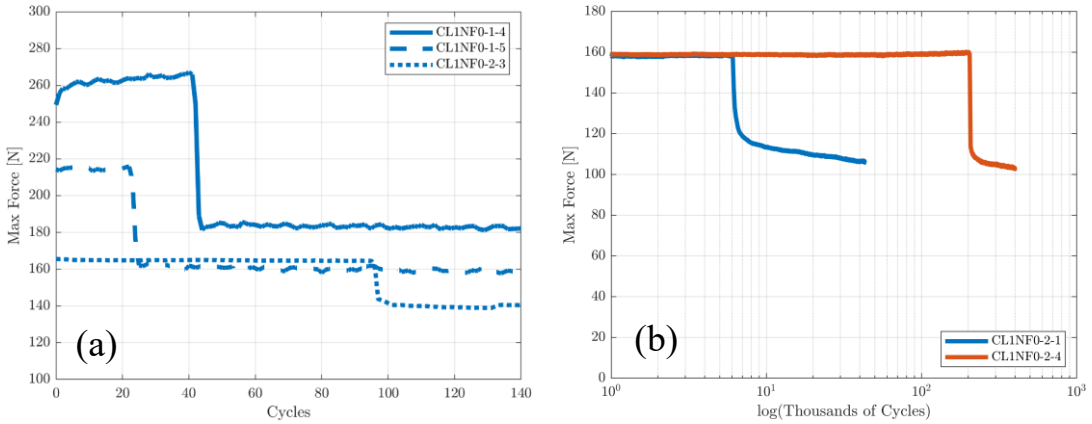

Figure 3: Max force during L-shaped fatigue tests: (a) Highest severity tests, (b) CL1NF0-2-1 and CL1NF0-2-4

The two specimens CL1NF0-1-4 and CL1NF0-1-5, tested at the highest severity, underwent a rapid delamination propagation within very few cycles (41 and 22 load cycles, respectively). The rapid drop of the force shown in Figure 3-(a) is a consequence of the rapid crack growth, which accelerated abruptly from the Teflon insert (initial defect length of 2 mm) along the curved region. Crack growth rate was significantly reduced after a specific load, which was 189 N for specimen CL1NF0-1-4 and 162 N for CL1NF0-1-5. The load drop was obtained in 3 cycles for CL1NF0-1-4, as well as for CL1NF0-1-5 (about 0.5 s)

The three specimens tested at the lowest severities (in the range 0.55 to 0.62) provided different responses. The trend of force vs. cycles for the specimen CL1NF-2-3 (effective severity 0.62) is plotted with those of the highest severities tests in Figure 3-(a), since it exhibited a similar rapid crack propagation just after 95 load cycles, with a force drop from 164 N to 141 N, in 6 cycles (about 1 s). Considering the test at 0.55 severity level (blue curve in CL1NF0-2-1, Figure 3-(b)), the number of cycles required to reach the region of rapid force drop increased to approximately 6000 cycles, and the rapid force drop went on until about 140 N after 40 cycles (about 6.5 s). The subsequent test was conducted at the same nominal load level (red curve in CL1NF0-2-4, Figure 3-(b)). It obtained the same qualitative response, with an initial stable force level followed by a rapid growth of the crack, but the onset of the rapid crack propagation required about 204,000 cycles. The rapid force drop arrested at about 139 N after 83 cycles (about 14 s).

During fatigue testing, damage accumulates at the pre-existing delamination tip until a critical threshold is reached, triggering a rapid crack propagation across the curved region, which corresponds to the load drop that was observed in the different tests. The load drop is not instantaneous, as in the unstable propagations that occurred in quasi-static tests, and its velocity tends to decrease if severity is reduced. Prior to this event, load fluctuations were minimal, indicating negligible crack growth. The initial rapid growth is arrested at different load levels. Thereafter, the load decreases gradually as the

delamination extends into the specimen legs. This behaviour highlights the existence of a threshold for the onset of the accelerated crack propagation phase and a transition from such phase to a slow crack propagation activated after a certain propagation length. The number of cycles required for these transitions vary from a few cycles to tens or hundreds of thousands of cycles, with maximum values that were obtained only in the tests with the lower severity levels.

In the quasi-static tests, the initial crack undergoes an initial unstable propagation. The propagation regime then changes to a stable slow-growth regime when the crack, approximately, reaches the end of the curved zones. Assuming a constant crack resistance for the material, such response is indicative of a strong variation of the Energy Release Rate (ERR) available to promote crack propagation with the crack length. In the fatigue tests, despite the quantitative differences in the number of cycles required to activate fast crack propagation, the qualitive responses are very similar for all the five tests. Although the propagations observed in the fatigue testing were not instantaneous, the occurrence of two regimes in the fatigue crack growth is evident in all the fatigue tests performed. The interpretation of these phenomena requires an analysis of the ERR variation, which is accomplished in the next section by applying the Irwin-Kies equation, linking the compliance of the specimens to the crack propagation. The simulations of these type of propagation with the fatigue damage accumulation laws validated for characterization specimens, like DCB and ENF, is particularly challenging due to the expected gradients in ERR and the presence of unstable propagation regimes in the quasi-static tests. The large scatter exhibited by the specimens tested at a nominal severity around 0.60 should be investigated, although such variability in fatigue test results is consistent with literature on similar specimens [16], [17], which emphasizes the need to model the statistical distributions of interfacial properties in fatigue analyses more than static ones.

3 NUMERICAL COMPLIANCE AND ENERGY RELEASE RATE EVOLUTION WITH CRACK LENGTH

The evaluation of the ERR for different crack lengths was performed via semi-analytical assessment based on the Irwin-Kies equation:

$$G = \frac{F^2}{2B}\frac{dC}{da} \tag{3}$$

This relation links applied load F, the specimen compliance C (or, better said, the effect of specimen geometry characteristics as a function of crack-length a) to the strain energy release rate G, the energy available for crack growth. A finite element model of the specimen was developed in Abaqus Standard [18] to numerically evaluate the compliance as a function of crack length.

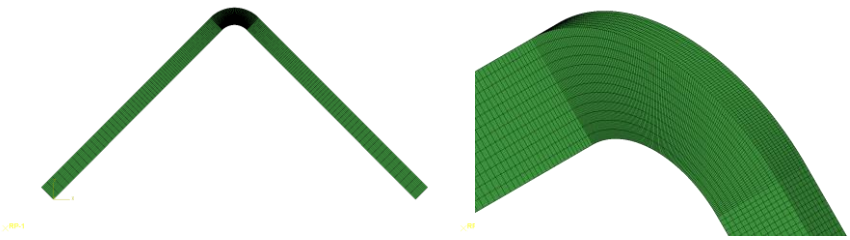

Figure 4: FE model of the angular specimen

The model is a 2-mm-wide strip of the specimen, meshed with laminated continuum shell elements (SC8R). Each shell comprises 4 plies A layer of zero-thickness cohesive elements (*COH3D8*) – containing a pre-crack at the centre of the curved region – was inserted between the 16th and 17th plies (i.e., between the 4th and 5th continuum shell layers). A total of 8 elements was used across the width. The mesh is coarse at the extremities of the legs and becomes finer in the curved region, where elements are approximately 0.1 mm long. Material properties are those reported Table 1. Loading was simulated by applying opening displacements to rigid bodies including the last 30 mm of each leg. Such boundary conditions were applied to the reference nodes of the rigid bodies, positioned in correspondence of the

hinges. Free rotations were allowed around the grip hinge axis, which replicates experimental boundary conditions. An implicit static analysis procedure was used, allowing for non-linear geometrical effects. Damage in cohesive elements was inhibited since the objective of these analyses was simply to evaluate the compliance at different crack lengths. A series of analyses was performed by removing cohesive elements in 0.2 mm increments to represent the development of an ideal crack from 1 mm to 13.4 mm (i.e., until the end of the curved region). The crack was symmetrically extended at both crack-tips. The compliances obtained in each analysis were interpolated with a polynomial, proving the result reported in Figure 5-(a) and then derived. By applying Eq. 3, the variation of the ERR with the crack length a was evaluated, as reported in Figure 5-(b), considering the load corresponding to an opening of 2 mm.

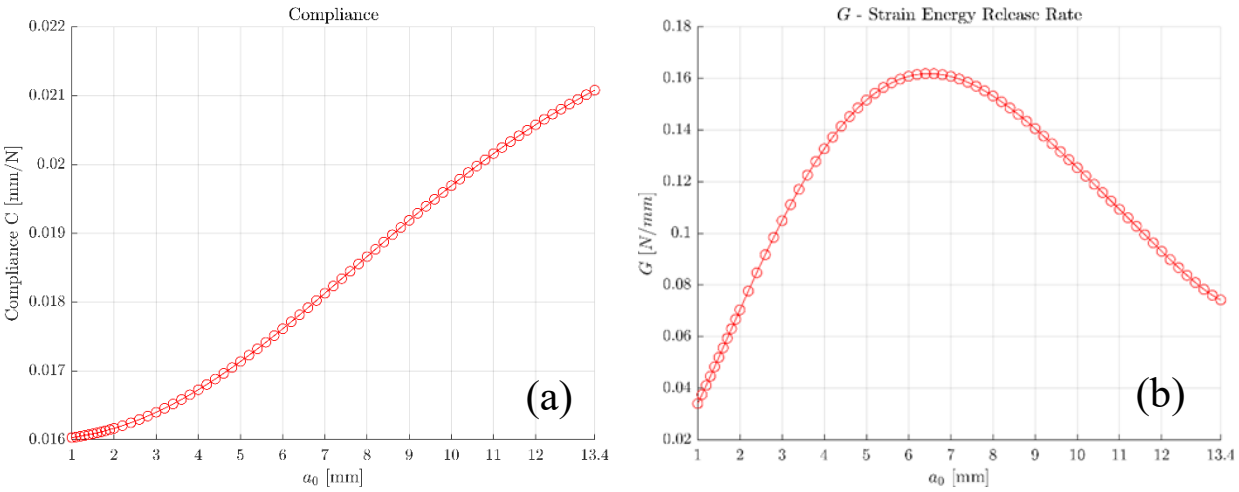

Figure 5: Numerical Compliance (a) and Energy Release Rate (b) of the L-shaped specimen as a function of crack length

Assuming a constant crack resistance, the sign of the derivative of the ERR curve, dG/da, determines the crack propagation regime: unstable if $dG/da > 0$ and stable if $dG/da < 0$. According to Figure 5-(b), the existence of a transition between unstable and stable regimes is evidenced at a = 6.4 mm. These results are consistent with those reported in [19], [20], where a similar approach was used to calculate G and the stability of delamination propagation in L-shaped laminates. Despite the differences in specimen geometry and loading conditions, the existence of a threshold for unstable-to-stable crack growth transition was found beyond a certain crack length (a = 6.55 mm in [18]).

This approach does not consider the presence of any fracture process zone (FPZ) at the crack tip. An estimate for the length can be evaluated using the formulation in [21]:

$$l_{pz}^{ss} = \gamma \frac{E' G_c}{\sigma_c^2} \text{ where } E' = \frac{E_{22}}{Q}, Q = \frac{1}{2}\sqrt{2\left[\sqrt{\frac{E_{22}}{E_{11}}} - \nu_{21}\right] + \frac{E_{22}}{G_{12}}} \tag{4}$$

which, using the values for γ reported in [22] ($\gamma = 0.73$) and [23] ($\gamma = 1.00$) and the material properties in Table 1, yields 0.16 mm and 0.22 mm as upper and lower bounds for the FPZ length. Although the process zone can be considered small, these values could affect the evaluation of the compliance as a function of the crack length used to obtain the results in Figure 5.

The experimental results can be interpreted by using the results of the semi-analytical procedure presented above. Since the tests were performed at fixed opening, the evolution of force and the relation between the compliance and the crack length in Figure 5-(a) can be used to estimate the crack length during the fatigue tests. The results, for the specimens tested with the lowest severity levels are similar. For CL1NF0-2-3, where rapid propagation was triggered after 95 cycles, the rapid crack growth was arrested at a force level that is compatible with a crack length of 7.5 mm. For the specimens CL1NF0-

2-1 and CL1NF0-2-4, the estimated crack lengths at the end of the rapid crack growth is of 6.7 mm and 7.2 mm. All these values are slightly beyond the maximum in the ERR-*a* curve, indicating the phase of rapid propagation ends when the crack enters the region of stable crack growth. For the specimens tested at the highest severity levels (CL1NF0-1-4 and CL1NF0-1-5), the estimation provides values larger than 13 mm. Such results can be explained by considering that the elastic energy stored in the specimens promoted a propagation of the crack into the region of stable propagation.

4 NUMERICAL SIMULATIONS

4.1 Static failure modelling

The same finite element model developed for the evaluation of the compliance with crack growth, was used to perform quasi-static simulation through a fully non-linear analysis, adopting an explicit time integration scheme with Simulia Abaqus/Explicit. The explicit solver can capture unstable propagation phenomena and transition to stable regimes without the convergence difficulties that are common with implicit codes. The model retains the continuum shell (SC8R) representation of the specimen, including the zero-thickness cohesive interface elements (COH3D8) positioned between the 16th and 17th interfaces, where the defect was located. The model was subjected to an opening displacement at the reference points coupled to the specimen legs. Quasi-static conditions were ensured by imposing a smoothly varying opening time history, and by checking that reaction forces read at the two reference points were identical. A user-defined Cohesive Zone Model (CZM) was used to characterize the fracture process. The CZM in [24], originally conceptualized for static fracture, was implemented in a VUMAT subroutine for COH3D8/COH2D4 cohesive elements in Abaqus/Explicit. The model is characterized by an initial linear elastic response (of penalty stiffness K_p). Damage initiates at the cohesive strength σ_0 (at the displacement δ_0) and progresses, gradually reducing the stress carrying capability according to a linear softening law, until a displacement δ_f, where the work spent in the damage process equals the prescribed interface toughness. The critical ERR and strengths used in the analyses are reported in Table 1 [14]. A quadratic strength criterion for damage initiation and the B-K model for damage progression were selected for mixed-mode propagation. The penalty stiffness was set at 1.25E+05 N/mm^3, following the formulation in [25].

The simulated force-displacement response in the analysis of the L-shaped specimen is presented in Figure 6, together with the corresponding experimental curves of the two specimens tested. The model accurately captures the linear elastic stiffness of the specimen during initial loading, as well as the predicted load at the onset of unstable delamination propagation from the pre-crack, which matches closely with the experimental failure loads.

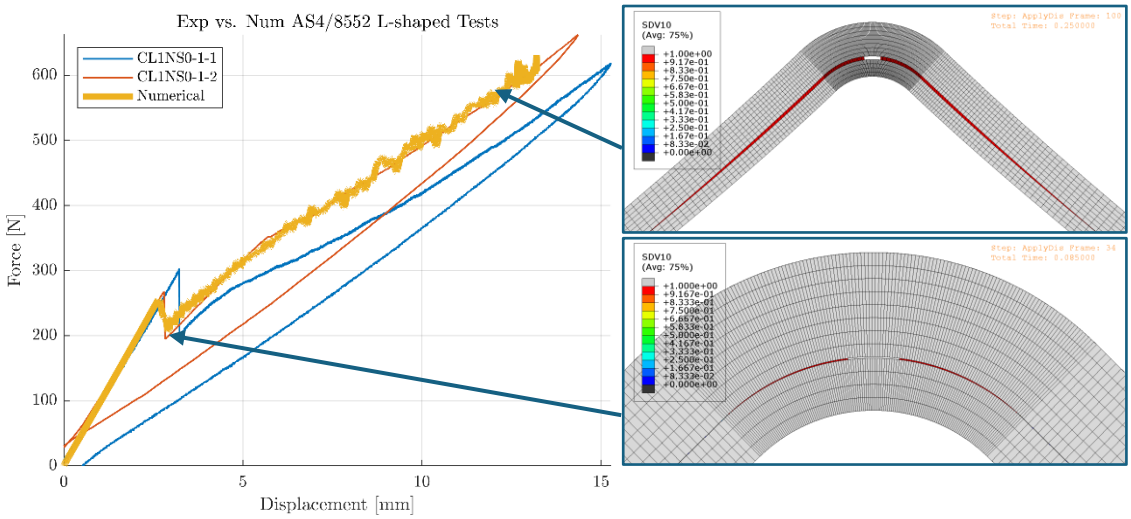

Figure 6: Numerical vs Experimental tests on L-shaped specimen

The sudden load drop that accompanies unstable delamination growth through the curved region was also captured by the simulation, as well as the response during the stable propagation of the crack along the legs of the specimens. This successful correlation of the static force-displacement response (including stiffness, first failure load, load drop, and crack stable propagation) provides confidence in the capability of the modelling approach to reliably model the loads required to propagate the initial delamination in quasi-static simulations, both for stable and unstable propagation regimes.

4.2 Modelling of fatigue damage accumulation and crack growth

Examples of cycle-by-cycle FE fatigue simulations exist in the literature but are only practical for Low and Ultra-Low Cycle Fatigue (LCF, ULCF) situations, which involve very few cycles with large plastic strains (such as seismic loading of steel structures [26]). For High Cycle Fatigue (HCF) applications, involving millions of cycles, simulating every cycle is computationally prohibitive. Therefore, simplified strategies are necessary for the practical FE simulation of structures under fatigue. A common class of simulation approaches is that of the "envelope load" methods [27]. They consist in the modelling of only the maximum (and/or minimum) loads in a fatigue load block, while relying on the CZM constitutive law to capture damage accumulation due to fatigue. Among the possible methods, the Simplified Cyclic Loading (SCL) is the one adopted here: it involves the quasi-static loading up to the block maximum load, after which fatigue damage accumulation is activated and continued, either until a specified cycle count or the (static) structural failure. A fatigue damage accumulation law can be easily integrated in the VUMAT subroutine previously used for quasi-static simulations. The fatigue model used here is based on Dávila's approach [9], [10], [11], using the SCL method and the suggested damage accumulation function, calibrated by fitting two parameters to the Paris data for mode I and II. The model applied is an updated version of the original approach proposed in [9] (CF18). It is based on the evaluation of a damage norm D. At each step in the simulation, the new values of the quasi-static and fatigue damage variables are evaluated independently of each other, and the larger of the two is selected as the one to be passed on to the next time increment. The typical response of a bi-linear cohesive zone element is shown in Figure 7-(a), showing the fatigue damage progression on a single cohesive element under a constant maximum stress. Load is applied quasi-statically from $\sigma = 0$ to $\sigma = \sigma_{max}$, and then kept constant while fatigue damage accumulates. As fatigue damage is accumulated, the damage norm degrades the penalty stiffness and λ increases. The traction-displacement state at the material point evolves along the path denoted as "Fatigue" in Figure 7-(a), until the softening branch of the static cohesive law is reached, at a displacement jump λ^*, at which point, the cohesive response is dominated by static tearing, which goes on until full separation of the cohesive interface.

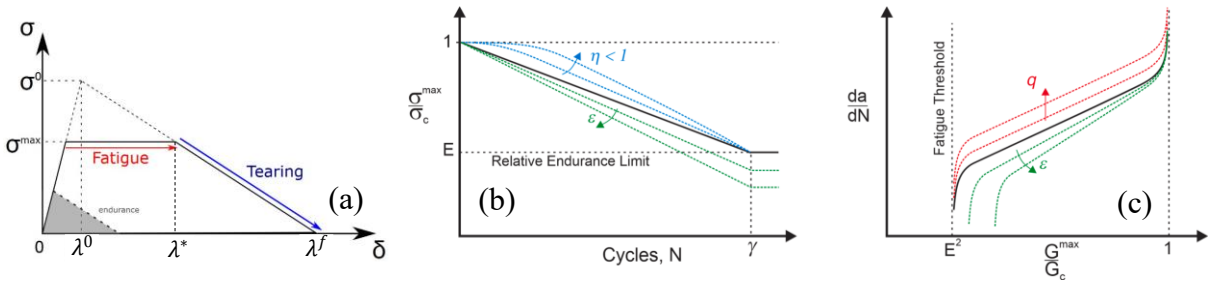

Figure 7: Fatigue damage accumulation law: (a) single element response in fatigue simulation, (b) effects of parameters η and ε in the S-N curve, and (c) effect of parameters q and ε in the Paris Curve

The CF22 fatigue damage accumulation law proposed in [11] is used herein within a VUMAT for explicit simulations. CF22 expresses the rate of change of the damage norm, D, with load cycles, N:

$$\frac{dD}{dN} = \frac{(1-D)^{-q}}{\gamma\, E^{\beta}(\beta+q+1)} \left(\frac{\lambda}{\lambda^*}\right)^{\beta} \tag{5}$$

where λ/λ^* is the ratio of current cohesive displacement jump λ to the corresponding static fracture displacement λ^* at the current residual fracture toughness; q is a fitting parameter to be calibrated, while

β, E and γ are parameters with a precise physical meaning in the S-N curve of the material. E is the infinite-life endurance threshold normalized with the static strength, i.e., the maximum allowable stress amplitude below which fatigue life is infinite, and γ is the number of cycles corresponding to this endurance limit. The threshold E is differentiated for the two opening modes, depends on the stress-ratio, and is interpolated between Mode I and Mode II endurance thresholds:

$$E = E_I + B(E_{II} - E_I) \text{ where: } E_I = \frac{2\varepsilon}{\varepsilon+1+R(\varepsilon-1)}, E_{II} = min\left(0.999,\ \phi\left(\left(\frac{2}{1-R}\right)^{\varpi}\right)\right) \quad (6)$$

here, ε and ϕ are the relative endurance values at fully reversed loading ($R = -1$) for Mode I and II, respectively; ϖ is a parameter controlling the variation of E_{II} as a function of R, and B is the mode mixity. The parameters β and q in Equation 5 are expressed as follows:

$$\beta = \frac{\eta \log(\gamma)}{\log(E)}, q = q_I + B(q_{II} - q_I) \quad (7)$$

where η is the brittleness parameter, and q_I and q_{II} parameters that allow the fitting of Paris crack growth rates in Mode I and II. The effect of the model parameters in the S-N curve and in the growth rate vs. severity plots are represented in Figure 7-(b) and Figure 7-(c), respectively. The calibration of the fatigue damage accumulation law for the AS4/8552 unidirectional (UD) prepreg was obtained via a trial-and-error procedure in [11]. Since the material is the same as used for the L-shaped specimens described in Section 2, the same calibration was adopted for the simulation of the fatigue tests.

In the explicit time integration scheme, each time step corresponds to a number of cycles ΔN. By discretizing the expression in Equation 5, the current value of the fatigue damage norm can be evaluated, as in Equation 8.

$$\frac{\Delta D}{\Delta N} = \frac{(1-D_{k-1})^{-q}}{\gamma E^{\beta}(\beta+q+1)}\left(\frac{\lambda}{\lambda^*}\right)^{\beta} \rightarrow D_k = D_{k-1} + \frac{(1-D_{k-1})^{-q}}{\gamma E^{\beta}(\beta+q+1)}\left(\frac{\lambda_k}{\lambda^*_k}\right)^{\beta}\Delta N \quad (8)$$

The fictitious frequency that links simulation time with cycle is selected to keep ΔD small enough at each integration step to avoid the numerical instabilities associated with excessive damage increments, but large enough to avoid a waste of computational power.

4.3 Simulation of the L-shaped specimen under fatigue loading

This section presents the results of simulations of the fatigue tests on the L-shaped laminated specimen. Figure 8 shows fatigue simulation results for specimens CL1NF0-1-5, tested at an initial severity of 0.70, and CL1NF0-2-1, at an initial severity of 0.55. Specimen CL1NF0-1-4 reaches the onset of unstable propagation during the quasi-static loading phase, so its fatigue simulation was not possible.

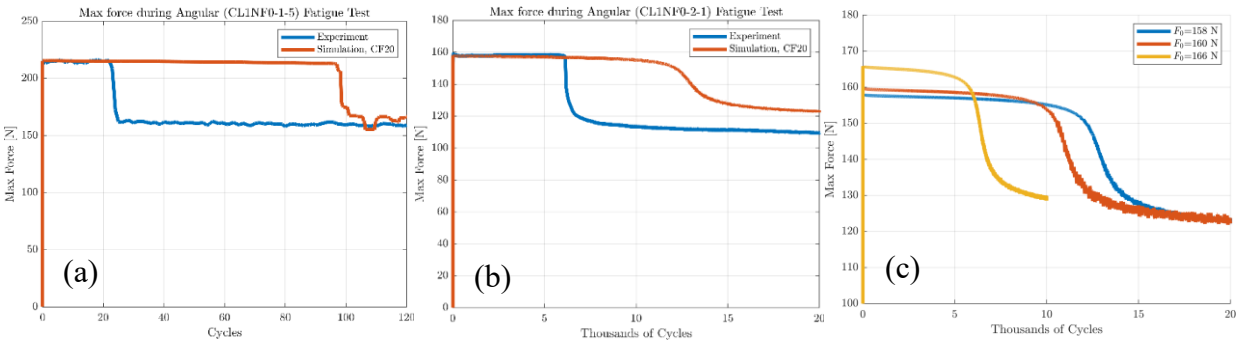

Figure 8: FE simulations compared with experimental fatigue tests on L-shaped specimens

The FE analyses show the onset of a rapid crack propagation after few cycles in CL1NF0-1-5 (96 cycles against 22 cycles in the test) and the need of thousands of cycles to activate the same phenomenon

in CL1NF0-2-1, where the model predicts the threshold at approximately 12,000 cycles, about twice the observed 6100 cycles. Considering the scatter of the experimental tests, the results are promising. In the CL1NF0-1-5 simulation, the crack growth is almost instantaneous and is arrested at a force level that matches the experimental level. In the simulation of CL1NF0-2-1, conducted at a severity of 0.55, the rate of the force reduction, related to the crack growth rate, is lower in the simulation than in the test. Moreover, the total crack propagation in the fast phase of the growth is lower than the experimental one, as indicated by the higher force level.

Despite these discrepancies, the qualitative aspects of the response are captured in both cases. Considering noticeable experimental variation of the response for the three tests performed at severity levels of 0.55, 0.57, and 0.62, two additional simulations were performed by applying slightly different openings, corresponding to 158 N and 166 N. The results are compared in Figure 8-(c) with the simulation performed at 160 N, already presented in Figure 8-(b). As can be seen, small variations in the applied load produce a large variation in the number of cycles required to activate the rapid growth propagation from 6000 to 12,500 cycles.

5 CONCLUSIONS

In this work, a study of delamination propagation under quasi-static and cyclic loading in L-shaped specimens was presented. Different regimes of propagation were found in quasi-static tests, in agreement with the results obtained with a semi-analytical evaluation of the ERR, through the application of an Irwin-Kies analysis. In the fatigue tests, very different quantitative responses were obtained by varying different severity levels, although three phases could be identified in all the experiments: a first phase of nucleation, without crack growth, a second phase of rapid crack growth, at a rate increasing with the severity, and a third phase of slow growth of the crack.

The availability of the ERR vs. crack length curve obtained through the semi-analytical procedure made possible an interpretation of the results. The energy available for crack opening increases with a significant gradient from the pre-cracked conditions until a crack length of about 6.4 mm (from 0.06 kJ/m2 to 0.16 kJ/m2 for an opening of 2 mm). This means the severity imposed at the beginning of the tests increases rapidly as the crack grows, promoting a very fast propagation phase. Interestingly, the experimental results indicate that this phase of rapid crack propagation ends after the maximum of the ERR curve, when severity starts decreasing with crack length.

The application of a cohesive-based approach within FE explicit simulation was able to capture the response in quasi-static tests. A fatigue damage accumulation law available in literature was described, implemented in a user-defined material subroutine and applied to model the fatigue tests. The three phases of the fatigue responses were qualitatively reproduced, with quantitative discrepancies that can be difficult to interpret, considering the limited number of experiments and the relevancy of typical scattering in fatigue propagation of delamination documented in the literature. The application of explicit time integration schemes made possible the identification of different propagation regimes with a good level of reliability. Results are promising for the possible application of the proposed approach in the presence of large variation of ERR with crack advancement, which can induce significantly different crack propagation rates in real-world damage scenarios.

REFERENCES

[1] “AC 20-107A - Composite Aircraft Structure.” Accessed: May 22, 2025. [Online]. Available: https://www.faa.gov/regulations_policies/advisory_circulars/index.cfm/go/document.information/documentID/22052

[2] J. A. Pascoe, “Slow-growth damage tolerance for fatigue after impact in FRP composites: Why current research won’t get us there,” *Theoretical and Applied Fracture Mechanics*, vol. 116, p. 103127, Dec. 2021, doi: 10.1016/J.TAFMEC.2021.103127.

[3] B. L. V. Bak, A. Turon, E. Lindgaard, and E. Lund, "A simulation method for high-cycle fatigue-driven delamination using a cohesive zone model," *Int J Numer Methods Eng*, vol. 106, no. 3, pp. 163–191, Apr. 2016, doi: 10.1002/NME.5117.

[4] B. L. V. Bak, A. Turon, E. Lindgaard, and E. Lund, "A benchmark study of simulation methods for high-cycle fatigue-driven delamination based on cohesive zone models," *Compos Struct*, vol. 164, pp. 198–206, Mar. 2017, doi: 10.1016/J.COMPSTRUCT.2016.11.081.

[5] L. Carreras *et al.*, "A simulation method for fatigue-driven delamination in layered structures involving non-negligible fracture process zones and arbitrarily shaped crack fronts," *Compos Part A Appl Sci Manuf*, vol. 122, pp. 107–119, Jul. 2019, doi: 10.1016/J.COMPOSITESA.2019.04.026.

[6] L. Carreras, B. L. V. Bak, S. M. Jensen, C. Lequesne, H. Xiong, and E. Lindgaard, "Benchmark test for mode I fatigue-driven delamination in GFRP composite laminates: Experimental results and simulation with the inter-laminar damage model implemented in SAMCEF," *Compos B Eng*, vol. 253, p. 110529, Mar. 2023, doi: 10.1016/J.COMPOSITESB.2023.110529.

[7] G. G. Trabal, B. L. V. Bak, B. Chen, L. Carreras, and E. Lindgaard, "An adaptive floating node based formulation for the analysis of multiple delaminations under high cycle fatigue loading," *Compos Part A Appl Sci Manuf*, vol. 160, p. 107036, Sep. 2022, doi: 10.1016/J.COMPOSITESA.2022.107036.

[8] A. Turon, J. Costa, P. P. Camanho, and C. G. Dávila, "Simulation of delamination in composites under high-cycle fatigue," *Compos Part A Appl Sci Manuf*, vol. 38, no. 11, pp. 2270–2282, Nov. 2007, doi: 10.1016/J.COMPOSITESA.2006.11.009.

[9] C. G. Dávila, "From S-N to the Paris law with a new mixed-mode cohesive fatigue model for delamination in composites," *Theoretical and Applied Fracture Mechanics*, vol. 106, p. 102499, Apr. 2020, doi: 10.1016/J.TAFMEC.2020.102499.

[10] C. G. Dávila and M. W. Joosten, "A cohesive fatigue model for composite delamination based on a new material characterization procedure for the Paris law," *Eng Fract Mech*, vol. 284, p. 109232, May 2023, doi: 10.1016/J.ENGFRACMECH.2023.109232.

[11] C. G. Davila, C. A. Rose, G. B. Murri, W. C. Jackson, and W. M. Johnston, "Evaluation of Fatigue Damage Accumulation Functions for Delamination Initiation and Propagation," 2020. Accessed: May 23, 2025. [Online]. Available: http://www.sti.nasa.gov

[12] I. Leciñana, J. Zurbitu, J. Renart, and A. Turon, "A robust fatigue parameter determination method for a local fatigue cohesive zone model," *Int J Fatigue*, vol. 171, p. 107582, Jun. 2023, doi: 10.1016/J.IJFATIGUE.2023.107582.

[13] Y. Ng, J. Tomblin, and E. Hooper, "Hexcel 8552 AS4 Unidirectional Prepreg at 190 gsm & 35% RC Qualification Material Property Data Report FAA Special Project Number SP4614WI-Q," 2011.

[14] S. Ghiasvand, "Modeling and monitoring of interface damage in composite in the presence of residual and combined stress states," 2023, Accessed: Jul. 01, 2025. [Online]. Available: https://www.politesi.polimi.it/handle/10589/183798

[15] W. C. Jackson and R. H. Martin, "An Interlaminar Tensile Strength Specimen," *ASTM Special Technical Publication*, no. 1206, pp. 333–354, 1993, doi: 10.1520/STP12638S.

[16] B. Tasdemir and D. Coker, "Comparison of damage mechanisms in curved composite laminates under static and fatigue loading," *Compos Struct*, vol. 213, pp. 190–203, Apr. 2019, doi: 10.1016/J.COMPSTRUCT.2019.01.072.

[17] B. Tasdemir and D. Coker, "Fatigue and static damage in curved woven fabric carbon fiber reinforced polymer laminates," *J Compos Mater*, vol. 56, no. 11, pp. 1693–1708, Jun. 2022, doi: 10.1177/00219983221078787/ASSET/82CB5E67-A985-4ADF-B041-3E44CFE1EB10/ASSETS/IMAGES/LARGE/10.1177_00219983221078787-FIG19.JPG.

[18] "Abaqus 2016 Documentation." Accessed: Jun. 29, 2025. [Online]. Available: http://130.149.89.49:2080/v2016/index.html

[19] R. H. Martin, "Delamination Failure in a Unidirectional Curved Composite Laminate," *ASTM Special Technical Publication*, no. 1120, pp. 365–383, 1992, doi: 10.1520/STP20170S.

[20] G. Wimmer and H. E. Pettermann, "A semi-analytical model for the simulation of delamination in laminated composites," *Compos Sci Technol*, vol. 68, no. 12, pp. 2332–2339, Sep. 2008, doi: 10.1016/J.COMPSCITECH.2007.10.022.

[21] A. Airoldi and C. G. Dávila, "Identification of material parameters for modelling delamination in the presence of fibre bridging," *Compos Struct*, vol. 94, no. 11, pp. 3240–3249, Nov. 2012, doi: 10.1016/J.COMPSTRUCT.2012.05.014.

[22] G. Bao and Z. Suo, "Remarks on Crack-Bridging Concepts," *Appl Mech Rev*, vol. 45, no. 8, pp. 355–366, Aug. 1992, doi: 10.1115/1.3119764.

[23] A. Hillerborg, M. Modéer, and P. E. Petersson, "Analysis of crack formation and crack growth in concrete by means of fracture mechanics and finite elements," *Cem Concr Res*, vol. 6, no. 6, pp. 773–781, Nov. 1976, doi: 10.1016/0008-8846(76)90007-7.

[24] P. P. Camanho and C. G. Dávila, "Mixed-Mode Decohesion Finite Elements for the Simulation of Delamination in Composite Materials," NASA/TM-2002-211737, 2002.

[25] A. Turon, C. G. Dávila, P. P. Camanho, and J. Costa, "An engineering solution for mesh size effects in the simulation of delamination using cohesive zone models," *Eng Fract Mech*, vol. 74, no. 10, pp. 1665–1682, Jul. 2007, doi: 10.1016/J.ENGFRACMECH.2006.08.025.

[26] H. R. Amiri, A. A. Aghakouchak, S. Shahbeyk, and M. D. Engelhardt, "Finite element simulation of ultra low cycle fatigue cracking in steel structures," *J Constr Steel Res*, vol. 89, pp. 175–184, Oct. 2013, doi: 10.1016/J.JCSR.2013.07.007.

[27] B. L. V. Bak, C. Sarrado, A. Turon, and J. Costa, "Delamination under fatigue loads in composite laminates: A review on the observed phenomenology and computational methods," *Appl Mech Rev*, vol. 66, no. 6, Nov. 2014, doi: 10.1115/1.4027647/443639.

[28] T. K. O'Brien, A. D. Chawan, R. Krueger, and I. L. Paris, "Transverse tension fatigue life characterization through flexure testing of composite materials," *Int J Fatigue*, vol. 24, no. 2–4, pp. 127–145, Feb. 2002, doi: 10.1016/S0142-1123(01)00104-9.

INSTITUT CLÉMENT ADER

ICCM24

24TH INTERNATIONAL CONFERENCE ON COMPOSITE MATERIALS

ICCM24 – 24TH INTERNATIONAL CONFERENCE ON COMPOSITE MATERIALS

Baltimore Convention Center – Baltimore, Maryland, USA

Modeling and Control of Polymerization Exotherm of an Acrylic Thermoplastic Resin in the Pultrusion Process

Farouk Zreika, Arthur Cantarel, Olivier De Almeida

Institut Clément Ader (ICA), Université de Toulouse, France

IMT Mines Albi-Carmaux École Mines-Télécom

INSA TOULOUSE

ISAE SUPAERO

UNIVERSITÉ TOULOUSE III PAUL SABATIER

cnrs

Université Fédérale Toulouse Midi-Pyrénées

Context – INFRAlight Project

INSTITUT CLÉMENT ADER

INFRAlight Project

Towards sustainable and digitalized mobility

Digitize and automate rail transport

Reduce costs and facilitate line operation and maintenance

Reduce the carbon footprint of transport



- **Continuous fibre recyclable thermoplastic composite rails**
- **Rails manufacturing by reactive thermoplastic pultrusion**

Pultrusion

ELIUM PMMA → **In-situ Polymerization**

Section of interest

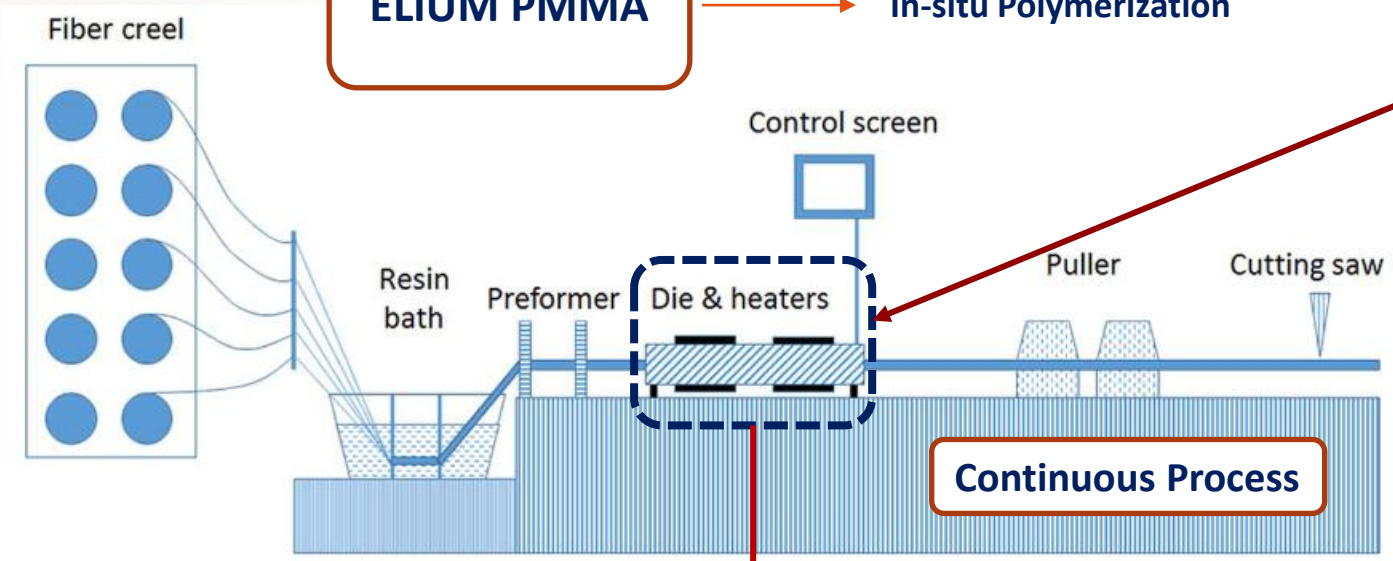



Alexander A. Safonov , Pierpaolo Carlone, Iskander Akhatov, 15 January 2018
doi : https://doi.org/10.1016/j.compstruct.2017.09.093

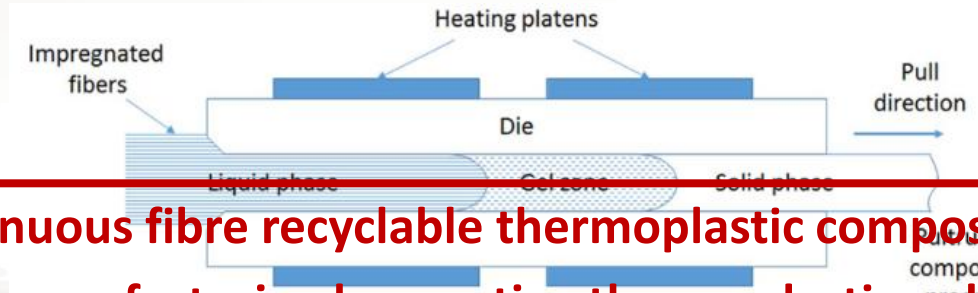

- **High production rate, high efficiency.**
- **Low production costs.**
- **Ability to produce profiles of infinite length.**

- **Continuous fibre recyclable thermoplastic composite rails**
- **Rails manufacturing by reactive thermoplastic pultrusion**

Experimental Thermal Study

Core temperature at 150°C

Surface temperature at 150°C

Core temperature at 110°C

Surface temperature at 110°C

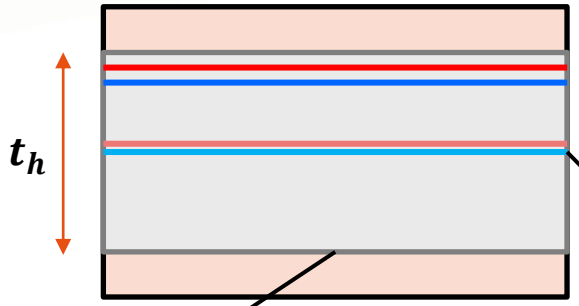

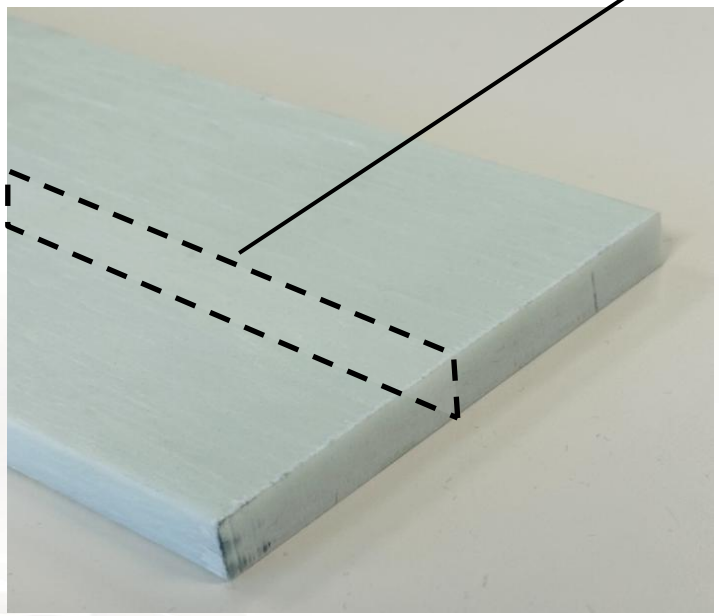

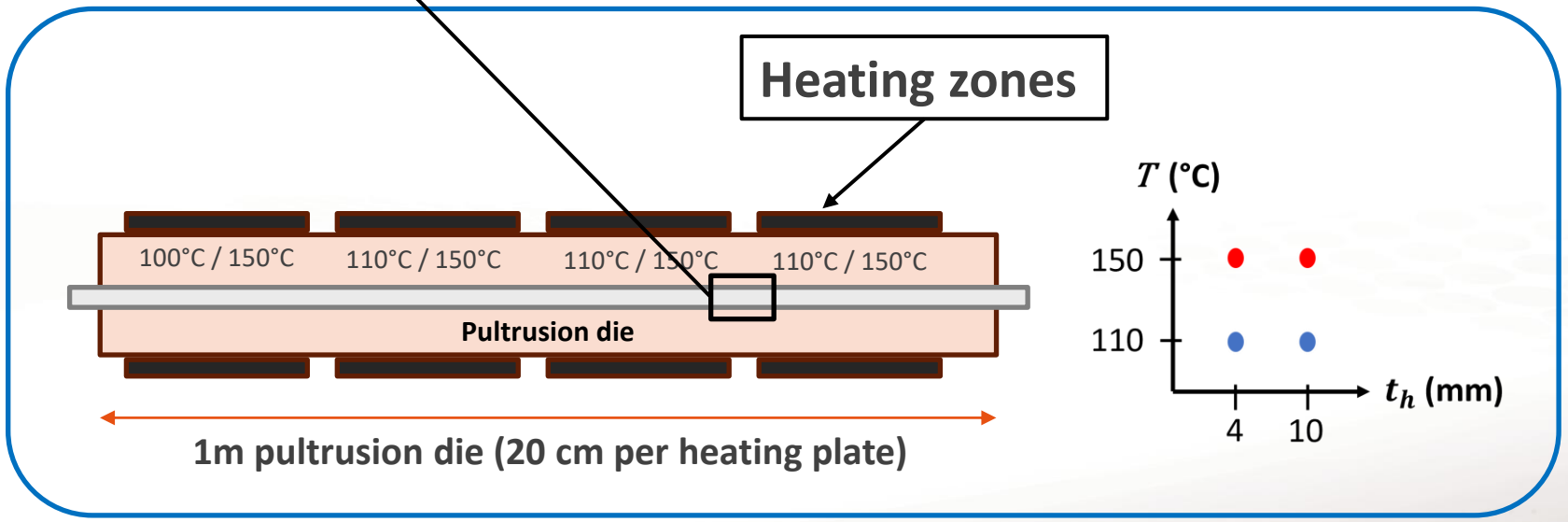

IRT M2P unidirectional Glass/ELIUM

Experimental Thermal Study

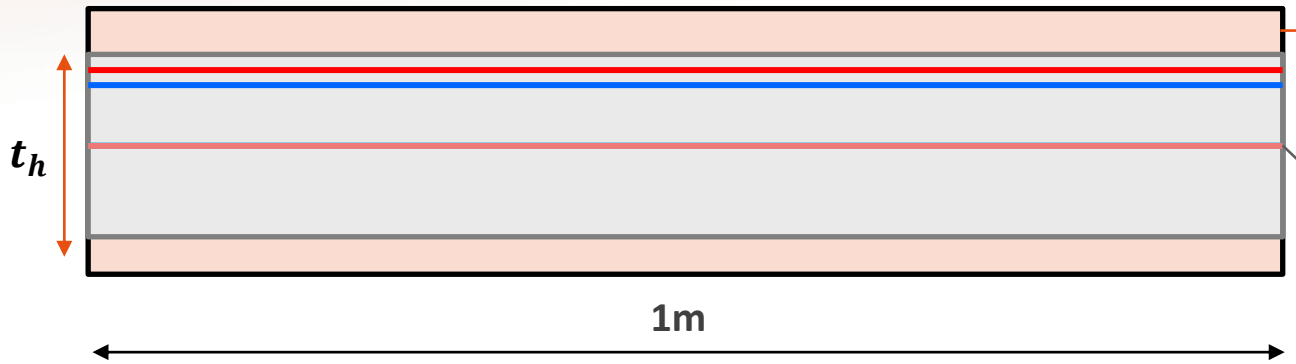

Pultrusion die

Composite

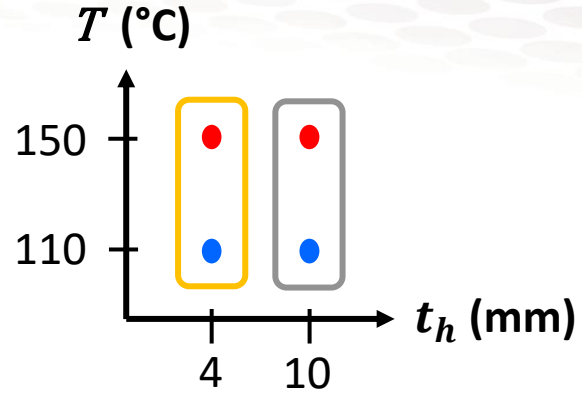

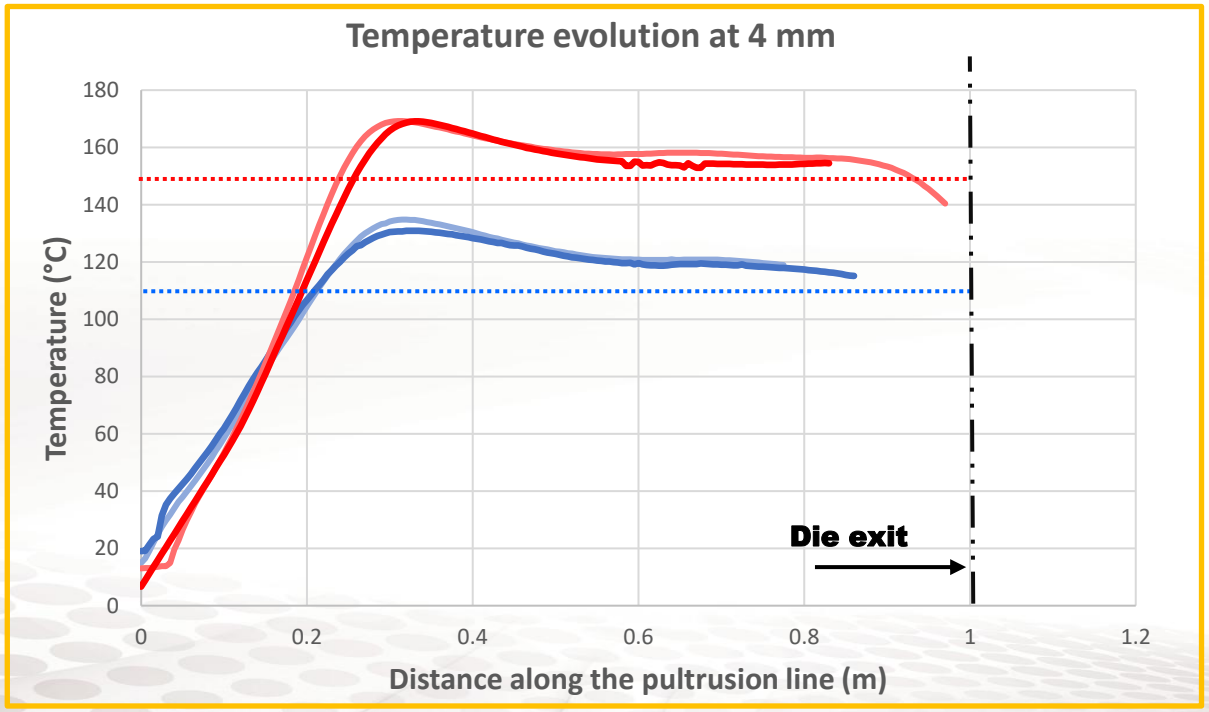

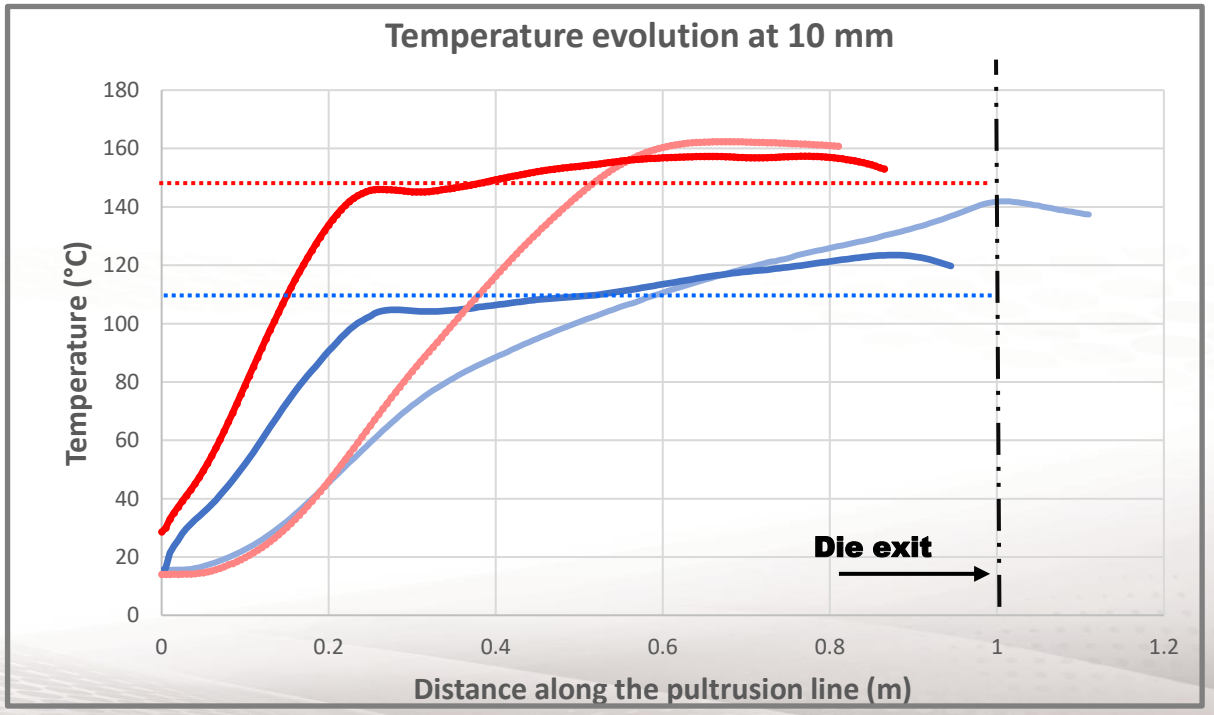

Experimental Manufacturing of Pultruded Plates Glass/ELIUM

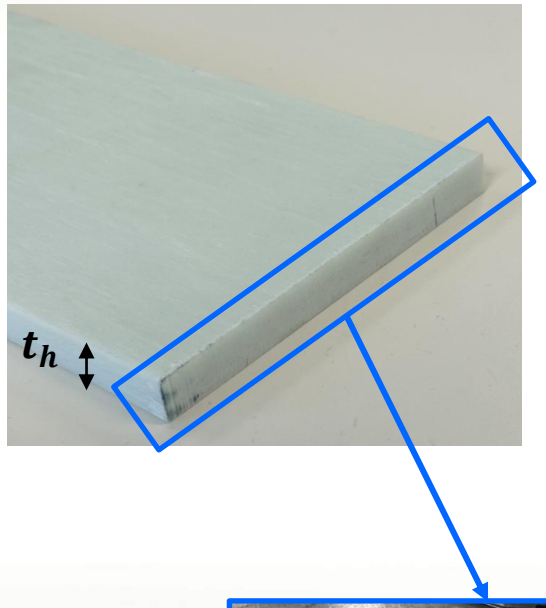



Micrographic characterization

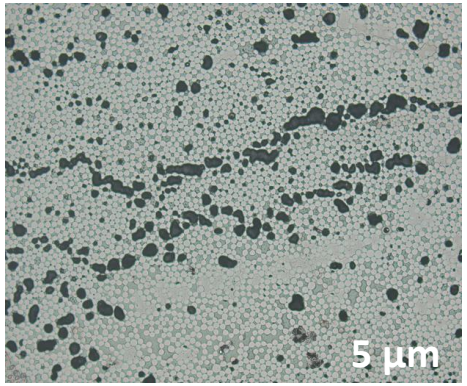

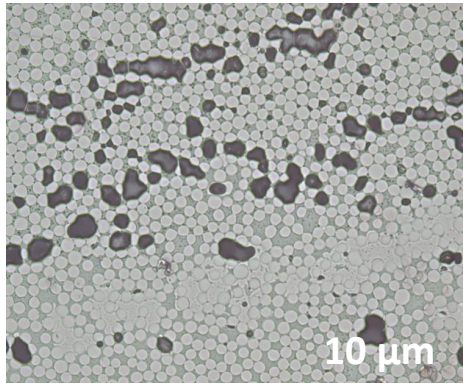

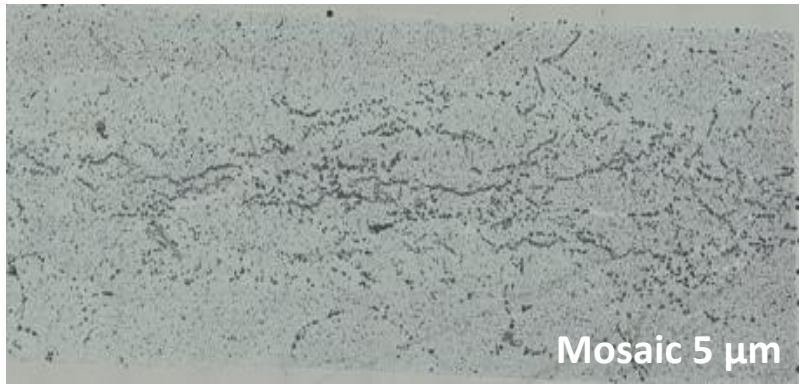



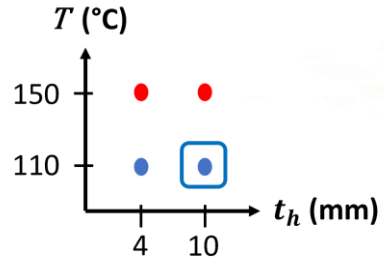

Pultruded 10 mm thick Plate Glass/ELIUM

IRT M2P – 110°C

Problem Statement and Approach

Overall Goal

- ✓ Optimize the process, to achieve a complete polymerization at the highest production speed
- ✓ Necessity of a fine and predictive model to support process control

Complex thermal behavior

- ➢ Strong thermo-kinetic coupling due to the complex polymerization of the Elium resin.
- ➢ Development of a numerical model of the pultrusion process by coupling heat transfer equations with the polymerization kinetics of the resin.
- ➢ Influence of Elium's specific kinetic behavior on the thermal regime during pultrusion.
- ➢ Evolution of material properties as a function of both temperature and degree of conversion.

The challenges of Pultrusion

INSTITUT CLÉMENT ADER

Thermal expansion $\frac{\Delta v}{v}$

Cure Shrinkage $\frac{\Delta v}{v}$

Boundary condition : $\sigma_{max} = \sigma_{adhesion}$

Mechanical state $\boldsymbol{\sigma}$

Mechanical properties $(E, \eta, \sigma, \gamma_s)$

$E(T)$
$\eta(T)$
$\rho(T)$

$E(\alpha)$
$\eta(\alpha)$
$\rho(\alpha)$

Kamal-Sourour Model

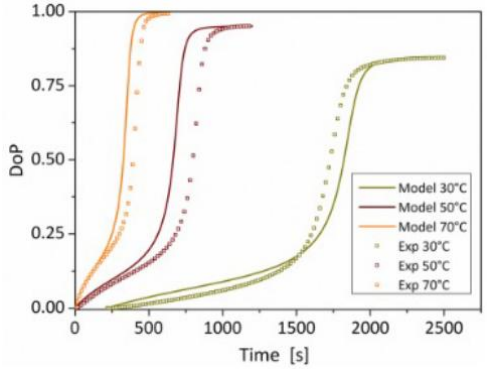

S. Sourour, M.R. Kamal, January 1976
doi : https://doi.org/10.1016/0040-6031(76)80056-1

E P

Thermal properties $(C_p(T), \lambda(T))$

Thermal state T

T λ

Nucleation / cracking porosity

Chemical properties (M_w, χ_{MMA})

Chemical state G

Polymerization kinetics α

$C_p(\alpha), \lambda(\alpha), \rho(\alpha)$

$\rho(T), \dot{\alpha}(T)$

Boundary conditions : RTC, h_c ...

Boundary condition : ϕ ?

Thermal Model & BC

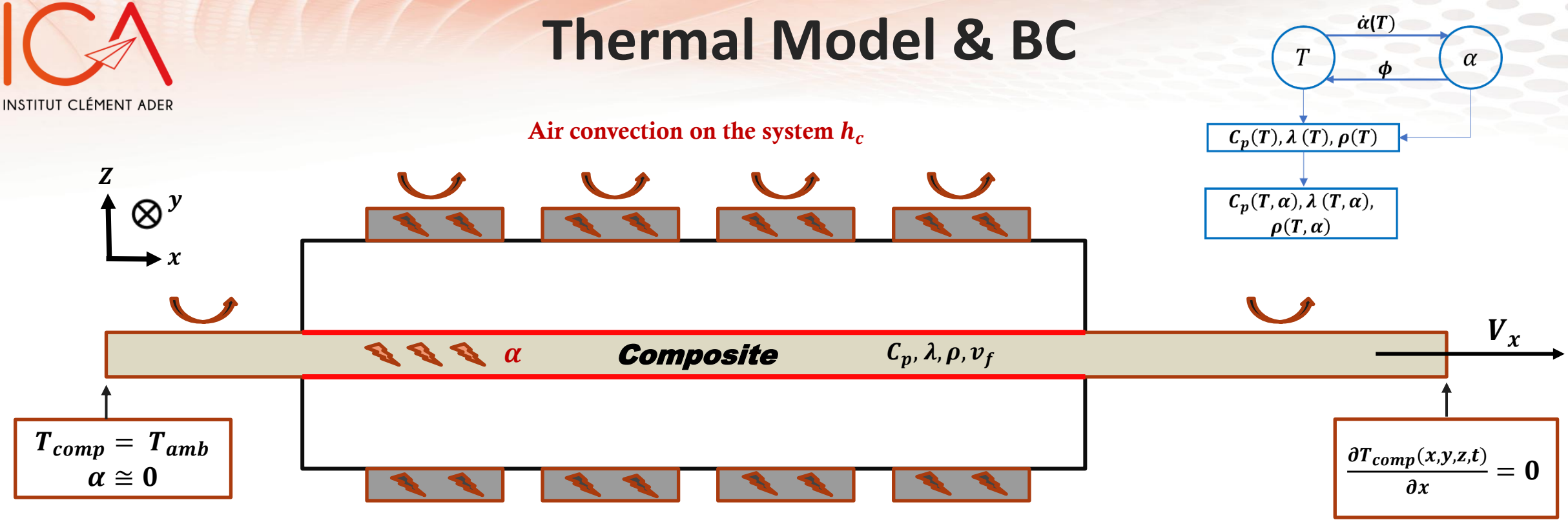

$$\frac{1}{\lambda_l} = \frac{1-v_f}{\lambda_r} + \frac{v_f}{\lambda_f}$$

$$\lambda_t = v_f\,\lambda_f + (1 - v_f)\,\lambda_r$$

$$C_P = v_f\,C_{Pf} + (1 - v_f)\,C_{Pr}$$

$$\rho = v_f\rho_f + (1 - v_f)\,\rho_r$$

$$\rho\,C_p\left(\frac{\partial T}{\partial t} + v_x\frac{\partial T}{\partial x}\right) + \nabla(-\lambda\nabla T) = \phi$$

$$\underbrace{\rho\,C_p v_x\frac{\partial T}{\partial x}}_{\text{Convection}} + \underbrace{\nabla(-\lambda\nabla T)}_{\text{Conduction}} = \underbrace{(1 - V_f)\rho_r\,\Delta H_{tot} v_x\frac{\partial \alpha}{\partial x}}_{\text{Exothermic source}}$$

??

Data sheet: *polymeres-netzsch-com/pmma-polymethacrylate-de-methyle*
Data sheet: *techniques-ingenieur/proprietes-des-fibres*

Kinetic Model of Elium Resin

$$\frac{d\alpha}{dt} = k_p \sqrt{\frac{2f(k_{d,P_1}[P_1] + k_{d,P_2}[P_2] + k_{d,P_3}[P_3]}{k_t}}(1-\alpha)$$

Damien Gacon et al., Composite Materials hal -04696743 (Jul 2024)

k_p : Radical polymerization rate constant
k_{d,P_i} : Dissociation rate constant
k_t : Termination rate constant
f : Efficiency of the peroxide initiator
$[P_i]$: Concentration of the peroxide initiator

- **Validation of the kinetic model using COMSOL**

Assumptions:

- **Thermal study under adiabatic conditions using COMSOL Multiphysics.**

- **Validation of the results obtained in COMSOL with the actual experimental data**

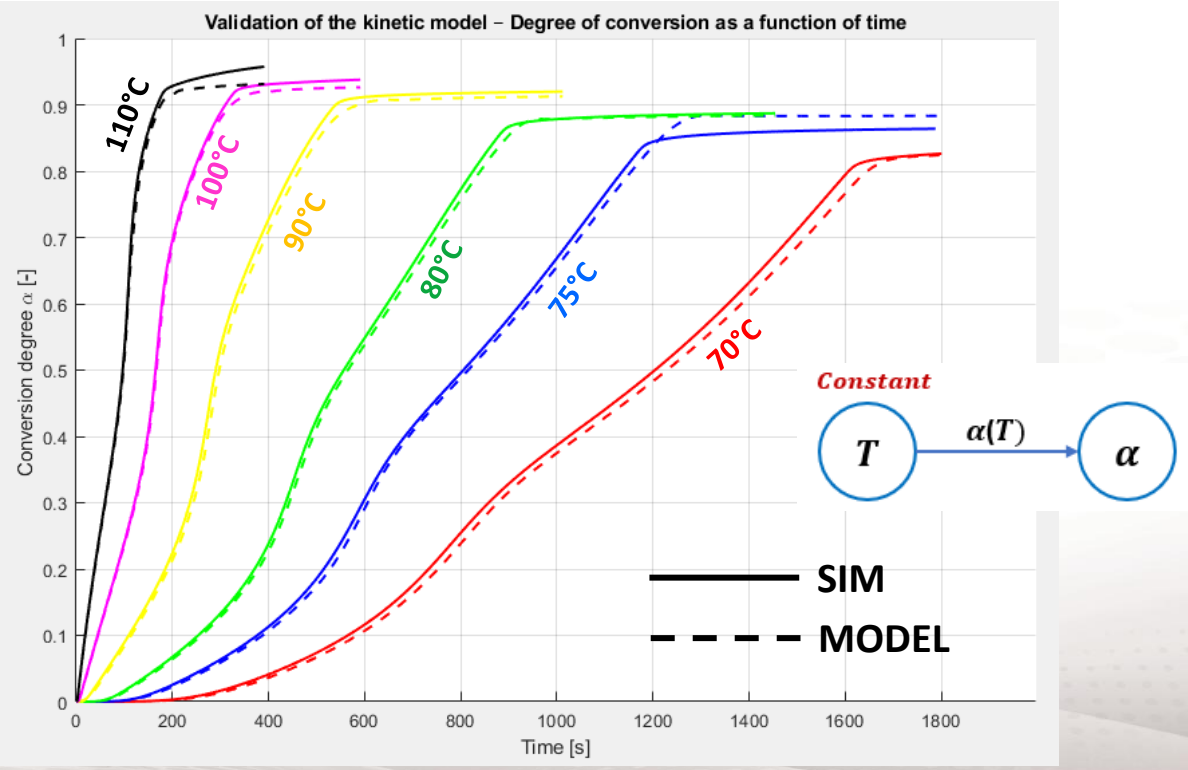

Influence of the source term at 110°C

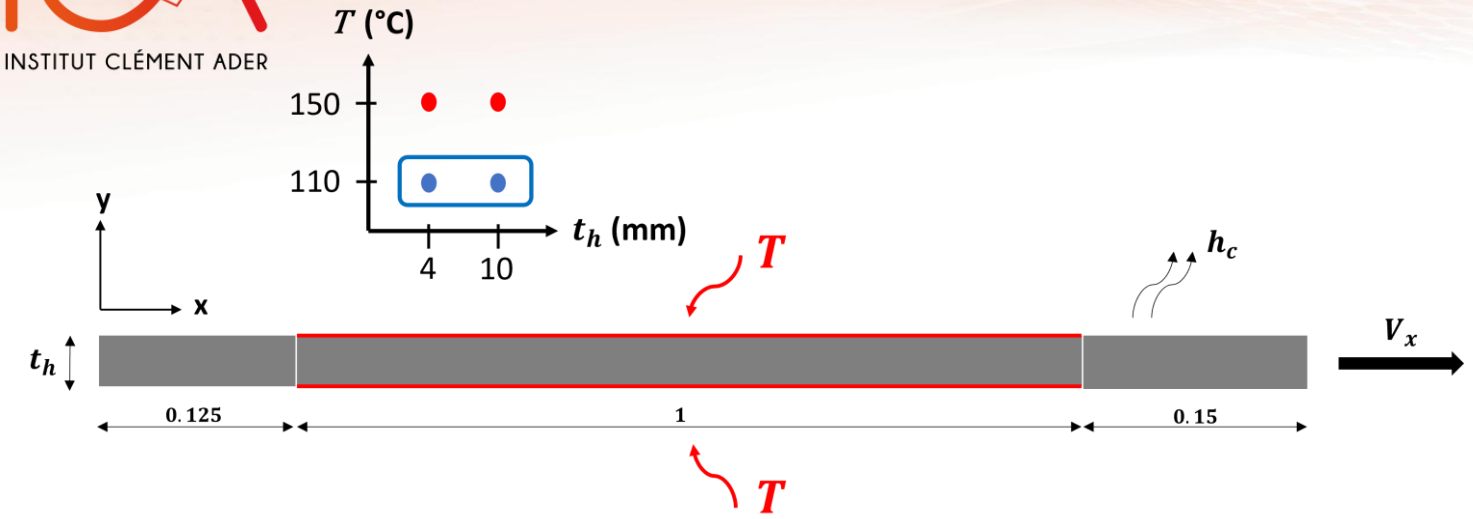

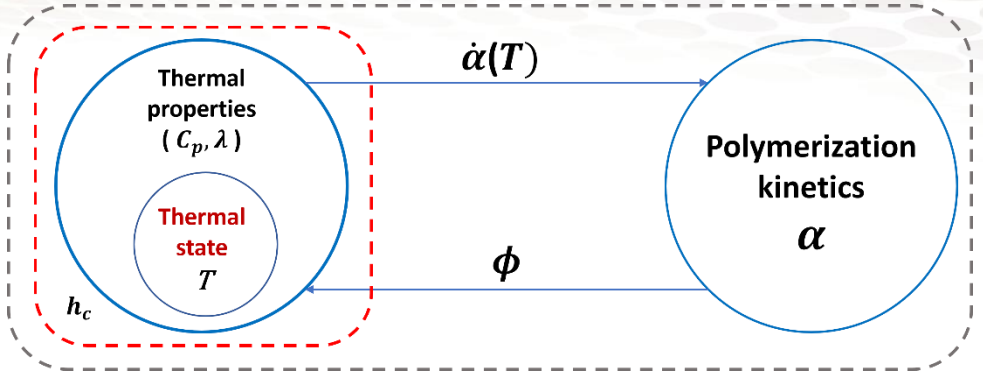

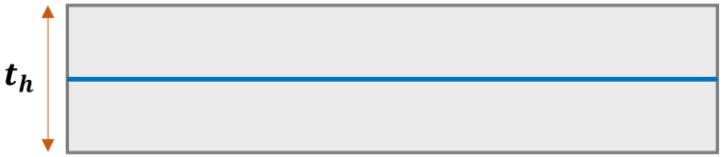

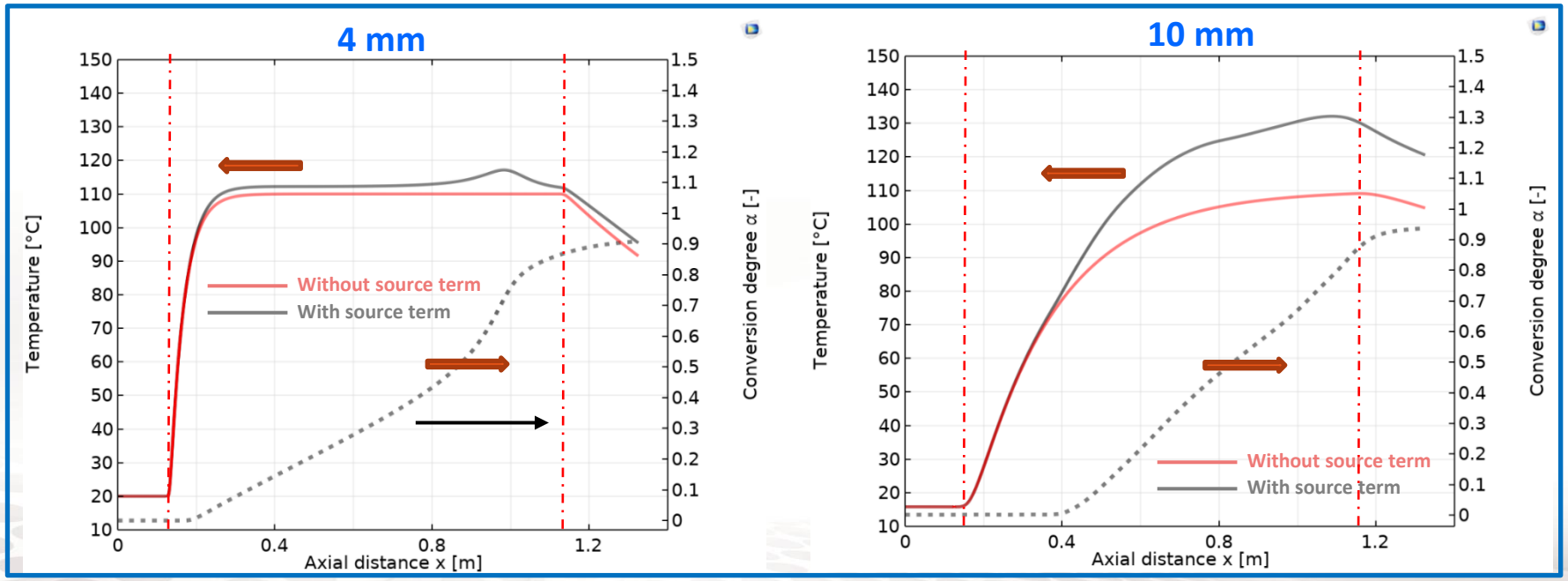

Conclusion

- A temperature rise due to the exothermic heat generated by polymerization.
- With a source term, the temperature exceeds the applied temperature

System setup in COMSOL

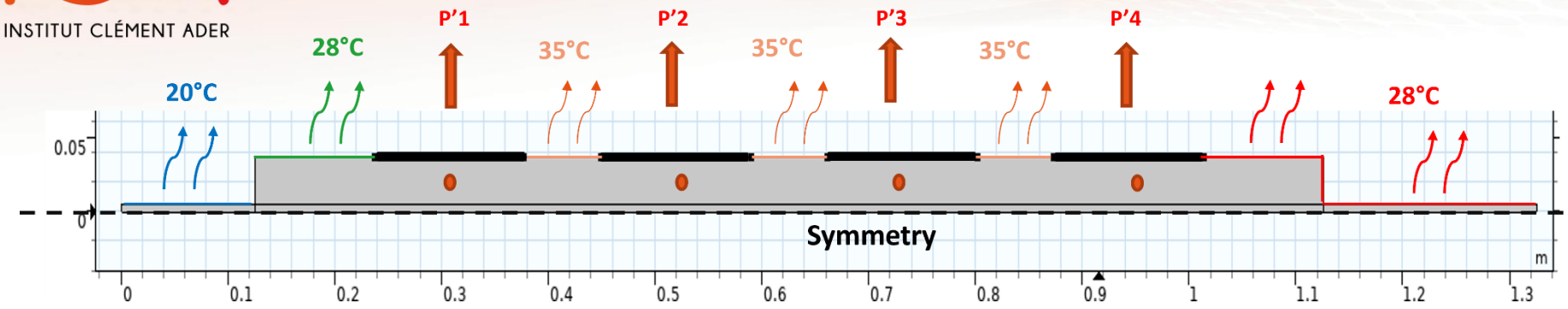

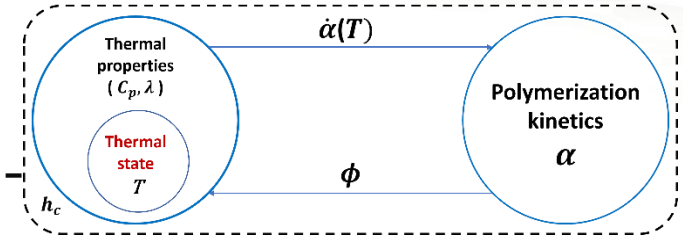

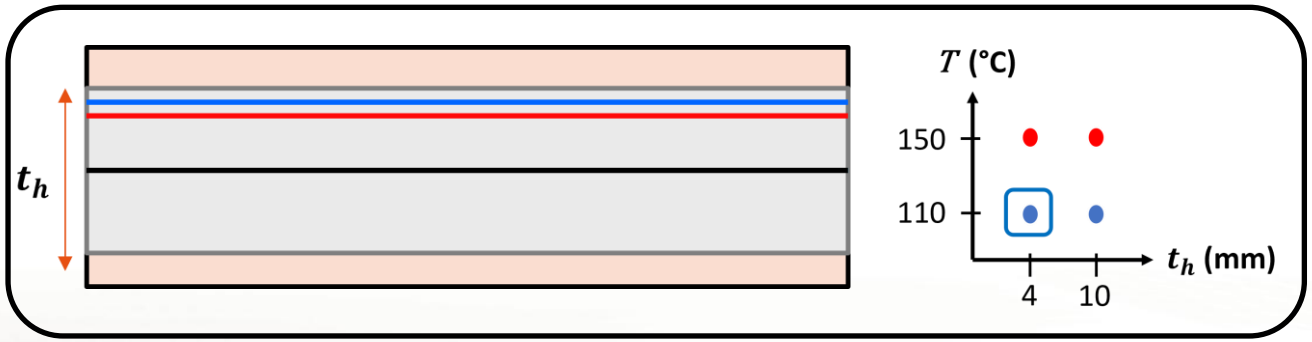

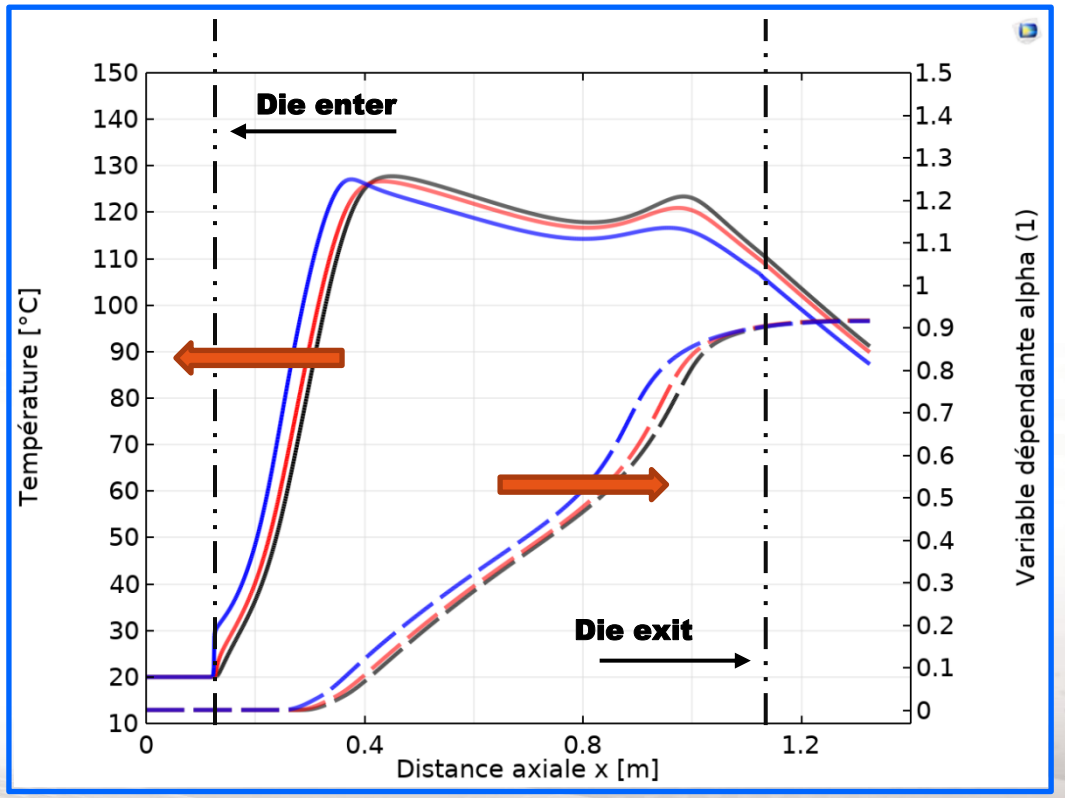

Conclusion

- Polymerization starts at the surface due to the high thermal conductivity of the die.
- Temperature and polymerization are delayed at the core.
- Homogeneous heat transfer.

System setup in COMSOL

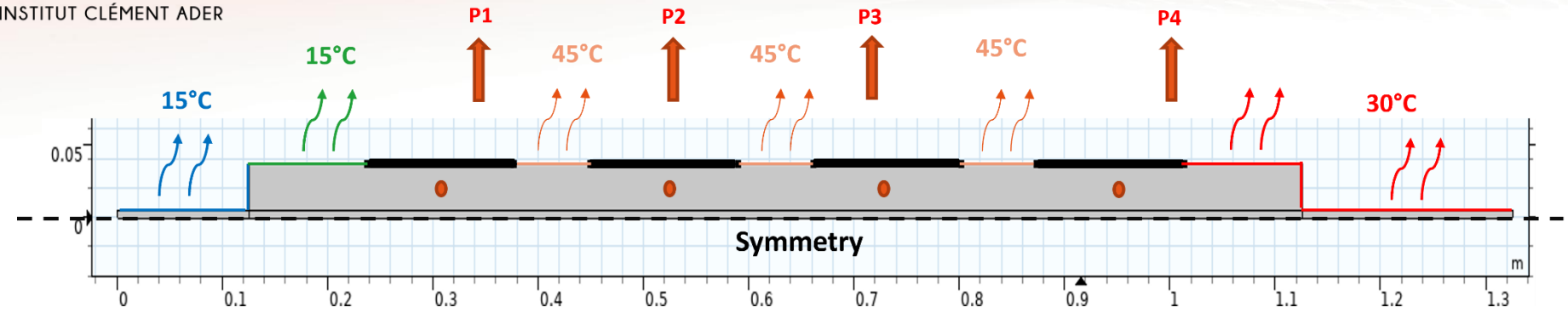

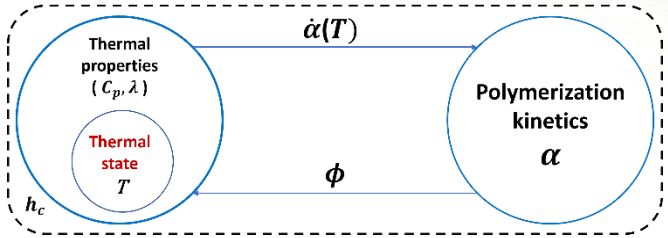

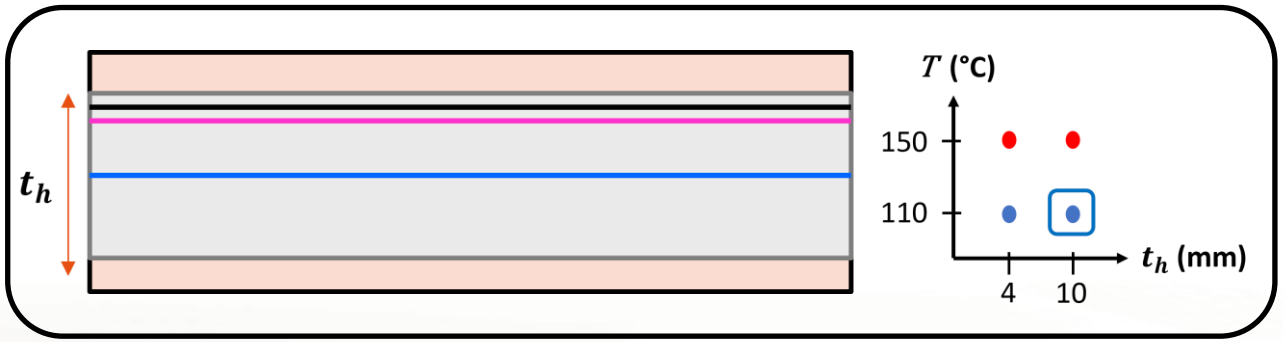

Conclusion

- Polymerization starts at the surface due to the high thermal conductivity of the die.
- Temperature and polymerization are delayed at the core.

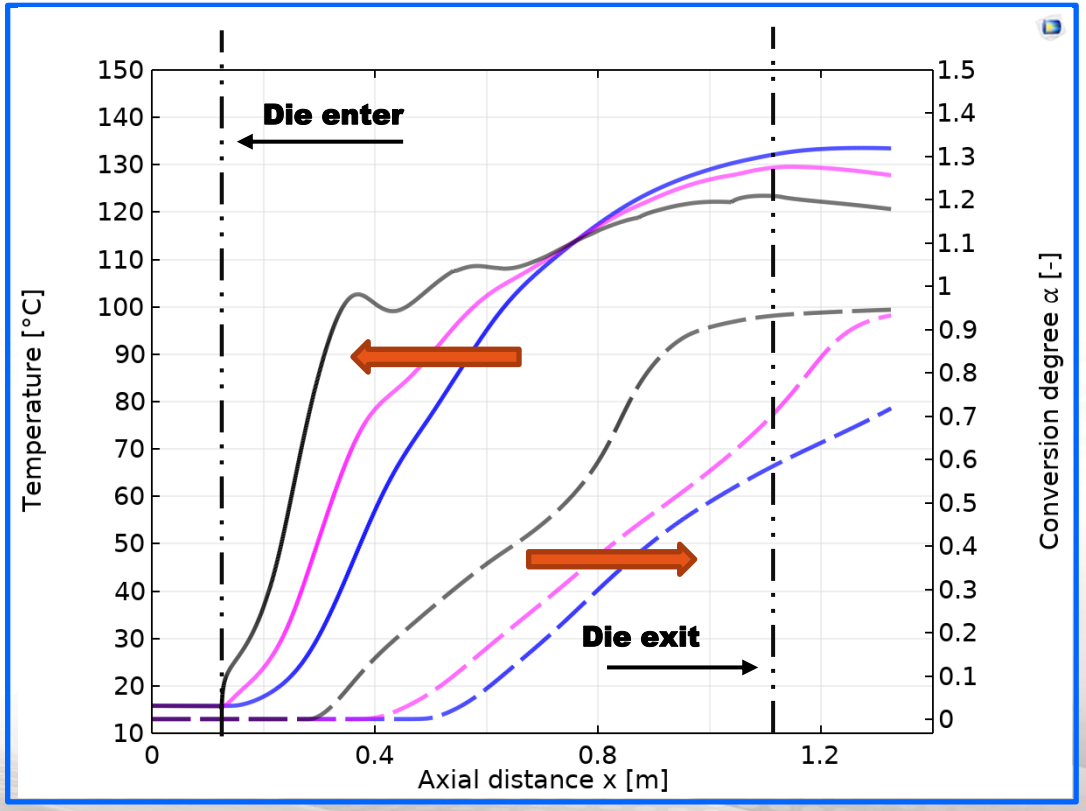

Intermediate conclusion

INSTITUT CLÉMENT ADER

Surface analysis

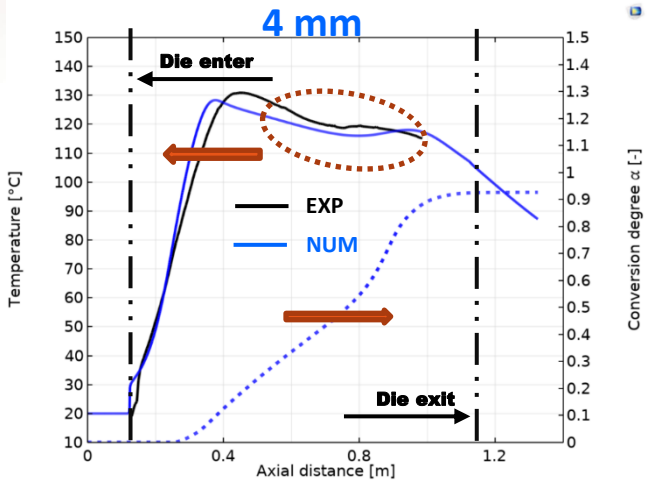

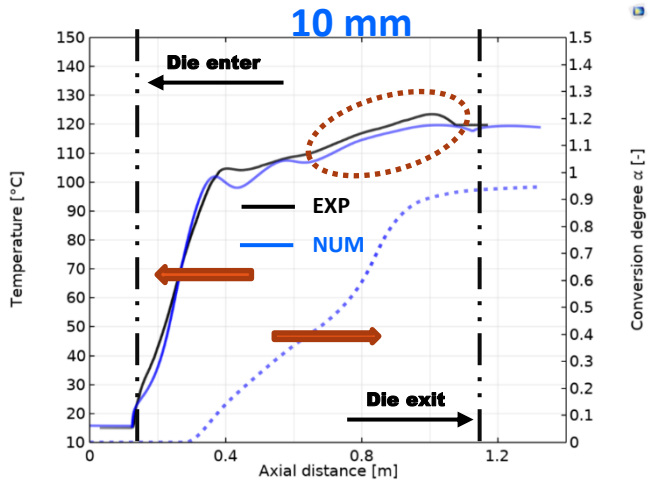

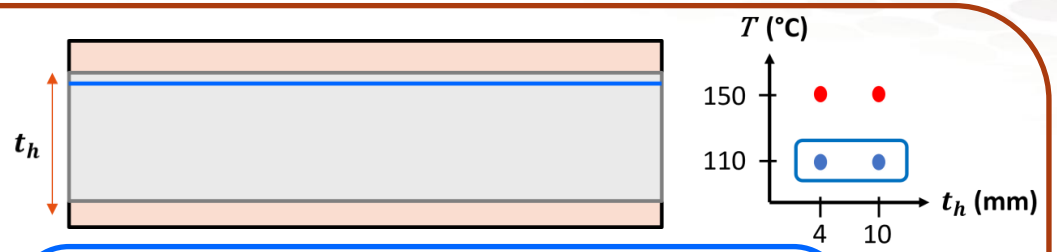

Relevant thermo-kinetic coupling

- Allows to capture the thermal evolution

But !!

- Slight shift in temperature at the surface !
- Problem for the thick part such as Rail !
  - **Thermal contact resistance ?**

Core analysis

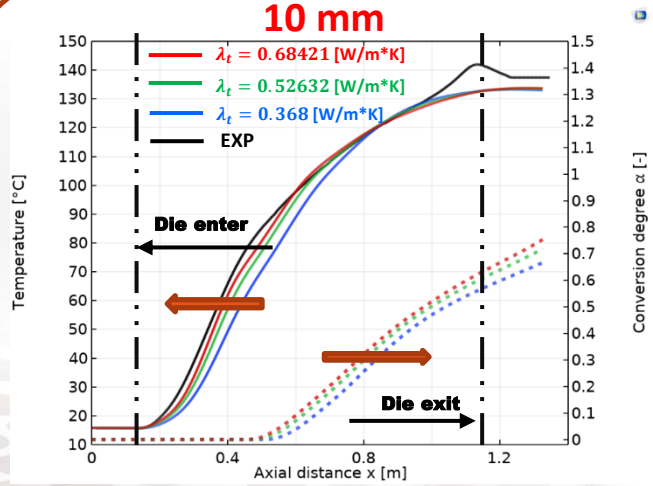

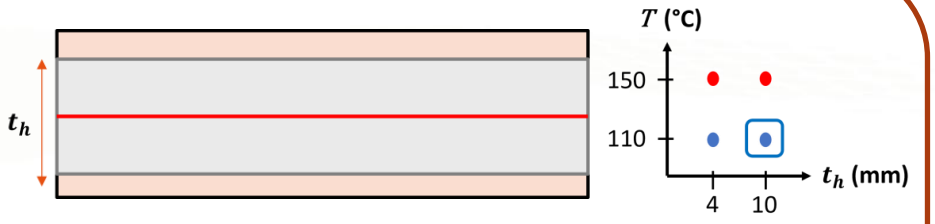

- A delay at the core is observed compared to experimental data
- **Can porosity affect thermal conductivity ?**

TCR ??

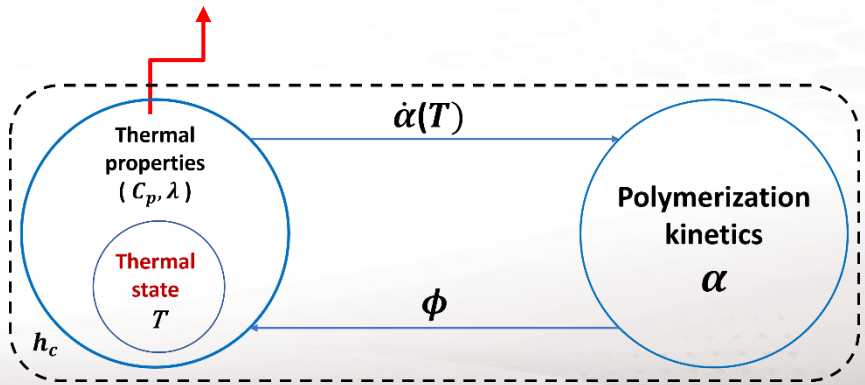

Thermal Optimization of TCR

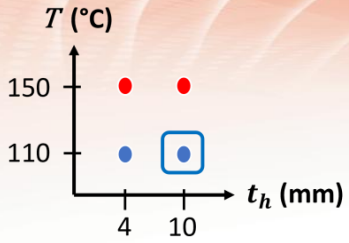

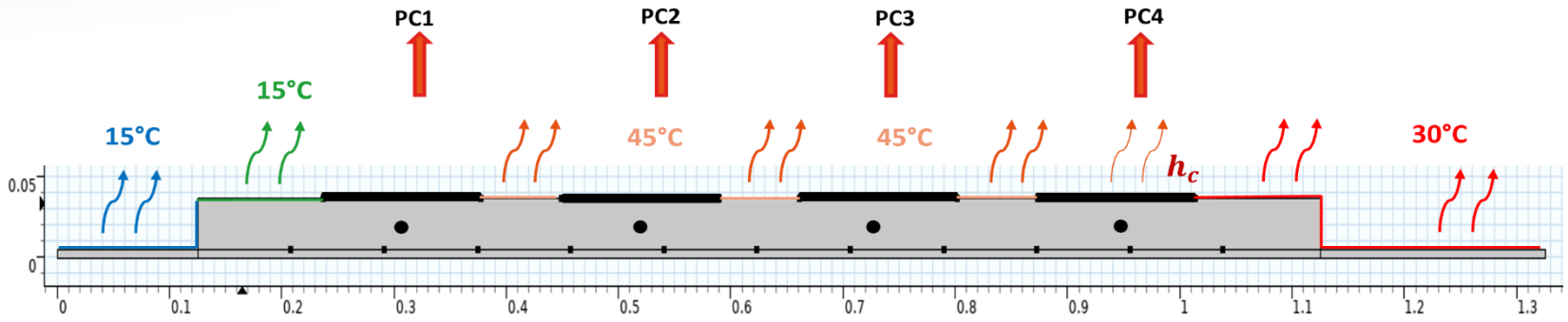

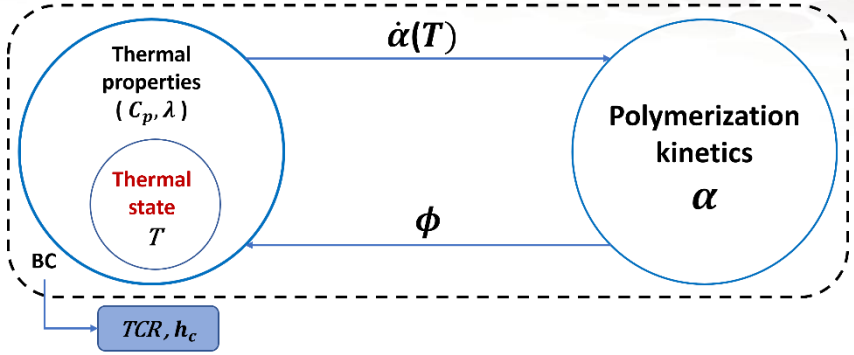

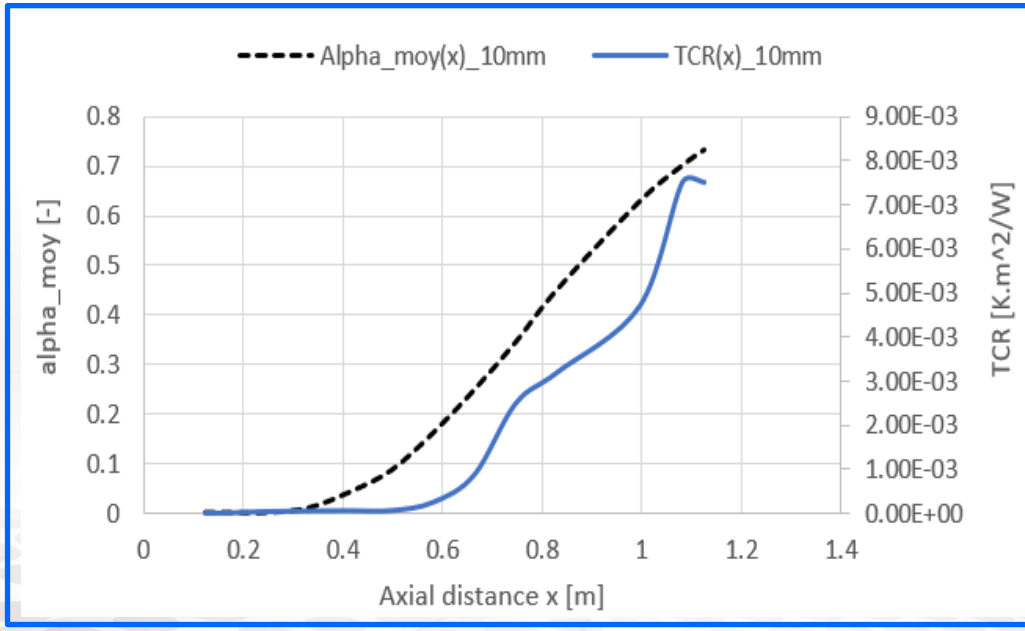

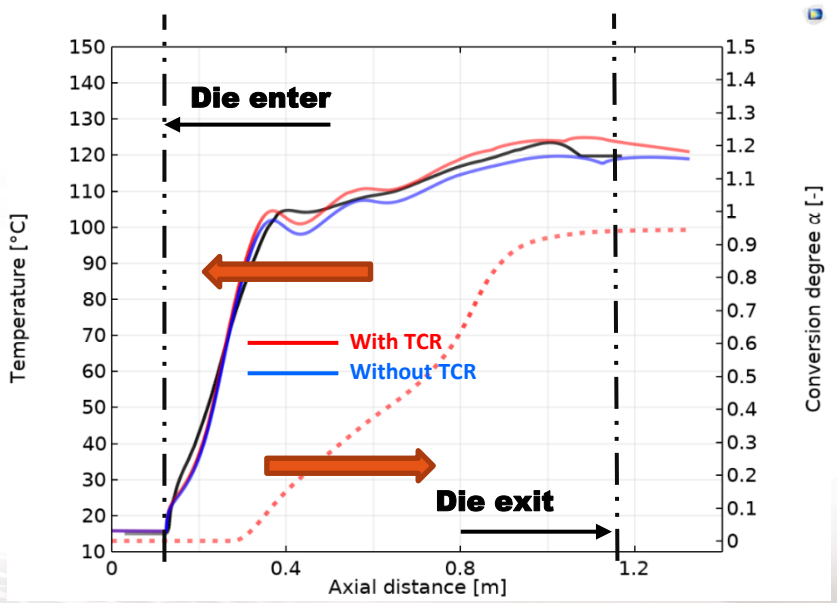

Conclusion

- The surface thermal profile shows better agreement with the experimental one with TCR
- Proportional relationship between TCR and the polymerization rate

Evolution of TCR as a function of conversion degree

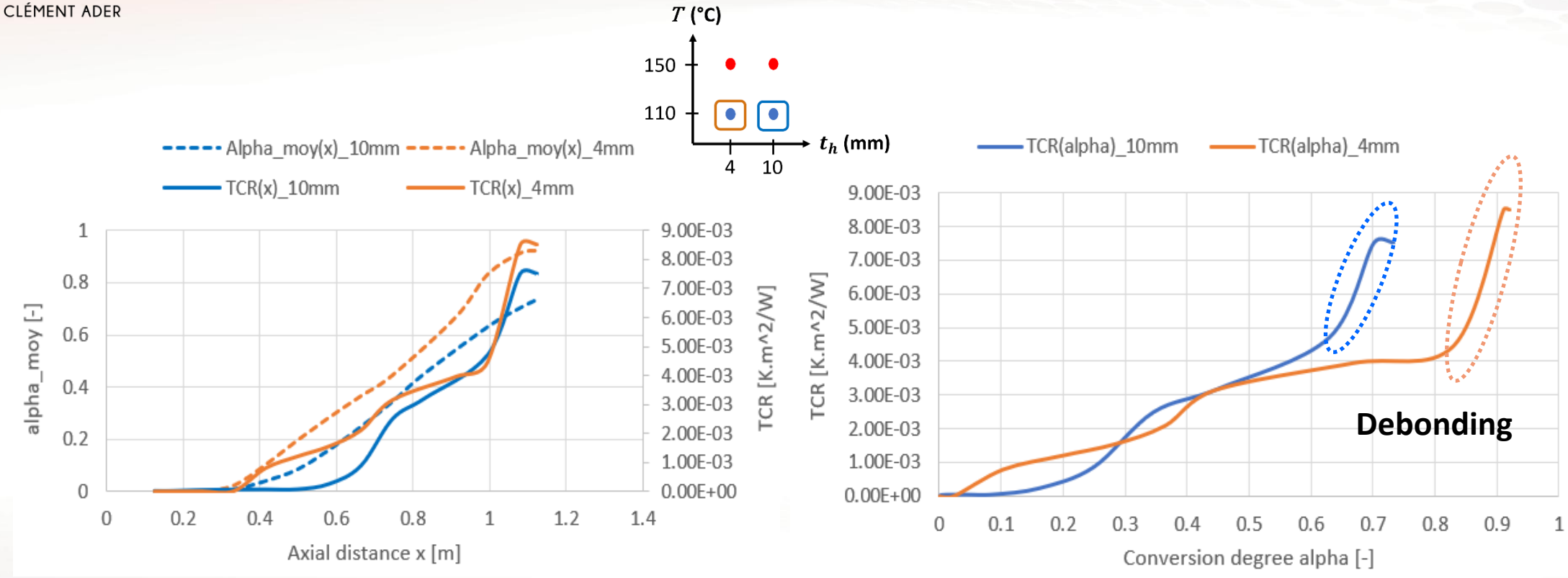

A linear relationship between shrinkage and alpha *(literature)*

$$\alpha_{moy} = \frac{\sum_i \alpha_i}{thickness}$$

- **Relationship between TCR and chemical shrinkage ?**
- **Sudden increase in TCR due to material debonding ?? possible link with mechanical effects ?**

Optimization of transverse thermal conductivity

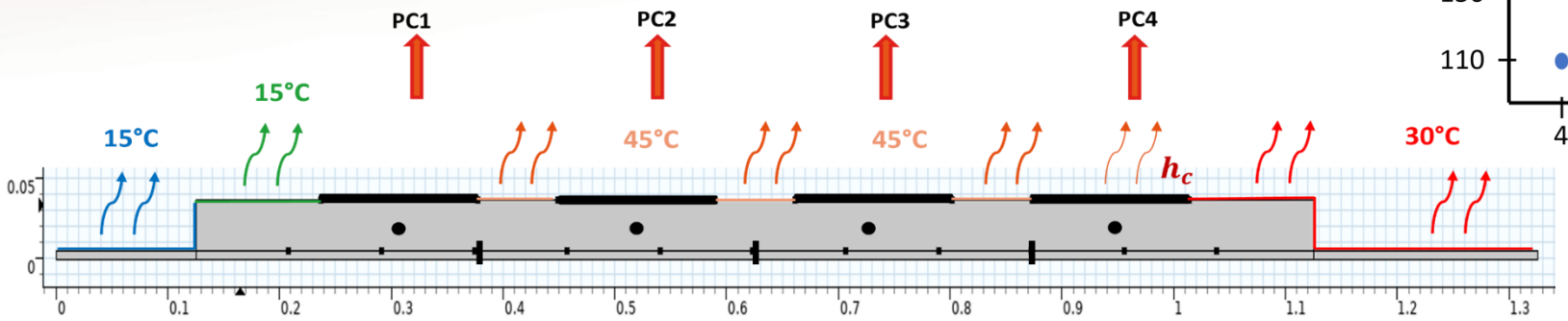

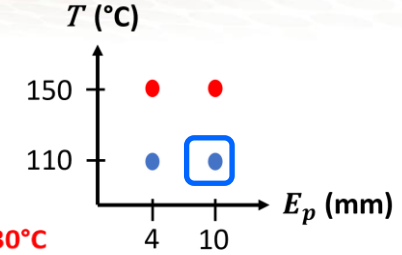

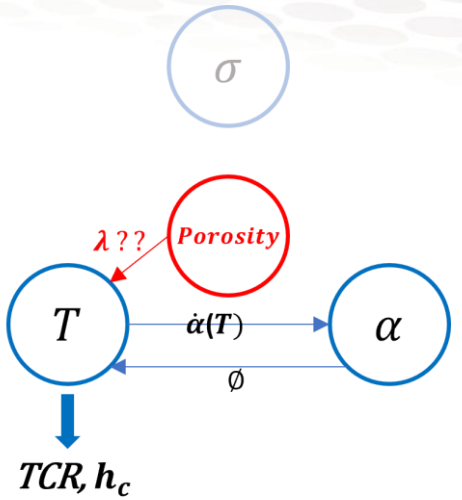

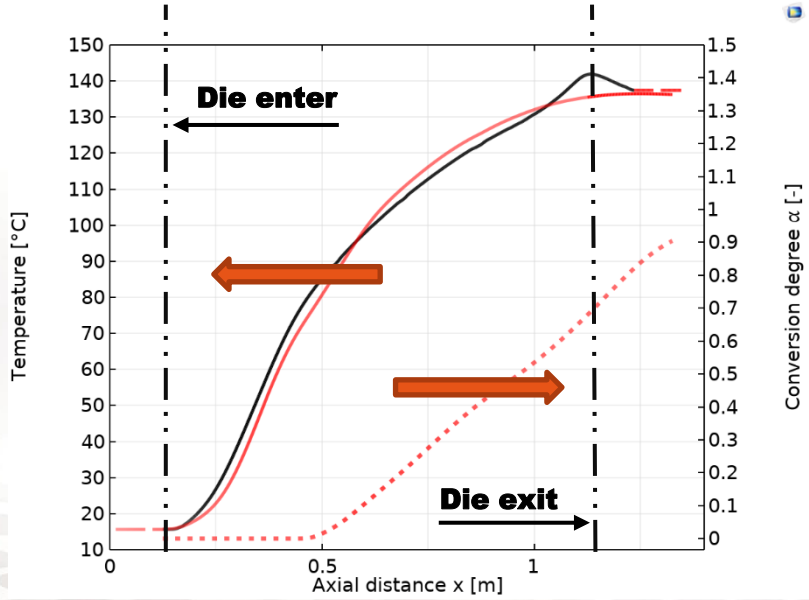

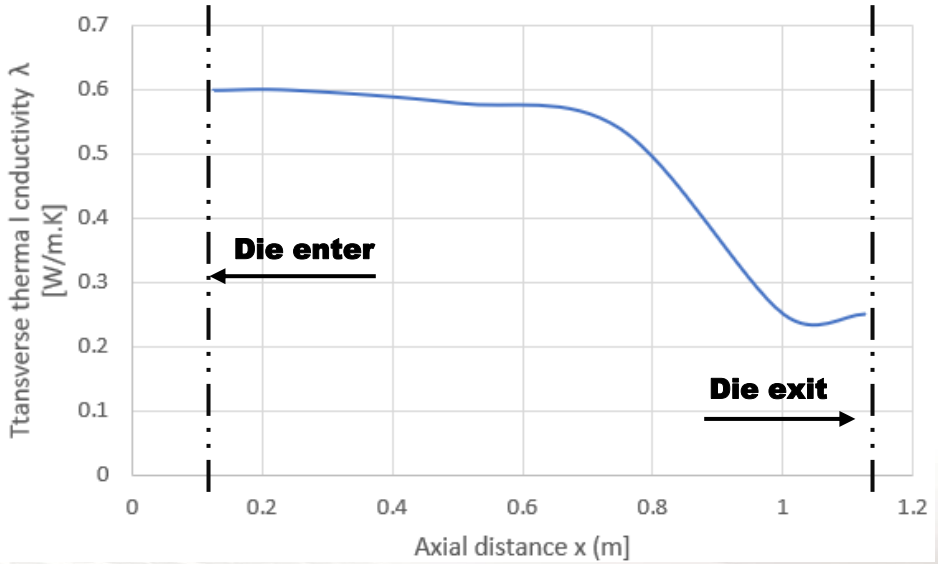

Conclusion

- **Thermal conductivity decreases along the die as the reaction progresses.**
- **Relation with porosity?**
- The central thermal profile shows better agreement with experimental one.

Conclusions and Perspectives

INSTITUT CLÉMENT ADER

Conclusion

- Implementation of thermo-kinetic coupling between the thermal behavior and the polymerization kinetics of the Elium resin.
- Comparison with experimental results shows a good phenomenological representation of exothermic effects and heat transfer.
- Representation of a possible effect of TCR and λ.

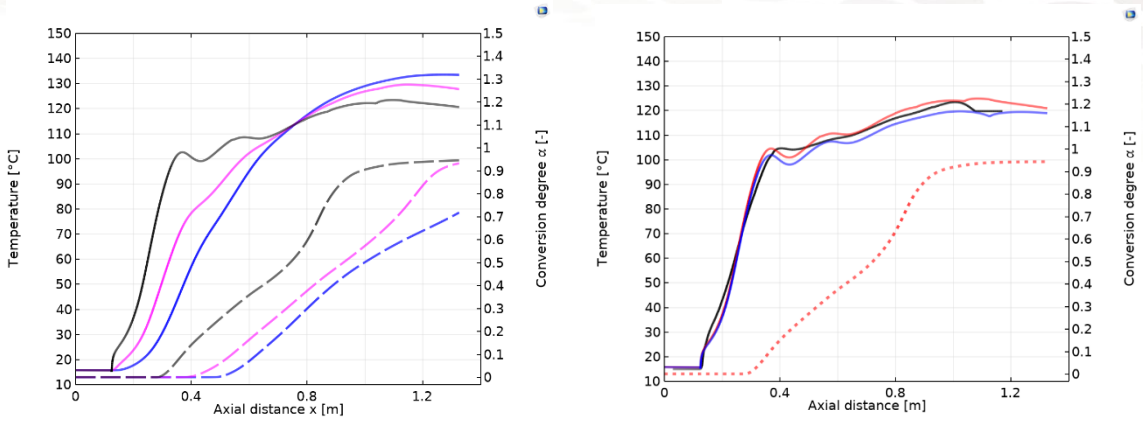

Perspectives

- **Consideration of additional physical phenomena :** TCR (α, T) as a function of chemical shrinkage, thermal conductivity as a function of porosity.
- **Development of a model**, that explains the presence of porosity at the core of the material by coupling physico-chemical phenomena with the mechanical behavior of the composite.
- Numerical thermal application in the case of the **pultruded rail**.

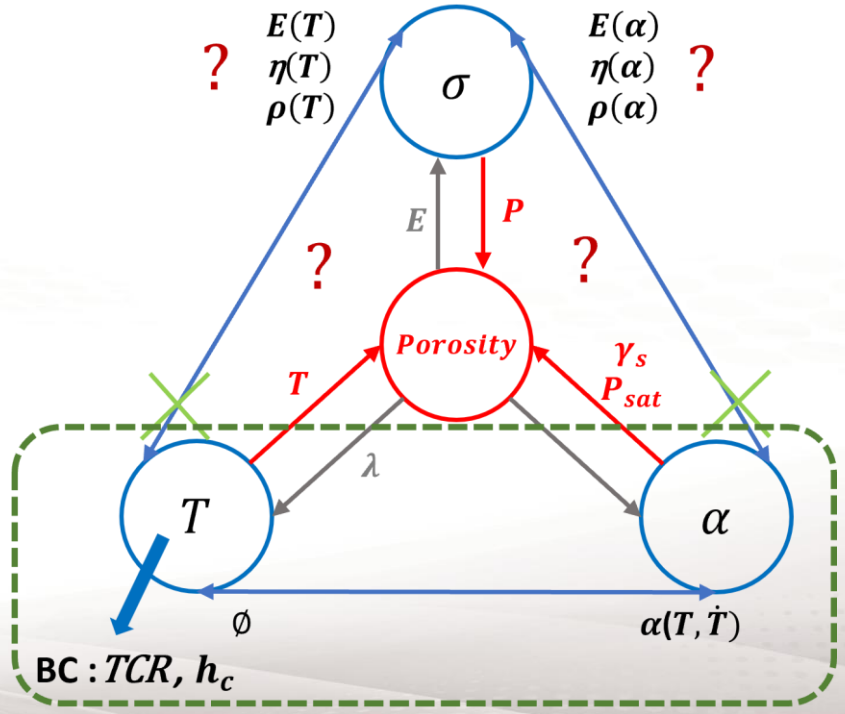

INSTITUT CLÉMENT ADER

ICCM24

24TH INTERNATIONAL CONFERENCE ON COMPOSITE MATERIALS

ICCM24 – 24TH INTERNATIONAL CONFERENCE ON COMPOSITE MATERIALS
Baltimore Convention Center – Baltimore, Maryland, USA

Modeling and Control of Exothermic Polymerization of an Acrylic Thermoplastic Resin in the Pultrusion Process

Thank you !

Farouk Zreika[a], Olivier De Almeida[a], Arthur Cantarel[b]

[a]Institut Clément Ader (ICA), Université de Toulouse, CNRS, Mines Albi, UPS, INSA, ISAE-SUPAERO, France

[b]Université de Technologie de Tarbes - UTTOP, France

IMT Mines Albi-Carmaux École Mines-Télécom

INSA TOULOUSE

ISAE SUPAERO

UNIVERSITÉ TOULOUSE III PAUL SABATIER

cnrs

Université Fédérale Toulouse Midi-Pyrénées

Back-up Slides
Composite Parameters

The longitudinal and transverse thermal conductivities (λ) are different :

$$[\lambda] = \begin{matrix} \lambda_l & 0 & 0 \\ 0 & \lambda_t & 0 \\ 0 & 0 & \lambda_t \end{matrix}$$

$$\frac{1}{\lambda_l} = \frac{1-v_f}{\lambda_r} + \frac{v_f}{\lambda_f}$$

$$\lambda_t = v_f\,\lambda_f + (1 - v_f)\,\lambda_r$$

- λ_r **= 0.25 [W/m*K]** : Thermal conductivity of the resin
- λ_f **= 1 [W/m*K]** : Thermal conductivity of the fiber

$$C_P = v_f\,C_{Pf} + (1 - v_f)\,C_{Pr}$$

$$\rho = v_f \rho_f + (1 - v_f)\,\rho_r$$

- C_{Pf} **= 830 [J/kg*K]** : Specific heat capacity of the fiber
- C_{Pr} **= 1470 [J/kg*K]** : Specific heat capacity of the resin
- ρ_r **= 1195 [kg/m^3]** : Density of the resin
- ρ_f **= 2550 [kg/m^3]** : Density of the resin

Thermal properties	10 mm plate	4 mm plate
v_f	0.7	0.67
λ_l	0.775 [W/m*K]	0.76 [W/m*K]
λ_t	0.52632 [W/m*K]	0.5102 [W/m*K]
C_P	1034.8 [J/kg*K]	1022 [J/kg*K]
ρ	2136 [kg/m^3]	2116.4 [kg/m^3]

Data sheet: *polymeres-netzsch-com/pmma-polymethacrylate-de-methyle*
Data sheet: *techniques-ingenieur/proprietes-des-fibres*

Back-up Slides
1D Thermal Analysis

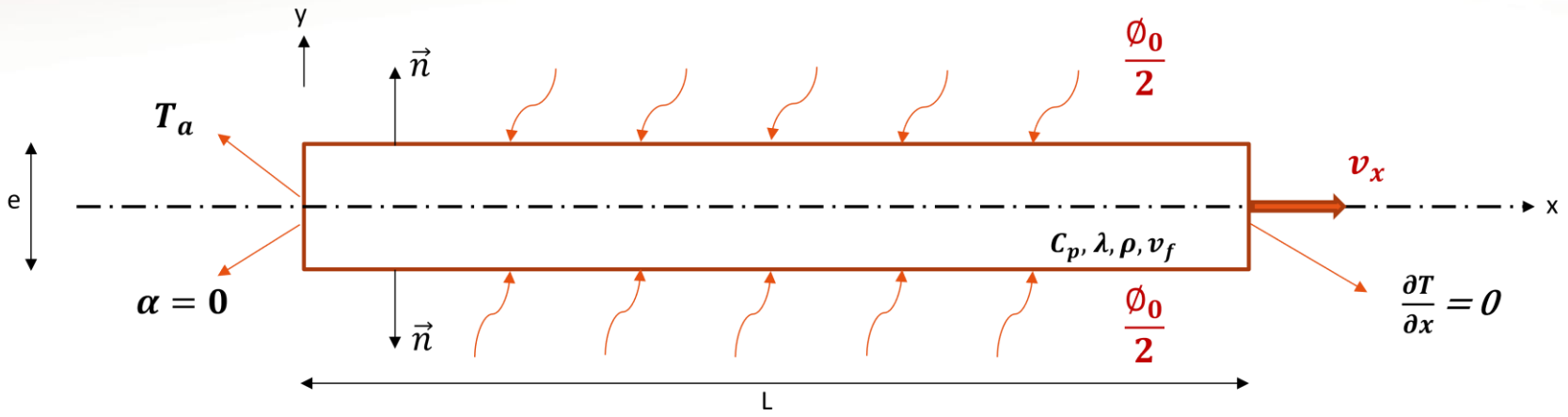

Assumptions

- The die's length (L) is much greater than the composite thickness(e) : L >> e
- Boundary conditions : $\alpha\ (\bar{x} = 0) = 0$ et $\bar{T}\ (\bar{x} = 0) = 0$
- Steady state; Homogeneous and isotropic material; Constant thermal properties

$$\rho\ C_p v_x \frac{\partial T}{\partial x} - \lambda \left(\frac{\partial^2 T}{\partial x^2} + \frac{\partial^2 T}{\partial y^2} \right) - \Delta H_v\ v_x \frac{\partial \alpha}{\partial x} = 0$$

$\bar{T}$ et $\bar{\alpha}$ are the average temperature and degree of conversion

$$\frac{\partial^2 \bar{T}}{\partial x^2} - \frac{\rho\ C_p v_x}{\lambda} \frac{\partial \bar{T}}{\partial x} + \frac{\phi_0}{\lambda e} + \frac{\Delta H_v\ v_x}{\lambda} \frac{\partial \bar{\alpha}}{\partial x} = 0$$

Adimensionnalisation : $\bar{\theta} = \frac{\bar{T}}{T_a}$; $\bar{x} = \frac{x}{L}$

$$\frac{\partial^2 \bar{\theta}}{\partial \bar{x}^2} - \frac{\rho\ C_p v_x L}{\lambda} \frac{\partial \bar{\theta}}{\partial \bar{x}} + \frac{\phi_0 L^2}{\lambda\ e\ T_a} + \frac{\Delta H_v v_x L}{\lambda\ T_a} \frac{\partial \bar{\alpha}}{\partial \bar{x}} = 0$$

Back-up Slides

1D Thermal Analysis

INSTITUT CLÉMENT ADER

$$P_e = \frac{convection}{conduction}$$

$$N_u = \frac{Heat\ flux}{conduction}$$

$$C = \frac{Exothermic\ reaction}{conduction}$$

$P_e \gg N_u , C \gg 1$

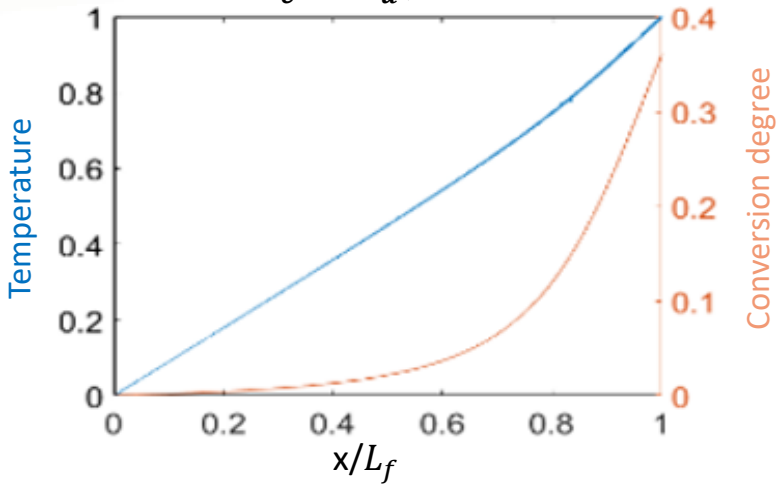

$N_u \gg P_e , C \gg 1$

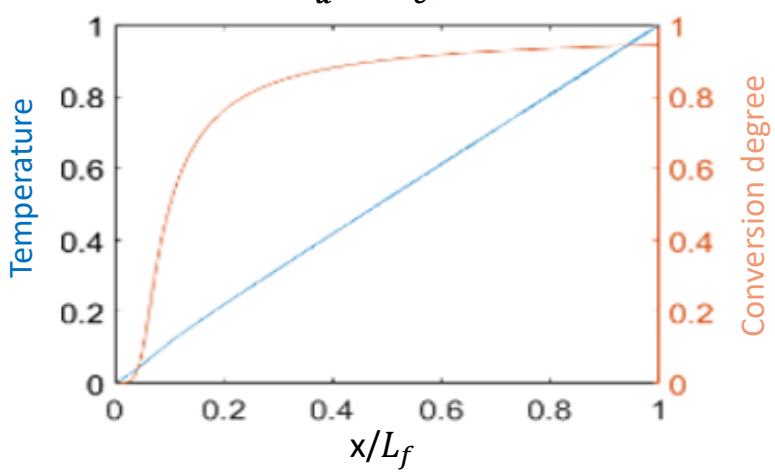

$C \gg N_u , P_e \gg 1$

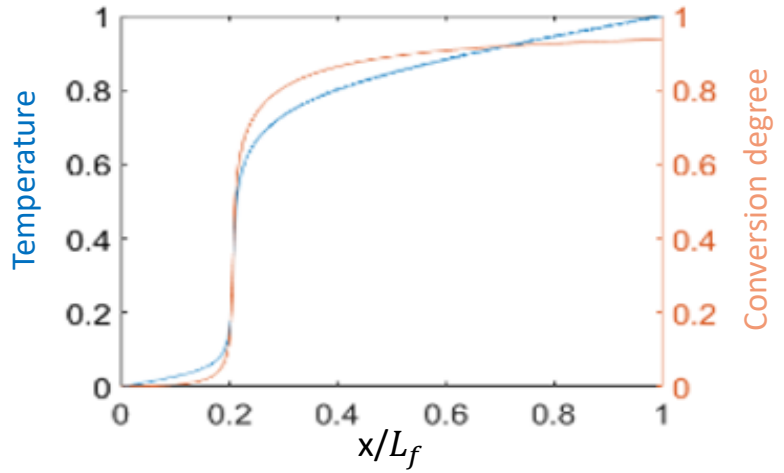

$P_e , N_u \gg C \gg 1$

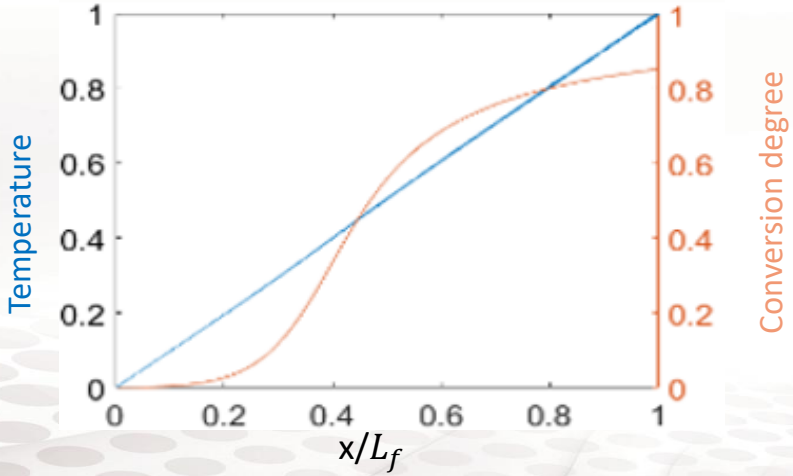

$1 \gg P_e , C , N_u$

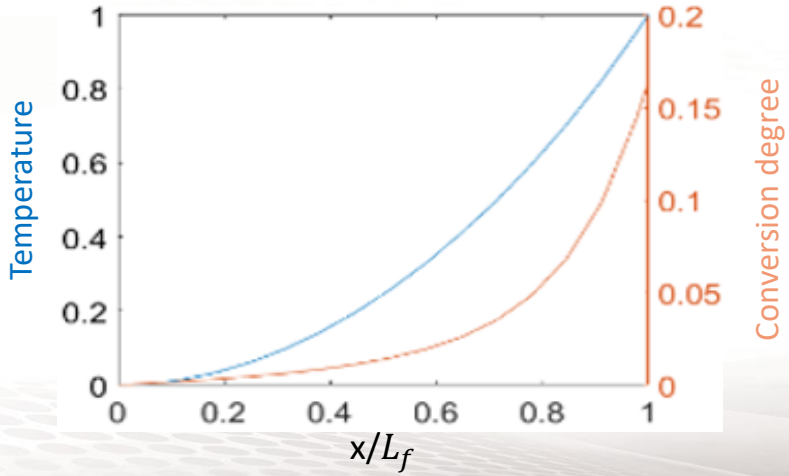

$P_e , C , N_u \gg 1$

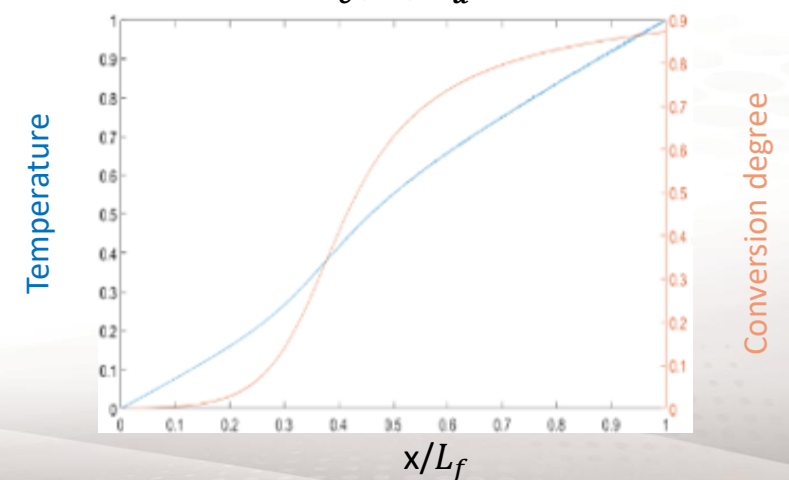

ICCM24
AUGUST 4-8, 2025
BALTIMORE CONVENTION CENTER
BALTIMORE, MARYLAND, USA

No Technical Paper Submission for:

Biltu Mahato

MODELLING RESIDUAL STRESSES IN THICK-SECTION THERMOPLASTIC COMPOSITES FOR WIND AND TIDAL ENERGY BLADES

Anastasia P. Tsavea[1], James Maguire[1], Colin Robert[2], Edward McCarthy[3], Eduardo Barocio[4],

R. Byron Pipes[4], Conchúr M. Ó Brádaigh[2]

[1] School of Mechanical, Aerospace, and Civil Engineering, University of Sheffield, Mapping Street, Sheffield S1 3JD, UK

[2] School of Chemical, Materials, and Biological Engineering, University of Sheffield, Sir Robert Hadfield Building, Mappin Street, Sheffield S1 3JD, UK

[3] School of Engineering, Institute for Materials and Processes, The University of Edinburgh, Sanderson Building, Robert Stevenson Road, Edinburgh EH9 3FB, Scotland, UK

[4] Composites Manufacturing and Simulation Center, Purdue University, West Lafayette 47906, IN, United States

Keywords: Elium® thermoplastic composites, Process-induced residual stresses, CHILE model

ABSTRACT

The adoption of Elium® acrylic thermoplastic composites in wind energy and marine applications offers significant sustainability advantages through end-of-life recyclability. Process-induced residual stresses during room-temperature polymerisation remain a critical manufacturing challenge, however, with large through-thickness temperature gradients developing during processing of thick-section composites. While viscoelastic models can predict these stresses, they require extensive material characterisation that is particularly challenging for the rapidly-evolving properties of room-temperature reactive thermoplastics. This paper presents the application of the Cure Hardening Instantaneously Linear Elastic (CHILE) model to reactive thermoplastic composites, offering computational efficiency without sacrificing accuracy. The CHILE framework is implemented through coupled thermal-chemical-mechanical finite element analysis in ABAQUS, incorporating autocatalytic polymerisation kinetics, conversion-dependent material properties and a critical gelation criterion ($\alpha = 0.4$) that governs the transition from liquid to solid behaviour. Simulations of thick UD E-glass/Elium® laminates demonstrate the model's capability to predict temperature profiles, through-thickness gradients, and resulting thermal and chemical residual stress distributions. Comparative analysis of forced convection at an elevated temperature (30°C) reveals that elevated-temperature processing can reduce spring-back by 33% and peak tensile stresses by up to 65%, despite fundamentally reversing the warpage mode from U-shape to Ω-shape through altered thermal-chemical shrinkage coupling during polymerisation. These findings provide manufacturers with an efficient tool for process optimisation and establish a framework for sustainable composite manufacturing. Future work will explore adaptive temperature control strategies to minimise residual stress formation, and a quantitative comparison of stress calculations using CHILE and full viscoelastic formulations.

1 INTRODUCTION

The International Energy Agency's Renewables 2024 Outlook [1] projects that the world will install more than 5.5 TW of new renewable power between 2024 and 2030, propelled by a doubling of annual wind-capacity additions. This will raise the amount of electricity from clean sources to about 46% of global electricity by the decade's end. Wind and marine renewable energy systems are positioned to play a critical role in this transition, requiring robust infrastructure capable of withstanding harsh operational environments for 20-25 year service lives [2]. The sustainability of these technologies remains limited, however, by the predominance of thermoset composite materials, which are difficult to recycle at end-of-life and contribute to growing composite waste streams, estimated at 62,000 tonnes annually, predominantly arising from wind turbines blades [3].

Elium® resin, a liquid methyl methacrylate infusible thermoplastic, offers a transformative solution by enabling room-temperature processing with the recyclability advantages of thermoplastics [4]. This resin system has been successfully demonstrated in full-scale renewable energy applications, including the TIGER project's 18-meter tidal turbine blades and the ZEBRA project's 62-meter recyclable wind turbine blade manufactured by Arkema and LM Wind Power [5], seen in Figure 1. These demonstrators have validated Elium®'s mechanical performance while highlighting manufacturing challenges that must be addressed for widespread adoption.



Figure 1 The world's then-largest recyclable Elium® wind blade, constructed as part of the ZEBRA project in 2022 – it has since been surpassed in length by a 77-metre blade manufactured by the same consortium [5].

Wind and tidal-turbine blades are designed to survive up to 10^8–10^9 variable-amplitude fatigue cycles over a 20-year life (IEC 61400-5), and recent full-scale tests at the University of Edinburgh's FastBlade facility confirm that tidal energy blades experience highly complex cyclic loads, enduring an entire lifetime's loading when exercised at 18–20 Hz for an equivalent 20 years [6]. Process-induced residual stresses significantly impact fatigue performance by superimposing on service loads, essentially acting as an internal mean load that accelerates fatigue damage in composites [7]. On wind-blade-grade glass/epoxy laminates, lowering residual stresses by 50 % triples the cycles to failure, while a 75% reduction extends life by roughly an order of magnitude, confirming residual-stress magnitude as a dominant lever in composite fatigue durability [8].

In reactive thermoplastic systems like Elium®, residual stresses arise from two coupled mechanisms during polymerisation. Chemical shrinkage, which in the case of Elium® is reported to result in a 13% volumetric reduction, according to Bamane et al. [9], occurs as polymer chains form and densify. Simultaneously, the exothermic polymerisation reaction generates temperature rises of up to 100°C in thick sections. This leads to thermal stresses due to global temperature gradients, as well as thermal expansion coefficient mismatches between the matrix and fibre phases [10]. The interaction between these mechanisms, combined with the material's transition from liquid to solid state during polymerisation, creates complex stress fields that vary significantly through component thickness.

Skin-core residual-stress and temperature gradients are a hallmark of thick composite laminates. Bogetti and Gillespie showed that the complex stress gradients which arise are sensitive to various factors including resin properties, laminate thickness, and processing history [13]. They showed that in cases where outside-to-inside curing arises, the laminate skins can be locked into compression while the solidifying core is put in tension; with the resulting stresses being sufficient to induce transverse cracking in some cases. In terms of wind and tidal turbine blades, Maguire et al. simulated the oven-curing of thick blade sections and showed that the use of low-exotherm resins and modified processing cycles can reduce thermal and cure gradients during critical periods (e.g. during gelation) [11]. In Elium® parts the exotherm peaks at the mid-plane [12], so polymerisation typically proceeds inside-out; the core

contracts first and is later restrained by the belatedly polymerised skins, giving the opposite stress sign (tensile centre, compressive outer plies). This effect creates a need for tailored polymerisation and temperature profiles to avoid warpage and residual-stress build-up.

Three primary modelling approaches exist for predicting process-induced residual stresses. Linear elastic models, while computationally efficient, cannot capture the evolving material state during polymerisation. Viscoelastic models provide the highest fidelity by tracking the complete stress history through polymerisation, as demonstrated in the seminal works of Bogetti and Gillespie [13] and White and Hahn [14]. However, the Cure Hardening Instantaneously Linear Elastic (CHILE) approach, introduced by Johnston et al. [15], has become widely adopted in process modelling of composites as it offers a compromise by assuming instantaneously elastic behaviour only after gelation while maintaining computational efficiency. While CHILE models typically overestimate residual stresses because they neglect matrix stress-relaxation [16], they provide a conservative, worst-case assessment that serves as an acceptable first-order approximation of material behaviour.

The application of viscoelastic models to Elium® composites faces unique challenges. Unlike high-temperature epoxy systems where reactions can be arrested by cooling, Elium® polymerises at room temperature, making it impossible to "freeze" intermediate conversion states for property characterisation. The rapid evolution from low-viscosity liquid (μ = 0.1 Pa·s) to solid polymer (E = 3.2 GPa) occurs within hours, requiring extensive time-dependent testing that is both technically challenging and computationally intensive to implement. With respect to the latter, full viscoelastic analyses typically require 20-50 times more computational resources than equivalent CHILE/pseudo-viscoelastic simulations, while offering moderate accuracy improvements for final residual stress predictions ([17], [18]). Nonetheless, no such comparative studies have been produced yet for Elium® room-temperature processing resins in particular, as of the current time of writing of this paper.

This paper presents the implementation of a CHILE framework specifically adapted for reactive thermoplastic composites, as a step towards addressing the critical need for efficient residual stress management in sustainable composite manufacturing. By capturing the essential physics of polymerisation-induced stresses while maintaining computational tractability, this approach enables practical process optimisation for next-generation recyclable composite structures.

2 CHILE MODEL FORMULATION AND THEORETICAL FRAMEWORK

The Cure Hardening Instantaneously Linear Elastic (CHILE) model offers a computationally efficient framework for predicting process-induced residual stresses while capturing the essential physics of polymerisation. The key distinction from viscoelastic models is that CHILE assumes the material responds purely elastically to each strain increment after gelation, using only the instantaneous modulus at the current conversion state. In contrast, viscoelastic models account for the entire loading history through hereditary integrals, where stresses depend on when strains were applied relative to the evolving relaxation modulus. The CHILE framework decomposes the total strain increment into three components:

$$d\varepsilon_{ij}^{\text{total}} = d\varepsilon_{ij}^{\text{elastic}} + d\varepsilon_{ij}^{\text{thermal}} + d\varepsilon_{ij}^{\text{chemical}} \quad (1)$$

where the thermal and chemical strains evolve continuously throughout polymerisation according to:

$$d\varepsilon^{\text{thermal}} = \alpha_{\text{CTE}}(T, \alpha) \cdot dT \quad (2)$$

$$d\varepsilon^{\text{chemical}} = \beta_{\text{CS}} \cdot d\alpha \quad (3)$$

Here, α represents the degree of conversion ($0 \leq \alpha \leq 1$), α_{CTE} is the coefficient of thermal expansion, and β_{CS} is the chemical shrinkage coefficient. The polymerisation kinetics follow an autocatalytic model with diffusion control:

$$\frac{d\alpha}{dt} = (k_1 + k_2\alpha^m)(1-\alpha)^n \cdot f_d(\alpha, T) \tag{4}$$

where k_1 and k_2 are temperature-dependent rate constants following Arrhenius relationships, m and n are reaction exponents, and $f_d(\alpha, T)$ represents diffusion limitations at high conversion, and is dependent on the degree of conversion and the temperature.

A critical aspect of CHILE residual stress calculation models is the gelation criterion. As liquid resin cannot sustain mechanical stress, the material accommodates all thermal and chemical strains through viscous flow prior to gelation. After the physical-gel point, these accumulated strains instantaneously generate elastic stresses based on the evolving stiffness tensor $C_{ijkl}(\alpha)$. The stiffness matrix is constructed using a given fibre-volume fraction and micromechanics, based on the evolving tensile modulus E (Figure 2), shear modulus G and Poisson's ratio ν of the resin. In the case of Elium® 191 XO/SA, where $\alpha_{\mathrm{gel}} \approx 0.4$ [9], the following holds true:

$$\sigma_{ij} = \begin{cases} 0 & \text{if } \alpha < 0.4 \\ C_{ijkl}(\alpha) \cdot \varepsilon_{ij}^{\mathrm{elastic}} & \text{if } \alpha \geq 0.4 \end{cases} \tag{5}$$

The CHILE model assumes that: (i) the material behaves as a nearly incompressible liquid before gelation, (ii) the transition to solid behaviour occurs instantaneously at the gel point (an approximation of this assumption was used for numerical stability), (iii) smooth transition to post-gelation behaviour is linear elastic with polymerisation-dependent properties, and (iv) no stress relaxation occurs after gelation. These assumptions, while simplifying the complex viscoelastic behaviour of polymerising systems, capture the dominant mechanisms of residual stress formation.

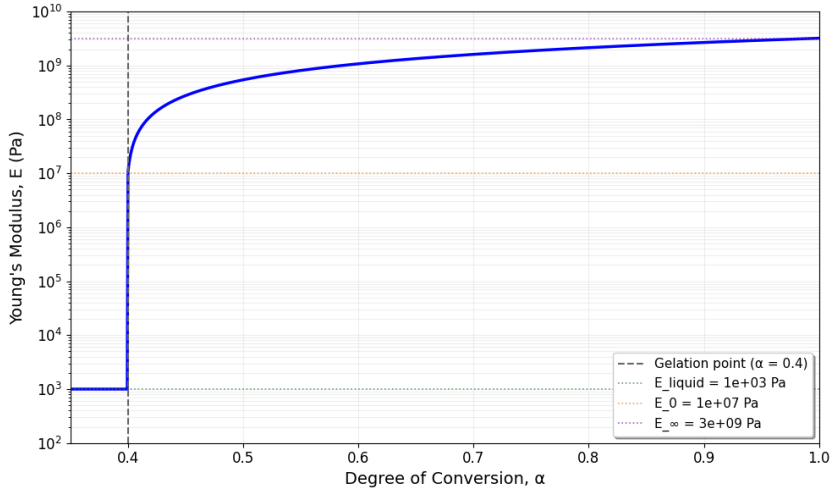

Figure 2 Evolution of resin's Young's Modulus in the CHILE formulation

3 NUMERICAL IMPLEMENTATION AND MATERIAL MODELLING

3.1 ABAQUS/Standard FEA simulation

The coupled thermal-chemical-mechanical analysis was implemented in ABAQUS/Standard using user-defined subroutines to capture the thermo-chemo-mechanical behaviour of Elium® polymerisation. The finite element model employs C3D8T coupled temperature-displacement elements, which provide simultaneous solution of heat transfer and mechanical equilibrium equations essential for capturing

process-induced residual stresses. The laminate geometry (200 mm by 200 mm, with an equivalent thickness of 60 plies, or 52.95 mm) was discretised with a structured mesh refined through the thickness. The mesh consists of over 70,000 nodes and 65,000 elements. The mesh was determined to be sufficient in calculating accurate residual stress and deformation results for this simulation. A two-step approach was used to reflect the polymerisation/consolidation phase, and the instantaneous tool-removal stage. Step 1 simulated the 24-hour polymerisation using coupled temperature-displacement analysis with automatic time incrementation (initial = 100s, minimum = 0.05s, maximum = 200s). The maximum temperature change per increment was limited to 2°C to ensure accurate capture of the exothermic peak. Step 2 modelled the tool removal as a static step, releasing the substrate constraint to reveal final part distortion.

The bottom surface (substrate interface) was constrained in the through-thickness z-direction to prevent rigid body motion while allowing in-plane deformation during the consolidation phase on a one-sided tool. Three reference nodes were constrained to prevent numerical singularities: a central node fixed in all directions, a second node constrained in x and z, and a third node constrained only in z-direction. These three nodes remain active in the second step of tool removal to permit free warpage of the laminate while still suppressing rigid-body modes, thereby capturing the true redistribution of residual stresses without numerical drift. Thermal boundary conditions specified natural convective heat transfer ($h = 10\ \mathrm{W/m^2 \cdot K}$) on the top surface with remaining surfaces insulated, representing typical open-mould processing. At this point, no thermal resistances have been implemented to represent the thermal effect of the tool (heat sink), in order to produce a first-order assessment of residual stress formation.

Four main ABAQUS user subroutines implemented the CHILE framework. USDFLD solved the autocatalytic kinetics using fourth-order Runge-Kutta integration, updating the degree of conversion field variable. HETVAL calculated internal heat generation from the polymerisation rate and heat of reaction. UEXPAN defined thermal and chemical strain increments based on composite micromechanics. UMAT implemented the gelation-dependent stiffness matrix, transitioning from liquid (E = 1 kPa) to the commencement of solid-like behaviour at α = 0.40. A flowchart overview of the model can be found in Figure 3.

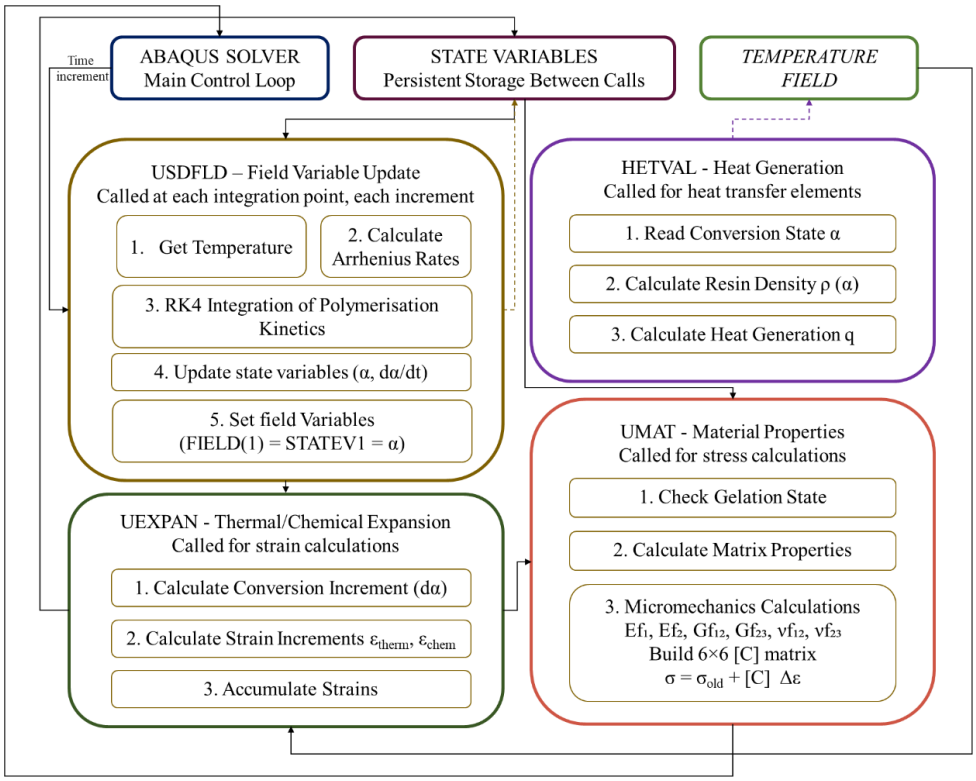

Figure 3 CHILE residual stress numerical scheme flowchart – key interactions.

Numerical stability was ensured through multiple strategies, including clamping degree of conversion between 0 and 0.999999, implementing overflow protection in exponential calculations, and checking for near-singular stiffness matrices.

3.2 Elium® 191 XO/SA Material Model

Elium® material properties were derived from resin molecular dynamics simulations by Bamane et al. [9]. The autocatalytic polymerisation kinetics were derived from best-fit DSC curves and incorporate both chemical reaction and diffusion limitations, seen in Table 1.

Table 1 Polymerisation kinetics.

Property	Symbol	Value	Unit
Fibre volume fraction	V_f	0.52	–
Heat of reaction	ΔH	253	kJ/kg
Pre-exponential factor 1	A_1	4.18	1/s
Pre-exponential factor 2	A_2	2.42×10^5	1/s
Activation energy 1	E_1	26.5	kJ/mol
Activation energy 2	E_2	41.8	kJ/mol
Autocatalytic exponent	m	2.86	–
Diffusion exponent	n	2.02	–
Gelation point	α_{gel}	0.40	–

Composite properties were calculated using micromechanics, with equivalent chemical shrinkage of -0.19% longitudinal strain and -0.37% transverse strain, reflecting fibre constraint effects, and equivalent coefficients of thermal expansion of 6.1 × 10^{-6} K^{-1} in the fibre direction and 25 × 10^{-6} K^{-1} in both transverse directions.

4 NUMERICAL RESULTS

4.1 Thick Laminate Case Study 1: Unidirectional Laminate

The through-thickness thermal profile of the laminate (Figure 4) shows lower temperature change ΔT from ambient (20°C) at the top surface, which is closest to the convective boundary. On the contrary, the bottom of the laminate reaches the highest temperature from ambient (82°C), as it is located furthest away from the convective boundary, resulting in through-thickness thermal gradients of approximately 30°C.

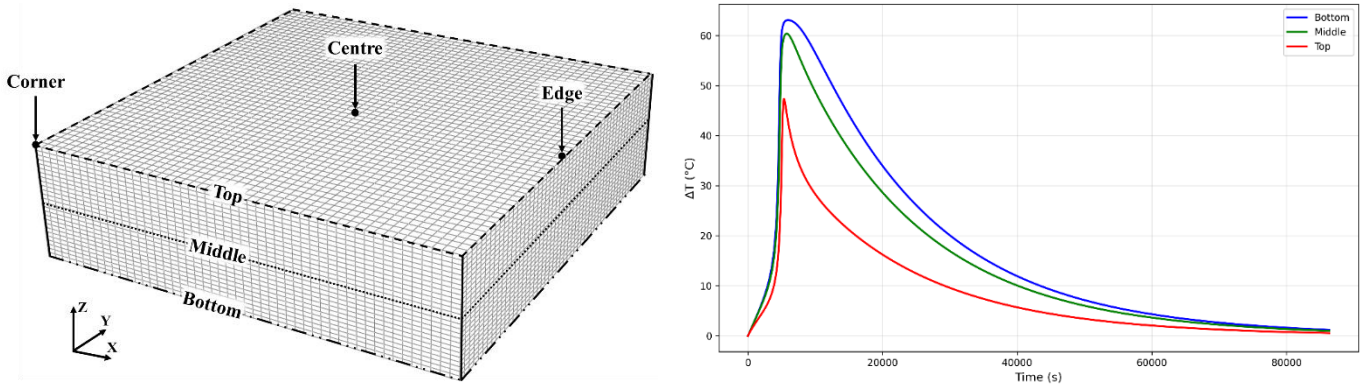

Figure 4 Left: Schematic of mesh and laminate location definitions. Right: Relative temperature increase from ambient 20°C, at the centre of a 52.95mm GF/Elium® laminate.

Similarly, the degrees of conversion were tracked, with a slight lag in the polymerisation of the top of the laminate being observed as a result of the convective heat loss boundary condition (Figure 5).

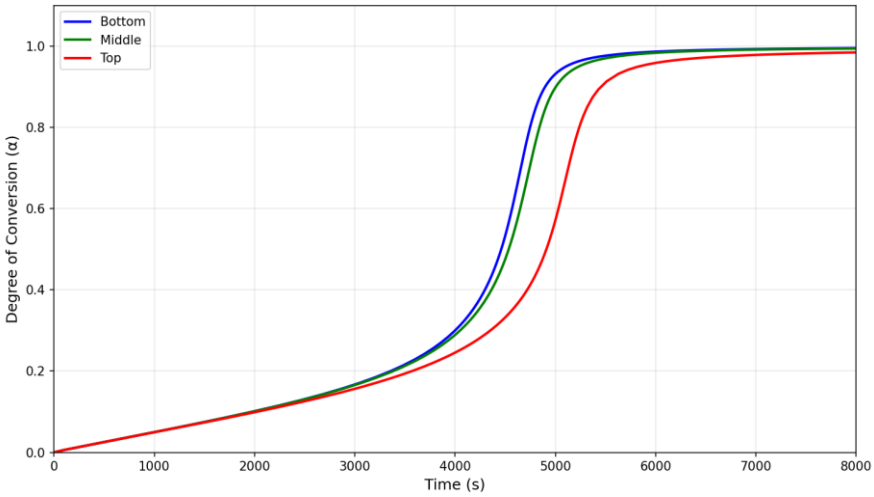

Figure 5 Through-thickness degrees of conversion at the centre of the laminate.

Following the removal of the tool, the unidirectional laminate experiences cylindrical bending as a result of the thermal and chemical stresses that developed during polymerisation. Displacement results are shown in metres in Figure 6. Owing to its omission of viscoelastic relaxation, the CHILE formulation would typically overpredict the deformation observed experimentally.

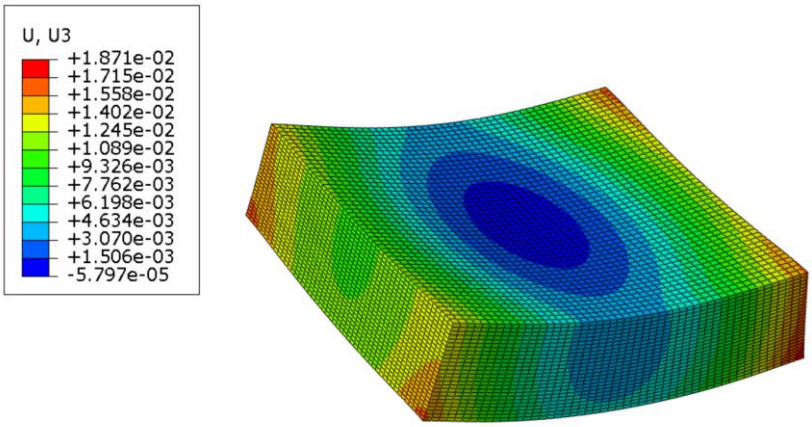

Figure 6 Cylindrical warpage of the 60-ply unidirectional GF/Elium® unidirectional laminate.

Chemical and thermal strains were also tracked (Figure 7), with results shown for the 1-direction - along the fibres. The maximum chemical strain (-0.00191) significantly dominates the maximum thermal strain (0.00038), showing that residual stress formation in the case of Elium® is a phenomenon largely driven by chemical shrinkage, and additionally due to the low temperature increase of the laminate from ambient (approximately 60°C relative temperature increase).

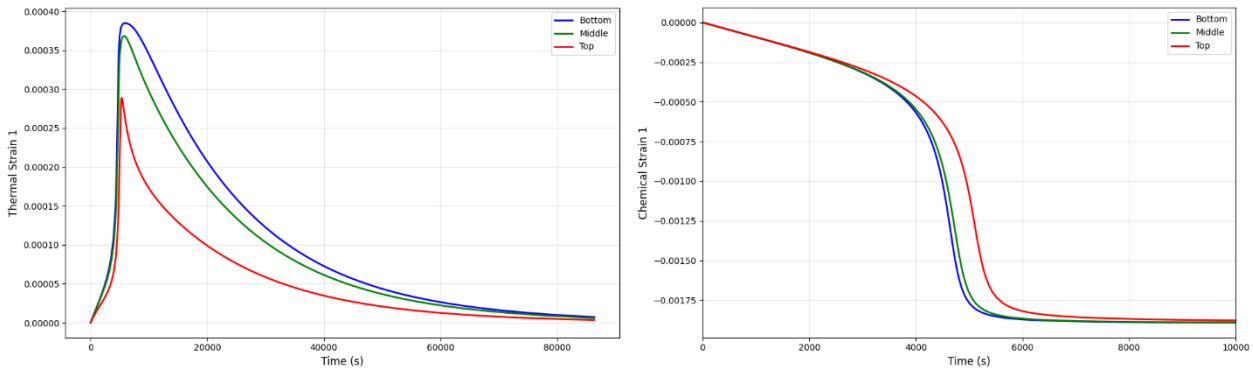

Figure 7 Thermal (left) and chemical (right) Strains during consolidation stage.

While strains occur from the beginning of the polymerisation, stresses do not become locked-in prior to gelation. Once the gelation condition is triggered (α = 0.4), chemical strains initially cause compression and subsequently the rate of thermal expansion surpasses the rate of chemical shrinkage, resulting in a bounce-back effect. Subsequently, as the exothermic reaction accelerates, and the rate of conversion increases, therefore resulting in a rapid increase of chemical stress. Afterwards, the laminate enters a cool-down phase, during which chemical stresses remain compressive, but in addition, thermal stresses become compressive as well ($\Delta T < 0$).

The fibre-direction stress (S11) evolution (Figure 8) during the polymerisation process exhibits significant spatial variation and magnitude differences across the composite laminate. At the geometric centre (left), substantial residual stresses develop, with the top layer reaching approximately 12.5 MPa of tensile stress, and the bottom layer developing compressive stresses of -5 MPa, while the middle layer remains at a much lower compressive stress state. This through-thickness gradient indicates significant bending moments induced by polymerisation shrinkage and thermal effects, and specifically the sequential polymerisation process: the middle and bottom layers polymerise and shrink first, then act as rigid constraints preventing the top layer from freely shrinking during its later polymerisation, forcing it into tension while the bottom layer experiences compression from the tool constraint. As seen later in section 4.3, upon tool removal, this asymmetric stress distribution creates a bending moment that causes the part to warp and the stress states to invert, with the previously compressed bottom surface transitioning to tension and the top surface stress transitioning to compression.

The corner region (right) demonstrates more complex transient behaviour, with the middle and bottom layers initially developing tensile stresses up to 0.12 MPa, followed by an asymptotic stress equilibrium toward 0.05MPa, while the top layer momentarily oscillates between tensile and compressive stresses before remaining at a very small compressive state throughout the end of consolidation. The marked difference in stress magnitudes between centre (±2.5-12.5 MPa) and corner (±0.12 MPa) locations reveals that the centre experiences substantially higher residual stresses, likely due to greater constraint from surrounding material, whereas the corner's proximity to free edges allows for stress relief through deformation.

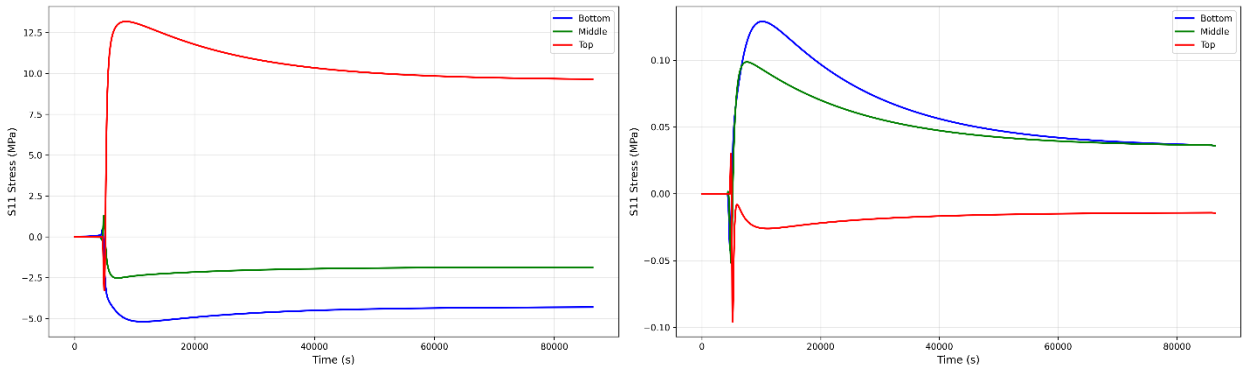

Figure 8 S11 stresses during consolidation stage at the centre (left) and a corner (right) of the laminate - stresses remain at zero pre-gelation as prescribed.

4.2 Thick Laminate Case Study 2: Elevated Temperature

To model the effect of oven heating at 30°C, an additional subroutine was employed to impose a forced convection to the top surface during the temperature rise in the centre of the laminate due to the exotherm. The aim was to gain further insight into residual stress mitigation strategies by reducing the skin-core effect present in Elium® laminates, where the core polymerises first due to heat not dissipating as effectively as the surfaces exposed to convection, therefore initiating premature shrinkage of the core earlier than the edges. The main differences implemented in the simulation are (a) longer consolidation time at room temperature following the forced convection phase, to allow for full cool-down prior to tool removal and (b) a supplementary FILM subroutine whereby the laminate top surface is exposed to forced convection condition with $h = 30\ \mathrm{W/m^2 \cdot K}$ at a pre-heated oven with a temperature of 30°C.

This heated condition is implemented until the temperature at centre of the laminate peaks (to promote concurrent polymerisation initiation at the middle and top of the laminate) and instantaneously removed and replaced by the natural convection at ambient temperature previously discussed.

The implementation of elevated temperature processing with controlled forced convection demonstrated significant mitigation of the skin-core thermal gradient characteristic of thick GF/Elium® laminate polymerisation, as seen in Figure 9. Application of 30°C forced convection until peak exotherm, followed by natural convection cooling, essentially broadens (resulting in a slight bimodality due to lagged heat transfer from inner-layer exotherm) and lowers the temperature profile at the top of the laminate (top). The result is higher through-thickness temperature gradients compare to the ambient case study. Nevertheless, the modified thermal profile promoted synchronised polymerisation initiation across the laminate thickness (bottom left), significantly reducing the temporal conversion gradient observed under ambient conditions (bottom right).

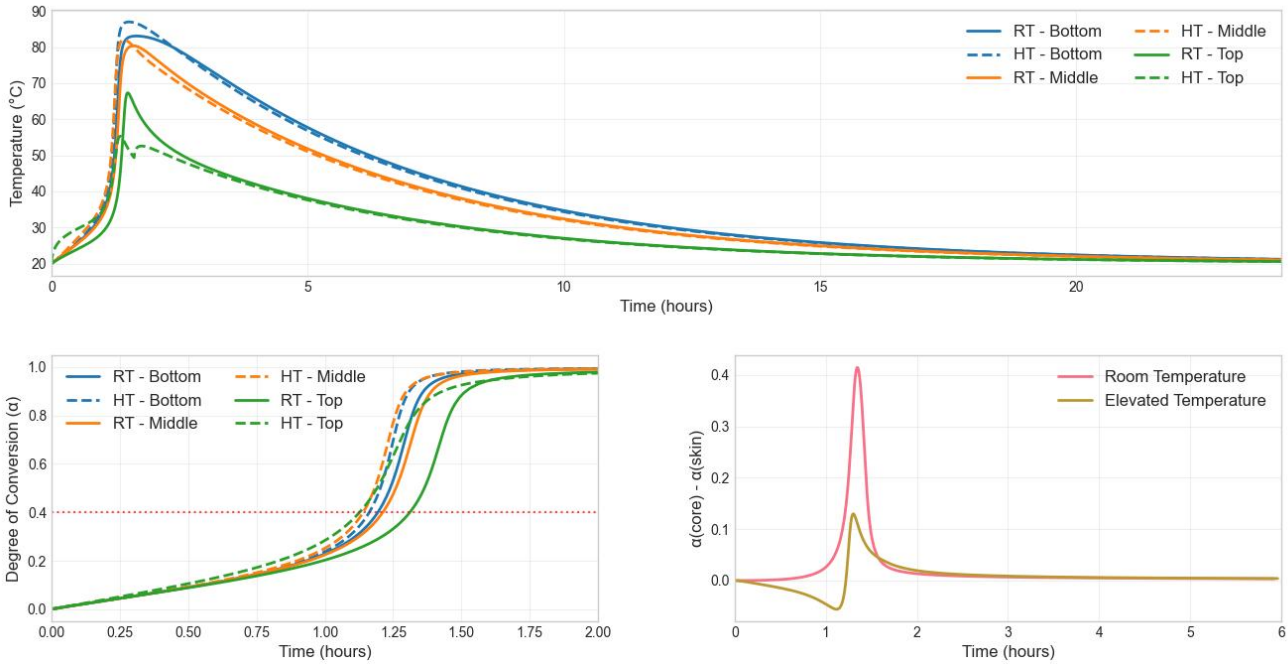

Figure 9 Comparison of ambient and elevated temperature processing case studies in terms of (top) temperature, (bottom left) degree of conversion, and (bottom right) skin-core temporal difference in degree of conversion.

4.3 Comparison of Case Studies: Post Tool-Removal

Following tool removal in both cases, the addition of forced convection fundamentally altered the residual stress state, manifesting as an inversion of the warpage mode from concave (U-shaped) to convex (Ω-shaped) curvature. The individual through-thickness stress states can be found in Figure 10. In absolute terms, there are reductions in final stresses in σ_{11}, σ_{22}, and σ_{23}, while σ_{33} and σ_{13} have remained essentially constant. A comparative summary of the worst-cases across all locations (centre and edges) of key parameters can be found in Table 2.

Investigating the edge effects, it becomes clear that there is significantly higher in-plane difference in the elevated temperature case, where the edge-to-centre stress ratio surpasses 500 for τ_{23}, as seen in Figure 11. This extreme stress concentration at edges in the elevated temperature case likely results from the more severe thermal gradients creating differential shrinkage patterns that are accommodated through interlaminar shear at the free boundaries, where the absence of constraint allows stress singularities to develop more prominently than in the room temperature case.

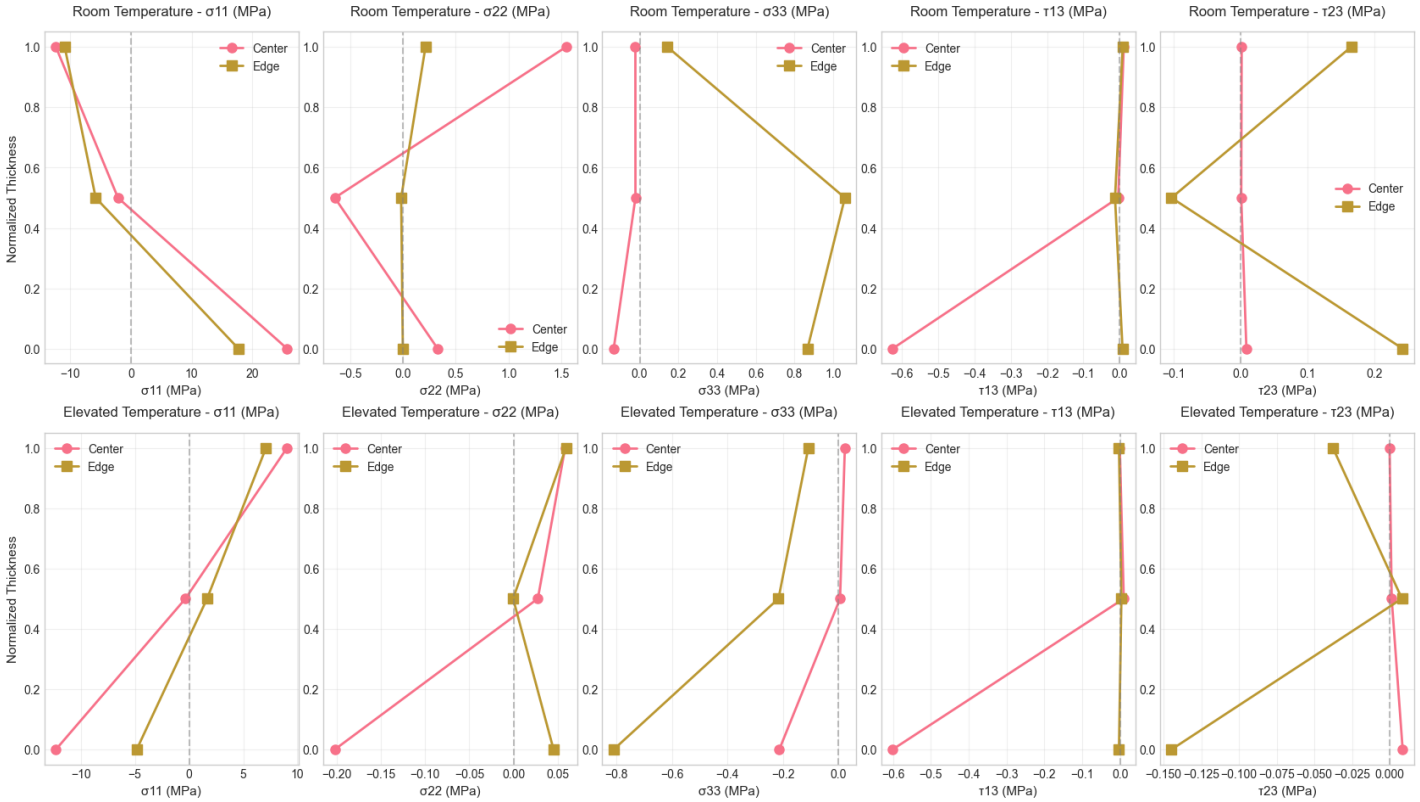

Figure 10 Through-thickness worst-cases stress states in ambient (top row) and forced convection (bottom row) cases.

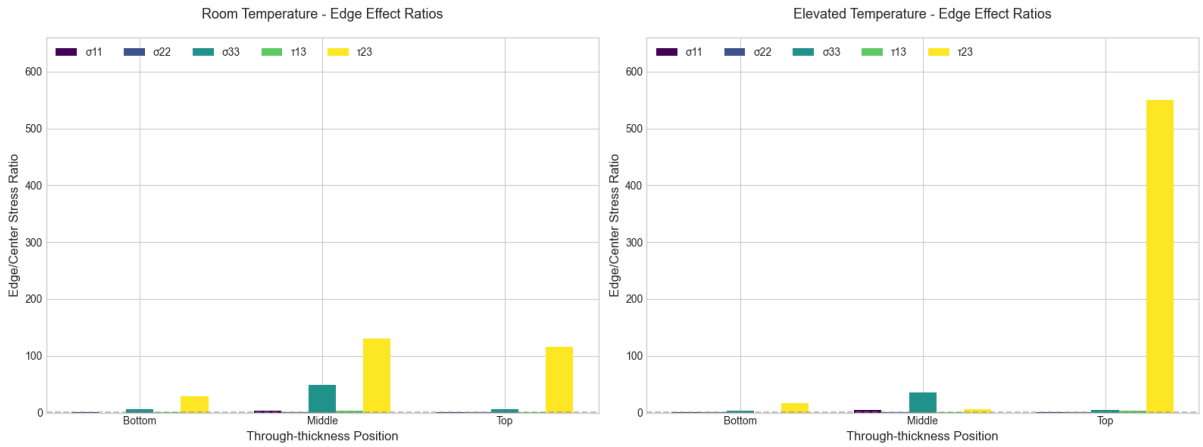

Figure 11 Summary of edge/centre stress ratios for room temperature (left) and elevated temperature (right) cases.

As seen in Table 2, the elevated temperature processing strategy achieved a 33% reduction in spring-back displacement (13.4 mm to 9.0 mm) despite generating 4.7% higher peak temperatures during the exothermic polymerisation of the thick UD Elium® laminate. Additionally, the fibre-direction stress (σ11) range (maximum tensile stress minus maximum compressive stress) reduced from 38.2 MPa to 21.3 MPa with a 65% reduction in peak tension (25.8MPa reduced to 9MPa), and the through-thickness normal stress (σ33) shifted from predominantly tensile (+1.06 MPa) to compressive (-0.81 MPa). The transverse stress (σ22) demonstrated a significant reduction, with the stress range decreasing from 2.1 MPa (room temperature) to 0.3 MPa (elevated temperature), representing an 86% reduction driven primarily by a 93% decrease in peak tensile stress (1.5 MPa to 0.1 MPa) while compressive stresses remained minimal in both cases. The interlaminar shear stress τ23 showed a 40% reduction, indicating improved mitigation of edge effects, while maintaining similar compressive stress magnitudes in both cases (~12.4 MPa). Despite these improvements, the 9.0 mm residual warpage in the elevated

temperature case still represents unacceptable dimensional instability for practical applications. Nonetheless, these findings indicate that relatively modest thermal control interventions during the polymerisation phase can substantially influence the development of manufacturing-induced residual stresses in thick thermoplastic structures.

Table 2 Summary of key comparative results between worst-case room temperature and elevated temperature processing, across all locations (centre and edges).

Parameter	Room Temperature (20°C)	Elevated Temperature (30°C)	Change (%)
Peak Temperature (°C)	83.1	87.0	+4.7
Final σ11 Compression (MPa)	-12.4	-12.3	-0.8
Final σ11 Tension (MPa)	25.8	9.0	-65.1
Final σ22 Compression (MPa)	-0.6	-0.2	-66.7
Final σ22 Tension (MPa)	1.5	0.1	-93.3
Final σ33 Compression (MPa)	-0.13	-0.81	+523.1
Final σ33 Tension (MPa)	1.06	0.02	-98.1
Final τ13 Shear (MPa)	0.625	0.601	-3.8
Final τ23 Shear (MPa)	0.242	0.145	-40.1
Max Spring-back (mm)	13.4	9.0	-32.8
Final Curvature Direction	U-shape (bottom tension)	Ո-shape (bottom compression)	—

5 CONCLUSIONS

This study demonstrated the application of the CHILE framework for predicting process-induced residual stresses in thick Elium® thermoplastic composites, providing manufacturers with a computationally efficient tool for process optimisation. The model captures the coupling between exothermic polymerisation, chemical shrinkage, and mechanical response, revealing that chemical shrinkage dominates thermal effects in driving residual stress formation. Comparative analysis of ambient versus elevated temperature processing revealed that modest thermal interventions can achieve 33% spring-back reduction and 65% decrease in peak tensile stresses, though the resulting 9 mm warpage remains unacceptable for industrial applications. Critically, the complete reversal of the warpage mode (U-shape to Ո-shape) demonstrates the extreme process sensitivity of thick unidirectional laminates, highlighting fundamental manufacturability challenges that cannot be overcome through process optimisation alone. The dramatic edge stress concentrations, particularly the 500-fold increase in τ_{23} for elevated temperature processing, underscore the three-dimensional nature of residual stress development in thick sections to reduce risk of delamination. As CHILE inherently overestimates residual stresses by neglecting viscoelastic relaxation, future implementation of full viscoelastic models may reveal lower stress magnitudes and reduced warpage predictions. Nevertheless, the severe dimensional instability and edge effects observed even in these conservative estimates suggest that achieving manufacturability in thick Elium® wind and tidal energy structures will require careful consideration of both layup architecture and processing strategies.

REFERENCES

[1] ‘Renewables 2024 – Analysis’, IEA. Accessed: Jun. 06, 2025. [Online]. Available: https://www.iea.org/reports/renewables-2024

[2] S. M. Woo and J. Whale, ‘A mini-review of end-of-life management of wind turbines: Current practices and closing the circular economy gap’, *Waste Manag. Res.*, vol. 40, no. 12, pp. 1730–1744, Dec. 2022, doi: 10.1177/0734242X221105434.

[3] A. Isa, N. Nosbi, M. Che Ismail, H. Md Akil, W. F. F. Wan Ali, and M. F. Omar, 'A Review on Recycling of Carbon Fibres: Methods to Reinforce and Expected Fibre Composite Degradations', *Materials*, vol. 15, no. 14, p. 4991, Jul. 2022, doi: 10.3390/ma15144991.
[4] M. L. Devine, 'Liquid acrylic resin-based composites for marine and renewable energy applications', PhD Dissertation, School of Engineering, The University of Edinburgh, Scotland, UK, 2025. [Online]. Available: https://era.ed.ac.uk/handle/1842/43530
[5] IRT Jules Verne, 'Breakthrough in Wind Turbine Blade Recycling: ZEBRA Project Demonstrates Closed-Loop System', Press release, Oct. 2024. [Online]. Available: https://www.arkema.com/files/live/sites/shared_arkema/files/downloads/news-attachments/global/en/press-release/2024/20241003_Press%20release%20Arkema%20Zebra.pdf
[6] S. Lopez Dubon, C. Vogel, D. Garcia Cava, F. Cuthill, E. D. McCarthy, and C. M. Ó Bradaigh, 'A Full-Scale Tidal Blade Fatigue Test using the FastBlade Facility', *Renew. Energy*, vol. 228, p. 120653, Jul. 2024, doi: 10.1016/j.renene.2024.120653.
[7] J. Hüther and P. Brøndsted, 'Influence of the curing cycles on the fatigue performance of unidirectional glass fiber reinforced epoxy composites: 37th Risø International Symposium on Materials Science', *O P Conf. Ser. Mater. Sci. Eng.*, vol. 139, 2016, doi: 10.1088/1757-899X/139/1/012023.
[8] M. A. Miranda Maduro, *Influence of Curing Cycle on the Build-up of Residual Stresses and the Effect on the Mechanical Performance of Fibre Composites*. Risø, Roskilde, Denmark: DTU Wind Energy, 2021.
[9] S. S. Bamane, P. P. Deshpande, S. U. Patil, M. Maiaru, and G. M. Odegard, 'Evolution of Physical, Thermal, and Mechanical Properties of Poly(methyl Methacrylate)-Based Elium Thermoplastic Polymer During Polymerization', *J. Phys. Chem. C*, vol. 128, no. 37, pp. 15639–15648, Sep. 2024, doi: 10.1021/acs.jpcc.4c04061.
[10] P. P. Parlevliet, H. E. N. Bersee, and A. Beukers, 'Residual stresses in thermoplastic composites—A study of the literature—Part I: Formation of residual stresses', *Compos. Part Appl. Sci. Manuf.*, vol. 37, no. 11, pp. 1847–1857, Nov. 2006, doi: 10.1016/j.compositesa.2005.12.025.
[11] J. M. Maguire, N. D. Sharp, R. B. Pipes, and C. M. Ó Brádaigh, 'Advanced process simulations for thick-section epoxy powder composite structures', *Compos. Part Appl. Sci. Manuf.*, vol. 161, p. 107073, Oct. 2022, doi: 10.1016/j.compositesa.2022.107073.
[12] S. F. Gayot, C. Bailly, T. Pardoen, P. Gérard, and F. Van Loock, 'Processing maps based on polymerization modelling of thick methacrylic laminates', *Mater. Des.*, vol. 196, p. 109170, Nov. 2020, doi: 10.1016/j.matdes.2020.109170.
[13] T. A. Bogetti and J. W. GillespieJr, 'Process-Induced Stress and Deformation in Thick-Section Thermoset Composite Laminates', *J. Compos. Mater.*, vol. 26, no. 5, pp. 626–660, Mar. 1992, doi: 10.1177/002199839202600502.
[14] S. R. White and H. T. Hahn, 'Cure Cycle Optimization for the Reduction of Processing-Induced Residual Stresses in Composite Materials', *J. Compos. Mater.*, vol. 27, no. 14, pp. 1352–1378, Dec. 1993, doi: 10.1177/002199839302701402.
[15] A. Johnston, R. Vaziri, and A. Poursartip, 'A Plane Strain Model for Process-Induced Deformation of Laminated Composite Structures', *J. Compos. Mater.*, vol. 35, no. 16, pp. 1435–1469, Aug. 2001, doi: 10.1106/YXEA-5MH9-76J5-BACK.
[16] W. Chen and D. Zhang, 'Improved prediction of residual stress induced warpage in thermoset composites using a multiscale thermo-viscoelastic processing model', *Compos. Part Appl. Sci. Manuf.*, vol. 126, p. 105575, Nov. 2019, doi: 10.1016/j.compositesa.2019.105575.
[17] M. Sandberg, O. Yuksel, I. Baran, J. Spangenberg, and J. H. Hattel, 'Steady-state modelling and analysis of process-induced stress and deformation in thermoset pultrusion processes', *Compos. Part B Eng.*, vol. 216, p. 108812, Jul. 2021, doi: 10.1016/j.compositesb.2021.108812.
[18] J. Dai, S. Xi, and D. Li, 'Numerical Analysis of Curing Residual Stress and Deformation in Thermosetting Composite Laminates with Comparison between Different Constitutive Models', *Materials*, vol. 12, no. 4, Art. no. 4, Jan. 2019, doi: 10.3390/ma12040572.

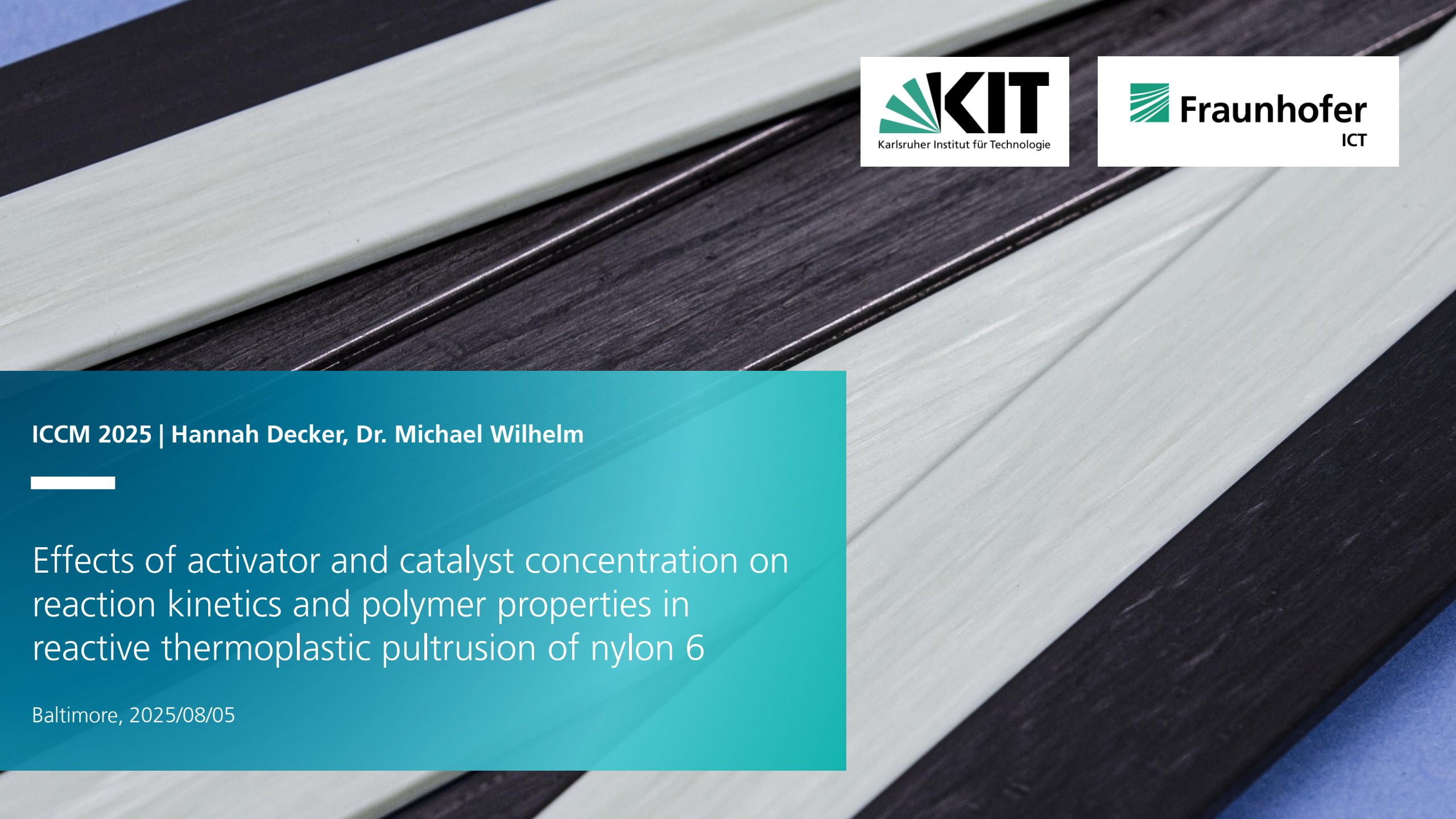

ICCM 2025 | Hannah Decker, Dr. Michael Wilhelm

Effects of activator and catalyst concentration on reaction kinetics and polymer properties in reactive thermoplastic pultrusion of nylon 6

Baltimore, 2025/08/05

Content

1 Motivation

2 State of research

3 Methodical approach

4 Formulation development

5 Effects on polymer properties

6 Conclusion and outlook

© Fraunhofer ICT

Motivation

Advantages of reactive anionic polyamide 6

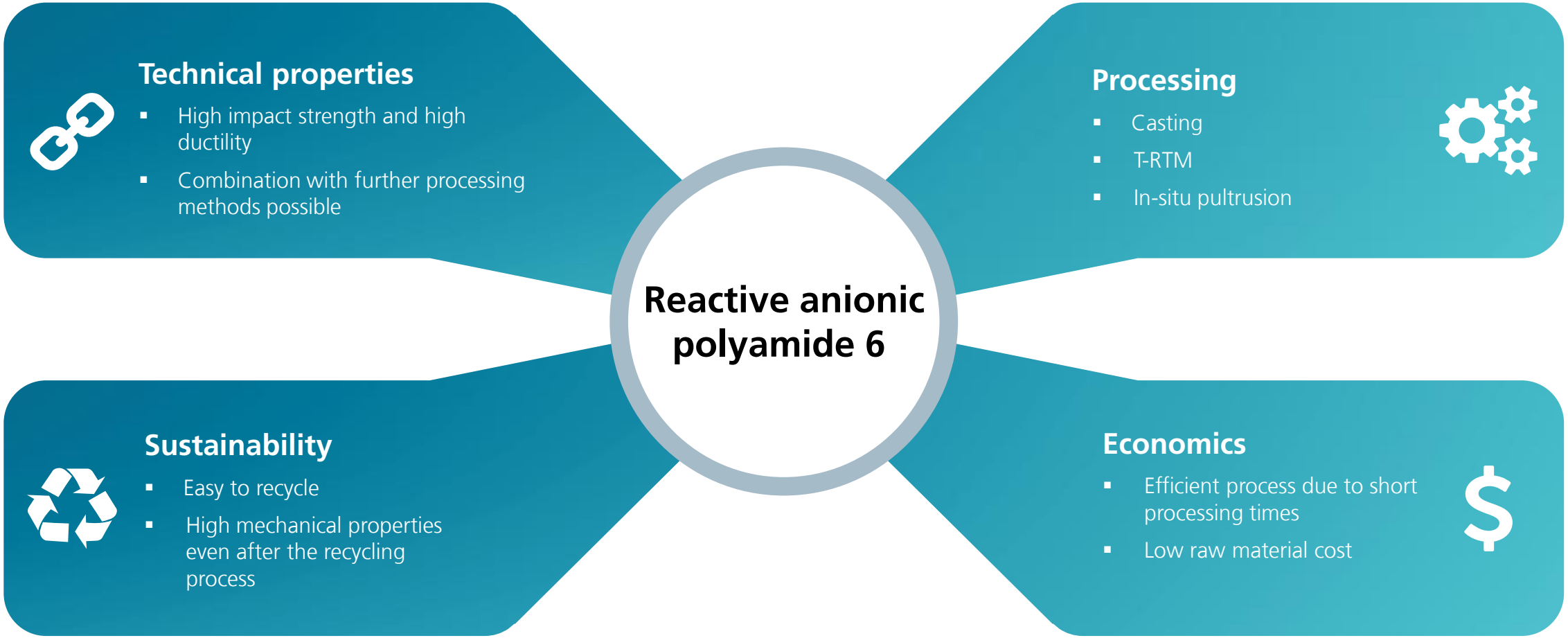

© Fraunhofer ICT

Motivation

Die length and pull-off speed: influence on the polymerization time

In-situ pultrusion line with caprolactam

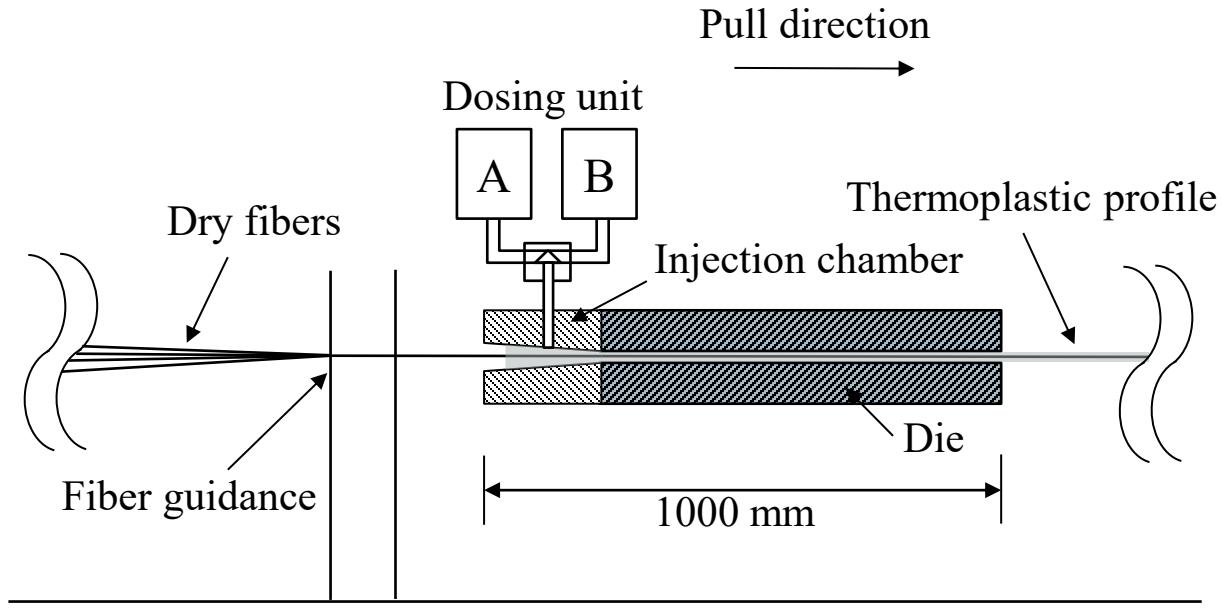

The polymerization time is determined by the pull-off speed and die length

Matrix dwell time in die

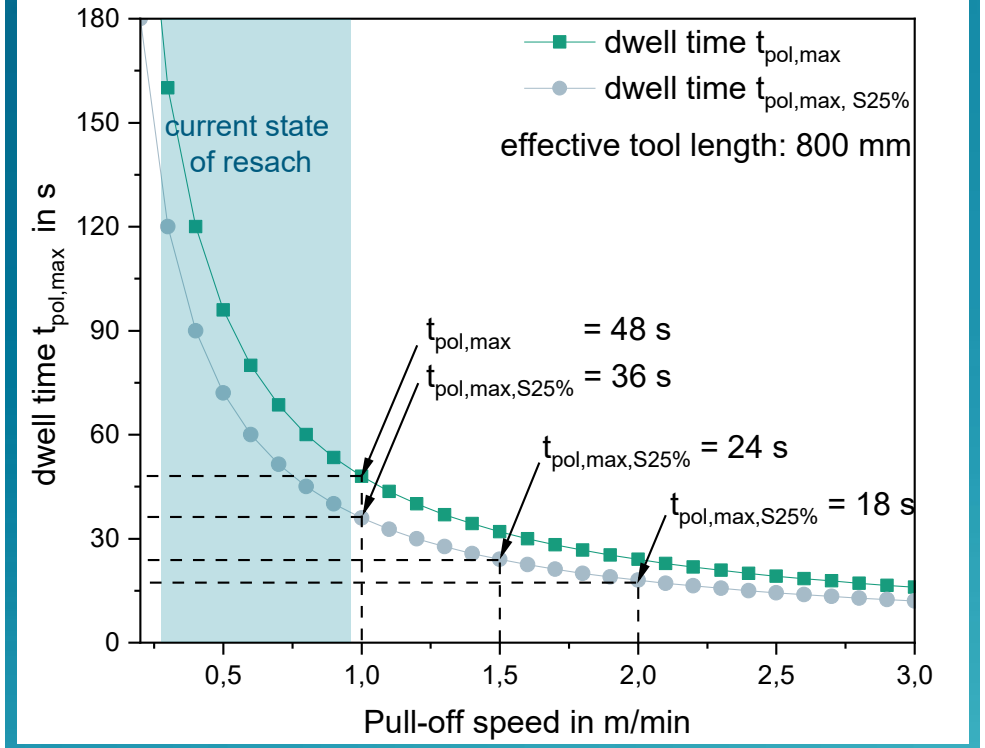

Polymerization times for economical in-situ pultrusion: < 36 s

© Fraunhofer ICT

State of research

Previous ratio regulations

Concentrations of Brüggolen C10 (NaCL) as catalyst and Brüggolen C20P (HDCL) as activator used in T-RTM

[A] : [C] in wt.-%	[A] : [C] in mol.-%	Relative ratio [A] : [C]	Source, year
3,0 : 4,5		1 : 1,5	Thomassey et al. [1], 2017
1,0 : 2,0 - 2,5 : 5,0		1 : 2	Wendel et al. [2], 2018
1,0 : 2,5 - 3,0 : 4,5		1 : 2,5 - 1 : 1,5	Choi et al. [3], 2019
3,2 : 3,2		1 : 1	Osváth et al. [4], 2020
	0,6 : 1,2	1 : 2	Murray et al. [5], 2021
3,0 : 3,0		1 : 1	Semperger et al. [6], 2022
1,5 : 2,2 - 4,0 : 6,0		1 : 1,5	Lagarinhos et al. [7], 2022

No standardized formulation for activator and catalyst concentration or ratio can be defined.

© Fraunhofer ICT

Formulation development

Investigation of polymerization kinetics

Semi-adiabatic beaker tests



Monomer (ε-CL)

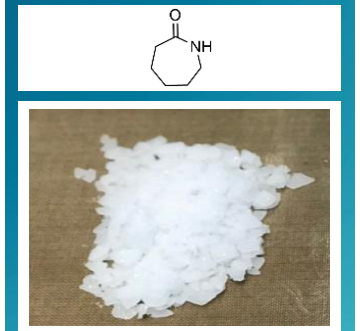

Activator (HDCL)

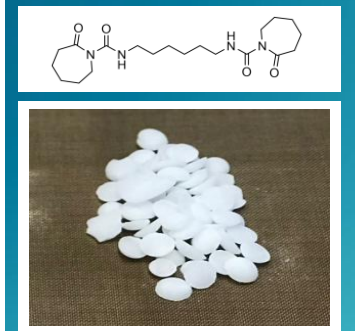

Catalyst (NaCL)

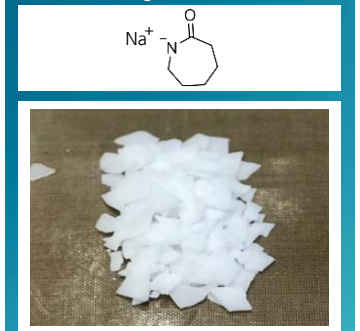

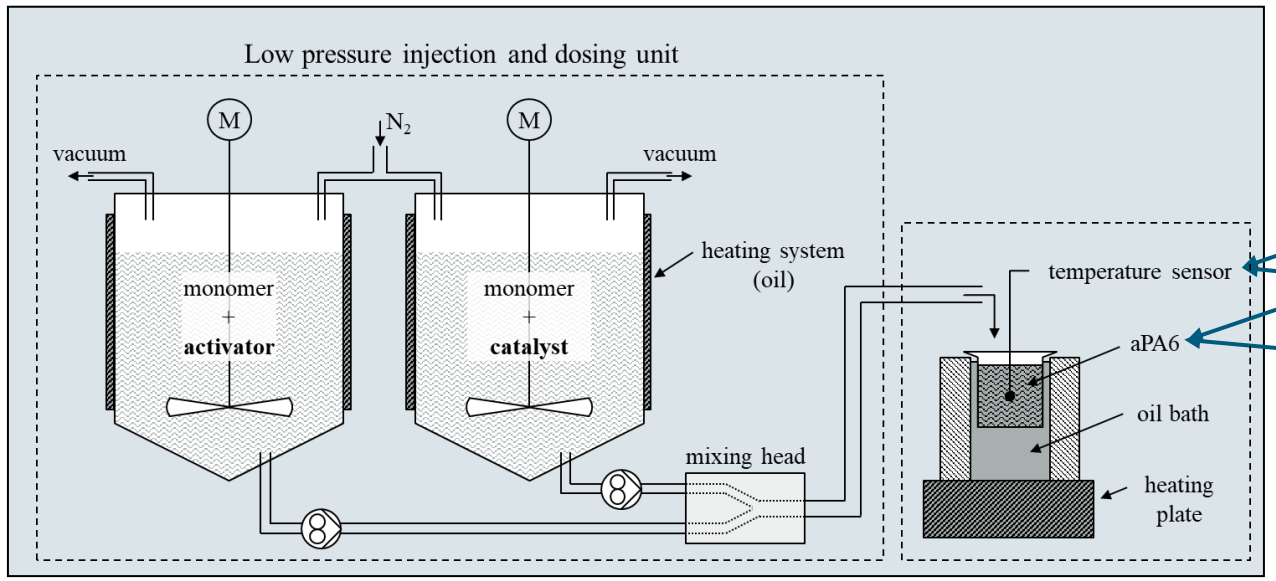

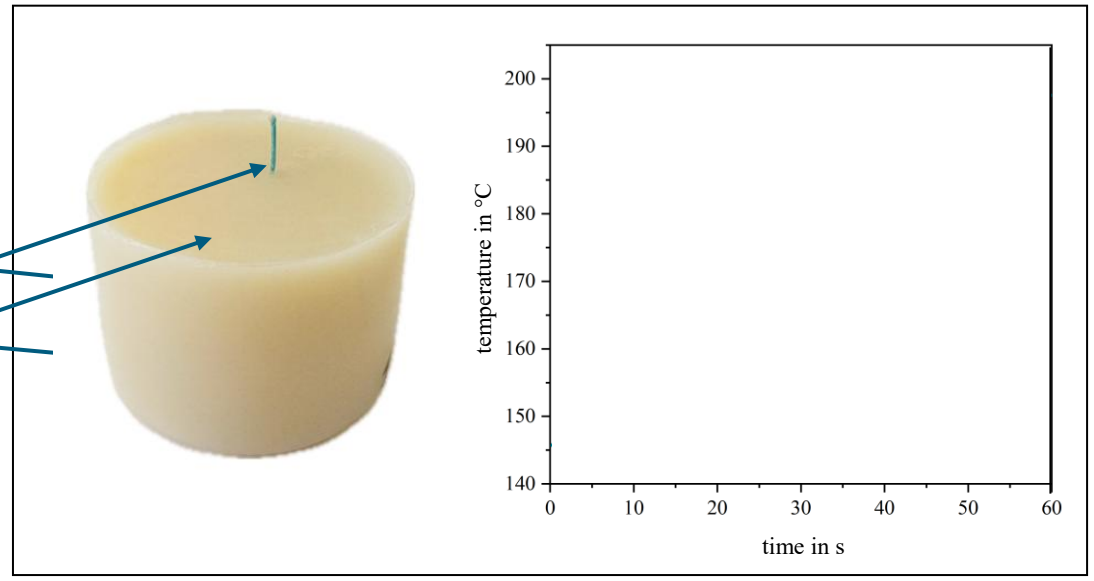

© Fraunhofer ICT

Formulation development

Determination of a suitable relative mixing ratio for the in-situ Pultrusion

Relative mixing ratio from activator to catalyst

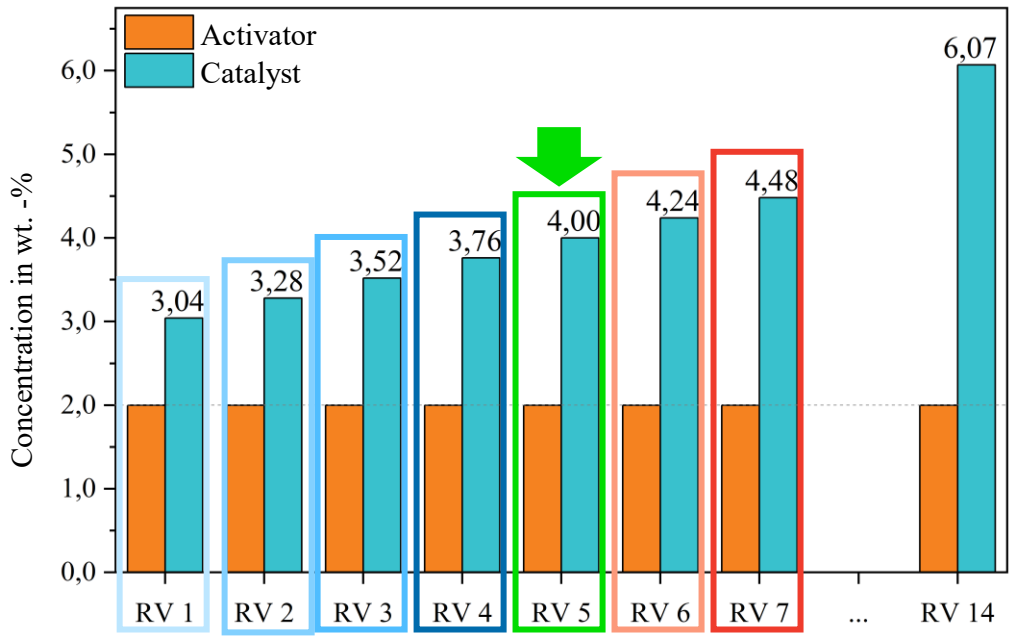

Ratio dependent polymerization kinetics

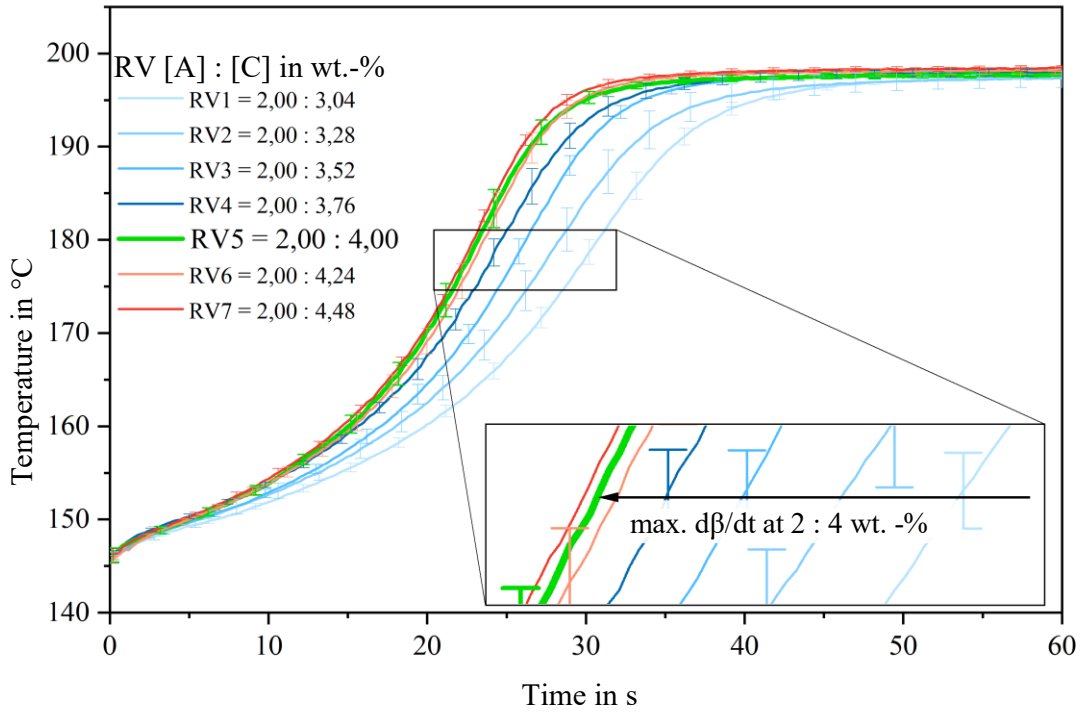

→ $(\text{max. } d\beta/dt)_{\text{min. Cat}} = [A] : [C] = 1{,}0 : 2{,}0$ wt.-%

Gradual increase of the catalyst concentration

© Fraunhofer ICT

Formulation development

Determination of suitable total concentrations

Concentration-dependent polymerization kinetics

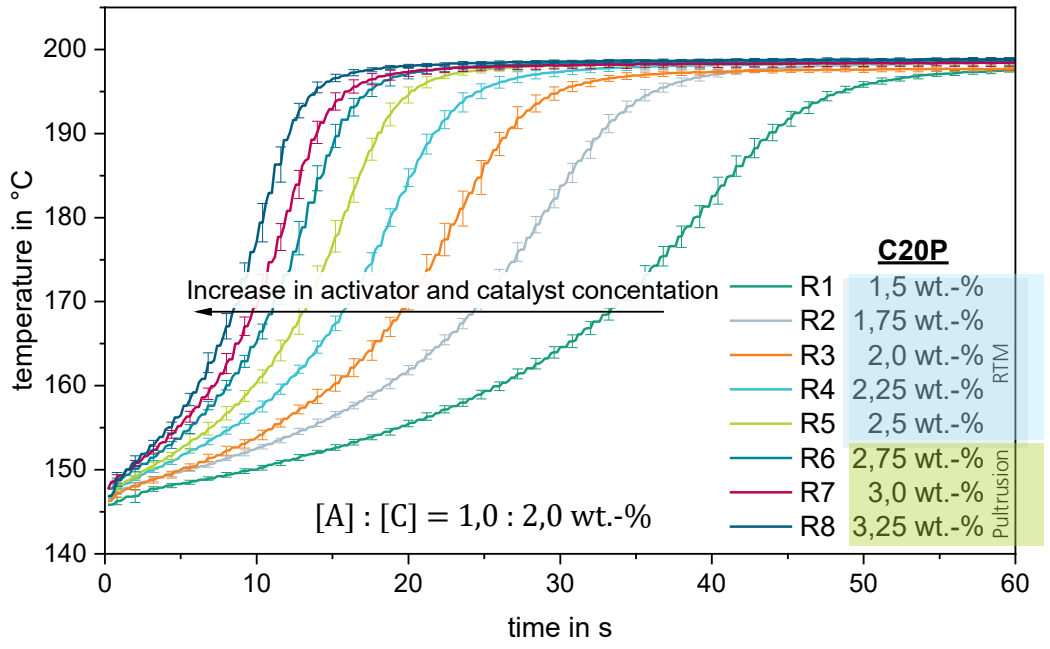

Polymerization time required for 98 % conversion

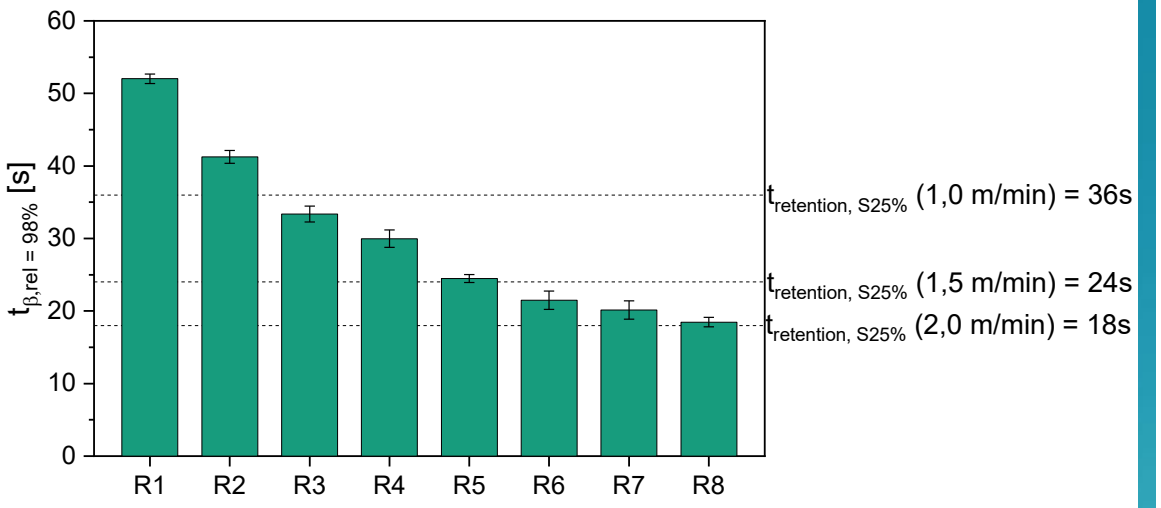

$$t_{ß,rel=98\,\%} = \left(T_{max,Rx} - T_{0,Rx}\right) * 98\,\%$$

With increasing total concentrations of Act./Cat., the polymerization rate increases disproportionately

Formulations **≥ R6** suitable for pull-off speeds up to **1.5 m/min**

© Fraunhofer ICT

Fraunhofer ICT

Formulation development

Influence of the activator and catalyst concentration on polymer properties

Influence on the weight-average molar mass

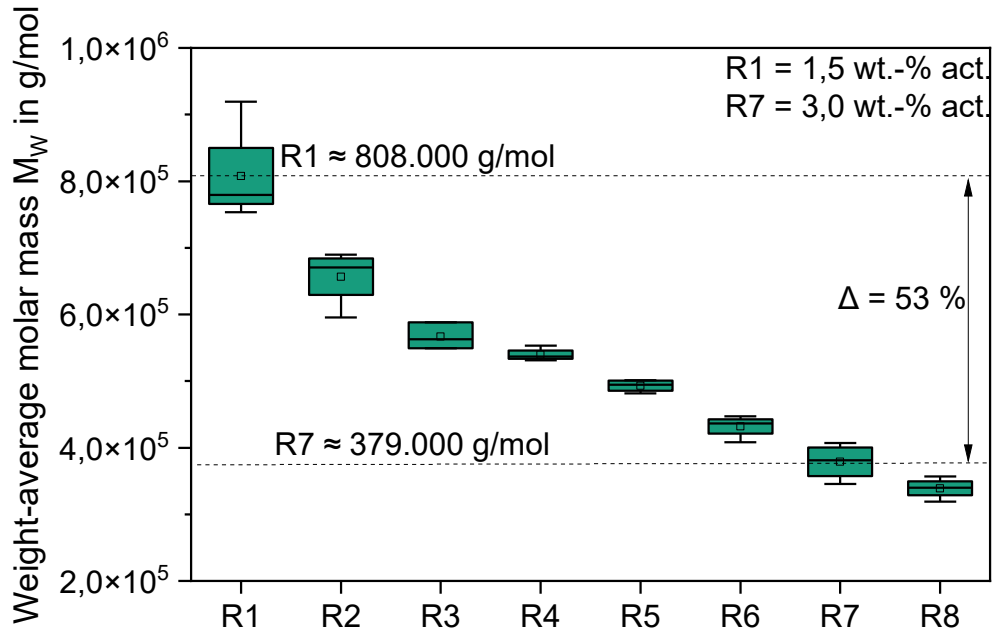

Approx. linear reduction of molar masses through increased proportion of activator and catalyst

Influence on the residual monomer content

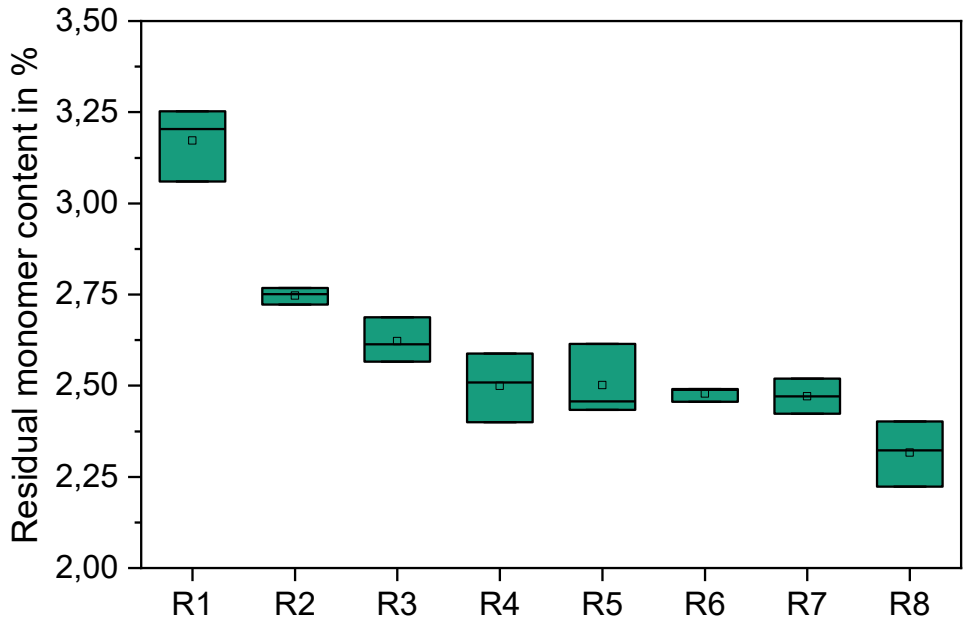

Constant low residual monomer content at relevant formulations (**≥ R6**)

© Fraunhofer ICT

Conclusion

Semi-adiabatic beaker tests are a valid method for investigating the influence of activator and catalyst concentration on kinetics and properties

The catalyst concentration can be limited to a minimum at an optimum ratio of [A] : [C] = 1.0 : 2.0 wt.% for max. reaction rate, high polymer properties and less side reactions.

From an activator concentration of 2.75 wt.% and a corresponding catalyst concentration of 5.5 wt.%, economical pultrusion is possible at a pull-off speed of ≥1.5 m/min

Increasing the activator and catalyst concentration even further showed no significant negative influence on the investigated polymer properties

© Fraunhofer ICT

References

[1] Thomassey, M., Paul Revol, B., Ruch, F., Schell, J. und Bouquey, M. "Interest of a Rheokinetic Study for the Development of Thermoplastic Composites by T-RTM" ujms, Jg. 5, Nr. 1, S. 15– 27, 2017, doi: 10.13189/ujms.2017.050103.

[2] Wendel, R., Rosenberg, P., Wilhelm, M. und Henning, F. "Anionic Polymerization of ε-Caprolactam under the Influence of Water: 2. Kinetic Model" J. Compos. Sci., Jg. 4, Nr. 1, S. 8– 20, 2020, doi: 10.3390/jcs4010008.

[3] Choi, C.-W., Jin, J.-W., Lee, H., Huh, M. und Kang, K.-W. "Optimal Polymerization Conditions in Thermoplastic-Resin Transfer Molding Process for Mechanical Properties of Carbon Fiber-Reinforced PA6 Composites Using the Response Surface Method" Fibers Polym, Jg. 20, Nr. 5, S. 1021–1028, 2019, doi: 10.1007/s12221-019-8901-4.

[4] Osváth, Z., Szőke, A., Pásztor, S., Szarka, G., Závoczki, L. B. und Iván, B. "Post-Polymerization Heat Effect in the Production of Polyamide 6 by Bulk Quasiliving Anionic Ring-Opening Polymerization of ε-Caprolactam with Industrial Components: A Green Processing Technique" Processes, Jg. 8, Nr. 7, Art. no. 856, 2020, doi: 10.3390/pr8070856.

[5] Murray, J. J. et al. "Thermoplastic RTM: Impact Properties of Anionically Polymerised Polyamide 6 Composites for Structural Automotive Parts" Energies, Jg. 14, Nr. 18, Art. no. 5790, 2021, doi: 10.3390/en14185790.

[6] Semperger, O. V., Osváth, Z., Pásztor, S. und Suplicz, A. "The effect of the titanium dioxide nanoparticles on the morphology and degradation of polyamide 6 prepared by anionic ringopening polymerization" Polym. Eng. Sci., Jg. 62, Nr. 6, 2022, doi: 10.1002/pen.25990

[7] Lagarinhos, J., Santos, L. und Oliveira, J. "Effect of Catalyst and Activator on Properties of Polyamide 6 Prepared by Thermoplastic Resin Transfer Molding Technology" J. of Materi Eng and Perform, Jg. 31, Nr. 31, S. 7098–7103, 2022, doi: 10.1007/s11665-022-07044-4.

Thanks!

Contact

Hannah Decker

Research assistant
Department Polymer Engineering
Tel. +49 721 4640 505
Hannah.decker@ict.fraunhofer.de

Fraunhofer ICT
Joseph-von-Fraunhofer Str. 7
76327 Pfinztal
www.ict.fraunhofer.de

Leveraging in-situ anionic polymerization of polyamide 6 for high performance basalt- and flax-fiber thermoplastic laminates

Giulia Cotti Comettini[1], Martino Valentini[1], Olivier De Almeida[2], Andrea Dorigato[1], Markus Kakkonen[3], Gerhard Kalinka[4], Pasi Kallio[5], Marco Papparotto[1], Alessandro Pegoretti[1], ***Giulia Fredi[1]***

[1]University of Trento, Italy; [2]Institut Clément Ader - IMT Mines Albi, France; [3]Fibrobotics Oy, Finland; [4]BAM Federal Institute for Materials Research and Testing, Germany; [5]Tampere University, Finland

24th International Conference on Composite Materials

Baltimore (MD, USA) - August 5, 2025

giulia.fredi@unitn.it

Thermoplastic composites: traditional and reactive processing

Thermoplastic composites

- shorter thermal cycles → increased production rate
- «infinite» shelf life
- post-thermoformability and recyclability
- High viscosity
- High-temperature processing

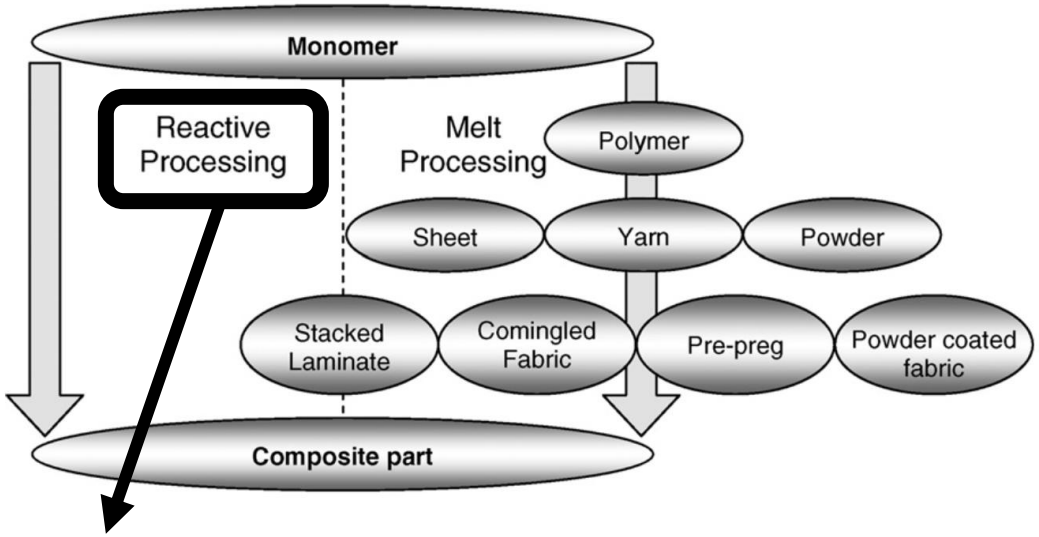

- **low-viscosity** precursors
- complete fiber **impregnation**
- **shorter and less complex** production cycles

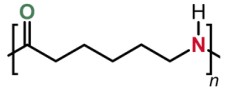

Polyamide 6 (PA6): reactive vs. melt processing

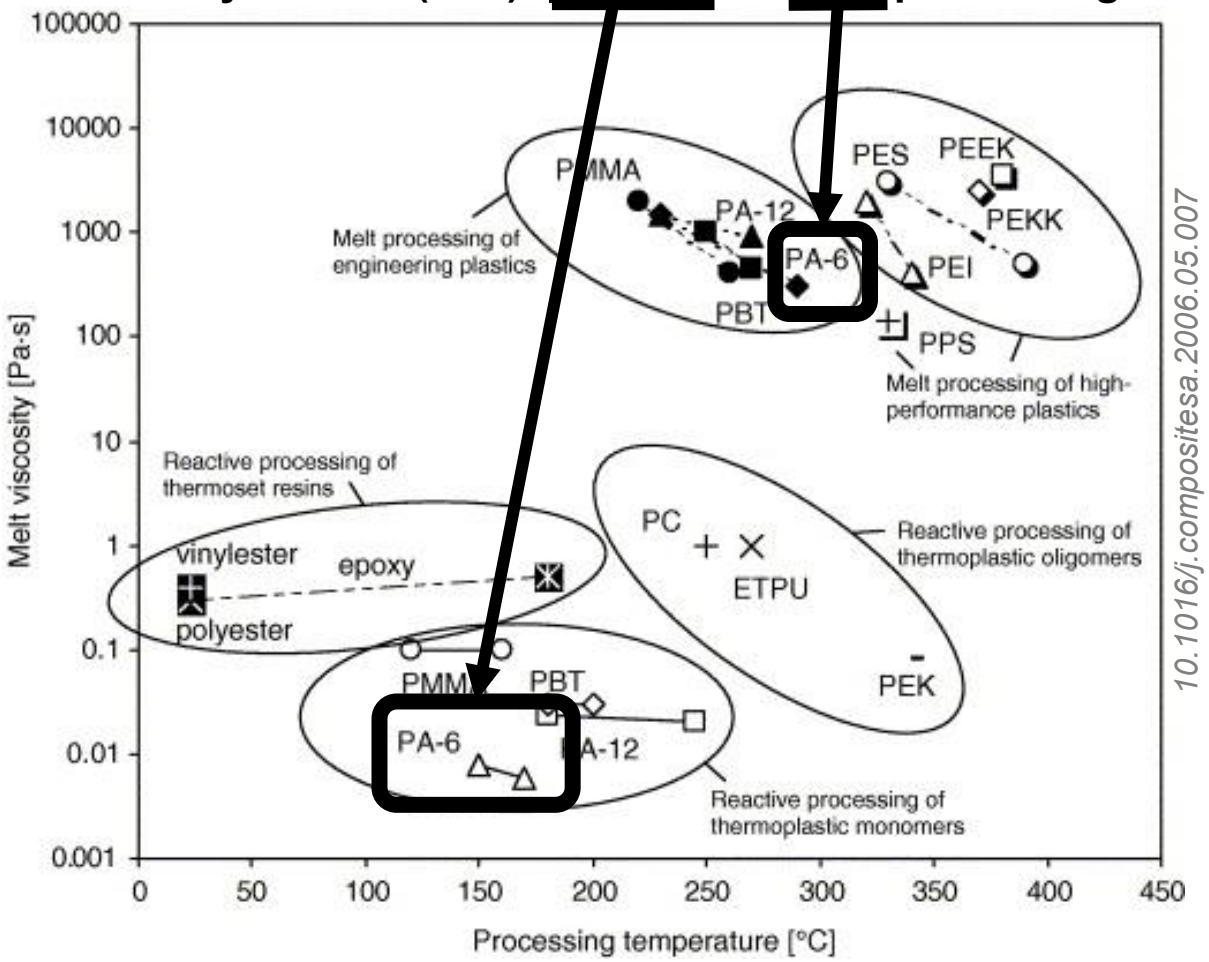

10.1016/j.compositesa.2006.05.007

PA6: hydrolytic vs. anionic polymerization

Hydrolytic polymerization

- T = 250 °C (> T_c)
- Hours-Days

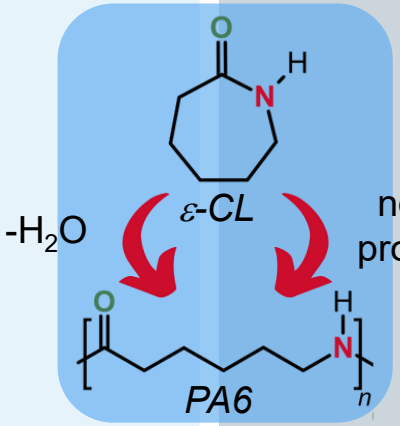

- Mw = 30 kg/mol
- Conv. > 90%
- X_c = 20-30 %
- E = 2-3 GPa

Anionic (ring-opening) polymerization

- T = 140-170 °C (< T_c)
- Seconds-minutes

no by-products → *suitable for reactive processing*

- Mw = 500 kg/mol
- Conv. >99%
- X_c = 40-50 %
- E = 3-4 GPa

extremely moisture-sensitive

Initiation

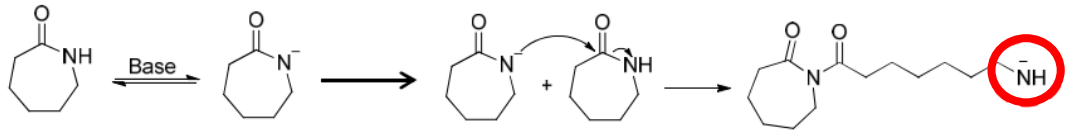

Initiation with an activator (faster)

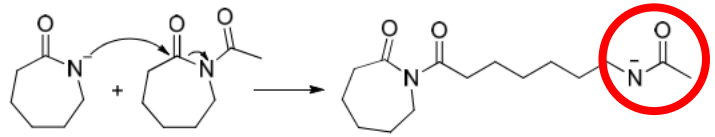

Common initiators:

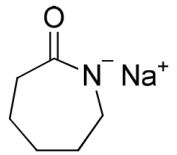

Bruggolen C10

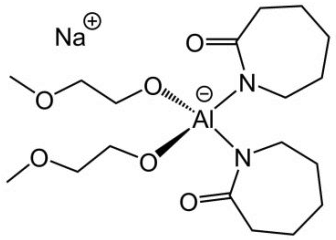

Dilactamate

Common activator:

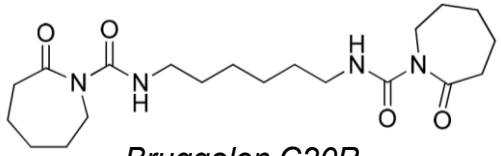

Bruggolen C20P

Aim of the work

Prepare and characterize aPA6-matrix composites with two types of continuous reinforcement:

1. Basalt fiber fabric

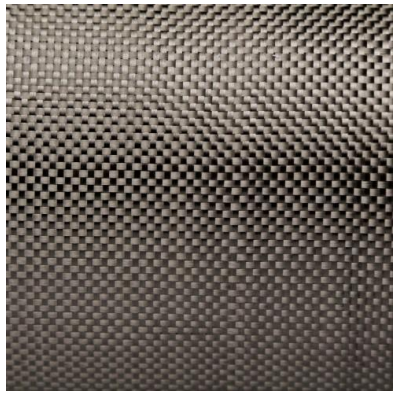

BAS220P (Basaltex NV)
- 220 g/m^2
- Plain
- (3-glycidyloxypropyl)trimethoxysilane sizing
- 3 types of surface state

2. Flax fiber fabric



Flax fabric Flaxdry BL200 (Eco-Technilin)
- 200 g/m^2
- Twill
- Twisted yarns
- 3 types of surface state

Outline

PA6/BF
- Monomer conversion
- Mechanical properties
- Fiber/matrix adhesion

PA6/FF
- Why plant fibers + anionic PA6?
- Fiber surface state
- Monomer conversion
- Mechanical properties

PA6/basalt fiber composites

Preparation of PA6/BF laminates via tRTM

Reactive in situ activated polymerization – Thermoplastic resin transfer molding

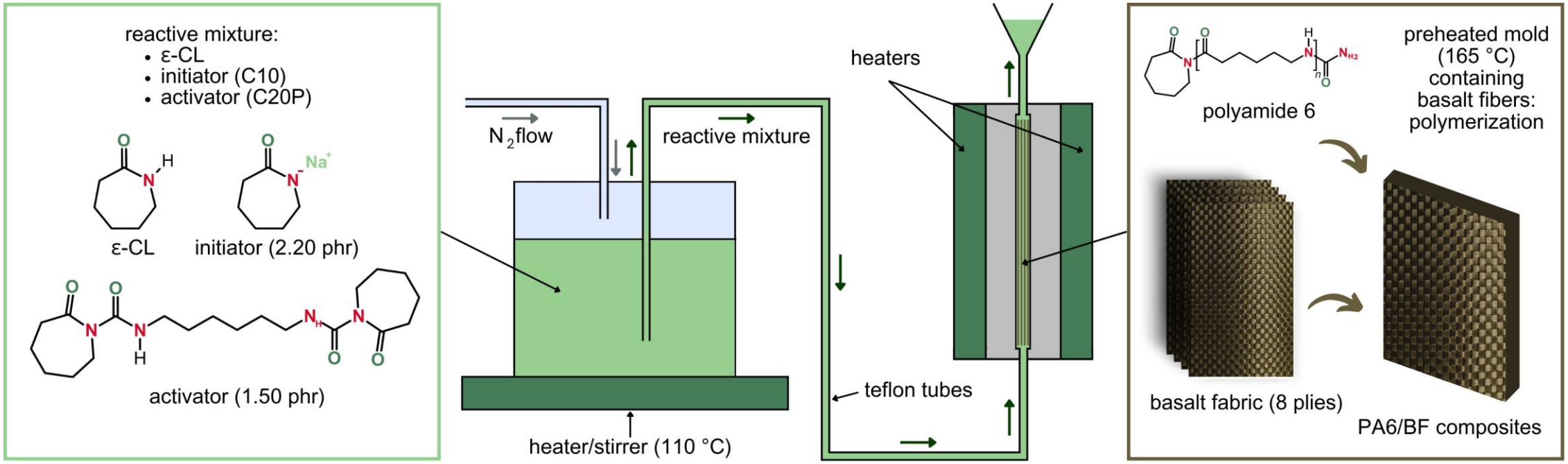

Sample	Reinforcement	Monomer conversion (%)	ϑ_v (vol%)	ϑ_f (vol%)
PA6/BFa	As-received BF	97.2	6.6	28.2
PA6/BFw	BF washed with ethanol	97.7	1.4	31.5
PA6/BFu	Thermally desized BF (400 °C – 4 h)	98.7	3.4	32.4

Valentini,… and Fredi, Composites A 2025, 190, 108681, 10.1016/j.compositesa.2024.108681

PA6/BF: microstructure

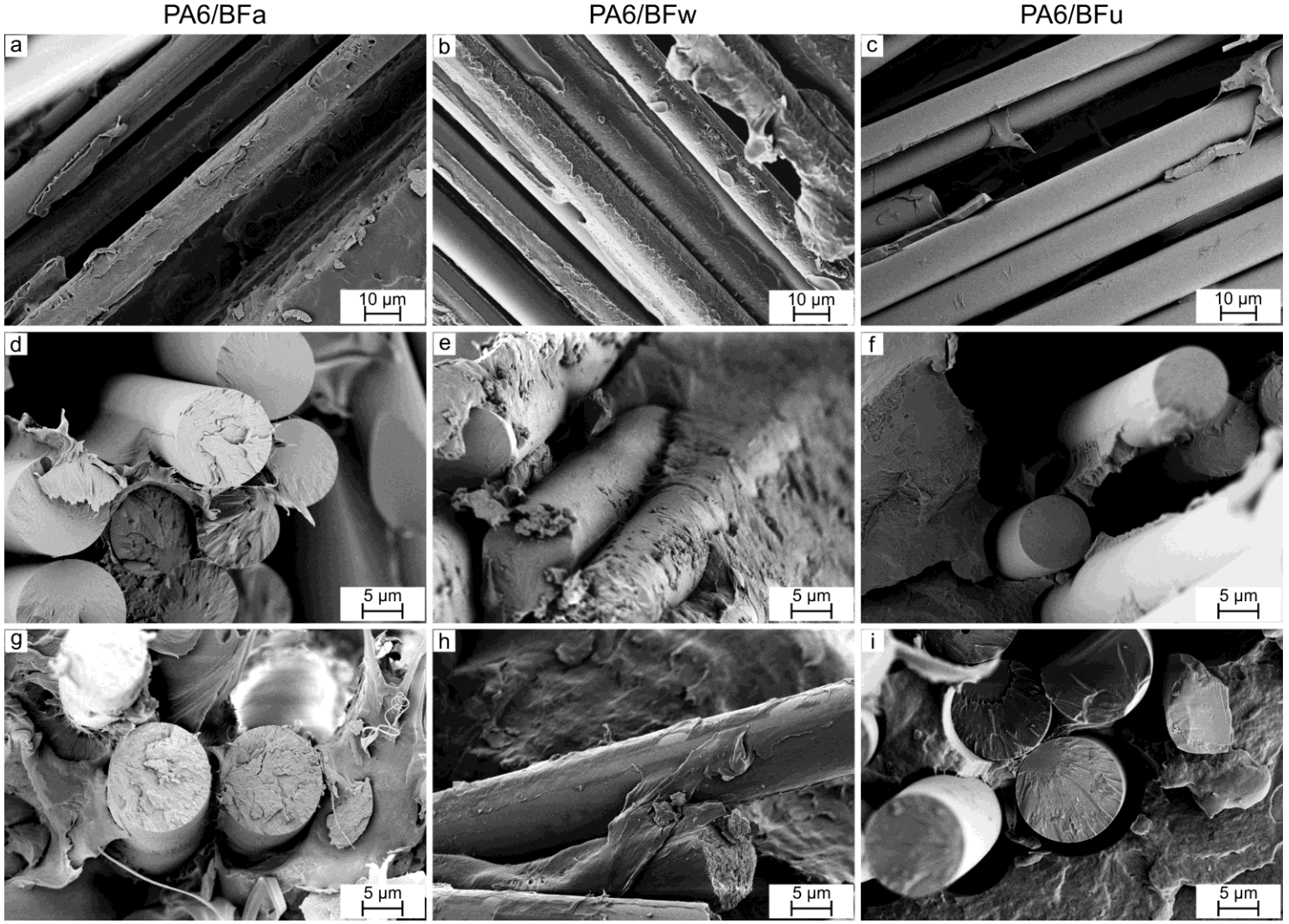

PA6/BFa and PA6/BFw:

- Matrix residues on the fibers
- Matrix deformation
- (slight) improvement with washing

→ good fiber/matrix adhesion

PA6/BFu:

- Clean fibers and grooves

→ scarce fiber/matrix adhesion

Valentini,… and Fredi, Composites A 2025, 190, 108681, 10.1016/j.compositesa.2024.108681

3-point bending test

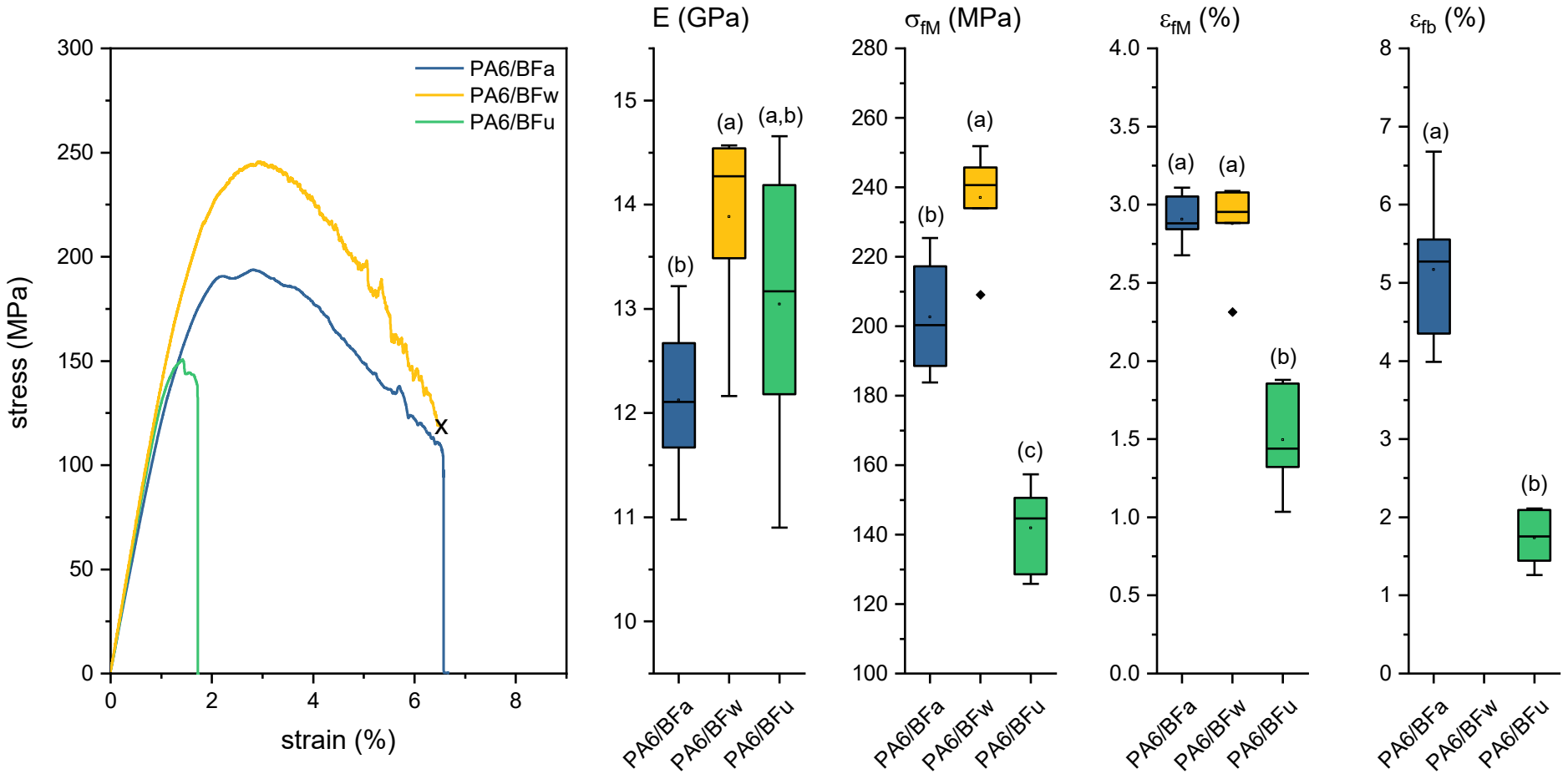

- Ethanol washing significantly increases the stiffness and strength
- Desizing decreases the mechanical properties
- TT at 400 °C may decrease the BF strength but not the stiffness
- Theoretical stiffness (mixture rule):
  - PA6/BFa: 13.0 GPa
  - PA6/BFw: 14.2 GPa
  - PA6/BFu: 14.5 GPa

Valentini,… and Fredi, Composites A 2025, 190, 108681, 10.1016/j.compositesa.2024.108681

Interfacial adhesion: three tests

Short beam shear (SBS) test

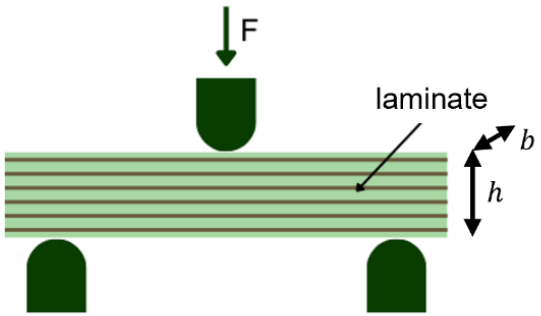

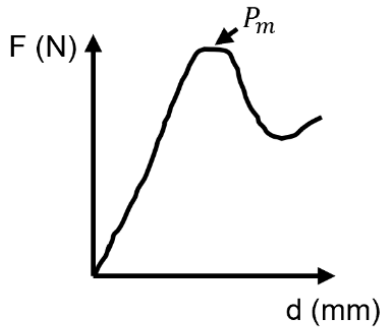

$$ILSS = F^{SBS} = \frac{3P_m}{4bh}$$

- 3-p bending with a short specimen
- Maximization of shear streses
- Delamination promoted

Single fiber push out (SFPO) test

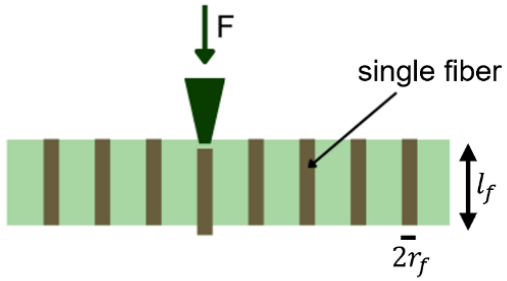

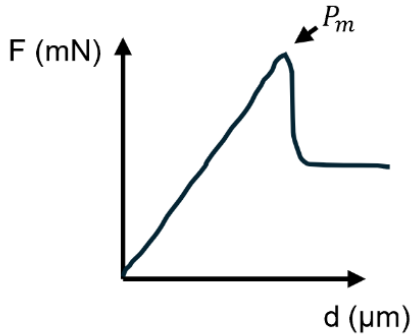

$$IFSS = F^{SFPO} = \frac{P_m}{2\pi r_f l_f}$$

- Thin (tens of μm) specimen
- Fiber is pushed out of the matrix

Microbond (MD) test

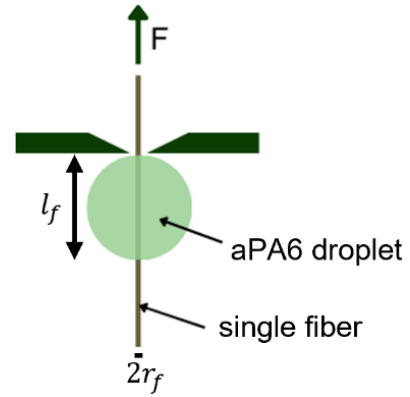

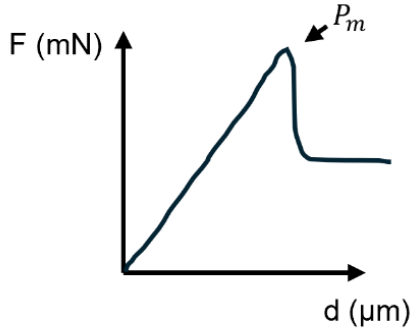

$$IFSS = F^{MD} = \frac{P_m}{2\pi r_f l_f}$$

- Droplets of matrix on the fiber
- Fiber is drawn out of the droplet

Valentini,… and Fredi, Composites A 2025, 190, 108681, 10.1016/j.compositesa.2024.108681

Interfacial adhesion

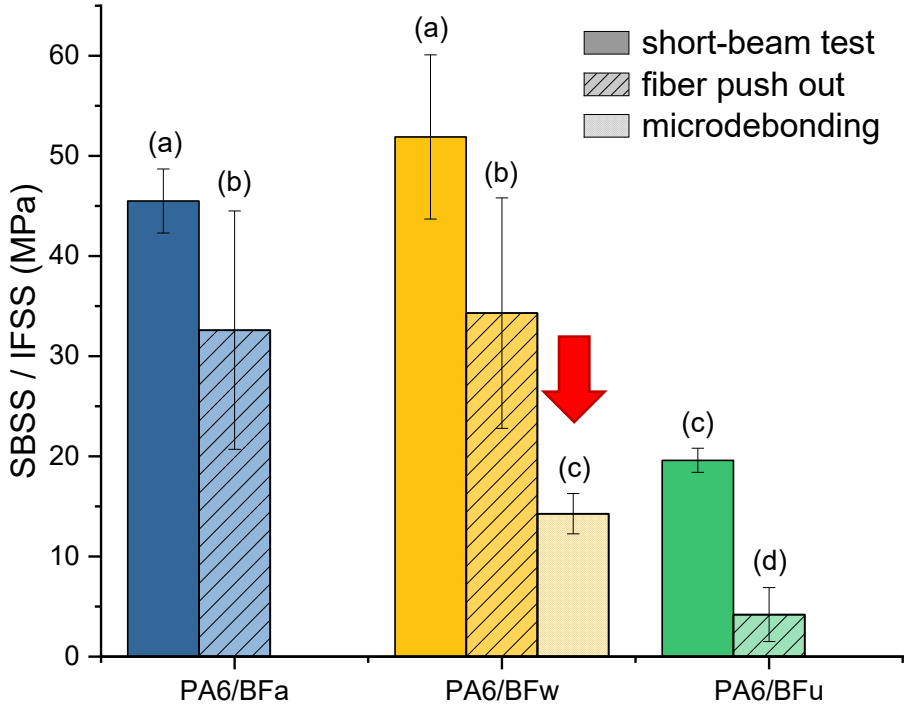

Short beam vs push out:

- Dispersion is higher with a micro-scale test but trends are similar:
  - PA6/BFw: washing increases adhesion
  - PA6/BFu: desizing decreases adhesion

Microdebonding:

- Lower adhesion

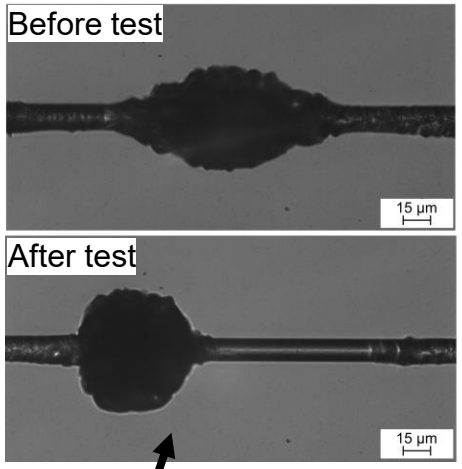

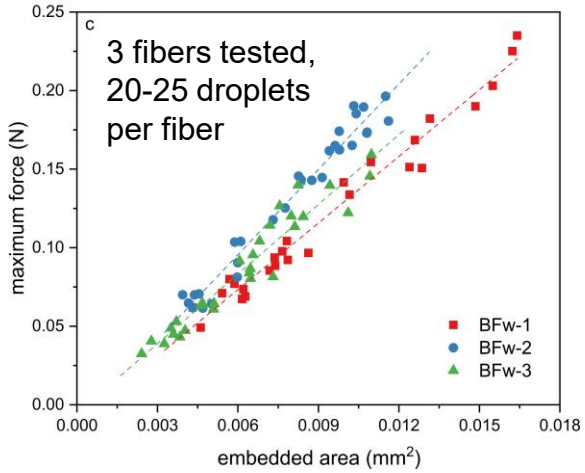

- **Ductile** droplets: residual monomer
- **Porous** droplets: overestimation of the interfacial area

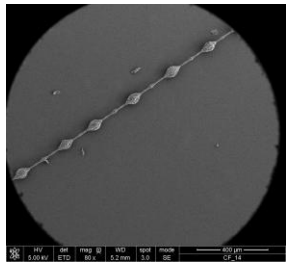

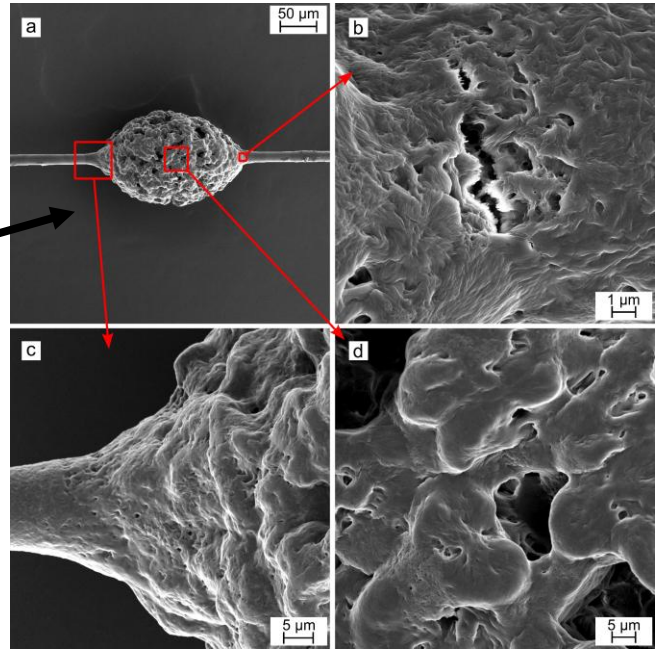

Valentini,… and Fredi, Composites A 2025, 190, 108681, 10.1016/j.compositesa.2024.108681

PA6/BF: conclusions

- **Fiber surface treatment critically determines fiber-matrix adhesion** (simple treatment effective with a sensitive polymerization reaction), **while the bulk matrix properties are not affected**

- **Ethanol washing** emerged as the most effective treatment, increasing short-beam shear strength by 14% compared to as-received fibers (51.9 ± 8.2 MPa vs 45.5 ± 3.2 MPa)
- Thermal desizing at 400°C significantly impaired interfacial bonding, reducing interfacial shear strength by ~50% (19.6 ± 1.2 MPa)

- **Multi-technique characterization** (short-beam shear, fiber push-out, microdebonding) provided complementary insights into interfacial behavior at different scales, but **the microdebonding test presents challenges that are unique of this matrix system**

aPA6/flax fiber composites

Lignocellulosic reinforcements: industrial applications

Key Benefits
(vs. glass)

- **High specific properties**
- Cost-effective production
- Bio-based
- Biodegradable
- Other functional properties (e.g., vibration-damping)

Automotive Industry
- Hemp, jute, flax, sisal fibers
- Seat cushions, interior panels, front grills

Transportation
- Aircraft interior components
- Boat hulls
- Pressure vessels (w/ thermosetting resins)

Construction & Building
- Wood-plastic composites for furniture & decking
- Hemp/lime concrete for soundproofing
- Recycled WPC in asphalt & concrete

Consumer & Sports Goods
- Musical instruments
- Sport equipment
- Packaging



pressure vessel



packaging



kenaf/PP inner-door panel



Sports-cycle frame


Mercedes Benz E-Class components

Lignocellulosic reinforcements in polymers: three main challenges

Challenge 1: Poor interfaces

Poor interfacial interaction with polymer matrices, for two main reasons:

1) **Hygroscopicity** and swelling (enhanced by fiber porosity)
2) **Hydrophilicity** and poor chemical compatibility with hydrophobic polymer matrices

Challenge 2: Poor stability

Poor thermal and environmental stability, so:

1) **Degradation during processing (T>200°C):** challenges with technical thermoplastics
2) **Degradation during use**: attack by microorganisms and fungi; flammability

Challenge 3: Property variability

Variability and challenges in measuring mechanical properties:

1) **Variable morphology** and irregular cross section
2) **Variability due to environmental conditions**

Bonus challenge
Decreased **durability** of durable composites (and of the biodegradable ones?)

Lignocellulosic reinforcements in polymers: poor thermal stability

Degradation during processing (T > 200°C)

- restricts manufacturing temperature
- limits the matrix selection to:

Thermosets
with curing temp.
below 200 °C

Low-melting-temperature thermoplastics
e.g., PE, PP, PLA

- Unfair competition with glass fibers
- Restricts broader industrial applications: **challenges with technical thermoplastics** like PET, PA, PEEK, etc.

https://doi.org/10.1016/j.jmrt.2024.04.085

Weight loss (%)	T (°C) at 5wt%	T (°C) at 25wt%	T (°C) at 50wt%	T (°C) at 75wt%
Hemp	105	329	341	458
Kenaf	64	313	341	371
Henequen	61	301	337	392
Flax	88	323	339	441
Glass	586	–	–	–

PA6/flax: aim of the work

Produce and characterize

polymer composites combining

lignocellulosic fibers and an

engineering polymer matrix (polyamide 6) exploiting

in situ reactive processing, which allows low precursor's viscosity and low processing temperatures

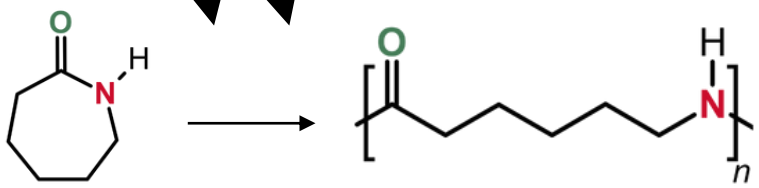

ε-caprolactam *PA6*

- Activated anionic ring-opening polymerization
- **Extremely sensitive to moisture and surface impurities** (initiator reacts with proton donating species and deactivates → lower degree of conversion)

Flax fabric Flaxdry BL200



Three surface states:

- **NT**: not treated (as received)
- **A**: silanized with APTES (spray coated)
- **HA**: treated with hexane, ethanol, acetone (HEA) and then silanized with APTES

Increase degree of conversion and interfacial adhesion

Characterization of the fibers: microstructure

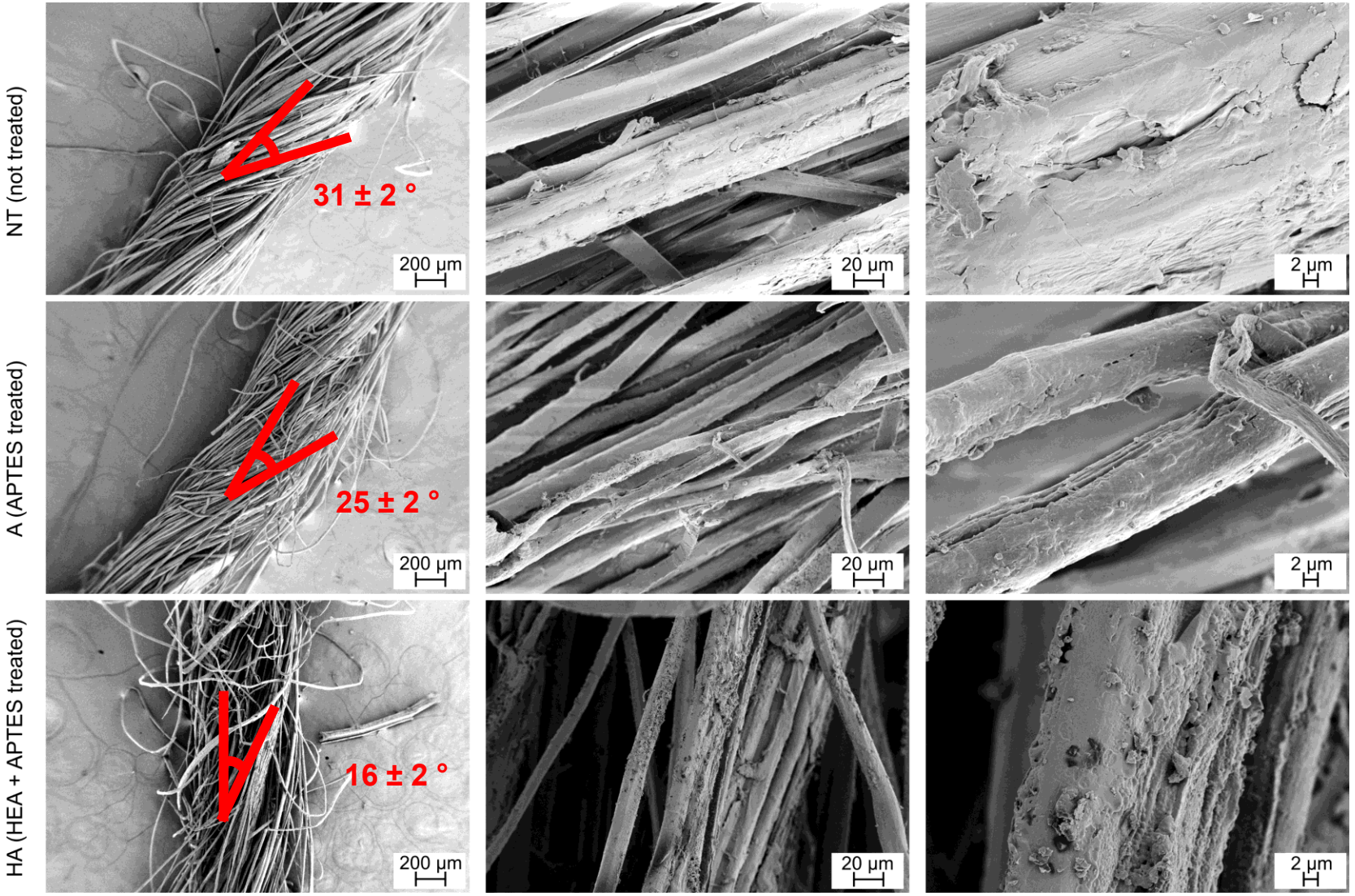

- Decrease in twist angle with both treatments
- No clear effects on the surface morphology

Twist angle (Orientation J – ImageJ)

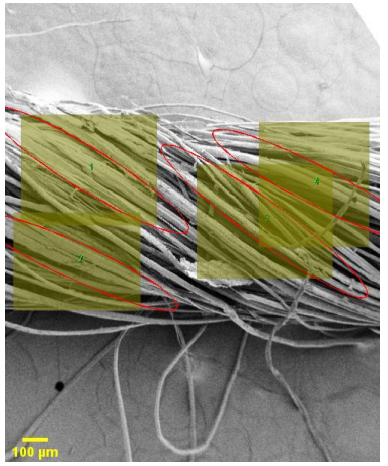

Characterization of the fibers: silanization

TGA

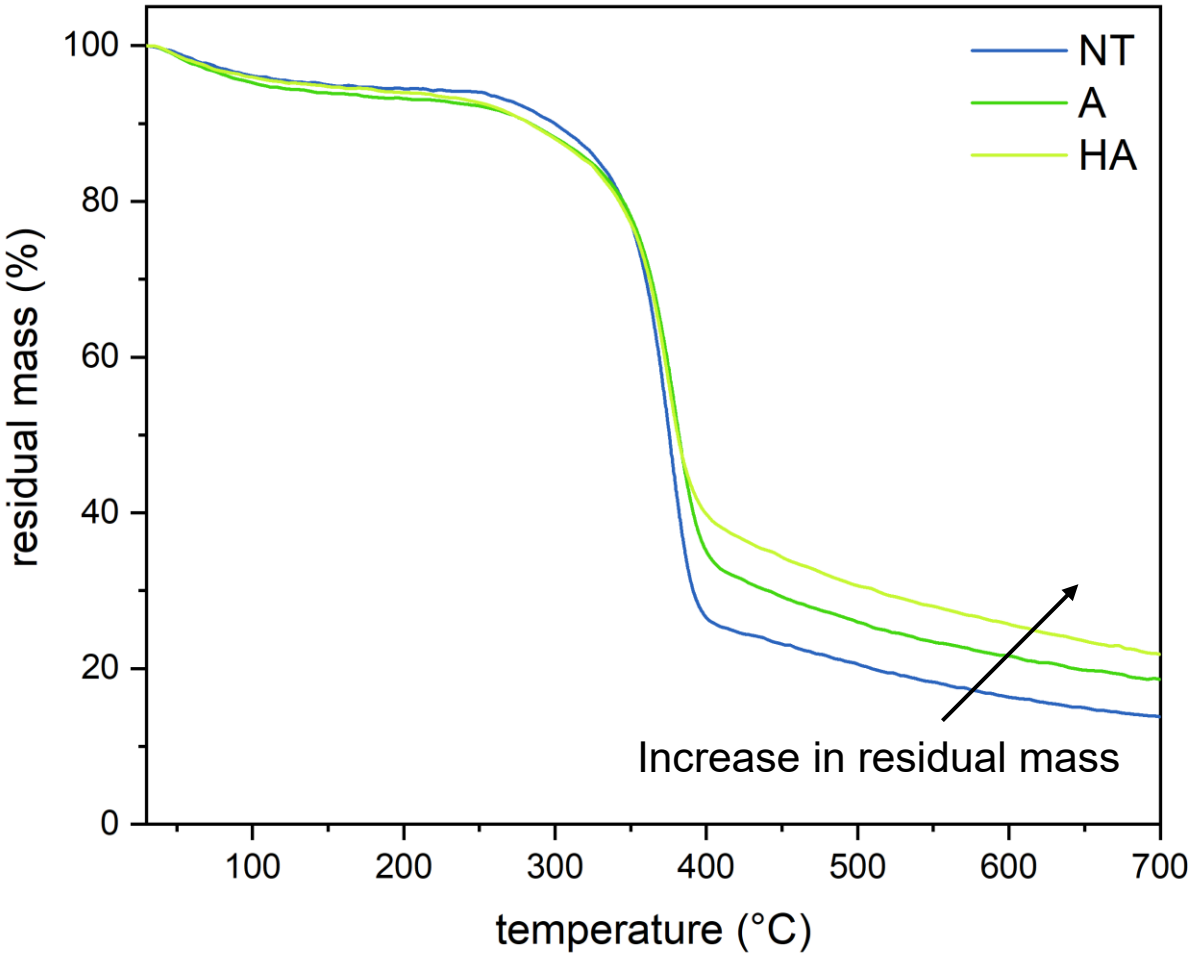

FT-IR

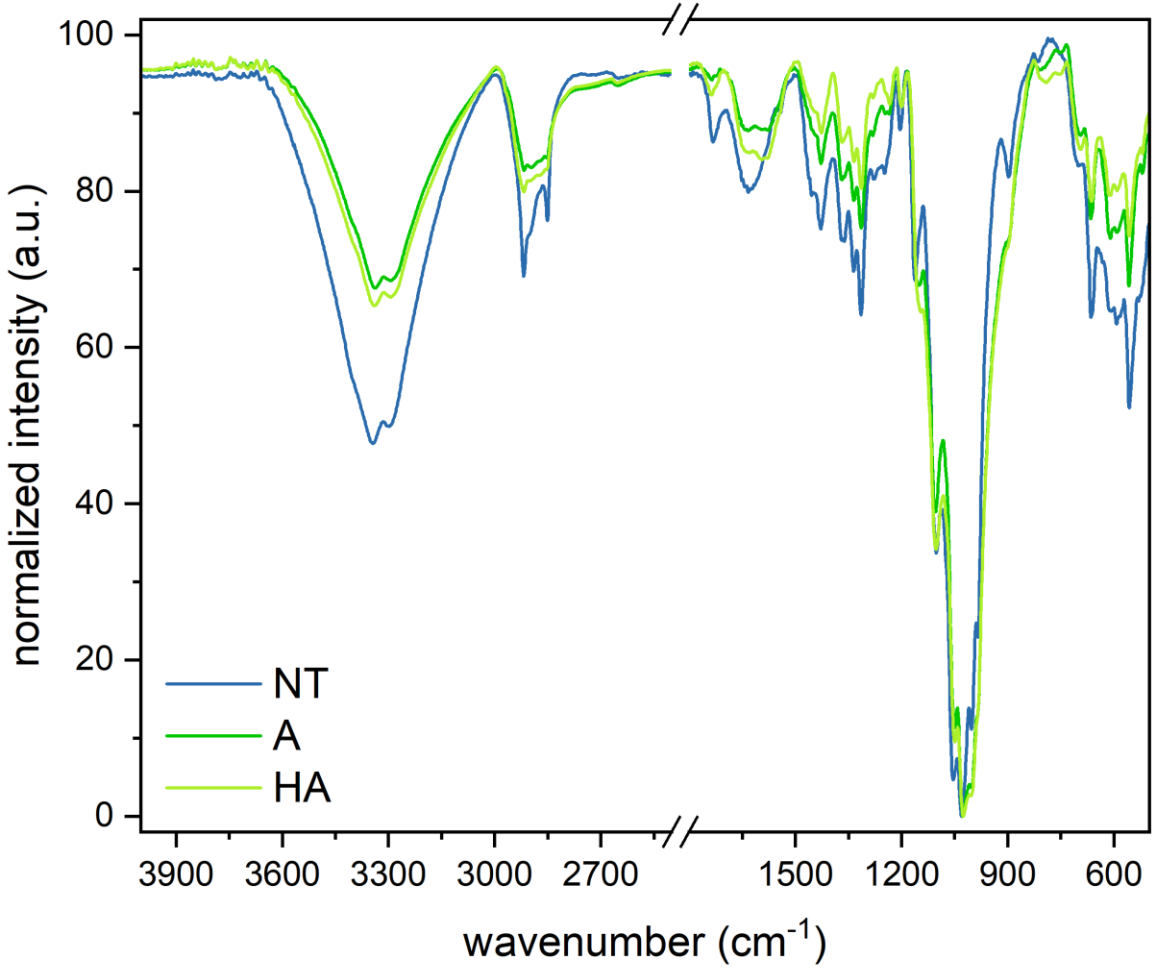

Characterization of the fibers: silanization

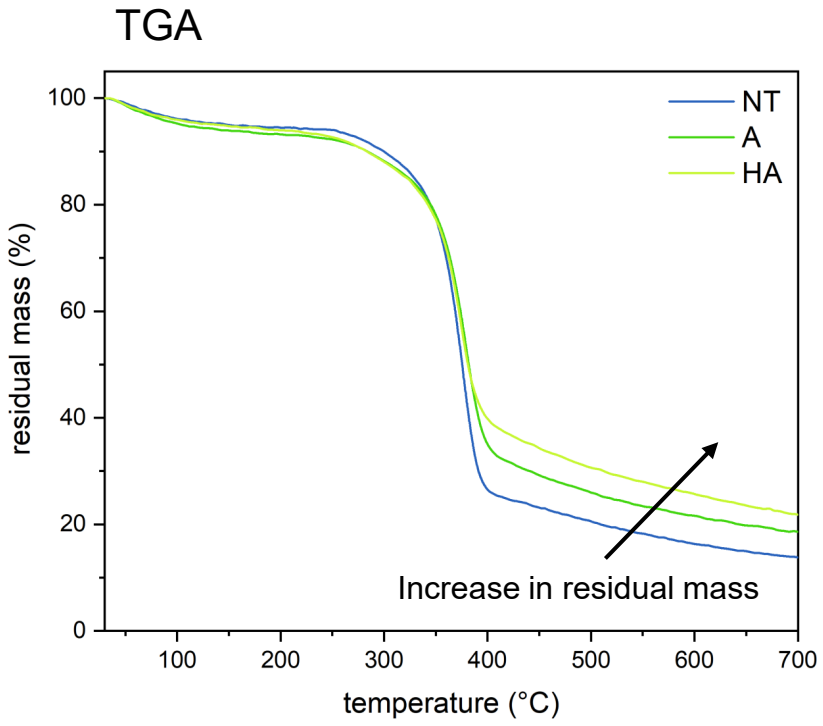

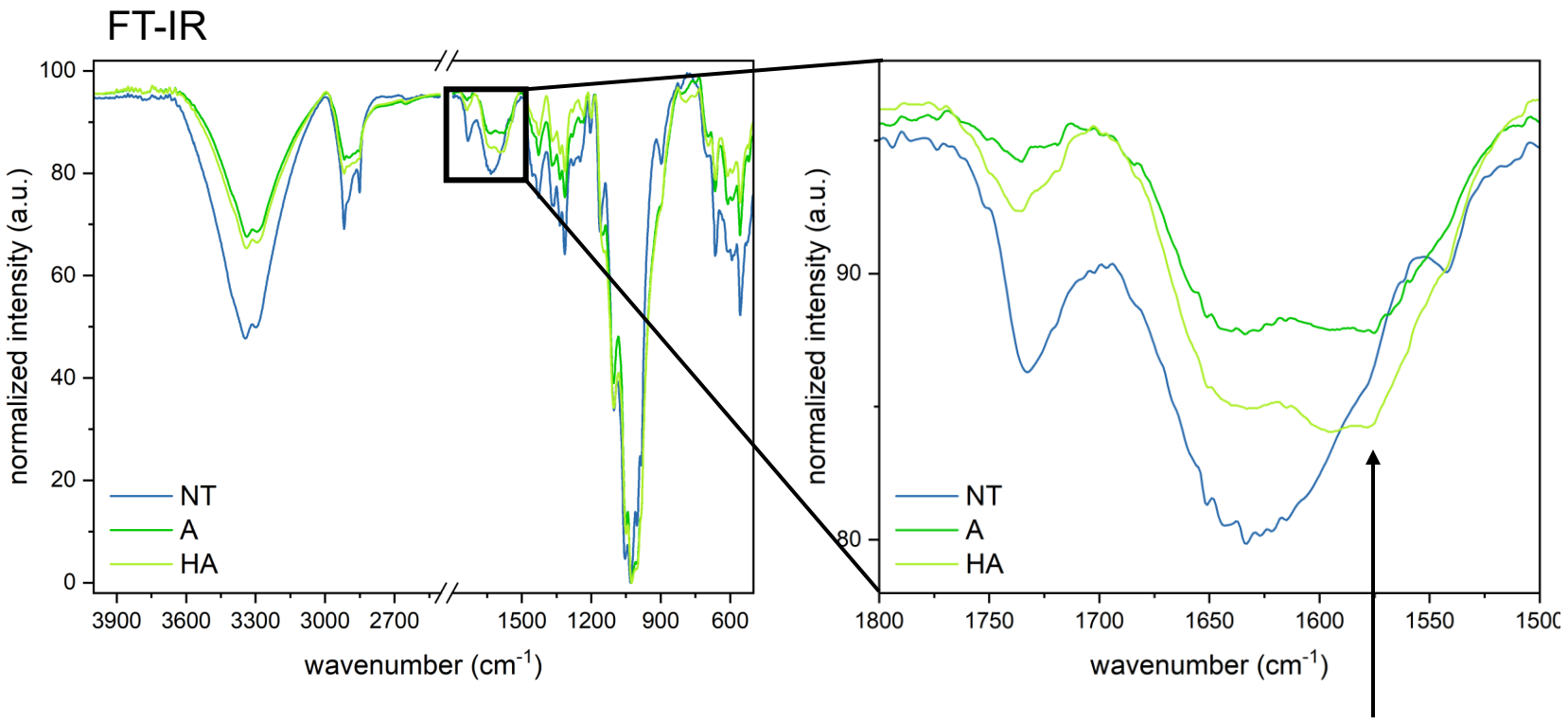

1590-1650 cm^{-1}: N-H bending

- Successful silanization
- Silanization seems more effective if preceded by HEA treatment

Characterization of the fibers: tensile tests

Tensile tests
- Single fibers
- Yarns →

- HA treatment **decreases the strain at break and the break tenacity**, but not the max load → increase in linear density

	Yarn (tex)	Staple (tex)
NT	107 ± 27	0.3483 ± 0.0007
A	115 ± 24	0.4248 ± 0.0007
HA	120 ± 34	0.4509 ± 0.0007

- the decrease is significant (for HA) but slight
- The **stiffness [N/tex]** is not significantly affected

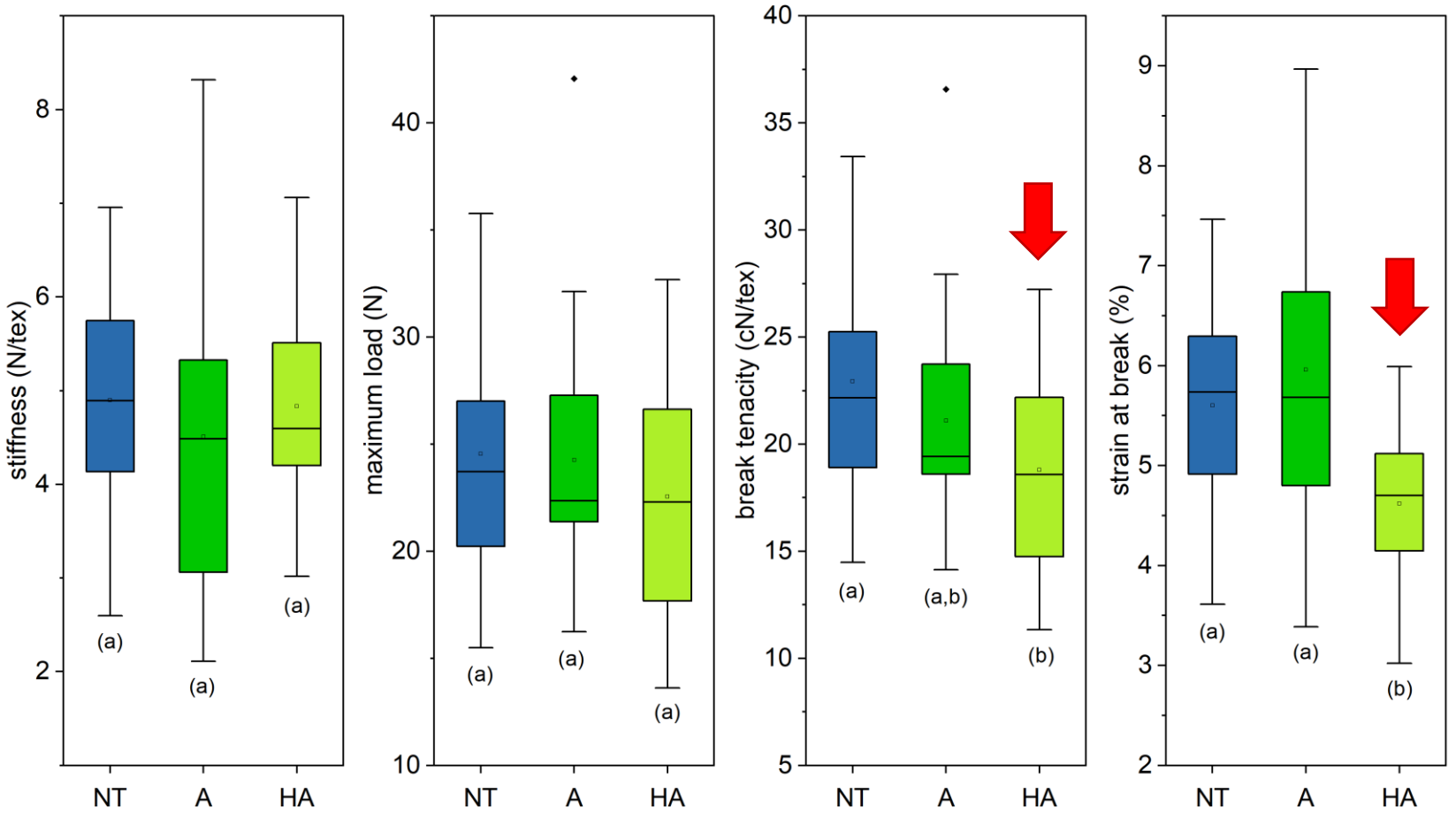

One-way ANOVA and Tukey's HSD test at p = 0.05

Preparation of PA6/flax laminates via tRTM

Reactive in situ activated polymerization – Thermoplastic resin transfer molding

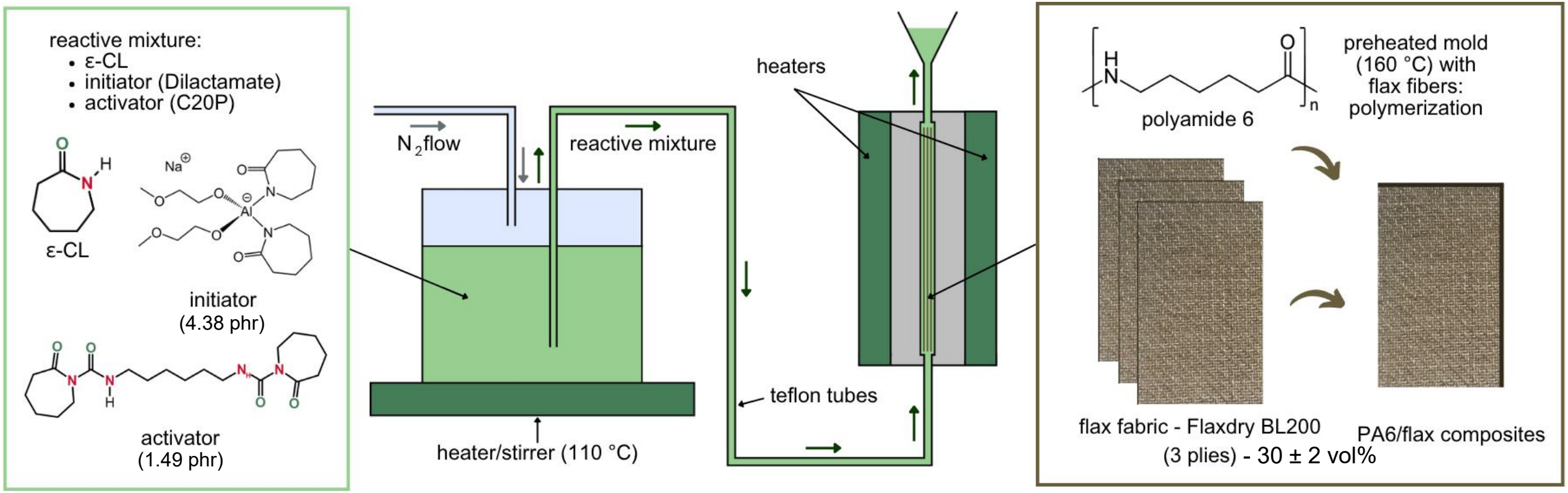

- Moisture-tolerant initiator (other initiators like NaCL perform worse)

PA6/flax composites: monomer conversion

DSC (first heating scan)

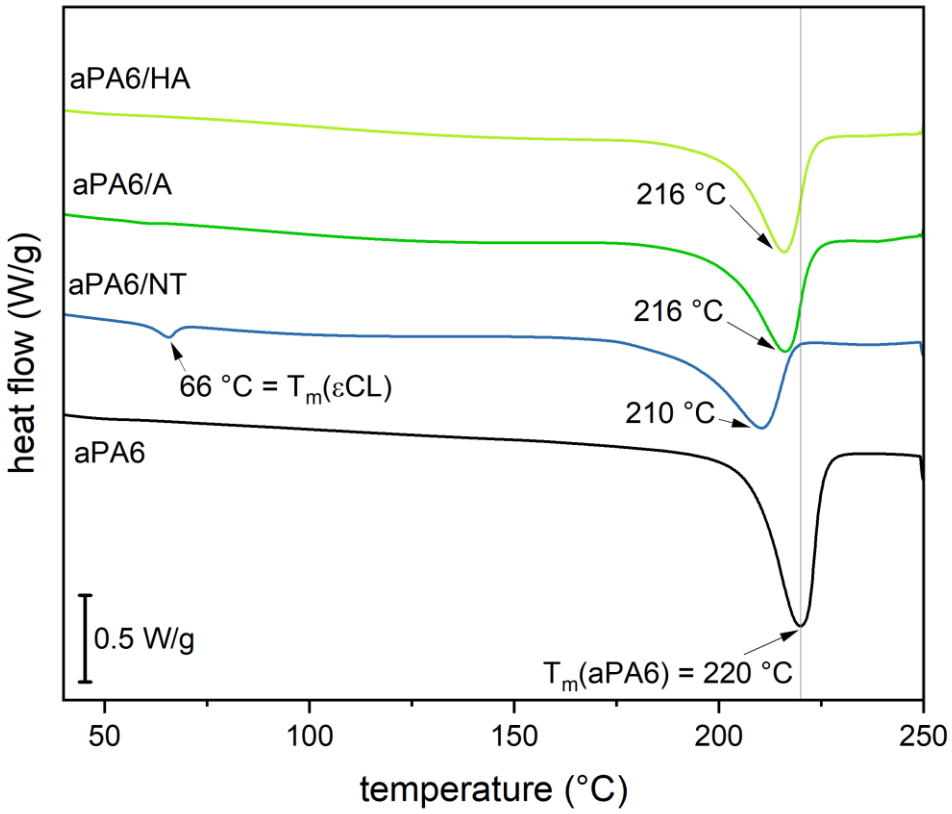

TGA

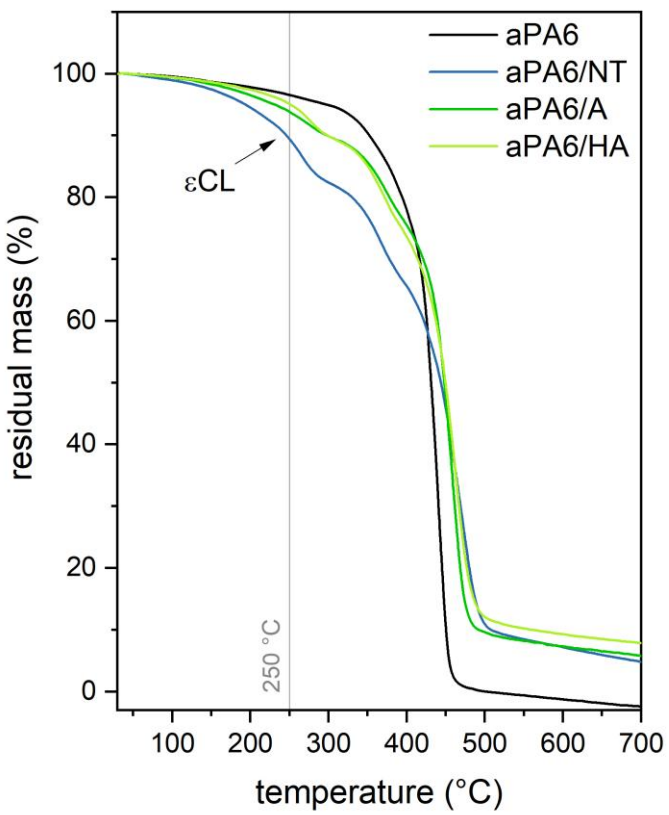

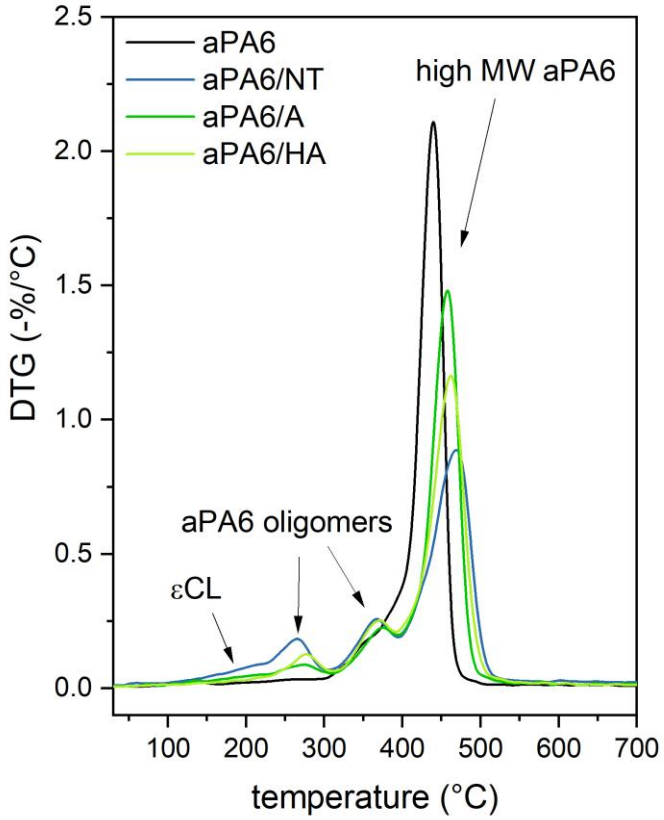

- aPA6 melting point decreases more with NT flax and less with A and HA flax
- Same trend for the conversion degree

Degree of conversion (%)	
aPA6	97.6
aPA6/NT	89.5
aPA6/A	93.9
aPA6/HA	95.1

Better than literature data (DL is an effective initiator)

PA6/flax composites: tensile tests

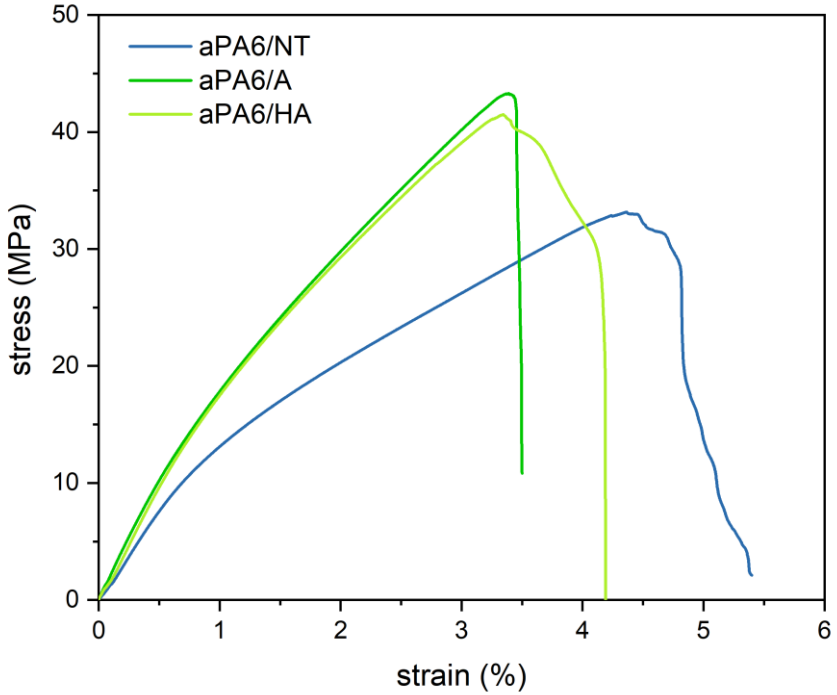

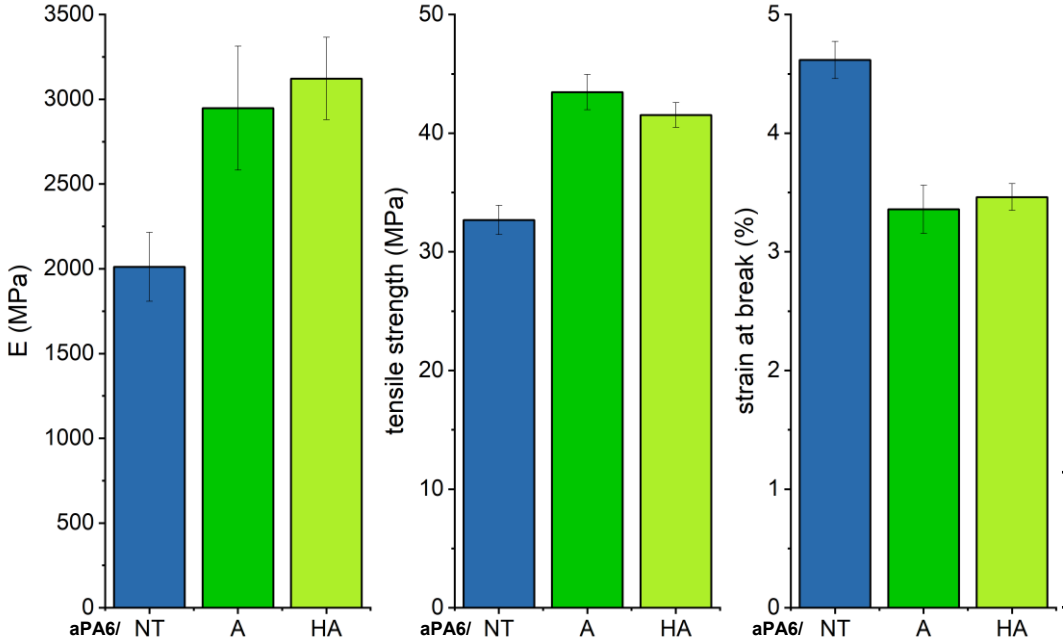

Unreinforced aPA6

E (GPa)	2.8 ± 0.3
UTS (MPa)	60 ± 1
Strain at break (%)	63 ± 19

Tensile fracture surface

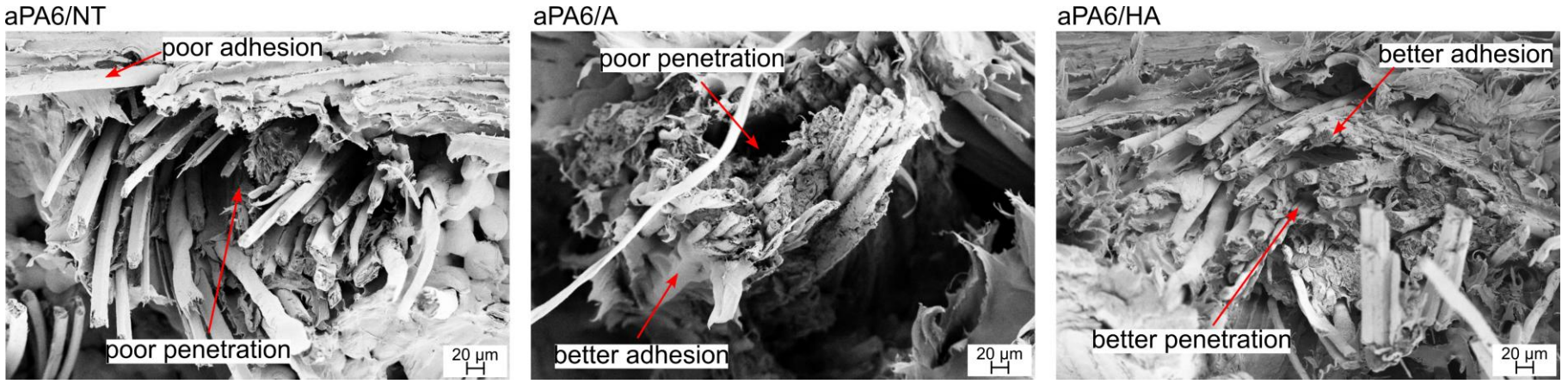

Matrix impregnation and packing factor (μ)

Convex hull

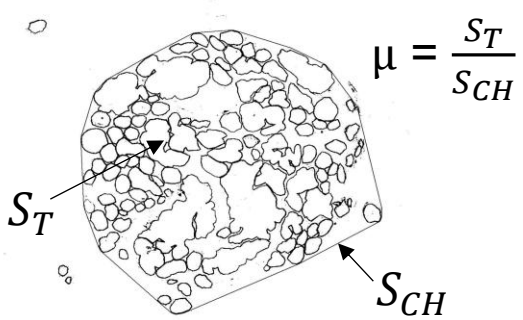

Concentric circles

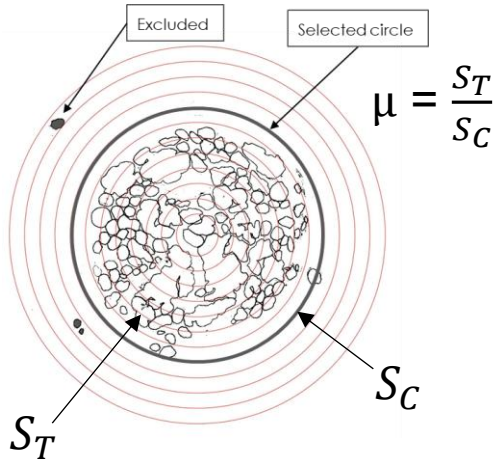

aPA6/NT

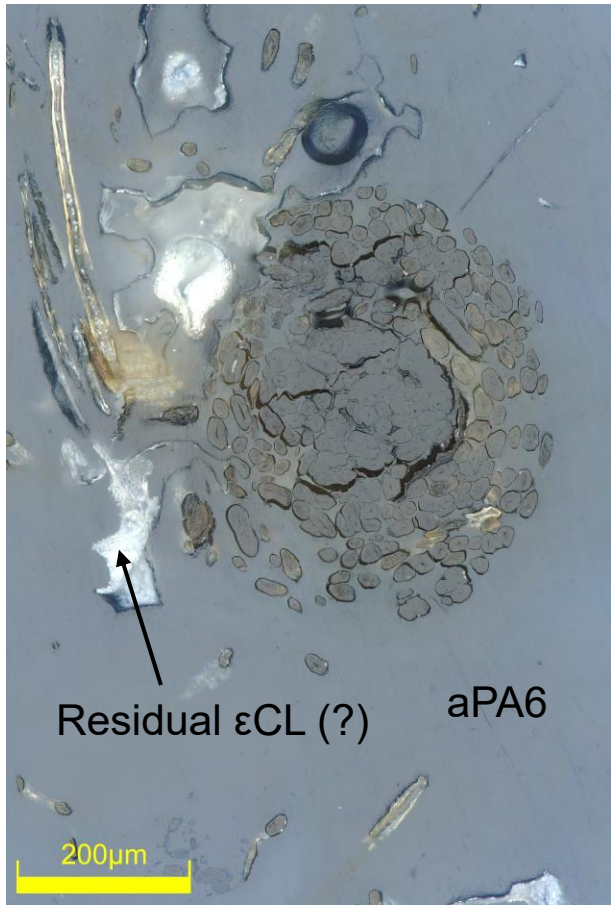

aPA6/A

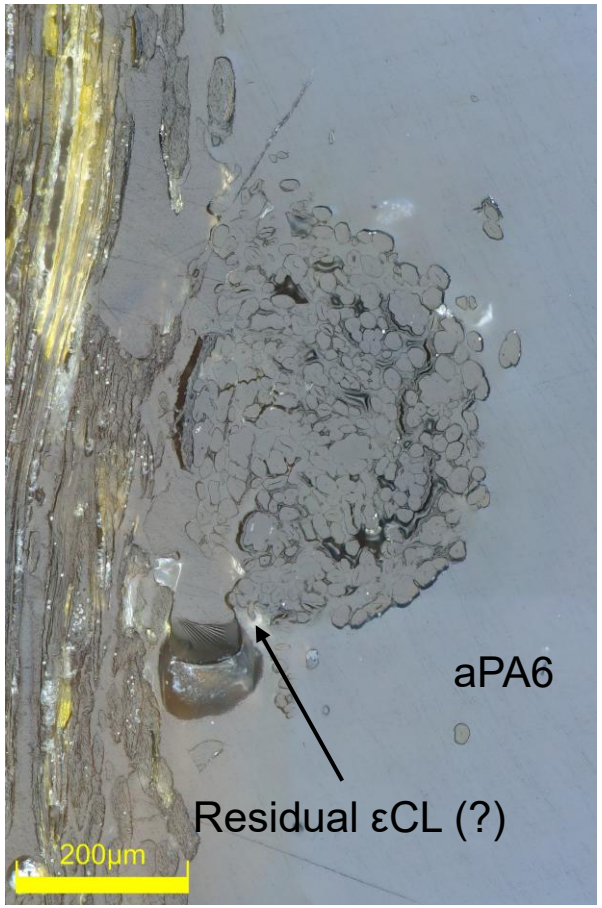

aPA6/HA

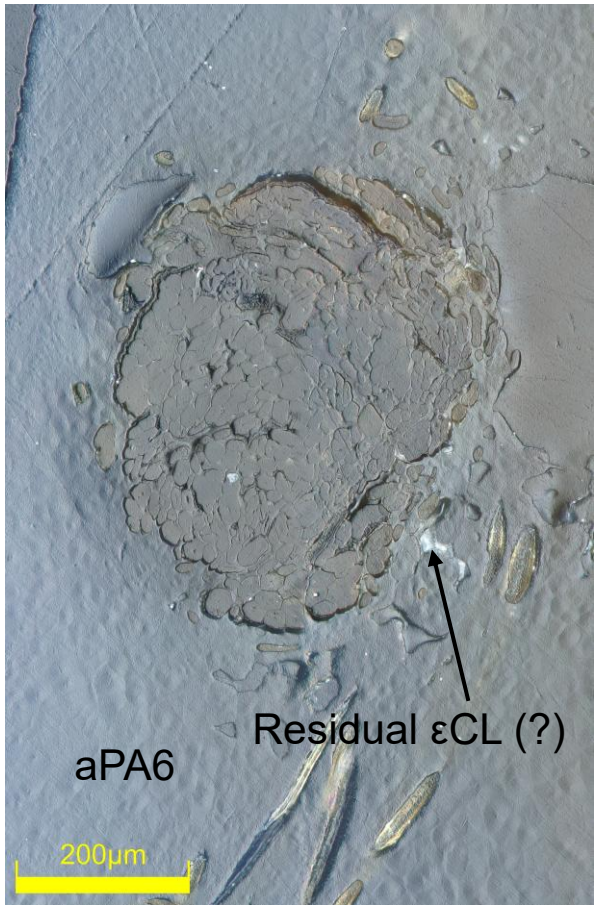

μ, convex hull method	0.62 ± 0.07	0.54 ± 0.05	0.64 ± 0.10
μ, concentric circles method	0.52 ± 0.08	0.42 ± 0.06	0.45 ± 0.07

Conclusions

- APTES silanization, especially if preceded by solvent treatment, **increases the monomer conversion, matrix penetration, interfacial adhesion and mechanical properties**
- The chosen initiator (Dilactamate) is suitable to reach **a high (89-95 %) degree of conversion** with a challenging reinforcement (moisture sensitivity of the anionic polymerization)
- The process and the surface treatment **has been proven effective** with a type of flax reinforcement (bidirectional highly twisted)

Current and future work

- Test the **impact** and **short-beam shear (SBS)** properties on the composites
- Explore **more environmentally sustainable surface treatments** (e.g., enzymatic treatment, collab. Univ. Ferrara, Italy)
- Look for **property maximization** with non-twisted UD fibers

References

[1] G. Fredi, L. Broggio, M. Valentini, M. Bortolotti, D. Rigotti, A. Dorigato, A. Pegoretti, Decoding the interplay of mold temperature and catalysts concentration on the crystallinity and mechanical properties of anionic polyamide 6: a combined experimental and statistical approach, **Polymer** 311 (2024) 127562. 10.1016/j.polymer.2024.127562

[2] S. Jalali, G. Greco, D. Rigotti, A. Dorigato, H. Mirbaha, G. Fredi, M. Bertolla, S. Guerra, T. Battistini, A. Dal Moro, A. Pegoretti, N.M. Pugno, Micromechanical Model for Single-Polymer Composites and Experimental Validation on Self-Reinforced PA6-Based Composites, **Composites Part A** 180 (2024) 108042. 10.1016/j.compositesa.2024.108042

[3] M. Valentini, O. De Almeida, M. Kakkonen, G. Kalinka, A. Dorigato, P. Kallio, G. Fredi, Effect of fiber surface state on the thermomechanical and interfacial properties of in situ polymerized polyamide 6/basalt fiber composites, **Composites Part A** 190 (2025) 108681. 10.1016/j.compositesa.2024.108681

[4] G. Cotti Comettini, M. Papparotto, A. Pegoretti, G. Fredi, Reactive processing of flax/polyamide6 laminates with different fiber surface modifications*, in preparation*

Giulia Fredi

Junior assistant professor, University of Trento (Italy)

Fulbright visiting scholar (2025), MIT AeroAstro (USA)

giulia.fredi@unitn.it

https://www.linkedin.com/in/giulia-fredi/

https://scholar.google.com/citations?user=nKeRFU0AAAAJ&hl=it&oi=ao

UNIVERSITÀ DI TRENTO Dipartimento di Ingegneria Industriale

IMT Mines Albi-Carmaux École Mines-Télécom

ICA

FIBROBOTICS

Tampere University

BAM

PON RICERCA E INNOVAZIONE

Co-funding of the FSE-REACT-EU, PON Research and Innovation 2014-2020 DM1062/2021

Leveraging in-situ anionic polymerization of polyamide 6 for high performance basalt- and flax-fiber thermoplastic laminates

Giulia Cotti Comettini[1], Martino Valentini[1], Olivier De Almeida[2], Andrea Dorigato[1], Markus Kakkonen[3], Gerhard Kalinka[4], Pasi Kallio[5], Marco Papparotto[1], Alessandro Pegoretti[1], ***Giulia Fredi[1]***

[1]University of Trento, Italy; [2]Institut Clément Ader - IMT Mines Albi, France; [3]Fibrobotics Oy, Finland; [4]BAM Federal Institute for Materials Research and Testing, Germany; [5]Tampere University, Finland

24th International Conference on Composite Materials

Baltimore (MD, USA) - August 5, 2025

giulia.fredi@unitn.it

Tensile tests on neat PA6

Instron 5969; ISO 527 1BA specimens; 10 mm/min.

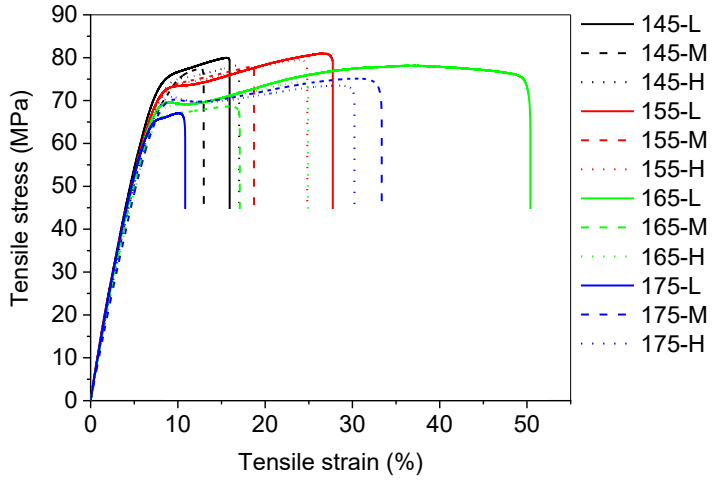

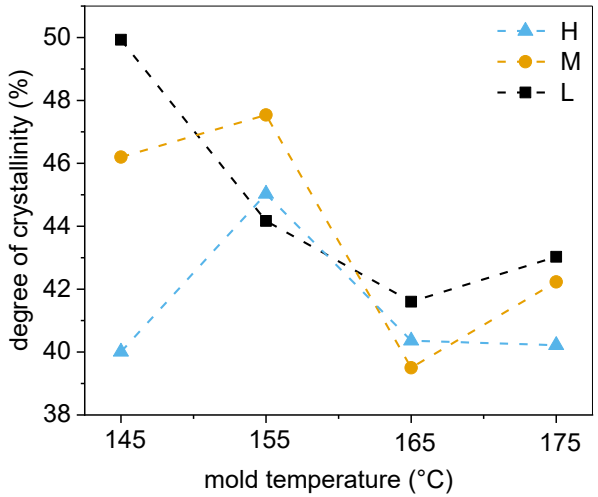

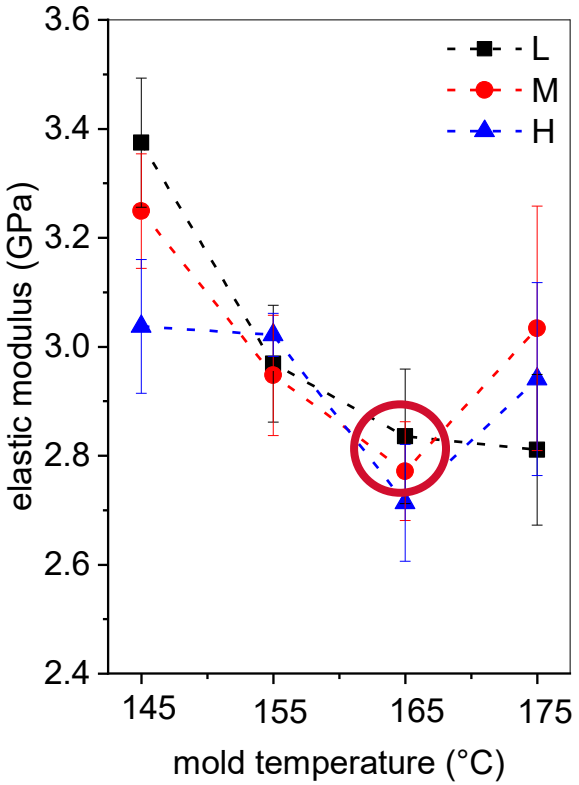

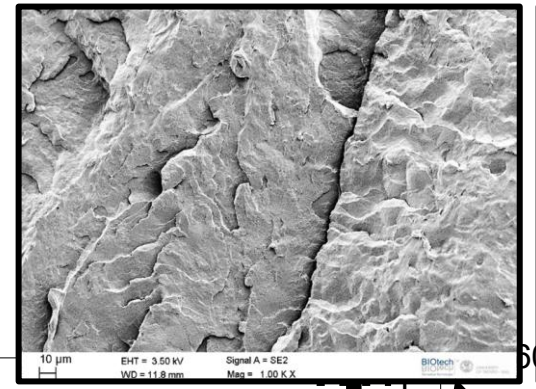

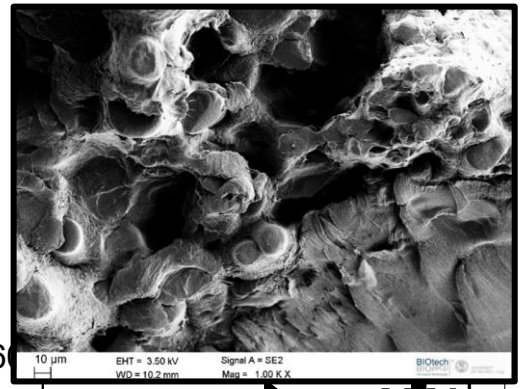

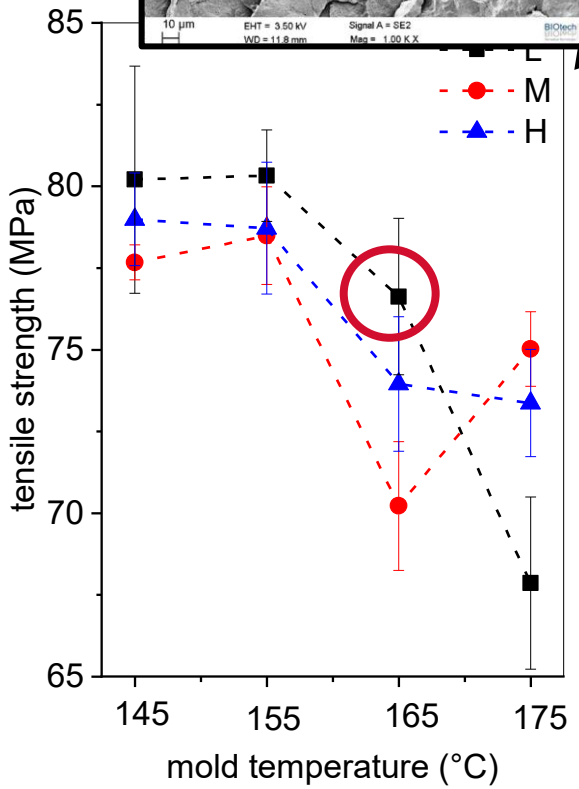

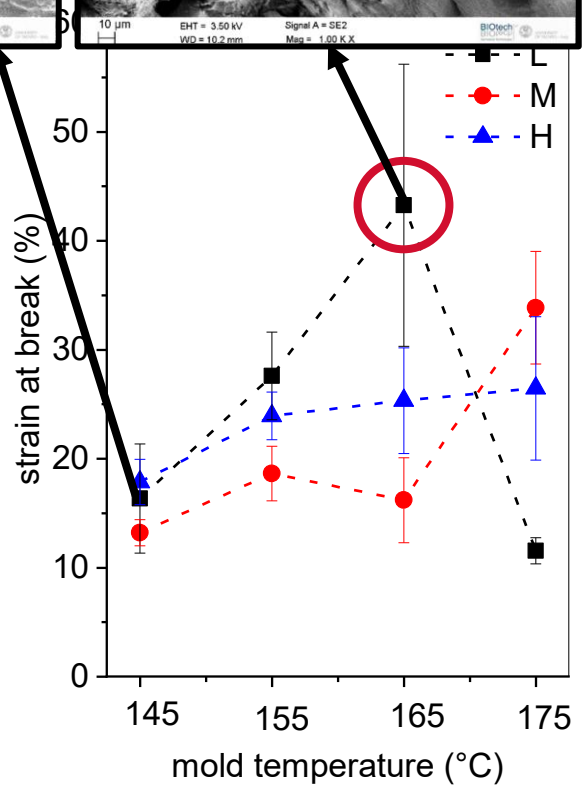

- trends of E follow the crystallinity; high ductility at intermediate temperatures
- 165-L: good compromise → **matrix for BF laminates**

Fredi et al, Polymer 2024, 311, 127562. 10.1016/j.polymer.2024.127562

ICCM24
AUGUST 4-8, 2025
BALTIMORE CONVENTION CENTER
BALTIMORE, MARYLAND, USA

No Technical Paper Submission for:

Sang-Woo Kim

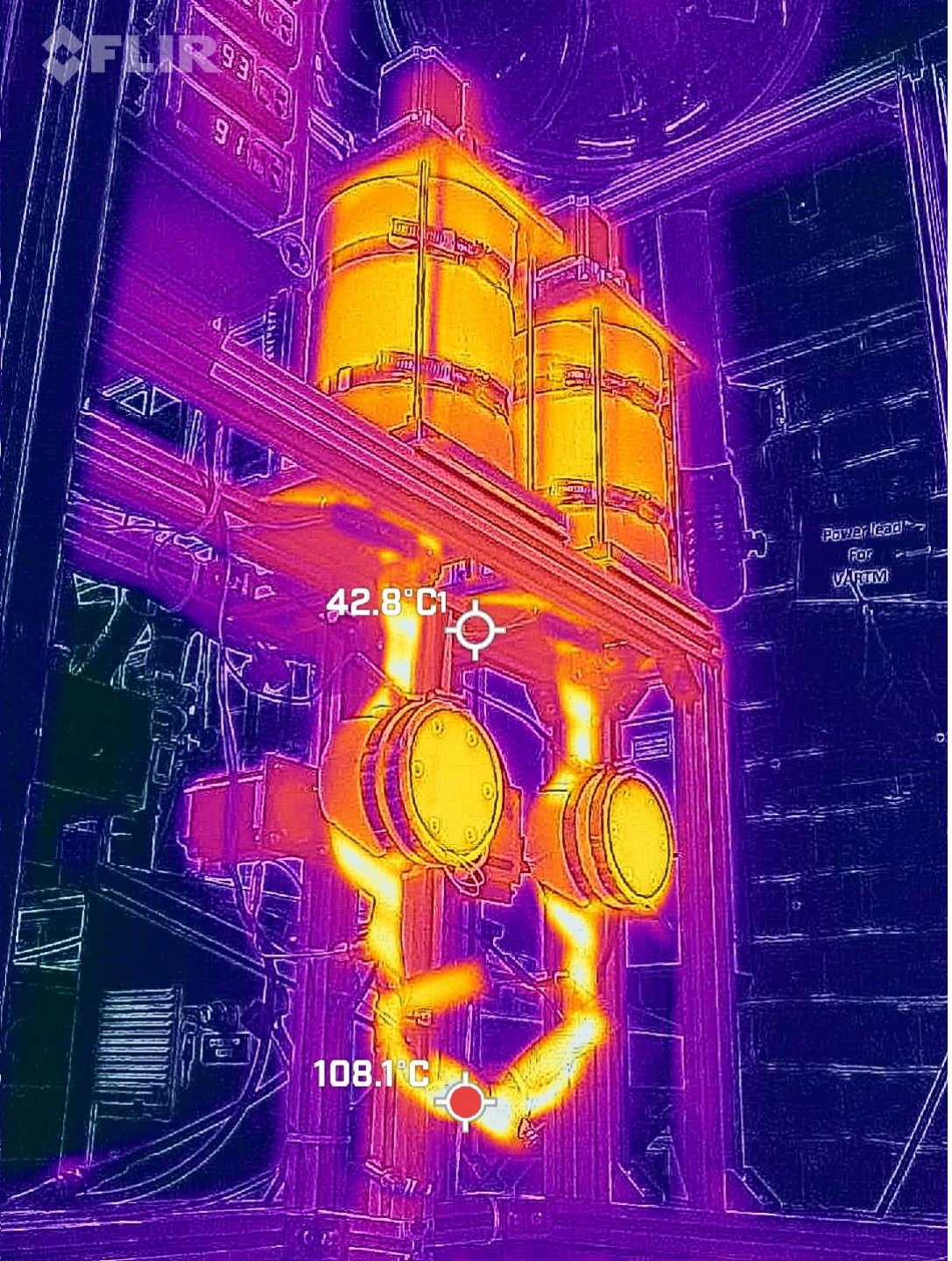

Thermoplastic Infusion, In-Situ Polymerisation (TPIIP) and Double Diaphragm Forming (DDF) for Complex Parts at Scale

Authors: G. Cerniauskas, A. Parsons, C.M. Ó Brádaigh, L. Harper, E.D. McCarthy

Affiliations: University of Edinburgh, University of Nottingham, University of Sheffield

Conference: ICCM24

Date: Tuesday, August 5, 2025

FastBlade - World's First Regenerative Fatigue Test Facility

What We Do at FastBlade:

- Specialise in accelerated fatigue testing for tidal turbine blades
- Use advanced technology to simulate real-world conditions



- Develop novel tidal turbine blades and marine structures
- Aim to improve durability and performance of structures
- Collaborate on projects in renewable energy, aerospace, and other industries
- Work towards developing standards for the tidal sector

FastBlade - World's First Regenerative Fatigue Test Facility

THE UNIVERSITY of EDINBURGH

FASTBLADE

UKRI Engineering and Physical Sciences Research Council

Research projects:

- **MaxBlade** - Maximising tidal energy generation through blade scaling & advanced digital engineering

MAX BLADE

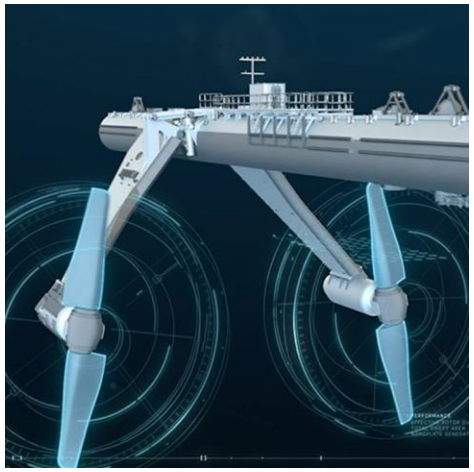



- **CoTide** - Developing and demonstrating holistic integrated tools and design processes for tidal stream energy

CoTide

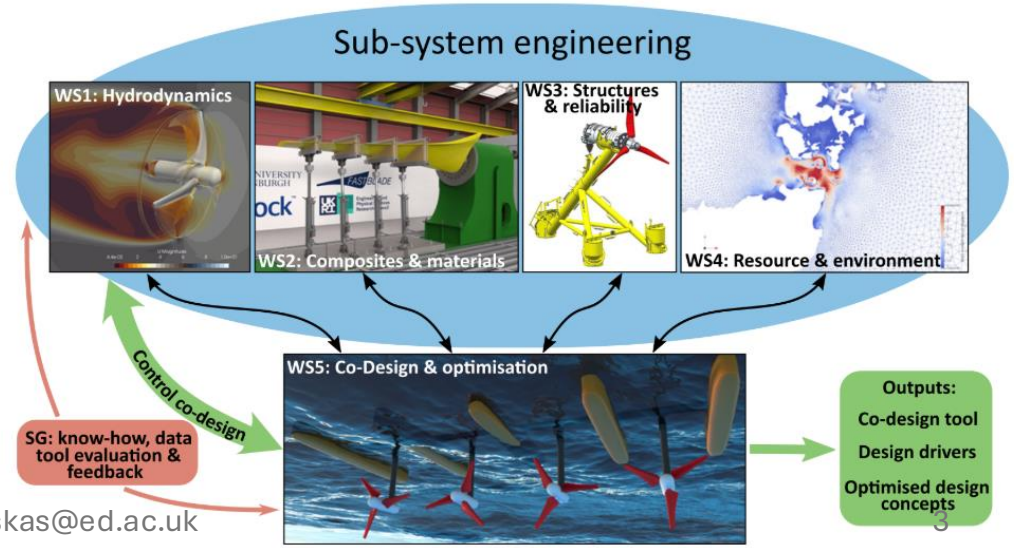

Thermoplastic Infusion, In-Situ Polymerisation (TPIIP) and Double Diaphragm Forming (DDF) for Complex Parts at Scale

Fibre Reinforced Thermoplastic Composites (TPC):

- Favoured for recyclability over landfill or pyrolysis
- Enables development of secondary markets

Importance:

- Growing demand across sectors like renewable energy, automotive, and aerospace.

Benefits:

- Welding
- Thermoforming
- Recyclability

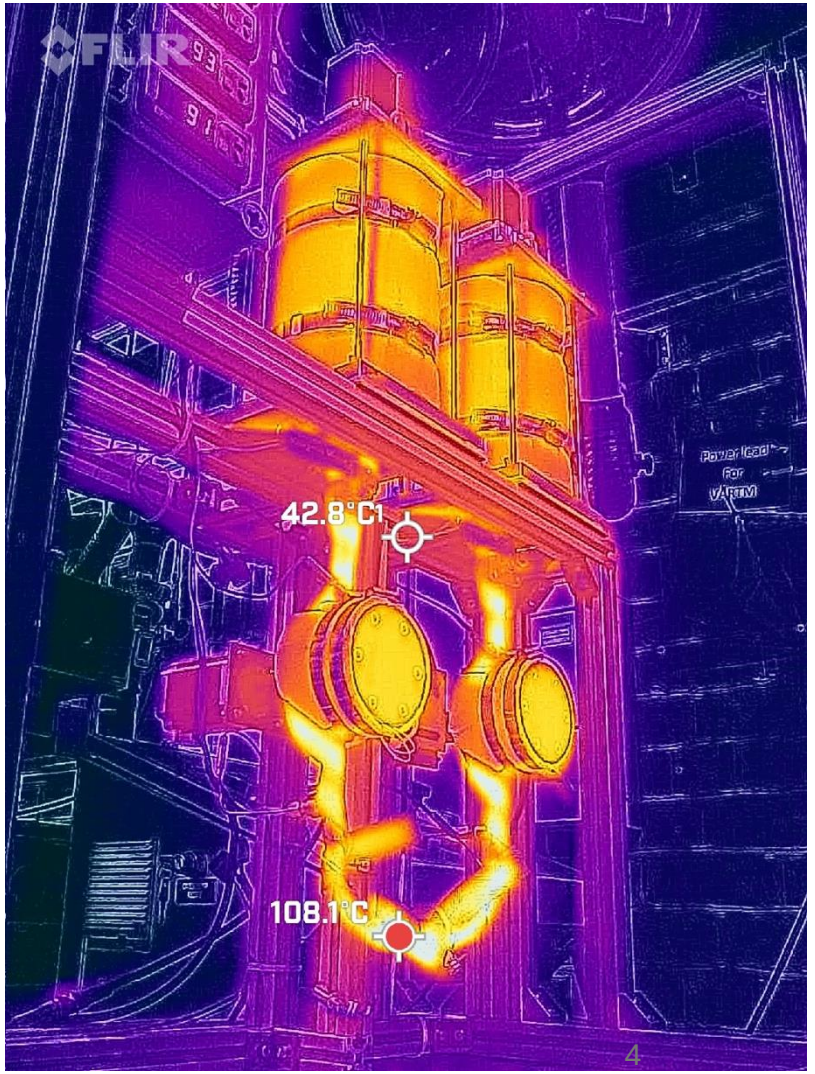

Objectives and Significance

Objective: Address barriers to adopting reactive thermoplastic resin transfer moulding (RTM) for glass fibre reinforced polyamide 6 composites.

Significance:

- Enables research and smaller-scale production using polyamide-6 (nylon-6) thermoplastic systems through reduced equipment costs
- Industrial-scale machines of a similar type are prohibitively expensive
- Offers insights into high-quality composite manufacturing and improved mechanical properties

Industrial scale



Tabletop size

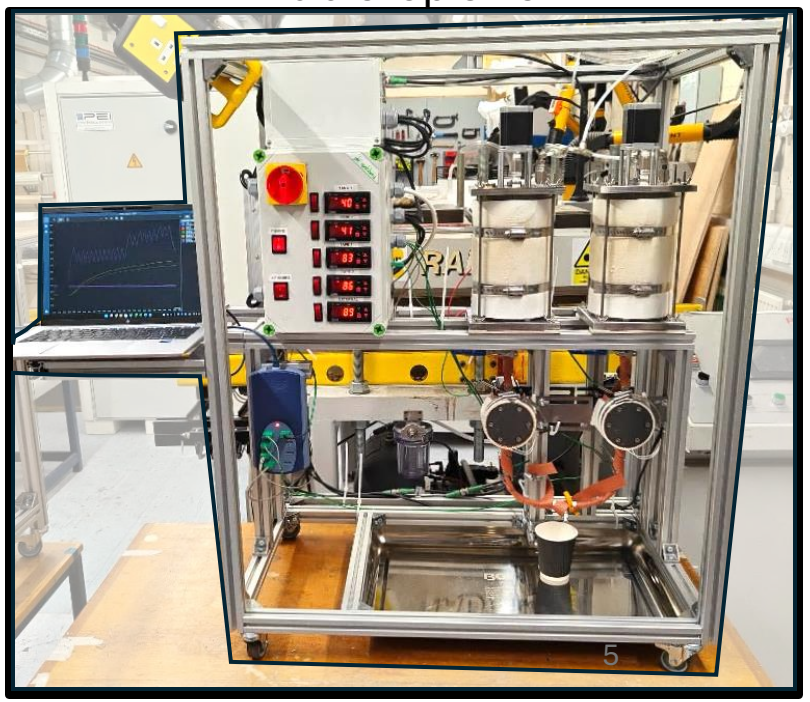

Methodology Overview

Materials Used:

- Monomer: ε-caprolactam
- Catalyst: Sodium caprolactamate
- Initiator: Hexamethylene-1,6-dicarbamoylcaprolactam
- Reinforcement: Polyester stitched UD glass fibre NCF

Equipment:

- Custom TP-RTM machine with heated tanks, gear pumps, and a static mixing head.
- Pneumatic press and aluminium mould for composite formation.

Process:

- Components heated and injected under low pressure.
- Polymerisation occurs in situ, forming the composite.

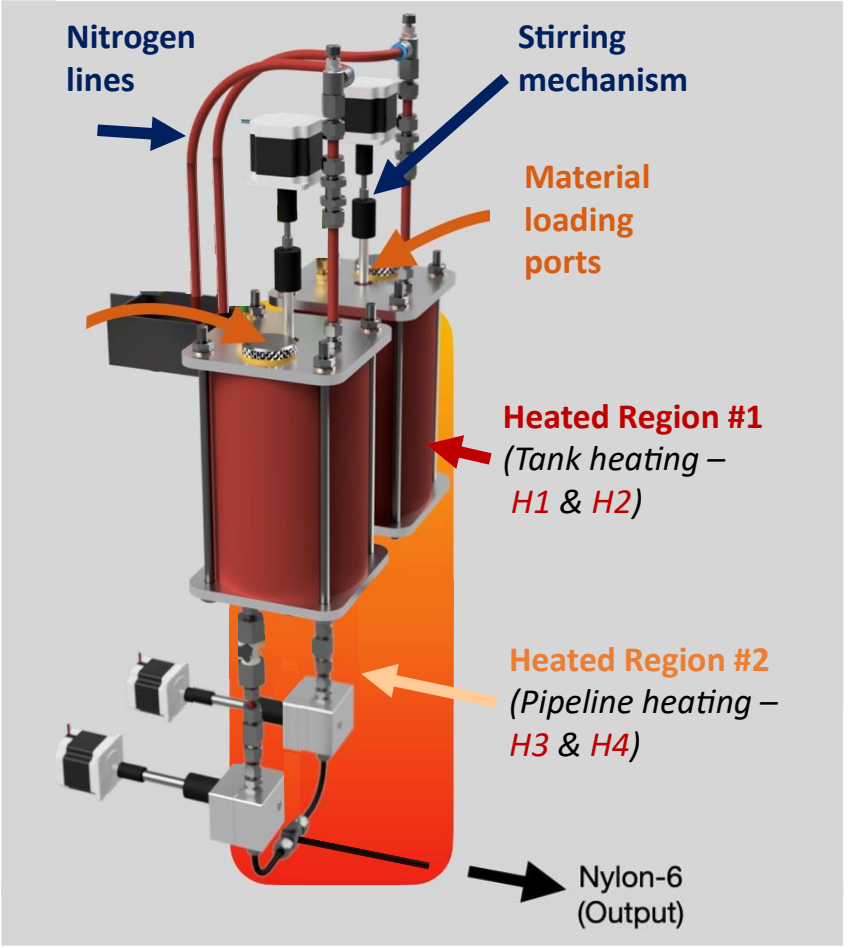

Manufacturing Process

Steps:

- Preparation: Drying of glass fibre fabric under vacuum.
- Injection: Low-viscosity monomers injected into the mould.
- Polymerisation: In-situ reaction forming polyamide 6 matrix.
- Cooling and Demoulding: Controlled cooling to ensure part quality.

Key Parameters:

- Injection pressure significantly lower than thermoset RTM.
- Temperature control critical for polymerisation and void reduction.

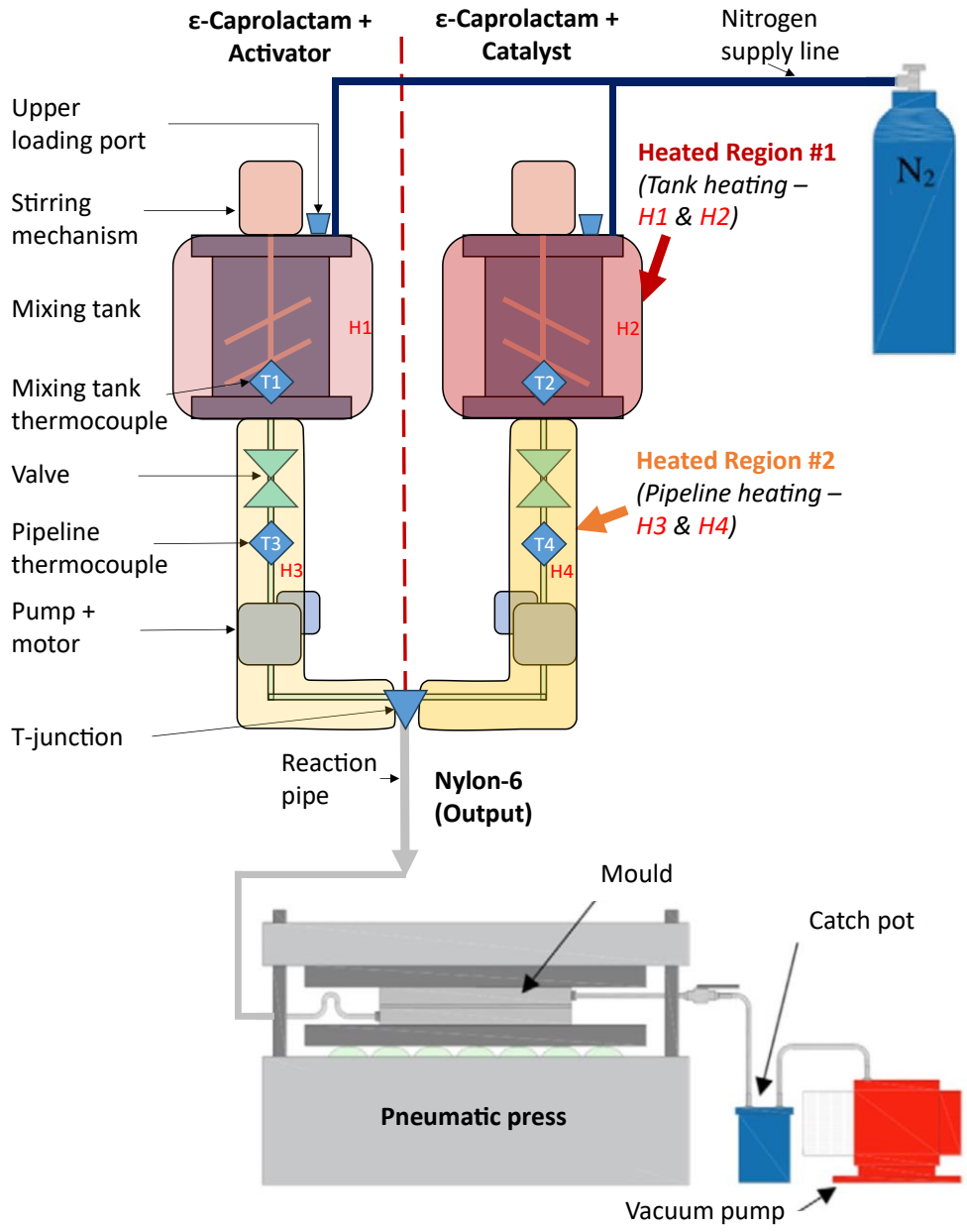

Polymerization and Manufacturing Process Overview

- After vacuum infusion, the reactant mixture polymerizes at 140–160 °C
- Benchmarked against Johns Manville's organosheet
- Successful infusion led to a manufacturing process using hot press tooling, demonstrating forming capabilities
- The "fill then form" process ensures even permeability before shaping, with polymerization below the 215 °C melt point allowing isothermal tool moulding

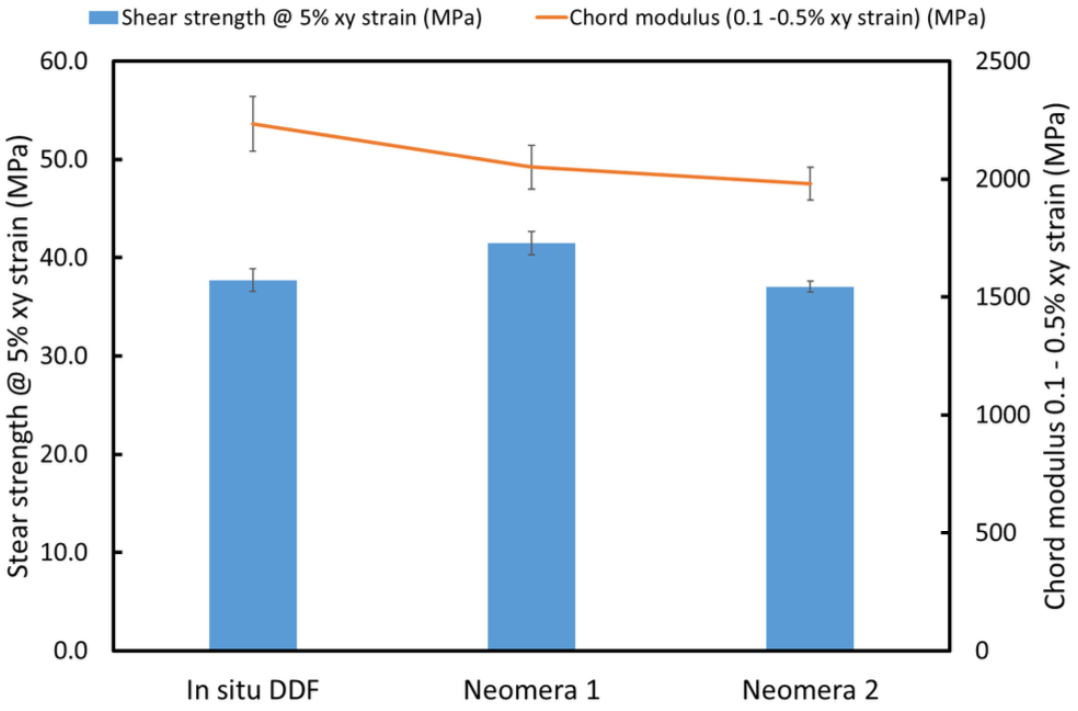

Figure 3: Results for in-plane shear testing comparing a flat panel produced using vacuum infusion between double diaphragms with two commercial organosheet panels (J. J. Murray *et al.*, Materials & Design, 2020).

Increasing TRL levels

- Constantly increasing TRL levels
- Equipment version progression

- Research collaborators
- Industry partners

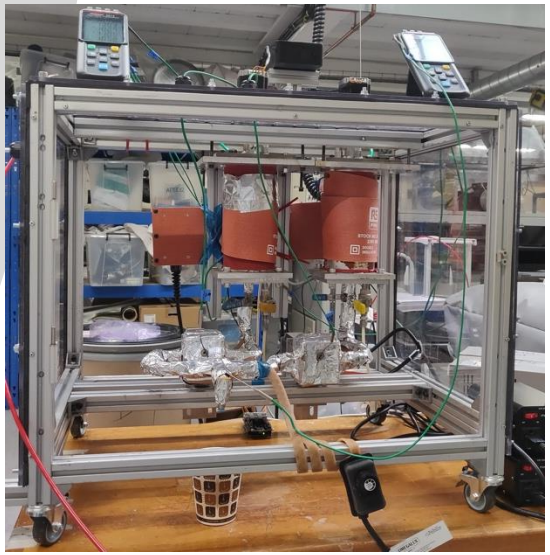

V1

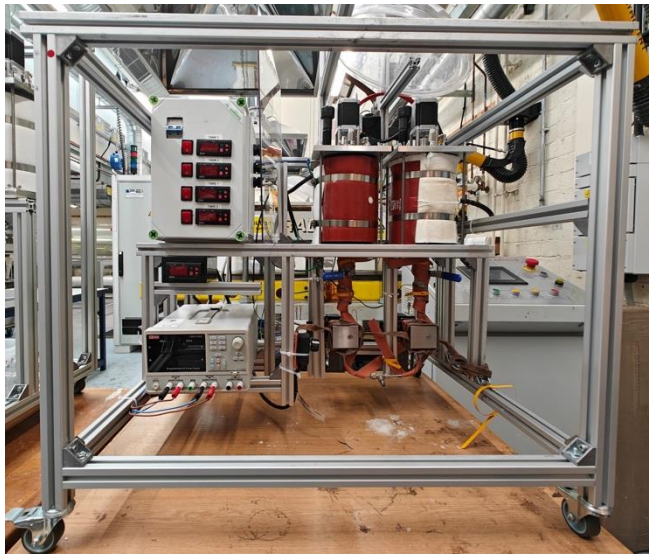

V2

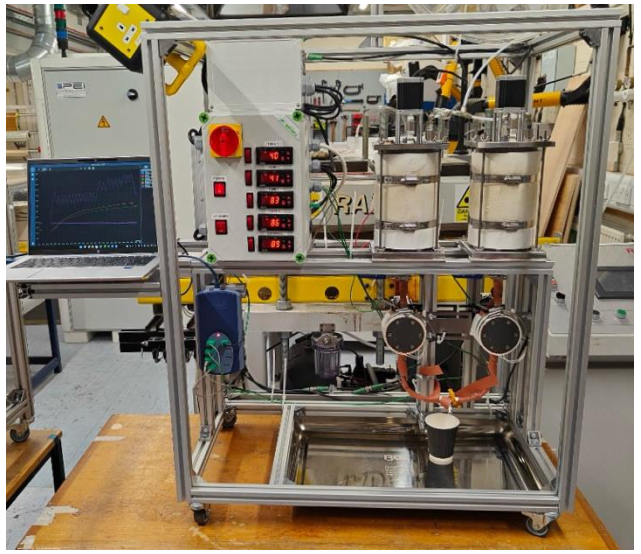

V3



V4

Benefits of DDF Process Variations

Dr Andrew Parsons - UoN

- Process Variations:
  - Immediate Part Formation:
    - Uses two tough, stretchable polymeric films.
    - Forms liquid thermoplastic composite blank before final polymerisation.
  - Flat Pre-Polymer Blank Production:
    - Creates a semi-polymerised oligomer resin system.
    - Can be reheated, formed, and polymerised in a press, stabilized against moisture.



Three-part frame with central vacuum channel

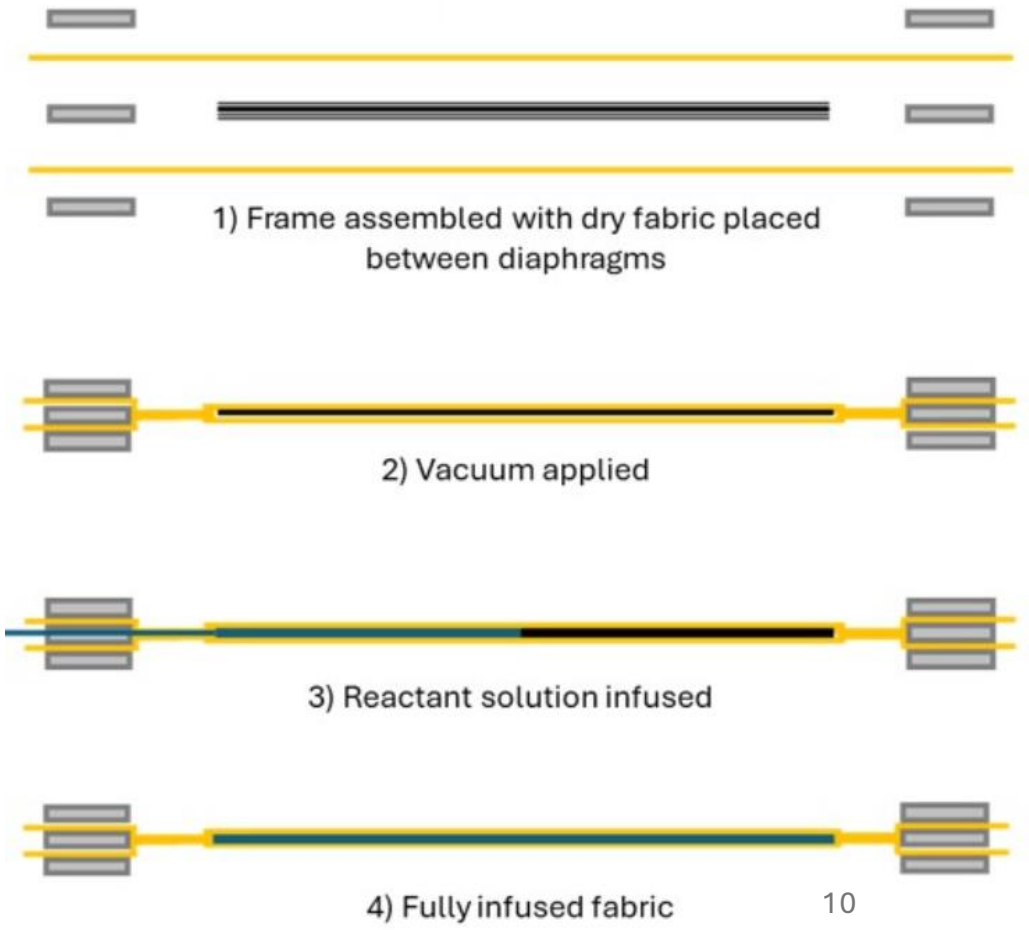

Benefits of DDF Process Variations

Dr Andrew Parsons - UoN

- Advantages and Efficiency:
  - Reduces metal tooling needs, leading to significant capital savings despite a slight increase in bagging consumables.
  - Fill-Form Process Sequence:
    - Lubricates fabric during forming.
    - Immediate forming follows infusion, reducing part wrinkling.

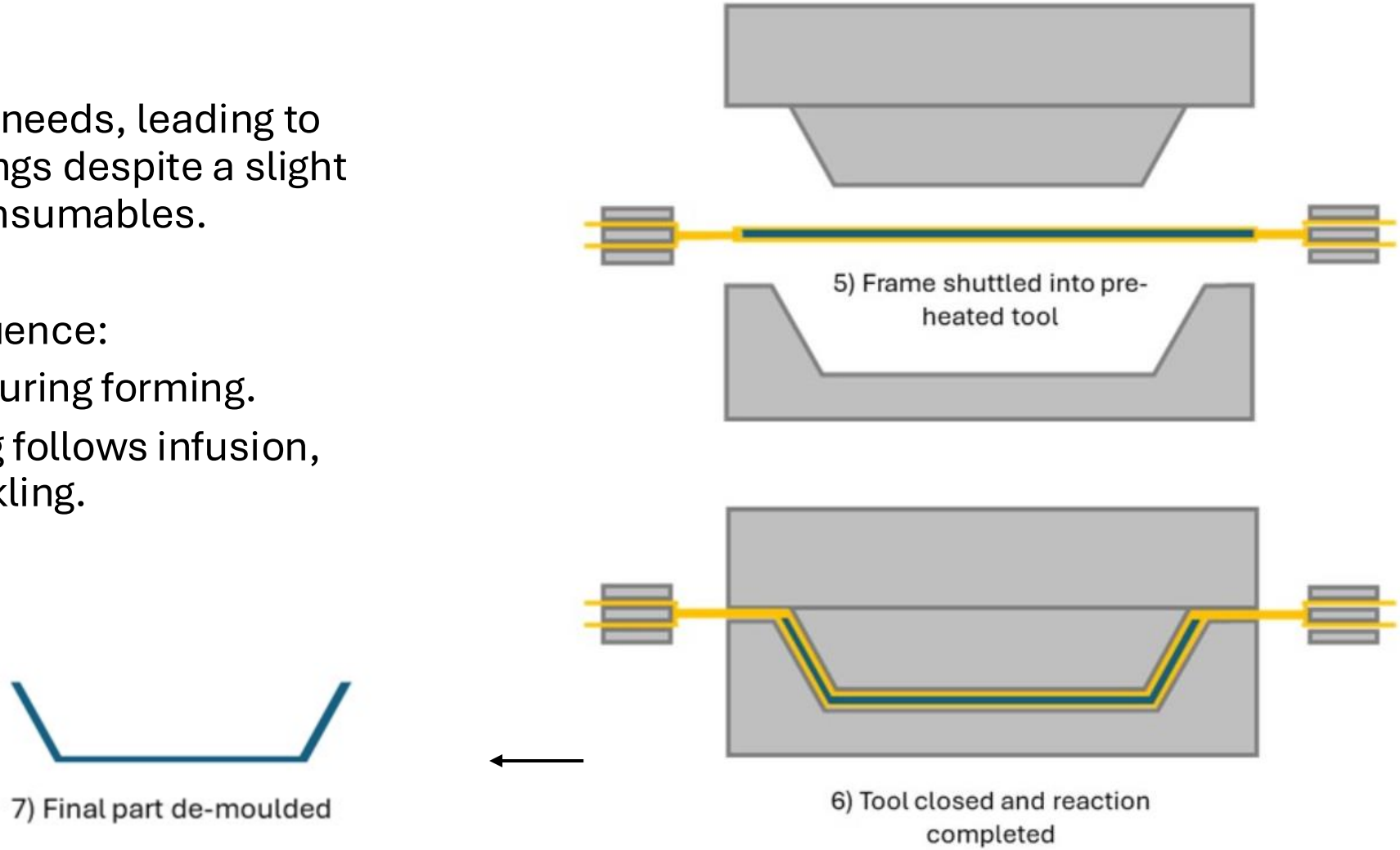

DDF Process: Current work and Challenges

Dr Andrew Parsons - UoN

- Process is temperature limited by available materials.
- Only Dahlar 9300Y, a high elongation fluoropolymer, meets mechanical and chemical demands.
- Bag strength is affected by temperature, risking pin-holing in high strain areas.
- Process is limited to a 145 °C ceiling for the tea tray tool.

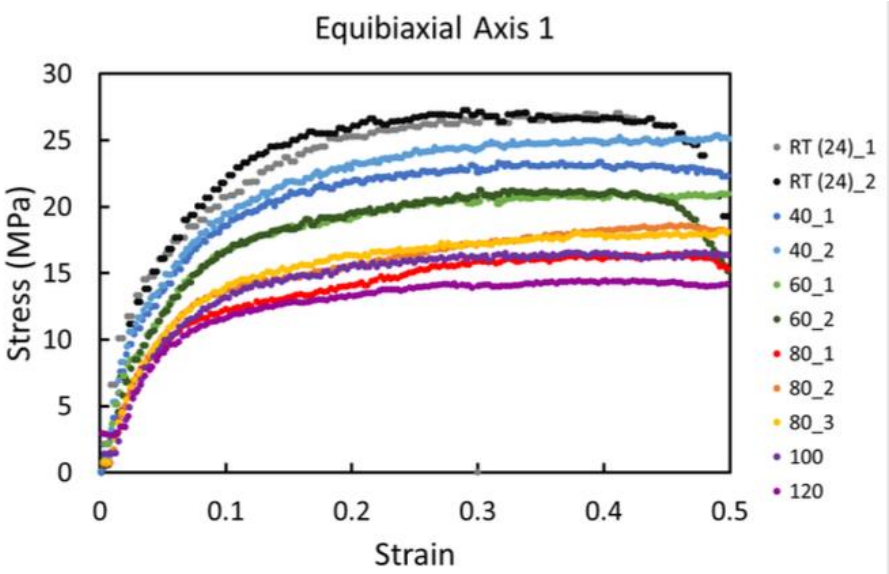

Figure 1: Temperature dependence of bagging in equibiaxial testing results.



Figure 2: Pin-holing observed at regions of high strain.

Summary: custom TP-RTM machine and the developed process

- Enables research which would not otherwise be possible due to high entry and operational costs
- Allows development work in thermoplastic (PA6), composite and other hybrid systems
- Project benefits from multidisciplinary expertise from a range of industrial partners and research institutions
- Happy to collaborate and develop custom solutions



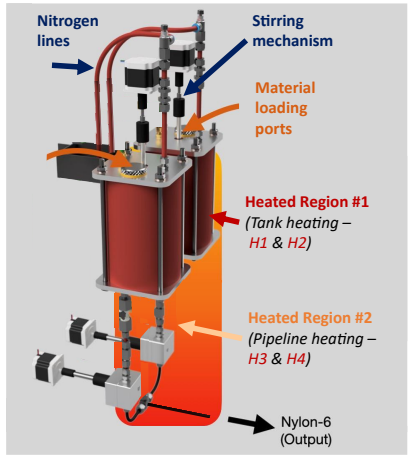

Tabletop size

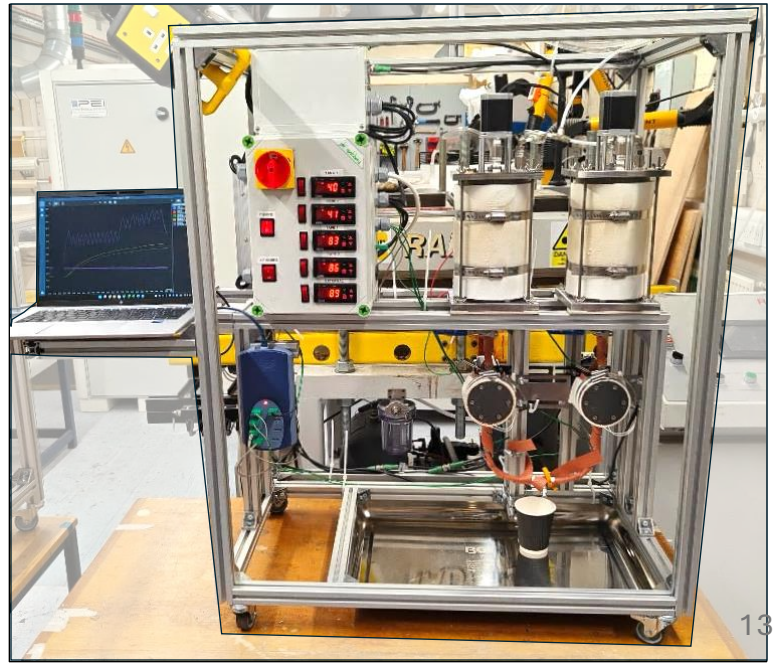

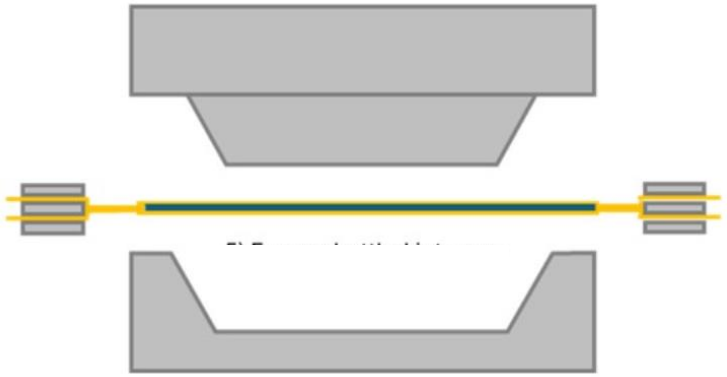

Thank you!

Importance of Shearing Deformation in Dynamical Mechanical Tests for Viscoelastic Properties of Continuous Fiber Thermoplastic Composites

R. Byron Pipes[1], Kwanchai Chinwicharnam[1,2] and Eduardo Barocio[1,3]
[1] Composites Manufacturing Simulation Center
bpipes@purdue.edu
[2] School of Aeronautics and Astronautics
kchinwic@purdue.edu
[3] School of Mechanical Engineering
ebarocio@purdue.edu
Purdue University
1105 Endurance Drive
West Lafayette, IN 47906

Keywords: flexural tests, Timoshenko beam theory, relaxation data, temperature

Abstract

The importance of shearing deformation when utilizing flexural tests to determine the relaxation properties of CF/PEKK [1] composites as a function of temperature is discussed in the context of Timoshenko beam theory with the goal of understanding differences between the 0-degree and 90-degree test results. Relaxation data are presented for relaxation moduli developed with the conventional dynamical mechanical test system. The range in temperature examined was 30 – 350 ^{0}C.

1 INTRODUCTION

The use of the three-point bending test to develop quasi-static and viscoelastic stress relaxation properties of polymers is well documented in the literature [2-3]. Furthermore, dynamic mechanical analysis (DMA) test facilities required to carry out these experiments as a function of temperature typically utilize property characteristics restricted to isotropic materials when converting imposed flexural deformation or force to determine the flexural stress within the test specimen. Of course, the correct relationship between applied deflection and the resulting stresses in the specimen for both orthotropic and isotropic systems is well known as Timoshenko beam theory [4].

$$\delta_T = \frac{PL^3}{48EI} + \frac{PL}{4k_s GA} \tag{1}$$

Where E and G are the appropriate Young's and shearing moduli of the orthotropic or isotropic medium for the 0-degree test geometry. In the present case, the two test geometries are in the 1-3 plane (0-degree test) and 2-3 plane (90-degree test) planes, where the fiber direction is 1, and the thickness direction is 3. The properties in equation (1) for the 0-degree specimen are thereby, E_{11} and G_{13}. For the 90-degree test, the Young's modulus is E_{22} and the shearing modulus, G_{23}. The other variables in equation (1) are the applied central load, P, the specimen span, L, the beam moment of inertia, I, cross-sectional area, A, and shear correction factor, k_s. Flexural stress calculation as a function of the applied load, P is identical for both beams of isotropic and orthotropic media.

The flexural test is typically used with confidence in prediction of Young's modulus for isotropic materials systems. However, for highly orthotropic materials this approach can produce misleading results, as discussed in reference [3]. Table 1 illustrates the conventional approach in utilizing only the first term of equation (1) to predict Young's modulus for a CF/PEKK composite. As discussed in reference [3], the modulus data developed within the Q800 DMA System of TA Instruments and utilized in the present study can yield moduli data for thin specimens that can be as much as 10-20 Percent in error.

2 APPARENT REDUCTION IN YOUNG'S MODULUS, E_{11}

The E_{11} modulus experimental data for the 0-degree flexure test are shown in Table 1. Furthermore, the data sheet of reference [1] shows the tensile and compressive moduli of the composite to be 139.0 GPa and 127.0 GPa, respectively. Thus, the ambient test results of 126. 42 GPa is only 5 percent less than the average of tensile and compressive modulus values reported in reference [1].

Temp. ^{0}C	30	120	150	180	210	240	270	300	330
E_{11}, GPa	126.42	130.89	128.27	120.40	115.30	107.55	99.29	80.61	18.05

Table 1 Values of E_{11} determined from deflection, δ and force, P utilizing classical beam theory (only first term in equation (1))

The data in Table 1 imply that the Young's modulus, E_{11}, is reduced from 126.42 GPa at 30 ^{0}C to 18.05 GPa at 330 ^{0}C. Yet the modulus of carbon fiber does not change over this temperature range and the contribution of the matrix phase to the composite tensile modulus is of second-order. Hence, it must be concluded that utilizing the conventional approach to determine E_{11} temperature dependence of the CF/PEKK composite will not yield the desired results. The following discussion explores the causes for this inconsistency.

3 RELATIVE SHEARING DEFORMATION TO FLEXURAL DEFORMATION

Equation (1) illustrates the relationship between the total beam central deflection, δ_T and that due to both the flexural stress, δ_f and to the shearing stress, δ_s. The constant, k_s is an area correction factor, typically taken as 5/6 for beams of rectangular cross-section. The important message of equation (1) is that both flexural stress and shearing stress contribute to the beam deflection and that their relative contributions can be measured by the ratio of the two terms, as shown in equation (2). Furthermore, the ratio of the Young's modulus to the shearing modulus and the square of the ratio of the beam height to beam span are shown to determine the relative contributions of the two deformation modes.

$$\frac{\delta_s}{\delta_f} = \left(\frac{1}{k_s}\right)\left(\frac{E_{11}}{G_{13}}\right)\left(\frac{h}{L}\right)^2 \tag{2}$$

Equation (2) can be utilized to determine the beam aspect ratio (L/h) that minimizes the influence of shearing deformation upon beam deflection, but its use requires knowledge of both the material

shearing modulus and Young's modulus. For isotropic materials, the shearing modulus and Young's modulus are related by the Poisson's ratio, ν.

$$\frac{\delta_s}{\delta_f} = \frac{12(1+\nu)}{5}\left(\frac{h}{L}\right)^2 \approx 3\left(\frac{h}{L}\right)^2 \tag{3}$$

Thus, for isotropic materials in bending, the ratio of the shearing to flexural displacements is less than 0.002 for L/h = 45, (ν = 0.3). In the present study, the DMA span was set at L = 50 mm and for the beam height of 1.08 mm, the ratio was 0.001. This ratio is clearly acceptable for isotropic systems, but this may not be the case for orthotropic materials where the ratio of Young's modulus to shearing modulus can be quite large.

4 FLEXURAL TESTS FOR VISCOELASTIC RELAXATION

Dynamic mechanical analysis (DMA) test facilities are often utilized to measure viscoelastic stress relaxation of composite materials such as CF/PEKK. A typical DMA test facility is shown in Figure 1 where the load or displacement control actuator and the pin supports are shown. The beam loading condition in Figure 1 is for three-point bending. The span length shown is 50 mm, but the apparatus can be adjusted for span length of 25 mm, as well.

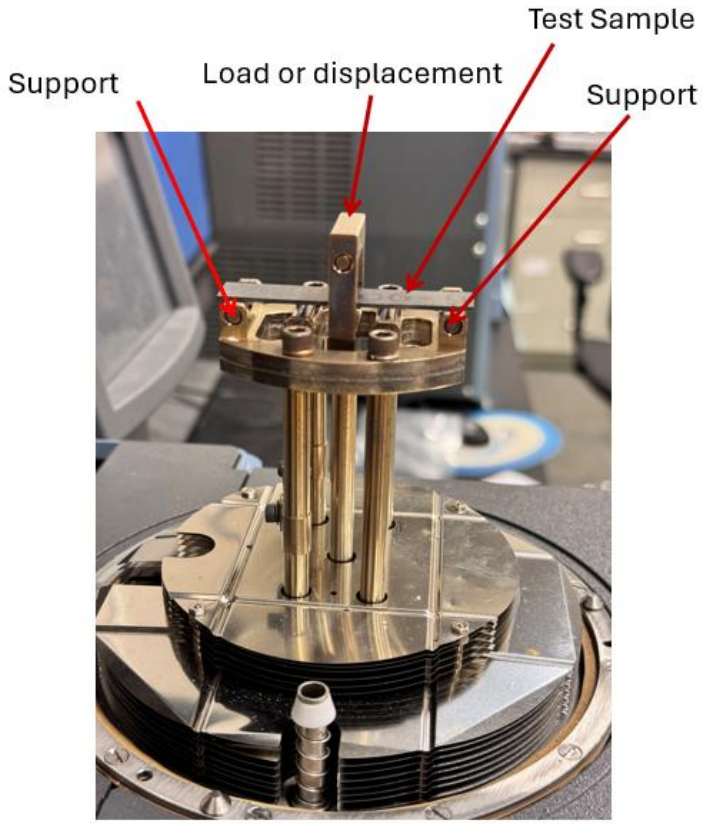

Figure1. Conventional DMA Test Facility for Three-point Flexure Tests

The DMA test facility allows for control of the time-temperature history of the test sample for harmonic or creep/relaxation loading conditions. Stress relaxation experiments are carried out by imposing a specified deflection at the mid-span of the beam and monitoring the reduction in the applied force with time. For isotropic materials, the relationship between beam deflection and flexural stress, utilizing Euler-Bernoulli beam theory, is well known and is correct for these materials for $L/h \geq 45$. However, as shown in the previous section, this is not true for highly orthotropic materials such as CF/PEKK in the 0-degree test geometry. Thus, issues with the role of shearing deformation in flexural testing under multiple temperature conditions are also present for viscoelastic stress relaxation. Furthermore, the relationship between total beam deflection and force involves both flexural and shearing deformation components in the viscoelastic case, just as it does in quasi-static testing.

The viscoelastic experimental results for the 0-degree composite beam composed of CF/PEKK is shown in Figure 2. The data presented in Figure 2 were determined by the conventional DMA system wherein a constant central displacement of 0.193 mm was imposed and the decay in force with time was recorded as a function of temperature.

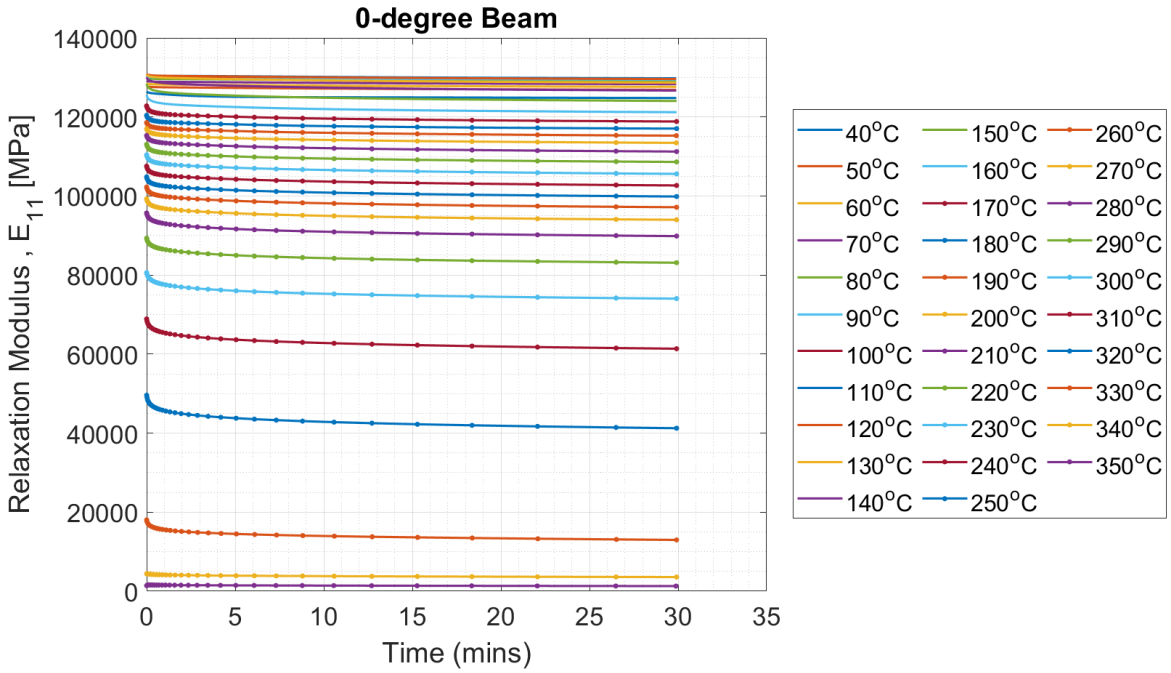

Figure 2. Apparent relaxation data for the 0-degree CF/PEKK composite beam in three-point bending

The dilemma presented in the foregoing discussion is that to separate the contributions of flexural and shearing deformations to determine beam total deformation requires knowledge of the very property that the test is designed to determine, namely E_{11} and G_{13}. Thus, a strategy must be

developed to quantify the relative contributions of the two deformation modes over the temperature range of interest. For the 0-degree specimen, test temperature provides the vehicle for this separation because the deformation due to shearing stress shows significant change with temperature, while the deformation due to flexural stress does not. This characteristic of the 0-degree specimen was illustrated earlier through equation (2). In Timoshenko beam theory [4], the two deformation modes are coupled in series and both support the same applied load, P, while contributing individually to the total deflection, δ_T. If the Young's modulus, E_{11} is taken as equal to the value measured at instantaneous, ambient conditions and to be independent of temperature, then deformation due to the flexural normal stress, δ_f can be calculated using Euler-Bernoulli beam theory (first term in equation 1) and subtracted from the total deflection to determine the deflection due to the shearing stress, δ_s.

Test data from the DMA in Figure 3 shows 90-degree modulus relaxation data taken for a CF/PEKK composite subjected to three-point bending of the 90-degree specimen over the temperature range of 40 ^{0}C to 300 ^{0}C. Hexagonal symmetry at the microscopic scale of the CF/PEKK implies that the 2-3 plane is a plane of transvers isotropy. Thus, the 90-degree flexure specimen satisfies minimization of the shearing contribution to lateral deflection at a specimen length to height ratio of 45. These results show that the relaxation modulus exhibits significant dependence upon temperature, falling from 9034 MPa at 30^{0}C to 273 MPa at 300 ^{0}C. Furthermore, significant relaxation in stress occurs in the first minute after application of the applied displacement.

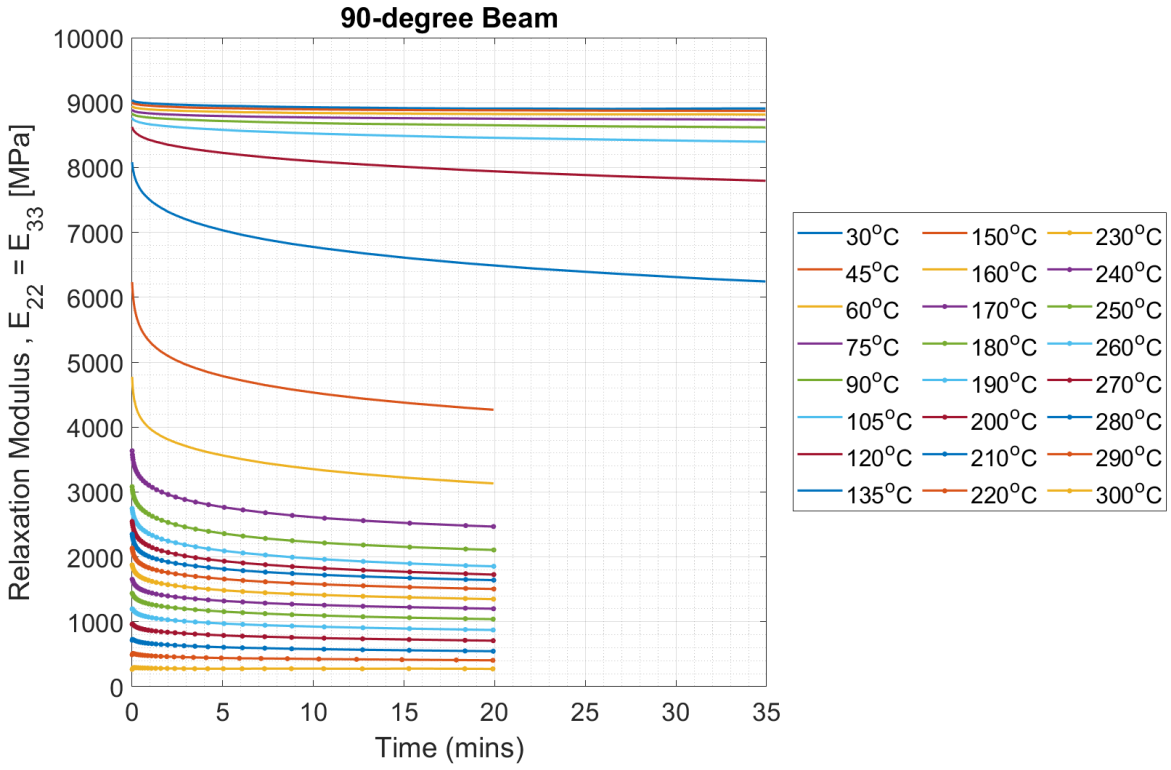

Figure 3 Relaxation of the transverse modulus, E_{22} from 30^{0}C to 300 ^{0}C

Given that the polymer matrix relaxation is largely responsible for relaxation of all matrix-dominated properties of the composite, the composite shearing modulus, G_{13} should exhibit quite similar behavior to E_{22}. Thereby, the authors chose to derive the relaxation properties in shear from the 90-degree data by fitting the form of the 90-degree relaxation data to the t = 0, T = 30 ^{0}C value for shearing modulus (5297 MPa) reported in the literature [5]. The resulting shearing modulus relaxation data for G_{13} are shown in Figure 4 where the primary relaxation occurs in the first 5 minutes at T $\geq$ 240 ^{0}C.

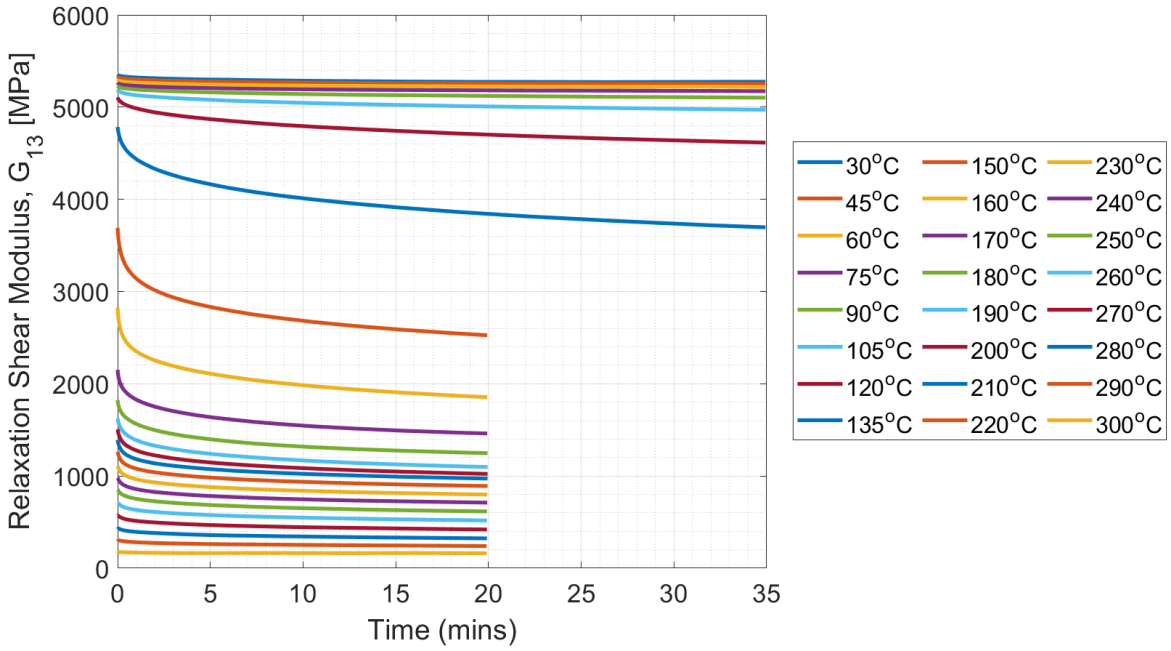

Figure 4 Relaxation data for the transverse shearing modulus, G_{13}

5 SHEAR MODULUS RELAXATION

Data for G_{13} presented in Table 2 were derived from the instantaneous values of the shearing modulus as a function of temperature shown in Figure 4. Experimental results and predictions (Equation 1) of the magnitude of the quasi-static, central force, P in three-point bending in the DMA Test system are presented for multiple temperatures and for a fixed displacement of 0.193 mm. The test specimen geometry was L = 50 mm, h = 1.08 mm and specimen width of 12.48 mm. If the Young's modulus, E_{11} is held constant at 126.42 GPa for the calculations and the shearing modulus is varied from 5297 MPa to 158 MPa, it is informative to examine the predicted force required to sustain the 0.193 mm in deflection as shown in Table 2. The close agreement between predictions and experiments for the magnitude of the force required to produce a deflection of 0.193 mm shows that the dominant contribution to the observed apparent relaxation of E_{11}, is actually due to relaxation of G_{13} and not relaxation of E_{11}.

^{0}C	G_{13}, GPa	E_{11}, GPa	$P^{Predicted}$, N	$P^{Experimental}$, N
60	5.297	126.42	12.11	12.58
90	5.232	126.42	12.11	12.75
120	5.106	126.42	12.11	12.81
150	3.691	126.42	12.04	12.57
160	2.827	126.42	11.97	12.30
170	2.151	126.42	11.88	12.02
180	1.824	126.42	11.82	11.79
190	1.625	126.42	11.76	11.61
200	1.507	126.42	11.72	11.46
230	1.110	126.42	11.54	10.82
240	0.980	126.42	11.45	10.55
250	0.852	126.42	11.33	10.28
260	0.708	126.42	11.16	10.03
270	0.569	126.42	10.92	9.75
280	0.425	126.42	10.52	9.40
290	0.293	126.42	9.89	8.78
300	0.158	126.42	8.48	7.94

Table 2 Predicted and experimental central force, P for three-point bending of the 0-degree test geometry at temperatures ranging from 60 – 300 ^{0}C for CF/PEKK composite

These results show that while the influence of temperature on deflection of the 0-degree beam would typically be expected to be due to a reduction of the Young's modulus, E_{11}, with temperature, the predictions of the force were carried out with equation (1) wherein E_{11} was held constant at 126.42 GPa. With temperature dependence of the shearing modulus, G_{13} utilized in the force predictions, good agreement between predicted force and observed force was demonstrated. This approach is counter to conventional interpretation of the use of the flexure test as a method to determine the temperature dependence of the Young's modulus. However, the general agreement between the predictions and experimental results demonstrate that when deflection is used as a measure of beam stiffness, there are two contributors to that stiffness and not one. Further, these results indicate that the major contributor to reduction in stiffness due to temperature in 0-degree flexure test is the shearing modulus, G_{13} and not E_{11}.

6 CONCLUSIONS

The first and primary conclusion of this work is that the 0-degree flexural test is inappropriate for the measurement of the time and temperature-dependent properties of the Young's modulus, E_{11}. Rather, this test yields data that reflects the time-dependent properties of the shearing modulus, G_{13}. Furthermore, extraction of G_{13} relaxation data from the 0-degree flexure sample test data, while plausible, is numerically difficult due to the form of equation (1) wherein G_{13} is in the denominator of the second term. This study also shows that the flexure test for the 90-degree fiber orientation geometry provides adequate data for the time dependent properties of the transvers Young's modulus, E_{22} so long as the beam aspect ratio, $L/h \geq 45$. Although the choice to derive the relaxation

data for the shearing modulus, G_{13} from that of the transverse Young's modulus, E_{22} is an approximation, it was shown to be useful in establishing the relationship between flexural deformation of the 0-degree sample and G_{13}, as witnessed by the agreement between predicted and observed relaxation force magnitudes. Finally, the difference between the tensile and compressive elastic modulus, E_{11} for the CF/PEKK materials system (139.0 GPa versus 127.0 GPa) was not considered in the present study, although results in reference [6] suggest the effect is of second order for CF/PEKK [1].

ACKNOWLEDGEMENTS

The authors acknowledge the support of the Institute for Advanced Composites Manufacturing Innovation of the Department of Energy and the State of Indiana IEDC.

REFERENCES

1. TECHNICAL DATA SHEET, APC (PEKK-FC), PEKK-FC THERMOPLASTIC POLYMER PREPREG, Solvay Composite Materials HQ, 4500 McGinnis Ferry Rd., Alpharetta, GA 30005-3914 USA.
2. Groenewoud, W. M. (Ed.), *Characterization of Polymers by Thermal Analysis*, Elsevier Science B.V., (2001).
3. Storage, T. C., et al, "Analysis of data reduction strategy used in TA Instruments Q800 DMA Test System," AFRL-RX-WP-TR-2013-0182, (2013).
4. Timoshenko, S. P. "LXVI. On the correction for shear of the differential equation for transverse vibrations of prismatic bars", The London, Edinburgh, and Dublin Philosophical Magazine and Journal of Science, 41(245): 744–746, (1921).
5. Barocio, E., Hicks, J., Kim, G., Favaloro, A., Ghosh, G., Goodsell, J. and Pipes, R. B., "Validation of shape change predictions for stamp forming of carbon fiber thermoplastic composite laminates," Composites Part B, 275, (2024).
6. Yao, W-J, Ye, Z-M, "Analytical Solution for Bending Beam Subject to Lateral Force with Different Modulus," Applied Mathematics and Mechanics, Vol. 25, No. 10, (2004).

ICCM24
24TH INTERNATIONAL CONFERENCE ON COMPOSITE MATERIALS
AUGUST 4-8, 2025
BALTIMORE CONVENTION CENTER • BALTIMORE, MARYLAND, USA

NUS National University of Singapore

A Mesoscale Model of Woven Fabric Thermoplastic Composites for Large Deformation

Yuhao Tan, K.M. Yeoh, K. Raju, Vincent BC Tan

Department of Mechanical Engineering, National University of Singapore

Outline

- Motivation
- Experimental campaign
- Mesoscale modeling
- Results and discussion
- Conclusions

1. Motivation



Carbon fiber woven thermoplastic composites

- High specific strength
- Excellent formability
- Sustainability

Draping

Fabric reinforcement

In-plane shear deformation

↓

Yarn reorientation

↓

Non-orthogonal fabric

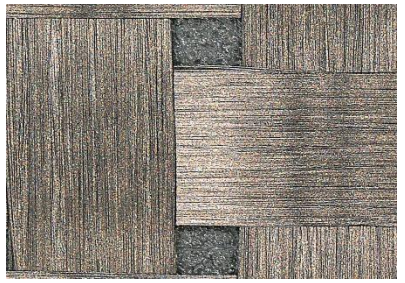

↓



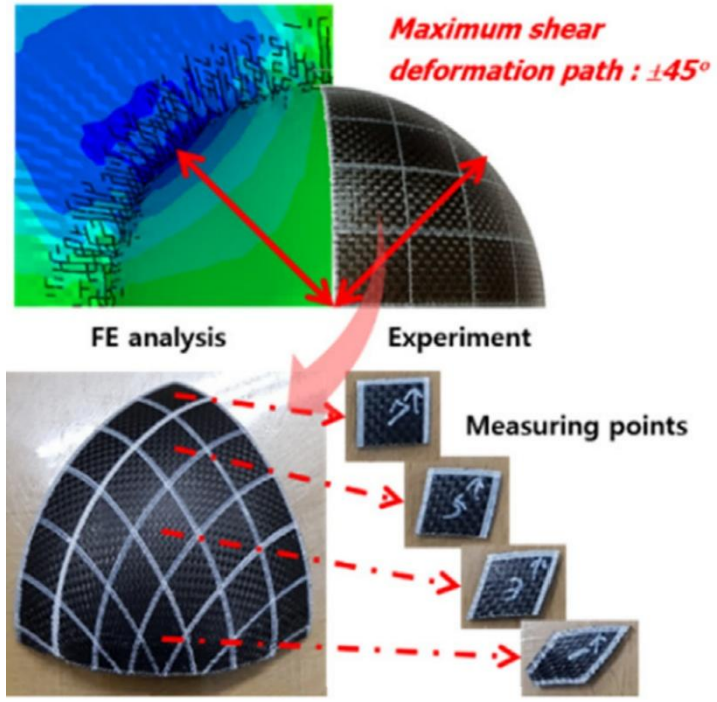

Various degrees of yarn reorientation [1]

↓

Spatially dependent mechanical behavior

Complex geometries



Helmet shell



Pressure vessel

[1] M.-G. Han et al., Composites Part A 110 (2018) 172–182.

1. Motivation

Finite element analysis (FEA)

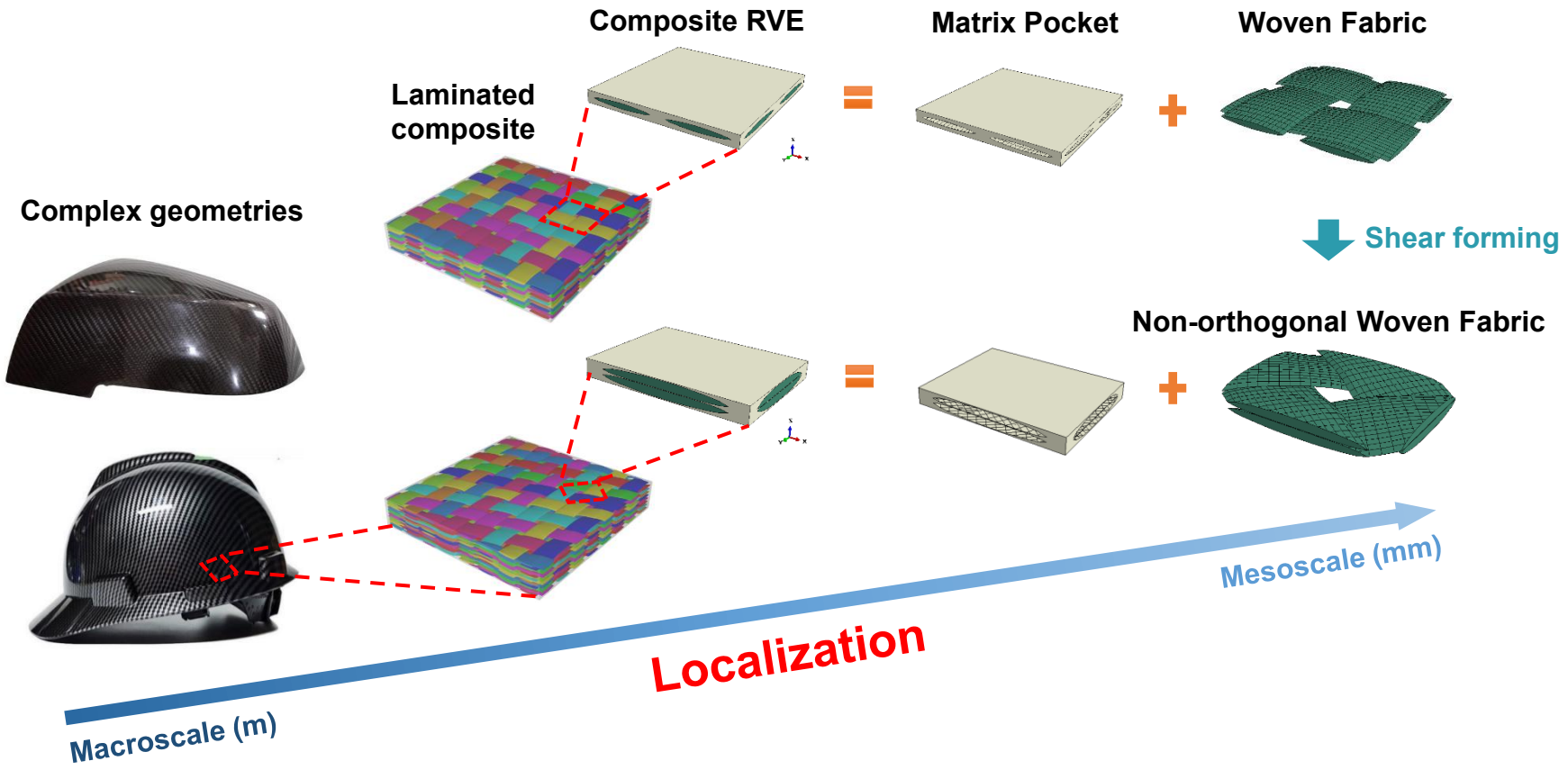

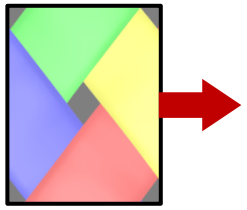

Off-axis loading

Potential large deformation of thermoplastic RVE

* Yarn rotation

Matrix plasticity

Combined non-linear effects

Challenging ?

Objective:

- Local mechanical behaviors of woven thermoplastic composites with complex geometries
- A mesoscale RVE damage model accounting for large deformation

2. Experimental campaign

Angle definition

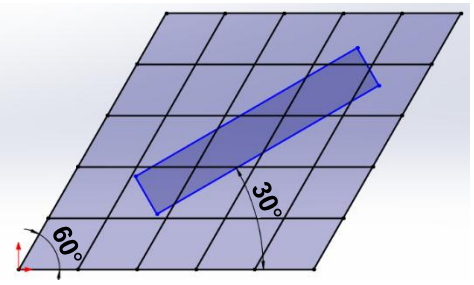

Fabric angle: 60°
Yarn angle: 30°

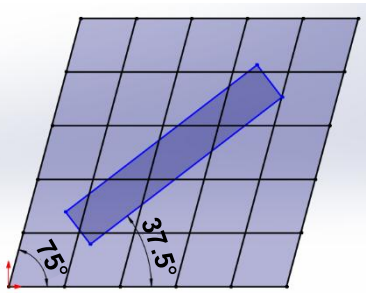

Fabric angle: 75°
Yarn angle: 37.5°

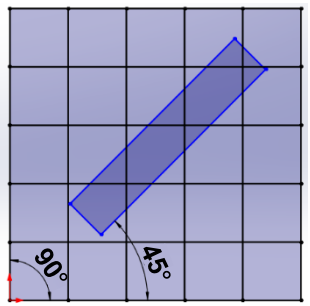

Fabric angle: 90°
Yarn angle: 45°

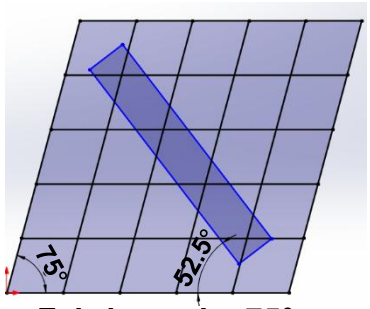

Fabric angle: 75°
Yarn angle: 52.5°

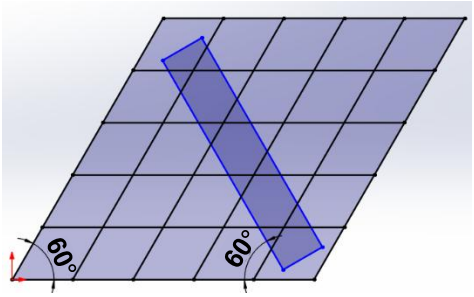

Fabric angle: 60°
Yarn angle: 60°

Shear forming of dry fabric

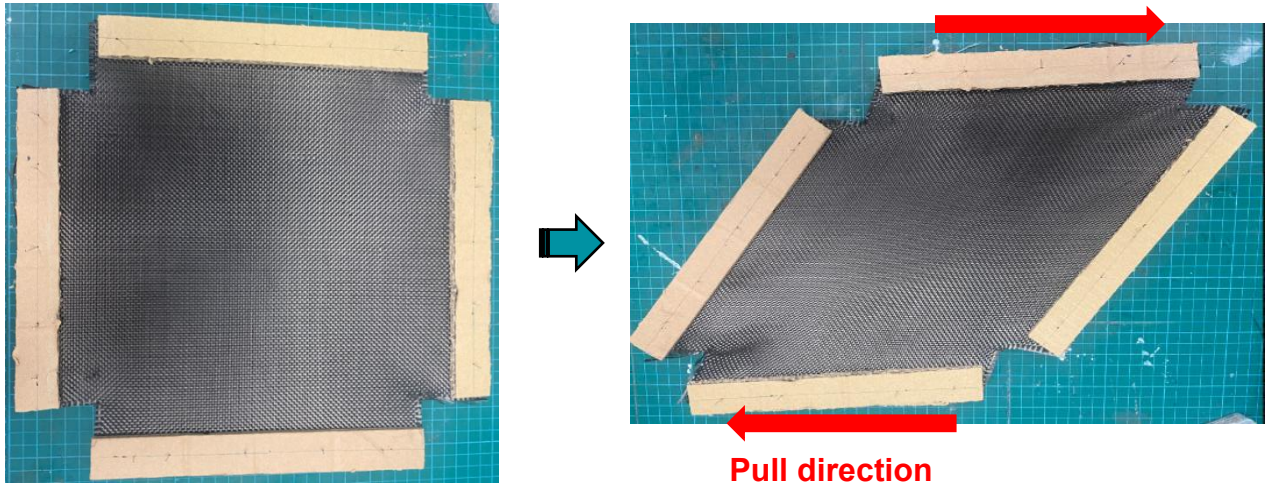

Specimen thermoforming

Stacking sequence



Polycarbonate (PC)

Carbon fabric

Temperature and pressure cycles

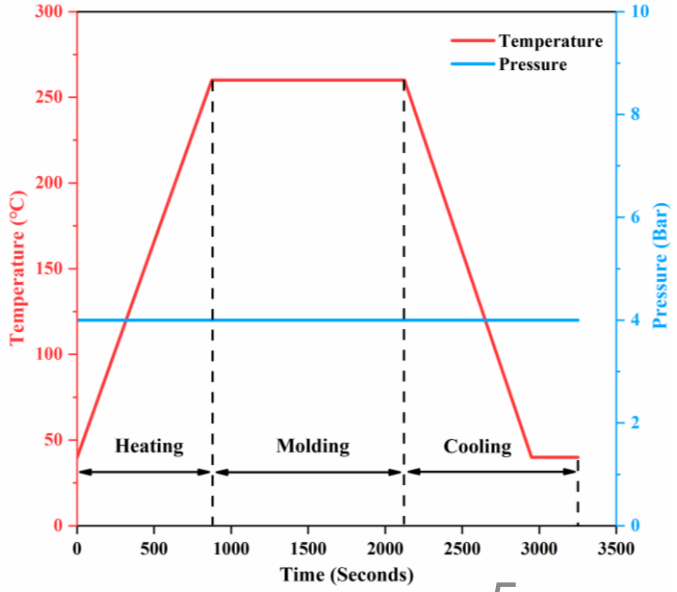

2. Experimental campaign

Off-axis uniaxial tests

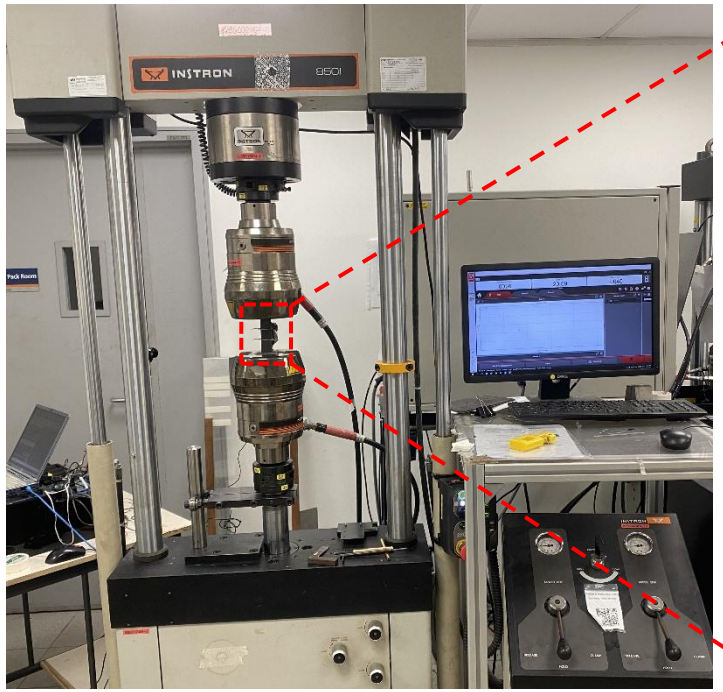

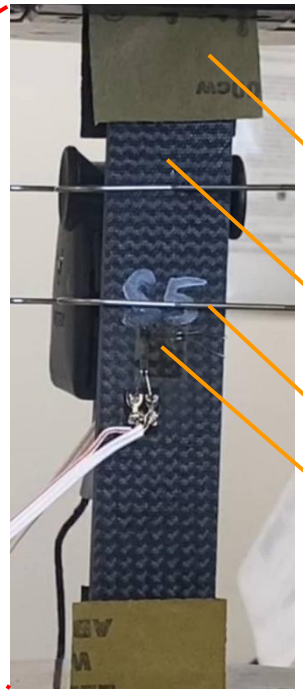

ASTM D3039

Digital image correlation (DIC) method

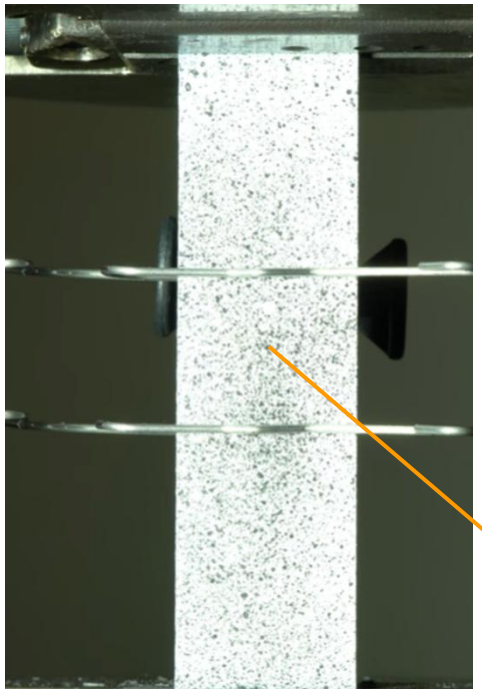

3. Mesoscale modeling

Morphologies of coupons

Yarn: transversely isotropic UD composite

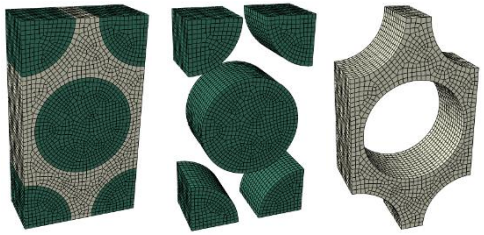

Yarn RVE Fibers Matrix

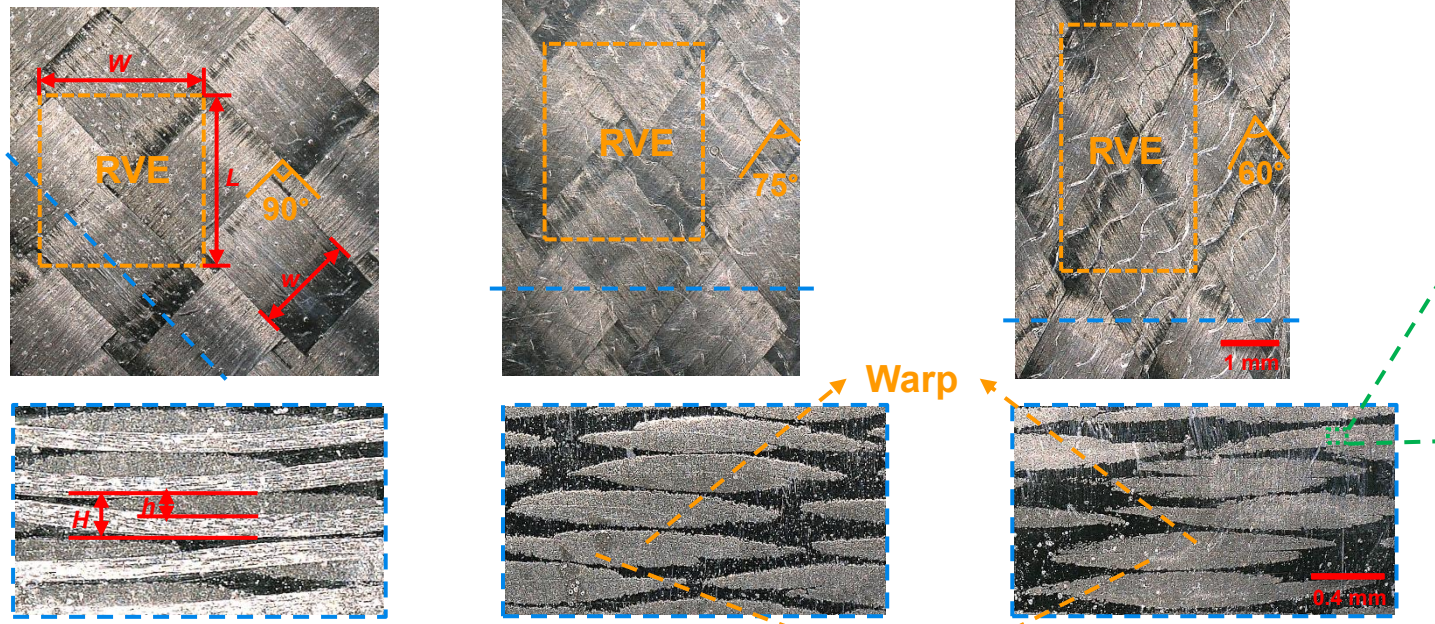

Fiber fill factor: 0.6518

Fabric angle 90° 75° 60°

- Size parameters
- Fiber volume fractions

Woven composite RVEs

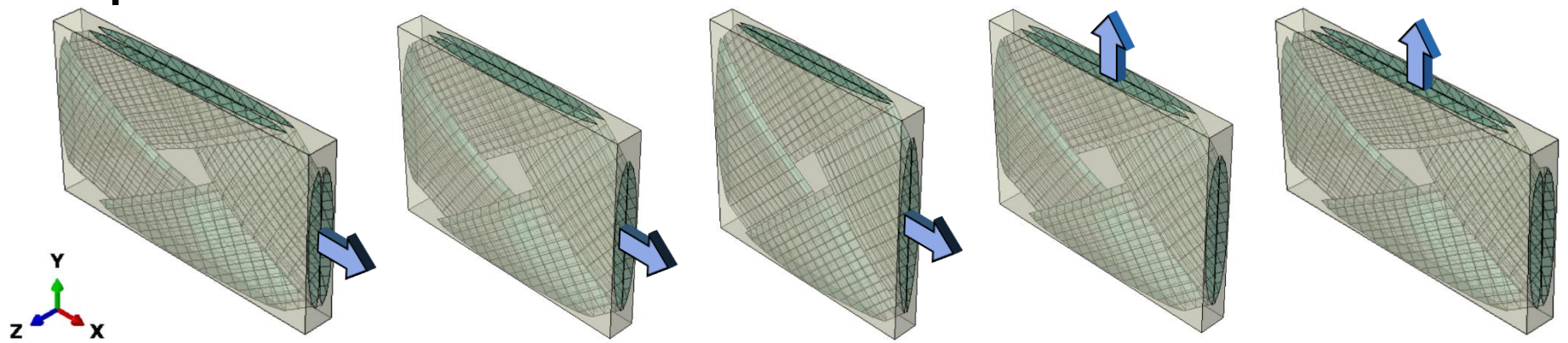

Yarn angle 30° 37.5° 45° 52.5° 60°

3. Mesoscale modeling

a. Material model-PC matrix

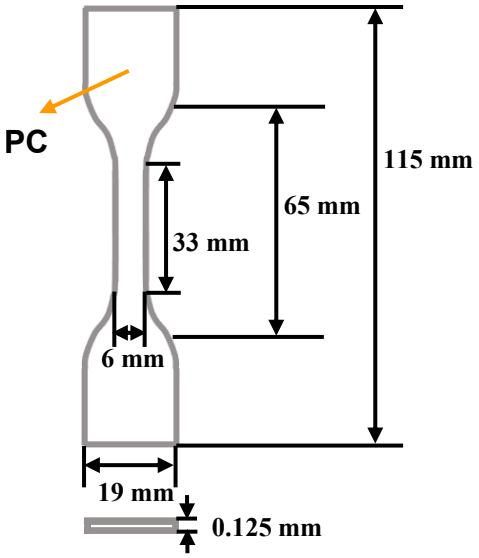

ASTM D638-14

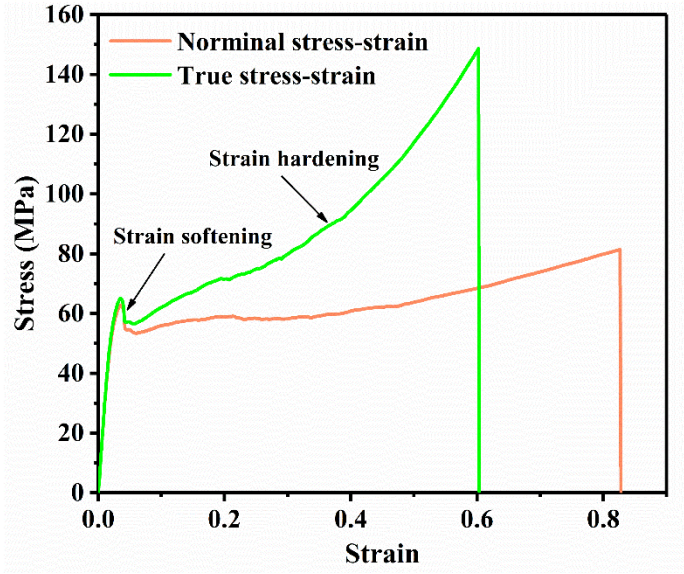

Elasto-plastic parameters

b. Material model-Yarn

Chamis' micromechanical model

Elastic constants

Properties	Carbon fiber []	PC matrix	Fiber yarn
E_{11} (GPa)	230	2.466	150.773
$E_{22} = E_{33}$ (GPa)	15		7.579
$v_{12} = v_{13}$	0.20	0.37	0.259
v_{23}	0.07		0.299
$G_{12} = G_{13}$ (GPa)	27	0.899	4.095
G_{23} (GPa)	7		3.034

Strength parameters

Carbon fiber		PC matrix		
X_{ft} (MPa)	X_{fc} (MPa)	S_{mt} (MPa)	S_{mc} (MPa)	S_{ms} (MPa)
3530	2470	65.04	80	40

Fiber yarn					
X_T (MPa)	X_C (MPa)	$Y_T = Z_T$ (MPa)	$Y_C = Z_C$ (MPa)	$S_{12} = S_{13}$ (MPa)	S_{23} (MPa)
2314.03	1619.17	56.59	69.61	33.56	27.45

3. Mesoscale modeling

a. Damage criterion-PC matrix pocket

Abaqus built-in Ductile failure criterion with exponential damage evolution laws

Facture strain: 0.6021

Fracture energy: 2.18 KJ/m²

b. Damage criterion-Yarn

Strain-based 3D Hashin failure criterion

Failure strains

$$\varepsilon_{XT}^{f}=\frac{X_T}{C_{11}} \quad \varepsilon_{XC}^{f}=\frac{X_C}{C_{11}} \quad \varepsilon_{YT}^{f}=\frac{Y_T}{C_{22}} \quad \varepsilon_{YC}^{f}=\frac{Y_C}{C_{22}} \quad \varepsilon_{S12}^{f}=\varepsilon_{S13}^{f}=\frac{S_{12}}{C_{44}} \quad \varepsilon_{S23}^{f}=\frac{S_{23}}{C_{66}}$$

Tensile failure in the longitudinal (fiber) direction ($\varepsilon_{11}\geq 0$)

$$F_{ft}=\sqrt{\left(\frac{\varepsilon_{11}}{\varepsilon_{XT}^{f}}\right)^2+\alpha\left[\left(\frac{\varepsilon_{12}}{\varepsilon_{S12}^{f}}\right)^2+\left(\frac{\varepsilon_{13}}{\varepsilon_{S13}^{f}}\right)^2\right]}>1$$

Compressive failure in the longitudinal (fiber) direction ($\varepsilon_{11}<0$)

$$F_{fc}=\sqrt{\left(\frac{\varepsilon_{11}}{\varepsilon_{XC}^{f}}\right)^2}>1$$

Tensile failure in the transverse (matrix) direction ($\varepsilon_{22}+\varepsilon_{33}\geq 0$)

$$F_{mt}=\sqrt{\left(\frac{\varepsilon_{22}+\varepsilon_{33}}{\varepsilon_{YT}^{f}}\right)+\left(\frac{\varepsilon_{22}+\varepsilon_{33}}{2\varepsilon_{S23}^{f}}\right)^2-\frac{\varepsilon_{22}\varepsilon_{33}}{\left(\varepsilon_{S23}^{f}\right)^2}+\left(\frac{\varepsilon_{12}}{\varepsilon_{S12}^{f}}\right)^2+\left(\frac{\varepsilon_{13}}{\varepsilon_{S13}^{f}}\right)^2+\left(\frac{\varepsilon_{23}}{\varepsilon_{S23}^{f}}\right)^2}>1$$

Compressive failure in the transverse (matrix) direction ($\varepsilon_{22}+\varepsilon_{33}<0$)

$$F_{mc}=\sqrt{\left[\left(\frac{\varepsilon_{YC}^{f}}{2\varepsilon_{S23}^{f}}\right)^2-1\right]\left(\frac{\varepsilon_{22}+\varepsilon_{33}}{\varepsilon_{YC}^{f}}\right)+\left(\frac{\varepsilon_{22}+\varepsilon_{33}}{2\varepsilon_{S23}^{f}}\right)^2-\frac{\varepsilon_{22}\varepsilon_{33}}{\left(\varepsilon_{S23}^{f}\right)^2}+\left(\frac{\varepsilon_{12}}{\varepsilon_{S12}^{f}}\right)^2+\left(\frac{\varepsilon_{13}}{\varepsilon_{S13}^{f}}\right)^2+\left(\frac{\varepsilon_{23}}{\varepsilon_{S23}^{f}}\right)^2}>1$$

Exponential progressive damage evolution

Damage variables d_{ft}, d_{fc}, d_{mt}, d_{mc}

$$d_{ft}=1-\frac{exp\left(-\frac{X_T\varepsilon_{XT}^{f}L_C(F_{ft}-1)}{G_{ft}}\right)}{F_{ft}} \qquad d_{fc}=1-\frac{exp\left(-\frac{X_C\varepsilon_{XC}^{f}L_C(F_{fc}-1)}{G_{fc}}\right)}{F_{fc}}$$

$$d_{mt}=1-\frac{exp\left(-\frac{Y_T\varepsilon_{YT}^{f}L_C(F_{mt}-1)}{G_{mt}}\right)}{F_{mt}} \qquad d_{mc}=1-\frac{exp\left(-\frac{Y_C\varepsilon_{YC}^{f}L_C(F_{mc}-1)}{G_{mc}}\right)}{F_{mc}}$$

Synthetic damage variables D_f, D_m

$$D_f=\begin{cases}d_{ft} & \varepsilon_{11}\geq 0\\ d_{fc} & \varepsilon_{11}<0\end{cases} \qquad D_m=\begin{cases}d_{mt} & \varepsilon_{22}+\varepsilon_{33}\geq 0\\ d_{mc} & \varepsilon_{22}+\varepsilon_{33}<0\end{cases}$$

Viscous regularization

Duvaut-Lions viscosity model

$$D^{v}|_{t_0+\Delta t}=\frac{\Delta t}{\eta+\Delta t}D|_{t_0+\Delta t}+\frac{\eta}{\eta+\Delta t}D^{v}|_{t_0}$$

$$\frac{\partial D^{v}}{\partial D}=\frac{\Delta t}{\eta+\Delta t}$$

4. Results and discussion

Woven composites with different yarn angles

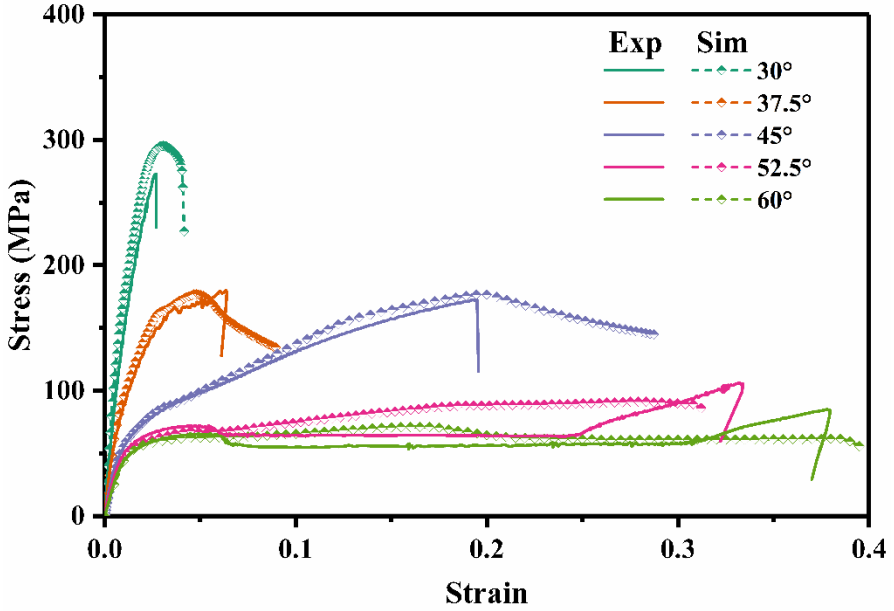

30° and 37.5°: Nearly linear

45°, 52.5° and 60°: Non-linear, large deformation

A transition of brittle to ductile characteristics

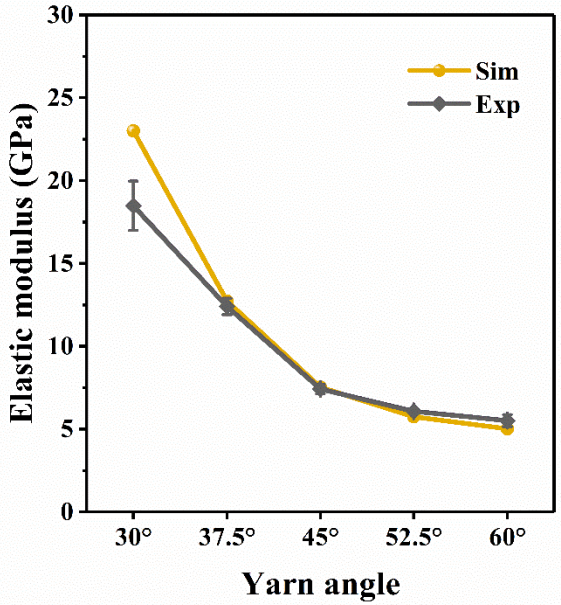

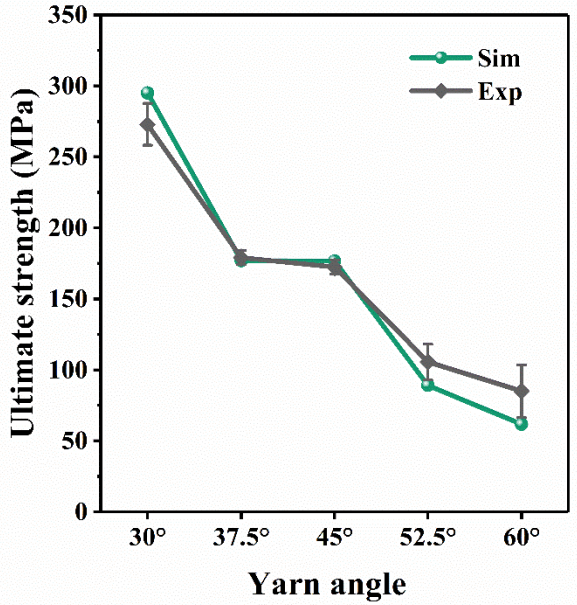

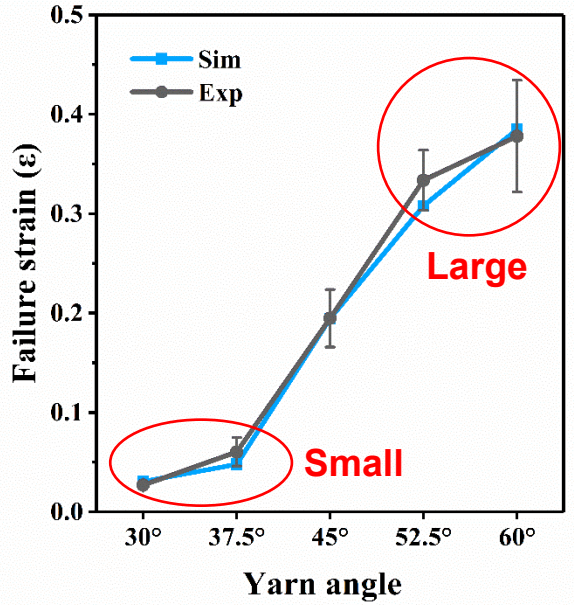

The experimental elastic moduli, ultimate strengths and failure strains validate the RVE model.

4. Results and discussion

Large deformation process of the 52.5° coupon

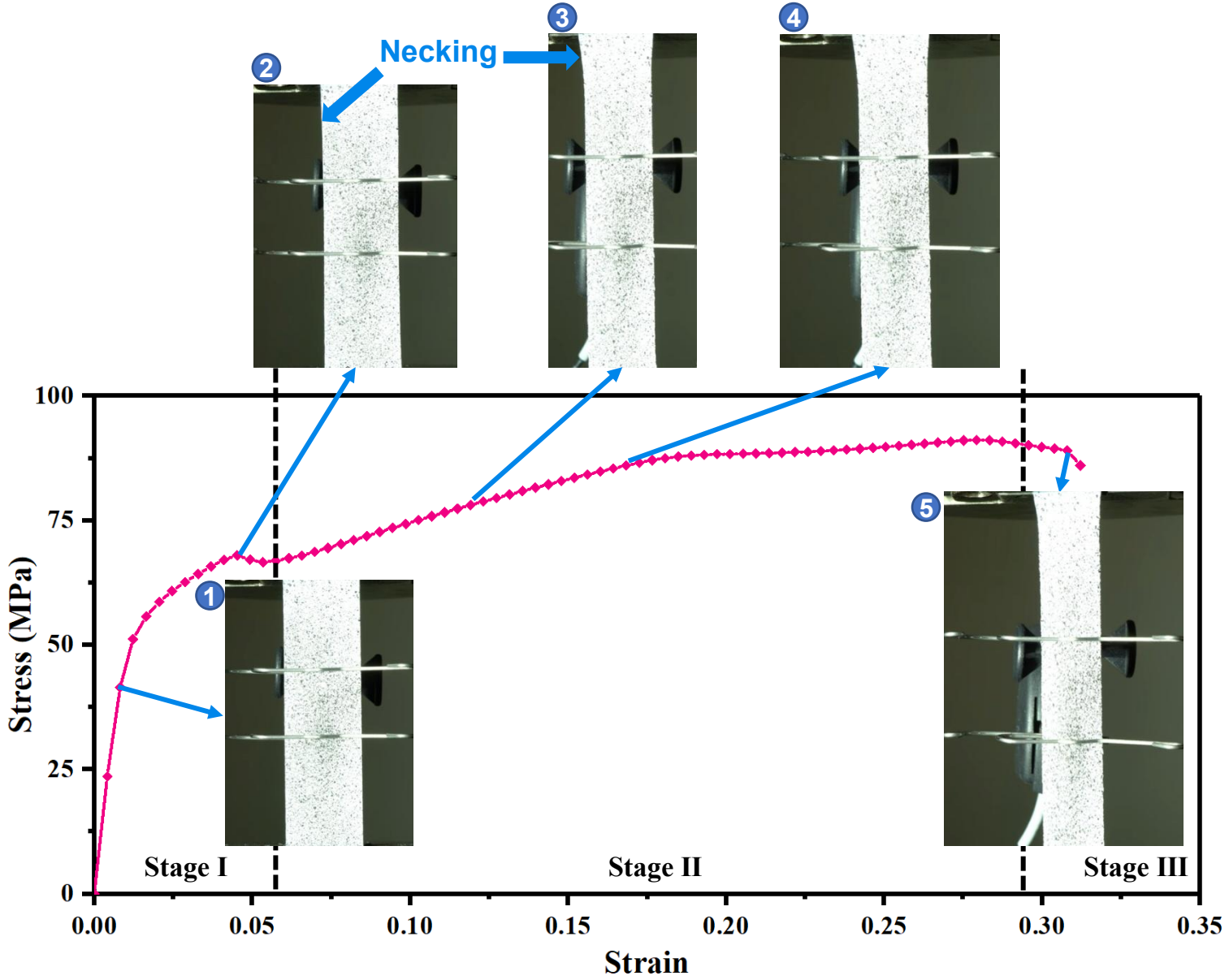

Post-test coupon morphologies



30°



37.5°

No necking



45°



60°

Significant necking

4. Results and discussion

- **Damage contours of the constituents within 30° RVE**

Coupon morphology

Carbon fiber

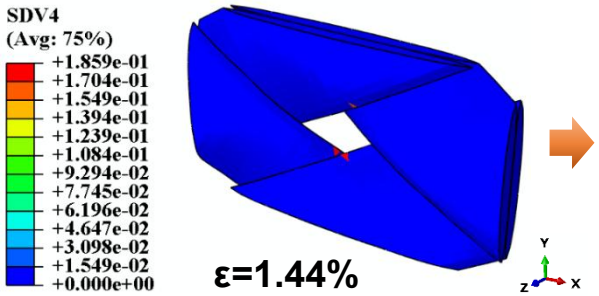

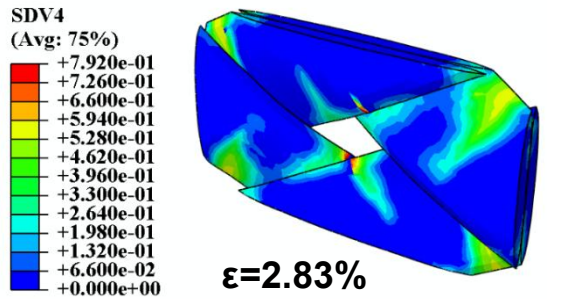

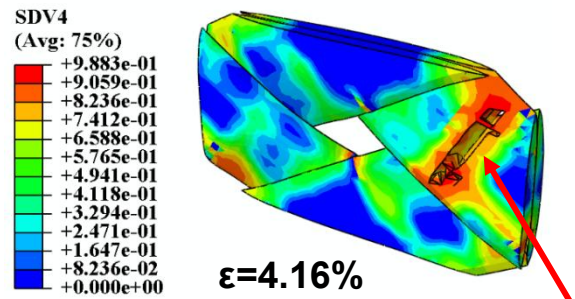



Damage initiation **Damage evolution** **Brittle failure**

PC pocket

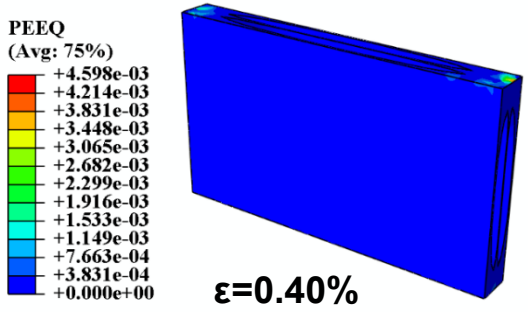

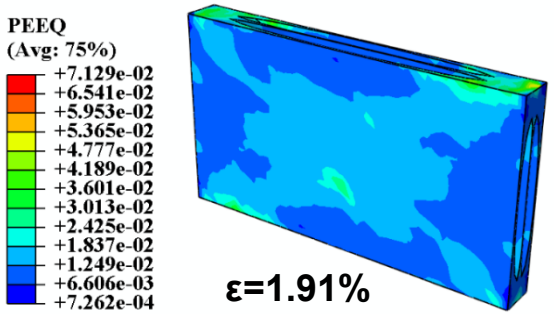

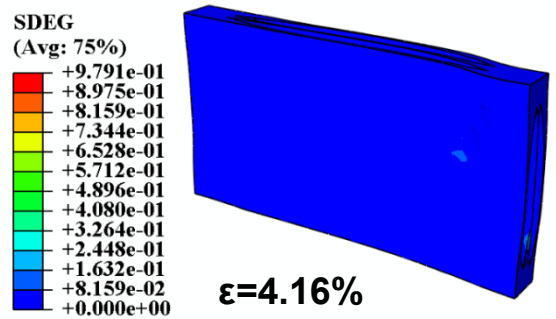



Plastic deformation **No matrix cracking**

Fiber fracture-dominated failure

4. Results and discussion

- **Damage contours of the constituents within 52.5° RVE**

Coupon morphology



Carbon fiber within yarn

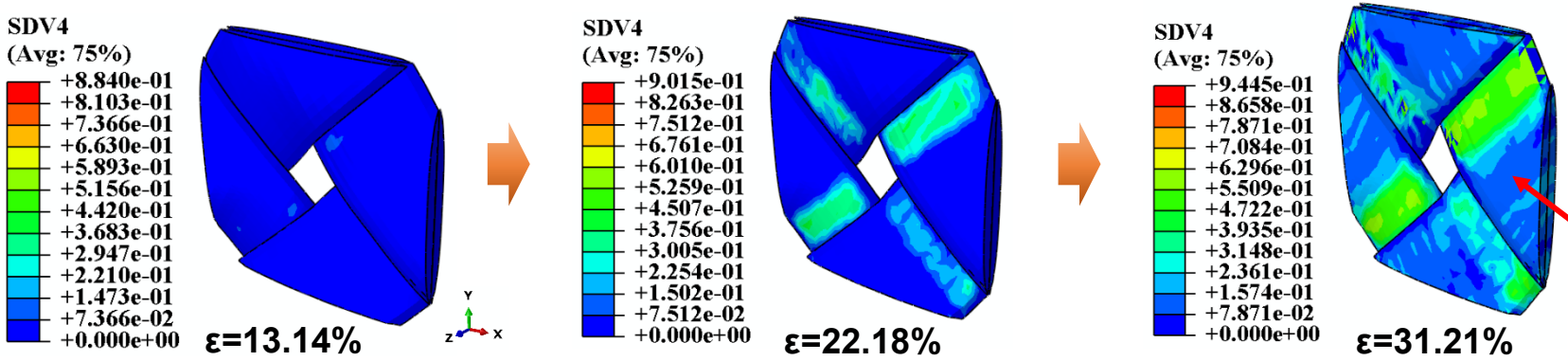

Ductile failure

PC within yarn

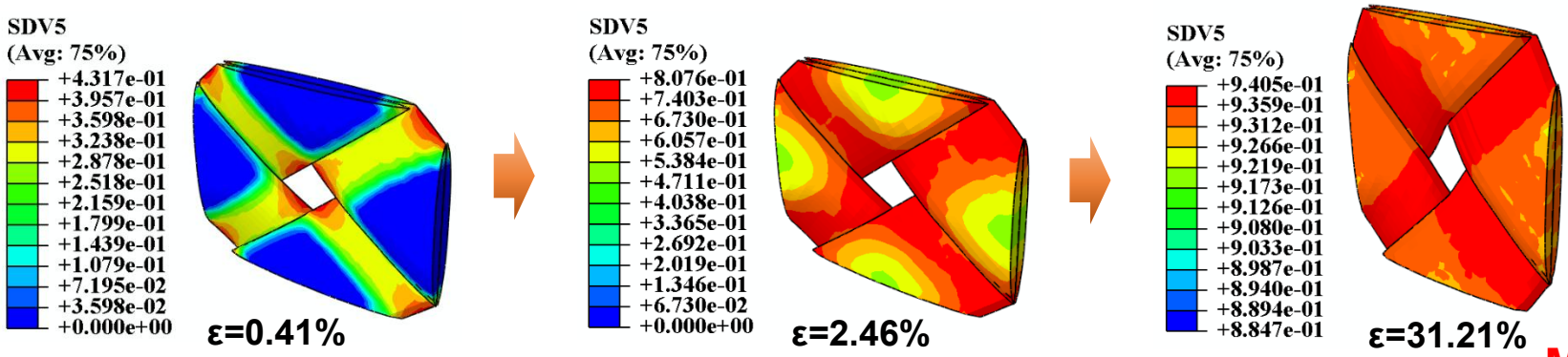

Fiber fracture and matrix cracking co-dominated failure mode

PC pocket

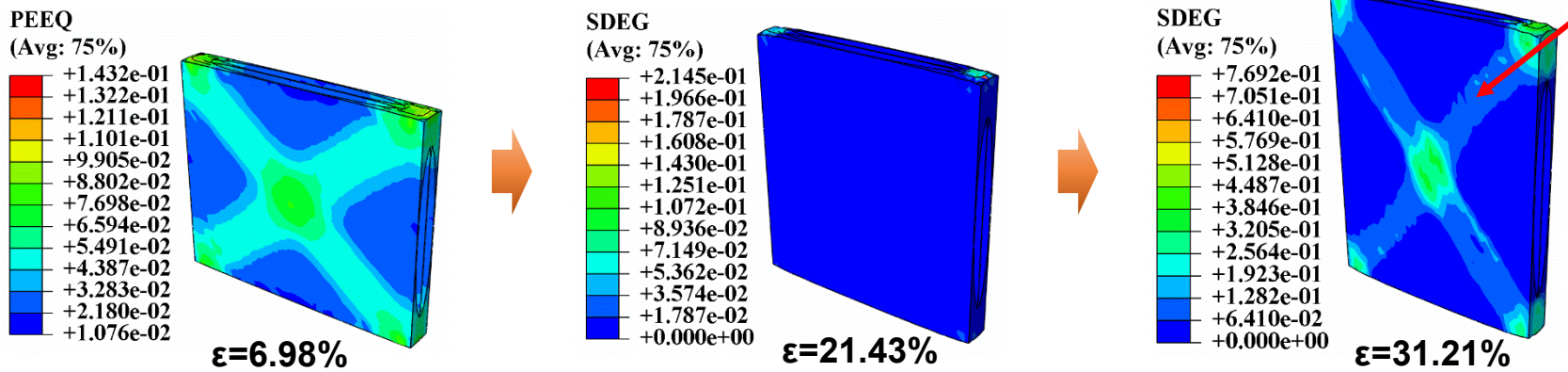

Massive matrix cracking

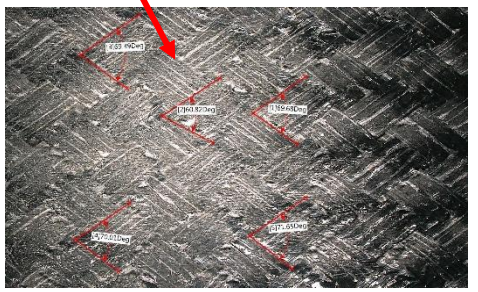

4. Results and discussion

Shear strains of the 52.5° coupon from DIC

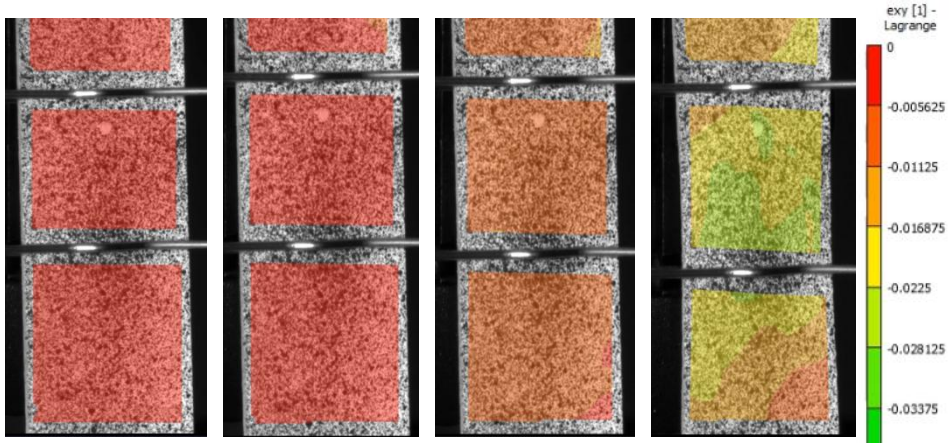

ε=1.41% ε=2.65% ε=5.08% ε=10.80%

Onset of necking

ε=17.63% ε=23.52% ε=28.22% ε=33.64%

Significant yarn displacement

Yarn rotation of large yarn angle RVEs

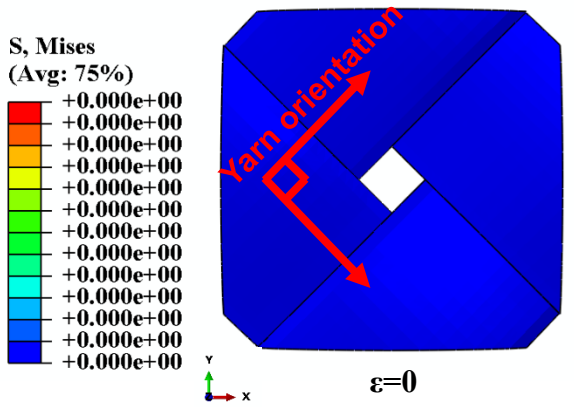

ε=0

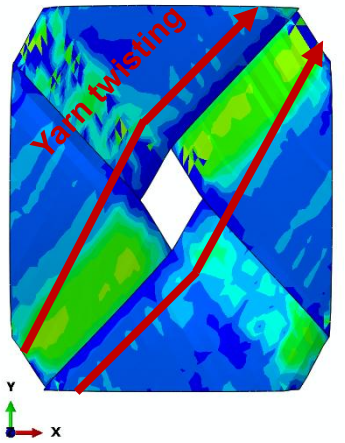

52.5° RVE

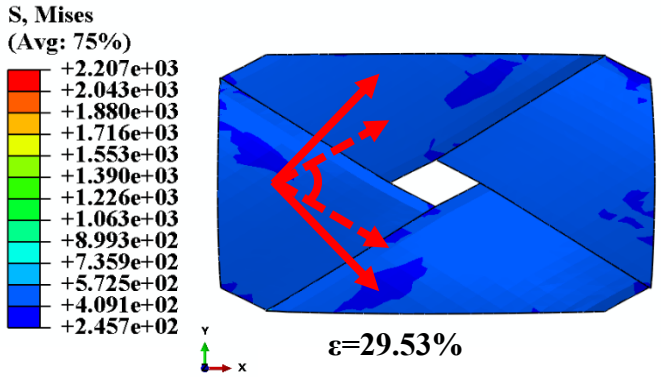

ε=29.53%

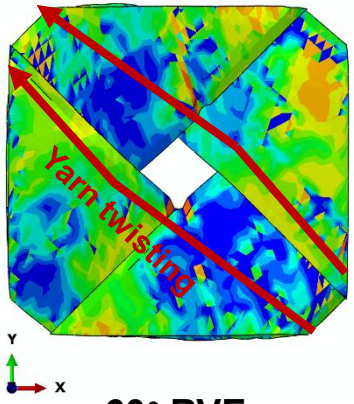

60° RVE

Fabric inter-locking effects

5. Conclusions

- A transition from brittle-like to ductile load response is found as the yarn angle increases.
- A mesoscale RVE model is developed to examine this transition as well as the progressive failure of woven thermoplastic composites.
- Large deformation with yarn rotation and fabric inter-locking effects are captured in large yarn angle RVEs.
- The failure mode changes from being dominated by fiber fracture in small yarn angle RVEs to being jointly dominated by fiber and matrix damage in large yarn angle RVEs.

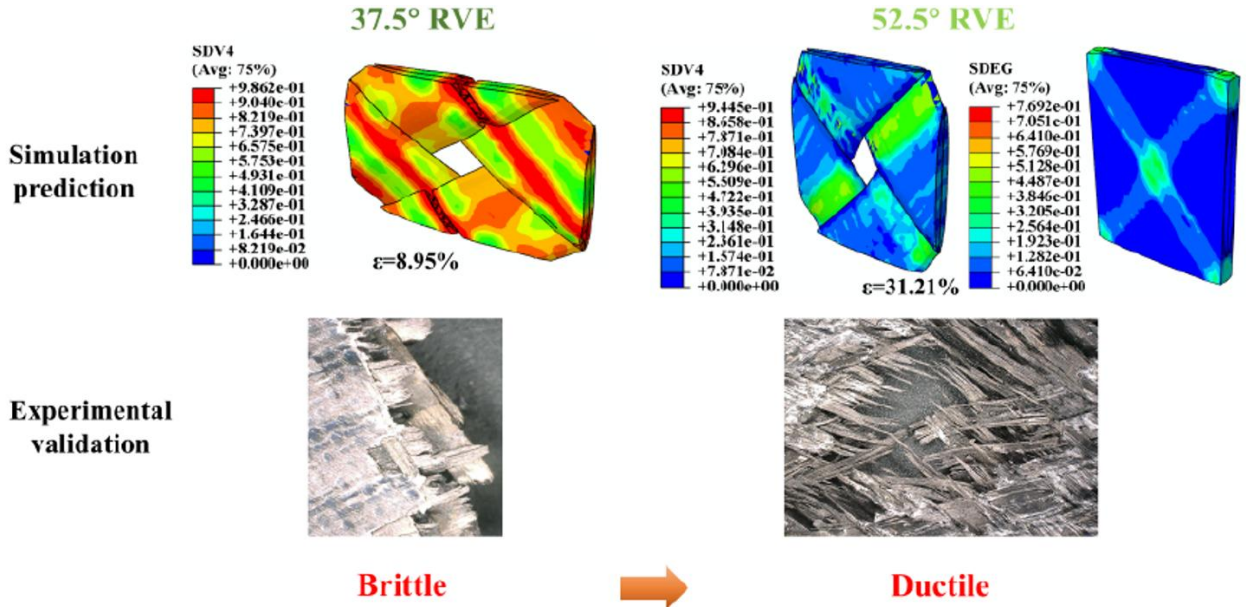

ICCM24
24TH INTERNATIONAL CONFERENCE ON COMPOSITE MATERIALS
AUGUST 4-8, 2025
BALTIMORE CONVENTION CENTER • BALTIMORE, MARYLAND, USA

NUS National University of Singapore

Thank you for your attention !

mpetanbc@nus.edu.sg

Tracking Ply Deformation during Thermoplastic Stamp Forming using Embedded Shape Sensor

K. Chikamori, S. Minakuchi*

The University of Tokyo

Background

Stamp forming process

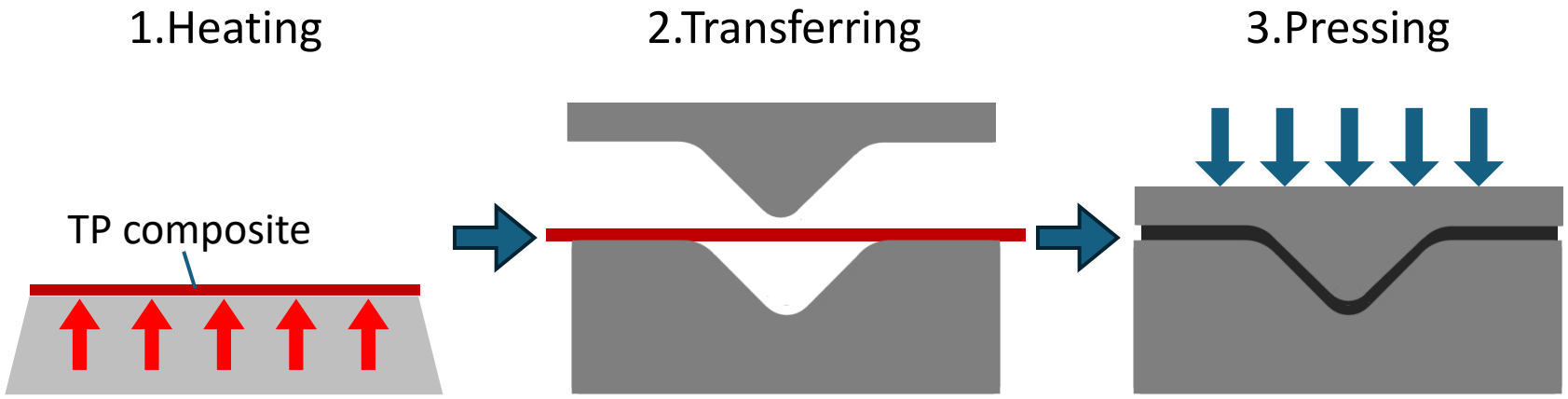

Advantage

✓ High-rate ✓ High-quality ✓ Complex structures

Background

Depending on forming conditions, heated composite plate is not properly pressed against mold….

- ✓ Areas of wavy plies and inadequate pressurization occur
- ✓ Mechanical properties of manufactured parts are reduced.

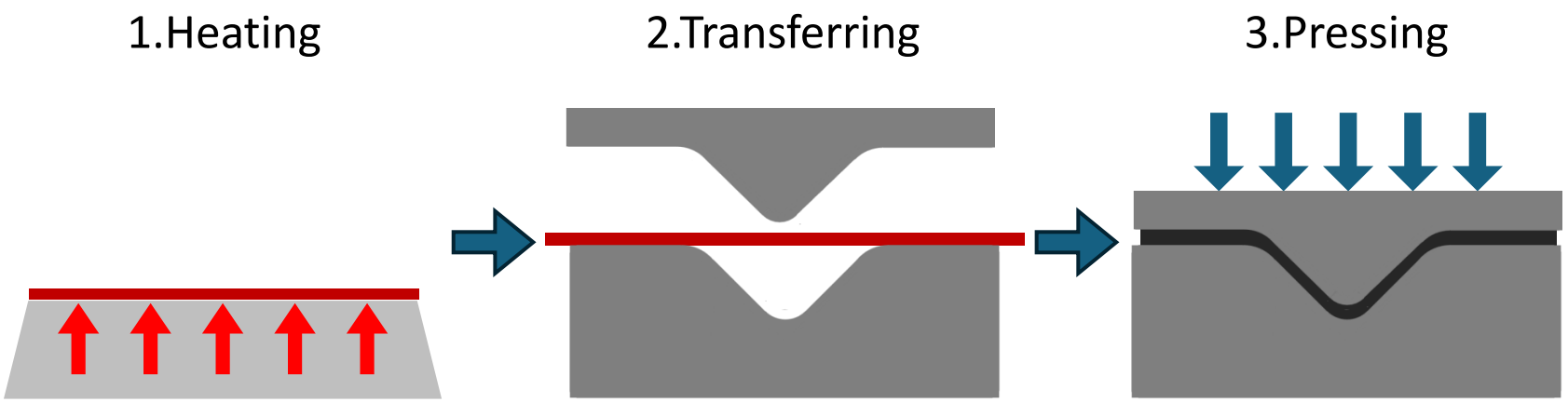

Now, forming conditions set by trial and error based on observations after forming

New in-situ measurement technology is needed to measure deformation of each ply during forming

Objective

- ✓ **Measure deformation of thermoplastic composites during stamp forming using shape sensor (originally for thermoset composites*)**
- ✓ **Investigate influence of forming parameters on deformation behavior**

*S. Minakuchi, S. Niwa, N. Takeda. "Strip-Type Embeddable Shape Sensor Based on Fiber Optics for In Situ Composite Consolidation Monitoring" Sensors 22, no. 17: 6604 (2022)
*T. Tamagawa, Y. Mori, S. Minakuchi. "Consolidation mechanism of composite corners cured on convex and concave tools" Composites Part A: Applied Science and Manufacturing 169, 107500 (2023)

Forming parameters to be investigated

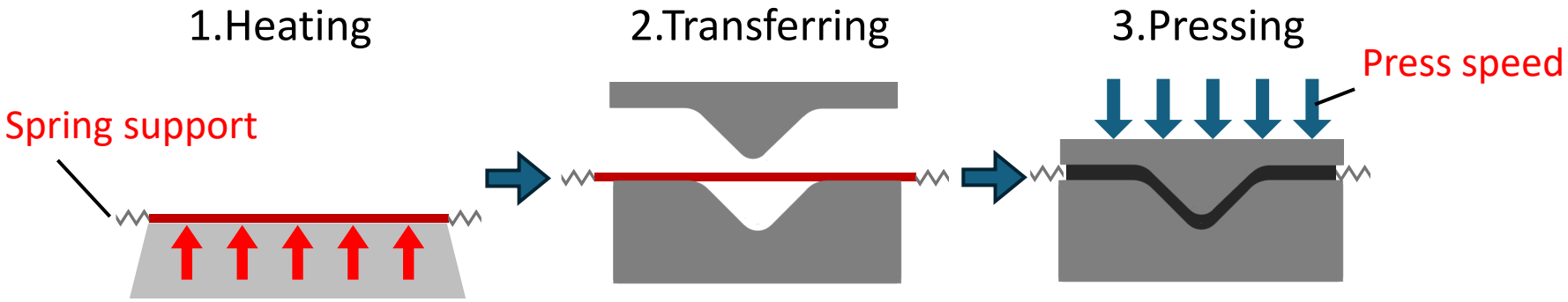

Strip-type shape sensor

- ✓ Two optical fibers embedded in upper and lower surfaces of thin polyimide sheet
- ✓ When bended along sensor axis, different strain (bending strain) is induced in two optical fibers and sensor shape can be back-calculated
- ✓ Deformation can be measured by embedding in composite

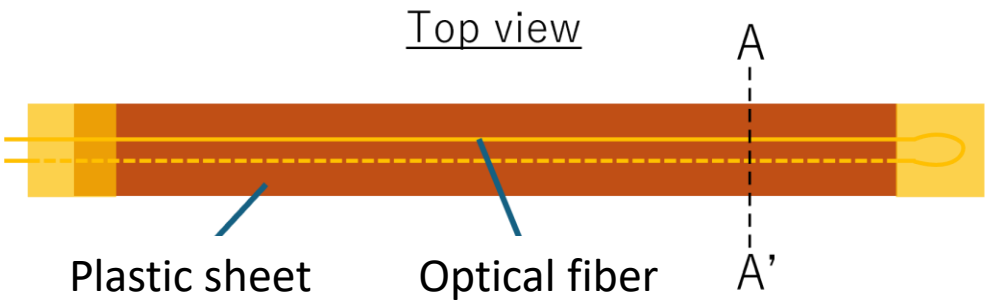

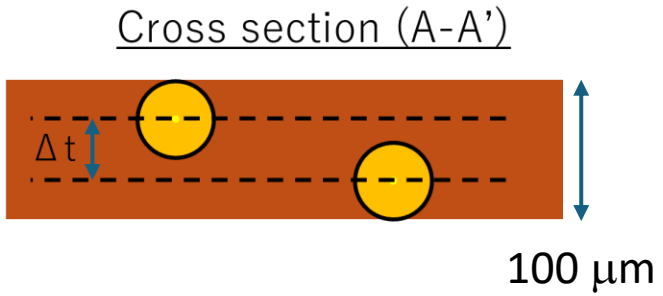



Strip-type shape sensor

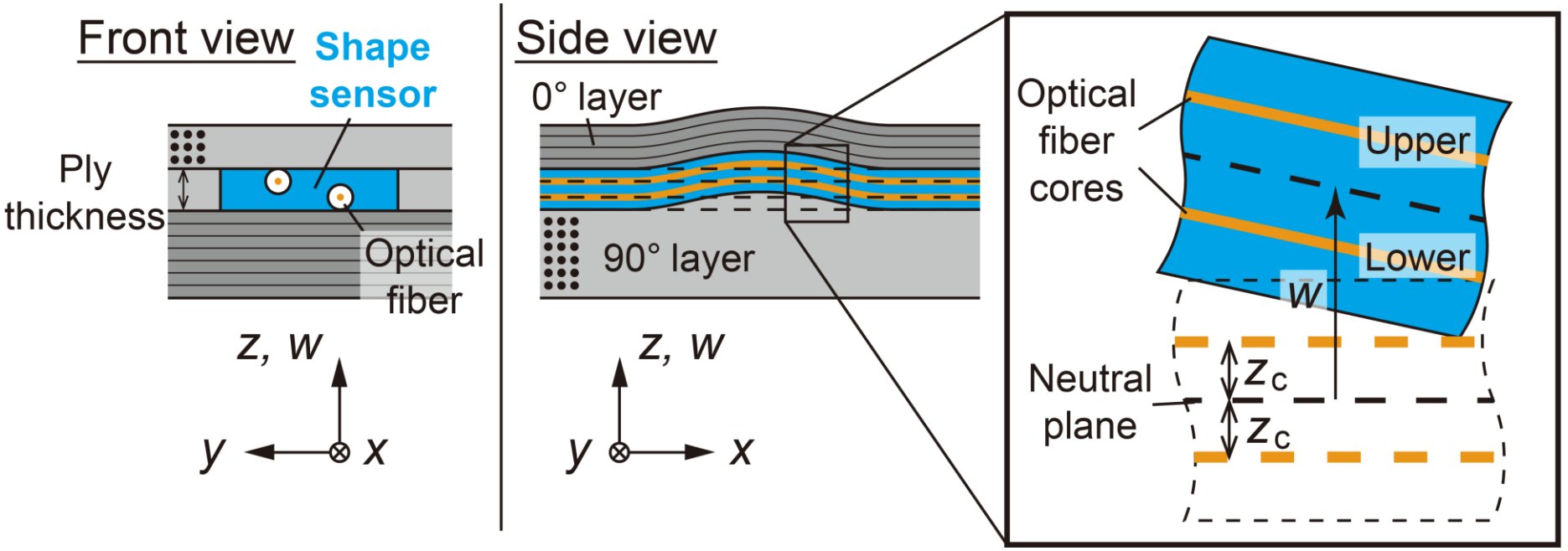

Curvature $\kappa = \dfrac{\varepsilon_{\text{lower}} - \varepsilon_{\text{upper}}}{2z_c}$,

- ✓ When this flexible sensor is embedded in composite part during lay-up, sensor deforms with surrounding plies
- ✓ By monitoring shape change of sensor, we can clarify dynamic deformation process during consolidation

Material and specimen

UD prepreg

- ✓ CF/PA6 (T_m: 219℃)
- ✓ Thickness：200μm
- ✓ Stacking sequence：$[0_{10}]$

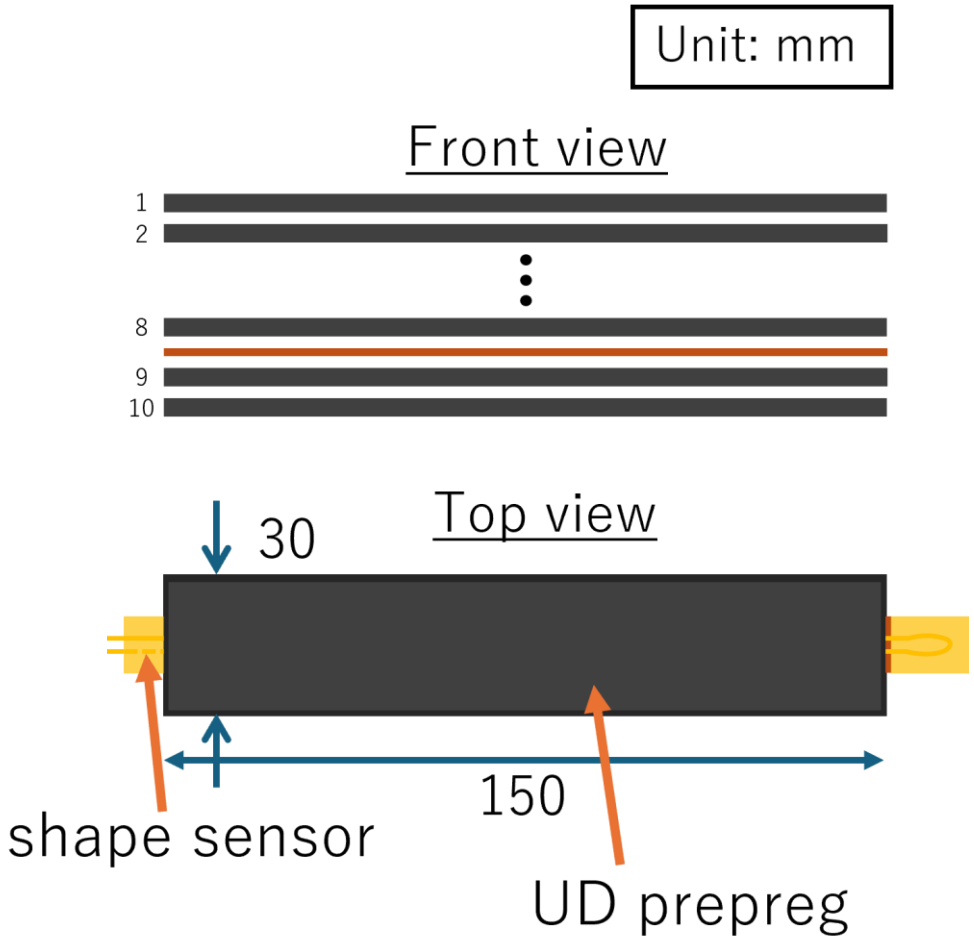

Stamp forming process

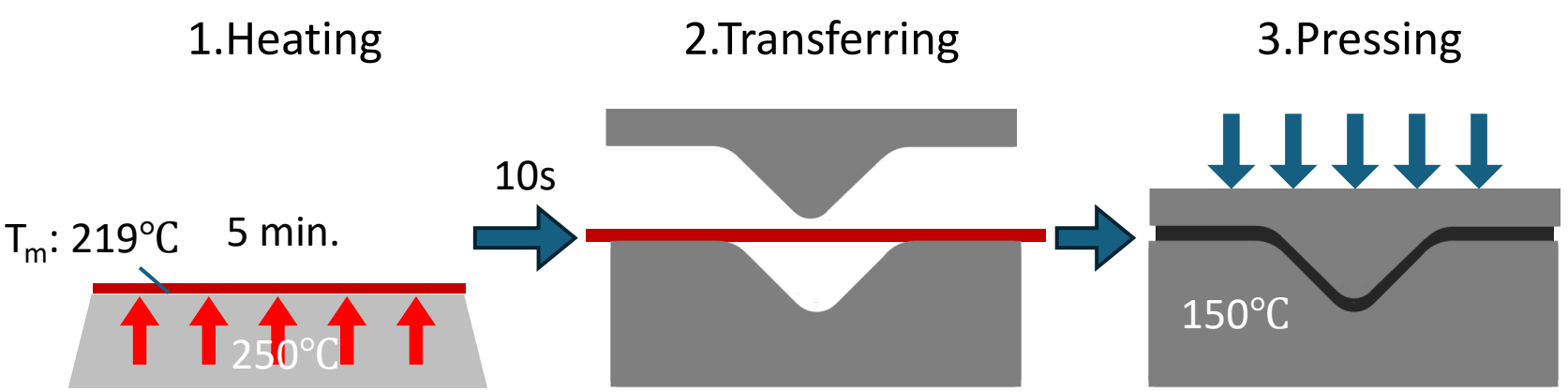

Spring support

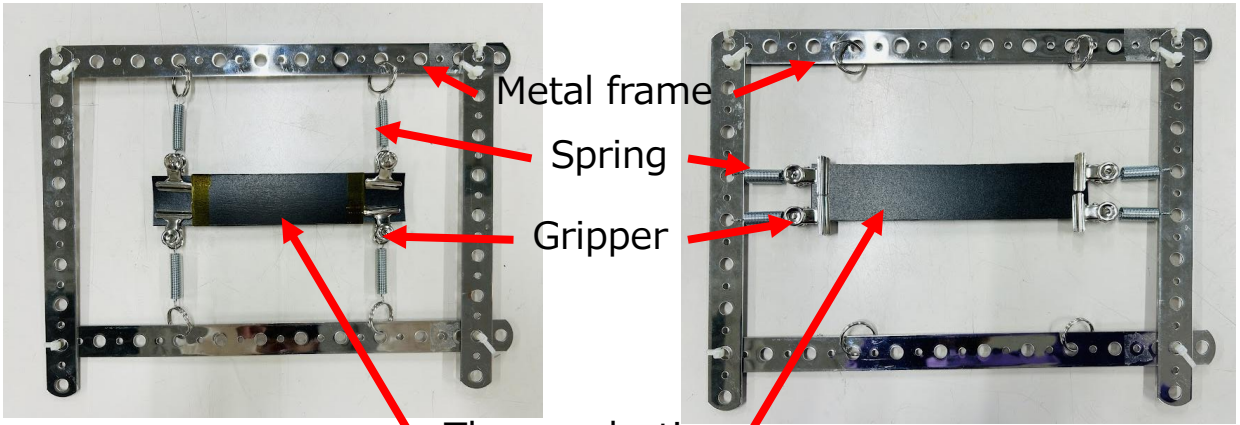

Mold

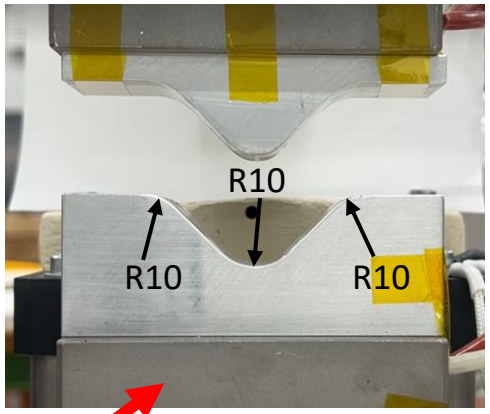

Measurement: sampling 10Hz, spatial resolution 0.65mm

Result

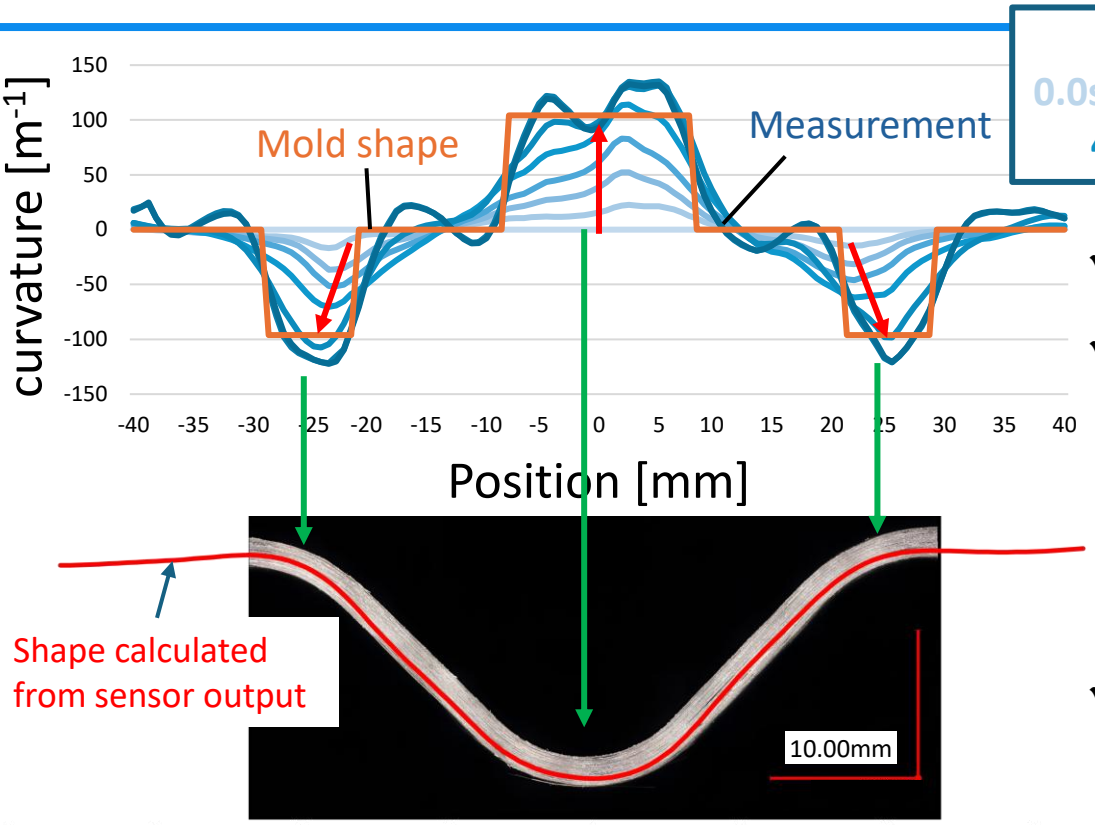

- ✓ Curvature increased in corners
- ✓ Left and right curvature peaks moved outward

  >>Contact point with mold moved outward as forming progressed.
- ✓ Curvature did not match mold shape >> Ply distortion

Movement of contact points outward

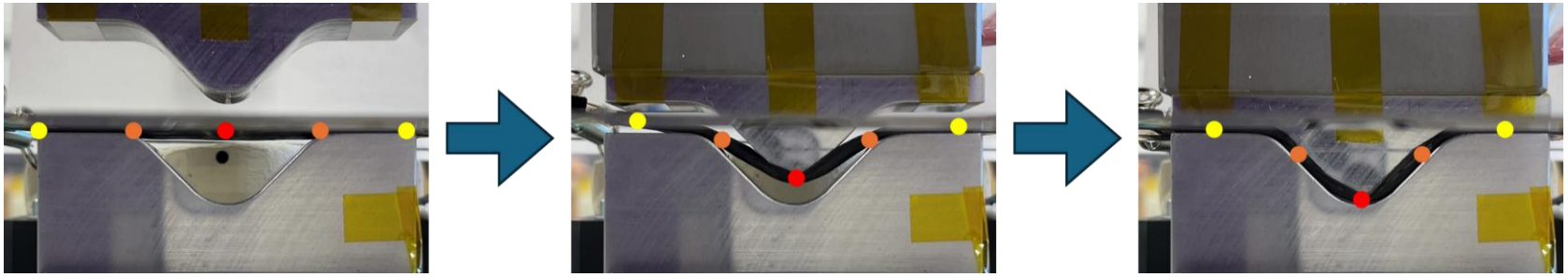

Effect of press speed

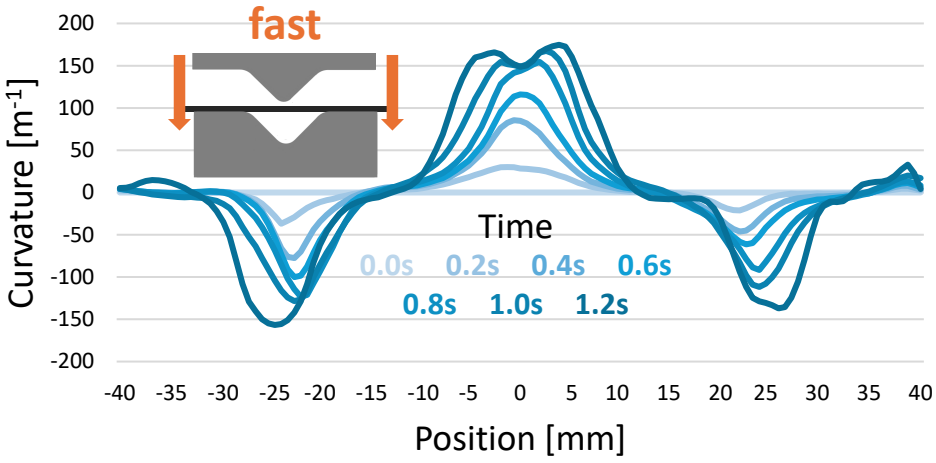

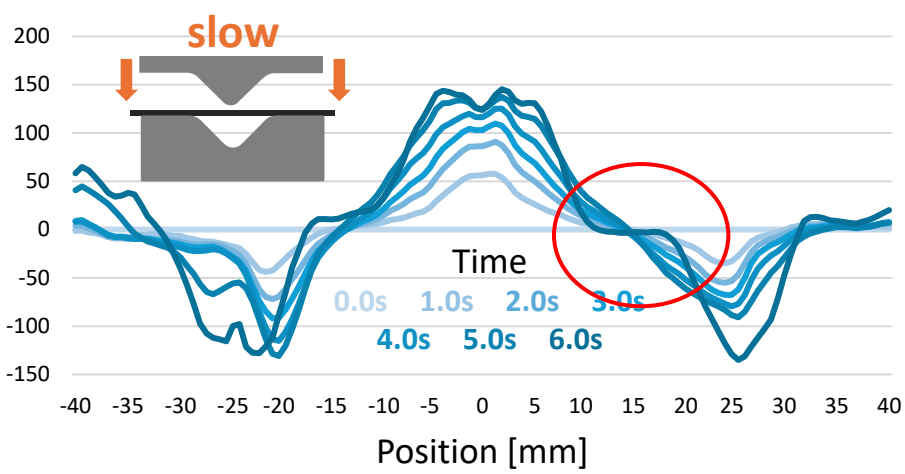

- ✓ When fast, curvature increased locally, and straight part remained unchanged (a)
- ✓ When slow, curvature increased over wide region, and straight part deformed once before returning to straight (b)

<u>Due to viscoelasticity of melted thermoplastic composite, deformation varied with press speed.</u>

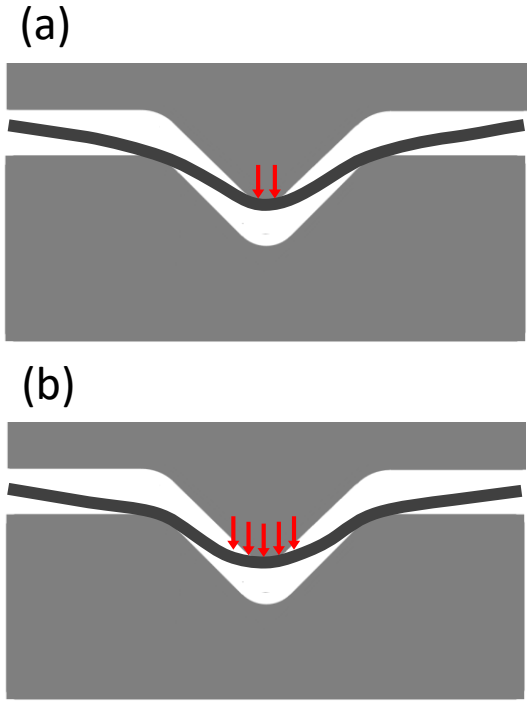

Effect of spring support

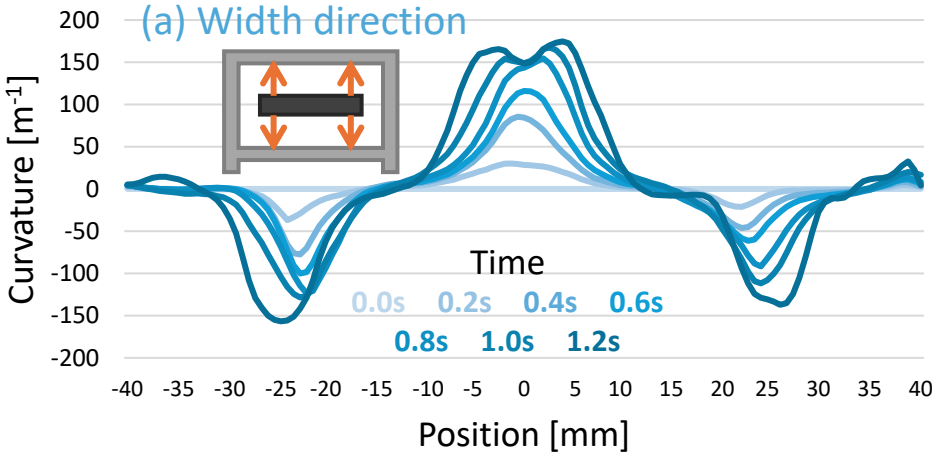

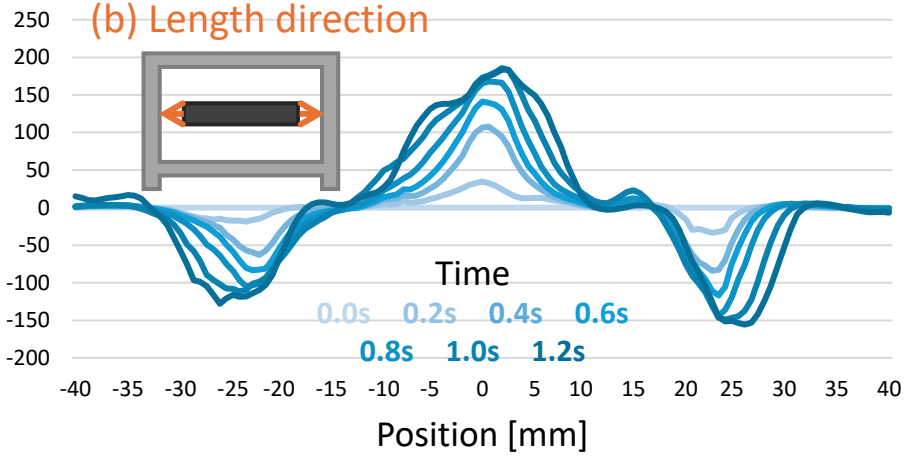

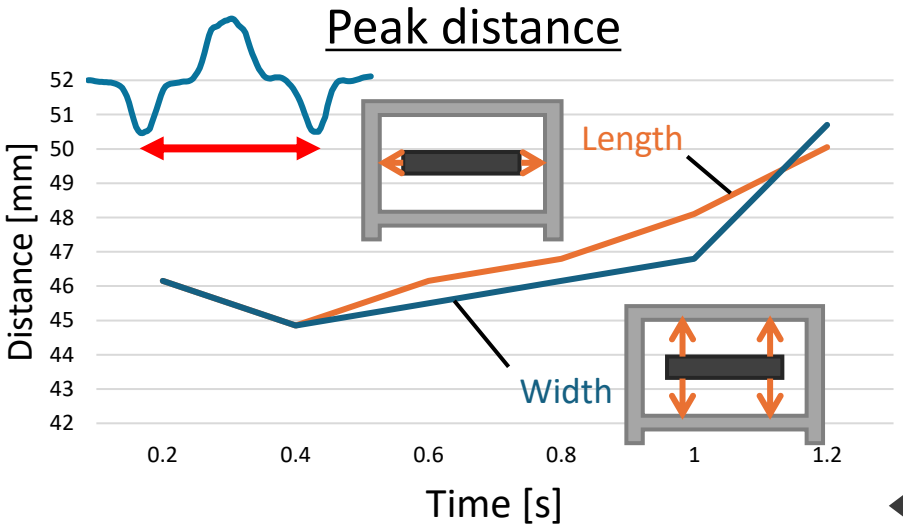

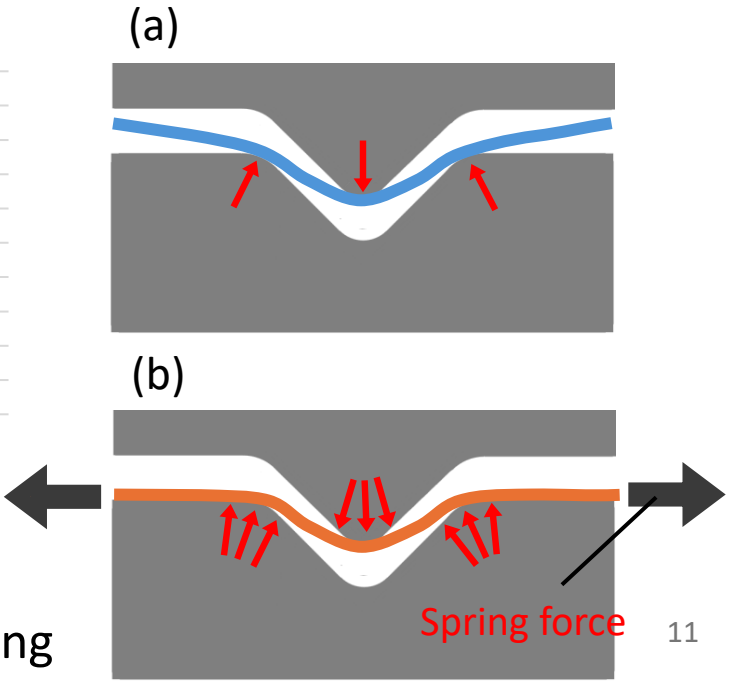

Longitudinal spring force changed corner shape
and caused gradual forming

Conclusions

- ✓ In-situ deformation monitoring technique was developed for stamp forming
- ✓ Technology will be applied to stamp forming with closed molds with large-scale

ICCM24
AUGUST 4-8, 2025
BALTIMORE CONVENTION CENTER
BALTIMORE, MARYLAND, USA

No Technical Paper Submission for:

Srikanth Pilla

ICCM24
AUGUST 4-8, 2025
BALTIMORE CONVENTION CENTER
BALTIMORE, MARYLAND, USA

No Technical Paper Submission for:

Gale Holmes

STUDY OF THE LONGITUDINAL COMPRESSIVE STRENGTH OF LAMINATED COMPOSITES USING VARIOUS CLASSICAL AND INNOVATIVE TESTS AT DIFFERENT TEMPERATURES

F. Laurin[1], A. Mavel[1], J. Berthe[1], C. Huchette[1]

[1]Onera, Paris-Saclay University
29 avenue de la division Leclerc, 932322 Chatillon France
Email: frederic.laurin@onera.fr, web page: http://www.onera.fr

Keywords: Fibre, Ply, Strength, Analytical modelling, Mechanical testing, Thermal analysis

ABSTRACT

In the design of aeronautical structures, determining the allowable values associated with failure criteria remains a key issue for the aeronautical industry, particularly the longitudinal compressive strength. Furthermore, this critical allowable value must be determined at various temperatures representative of flight conditions, or even in the event of a fire, which adds complexity to the multi-instrumented testing procedure and the associated analysis methods. This study has determined the longitudinal compressive strength of T700GC/M21 unidirectional carbon/epoxy plies by considering different classical and innovative tests performed at various temperatures (from ambient to 120 °C) and analysing them using an original hybrid failure approach.

1 INTRODUCTION

Composite materials, especially carbon fibre reinforced plastics (CFRP), are widely used in modern aircraft. Currently, design methods for laminated composite structures mainly rely on linear elastic structural analysis combined with failure criteria [1] defined at the scale of the unidirectional (UD) ply. Therefore, determining the design allowable — the ply strengths that take into account material scattering, as recommended in aeronautical standards [2]— is a major concern for designers. Determining the design allowable is a time-consuming and expensive process since many tests are required, especially at different temperatures representative of flight or fire conditions. To reduce costs and product lead times, fast and simple identification tests and analysis methods are required. Furthermore, identifying tests with low coefficients of variation (CV) would increase the A- and B-basis allowable [2], resulting in higher-performance designs. Among the in-plane strengths of a unidirectional ply, determining the longitudinal compressive strength of the ply currently remains a technical and scientific challenge.
This article analyses existing tests for determining the longitudinal compressive strength of unidirectional plies at different temperatures, from ambient temperature to 120°C. It considers classical compressive tests described in Section 2.1, but also classical and innovative bending tests in sections 3.1 and 3.2. An approach based on failure analysis has been developed to predict fibre kinking in composite laminates subjected to different loadings and temperatures in section 2.2. This approach considers the unidirectional ply as the elementary modelling entity, but some material parameters are updated using a micromechanical model. The model is applied to different test configurations performed at various temperatures in compression (section 2.3) and bending (section 3.3).

2 COMPRESSION TESTS ON UD PLY AT DIFFERENT TEMPERATURES

2.1 Presentation of compression test results on UD ply

The longitudinal compressive strength of carbon/epoxy T700GC/M21 unidirectional plies (aeronautical quality) with a weight area of 268 g/m² has been determined using classical compression tests on 16 0° laminates. All composite specimens were manufactured at ONERA using an autoclave, with a curing cycle corresponding to that recommended by the material provider.

The longitudinal compressive strength, associated with the onset of fibre kinking, is usually identified using standards based on uniaxial compressive tests on unidirectional 0° laminates. There are many standards regarding testing methods and fixtures in the literature. As initially proposed by [3] and subsequently refined in ASTM D3410/D3410M-16 [4], compressive force can be transferred to the specimen via shear at the wedge grip interfaces. This experimental device requires the use of tabbed specimens and complex, heavy fixtures. Alternatively, the EN2850 AECMA standard [5] recommends transmitting the compressive force into the specimen through end-loading [6], thus avoiding the use of additional tabs. [5] recommends transmitting the compressive force into the specimen through end-loading [6], thus avoiding the need for additional tabs. This method is currently the most commonly used in the aeronautical industry and corresponds to the ASTM D695-15 standard [7]. Finally, the ASTM D6641/D6641M standard [8] combines shear and end-loading to transmit the compressive force.

Since a higher compressive strength can be obtained using the latter method [9,10], the experimental device shown in Fig. 1 has been considered in the present study. It is associated with an Instron hydraulic testing machine with a maximum load capacity of 300 kN. Compression tests were performed at ONERA Lille with a loading rate of 1.5 mm/s. Longitudinal strain was measured using a QFLAB-3-11 strain gauge. The experimental device was introduced into a furnace, as illustrated in Fig. 1b. Compression tests have been carried out at four different temperatures: 20 °C, 80 °C, 100 °C and 120 °C. Three specimens were tested for each configuration of tests to estimate the scattering.

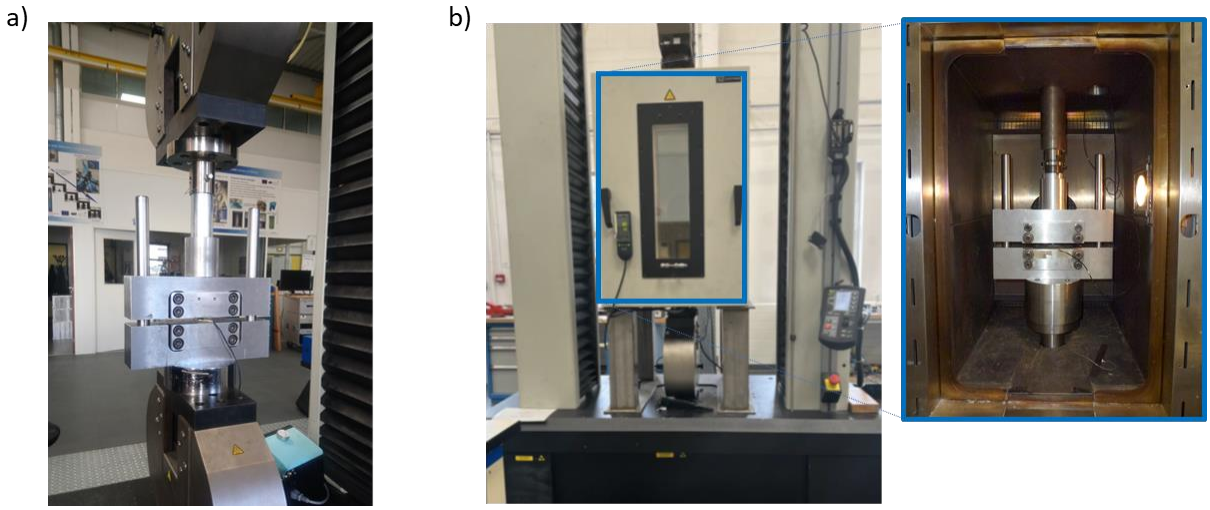

Figure 1: a) compression test device available at ONERA, b) compression test performed in a furnace.

Fig. 2a shows that the behaviour in the fibre direction appears to be insensitive to the applied temperature and exhibits slight nonlinearity up to failure. Experimental results have already demonstrated that this nonlinearity is due to the nonlinear elastic behaviour imposed by the carbon fibres [11,12], which is consistent with the observations performed in this study. Fig. 2b shows the evolution of the measured longitudinal compressive strength as a function of temperature. The evolution is almost linear and consequent (the strength is decreased by 40% at 120°C). It should be noted that the scatter of the measured strength increases with temperature. The failure patterns of the different specimens, as shown in Fig. 2b, are not located at the ends of the jaws, and the tests appear to be relevant for measuring the longitudinal compressive strength at different temperatures using the proposed experimental device.

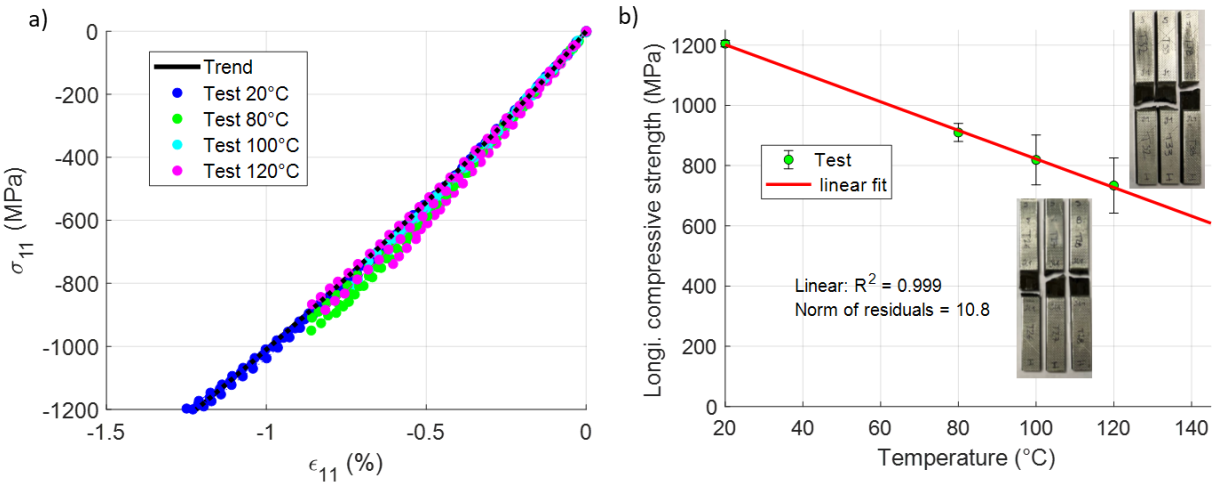

Figure 2: a) Longitudinal behavior and b) evolution of the longitudinal compressive strength of UD ply subjected to compression loading at different temperatures

2.2 Micromechanical model to predict the longitudinal compressive strength of a UD ply

A model defined at the micromechanical scale has been proposed by Grandidier [13,14]. This model is based on finite element simulations with enhanced elements to capture the fibre buckling embedded within the matrix. Based on this work, a simplified analytical model has been proposed by Grandidier [15] later in order to be used in design office to determine the longitudinal compressive strength, considering compressive loading or bending. The model accounting for the combined contributions of fibre micro-buckling [16] and the structural effect (stacking sequence, strain gradient) [17–19] was proposed to describe the mechanism of failure under compression or flexural loading [15]. The local failure mechanism accepted by the scientific community puts together a sequence of phenomena: under compression load a little fibre misalignment triggers fibre buckling, the matrix provides the assembly of the fibres but evolves to plasticity which amplifies therefore the instability, fibre failure appears successively by developing a kink band [16]. The main governing parameters of this mechanism are the nonlinearity of matrix properties and fibres initial undulation defects noted ϕ_0.
The most efficient models existing in the literature account quite well for these effects. Budiansky and Fleck [16] modelled the non-linear shear behaviour of UD (shear strain) vs. (shear stress) by using a Ramberg-Osgood (RO) description, reported in Eq. 1:

$$\frac{\gamma}{\gamma_{UD}^{y}} = \frac{\tau}{\tau_{UD}^{y}} + \frac{3}{7}\left(\frac{\tau}{\tau_{UD}^{y}}\right)^{n_{UD}} \tag{1}$$

It involves three material parameters (τ_{UD}^{y}, G_{UD}, n_{UD}) or (γ_{UD}^{y}, τ_{UD}^{y}, n_{UD}). G_{UD} is the in-plane shear modulus of the composite, τ_{UD}^{y} is a nominal shear yield stress for which the secant modulus is reduced to 70% of its initial value G_{UD}. γ_{UD}^{y} is defined as the elastic strain at the shear stress τ_{UD}^{y} so that $\tau_{UD}^{y} = G_{UD} \,.\, \gamma_{UD}^{y}$. The compressive strength, referred to as σ_{UD}^{stab}, and calculated using Budiansky and Fleck's model, is defined as the maximum stress applied on UD before the fibre instability, as reported in Eq. 2.

$$\sigma_{UD}^{stab} = \frac{1}{1 + n_{UD}\left(\frac{3}{7}\right)^{\frac{1}{n_{UD}}}\left(\frac{\phi_0/\gamma_{UD}^{y}}{n_{UD}-1}\right)^{\frac{n_{UD}-1}{n_{UD}}}} \tag{2}$$

The structural effect results in the increase of UD failure compressive strain and stress with respect to σ_{UD}^{stab}. It is due to several mechanisms that do not take place at the UD mesoscopic scale but rather at a larger, macroscopic scale (laminate).

Three factors are included in the structural effect, namely the deformation gradient through the thickness due to bending loadings, the thickness of UD ply and the stiffness of off-axis neighbouring plies. Experimental observations on the structural effect have been experimentally detailed and compared by Grandidier [15], ending with the proposal of an analytical model (reported in Eq. 3) to predict the stress due to structural application.

$$\sigma_{UD}^{struct} = 2r_{gf}\frac{\pi}{e_b}\sqrt{\frac{E_m E_f}{1-\nu_m^2}V_f(1-V_f)} \quad (3)$$

where r_{gf} is the gyration radius of fibre r_{gf}= *I/S* , with *I* the second moment of area of the fibre, and *S* the area of the fibre's cross section (it is equivalent to the fibre diameter divided by 4, in case of fibres are considered circular), E_m and ν_m are respectively the Young's modulus and the Poisson's ratio of the matrix, E_f the longitudinal elastic modulus of the fibre, V_f the volume fraction of fibres and e_b the characteristic thickness of UD involved in the instability mode (a fraction of the total thickness of UD), which is discussed below. For a UD layer subjected to bending, only the part in compression is considered for critical thickness (e_c). A reduced part of thickness is considered to contribute to compression failure due to the distribution of the strain and is considered equal to $e_b = 0.5\, e_c$ which permits correlation with experimental results considering the evolution of the middle plan during bending loading because the longitudinal behaviour in tension and in compression is different. For a UD layer subjected to compression, $e_b = \infty$ to deactivate the structural part in the model.

To summarize, the proposed model considers both the micro-buckling mechanism ($\sigma_{\mathrm{UD}}^{\mathrm{stab}}$) and the structural effect ($\sigma_{\mathrm{UD}}^{\mathrm{struct}}$). The estimated compressive strength is called critical, referred to as σ_{UD}^{crit}, is higher than σ_{UD}^{stab}, since it is defined in Eq. 4:

$$\sigma_{UD}^{crit} = \sigma_{UD}^{stab} + \sigma_{UD}^{struct} \quad (4)$$

2.3 Analysis of compression tests with an advanced micromechanical model

The micromechanical model proposed by Grandidier has been fully validated for the T700GC/M21 material. In order to use the model, however, several pieces of experimental data are required.

Firstly, the analysis of the microstructure has been performed to measure parameters related to the structural effect, such as the volume fraction of fibres and their radius, thanks to the analysis of CT scans. The distribution of fibre radii has been determined, yielding an average Weibull value of r_f=3.25µm and a fibre volume ratio of V_f =56%. In a previous study, the mechanical properties of the fibres and the matrix were determined using an inverse method based on the Mori-Tanaka approach. This method was used to obtain the relevant mechanical properties measured at the ply scale, based on tensile tests performed on 0-ply, 90-ply and [±45] laminates. The values identified were E_f=240GPa, E_m=3100MPa, and ν_m=0.3.

Then, the plasticity of the matrix, which is modelled using a Ramberg-Osgood law, requires the identification of three parameters ($\tau_{UD}^{y}, G_{UD}, n_{UD}$) at different temperatures. These parameters can be determined by inverse identification using tensile tests on a $[\pm 45]_s$ laminate tested at 20 °C, 70 °C and 120 °C at ONERA, as reported in Fig. 3 [20]. The tensile tests were performed at ONERA Lille in accordance with AITM1-002 [21], but with a displacement rate of 1 mm/s, which is consistent with the loading rate applied to the 0-ply compression tests. Longitudinal and transverse strain gauges were used to measure the in-plane shear strain in the tested specimens at different temperatures. The Ramberg-Osgood parameters for each temperature were identified independently using an automated identification method based on the simplex method [22] to calibrate the three parameters. It was observed that these three parameters evolve linearly as a function of temperature. Therefore, a first-order polynomial has been fitted to each of the three parameters to successfully describe the available experimental data at different temperatures, as shown in Fig. 3.

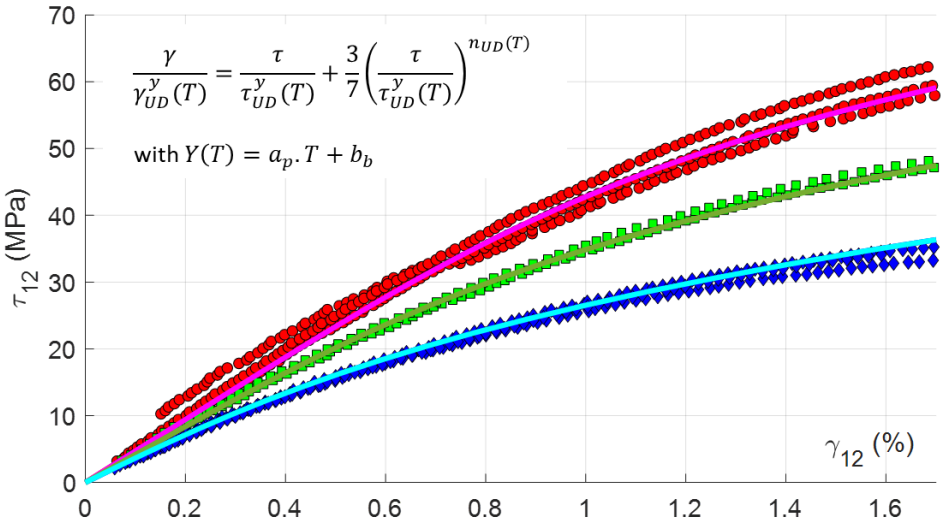

Figure 3: Tensile test on $[\pm 45]_s$ laminates at different temperatures and comparison with simulated Ramberg-Osgood model predictions

The final parameter to identify is the initial misalignment of the fibres, which causes them to kink within the composite material. This value was determined using inverse identification in conjunction with a tensile test on a specific laminate that failed in compression. The identified value is $\phi_0 = 2°$, which is consistent with data found in the literature [15,23].

Fig. 4a shows a successful comparison between experimental stress/strain curves at different temperatures and the predicted elastic nonlinear behaviour introduced in the OPFM model which is assumed to be insensitive to temperature. The details of the nonlinear elastic behaviour are given in [24]. Finally, Fig. 4b presents a comparison of the test results for 0 ply at different temperatures with the predictions of the identified micromechanical model. The evolution of strength with temperature is predicted very accurately from ambient temperature to 120°C. The decrease in strength with temperature is approximately -40% compared to ambient temperature, which is significant and must be considered in the design of composite structures.

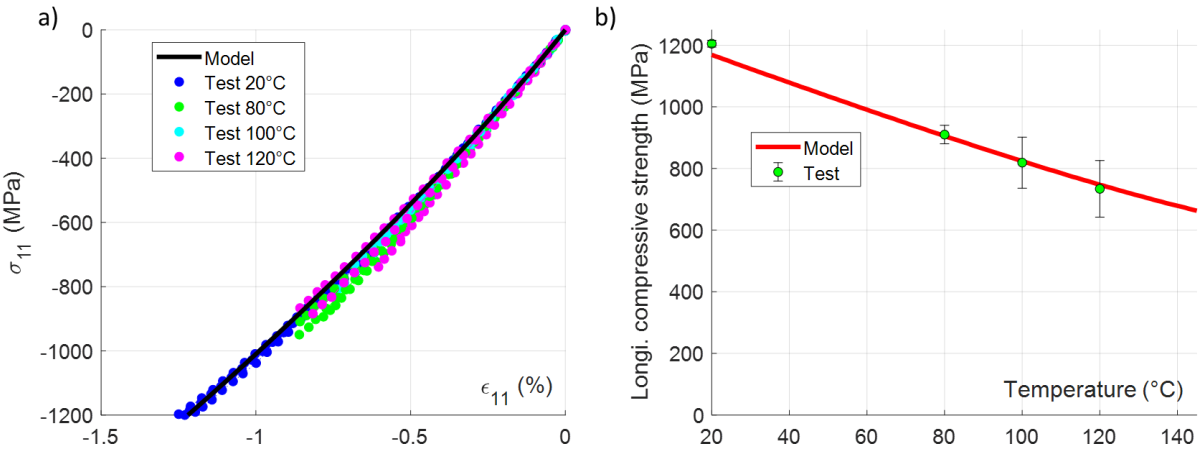

Figure 4: Experimental and predicted a) longitudinal behavior and b) evolution of the longitudinal compressive strength of UD ply subjected to compression at different temperatures

3. BENDING TESTS ON UD PLY AT DIFFERENT TEMPERATURES

3.1 Presentation of four-point bending test results on UD ply at different temperatures

The longitudinal compressive strength of 268 g/m² carbon/epoxy T700GC/M21 unidirectional plies has also been determined using classical four-point bending tests on 0° laminates. Several authors have indeed proposed using bending tests to overcome the challenges associated with compressive testing of unidirectional laminates. For a carbon/epoxy unidirectional ply, the longitudinal compressive strength is much lower than the longitudinal tensile strength. Therefore, three-point bending tests [25,26] and four-point bending tests [27] are useful for identifying compressive strength in the fibre direction.

Therefore, four-point bending tests have been performed on specimens constituted with 8 0-plies at ONERA Châtillon using an electromechanical testing machine with a maximum loading capacity of 150kN. The specimens measured 120×10×2.23 mm. The loading rate was fixed at 1 mm/min. The distance between the support spans is 100 mm, and the distance between the loading spans is 30 mm. The span radius has been set to 5 mm. The experimental device was introduced into a furnace that allowed a temperature to be applied ranging from -100°C to 500°C. Furthermore, a large window in the furnace door enables measurement of the strain field on one of the specimen's free edges, where a black-and-white speckle pattern has been applied. This is achieved using digital image correlation with Vic2D software, with one camera focused between the loading span to observe the failure pattern and another observing the global view of the setup to control the boundary conditions. The experimental setup is described in Fig. 5. Four-point bending tests were performed at different temperatures: 20 °C, 45 °C, 120 °C, 145 °C and 165 °C. Only one specimen was tested for each temperature studied.

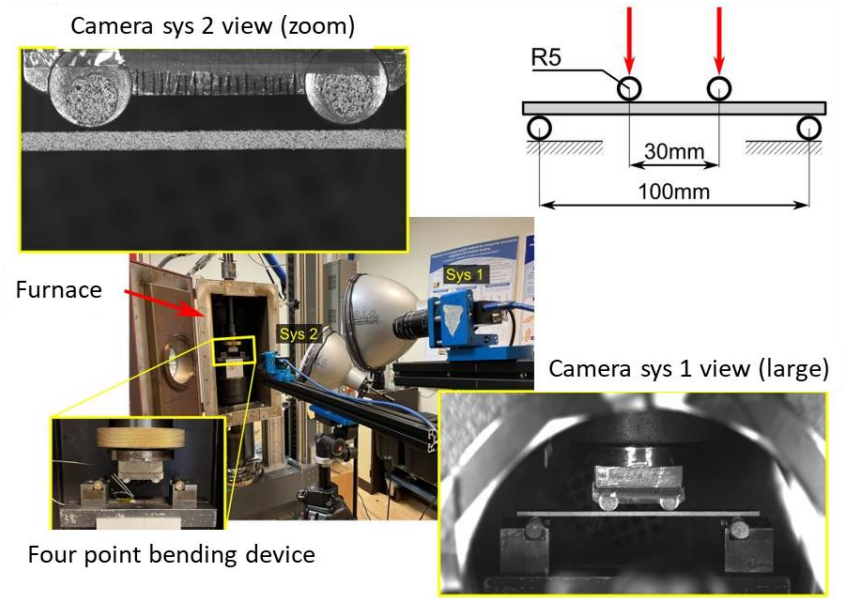

Figure 5: Four-point bending tests performed in a furnace at different temperatures, from ambient temperature to 165°C.

The failure pattern has been analysed at different temperatures. At temperatures above 100°C, failure of the specimen is more progressive, with compressive fibre failure occurring between the loading spans. The measured strains at failure for these high temperatures are reported in Fig. 6. A typical failure pattern is observed at 120 °C, and these results can be considered valid. Linear evolution of apparent longitudinal strain at failure as a function of temperature is observed. However, at 20°C and 45°C, failure occurs prematurely within the loading spans. These strains at failure, which are also reported in Fig. 6, are not considered valid for the purposes of the following analysis. It is well known that four-point bending test set-ups generate high stress concentrations under the rollers, which can lead to local indentation and premature specimen failure.

To avoid this, some authors introduced polymer pads between the rollers and the specimens [23]. However, this necessitates the characterisation of the additional material's mechanical behaviour. To overcome this difficulty, an alternative bending device has been developed, which is presented in the next section.

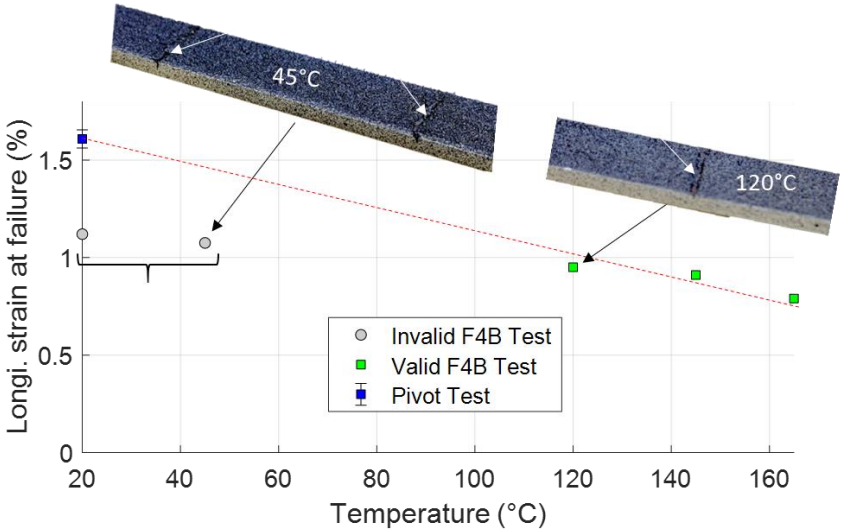

Figure 6: Evolution of the longitudinal strain at failure as a function of the temperature considering test results from four-point bending and compressive with pivot tests.

3.2 Presentation of compression with pivot test on UD ply at ambient temperature

The compression with pivots testing device [28] enables bending loading to be generated by offsetting the mid-plane of the laminate with respect to the rotation axes of the pivots. This is an alternative to existing bending testing devices [11,14,29–31]. This device avoids local stress concentrations close to the jaws and the indentation issues experienced with the aforementioned testing set-ups. Furthermore, it enables direct observation of compressive failure in the surface plies of the laminate. Due to the use of a bending loading mode, the failure mechanism can be observed in the gauge section, which is far from the jaws.

Figure 7a shows an original experimental compression device with pivots. The concept involves applying uniform compression to a laminate plate that is clamped between two jaws with pivots. The eccentricity of a given test relates to the offset of the plate's mid-surface and imposes the compression-to-bending ratio. This is controlled by inserting a couple of wedges adequately into the jaws of the tabs. In the present study, large eccentricities equal to half the total thickness of the specimen being tested are used to obtain a quasi-pure bending moment in the gauge length.

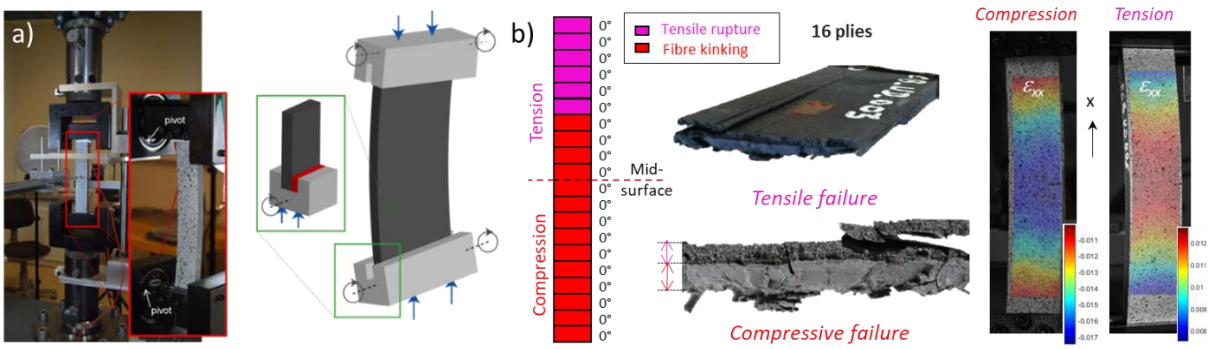

Figure 7: a) Presentation of the compression with pivots experimental device, b) Failure pattern of the 16 0-plies subjected to bending loading

Bending tests on 16 0-plies specimens have been performed at ONERA Châtillon, but only at ambient temperature. The specimens measured 130 mm x 30 mm x 4.2 mm. Three specimens were tested. Different measurement techniques were used to improve understanding of the physical mechanisms involved and to obtain global and local information, as reported in Fig. 7a: (i) a LVDT sensor; (ii) acoustic emission to detect damage events during loading (no acoustic events were detected prior to final failure); (iii) strain gauges bonded to the upper and lower faces of the unnotched specimens to measure strain; and (iv) stereo digital image correlation (using the Vic3D system) on the two faces of the specimen painted with black-and-white speckles to measure in-plane strains on the outer surfaces, as shown in Fig. 6b, (v) post-mortem micrographs to study the failure pattern of the specimens. The distribution of fibre failure in tension and compression through the thickness can easily be observed in the post-mortem pictures since the grey colours correspond to different failure mechanisms. The evolution of the mid-plane during the tests is also clearly visible. Furthermore, failure occurs far from the jaws and can be considered a valid compressive fibre failure mode. The strain at failure on the compression face, measured with DIC and a strain gauge at ambient temperature, is -1.6%, with a covariance of 2.9%. This has been added to Fig. 6 (blue point) and should be considered instead of the test results at 20 °C and 45 °C obtained using four-point bending device. The evolution of the strain at failure appears to be linear again, with a -50% decrease in strain at failure for compression with a pivot test at ambient temperature compared to that measured in four-point bending tests at 165°C.

3.3 Analysis of the bending tests with the micromechanical model

The micromechanical model was applied to estimate the longitudinal compressive strength of bending tests carried out at different temperatures. The strain at failure was estimated by considering the elastic nonlinear behaviour mentioned in Section 2.2 and previously identified. It should be noted that the effective thickness considers the evolution of the middle plane during the bending test due to the hardening observed in longitudinal tension and the softening observed in longitudinal compression. Fig. 8 shows a comparison of the predicted and measured strain at failure obtained from the bending test. Initially, the predicted evolution of the failure strain appears slightly nonlinear and is consistent with the experimental data.

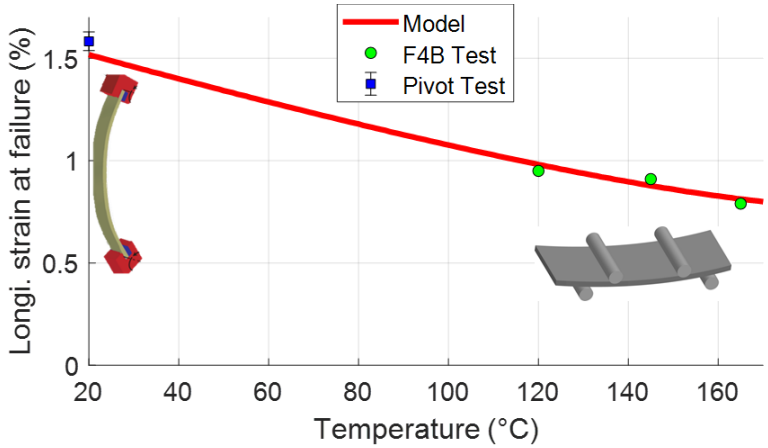

Figure 8: Predicted and measured evolution of the longitudinal strain at failure as a function of the temperature considering bending tests

The same identification has been used for the micromechanical model in order to predict the evolution of the longitudinal compressive strength (or longitudinal strain at failure) when 0-ply is subjected to compression or bending at different temperatures. The results obtained are promising.

4 CONCLUSIONS

This study determined the longitudinal compressive strength of T700GC/M21 unidirectional carbon/epoxy plies by performing compression and bending tests at different temperatures (from ambient to 145 °C) and analysing the results using an original micromechanical approach.

The longitudinal compressive strength was determined from the results of standardised compression tests on sixteen 0-plies at different temperatures. The longitudinal compressive strength and the associated strain at failure decreased linearly with temperature, dropping by -40% at 120°C. Furthermore, four-point bending tests were carried out on 8 0-plies at different temperatures. The longitudinal strain was measured using digital image correlation to observe the specimen through a large window into the furnace. Once again, the evolution of the measured strain at failure is almost linear as a function of temperature, dropping by -50% at 145°C.

The micromechanical model proposed by Grandidier was used to determine the apparent longitudinal compressive strength of the ply. This model takes into account the nonlinearity of the matrix and was calibrated at different temperatures through the analysis of tensile tests on $[\pm 45]_s$ laminates, and the nonlinear behaviour in the fibre direction. Analysis of the various tests using the current failure approach has demonstrated consistency between the test data obtained at different temperatures, which is encouraging.

ACKNOWLEDGEMENTS

The authors would like to express their sincere gratitude to DGA-TA for funding this experimental and numerical study.

REFERENCES

[1] P.D. Soden, M.J. Hinton, A.S. Kaddour, A comparison of the predictive capabilities of current failure theories for composite laminates, Compos. Sci. Technol. 58 (1998) 1225–1254.
[2] MIL-HDBK-17-1F: Composite Materials Handbook, Volume 1 - Polymer Matrix Composites Guidelines for Characterization of Structural Materials, U.S. Department of Defence, 2002.
[3] K. Hofer, P. Rao, A New Static Compression Fixture for Advanced Composite Materials, J. Test. Eval. 5 (1977) 278–283.
[4] ASTM D3410 / D3410M - 16, Standard Test Method for Compressive Properties of Polymer Matrix Composite Materials with Unsupported Gage Section by Shear Loading, 2016.
[5] AECMA, AECMA standard EN-2850, Aerospace series carbon fibre thermosetting resin unidirectional laminates. Compression test parallel to fibre direction, 1997.
[6] C. Soutis, J. Lee, C. Kong, Size effect on compressive strength of T300/924C carbon fibre-epoxy laminates, Plast. Rubber Compos. 31 (2002) 364–370.
[7] ASTM D695-15, Standard Test Method for Compressive Properties of Rigid Plastics, 2015.
[8] ASTM D6641 / D6641M-16, Standard Test Method for Compressive Properties of Polymer Matrix Composite Materials Using a Combined Loading Compression (CLC) Test Fixture, 2016.
[9] D. Adams, J. Welsh, The Wyoming Combined Loading Compression (CLC) Test Method, J. Compos. Technol. Res. 19 (1997) 123–133.
[10] I.M. Daniel, H.M. Hsiao, Is there a thickness effect on compressive strength of unnotched composite laminates?, Int. J. Fract. 95 (1999) 143–158.
[11] O. Allix, P. Ladeveze, E. Vittecoq, Modelling and identification of the mechanical behaviour of composite laminates in compression, Compos. Sci. Technol. 51 (1994) 35–42.
[12] T. Yokozeki, T. Ogasawara, T. Ishikawa, Nonlinear behavior and compressive strength of unidirectional and multidirectional carbon fiber composite laminates, Compos. Part A 37 (2006) 2069–2079.
[13] S. Drapier, J.-C. Grandidier, M. Potier-Ferry, Towards a numerical model of the compressive strength for long fibre composites, Eur. J. Mech. - ASolids 18 (1999) 69–92.
[14] J.-C. Grandidier, G. Ferron, M. Potier-Ferry, Microbuckling and strength in long-fiber composites: theory and experiments, Int. J. Solids Struct. 29 (1992) 1753–1761.

[15] J.-C. Grandidier, P. Casari, C. Jochum, A fibre direction compressive failure criterion for long fibre laminates at ply scale, including stacking sequence and laminate thickness effects, Compos. Struct. 94 (2012) 3799–3806. http://dx.doi.org/10.1016/j.compstruct.2012.06.013.
[16] B. Budiansky, N.A. Fleck, Compressive failure of fibre composites, J. Mech. Phys. Solids 41 (1993) 183–211.
[17] S. Drapier, C. Gardin, J.-C. Grandidier, M. Potier-Ferry, Structure effect and microbuckling, 9th Fr. Natl. Colloq. Compos. Mater. 56 (1996) 861–867. https://doi.org/10.1016/0266-3538(96)00033-4.
[18] C. Gardin, J.C. Grandidier, M. Potier-Ferry, Homogenized models for the modelling of instability in long fibre media, Rev. Mec. Appliquée ThÉorique 1 (2002) 171–203.
[19] M.R. Wisnom, J.W. Atkinson, Constrained buckling tests show increasing compressive strain to failure with increasing strain gradient, Compos. Part Appl. Sci. Manuf. Inc. Compos. Compos. Manuf. 28 (1997) 964.
[20] J. Berthe, M. Brieu, E. Deletombe, Thermo-viscoelastic modelling of organic matrix composite behaviour – Application to T700GC/M21, Mech. Mater. 81 (2015) 18–24. https://doi.org/10.1016/j.mechmat.2014.10.005.
[21] AITM, AITM standard 1-0002, Fibre reinforced plastics - Determination of in-plane shear properties (+-45 tensile test), 1998.
[22] J.C. Lagarias, J.A. Reeds, M.H. Wright, P.E. Wright, Convergence properties of the Nelder-Mead simplex method in low dimensions, SIAM J. Optim. 9 (1998) 112–147. https://doi.org/10.1137/S1052623496303470.
[23] P.-Y. Mechin, V. Keryvin, J.-C. Grandidier, D. Glehen, An experimental protocol to measure the parameters affecting the compressive strength of CFRP with a fibre micro-buckling failure criterion, Compos. Struct. 211 (2019) 154–162. https://doi.org/10.1016/j.compstruct.2018.12.026.
[24] F. Laurin, N. Carrere, J.-F. Maire, Strength analysis methods for high stress gradient parts in composite structures ensuring design office requirements, ProcIMechE PartG JAerospace Eng. 225 (2011) 291–301.
[25] N. Carbajal, F. Mujika, Determination of compressive strength of unidirectional composites by three-point bending tests, Polym. Test. 28 (2009) 150–156.
[26] N. Carbajal, F. Mujika, Determination of longitudinal compressive strength of long fiber composites by three-point bending of [0$_m$/90$_n$/0$_p$] cross-ply laminated strips, Polym. Test. 28 (2009) 618–626.
[27] P.J. Callus, The effects of hole-size and environment on the mechanical behaviour of a quasi-isotropic AS4/3501-6 laminate in tension, compression and bending, Defence Science and Technology Organisation of Australian Government, 2007.
[28] F. Laurin, C. Julien, P. Paulmier, Damage and strength analysis of open-hole laminated plates under tensile, compressive and bending loadings, in: 2016: pp. 1–8.
[29] M.R. Wisnom, On the Increase in Fracture Energy with Thickness in Delamination of Unidirectional Glass Fibre-Epoxy with Cut Central Plies, J. Reinf. Plast. Compos. 11 (1992) 909.
[30] M.R. Wisnom, T. Reynolds, N. Gwilliam, Reduction in interlaminar shear strength by discrete and distributed voids, Compos. Sci. Technol. 56 (1996) 101.
[31] C. Hochard, J. Payan, O. Montagnier, Design and computation of laminated composite structures, Compos. Sci. Technol. 65 (2005) 474.



Monitoring The Structural Condition of Composite Industrial Parts Through Embedded Optical Sensorization

ICCM24 – 24th International Conference on Composite Materials
August 4 – 8, 2025, Baltimore – USA

Helena Rocha
Carlos Fonte, Sara Gomes, Rui Santos, Hugo Gomes,
Pedro Mendes, Pedro Grilo, Pedro Vieira, Paulo Antunes

Contents

- Introduction
- Case Study 1 – Monitoring of Composite Overwrapped Pressure Vessels
- Case Study 2 – Monitoring of a UAV's spar
- Conclusions



INTRODUCTION

Damage in Composite Materials

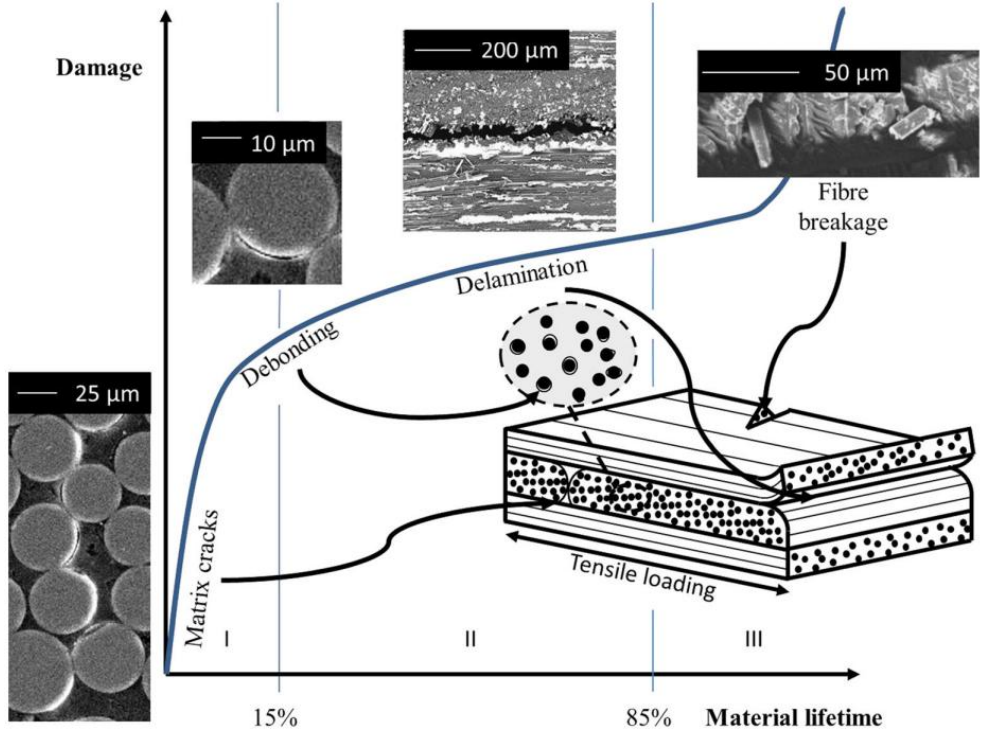

Damage evolution in continuous fiber composites during **fatigue loading** and occurring damage mechanisms

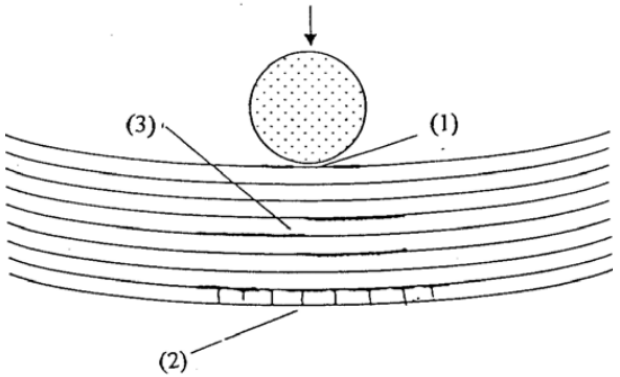

(1) Compression failure
(2) Tension failure
(3) Shear-driven delamination at multiple interfaces

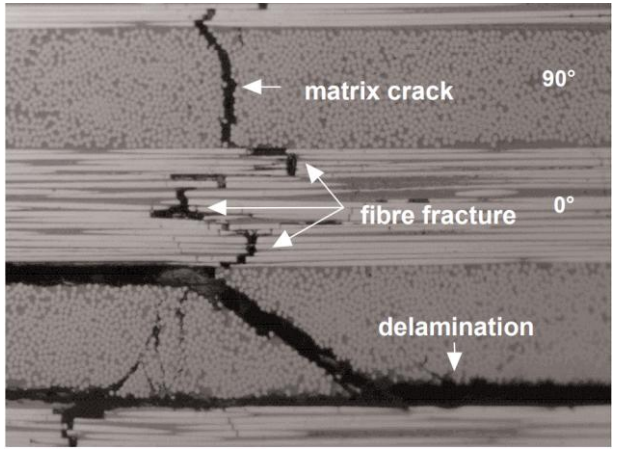

Damage mode types on **impacted** composite laminate

Davies, G. A. O., Olsson, R. Impact on composite structures. The Aeronautical Journal (2004), 108 (1089), 541–563
Duchene, P., Chaki, S., Ayadi. A., Krawczak, P. A review of non-destructive techniques used for mechanical damage assessment in polymer composites. J Mater Sci (2018) 53: 7915–7938

Embedded Sensorization:

A Smart Solution for Composite Health Monitoring

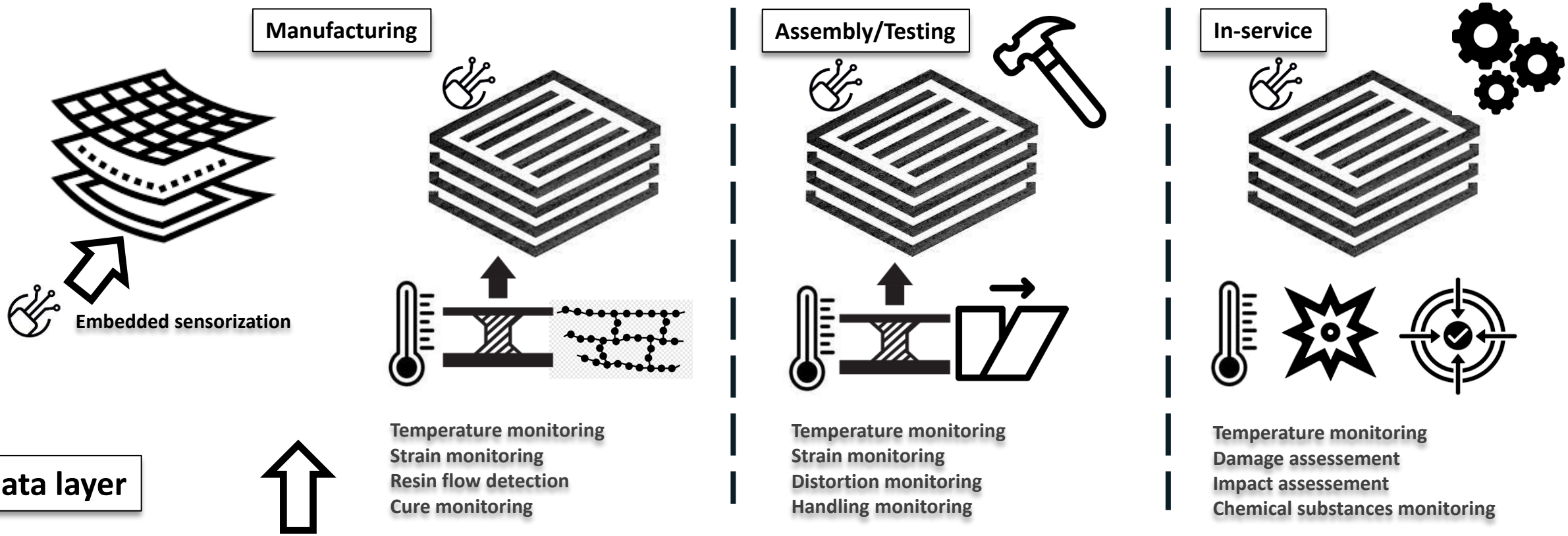

Optical Fiber Sensors:
Fibre Bragg Grating (FBG) sensors

Advantages

+ compatibility with composites fabrication
+ reduced cabling as several FBG sensors can be multiplexed in the same OF
+ high sensitivity
+ ability to monitor the fabrication process and curing
+ capability of impact damage detection
+ localized strain measurement
+ immunity to electromagnetic interference
+ Durability

Disadvantages

- expensive optoelectronic interrogation system
- fragility
- localized strain measurement

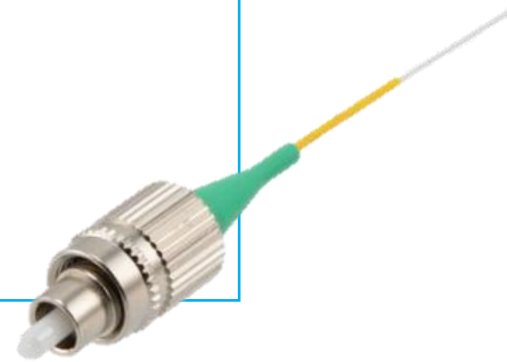

Fibre Gragg Grating (FBG) sensors

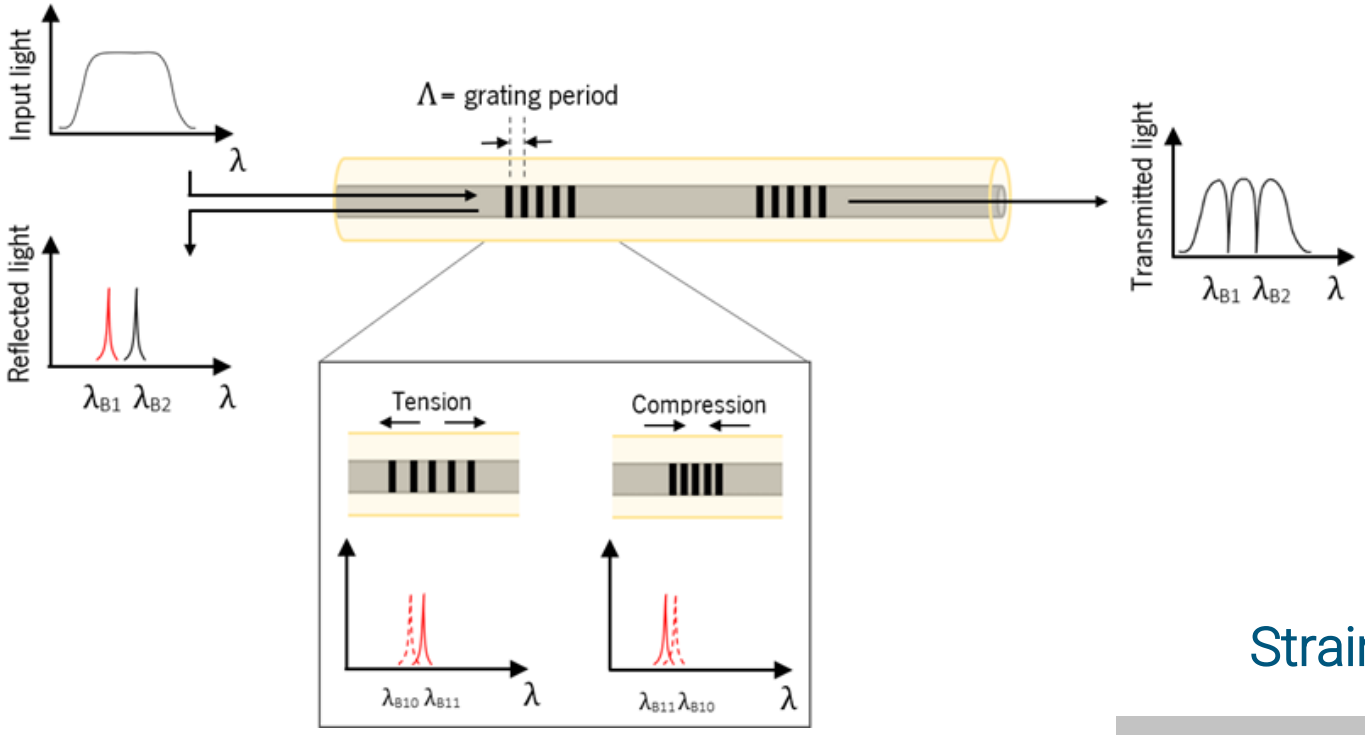

$$\Delta\varepsilon = \Delta\lambda_S \times S_\varepsilon$$

$$\Delta T = \Delta\lambda_T \times S_T$$

Strain – Temperature compensation

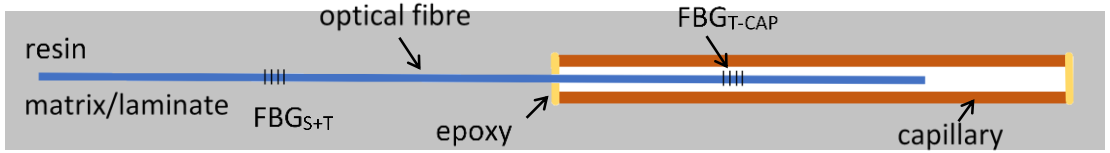



CASE STUDY 1

Monitoring of Composite Overwrapped Pressure Vessels

Objectives

- Establish a baseline of FBG sensors data for the current manufacturing process (Winding, Curing and *Autofrettage*) and pressure cycling fatigue test
- Measurement of strain in all manufacturing and testing stages
- Assess the contribution of different layers (at location of FBG sensors) to the overall mechanical resistance of the SCBA tanks

SCBA tank specimens

Specimen	OF Supplier	Manufacturing variations
1	A	External heating during heating of CF/epoxy prepreg tape winding
2	B	No use of external heating

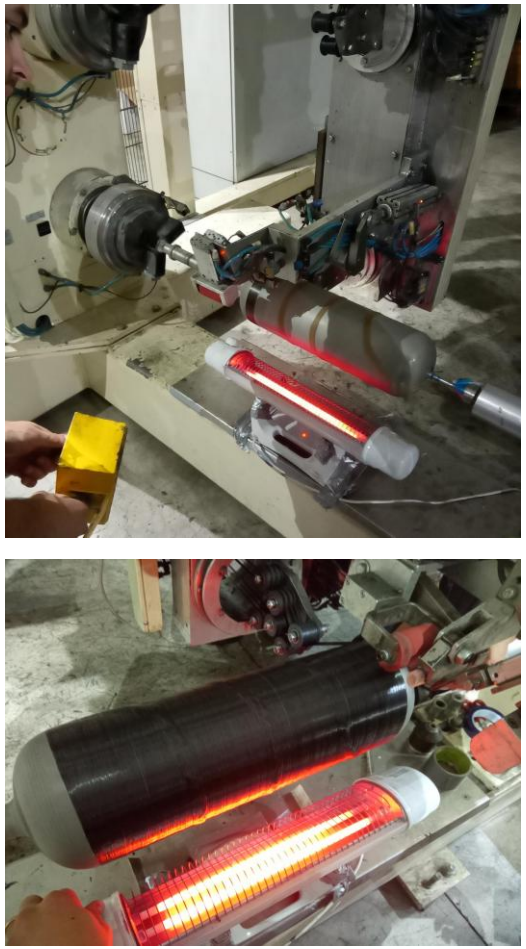

Winding of CF composite layers of SCBA tank 1 with applied external heating

FBG sensors Integration Methodology

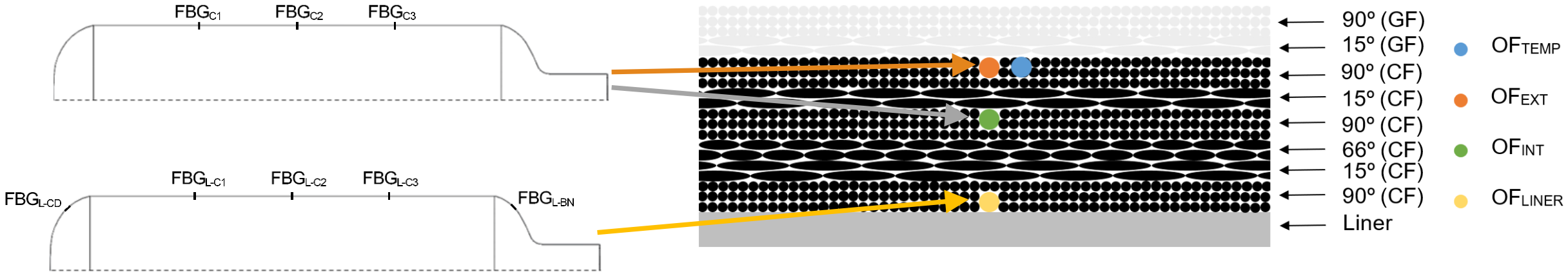

Summary of embedded OFs

OF	No. FBG sensors	Sensor type	Location
OF$_{LINER}$	5	mechanical and thermal strain	Liner Surface
OF$_{INT}$	3		In between internal CF circumferential layers and helical layers
OF$_{EXT}$	3		In between last circumferential CF and GF layers
OF$_{TEMP}$	1	temperature variations	In between same layers as OF$_{EXT}$. FBG$_{TEMP}$ positioned next to FBG1 on OF$_{EXT}$

FBG sensors Integration

OF_{LINER}



OF_{INT}

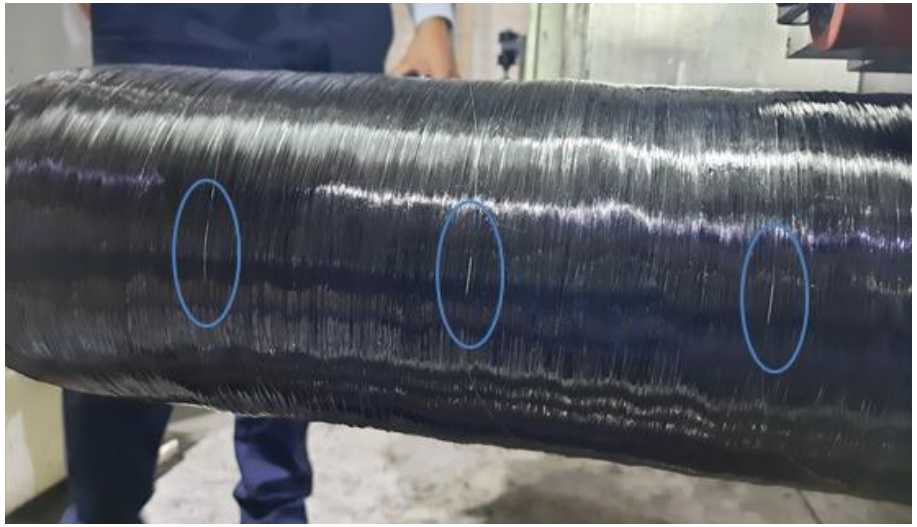

OF_{EXT} & OF_{TEMP}

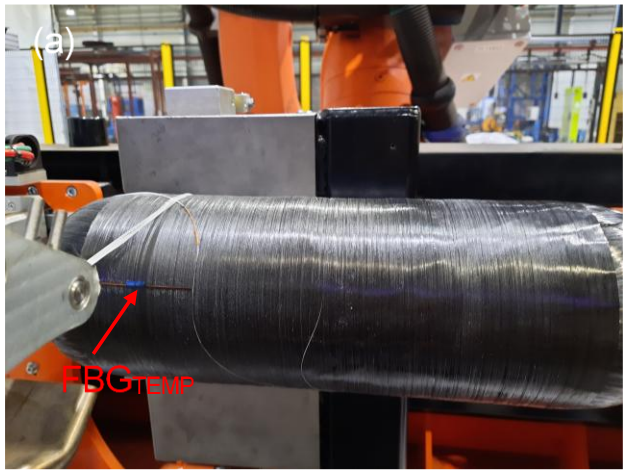

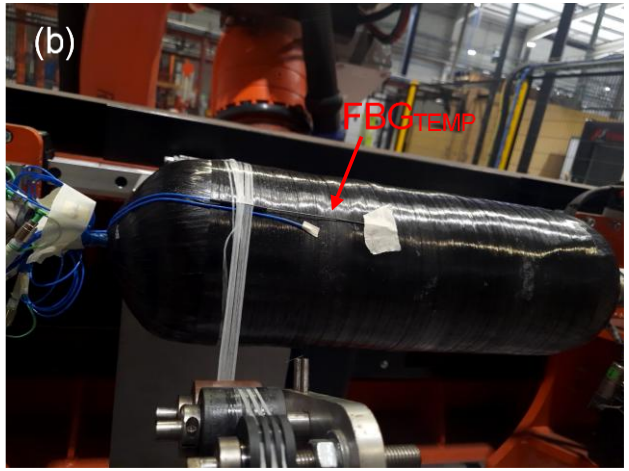

Manufacturing – Winding



Loading of the instrumented liner on the winding equipment



Winding of first intermediate helical layer



Loading of SCBA tank specimen in the GF winding equipment

Winding Monitoring

Measured strain, by FBG_{L-C2} close to the liner, during winding of different layers

Winding Stages		Tank 1 (FBG L-C2)	Tank 2 (FBG L-C2)
0	Before Winding	0	0
1	1Circf	795	-77
2	2Circf	1333	-103
3	3Circf	1282	-128
4	4Circf	1205	-154
5	Hel15	1385	-77
6	Hel66	1256	-179
7	1Circf int	1231	-256
8	2Circf int	564	-179
9	Hel int	-	-128
10	1Circf ext	-	-179
11	Hel GF	-	-26
12	1Circf GF	-	-103
13	2Circf GF	-	-77
14	3Circf GF	-	-128

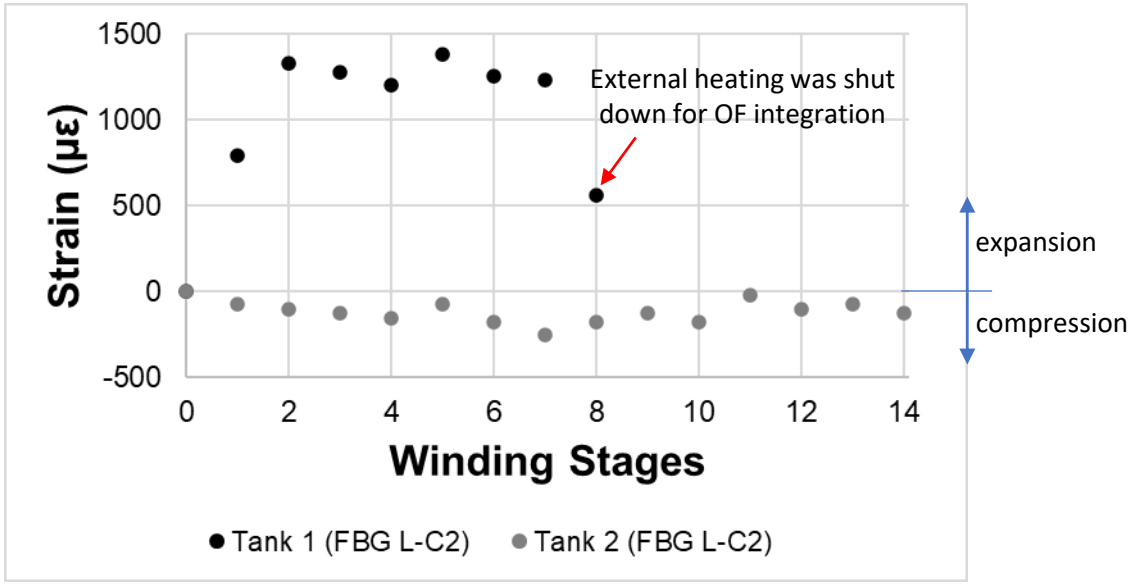

Manufacturing – Curing

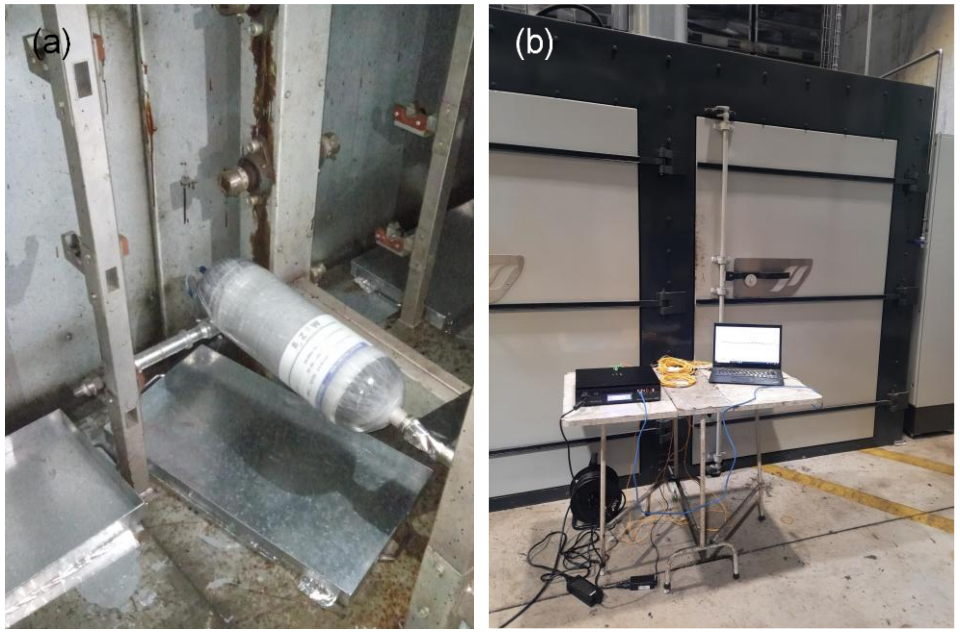

(a) instrumented SCBA tank specimen in the oven for curing and (b) data acquisition set up outside of it

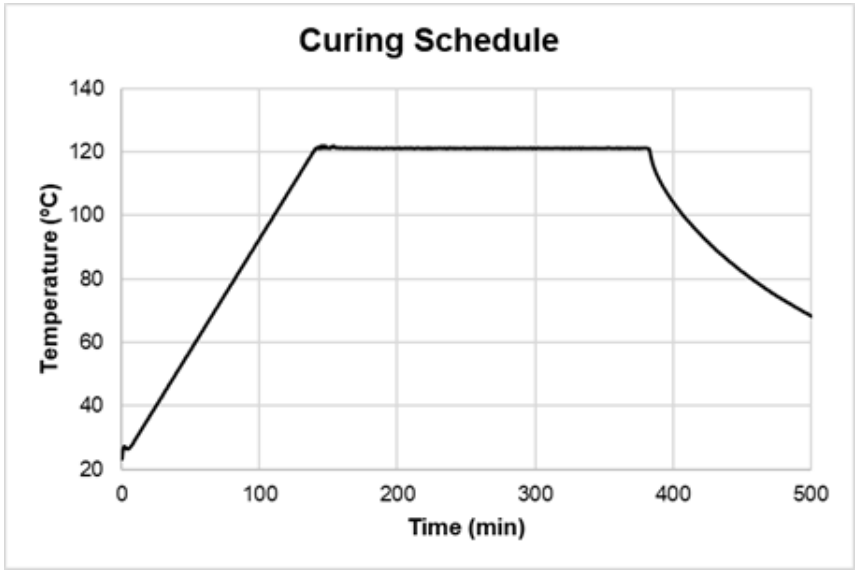

Typical curing schedule

Curing Monitoring

SCBA tank 1

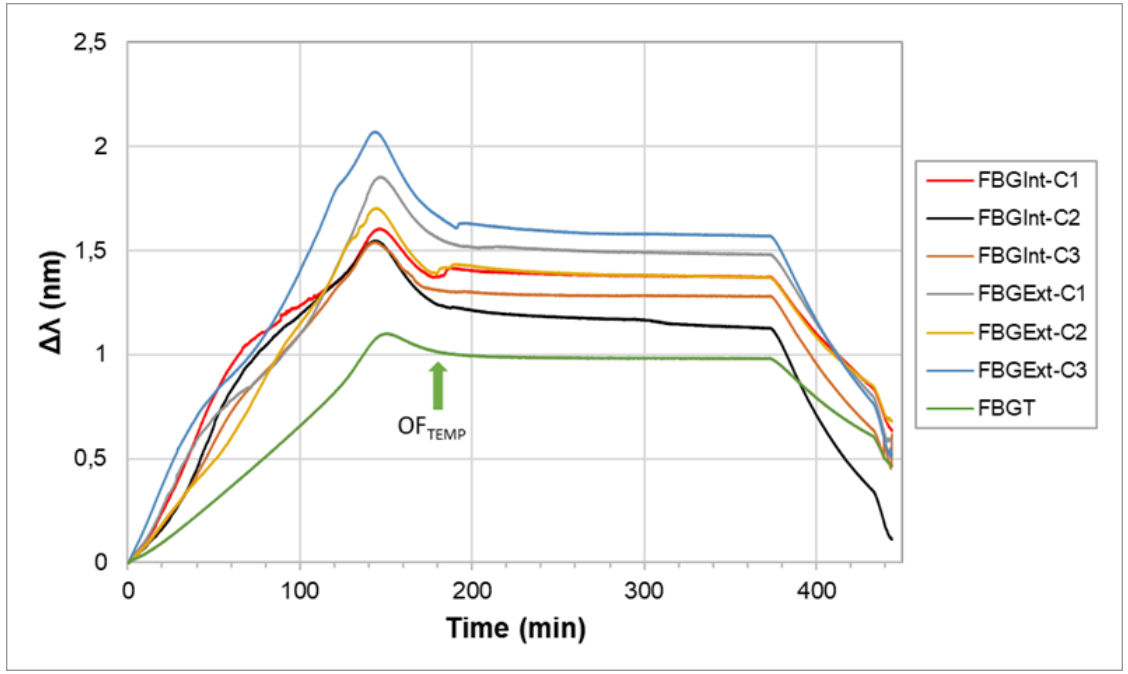

Central wavelength changes measured by FBG sensors in the SCBA tank 1

SCBA tank 2

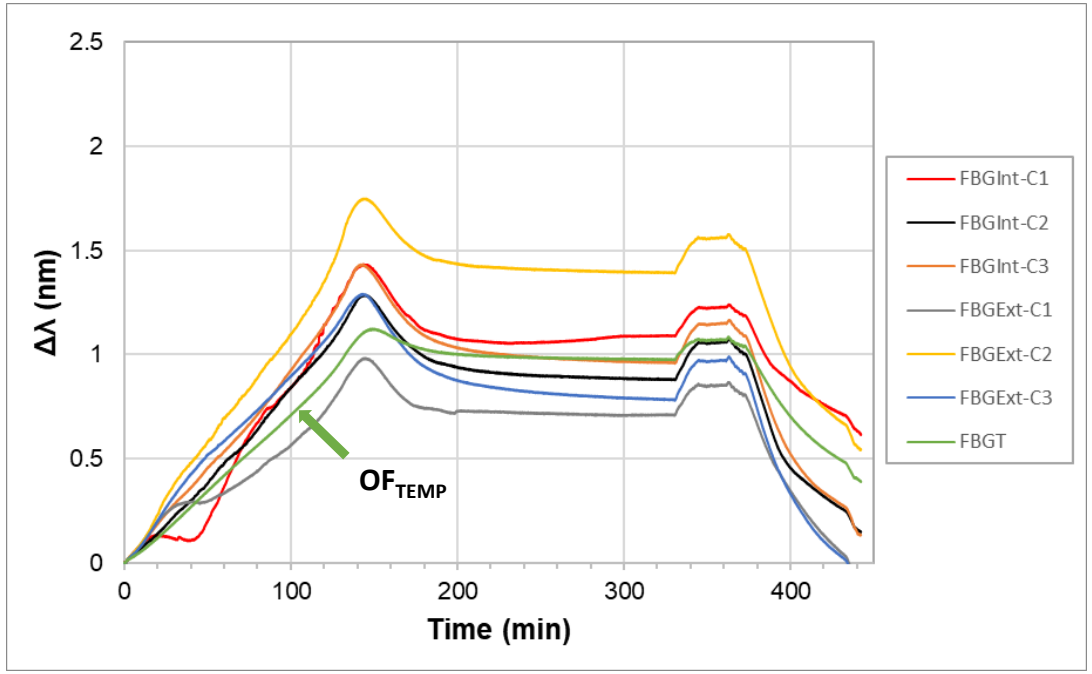

Central wavelength changes measured by FBG sensors in the SCBA tank 2

Curing Monitoring

SCBA tank 1

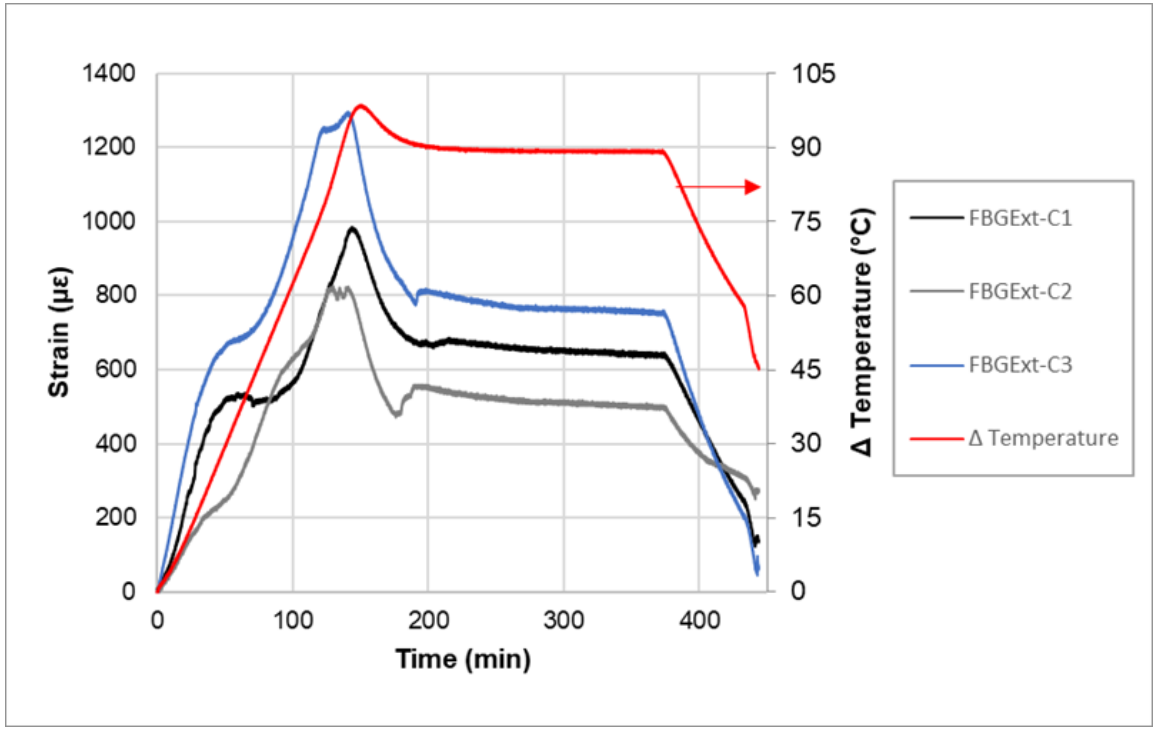

SCBA tank 2

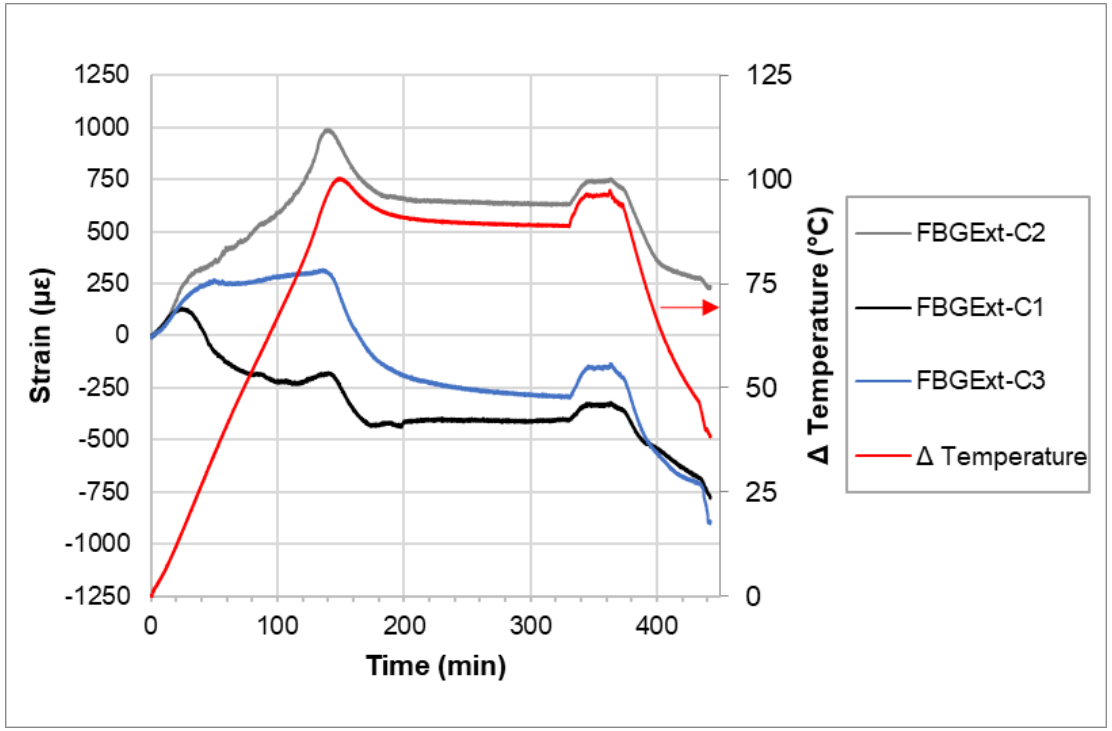

Strain and temperature changes for FBG sensors in the OF_{EXT} and OF_{TEMP} placed in between last CF layer and first GF layer in the SCBA tank 1 (left) and tank 2 (right)

Manufacturing – *Autofrettage*

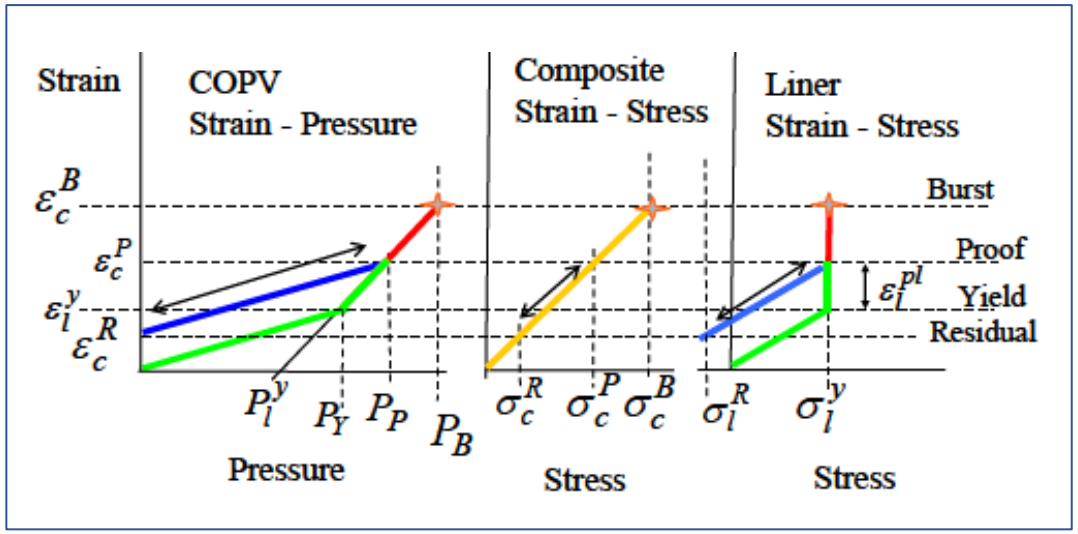

Stress/strain behaviour of liner, composite overwrap and overall COPV when subject to pressurization during autofrettage and following pressure cycles

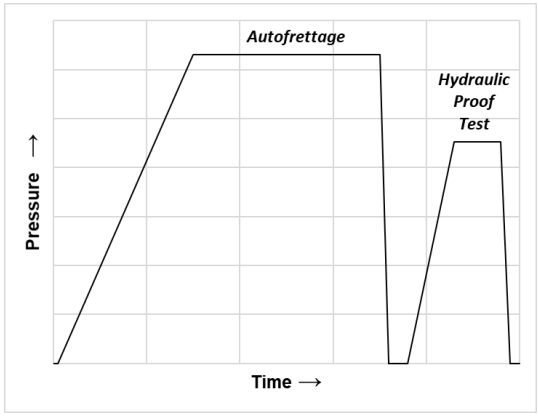

Theoretical pressure schedule of the autofrettage process and subsequent hydraulic proof pressure test

J. C. Thesken, P. Murthy, and L. Phoenix, "Composite overwrap pressure vessels: Mechanics and stress rupture lifing philosophy," 2009.

Fatigue Pressure Cyclic Test



Instrumented SCBA tank specimen in the fatigue test equipment ready for testing

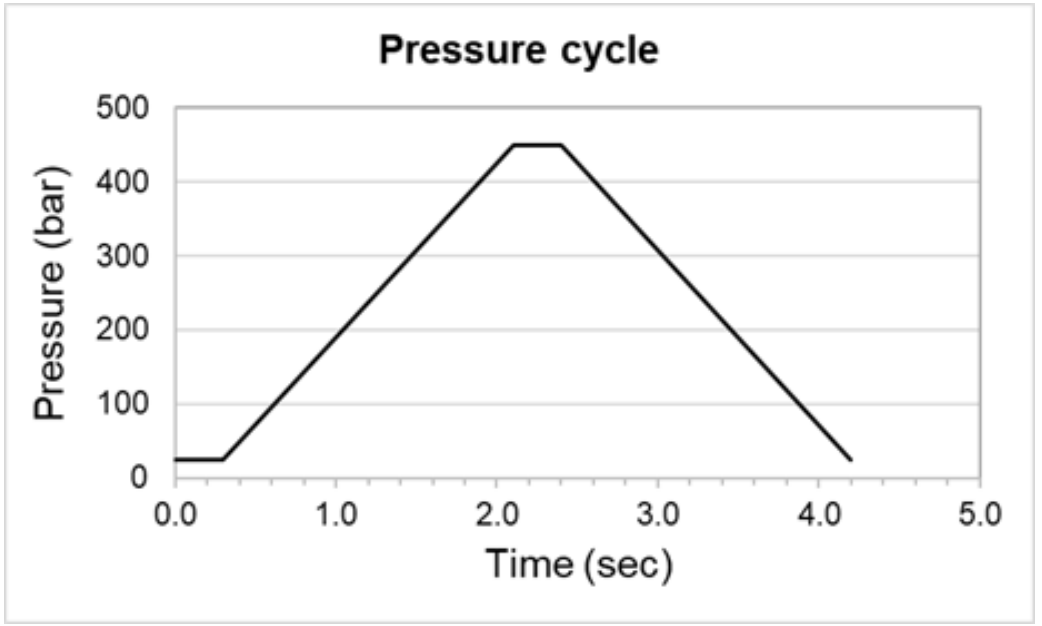

Pressure cycle employed in the fatigue test

Autofrettage and Fatigue Testing Monitoring

Autofrettage Process

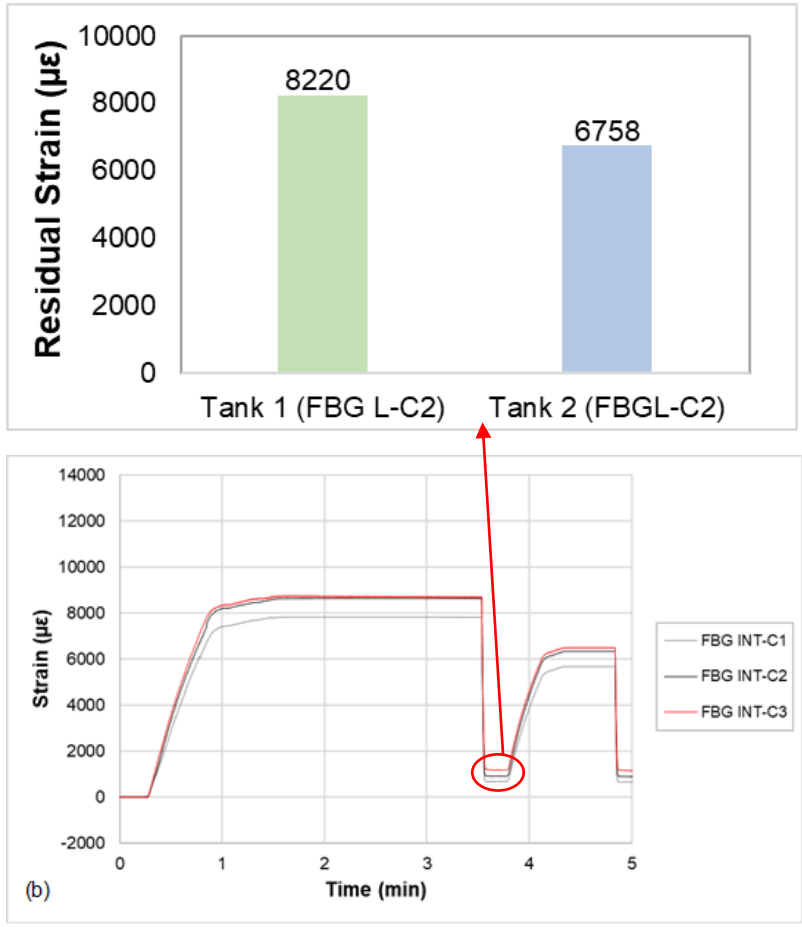

Example of strain measured by FBG sensors in OF_{INT} in SCBA tank 1

Fatigue Testing

Specimen	Number of endured cycles in fatigue test
1	16 281
2	8 234

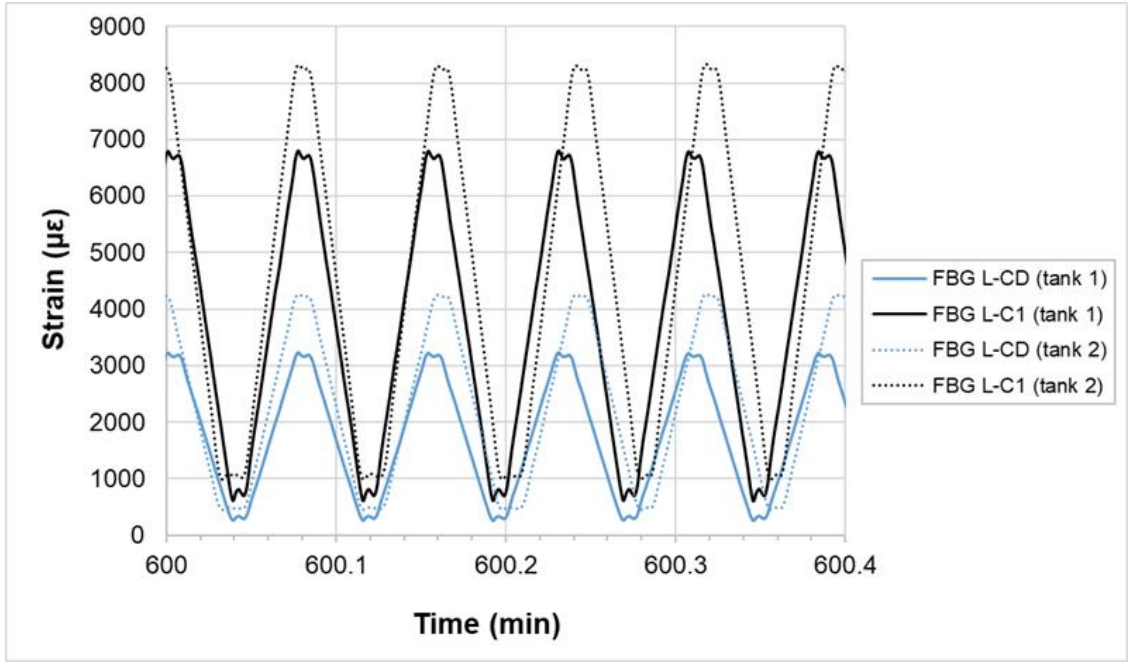

Comparison of strain measured in $FBG_{L\text{-}CD}$ and $FBG_{L\text{-}C1}$ sensors, bonded to the liner, on the different SCBA tank specimens

Conclusions

Winding Process: Heating of the wound setup promoted expansion of the liner (tank 1);

Curing: it is possible that full curing conversion is not achieved by the end of the isothermal period, as strain is still slightly decreasing;

Autofrettage:

- The residual strain measured by the FBG sensors confirm that plasticity is successfully imposed on the liner;
- It is possible that tank 1 has suffered higher plasticity in the *autofrettage* process (increased volumetry);

Fatigue Testing:

- FBG sensors in the liner show higher amplitude deformation in SCBA tank 2 (non-heated), which may explain the much faster failure of this specimen;
- The lower strain amplitudes measured in FBG sensors in OF_{LINER} of tank 1 could be linked with the increase of liner's volumetry (plastic deformation) and the consequent higher compression loading induced from the composite (elastic behavior) on the liner;
- Heating of the wound setup during winding, may have contributed to improved fatigue strength due to two factors:

  (1) the initial expansion of the liner makes the composite to be wound at a larger radius, closer to the final one after autofrettage, causing less fibre breakage after curing and autofrettage;

  (2) the higher temperature increases resin viscosity promoting improved consolidation of the composite.



CASE STUDY 2

Monitoring of a UAV's spar

Objectives

- Monitor the manufacturing process
- Monitor the structural health condition of the spar, through static and flight testing
- Determine the Remaining Useful Life of the Structure

Optical Sensors Integration

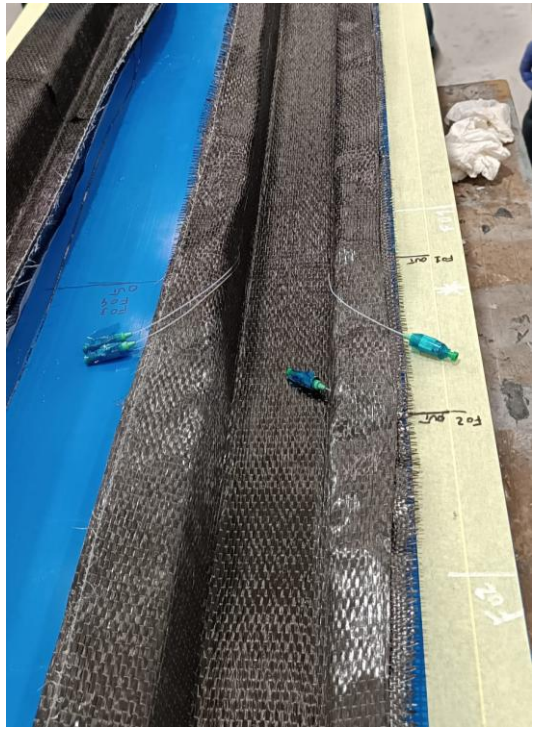

Placement of Optical Fiber Sensors during Manufacturing



Vacuum Bag sealed

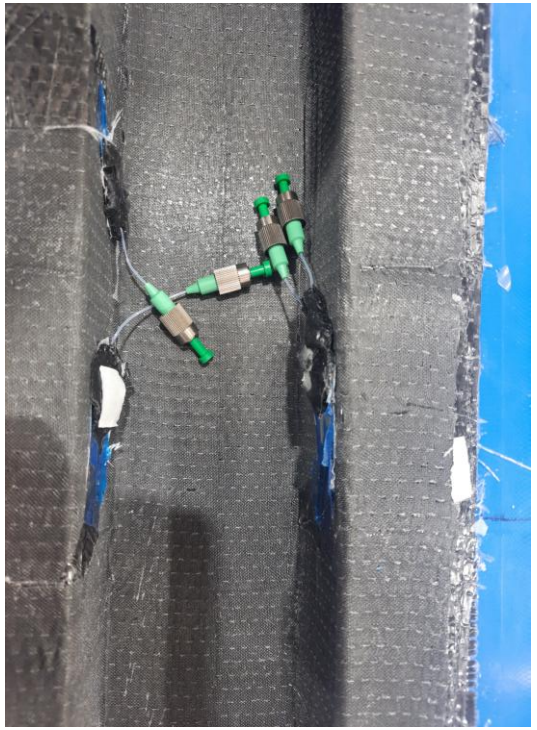

Demolded piece after curing

Optical Sensors Integration

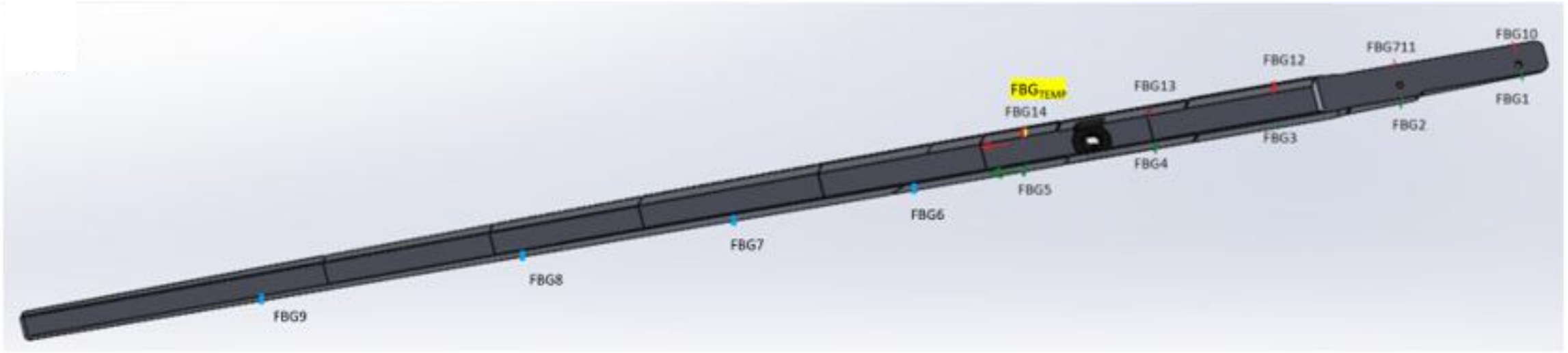

Cure Monitoring

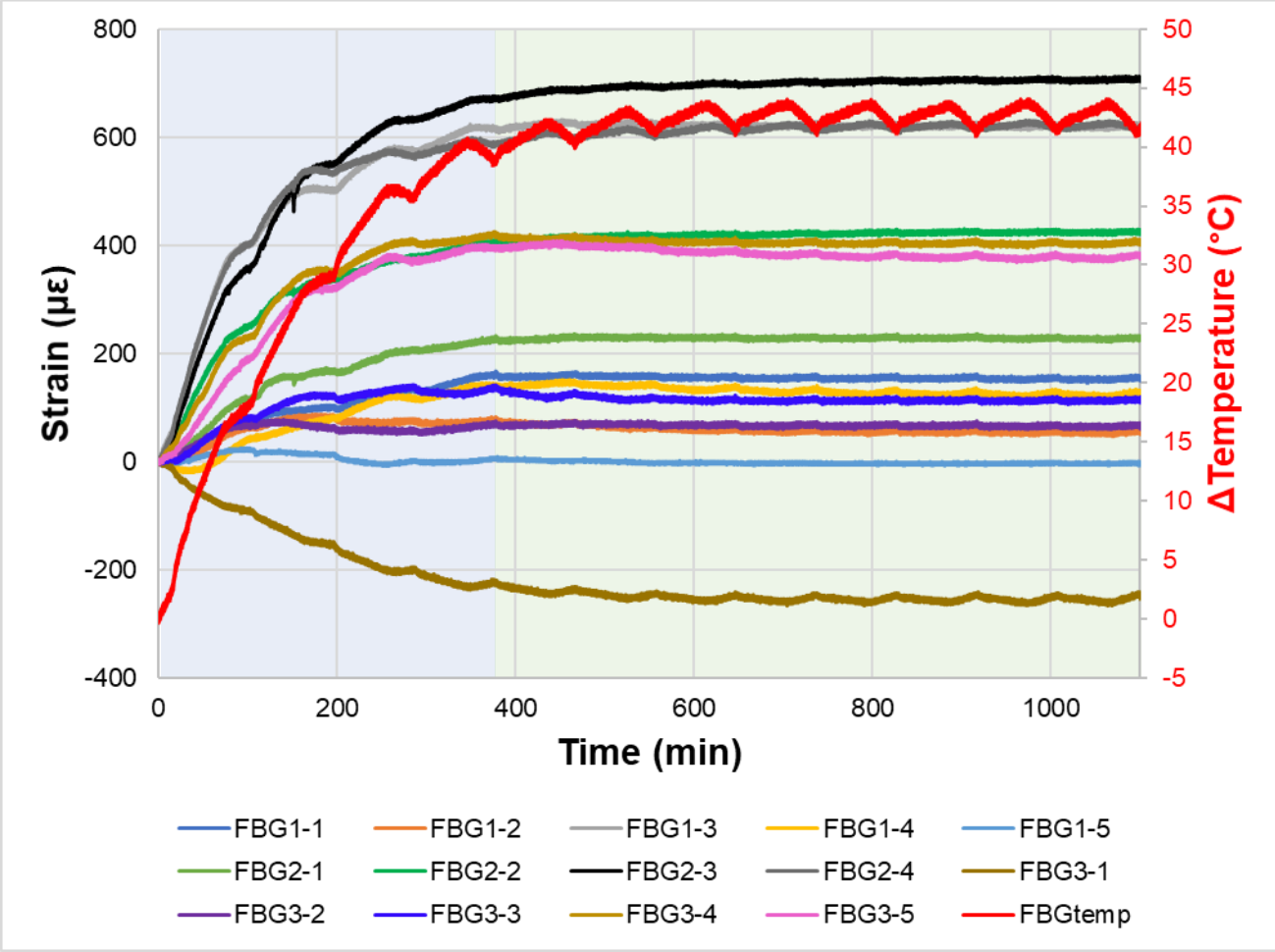

Static Test Monitoring

Strain change during Static Loading test

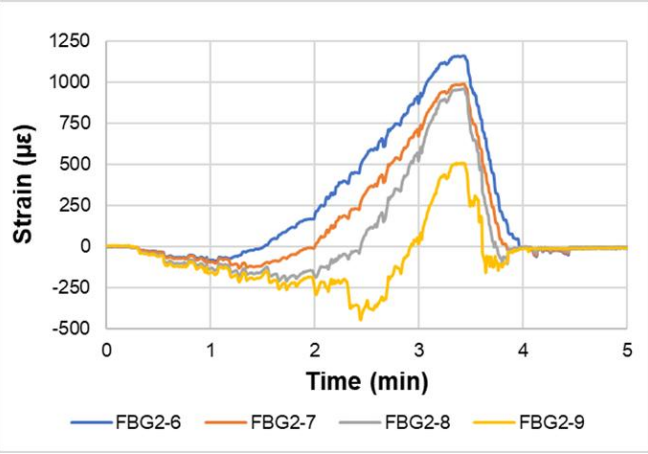

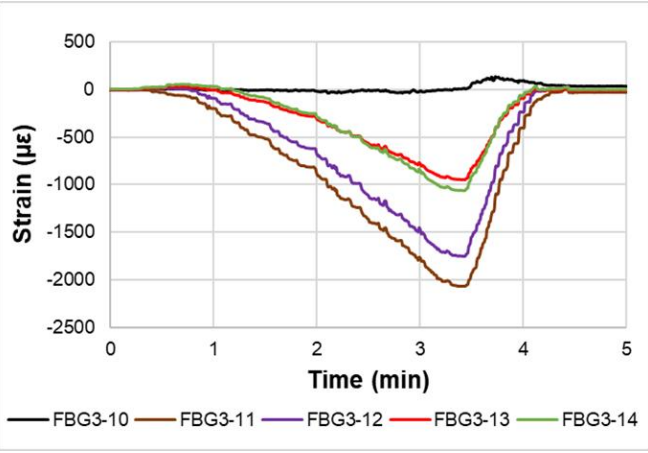

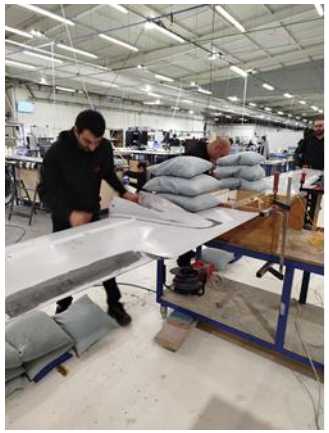



Maximum strain measured during test and residual strain after static test

Sensor	Max. strain (με)	Residual strain (με)
FBG2-6	1159.4	-10.9
FBG2-7	989.9	-7.7
FBG2-8	958.3	-4.8
FBG2-9	504.7	-12.6
FBG3-14	-1068.4	-4.3
FBG3-13	-952.3	-4.3
FBG3-12	-1757.2	-4.7
FBG3-11	-2072.7	-23.8
FBG3-10	132.1	36.7

Prediction of the Remaining Useful Life

Strain Analysis of Real-World Irregular Loads

- Real-world strain transient data exhibit irregular behavior over time, making it difficult to count the number of cycles and the life span of that part
- Some methods and algorithms must be implemented to analyze this irregular data;
- Two of them are the Four-Point Method and the RainFlow method

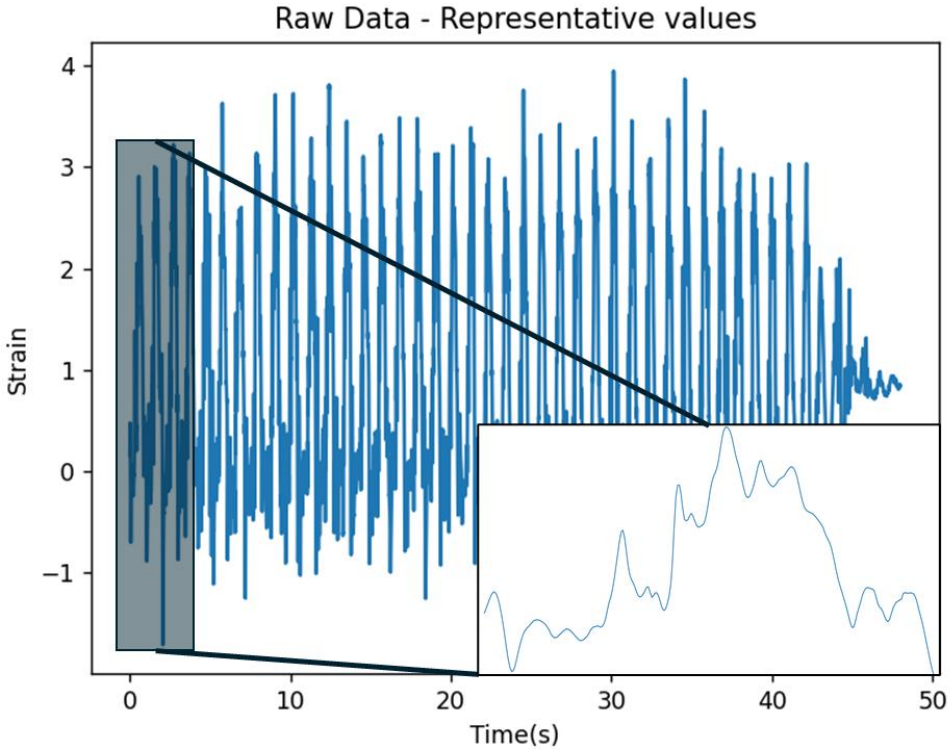

Prediction of the Remaining Useful Life

Four-Point counting Method

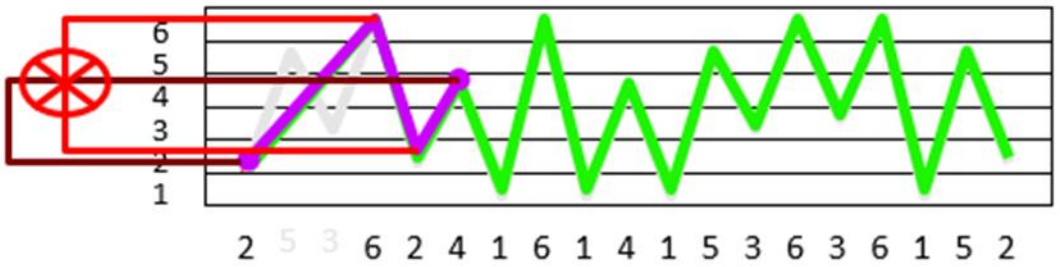

The Four-Point Method is a simple algorithm to rapidly assess the incurred cycles across the transient data and indirectly acknowledge the part's fatigue life

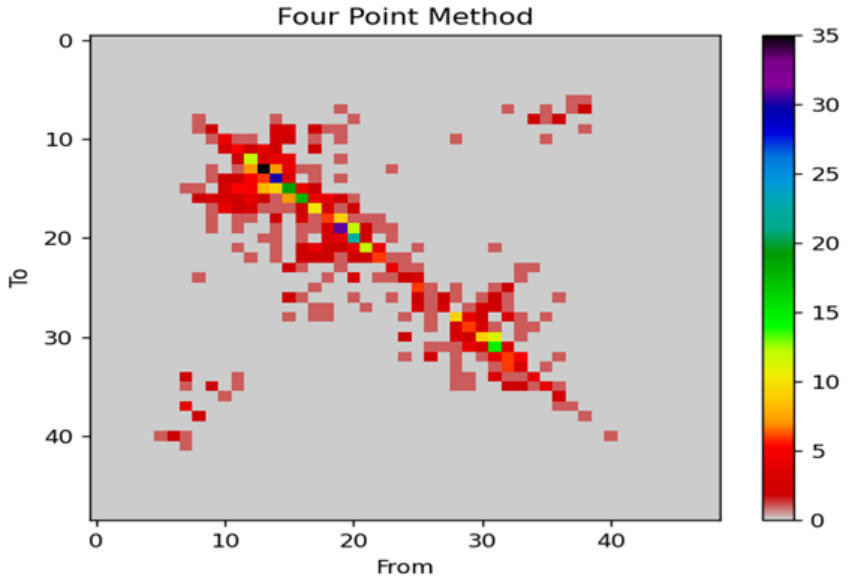

Prediction of the Remaining Useful Life

RainFlow counting Method

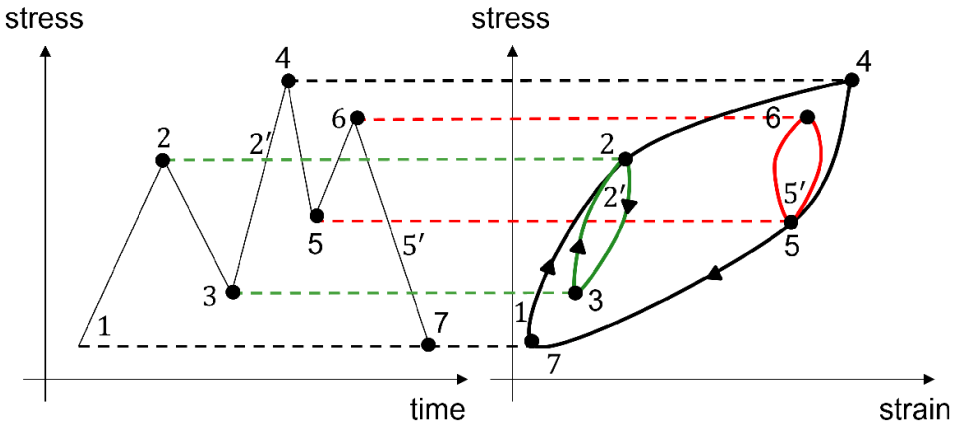

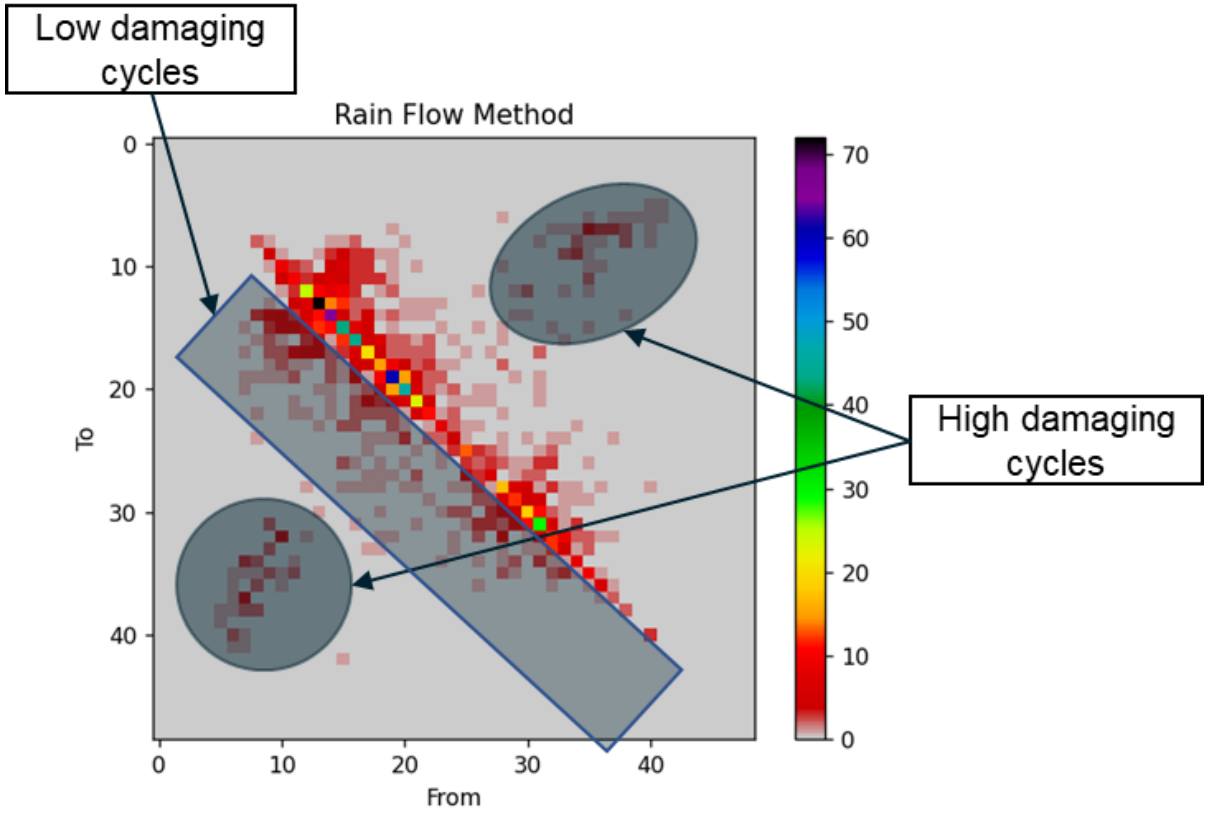

The Rainflow method is a more robust approach to cycle counting and fatigue assessment;

It extracts the hysteresis cycles and is more precise to extract the damage caused by the “accumulation” of fatigue

Conclusions and Future Work

- The localized strain data allowed to verify the correct curing of the part
- The FBG sensors were able to accurately measure strain during static testing
- The application of cycle counting methods will give important in-situ information about the parts' lifespan, even extending their longevity. Furthermore, the information can be used to predict the most efficient way to plan maintenance operations, reducing the operational costs. Algorithms for the prediction of the Remaining Useful Life of the spar will be developed
- The same spar will be subjected to flight test, with sensing data being acquired in real-time



(+351) 253 510 072
helena.rocha@piep.pt
www.piep.pt

PIEP - Pólo de Inovação em Engenharia de Polímeros,
Universidade do Minho, Campus de Azurém, Edifício 15
4800-058 Guimarães, Portugal

Follow PIEP on social networks

Thank you for your attention!

ICCM24
AUGUST 4-8, 2025
BALTIMORE CONVENTION CENTER
BALTIMORE, MARYLAND, USA

No Technical Paper Submission for:

Shridhar Yarlagadda

ICCM24
AUGUST 4-8, 2025
BALTIMORE CONVENTION CENTER
BALTIMORE, MARYLAND, USA

No Technical Paper Submission for:

Emiliano Bilotti

ICCM24
AUGUST 4-8, 2025
BALTIMORE CONVENTION CENTER
BALTIMORE, MARYLAND, USA

No Technical Paper Submission for:

Nuno Curado Correia

GENERATIVE DESIGN OF COMPOSITE WEARABLE DEVICES

Mariana Hernandez Rocha[1], Aytac Teker[2] and Kishore Pochiraju[3]

[1]Department of Mechanical Engineering, Stevens Institute of Technology
Castle Point Terrace, Hoboken, 07030, New Jersey, United States
Email: mhernan7@stevens.edu

[2]Department of Mechanical Engineering, Stevens Institute of Technology
Castle Point Terrace, Hoboken, 07030, New Jersey, United States
Email: ateker@stevens.edu

[3]Department of Systems Engineering, Stevens Institute of Technology
Castle Point Terrace, Hoboken, 07030, New Jersey, United States
Email: kpochira@stevens.edu

Keywords: Composite materials, generative design, wearable devices, orthosis, additive manufacturing, optimization

ABSTRACT

Design of lightweight (weight-minimized) composite structures that can meet stiffness, strength, and manufacturing constraints is challenging and time-consuming. Numerous constraints from wearable medical devices such as orthotics and exoskeletons, have geometric constraints from the user's anatomy determining their fit, comfort, and safety during wear. This paper presents a generative design methodology to create composite wearables customized to the user's anatomy. Design automation begins with a 3D scan of the relevant anatomy as input and produces 3D printable composite structure components. Through constrained optimization, the design process is accelerated by establishing the structural geometry, reinforcement fiber insertion paths, and manufacturing process plans. The methodology is illustrated on a patient-customized active ankle orthosis design. The geometric constraints are derived from a lower limb scan, and a patient-customized contact surface was generated and the fit is evaluated based on curvature and smoothness metrics. The surface is thickened to create a 3D structure, and the fiber reinforcement paths are determined based on the strength, stiffness, and limitations of additive manufacturing machinery. Considerations from the composite Process–Structure–Property–Performance (PSPP) relationships allow the considerations void and defect introduction by the 3D printing process. The insertion of generative design, automation, and optimization techniques reduced the scan to a real part cycle from several days to about 18 hours. The paper presents treadmill walk testing results from 15 healthy subjects.

1 INTRODUCTION

The development of personalized wearable medical devices, particularly orthotics and exoskeletons, represents a significant challenge in the intersection of biomechanics, materials science, and manufacturing technology. Traditional approaches to designing these devices often rely on manual processes that are time-intensive, costly, and may not fully optimize the mechanical properties required for individual users. The emergence of generative design methodologies, combined with advances in composite manufacturing and 3D printing technologies, offers unprecedented opportunities to create patient-specific devices that maximize performance while minimizing weight and production time [6].

Composite materials have gained prominence in wearable device applications due to their exceptional strength-to-weight ratio, design flexibility, and ability to be tailored for specific loading conditions [1,2]. However, the design of composite structures for wearable applications presents unique challenges,

including complex geometric constraints imposed by human anatomy, the need for comfortable user interfaces, and manufacturing limitations inherent in additive manufacturing processes. Additive Manufacturing (AM) has revolutionized the fabrication of composite structures by enabling complex geometries and customized fiber architectures. Fused filament fabrication (FFF) with continuous fiber reinforcement has emerged as a leading technique for producing high-performance composite components [3, 5]. Carbon fiber-reinforced polymers (CFRPs) and glass fiber-reinforced polymers (GFRPs) have demonstrated superior mechanical properties compared to traditional metallic materials, making them particularly attractive for lightweight wearable applications [7]. The biocompatibility and corrosion resistance of certain composite systems have further expanded their adoption in direct-contact medical applications [2]. Recent advances have enabled the development of patient-specific orthotic devices with tailored mechanical properties, achieving a weight reduction of up to 40% while maintaining equivalent stiffness characteristics compared to conventional materials [16].

The Process–Structure–Property–Performance (PSPP) framework provides a systematic approach to understanding the relationships between manufacturing parameters, resulting microstructure, material properties, and ultimate device performance. This framework becomes particularly critical when designing composite structures using additive manufacturing, where process-induced defects and anisotropic properties significantly influence the final product characteristics [6,8].

The Taguchi method, developed by Genichi Taguchi, provides a systematic approach to experimental design that maximizes information extraction while minimizing the number of required experiments [9]. This methodology is particularly valuable in composite design applications where computational analysis can be expensive and time-consuming for complex geometries [12]. The method employs orthogonal arrays to systematically explore the design space and identify optimal parameter combinations through statistical analysis of variance (ANOVA) [10].

This paper presents a comprehensive generative design methodology that integrates anatomical scanning, constrained optimization, and composite manufacturing considerations to create patient-customized wearable devices. The methodology is demonstrated through the design and testing of an ankle orthosis, showcasing the potential for significant reductions in design cycle time while maintaining or improving device performance. Taguchi method enables efficient exploration of geometric parameters while maintaining statistical rigor in the analysis of mechanical performance metrics [11].

2 METHODOLOGY

2.1 Generative Design Framework

The proposed generative design methodology follows a systematic approach that begins with the acquisition of anatomical data and progresses through geometric modeling, optimization, and manufacturing planning. The framework consists of three primary phases: anatomical scanning and constraint definition, surface generation and parametric modeling, and peridynamics-based structural analysis.

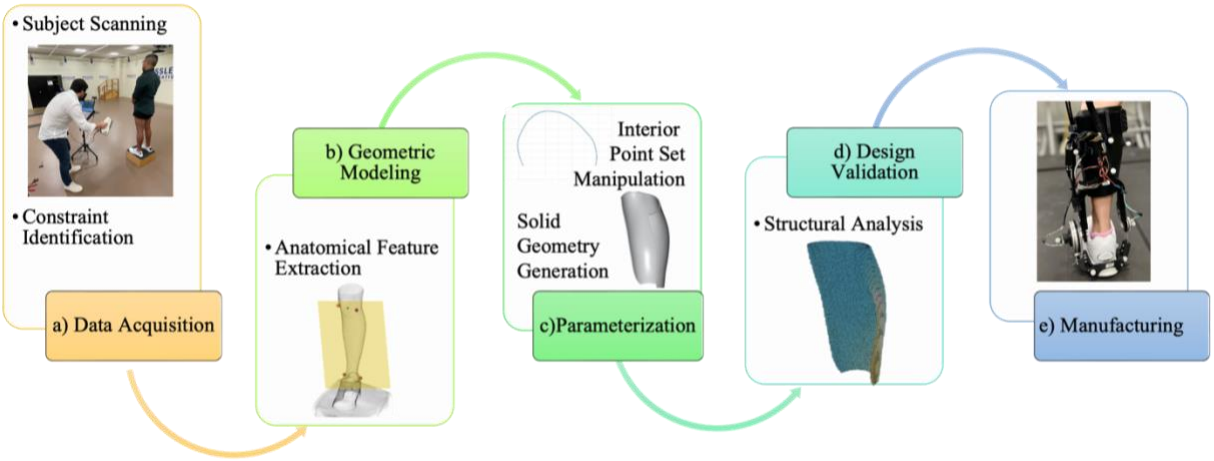

Figure 1: Geometric Design Pipeline.

The anatomical scanning phase, Figure 1a), utilizes high-resolution 3D scanning technology to capture the precise geometry of the relevant body segments. For the ankle orthosis application, this includes detailed scanning of the lower limb from the knee to the foot, capturing critical anatomical landmarks and surface variations that influence device fit and comfort. The scanning data is processed to remove noise and artifacts while preserving essential geometric features.

Constraint identification involves establishing geometric, mechanical, and manufacturing boundaries that guide the optimization process. Geometric constraints are derived directly from the anatomical scan data Figure 1(b), ensuring that the final device maintains appropriate clearances and contact areas. Mechanical constraints include minimum stiffness requirements, maximum stress limitations, and fatigue considerations based on anticipated loading conditions. Manufacturing constraints include limitations imposed by the additive manufacturing process, including minimum feature sizes, support requirements, and fiber placement capabilities.

Patient-customized contact surfaces are generated using advanced surface modelling techniques that balance conformity to the anatomical geometry with mechanical performance requirements. This step produces a solid geometry and is depicted in Figure 1(c) within the design pipeline. The surface generation process utilizes surface reconstruction algorithms, such as the Poisson Reconstruction Algorithm [17], which create smooth, continuous surfaces while maintaining proximity to the scanned anatomy.

2.2 Parametric Design Space Definition

A parameterization step follows the surface reconstruction to produce a solid geometry— the definition of key variables that control the geometric characteristics of the orthotic shank. The solid geometry is generated by converting a 2D surface mesh into a 3D solid by slicing it horizontally at various heights to extract contour points. These raw contour points are fitted with NURBS curves to create parameterized cross-sections. Afterward, new points are generated by extending perpendicular vectors from each point according to the specified thickness value. The process concludes by connecting the inner and outer curve endpoints with smooth arcs, resulting in continuous, watertight slices that form the final 3D solid structure. The structural analysis is performed on two parameters that control the shape of the contours: the thickness value and the profiling values.

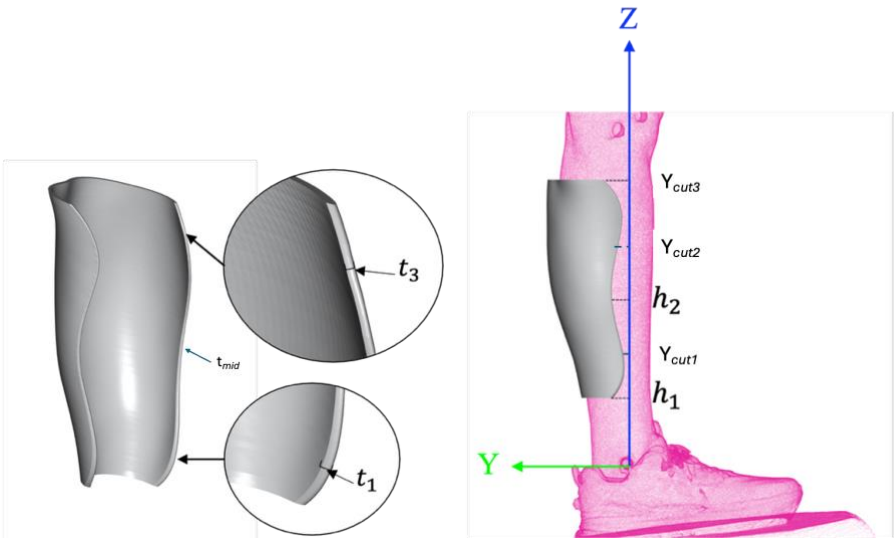

Figure 3: Variables corresponding to the thickness and profile of the shank. Geometry is parametrically varied by adjusting four variables, t_{mid}, Y_{cut1}, Y_{cut2}, and Y_{cut3}.

2.3 Taguchi L9 Orthogonal Array Design

The complete design space was systematically explored using Taguchi L9 fractional factorial analysis methodology. The full factorial design space encompasses 81 possible combinations, but the L9 array reduces this to nine strategically selected configurations that provide comprehensive coverage of the parameter space. We selected four variables to control the geometry of the shank as shown in Table 1.

Variable	Level1 (mm)	Level 2 (mm)	Level 3 (mm)
t_{mid}	3	4	5
Y_{cut1}	5	10	20
Y_{cut2}	15	20	25
Y_{cut3}	20	30	40

Table 1: Fractional Factorial (L9) Design Space.

Run	t_{mid} (mm)	Y_{cut1} (mm)	Y_{cut2} (mm)	Y_{cut3} (mm)
1	3	5	15	20
2	3	10	20	30
3	3	20	25	40
4	4	5	20	40
5	4	10	25	20
6	4	20	15	30
7	5	5	25	30
8	5	10	15	40
9	5	20	20	20

Table 2: Taguchi L9 Orthogonal Array.

2.3 Peridynamics-Based Structural Analysis

The structural analysis framework employs peridynamics theory to evaluate the mechanical behavior of composite shank designs under physiological loading conditions. Peridynamics provides a non-local continuum mechanics formulation that is particularly well-suited for analyzing composite materials with complex microstructures and potential damage mechanisms [13].

The peridynamics formulation replaces the classical partial differential equations of continuum mechanics with integro-differential equations, allowing for natural treatment of discontinuities such as cracks, delaminations, and material interfaces [14]. This approach is particularly advantageous for composite structures where traditional finite element methods may encounter difficulties in capturing damage initiation and propagation.

The implementation utilizes a mesh-free discretization approach, where the material domain is represented by a collection of material points, each interacting with neighbouring points within a defined horizon. The interactions between material points are governed by pairwise force functions that encode the material's constitutive behavior, including elastic response, damage initiation criteria, and failure mechanisms [15].

2.5 Taguchi Analysis Methodology

The Taguchi analysis methodology systematically evaluates the mechanical performance metrics obtained from peridynamics simulations. The analysis focuses on maximum stress, reaction forces, deformation, damage evolution, and fatigue as key performance indicators.

The analysis employs Signal-to-Noise (S/N) ratios to quantify the robustness of each design configuration [19]. For mechanical properties where smaller values are preferred, like stress and deformation, the ratio used is defined as:

$$\text{S/N} = -10log_{10}(\frac{1}{n}\sum y^2) \quad (1)$$

For properties where larger values are preferred, like load capacity, the "larger-is-better" S/N ratio is used:

$$\text{S/N} = -10log_{10}(\frac{1}{n}\sum \frac{1}{y^2}) \quad (2)$$

Analysis of Variance (ANOVA) is conducted to determine the relative contribution of each design parameter to the overall performance metrics, allowing us to identify the most influential parameters and optimal design configurations [20].

3 RESULTS AND DISCUSSION

3.1 Design Cycle Time Reduction

The implementation of the generative design methodology resulted in a dramatic reduction in design cycle time from the initial anatomical scan to the production of a functional composite device. Traditional manual design approaches typically required several days of skilled designer time, involving iterative modeling, analysis, and refinement cycles. The automated generative design process reduced this timeline to approximately 10 hours, representing a significant improvement in design efficiency.

The print direction received specific attention to match the anatomical complexity of the shank orthosis and to fulfil the mechanical requirements of dynamic gait loading. The orthosis in Batch 1,

Figure 4 left, is placed in the upright printing position as a single continuous piece to maintain the natural curvature and medial-lateral asymmetry of the patient's limb. The orientation of the print ensured that the layer lines followed the main loading direction because this direction is crucial for resisting torque during the gait cycle. To comply with the Bambu X1 printer's maximum Z-height of 256 mm, the generative design algorithm set the maximum length of the shank component to 250 mm. The upright configuration proved biomechanically superior; however, it required extensive support structures, which exceeded print stability limits due to the high aspect ratio.

The design of Batch 2, Figure 4, on the right, consisted of multiple parts arranged flat on the print bed to decrease the build height and enhance print reliability. The flat printing orientation reduced the likelihood of warping and resulted in improved surface quality throughout curved sections. The printing process utilized a 0.6 mm nozzle, combined with a 0.18 mm layer height, to achieve both mechanical strength and surface resolution. The orthosis features a 100% concentric infill pattern to enhance strength, adhering to the part contours and creating uniform torsional resistance. The chosen infill pattern minimized the chance of interlayer delamination and internal voids, which are essential for maintaining orthotic structural integrity when subjected to cyclic gait loading. The approach combines anatomical geometry with mechanical requirements to support both performance and manufacturability in patient-customized wearable devices.

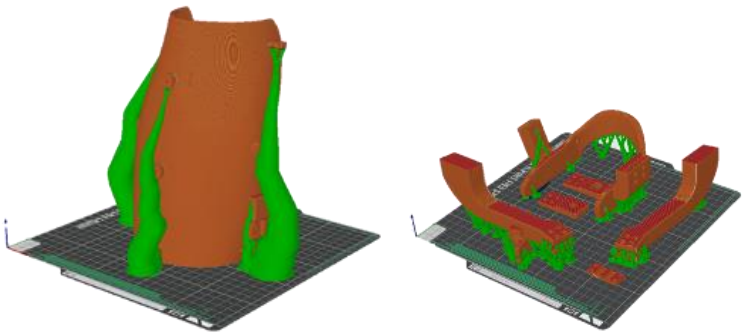

Figure 4: Printing batches in parallel allows for compliance with the machining time constraint.

The time reduction was achieved through several key innovations, including automated surface generation algorithms, parallel optimization processing, and integrated manufacturing planning. The automated surface generation eliminated the need for manual surface modeling, while the parallel optimization approach allowed simultaneous evaluation of multiple design candidates. The integrated manufacturing planning ensured that manufacturability constraints were considered throughout the optimization process, eliminating the need for post-optimization design modifications.

3.2 Peridynamics Simulation Results

A comprehensive peridynamics analysis was conducted on all nine shank configurations from the L9 orthogonal array presented in Figure 5. The simulations were performed under a 2mm deflection scenario representative of the loading conditions resulting from the Series of Elastic Actuators (SEA) system. The analysis setup is shown in Figure 6. The left side represents the arrangement of particles for that shank, while the picture on the right illustrates the boundary conditions, represented by the points at the top, and the points at the bottom indicate the area subject to a deflection of 2 mm. Table 3 contains the mechanical properties data for each of the L9 configurations.

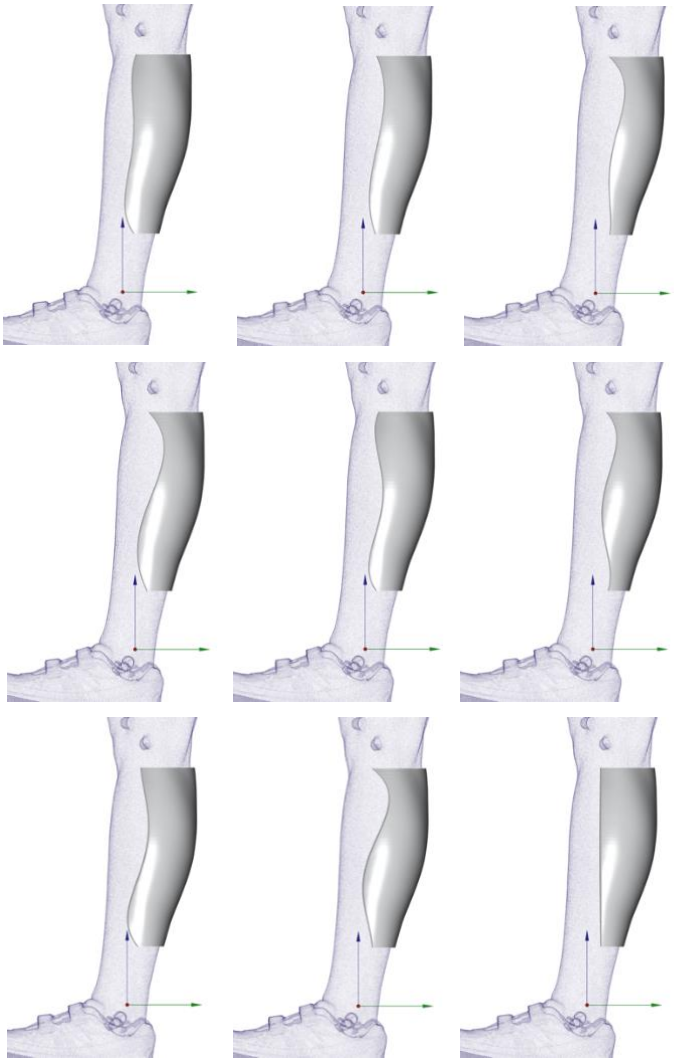

Figure 5: Profiles of the shanks analyzed with fractional factorial analysis.

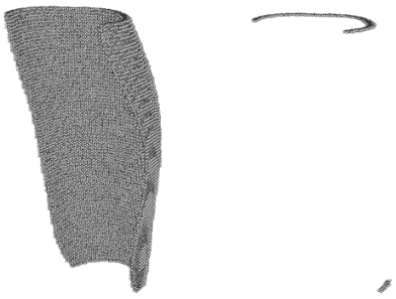

(a) (b)

Figure 6: Point mesh used for the analysis and the locations where boundary conditions are applied (a) Point Mesh (b) Top surface is constrained, and bottom surface is pushed in to reflect the forces from the compliant actuator

Run	Mises Stress (MPa)	Max Displacement Magnitude (mm)	Reaction Force (N)
1	-1.85	7.9	4603
2	-1.40	6.2	2964
3	-1.00	7.2	2614
4	-1.05	8.7	2536
5	-1.05	8.2	4654
6	-0.70	7.1	3415
7	-0.67	5.5	3354
8	-0.41	6.2	2184
9	-0.64	11.2	2532

Table 3: Results from the simulations with factors from the Taguchi L9 array

3.3 Taguchi Analysis of Mechanical Properties

The Taguchi analysis reveals the relative importance of each design parameter in determining the stiffness performance of the orthotic shank designs. The study examines the sensitivity of mechanical properties to parameter variations and identifies optimal parameter combinations.

The main effect plots in Figure 7 illustrate how the response variable changes across different levels of each factor. The thickness level (T_{mid}) behavior suggests an optimal mid-range value. The variable Ycut3 exhibits the steepest and most consistent decline, which aligns with the ANOVA results indicating that this factor had the largest effect size.

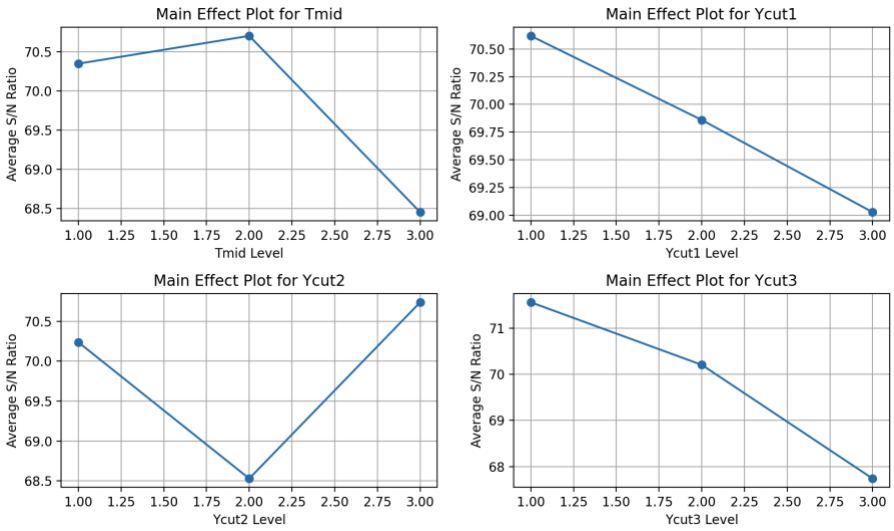

Figure 7: Effect tables for each level.

Source of Variation	Sum of Squares	Degrees of Freedom	F-Statistic	P-Value	Contribution (%)
t_{mid}	1,229,146	2	1.924	0.342	18.996
Y_{cut2}	1,288,155	2	2.016	0.332	19.908
Y_{cut3}	3,314,373	2	5.188	0.162	51.222
Residual	638,909	2	-	-	9.874

Table 4: ANOVA Table

Key findings from these results, presented in Table 4, show that $\boldsymbol{Y_{cut3}}$ shows the strongest effect, explaining 51.2% of the total variance with a large effect size. The low residual variance (9.9%) suggests that the model accounts for most of the systematic variation.

4 CONCLUSIONS AND FUTURE WORK

This paper has presented a comprehensive generative design methodology for creating patient-customized composite wearable devices. The methodology successfully integrates anatomical scanning, constrained optimization, and additive manufacturing considerations to produce high-performance devices with significantly reduced design cycle times. In addition, we present a systematic approach for analyzing composite orthotic shank designs using Taguchi's experimental design methodology combined with peridynamics-based structural analysis. The methodology successfully reduces the computational burden while maintaining statistical rigor in evaluating mechanical performance.

The key contributions of this work include the development of an automated surface generation algorithm that creates patient-specific contact surfaces, a multi-objective optimization framework that simultaneously considers mechanical performance and manufacturing constraints. The significant reduction in design cycle time from days to hours represents a major advancement in the practical implementation of personalized wearable devices.

The Taguchi method proves particularly effective for composite design applications where computational analysis can be expensive and time-consuming. The approach enables the identification of optimal design parameters while providing insights into parameter sensitivity and robust design practices.

Future work will focus on extending the methodology to other types of wearable devices. The integration of artificial intelligence techniques into the optimization framework represents another promising area for future development, potentially allowing for further reductions in design cycle time and improvements in optimization convergence. And the development of predictive models for mechanical performance based on Taguchi results.

REFERENCES

[1] Rajak, D. K., Pagar, D. D., Menezes, P. L., & Linul, E. (2019). Fiber-reinforced polymer composites: manufacturing, properties, and applications. *Polymers*, 11(10), 1667.

[2] Ramakrishna, S., Mayer, J., Wintermantel, E., & Leong, K. W. (2001). Biomedical applications of polymer-composite materials: a review. *Composites science and technology*, 61(9), 1189-1224.

[3] Zhang, L., Chen, Y., & Liu, M. (2022). Continuous fiber-reinforced thermoplastic composites for patient-specific orthotic devices. *Composites Part A: Applied Science and Manufacturing*, 156, 106891.

[4] Liu, Y., Chen, J., & Wang, X. (2023). Shape memory alloy reinforced composites for adaptive orthotic systems. *Smart Materials and Structures*, 32(7), 075012.

[5] Blok, L. G., Longana, M. L., Yu, H., & Woods, B. K. (2018). An investigation into 3D printing of fibre reinforced thermoplastic composites. *Additive Manufacturing*, 22, 176-186.

[6] Dutra, T. A., Ferreira, R. T., Resende, H. B., & Guimarães, A. (2019). Mechanical characterization and asymptotic homogenization of 3D-printed continuous carbon fiber-reinforced thermoplastic. *Journal of the Brazilian Society of Mechanical Sciences and Engineering*, 41(3), 1-15.

[7] Tekinalp, H. L., Kunc, V., Velez-Garcia, G. M., Duty, C. E., Love, L. J., Naskar, A. K., ... & Ozcan, S. (2014). Highly oriented carbon fiber–polymer composites via additive manufacturing. *Composites Science and Technology*, 105, 144-150.

[8] Jin, Z., Zhang, Z., Demir, K., & Gu, G. X. (2019). Machine learning for advanced additive manufacturing. *Matter*, 3(5), 1541-1556.

[9] Krish, S. (2011). A practical generative design method. *Computer-Aided Design*, 43(1), 88-100.

[10] Bendsøe, M. P., & Sigmund, O. (2003). *Topology optimization: theory, methods, and applications*. Springer Science & Business Media.

[11] Banga, S., Gehani, H., Bhilare, S., Patel, S., & Kara, L. (2018). 3D topology optimization using convolutional neural networks. *arXiv preprint arXiv:1808.07440*.

[12] Papapetrou, V. S., Patel, C., & Tamijani, A. Y. (2020). Stiffness-based optimization framework for the topology and fiber paths of continuous fiber composites. *Composites Part B: Engineering*, 183, 107681.

[13] Silling, S. A. (2000). Reformulation of elasticity theory for discontinuities and long-range forces. *Journal of the Mechanics and Physics of Solids*, 48(1), 175-209.

[14] Xu, J., Askari, A., Weckner, O., & Silling, S. (2008). Peridynamic analysis of impact damage in composite laminates. *Journal of Aerospace Engineering*, 21(3), 187-194.

[15] Kilic, B., & Madenci, E. (2010). Peridynamic theory for thermomechanical analysis. *IEEE transactions on advanced packaging*, 33(1), 97-105.

[16] Dombroski, C. E., Balsdon, M. E., & Froats, A. (2014). The use of a low-cost 3D scanning and printing tool in the manufacture of custom-made foot orthoses: a preliminary study. *BMC research notes*, 7(1), 1-8.

[17] Kazhdan, M., Bolitho, M., & Hoppe, H. (2006). Poisson surface reconstruction. *Proceedings of the fourth Eurographics symposium on Geometry processing*, 7.

[18] Cagle, J. C., Reinhall, P. G., Hafner, B. J., & Sanders, J. E. (2018). Development of standardized material testing protocols for prosthetic liners. *Journal of biomechanical engineering*, 140(4), 041004.

[19] Deb, K., Pratap, A., Agarwal, S., & Meyarivan, T. (2002). A fast and elitist multiobjective genetic algorithm: NSGA-II. *IEEE transactions on evolutionary computation*, 6(2), 182-197.

[20] Beyer, H. G., & Sendhoff, B. (2007). Robust optimization–a comprehensive survey. *Computer methods in applied mechanics and engineering*, 196(33-34), 3190-3218.

SUSTAINABLE COMPOSITES START WITH LCA: SEEING THE WHOLE PICTURE

Martina Salzano de Luna[1]

[1]Department of Chemical, Materials and Production Engineering, University of Naples Federico II
Piazzale Tecchio 80, 80125 Naples, Italy
Email: martina.salzanodeluna@unina.it, web page: https://www.polyfun.unina.it/

Keywords: Green composites, Biopolymers, Natural fibers, Life cycle assessment, Environmental sustainability

ABSTRACT

The increasing urgency to address environmental challenges and reduce the environmental footprint of industrial processes has led to significant interest in the development of sustainable composite materials, commonly referred to as green composites or biocomposites. These materials usually consist of a bio-based or biodegradable polymer matrix reinforced with natural fibers.

In principle, biocomposites combine environmental benefits — such as reduced greenhouse gas emissions, lower energy consumption and better disposal options — with promising mechanical properties and low weight.

However, the concept of "sustainability" in the context of green composites is multidimensional and encompasses not only the origin of the material and biodegradability, but also metrics of life cycle assessment, durability, resource renewability and socio-economic impact. A holistic assessment of these aspects is essential to avoid the risk of greenwashing and to ensure the true environmental benefits of these new materials.

In this work, a representative case study from the literature is presented to highlight the importance of critically assessing the environmental impact of supposedly green materials such as biocomposites. The aim is to emphasize the crucial role of LCA analysis as an additional tool to characterize newly proposed materials.

1 INTRODUCTION

In recent decades, the transition to sustainable materials and production systems has become an urgent global priority. This change is driven by the growing awareness of environmental degradation, climate change, resource depletion and the unsustainable nature of many conventional production processes. In this context, green composites and especially biocomposites have emerged as one of the most promising material families to support a circular economy with low environmental impact. In the broadest sense, biocomposites are composite materials in which either the matrix, the reinforcement or both are derived from renewable, natural or biodegradable sources [1].

Biocomposites usually consist of natural fibers (such as flax, jute, hemp, sisal or agricultural residues) embedded in a polymer matrix that is either biodegradable (e.g. PLA, PHB) or bio-based (e.g. bio-polyethylene, bio-epoxy resins). These materials represent an attractive and increasingly feasible alternative to conventional composite materials based on synthetic fibers and petroleum-based resins. Their attractiveness lies not only in their use of renewable raw materials, but also in their potential to lower carbon emissions, reduce energy consumption during manufacture and improve end-of-life options, including composting and recyclability [2,3].

The environmental motivation for the development of biocomposites stems from their potential to mitigate various impacts associated with conventional composites. For example, life cycle assessment (LCA) studies have shown that natural fibers can reduce the global warming potential (GWP) of composites by 20–50% compared to synthetic alternatives [4]. This is mainly due to carbon sequestration during plant growth and the lower embodied energy of natural fibers. In addition, many bio-based polymers are derived from agricultural waste streams or non-food biomass, which underlines their sustainability and reduces competition with food resources.

Economically, biocomposites offer the opportunity to utilize local biomass resources, especially in rural or developing regions, thus promoting green value chains and decentralized production systems. The growing market demand for sustainable solutions, particularly in the automotive, packaging, consumer goods and construction industries, has created further incentives for research and innovation in this area.

Despite these advantages, the development and introduction of green composites still faces a number of technical and systemic challenges. First, natural fibers exhibit variations in their mechanical properties due to different growing conditions, harvesting and processing techniques. This inconsistency can affect the predictability and repeatability of composite performance [5]. In addition, natural fibers are hydrophilic, which can lead to poor interfacial bonding with hydrophobic matrices and moisture absorption, reducing long-term durability, especially in humid environments [6].

Another limitation concerns the trade-offs in mechanical properties: while biocomposites are lightweight and often sufficiently strong for semi-structural applications, they may not achieve the stiffness, heat resistance or impact strength of high-performance synthetic composites such as carbon or glass fiber systems. Advanced fiber treatments (e.g. silanization, acetylation) and matrix modifications (e.g. compatibilizers, nanofillers) are currently being explored to address these issues, but they may result in environmental impacts or higher costs, negating some of the original sustainability benefits.

It is crucial to emphasize that sustainability in materials science is not a topic that is limited to a single variable. It must be evaluated through a holistic and multi-criteria lens. While bio-based origin and biodegradability are important, they alone are not enough to claim true environmental sustainability. Factors such as durability, toxicity, ethics in the supply chain, renewal rate and overall life cycle performance must also be considered. Indeed, some bio-based polymers require high energy inputs or generate significant emissions during synthesis, necessitating a careful LCA comparison with petrochemical alternatives [7]. Furthermore, end-of-life scenarios remain a complex issue. While certain biocomposites are marketed as biodegradable, actual degradation rates vary widely depending on conditions, and industrial composting facilities may be required for effective degradation. In parallel, thermoplastic-based biocomposites can be recycled, but the separation of fibers and matrix remains a technical challenge. As a result, many green composites are still incinerated or landfilled unless they are specifically designed for the circular economy [8].

Overall, the future of biocomposites lies in the balance between performance, sustainability and scalability. From a system perspective, there is a growing need for standardization, certification systems and eco-labels that can validate the sustainability claims of green composites. This includes harmonized methods for life cycle assessment, toxicity screening and biodegradability testing. Such frameworks are essential to avoid the pitfalls of greenwashing and to inform both consumers and industrial users about the real benefits and limitations of these materials.

2 CASE STUDY

In a recent review by Suarez et al. the aspects related to sustainability of polymer composites were assessed, with the goal of highlighting if natural-based composites are actually sustainable [9]. The authors concluded that “there is a wide number of publications dealing with the use of natural fibers or natural, biodegradable or biobased matrices, which claims to be producing a more sustainable or more environmentally friendly material than those based on fuel, although very few of them have performed environmental analysis to really demonstrate this point”. Although the number of studies using LCA analyzes to quantify the environmental impact of biocomposites together with their technical performance is increasing, much remains to be done to understand the relationship between materials, processing and performance, both in terms of final application and environmental impact. As a representative case study in this direction, the work done by Filippone and co-workers [10] is considered in the following. In particular, the environmental implications due to the presence of the lignocellulosic microfibers were assessed by using unfilled PLA as benchmark. A “cradle-to-gate” life cycle analysis was carried out, considering the following three processes: a) production of the microfibers; b) production of the PLA; c) manufacturing of the bio-pellets (Fig. 1).

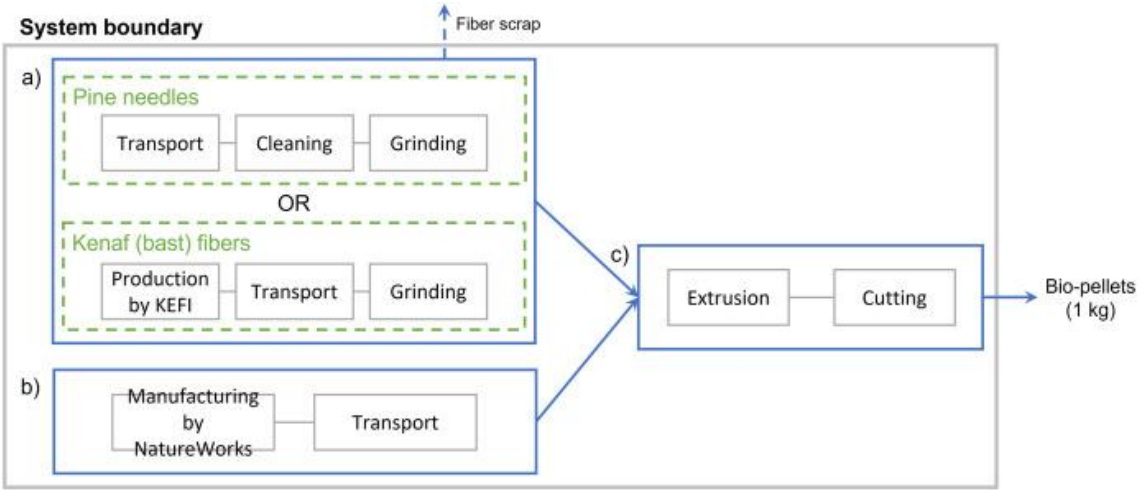

Figure 1: System boundary (*cradle-to-gate* life cycle). The process is divided into three sub-processes: a) production of the microfibers; b) production of the PLA; c) manufacturing of the bio-pellets. Taken from [10].

Moreover, since the origin of natural fibers has a strong effect on their environmental impact, two types of fibers are considered in the study, namely kenaf and pine needles microfibers, in order to compare cultivated and naturally grown feedstocks. Original fibers and microfibers obtain after the grinding process are shown in Fig. 2.

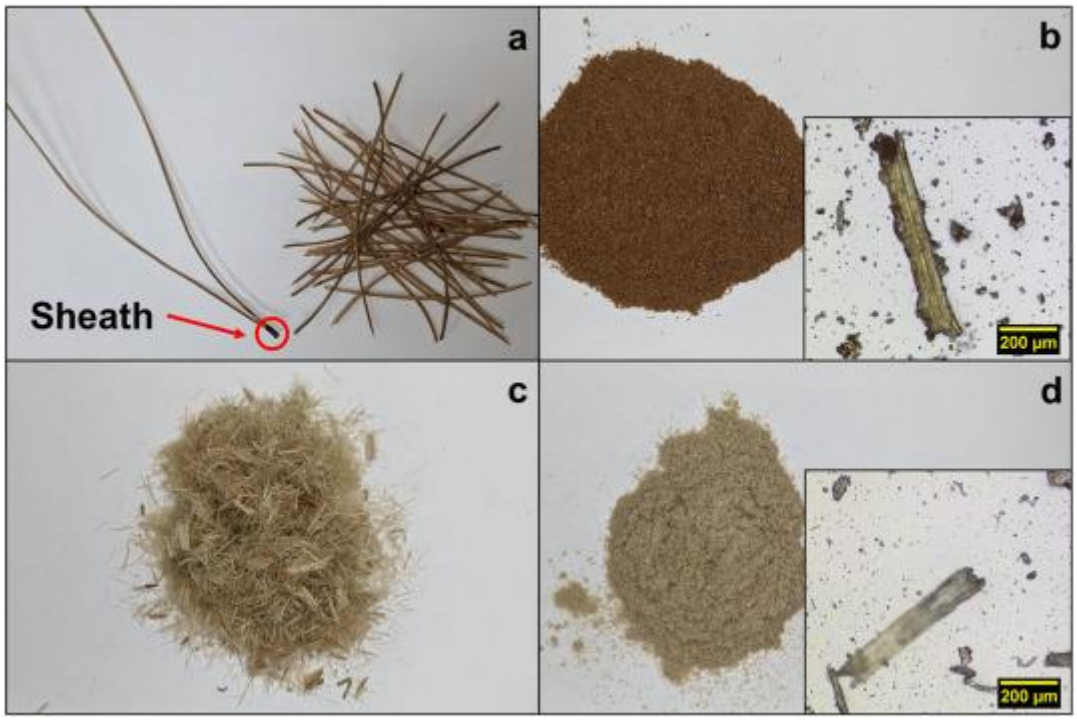

Figure 2: Pine needles and kenaf fibers before (a, c) and after (b, d) the grinding process. The arrow in a) indicates the fascicle sheath. Magnifications in b) and d) show the microfibers obtained after grinding that were used for producing the green composites. Taken from [10].

Interestingly, the LCA analysis revealed that fibers obtained from naturally grown raw material are only slightly better than cultivated ones in terms of environmental impacts. The main advantages of using natural raw materials concern the indicators for human toxicity and ecotoxicity. This is mainly

due to the impact of the washing and drying phases of the pine needles. Greater advantages of naturally grown raw materials are expected in the event of an industrial scale-up of fiber production. More importantly, the environmental impact of composites resulting from the combination of the effects of polymer and fillers and the contribution of the melt mixing process is much lower than that of pure PLA. The higher the fiber content, the greater the benefits (Fig. 3). The reason for this is that the fibers represent a negligible environmental impact compared to the polymer matrix. Therefore, replacing "high impact" PLA with "low impact" natural fibers is always preferable.

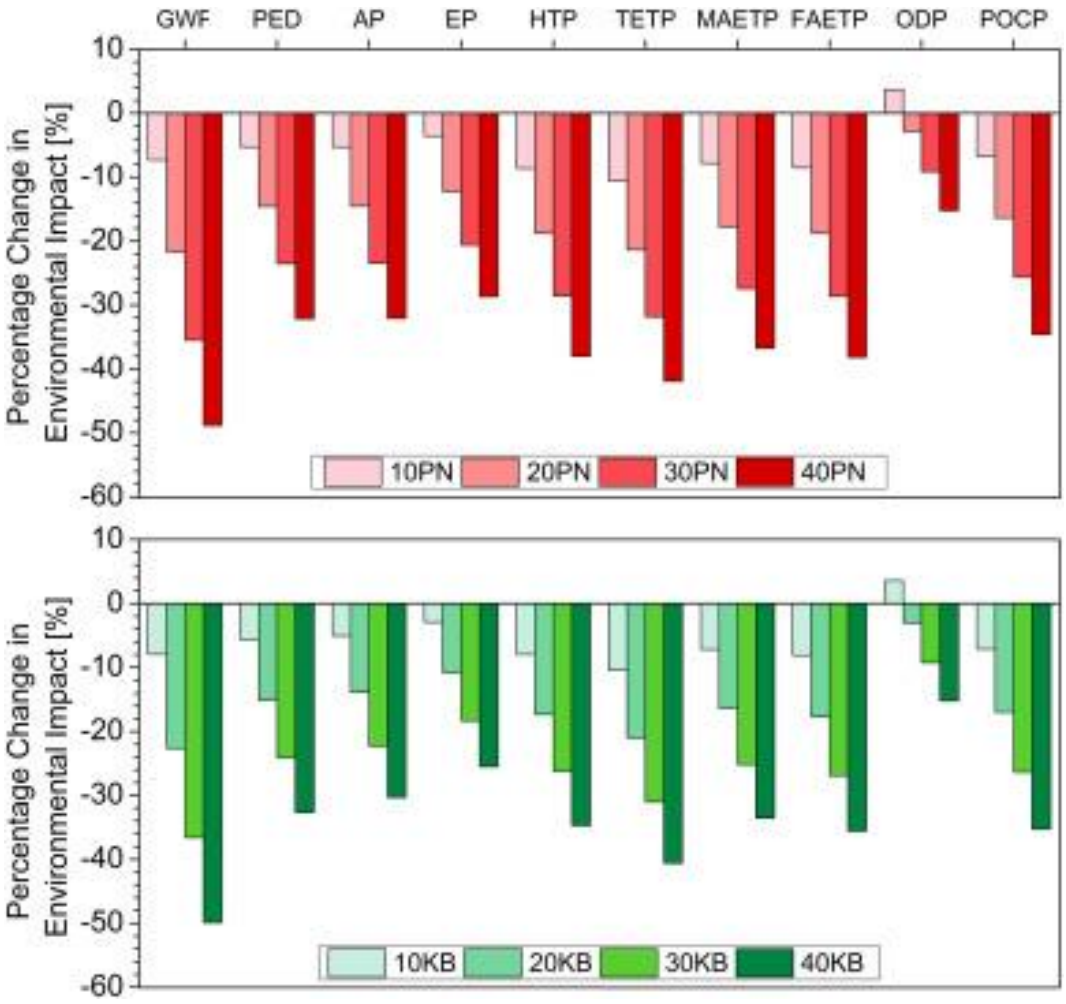

Figure 3: Percentage change in the environmental impacts of *x*PN and *x*KB bio-pellets with respect to pure PLA pellets (*x* indicates the percentage volume fraction of microfibers in the composite). Taken from [10].

In addition to the benefits arising from the improved environmental fingerprint, the selected fibers are also expected to improve the performance of the tested materials to a certain extent. This has an indirect impact on the overall sustainability of the composites, as improved performance potentially enables material savings [11]. For this reason, the mechanical performance of the composite samples was estimated and converted into weight reductions (Fig. 4).

A stiffness-limited design of a panel proves that the use of green composites instead of pure PLA leads to material savings of up to 8% (at 30% of the KB). By optimizing the formulation, e.g. by using surface-treated natural fibers to improve the polymer-fiber interaction, a much greater weight reduction could be achieved. In the latter case, a functionality-based LCA would be also necessary to assess whether this material saving outweighs the environmental impact of the fiber treatment.

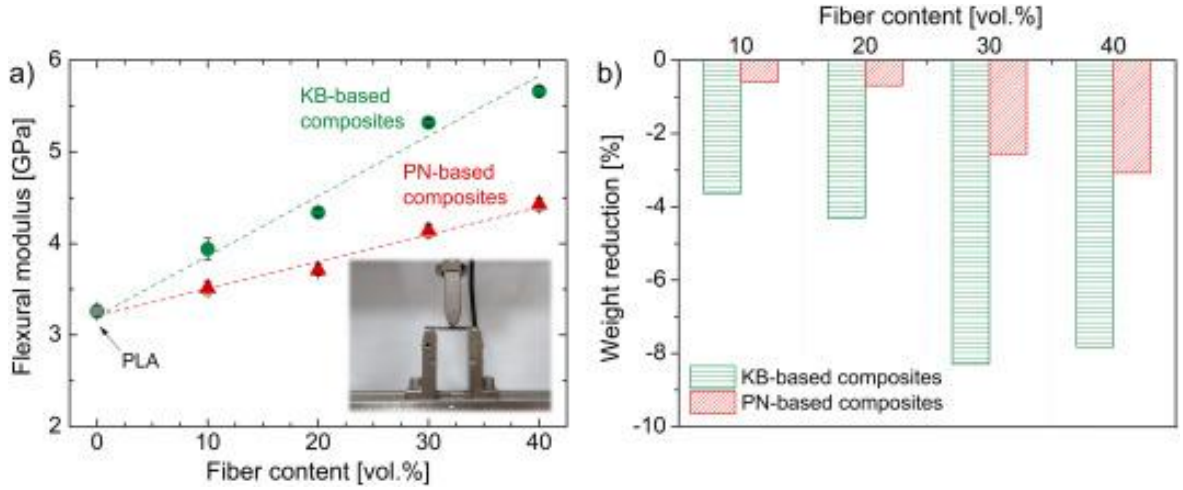

Figure 4: a) Flexural modulus of green composite samples as function of the fiber content. The testing setup for 3-point bending measurements is shown in the inset (dashed lines are guides for the eye). b) Percentage weight reduction achievable using green composites at different fiber content to realize a rectangular panel at fixed bending stiffness. Taken from [10].

3 CONCLUSIONS

In summary, green composites are a rapidly developing area with great potential to support the transition to sustainable and circular material systems. Their environmental attractiveness is obvious, but scientific rigor and holistic assessment are essential to ensure that their development leads to real environmental and social benefits. Collaboration between materials scientists, environmental engineers, industrial designers and policy makers will be crucial to overcome the current barriers and make biocomposites mainstream across all industries.

REFERENCES

[1] A.K. Mohanty, M. Misra, and L.T. Drzal, Sustainable bio-composites from renewable resources: Opportunities and challenges, *Journal of Polymers and the Environment*, **10**, 2000, pp. 19-26 (https://doi.org/10.1023/A:1024696314410).

[2] K.L. Pickering, M.G.A. Efendy, and T.M. Le, A review of recent developments in natural fibre composites and their mechanical performance, *Composites Part A*, **83**, 2016, pp. 98-112 (https://doi.org/10.1016/j.compositesa.2015.08.038).

[3] O. Faruk, A.K. Bledzki, H.P. Fink, and M. Sain, Biocomposites reinforced with natural fibers: 2000–2010, *Progress in Polymer Science*, **37**, 2012, pp. 1552-1596 (https://doi.org/10.1016/j.progpolymsci.2012.04.003).

[4] A.D. La Rosa, G. Cozzo, A. Latteri, A. Recca, A. Björklund, E. Parrinello, and G. Cicala, Life cycle assessment of a novel hybrid glass-hemp/thermoset composite, *Journal of Cleaner Production*, **44**, 2013, pp. 69-76 (https://doi.org/10.1016/j.jclepro.2012.11.038).

[5] V. Fiore, T. Scalici, G. Di Bella, and A. Valenza, A review on basalt fibre and its composites. *Composites Part B: Engineering*, **74**, 2015, pp. 74-94 (https://doi.org/10.1016/j.compositesb.2014.12.008).

[6] N. Saba, M. Jawaid, and O.Y. Alothman, An overview of natural fibre reinforced thermoplastic composites, *Journal of Renewable Materials*, **4**, 2016, pp. 23-34. (https://doi.org/10.7569/JRM.2015.634115).

[7] V. Siracusa, P. Rocculi, S. Romani, and M. Dalla Rosa, Biodegradable polymers for food packaging: a review, *Trends in food science & technology*, **19**, 2008, pp. 634-643 (https://doi.org/10.1016/j.tifs.2008.07.003).

[8] F. Aeschelmann, and M. Carus, Bio-based building blocks and polymers—Global capacities and trends 2015–2020. *Industrial Biotechnology*, **11**, 20156, pp. 274-279 (https://doi.org/10.1089/ind.2015.29030.fae).

[9] L. Suárez, J. Castellano, S. Díaz, A. Tcharkhtchi, and Z. Ortega, Are natural-based composites sustainable?, *Polymers*, **13**, 2021, pp. 2326 (https://doi.org/10.3390/polym13142326).

[10] L. Operato, L. Vitiello, P. Aprea, V. Ambrogi, M. Salzano de Luna, and G. Filippone, Life cycle assessment of poly (lactic acid)-based green composites filled with pine needles or kenaf fibers, *Journal of Cleaner Production*, **387**, 2023, pp. 135901 (https://doi.org/10.1016/j.jclepro.2023.135901).

[11] S.C. Carroccio, P. Scarfato, E. Bruno, P. Aprea, N.T. Dintcheva, and G. Filippone, Impact of nanoparticles on the environmental sustainability of polymer nanocomposites based on bioplastics or recycled plastics-A review of life-cycle assessment studies, *Journal of Cleaner Production*, **335**, 2022, pp. 130322 (https://doi.org/10.1016/j.jclepro.2021.130322).

Development of a Non-Iterative Artificial Neural Network Model for Enhanced Finite Element Analysis of Short Fiber-Reinforced Plastics

2025.8.6

Minjun Kwak and **Woong-Ryeol Yu***

Department of Materials Science and Engineering (MSE) and Research Institute of Advanced Materials (RIAM), Seoul National University, Seoul, 08826, Republic of Korea

Contents

I. Introduction

II. Non-iterative artificial neural network constitutive model

- Initial approach: series ANN structure
- Alternative approach: integrated ANN for pseudograin

III. Conclusion

Introduction

Short fiber-reinforced plastics (SFRPs)

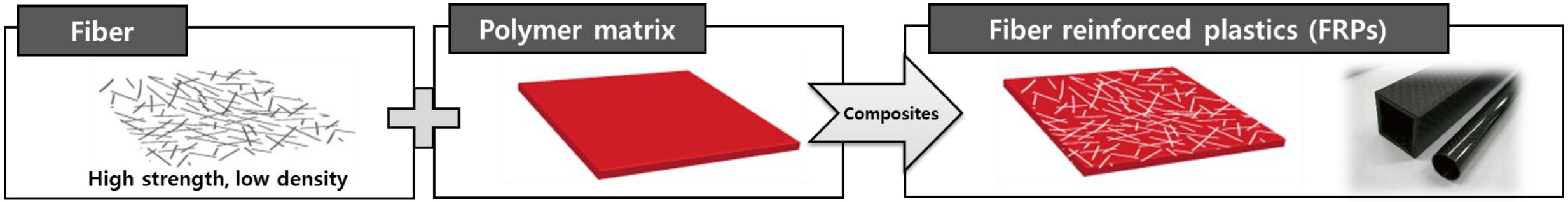

Classification of fiber reinforcement

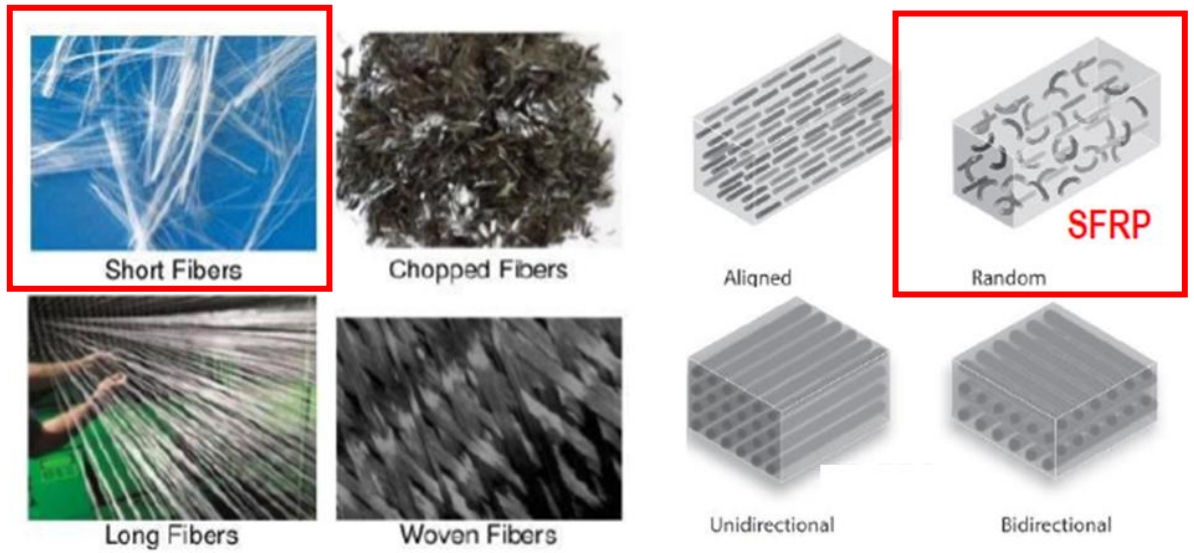

Advanced Functional Materials 32.40 (2022) 2205723

Industrial application of SFRP

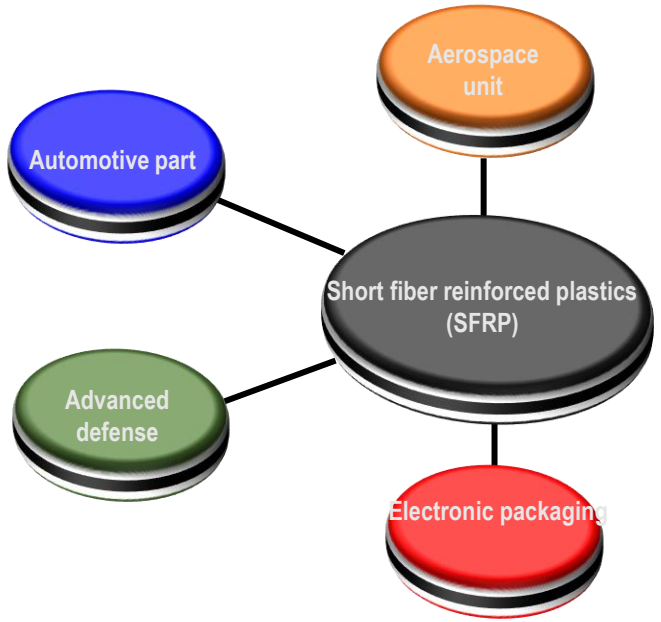

- Excellent manufacturing ease
- Low manufacturing cost
- Outstanding mechanical performance with light weight

Anisotropic mechanical behavior of SFRPs

Injection molding process

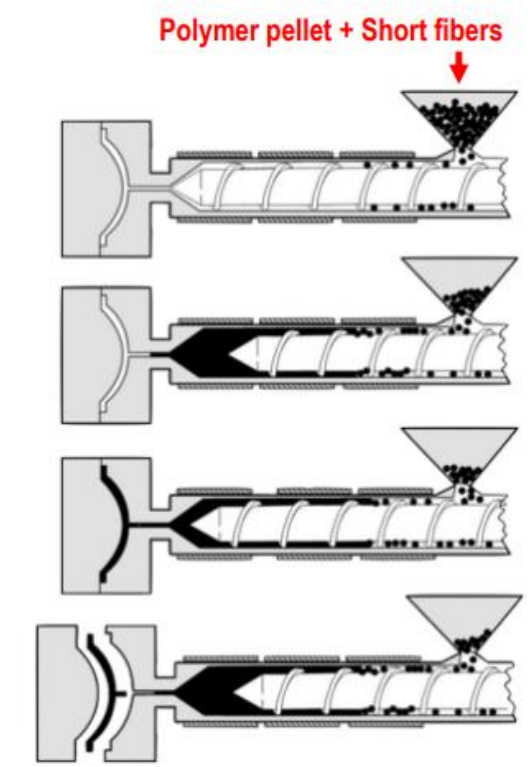

Manufacturing Techniques for PMCs (2012)

Variation of microstructure

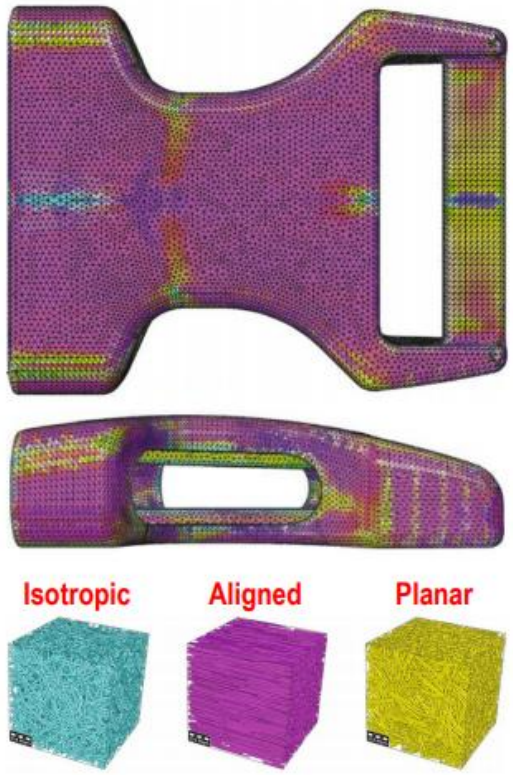

Computational Mechanics 61 (2018) ***729-750***

Anisotropic dependence on mechanical behavior

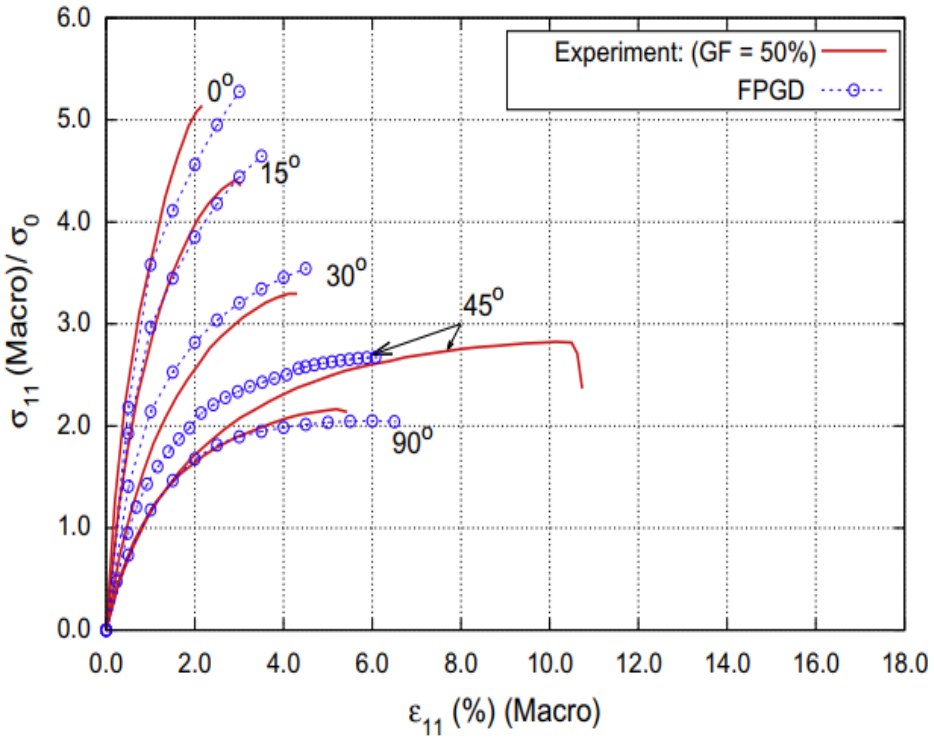

Composites: Part A 73 (2015) 166–175

- Tensile behavior of SFRP has strong dependence on local anisotropy induced by injection molding process.
- Mechanical behavior prediction method maintaining high accuracy and low computation cost is necessary for properly using SFRP in industrial field.

Prediction of the static failure behavior of SFRP Parts

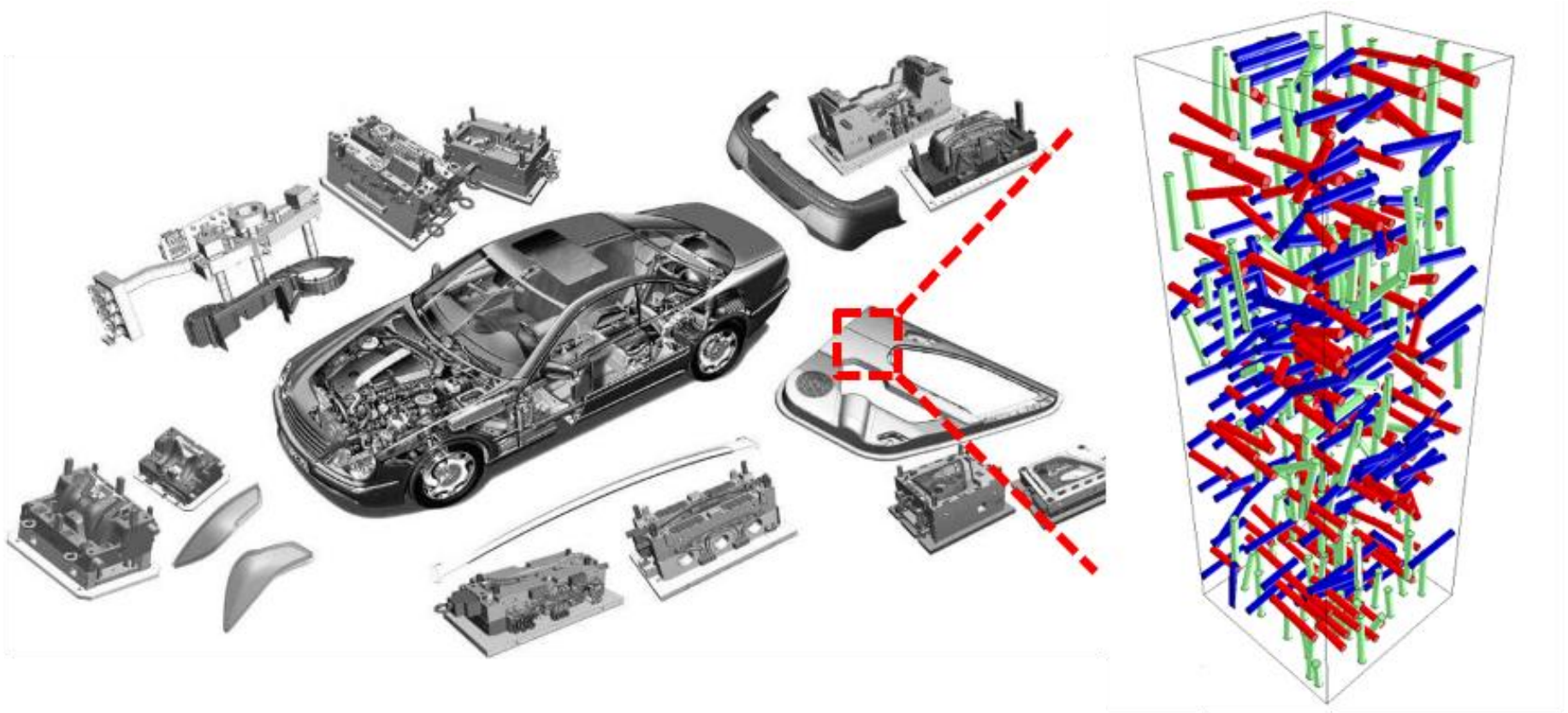

How can we predict the mechanical failure behavior of this anisotropic composite?

Mechanical models for SFRPs

Phenomenological models

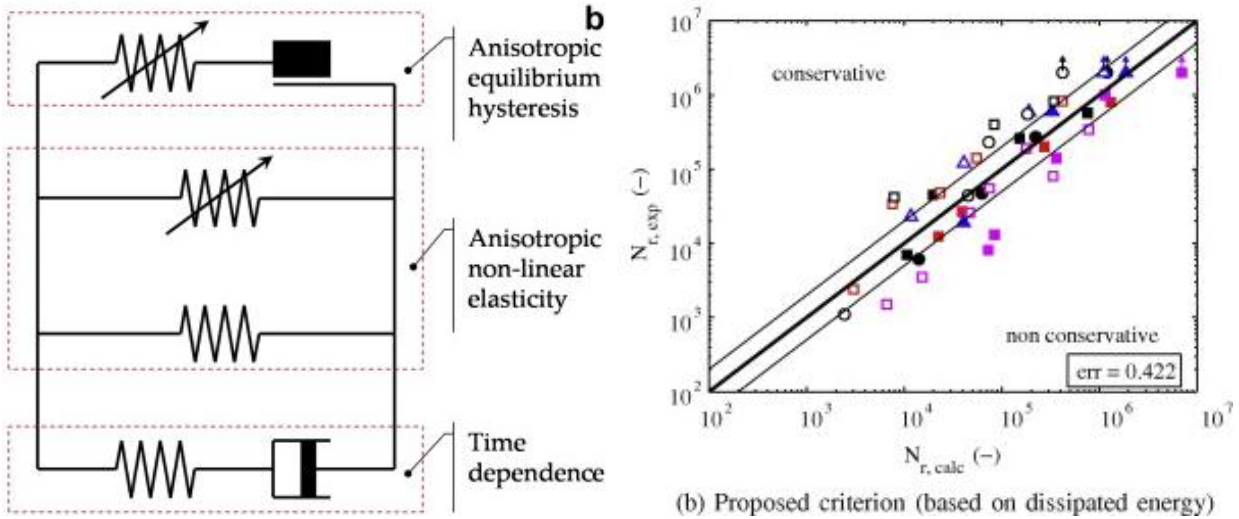

(b) Proposed criterion (based on dissipated energy)

European Journal of Mechanics-A/Solids 29(6) (2010) 1065-1077

International Journal of Fatigue 136 (2020) 105571

- Require labor-intensive experiments to characterize the fatigue properties considering the properties of constituents (fiber volume fraction, aspect ratio or orientation tensor).
- → **Difficult for modeling SFRP parts** that have significantly different mechanical properties due to varying the **local fiber orientation**.

Micromechanical models

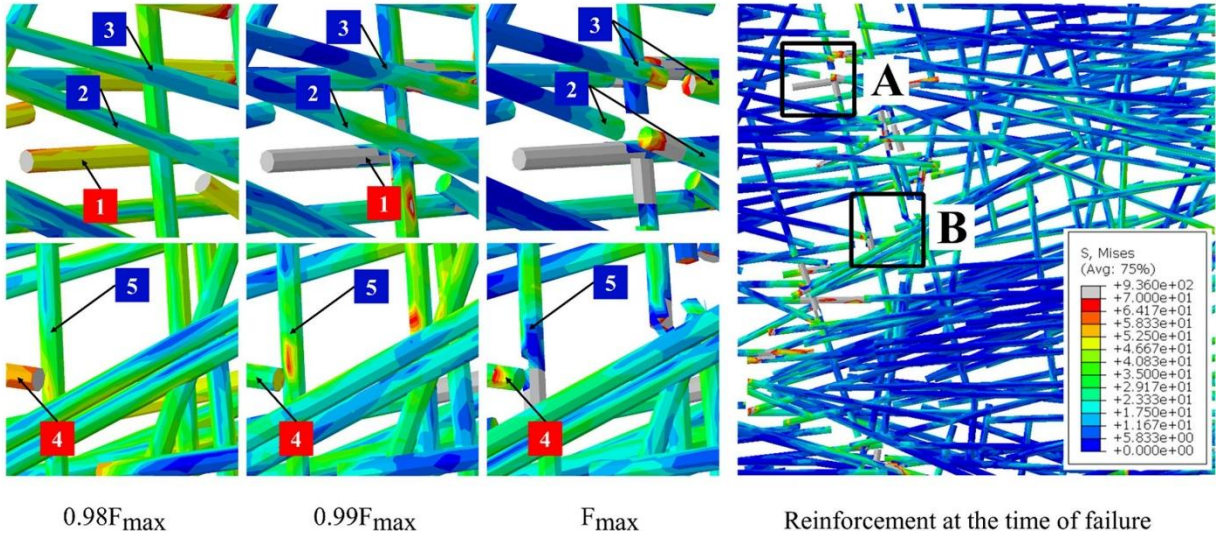

$0.98F_{max}$ $0.99F_{max}$ F_{max} Reinforcement at the time of failure

International Journal of Fatigue 160 (2022) 106880

- Describe the fatigue failure of SFRPs considering individual constituents (fiber, matrix, and interface).
- → **Time-intensive** because stress calculation of all fibers, matrix and interfaces is enormous.

Two-step homogenization for SFRPs

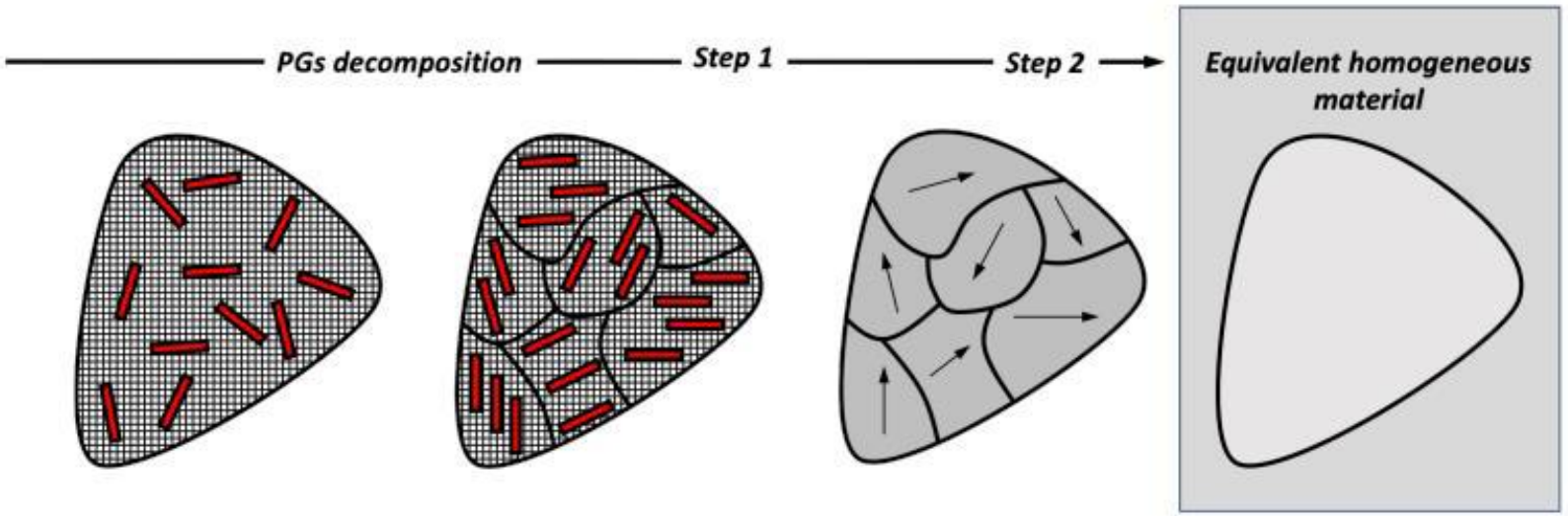

1. **Pseudograin decomposition**: Gommers (1998), Weber (1999), Ogierman (2017)
2. **1st Homogenization**: Mori-Tanaka (1973)

$$\langle C \rangle_\Omega = [(1 - v_i)C_m + v_i C_i : A^\varepsilon] : [(1 - v_i)I + v_i A^\varepsilon]^{-1}$$
$$A^\varepsilon{}_{MT} = [I + S : (C_m{}^{-1} : C_i - I)]^{-1}$$

3. **2nd homogenization**: Voigt (1889)

$$\langle C \rangle_\Omega = [(1 - v_i)C_m + v_i C_i]$$

Thesis Ecole Polytechnique de Louvain *61* (2019)

- **Two step homogenization method** was suggested to predict the mechanical behavior of SFRPs considering the **local orientation** and **computational cost**.
- Two-step homogenization is composed of following procedures.
  - Pseudograin decomposition: Gommers (1998), Weber (1999), Ogierman (2017)
  - 1st Homogenization: Mori-Tanaka (1973), Miller (2013)
  - 2nd Homogenization: Voigt (1889)
- DIGIMAT software allowed static failure prediction by using two-step homogenization, but failure behavior prediction showed high dependence on **user-defined failed weight fraction of entire pseudograin.**

We decided to develop ABAQUS user material subroutine (UMAT)

Based on two-step homogenization framework utilizing pseudograin approach.

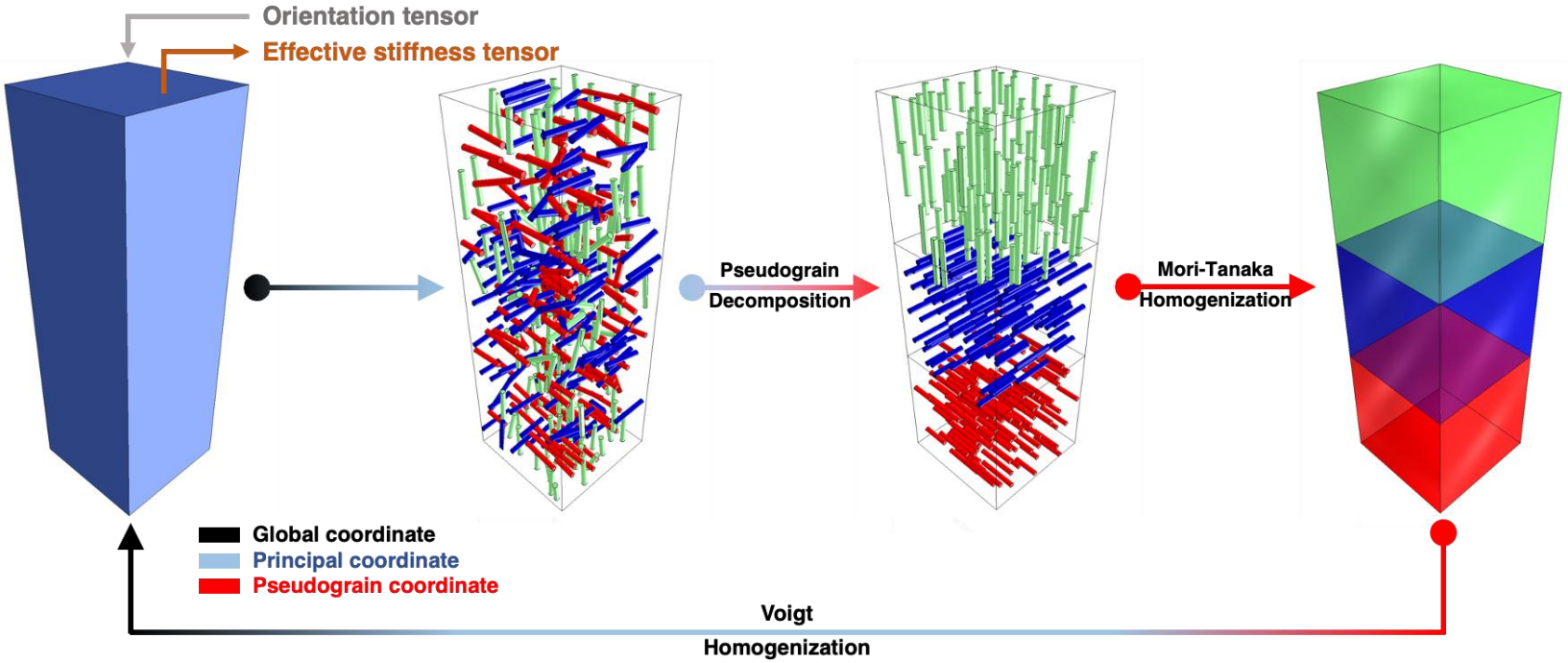

Fiber - elastic

$\langle \Delta\varepsilon_f \rangle$

$$\langle \Delta\varepsilon_f \rangle = B : [v_f B + v_m I]^{-1} : \langle \Delta\varepsilon \rangle$$

Matrix – viscoelastic viscoplastic

$\langle \Delta\varepsilon_m \rangle$

$$\langle \Delta\varepsilon_m \rangle = [v_f B + v_m I]^{-1} : \langle \Delta\varepsilon \rangle$$

Mori-Tanaka 1st homogenization

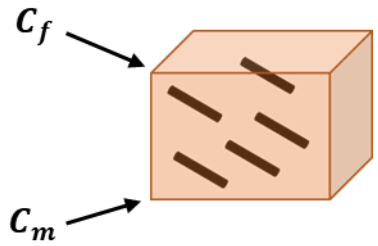

$$C_{PG} = [v_m C_m + v_f C_f : B^{\varepsilon}] : [v_f B + v_m I]^{-1}$$

$$\Delta\sigma_{PG} = C_{PG} : \Delta\varepsilon_{PG}$$

What are the main obstacles to achieve our goal?

Nested loop structure in 2-step homogenization algorithm

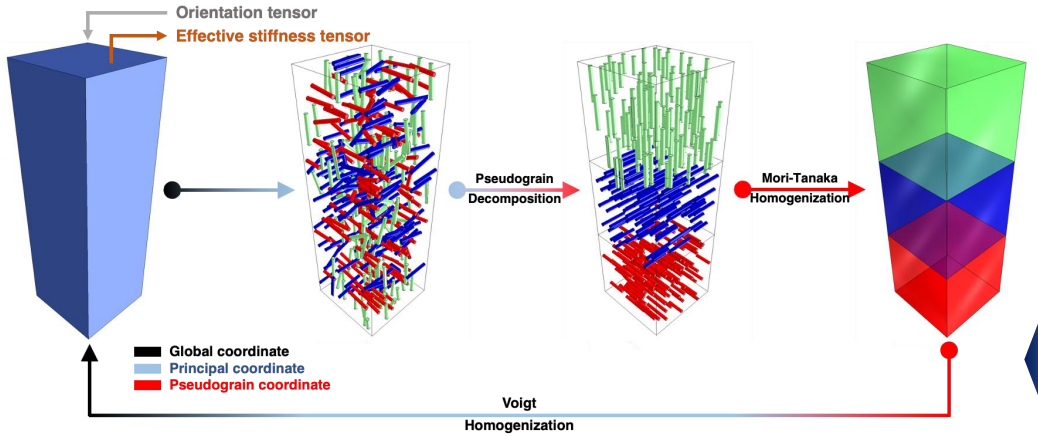

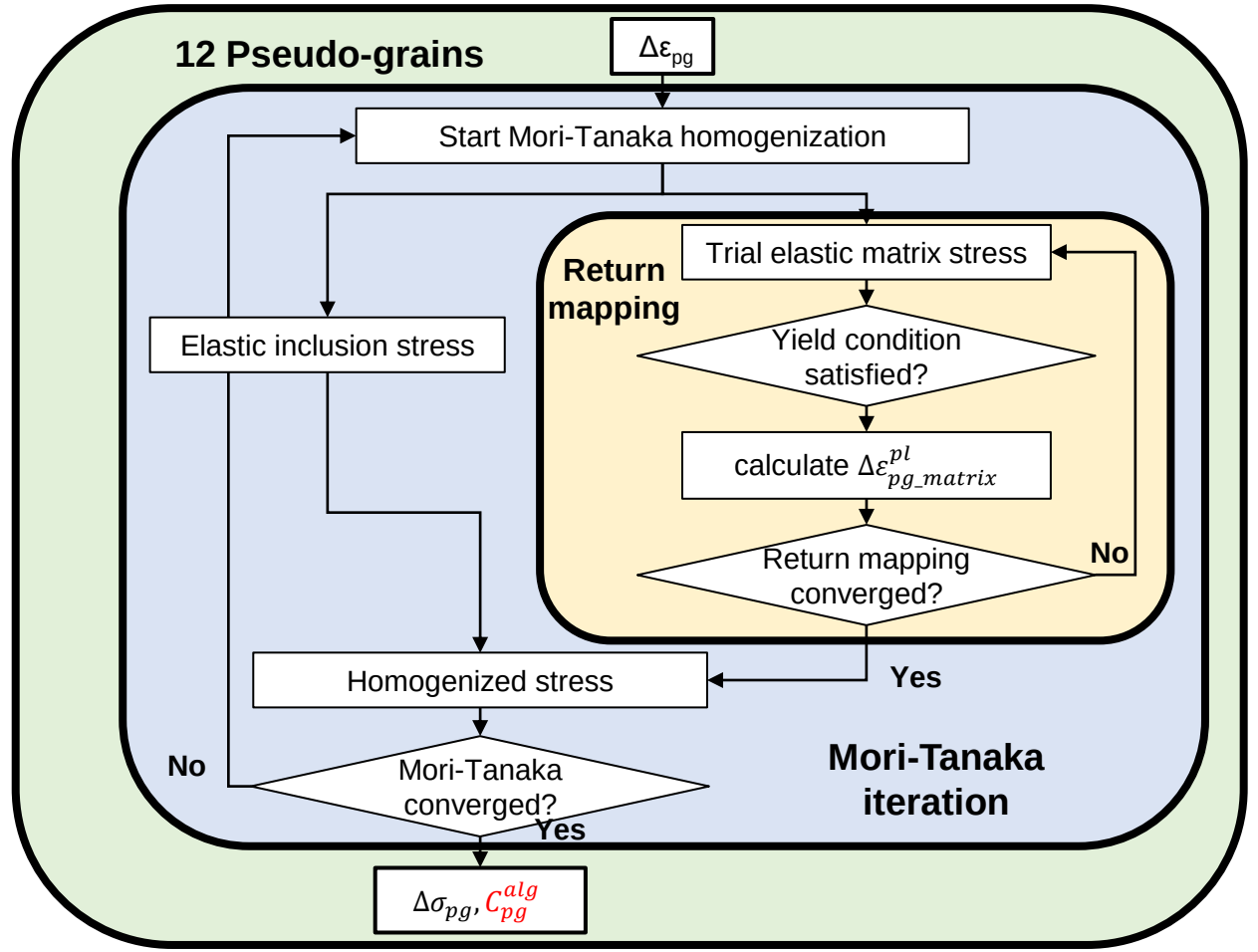

- ✓ 2-step homogenization using the pseudograin approach involves nested loops for calculation.

- → **The excessive number of iterations leads to increased computational time and lower vectorization efficiency.**

Comput. Methods Appl. Mech. Eng. 283 (2015) 1032–1060.

ANN-based constitutive equation

$\Delta\varepsilon$

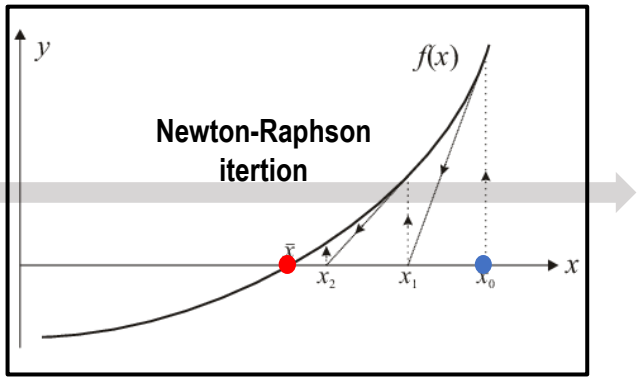

$\Delta\sigma$
C^{alg}

Conventional constitutive equation

- ✓ Need to fully capture and understand the constitutive behavior of materials
- ✓ Iterative calculations to model non-linear plastic deformation

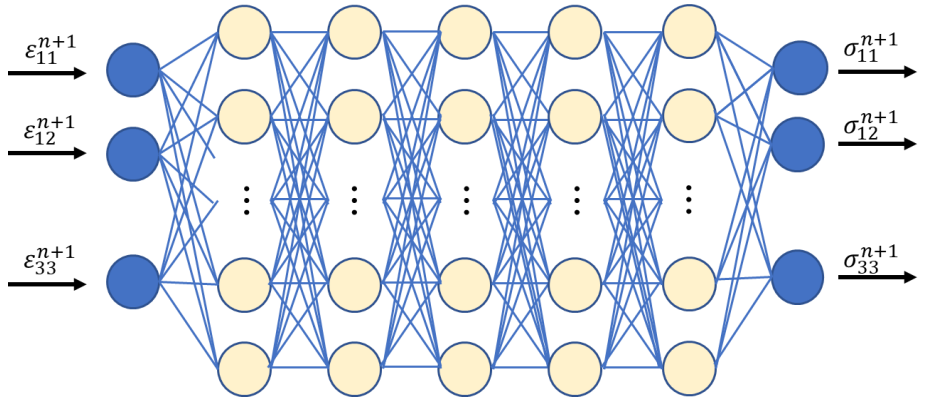

Artificial neural network (ANN)

- ✓ Highly nonlinear regression method predicting response without explicit function expressions
- ✓ Reduces the number of iterations and enhance vectorization efficiency

Comput. Methods Appl. Mech. Eng. 283 (2015) 1032–1060.

Initial approach: Modular ANN Architecture

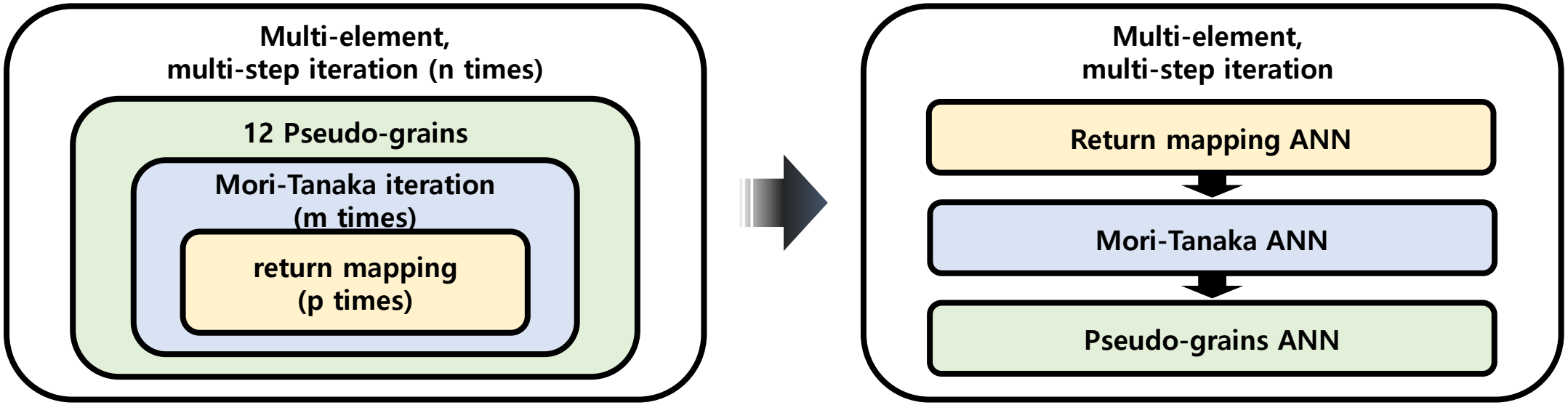

Modularize each loop instead of creating multiple loops all at once.

1. Easy to focus on each system's physics, making pattern recognition and learning more effective.
2. Easy to modify each model when system changes occur, such as material changes.

Modular ANN (1): return mapping

Return mapping

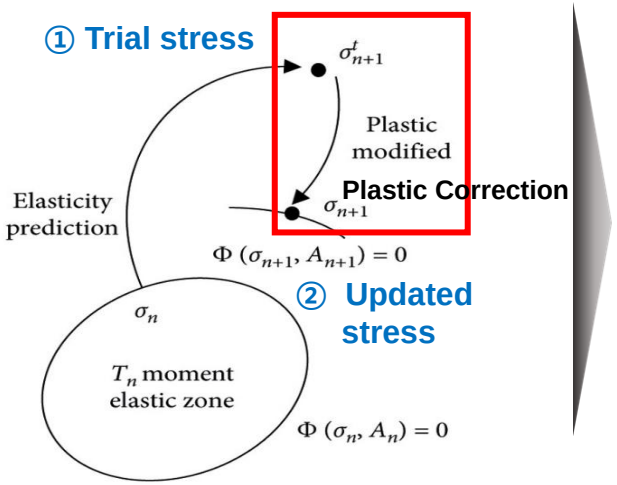

① Trial stress

σ_n^{TR}

ANN

② Updated stress

σ_{n+1}

Deviatoric stress

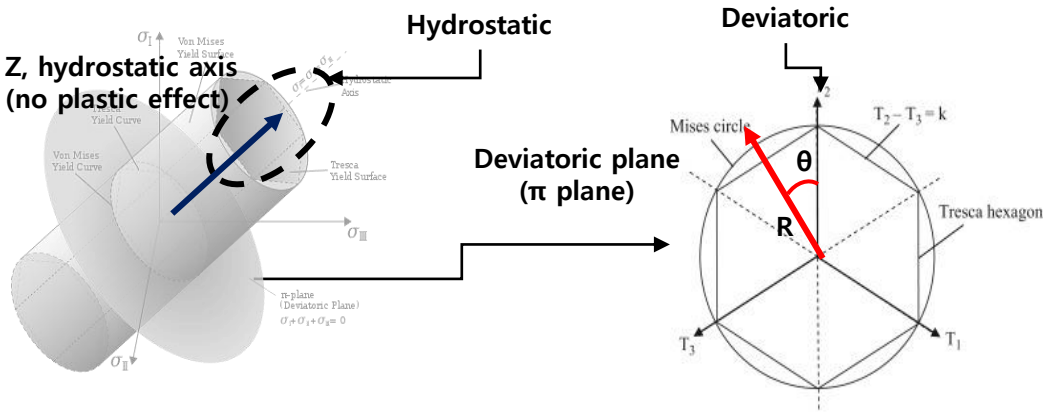

Deviatoric trial stress (scalar)
Flow stress
Viscoplastic function

$$\left\{ \begin{matrix} \mathrm{S}_R^{TR} \\ \rho(\bar{\varepsilon}^{p,n}) \\ g_v(f)\Delta t \end{matrix} \right\} \rightarrow \left\{ \begin{matrix} \mathrm{S}_R^{n+1} \\ \rho(\bar{\varepsilon}^{p,n+1}) \end{matrix} \right\}$$

Deviatoric corrected stress (scalar)
Flow stress

Trial **Corrected**

Modular ANN (1): return mapping

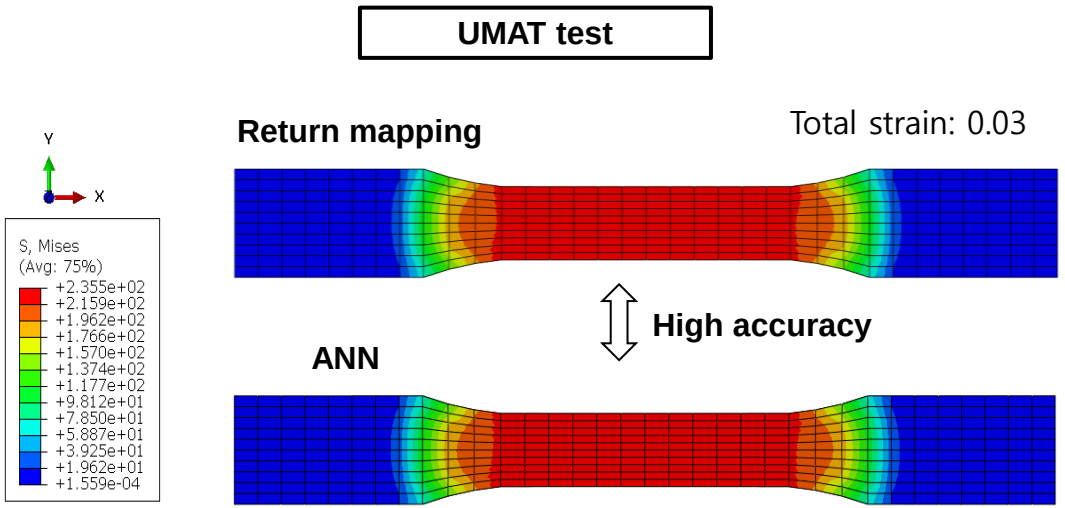

CPU calculation time for each algorithm

	Return mapping	ANN	Reduction rate
1000 elements	111 sec	108 sec	**3 %**
loop only	2.9 msec	1.6 msec	55 %

✓ Specimen level simulation showed both methods achieve high accuracy.

✓ The ANN model achieved a 55% reduction at the loop level, but only about 3% across the full 1000-element analysis.

Modular ANN (2): Mori-Tanaka homogenization ANN

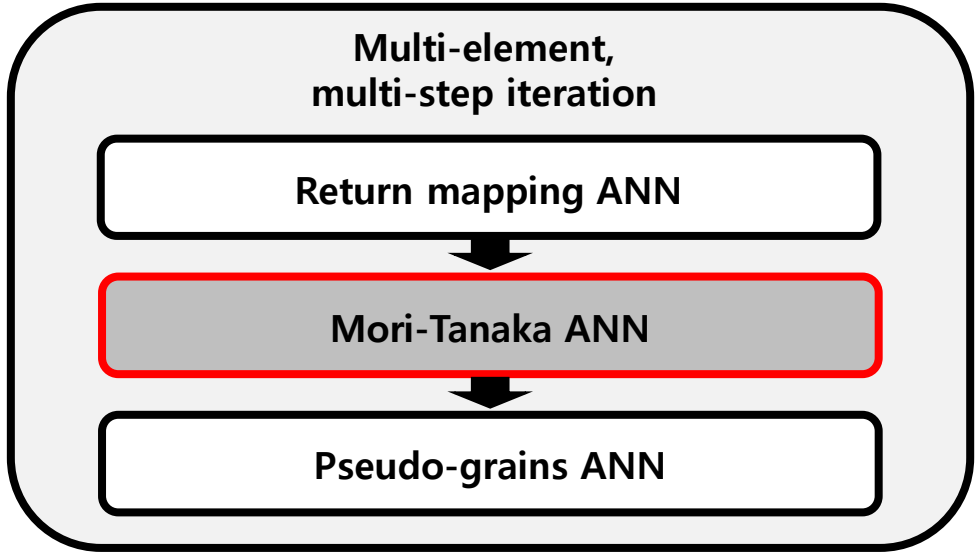

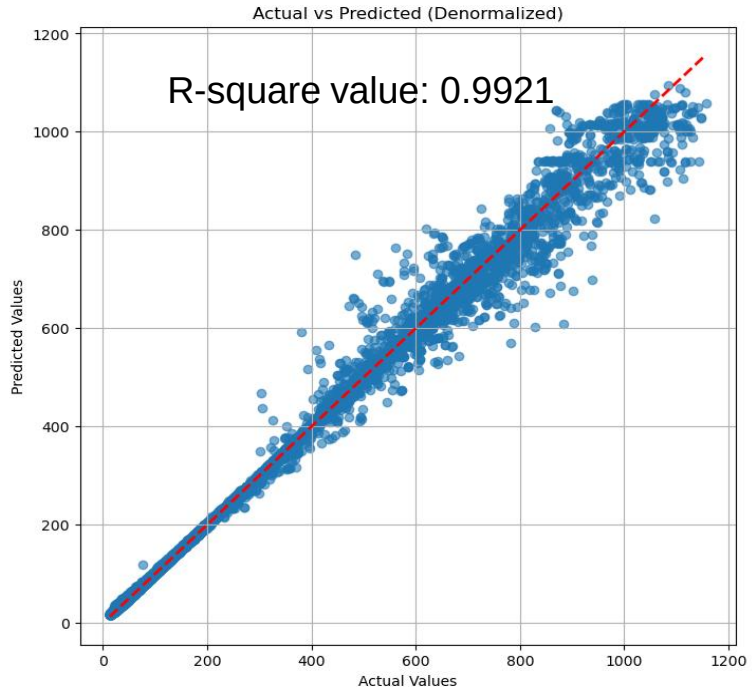

- ✓ Error accumulation occurs due to the consecutive use of two neural networks.
- ✓ Since accurate prediction requires the output of one ANN as input for the other, using the first ANN's output as input was challenging.

Alternative strategy: Integrated ANN

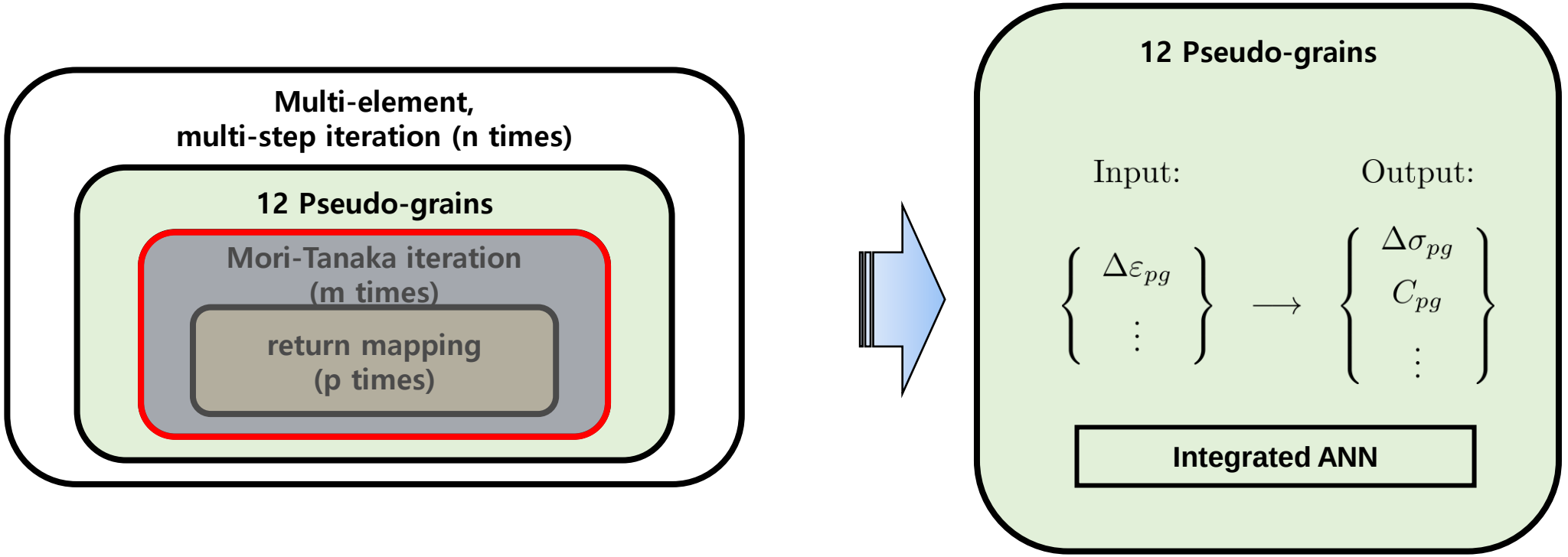

✓ Instead of sequentially connecting neural networks, a single integrated neural network that can simultaneously represent both systems is needed.

Mori-Tanaka iteration loop

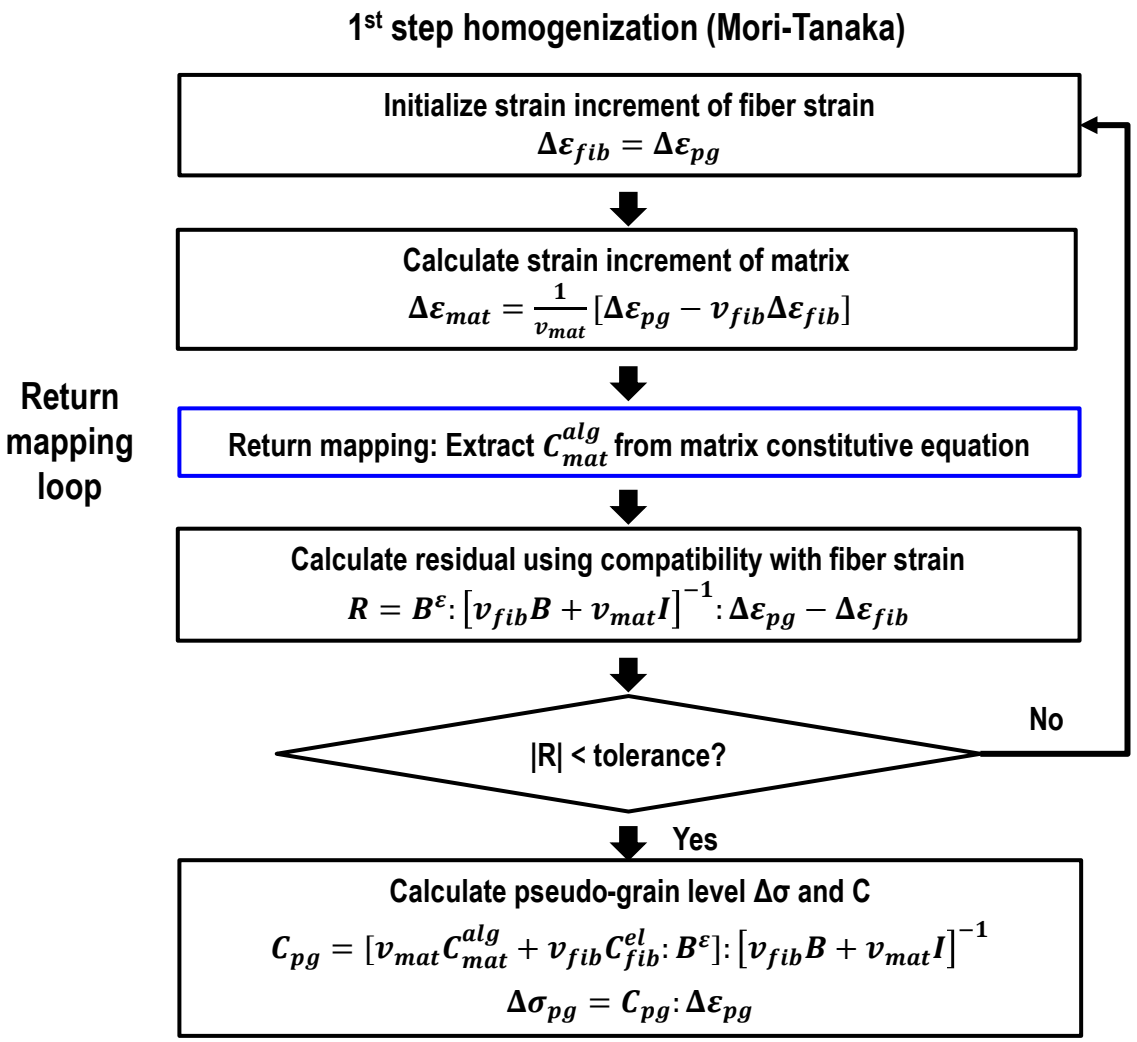

- To estimate the macroscopic behavior of pseudo grain, the Mori–Tanaka homogenization method is used.
- Repeat until convergence:
  a. Decompose pseudo grain strain into matrix and fiber strain
  b. Update plastic matrix stress and elastic fiber stress
  c. Update average stiffness and recompute matrix strain
  d. Check convergence of matrix and fiber strain
- As a result, pseudo-grain level stiffness and stress are computed analytically.

Problem when using Integrated ANN

What we need is…

$\Delta\varepsilon_{pg}$

$\Delta\sigma_{pg}$ or C_{pg}^{alg}

Stress increment

Consistent tangent stiffness

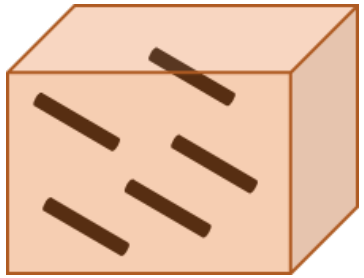

Pseudo-grain

$$\Delta\sigma_{pg} = C_{pg}^{alg}\Delta\varepsilon_{pg}$$

Input:

$$\left\{\begin{array}{l}\Delta\varepsilon_{pg,11}\\ \Delta\varepsilon_{pg,22}\\ \Delta\varepsilon_{pg,33}\\ \vdots\end{array}\right\}$$

9+α inputs

$\longrightarrow$

Output:

$$\left\{\begin{array}{l}\Delta\sigma_{pg,11}\\ \Delta\sigma_{pg,22}\\ \vdots\\ C_{pg,11}\\ C_{pg,12}\\ \vdots\end{array}\right\}$$

9 outputs

36 outputs

- ✓ The ANN is designed to approximate Mori–Tanaka homogenization by mapping pseudo-grain strain to stress increment and tangent stiffness.
- ✓ However, directly using full 3D stress and stiffness tensors as ANN outputs makes the network excessively large and computationally inefficient.

→ **Need to reduce input and output features**

Strategy for integrated ANN (1): output feature

$$\left\{ \begin{matrix} \Delta\varepsilon_{mat} \\ \Delta\varepsilon_{fib} \end{matrix} \right\} \quad V_{mat}\Delta\varepsilon_{mat} + (1 - V_{mat})\Delta\varepsilon_{fib} = \Delta\varepsilon_{pg}$$

$$\left\{ \ \Delta\varepsilon_{fib} \ \right\} \quad B^{\varepsilon} : [V_{fib}B^{\varepsilon} + V_{mat}I]^{-1} : \Delta\varepsilon_{pg} = \Delta\varepsilon_{fib}$$

$$B^{\varepsilon} = \left[I + S : \left((C_{mat}^{iso})^{-1} : C_{fib} - I \right) \right]^{-1}$$

$$\left\{ \ C^{iso} \ \right\} \quad C^{\mathrm{iso}} \equiv 3\kappa^{ve} I^{\mathrm{vol}} + 2\mu^{reg} I^{\mathrm{dev}}$$

$$\left\{ \ \mu_{reg} \ \right\} \quad \mu^{\mathrm{reg}}(t_{n+1}) = \mu^{vep}(t_{n+1}) + (\mu^{\mathrm{reg}}(t_n) - \mu^{vep}(t_{n+1})) \exp\left(-\frac{h_{vep}}{h_v - h_{vep}} \right)$$

$$\mu^{vep} = \mu^{ve} \left(1 - \frac{3\mu^{ve}}{3\mu^{ve} + \frac{dR}{dp}(\bar{\varepsilon}^{p})} \right)$$

Regularized shear moduli

Knowing the matrix's **effective plastic strain ($\bar{\varepsilon}^{p}_{mat}$)** allows determination of $\Delta\varepsilon_{mat}$ and $\Delta\varepsilon_{fib}$.

Calculate matrix's stress and stiffness

$$\boldsymbol{\sigma}_{mat} = \mathbf{C} : \Delta\boldsymbol{\varepsilon}_{mat} - 2\mu\Delta\bar{\varepsilon}^{p}\mathbf{N}^{\mathrm{trial}}$$

$$\mathbf{C}_{mat}^{\mathrm{alg}} = \widetilde{\mathbf{E}} - \frac{(2\widetilde{G})^2}{h_v}\mathbf{N}\otimes\mathbf{N} - \left(2\widetilde{G}\right)^2 \frac{\sigma_{eq}\Delta\bar{\varepsilon}^{p}}{\sigma_{eq}+3\widetilde{G}\Delta\bar{\varepsilon}^{p}}\frac{\partial\mathbf{N}}{\partial\sigma}$$

- C_{pg} using rule of mixture
- Damaged stiffness and stress

∴ **The ANN requires only $\bar{\varepsilon}^{p}_{mat}$ as output.**

Strategy for integrated ANN (2): input features

Prior effective plastic strain of matrix

✓ Need to monitor the degree of plastic strain.

→ Use the effective plastic strain from the previous increment.

$$\bar{\varepsilon}^{p} = \sqrt{\frac{2}{3}\,\varepsilon_{ij}^{p}\,\varepsilon_{ij}^{p}}$$

Von-Mises pseudo-grain effective strain

✓ Need to provide scalar input for yield evaluation and plastic strain increment

→ Use von Mises equivalent strain derived from pseudo-grain level strain

$$\widehat{\varepsilon} = \sqrt{\frac{2}{3}\,\varepsilon_{\mathrm{dev}} : \varepsilon_{\mathrm{dev}}}$$

$$= \sqrt{\frac{2}{3}\left[(\varepsilon_{xx}-\varepsilon_{yy})^2 + (\varepsilon_{yy}-\varepsilon_{zz})^2 + (\varepsilon_{zz}-\varepsilon_{xx})^2 + 6(\varepsilon_{xy}^2+\varepsilon_{yz}^2+\varepsilon_{zx}^2)\right]}$$

Final ANN structure

$$(\bar{\varepsilon}_{mat}^{p,n}) = f_{\text{ANN-2}}\left(\widehat{\varepsilon}_{pg}, \bar{\varepsilon}_{mat}^{p,n-1}\right)$$

→ Two scalar values are used as input to predict one scalar output.

Dataset for integrated ANN (1)

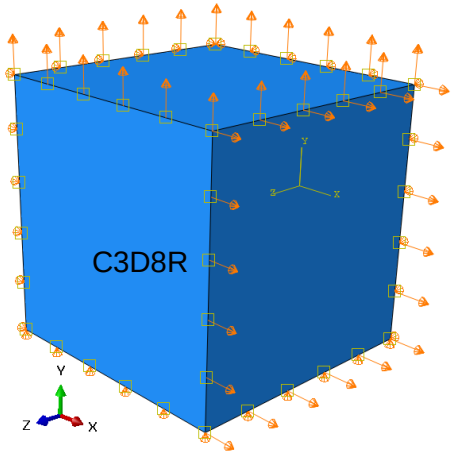

$$\mathbf{u} = \begin{bmatrix} \varepsilon_{11}x + \varepsilon_{12}y + \varepsilon_{31}z \\ \varepsilon_{22}y + \varepsilon_{12}x + \varepsilon_{23}z \\ \varepsilon_{33}z + \varepsilon_{23}y + \varepsilon_{31}x \end{bmatrix}$$

Viscoplastic parameter	
Yield stress (MPa), σ_y	32.91
Hardening exponent, B	0.5446
Hardening modulus, C	39.35
Viscoplastic coefficient, η	6481
Viscoplastic exponent, VN	1.48

Fiber properties	
Elastic modulus (GPa)	72.0
Poisson ratio	0.22
Density (g/cm³)	1.80
Fiber volume fraction	0.208 (≈ W_f: 0.4)
Fiber aspect ratio	25

Dataset with various loading path

Longitudinal tension
Transverse tension
Longitudinal pure shear
Biaxial tension + shear
Biaxial mixed load + shear
biaxial compression + shear
…

- ✓ Finite element simulations with 100 increments were used to generate each database.
- ✓ Various loading paths were considered under a simple linear loading condition.

Dataset for integrated ANN (2)

	#	ε11	ε22	ε33	ε12	ε31	ε23	
Longitudinal tension	1	0.04	0	free	0	0	0	Training dataset
Transverse tension	2	0	0.06	free	0	0	0	
Longitudinal pure shear	3	0	0	0	0.06	0	0	
Biaxial load with shear	4	0.02	0.024	free	0.06	0	0	
	5	-0.02	0.03	free	0.045	0	0	
	6	0.016	-0.04	free	0.05	0	0	
	7	0.016	0.04	free	0.04	0	0	
	8	0.02	0.06	free	0.04	0	0	
	9	0.016	0.06	free	0.03	0	0	
	10	0.016	0.06	free	0.02	0	0	
	11	-0.02	-0.02	free	0.06	0	0	
	12	-0.02	-0.04	free	0.04	0	0	
	13	-0.02	-0.06	free	0.02	0	0	
Test loading set 1	14	0.02	0.036	free	0.027	0	0	Test dataset
	15	-0.02	-0.04	free	0.027	0	0	
	16	0.02	0.075	free	0.03	0	0	
	17	0.02	0.02	free	0.06	0	0	
Test loading set 2	18	0.02	0.04	free	0.04	0	0.02	
	19	0.02	0.03	free	0.03	0	0.03	

→ 1300 training datasets were generated.

13 random loading path for training

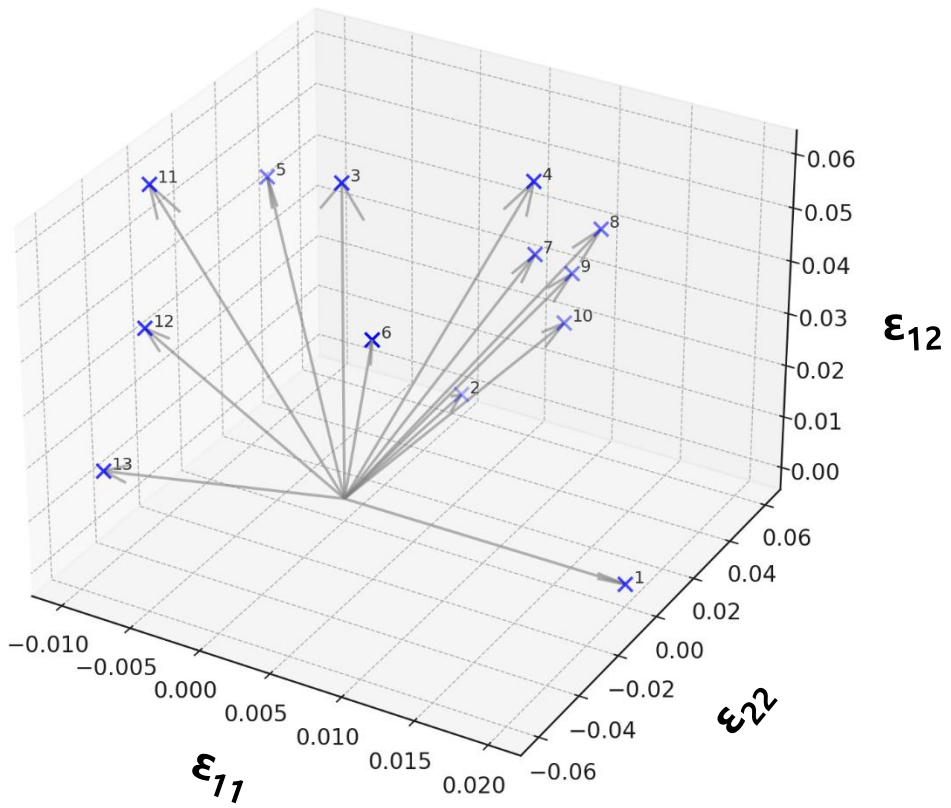

Training integrated ANN

Hyperparameter search: hyperband algorithm

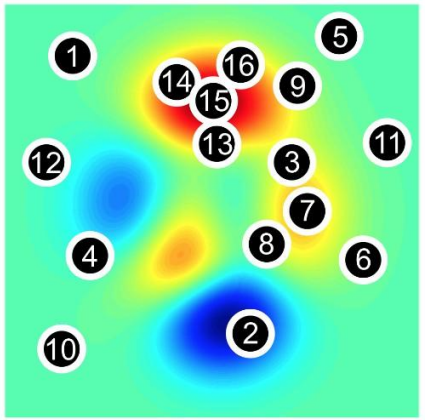

Hyperband

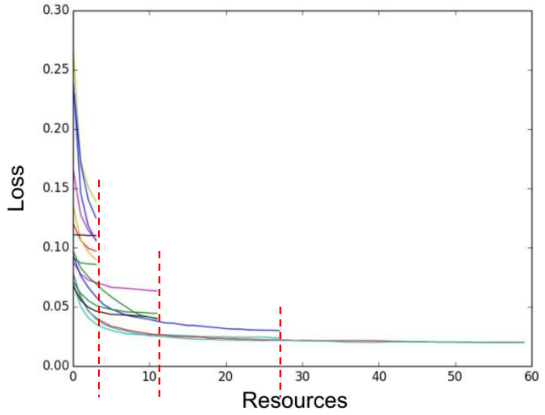

Prediction test

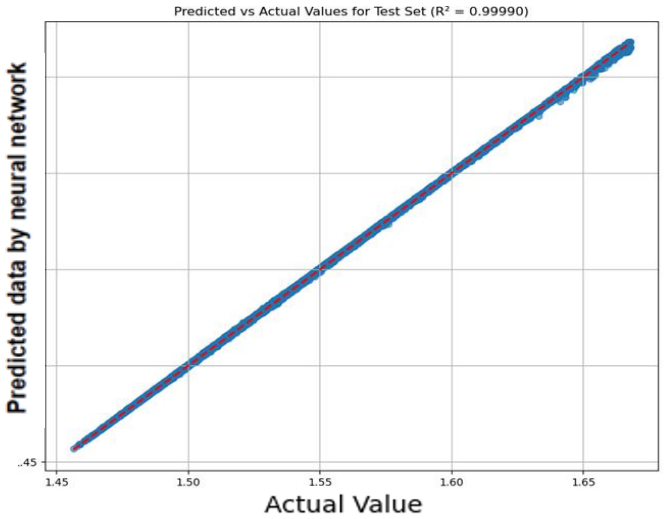

- ✓ In order to find the appropriate hyperparameter of ANN such as the number of neurons and hidden layers, hyperband algorithm was used.
- ✓ The predicted and actual values plot of output variables showed remarkably high accuracy with an R-squared value of over 0.9999

Mori-Tanka ANN test results

Test results (loading path #14~17)

→ Test dataset within the training range.

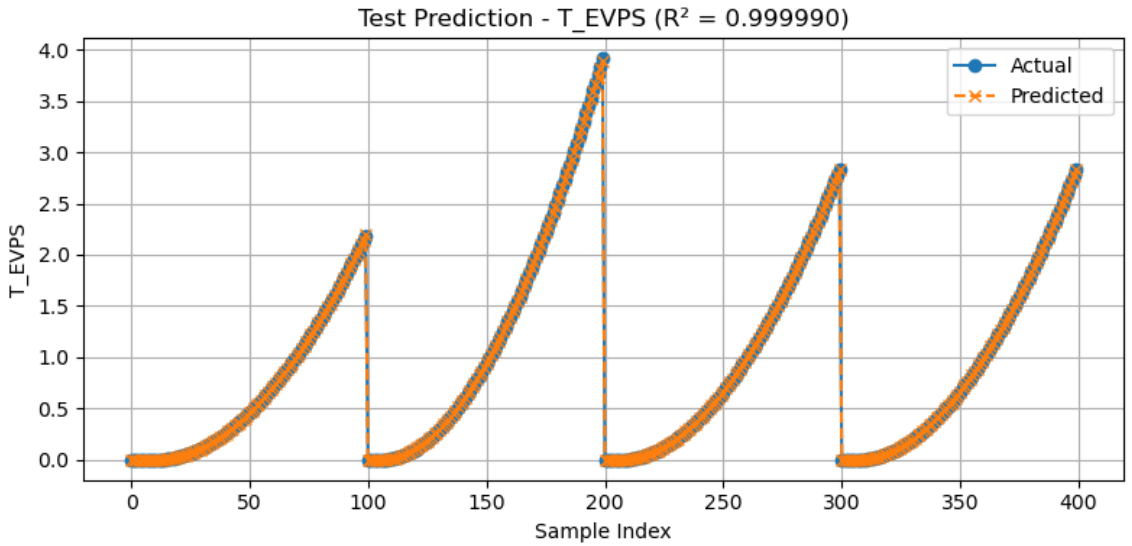

Test results (loading path #18~19)

→ 23-direction strain not included in training was used.

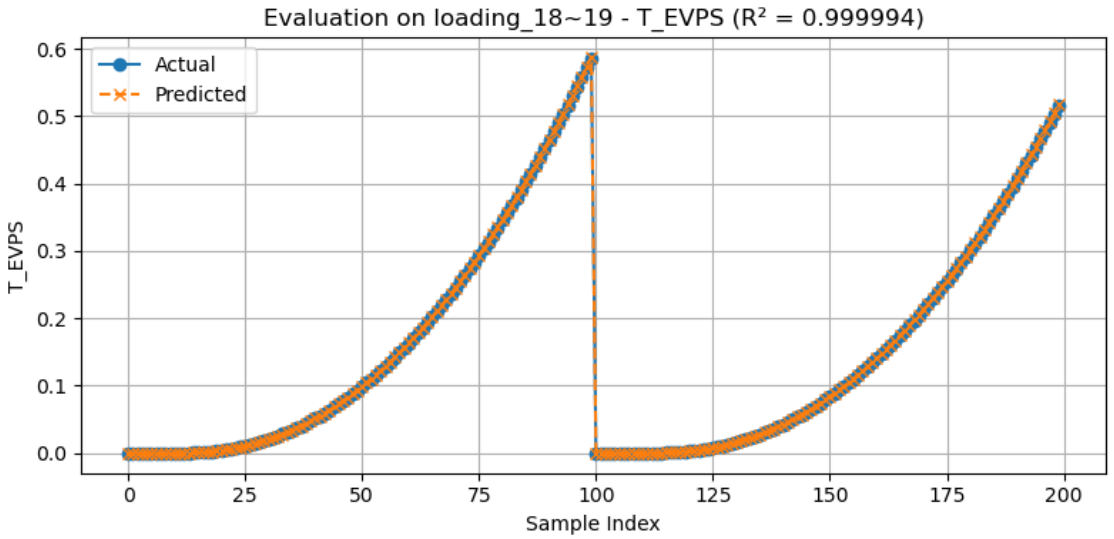

- ✓ The neural network shows high accuracy within the training range.
- ✓ The use of effective strain enables accurate predictions even when shear components not included in training are applied.

ABAQUS User Subroutine(UMAT) implementation results

Loading beyond the training range

$$\{\varepsilon_{11}, \varepsilon_{22}, \varepsilon_{33}, \varepsilon_{12}, \varepsilon_{13}, \varepsilon_{23}\} = \{0.05,\ 0,\ \text{free},\ \varepsilon_3,\ 0,\ 0\}$$

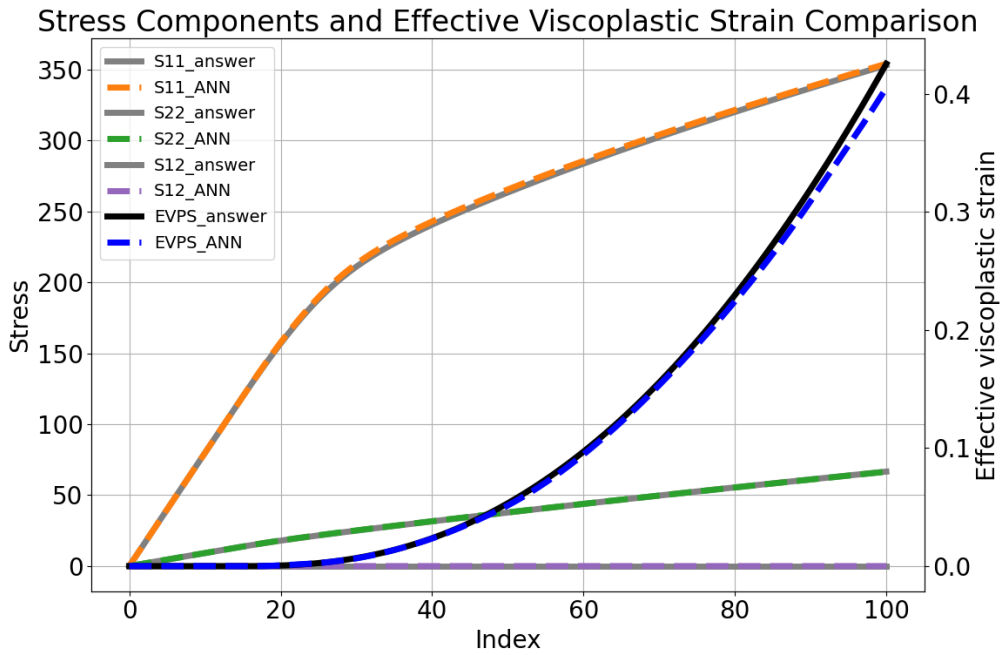

Non-proportional loading

→ The loading path was altered through multiple steps

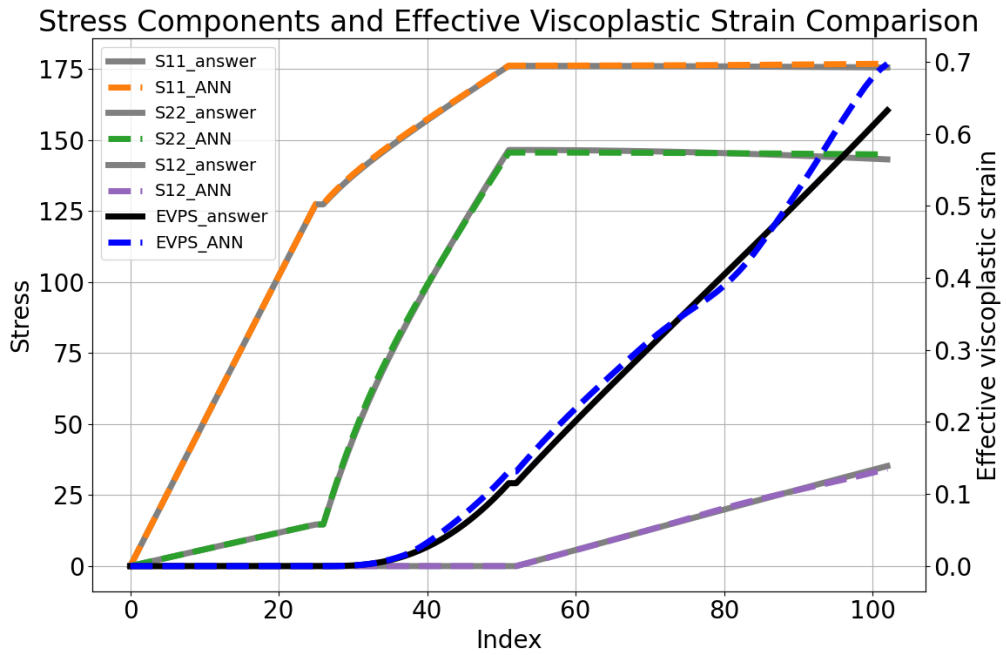

- ✓ The trained neural network was implemented and tested using an ABAQUS user-defined subroutine (UMAT).
- ✓ The model performs well beyond the training domain, effectively handling even non-proportional loading cases.

Calculation time comparison (1): multi-element test

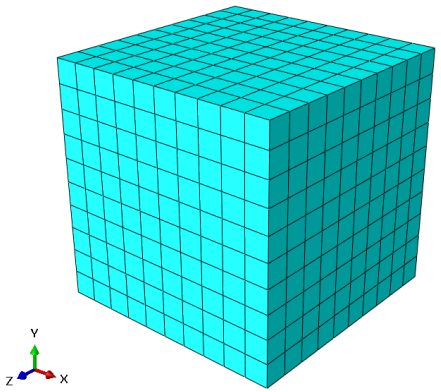

Single pseudo grain test (1000 elements)

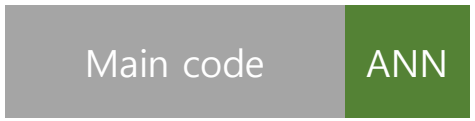

63 sec



68 sec

7.5% reduction

12 pseudo grain test (1000 elements)



120 sec

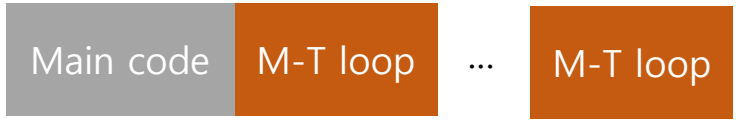

179 sec

33% reduction

- ✓ Computational time was reduced by employing neural networks, especially in cases involving 12 pseudo-grains.
- ✓ This reduction is expected to become more significant as the number of elements increases.

Concluding remarks

Non-iterative artificial neural network constitutive model

- ANN-based constitutive model to predict the properties of polymer matrix and combined fiber composite materials was developed.
- The proposed ANN successfully approximates Mori–Tanaka homogenization with high accuracy, even under loading conditions beyond the training domain.
- By reducing computational cost, the ANN demonstrates strong potential for integration into large-scale finite element simulations.

Thank you very much for your attention

DEEP LEARNING-BASED GEOMETRICAL ANALYSIS AND TENSION STRAIN MAPPING OF BAMBOO FIBRE MICROSTRUCTURE

Carlos I. Cardona[1,2], Lina M. García[3] and C. A. Fuentes[1,4]

[1]Luxembourg Institute of Science and Technology (LIST), Department of Materials Research and Technology, 5, rue Bommel L-4940 Hautcharage, Luxembourg
Email: carlos.cardona@list.lu, web page: https://www.list.lu/

[2] University of Luxembourg, Department of Physics and Materials Science, 2, place de l'Université L-4365 Esch-sur-Alzette, Luxembourg
web page: https://www.uni.lu/en/

[3]Department of Electronics and Automation, Autonomous University of Manizales, 170001 Edificio Sacatín. Manizales, Colombia
Email: linam.garciap@autonoma.edu.co, web page: http://www.autonoma.edu.co

[4]KU Leuven, Department of Materials Engineering, Kasteelpark Arenberg 44/bus 2450, 3001 Leuven, Belgium
Email: carlos.fuentes@list.lu, web page: https://www.kuleuven.be/english/kuleuven

Keywords: Bamboo fibre, Microstructure, Deep-Learning Geometrical Analysis, Tension Strain Mapping, vector fields.

ABSTRACT

Bamboo technical fibre is a structurally graded natural composite material consisting of tubular elementary fibres bonded by a middle lamella. Its hierarchical design exhibits localized distortions of unknown configuration. We applied a deep learning-based geometrical analysis to extract the spatial distribution of fibre hierarchies in the cross-section, correlating this with tensile strain maps in the longitudinal direction. The lumen fraction, representing the percentage of the total technical fibre cross-sectional area occupied by lumens, averaged 7 to 13%. In the middle part of the cross-section, the middle lamella had an average thickness of 0.48 μm, while the elementary fibres averaged 13.79 μm in diameter and their lumens averaged 2.7 μm in diameter. Using vector fields derived from gradient cubic approximations, we evaluated the positional distribution of elementary fibres on the cross-section and contrasted this with micro-tensile strain maps. This analysis categorized fibre failure origins as asymmetric defibrillation and cell wall cracking, identifying key parameters for physics-informed models.

1 INTRODUCTION

One of the main challenges in understanding the structural behaviour of technical bamboo fibres lies in establishing a clear relationship between their mechanical response and their complex microstructure present in the cross section. These fibres, composed of tubular elementary units bonded together by the middle lamella, form a hierarchical natural composite that features unique polygonal cell wall morphologies with internal lumens. At both the technical (fibre bundle) and elementary fibre levels, bamboo displays significant microstructural variability including distortions, surface irregularities, and cross-sectional asymmetries that have largely remained underexplored [1].

The area fraction of each anatomical phase (elementary fibre wall, lumen, and middle lamella) plays a role in defining the fibber's load-bearing capacity, as it dictates the effective cross-sectional area available for stress transfer. Such geometrical complexity results in non-uniform stiffness distributions, which may govern how damage initiates and propagates for samples without pre-existent defects. Specifically, the spatial variation in fibre cross-section is proposed as a design signature potentially linked to flexural loads experienced during the plant's growth. However, quantifying this link has been

limited by challenges in resolving these microstructures using conventional imaging. Bamboo has gained considerable attention as a natural, sustainable alternative for reinforcing composite materials due to its high strength to weight ratio, functional grading, and unique fibre architecture. Among the most studied species, Guadua angustifolia exhibit complex hierarchical structures, where tubular elementary fibres are bound by middle lamellae and contain central lumens. These microstructural features influence the fiber's mechanical properties, including tensile strength and stiffness, which can reach up to 800 MPa and 43 GPa, respectively [1].

Several studies have explored the mechanical behaviour of bamboo under varying loading conditions. For example, Hu et al. [2] demonstrated that strain rate sensitivity significantly affects bamboo's failure mechanisms, including fibre buckling, delamination, and intercellular cracking. Likewise, Wang et al. [3] highlighted the asymmetric bending behaviour of bamboo, driven by its gradient fiber distribution, and showed how failure initiates preferentially in parenchyma-rich zones. These investigations confirm that mechanical behaviour in bamboo is intimately tied to its internal architecture, but they often lack quantitative links between microstructure and local strain behaviour.

While scanning electron microscopy (SEM) and micro-computed tomography (μCT) have been used to visualize damage modes and structural defects, they often fall short in segmenting distinct anatomical phases such as lumen, middle lamella, and fibre wall at the resolution needed for geometric modelling. Osorio et al. [4] conducted detailed microscopy-based studies of bamboo fibres and confirmed that variations in fiber diameter, layering patterns, and microfibrillar angles play a critical role in determining stiffness and failure. However, quantitative segmentation of these regions and their influence on strain maps remain largely unaddressed. Recent approaches have proposed nature-inspired geometrical models to replicate bamboo's toughness in synthetic structures, validating that geometry particularly gradient patterns and void distributions can drastically alter fracture behavior [5]. Yet, within the bamboo research community, there is a critical gap; the lack of computational tools to decode the spatial distribution of microstructural phases and correlate them directly with strain localization and damage asymmetry.

Despite the potential of micro-computed tomography (μCT) to visualize complex vascular and fibrous networks in natural composites, its limited poor contrast at biological interfaces presents challenges for identifying key anatomical features, such as the middle lamella in bamboo. Recent studies have explored combining μCT with deep learning to improve interpretability. For example, Badran et al. Badran et.al [6] validated the use of deep learning for segmenting low-contrast CT images of fiber-reinforced composites yet emphasized the difficulty of capturing fine features below the voxel size threshold. Similarly, deep learning-based approaches have shown promise for automating structural defect segmentation and microstructure labelling in polymer and natural composites, but their success depends heavily on high quality annotations and the amount of available domain specific training data [7, 8]. These challenges underscore the need for complementary imaging strategies. In this context, optical microscopy paired with deep learning segmentation offers a high-resolution, label-specific approach for analysing microstructural features like lumen expansion and fibre wall gradients essential for quantifying the architectural parameters that drive bamboo fibre behaviour.

However, traditional image analysis techniques such as thresholding, edge detection, and clustering are often inadequate for capturing the complex and inhomogeneous microstructures of natural fibers like bamboo [9]. To address these challenges, advanced convolutional neural networks (CNNs) have been developed to enable precise semantic segmentation of hierarchical fiber structures. For instance, the CA-DeepLabv3+ model proposed by Lv et al. achieved a mean pixel accuracy of 95.2% and mean Intersection over Union (mIoU) of 90.7% across a range of natural fiber types, thanks to its attention-enhanced feature extraction and multi-scale segmentation capabilities [10]. Such architecture enables pixel-wise differentiation of critical regions such as lumens, fiber walls, and bonding interfaces. These tools offer a pathway to quantify geometrical gradients and interphase distributions, which are essential to link fiber architecture with mechanical response.

In this context, our study introduces a deep learning-based segmentation framework combined with micro-scale strain mapping to resolve the spatial hierarchy of bamboo fibre microstructures. By distinguishing lumen, middle lamella, and elementary fibre areas, and analysing their expansion gradients, we demonstrate how microstructural geometry modulates strain propagation and damage modes. This work provides novel insight into the cooperative behaviour of elementary fibres, providing quantitative geometrical links with strain and failure evolution, offering offers a foundation for bio-inspired design strategies in fibre reinforced materials.

2 MATERIALS AND METHODS GENERAL SPECIFICATIONS

Single bamboo fibers were embedded in Clarocit cold-curing resin (Struers) by manually mixing 20 g of powder with 12 g of liquid hardener. The mixture was poured into silicon rubber molds initially filled halfway to position the fiber centrally before topping off to fully encapsulate it. After curing for 30 minutes and stabilizing for 24 hours at room temperature. Sectioning was performed perpendicular to the fiber's axis with the initial cutting pitch of 3 mm using a fast-trimming device for locating the fiber in the resin. Transverse finer sections were prepared using a Leica UltraCut MZ6 ultramicrotome equipped with a DIATOME Histo diamond knife (HI-14910), with cutting pitch progressively reduced from 700 nm to 250 nm. Final cuts were made at 250 nm with a holder oscillation speed of 10 mm/s to ensure flat surfaces and minimal artifact generation (see **Figure 1a** and **1b)**.

Following sectioning, optical micrographs were acquired using an Olympus microscope at magnifications of 20×, 50×, and 100×. These scales were selected to first locate the fiber and then capture detailed regions of interest, such as lumens, middle lamella, and fiber walls. Images were recorded at a resolution of 2053 × 1086 pixels, enabling high-fidelity input for subsequent deep learning segmentation and morphological analysis with the deep learning root painter model database trained with 1500 images.

Bamboo fibers were tested under single fiber tensile testing with a loading rate of 0.2 mm/min using FAVIMAT single fiber tensile testing equipment. The sample preparation protocol consisted of embedding the fiber to test in epoxy (28% hardener) resin blocks at each side to use them as supports avoiding damage by conventional gripping or slippage. Gage length of 15 mm was defined for the tensile tests with a total span length of 55 mm, which means that 20 mm of fiber is embedded in the resin block at each side. The protocol was designed to load the fiber from adhesive gripping from the resin with the fiber and create a homogeneous force distribution in the cross section to facilitate the damage initiation occurs in a track between the gauge length.

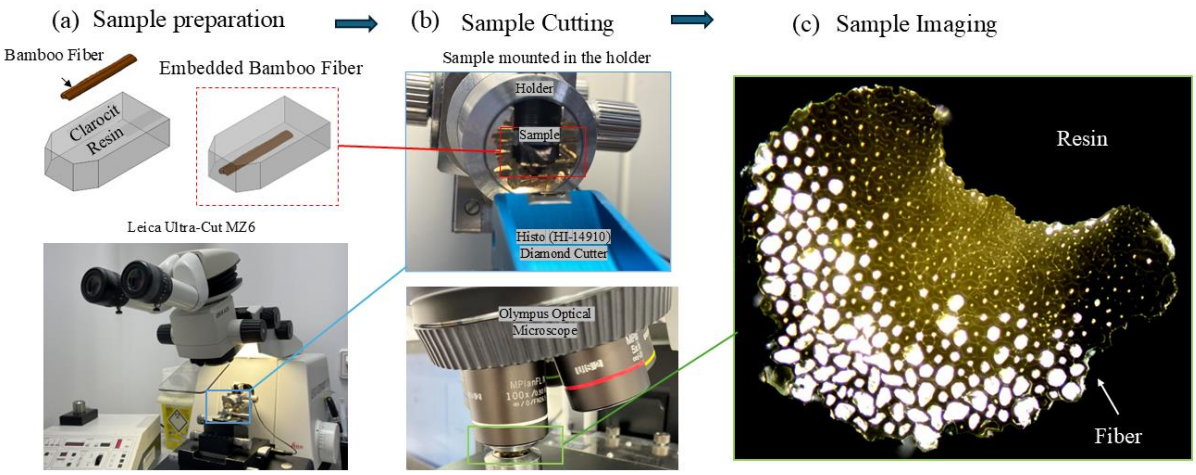

Figure 1. a) Fiber Sample preparation. b) Fiber Cutting by Ultramicrotomy. c) Fiber cross Section Imaging.

3 RESULTS AND DISCUSSION

Using Root Painter deep learning segmentation tool, we successfully resolved the three primary anatomical phases in cross-sections of bamboo technical fibres: elementary fibre walls, middle lamella, and lumens. Quantitative analysis revealed that elementary fibre walls constituted approximately 78% of the technical fibre cross-sectional area, while the middle lamella and lumens accounted for 12.9 % and 8.20%, respectively for the tested sample 1, see **Figure 2a** and **2b** (Sample1). Within an analysed area of 8214 μm² in the fibre cross-section (1033 × 541 sampled pixels), 25 lumen areas were calculated and sorted from minimum to maximum to determine the rate of change of lumen size within this area, based on a linear fitting with a growth rate of 0.2 per lumen.

To sample a larger portion of the cross-section, a deeper analysis of the segmented images was performed to investigate the localised expansion and shrinkage patterns governing the area distributions and, consequently, the fibre's hierarchical organisation (see **Figure 2c**). Using the equations presented in Section 5, the scattered values (X, Y, and lumen area magnitudes) were interpolated onto a regular grid via 2D cubic interpolation, yielding a continuous vector field contour map shown in Figure 3d.

The contour-streamline map reveals a distinct pattern of peripheral intensification and central stability in pore-area ratio. Along both the left and right borders, broad bands of high gradient ($\|\nabla A\| \gtrsim 20$) indicate pronounced expansion fronts pushing outward, likely reflecting material inhomogeneities. In contrast, the central plateau (around X ≈ 100–150 μm, Y ≈ 40–80 μm) remains cool and uniform ($\|\nabla A\| \lesssim 10$), indicating regions where pore sizes change minimally, suggesting a stable microstructure in the fibre core.

Superimposed hotspots of rapid expansion such as those near (X,Y) ≈ (230,15) and (30,105) highlight localized abrupt changes area flux intensity, which may correspond to defects or transitional microdomains (see **Figure 2c** and **d**). Streamlines coherently trace these flows, converging at local maxima (possible lumens coalescence) and diverging from local minima (lumen collapse zones). Quantitatively segmenting regions above a chosen gradient threshold could enable measurement of their spatial extent providing objective metrics for comparing specimens or assessing fibre conditions.

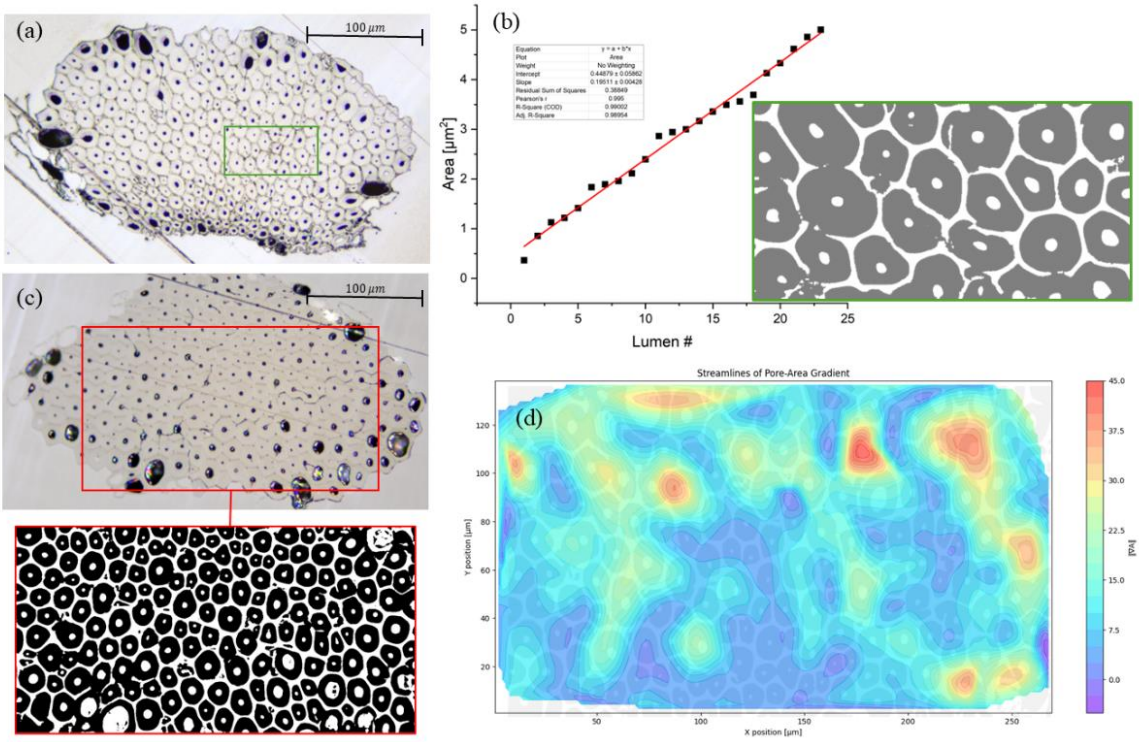

Figure 3. (a) (b) Calculation of the Lumen expansion variation with a linear approximation applied on a lumen count on 8-bit image segmented by the deep learning approach. (c)(d) calculation of the vector field of lumen area variation

For the samples tested under tension, strain maps were calculated for two bamboo fibres. The resulting strain fields exhibited distinct oscillatory waveforms up to the point of failure, with varying percentages of strain initiation. In Sample 1, over approximately 1600 µm of fibre length, strain began to localise at around 10% of the total elongation. The characteristic damage pattern in this sample was a combination of defibrillation and partial cell wall breakage, occurring with less depth compared to Sample 2 (see **Figure 3a** and **3b**).

In contrast, Sample 2 was examined laterally, with the observation direction perpendicular to the minor width of the fibre cross section. In this case, over a 3700 µm fibre length, more pronounced oscillations were observed, with strain concentration peaking at around 40% elongation. The failure mechanism in this sample was more strongly influenced by central defibrillation, where interfacial shear stress appeared to be the dominant factor. Notably, Sample 2 also exhibited greater elongation before failure compared to Sample 1 (see **Figure 3c** and **3d**).

These patterns suggested alternating regions of higher and lower strain intensity corresponding to variations in local phase composition demonstrated in the vector fields of the cross section. Particularly, higher lumen area regions versus lower lumen area regions. Such observations support the hypothesis of mechanical cooperation among elementary fibres, where load sharing occurs along complex and asymmetric paths, likely driven by the internal geometry.

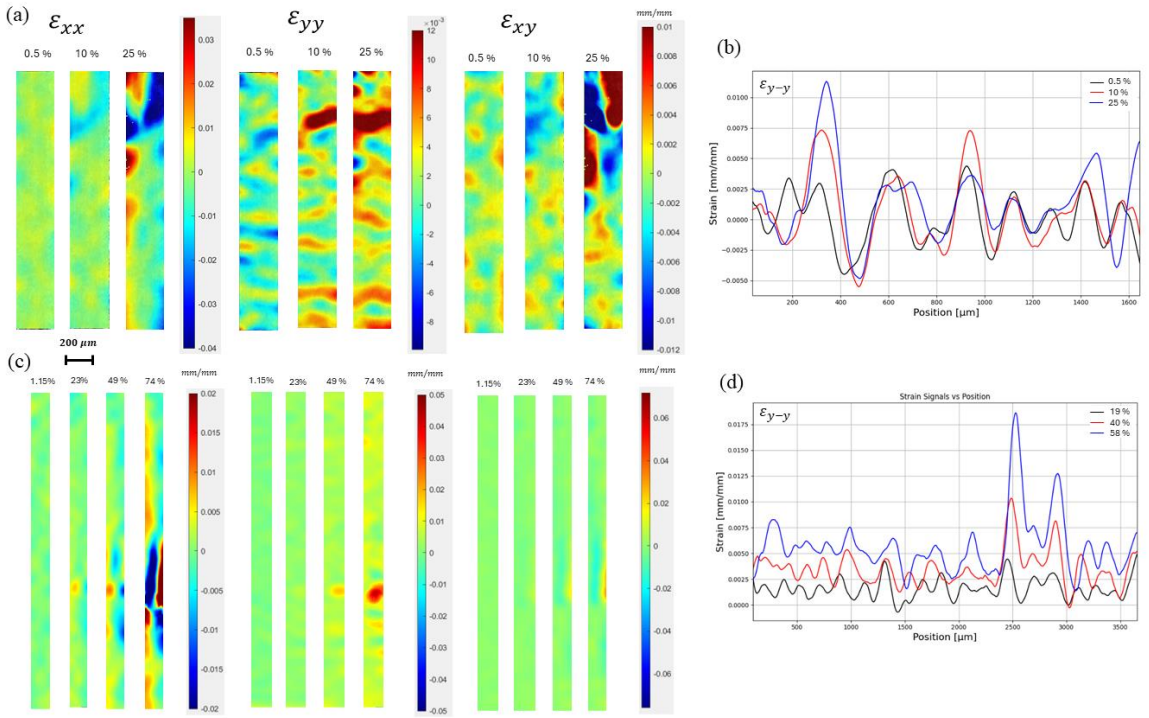

Figure 3. Strain maps applied on two bamboo fibers tested by tensile loading and strain oscillation functions. (a)(b). Sample 1. (c)(d). Sample 2

The oscillatory strain response observed along the central path of the bamboo fibre cross section is strongly indicative of an underlying structural heterogeneity presented in the cross sections studied by segmentation and gradients. Given the known anatomical features of bamboo alternating regions of vascular bundles, the higher strain amplitudes are likely associated with larger lumen fibres, while the lower amplitudes reflect more densely packed, small-lumen fibres. This interpretation is supported by the consistent periodicity and amplitude increase across different levels of applied strain, suggesting a

stable and load-sensitive mechanical differentiation and fibre cooperation. As for example, amplitude difference between the first two peaks of the strain signals was 22% in amplitude difference considering between 200 to 800 μm of fibre range at 25% of total fibre elongation in Y direction.

By analyzing the spatial strain oscillations within the 200–800 μm region, an oscillatory waveform pattern was observed in the strain signal extracted from the strain map, indicating energy dissipation along the length of the technical fiber. This behavior supports the hypothesis that internal geometry driven stiffness gradients contribute to a functionally graded mechanical response. The observed spatial damping suggests that elementary fibers cooperate mechanically, alternating in stiffness and compliance to distribute load and manage localized stress. This cooperative behavior delays failure initiation and governs the asymmetric damage evolution characteristic of bamboo technical fibers. Moreover, this difference in peak amplitude values reflect cooperative load sharing among elementary fibres. Notably, damage initiation and propagation are shown to be spatially dependent on fibre geometry and stiffness gradients. These findings support the hypothesis that microstructural geometry is a governing design parameter influencing not only failure modes (e.g., clean breakage, defibrillation, or mixed failure) but also energy dissipation and mechanical resilience.

4 EQUATIONS

To quantify the growth and shrinkage rates of the lumen size in area distributions sampling the gradient map obtained for the geometry the following equation was used:

$$\|\nabla A(x,y)\| = \sqrt{\left(\frac{\partial A}{\partial x}\right)^2 + \left(\frac{\partial A}{\partial y}\right)^2}\,, \tag{1}$$

where $(\partial A/\partial A)$ is the partial derivative of the area in x and y direction. The expansion rate provides information regarding the geometrical features linked to dominant regions of the microstructure which can be attributed to structural changes and density variations. We point out that these regions can be extracted as indicators of stress transfer and elementary fiber cooperation. See table 1

Engineering constant	Units	Values
Rate	[μm²/ μm]	0.90
Peak rate	[μm²/ μm]	5.85
Median rate	[μm²/ μm]	0.71
Percentiles	[%]	[0.02417066 0.06871499 0.14725231]

Table 1: rates of change of lumen area size.

6 CONCLUSIONS

This study confirms that bamboo technical fibres behave as functionally graded materials, exhibiting vector fields that can be interpreted as geometrical signatures for understanding how stress is distributed and transferred axially. Fibres that demonstrated greater elongation before failure such as the second sample in the strain map showed damage initiation at approximately 20% of total elongation, compared to earlier onset in Sample 1. Microstructural geometry, including lumen expansion and phase area distribution, governs both mechanical performance and damage behaviour.

Through deep learning–based segmentation and microscale strain mapping, we identified localised regions of rapid expansion particularly around coordinates (230, 15) and (30, 105), that indicate concentrated flux activity within the lumen areas, potentially corresponding to transitional microstructural domains. The flow streamlines exhibit organised patterns, converging at areas of

maximum flux, suggestive of void coalescence, and diverging from minima, which may represent zones of maximum lumen size.

The resulting strain fields reflect cooperative mechanical behaviour, with oscillatory patterns linked to variations in material density and phase distribution. This internal structural organisation leads to asymmetric damage evolution, with clear implications for predicting failure modes. These insights suggest that geometrical characteristics can serve as predictive design parameters in composites based on bamboo, supporting quality control, process optimisation, and performance modelling.

The quantified phase proportions highlight the dominant structural role of the fibre walls in bearing load, while the middle lamella governs inter-fibre bonding and stress transfer, and the lumens influence local stress distribution and contribute to damage initiation pathways. Together, these three components define the hierarchical architecture that underpins the fibre's mechanical performance and failure behaviour. Ongoing work aims to further validate the presence of alternating regions of stiffness and compliance that enable load sharing, delay failure initiation, and govern the asymmetric damage patterns observed in bamboo technical fibres.

ACKNOWLEDGEMENTS

The authors would like to express their gratitude to the Luxembourg National Research Fund (FNR) for supporting the SusPoCo (Sustainable Polymer Composites) project under grant agreement PRIDE21/167482260.

REFERENCES

[1] L. Osorio, E. Trujillo, A. W. Van Vuure, and I. Verpoest, "Morphological aspects and mechanical properties of single bamboo fibers and flexural characterization of bamboo/epoxy composites," J. Reinf. Plast. Compos., vol. 30, no. 5, pp. 396–408, Apr. 2011, doi: 10.1177/0731684410397683.

[2] D. Hu, B. Song, L. Dang, and Z. Zhang, "Effect of strain rate on mechanical properties of the bamboo material under quasi-static and dynamic loading condition," Composite Structures, vol. 200, pp. 635–646, 2018, doi: 10.1016/j.compstruct.2018.05.107.

[3] Wang, X., Luo, X. Y., Ren, H. Q., & Zhong, Y. Q. (2023). Asymmetric bending characteristics and failure mechanism of bamboo under different loading directions. Industrial Crops and Products, 201, 116721. https://doi.org/10.1016/j.indcrop.2023.116721

[4] L. Osorio, E. Trujillo, F. Lens, J. Ivens, I. Verpoest, and A. W. Van Vuure, "In-depth study of the microstructure of bamboo fibres and their relation to the mechanical properties," J. Reinf. Plast. Compos., vol. 37, no. 17, pp. 1099–1113, 2018. doi: 10.1177/0731684418783055

[5] Zhu, X. D., Liu, J., Tertuliano, O. A., & Raney, J. R. (2023). Improving structural damage tolerance and fracture energy via bamboo-inspired void patterns. *arXiv preprint*, arXiv:2306.05365. https://doi.org/10.48550/arxiv.2306.05365

[6] A. Badran, D. Parkinson, D. Ushizima, D. Marshall, and E. Maillet, "Validation of deep learning segmentation of CT images of fiber-reinforced composites," J. Compos. Sci., vol. 6, no. 2, art. 60, Feb. 2022, doi: 10.3390/jcs6020060.

[7] R. Vorobev, I. Vasilev, and I. Kremnev, "Segmentation of structural defects in polymer composite computed tomography images with deep learning models," Tomogr. Mater. Struct., vol. 3, p. 100014, Sep. 2023, doi: 10.1016/j.tmater.2023.100014.

[8] X. Wang, H. Su, N. Li, Y. Chen, Y. Yang, and H. Meng, "A Deep Learning Labeling Method for Material Microstructure Image Segmentation," Processes, vol. 11, no. 12, art. 3272, Nov. 2023, doi: 10.3390/pr11123272.

[9] A. G. Smith, E. Han, J. Petersen, N. A. F. Olsen, C. Giese, M. Athmann, et al., "RootPainter: deep learning segmentation of biological images with corrective annotation," New Phytol., vol. 236, no. 2, pp. 774–791, Oct. 2022, doi: 10.1111/nph.18387.

[10] Lv, S., Li, X., Takagi, H., Hou, Z., Zhai, Y., Chen, L., & Ni, H. (2024). Research on Natural Fiber Microstructure Detection Method Based on CA-DeepLabv3+. Materials, 17(23), 5942.

Bayesian Calibration of Finite Element C-spar Models using Digital Image Correlation

Carl Scarth[1], Jean Bénézech[1], Geir Olafsson[2], Vincent K. Maes[2], Janice M. Dulieu-Barton[2], Richard Butler[1], Andrew T. Rhead[1]

[1]Centre for Integrated Materials, Processes and Structures, University of Bath, Bath, UK
[2] Bristol Composites Institute, University of Bristol, Bristol, UK

AI Empowering Composites
24th International Conference on Composite Materials (ICCM 24)
Baltimore, Maryland, USA, 4th-8th August 2025

Bayesian inference

- All predictions are subject to uncertainty:
  - Manufacturing uncertainty.
  - How accurate are models?
  - Are tests representative of reality? Noisy measurements?
  - Unknown quantities e.g. internal defects/features, damage.
- **Bayesian inference** helps us quantify and reduce this uncertainty by using new data to learn about uncertain quantities

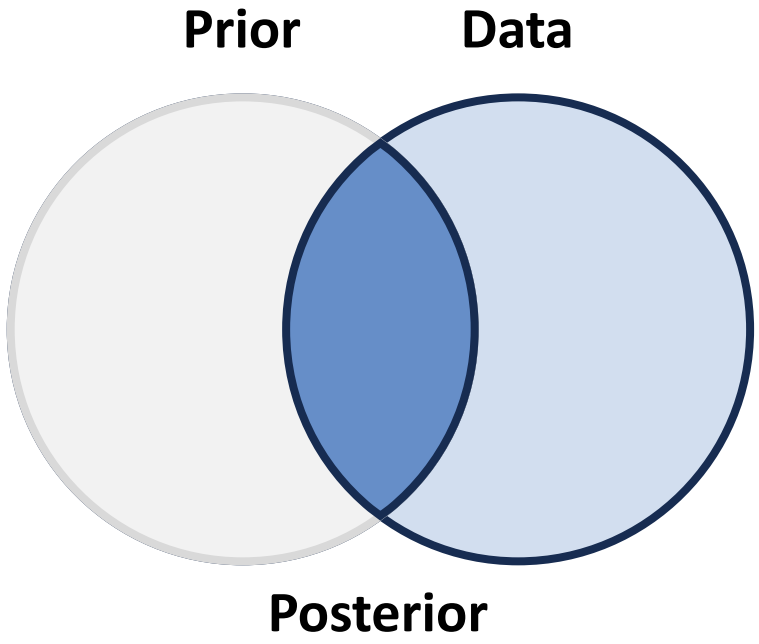

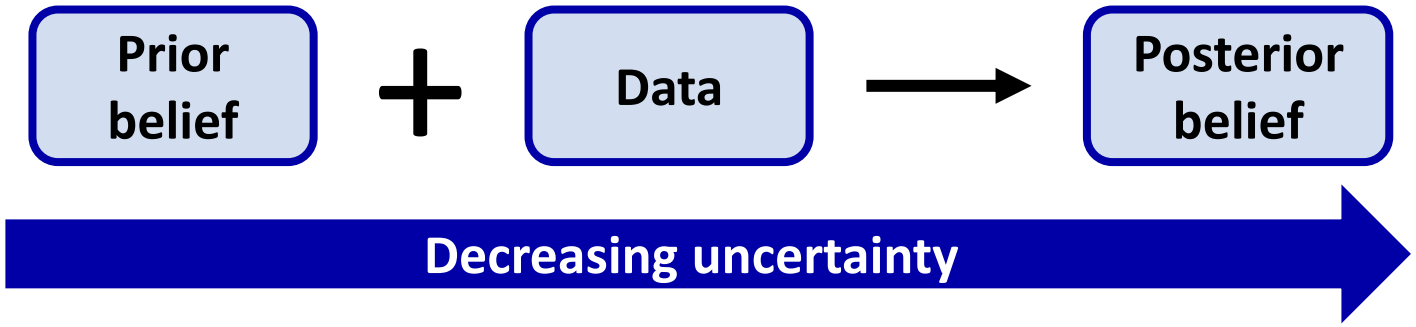

Bayesian model calibration

- Bayesian model calibration uses **model outputs** and **experimental data** to inform predictions.
- Can account for uncertainties in model inputs, model physics, and in the test data.
- Example case study using:
  - Stereo DIC from Compression tests on a C-spar.
  - ABAQUS model with material, boundary condition, and geometric uncertainty.
  - Main challenge is handling large quantities of data spanning both **time and space**.

Can we use the DIC to verify the accuracy of the model despite the uncertain inputs?

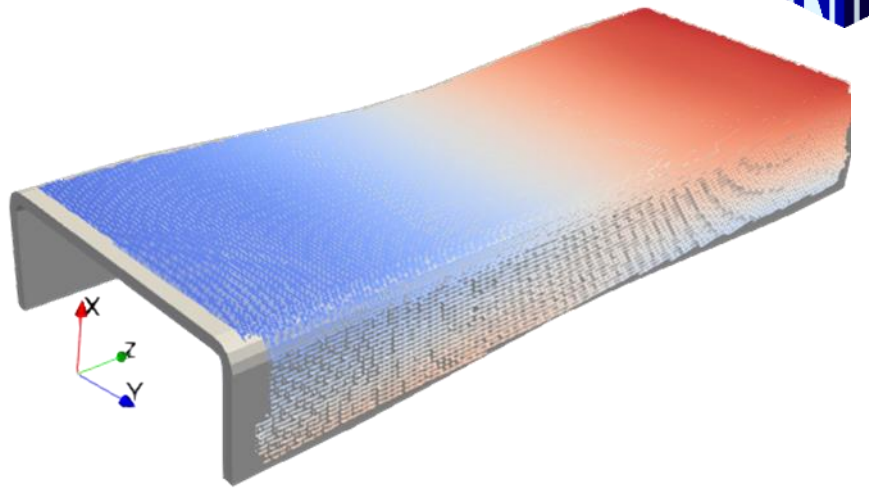

Longitudinal displacement from DIC at 200kN

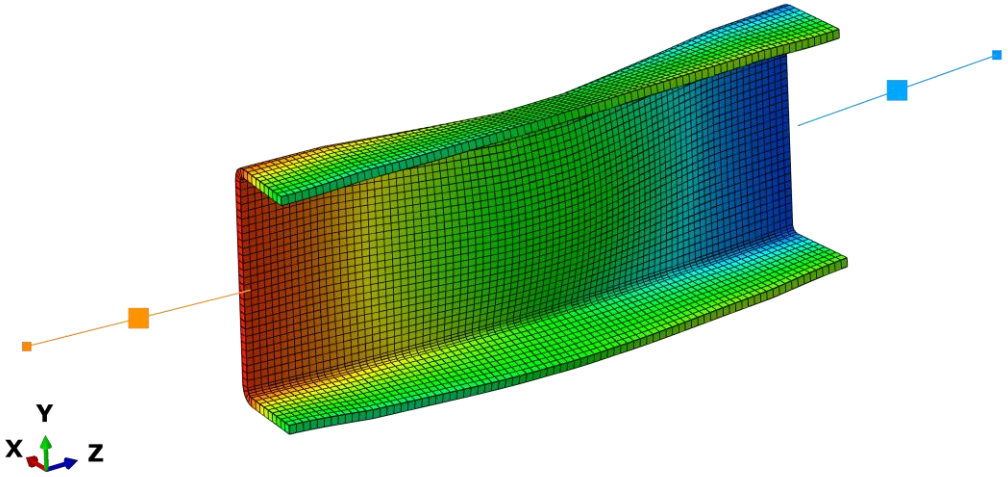

Longitudinal displacement from ABAQUS at 200kN

Experimental data

- Stereo DIC captured using MatchID, from compression tests on a composite C-spar undertaken at the University of Bristol.
- 48 plies of IM7/8552, QI layup.
- +4mm eccentric loading relative to neutral axis.
- Separate datasets from two camera pairs, each focussed on one flange + the web.
- Limit analysis to longitudinal and out-of-plane displacement, maximum load 150 kN.

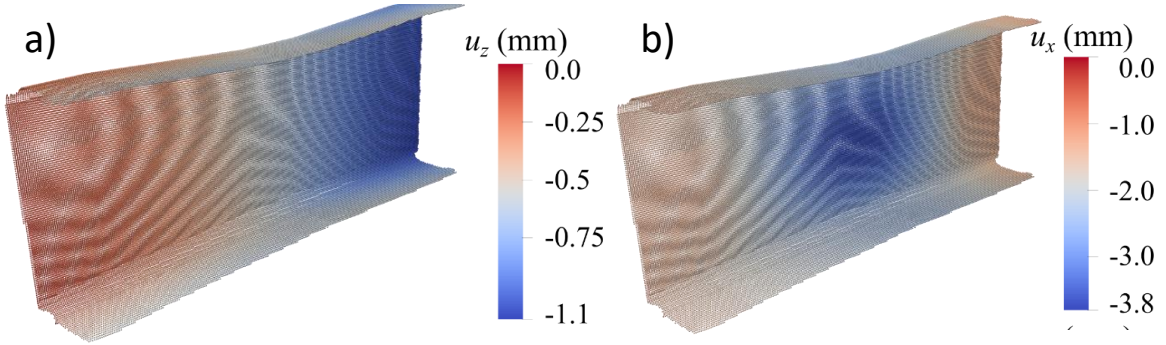

DIC showing a) Longitudinal and b) out-of-plane displacement at 150 kN

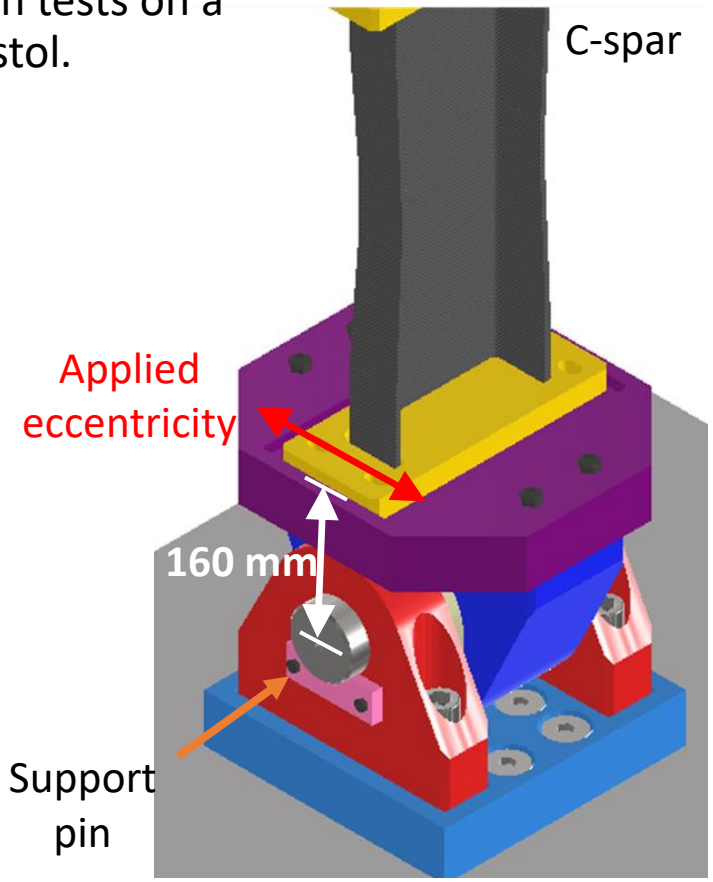

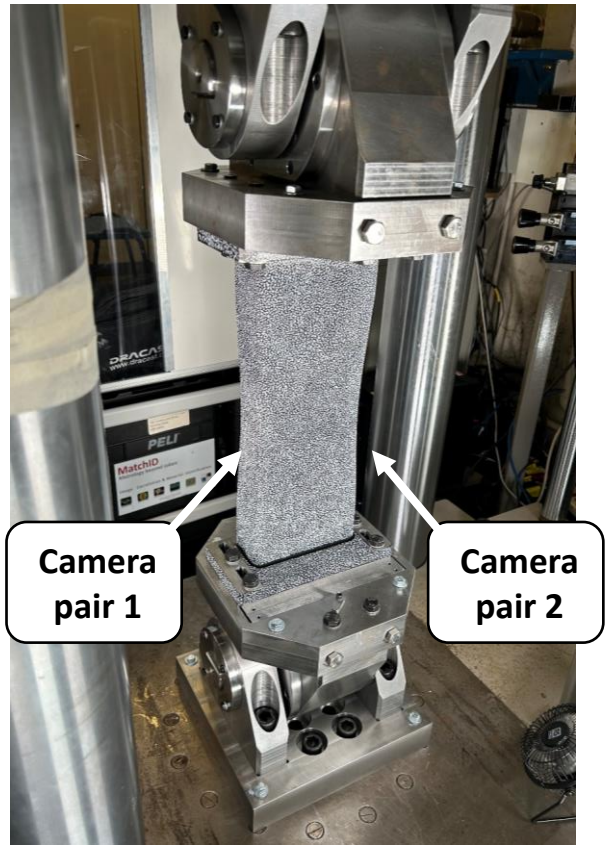

Experimental configuration showing rig design and camera pair focus

ABAQUS model and uncertainties

- Modelled with 4536 SC8R continuum shell elements (9354 nodes).
- Simply supported at reference nodes.
- Uncertainty in illustrated boundary conditions.
- Geometric uncertainty in ply thickness (t_{ply}) and corner thinning (t_{thin}).
- Uncertainty in E_{11}, E_{22} and G_{12}.

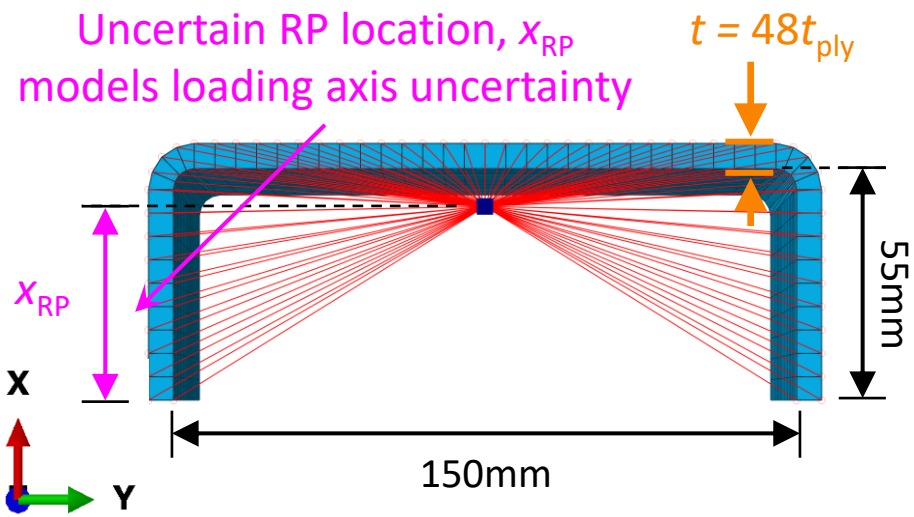

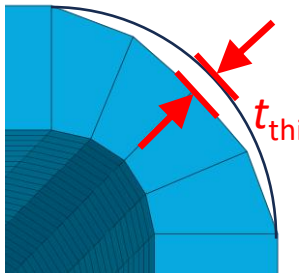

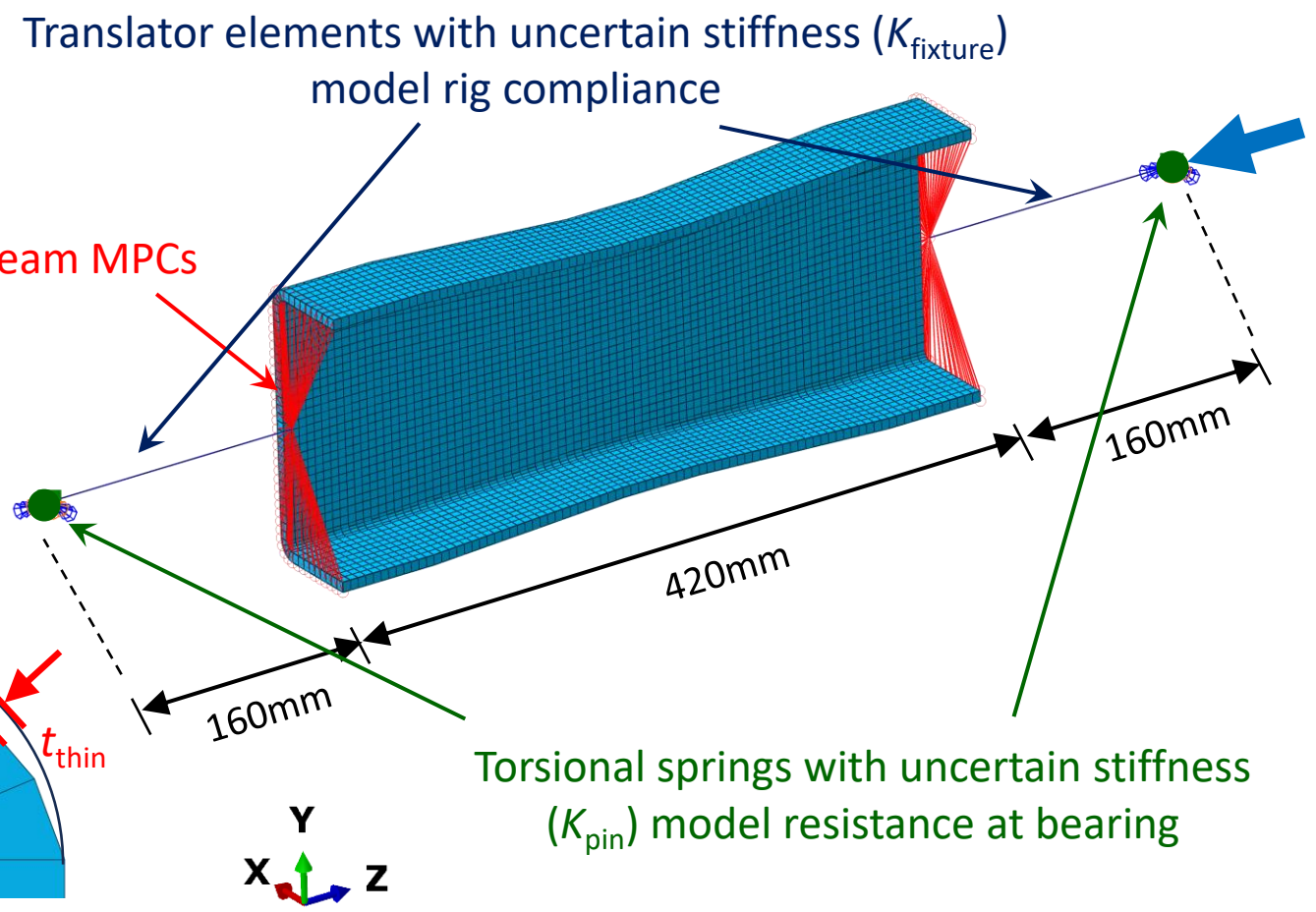

Calibration methodology

- Following Higdon et al.[1], method for calibrating models with vector-valued output:

$$\boldsymbol{y} = \boldsymbol{\eta}(\boldsymbol{\theta}^*) + \boldsymbol{\varepsilon}$$

DIC point cloud **Abaqus model** **Error**

$\boldsymbol{\theta}^*$ = uncertain inputs we want to learn about:

E_{11}, E_{22}, G_{12}, t_{ply}, x_{RP}, $K_{fixture}$, t_{thin}, K_{spring}

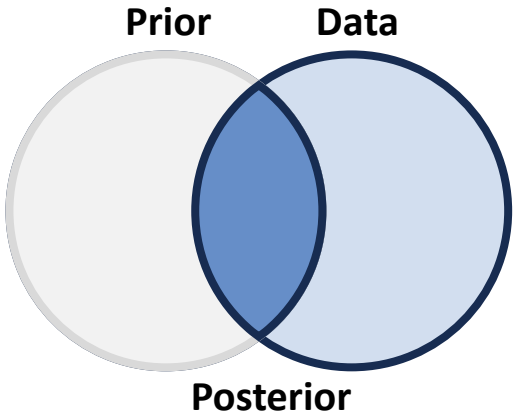

- An inverse problem:
  - $\boldsymbol{y}$ is known, $\boldsymbol{\theta}^*$, hyperparameters for $\boldsymbol{\eta}$, and magnitude of error $\boldsymbol{\varepsilon}$ are uncertain.
- Solve by:
  1) Specify **prior distributions** for uncertain parameters from coupon data, parametric studies & engineering judgement.
  2) Feed in **data**: combined dataset of DIC, plus 100 Latin Hypercube Samples of ABAQUS model output.
  3) Sample from the **posterior distribution** using Hamiltonian Monte Carlo (No-U-Turn Sampler, NUTS) in Stan[2].

[1] *D. Higdon et al, "Computer model calibration using high-dimensional output", Journal of the American Statistical Association, 2008*
[2] *Stan modeling language users guide and reference manual, Version 2.26.1, https://mc-stan.org*

Output decomposition

- Total of **299,328** model output values from each of the 100 training samples, and **1,227,163** DIC displacements.
- Decompose into first p = 7 principal components of model output using SVD:

$$\boldsymbol{\eta}(\boldsymbol{\theta}^*) \approx \sum_{i=1}^{p} \boldsymbol{\phi}_i(\boldsymbol{x}, t)\, w_i(\boldsymbol{\theta}^*)$$

- Basis vectors $\boldsymbol{\phi}_i$ capture spatial & temporal dependency.
- Gaussian process emulators for coefficients w_i capture dependency on uncertain model inputs.

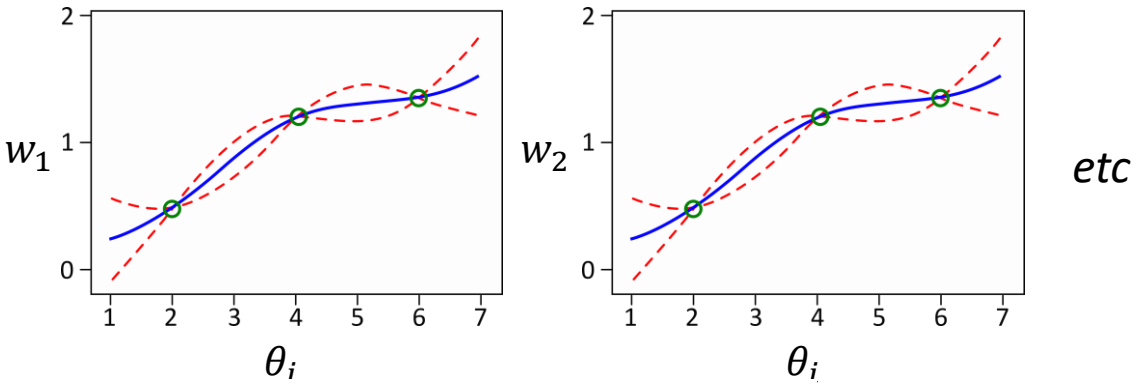

Gaussian process emulator illustration

etc

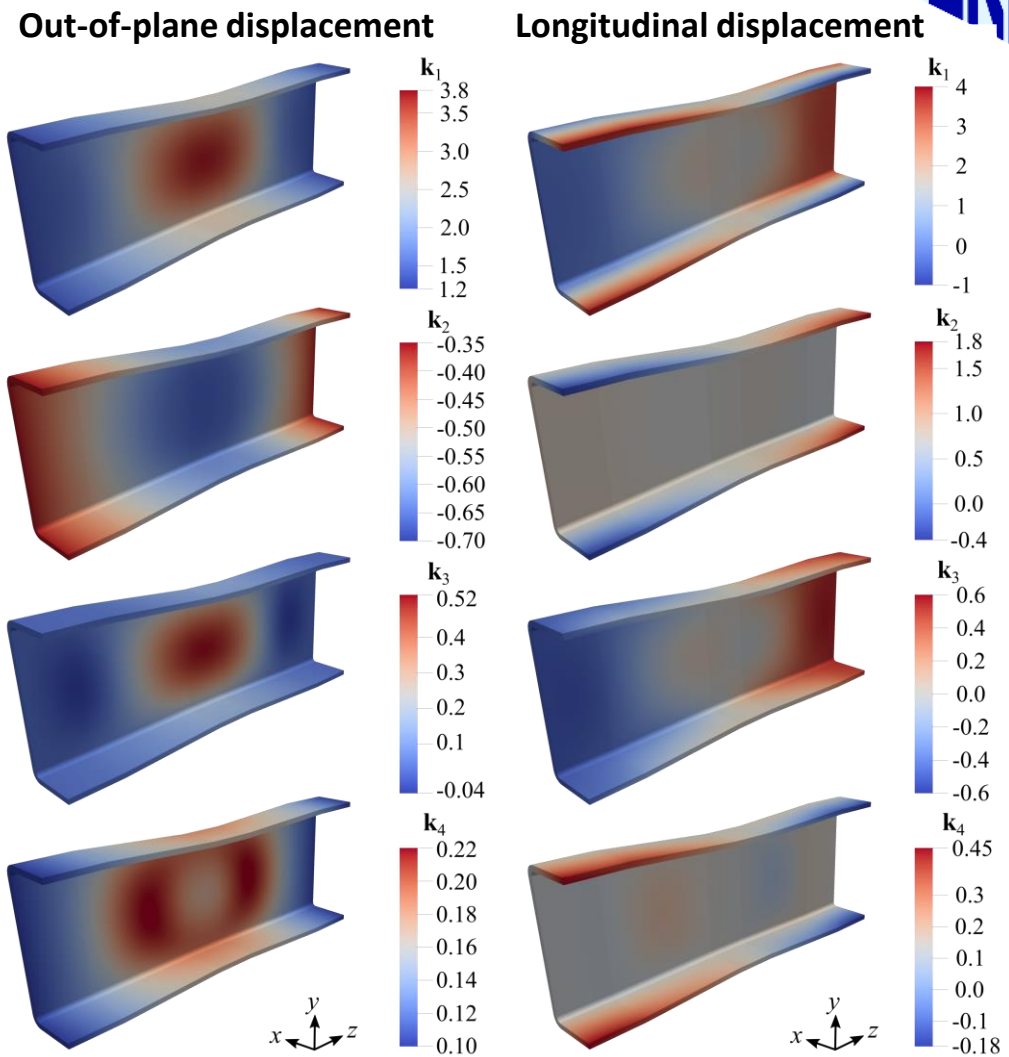

First 4 principal components at 150kN

Prior distributions

What do I **believe** about the uncertain inputs before the test?
Not a measure of variability.

Prior parameters: mean and standard deviation for Gaussian and Half-normal, upper and lower bounds for uniform

	Distribution	Parameter 1	Parameter 2
E_{11} (GPa)[3]	Gaussian	150.0	9.0
E_{22} (GPa)[4]	Gaussian	8.96	0.538
G_{12} (GPa)[4]	Gaussian	4.69	0.281
t_{ply} (mm)	Gaussian	0.125	0.00625
x_{RP} (mm)	Gaussian	46.0	0.667
$\log(K_{fixture})$	Uniform	5.9	12.0
$\log(K_{pin})$	Half-normal	4.0	2.5
t_{thin} (mm)	Half-normal	0.0	0.51

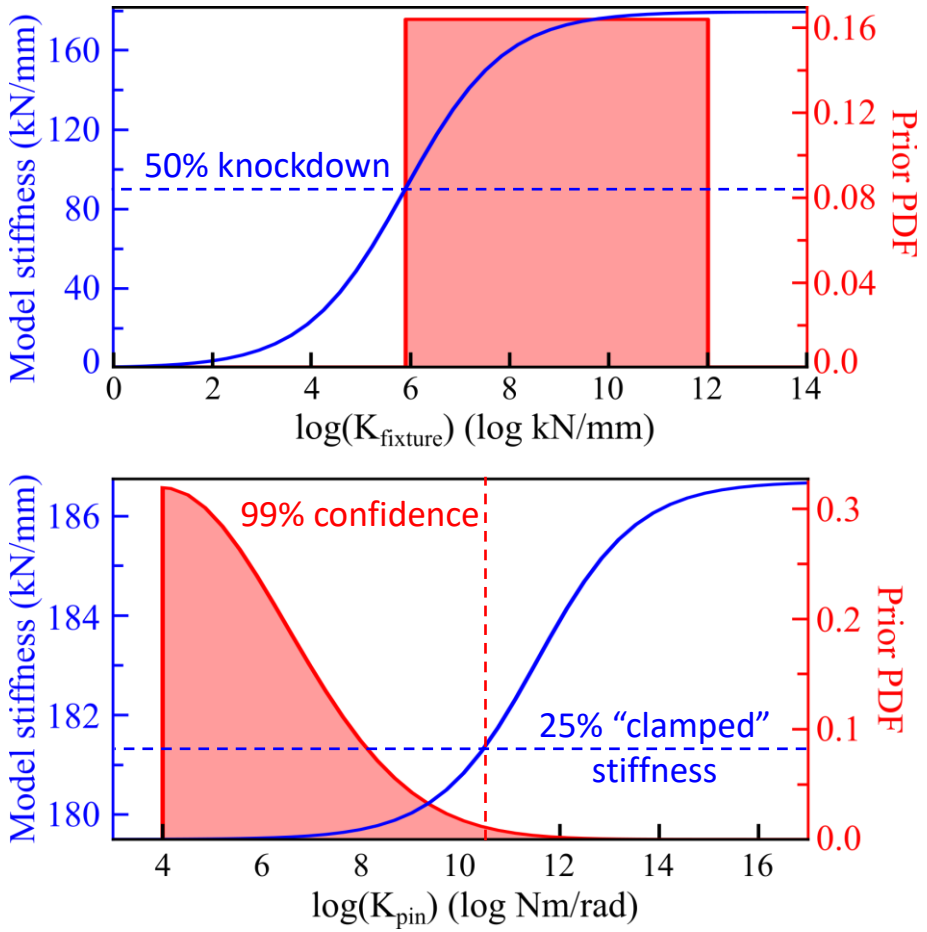

Initial mode force-displacement gradient at reference node vs $\log(K_{fixture})$ and $\log(K_{rig})$, overlaid with prior distributions

[3] *HexTow® IM7 Carbon Fibre, Product Data Sheet, HEXCEL*
[4] *E. Clarkson. "Hexcel 8552 IM7 unidirectional prepreg 190 gsm & 35% qualification statistical analysis report." NCAMP, 2019.*

Results: Posterior distributions

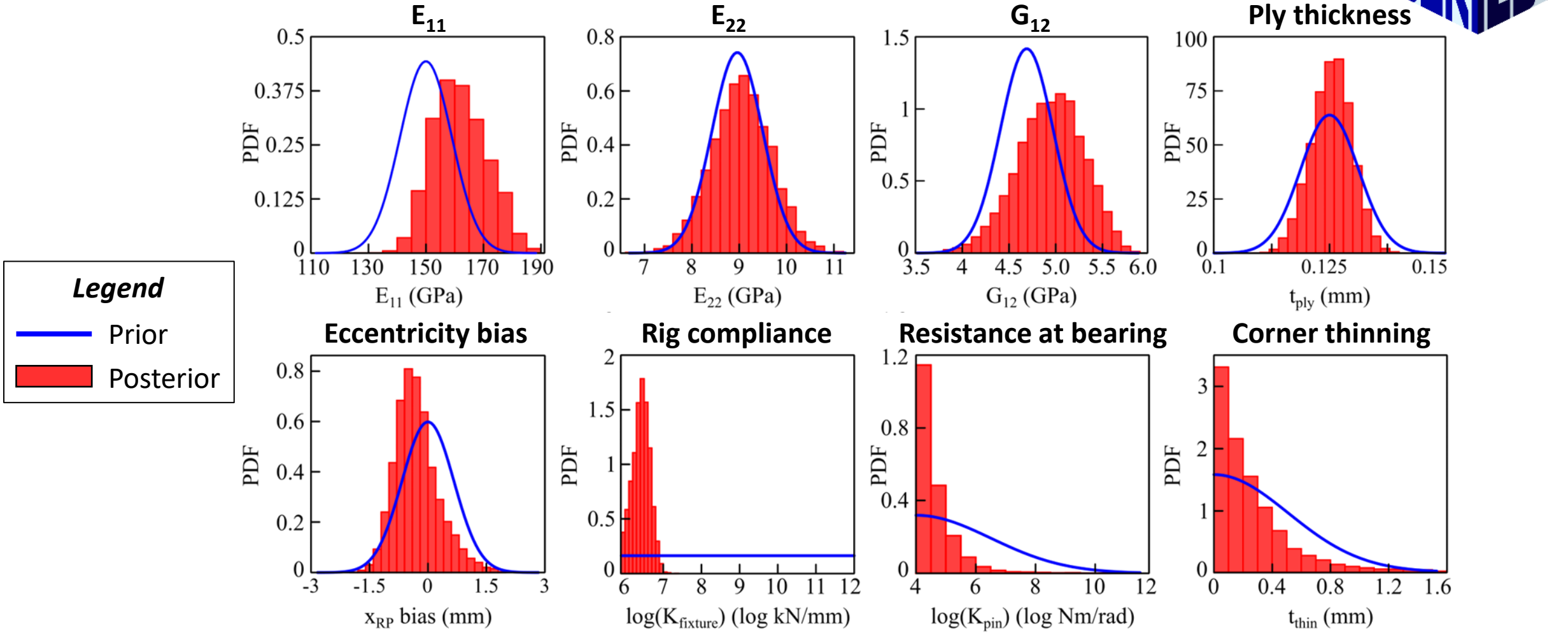

Prior & posterior heatmaps

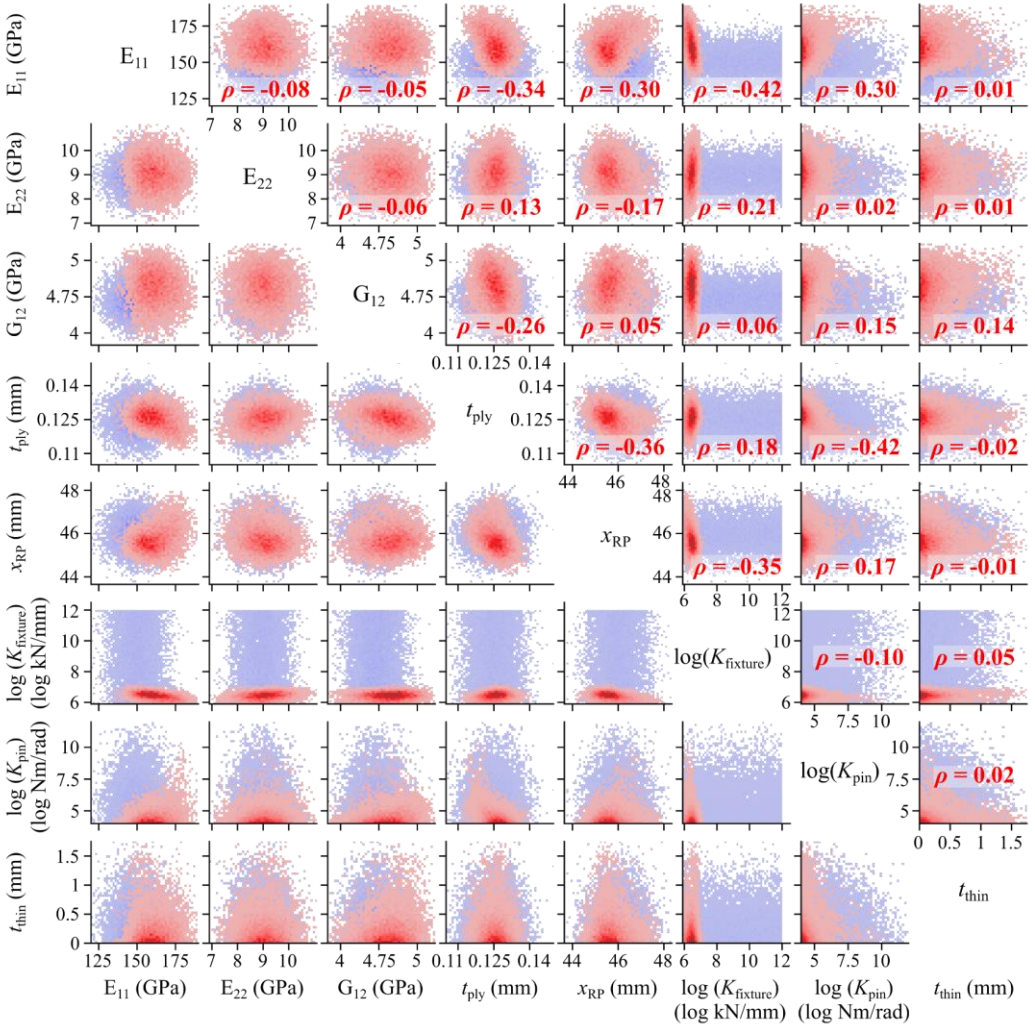

- Differences between blue and red show reductions in uncertainty
- Strong correlations indicate inputs have complementary or antagonistic effects

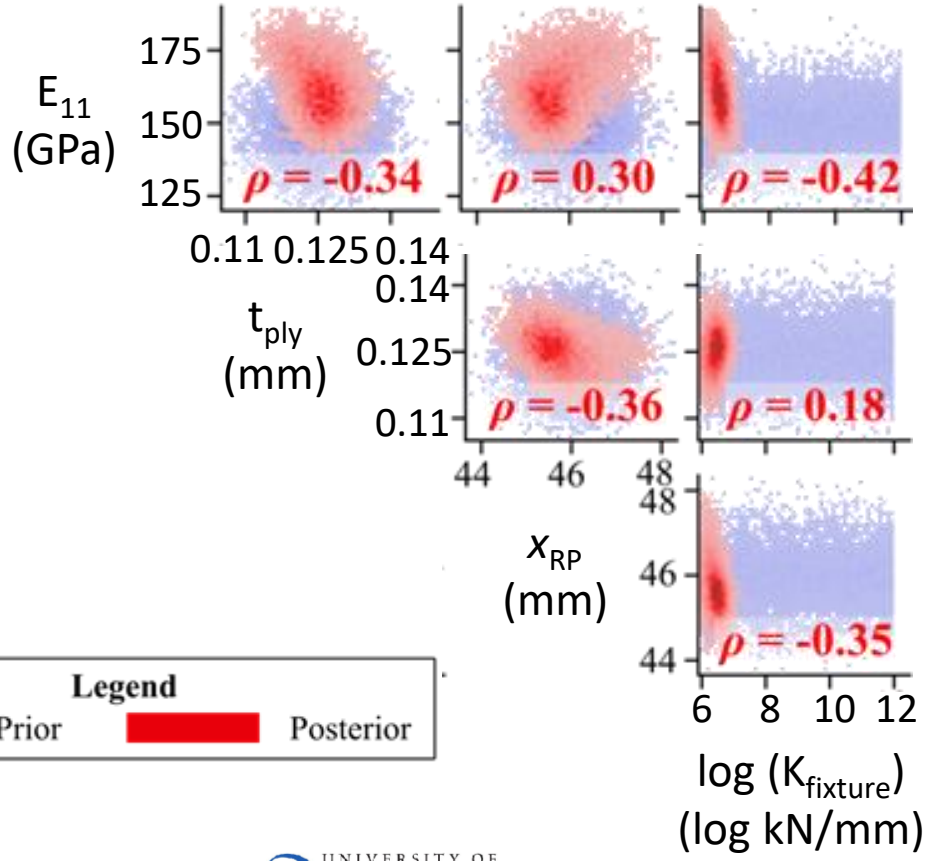

Posterior Predictions

- Run posterior samples back through model to get posterior prediction given “true” input values

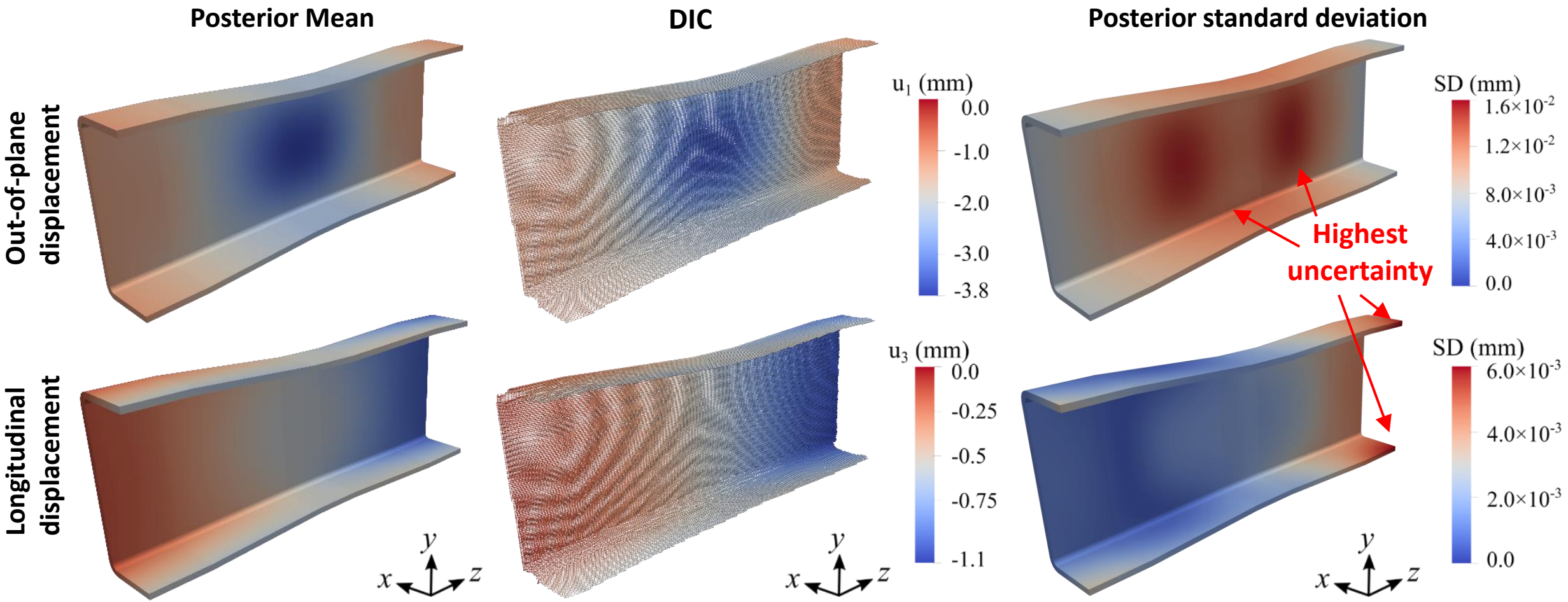

Prior & posterior residuals

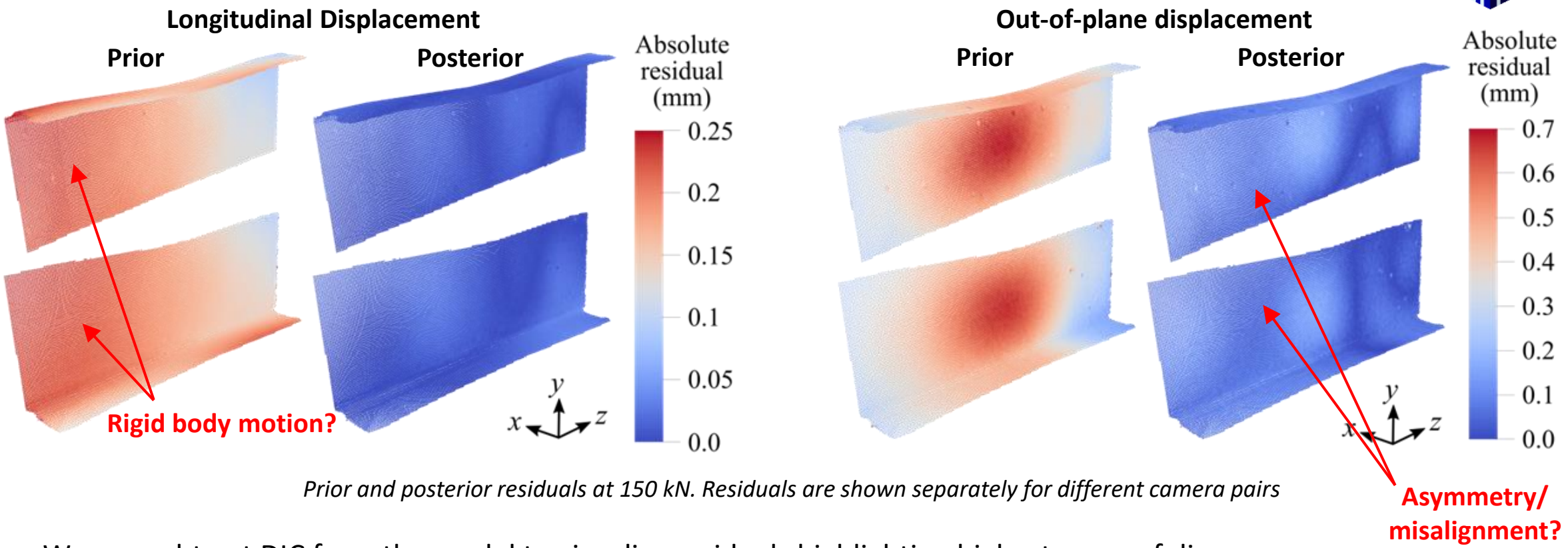

Prior and posterior residuals at 150 kN. Residuals are shown separately for different camera pairs

- We can subtract DIC from the model to visualise residuals highlighting highest areas of discrepancy.
- "Prior" residuals taken relative to model output using deterministic input values.
- Posterior residuals taken relative to posterior predictive mean.

Force-Displacement Trends

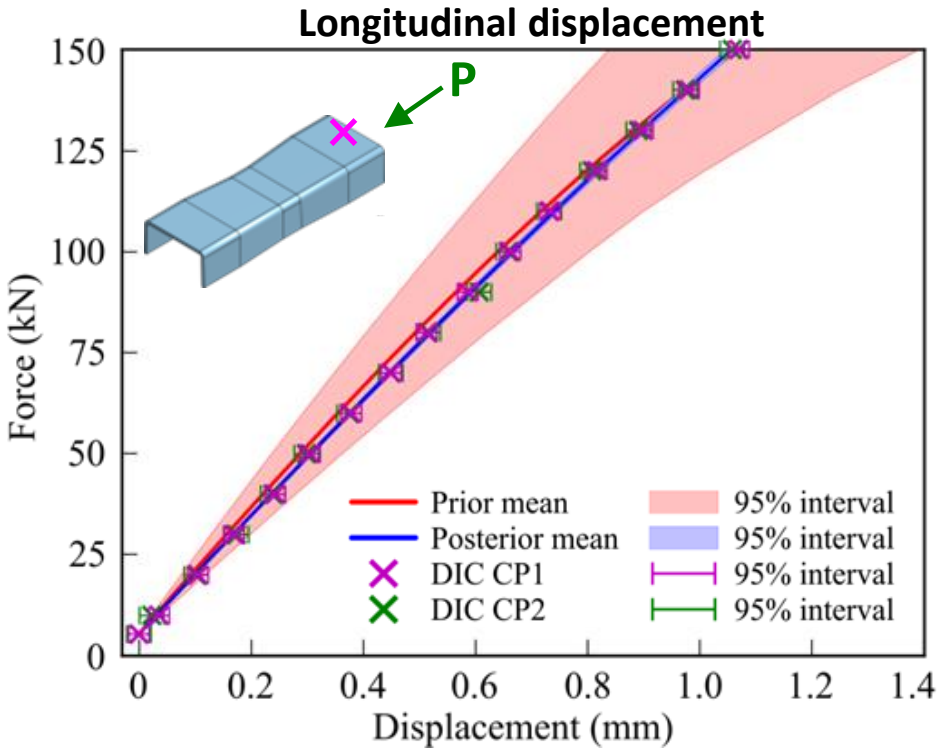

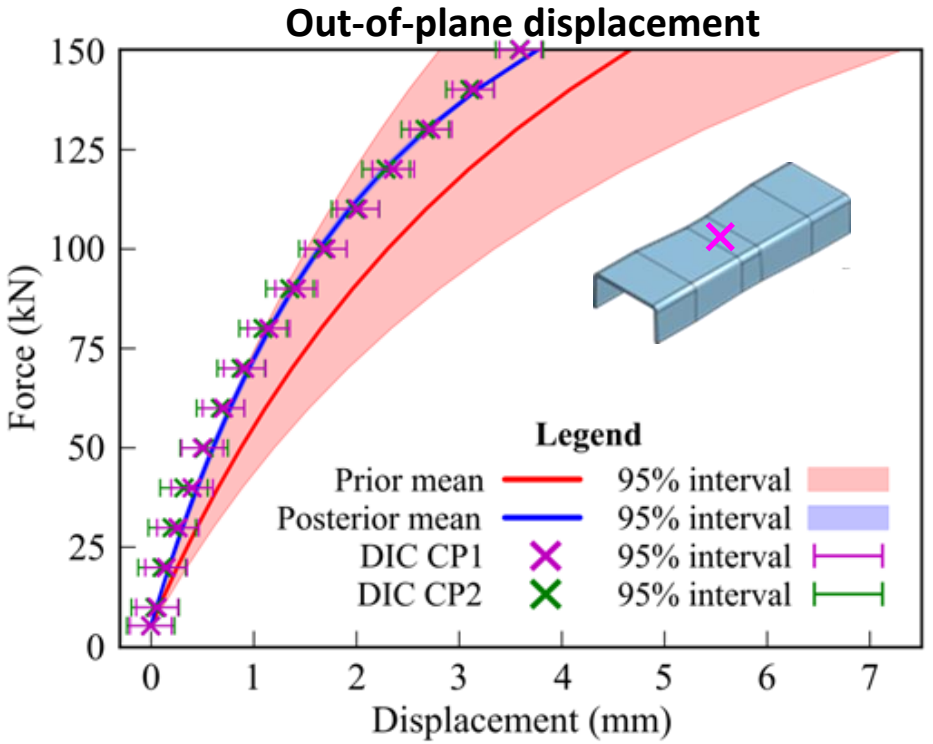

Prior and posterior force-displacement trends at fixed point X on spar surface

- Significant reduction in prediction uncertainty. Discrepancies attributed to observation error.
- Stiffer material response due to increased E_{11} better fits both longitudinal and out-of-plane DIC.
- Higher error inferred for out-of-plane displacement

Conclusions and outlook

- Demonstrated a powerful statistical toolkit for comparing FE models against DIC, while accounting for uncertainty in model inputs and test data.
- Overcame challenge of calibrating full-field model output using high volumes of data.
- Useful for validating virtual tests.
- Uncertainty in boundary conditions very important.
- Shift in modulus also noteworthy. Using a homogeneous linear value across structure in may be overly simplistic.
- Future work will extend further into nonlinear regime and consider failure.
- Long term aim to decide most informative future experiments via Bayesian Design of Experiments.

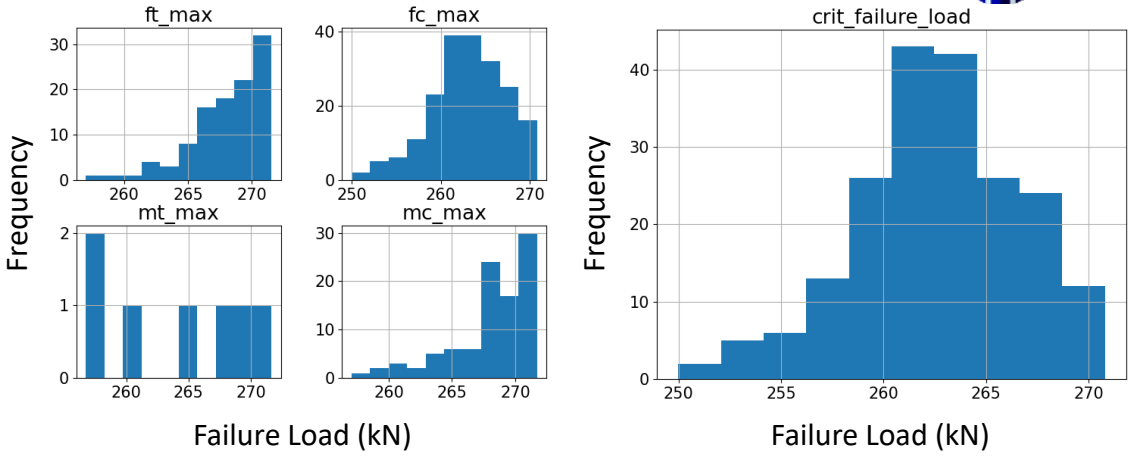

Preliminary uncertainty quantification study using Hashin failure criteria

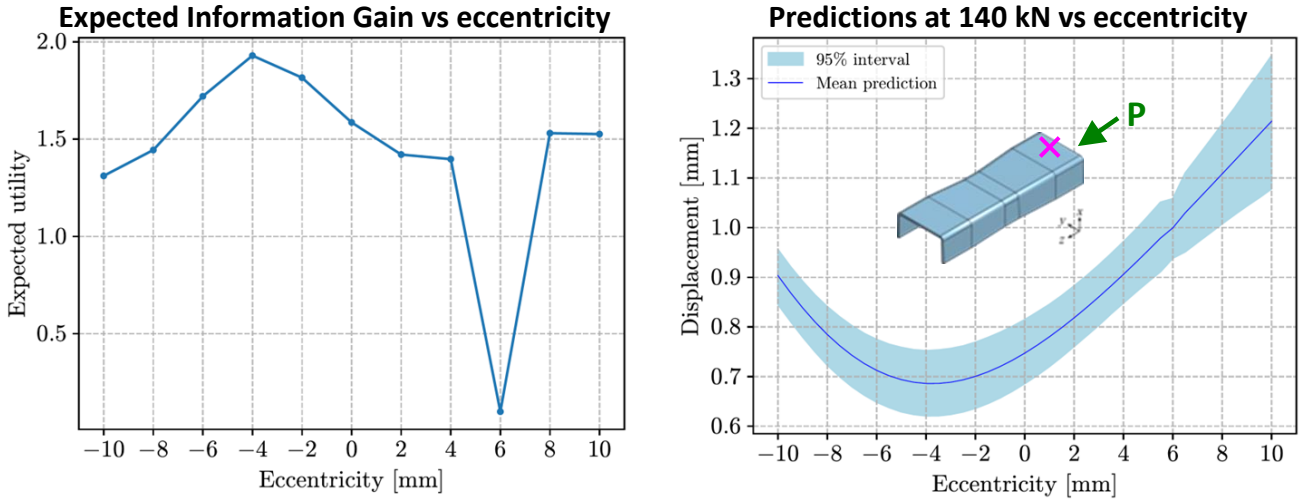

Preliminary Design of Experiments using displacement at fixed location on spar

The research presented was supported by the EPSRC Programme Grant
‘Certification for Design – Reshaping the Testing Pyramid’
(CerTest, EP/S017038/1)



























Engineering and Physical Sciences Research Council

Thank you for listening!

University of BRISTOL · UNIVERSITY OF BATH · University of Southampton · UNIVERSITY OF EXETER

ICCM24
AUGUST 4-8, 2025
BALTIMORE CONVENTION CENTER
BALTIMORE, MARYLAND, USA

No Technical Paper Submission for:

Lauren Thomas



Center for Composite Materials

Characterization and Modeling of Deformation Mechanisms of Aligned Discontinuous Fiber Prepreg during Thermoforming

Aidan Ford, Andrew Stack, Tom Cender, Suresh Advani



DISTRIBUTION STATEMENT A. Approved for public release: distribution unlimited. AFRL-2025-3663



TuFF: Tailored universal Feedstock for Forming

- **Chopped fibers are aligned** by water flow onto a film
- Films of aligned fiber are prepregged with resin
- Prepreg can be used in **thermoforming process**
  - **Allows for stretch** during forming
  - Final properties comparable to continuous UD prepreg

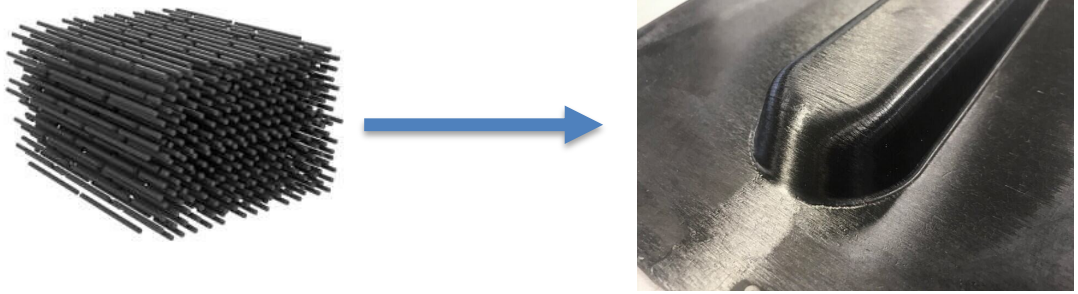

UNIVERSITY OF DELAWARE CENTER FOR COMPOSITE MATERIALS AFRL
DISTRIBUTION STATEMENT A. Approved for public release: distribution unlimited
AFRL-2025-3663.

Role of Numerical Model

- **Goal:** Develop tool to:
  - Guide geometry and process conditions to minimize failed parts.
  - Maximize manufacturing rate.
- **Modeling optimizes process** without spending material, energy, labor.
- **Develop** and **validate** model's prediction of **deformation**

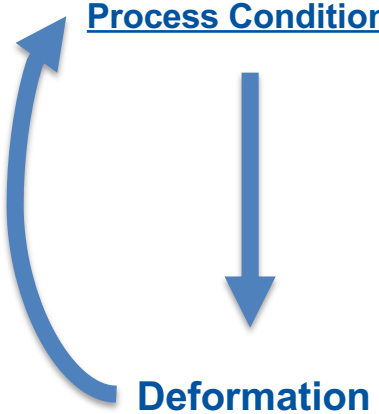

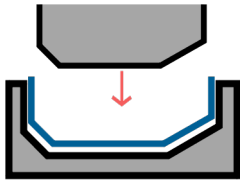

Tool displacement rate, Temperature

or

Gas pressure, Temperature

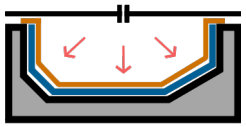



4 main deformation mechanisms:



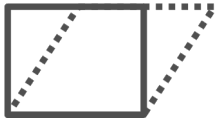



Stretch Interface slip In-plane shear Bending

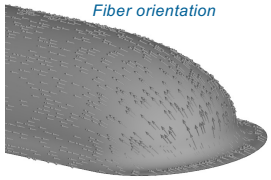

Design Criteria:
Thickness, Fiber Orientation

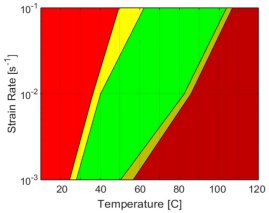

Forming window:
stress, strain rate

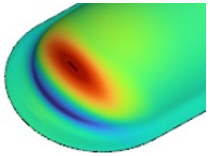

Deformation Limits

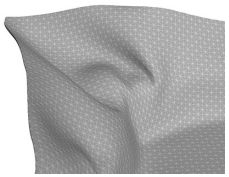

Defects:
Wrinkles, Buckling

UNIVERSITY OF DELAWARE CENTER FOR COMPOSITE MATERIALS AFRL

DISTRIBUTION STATEMENT A. Approved for public release: distribution unlimited
AFRL-2025-3663.

Model Development Framework

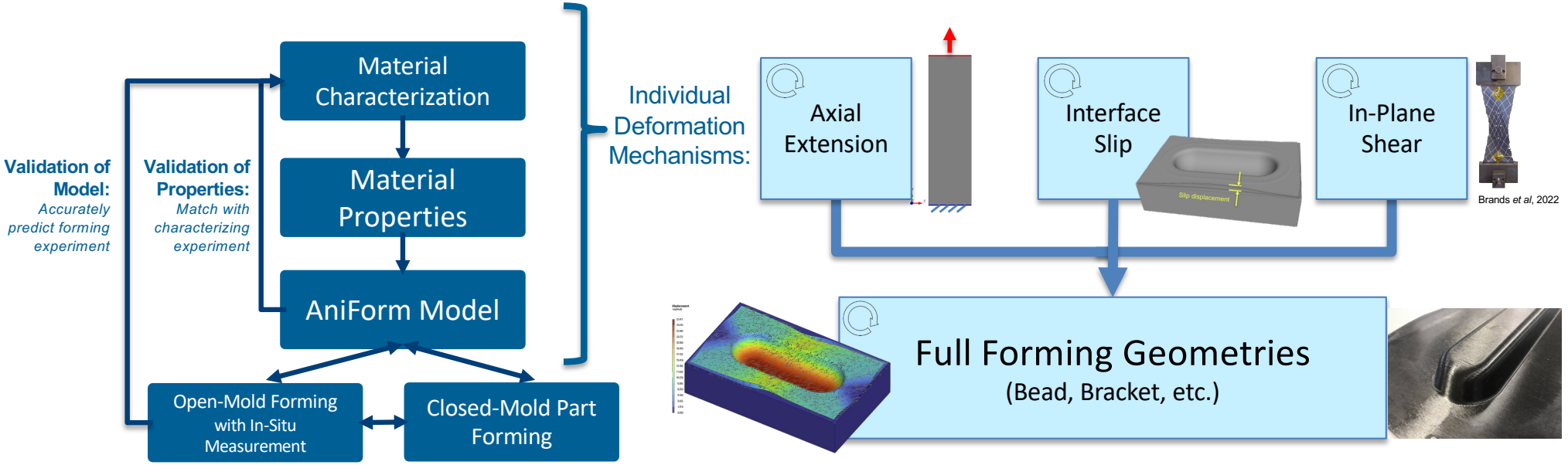

UNIVERSITY OF DELAWARE CENTER FOR COMPOSITE MATERIALS AFRL
DISTRIBUTION STATEMENT A. Approved for public release: distribution unlimited
AFRL-2025-3663.

Model Development Framework

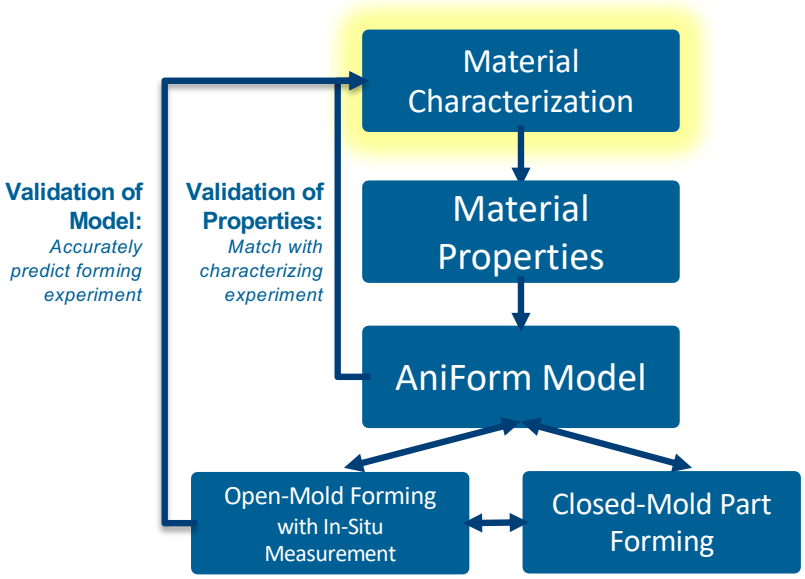

Example, Longitudinal Extension:

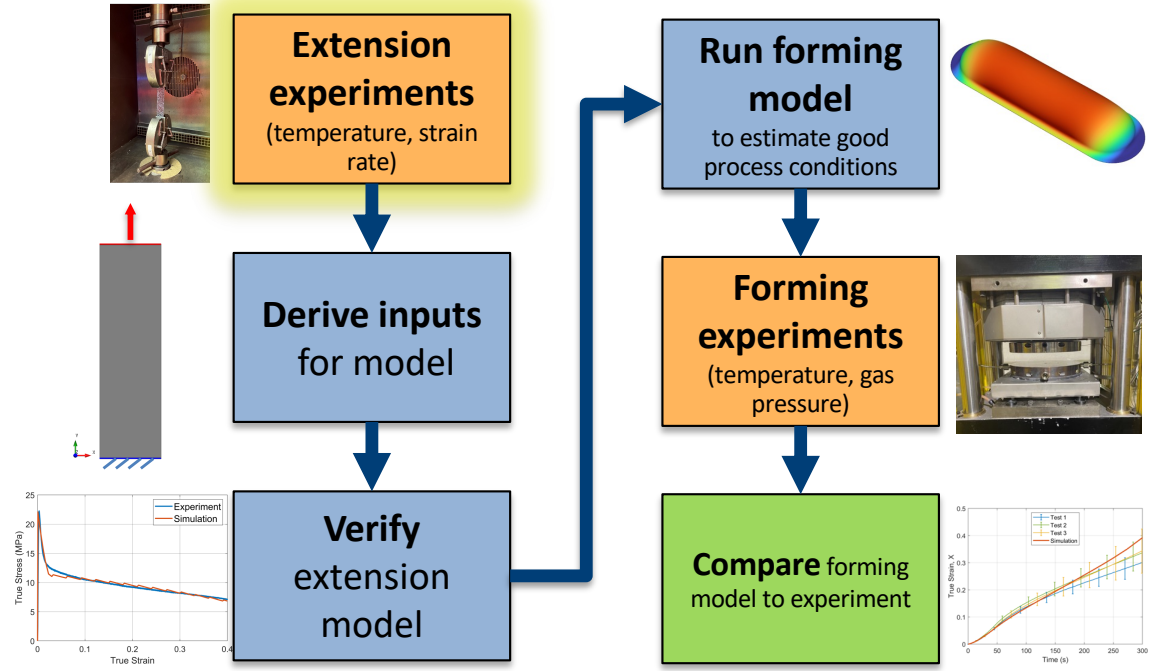

UNIVERSITY OF DELAWARE CENTER FOR COMPOSITE MATERIALS AFRL

DISTRIBUTION STATEMENT A. Approved for public release: distribution unlimited AFRL-2025-3663.

Axial Extension Experiments:
Setup and Data Measurement

- **Axial extension tests** characterize TuFF in a primary deformation mechanism
- Goal:
  - **Measure** strain + stress as a function of strain rate + temperature
- Procedure:
  - Stretch a 25.4 × 90 mm sample at known strain rates (s^{-1}) and temperatures (^oC)
  - Extension at constant strain rate

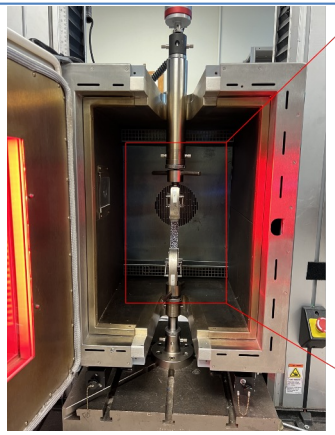

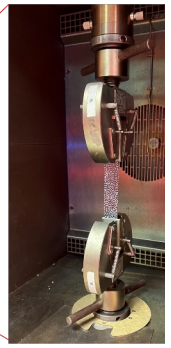

Test setup: a sample is gripped and stretched inside an environment chamber

Data analysis: Digital image correlation (DIC) tracks local strains over time.

Force is measured by a load cell to calculate stress (not shown)

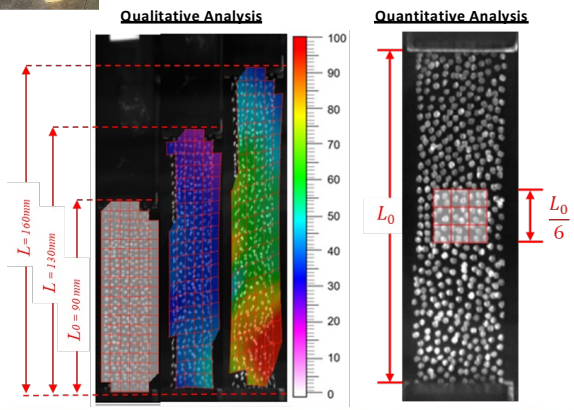

UNIVERSITY OF DELAWARE CENTER FOR COMPOSITE MATERIALS AFRL

DISTRIBUTION STATEMENT A. Approved for public release: distribution unlimited
AFRL-2025-3663.

Model Development Framework

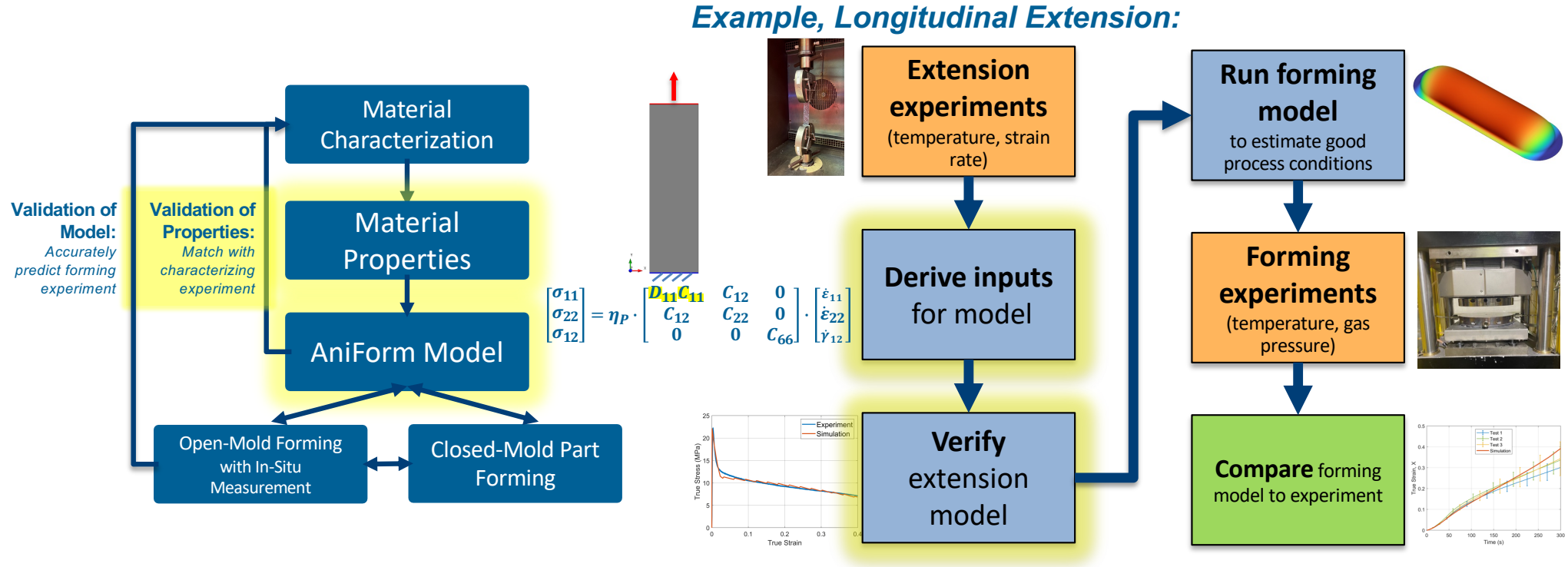

UNIVERSITY OF DELAWARE CENTER FOR COMPOSITE MATERIALS AFRL THE AIR FORCE RESEARCH LABORATORY
DISTRIBUTION STATEMENT A. Approved for public release: distribution unlimited AFRL-2025-3663.

Axial Extension Simulation:
Constitutive Equation and Acquiring Inputs

- Developed a model that **matches uniaxial extension data**
- Constitutive equation:
  - Viscous equation with strain softening component

$$\begin{bmatrix}\sigma_{11}\\ \sigma_{22}\\ \sigma_{12}\end{bmatrix} = \eta_P \cdot \begin{bmatrix}D_{11}C_{11} & C_{12} & 0\\ C_{12} & C_{22} & 0\\ 0 & 0 & C_{66}\end{bmatrix} \cdot \begin{bmatrix}\dot{\varepsilon}_{11}\\ \dot{\varepsilon}_{22}\\ \dot{\gamma}_{12}\end{bmatrix}$$

Stresses = **Polymer viscosity** · **Directional magnification from fibers** · **Strain rates**

$$D_{11} = \mathrm{C} \cdot \left(1 - \frac{\varepsilon_{11}}{D}\right) + (1.0 - \mathrm{C}) \cdot \left(1 - \frac{\varepsilon_{11}}{F}\right)$$

Strain softening = First phase [peak] + Second phase [long-term]

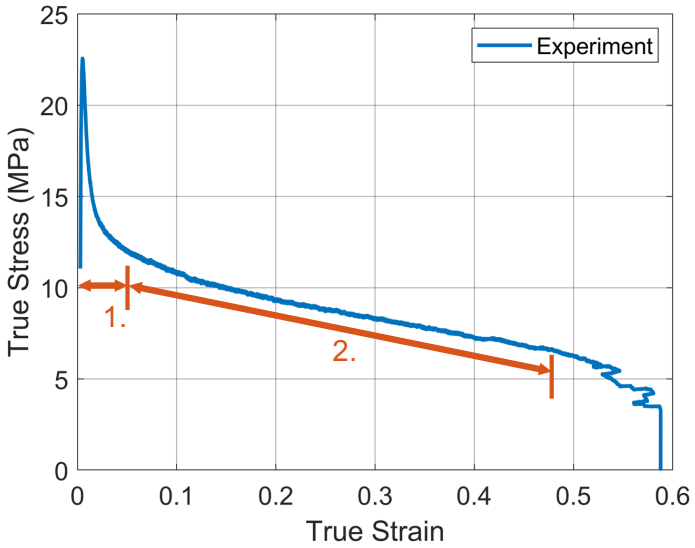

Stress-strain behavior of one TuFF ply: experimental data.
($\dot{\varepsilon} = 0.001\ s^{-1},\ T = 40°C$)

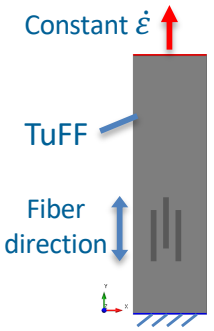

UNIVERSITY OF DELAWARE CENTER FOR COMPOSITE MATERIALS AFRL
DISTRIBUTION STATEMENT A. Approved for public release: distribution unlimited
AFRL-2025-3663.

Axial Extension Simulation:
Constitutive Equation and Acquiring Inputs

- Developed a model that **matches uniaxial extension data**
- Constitutive equation:
  - Viscous equation with strain softening component

$$\begin{bmatrix}\sigma_{11}\\ \sigma_{22}\\ \sigma_{12}\end{bmatrix} = \eta_P \cdot \begin{bmatrix}D_{11}C_{11} & C_{12} & 0\\ C_{12} & C_{22} & 0\\ 0 & 0 & C_{66}\end{bmatrix} \cdot \begin{bmatrix}\dot{\varepsilon}_{11}\\ \dot{\varepsilon}_{22}\\ \dot{\gamma}_{12}\end{bmatrix}$$

Stresses = Polymer viscosity · Directional magnification from fibers · Strain rates

$$D_{11} = \mathrm{C} \cdot \left(1 - \frac{\varepsilon_{11}}{D}\right) + (1.0 - \mathrm{C}) \cdot \left(1 - \frac{\varepsilon_{11}}{F}\right)$$

Strain softening = First phase [peak] + Second phase [long-term]

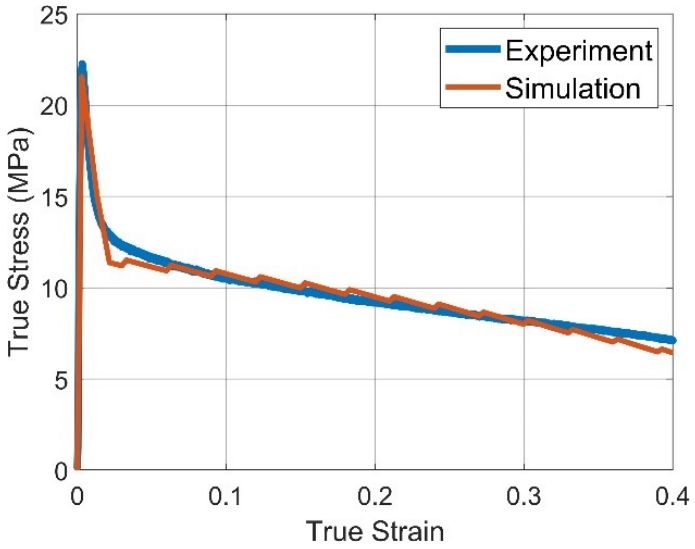

Stress-strain behavior of one TuFF ply: comparison between experiment and simulation ($\dot{\varepsilon} = 0.001\ s^{-1},\ T = 40°C$)

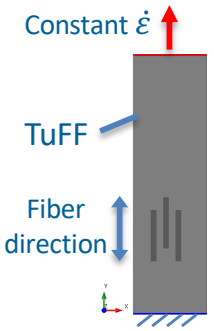

UNIVERSITY OF DELAWARE CENTER FOR COMPOSITE MATERIALS AFRL
DISTRIBUTION STATEMENT A. Approved for public release: distribution unlimited
AFRL-2025-3663.

Axial Extension Simulation:
Validation of Model

Local strain over time of DIC capture (left) and simulation (right)

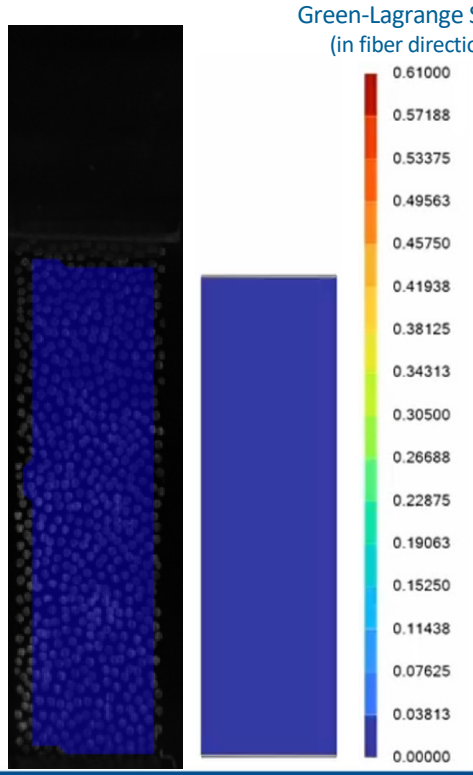

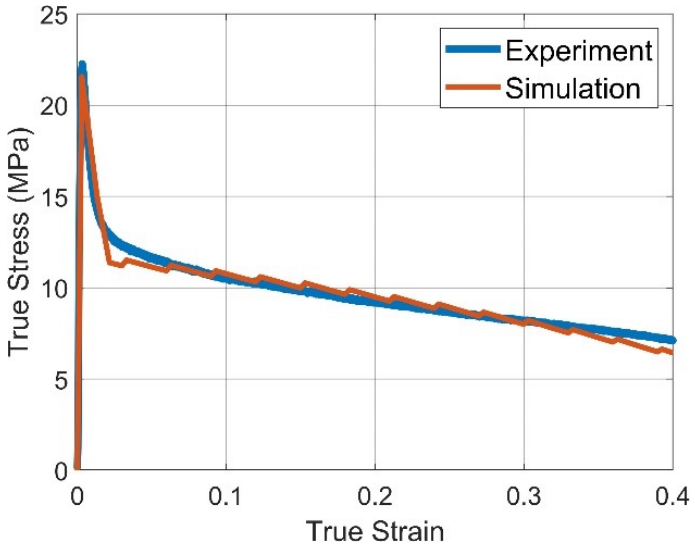

Stress-strain behavior of one TuFF ply: comparison between experiment and simulation ($\dot{\varepsilon} = 0.001\ s^{-1},\ T = 40°C$)

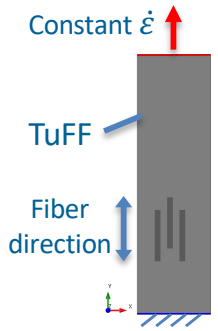

UNIVERSITY OF DELAWARE CENTER FOR COMPOSITE MATERIALS AFRL
DISTRIBUTION STATEMENT A. Approved for public release: distribution unlimited
AFRL-2025-3663.

Model Development Framework

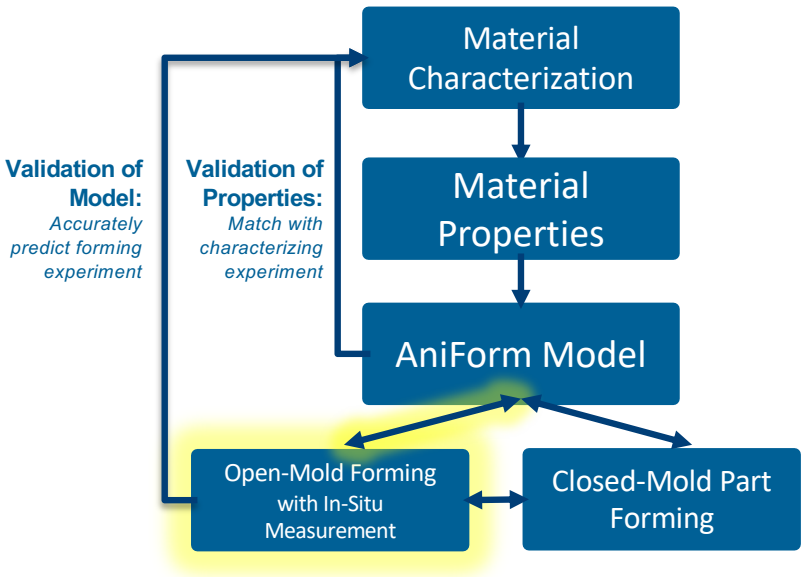

Example, Longitudinal Extension:

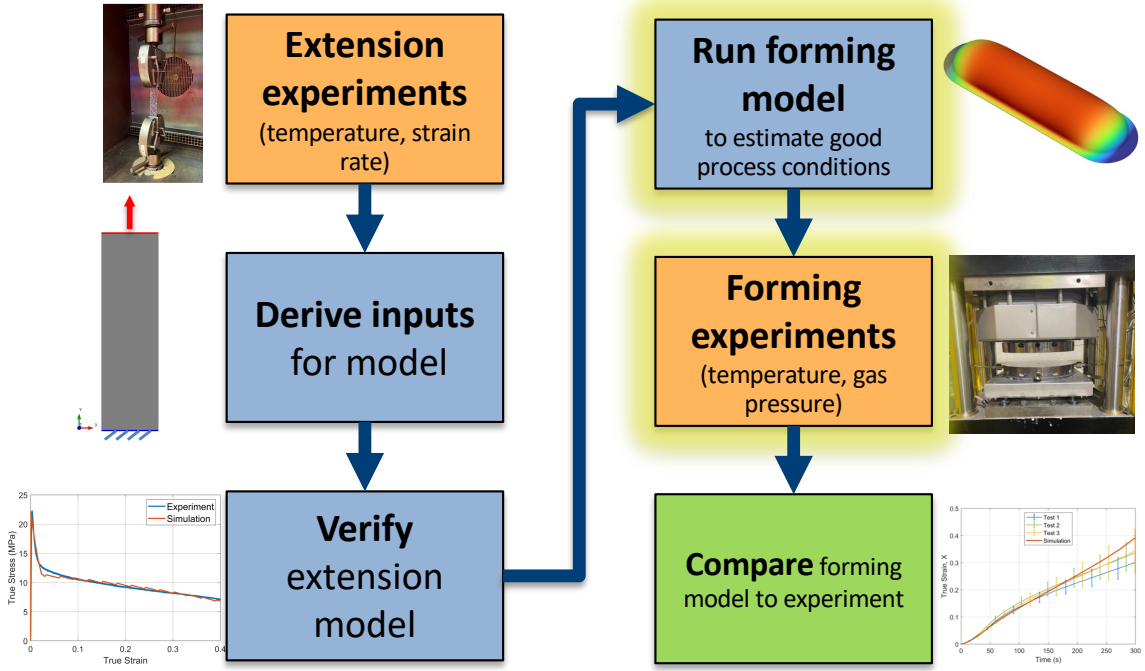

UNIVERSITY OF DELAWARE CENTER FOR COMPOSITE MATERIALS AFRL

DISTRIBUTION STATEMENT A. Approved for public release: distribution unlimited AFRL-2025-3663.

Forming Characterization System

Equipment developed and acquired under
ONR Grant No. N00014-22-1-2124



GOM ARAMIS 12MP DIC

Forming Characterization System
Interlaken SP75

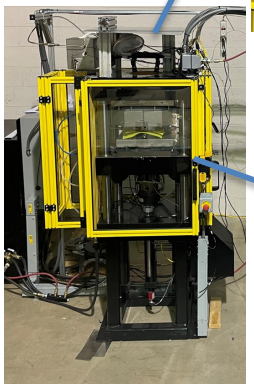

Plane Strain Gas Bulge Tool Set

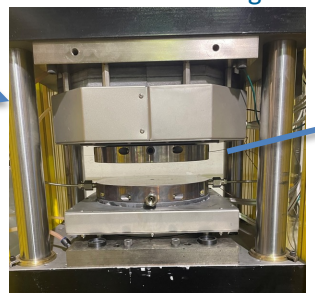

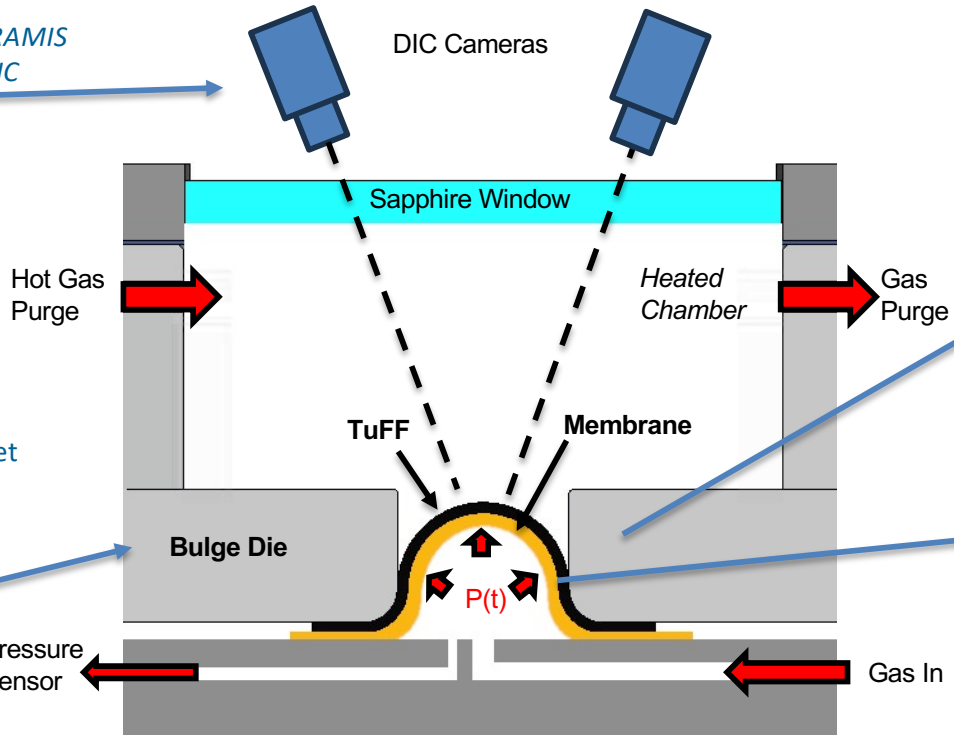

Bulge Die

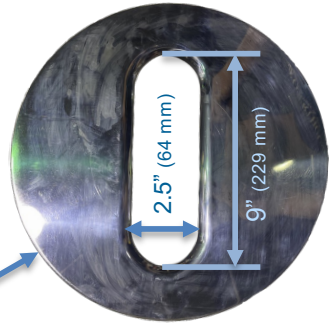

$[0/90]_S$ TuFF laminate with bagging membrane.

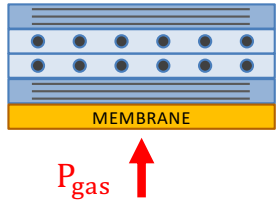

UNIVERSITY OF DELAWARE CENTER FOR COMPOSITE MATERIALS

AFRL

DISTRIBUTION STATEMENT A. Approved for public release: distribution unlimited
AFRL-2025-3663.

Open-Mold Bead Simulation

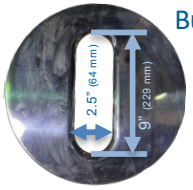

Bulge die used in experiments.

Layup

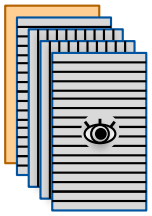

Coordinate system

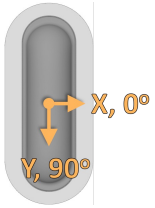

Input gas pressure

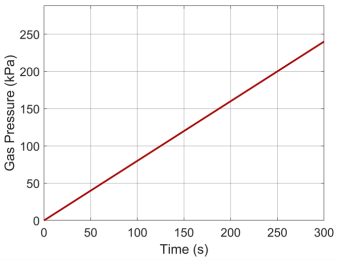

- **Matching conditions of experiment:**
  - Layup: $[0/90]_s$ TuFF with single bladder membrane.
  - Inputs from **40°C**, $\dot{\varepsilon} = 0.001\ s^{-1}$ test.
  - Gas pressure: 0.8 kPa/s ramp for 250 seconds.
  - Boundary condition: clamped around bead for no slip-in.
- **Strain** and **strain rate** over **time** are tracked at center of outermost ply.

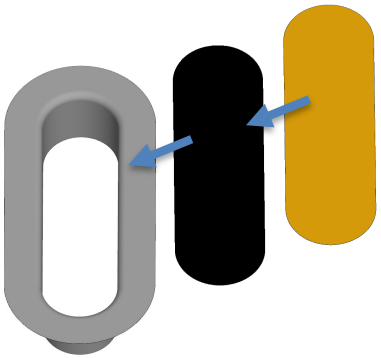

Simplified model is constructed.

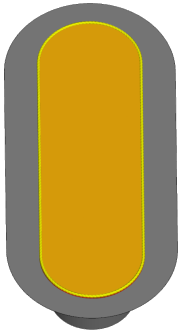

Edges' DOF are locked.

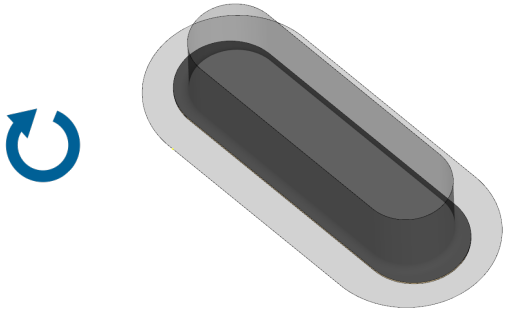

Laminate expands through the tool.

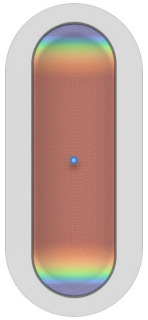

Data is tracked at center of outermost ply.

UNIVERSITY OF DELAWARE CENTER FOR COMPOSITE MATERIALS AFRL
DISTRIBUTION STATEMENT A. Approved for public release: distribution unlimited
AFRL-2025-3663.

Obtaining Gas Pressure Profile

- Forming window suggests process conditions
  - Strain Rate + Temperature

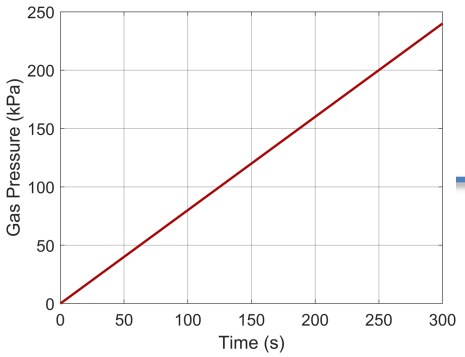

Gas Pressure vs. Time

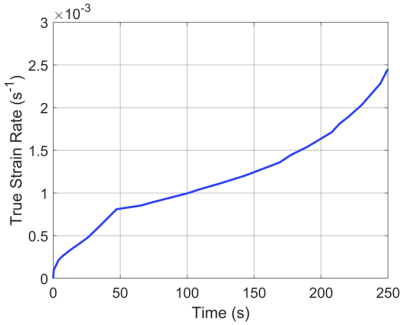

Strain Rate vs. Time

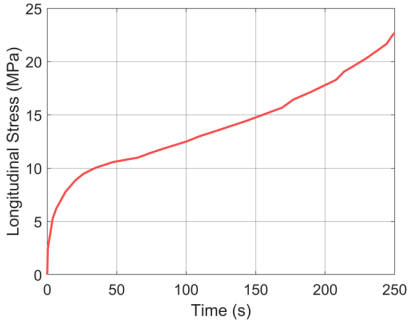

Stress vs. Time

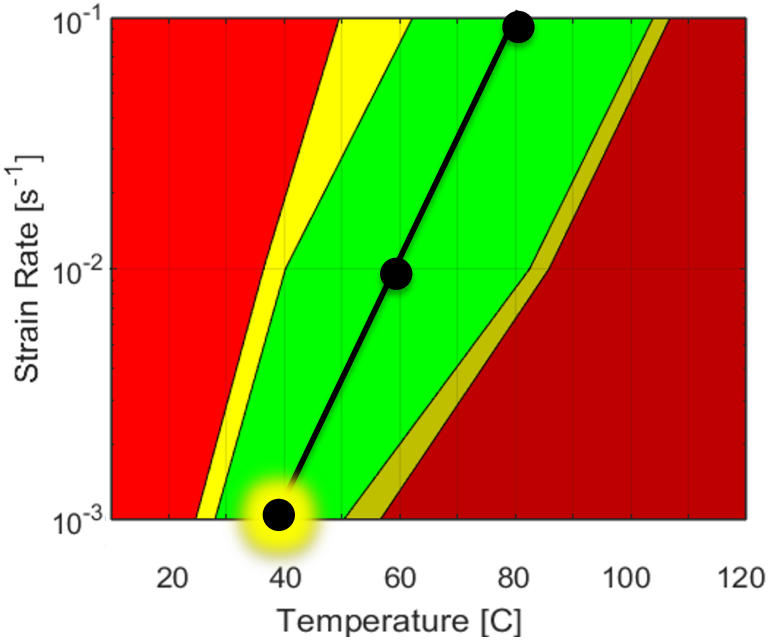

TuFF needs range of stress to stretch

DISTRIBUTION STATEMENT A. Approved for public release: distribution unlimited
AFRL-2025-3663.

Model Development Framework

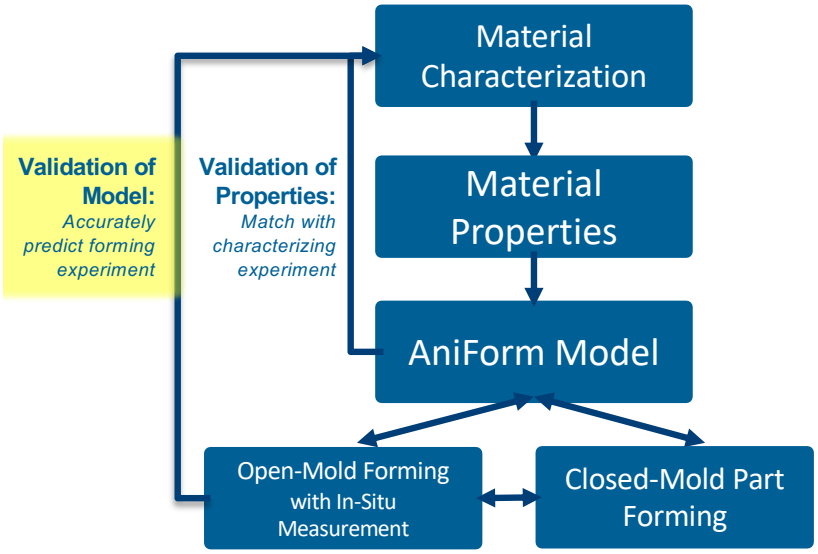

Example, Longitudinal Extension:

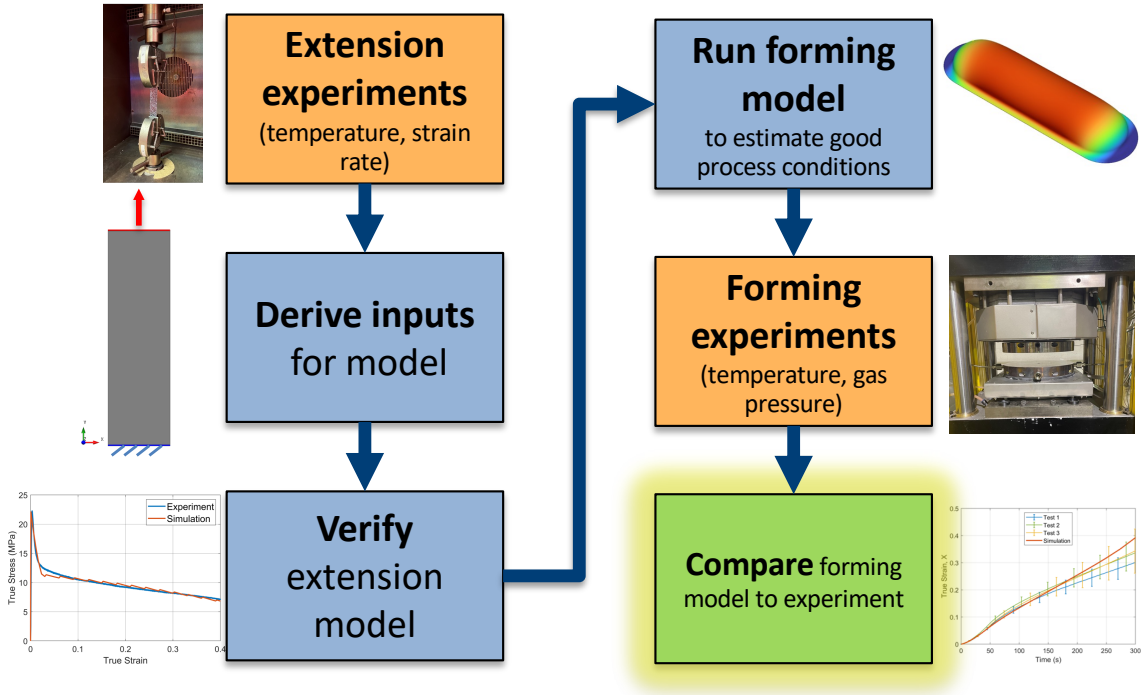

UNIVERSITY OF DELAWARE CENTER FOR COMPOSITE MATERIALS AFRL

DISTRIBUTION STATEMENT A. Approved for public release: distribution unlimited AFRL-2025-3663.

Accuracy of Forming Model

Conditions

- Temp = 40°C
- Pressure = 0.8 kPa/s ramp for 250 seconds.
- Layup = $[0/90]_S$ with single diaphragm
- Interfaces have Coulomb friction, $\mu = 0.4$

Layup

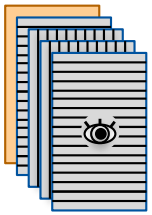

Coordinate system

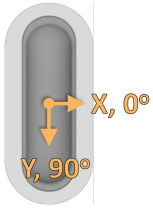

Input gas pressure

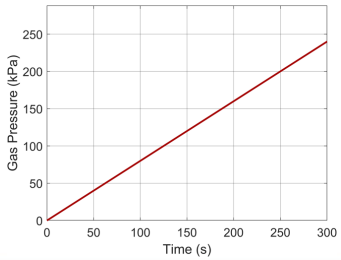

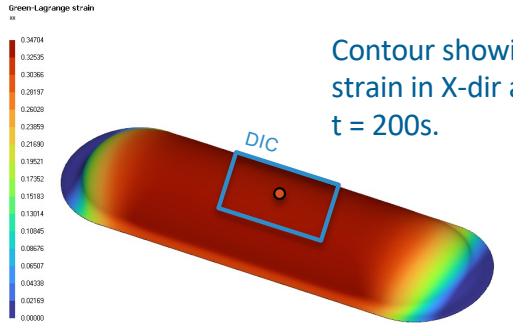

Contour showing strain in X-dir at t = 200s.

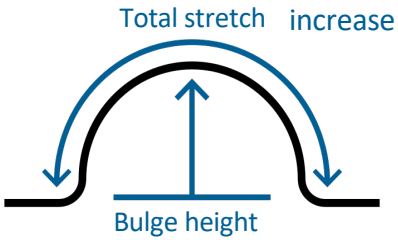

Strains add up to increase bulge height.

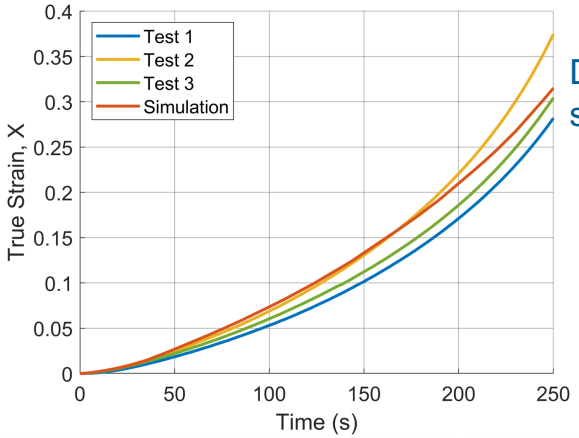

Development of strain over time.

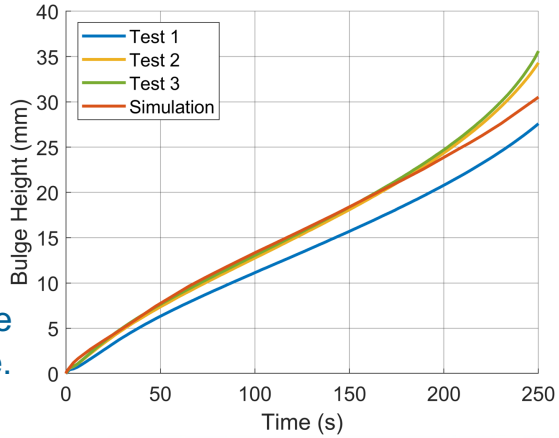

Development of bulge height over time.

DISTRIBUTION STATEMENT A. Approved for public release: distribution unlimited
AFRL-2025-3663.

Conclusions

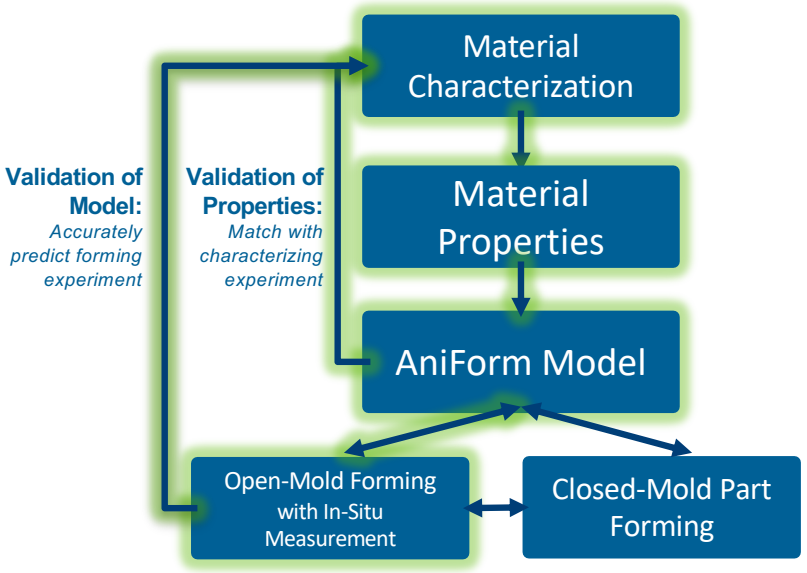

Extensional properties predicts stretch in forming

- **Validated model** to predict **longitudinal extensior** in forming.
- Simple equation + properties works:

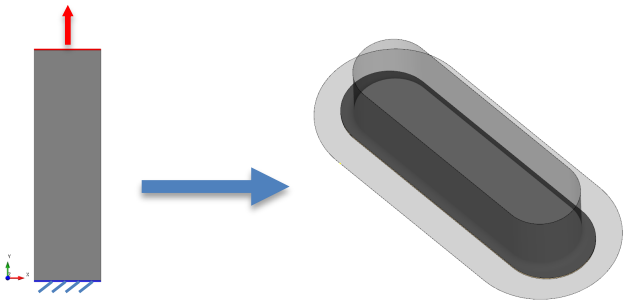

Longitudinal Extension:
- Constant strain rate, impulsively started
- Single ply
- No transverse pressure

Forming:
- Gas pressure-driven
- Multi-ply with bladder
- Transverse pressure

- Suggests continuum-scale viscosity behaves in the same manner for single ply extension and multi-ply blanks in bead forming

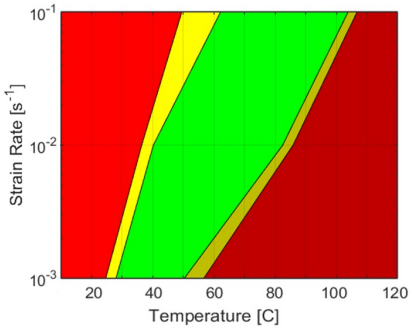

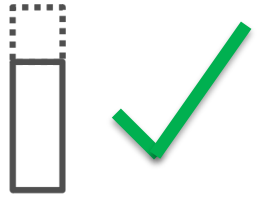

Stretch

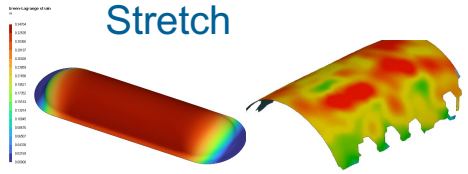

UNIVERSITY OF DELAWARE CENTER FOR COMPOSITE MATERIALS AFRL
DISTRIBUTION STATEMENT A. Approved for public release: distribution unlimited
AFRL-2025-3663.

Questions?

DISTRIBUTION STATEMENT A. Approved for public release: distribution unlimited
AFRL-2025-3663.



Center for Composite Materials

Transverse Shear Characterization of Aligned Discontinuous Fiber Prepregs using Squeeze Flow

Rafe Garcia-Hidalgo, Dr. Pavel Simacek, Prof. Suresh Advani



DISTRIBUTION STATEMENT A. Approved for public release: distribution unlimited. AFRL-2025-3653.

UNIVERSITY OF DELAWARE

TuFF Introduction

DISTRIBUTION STATEMENT A. Approved for public release: distribution unlimited. AFRL-2025-3653.

TuFF: Tailored Universal Feedstock for Forming

- **Chopped fibers** are highly **aligned** by water flow onto thin film
- Films of aligned fiber are prepregged with resin
- Prepreg can be used in **thermoforming process**
  - **Allows for stretch** during forming
  - Final properties comparable to continuous unidirectional prepreg











UNIVERSITY OF DELAWARE CENTER FOR COMPOSITE MATERIALS AFRL

DISTRIBUTION STATEMENT A. Approved for public release: distribution unlimited. AFRL-2025-3653.

Outline

- **Motivation**
- Objectives
- Test Methodology
- Results and Future Work

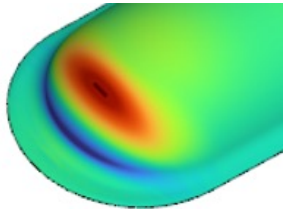

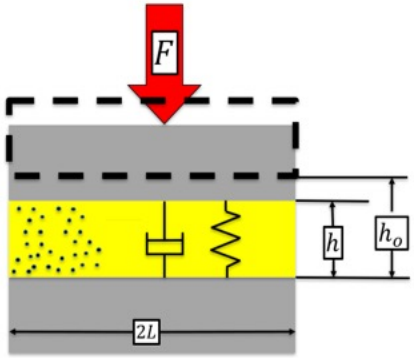

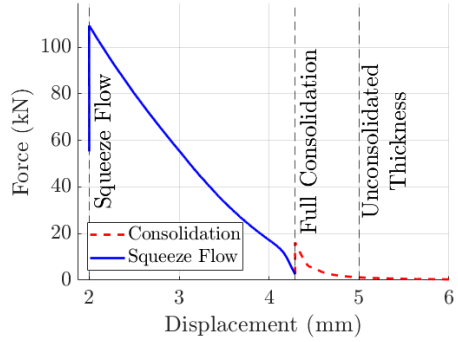

DISTRIBUTION STATEMENT A. Approved for public release: distribution unlimited. AFRL-2025-3653.

Motivation

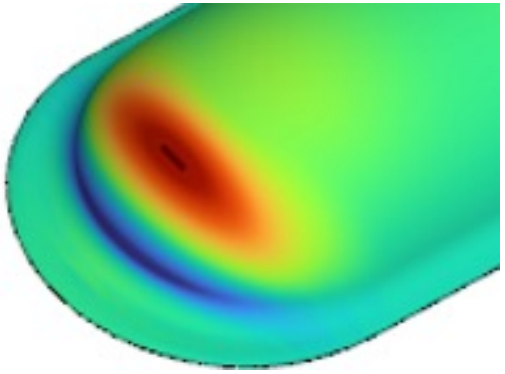



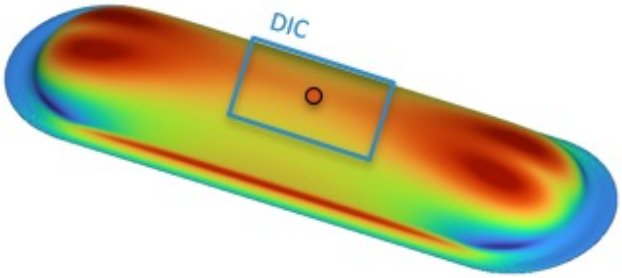

DISTRIBUTION STATEMENT A. Approved for public release: distribution unlimited. AFRL-2025-3653.

Motivation

Forming:

TuFF Blank

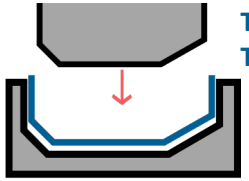

Tool displacement rate, Temperature

or

Gas pressure, Temperature

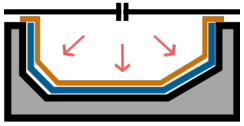

DISTRIBUTION STATEMENT A. Approved for public release: distribution unlimited. AFRL-2025-3653.

Motivation

Forming:

TuFF Blank

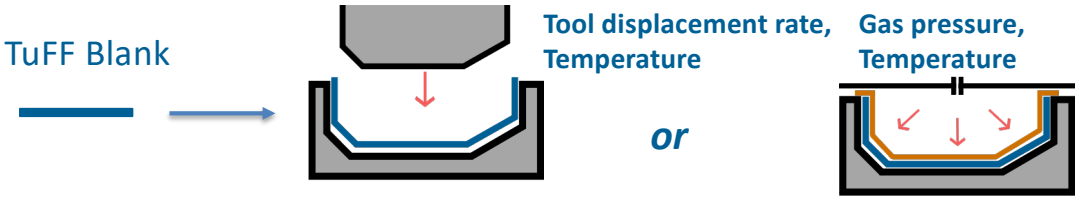

5 main deformation mechanisms:

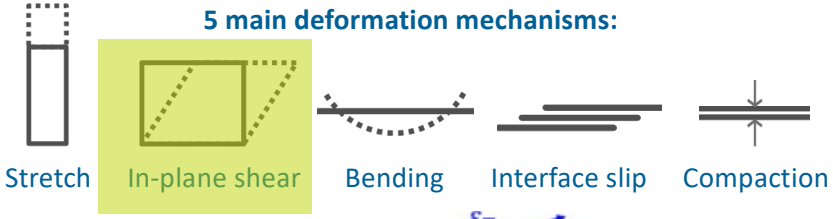

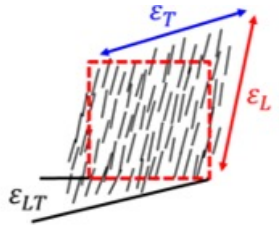

UNIVERSITY OF DELAWARE CENTER FOR COMPOSITE MATERIALS AFRL

DISTRIBUTION STATEMENT A. Approved for public release: distribution unlimited. AFRL-2025-3653.

Motivation

Forming:

TuFF Blank

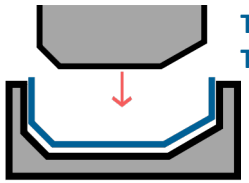

Tool displacement rate, Temperature

or

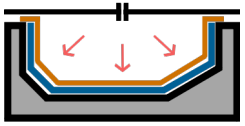

Gas pressure, Temperature

5 main deformation mechanisms:

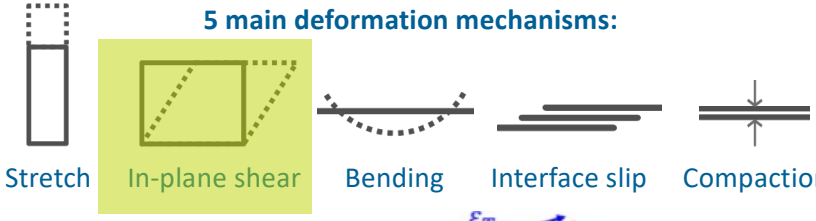

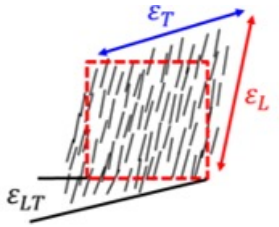

Virtual Modeling:

ANIFORM
VIRTUAL FORMING

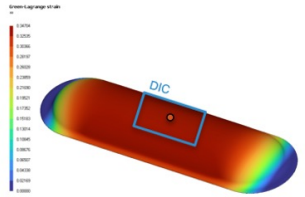

$$\begin{bmatrix}\sigma_{11}\\ \sigma_{22}\\ \sigma_{12}\end{bmatrix} = \eta_P \cdot \begin{bmatrix}D_{11}C_{11} & C_{12} & 0\\ C_{12} & C_{22} & 0\\ 0 & 0 & C_{66}\end{bmatrix} \cdot \begin{bmatrix}\dot{\varepsilon}_{11}\\ \dot{\varepsilon}_{22}\\ \dot{\gamma}_{12}\end{bmatrix}$$

Stresses = Polymer viscosity · Directional magnification from fibers · Strain rates

UNIVERSITY OF DELAWARE CENTER FOR COMPOSITE MATERIALS AFRL

DISTRIBUTION STATEMENT A. Approved for public release: distribution unlimited. AFRL-2025-3653.

Objectives

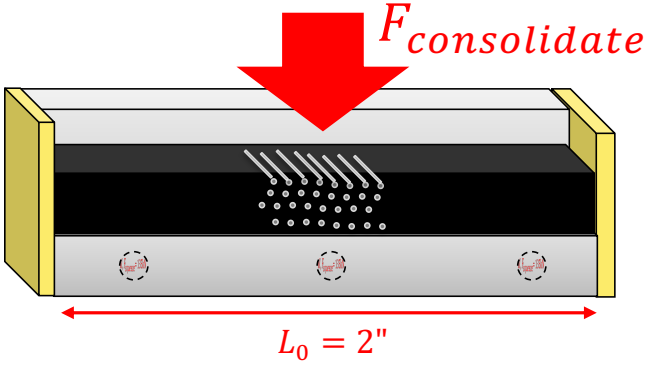

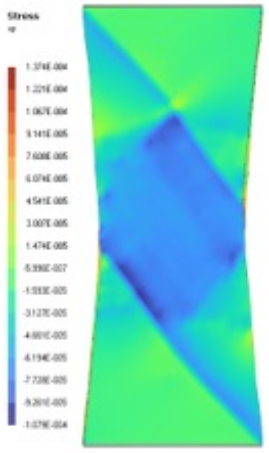

UNIVERSITY OF DELAWARE CENTER FOR COMPOSITE MATERIALS AFRL
DISTRIBUTION STATEMENT A. Approved for public release: distribution unlimited. AFRL-2025-3653.

Constitutive model to describe TuFF Deformation in Aniform

- Develop an anisotropic material model to relate the **stress(σ)** vs **strain rate ($\dot{\varepsilon}$)** for **forming**.
- Magnification matrix modifies **polymer viscosity**.

$$\begin{bmatrix}\sigma_{11}\\ \sigma_{22}\\ \sigma_{12}\end{bmatrix} = \eta_P \cdot \begin{bmatrix}D_{11}C_{11} & C_{12} & 0\\ C_{12} & C_{22} & 0\\ 0 & 0 & C_{66}\end{bmatrix} \cdot \begin{bmatrix}\dot{\varepsilon}_{11}\\ \dot{\varepsilon}_{22}\\ \dot{\gamma}_{12}\end{bmatrix}$$

Stresses = Polymer viscosity · Directional magnification from fibers · Strain rates

ANIFORM
VIRTUAL FORMING

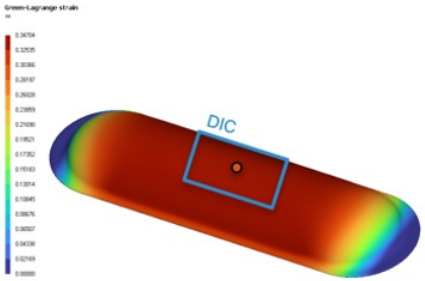

$D_{11}C_{11}$:

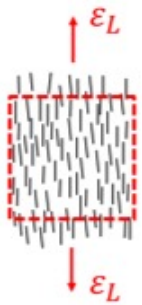

C_{22}:

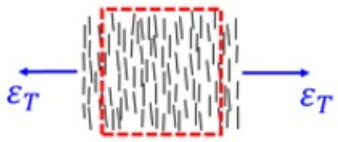

C_{66}:

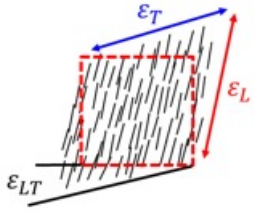

UNIVERSITY OF DELAWARE CENTER FOR COMPOSITE MATERIALS AFRL

DISTRIBUTION STATEMENT A. Approved for public release: distribution unlimited. AFRL-2025-3653.

Effect of C_{66} on Biased Extension Test

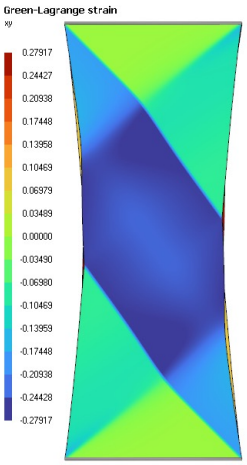

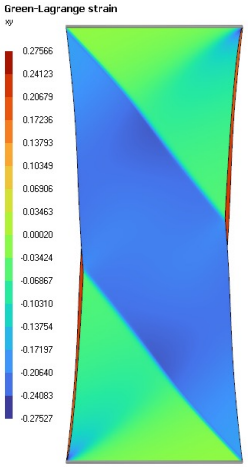

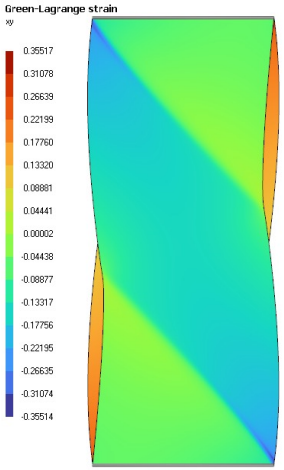

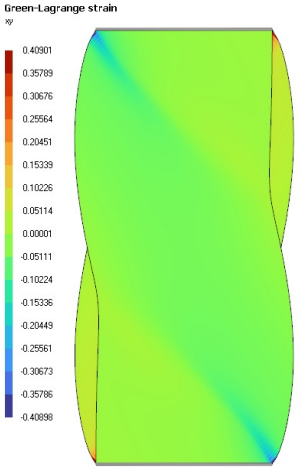

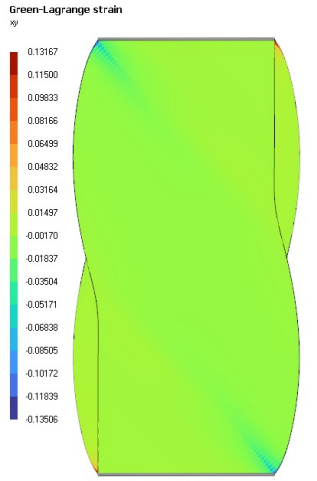

$C_{66} =$	$1e2$	$1e3$	$1e4$	$1e5$	$1e6 \sim C_{11}$
$\varepsilon_{LT} =$	0.27	0.21	0.16	0.04	0.005

DISTRIBUTION STATEMENT A. Approved for public release: distribution unlimited. AFRL-2025-3653.

Test Methodology

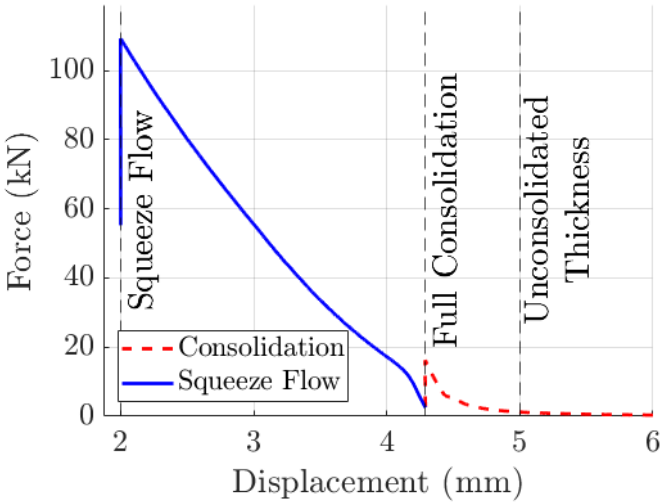

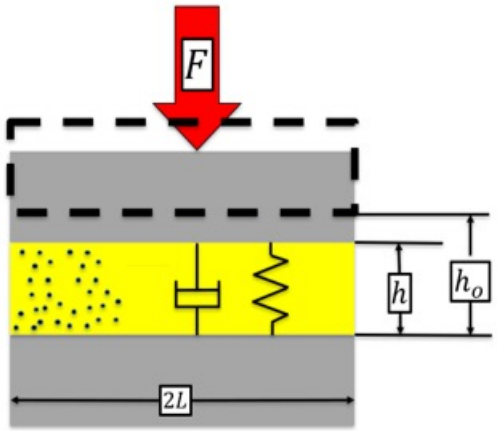

UNIVERSITY OF DELAWARE CENTER FOR COMPOSITE MATERIALS AFRL

DISTRIBUTION STATEMENT A. Approved for public release: distribution unlimited. AFRL-2025-3653.

Experimental Procedure

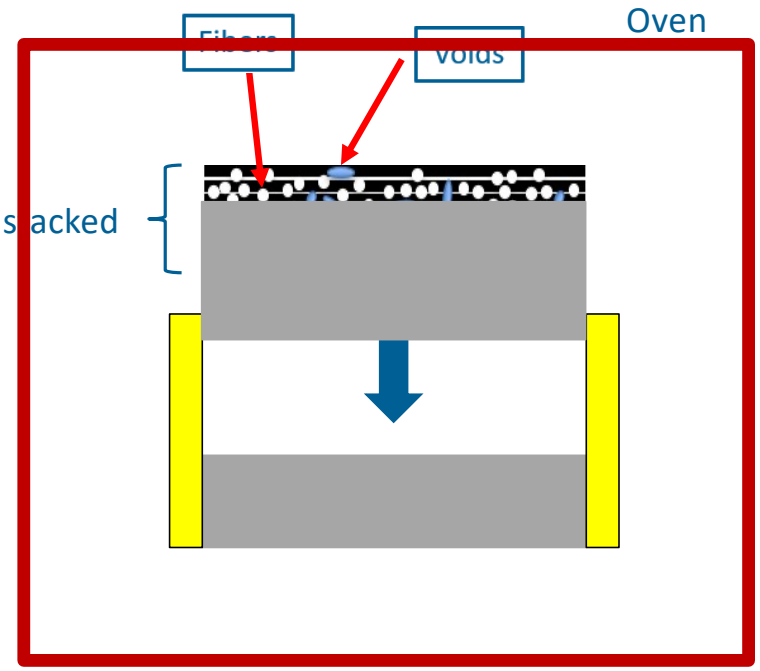

UNIVERSITY OF DELAWARE CENTER FOR COMPOSITE MATERIALS AFRL
DISTRIBUTION STATEMENT A. Approved for public release: distribution unlimited. AFRL-2025-3653.

Experimental Procedure

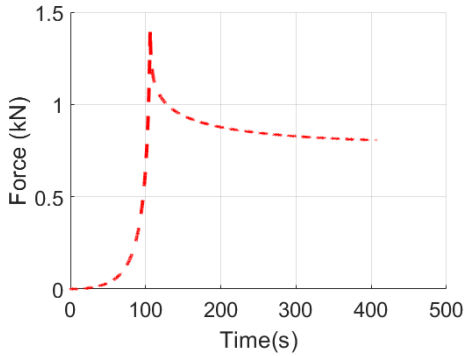

≈ 30 Minute hold

Constant displacement rate ($\dot{h}$)

Oven

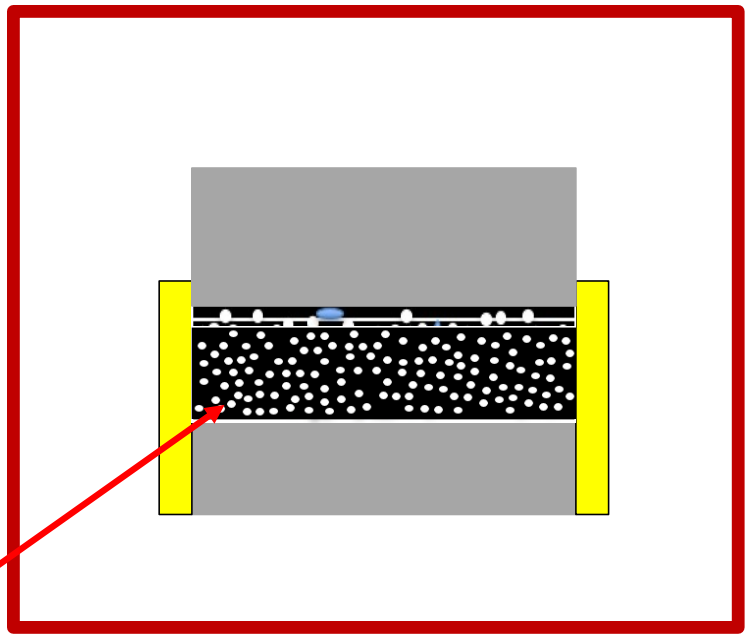

Remove voids

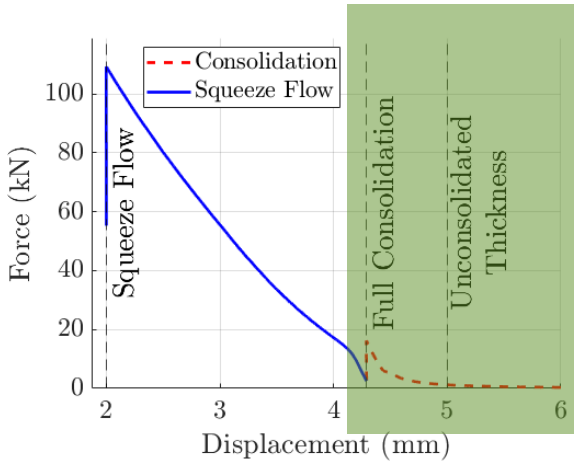

$$h_{consolidation} = \frac{Sample\ mass}{TuFF\ density \times Fixture\ area} \approx 4.3mm$$

UNIVERSITY OF DELAWARE CENTER FOR COMPOSITE MATERIALS AFRL

DISTRIBUTION STATEMENT A. Approved for public release: distribution unlimited. AFRL-2025-3653.

Experimental Procedure

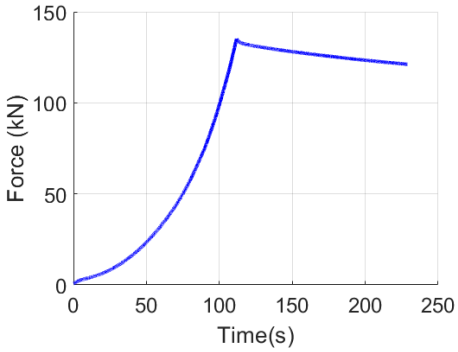

Constant displacement rate ($\dot{h}$)

Oven

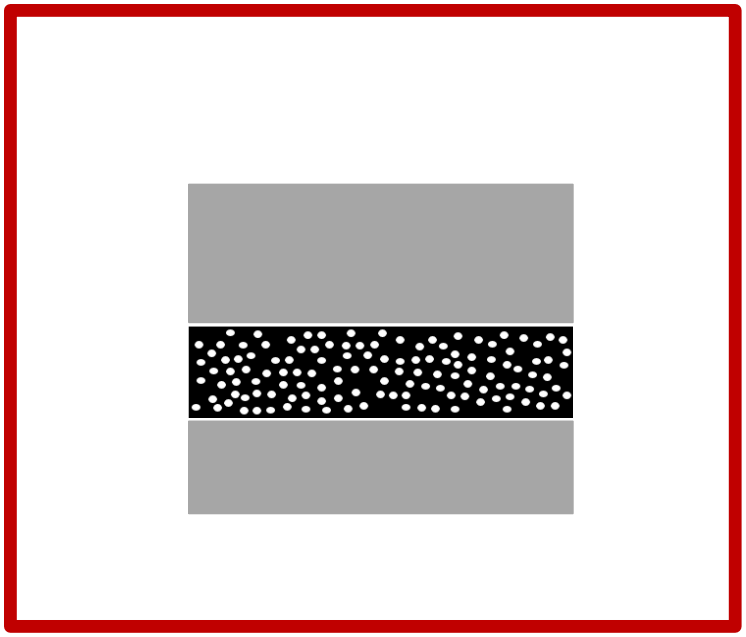

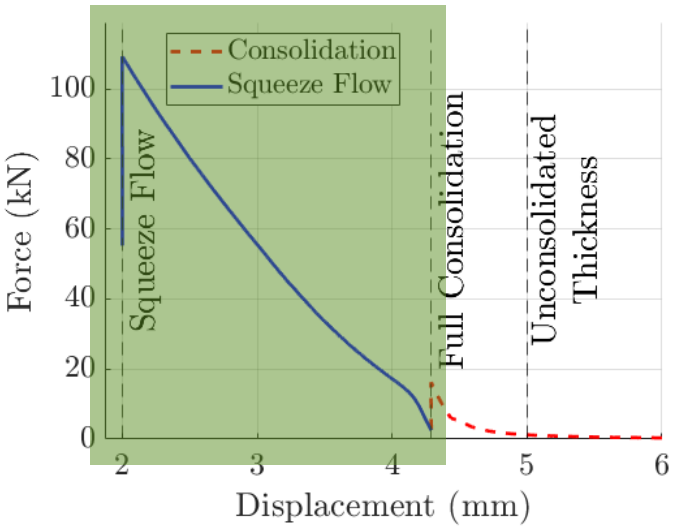

DISTRIBUTION STATEMENT A. Approved for public release: distribution unlimited. AFRL-2025-3653.

Squeeze Flow Experiment to Determine C_{66}

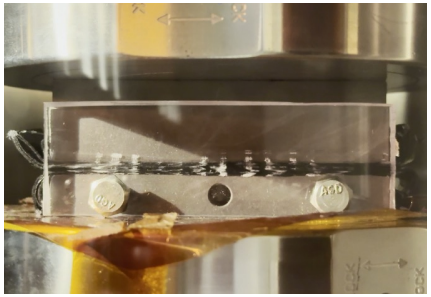



Consolidate sample:

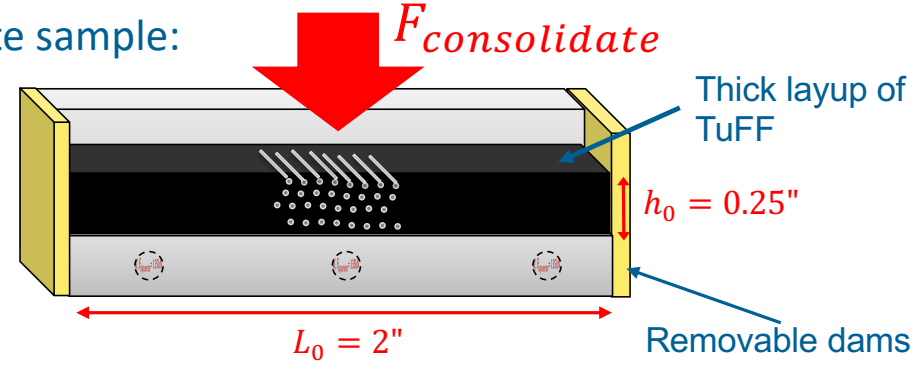

Drive squeeze flow:

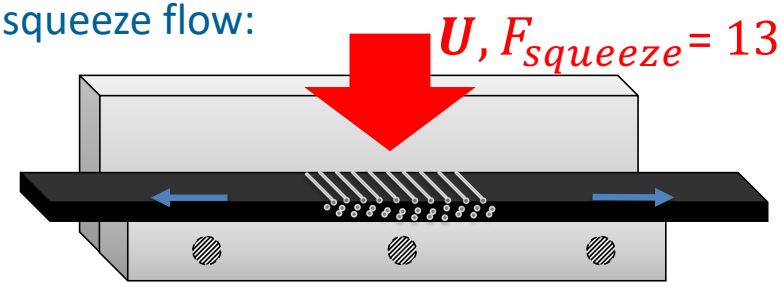

Squeeze flow creates a **shearing deformation** in the sample which allows C_{66} to be characterized

DISTRIBUTION STATEMENT A. Approved for public release: distribution unlimited. AFRL-2025-3653.

Squeeze Flow Visualization with Markers

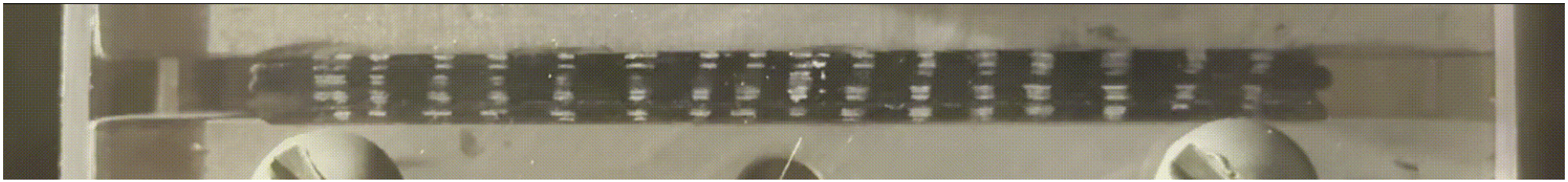

- Initial **parabolic** flow -> no slip boundary condition at **TuFF-tool** interface
- Analytical solution for force available from dimensions, viscosity (η), and closing rate ($\dot{h}$)

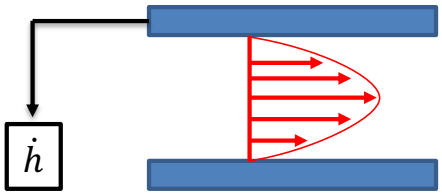

$$F = \frac{4\,L^3 W \eta \dot{h}}{h^3}$$

- Transition to plug or partial slip flow → evidence of **interfacial slip** developing at the TuFF-tool interface in later stages of the test

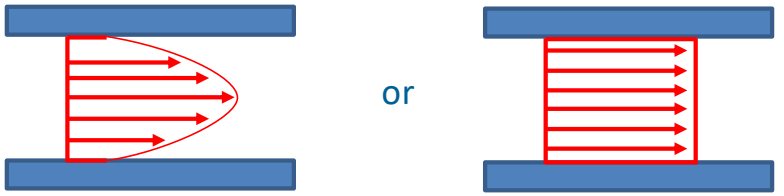

DISTRIBUTION STATEMENT A. Approved for public release: distribution unlimited. AFRL-2025-3653.

Model Formulation

- TuFF prepreg in squeeze flow is not only a viscous reaction, acts like a **spring and damper** system when squeezed:

Viscous Resin Force:

$$F_{Resin} = \frac{4L^3 W \dot{h} \eta_P C_{66}}{h^3}$$

Spring Fiber Force:

$$F_{Fiber} = \sum_{i=1}^{n} k_i \, (h_o - h)^i$$

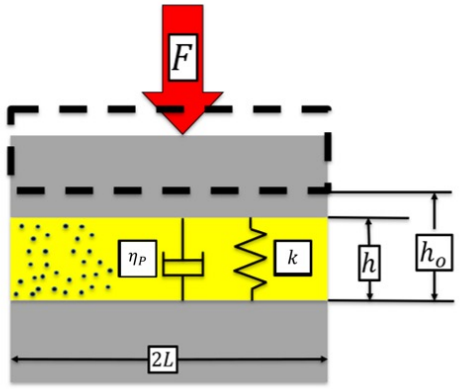

- The addition of these two reaction forces will describe the no slip portion of the experiment

$$F_{Sample} = F_{Resin} + F_{Fibers}$$

- h_o has been selected to be the displacement where the force begins to increase at $h = 4.68mm$

UNIVERSITY OF DELAWARE CENTER FOR COMPOSITE MATERIALS AFRL
DISTRIBUTION STATEMENT A. Approved for public release: distribution unlimited. AFRL-2025-3653.

Results and Future Work

DISTRIBUTION STATEMENT A. Approved for public release: distribution unlimited. AFRL-2025-3653.

Squeeze Flow Experimental Results

- Squeeze flow experiments produce repeatable results

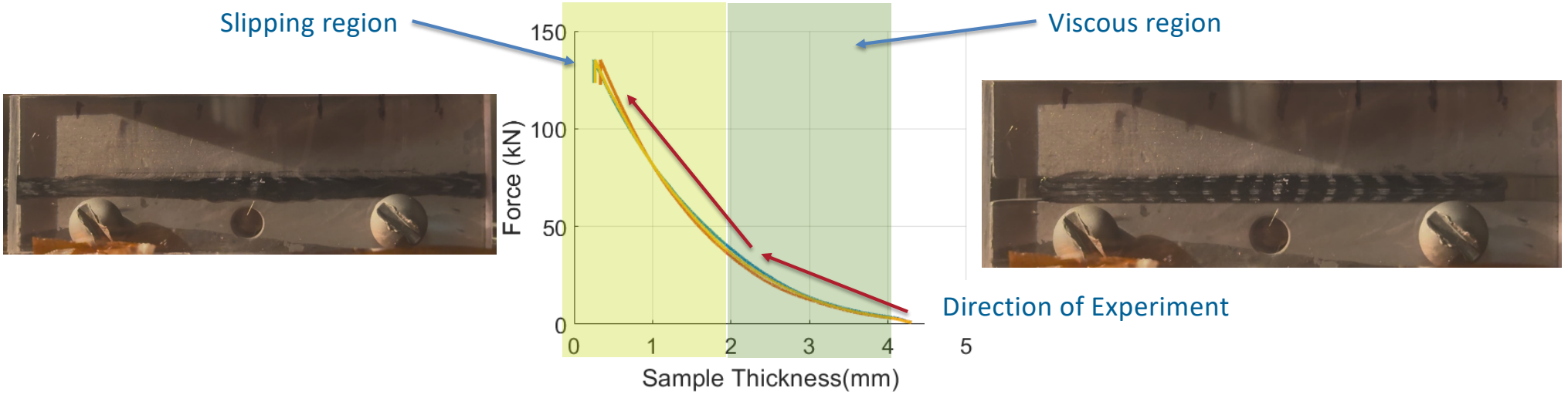

DISTRIBUTION STATEMENT A. Approved for public release: distribution unlimited. AFRL-2025-3653.

Modeling The Spring Response

- To fully describe spring response, sample squeezed to consecutive displacements
- Fiber spring response tracked

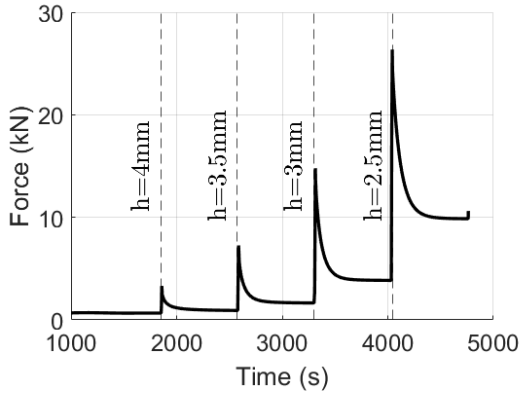

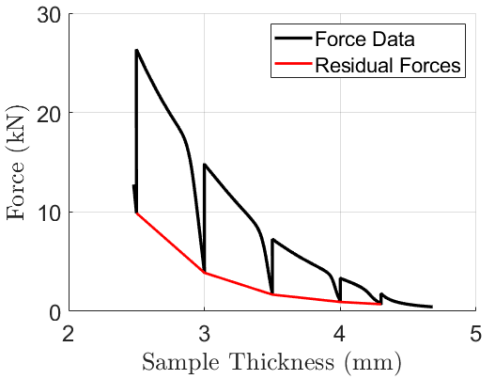

Fiber Response:

$$F_{Fibers} = 0.44(4.68 - h)^4$$

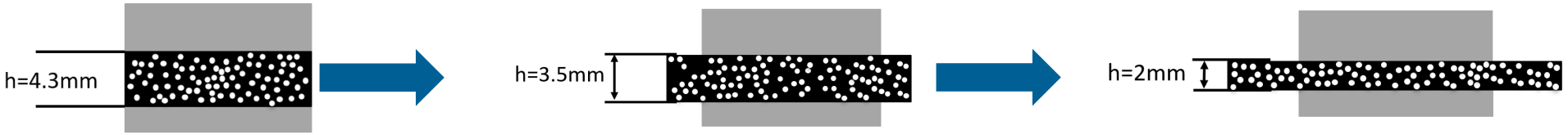

DISTRIBUTION STATEMENT A. Approved for public release: distribution unlimited. AFRL-2025-3653.

Fitted Parameters

- By isolating the viscous response to squeeze flow, C_{66} can be found using least squares optimization.
- For characterization to be correct, C_{66} remain constant at different dimensions and closure rates

$$F = \frac{4L^3 W \dot{h} \eta_P C_{66}}{h^3} + k_4 (h_o - h)^4$$

Parameters:
C_{66}: 17853
k_4: 0.44

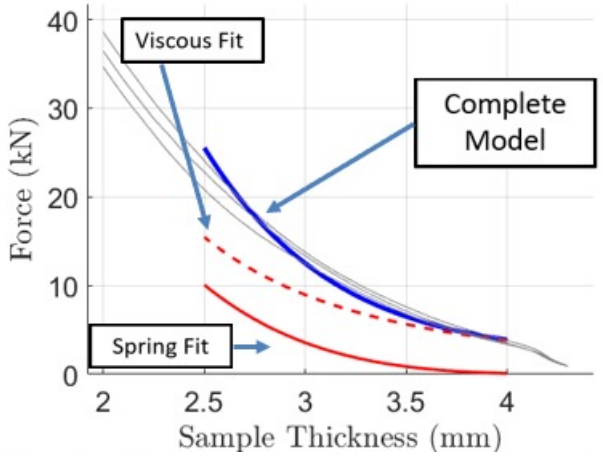

- Prepreg viscosity is 18000 time larger than the polymer viscosity

UNIVERSITY OF DELAWARE CENTER FOR COMPOSITE MATERIALS AFRL
DISTRIBUTION STATEMENT A. Approved for public release: distribution unlimited. AFRL-2025-3653.

Summary

- A model was formulated to characterize the transvers viscosity of TuFF prepreg.
- Squeeze flow experiments were conducted in a 2”x1” fixture, all fibers were aligned in the direction perpendicular to flow.
- Three consistent experiments were performed and the viscosity was found to be 1e4 times larger than the polymer viscosity.
- Same methodology will be used to find viscosity using 4”x1” fixture.
- The characterized value will be used in Aniform.

$$\begin{bmatrix}\sigma_{11}\\ \sigma_{22}\\ \sigma_{12}\end{bmatrix} = \eta_P \cdot \begin{bmatrix}D_{11}C_{11} & C_{12} & 0\\ C_{12} & C_{22} & 0\\ 0 & 0 & C_{66}\end{bmatrix} \cdot \begin{bmatrix}\dot{\varepsilon}_{11}\\ \dot{\varepsilon}_{22}\\ \dot{\gamma}_{12}\end{bmatrix}$$

Stresses = Polymer viscosity · Directional magnification from fibers · Strain rates

UNIVERSITY OF DELAWARE CENTER FOR COMPOSITE MATERIALS AFRL
DISTRIBUTION STATEMENT A. Approved for public release: distribution unlimited. AFRL-2025-3653.

Fitted Parameters

- There have been two different sample dimensions tested, 4”x1” and 2”x1”
- Even with varying dimensions, C_{66} should be the same between experiments

$$F = \frac{4L^3 W \dot{h} \eta_P C_{66}}{h^3} + k_1(h_o - h) + k_3(h_o - h)^3$$

2”x1” Fixture Fit

Parameters:

C_{66}: 3940

k_1: 1.66

k_2: 1.22

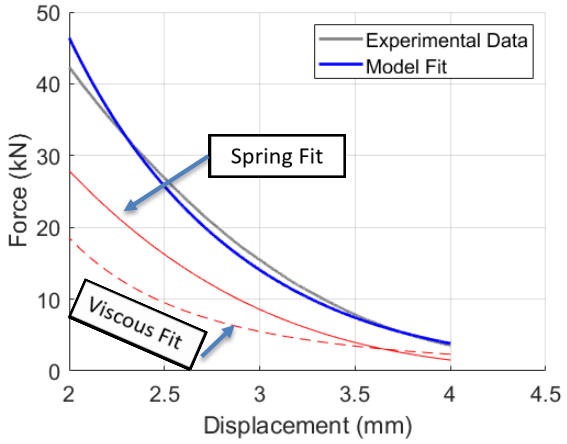

4”x1” Fixture Fit

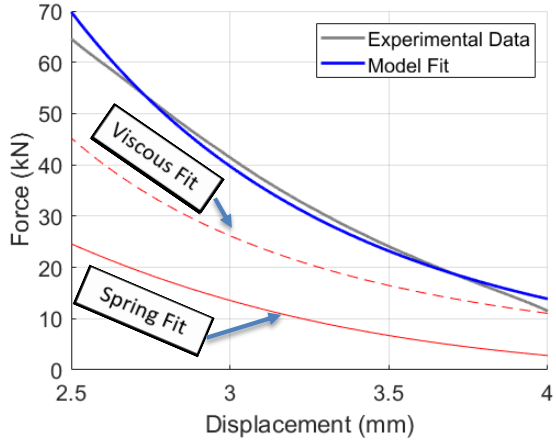

Parameters:

C_{66}: 2850

k_1: 3.38

k_3: 1.66

UNIVERSITY OF DELAWARE CENTER FOR COMPOSITE MATERIALS AFRL

DISTRIBUTION STATEMENT A. Approved for public release: distribution unlimited. AFRL-2025-3653.

Other Method for Defining the Spring Response

Consolidation

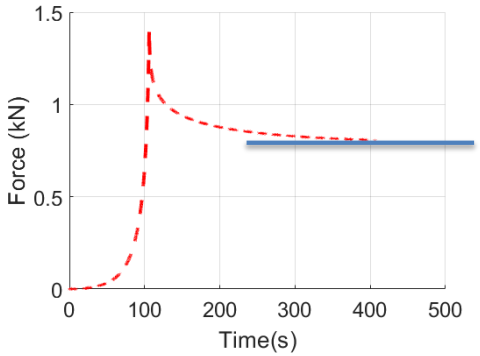

Residual Force

Final Displacement

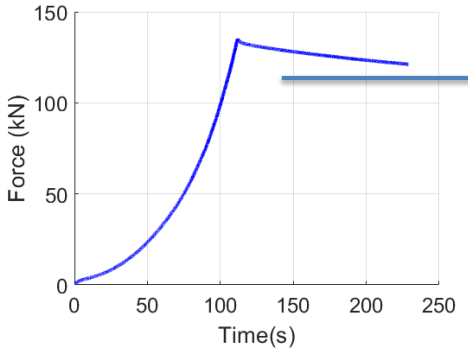

Residual Force

- Residual force is taken from consolidation and final displacement
- Polynomial spring is created and then C_{66} is found

Spring Equation

$$k_1(h_o - h) + k_3(h_o - h)^3$$

UNIVERSITY OF DELAWARE CENTER FOR COMPOSITE MATERIALS AFRL

DISTRIBUTION STATEMENT A. Approved for public release: distribution unlimited. AFRL-2025-3653.



Center for Composite Materials

Forming with Partially Cured TuFF/Thermoset Prepregs

Matt Abraham, Thomas Cender (PhD), Pavel Simacek (PhD), Prof. S.G. Advani

ICCM24 Slides| 05/28/2025



DISTRIBUTION STATEMENT A. Approved for public release: distribution unlimited. AFRL-2025-3651

UNIVERSITY OF DELAWARE

TuFF: Tailored Universal Feedstock for Forming

- **Chopped fibers** are highly **aligned** by water flow onto thin film
- Films of aligned fiber are prepregged with resin
- Prepreg can be used in **thermoforming process**
  - **Allows for stretch** during forming
  - Final properties comparable to continuous unidirectional prepreg











UNIVERSITY OF DELAWARE CENTER FOR COMPOSITE MATERIALS AFRL

DISTRIBUTION STATEMENT A. Approved for public release: distribution unlimited. AFRL-2025-3651

Outline

Process Development

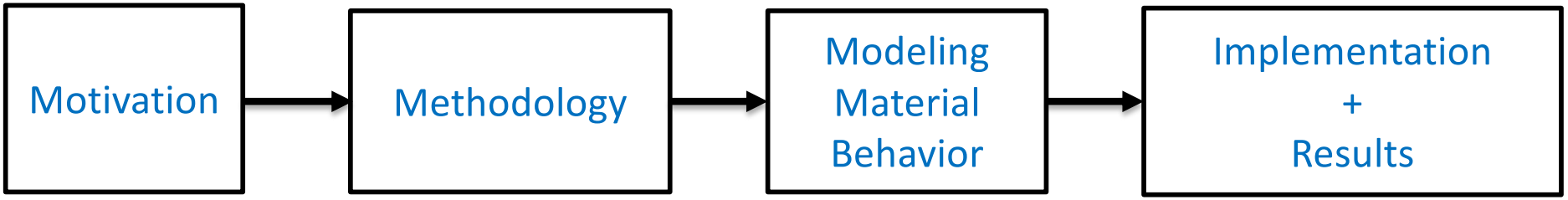

UNIVERSITY OF DELAWARE CENTER FOR COMPOSITE MATERIALS AFRL

DISTRIBUTION STATEMENT A. Approved for public release: distribution unlimited. AFRL-2025-3651

Outline

Process Development

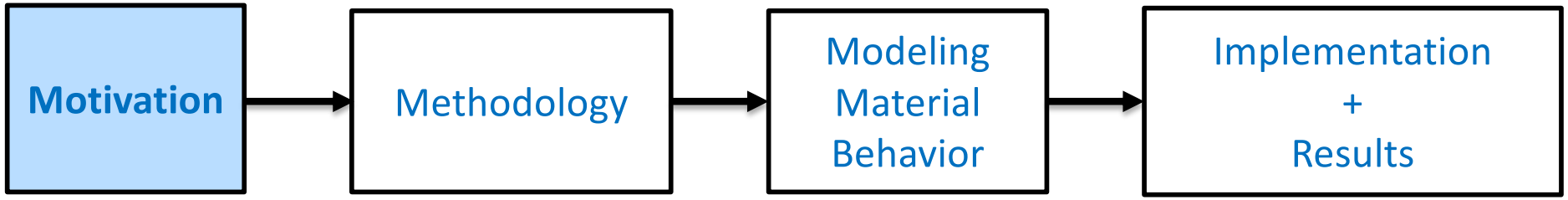

UNIVERSITY OF DELAWARE CENTER FOR COMPOSITE MATERIALS AFRL

DISTRIBUTION STATEMENT A. Approved for public release: distribution unlimited. AFRL-2025-3651

Problem Motivation

- Is it possible to implement progressive forming with TuFF/**thermoset** prepreg?

- Challenges
  - Thermoset low viscosity at temperature leads to resin bleed
  - Requires curing to hold structure between forming steps
  - Limited working time

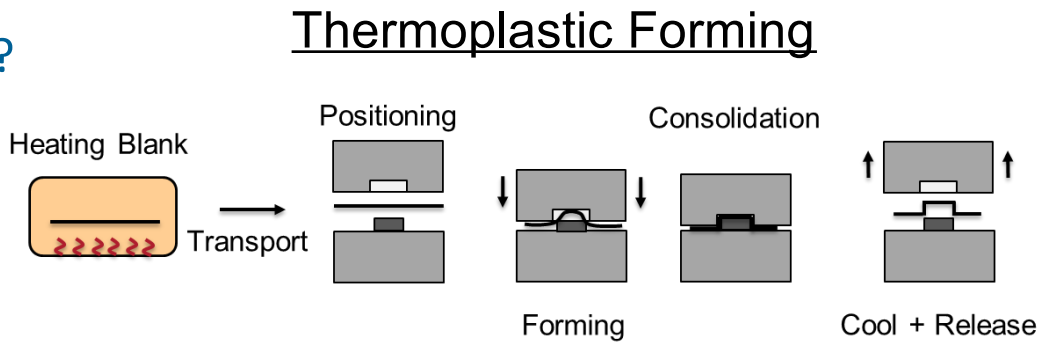





UNIVERSITY OF DELAWARE CENTER FOR COMPOSITE MATERIALS AFRL
DISTRIBUTION STATEMENT A. Approved for public release: distribution unlimited. AFRL-2025-3651

Outline

Process Development

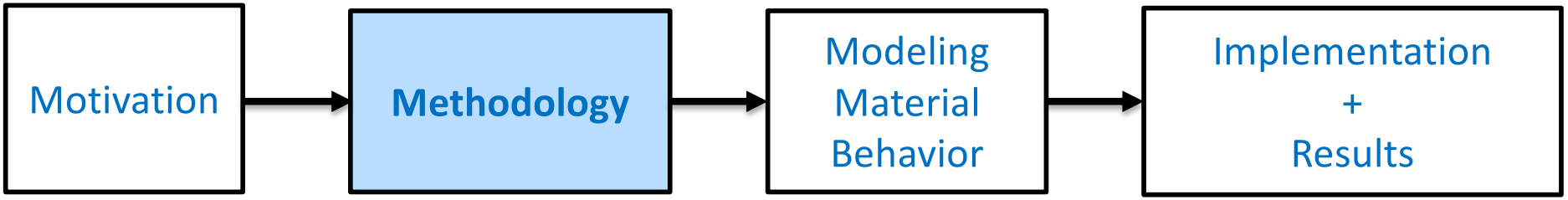

UNIVERSITY OF DELAWARE CENTER FOR COMPOSITE MATERIALS AFRL

DISTRIBUTION STATEMENT A. Approved for public release: distribution unlimited. AFRL-2025-3651

Partial Curing of TuFF/977-3

PROCESS METHODOLOGY

UNIVERSITY OF DELAWARE CENTER FOR COMPOSITE MATERIALS AFRL

DISTRIBUTION STATEMENT A. Approved for public release: distribution unlimited.

Traditional Forming with Thermosets

- Why Thermosets?
  - Durable
  - Heat resistant

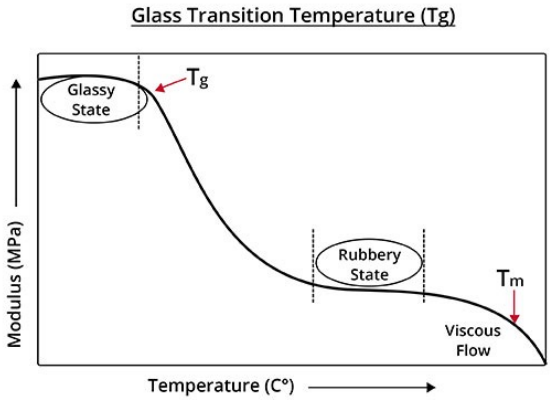

Forming + Part Ejection above T_g

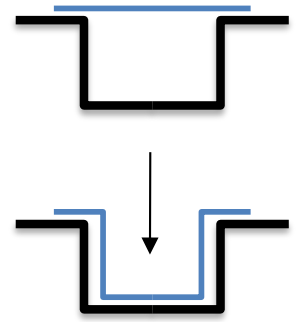

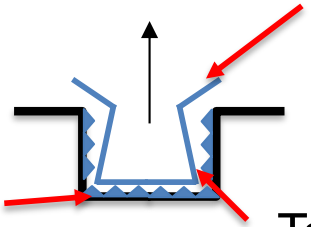

Loss of Shape

Resin Bleed Out

Tacky Surface

UNIVERSITY OF DELAWARE CENTER FOR COMPOSITE MATERIALS AFRL

DISTRIBUTION STATEMENT A. Approved for public release: distribution unlimited. AFRL-2025-3651

Proposed Solution

Stage Resin



Pre-form blank

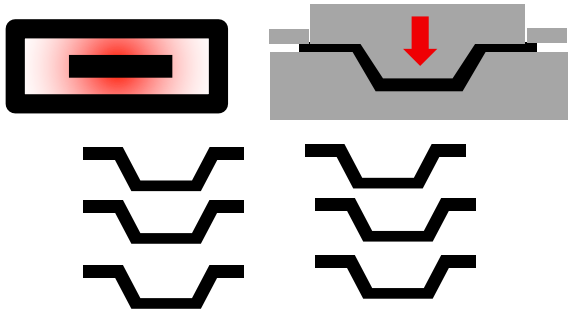

Final Form + Cure



Benefits:

1. Reduces TuFF/977-3 porosity issues:
   a. Vent volatiles with oven-vacuum (no pressure and no bleed)
   b. Reduces resin bleed during cure (higher visc. and shorter time to gel)
2. Reduces risk:
   a. Inspect after preforming (visual)
   b. Splitting the forming process: deep draw vs detailed feature
3. Reduces cycle time:
   a. Stamping press at constant temp.
   b. Parallel processes

UNIVERSITY OF DELAWARE CENTER FOR COMPOSITE MATERIALS AFRL

DISTRIBUTION STATEMENT A. Approved for public release: distribution unlimited. AFRL-2025-3651

Proposed Solution

Stage Resin



⇨ Partially Cure w/ Oven

Pre-form blank

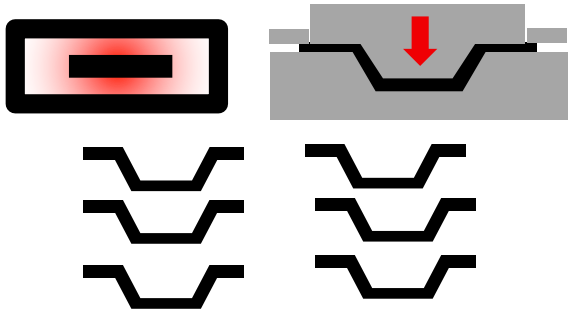

Final Form + Cure



UNIVERSITY OF DELAWARE CENTER FOR COMPOSITE MATERIALS AFRL

DISTRIBUTION STATEMENT A. Approved for public release: distribution unlimited. AFRL-2025-3651

Proposed Solution

Stage Resin



Pre-form blank

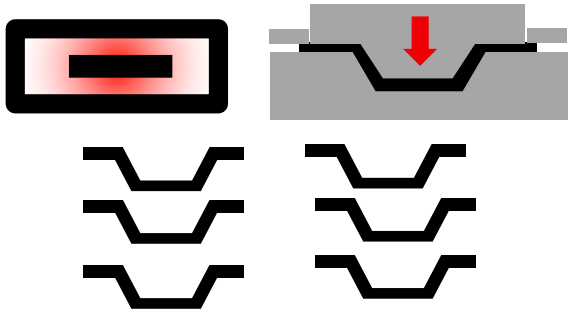

⇨ Deep Draw (Coarse Features)

Final Form + Cure



UNIVERSITY OF DELAWARE CENTER FOR COMPOSITE MATERIALS AFRL

DISTRIBUTION STATEMENT A. Approved for public release: distribution unlimited. AFRL-2025-3651

Proposed Solution

Stage Resin



Pre-form blank

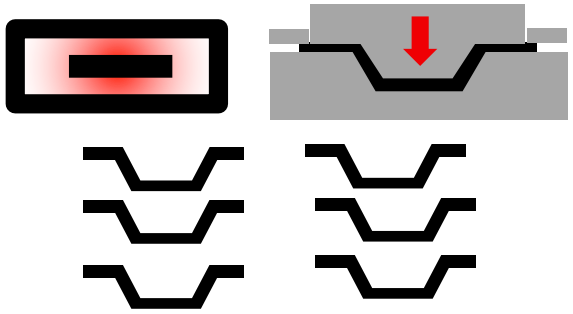

⇨ Deep Draw (Coarse Features)
(At Temperature)

Final Form + Cure



UNIVERSITY OF DELAWARE CENTER FOR COMPOSITE MATERIALS AFRL

DISTRIBUTION STATEMENT A. Approved for public release: distribution unlimited. AFRL-2025-3651

Proposed Solution

Stage Resin



Pre-form blank

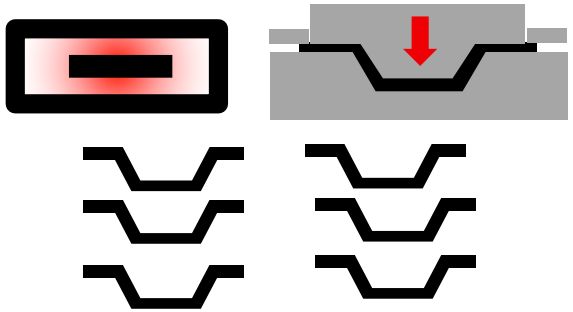

⇨ Deep Draw (Coarse Features)

⇨ Visual Inspection of Parts

Final Form + Cure



UNIVERSITY OF DELAWARE CENTER FOR COMPOSITE MATERIALS AFRL

DISTRIBUTION STATEMENT A. Approved for public release: distribution unlimited. AFRL-2025-3651

Proposed Solution

Stage Resin



Pre-form blank

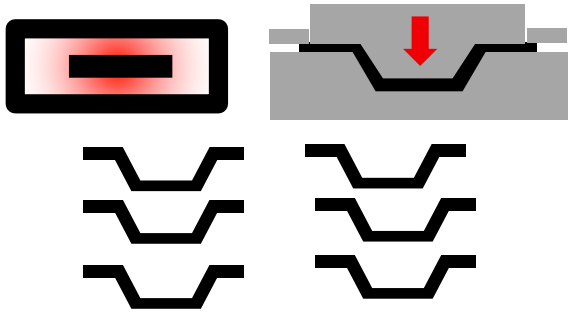

Final Form + Cure



⇨ Final Forming + Curing in Batch Process

UNIVERSITY OF DELAWARE CENTER FOR COMPOSITE MATERIALS AFRL

DISTRIBUTION STATEMENT A. Approved for public release: distribution unlimited. AFRL-2025-3651

Proposed Solution

Part Production Quality

Benefits:

1. **Reduces TuFF/977-3 porosity issues:**
   a. Vent volatiles with oven-vacuum (no pressure and no bleed)
   b. Reduces resin bleed during cure (higher visc. and shorter time to gel)
2. **Reduces risk:**
   a. Inspect after preforming (visual)
   b. Splitting the forming process: deep draw vs detailed feature
3. Reduces cycle time:
   a. Stamping press at constant temp.
   b. Parallel processes

UNIVERSITY OF DELAWARE CENTER FOR COMPOSITE MATERIALS AFRL
DISTRIBUTION STATEMENT A. Approved for public release: distribution unlimited. AFRL-2025-3651

Proposed Solution

Benefits:

1. Reduces TuFF/977-3 porosity issues:
   a. Vent volatiles with oven-vacuum (no pressure and no bleed)
   b. Reduces resin bleed during cure (higher visc. and shorter time to gel)
2. Reduces risk:
   a. Inspect after preforming (visual)
   b. Splitting the forming process: deep draw vs detailed feature

Part Production Speed

3. Reduces cycle time:
   a. Stamping press at constant temp.
   b. Parallel processes

UNIVERSITY OF DELAWARE CENTER FOR COMPOSITE MATERIALS AFRL
DISTRIBUTION STATEMENT A. Approved for public release: distribution unlimited. AFRL-2025-3651

Outline

Process Development

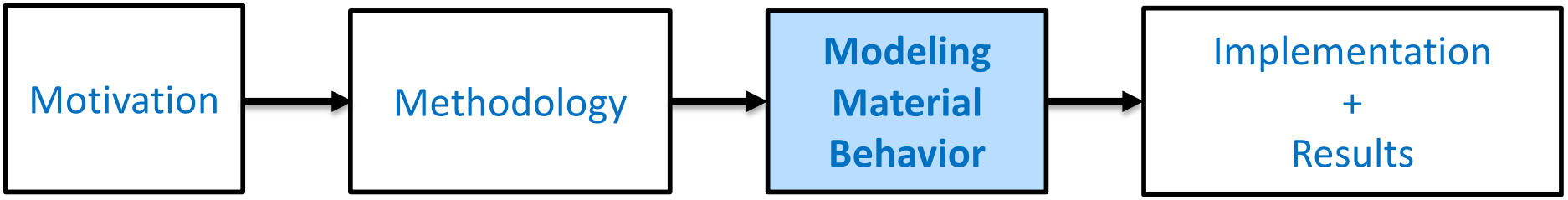

UNIVERSITY OF DELAWARE CENTER FOR COMPOSITE MATERIALS AFRL
DISTRIBUTION STATEMENT A. Approved for public release: distribution unlimited. AFRL-2025-3651

Rheo-Cure Behavior

PROCESS MODELING

DISTRIBUTION STATEMENT A. Approved for public release: distribution unlimited.

Modeling Resin Behavior

Degree Of Cure
(α)

≤ 5% Error

Glass Transition
Temperature
(T_g)

Viscosity Model

$\eta^P(\alpha, T, \dot{\gamma})$ → Tune η^P using α

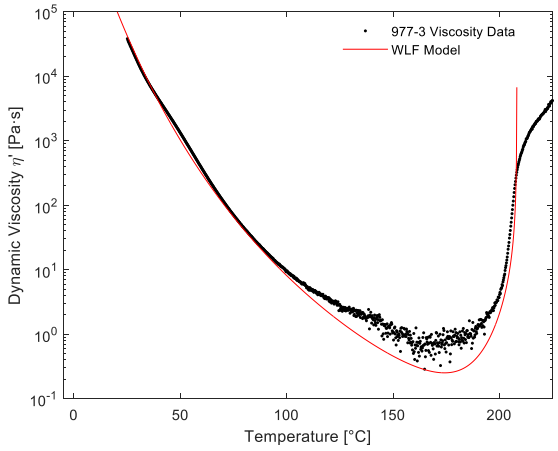

UNIVERSITY OF DELAWARE CENTER FOR COMPOSITE MATERIALS AFRL

DISTRIBUTION STATEMENT A. Approved for public release: distribution unlimited. AFRL-2025-3651

Modeling Resin Behavior

Degree Of Cure
(α)

≤ 5% Error

Glass Transition
Temperature
(T_g)

Polymer Viscosity

$\eta^P(\alpha, T, \dot{\gamma})$

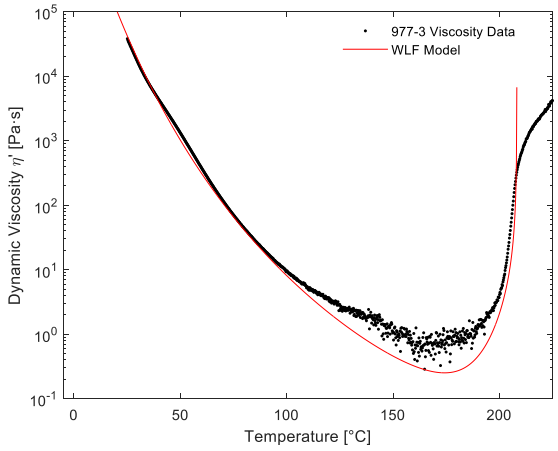

Tune η^P using α

$$\begin{bmatrix}\sigma_{11}\\ \sigma_{22}\\ \sigma_{12}\end{bmatrix} = \eta_P \cdot \begin{bmatrix}D_{11}C_{11} & C_{12} & 0\\ C_{12} & C_{22} & 0\\ 0 & 0 & C_{66}\end{bmatrix} \cdot \begin{bmatrix}\dot{\varepsilon}_{11}\\ \dot{\varepsilon}_{22}\\ \dot{\gamma}_{12}\end{bmatrix}$$

Stresses = Polymer viscosity · Directional magnification from fibers · Strain rates

TuFF Constitutive Eq.

UNIVERSITY OF DELAWARE CENTER FOR COMPOSITE MATERIALS AFRL

DISTRIBUTION STATEMENT A. Approved for public release: distribution unlimited. AFRL-2025-3651

Modeling Degree of Cure

- Experimental Runs on DSC
  - Isothermal hold 140-200C (30hr)
  - 4 Trials at each temperature
- Simple Model Fit
  - High accuracy desired for $\alpha \leq 0.4$
  - Optimization script used for fitting

$$\frac{d\alpha}{dt} = K_1(1-\alpha)^{n_1} + K_2\alpha^m(1-\alpha)^{n_2}$$

$$k = A \cdot e^{-\frac{Ea}{RT}}$$

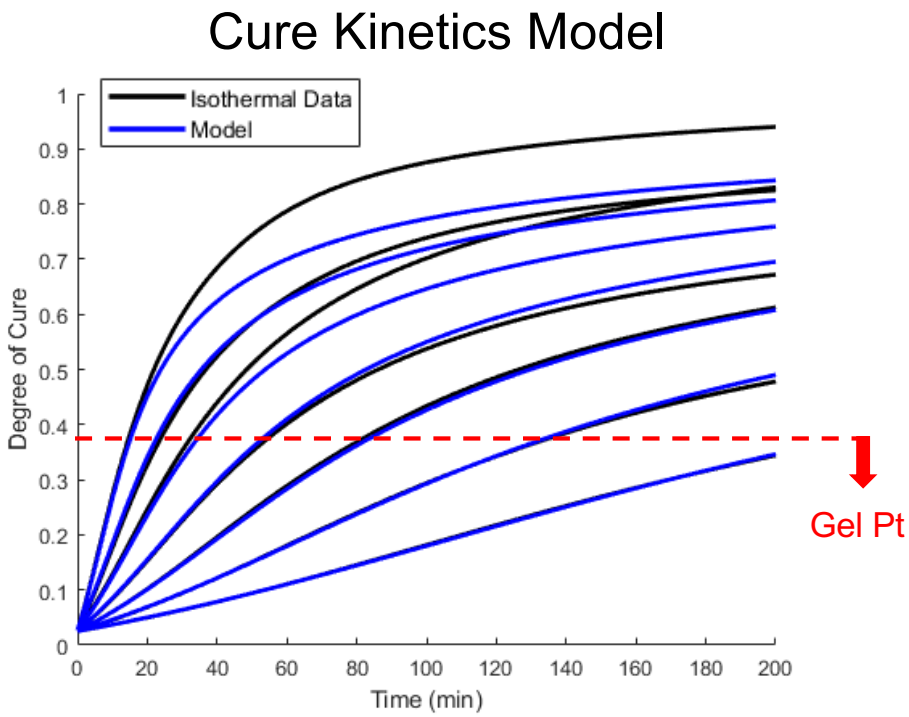

UNIVERSITY OF DELAWARE CENTER FOR COMPOSITE MATERIALS AFRL
DISTRIBUTION STATEMENT A. Approved for public release: distribution unlimited. AFRL-2025-3651

Glass Transition/Cure Relationship

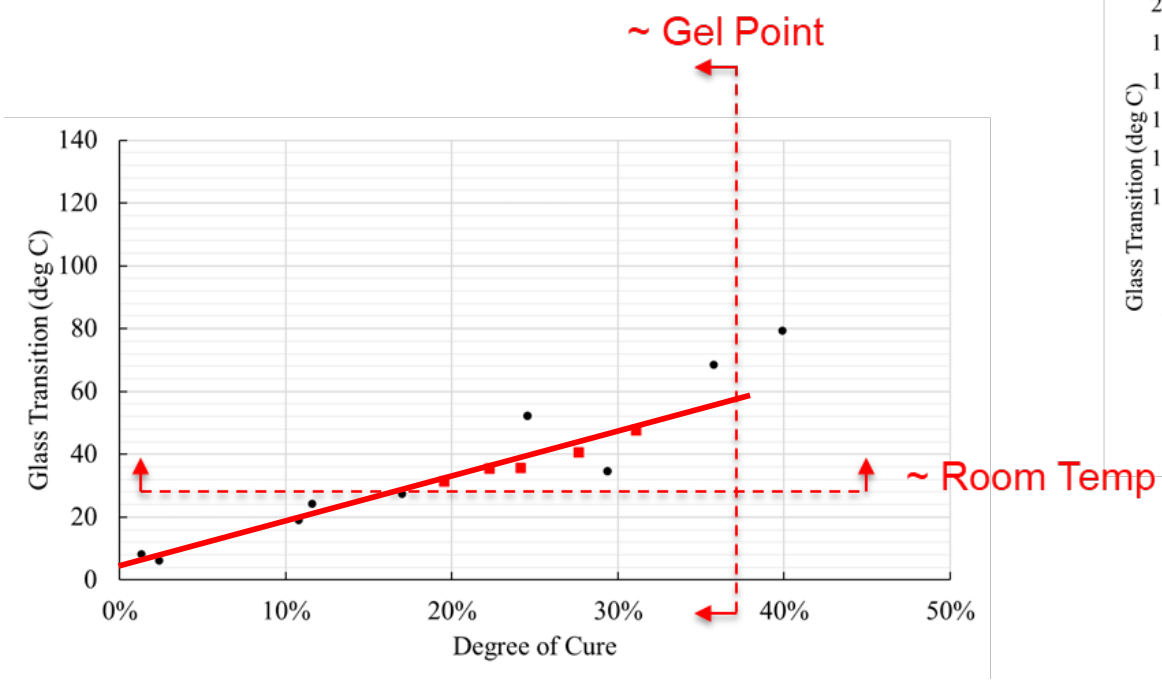

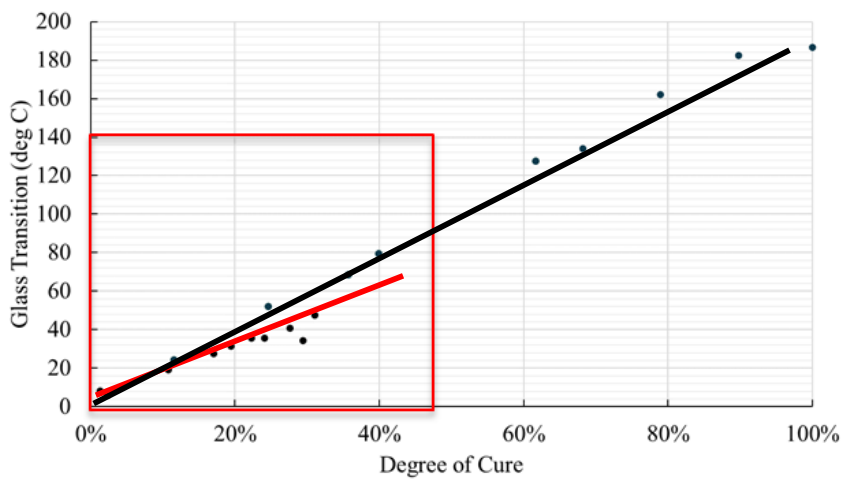

UNIVERSITY OF DELAWARE CENTER FOR COMPOSITE MATERIALS AFRL

DISTRIBUTION STATEMENT A. Approved for public release: distribution unlimited. AFRL-2025-3651

Process Model

Start with:

Tg > 25°C

$\alpha < \alpha_{gel}$

15% < α < 38%

Choose α = 20%

Define viscosity targets

Obtain temperature/strain rate

Extension Test Forming Window

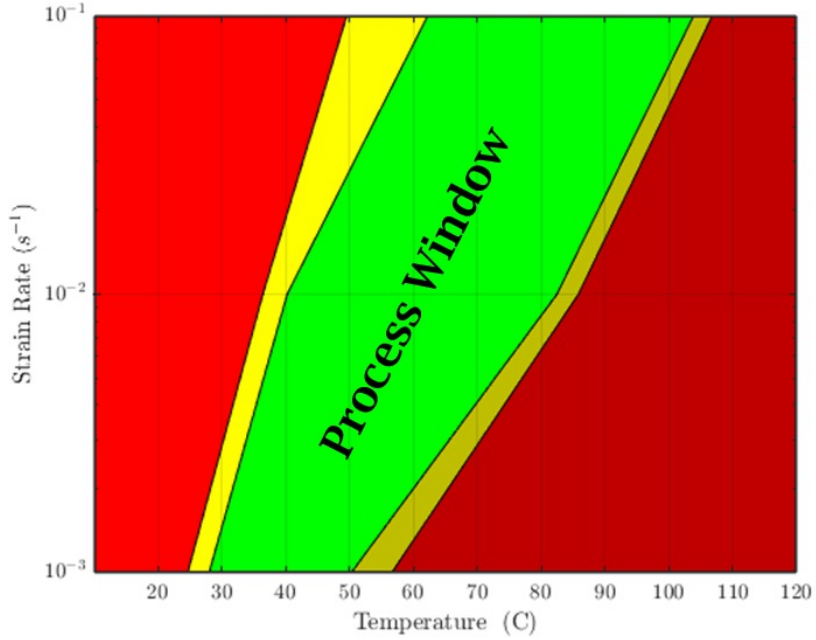

UNIVERSITY OF DELAWARE CENTER FOR COMPOSITE MATERIALS AFRL

DISTRIBUTION STATEMENT A. Approved for public release: distribution unlimited. AFRL-2025-3651

Outline

Process Development

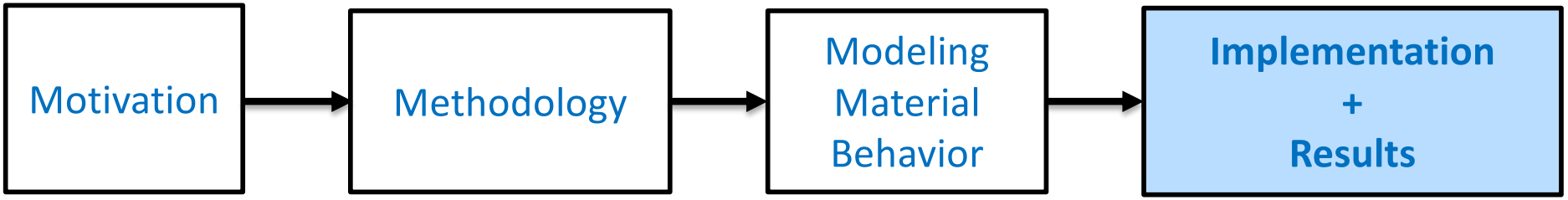

UNIVERSITY OF DELAWARE CENTER FOR COMPOSITE MATERIALS AFRL
DISTRIBUTION STATEMENT A. Approved for public release: distribution unlimited. AFRL-2025-3651

Material Characterization w/ Partial Cure Process

MECHANICAL TESTING RESULTS

DISTRIBUTION STATEMENT A. Approved for public release: distribution unlimited.

Comparing Processes

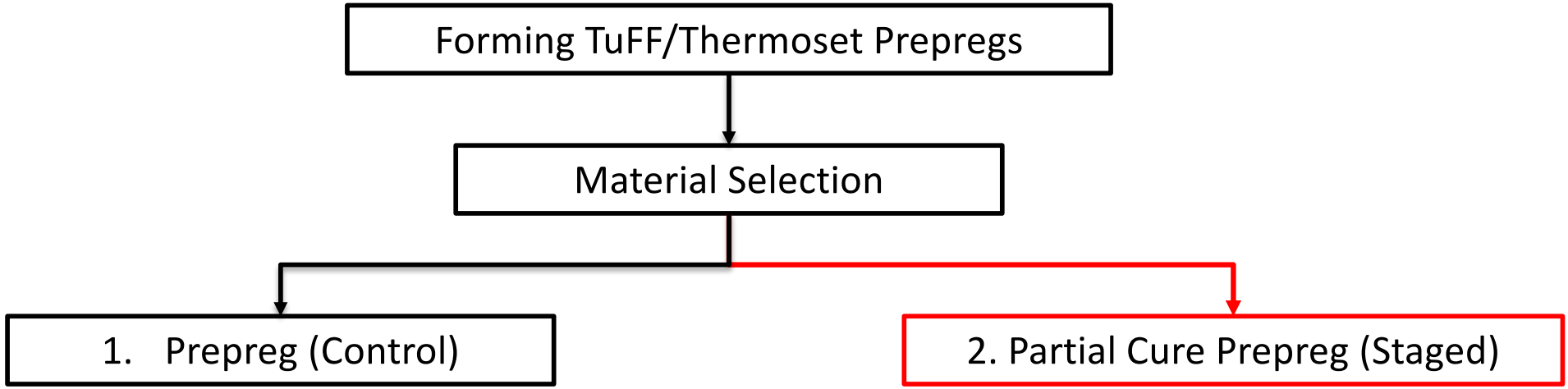

Main Questions:

- *Can we accurately model the partial curing process?*
- *Does processing method affect material quality?*

UNIVERSITY OF DELAWARE CENTER FOR COMPOSITE MATERIALS AFRL
DISTRIBUTION STATEMENT A. Approved for public release: distribution unlimited. AFRL-2025-3651

Fabricating Panels

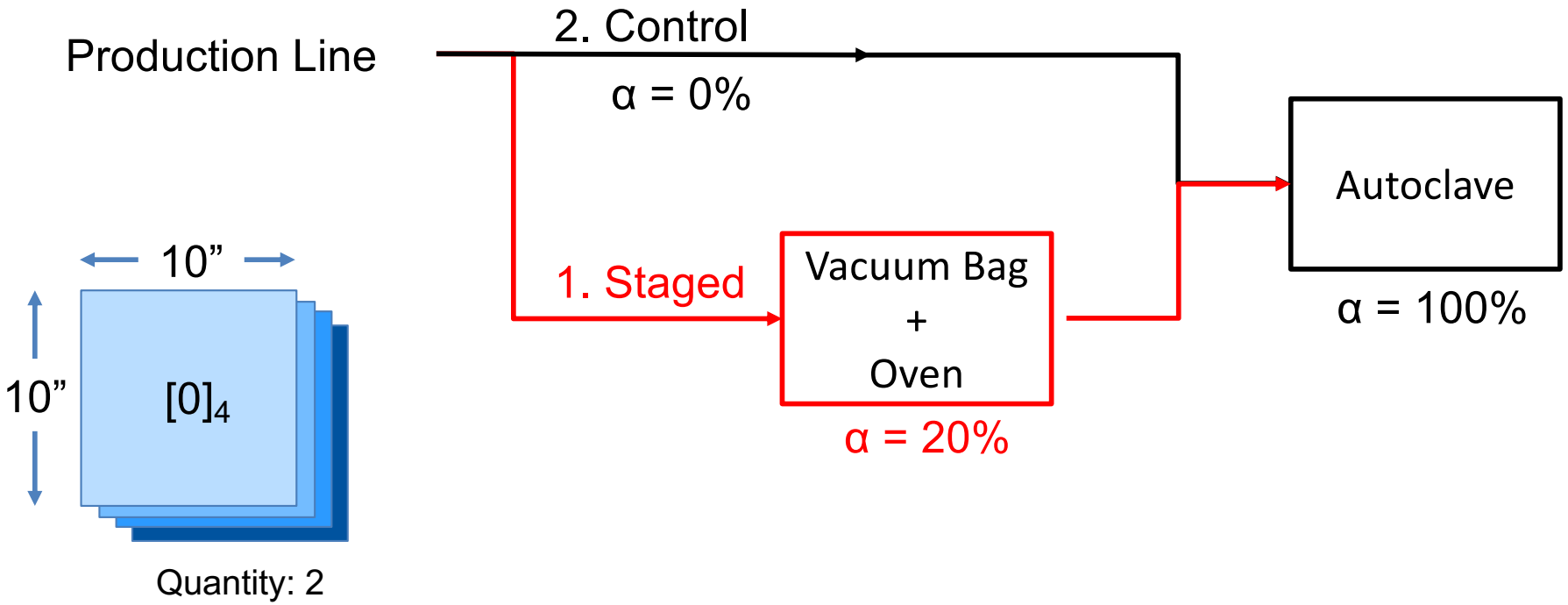

UNIVERSITY OF DELAWARE CENTER FOR COMPOSITE MATERIALS AFRL
DISTRIBUTION STATEMENT A. Approved for public release: distribution unlimited. AFRL-2025-3651

Fabricating Panels

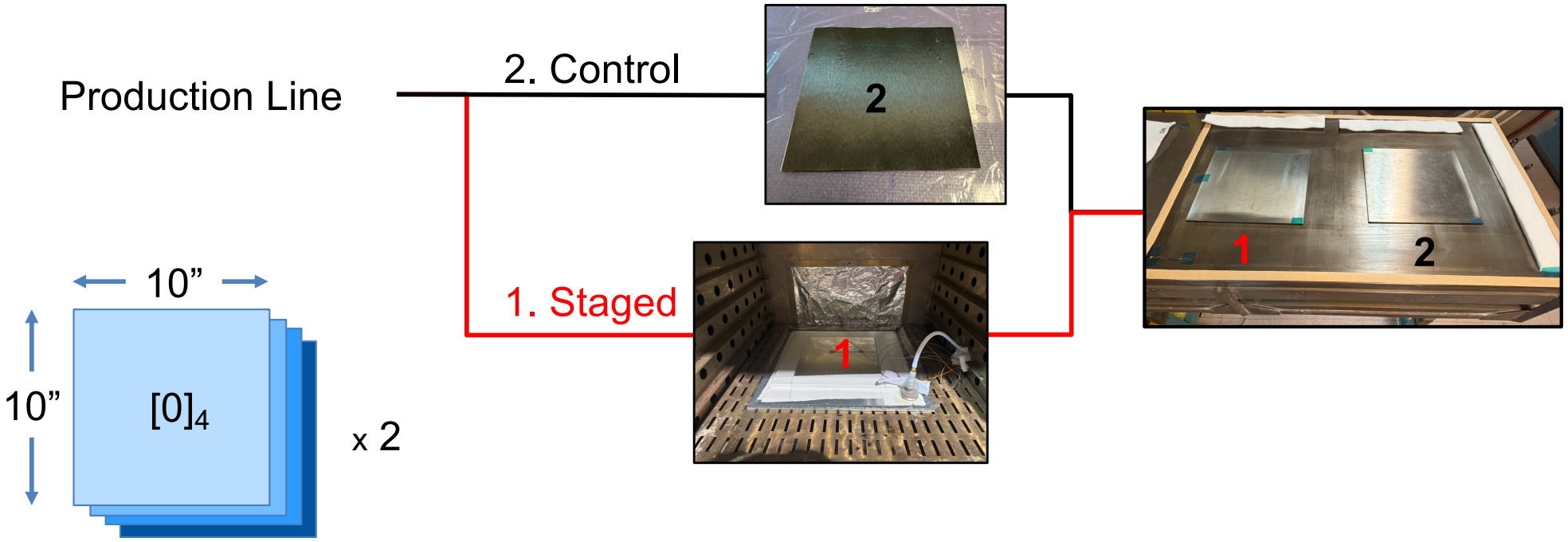

UNIVERSITY OF DELAWARE CENTER FOR COMPOSITE MATERIALS AFRL
DISTRIBUTION STATEMENT A. Approved for public release: distribution unlimited. AFRL-2025-3651

Resin Bleed Out

1. Staged
$\alpha_0 = 20\%$
$T_g = 35℃$

2. Control
$\alpha_0 = 0\%$
$T_g = -3℃$

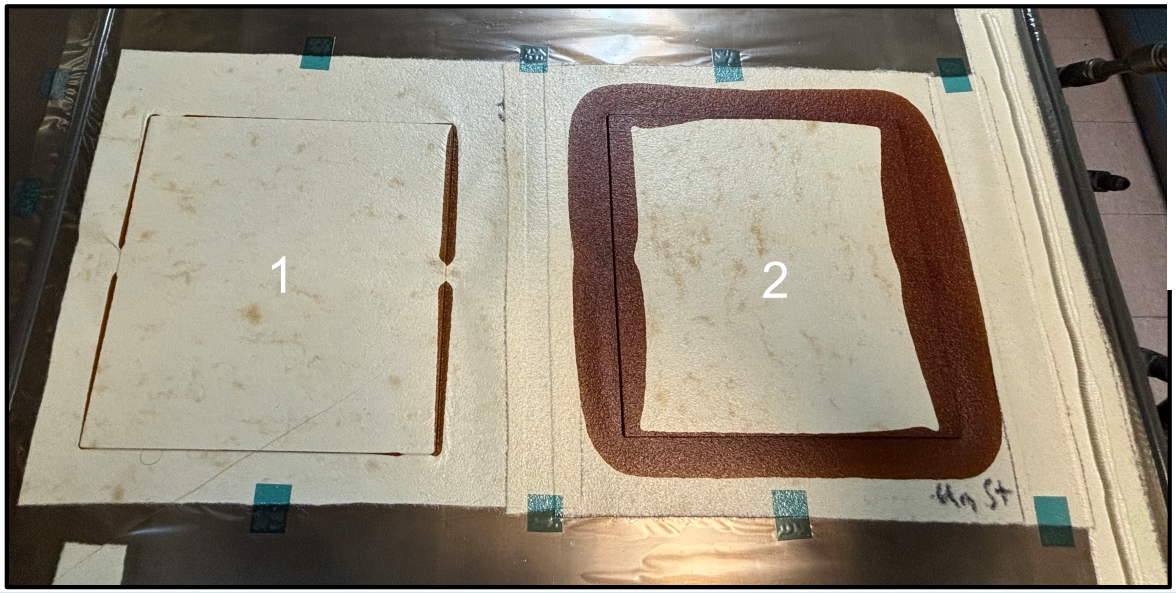

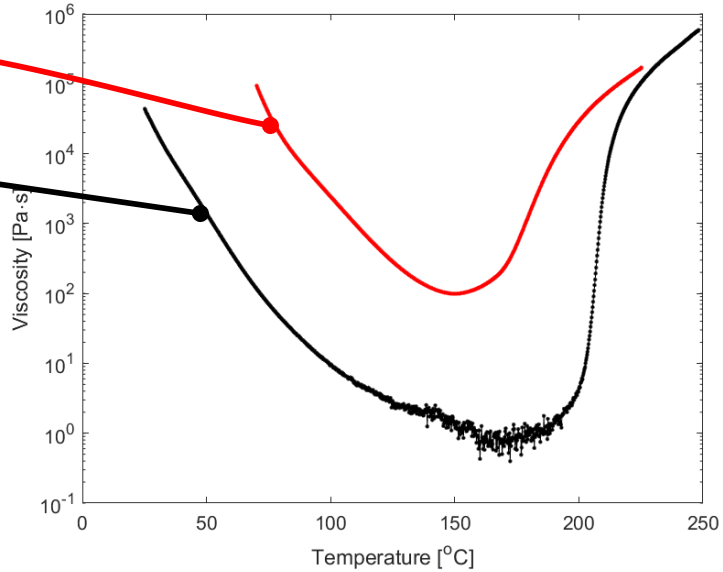

	Mass Difference (g)	
	Staged	Control
Panel	- 1.0	- 6.0
Breather	+ 1.1	+ 6.4
% Mass Loss	-1.5%	-8.8%

UNIVERSITY OF DELAWARE CENTER FOR COMPOSITE MATERIALS AFRL
DISTRIBUTION STATEMENT A. Approved for public release: distribution unlimited. AFRL-2025-3651

C-SCAN

Porosity from resin bleed out

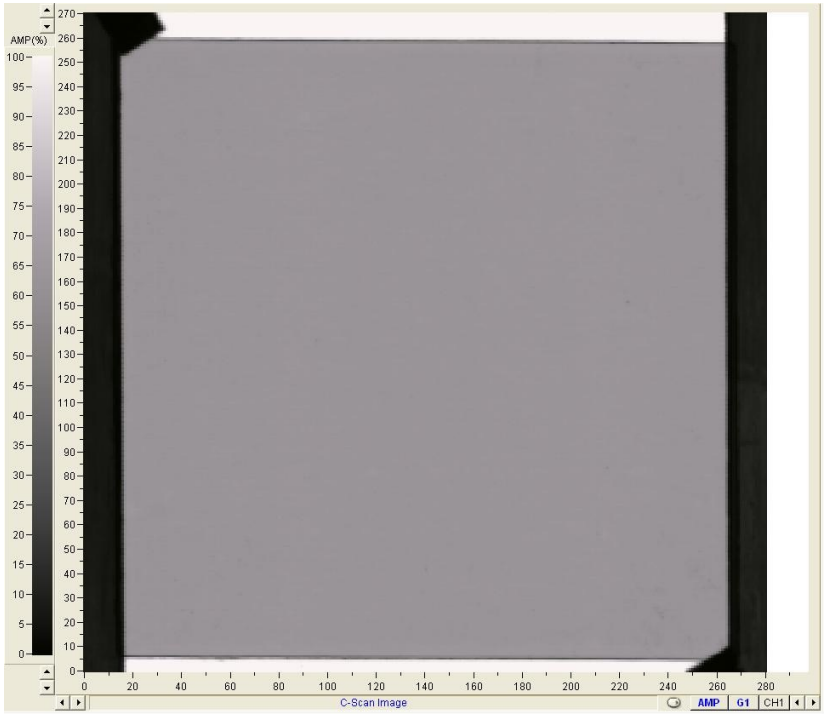

1. Staged

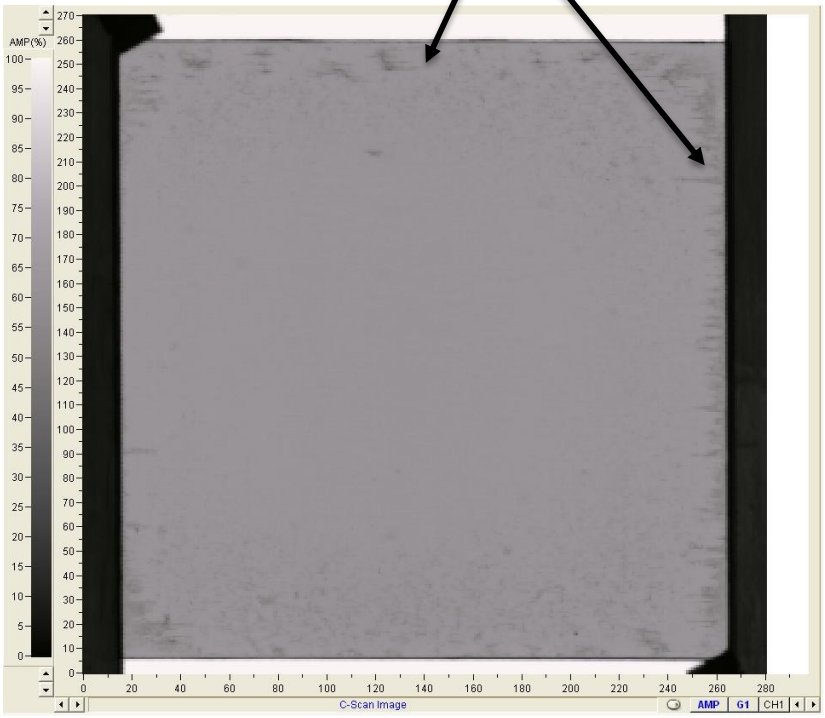

2. Control

UNIVERSITY OF DELAWARE CENTER FOR COMPOSITE MATERIALS AFRL

DISTRIBUTION STATEMENT A. Approved for public release: distribution unlimited. AFRL-2025-3651

Uniaxial Tension Test Results

- ASTM D3039 standard used
- $[0]_4$ Layup
- 7 samples from each panel (14 total samples tested)

	Failure Strength (ksi)	Failure Strain (%)	Modulus (Msi)
Control Panel	260 ± 34.6	1.13 ± 0.21	21.5 ± 0.23
Staged Panel	287 ± 15.1	1.38 ± 0.07	19.8 ± 0.14
Previous Work	290 ± 16.8	1.31 ± 0.07	21.3 ± 0.08

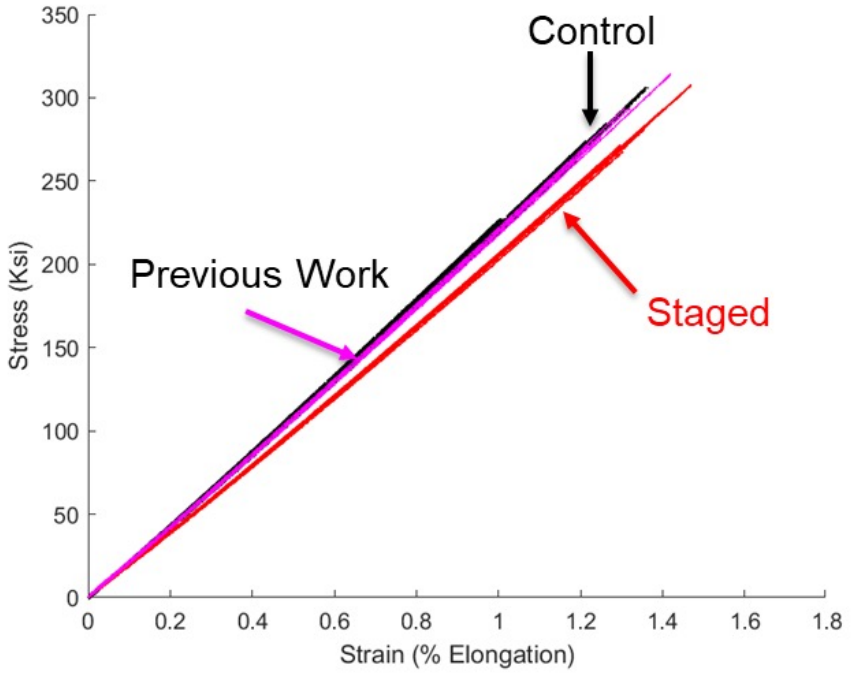

UNIVERSITY OF DELAWARE CENTER FOR COMPOSITE MATERIALS AFRL
DISTRIBUTION STATEMENT A. Approved for public release: distribution unlimited. AFRL-2025-3651

Extension Testing w/ Partial Cure Material

DEFORMATION CHARACTERISTICS

UNIVERSITY OF DELAWARE CENTER FOR COMPOSITE MATERIALS AFRL
DISTRIBUTION STATEMENT A. Approved for public release: distribution unlimited.

Model Development Framework

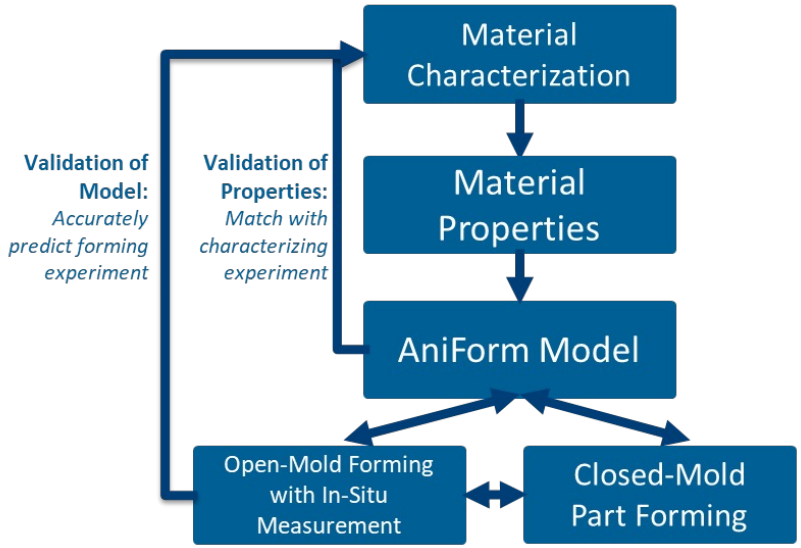

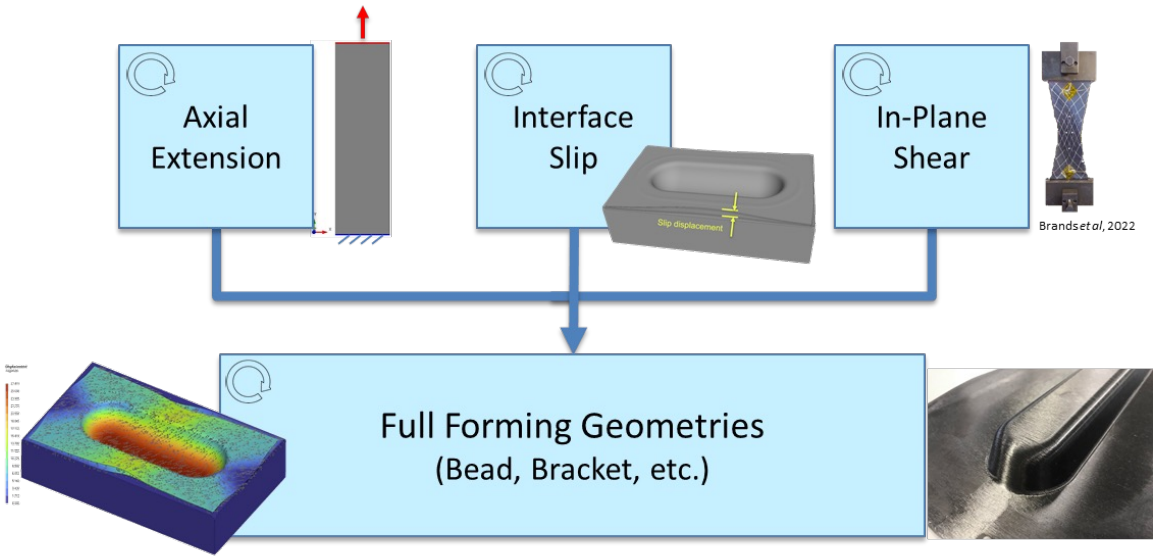

UNIVERSITY OF DELAWARE CENTER FOR COMPOSITE MATERIALS AFRL
DISTRIBUTION STATEMENT A. Approved for public release: distribution unlimited. AFRL-2025-3651

Model Development Framework

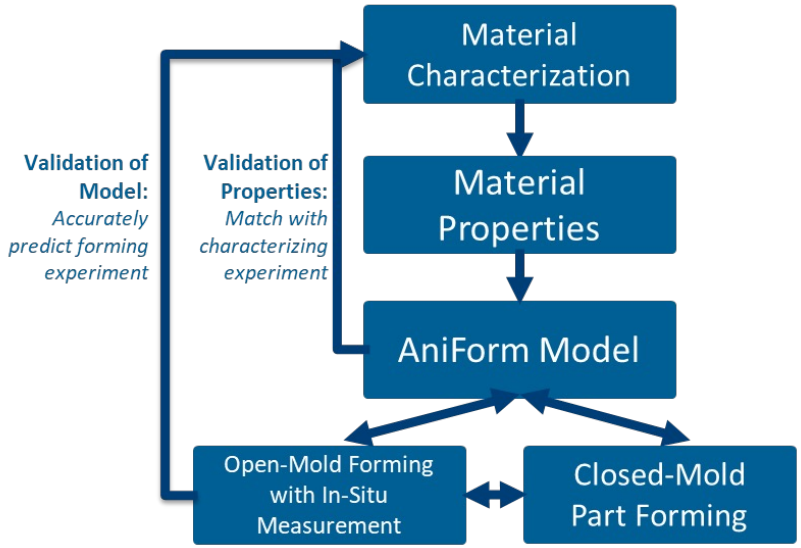

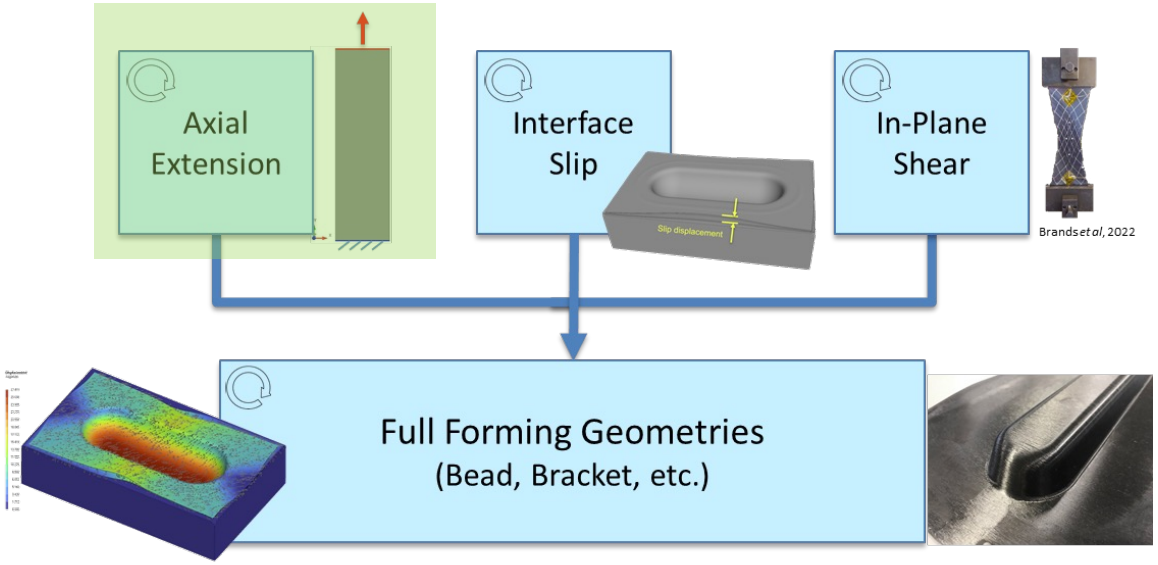

UNIVERSITY OF DELAWARE CENTER FOR COMPOSITE MATERIALS AFRL
DISTRIBUTION STATEMENT A. Approved for public release: distribution unlimited. AFRL-2025-3651

Defining a New Forming Window

✓ Micromechanical Model

Change α → Change Temperatures

✓ Composite Forming Process Window (Prepreg)

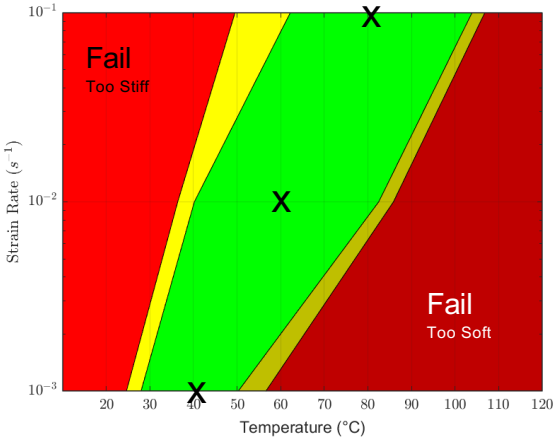

✓ Resin Viscosity Targets

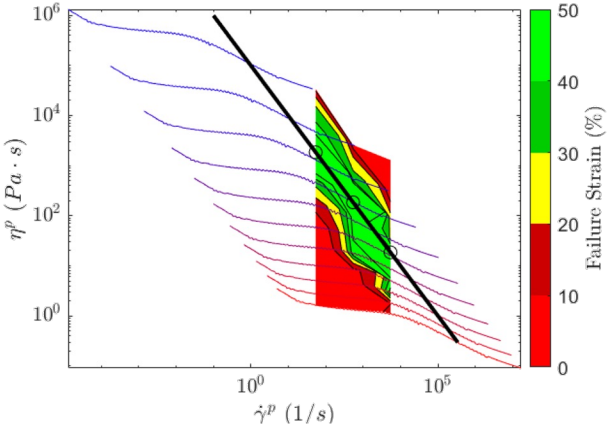

Composite Forming Process Window (Staged)

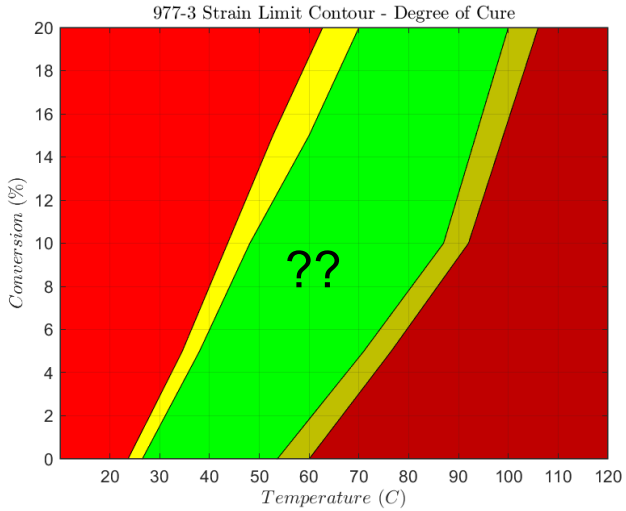

DISTRIBUTION STATEMENT A. Approved for public release: distribution unlimited. AFRL-2025-3651

Estimating Temperature/Viscosity Relationships

- Initial Estimation:
  - Polymer viscosity curves used to guess forming window for partial cure material
  - Provides a starting point for testing

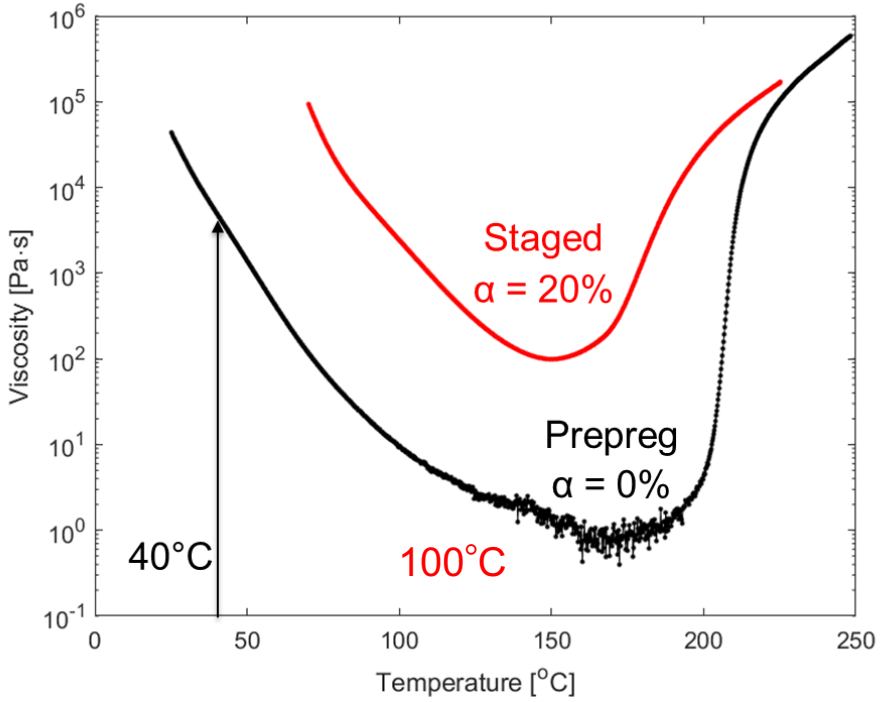

UNIVERSITY OF DELAWARE CENTER FOR COMPOSITE MATERIALS AFRL
DISTRIBUTION STATEMENT A. Approved for public release: distribution unlimited. AFRL-2025-3651

Estimating Temperature/Viscosity Relationships

- Initial Estimation:
  - Polymer viscosity curves used to guess forming window for partial cure material
  - Provides a starting point for testing

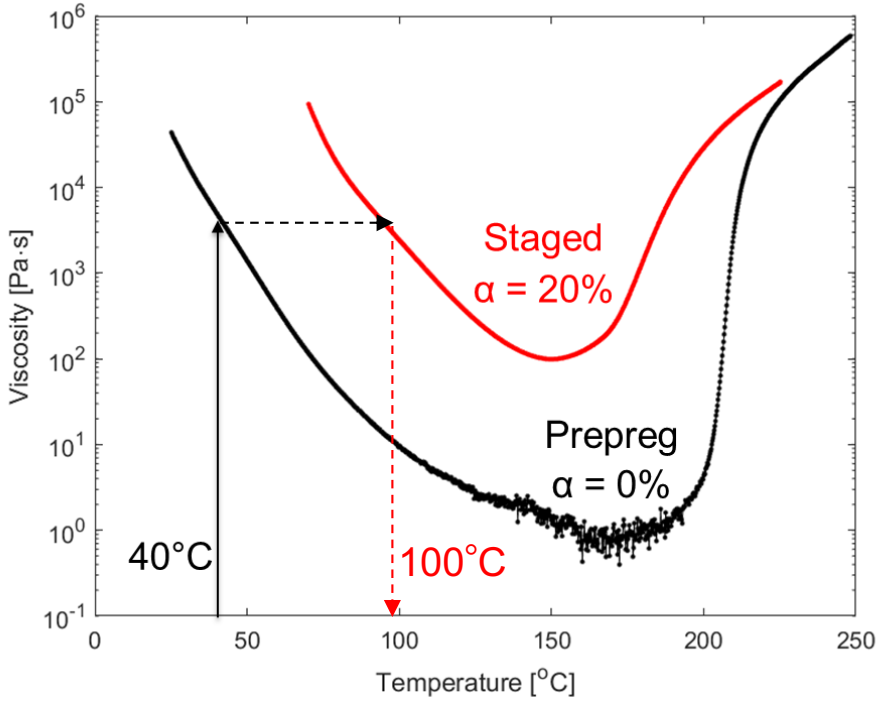

DISTRIBUTION STATEMENT A. Approved for public release: distribution unlimited. AFRL-2025-3651

Estimating Temperature/Viscosity Relationships

- Initial Estimation:
  - Polymer viscosity (n_p) used to guess forming window for partial cure material
  - Provides a starting point for testing

Measured via Instron Testing

$$\frac{\sigma}{\dot{\varepsilon}} = \underbrace{n_p \cdot c}_{\text{Apparent Viscosity } (\eta_L)}$$

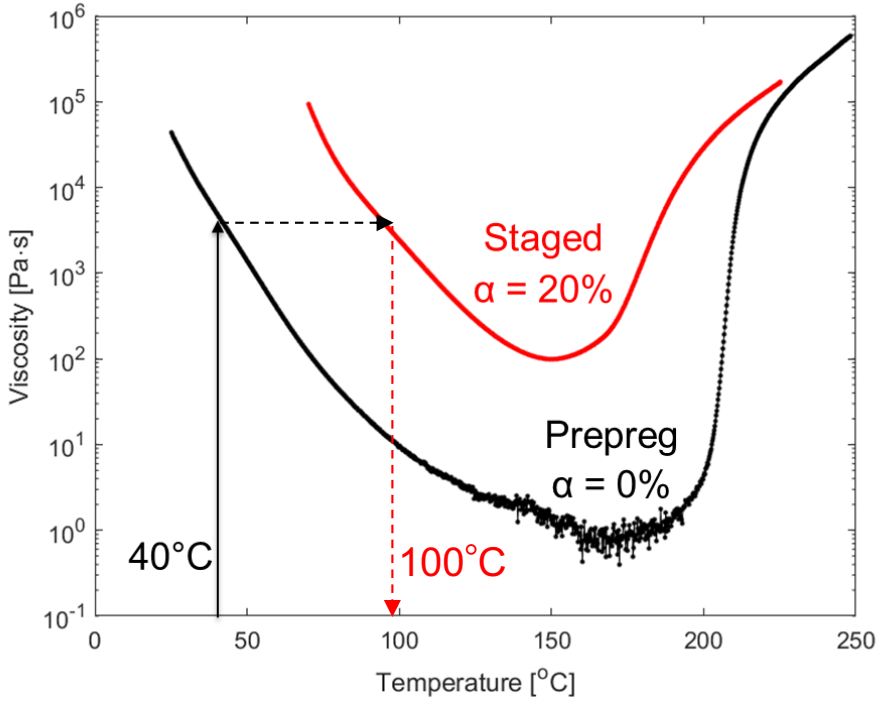

UNIVERSITY OF DELAWARE CENTER FOR COMPOSITE MATERIALS AFRL
DISTRIBUTION STATEMENT A. Approved for public release: distribution unlimited. AFRL-2025-3651

Forming Process Window Development

- Objective:
  - Identify ideal forming temperatures
- Method:
  - Extension Test (1” wide samples)
  - Digital Image Correlation (DIC) for strain limit calculation
- Procedure:
  - Stretch 25.4 × 90 mm partially cured sample
  - Fixed $\dot{\varepsilon}$ (s^{-1}) and T (°C)



Test setup: a sample is gripped and stretched inside an environment chamber

Data analysis: Digital image correlation (DIC) tracks local strains over time.

Force is measured by a load cell to calculate stress (not shown)

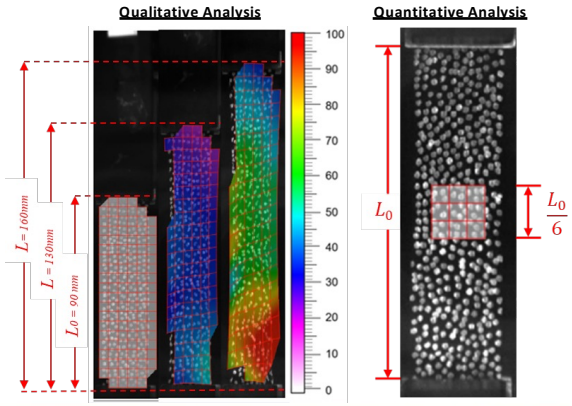

UNIVERSITY OF DELAWARE CENTER FOR COMPOSITE MATERIALS AFRL
DISTRIBUTION STATEMENT A. Approved for public release: distribution unlimited. AFRL-2025-3651

Forming Improvements of Partially Cured Blanks

- Observed Differences (Visual)
  - Staged samples exhibit:
    - Greater uniformity and necking
    - Failure typically in center 1/3
    - Almost all samples remained intact
- Potential Reasons:
  - Partial cure = Longer polymer chains
  - Increases viscous length scale → better stability

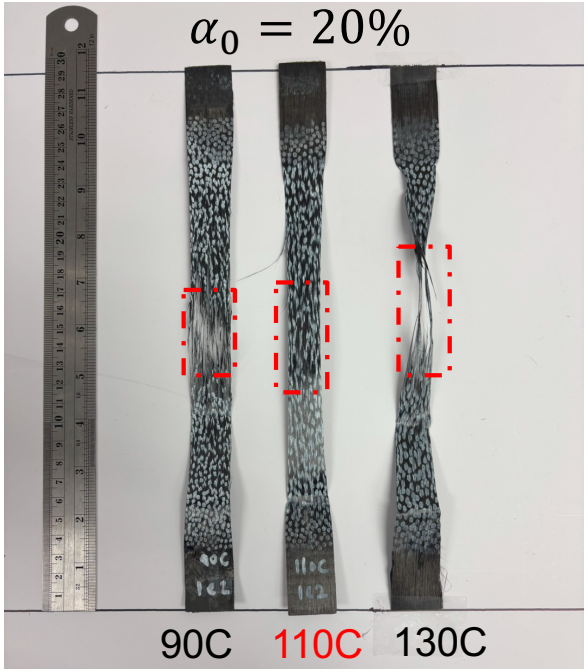

UNIVERSITY OF DELAWARE CENTER FOR COMPOSITE MATERIALS AFRL
DISTRIBUTION STATEMENT A. Approved for public release: distribution unlimited. AFRL-2025-3651

Forming Process Window (Staged)

Forming Rate of 0.01 s^{-1}

- B-staged prepreg (uncured) showed maximum formability at 60C
- Increasing the cure to 20% (staged) showed maximum formability at 110C

Anticipate forming window increase of +20°C for every x10 increase in $\dot{\varepsilon}$

Forming Window Temperatures (°C)		
Strain Rate	**α = 0%**	**α = 20%**
0.001	40	90
0.01	60	110
0.1	80	130

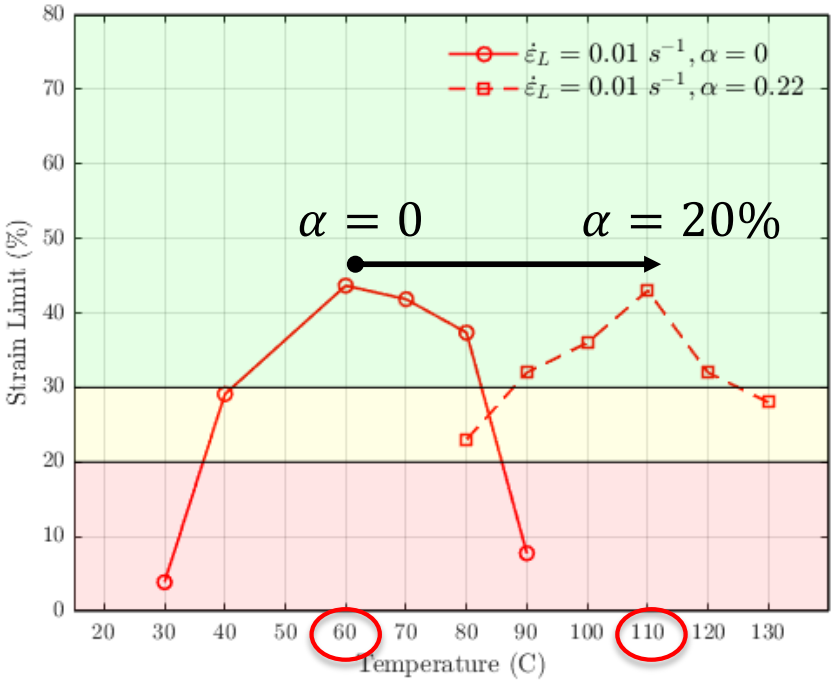

UNIVERSITY OF DELAWARE CENTER FOR COMPOSITE MATERIALS AFRL
DISTRIBUTION STATEMENT A. Approved for public release: distribution unlimited. AFRL-2025-3651

Extension Test Results (Staged)

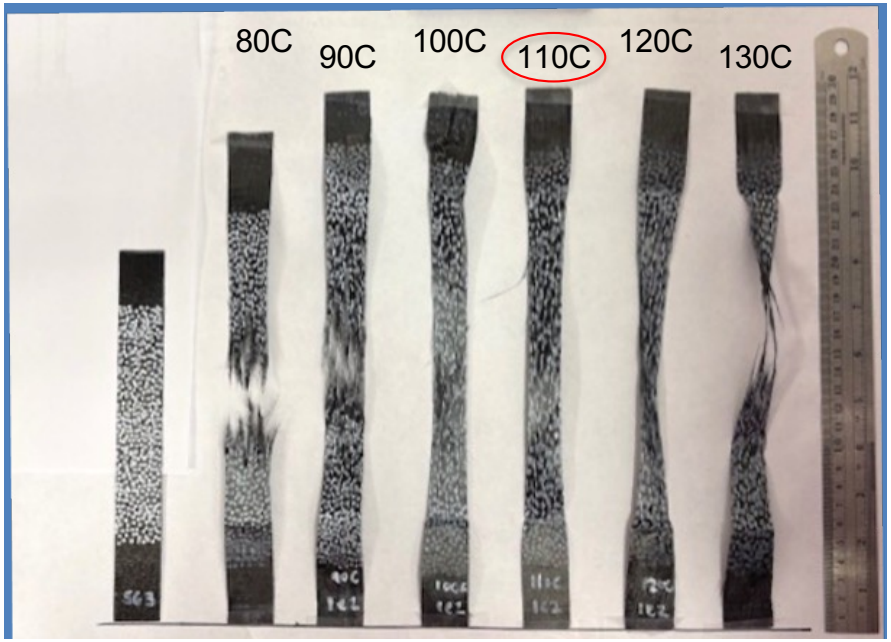

Strain Rate = 0.01 /s

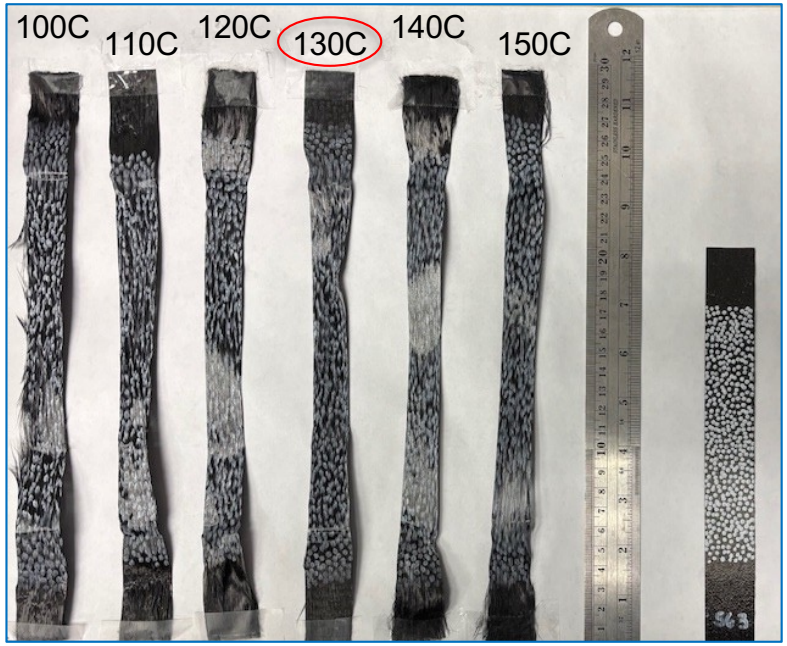

Strain Rate = 0.1 /s

UNIVERSITY OF DELAWARE CENTER FOR COMPOSITE MATERIALS AFRL

DISTRIBUTION STATEMENT A. Approved for public release: distribution unlimited. AFRL-2025-3651

Summary

- **Developed** a process for rapid manufacturing of TuFF/977-3
  - Increase cure to 20% (cure cycle/model dev.)
  - Rapid Stamp/Eject (forming process window shift)
- **Demonstrated**: Accurate cure kinetics below 40% cure
- **Demonstrated**: Reduced resin bleed out during curing of staged material
- **Demonstrated:** Tensile properties of staged blanks
- **Demonstrated**: Extension characteristics of staged blanks

UNIVERSITY OF DELAWARE CENTER FOR COMPOSITE MATERIALS AFRL
DISTRIBUTION STATEMENT A. Approved for public release: distribution unlimited. AFRL-2025-3651

Summary

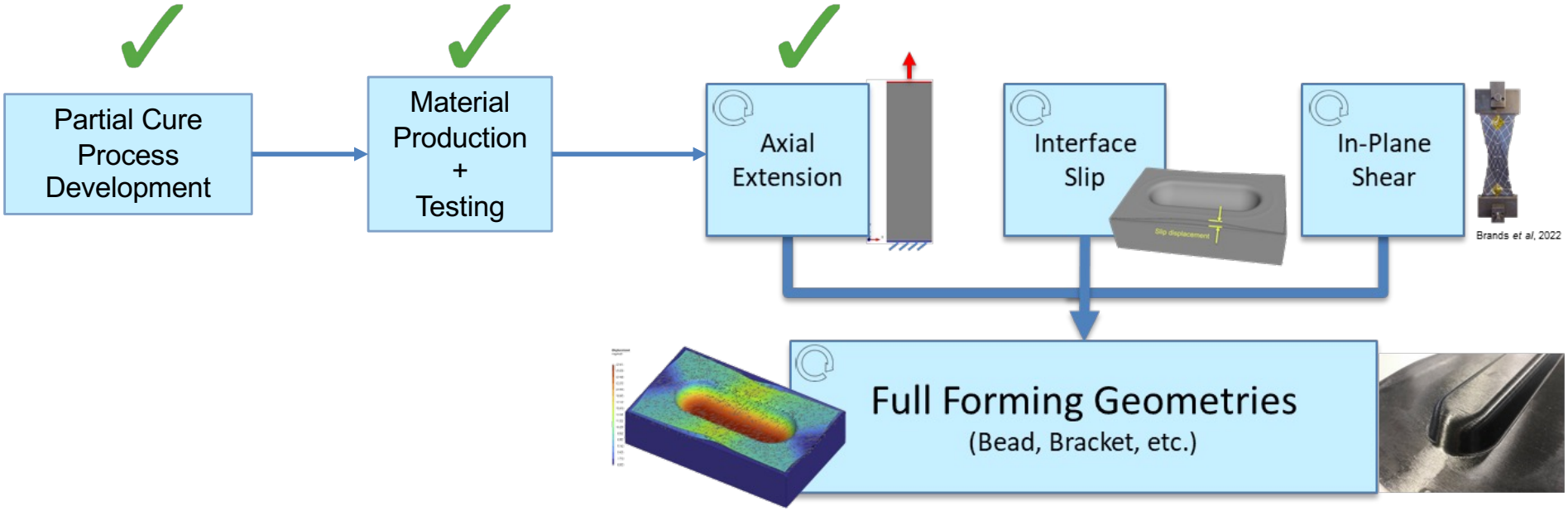

UNIVERSITY OF DELAWARE CENTER FOR COMPOSITE MATERIALS AFRL

DISTRIBUTION STATEMENT A. Approved for public release: distribution unlimited. AFRL-2025-3651

Summary

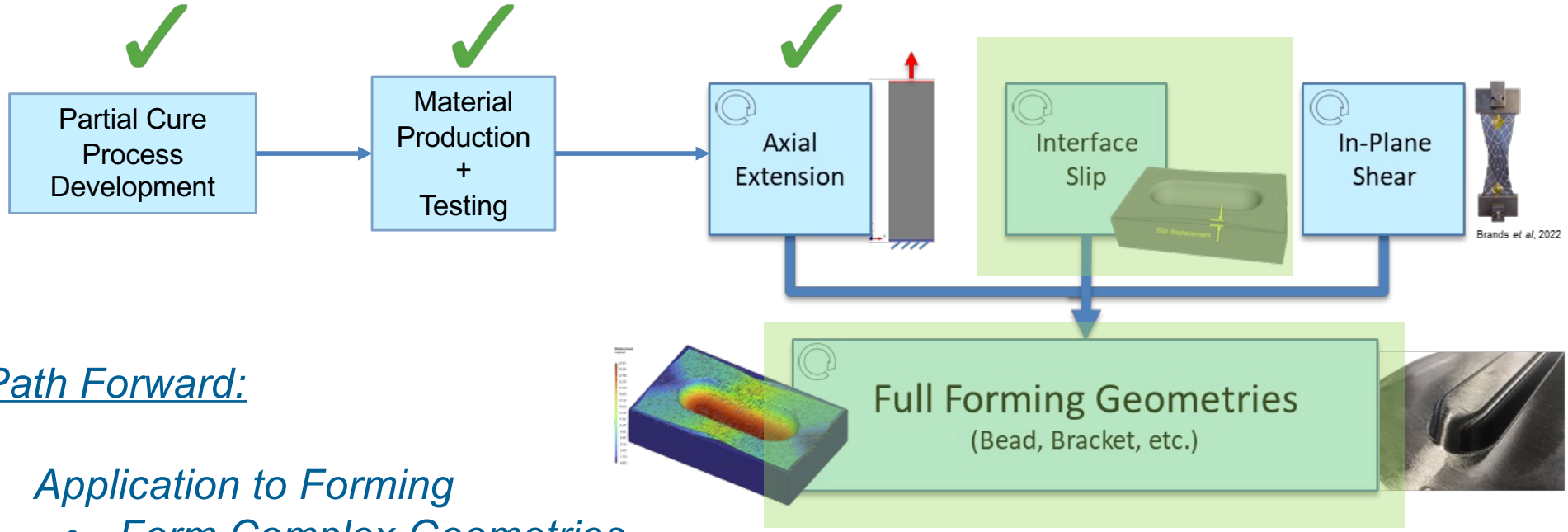

Path Forward:

- *Application to Forming*
  - *Form Complex Geometries*
  - *AniForm Modeling of Interface*

UNIVERSITY OF DELAWARE CENTER FOR COMPOSITE MATERIALS AFRL
DISTRIBUTION STATEMENT A. Approved for public release: distribution unlimited. AFRL-2025-3651

ICCM24
AUGUST 4-8, 2025
BALTIMORE CONVENTION CENTER
BALTIMORE, MARYLAND, USA

No Technical Paper Submission for:

Miguel de Carvalho

Tensile Behavior and Stress Relaxation of Uncured Prepreg of Aligned Discontinuous Fiber Materials

Presenter: Navid Niknafs



UNIVERSITY OF DELAWARE
CENTER FOR
COMPOSITE MATERIALS
Celebrating 50 Years

Project Overview

UNIVERSITY OF DELAWARE
CENTER FOR COMPOSITE MATERIALS
Celebrating 50 Years

"Tensile Behavior and Stress Relaxation of Uncured Prepreg of Aligned Discontinuous Fiber Materials"

Objectives

- Characterize tensile behavior of uncured TuFF under uniaxial loading.
- Develop and validate a continuum constitutive model.
- Enable forming process simulations for TuFF prepreg.
- Approach
  - Perform room temperature tensile tests over wide range of strain rates.
  - Analyze recorded video for strain measurement.
  - Formulate and validate constitutive expressions.
  - Implement model in commercial forming software.
  - Validate forming simulations with experimental results.

Research Team:



Navid Niknafs
Research Associate III

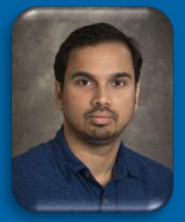

Nithin Parambil
Research Associate III

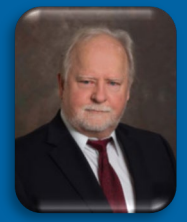

John W. Gillespie, Jr.
Professor



Shridhar Yarlagadda
Associate Professor



David Roseman
Manufacturing Process Engineer

NASA ULI UNIVERSITY LEADERSHIP INITIATIVE

Introduction

- Forming of Fiber-Reinforced Composites
  - Continuous fibers offer strength, but poor formability.
  - Aligned Discontinuous Fiber (ADF) composites (like TuFF) balance formability and performance.

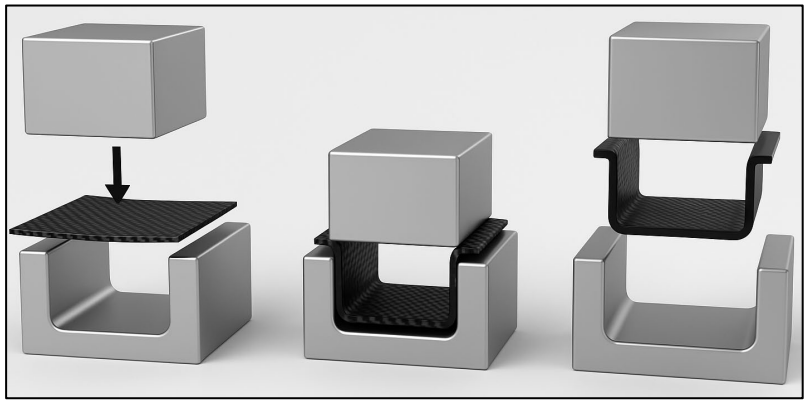

- TuFF Forming Opportunities and Challenges
  - **Significant** fiber-direction stretchability (e.g. local maximum strain 42%)
  - **Lack of constitutive models** capturing anisotropic mechanical behavior of uncured prepreg.

- Methodology:
  - **I.** **Design** experimental framework for tensile testing of uncured TuFF prepreg.
  - **II.** **Characterize** strain-rate dependent viscous response in fiber direction.
  - **III.** **Develop** continuum constitutive model using normalized master curve.
  - **IV.** **Implement** model in composite forming simulation software.



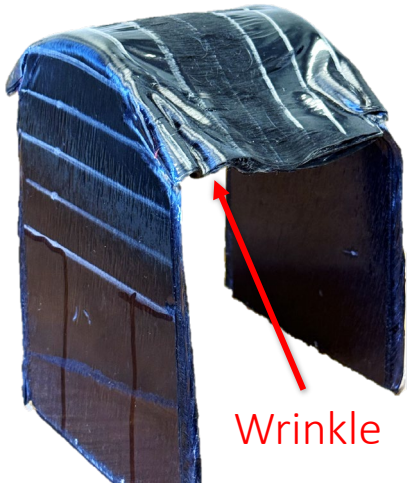

Experimental Procedure

- Materials and Conditions
  - Prepreg: 3mm IM7 carbon fiber with Axiom (Ax-2201FR) thermoset resin.
  - Volume fraction: 40%
  - Areal Weight: 120gsm
  - Specimens: 4” gauge length x 1” width x 0.25mm Thickness.
  - Room temperature conditioning.
- Sample Preparation
  - Utilized mirror-finished aluminum fixture for end-tab bonding.
  - Applied a dot-grid pattern on specimens surface using an acrylic stencil.
- Experimental Setup
  - Captured force and cross-head displacement via Instron (2kN load cell - 1000Hz)
  - Recorded deformation by HD digital video camera (24 fps)

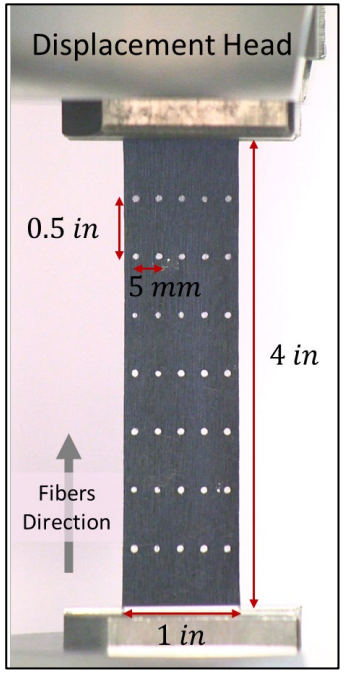

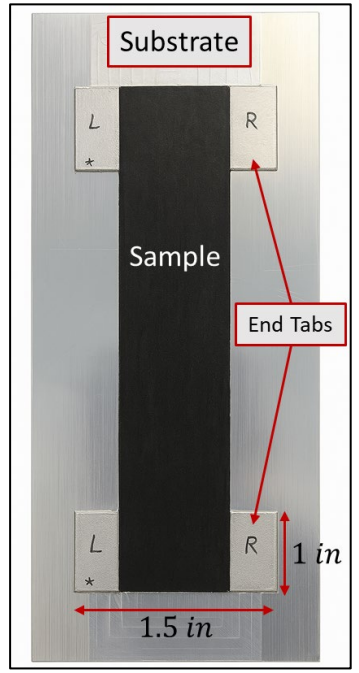

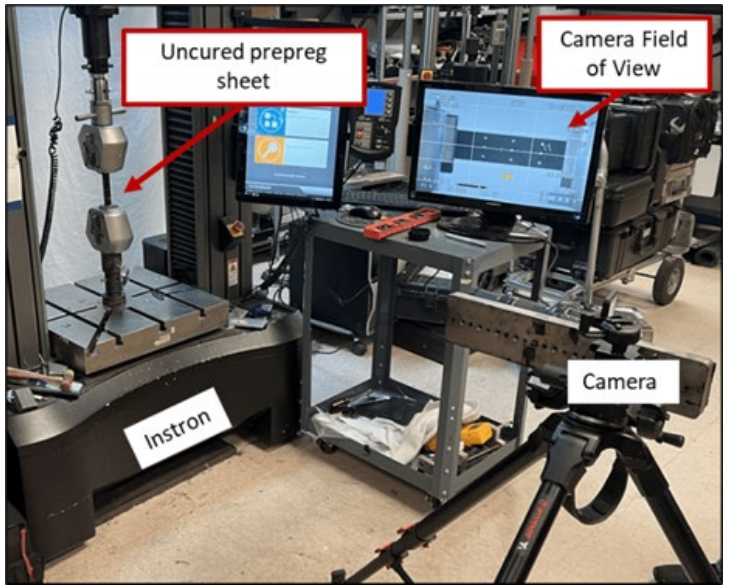

Experimental Procedure – Uniaxial Tensile in Fiber Direction

- Preliminary Data
  - Uniaxial tensile test at **constant strain rates** (x3/x5 replicates per strain rate).
  - Strain rates (displacement velocity) spanning three orders of magnitude (displacement velocities:0.02 to 20 $^{in}/_{min}$).

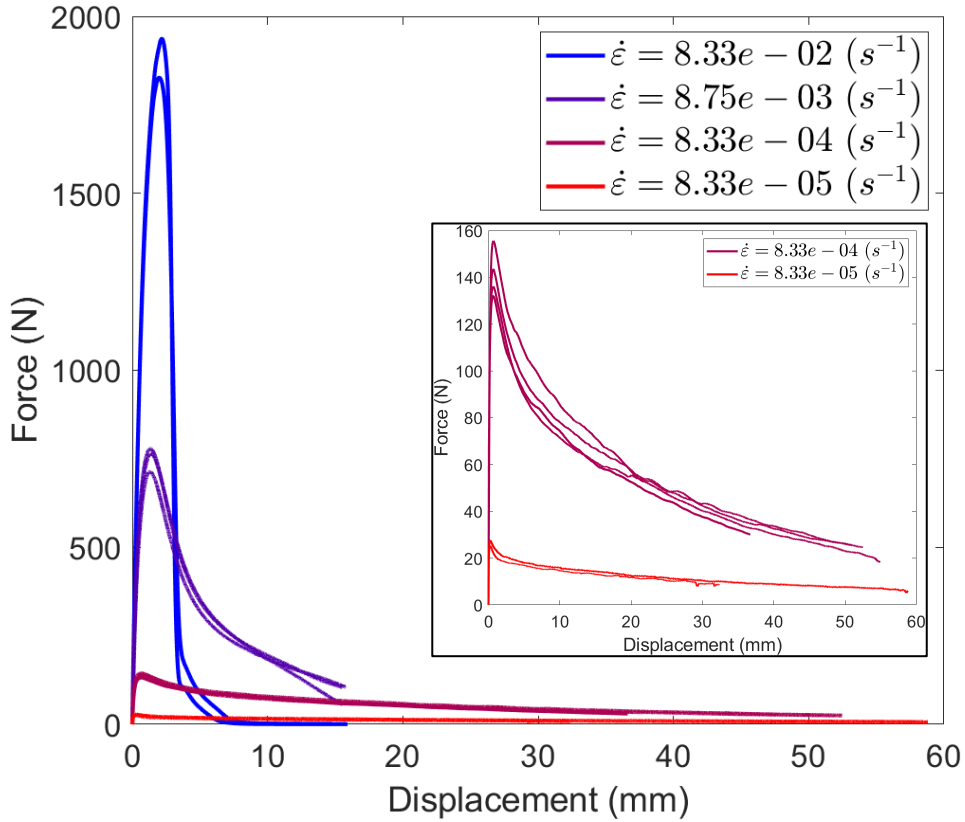

Displacement Rate (inch/min)	Strain Rate (1/s)	Yield Stress (MPa)		Yield Strain (%)	
		Mean	Standard Deviation	Mean	Standard Deviation
0.02	8.33e-05	4.16	0.19	0.23	0.025
0.2	8.33e-04	21.60	0.92	0.61	0.007
2.1	8.75e-03	118.36	5.41	1.33	0.031
20	8.33e-02	296.29	12.23	2.05	0.134

- Reliable Experimental Data
  1. High experimental repeatability (< 5%).
  2. Low material variability.
- Similar Normalized Response.

Constitutive Model Formulation – Approach

- Approach

1. Convert *Force-Displacement* to *Eng. Stress-Strain*.

2. Split material response in two distinct regions:
   a) Pre-Yield (Region I)
   b) Post-Yield (Region II)

3. Propose Individual rate-dependent models for Pre-Yield and Post-Yield regions with smooth transition at yield.

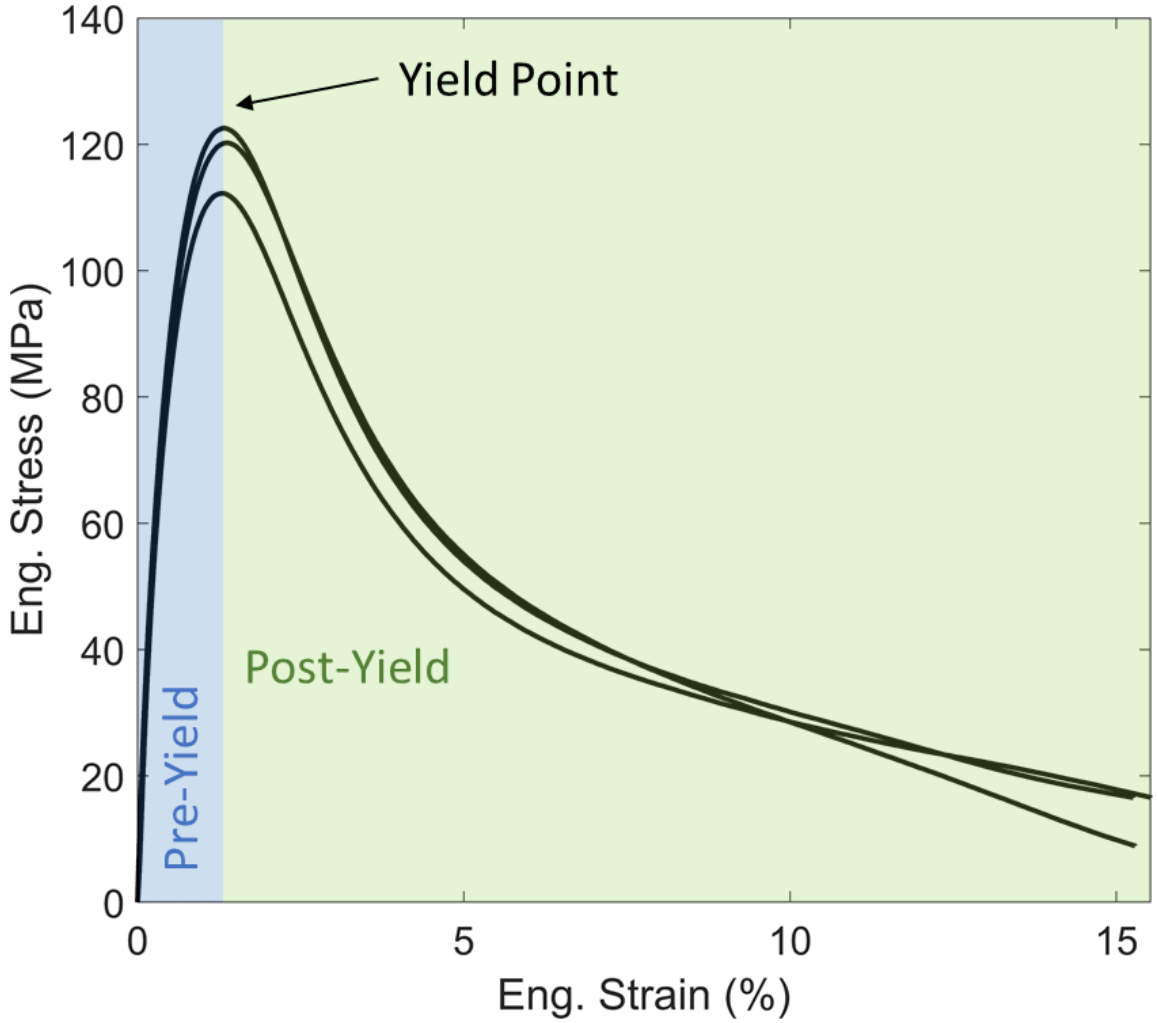

Constitutive Model Formulation – Constant Strain Rate Loading

- Yield Stress (σ_0) increase with increasing Strain Rate ($\dot{\varepsilon}$)
- Implemented Model (Eyring Yielding model):

$$\sigma_{0(\dot{\varepsilon})} = A.\ln\left(\frac{\dot{\varepsilon}}{C_1}\right) + B.\sinh^{-1}\left(\frac{\dot{\varepsilon}}{C_2}\right) + D$$

- Assumptions:
  - Plateau at very low strain rates (half the yield stress). $D = \frac{\dot{\varepsilon}_{min}}{2}$
  - Keep yield stress positive at very low strain rates. $C_1 = \dot{\varepsilon}_{min}$

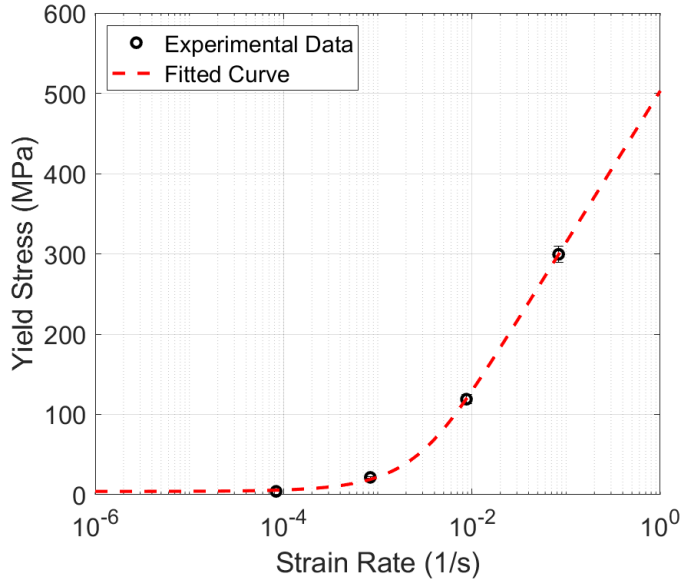

- Similar procedure for Yield Strain (ε_0)

Yield Stress	Yield Strain
$\sigma_{0(\dot{\varepsilon})} = A\ln\left(\frac{\dot{\varepsilon}}{C_1}\right) + B\sinh^{-1}\left(\frac{\dot{\varepsilon}}{C_2}\right) + D$	$\varepsilon_{0(\dot{\varepsilon})} = a\ln\left(\frac{\dot{\varepsilon}}{c_1}\right) + b\sinh^{-1}\left(\frac{\dot{\varepsilon}}{c_2}\right) + d$
$A = 8.50\ \mathrm{e} - 03$	$a = 6.65e - 06$
$B = 5.93e + 01$	$b = 2.92e - 03$
$C_1 = 8.33e - 05$	$c_1 = 8.33e - 05$
$C_2 = 2.50e - 03$	$c_2 = 2.97e - 04$
$D = 2.08$	$d = 1.20e - 03$

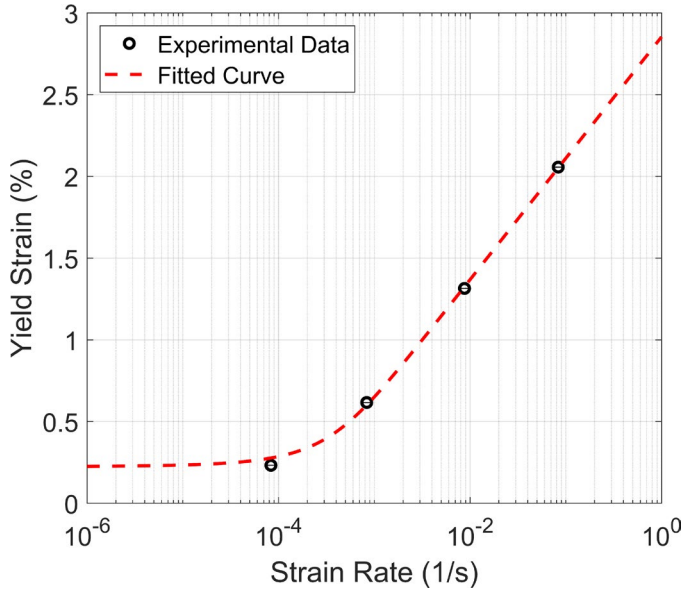

Constitutive Model Formulation – Constant Strain Rate Loading

- Pre-Yield (Region I) Modeling: Non-linear Hardening
  - Normalized Stress ($\bar{\sigma}$) – Normalized Strain ($\bar{\varepsilon}$) (with respect to *Yield Stress* and *Yield Strain)*.

- Implemented Model :

$$\bar{\sigma}_{(\bar{\varepsilon},\ \dot{\varepsilon})} = \frac{\bar{E}_{(\dot{\varepsilon})} . \bar{\varepsilon}}{\left(1 + \left(\bar{E}_{(\dot{\varepsilon})} . \bar{\varepsilon}\right)^{\bar{n}_{(\dot{\varepsilon})}}\right)^{\frac{1}{\bar{n}_{(\dot{\varepsilon})}}}}$$

- Fitting Parameters:
  - $\bar{E}_{(\dot{\varepsilon})}$: Initial Slope (Initial Normalized Stiffness)
  - $\bar{n}_{(\dot{\varepsilon})}$: Asymptotic Plateau shape

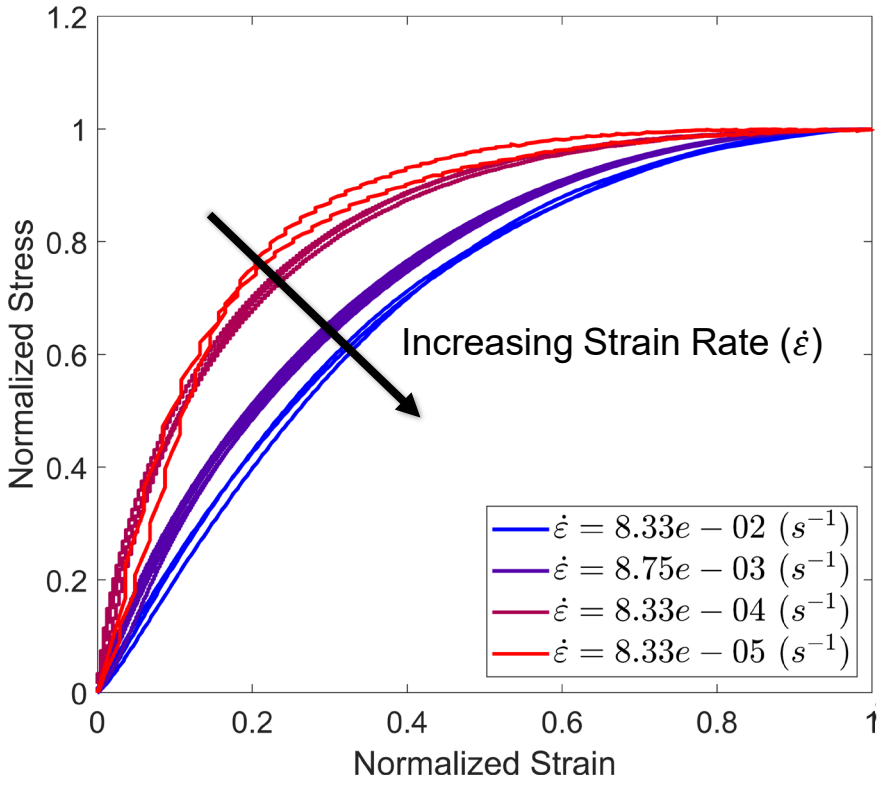

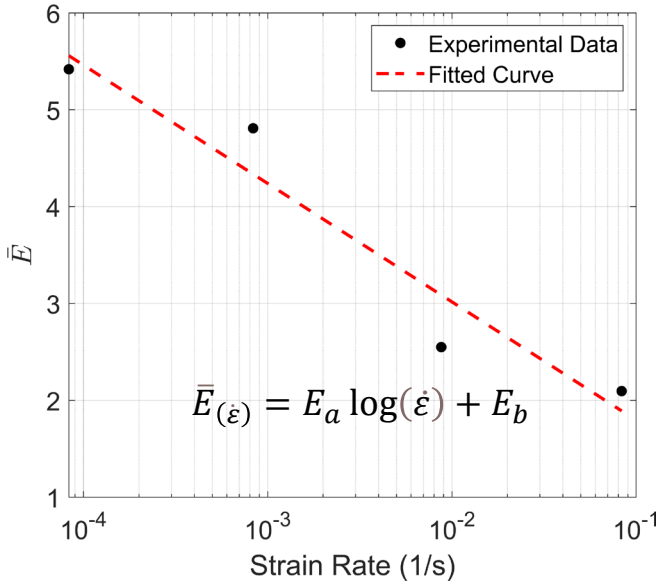

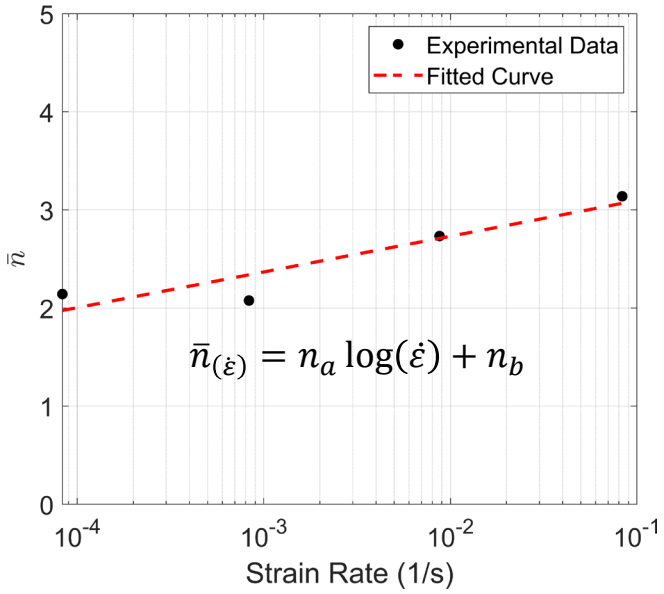

Constitutive Model Formulation – Constant Strain Rate Loading

- Pre-Yield (Region I) Model Validation
  - Denormalizing the model prediction (normalized stress - strain) by multiplying them to yield stress and yield strain.

$$\sigma_{(\bar{\varepsilon},\ \dot{\varepsilon})} = \sigma_{0(\dot{\varepsilon})} \cdot \frac{\bar{E}_{(\dot{\varepsilon})} \cdot \bar{\varepsilon}}{\left(1 + \left(\bar{E}_{(\dot{\varepsilon})} \cdot \bar{\varepsilon}\right)^{\bar{n}_{(\dot{\varepsilon})}}\right)^{\frac{1}{\bar{n}_{(\dot{\varepsilon})}}}}$$

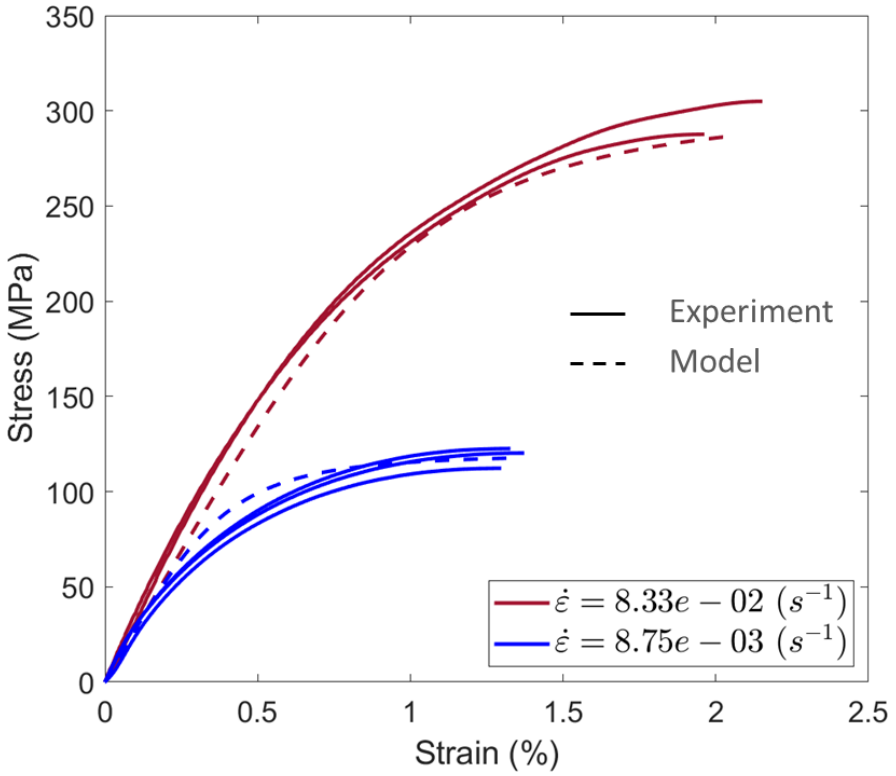

- High Strain Rate Data

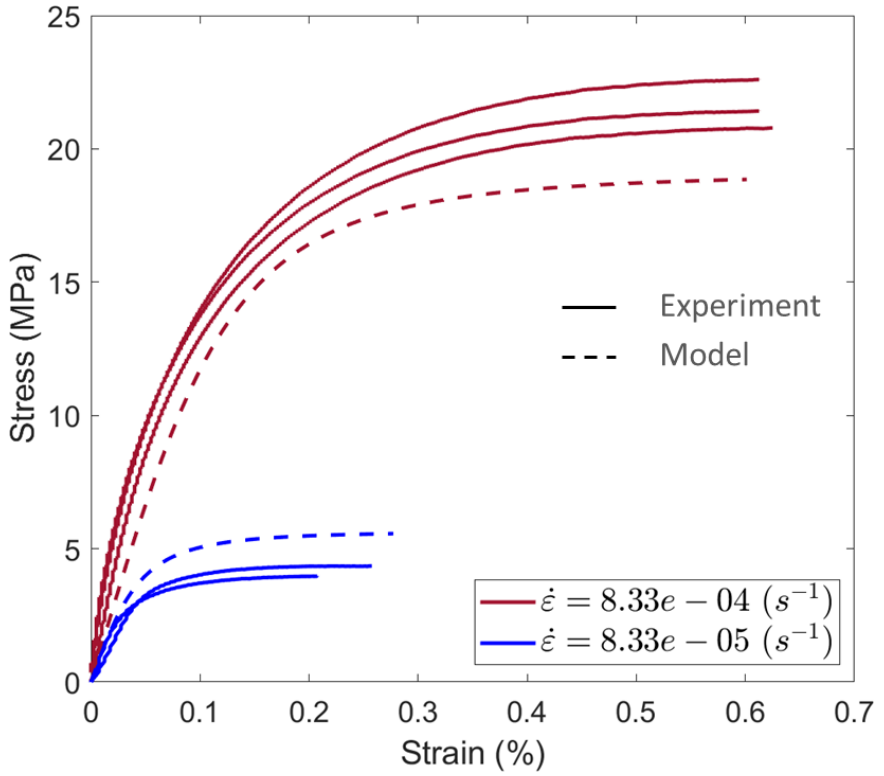

- Low Strain Rate Data

Constitutive Model Formulation – Constant Strain Rate Loading

- Post-Yield (Region II) Modeling: Exponential Softening
  - Normalized Stress ($\bar{\sigma}$) – Relative Strain ($\varepsilon - \varepsilon_0$)
- Implemented Model :

$$\bar{\sigma}(\varepsilon, \dot{\varepsilon}) = \frac{1}{2}\left(\exp\left[-\left(\frac{\varepsilon - \varepsilon_0}{\varepsilon^*_{(\dot{\varepsilon})}} \right)^{m_{(\dot{\varepsilon})}} \right] + \exp\left[-\left(\frac{\varepsilon - \varepsilon_0}{\varepsilon^{**}_{(\dot{\varepsilon})}} \right)^{M_{(\dot{\varepsilon})}} \right] \right)$$

- Fitting Parameters:
  - $\varepsilon^*_{(\dot{\varepsilon})}$ / $\varepsilon^{**}_{(\dot{\varepsilon})}$: Decay Coefficient
  - $m_{(\dot{\varepsilon})}$ / $M_{(\dot{\varepsilon})}$: Softening Strain Scales

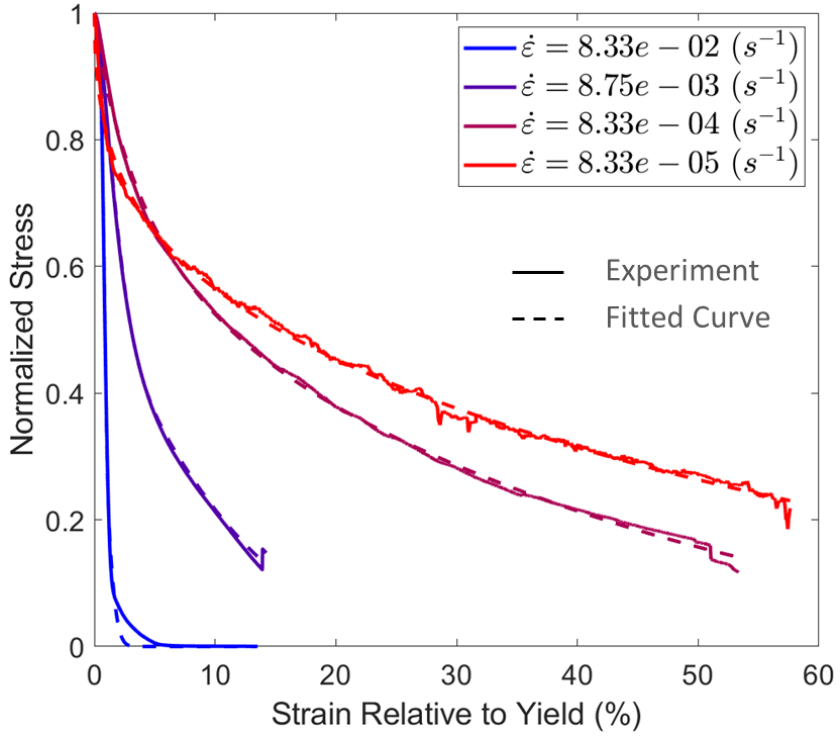

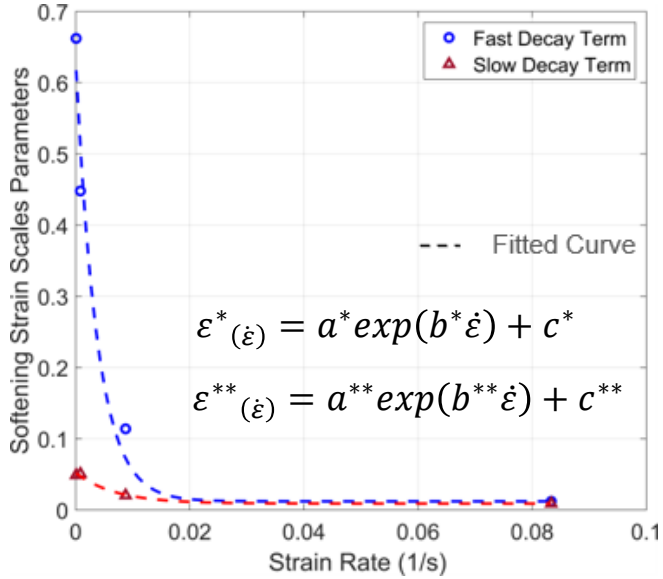

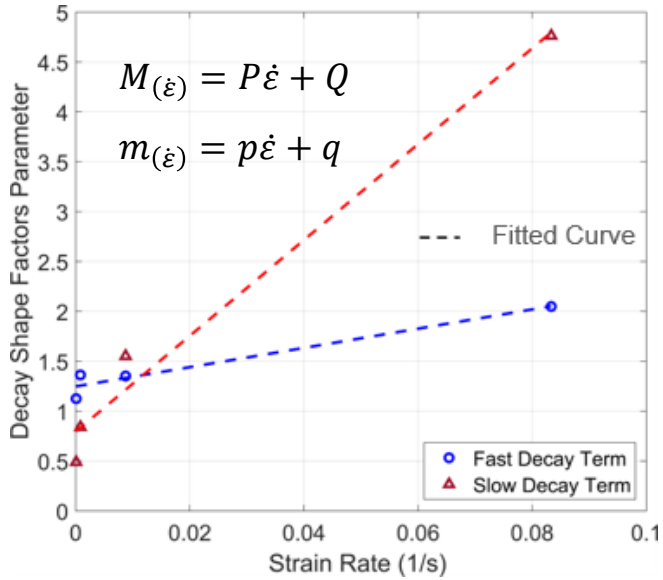

Constitutive Model Formulation – Constant Strain Rate Loading

- Post-Yield (Region II) Model Validation

1. Stress decays exponentially toward zero in the post-yield regime (desirable for implementation in forming simulations).
2. Prediction error is comparable to variation across replicates.
3. Stress can get de-normalized with respect to yield stress.

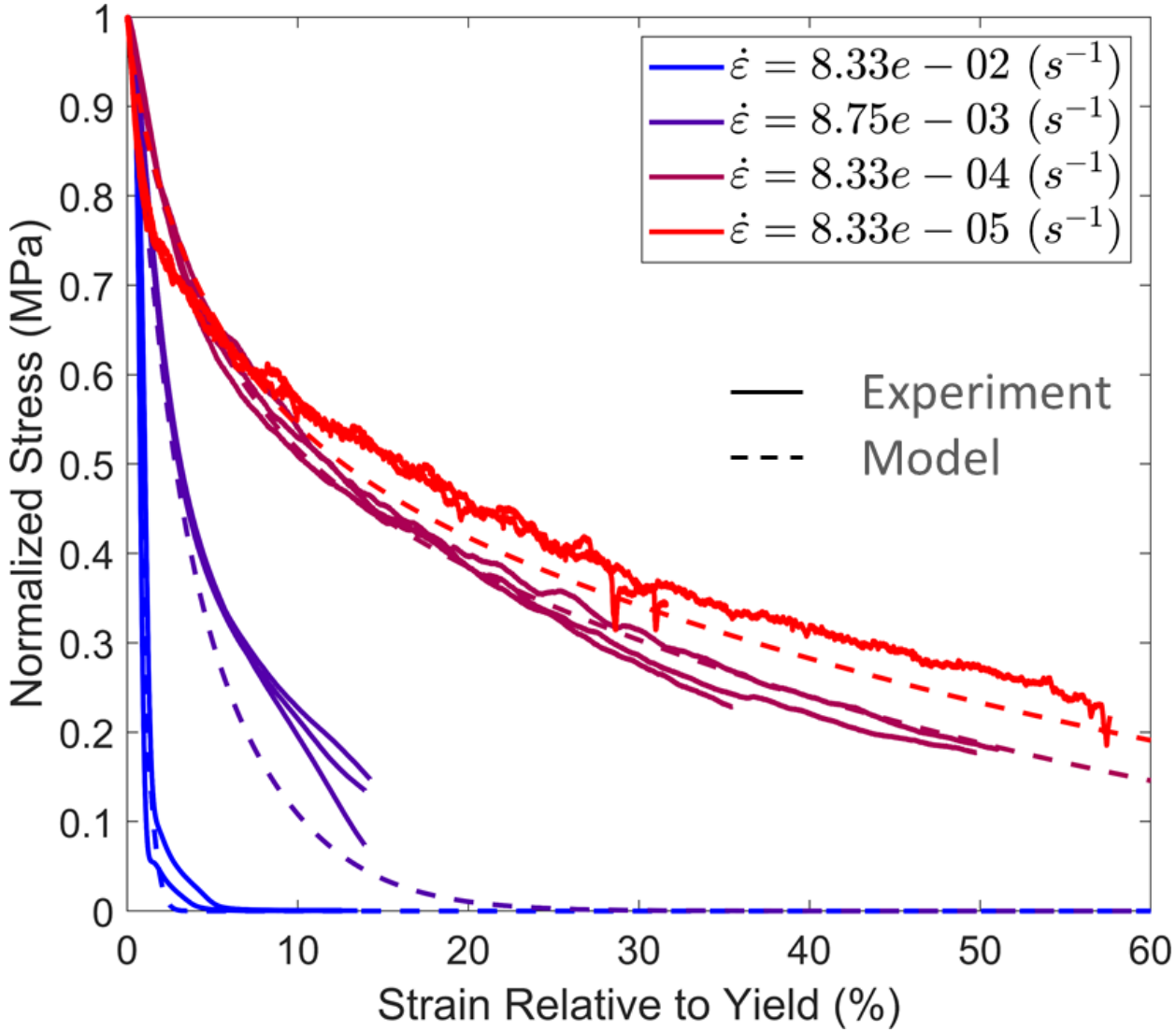

Constitutive Model Formulation – Constant Strain Rate Loading

- Characterized Models

- Yield Stress (σ_0) and Strain (ε_0)

$$\sigma_{0(\dot{\varepsilon})} = A.\ln\left(\frac{\dot{\varepsilon}}{C_1}\right) + B.\sinh^{-1}\left(\frac{\dot{\varepsilon}}{C_2}\right) + D$$

$$\varepsilon_{0(\dot{\varepsilon})} = a.\ln\left(\frac{\dot{\varepsilon}}{c_1}\right) + b.\sinh^{-1}\left(\frac{\dot{\varepsilon}}{c_2}\right) + d$$

- Pre-Yield Non-linear Hardening

$$\sigma(\varepsilon,\dot{\varepsilon}) = \sigma_{0(\dot{\varepsilon})}.\frac{\bar{E}_{(\dot{\varepsilon})}.\bar{\varepsilon}}{\left(1 + \left(\bar{E}_{(\dot{\varepsilon})}.\bar{\varepsilon}\right)^{\bar{n}_{(\dot{\varepsilon})}}\right)^{\frac{1}{\bar{n}_{(\dot{\varepsilon})}}}}$$

$$\bar{E}_{(\dot{\varepsilon})} = E_a \log(\dot{\varepsilon}) + E_b$$

$$\bar{n}_{(\dot{\varepsilon})} = n_a \log(\dot{\varepsilon}) + n_b$$

$$\bar{\varepsilon} = \frac{\varepsilon}{\varepsilon_{0(\dot{\varepsilon})}}$$

- Post-Yield Softening

$$\sigma(\varepsilon,\dot{\varepsilon}) = \frac{\sigma_{0(\dot{\varepsilon})}}{2}\left(\exp\left[-\left(\frac{\varepsilon-\varepsilon_0}{\varepsilon^*_{(\dot{\varepsilon})}}\right)^{m_{(\dot{\varepsilon})}}\right] + \exp\left[-\left(\frac{\varepsilon-\varepsilon_0}{\varepsilon^{**}_{(\dot{\varepsilon})}}\right)^{M_{(\dot{\varepsilon})}}\right]\right)$$

$$\varepsilon^*_{(\dot{\varepsilon})} = a^* exp(b^*\dot{\varepsilon}) + c^*$$

$$\varepsilon^{**}_{(\dot{\varepsilon})} = a^{**} exp(b^{**}\dot{\varepsilon}) + c^{**}$$

$$M_{(\dot{\varepsilon})} = P\dot{\varepsilon} + Q$$

$$m_{(\dot{\varepsilon})} = p\dot{\varepsilon} + q$$

Constitutive Model Formulation – Constant Strain Rate Loading

- Material response validation across 3 orders of strain rate magnitude (22 fitting parameters).

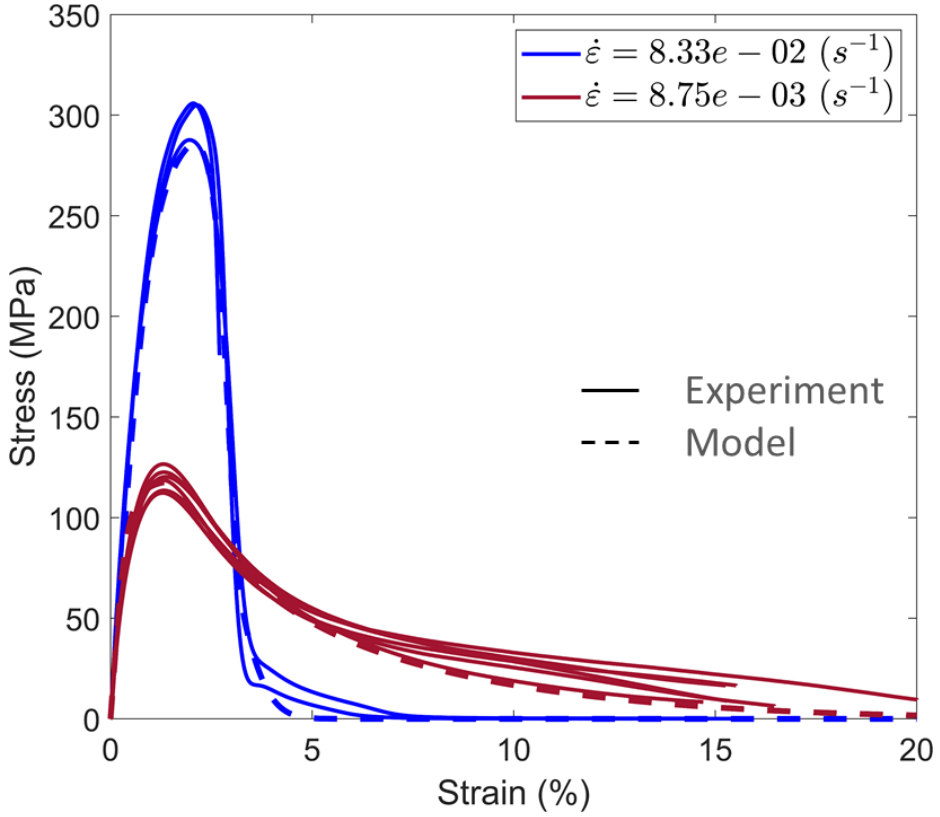

- High Strain Rate Data

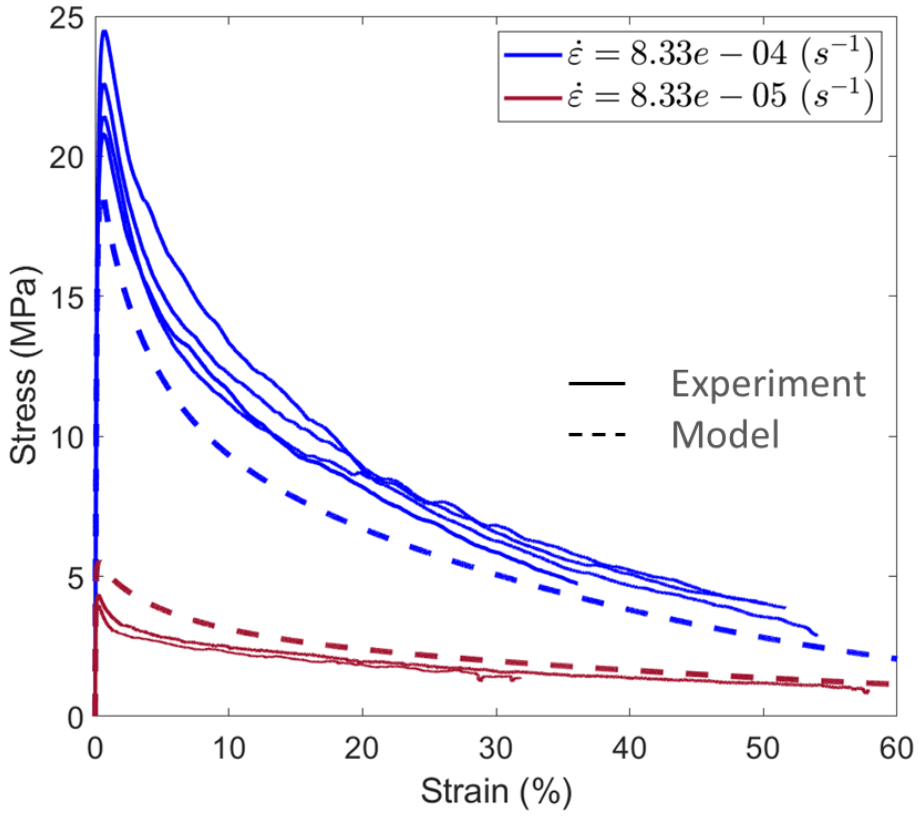

- Low Strain Rate Data

Constitutive Model Formulation – Constant Strain Rate Loading

- Strain Rate Dependent Constitutive Tensile Behavior (Family of curves)
  - Predicted curves covering strain rates from very low to very high levels
  - Lower Strain Rates:
    i. Lower yield stress,
    ii. Earlier yielding at smaller strains,
    iii. Gradual softening.
  - Higher Strain Rate:
    i. Higher yield stress,
    ii. Larger strain before yielding,
    iii. Sharp stress decay after yield.
  - Tabular inputs for ABAQUS explicit solver

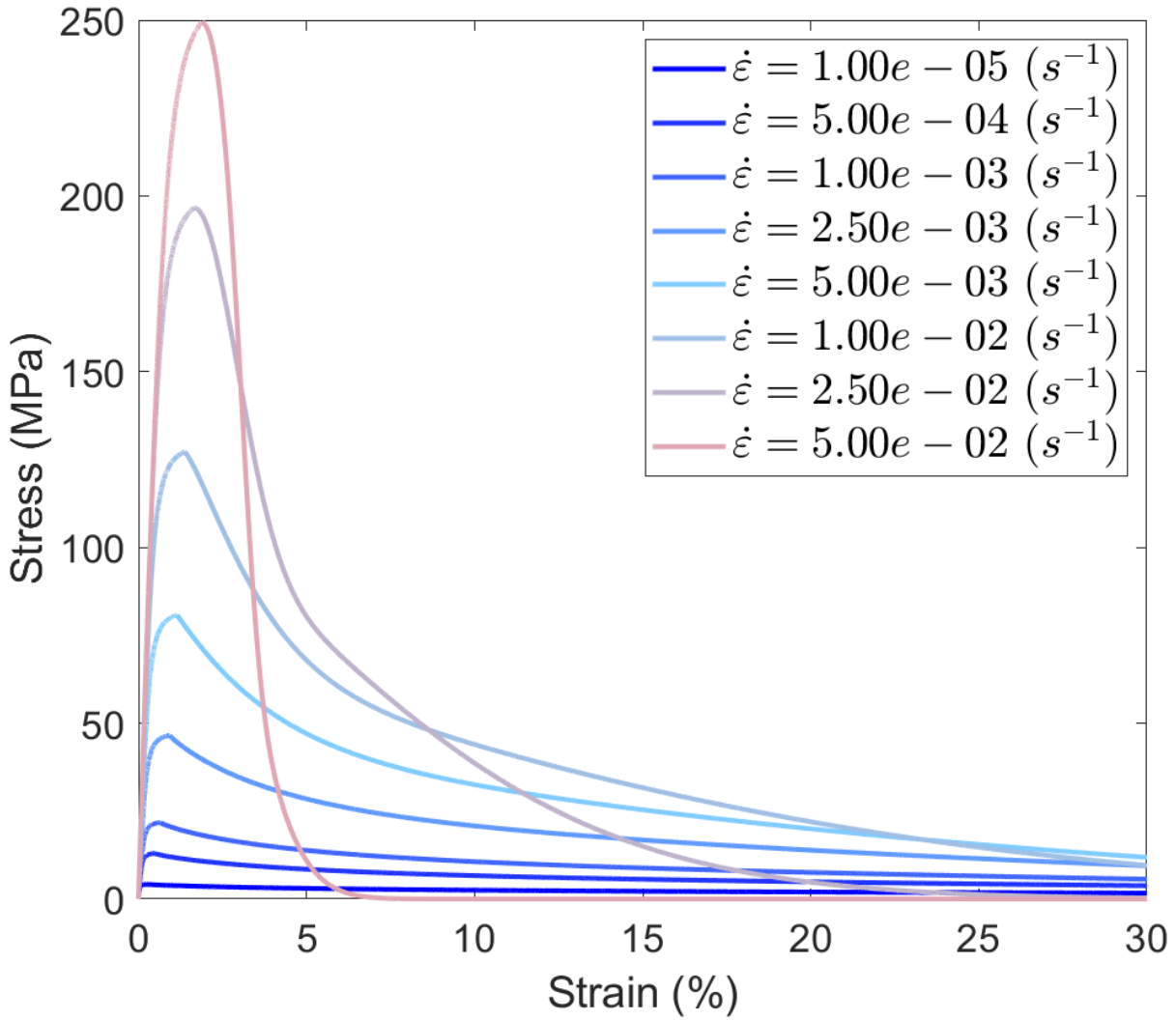

Constitutive Model Formulation – Stress Relaxation

- Experimental Procedure and Data
  - **Loading at constant strain** rate, followed by **stress relaxation** hold at defined strain levels.
  - **Strain levels** : $\left[\frac{1}{4}, \frac{1}{2}, \frac{3}{4}, 1, \frac{5}{4}, \frac{6}{4}\right] * \varepsilon_0$
  - Each test includes 6 sequential loading –relaxation cycles.
  - The first Loading-Relaxation cycle results.
  - Stress decay curves isolated for relaxation model fitting.

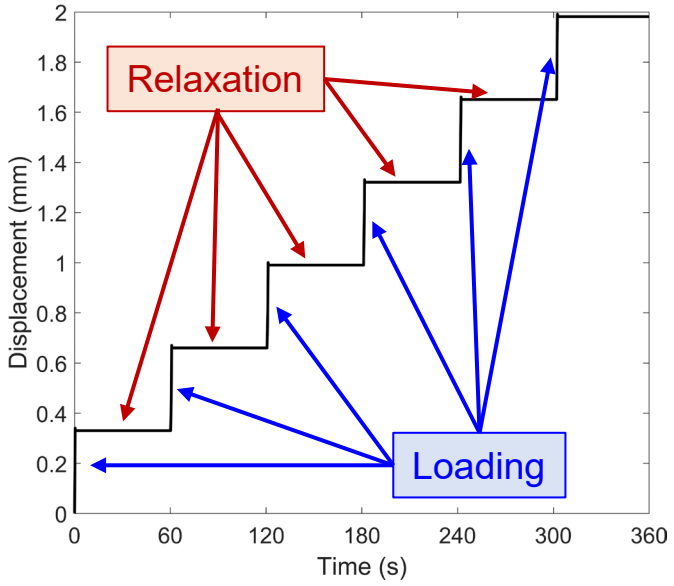

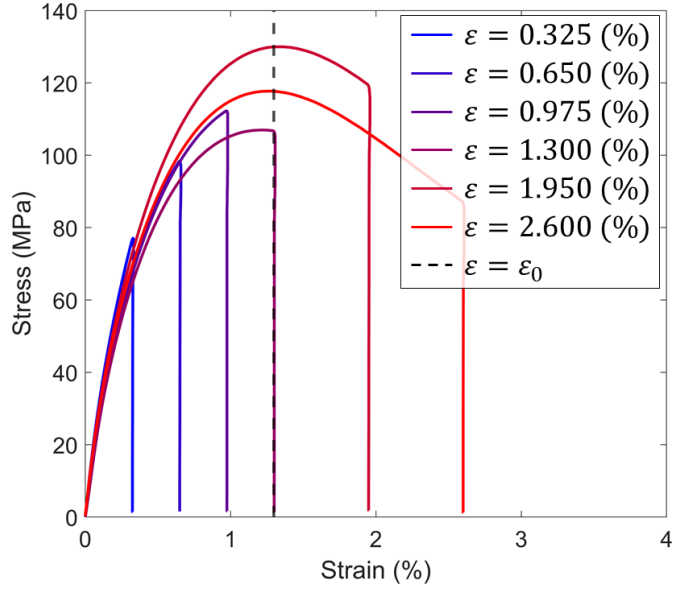

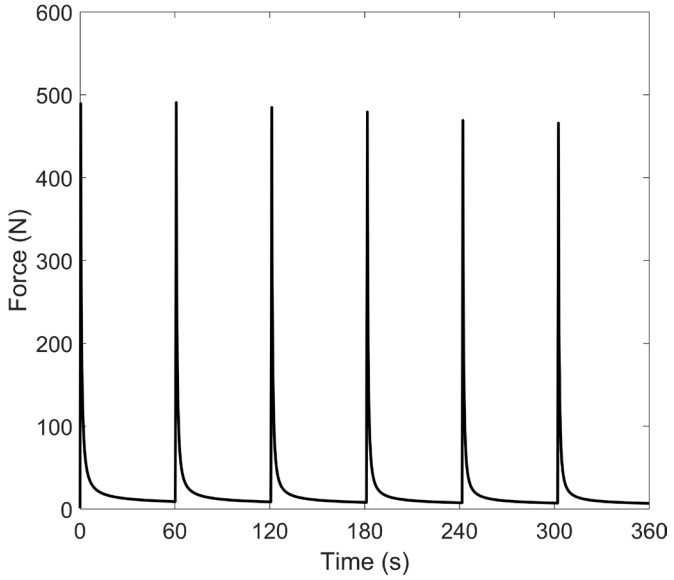

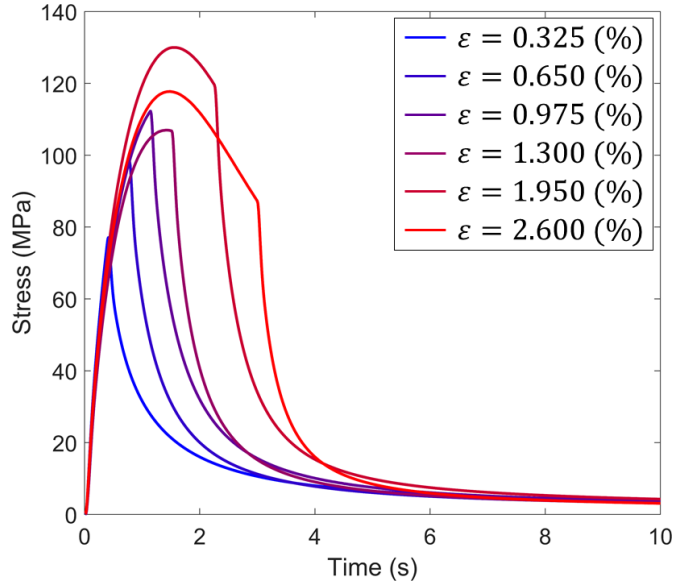

Constitutive Model Formulation – Stress Relaxation

- Stress Decay Model
  - Fully viscous response.
  - Dependency on the strain rate of the prior loading interval.
  - No significant strain dependency.

- Implemented Model :

$$\bar{\sigma}(t,\dot{\varepsilon}) = \exp\left[-\left(\frac{t}{\tau_{(\dot{\varepsilon})}}\right)^{n_{(\dot{\varepsilon})}}\right]$$

- Parameters:
  - $\tau_{(\dot{\varepsilon})}$: Characteristic Time
  - $n_{(\dot{\varepsilon})}$: Exponent Parameter

- Stress Relaxation Time scales: 1-10 seconds

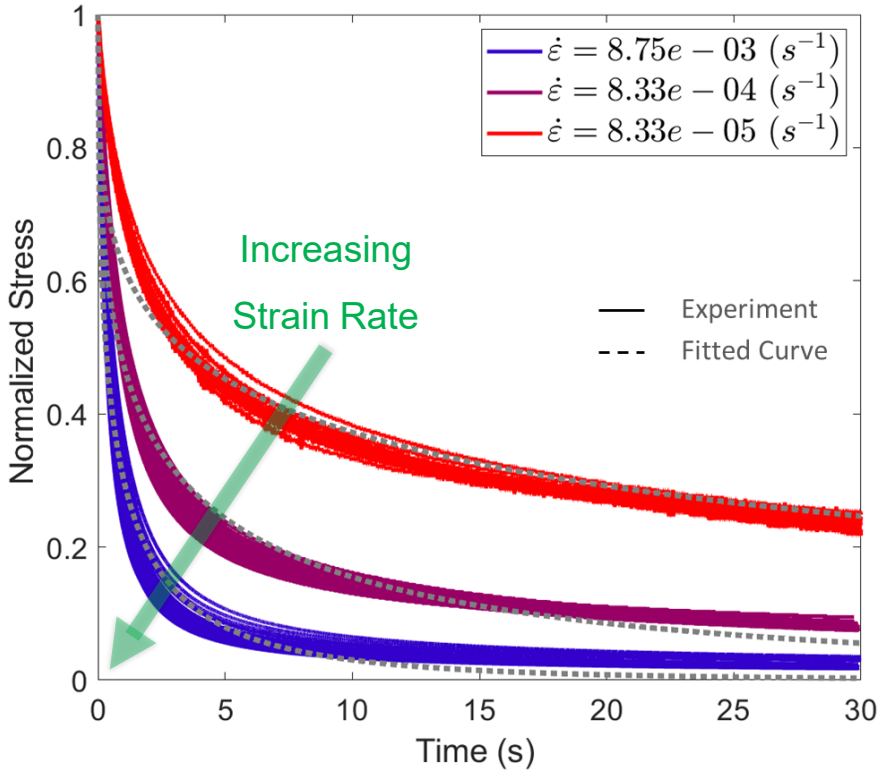

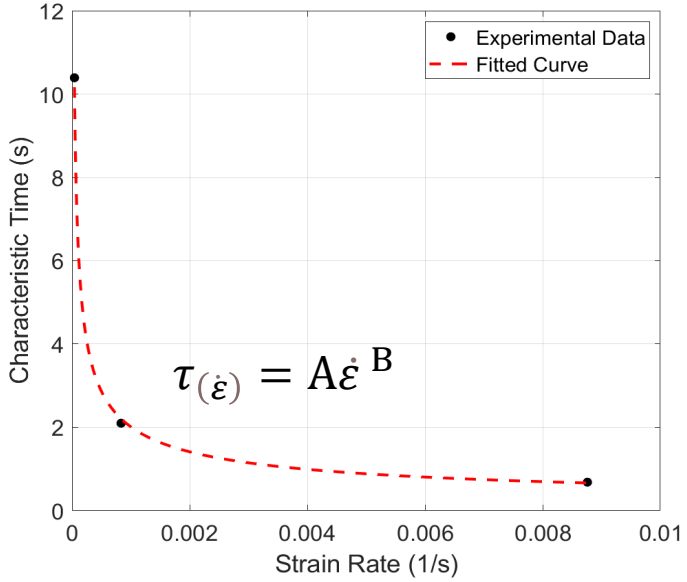

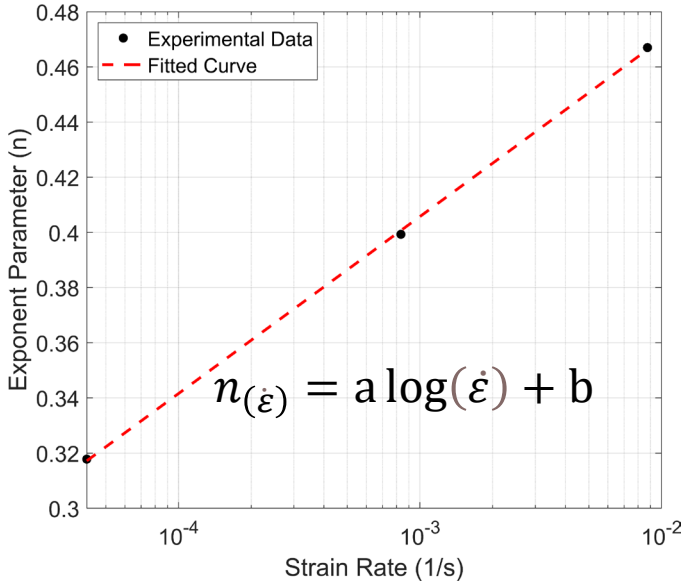

Constitutive Model Formulation – Stress Relaxation

- Stress Relaxation Model Validation

- Constant strain rate (8.75e-5 s^{-1})
- Up to 0.64% strain.
- 30s of stress decay

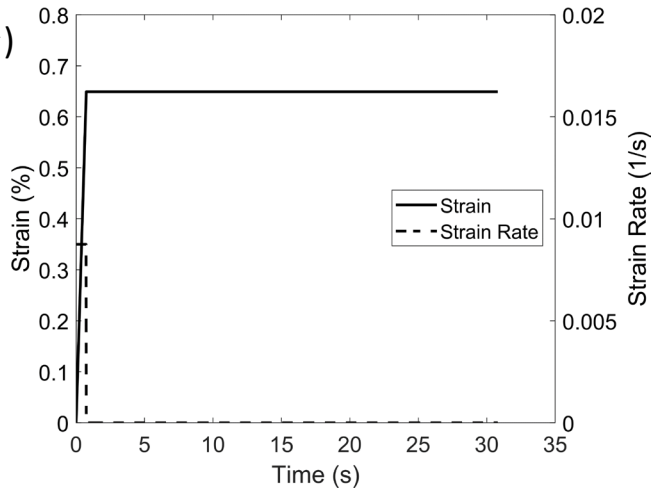

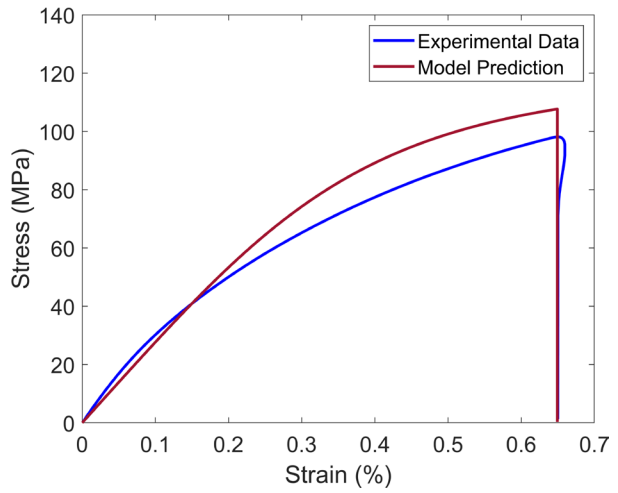

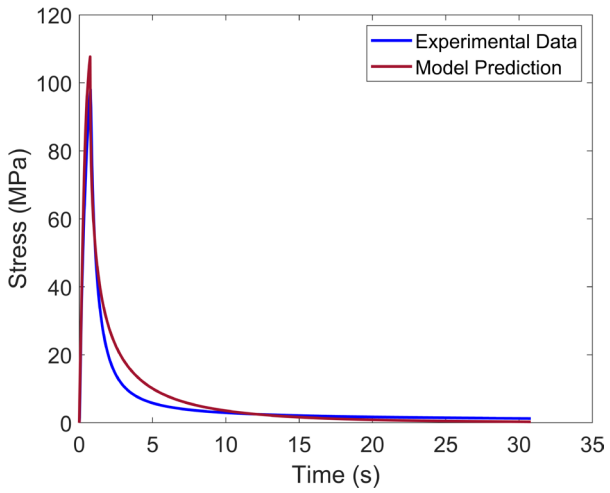

- Constant strain rate (8.75e-5 s^{-1})
- Up to 2.6% strain.
- 30s of stress decay

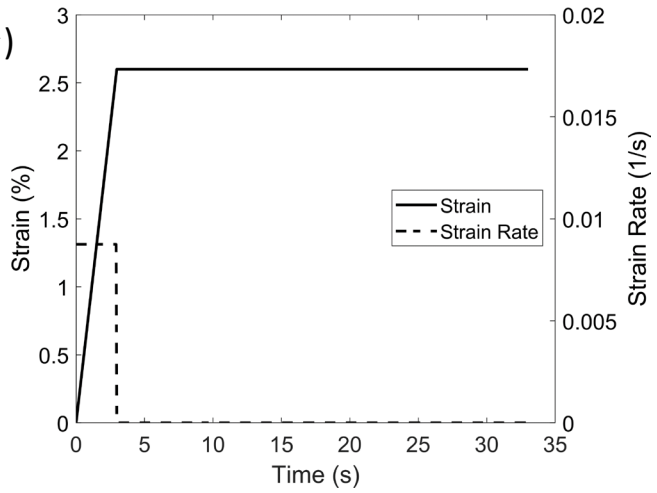

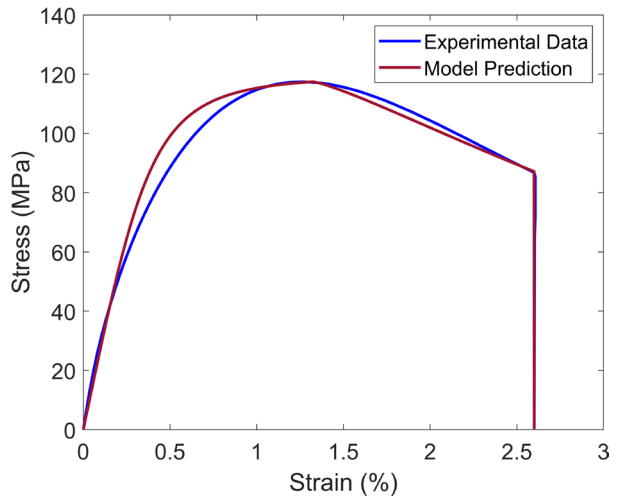

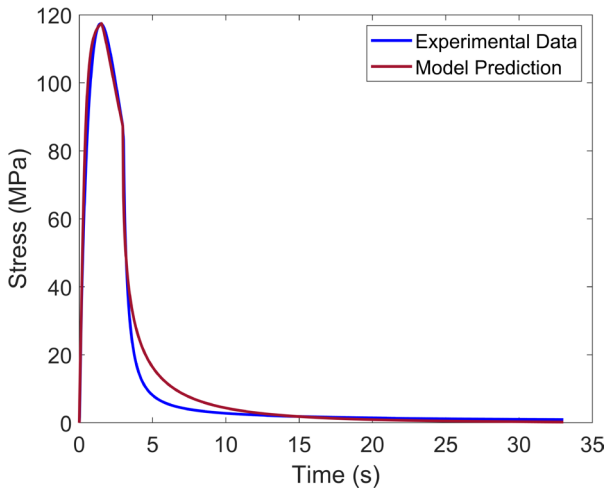

Constitutive Model Formulation – Incremental Formulation

- Incremental Formulation for Software Implementation

$$\sigma^{new} = \sigma^{old} + \Delta\sigma$$

- Stress increment formulations:

$$\Delta\sigma = \frac{\partial\sigma}{\partial\varepsilon}\Delta\varepsilon + \frac{\partial\sigma}{\partial\dot{\varepsilon}}\Delta\dot{\varepsilon}$$

- Chain rule differentiation

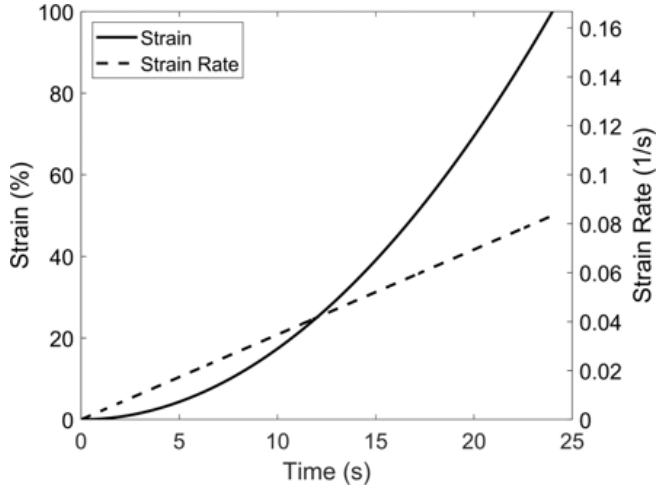

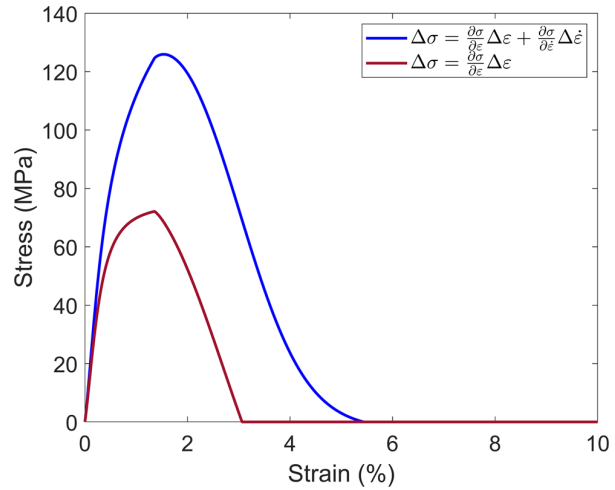

Pre-Yield

$$\sigma(\varepsilon,\dot{\varepsilon}) = \sigma_{0(\dot{\varepsilon})}.\frac{\bar{E}_{(\dot{\varepsilon})}.\bar{\varepsilon}}{\left(1+\left(\bar{E}_{(\dot{\varepsilon})}.\bar{\varepsilon}\right)^{\bar{n}_{(\dot{\varepsilon})}}\right)^{\frac{1}{\bar{n}_{(\dot{\varepsilon})}}}}$$

Post-Yield

$$\sigma(\varepsilon,\dot{\varepsilon}) = \frac{\sigma_{0(\dot{\varepsilon})}}{2}\left(\exp\left[-\left(\frac{\varepsilon-\varepsilon_0}{\varepsilon^*_{(\dot{\varepsilon})}}\right)^{m_{(\dot{\varepsilon})}}\right] + \exp\left[-\left(\frac{\varepsilon-\varepsilon_0}{\varepsilon^{**}_{(\dot{\varepsilon})}}\right)^{M_{(\dot{\varepsilon})}}\right]\right)$$

Stress Relaxation

$$\sigma(t,\dot{\varepsilon}) = \sigma_{0(\dot{\varepsilon})}.\exp\left[-\left(\frac{t}{\tau_{(\dot{\varepsilon})}}\right)^{n_{(\dot{\varepsilon})}}\right]$$

CAD/CAM Software Implementation

- Constitutive Model in Fiber Direction
  - Pre-Yield

$$\sigma(\varepsilon,\dot{\varepsilon}) = \sigma_{0(\dot{\varepsilon})}\cdot\frac{\bar{E}_{(\dot{\varepsilon})}\,.\,\bar{\varepsilon}}{\left(1+\left(\bar{E}_{(\dot{\varepsilon})}\,.\,\bar{\varepsilon}\right)^{\bar{n}_{(\dot{\varepsilon})}}\right)^{\frac{1}{\bar{n}_{(\dot{\varepsilon})}}}}$$

  - Post-Yield

$$\sigma(\varepsilon,\dot{\varepsilon}) = \frac{\sigma_{0(\dot{\varepsilon})}}{2}\left(\exp\left[-\left(\frac{\varepsilon-\varepsilon_0}{\varepsilon^{*}_{(\dot{\varepsilon})}}\right)^{m_{(\dot{\varepsilon})}}\right]+\exp\left[-\left(\frac{\varepsilon-\varepsilon_0}{\varepsilon^{**}_{(\dot{\varepsilon})}}\right)^{M_{(\dot{\varepsilon})}}\right]\right)$$

SIMULIA ABAQUS

Explicit Implementation

(Tabular inputs by family curves)

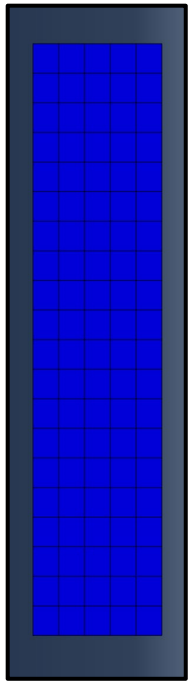

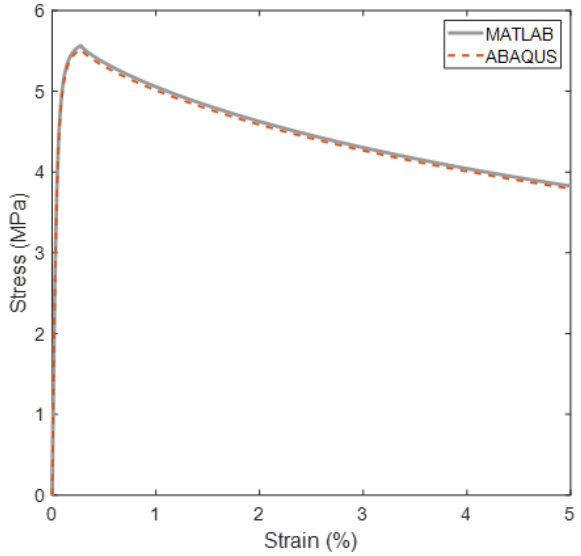

ANIFORM VIRTUAL FORMING

Implicit Implementation

(Incremental Formulation)

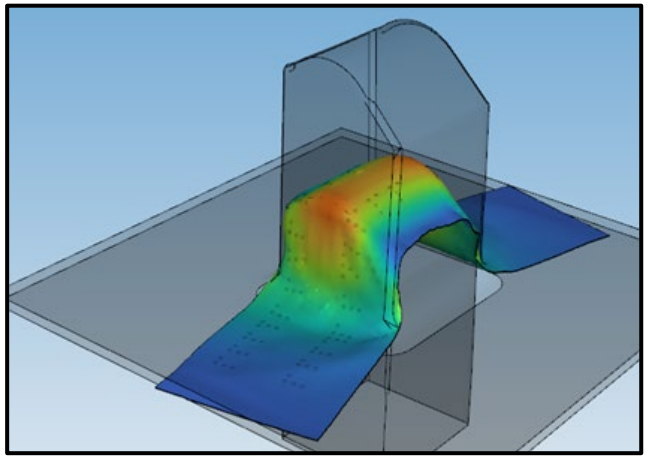

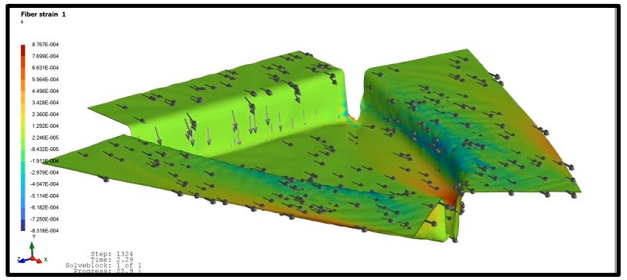

Conclusions

- Developed an **experimental and analysis methodology** for characterization of uncured highly aligned discontinuous fiber prepreg at room temperature.
- Demonstrated normalized stress-strain curves **collapse onto a master curve**.
- Formulated a **strain-rate-dependent anisotropic model** capturing:
  - i. Pre-yield non-linear hardening,
  - ii. Post-yield exponential softening, and
  - iii. Exponential stress decay during relaxation.
- **Validated** model predictions against experimental results.
- Generated a **family of rate-dependent input curves** for forming simulations.
- Formulated Constitutive model in **incremental form** for software implementation.
- Implemented the constitutive model in CAM/CAD software (**AniForm / Abaqus**).
- **Simulated complex** part geometries using Axiom TuFF model.

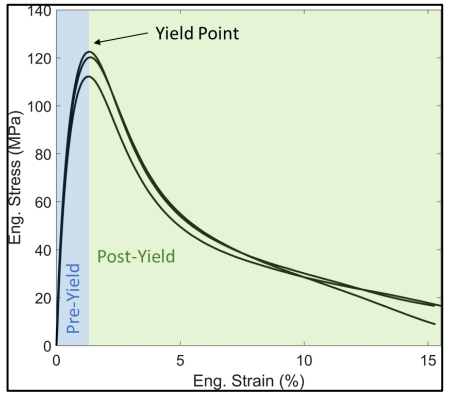

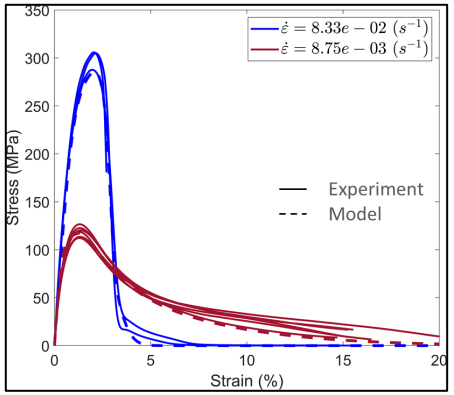

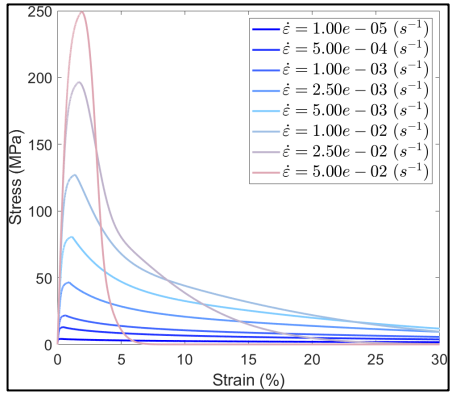

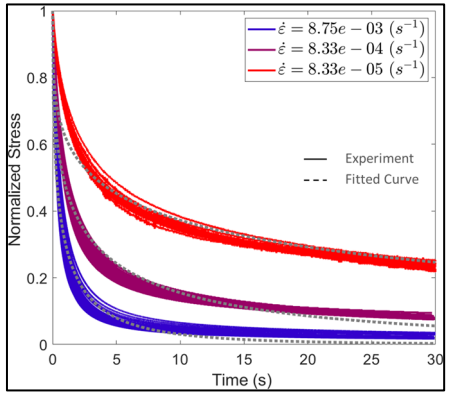

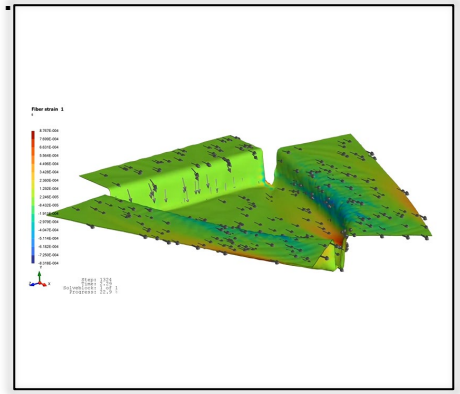

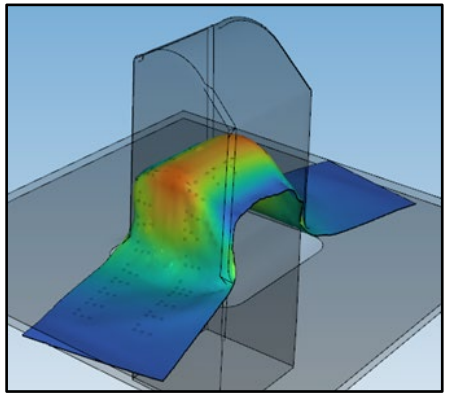

Future Directions

- Expand mechanical characterization to additional in-plane loading conditions
  i. Transverse direction (90° to fiber alignment),
  ii. In-plane shear,
  iii. Off-axis loading scenarios,

  that enables a more complete anisotropic material model.

- Investigate thickness deformation (thinning response).

- Characterize temperature-dependent behavior at elevated temperatures.
  - Supports non-isothermal forming simulations.

Acknowledgments

- This work is supported by the National Aeronautics and Space Administration (NASA) through grant No. 80NSSC20M0164, provided by the Aeronautics Research Mission Directorate's Transformative Aeronautics Concepts Program, as part of the University Leadership Initiative.



- The support provided by the AniForm Engineering, especially *Dr. Sebastiaan Haanappel* and *Dr. Rene ten Thije*, for simulation resources and technical guidance during the implementation of the constitutive model in Aniform is gratefully acknowledged.





Impact of fiber aspect ratio on the mechanical performance of short fiber composites

Uday Kiran Balaga[1,2], Chris Blackwell[3], Joseph Deitzel[1], Dirk Heider[1,3], Suresh G Advani[1,2]

1 Center for Composite Materials

2 Department of Mechanical Engineering

3 Composites Automation LLC



Outline

- Background & Motivation
- Objectives
- Experimental Approach
- Results & Discussions
- Conclusions

- **Background & Motivation**
- Objectives
- Experimental Approach
- Results & Discussions
- Conclusions

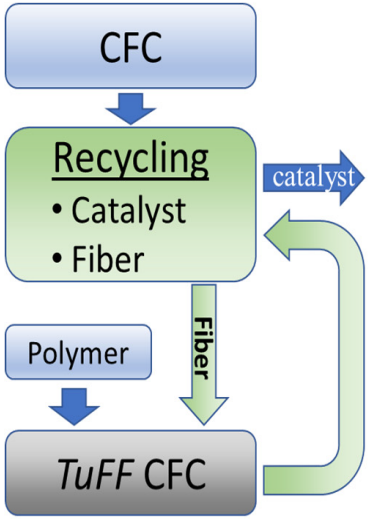

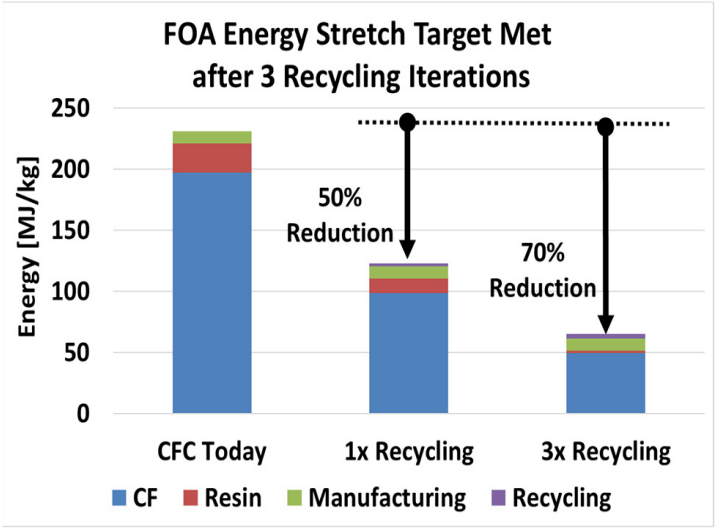

Background

› Conventional processing flow chart of composite parts

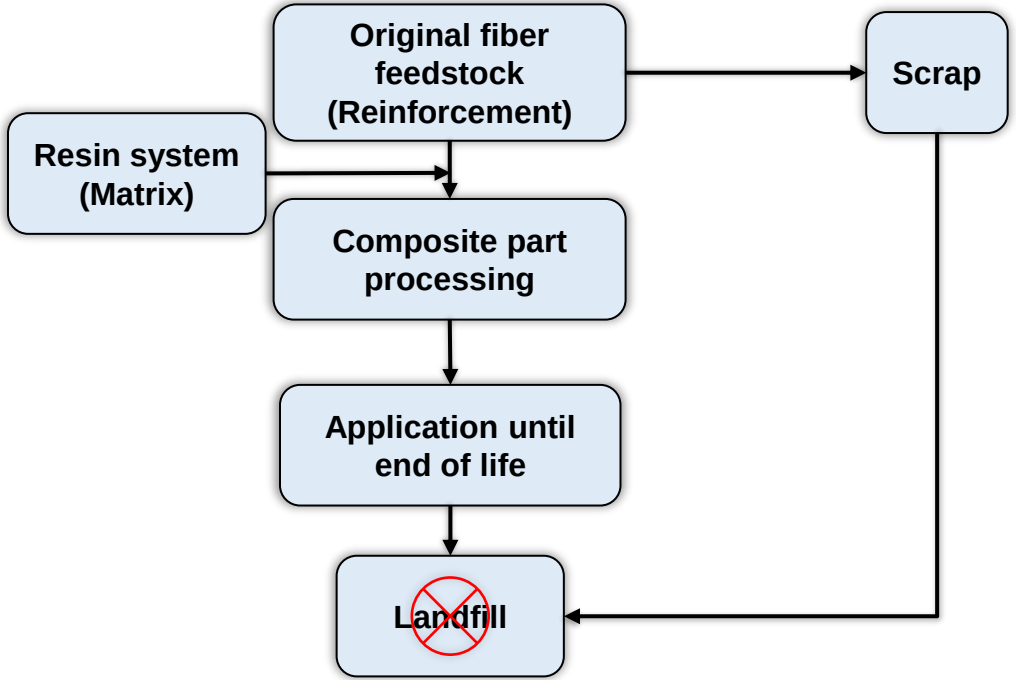

Background

- Conventional processing flow chart of composite parts
- Fibers recycling from composite scrap or end of life parts
  - Fiber length reduction (Aspect ratio (ξ))
  - Fiber strength
  - Interface quality
  - Alignment & orientation
  - Volume fraction

Recycling approach

Re-processing approach

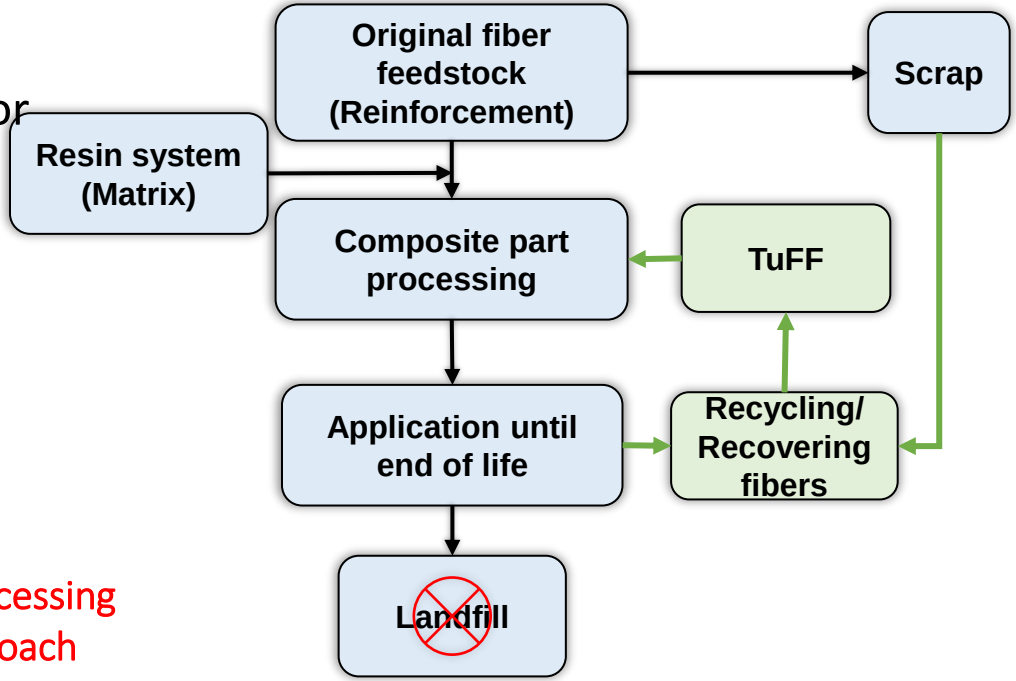

Motivation

- Conventional processing flow chart of composite parts
- Fibers recycling from composite scrap or end of life parts
  - Fiber length reduction (Aspect ratio (ξ))
  - Fiber strength
  - Interface quality
  - Alignment & orientation
  - Volume fraction

Recycling approach

Re-processing approach

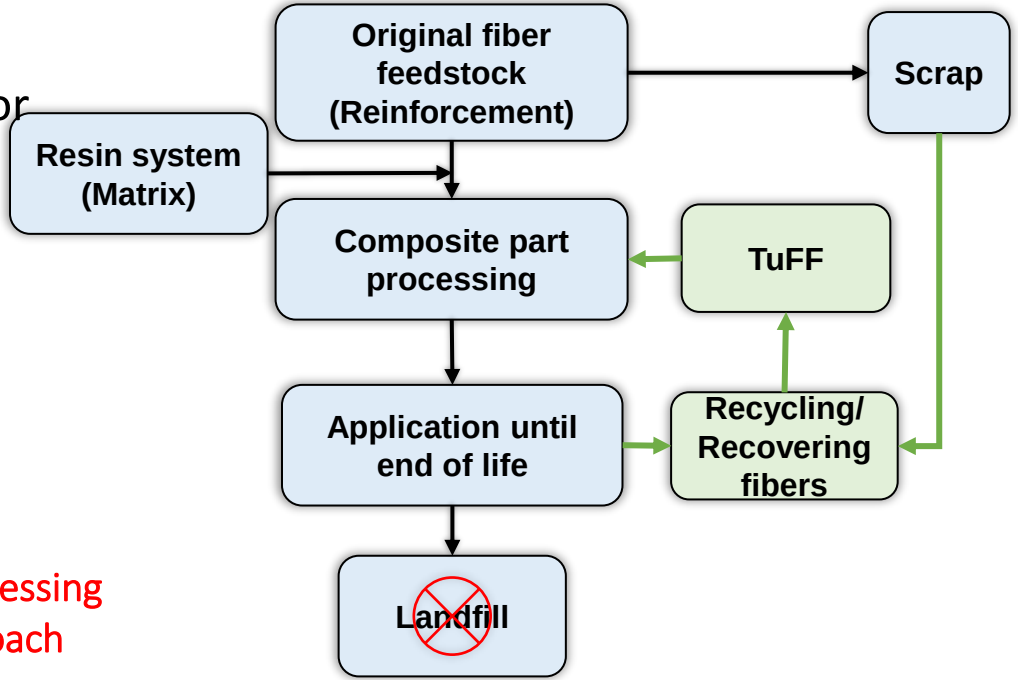

TuFF Background

Tailored **u**niversal **F**eedstock for **F**orming (**TuFF**) Process

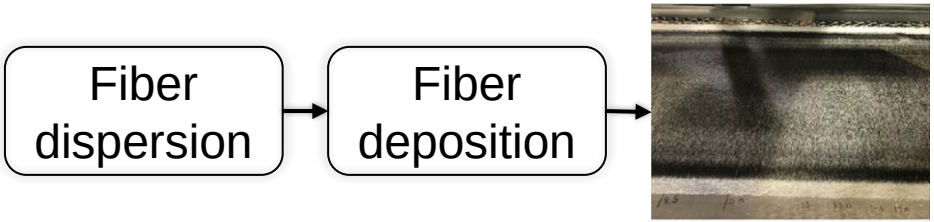

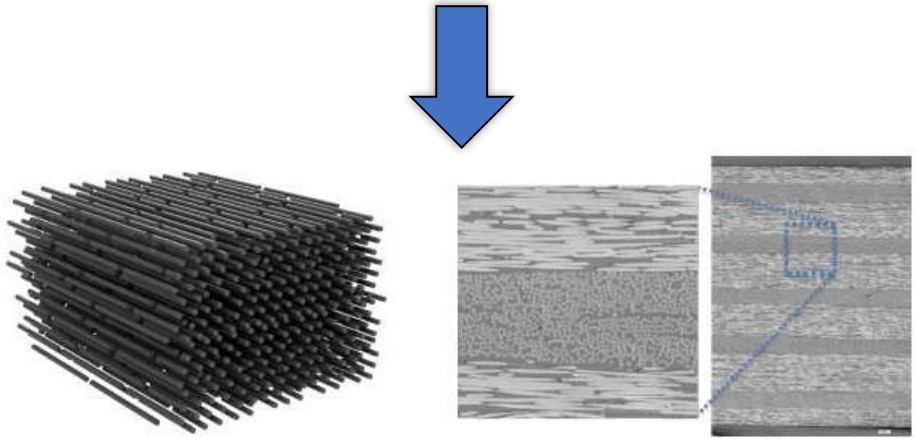

- Water based fiber deposition process
- Highly aligned short fiber preforms
- Performance similar to continuous composites

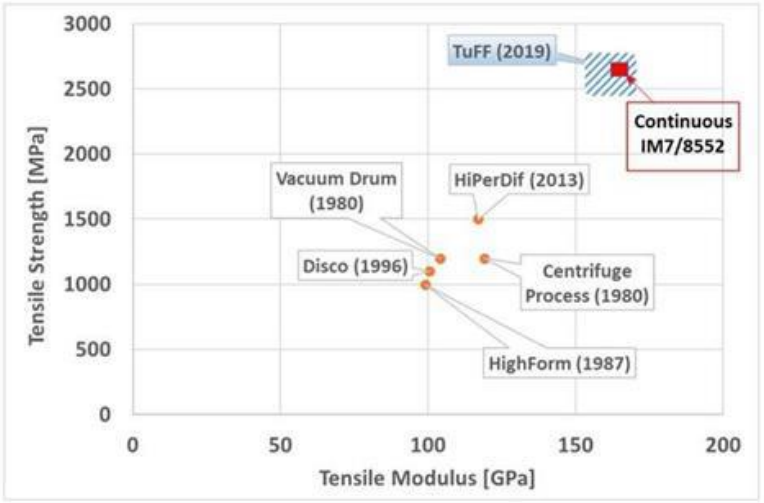

Outline

- Background & Motivation
- **Objectives**
- Experimental Approach
- Results & Discussions
- Conclusions

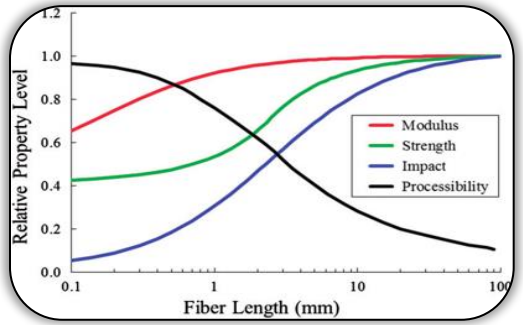

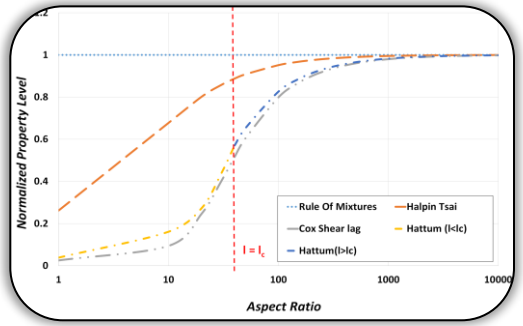

Objectives

- Mechanical performance as a function of fiber ξ(length / diameter)
- Investigating the processing quality
- Comparison of experimental data with analytical models

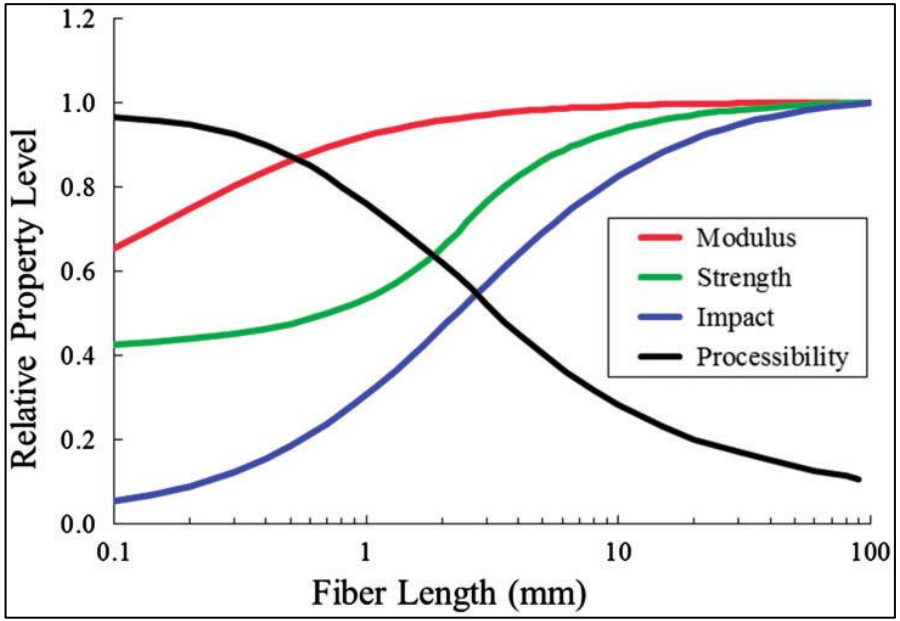

Wang, Qiushi & Jones, Joydan & Lu, Na & Johnson, Ralph & Ning, Haibin & Pillay, Selvum. (2017). Development and characterization of high-performance kenaf fiber–HDPE composites. Journal of Reinforced Plastics and Composites. 37. 073168441773912. 10.1177/0731684417739127.

Earlier Work

- Previous work on individual fiber lengths with increasing ξ
- Consistent stiffness irrespective of fiber ξ
- Increasing strength with increased ξ
- Similar to continuous at ~600 ξ
- Mixed ξ ???

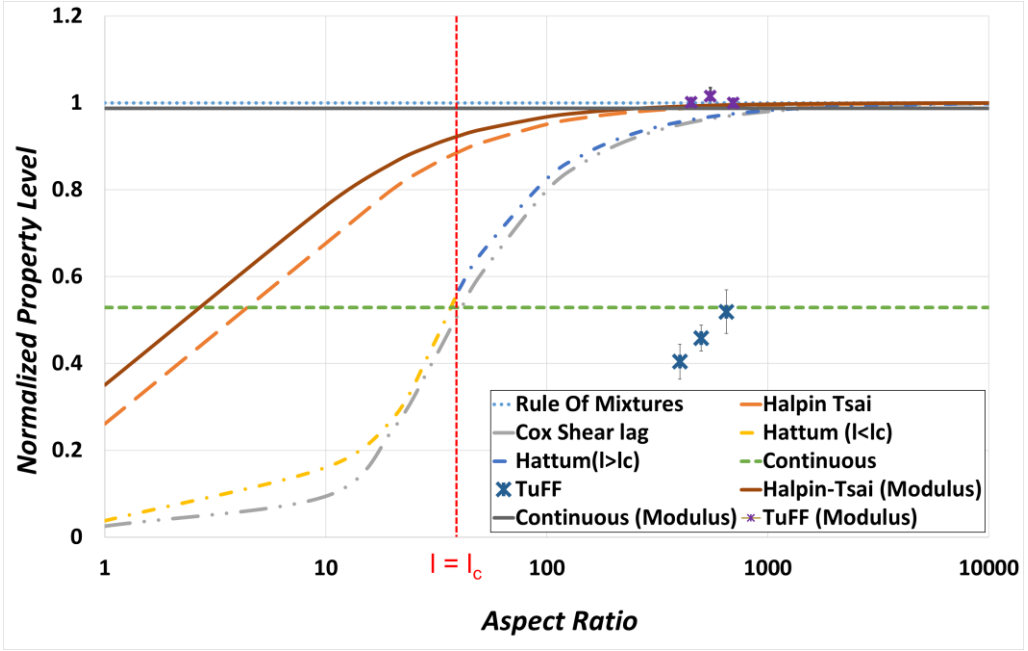

Balaga, U.K., et. al. (2024). Influence of fiber aspect ratio on the mechanical performance of highly aligned short fiber composites. ASC Conference, San Diego.

Outline

- Background & Motivation
- Objectives
- **Experimental Approach**
- Results & Discussions
- Conclusions







Design of Experiments

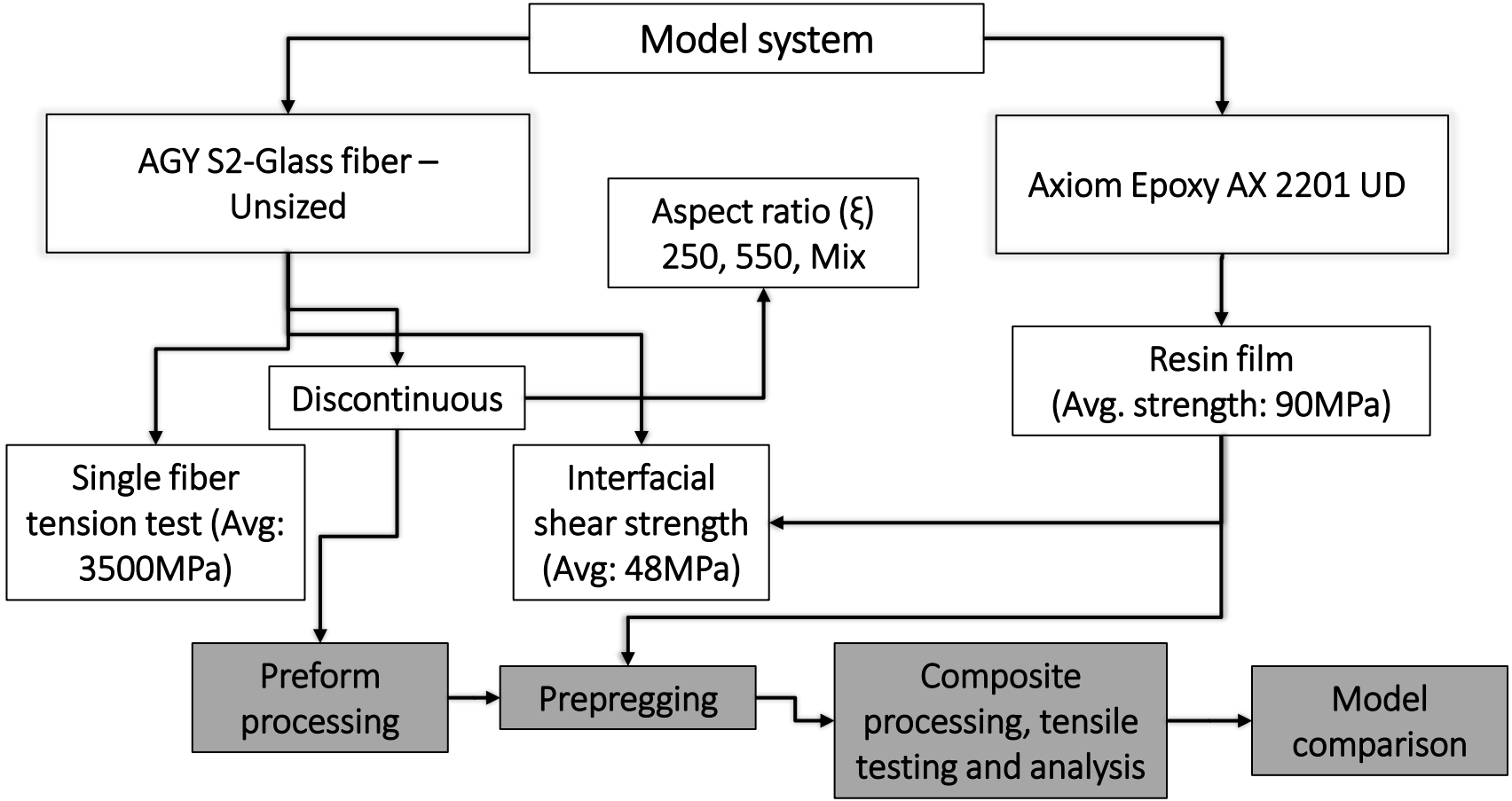

Composite Processing

Preform processing

ID	ξ
P1 (3.25mm)	250
P2 (7.15mm)	550
P12 (mixed)	mix

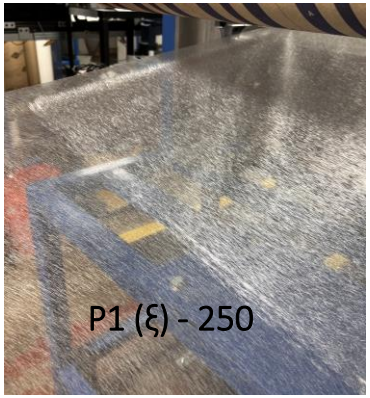

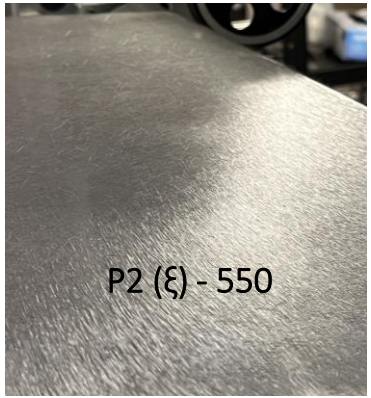



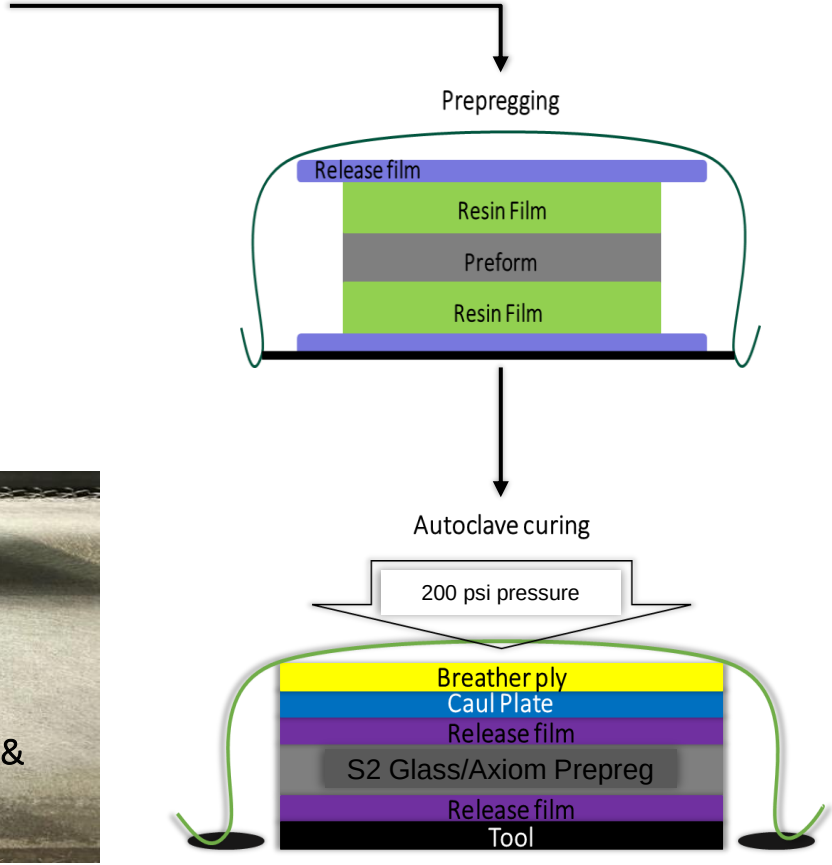

Outline

- Background & Motivation
- Objectives
- Experimental Approach
- **Results & Discussions**
- Conclusions

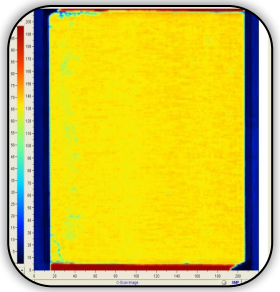

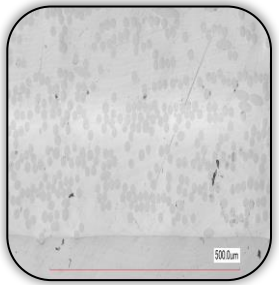

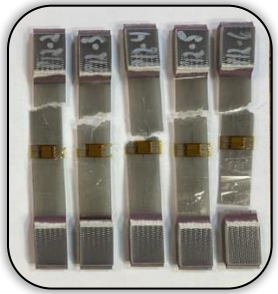

C-Scans and Microscopy

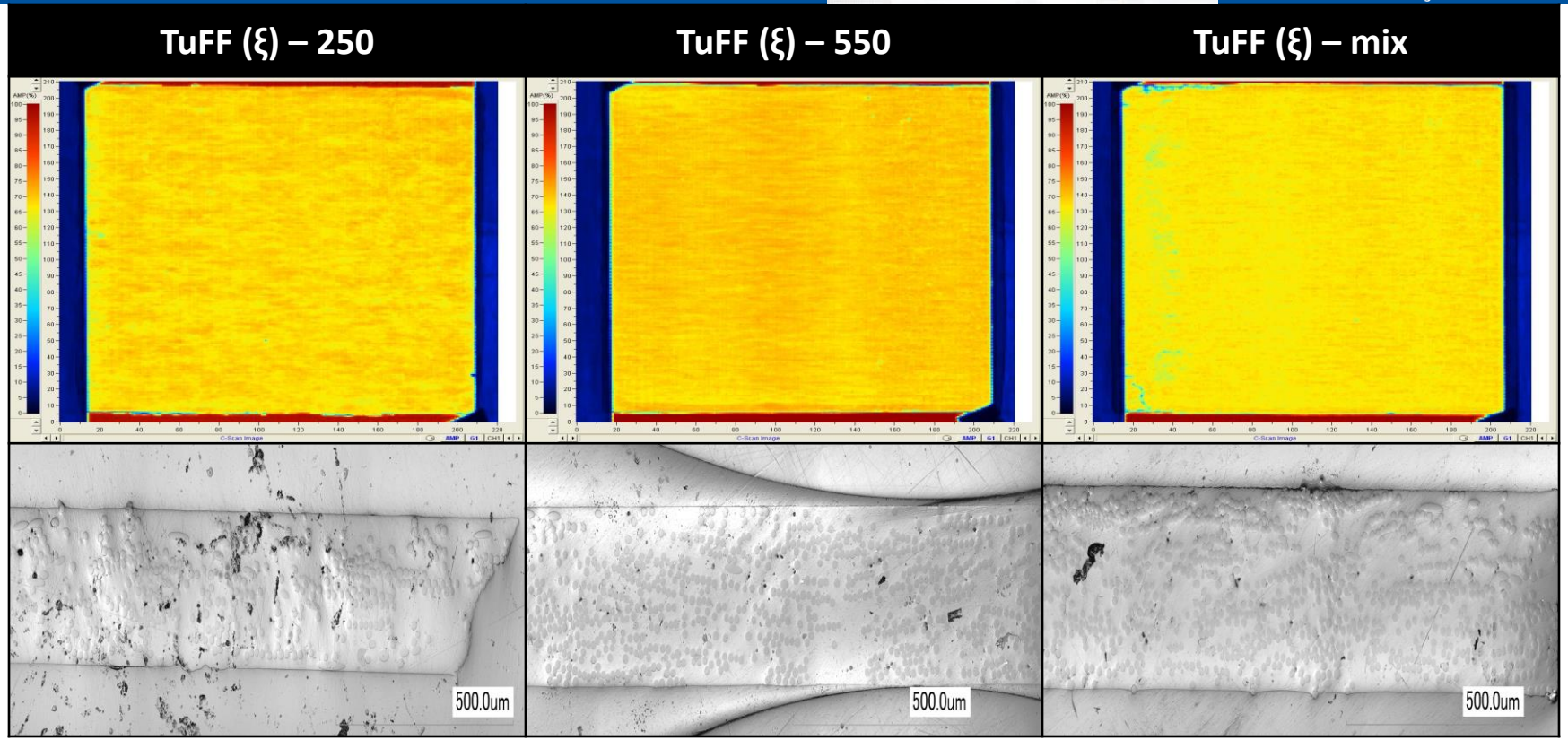

*ξ – Aspect ratio

- Uniform distribution in Tuff composite (minimal voids or porosity in all cases)

Orientation Analysis

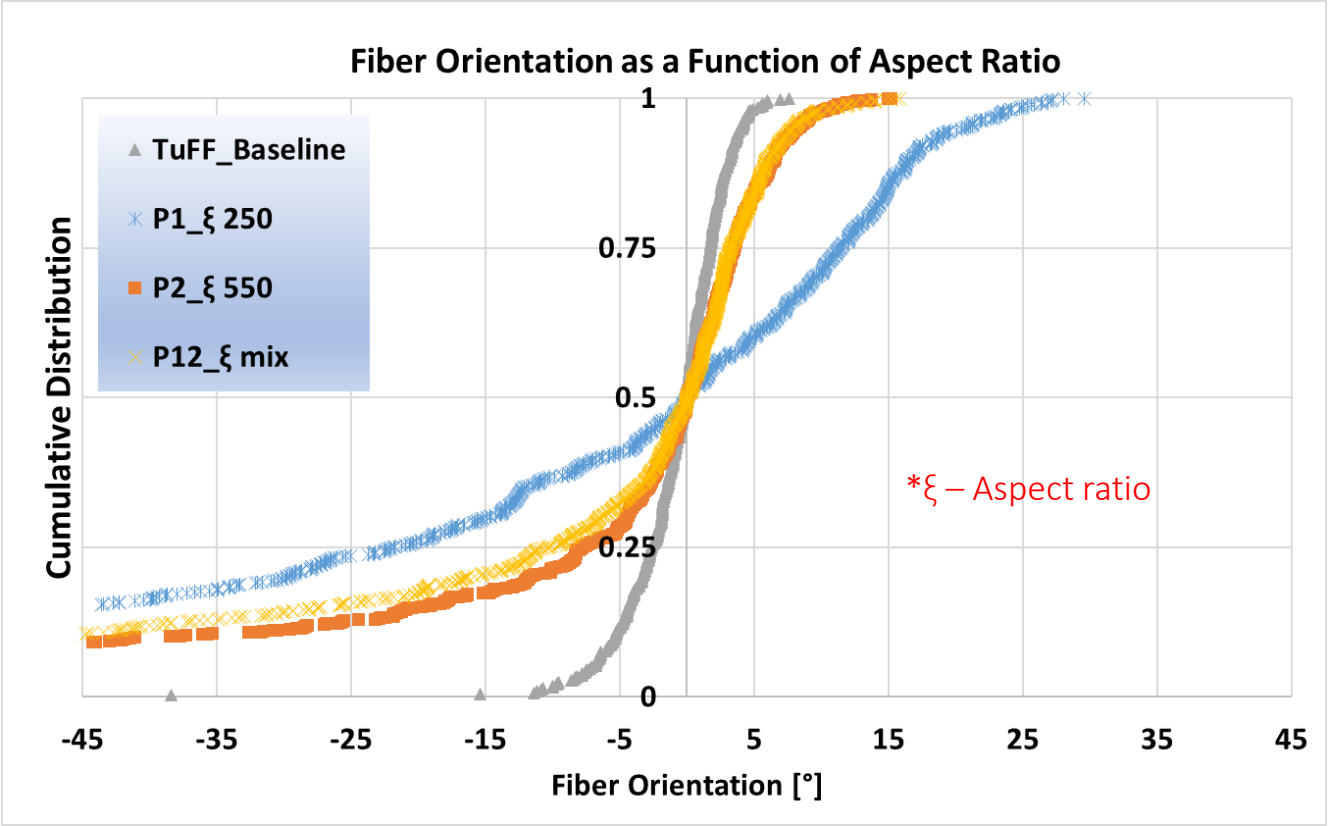

- TuFF baseline
  - Tight orientation
  - Higher FVF
- TuFF P1, P2 & P12
  - Broader spread
  - As fiber ξ reduces, orientation reduces
  - More than 60% fibers within ±15°

Mechanical Performance

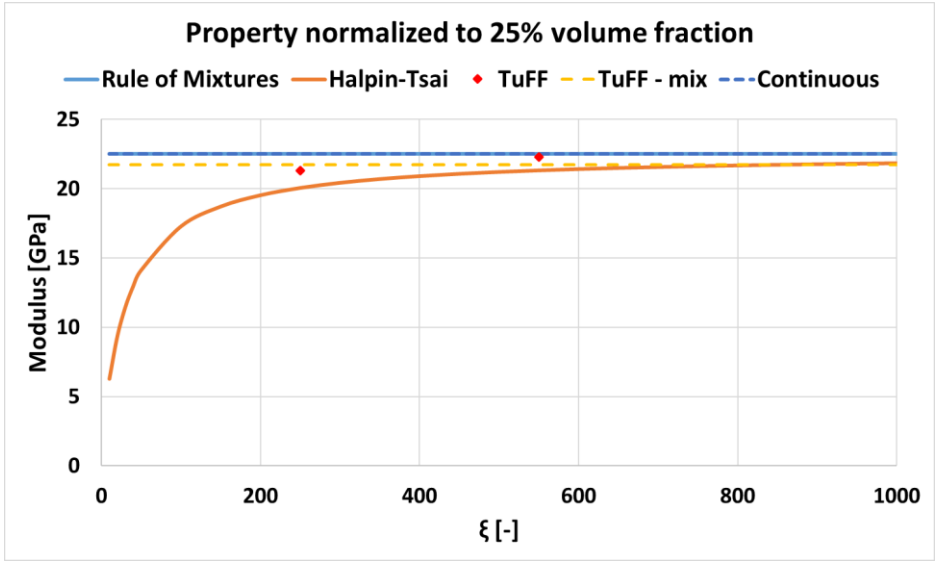

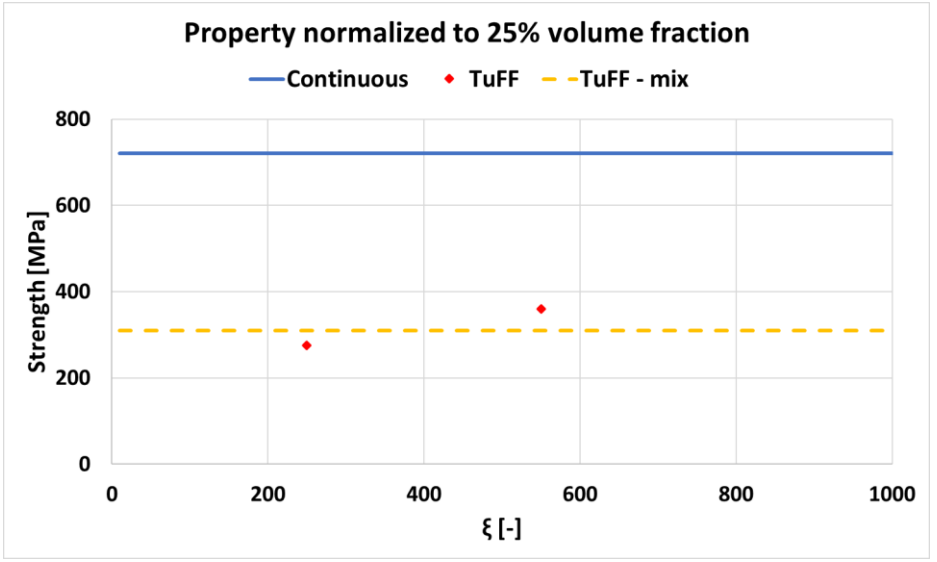

› Modulus

- Independent of Aspect Ratio
- Continuous composite data from technical data sheet

› Strength

- Increases with increasing ξ
- Mixed ξ strength between the two data points with higher inclination towards smaller ξ

Mechanical Failure Behavior

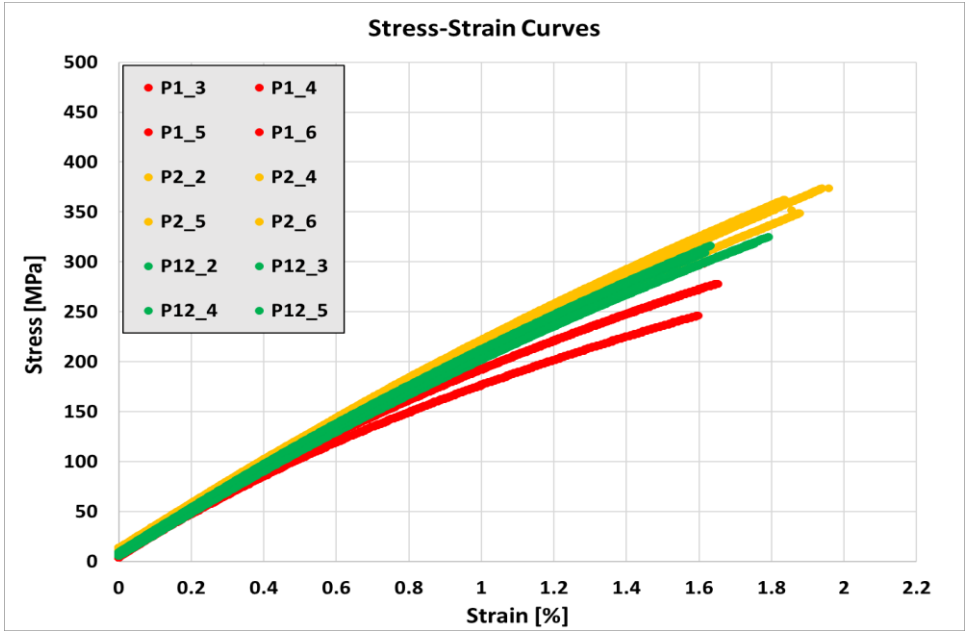

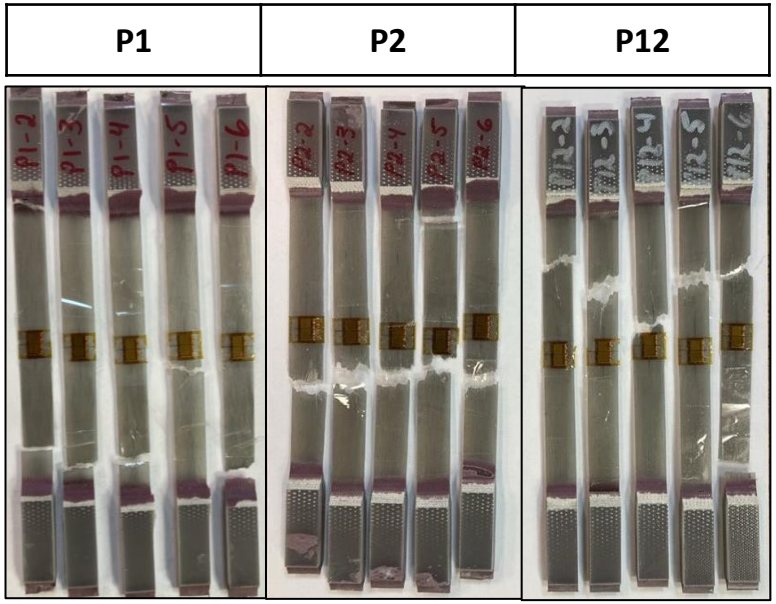

› Matrix dominated failure in the shorter fibers (low volume fraction, poor interface or inefficient load transfer)

› Displacement – 0.05 inch/min

› Failure Mode - LGM (ASTM 3039)

(lateral gage middle)

Analytical Models

- Modelling: Property vs Aspect ratio

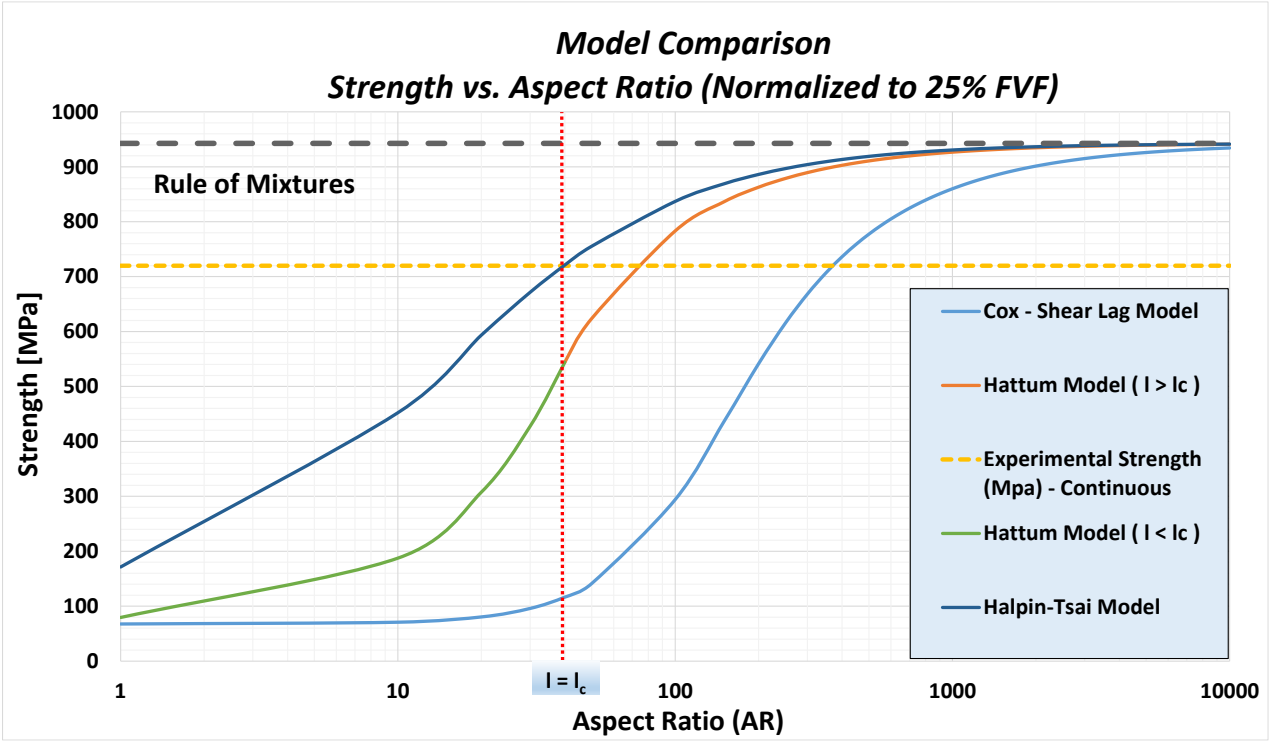

Model inputs	
Fiber volume fraction	0.25
Matrix volume fraction	0.75
Fiber strength	3500 MPa
Matrix strength	90 MPa
Fiber matrix interface strength	48 MPa
Diameter	13 um

l = Fiber length, l_c = Critical length

Analytical Model Comparisons

- Model limitations in comparison with experimental results

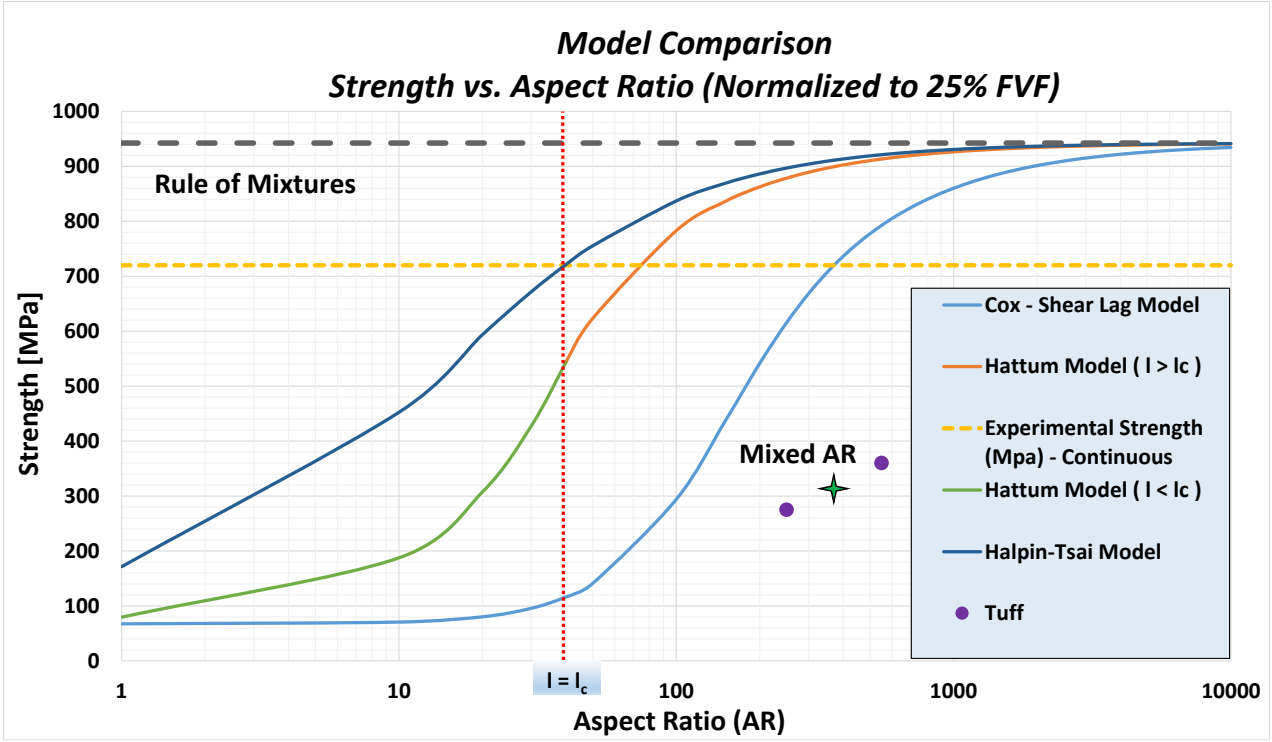

- Stochastic fiber strengths
- Intensity of microcracking progressions
- Interface failures in short fiber composite
- Non – uniform fiber volume fractions and orientation

Outline

- Background & Motivation
- Objectives
- Experimental Approach
- Results & Discussions
- **Conclusions**

Conclusions

Current:

- Experimental investigations of continuous and discontinuous composites.
- Alignment and packing efficiency analysis.
- Mechanical performance vs aspect ratio investigations with analytical models, experimental validations and interpretations.

Future Scope:

- Mechanical performance vs aspect ratio curve with fibers ranging lower and higher end of S-curve.
- Mixing of multiple fiber lengths at higher and lower end to investigate the mechanical behaviors.

Long term goals:

- Enabling closed loop recycling for sustainable manufacturing.
- High performance short fiber composites.

Acknowledgements

- This research is based upon work supported by the U.S. Department of Energy's Office of Energy Efficiency and Renewable Energy (EERE) under the Advanced Manufacturing Office Award Number DE-EE0009303.
- The C-scan results were generously provided by Dr. Nicholas Shevchenko from the Center for Composite Materials at the University of Delaware.



VOLUMETRIC QUANTIFICATION OF BRIDGING AND WRINKLING DEFECTS IN COMPOSITE LAMINATES

Cooper Williams[1], Dr. Cecily Ryan[1], Dr. Jared Nelson[2], Dr. Douglas Cairns[1]*, and Christopher Ridgard[1]*

[1]Department of Mechanical and Industrial Engineering, Montana State University
220 Roberts Hall, Bozeman, Montana, 59715, United States of America
Email: cooper.williams2@student.montana.edu, cecily.ryan@montana.edu
web page: https://www.montana.edu/advancedcomposites/

[2]Department of Mechanical Engineering, Keene State University
229 Main St, Keene, New Hampshire, 03431, United States of America
Email: jared.nelseon@keene.edu

*Corresponding Author(s)
Email: dcairns@montana.edu, Christopher.ridargd@montana.edu

Keywords: Carbon Fiber Composites, Laminates, Prepreg, Defects, Discontinuous Fibers

ABSTRACT

Stretch broken carbon fiber (SBCF) offers enhanced formability over traditional continuous carbon fiber (CCF) while retaining comparable mechanical properties. Leveraging this advantage, SBCF has the potential to reduce the formation and severity of common laminate defects such as wrinkling and bridging. This study introduces and applies volumetric methods for quantifying these defects with improved accuracy and resolution. Two SBCF and two CCF quasi-isotropic laminates were manufactured in a curved c-channel geometry and analyzed using 3D scan data and updated image processing methods. Results showed that the Montana State University (MSU)-developed SBCF laminates outperformed their CCF counterparts in terms of bridging behavior, exhibiting significantly lower average bridging volume and variability across both inner and outer radii of the channel. In contrast, both material systems yielded comparable wrinkling based on the defect scoring method discussed herein. However, there were differences observed in the wrinkling behavior between CCF and SBCF laminates with similar scores. While CCF laminates exhibited a higher frequency of and more broadly located wrinkles, SBCF laminates showed fewer wrinkles of larger average magnitude, particularly in non-critical regions. These findings reinforce SBCF as a promising material system for complex forming applications and highlight the need for further optimization to reduce wrinkling, particularly when occurring in critical regions.

INTRODUCTION

Carbon fiber (CF) composites are widely employed in performance-driven industries such as aerospace, automotive, and sporting goods due to their high tensile strength-to-weight ratio and design flexibility. These properties make them particularly desirable for structural applications where being lightweight and stiffness are critical material considerations. Fiber-reinforced composites are generally categorized into two groups: continuous fiber and discontinuous fiber systems. Continuous carbon fibers (CCF) are commonly used in pre-impregnated (prepreg) laminates for specific, efficiency focused applications. However, the limited maximum strain and inability for fibers within a CF tow to stretch and displace with respect to other fibers, can present significant challenges during the layup of complex geometries. Defects such as bridging and wrinkling are likely to occur in these geometries, limiting application due to manufacturability and performance [5, 6, 8].

Aligned, discontinuous fiber systems, such as stretch broken carbon fiber (SBCF), have been proposed as a more formable alternative for complex laminate geometries. SBCF laminates offer an improved ability to conform to complex geometries, making it a promising candidate for next-generation composite structures. Researchers at Montana State University (MSU) [1-3,7,10] have made significant

progress in developing an SBCF prepreg system and are actively evaluating its forming behavior in geometrically challenging applications, using CCF laminates as a performance benchmark.

This study focuses on two critical laminate defects: wrinkling and bridging [4]. By quantifying these defects across both SBCF and CCF material systems within a specified complex geometry, the curved c-channel, this work aims to assess the formability of MSU SBCF material, identify successful forming strategies, and evaluate metrics related to the material's potential for use in industrial composite component manufacturing.

METHODOLOGY

Laminate Manufacturing

Six laminates were manufactured for this study; three of which were continuous unidirectional Syensqo Hexcel 12k IM7 CYCOM® 977-3 carbon fiber prepreg [12]. The remaining three laminates were made with unidirectional MSU SBCF carbon fiber prepreg. This SBCF prepreg was made in conjunction with the University of Southern Mississippi using MSU stretch broken Hexcel 12k IM7 fibers and CYCOM® 977-3 resin system [11-12]. All laminates, CCF and SBCF, were eight-ply, quasi-isotropic, $[45/0/-45/90]_S$ to maintain consistency with laminates evaluated in previous MSU SBCF program studies [1]. The laminates for this study were formed into a curved c-channel geometry, Figure 1, following the layup method used in previous studies, also with the purpose of maintaining consistency [1]. This method is described briefly below.

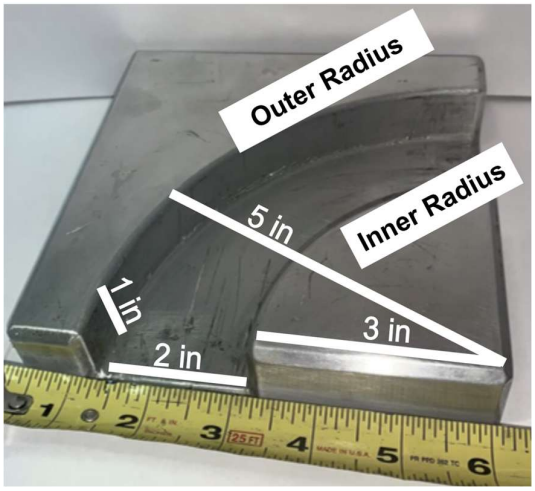

Figure 1: Curved c-channel aluminum mold used for previous program laminates in [1].

During manufacturing, 9-inch square plies were laid up in pairs and formed to the mold starting in the corner where the radii are centered. The plies were then worked across the surface of the mold, down the inner radius face, across the bottom of the channel, up the outer radius face, and onto the larger flat area towards the diagonal corner of the start. The newest curved c-channel mold, the mold for these studies, has been expanded by 1.5 inches in length and width from the mold used in previous studies to accommodate grit strips to secure material edges during forming. During the layup, plies were formed by hand using 200°F [93.3°C] via heat gun to increase the pliability of the two-ply sub-laminate. Once initially placed, the same heat and force was then applied to the pair of plies to enhance forming and smooth out wrinkles that may have formed. A silicon intensifier was placed onto the laminate after the layup was completed. Figure 2 shows the completed layup with the grit strips and intensifier. The laminate was then vacuum bagged and debulked for 20 minutes before curing in an autoclave. The autoclave recipe for all laminates in this study follows the current recipe for curing MSU SBCF parts: the autoclave is initially ramped to 200°F [93.3°C] for 30 minutes before a 4-hour dwell at 250°F [121°C]. This cure cycle has been developed from forming evaluations of SBCF parts during autoclave

curing in previous program studies [1-2]. During the autoclave cure, the grit strips mitigate slipping on the ply-mold interface. After curing completed, the laminate was demolded and trimmed to a 6 inch by 6-inch square. Sharp edges were then sanded away for handling.

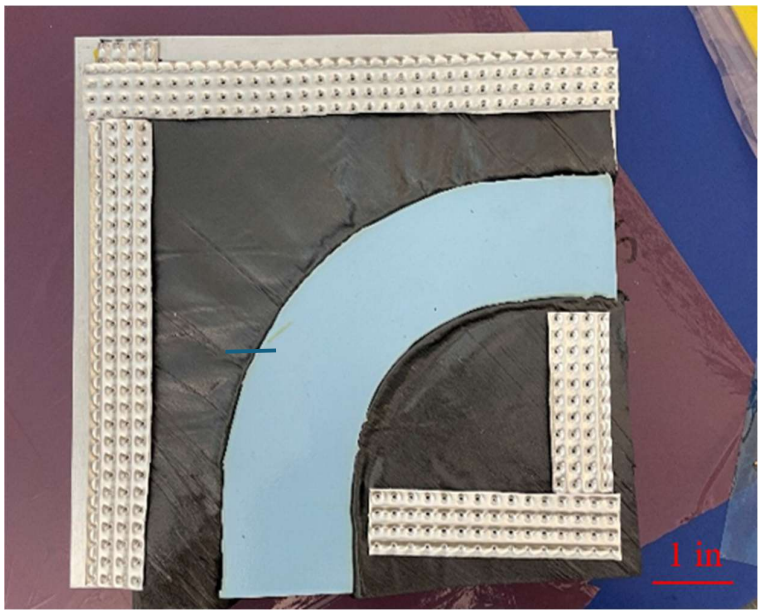

Figure 2: Complete curved c-channel layup ready for bag.

Wrinkling Analysis

After the laminate was cured, trimmed, and sanded, it was scanned in 3-dimensions using a Keyence VL-800 Series 3D scanner. The scan produces a point cloud with about 300,000 points and an STL mesh of the scanned laminate. Once scanning was completed, the rectangular footprint (boxed in Figure 3) of each observable wrinkle was directly measured and recorded with dial calipers for later use. The critical area–the main channel and circled in Figure 3 – is where wrinkles would be most concerning. The non critical area outside of the circle is of lesser, but substantial, concern.

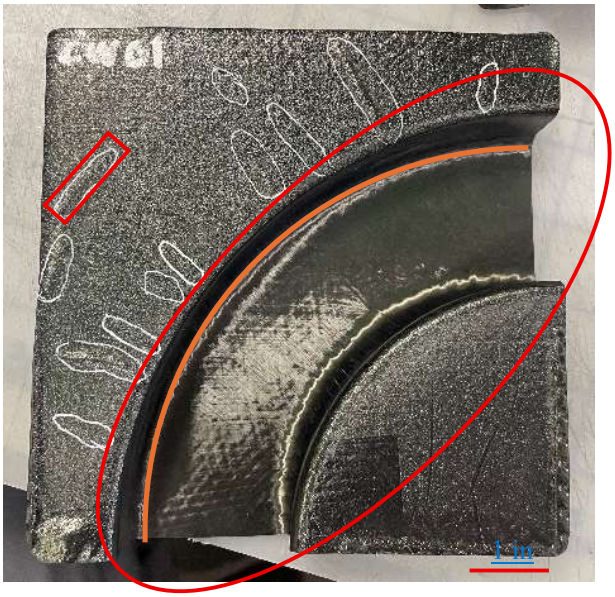

Figure 3: Curved c-channel laminate after complete wrinkle measurement.

3D scans of laminates were analyzed using CloudCompare. A reference mesh of the as-designed, ideal laminate is imported into the software as is the STL mesh of the scanned laminate. These two meshes are then scaled and aligned. Using CloudCompare's cloud to mesh (C2M) comparison tool, the distance between the reference mesh and various groups of points in the scanned mesh–usually around 50,000 groups–can be calculated. This analysis yields a displacement mapping of the scanned laminate onto the original, highlighting where the greatest distances between the two are. An example of results from this process is shown in Figure 6 below. Wrinkles are easily visible; they can be easily identified, isolated, and labeled for individual analysis. Using a Gaussian distribution tool in CloudCompare, the Gaussian mean distance of each wrinkle from the reference was determined and recorded. This mean was then multiplied across the rectangular footprint of each wrinkle to determine a volumetric approximation of the wrinkle size.

With the 3D scans, all laminate wrinkles were analyzed to create a more complete understanding of SBCF wrinkling during forming. Therefore, wrinkles can be analyzed both in the critical area, circled in Figure 3, as done in prior studies and in the submitted conference abstract, as well as more broadly across the parts. This full-part analysis allows for a more complete understanding and quantification of wrinkling frequency, magnitude, and location during forming. Additionally, it is important to note that the techniques of the MSU SBCF Parts and Structures Manufacturing group have progressed to where wrinkling rarely occurs on critical surfaces. Wrinkles on the critical area and noncritical areas of each laminate are denoted separately for further analysis.

Bridging Analysis

After the wrinkling analysis was complete, each laminate is cut every 15° from 0° to 90°, as depicted in Figure 4. Section faces were sanded for imaging at the inner and outer radii to obtain the cross-sectional area for bridging measurements and calculations.

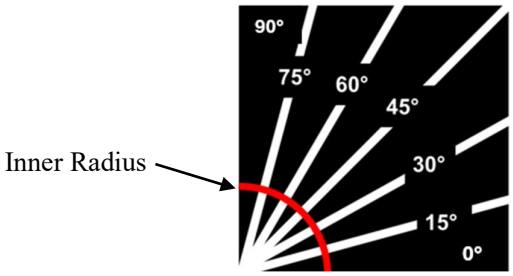

Figure 4: Sectioned curved c-channel showing the slices made for the bridging analysis.

Figure 5 depicts the cross section of both the inner and outer radii of Figure 1, as both have the same cross-sectional geometry and a fillet of 0.125 in radius. Using ImageJ, measurements of the distance, L_x and L_y, between the laminate-mold contact point and the perpendicular mold surface were collected from images. The lengths measured were used to calculate the cross-sectional area of the bridging space. L_x and L_y were first used to find the area of the red rectangle, Figure 5, and then used to find the area of the ellipse formed by the laminate. The area of the ellipse was then subtracted from the areas of the rectangle and fillet. The result of this calculation is the area of space generated from bridging, measured in square inches. This area was then extended over a fraction of the length of the curve perpendicular to the cross section in such that each area possesses equal length relative to all other calculated areas for a given radius. For example, if there are twelve faces, that of Figure 4, created along a radius of curvature with an arc length –such as the orange arc of Figure 3– of six inches, the cross-sectional area of each face is extrapolated over 0.5 inches of the total six inches. This analysis assumes that the surface created when the laminate was cut is an adequate representation of bridging for the surrounding area of the radius through this extreme region of the geometry.

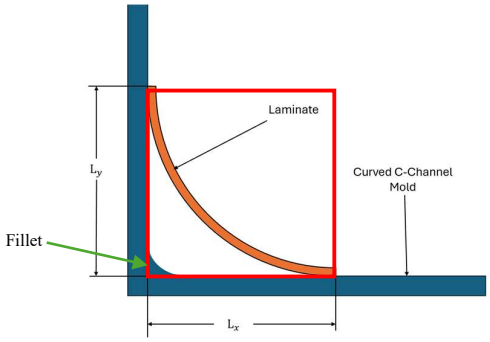

Figure 5: Curved c-channel cross-section and location of measurements to calculate bridging volume.

Table 1: Variables for Calculating Bridging Volume

Variable	Definition
r_f	Fillet radius, 0.25 in.
i	Cross-sectional face being measured, ND*.
L_{yi}	Vertical length from point of tangency to perpendicular mold surface at i, in.
L_{xi}	Horizontal length from point of tangency to perpendicular mold surface at i, in.
A_e	Cross-sectional Ellipse area, in.^{2}
A_R	Cross-sectional Rectangle area, in.^{2}
A_B	Cross-sectional Bridging area, in.^{2}
l_{ARC}	Length of curvature of concern, in.
N	Total number of cross-sectional faces created, ND*.
V_B	Volume of Bridging, in.^{3}

*ND: Non-dimensional

Equation 1, below, describes the summation of small sections of volumes for each face created when cutting the laminate at the specified angles shown in Figure 4. These volumes are generated by multiplying the cross-sectional area of bridging (blue boxed term in Equation 1) by a fraction of the area's guide curve (orange boxed term in Equation 1). The terms in the blue box of Equation 1 represent the subtraction of the ellipse's area from the red rectangle's area plus the small cross-sectional area of the fillet, Figure 5. The term boxed in orange, below, describes a fraction of the cross-sectional area's guide curve. The outer and inner radii are the guide curves of this geometry. The length of the arc, l_{ARC}, is simply the total length of the outer or inner radius, depending on the radius of curvature. Multiplying the blue and orange terms of Equation 1 generates the volumetric measurement of bridging in cubic inches.

$$\sum_{n=0}^{N}\left[\left((L_y \cdot L_x) - \frac{\pi \cdot L_{yi} \cdot L_{xi}}{4} + ({r_f}^2 - \frac{\pi * {r_f}^2}{4})\right) * \left[\frac{l_{ARC}}{N}\right]\right] = V_B \qquad (1)$$

Cutting a curved c-channel laminate, as previously discussed, creates twelve cross-sectional faces: one at 0°, another at 90°, and two at every remaining cut site. Thus, in Equations 1 and 2, the inner and outer radii lengths were sectioned into twelfths for the purpose of these equations. These equations were used to extrapolate the cross-sectional area along a portion of the extreme radius such that each volume was equal in the length it spans. The summation of these twelve volume approximations formed a 3D model of the total volume created by bridging for the geometry under inspection (variables are listed in Table 1).

Equation 2 is a simplified version of Equation 1. It uses the same variables but establishes a constant that represents subtracting one-quarter of an ellipse from a rectangle whose sides are equal to the major and minor axes of the ellipse. This constant, in the purple box of Equation 2, assumes that the laminate maintains a smooth, elliptical cross-sectional profile. Equation 2 also introduces the constant

cross-sectional area of the fillet in square inches, the green box, since the fillet is of a known, constant value. Equation 2 was used to determine the total bridging volume estimate.

$$\sum_{n=0}^{N}\left[\left(\left(L_{yi}L_{xi}\right)*\left(1-\frac{\pi}{4}\right)+0.00353\right)*\frac{l_{ARC}}{N}\right]=V_B \qquad (2)$$

It is important to note that equations 1 and 2 are specific to calculations for this geometry and represent the application of this quantification process to the curved c-channel. The principles of this method can be applied to any concave laminate of interest where bridging may occur. In future work, similar calculations will be extended for use in other geometries. The key feature of this approach is that a model of the space created by bridging can be established using cross-sectional measurements to define bridging and extrapolated over an appropriate perpendicular arc length. This calculation is repeated at each face created from cutting, and the resulting volumes are summed to form a comprehensive volumetric bridging model of the laminate.

NOMENCLATURE

Table 2: Sample Laminate Labelling

Sample Number	Continuous Fiber (CF)	Stretch Broken Carbon Fiber (SBCF)
1	CF01	SBCF01
2	CF02	SBCF02
3	CF03	SBCF03

RESULTS

Due to a layup error, laminate SBCF01 was found to be asymmetric and was therefore excluded from further wrinkling analysis in this study. The nonconformity rendered its scans unusable for 3D wrinkle characterization. To maintain balanced sample sizes between SBCF and CCF groups, wrinkling data for CF02 are also withheld.

Wrinkling Analysis Results

The greatest number of wrinkles was observed in CF01, which exhibited twelve distinct wrinkles. All the other laminates presented eight wrinkles each. Wrinkles were primarily located in non-critical regions of the laminate geometry, with the exception of a single critical-region wrinkle observed in CF03. SBCF01 and SBCF03 exhibited larger average wrinkle volumes than either of the continuous fiber laminates: 0.00589 in^3 and 0.00711 in^3, respectively. In comparison, CF01 and CF03 had average wrinkle volumes of 0.00221 in^3 and 0.00309 in^3, respectively. The stretch-broken fiber laminates also demonstrated greater variability in wrinkle size, with standard deviations of 0.00745 in^3 in SBCF02 and 0.006013 in^3 in SBCF03.

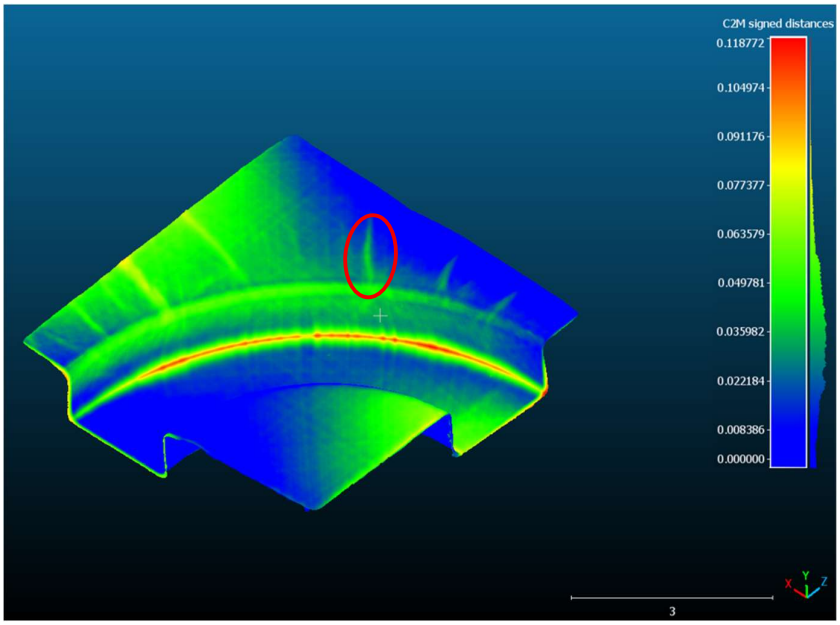

Figure 6: Complete CloudCompare C2M analysis of SBCF03. Both scales display inches, which may marginally deviate through a scaling factor.

Figure 6 depicts a completed CloudCompare C2M (Cloud-to-Mesh) analysis used to quantify wrinkle geometry. This analysis was similarly performed for CF01, CF02, and SBCF02, isolated wrinkles are displayed in Table 3. In Figure 6, wrinkle locations correspond to areas of maximum deviation from the nominal surface geometry. Areas near 0 in of deformation are shown in blue while areas of high deformation approaching 0.01188 in are shown in red. Green, yellow, and orange areas depict increasing distances from the designed part, respectively. Wrinkles were shown highlighted and easily observed as green and yellow areas of Figure 6. All eight wrinkles in SBCF03 were located on the large, non-critical zone of the part, a trend observed across most laminates in the study. Notably, SBCF02 exhibited both the largest and smallest wrinkles by volume, measured at 0.228 in^3 and 0.0005 in^3, respectively. This range underscores the variability in wrinkle severity found in stretch broken laminates compared to their continuous fiber counterparts.

Table 3 below shows the isolated wrinkles of each laminate after the initial alignment is completed. These wrinkles are located mainly on the top flange as previously discussed and can dramatically vary in size. Many of the wrinkles are either aligned with the fiber axis of the +45° plies or the corner where layup begins. Color scales for these wrinkles also widely vary as they are typically one of the largest deformations in a laminate and can have varying prominence, meaning that the height of the wrinkle itself varies with respect to the height of the surface it propagates on.

Table 3: Images of isolated wrinkles of all analyzed laminates

CF01	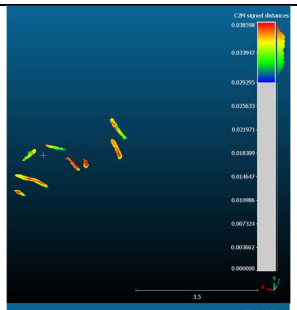
CF03	
SBCF02	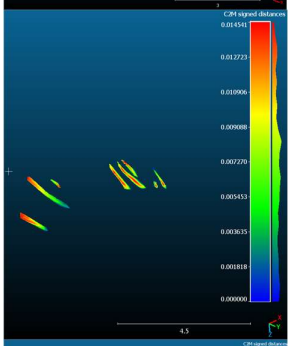
SBCF03	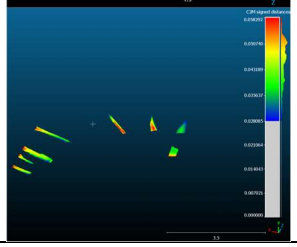

*Laminate scales are in inches and marginally deviate from designed laminate part through a scaling factor.

Bridging Analysis Results

CF02 exhibited the highest average bridging volume along both the inner and outer radii, measured at 0.01182 in^3 and 0.00916 in^3, respectively. The variance of CF02 was also larger than all other laminates: 5.81130E-05 in^6 at the inner radius and 2.15772E-05 in^6 at the outer radius. SBCF02 showed the lowest average bridging volumes across both regions, 0.00230 in^3 (inner) and 0.00381 in^3(outer), and also exhibited the lowest variance: 3.75586E-07 in^6 (inner) and 3.99120E-07 in^6 (outer). At both radii, SBCF01 displayed average bridging comparable to CF01–the best CF laminate in terms of bridging–but performed the worst among SBCF laminates with average bridging at the inner radius of 0.00643 in^3 and 0.00584 in^3 at the outer radius. SBCF02 and SBCF03 showed low bridging with maximum average bridging at either radius of 0.00381 in^3 and 0.00412 in^3, respectively.

.

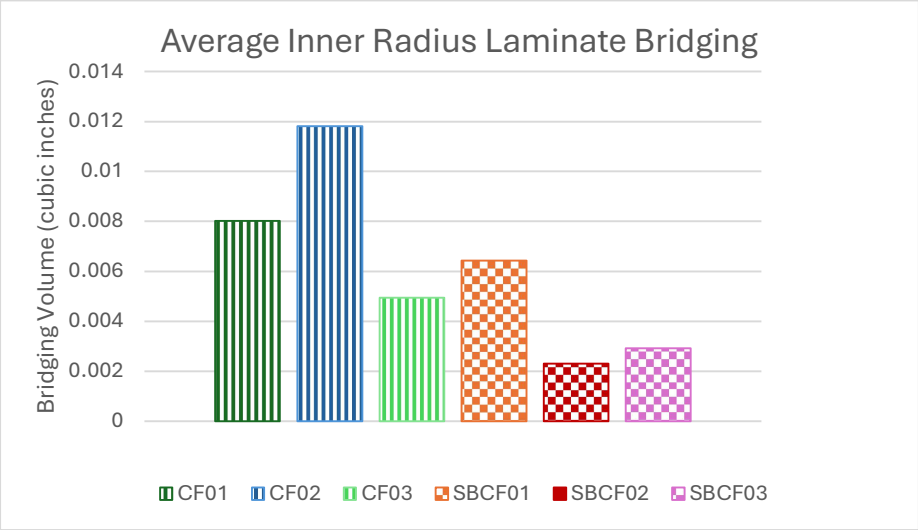

Figure 7: Average inner radius bridging volume of all laminates.

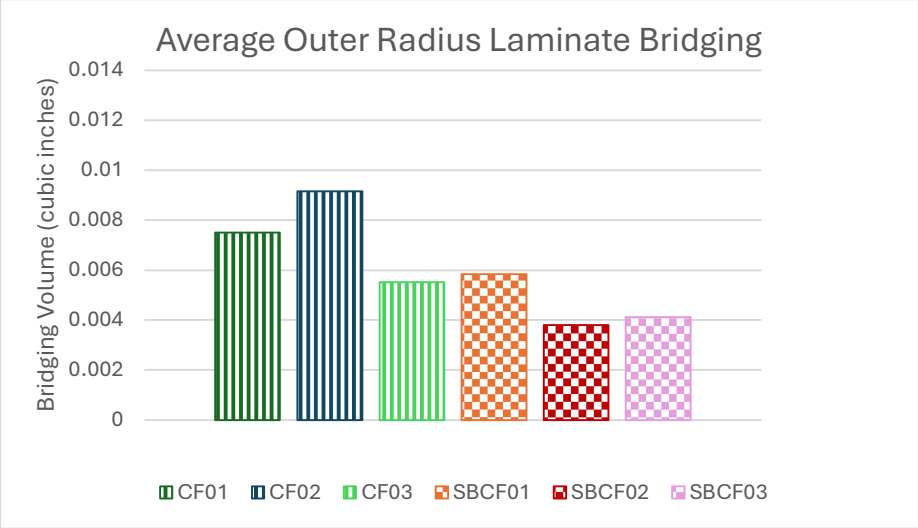

Figure 8: Average outer radius bridging volume of all laminates.

The x-axes of Figure 9 and Figure 10 correspond with the cuts shown in Figure 4, not ply fiber angle. All laminates exhibit a local peak in bridging volume near the 45° face cuts, Figure 4, with this effect more pronounced in the continuous fiber laminates. In addition to having the highest average bridging volumes, CF02 also shows both the highest and lowest bridging occurrences at the outer radius, indicating a broader spread in localized bridging severity. Similar to the average bridging behavior, the forming of SBCF01 is comparable to that of the CF laminates but is much greater than other SBCF laminates, especially at extreme geometry. In contrast, SBCF02 and SBCF03 laminates demonstrate the most consistent bridging behavior across both radii while maintaining low bridging volumes, as shown in Figure 9 and Figure 10. At the inner radius, continuous fiber laminates demonstrate poor forming to the concave radius as the curve of the channel becomes more aggressive; but bridging decreases at the 0° and 90° cuts. Conversely, SBCF laminates exhibit low amounts of bridging across the curve with fluctuations throughout.

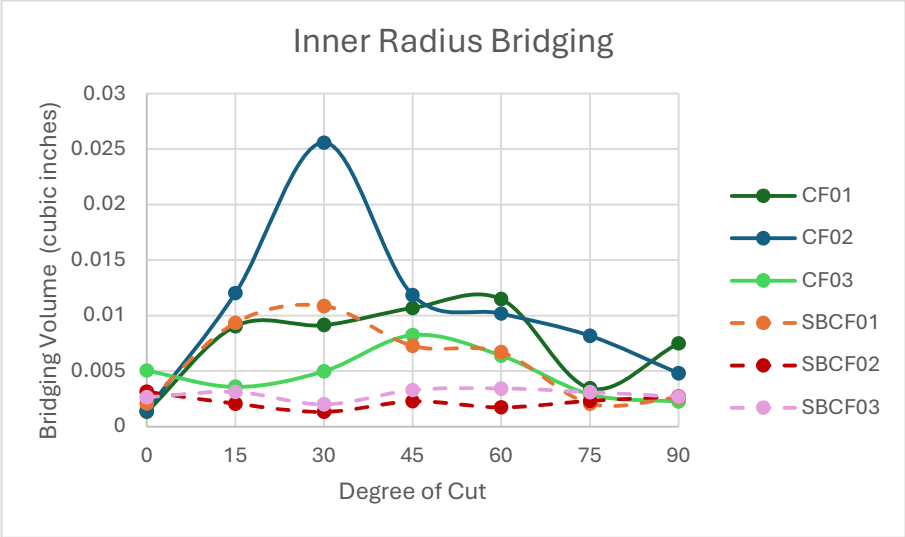

Figure 9: Inner radius bridging volume mapping.

Similar to their behavior at the inner radius, continuous fiber laminates at the outer radius of the curved c-channel exhibited greater bridging towards the extreme portions of the curve, with better conformity before and after this section of geometry. The stretch broken laminates outer bridging performance was also comparable to their bridging performance at the inner radius, again with SBCF01 as an outlier. SBCF03 had a lower range of bridging volume throughout the laminate with stronger local fluctuations at the most aggressive portions of the geometry. Notably, SBCF02 demonstrated outstanding bridging performance, maintaining a low, nearly constant bridging volume around the curvature.

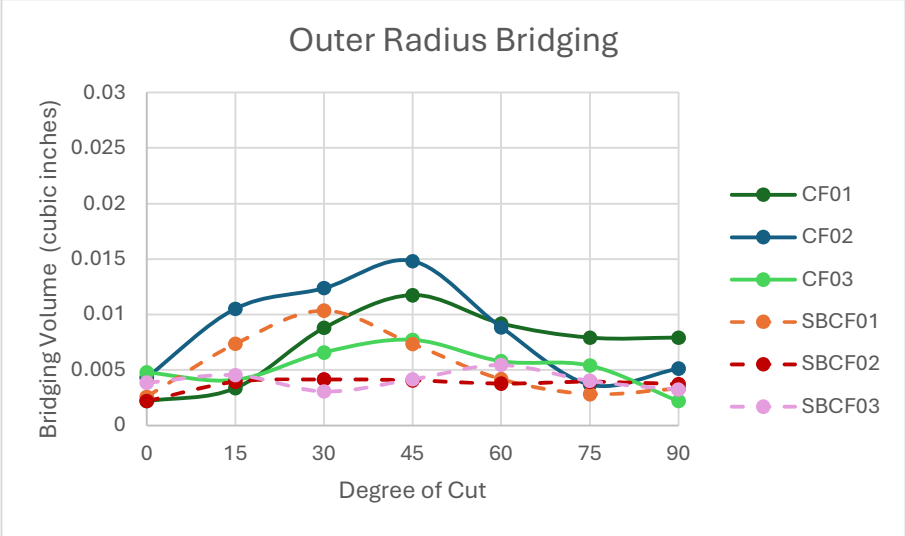

Figure 10: Outer radius bridging volume mapping.

DISCUSSION

Wrinkling Analysis Discussion

The higher variability of wrinkle magnitude and comparable wrinkle propagation in SBCF laminates compared to CCF laminates indicates that SBCF may also be more sensitive to local

disturbances during layup and curing given that the current MSU SBCF laminate manufacturing practices are under continual development, and current practices may still allow small process inconsistencies to manifest as wrinkles and other defects. The consistent wrinkle locations of this study loosely align with wrinkling from previous studies, despite more refined manufacturing processes [1]. The larger non-critical flange regions are more susceptible to wrinkling, likely due to the layup technique and residual forming forces induced during layup and curing. Wrinkling at this flange emphasizes the consideration placed on tooling design and layup practices, such as tension control when working with this material.

The present wrinkling analysis between CCF and SBCF materials does not clearly indicate which material is better suited to avoiding laminate wrinkling. The consistent presence of wrinkles in both materials highlights residual challenges in achieving defect-free forming. The wrinkling behavior of CCF laminates may be within the expected bounds for unidirectional laminates of this geometry, but the ceiling for formability for SBCF laminates is much higher than demonstrated in this study. As optimal SBCF laminate manufacturing practices such as tooling design, vacuum bag configuration, layup technique, and strategic intensifier use continue to be identified and refined, it is probable that SBCF part conformity will improve, especially for this geometry.

Bridging Analysis Discussion

As the laminates form to the mold geometry during forming, the 0° and 90° plies are primarily subjected to transverse in-plane tension, particularly near the extreme regions of curvature where stress concentrations are highest. The ±45° plies behave differently under deformation: the +45° plies experience in-plane longitudinal tension, while the -45° plies are subjected to in-plane orthogonal tension. At both the inner and outer radii, CCF tend to bridge as they span the concave geometry, constrained by their high tensile stiffness and limited ability to stretch. In contrast, the SBCF laminates demonstrate improved conformity in these regions. This increased geometric conformity is attributed to the shorter, discontinuous but aligned fiber segments that characterize SBCF materials, which allow for higher effective stretch ratio without theoretically significantly sacrificing composite properties. The reduced fiber lengths in SBCF laminates not only improve formability but also significantly lower the likelihood of bridging in concave regions.

While Figure 9 and Figure 10 may initially suggest that bridging is more severe at the outer radius than the inner, this comparison is misleading due to differences in arc length between the two regions. The outer radius spans a longer arc (7.854 in) than the inner radius (4.712 in), which inherently increases the calculated bridging volume at the outer radius (Equation 2), regardless of actual bridging severity. This difference allows for the direct comparison of a specific radii between laminates but not between the inner and outer radii of a given laminate.

In addition, the use of a silicon intensifier during autoclave processing has become a critical feature of MSU's SBCF laminate manufacturing approach. In this study, it played an important role in enhancing forming quality by reducing bridging and alleviating layup "touch" time. Bridging has been a challenge for previous SBCF programs due to fiber length [9]; however, the MSU SBCF laminates significantly outperformed the continuous fiber laminates in terms of bridging behavior in the c-channel geometry of this study. The results of this study have direct implications for manufacturing curved composite components where conformability, labor efficiency, and defect tolerance are critical, such as an aerospace stiffener design or automotive reinforcements.

CONCLUSION

Forming an eight-ply quasi-isotropic prepreg laminate into a curved c-channel geometry provided valuable insights into the layup, forming, and curing procedures and preliminary defect behavior of MSU's SBCF material system in complex structures. Using CCF laminates as a control enabled direct benchmarking of bridging and wrinkling performance under identical geometric and process constraints.

The CCF laminates exhibited significant bridging, particularly in regions of high curvature, along with wrinkling defects in both critical and non-critical areas. In contrast, two of the SBCF laminates demonstrated improved bridging performance, with reduced defect volume and variability across the inner and outer radii. However, SBCF laminates also showed comparable, yet slightly higher average wrinkle volumes compared to their continuous fiber counterparts, despite similar wrinkle counts. None of the wrinkles in SBCF laminates were in critical regions. While no definitive material preference can be established from this study alone, the findings suggest that with further refinement in processing techniques, SBCF materials have strong potential for use in complex-forming applications, especially where bridging is a limiting defect.

Additionally, this work provides valuable insights regarding the effectiveness of these new quantification methods. The bridging system worked as intended without any unforeseen challenges. The wrinkling system, however, was particularly challenged in the analysis of laminates with high macroscopic deviation from the designed laminate, such as SBCF01. This challenge will be overcome as the wrinkling analysis process is refined, and knowledge gaps will be filled accordingly.

FUTURE WORK

Subsequent studies will focus on expanding the defect characterization framework by employing next-generation metrics similar to those used for bridging and wrinkling in this study. Particular attention will be given to understanding the behavior of SBCF materials in concave radii, where corner thickening is observed; furthermore, the mechanisms and mitigation strategies for this phenomenon are outside the scope of the present study, they will be addressed in future work. Understanding, quantifying, and potentially mitigating this effect will be essential for enabling the broader adoption of SBCF laminates in geometrically complex structural components, including the curved c-channel. Another future focus will be to expand the types of complex geometries that are evaluated for forming complex structures using this rigorous defect quantification scheme. As the production of MSU SBCF output increases in volume and quality, as outlined in [3], a growing catalog of laminate quality evaluations will guide the optimization of MSU SBCF applications and manufacturing techniques.

ACKNOWLEDGEMENTS

Montana State University would like to acknowledge the contribution of the US Army which has funded much of the recent development work. Agency: US Department of the Army; Award Number: W911W6-18-C-0050. The views and conclusions contained in this document are those of the authors and should not be interpreted as necessarily representing the official policies, either expressed or implied, of the Government.

REFERENCES

[1] Dube, M. E., *Forming Evaluation Metrics and Methods for Complex Stretch Broken and Continuous Carbon Fiber Parts*, Montana State University, Bozeman, MT, 2023.

[2] J. Janiki, *Forming Parameters and Quantification of Continuous and Stretch Broken Carbon Fibers*, Montana State University, Bozeman, MT, 2021.

[3] C. Ridgard et al, *Scalability, Production, and Application of Stretch Broken Carbon Fiber for Primary Aircraft Structure*, Vertical Flight Society: Forum 81, Virginia Beach, United States of America, May 19-23, 2025.

[4] M. H. Hassan, A. R. Othman, and S. Kamaruddin, *A review on the manufacturing defects of complex-shaped laminate in aircraft composite structures*, International Journal of Advanced Manufacturing Technology, vol. 91, no. 9–12. Springer London, pp. 4081–4094, August 1, 2017, doi: 10.1007/s00170-017-0096-5

[5] Luthada, P. "Defects and Damage in Composite Materials and Structures," *Addcomposites*, July 30, 2021, https://www.addcomposites.com/post/defects-and-damage-in-composite-materials-and-structures.

[6] Heslehurst, R. B., *Defects and Damage in Composite Materials and Structures*, 2014.

[7] Ridgard, C., Cairns, D., Boothe, E., "Advances in the development of stretch broken carbon fiber for primary aircraft structure," CAMX 2022, 2022.

[8] Potter, K. D., "Understanding the Origins of Defects and Variability in Composites Manufacture", International Conference on Composite Materials 17, Edinburgh, United Kingdom, 2009.

[9] Dillon, G. P., Stiver III, D. H., Application of Stretch Broken Carbon Materials to Rotorcraft Structure, Pennsylvania State University.

[10] Shchemelinin, Y., Nelson J. W., Ryan, C., Bajwa, D., Cairns, D., and Amendola, R., "Hydraulic bulge testing to compare formability of continuous and stretch broken carbon fiber reinforced polymer composites," International Journal of Material Forming, vol. 16, no. 2, Mar. 2023, doi: 10.1007/s12289-023-01743-6.

[11] "HexTow® IM7 Carbon Fiber.", https://www.hexcel.com/Resources/DataSheets/Carbon-Fiber

[12] "CYCOM® 977-3", https://www.solvay.com/en/product/cycom-977-3#

Interply Friction Characterization of Continuous and Stretch Broken Carbon Fiber (SBCF) Composites during Forming

Presenter: Tasnia Javin Nur

PhD Candidate, Material Science

Montana State University, Bozeman, MT

Outline

- Challenges in composite forming
- Introduction to stretch broken carbon fiber (SBCF)
- Relevance of friction during forming
- Interply friction characterization
  - Test materials
  - Test method
  - Test matrix
- Results and discussion
- Future work and conclusion

Challenges during Composite Forming

- Conventional CFRP composites made of continuous fibers –
  - -high axial stiffness
  - -low strain-to-failure
- Poor drapability and limited formability over double-curved or complex geometries
- Leads to forming defects: wrinkling, buckling, bridging, misalignment
- Limits large-scale adoption of CFRPs as replacement for metals in aerospace structures



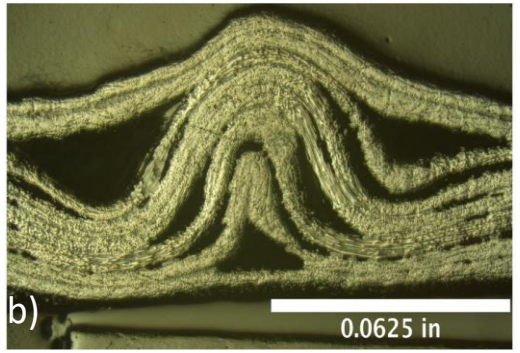



Forming defects : (a,b) Ply wrinkling and fiber buckling (c) Bridging

Stretch Broken Carbon Fiber (SBCF)

Metal-like formability in carbon fiber composites without compromising stiffness or strength





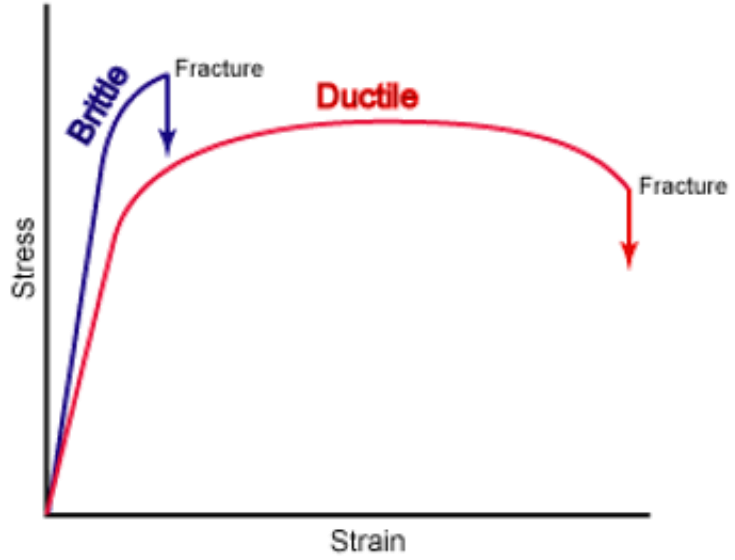

Stretch Broken Carbon Fiber (SBCF)

- Discontinuous, aligned short fibers with variable lengths (1- 40 mm)
- Continuous carbon fiber tows broken in tension, with breaks occurring at natural flaws
- Forming facilitated by axial stretching of the fibers when impregnated with resin (pseudo-ductility)
- Tensile strength retained through local shear load transfer

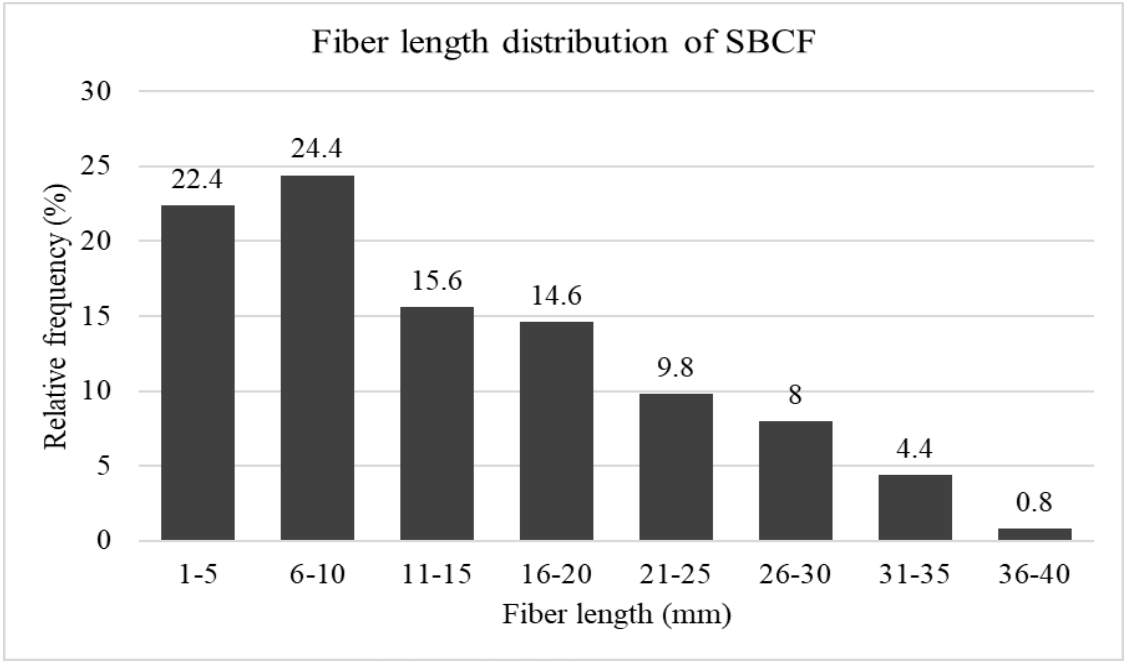

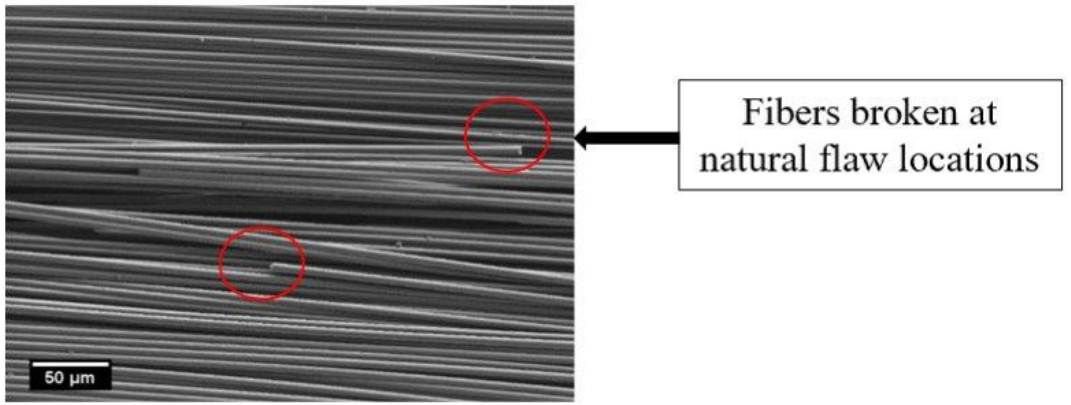

Relevance of Friction during Composite Forming

- Interply shear and slippage are essential deformation mechanisms for forming laminates into complex geometries
- Slippage is governed by interply friction, involves relative movement between adjacent uncured plies
- High frictional resistance limits interply shear, leading to forming defects
- SBCF introduces stretch deformation mode, reduces influence of friction and shear

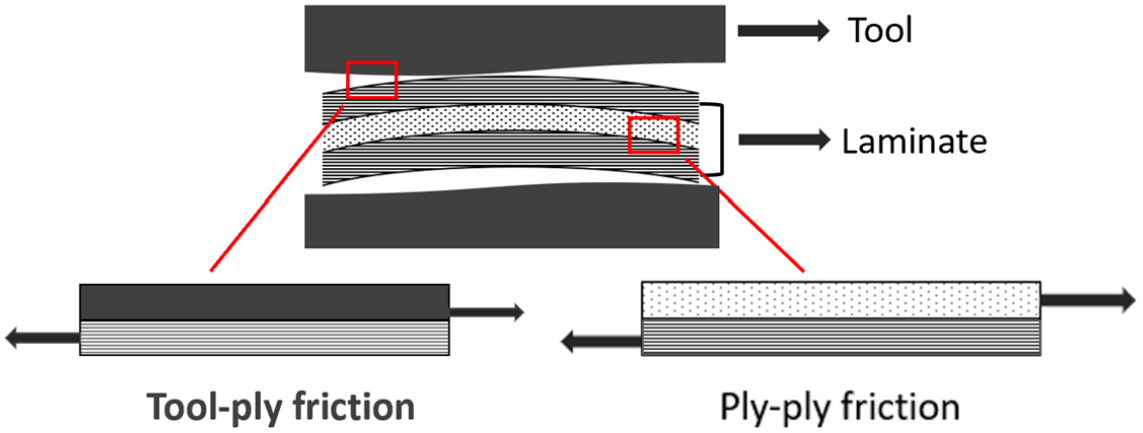

Interply Friction Characterization: Materials

Two carbon/epoxy prepregs :

- **Stretch broken carbon fiber (SBCF) prepregs** –

MSU Hexcel IM7 SBCF fibers impregnated with CYCOM® 977-3 resin in collaboration with USM (RC=37.5 %, FAW=139.6 gsm, Water Pickup (%) = 0.53)

- **Continuous carbon fiber (CCF) prepregs** –

Syensqo Hexcel 12k IM7 continuous fiber impregnated with CYCOM® 977-3 resin (RC = 32.7, FAW= 137.9 gsm, Water Pickup (%) = 0.57)



Novel stretch-breaking process developed at MSU

Interply Friction Characterization: Pull-through Test Method

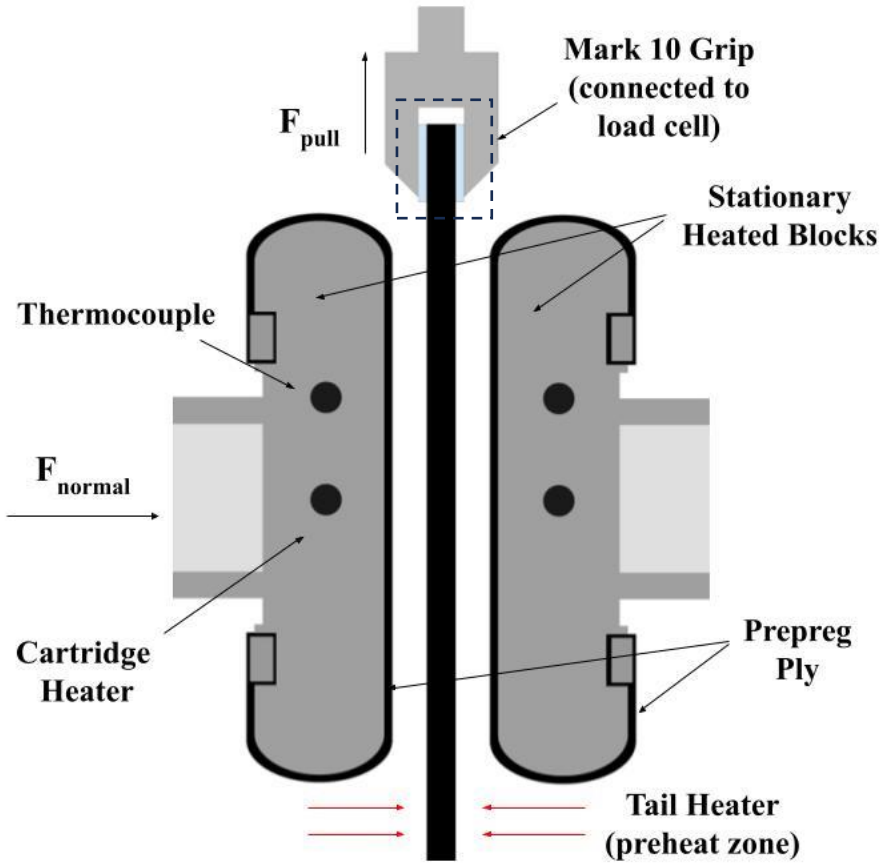

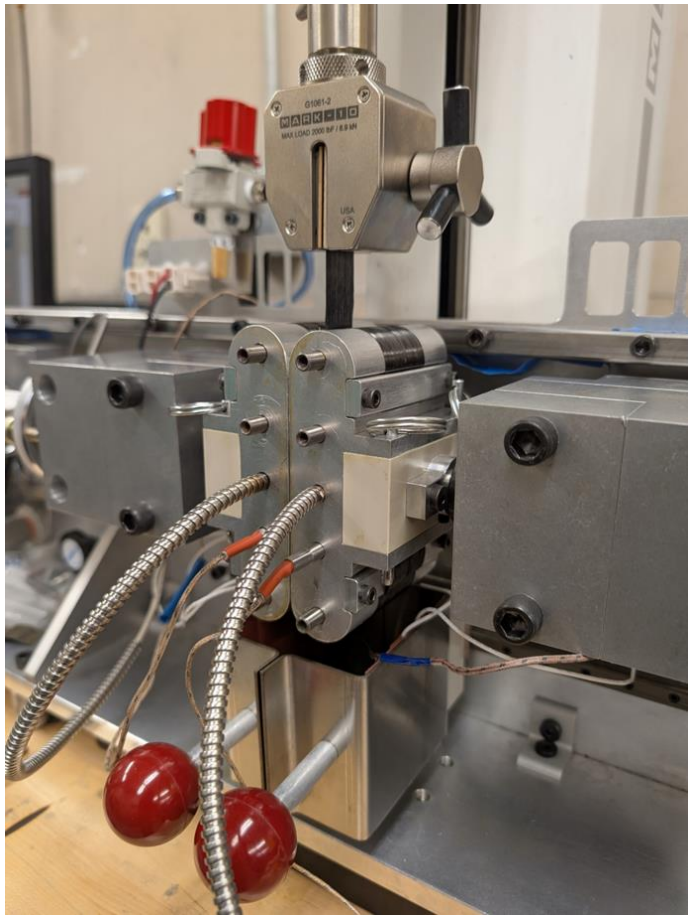

Test configuration and test matrix

	Clamping block	Central specimen	Clamping block
SBCF test	0° CCF	$[0]_{12}$=All 0° SBCFs	0° CCF
CCF test	0° CCF	$[0]_{12}$=All 0° CCFs	0° CCF

Test *	Temperature (°C)	Normal pressure (MPa)	Pulling rate (mm/min)
1	121	0.1	1
2	121	0.3	1
3	121	0.6	1

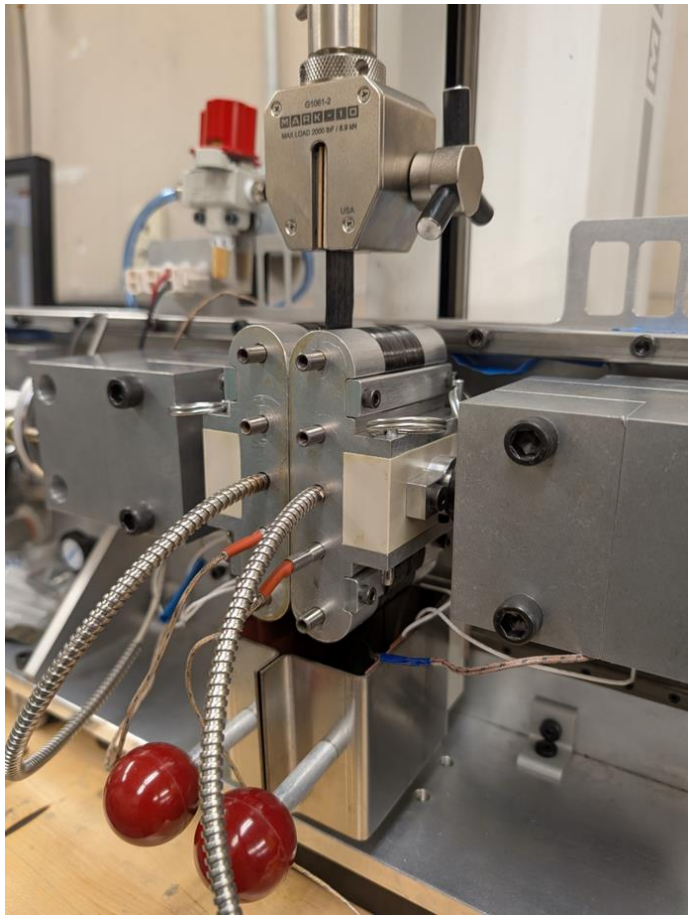

*Each test corresponds to three replicates and results are averaged for three tested samples

Results : CCF vs SBCF

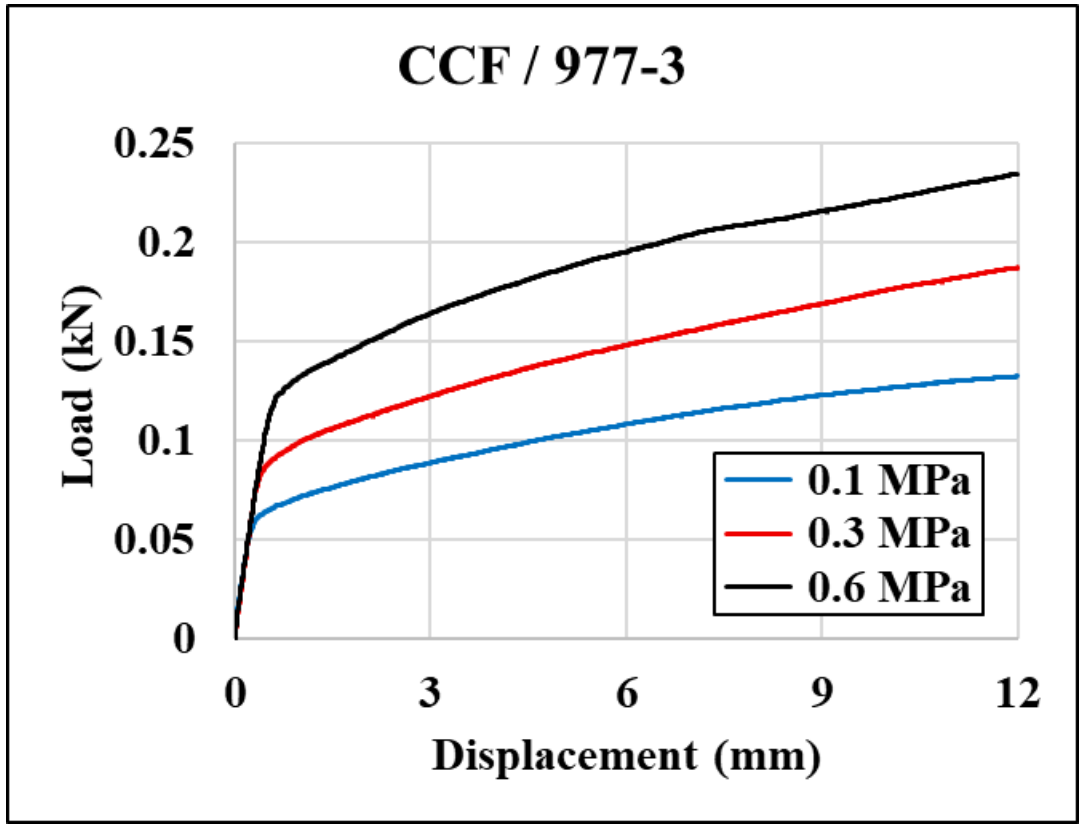

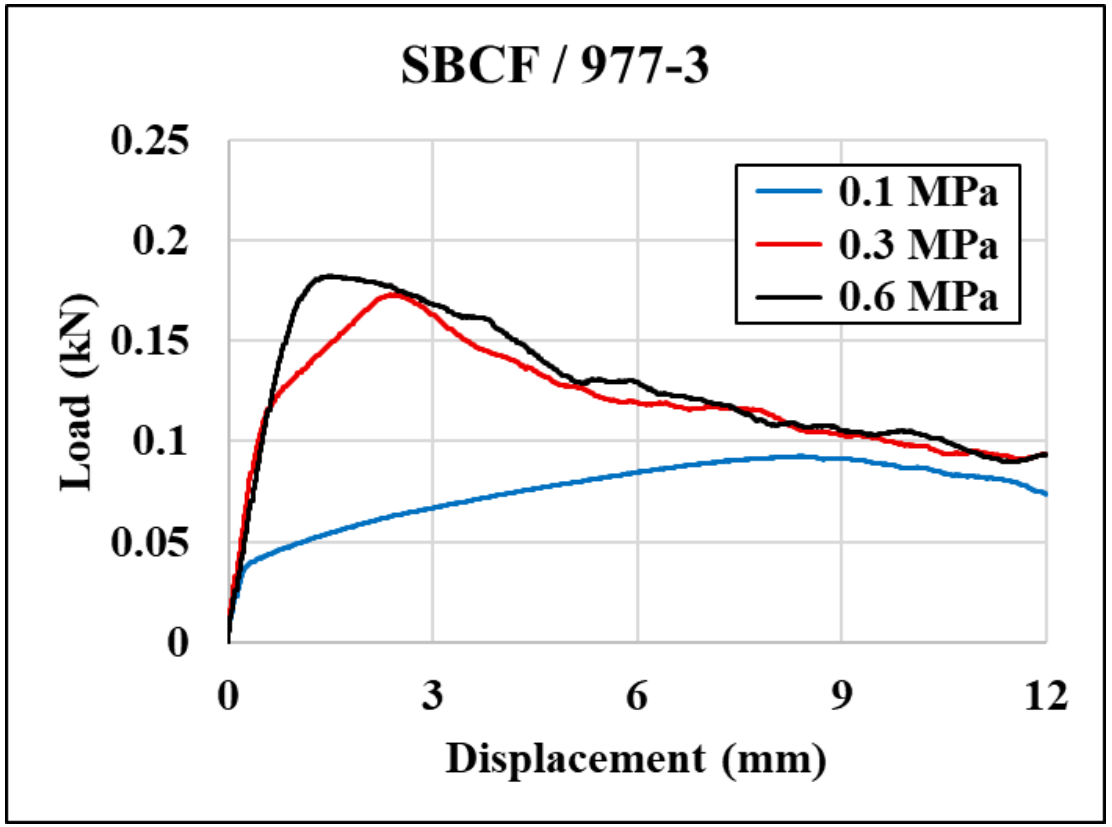

Load due to frictional resistance increases with displacement and normal pressure

Load relaxation for each test after frictional resistance reached a threshold value

Results: continued

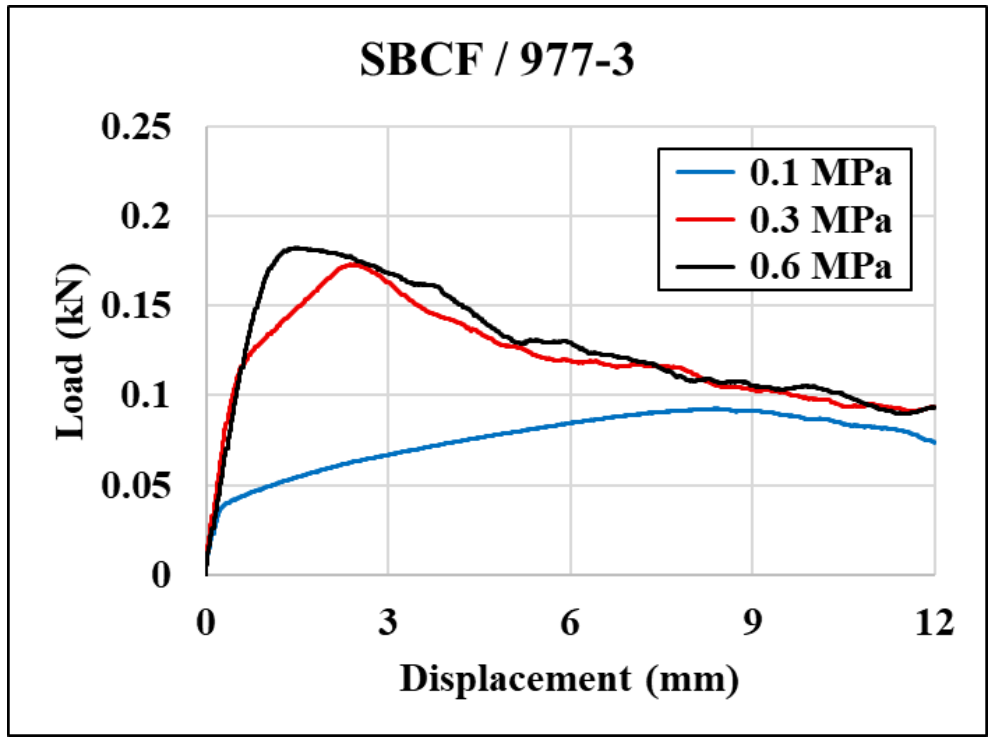

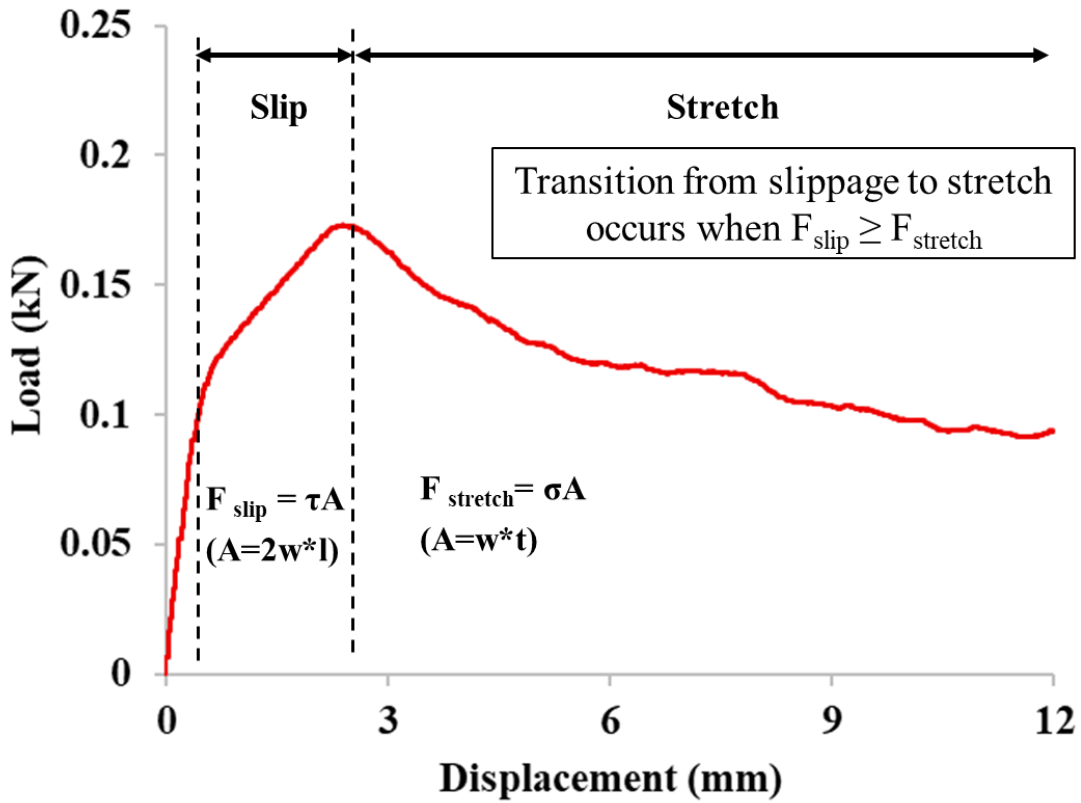

Results: continued

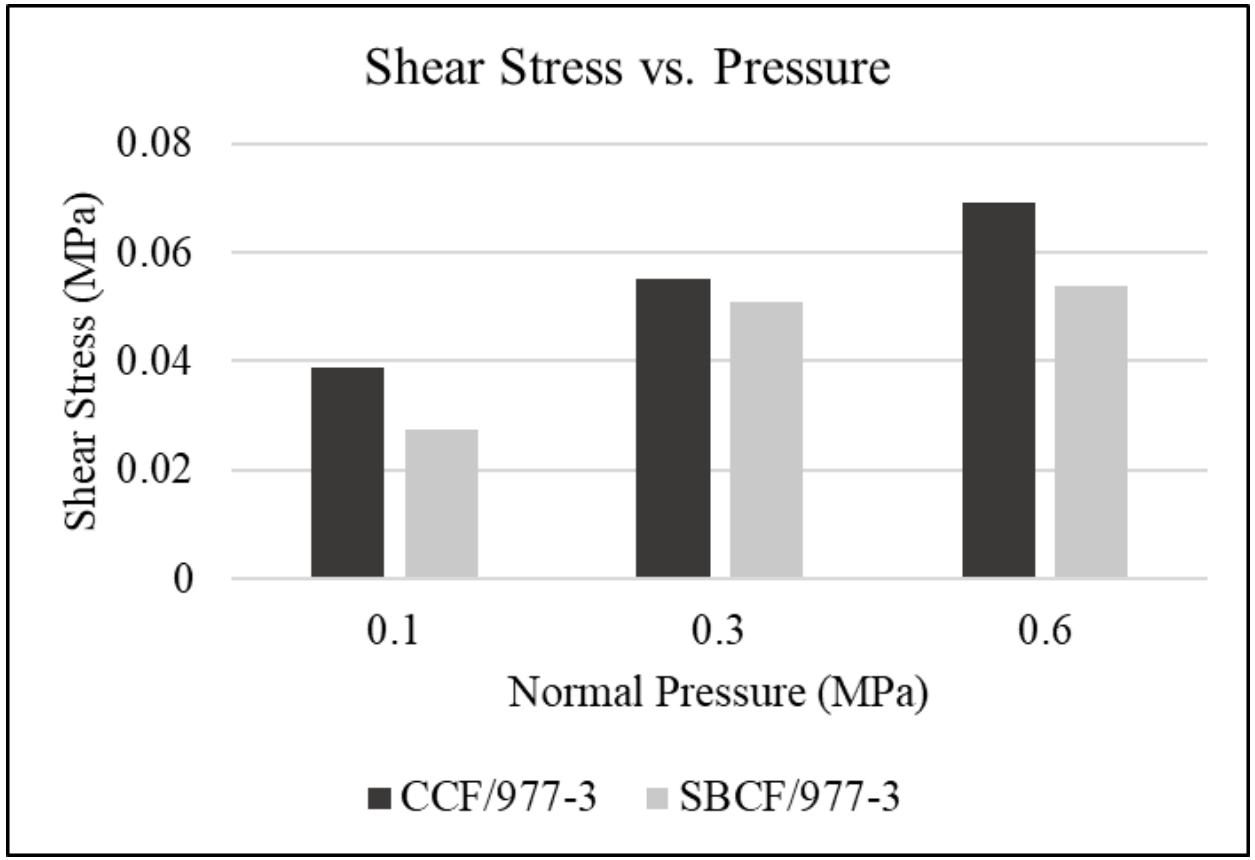

Shear stress, $\tau = F/A$

F = max load from load displacement curve (in N)

A = area = (w * l) * 2 =3386 mm^2

Conclusion

- Differences in the material deformation behavior between CCF and SBCF laminates during interply friction testing -

➢For CCF laminates -

  - primarily frictional interply shear, higher normal pressure increases resistance

➢For SBCF laminates -

  - axial stretching at the onset of high interply frictional resistance

- Unique SBCF deformation behavior can help mitigate excessive shear stress generation

Future work

- Continue testing to study effect of temperature and ply orientation
- Determine threshold between stretch and slippage response under various forming conditions

Acknowledgement

This work was supported by US Army Combat Capabilities Development Command Aviation & Missile Center Technology Development Directorate (Contract number: W911W6-18-0050). The views and conclusions contained in this presentation are those of the authors and should not be interpreted as necessarily representing the official policies, either expressed or implied, of the Government

Thank you

SUSTAINABLE ALIGNED SHORT CARBON FIBRE REINFORCED COMPOSITES WITH ELECTROSPUN POLYMER MATRIX

Shivdarshan Sherugar[1], Houng Xuen Ooi[1], Edwin Rosario[1], Xiang Ding[2], Hannah Leese[2] and HaNa Yu[1]

[1]Mechanical Engineering dept., University of Bath
Claverton down, Bath, BA2 7AY, United Kingdom
Email : sbs79@bath.ac.uk, web page: www.bath.ac.uk

[2]Department of Chemical Engineering, University of Bath
Claverton down, Bath, BA2 7AY, United Kingdom

Keywords: HiPerDiF, aligned discontinuous carbon fibre preforms, Rapid fibre alignment assessment (RFAA), electrospun material, PLA

ABSTRACT

Aligned short fibre composites have demonstrated exceptional tensile strength, stiffness, and load-bearing capabilities, as evidenced by both theoretical and experimental [1, 2] studies over the past decade, establishing them as a promising material for future advanced applications. Additionally, they provide an opportunity to better utilise recycled fibres, further promoting sustainability in composite materials. Short fiber alignment techniques, such as HiPerDiF [2] and TuFF [3], produce dry preforms that must be combined with a resin system. The most effective method to fabricate composites with aligned fibres involves stacking epoxy resin films with aligned fibre preforms, followed by compression using autoclave vacuum bag moulding. Another approach has been to use resin infusion processes with infusible epoxy resin or thermoplastic (Elium®) resin systems. Though they have shown great success in proving superior mechanical properties, challenges remain: 1) thermoset resin systems are difficult to recycle, and 2) there is limited understanding of how the resin combining process affects the structural integrity of aligned fibre assemblies during fabrication. This study therefore investigates the role of matrix material and its microstructure in composites fabricated with aligned carbon fibres by comparing two distinct matrices: electrospun thermoplastic polymer and conventionally fabricated polymer films. The electrospun polymer matrix features a fine, partially aligned fiber architecture and a high surface area, enhancing fiber-matrix impregnation unlike conventional polymer films. Both composite configurations are fabricated with aligned carbon fibres and subjected to mechanical testing, including tensile properties, to evaluate their performance. This paper highlights the potential of leveraging advanced matrix fabrication techniques to maximise the mechanical advantages offered by aligned carbon fibres, paving the way for lightweight, high-performance composite materials suitable for engineering and aerospace applications.

1 INTRODUCTION

Highly aligned discontinuous fibre composites have drawn attention not only for their comparable stiffness and strength to continuous fibre composites [4], but also for their formability and recyclability. Several methods have been developed to produce such composites, e.g., HiPerDiF [5], rotating drum [6] and TuFF [7].

Studies show that the mechanical performance of the composite increases with greater fibre alignment [2, 5, 8]. In addition to improved mechanical properties, manufacturing complex parts with aligned discontinuous fibre is easier, as the fibres can adjust their position during forming, preventing buckling and wrinkling [7, 9]. Also, aligned discontinuous fibre composites possess some level of ductility, making them a suitable choice for applications that require pseudo-ductile materials [10]. Most importantly, the greatest protentional of aligned discontinuous fibre composites is their ability to

support recyclability. Fibres reclaimed after their lifecycle in applications can be used to produce new aligned discontinuous fibre composites. In this way, recycled fibres are utilised in higher-value materials, supporting a circular economy and reducing landfill waste [4]. Case studies and application prototypes, such as flexi wings on formula 1 car, tennis rackets, provide good examples of this potential [11].

However, to take full advantage of the recyclability of aligned discontinuous fibre composites, thermoplastic type polymer is preferred over thermoset type polymer [12]. Thermoplastics, however, have higher melt viscosities, which lead to insufficient impregnation of the fibre bundles [13]. Poor impregnation results in inefficient load transfer between the fibres and matrix [14], reducing the overall strength of the composite.

One approach to improving impregnation is to use the electrospun form of thermoplastic polymers. Electrospun thermoplastic polymer sheets have higher porosity and surface area than conventional films, which can enhance impregnation [15]. Using electrospun polymer sheets in aligned short fibre composites offers additional benefits beyond improved impregnation. One such benefit is that electrospun sheets exhibit a unique structure, with nano/micro-fibres partially aligned in a single direction. This, combined with their porosity, could help retain fibre alignment during compression moulding. Moreover, this is particularly beneficial when using HiPerDiF or TuFF processes to produce aligned fibre preforms, as these methods may leave a small amount of moisture after fibre alignment. The porous structure of electrospun sheets can help remove this moisture effectively.

This study attempts to use electrospun thermoplastic polymer material as a matrix in manufacturing aligned short carbon fibre composites, in order to compare them with conventional aligned short carbon fibre composites. Aligned short carbon fibres are combined with two types of PLA material: i) Conventional PLA film and ii) Electrospun PLA film, to form composites whose tensile properties are then compared.

2 ALIGNED SHORT CARBON FIBRES

An experimental setup was developed to prepare aligned carbon fibre preforms. This setup is based on the principle of HiPerDiF method [2], which uses a sudden change in momentum of a fibre-water suspension onto a plate to align the fibres. The fibre alignment head consists of thin parallel plates that capture the fibre-water suspension jets. Below the head is a moving conveyor belt, which collects the aligned fibres and allows the water drain out, resulting in an aligned fibre preform on the belt. This setup is of smaller size than HiPerDiF and can generate a preform of around 5 mm in width. 3 mm length of carbon fibres (Tenax-A HT C124- 3 mm [16]) were used in this study which resulted in an aspect ratio of around 428. To assess the alignment of fibres in a preform, the Rapid Fibre Alignment Assessment (RFAA) method was adopted [17, 18]. To apply this method (See Figure 1), a section of preform was first imaged. The whole image was then sectioned into equally spaced, same-sized 'Region Of Interest (ROI)'. This code was applied to each ROI individually. Based on the defined formula, the image in each ROI was transformed in the x and y directions, and the transformed image was then subtracted from the original image. The resultant pixel density in x and y directions after subtraction indicated the fibre alignment in each ROI.

This method is quicker and effective [18, 19]. The RFAA method was applied to five images of the dry preforms before they were combining with the resin matrix, and the mean fibre alignment was found to be $\pm$ 8 deg.

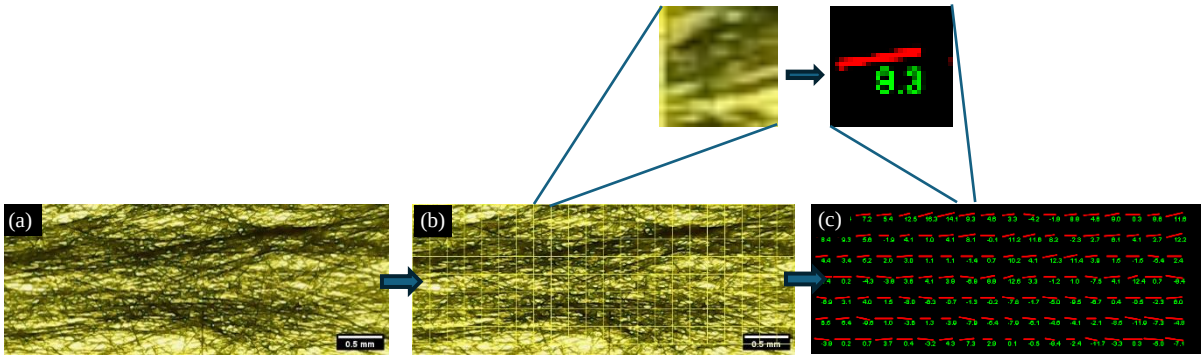

Figure 1: (a) Aligned fibres image, (b) Segmented into small region of interest (ROI), and (c) Applied RFAA method to assess alignment in each ROI

3 PLA MATERIAL AS MATRIX

The conventional PLA film was obtained from Goodfellow, Cambridge UK (product: ME34-FM-000100). This film has a thickness of 0.05 mm, with a tensile strength of 53 MPa and a tensile modulus of 3.5 GPa. For electrospun PLA, granules were acquired from the same manufacturer and have similar mechanical properties. These granules were then dissolved in chloroform and dimethylformamide, and stirred for 4 hours at 50° C to produce a PLA solution. This solution was then fed through a syringe, where it was stretched and deposited as a porous film (containing PLA micro-fibers) onto a collector, similar to a typical electrospinning process [20], except that a roller type collector was used instead of a flat one. Since the roller rotates at a constant speed, the deposited micro-fibers are aligned in the direction of rotation. A voltage of 25 kV was applied between the syringe and the collector, and with the collector rotating at 3500 RPM, a 20 µm thick, porous film containing PLA micro-fibers was formed.

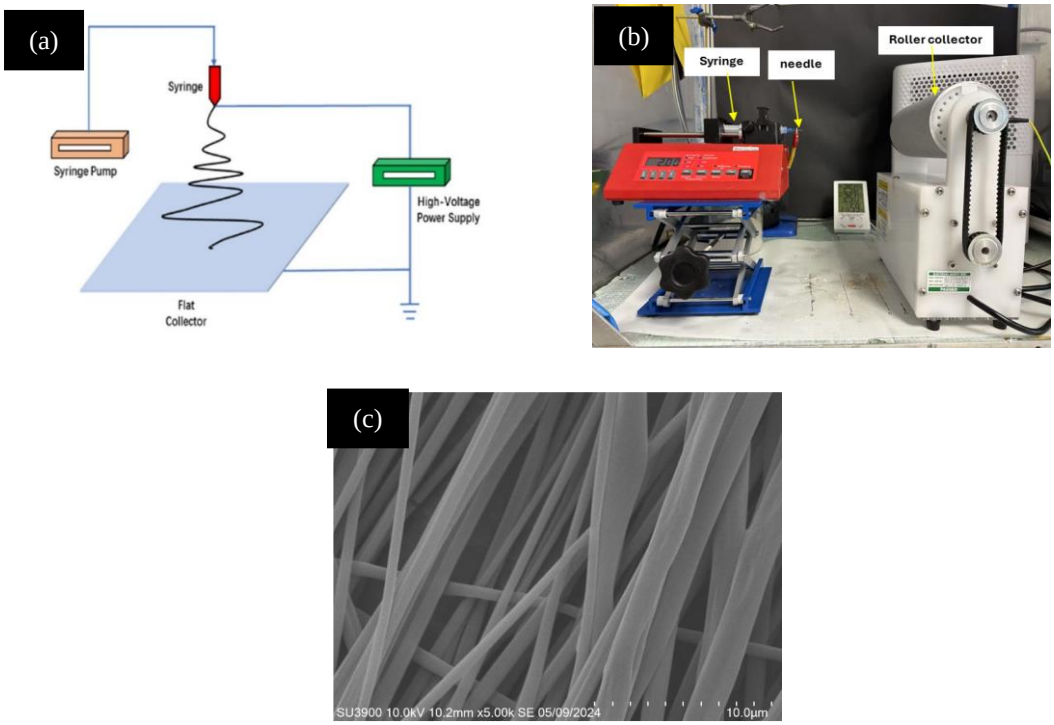

Figure 2. (a)Typical Electrospinning set-up, (b) Electrospinning setup with roller collector and (c) micro-fibres of PLA in electrospun film.

4 TENSILE TEST SAMPLE PREPARATION

Two sets of samples were prepared: one using conventional PLA film and the other using electrospun PLA sheets, and tensile tests were performed in accordance with ASTM D3039 standards. In both cases, the same number of dry aligned carbon fibre preform layers (eight in total) was used. To achieve a consistent fibre volume fraction of approximately 23%, the preforms were stacked differently according to the stacking sequence as follows:

For conventional PLA - ***P*** + aligned carbon fibre – ***f*** :

$$[P/f_4]_s$$

For electrospun PLA - ***EP*** + aligned carbon fibre – ***f*** :

$$[EP_5/[f/EP]_4/EP/[EP/f]_4/EP_5]$$

These stacked layers were subjected to compression moulding by vacuum bagging and then placed in an oven. The pressure and temperature were set to 1 bar and 200° C, respectively. The samples measured 5 mm in width, 150 mm in length and 0.2 mm in thickness. Conventional PLA required 30 mins at 200°C to form composites, while electrospun PLA formed composites in 20 mins at the same temperature (see Figure 3).

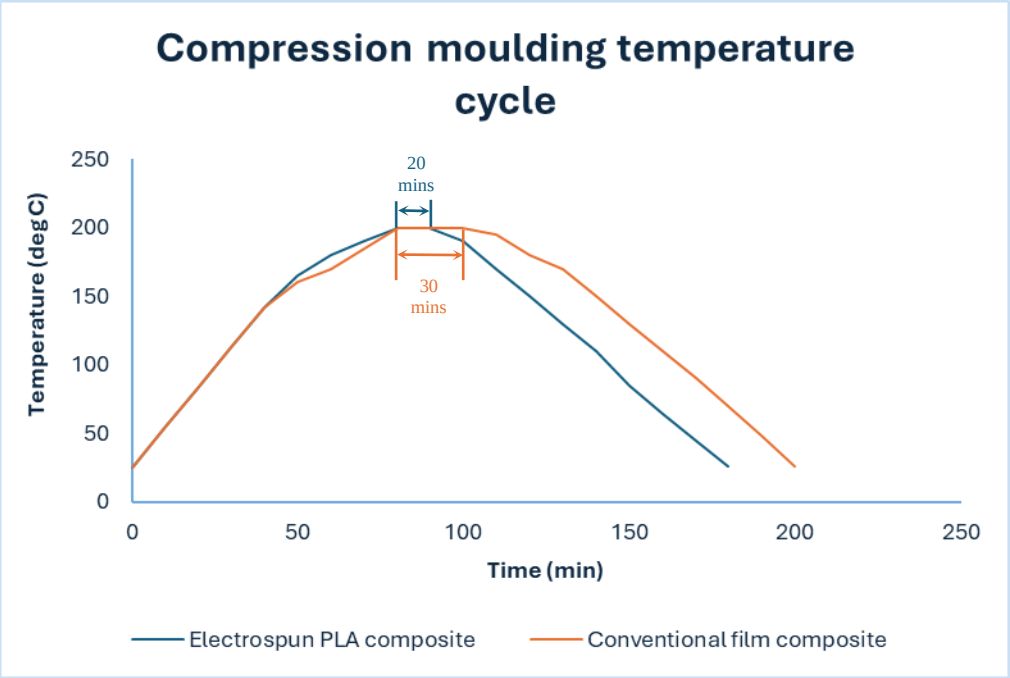

Figure 3: Heating cycle for electrospun and conventional PLA composites (Note: Constant vacuum applied.)

5 RESULTS AND DISCUSSION

Three specimens were tested in each sample set using a tensile testing machine (Instron D5967, 30 kN load cell). The results are shown in Figure 4. The use of electrospun PLA as a matrix resulted in a meaningful increase in mechanical properties compared to conventional PLA film. The tensile strength increased from 285 MPa to 337 MPa, an improvement of approximately 18%. Likewise, the tensile

modulus rose from 17.6 GPa to 19 GPa, reflecting an increase of about 8.0%. These results show that electrospun PLA can contribute to enhancing the mechanical performance of aligned short fibre composites. This can be attribute to more uniform and thermal behaviour of electrospun film. Due to its fine fibre structure, it heats and melts evenly and quickly. Also, it's higher surface area due to fine fibre structure helps it to flow more effectively between fibre bundles without affecting fibre alignment, resulting in good impregnation. In contrast, the conventional PLA film with its lower thermal responsiveness results in incomplete impregnation and its lower surface area may disrupt fibre alignment.

.

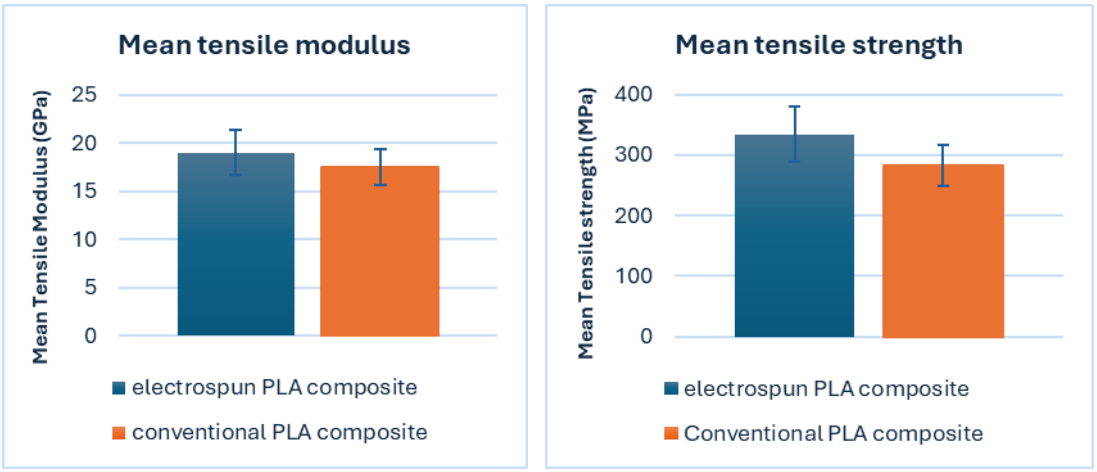

Figure 4. Tensile strength and modulus between electrospun and conventional PLA composites with aligned discontinuous carbon fibres.

6 CONCLUSION AND FUTURE WORKS

In this study, a simple comparison was made between the tensile properties of composites manufactured from two different forms of PLA. The conventional PLA film and electrospun PLA film were compression moulded with aligned short carbon fibres for 30 mins and 20 mins respectively, at 200° C. The results show that the electrospun PLA composite achieved higher tensile modulus and tensile strength than the conventional PLA composite, despite requiring less processing time. Therefore, using the electrospun form of the thermoplastic matrix material could be a potential solution for improving the sustainability of carbon fibre composites. This is largely attributed to its better impregnation capability, which leads to fewer defects during processing. The fine fibre structure and porosity of the electrospun PLA allow the matrix to flow more efficiently between the carbon fibre bundles, reducing voids and enhancing composite quality with shorter moulding times.

However, further research is needed to fully understand the effects of the moulding process on fibre alignment. The high viscosity of melted PLA can disrupt the alignment and structure of the carbon fibre preforms during processing. This disruption is expected to be less significant when using electrospun PLA, due to its porous structure and fine fibre morphology, which promote more uniform melting and better flow. Ongoing studies aim to investigate how these characteristics influence fibre alignment during composite fabrication.

ACKNOWLEDGEMENTS

We would like to thank Lineat for providing their technical expertise. We would also like to thank Mr. Jeff Boston, Mr. Gary Barter, Mr. Angus Tillotson and team from workshop, 3D printing lab and biomechanics lab in mechanical engineering dept., University of Bath for their help in building experimental setup and testing.

REFERENCES

1. Such, M., C. Ward, and K. Potter, *Aligned Discontinuous Fibre Composites: A Short History.* Journal of Multifunctional Composites, 2014. **2**.
2. Yu, H., K.D. Potter, and M.R. Wisnom, *A novel manufacturing method for aligned discontinuous fibre composites (High Performance-Discontinuous Fibre method).* Composites Part A: Applied Science and Manufacturing, 2014. **65**: p. 175-185.
3. John Tierney, A.V., Dirk Heider , Shridhar Yarlagadda , John W. Gillespie , Jr, *ALIGNED DISCONTINUOUS FIBER PREFORMS , COMPOSITES AND SYSTEMS AND PROCESSES OF MANUFACTURE* U.S. Patent, Editor. 2020, University of Delaware , Newark , DE: United States. p. 7.
4. Lewis, C., et al., *A Review on the Modelling of Aligned Discontinuous Fibre Composites.* Journal of Composites Science, 2024. **8**(8): p. 318.
5. Yu, H., K.D. Potter, and M.R. Wisnom. *Aligned short fibre composites with high performance*. in *19th International Conference on Composite Materials (ICCM19)*. 2013.
6. Pickering, S.J., et al., *Applications for carbon fibre recovered from composites.* IOP Conference Series: Materials Science and Engineering, 2016. **139**(1): p. 012005.
7. Yarlagadda, S., et al., *Formability of TuFF composite blanks.* SAMPE 2019-Charlotte, NC, May 2019, 2019.
8. Yarlagadda, S., et al., *Tailorable universal feedstock for forming (TUFF): overview and performance.* SAMPE 2019-Charlotte, NC, May 2019, 2019.
9. Eguemann, N., et al. *Compression moulding of complex parts for the aerospace with discontinuous novel and recycled thermoplastic composite materials*. in *19th International conference on composite materials*. 2013.
10. Yu, H., et al., *Pseudo-ductility in intermingled carbon/glass hybrid composites with highly aligned discontinuous fibres.* Composites Part A: Applied Science and Manufacturing, 2015. **73**: p. 35-44.
11. Lineat. *Sectors*. 2025; Available from: https://lineat.co.uk/automotive/.
12. Nishida, H., et al., *Thermoplastic vs. thermoset epoxy carbon textile composites.* IOP Conference Series: Materials Science and Engineering, 2018. **406**(1): p. 012043.
13. Erber, A. and S. Spitko, *Expanded role for thermoplastic composites.* Reinforced Plastics, 2014. **58**(4): p. 29-33.
14. Huang, S., et al., *Characterization of interfacial properties between fibre and polymer matrix in composite materials – A critical review.* Journal of Materials Research and Technology, 2021. **13**: p. 1441-1484.
15. Yang, X., et al., *Electrospun carbon nanofibers and their reinforced composites: Preparation, modification, applications, and perspectives.* Composites Part B: Engineering, 2023. **249**: p. 110386.
16. Teijin, *Tenax short fibres*, in *Tenax chopped fibres(C-series & P-series)*, T. limited, Editor. 2024: https://www.teijincarbon.com/products/short-fibers.
17. Boudaoud, A., et al., *FibrilTool, an ImageJ plug-in to quantify fibrillar structures in raw microscopy images.* Nature Protocols, 2014. **9**(2): p. 457-463.
18. Wright, W.J., et al., *Rapid fiber alignment quantification in direct write printing of short fiber reinforced composites.* Composites Part B: Engineering, 2022. **236**: p. 109814.
19. Boudaoud, A., et al., *FibrilTool, an ImageJ plug-in to quantify fibrillar structures in raw microscopy images.* Nat Protoc, 2014. **9**(2): p. 457-63.

20. Zhang, W., et al., *Structural design and environmental applications of electrospun nanofibers.* Composites Part A: Applied Science and Manufacturing, 2020. **137**: p. 106009.

IS THERE A HYBRID EFFECT IN TENSILE AND COMPRESSIVE FAILURE OF CARBON FIBRE COMPOSITES?

Michael R. Wisnom

Bristol Composite Institute, University of Bristol

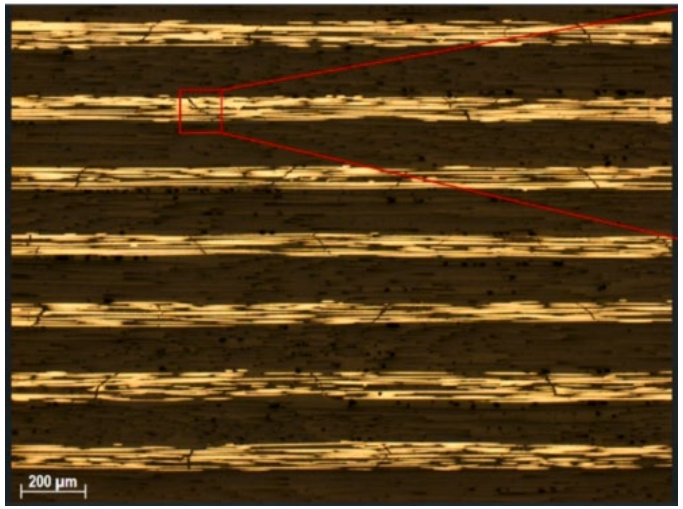

Next Generation Fibre-Reinforced Composites

IMPERIAL

The Composites Centre
for research, modelling, testing and training in advanced composites

University of BRISTOL
Bristol Composites Institute

UK Research and Innovation

Engineering and Physical Sciences Research Council

HYBRID EFFECT

- Can be defined as an increase in failure strain in a hybrid composite compared with when tested on its own
- Reports of hybrid effects from the early days of composites generated much debate, e.g. Hayashi, 1972

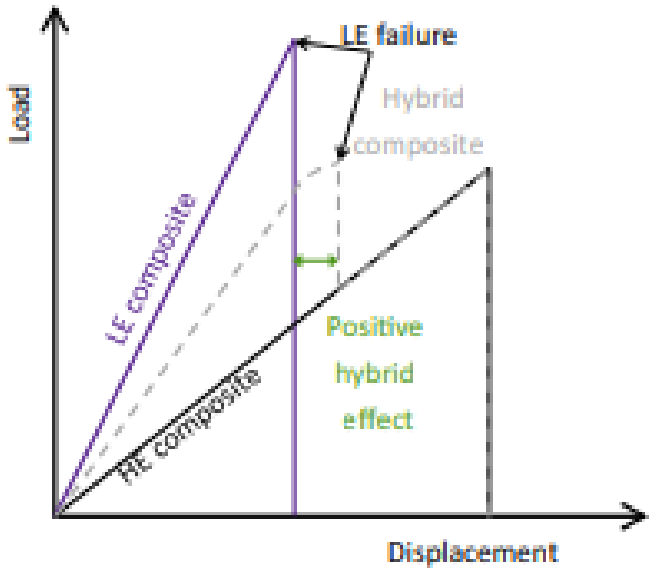

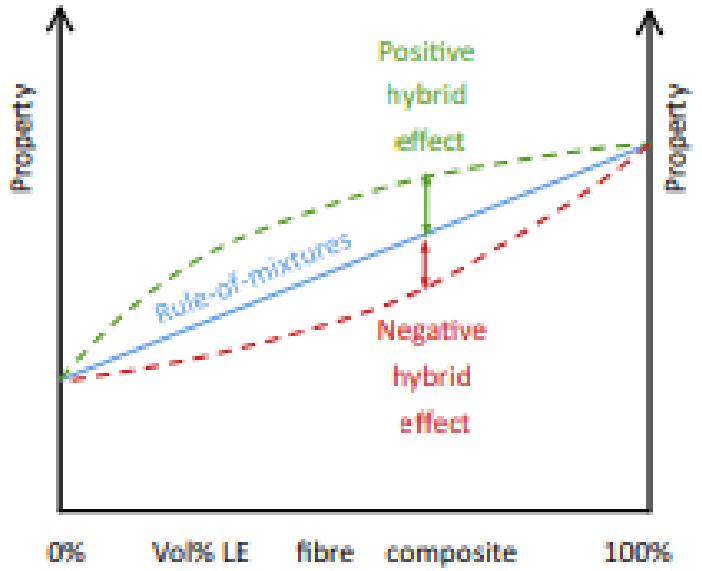

- Low extension (LE) fibre e.g. carbon
- High extension (HE) fibre e.g. glass
- Deviation from Rule of Mixtures

Swolfs, 2014

NEED FOR A GOOD BASELINE

- Testing of composites is very challenging
- Failures often occur prematurely at grips
- Compression testing is particularly difficult
- Makes it hard to accurately compare strengths
- Reliable baseline failure strains are crucial for proper assessment of hybrid effects

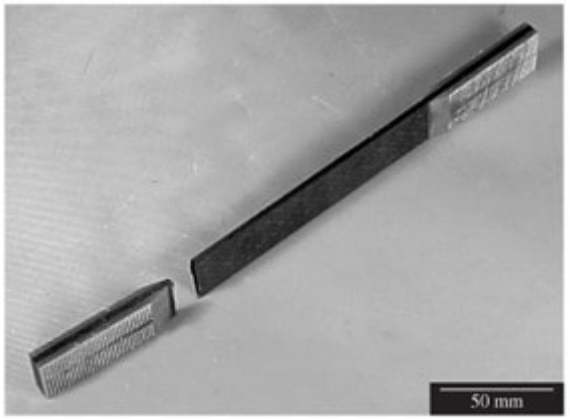



OUTLINE

- Obtaining a good baseline
- Hybrid effects in tension
  - UD glass/carbon
  - UD high modulus/high strength carbon
  - QI glass/carbon
- Hybrid effects in compression
  - UD high strength carbon / S-glass
  - UD high modulus/high strength carbon

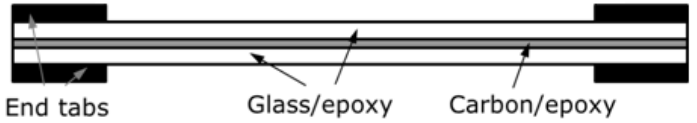



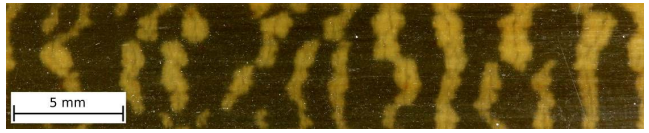

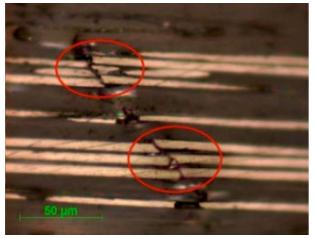

AN ACCURATE SIMPLE TENSILE TEST

- Sandwich specimen eliminates stress concentration
- Strain in carbon LOWER at tab
- Eliminates grip failures

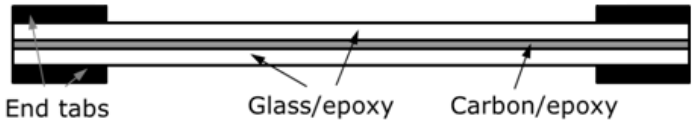

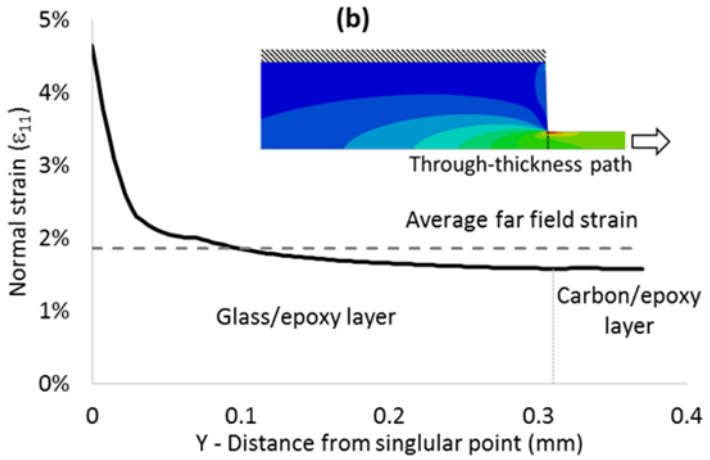

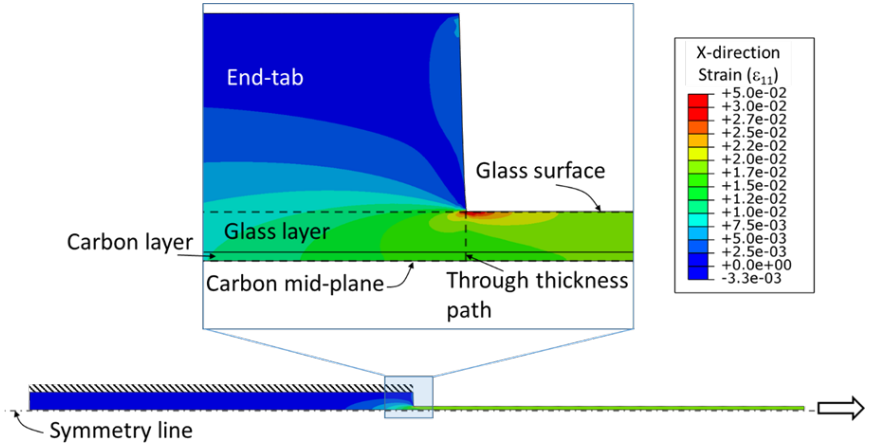

Czél, Jalalvand, Wisnom, 2016

CONSISTENT TENSILE FAILURES

- Gauge section failure followed by delamination
- Much higher failure strain, lower variability
- E.g. 1.86% vs. 1.5% strain for TR30 carbon/epoxy
- Gauge section failure even without end-tabs

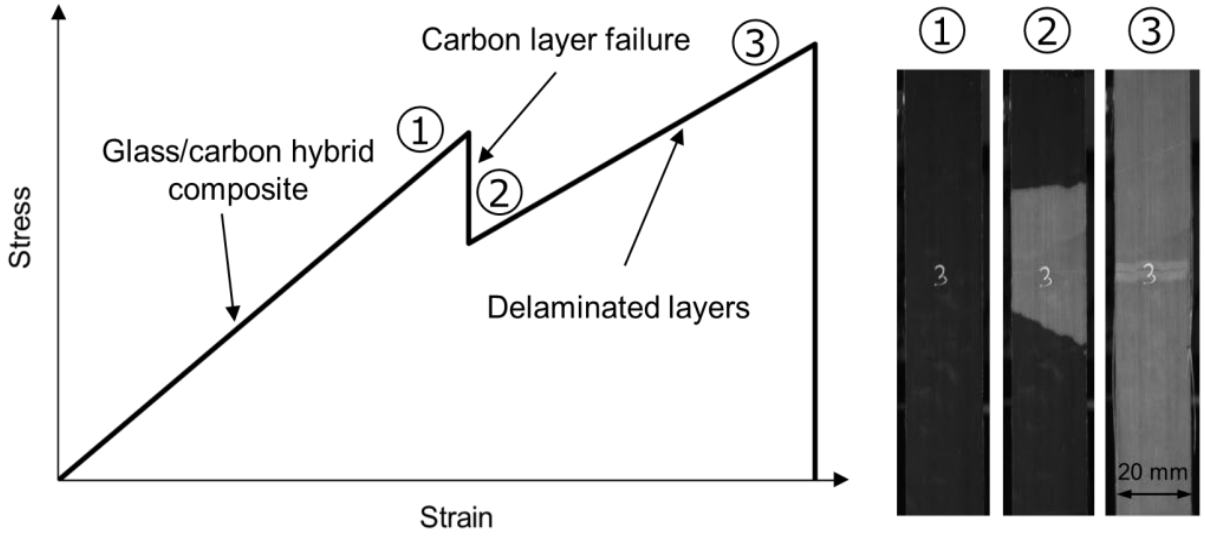

SANDWICH BEAM COMPRESSION TEST

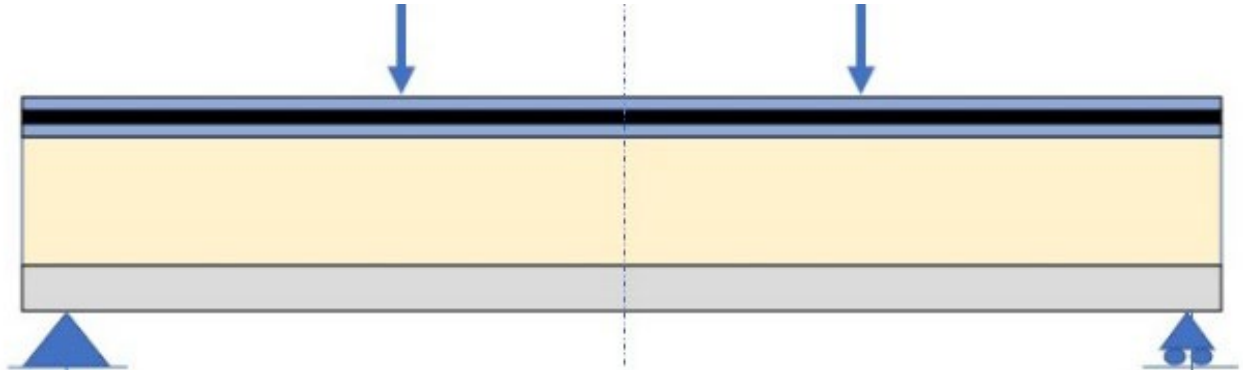

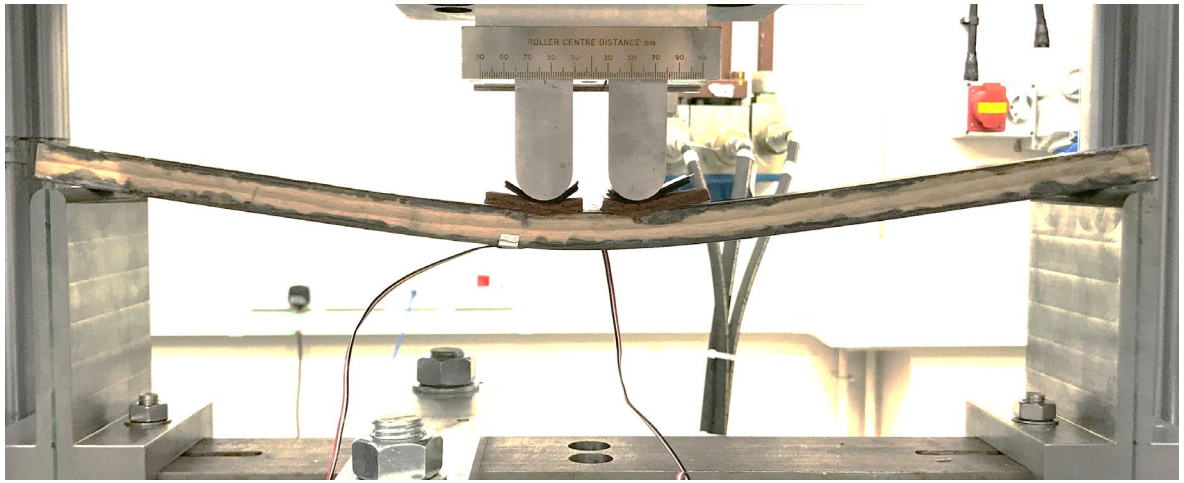

Wu & Wisnom, 2023

- Four-point bending
- Hybrid compression skin
- Carbon tension skin
- Wood or PMMA core
- Large rollers avoid local failures
- Strain gradient effect?

VALIDATION OF TEST

- IM7/8552 carbon/epoxy skins, t = 0.5 mm
- Little effect of strain gradient above 10 mm thickness
- 1.36% strain - 14% higher than 1.19% in direct compression

(Thomson et al, 2019)

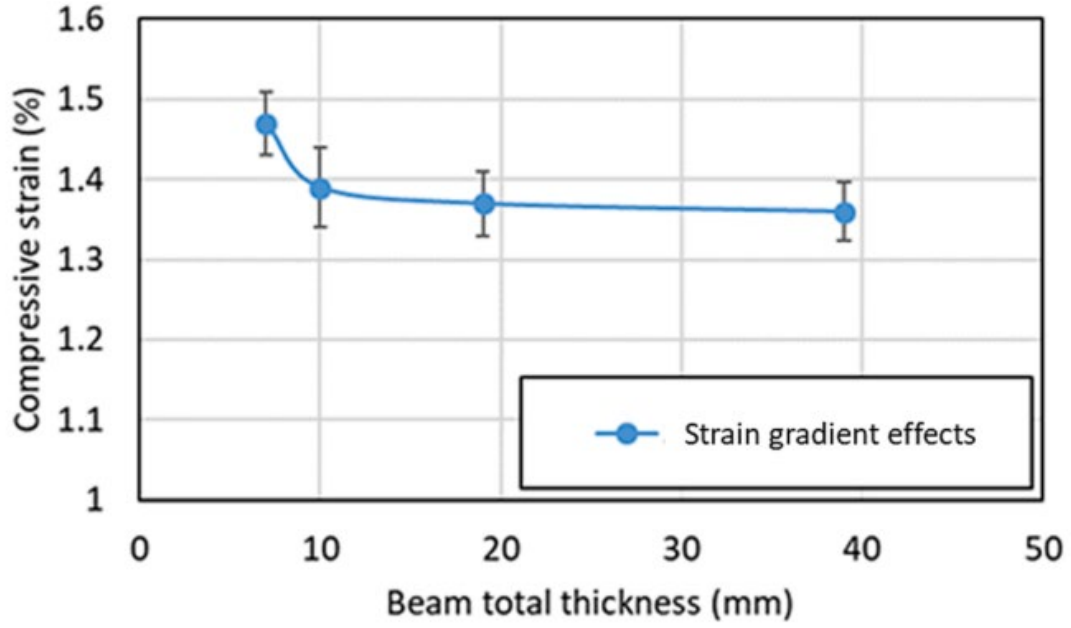

Wu & Wisnom, 2023

HYBRID TENSION TESTS

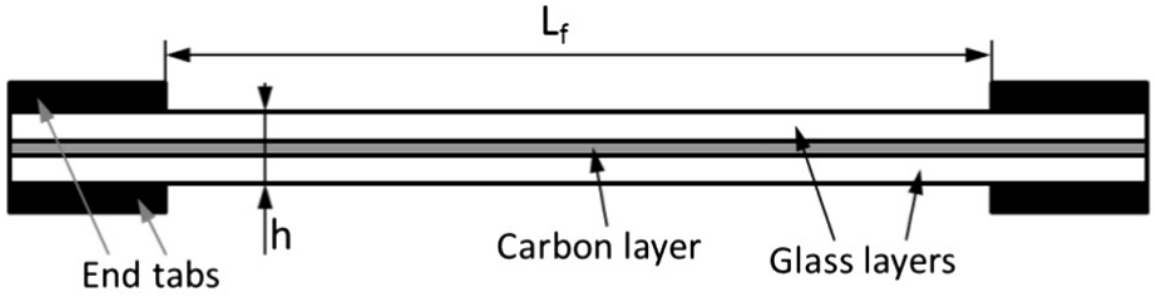

- Skyflex TR30 high strength carbon/epoxy (0.029 mm)
- Hexcel S2 glass/epoxy plies (0.155 mm) either side

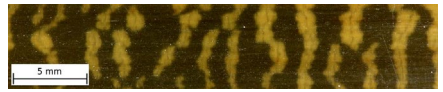

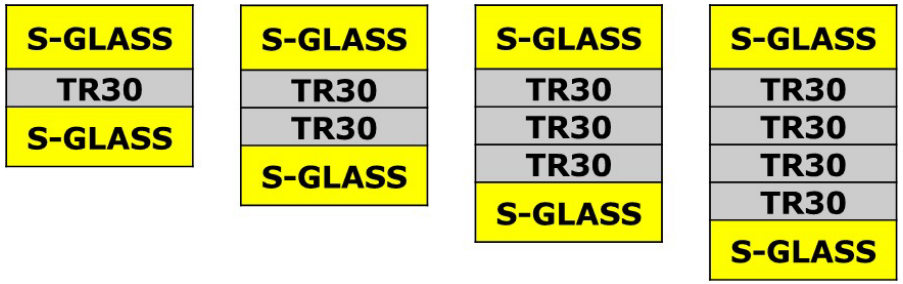

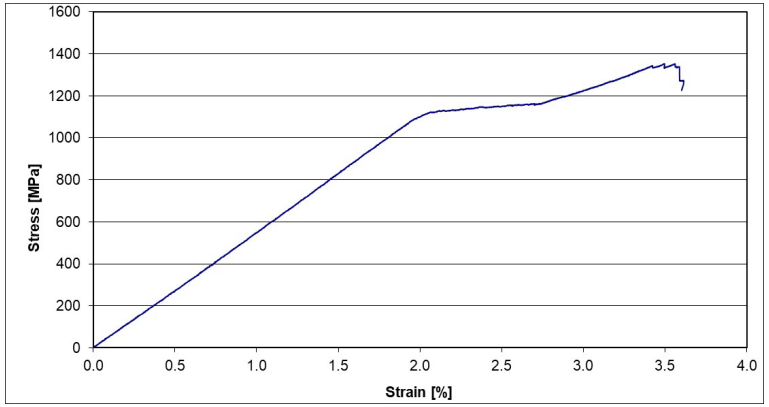

- 3 and 4 ply specimens delaminated with clear load drop
- 1 and 2 ply specimens exhibited pseudo-ductile behaviour

Wisnom et al, 2016

DEFINITION OF FAILURE STRAIN

- Thick specimens: strain at load drop
- Thin specimens: knee point in stress-strain curve
- Corresponds to point of establishment of ply fragmentation
- All results corrected for thermal strains

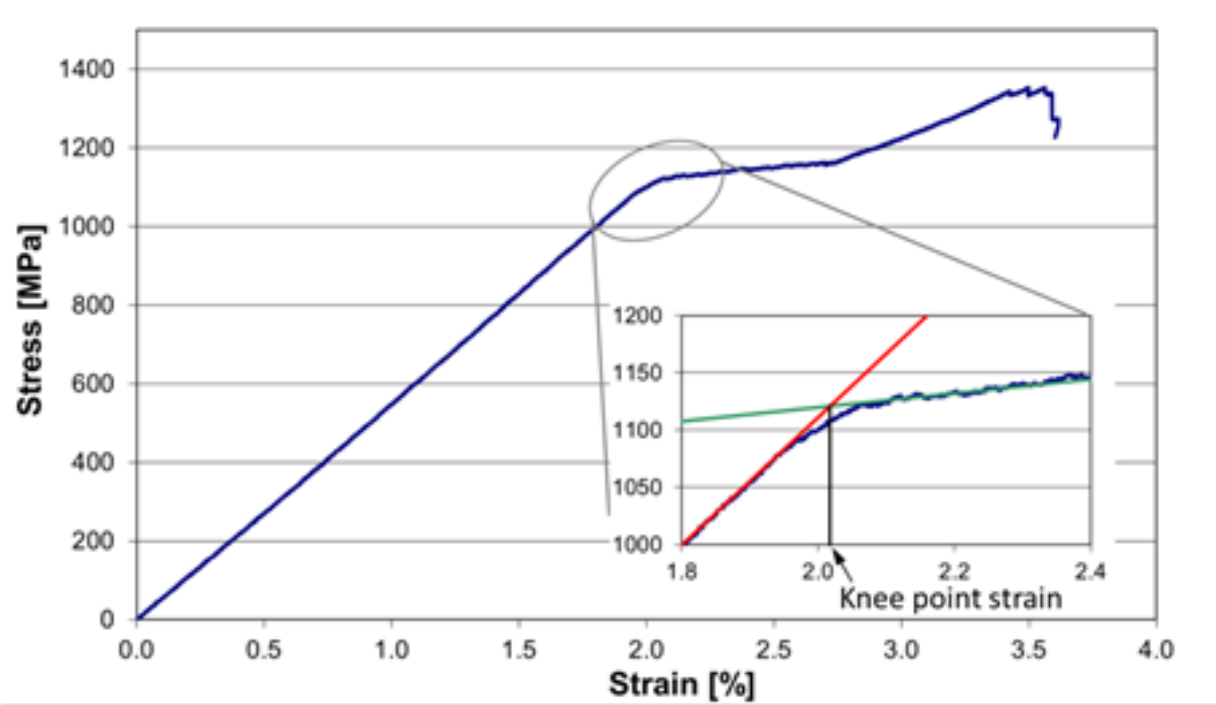

HYBRID EFFECT IN GLASS / CARBON

- 3 and 4 carbon plies similar, close to expected fibre strain
- 1.86% baseline cf 1.5% with conventional test
- 20% increase in strain to 2.2% for single ply case
- Due to restriction on forming critical cluster

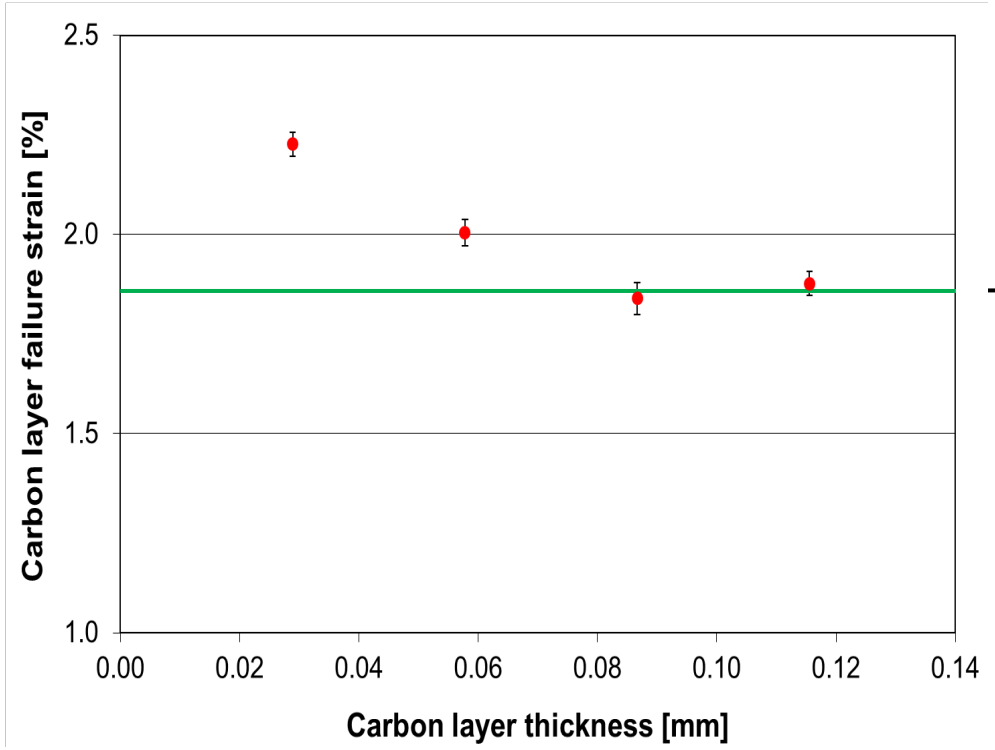

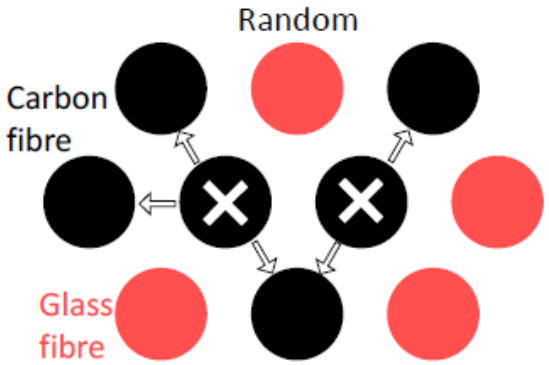

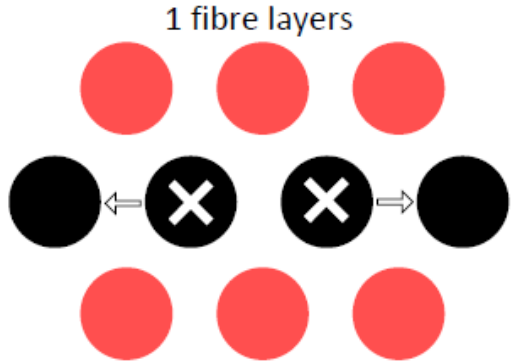

Wisnom et al, 2016

HYBRID EFFECT IN ALL CARBON LAMINATES

- Carbon /carbon hybrids also show hybrid effect
- Ultra high modulus XN80 (0.047 mm ply t)
- T1000 intermediate modulus (0.032 mm ply t)
- $[T1000_2/XN80_2/T1000_2]$ versus $[T1000_1/XN80_1/T1000_1]_2$
- ~30% higher than datasheet laminate failure strain of 0.31%
- 6% increase in knee point strain for single XN80 ply

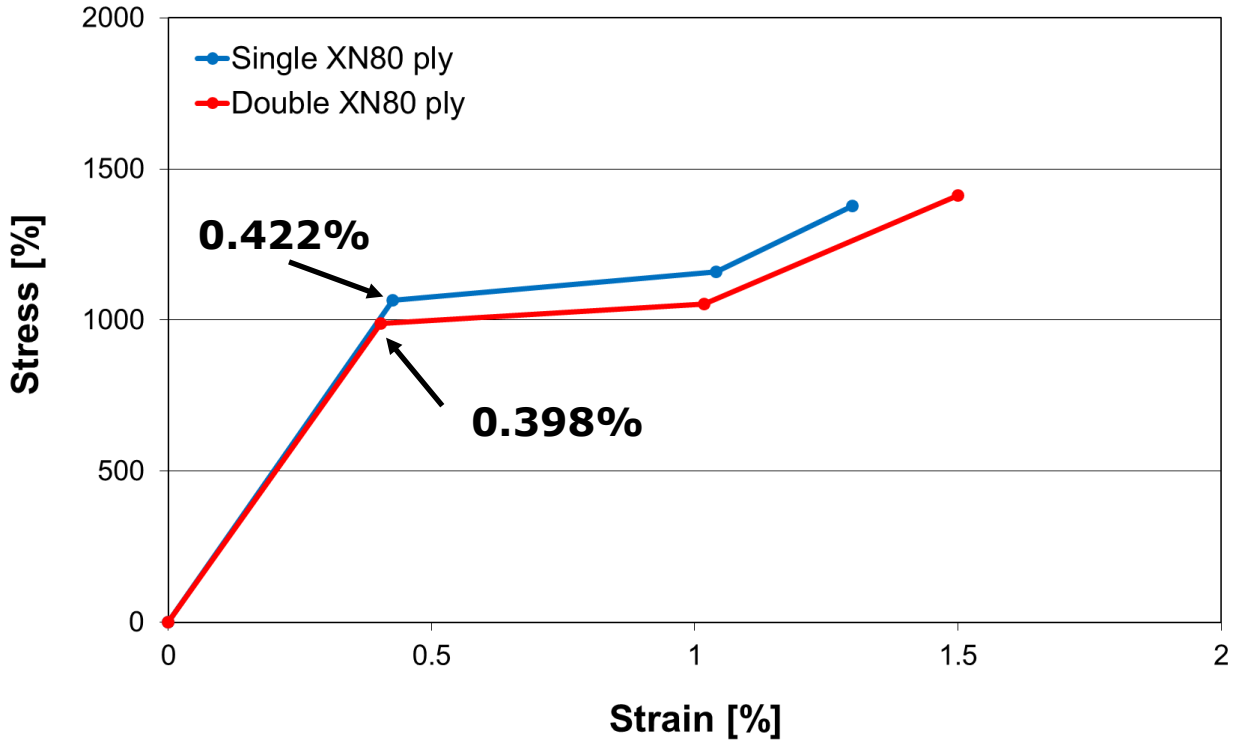

Czél, Jalalvand, Wisnom, Czigány 2017

QUASI-ISOTROPIC PSEUDO-DUCTILE HYBRIDS

- $[\underline{QI}_{G60}/\underline{QI}_{C60}]_s$ tested in 0, 60 and -60 directions
- 13% higher strain when loaded in 0° direction
- Due to higher stiffness of adjacent 0° glass ply
- Can be correlated with stress concentrations in adjacent plies (**Idarraga et al, 2025**)

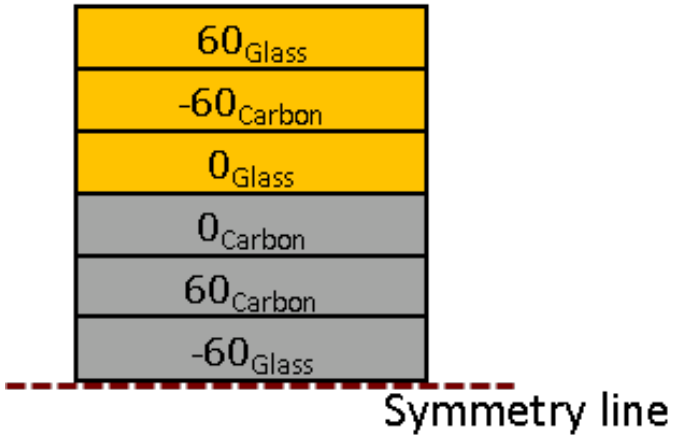

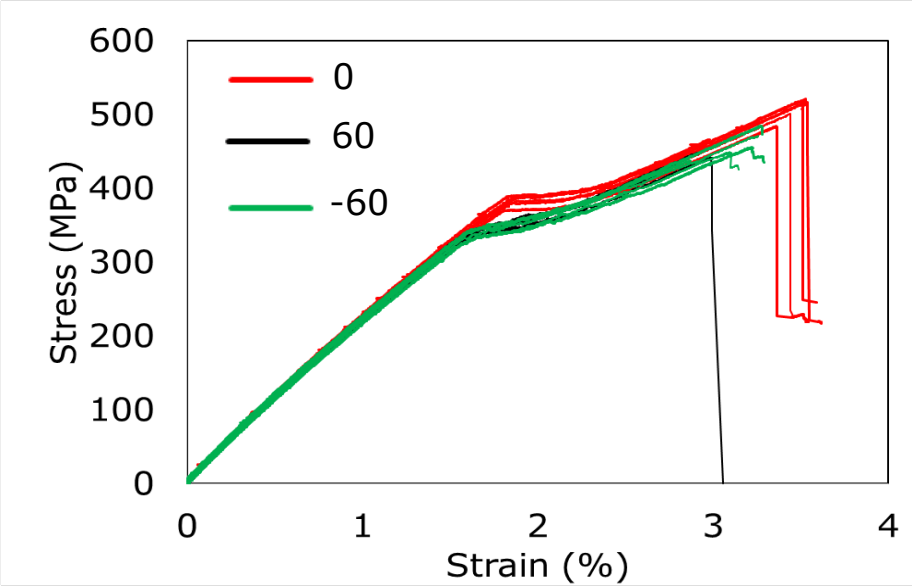

Fotouhi, Jalalvand, Wisnom, 2017

COMPRESSIVE FAILURE OF CARBON/GLASS HYBRIDS

- High strength TC33 carbon, 95 GPa, 0.03 mm
- S-glass, 45 GPa, 0.155 mm ply thickness
- Tested in 4-point bending
- Sudden failures with kink bands
- Large hybrid effect - 54% increase in strain
- Similar stresses – instability more related to stress than strain



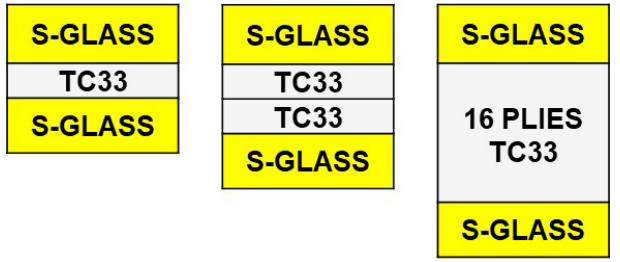

Specimen configuration	Compressive failure strain (%) CV(%)	Laminate failure stress (MPa)
SG/TC33$_1$/SG	2.609 (8)	1271
SG/TC33$_2$/SG	2.234 (8)	1232
SG/TC33$_{16}$/SG	1.691 (6)	1121

Tongloet, 2025

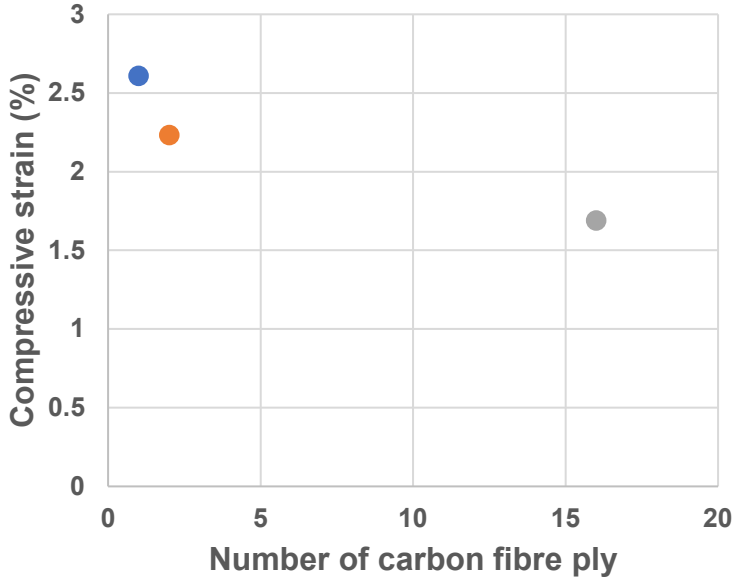

HIGH MODULUS CARBON / GLASS HYBRIDS

Direct compression

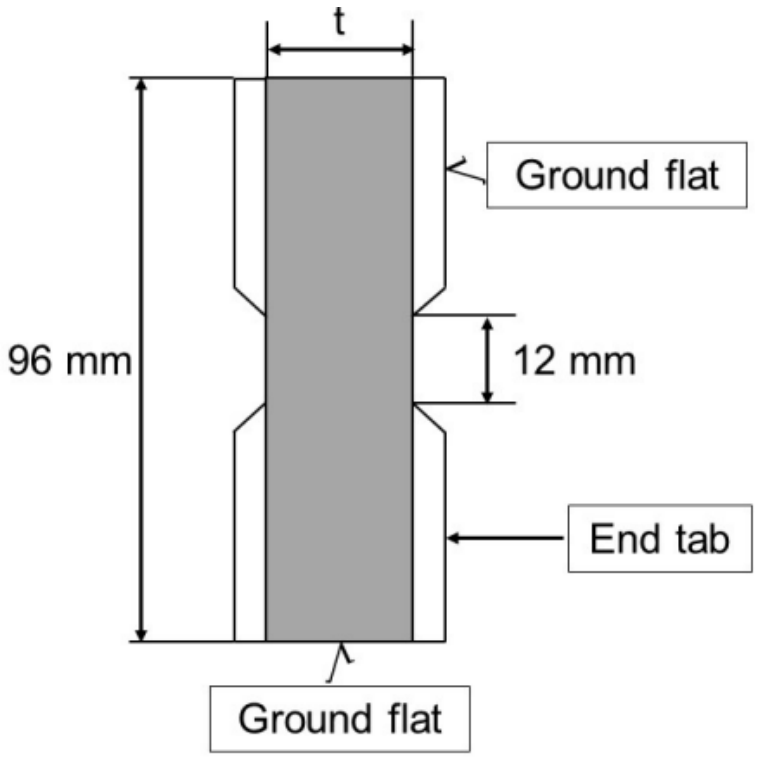

Suwarta et al., 2025

- M55J high modulus PAN, ply t=0.03 mm, 240 GPa
- S-glass, t=0.155 mm, 45 GPa
- 17 repeats with single glass ply between each carbon sublaminate
- Thickness 3.31 to 4.35 mm

Layup 1
S-glass
M55J
S-glass

Layup 2
S-glass
M55J
M55J
S-glass

Layup 3
S-glass
M55J
M55J
M55J
S-glass

S-GLASS / HIGH MODULUS CARBON HYBRID EFFECT

- Pseudo-ductile response with fragmentation
- Controlled by fibre failure not shear instability
- Final failure by delamination
- Knee point at 0.5% for all cases
- No hybrid effect?

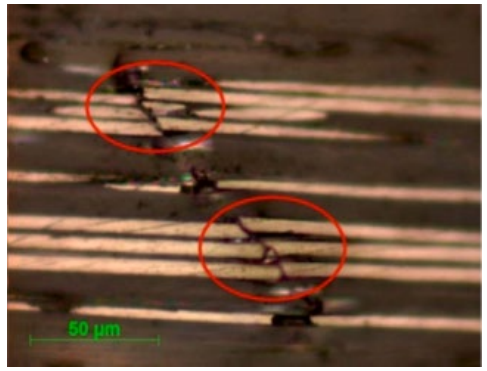

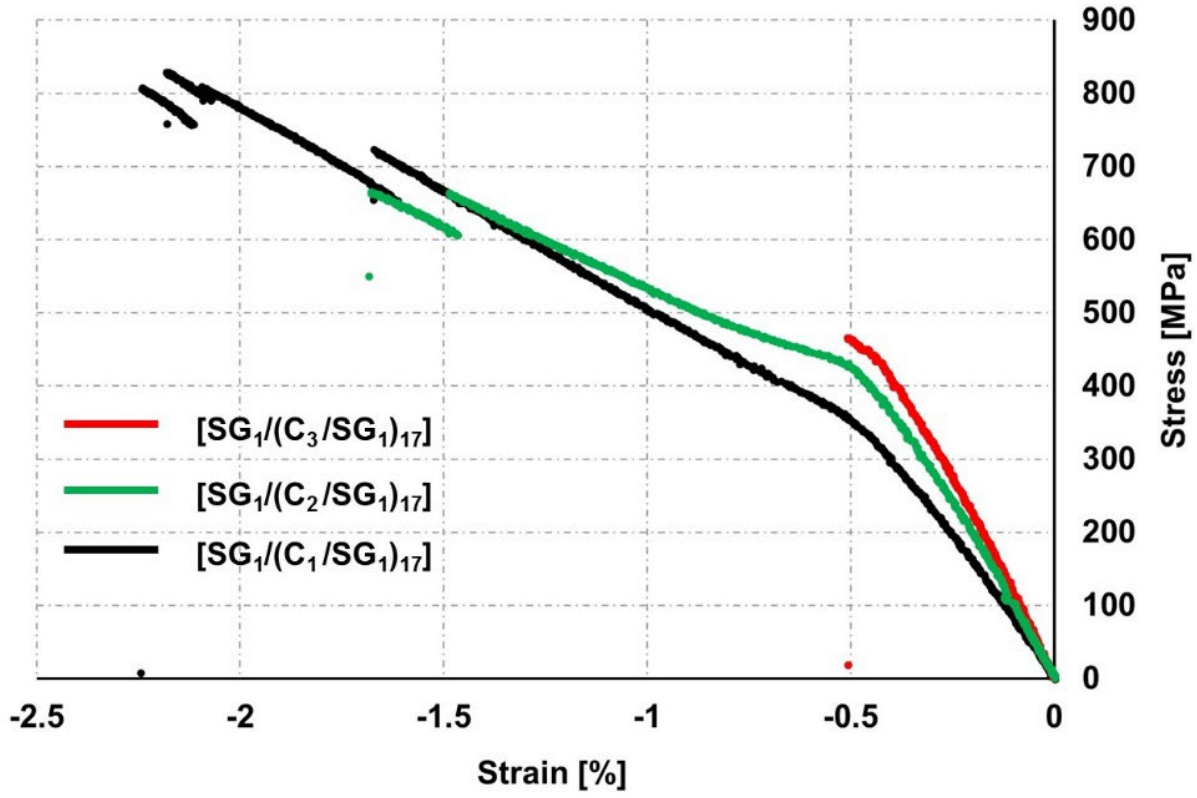

S-GLASS / HIGH MODULUS CARBON HYBRID EFFECT

- Knee point at ~0.5% for all cases
- But failure strain of monolithic M55J composite reported ~0.31% **(Montagnier & Hochard, 2004)**
- Hybrid effect – fibre failure is delayed by support from Glass
- But fragmentation still occurs at similar strains

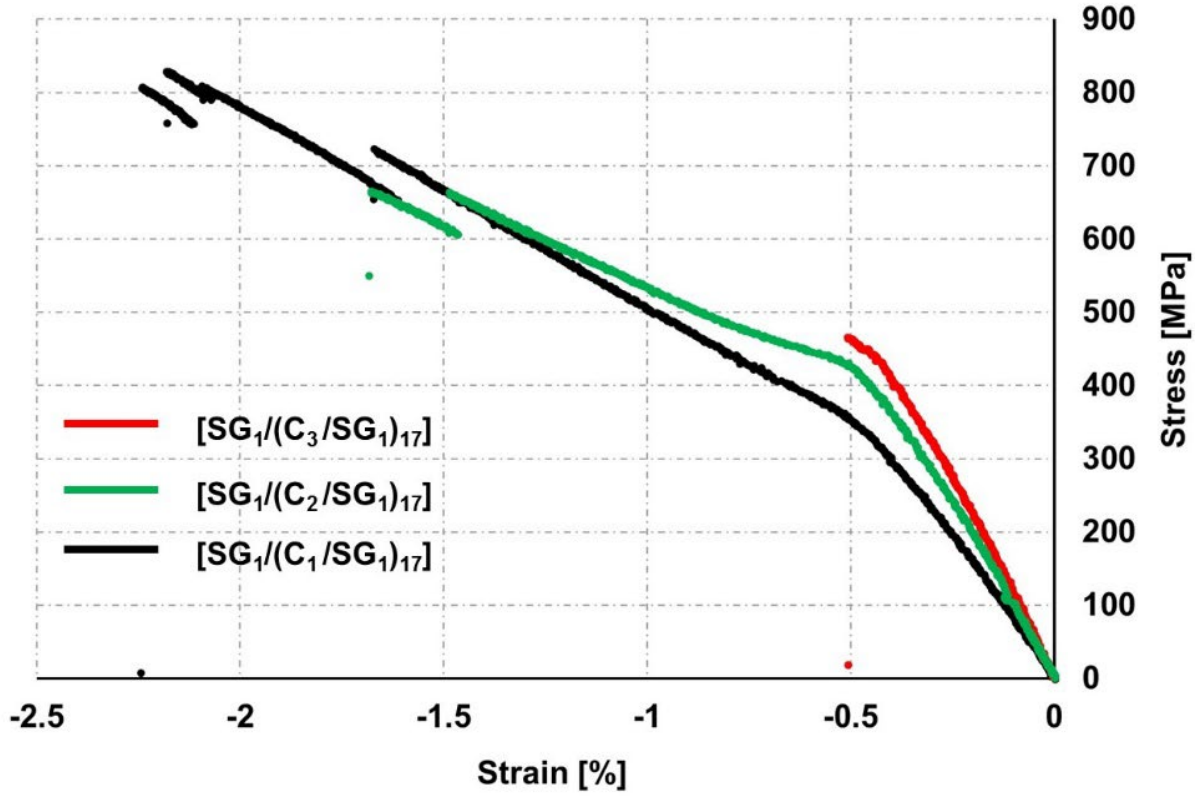

HIGH MODULUS / HIGH STRENGTH CARBON HYBRIDS

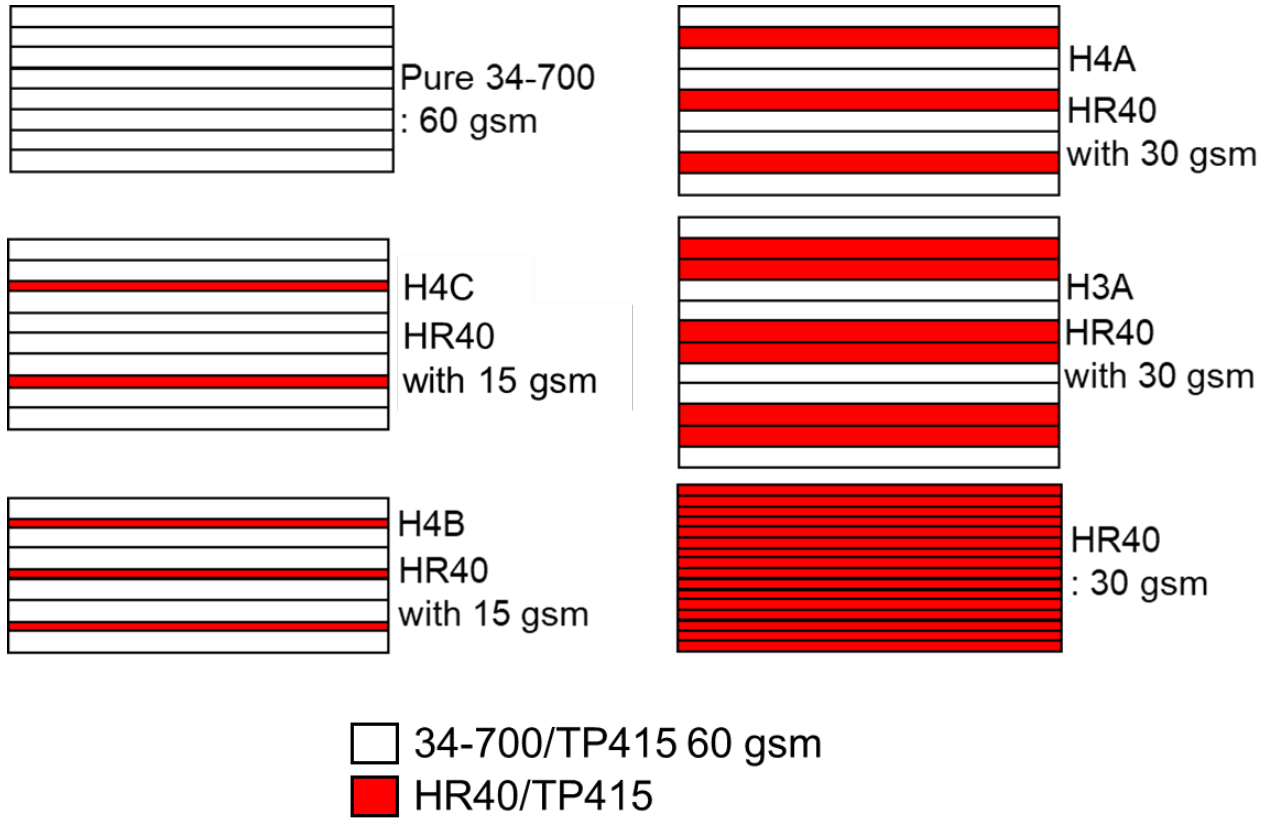

Unidirectional laminates

Fibre type	Fibre tensile modulus (GPa)
34-700	234
HR40	390

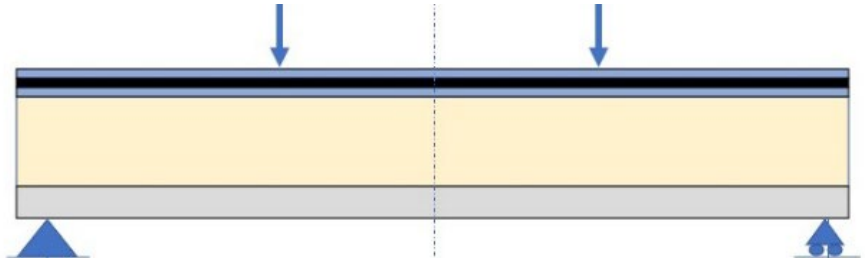

Sandwich 4 point bending test

Tongloet et al, 2025

HIGH MODULUS / HIGH STRENGTH CARBON HYBRIDS

- No fragmentation or pseudo-ductility
- All failures show kink bands
- HR40 failure strain nearly doubled
- Due to support from 34-700
- Hybrid effect
- Fibre failure initiates by instability
- Before fibre fracture, failure transitions to composite instability

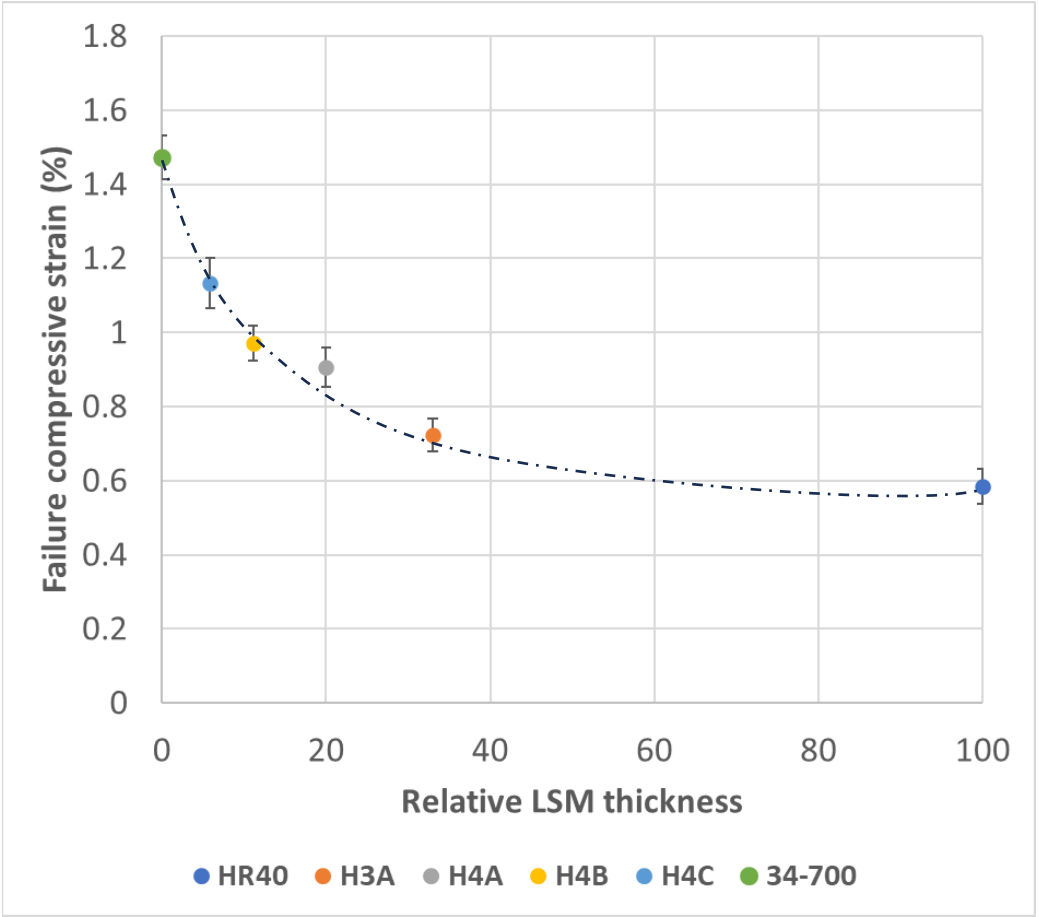

IS THERE A HYBRID EFFECT?

- Yes - significant effects in tension and compression
- But - need good baseline for valid comparison
- Tension – up to 20% increase in strain for thin plies
- Due to restriction in forming critical cluster
- Compression – large increases in failure strain when failure by composite shear instability (Std. Mod. C/G)
- Fibre failure instability delayed (HM C) but similar fragmentation strain
- Hybrid effects in compression due to support against instability

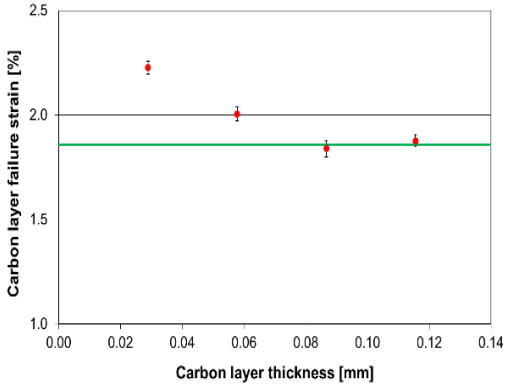

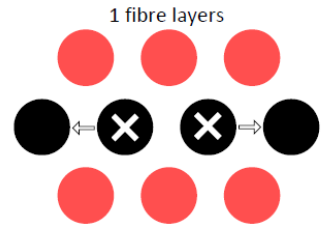

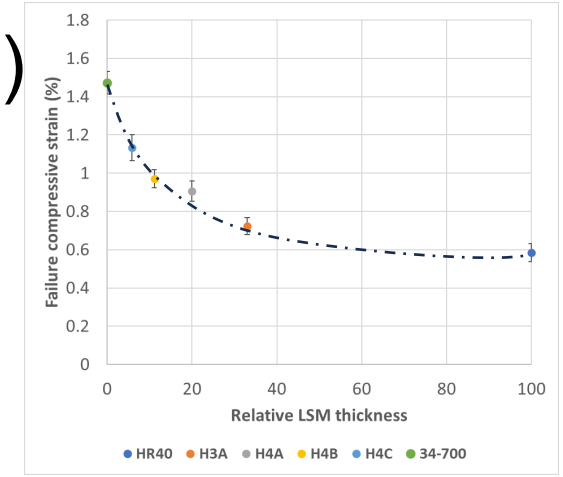

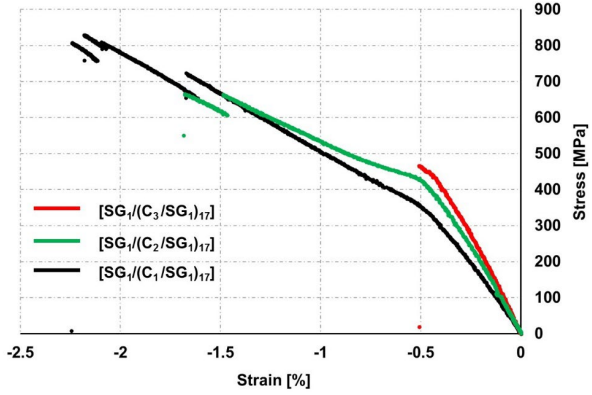

REFERENCES

1. Czél, G., M. Jalalvand, and M.R. Wisnom, *Hybrid specimens eliminating stress concentrations in tensile and compressive testing of unidirectional composites*. Composites Part A-Applied Science and Manufacturing, 2016. **91**: p. 436-447. https://doi.org/10.1016/j.compositesa.2016.07.021
2. Czel, G., et al., *Design and characterisation of high performance, pseudo-ductile all-carbon/epoxy unidirectional hybrid composites*. Composites Part B-Engineering, 2017. **111**: p. 348-356. https://doi.org/10.1016/j.compositesb.2016.11.049
3. Fotouhi, M., M. Jalalvand, and M.R. Wisnom, *High performance quasi-isotropic thin-ply carbon/glass hybrid composites with pseudo-ductile behaviour in all fibre orientations*. Composites Science and Technology, 2017. **152**: p. 101-110. https://doi.org/10.1016/j.compscitech.2017.08.024
4. Hayashi T, K.K., Yamazaki A, Kihira M, *Development of new material properties by hybrid composition*. 2nd report. Fukugo Zairyo (Composite Materials) 1972. **1**: p. 21-25.
5. Idarraga G, J. Acosta, M. Jalalvand, J. Meza and M. R. Wisnom, *Hybrid Effect in Multi-directional Carbon/Glass Composites,* Composites Science and Technology, 2025. p. 111285. https://doi.org/10.1016/j.compscitech.2025.111285
6. Suwarta, P., et al., *Pseudo-ductile compressive behaviour of unidirectional thin-ply carbon /glass fibre-epoxy hybrid composites*. Composites Part A-Applied Science and Manufacturing, 2025. **195**:108877. https://doi.org/10.1016/j.compositesa.2025.108877
7. Swolfs, Y., L. Gorbatikh, and I. Verpoest, *Fibre hybridisation in polymer composites: A review*. Composites Part A-Applied Science and Manufacturing, 2014. **67**: p. 181-200. https://doi.org/10.1016/j.compositesa.2014.08.027
8. Tongloet, A., Wisnom, M.R., Wu, X., Argyropoulos, A., Cugnoni, J., Michaud, V., *Compressive behaviour of high modulus/high strength thin-ply carbon fibre hybrid composites*. To be published, 2025.
9. Tongloet, A, *Compressive Behaviour of Longitudinal Hybrid Composites*, PhD thesis, 2025. University of Bristol.
10. Wisnom, M.R., et al., *Hybrid effects in thin ply carbon/glass unidirectional laminates: Accurate experimental determination and prediction*. Composites Part A-Applied Science and Manufacturing, 2016. **88**: p. 131-139. https://doi.org/10.1016/j.compositesa.2016.04.014
11. Wu, X. and M.R. Wisnom, *Compressive failure strain of unidirectional carbon fibre composites from bending tests*. Composite Structures, 2023. **304**: p. 116467. https://doi.org/10.1016/j.compstruct.2022.116467



Next Generation
Fibre-Reinforced Composites

https://nextcomp.ac.uk

I would like to acknowledge funding which supported this work from the UK Research and Innovation - EPSRC Programme Grant; Next Generation Fibre-Reinforced Composites: A Full Scale Redesign for Compression (EP/T011653/1)

A collaboration between Imperial College London and University of Bristol

IMPERIAL

University of BRISTOL

Bristol Composites Institute

FE SIMULATIONS OF LARGE UD-FRP MICROSTRUCTURES UNDER LONGITUDINAL COMPRESSION

ICCM24 24TH INTERNATIONAL CONFERENCE ON COMPOSITE MATERIALS
AUG 4-8, 2025 · BALTIMORE CONVENTION CENTER · BALTIMORE, MARYLAND

Dr Dimitrios Bikos[1]

Prof Richard Trask[2], Prof Paul Robinson[3] , Dr Soraia Pimenta[1]

[1] Mechanical Engineering, Imperial College London, UK

[2] Bristol Composites Institute, University of Bristol, UK

[3] Aeronautics, Imperial College London, UK

d.bikos17@imperial.ac.uk

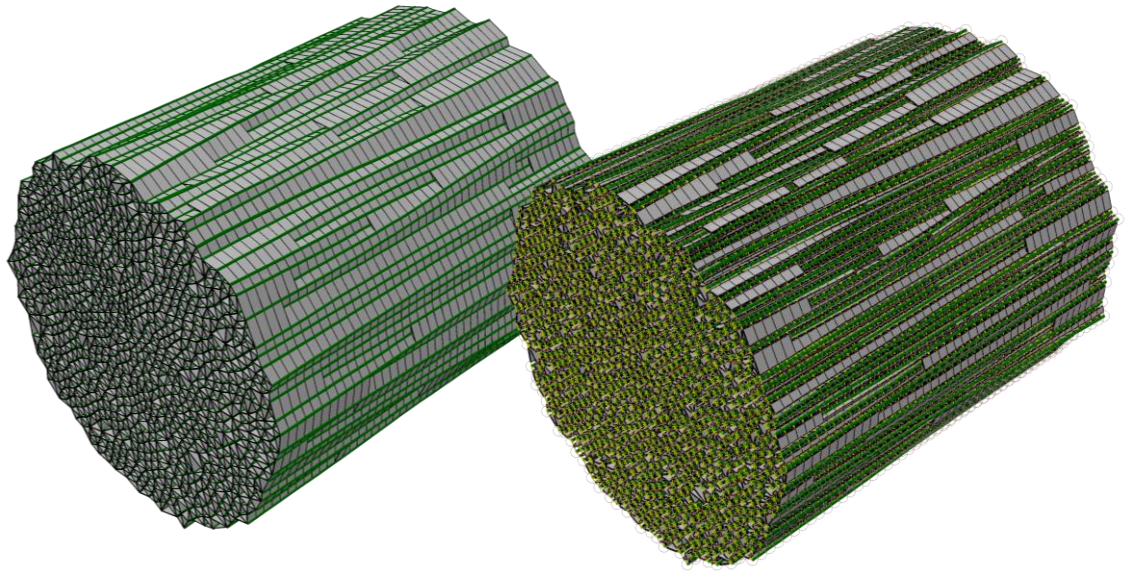

Next Generation Fibre-Reinforced Composites

IMPERIAL

The Composites Centre
for research, modelling, testing and training in advanced composites

University of BRISTOL
Bristol Composites Institute

UK Research and Innovation

Engineering and Physical Sciences Research Council

BUILDING ON PREVIOUS WORK

ECCM21: "*FE-Simulation of real microstructures: 1000 fibres, 1 mm long*"

12 hours

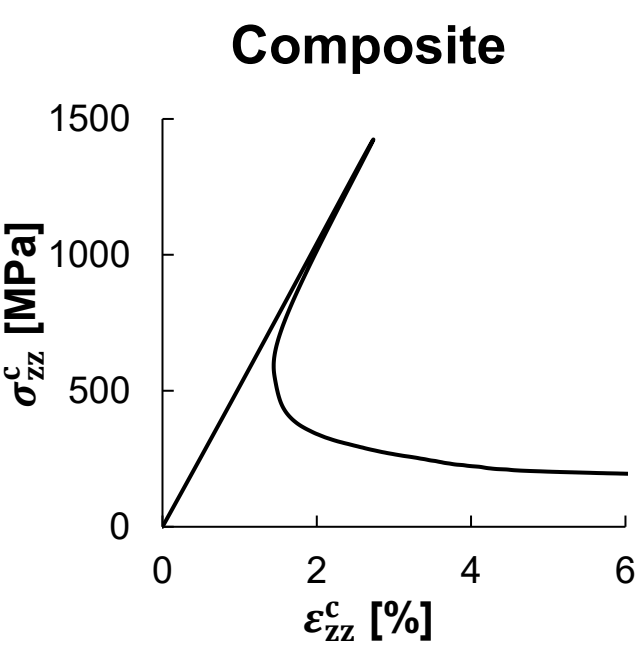

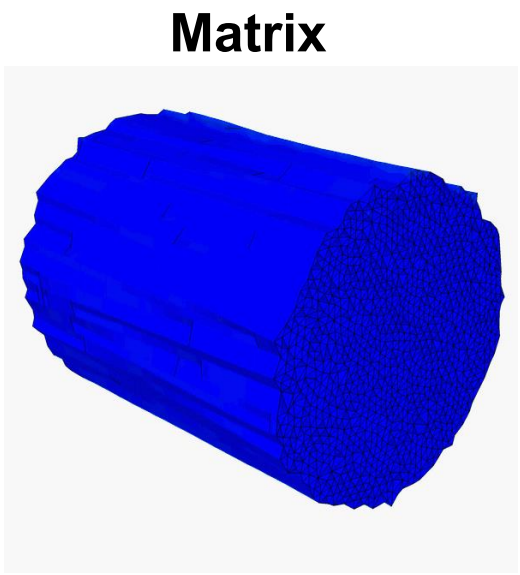

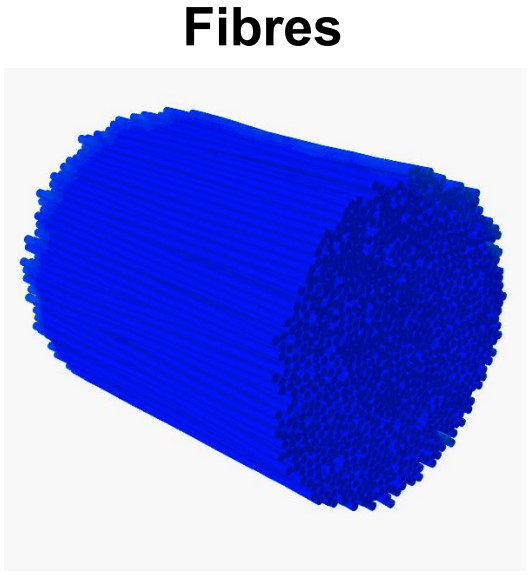



In-depth analysis of fibre imperfections and compressive failure mechanisms.

LAYOUT

Aims

Why the need of 3D micromechanical FE-Models.

Importance of simulating real microstructures:

- *Why average metrics are not enough.*

Demonstration

SB FE-simulations on a LARGE CFRP microstructure with our most accurate and computationally-efficient model.

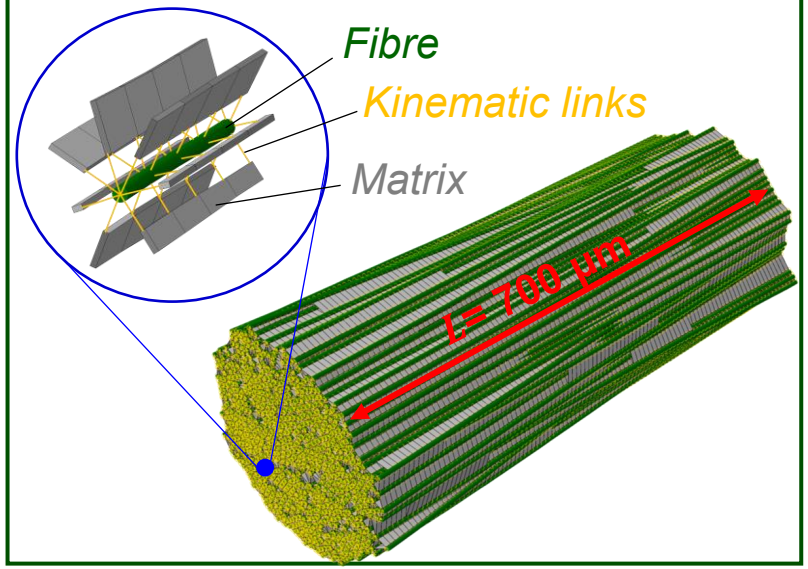

Opportunities

An in-depth analysis of compressive failure mechanisms of real FRP microstructures.

Analysis of coupled torsion-kinking behaviour of RVE.

Bonus study: Effect of real microstructures with similar average fibre imperfections.

Analysis of real CFRP imperfections

800 CF paths from μCT (Emerson *et al.* 2017).

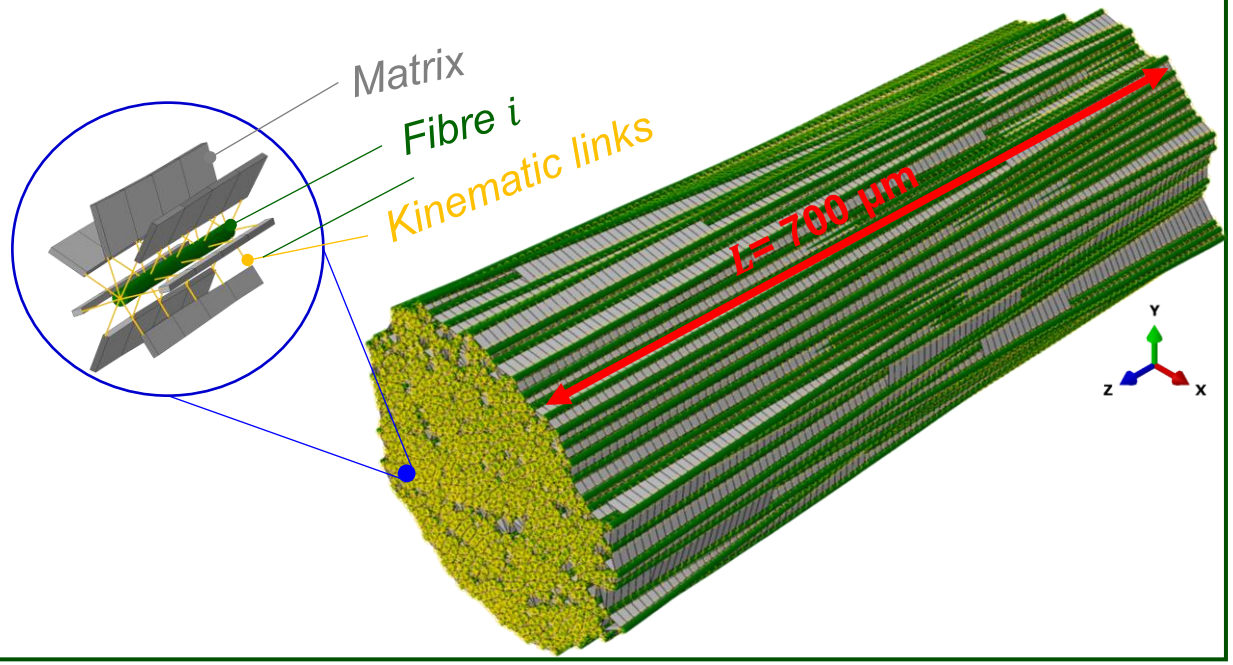



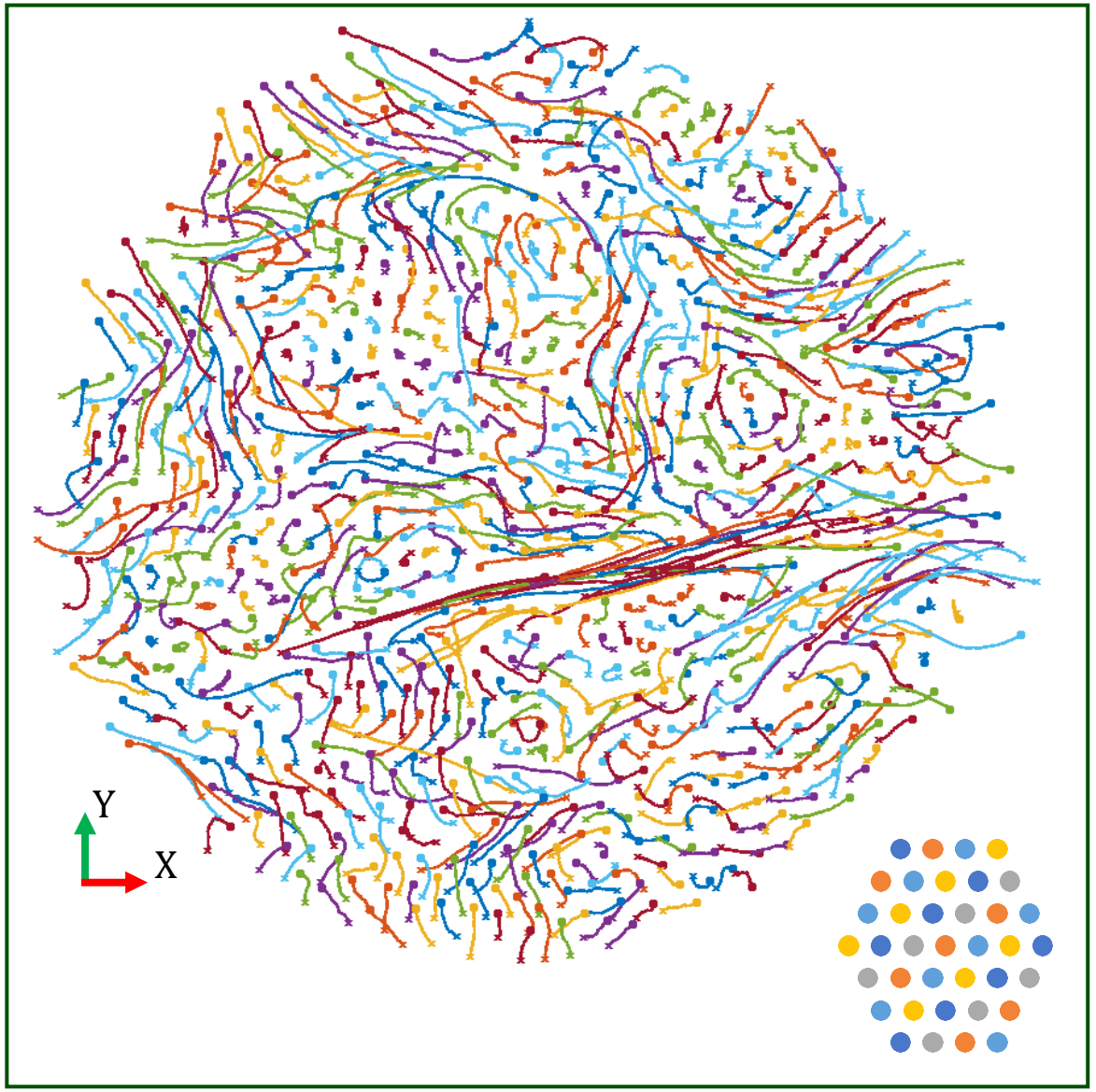

ANALYSIS OF REAL CFRP IMPERFECTIONS

800 CF paths from μCT (Emerson *et al.* 2017).

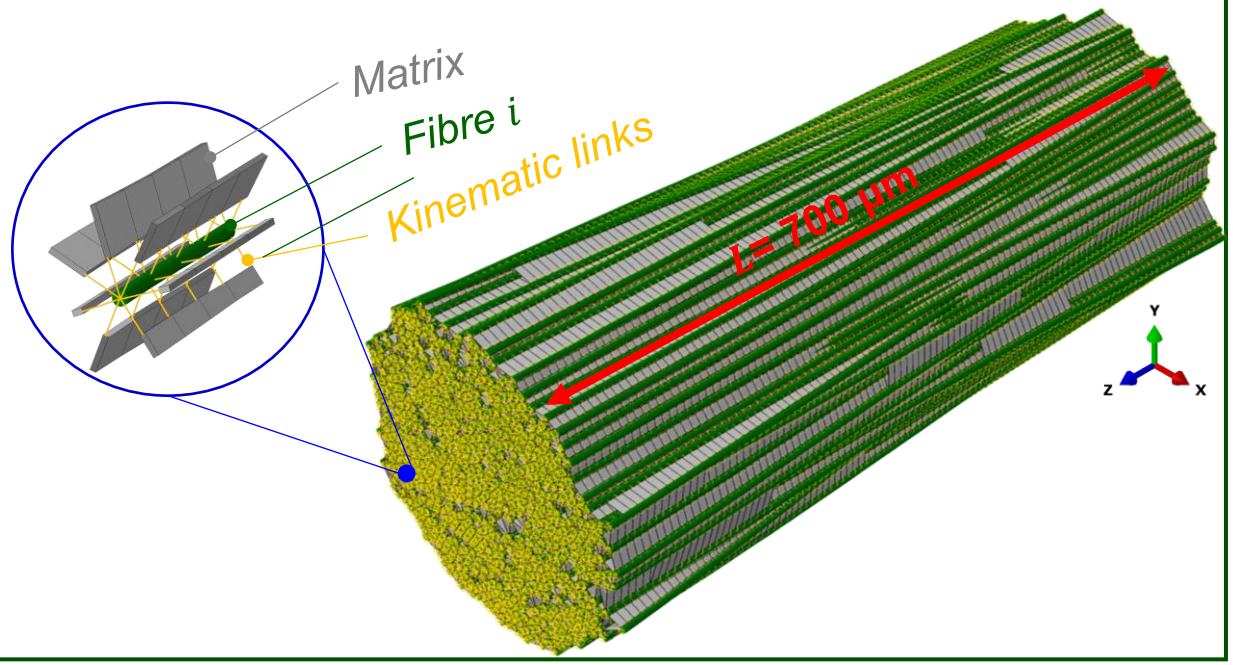

The misalignment angle of a given fibre i is defined by its:

i. Magnitude, $\boldsymbol{\theta_i^f}$
ii. Planar orientation, phase angle, $\boldsymbol{\varphi_i^f}$

Magnitude of fibre misalignment angle, $\boldsymbol{\theta_i^f}$

$\overline{\boldsymbol{\theta^f}}$**=1.39** $\pm$ **1.03°**

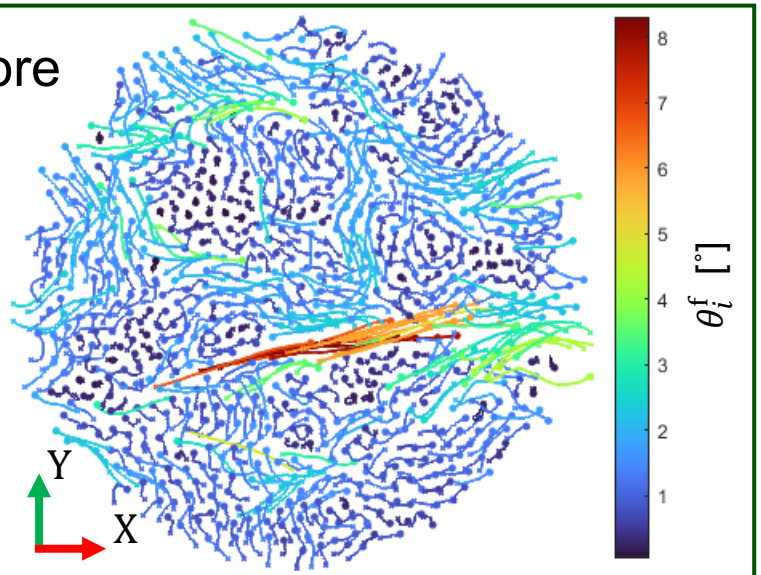

Global fibre phase angle, $\boldsymbol{\varphi_i^f}$

$\overline{\boldsymbol{\varphi^f}}$**=-14.7°**
IQD=138.9°

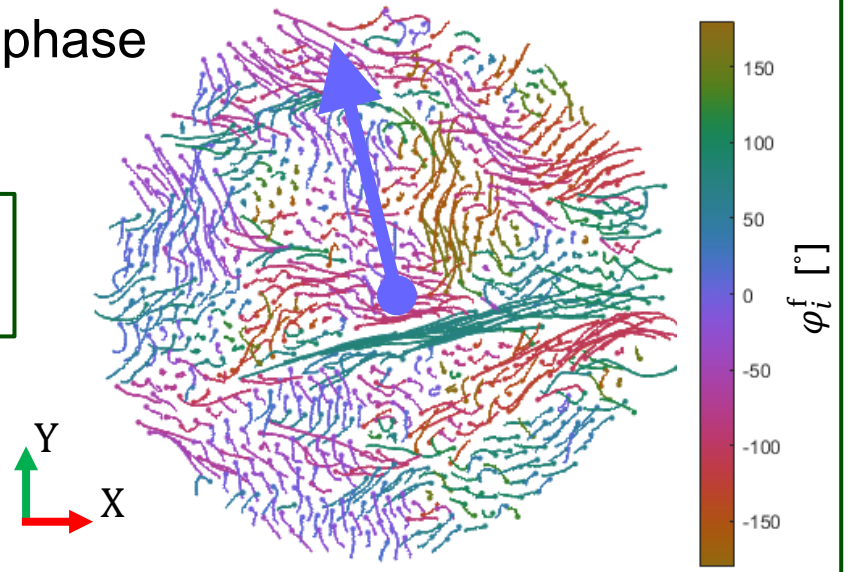

ANALYSIS OF REAL CFRP IMPERFECTIONS

800 CF paths from μCT (Emerson *et al.* 2017)

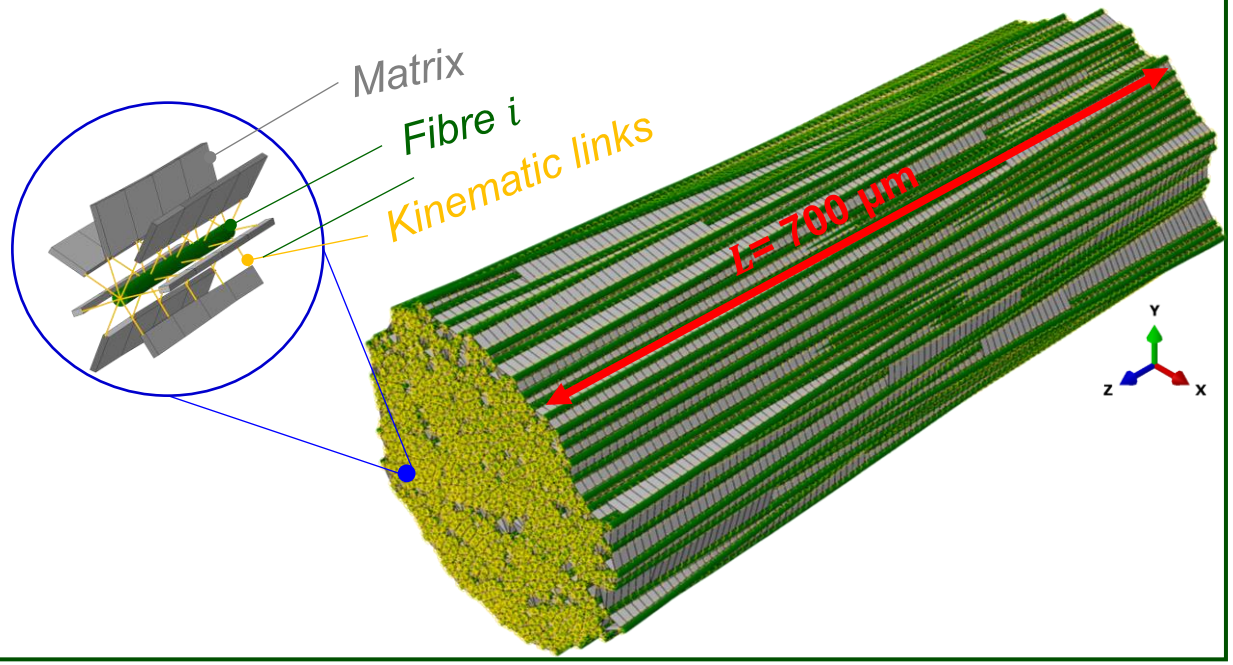

- A distribution of fibre diameters is assumed due to lack of available tracking data;
- A normal distribution with: $\overline{\emptyset^f}$=6.6 ± 0.3 μm*

Distribution of fibres diameter, $\emptyset^f$ [μm]

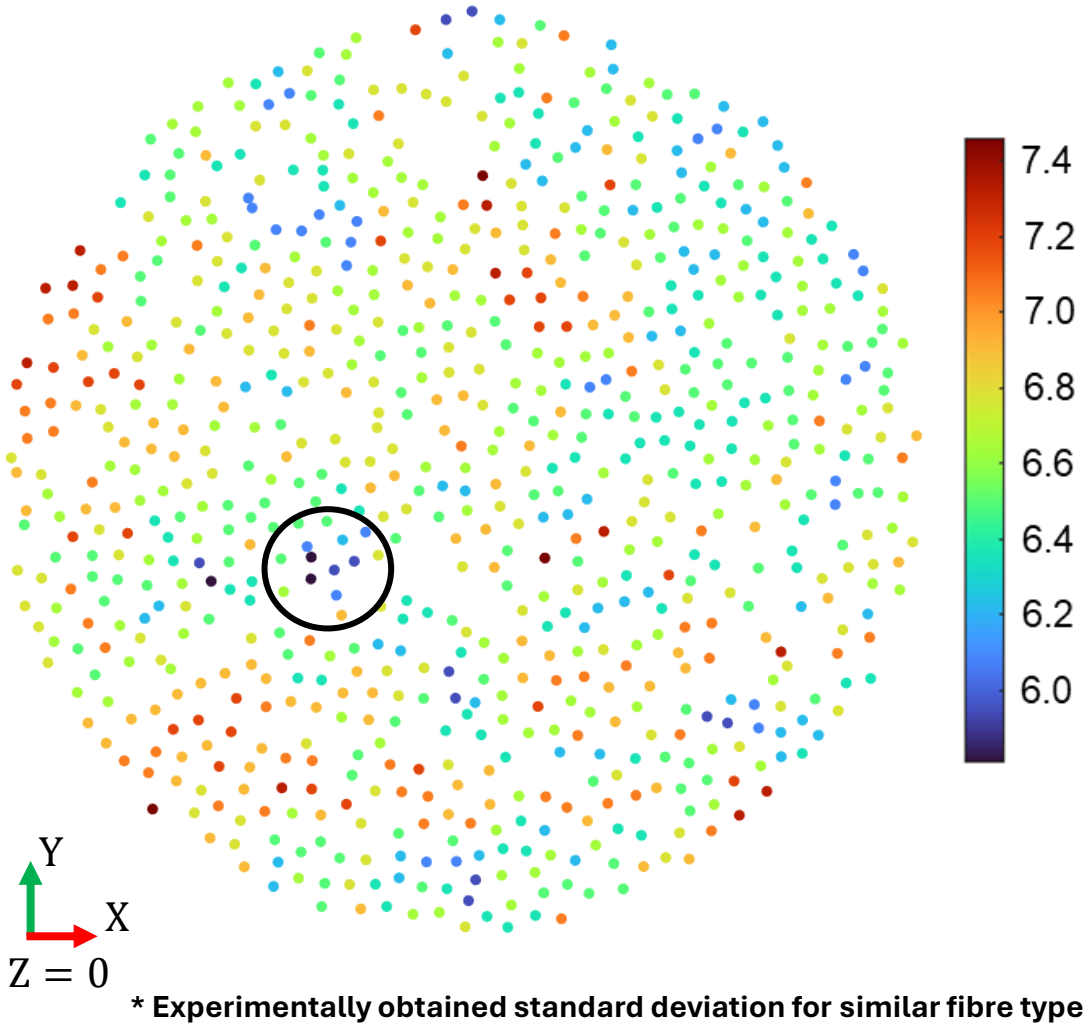

* Experimentally obtained standard deviation for similar fibre type (Mesquita *et al.* 2021)

Analysis of real CFRP imperfections

800 CF paths from µCT (Emerson *et al.* 2017)

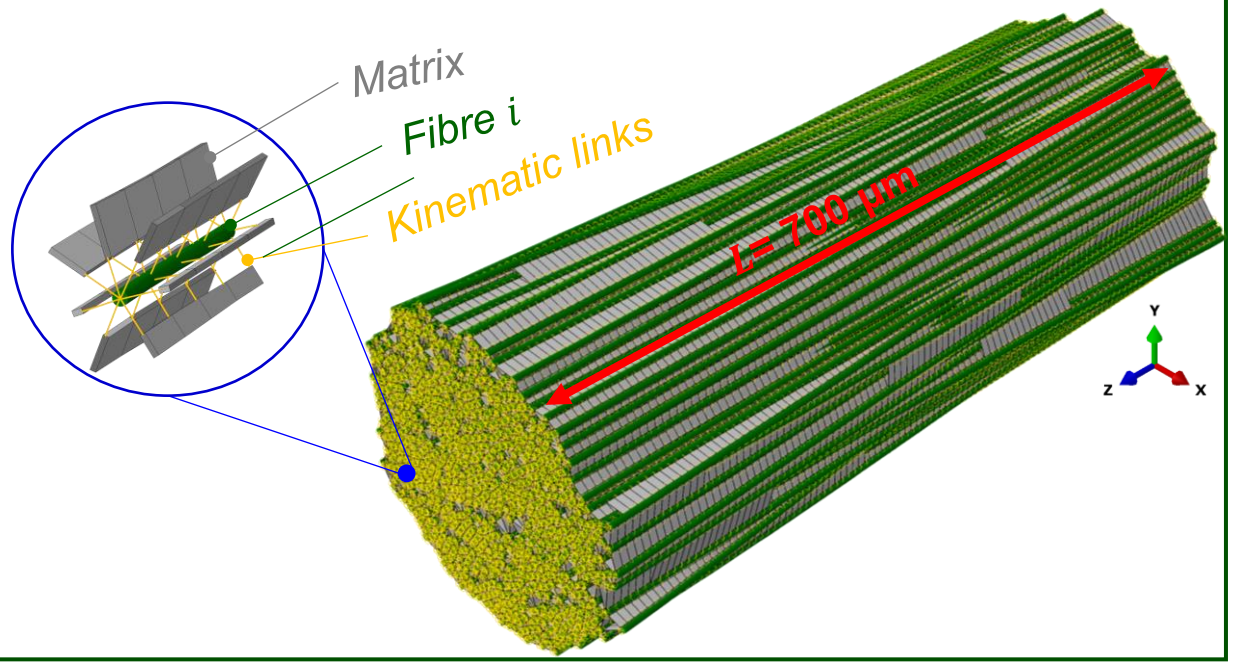

- The local fibre volume fraction of the RVE ($\mathbf{V^f}$) is calculated employing the Voronoi Network for each Z section;
- A large variation in $\mathbf{V^f}$ is observed → $\overline{\mathbf{V^f}}$**=49.2 ± 8.4 %**

Local fibre volume fraction, $\mathbf{V^f}$

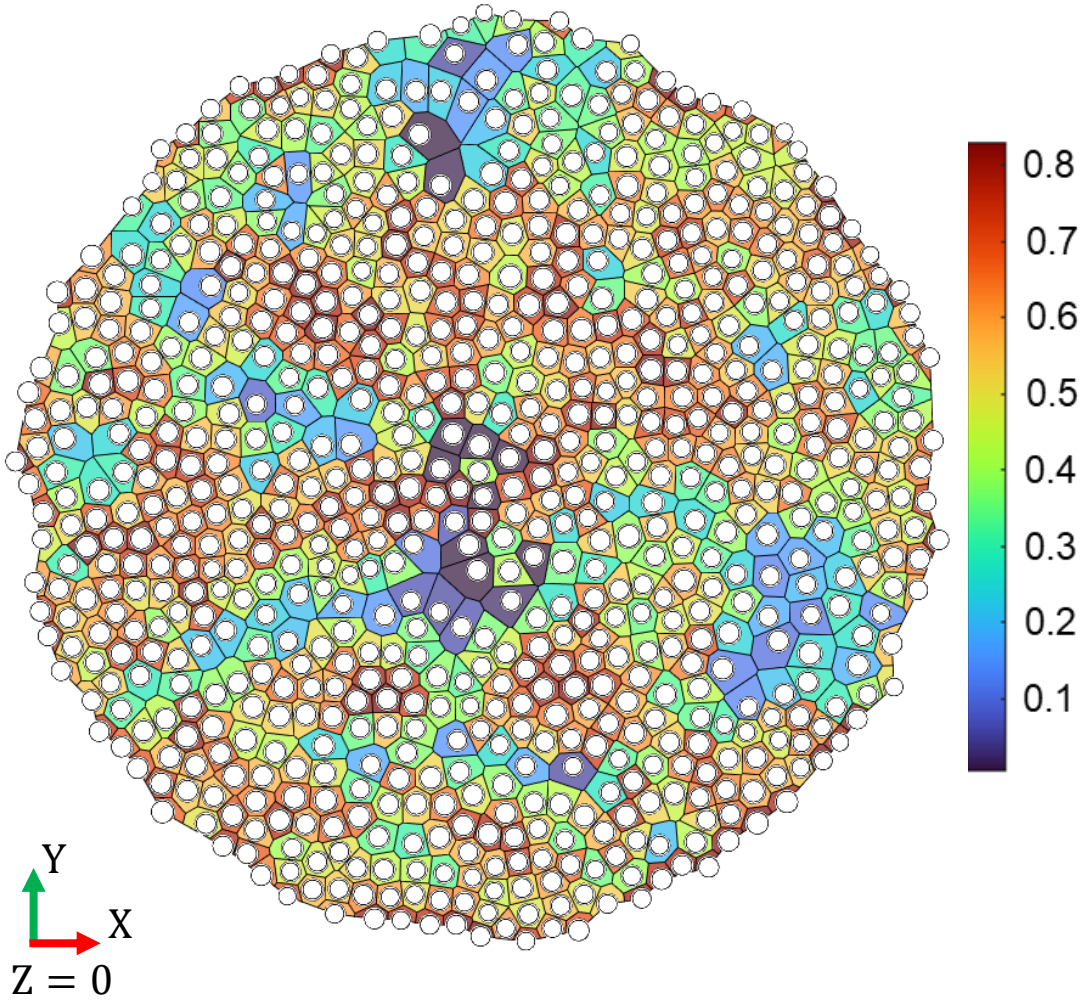

SIMULATING REAL CFRP-RVEs

Matrix: Yield-band

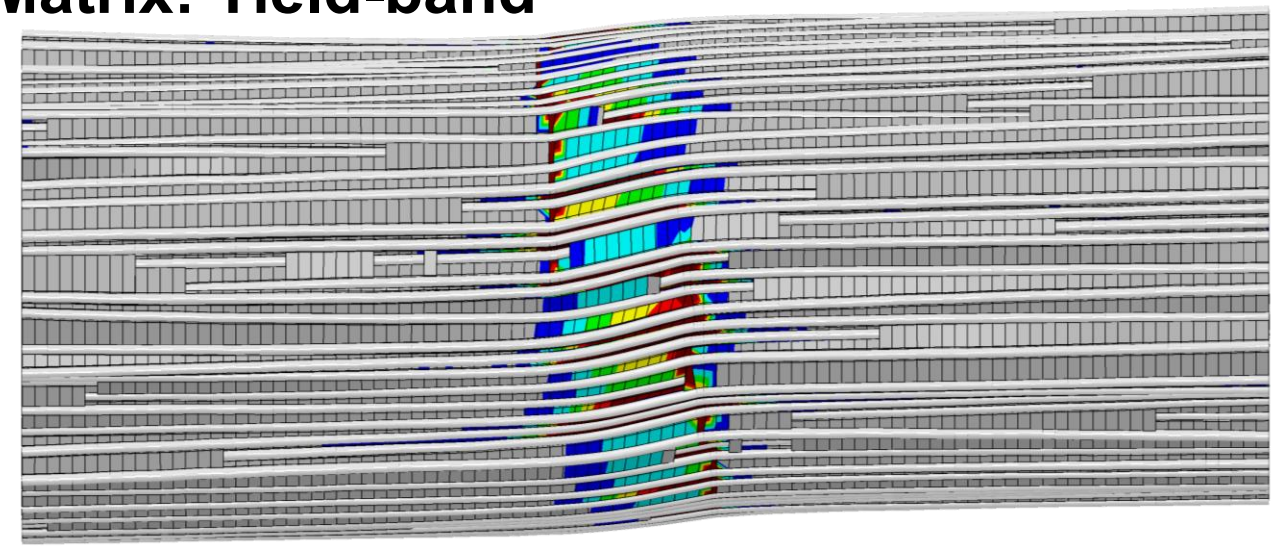

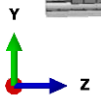

Fibres: Fibre kinking

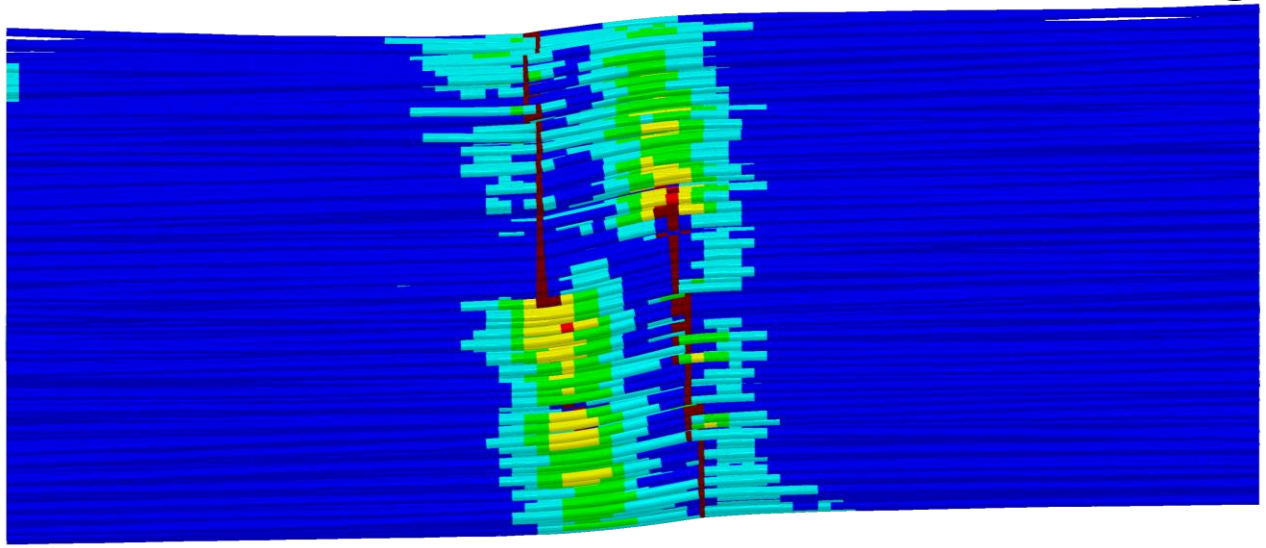

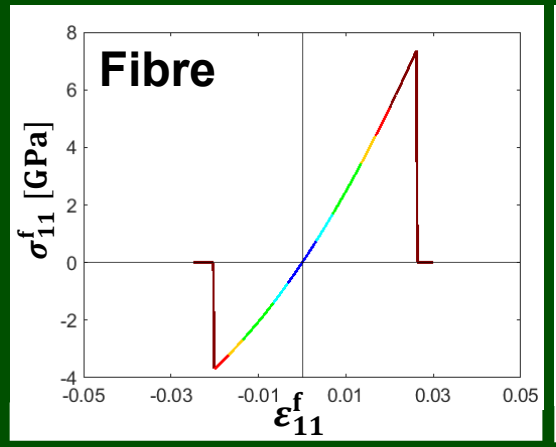

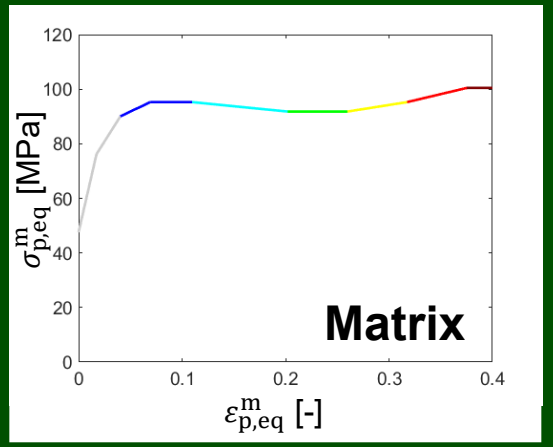

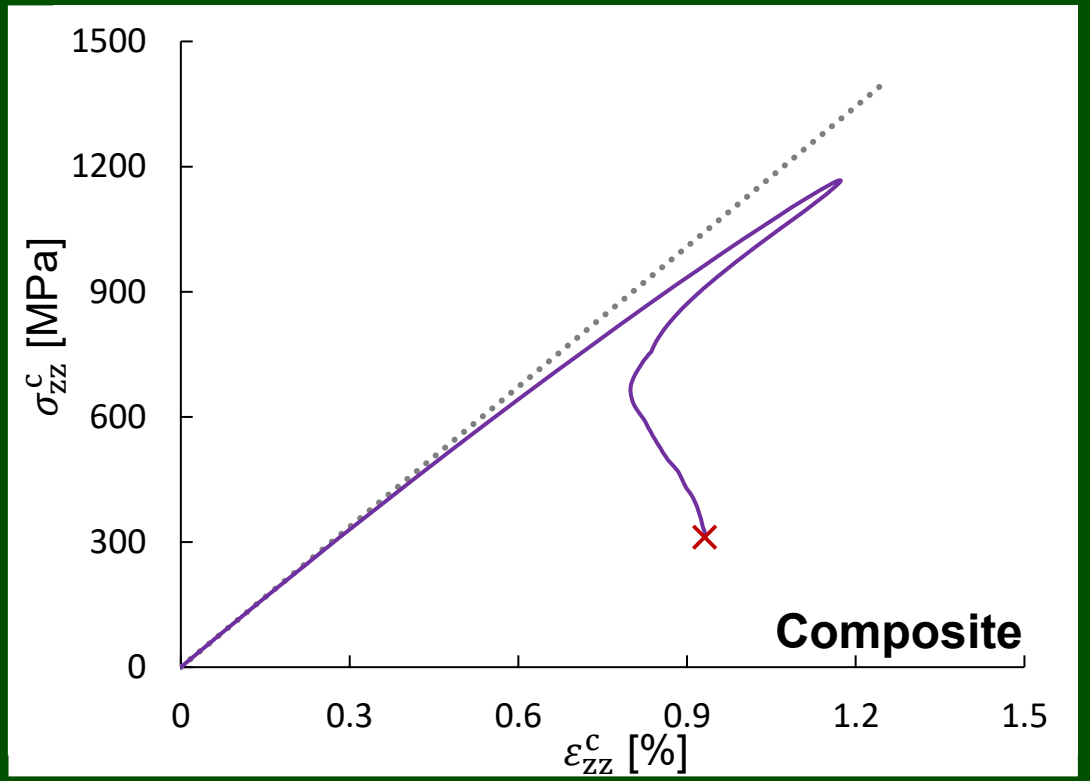

SIMULATING REAL CFRP-RVES

- A 3D torsional deformation occurs and becomes more pronounced during matrix yielding.
- The direction of torsion is not constant.

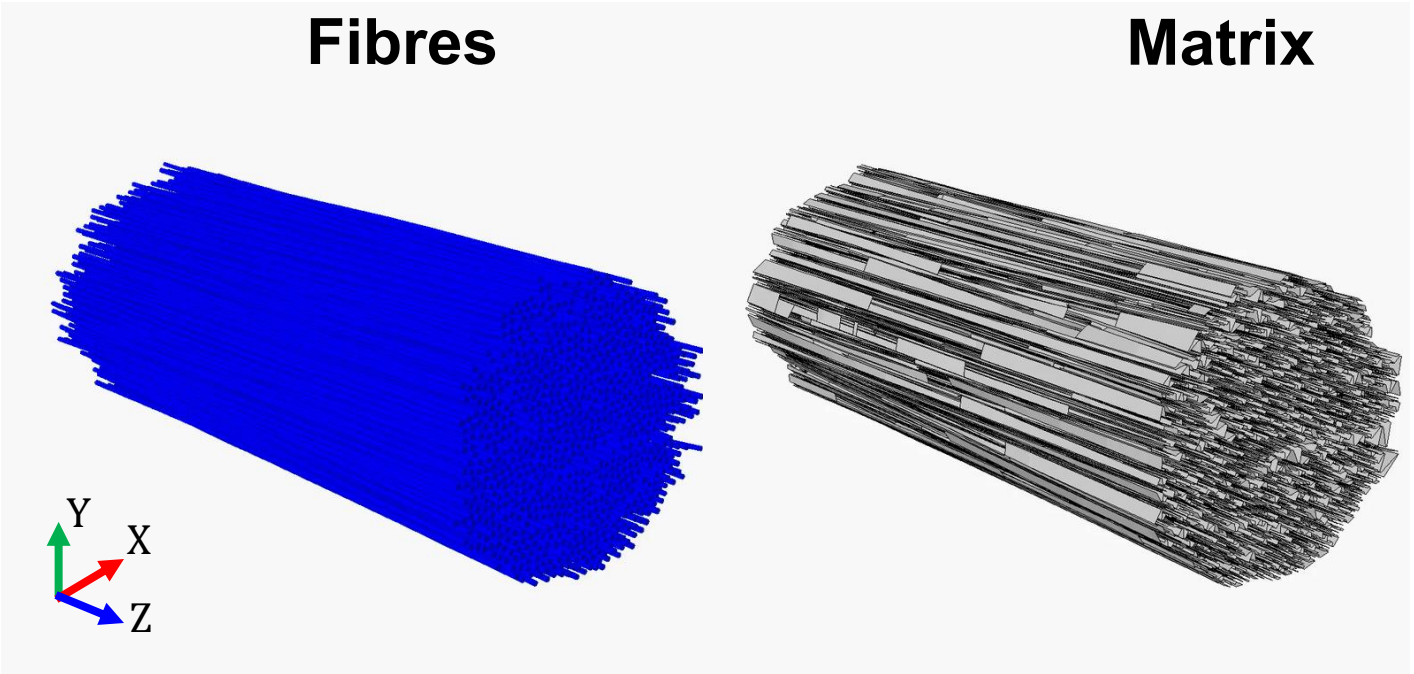

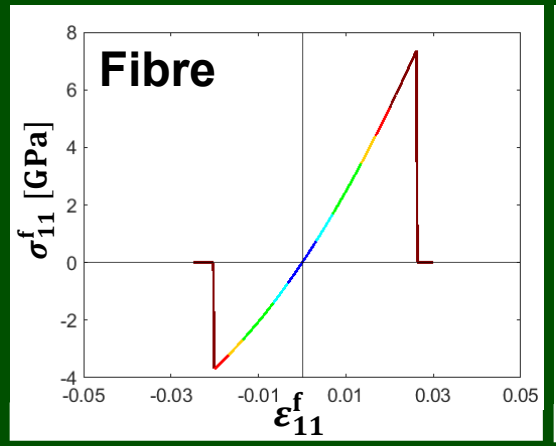

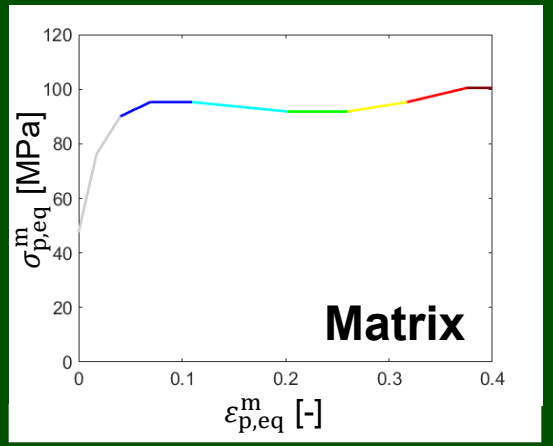

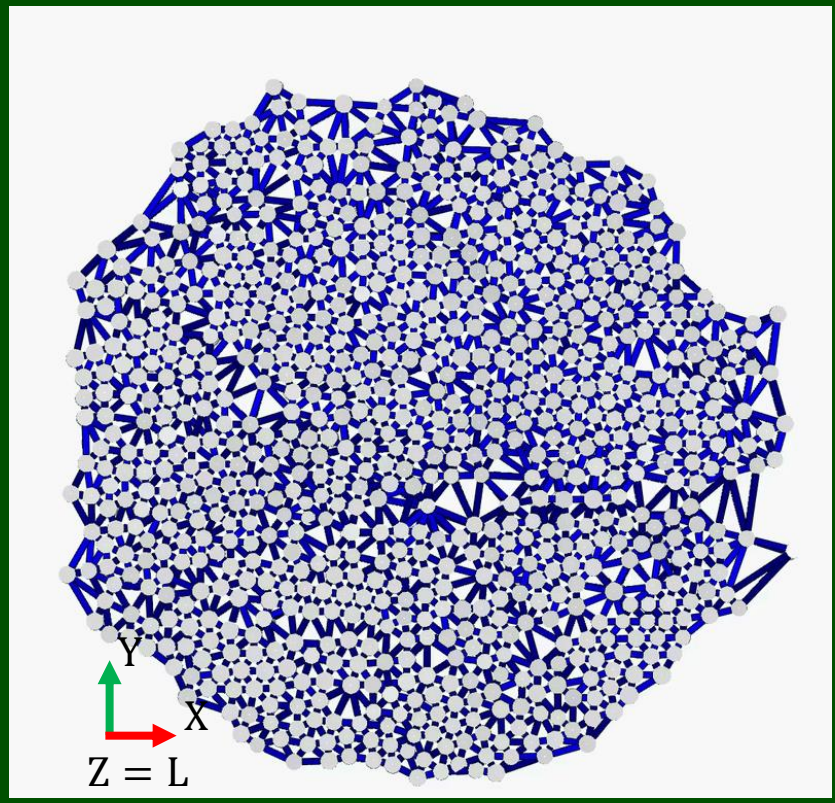

FRAME BY FRAME ANALYSIS

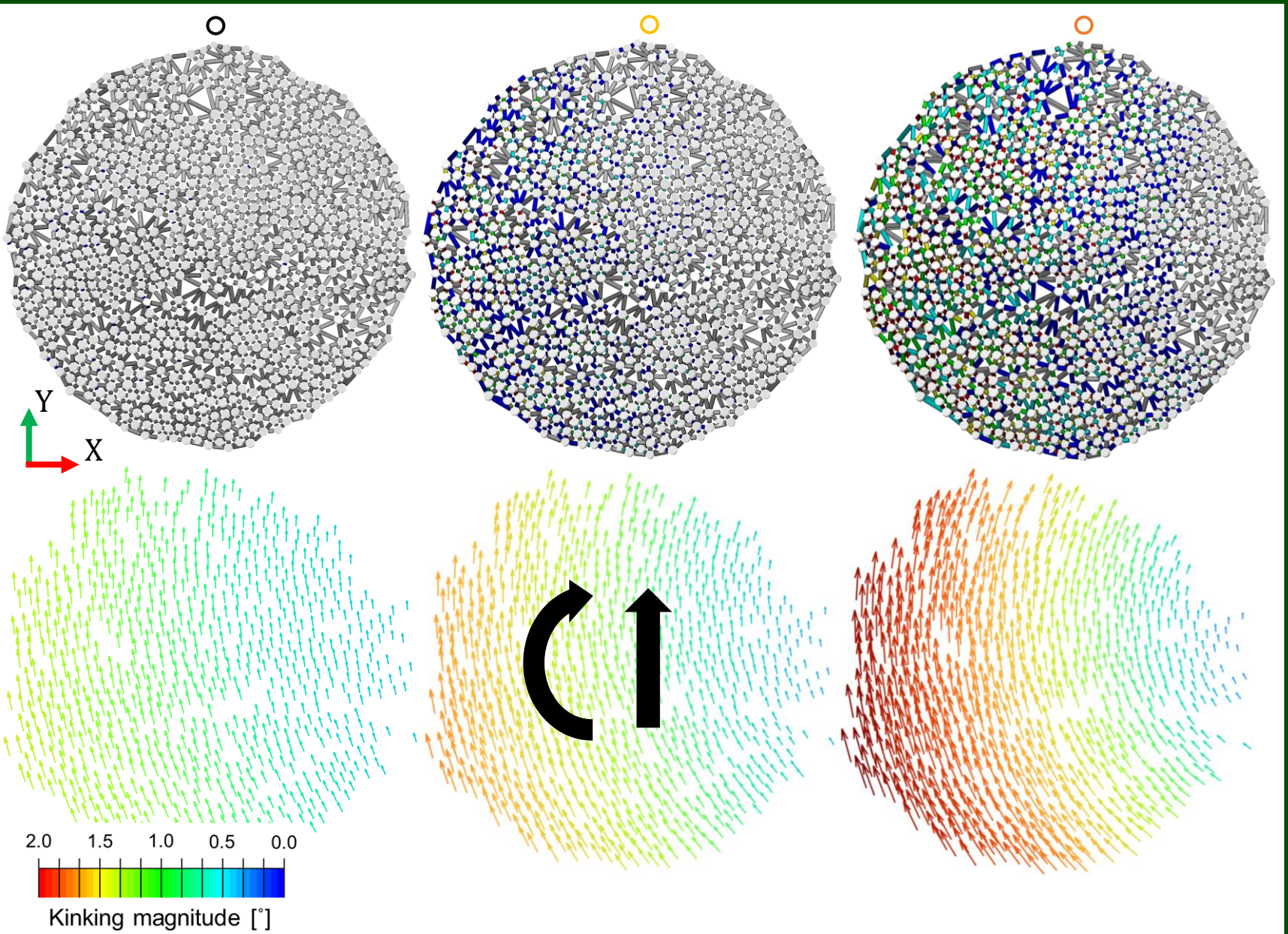

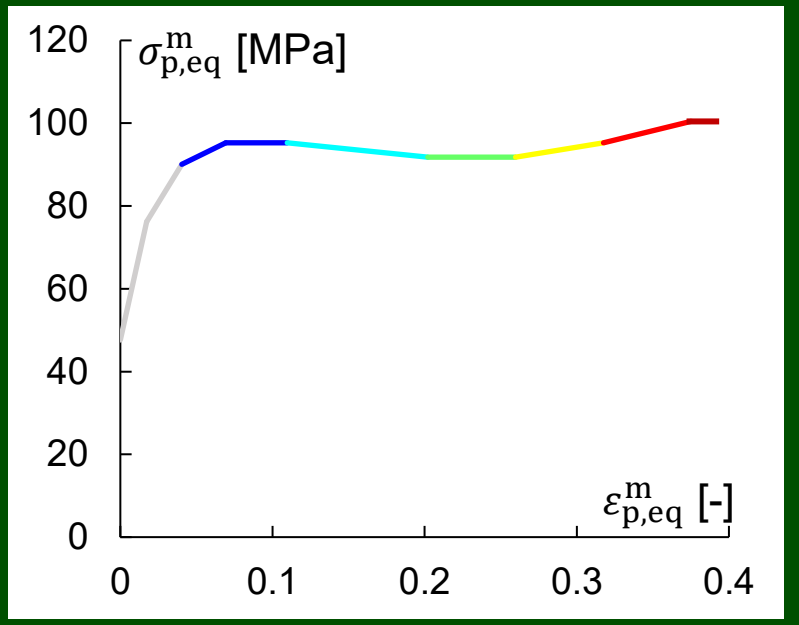

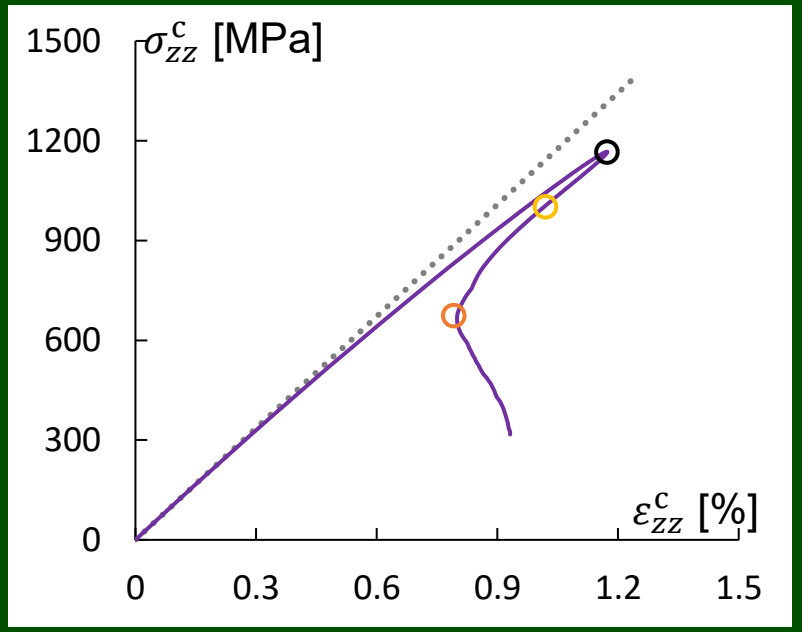

FIBRE MOTION – PEAK GLOBAL STRESS

Fibre motion can be decoupled to kinking and torsional motion
A small (~1.25˚) but perfect circular motion is observed.

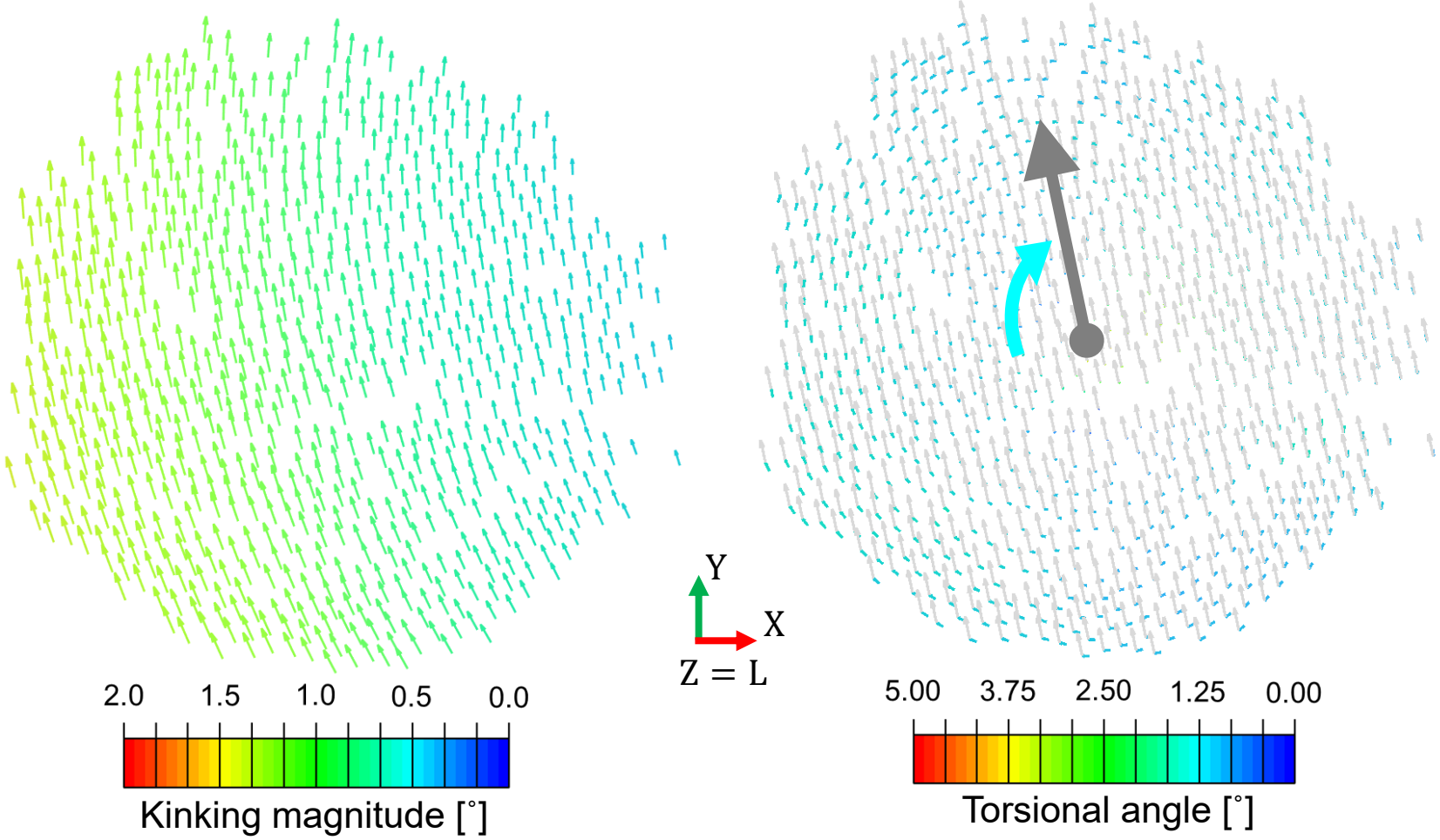

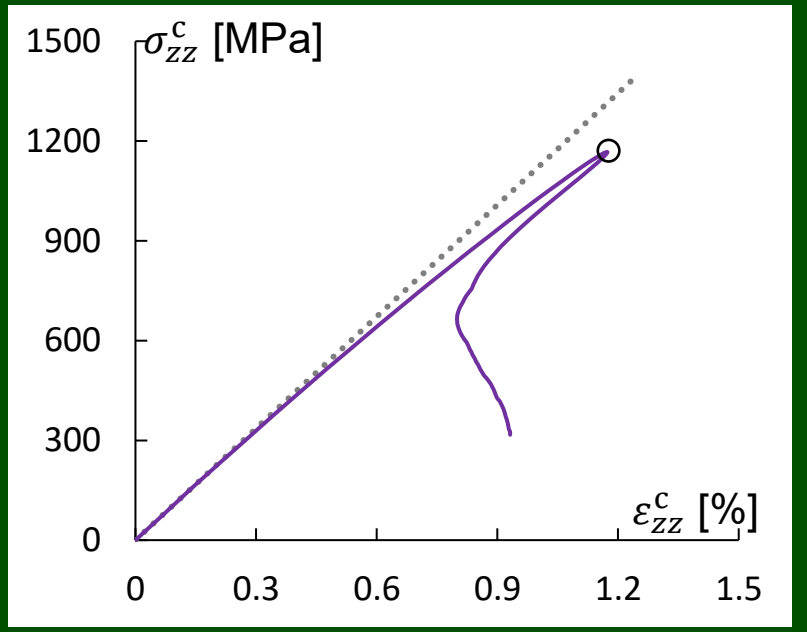

Key questions:

"What drives the torsional deformation?"

"Why is this even important?"

FIBRE TWISTING – PEAK GLOBAL STRESS

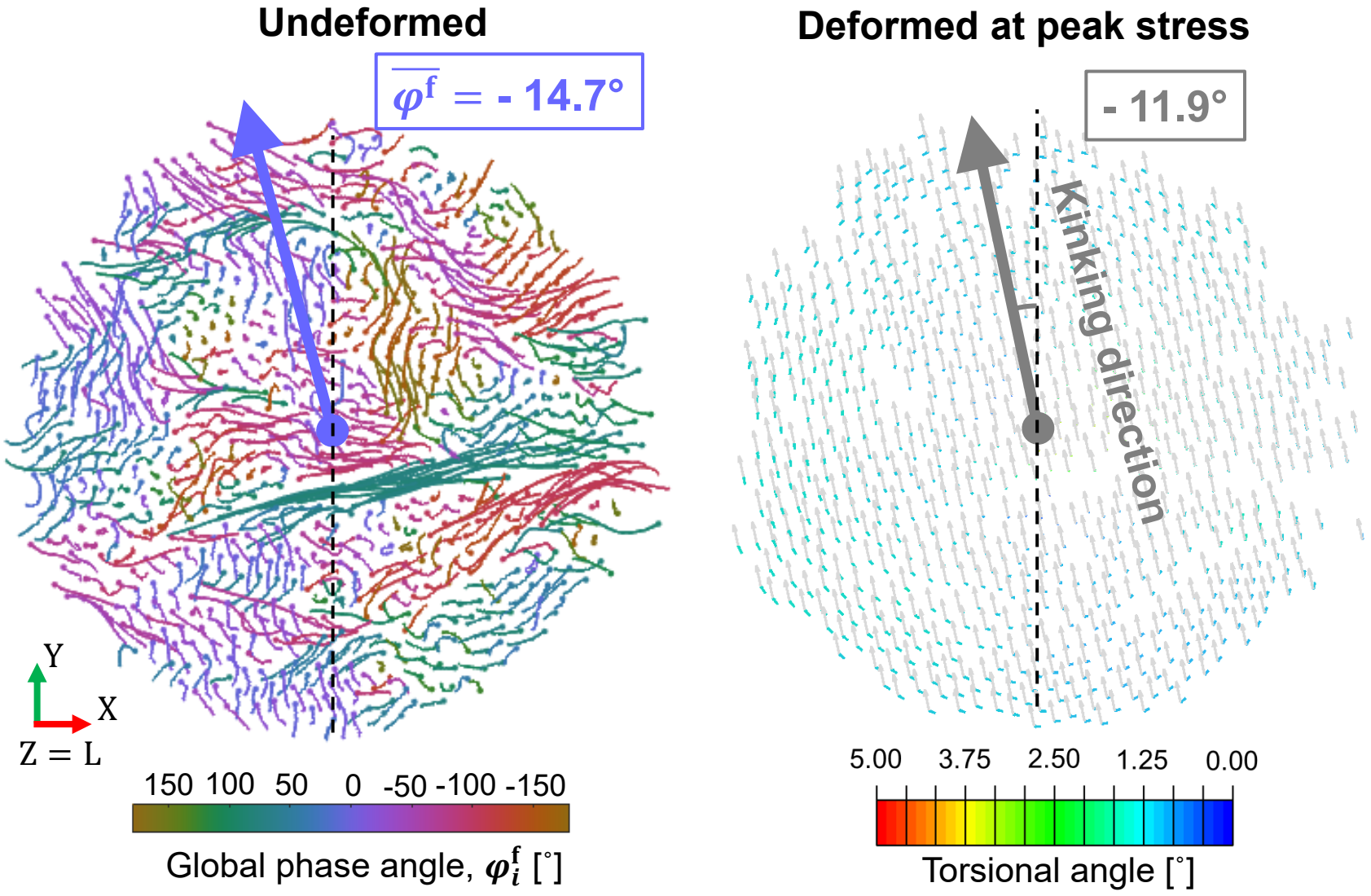

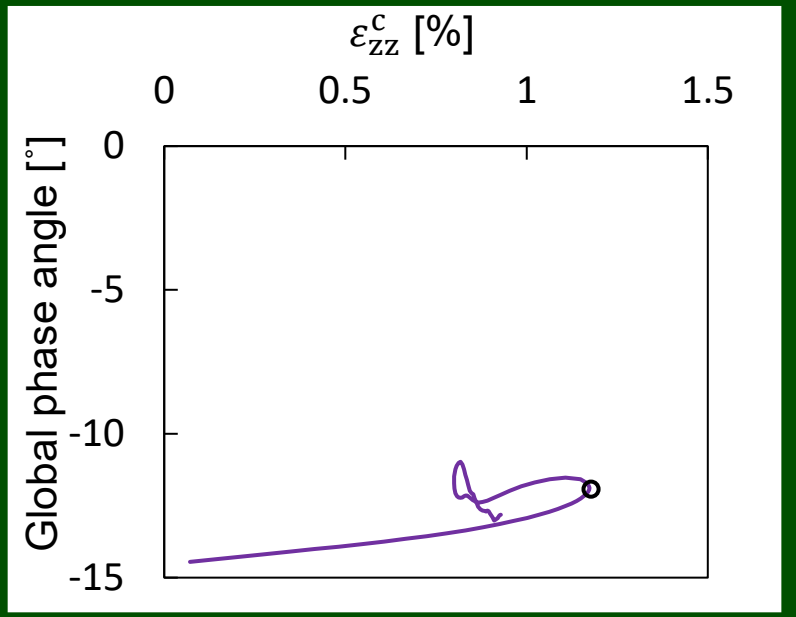

Torsional deformation potentially occurs because of the initial twist of fibre architecture!

ASSESSMENT OF FIBRE TWISTING

Decouple the mean misalignment from mean twisting of fibres.

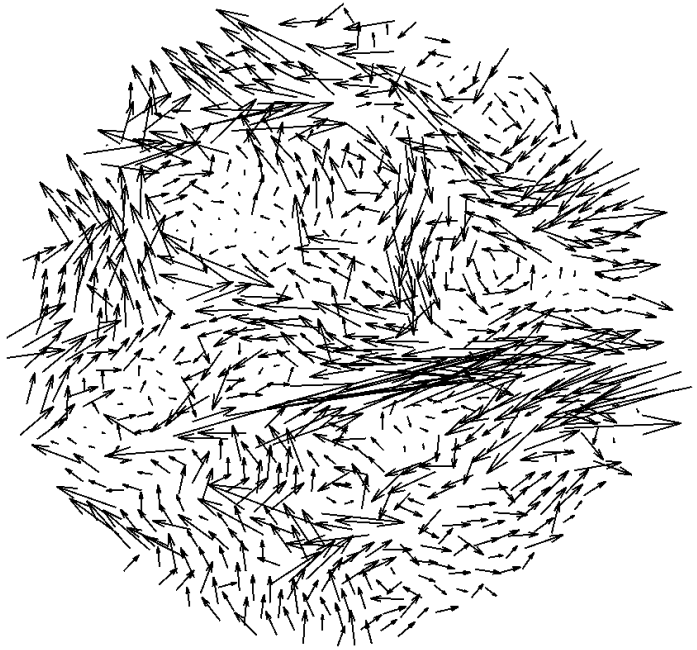

The average twisting angle of the initial fibre architecture:

$$\overline{\Psi_0^{\mathrm{f}}} = 16.4\ °$$

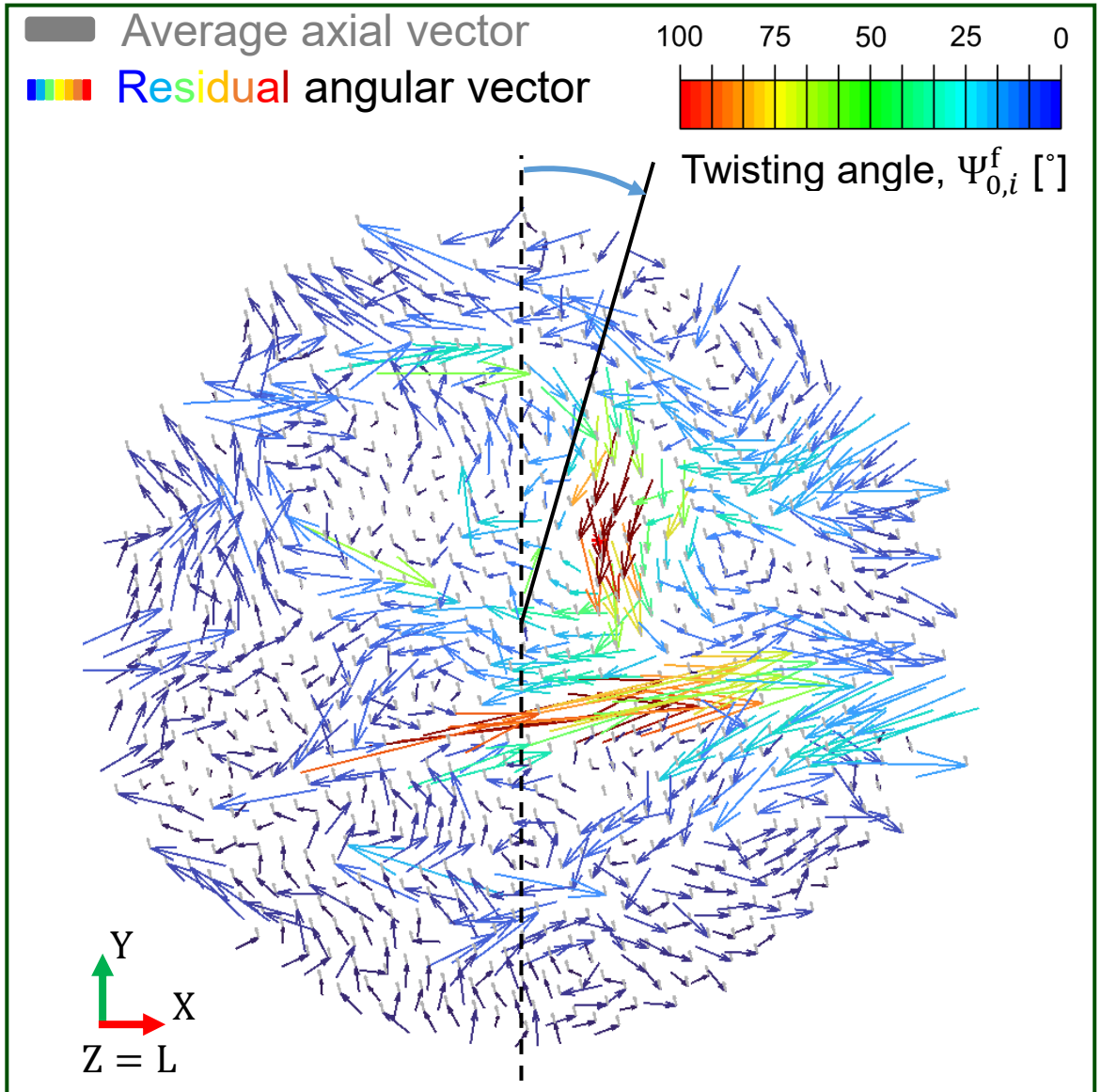

Case study: Effect of real fibre imperfections

Compressive failure in RVEs with similar microstructural features

To be continued at my talk…

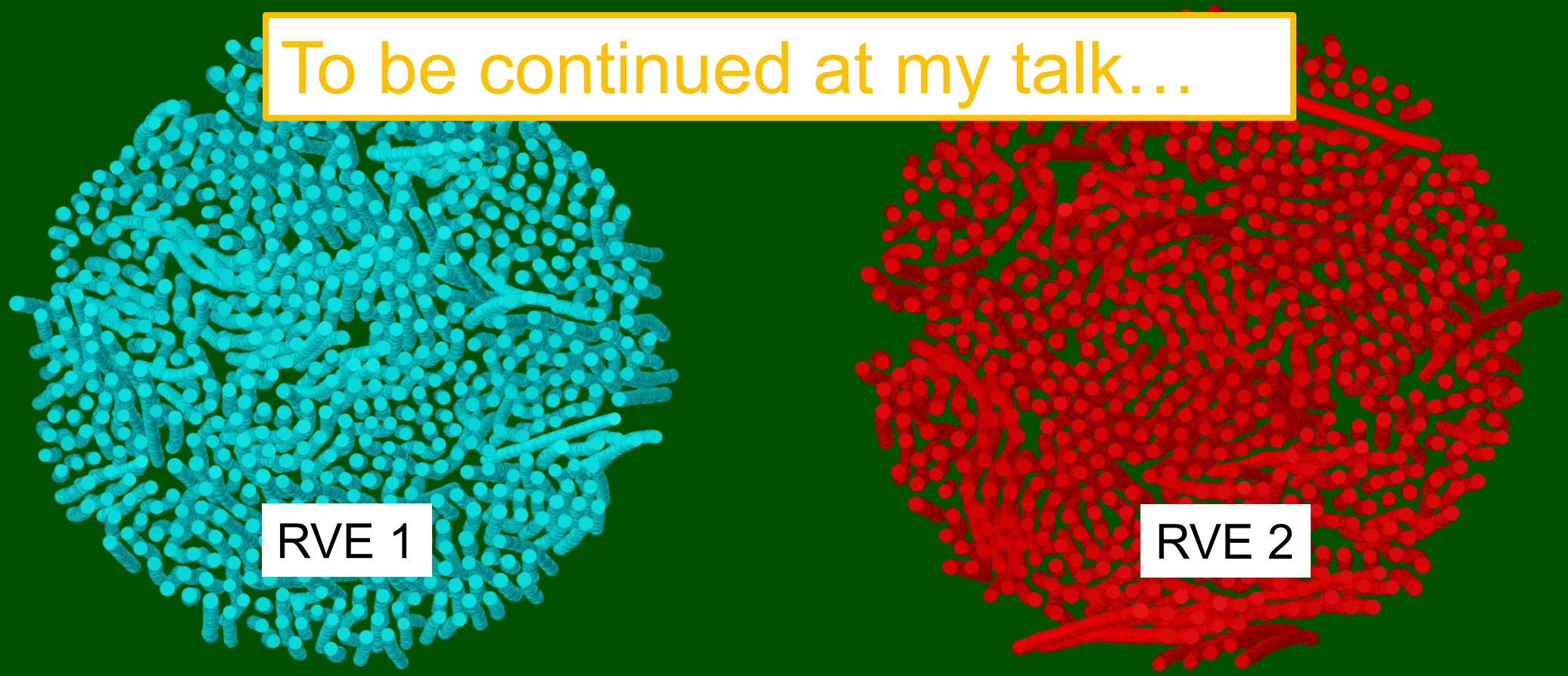

RVEs with 600 fibres and L =450 μm but in different region in the CT specimen



Next COMP

Next Generation
Fibre-Reinforced Composites

https://nextcomp.ac.uk

I would like to acknowledge funding which supported this work from the UK Research and Innovation - EPSRC Programme Grant; Next Generation Fibre-Reinforced Composites: A Full Scale Redesign for Compression (EP/T011653/1)

A collaboration between Imperial College London and University of Bristol

IMPERIAL

University of BRISTOL

Bristol Composites Institute

Unusual Effect of the Degree of Cure of some Epoxy Resins on the Compressive Strength of Continuous Fibre Composites

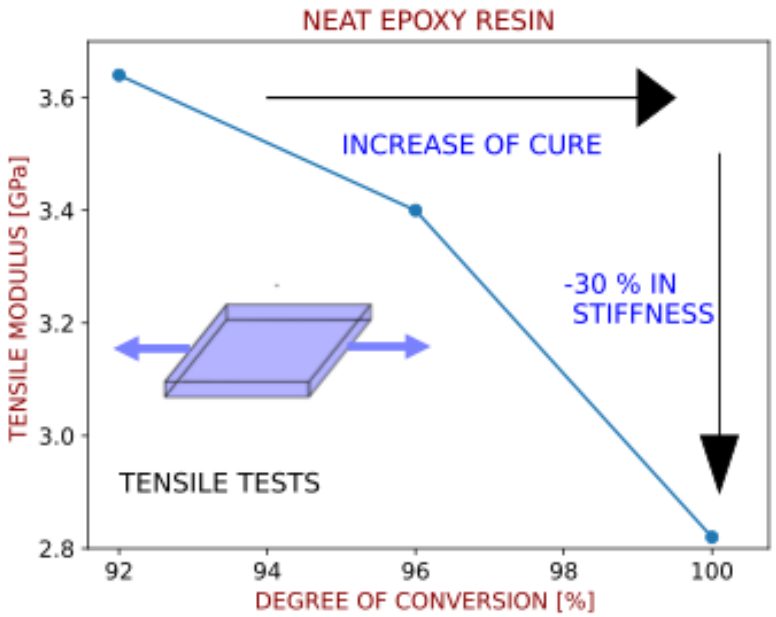

ANALYTICAL MODEL

UNDERSTANDING
ESTIMATING

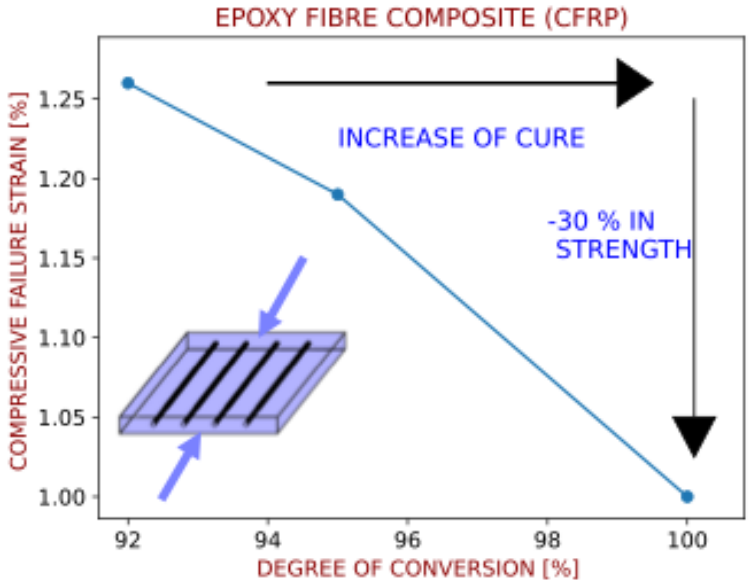

Vincent Keryvin

IRDL UMR CNRS 6027

Univ. Bretagne Sud, Lorient, France

vincent.keryvin@univ-ubs.fr

Université Bretagne Sud

Institut de Recherche Dupuy de Lôme

Context





Compressive failure of hydrofoils in bending

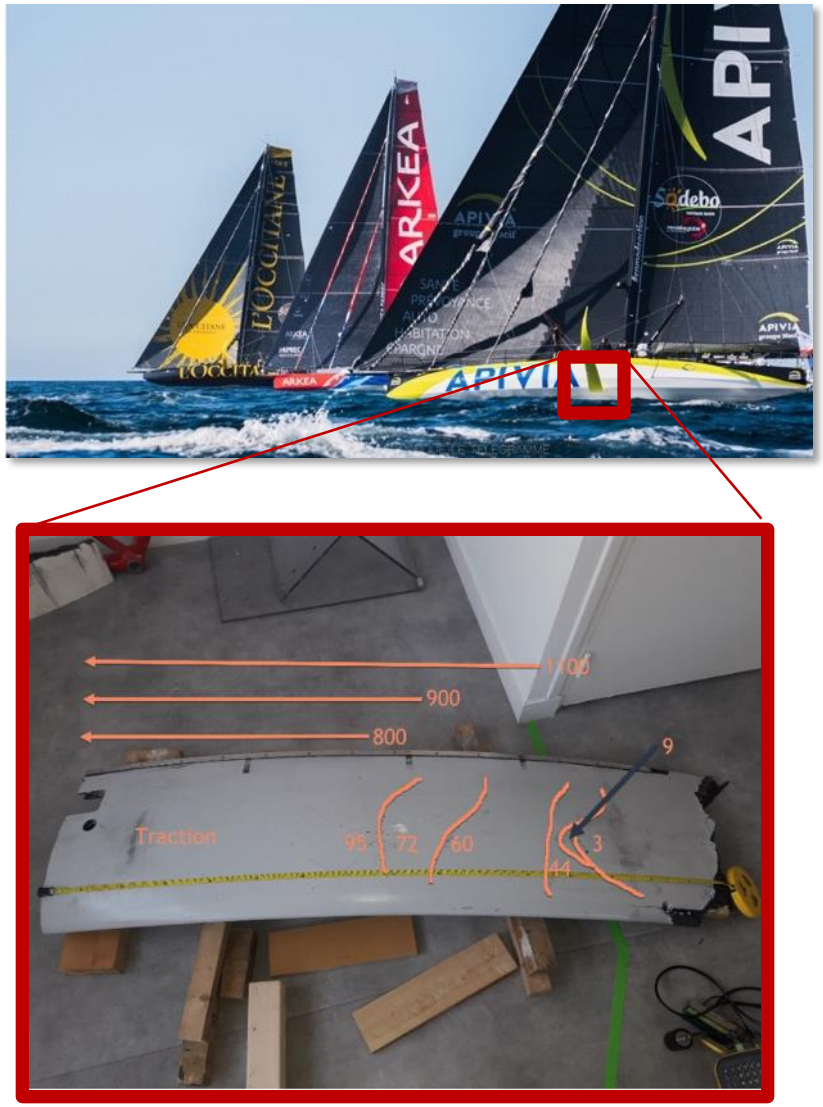

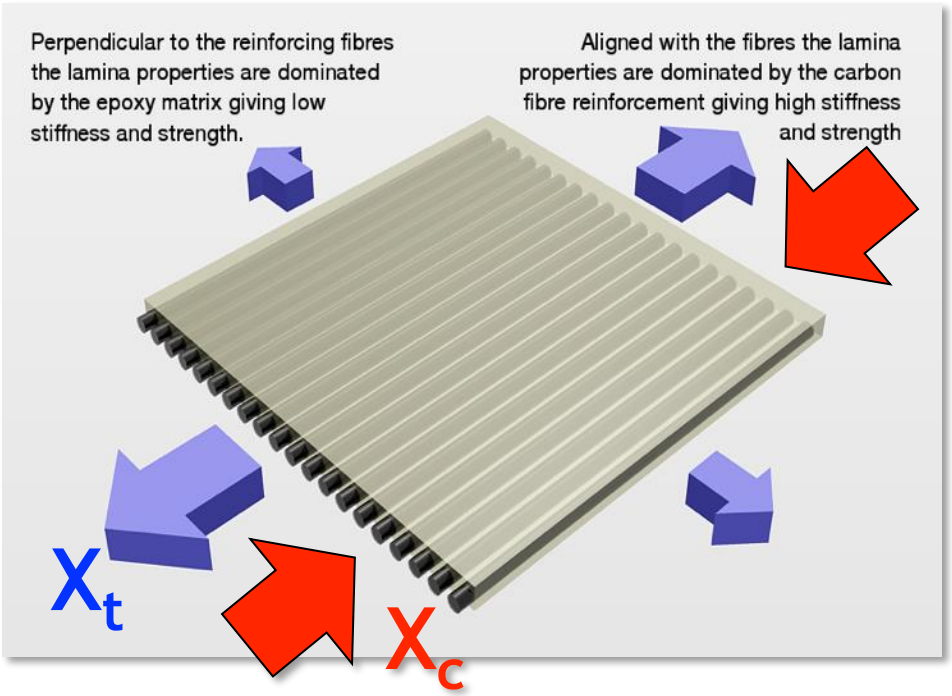

$$X_c < X_t$$

Compressive strength is a key design parameter

Fibre micro-buckling mechanism

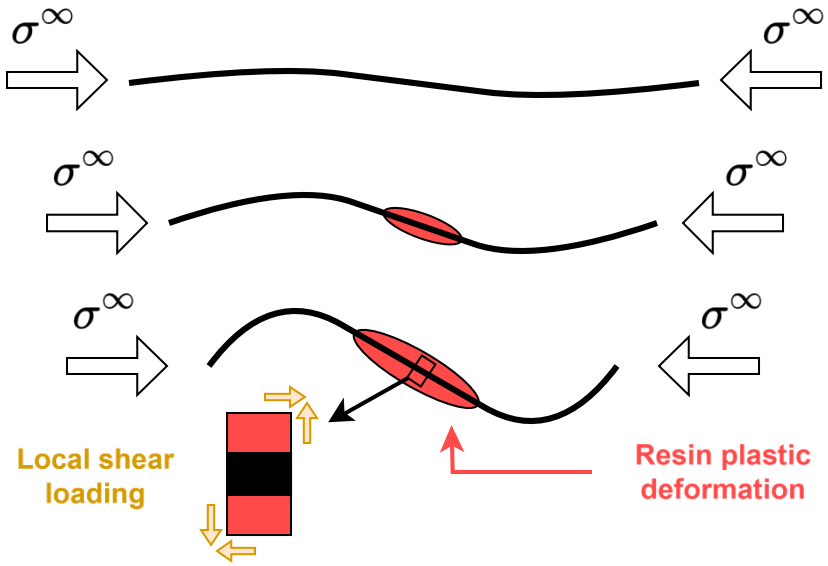

Process

Fibre misalignment

Material

UD non-linear shear behaviour

[Mechin, PhD (2017)]

Estimation of compressive strength requires knowledge of the non-linear shear behaviour of the ply

Common opinion on curing thermosets CFRP

« For best mechanical performance, complete curing is sought »

Curing

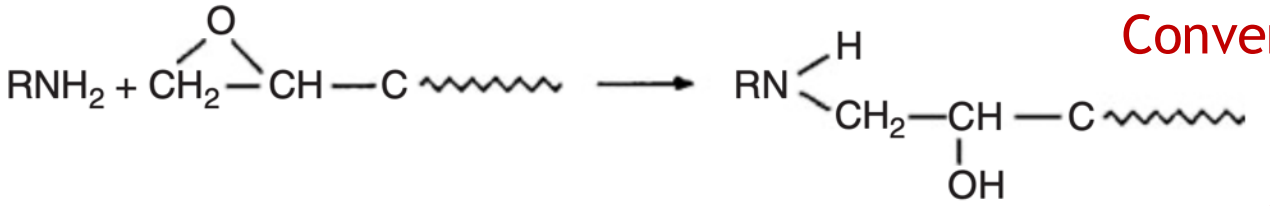

Amine + Epoxy

Resin

Conversion from liquid/reactive state to thermoset

Cross-linking between polymeric chains

Context

TYPICAL CURE TIME & TEMPERATURES

0.3°C (0.5°F)/min should be considered the minimum ramp rate. Alternative cure cycles and processes can be used.

PROPERTY	70°C CURE (158°F)	80°C CURE (176°F)	120°C CURE (248°F)	TEST STANDARD
Processing Method	Vacuum Bag / Autoclave	Vacuum Bag / Autoclave	Vacuum Bag / Autoclave	
Typical Ramp Rate	0.3 – 2°C/minute	0.3 – 2°C/minute	0.3 – 2°C/minute	-
Cure Time	12 hrs*	6hrs*	45 minutes*	-
Cure Pressure	-1 Bar / +6 Bar	-1 Bar / +6 Bar	-1 Bar / +6 Bar	-
Dry Tg (DMA)	85°C	98°C	125°C	ASTM D7028

MECHANICAL PROPERTIES

CURED RESIN PROPERTIES

Resin cast oven cured for 12 hours at 70°C (158°F). Mean values.

PROPERTY	SYMBOL	UNIT	12 HOURS @ 70 °C (158°F)	6 HOURS @ 80°C (176°F)	45 MINUTES @ 120°C (248°F)	TEST STANDARD
Cured resin density	ρ_{cured}	g/cm³	1.19	1.19	1.19	Archimedean principle
Tensile Strength	σ_T	MPa	68	82	83	ISO 527-2
Tensile Modulus	E_T	GPa	3.8	3.4	3.0	ISO 527-2
Flexural Strength	σ_F	MPa	117	123	117	ISO 178
Flexural Modulus	E_F	GPa	3.8	3.5	2.9	ISO 178
Compressive Yield Strength	σ_C	MPa	147	140	117	ISO 604

[Se75 data sheet, Gurit (2022)]

Stiffness decreases when cross-linking increases!

Objective

I

II

graphene layers

fibre

Effect on compressive strength of the ply in a laminate?

III

matrix

polymer chains

composite

unidirectional ply

IV

tape laminate

V



composite structure

Stiffness decreases when cross-linking increases

Five scales from the structure of fibres and resins to composite structures

Questions

Q1 – Estimation of consequences on Xc

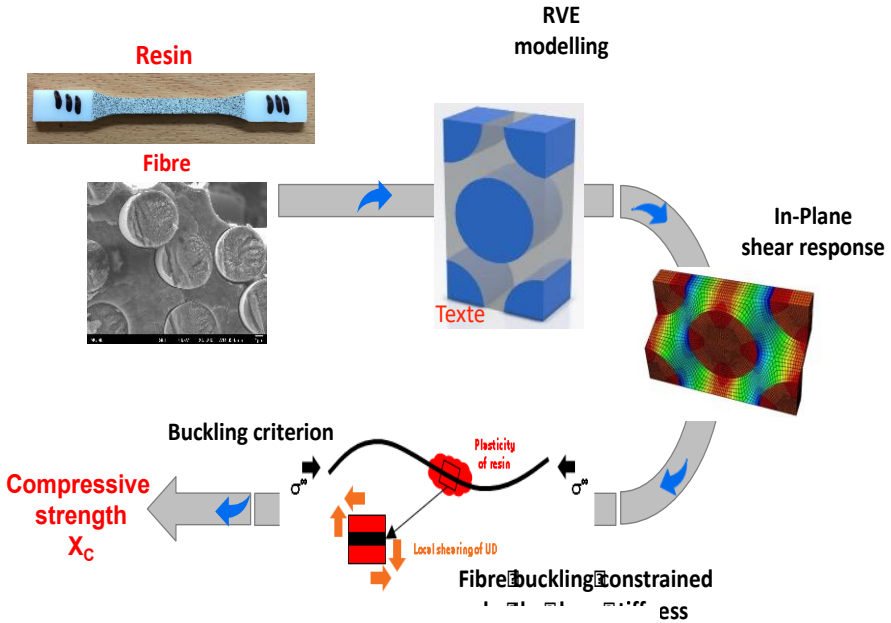

[Mechin, COST (2023)]

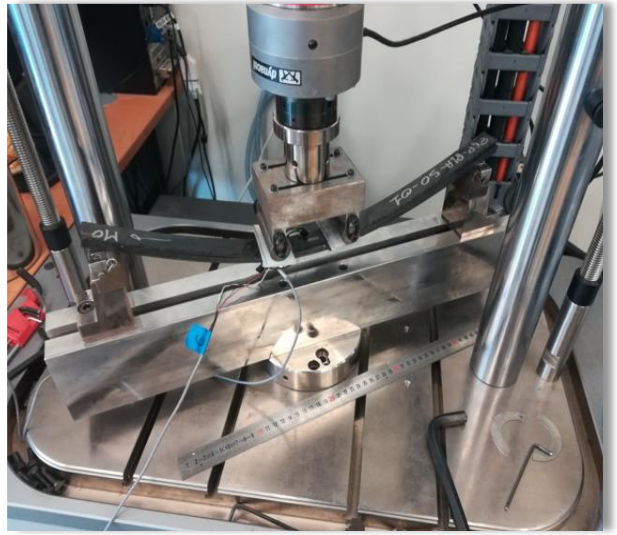

Q3 – Origins

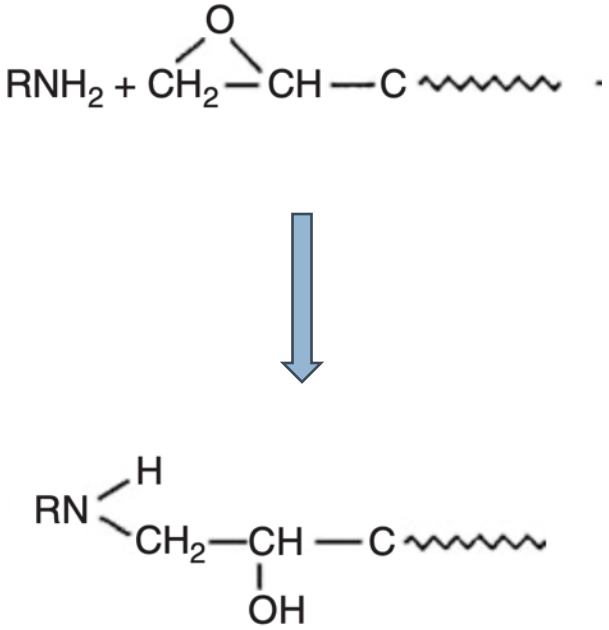

Q2 – Experimental confirmation

Q1

Can we predict the influence of curing on the compressive strength?

Our methodology for compression

UD non-linear shear behaviour

- Fibre anisotropic elastic properties
- Matrix non-linear behaviour
- Arrangement of fibres

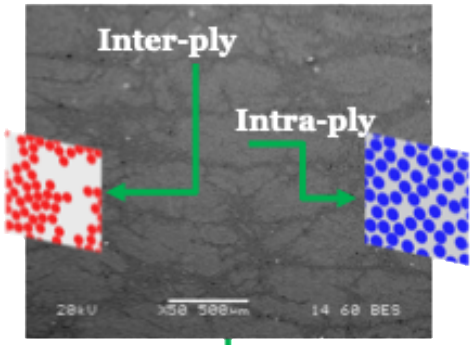

Estimation/Validation/Measurement

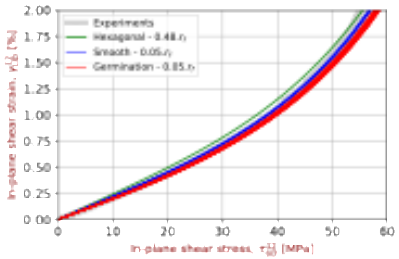

[Mechin, COST (2023)]

Mechanisms

- UD shear behaviour
- Initial fibre misalignment

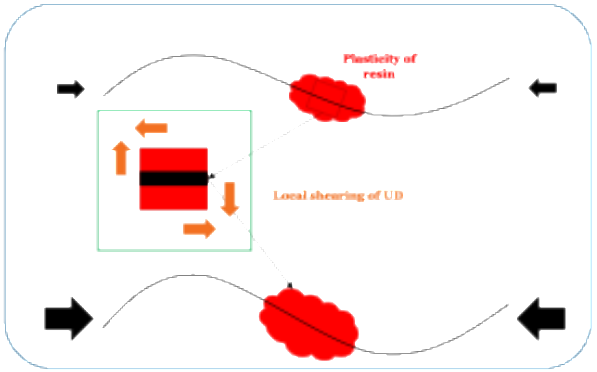

Estimation/Validation Compressive strength

- Material: ply scale
- Manufacturing defects
- Structural effect : laminate scale

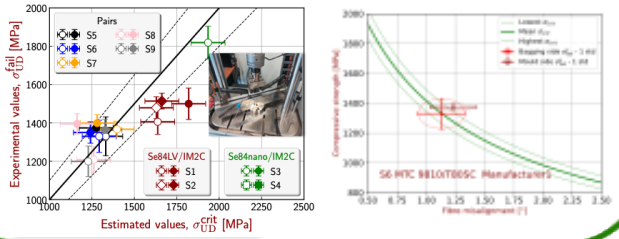

Manufacturing defects

- Initial fibre misalignment

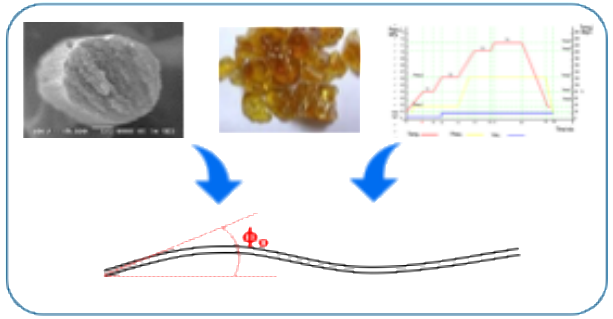

Measurement

[Yurgartis, CSTE (1987)]

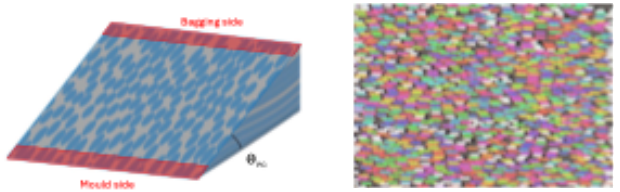

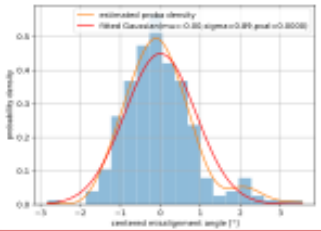

[Mechin et al., CPA (2025)]

V. Keryvin – Univ. Bretagne Sud, France - Conference ICCM24 - Baltimore – August 2025

Understanding – Validating – Estimating – Designing

Multiscale modelling

From scale II to scale III

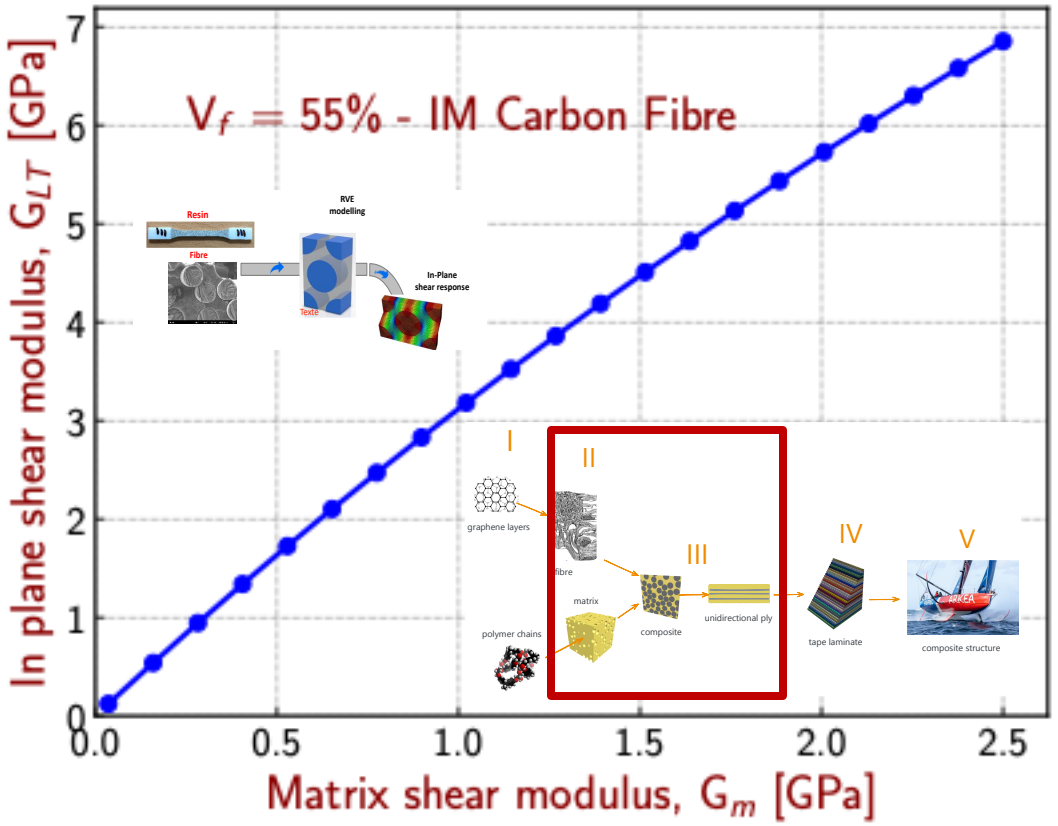

[Mechin et al., COST (2023)]

From scale III to scale IV

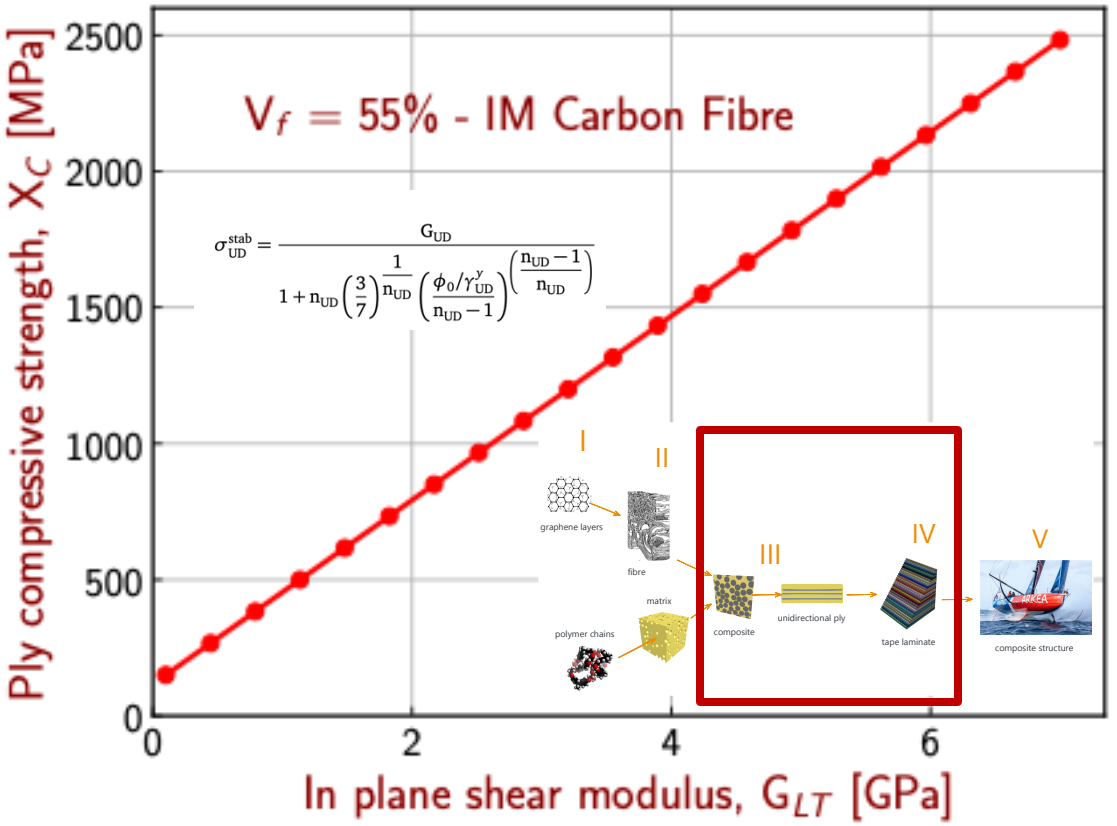

[Budiansky, JMPS (1993)]

Influence of the resin behaviour on the compressive strength of the ply

Q2

Can we validate the propagation from the neat cast resin to the composite laminate?

Materials

Neat cast resin Se75 Gurit

MECHANICAL PROPERTIES

CURED RESIN PROPERTIES

Resin cast oven cured for 12 hours at 70°C (158°F). Mean values.

PROPERTY	SYMBOL	UNIT	12 HOURS @ 70 °C (158°F)	6 HOURS @ 80°C (176°F)	45 MINUTES @ 120°C (248°F)
Cured resin density	ρ_{cured}	g/cm³	1.19	1.19	1.19
Tensile Strength	σ_T	MPa	68	82	83
Tensile Modulus	E_T	GPa	3.8	3.4	3.0
Flexural Strength	σ_F	MPa	117	123	117
Flexural Modulus	E_F	GPa	3.8	3.5	2.9
Compressive Yield Strength	σ_C	MPa	147	140	117

$$T_g^{\infty} = 125°C$$



II

II

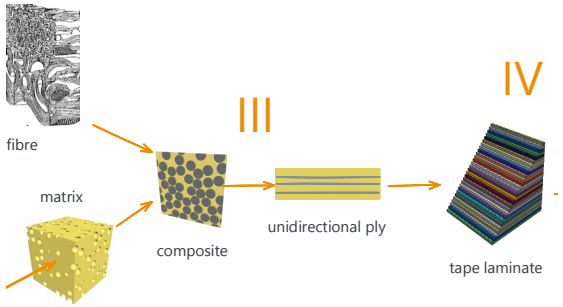

Tape prepreg with Hexcel IM (IM2C) carbon fibres

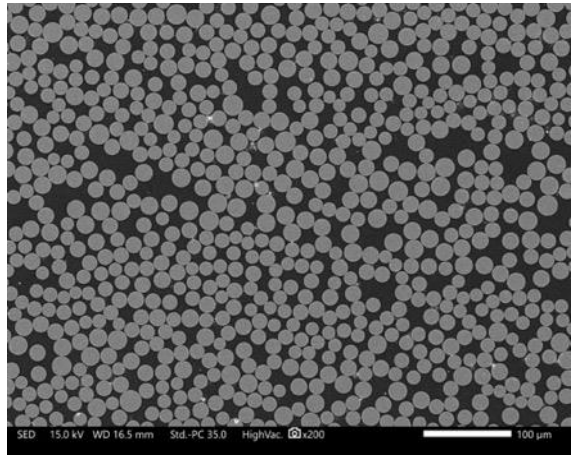

III

IV

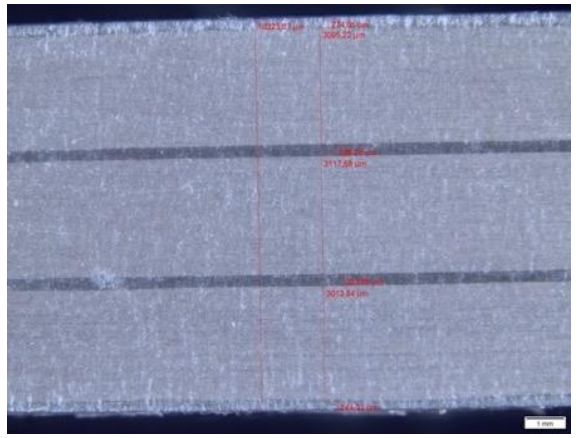

10 mm

Three scales: resin (II), lamina (III), laminate (IV)

Curing

(DOC) Degrees of conversion (w.r.t. uncured prepregs) – 92%, 95%, 100%

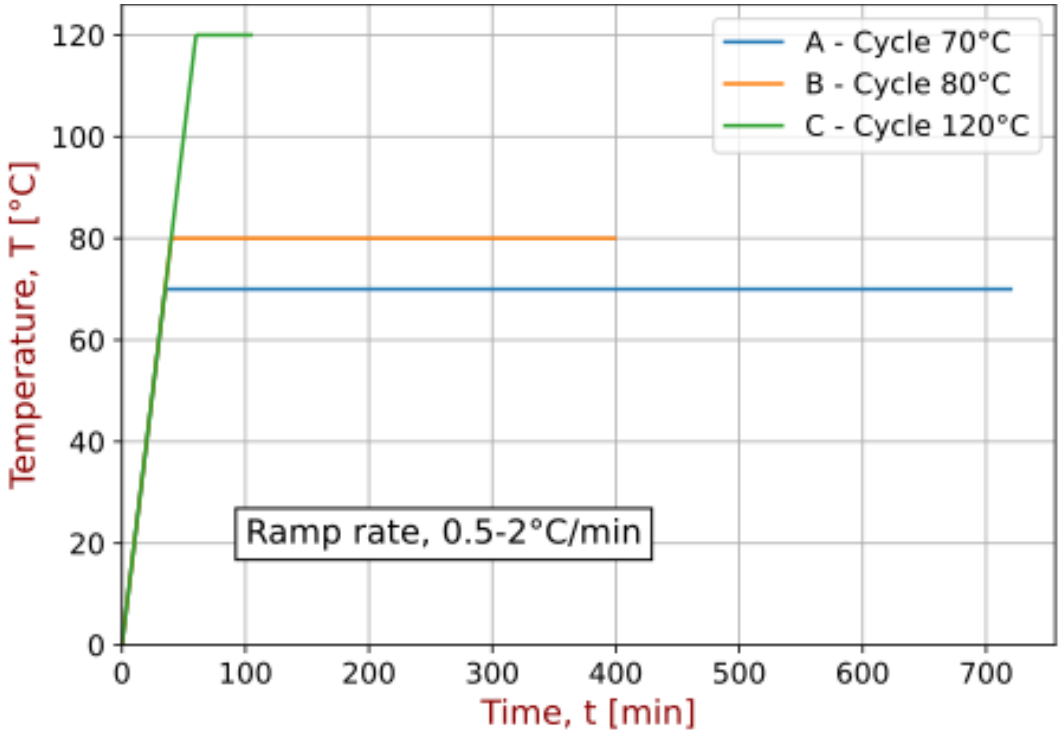

[Keryvin et al., CPB (2024)]

Neat cast resin

II



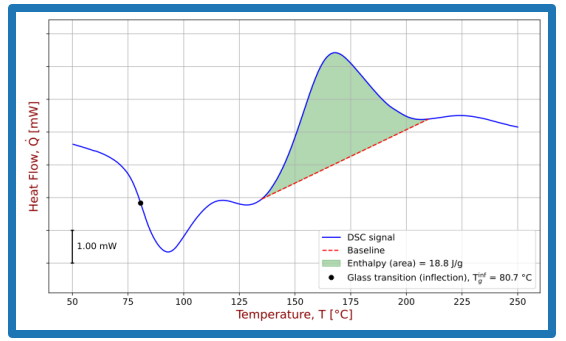

Lamina

III

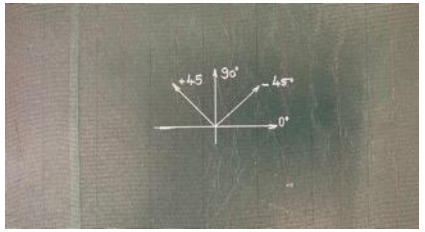

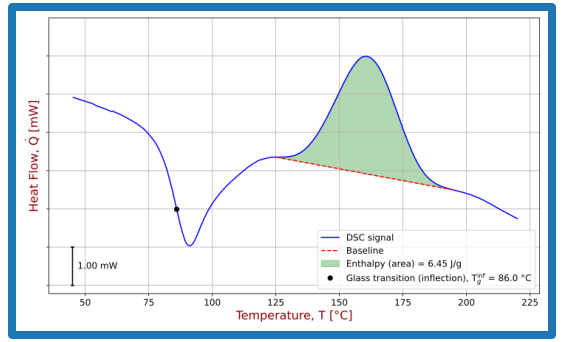

Laminate

IV

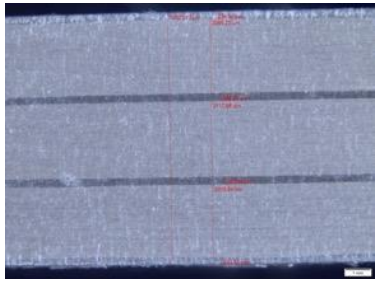

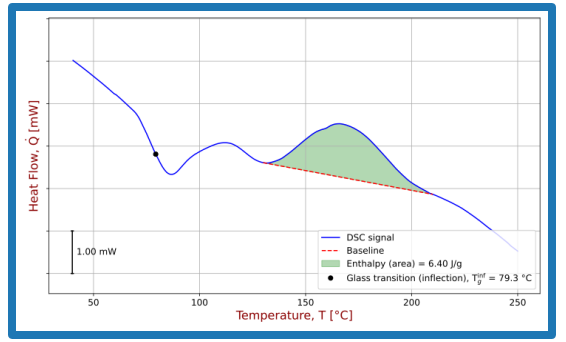

Same DOC (~1%) at all scales – from DSC measurements

Mechanical testing

Scale II - Neat cast resin



tensile tests

Scale III – Lamina (ply)

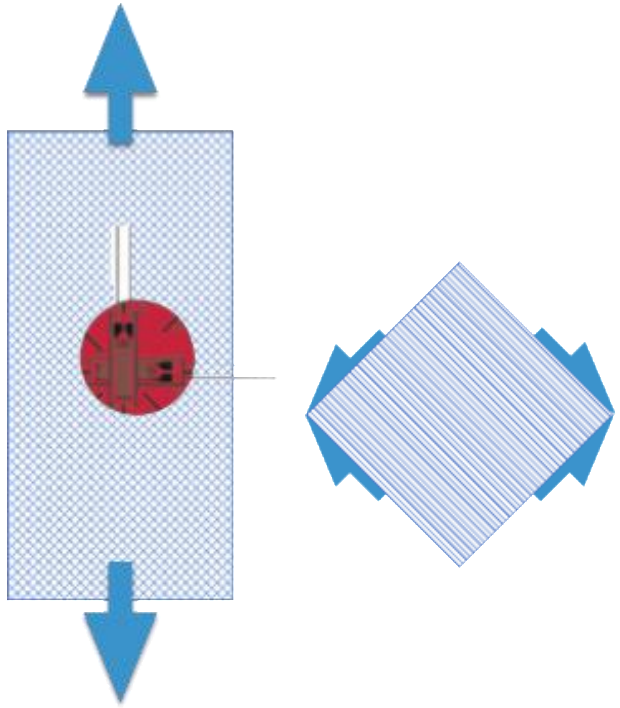

±45° tensile tests → ply shear behaviour

Scale IV - Laminate

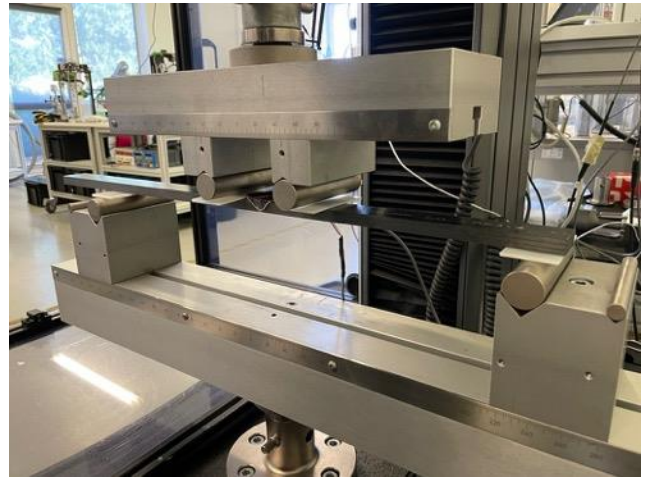

4 point-bending

→ compressive failure strain

Thick laminates representative of composite parts for racing yachts

Constituent scale (II)– Se75 epoxy (neat cast resin)

Degrees of conversion (w.r.t. uncured prepregs) – 92%, 95%, 100%

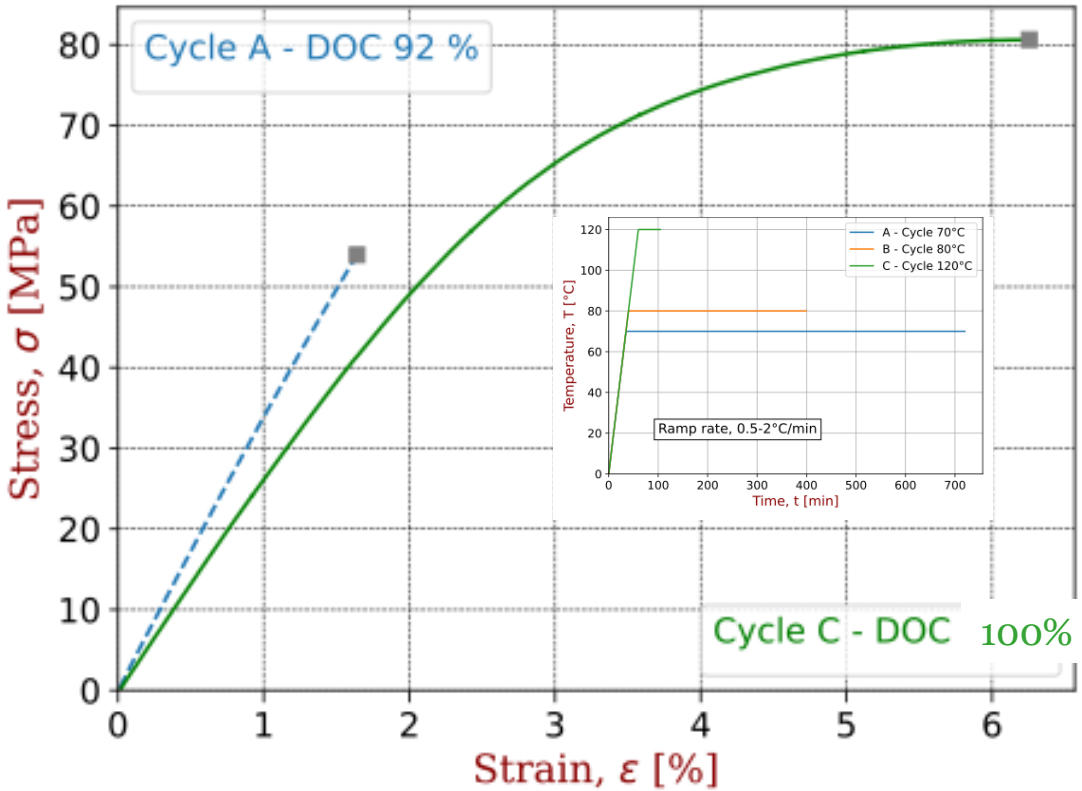

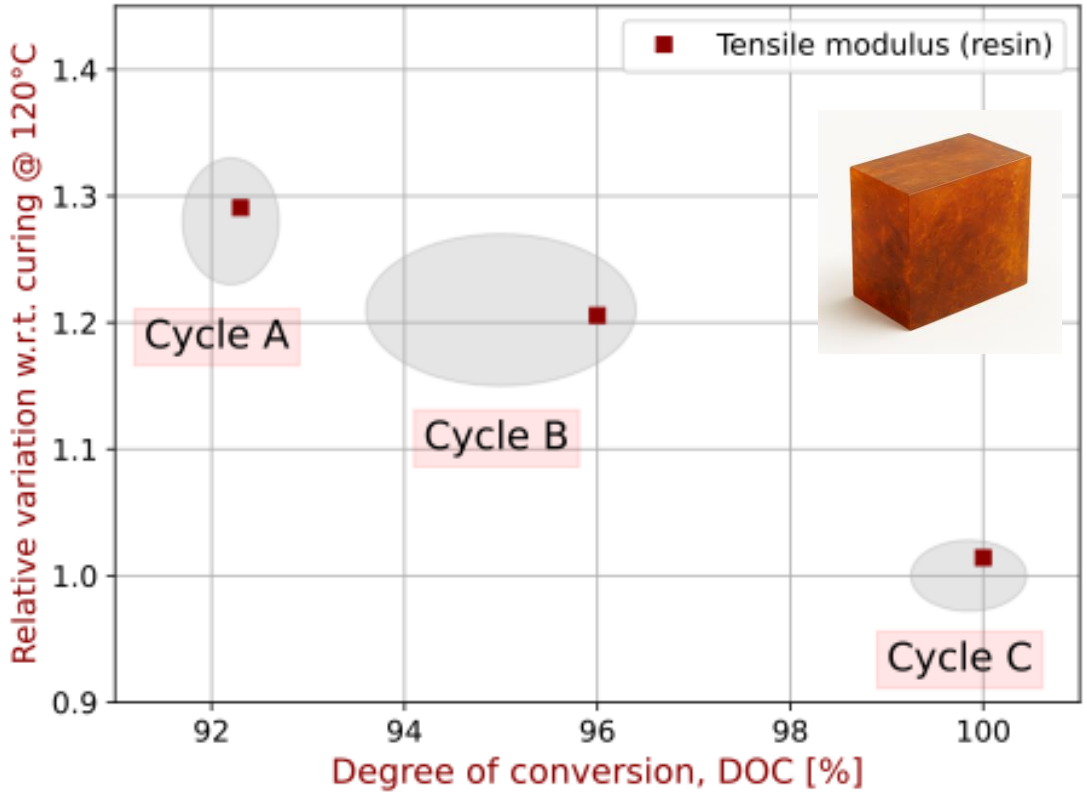

[Keryvin et al., CPB (2024)]

High stiffness and brittleness (low DOC) to ductility and lower stiffness (high DOC)

Lamina scale (III, Se75/IM2C) - Shear

Degrees of conversion (w.r.t. uncured prepregs) – 92%, 95%, 100%

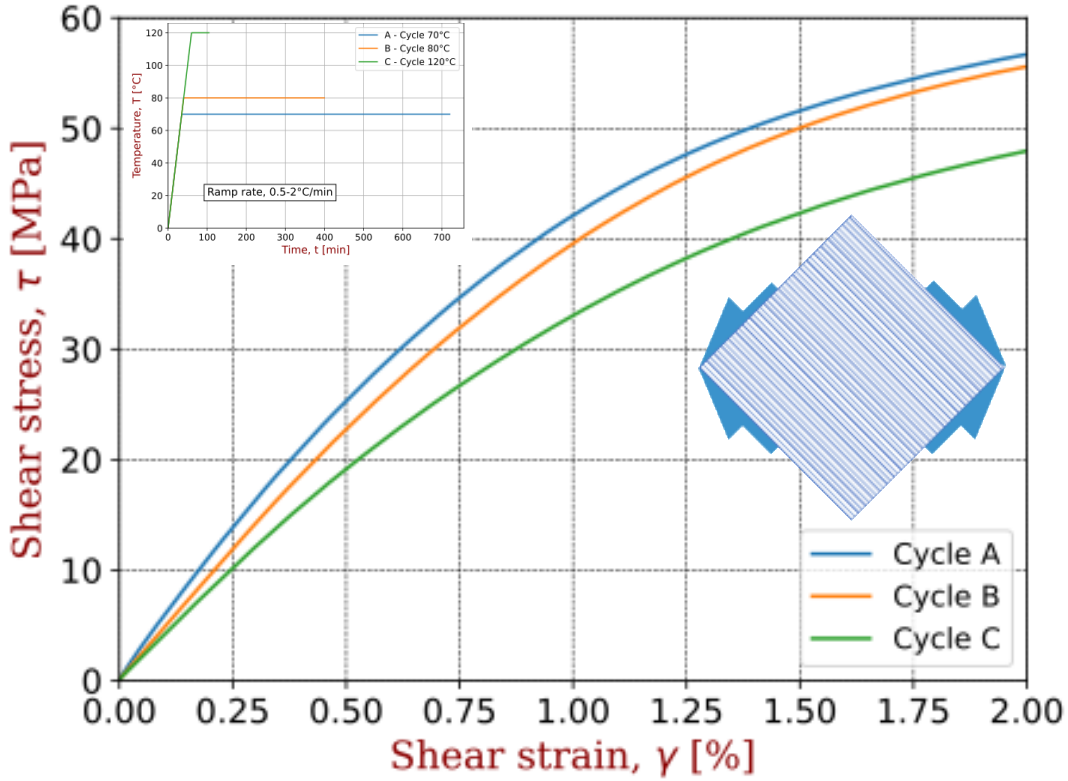

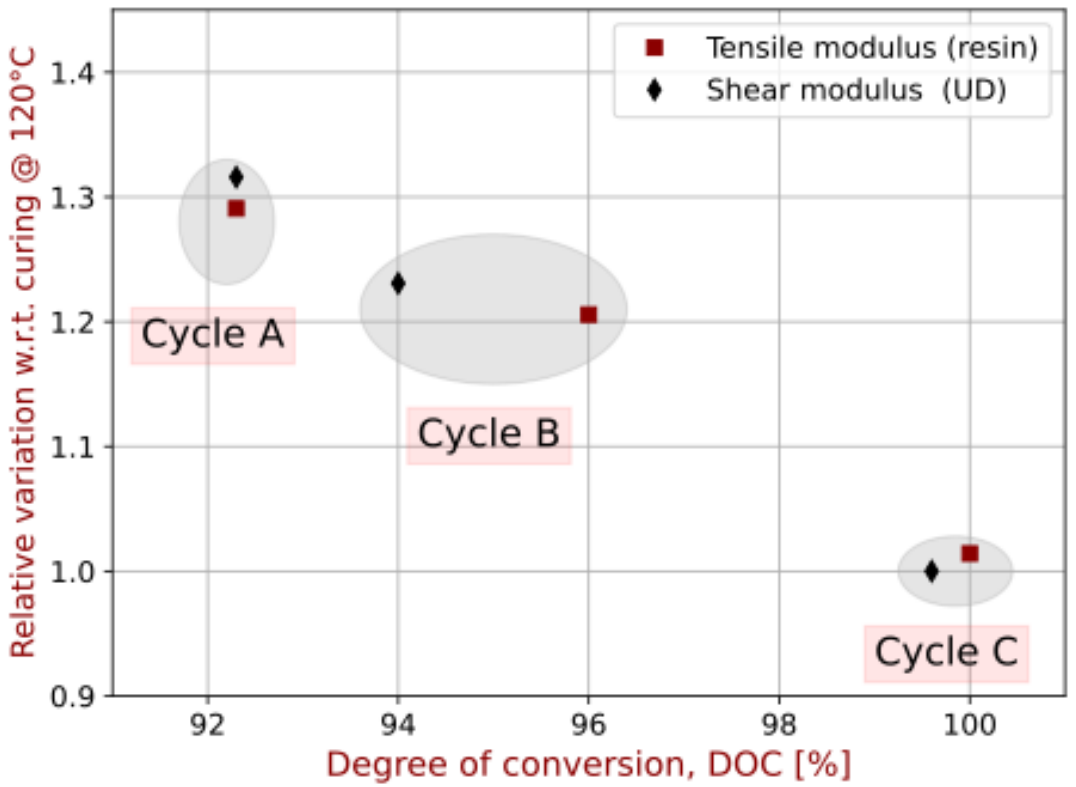

[Keryvin et al., CPB (2024)]

The resin behaviour quantitatively transferred to the composite ply

Laminate scale (IV, Se75/IM2C)
Compressive strength of the ply in the laminate

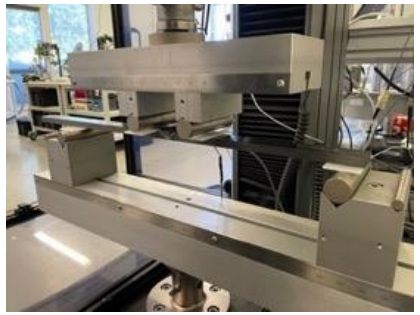

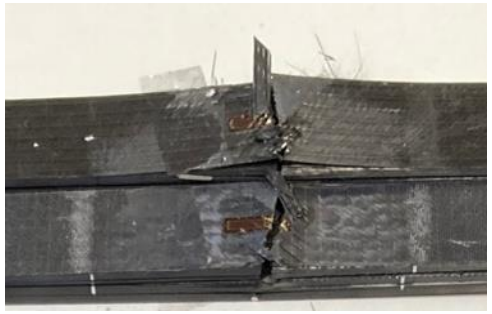

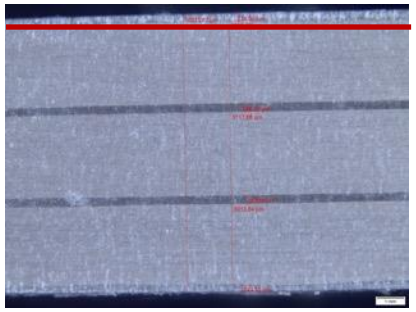

Initial fibre misalignment
ϕ_0 ~ 1°
(whatever the cure)

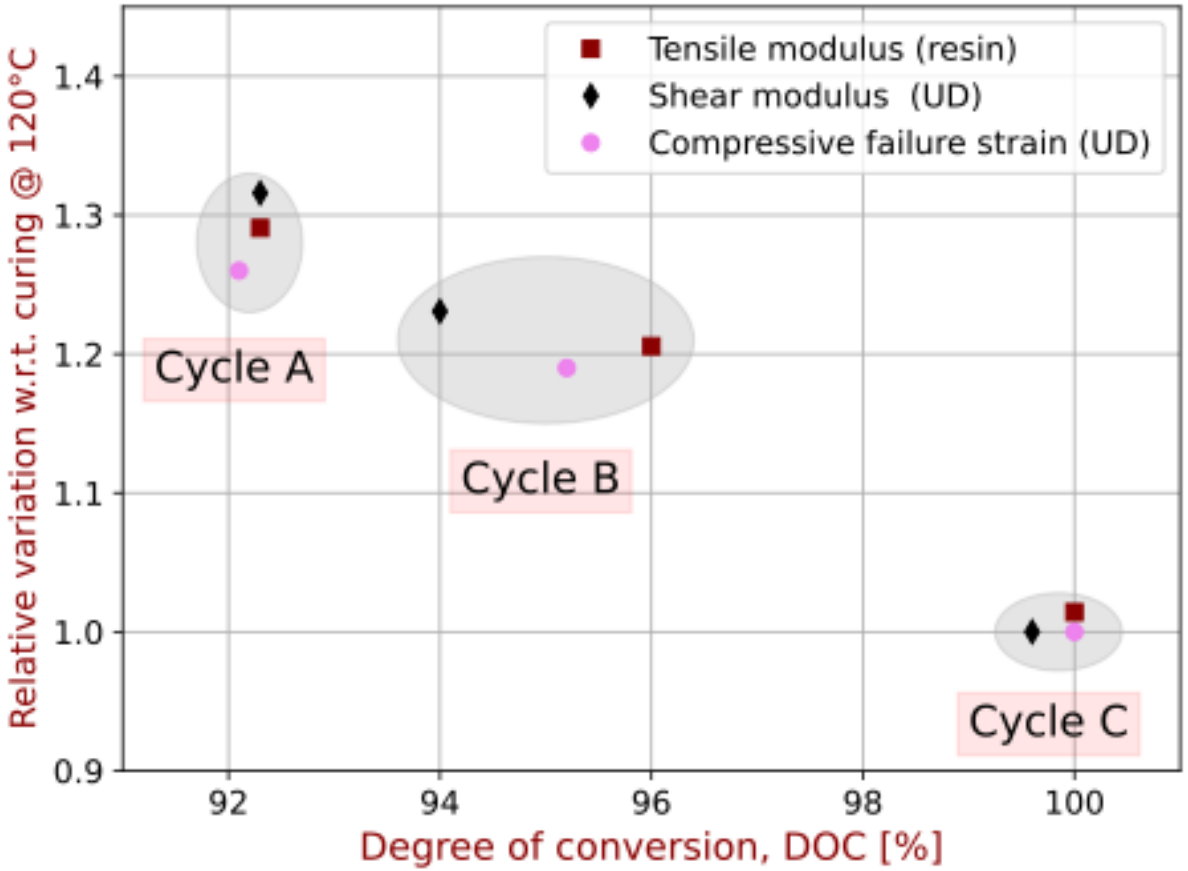

[Keryvin et al., CPB (2024)]

The difference in mechanical performance is found at all scales

Q3

Origins and uniqueness of this resin behaviour?

Unique case?

[Noordam et al., 1987]

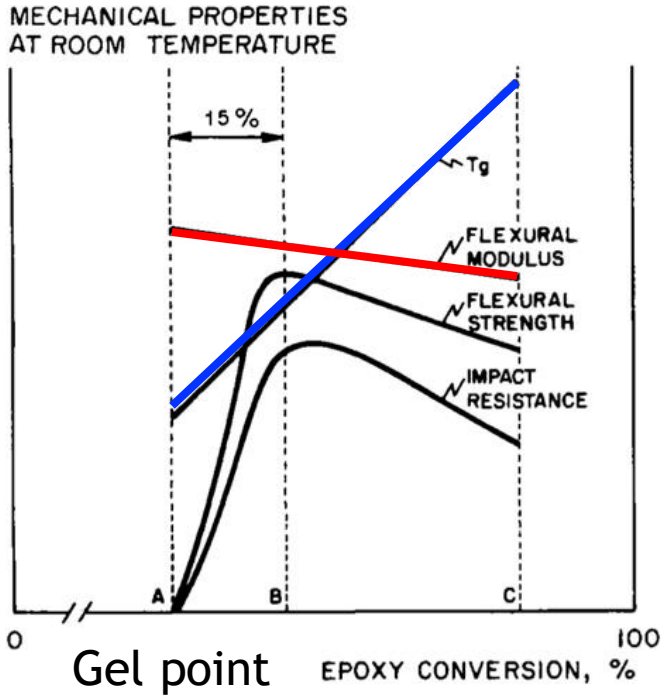

Figure 2. Schematic presentation of the development of mechanical properties as a function of the degree of cure.

Epikote epoxies (Shell)

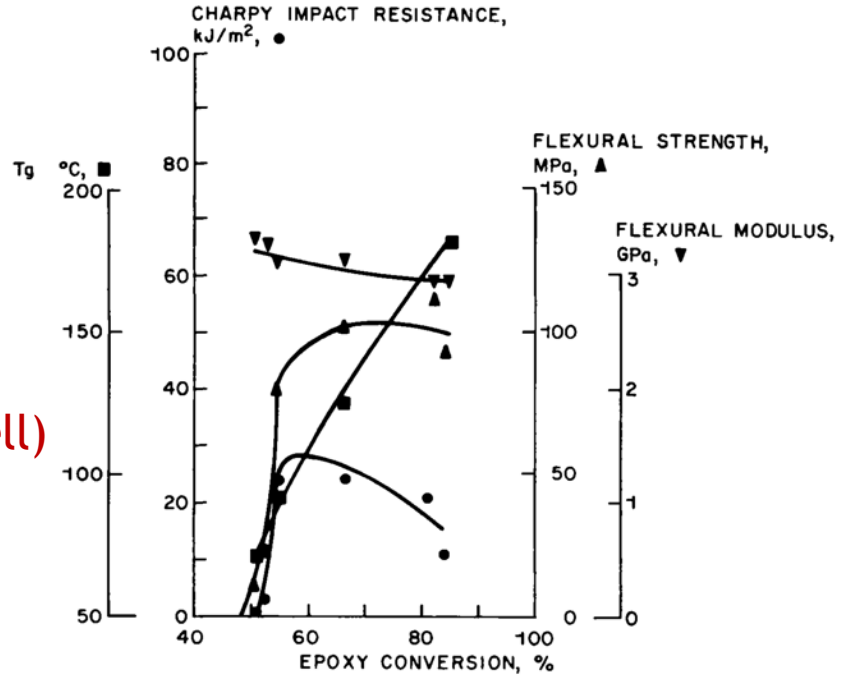

Figure 5. Mechanical properties of "EPIKOTE" 155/DMACM as a function of the degree of cure.

Known from a long time ago by epoxy chemists

Unique case?

[Marks et al., ACS AMI (2009)]

Dow Chemical, Epoxy R&D

« It is widely assumed that optimum properties of epoxy thermosets are achieved upon full cure »

« In practice cure conditions are typically controlled to balance the final properties and processing time rather than to achieve complete functional group conversion »

Same belief as in our marine engineering circles

DGEBA + 4,4'-DDS

[Marks et al., ACS AMI (2009)]

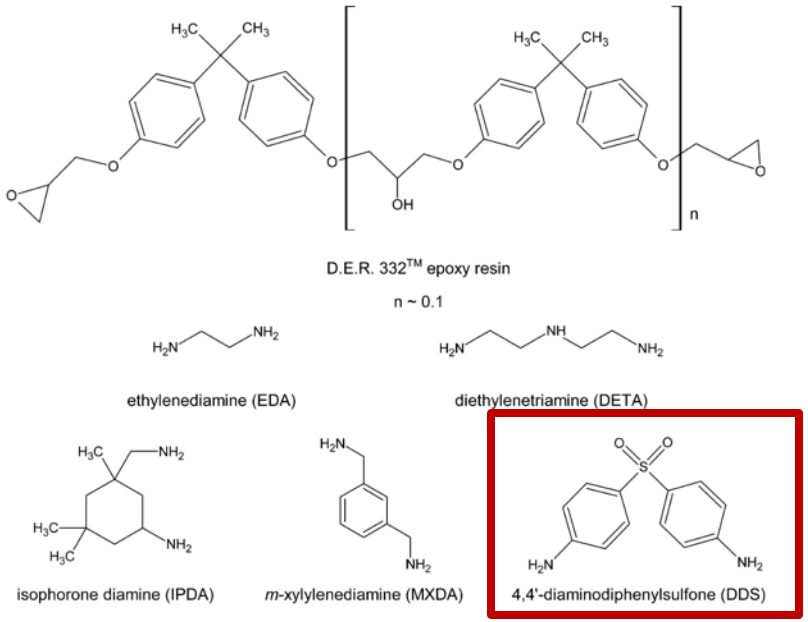

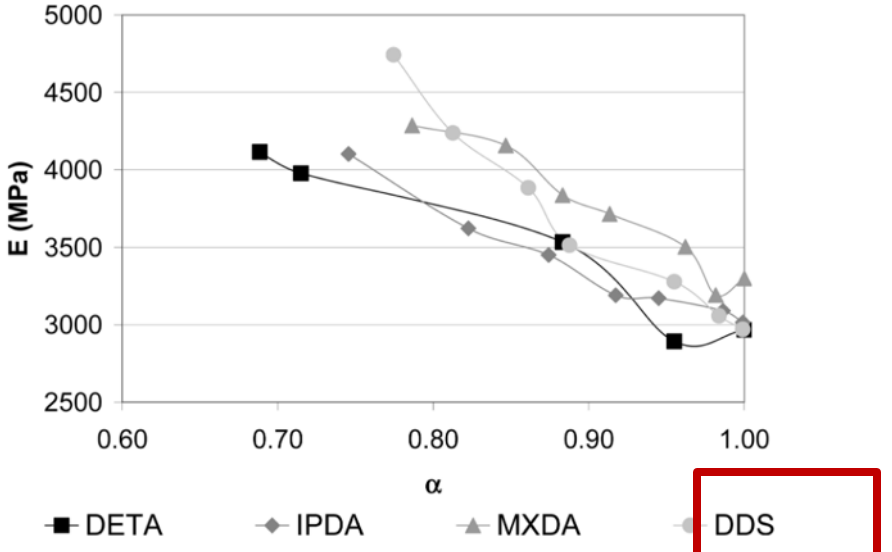

FIGURE 7. *E* vs α for DER 332—DETA, —IPDA, —MXDA and —DDS thermosets.

Formation of covalent bonds → constraints → density decreases

E decreases with the degree of conversion

DGEBA + 3,3'-DDS

[Pramanik et al., Polym Engng Sci (2014)]

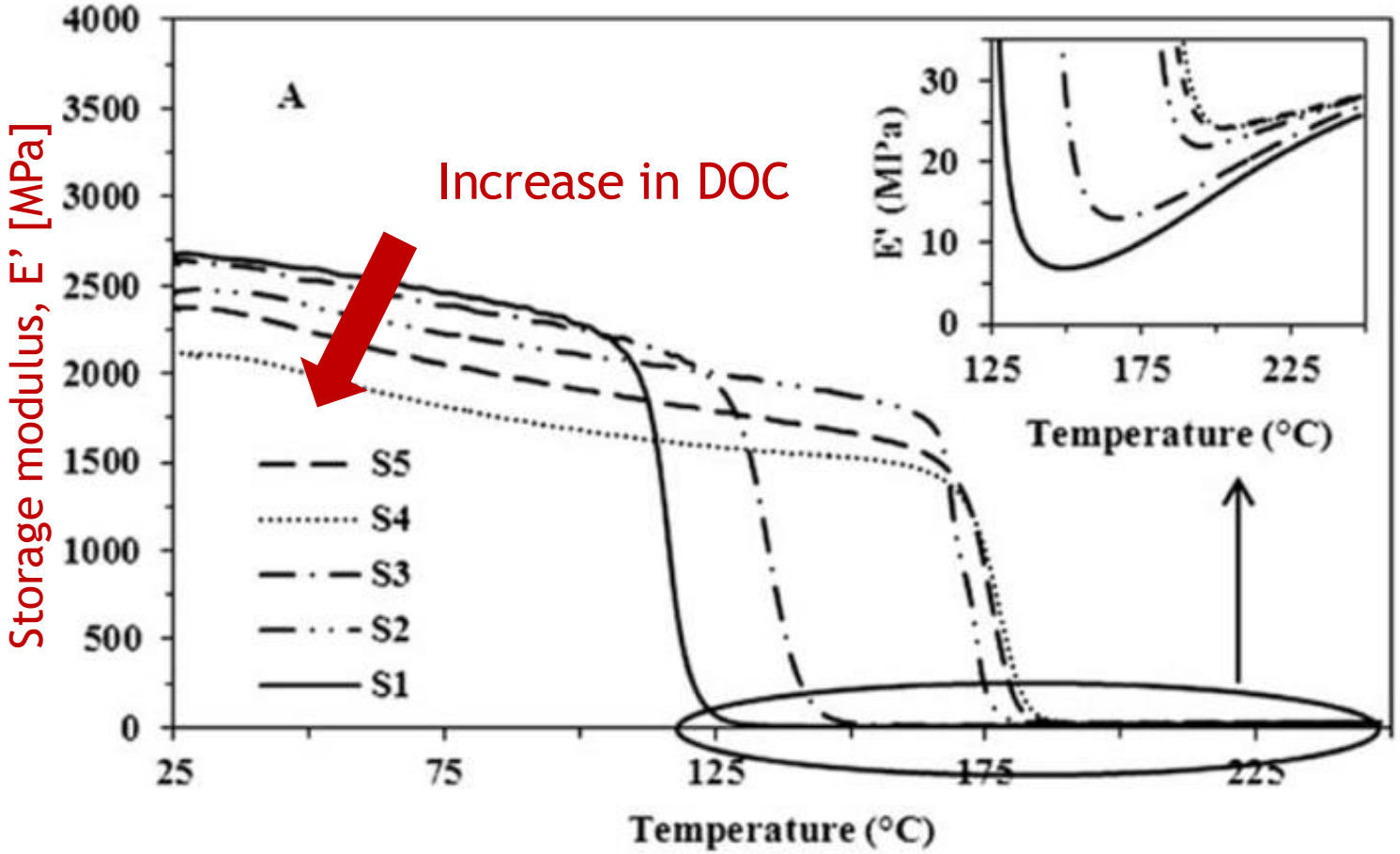

E' (RT) decreases with DOC



Summary and outlook

Unexpected effect of curing on the compressive strength of the composite ply

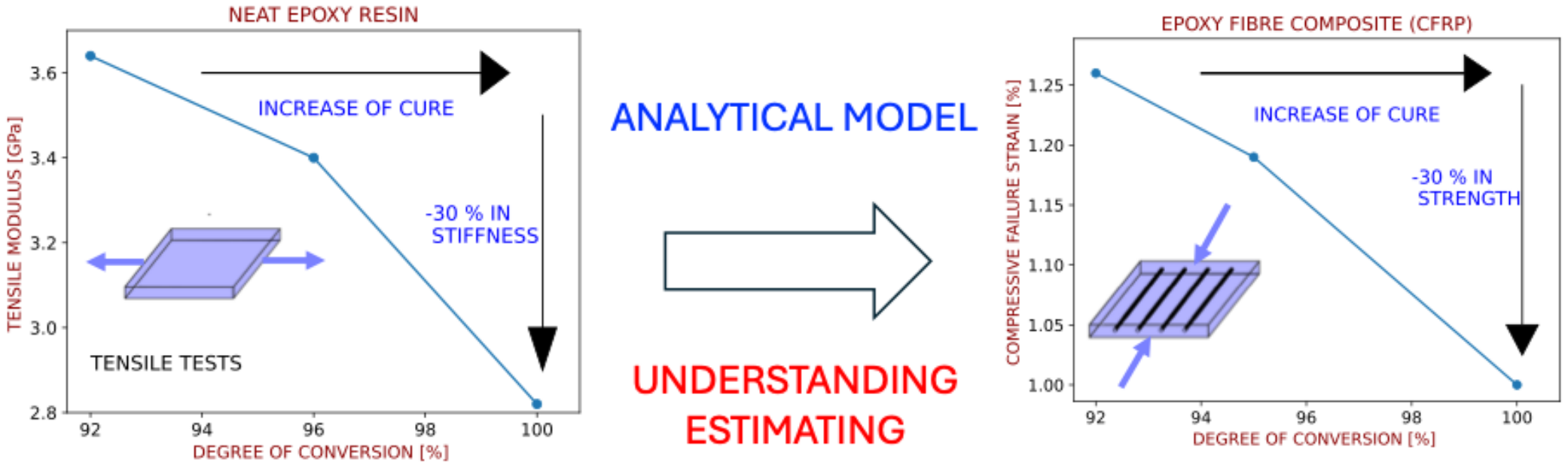

[Keryvin et al., CPB (2024)]

Complete curing does not give the optimal mechanical properties

Contributions to this work

- P.-Y. Méchin
- E. Fabing

- A. Le Palabe
- K. Mahé-Flahaut
- I. Pillin

See V. Keryvin et al., Composites Part B (2024) 287:11836

IMPROVING FRP COMPRESSIVE PERFORMANCE THROUGH **INTERMITTENT MATRIX PROPERTY MODIFICATION**

Hwei Linn Khoo*[1,2]

[3] R. Trask, [2]S. Pimenta, and [1] P. Robinson

[1]Department of Aeronautics, Imperial College London, London, UK

[2]Department of Mechanical Engineering, Imperial College London, London, UK

[3]Bristol Composites Institute, University of Bristol. Bristol, UK

* hlk18@ic.ac.uk



Next Generation Fibre-Reinforced Composites

IMPERIAL

The Composites Centre

for research, modelling, testing and training in advanced composites

University of BRISTOL

Bristol Composites Institute

UK Research and Innovation

Engineering and Physical Sciences Research Council

FRP COMPRESSIVE FAILURE

MOTIVATION

- Matrix-dominated failure under compression (*e.g. kink-band formation*) remains a limiting factor in FRPs.
- This consequently limits FRPs' range of applicability and design.

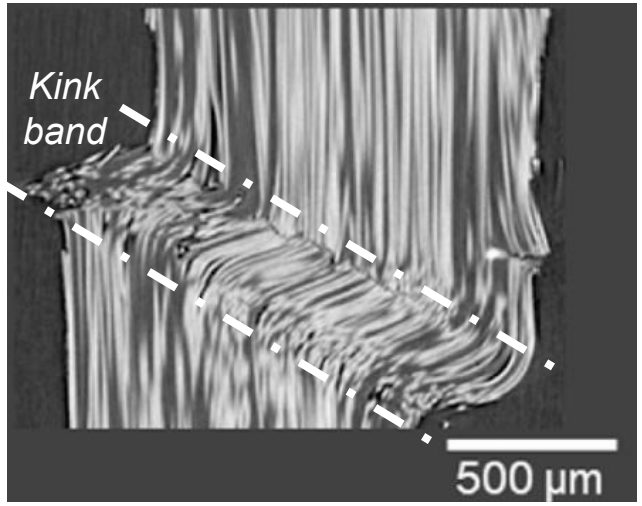

FRP Compressive failure

Wang, Y. *et al.* (2021) doi:10.1016/j.compscitech.2021.108929.

Traditional improvement strategy:

- Uniform strengthening

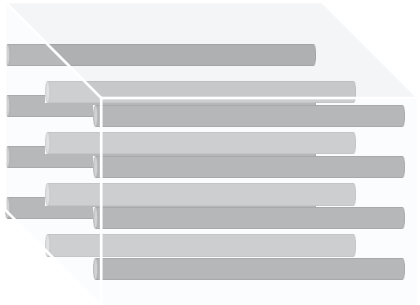

Novel strategy:

- Targeted strengthening

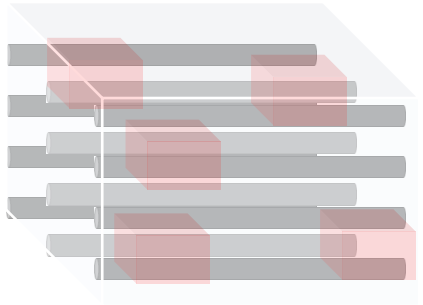

Aim

*To what extent can intermittent **strong–weak matrix modification** benefit **CFRPs in compression**?*

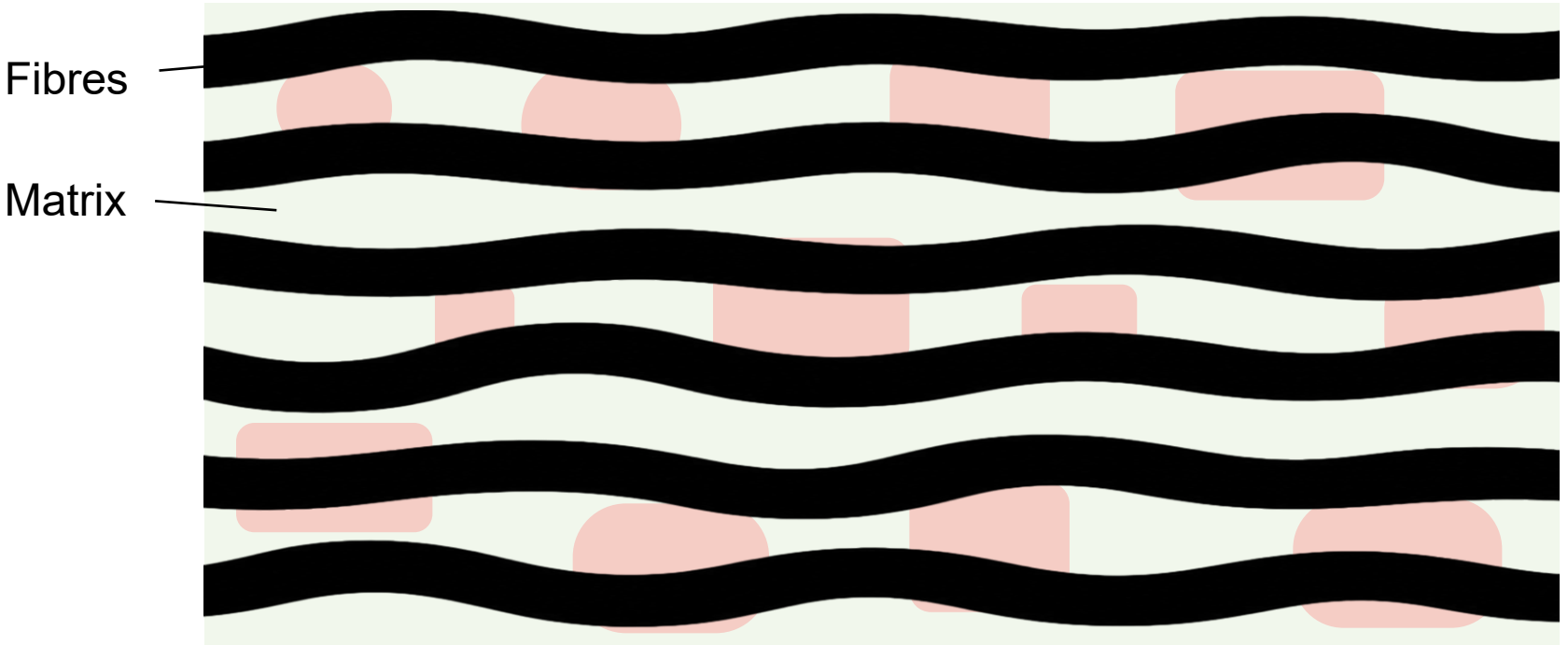

WORKFLOW

1) Select

FRP architecture

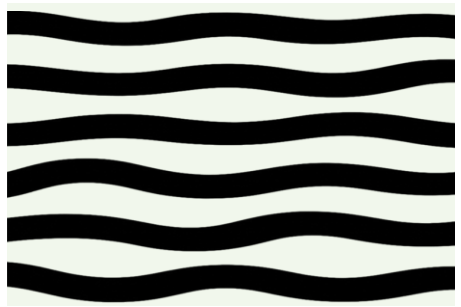

2) Develop and explore

intermittent modification strategies

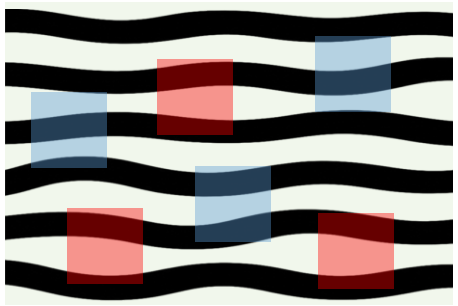

?

3) Benchmark against

homogenous matrix baselines

Strong matrix strength and stiffness is 1.5 X that of the weak matrix.

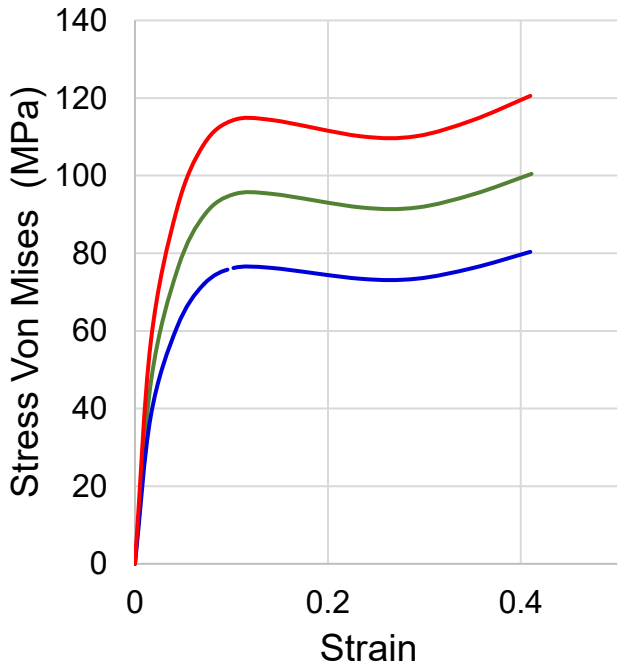

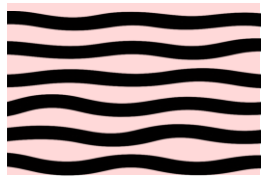

Strong matrix



RoM matrix

(50% strong + 50% weak)

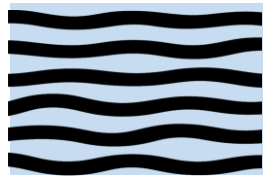

Weak matrix

UNIDIRECTIONAL FRPS

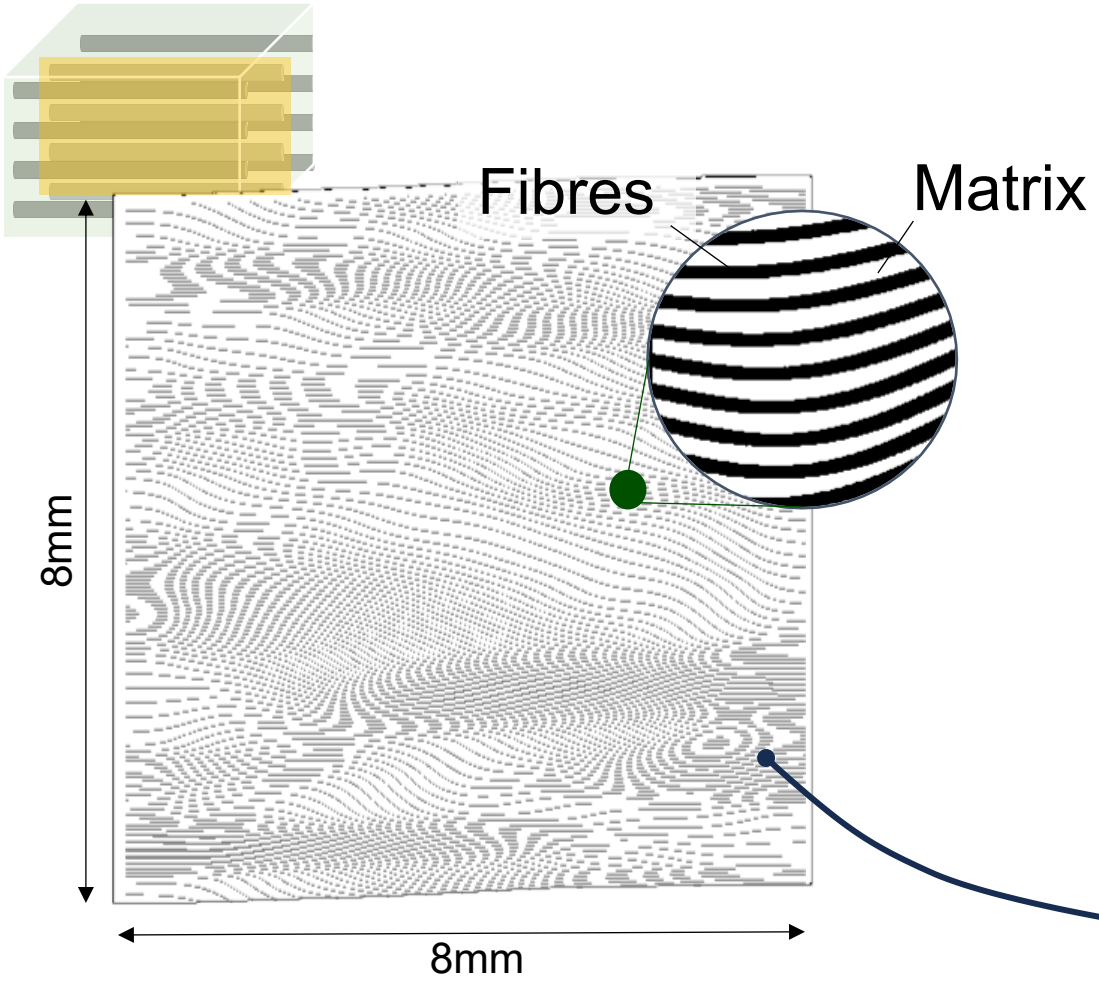

2D longitudinal slice of UD FRP

- Optimised architecture for composite strength and stiffness
- Most influential geometric defect: fibre misalignment angle θ^{f}

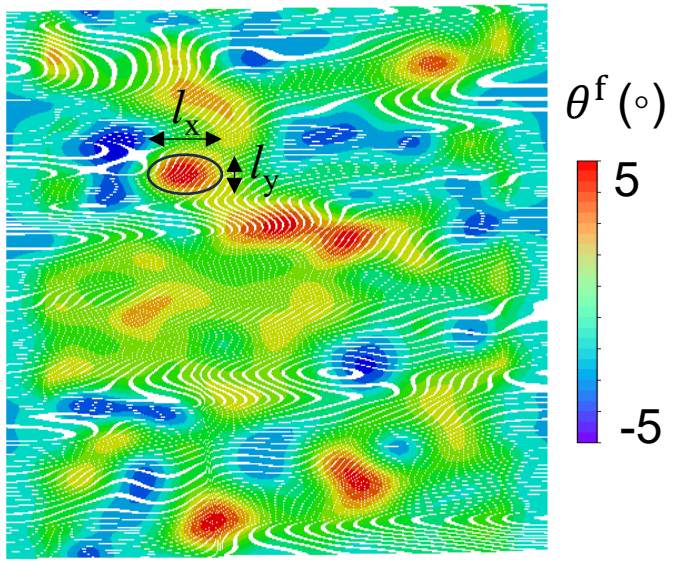

HOMOGENEOUS MATRIX BASELINE RESPONSE

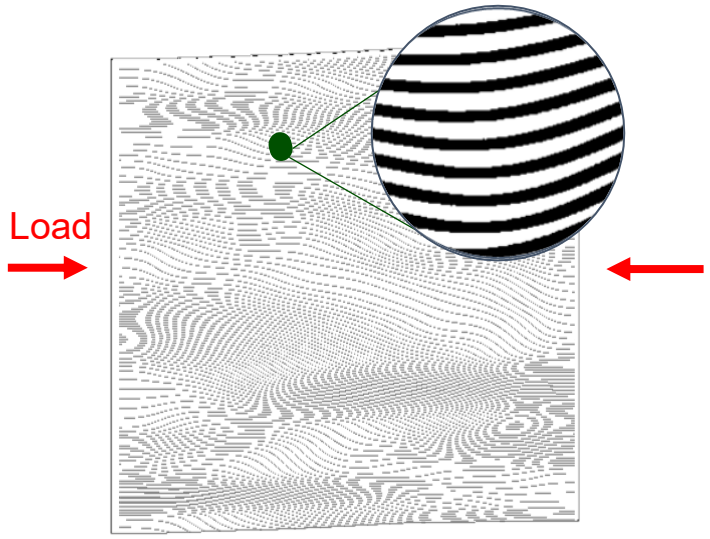

FE simulation

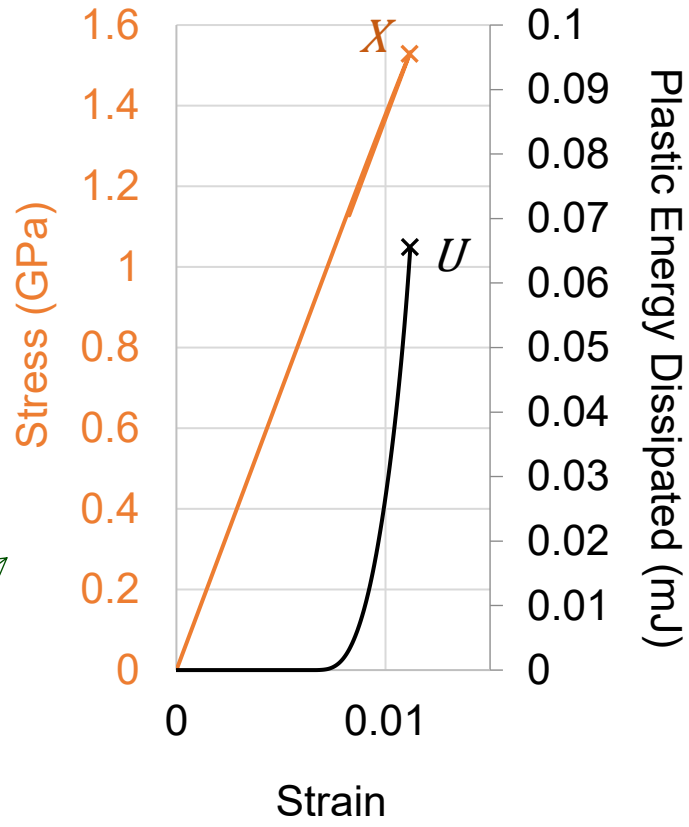

At peak stress X

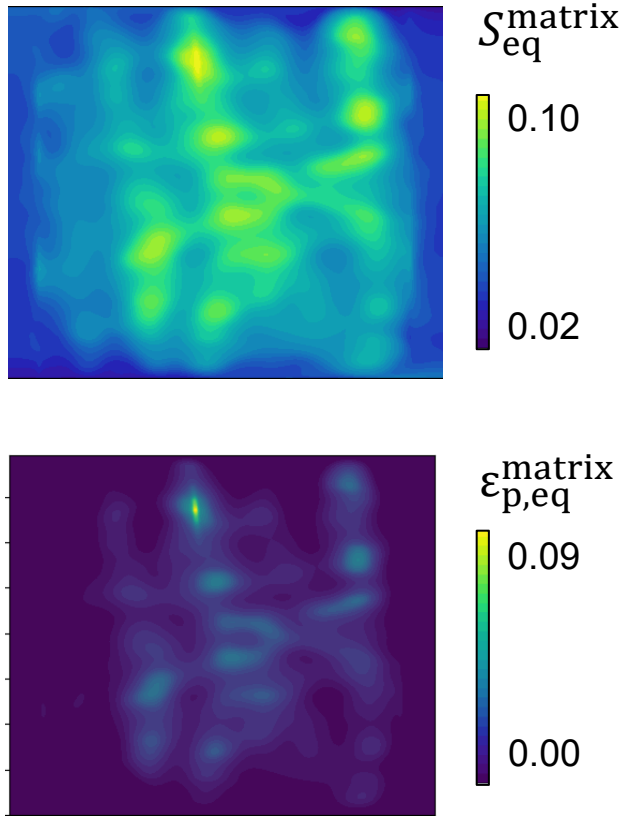

UNIDIRECTIONAL FRPS

HOMOGENEOUS MATRIX BASELINE RESPONSE

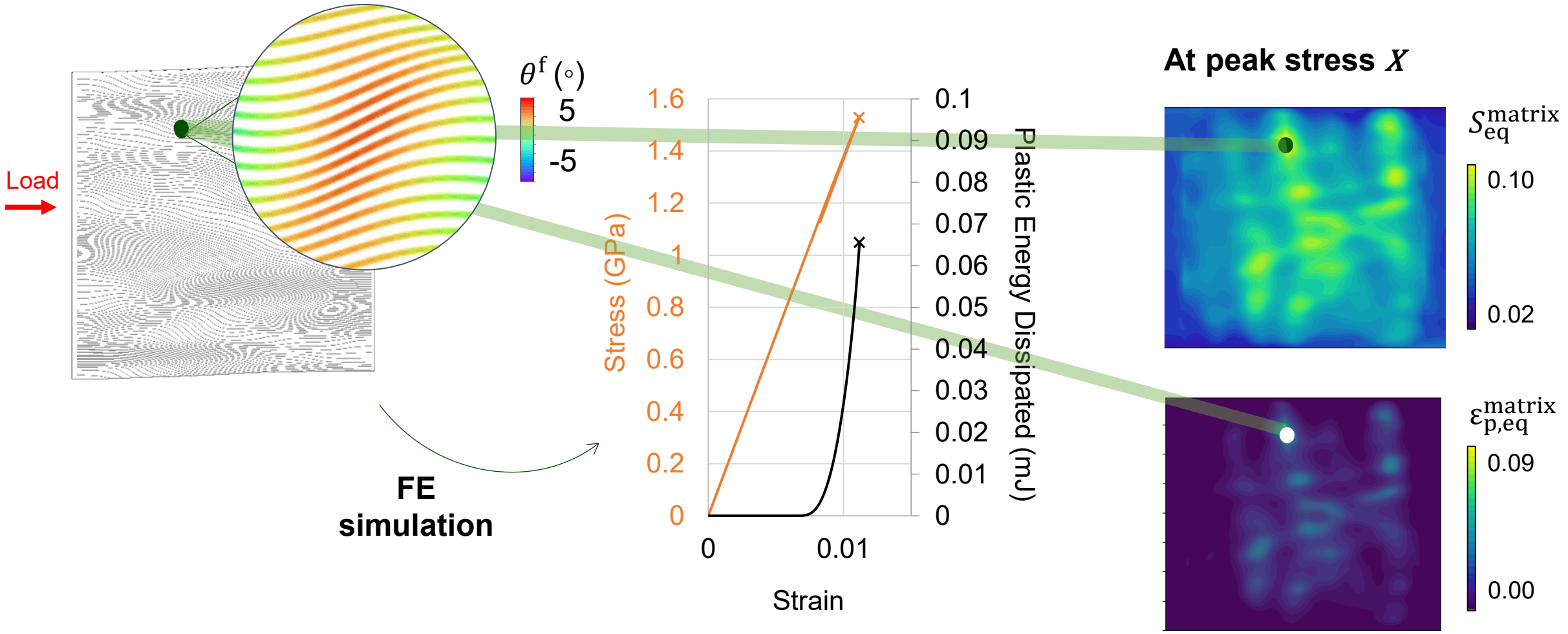

UNIDIRECTIONAL FRPS

HOMOGENEOUS MATRIX BASELINE RESPONSE

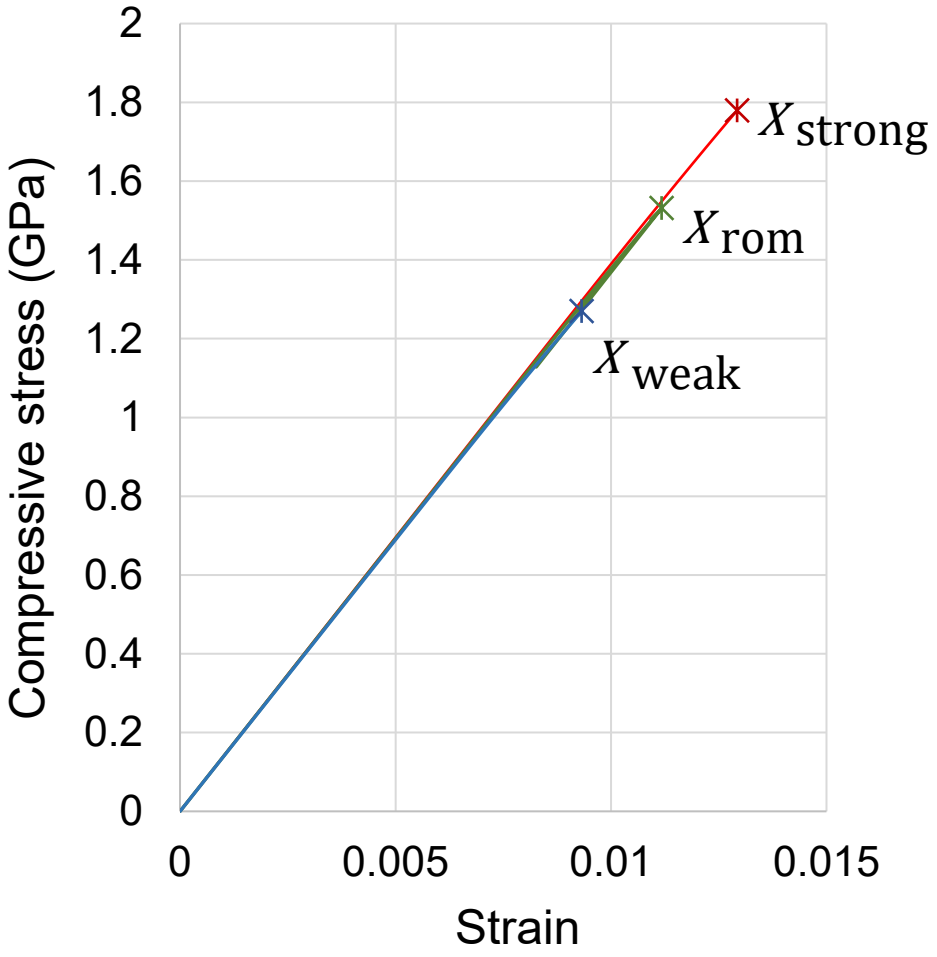

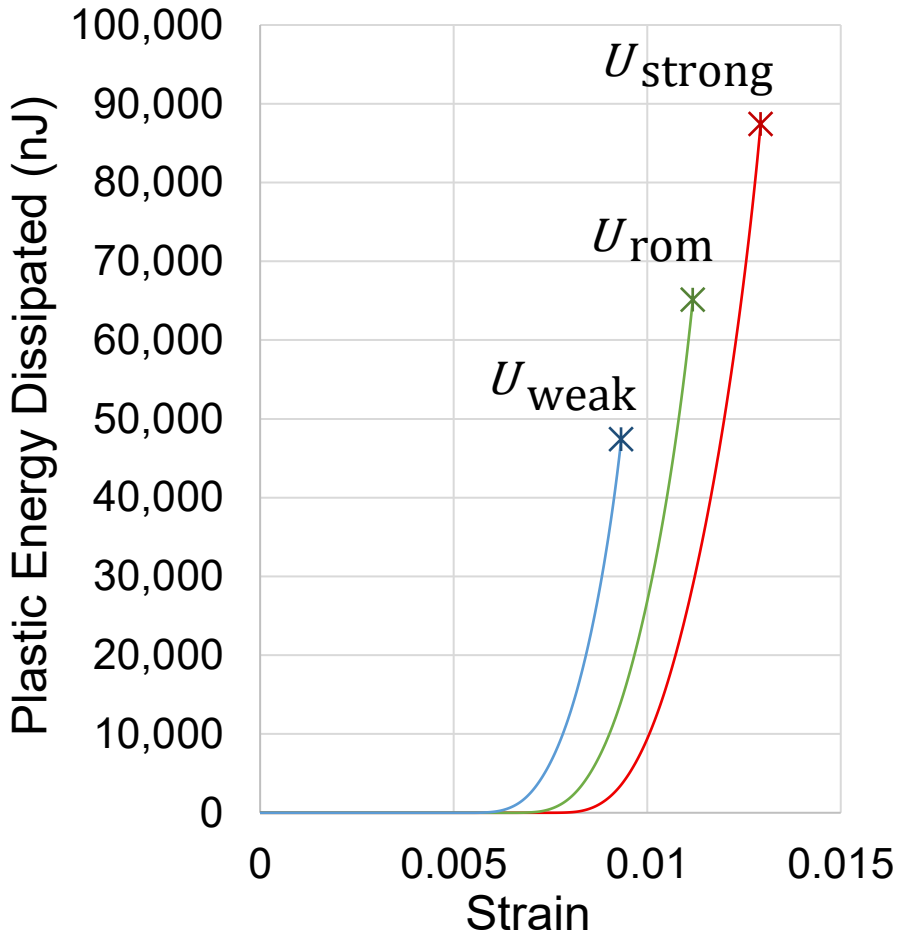



Strong matrix



RoM matrix
(50% strong +
50% weak)

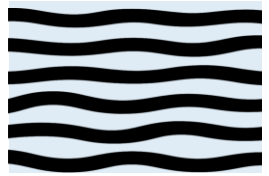

Weak matrix

HOMOGENEOUS MATRIX BASELINES AS BENCHMARKS

Normalised Compressive Strength

$$\tilde{X} = \frac{X - X_{\text{weak}}}{X_{\text{strong}} - X_{\text{weak}}}$$

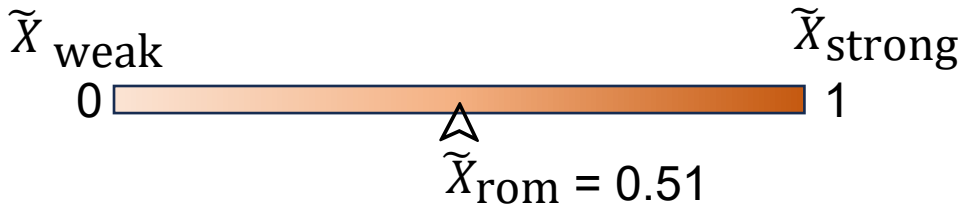

Normalised Plastic Energy Dissipated (at failure)

$$\tilde{U} = \frac{U - U_{\text{weak}}}{U_{\text{strong}} - U_{\text{weak}}}$$

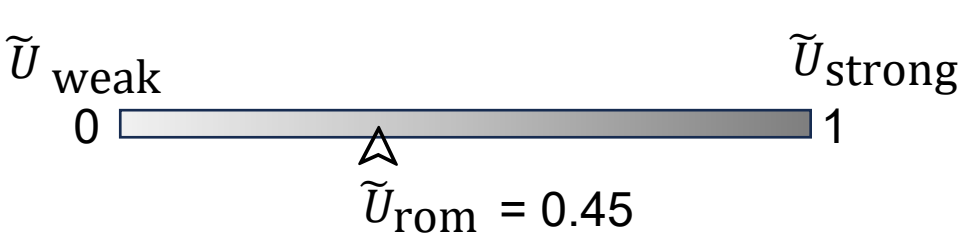



Strong matrix performance = 1

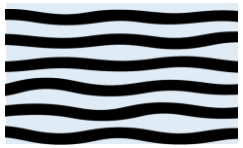

Weak matrix performance = 0

INTERMITTENT MODIFICATION STRATEGY

A. MANUFACTURE-FRIENDLY

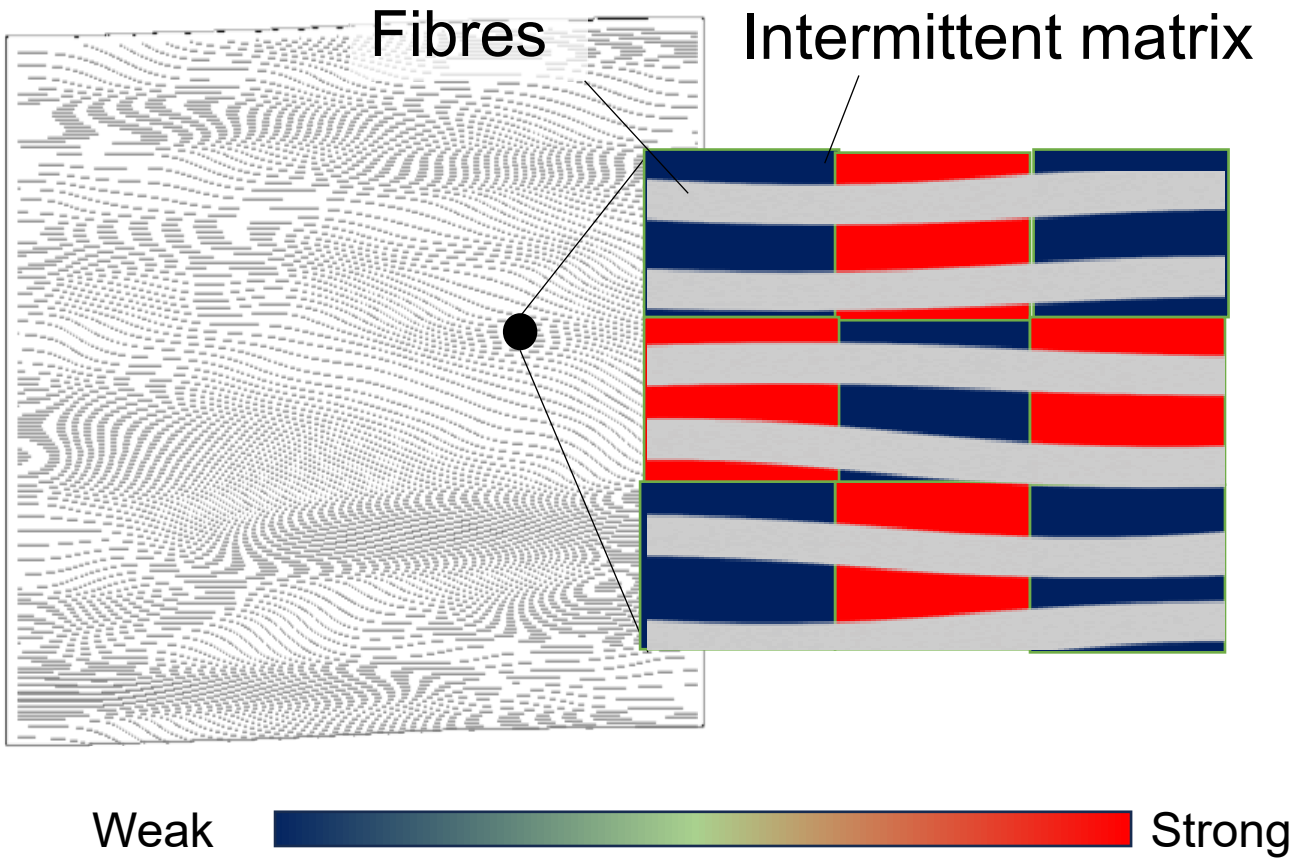

- Intermittent matrix follows **regular checkerboard grid pattern**
- Discretised transitions
- Size of grid determined from spatial parameters of FRP θ^{f} field

INTERMITTENT MODIFICATION STRATEGY

A. MANUFACTURE-FRIENDLY

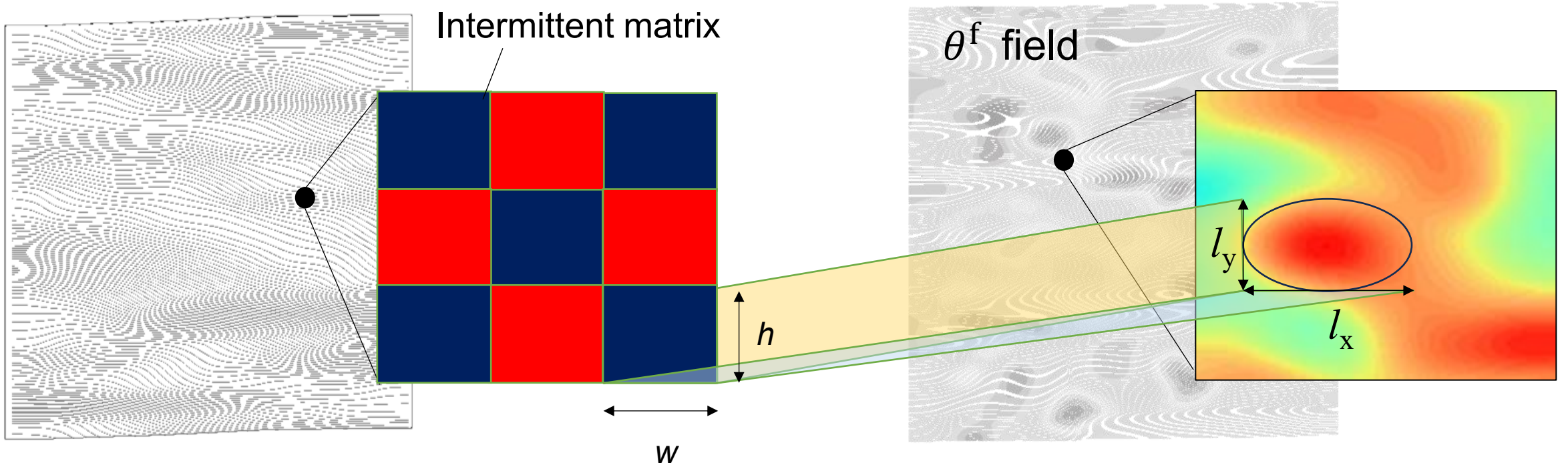

UD FRPS ~ MANUFACTURE-FRIENDLY

INTERMITTENT MATRIX MODIFIED FRPS

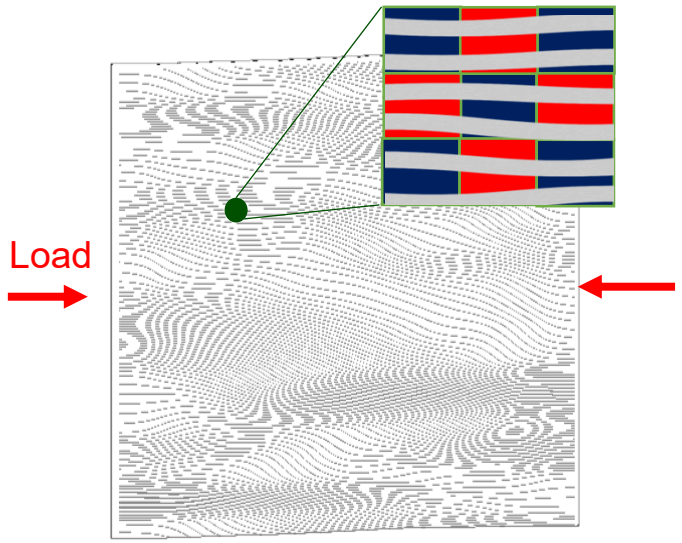

FE simulation

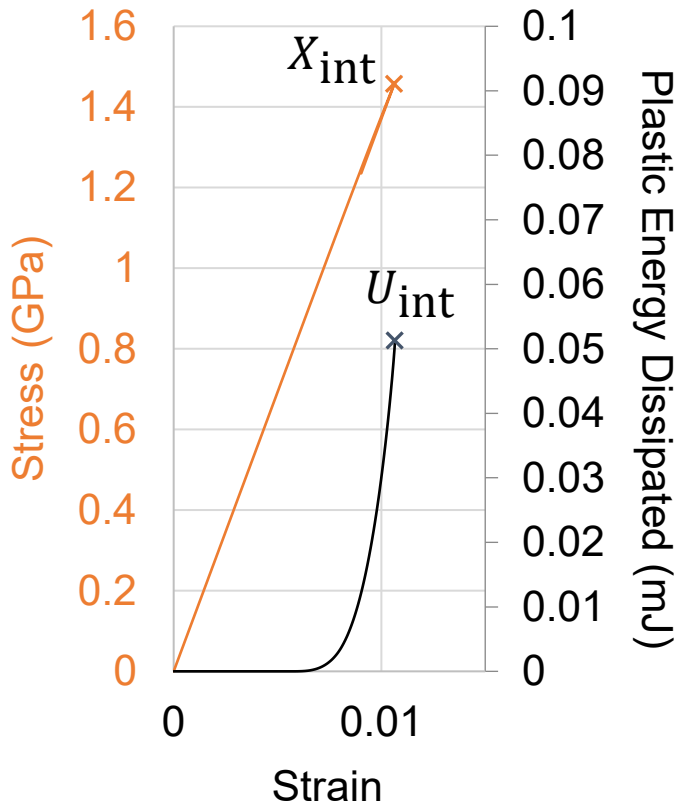

At peak stress X

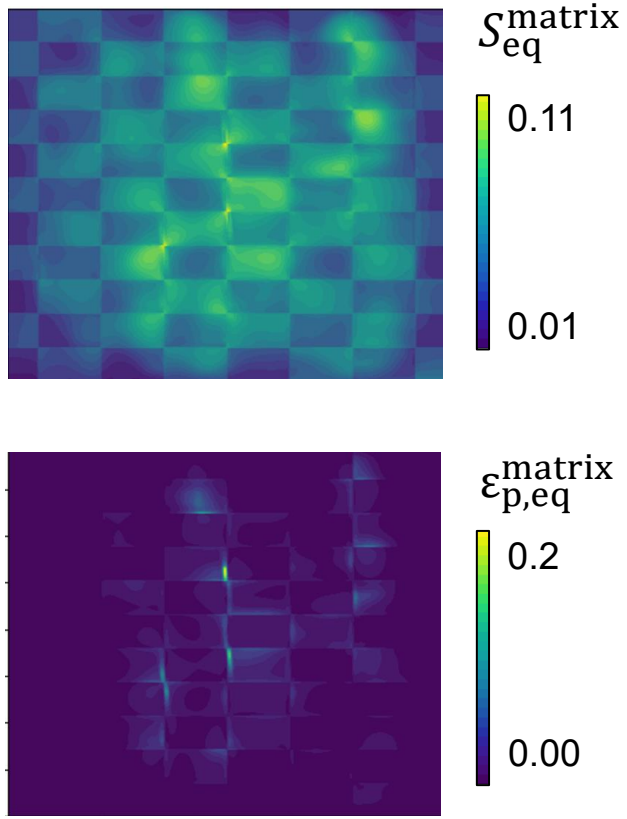

INTERMITTENT MATRIX MODIFIED FRPS

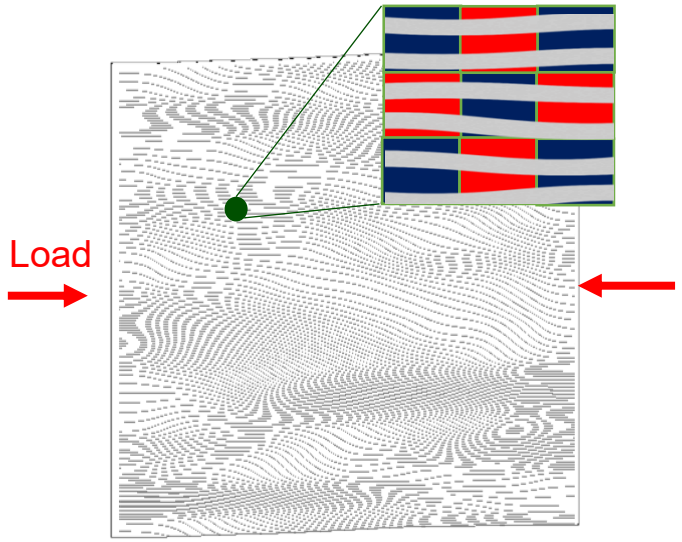

FE simulation

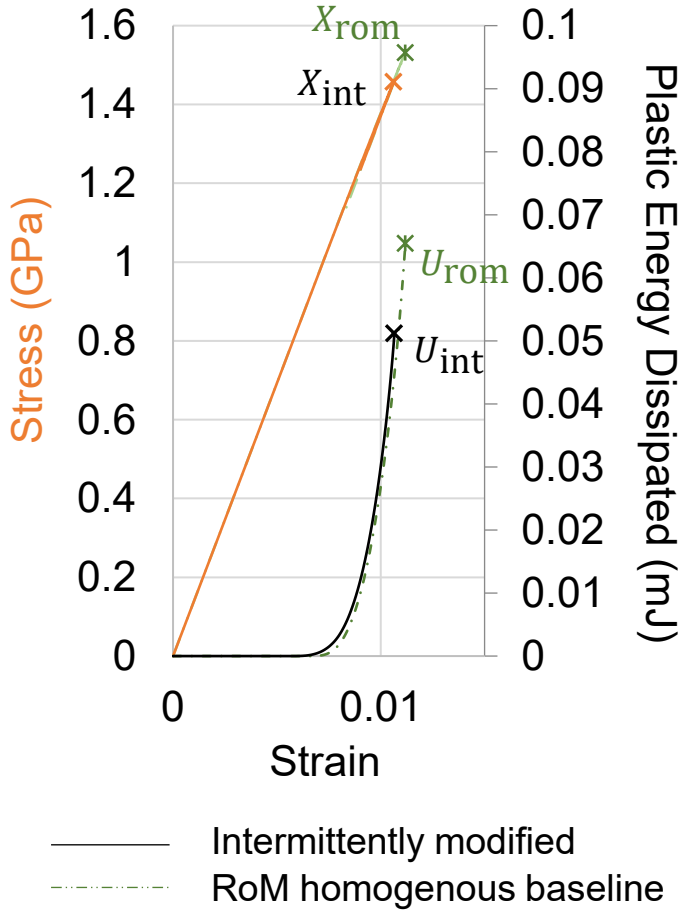

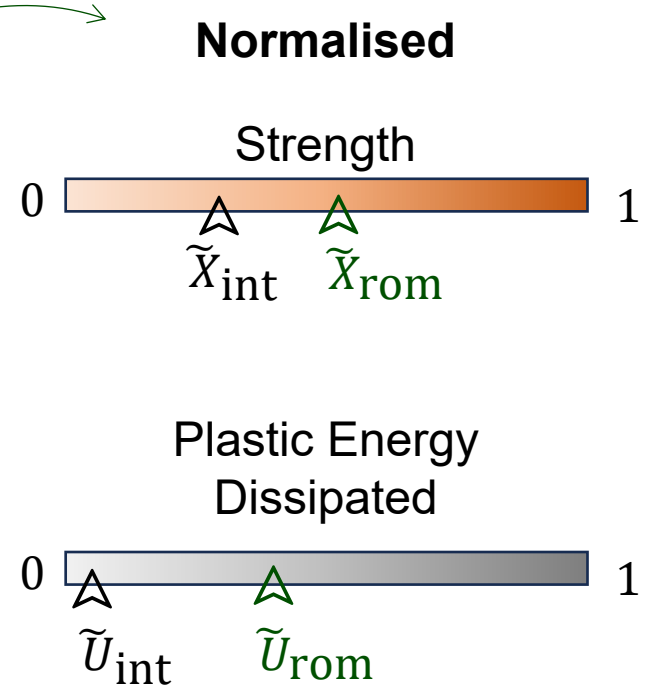

UD FRPS ~ MANUFACTURE-FRIENDLY

EFFECT OF PATTERN SIZE

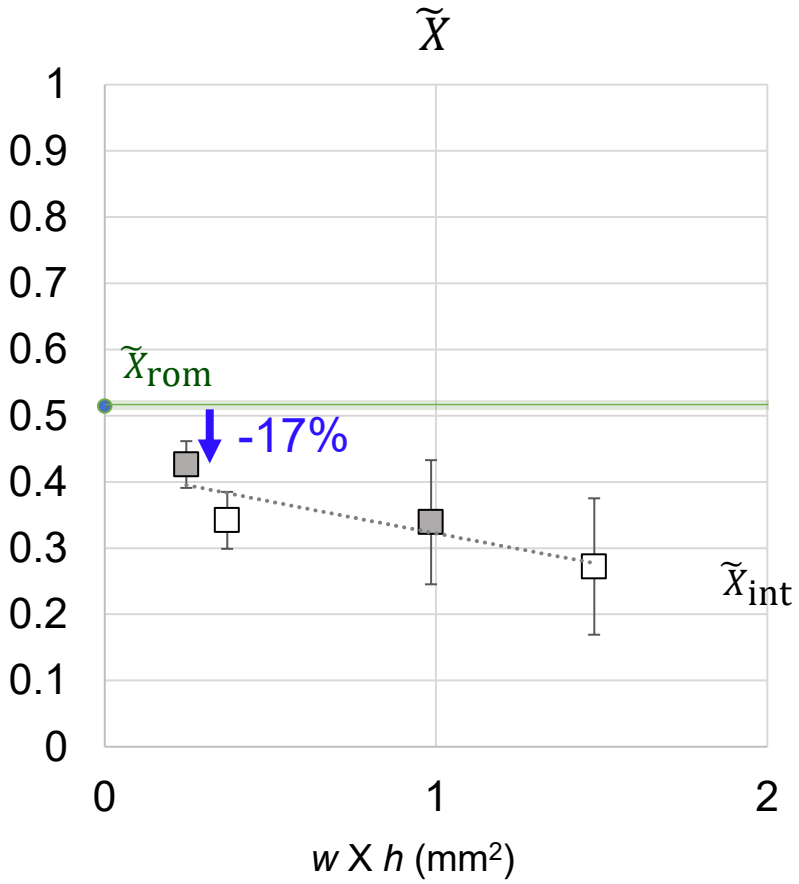

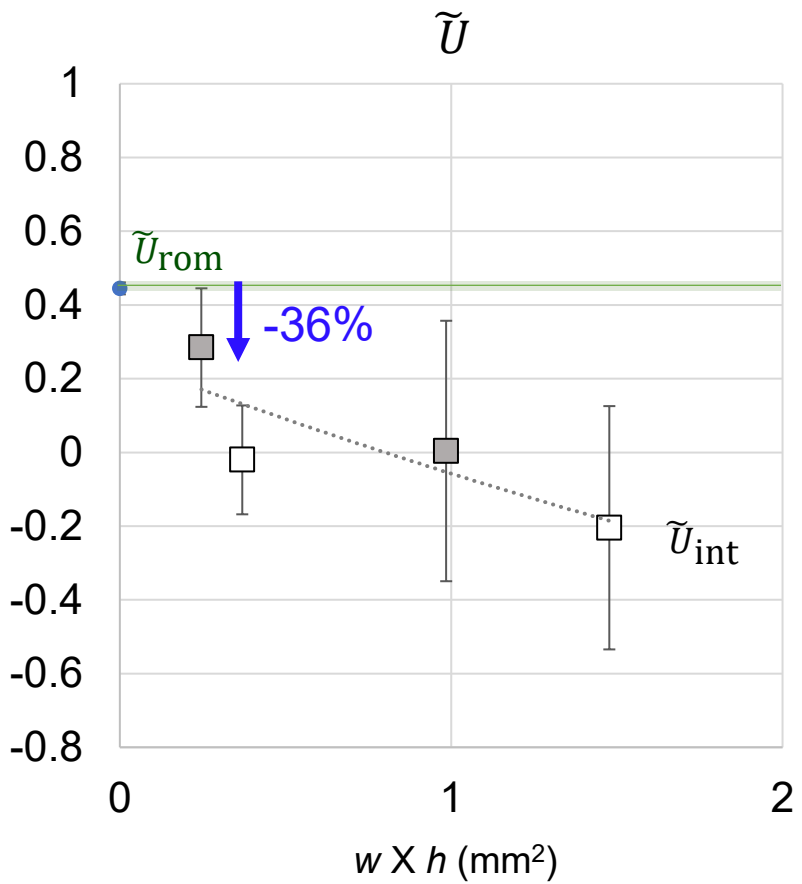

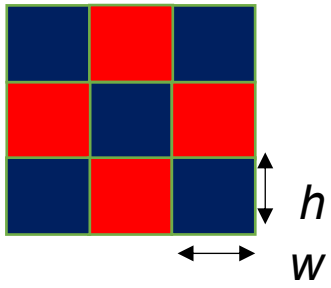

w	h
$l_x = 0.73$ mm	$l_y = 1.35$ mm
l_x	$1.5 \cdot l_y$
$2 \cdot l_x$	$2 \cdot l_y$
$2 \cdot l_x$	$3 \cdot l_y$

INTERMITTENT MODIFICATION STRATEGY

B. DEFECT-ORIENTED

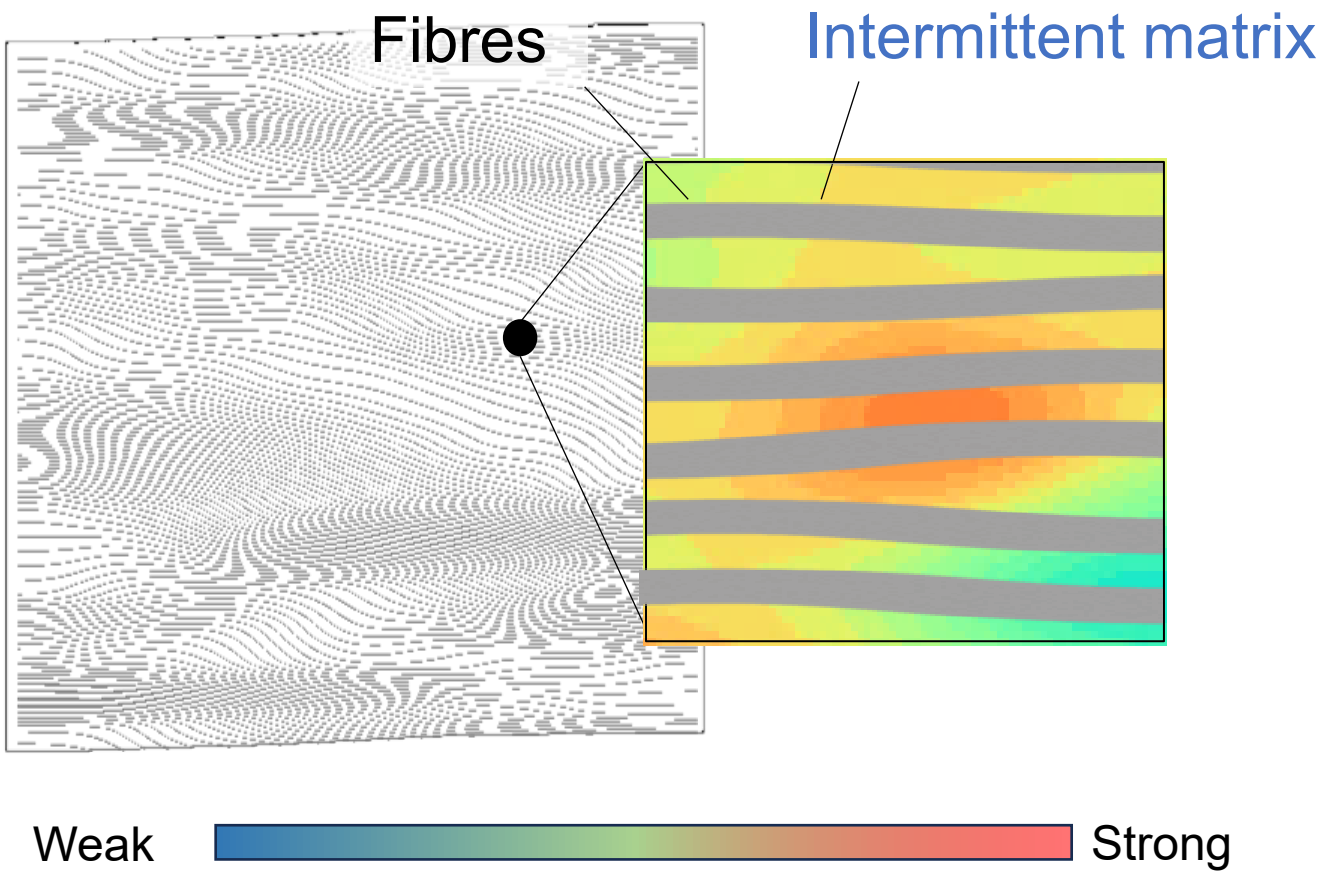

- Intermittent matrix variation follows variation of **FRP** $\left|\boldsymbol{\theta}^{\boldsymbol{f}}\right|$ **field.**
- Enables targeted strengthening of weakest regions
  - i.e. regions with high $\left|\theta^{\mathrm{f}}\right|$

UD FRPS ~ DEFECT-ORIENTED

INTERMITTENT MATRIX MODIFIED FRPS

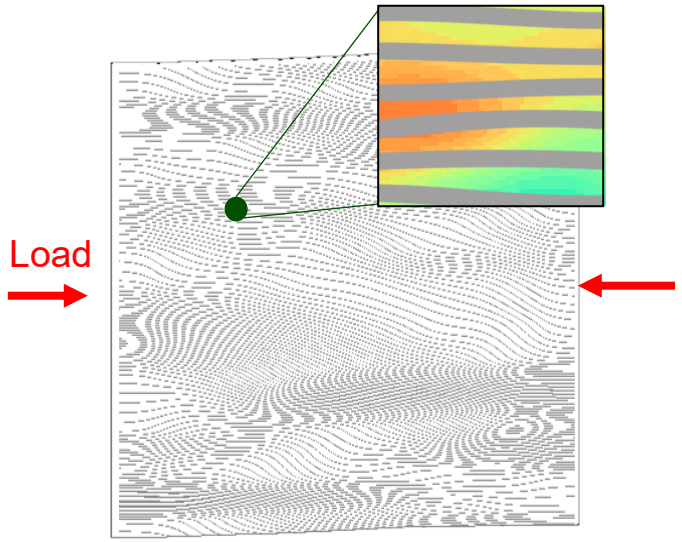

FE simulation

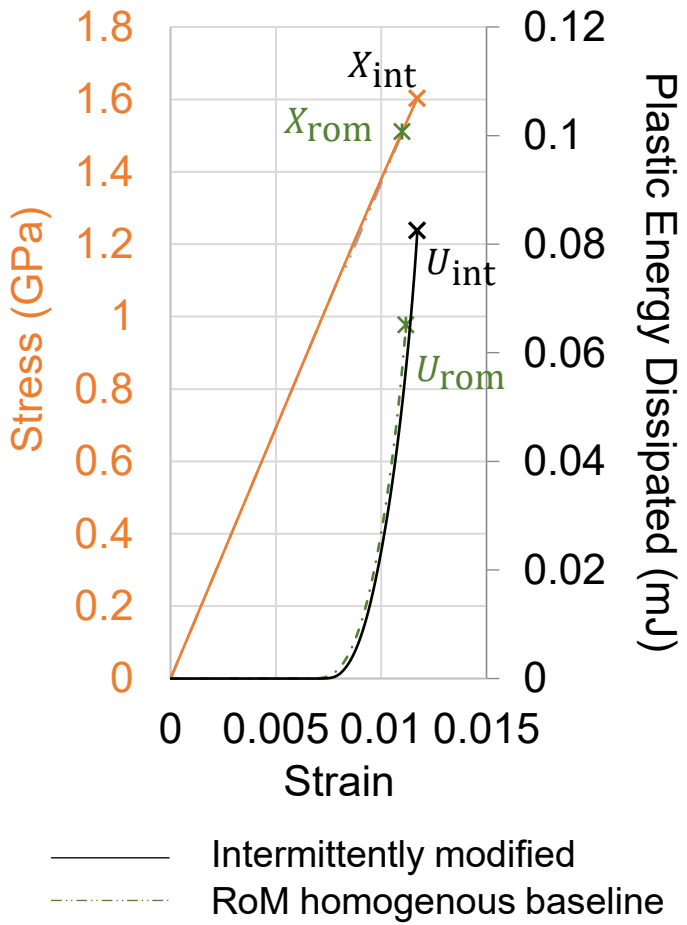

At peak stress X_{int}

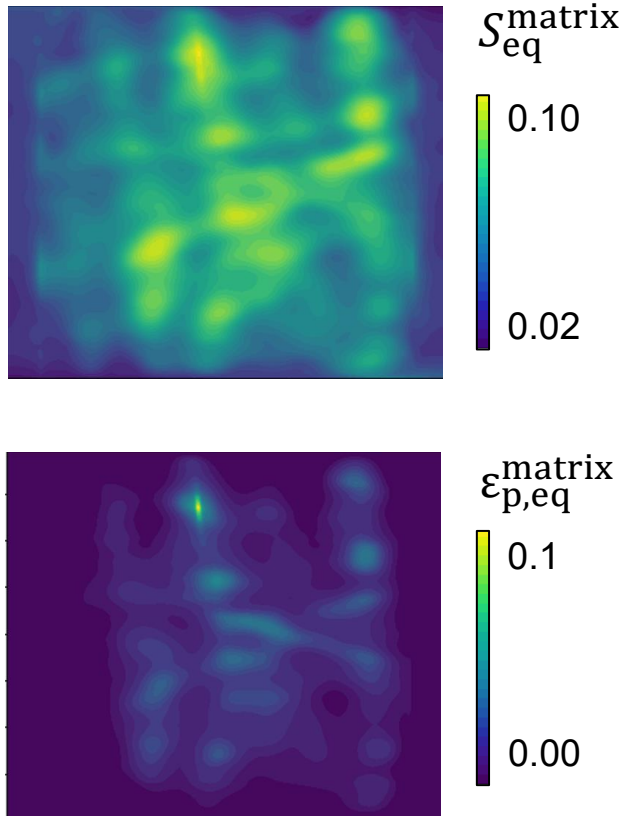

UNIDIRECTIONAL FRPS

COMPARING INTERMITTENT MATRIX MODIFICATION STRATEGIES

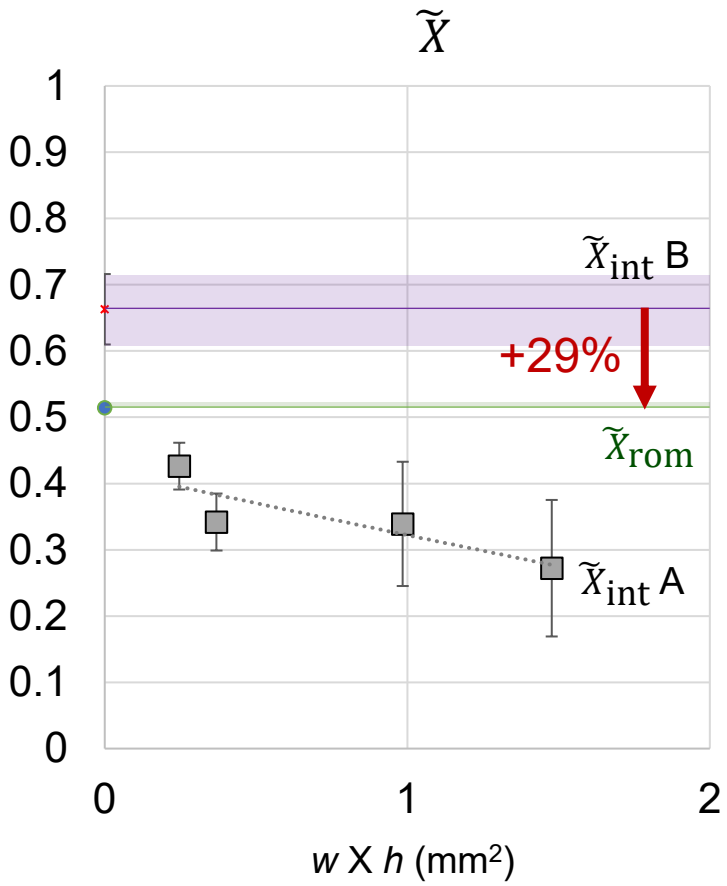

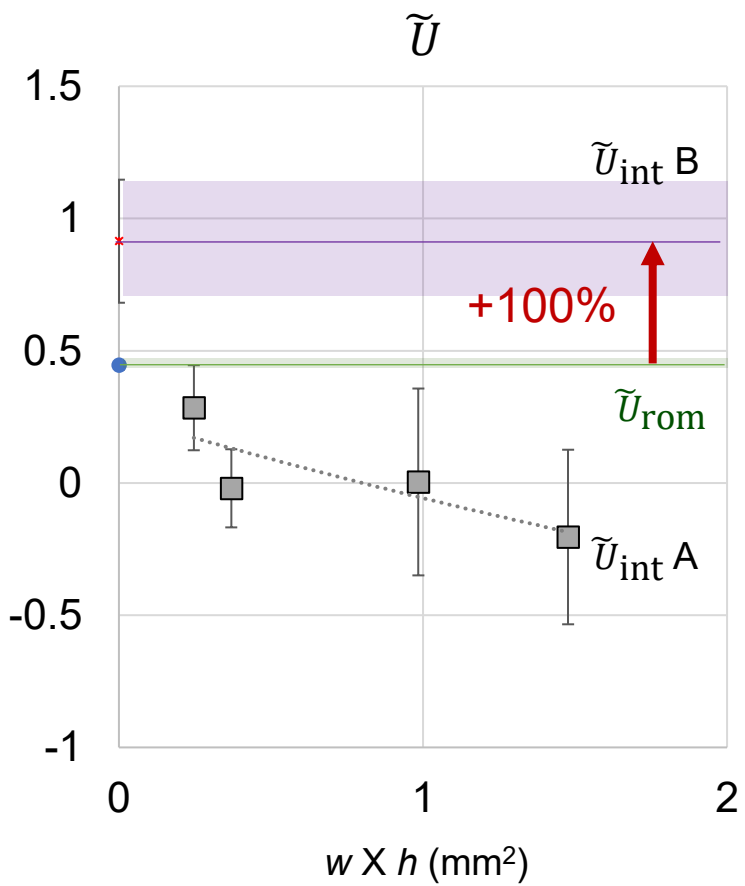

$\tilde{}_{\text{int}}$ B

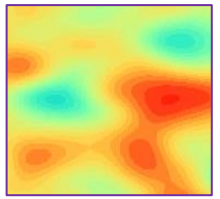

Strategy B: defect –oriented
Follow FRP $|\theta^f|$ field

$\tilde{}_{\text{int}}$ A

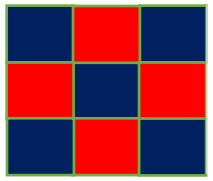

Strategy A: manufacture-friendly
Regular checkerboard

Woven FRPs

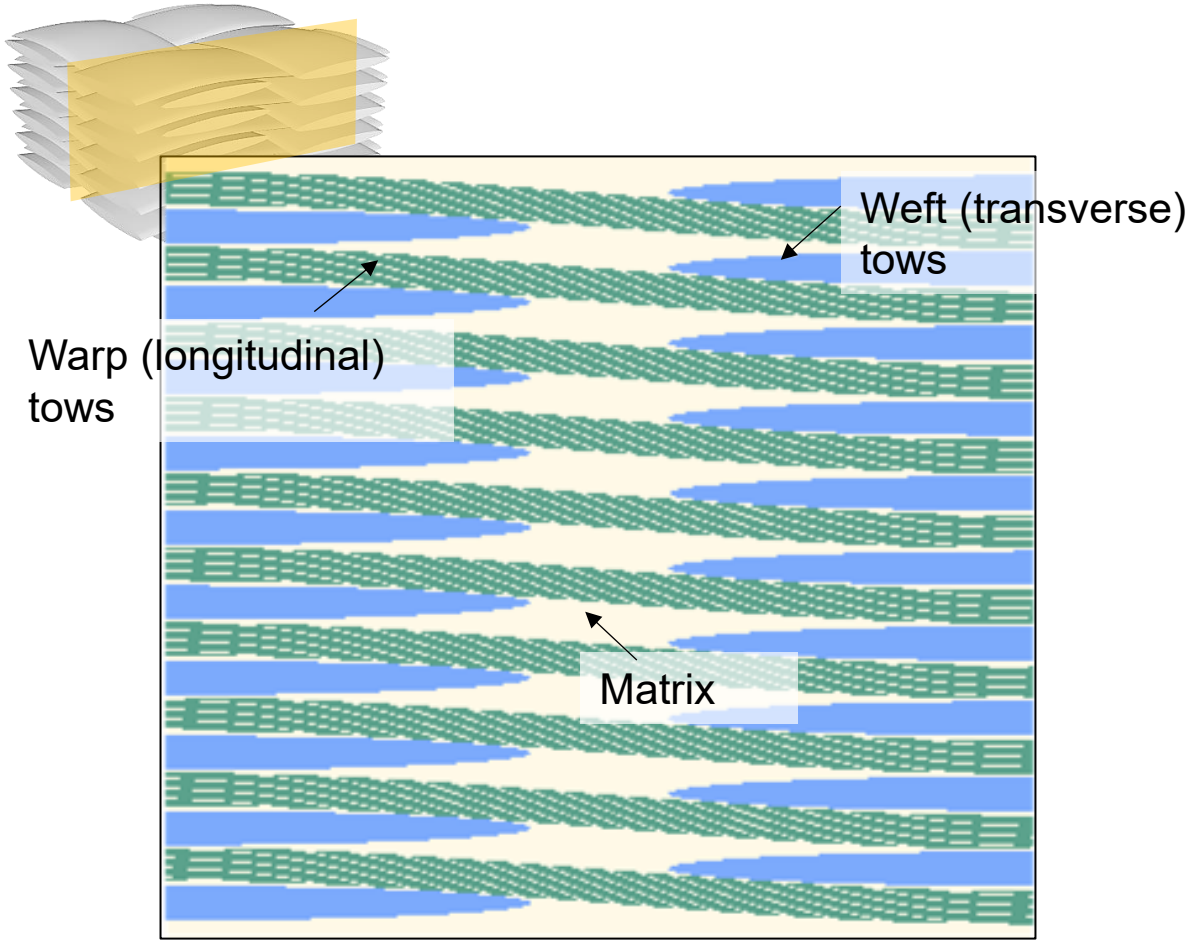

2D cross-sectional slice of a woven FRP

- Efficient at reinforcing multiple directions within single ply
- Increased drapability and conformability for complex structures
- Fail by initial kink-banding of individual tows, followed by global failure.

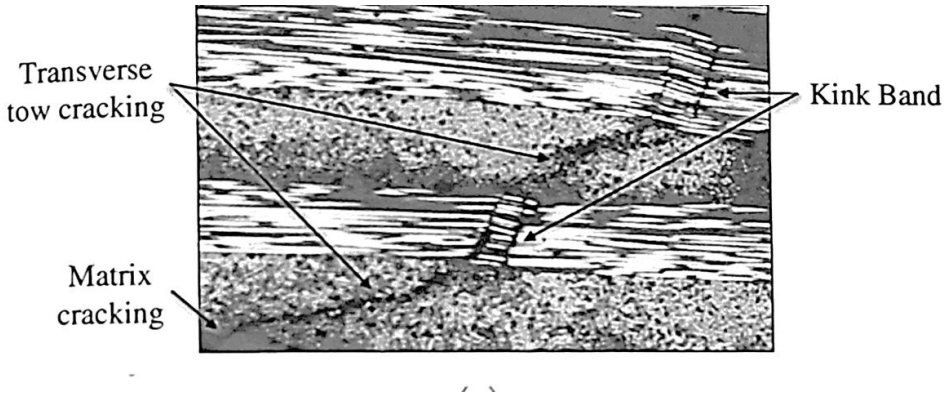

HOMOGENEOUS MATRIX BASELINE RESPONSE

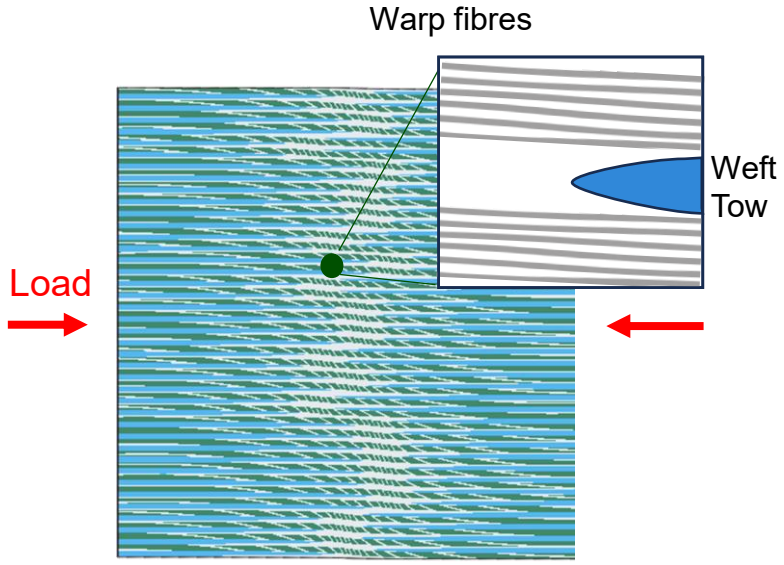

Low stacking randomness

FE simulation

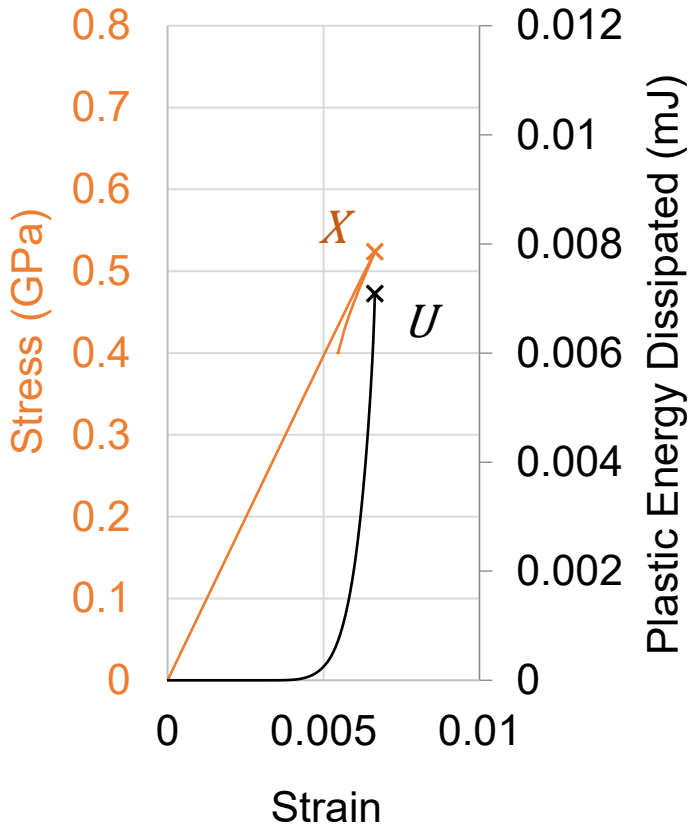

At peak stress X

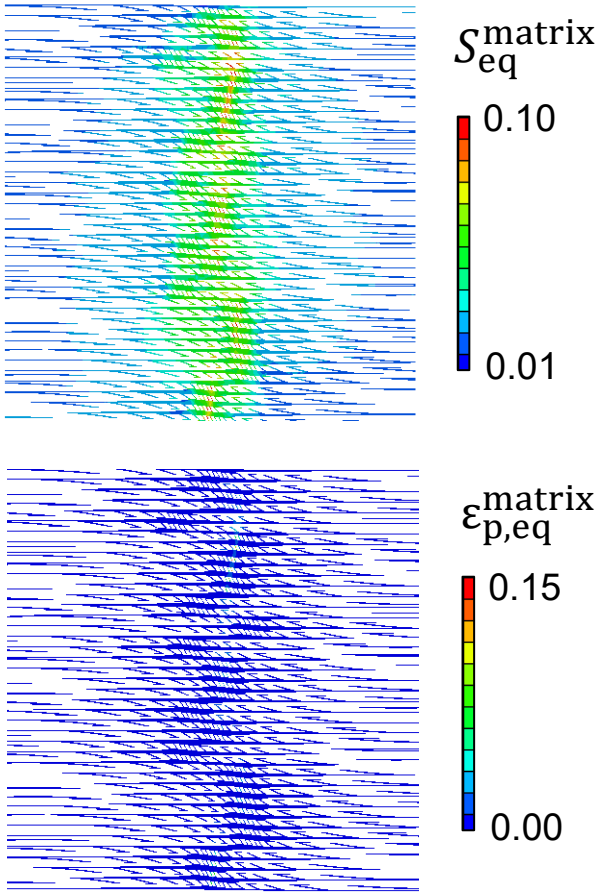

WOVEN FRPS

HOMOGENEOUS MATRIX BASELINE RESPONSE

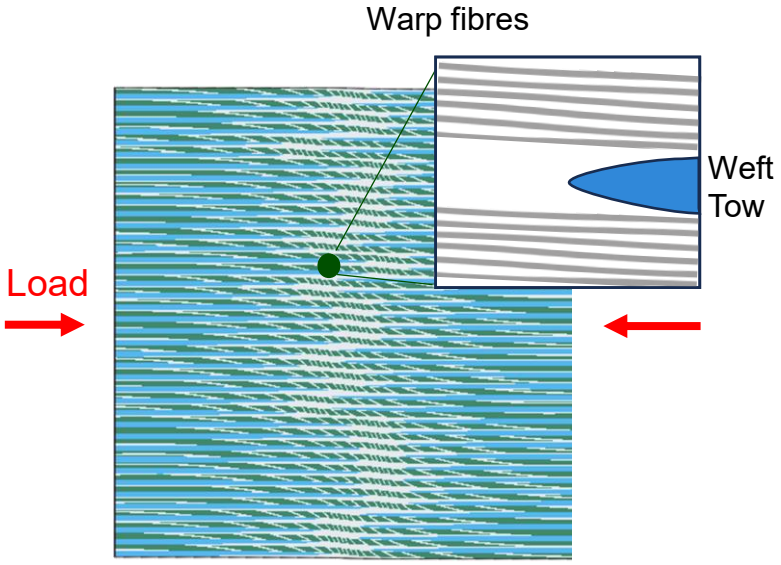

Low stacking randomness

FE simulation

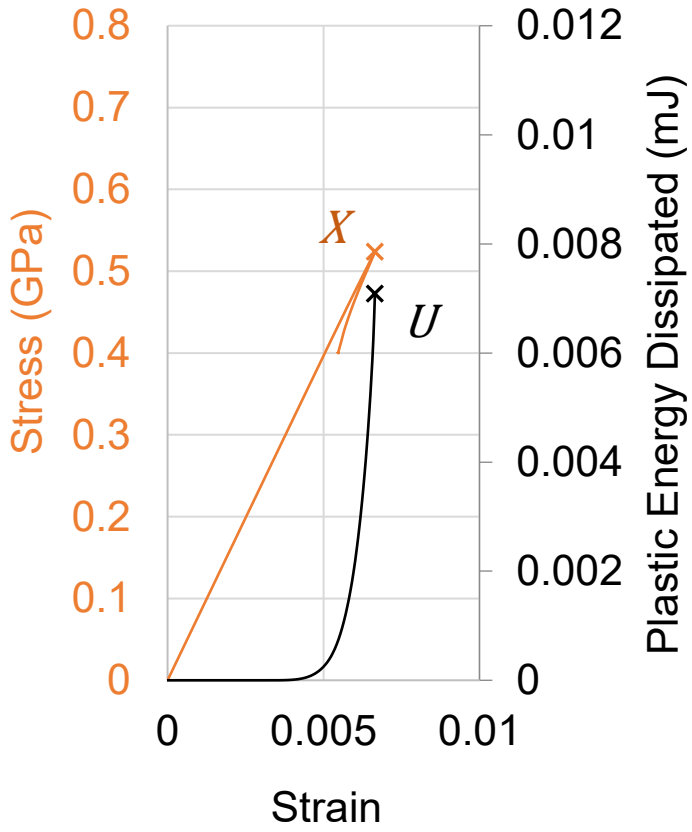

At peak stress *X*

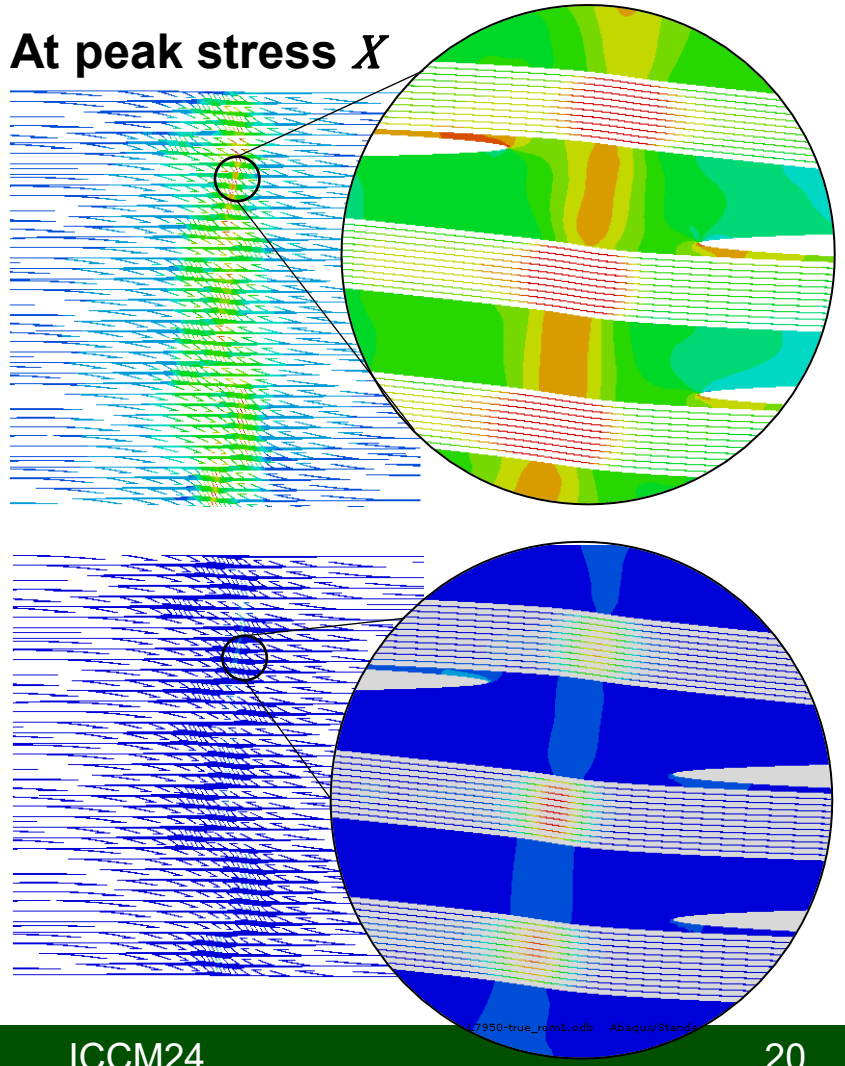

HOMOGENEOUS MATRIX BASELINE RESPONSE

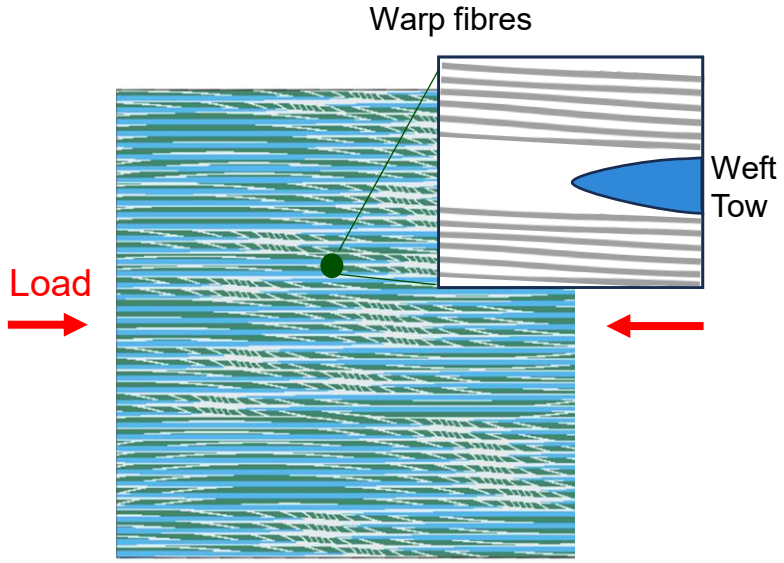

High stacking randomness

FE simulation

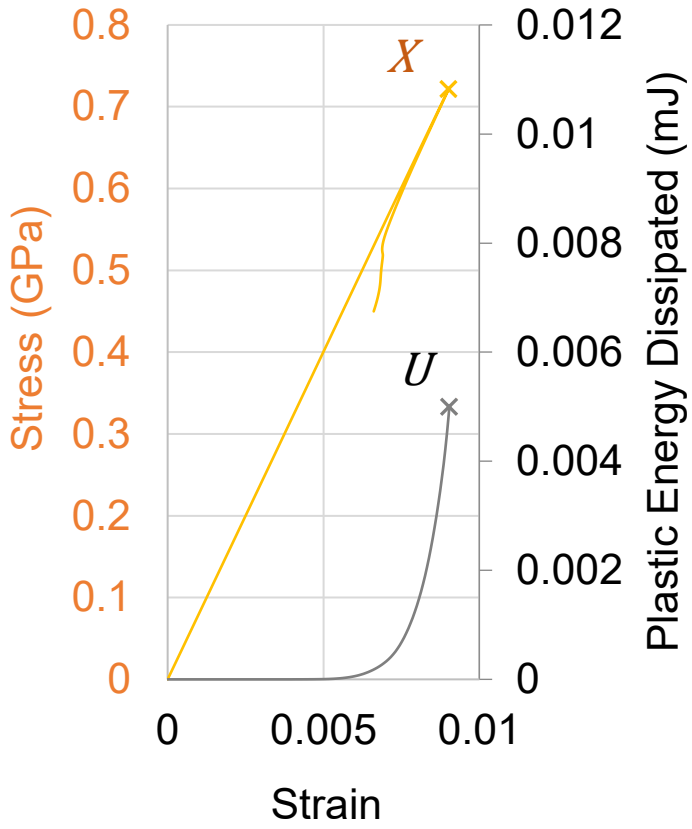

At peak stress X

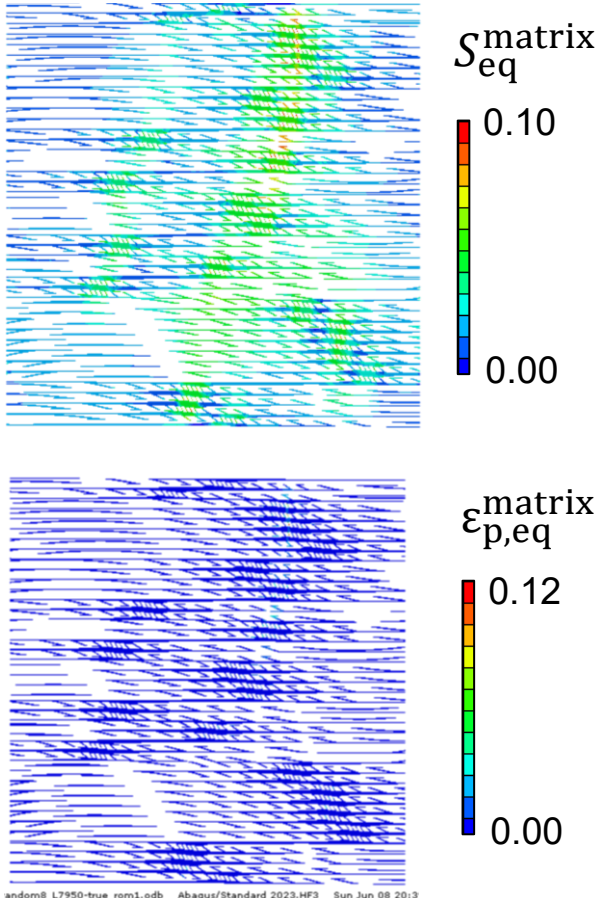

WOVEN FRPS

HOMOGENEOUS MATRIX BASELINE RESPONSE

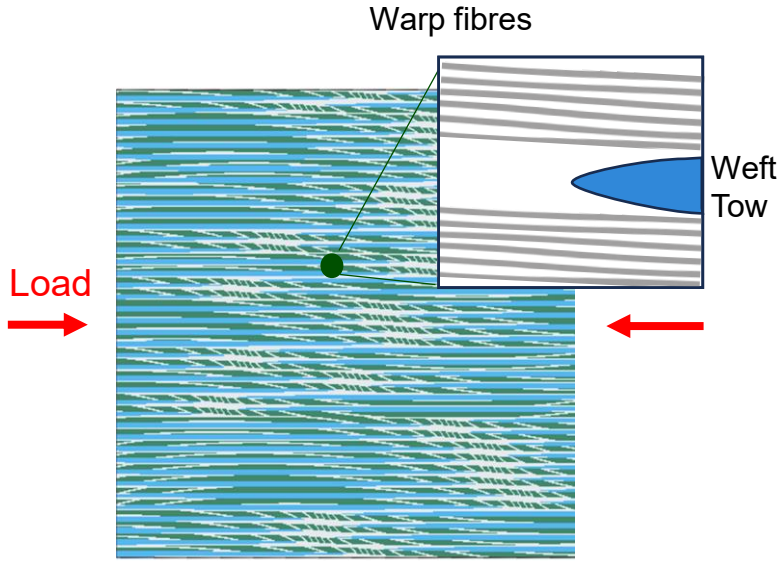

High stacking randomness

FE simulation

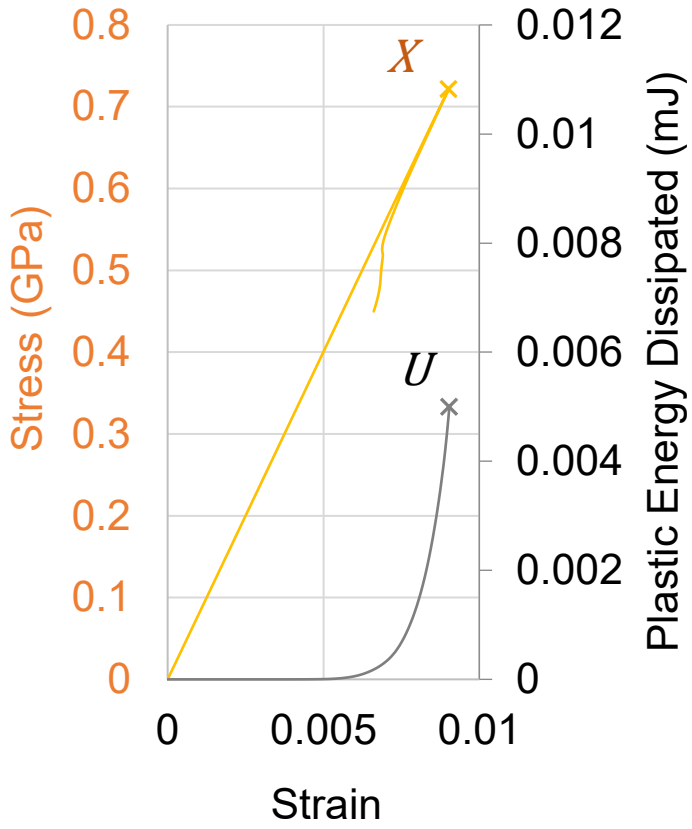

At peak stress X

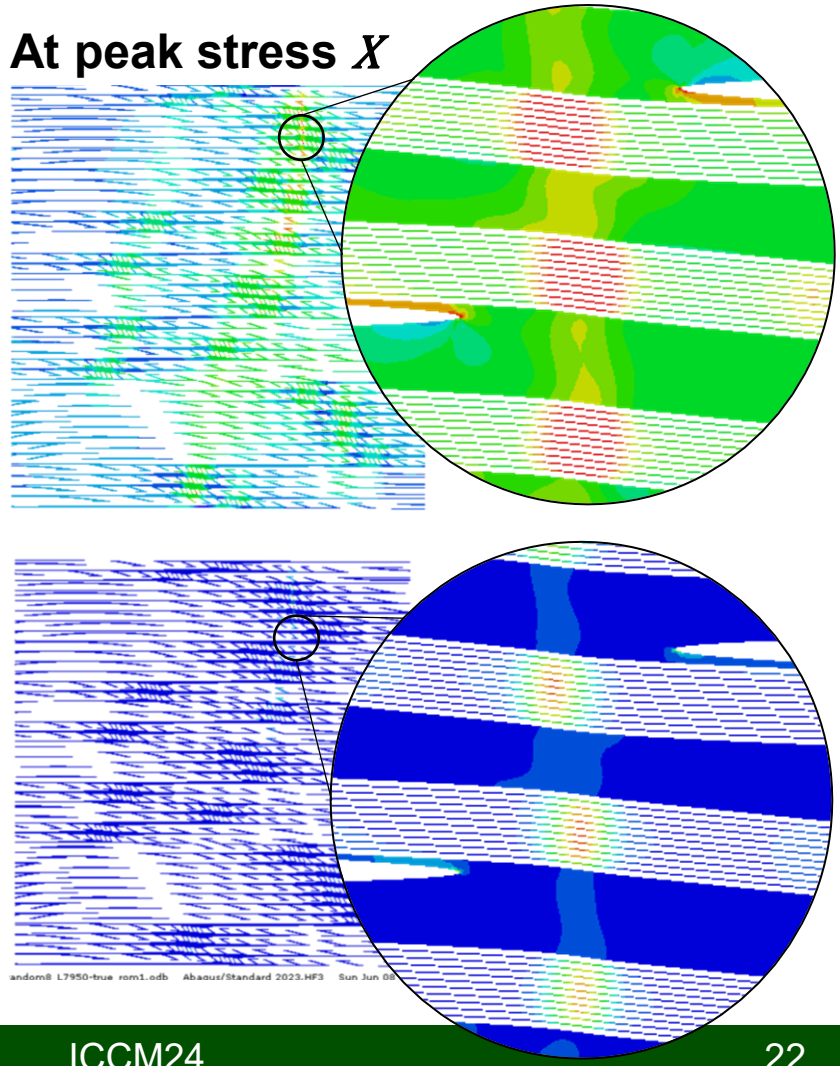

INTERMITTENT MODIFICATION STRATEGY

C. MANUFACTURE-FRIENDLY + DEFECT-ORIENTED

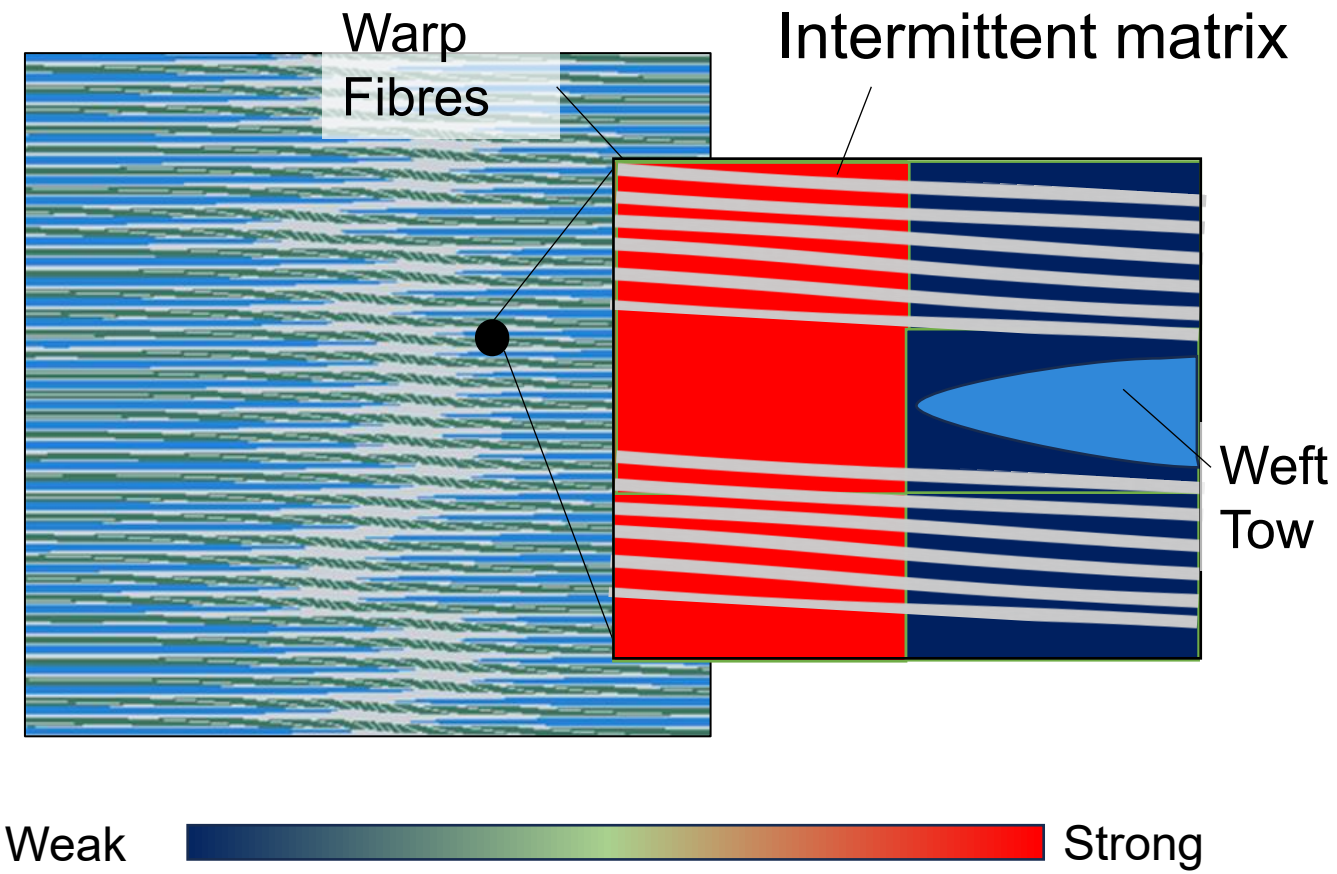

- Strong matrix regions are centred on the max-crimp (high $\left|\theta^{\mathrm{f}}\right|$) region.
- Discretised transitions.

WOVEN FRPS

INTERMITTENT MATRIX MODIFIED FRPS

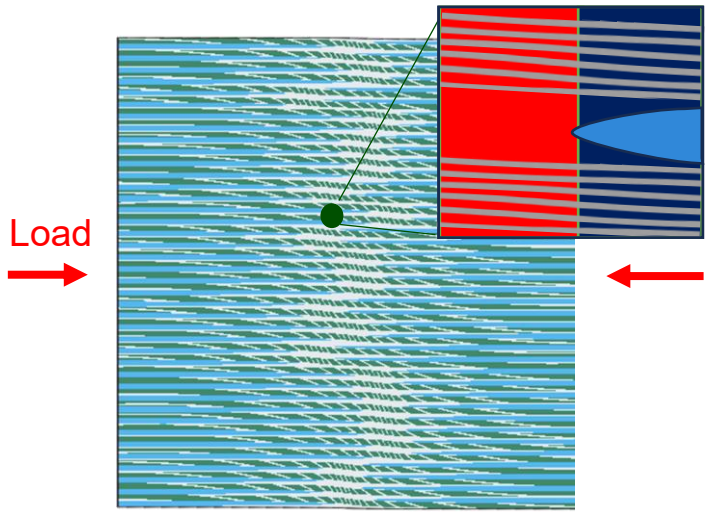

Low stacking randomness

FE simulation

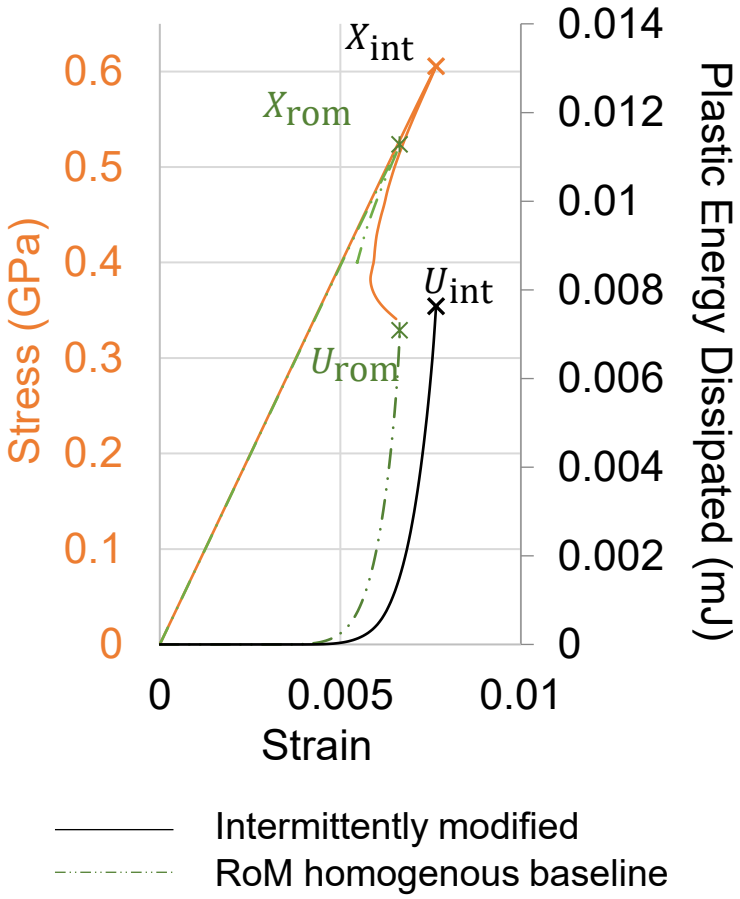

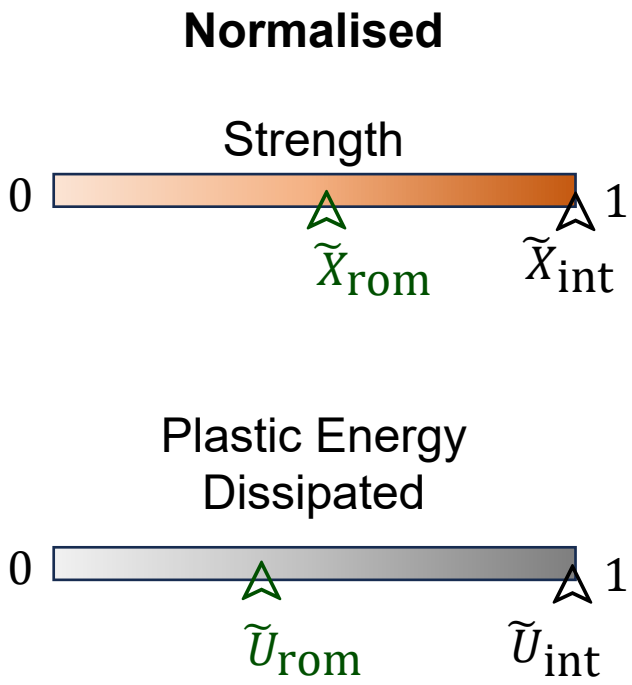

WOVEN FRPS

INTERMITTENT MATRIX MODIFIED FRPS

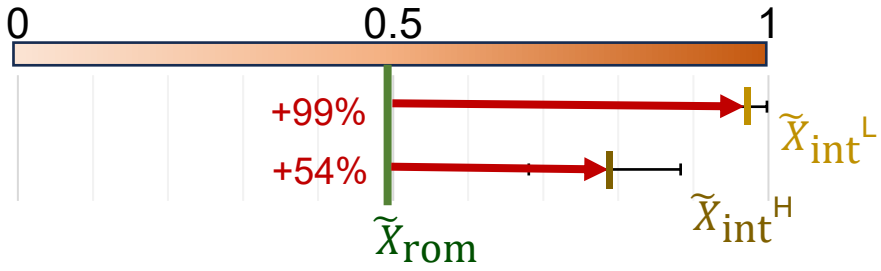

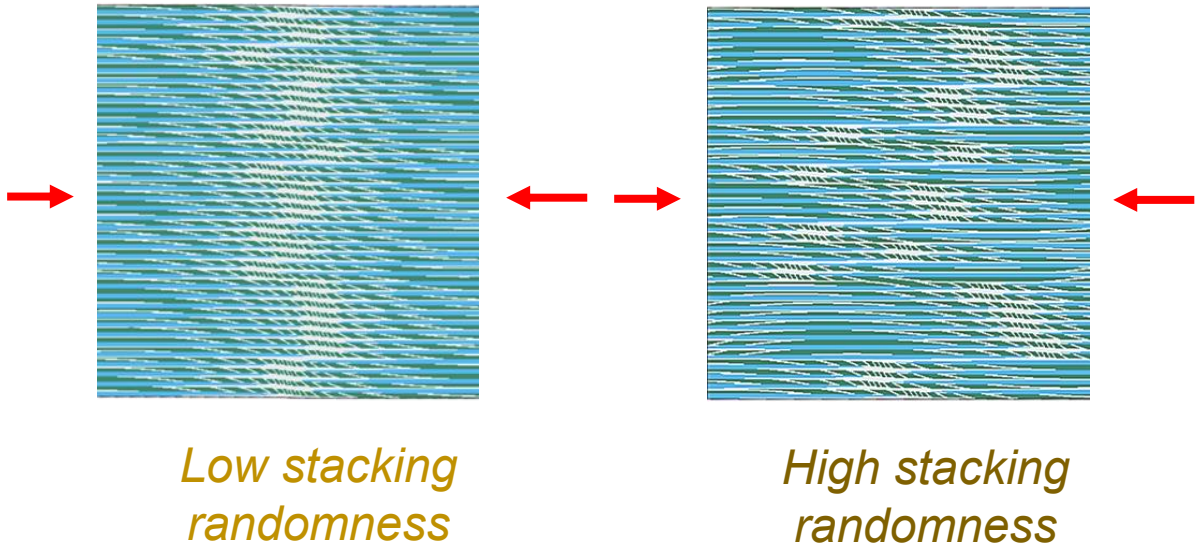

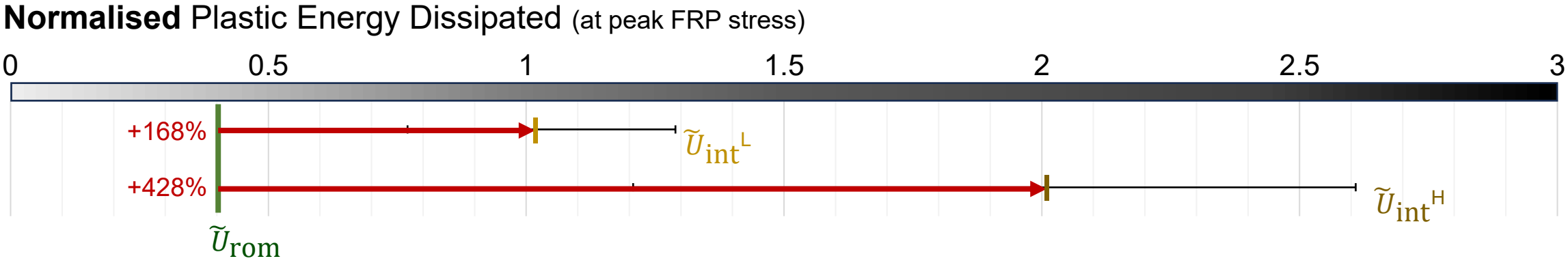

KEY TAKEAWAYS

- Intermittent matrix modification strategies are **most useful** if the FRP architecture allows for **high predictability of failure locations**.
- If critical defects can be easily predetermined, those areas can be feasibly targeted and strengthened, allowing for significant benefit to be gained.

UD FRP	**Woven FRP**
	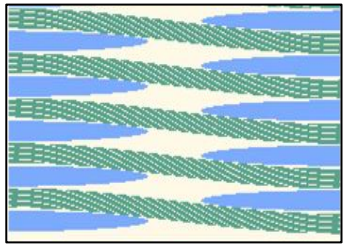
Low damage predictability	High damage predictability
Limited potential for intermittent matrix modification	High potential for intermittent matrix modification



Next COMP

Next Generation
Fibre-Reinforced Composites

https://nextcomp.ac.uk

I would like to acknowledge funding which supported this work from the UK Research and Innovation - EPSRC Programme Grant; Next Generation Fibre-Reinforced Composites: A Full Scale Redesign for Compression (EP/T011653/1)

A collaboration between Imperial College London and University of Bristol

IMPERIAL

University of BRISTOL

Bristol Composites Institute

ICCM24 24TH INTERNATIONAL CONFERENCE ON COMPOSITE MATERIALS
AUG 4-8, 2025 • BALTIMORE CONVENTION CENTER • BALTIMORE, MARYLAND

POLYMER COMPOSITES REINFORCED BY CONTINUOUS IRREGULAR NETWORKS:
FROM BIOINSPIRED DESIGN TO FRACTURE

T. Magrini[1]

[1]Department of Mechanical Engineering, Eindhoven University of Technology
5600MB, Eindhoven, The Netherlands
Email: t.magrini@tue.nl, web page: https://www.tue.nl/en/our-university/departments/mechanical-engineering

Keywords: Additive Manufacturing, Bioinspiration, Composites, Mechanics, Metamaterials.

ABSTRACT

Biological materials are often reinforced by irregular structures that provide outstanding mechanical properties, ranging from high stiffness-to-weight ratios to excellent energy absorption. Unfortunately, replicating the complex design of non-periodic biological structures in synthetic materials still proves a significant design and fabrication challenge. In this context, the recent development of virtual growth algorithms, a tile-based material design tool, can pave the way to a new class of bioinspired architected materials, with superior structural properties. The algorithms can independently tailor the global topology and the local geometry of the generated structures, allowing precise control over the final mechanical properties of the generated materials. Using the algorithm, polymer composites can be designed and then fabricated by additive manufacturing, achieving control over global mechanical properties, like strength and rigidity, as well as local mechanisms of fracture nucleation and propagation, and of fracture energy dissipation. Furthermore, VGAs can be used for bioinspired materials design, by converting complex non-periodic biological structures into a network of building blocks and rules that determine their relative connectivity. Rather than creating an exact replica of the biological material, the method generates synthetic polymer composites with equivalent global- and local descriptors to the biological material, allowing for the emergence of analogous structure-to-property relationships. The method is demonstrated using the pericarp of an orange, a biological material known for its high energy-absorbing capabilities and its gradual rigidity variations. Starting from high resolution micrographs of the biological material, design guidelines for the creation of materials inspired by the orange pericarp can be extracted. Using additive manufacturing, orange-inspired polymer composites can be fabricated and tested under quasi-static and dynamic compressive loading. While the quasi-static results reveal spatially varying mechanical properties, dynamic loading experiments highlight the local mechanisms of deformation responsible for the dissipation of impact energy.

1 INTRODUCTION

Over the process of evolution, nature has generated a multitude of materials that display excellent mechanical properties, ranging from high rigidity, load-bearing capacity, resistance against the initiation and propagation of fractures, and resistance against unpredictable impacts. Using readily available resources, nature achieves these properties by fine-tuning the internal architecture of the materials, arranging reinforcing elements, such as particles, rods, and platelets, in complex and often hierarchical assemblies. Bone and mother-of-pearl are examples of such hierarchically reinforced materials, whose mechanical properties exceed those of their constituents. Nacre, another name for mother-of-pearl, is the inner lining of pen, oysters and abalone shells, and is composed of 95% of calcium carbonate platelets, in the form of aragonite. Despite aragonite is a brittle constituent, nacre displays a fracture resistance that is two orders of magnitude higher than its monolithic equivalent. This remarkable improvement in fracture resistance is due to the internal arrangement of the platelets, organized in a highly regular and periodic, brick-and-mortar configuration [1]. This structure can deflect incoming cracks on long and tortuous trajectories, dissipating enormous amounts of fracture energy. Over the last decades, efforts have targeted the reproduction, at the laboratory scale, of brick-and-mortar architectures, leveraging

freeze casting,[2], [3] magnetic alignment,[4], [5], [6] and gravitational sedimentation,[7], [8], [9] as means to control the alignment of large aspect ratio reinforcing elements in high-volume fraction nacre-inspired composites. Replicating the internal architecture of biological nacre in synthetic composites, using high-performance ceramics, like alumina or glass, has enabled the design and manufacturing of composites which display a combination of strength, stiffness, and toughness, properties that are often mutually exclusive in manmade materials.[10] Similarly to nacre, the club of the mantis shrimp and cortical bone[11], [12], [13] are other examples of materials that display periodic internal architectures, with their reinforcing elements arranged in Bouligand or in concentric lamellar domains, respectively.

Periodic bioinspired materials have been widely studied and replicated in the laboratories, due to their ease of manufacturing, through particle-assembly methods or additive manufacturing. However, nature does not always resort to highly periodic structures for its structural materials. Trabecular bone[14], [15] and the citrus fruit pericarp[16] are examples of biological structural materials that display a highly irregular, non-periodic internal architecture. Trabecular bone, also called spongy bone, constitutes the highly porous internal portion of our bones. It is formed by trabecular struts and plates, and despite its mechanical properties are highly dependent on its mineral and collagen content, it is critical to transfer stresses to cortical (or compact) bone and to carry loads, while maintaining an overall low weight.[17] Fruit pericarps are instead formidable impact absorbers. When the fruits fall from the tree, citrus fruit pericarps protect the pulp and the seeds, efficiently absorbing impact energy and leaving the fruit intact. Taking inspiration from irregular biological structural materials and replicating their complex structures using higher-performance engineering constituents is extremely relevant, from safety critical applications, where preventing damage from impacts with objects is paramount, to soft robotics and smart skins, where damage avoidance is critical for object manipulation and human-robot interactions.

Unfortunately, replicating the internal structure of an irregular biological material is complex. High-fidelity replication requires microcomputed tomography[18], [19] or investment casting.[20] Stochastic processes, like foaming,[21], [22] prove limited, because they are often unable to imitate the complex internal structure of the biological material, as well as its structural logic. In this context, computational approaches, like tile-based assembly methods and virtual growth algorithms, VGAs, can provide the level of control that is necessary to replicate the irregular arrangement of domains across lengthscales and their spatially varying density, critical aspects when replicating the internal architecture of biological materials.

In this work, I will highlight a VGA-based material design method that recently emerged as a promising platform to replicate non-periodic biological materials and to generate non-periodic reinforcing materials architectures. Starting from the pericarp of an orange, its irregular structure is discretized into a network of tiles, connected through a precise set of connectivity rules, allowing the generation of countless equivalent irregular architectures that display analogous topology, the connectivity between adjacent tiles, and geometry, the shape of the generated domains or mesostructures. The generated materials are then fabricated using additive manufacturing and tested in quasi-static and dynamic compression, with the goal of determining their architecture-to-properties relationship, along with the role of the tiles or of their assembly into mesostructures, on the global and local mechanical response of the materials.

2 METHODS AND RESULTS

2.1 Tile-based Material Generation: Virtual Growth Algorithms

Virtual Growth Algorithms (VGAs) are a powerful platform for materials design and generation that gained significant traction for their ability to develop non-periodic structures and networks through local growth processes, that have been recently exploited for the generation of reinforcing networks in composites and lattices. Introduced by Liu and co-authors, VGAs are graph-based and rely on the assembly of simplified building blocks, or tiles.[23] The assembly of the tiles occurs stochastically over a predefined grid or mesh, following a precise set of connectivity or adjacency rules, paramount to determine the tile-to-tile connections that are allowed or not. The final structure that is generated depends on the geometry and connectivity of the tiles, as well as on their availability and relative connectivity

(Figure 1). These are all inputs that are provided by the user. As a result, VGAs are extremely powerful as they allow to decouple the topology of the network, or its connectivity, and its geometry, emerging from the shape of the chosen tiles. The VGAs developed by Liu and co-authors implemented a *WaveFunctionCollapse* algorithm.[24] The structure gets formed iteratively; the algorithm evaluates eligible sites for growth and selects the location with the minimal nodal entropy for the next tile assignment. For each location, the nodal entropy depends on the total number of tiles that satisfies the connectivity rules. As the structure gets formed, structural features, also called mesostructures, emerge. Preventing the formation of mesostructures that are disconnected from the rest of the network is paramount, and connections that can lead to closed-loops are often forbidden.

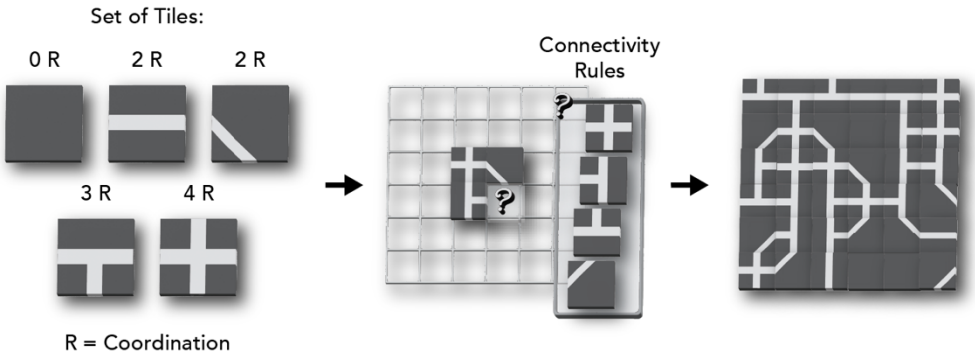

Figure 1: Sketch depicting the virtual growth algorithm and its working principle. Figure adapted from Magrini et al.[25] and Fox et al.[26]

2.2 Bioinspired Materials Generation

2-dimensional cross-sectional microscopy images of the pericarp of an orange were retrieved. The detailed procedure to cut and stain the biological tissues for histological imaging has been carefully reported by Fox and co-authors.[26] Orange pericarps display a density gradient, as they are composed by two primary regions. The external region, called flavedo, is rigid and highly interconnected. The internal region, called albedo, contains large intercellular spaces, that due to their high compressibility are responsible for the great energy absorbing capability of the pericarp (Figure 2).[27], [28]

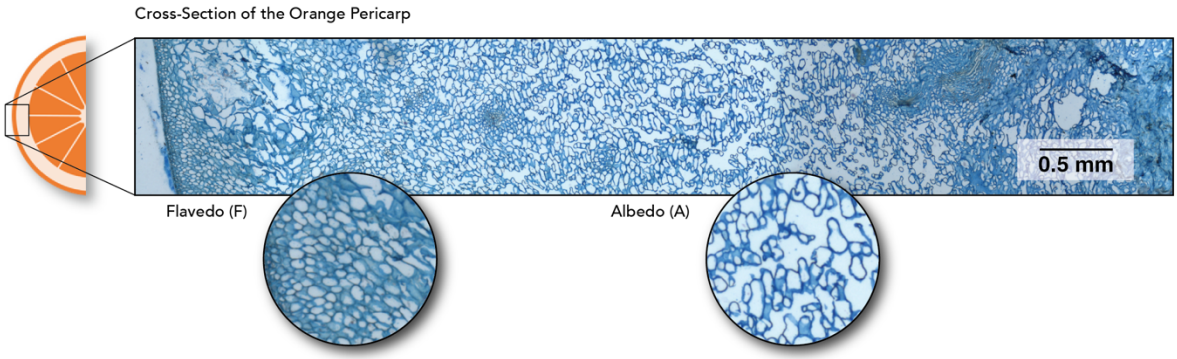

Figure 2: The orange pericarp (cross-sectional view). Microscopy image credits: M. Antonini.

Leveraging the image processing software Fiji,[29] the histological cross-section of the pericarp is first converted into a skeleton,[30] a line with a single pixel thickness. The skeleton is then subdivided into a collection of irregular tiles, using a regular grid. The size of the grid elements is chosen to ensure that no more than one node per element is included (Figure 3a). Despite each tile extracted from the biological material is irregular and different from the neighbouring ones, a conversion must be carried out, with the goal of simplifying the extracted tile into one of the five pre-selected VGA-tiles. This

conversion is performed by analyzing the perimeter of the irregular tiles, and assigning a value to each intersection of the branches with the external perimeter. Using binary code values, 1, 10, 100 and 1000, representing left, top, right and bottom respectively, it is possible to uniquely assign a simplified VGA-tile equivalent to each irregular element extracted from the starting image. Each simplified VGA-tile is defined by its coordination number, the number of connections it forms, and its orientation (Figure 3b).

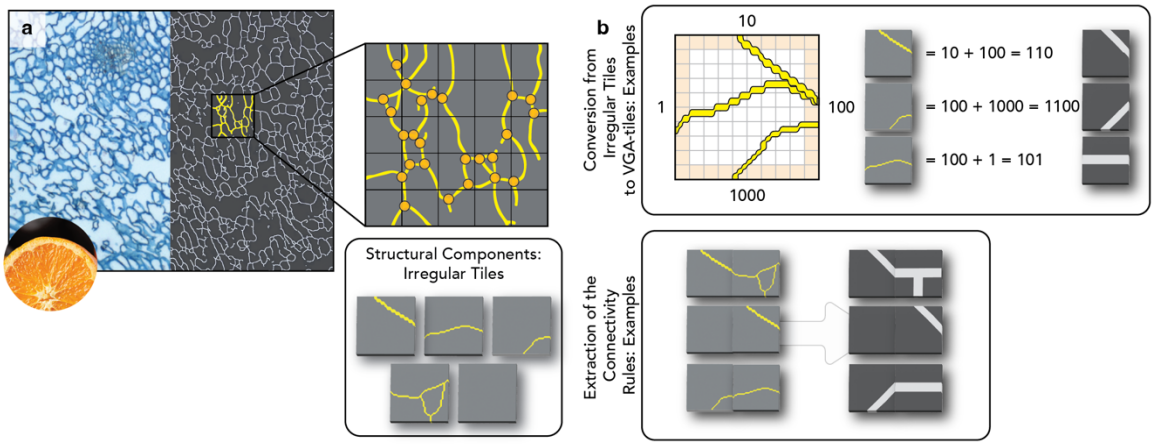

Figure 3: The conversion method. a) Image processing to extract the irregular tiles from the skeletonized image. b) Conversion in simplified VGA-tiles and relative connectivity rules (examples). Figure adapted from Fox et al.[26]

Once all grid elements have been converted into simplified VGA-tiles, the connections between VGA-tiles are analysed, with the goal of determining the connectivity rules that allow the reconstruction of the orange peel. As expected, the composition, intended as the frequency of each simplified VGA-tile, as well as the rules that determine the connectivity between the tiles, both depend on the region of the pericarp that is studied. For example, the flavedo region of the pericarp features a higher frequency of 3- and 4-coordinated tiles than the albedo region. This is representative of the higher density and interconnectivity of the external layer of the pericarp. On the other hand, the albedo region features a higher frequency of empty tiles, due to the presence of larger intercellular spaces in the inner portion of the peel (Figure 4a). Analogous conclusions can be drawn from the extracted connectivity rules. The flavedo-inspired portion features a higher frequency of 3-to-3 coordinated tiles and 3-to-2 coordinated tiles connections than the albedo-inspired portion, while the empty-to-empty tile connections are more representative in the albedo than in the flavedo (Figure 4b).

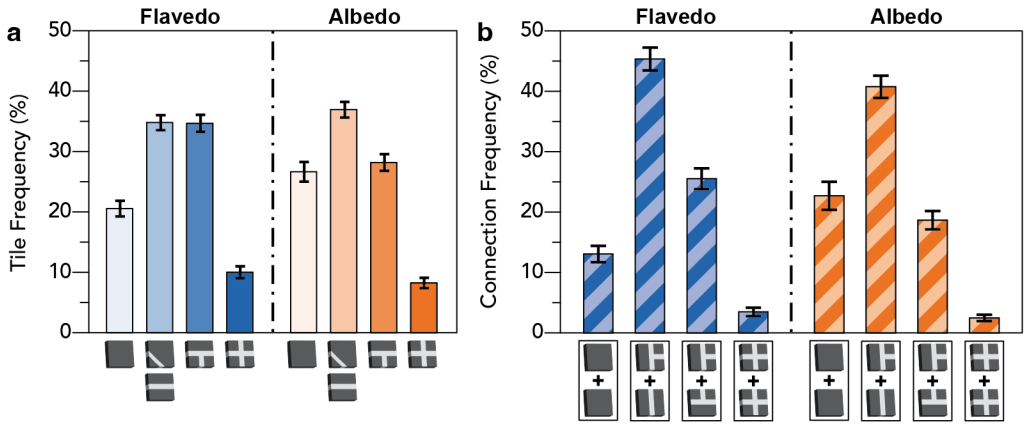

Figure 4: Extracting tile composition and connectivity rules from the orange pericarp. a) Tile frequency. b) Examples of the connectivity rules. Figure adapted from Fox et al.[26]

2.3 Material Fabrication

With the tile frequencies and connectivity rules extracted from the flavedo and albedo portions of the pericarp, the virtual growth algorithm is used to reconstruct flavedo-inspired (F) VGA-samples and albedo-inspired (A) VGA-samples, with a size of 50-by-50 tiles. As the flavedo accounts for 10-20% of the overall peel thickness, and the albedo for the remaining 80-90%, the generated structures are then combined, recreating the full-pericarp (P) VGA-samples (Figure 5). To carry out the mechanical characterization of the structures, samples with a height of 2.5 cm, width of 2.5 cm and thickness of 1.0 cm were manufactured using a polyjet printer (Stratasys Objet500 Connex3), using two commercially available photoresins, Stratasys VeroWhite Polyjet Resin (VW) and Stratasys TangoBlack Polyjet Resin (TB). VW, a stiff viscoelastic polymer, is used for the reinforcing network, while TB, a soft elastomeric polymer, is used for the matrix, filling the gaps within the network. Accounting for the limitation of the polyjet printer, a tile size of 0.5 mm by 0.5 mm was chosen, with individual network struts of 0.1 mm. In this study, contrary to the biological material, generating a two-phase material was preferred, leading to polymer-composite specimens suitable for mechanical testing and for mapping of strains through 2D digital image correlation (DIC). The mechanical properties of the resins used in this study fall within the ranges reported in literature. [31], [32]

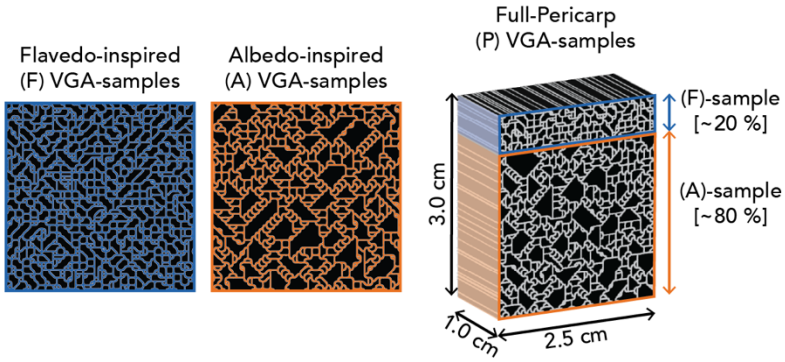

Figure 5: VGA-generated samples: (F), (A), and (P). Flavedo-, Albedo-, and full-Pericarp inspired samples. Figure adapted from Fox et al.[26]

2.4 Quasi-static Mechanical Testing: Compression

Quasi-static mechanical testing was carried out using a universal testing machine (UTS) (Instron E3000, Instron, USA), with a 5kN load cell equipped with flat compression plates, at a rate of 1mm/min and up to a 10% compressive strain. Three set of samples have been tested: flavedo-inspired (F) VGA-samples, albedo-inspired (A) VGA-samples, and full-pericarp (P) VGA-samples. From the stress-strain curves, the modulus of elasticity was extracted. As one could expect from their biological counterparts, the F-samples proved 116% stiffer than the A-samples, while P-samples displayed intermediate values (Figure 6).

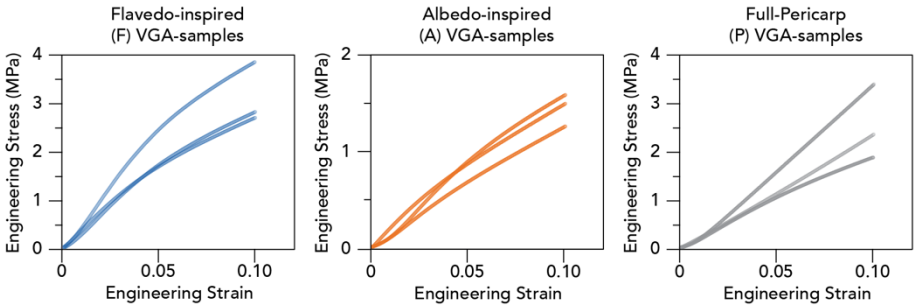

Figure 6: Stress-strain curves recorded on flavedo-inspired (F) VGA-samples (left), albedo-inspired (A) VGA-samples (middle) and full-pericarp (P) VGA-samples (right). Adapted from Fox et al.[26]

To determine the role of local mesostructures (the local domains formed by adjacent VGA-tiles) during compression loading, 2D DIC was performed to track the strain field. The composites were spray painted using a flat white paint and speckled with flat black paint, generating a speckle size of 0.1 to 0.3 mm. Commercially available DIC software (VIC 2D, Correlated Solutions, USA) was used to reconstruct the Lagrangian strain field (subset size 35, step size 2). Through DIC it was possible to elucidate the strain distribution during compressive loading. Up to 10% global compressive strain, F-samples displayed uniform strain fields, without exceeding 15% strain at the local scale (Figure 7a). This is due to the extensive presence of stretching-dominated mesostructures, formed by high-coordination tiles (3- and 4-coordinated tiles). On the contrary, A-samples displayed highly localized strain field, with mesostructures reaching up to 30% local strain, at an applied 10% global compressive strain (Figure 7b). This was observed in large and highly compressible mesostructures, composed of consecutive low-coordination tiles (2-coordinated tiles and empty tiles). These mesostructures often featured concave edges and 2-coordinated tiles arranged diagonally in series, which can rotate, during deformation, around 3-coordinated nodes.

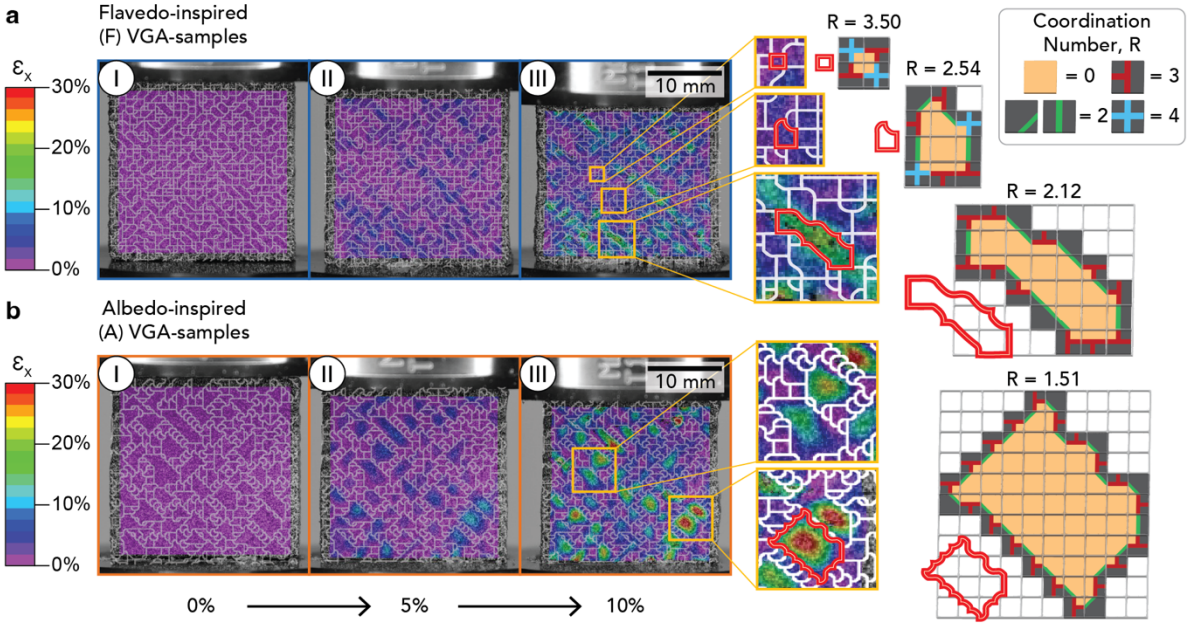

Figure 7: Compression tests. 2D DIC recorded at 0%, 5% and 10% global strain on flavedo-inspired (F) VGA-samples (a) and albedo-inspired (A) VGA-samples (b). Figure adapted from Fox et al.[26]

2.5 Dynamic Mechanical Testing: Compression

Finally, the energy absorption capabilities of the samples were characterized using drop tower tests conducted at a strain rate of ~100 s^{-1}. For the purpose, a drop tower of 3 m height and 2.7 cm inner diameter and a cylindrical striker of 10 cm height, 2.5 cm diameter and a 400 g mass were chosen. The experiments were recorded using a high-speed camera (Phantom v1610, Vision Research, AMETEK, USA), triggered by a photodiode mounted in proximity of the tower's lower opening, set to an acquisition rate of 50k fps at a resolution of 512 pixel by 512 pixel (Figure 8a). Analysing the recorded videos with the image processing software Fiji,[29] the time in contact between the striker and the sample, along with the coefficient of restitution (*e*), defined as the ratio between the velocity of the striker before and after the impact with the sample, were extracted (Figure 8b and 8c). The results were compared to periodic honeycomb (H) and graded honeycomb (gH) samples having the same volume fraction of reinforcing phase. Among all the conducted tests, the flavedo-inspired (F) VGA-samples displayed the highest *e* and the shortest time in contact with the striker. On the other hand, the full-pericarp (P) VGA-samples, similarly to the albedo-inspired (A) VGA-samples, displayed a 7.5% and 10% lower *e* than the H- and gH-samples respectively. In parallel to a lower coefficient of restitution,

(P)- and (A) VGA-samples display a 16% and 25% longer time in contact with the striker with respect to H- and gH-samples, respectively. Such a striking difference in energy absorption performance is due to the reinforcing architecture of the materials. There is indeed a correlation between the mesostructures size and shape, and the deformation they are subjected to during compressive loading. For example, the presence of large, concave mesostructures formed by low coordination tile assemblies, often observed in the albedo-inspired (A) VGA-samples (and therefore in the full-pericarp (P) VGA-samples), leads to less constrained strut bending and buckling. These mechanisms of deformation, already observed in the quasi-static compression loading tests, are analogous to what is observed in the biological material counterpart, where large and compressible intercellular spaces in the orange albedo are responsible of dissipating most of the energy caused by unpredictable impacts, like when the fruit falls from the tree.

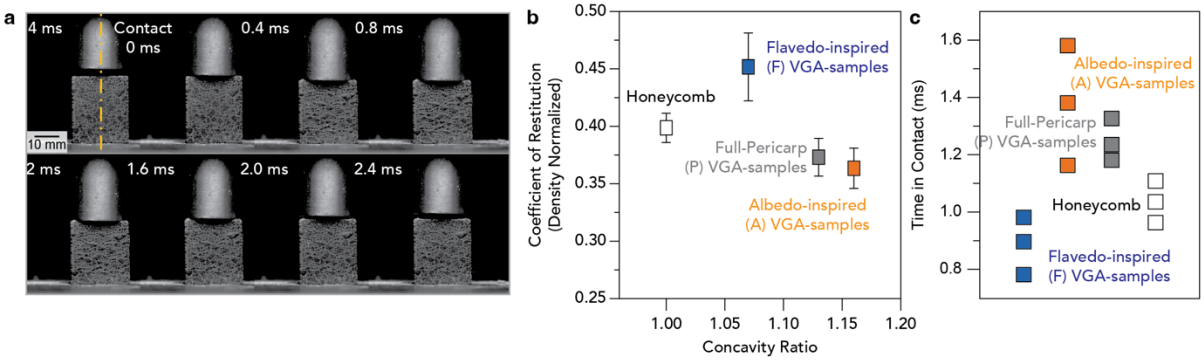

Figure 8: a) time-lapse of the striker impact on a full-pericarp (P) VGA-sample. b) The measured coefficient of restitution. c) The recorded time in contact. Figure adapted from Fox et al.[26]

3 CONCLUSIONS

In summary, using computer-aided tile-based material design methods, it is possible to extract the topology and the geometry of irregular biological materials, like the pericarp of an orange, and recreate their structure-to-properties relationship in bioinspired equivalents. The bioinspired structures are fabricated using multi-material additive manufacturing and tested in quasi-static and dynamic compression. Using DIC and image analysis, it is possible to analyze the mechanisms of deformation that occur at the local scale, correlate them to the global mechanical performance of the materials and to the mesostructures that emerge during sample generation.

ACKNOWLEDGEMENTS

T.M. thanks the co-authors of the articles Adv. Mater. 2024, 36, 2305198 and Adv. Mater. 2024, 36, 2405567 upon which this conference proceeding entry is based upon.

REFERENCES

[1] T. Magrini, F. Bouville, and A. R. Studart, “Transparent materials with stiff and tough hierarchical structures,” *Open Ceramics*, vol. 6, Jun. 2021, doi: 10.1016/J.OCERAM.2021.100109.

[2] E. Munch, M. E. Launey, D. H. Alsem, E. Saiz, A. P. Tomsia, and R. O. Ritchie, “Tough, bio-inspired hybrid materials,” *Science*, vol. 322, no. 5907, pp. 1516–1520, Dec. 2008, doi: 10.1126/SCIENCE.1164865.

[3] F. Bouville, E. Maire, S. Meille, B. Van De Moortèle, A. J. Stevenson, and S. Deville, “Strong, tough and stiff bioinspired ceramics from brittle constituents,” 2014, doi: 10.1038/NMAT3915.

[4] M. Grossman, F. Bouville, F. Erni, K. Masania, R. Libanori, and A. R. Studart, “Mineral Nano-Interconnectivity Stiffens and Toughens Nacre-like Composite Materials,” *Advanced Materials*, vol. 29, no. 8, 2017, doi: 10.1002/adma.201605039.

[5] R. M. Erb, R. Libanori, N. Rothfuchs, and A. R. Studart, "Composites reinforced in three dimensions by using low magnetic fields," *Science (1979)*, vol. 335, no. 6065, pp. 199–204, Jan. 2012, doi: 10.1126/SCIENCE.1210822/SUPPL_FILE/ERB.SOM.PDF.

[6] H. Le Ferrand, F. Bouville, T. P. Niebel, and A. R. Studart, "Magnetically assisted slip casting of bioinspired heterogeneous composites," *Nat Mater*, vol. 14, no. 11, pp. 1172–1179, 2015, doi: 10.1038/nmat4419.

[7] T. Magrini, F. Bouville, A. Lauria, H. Le Ferrand, T. P. Niebel, and A. R. Studart, "Transparent and tough bulk composites inspired by nacre," *Nat Commun*, vol. 10, no. 1, Dec. 2019, doi: 10.1038/s41467-019-10829-2.

[8] T. Magrini, S. Moser, M. Fellner, A. Lauria, F. Bouville, and A. R. Studart, "Transparent Nacre-like Composites Toughened through Mineral Bridges," *Adv Funct Mater*, vol. 30, no. 27, Jul. 2020, doi: 10.1002/adfm.202002149.

[9] T. Magrini, F. Bouville, and A. R. Studart, "Transparent materials with stiff and tough hierarchical structures," *Open Ceramics*, vol. 6, Jun. 2021, doi: 10.1016/j.oceram.2021.100109.

[10] R. O. Ritchie, "The conflicts between strength and toughness," *Nature Materials 2011 10:11*, vol. 10, no. 11, pp. 817–822, Oct. 2011, doi: 10.1038/nmat3115.

[11] E. A. Zimmermann, B. rn Busse, and R. O. Ritchie, "The fracture mechanics of human bone: influence of disease and treatment," *Bonekey Rep*, vol. 4, p. 743, 2015, doi: 10.1038/bonekey.2015.112.

[12] T. Magrini, R. Libanori, A. Kan, and A. R. Studart, "Complex Materials: The Tough Life of Bone," *Revista Brasileira de Ensino de Fisica*, vol. 43, pp. 1–17, 2021, doi: 10.1590/1806-9126-RBEF-2020-0438.

[13] M. E. Launey, M. J. Buehler, and R. O. Ritchie, "On the mechanistic origins of toughness in bone," *Annu Rev Mater Res*, vol. 40, no. Volume 40, 2010, pp. 25–53, Aug. 2010, doi: 10.1146/ANNUREV-MATSCI-070909-104427/CITE/REFWORKS.

[14] W. J. Whitehouse, "The quantitative morphology of anisotropic trabecular bone," *J Microsc*, vol. 101, no. 2, pp. 153–168, 1974, doi: 10.1111/J.1365-2818.1974.TB03878.X.

[15] W. J. Whitehouse and E. D. Dysont, "Scanning electron microscope studies of trabecular bone in the proxinal end of the human femur," 1974.

[16] M. Jentzsch, V. Albiez, T. C. Kardamakis, and T. Speck, "Analysis of the peel structure of different Citrus spp. via light microscopy, SEM and μCT with manual and automatic segmentation," *Soft Matter*, vol. 20, no. 12, pp. 2804–2811, Mar. 2024, doi: 10.1039/D3SM01511D.

[17] R. Oftadeh, M. Perez-Viloria, J. C. Villa-Camacho, A. Vaziri, and A. Nazarian, "Biomechanics and Mechanobiology of Trabecular Bone: A Review," *J Biomech Eng*, vol. 137, no. 1, p. 0108021, Jan. 2015, doi: 10.1115/1.4029176.

[18] A. Mao, N. Zhao, Y. Liang, and H. Bai, "Mechanically Efficient Cellular Materials Inspired by Cuttlebone," *Advanced Materials*, vol. 33, no. 15, p. 2007348, Apr. 2021, doi: 10.1002/ADMA.202007348

[19] N. Kumar *et al.*, "Mimicking high strength lightweight novel structures inspired from the trabecular bone microarchitecture," *Philosophical Transactions of the Royal Society A: Mathematical, Physical and Engineering Sciences*, vol. 378, no. 2167, Mar. 2020, doi: 10.1098/RSTA.2019.0448,.

[20] S. F. Fischer *et al.*, "Pummelos as concept generators for biomimetically inspired low weight structures with excellent damping properties," *Adv Eng Mater*, vol. 12, no. 12, pp. B658–B663, Dec. 2010, doi: 10.1002/ADEM.201080065

[21] J. A. Carpenter *et al.*, "Hierarchical Porous Monoliths of Steel with Self-Reinforcing Adaptive Properties," *Advanced Materials*, vol. 35, no. 10, p. 2207181, Mar. 2023, doi: 10.1002/ADMA.202207181.

[22] M. Bianchi, F. Scarpa, and C. W. Smith, "Shape memory behaviour in auxetic foams: Mechanical properties," *Acta Mater*, vol. 58, no. 3, pp. 858–865, Feb. 2010, doi: 10.1016/J.ACTAMAT.2009.09.063.

[23] K. Liu, R. Sun, and C. Daraio, "Growth rules for irregular architected materials with programmable properties," *Science*, 2022, [Online]. Available: https://www.science.org

[24] I. Karth and A. M. Smith, “WaveFunctionCollapse: Content Generation via Constraint Solving and Machine Learning,” *IEEE Trans Games*, vol. 14, no. 3, pp. 364–376, Sep. 2022, doi: 10.1109/TG.2021.3076368.
[25] T. Magrini, C. Fox, A. Wihardja, A. Kolli, and C. Daraio, “Control of Mechanical and Fracture Properties in Two-Phase Materials Reinforced by Continuous, Irregular Networks,” *Advanced Materials*, p. 2305198, 2023, doi: 10.1002/ADMA.202305198.
[26] C. Fox, K. Chen, M. Antonini, T. Magrini, and C. Daraio, “Extracting Geometry and Topology of Orange Pericarps for the Design of Bioinspired Energy Absorbing Materials,” *Advanced Materials*, Jul. 2024, doi: 10.1002/ADMA.202405567.
[27] M. Jentzsch, M. C. Badstöber, F. Umlas, and T. Speck, “Damage protection in fruits: Comparative analysis of the functional morphology of the fruit peels of five Citrus species via quasi-static compression tests,” *Front Mater*, vol. 9, p. 979151, Dec. 2022, doi: 10.3389/FMATS.2022.979151/BIBTEX.
[28] M. Jentzsch, S. Becker, M. Thielen, and T. Speck, “Functional Anatomy, Impact Behavior and Energy Dissipation of the Peel of Citrus × limon: A Comparison of Citrus × limon and Citrus maxima,” *Plants 2022, Vol. 11, Page 991*, vol. 11, no. 7, p. 991, Apr. 2022, doi: 10.3390/PLANTS11070991.
[29] J. Schindelin *et al.*, “Fiji: An open-source platform for biological-image analysis,” *Nat Methods*, vol. 9, no. 7, pp. 676–682, 2012, doi: 10.1038/nmeth.2019.
[30] I. Arganda-Carreras, R. Fernández-González, A. Muñoz-Barrutia, and C. Ortiz-De-Solorzano, “3D reconstruction of histological sections: Application to mammary gland tissue,” *Microsc Res Tech*, vol. 73, no. 11, pp. 1019–1029, 2010, doi: 10.1002/JEMT.20829,.
[31] J. Ryan, C. Dizon, A. H. Espera, Q. Chen, and R. C. Advincula, “Mechanical characterization of 3D-printed polymers,” *Addit Manuf*, vol. 20, pp. 44–67, 2018, doi: 10.1016/j.addma.2017.12.002.
[32] D. Bell and T. Siegmund, “3D-printed polymers exhibit a strength size effect,” *Addit Manuf*, vol. 21, pp. 658–665, May 2018, doi: 10.1016/J.ADDMA.2018.04.013.

SILICA-EPOXY INTERFACES IN BICONTINUOUS NANOCOMPOSITES

Charles M. D. Shaw[1], David B. Anthony[1], Ian Hamerton[2], Milo S. P. Shaffer[1]

[1] Department of Chemistry, Imperial College London, London, UK
c.shaw20@imperial.ac.uk

[2] Department of Chemistry, Imperial College London, London, UK
d.anthony08@imperial.ac.uk, https://www.imperial.ac.uk/people/d.anthony08

[3] Bristol Composites Institute, University of Bristol, Bristol, UK
ian.hamerton@bristol.ac.uk, https://research-information.bris.ac.uk/en/persons/ian-hamerton

[4] Department of Chemistry and Department of Materials,
Imperial College London, London, UK
m.shaffer@imperial.ac.uk, https://www.imperial.ac.uk/people/m.shaffer

Keywords: Nano-structures, 3-Dimensional reinforcement, Interface, Micro-mechanics, Hardness

ABSTRACT

In classic discontinuous silica-epoxy nanocomposites, strong matrix-reinforcement interactions may enhance toughness by introducing new energy absorption mechanisms. These silica-epoxy interactions are mediated either directly through inherent silica silanol groups or *via* tethering of reactive amine or epoxide groups. Recently, bicontinuous silica-epoxy nanocomposites have been formed by backfilling monolithic silica aerogel with epoxy resin. The continuous reinforcement network provides long-range load transfer, inherently uniform silica distribution, and synergistic interlocking effects. When preparing these nanocomposites, the silica aerogel is typically hydrophobised to prevent moisture absorption which can lead to shrinkage or cracking prior to backfilling. However, the aggressive reagents used (typically trimethylchlorosilane,TMCS) give almost complete conversion of silanol groups, leading to an inert surface which forms only very weak interactions with epoxy resin. Under shear loading, this poor interface leads to brittle failure at relatively low strain. Mild hydrophobisation agents such as dimethyldimethoxysilane (DMDMS), instead give incomplete conversion of silanols to yield a "part-methylated" surface which, while providing some hydrophobic character, forms a stronger silica-epoxy interface. Furthermore, as it does not form acidic byproducts, which would otherwise catalyse ring opening, DMDMS may be used alongside (3-glycidyloxypropyl)trimethoxysilane (GPTMS) to give a "part methylated + epoxidated" surface. Across a broad range of silica aerogel densities, both surface types give significantly lower moisture content ("part methylated" ≈ 2.6 wt.%, "part methylated + epoxidated" ≈ 1.4 wt.%) when compared with unmodified silica aerogel (≈ 9.8 wt.%). These values are greater than those of TMCS-methylated silica aerogel, however, in contrast to unmodified silica aerogel, uncracked monoliths are formed in all cases.

1 INTRODUCTION

For unidirectional carbon fibre composites (UD CFRPs), conventional polymer matrices provide insufficient shear support against fibre micro-buckling in compression. Consequently, the compressive strength of UD CFRPs is typically less than 60% of their tensile strength. Commercial nanosilica reinforcements improve matrix shear strength and modulus leading to enhanced fibre composite compressive strength [1]. These nanocomposite matrices typically contain dispersed discontinuous nanofillers with no direct load transfer within the reinforcement phase. Furthermore, above very modest loadings (6 SiO_x vol.%) nanofiller agglomeration leads to decreased compressive performance in unidirectional fibre composites. Bicontinuous nanocomposites feature a macroscopically continuous reinforcement which interlocks with the matrix phase to give synergistic mechanical property enhancement [2]. Silica-epoxy bicontinuous nanocomposites have been formed with loadings of up to 10 SiO_x vol.% by backfilling a continuous silica reinforcement (silica aerogel) with epoxy resin [3]. These novel materials display distinct super-linear power law loading-property relationships owing to fractal branching of the silica network. In contrast, the equivalent trends for discontinuous nanocomposites are distinctly linear or sub-linear [4-6]. At present, modulus enhancement in silica-epoxy bicontinuous nanocomposites is curtailed by low reinforcement loadings and a weak matrix-reinforcement interface. To aid aerogel processing (decreased network shrinkage and moisture absorption), reinforcement networks were previously formed with fully-methylated surfaces. However, this functionalisation precludes covalent bonding at the matrix-reinforcement interface. In particulate systems, specimens with inert interfaces have significantly worse strength, stiffness and toughness *vs*. otherwise-equivalent specimens with covalently-bound interfaces [7]. Commercial discontinuous nanosilica reinforcements feature reactive surface silanol groups for improved toughness through strong covalent bonding with the epoxy resin matrix [8, 9]. Here, novel part-methylated silica aerogel surface chemistries are developed to balance the processing benefits of methylation with the superior mechanical properties of reactive surfaces.Two new surface types are introduced: “part-methylated” and “part-methylated + epoxidated” (Figure 1). The former features reactive silanol groups while the latter has silanols and additional tethered epoxide groups. Both surfaces were partially methylated with dimethyldimethoxysilane (DMDMS), a mild methylating agent. Unlike trimethylchlorosilane (TMCS) – a classic methylating agent for silica aerogel, DMDMS produces no acidic byproducts and is therefore well-suited for co-functionalisation in the presence of acid-sensitive epoxide groups. Synthesis of the silica skeleton is described in [10]. To confirm compatibility with a range of silica content, the tetramethylorthosilicate (TMOS) volume fraction in the sol-gel precursor was varied for measurement of aerogel physical properties relevant to epoxy backfilling.

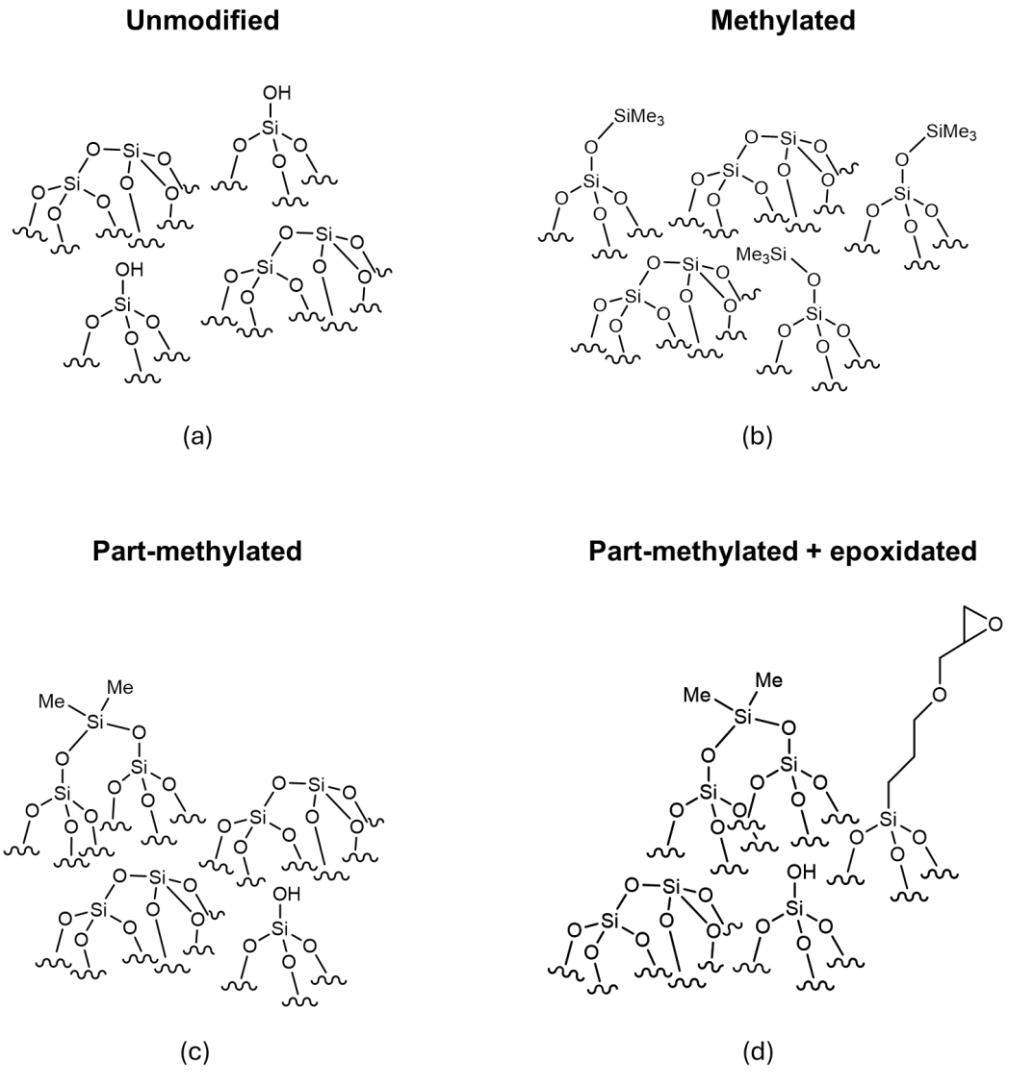

Figure 1. Chemical structures of silica aerogel surfaces discussed in this paper.

2 SURFACE MODIFICATION METHODS

Part-methylated and part-methylated + epoxidated silica aerogel monoliths were formed by functionalisation of TMOS-derived wet silica gel monoliths. Cylindrical monoliths (d = 6 mm, l = 15 mm) were prepared by stirring the appropriate mixture of TMOS, water and ethanol (TMOS volume fraction, φ_{TMOS} = 0.23) for 3 h at 25 °C before transfer of the liquid sol to high density polyethylene moulds [3]. After gelation, samples were aged in the supernatant for 4 days at room temperature to consolidate the silica network through increased inter-particle crosslinking. After demoulding, samples were transferred to ethanol prior to functionalisation. After functionalisation, samples were exchanged first into ethanol and then acetone before drying. Samples were dried from supercritical CO_2 to minimise the capillary forces that drive pore collapse and overall sample shrinkage. Infra-red spectroscopy was used to identify surface-bound groups. All IR spectra are normalised to the transmittance of the largest Si-O-Si (siloxane) signal (1050 cm^{-1} – 1080 cm^{-1}) at an arbitrary transmittance (T) value of T = 64.2. This signal has been chosen as it represents the bulk amorphous silica (SiO_x) only and hence will not change as a result of new siloxane linkages formed during surface modification [11]. Consequently, by

using the same feedstock aerogel, intensities of all other relevant signals may be compared semi-quantitatively between candidate surfaces to contrast relative loadings of various surface groups.

Table 1. IR signals relevant to the functionalisation of silica aerogel surfaces [11].

Bond	Si-O-H	Si-C-H	Si-O-Si	Si-O-C-H	Epoxide
Wavenumber [cm^{-1}]	3300 – 3500 (*O-H stretch*)	2975 (*C-H stretch*)	1080 (*stretch*)	2855 (*C-H stretch*)	910 *(asymm. Stretch)*
	950 (*Si-O stretch*)	1250 (*Si-C-H bend*)	800 (*bend*)		
		840 (*Si-C stretch*)	455 (*rocking*)		
		755 (*Si-C stretch*)			

To achieve a part-methylated + epoxidated surface, a simultaneous functionalisation reaction was trialled using the mild methylating agent DMDMS. This reagent replaces TMCS which was found to catalyse epoxide ring opening by releasing HCl during grafting [12]. Functionalisation solutions were prepared by first, separately hydrolysing GPTMS and DMDMS (1 $mol.dm^{-3}$) in an ethnanol-water mixture (n_{water}/n_{silane} = 1.33). Solutions were then combined in various volume ratios to vary the relative silane concentrations. The mole fraction of GPTMS out of the total number of moles of silane (χ_{GPTMS}) is used when discussing the effect of functionalisation solution on aerogel properties. Functionalisation was performed by immersing wet silica gel monoliths in functionalisation solution for 48 h at 65 °C. 50 mL of functionalisation solution was used for every 4 mL of wet silica gel. Samples were then exchanged to acetone *via* ethanol and dried by critical point drying (CPD). Relative intensity (decreased transmittance) of the 910 cm^{-1} (epoxide) signal increases with increasing χ_{GPTMS} (Figure 2 (a)). This relative intensity is quantified as the difference in transmittance between the Si-alkyl (850 cm^{-1}) and epoxide (910 cm^{-1}) signals ($\Delta T_{850\ cm^{-1} - 910\ cm^{-1}}$) (b)). A greater value of $\Delta T_{850\ cm^{-1} - 910\ cm^{-1}}$ indicates a greater degree of GPTMS grafting relative to methylating agent (DMDMS) grafting. The systematic change in relative intensity of these two signals with functionalisation solution composition shows that both 3-(glycidyloxypropyl)silyl (GPS) and dimethylsilyl (DMS) residues are bound to the surface. A constant ratio would indicate that only GPS residues were bound. $\Delta T_{850\ cm^{-1} - 910\ cm^{-1}}$ increases sharply with GPTMS content before levelling off. This gradient decrease commences between χ_{GPTMS} = 6 mol.% and χ_{GPTMS} = 13 mol.%. DMDMS should bind to the surface more rapidly than GPTMS due to its smaller steric bulk. At χ_{GPTMS} = 38 mol.% $\Delta T_{850\ cm^{-1} - 910\ cm^{-1}}$ approaches the value seen for the χ_{GPTMS} = 100 mol.% sample, hence, in this range of GPTMS content, GPS residues dominate the grafting. This dominance may result from the ability of a single GPS residue to prevent binding of DMDMS at a relatively large number of neighbouring silanol sites due to the large steric bulk (relatively large radius of gyration) of its longer chain. The trend in specimen shrinkage with χ_{GPTMS} approximately follow the $\Delta T_{850\ cm^{-1} - 910\ cm^{-1}}$ trend (Figure 2 (b)). Uncracked monoliths were formed with functionalisation solutions containing up to and including χ_{GPTMS} = 21 mol.% (Figure 2 (c)). Beyond this value, the capillary pressures associated with moisture absorption caused specimen disintegration. The χ_{GPTMS} = 6 mol.% functionalisation solution composition was selected for further study due to its relatively high $\Delta T_{850\ cm^{-1} - 910\ cm^{-1}}$ and relatively low shrinkage. Silica aerogel formed with a DMDMS-only functionalisation solution is also a suitable candidate reinforcement as it produces uncracked "part-methylated" monoliths bearing reactive silanol groups.

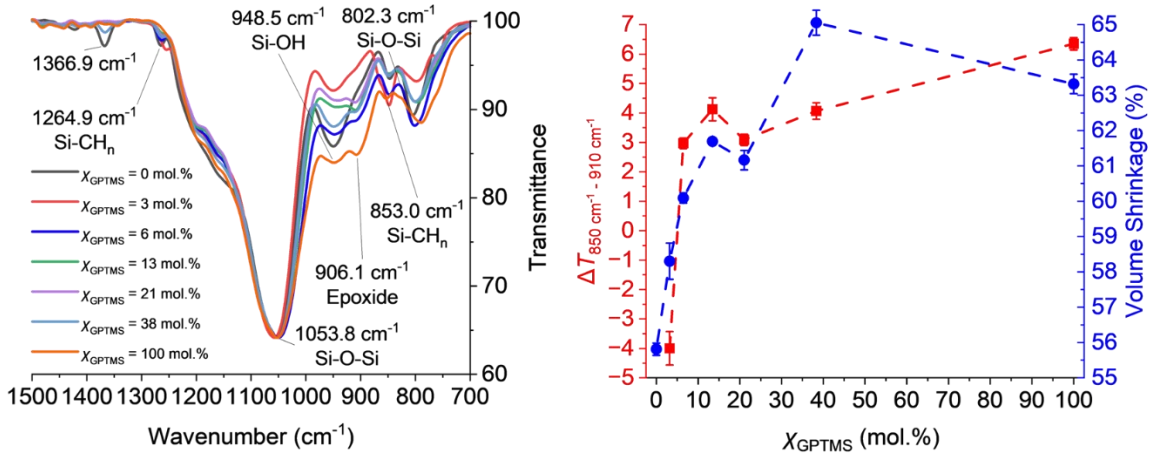

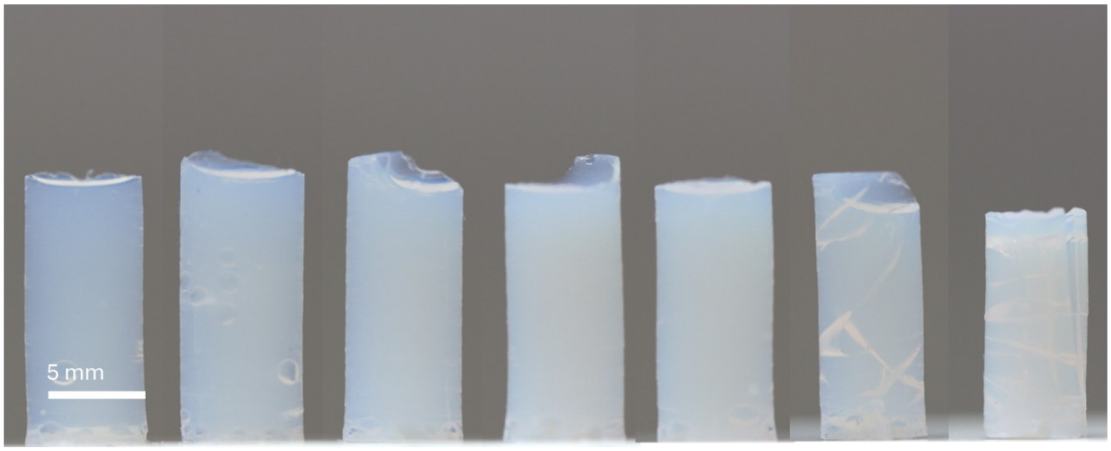

(c)

Figure 2. (a) Overlaid IR spectra for silica aerogel monoliths formed after treatment with functionalisation solutions containing varying ratios of DMDMS and GPTMS. (b) Volume shrinkage and difference in transmittance ($\Delta T_{850\ cm^{-1}-910\ cm^{-1}}$) between IR signals at 850 cm-1 and 910 cm-1 plotted against χ_{GPTMS} for silica aerogel monoliths formed after treatment with functionalisation solutions containing varying ratios of DMDMS and GPTMS. (c) Silica aerogel monoliths formed after treatment with functionalisation solutions containing varying ratios of DMDMS and GPTMS. From left to right: χ_{GPTMS} = 0 mol.%, χ_{GPTMS} = 3 mol.% , χ_{GPTMS} = 6 mol.%, χ_{GPTMS} = 13 mol.%, χ_{GPTMS} = 21 mol.%, χ_{GPTMS} = 38 mol.%, χ_{GPTMS} = 100 mol.%. For (b) bars show one standard error.

3 PHYSICAL PROPERTIES OF FUNCTIONALISED AEROGEL

This section investigates the application of part-methylated and part-methylated + epoxidated functionalised surfaces to silica aerogel of varying silica content and provides a detailed discussion of physical properties. Silica content was controlled by varying sol-gel precursor TMOS volume fraction (φ_{TMOS}) in the range of $0.15 > \varphi_{TMOS} > 0.41$. For each φ_{TMOS} value, four surface types (methylated, unmodified, part-methylated, and part-methylated + epoxidated) were prepared from a single batch of monolithic wet silica gel. Therefore, prior to functionalisation, the primary structure should be identical for each surface type at a given φ_{TMOS}. . Thermogravimetric analysis (TGA) is used to quantify the moisture content of these mildly-hydrophilic aerogels to determine how this content varies between

different surface functionality and pore characteristics. This moisture content is also used to renormalise mass-dependent properties to the actual silica aerogel mass after moisture removal. Mass loss from silica aerogel is also given by renormalisation of the mass loss at 150 °C, which is the temperature at which removal of physisorbed water is observed to be complete. However, these TGA data give only a semi-quantitative measure of the quantity of surface-bound groups for two reasons: Firstly, the Si atoms of surface-bound residue remain bound to the silica surface as Si-O bonds are not broken in this temperature range and consequently only the organic components are removed (as methane or methanol in the case of TMS or DMS residues) [13]. Secondly, above 200 °C silanol groups will undergo condensation to form new siloxane linkages resulting in loss of water which increases the overall mass loss. Consequently, TGA dry mass loss values are compared only in terms of their relative magnitudes for each surface type at a given φ_{TMOS} [14]. The various samples synthesised for this study are identified by their φ_{TMOS} and surface type (Figure 1). Surface-bound groups are identified by the following names: TMS (from TMCS), silanol (Si-OH), methoxy (residual methoxy groups in unmodified silica aerogel), DMS (from DMDMS), and GPS (from GPTMS). The structures of these surface-bound groups are shown in Figure 3.

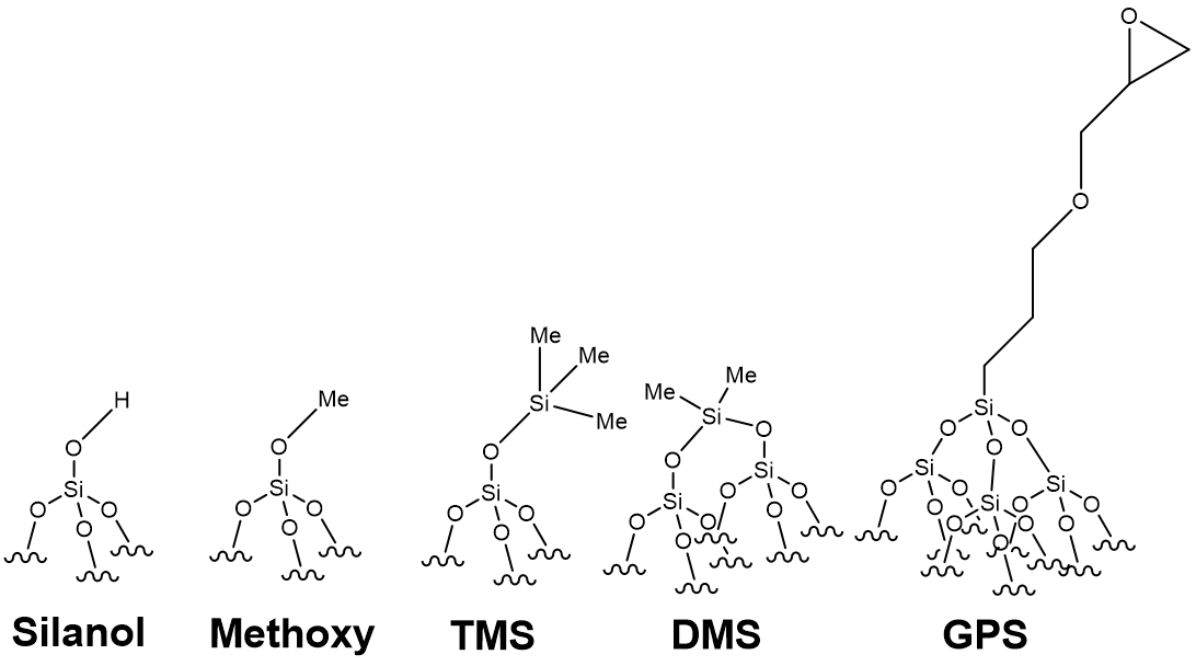

Figure 3. Chemical structures of surface-bound groups. TMS = trimethylsilyl, DMS = dimethylsilyl, GPS = (3-glycidyloxypropyl)silyl.

Density and porosity

Envelope densities were measured by mass and volume measurement due to the incompatibility of hydrophilic porous materials with Archimedes' density measurement in water. However, due to the high precision of the balance and callipers used, repeat measurement yielded low uncertainties. For each surface type, envelope density generally increases with increasing φ_{TMOS}. Methylated aerogel shows a reasonably-linear envelope density trend and is a good match for the TMOS-water aerogel reported previously [3]. The trends for the other three surfaces are far less linear and are shifted to higher densities relative to the methylated surface due to greater volume shrinkage (Figure 4 (b)). Although the shrinkage of the unmodified aerogel (at any φ_{TMOS}) is greater than that of the part methylated + epoxidated aerogel, the unmodified aerogel has the lower envelope density. This difference is due to the significantly greater relative surface-bound mass fraction of the part-methylated + epoxidated aerogel due to the large

molecular mass of the GPS chains. The skeletal densities of methylated silica aerogel agree with TMOS-water aerogel reported previously for $\varphi_{TMOS} > 0.2$ [3]. These skeletal densities are significantly lower than the density of amorphous silica (2.3 $g.cm^{-3}$) due to the contribution of the low-density TMS surface coating [15]. However, at lower values of φ_{TMOS}, the skeletal density increases sharply. This increase is indicative of a lower contribution of the low density TMS surface to the overall skeletal density. This lower contribution results from the decreased specific surface area of the particles due to the significantly slower gelation kinetics at lower [TMOS] (lower φ_{TMOS}) which leads to a smaller TMS volume fraction. From literature, the surface loading of these alkoxy groups is approximately 3.5 nm^{-2} [14, 16]. Skeletal densities of unmodified silica aerogel are an excellent match for literature values for neutral unmodified TMOS aerogel (1.8 $g.cm^{-3}$ – 1.9 $g.cm^{-3}$) [17]. Despite the lack of intentional surface modification, this skeletal density is still lower than the density of amorphous silica (2.3 $g.cm^{-3}$) due to the presence of residual surface alkoxy groups resulting from incomplete precursor hydrolysis. From literature, alkoxy surface loading is approximately 2.4 nm^{-2} [14]. In surface-modified silica aerogels, these methoxy groups are displaced during grafting reactions. The skeletal densities of part-methylated, and part-methylated + epoxidated silica aerogel are intermediate between the unmodified and methylated silica aerogels. These relative skeletal densities imply that the surface-bound loading of these samples fall between the surface-bound loadings of unmodified and methylated aerogel. The greater molar volume of the GPS residues vs. DMS residues cancels out their greater mass leading to no net change in skeletal density vs. the part-methylated surface (Figure 4 (c)).

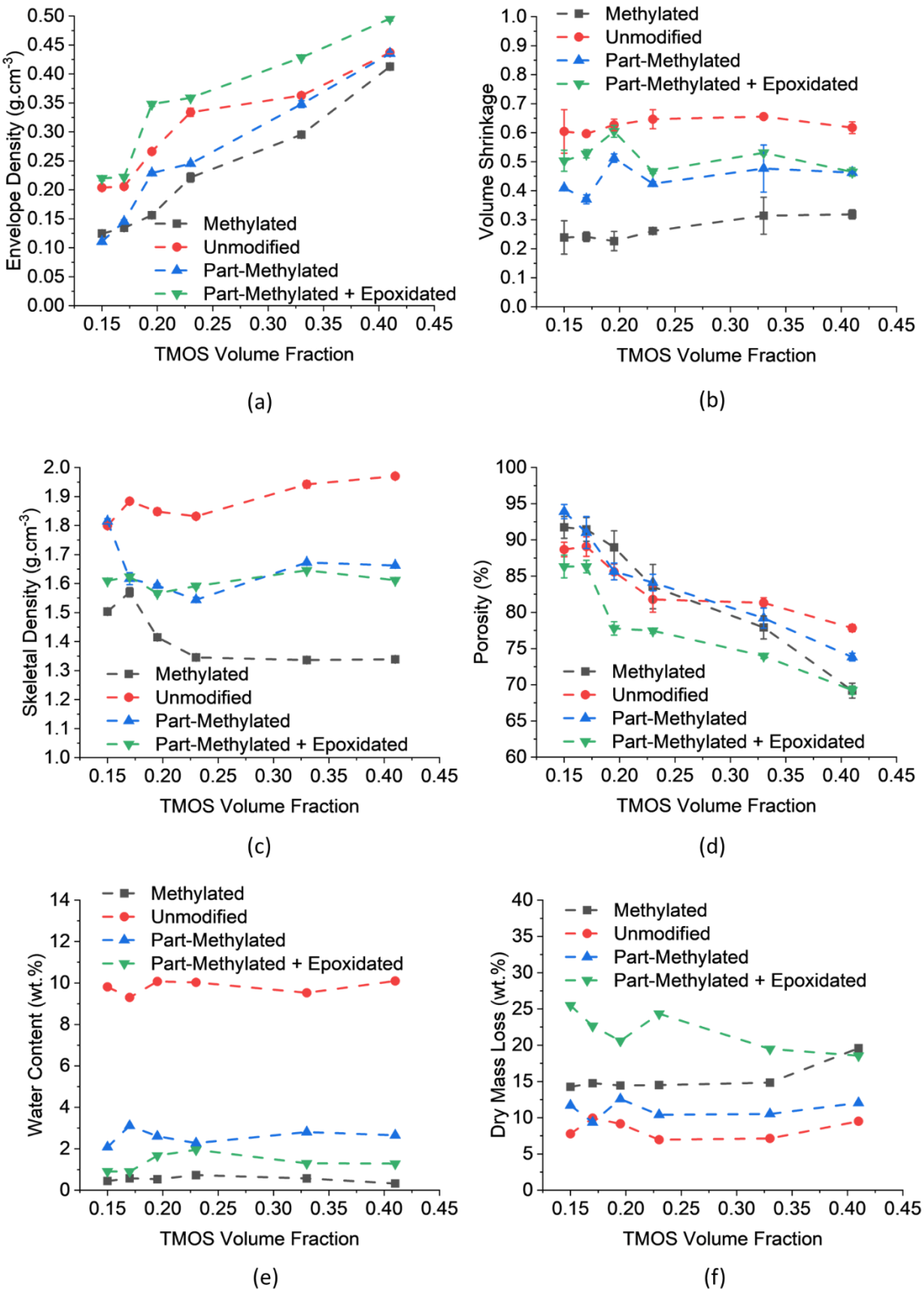

Figure 4 (a) Envelope density (Archimedes method), (b) volume shrinkage, (c) skeletal density (AccuPyc), (d) porosity (calculated from envelope and skeletal densities), (e) water content (TGA), and (f) Mass loss (TGA) of dry silica aerogel monoliths with various surface types plotted against aerogel precursor TMOS volume fraction. Bars show one standard error.

Thermogravimetric analysis

The water content of aerogel monoliths was measured by TGA (Figure 4 (e)). This water content is calculated from the mass loss at the first TGA first derivative minimum. This minimum occurs in the range of 100 °C – 150 °C. Water content is lowest (≈ 0.5 wt.%) for methylated specimens and highest for unmodified specimens (≈ 9.8 wt.%) reflecting their respective superhydrophobicity and hydrophilicity (Figure 5). Accordingly, the water content of the part-methylated aerogel is intermediate of these values (≈ 2.6 wt.%). Interestingly, the water content of part-methylated + epoxidated aerogels is consistently around half that of their part-methylated counterparts (≈ 1.4 wt.%). Decreased water absorbance indicates that binding of GPS residues has a net hydrophobising effect on the aerogel surface which is likely due to the replacement of three highly hydrophilic silanol groups with a single less hydrophilic epoxide group during tripodal binding of GPS. This finding helps justify the choice of GPTMS over hydrophilic (3-aminopropyl)triethoxysilane (APTES) as a linking group. This water content is similar to that reported for GPTMS-functionalised particulate nanosilica (0.7 wt.% – 1.1 wt.%) [18]. Methylated specimens formed from precursors with $\varphi_{TMOS} = 0.15$ to $\varphi_{TMOS} = 0.33$ have similar TGA first derivative profiles with a large mass loss event centred at 360 °C which overlaps with a secondary mass loss event centred at 480 °C (Figure 5 (a)). Decomposition of silica-bound TMS residues is known to produce methane and methanol by methyl displacement in this temperature range [13]. For $\varphi_{TMOS} = 0.41$, the positions of maxima are shifted slightly. However, most organic decomposition still occurs in the range of 300 °C – 600 °C. For $\varphi_{TMOS} = 0.33$ and $\varphi_{TMOS} = 0.41$ a third mass loss event is seen at 730 °C. $\varphi_{TMOS} = 0.17$ is the only sample which has an additional mass loss event at 640 °C. These higher temperature decomposition events are the result of Si-C homolysis. It is not understood why these further events are only seen for these three specimens. The mass loss at 200 °C is due to condensation of surface silanol groups and the resulting water loss. This condensation is most significant for higher φ_{TMOS} values where the lower porosity likely generates a greater number of silanol groups inaccessible to TMS modification which are, therefore, available for condensation prior to TMS decomposition [12]. Unmodified specimens begin to lose additional mass immediately after drying (≈ 150 °C) (Figure 5 (b)). This mass loss is due to condensation of the large concentration of silanol groups. A second, broad peak in the TGA first derivative commences at 400 °C due to loss of surface-bound methoxy groups through a hydrolysis mechanism facilitated by moisture generated from silanol condensation. A similar mass loss profile is seen in literature for unmodified TMOS-derived silica aerogel specimens [19]. The TGA first derivative profile of part-methylated silica shows several distinguishable overlapping signals (Figure 5 (c)). Decomposition of dry aerogel again commences at a lower temperature than observed for methylated silica aerogel (≈ 200 °C vs. 350 °C) due to silanol condensation. Loss of methane and methanol follow at higher temperatures as seen for methylated aerogel. The TGA first derivative profiles of $\varphi_{TMOS} = 0.33$, and $\varphi_{TMOS} = 0.41$ differ from the other samples in the form of a smoother broad peak ($\varphi_{TMOS} = 0.33$ and $\varphi_{TMOS} = 0.41$) which again replicates the behaviour seen for methylated silica aerogel. This broader peak may result from a greater degree of mass loss through silanol condensation resulting from a lower degree of surface functionalisation due to a greater proportion of very small pores in the higher density aerogel. The sharp signal seen for $\varphi_{TMOS} = 0.20$ at 650 °C may be due to contamination. The TGA first derivative profile of part-methylated + epoxidated silica aerogel is more like that of methylated silica aerogel than the other surfaces with both showing a large maximum at approximately 350 °C (Figure 5 (d)). The distinct shoulder preceding this peak (starting at 150 °C) may be due to significant loss of condensation products (water) resulting from the self-polymerisation of surface-bound epoxide (GPS residues) in addition to the previously described silanol condensation. Again, $\varphi_{TMOS} = 0.33$ and $\varphi_{TMOS} = 0.41$ show a smoother peak likely due to greater surface silanol concentrations.

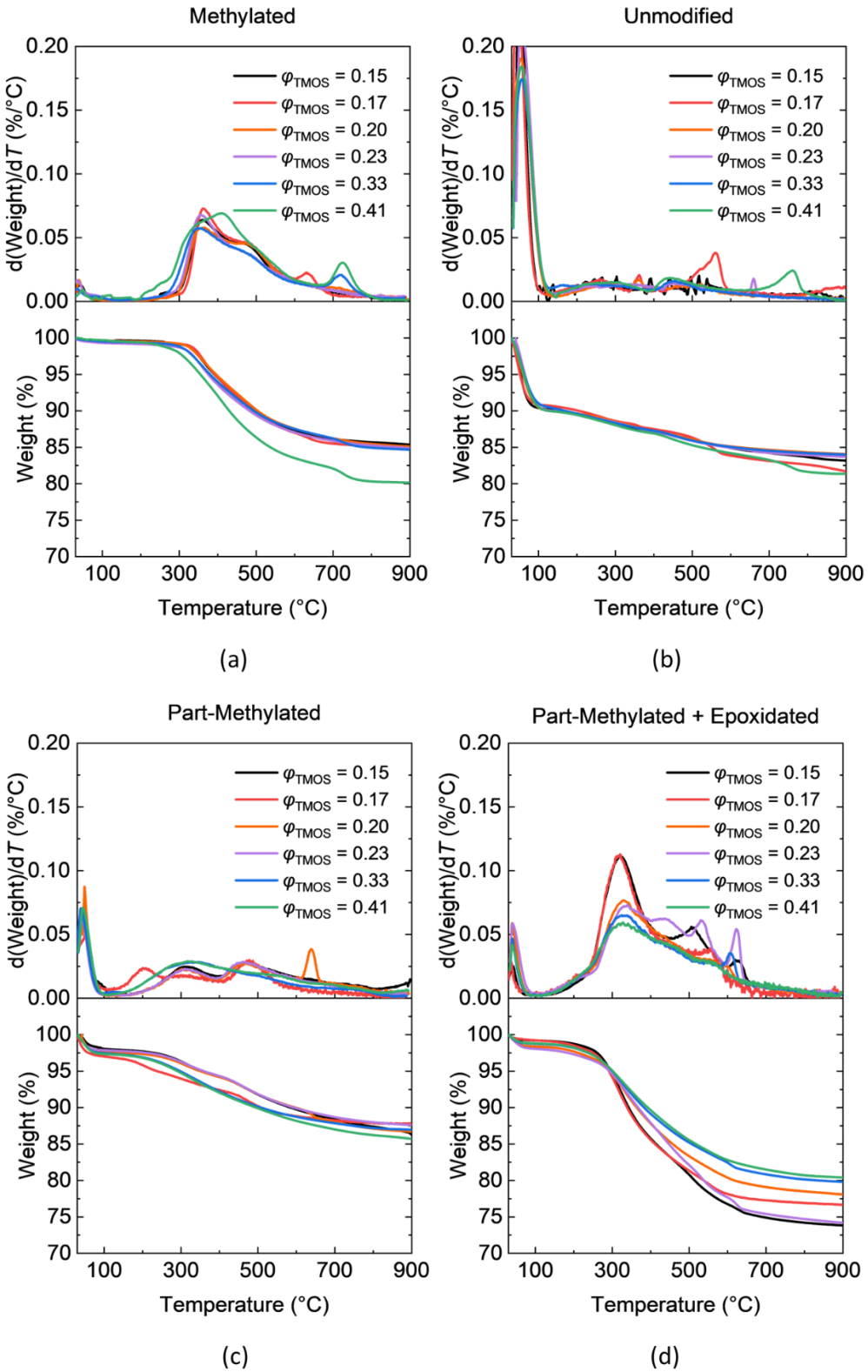

Figure 5. TGA data for (a) methylated, (b) unmodified, (c) part-methylated, and (d) part-methylated + epoxidated silica aerogel monoliths with various TMOS volume fractions (φ_{TMOS}).

CONCLUSIONS

Two new silica aerogel surface types were synthesised and characterised: part-methylated, and part-methylated + epoxidated. These surfaces enable the formation of moisture-stable, high-density, silica aerogel monoliths with amphiphilic reactive interfaces. The simultaneous independent binding of dimethylsilyl (DMS) and (3-glycidyloxypropyl)silyl (GPS) residues in part-methylated + epoxidated silica aerogel has been confirmed by IR analysis. This bi-functionalisation forms silica aerogel with a surface featuring DMS, GPS and silanol groups. The GPS and silanol groups act as reactive sites and DMS groups provide hydrophobic character for decreased moisture uptake. The shrinkage of part-methylated + epoxidated silica aerogel monoliths was found to decrease with increased proportion of DMS binding relative to GPS binding. A suitable GPTMS/DMDMS ratio (χ_{GPTMS} = 6 mol.%) was chosen to trade-off shrinkage against GPS loading. Part-methylated and part-methylated + epoxidated surfaces were found to be mildly hydrophilic by thermogravimetric analysis (TGA). However, moisture uptake was far less than that of the equivalent unmodified silica aerogel. These reinforcement networks are therefore suitable for backfilling with epoxy resin to form bicontinuous nanocomposites, which may themselves be applied as nanostructured matrices for fibre-reinforced composites.

ACKNOWLEDGEMENTS

The authors kindly acknowledge the funding for this research provided by UK Engineering and Physical Sciences Research Council (EPSRC) programme Grant EP/T011653/1, Next Generation Fibre-Reinforced Composites (NextCOMP): a Full Scale Redesign for Compression a collaboration between Imperial College London and the University of Bristol. For the purpose of open access, the authors have applied a Creative Commons Attribution (CC BY) license to any author accepted manuscript version arising. Supporting data can be requested from the corresponding author but may be subject to confidentiality obligations.

REFERENCES

[1] A. Jumahat, C. Soutis, F.R. Jones, A. Hodzic. Improved Compressive Properties of a Unidirectional CFRP Laminate Using Nanosilica Particles. *Advanced Composites Letters*. 2010;**19**(6): pp. 204-7.
[2] D.R. Clarke. Interpenetrating Phase Composites. *Journal of the American Ceramic Society*. 1992;**75**(4): pp. 739-58.
[3] C.M.D. Shaw, D.B. Anthony, I. Hamerton, M.S.P. Shaffer. Bicontinuous silica-epoxy nanocomposites by aerogel infusion. *Composites Part A: Applied Science and Manufacturing*. 2024;**182**: pp. 108164.
[4] A. Jumahat, C. Soutis, F.R. Jones, A. Hodzic. Effect of silica nanoparticles on compressive properties of an epoxy polymer. *Journal of Materials Science*. 2010;**45**(21): pp. 5973-83.
[5] D. Tzetzis, G. Mansour. Nanoindentation, compression and fractural characterization of highly dispersed epoxy silica nanocomposites. *Journal of Reinforced Plastics and Composites*. 2016;**35**(7): pp. 541-55.
[6] Bernt Brønmo Johnsen, Marie Bourgeaux-Goget, T. Olsen. Material properties of silica/epoxy nanocomposites. Norwegian Defence Research Establishment (FFI); 2015.
[7] T. Nazir, A. Afzal, H.M. Siddiqi, S. Saeed, M. Dumon. The influence of temperature and interface strength on the microstructure and performance of sol–gel silica–epoxy nanocomposites. *Polymer Bulletin*. 2011;**67**(8): pp. 1539-51.
[8] Adam J, Roscher C, Eger C, Adebahr T, Wieczorreck R, Pyrlik M. Evonik Hanse GmbH. Silicon Dioxide Dispersion. Patent: US9376544B2. 28/06/2016.
[9] S. Sprenger. Nanosilica-Toughened Epoxy Resins. *Polymers*. 2020;**12**(8): pp. 1777.
[10] C.M.D. Shaw, D.B. Anthony, I. Hamerton, M.S. Shaffer. Bicontinuous Silica-Epoxy Nanocomposites. *In proceedings of: 23rd International Conference on Composite Materials Belfast. 2023*.
[11] B. Arkles, G. Larson. Silicon Compounds: Silanes & Silicones. Morrisville, PA: Gelest Inc.; 2013.
[12] C. Shaw. Bicontinuous Silica-Epoxy Matrices for Fibre-Reinforced Composites. London: Imperial College London; 2025.

[13] Y.W. Ngeow, A.V. Chapman, J.Y.Y. Heng, D.R. Williams, S. Mathys, C.D. Hull. Characterization of silica modified with silanes by using thermogravimetric analysis combined with infrared detection. *Rubber Chemistry and Technology*. 2018;**92**(2): pp. 237-62.
[14] Z. Li, S. Zhao, M.M. Koebel, W.J. Malfait. Silica aerogels with tailored chemical functionality. *Materials & Design*. 2020;**193**: pp. 108833.
[15] S. Brunauer, D. Kantro, C. Weise. The surface energies of amorphous silica and hydrous amorphous silica. *Canadian Journal of Chemistry*. 1956;**34**(10): pp. 1483-96.
[16] W.J. Malfait, R. Verel, M.M. Koebel. Hydrophobization of Silica Aerogels: Insights from Quantitative Solid-State NMR Spectroscopy. *The Journal of Physical Chemistry C*. 2014;**118**(44): pp. 25545-54.
[17] T. Woignier, J. Phalippou. Skeletal density of silica aerogels. *Journal of Non-Crystalline Solids*. 1987;**93**(1): pp. 17-21.
[18] H. Bahramnia, H.M. Semnani, A. Habibolahzadeh, H. Abdoos. The Effect of 3-(Glycidoloxy Propyl) Trimethoxy Silane Concentration on Surface Modification of SiO2 Nanoparticles. *Silicon*. 2022;**14**(9): pp. 4969-77.
[19] A.V. Rao, M.M. Kulkarni. Hydrophobic properties of TMOS/TMES-based silica aerogels. *Materials Research Bulletin*. 2002;**37**(9): pp. 1667-77.

Cure-induced wrinkles and compression strength knock-down in uni-directional composites.

Lars P. Mikkelsen, Jesper K. Jørgensen, Sérgio Costa
Composites Manufacturing and Testing,
DTU Wind and Energy Systems

Acknowledgement:

- Turbo: Towards tURbine Blade production with zerO waste, Horizon Europe

Funded by the European Union

Fatigue failure of wrinkles in load carrying laminates

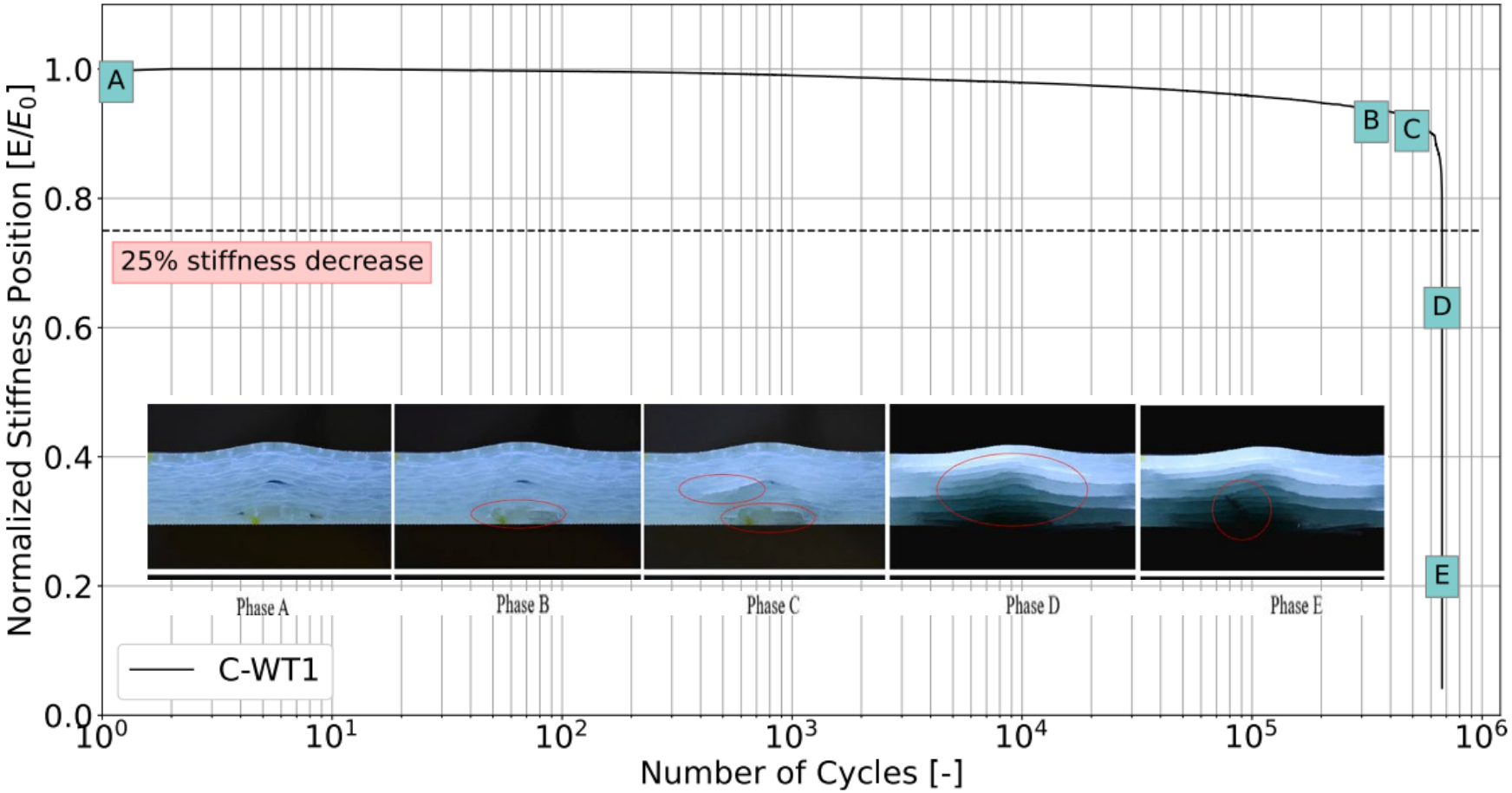

Mendonça, H.G., Mikkelsen, L.P., Zhang, B., Allegri, G., Hallet, S.R., Fatigue Delaminations in Composites for Wind Turbine Blades with Artificial Wrinkle Defects, *Int. J. of Fatigue,* **170**, 107822, https://doi.org/10.1016/j.ijfatigue.2023.107822, 2023.

The concept of cure-induced wrinkles

Wind turbine blade composite consists of fibres embedded in polymer ”resin”.

- The polymer will have to polymerise to give the blade its mechanical properties.
  - This process is referred to as **curing**.
  - Performed at elevated temperatures
- **Temperature gradients** occur during **heating** or **exothermal heat release** from the resin.
- The temperature gradients results in varying build-up of resin stiffness.
- This allows the fibres to buckle, driven by variations in thermal expansion and chemical shrinkage of the resin.
- This results in the phenomenon called ***”Cure-induced wrinkles”.***

Cure-induced Wrinkles

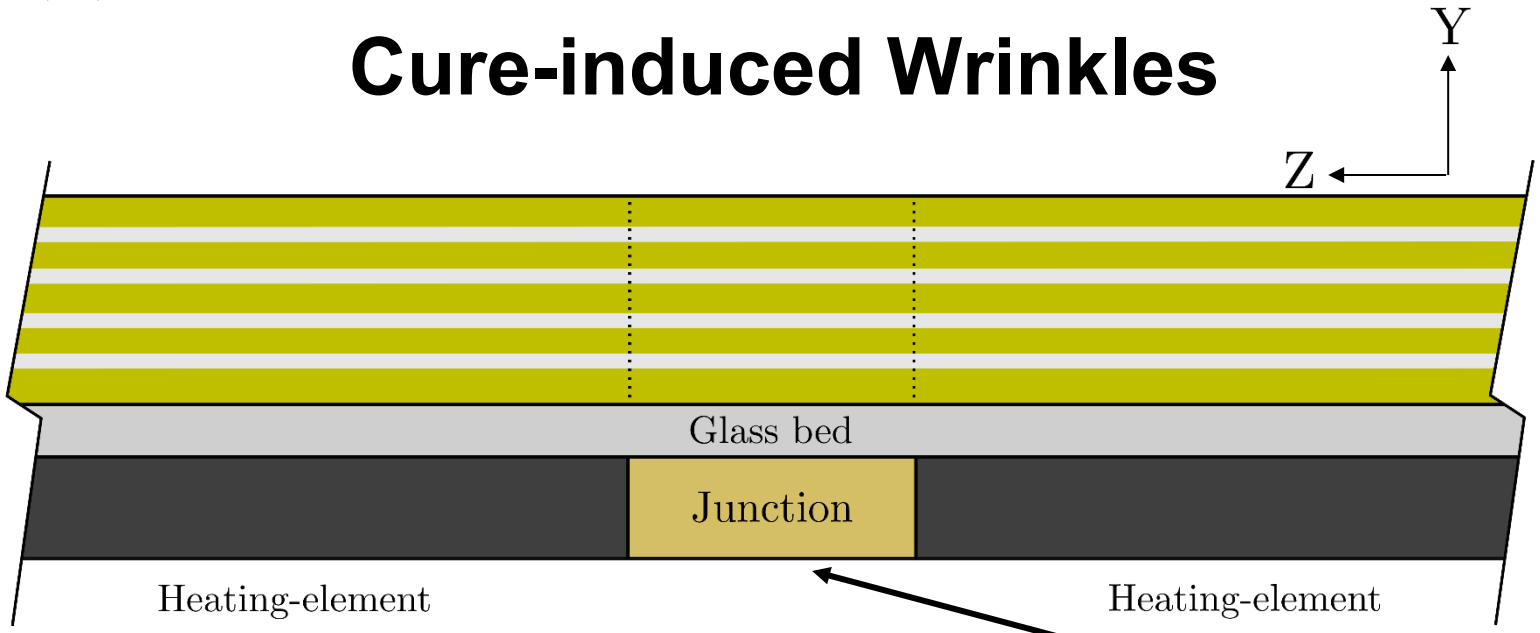

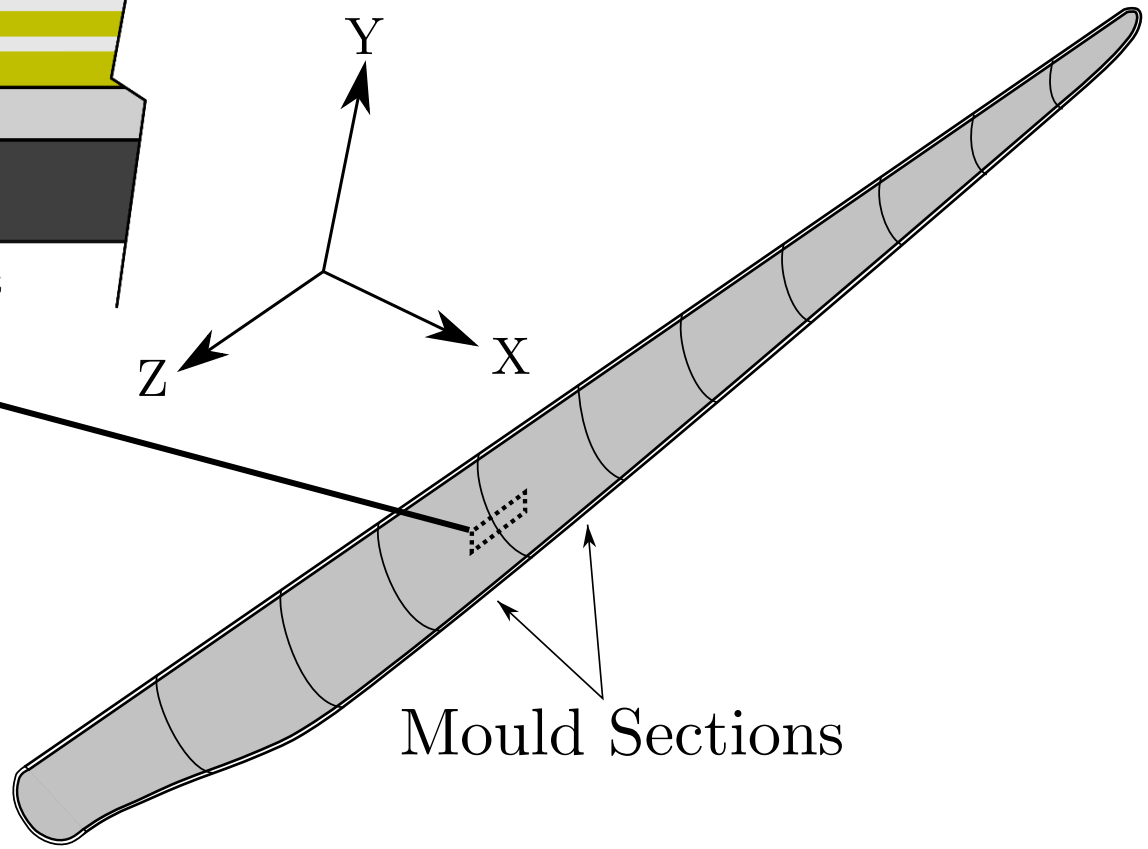

Jørgensen, J. K., Mikkelsen, L. P., and Maes, V. (2024). Finite element simulation of the driving mechanisms for cure-induced wrinkles. In *Proceedings of the 21st European Conference on Composite Materials - Special Sessions,* Binetruy, C. & Jacquemin, F. (eds.). European Society for Composite Materials, **vol. 8**, 31-36, 2-5 July, 2024, Nantes, France, https://doi.org/10.60691/yj56-np80.

Cure-induced Wrinkles

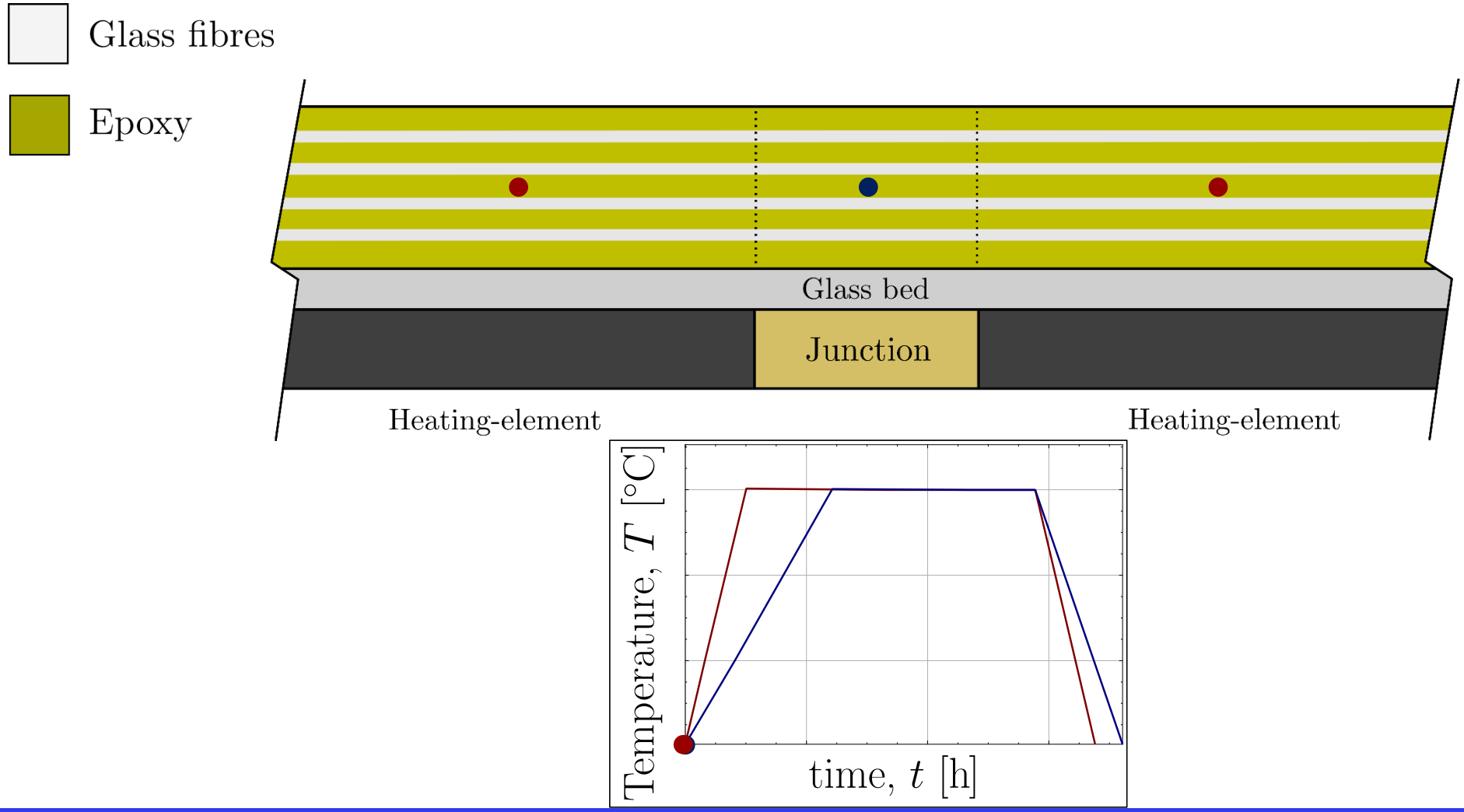

Cure-induced Wrinkles

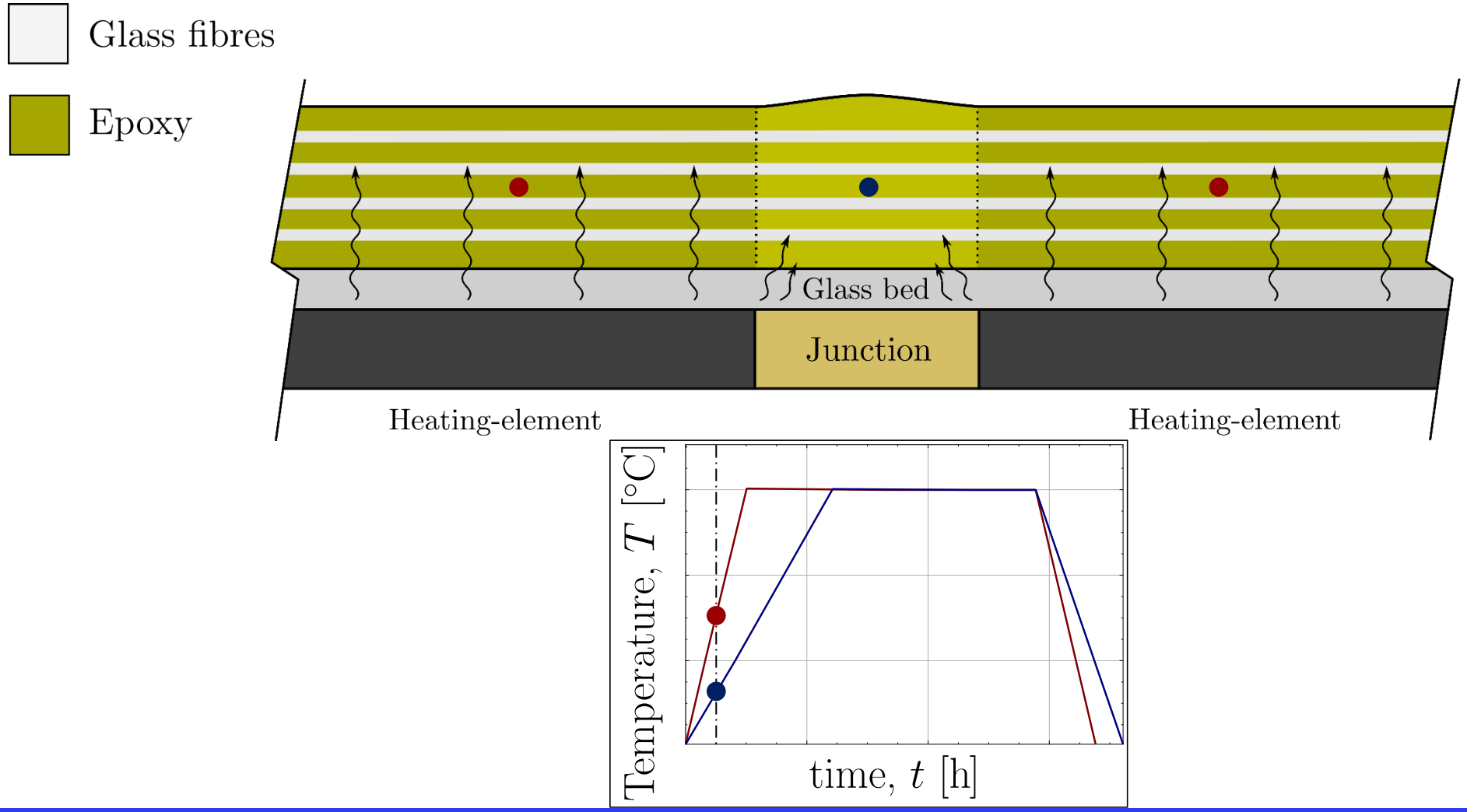

Cure-induced Wrinkles

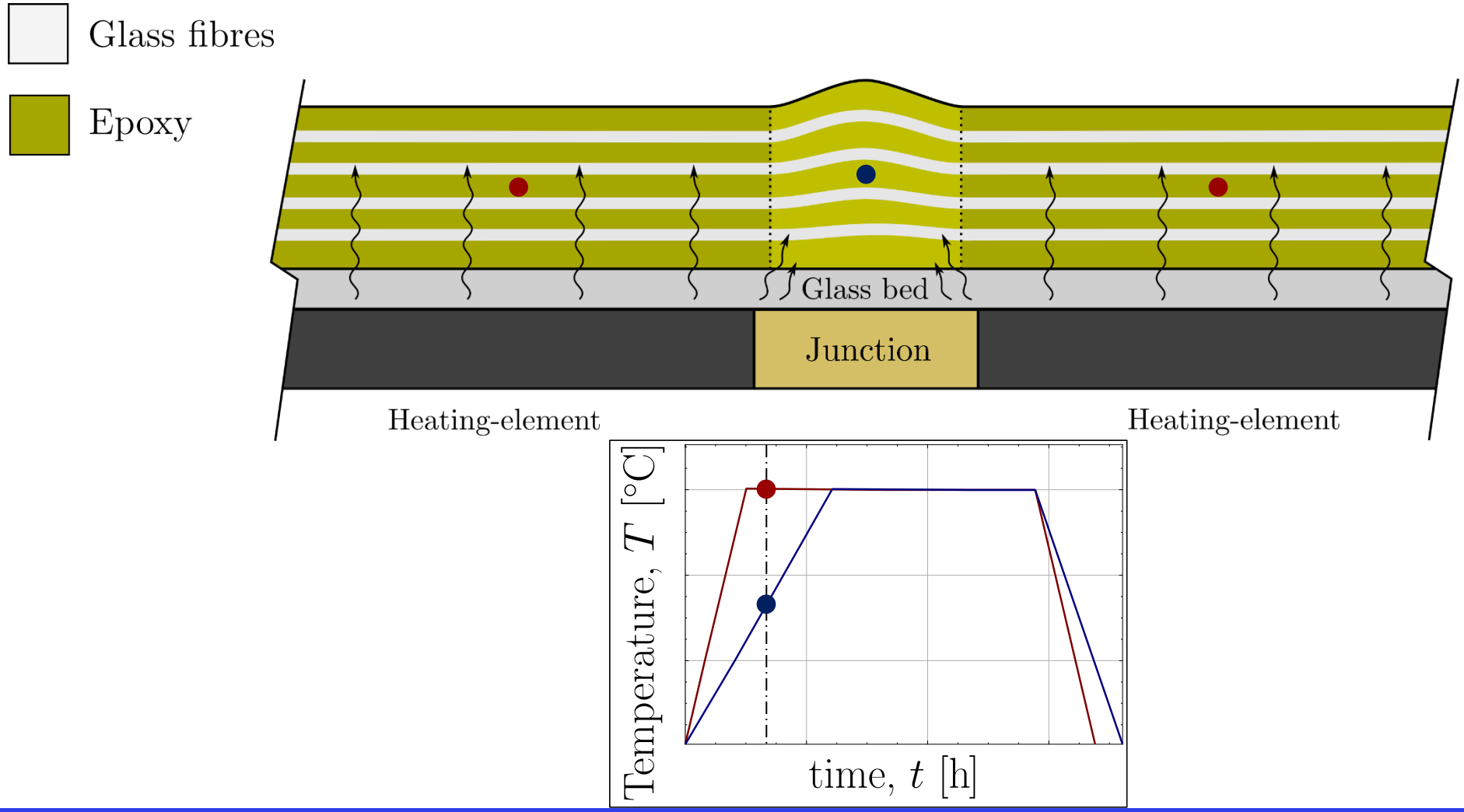

Cure-induced Wrinkles

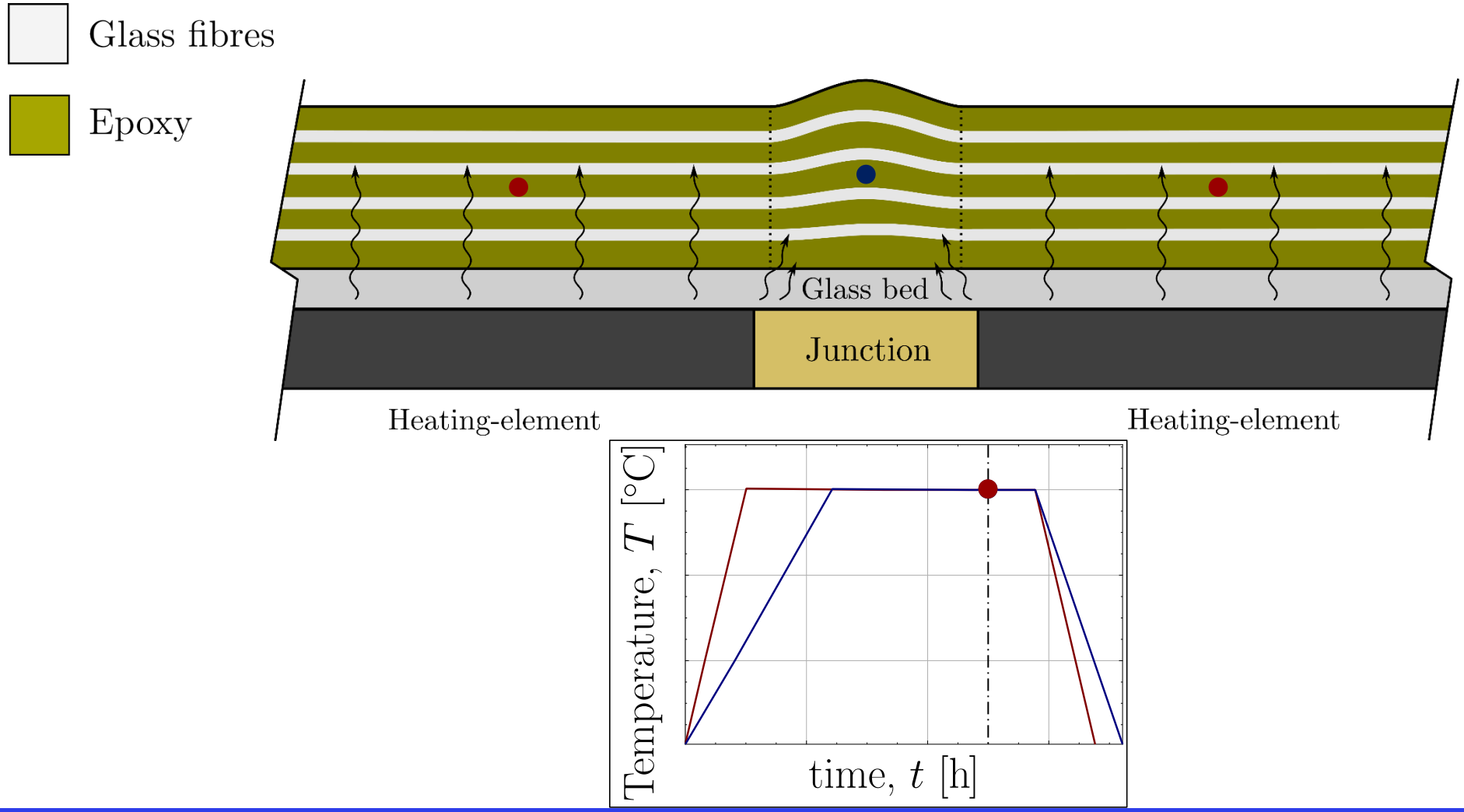

Cure-induced Wrinkles

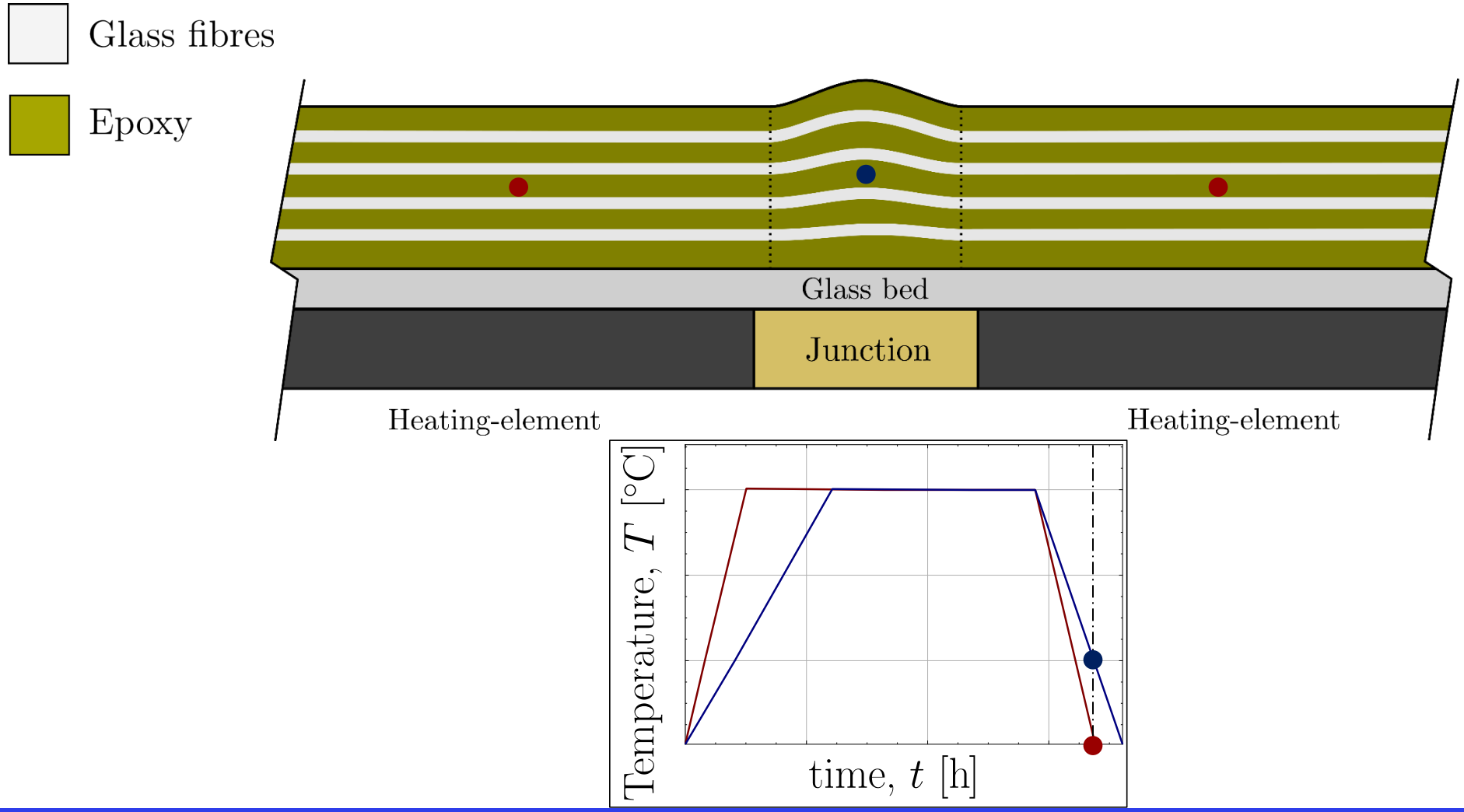

Model for precise cure shrinkage predictions

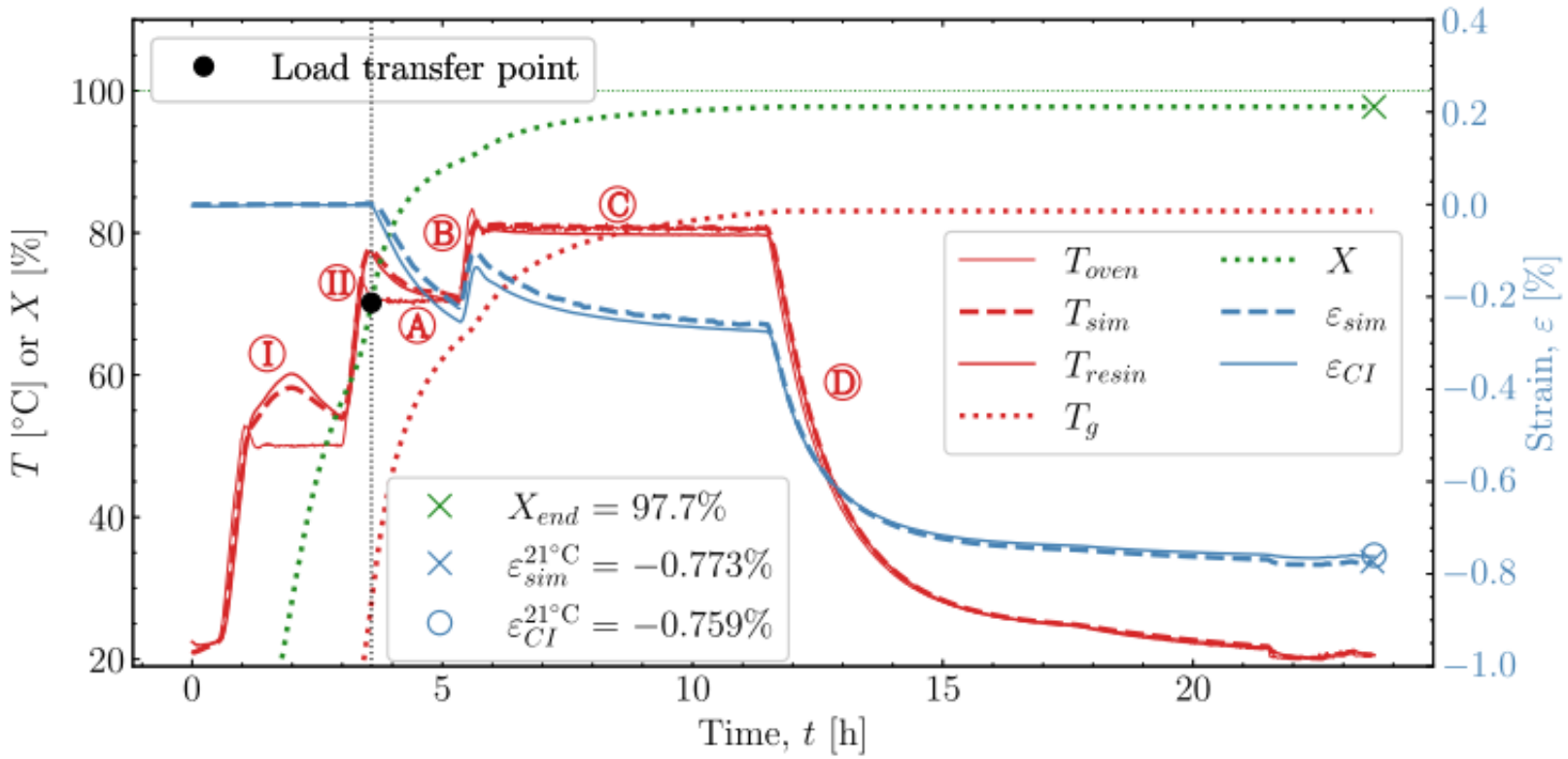

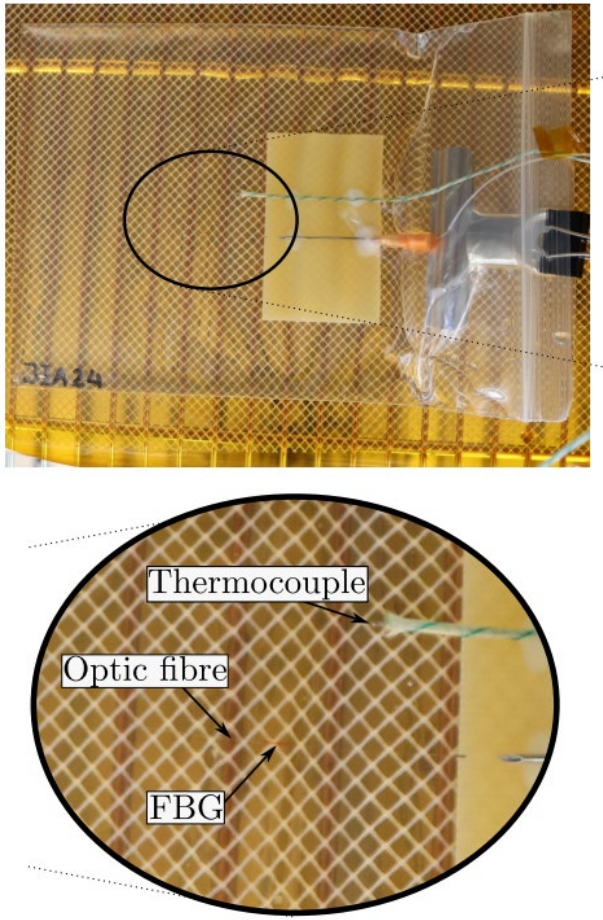

Jørgensen, J. K., Maes, V. K., Mikkelsen, L. P., & Andersen, T. L., A Precise Prediction of the Chemical and Thermal Shrinkage during Curing of an Epoxy Resin. *Polymers*, 16(2435), 1–22. https://doi.org/10.3390/polym16172435, 2024

Experimental measured and numerical predicted cure-induced shrinkage

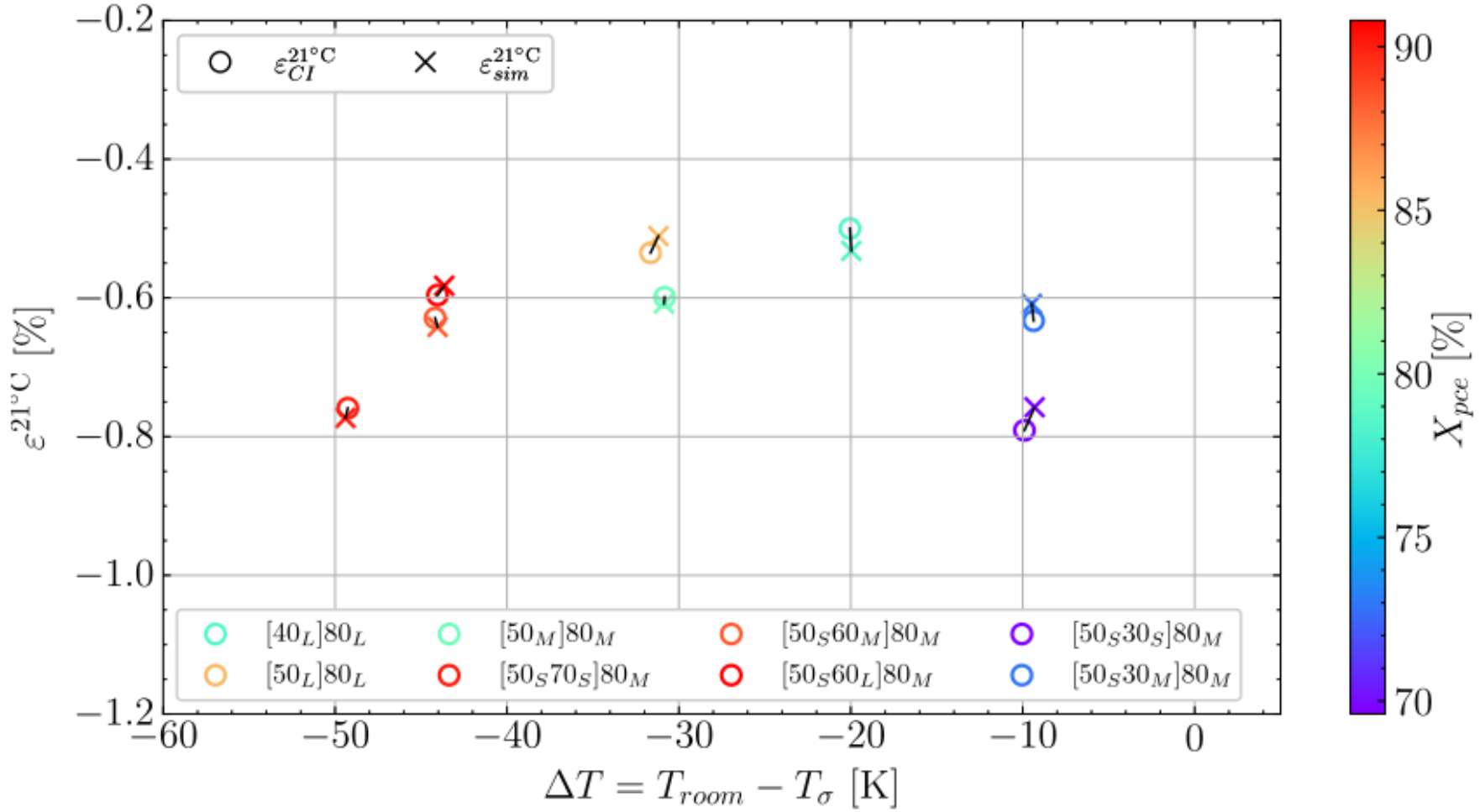

Material characterizations of the resin system

- DSC measurements

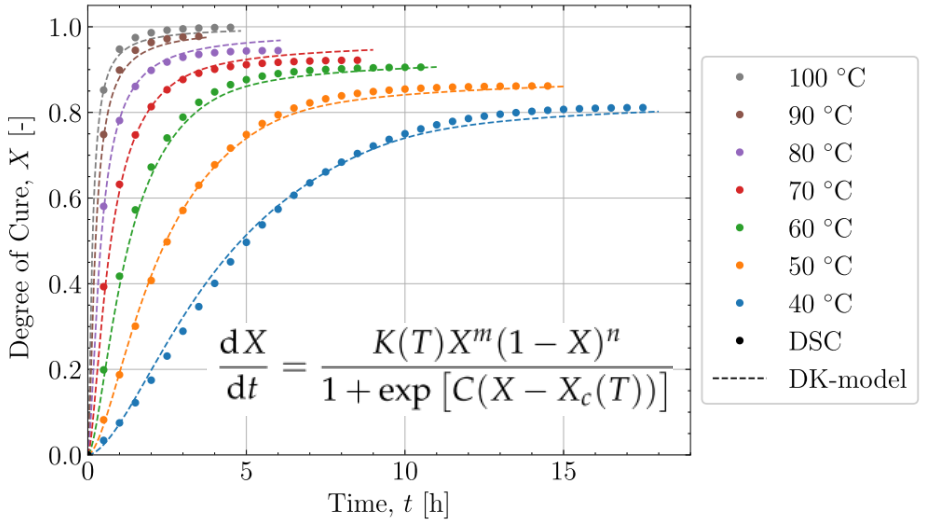

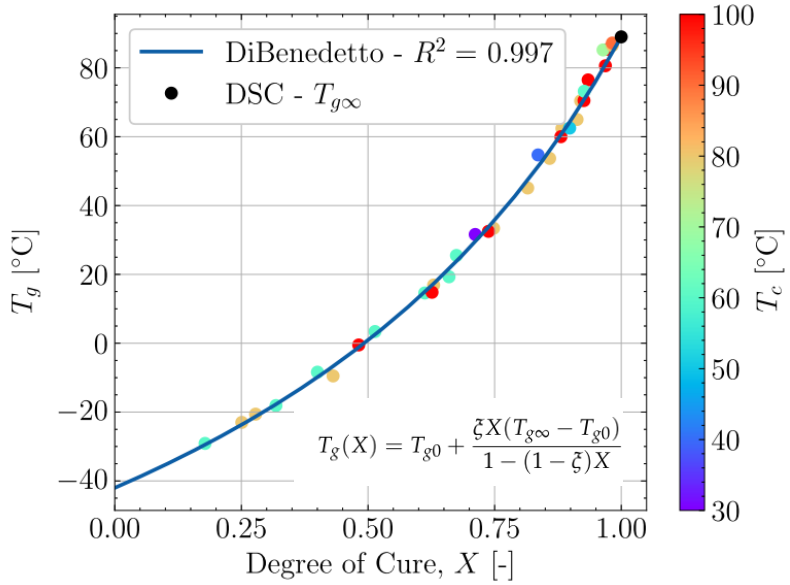

- Chemical shrinkage

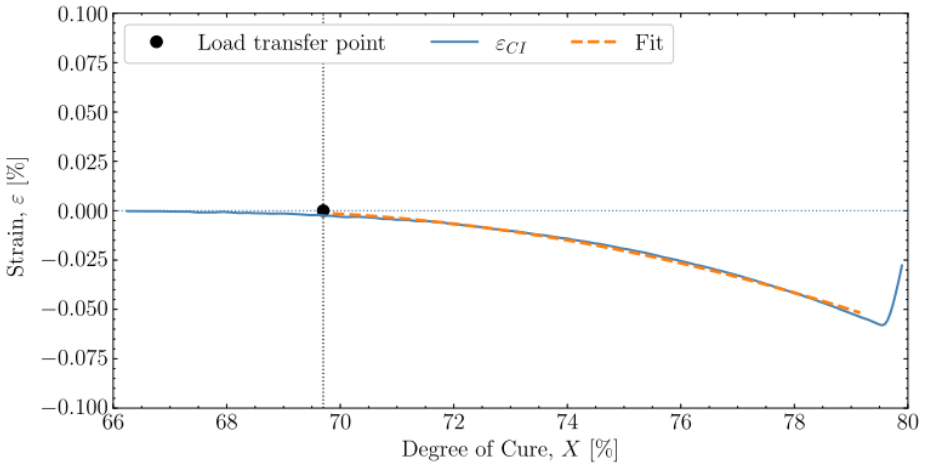

- Thermal contraction/expansion

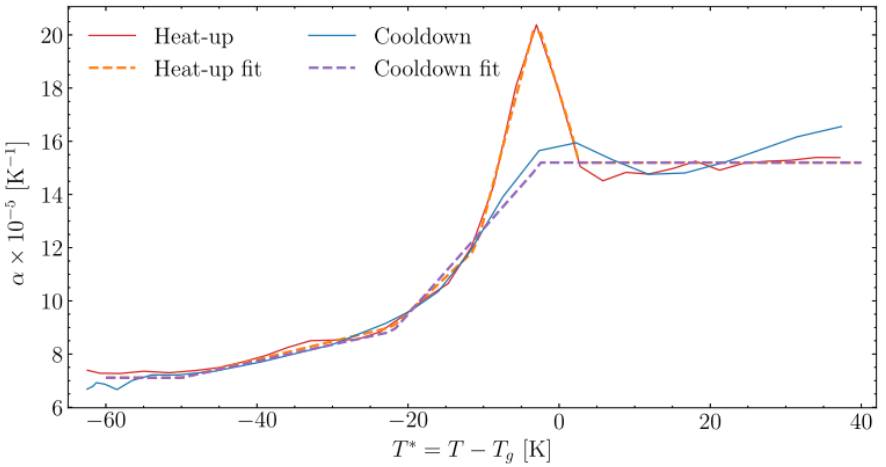

Stiffness build-up during curing

$$E_m = \begin{cases} E_m^0, & X < X_\sigma \\ E_m^0 (1 - X_m) + X_m E_m^\infty, & X_\sigma \leq X < X_{\text{end}} \\ E_m^\infty, & X \geq X_{\text{end}} \end{cases}, \text{ with}$$

$$X_m = \left(\frac{X - X_\sigma}{X_{\text{end}} - X_\sigma} \right).$$

$$\Delta\sigma_m = E_m \varepsilon_m^{mech},$$

$$\Delta\sigma_f = E_f \varepsilon_f^{mech}.$$

$$E_{f,c}(X) = \left(0.01 + \frac{0.99}{1 + \exp\left(q(X - X_\sigma)\right)} \right) E_f, \qquad \varepsilon_f^{mech} < 0.$$

Jørgensen, J. K., Mikkelsen, L. P., Maes, V. K., Prediction of cure-induced wrinkles aimed at the manufacturing of largewind turbine blades. Submitted 2025.

Predict the cure-induced wrinkle formation

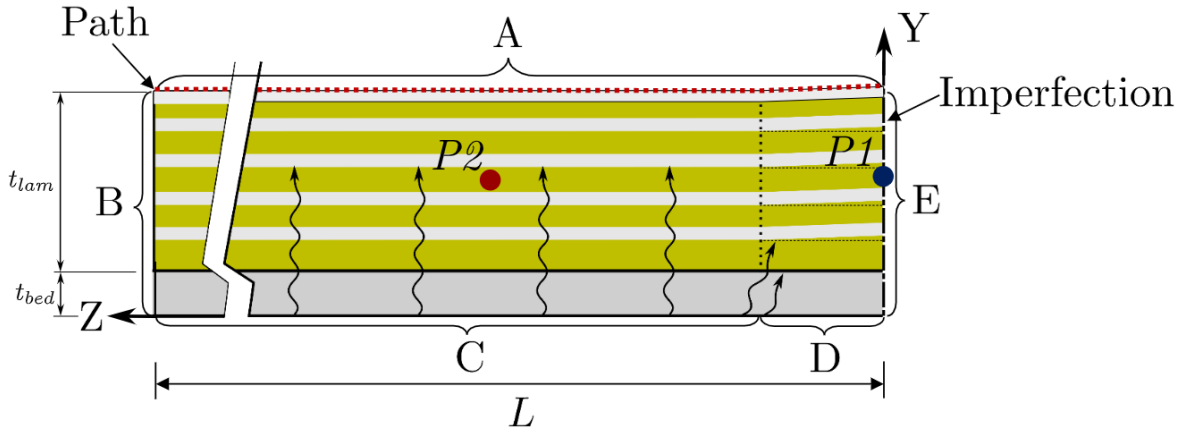

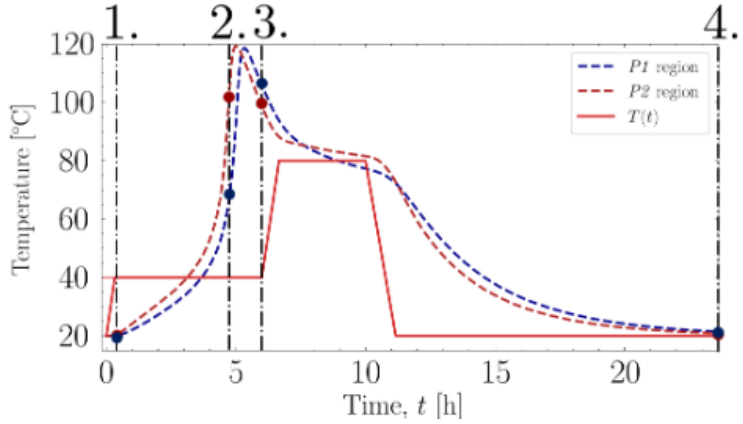

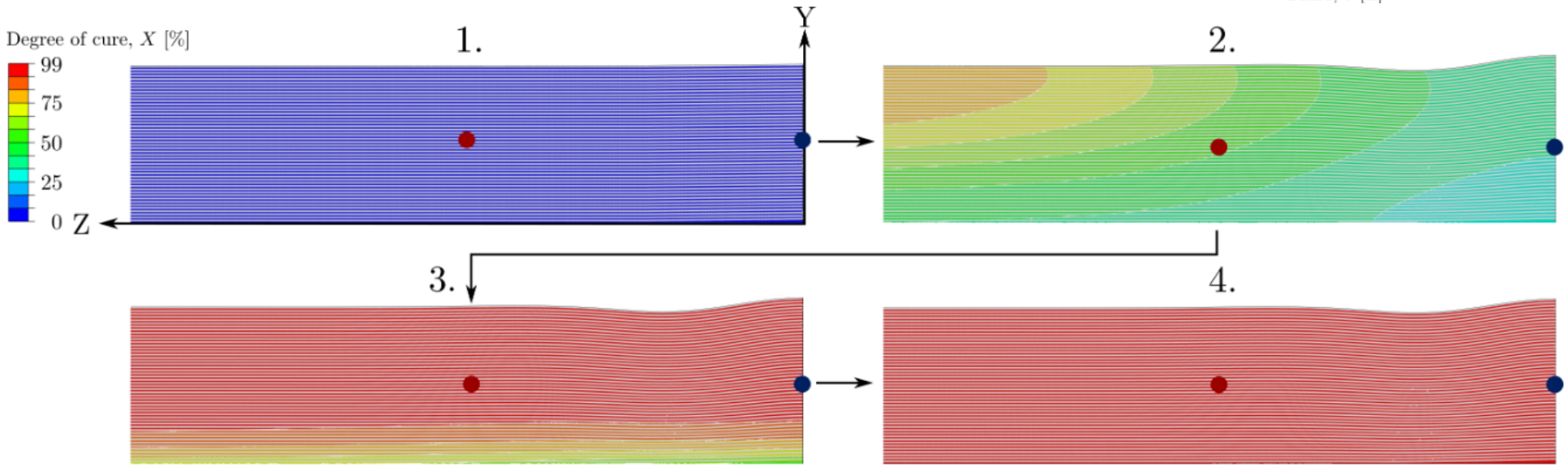

Final wrinkle shape

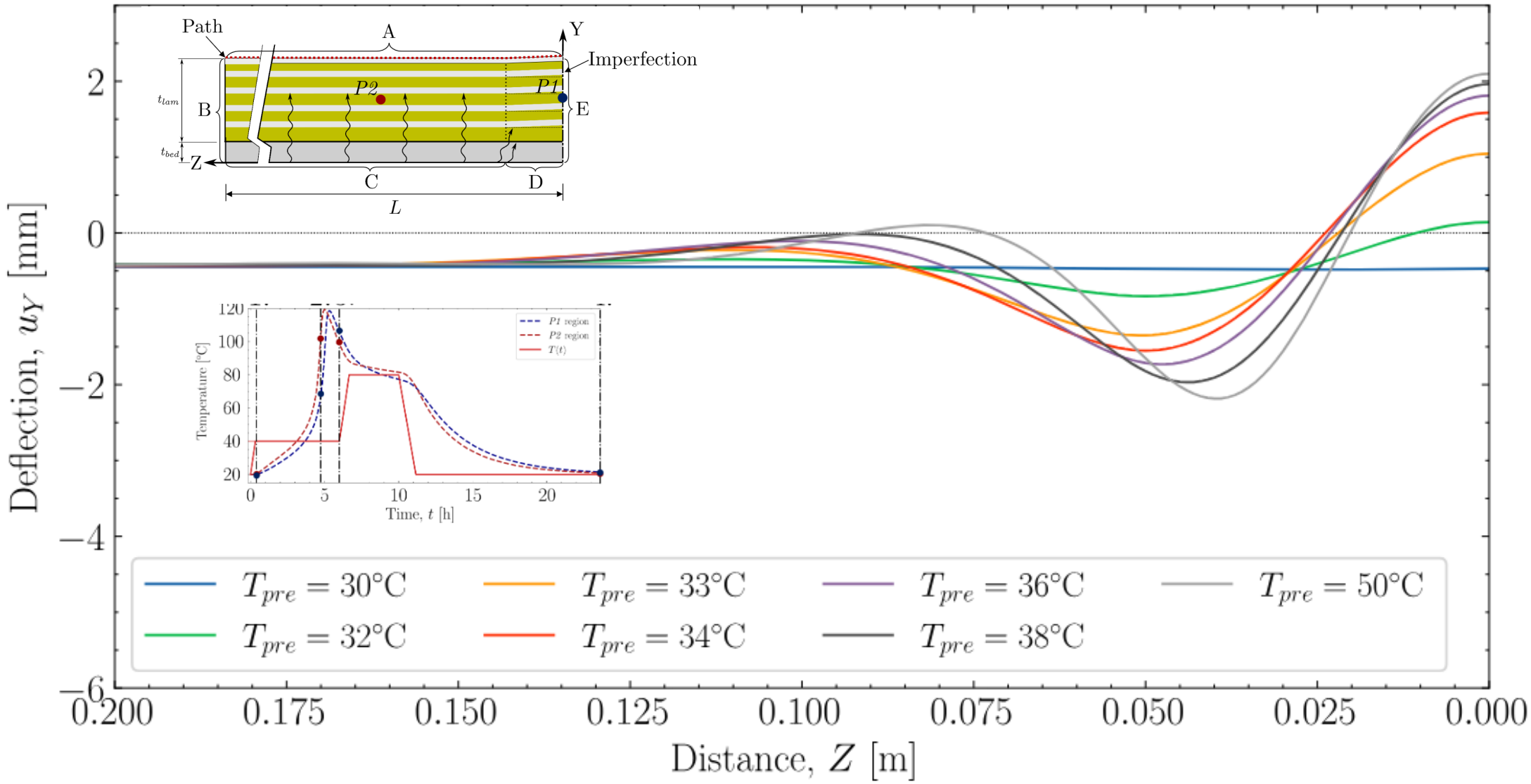

Compressive failure mechanism

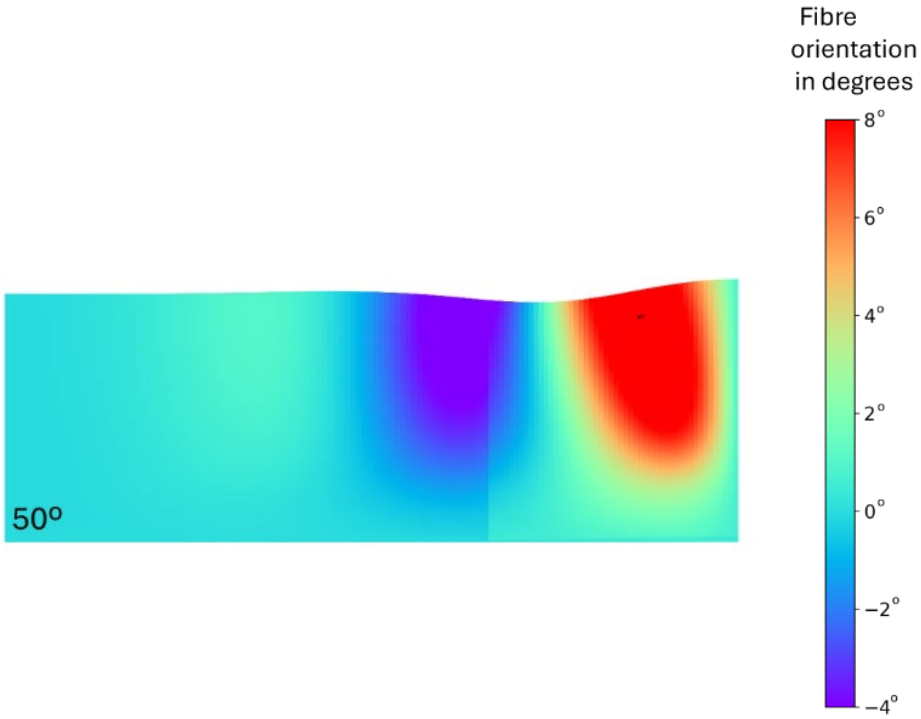

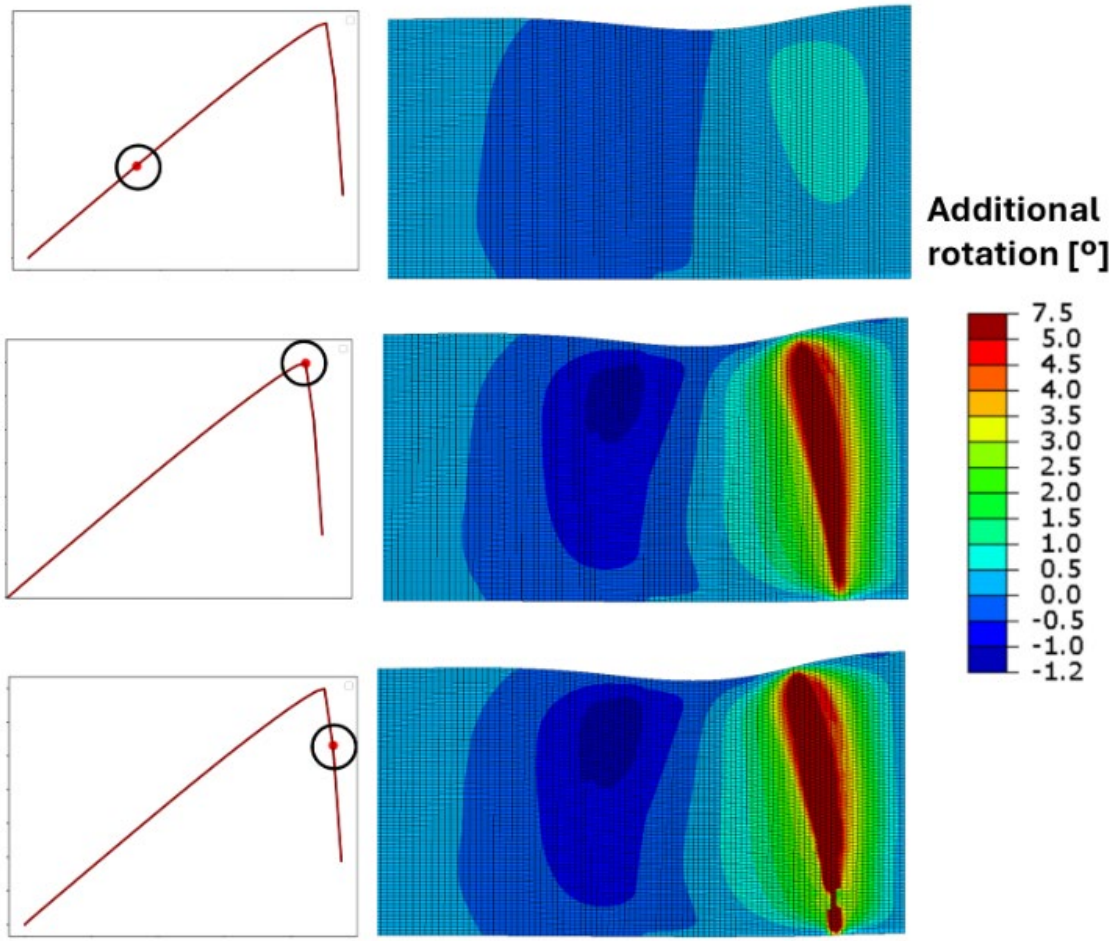

Figure 15: Contour plot of additional fibre rotation at three different loading stages for the $T_{\text{pre-cure}} = 50\,^{\circ}\text{C}$.

Costa, S, Jørgensen, J. K., Mikkelsen, L. P., Effect of curing temperature on the longitudinal compressive strength of unidirectional composites. Under preparation 2025.

Compression strength knock-down

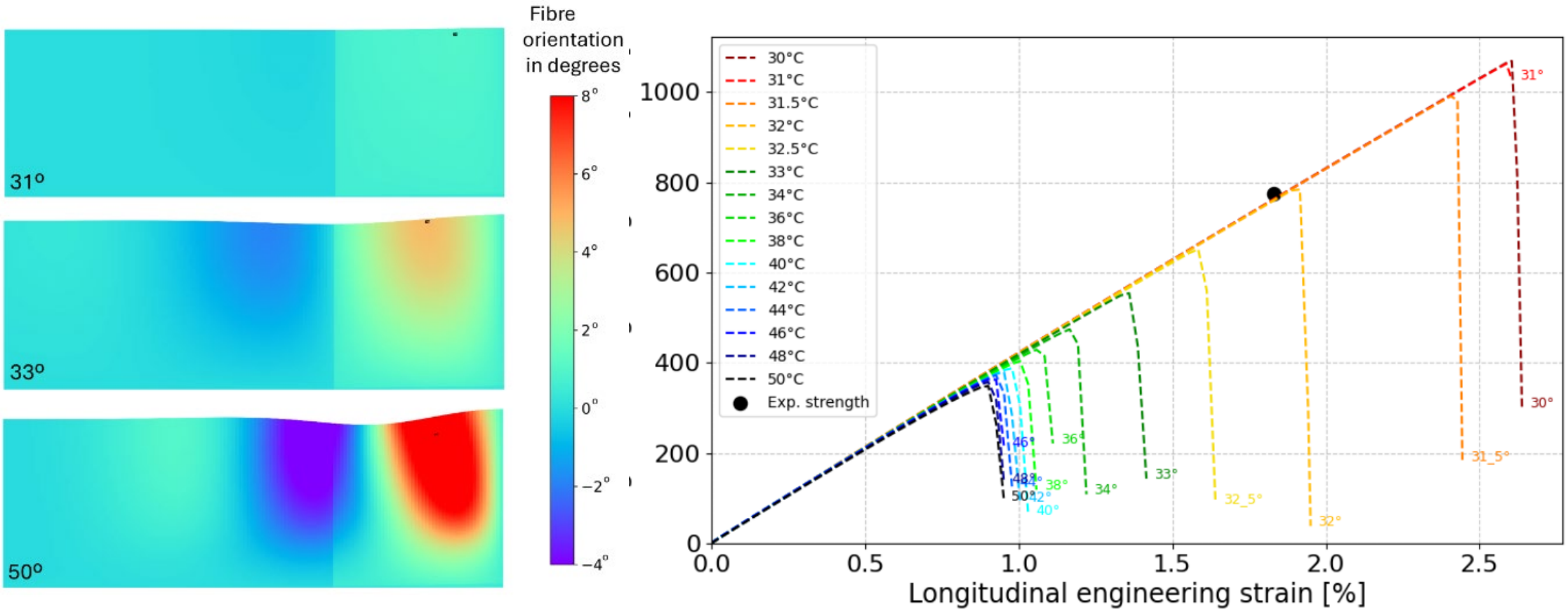

Costa, S, Jørgensen, J. K., Mikkelsen, L. P., Effect of curing temperature on the longitudinal compressive strength of unidirectional composites. Under preparation 2025.

Currently ignoring visco-elastic relaxation during curing

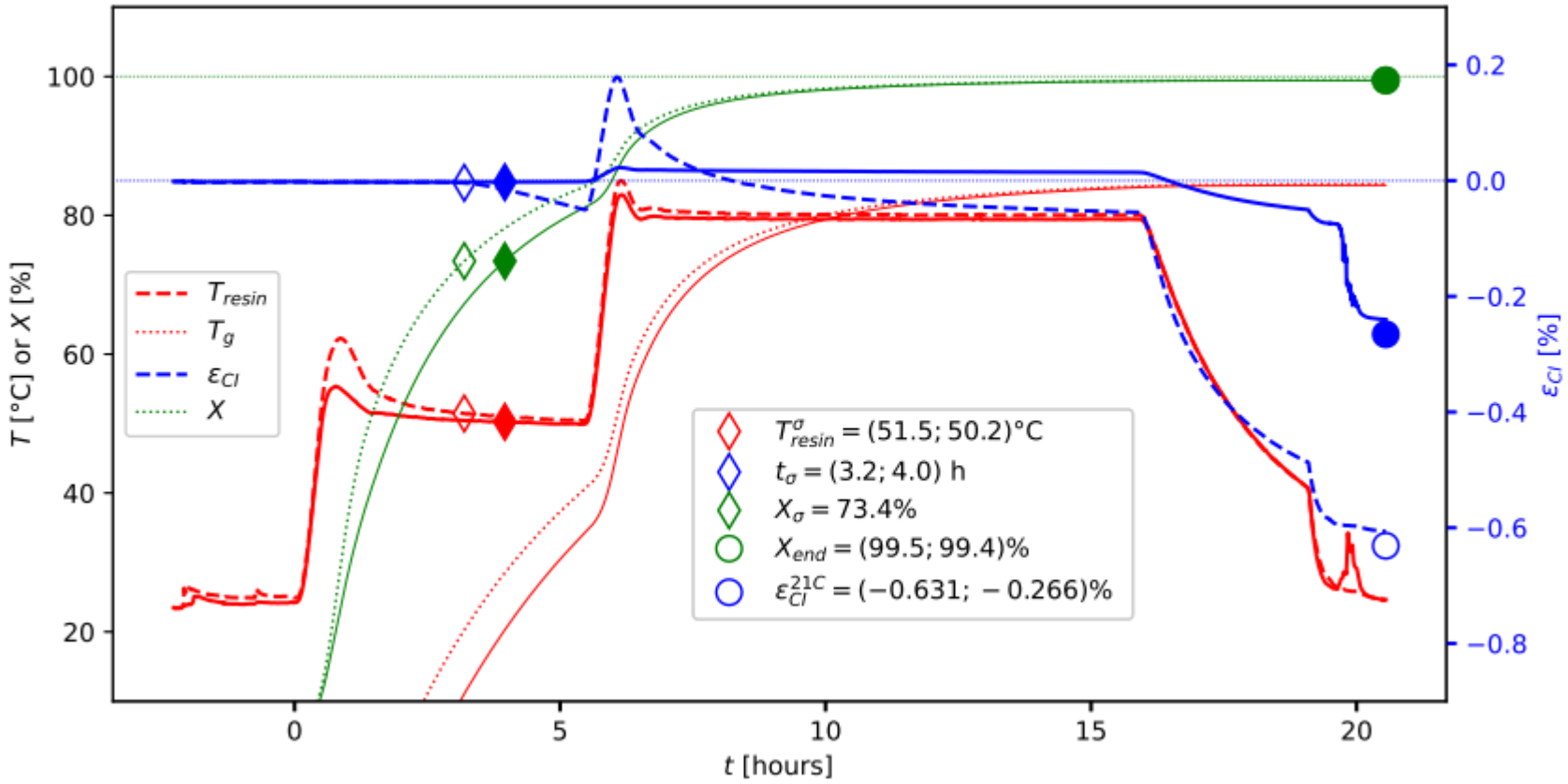

Mikkelsen, L.P., Jørgensen, J.K, Mortensen, U.A., Andersen, T.L., In-situ cure-induced strain measurements using optical fiber Bragg gratings for residual stress determinations in thermosets, *Solids,* 6(1), https://doi.org/10.3390/solids6010003, 2025.

Conclusion

- Demonstrate that curing under varying temperature may lead to cure-induced wrinkles
- Cure-induced wrinkles may reduce the compression strength significantly
- Small variations in the cure-conditions may lead to large strength reduction due to the present of cure-induced wrinkles

ICCM24 24TH INTERNATIONAL CONFERENCE ON COMPOSITE MATERIALS
AUG 4-8, 2025 • BALTIMORE CONVENTION CENTER • BALTIMORE, MARYLAND

INFLUENCE OF TRANSIENT RADIATIVE HEAT FLUX ON DEGREE OF CRYSTALLINITY IN THERMOPLASTIC COMPOSITES

Mark Smeets[a], Arian Tashakori[a], Sandesh Amgai[a], Vishnu V Ganesan[a], Ankur Jain[a], Paul Davidson[a,]

[a]*Department of Mechanical and Aerospace Engineering, University of Texas at Arlington, Arlington, TX 7601-0018*

Keywords: Composite failure, compression strength

ABSTRACT

Automated Fiber Placement (AFP) enables high-speed, precise deposition of fiber-reinforced composites, making it ideal for complex, high-performance structures. Understanding the transient thermal behavior of thermoplastic composites during AFP is critical, as it affects bonding, residual stress, and final properties. This study presents a systematic experimental characterization of thermal evolution and resulting crystallinity in CF/LM-PAEK composites exposed to a moving Xenon-arc flash lamp. A robotic setup was developed to map the lamp's irradiance profile, and infrared thermography was used to capture surface temperature during heating. Differential Scanning Calorimetry (DSC) measured crystallinity across varying process conditions. Results show that temperature and crystallization are governed by radiant exposure, thermal diffusivity, cooling rates, and process parameters such as power and speed. These insights support improved AFP thermal control and process optimization.

1 INTRODUCTION

Carbon fiber reinforced polymer (CFRP) composites are widely used in aerospace applications due to their high strength-to-weight ratio. Traditional methods like hand layup are labor-intensive and inefficient [1], whereas Automated Fiber Placement (AFP) enables scalable manufacturing by robotically depositing pre-impregnated CFRP tows with improved precision [2, 3]. Both thermoset and thermoplastic CFRPs can be manufactured via AFP. Thermosets require curing post-laydown, while thermoplastics offer the advantage of in-situ consolidation, eliminating autoclave requirements and shortening cycle times [4–6]. However, controlling crystallinity and achieving strong interlaminar bonding in thermoplastics is challenging due to rapid thermal cycles.

In AFP of thermoplastics, tows must be rapidly heated to 320°C–350°C [7] to allow polymer chain mobility and subsequent crystallization, forming lamellae and spherulites that determine mechanical performance [8, 9]. Studies indicate that rapid cooling reduces crystallinity, while prolonged heating enhances it [10]. Thus, uniform and efficient heating becomes essential. Various non-contact heating systems have been examined, including Hot Gas Torch (HGT) [11–13], induction heating [14–16], and Near-Infrared (NIR) lasers [17–19]. A newer alternative is Xenon-arc flash lamp heating [20–22], which delivers high-energy broadband UV–IR pulses.

Heating strategies strongly affect temperature gradients and resulting microstructure. Tafreshi et al. [12] showed that while HGT effectively heats the surface, inner plies remain under-heated. Similarly, Shafaq et al. [23] linked cooling rate variations to crystallinity fluctuations. Laser heating improves interlaminar bonding but has limited penetration, causing lower crystallinity in core plies [24]. Xenon-arc flash lamps, emitting diffuse radiation unlike lasers' collimated beams, may enable better thermal penetration and uniformity [25]. However, few studies to date explore their behavior and process optimization in AFP.

Challenges in Xenon-arc flash AFP heating include energy distribution control, consistent material exposure, and understanding crystallization effects. Heating effectiveness is governed by the radiative heat flux and the temperature evolution rate in the laydown zone [7]. While prior studies have used thermocouples [26], fiber Bragg gratings [27], and IR thermography [28, 29] to map AFP thermal profiles, limited data exists on Xenon-arc systems. Danezis et al. [30] developed a 3D optical ray-tracing model to simulate lamp behavior, highlighting the complexity of diffuse source modeling.

This study focuses on the thermal characteristics of Xenon-arc flash heating in AFP. It aims to isolate key parameters—irradiance, exposure time, and thermal response—and quantify their effects on surface temperature and crystallization. A spatially resolved irradiance field is characterized and linked to temperature evolution and crystallinity, as measured by Differential Scanning Calorimetry (DSC). Experiments are conducted using a KUKA robotic AFP platform, a Xenon-arc flash lamp as the heating source, and LM-PAEK carbon fiber tows as the material system [31]. The results aim to bridge critical gaps in understanding AFP thermal behavior and to optimize Xenon-arc based heating strategies for next-generation thermoplastic composites.

2 EXPERIMENTS

2.1 Flux Measurement

A measurement setup was developed to characterize irradiance (Ee) near the Xenon-arc flash lamp of a humm3 heating system [20]. The lamp, enclosed in a 26 mm × 70 mm cavity, was mounted vertically, and irradiance was measured using a water-cooled Gordon gauge heat flux sensor (Hukseflux) mounted on a six-axis robotic arm. The sensor, with a 4.3 mm port and up to 1 MW/m² measurement capacity, recorded data at 200 Hz using a DI-245 system (Dataq). Irradiance output was controlled by adjusting pulse width (tp), while keeping voltage (200 V) and frequency (90 Hz) constant. Based on the relation P=Ie ω tpV, with Ie=230 A, pulse widths of 0.3 ms, 1 ms, and 1.7 ms yielded power outputs of 1240 W, 4132 W, and 7025 W, respectively.

A KUKA robotic arm, programmed using Grasshopper UI in Rhino 7, was used to move a heat flux sensor through a 3D grid above the Xenon-arc flash lamp. At each grid point, the sensor held position for four seconds to record voltage, which was averaged and converted to irradiance. Measurements were taken from 36 mm to 12 mm vertically (Z-axis), and across a 52 mm × 36 mm area in the horizontal plane (X–Y), with 4 mm step sizes. Due to housing constraints, data below 12 mm was linearly extrapolated.

Three power levels (1240 W, 4132 W, and 7025 W) were tested. A full 3D irradiance field was mapped at 4132 W using 1078 measured and 462 extrapolated points, covering one quadrant and mirrored to form the full field. Radial Basis interpolation in Python was used to generate the 3D irradiance map, which was then scaled linearly for the other two power levels. This enabled development of a power-based scaling law for estimating irradiance fields between 1240 W and 7025 W.

2.2 Thermal Measurement

Following irradiance field characterization, a new setup was implemented to measure the surface temperature profile on a CF/LM-PAEK panel (VICTREX AE™ 250 UDT) as the Xenon-arc flash lamp moved across it. A FLIR A655sc infrared camera operating in the 7.5–14 µm spectral range at 60 Hz captured real-time thermal data during lamp traversal at various speeds (Figure 1).

The setup included a four-rod frame supporting a panel made of ten evenly spaced CF/LM-PAEK tows, secured using double-sided tape. The lamp, mounted on the robot arm, moved along a path aligned with the center of the panel and tows, ensuring radiation incidence was normal to the surface. The fiber direction matched the direction of lamp motion. The IR camera was positioned to monitor the full temperature field, while a flux sensor placed beneath the panel verified irradiance during lamp motion. The robot's path was carefully calibrated to ensure accurate tracking over the panel.

The interpolated irradiance field guided the selection of a 28 mm lamp height for the moving lamp experiments—sufficient to avoid blocking the thermal camera's view. The robotic arm was programmed to traverse a path beyond the lamp's irradiance footprint, ensuring full coverage over the CF/LM-PAEK tows (Figure 1).

Twelve tests were conducted in two phases. The first phase studied how varying speeds affected surface temperature evolution. For lamp powers of 2066 W, 4132 W, and 7025 W, speeds of 200, 300, and 400 mm/s were tested (nine experiments). The second phase aimed to reach the optimal crystallization temperature range (320–340 °C). Speeds were adjusted accordingly: 35 mm/s (2066 W), 130 mm/s (4132 W), and 210 mm/s (7025 W), with additional runs at 100 mm/s and 500 mm/s (4132 W).

Each test followed a consistent procedure: the lamp was set to simmer mode, IR recording began, then after five seconds, the lamp switched to flash mode and the robot initiated motion. The FLIR camera recorded the full heating and cooling cycle, while the flux sensor captured irradiance over time to validate the empirical irradiance model. A new panel was used for each test and preserved for post-experiment material characterization.

2.3 Material Characterization

After the moving lamp experiments, the irradiated CF/LM-PAEK tows within a panel were sectioned to measure the degree of crystallization corresponding to their distance from the lamp, the lamp power, and the lamp speed across the tow. The tows which exceeded the glass transition (Tg) temperature of 150 ◦C were considered for Differential Scanning Calorimetry (DSC) and further analysis. Certain experiments were excluded from mate- rial analysis, since the panel never exceed the Tg. These experiments were: 200 mm/s, 300 mm/s, and 400 mm/s for a power of 2066 W and 500 mm/s for a power of 4132 W .

For each measurement, a hole puncher was used to cut out a disc in the center of an irradiated tow. For the DSC measurements, temperature sweep was set from 40 ◦C to 360 ◦C at a rate of 10 ◦C/m. For all experiments, only tows 1-3 were chosen, since these crossed the Tg threshold. A total of 33 samples were analyzed using DSC including the three as-received pristine (unheated) samples and three oven-baked samples. The pristine samples represented the lower benchmark of CF/LM-PAEK tape crystallinity. On the other hand, the oven-baked samples represented the upper benchmark of crystallinity through a slow heating and cooling process, allowing for increased spherulite growth [33]. Specifically, the oven-baked samples were heated to 310 ◦C and held at 280 ◦C for 60 minutes. The samples were then cooled at a rate of 18 ◦C/min to room temperature. Crystallinity in each sample was estimated using the following standard procedure [10]:

Bulk crystallization is a result of multiple factors during the experiments, but is most influenced by the resulting temperature-time profile during the cooling phase. The temperature data from the IR camera for each experiment was converted to a multidimensional array. Each pixel at any location on the tows exhibited a heating and cooling phase, and is easily extracted for analysis.

3 SUMMARY OF RESULTS

3.1 Irradiance Field Characterization

A 3D irradiance field around the Xenon-arc flash lamp (at 4132 W) was generated using Radial Basis Function interpolation (Figure 2). The irradiance profile revealed a conical decay from the lamp center, dropping from ~0.7 MW/m² near the origin to ~0.2 MW/m² at 20 mm. While the spatial shape remained consistent across power levels, magnitudes scaled with a third-order polynomial function accounting for voltage, frequency, and pulse width. This enables prediction of transient irradiance at any speed or location on the panel.

3.2 Transient Irradiance and Radiant Exposure

As the lamp traverses the panel, the irradiance on a point varies over time. Radiant exposure (He) is computed by integrating irradiance over exposure time. Experimental validation with a flux sensor confirmed strong correlation with the predicted irradiance. Increasing lamp speed narrows the irradiance profile and reduces peak irradiance. Multiple combinations of power and speed can yield the same radiant exposure (Figure 3).

3.3 Temperature Evolution Across the Panel

IR camera measurements show that the surface temperature lags behind the peak irradiance due to thermal diffusion (Figure 4). At high speeds and powers (e.g., 7025 W at 400 mm/s), the temperature front moves slower than the lamp, with increasing lag. Table 1 summarizes this lag, showing temperature front speeds are typically 30–67% of the lamp speed, decreasing with higher lamp power.

3.4 Linking Temperature, Radiant Exposure, and Speed

Bubble plots (Figure 5) reveal that even with equal radiant exposure, different power-speed combinations yield different peak temperatures due to location effects and thermal inertia. Tow 1 (closest to the lamp center) did not always show the highest temperature, likely due to dynamic heat accumulation and loss mechanisms. There is no one-to-one mapping between radiant exposure and peak temperature—thermal response is a function of power, speed, and thermal transport properties.

3.5 Crystallinity Trends

DSC analysis showed only slight increases in crystallinity across samples compared to the as-received material. The highest crystallinity (5.45%) was obtained at 7025 W and 200 mm/s. Most experimental runs yielded crystallinity in the 2.4–3.3% range, similar or slightly above baseline. Oven-baked samples reached much higher crystallinity (18.8%) due to longer controlled cooling. Key factors influencing crystallinity were maximum temperature and cooling duration. However, given the short exposure and rapid cooling inherent to AFP, significant increases in crystallinity are limited without further thermal management (Figure 6).

4 CONCLUSIONS

This study developed a systematic method to quantify the thermal history and resulting crystallinity of CF/LM-PAEK composite tape heated by a Xenon-arc flash lamp. A robotic test setup was used to map the 3D irradiance field and then simulate a moving heat source over a stationary panel. The resulting transient temperature behavior was captured using infrared thermography, and the crystallinity outcomes were analyzed via DSC.

Key findings include:

- A complete irradiance field model was created using robotic measurements, RBF interpolation, and a power-based scaling law, enabling prediction under any lamp setting.
- A clear thermal lag was observed between lamp motion and temperature front, which increases with speed.
- Radiant exposure depends on lamp power, position, and speed; different parameter combinations can result in the same exposure.
- Peak material temperature correlates with radiant exposure and spatial position, not just power and speed, making simple process control insufficient.
- DSC results showed that rapid cooling under the Xenon-arc leads to crystallinity levels significantly lower than those achieved via slow cooling, even when peak temperatures exceeded the melt point.

Overall, the study underscores the need for precise thermal control in AFP of thermoplastics. The experimental framework established here lays the foundation for predictive modeling of thermal behavior and microstructure evolution in advanced manufacturing of CF/LM-PAEK composites.

ACKNOWLEDGEMENT

The Automated Fiber Placement (AFP) system was developed through the University of Texas System's Science and Technology Acquisition and Retention (STAR) program and PD Start-up funding. Authors are grateful to Dr. Rassel Raihan for use of DSC system.

REFERENCES

[1] A. M. Almushaikeh, S. O. Alaswad, M. S. Alsuhybani, B. M. AlOtaibi, I. M. Alarifi, N. B. Alqahtani, S. M. Aldosari, S. S. Alsaleh, A. S. Haidyrah, A. A. Alolyan, et al., Manufacturing of carbon fiber reinforced thermoplastics and its recovery of carbon fiber: A review, Polymer Testing 122 (2023) 108029.

[2] D. Balaji, B. Arulmurugan, V. Bhuvaneswari, An overview of the additive manufacturing of bast fiber-reinforced composites and envisaging advancements using the patent landscape, Polymers 15 (2023).

[3] A. Brasington, C. Sacco, J. Halbritter, R. Wehbe, R. Harik, Automated fiber placement: A review of history, current technologies, and future paths forward, Composites Part C: Open Access 6 (2021) 100182.

[4] V. Balasubramani, K. Nagarajan, Experimental and optimization of interlaminar shear strength and flexural modulus of laminated composite materials under flexural loading, Materials Today Proceedings (2023).

[5] M. H. Nguyen, A. A. Vijayachandran, P. Davidson, D. Call, D. Lee, A. M. Waas, Effect of automated fiber placement (afp) manufacturing signature on mechanical performance, in: AIAA scitech 2019 forum, 2019, p. 0516.

[6] M. H. Nguyen, A. A. Vijayachandran, P. Davidson, D. Call, D. Lee, A. M. Waas, Effect of automated fiber placement (afp) manufacturing signature on mechanical performance of composite structures, Composite Structures 228 (2019) 111335.

[7] Z. Cao, M. Dong, K. Liu, H. Fu, Temperature field in the heat transfer process of peek thermoplastic composite fiber placement, Materials 13 (2020).

[8] X. Guan, R. Pitchumani, Modeling of spherulitic crystallization in thermoplastic tow-placement pro- cess: heat transfer analysis, Composites science and technology 64 (2004) 1123–1134.

[9] Y. Jia, Z. Mao, W. Huang, J. Zhang, Effect of temperature and crystallinity on the thermal conductivity of semi-crystalline polymers: A case study of polyethylene, Materials Chemistry and Physics 287 (2022) 126325.

[10] H. P´erez-Mart´ın, P. Mackenzie, A. Baidak, C. M. Ó Brádaigh, D. Ray, Crystallisation behaviour and morphological studies of pekk and carbon fibre/pekk composites, Composites Part A: Applied Science and Manufacturing 159 (2022) 106992.

[11] N. Hassan, J. E. Thompson, R. Batra, A. B. Hulcher, X. Song, A. C. Loos, A heat transfer analysis of the fiber placement composite manufacturing process, Journal of reinforced plastics and composites 24 (2005) 869–888.

[12] O. A. Tafreshi, S. V. Hoa, F. Shadmehri, D. M. Hoang, D. Rosca, Heat transfer analysis of automated fiber placement of thermoplastic composites using a hot gas torch, Advanced Manufacturing: Polymer & Composites Science 5 (2019) 206–233.

[13] O. Aghababaei Tafreshi, S. Van Hoa, F. Shadmehri, D. M. Hoang, D. Rosca, Determination of con- vective heat transfer coefficient for automated fiber placement (afp) for thermoplastic composites using hot gas torch, Advanced Manufacturing: Polymer & Composites Science 6 (2020) 86–100.

[14] T. Ahmed, D. Stavrov, H. Bersee, A. Beukers, Induction welding of thermoplastic composites—an overview, Composites Part A: Applied Science and Manufacturing 37 (2006) 1638–1651.

[15] R. Rudolf, P. Mitschang, M. Neitzel, Induction heating of continuous carbon-fibre-reinforced thermo- plastics, Composites Part A: Applied Science and Manufacturing 31 (2000) 1191–1202.

[16] T. Bayerl, M. Duhovic, P. Mitschang, D. Bhattacharyya, The heating of polymer composites by electromagnetic induction–a review, Composites Part A: Applied Science and Manufacturing 57 (2014) 27–40.

[17] E. Beyeler, W. Phillips, S. I. Güçeri, Experimental investigation of laser-assisted thermoplastic tape consolidation, Journal of thermoplastic composite materials 1 (1988) 107–121.

[18] C. Stokes-Griffin, P. Compston, Optical characterisation and modelling for oblique near-infrared laser heating of carbon fibre reinforced thermoplastic composites, Optics and Lasers in Engineering 72 (2015) 1–11.

[19] C. Stokes-Griffin, P. Compston, An inverse model for optimisation of laser heat flux distributions in an automated laser tape placement process for carbon-fibre/peek, Composites Part A: Applied Science and Manufacturing 88 (2016) 190–197.

[20] H. Nobelight, Humm3 heating systemr, 2024. URL: https://www.heraeus.com/en/hng/products_and_solutions/arc_and_flash_lamps/humm3/humm3_1/humm3.html.

[21] D. Tavkari, P. Davidson, Thermal characterization of xenon flash lamp system for automated fiber placement, in: ASME Aerospace Structures, Structural Dynamics, and Materials Conference, volume 87745, American Society of Mechanical Engineers, 2024, p. V001T03A002.

[22] D. Tavkari, V. V. Ganesan, S. Amgai, A. Jain, P. Davidson, Thermal characterization of xenon-arc flash lamp heating system for automated fiber placement (afp) of

thermoplastic composites, Composites Part A: Applied Science and Manufacturing 190 (2025) 108568.

[23] S. Shafaqa, M. J. Donough, A. L. Farnsworth, A. W. Phillips, G. Chirima, N. A. S. John, B. B. Arber,
K. Murphy, G. Prusty, On the ply-wise investigation of the crystalline morphology distribution of in-situ consolidated cf/peek composite using wide-angle x-ray scattering (waxs), Composites Part A: Applied Science and Manufacturing 190 (2025) 108792.

[24] D. Ray, A. J. Comer, J. Lyons, W. Obande, D. Jones, R. M. O. Higgins, M. A. McCarthy, Fracture toughness of carbon fiber/polyether ether ketone composites manufactured by autoclave and laser- assisted automated tape placement, Journal of Applied Polymer Science 132 (2015) 41643.

[25] M. Edwards, A. Page, D. Williams, A. Danezis, M. Schilling, T. Jenek, Optimization of xenon flashlamp heating in thermoplastic automated fibre placement, 2021.

[26] R. Lichtinger, P. Hörmann, D. Stelzl, R. Hinterhölzl, The effects of heat input on adjacent paths during automated fibre placement, Composites Part A: Applied Science and Manufacturing 68 (2015) 387–397.

[27] E. Oromiehie, N. D. Chakladar, G. Rajan, B. G. Prusty, Online monitoring and prediction of thermo- mechanics of afp based thermoplastic composites, Sensors 19 (2019) 1310.

[28] I. Schiel, L. Raps, A. R. Chadwick, I. Schmidt, M. Simone, S. Nowotny, An investigation of in-situ afp process parameters using cf/lm-paek, Advanced Manufacturing: Polymer & Composites Science 6 (2020) 191–197.

[29] P. Juarez, E. Gregory, In situ thermal inspection of automated fiber placement for manufacturing induced defects, Composites Part B: Engineering 220 (2021) 109002.

[30] A. Danezis, D. Williams, M. Edwards, A. A. Skordos, Heat transfer modelling of flashlamp heating for automated tape placement of thermoplastic composites, Composites Part A: Applied Science and Manufacturing 145 (2021) 106381.

[31] Victrex, Victrex carbon fiber-paek pre-preg tape, 2024. URL: https://www.victrex.com/en/products/peek-forms/composite-tape.

[32] Hukseflux, Hukseflux sensor, 2024. URL: https://www.hukseflux.com/products/heat-flux-sensors/heat-flux-sensors/gg01-gardon-gauge.

[33] R. Zhang, E. Zhuravlev, R. Androsch, C. Schick, Visualization of polymer crystallization by in situ combination of atomic force microscopy and fast scanning calorimetry, Polymers 11 (2019) 890.

Table 1: Maximum temperature achieved (T_m) for combinations of lamp speed (S_L), speed of maximum temperature front (S_T), and maximum temperature of tape achieved (T_m)

P (W)	*S_L(mm/s)*	*S_T (mm/s)*	*T_m(°C)*
2066	*35*	*33.33*	*339.3*
2066	*200*	*175*	*107.2*
2066	*300*	*271.43*	*83.5*
2066	*400*	*354.17*	*66.9*
4132	*100*	*93.75*	*406*
4132	*130*	*125*	*315.5*
4132	*200*	*189.58*	*238*
4132	*300*	*287.5*	*178.1*
4132	*400*	*341.67*	*143.26*
7025	*200*	*183.93*	*399.3*
7025	*290*	*275.34*	*321.6*
7025	*300*	*277.68*	*292.9*
7025	*400*	*360.71*	*248.6*

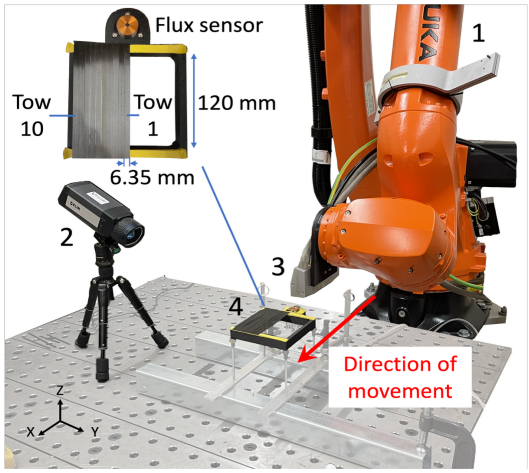

Figure 1: Left: Experimental setup for CFRP tows exposed to irradiance. The KUKA robot (1) controls the movement of the Xenon-arc flash lamp (2). The thermal camera (3) records surface temperature of the tows mounted to a fixture (4). On the fixture, a flux sensor and the first tow are aligned with the straight move path of the lamp.

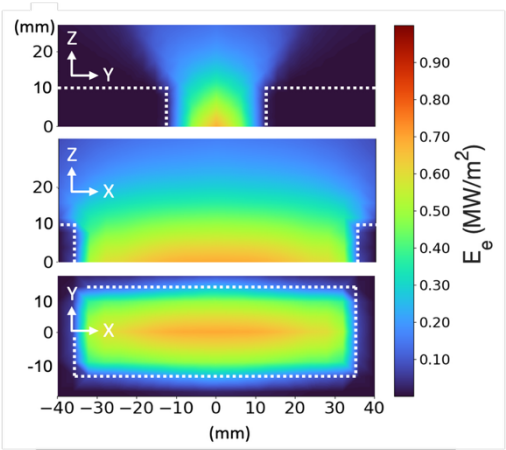

Figure 2: Measured irradiance envelope around the Xenon-arc flash lamp for a power of 4132 W . Dotted white line depicts the lamp head cavity.

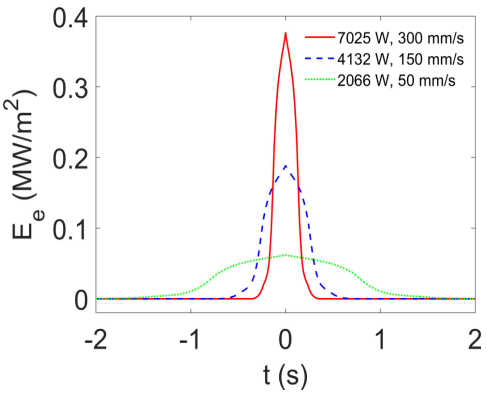

Figure 3: Irradiance profile with the same radiant exposure of 141 KJ/m2 at tow 1 center for difference power and speeds of [7025 W , 200 mm/s],[4132 W , 100 mm/s],[2066 W , 35 mm/s].

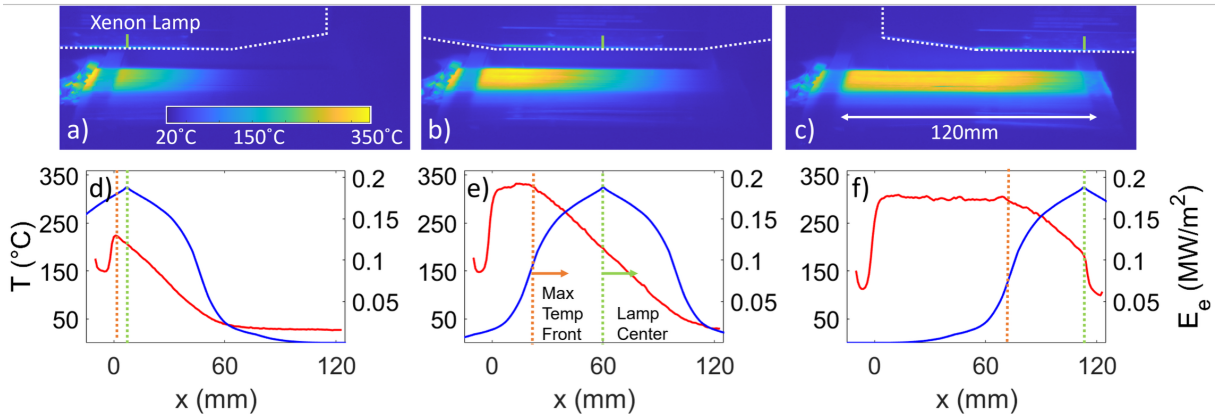

Figure 4: Progression of the surface temperature of CFRP tows subjected to radiation from a moving Xenon- arc flash lamp with a speed of 130 mm/s and power set to 4132 W . Surface temperatures shown are taken at a) t = 0 s, b) t = 0.46 s and c) t = 0.92 s. (d-f) are the corresponding temperatures measured across the length of the first tow directly below the lamp's path. The vertical green lines represents the position of the lamp's center while the vertical orange line represents the peak temperature front moving across the tow for the three frames. Solid red line refers to temperature, and solid blue line refers to irradiance across tow 1 due to lamp motion.

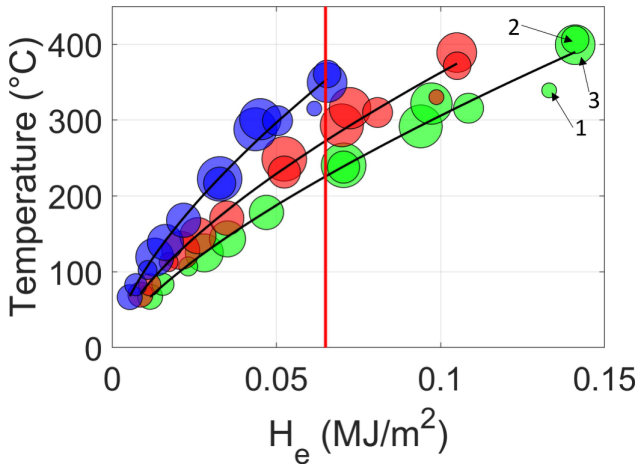

Figure 5: Bubble plot showing variation of temperature with radiant exposure. Bubble size represents the speed of lamp motion.

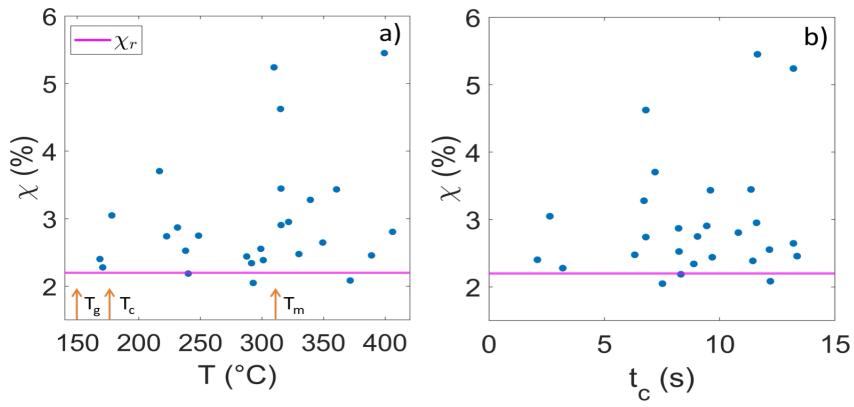

Figure 6: Measured crystallinity for tows 1-3 of all experiments with respect to a) Maximum Temperature and b) cooling duration from peak temperature to 150C.

FIBER WAVINESS IN THERMOPLASTIC CFRP: MECHANISMS OF FORMATION AND MECHANICAL INFLUENCE

Takayu Nishioka[1], Ryo Higuchi[2] and Tomohiro Yokozeki[3]

[1]Department of Aeronautics and Astronautics, The University of Tokyo
7-3-1 Hongo, Bunkyo-ku, Tokyo, Japan
Email: nishioka-takayu687@g.ecc.u-tokyo.ac.jp, web page: https://www.aerospace.t.u-tokyo.ac.jp/en/

[2] Department of Aeronautics and Astronautics, The University of Tokyo
7-3-1 Hongo, Bunkyo-ku, Tokyo, Japan
Email: higuchi@aastr.t.u-tokyo.ac.jp, web page: https://www.aerospace.t.u-tokyo.ac.jp/en/

[3] Department of Aeronautics and Astronautics, The University of Tokyo
7-3-1 Hongo, Bunkyo-ku, Tokyo, Japan
Email: yokozeki@aastr.t.u-tokyo.ac.jp, web page: https://www.aerospace.t.u-tokyo.ac.jp/en/

Keywords: Composite Materials, Thermoplastics, Fiber Waviness

ABSTRACT

In recent years, carbon fiber-reinforced thermoplastics (CFRTPs) have been increasingly applied, particularly in the aerospace field, due to their high productivity and recyclability. However, various molding defects caused by complex molding behaviors and high processing temperatures have hindered their application to critical structural components. Among these, in-plane fiber waviness on the surface of component surfaces is known to reduce longitudinal strength and induce complex damage propagation behavior. While numerous studies have investigated the geometric characteristics of fiber waviness and its influence on mechanical performance, the effects of process-induced phenomena during molding, especially crystallization behavior in thermoplastics, remain largely unexplored. This study aims to develop a numerical analysis framework that captures the entire process, from molding to mechanical performance of fiber waviness, incorporating the effects of the crystallization behavior of thermoplastics during the forming process. The validity of the proposed method is assessed through comparison with experiments, enabling a comprehensive evaluation of residual stresses and their influence on the mechanical performance of CFRTPs with fiber waviness.

1 INTRODUCTION

In recent years, as the application of carbon fiber-reinforced plastic (CFRP) components in aerospace structures has advanced, there has been a growing demand not only for their excellent mechanical properties but also for additional functional innovations, such as recyclability or manufacturing productivity. In response, significant efforts have been directed toward the development of carbon fiber-reinforced thermoplastics (CFRTPs), which use thermoplastic matrices that solidify upon cooling and can be re-melted upon heating. Owing to these characteristics, CFRTPs have attracted considerable attention as recyclable and highly productive materials. However, the high flowability of thermoplastic resins and the elevated processing temperature required during molding pose challenges, resulting in various manufacturing defects that continue to hinder the widespread application of CFRTPs to structural components.

Among these defects, fiber waviness caused by misalignment of fiber orientation is one of the most critical issues [1]. In CFRTP laminates, fiber waviness typically occurs in the in-plane direction of the surface, inducing inhomogeneous stress fields that lead to a reduction in mechanical strength and the emergence of complex fracture modes. These issues are further compounded by the relatively high processing temperatures and crystallization behavior characteristics of thermoplastic matrices, which are known to generate substantial residual strain during molding and cooling [2]. Notably, CFRTPs employed in structural components primarily utilize semicrystalline thermoplastic resins as their matrix

materials, which exhibit distinct crystallization behavior that significantly influences the development of residual strain. While the influence of fiber waviness on mechanical properties has been widely investigated through various numerical analysis methods [3-5], the potential impact of process-induced residual strains on fiber waviness and structure strength has raised increasing concern. Nevertheless, only a limited number of studies have incorporated the effects of molding-induced residual strain into numerical simulations.

Numerous experimental studies have explored the mechanisms of fiber waviness formation in CFRP laminates [6]. Among the various types of fiber waviness, in-plane fiber waviness occurring on the laminate surfaces is known to result from the interaction of multiple factors. Kugler et al. [7] identified key factors, such as tool plate/part coefficient of thermal expansion (CTE) mismatch, temporal temperature gradients, and spatial temperature gradients through comparative investigations of amorphous CFRTPs. Krämer et al. [8] conducted real-time observations of crystalline CFRTPs and revealed the effects of molding conditions on fiber waviness formation. However, the influence of the parameters of molding conditions on fiber waviness formation and the effects on the mechanical properties of CFRTP laminates remain unclear.

This study proposes a numerical analysis framework to investigate the effects of molding conditions on in-plane fiber waviness in CFRTP laminates, with a particular focus on geometric characteristics and mechanical behavior. By comparing numerical simulation results with experimental data, the validity of the proposed approach is evaluated, and the influence of residual stresses generated around the fiber waviness on component strength is examined. This research establishes a link between molding conditions and the structural performance of CFRTP components, thereby contributing to the advancement of forming technologies for CFRTPs.

2 EXPERIMENT

MCCP1223 (CF/PA6 based unidirectional prepreg, Maruhachi Co.) is used as the material in this study. To intentionally induce in-plane fiber waviness through longitudinal compression during molding, A5052 aluminum molds with intentionally poor release agent coverage near the edges are employed, as illustrated in Figure 1. The release agent failure localizes the constraint during the cooling process, promoting localized compressive stress and fiber buckling (see Figure 1). A unidirectional 6-ply laminate (0° stacking) of 200 × 200 mm is prepared, with a total thickness of approximately 1 mm. The laminate is heated and pressed at 280 °C and 1 MPa for 15 minutes.

Three different cooling conditions were applied: Slow cooling (in the hot press), Medium cooling (at room temperature), and Fast cooling (using water). Two laminates were molded under each condition. The average cooling rate between 250 °C and 200 °C was defined as the representative cooling rate: Slow (0.02 K/s), Medium (2.06 K/s), and Fast (24.30 K/s).

After molding, the geometric shape of the fiber waviness is measured using an optical microscope (see Figure 2). Furthermore, mechanical performance is evaluated using four-point bending tests (according to JIS K7074) and tensile tests (according to JIS K7165), with ten specimens tested for each cooling condition (n = 10). Load–displacement curves are used to determine the mechanical strength of the specimens, and the failure modes are identified through post-fracture observations of the tested specimens.

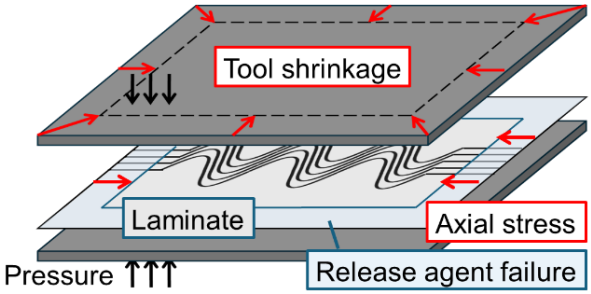

Figure 1: Formation mechanism of fiber waviness in CFRTP laminates

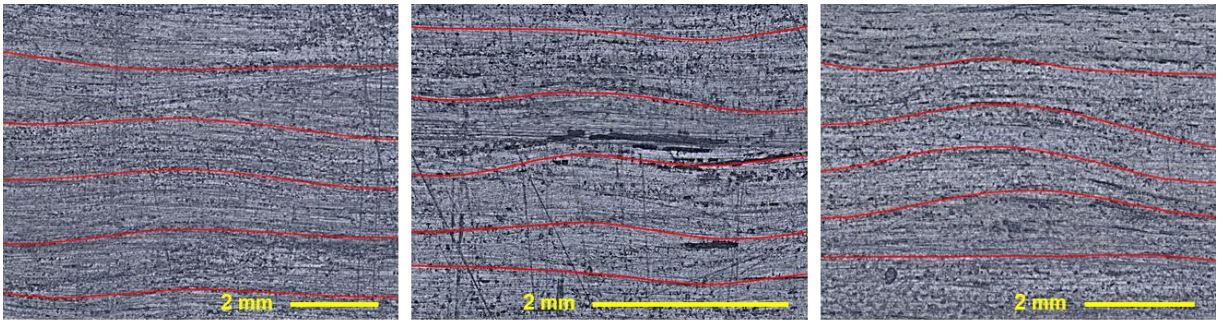

Slow Medium Fast

Figure 2: Optical microscopic images of fiber waviness

3 NUMERICAL ANALYSIS METHOD

3.1 Molding analysis

According to Kugler et al. [7], the primary mechanisms responsible for fiber waviness formation in amorphous CFRTPs include tool plate/part CTE mismatch, temporal temperature gradients, and spatial temperature gradients. Furthermore, in a study on crystalline CFRTPs, Krämer et al. [8] reported that fiber waviness forms during the cooling process within the temperature range between the processing temperature $T_{\max}$ and the crystallization temperature T_c, referred to as the waviness formation temperature interval $\Delta T_w = T_{\max} - T_c$. It was also found that the width of this interval ΔT_w significantly affects the severity of the fiber waviness. Since both the waviness formation temperature interval ΔT_w and the crystallization behavior of thermoplastics are highly dependent on the cooling rate, this study treats the cooling rate as a key molding parameter and investigates its influence on the mechanical characteristics of fiber waviness.

Considering the above findings and the molding characteristics of crystalline thermoplastics, the fiber waviness formation process can be modeled in the following three stages:

(i) Molten phase (Processing temperature $T_{\max}$ to crystallization temperature T_c):
This stage is governed by the fluidity of the thermoplastic matrix.

(ii) Solidification phase (Crystallization temperature T_c to glass transition temperature T_g):
The solidification of the matrix and the generation of residual stresses are considered.

(iii) Solid phase (Glass transition temperature T_g to room temperature T_r):
The matrix is assumed to behave as a fully elastic material.

(i) Molten phase (Processing temperature $T_{\max}$ ~ crystallization temperature T_c)

Above the crystallization temperature T_c, thermoplastics exhibit fluid-like behavior. Therefore, axial compressive stress acting on the fibers due to differential thermal shrinkage between mold and laminate is considered the primary cause of fiber waviness formation. Based on this assumption, the difference in shrinkage between the mold and the laminate during the cooling process is presumed to correspond to the amount of longitudinal shrinkage caused by the formation of fiber waviness.

The difference in thermal strain between the fiber and the mold ε_t can be expressed as:

$$\varepsilon_t = -(\alpha_t - \alpha_f)\Delta T_w, \tag{1}$$

where α_t and α_f are the CTE of mold and fiber. Based on the experimental observations, the geometric shape of fiber waviness is fitted to be sinusoidal as:

$$Y(x,y,z) = 2A_0(z)\cos^2(\pi y/2U)\cos^2(\pi x/\lambda) \tag{2}$$

$$A_0(z) = \begin{cases} A_0^{\max} z \text{ (under compression)} \\ A_0^{\max} \text{ (under tensile)} \end{cases} \tag{3}$$

where x, y: in-plane fiber direction and transverse direction, respectively; z: out-of-plane direction. $A_0^{\max}$: maximum amplitude; λ: wavelength; U: width of the waviness region (Figure 3). The strain caused by the fiber waviness ε_w is then given by:

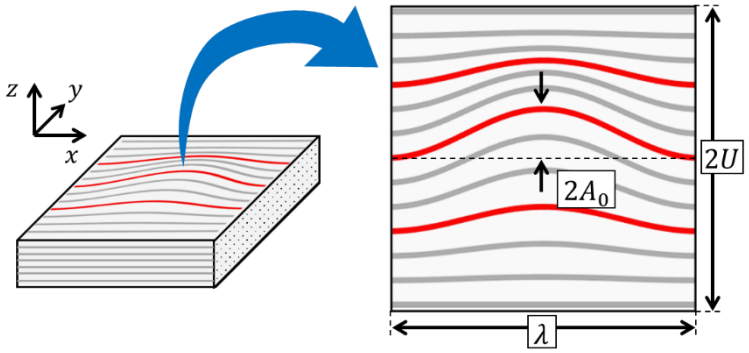

Figure 3: Geometry of fiber waviness

$$\varepsilon_{\mathrm{w}} = \ln\left(\lambda \Big/ \int_{-\lambda/2}^{-\lambda/2} \sqrt{1 + \left(\partial Y/\partial x|_{y=0}\right)^2}\, dx\right). \tag{4}$$

Since fiber waviness is generated locally in CFRTP laminates, the relationship between ε_{t} and ε_{w} can be described using the length subjected to axial fiber compression L_{t} and the length of the waviness region L_{w}:

$$L_{\mathrm{t}}\varepsilon_{\mathrm{t}} = L_{\mathrm{w}}\varepsilon_{\mathrm{w}}. \tag{5}$$

From Equations (1) to (5), the crystallization temperature T_{c} can be associated with the resulting geometric shape of the fiber waviness. Since T_{c} is significantly affected by the cooling rate, this establishes a direct relationship between the cooling rate and the geometric characteristics of fiber waviness. The stiffness of the thermoplastics is sufficiently low, and thus, the residual stress generated during this process is assumed to be negligible.

(ii) Solidification phase (Crystallization temperature T_{c} to glass transition temperature T_{g}):

Below the crystallization temperature T_{c}, it becomes necessary to consider the residual stresses generated during the cooling process due to the increase in matrix stiffness. In thermoplastics, shrinkage during the cooling process can be broadly classified into two categories: thermal shrinkage, caused by reduced molecular mobility with decreasing temperature, and crystallization shrinkage, resulting from the formation of crystalline structures. An incremental linear elasticity (ILE) model [9,10], which employs representative material properties in segments, introduced, is introduced to implement these effects of thermal shrinkage in numerical analysis.

Crystallization kinetics are modeled using the Ziabicki–Nakamura equation [11,12], a non-isothermal crystallization model:

$$\tilde{\theta}(t) = 1 - \exp\left[-\left(\int_0^t K(T)dt\right)^n\right], \tag{6}$$

$$K(T) = K_{\max} \exp\left[\frac{-4\ln 2\,(T-\bar{T})^2}{D^2}\right], \tag{7}$$

where $\tilde{\theta}(t)$: the relative degree of crystallinity with respect to the maximum degree of crystallinity at time t, $K(T)$: the crystallization rate constant at temperature T, n: the Avrami index representing the fractal dimension of the crystals, and $K_{\max}, \bar{T}, D$: fitting parameters in the Gaussian approximation of the crystallization rate.

In this study, it is assumed that the mechanical properties of the thermoplastic matrix are proportional to its degree of crystallinity. The total shrinkage strain is considered to consist of two components: thermal shrinkage, which is proportional to the temperature change, and crystallization shrinkage, which is proportional to the degree of crystallinity. The magnitude of the crystallization shrinkage strain is estimated based on the warpage deformation in asymmetric laminates with a [0/90/90] stacking sequence, according to reference [13].

(iii) Solid phase (Glass transition temperature T_g to room temperature T_r)

Since no further crystallization is assumed to occur below the glass transition temperature T_g, the mechanical properties of the matrix are considered constant. Therefore, only the effects of thermal shrinkage are considered in this process. Finally, the demolding process is modeled by imposing a stress-free boundary condition on the model.

3.2 Strength analysis

Around the fiber waviness, complex damage behavior can arise due to the combined effects of the geometric shape of the fiber waviness and applied load conditions. To investigate this phenomenon, a high-fidelity numerical approach is introduced, in which fiber- and matrix-dominated damage mechanisms are modeled separately.

In fiber-dominated damage, it is well known that distinct failure mechanisms occur under longitudinal compressive and tensile loading. Under compressive loading, inhomogeneous shear stress fields arising from the initial fiber misalignment trigger the shear yielding of the matrix, leading to the formation of kink bands. In this study, the LaRC03 failure criterion [14], which accounts for fiber misalignment, is introduced for the onset of kink band. In addition, the physical based model (PBM) [15,16] is implemented to represent energy dissipation due to matrix plastic deformation. Under tensile loading, brittle damage associated with fiber fracture progresses, with failure initiation occurring randomly. This introduces a size effect, which is addressed in this study using the Weibull failure criterion [17].

In matrix-dominated damage, it is essential to capture displacement discontinuities caused by matrix cracking. In CFRP laminates, matrix cracks typically propagate along the fiber direction and can exhibit complex geometries. To efficiently model this cracking behavior, this study employs the extended finite element method (XFEM) [18,19], which allows for the representation of displacement discontinuities independently of the mesh geometry. Furthermore, to capture the plastic zone around the crack tip, a cohesive zone model (CZM) [20] is incorporated in conjunction with XFEM.

4 RESULTS AND DISCUSSION

4.1 Simulation conditions

Numerical simulations are performed under three different cooling conditions: Slow (0.02 K/s), Medium (2.06 K/s), and Fast (24.30 K/s), in accordance with the experimental setup. The influence of cooling conditions on the geometric shape of the fiber waviness and its mechanical effects are investigated.

The dimensions of the finite element model are shown in Figure 4. Since fiber waviness forms continuously on the surface of the component, a representative volume element (RVE) with periodic boundary conditions is used as the analysis domain. In the four-point bending analysis, macroscopic curvature is applied, and the analysis is terminated when a 5% load drop is observed. In the tensile test simulation, macroscopic in-plane strain is applied, and the analysis is terminated when the Weibull failure criterion is satisfied. Structural strength is evaluated based on the surface stress of the RVE at the termination point of each analysis.

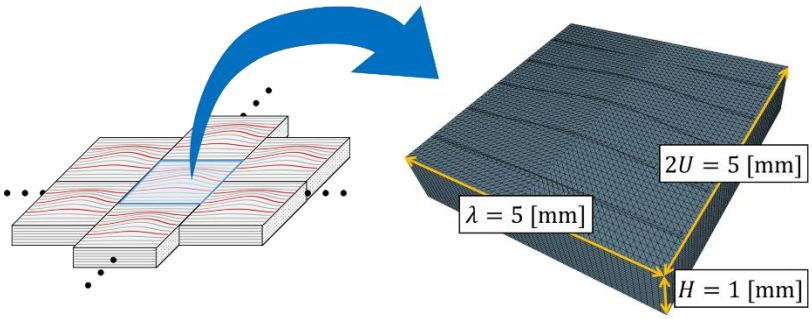

Figure 4: Finite element model and its dimensions

4.2 Experimental and simulation results

The effect of the cooling rate on the geometric characteristics of fiber waviness is shown in Figure 5. The vertical axis represents the severity of waviness, which is commonly used as a geometric metric of fiber waviness and is defined as:

$$w = A_0^{\max}/\lambda. \tag{8}$$

The simulation results show reasonable agreement with experimental data. These results indicate that the severity of fiber waviness increases with higher cooling rates. This is because higher cooling rates lead to lower crystallization temperature, thereby widening the waviness formation temperature interval ΔT_{w} in which fiber waviness forms. However, it should be noted that the Fast cooling condition exceeds the validated range of the cooling rate range of the DSC device (DSC 8500, Perkin Elmer Co.) used in the measurements of crystallization temperature, and further investigation is required.

Figure 6 presents both experimental and numerical results for the dependence of compressive and tensile strength on cooling rate. The vertical axis indicates the normalized strength obtained by dividing the measured or simulated strength by the reference strength of a specimen without fiber waviness. The numerical results show good agreement with the experimental data. Additionally, simulation results without residual stresses are included in Figure 6 to assess the effect of residual stresses on the mechanical behavior associated with fiber waviness. These results indicate that residual stresses generated around the fiber waviness region contribute to an increase in compressive strength while causing a reduction in tensile strength.

In the next section, the effects of the residual stress fields induced around the fiber waviness on the mechanical properties and the underlying mechanisms are discussed.

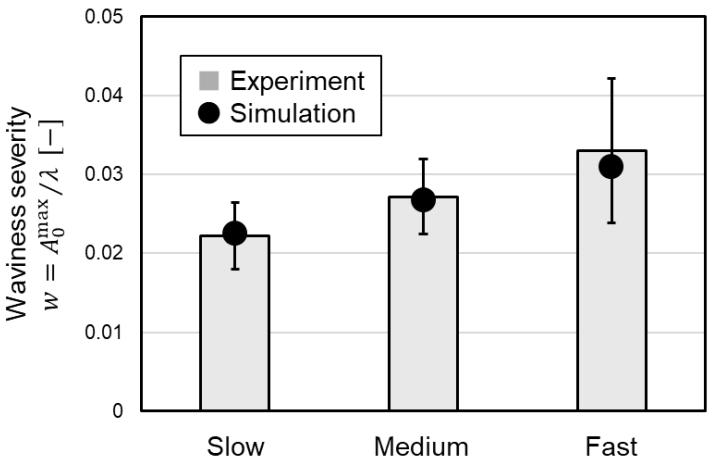

Figure 5: Cooling rate-dependent waviness geometry

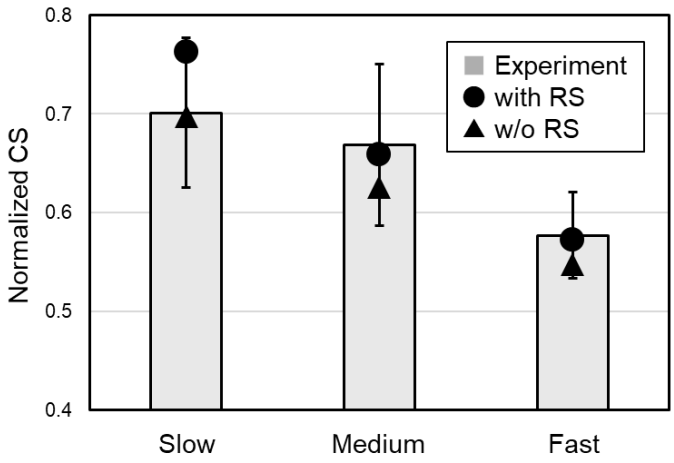

(a) Compressive strength

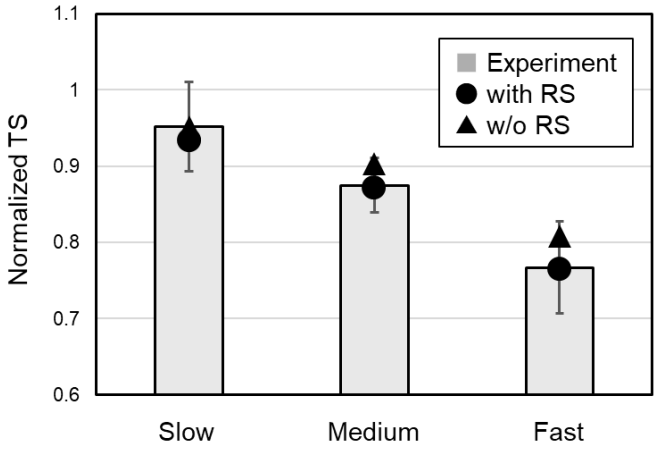

(b) Tensile strength

Figure 6: Cooling rate-dependent structural strength

4.3 Discussion

The residual stresses around the fiber waviness contribute to an increase in compressive strength while leading to a reduction in tensile strength. This behavior is closely related to the dominant damage mechanisms occurring near the fiber waviness.

Under compressive loading, kink bands and matrix cracks are initiated around the fiber waviness due to localized shear stress, ultimately resulting in failure (Figure 7). In contrast, under tensile loading, matrix cracking caused by localized shear stress induces stress concentration, which subsequently leads to fiber breakage (Figure 8). As shown in Figure 9 and Figure 10, the residual shear stress field generated by fiber waviness acts in the opposite direction to the shear stress field induced under compressive loading but in the same direction as that induced under tensile loading. This observation suggests that the residual stress field helps to suppress damage under compressive loading while it facilitates damage initiation under tensile loading.

Among the three cooling conditions, the residual shear stress field is found to be most pronounced under the slow cooling condition. Although both the geometric nonlinearity of fiber waviness and the magnitude of matrix shrinkage during cooling contribute to the development of the residual shear stress field, the results indicate that matrix shrinkage has a more dominant influence.

Considering the residual stresses, the simulation results for the Medium and Fast cooling conditions show good agreement with the experimental data. However, this is not the case for the Slow condition. The proposed analysis approach does not account for time-dependent effects in the resin, such as the relaxation of residual stresses. Therefore, the development of numerical methods capable of capturing these effects is needed in future work.

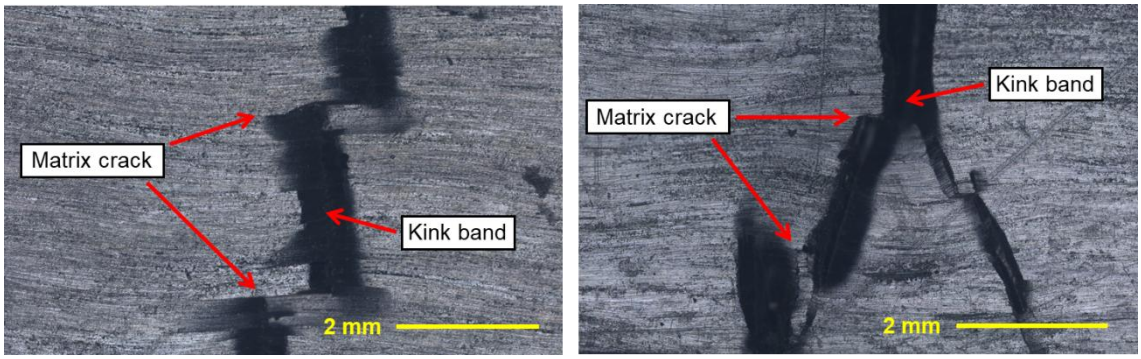

Slow Fast

(a) Experimental observation

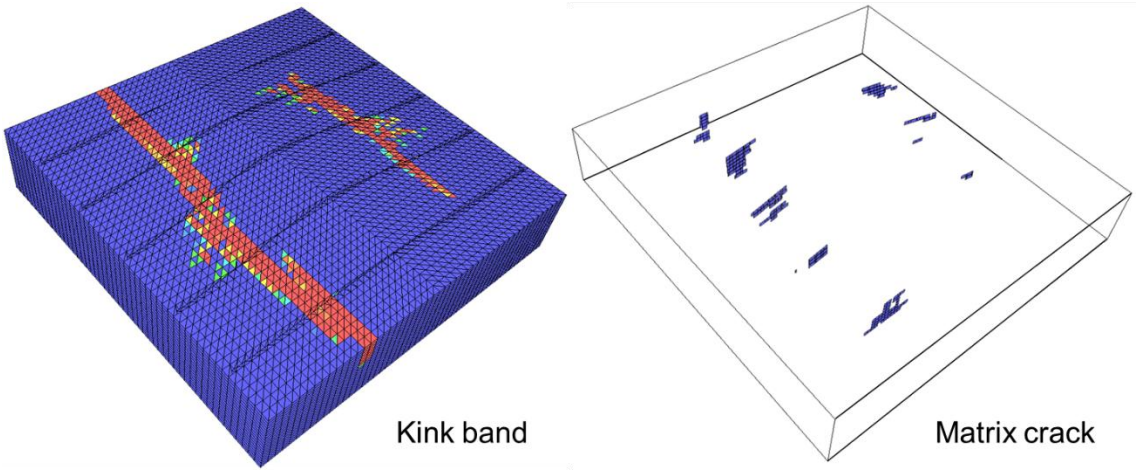

(b) Simulation (Fast cooling rate)

Figure 7: Fracture mode under compressive loading

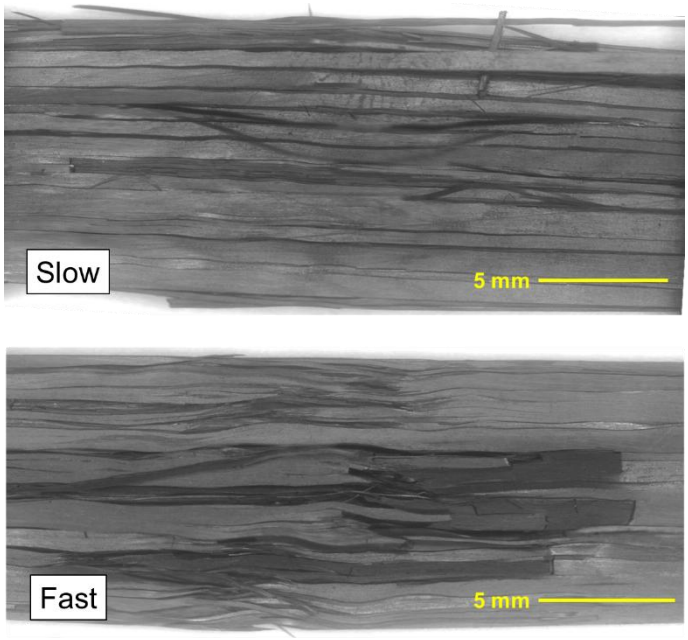

(a) Experimental observation

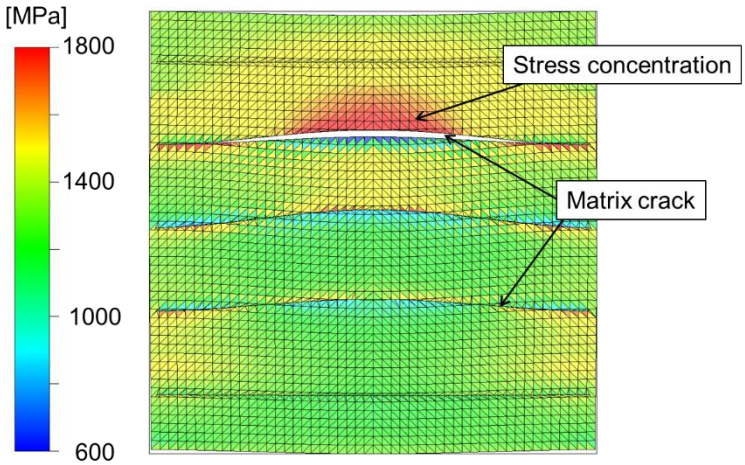

(b) Simulation (Fast cooling rate)

Figure 8: Fracture mode under tensile loading

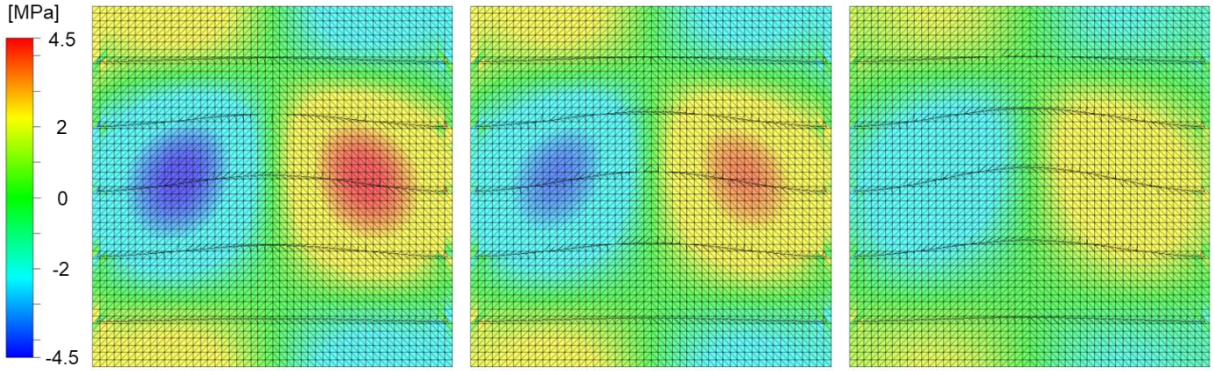

Slow Medium Fast

Figure 9: Residual shear stress around fiber waviness

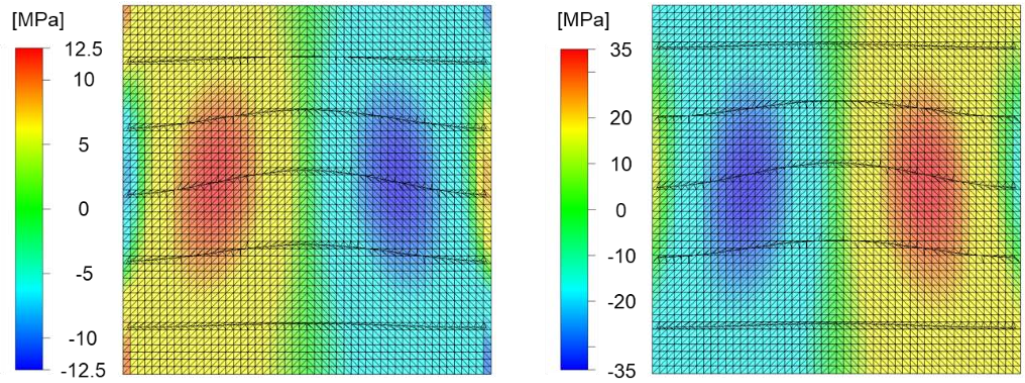

Figure 10: Shear stress field around fiber waviness
(Left: Under compressive loading $K = 0.01$, Right: Under tensile loading $E = 0.01$)

5 CONCLUSION

In this study, a numerical analysis framework is developed to investigate the relationship between molding conditions, specifically cooling rate, and the geometric and mechanical characteristics of in-plane fiber waviness in CFRTP laminates. The proposed method incorporates a process-dependent residual stress formulation based on the crystallization behavior of semicrystalline thermoplastics and evaluates its influence on mechanical performance through comparison with experimental data.

The results demonstrated that higher cooling rates lead to more severe fiber waviness due to a wider waviness formation temperature interval associated with a lower crystallization temperature. The severity of fiber waviness is found to significantly affect both compressive and tensile strength, and the proposed simulation framework showed good agreement with experimental results under Medium and Fast cooling conditions.

Residual stresses generated around the fiber waviness region are shown to enhance compressive strength by offsetting the externally applied shear stress field, while they promoted failure under tensile loading due to reinforcement of the local stress field. These mechanisms were validated by both experimental observations and simulation results.

However, discrepancies between simulation and experiment under the Slow cooling condition highlight the limitations of the current framework, which does not account for time-dependent effects such as residual stress relaxation during slow cooling. Future work should focus on incorporating viscoelastic behavior and long-term stress relaxation models into the process simulation in order to further improve the accuracy and predictive capability of fiber waviness modeling in CFRTPs.

ACKNOWLEDGEMENTS

This work was supported by the International Graduate Program for Excellence in Earth-Space Science (IGPEES), a World-leading Innovative Graduate Study (WINGS) Program at the University of Tokyo, and by the Japan Society for the Promotion of Science (JSPS) KAKENHI (Grant No. 24KJ0958).

REFERENCES

[1] P. Kulkarni, K. D. Mali and S. Singh, An overview of the formation of fibre waviness and its effect on the mechanical performance of fibre reinforced polymer composites, *Composites Part A: Applied Science and Manufacturing,* **137**, 2020, 106013 (doi: 10.1016/j.compositesa.2020.106013).

[2] P.P. Parlevliet, H.E.N. Bersee and A. Beukers, Residual stresses in thermoplastic composites—A study of the literature—Part I: Formation of residual stresses, *Composites Part A: Applied Science and Manufacturing,* **37**, 2006, pp. 1847-1857 (doi: 10.1016/j.compositesa.2005.12.025).

[3] S.N. Nair, A. Dasari, C.Y. Yue and S. Narasimalu, Failure behavior of unidirectional composites under compression loading: effect of fiber waviness, *Materials*, **10**, 2017, 909 (doi: 10.3390/ma10080909).

[4] D. Wilhelmsson, R. Gutkin, F. Edgren and L.E. Asp, An experimental study of fibre waviness and its effects on compressive properties of unidirectional NCF composites, *Composites Part A: Applied Science and Manufacturing,* **107**, 2018, pp. 665-674 (doi: 10.1016/j.compositesa.2018.02.013).

[5] T. Yokozeki, H. Takemura and T. Aoki, Numerical analysis on the flexural strength of unidirectional CFRTP composites with in-plane fiber bundle waviness, *Advanced Composite Materials*, **29**, 2020, pp. 89–100 (doi: 10.1080/09243046.2019.1650322).

[6] M. P. Alves, C. A. Cimini Junior and S. K. Ha, Fiber waviness and its effect on the mechanical performance of fiber reinforced polymer composites: An enhanced review, *Composites Part A: Applied Science and Manufacturing*, **149**, 2021, 106526 (doi: 10.1016/j.compositesa.2021.106526).

[7] D. Kugler and T. J. Moon, Identification of the Most Significant Processing Parameters on the Development of Fiber Waviness in Thin Laminates, *Journal of Composite Materials*, **36**, 2002, pp. 1451–1479 (doi: 10.1177/0021998302036012575).

[8] E. T. M. Krämer, W. J. B. Grouve, S. Koussios, L. L. Warnet and R. Akkerman, Real-time observation of waviness formation during C/PEEK consolidation, *Composites Part A: Applied Science and Manufacturing*, **133**, 2020, 105872 (doi: 10.1016/j.compositesa.2020.105872).

[9] C. Brauner, C. Peters, F. Brandwein and A. S. Herrmann, Analysis of process induced deformations in thermoplastic composite materials, *Journal of Composite Materials*, **48**, 2014, pp. 2779–2791 (doi: 10.1177/0021998313502101).

[10] T. Tsukada, S. Minakuchi and N. Takeda, Assessing residual stress redistribution during annealing in thick thermoplastic composites using optical fiber sensors, *Journal of Thermoplastic Composite Materials*, **33**, 2020, pp. 53-68 (doi: 10.1177/0892705718804580).

[11] A. Ziabicki, *Fundamentals of Fibre Formation: The Science of Fibre Spinning and Drawing*, John Wiley, London, 1976.

[12] K. Nakamura, T. Watanabe, K. Katayama and T. Amano, Some aspects of nonisothermal crystallization of polymers. I. Relationship between crystallization temperature, crystallinity, and cooling conditions, *Journal of Applied Polymer Science*, 16, 1972, pp. 1077–1091 (doi: 10.1002/app.1972.070160503).

[13] K.D. Cowley and P.W.R. Beaumont, The measurement and prediction of residual stresses in carbon-fibre/polymer composites, *Composites Science and Technology,* **57**, 1997, pp. 1445-1455 (doi: 10.1016/S0266-3538(97)00048-1).

[14] C. G. Dávila and P. P. Camanho, Failure Criteria for FRP Laminates in Plane Stress, NASA/TM-2003-212663, 2003.

[15] S. Costa, R. Gutkin and R. Olsson, Mesh objective implementation of a fibre kinkingmodel for damage growth with friction, *Composite Structures*, **168,** 2017, pp. 384–391 (doi: 10.1016/j.compstruct.2017.02.057).

[16] S. Costa, M. Fagerström and R. Olsson, Development and validation of a finite deformation fibre kinking model for crushing of composites, *Composites Science and Technology,* **197**, 2020, 108236 (doi: 10.1016/j.compscitech.2020.108236).

[17] S.R. Hallett, B.G. Green, W.G. Jiang and M.R. Wisnom, An experimental and numerical investigation into the damage mechanisms in notched composites, *Composites Part A: Applied Science and Manufacturing,* **40**, 2009, pp. 613-624 (doi: 10.1016/j.compositesa.2009.02.021).

[18] N. Moës, J. Dolbow, and T. Belytschko, A finite element method for crack growth without remeshing, *International Journal for Numerical Methods in Engineering*, **46**, 1999, pp. 131–150 (doi: 10.1002/(SICI)1097-0207(19990910)46:1<131::AID-NME726>3.0.CO;2-J).

[19] T. Belytschko and T. Black, Elastic crack growth in finite elements with minimal remeshing, *International Journal for Numerical Methods in Engineering*, **45**, 1999, pp. 601–620 (doi: 10.1002/(SICI)1097-0207(19990620)45:5<601::AID-NME598>3.0.CO;2-S).

[20] P. P. Camanho and C. G. Dàvila, Mixed-Mode Decohesion Finite Elements for the Simulation of Delamination in Composite Materials, NASA/TM-2002-211737, 2002.

LUNAR: a tool for setting up process modeling based molecular dynamics simulations

Josh Kemppainen[1*]
Gregory M. Odegard[1]
08/06/2025

[1] Michigan Technological University, Houghton, MI 49931

*Corresponding Author: jdkemppa@mtu.edu

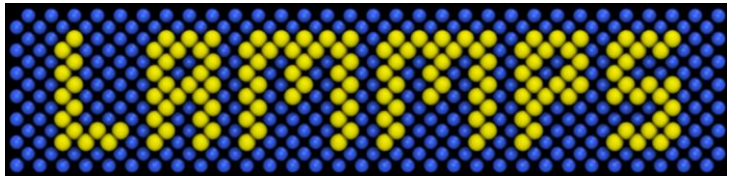

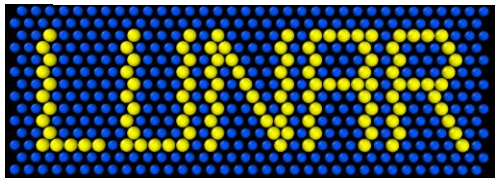

Outline

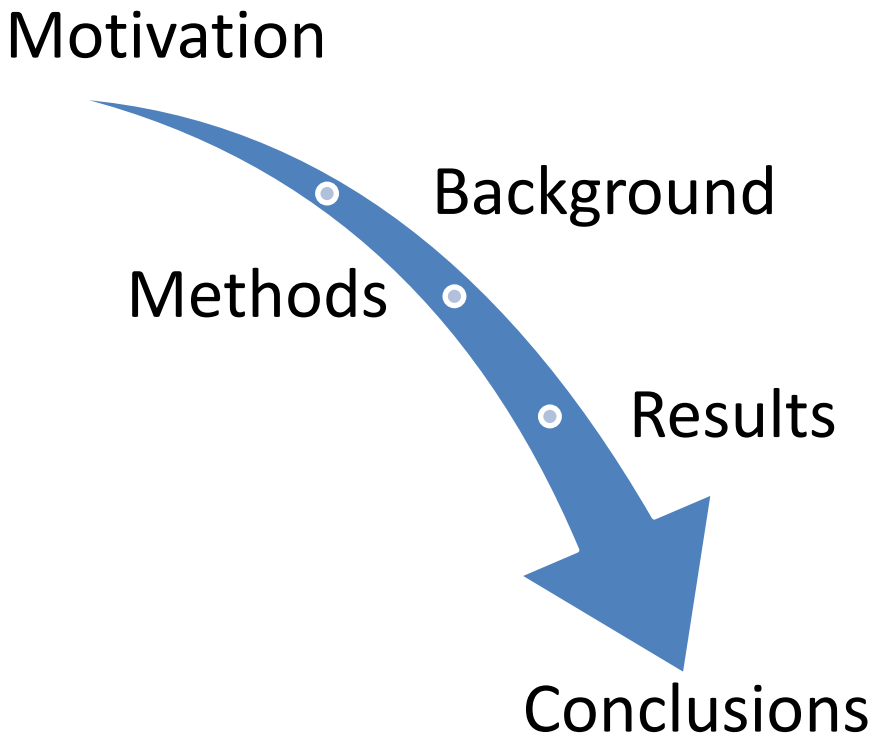

Motivation – Lightweight and tailorable properties

“Polymer matrix composites are lighter, stronger, and stiffer than traditional materials—and they can be tailored for specific needs.”

— National Academies

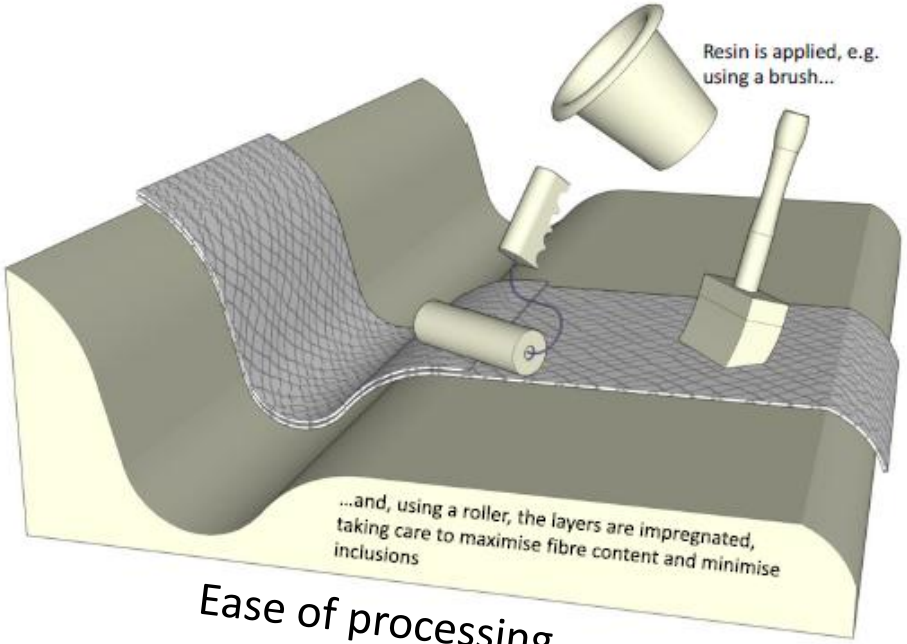

Ease of processing

National Academies - High-Performance Structural Fibers for Advanced Polymer Matrix Composites: https://doi.org/10.17226/11268.
Nijssen – Composite Materials an introduction

Background - ICME (Integrated computational materials engineering)

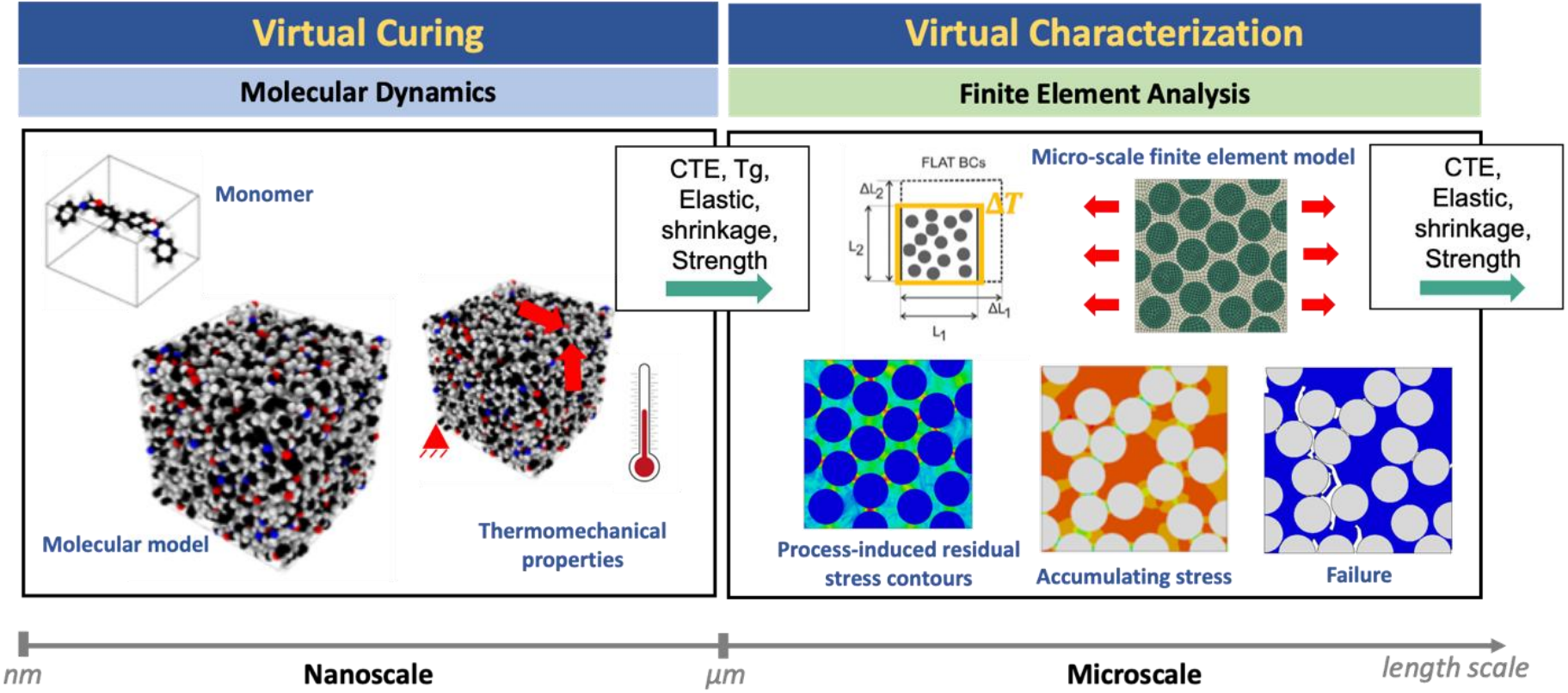

Deshpande, 2023: Multiscale Process Modeling of a Carbon Fiber/Epoxy Composite for Predicting Residual Stress and Strength

Background - MD simulation

$$\boldsymbol{r_A}(t+\Delta t) = \boldsymbol{r_a}(t) + \boldsymbol{v_a}(\Delta t) + \left(\frac{1}{2}\boldsymbol{a_A}\right)(\Delta t)^2$$

- $\mathbf{F_A}$ force on an atom
- U_A potential energy
- m_A mass of an atom
- $\boldsymbol{v_A}$ velocity of an atom
- $\boldsymbol{a_A}$ acceleration of an atom
- $\mathbf{r_A}$ position of an atom
- Δt timestep

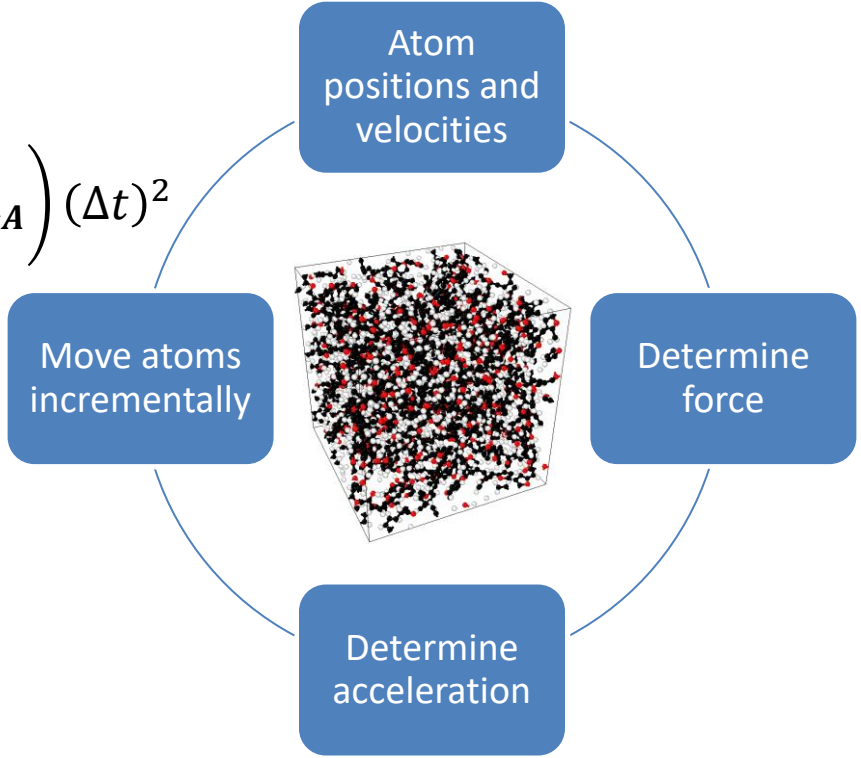

$$\boldsymbol{F_A} = -\nabla U_A$$

$$\boldsymbol{a_A} = \frac{\boldsymbol{F_A}}{m_A}$$

Molecular Modelling for Beginners by Alan Hinchliffe

Background - MD simulation

$$\boldsymbol{r_A}(t+\Delta t) = \boldsymbol{r_a}(t) + \boldsymbol{v_a}(\Delta t) + \left(\frac{1}{2}\boldsymbol{a_A}\right)(\Delta t)^2$$

- $\mathbf{F_A}$ force on an atom
- U_A potential energy
- m_A mass of an atom
- $\boldsymbol{v_A}$ velocity of an atom
- $\boldsymbol{a_A}$ acceleration of an atom
- $\mathbf{r_A}$ position of an atom
- Δt timestep

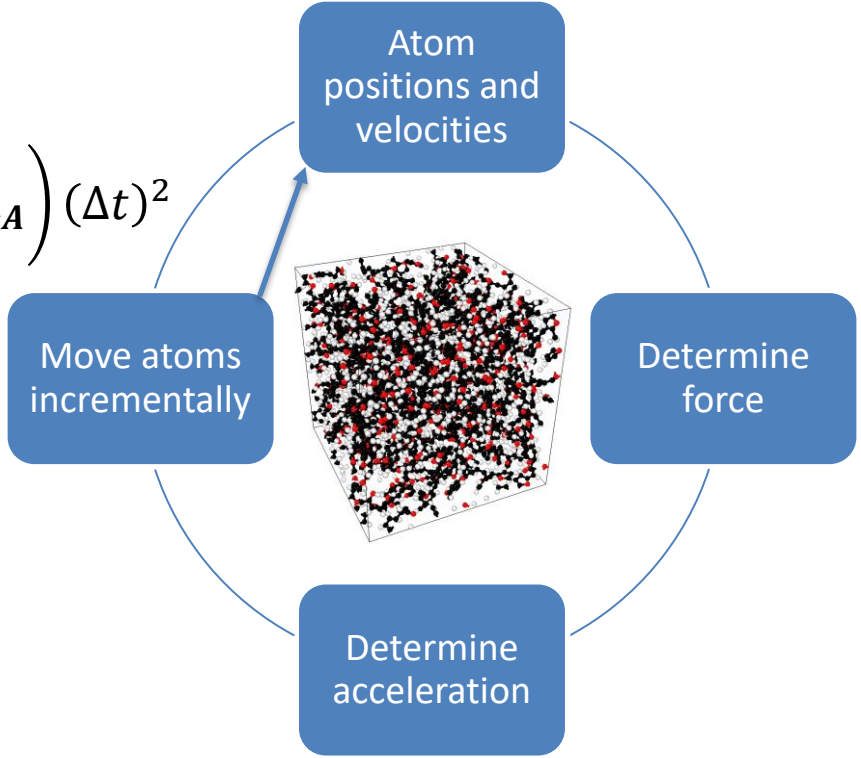

$$\boldsymbol{F_A} = -\nabla U_A$$

$$\boldsymbol{a_A} = \frac{\boldsymbol{F_A}}{m_A}$$

Molecular Modelling for Beginners by Alan Hinchliffe

Background – MD fixed bond force field basics

Bond

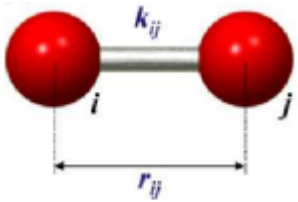

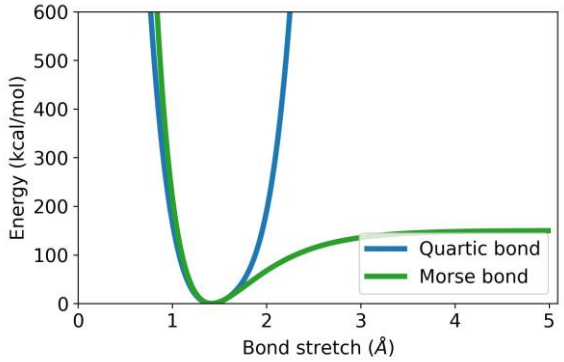

$$E = K_2 (r - r_0)^2 + K_3 (r - r_0)^3 + K_4 (r - r_0)^4$$

$$E = D\left[1 - e^{-\alpha(r - r_0)}\right]^2$$

Angle

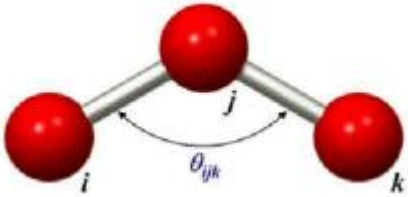

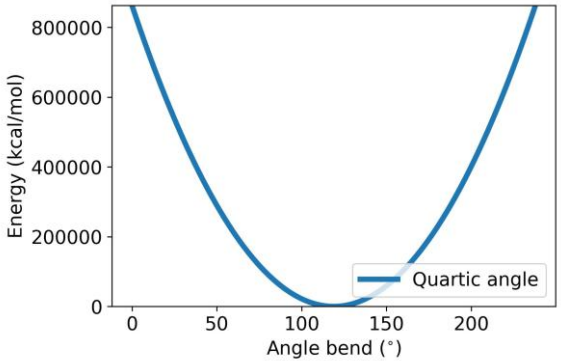

$$E = K_2 (\theta - \theta_0)^2 + K_3 (\theta - \theta_0)^3 + K_4 (\theta - \theta_0)^4$$

Dihedral

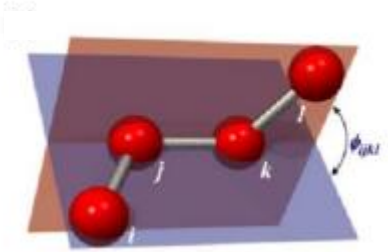

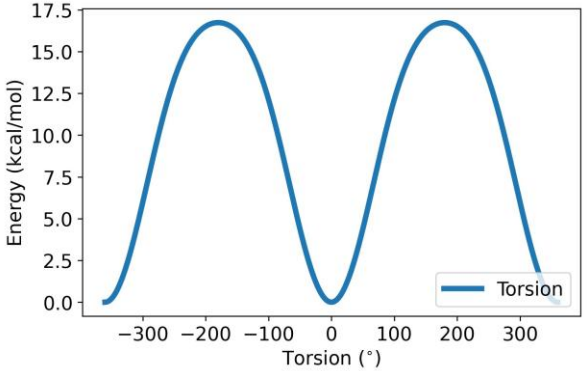

$$E = \sum_{n=1}^{3} K_n[1 - cos(n\varphi - \varphi_n)]$$

Background – MD fixed bond force field basics

Improper

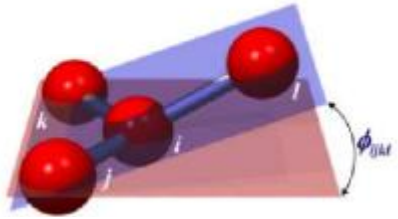

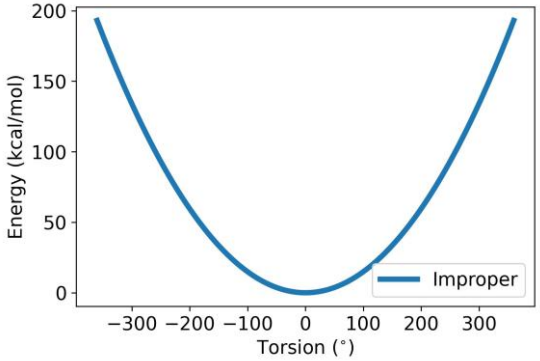

$$\mathbf{E} = \mathbf{K}\left[\frac{\boldsymbol{\phi_{ijkl}} + \boldsymbol{\phi_{kjli}} + \boldsymbol{\phi_{ljik}}}{\mathbf{3}} - \boldsymbol{\phi_0}\right]^2$$

van der Waals

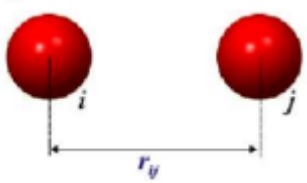

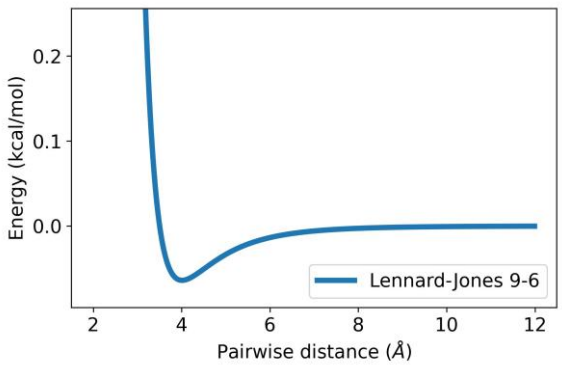

$$\mathbf{E} = \boldsymbol{\epsilon}\left[\mathbf{2}(\frac{\boldsymbol{\sigma}}{\boldsymbol{r}})^{\mathbf{9}} - \mathbf{3}(\frac{\boldsymbol{\sigma}}{\boldsymbol{r}})^{\mathbf{6}}\right]$$

Electrostatics

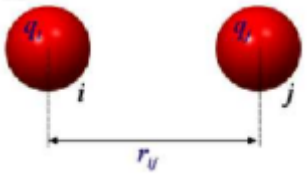

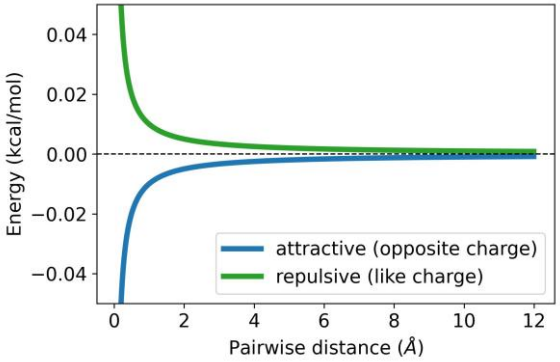

$$\mathbf{E} = \frac{\boldsymbol{C q_i q_j}}{\boldsymbol{\epsilon r}}$$

LUNAR overview

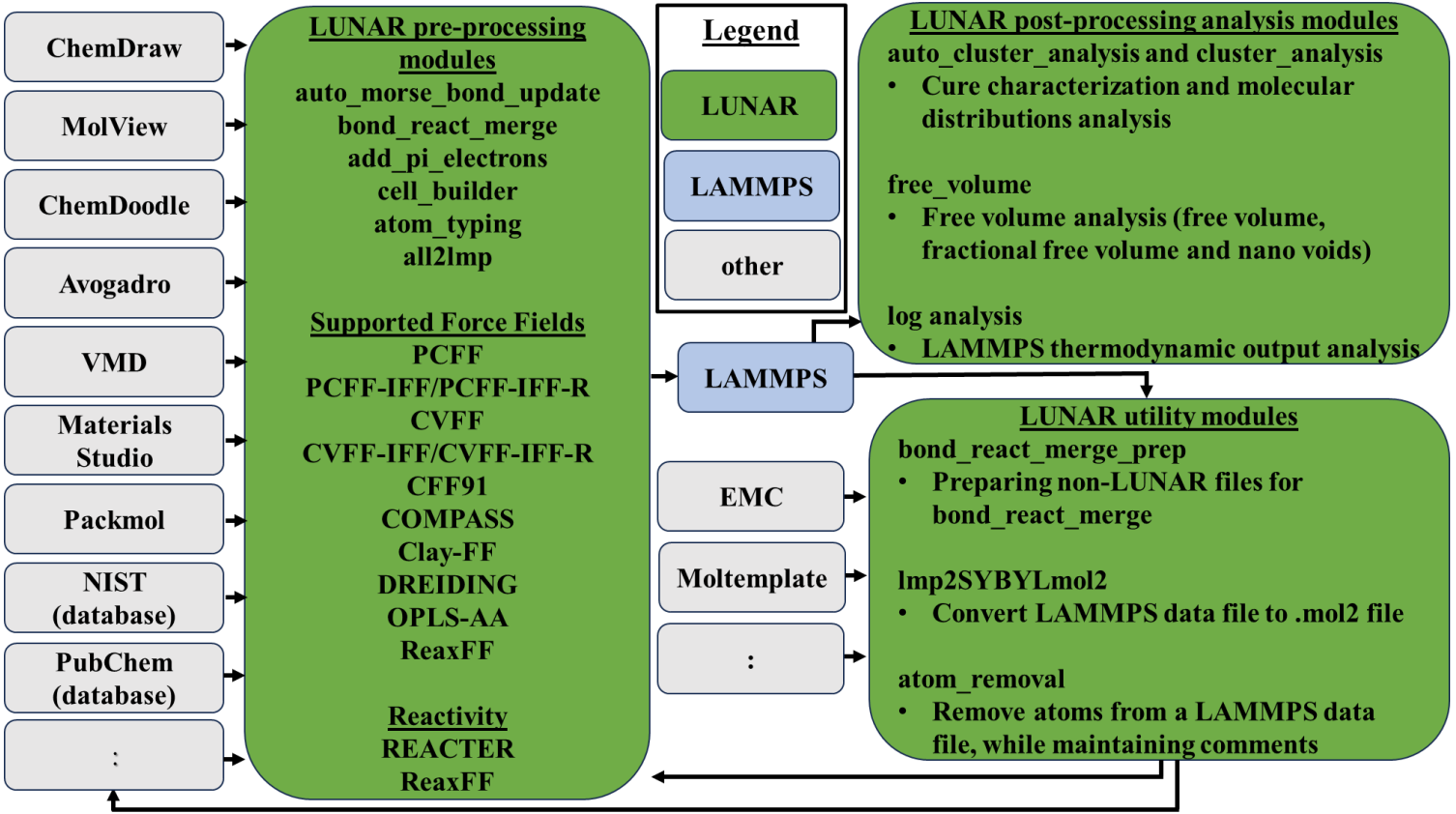

Benchmark systems

Cyanate ester

bisphenol E dicyanate

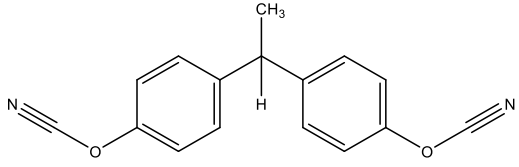

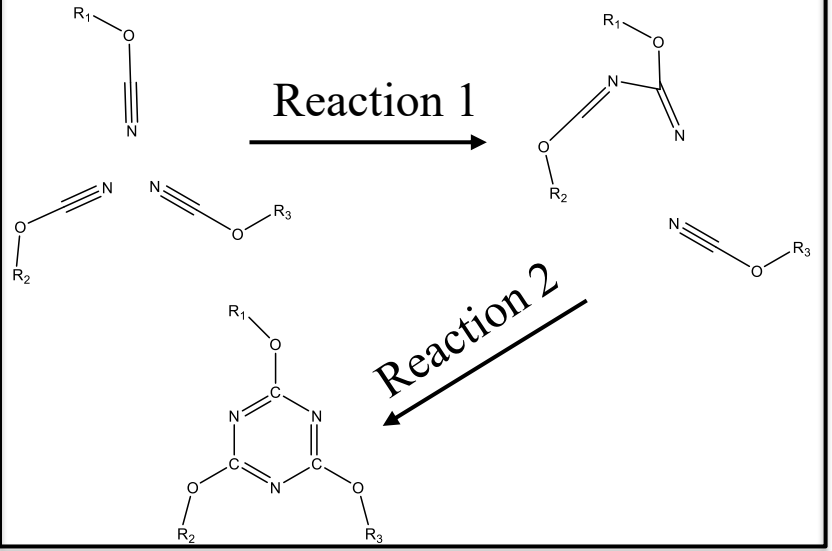

DGEBF (Qty: 2)

diglycidyl ether bisphenol F

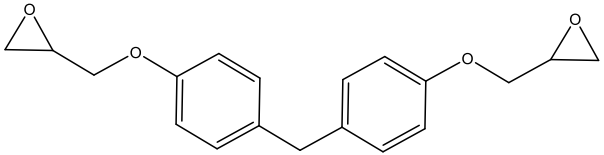

DETDA (Qty: 1)

diethyltoluenediamine

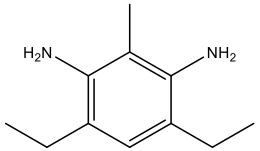

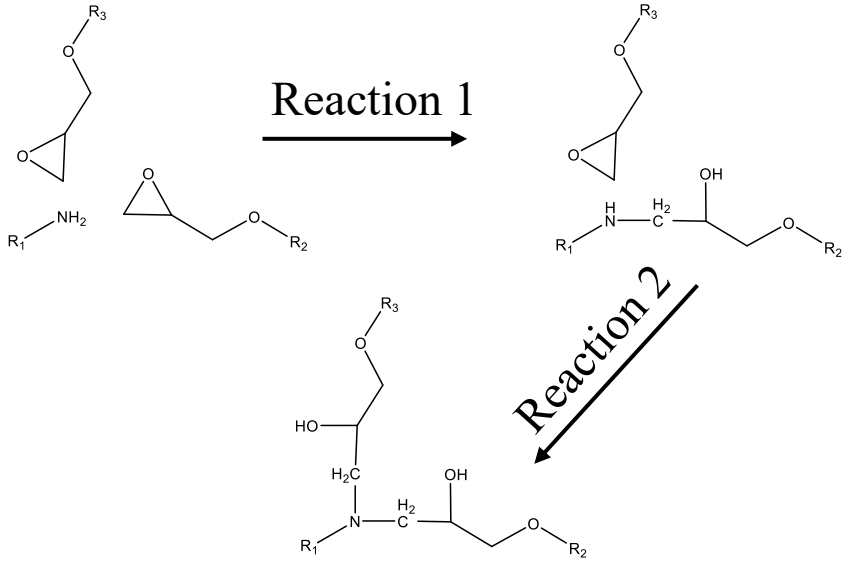

Mix: Randomly place and orientate molecules

cell_builder (random)

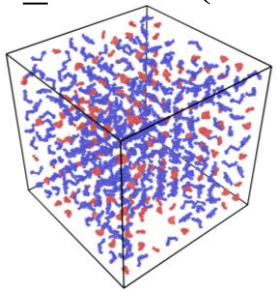

cell_builder (amorphous)

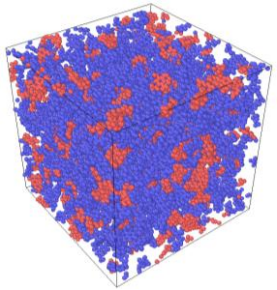

cell_builder (grouped)

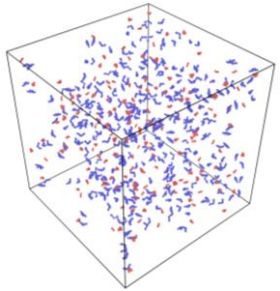

LAMMPS *"create_atoms"*

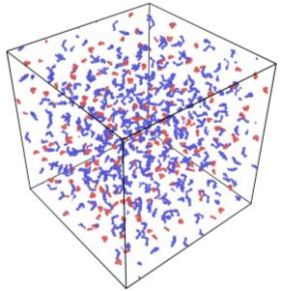

LAMMPS *"replicate"*

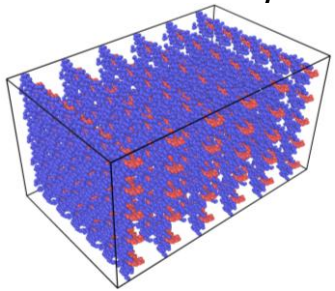

Packmol gas

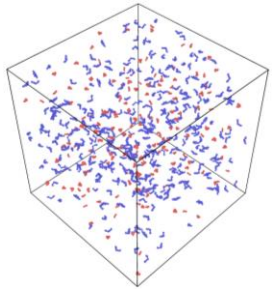

Packmol liquid

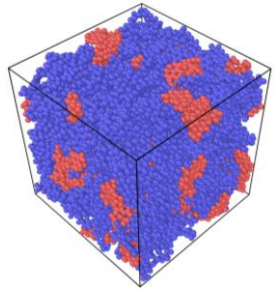

DGEBF DETDA

Mix: Randomly place and orientate molecules

LUNAR/cell_builder.py options

Random (r)

Grouped locally (g)

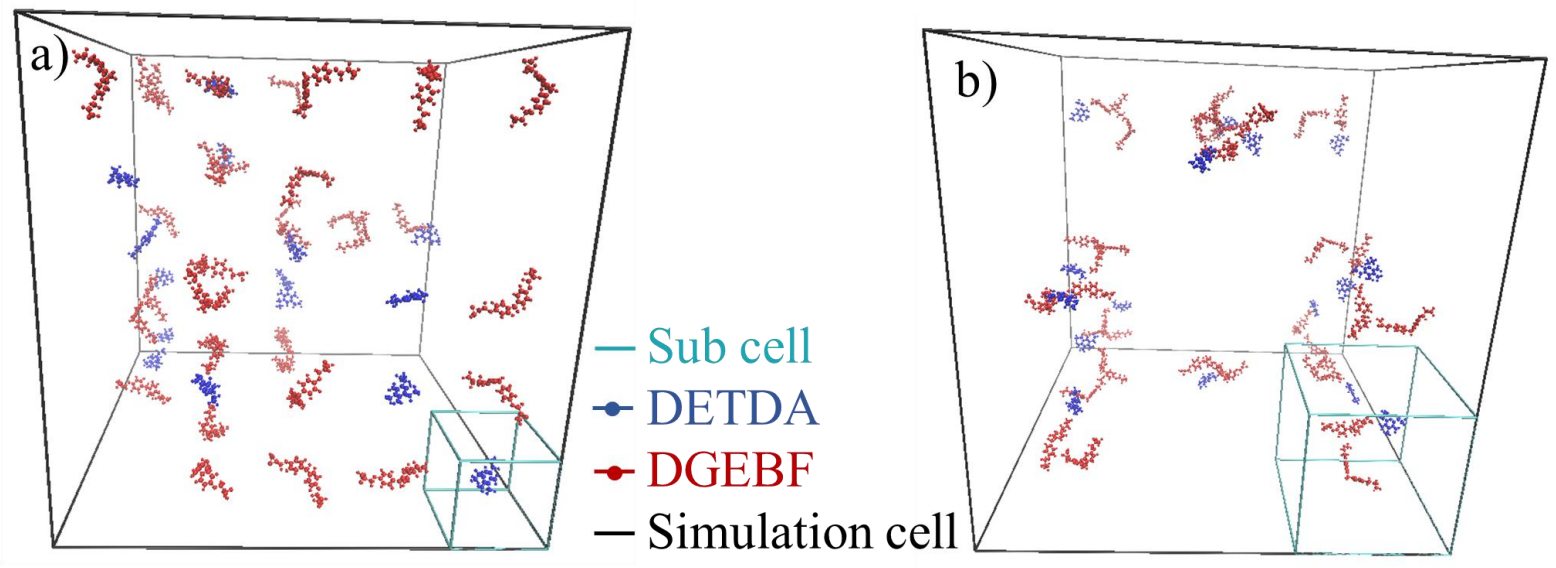

Packing results: density

DGEBF/DETDA

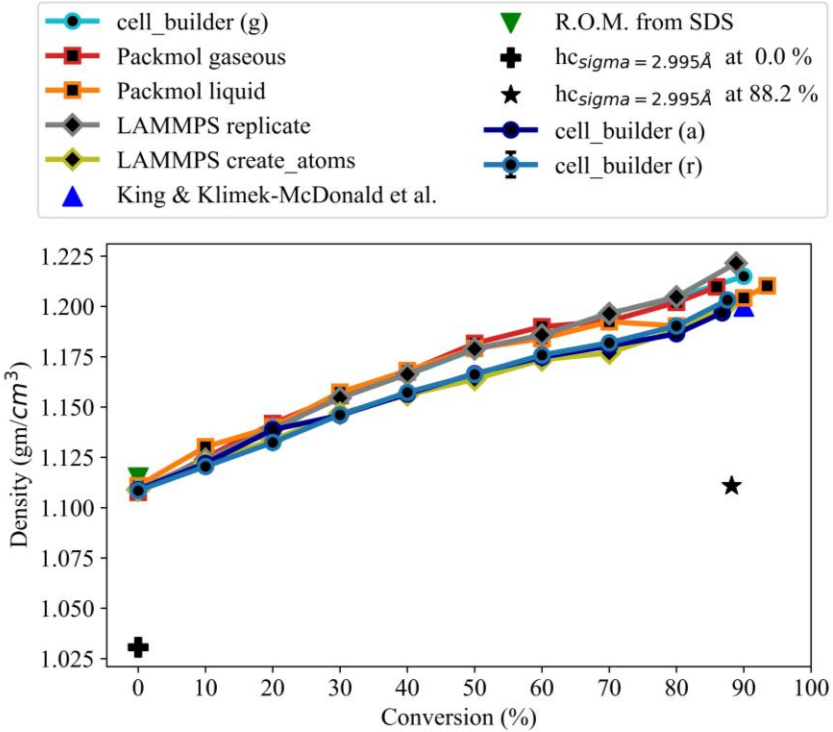

Cyanate Ester

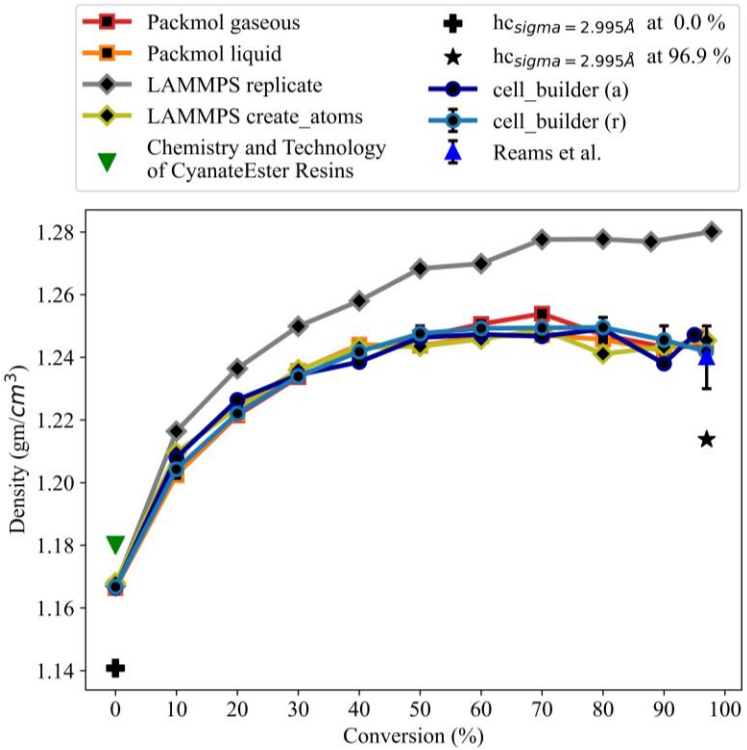

Packing results: shrinkage

DGEBF/DETDA

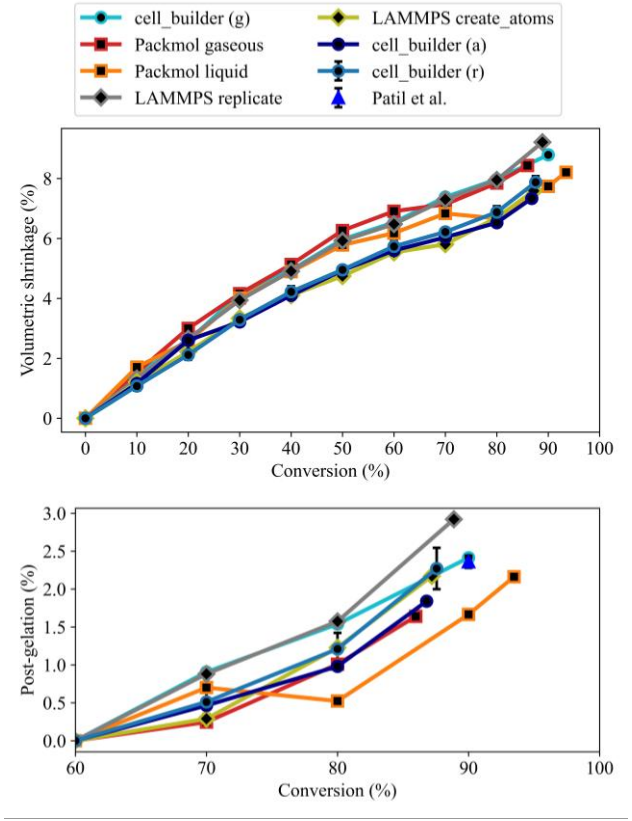

Cyanate Ester

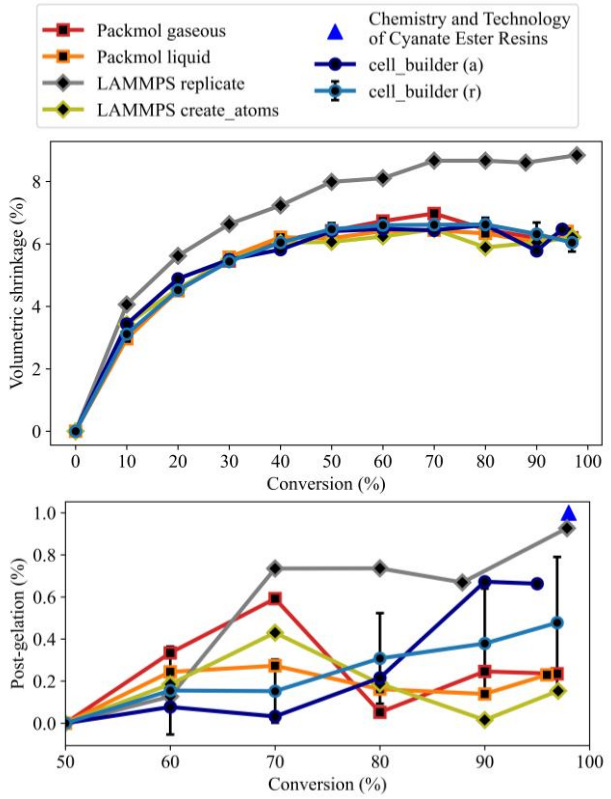

Packing results: free volume

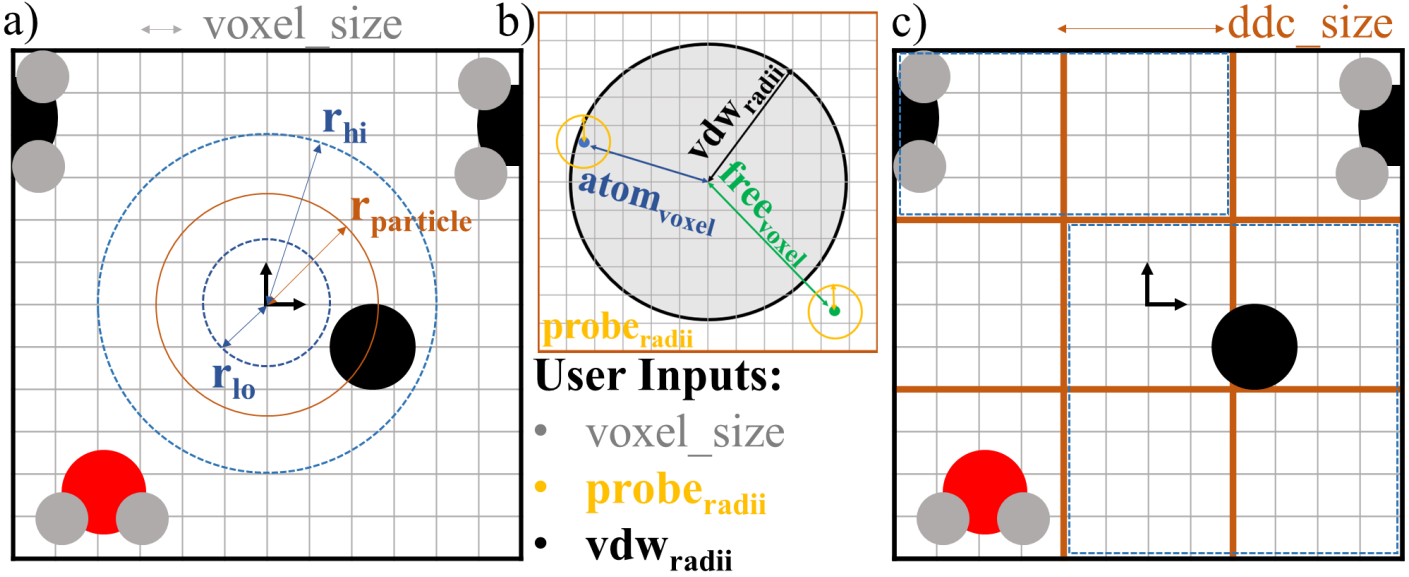

User Inputs:

- voxel_size
- $probe_{radii}$
- vdw_{radii}

$ddc\_size = 2.1*\max(\text{system } vdw_{radii}) + 2*voxel\_size + 2*probe_{radii}$

$r_{lo} = r_{particle} - 2*probe_{radii} - voxel\_size$

$r_{hi} = r_{particle} + 2*probe_{radii} + voxel\_size$

Packing results: free volume

DGEBF/DETDA

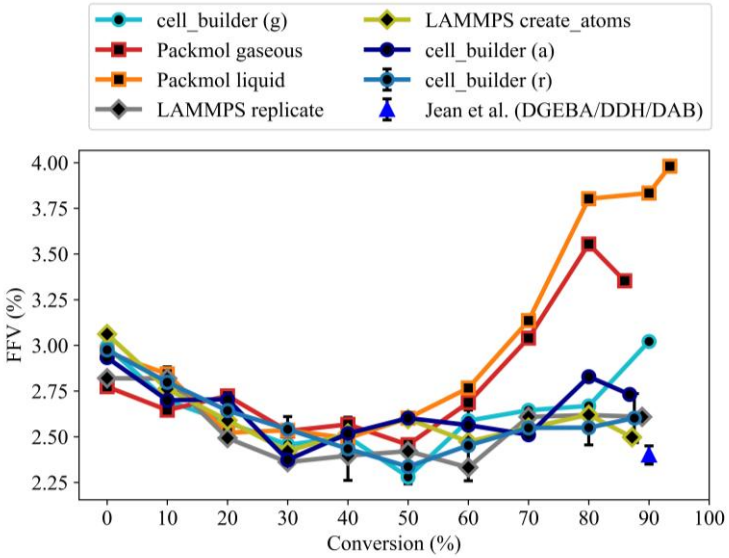

Cyanate Ester

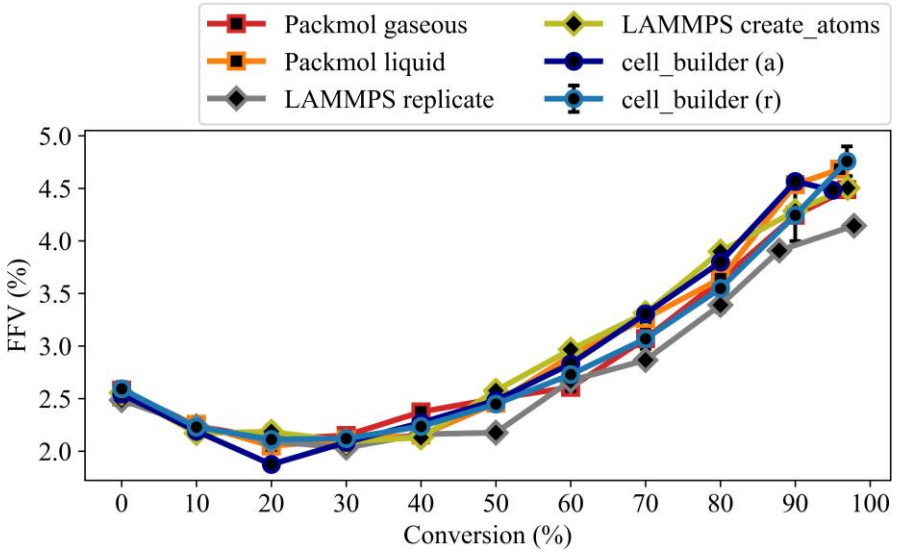

Packing results: free volume

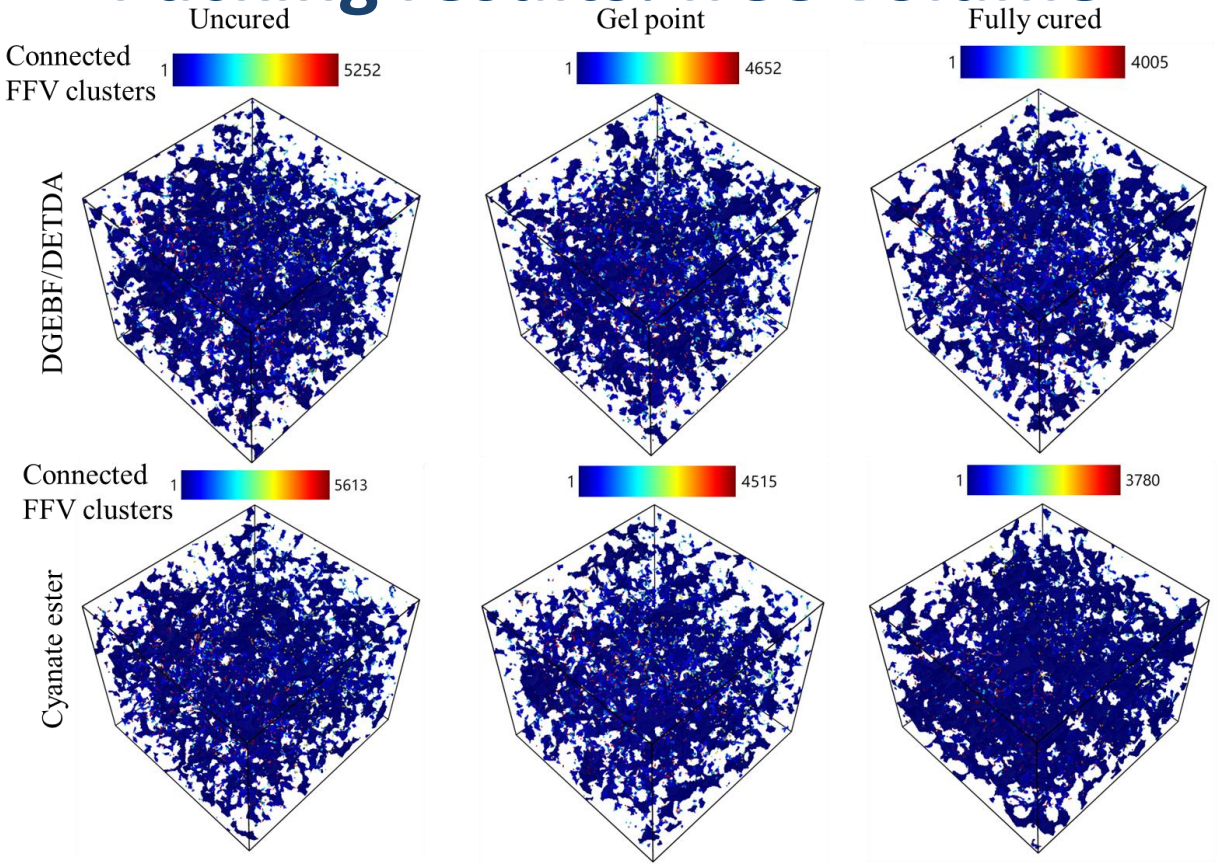

Conclusions

- The random packing methods generate the initial simulation cell produces the best model when looking at:
  - Density predictions
  - Post gelation shrinkage
  - FFV
- LUNAR has everything needed for ICME based process modeling using Molecular dynamics
- LUNAR is published at Journal of Chemical Information and Modeling (JCIM)
  - https://doi.org/10.1021/acs.jcim.4c00730
- LUNAR is free to download at:
  - https://github.com/CMMRLab/LUNAR

Acknowledgements

- Dr. Gregory Odegard
- CMMR Lab Group
- Superior: Dr. Gowtham



1885

CMMR Lab
COMPUTATIONAL MECHANICS
& MATERIALS RESEARCH

Motivation – Materials for high heat and extreme environments

Systems:

- Heat shields
- Rocket nozzles
- Braking systems



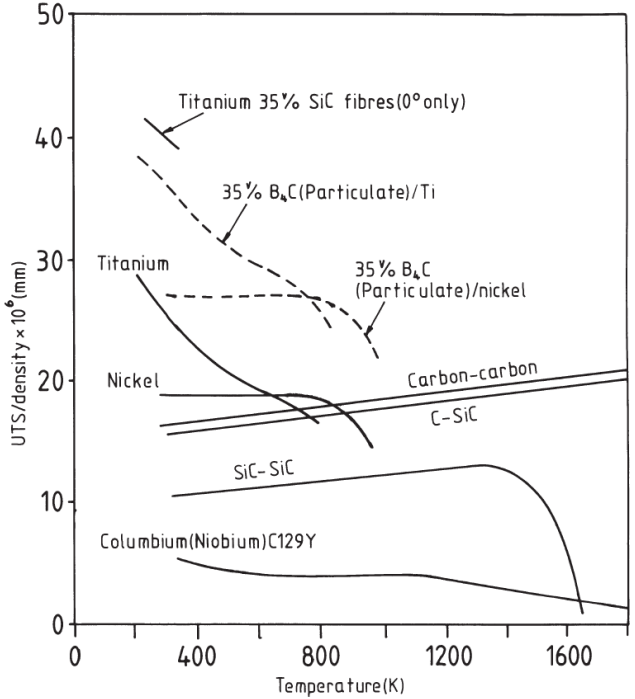

Carbon-Carbon Composites, G. Savage, 1994

Orion Crew modules: https://lockheedmartin.com/en-us/news/features/2022/orion-heat-shield.html

Background: Carbon-carbon composites (PIP method)

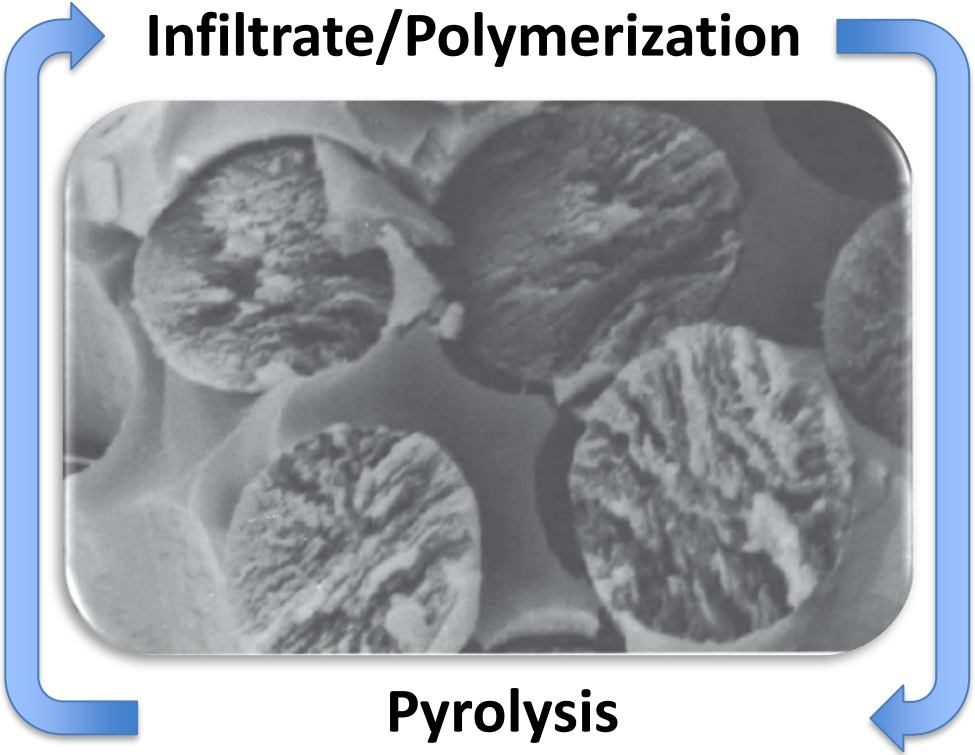

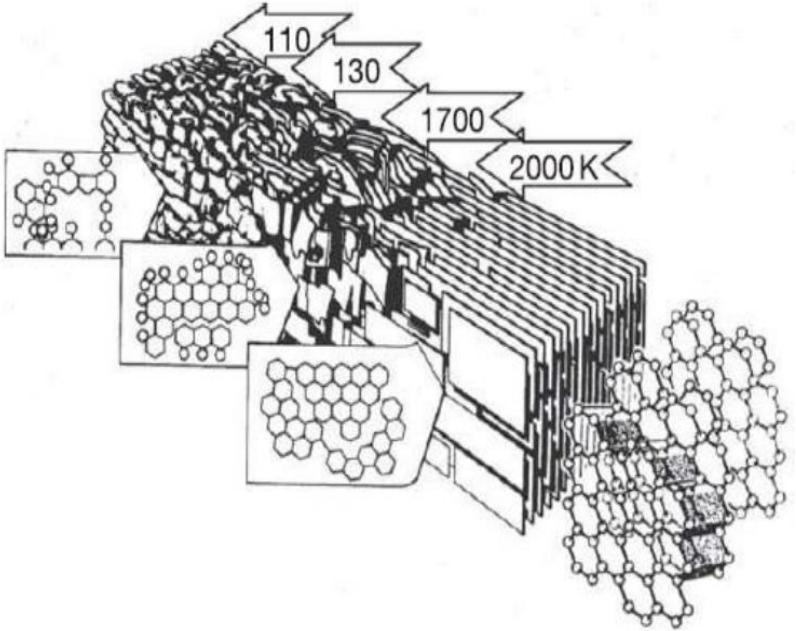

Carbon-Carbon Composites, G. Savage, 1994
Comprehensive inorganic chemistry II: From elements to applications. Burlington: Elsevier, 2013

Packing results: potential energy

DGEBF/DETDA

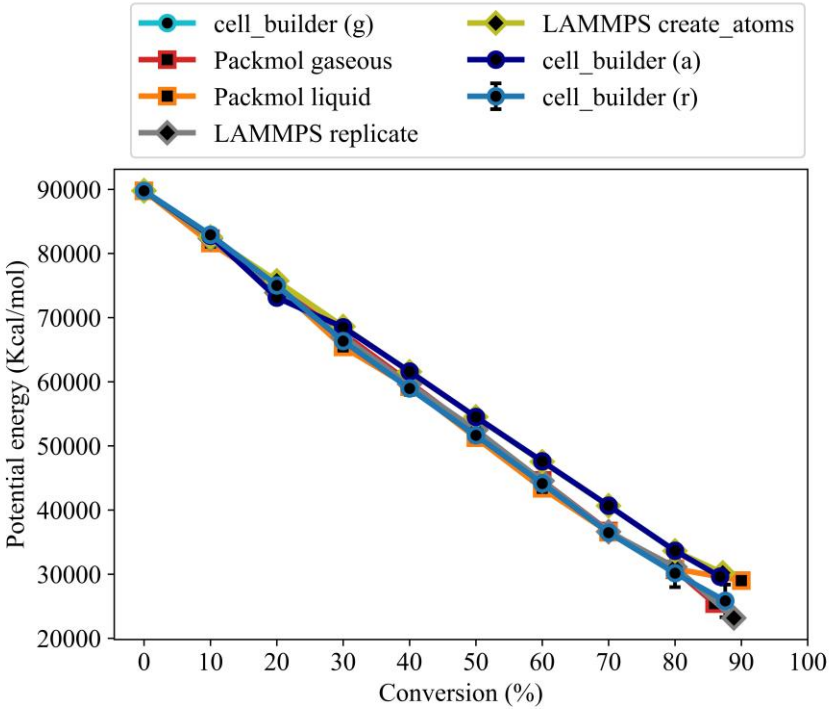

Cyanate Ester

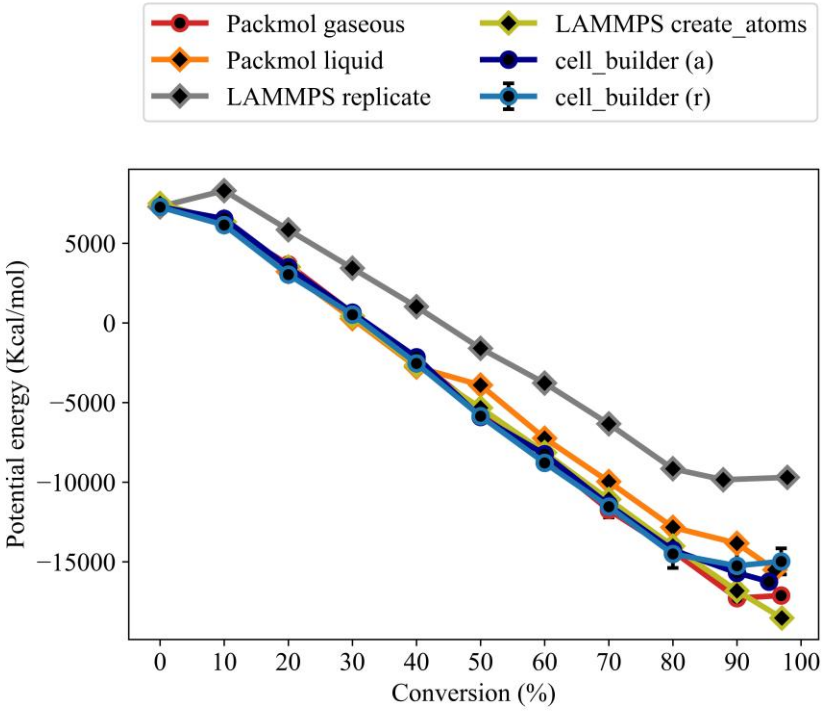

LUNAR performance

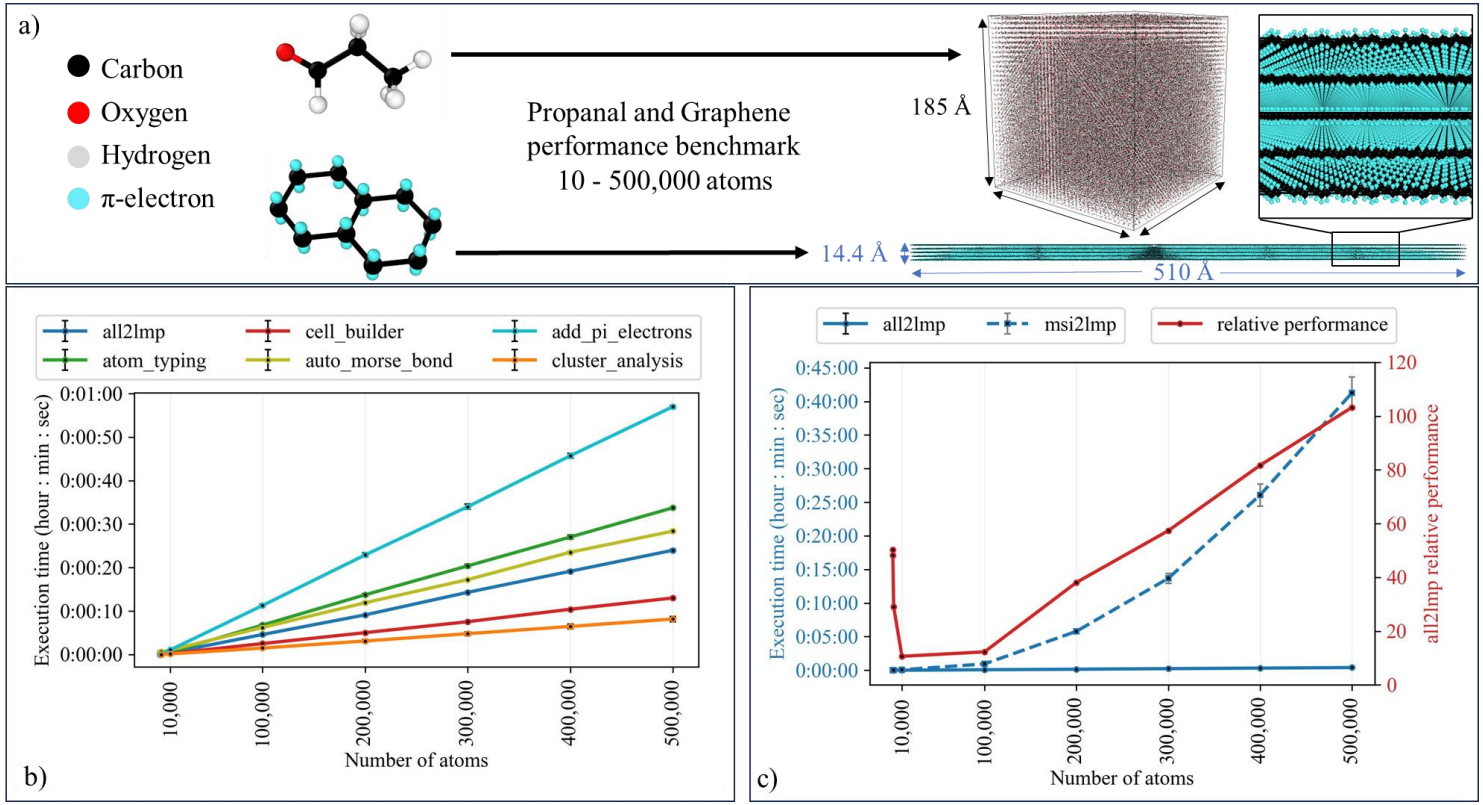

DGEBF/DETDA and AroCy L10 Modeling procedure

ChemDraw | LUNAR | LAMMPS | Combinations

Draw: Initialize start monomer connectivity and positions in ChemDraw

↓

Atom type and apply PCFF-IFF parameters: Using LUNAR

↓

Unify energy coeffs and generate REACTER template: Using LUNAR

↓

Mix: Randomly place and orientate molecules

↓

Densify: 1.18 g/cm^3 at 27 C° NVT (experimental liquid density)

↓

Equilibrate: 27 C° 1 atm for 2 ns NPT (liquid density)

↓

Polymerize: 240 C° for 2 ns NVT using REACTER

↓

Equilibrate: 27 C° 1 atm for 2 ns NPT (polymer density)

5-replicates built

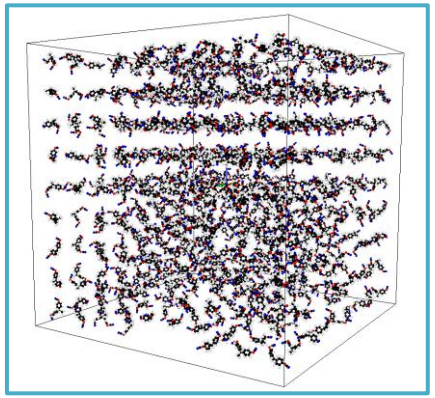

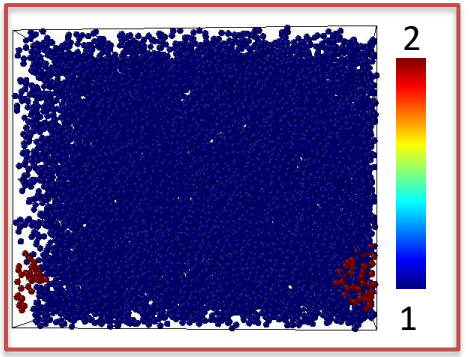

Gelation behavior

DGEBF/DETDA

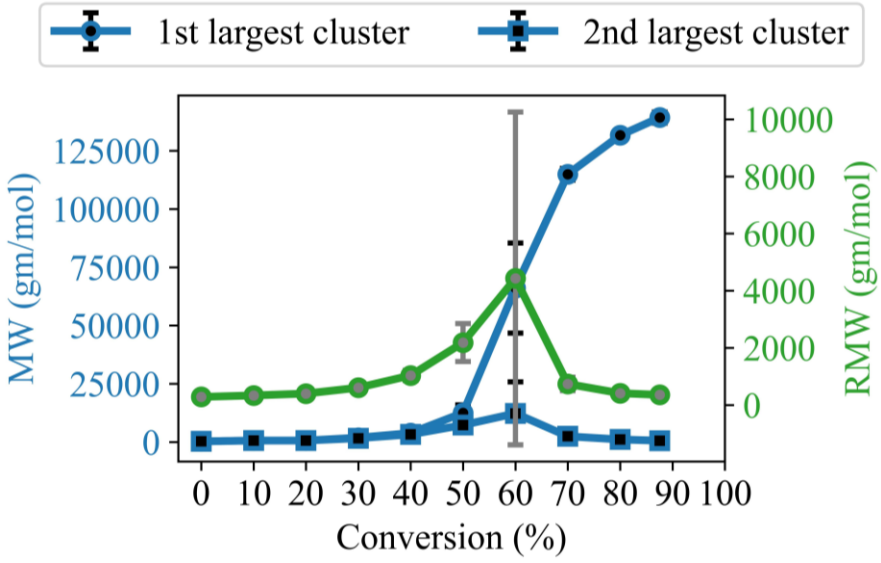

$$Conversion_{DGEBF/DETDA} = \frac{reaction\ 1_{count} + reaction\ 2_{count}}{720}$$

AroCy L10

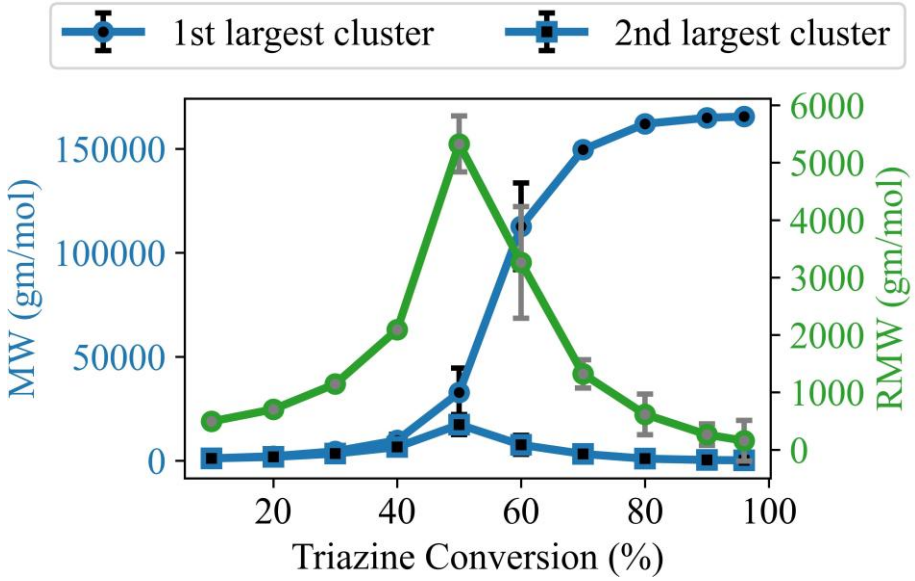

$$Conversion_{L10} = \frac{reaction\ 2_{count}}{2 * (627/3)}$$

Free volume analysis

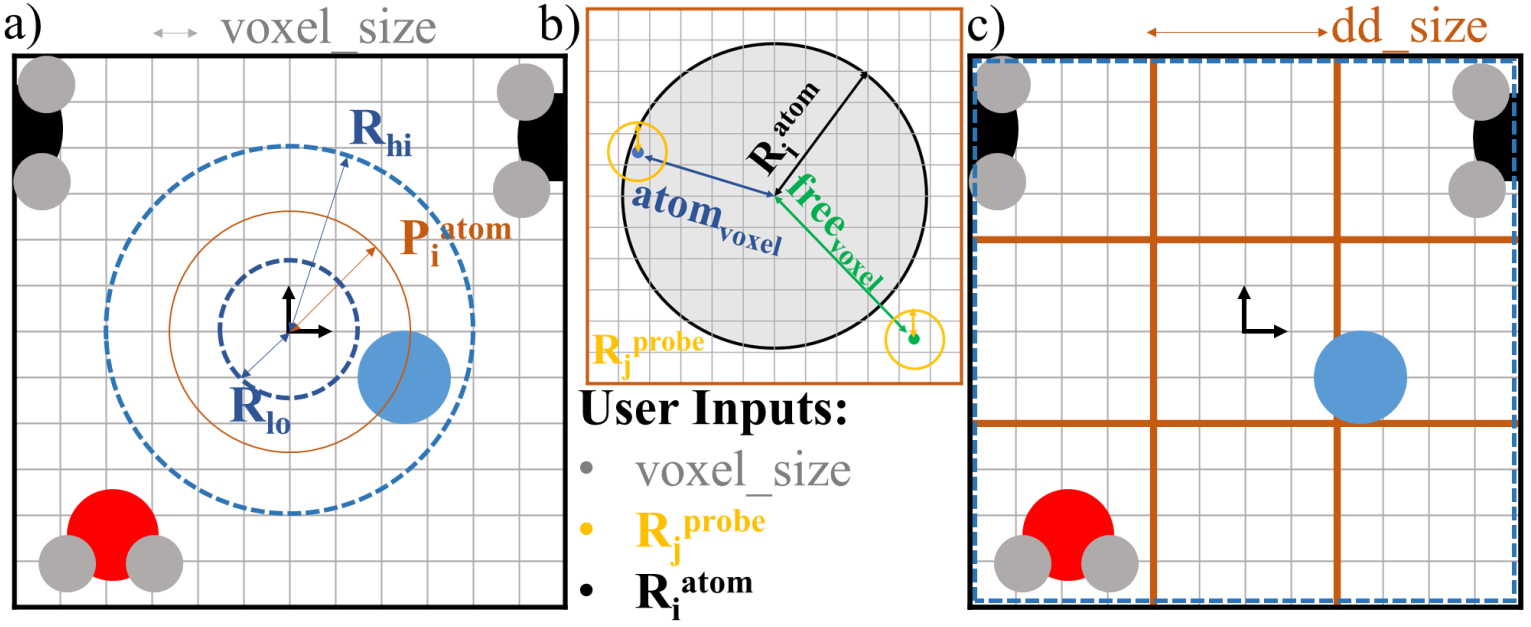

User Inputs:

- voxel_size
- R_j^{probe}
- R_i^{atom}

$$dd\_size = 2.1*\max(\text{system } R_i^{atom}) + 2*voxel\_size + 2*R_j^{probe}$$

$$R_{lo} = P_i^{atom} - 2*R_j^{probe} - voxel\_size$$

$$R_{hi} = P_i^{atom} + 2*R_j^{probe} + voxel\_size$$

Example atom

Free volume convergence and performance

DGEBF/DETDA L10

Uncured

Fully cured

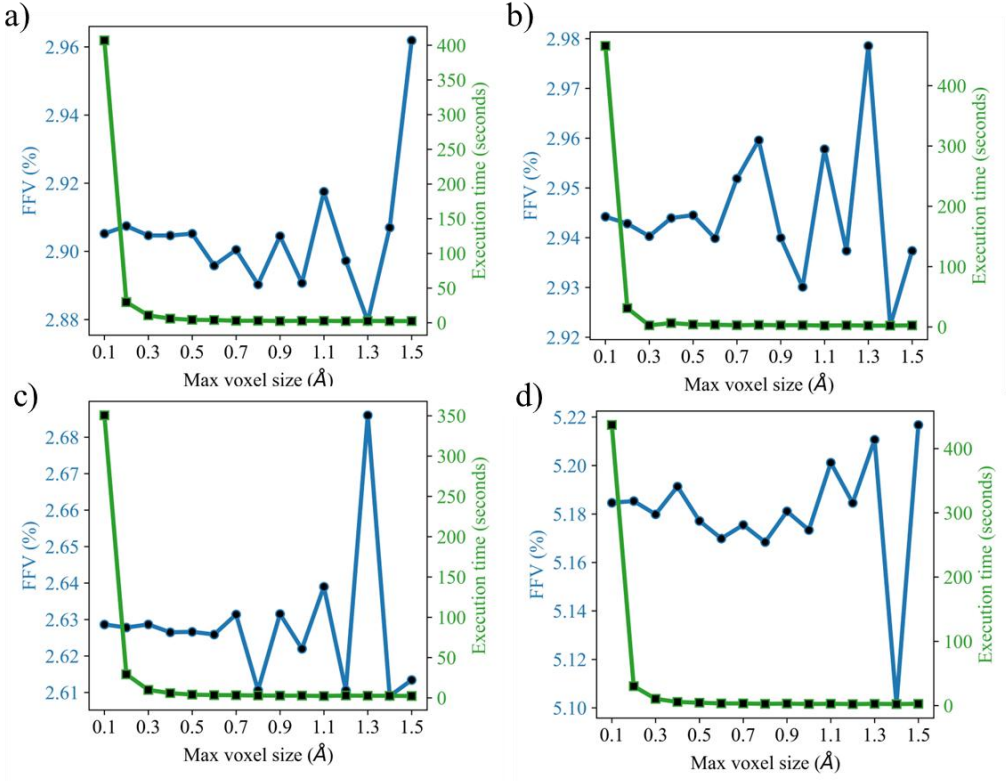

Mix: Randomly place and orientate molecules

LUNAR/cell_builder.py options

Random (r)

Grouped locally (g)

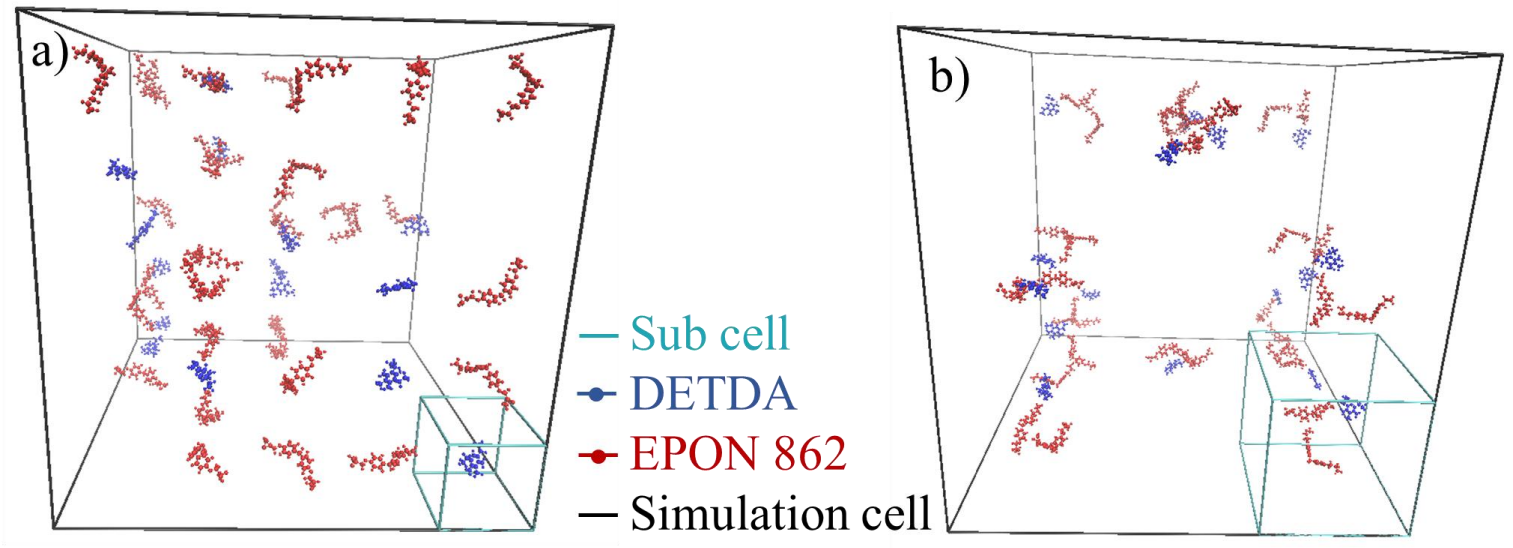

MD parameterizing: Atom types

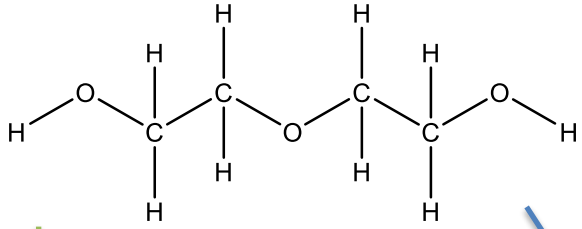

IFF

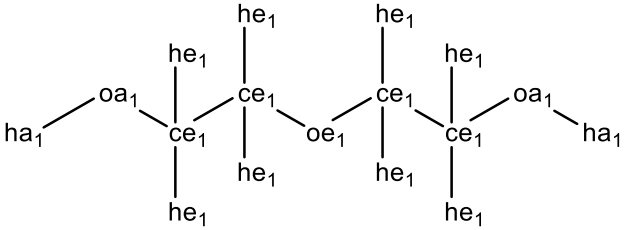

Dreiding - Implicit hydrogens (coarse grained)

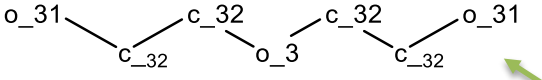

Dreiding

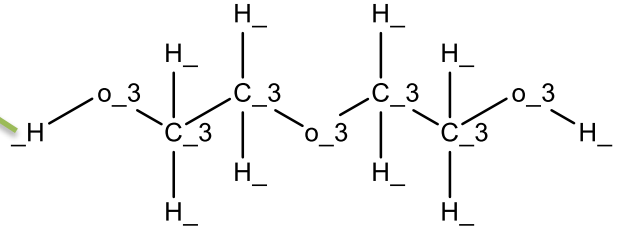

PCFF

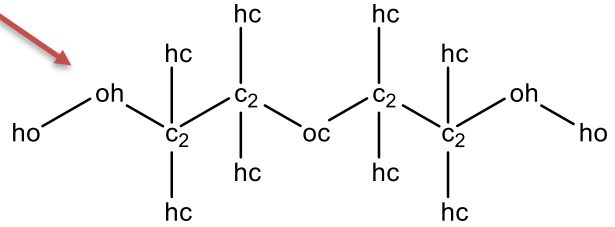

MD parameterizing

Element representation

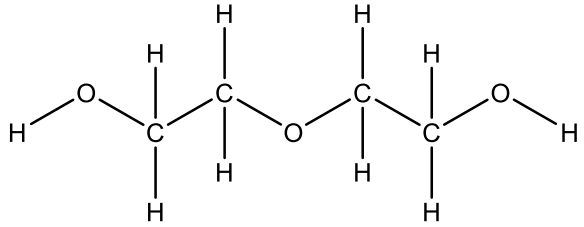

atom typing

PCFF atom typed

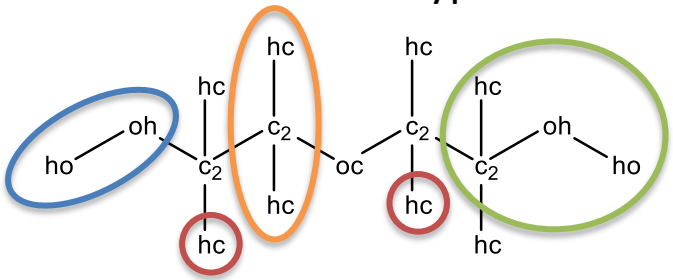

parameterization

$$E_{hc-hc} = \epsilon\left[2\left(\frac{\sigma}{r}\right)^9 - 3\left(\frac{\sigma}{r}\right)^6\right]$$

$$E_{hc-hc} = \frac{Cq_{hc}q_{hc}}{\epsilon r}$$

$$E_{ho-oh} = K_2\,(r - r_o)^2 + K_3\,(r - r_o)^3 + K_4\,(r - r_o)^4$$

$$E_{hc-c2-hc} = K_2\,(\theta - \theta_o)^2 + K_3\,(\theta - \theta_o)^3 + K_4\,(\theta - \theta_o)^4$$

$$E_{hc-c2-oh-ho} = K_1[1 - cos(1\varphi - \varphi_n)] + K_2[1 - cos(2\varphi - \varphi_n)] + K_3[1 - cos(3\varphi - \varphi_n)]$$

MD parameterizing: Transferability

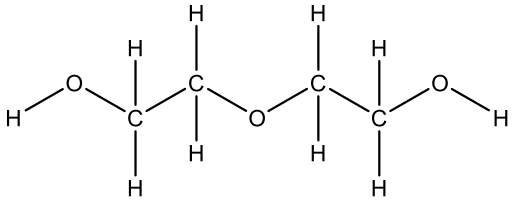

IFF (atom types and parameters are **NOT** transferable to other molecules)

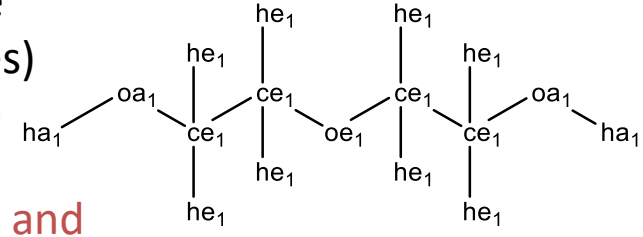

PCFF (atom types and parameters **ARE** transferable to other molecules)

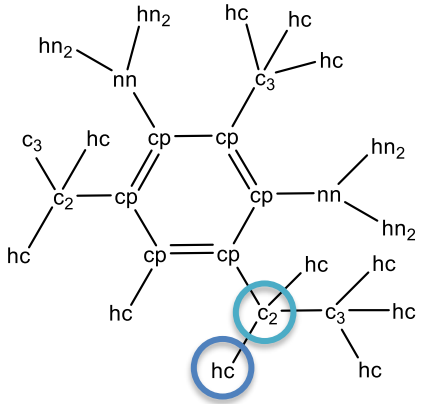

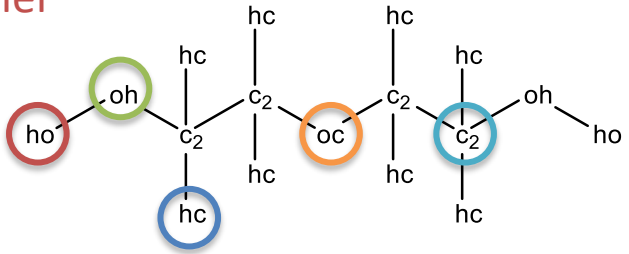

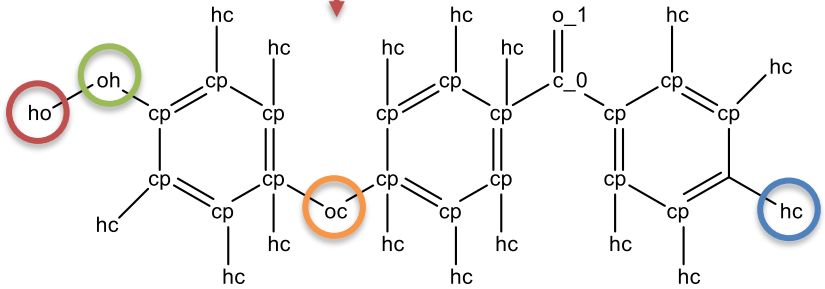

IFF <50 materials

PCFF >100's materials

IFF <0.5% error

PCFF <~10.0% error

ICCM24
AUGUST 4-8, 2025
BALTIMORE CONVENTION CENTER
BALTIMORE, MARYLAND, USA

No Technical Paper Submission for:

Meng Yi Song

ICCM24
AUGUST 4-8, 2025
BALTIMORE CONVENTION CENTER
BALTIMORE, MARYLAND, USA

No Technical Paper Submission for:

Shiyao Lin

ICCM24
AUGUST 4-8, 2025
BALTIMORE CONVENTION CENTER
BALTIMORE, MARYLAND, USA

No Technical Paper Submission for:

Wenkai Chang

ICCM24
AUGUST 4-8, 2025
BALTIMORE CONVENTION CENTER
BALTIMORE, MARYLAND, USA

No Technical Paper Submission for:

Ahmadreza Ravangard

Accelerating Progressive Damage and Failure Analysis of Composites using a Hybrid Implicit-Explicit Approach

Shiyao Lin, Assistant Professor
Department of Mechanical and Aerospace Engineering
Institute for Predictive Performance Methodologies
University of Texas at Arlington (UTA)

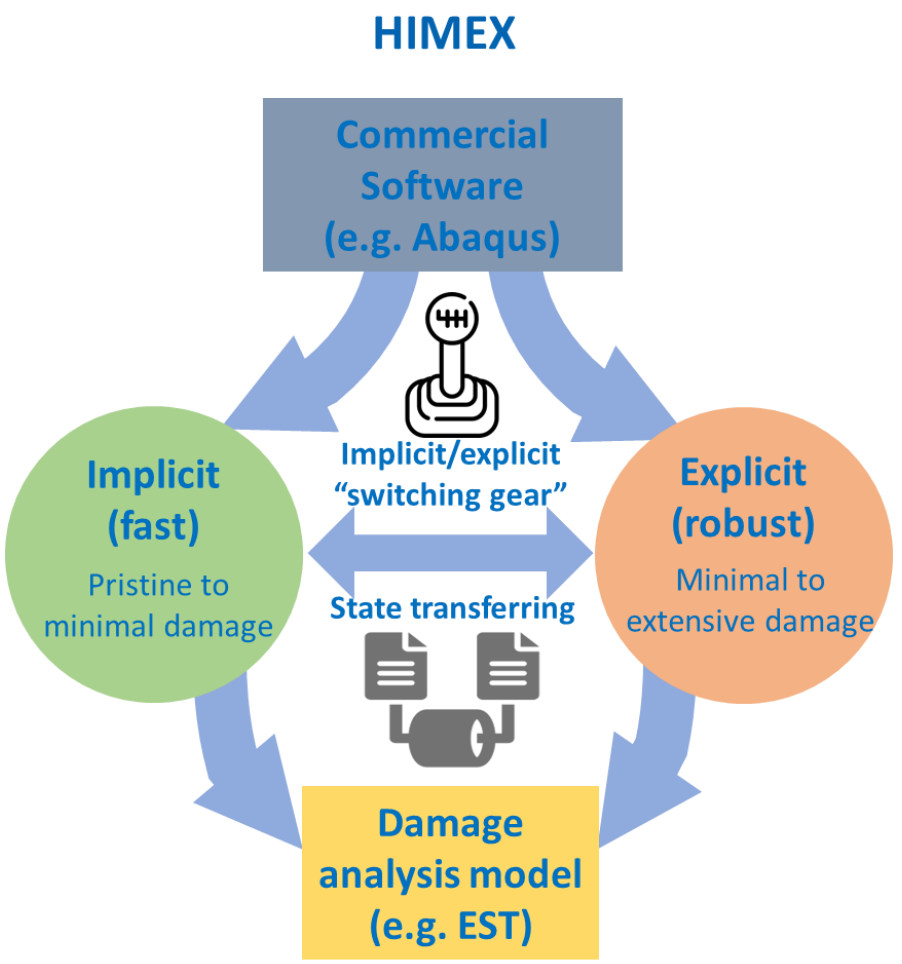

Content

1. Numerical Accuracy, Efficiency, and Robustness in Progressive Damage and Failure Analysis (PDFA)
2. **HIMEX**: **H**ybrid **Im**plicit-**Ex**plicit PDFA
3. Application Examples: Open-hole Tension
4. Discussions
5. Conclusions and Vision

1. Accuracy, Efficiency, and Robustness in PDFA

Multiscale Composite Damage

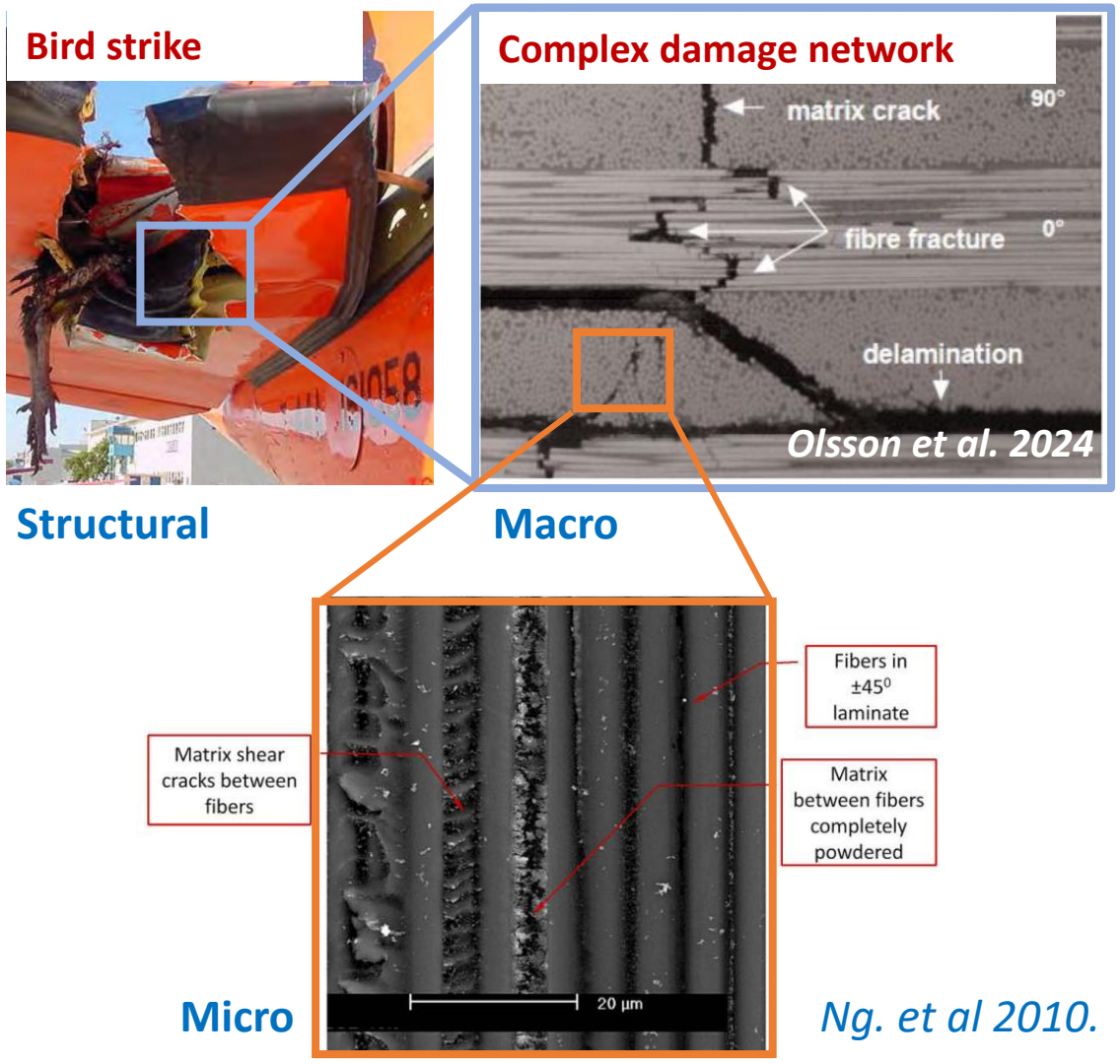

Ng. et al 2010.

Progressive Damage Analysis across Length Scales

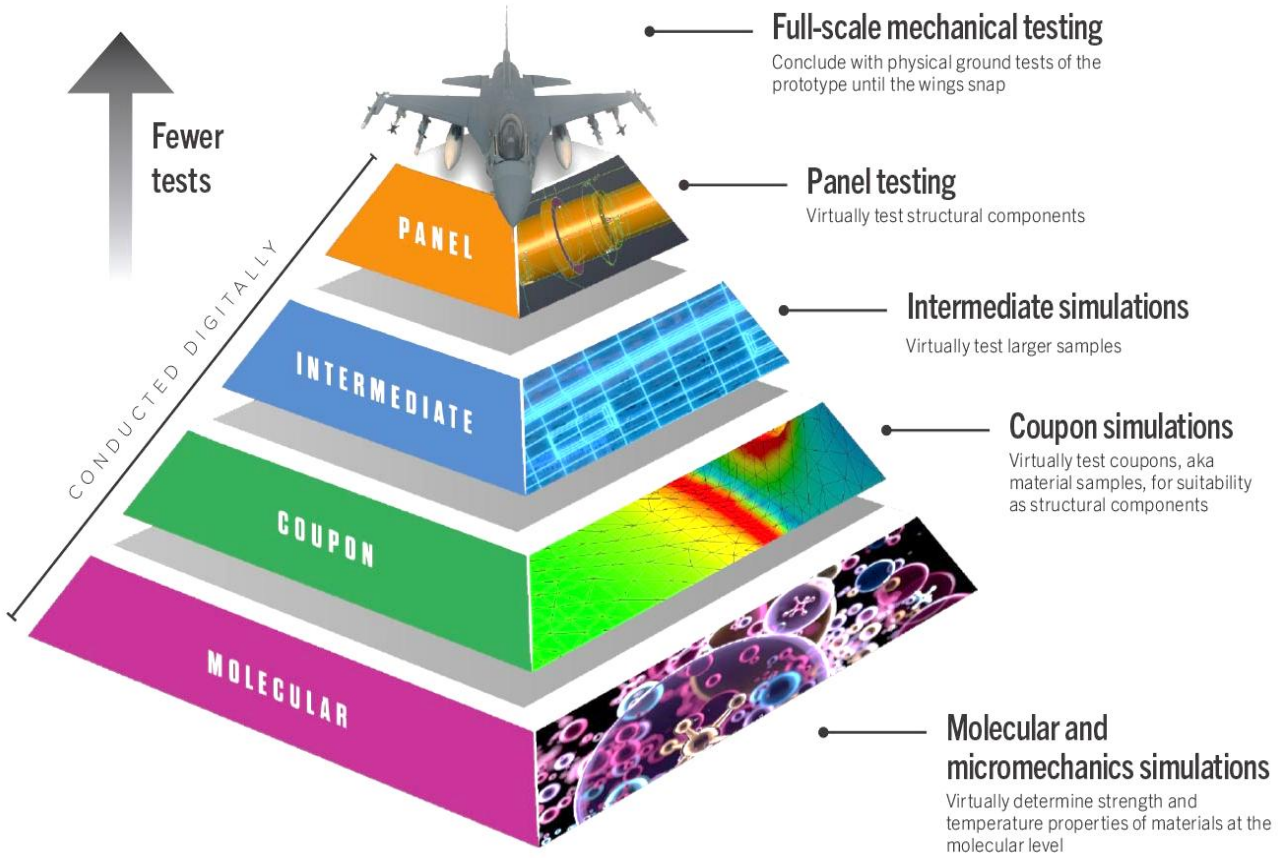

Waas, A., 2022. The case for more virtual testing. AEROSPACE AMERICA, 60(6), pp.22-24.

1. Accuracy, Efficiency, and Robustness in PDFA

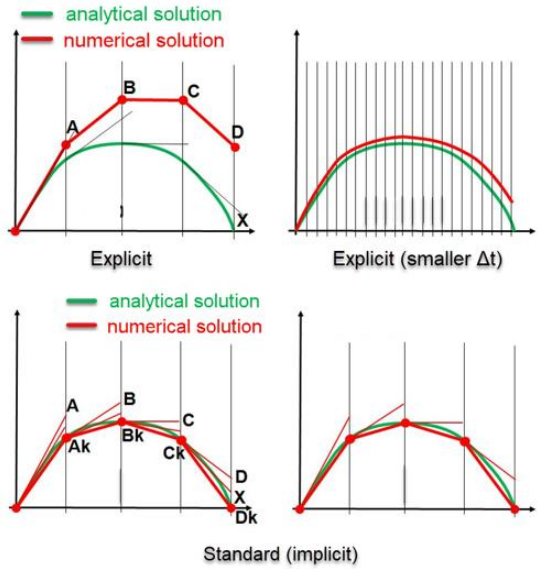

https://simulation-blog.technia.com/simulation/implicit-vs-explicit-finite-element-analysis

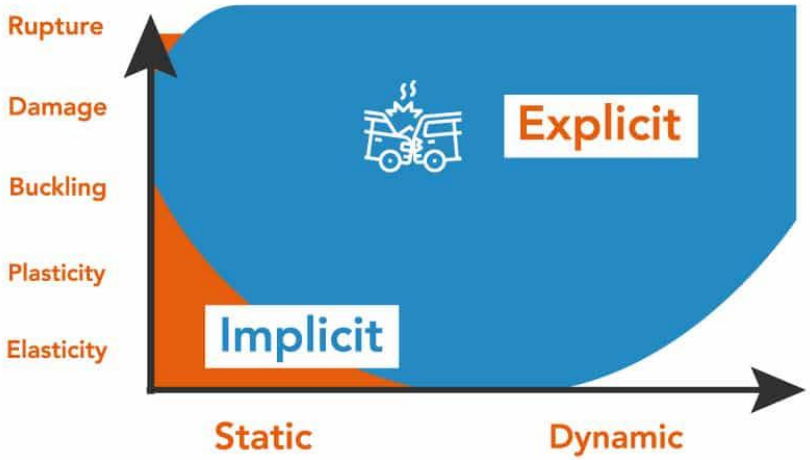

https://featips.com/2022/09/29/implicit-vs-explicit-analysis/

	Implicit PDFA (Backward Euler)	Explicit PDFA (Forward Euler)
Stable time increment size	Large	Small, proper mass scaling may be used
Analysis Accuracy	High	High only when sufficiently small time increment is used
Analysis Efficiency	High	Low
Analysis Robustness	Low	High, more suitable for damage propagation analysis
Abaqus subroutine implementation	Request Jacobian, stress, and state variable updates	Request stress, and state variable updates

1. Accuracy, Efficiency, and Robustness in PDFA



Load-displacement

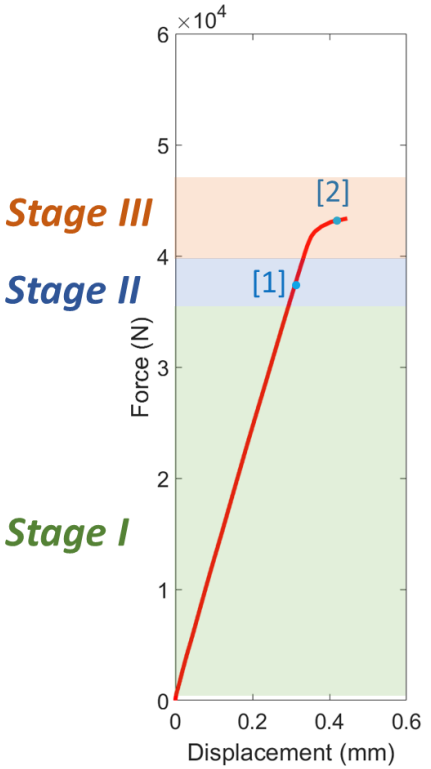

(a)

Damage development

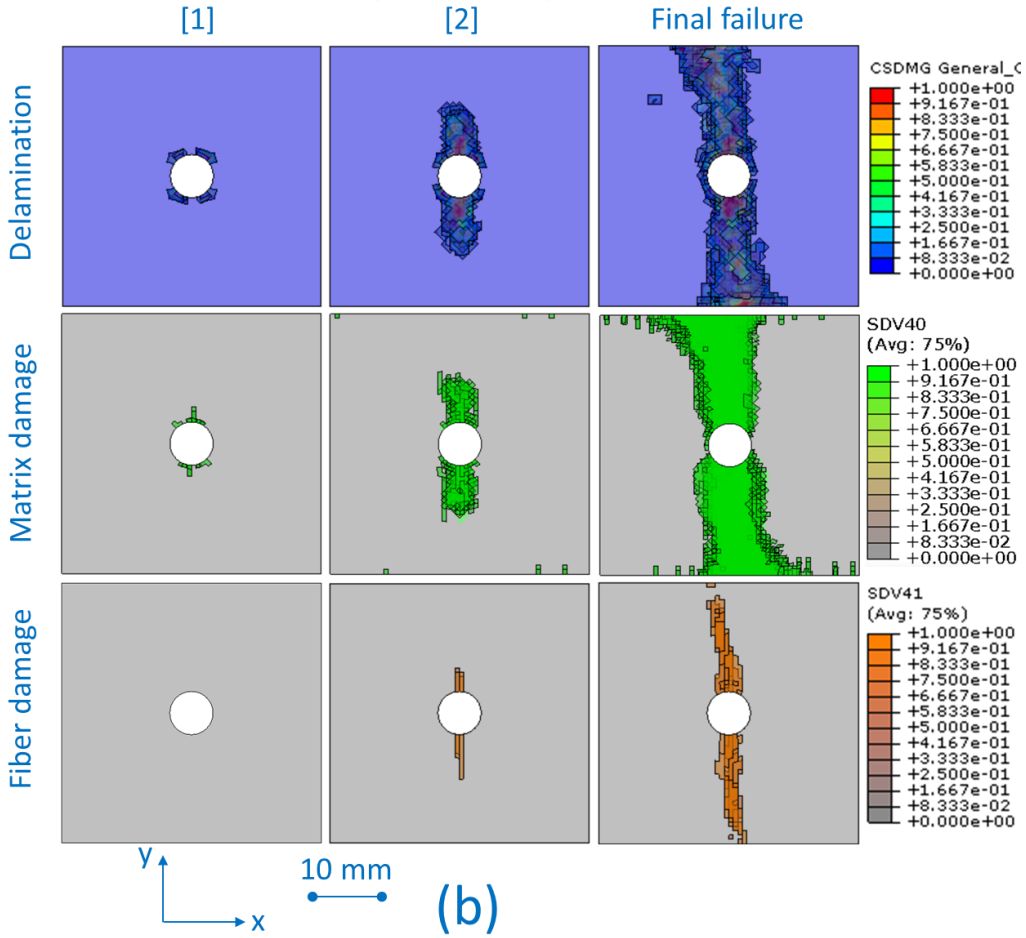

(b)

- Most of the OHT loading history (**Stage I**) is without damage initiation or propagation.
- At **stage II**, minimal matrix damage and delamination start to happen.
- At **stage III**, extensive damage of all the three modes keep growing, leading to the final catastrophic failure.
- **Most of the OHT analyses are done with explicit PDFA**. Some implicit PDFA may be conducted but most likely convergent until the beginning of **stage III** -- **no extensive damage propagation could be effectively predicted by implicit PDFA**.

1. Accuracy, Efficiency, and Robustness in PDFA

Commercial Software (e.g. Abaqus)

Implicit (fast)

Pristine to minimal damage

Damage analysis model (e.g. EST)

Load-displacement **Damage development**

[1] [2] Final failure



- Fast implicit PDFA analysis only applicable to Stage I and partially Stage II.

1. Accuracy, Efficiency, and Robustness in PDFA

Commercial Software (e.g. Abaqus)

Explicit (robust)

Minimal to extensive damage

Damage analysis model (e.g. EST)

Load-displacement

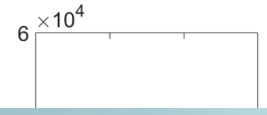

Damage development





Analogy: Driving on a rugged uphill road with low gears

- **Rugged:** High numerical difficulty (e.g., damage propagation)
- **Low gears**: Slow and robust **explicit solver**

- Robust explicit PDFA applies to all the stages, but **not necessary for stage I**.

1. Accuracy, Efficiency, and Robustness in PDFA

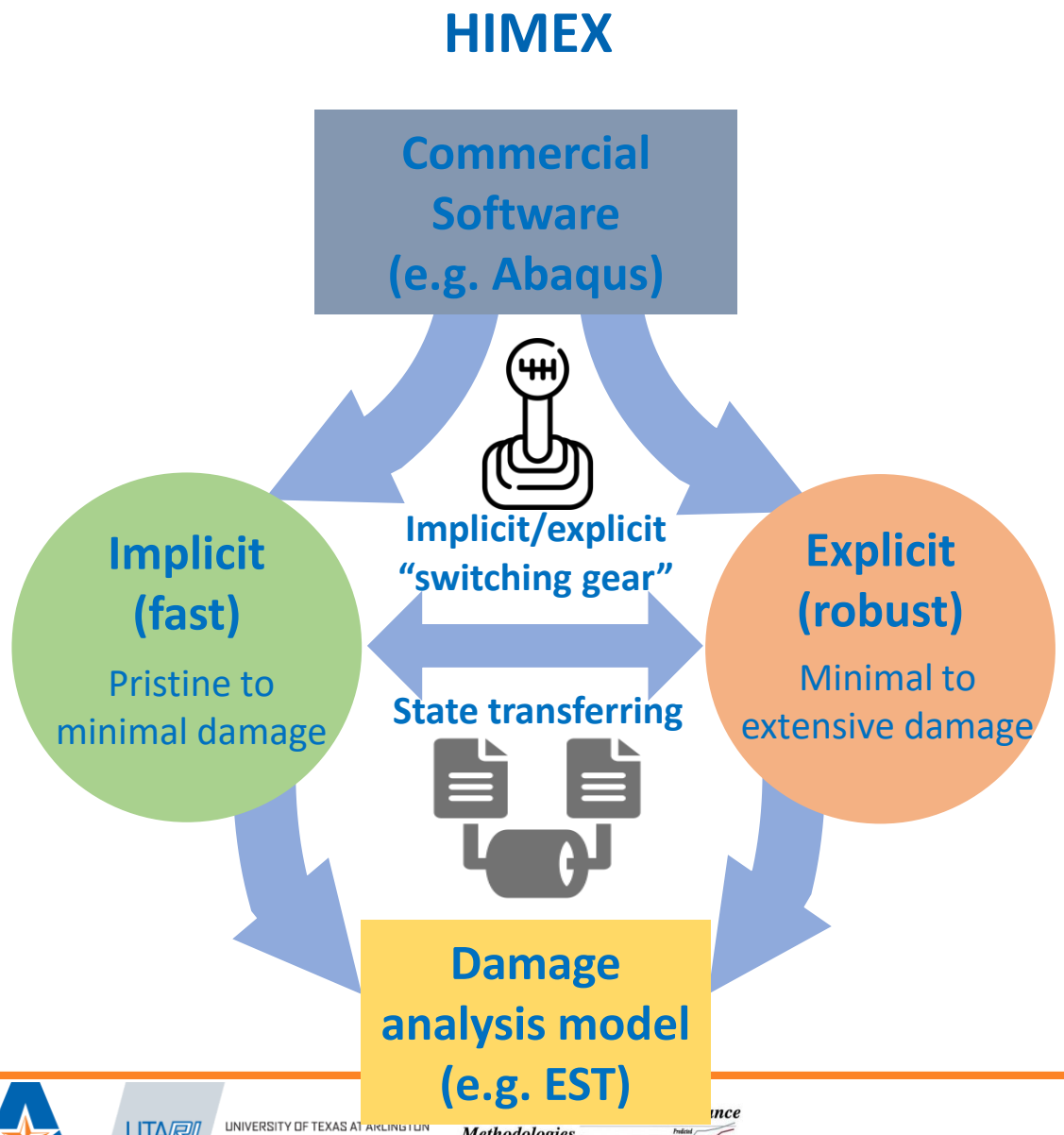

- Many PDFA analysis cases (e.g., OHT/OHC, single-edge notched tension, compression after impact, etc.,) are initially and majorly with no or minimal damage initiation and propagation, followed by drastic/catastrophic damage propagation.
- Elastic implicit stress analysis is applicable to the undamaged stage for high efficiency. When damage is about to happen, explicit PDFA is activated to predict damage evolution and structural failure.
- The key questions are **how and when to transfer from implicit analysis to explicit analysis**.

Content

1. Numerical Accuracy, Efficiency, and Robustness in Progressive Damage and Failure Analysis (PDFA)
2. **HIMEX**: **H**ybrid **Im**plicit-**Ex**plicit PDFA
3. Application Examples: Open-hole Tension
4. Discussions
5. Conclusions and Vision

2. HIMEX: Hybrid Implicit-Explicit PDFA

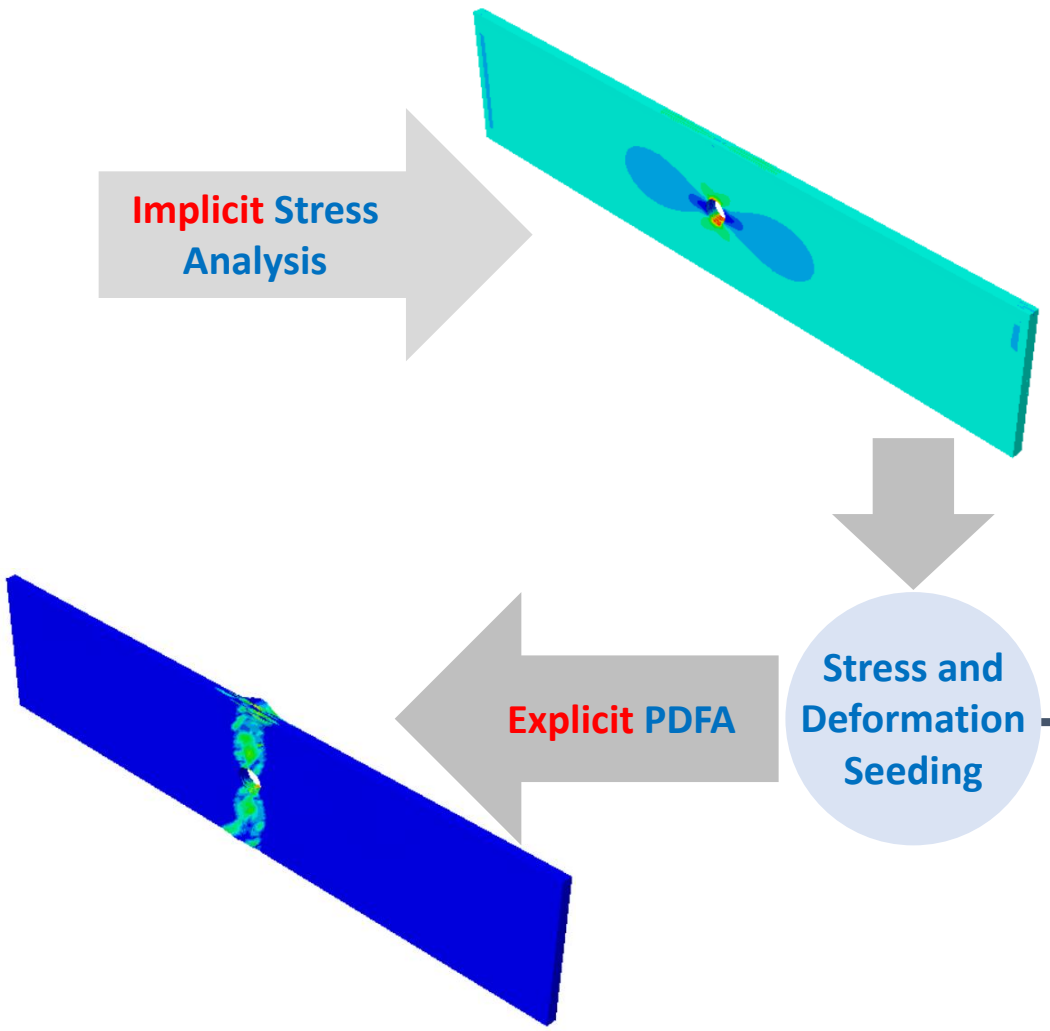

- Implicit stress analysis → state transferring → explicit PDFA.
- For most quasi-static testing of composites, **only one** "switching gear" is needed. Therefore, HIMEX may not be applied to impact or fatigue analyses yet.
- Deformed **geometry**, full-field **strains**, and **stresses** are to be transferred from the implicit stress analysis to the explicit PDFA.

2. HIMEX: Hybrid Implicit-Explicit PDFA: Deformation Transferring

Implicit Stress Analysis

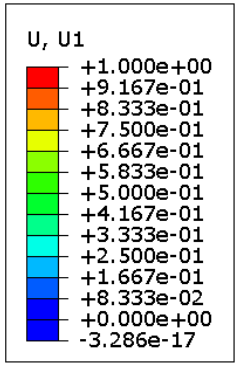

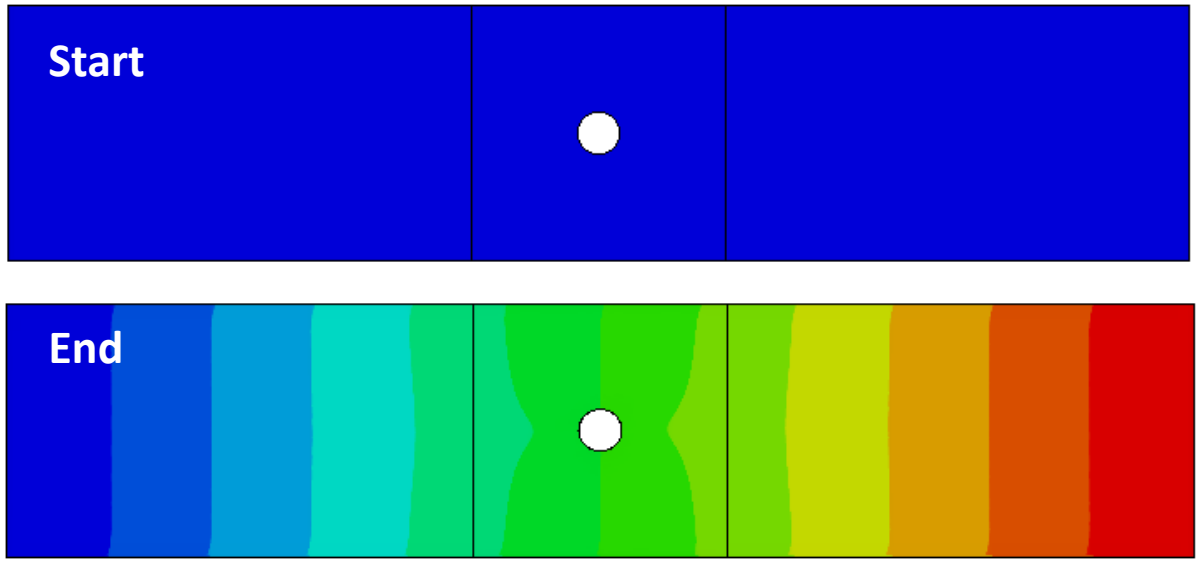



Explicit PDFA: starting with a deformed mesh

Deformed mesh imported from the end of the implicit analysis

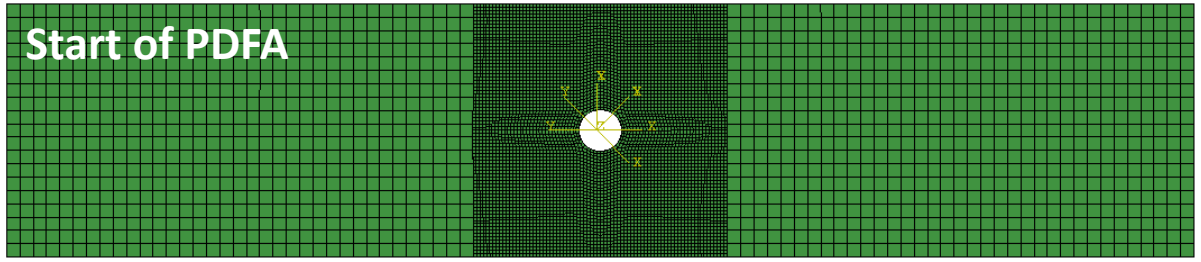

- Implicit stress analysis is the first step of HIMEX.
- Deformation transferring is ensured by **importing nodal coordinates of the deformed mesh** at the end of the implicit analysis to the explicit PDFA mesh.
- Deformation interpolation can be achieved **between different meshes**, enhancing the flexibility of HIMEX.
- Explicit PDFA starts with a deformed mesh and **pre-existing stresses and strains** need to be imported.
- A **semi-automated Python script** has been developed to facilitate fast deformation transferring.

2. HIMEX: Hybrid Implicit-Explicit PDFA: Stress and Strain Transferring

Implicit Stress Analysis

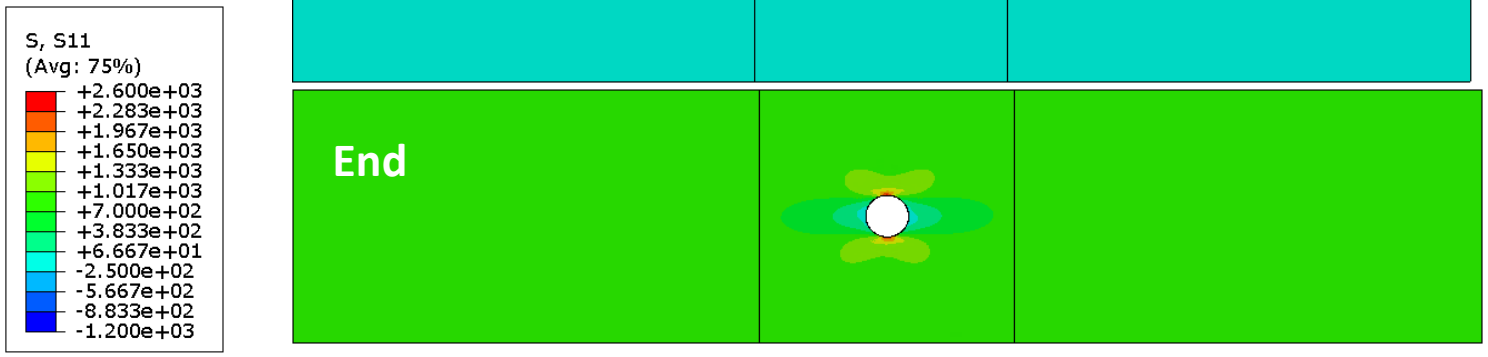

Explicit PDFA: starting with pre-existing stresses and strains

Stress states imported from the end of the implicit analysis

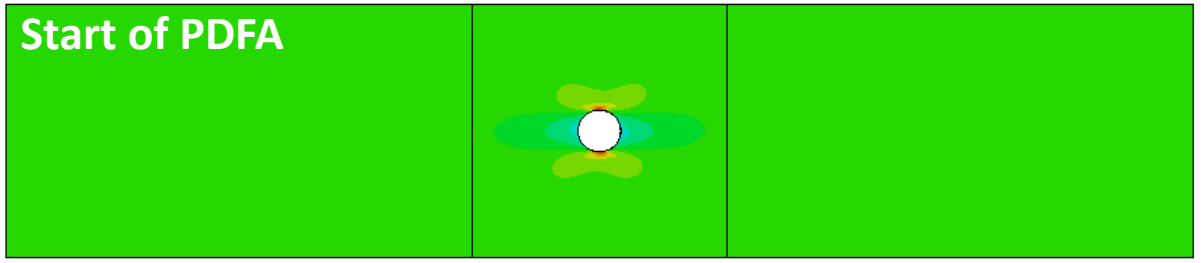

- Stress transferring is ensured by **importing stresses from the integration points** of the implicit mesh to the corresponding **integration points** of the explicit mesh.
- Strain transferring is ensured by calculating the pre-existing strains of the PDFA model by:

$$\{\epsilon^{pre}\} = [S]\{\sigma^{pre}\}.$$

where, $[S]$ is the elastic **compliance matrix**.

- A **semi-automated Python script** has been developed to facilitate fast **stress transferring**.
- The PDFA model enhanced Schapery theory (**EST**) **has been modified** to facilitate fast **strain transferring**.

Content

1. Numerical Accuracy, Efficiency, and Robustness in Progressive Damage and Failure Analysis (PDFA)
2. HIMEX: **H**ybrid **Im**plicit-**Ex**plicit PDFA
3. Application Examples: Open-hole Tension
4. Discussions
5. Conclusions and Vision

3. Application Example: OHT – Model and Mesh

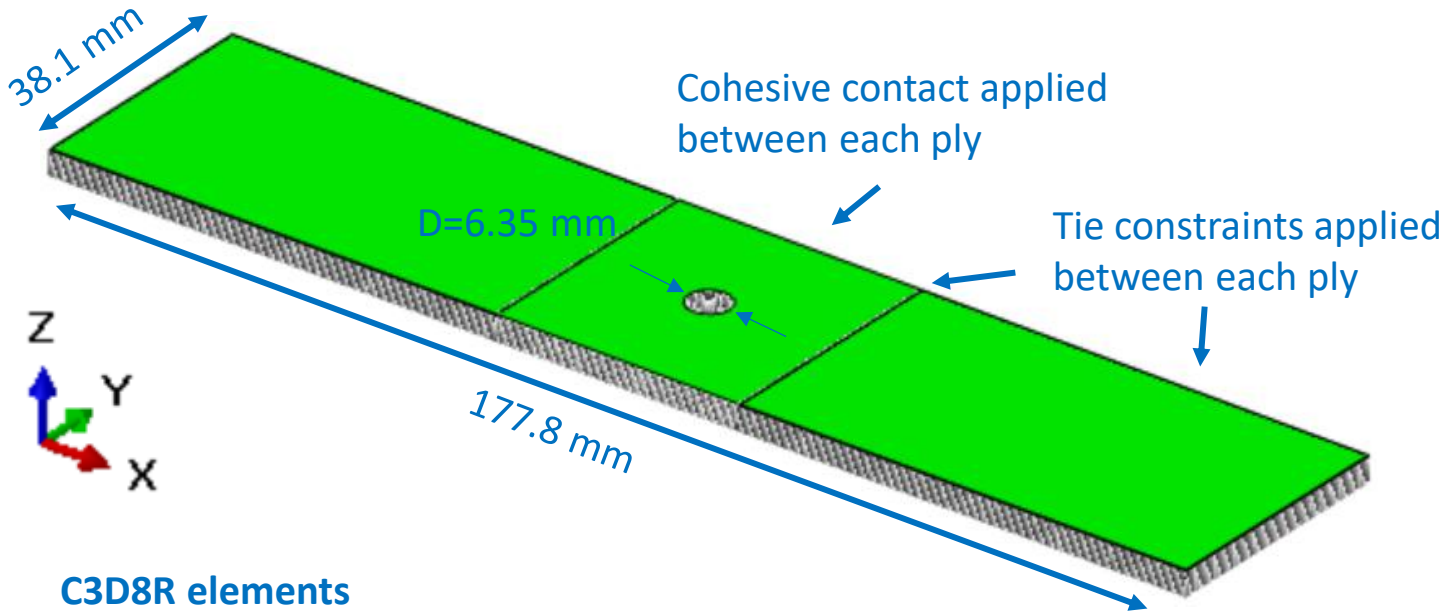

C3D8R elements
HIMEX Analysis
Mass scaling target time increment 1e-5 s

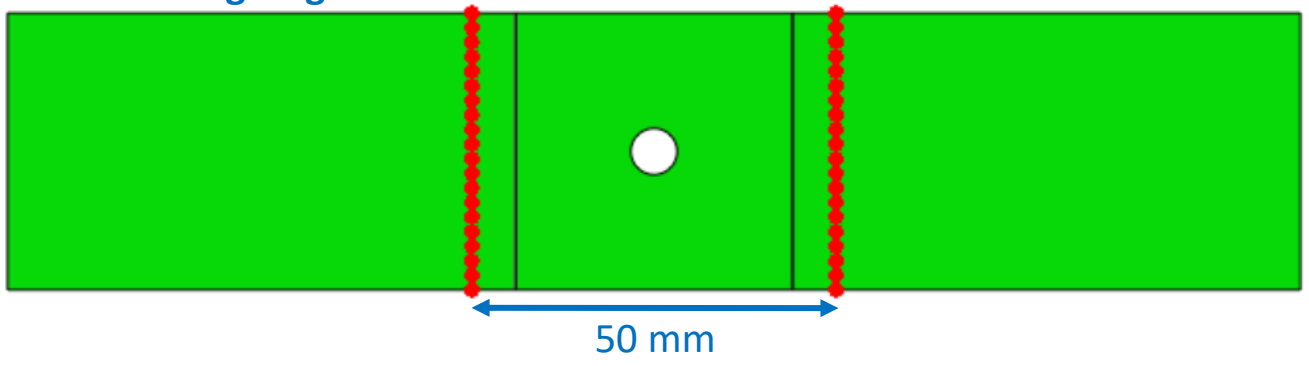

Virtual extensometers

0°- or 90°-ply mesh

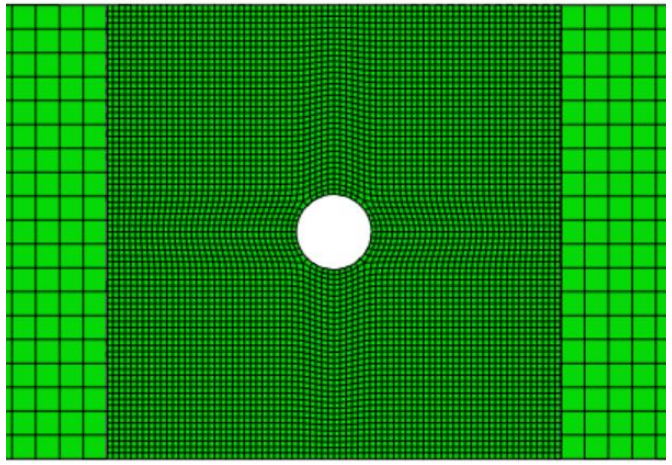

45°- or -45°-ply mesh

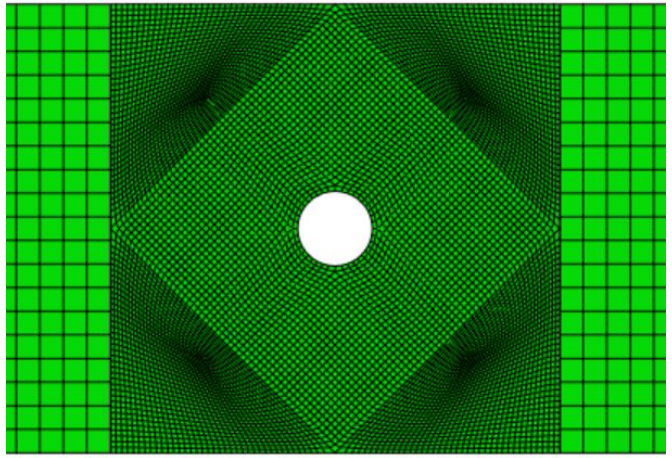

Fine: 0.5 ~ 0.6 mm, Coarse: 2 mm

3. Application Example: OHT – PDFA Model EST

Damage modes of 3D EST

Fiber tensile/compressive damage

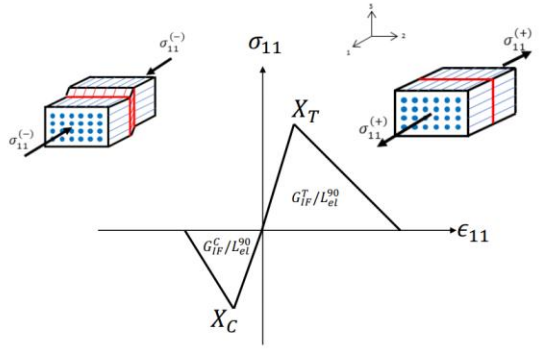

Matrix transverse tensile/compressive damage

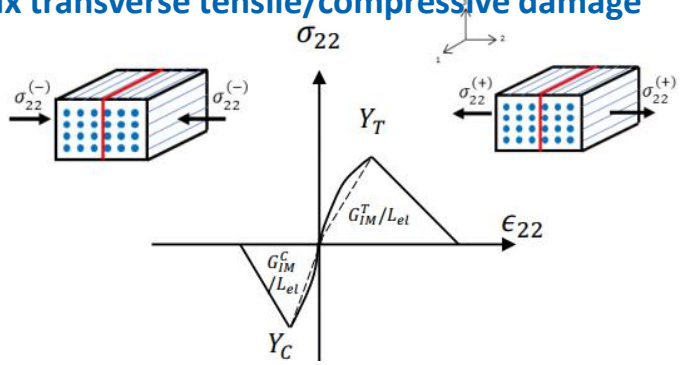

Matrix in-plane shear damage

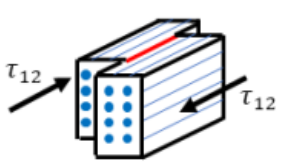

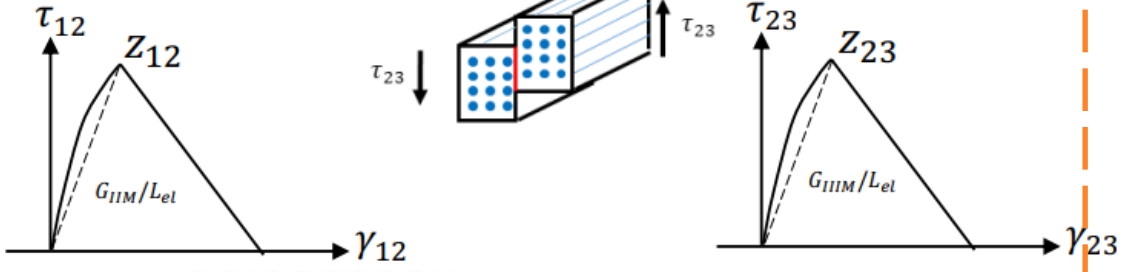

Matrix transverse shear damage

- Enhanced Schapery Theory (**EST**) combines Schapery Theory (**ST**) (Schapery, 1989) and the Bazant-Oh Crack Band (**CB**) (Bazant, 1983) model to analyze the intra-ply damage and failure of a lamina
- Implemented with Abaqus VUMAT.

3. Application Example: OHT Results [25/50/25] Layup

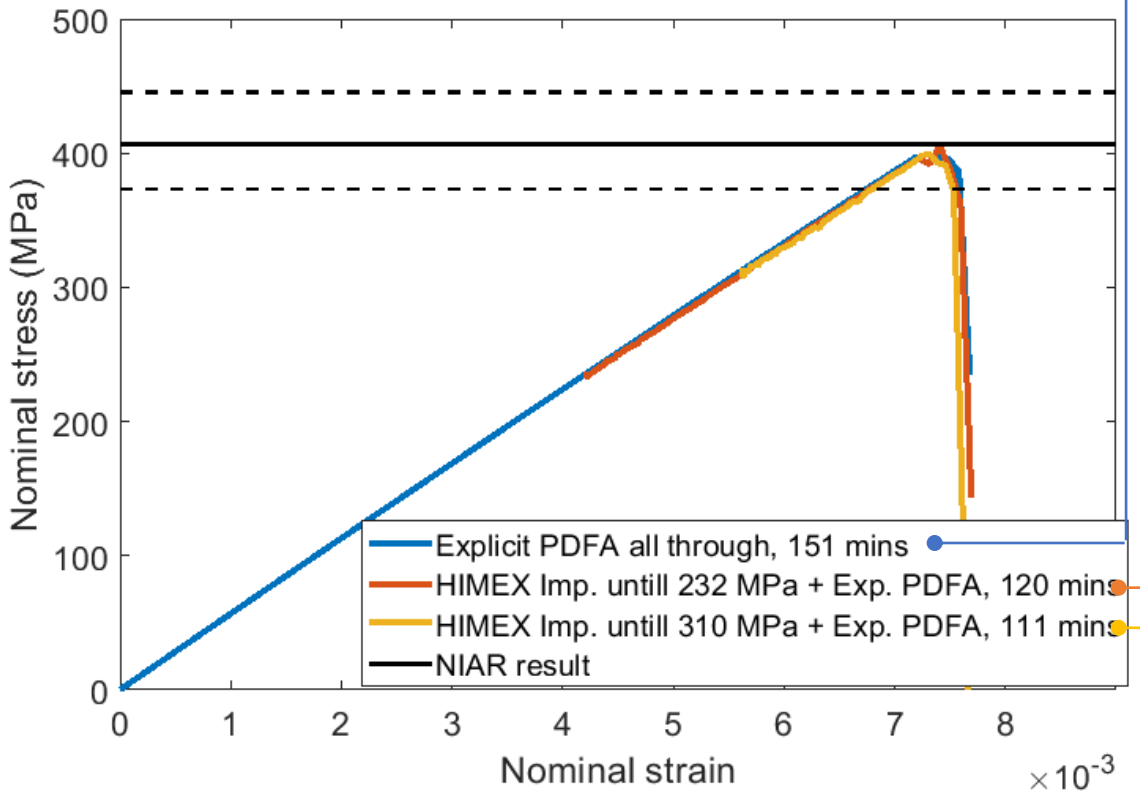

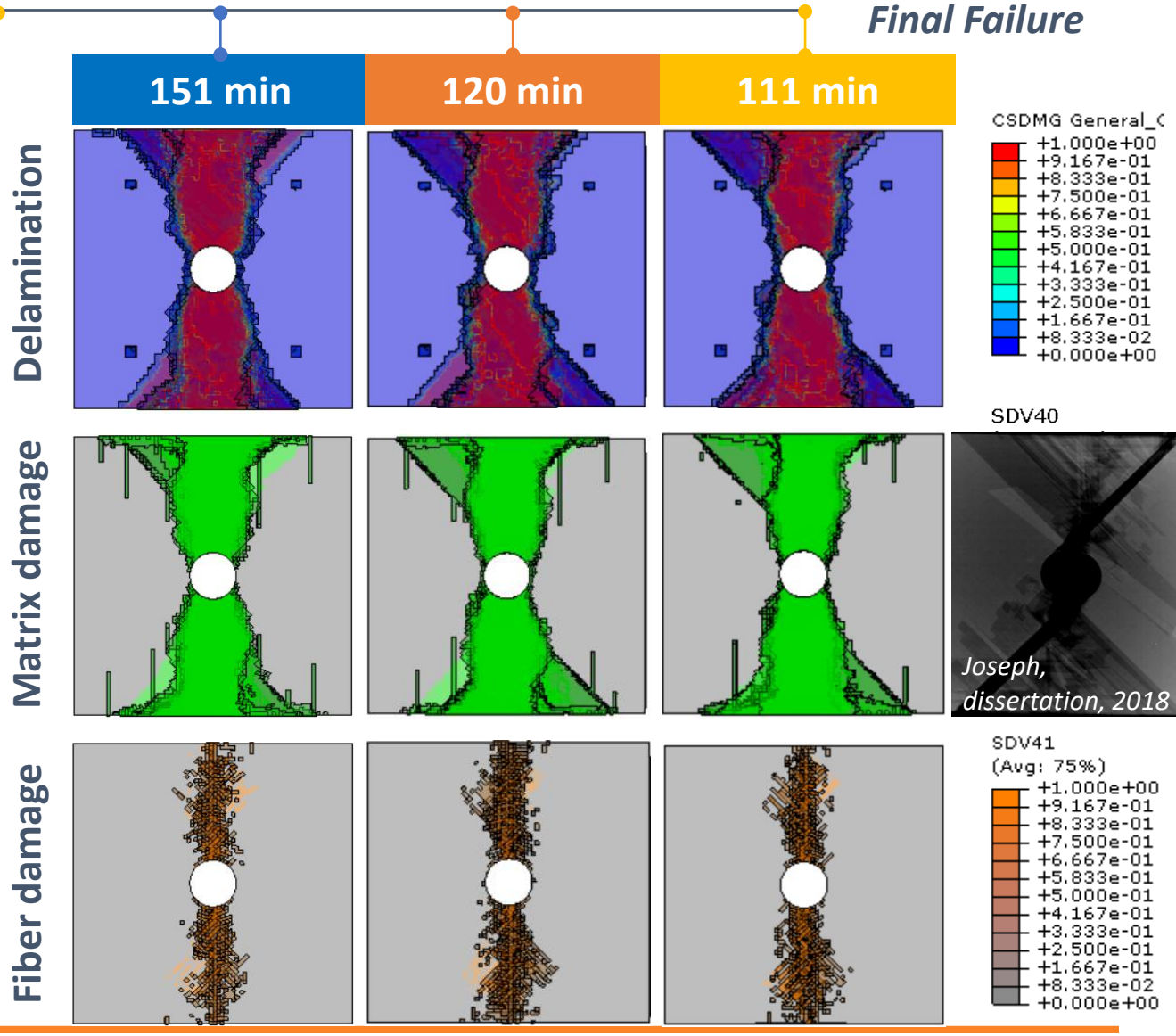

- Max time saving: 26.5%
- No accuracy loss.

3. Application Example: OHT Results [50/40/10] Layup

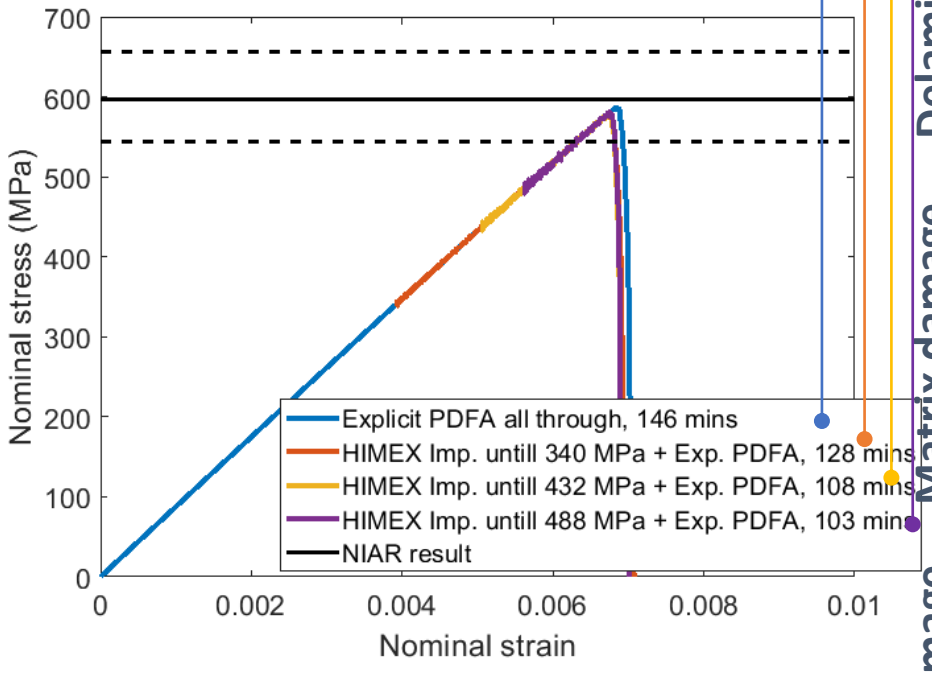

- Max time saving: 29.5%
- No accuracy loss.

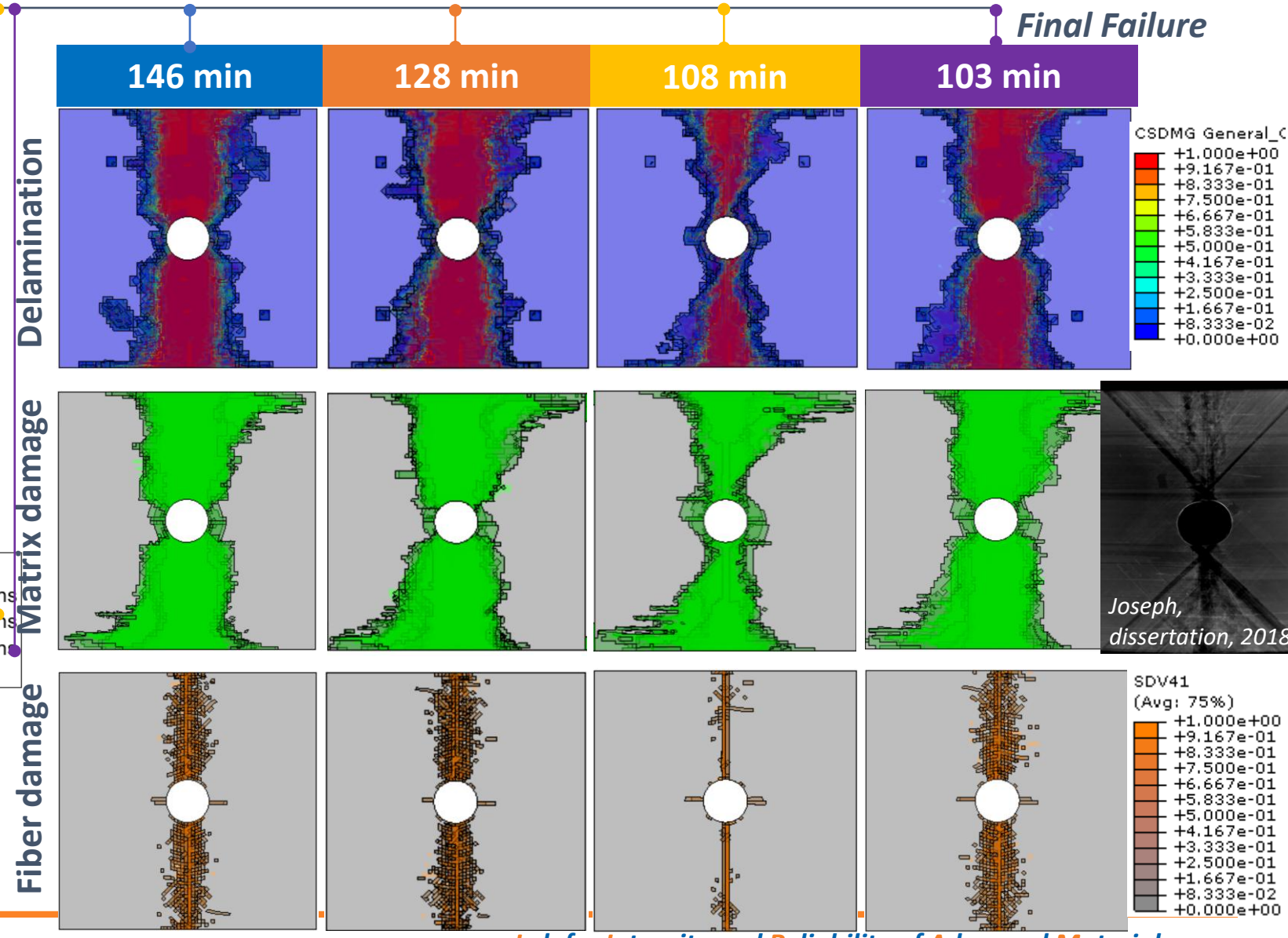

3. Application Example: OHT Results: Damage History of the [25/50/25] Layup

Explicit PDFA All Through: 151 mins

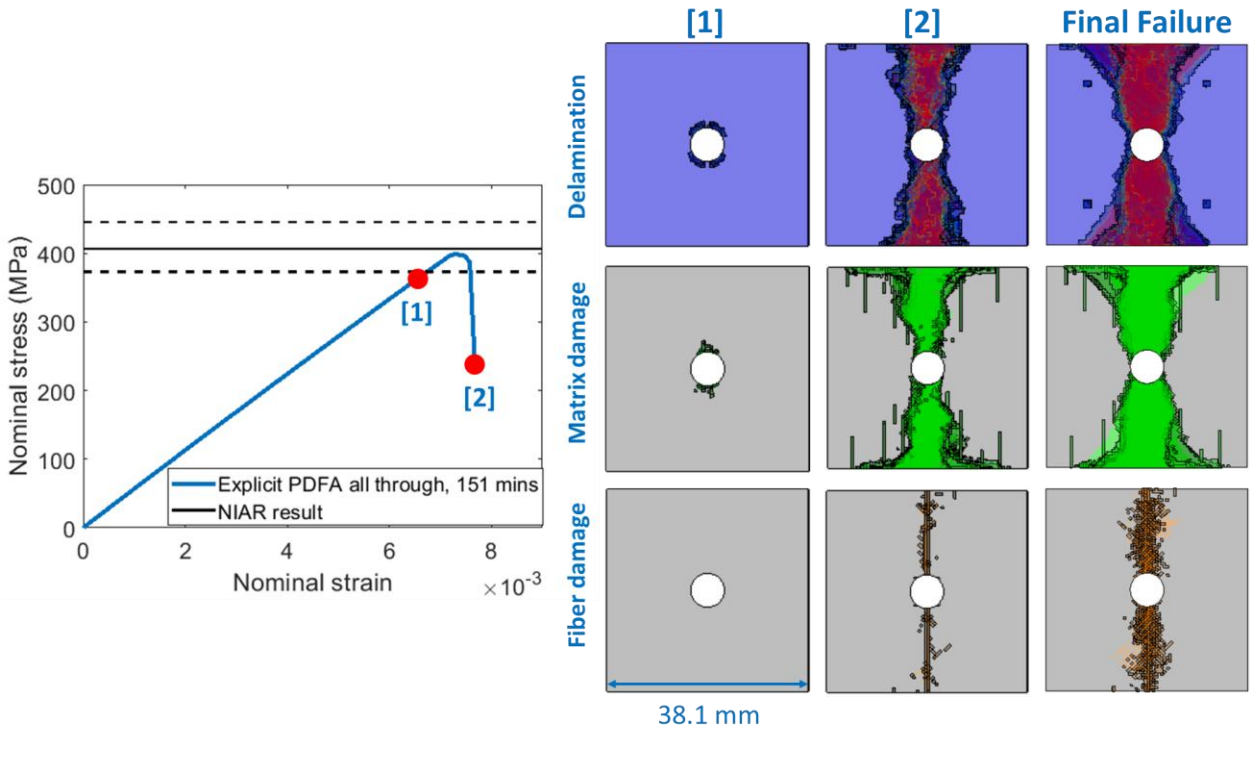

HIMEX: Implicit analysis (29 mins) + Explicit PDFA (82 mins)

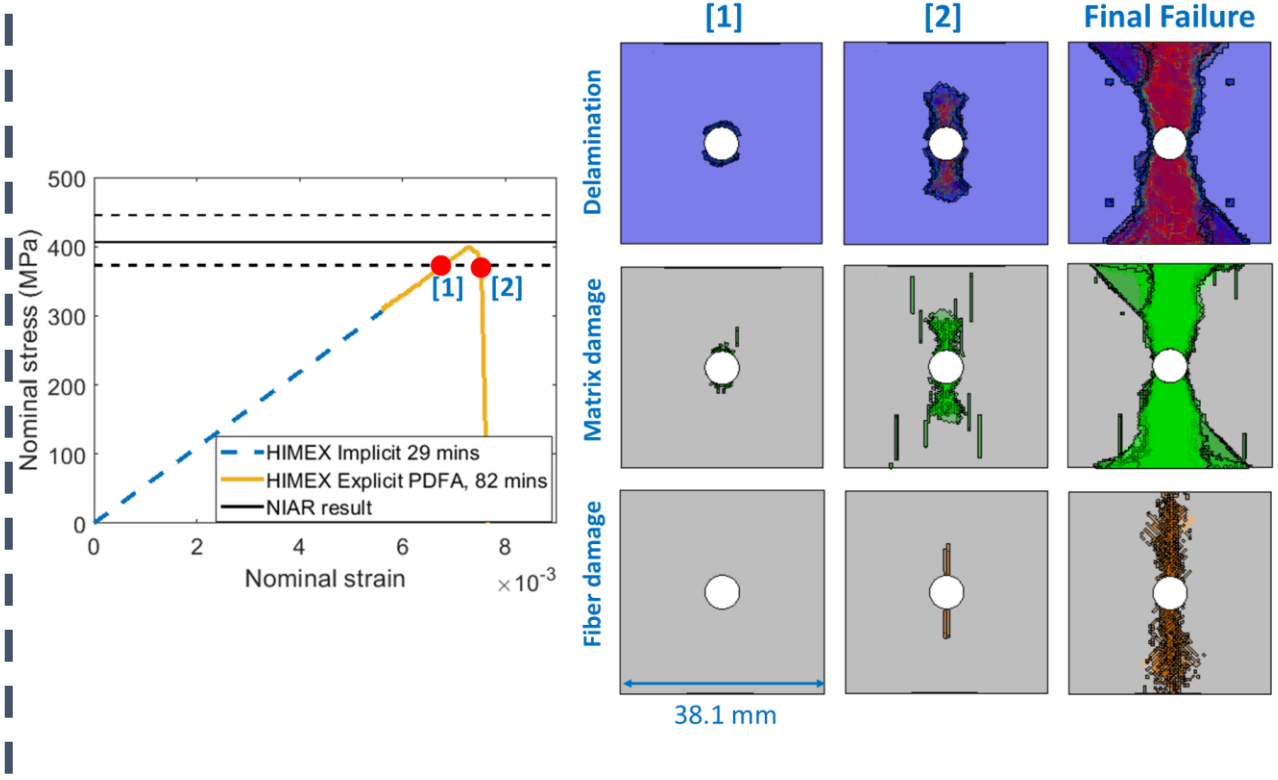

- The predicted damage development histories are highly similar.
- Snapshots of damage taken at slightly different time due to the mismatch of starting points.

Content

1. Numerical Accuracy, Efficiency, and Robustness in Progressive Damage and Failure Analysis (PDFA)
2. HIMEX: **H**ybrid **Im**plicit-**Ex**plicit PDFA
3. Application Examples: Open-hole Tension
4. Discussions
5. Conclusions and Vision

4. Discussions: Numerical Oscillations induced by HIMEX

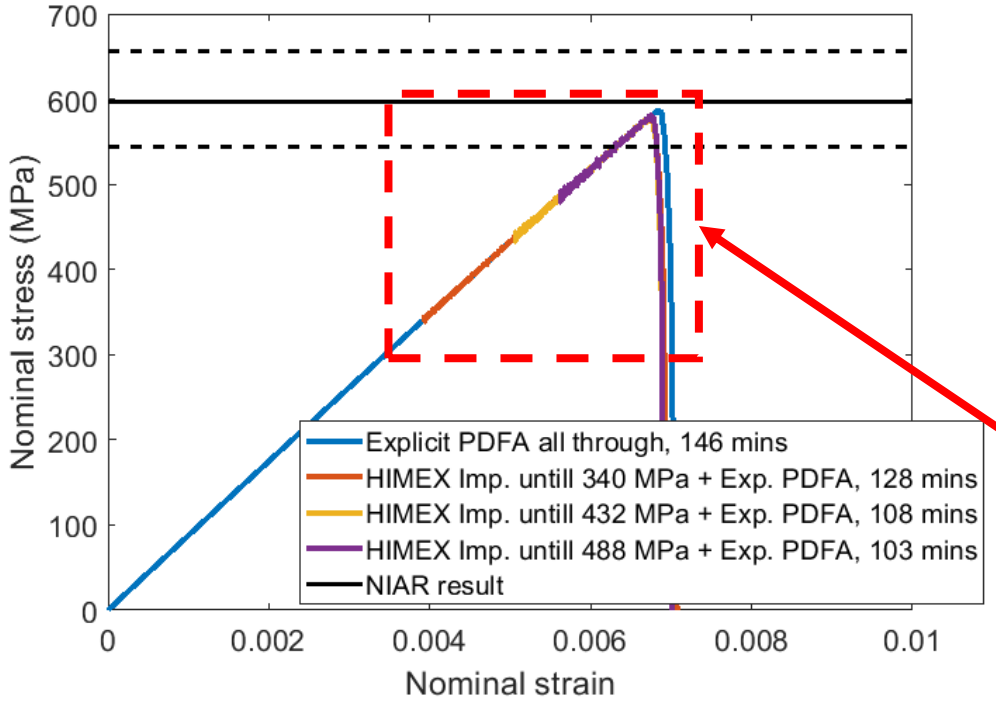

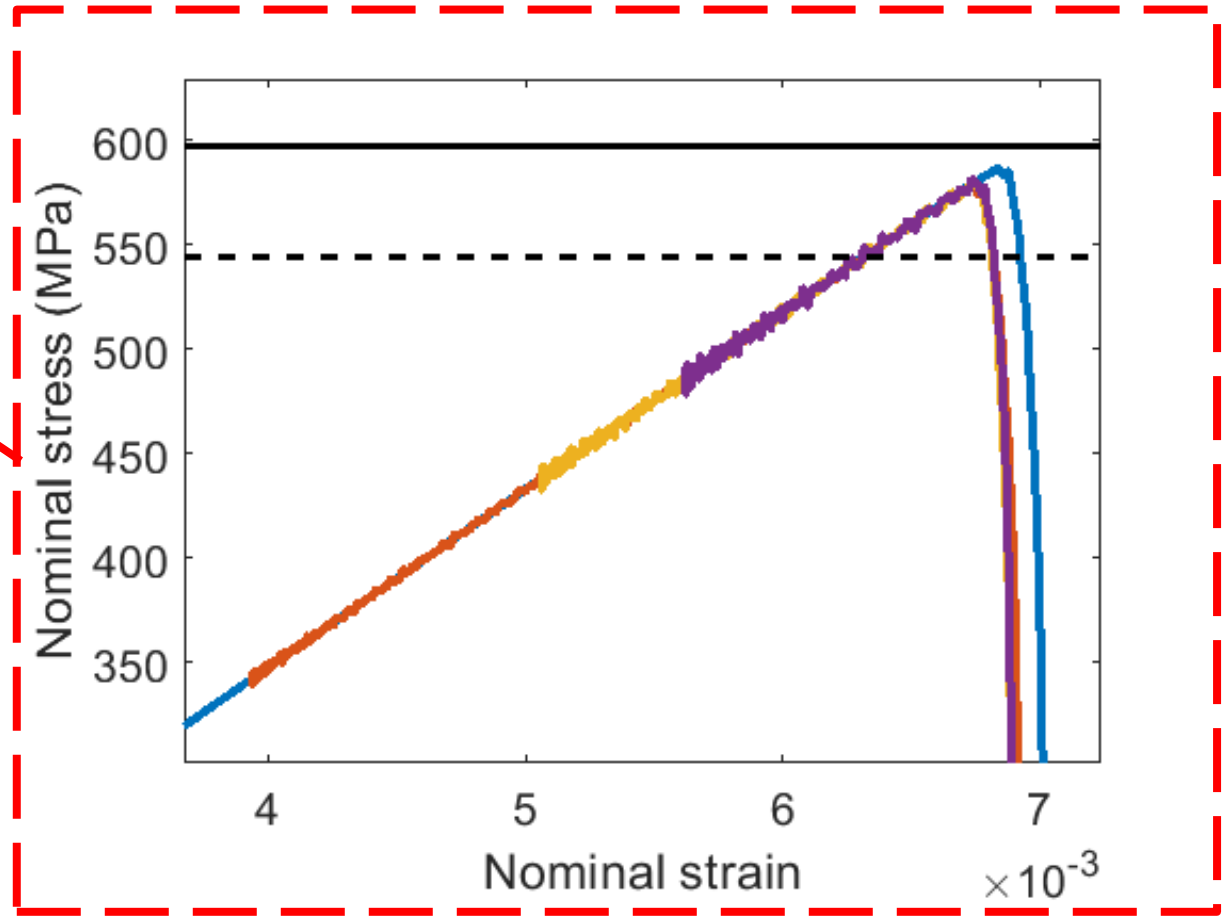

- After the implicit-explicit transitioning, **numerical oscillations** are seen. The later the transition, the higher the oscillations.
- The numerical oscillations are likely to be induced by 1) **precision** of stress and strain transferring. 2) **damage initiates** shortly after transition, and 3) exact **force equilibrium** is inherently **not ensured** in explicit analysis.

4. Discussions: When to "Switch Gears" in HIMEX

Matrix Damage

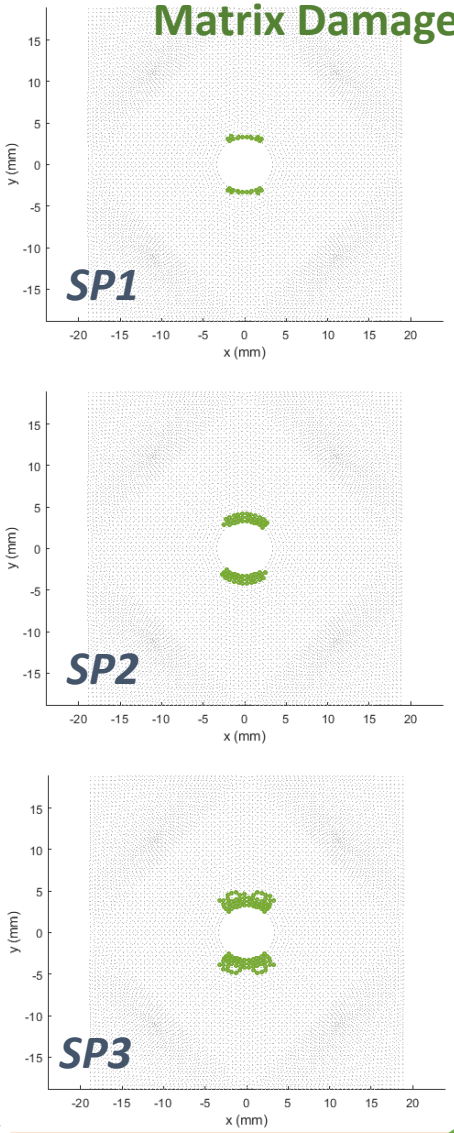

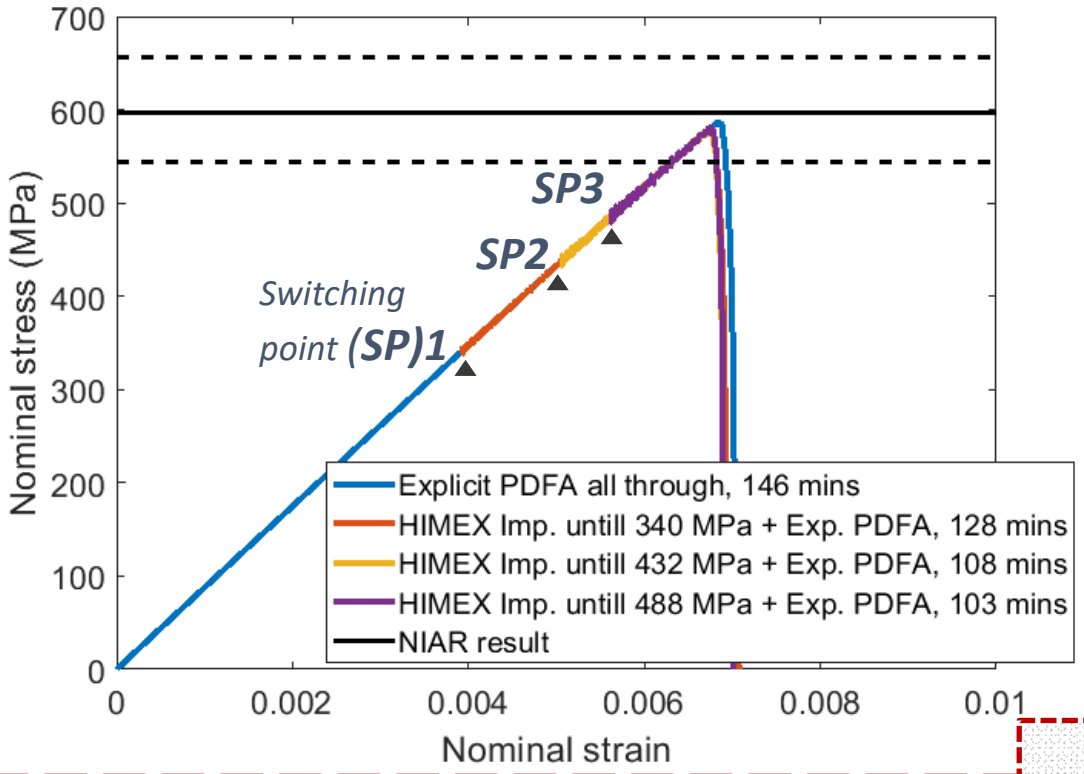

Fiber Damage

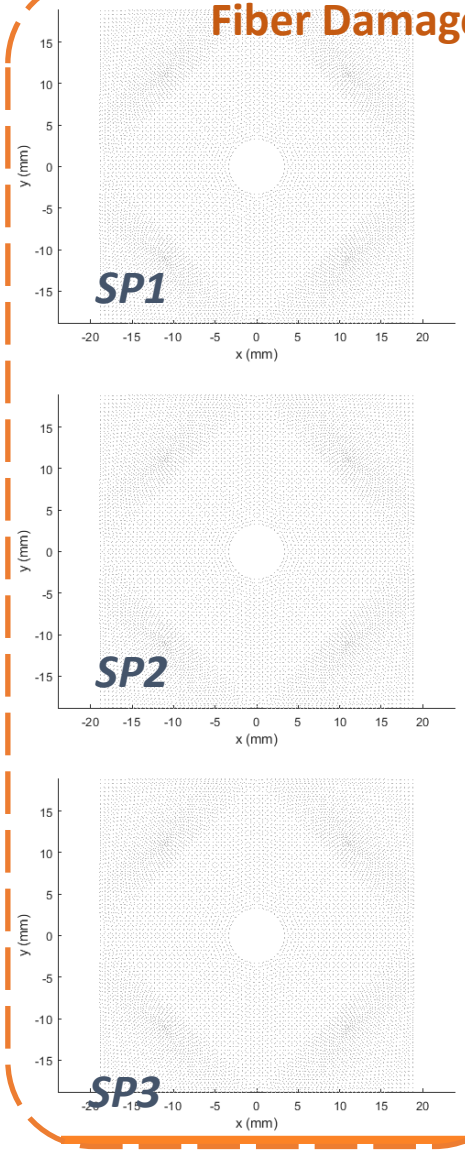

Delamination

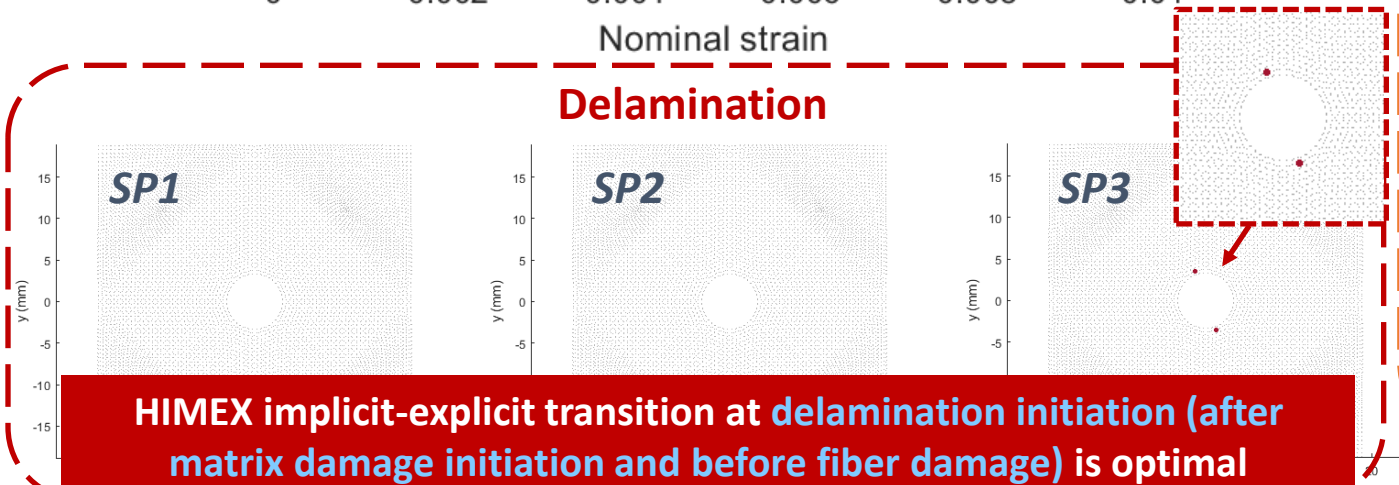

HIMEX implicit-explicit transition at delamination initiation (after matrix damage initiation and before fiber damage) is optimal

Content

1. Numerical Accuracy, Efficiency, and Robustness in Progressive Damage and Failure Analysis (PDFA)
2. HIMEX: **H**ybrid **Im**plicit-**Ex**plicit PDFA
3. Application Examples: Open-hole Tension
4. Discussions
5. Conclusions and Vision

5. Conclusions

- A new **h**ybrid **im**plicit-**ex**plicit (**HIMEX**) PDFA framework has been developed to accelerate the PDFA. HIMEX leverages the advantages of both the implicit (high efficiency) and explicit (robustness) algorithms.
- Demonstrated by the OHT application cases, HIMEX **saves the computation time up to 29.5% without compromising accuracy**.
- HIMEX is **transferrable across analysis software packages and PDFA subroutines**, generally applicable to quasi-static damage analysis of composites (e.g., OHT/OHC, SENT, SLP, DCB/ENF/MMB, etc.)
- Future directions include applying HIMEX to more complex cases (e.g., postbuckling and CAI) and developing HIMEX with **multiple explicit-implicit transitioning** for fatigue analysis.

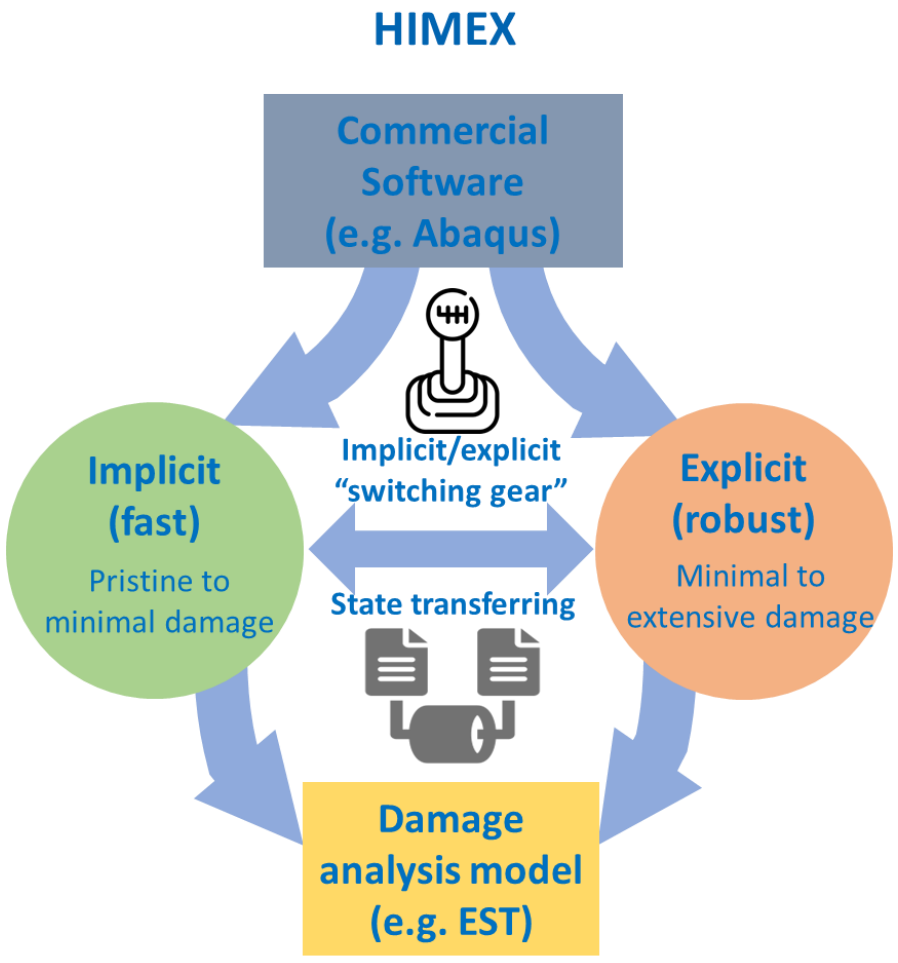

Thank you, Question?

Shiyao Lin, Assistant Professor
Department of Mechanical and Aerospace Engineering
Institute for Predictive Performance Methodologies
University of Texas at Arlington (UTA)
shiyao.lin@uta.edu

We are hiring Ph.D. students.

ICCM24
AUGUST 4-8, 2025
BALTIMORE CONVENTION CENTER
BALTIMORE, MARYLAND, USA

No Technical Paper Submission for:

Bowen Cao

Center for Composite Materials

Role of Modeling and Simulation in the Development and Application of Digital Twin for Liquid Composites Molding Processes

Suresh G. Advani and Pavel Simacek

University of Delaware

Outline

- Liquid Injection Molding
  - Process and Process Variations
- Digital Twin Role in Process Control
  - Possible Constructions of Digital Twin
- Simulation Approach, Uses and Capabilities
- Connecting the Digital and Physical
  - Direct Full Model Simulation as a Part of Digital Twin
  - Note on Machine Learning Approaches
- Real Time Challenge

LCM (RTM) Manufacturing Process

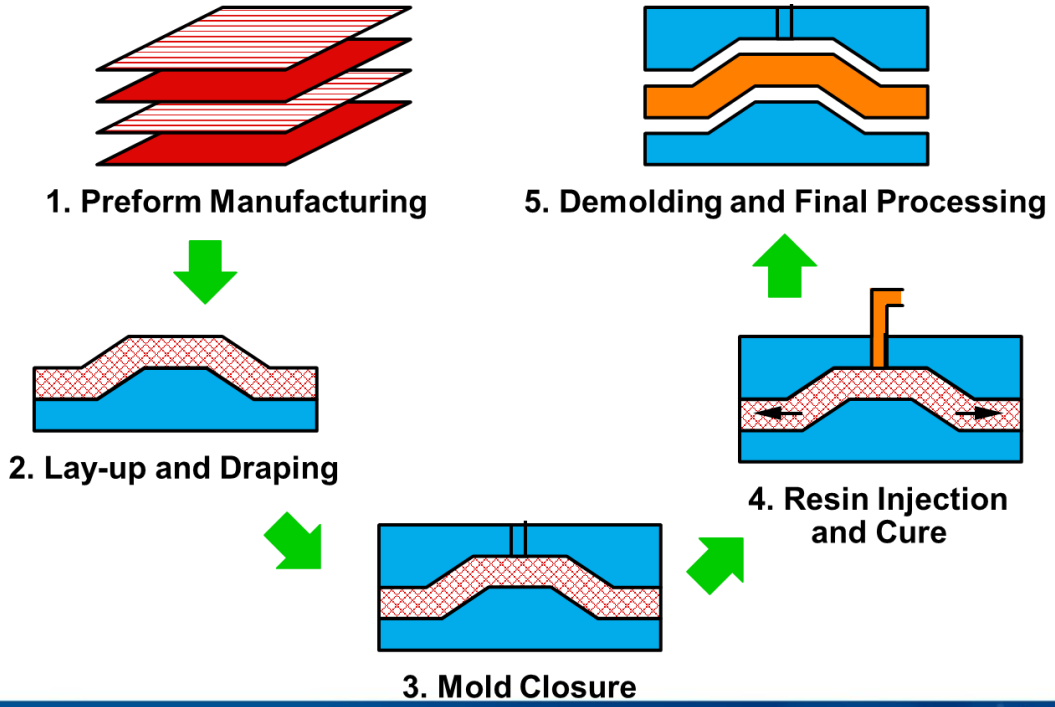

Variety of Processing Methods

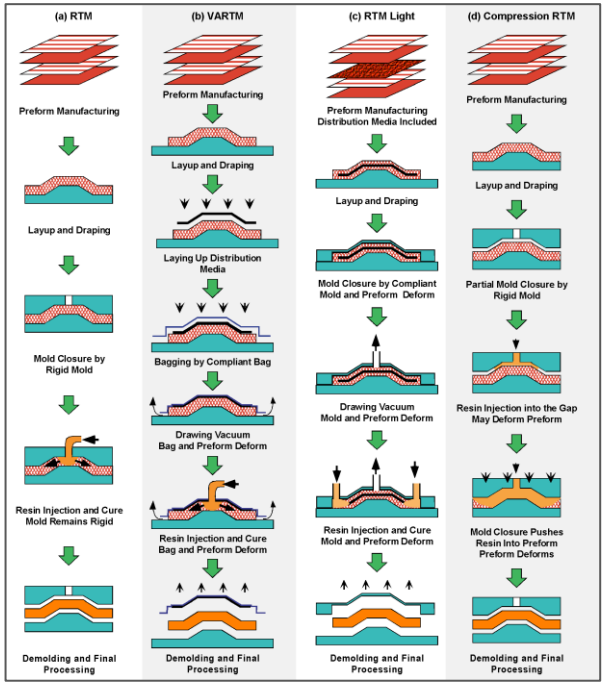

Variety of Process Variants

Flexible Infusion Settings

Lots of Ways to Do It Wrong:
Numerical Simulation Helps with Choices

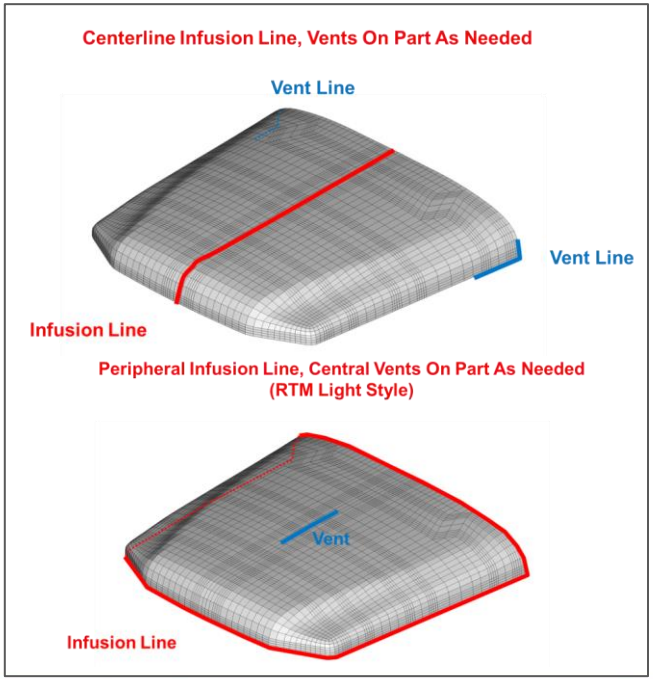

Flow Variability: Race-tracking

Transverse racetracking in ribs

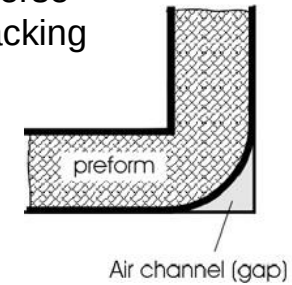

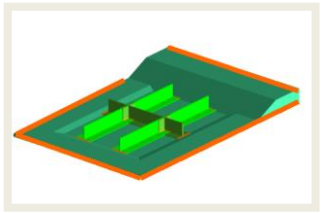

Racetracking along mold walls

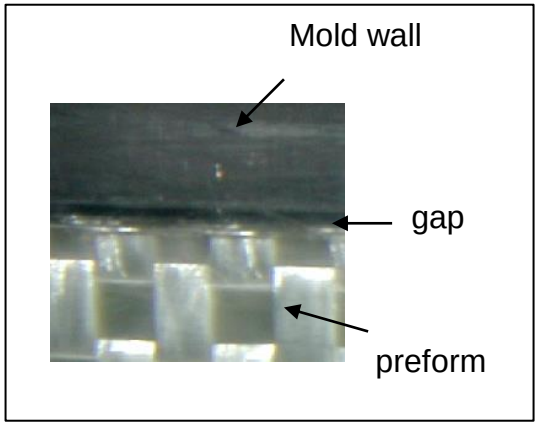

Transverse racetracking in tapered regions

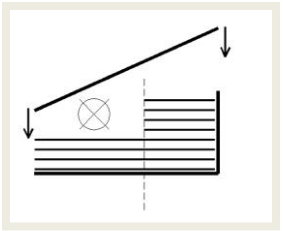

Ribs cut too short

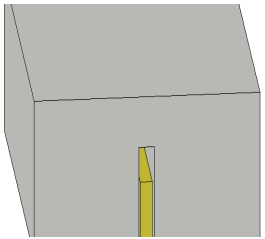

Source: Uneven Spacing and Gaps
Impact: Changed Flow Patterns
Prevention: Difficult

LCM Process Variability: Racetracking Impact

- **Same Part Being Infused, Different Outcomes Possible Depending on Gaps**
- **This Phenomenon Cannot Be Prevented**
- **The Racetrack Must Be Detected and Identified**
- **Corrective Action Must Be Taken**
- **Reason to Deploy AI in Some Form**

Resin Infusion Designed in Absence of Racetracking Channels:

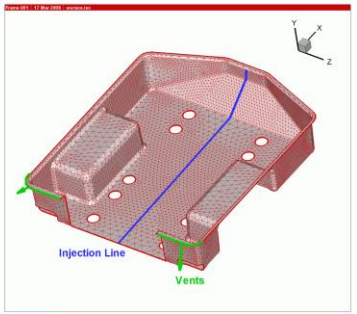

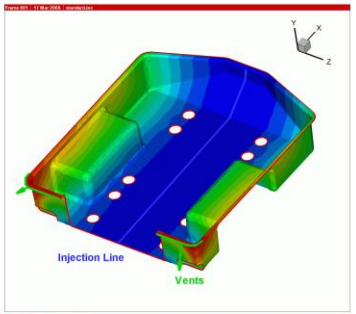

Effect of a Single Racetracking Channel on Flow:

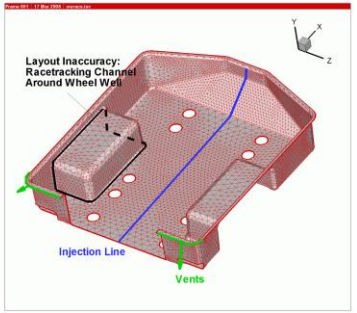

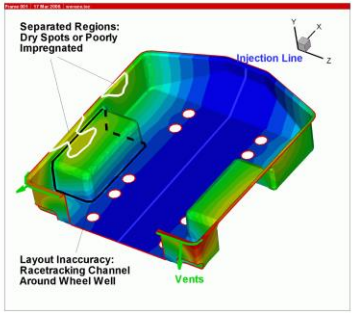

Digital Twin Idea

Physical Part Manufacturing

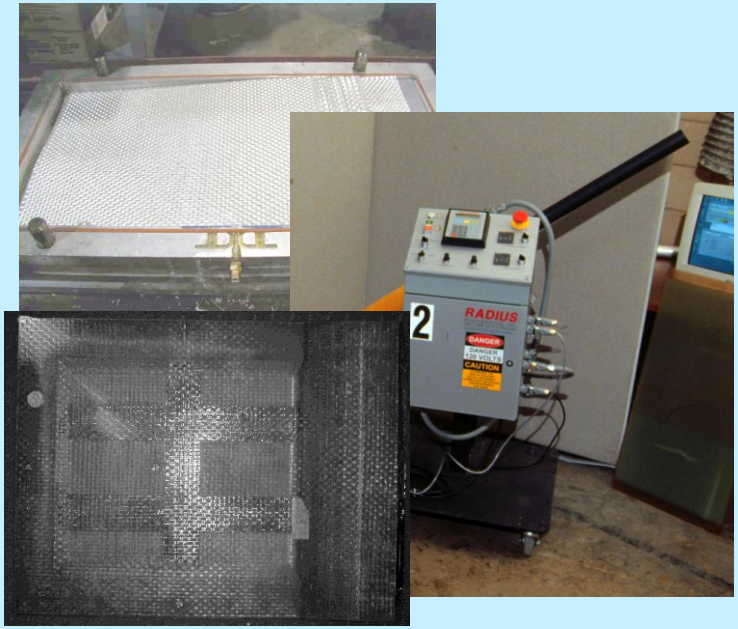

Create Model

Updates of State

Suggested Controls

Accurate Digital Representation

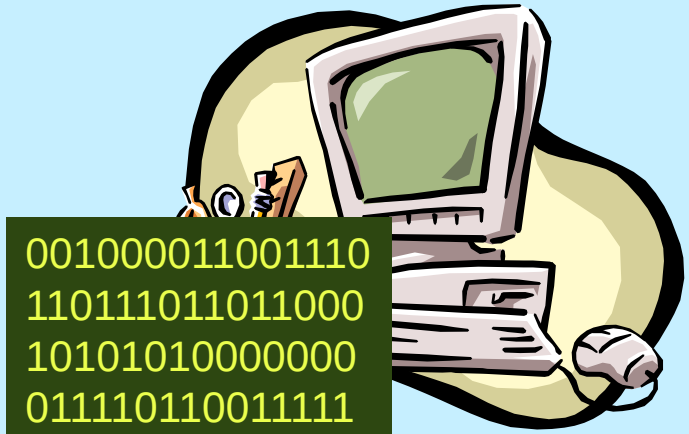

```
001000011001110
110111011011000
10101010000000
011110110011111
01110100010101
01001010101001
100111000110011
110000000_
```

Early Attempts on Digital Twin

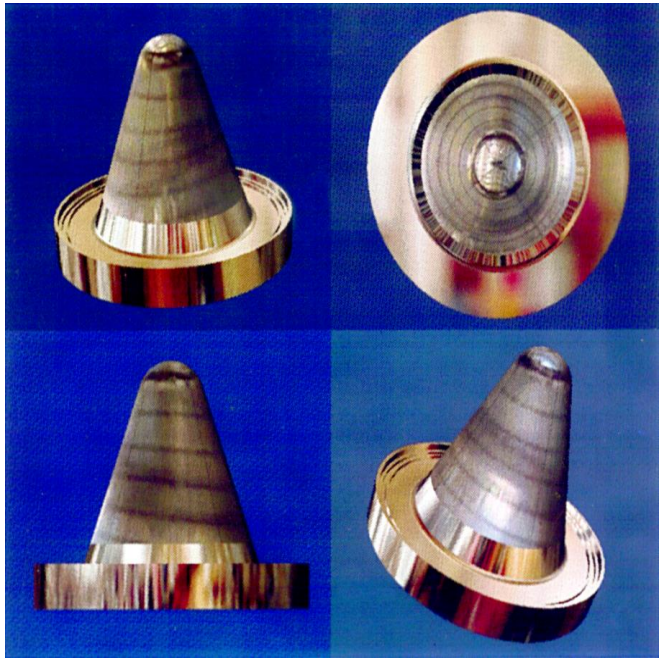



Simulation:
Always the Same Result

Note:
Needs Work on Feedback,
Physical World Sabotages This!



Requirements to Be of Use

Physical Setup

- Sensor System That Can Provide Feedback before Process Is Finalized
- Some Control Option to Reverse Negative Development as Directed by Digital Twin

Digital Twin

- Sufficient Accuracy of Model Description
  - Inclusion of Any Uncertain Aspects as Parameters to Be Modified on the Fly!
- Ability to React (Update Model as Needed) to Parameter Changes/Feedback in ***real time***
  - This Includes Finding Some Solution

Possible Approaches to Building Digital Twin

- Tweak Some Controls
- Observe Outcome
- Machine Learn from Physical Mistakes

- **This is Prohibitively Expensive!**

- Run Realtime Process Simulation if You Can
- Add Some Control/Solution Search Algorithm
- **Base Control on Gradual Reduction of Uncertainty in Model**

- Run Process Simulation with as Many Disturbances, Control Actions and So On
- **Feed This To Machine Learning**
- **Use AI to "Do" Digital Twin**

Connected: We Need Simulation!

Simulation Development and Uses (1)

Initially:
Process Design, Injection and Venting Strategies

Outcome:
Sufficiently Accurate Model
Simulation Time (Lower Fidelity) in Seconds

Injection Location=>
Flow Patterns=>
Last Separate Regions to Fill=>
Vent Location

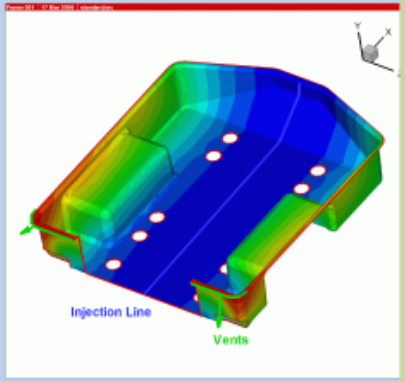

Injection Lines=>
Flow Time and Patterns=>
Sequential Injection Location
And Timing

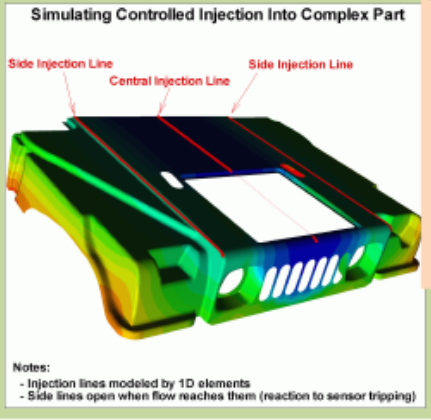

Distribution Media layout
=>
Lead Length(s)
=>
Delay Lines, Gaps and Timing

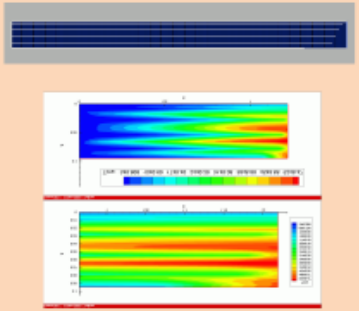

Simulation Development and Uses (2)

Handling Process Variations and "Features":

RTM Model Expanded to VARTM, CRTM, Pulltrusion

Model Can Handle Distribution Channels, Fabric Deformation, etc.

Preform Deformation And Effects on Material Data

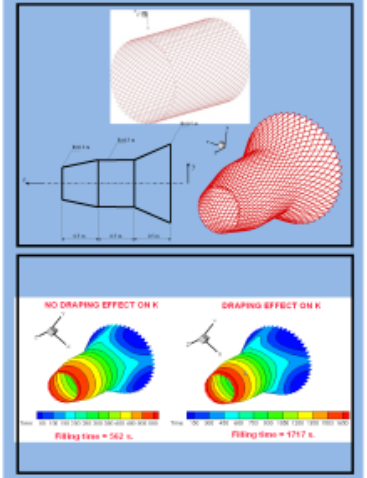

Better Flow Modeling in Doubly Curved Parts

Model for Distribution Media and Channels

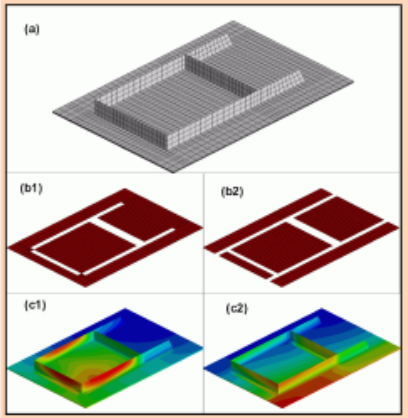

Modeling VARTM, CRTM Optimizing Distribution Network

Varying Material Properties and Creating Resin Sources/Sinks During Infusion

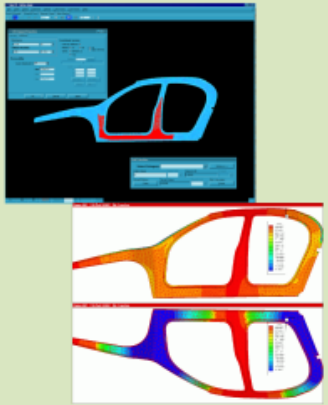

Modeling Compression RTM, Infusion in Pultrusion, Post Filling Flows

Simulation Development and Uses (3)

Handling Process Variability:

Modeling Individual Disturbances

Generating Multiple Scenarios "Automatically"

Sufficient Throughput to "Have Them All"

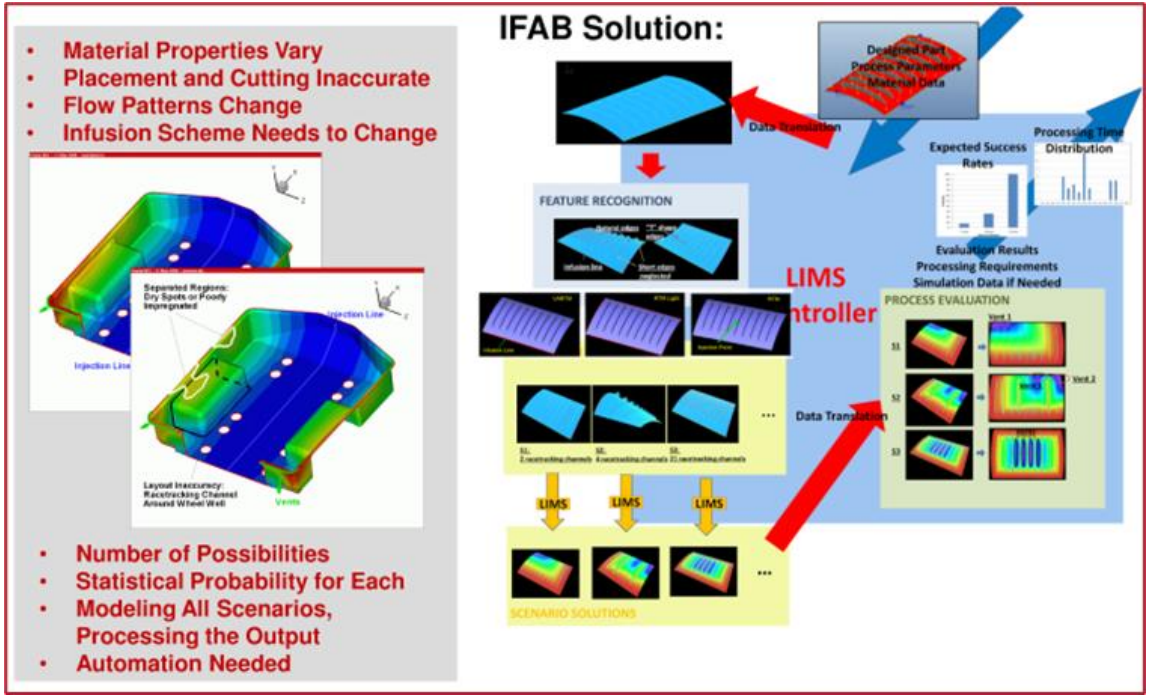

Process Control and Sensing

To Use Simulation for Digital Twin It Must Allow Control of Model Process

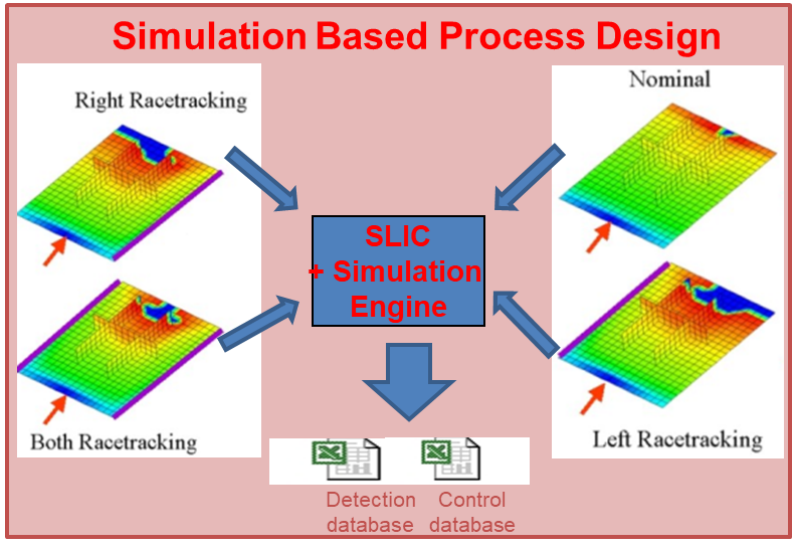

- Simulation of Sensor Action Needed!
- Implementation of Control Elements (Say, Additional Gates) Needed



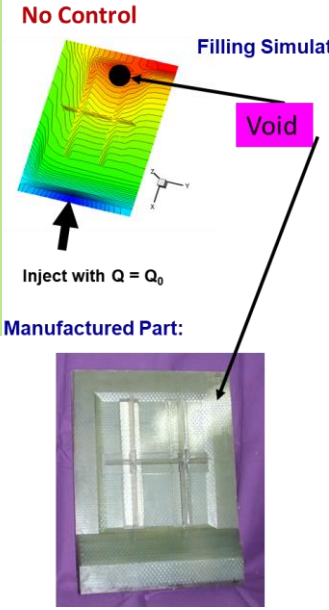

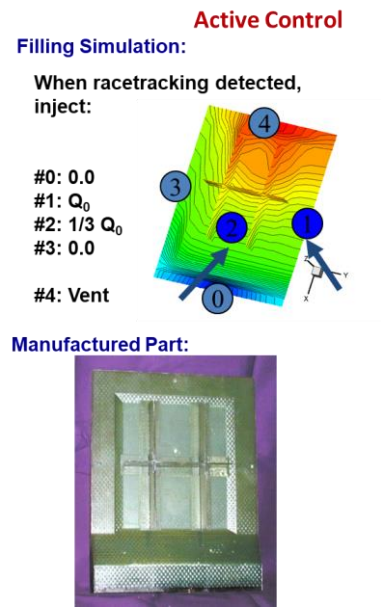

Simulation Capability Available for Digital Twin Development

- Most Liquid Composite Molding Processes Can Be Satisfactorily Modeled
  - Performance is *Very* Acceptable even for Large Number of Possibilities
  - Variations of LCM Processing Have Been Addressed
  - Modeling Extra Distribution Hardware (Tubing, Distribution Media) Has Been Fully Resolved
- Process Variability Has Been Addressed. Disturbances Based on Part Geometry Have Been Successfully Generated
- Control Actions Can Be Designed and Modelled
  - Approaches Vary, Generic Recipe Still Ahead (Space for ML Here)
  - Actual Implementation Remains Task for Digital Twin Development

Communication Between Simulation and Outside World

What Is Needed to Use Simulation On-Line Within Digital Twin

- Simulation Flexibility to Change Settings Mid-Way of Run
- Mechanism for Digital Twin Code to Send Commands to Simulation
  - Change the State of Parameters As Needed (Determined from Physical Realm)
  - Modify Simulation State on the Fly Including Injection Control Option(s)
- Mechanism to Transfer Simulation Data Between Executed Programs
  - This Can Be Used to Chain Other Models "In" as Needed (Volatiles, Heat….)
  - It Can Facilitate Parallelization

Current LIMS Approach Through MPI Interface:

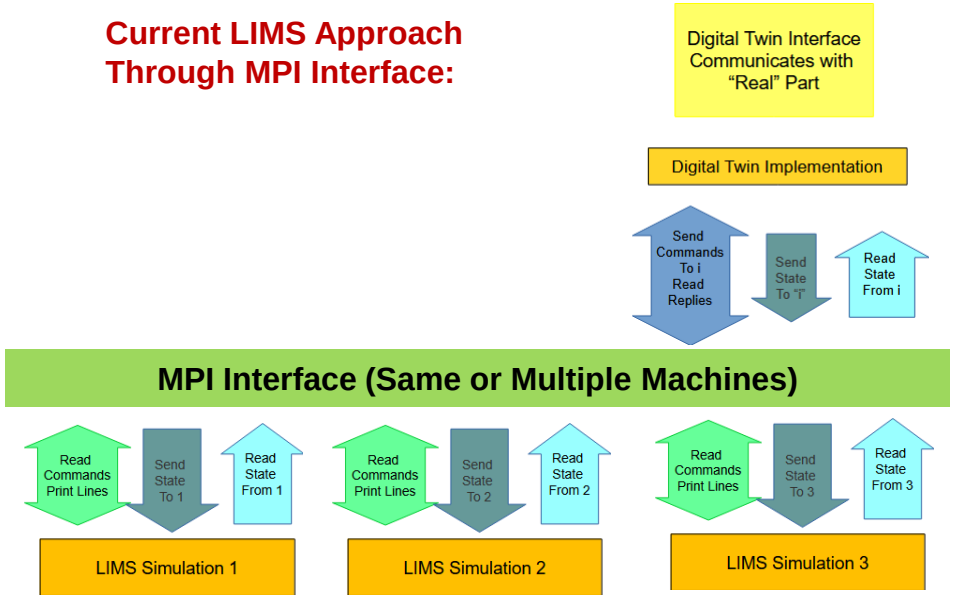

MPI Connectivity and Coupling LIMS Simulation with Additional Process Physics Models (Volatile Transport)

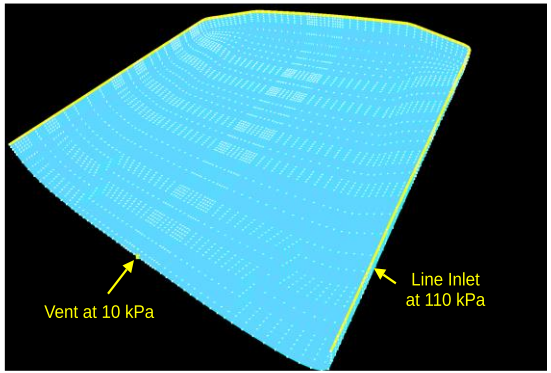

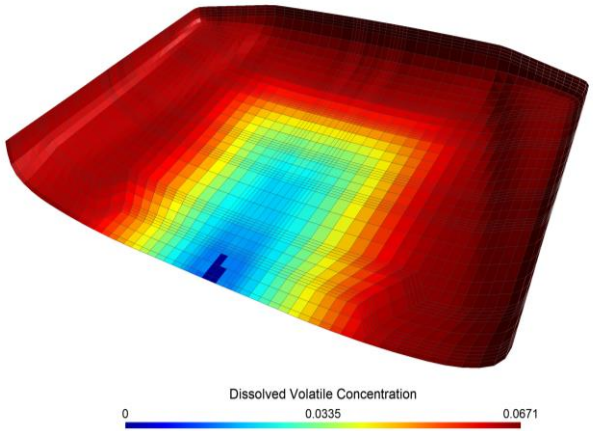

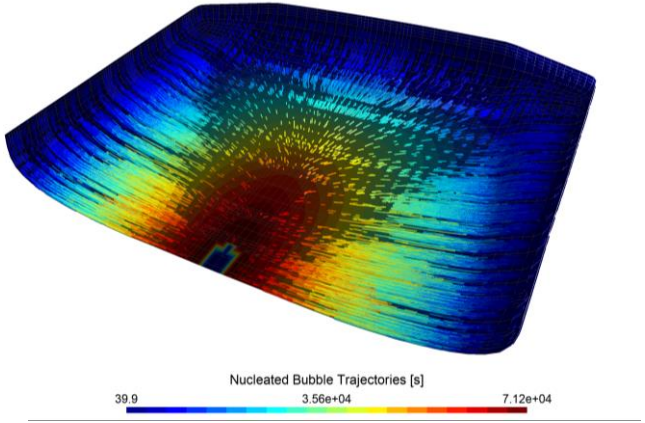

Properly Resolved Communication (In This Case over MPI) Broadens the Process Model Applicability

Conclusions

- The Construction of Digital Twin for LCM Requires Process Modeling
  - Either Directly or to Train AI
- Process Model Must Handle The Usual Trappings of LCM Processes (Most Do)
- Process Model Must Simulate Process Variability (Most Do)
  - To use On-line Modeling, The Model Parameters Must Be Accessible *During* the Simulation (LIMS Allows This)
- Process Model Must Simulate Control Action (Some Do)
  - To use On-line Modeling, The Controls Must Be Accessible *During* the Simulation (LIMS Allows This)
- Important Features for Actually Using Simulation are Inter-Process Communication and Computational Performance

Acknowledgement

- This material is based upon work supported by the U.S. Department of Energy's Office of Energy Efficiency and Renewable Energy (EERE) under the Advanced Manufacturing Office, Award Number DE-EE0010205

NUMERICAL MODELING OF FIBER BUNDLE ARCHITECTURE IN THE ROBOTIC CORELESS FILAMENT WINDING PROCESS

S. Hügle[1], M. Bellmann[1], L. Balangé[2], A. J. Thompson[3], M. Pei[3], S. Carosella[1], S. R. Hallett[3], V. Schwieger[2] and P. Middendorf[1]

[1]Institute of Aircraft Design, University of Stuttgart
Pfaffenwaldring 31, 70569 Stuttgart, Germany
Email: huegle@ifb.uni-stuttgart.de, bellmann@ifb.uni-stuttgart.de, carosella@ifb.uni-stuttgart.de, middendorf@ifb.uni-stuttgart.de web page: https://www.ifb.uni-stuttgart.de/

[2]Institute of Engineering Geodesy, University of Stuttgart
Geschwister-Scholl-Str. 24D, 70174 Stuttgart, Germany
Email: laura.balange@iigs.uni-stuttgart.de, volker.schwieger@iigs.uni-stuttgart.de, web page: https://www.iigs.uni-stuttgart.de/

[3]Bristol Composites Institute, University of Bristol,
Beacon House, Queens Road, Bristol, BS8 1QU, United Kingdom
Email: michael.yuan.pei@bristol.ac.uk, stephen.hallett@bristol.ac.uk, web page: https://www.bristol.ac.uk/composites/

Keywords: Computational modeling, Finite element analysis FEA, Filament winding

ABSTRACT

The coreless filament winding (CFW) is a novel robot assisted manufacturing process, where impregnated fiber bundles are wound around sleeves in a defined chronological order. Unlike conventional winding, there is no mandrel available to define the resulting shape. Instead the fiber-fiber and fiber-sleeve interaction, influenced by winding sequence and prestress, is forming the final fiber architecture. Depending on the load case of the subsequent area of application, a precise knowledge on the cross-section of the resulting fiber structure is required for a reliable structural evaluation. In order to enable virtual modeling of the forming process, an expansion-based multifilament method is presented. The values for influencing parameters, such as filament diameter, static coefficient of friction, Young's modulus, pretension and penalty stiffness require a balanced interaction and therefore need to be optimised to experimental results during an optimization loop. To evaluate the deviation between simulation results and experimental data, the area and maximal dimensions in a cross-section of a specimen is used.

1 INTRODUCTION

The coreless filament winding technique is a novel robot assisted manufacturing process, where pre-impregnated tows are wound around sleeves in a predefined pattern without a mould resulting in shell-like truss or lattice structures. The flexibility in shape design and its potential for lightweight construction make the process suitable not only for the architectural sector, but also as topology-optimized fiber-reinforced connecting elements or satellite structures. For this highly interconnected structure a sufficient fiber-fiber interaction is required to ensure a reduced buckling length for each free-spanning fiber segment between two fiber connection points [1]. The non-cured, impregnated fibers exhibit no bending resistance during fabrication so that each newly added fiber segment deforms the previous ones [2]. This deformation significantly influences the final shape of the structure and introduces tension in the previously wound fibers. The final structural architecture thus results from fiber-fiber and fiber-sleeve-interaction during the process as well as sleeve point positioning and orientation [3]. A precise cross-section is required to reduce over-dimensioning and material waste. Due to compaction of the fibers during the process and the typically large number of tow crossing points in coreless wound structures, analytical calculation of fiber architecture and bundle cross-sections of

complex structures is challenging. To obtain detailed data prior to fabrication and virtually replicate manufacturing as basis for structural and process optimization, a process simulation workflow has been developed by Hügle et al. using an explicit finite element approach [4]. The finite element approach is able to capture the elastic deformation and friction but requires a long computation time, thus limiting the applicability for large structures. Furthermore, it indicates that modeling of fiber deformation must be included in the simulation for a realistic prediction of fiber architecture and cross-sections. Modeling of a realistic tow shape is a wide-ranging research topic during the generation of unit cell models in woven composite simulation. Here, single and multifilament relaxation models have been used to simulate the fiber-fiber-interaction that form the resulting structure on a sub mesoscale model as reviewed by Wielhorski et al [5]. The approach has been continued by Jones [6] to model the influence of winding sequence and pin configuration on a mandrel for a wound truss structure. In this work the multifilament approach is extended to predict the fiber architecture and cross-sectional yarn deformation of a coreless-wound structure. As a mandrel is not used for this manufacturing technology, an expansion-based approach is applied, which requires a parameter fitting to experimental data to obtain information on realistic fiber bundle deformation.

2 METHODOLGY

In the following section the fundamentals for the methodology of the simulation approach will be explained. Afterwards the implemented procedure to evaluate selected cross-sections of a simulation result and quantify the deviation to experimental results are described. The methods are then implemented in an optimization loop with the software tool LS-Opt to identify values for the following parameters: virtual fiber diameter, static coefficient of friction, Young's modulus, internal loading and penalty stiffness.

2.1 MODELING APROACH

The software used for the expansive modeling approach is the solver SimTex, developed by the Bristol Composites Institute. This explicit finite element solver was originally created for digital element simulation with an implementation of fast contact algorithms to reduce computation time for textile forming processes. The digital element method uses chains of artificial beam elements with a reduced stiffness matrix that are connected with joints [7]. This enables a reduced computational effort under usage of non-physically related material data. During multifilament textile forming processes, an initial single tow and respective fiber path, that represents an initial geometry of the fiber architecture, is transferred into arrays of multiple virtual fibers that interact with each other to form the deformed tow shape. This multifilament cross-section is derived by a division of the single virtual filament of the initial fiber path into multiple virtual filaments with a smaller diameter. By varying the number n_{virt_fibers} of virtual fibers per tow that represent it in the simulation and the diameter of this fibers d_{virt_fibers}, a realistic virtual textile architecture and cross-sectional shape can be modelled.

In the modeling approach, a single virtual filament fiber path out of a process simulation by Hügle et al. is transferred in an overlapping multi-filament cross-section (Fig. 1 a)) by scaling of the tow cross-section. In Fig. 1 c) a comparison of different amounts of virtual fibers for a circular virtual tow is displayed, where a single virtual fiber represents several physical fibers. This virtual tow is subsequently expanding due to penalty stiffness in the contact among the individual overlapping virtual filaments (Fig. 1 b)). The initial contact space between the filaments is defined by the dimensions of the mesoscopic fiber path out of the process simulation, where the initial dimension needs to be larger than the scaled virtual tow cross-section, but not too large to enable a sufficient interaction of the virtual filaments. To address this issue an additional internal loading and thus axial shrinking of the elements is applied to control the expansion and fiber interaction in SimTex. This expanding approach enables modeling of large cross-sectional deformations as they occur at intersections of fibers or at sleeves as shown in Fig. 3.

In the virtual filament approach by Jones, the diameter of the virtual filaments is dimensioned to preserve the total area of all physical fibers. The resulting calculated cross-section is then scaled to enable an expansion of the virtual tow. The methodology is also part of a pre-processor for SimTex. As the coreless winding uses pre-impregnated fiber bundles, this approach is extended to preserve the

theoretical wet yarn cross-section A_{wet} for a defined fiber volume ratio FVR, presuming that the total area of the real roving (including resin and neglecting pores) corresponds to the total area of the virtual roving.

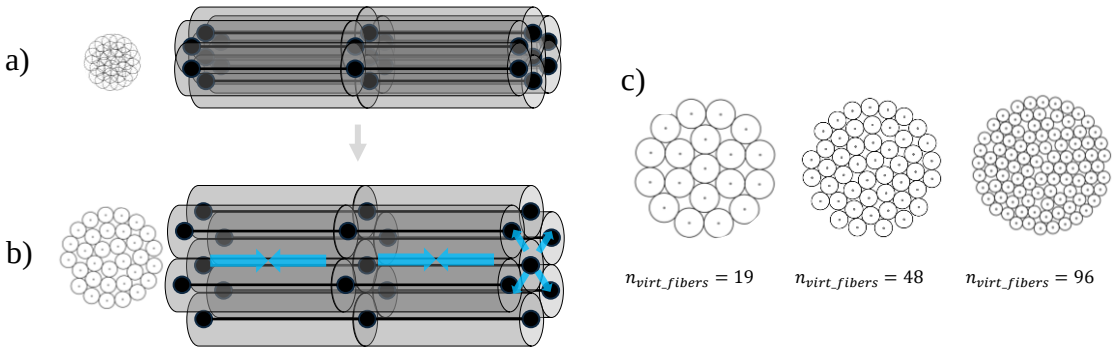

Figure 1: Schematic representation of the simulation approach: Initial overlapping virtual filaments (a) of a virtual tow that expand due to contact forces among the filaments controlled by additional internal contraction loading to a final expanded stage (b). Cross section of a circular virtual tow consisting of an increased number of virtual fibers and their respective centroid points (c).

Assuming a complete expansion of the virtual fiber bundle, the required diameter d_{virt_fibers} of a virtual filament in the impregnated modeling approach can be calculated by additional scaling. As the sum of cross-sectional areas of the finite number of virtual elements A_{virt_fibers} is not able to fill the circular cross-sectional wet tow area A_{wet} without free space, the packing density p_d of the virtual fiber bundle needs to be considered. the following equation (Eq. 1) must be satisfied:

$$A_{virt\_Fil} = p_d \cdot A_{wet} \tag{1}$$

The value of the fiber volume ratio (FVR) of the wet tow can be calculated according to Eq. 2 using the physical diameter d_{fiber} and number of filaments n_{fibers}:

$$A_{wet} = \frac{n_{fibers} \cdot \pi \cdot \left(\frac{d_{fiber}}{2}\right)^2}{FVR} \tag{2}$$

Considering a FVR of one, the same formula applies for A_{virt_Fil} and thus the diameter of a virtual filament d_{virt_fibers} can be calculated:

$$d_{virt\_fibers} = d_{fibers} \sqrt{\frac{p_d \cdot n_{fibers}}{n_{virt\_fibers} \cdot FVR}} \tag{3}$$

As shown in Fig. 2, the packing density of the cross-section can change during usage of different numbers of virtual filaments. The packing density of a centroid configuration can be calculated by dividing the total area of all virtual fibers by the resulting diameter d_{virt_tow} of the resulting virtual tow during a pre-calculation with $p_d = 1$ according to Eq. 4.

$$p_d = \frac{n_{virt\_fibers} \cdot \ {d_{virt\_fibers}}^2}{{d_{virt\_tow}}^2} \tag{4}$$

The resulting unscaled cross-section of a virtual tow with 48 virtual fibers and the respective theoretical diameter of the impregnated wet yarn cross-section for the experimental data used in this study with a radius of $1.704\ mm$ is shown in Fig. 3 a). A scaling factor of 0.5 enables a reasonable fiber interaction during expansion and usage of the process simulation results with a bundle thickness of $2.5\ mm$ thickness without overlapping of individual fiber layers resulting in intertwined virtual fibers. A scaled

cross-section with a target scale factor of 0.5 and a resulting radius of 0.961 *mm* is illustrated in Fig. 3 b). The actual scale factor for this input data is 0.564 as the scaling is applied to the centroids of the fibers neglecting the influence of fiber bundle dimensions.

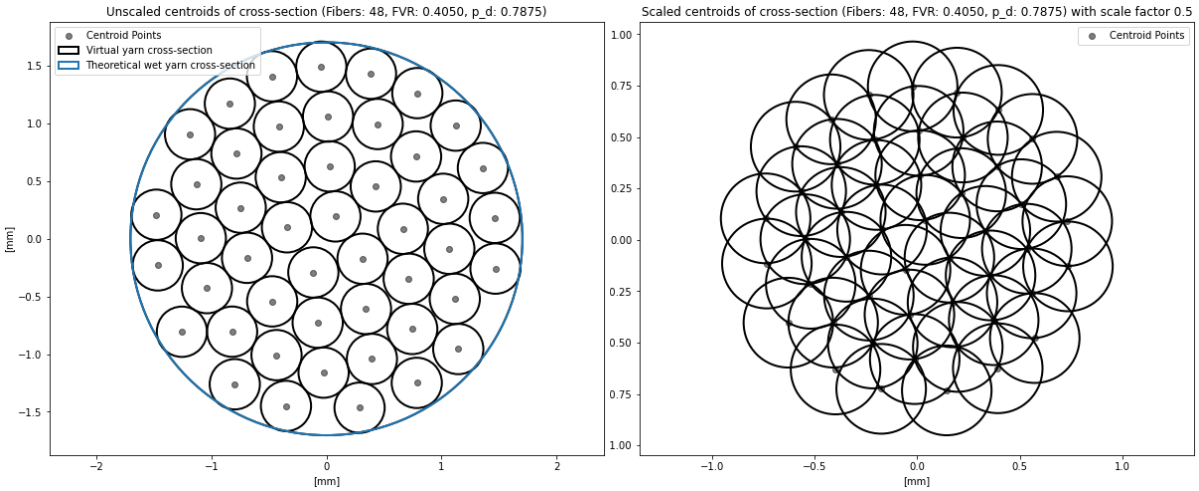

Figure 2: a) Unscaled cross-section of a virtual tow with 48 virtual fibers and the respective theoretical wet yarn cross-section. B) Scaled virtual tow with a target scale factor of 0.5.

In Fig. 3 shows a simulation model for the analyzed structure and the result after an interaction of the multiple fibers (Fig. 3 b)). The model of the sleeve (detail in Fig. 3 a)) is discretized with triangular *Tri*-elements, that are only used as rigid contact surface and are fixed in their translational and rotational degrees of freedom. The virtual fiber elements are modeled in SimTex as spherocylindrical *Line*-elements. These are defined by a discretization of the initial fiber path into elements of a user defined length. A high amount of virtual fibers with a resulting small diameter will result in a large aspect ratio (element length over diameter) and may cause penetrations at contact areas with a high curvature. To prevent these penetrations, the user-defined length is reduced when setting up the model to ensure an aspect ratio of 4 according to empirical results from Jones. The ends of the fiber path are fixed in fiber direction, but free to move in the cross-sectional plane perpendicular to it, allowing the filaments to move freely in crossing areas or at contact areas with anchors. The end of the yarn must be positioned so that the fibers are pulled towards the sleeve under tensile load. To define this boundary condition, a local coordinate system at each end point is used. As this local coordinate system is depending on fiber path and its discretization, the adjoining elements are used to define the new local x-axis with its direction pointing outward. The new local y-axis is defined with a rotation of the global coordinate system using the Gram-Schmidt orthogonalization method and the z-axis as a cross-product of these two axis vectors.

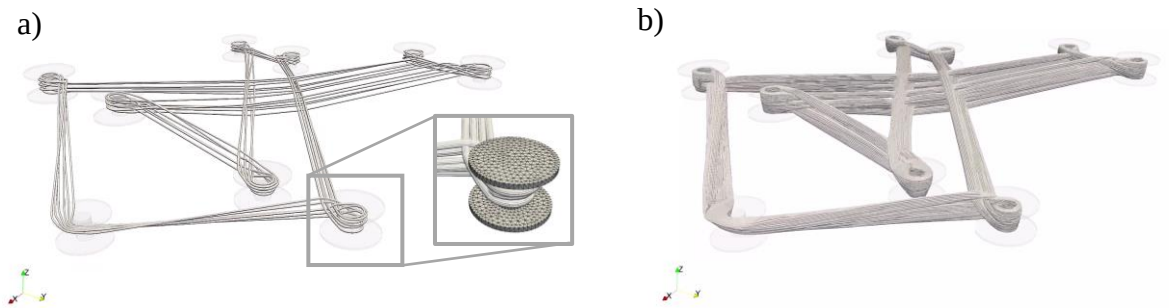

Figure 3: a) Initial configuration of the overlapping virtual fibers with a fiber path extracted out of a previous simulation of the winding process. The detail shows the discretization of the sleeve model. b) SimTex simulation result after interaction of the virtual fibers with each other.

2.2 APPROACH FOR GEOMETRIC ANALYSIS

To enable a comparison of the simulation results with experimental data, a fast but representative approach for the geometrical evaluation of a cross-sectional shape out of a point cloud is required. A convex hull is not sufficient for the irregular convex and non-convex shaped cross-section of those structures. Green et al [8] used a modified version of the convex hull with a finite search radius for a yarn cross-section, showing good agreement with a curved yarn cross-section. The approach is controlled by the local search radius during the construction of a polygon line. A varying average point distance in the data set is disadvantageous and requires an iterative increasing of the search length if no point is found. The same might apply for an alpha-shape, the generalization of a convex hull that calculates the boundary of a point cloud by removing edges from an initial Delaunay triangulation based on an alpha parameter that controls the degree of detail. Balangé et al [9] suggested a convex hull for a limited number of points and a B-spline based approach for the envelope of a more complex cross-section. As the B-spline approach reduces usage for further analysis, a segmented convex hull approach is used in this paper to evaluate a cross-sectional area at a point selected for analysis.

While an exact match between the simulation points and an experimentally determined point cloud cannot be guaranteed, a point cluster is initially extracted using a cylindrical search volume defined by a start and endpoint and a radius. These points are then projected onto a plane with two-dimensional coordinate system defined by a rotation of the global coordinate system with the Gram-Schmidt orthogonalization, so that the new x-axis matches the cylinder axis. The origin of this projection coordinate system is defined as the first point. The vertical axis is the rotated z-axis (coordinates defined as v) and the horizontal axis is defined as the inverted rotated y-axis (coordinates defined as h).

To calculate the cross-sectional envelope, the centroid (v_c, h_c) of the projected points is calculated and used as center for a segmentation of the points into a user-defined number of subsections defined by their angular range. For each subsection an individual convex hull is calculated and all hulls are then combined to a single hull curve, where duplicate points are removed and the area of the subsegments hulls are added up to calculate the area of the combined cross-section.

To define the segments based on angular values, Eq. 5 is used to calculate the angle of each projected point with coordinates (v_i, h_i) relative to the centroid and additionally converted in a value range of $[0,\ 2\pi]$.

$$\theta_i = \operatorname{atan}^2(h_i - h_c, v_i - v_c) \tag{5}$$

Starting from the first segment (with lower boundary $\theta = 0$) the points in this segment are extracted on the border angle θ_{start} and θ_{end} of this segment and a convex hull is calculated for the points. In addition to the number of sections the shape of each segment hull and thus the accuracy of the approach is highly depending on the point of the transition boundary between the sections. In the absence of a point on the boundary, an artificial point must be created to prevent an indentation between two segments, which could significantly impact the results. A search area with a defined threshold is used to identify a point with the maximal distance to the centroid point in each of the neighbouring sections of a border. If no point is found in a section, the threshold is iteratively increased with a threshold delta until a maximum number of iterations is reached. To define the distance of this boundary point to the centroid, the mean value of both distances in the neighbouring segments are used. If the maximum distance of the current segment is more than 1.5 times smaller than that of the adjacent segment, this smaller value is used. This avoids an overprediction of the segments hull, if a small sized segment is neighbouring a larger one.

Since the usability of the approach depends on the density of the point distribution, two approaches are used to identify the border points. For a high-density distribution, a rectangular shaped search area with the angular boundary line as center line is applied. Points with the greatest distance from the centroid can be effectively identified, even when the distribution follows a grid-like configuration as it can occur with the previous mentioned approach. As the threshold and the delta of the iteration needs to be as low as possible to avoid an overprediction of the hulls, the rectangular approach is more time consuming for a low point distribution. With an angular based and thus circular search area, the coverage expands proportionally with increasing distance from the centroid. While the search area can be rapidly expanded, the likelihood of selecting suboptimal points increases in the presence of large spatial

discontinuities within the search region. The centroid and the calculated points on the boundary line are then added to the point cloud of the segment. An individual convex hull is calculated for the subsection, where the segment area A_{seg} of the segments convex hull polygon can be calculated according to Bronstein et al. [10] with Eq. 6.

$$A_{seg} = \frac{1}{2}\sum_{j=0}^{n}(h_i v_{i+1} - h_{i+1} v_i) \tag{6}$$

The result for the segment area and the convex hull points without the centroid can then be added to data defining the full hull envelope. This procedure is executed in an anti-clockwise direction until the initial segment reached, completing the loop. If during calculation a segment is reached that contains less than the required three points to calculate a convex hull its angular range is merged with the next segment. Fig. 4 shows a comparison of a convex hull (Fig. 4 a)) to the segmented hull approach with a low segment number of 12 (Fig. 4 b)) and the respective boundary points. With the convex hull the shape and area of 156.8 mm^2 are overpredicted, whereas the segmented approach results in a better prediction with an area of 138.6 mm^2. Increasing the number of segments to 360 further improves the accuracy of the calculation to an area of 134.2 mm^2. To avoid artifacts and indentations resulting from isolated internal points, the threshold parameter needs to be increased to ensure that smaller segments are integrated into larger ones.

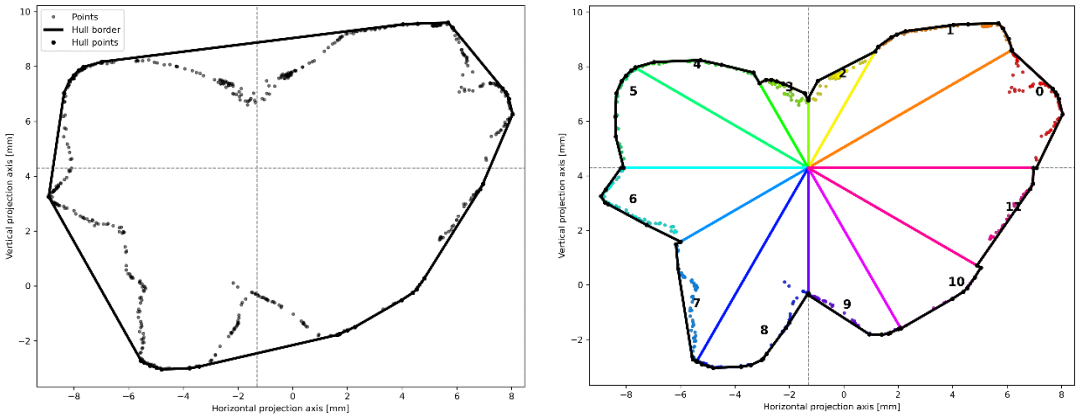

Figure 4: a) Projected points with a hull border resulting out of convex hull that is overpredicting the shape of specimen cross-section. b) Hull using the segmented approach with a low number of 12 segments enabling a more precise calculation of the envelope curve.

Analogous to the method proposed by Jones, the fiber volume ratio of the calculated cross-section can be estimated by dividing the amount n_{Fil} of physical filaments d_{fiber} within the cross-section by the summed area A_{Env} of the hull envelope curve representing the deformed cross-sectional boundary, as defined in Equation 7.

$$FVR = p_d \frac{n_{Fil} \cdot \pi \cdot \left(\frac{d_{fiber}}{2}\right)^2}{A_{\mathrm{Env}}} \tag{7}$$

Since the cross-sectional area alone is insufficient to fully characterize the shape or quantify deviation, additional geometric parameters are required. In this paper, the moments of inertia I_{hh}, I_{vv} and I_{hv} in the two-dimensional coordinate system are used. As the points that define the envelope of the hull curve is a closed polynomial with already anti-clockwise sorted points, a mathematical approach by Steger [11] based on the Gaussian trapezoidal formula is used (Eq. 8 to 11).

$$I_{hh} = \frac{1}{12}\sum_{i=1}^{n-1}\left(v_i^2 + v_i v_{i+1} + v_{i+1}^2\right) \cdot a_i \tag{8}$$

$$I_{vv} = \frac{1}{12}\sum_{i=1}^{n-1}\left(h_i^2 + h_i h_{i+1} + h_{i+1}^2\right) \cdot a_i \tag{9}$$

$$I_{hv} = -\frac{1}{24}\sum_{i=1}^{n-1}\left(h_i v_{i+1} + 2h_i v_i + 2h_{i+1} v_{i+1} + h_{i+1} v_i\right) \cdot a_i \tag{10}$$

$$a_i = h_i v_{i+1} - h_{i+1} v_i \tag{11}$$

As an alternative approach, the maximal dimension $d_{\max\_h}$ in horizontal and $d_{\max\_v}$ in vertical direction in the cross-sections coordinate system are calculated for the hull points of the cross-section according to Eq. 12 and 13.

$$d_{\max\_h} = h_{max} - v_{min} \tag{12}$$

$$d_{\max\_v} = v_{max} - v_{min} \tag{13}$$

This approach enables fast and, in most cases, a stable estimation of irregular cross-sectional areas without requirement for iterations. However, local variations in the computed area may arise due to the choice of the number of segments and the method used to determine points along the boundary between segments, as well as the corresponding threshold value. As the centroid of all points is used as the center for the circular segmentation, concave regions with slender overhangs encompassing multiple circular segments simultaneously, or cross-sections with a predominantly rectangular geometry cannot be accurately represented using this method. To address such cases and use more circular input data for the approach, an additional grid-based subdivision before the aforementioned approach needs to be implemented. This requires an additional consideration of the additional grid boundaries and sorting of edge points along the outer hull curve.

2.3 OPTIMIZATION APPROACH

The framework for the scripted implementation of the optimization problem of parameter identification for the expansion process is based on a LS-Opt workflow. The software is a multiparameter, multi-objective optimization platform for highly user specific approaches. Although it was originally created for LS-Dyna it supports any scriptable software and FE-solver. The flowchart in Fig. 6 shows the optimization strategy and workflow.

A successive response surface method was utilized for the optimization problem. In this approach, the solver selects D-Optimal points from the initial design space, evaluates the corresponding responses, and constructs a polynomial metamodel to estimate optimal design points. These design points are used to generate a solver input file for the SimTex simulation via an implementation of the methods in subsection 2.1 in a Python script. The results of each simulation are then post-processed using BetaCAE Meta, a software tool tightly integrated into LS-OPT, providing a user-friendly Python interface for post-processing. To address the challenges posed by highly nonlinear response surfaces, sequential domain reduction is employed. This technique refines the design space iteratively, improving convergence towards optimal solutions. For the expansion simulation the following parameters were identified as influential and were included in the optimization process.

Percentage strain via fiber modulus and internal loading: A combination of the Young's modulus of the fiber and internal contraction loading applies a direct nodal load. This induces up to 0.25 % elastic strain, acting effectively as a global tensile force. With increased nodal loading, the force equilibrium shifts toward a more compact cross-sectional configuration.

Fiber volume ratio: This parameter scales the combined surface area of virtual fibers and affects the cross-sectional area of bar elements during preprocessing.

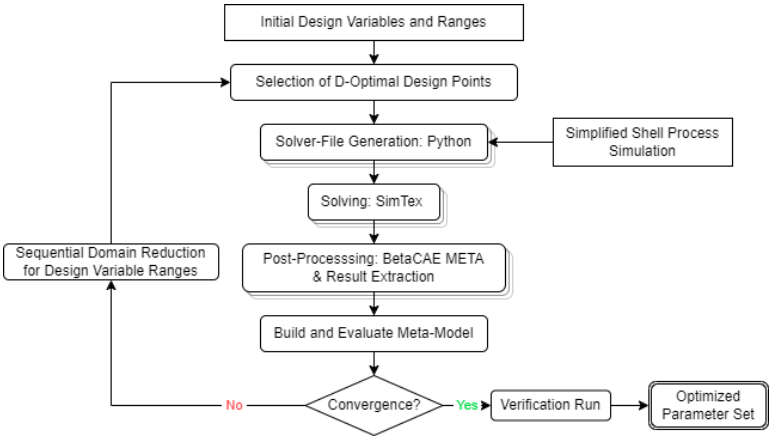

Figure 5: Flowchart of the optimization workflow.

Contact stiffness between fibers: It determines the degree of overlap at contact areas between fibers, particularly at termination time or converged nodal force equilibrium. This parameter scales and balances the cross-sectional area for locations of different interacting nodal forces.

Contact properties: This includes parameters such as contact thickness and penalty stiffness. These values are crucial for defining realistic interactions and avoid interpenetrations.

Friction parameters for fiber-fiber and sleeve-fiber interaction: The friction affects the deformation behavior and shape of fiber cross sections under tension by influencing sliding and sticking between contact surfaces.

Fiber density: The density of the fibers acts as a mass scaling factor to adjust the time step size and maintain contact stability, especially for the sleeve regions with high tension and contact forces. This compensates for current limitations in the SimTex solver's capabilities.

Simulation time: The simulation time is set as a fixed parameter for all simulations. Kinetic energy convergence is not used as a termination criterion, as local fiber movements introduce oscillations that reduce numerical performance without significantly enhancing accuracy. As a result, the optimized parameter sets are only representative for the selected simulation run time.

Furthermore, the accuracy of the optimization, regarding cross-sectional shapes and the position of their center of gravity highly depends on an accurate base model. The primary goal is to derive realistic approximations of cross sections to support subsequent structural analyses. The target function used for optimization is the mean square root error calculated from a set of identifying metrics for multiple cross sections. The selected cross sections represent key structural interaction mechanisms: the interaction between sleeve and fiber, the interaction between mostly parallel fibers and at the intersection points of multiple crossing tows.

Each cross section with additional points added to discretize the contact area during analysis is characterized by its surface area and the maximum extents $d_{\max\_h}$ and $d_{\max\_v}$ (Eq. 12 and 13) within the projection plane. These geometric descriptors are sufficient for identifying and comparing structural responses across design variants. While more detailed metrics, such as moments of inertia (Eq. 8 to 1), can be more descriptive especially for subsequent evaluation of mechanical performance. Specifically, these values inherently scale with the square of the distance from a reference point, which must itself be accurately defined and matched between datasets. This dependency adds numerical weighting that can reduce the convergence rate of the optimization algorithm by overemphasizing deviations in geometry relative to location. Consistency in cross section analysis between reference and simulation data is achieved by using identical extraction methods respectively. This alignment ensures that the evaluated parameters reflect true physical variations rather than differences arising from analysis methodology.

3 EXPERIMENTAL DATA GENERATION

In order to validate simulation results, different sizes of robotically wound specimen are used. The basis for the optimization of parameters is a small model with two anchors of 200 mm distance and an

intersection of the fibers in the middle of the anchors. For an evaluation of the approach a middle-sized model with four anchors and a dimension of $320\ mm\ x\ 160\ mm$ is used. Both of the specimen consist of a fiber bundle out of two fibers of type Teijin Carbon Tenax-E STS40 F13 48K with a filament diameter of $0.007\ mm$. The fibers are impregnated with the resin MGS LR 135 and the curing agent combination MGS LH 138 / LH287 with a fiber volume ratio of $40\ \%$. The structures were impregnated in an inline impregnation process within the winding head, so that the influence of different resin viscosities is negligible. For both specimen, six layers of fibers are used, resulting in a total number of 12 fiber bundles at fiber intersection points. The specimens where scanned with a terrestrial laser scanner (TLS) of type Trimble X7 with a 3D Point accuracy of $2.4\ mm$ at a distance of $10\ m$. A target-based registration and a Statistical Outlier Removal (SOR) filter in CloudCompare was applied to the data to remove isolated points. To increase the point density for evaluation, especially during the optimization approach, the specimen where additionally scanned with a structured light 3D scanning (ATOS III Rev. 02 800) with a measurement volume of $560\ mm\ x\ 420\ mm\ x\ 420\ mm$ (CP40/MV560) with a measuring point distance of $0.176\ mm$. Target points on the specimen mounting device and scanning spray was used during the measurements. The data was processed, referenced and cropped with the associated manufacturer software GOM Inspect. As the specimen do consist of an irregular and curved surface, three tilting angles of the sample holder and multiple repositions around the rotation axis were used for a high coverage ratio during this scanning. Nevertheless, areas around the sleeve and in the area between sleeve and intersection point in the middle of the structure cannot be fully captured using this approach. However, a comparison of the two measurement methods in Fig. 6 b) shows a more precise capturing of the specimen for the structured light scanning. The measured points of the TLS are more distributed, but a scanning of large structures in a short time as a higher field of view is available and fewer scanning positions are required. As the sleeve positions were taught manually during production, a deviation of the sleeve positions measured in the teach-in and the specimen mounting devices in the lower millimetre range cannot be avoided. In order to use the scanned data for a comparison between experiment and simulation, the sleeve positions were manually adjusted to the point clouds in CloudCompare.

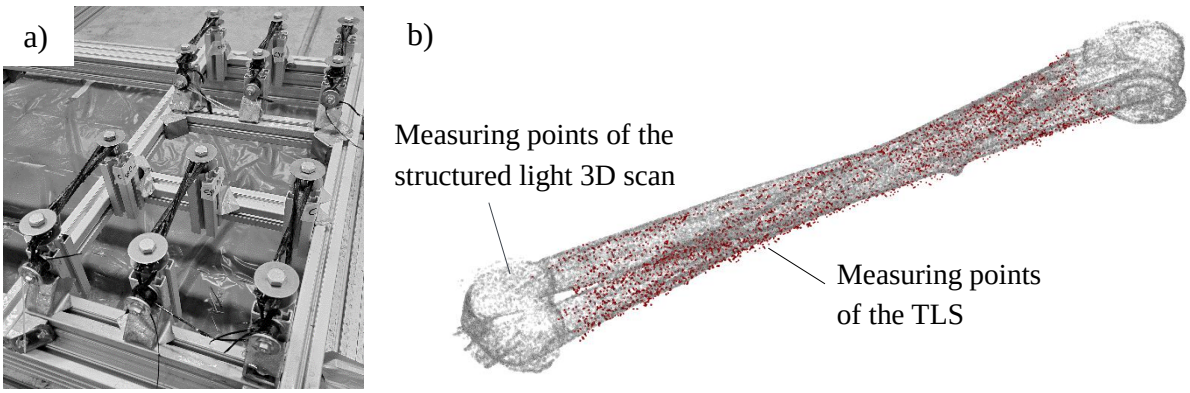

Figure 6: a) Result of the winding process for the small specimen used for optimization. b) Comparison of scanning results: The TLS measuring points (red) are more distributed compared to the structured light 3D scan, but enable a measurement of larger structures.

4 RESULTS

The discrete simulation effects and respective displacements are shown in Fig. 7. The initial virtual tow with overlapping elements (Fig. 7 a)) is expanding due to contact (Fig. 7 b)) without internal loading with limited displacements. With a global tension force, applied as internal loading, without fiber-fiber friction a high level of compaction of the tow can be achieved (Fig. 7 c)). The fiber deformation is significantly influenced by the parameter set used and the results are depending on time of evaluation. It should be noted that numerical optimization approaches furthermore always directly depend on a representative model, and accurate results extraction. The simulation results are evaluated after a runtime of 2.25 s with an increased stabilizing damping factor of 0.4 during the first second of the simulation.

After this a damping value of 0.05 is used. A cross-section (Fig. 7 d)) at the intersection in the middle of the specimen (point 1) and at one fiber strand (point 2) are used for optimization. The optimized results for 32 fibers model provide a parameter set of inputs (Table 1) that show good accuracy for deviation of area (< 5.5 % for point 1 and < 1 % for point 2) and maximal dimensions simultaneously (vertical and horizontal deviation < 10.0 % for point 1 and < 13.0 % for point 2). A usage of 16 fibers increases the area deviation for point 1 and dimension deviation for point 2 by 1.5 %. However, the moments of inertia are overestimated by up to 30%.

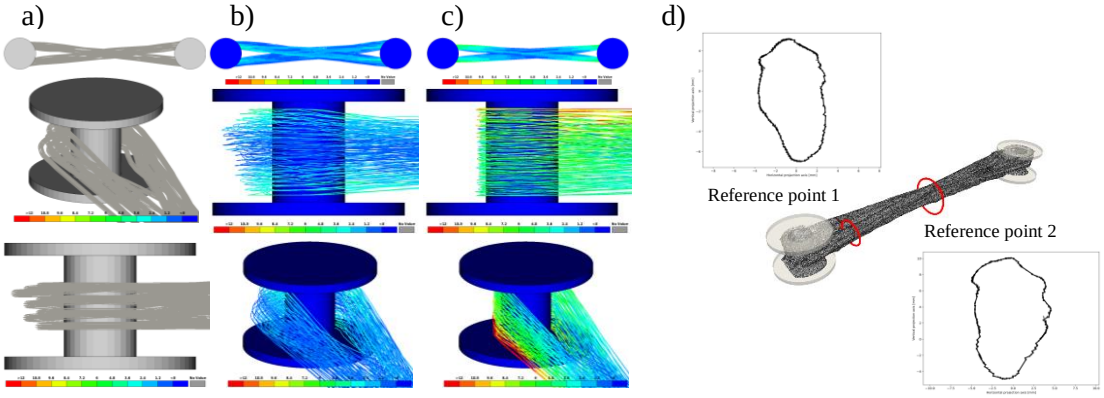

Figure 7: Discrete simulation effects and displacements: a) Initial model setup. b) Expansion of filaments due to contact resolution without fiber-fiber friction. c) Applied global tension force as internal loading. d) Optimization reference points and respective cross-sections.

The optimized parameter set for the non-physical digital element simulation shows that FVR is comparable to target values during manufacturing and that the scale factor (s) for the cross-section matches initial suggestions. The friction values for fiber-fiber friction μ_{FF} are nearly identical for both numbers of virtual fibers, with a slightly increased value for 16 fibers virtual to endure the shape of the expanding cross-section. The fiber stiffness E_{Fiber} and density ρ_{fiber} are adjusted to enable a fast computation as anticipated during a digital element simulation, but still enable an enhanced dynamic response and stiffness of the fibers during the simulation. The penalty stiffness for the sleeve-fiber contact $E_{Penalty\_SF}$ is higher than that of the inter-fiber contacts $E_{Penalty\_FF}$ to reduce interpenetrations at the sleeve. A sleeve thickness h_{sleeve} of $2.0\ mm$ is additionally prescribed to meet this requirement. The optimized value for the number of virtual fibers indicates that a relatively small number of virtual fibers is sufficient for a low aerial deviation, which is also advantageous for larger structures.

Parameter	Description		Optimum for 16 fibers	Optimum for 32 fibers
FVR	Fiber Volume Ratio	–	0.38	0.38
n_{virt_fibers}	Number of virtual fibers	–	16	32
l_{fiber}	Length of fiber element	[mm]	2.0	2.0
h_{sleeve}	Thickness of sleeve	[mm]	2.0	2.0
s	Scale factor	–	0.53	0.53
μ_{FF}	Inter-Fiber friction	–	0.11	0.08
μ_{SF}	Sleeve-Fiber friction	–	0.26	0.26
$E_{Penalty\_FF}$	Inter-Fiber penalty stiffness	[MPa]	1197.59	1225.7
$E_{Penalty\_SF}$	Sleeve-Fiber penalty stiffness	[MPa]	15000.00	15000.00
E_{fiber}	Young's modulus of fiber	[MPa]	96857.0	98279.4
E_{sleeve}	Young's modulus of sleeve	[MPa]	50000.0	50000.0
ρ_{fiber}	Density of fiber	$\left[\frac{t}{mm^3}\right]$	0.01	0.01
ρ_{sleeve}	Density of sleeve	$\left[\frac{t}{mm^3}\right]$	0.5	0.5
IL_{fiber}	Fiber internal loading	[N]	-0.1	-0.1

Table 1: Optimized values for 16 and 32 virtual fibers.

To examine the transferability of the optimized parameters to larger structures, the methodology and the optimized values for 16 fibers were evaluated for a model with four sleeves. In Fig. 9 the respective results of geometry and a cross-section (A-B) for process simulation (Fig. 9 a)), multifilament approach (Fig. 9 b)) and scanned data (Fig. 9 c)) are shown. As the process simulation uses a two-dimensional modeling approach the volume defined by the contact is replicated with artificial nodes. The results show, that the cross-sectional shape at the intersection point in the middle of the structure (A-B) cannot be fully captured using this approach. In addition, the clustered distribution of the virtual fibers implies an insufficient influence of the internal contraction force so that the initial distance of the fiber path out of the process simulation cannot be compensated. Since such a clustering of the elements limits the application of the segmented hull, an evaluation is carried out with a single segment as a normal convex hull. The calculated area of 266.0 mm^2 for the multifilament approaches has a smaller deviation to the scan data (187.7 mm^2) compared to the initial result of the process simulation (316.8 mm^2). The vertical dimension is overestimated by 20 % and the horizontal dimension by 39 % resulting in a large deviation in the moment of inertia. Nevertheless, the multifilament approach shows comparable fiber alignment to the scan data at the fiber junction area at the sleeves (Fig. 9, blue frame). In addition to a longer simulation duration that may cause penetrations at the sleeves, additional consideration of the internal loading as an optimization parameter and a reduction of the yarn geometry of the process simulation could reduce the deviations.

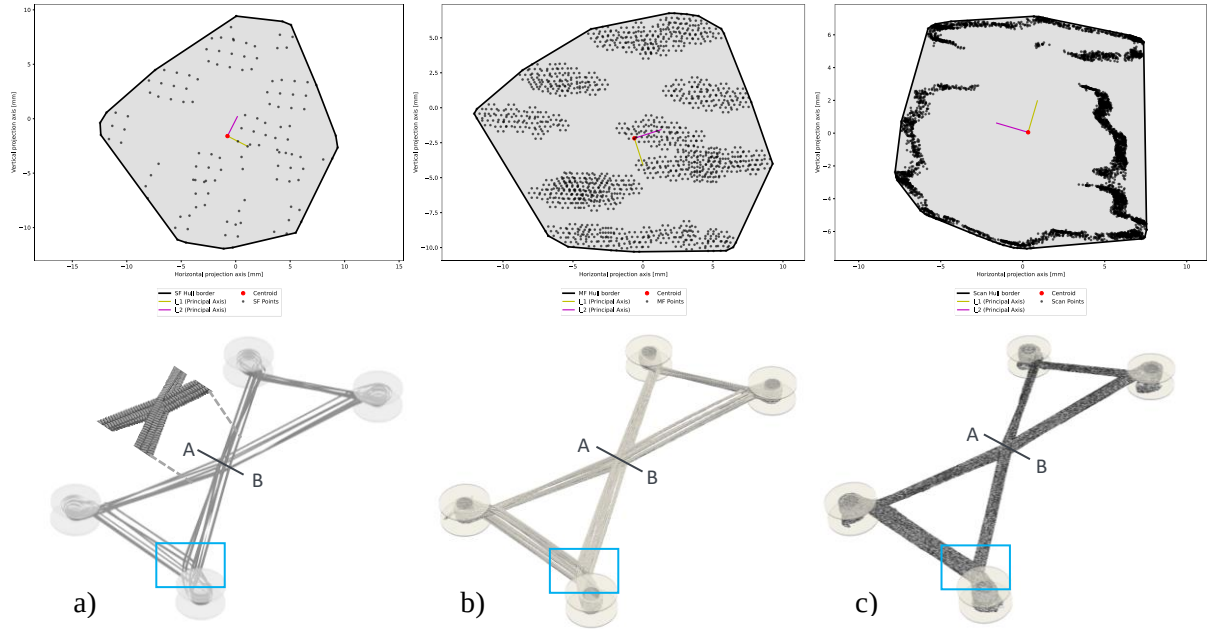

Figure 9: Comparison of modeling and simulation models and a respective cross-section showing convex hull and principal moments of inertia (A-B): a) Simulation result of the process simulation and respective point cloud to replicate the contact volume. b) Result multifilament approach using optimized values for 16 fibers. c) Scanned structure with additional (unscanned) sleeve geometry.

5 CONCLUSION AND OUTLOOK

The presented work employs a multifilament and parameter optimization approach in the solver SimTex to improve the prediction of final fiber architecture and enables the simulation of complex bundle deformations during the coreless winding process. The paper describes relations between design variables and respective interactions and provides an optimized parameter set that is showing good accuracy in area estimation to a real-world equivalent used during optimization. It showed that a relative low number of filaments can be sufficient for a reasonable prediction of a cross-sectional area, thus reducing the computational expenditure. However, to enhance the stability of the optimization, the area has a greater influence than the maximal dimensions of a cross-section. As the shape is not considered

sufficiently this further reduces a transferability of the optimized parameter results to a larger structure. In further optimizations, an equal weighting of the parameters should be considered to improve the predictive capabilities for the shape of a cross-section. Furthermore, a more representative basis model should be used and interrelations of fiber bundle modelling during process simulation and multifilament simulation results need to be studied to improve the transferability to more complex simulation models.

In a continuation of the work, the proposed simulation chain can be used to generate discretised geometrical data for a simplified but fast beam model. Using the local center of mass and moments of inertia, the mechanical behaviour of a structure could be predicted with reasonable accuracy. A complete simulation chain can thus be used to virtually validate or optimize a structural design on a high detail level.

ACKNOWLEDGEMENTS

The present work is supported by the Deutsche Forschungsgemeinschaft (DFG, German Research Foundation) under Germany´s Excellence Strategy – EXC 2120/1 – 390831618.

REFERENCES

[1] M. Prado, J. Doerstelmann, J. Solly, A. Menges, J. Knippers (2017). Elytra Filament Pavilion: Robotic Filament Winding for Structural Composite Building Systems. In Fabricate – Rethinking Design and Construction [Proceedings of the Fabricate Conference 2017], Stuttgart, pp. 224–233. (ISBN: 978 1 78735 001 4; JSTORE: j.ctt1n7qkg7.35).

[2] F. Waimer, R. La Magna, J. Knippers (2013). Integrative Numerical Techniques for Fiber Reinforced Polymers - Forming Process and Analysis of Differentiated Anisotropy. Journal of the International Association for Shell and Spatial Structures. 54.

[3] Gil Pérez, M., Mindermann, P., Zechmeister, C., Forster, D., Guo, Y., Hügle, S., Kannenberg, F., Balangé, L., Schwieger, V., Middendorf, P., Bischoff, M., Menges, A., Gresser, G. T., Knippers, J. (2023). Data processing, analysis, and evaluation methods for co-design of coreless filament-wound building systems. Journal of Computational Design and Engineering,10(4), Article4. https://doi.org/10.1093/jcde/qwad064

[4] S. Hügle, E. Genc, J. Dittmann and P. Middendorf (2022). Offline robot-pathplanning and process simulation for the structural analysis of coreless wound fiber-polymer composite structures, Key Engineering Materials 926, 2022, 1445–1453, https://doi.org/10.4028/p-970 esd

[5] Y. Wielhorski, A. Mendoza, M. Rubino, S. Roux, (2022). Numerical modeling of 3D woven composite reinforcements: A review, Composites Part A: Applied Science and Manufacturing, Volume 154, 2022, 106729, ISSN 1359-835X, https://doi.org/10.1016/j.compositesa.2021.106729.

[6] J. L Jones (2019). Novel interfaces in hybrid composite-metal, PhD Thesis, University of Bristol

[7] Y. Wang, X. Sun (2001). Digital-element simulation of textile processes, Composites Science and Technology, 61:311–9, https://doi.org/10.1016/S0266-3538(00)00223-2.

[8] S.D. Green, M.Y. Matveev, A.C. Long, D. Ivanov, S.R. Hallett (2014). Mechanical modeling of 3D woven composites considering realistic unit cell geometry, Composite Structures, Volume 118, Pages 284-293, https://doi.org/10.1016/j.compstruct.2014.07.005

[9] L. Balangé, C. Harmening, R. Duque Estrada, A. Menges, H. Neuner, V. Schwieger (2022). Monitoring the production process of lightweight fibrous structures using terrestrial laser scanning. 5th Joint International Symposium on Deformation Monitoring, Valencia, Spain. https://doi.org/10.4995/JISDM2022.2022.13830

[10] I. N. Bronstein, K. A. Semendjajew, G. Musiol, H. Mühlig (2001). Taschenbuch der Mathematik. Überarbeitete und erweiterte Auflage 5. Frankfurt am Main: Verlag Harri Deutsch.

[11] C. Steger (1996). On the Calculation of Arbitrary Moments of Polygons, https://api.semanticscholar.org/CorpusID:17506973

ICCM24
AUGUST 4-8, 2025
BALTIMORE CONVENTION CENTER
BALTIMORE, MARYLAND, USA

No Technical Paper Submission for:

Takuma Sugiyama

ICCM24 24TH INTERNATIONAL CONFERENCE ON COMPOSITE MATERIALS
AUG 4-8, 2025 • BALTIMORE CONVENTION CENTER • BALTIMORE, MARYLAND

VIRTUAL TESTING OF RECYCLED GLASS FIBER REINFORCED POLYMER SANDWICH CORES

Michael Paulitsch[1], Bianca Purgleitner[2], Andreas Pfleger[3], Peter Pangerl[4] and Roland M. Hinterhölzl[1]

[1]Research Group of Lightweight Design and Composite Materials, University of Applied Sciences Upper Austria, Stelzhamerstraße 23, 4600 Wels, Austria
Email: Michael.Paulitsch@fh-wels.at, web page: https://fh-ooe.at/

[2]Transfercenter für Kunststofftechnologie,
Franz-Fritsch-Straße 11, 4600 Wels, Austria
Email: Bianca.purgleitner@tckt.at, web page: https://www.tckt.at/

[3]Tripan Leichtbauteile GmbH & Co KG
Am Kirchenholz 2, 4063 Hörsching, Austria
Email: andreas.pfleger@tripan.at, web page: https://www.tripan.at/

[4]Synron GmbH
Bahnhofstraße 35a, 4910 Ried im Innkreis, Austria
Email: peter.pangerl@synron.at, web page: https://www.synron.at/

Keywords: Recycling, Glass fibres; Finite Element Analysis; Buckling; Thermosetting resin

ABSTRACT

End of life strategies for wind turbine blades become increasingly important, as an ever-growing number of wind turbines reaches its decommissioning date. Various types of recycling i. e. mechanical, thermal and chemical, are currently the subject of research.

The goal of this study is, to assess the suitability of recycled glass fibre reinforced polymers (rGFRP) from wind turbine blade as a raw material for truck trailer floor panels. In order to achieve weight-wise competitive material properties with the currently used plywood, rGFRP is used in a sandwich part, as both skin and core material. A static simulation and a linear buckling analysis of established and rare core types have been conducted to compare these options regarding stiffness, mechanical stresses and susceptibility for buckling. Compared to the currently used plywood, rGFRP sandwich parts show significantly higher stiffness. However, stresses exceeding the tensile strength of rGFRP in the skins occur, highlighting the need to either further improve the recycled material or to add virgin GFRP. Equally high stresses in the core have to be investigated further, as stress concentrations occur on sharp edges and corners in the core geometries. Preliminary analysis of buckling behaviour indicates that buckling is not an issue for the used wall thickness at the expected loads.

1. INTRODUCTION

Wind turbines are essential for producing clean and renewable energy. With the rapid growth of the wind energy industry, the extensive use of composite materials in wind turbine blades is posing significant environmental challenges [1]. To fulfill the design criteria of durability and high strength to weight ratio, wind turbine blades are manufactured from non-biodegradable materials such as glass fibers and thermoset polymers like epoxy resin. An exceeding number of turbines reach their end-of-life, necessitating the need for comprehensive recycling and reuse strategies. As of right now, wind turbine blades at their end of life are either burnt or stored at landfills [2]. These strategies however, lead to a waste of resources and could also be legally prohibited in the future. For example, WindEurope, a leading non-profit association that represents and promotes the wind energy industry across Europe, proposed a landfill ban for wind turbine blades in Europe from 2025 onwards [3]. Of the currently known recycling methods [4], mechanical recycling is still the only economically and ecologically sensible process according to literature [5].

The goal of this study is to evaluate the suitability of mechanically recycled glass fiber reinforced polymer (rGFRP) as a raw material for truck trailer floor panels. Plywood, with a density of 680 kg/m³, is currently used in truck trailer floors. With a density of more than 1500 kg/m³ and similar tensile strength as plywood, the use of rGFRP only makes sense if used as a sandwich part. To determine the ideal core geometry, different core geometries were virtually tested regarding the stresses that occur and their sensitivity towards buckling using Finite Element Analysis.

2. MATERIAL

The starting point for this study was unsorted shredded wind turbine blade material. Besides glass fibre reinforced polymer (GFRP), this material contained metals such as copper (likely from lightning rod) and lead (likely from balancing weights) among other things. While no lead was found after further refinement, the copper could only be partially removed by the available metal separator using eddy currents.

Plates of shredded material mixed with virgin epoxy resin were manufactured by a press process, curing the material at 80 °C for 90 minutes. Density was measured using the immersion method according to ISO 1183-1:2019. To determine E1 and E2 for rGFRP, uniaxial tensile tests in accordance with ISO 527-4 were carried out. The Poisson ratio was measured by applying strain gauges. Samples with a size of 100 x 10 mm were cut out in 0°, 45° and 90° to the length axis of the panel. These angles are not corresponding to any fibre direction. No significant difference was found, which is why isotropic in-plane behaviour was assumed. Tests in thickness direction were not carried out and isotropic behaviour was assumed. A simulation was carried out to estimate the effect of that assumption.

Three different grain sizes were investigated (0-0.355 mm, 0.355-1.4 mm, 1.4 mm-2.8 mm). The middle fraction (0.355-1.4 mm) showed a slightly weaker mechanical performance in bending and tensile tests than the finest grain size but was available in a larger quantity and therefore selected for further steps in the project. Different epoxy resins were investigated of which KR 44.39 showed the best performance in tensile tests. The weight percentage of the shredded material is approximately 60%, resulting in a fibre volume ratio of approximately 30%.

A comparison between the values of rGFRP and the currently used plywood are given in Table 1. The values for plywood are from the “Finnish plywood-27 mm birch” entry in the Altair ESA-Comp database.

Table 1 Important mechanical quantities of rGFRP and plywood

Property		rGFRP	Plywood
E_1	[GPa]	10.03±0.4	7.67
E_2	[GPa]	10.03±0.4	7.21
E_3	[GPa]	10.03±0.4	3
σ_{1t}	[MPa]	53.1±3.3	38.7
σ_{2t}	[MPa]	53.1±3.3	36.3
ν_{12}	–	0.3	0.05
ρ	[kg/m³]	1540±10	680

rGFRP is the raw material for both, the skins and the core.

3. PROBLEM DESCRIPTION AND DESIGN CONSTRAINTS

The planned application for the material is as floor panel in a truck trailer. The truck trailer substructure consists of a steel frame (*Figure 1*) and floor panels screwed onto the steel frame. The largest unsupported span of a panel in the truck trailer has dimensions of 1600 mm x 500 mm. The total height of the floor panels is limited to 28 mm.

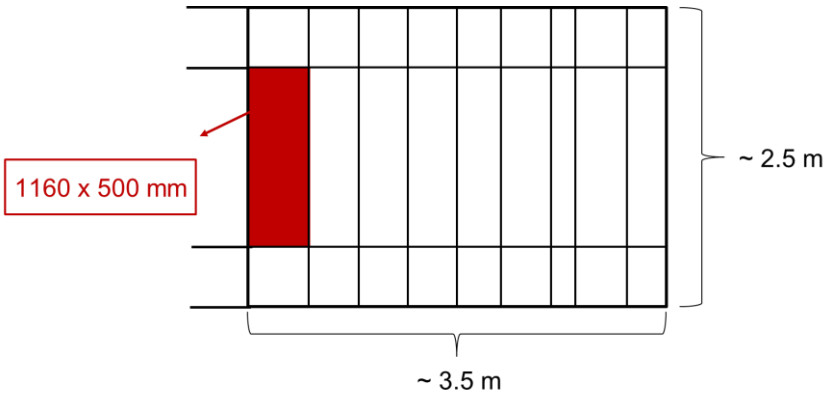

Figure 1 Schematic top view of truck trailer steel frame segment: steel beams (black lines) and panels (white spaces in between), of which the largest unsupported span is highlighted in red

The critical load case is a forklift with a weight of 3600 kg per wheel standing at the weakest point, which is usually the center of the panel, for 5 minutes. The contact area of a wheel based on dimensioning guidelines for plywood panels is 180 x 80 mm. The load applied on the contact area amounts to a pressure of 2.45 MPa.

From a manufacturing perspective, project partners agreed to focus predominantly on core patterns that are easy to manufacture while using a pressing process.

The grain size of the shredded material of 1.4 mm determines the theoretical lower limit for the thickness of a pressed structure.

The weight of the sandwich panel should be equal to or less than the weight of the plywood panel. Furthermore, the stiffness of the panel should be equal to or higher than the stiffness of the plywood panel.

4. INVESTIGATED CORE TYPES

In the current analysis, sandwich parts consisting of 4 mm thick skins and a core with a height of 20 mm have been investigated. The only factor, that has been varied was the core geometry.

The investigated core types can be divided into four groups: Corrugated, honeycombs, Miura-ori foldcore geometries and generalized Resch pattern foldcore geometries. Corrugated and honeycombs are well-established core types. Honeycombs are difficult to manufacture using a pressing process due to their vertical elements. They were nevertheless included as benchmark, as literature indicates great bending, compression and shear properties [8]–[10]. Miura-ori cores and cores inspired by generalized Resch pattern geometries represent rare core types but have also been investigated in the literature [11], [12]. For an overview of all investigated core geometries, see Table 2.

A wall thickness of 2 mm was chosen for all geometries. Dimensions of the cores were chosen so that the volume filling degree was between 18-22%. By that, equivalent weight with the plywood panel was achieved.

5. SIMULATION SETUP

For virtual testing, a geometrically non-linear static simulation and a linear buckling analysis (LBA) were set up using the Finite Element software Abaqus CAE 2020. The goal of the static simulation was to determine the stresses and displacements in skins and core when the forklift stands in the center of the panel. Therefore, a load of 2.45 MPa (see Section 3) was used. A static simulation of the plywood panel was carried out for comparison. In the LBA, an initial value of 1 was used, which is common in literature. The analysis then solves for eigenvalues which will give you the factor by which the initial load has to be multiplied to reach the buckling loads. In either case, the load was distributed evenly over the entire contact area. For the static simulations, a symmetry condition was used, allowing to calculate only half of the geometry. For the buckling simulations, the entire model had to be calculated.

As core cell dimensions (i. e. 20 mm square honeycomb cell length) are in the same order of magnitude as the overall sandwich thickness (28 mm), the cores were not homogenized but simulated as discrete structures, allowing a visualization of local effects to some extent.

Table 2 Investigated core geometries; length-direction is roughly horizontal and width direction roughly vertical

Core Type			
Corrugated	Triangular (C Tri)	Rectangular (C Rec)	Trapezoidal (C Trap)
	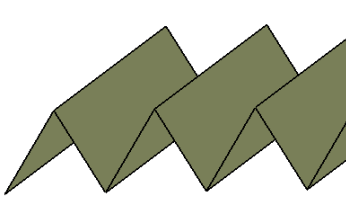	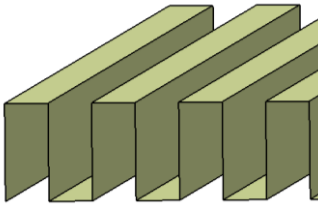	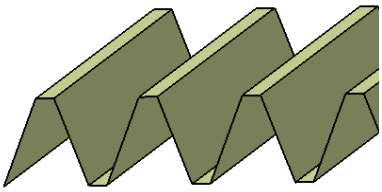
Honeycombs	Square (H Square)	Rectangular (H Rec)	Hexagonal (H Hex)
	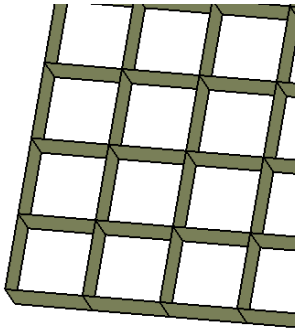	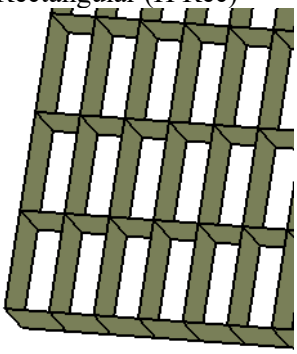	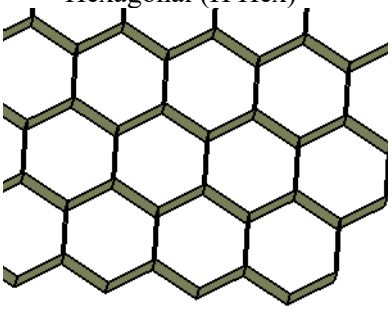
Miura-ori	V longitudinal (M V L)	V transversal (M V T)	M longitudinal (M M)
	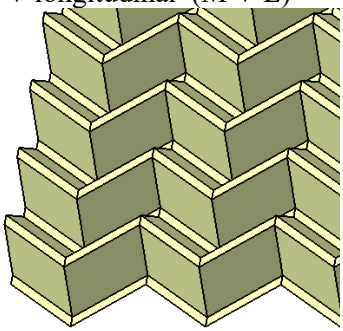	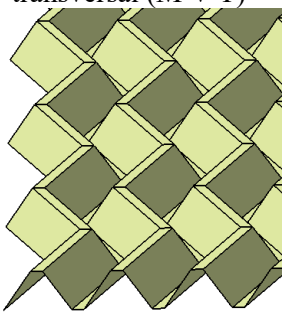	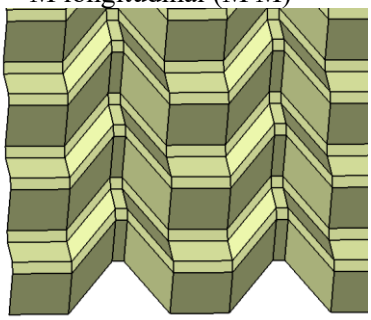
Resch	Triangular (R Tri)	Quadrangular (R Quad)	Hexagonal (R Hex)
	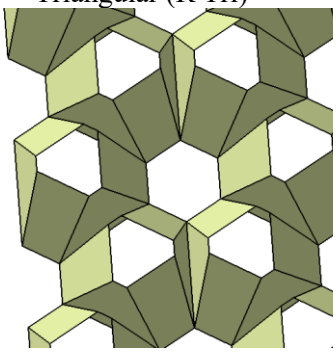	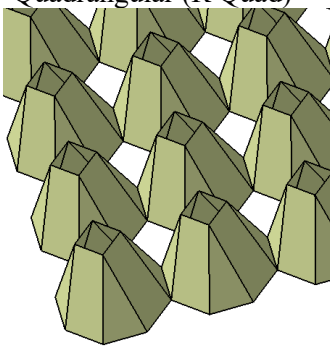	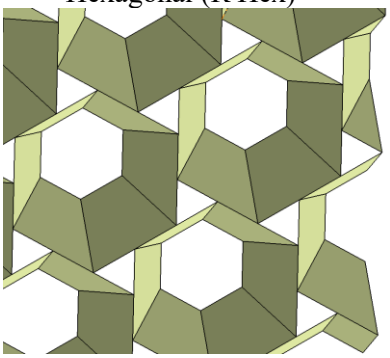

For both simulations, “Tie”-contacts, simulating perfect bonding, were defined between the core top and bottom surfaces and the respective skin surfaces. For the LBA, movement in z-direction was prohibited (U3 = 0) on all 4 edges, modelling the rigid connection via screws onto the trailer. On one side, in plane-movement was additionally constrained (U1, U2 = 0). For the static simulation, the boundary condition of one edge with prohibited movement in z-direction war replaced by the symmetry condition (U2=UR!=UR3=0).

For the skins, quadratic shell elements (S8R) and for the core quadratic solid elements (C3D20R for corrugated and honeycomb cores, C3D10 for Miura-ori and Resch cores) were used. A 2 mm mesh was specified for the load area for the skins, while a 5 mm mesh was used outside of the load area. For the core, this general criterion was used as well – however for all Miura-ori or Resch cores at least two elements were assigned over any dimension (thickness, width and length) in the load area. For corrugated and honeycomb cores, there are at least three elements.

Mesh convergence studies were carried out for each core geometry groups i. e. corrugated cores, honeycombs, etc. for both, the static simulation and the LBA.

6. RESULTS

6.1. Static simulation

6.1.1. Estimation of thickness property influence

A simulation of a H-Rec sandwich with E1, E2 of the rGFRP and 5 MPa for E3 (approximately half of E1, E2) was set up to determine the effect of assumption of isotropic material behaviour. The other properties to describe the material behaviour (G_{12} = 3.03 GPa, G_{13} = G_{23} = 2.5 GPa, ν_{13} = ν_{23} = 0.3) were taken from the “7781 Glass Fabric / MGS418” entry in the Altair ESA-Comp database – a typical glass fibre fabric in epoxy matrix. The simulation showed a slight increase of 8.3% in displacement compared to isotropic properties, indicating that thickness properties only slightly influence the displacement results.

6.1.2. Displacement

Several plots were derived from the results of the static simulation. One of the key takeaways is that all investigated core geometries have a significantly smaller displacement (max. 13.7 mm) than the plywood panel (16.5 mm, Figure 2). With the exception of the corrugated rectangular core, a clear trend by core type can be established: Miura-ori cores and Resch pattern cores are less stiff under bending (11.5-11.8 mm). Corrugated and honeycomb cores have lower displacements (10.9-11.2 mm), with the lowest values experienced by the corrugated trapezoidal and the rectangular honeycomb cores.

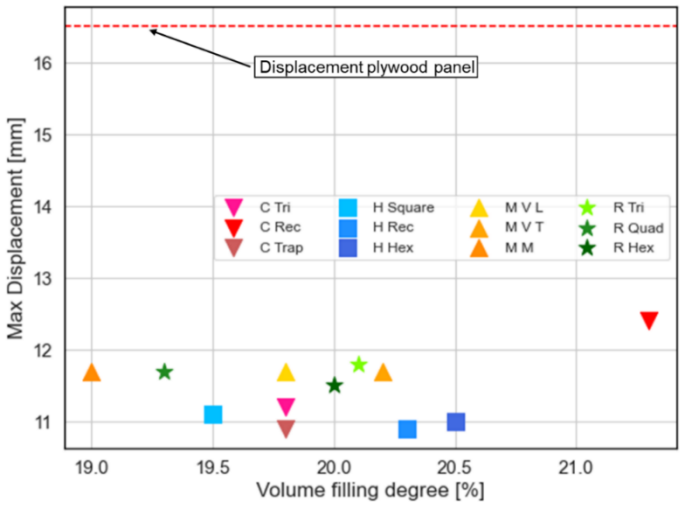

Figure 2 Maximum displacement in static simulation of different core types as a function of volume filling degree

The lower displacement of the rectangular honeycomb compared to the square honeycomb can be explained by its tighter spaces between the beam elements in the width direction. This feature was specifically put in place to increase stiffness. When the length to width ratio exceeds factor of 2, stresses occur predominantly in width direction, as that direction is much stiffer. Therefore, stiffening in the width direction improves the stiffness more than stiffening in the length direction. This is also the reason why corrugated cores are as stiff as honeycomb cores in this example and Miura-ori and Resch pattern cores are less stiff.

6.1.3. Skin stresses

The maximum tension stresses in skins for the different core geometries can be seen in Figure 3. For this analysis, stress maxima at the edges where boundary conditions were applied, were ignored. Overall, skin stresses are quite similar for all cores. A similar trend as in Figure 2 can be seen: stiff cores lead to less stress in the skins. For all core geometries, the maximum stress exceeds the ultimate tensile strength of GFRP by a significant margin. Figure 3 could have also been plotted for compression stresses, which show a very similar trend to the tensile stresses.

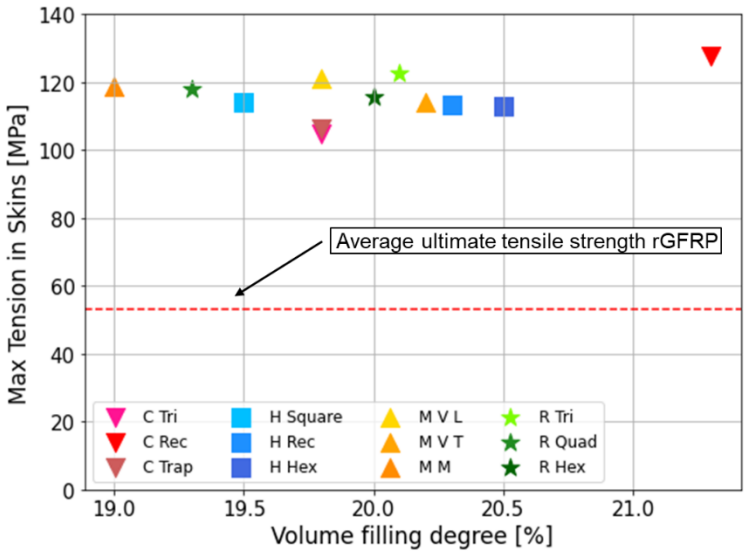

Figure 3 Maximum tension in skins in static simulation of different core types as a function of volume filling degree

6.1.4. Core stresses

Core stresses were evaluated as well and were in the same order of magnitude as the skin stresses and higher (peak stresses between 90 MPa and 300 MPa). However, a sensible evaluation is challenging: While Mesh convergence studies converge for skin stresses and displacements, they linearly increase or even slightly diverge for core stresses due to stress concentrations on corners and edges (i. e. Figure 4, Figure 5).

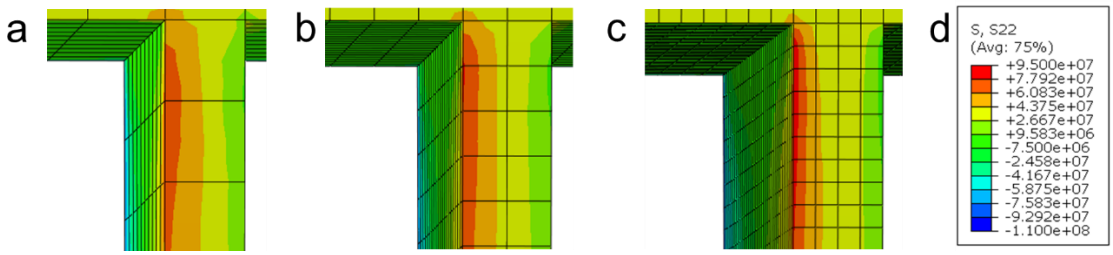

Figure 4 Edge of load area of square honeycomb with 1 (a), 2 (b) and 4 elements (c) over the width resulting in 74,7 MPa, 80,3 MPa and 91,7 MPa peak stress respectively; d: scale for all three simulations

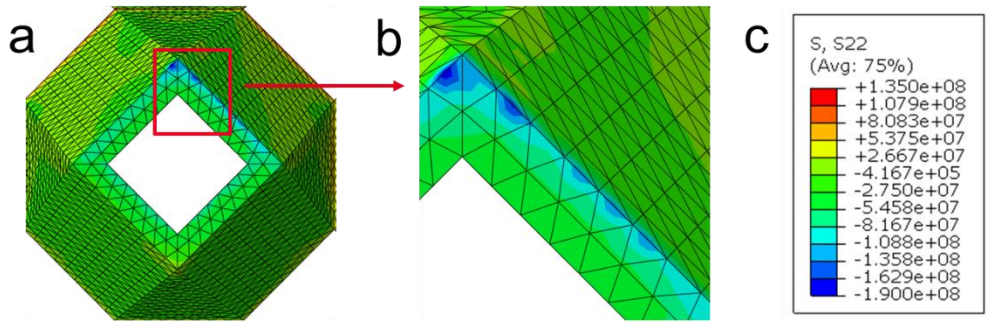

Figure 5 Stress concentrations in quadratic Resch pattern in load area (a, b) with the corresponding scale (c)

Further investigations will take place to accurately evaluate the core stresses.

6.2. LBA

By employing an LBA, a preliminary investigation of the buckling load for each core geometry has been established. None of the core geometries failed at loads less than twice the currently used static load (Figure 6).

Further investigation by using a non-linear buckling analysis would be necessary to accurately determine the exact buckling loads. However, given the magnitude of the normal skin and core stresses in the static simulation, focus will be placed on evaluating the core stresses and improving static performance.

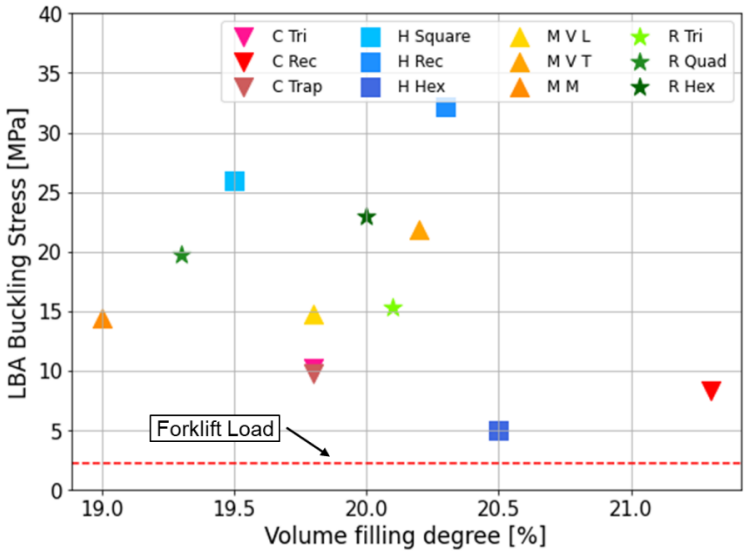

Figure 6 LBA buckling stress of different core types as a function of volume filling degree

7. CONCLUSION AND OUTLOOK

A geometrically non-linear static simulation and a linear buckling analysis (LBA) were set up for sandwich parts differing in employed core geometry (different corrugated cores, honeycomb cores, Miura-ori cores and generalized Resch pattern cores). To evaluate their suitability for truck trailer floor panels, the results of the static simulation were compared to the simulation of the currently used plywood floor panel. All investigated core geometries showed significantly increased stiffness than the plywood panel. For all geometries, the skin stresses exceeded 100 MPa. Given the tensile strength of

rGFRP of 55 MPa, additional reinforcement or the use of virgin GFRP as skins is needed. Stresses in the core were in the same magnitude as the stresses in the skins. They need to be further investigated as stress concentrations occur on edges and at corners in the load area (global-local submodelling techniques). As a possible alternative, rGFRP foam cores, consisting of epoxy resin, blowing agents and shredded blade material, will be investigated. The LBA indicates that no core geometry is susceptible to buckling.

All investigations have been carried out for the load case where the load is applied centrally onto the panel for maximum bending stress. However, shear stress is maximized with the load closer to the panel edge, decreasing the area where shear can be relieved. This load case has to be investigated as well to accurately determine the highest shear loads.

ACKNOWLEDGEMENTS

We gratefully acknowledge the financial support of the Austrian Research Promotion Agency (FFG) and the Upper Austrian government in the OOE2022 – Future Mobility Program (Project ‘rGFK goes Trailer’, Grant No.901698).

REFERENCES

[1] Y. Zhang, Y. Pontikes, L. Lessard, and A. Willem van Vuure, “Recycling and valorization of glass fibre thermoset composite waste by cold incorporation into a sustainable inorganic polymer matrix,” *Compos. Part B Eng.*, vol. 223, no. June, p. 109120, 2021, doi: 10.1016/j.compositesb.2021.109120.

[2] G. Lichtenegger, A. A. Rentizelas, N. Trivyza, and S. Siegl, “Offshore and onshore wind turbine blade waste material forecast at a regional level in Europe until 2050,” *Waste Manag.*, vol. 106, pp. 120–131, 2020, doi: 10.1016/j.wasman.2020.03.018.

[3] “Wind Europe.” https://windeurope.org/about-wind/wind-energy-and-the-environment/ (accessed Nov. 05, 2024).

[4] P. Liu, F. Meng, and C. Y. Barlow, “Wind turbine blade end-of-life options: An economic comparison,” *Resour. Conserv. Recycl.*, vol. 180, no. February, p. 106202, 2022, doi: 10.1016/j.resconrec.2022.106202.

[5] E. B. Paulsen and P. Enevoldsen, “A multidisciplinary review of recycling methods for end-of-life wind turbine blades,” *Energies*, vol. 14, no. 14, pp. 1–13, 2021, doi: 10.3390/en14144247.

[6] K. Bhavith, M. Prashanth Pai, M. Sudheer, C. G. Ramachandra, B. H. Maruthi Prashanth, and B. Kiran Kumar, “The Effect of Metal Filler on the Mechanical Performance of Epoxy Resin Composites,” *Eng. Proc.*, vol. 59, no. 1, 2023, doi: 10.3390/engproc2023059200.

[7] Z. He, E. Tang, W. Yao, and R. Wang, “Response characteristics and particle contributions of epoxy resin composite embedded with Al particles under different loading modes,” *J. Mater. Res. Technol.*, vol. 34, no. July 2024, pp. 2260–2272, 2025, doi: 10.1016/j.jmrt.2024.12.149.

[8] L. Valdevit, J. W. Hutchinson, and A. G. Evans, “Structurally optimized sandwich panels with prismatic cores,” *Int. J. Solids Struct.*, vol. 41, no. 18–19, pp. 5105–5124, 2004, doi: 10.1016/j.ijsolstr.2004.04.027.

[9] M. R. M. Rejab and W. J. Cantwell, “The mechanical behaviour of corrugated-core sandwich panels,” *Compos. Part B Eng.*, vol. 47, pp. 267–277, 2013, doi: 10.1016/j.compositesb.2012.10.031.

[10] F. Côté, V. S. Deshpande, N. A. Fleck, and A. G. Evans, “The compressive and shear responses of corrugated and diamond lattice materials,” *Int. J. Solids Struct.*, vol. 43, no. 20, pp. 6220–6242, 2006, doi: 10.1016/j.ijsolstr.2005.07.045.

[11] Y. Deng and S. Zhang, “Quasi-static compression response of foldcore sandwich structure based on core evolution,” *Mech. Adv. Mater. Struct.*, vol. 32, no. 10, pp. 2369–2380, 2024, doi: 10.1080/15376494.2024.2378507.

[12] A. Deng, B. Ji, X. Zhou, and Z. You, “Geometric design and mechanical properties of

foldcores based on the generalized Resch patterns," *Thin-Walled Struct.*, vol. 148, no. 800, p. 106516, 2020, doi: 10.1016/j.tws.2019.106516.

Fatigue Life Prediction of Dissimilar Material Joints using Neural Networks

Young Bin Kim[1], Hee-Chan Song[1], Suji Kim[1], Junghee Seo[1], Kyoungsik Kim, Heoung-Jae Chun[1]*

[1]Department of Mechanical Engineering, Yonsei University, Seoul, Republic of Korea

Defense Vertical Takeoff and Landing Aircraft Specialized Research Center, Republic of Korea

Introduction

Background of the Study

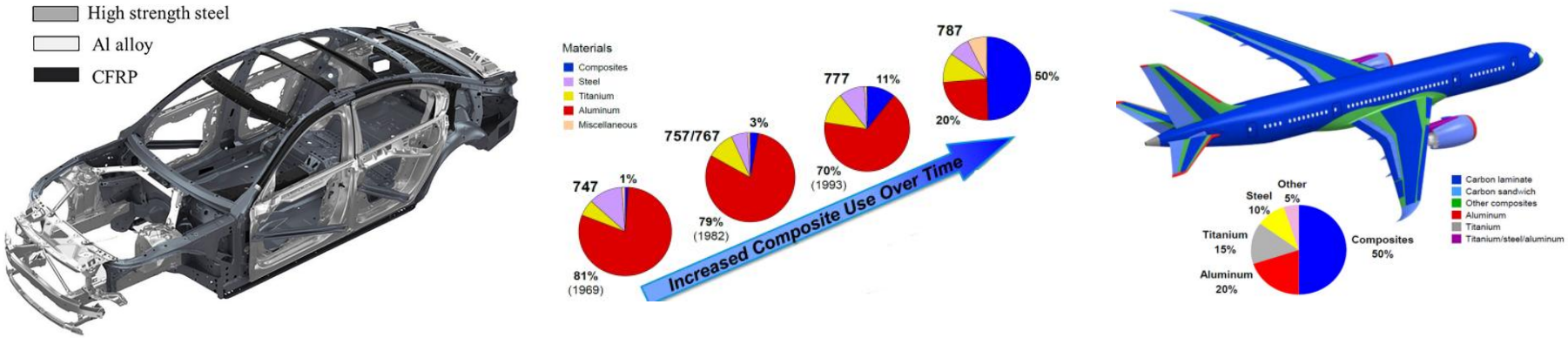

< Composite materials trends>

- Dissimilar material joints, which combine composite materials with metals, are widely used in aerospace and automotive industries due to their high specific strength, stiffness, and long fatigue life
- With the trend of replacing metal materials with composites, there is a growing need for research on composite-metal joints
- Since fatigue damage is one of the principal causes of joint failure, predicting the fatigue life of joints is essential

Introduction

Research Objectives

Propose a neural network-based method to predict fatigue life of dissimilar material joints with improved accuracy and reduced computational cost

- **Investigate fatigue behavior of bonded and hybrid joints with varying overlap lengths**
- **Predict fatigue life using neural networks trained on experimental data**
- **Bayesian regularized to prevent overfitting and enhance model generalization**
- **Compare neural network predictions with experimental S-N curves for validation**

YONSEI UNIVERSITY
DEPARTMENT OF MECHANICAL ENGINEERING
ISID Intelligent Structure & Integrated Design Lab

Materials and Methods

Specimen preparation & Experiment

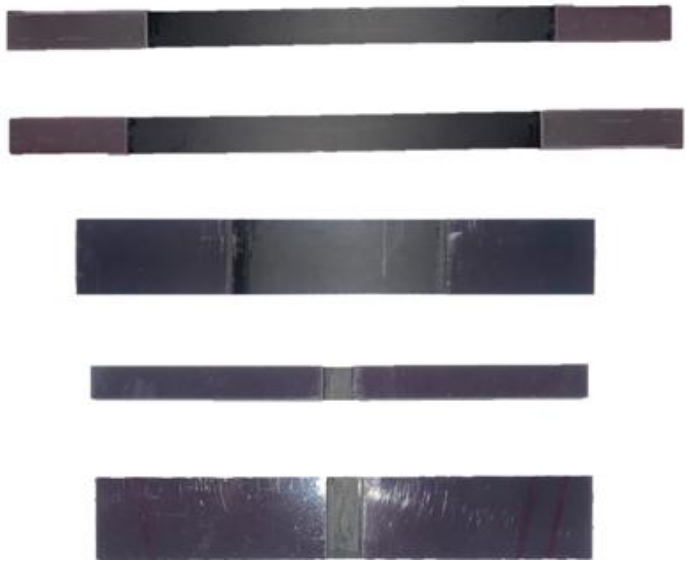

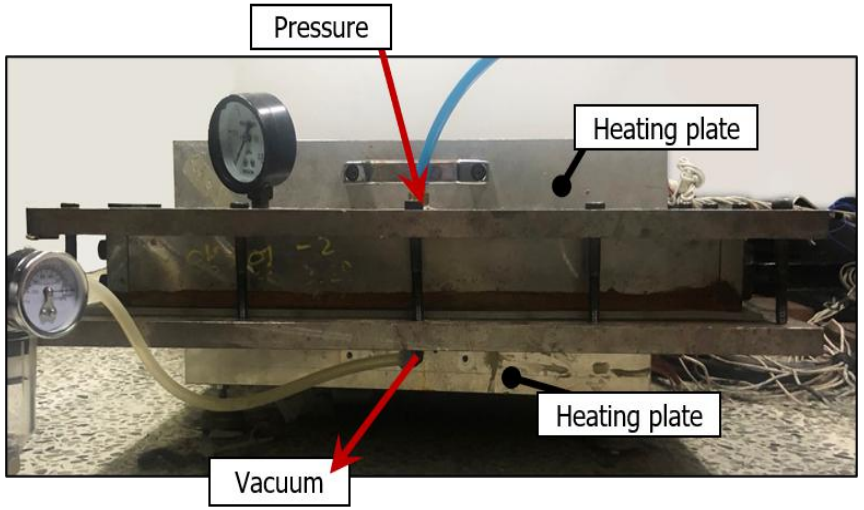

<Specimen preparation >

- Composite specimens made by cutting unidirectional prepregs into 250 mm×250 mm
- Hand lay-up lamination $[0/90]_{5s}$, autoclave curing and machining
- Glass fiber reinforced plastic tabs, Specimen bonding surface treated with #400 silicon carbide paper and acetone degreasing, Tabs attached with EA9309.3NA adhesive
- SS400 steel specimens were prepared similarly, with a GFRP tab, acetone treatment, and Teroson EP 5016 adhesive bonding

Materials and Methods

Specimen preparation & Experiment

(a) (b)



<Geometry of joint specimen
(a) Bonded joint (b) Hybrid joint >

(a)

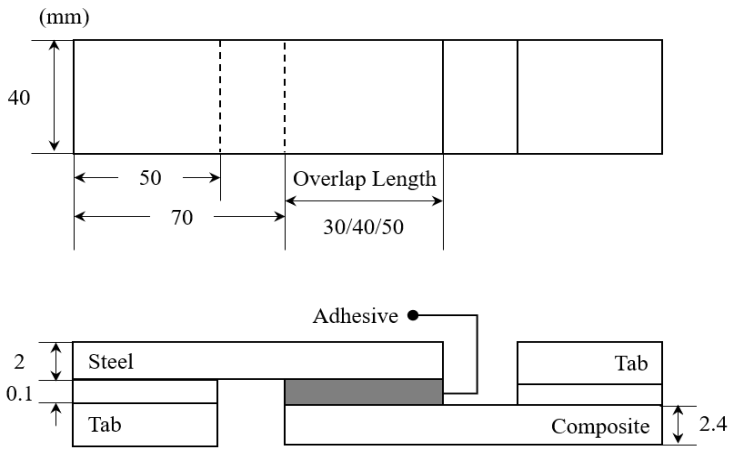

(b)

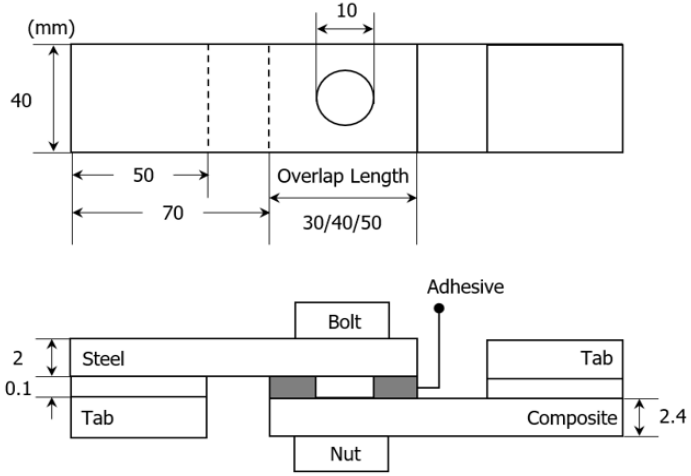

<Geometry of joint specimen
(a) Bonded joint (b) Hybrid joint >

Tensile Test

- 6 tests per joint; average values used
- Universal Testing Machine at room temperature
- Displacement control: 0.2 mm/min
- Force–displacement curves obtained for reference

Fatigue Test

- Load levels selected from the elastic range of tensile results
- Bonded Joint: 65%, 60%, 57% of failure load
- Hybrid Joint: 60%, 55%, 50% of failure load (Hydraulic servo-type machine (SALT Co.))
- Load control, sinusoidal wave, 3 Hz frequency
- Tension–tension fatigue, R = 0.1, 6 tests per load level; F–N diagrams constructed

Materials and Methods

Bayesian Regularized Neural Network (BNN)

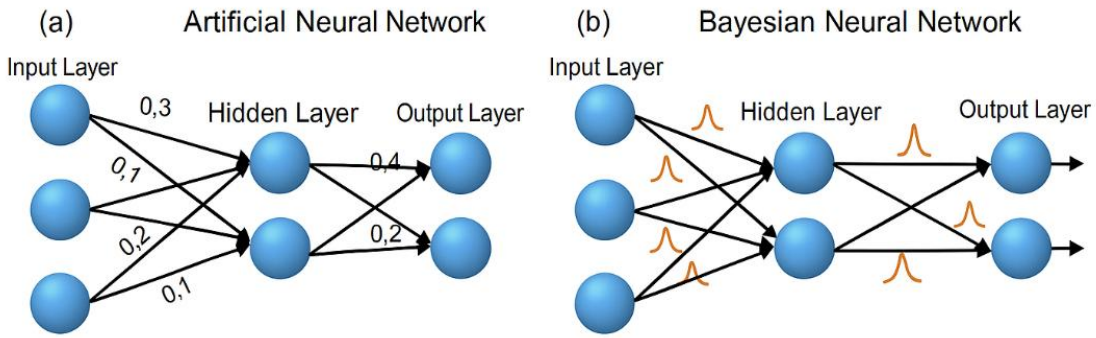

< Comparison of an artificial neural network (ANN) and a Bayesian Regularized Neural Network (BNN)>

Feature	Standard Neural Network (ANN)	Bayesian Regularized Neural Network (BRANN)
Goal	Minimize prediction error only	Minimize both prediction error and model compl exity
Loss function	E_D –> focuses only on data error	$\beta E_D + \alpha E_W$ –> balances error and weight size
Weight treatment	Single fixed optimal value	Treated as a probability distribution (uncertainty -aware)
Generalization	Higher risk of overfitting	Better generalization and robustness
Data requirement	Needs a large dataset to perform well	More stable with small or noisy datasets
Overfitting	Likely if regularization is weak	Actively avoids overfitting by penalizing complex ity

Materials and Methods

Loss function

- In general, neural networks aim to minimize the sum of squared errors E_D

$$E_D = \sum_{i=1}^{n} (t_i - a_i)^2$$

- t_i : the target value of the training data
- a_i : the predicted value produced by the neural network

- However, to reduce model complexity and prevent overfitting, a regularization term E_W , which represents the sum of squared network weights, is added. The objective function becomes:

$$F = \beta E_D + \alpha E_W$$

- α: the weighting factor for the weight magnitude term
- β : the weighting factor for the data error term

Materials and Methods

Bayes' theorem

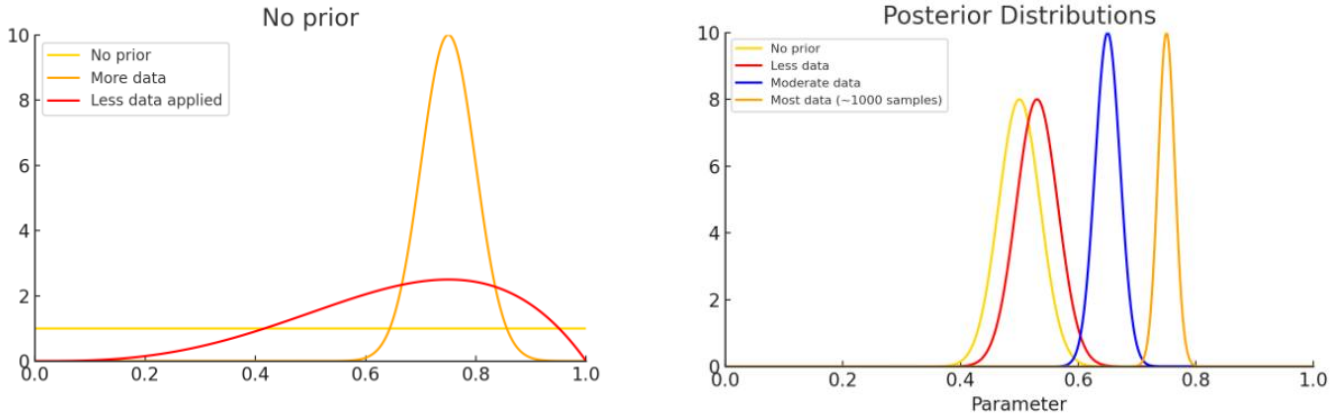

- **Without prior knowledge:**
  Distribution narrows around 0.78 as more data are added, increasing confidence.

- **With a prior following a Normal distribution 0.5:**
  Estimate keeps a shape similar to the prior while progressively approaching the true value

➔ By applying such Bayesian prior probabilities to constrain the weights, this approach aims to prevent overfitting caused by excessively large weights

Materials and Methods

Bayesian regularization

$$P(\alpha, \beta \mid D, M) = \frac{P(D \mid \alpha, \beta, M) P(\alpha, \beta \mid M)}{P(D \mid M)}.$$

- w: the weight vector (connection strengths) of the neural network
- D: the training dataset
- M: the neural network architecture (model)
- α,β: hyperparameters used for regularization

1. $P(w|\alpha,M)$: the Gaussian prior distribution that encourages the weights to remain small

2. $P(D|w,\beta,M)$: the likelihood, representing how well the data fit given the current weights

➔ This formulation means that as more data are observed, the posterior becomes narrower, while a strong prior keeps the estimate close to the prior beliefs

➔ In other words, it balances data fit and prior constraints to prevent excessively large weights (model complexity) and reduce overfitting

Materials and Methods

Flow chart for Bayesian optimization of regularization parameters

Error Term Calculation

- The objective function combines data error and weight decay error from training data.

Application of the Levenberg–Marquardt Algorithm

- The algorithm updates the weights in the direction that minimizes the objective function.

Effective Number of Parameters γ

- The Gauss–Newton approximation is used to compute the model complexity γ

Updating α and β

- Using the newly calculated γ, update the regularization parameters α and β.

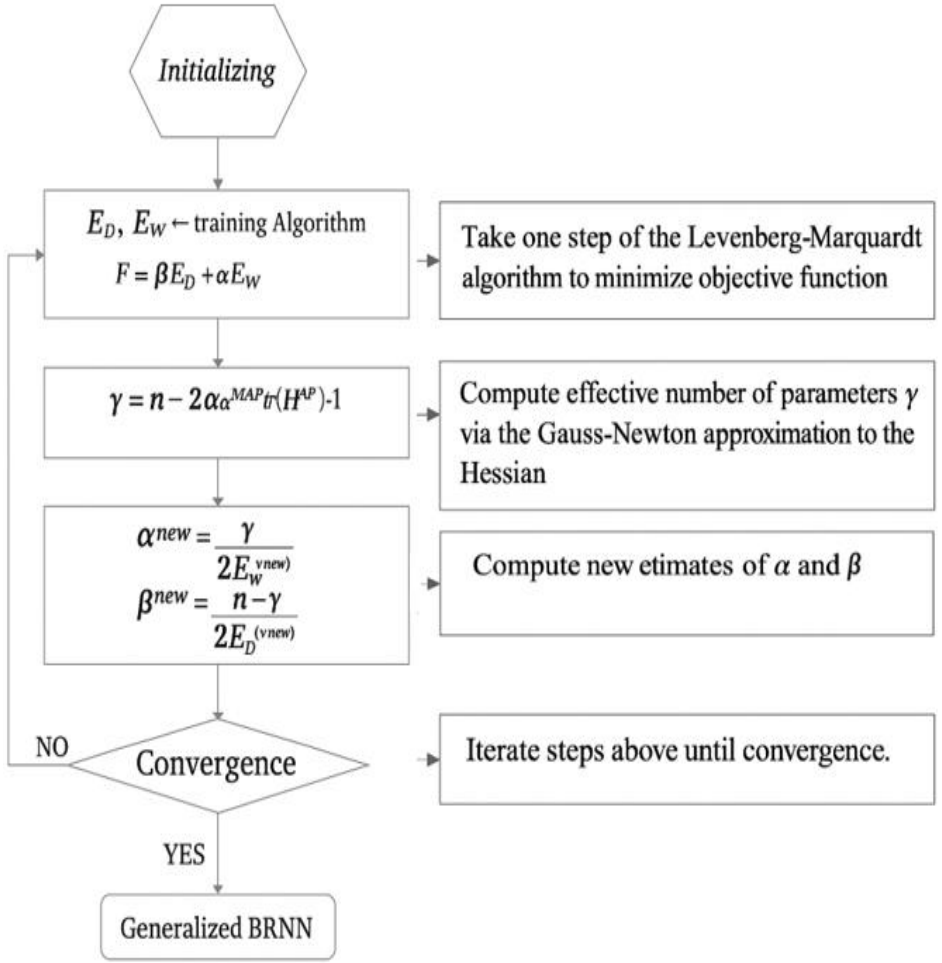

Convergence Check

- **YES** → Training complete → **Generalized BRANN model** is formed
- **NO** → Repeat the above steps

Materials and Methods

Levenberg-Marquardt

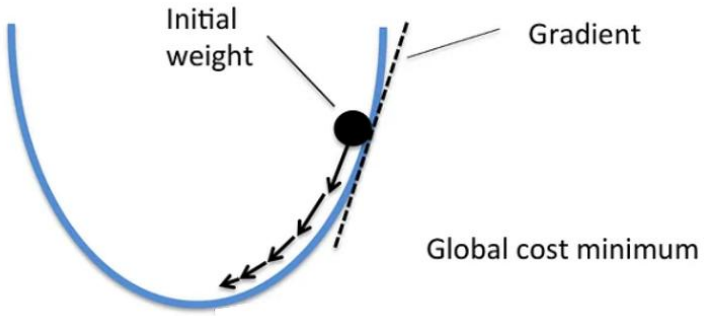

- **A hybrid between Gradient Descent and the Gauss–Newton method**

  Minimize $F = \beta E_D + \alpha E_W$

- **Weight Update Rule:** $w_{new} = w_{old} - (J^T J + \lambda I)^{-1} J^T e$

- J: **Jacobian matrix (partial derivatives of the error function with respect to weights)**
- e: **Error vector (e.g.,** $e = y - f(x,w)$**e=y−f(x,w))**
- λ: **Damping factor (adjusts between gradient descent and Gauss–Newton behavior)**

If λ **is large → behaves like gradient descent (slow but stable)**
If λ **is small → behaves like Gauss–Newton (faster but potentially unstable)**

YONSEI UNIVERSITY
DEPARTMENT OF MECHANICAL ENGINEERING
ISID Intelligent Structure & Integrated Design Lab

Materials and Methods

Gauss–Newton Approximation & Parameter Update

This is the stage where the model complexity (γ) is estimated, and the regularization parameters (α and β) are updated accordingly

- **Estimating the Effective Number of Parameters (γ)**
- **γ quantifies how complex the model is**
- **The computed value of γ is used in the regularization parameter update step:**

$$\gamma = n - 2\alpha^{MAP} tr(H^{MAP})^{-1}$$

- **n: Total number of parameters**
- **$(H^{MAP})^{-1}$: Approximate inverse Hessian matrix at the MAP estimate**

$$\alpha^{new} = \frac{\gamma}{2E_w(w^{new})}$$

$$\beta^{new} = \frac{n-\gamma}{2E_D(w^{new})}$$

YONSEI UNIVERSITY
DEPARTMENT OF MECHANICAL ENGINEERING
ISID Intelligent Structure & Integrated Design Lab

Materials and Methods

BRANN-Based Fatigue Life Prediction

Levenberg–Marquardt Algorithm

- Minimizes the objective function:

$$F = \beta E_D + \alpha E_W$$

- Efficiently finds weights that balance accuracy and smoothness
- Enables fast convergence and stable learning even with small datasets

BRANN uses this algorithm to update weights while preserving generalization

Gauss–Newton Approximation & Parameter Update

- Approximates the Hessian matrix using the Gauss–Newton method
- Repeats until convergence

→ well-regularized, generalized BRANN model

$$\alpha^{new} = \frac{\gamma}{2E_w(w^{new})}$$

$$\beta^{new} = \frac{n-\gamma}{2E_D(w^{new})}$$

This Bayesian framework allows BRANN to prevent overfitting automatically

Materials and Methods

Fatigue life prediction methodology

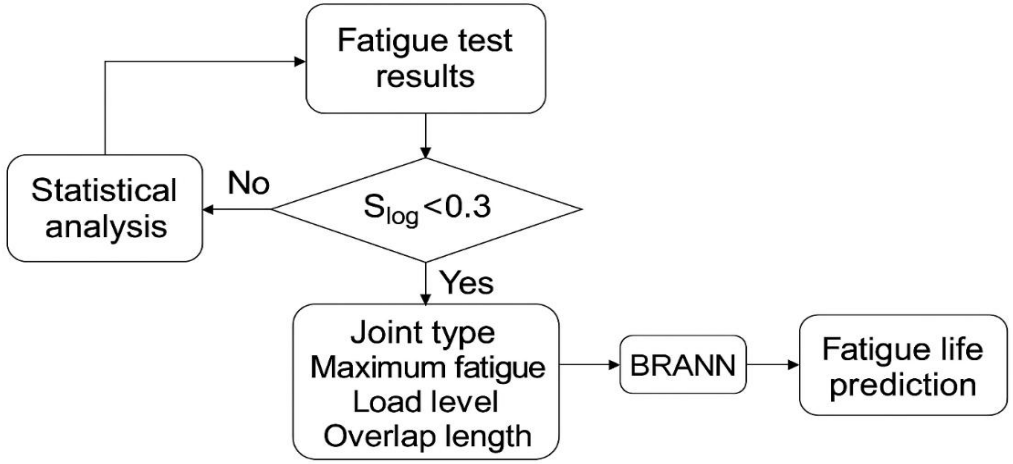

< Fatigue life prediction methodology>

- Fatigue test results are obtained from experimental data.
- Statistical analysis is performed to check the data quality
- If the logarithmic standard deviation S_{log}<0.3S, the data is considered reliable
- Input features such as joint type, maximum fatigue, load level, and overlap length are selected
- These inputs are fed into the BRANN model to predict fatigue life

Results

Material Characterization

- USN 125B carbon/epoxy composite

-	E_1	E_2	G_{12}	ν	F_{1t}	F_{2t}	F_{1c}	F_{2c}	F_6
Unit	GPa	GPa	GPa	-	MPa	MPa	MPa	MPa	MPa
USN-125 B	142	7.97	3.98	0.312	2419	48	1231	178	46

- SS400 Steel

-	E	σ_T	ν
Unit	GPa	MPa	-
SS400 Steel	206	313	0.29

- Type D adhesive

-	E	σ_T	ν
Unit	GPa	MPa	-
SS400 Steel	206	313	0.29

Results

Tensile tests of bonded joint

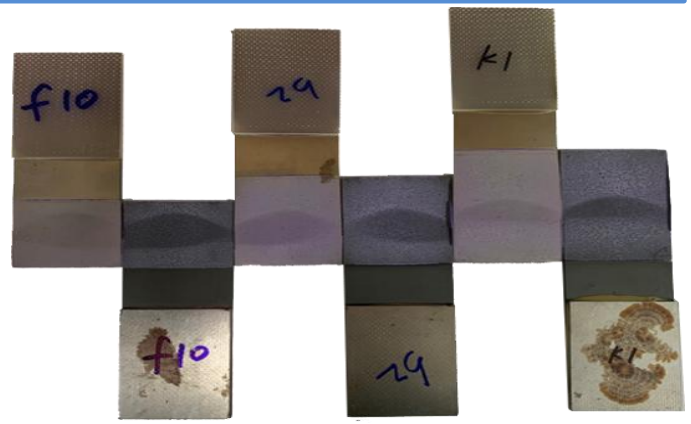

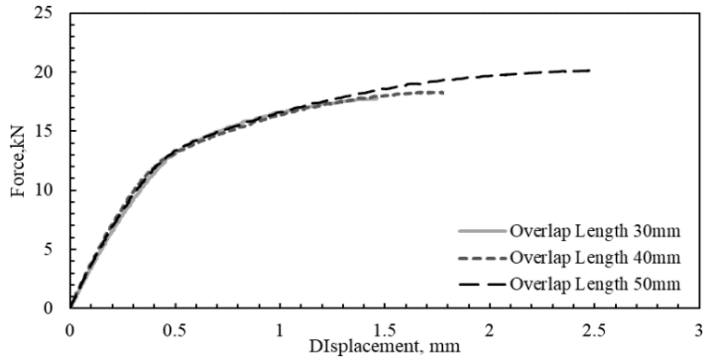

< Failure loads for each overlap length >

< Tensile test result data >

	Overlap Length 30 mm	Overlap Length 40 mm	Overlap Length 50 mm
Failure Load (kN)	17.001	18.645	19.507
	17.445	18.289	19.582
	17.597	18.11	19.509
	17.727	18.710	19.236
	17.774	18.5545	19.206
	18.043	18.793	20.152
Average	17.598	18.517	19.532

- An increase in overlap length by 10 mm resulted in approximately a 5% increase in the failure load
- The increase in bonded area distributed the applied load and reduced internal stress

Results

Tensile tests of hybrid joint

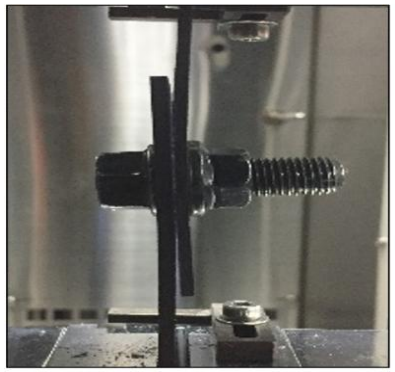

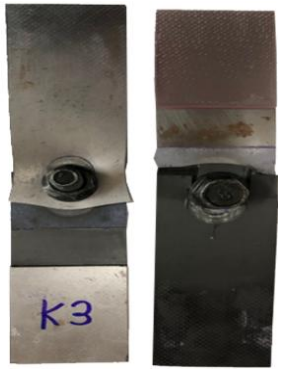

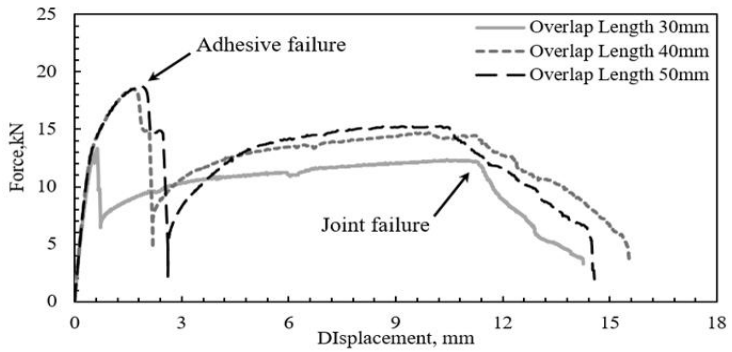

< Failure loads for each overlap length >

< Tensile test result data >

	Overlap Length 30mm	Overlap Length 40mm	Overlap Length 50mm
Failure load (kN)	13.321	17.856	18.751
	13.326	17.891	18.728
	13.439	18.833	18.315
	13.349	18.471	18.988
	14.152	18.2	18.125
	14.241	18.149	17.619
Average	13.638	18.233	18.421

- Two stages of failure behavior were observed: the first stage involved deformation and failure of the adhesive, and in the second stage, the load was transferred to the bolt, resulting in the second peak
- Performance varied depending on the effectiveness of load sharing
- An increase in overlap length by 10 mm resulted in increase in the failure load

YONSEI UNIVERSITY
DEPARTMENT OF MECHANICAL ENGINEERING
ISID Intelligent Structure & Integrated Design Lab

Results

Fatigue tests bonded joint

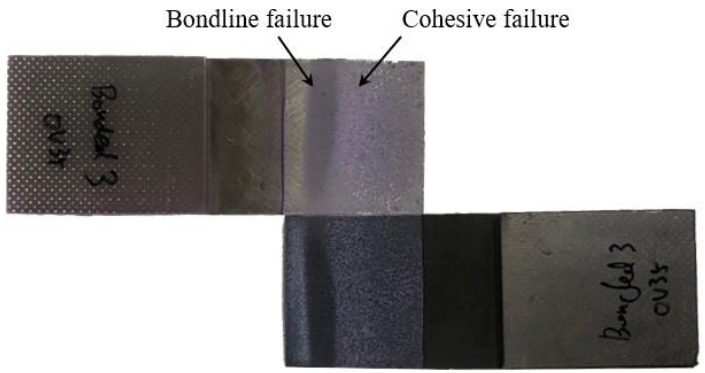

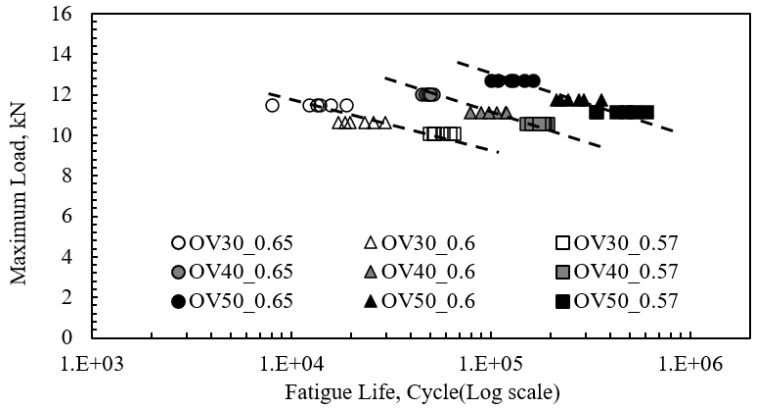

< F-N curves of the bonded single lap joints >

< The fatigue life data of the bonded single lap joints >

Overlap length 30mm			Overlap length 40mm			Overlap length 50mm		
Maximum fatigue load (kN)	Load level	Fatigue life (Cycle)	Maximum fatigue load (kN)	Load level	Fatigue Life (Cycle)	Maximum fatigue load (kN)	Load level	Fatigue Life (Cycle)
11.5043	0.65	7991	12.0354	0.65	45078	12.6962	0.65	162929
		12293			47200			109119
		13498			48793			130703
		13968			51569			100160
		15806			48972			125474
		18919			50148			147867
10.6194	0.6	17341	11.1096	0.6	79394	11.7196	0.6	361460
		18780			119575			293621
		19783			107701			276143
		23344			120143			245876
		25825			89724			224174
		29546			98271			214876
10.0884	0.57	49587	10.5541	0.57	193951	11.1332	0.57	335947
		51487			150167			477797
		52425			186606			607073
		57945			159846			524792
		62438			182546			340202
		65090			175483			425071

- All specimens had a failure at the joint with the adhesive
- Increasing the overlap length by 10 mm increased the joint's fatigue life by about 5 times

YONSEI UNIVERSITY
DEPARTMENT OF MECHANICAL ENGINEERING
ISID Intelligent Structure & Integrated Design Lab

Results

Fatigue tests hybrid joint



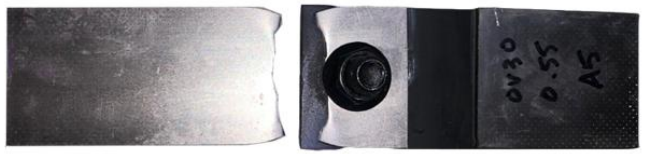

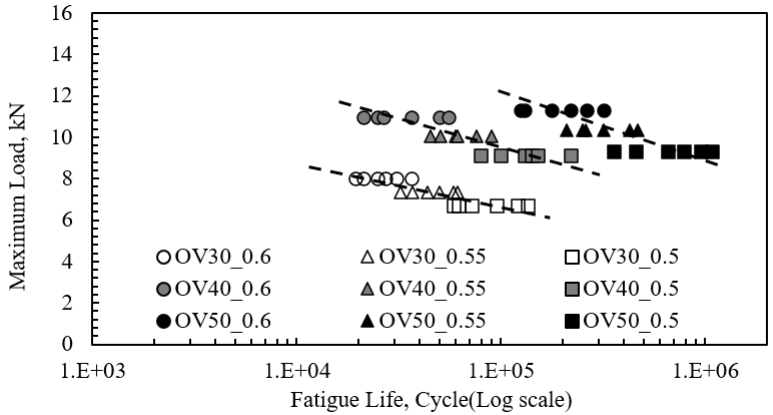

< F-N curves of the hybrid joint>

< The fatigue life data of the hybrid joint>

Overlap length 30mm			Overlap length 40mm			Overlap length 50mm		
Maximum fatigue load (kN)	Load level	Fatigue life (Cycle)	Maximum fatigue load (kN)	Load level	Fatigue Life (Cycle)	Maximum fatigue load (kN)	Load level	Fatigue Life (Cycle)
11.5043	0.65	7991	12.0354	0.65	45078	12.6962	0.65	162929
		12293			47200			109119
		13498			48793			130703
		13968			51569			100160
		15806			48972			125474
		18919			50148			147867
10.6194	0.6	17341	11.1096	0.6	79394	11.7196	0.6	361460
		18780			119575			293621
		19783			107701			276143
		23344			120143			245876
		25825			89724			224174
		29546			98271			214876
10.0884	0.57	49587	10.5541	0.57	193951	11.1332	0.57	335947
		51487			150167			477797
		52425			186606			607073
		57945			159846			524792
		62438			182546			340202
		65090			175483			425071

- The failure point was defined as the moment when the adhesive was completely failed
- As the overlap length increased from 30 mm to 40 mm, the fatigue life increased approximately 18 times, and as the overlap length increased from 40 mm to 50 mm, the fatigue life increased approximately 7 times

Results

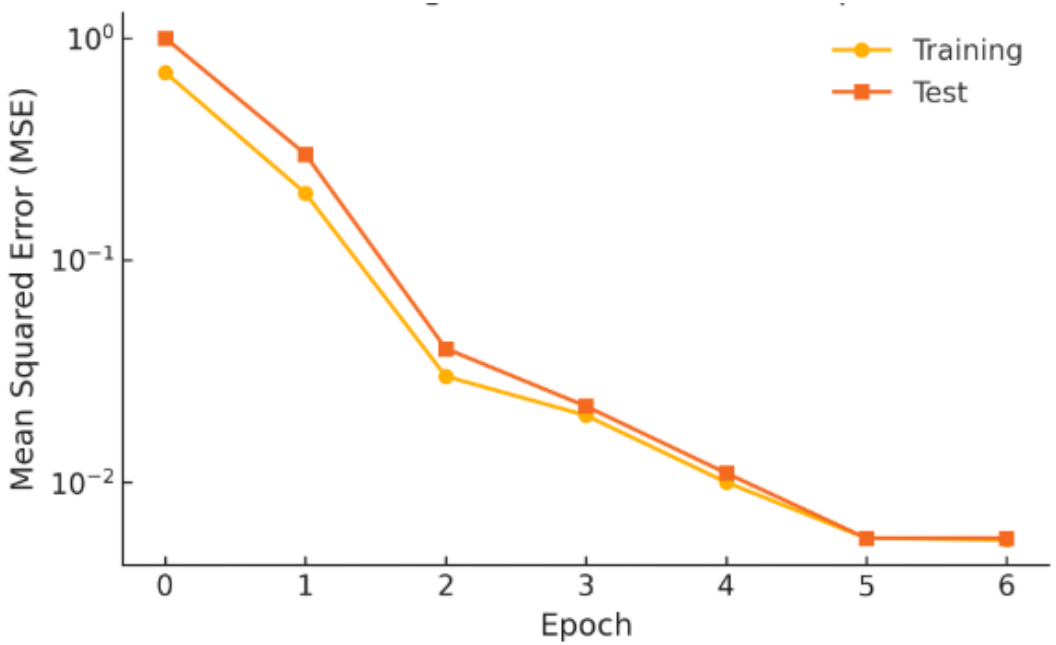

<Neural Network Learning Performance>

- **Both training and test errors show a decreasing trend**
- **Minimum test MSE achieved at Epoch 4 (0.00399)**
- **Stable learning without signs of overfitting**

Results

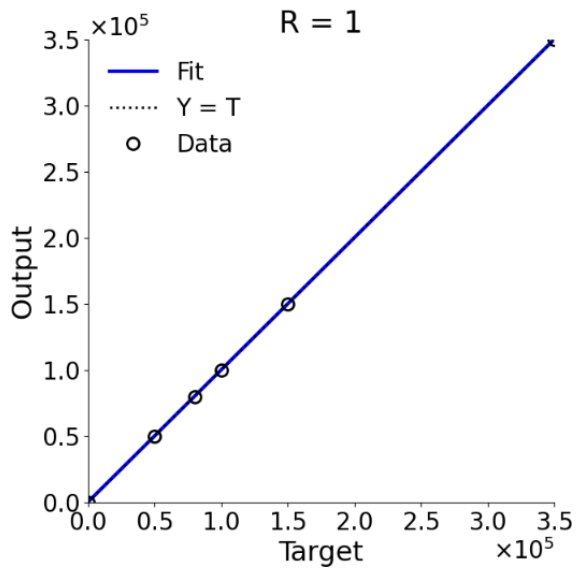

<Training>

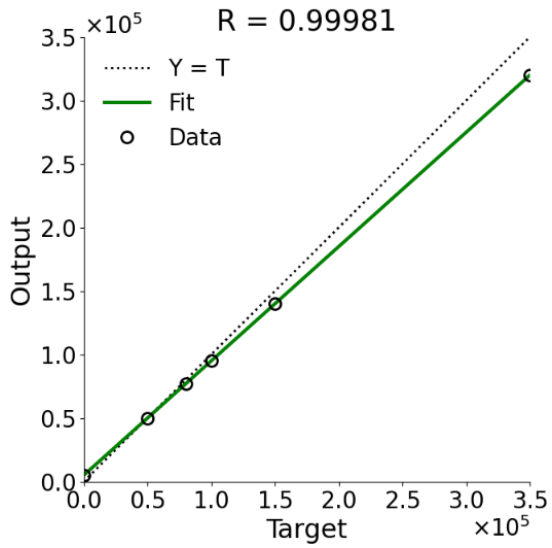

<Test>

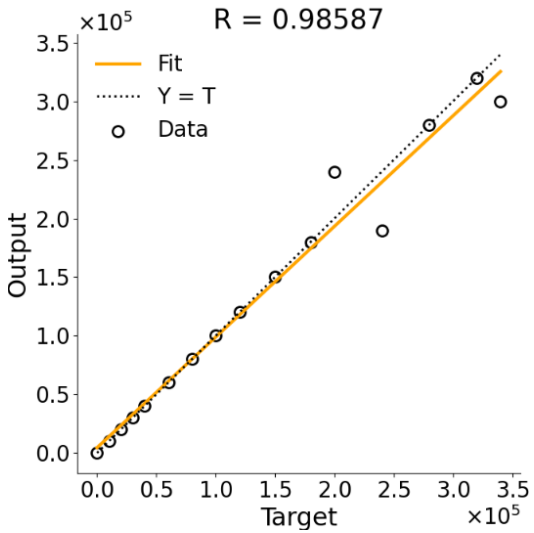

<All>

- Strong linear correlation observed between predicted and target values
- R-values: Training = 1.00000, Validation = 0.99981, All = 0.99383
- These results confirm excellent model performance and generalization ability

YONSEI UNIVERSITY
DEPARTMENT OF MECHANICAL ENGINEERING
ISID Intelligent Structure & Integrated Design Lab

Results

Training Convergence

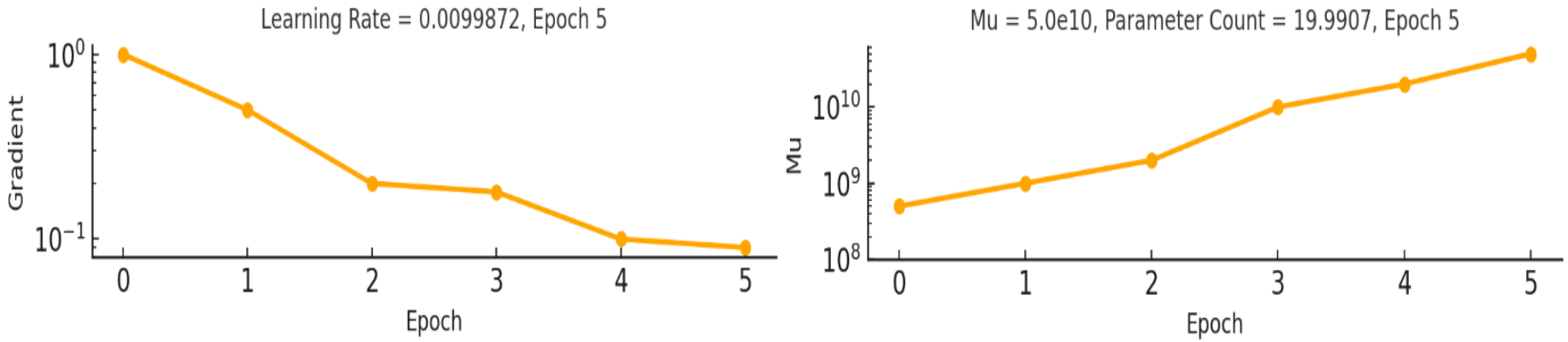

- **Gradient decreased steadily, indicating smooth convergence of the training process**
- **Mu (damping factor) increased, showing that the Levenberg-Marquardt algorithm approached convergence**
- **Gamma (Effective Parameters) stabilized around 20, suggesting efficient model complexity**
- **Sum of Squared Weights (ssX) remained bounded, preventing overfitting**
- **Validation Failures stayed at zero, confirming no degradation in generalization**

Results

Training Convergence

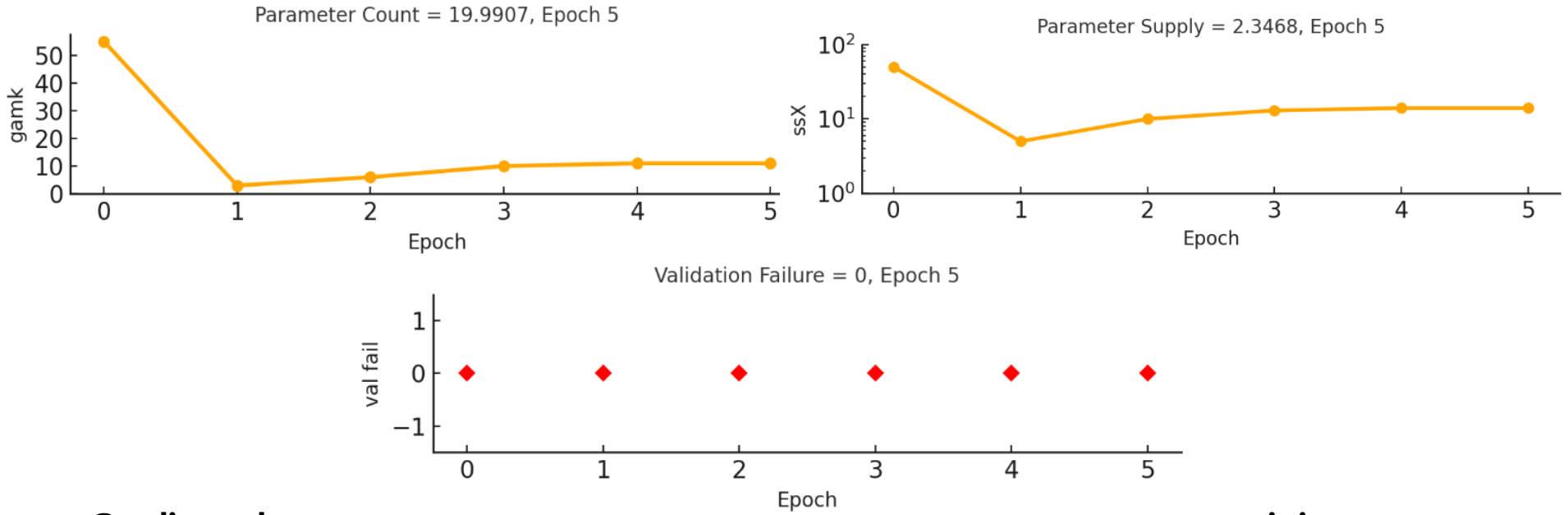

- Gradient decreased steadily, indicating smooth convergence of the training process
- Mu (damping factor) increased, showing that the Levenberg-Marquardt algorithm approached convergence
- Gamma (Effective Parameters) stabilized around 20, suggesting efficient model complexity
- Sum of Squared Weights (ssX) remained bounded, preventing overfitting
- Validation Failures stayed at zero, confirming no degradation in generalization

YONSEI UNIVERSITY
DEPARTMENT OF MECHANICAL ENGINEERING
ISID Intelligent Structure & Integrated Design Lab

Results

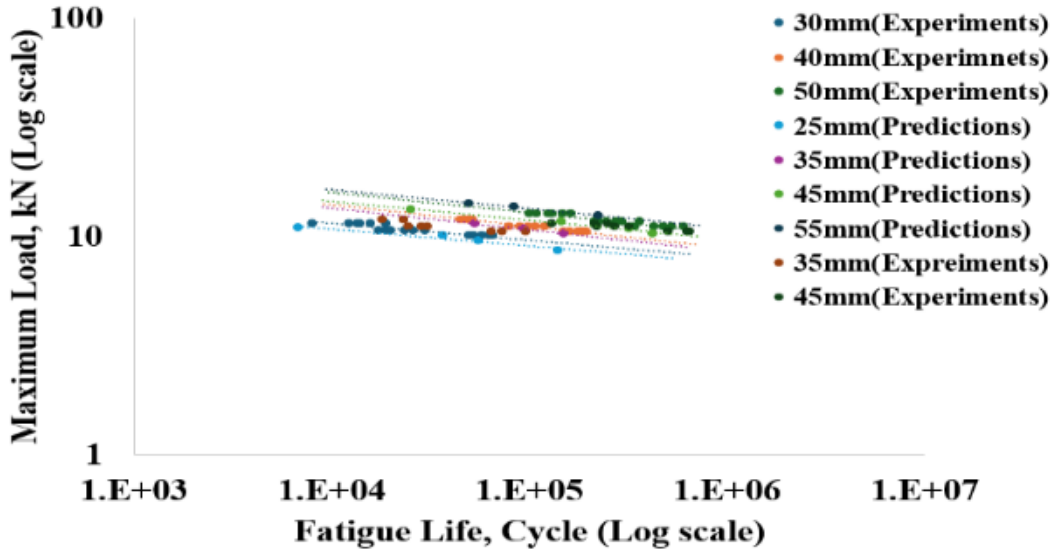

<Experimental and predicted fatigue life of bonded joints>

- A neural network was trained using hybrid joint fatigue data for 30, 40, and 50mm overlaps.
- The model predicted F–N curves for unseen lengths: 25, 35, 45, and 55 mm
- Experimental validation at 35 mm and 45 mm confirmed high prediction accuracy
- The model demonstrates strong generalization for fatigue life prediction

YONSEI UNIVERSITY
DEPARTMENT OF MECHANICAL ENGINEERING
ISID Intelligent Structure & Integrated Design Lab

Results

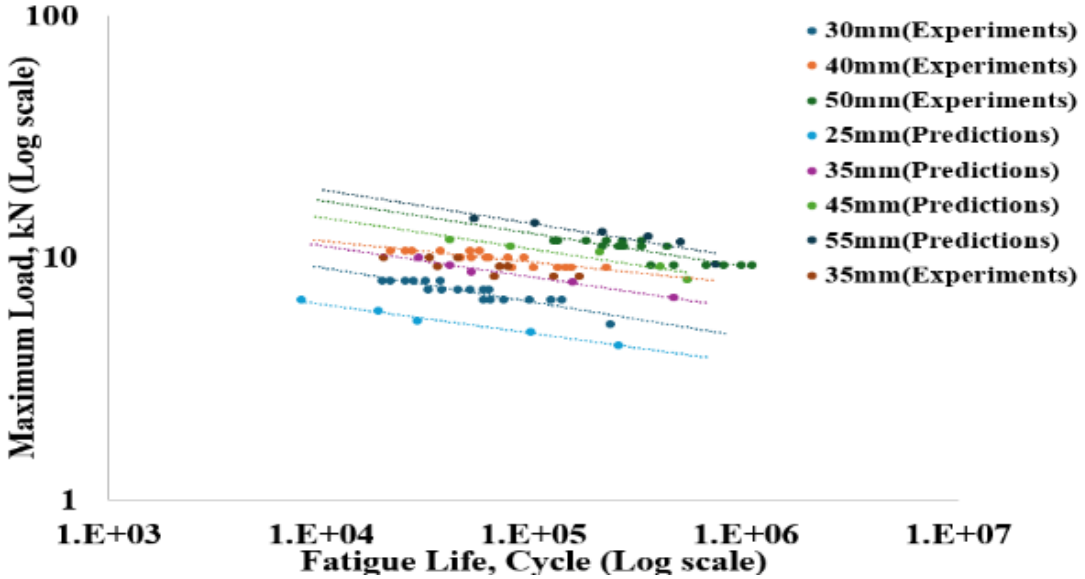

<Experimental and predicted fatigue life of hybrid joints>

- F-N (Force–Cycle) curves were predicted using a neural network trained on 30, 40, and 50mm overlap data.
- Predictions were extended to new overlap lengths: 25, 35, 45, and 55 mm
- The 35 mm prediction was experimentally validated, showing strong agreement
- The model demonstrates strong generalization for various hybrid joint configurations

Results

Expected Effects of Research

Original fatigue life forecasting method

Inaccurate when applied to dissimilar material joints
Prone to overfitting and poor generalization

Fatigue life prediction method in this study

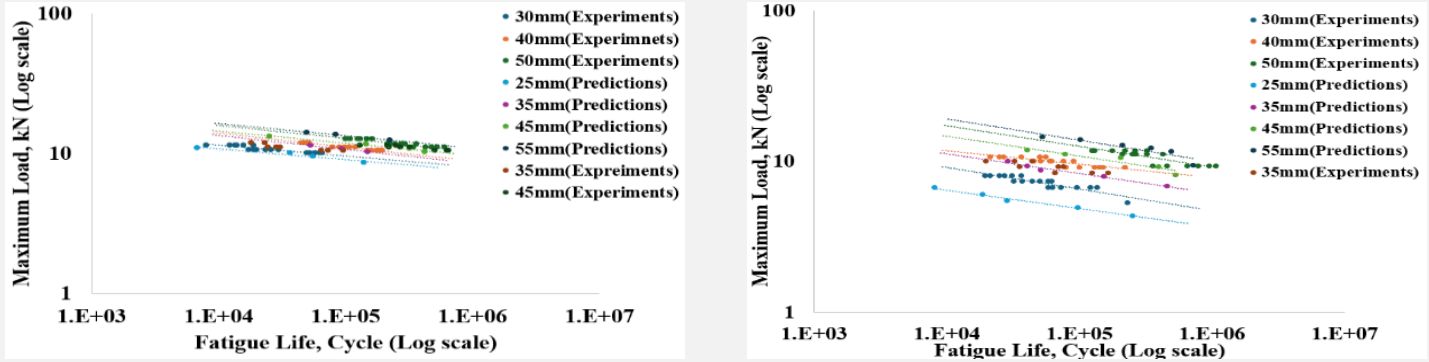

<Experimental setup for fatigue tests of single lap joints and hybrid joints>

- Accurate fatigue life prediction for bonded and hybrid joints with varying overlap lengths
- Effective overfitting mitigation via Bayesian regularization

YONSEI UNIVERSITY
DEPARTMENT OF MECHANICAL ENGINEERING
ISID Intelligent Structure & Integrated Design Lab

Summary & Future Works

Summary

- Proposed a fatigue life prediction method for dissimilar material joints using a neural network
- Constructed experimental F-N data for bonded and hybrid joints with varying overlap lengths
- Trained a Bayesian Regularized Neural Network (BRANN) using fatigue data from 30, 40, and 50mm overlaps
- Predicted fatigue life for unseen overlap lengths (25, 35, 45, 55 mm) using the trained model
- Prediction accuracy was validated at 35 mm and 45 mm overlaps, showing good agreement with experiments

Future Works

- Expand training dataset to cover more diverse joint configurations and loading conditions
- Apply model to multi-axial fatigue cases and real structural joint geometries

YONSEI UNIVERSITY
DEPARTMENT OF MECHANICAL ENGINEERING
ISID Intelligent Structure & Integrated Design Lab

Q & A

Thank you

ICCM24
AUGUST 4-8, 2025
BALTIMORE CONVENTION CENTER
BALTIMORE, MARYLAND, USA

No Technical Paper Submission for:

John Finder

COMPOSITE 3D-PRINTED PLATE-BASED MECHANICAL METAMATERIALS

Aya Hosoi[1,2], Jier Wang[1] , Yuki Fujita[1,2] , Tatsuo Tanaka[3] , Junichi Takahashi[2] and Ajit Panesar[1]

[1]Department of Aeronautics, Imperial College London
Exhibition Road, SW7 2AZ, UK
Email: a.hosoi24@imperial.ac.uk, web page: https://idea-lab-ic.github.io/#/

[2] Asahi Kasei Corporation
1-3-1, Yakoh, Kawasaki-ku, Kawasaki-city, Kanagawa 210-0863, Japan
Email: second.author@m-tech.aau.dk, web page: https://www.asahi-kasei.com/

[3]Asahi Kasei Plastics Vietnam
703-704, 29 Le Duan, Ben Nghe Ward, 71000, Vietnam
web page: https://www.asahi-kasei-plastics.com/en/

Keywords: Computational modelling, Additive Manufacturing, Composites, Mechanical testing

ABSTRACT

Metamaterials have attracted interest in both academia and industry due to their outstanding properties across various fields, such as mechanical, thermal, electromagnetic and acoustic. Those properties are realised by underlying architectures of metamaterials. Controlling the micro-architecture in a multiscale metamaterial opens the possibility for multifunctional applications relevant to diverse sectors including aerospace, automotive, biomedical and sports.

Innovative metamaterial designs have been effectively derived from approaches such as inverse homogenisation and dehomogenisation, which have evolved from traditional density-based topology optimisation. Alternatives to these approaches, leveraging machine learning-based inverse generation strategies have also been developed. Our recent work has proposed a two-step metamaterial designing approach that combined topology optimisation and machine learning.

This study advances the proposed two-step approach by extending the geometry space to include 3D unit lattice cells and accommodating material anisotropy, specifically orthotropy in this study, opening the opportunity to utilise fibre-reinforced additive manufacturing. Numerical evaluation using finite element analysis confirmed that the optimal structures performed better than their uniformly designed counterparts, while the difference was marginal in isotropic materials due to the difference in boundary conditions applied in optimisation and numerical validation. The 3D extension was achieved by applying two types of unit lattice cells: truss-based BCC and plate-based BCC. The numerical evaluation showed that the plate-based BCC lattice structure outperformed the truss-based BCC, indicating the effectiveness of plate-based metamaterials.

This study aims to accelerate the development in the field of composite metamaterials by presenting the validated computational ML-based inverse design framework, considering practical fabrication and use cases. Future work will include the extension to other objective functions incorporating buckling, vibration, thermal etc. along with experimental validations.

1 INTRODUCTION

Metamaterials (MMs) are intentionally designed architectures that exhibit effective properties surpassing those of their constituent materials. These properties range from electromagnetic to acoustic, thermal and mechanical characteristics, attracting researchers in various fields such as aerospace, automotive, biomedical and sports. [1] The properties of MMs are realised by their underlying micro-architectures, also known as unit lattice cells. Designing these lattice cells enables MMs to exhibit outstanding behaviours not found in nature.

A variety of lattice cell structures have been proposed as micro-architectures for MMs, such as truss-based, surface-based and plate-based lattices. Truss-based lattices are the most widely studied due to their geometric simplicity. Representative examples include Body-Centred Cubic (BCC) and Face-Centred Cubic (FCC) lattices, which are typically bending-dominated and thus relatively compliant at low volume fractions. Plate-based lattices, introduced by Berger et al. [2], are characterized by interconnected flat panels. Plate-based lattices have attracted interest because of their ability to approach the Hashin–Shtrikman (HS) bound, the theoretical limit of the elastic moduli in accordance with the volume fractions of isotropic lattices. Several research group have designed mechanical MMs utilising plate-based lattices. [3], [4]

Numerous approaches have been developed to effectively design the MMs' micro-architectures. For example, inverse homogenisation was proposed by utilising a density-based topology optimisation (TO) to minimise the error between the predefined target properties and the effective properties calculated by numerical homogenisation. [5] Dehomogenisation has been developed to concurrently optimise the macro and micro-architecture of MMs by parameterising pre-defined micro-architectures and applying homogenisation-based TO. [6], [7] As an alternative to these TO-based approaches, optimisation leveraging machine learning (ML) has gained interest as a computationally efficient approach. [8] Our recent study [9] has proposed a two-step designing approach for realising multi-scale architecture, i.e., lattice structure, by combining TO and ML. Various 2D lattice geometries considering isotropic material properties were explored. The lattice geometries were parameterised and optimised by a ML-based inverse generator to map architectures based on specified target properties.

This study advances on the proposed TO and ML-based lattice optimisation approach by extending the geometry space to include 3D unit lattice cells and considering material anisotropy, opening the opportunity to utilise fibre-reinforced additive manufacturing (FRAM). A FRAM material is simplified as a transversely isotropic, i.e., orthotropic, material in this study. The 3D lattice optimisation considers two types of 3D unit lattice cells: truss-based BCC and plate-based BCC. Finite element analysis (FEA) for a three-point bending (3PB) test is conducted to numerically evaluate the performance of the optimised lattice structures.

This study aims to accelerate the development in the field of composite metamaterials by presenting the validated computational ML-based inverse design framework, considering practical fabrication and use cases.

2 METHODOLOGY

2.1 TO and ML-based lattice optimisation

As described in Jier and Panesar (2022)[9], the lattice generation approach consists of two steps: 1) optimise mechanical property for each unit cell from density and stress distribution obtained by low resolution TO; 2) generate lattice unit cell to realise the optimal mechanical property using the ML-based inverse generator.

This study considered the Messerschmitt-Bölkow-Blohm (MBB)-beam problem shown in Fig. 1. The objective of the lattice optimisation is to minimise the mechanical compliance $\boldsymbol{C}$ (a measure of the inverse of stiffness) defined as:

$$\boldsymbol{C} = \frac{1}{2}\boldsymbol{U}^T\boldsymbol{K}\boldsymbol{U} \tag{1}$$

where $\boldsymbol{K}$ is the global stiffness matrix and $\boldsymbol{U}$ is the global displacement vector. The optimisation starts with density-based low resolution TO described in Eqs. 2.

$$\begin{aligned} &\min_{\boldsymbol{\rho}} \boldsymbol{C} \\ &s.t.: \sum_{i=1}^{N} V_i\rho_i - V_f \leq 0 \\ &\boldsymbol{K}\boldsymbol{U} = \boldsymbol{F} \\ &0 \leq \rho_i \leq 1 \end{aligned} \tag{2}$$

where N is the number of elements in the design domain, V_i is the elemental volume, ρ_i is the elemental density ($\rho_i = 1$ means that the element is filled with material while $\rho_i = 0$ means void), V_f is the volume fraction and $\boldsymbol{F}$ is the global load vector. V_f was set to be as 0.5 in this study. Solid Isotropic Material Penalisation (SIMP) method is applied to calculate the elastic properties, i.e., Young's modulus, in each element by interpolating with the value of density ρ_i:

$$E(\rho_i) = E_{min} + E_0 {\rho_i}^p \tag{3}$$

where E_{min} is the minimal value that the elemental Young's modulus can take ($E_{min} = 1.0 \times 10^{-9}$ in this study) and p is the penalisation factor in SIMP. In this study, p was set to be 2.6 in 2D cases based on the precious study [9] and 3 in 3D cases as a generalised value. As an example for the lattice optimisation, an optimal lattice structure having 20×10 unit cells (as Fig. 2b) is derived from the low resolution TO in 20×10 elements (as Fig. 2a).

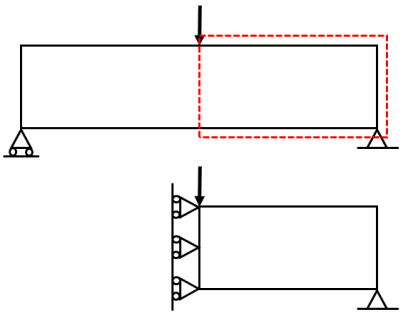

Figure 1: The MBB-beam problem

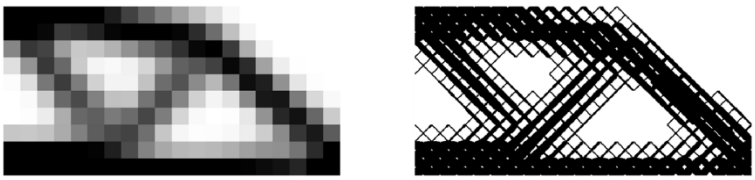

(a) (b)

Figure 2: Examples of (a) low resolution TO and (b) lattice structure for MBB-beam problem

2.1.1 Optimisation of mechanical property

This study applied elastic stiffness tensor $\boldsymbol{D}$ as a mechanical property to be optimised in the first step. Elastic stiffness tensor $\boldsymbol{D}$ represents the relationship between strain ε and stress σ as described in 2D and 3D in Eqs.4 and 5, respectively. The tensor in 2D and 3D has 6 and 21 independent entries because of its symmetry as shown in Eq. 6.

$$\begin{bmatrix}\sigma_{11}\\ \sigma_{22}\\ \sigma_{12}\end{bmatrix} = \begin{bmatrix}D_{1111} & D_{1122} & D_{1112}\\ D_{2211} & D_{2222} & D_{2212}\\ D_{1211} & D_{1222} & D_{1212}\end{bmatrix}\begin{bmatrix}\varepsilon_{11}\\ \varepsilon_{22}\\ \varepsilon_{12}\end{bmatrix} \tag{4}$$

$$\begin{bmatrix}\sigma_{11}\\ \sigma_{22}\\ \sigma_{33}\\ \sigma_{12}\\ \sigma_{23}\\ \sigma_{31}\end{bmatrix} = \begin{bmatrix}D_{1111} & D_{1122} & D_{1133} & D_{1112} & D_{1123} & D_{1131}\\ D_{2211} & D_{2222} & D_{2233} & D_{2212} & D_{2223} & D_{2231}\\ D_{3311} & D_{3322} & D_{3333} & D_{3312} & D_{3323} & D_{3331}\\ D_{1211} & D_{1222} & D_{1233} & D_{1212} & D_{1223} & D_{1231}\\ D_{2311} & D_{2322} & D_{2333} & D_{2312} & D_{2323} & D_{2331}\\ D_{3111} & D_{3122} & D_{3133} & D_{3112} & D_{3123} & D_{3131}\end{bmatrix}\begin{bmatrix}\varepsilon_{11}\\ \varepsilon_{22}\\ \varepsilon_{33}\\ \varepsilon_{12}\\ \varepsilon_{23}\\ \varepsilon_{31}\end{bmatrix} \tag{5}$$

$$D_{ijkl} = D_{klij} \tag{6}$$

The elastic stiffness tensor $\boldsymbol{D}$ in each low-resolution element is optimised based on the minimisation problem as in Eq. 7 so that the elemental mechanical compliance c_e be minimised.

$$\min_{\boldsymbol{D_e}} c_e = \frac{1}{2}\boldsymbol{\sigma}^T \boldsymbol{D_e}^{-1}\boldsymbol{\sigma} \qquad (7)$$
$$s.t.: P(\boldsymbol{D_e}, vf_e) \geq \epsilon$$
$$|vf_e - \rho_e(SIMP)| \leq \delta$$

where $\boldsymbol{D_e}$ is the elemental elastic tensor to be optimised, $\boldsymbol{\sigma}$ is stress derived from the result of the low resolution TO, $P(\boldsymbol{D_e}, vf_e)$ is the probability of the combination of the values of $\boldsymbol{D_e}$ and the lattice cell volume fraction vf_e, which are constrained by the elemental density from the low resolution TO ($\rho_e(SIMP)$). ϵ and δ is the predefined limit of the probability and the volume fraction error.

2.1.2 Inverse generator for multi-scale lattice

This study advanced the previous study [9], which considered 2D truss-based BCC lattices, by extending unit cell types into 3D truss-based and plate-based BCC lattices. Each cell type was parameterised as shown in Fig. 3. 2D unit cells had 4 representative parameters, $a_1 - a_4$, while 3D unit cells had 8, $a_1 - a_8$. Based on the unit cell structure, a corresponding mechanical property, an effective elastic tensor $\boldsymbol{D}$ described in 2.1.1, was calculated by applying numerical homogenization [10], [11]

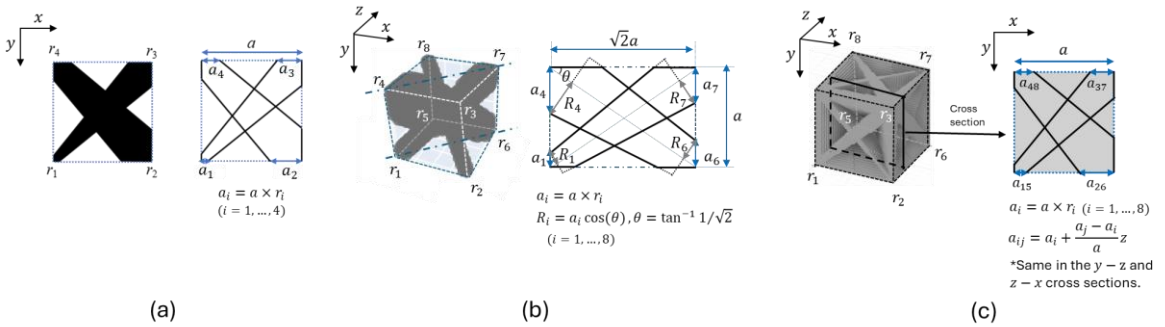

Figure 3: Unit cells parameterisation for (a)2D truss-based BCC, (b)3D truss-based BCC and (c)3D plate-based BCC

Based on the optimisation results of mechanical properties in 2.1.1, a corresponding structure of the lattice unit cell is obtained. This lattice unit cell generation is realised by a pretrained ML-based inverse generator. This study applied multi-layer perceptron (MLP) as a model utilised in the inverse generator. The input of the inverse generator is independent components of $\boldsymbol{D_e}$ (6 components in 2D and 21 components in 3D) and the volume fraction vf_e. The output is a set of unit cell parameters ($r_1 - r_4$ in 2D and $r_1 - r_8$ in 3D). In the training processes, 5000 randomly generated sets of unit cell parameters along with computed volume fractions and numerically homogenised elastic tensors $\boldsymbol{D}$ were applied as a training or testing data.

2.2 Materials and numerical validation

This study considered two materials, Nylon (Polyamide 6) and a short fibre-reinforced nylon called Onyx. The mechanical properties described in Table 1 were defined based on the datasheets by *Markforged Inc.* [12]. Onyx was assumed as isotropic material in 3D lattices as orthotropy in 3D was out of scope in this study.

The 2D lattice unit cell considering orthotropic material was divided into 4 regions, described as i-iv in fig. 5. Each region was assumed to have material properties specified in Table 2 by considering short fibre orientation in the printing process.

	2D lattice		3D lattices
Material type	Isotropic	Orthotropic	Isotropic
Mechanical properties used on optimisation process	$\rho = 1.1$ kg/m^3 $E = 1.7$ GPa $\nu = 0.3$	$\rho = 1.2$ kg/m^3 $E_{11} = 2.4$ GPa, $E_{22} = 1.7$ GPa $\nu = 0.3$, $G_{12} = E_{11}/2(1+\nu)$	$\rho = 1.2$ kg/m^3 $E = 2.4$ GPa $\nu = 0.3$
Corresponding materials	Nylon (PA 6)	Onyx (PA with short CF)	Onyx (PA with short CF)

Table 1: Material properties

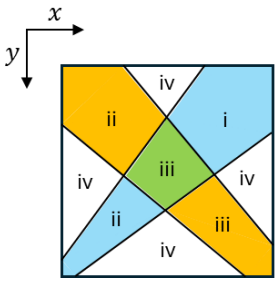

Figure 5: Assumption of material distribution in 2D unit cell with orthotropic material

Region in Figure 5	i	ii	iii	iv
Material type	Orthotropic	Orthotropic	Isotropic	Void
Fibre orientation (direction of E_{11})	45 deg	-45 deg	-	-
Mechanical properties	$\rho = 1.2$ kg/m^3 $E_{11} = 2.4$ GPa $E_{22} = 1.7$ GPa $\nu = 0.3$ $G_{xy} = E_{11}/2(1+\nu)$		$\rho = 1.2$ kg/m^3 $E = 1.7$ GPa $\nu = 0.3$	$\rho = 0$ kg/m^3 $E = 0$ GPa

Table 2: Material properties in 2D unit cell with orthotropic material

Three-point bending (3PB) tests, which corresponds to the half MBB-beam problem, were simulated using finite element analysis (FEA) with *Abaqus CAE* based on the ASTM D7264/D7264M – 15 standard (Fig.4(b) [13]). All lattice structures were set to have the same size of $120 \times 30 \times 10mm$ as shown in Fig. 4(a). Flat plates with the thickness of 2mm were added where the specimens contacted the loading nose and the supports (middle of the top surface and the left and the right corner of the bottom surface). This is to smoothly load the specimens throughout the test as the contacting points change during the 3PB test. In this study, both materials, Nylon and Onyx were set as isotropic in the FEA validation for simplicity, though orthotropy in validation is to be considered in the future work.

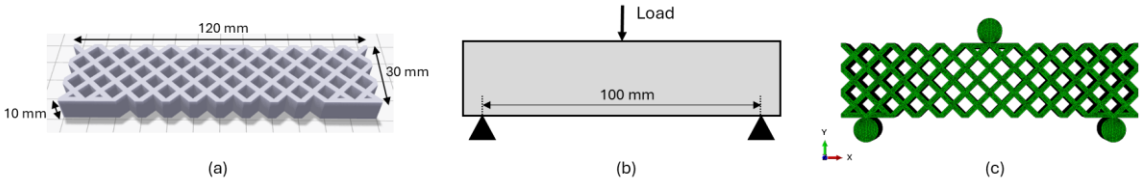

Figure 4: Numerical validation (a) Sizing specification of the specimens, (b) Three-point bending test based on ASTM D7264/D7264M – 15 and (c) Corresponding FEA model

3 RESULTS AND DISCUSSIONS

3.1 2D truss-based metamaterials

The application of the TO and ML-based lattice optimisation to 2D truss-based BCC using isotropic and orthotropic materials is detailed in Table 3. This table includes structural performance, i.e., mechanical compliance and mass, which is the volume fraction multiplied by material density. The number of unit cells were varied by changing the mesh resolution of low resolution TO.

Low resolution	Cell size	Material type	Lattice design	Compliance	Mass ($V_f \times \rho$)
20×10	30×30	Isotropic (Nylon)	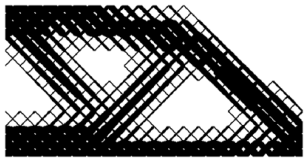	59.8	$0.52 \times 1.1 = 0.57$
		Orthotropic (Onyx)	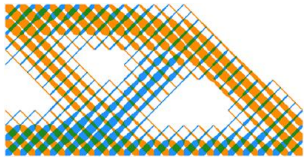	40.3	$0.46 \times 1.2 = 0.55$
8×4	30×30	Isotropic (Nylon)		202.6	$0.50 \times 1.1 = 0.55$
		Orthotropic (Onyx)		78.2	$0.48 \times 1.2 = 0.58$
6×3	30×30	Isotropic (Nylon)	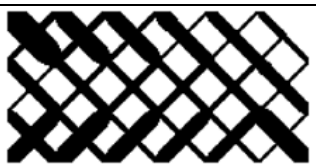	319.7	$0.50 \times 1.1 = 0.55$
		Orthotropic (Onyx)		110.9	$0.48 \times 1.2 = 0.58$

Table 3: Optimisation results with isotropic and orthotropic materials in 2D truss-based BCC

The optimal structures having 6×3 lattice unit cells in Table 3 along with the uniform counterparts were extruded into the 2.5D structures as shown in the Fig.4(a) and numerically evaluated using FEA corresponding to the 3PB test, which are summarised in Table 4. The uniform counterparts had more widely distributed region having higher strain energy above the average while the optimal structures had higher values in specific regions (orange rectangles in the strain energy distribution in Table 4). This results in lower total strain energy, i.e., mechanical compliance, calculated by integrating the elemental strain energies. A stress-based constraint is needed to reduce stress in higher strain energy region in the optimal structures.

The specific stiffnesses, defined as a measure of the flexural stiffness of the structures, were higher in the optimal structures than in the uniform counterparts whereas the difference with Nylon was marginal. One of the reasons is considered to be a difference in boundary conditions used in the

optimisation (half MBB beam) and the FEA. Spatial positions of the supports were at the corner in the half MBB beam (Fig. 1) while at 10mm from the corners in the FEA (Fig. 4(b)). The assumption of the interaction between the lattice structures and the load / supports were also different; the half MBB beam applied fixed boundary condition while the FEA applied contact boundary condition. More investigation is needed for the boundary condition.

Material	Structure	Strain energy distribution at displacement 2mm	Specific stiffness N/mm (Load / displacement/ V_f)
Nylon	Uniform (benchmark)	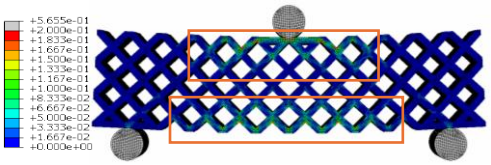	162.5
	Optimal	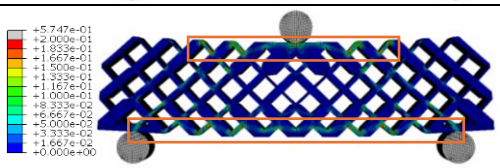	165.1
Onyx	Uniform (benchmark)	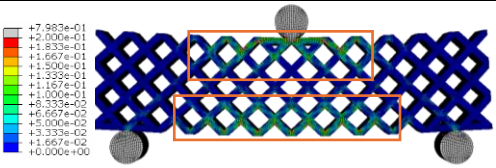	229.4
	Optimal	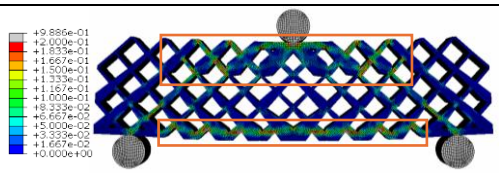	335.6

Table 4: Maximum principal strain distribution of each structure

3.2 3D truss and plate-based metamaterials

Optimisation results with 3D lattices are summarised in Table 5. Unlike the truss-based BCC, plate-based BCC had less thickness variant structure because of its high surface area. Nevertheless, the thicker plates were seen in the cells connected to the load i.e., top left corner, and the support, i.e., bottom right corner. This was the same tendency as the 2D lattices in Table 3. The specific stiffness calculated from the FEA result was higher in the plate-based BCC than in the truss-based BCC, confirming the efficiency of the plate-based lattices in the same volume fraction. This result complies to the experimental work conducted by Tancogne-Dejean et al. [14], where the normalised Young's moduli of plate-based lattices surpassed those of truss-based lattices.

Low resolution	Cell type	Cell size	Lattice design	Specific stiffness N/mm (Load / displacement/ V_f)
$6 \times 3 \times 1$	Truss-based BCC	$30 \times 30 \times 30$	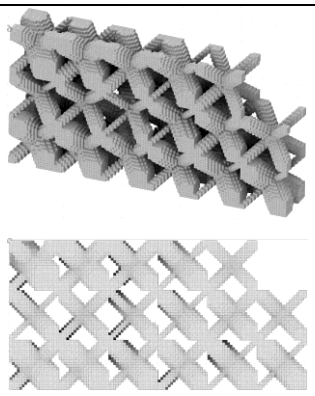	143.9
	Plate-based BCC	$50 \times 50 \times 50$	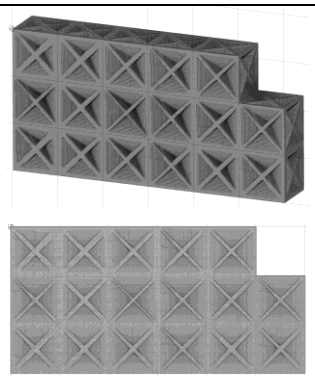	671.4

Table 5: Lattice optimisation results in 3D truss-based and lattice-based BCC

4 CONCLUSIONS

The TO and ML-based lattice optimisation approach was advanced to consider orthotropic material properties and 3D lattice structures. The optimal structures in both orthotropic and isotropic materials were numerically evaluated by computing 3PB test using FEA. The results showed that the optimal lattice structures were stiffer, i.e., had better performance, than their uniform counterparts while the difference was marginal in isotropic materials, possibly due to the difference in boundary conditions. The optimal structures had smaller regions having higher strain energy, resulting in the lower total strain energy, i.e., mechanical compliance.

The 3D lattice optimisation results considering truss-based BCC and plate-based BCC lattices showed a tendency for the graded lattice structures similar to those in 2D cases. The optimal plate-based BCC lattice structure had less-graded structures than the truss-based BCC due to its high surface area. The plate-based BCC lattice outperformed the truss-based BCC lattice, indicating the effectiveness of applying plate-based lattices in the proposed lattice optimisation approach.

This study presented a numerically validated TO and ML-based MM design framework to accelerate the development in the field of composite MMs. Future works will include the extension to other objective functions incorporating buckling, vibration, thermal etc. along with experimental validations.

REFERENCES

[1] J. Fan *et al.*, 'A review of additive manufacturing of metamaterials and developing trends', *Materials Today*, vol. 50, pp. 303–328, Nov. 2021, doi: 10.1016/j.mattod.2021.04.019.

[2] J. B. Berger, H. N. G. Wadley, and R. M. McMeeking, 'Mechanical metamaterials at the theoretical limit of isotropic elastic stiffness', *Nature*, vol. 543, no. 7646, pp. 533–537, Mar. 2017, doi: 10.1038/nature21075.

[3] B. Sun, X. Yan, P. Liu, Y. Xia, and L. Lu, 'Parametric plate lattices: Modeling and optimization of plate lattices with superior mechanical properties', *Additive Manufacturing*, vol. 72, p. 103626, Jun. 2023, doi: 10.1016/j.addma.2023.103626.
[4] Y. Zhu, J. Pan, E. Polyzos, J. Wang, and L. Pyl, 'Design and numerical analysis of perforated plate lattice structures', *Thin-Walled Structures*, vol. 204, p. 112339, Nov. 2024, doi: 10.1016/j.tws.2024.112339.
[5] O. Sigmund, 'Materials with prescribed constitutive parameters: An inverse homogenization problem', *International Journal of Solids and Structures*, vol. 31, no. 17, pp. 2313–2329, Sep. 1994, doi: 10.1016/0020-7683(94)90154-6.
[6] J. P. Groen and O. Sigmund, 'Homogenization-based topology optimization for high-resolution manufacturable microstructures', *International Journal for Numerical Methods in Engineering*, vol. 113, no. 8, pp. 1148–1163, 2018, doi: 10.1002/nme.5575.
[7] R. V. Woldseth, O. Sigmund, and P. D. L. Jensen, 'An 808 line phasor-based dehomogenisation Matlab code for multi-scale topology optimisation', *Struct Multidisc Optim*, vol. 67, no. 12, p. 205, Nov. 2024, doi: 10.1007/s00158-024-03880-1.
[8] D. Lee, W. (Wayne) Chen, L. Wang, Y.-C. Chan, and W. Chen, 'Data-Driven Design for Metamaterials and Multiscale Systems: A Review', *Advanced Materials*, vol. 36, no. 8, p. 2305254, 2024, doi: 10.1002/adma.202305254.
[9] J. Wang and A. Panesar, 'Machine learning based lattice generation method derived from topology optimisation', *Additive Manufacturing*, vol. 60, p. 103238, Dec. 2022, doi: 10.1016/j.addma.2022.103238.
[10] E. Andreassen and C. S. Andreasen, 'How to determine composite material properties using numerical homogenization', *Computational Materials Science*, vol. 83, pp. 488–495, Feb. 2014, doi: 10.1016/j.commatsci.2013.09.006.
[11] G. Dong, Y. Tang, and Y. F. Zhao, 'A 149 Line Homogenization Code for Three-Dimensional Cellular Materials Written in matlab', *Journal of Engineering Materials and Technology*, vol. 141, no. 1, p. 011005, Jan. 2019, doi: 10.1115/1.4040555.
[12] 'Datasheets'. Accessed: Jun. 23, 2025. [Online]. Available: https://markforged.com/datasheets
[13] 'Standard Test Method for Flexural Properties of Polymer Matrix Composite Materials'. Accessed: Jun. 23, 2025. [Online]. Available: https://store.astm.org/d7264_d7264m-15.html
[14] T. Tancogne-Dejean, M. Diamantopoulou, M. B. Gorji, C. Bonatti, and D. Mohr, '3D Plate-Lattices: An Emerging Class of Low-Density Metamaterial Exhibiting Optimal Isotropic Stiffness', *Advanced Materials*, vol. 30, no. 45, p. 1803334, 2018, doi: 10.1002/adma.201803334.

ICCM24
AUGUST 4-8, 2025
BALTIMORE CONVENTION CENTER
BALTIMORE, MARYLAND, USA

No Technical Paper Submission for:

Ahmed Afzal

MECHANICAL RECYCLING OF GLASS FIBER REINFORCED WIND TURBINE BLADE COMPONENTS INTO PELLET-BASED FEEDSTOCKS FOR ADDITIVE MANUFACTURING

Dimitrij Seibert[1,*], Andrej Fehler[1], Jan Bürgener[1], Philipp Johst[1], Robert Böhm[1]

[1]Faculty of Engineering, HTWK Leipzig – University of Applied Sciences
Karl-Liebknecht-Straße 132, D-04277 Leipzig, Germany
Email: dimitrij.seibert@htwk-leipzig.de (corresponding author), andrej.fehler@htwk-leipzig.de, jan.buergener@htwk-leipzig.de, philipp.johst@htwk-leipzig.de, robert.boehm@htwk-leipzig.de
web page: https://fing.htwk-leipzig.de/forschung-transfer/leichtbau-mit-verbundwerkstoffen/composite-circularity-lab

Keywords: Wind turbine blades, Composite material, Mechanical recycling, 3D printing, Computed Tomography

ABSTRACT

The rapid growth of the wind energy sector is expected to generate a significant amount of end-of-life (EoL) fiber-reinforced polymer (FRP) waste as wind turbines reach their 20–25-year lifespan. By 2050, Europe is expected to accumulate around 7.6 million tons of FRP from decommissioned wind turbine blades (WTBs). Among the different disposal strategies, mechanical recycling is the most discussed due to its sustainability. This research investigates the reuse of mechanically recycled glass fiber reinforced polymers (GFRP) in 3D printing, specifically in the production of reinforced acrylonitrile butadiene styrene (ABS) pellets. Tensile samples with different fiber content are produced using a fused granulate fabrication (FGF) 3D printer and analyzed by X-ray micro-computed tomography (µCT) and mechanical testing. The findings demonstrate the viability of incorporating recycled WTB materials into engineering thermoplastic composites, thereby enhancing their mechanical properties. Further research is needed to maximize the recycled content while meeting the performance criteria for demanding applications.

1 INTRODUCTION

The rapid expansion of the wind energy sector is expected to lead to a significant amount of end-of-life (EoL) fiber reinforced polymer (FRP) material stream in the coming years. This challenge arises as wind turbines blades (WTBs), which are primarily made of FRPs [1], reach the end of their initial 20 - 25 year life cycle [2]. According to Lahuerta *et al.* [3], approximately 7.6 million tons of FRP EoL WTB material mass will be generated in Europe by 2050. For Germany a total mass of EoL WTB of 689 kt is estimated [4].

Various strategies have been proposed and implemented in response to this impending material stream. The concept of different ‘R's’ to manage EoL WTB materials, emphasizing reduction, reuse, recycling, recovery, and redesign [5]. According to Lund and Madsen [6], mechanical recycling is the most frequently discussed ‘R’-strategy in the literature for the management of EoL WTB materials. The recycling process includes a series of mechanical operations, such as cutting, shredding, grinding or crushing the WTB. These operations are intended to reduce the size of the resin and fibers or to separate them for further processing or direct use in secondary products [7]. Studies, such as those by Delvere *et al.* [8], have concluded that mechanical recycling is currently the most sustainable recycling technology for FRP WTBs, based on comprehensive sustainability criteria.

Mamanpush *et al.* [9] demonstrated the feasibility and potential of mechanically recycled WTB materials in the production of high-performance composites. For instance, recycled glass fiber reinforced polymers (rGFRPs) have been used in noise barriers [10], as a filler in concrete [11], and in sheet molding compounds [12]. Recent advancements have also explored the use of mechanically recycled fibers in 3D printing materials. In [13] it is demonstrated that recycled FRP could replace virgin fibers in additive manufacturing while maintaining mechanical integrity. Furthermore, several studies

by Rahimizadeh *et al*. ([14-17]) have investigated the integration of rGFRP materials with polylactic acid (PLA) in 3D printing, showing improvements in strength and modulus compared to neat PLA samples, despite some reductions in tensile strength and failure strain.

Building on recent advancements in the field of composite mechanical recycling, this research investigates the reuse of mechanically recycled GFRP materials in 3D-printing applications. The focus is on the optimized production of reinforced acrylonitrile butadiene styrene (ABS) composites incorporating rGFRP. Employing a pellet-based approach using fused granular fabrication (FGF) instead of filament-based fused deposition modeling (FDM) simplifies the printing process by reducing feedstock quality requirements. Furthermore, FGF and large-format additive manufacturing enable the direct reuse of recycled fiber-reinforced polymer (rFRP) granulate, making them highly effective for industrial-scale recycling and the scalable integration of composite EoL material into new large-scale applications [18, 19]. This approach aims to increase recyclate incorporation while ensuring the mechanical integrity required for technical-grade applications.

2 MATERIALS AND METHODS

2.1 EoL WTB Material

For the present study, EoL WTB segments from an E40/6 wind turbine (Enercon, Germany) are selected as the source material. These segments are obtained through perpendicular cuts along the WTB length (see Figure 1a). The spar caps are cut out of the WTB segment through the utilization of a panel saw equipped with a diamond-tipped circular blade. The selection of these components is driven by their high glass fiber volume content and structural homogeneity, especially in comparison to the shear web and sandwich regions (see Figure 1b). The resulting spar cap material (see Figure 1c), which serves as the feedstock for subsequent mechanical size reduction, is composed of unidirectional glass fiber laminates embedded in an epoxy matrix. The glass fiber volume content of the spar cap material in an E40/6 WTB is estimated at approximately 57 % (calculated with a calcination process using a glass fiber density of 2.48 g*cm^{-3} (measured with a pycnometer) and a matrix density of 1.2 g*cm^{-3} [20]).

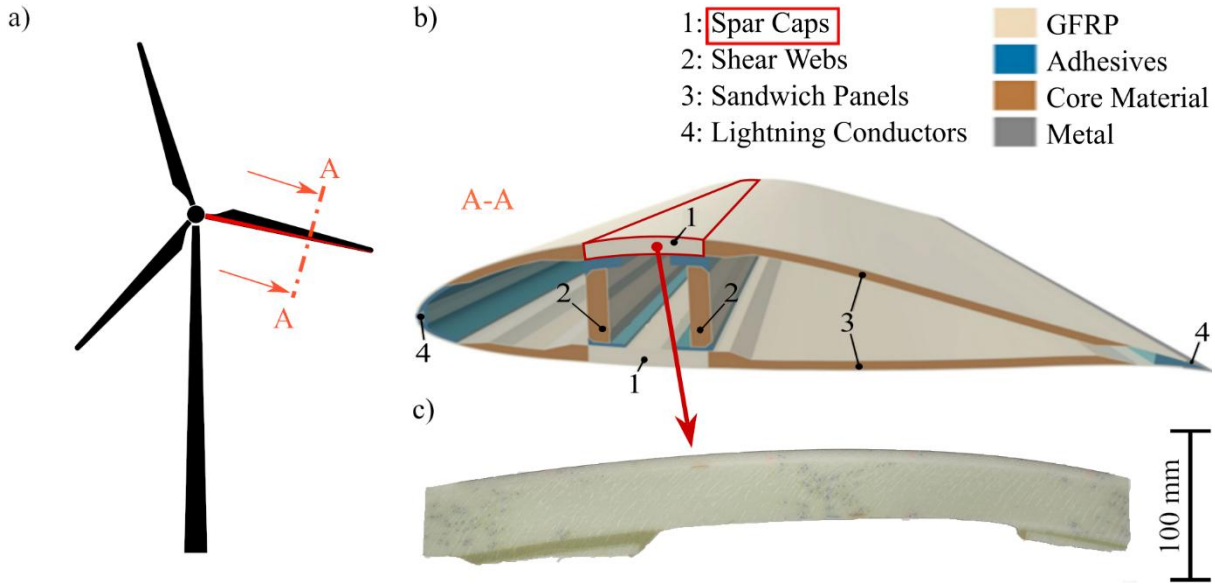

Figure 1: (a) Cutting section perpendicular to the length of the wind turbine blade (WTB); (b) Schematic cross-section of an E40/6 WTB (based on [21]); (c) Spar cap material used in this study for the shredding process.

2.2 Shredding and Sieving Process

To enable further processing, the previously prepared material is shredded using the GP20 Hybrid granulation system (3devo B.V., Utrecht, Netherlands), which combines a twin-shaft shredder and a rotary mill. The shredder features two counter-rotating shafts, each with seven blades bearing three teeth, while the milling stage includes a rotary cutter with three edges and a 3.4 mm sieve. The material is processed three times to ensure consistent fiber shortening and homogenization. The mixture is then dry-sieved using a sieve shaker (AS 200 Control, Retsch GmbH, Haan, Germany) with mesh sizes of 250 µm, 100 µm, and 63 µm. In the following, remaining material on the sieves (see Figure 2) is referred to as the "oversize fraction" (OF) in combination with the corresponding mesh size, e.g. OF>100. The OF>250 was further milled using a laboratory cutting mill (MF 10 basic Cutting Mill, IKA-Werke GmbH & Co. KG, Staufen, Germany) fitted with a 2 mm sieve to increase yield in the desired size ranges. For subsequent processing the OF>100 and OF>63 are selected.

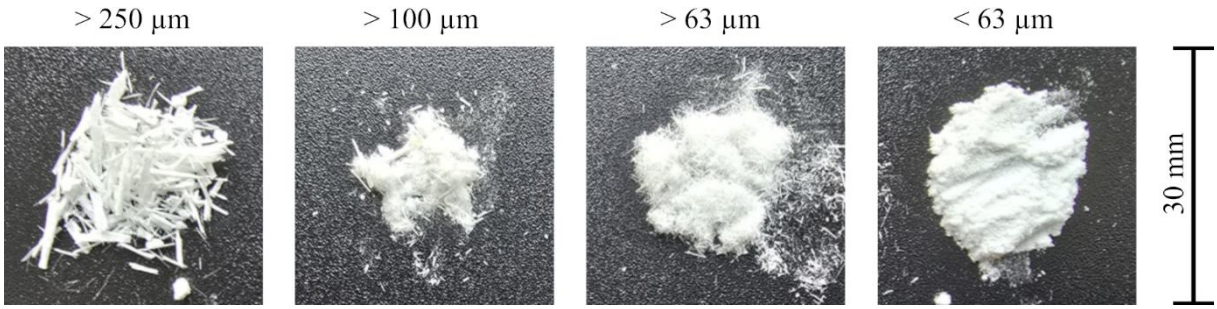

Figure 2: Comparison of the oversize fractions.

2.3 Compounding and 3D-Printing

The OF>100 and OF>63 are compounded with virgin ABS (vABS) powder (Magnum™ 3513, INEOS Styrolution, Germany) with two different weight ratios. This results in five material variants: Neat vABS and four rGFRP compounds. ABS-rGF10/100 and ABS-rGF20/100 containing 10 wt% and 20 wt% rGFRP from the OF>100, respectively, as well as ABS-rGF10/63 and ABS-rGF20/63 containing 10 wt% and 20 wt% rGFRP from the OF>63 (Figure 3).

Dry mixing is followed by homogenization in a low-speed laboratory mixer until visual uniformity in fiber distribution and color is achieved. According to the specifications outlined in the Magnum™ 3513 datasheet, all materials are dried at a temperature of 80 °C for a duration of four hours in a convection oven. This procedure is conducted to remove residual moisture and prevent pore formation and surface defects caused by vapor expansion during extrusion.

The resulting compounds, along with vABS as reference, are extruded into continuous filaments using a Filament Maker ONE Composer 450 single-screw extruder (3devo, Netherlands). Parameters are chosen according to 3devo extrusion report for Magnum™ 3513 (heat zones h4-h1: 215, 225, 235, 245 °C with 2 mm nozzle diameter). The filaments are pelletized using an open-source pelletizer, printed out of vABS to minimize contamination.

Tensile samples are manufactured using a FGF 3D printer (Tumaker NX300 Modular, Tumaker S.L., Irun, Spain), equipped with a pellet extruder comprising two independently controlled heating zones and a 0.8 mm diameter hardened steel nozzle to mitigate abrasive wear from the rGFRP feedstocks. Tensile sample dimensions follow ISO 527-4 (Type 2) and are 250 × 25 × 2 mm (L × W × T). They are printed sequentially on a heated build plate set to 100 °C, with cooling fans deactivated. Slicing is performed using Simplify3D (Simplify3D LLC, Cincinnati, USA), applying a layer height of 0.2 mm, no outer perimeters, no top or bottom layers, and a 100 % infill with aligned pattern oriented parallel to the tensile load direction. Extrusion multipliers are calibrated individually for each compound to ensure closed layers and dimensional accuracy. Values range from 100 % for vABS to 118 % for ABS-rGF20/100. To provide an overview of the processing of the 3D-printed tensile samples, the procedure is summarized schematically in Figure 3.

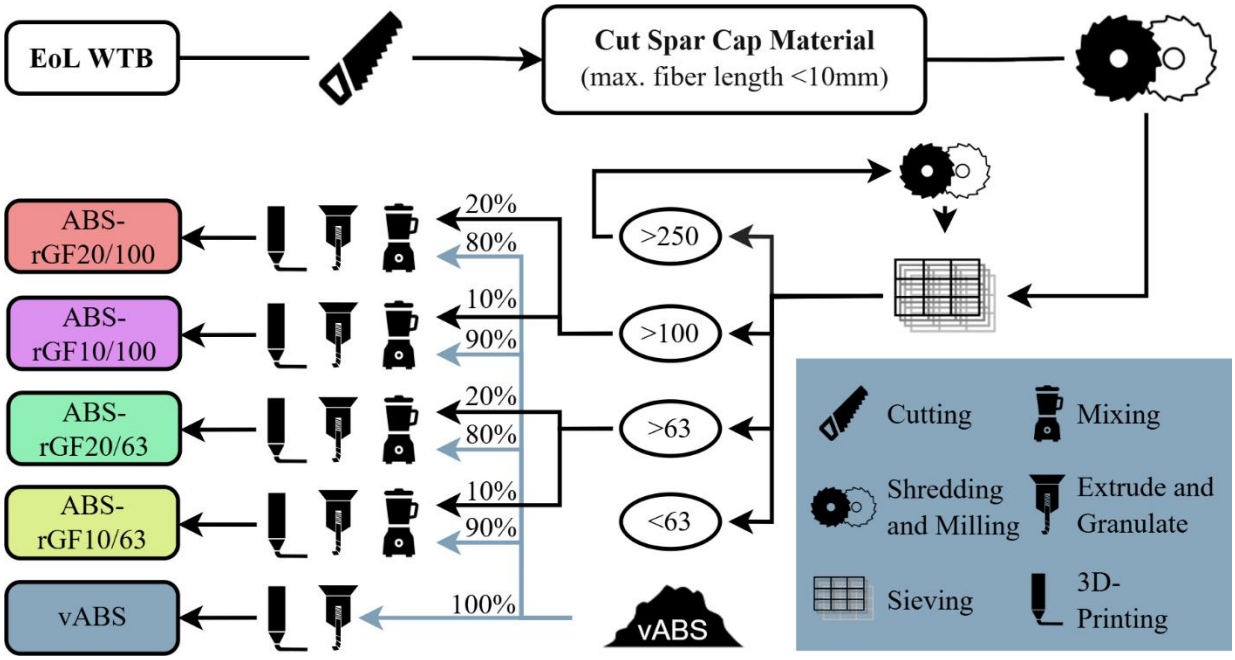

Figure 3: Schematic representation of the processing route from EoL WTB to 3D-printed tensile samples.

2.4 Material Characterization of recyclates and tensile samples

In order to characterize the EoL WTB recyclates, the fiber mass and volume content of each OF is determined through calcination tests according to ISO 1172 and ISO 1183-1 (glass fiber density of 2.48 g*cm^{-3} and matrix density of 1.2 g*cm^{-3}). Particle size and shape are analyzed using the dynamic image analysis system QICPIC with the LIXELL wet dispersion module (Sympatec GmbH, Clausthal-Zellerfeld, Germany), following ISO 9276 and ISO 13322-2. Samples are dispersed in distilled water, homogenized by stirring, and treated with surfactant. Each sample is measured three times from two independent subsamples to ensure repeatability. Size distributions are evaluated as volume-based density $q_3^*(x)$. Calcinated fiber samples (OF>63 and OF>100) are described by fiber length (LEFI) and fiber diameter (DIFI). Particle shape is assessed via elongation and straightness. Volume is calculated using a cylindrical mode. Characterization of vABS is estimated by equal projected circle diameter (EQPC).

To characterize the tensile samples, X-ray micro-computed tomography (µCT) is conducted on one randomly chosen printed rGFRP sample per compound using a high-resolution system (Phoenix Nanotom M, Waygate Technologies GmbH, Wunstorf, Germany) to evaluate internal structure, porosity and fiber volume content. Scans are performed using *datos|x* software. Image processing and volumetric analysis are carried out using *VGSTUDIO MAX 2023.1* (Volume Graphics GmbH, Heidelberg, Germany). Fiber volume content and porosity are quantified via manual segmentation of a selected region of interest (ROI), located within the interior of the sample to exclude surface effects and ensure that surface roughness does not affect the measurements. Segmentation was based on the gray value histogram using the ISO50 threshold method, in accordance with the general guidelines of ISO 15708-3. The applied scan parameters are listed in Table 1.

Mechanical testing of the printed samples (n=20 for each variant) is conducted in accordance with ISO 527-1. Prior to testing, samples are conditioned under standard laboratory climate (23 °C, 50 % relative humidity). A universal testing machine (Zwick Roell Z050, ZwickRoell GmbH & Co. KG, Germany) is used to determine tensile strength, Young's modulus, strain at break and tensile stress at break.

Table 1: Parameters used for µCT-scans.

Parameter	Unit	Value
Tube voltage	kV	100
Tube current	µA	110
Focus-detector-distance (FDD)	mm	290
Focus-object-distance (FOD)	mm	7.5
Voxel size	µm	2.6
Number of projections	-	2500
Binning	-	1
Averaging	-	3

3 RESULTS

3.1 Characterization of recyclates

The mean fiber mass content of the OF>63 and OF>100 are 76.03 wt% and 78.36 wt%, respectively. This corresponds to fiber volume content of approximately 60.54 % and 63.67 %. The distribution curves of OF>63 and OF>100 are shown in Figure 4.

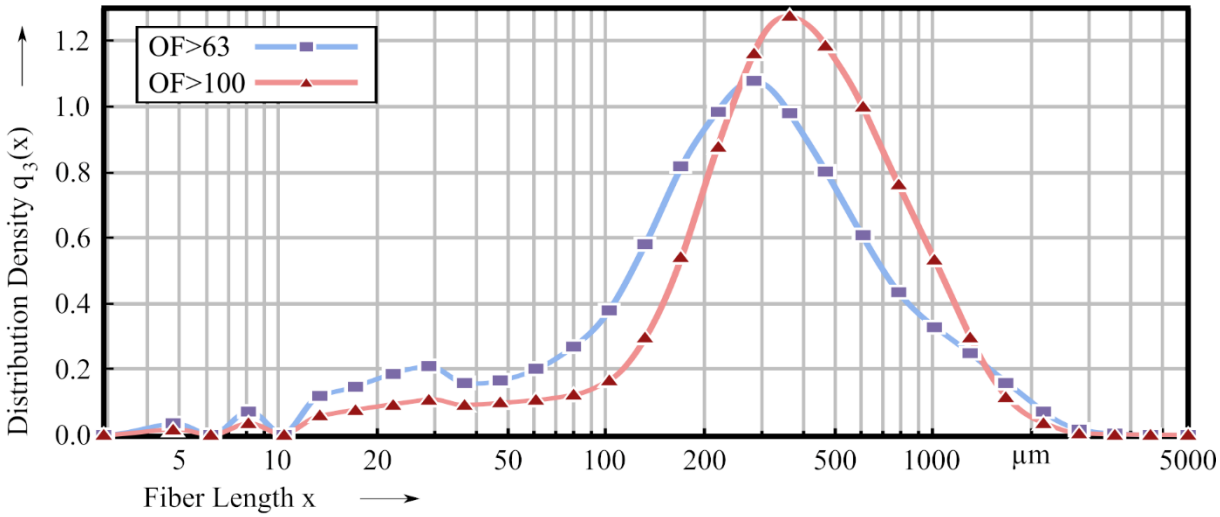

Figure 4: Fiber length distribution density curves of the OF>63 and OF>100.

Both curves show right-skewed profiles with a broad spread of fiber lengths. OF>63 exhibits a wider distribution in the lower length range, with a gradual rise and a long tail extending toward higher lengths. The cumulative curve increases more steadily, indicating a relatively even spread of shorter and medium-length fibers. In contrast, OF>100 shows a steeper rise in the cumulative curve at longer lengths, reflecting a larger proportion of long fibers. Its density curve is shifted to the right, with a more pronounced peak at longer fiber lengths compared to OF>63.

The vABS sample shows a median EQPC of 147 µm. OF>63 fibers range (Figure 4) from 40 to 852 µm in length (x_{50}=263 µm), while OF>100 fibers are longer overall, ranging from 106 to 926 µm (x_{50}=371 µm). The shift toward higher fiber lengths in OF>100 is also reflected in the cumulative distribution. Fiber diameters are similar in both samples, with median values of approximately 22 µm. This indicates a higher proportion of long fibers in OF>100 compared to OF>63. The key parameters are summarized in Table 2.

Table 2: Key parameters for all analyzed materials.

Variant	Value	Unit	X_{10}	X_{50}	X_{90}
vABS	EQPC	µm	45.76	147.42	345.56
OF>63	LEFI	µm	40.46	262.55	851.81
	DIFI	µm	15.59	22.01	28.07
OF>100	LEFI	µm	105.56	371.01	925.58
	DIFI	µm	17.18	22.42	28.31

3.2 Characterization of tensile samples

The µCT analysis shows clear differences in internal structure, porosity and fiber volume content among the different compounds used for the tensile samples (see Figure 5).

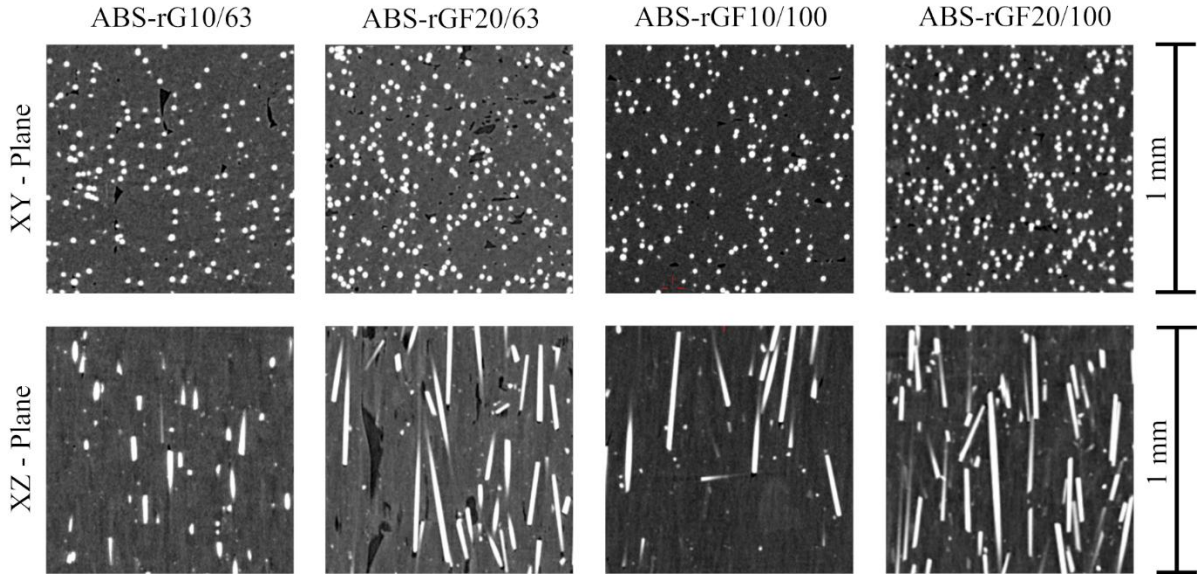

Figure 5: Cut out of cross-sections from the ROI in XY- and XZ-plane from the tensile samples of each compound.

For ABS-10rGF/63 and ABS-10rGF/100, the fiber volume content is approximately 5 vol%. ABS-20rGF/63 and ABS-20rGF/100 variants show an increased amount of approximately 9 vol%. A generally homogeneous fiber distribution is visible, with occasional fiber agglomerations. A preferred fiber orientation corresponding to the 3D printing paths is observed. Porosity within the ROIs ranges from 0.62 vol% to 1.58 vol%. The fiber volume content and porosity are summarized in Table 3.

Table 3: µCT-based quantification of fiber volume content and porosity in tensile samples of different compounds using ISO50 threshold values.

Parameter	Value	ABS-10rGF/63	ABS-20rGF/63	ABS-10rGF/100	ABS-20rGF/100
Fiber volume content	%	5.04	9.26	5.01	9.04
Porosity	%	1.04	1.58	0.62	0.91

The tensile tests results show improvements in stiffness and strength for all tested rGFRP samples compared to the vABS. Fracture occurs perpendicular to the loading axis in all variants (see Figure 6a). While vABS exhibits a distinct yield point, stress plateau, and extensive post-yield deformation, all rGFRP samples show a steeper slope with nearly linear elastic behavior up to failure with lower strain, lacking a visible yield point, except ABS-rGF10/63 (see Figure 6b and 6e). This finding suggests a shift in failure behavior due to the reinforcement with chopped fibers coming from EoL WTB spar cap material. An increase in mechanical properties from 10 wt% to 20 wt% compounds is observed. The greatest improvements in mechanical properties are observed for ABS-rGF20/63 with an increase of 101 % in Young's modulus and 27 % in tensile strength in comparison to vABS (see Figure 6c and Figure 6d). Tensile strain at failure reduces among all rGFRP compounds. Values decreased by 79 to 89 % compared to the reference. The increase in Young's modulus and tensile strength by increasing the fiber mass content from 10 wt% to 20 wt% is greater for OF>63 than for OF>100. Furthermore, the greatest dispersion was observed for ABS r20GF/100.

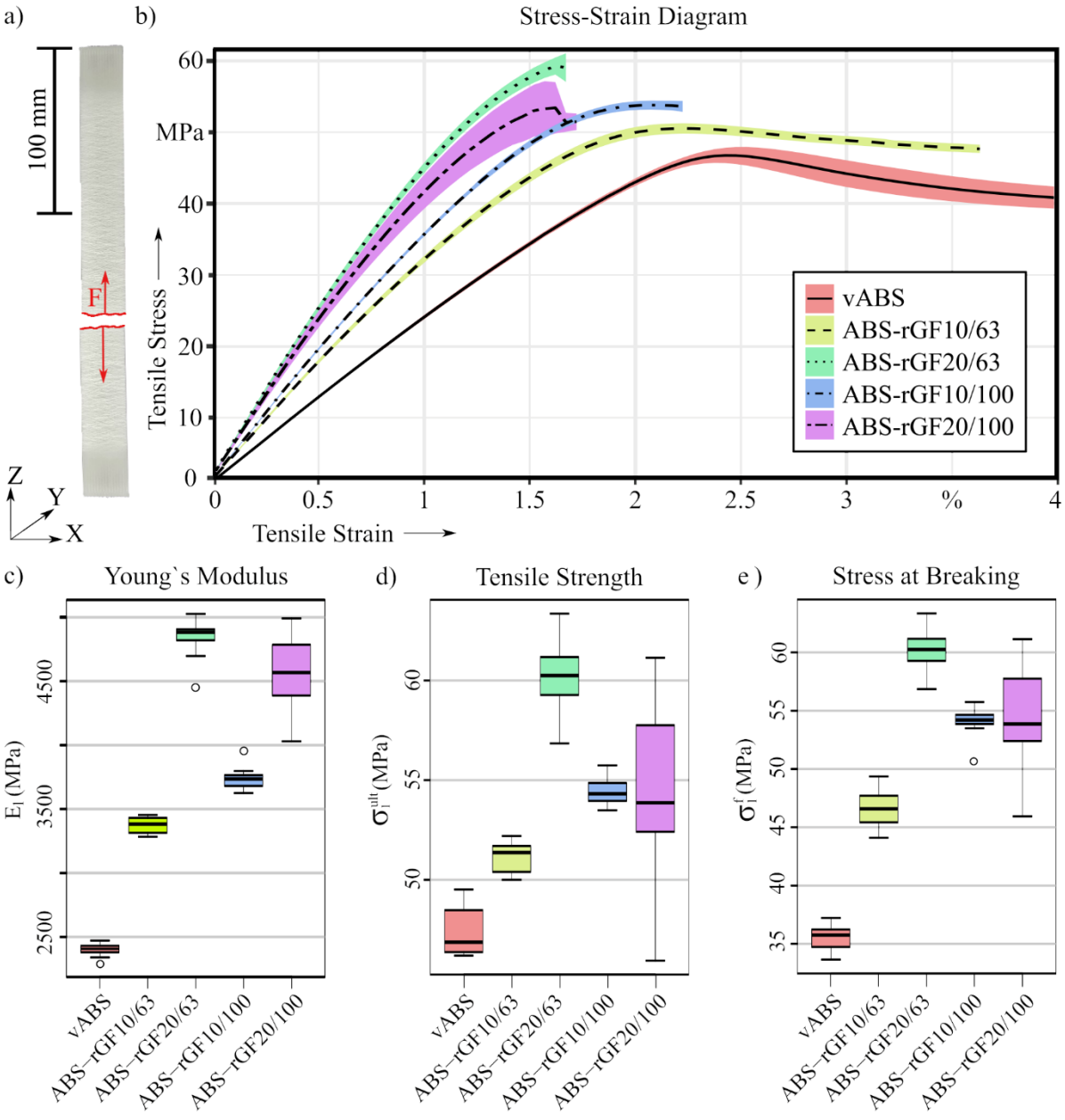

Figure 6: Mechanical testing of vABS and rGFRP samples: (a) tensile sample after testing; (b) mean stress–strain curves; (c) Young's modulus; (d) ultimate tensile strength; (e) stress at break.

The tensile test results are summarized in Table 4, which lists the engineering constants with mean values and standard deviations.

Table 4: Tensile test results: Youngs-Modulus (E_1), tensile strength (σ_1^{ult}), stress at break (σ_1^f) and strain at break (ε_1^f).

Engineering constant	Unit	vABS	ABS-rGF10/63	ABS-rGF20/63	ABS-rGF10/100	ABS-rGF20/100
E_1	MPa	2402±42	3367±61.4	4839±142	3734±74.3	4587±237
σ_1^{ult}	MPa	47.4±1.16	51.1±0.74	60.2±1.72	54.4±0.64	54.6±3.61
σ_1^f	MPa	35.6±1.57	46.6±1.57	60.2±1.72	54.2±1.02	54.6±3.62
ε_1^f	%	30.9±10	6.3±0.79	3.3±0.14	3.9±0.21	3.4±0.26

4 DISCUSSION

The incorporation of 10 wt% rGFRP into printed samples resulted in an enhancement in stiffness and strength, without compromising printability for either OF. The low porosity values and homogeneously distributed fibers in µCT scans provide further evidence to support these findings. The use of vABS powder in the compounding process facilitates generally homogeneous fiber distribution, thereby ensuring consistent processing and mechanical behavior.

Conversely, combinations of elevated recyclate content and coarser sieve fractions (OF>100) result in increased variability in mechanical properties and diminished surface quality. This phenomenon is likely attributable to impaired flow and printability, particularly when employing a 0.8 mm nozzle. Local printing defects and material inhomogeneities, including fiber agglomerations, have been identified as additional contributing factors to the observed deviations. These findings underscore the necessity of optimizing print parameters.

The measured fiber volume content of the rGFRP indicates that only small amounts of matrix material are lost during the mechanical recycling. In comparison to the initial spar cap material with approximately 57 vol%, the OF>63 and OF>100 show an increase of about 6.2 % and 11.7 %, respectively.

Fiber length and distribution have been identified as pivotal factors influencing both mechanical performance and processing behavior. The successful integration of short, mechanically recycled GFRP, which is often considered low-value residue, demonstrates its potential for use in circular material flows. The purely mechanical preparation route avoids pyrolysis or chemical treatment, thereby simplifying material recovery and enabling direct reuse in thermoplastic matrices.

The present study focuses on ABS in powder form and GFRP derived from EoL WTB spar cap material. While the method is applicable to other thermoplastics and WTB sections, components such as shear webs or sandwiches generally exhibit lower fiber content and higher levels of contaminants (e.g., balsa wood, polyurethane foam). These materials may necessitate supplementary separation or pretreatment procedures, such as air classification or density-based sorting, to yield recyclates suitable for further utilization. Furthermore, the mechanical test data and µCT-based structural information may serve as a valuable basis for developing numerical simulation models of rGFRP-based components. These models have the potential to facilitate design optimization and material performance prediction in the field of additive manufacturing. In order to further validate these findings, it will be necessary to characterize additional parameters in subsequent studies. These additional parameters may include, but are not limited to, local fiber orientation, orientation distribution, and fiber-matrix interface quality.

5 CONCLUSIONS

The present study demonstrates the feasibility of mechanically recycled GFRP materials from EoL WTB spar caps into thermoplastic composites suitable for large-scale additive manufacturing. The applied process chain, which is entirely dependent on mechanical recycling steps such as cutting, shredding, milling, and sieving, enables the production of high-fiber-content recyclates. These recyclates are successfully compounded with ABS powder and processed via FGF.

These findings indicate that energy- and resource-intensive recycling methods, such as pyrolysis, are not necessary to produce compatible feedstocks for thermoplastic matrices. This contributes to the expansion of existing recycling strategies for WTBs beyond the practices of downcycling or incineration, thereby facilitating more circular material flows in accordance with established R-strategies. The developed process chain provides a scalable and transferable framework for the further utilization of fiber-rich WTB residues. To achieve the optimal utilization of this material, future research should prioritize increasing the recycled content while maintaining the processability and performance of the material.

ACKNOWLEDGEMENTS AND FUNDING

Our thanks go to Sebastian Blanke from the chemistry laboratory at MNZ, HTWK Leipzig, for his invaluable technical support. We also gratefully acknowledge Sympatec GmbH for conducting the fiber length and particle size analyses. Furthermore, we thank Enercon GmbH, Magdeburg, for kindly providing end-of-life wind turbine blades used in this study.

The study has been performed within the HORIZON-CL4-2021-RESILIENCE-01 project "European recycling and circularity in large composite components (EuReComp)", call "A Digitized, Resource-Efficient and Resilient Industry 2021", HORIZON Research and Innovation Actions, Contract Number 101058089. Views and opinions expressed are however those of the author(s) only and do not necessarily reflect those of the European Union or HADEA. Neither the European Union nor HADEA can be held responsible for them. This research was supported by the Deutsche Forschungsgemeinschaft (DFG), which funded the acquisition of the X-ray CT system.

REFERENCES

[1] L. Fingersh, M. Hand, and A. and Laxson, Wind Turbine Design Cost and Scaling Model, Accessed: Feb. 2, 2023. [Online]. Available: https://www.nrel.gov/docs/fy07osti/40566.pdf

[2] S. K. Gopalraj and T. Kärki, A review on the recycling of waste carbon fibre/glass fibre-reinforced composites: fibre recovery, properties and life-cycle analysis, *SN Appl. Sci.*, **2**, *2020* (doi: 10.1007/s42452-020-2195-4).

[3] F. Lahuerta *et al.,* Decommissioning Inventory for Wind Turbine Blades Installed Until 2022 in Europe, *Mater Circ Econ*, **5**, *2023* (doi: 10.1007/s42824-023-00084-8).

[4] P. Johst, M. Bühl, C. Enderle, R. Kupfer, N. Modler and R. Böhm, Forecasting wind turbine blade waste with material composition and geographical distribution: Methodology and application to Germany, *Resources, Conservation and Recycling*, **211**, *2024* (doi: 10.1016/j.resconrec.2024.107876).

[5] J. Potting, M. Hekkert, E. Worrell and A. and Hanemaaijer, Circular Economy: Measuring innovation in the product chain, *2017* Accessed: Jan. 25, 2023. [Online]. Available: https://www.pbl.nl/sites/default/files/downloads/pbl-2016-circular-economy-measuring-innovation-in-product-chains-2544.pdf

[6] K. W. Lund and E. S. Madsen, State-of-the-art value chain roadmap for sustainable end-of-life wind turbine blades, *Renewable and Sustainable Energy Reviews*, **192**, *2024* (doi: 10.1016/j.rser.2023.114234).

[7] J. P. Jensen and K. Skelton, Wind turbine blade recycling: Experiences, challenges and possibilities in a circular economy, *Renewable and Sustainable Energy Reviews*, **97**, *2018*, pp. 165–176 (doi: 10.1016/j.rser.2018.08.041).

[8] I. Delvere, M. Iltina, M. Shanbayev, A. Abildayeva, S. Kuzhamberdieva and D. Blumberga, Evaluation of Polymer Matrix Composite Waste Recycling Methods, *Environmental and Climate Technologies*, **23**, *2019*, pp. 168–187 (doi: 10.2478/rtuect-2019-0012).

[9] S. H. Mamanpush, H. Li, K. Englund and A. T. Tabatabaei, Recycled wind turbine blades as a feedstock for second generation composites, *Waste management (New York, N.Y.)*, **76**, *2018*, pp. 708–714 (doi: 10.1016/j.wasman.2018.02.050).

[10] R. Fonte and G. Xydis, Wind turbine blade recycling: An evaluation of the European market potential for recycled composite materials, *Journal of environmental management*, **287**, *2021* (doi: 10.1016/j.jenvman.2021.112269).
[11] A. Yazdanbakhsh, L. C. Bank, K.-A. Rieder, Y. Tian and C. Chen, Concrete with discrete slender elements from mechanically recycled wind turbine blades, *Resources, Conservation and Recycling*, **128**, *2018*, pp. 11–21 (doi: 10.1016/j.resconrec.2017.08.005).
[12] A. Azapagic, L. Stamford, L. Youds and C. Barteczko-Hibbert, Towards sustainable production and consumption: A novel DEcision-Support Framework IntegRating Economic, Environmental and Social Sustainability (DESIRES), *Computers & Chemical Engineering*, **91**, *2016*, pp. 93–103 (doi: 10.1016/j.compchemeng.2016.03.017).
[13] A. Romani, A. Mantelli, R. Suriano, M. Levi and S. Turri, Additive Re-Manufacturing of Mechanically Recycled End-of-Life Glass Fiber-Reinforced Polymers for Value-Added Circular Design, *Materials (Basel, Switzerland)*, **13**, *2020* (doi: 10.3390/ma13163545).
[14] A. Rahimizadeh, J. Kalman, K. Fayazbakhsh and L. Lessard, Recycling of fiberglass wind turbine blades into reinforced filaments for use in Additive Manufacturing, *Composites Part B: Engineering*, **175**, *2019* (doi: 10.1016/j.compositesb.2019.107101).
[15] A. Rahimizadeh, J. Kalman, K. Fayazbakhsh and L. Lessard, Mechanical and thermal study of 3D printing composite filaments from wind turbine waste, *Polymer Composites*, **42**, *2021*, pp. 2305–2316 (doi: 10.1002/pc.25978).
[16] A. Rahimizadeh, J. Kalman, R. Henri, K. Fayazbakhsh and L. Lessard, Recycled Glass Fiber Composites from Wind Turbine Waste for 3D Printing Feedstock: Effects of Fiber Content and Interface on Mechanical Performance, *Materials (Basel, Switzerland)*, **12**, *2019* (doi: 10.3390/ma12233929).
[17] A. Rahimizadeh, M. Tahir, K. Fayazbakhsh and L. Lessard, Tensile properties and interfacial shear strength of recycled fibers from wind turbine waste, *Composites Part A: Applied Science and Manufacturing*, **131**, *2020* (doi: 10.1016/j.compositesa.2020.105786).
[18] M. Korey *et al.,* Recycling polymer composite granulate/regrind using big area additive manufacturing, *Composites Part B: Engineering*, **256**, *2023* (doi: 10.1016/j.compositesb.2023.110652).
[19] F. Pignatelli and G. Percoco, An application- and market-oriented review on large format additive manufacturing, focusing on polymer pellet-based 3D printing, *Prog Addit Manuf*, **7**, *2022*, pp. 1363–1377 (doi: 10.1007/s40964-022-00309-3).
[20] H. Schürmann, Konstruieren mit Faser-Kunststoff-Verbunden: *Mit 39 Tabellen,* 2nd ed. (VDI-/Buch]). Berlin, Heidelberg: Springer, 2007.
[21] P. Johst *et al.,* Identification and Environmental Assessments for Different Scenarios of Repurposed Decommissioned Wind Turbine Blades, *Mater Circ Econ*, **5**, *2023* (doi: 10.1007/s42824-023-00085-7).

Enabling All-Composite Pressure Vessels Through Integrated Electrospun Nanofiber Architectures

Jaejun Bae[1], Jeho Jin[1], Sunghwan Park[2], Jaeho Yun[2], Jeonyoon Lee[1,†]

[1] Department of Aerospace Engineering, Korea Advanced Institute of Science and Technology (KAIST)

[2] Technologies R&D Team 2, Launch Vehicle R&D Center, Hanwha Aerospace

ICCM24

24TH INTERNATIONAL CONFERENCE ON COMPOSITE MATERIALS

KAIST

Copyright 2025 All rights reserved.

Laboratory for Advanced Materials and Processes

Contents

1. Research background
2. Objective & Approach
3. Fabrication & Process
4. Result & Discussion
5. Conclusion

Research background

Increase in Utilization of Composites in Aerospace Structure

- Due to the need for **lightweight structures** in the aerospace industry, demand for composites has significantly increased.
- For instance, the **Boeing 787** uses **composite materials** about 50% of its weight. [1]
- Furthermore, **1st and 2nd stage forward fuselage** and **payload fairing** of **Nuri (Korea Space Launch Vehicle-Ⅱ).** use **composite material** to reduce the weight of launch vehicle.

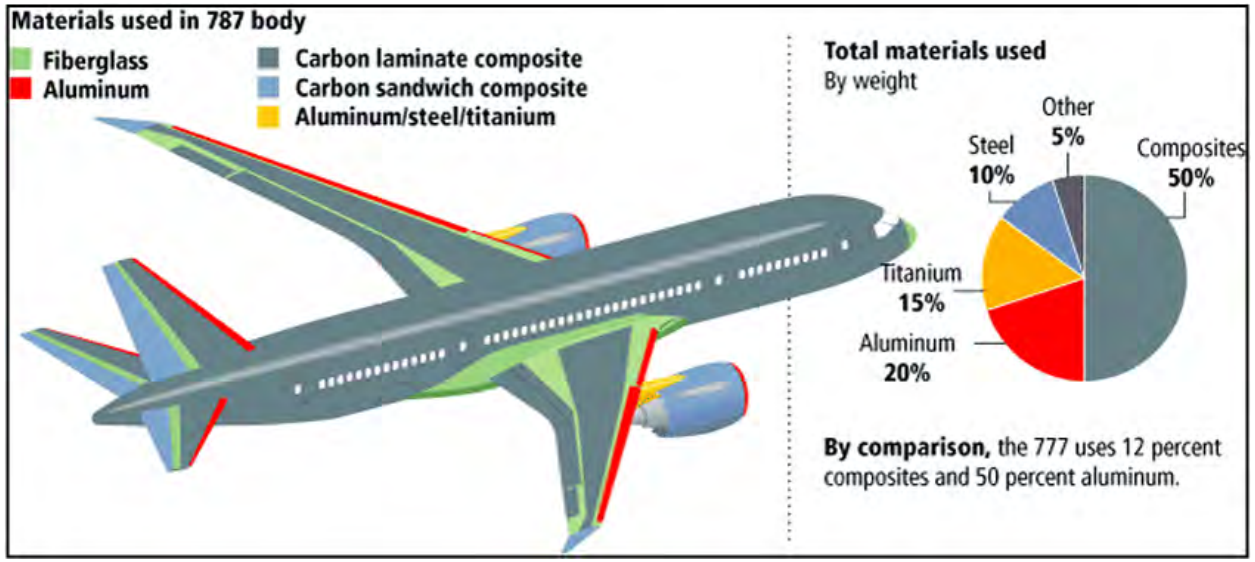

<Use of composite materials in Boeing 787 [1]>

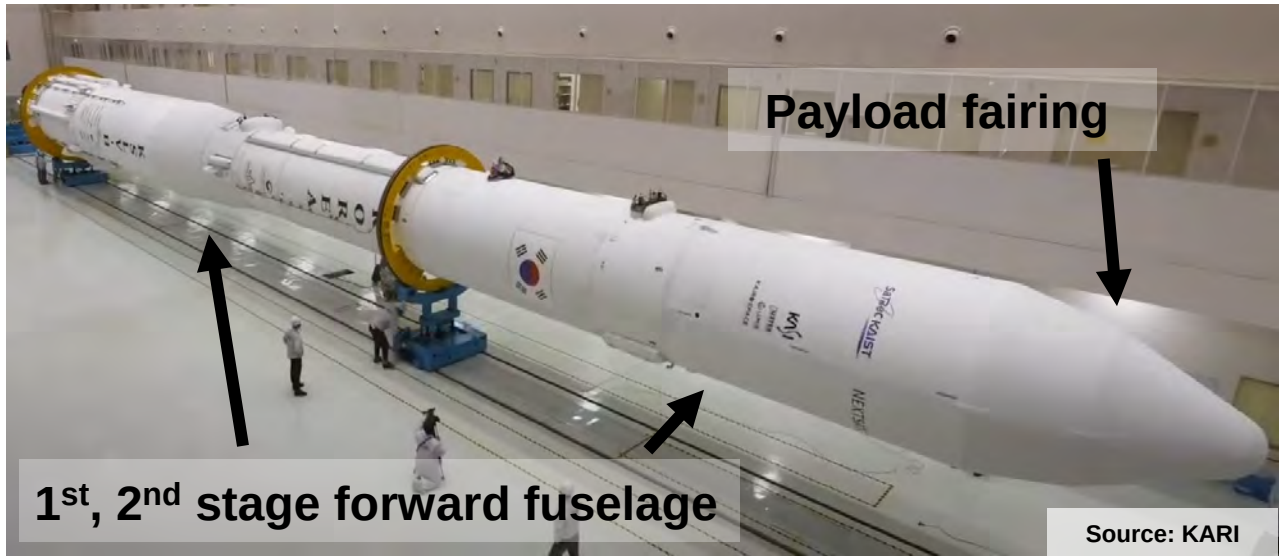

<Use of composite materials in Nuri>

[1] Tanasa F et al. Int. conf. of scientific paper AFASES, Brasov, 2013. 23-25 May.

Composite Application in Aerospace Industry: Composite Overwrapped Pressure Vessel (COPV)

- By changing the **material from metal to composites** in a pressure vessel, approximately **70% weight reduction** can be achieved. [2]
- Space launch companies and research institutions are continuously conducting research to replace **metal fuel tanks in launch vehicles with COPVs**.



<Composite LOX tank for launch vehicle>

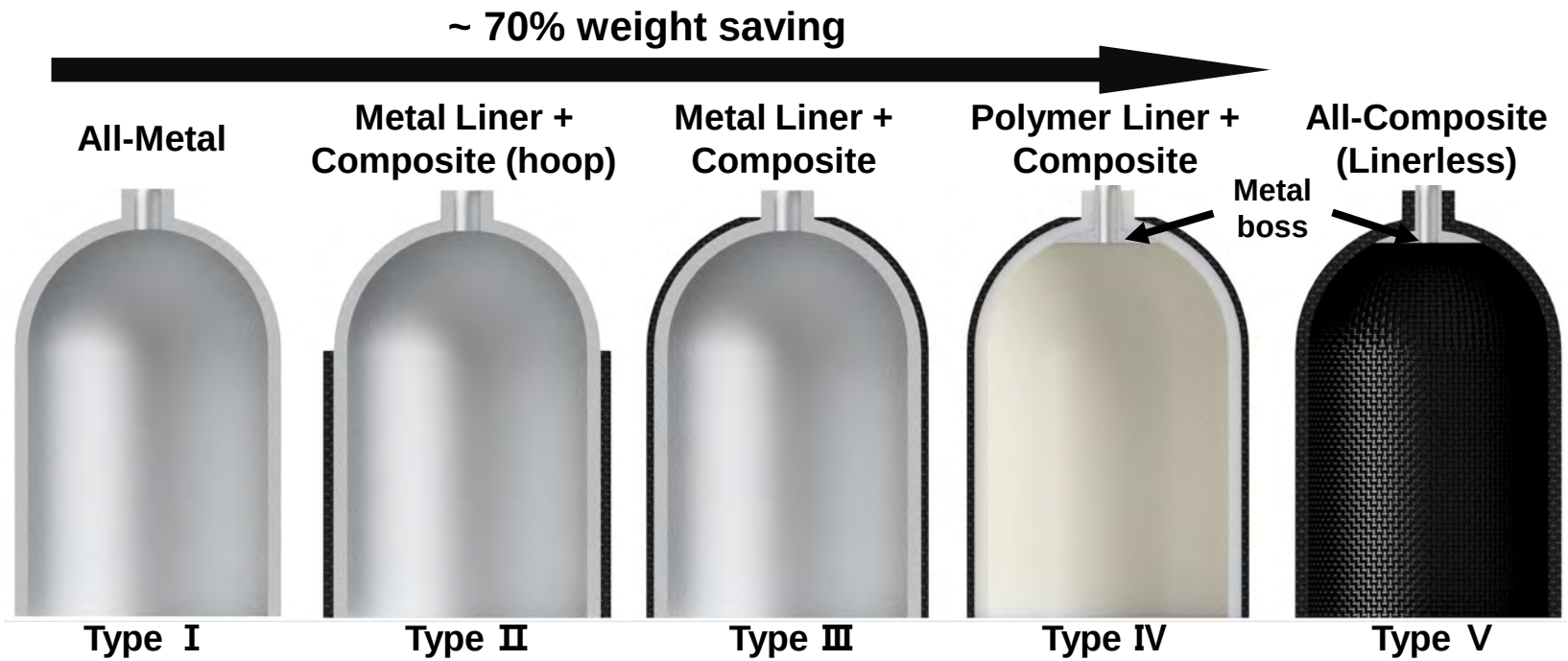

<Schematic of COPV for different types>

[2] Azeem, M., et al. (2022). Journal of Energy Storage.

Void Defects Occur Due to Low Pressure in COPV Manufacturing Processes

- Aerospace composites are manufactured using the **autoclave process** for **high quality structure.** [3]
- However, **autoclave process** cannot be used for **COPV manufacturing**, due to the high cost and **external pressure** applied in **radial direction.**
- Due to a manufacturing process restrictions, COPVs have a **high void content,** approximately 3 to 9%. [4]

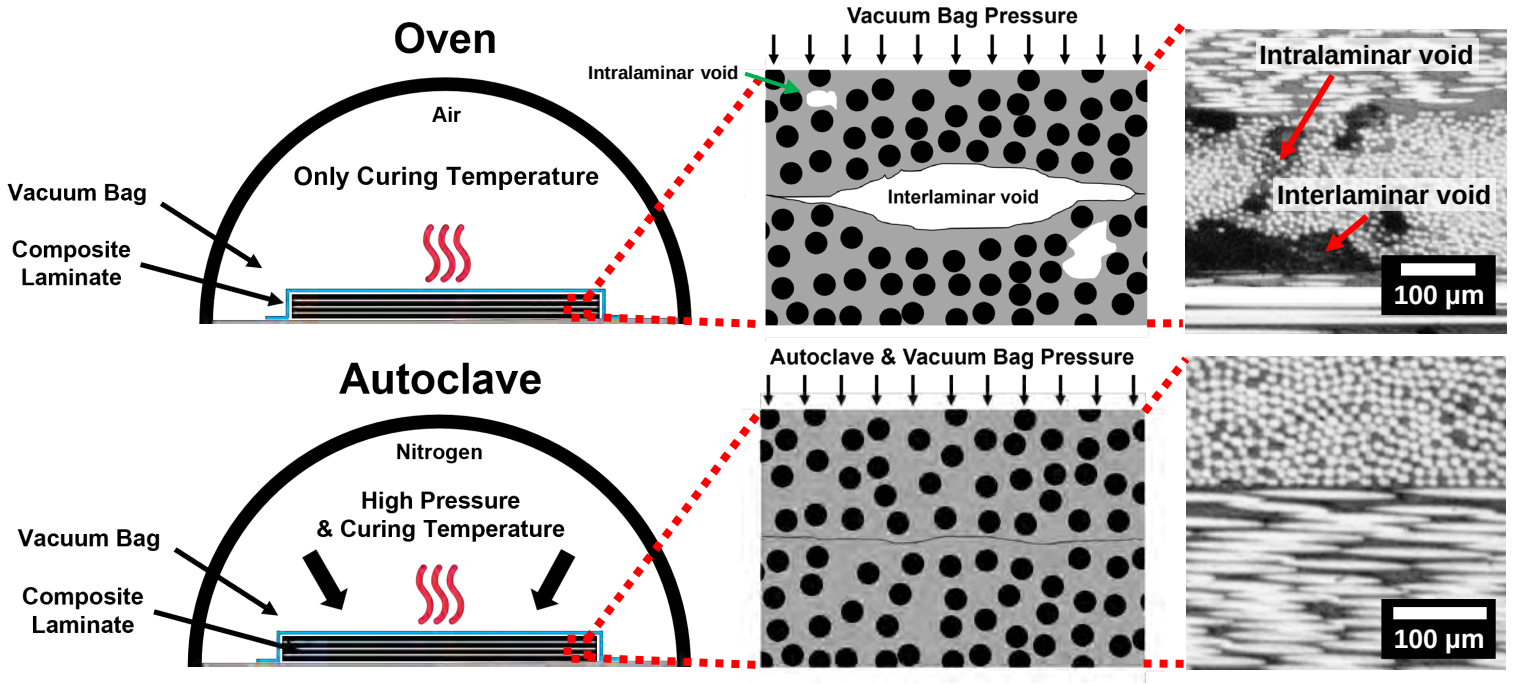

<Composite manufacturing process>

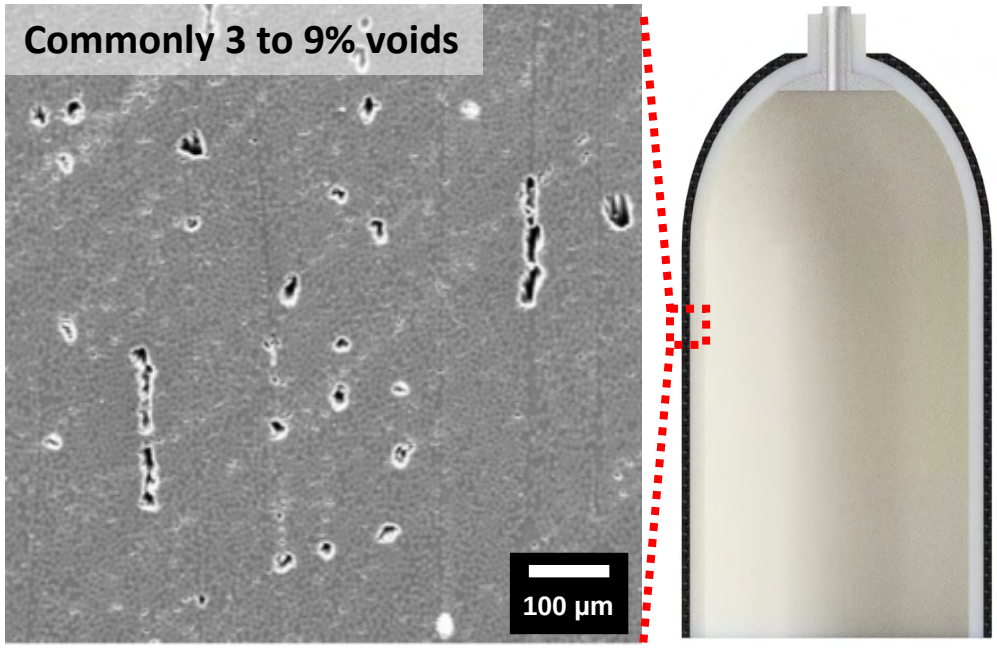

<Cross-section image of composite in COPV [4]>

[3] Centea, T., et al. (2015). Composites Part A: Applied Science and Manufacturing.
[4] Edgecombe, B. (2018). Materia, Inc., Pasadena, CA (United States).

Influence of Void Content in Mechanical Properties and Gas Permeability of Composite

- **Void defects** that occur during the oven curing process **significantly reduce the mechanical strength.** [5-6]
- **Enclosed damage (e.g., void defect)** in composite can **increase gas permeability.** [7]

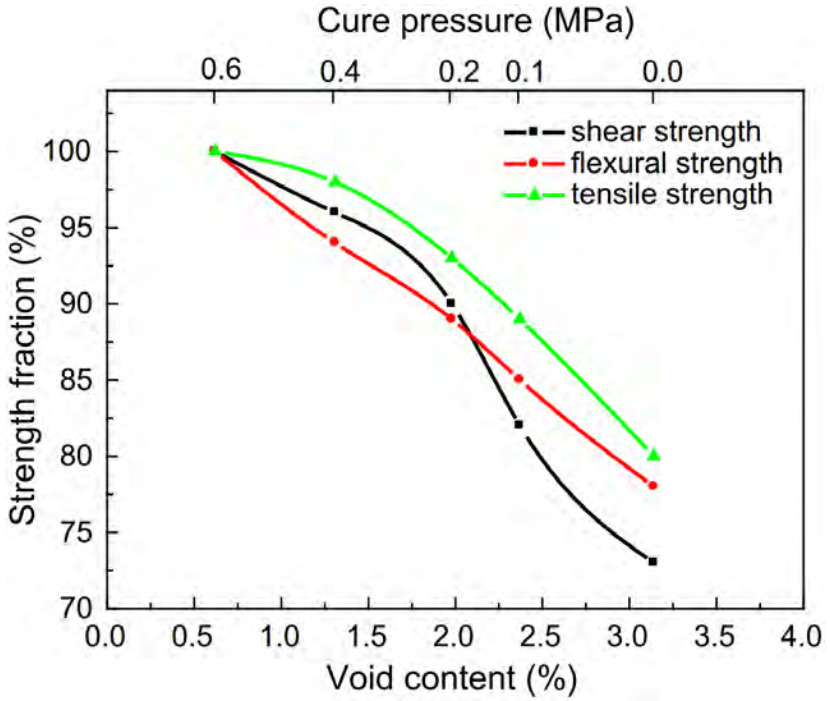

<Relationship between mechanical properties and void content [6]>

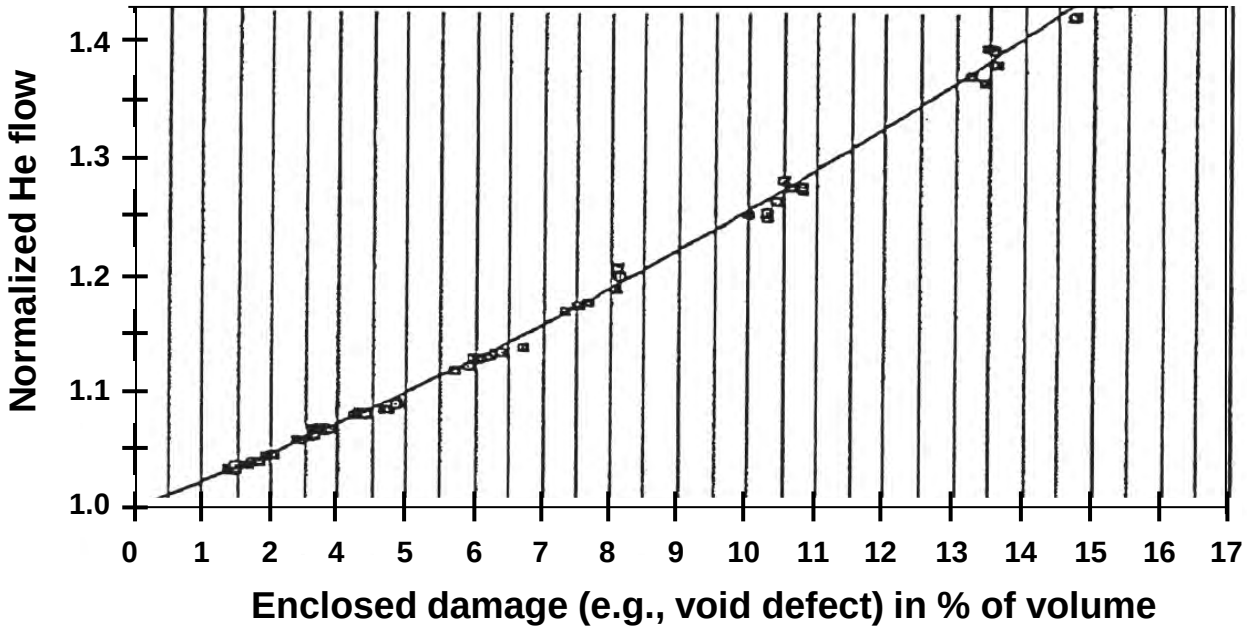

<Relationship between helium permeability and enclosed damaged in CFRP laminate [7]>

KAIST

[5] Olivier, P. B. A. U. P. S., et al. (1995). Composites.
[6] Liu, L., et al. (2006). Composite Structures.
[7] Disdier, S., et al. (1998). Cryogenics.

Microcracks and Delamination Between Layers Caused by Thermal Cycling

- Composites have **different Coefficients of Thermal Expansion** (CTE) between the laminated layers. [8]
- CTE mismatch between composite laminates during rapid **temperature changes** induces internal **microcracks** and **delamination**. [9-10]
- Microcracks and delamination adversely affect the **gas permeability** and **mechanical properties**. [10-13]

ε_T: Transverse thermal strain
ε_L: Longitudinal thermal strain

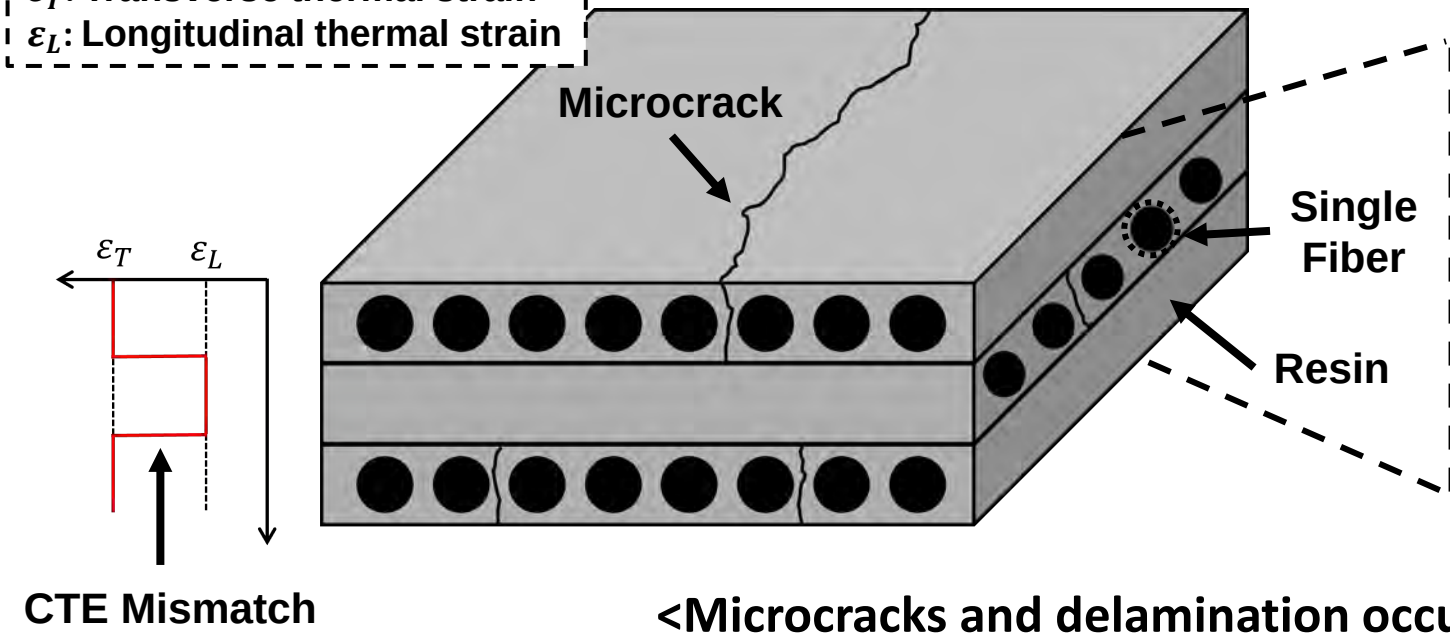

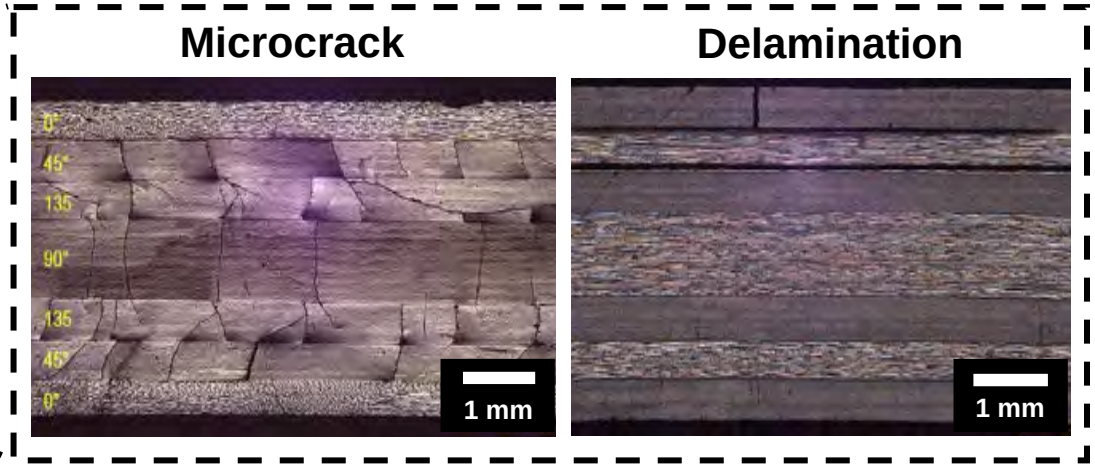

<Microcracks and delamination occur due to CTE mismatch [9]>

[8] Ran, Z., et al. (2014). Chinese Journal of Aeronautics.
[9] Grogan, D. M., et al. (2014). Composites Part A: Applied Science and Manufacturing.
[10] Saha, S., et al. (2024). Journal of Composite Materials.
[11] Flanagan, M., et al. (2017). Composites Part A: Applied Science and Manufacturing,
[12] Bechel, V. T., et al. (2006). Composites science and Technology
[13] Meng, J., et al. (2020). Composites Science and Technology

Microcracks and Delamination Between Layers Caused by Thermal Cycling

- Composites have **different Coefficients of Thermal Expansion** (CTE) between the laminated layers. [8]
- CTE mismatch between composite laminates during rapid **temperature changes** induces internal **microcracks** and **delamination**. [9-10]
- Microcracks and delamination adversely affect the **gas permeability** and **mechanical properties**. [10-13]

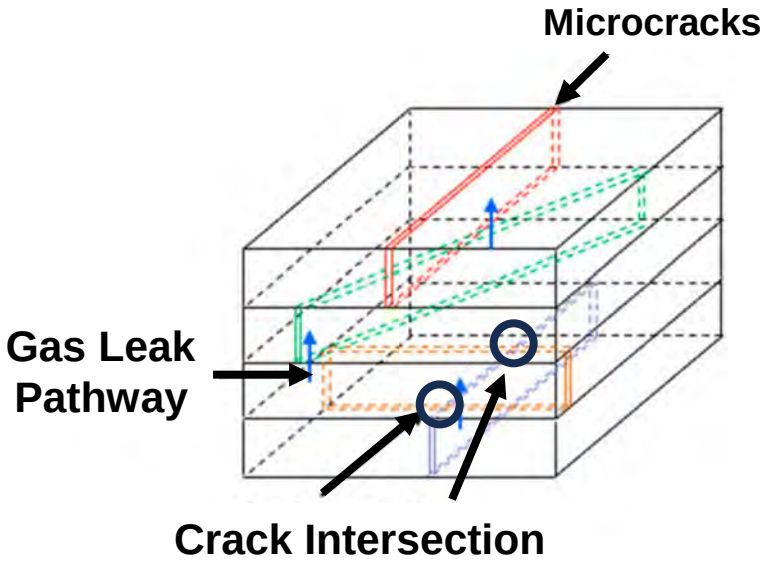

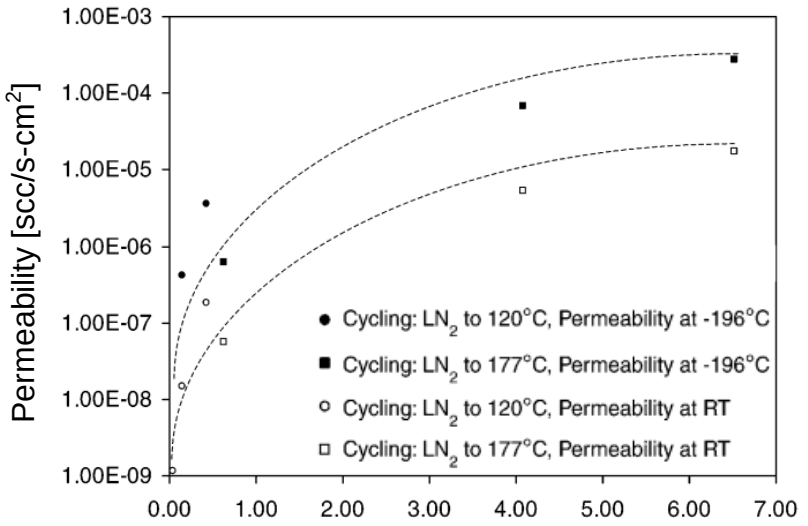

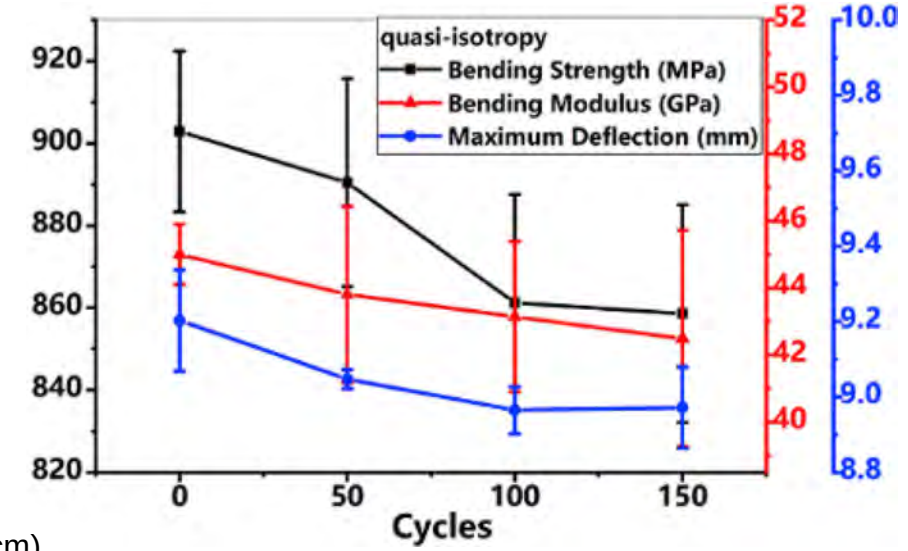

<Microcracks and delamination lead to an increase in gas permeability and a decrease in the mechanical strength of the composite material [10, 12, 13]>

[8] Ran, Z., et al. (2014). Chinese Journal of Aeronautics.
[9] Grogan, D. M., et al. (2014). Composites Part A: Applied Science and Manufacturing.
[10] Saha, S., et al. (2024). Journal of Composite Materials.
[11] Flanagan, M., et al. (2017). Composites Part A: Applied Science and Manufacturing,
[12] Bechel, V. T., et al. (2006). Composites science and Technology
[13] Meng, J., et al. (2020). Composites Science and Technology

Objective and Approach

Research Approach

Nanomaterial architectures in composite interlaminar region

#1. Nano-structured interlaminar toughening as a CTE mismatch buffer

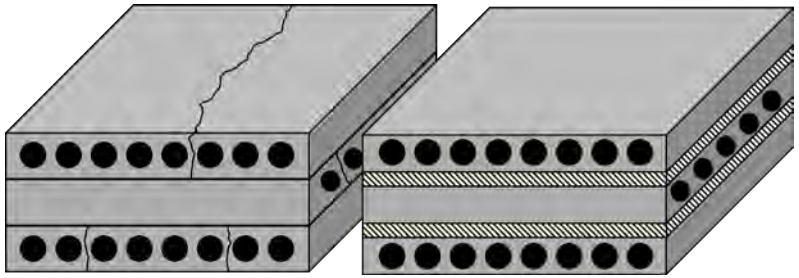

- Prohibit microcrack and delamination due to thermal cycling

#2. Capillary-enhanced void-free manufacturing

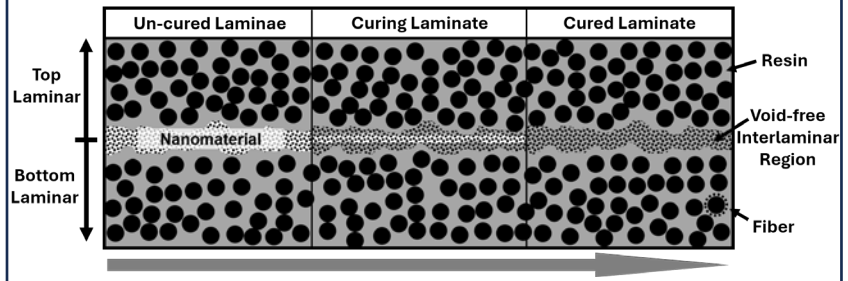

- Void defect-free next-generation composite production process

#3. Nanomaterials act as a gas permeation barrier

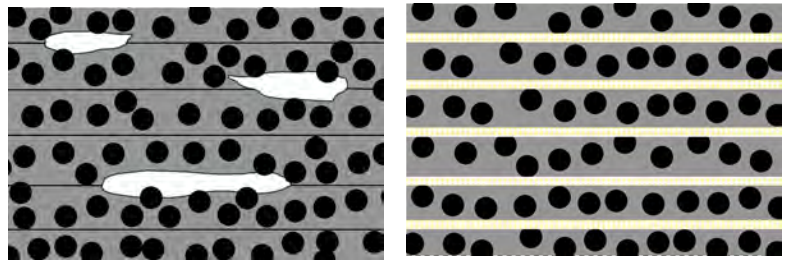

- Nanomaterials perform as a thin yet multi-layered permeation barrier

Nano-Structured Interlaminar Toughening as a CTE Mismatch Buffer

- High-toughness nanomaterials are layered between composite laminate layers and co-cured.
- The **high-toughness nanomaterials** act as a **CTE mismatch buffer** in the laminate, preventing microcracks and delamination.

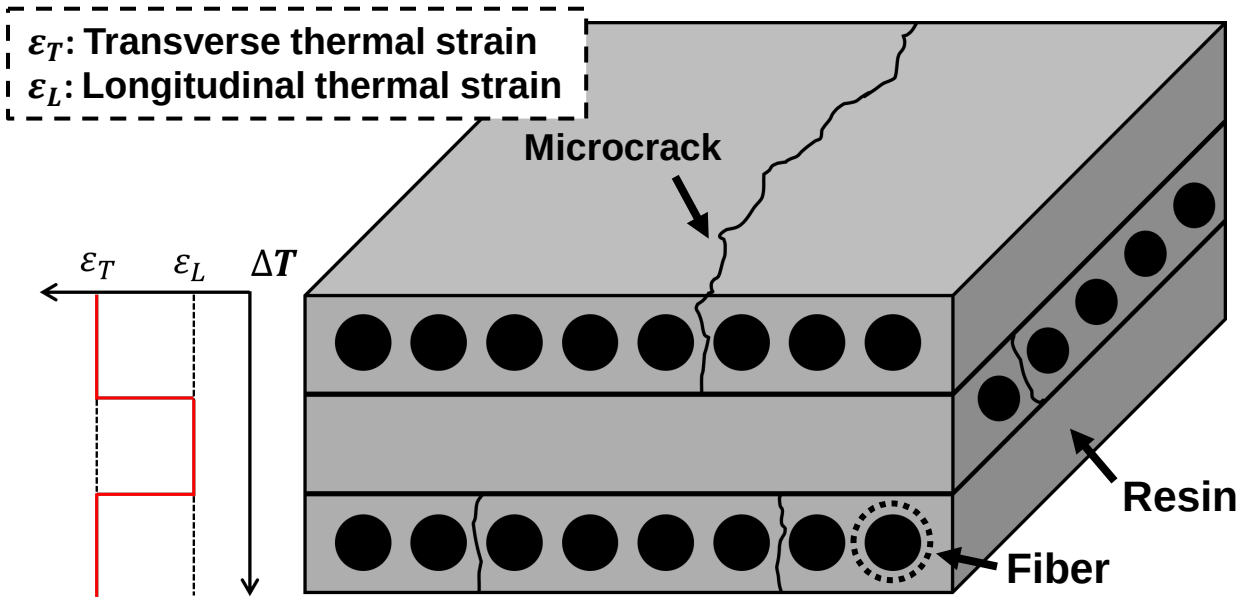

<Microcracks, delamination in composite induced by thermal cycling>

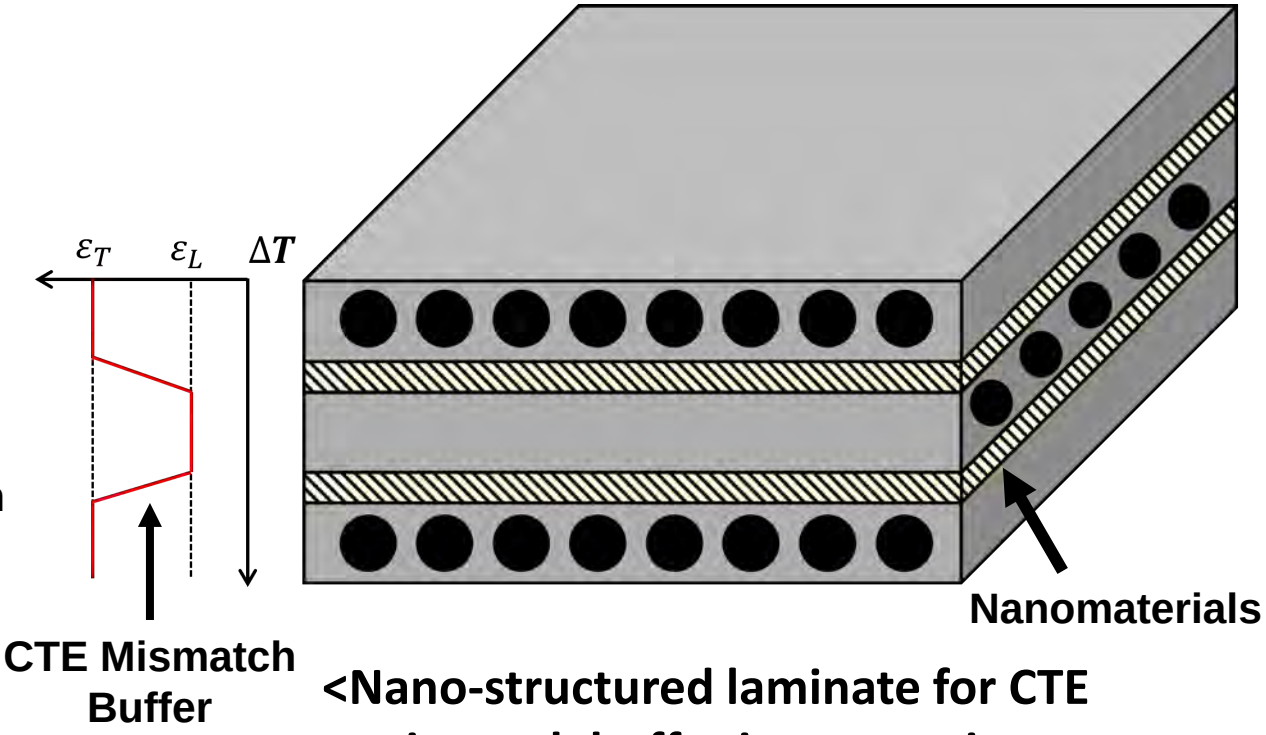

<Nano-structured laminate for CTE mismatch buffer in composite>

Capillary-Enhanced Void-Free Manufacturing

- Due to limitations in the manufacturing process, void defects occur between laminate interfaces.
- By utilizing the **capillary action of nanostructures**, it is possible to **provide additional pressure** to the composite without using an autoclave. [14]

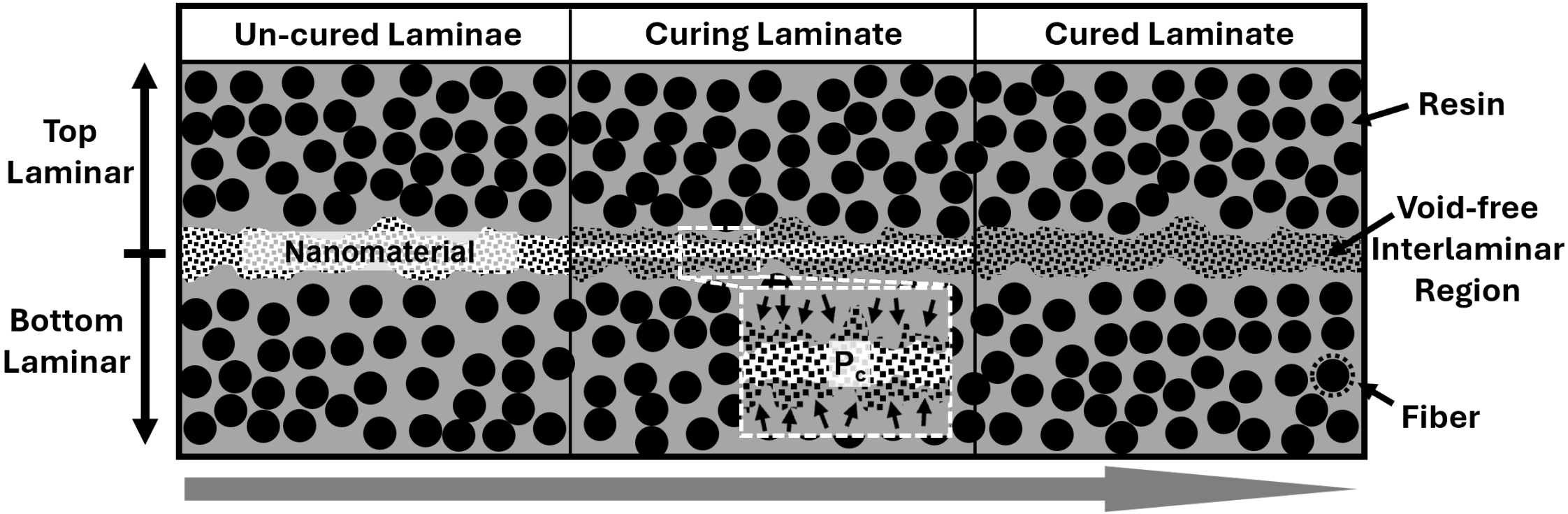

<Capillary pressure can act as additional pressure for reducing void contents>

[14] Lee, J., et al. (2020). Advanced Materials Interfaces.

Nanomaterials as a Gas Permeation Barrier

- **Void defects** in the composite act as **gas leakage paths**, permanently increasing the **steady state leak rate**.
- Further, microcracks and delamination caused by thermal cycling hinder the use of composite as a gas permeation barrier.
- **Nanomaterials** layered between the composite laminate serve as a **gas permeation barrier**.

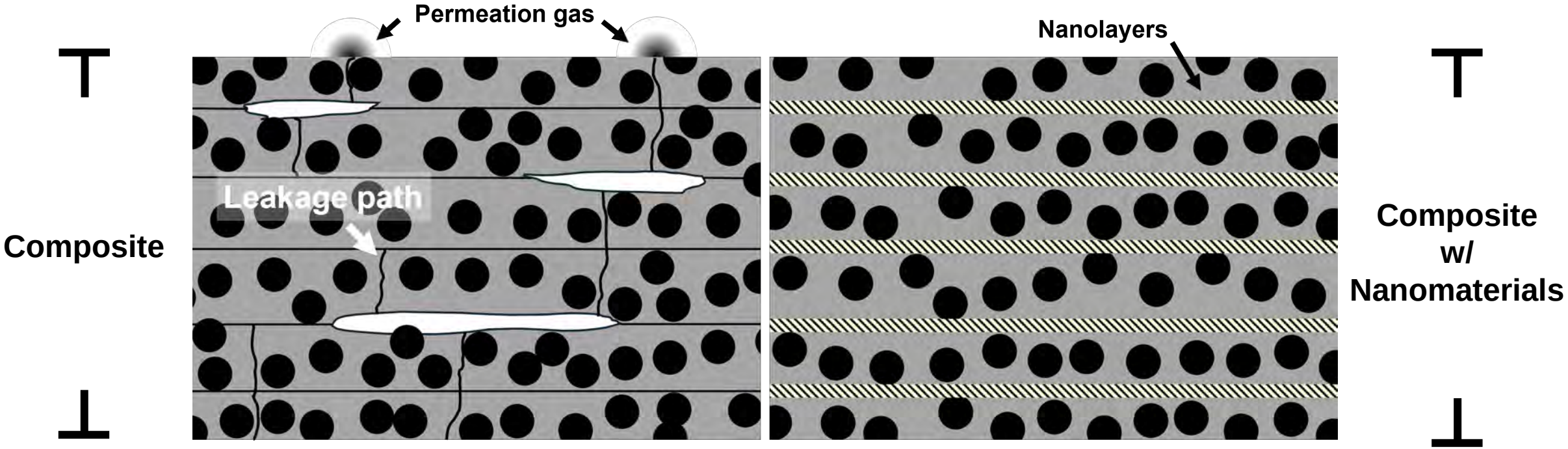

<Nano-structured laminate for a gas permeation barrier>

Fabrication and Process

Synthesis Process of Nanofibers: Electrospinning

- **Electrospinning** is used as a method for synthesizing polymer nanomaterials (**high productivity**, **low cost**).
- **High voltage** is applied to create an **electric field;** the **polymer** dissolved in the solvent is emitted through a nozzle.
- The solvent **evaporates** before reaching the substrate, forming **polymer fibers** with **nanoscale structures.**

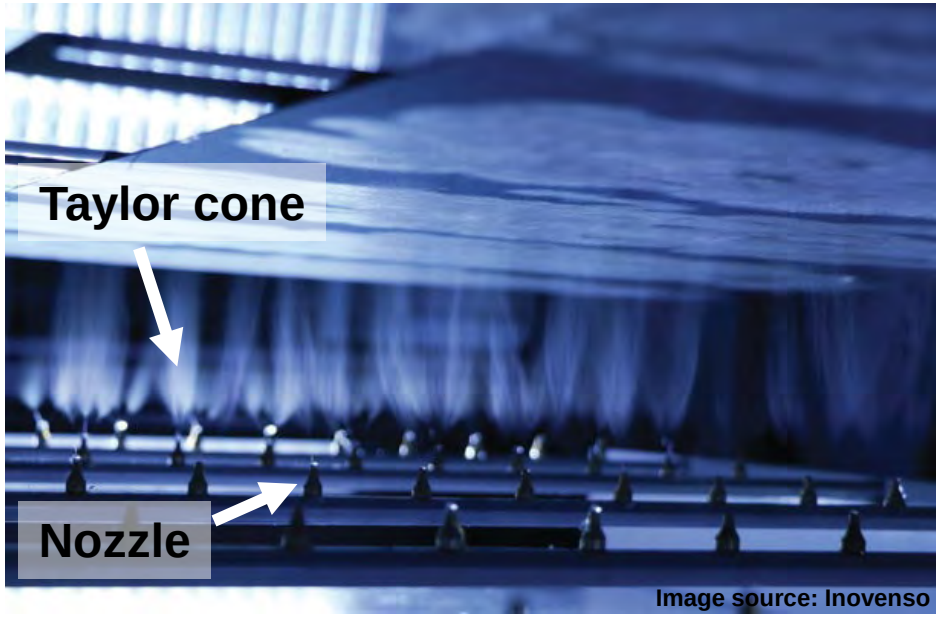

<Electrospinning process>

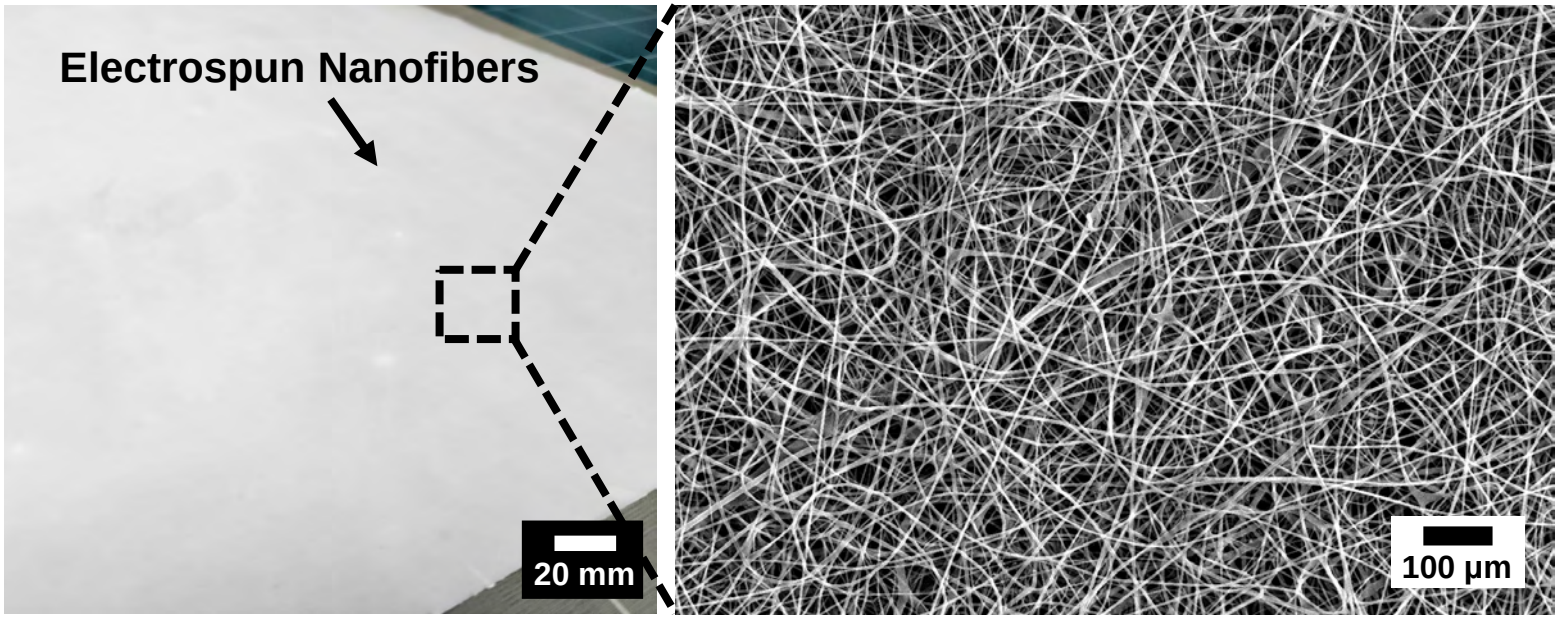

<Morphology of electrospun nanofibers>

SEM Images of Electrospun Nanofibers

- **Nanolayers** used in this study were Nanolayr® electrospun PA6 (XLB).
- **Nanofibers** have **smooth surface** without any beading, as observed through Scanning Electron Microscope (SEM).
- **Cross-sectional SEM images** showed that the **thickness** of the **nanolayer** was ~**24 µm** per layer for **4.5 gsm**.
- **Average fiber diameter** was **414 nm (SE = 30.9 nm),** based on manual measurement.

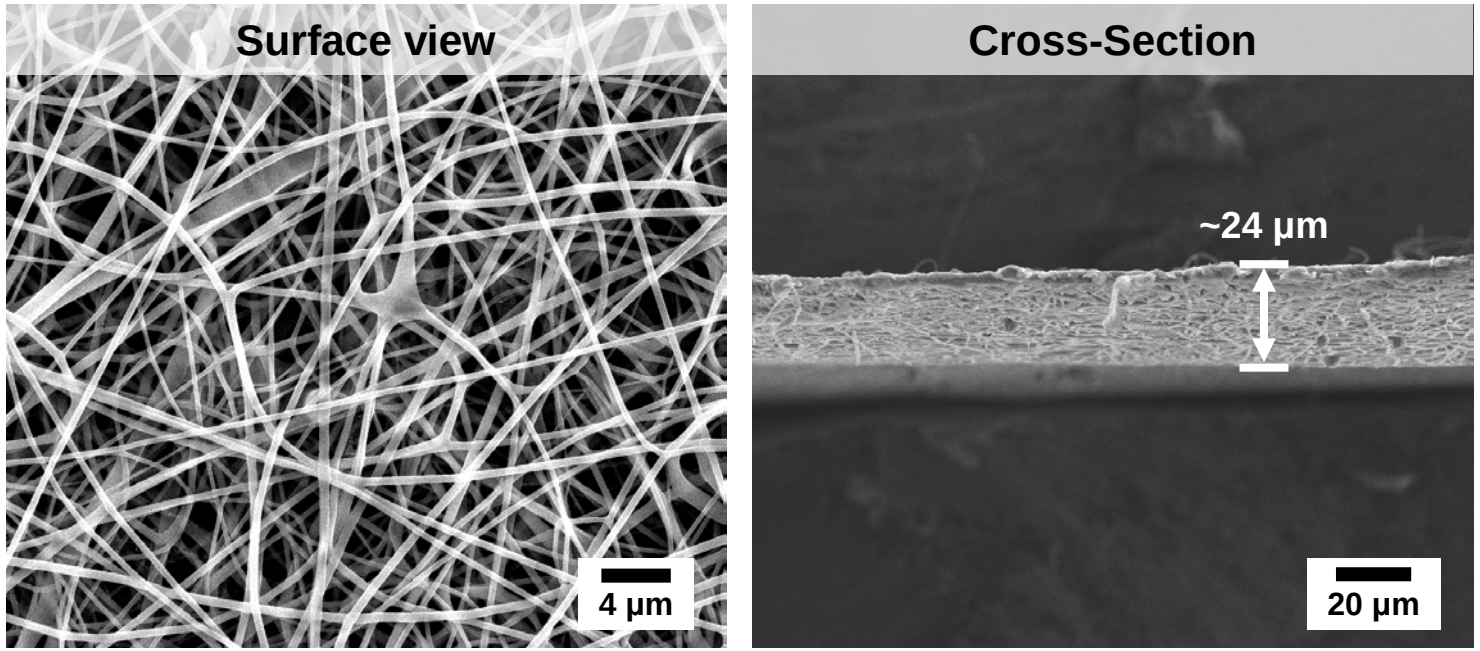

<SEM image of nanolayers (4.5 gsm)>

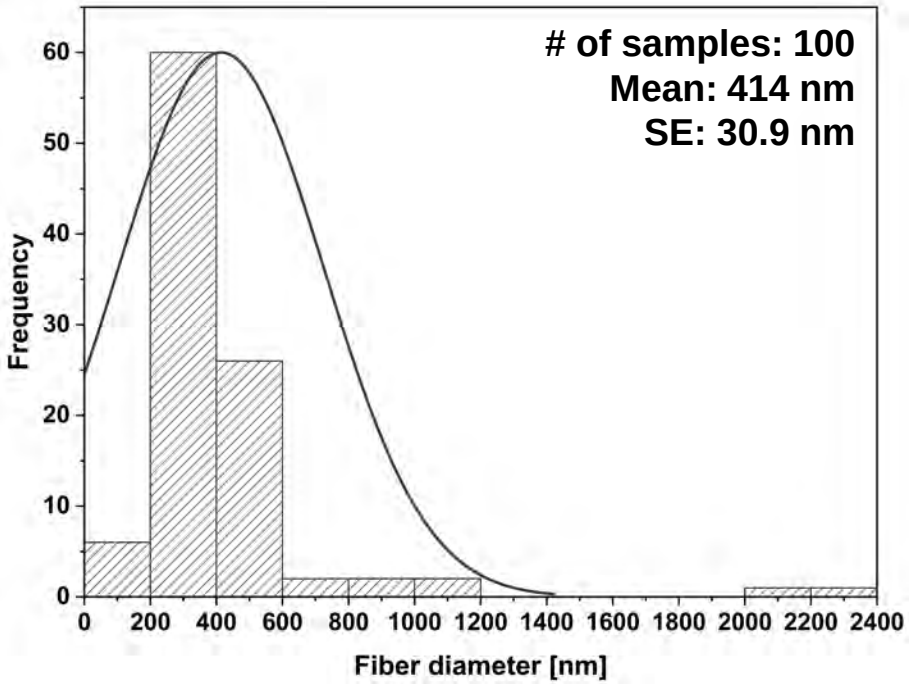

<Histogram of nanofibers diameter>

Fabrication, Curing Process of Composite Laminates with Electrospinning Nanolayers

- Considering the mechanism of microcracks and delamination due to CTE mismatch, the laminate **lay-up** is selected as **cross-ply $[0/90]_{4s}$** to evaluate the **worst-case scenario**. [15]
- **Nanolayers** are **transferred** between **all the laminae** (SK chemicals T700/H18 UD prepreg, USN-125B).
- Vacuum bagging is a commonly used method, and the surface film varies depending on the type of experiment.

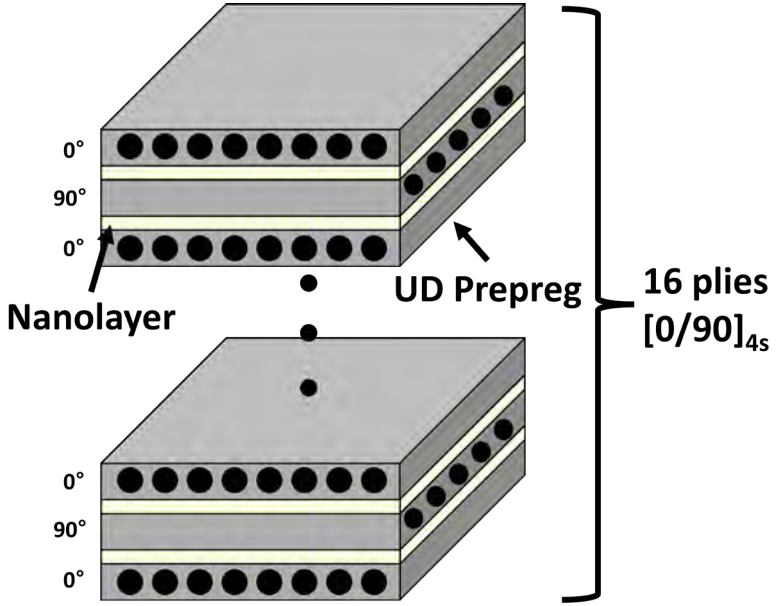

<Lay-up of laminate with nanolayers>

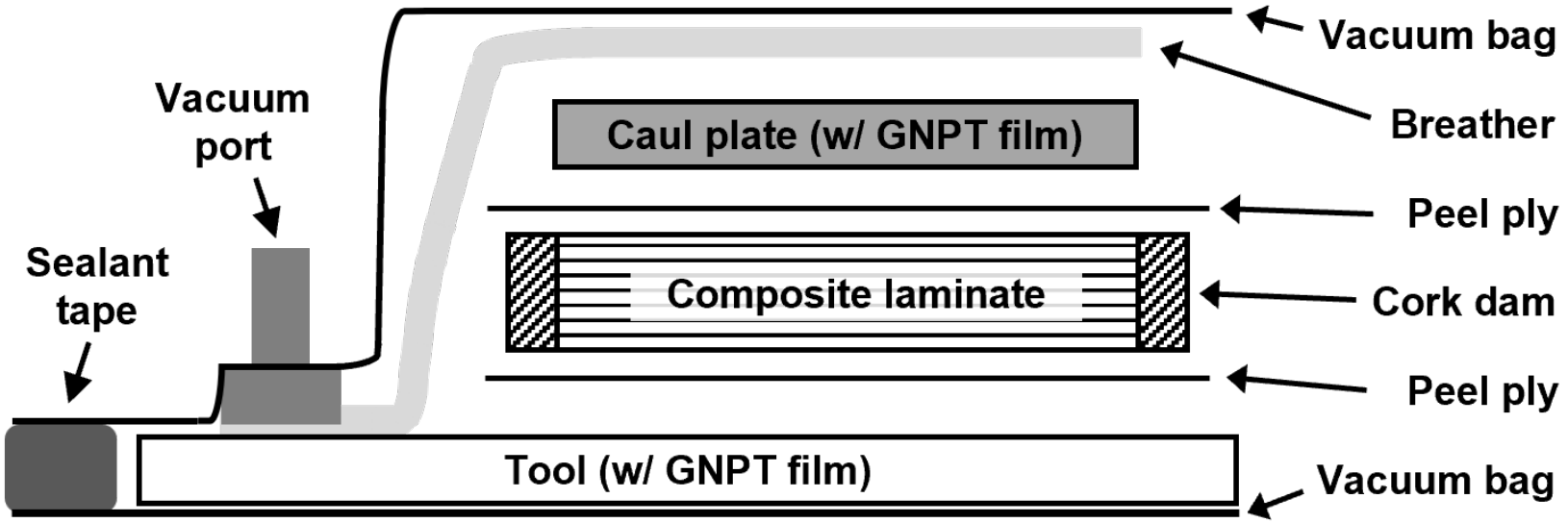

<Vacuum bagging of the composite laminate>

[15] Meng, Jinxin, et al. Composites Science and Technology (2022)

Fabrication, Curing Process of Composite Laminates with Electrospinning Nanolayers

- Nanolayers are cut slightly larger than the prepreg to cover all surfaces of the composite.
- Curing is performed in an **oven** and **autoclave** according to the **Manufacturer Recommended Cure Cycle** (MRCC) of the prepreg resin.
- Oven-cured laminate w/o nanolayer and oven-cured laminate w/ nanolayers are cured simultaneously in oven
- **Autoclave-cured laminates** are cured using the same cure cycle as oven-cured laminates, under an applied pressure of **5 bar** (nominal cured thickness: 1.92 mm).

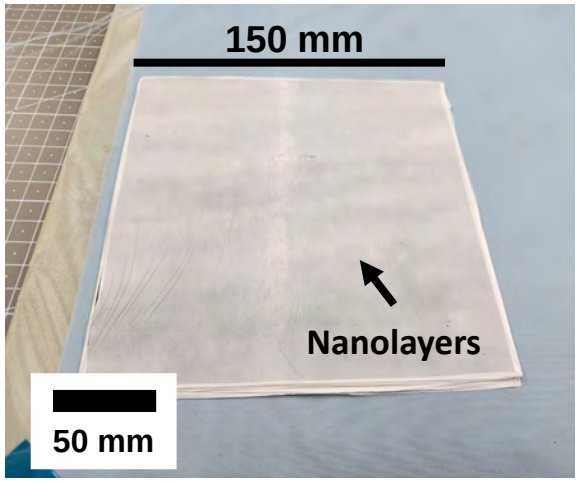

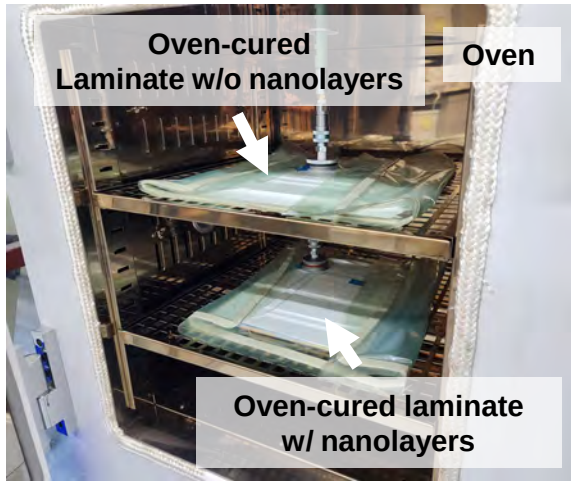

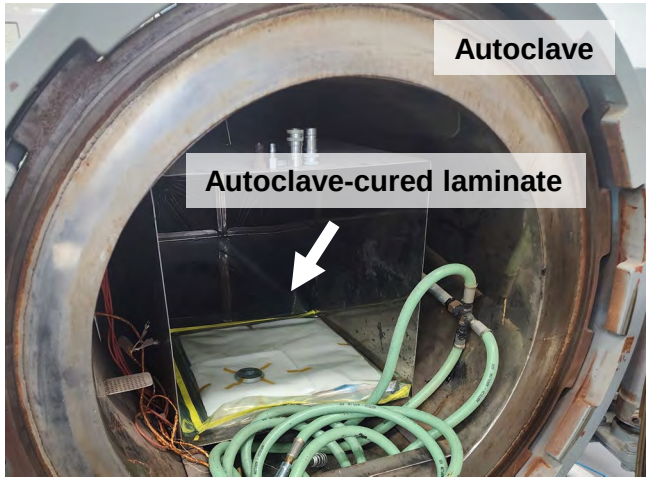

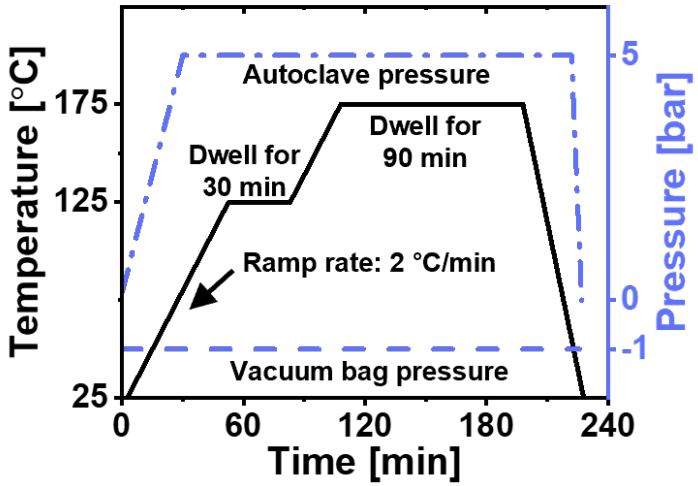

<Fabrication, curing process, and cure cycle of composite laminate>

Result and Discussion

Void Analysis: Void Contents & 3D Rendering

- The **oven-cured laminate w/ nanolayers** was found to have approximately **98% fewer voids** compared to the oven-cured laminate w/o nanolayers (same as autoclave-cured laminate w/o nanolayers).

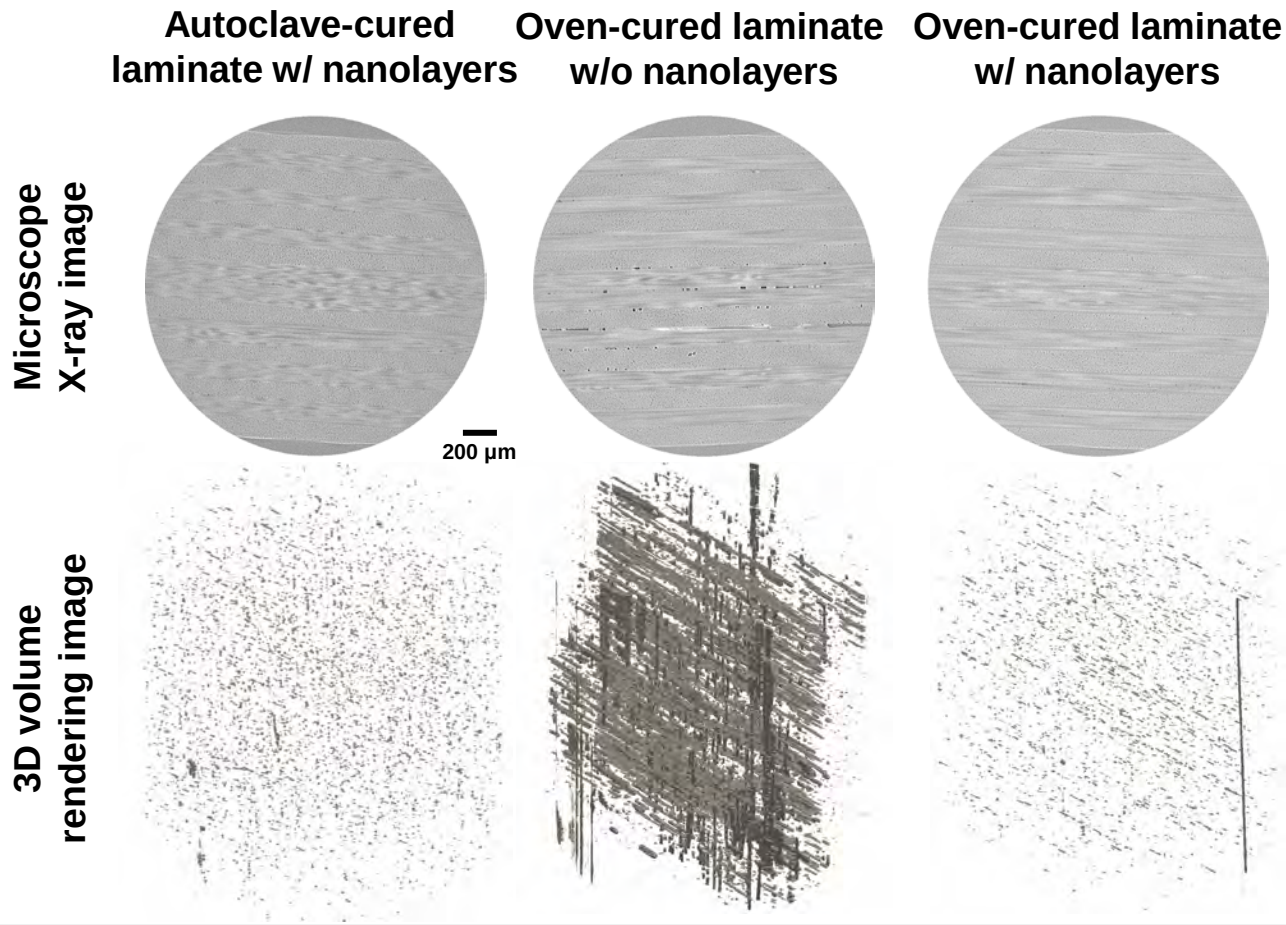

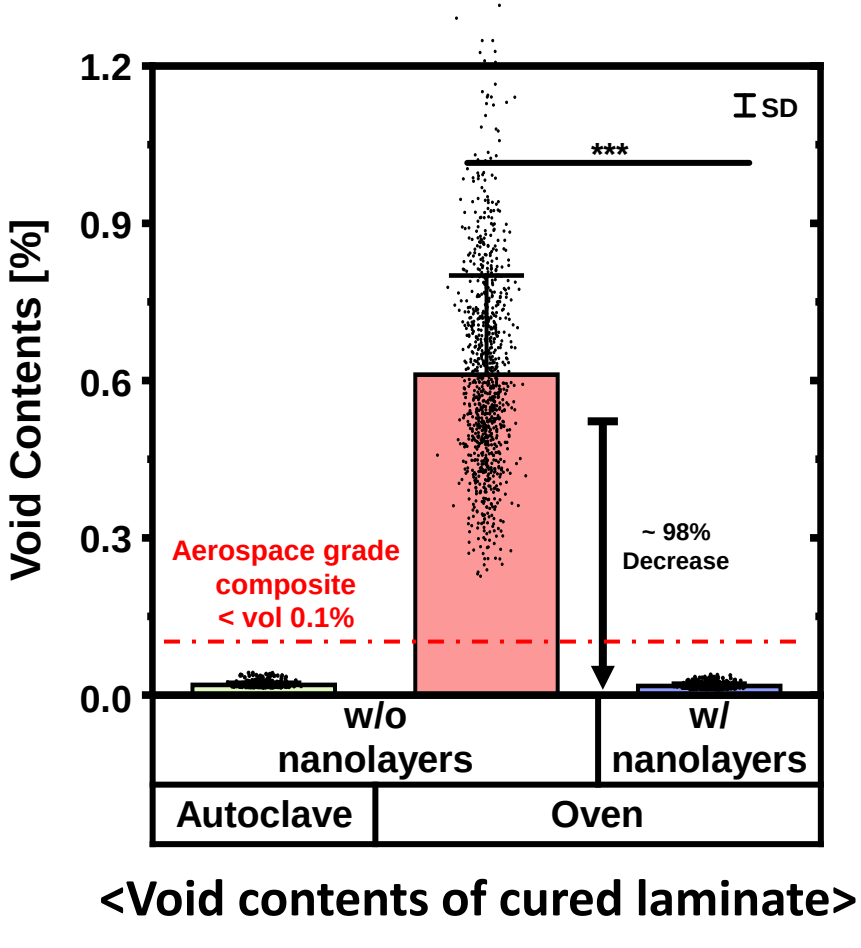

<Void contents of cured laminate>

Apparatus of Gas Permeability Test

- **Concentration gradient** between the upper and lower chambers induce **diffusion** in the **out-of-plane direction** of the specimen.
- The **permeation gas** is **helium** (10 bar), which has a **small molecular size** and **high diffusion rate**. [16]

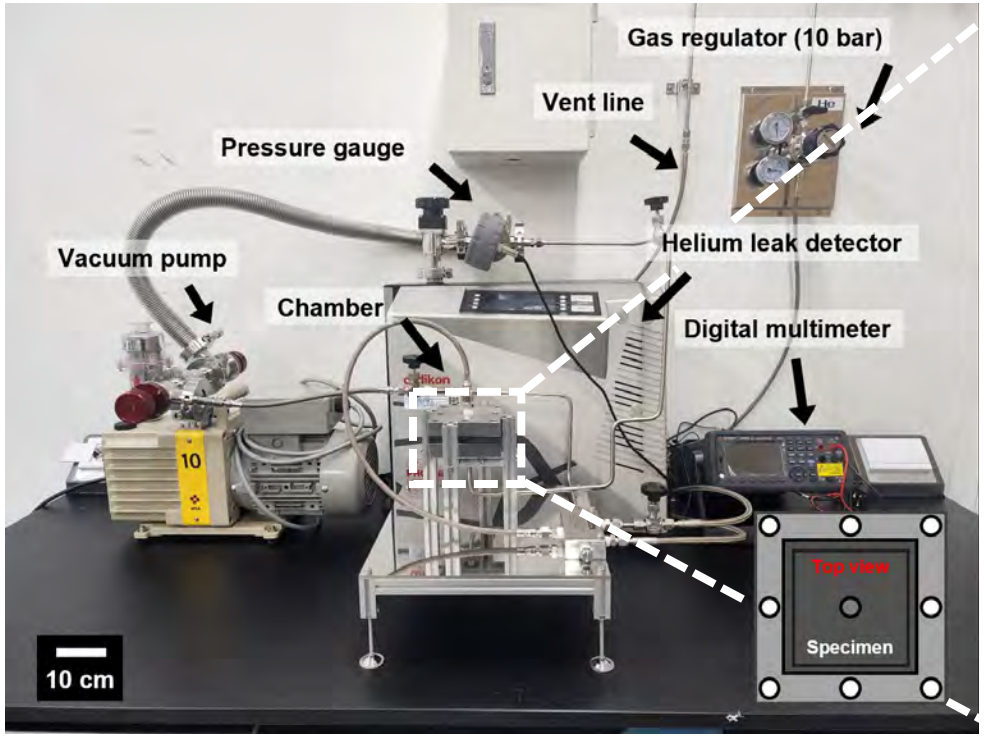

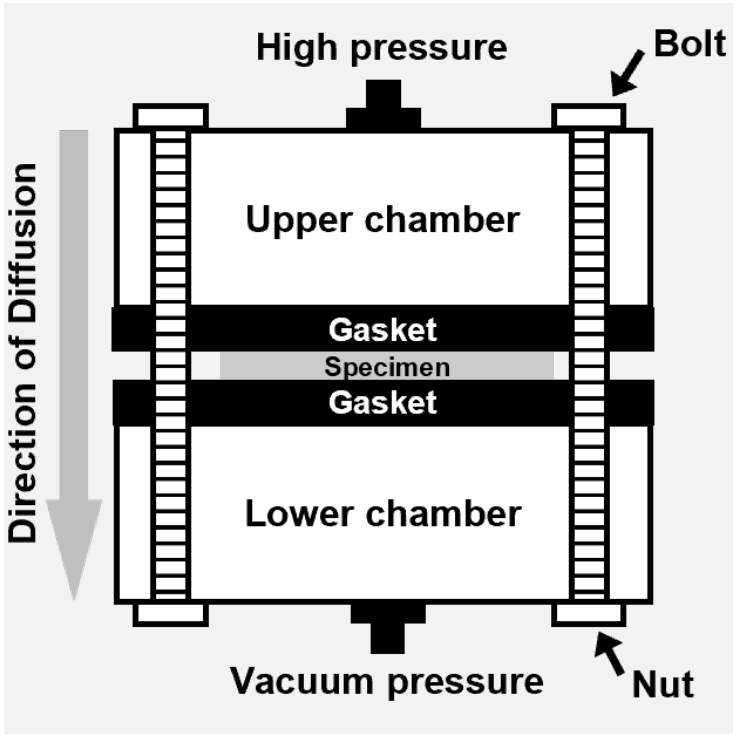

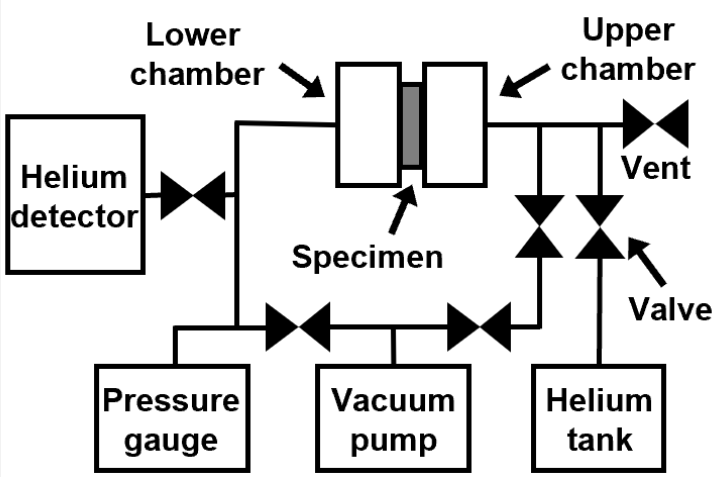

<Schematic of apparatus for helium gas permeability testing>

<Apparatus for helium gas permeability measurement of composite laminate>

[16] Choi, Sukjoo, et al. Composites Part B: Engineering (2008)

Results of Gas Permeability Test

- There are **no significant difference of steady state leak rate** in **autoclave-cured** and **oven-cured laminate.**
- The **gas permeability** was calculated to remove the influence of **thickness**, **temperature**, **concentration**, and **area**.
- The **gas permeability** of **oven-cured laminate w/ nanolayers was 21% reduction** compared to the w/o nanolayer.

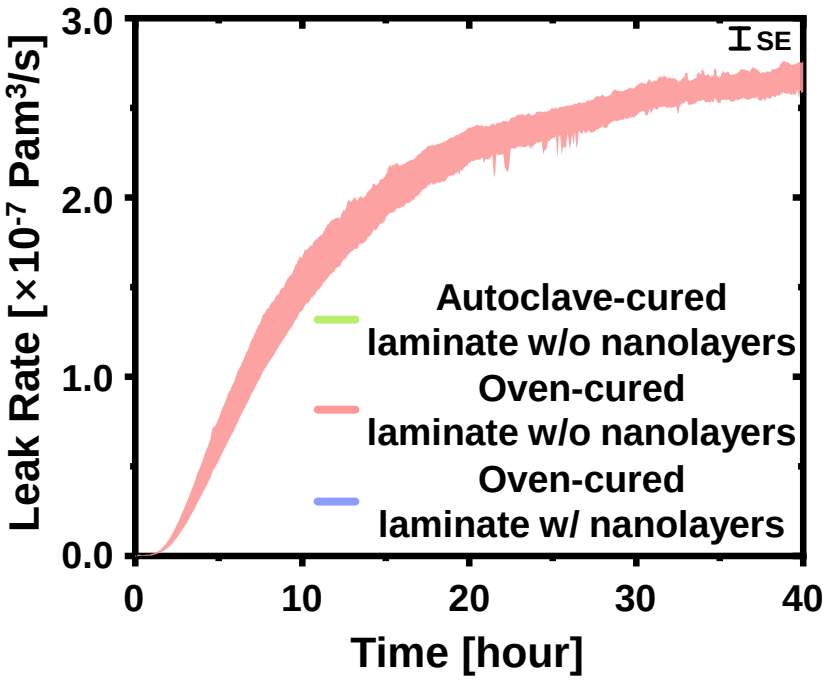

<Leak rate-time curve>

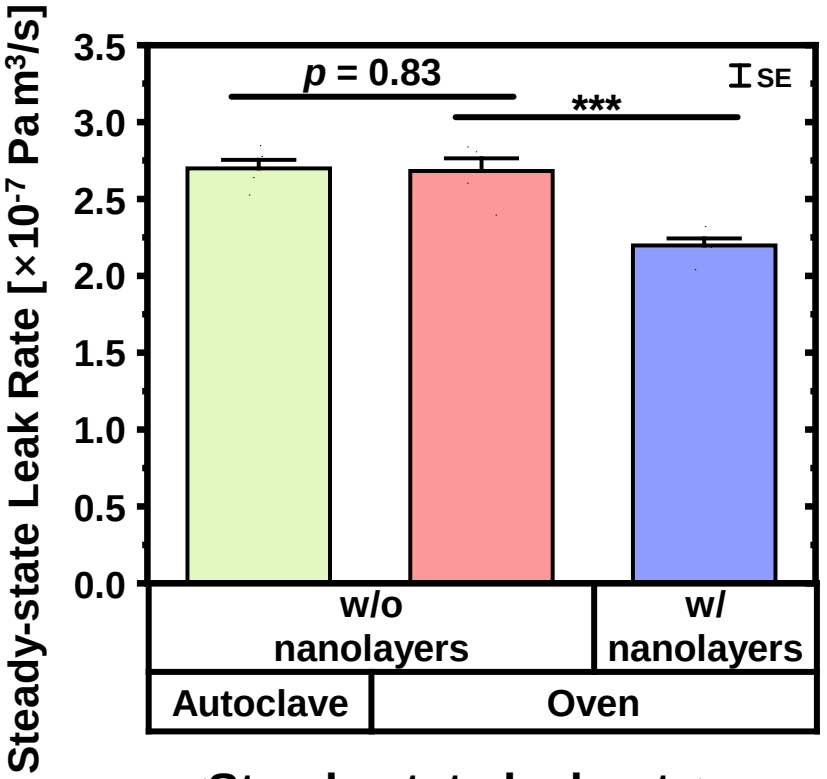

<Steady state leak rate>

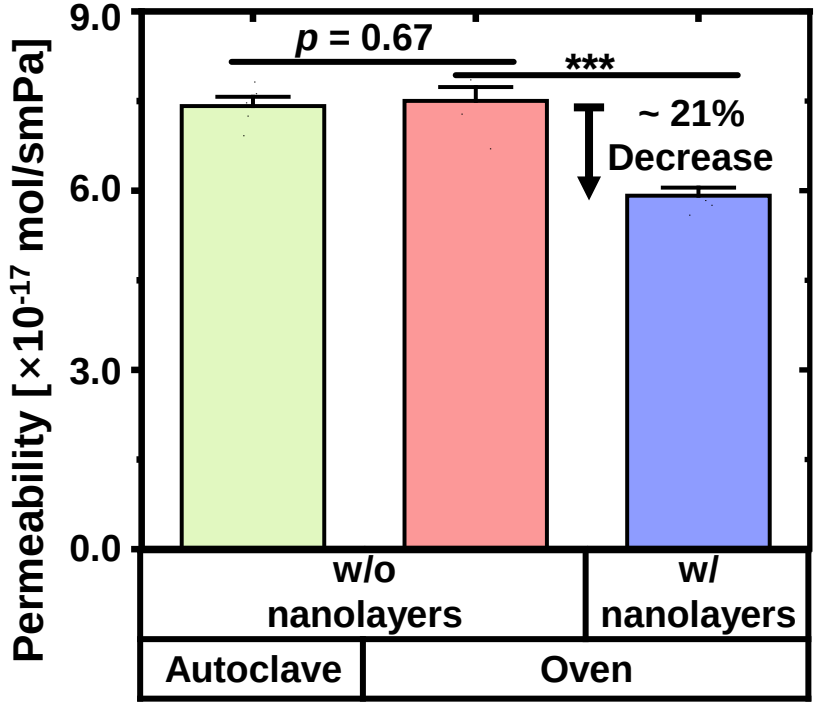

<Helium gas permeability>

Microcrack in Oven-cured Laminate w/o Nanolayers

- The cryogenic cycling test oven-cured laminate was performed for **300 cycles** from room temperature to cryogenic temperature (-196 °C).
- The **microcracks** were **observed** in **oven-cured laminate w/o nanolayers** after 300 cryogenic cycling.

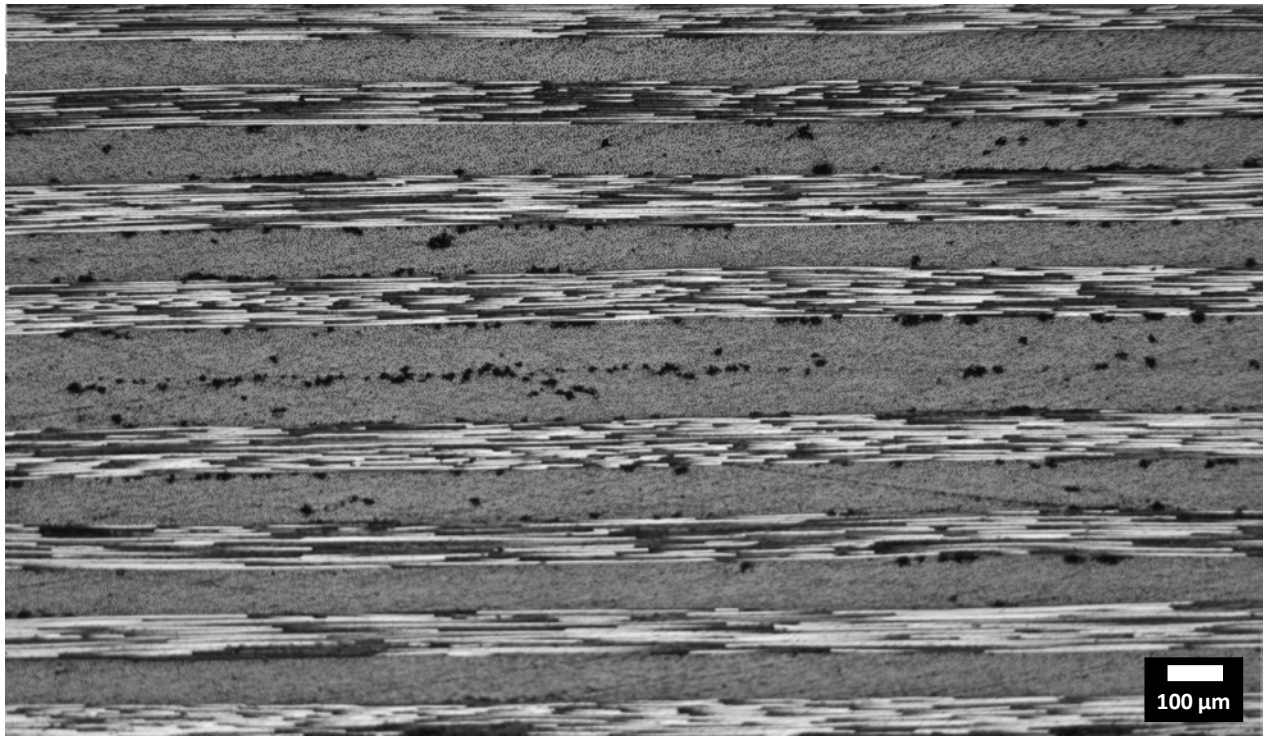

<# of cycles: 0>

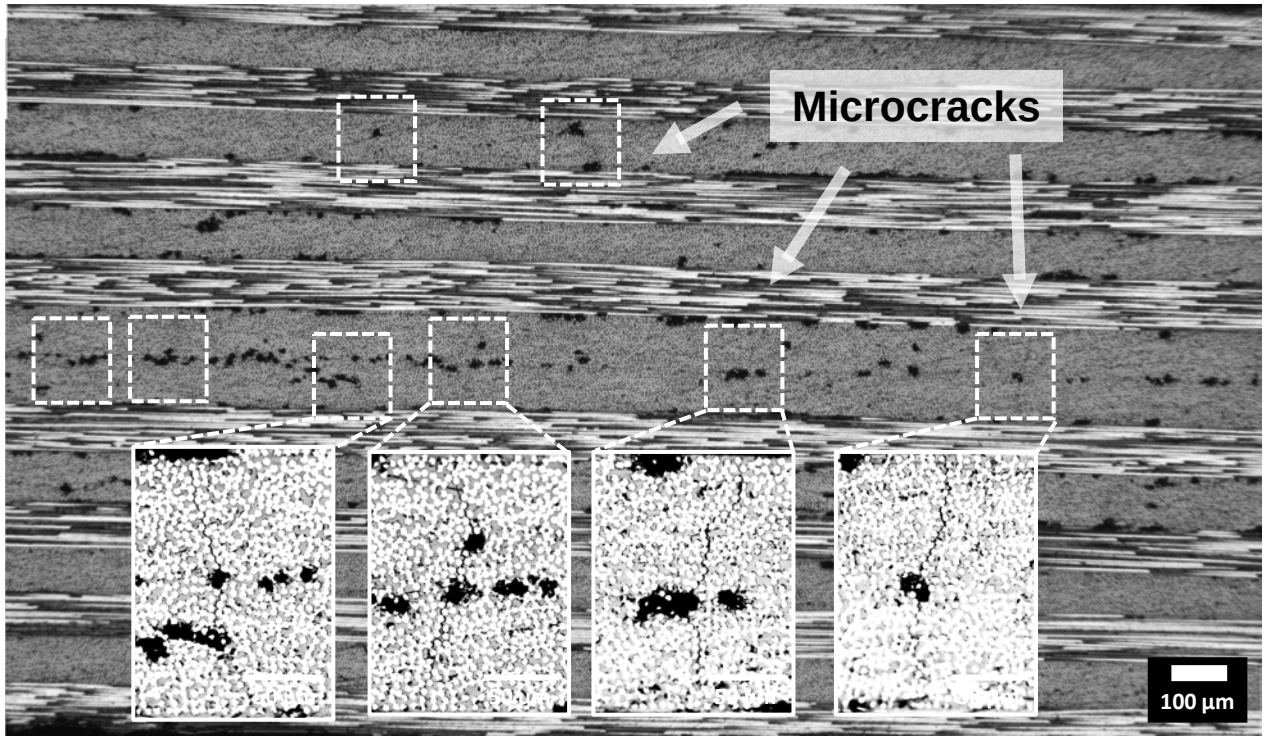

<# of cycles: 300>

Microcrack in Oven-cured Laminate w/ Nanolayers

- The cryogenic cycling test oven-cured laminate was performed for **300 cycles** from room temperature to cryogenic temperature (-196 ˚C).
- The **microcrack** was **not observed** in **oven-cured laminate w/ nanolayers** after 300 cryogenic cycling.

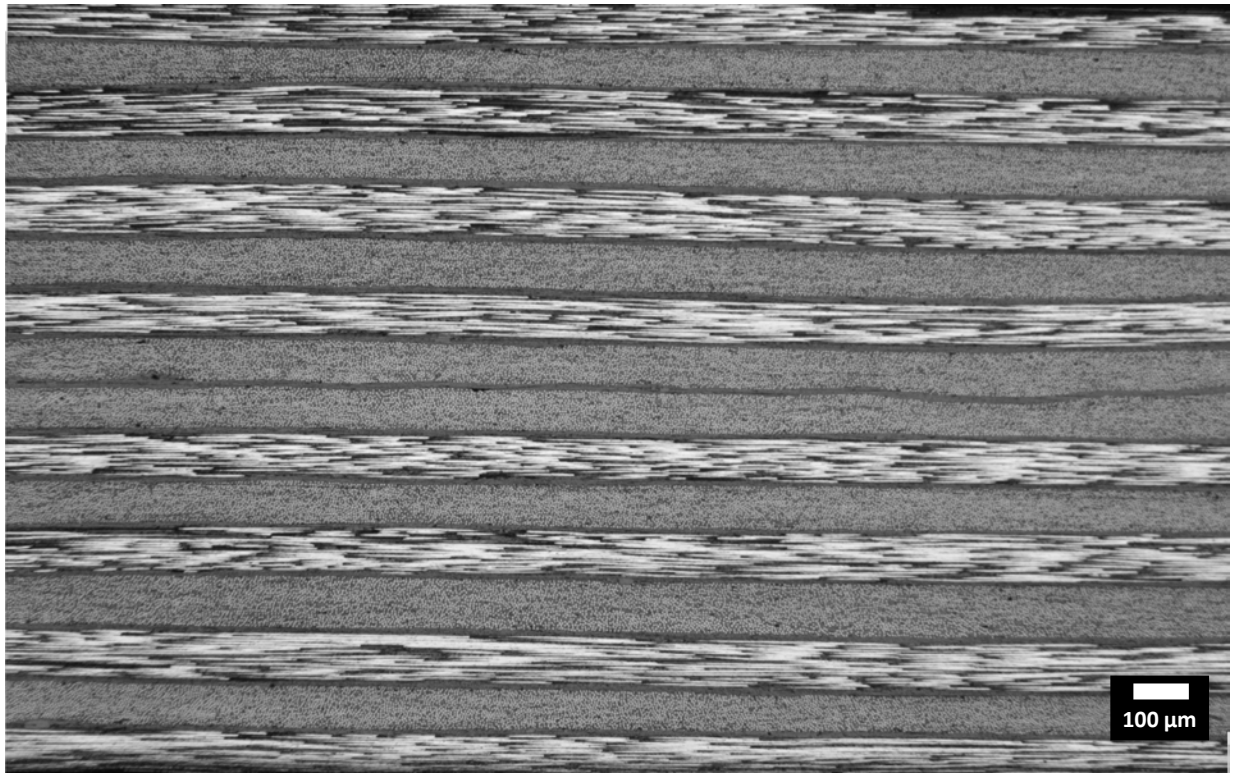

<# of cycles: 0>

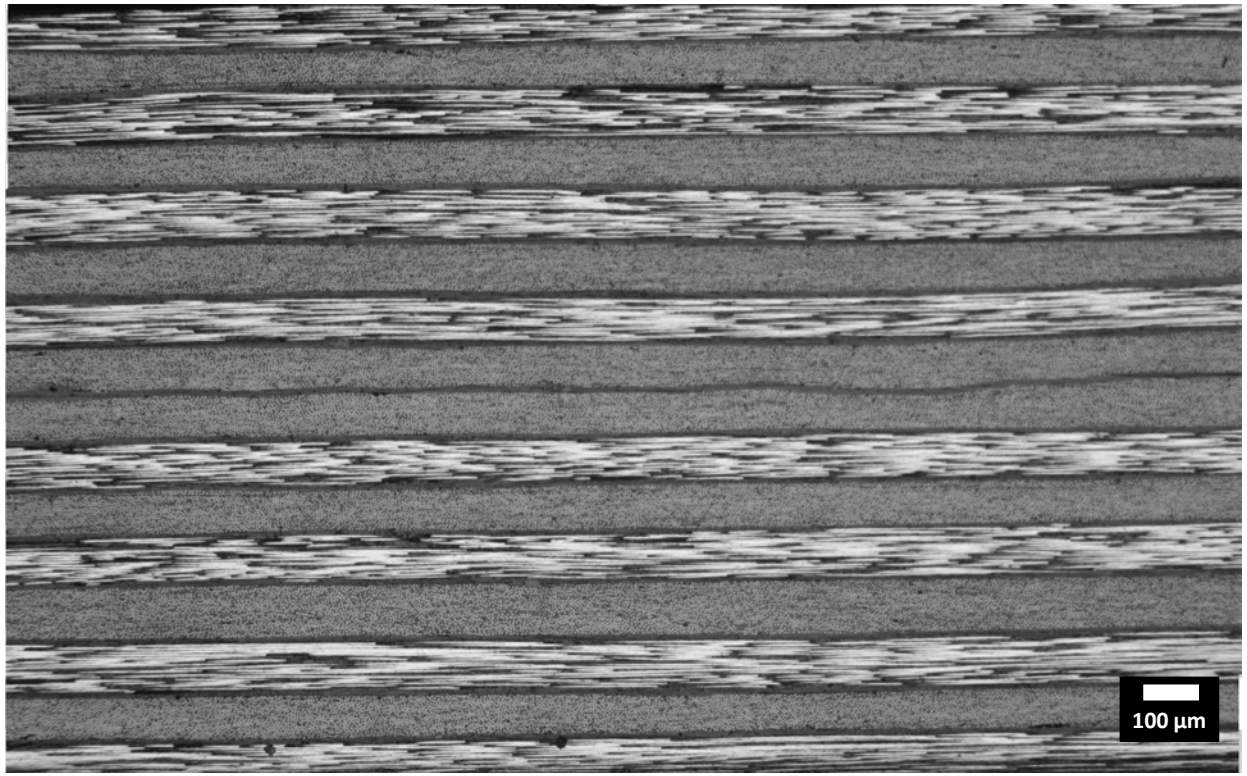

<# of cycles: 300>

Results of Double-Edge Notched Tensile Test

- Double-Edge Notched Tensile specimens (**cross-ply, $[0/90]_{4s}$**) are machined using a **water jet**.
- The tensile test was conducted using a hydraulic Instron 1350. **Pilot test** results confirmed that **failure occurred** at the **exact center** of the **specimen**.
- The **laminate with nanolayers** can **withstand higher tensile loads** compared to the baseline laminate.

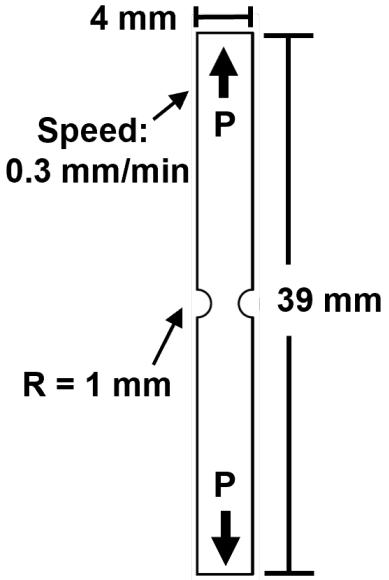

<Schematic of DENT test>

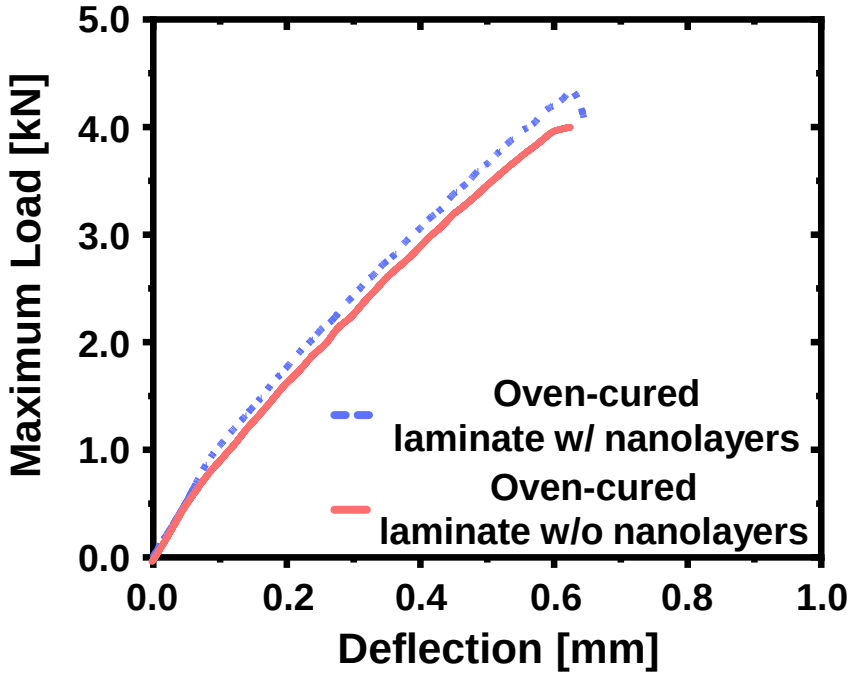

<Load-deflection curve>

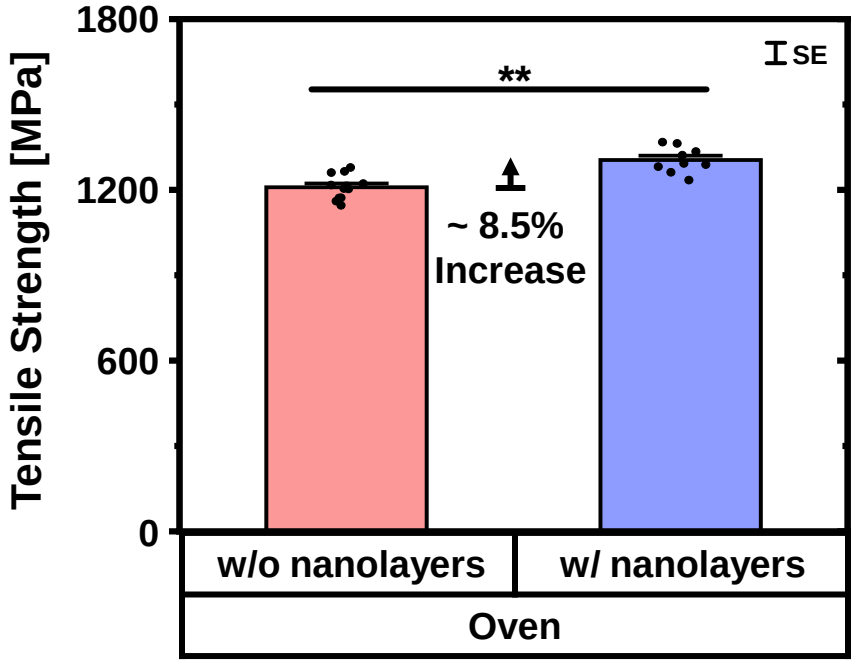

<Ultimate Tensile Strength>

Results of Short-beam Shear Test

- **Short-beam Shear Test** was conducted based on **ASTM D2344** for measurement of **bending** and **shear failure.**
- The composite lay-up consists of **18 unidirectional** (**UD**) **prepregs** (100 mm x 100 mm).
- The **short-beam strength** of the oven-cured laminate w/ nanolayers is significantly **higher** than oven-cured laminate w/o nanolayers (but, slightly lower than the autoclave-cured laminate w/o nanolayers).

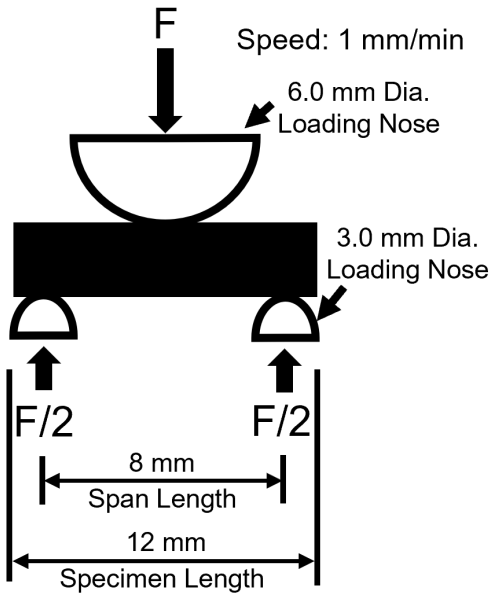

<Schematic of Short-beam shear test>

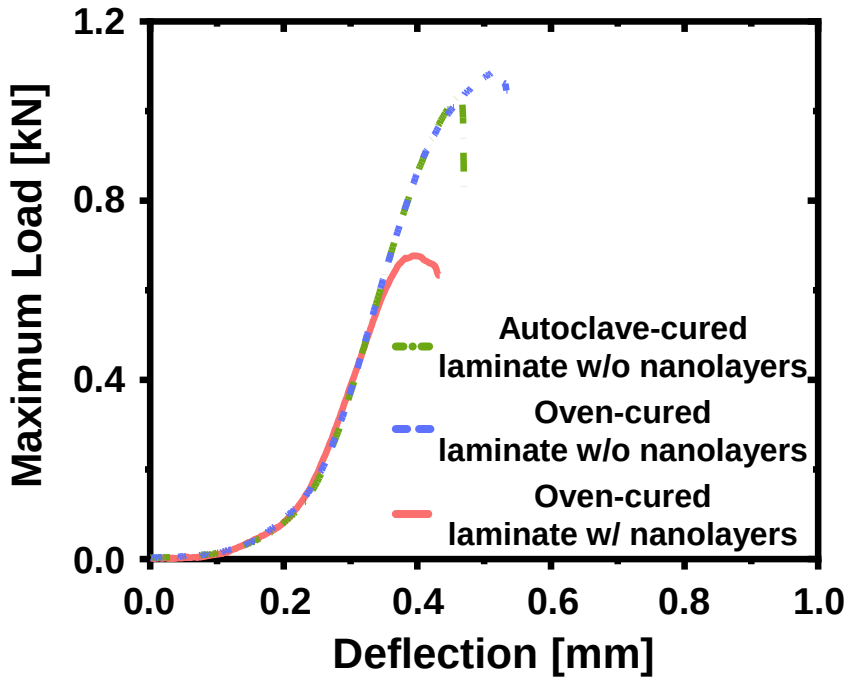

<Load-deflection curve>

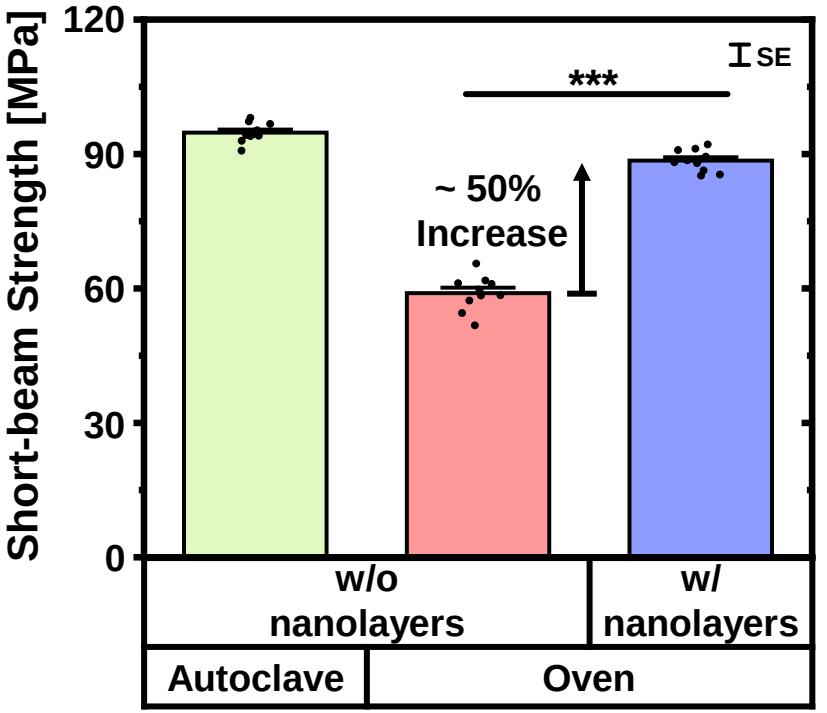

<Short-beam strength>

Conclusion

- We investigated the effects of layering **electrospun nanofiber** at the interfaces of composite laminates.
- Due to nanolayer's conformable morphology and the **capillary action** resulting from the small fiber diameter, nanolayers effectively **reduce voids** in a vacuum-bag-only process.
- Nanolayers **reduce the gas permeability** of the composites, serving as an effective permeation barrier.
- Integration of **nanolayers** in laminate can provides a significant effect on **microcracks prevention**.
- The incorporation of nanolayers **enhances** both the **ultimate tensile strength** and **short beam strength** of the composites.

Acknowledgements

This research was supported by Hanwha Space Hub and the KAIST Space Institute.

Part of the experimental work was performed using the facilities of the KAIST Analysis Research Advancement (KARA).





Thank you for your attention

Contact email: jlee@kaist.ac.kr

COMPARING THE LOCAL PREDICTIONS OF THE STRAIN ENERGY RELEASE RATE BY CZM AND VCCT IN LARGE AND CURVED DELAMINATIONS

Luca M. Martulli[1], Andrea Bernasconi[1], Albert Turon[2] and Laura Carreras[2]

[1]Department of Mechanical Engineering, Politecnico di Milano
Via La Masa 1, 20156 Milan, Italy
Email: lucamichele.martulli@polimi.it

[2]AMADE, Polytechnic School, University of Girona
C/Universitat de Girona 4, 17003 Girona, Spain

Keywords: Composite plates, Modal analysis, Identification, Properties, Finite elements

ABSTRACT

The two most common numerical methods to predict delaminations in composite laminates are the Cohesive Zone Model (CZM) and the Virtual Crack Closure Technique (VCCT). The available literature on the topic has shown comparable performance for CZM and VCCT, but is limited to the comparison of global descriptors, like the load-displacement curve. A local comparison is thus still lacking, especially for large and curved delamination fronts, for which more significant differences are expected. This work thus aims to compare the predictions of CZM and VCCT considering the local calculations of the strain energy release rate G and its components. To address this, we simulated the response of a special reinforced end-notch flexure specimen featuring a curved delamination front. A reference CZM simulation was first performed; since G is not an immediate output of cohesive elements, a J-integral formulation was implemented in this simulation. Delamination fronts were then extracted at different damage levels and then mapped in VCCT simulations. A smoothing algorithm was successfully adopted to compensate the discontinuities due to the discontinuous nature of VCCT. The comparison showed that both methods predicted similar trends in G and its mode I, mode II, and mode III components, but significant differences were observed in absolute values. Overall, this work presents a comparison methodology for the comparison of VCCT and CZM predictions, overcoming the previous limitations of both approaches.

1 INTRODUCTION

Delaminations is a critical failure mode of composite laminates. Predicting it is thus crucial in the safe design of composite structures. The two most commonly adopted numerical approaches for this task are the Cohesive Zone Model (CZM) and the Virtual Crack Closure Technique (VCCT) [1-2]. The former relies on the use of cohesive elements, that are special purpose elements whose constitutive law is in the form of a traction-separation law. Through a damage variable, CZM can model the fracture process zone ahead of the delamination front. Conversely, VCCT is a linear elastic fracture mechanics approach, and does not model any process zone.

Several work in the literature compare the performance of both approaches and under different loading conditions, including static and fatigue loading [1-4]. However, this comparison is often performed at a global scale using global descriptors, most commonly the load-displacement curve. While this allows a first comparison, it provides only limited insights into the capabilities of the two approaches. Moreover, it prevents an understanding of the causes of any possible discrepancy. A more accurate and deep analysis would compare the calculations of the strain energy release rate G at the delamination front, and how G is decomposed in the different modes of fractures. However, this was so far prevented for the following causes:

1. G is not a direct output of the CZM [5-7];
2. The CZM does not make a distinction between mode II and mode III [5-7];

3. The VCCT is often affected by discontinuities and concentrations of G for large and curved crack fronts [8].

This work presents a procedure to overcome these limitations and compare the local readings of G and its components by the CZM and the VCCT. The first two limitations above are overcome by adopting a J-integral formulation of the cohesive elements. The third limitation is addressed by adopting a smoothing algorithm for the description of the delamination front. A large partially reinforced End-Notched Flexure (ENF) specimen was used as study case, since it features large and curved delamination fronts.

2 MATERIALS AND METHODS

2.1 Numerical case-study

Abaqus 2024 was used in all the numerical simulations [9]. Figure 1a shows the partially reinforced ENF specimen considered, which was previously introduced in [6]. It is composed by two 140 mm x 60 mm x 1.5 mm composite plates, featuring an initial 40 mm delamination. Two reinforcing arms, of dimensions 85 mm x 25 mm x 1.5 mm, are bonded on both the top and bottom sides of the ENF: these promote a curved delamination front that evolves during loading.

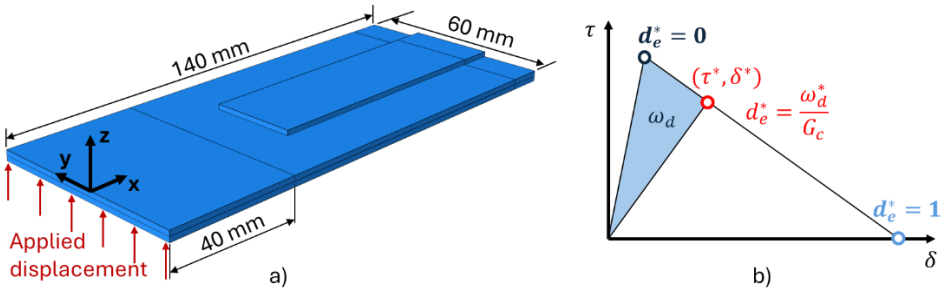

Figure 1: a) The ENF model adopted in this work; b) a triangular traction-separation law.

A vertical displacement is imposed in the front edge of the specimen. Following [6], the material properties of both laminates (large arms and reinforcing arms) and those of the interface are reported in Table 1. In the table, G_{Ic}, G_{IIc} and G_{IIIc} are the mode I, mode II and mode III fracture toughnesses, respectively, while η is the BK law exponent [10]. Note that these toughnesses are used only in the CZM simulations, while the VCCT simulations employ virtually infinite toughnesses (see Section 2.2). For the CZM simulations, bilinear traction-separation laws are considered and described by the stiffnesses K_I, K_{II} and K_{III} and the maximum stresses τ_I, τ_{II} and τ_{III} in mode I, mode II and mode III, respectively. Note that these stresses are adopted to cause an extended process zone: although less realistic, this would better highlight the main differences between VCCT and CZM and facilitate the extraction of the different delamination fronts.

Table 1: Laminate and interface property adopted [6].

Laminate elastic properties					
E_{11} (GPa)	$E_{22} = E_{33}$ (GPa)	$G_{12} = G_{13}$ (GPa)	G_{23} (GPa)	$\nu_{12} = \nu_{13}$ (-)	ν_{23} (-)
154	8.5	4.2	3.036	0.35	0.4
Interface properties for all simulations			**Traction-separation law parameters**		
G_{Ic} (kJ/m^2)	$G_{IIc} = G_{IIIc}$ (kJ/m^2)	η (-)	τ_I (MPa)	$\tau_{II} = \tau_{III}$ (MPa)	$K_I = K_{II} = K_{III}$ (N/mm^3)
0.3	3	2	35	35	10^5

The mesh size in the area of the delamination front was always kept equal to 1 mm or below; in the other regions it was increased for computational efficiency, but it was never higher than 5 mm. For the CZM simulations, solid C3D8I elements were used for all laminates, with three elements in the thickness direction; zero-thickness cohesive elements were used via an UEL subroutine developed in [7]. For the

VCCT simulations, continuum shell SC8R were used for all laminates, with one element in the thickness direction; the standard VCCT interaction of Abaqus was considered [9].

2.2 Adopted approach

A meaningful comparison of the CZM and VCCT readings of G would require the same delamination front and the same imposed displacement. To this end, a first reference CZM simulation was performed with a maximum applied displacement of 30 mm. This simulation was performed considering the initial delaminated 40 mm. As mentioned in Section 1, G is not a direct output of the CZM and a decomposition between mode II and mode III cannot be obtained. Therefore, the J-integral approach developed and implemented in [7] is adopted for the CZM simulation: through the identification of the delamination growth direction, this approach can compute all three G components in a simulation featuring cohesive elements.

The reference CZM simulation thus allows to identify a process zone, defined as:

$$0 < d_e = \frac{\omega_d}{G_c} < 1 \tag{1}$$

where d_e is the energy damage and ω_d is the dissipated energy (both quantities are defined in the traction-separation law reported in Figure 1b). In [7], the iso-damage lines were considered as perpendicular to the delamination growth direction. Therefore, in this work, these are extracted from the CZM process zone and used as delamination fronts for the VCCT simulations. In particular, for specific increments of the CZM simulation, five delamination fronts are extracted corresponding to a damage variable d_e equal to 0, 0.25, 0.5, 0.75 and1.

These delamination fronts are thus described via the nodes whose damage variable d_e is closer to these values. This, however, causes a discontinuous description of the delamination front, since the mesh is not conformal to the shape of the front. As a result, strain energy release rate concentrations arise in corner nodes; moreover, in these nodes, the directions of mode II and mode III propagation cannot be distinguished [6-7]. This is issue is even more critical for the ELS considered in this work, since it is characterised by a very large and curved crack front [8]. Therefore, the coordinates of the nodes composing the delamination front were smoothed using a moving average algorithm with window size of 15. The smoothed coordinates are then mapped to a the VCCT simulation to create the delamination front. Finally, the VCCT simulations can be run with the smoothed delamination front extracted from the CZM simulation: note that, for these simulations, an infinite fracture toughness is considered to prevent propagation and allow the readings of G. A simple schematic of the procedure is reported in Figure 2.

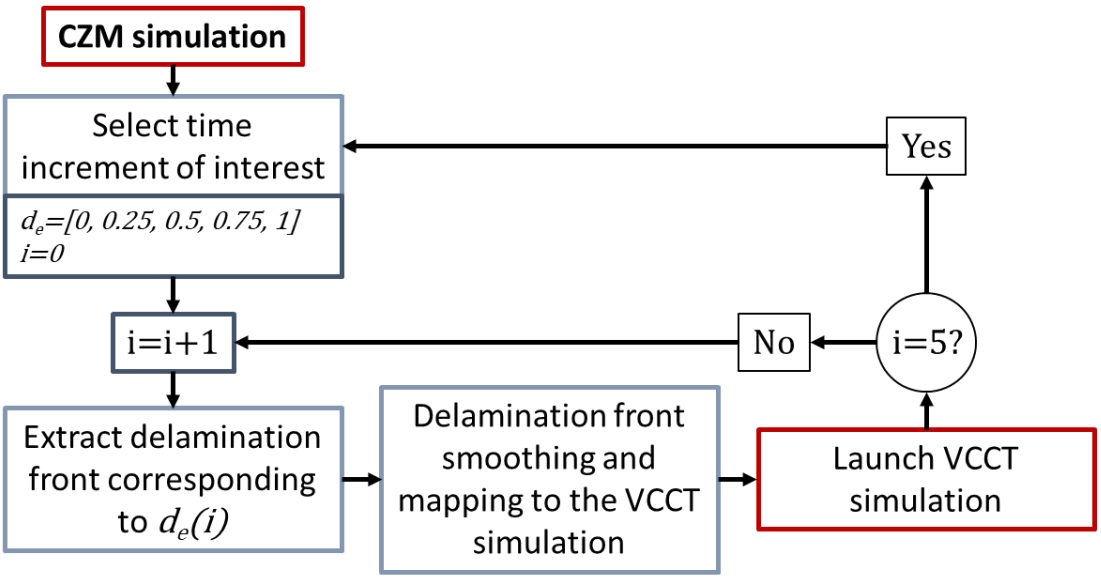

Figure 2: the adopted comparative procedure.

3 RESULTS AND DISCUSSION

Figure 3a shows the load-displacement curve obtained from the CZM simulation. As shown, we have selected two increments on this curve for the present analysis, corresponding to specific values of applied displacement and resulting load. These were selected to ensure the delamination front propagated enough to allow a meaningful comparison. The delamination fronts extracted for both points are reported in Figure 3b and Figure 3c. The delamination fronts of the Figure 3b increment are close to the beginning of the reinforcing arm: the fronts are relatively straight, with some curves starting to form towards lower values of damage. Conversely, the delamination fronts relative to Figure 3c are well developed below the reinforcing arm, being significantly more curved.

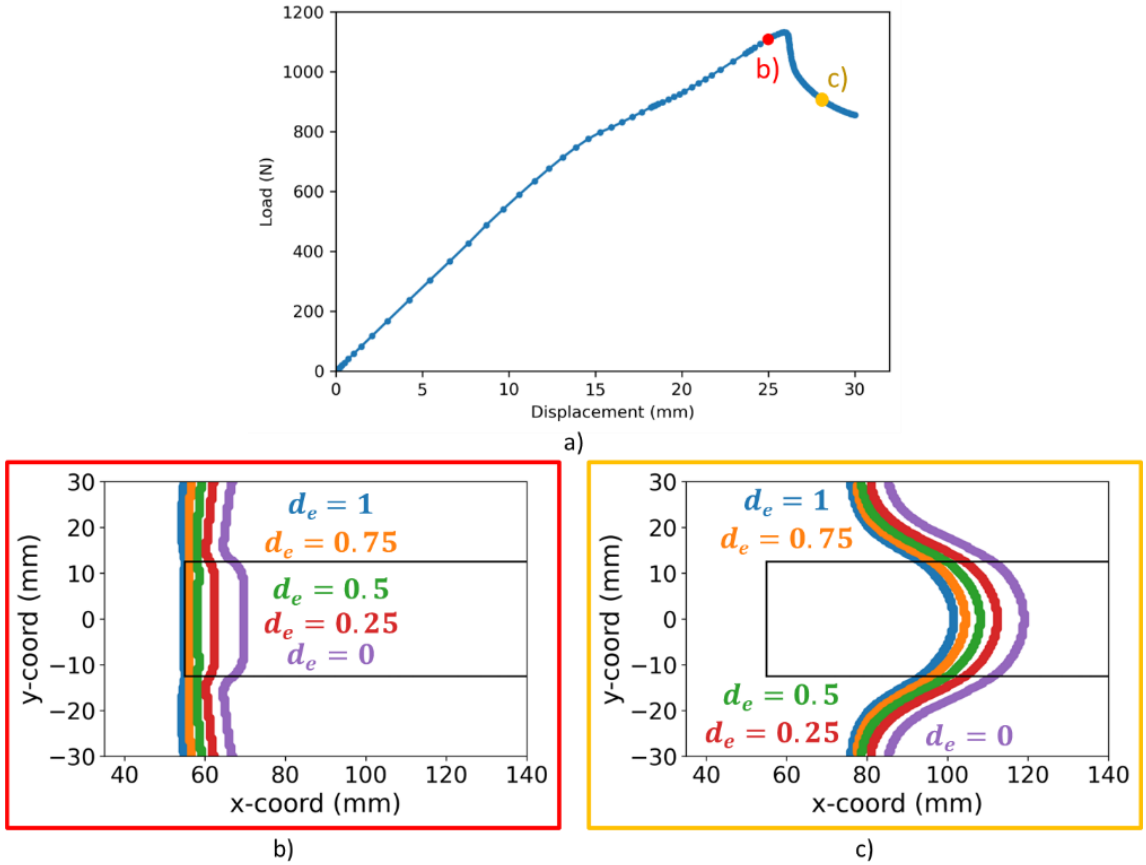

Figure 3: a) load displacement curve of the simulated ELS and b-c) delamination fronts at different increments of the CZM simulation.

The calculated strain energy release rate components by both the VCCT and the CZM (through the implemented J-integral formulation) are reported in Figure 4 and Figure 5 for the delamination fronts reported in Figure 3a and Figure 3b, respectively. Overall, the two techniques seem to lead to similar trends but generally different results.

Regarding Figure 4, the discrepancies between the different fronts appear significant. In particular, the VCCT calculates very high values of the strain energy release rate, especially for the fronts with the higher damage. This higher discrepancy can be explained by the fact that the higher damage fronts are located below the front edge of the reinforcing arms (see Figure 3b). One of the fundamental assumptions of the VCCT is that the propagation of the front is self-similar. The sudden thickness variation cause by the presence of the reinforcing arms makes this assumption not applicable, since the crack propagation is locally altered by the increased thickness and thus stiffness. Indeed, for the lower damage fronts, this effect seems mitigated. This is interesting, since these fronts are more curved than the higher damage ones (see Figure 3b): the thickness variation thus seems to have a stronger effect than the curvature of the delamination fronts.

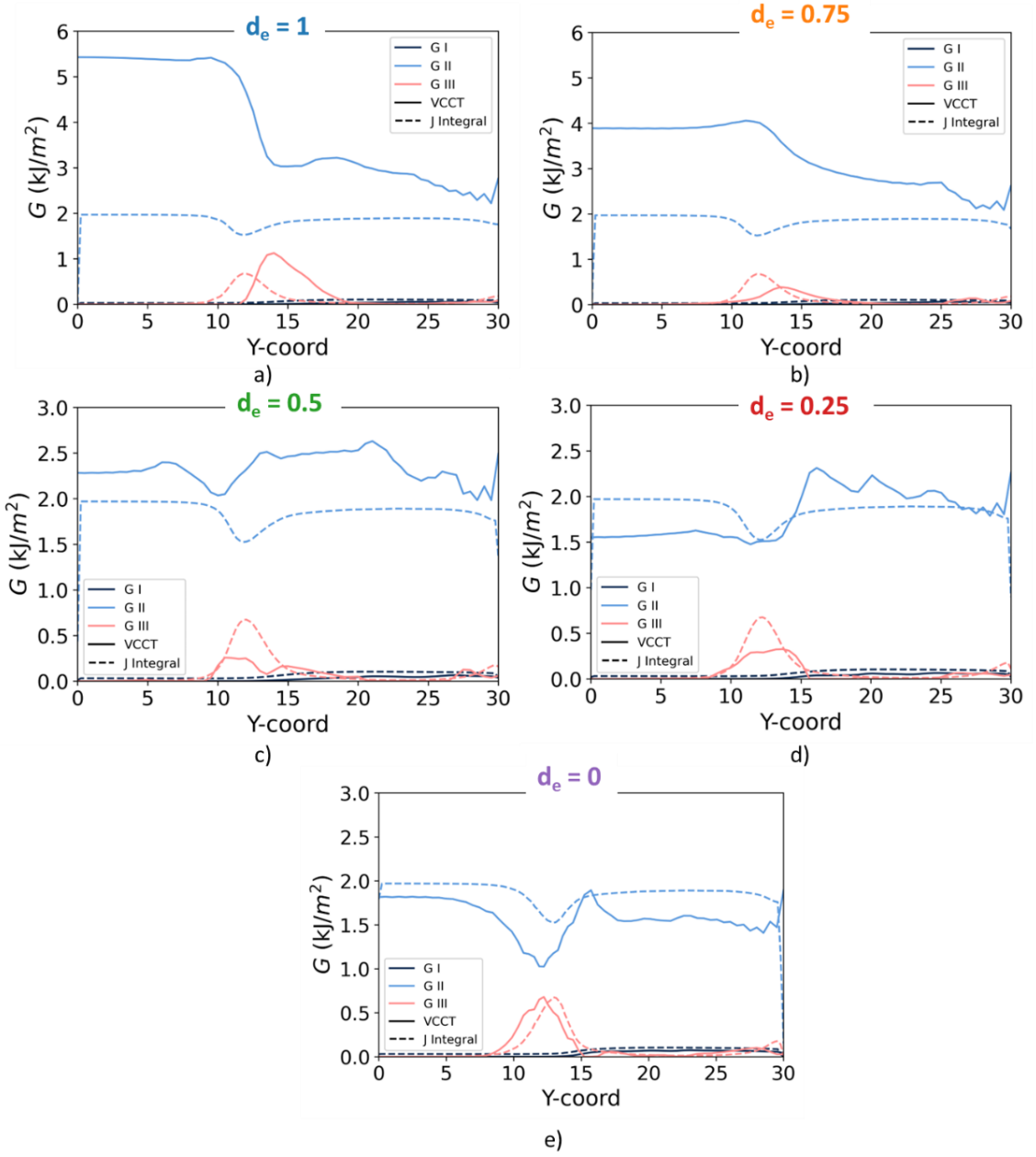

Figure 4: a-e) The calculated components of the strain energy release rate by both the VCCT and the CZM for the five delamination fronts of Figure 3b.

Figure 5 shows, instead, a much closer agreement between the two tested methods. In this case, VCCT and CZM show more similar results for the higher damage fronts. In all cases, the highest discrepancy is observed for the GIII peak in correspondence of about 15 mm of the y-coordinate. Considering the mode III direction, thus parallel to the delamination front, this is also a location of thickness variation still due to the presence of a reinforcing arms' bounding edge (see Figure 3c). Both this discrepancy and the general better agreement seem to confirm that the reinforcing arms affect the accuracy of the VCCT.

In all cases, discrepancies are always observed in at least one of the components of G. Moreover, the discrepancies between the methods seem to be independent between each other, which implies that the total strain energy release rate G_{tot}, the sum of the components, is also calculated differently. Therefore, the discrepancies are not due different decomposition in the modes of fracture.

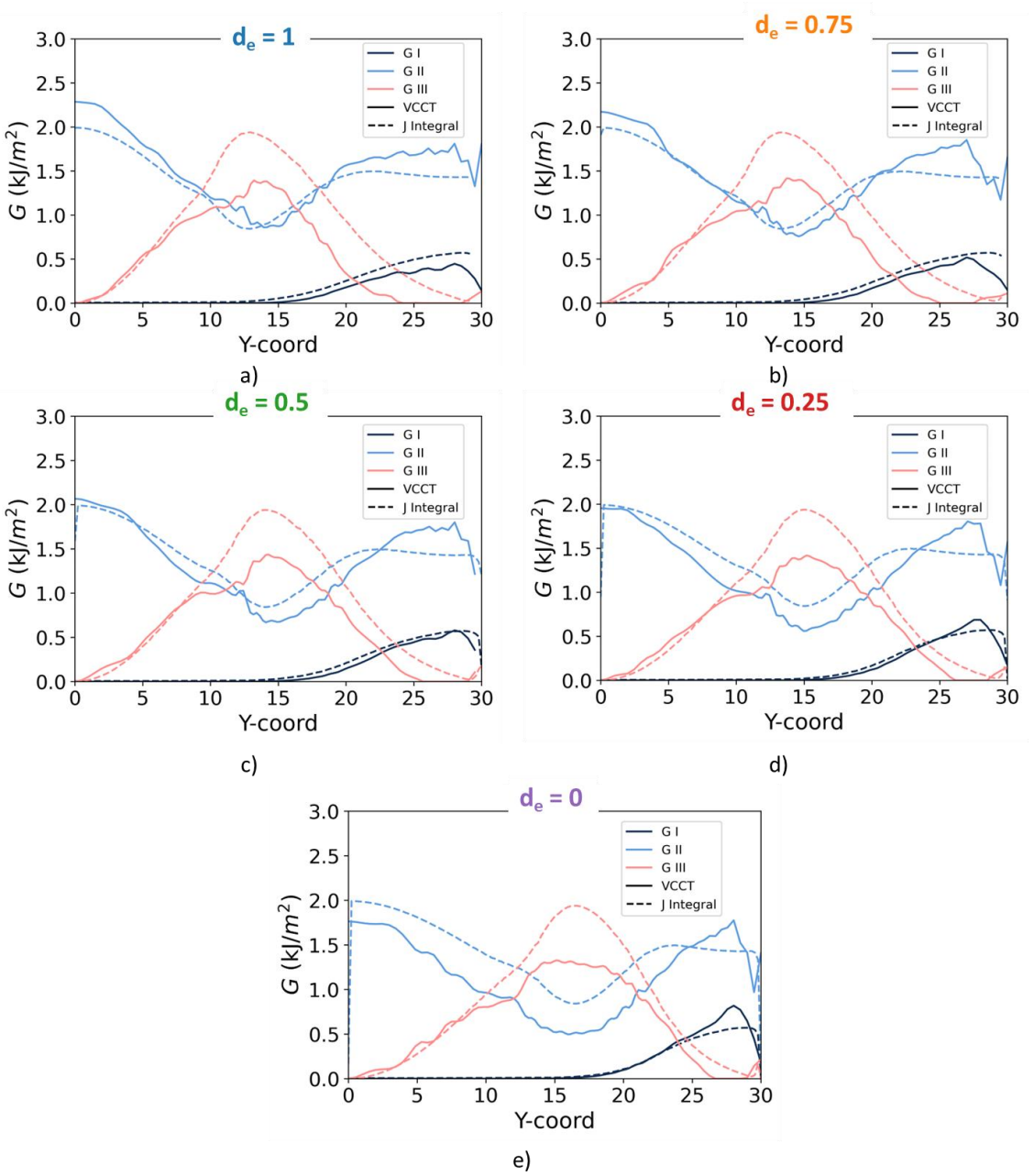

Figure 5: a-e) The calculated components of the strain energy release rate by both the VCCT and the CZM for the five delamination fronts of Figure 3c.

4 CONCLUSIONS AND FUTURE WORKS

This work presented a comparative analysis on the strain energy release rate (G) calculation by the VCCT and the CZM. The two techniques were already compared earlier, but always at a global level, while in this work their local capabilities are investigated. The considered study-case is a reinforced ENF specimen, which causes large and curved delamination fronts.

A specific procedure was thus developed. First, a CZM simulation is run using a J-integral algorithm to compute G at the delamination front from the cohesive elements. For two simulation increments, five delamination fronts were extracted corresponding to damages equal to 0, 0.25, 0.5, 0.75 and 1. These fronts are then smoothed with a moving average algorithm, as their discontinuous nature would prevent correct readings from the VCCT. The smoothed coordinates of the fronts are then mapped onto a new simulation to be run with the VCCT.

All the tested delamination fronts highlighted some level of discrepancy. In particular, the thickness variations caused by the reinforcing arms seemed to be the main source of inaccuracy from the VCCT: indeed, such thickness variations violate the VCCT assumption of a self-similar crack propagation. Conversely, the curvature of the delamination fronts does not seem to cause significant discrepancies: this further confirms the importance of the smoothing algorithm that allows a mesh conformal to the delamination front.

The work investigated mainly two increments of the ENF specimen, which is mainly loaded in mode II and mode III. Further investigations are planned, involving more increments of the ENF as well as the study of a reinforced Double Cantilever Beam (DCB) specimen. The reinforced DCB would allow a mode I comparison, thus extending the scope of this work, but also give a more informed feedback, since experimental results are available for the reinforced DCB. Moreover, the comparison presented in this work is performed considering an extended process zone to better distinguish the different fronts. Considering that the process zone is a key difference between VCCT and CZM, performing this comparison with more realistic process zones is an important future planned work.

REFERENCES

[1] J.A. Pascoe, R.C. Alderliesten, R. Benedictus, Methods for the prediction of fatigue delamination growth in composites and adhesive bonds – A critical review, *Engineering Fracture Mechanics,* **112**, 2013, pp. 72-96.

[2] M. Heidari-Rarani, M- Sayedain, Finite element modeling strategies for 2D and 3D delamination propagation in composite DCB specimens using VCCT, CZM and XFEM approaches, *Theoretical and Applied Fracture Mechanics*, **103**, 2019, 102246.

[3] A. Pirondi, G. Giugliese, F. Moroni, A. Bernasconi, A. Jamil, Comparative Study of Cohesive Zone and Virtual Crack Closure Techniques for Three-Dimensional Fatigue Debonding, *The Journal of Adhesion*, **90**, 2014, pp. 457-481.

[4] R. Liu, Z. Yu, F. Nasonov, Evaluations on VCCT and CZM methods of delamination propagation simulation for composite specimens, *Aerospace systems*, **6**, 2023, pp. 621-632.

[5] A. Turon, P.P. Camanho, J. Costa, C.G. Davila, A damage model for the simulation of delamination in advanced composites under variable-mode loading, *Mechanics of materials*, **38**, 2006, pp. 1072-1089.

[6] L. Carreras, B.L.V. Bak, A. Turon, J. Renart, E. Lindgaard, Point-wise evaluation of the growth driving direction for arbitrarily shaped delamination fronts using cohesive elements, *European Journal of Mechanics / A Solids*, **72**, 2018, pp. 464-482.

[7] L. Carreras, E. Lindgaard, J. Renart, B.L.V. Bak, A. Turon, An evaluation of mode-decomposed energy release rates for arbitrarily shaped delamination fronts using cohesive elements, *Computer methods in Applied Mechanical Engineering*, **347**, 2019, pp. 218-237.

[8] L.M. Martulli, A. Bernasconi, J. Renart, B.L.V. Bak, A. Turon, An efficient and versatile use of the VCCT for composites delamination growth under fatigue loadings in 3D numerical analysis: the Sequential Static Fatigue algorithm, *International Journal of Fatigue*, **170**, 2023, 107493.

[9] Dassault Systemès. Abaqus 2024 manual.

[10] M.L. Benzeggagh and M. Kenane, Measurement of mixed-mode delamination fracture toughness of unidirectional glass/epoxy composites with mixed-mode bending apparatus, *Composite Science and Technology*, **56**, 1996, pp. 439-449.

CFRP RECYCLING METHOD COMPATIBLE WITH A WIDE RANGE OF EPOXY MATRICES

Naoki Mori[1], Masatoshi Kubouchi[1] and Saiko Aoki [1]

[1] School of Materials and Chemical Technology
Department of Chemical Science and Engineering, Institute of Science Tokyo,
2-12-1, Ookayama, Meguro-ku, Tokyo 152-8552, Japan
Email: naoki.m.aa@m.titech.ac.jp web page: https://educ.titech.ac.jp/cap/eng/

Keywords: Composite, CFRP, Recycling,

ABSTRACT

We have developed a chemical recycling method for carbon fiber reinforced plastics (CFRP) using nitric acid decomposition. While carbon fiber (CF) recycling has been widely studied, reports focusing on the chemical recycling of the resin matrix in CFRP remain limited. In this study, we targeted the resin fraction of epoxy-based prepreg CFRP and successfully decomposed it under mild conditions (3 hours at 80 °C) using nitric acid. This process enabled the efficient separation and recovery of carbon fiber with minimal damage, while also allowing for the isolation of decomposed resin fragments.

Characterization of the resin decomposition products revealed the formation of nitro-containing aromatic compounds. Subsequent catalytic hydrogenation of these nitroaromatics yielded amine-functionalized compounds, which were evaluated as potential curing agents for new epoxy resins. The resulting recycled amines demonstrated reactivity comparable to conventional amine hardeners, indicating their applicability as a value-added recycled product. This approach not only contributes to the full recycling of CFRP components but also provides a pathway to upcycle the resin fraction into functional intermediates for polymer synthesis.

Our work highlights a viable strategy for the holistic recycling of thermoset-based CFRPs, addressing the sustainability challenges associated with composite materials. Further research is underway to optimize the reaction parameters, improve product yields, and evaluate the performance of resins cured with the recycled amines in real applications. This study represents a significant step toward establishing a closed-loop material cycle for CFRPs.

1 INTRODUCTION

Carbon fiber reinforced plastics (CFRPs) are composite materials that combine high-strength carbon fiber with a thermosetting polymer matrix, typically based on epoxy resins. Owing to their superior mechanical properties, low weight, and excellent corrosion resistance, CFRPs are widely adopted in high-performance applications such as aerospace structures, automotive parts, wind turbine blades, and sporting goods. While the production of CFRPs is energy-intensive, their lightweight nature allows for significant energy savings during service, particularly in transportation applications, resulting in reduced fuel consumption and carbon dioxide emissions [1]. From a life cycle assessment (LCA) perspective, CFRPs are thus considered environmentally favorable materials [2]. However, the end-of-life (EoL) treatment of CFRPs presents a major sustainability challenge. The difficulty of recycling thermosetting resins, which cannot be remelted or reshaped, has led to widespread incineration or landfilling of CFRP waste, undermining efforts toward resource circulation and environmental conservation [3].

To address these issues, several CFRP recycling techniques have been investigated, including mechanical shredding, pyrolysis, and chemical solvolysis [4-8]. Mechanical recycling involves cutting or grinding CFRP into short-fiber-reinforced fillers. Although this method is relatively simple and low-cost, it significantly degrades fiber properties and limits the reuse of recovered materials to low-performance applications [9]. Pyrolysis processes, which decompose the resin at high temperatures (typically 450–700 °C) in an inert atmosphere, can recover carbon fiber with moderate structural preservation. However, these methods suffer from high energy demand, degradation of fiberurfaces, and emission of volatile organic compounds[6]. Chemical recycling approaches, such as solvolysis, utilize

solvents to depolymerize the matrix resin, offering greater selectivity. Yet, these techniques often face limitations in scalability, solvent recovery, and economic feasibility [7].

A critical limitation of these conventional strategies is their emphasis on recovering carbon fiber while neglecting the thermoset resin fraction. In most cases, the resin is either thermally evaporate or discarded as waste, despite comprising 30–40% of the CFRP mass [8]. This practice not only results in material loss but also generates environmental concerns related to emissions and residues [9]. The limited research on resin recycling can be attributed to technical challenges such as the crosslinked nature of thermoset networks, low intrinsic value of the resin relative to fiber, and the historical focus on maximizing fiber performance [10]. However, for CFRP recycling to align with the principles of a circular economy, it is essential to develop approaches that recover and valorize both components of the composite.

In this study, we present a nitric acid-based chemical recycling method that simultaneously enables the recovery of high-quality carbon fiber and the upcycling of resin decomposition products into functional curing agents. Nitric acid has been previously studied for its ability to depolymerize epoxy model compounds and introduce nitro groups into aromatic moieties under controlled conditions [11-12]. Compared to pyrolysis and solvolysis, nitric acid decomposition offers milder operating conditions, better selectivity, and the potential for downstream chemical transformation of the degraded resin.

To enhance the practicality and efficiency of the proposed method, we selected CFRP prepreg waste as the feedstock material. Prepregs are composed of partially cured epoxy resins and carbon fiber, and they represent a common form of production scrap in composite manufacturing [12]. One key advantage of using prepreg over fully cured CFRP is that partially crosslinked matrices are more susceptible to chemical cleavage, enabling faster and more efficient decomposition. While fully cured CFRP components exhibit dense three-dimensional crosslinking, prepregs retain unreacted or semi-reacted functional groups, reducing the energy, uptimes and reagent requirements for matrix breakdown. In our laboratory, we confirmed that the recovered fiber retained their morphology and mechanical integrity, with some batches even showing improved tensile properties compared to virgin carbon fiber so far [13]

In our experiments, CFRP prepreg samples were treated with concentrated nitric acid at 80 °C for 3 hours. This condition was sufficient to dissolve the matrix and release the embedded carbon fiber with minimal structural damage.

Chemical analysis of the liquid-phase degradation products revealed the formation of nitroaromatic intermediates, derived from the nitration of the epoxy resin's aromatic backbone [14]. These compounds were subsequently subjected to catalytic hydrogenation using palladium on carbon ($Pd(OAc)_2$) under mild conditions (r.t.), yielding amine-functionalized compounds. These recycled amines were then evaluated as potential curing agents for new epoxy systems. Reactivity tests demonstrated comparable performance to commercial hardeners such as polyetheramines, indicating the feasibility of reintroducing the resin-derived products into composite manufacturing workflows.

The novelty of this study lies in the integrated approach that targets both the fiber and resin fractions of CFRP, transforming waste materials into reusable and functional components. By choosing prepreg as a feedstock, the process circumvents some of the chemical intractability associated with fully cured CFRP, thus improving decomposition kinetics and reaction control. Moreover, the nitric acid-based pathway offers a promising route to closed-loop CFRP recycling, combining environmental responsibility with industrial utility.

In contrast to traditional methods that focus solely on carbon fiber preservation, our approach demonstrates the possibility of full-component CFRP valorization under mild and scalable conditions. The dual recovery strategy not only addresses the technical gap in thermoset resin recycling but also contributes to the reduction of emissions and waste associated with CFRP disposal. From an economic standpoint, the ability to obtain both high-quality fiber and value-added resin-derived products enhances the overall material efficiency of the recycling process.

In conclusion, this work establishes a new paradigm in CFRP recycling by leveraging the reactivity of prepreg-based waste and utilizing nitric acid chemistry to achieve simultaneous fiber recovery and resin upcycling. Through the formation of amine curing agents from nitro intermediates, we provide a rare example of thermoset polymer circularity. Ongoing work is focused on optimizing reaction parameters, improving product separation, and scaling up the process for broader industrial application.

The findings presented here lay the foundation for a holistic, sustainable approach to CFRP waste management.

2 EXPERIMENTAL SECTION

2.1 Materials

In this study, the recycle target is Prepreg offcuts derived from actual CFRP manufacturing processes, but in practice new Prepreg were used as raw materials. The material used was TORAYCA® T800SC/3900-2B (Toray Industries, Inc.), consisting of T800SC carbon fiber fabric pre-impregnated with an epoxy-based matrix resin. The precise formulation of the epoxy resin was not disclosed by the manufacturer.

All chemical reagents were purchased from Kanto Chemical Co., Inc. (Tokyo, Japan), and used as received without further purification.

2.2 Nitric acid decomposition

A custom-made 500mL separable flask with fins was used (Figure 1) as decomposition reactor vessel. 10g of prepreg sheet (40mm x 40mm x 0.1mm) was placed in the flask and immersed in 200g of 7.5M nitric acid.

The separable flask was attached to a rotary evaporator, and the reaction temperature was set to 80 °C, and the flask was rotated and stirred at 60rpm for 180 minutes at a constant temperature. After that, the CF and resin decomposition products were removed with tweezers. The CF and resin decomposition products were then washed with 400mL of ion-exchanged water and 300mL of ethyl acetate. The ethyl acetate was evaporated, and 1.6g of resin decomposition products were collected.

On the other hand, to recover the resin digest dissolved in nitric acid, the HNO_3 solution was subjected to liquid-liquid extraction with 200 mL of ethyl acetate. This procedure was repeated three times. The ethyl acetate phase was neutralized with 1 M $NaHCO_3$ aqueous solution before being evaporated to obtain the resin digest, and the ethyl acetate was washed with 200 mL of pure water to remove the salt. Resin decomposition products obtained weighed 1.5 g.

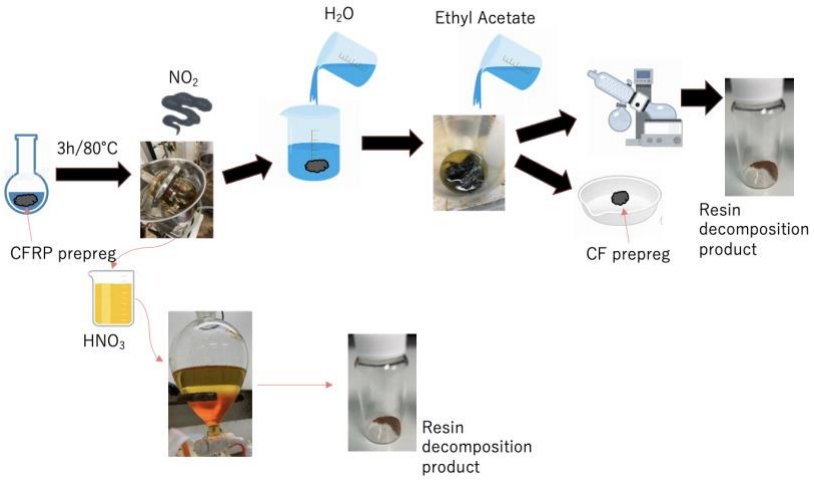

Fig. 1. Carbon fiber decomposition process using nitric acid in the modified separable flask.

2.3 Hydrogenation reaction of resin decomposition

The resin decomposition product (0.5 g) was dissolved in THF (3 mL) at room temperature. Then, the catalyst Palladium (II) acetate (0.5 mmol, 11 mg) and KF (2 mmol, 116 mg) were dissolved in 2 mL of water, and the hydrogenation agent polymethylhydrosiloxane (PMHS) (4 mmol, 0.24 mL) was mixed and stirred for 30 min. After that, the reaction product (approximately 0.2 g) was obtained by filtration through Celite. The obtained reaction product was analyzed by FT-IR to confirm the progress of the

reaction.

2.4 Analytical methods

A thermogravimetric analysis (TGA) was conducted using DTG-60 (Shimadzu) to investigate the amount of the residual resin on the recovered carbon fiber. Fourier transform infrared (FT-IR) spectroscopy was carried out using FTIR-8300 (Shimadzu) to evaluate the functional groups in the decomposed products. Molecular weight distribution was measured using Size Exclusion Chromatography(SEC) (PU-980, JASCO Corporation, Tokyo, Japan). Tetrahydrofuran (THF) was used as mobile phase of SEC analysis.

3 RESULTS AND DISCUSSION

3.1 Optimization of Nitric Acid Decomposition Conditions

To investigate the decomposition behavior of CFRP prepreg under, we employed a custom-built 500 mL separable flask mounted on a rotary evaporator platform, rotated at 60 rpm to ensure gentle agitation and uniform exposure to the acid. Prepreg sheets were immersed in 38 mass% nitric acid at 80 °C for varying durations (5 min to 8 h). The residual resin mass was measured after each time point to evaluate decomposition progress.

As shown in Figure 2, the resin mass began to decrease rapidly within the first hour, reaching a plateau at 3 h, where more than 45% of the matrix resin had decomposed. Beyond this point, no significant change in mass was observed up to 8 h. Therefore, 3 h was adopted as the optimal decomposition time for further processing.

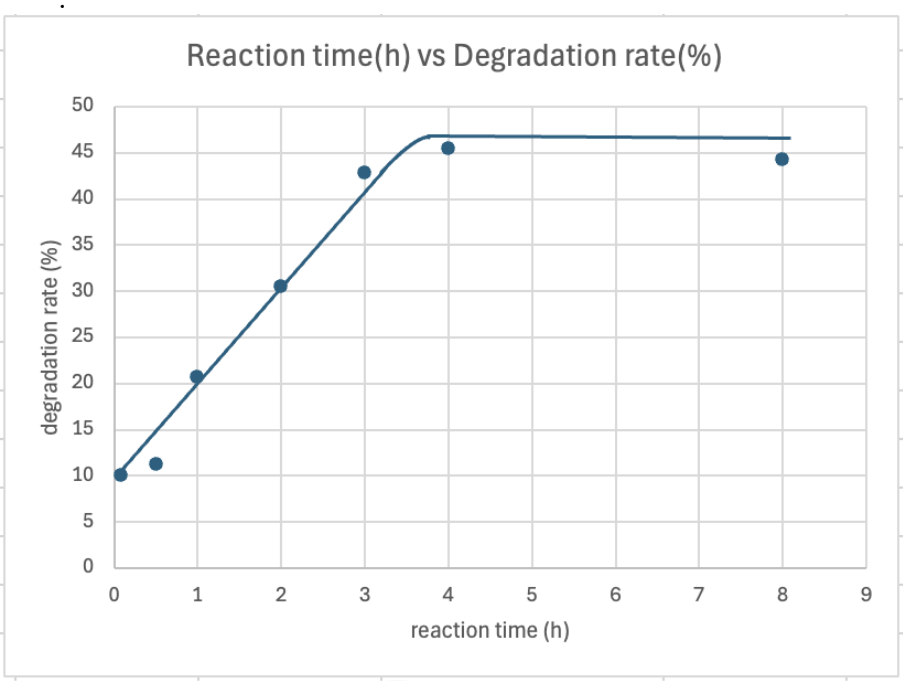

Figure 2: Reaction time(min) vs Degradation rate(%)

To clarify the material flow during the decomposition process, a mass balance summary is provided in Figure 3, which includes input prepreg mass, recovered carbon fiber, and decomposed resin yields. In the optimized 3 h reaction, 10.0 g of prepreg yielded 6.5g of carbon fiber and 3.5 g of organic decomposition products, with the remainder attributed to gaseous losses and trace residues.

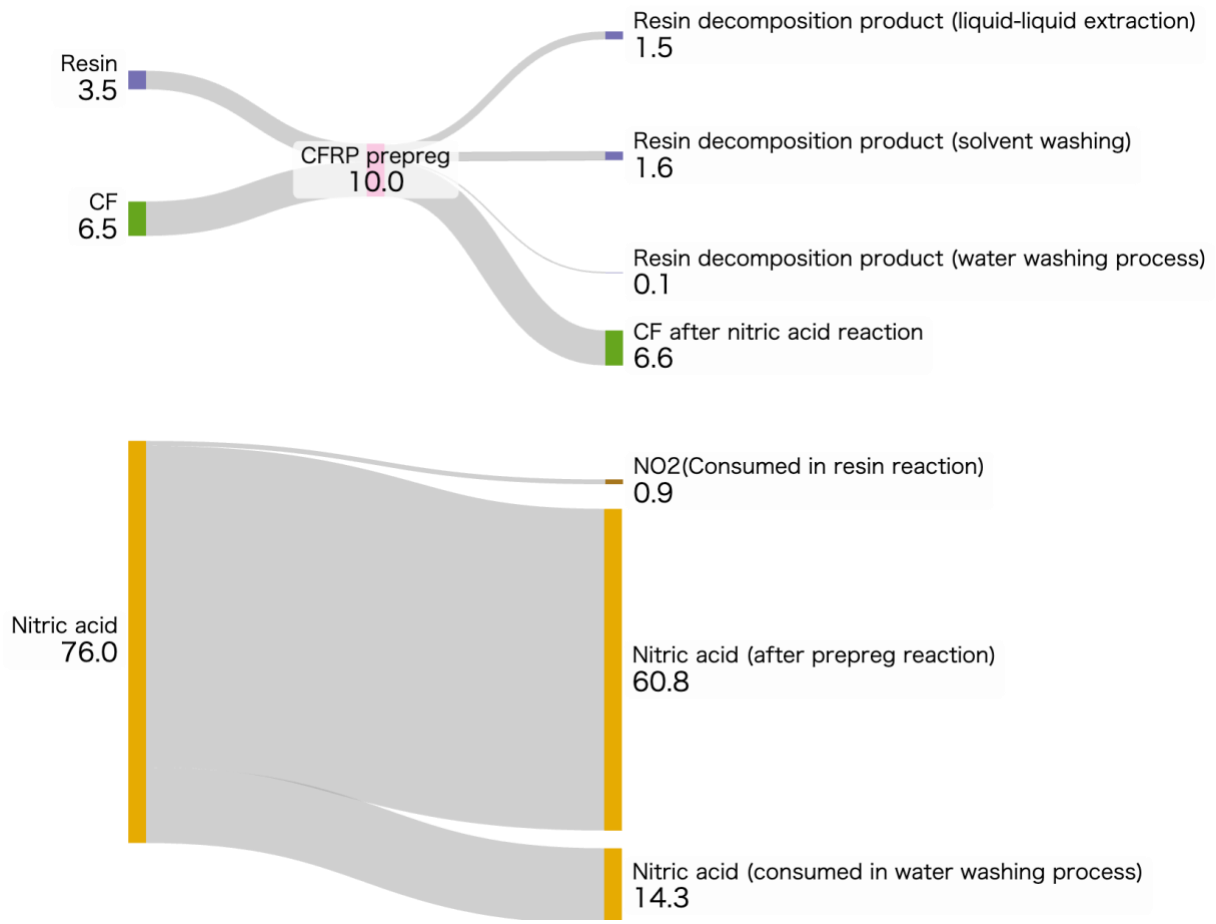

Figure.3 A mass balance summary

3.2 Structural Analysis of Decomposed Resin

Visual observation during the reaction revealed a distinct color change from pale yellow to deep orange, indicating oxidative nitration. FT-IR spectra of the isolated resin decomposition products (Figure 4) exhibited characteristic nitro group peaks at 1550 cm^{-1} (asymmetric stretch) and 1330 cm^{-1} (symmetric stretch), consistent with aromatic nitration. This suggests that the nitric acid preferentially attacked the aromatic backbone of the epoxy network.

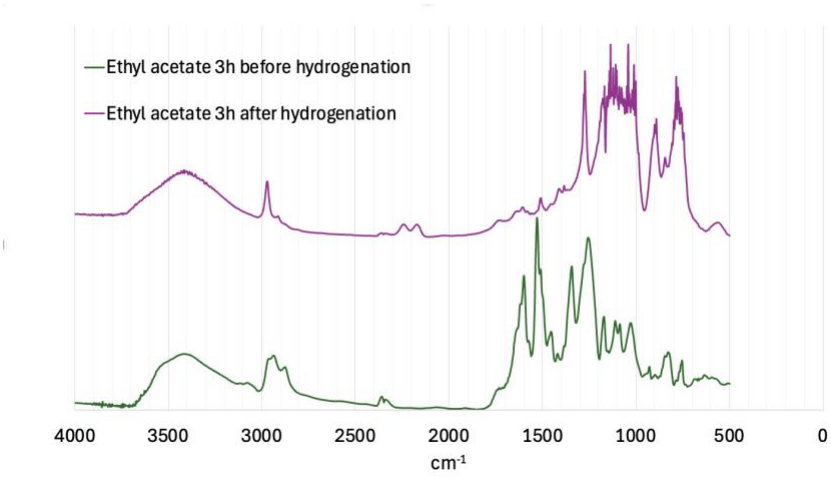

Figure 4: FT-IR of CFRP prepreg and decomposed resin

Molecular weight changes were evaluated using size exclusion chromatography (SEC). The number-average molecular weight (Mw) decreased from 1830 g/mol (original resin) to 1050 g/mol (decomposed resin) after 3 h of treatment.

3.3 Amination and Amine Value Determination

The nitrated resin was subsequently subjected to catalytic hydrogenation using $Pd(OAc)_2$ in THF to obtain amine-functionalized compounds. The reaction product was a black solid with a recovery rate of 62.3 mass%, based on the mass of nitrated intermediates. FT-IR analysis after reduction showed

The disappearance of the peaks at around 1550 cm-1 and 1330 cm-1 due to the nitro group confirmed that the hydrogenation reaction had progressed. (Figure 5).

Amine value titration was conducted in methanol using perchloric acid titrant and crystal violet as the indicator (ASTM D2073-modified method). The resulting amine value was 138 mg KOH/g, corresponding to an amine equivalent weight of 406 g/mol. These results indicate that the recycled amine mixture has sufficient nucleophilicity and basicity for potential use as an epoxy curing agent.

3.4 Application as Epoxy Resin Curing Agent

To test its applicability, the recycled amine was mixed with JER 828 epoxy resin at an equivalent stoichiometric ratio and cured at 60 °C for 1 h followed by 150 °C for 11 h. The resulting cured resin exhibited good crosslinking without surface defects. Mechanical testing revealed a flexural strength of 51 MPa, compared to 62 MPa for the control system cured with commercial Jeffamine D-230. Although approximately 20% lower in strength, the recycled system achieved sufficient hardness and structural integrity, demonstrating practical potential, especially for secondary applications where ultra-high strength is not required.

4 CONCLUSIONS

This study demonstrates that nitric acid decomposition is an effective and scalable method for simultaneous recovery of both carbon fiber and epoxy resin-derived intermediates from CFRP prepreg. The moderate operating conditions (80 °C, 3 h, mild rotation) facilitate high resin decomposition rates while preserving fiber morphology. Subsequent conversion of nitrated oligomers into amine compounds enables their reuse as curing agents, achieving a closed-loop recycling pathway.

The resin recovery and the amine functionality of the final product confirm the feasibility of upcycling CFRP matrices into chemically useful forms. Although the mechanical performance of the recycled resin is modestly lower than that of virgin materials, this can be improved through purification, formulation optimization, or blending strategies. Future work will explore continuous processing configurations and lifecycle analysis to assess environmental and economic advantages of this approach.

ACKNOWLEDGEMENTS

Declaration of Competing Interest

The authors declare that they have no known competing financial interests or personal relationships that could have appeared to influence the work reported in this paper.

REFERENCES

[1] Alam, P., Mamalis, D., Robert, C.; Floreani, C., Brádaigh, C.M.Ó. The fatigue of carbon fibre reinforced plastics—A review. Compos.Part B Eng. **166**,2019, pp. 555–579.

[2] Keith, M.J.; Al-Duri, B., McDonald, T.O., Leeke, G.A., Solvent-Based Recycling as a Waste Management Strategy for Fibre-Reinforced Polymers: Current State of the Art. Polymers 2025, **17**, pp.843. https://doi.org/10.3390/polym17070843

[3] Witik, R.A.; Teuscher, R.; Michaud, V.; Ludwig, C.; Månson, J.-A.E. Carbon fibre reinforced composite waste: An environmental assessment of recycling, energy recovery and landfilling. Compos. Part. A Appl. Sci. Manuf. **49**, 2013, pp. 89–99.

[4] J. M. Park, D. J. Kwon, Z. J. Wang, G. Y. Gu, K. L. Devries, Effect of thermal treatment temperatures on the reinforcing and interfacial properties of recycled carbon fiber-phenolic composites, Composites Part A: Applied Science and Manufacturing, **47**, 2013, pp. 156–164. https://doi.org/10.1016/j.compositesa.2012.12.002.

[5] R. A. Witik, R. Teuscher,V. Michaud, C. Ludwig, J. A. E. Månson, Carbon fibre reinforced composite waste: An environmental assessment of recycling, energy recovery and landfilling, Composites Part A: Applied Science and Manufacturing, **49**, 2013, pp. 89–99.

[6] R .M. Ibarra, M. Sasaki, M. Goto, A. T. Quitain, S. M. G. Montes, J. A. Aguilar-Garib, Carbon Fiber Recovery Using Water and Benzyl Alcohol in Subcritical and Supercritical Conditions for Chemical Recycling of Thermoset Composite Materials, Journal of Material Cycles Waste Management, **17**. 2015. pp. 369–379.

[7] K. W. Kim, H. M. Lee, J. H. An, D. C. Chung, K. H. An, B. J. Kim, Recycling and characterization of carbon fiber from carbon fiber reinforced epoxy matrix composites by a novel super-heated-steam method, Journal of Environmental Management, **203**, 2017, pp. 872–879.

[8] G. Caia, M. Wada, I. Ohsawa, S. Kitaoka, J. Takahashi, Tensile properties of recycled carbon fiber subjected to superheated steam treatment under various conditions, Composite Part A Applied Science Manufacture, **133**, 2020. pp. 195869 https://doi.org/10.1016/j.compositesa.2020.105869

[9] E. Butler, G. Devlin, D. Meier, K. McDonnell, A review of recent laboratory research and commercial developments in fast pyrolysis and upgrading, Renewable and Sustainable Energy Reviews, **15**, 2011. 8 4171-4186. https://doi.org/10.1016/j.rser.2011.07.035.

[10] J. Zhang, V. S. Chevali, H. Wang, C. H. Wang, Current status of carbon fibre and carbon fibre composites recycling, Composites Part B: Engineering, **193**, 2020. pp. 108053 https://doi.org/10.1016/j.compositesb.2020.108053.

[11] W. Dang, M. Kubouchi, S. Yamamoto, H. Sembokuya, K. Tsuda, An approach to chemical recycling of epoxy resin cured with amine using nitric acid, *Polymer*, **43**, 10, 2002, pp. 2953-2958 https://doi.org/10.1016/S0032-3861(02)00100-3.

[12] T. Hanaoka, Y. Arao, Y. Kayaki, S. Kuwata, M. Kubouchi, New Approach to Recycling of Epoxy Resins Using Nitric Acid: Regeneration of Decomposed Products through Hydrogenation, ACS Sustainable Chemistry & Engineering, **9**, 37,2021, pp. 12520-12529, https://doi.org/10.1021/acssuschemeng.1c01737.

[13] Sakai, A., Kurniawan, W., Kubouchi. M., Chemical Recycling of CFRP in an Environmentally Friendly Approach. Polymers **16**, 2024, pp. 143.https://doi.org/10.3390/polym16010143

[14] Hanaoka.T., Arao.Y., Kayaki.Y.,Kuwata.S., Kubouchi.M., Analysis of nitric acid decomposition of epoxy resin network structures for chemical recyclingPolymer Degradation and Stability Volume **186**, 2021, pp.109537

ATA ENGINEERING, INC.

Uncertainty Quantification of X-ray CT Segmentation of Multiclass Microdamage in Advanced Composites via Deep Learning

Reed Kopp, Rohan Patel, and Chiemeka Nzerue

ATA Engineering, Inc., San Diego, CA

24th International Conference on Composite Materials

August 6, 2025

NAVAIR Public Release SPR# 2025-0376. Distribution Statement A - Approved for public release; Distribution is unlimited.

(858) 480-2000 www.ata-e.com ata-engineering

San Diego • Los Angeles • Berkeley • Albuquerque • Denver • Huntsville • Washington D.C. • Boston • Madison



Overview

- Motivation and Background
- Approach and Results
- Conclusions and Future Work

NAVAIR Public Release SPR# 2025-0376. Distribution Statement A - Approved for public release; Distribution is unlimited.

Carbon Fiber Reinforced Polymers (CFRPs) Exhibit Complex Micro/Mesoscale Failure Modes under Mechanical Loading

- Consider general loadings of a **single CFRP unidirectional ply**:

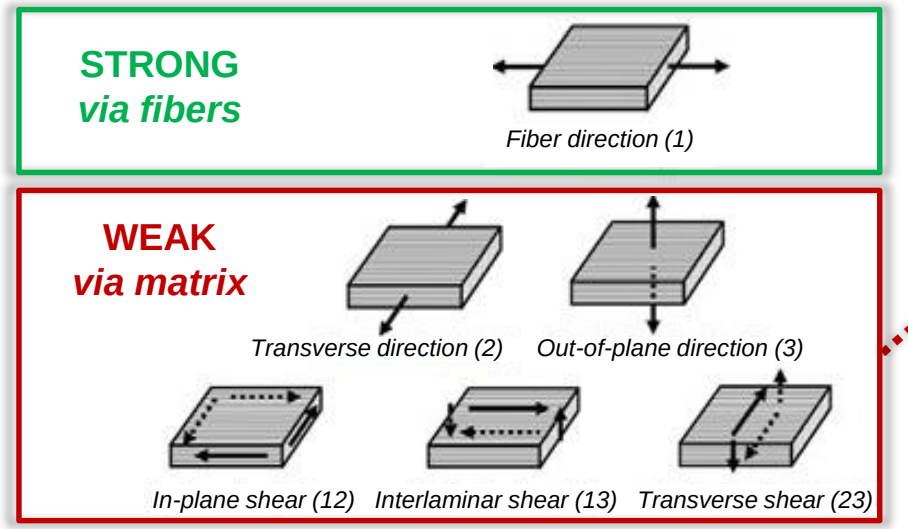

Source: Composites World

Intra-ply (single ply) damage modes

Failure via multiple damage modes

Inter-ply (ply-ply) damage modes

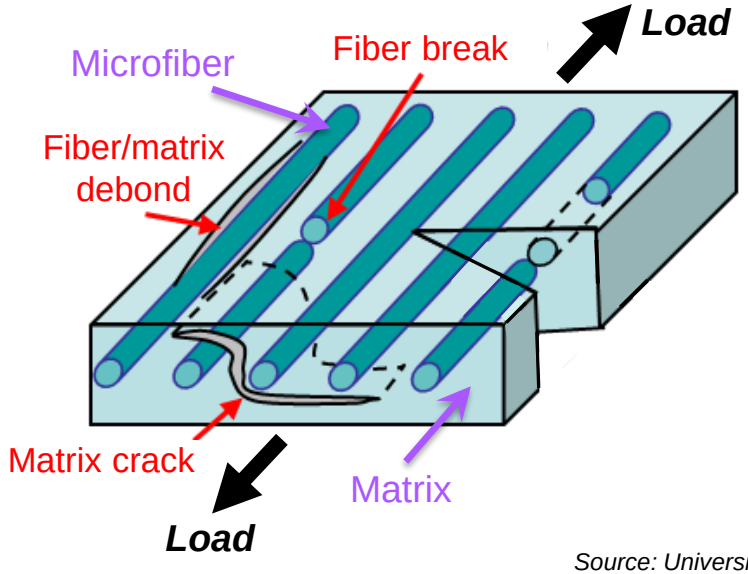

Source: University of Liège (adapted)

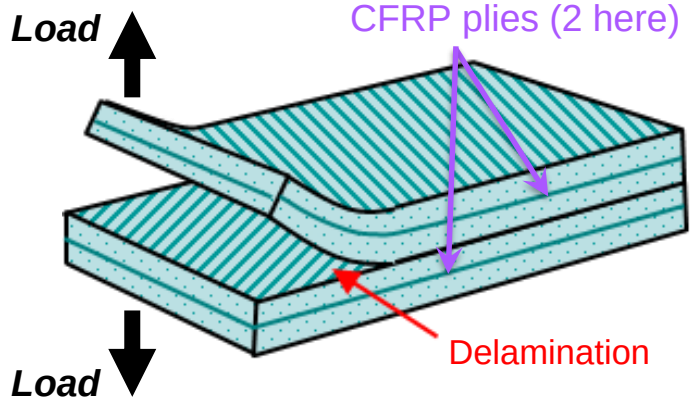

NAVAIR Public Release SPR# 2025-0376. Distribution Statement A - Approved for public release; Distribution is unlimited.

Progressive Damage Characterization Underpins CFRP Strength/Toughness Understanding but is Limited

Characterizing progressive damage requires imaging of several material features:

- constituent morphology *(micro-/meso-structure)*
- manufacturing defects & damage precursors
- multi-scale damage *(micro-, meso-, macro-)*

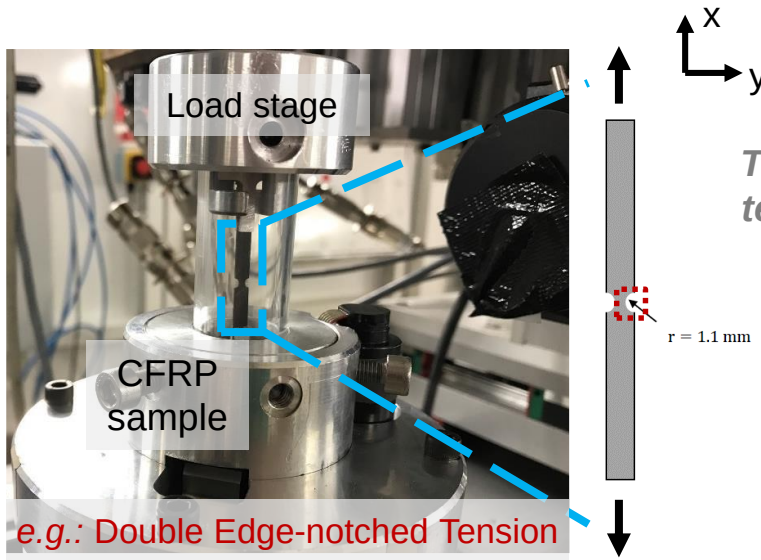

e.g.: Double Edge-notched Tension

Traditional techniques

1. **Exterior:** Microscopy (optical, **scanning electron**)
   - High-resolution, but only 2D
   - Can be destructive to expose interior

Scanning electron microscopy (SEM)



e.g. **Nanostitch** effects on damage *[Lewis et al. 2016]*

2. **Interior:** **Ultrasound** (**C-scan**, tomography), 2D X-ray
   - C-scan: low-resolution, "quasi-3D", underwater
   - Step-wise *ex situ* with cyclic imaging/reloading

C-scan



e.g. **Ply thickness** effects on damage *[Amacher et al. 2014]*

Challenge: How can we characterize 3D micro-failure behavior?

NAVAIR Public Release SPR# 2025-0376. Distribution Statement A - Approved for public release; Distribution is unlimited.

Modern Progressive Damage Characterization:
X-ray µCT Reveals 3D Material Interior

Characterizing progressive damage requires imaging of several material features:

- constituent morphology *(micro-/meso-structure)*
- manufacturing defects & damage precursors
- multi-scale damage *(micro-, meso-, macro-)*

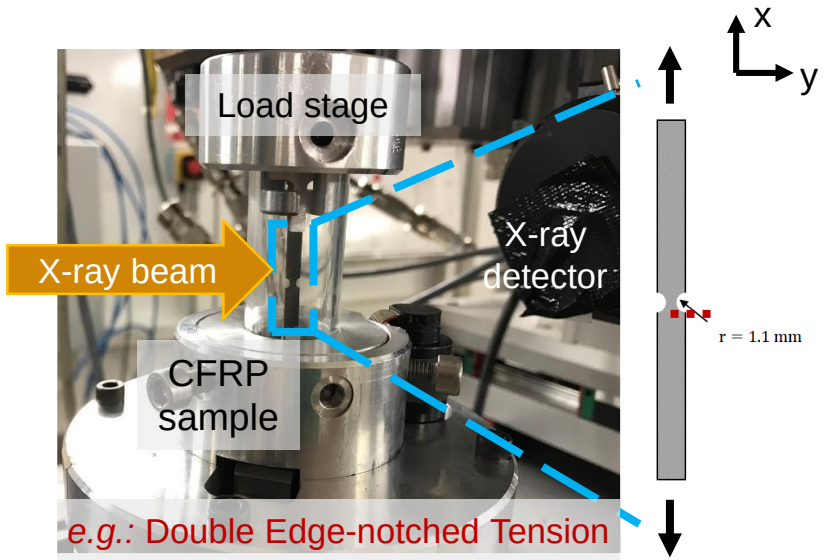

Challenge: How can we characterize 3D micro-failure behavior?

X-ray Micro-computed Tomography (µCT) → Nondestructive high-resolution imaging of material interior

2D Virtual Cross-sections

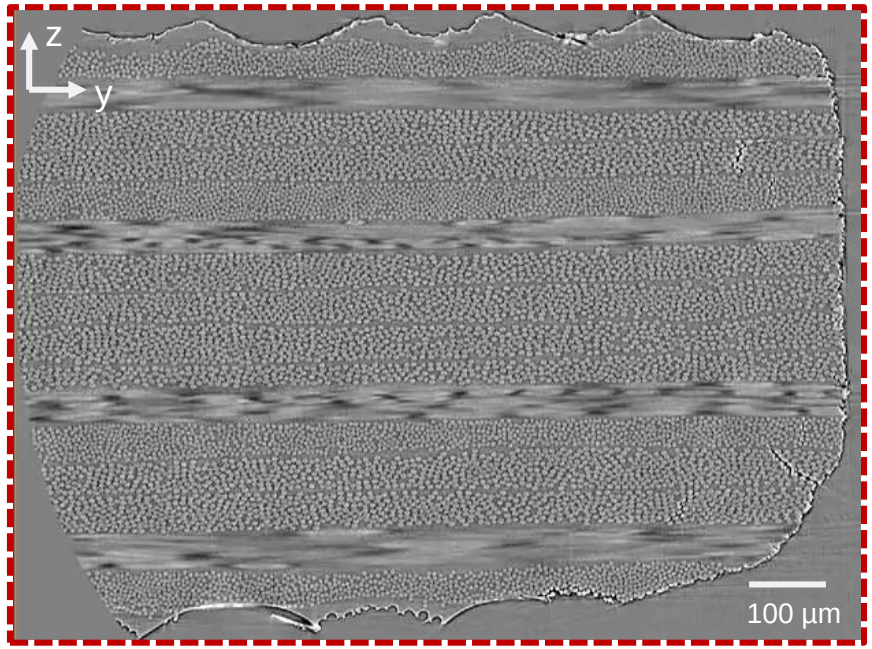

NAVAIR Public Release SPR# 2025-0376. Distribution Statement A - Approved for public release; Distribution is unlimited.

Modern Progressive Damage Characterization:
X-ray µCT Reveals 3D Material Interior

Characterizing progressive damage requires imaging of several material features:

- constituent morphology *(micro-/meso-structure)*
- manufacturing defects & damage precursors
- multi-scale damage *(micro-, meso-, macro-)*

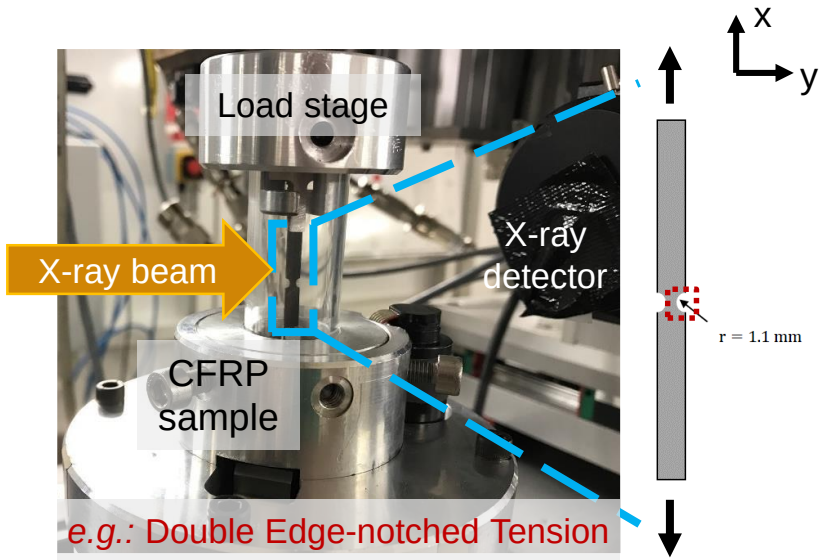

Challenge: How can we characterize 3D micro-failure behavior?

X-ray Micro-computed Tomography (µCT) → Nondestructive high-resolution imaging of material interior

Mutually ⊥ 2D Cross-sections

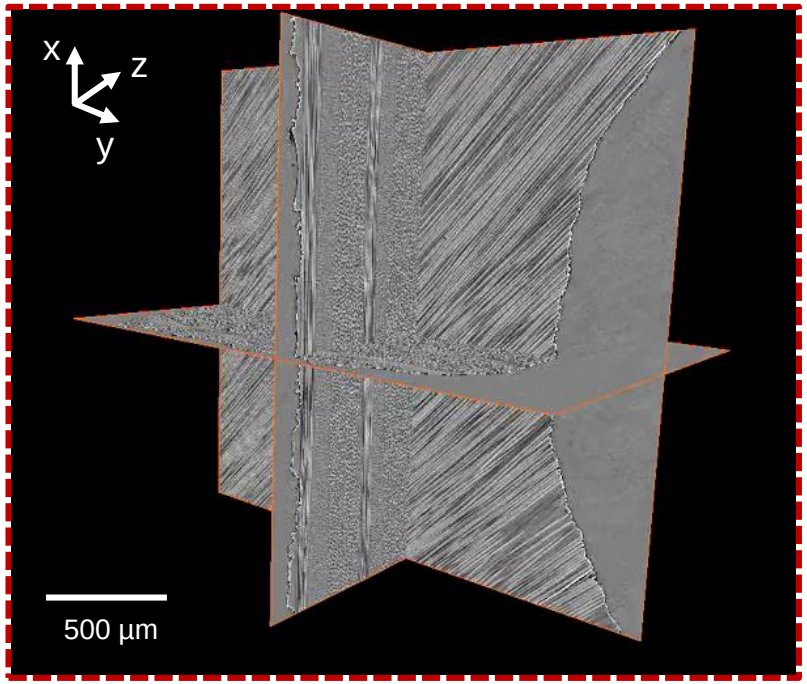

NAVAIR Public Release SPR# 2025-0376. Distribution Statement A - Approved for public release; Distribution is unlimited.

Multiclass 3D Microdamage Characterization in Heterogeneous Materials

- What is the current segmentation problem and why is it hard (**no rule-based feasible solutions**)?

Heterogeneous materials → **μCT-based *in situ* visualization** → **BIG data**

Advanced composites

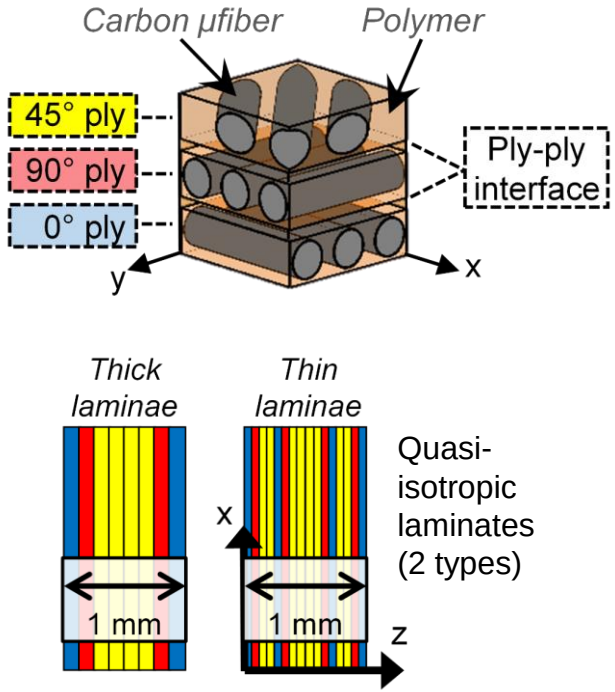

3D damage progression (artifact prone)

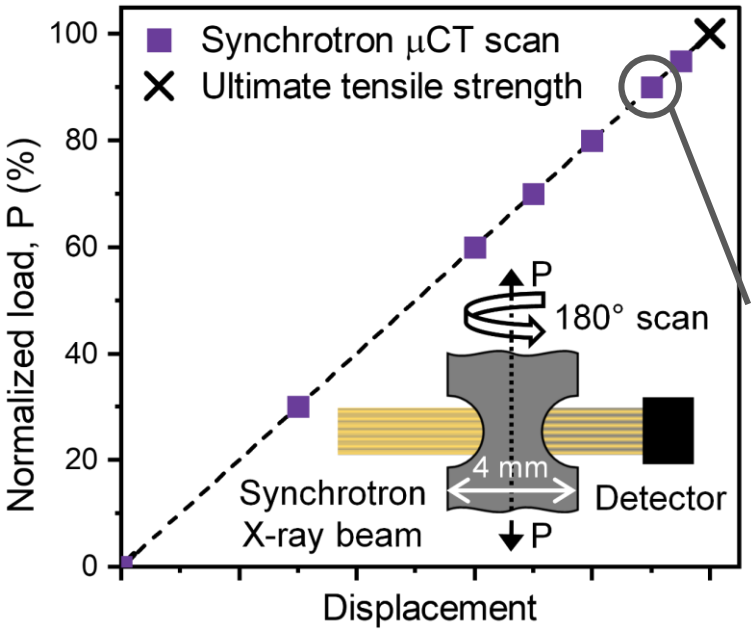

Stack of virtual cross-sections (bottleneck)

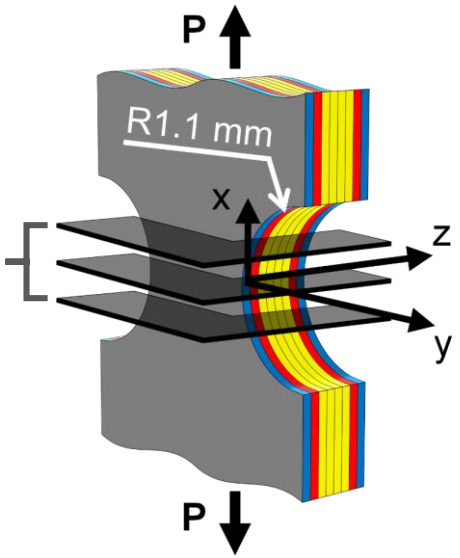

NAVAIR Public Release SPR# 2025-0376. Distribution Statement A - Approved for public release; Distribution is unlimited.

Multiclass 3D Microdamage Characterization in Heterogeneous Materials

- What is the current segmentation problem and why is it hard (**no rule-based feasible solutions**)?

μCT-based *in situ* visualization → **BIG data** → **Sparse, complex damage**

3D progressive damage (artifact prone)

Stack of virtual cross-sections (bottleneck)

*Multiclass, interacting **polymer-related microdamage** nondestructively observed in heterogeneous material*

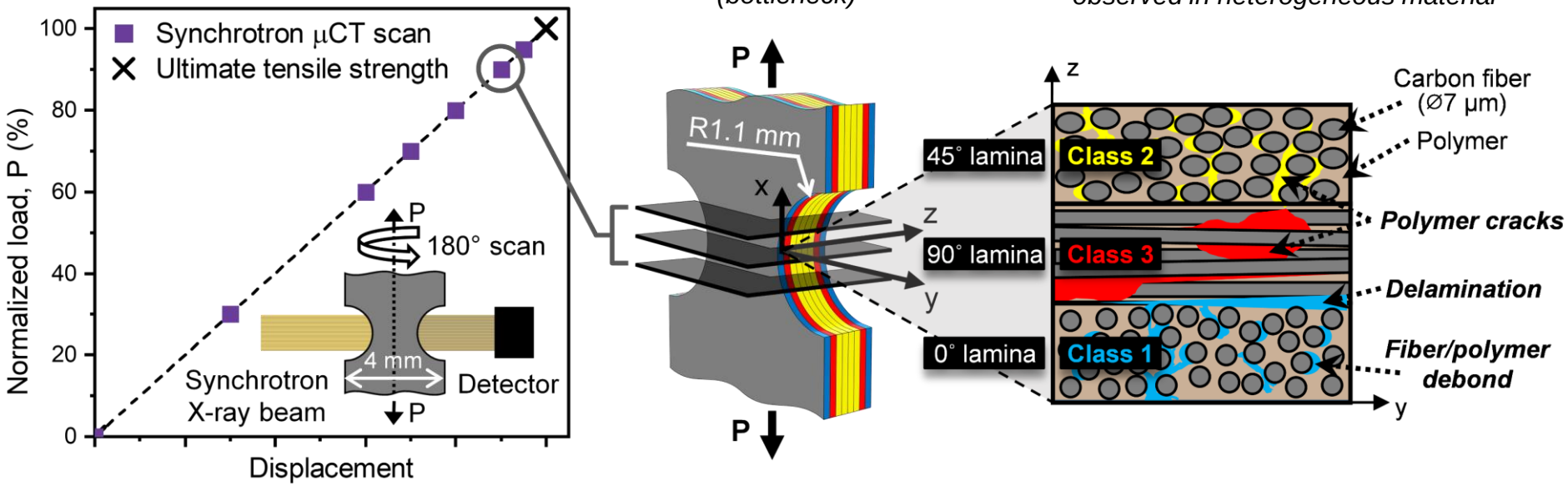

NAVAIR Public Release SPR# 2025-0376. Distribution Statement A - Approved for public release; Distribution is unlimited.

Modern Progressive Damage Characterization:
How to achieve objective analysis of X-ray µCT data?

- Consider an artifact-prone raw (unsegmented) tomogram, following minimal pre-processing:

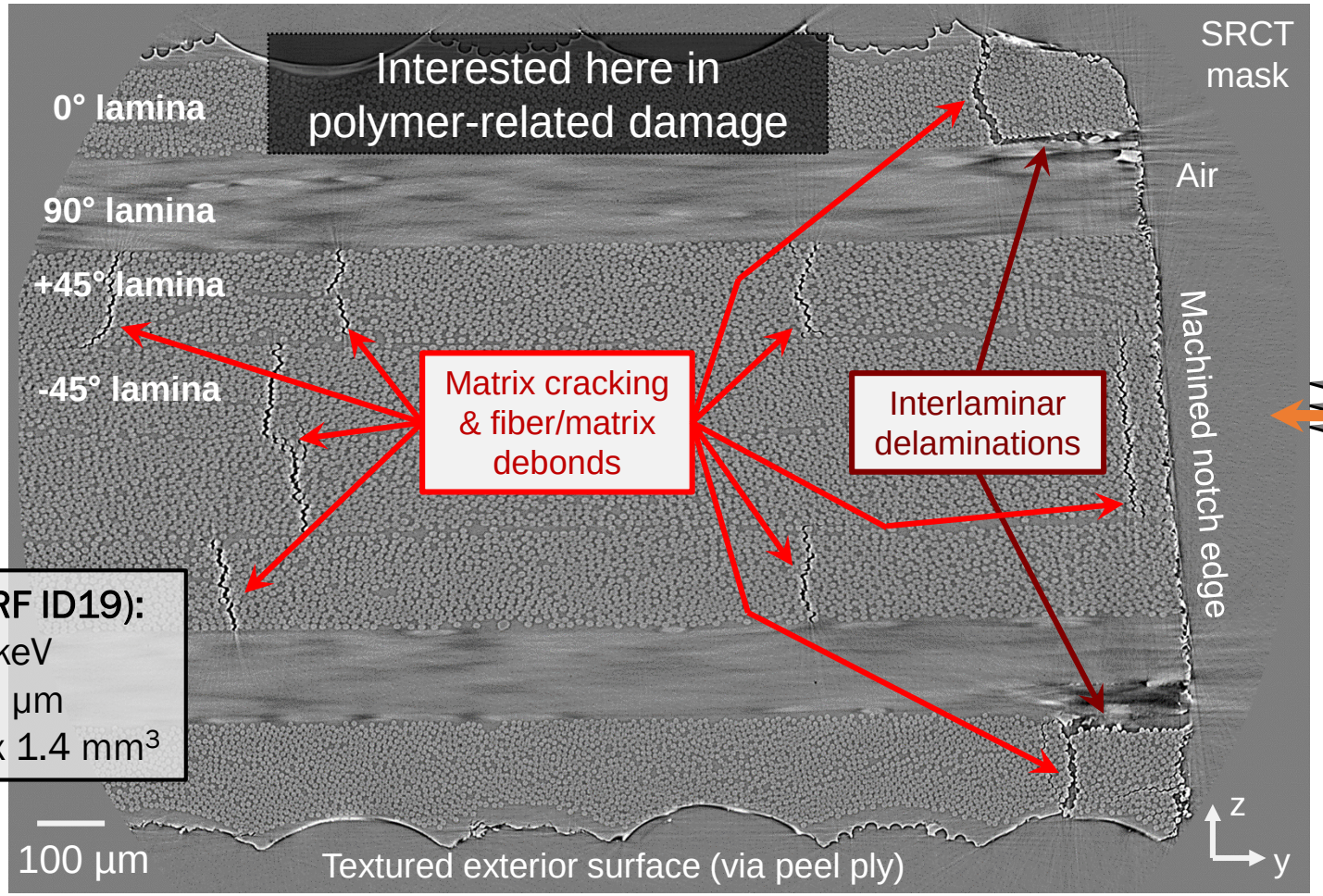

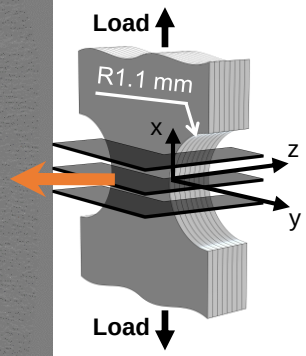

SRCT parameters (ESRF ID19):

X-ray energy:	20 keV
Voxel (vx) size:	0.65 µm
Field-of-view:	1.6 x 1.6 x 1.4 mm^3

NAVAIR Public Release SPR# 2025-0376. Distribution Statement A - Approved for public release; Distribution is unlimited.

Modern Progressive Damage Characterization:
How to achieve objective analysis of X-ray µCT data?

- **Semi-auto human segmentation** of multiclass matrix damage (general state-of-the-art method*):

Class imbalance challenge

Background pixel count: 99.74% *(bulk, air, mask)*
0° damage pixel count: 0.08%
±45° damage pixel count: 0.18%
90° damage pixel count: 0.00% *(user error)*

Sparse damage *(0.26% of pixels here)*

Matrix damage
- 0° ply
- ±45° ply
- 90° ply

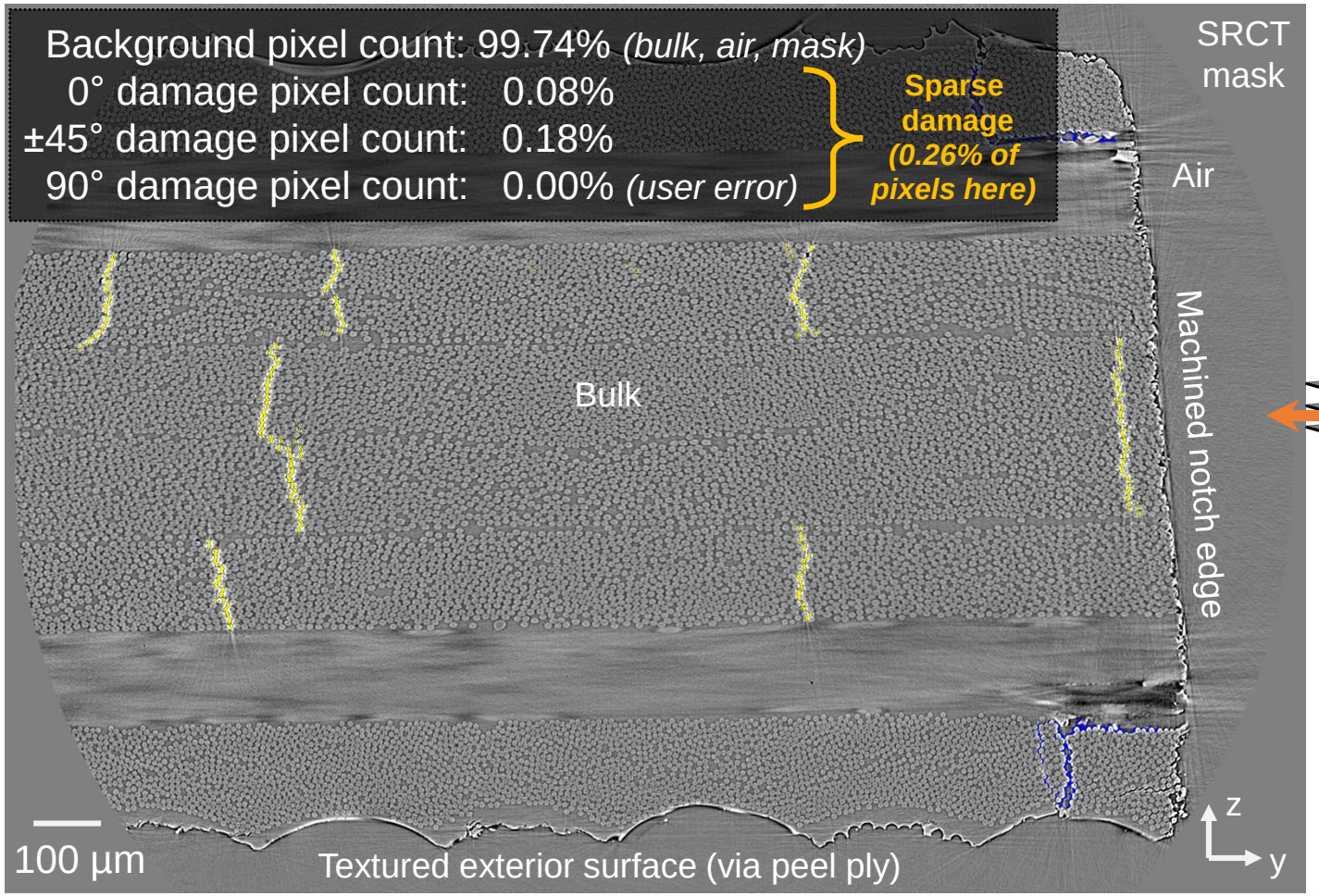

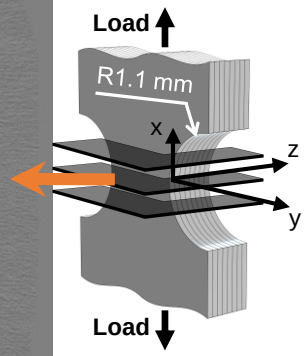

*Approx. 10 h per scan segmentation

NAVAIR Public Release SPR# 2025-0376. Distribution Statement A - Approved for public release; Distribution is unlimited.

Deep Learning (DL)-based computer vision for complex, sparse defect segmentation (1/2)

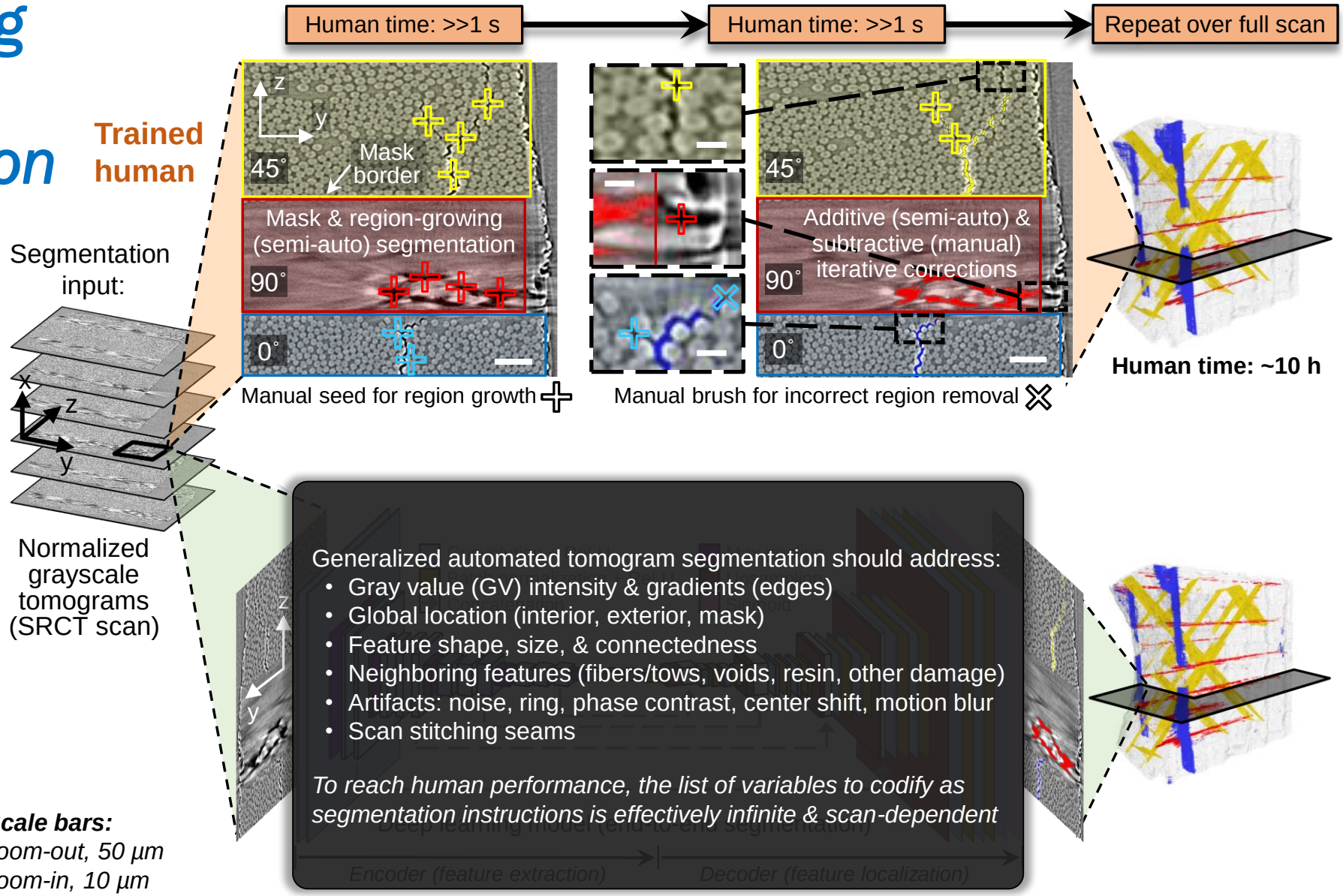

Scale bars:
zoom-out, 50 µm
zoom-in, 10 µm

NAVAIR Public Release SPR# 2025-0376. Distribution Statement A - Approved for public release; Distribution is unlimited.

DL-based computer vision for complex, sparse defect segmentation (2/2)

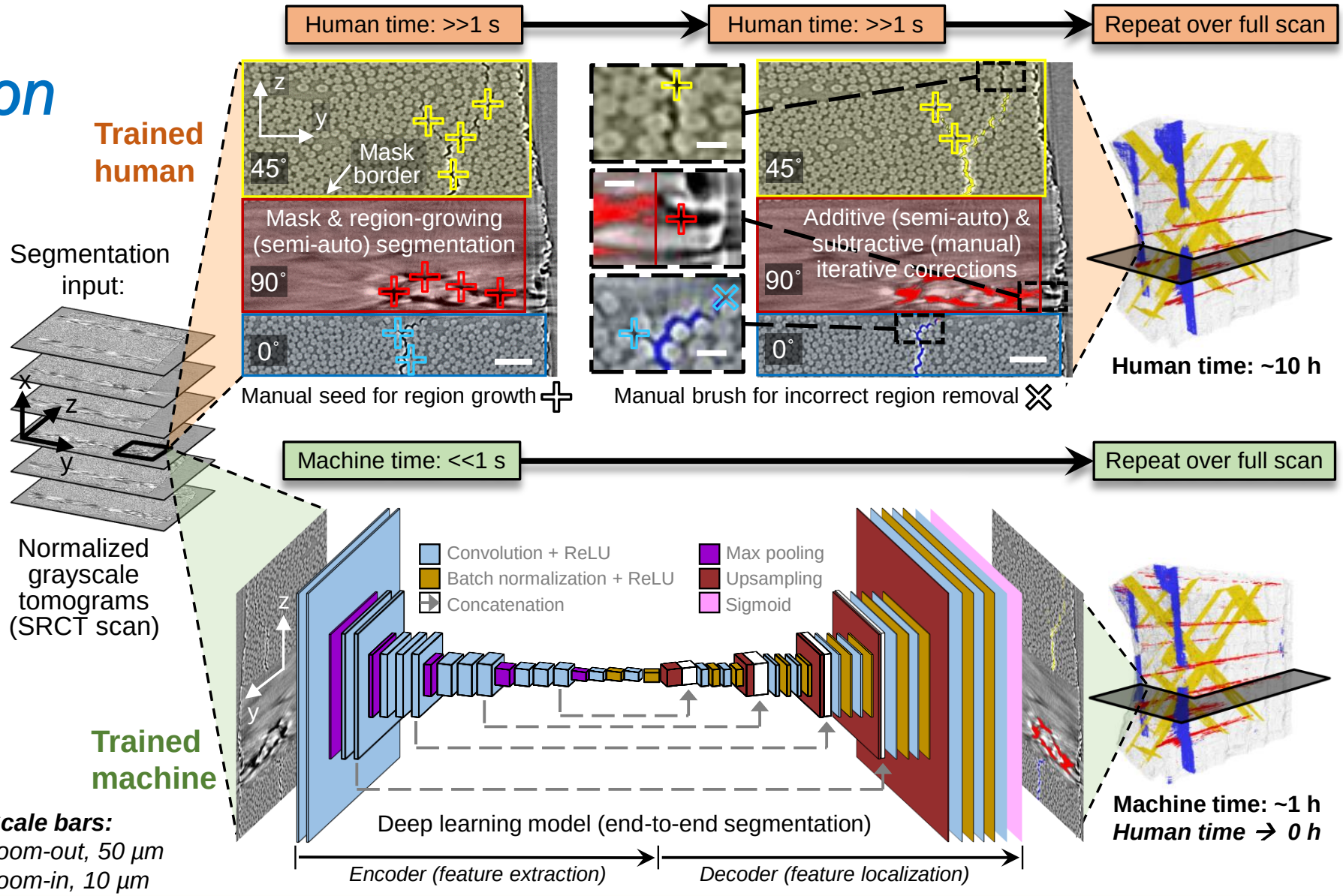

NAVAIR Public Release SPR# 2025-0376. Distribution Statement A - Approved for public release; Distribution is unlimited.

DL-based computer vision for complex, sparse defect segmentation (2/2)

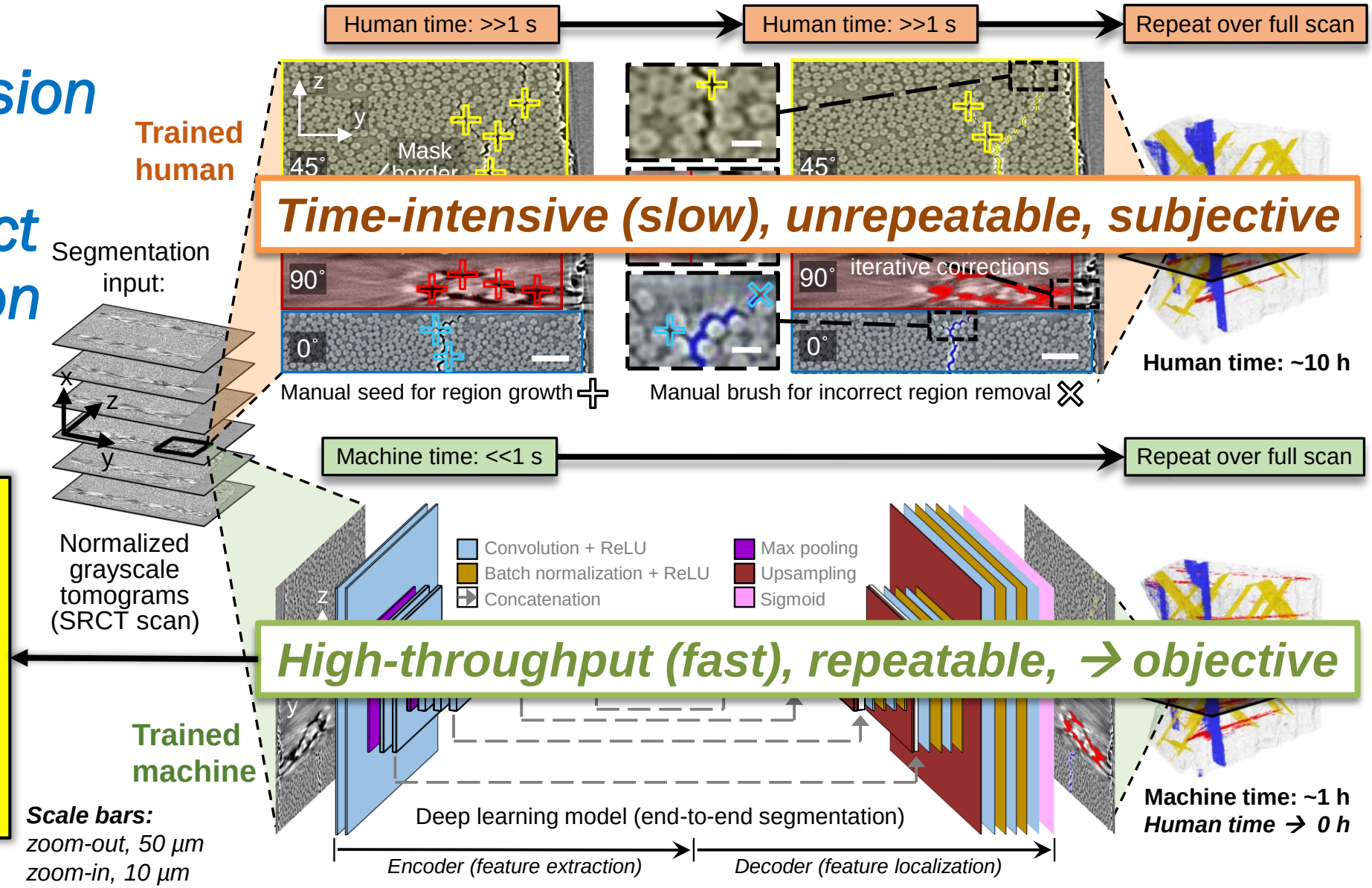

However, broader body of related literature still focused on deterministic methods.

Scale bars:
zoom-out, 50 µm
zoom-in, 10 µm

NAVAIR Public Release SPR# 2025-0376. Distribution Statement A - Approved for public release; Distribution is unlimited.

Study Goals at the Intersection of Advances in Composites Damage and Computer Vision for Materials XCT Segmentation

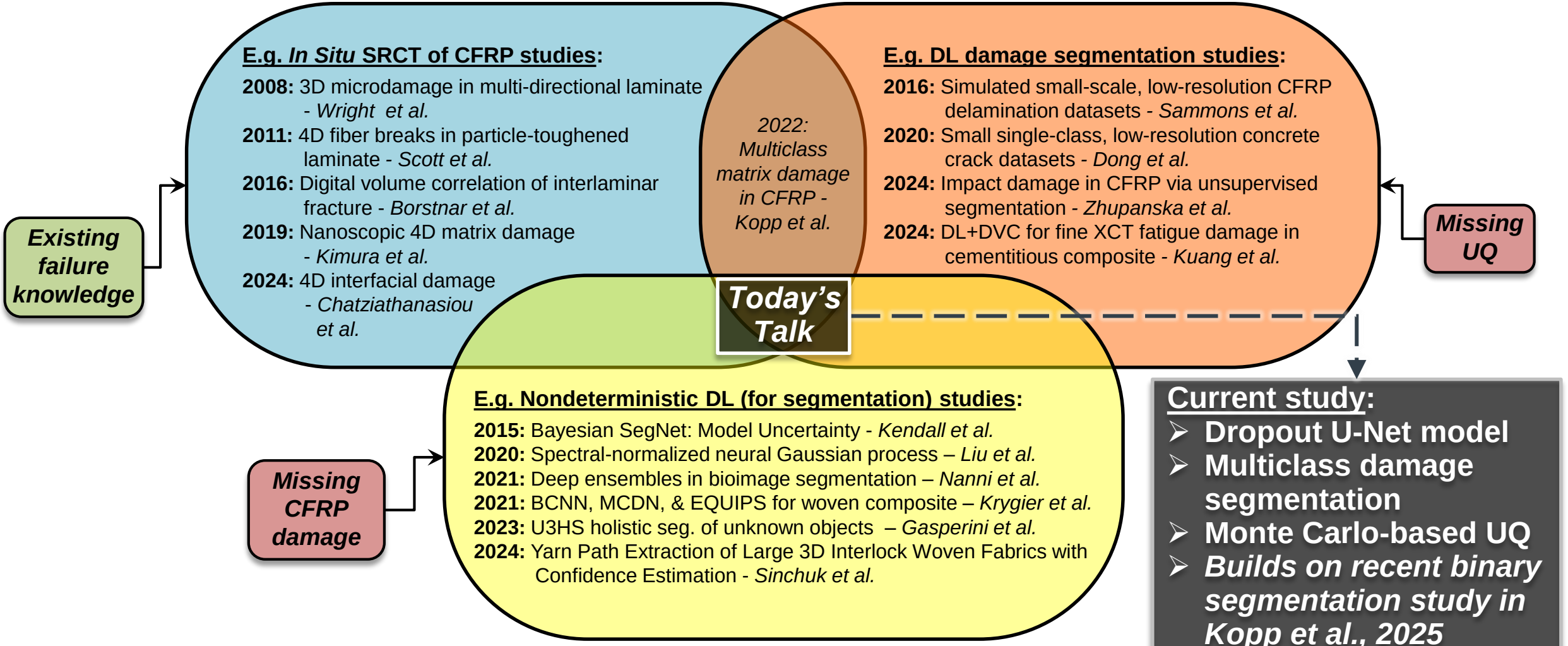

NAVAIR Public Release SPR# 2025-0376. Distribution Statement A - Approved for public release; Distribution is unlimited.

Paper and Public Data Leveraged for Current Study

➢Relevant Literature – Advanced Materials:

- Kopp, R., Joseph, J., Ni, X., Roy, N., Wardle, B.L., Deep Learning Unlocks X-ray Microtomography Segmentation of Multiclass Microdamage in Heterogeneous Materials. *Adv. Mater.* 2022, 34, 2107817. https://doi.org/10.1002/adma.202107817



➢Relevant Public Data – Dryad:

- Kopp, Reed et al. (2021), Data from: Deep learning unlocks X-ray microtomography segmentation of multiclass microdamage in heterogeneous materials, Dryad, Dataset, https://doi.org/10.5061/dryad.ffbg79cwb
  - ***200+ GB of raw & labeled SRCT tomograms***

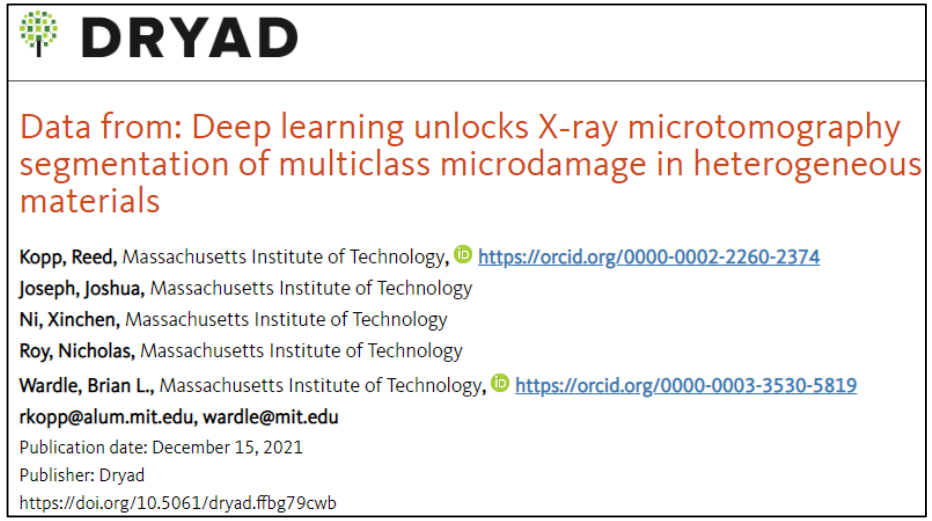

NAVAIR Public Release SPR# 2025-0376. Distribution Statement A - Approved for public release; Distribution is unlimited.

Kopp et al. 2022: Dataset Preparation & Key Variables

Summary of key details and variables studied in deep learning machine development:

Establishing trained machine

Human segmentation database *(~65,000 SRCT tomograms)*[1] → **SRCT scan composition of datasets** *(cropped tomograms sampled from scans)* → **Hyperparametric study and machine downselection** *(effects of train set composition/size/sequence, epochs)*

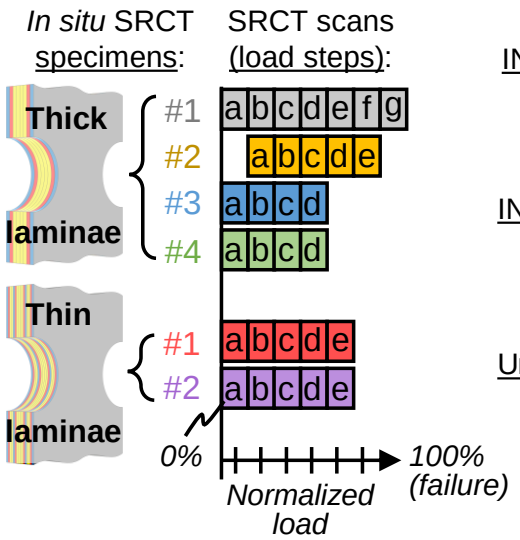

IND-datasets: *independent specimens*
Train: a b c d e a b c d e
Validation: a b c d e f g a b c d

INL-datasets: *interleaved specimens*
Train: a c e b d f a c b d
Validation: b d a c e g b d a c e

Universal dataset (same for IND & INL):
Test: a b c d a b c d e

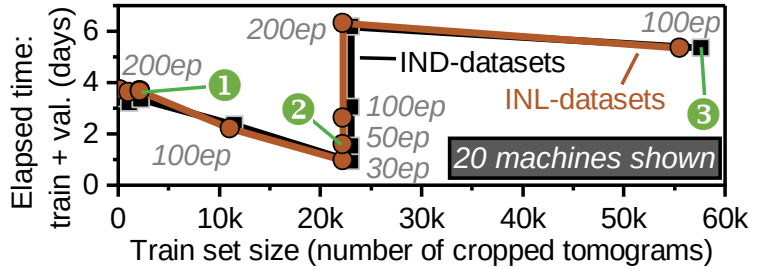

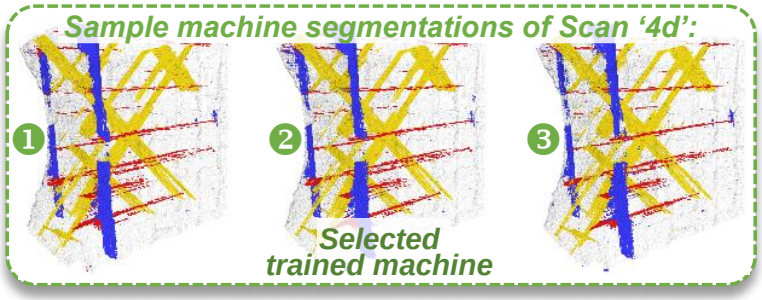

Matrix damage:
0˚ laminae | ±45˚ laminae | 90˚ laminae

[1]*Ni*, Kopp* et al. 2021*

NAVAIR Public Release SPR# 2025-0376. Distribution Statement A - Approved for public release; Distribution is unlimited.

Kopp et al. 2022: Model Testing Comparison & Hyperparameter Selection

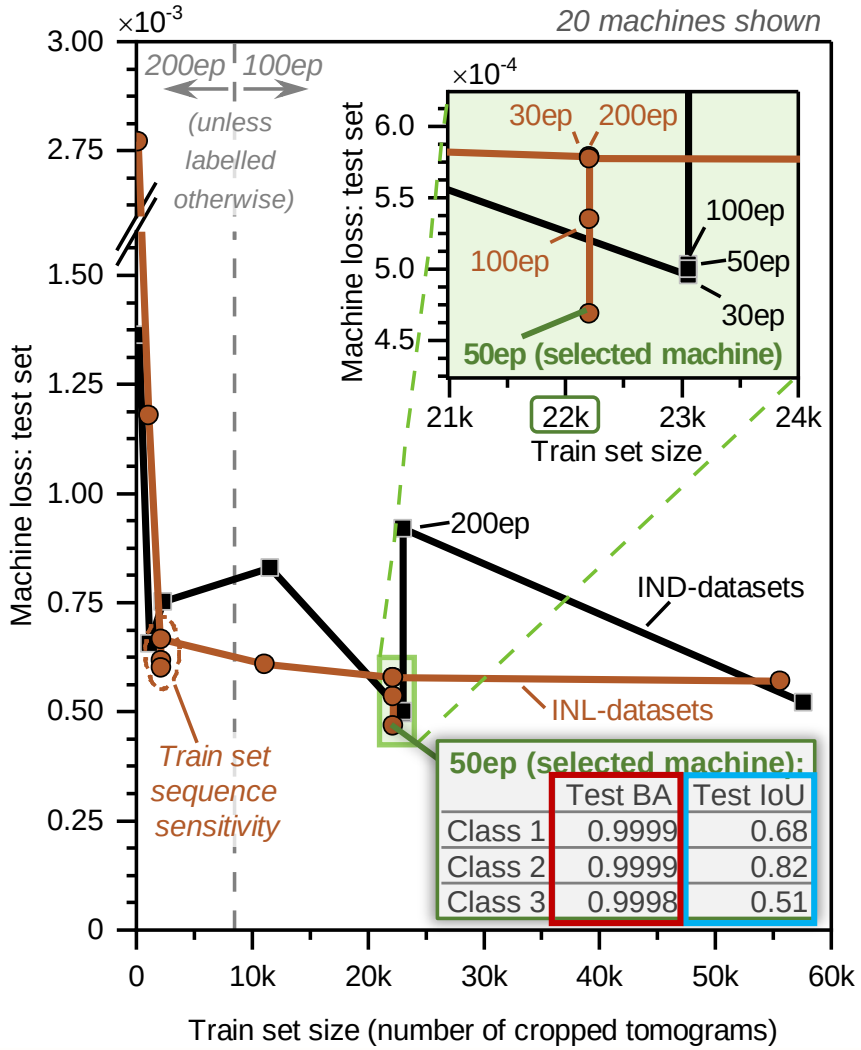

$$\text{IoU Score} = \frac{\text{Intersection Set}}{\text{Union Set}} =$$



$$\text{IoU Score} = \frac{\text{True Pos.}}{\text{True Pos.} + \text{False Pos.} + \text{False Neg.}}$$

→ *dominated by positive damage performance*

Needle: *Damage*

Haystack: *Bulk, air, mask*

$$\textbf{Binary accuracy} = \frac{\text{True Pos.} + \text{True Neg.}}{\text{All Pixels}}$$



Matrix damage:		
0˚ laminae *(Class 1)*	±45˚ laminae *(Class 2)*	90˚ laminae *(Class 3)*

NAVAIR Public Release SPR# 2025-0376. Distribution Statement A - Approved for public release; Distribution is unlimited.

Kopp et al. 2022: Model Testing Comparison & Hyperparameter Selection

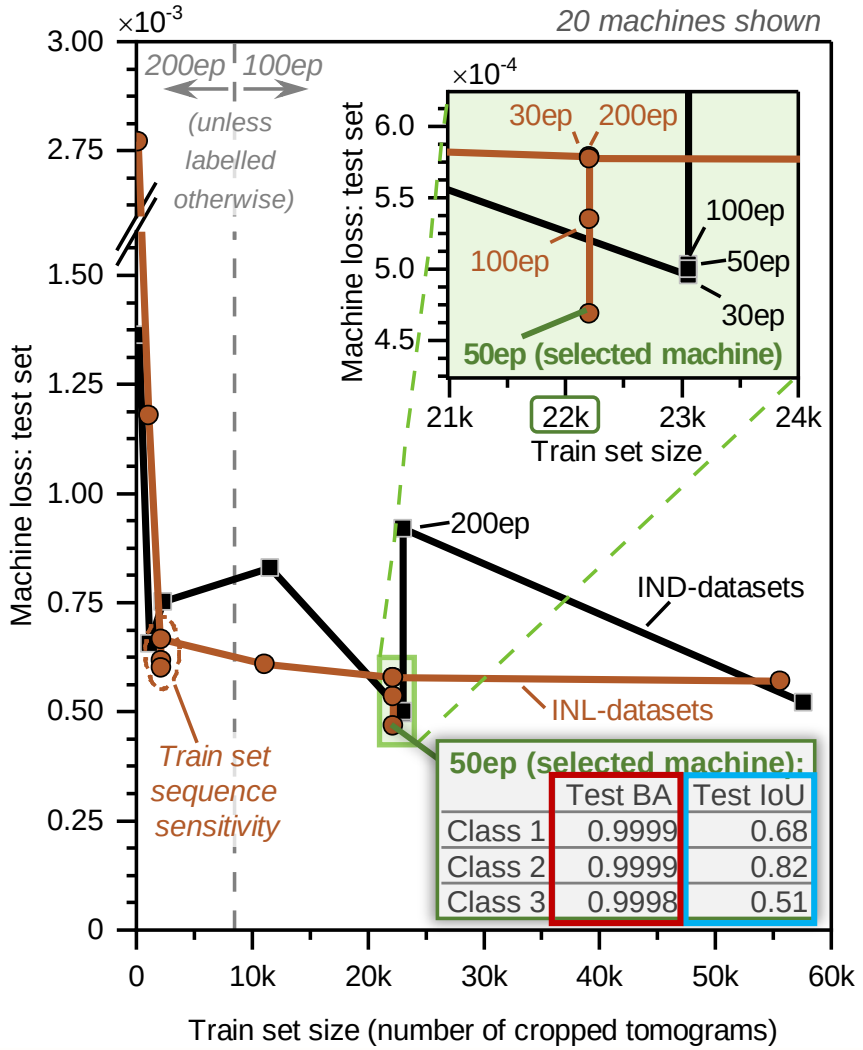

Downselection of machine based on:

- **20 different machines**
- **12 different datasets** *(patch size: 512 x 512)*
  - 6 different training set sizes (“1” [sm] – “6” [lg])
  - 2 different scan set splits evaluated (INL vs. IND)
- **4 different epoch # cases**
- 3 different random train seeds (sequence)
- **2 different loss functions (binary vs. categorical cross entropy)**
- 53 different scan/machine inferences
- 19 different 3D visualizations with inferred data

Performance elbow point occurs around 2,000 train patches

Matrix damage:		
0˚ laminae *(Class 1)*	±45˚ laminae *(Class 2)*	90˚ laminae *(Class 3)*

NAVAIR Public Release SPR# 2025-0376. Distribution Statement A - Approved for public release; Distribution is unlimited.

DL Model Architecture: U-Net-based Monte Carlo Dropout Network (MCDN)

- **MCDN model architecture (based on Krygier et al., 2021]) was the primary motivation** of the current study of key hyperparameter effects on nondeterministic segmentation predictions
  - *~10X fewer parameters than model in Kopp et al. 2022*
- **MCDN spatial dropout layers** enable user definition of their spatial dropout factor/magnitude *(i.e., the fraction of neural network nodes that are eliminated in each forward pass)*
- **Observations from Kopp et al., 2025 (AIAA SciTech): Increasing the dropout factor generally increased the prediction variability and thus capacity for UQ, though often at the cost of predictive accuracy**

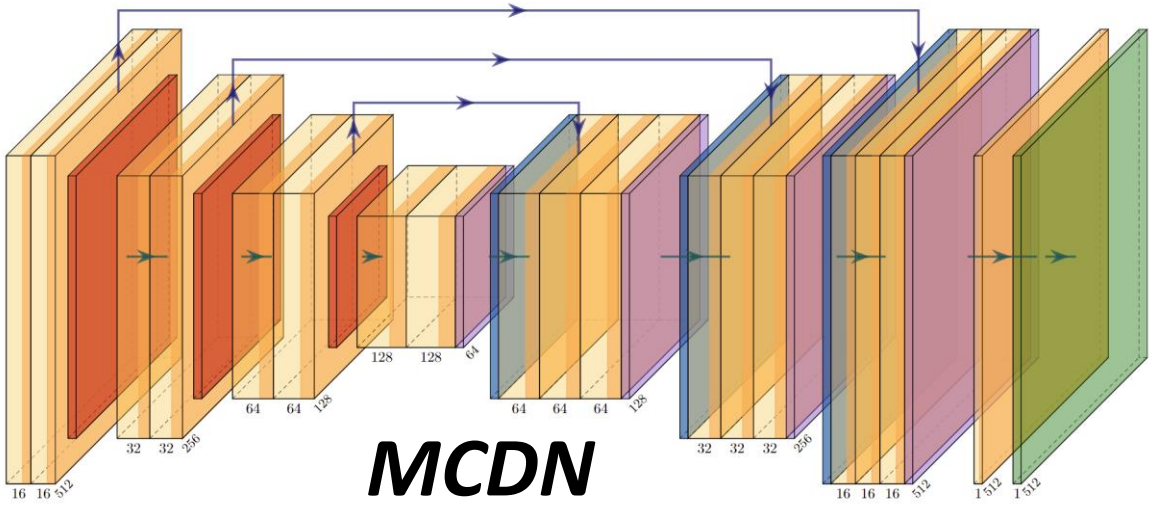

Customizable DL model architecture* of the Monte Carlo U-Net dropout network (MCDN).

Layers are colored as follows:

Yellow: Conv2d + RELU *Blue: Upsample*
Orange: Max pooling *Green: Sigmoid*
Purple: Spatial dropout

**Configuration shown here has a depth of 3 and 16 initial channels*

NAVAIR Public Release SPR# 2025-0376. Distribution Statement A - Approved for public release; Distribution is unlimited.

Nondeterministic Segmentation Development on Public Multiclass Matrix Microdamage XCT Data (1/5)

Summary of multiclass dataset targets *used to develop DL segmentation of matrix microdamage.*

- Optimal sizing of training and validation datasets based on prior deterministic work by [Kopp, 2022]

Similar to [Kopp, 2022]

Dataset case	Dataset split	Number of scans	Patch width	Patch height	Patch depth	Target number of patches per scan	Target maximum voxel count per scan	Target maximum number of patches	Target patch class sampling split: E/0°/45°/90°
1	Train	10	512	512	1	250	6.55E+07	2,500	40%/20%/20%/20%
	Validation	11				125	3.28E+07	1,375	
2	Train	10	512	512	1	2,000	5.24E+08	20,000	
	Validation	11				125	3.28E+07	1,375	
3	Train	10	256	256	1	2,000	1.31E+08	20,000	
	Validation	11				250	1.64E+07	2,750	
4	Train	10	128	128	1	2,000	3.28E+07	20,000	
	Validation	11				250	4.10E+06	2,750	
5	Train	10	512	512	8	250	5.24E+08	2,500	
	Validation	11				125	2.62E+08	1,375	
6	Train	10	256	256	32	250	5.24E+08	2,500	
	Validation	11				125	2.62E+08	1,375	
7	Train	10	128	128	128	250	5.24E+08	2,500	
	Validation	11				125	2.62E+08	1,375	

Colored largest (green) to smallest (red)

NAVAIR Public Release SPR# 2025-0376. Distribution Statement A - Approved for public release; Distribution is unlimited.

Nondeterministic Segmentation Development on Public Multiclass Matrix Microdamage XCT Data (2/5)

Summary of multiclass dataset size and composition *used to develop DL segmentation of matrix microdamage.*

- Quantity of labeled damage region ground truth pixels is much lower than the quantity of background pixels (i.e., **sparse labels**), which generally makes effective model learning challenging to achieve.

Dataset case	Patch width	Patch height	Patch depth	Dataset split	Number of patches	Exterior (% of all voxels)	0°-ply damage (% of all voxels)	45°-ply damage (% of all voxels)	90°-ply damage (% of all voxels)
1	512	512	1	Train	2,350	99.84%	0.03%	0.07%	0.05%
				Validation	1,300	99.82%	0.03%	0.08%	0.07%
2	512	512	1	Train	18,031	99.83%	0.03%	0.08%	0.06%
				Validation	1,300	99.82%	0.03%	0.08%	0.07%
3	256	256	1	Train	17,025	99.64%	0.09%	0.13%	0.15%
				Validation	2,580	99.60%	0.11%	0.13%	0.16%
4	128	128	1	Train	16,082	99.18%	0.22%	0.28%	0.32%
				Validation	2,522	99.09%	0.24%	0.29%	0.37%
5	512	512	8	Train	2,350	99.85%	0.03%	0.07%	0.05%
				Validation	1,300	99.84%	0.03%	0.08%	0.05%
6	256	256	32	Train	2,350	99.75%	0.07%	0.10%	0.08%
				Validation	1,300	99.73%	0.08%	0.11%	0.07%
7	128	128	128	Train	2,345	99.69%	0.14%	0.12%	0.06%
				Validation	1,300	99.67%	0.15%	0.12%	0.06%

Colored largest (green) to smallest (red)

NAVAIR Public Release SPR# 2025-0376. Distribution Statement A - Approved for public release; Distribution is unlimited.

Nondeterministic Segmentation Development on Public Multiclass Matrix Microdamage XCT Data (3/5)

Sample test set images *selected due to their inclusion of the full range of microstructural feature/damage/artifact complexity, e.g., air, exterior corners, damage in all ply directions, manual mask for region-growing, interior.*

<u>Raw tomograms via SRCT</u> *(test set 2D patches shown)*

Thick specimen (sample test set data)

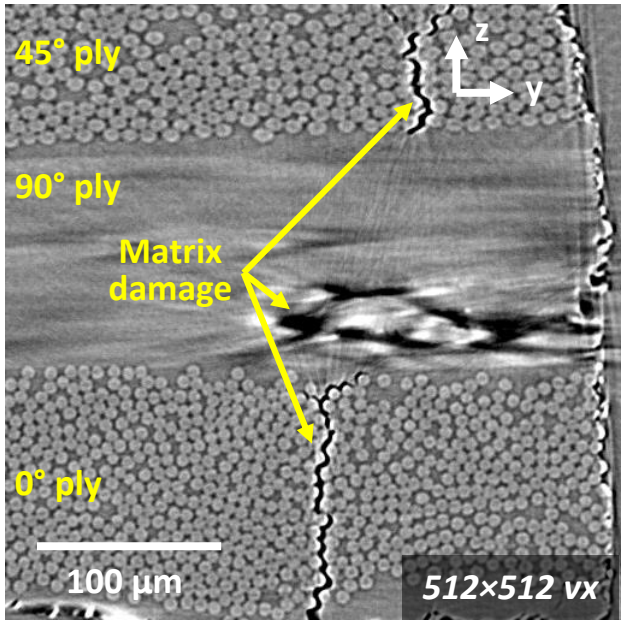

Thick nominal cured ply thickness: 130 µm = 200 vx

Thin specimen (sample test set data)

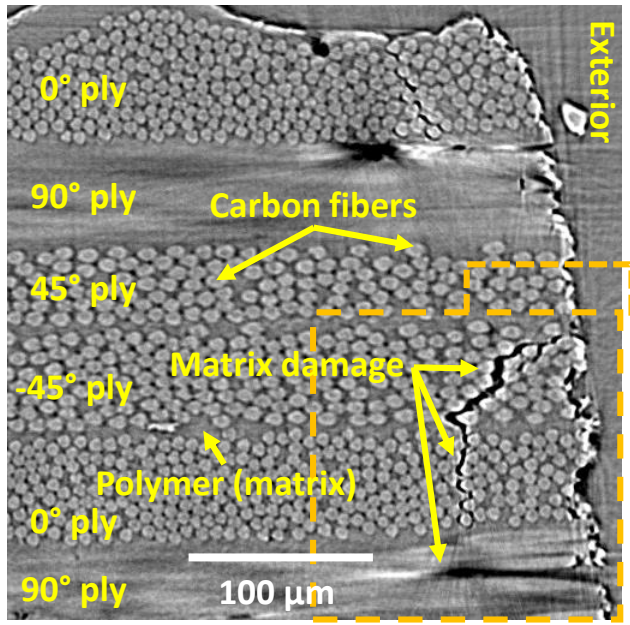

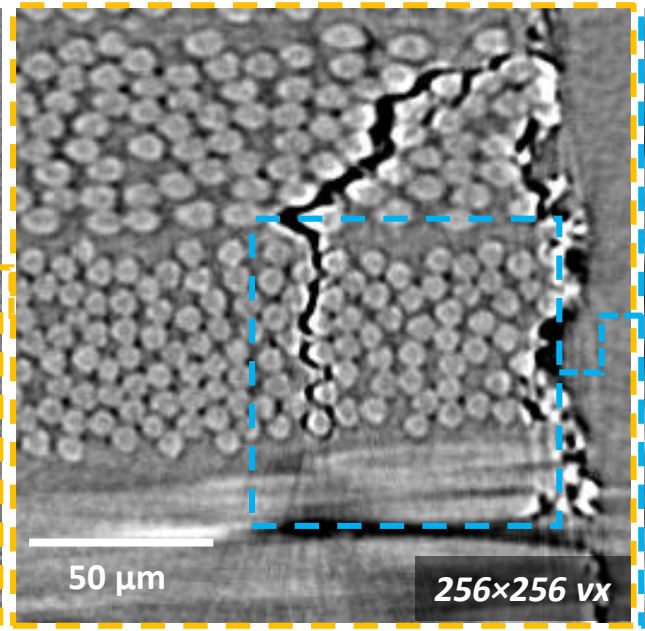

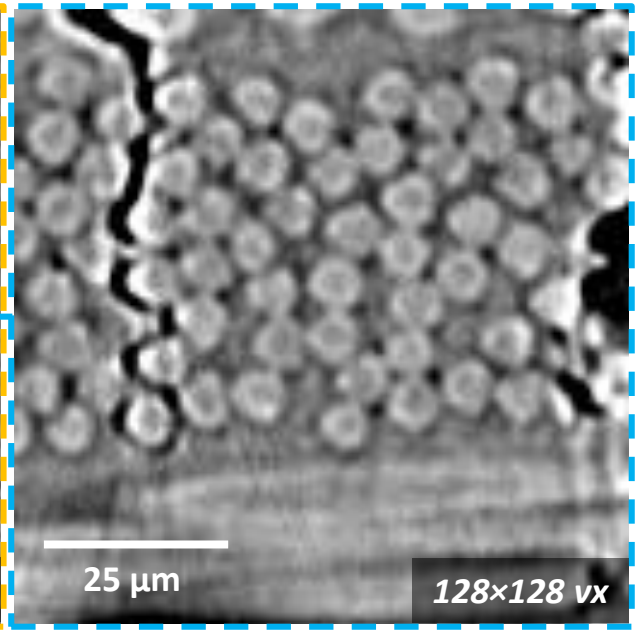

512 px

256 px

128 px

Thin nominal cured ply thickness: 54 µm = 83 vx

NAVAIR Public Release SPR# 2025-0376. Distribution Statement A - Approved for public release; Distribution is unlimited.

Nondeterministic Segmentation Development on Public Multiclass Matrix Microdamage XCT Data (4/5)

Raw tomograms via SRCT *(Thin specimen sample test set 2D & 3D patches shown)*

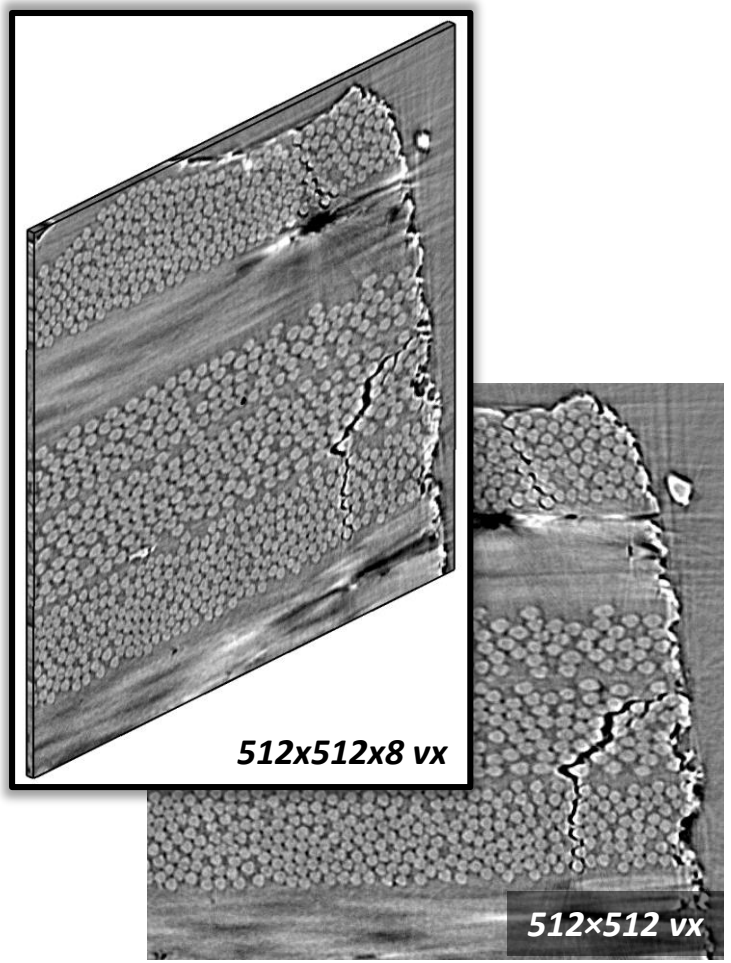

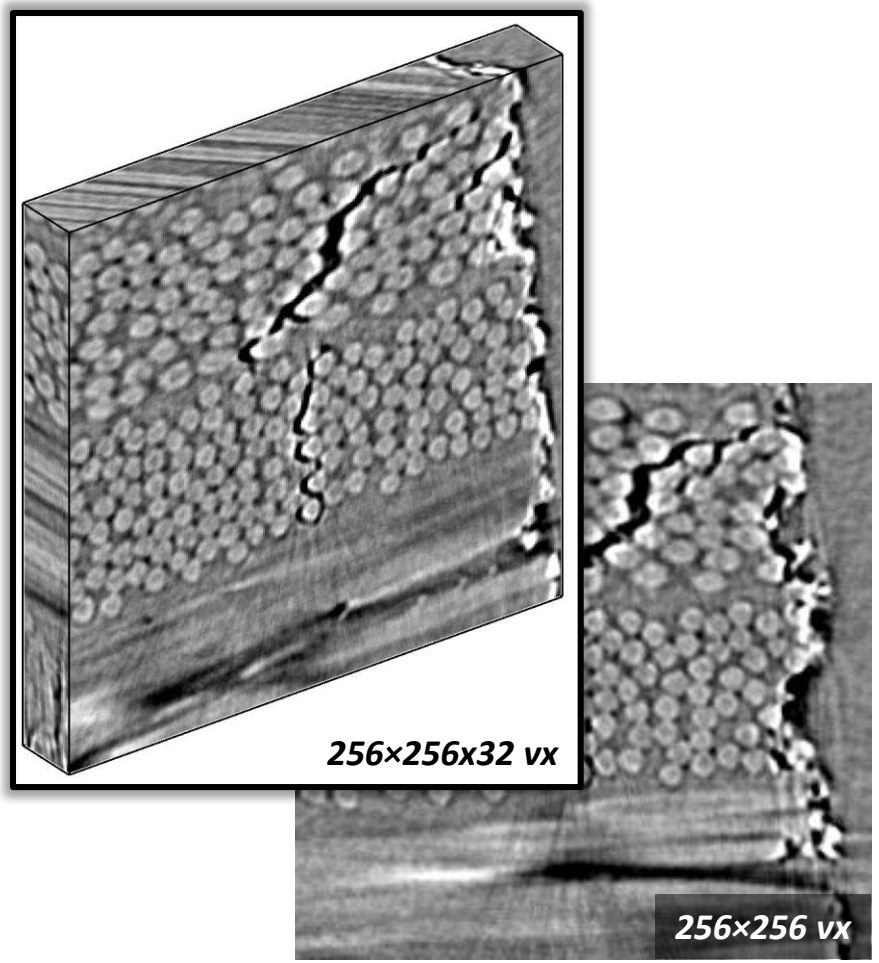

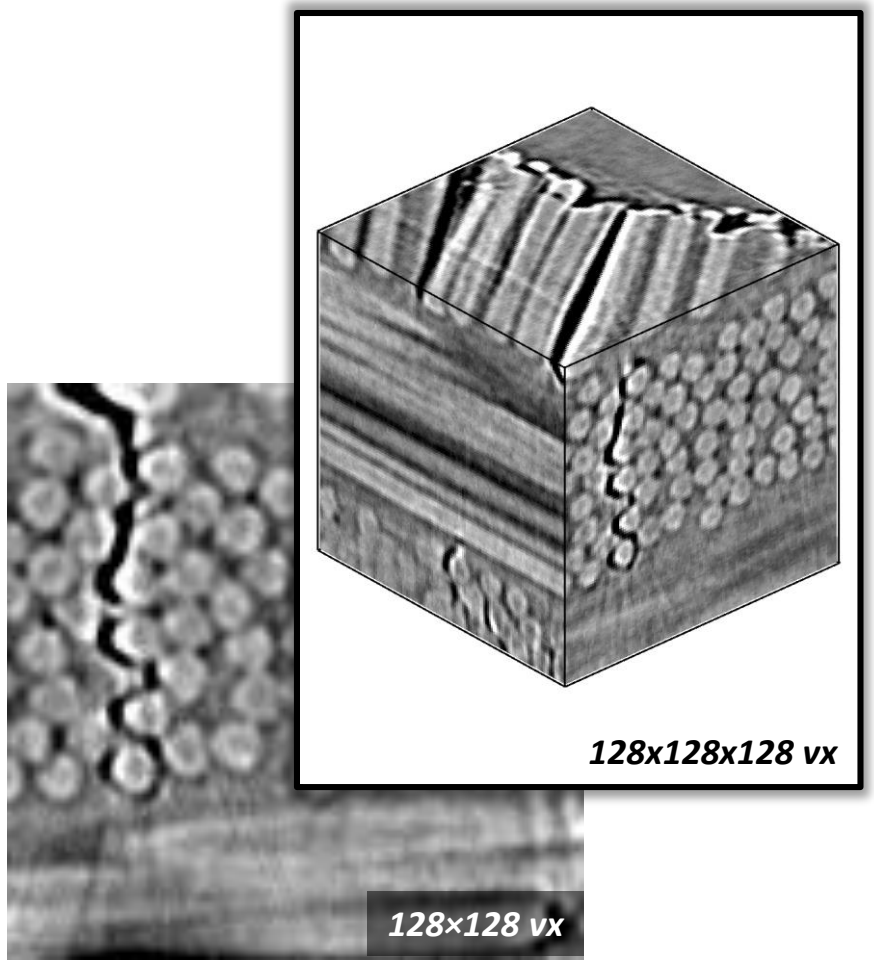

NAVAIR Public Release SPR# 2025-0376. Distribution Statement A - Approved for public release; Distribution is unlimited.

Nondeterministic Segmentation Development on Public Multiclass Matrix Microdamage XCT Data (5/5)

Human semi-automatic 3D scan-level labeling of ground truth *(test set 3D patches shown)*

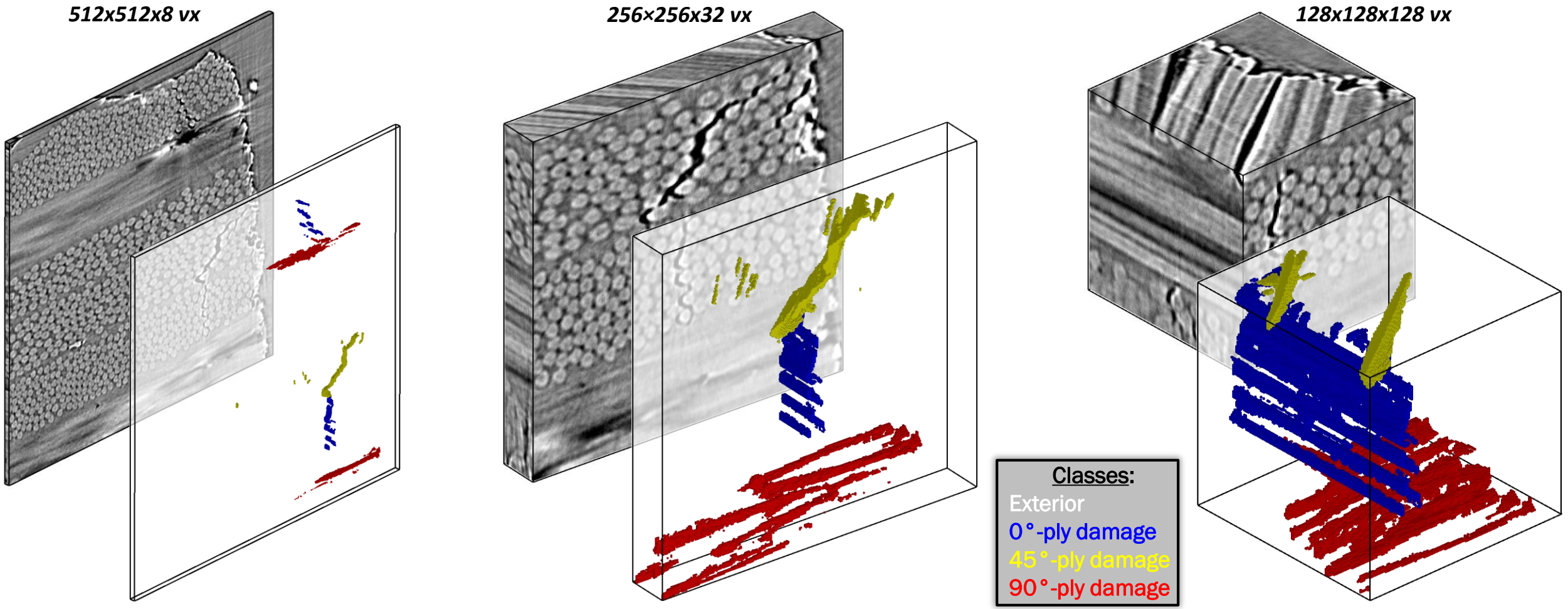

NAVAIR Public Release SPR# 2025-0376. Distribution Statement A - Approved for public release; Distribution is unlimited.

Key DL configurations to study hyperparameter effects

Primary DL hyperparameters assessed in the current study:

- Train set size (patch count)
- Loss weighting
- Data augmentation
- Batch size
- U-Net architecture and size
- Patch dimensions
- MC dropout magnitude *(focus)*

Additionally, an initial study was done to verify general reproduction of Kopp et al. 2022 results with the current methods (not shown here)

Model case	Dataset case	MCDN dropout factor	U-Net depth, initial channels	U-Net parameter count	Loss weighting	Data augmentation	Epochs	Batch size	Initial learning rate	Pretrained model case
1-1	1	0.1	4, 16	2.2E+06	Class volume inverse	90° rotate, flip	100	16	1E-03	None
1-2.1	1	0.1	4, 16	2.2E+06	None	90° rotate, flip	100	16	1E-03	None
1-3	1	0.1	4, 16	2.2E+06	0.1, 0.3, 0.3, 0.3	90° rotate, flip	100	16	1E-03	None
1-4	1	0.1	4, 16	2.2E+06	None	None	100	16	1E-03	None
2-1	2	0.1	4, 16	2.2E+06	None	90° rotate, flip	100	16	1E-03	None
2-2	2	0.1	4, 16	2.2E+06	0.1, 0.3, 0.3, 0.3	90° rotate, flip	100	16	1E-03	None
2-3	2	0.1	4, 16	2.2E+06	Class volume inverse	90° rotate, flip	100	16	1E-03	None
2-4	2	0.1	4, 8	5.4E+05	None	90° rotate, flip	100	16	1E-03	None
2-5	2	0.1	3, 16	5.4E+05	None	90° rotate, flip	100	16	1E-03	None
2-6	2	0.0	4, 16	2.2E+06	None	90° rotate, flip	100	16	1E-03	None
2-7	2	0.3	4, 16	2.2E+06	None	90° rotate, flip	100	16	1E-03	None
2-8	2	0.5	4, 16	2.2E+06	None	90° rotate, flip	100	16	1E-03	None
2-9	2	0.7	4, 16	2.2E+06	None	90° rotate, flip	100	16	1E-03	None
2-10	2	0.9	4, 16	2.2E+06	None	90° rotate, flip	100	16	1E-03	None
3-1	3	0.1	4, 16	2.2E+06	None	90° rotate, flip	100	16	1E-03	None
4-1	4	0.1	4, 16	2.2E+06	None	90° rotate, flip	100	16	1E-03	None
4-2.1	4	0.1	4, 16	2.2E+06	None	90° rotate, flip	100	2	1E-03	None
4-2.2	4	0.1	4, 16	2.2E+06	None	90° rotate, flip	100	2	1E-03	None
4-3	4	0.1	4, 16	2.2E+06	None	90° rotate, flip	100	8	1E-03	None
4-4	4	0.1	4, 16	2.2E+06	None	90° rotate, flip	100	4	1E-03	None
5-1	4	0.1	4, 8	1.6E+06	None	90° rotate, flip	100	4	1E-03	None
6-1.1	6	0.1	4, 8	1.6E+06	None	90° rotate, flip	100	8	1E-03	None
6-1.2	6	0.1	4, 8	1.6E+06	None	90° rotate, flip	16	8	1E-03	6-1.1
6-1.3	6	0.1	4, 8	1.6E+06	None	90° rotate, flip	25	8	1E-04	6-1.2
6-1.4	6	0.1	4, 8	1.6E+06	None	90° rotate, flip	25	8	1E-05	6-1.3
7-1	7	0.1	3, 16	1.6E+06	None	90° rotate, flip	40	8	1E-03	None
7-2.1	7	0.1	4, 8	1.6E+06	None	90° rotate, flip	100	8	1E-03	None
7-2.2	7	0.1	4, 8	1.6E+06	None	90° rotate, flip	16	8	1E-03	7-2.1
7-2.3	7	0.1	4, 8	1.6E+06	None	90° rotate, flip	25	8	1E-04	7-2.2
7-2.4	7	0.1	4, 8	1.6E+06	None	90° rotate, flip	25	8	1E-05	7-2.3

NAVAIR Public Release SPR# 2025-0376. Distribution Statement A - Approved for public release; Distribution is unlimited.

Key DL configurations to study hyperparameter effects

Primary DL hyperparameters assessed in the current study:

- Train set size (patch count)
- Loss weighting
- Data augmentation
- Batch size
- U-Net architecture and size
- Patch dimensions
- MC dropout magnitude *(focus)*

- Across all models shown, each model learning metric was color-coded from best (green) to worst (red)
- Subsequent slides focus on specific hyperparameter effects via metrics
- *Using training loss as the save checkpoint provided best results*

saved at min trn loss

Model case	Dataset split	Last saved epoch	Average loss	Exterior class IoU	0°-ply damage class IoU	45°-ply damage class IoU	90°-ply damage class IoU	Runtime (h)	Runtime (s)
1-1	Training	95	3.47E-02	0.98	0.06	0.11	0.08	2.8	10199.0
	Validation		7.13E-02	0.98	0.06	0.13	0.10		
1-2.1	Training	97	1.62E-03	1.00	0.64	0.80	0.54	2.8	10216.0
	Validation		2.12E-03	1.00	0.64	0.77	0.50		
1-2.2	Training	99	1.65E-03	1.00	0.63	0.80	0.57	3.0	10776.0
	Validation		2.56E-03	1.00	0.68	0.71	0.52		
1-2.3	Training	100	1.65E-03	1.00	0.62	0.80	0.56	3.0	10736.0
	Validation		2.72E-03	1.00	0.36	0.69	0.50		
1-3	Training	96	2.88E-03	1.00	0.62	0.79	0.56	2.8	9964.9
	Validation		4.63E-03	1.00	0.66	0.73	0.47		
1-4	Training	84	1.43E-03	1.00	0.68	0.82	0.59	2.8	10242.0
	Validation		2.68E-03	1.00	0.61	0.74	0.49		
2-1	Training	95	1.06E-03	1.00	0.74	0.86	0.71	17.9	64429.0
	Validation		1.93E-03	1.00	0.68	0.78	0.60		
2-2	Training	99	1.80E-03	1.00	0.74	0.84	0.70	17.9	64451.0
	Validation		3.97E-03	1.00	0.70	0.75	0.60		
2-3	Training	94	1.69E-02	0.99	0.11	0.17	0.17	18.5	66577.0
	Validation		5.53E-02	0.99	0.13	0.17	0.18		
2-4	Training	99	1.22E-03	1.00	0.71	0.84	0.68	11.4	41193.0
	Validation		2.13E-03	1.00	0.67	0.77	0.55		
2-5	Training	92	1.15E-03	1.00	0.73	0.84	0.68	17.1	61440.0
	Validation		1.97E-03	1.00	0.68	0.78	0.59		
2-6	Training	91	8.54E-04	1.00	0.80	0.88	0.75	17.7	63739.0
	Validation		2.07E-03	1.00	0.69	0.78	0.60		
2-7	Training	99	1.17E-03	1.00	0.72	0.84	0.69	17.9	64377.0
	Validation		2.04E-03	1.00	0.67	0.77	0.59		
2-8	Training	99	1.51E-03	1.00	0.67	0.81	0.62	17.9	64574.0
	Validation		2.32E-03	1.00	0.65	0.75	0.54		
2-9	Training	99	2.30E-03	1.00	0.49	0.76	0.51	17.9	64524.0
	Validation		2.92E-03	1.00	0.49	0.71	0.49		
2-10	Training	72	5.50E-03	1.00	0.00	0.35	0.00	17.9	64609.0
	Validation		6.42E-03	1.00	0.00	0.35	0.00		
3-1	Training	97	2.56E-03	1.00	0.74	0.86	0.69	5.1	18506.0
	Validation		4.39E-03	1.00	0.68	0.76	0.60		
4-1	Training	99	6.33E-03	1.00	0.69	0.85	0.67	2.4	8746.3
	Validation		9.41E-03	1.00	0.66	0.83	0.57		
4-2.1	Training	93	8.06E-03	1.00	0.65	0.84	0.59	10.5	37805.0
	Validation		9.40E-01	0.99	0.55	0.31	0.02		
4-2.2	Training	93	7.96E-03	1.00	0.65	0.83	0.59	10.6	38073.0
	Validation		1.71E-02	1.00	0.54	0.70	0.25		
4-3	Training	99	7.30E-03	1.00	0.67	0.84	0.61	3.4	12269.0
	Validation		1.05E+04	1.00	0.64	0.81	0.48		
4-4	Training	74	7.14E-03	1.00	0.67	0.84	0.62	5.7	20657.0
	Validation		2.56E-02	1.00	0.62	0.76	0.36		
5-1	Training	96	1.29E-03	1.00	0.66	0.81	0.67	41.4	149050.0
	Validation		1.82E-03	1.00	0.67	0.79	0.53		
6-1.1	Training	96	2.99E-03	1.00	0.62	0.76	0.57	25.7	92471.0
	Validation		4.14E-03	1.00	0.59	0.77	0.44		
6-1.2	Training	14	3.12E-03	1.00	0.62	0.75	0.54	4.1	14846.0
	Validation		4.24E-03	1.00	0.57	0.73	0.43		
6-1.3	Training	24	2.73E-03	1.00	0.65	0.78	0.59	6.4	23182.0
	Validation		2.86E-03	1.00	0.65	0.76	0.58		
6-1.4	Training	17	2.68E-03	1.00	0.66	0.78	0.59	6.4	23101.0
	Validation		4.11E-03	1.00	0.60	0.74	0.47		
7-1	Training	40	5.09E-03	1.00	0.51	0.68	0.39	11.7	42000.0
	Validation		5.21E-03	1.00	0.55	0.75	0.45		
7-2.1	Training	99	4.09E-03	1.00	0.60	0.73	0.43	21.5	77556.0
	Validation		4.39E-03	1.00	0.60	0.75	0.33		
7-2.2	Training	16	3.86E-03	1.00	0.61	0.75	0.44	3.6	13072.0
	Validation		4.38E-03	1.00	0.62	0.74	0.39		
7-2.3	Training	20	3.44E-03	1.00	0.65	0.77	0.47	8.0	28830.0
	Validation		4.15E-03	1.00	0.61	0.76	0.44		
7-2.4	Training	4	3.40E-03	1.00	0.66	0.77	0.48	5.3	19118.0
	Validation		4.15E-03	1.00	0.61	0.76	0.45		

saved at min val loss

Model case	Dataset split	Last saved epoch	Average loss	Exterior class IoU	0°-ply damage class IoU	45°-ply damage class IoU	90°-ply damage class IoU	Runtime (h)
1-1	Training	84	4.16E-02	0.98	0.06	0.10	0.08	2.8
	Validation		6.39E-02	0.98	0.06	0.12	0.10	
1-2.1	Training	99	1.64E-03	1.00	0.63	0.79	0.53	2.8
	Validation		2.09E-03	1.00	0.66	0.77	0.55	
1-2.2	Training	93	1.76E-03	1.00	0.62	0.80	0.53	3.0
	Validation		2.22E-03	1.00	0.68	0.79	0.51	
1-2.3	Training	98	1.67E-03	1.00	0.64	0.79	0.56	3.0
	Validation		2.17E-03	1.00	0.67	0.77	0.56	
1-3	Training	91	2.96E-03	1.00	0.62	0.78	0.55	2.8
	Validation		4.13E-03	1.00	0.65	0.74	0.53	
1-4	Training	93	1.63E-03	1.00	0.63	0.80	0.57	2.8
	Validation		2.46E-03	1.00	0.63	0.76	0.47	
2-1	Training	48	1.15E-03	1.00	0.72	0.85	0.68	17.9
	Validation		1.86E-03	1.00	0.67	0.78	0.59	
2-2	Training	53	2.32E-03	1.00	0.69	0.81	0.65	17.9
	Validation		3.45E-03	1.00	0.69	0.74	0.60	
2-3	Training	52	3.07E-02	0.99	0.08	0.15	0.13	18.5
	Validation		4.93E-02	0.99	0.08	0.14	0.13	
2-4	Training	75	1.45E-03	1.00	0.67	0.81	0.62	11.4
	Validation		1.94E-03	1.00	0.68	0.79	0.60	
2-5	Training	36	1.46E-03	1.00	0.68	0.81	0.62	17.1
	Validation		1.83E-03	1.00	0.69	0.80	0.58	
2-6	Training	41	1.23E-03	1.00	0.73	0.84	0.66	17.7
	Validation		1.79E-03	1.00	0.68	0.79	0.58	
2-7	Training	47	1.44E-03	1.00	0.68	0.81	0.64	17.9
	Validation		1.92E-03	1.00	0.70	0.77	0.60	
2-8	Training	93	1.52E-03	1.00	0.67	0.81	0.63	17.9
	Validation		2.12E-03	1.00	0.65	0.76	0.56	
2-9	Training	91	2.41E-03	1.00	0.47	0.75	0.50	17.9
	Validation		2.75E-03	1.00	0.46	0.71	0.50	
2-10	Training	76	5.51E-03	1.00	0.00	0.35	0.00	17.9
	Validation		5.95E-03	1.00	0.00	0.36	0.00	
3-1	Training	64	3.21E-03	1.00	0.69	0.83	0.62	5.1
	Validation		4.24E-03	1.00	0.69	0.76	0.60	
4-1	Training	83	6.63E-03	1.00	0.69	0.85	0.65	2.4
	Validation		9.02E-03	1.00	0.67	0.83	0.58	
4-2.1	Training	23	1.10E-02	1.00	0.59	0.78	0.44	10.5
	Validation		2.07E-02	0.99	0.51	0.57	0.07	
4-2.2	Training	30	1.03E-02	1.00	0.60	0.79	0.49	10.6
	Validation		1.52E-02	1.00	0.43	0.67	0.33	
4-3	Training	34	9.92E-03	1.00	0.62	0.80	0.49	3.4
	Validation		1.09E-02	1.00	0.62	0.80	0.52	
4-4	Training	38	9.43E-03	1.00	0.63	0.81	0.51	5.7
	Validation		1.38E-02	1.00	0.64	0.77	0.38	
5-1	Training	93	1.30E-03	1.00	0.66	0.81	0.67	41.4
	Validation		1.76E-03	1.00	0.66	0.79	0.53	
6-1.1	Training	97	3.01E-03	1.00	0.64	0.76	0.56	25.7
	Validation		4.06E-03	1.00	0.61	0.74	0.47	
6-1.2	Training	5	3.29E-03	1.00	0.61	0.74	0.53	4.1
	Validation		4.18E-03	1.00	0.59	0.75	0.46	
6-1.3	Training	4	3.99E-03	1.00	0.59	0.76	0.48	6.4
	Validation		3.92E-03	1.00	0.60	0.76	0.47	
6-1.4	Training	18	2.76E-03	1.00	0.65	0.77	0.58	6.4
	Validation		3.95E-03	1.00	0.60	0.77	0.48	
7-1	Training	40	5.09E-03	1.00	0.51	0.68	0.39	11.7
	Validation		5.21E-03	1.00	0.55	0.75	0.45	
7-2.1	Training	91	4.24E-03	1.00	0.60	0.72	0.41	21.5
	Validation		4.26E-03	1.00	0.60	0.75	0.45	
7-2.2	Training	9	4.05E-03	1.00	0.60	0.74	0.42	3.6
	Validation		4.35E-03	1.00	0.62	0.75	0.41	
7-2.3	Training	22	3.49E-03	1.00	0.65	0.76	0.48	8.0
	Validation		4.13E-03	1.00	0.62	0.76	0.46	
7-2.4	Training	13	3.50E-03	1.00	0.65	0.76	0.47	5.3
	Validation		4.09E-03	1.00	0.60	0.76	0.46	

NAVAIR Public Release SPR# 2025-0376. Distribution Statement A - Approved for public release; Distribution is unlimited.

Key DL results to assess hyperparameter effects (1/5)

Hyperparameters of interest here:

- Train set patch qty. (*"Dataset case"*): *2K ("1"), 20K ("2")*
- Loss weighting: *None, slight, inverse class vol.*
- Data augmentation: *None, flip/rotate*

- *Suggested practice: Larger train sets, no loss weighting, and flip/rotate data augmentation*

Patch size for these cases: 512 x 512

Model case	Dataset case	MCDN dropout factor	U-Net depth, initial channels	U-Net parameter count	Loss weighting	Data augmentation	Epochs	Batch size	Initial learning rate
1-2.1	1	0.1	4, 16	2.2E+06	None	90° rotate, flip	100	16	1E-03
1-4	1	0.1	4, 16	2.2E+06	None	None	100	16	1E-03
2-1	2	0.1	4, 16	2.2E+06	None	90° rotate, flip	100	16	1E-03
2-2	2	0.1	4, 16	2.2E+06	0.1, 0.3, 0.3, 0.3	90° rotate, flip	100	16	1E-03
2-3	2	0.1	4, 16	2.2E+06	Class vol. inverse	90° rotate, flip	100	16	1E-03

Training & validation, save based on min. train loss

Additional 2K dataset case results not shown here

Model case	Dataset split	Last saved epoch	Average loss	Exterior class IoU	0°-ply dmg class IoU	45°-ply dmg class IoU	90°-ply dmg class IoU	Runtime (h)
1-2.1	Training	97	1.62E-03	1.00	0.64	0.80	0.54	2.8
	Validation		2.12E-03	1.00	0.64	0.77	0.50	
1-4	Training	84	1.43E-03	1.00	0.68	0.82	0.59	2.8
	Validation		2.68E-03	1.00	0.61	0.74	0.49	
2-1	Training	95	1.06E-03	1.00	0.74	0.86	0.71	17.9
	Validation		1.93E-03	1.00	0.68	0.78	0.60	
2-2	Training	99	1.80E-03	1.00	0.74	0.84	0.70	17.9
	Validation		3.97E-03	1.00	0.70	0.75	0.60	
2-3	Training	94	1.69E-02	0.99	0.11	0.17	0.17	18.5
	Validation		5.53E-02	0.99	0.13	0.17	0.18	

NAVAIR Public Release SPR# 2025-0376. Distribution Statement A - Approved for public release; Distribution is unlimited.

Key DL results to assess hyperparameter effects (2/5)

Hyperparameters of interest here:

- Mini-batch size: *2, 4, 8, 16*
- *Note: For current GPU, full VRAM for 4 to 8 3D patches; larger batches use shared memory*

- *Suggested practice: Larger mini-batch sizes improve generalizability and validation set convergence*

Patch size for these cases: 128 x 128

Model case	Dataset case	MCDN dropout factor	U-Net depth, initial channels	U-Net parameter count	Loss weighting	Data augmentation	Epochs	Batch size	Initial learning rate
4-1	4	0.1	4, 16	2.2E+06	None	90° rotate, flip	100	16	1E-03
4-2.1	4	0.1	4, 16	2.2E+06	None	90° rotate, flip	100	2	1E-03
4-2.2	4	0.1	4, 16	2.2E+06	None	90° rotate, flip	100	2	1E-03
4-3	4	0.1	4, 16	2.2E+06	None	90° rotate, flip	100	8	1E-03
4-4	4	0.1	4, 16	2.2E+06	None	90° rotate, flip	100	4	1E-03

Model case	Dataset split	Last saved epoch	Average loss	Exterior class IoU	0°-ply dmg class IoU	45°-ply dmg class IoU	90°-ply dmg class IoU	Runtime (h)
4-1	Training	99	6.33E-03	1.00	0.69	0.85	0.67	2.4
	Validation		9.41E-03	1.00	0.66	0.83	0.57	
4-2.1	Training	93	8.06E-03	1.00	0.65	0.84	0.59	10.5
	Validation		9.40E-01	0.99	0.55	0.31	0.02	
4-2.2	Training	93	7.96E-03	1.00	0.65	0.83	0.59	10.6
	Validation		1.71E-02	1.00	0.54	0.70	0.25	
4-3	Training	99	7.30E-03	1.00	0.67	0.84	0.61	3.4
	Validation		1.05E+04	1.00	0.64	0.81	0.48	
4-4	Training	74	7.14E-03	1.00	0.67	0.84	0.62	5.7
	Validation		2.56E-02	1.00	0.62	0.76	0.36	

NAVAIR Public Release SPR# 2025-0376. Distribution Statement A - Approved for public release; Distribution is unlimited.

Key DL results to assess hyperparameter effects (3/5)

Hyperparameters of interest here:

- U-Net architecture and size *(depth, initial channels)*: *3, 16 | 4, 8 | 4, 16*

- *Suggested practice: Increasing model depth maintains performance and reduces runtime, even with reduced initial channels*

Model case	Dataset case	MCDN dropout factor	U-Net depth, initial channels	U-Net parameter count	Loss weighting	Data augmentation	Epochs	Batch size	Initial learning rate
2-1	2	0.1	4, 16	2.2E+06	None	90° rotate, flip	100	16	1E-03
2-4	2	0.1	4, 8	5.4E+05	None	90° rotate, flip	100	16	1E-03
2-5	2	0.1	3, 16	5.4E+05	None	90° rotate, flip	100	16	1E-03

Model case	Dataset split	Last saved epoch	Average loss	Exterior class IoU	0°-ply dmg class IoU	45°-ply dmg class IoU	90°-ply dmg class IoU	Runtime (h)
2-1	Training	95	1.06E-03	1.00	0.74	0.86	0.71	17.9
	Validation		1.93E-03	1.00	0.68	0.78	0.60	
2-4	Training	99	1.22E-03	1.00	0.71	0.84	0.68	11.4
	Validation		2.13E-03	1.00	0.67	0.77	0.55	
2-5	Training	92	1.15E-03	1.00	0.73	0.84	0.68	17.1
	Validation		1.97E-03	1.00	0.68	0.78	0.59	

Patch size for these cases: 512 x 512

NAVAIR Public Release SPR# 2025-0376. Distribution Statement A - Approved for public release; Distribution is unlimited.

Key DL results to assess hyperparameter effects (4/5)

Hyperparameters of interest here:

- Patch dimensions (*"Dataset case"*): *512x512 ("2"), 256x256 ("3"), 128x128 ("4"), 512x512x8 ("5"), 256x256x32 ("6"), 128x128x128 ("7")*
- *Suggested practice: Larger 2D patches appear to lead to higher-performance models, albeit at increased runtime*

Model case	Dataset case	MCDN dropout factor	U-Net depth, initial channels	U-Net parameter count	Loss weighting	Data augmentation	Epochs	Batch size	Initial learning rate
2-1	2	0.1	4, 16	2.2E+06	None	90° rotate, flip	100	16	1E-03
3-1	3	0.1	4, 16	2.2E+06	None	90° rotate, flip	100	16	1E-03
4-1	4	0.1	4, 16	2.2E+06	None	90° rotate, flip	100	16	1E-03
5-1	5	0.1	4, 8	1.6E+06	None	90° rotate, flip	100	4	1E-03
6-1.4	6	0.1	4, 8	1.6E+06	None	90° rotate, flip	166	8	1E-03
7-2.4	7	0.1	4, 8	1.6E+06	None	90° rotate, flip	166	8	1E-03

Model case	Dataset split	Last saved epoch	Average loss	Exterior class IoU	0°-ply dmg class IoU	45°-ply dmg class IoU	90°-ply dmg class IoU	Runtime (h)
2-1	Training	95	1.06E-03	1.00	0.74	0.86	0.71	17.9
	Validation		1.93E-03	1.00	0.68	0.78	0.60	
3-1	Training	97	2.56E-03	1.00	0.74	0.86	0.69	5.1
	Validation		4.39E-03	1.00	0.68	0.76	0.60	
4-1	Training	99	6.33E-03	1.00	0.69	0.85	0.67	2.4
	Validation		9.41E-03	1.00	0.66	0.83	0.57	
5-1	Training	96	1.29E-03	1.00	0.66	0.81	0.67	41.4
	Validation		1.82E-03	1.00	0.67	0.79	0.53	
6-1.4	Training	158	2.68E-03	1.00	0.66	0.78	0.59	42.7
	Validation		4.11E-03	1.00	0.60	0.74	0.47	
7-2.4	Training	145	3.40E-03	1.00	0.66	0.77	0.48	38.5
	Validation		4.15E-03	1.00	0.61	0.76	0.45	

NAVAIR Public Release SPR# 2025-0376. Distribution Statement A - Approved for public release; Distribution is unlimited.

Key DL results to assess hyperparameter effects (5/5)

Hyperparameters of interest here:

- Dropout factor magnitude:
  0.0 (deterministic), 0.1, 0.3, 0.5, 0.7, 0.9

- *Suggested practice: Lower MC dropout magnitude improves accuracy and convergence*

Patch size for these cases: 512 x 512

Model case	Dataset case	MCDN dropout factor	U-Net depth, initial channels	U-Net parameter count	Loss weighting	Data augmentation	Epochs	Batch size	Initial learning rate
2-1	2	0.1	4, 16	2.2E+06	None	90° rotate, flip	100	16	1E-03
2-6	2	0.0	4, 16	2.2E+06	None	90° rotate, flip	100	16	1E-03
2-7	2	0.3	4, 16	2.2E+06	None	90° rotate, flip	100	16	1E-03
2-8	2	0.5	4, 16	2.2E+06	None	90° rotate, flip	100	16	1E-03
2-9	2	0.7	4, 16	2.2E+06	None	90° rotate, flip	100	16	1E-03
2-10	2	0.9	4, 16	2.2E+06	None	90° rotate, flip	100	16	1E-03

Model case	Dataset split	Last saved epoch	Average loss	Exterior class IoU	0°-ply dmg class IoU	45°-ply dmg class IoU	90°-ply dmg class IoU	Runtime (h)
2-1	Training	95	1.06E-03	1.00	0.74	0.86	0.71	17.9
	Validation		1.93E-03	1.00	0.68	0.78	0.60	
2-6	Training	91	8.54E-04	1.00	0.80	0.88	0.75	17.7
	Validation		2.07E-03	1.00	0.69	0.78	0.60	
2-7	Training	99	1.17E-03	1.00	0.72	0.84	0.69	17.9
	Validation		2.04E-03	1.00	0.67	0.77	0.59	
2-8	Training	99	1.51E-03	1.00	0.67	0.81	0.62	17.9
	Validation		2.32E-03	1.00	0.65	0.75	0.54	
2-9	Training	99	2.30E-03	1.00	0.49	0.76	0.51	17.9
	Validation		2.92E-03	1.00	0.49	0.71	0.49	
2-10	Training	72	5.50E-03	1.00	0.00	0.35	0.00	17.9
	Validation		6.42E-03	1.00	0.00	0.35	0.00	

NAVAIR Public Release SPR# 2025-0376. Distribution Statement A - Approved for public release; Distribution is unlimited.

Nondeterministic Segmentation on Test Set: Effects of Model Input Dimensions (1/6)

***Test set Thin sample:** Argmax of the mean probability distribution (generated via 32 MC samples during inference)*

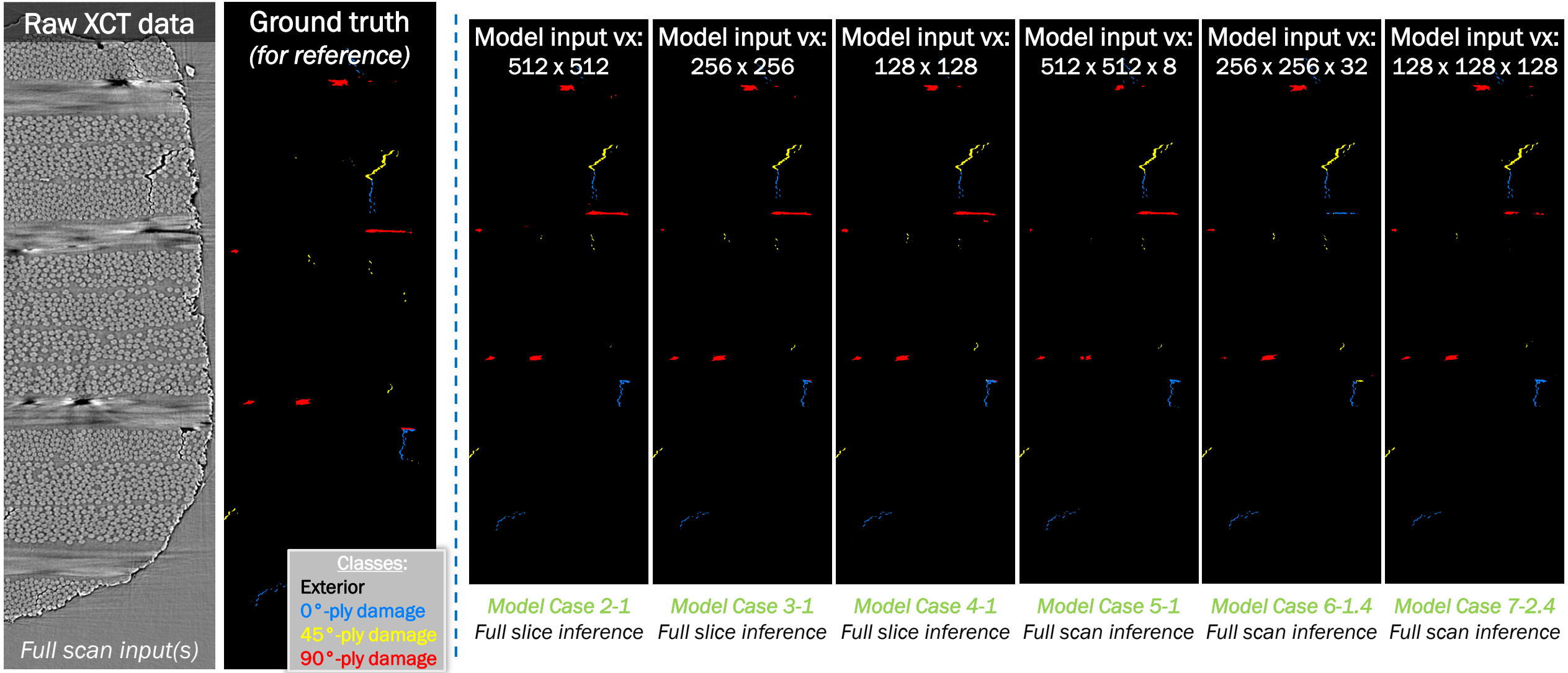

NAVAIR Public Release SPR# 2025-0376. Distribution Statement A - Approved for public release; Distribution is unlimited.

Note: 0.5 is an ideal binary threshold value

Nondeterministic Segmentation on Test Set: Effects of Model Input Dimensions (2/6)

***Test set Thin sample:** [Argmax class mean] of the probability distribution (generated via 32 MC samples during inference)*

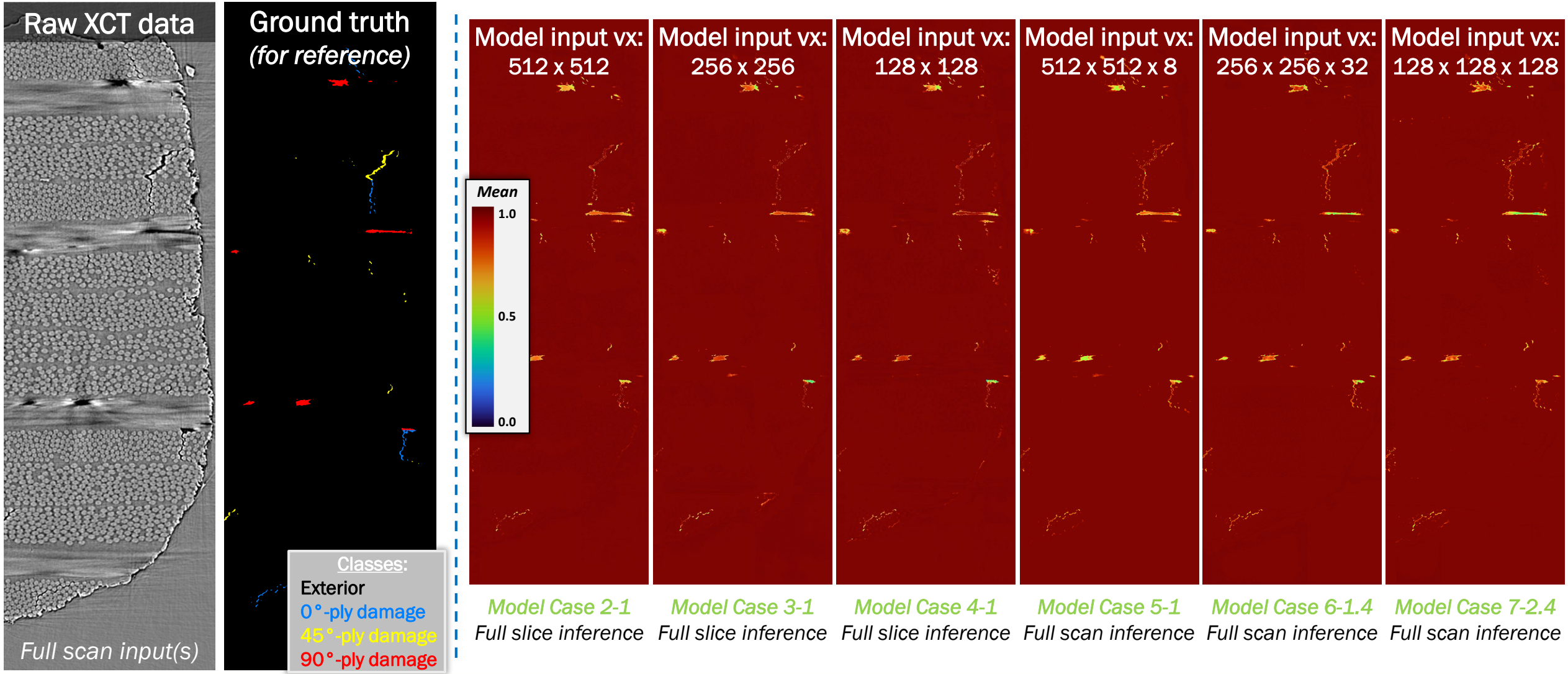

NAVAIR Public Release SPR# 2025-0376. Distribution Statement A - Approved for public release; Distribution is unlimited.

*Uncertainty refers to interquartile range

Nondeterministic Segmentation on Test Set: Effects of Model Input Dimensions (3/6)

Test set Thin sample: Argmax class uncertainty of the probability distribution (generated via 32 MC samples during inference)*

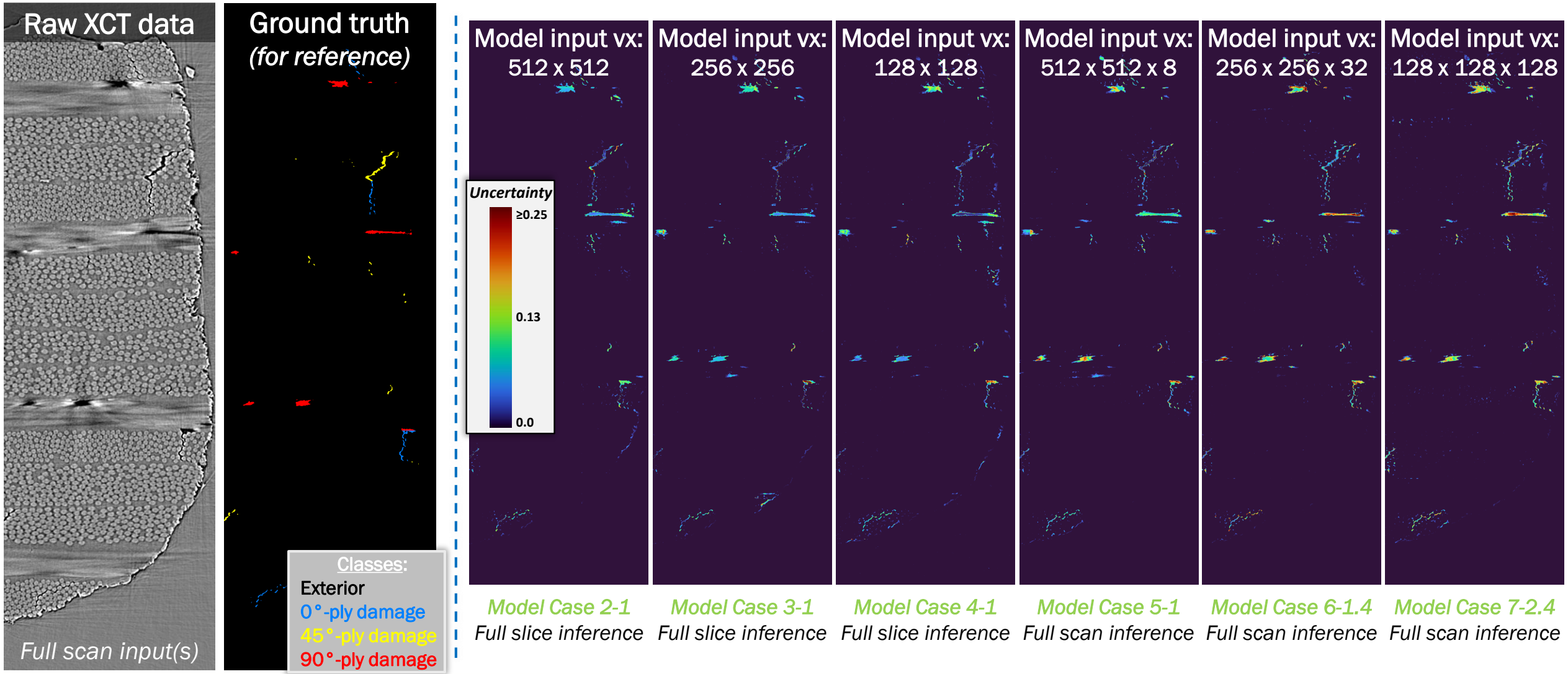

Model Case 2-1	Model Case 3-1	Model Case 4-1	Model Case 5-1	Model Case 6-1.4	Model Case 7-2.4
Full slice inference	Full slice inference	Full slice inference	Full scan inference	Full scan inference	Full scan inference

NAVAIR Public Release SPR# 2025-0376. Distribution Statement A - Approved for public release; Distribution is unlimited.

Nondeterministic Segmentation on Test Set: Effects of Model Input Dimensions (4/6)

Test set Thick sample: Argmax of the mean probability distribution (generated via 32 MC samples during inference)

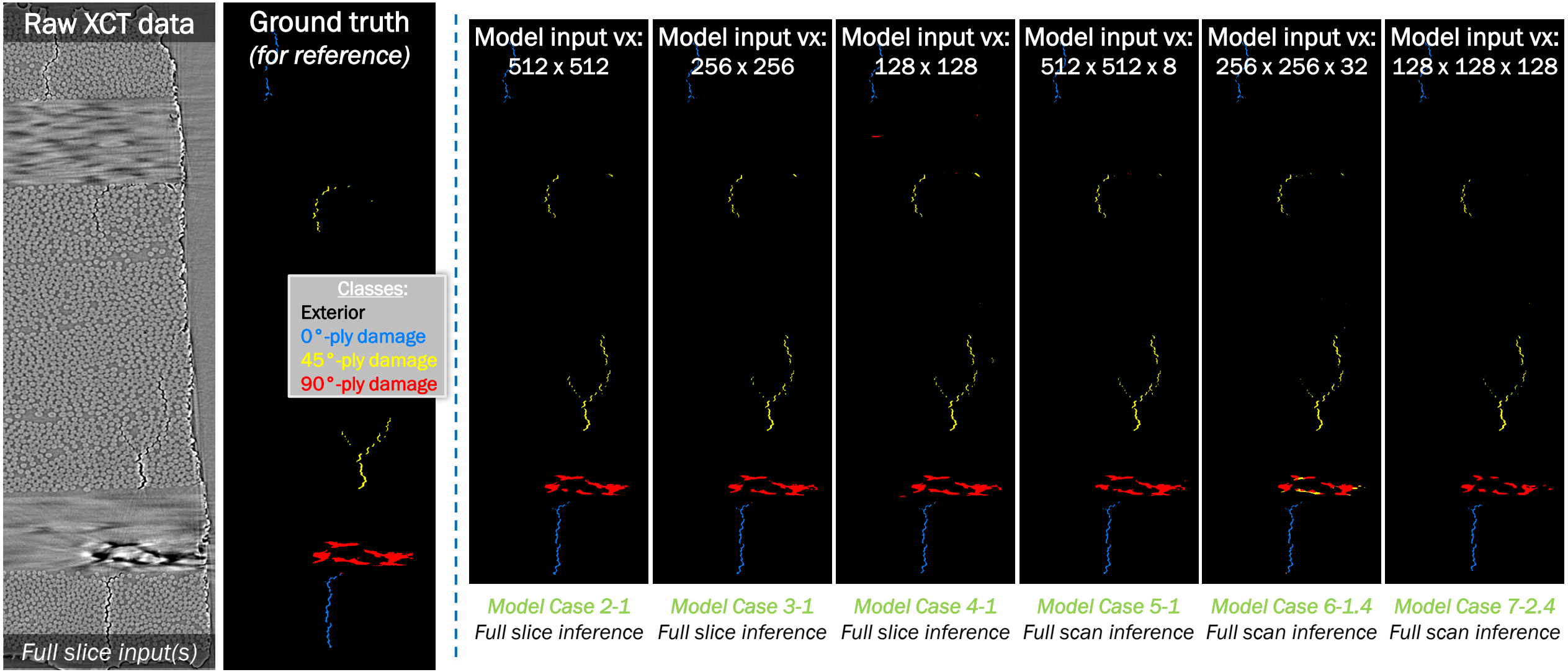

NAVAIR Public Release SPR# 2025-0376. Distribution Statement A - Approved for public release; Distribution is unlimited.

Note: 0.5 is an ideal binary threshold value

Nondeterministic Segmentation on Test Set: Effects of Model Input Dimensions (5/6)

***Test set Thick sample:** [Argmax class mean](#) of the probability distribution (generated via 32 MC samples during inference)*

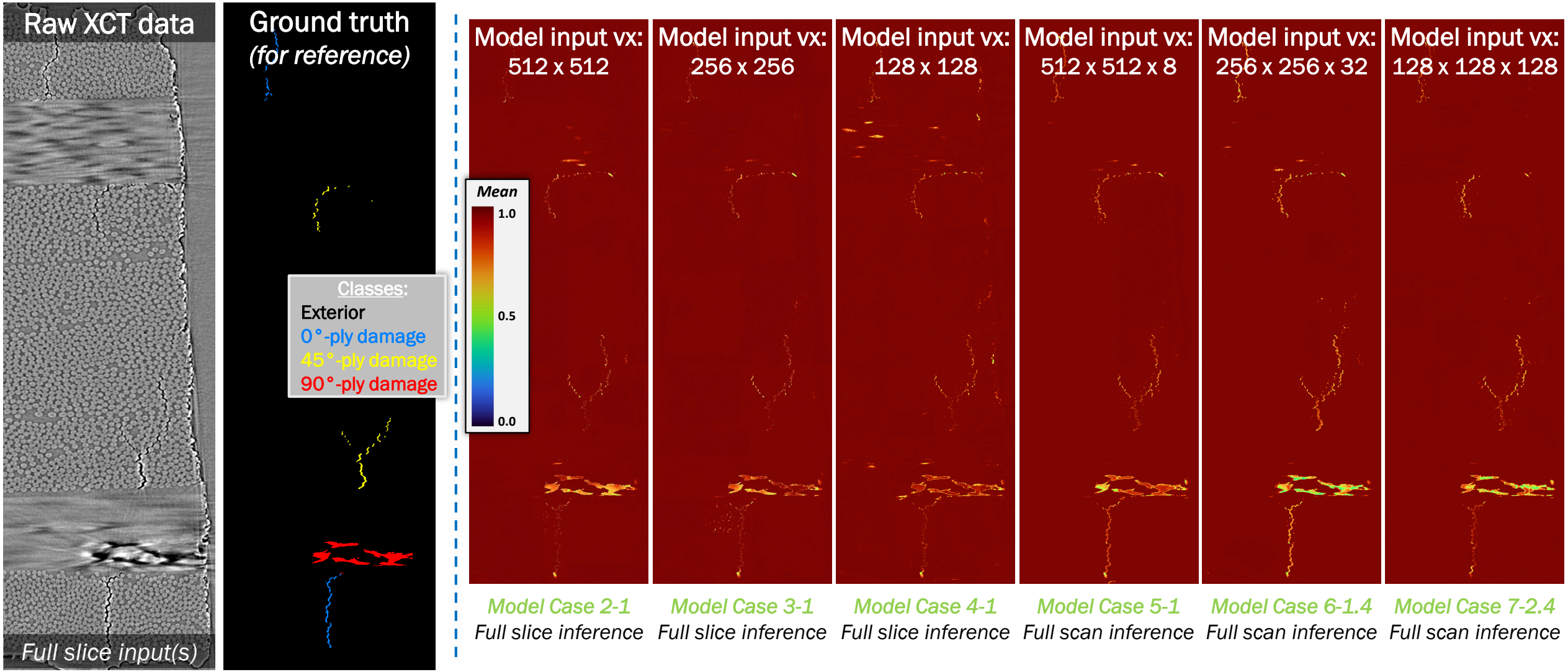

NAVAIR Public Release SPR# 2025-0376. Distribution Statement A - Approved for public release; Distribution is unlimited.

*Uncertainty refers to interquartile range

Nondeterministic Segmentation on Test Set: Effects of Model Input Dimensions (6/6)

Test set Thick sample: Argmax class uncertainty of the probability distribution (generated via 32 MC samples during inference)*

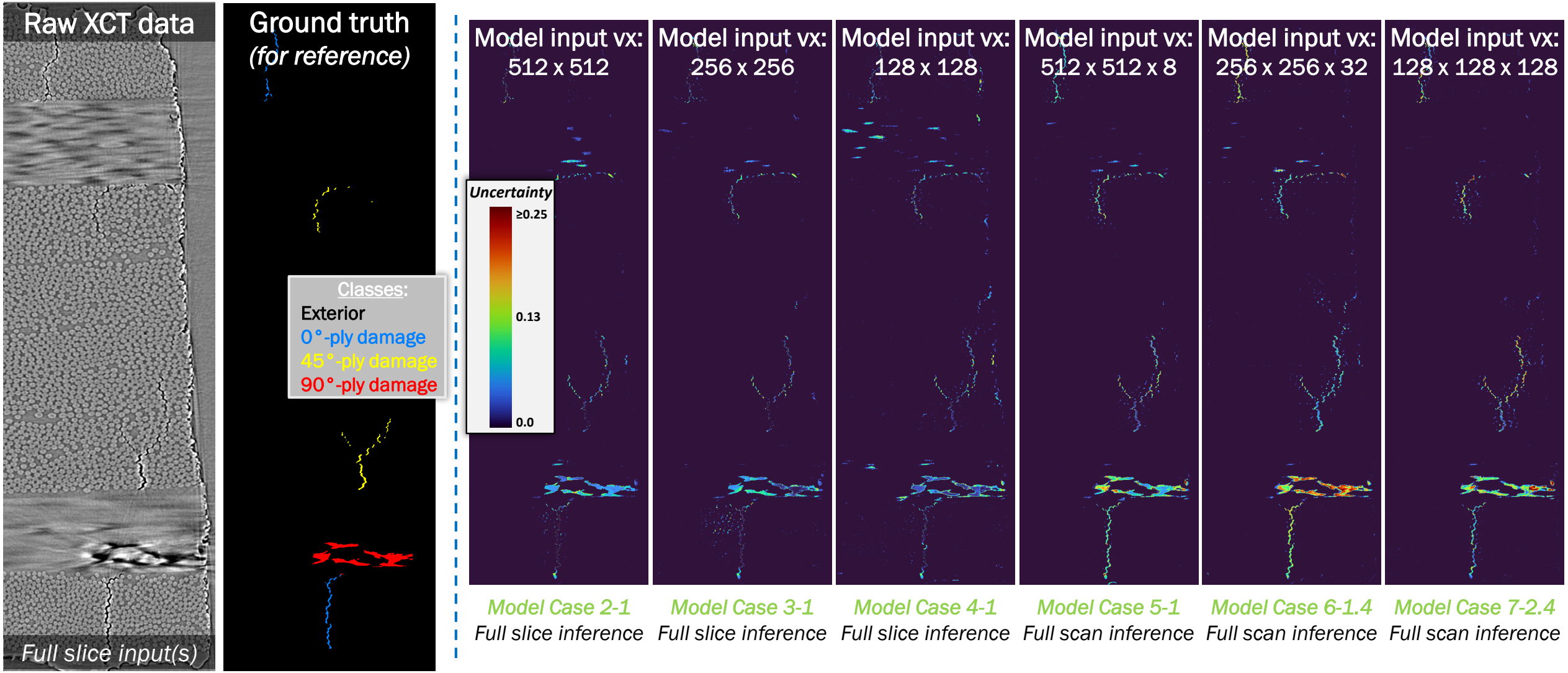

NAVAIR Public Release SPR# 2025-0376. Distribution Statement A - Approved for public release; Distribution is unlimited.

Note: Model input of 512 x 512 vx for below results

Nondeterministic Segmentation on Test Set: Effects of Dropout Magnitude (1/6)

Test set Thin sample: Argmax of the mean probability distribution (generated via 32 MC samples during inference)

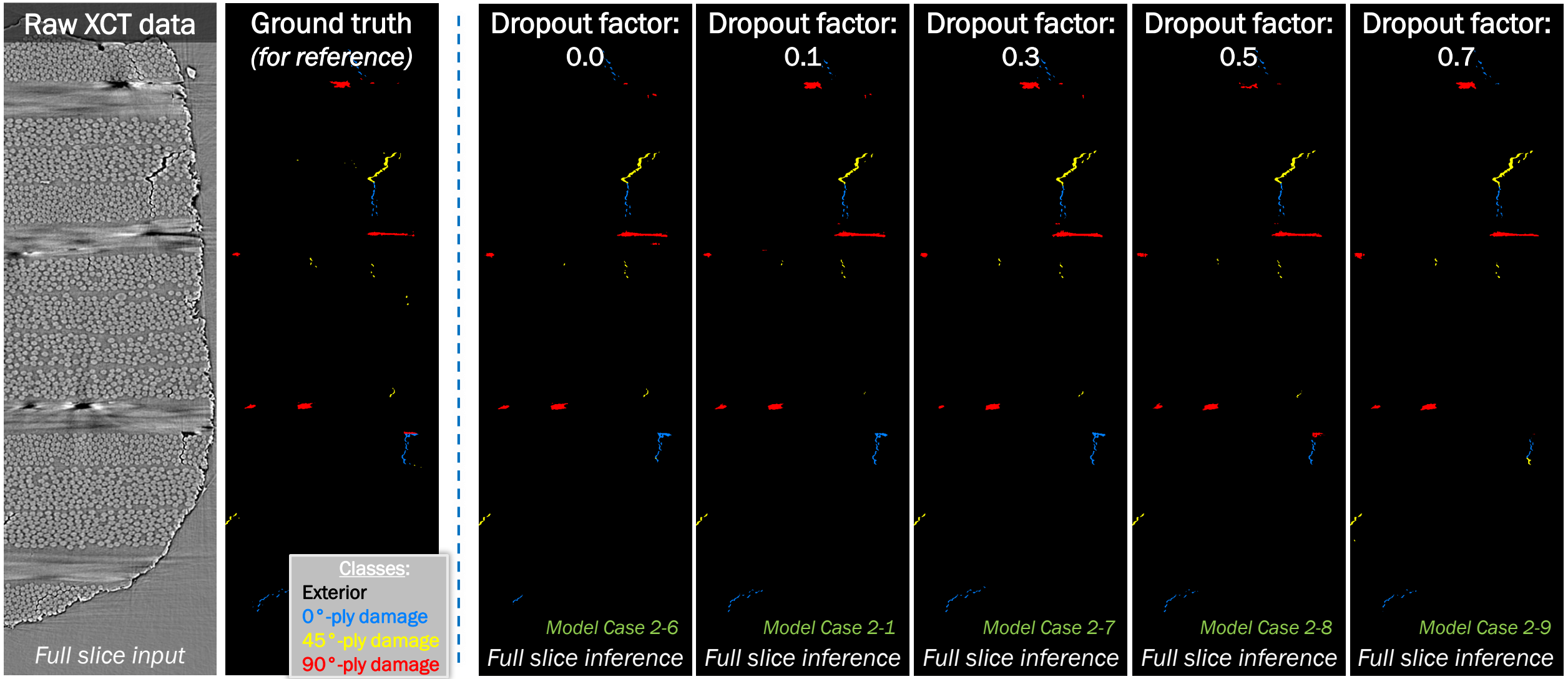

NAVAIR Public Release SPR# 2025-0376. Distribution Statement A - Approved for public release; Distribution is unlimited.

Note: 0.5 is an ideal binary threshold value

Nondeterministic Segmentation on Test Set: Effects of Dropout Magnitude (2/6)

***Test set Thin sample:** [Argmax class mean](#) of the probability distribution (generated via 32 MC samples during inference)*

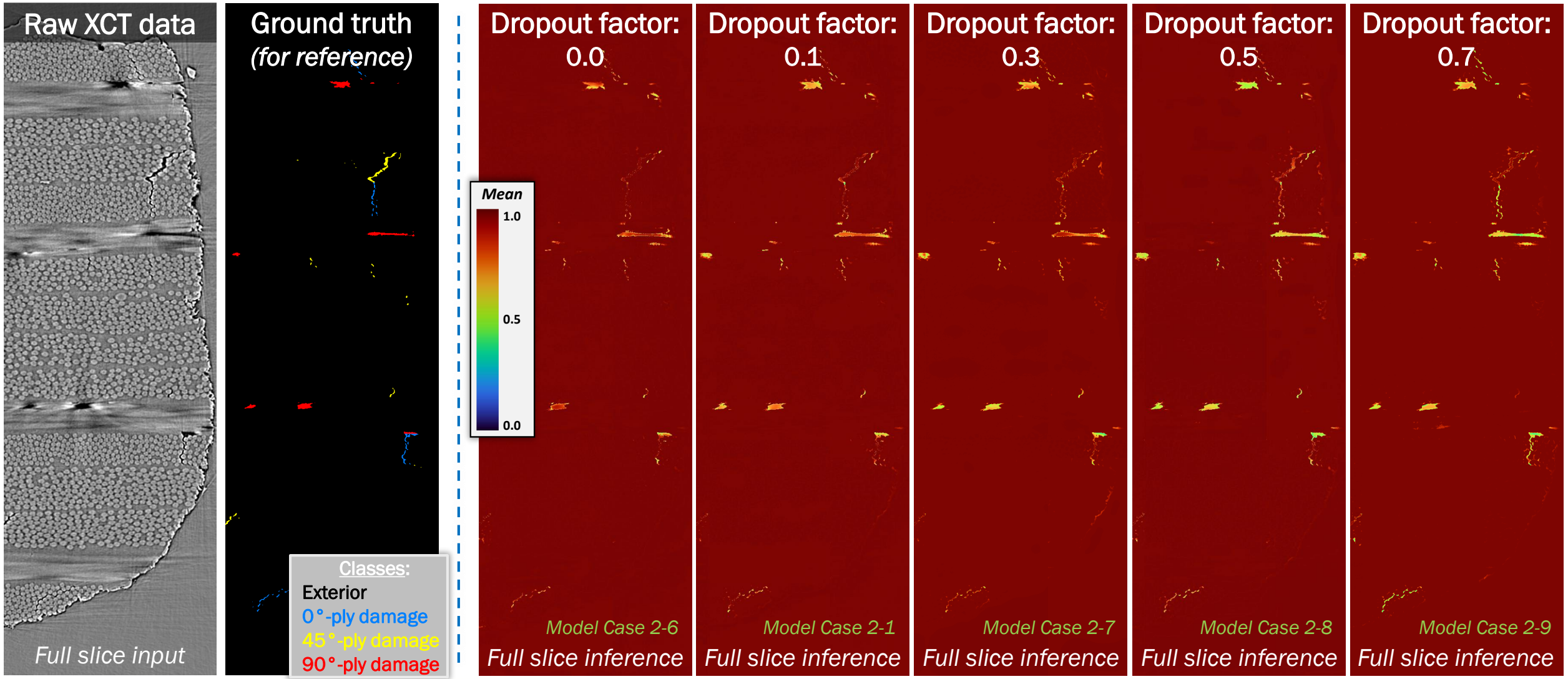

NAVAIR Public Release SPR# 2025-0376. Distribution Statement A - Approved for public release; Distribution is unlimited.

*Uncertainty refers to interquartile range

Nondeterministic Segmentation on Test Set: Effects of Dropout Magnitude (3/6)

Test set Thin sample: Argmax class uncertainty of the probability distribution (generated via 32 MC samples during inference)*

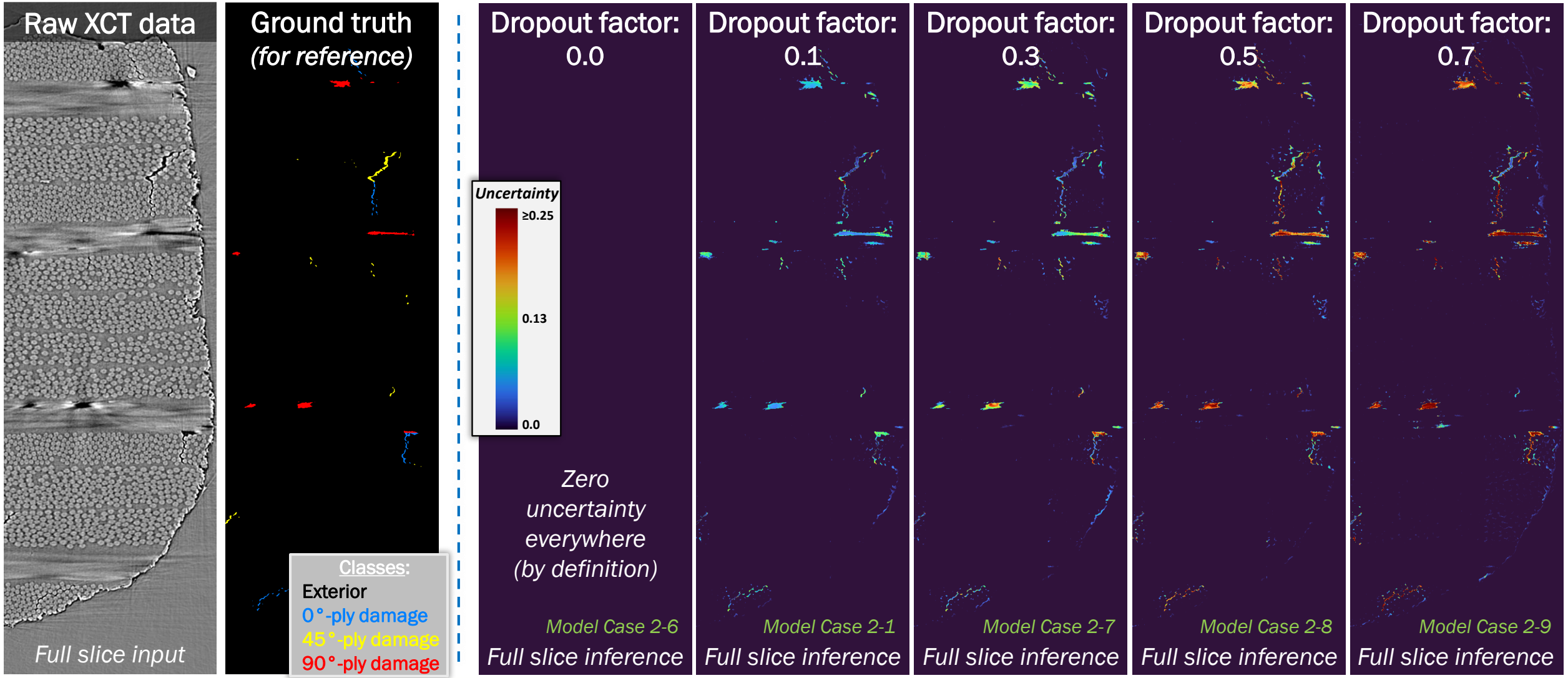

NAVAIR Public Release SPR# 2025-0376. Distribution Statement A - Approved for public release; Distribution is unlimited.

Note: Model input of 512 x 512 vx for below results

Nondeterministic Segmentation on Test Set: Effects of Dropout Magnitude (4/6)

Test set Thick sample: Argmax of the mean probability distribution (generated via 32 MC samples during inference)

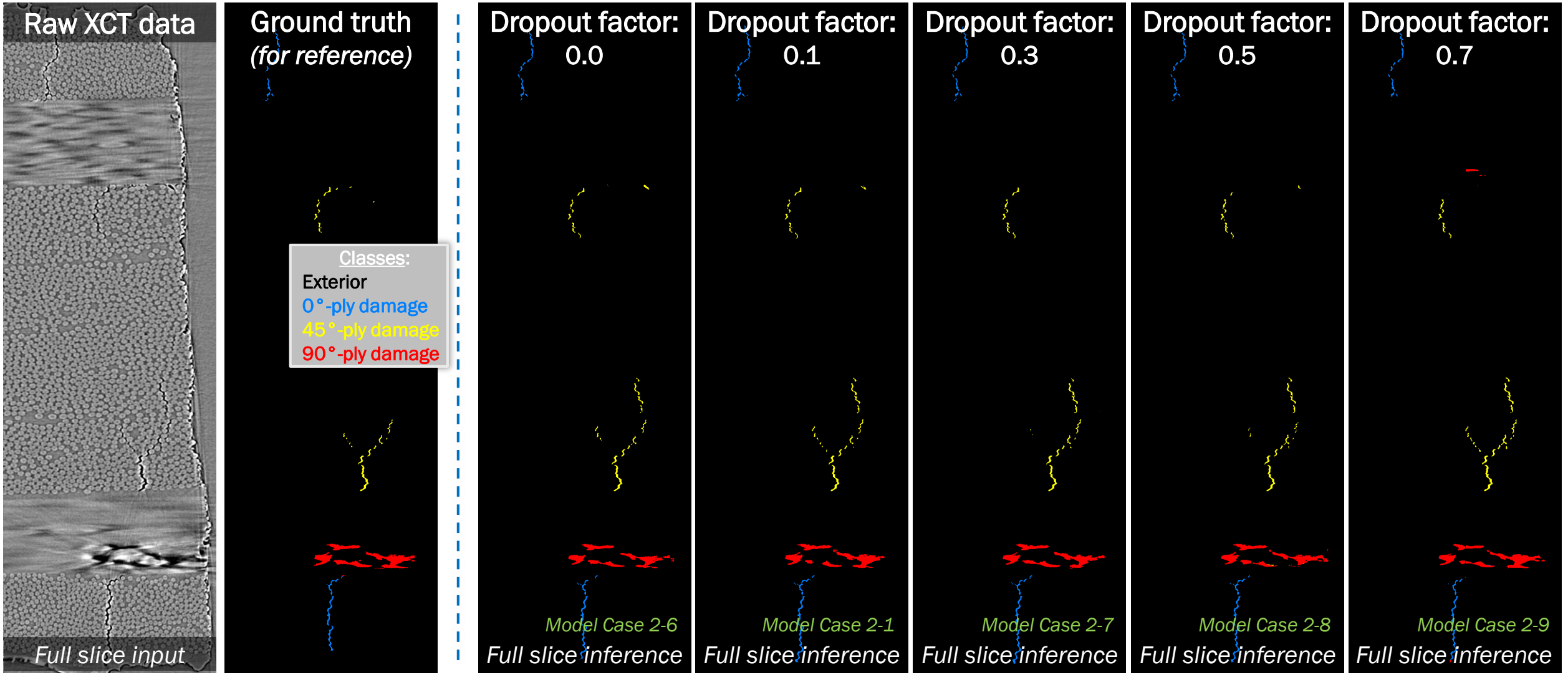

NAVAIR Public Release SPR# 2025-0376. Distribution Statement A - Approved for public release; Distribution is unlimited.

Note: 0.5 is an ideal binary threshold value

Nondeterministic Segmentation on Test Set: Effects of Dropout Magnitude (5/6)

***Test set Thick sample:** [Argmax class mean] of the probability distribution (generated via 32 MC samples during inference)*

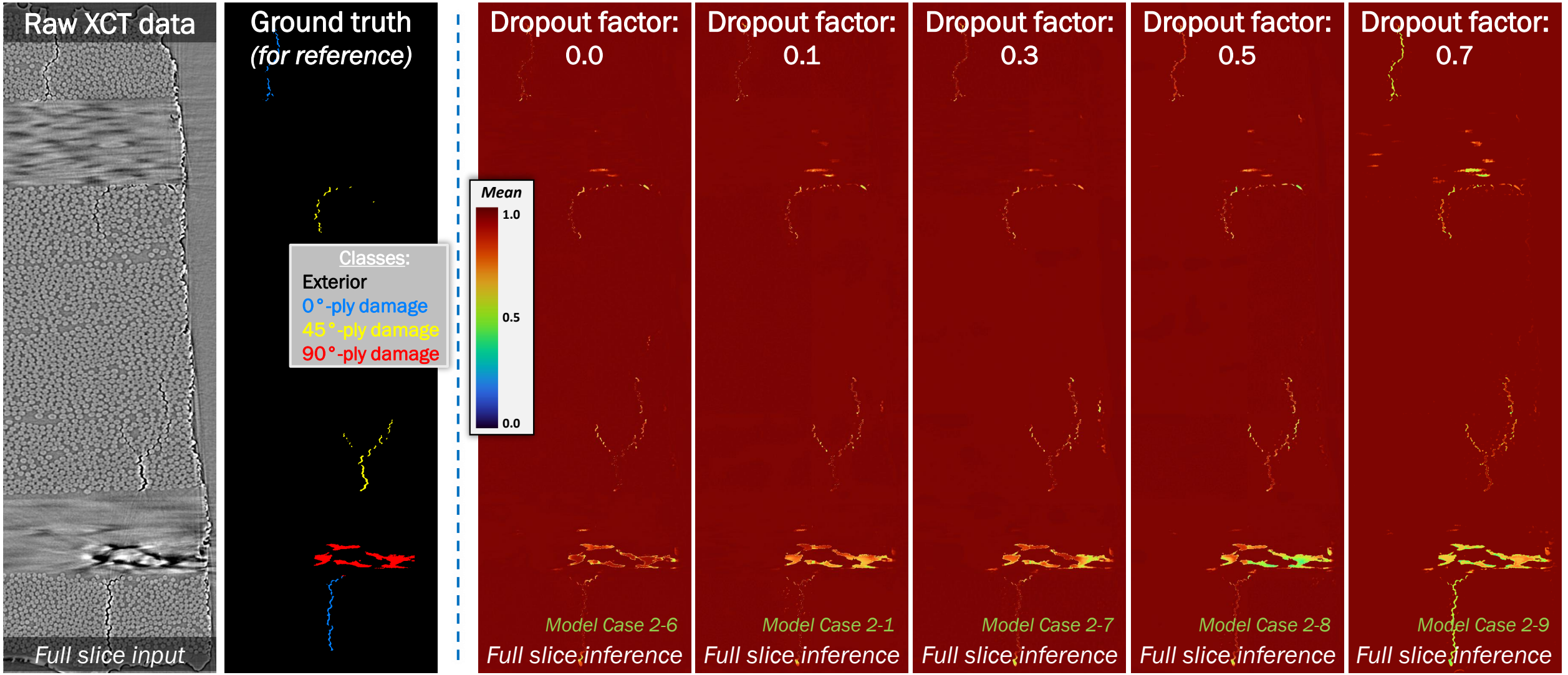

NAVAIR Public Release SPR# 2025-0376. Distribution Statement A - Approved for public release; Distribution is unlimited.

*Uncertainty refers to interquartile range

Nondeterministic Segmentation on Test Set: Effects of Dropout Magnitude (6/6)

Test set Thick sample: Argmax class uncertainty of the probability distribution (generated via 32 MC samples during inference)*

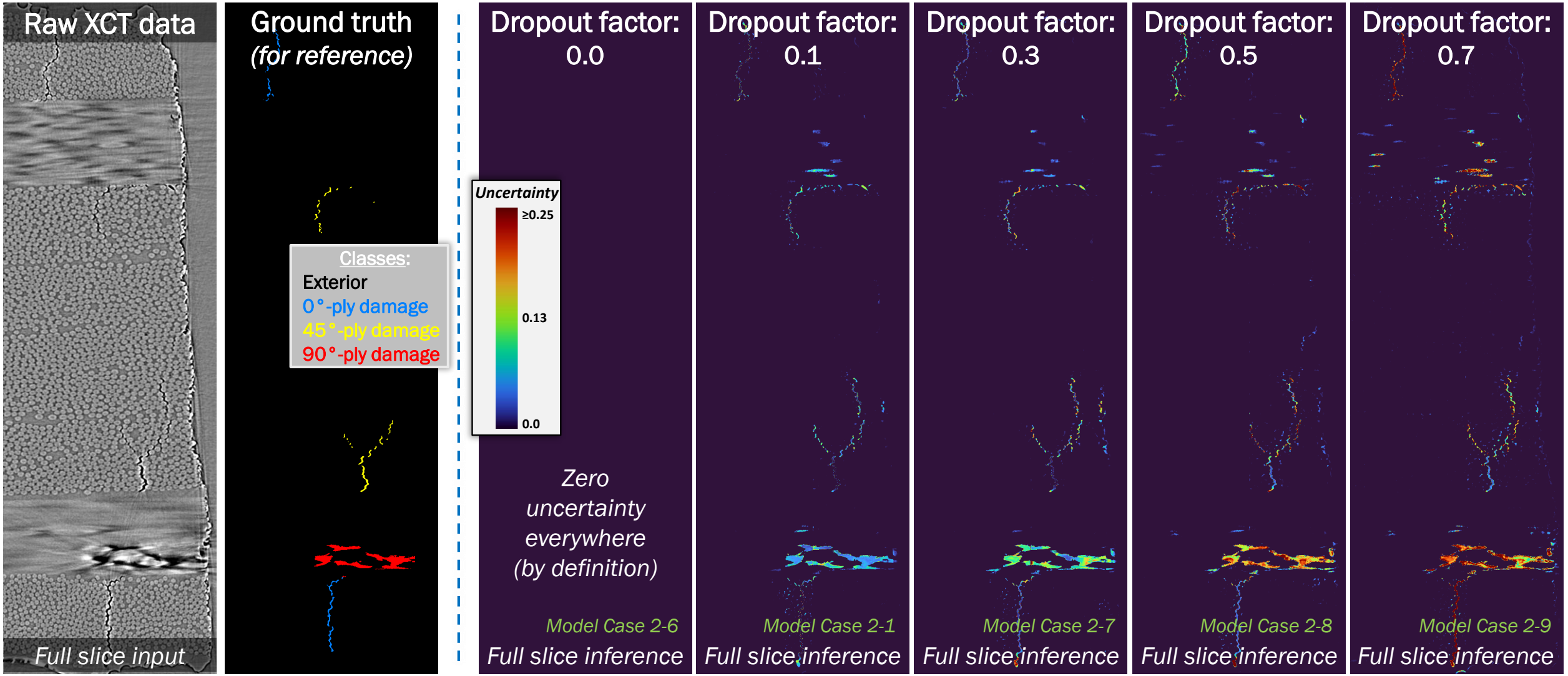

NAVAIR Public Release SPR# 2025-0376. Distribution Statement A - Approved for public release; Distribution is unlimited.

*Uncertainty contribution refers to given class IQR normalized by sum of all class IQRs

Nondeterministic Segmentation on Test Set: Class Contributions to Uncertainty (1/2)

Test set Thin sample: Uncertainty of each class's probability distribution (generated via 32 MC samples during inference)*

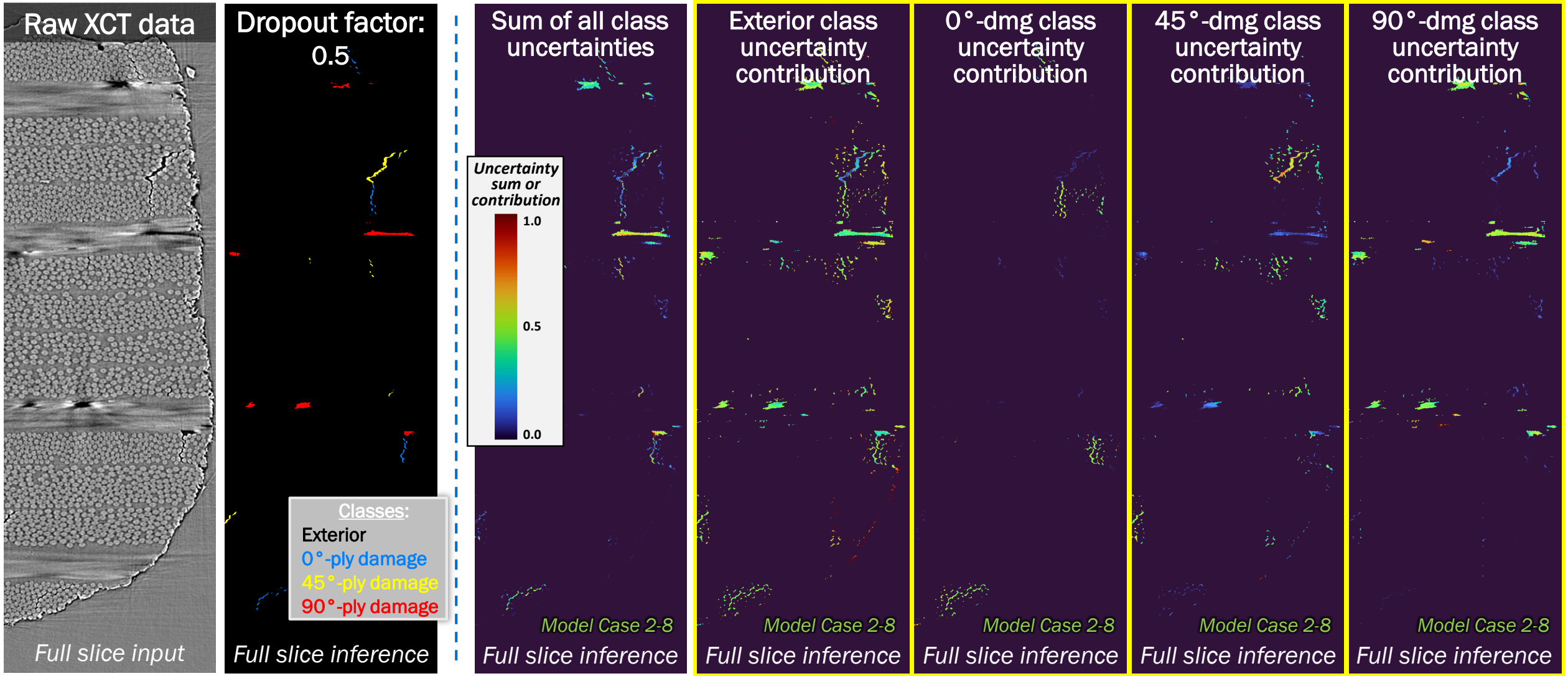

NAVAIR Public Release SPR# 2025-0376. Distribution Statement A - Approved for public release; Distribution is unlimited.

*Uncertainty contribution refers to given class IQR normalized by sum of all class IQRs

Nondeterministic Segmentation on Test Set: Class Contributions to Uncertainty (2/2)

Test set Thick sample: Uncertainty of each class's probability distribution (generated via 32 MC samples during inference)*

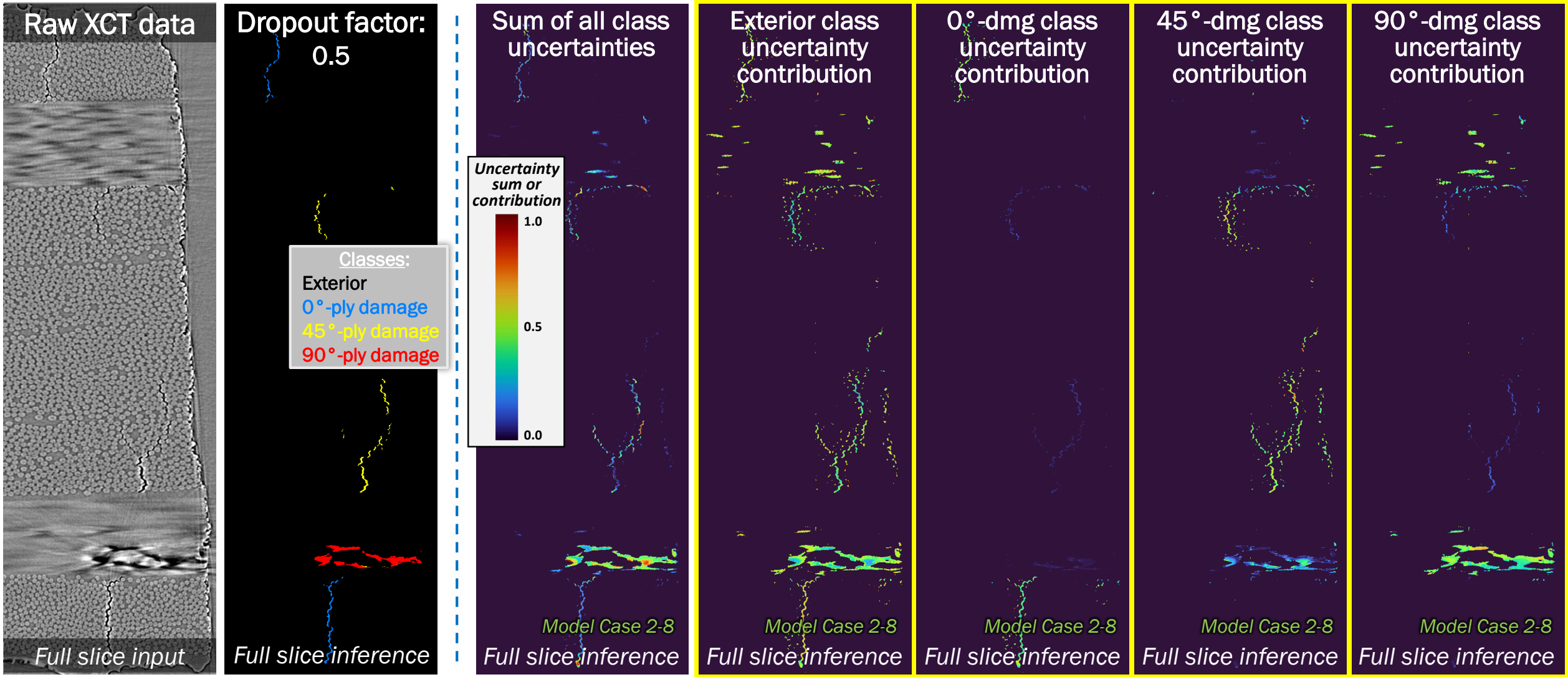

NAVAIR Public Release SPR# 2025-0376. Distribution Statement A - Approved for public release; Distribution is unlimited.

Conclusions:

- Established **suggested practices for developing MCDN models** based on: Train set size, loss weighting, data augmentation, batch size, U-Net architecture/size, patch dimensions, and MC dropout magnitude.
- MCDN models including a **relatively high dropout factor of up to 0.7 can relatively effectively learn** the sparse multiclass segmentation task with useful levels of uncertainty/confidence *(here, IQR used as a simple first-pass)* and without any appreciable increase in training times.
- Highest uncertainty is unsurprisingly typically observed at the borders of classes.
- The qualitative results suggest an **inverse relationship between segmentation predictive accuracy (decreased) and UQ capacity (increased) when the dropout factor is increased**.
- Additionally, the **models correct many ground truth errors**, albeit at the expense of metric scores that assume label set perfection.

Future/Ongoing Work:

- Develop and assess alternative 2D/3D nondeterministic model architectures and multiclass uncertainty approaches
- Explore uncertainty-guided DL-segmentation model fine-tuning and active learning

NAVAIR Public Release SPR# 2025-0376. Distribution Statement A - Approved for public release; Distribution is unlimited.

Acknowledgments

- This material is based upon work supported by the Naval Air Warfare Center under Contract No. N68335-22-C-0370.
- Thank you to the NAVAIR engineers involved in this study for their feedback and guidance.
- Thank you to additional ATA Engineering staff: David Najera, Matthew Mueller, Elliot Haag, and Joshua Davis.

Thank you! — Any Questions?



Dr. Reed Kopp

reed.kopp@ata-e.com

Project Engineer

ATA Engineering, Inc.

NAVAIR Public Release SPR# 2025-0376. Distribution Statement A - Approved for public release; Distribution is unlimited.

APPENDIX

NAVAIR Public Release SPR# 2025-0376. Distribution Statement A - Approved for public release; Distribution is unlimited.

Common details/parameters used for dataset management and DL model development that were applied to all DL models

Model initialization	Random/default
Loss function	Categorical cross entropy
Model performance metrics (probability threshold: 0.5)	Binary accuracy, intersection over union
Training optimizer algorithm	Adam
Learning rate schedule	Reduce learning rate on plateau
Model checkpoint saving during training	Best train and validation losses
Number of Monte Carlo samples used during testing	32
Machine learning framework	PyTorch v2.4.1, Python 3.10
Machine hardware (Windows 10 desktop)	1 GPU (NVIDIA Quadro RTX 5000, 16 GB of GPU memory), 128 GB of memory, 8 CPU cores

NAVAIR Public Release SPR# 2025-0376. Distribution Statement A - Approved for public release; Distribution is unlimited.

Nondeterministic Segmentation on Test Set: Effects of Model Input Dimensions (1/6)

***Test set Thin sample:** [Argmax](#) of the mean probability distribution (generated via 32 MC samples during inference)*

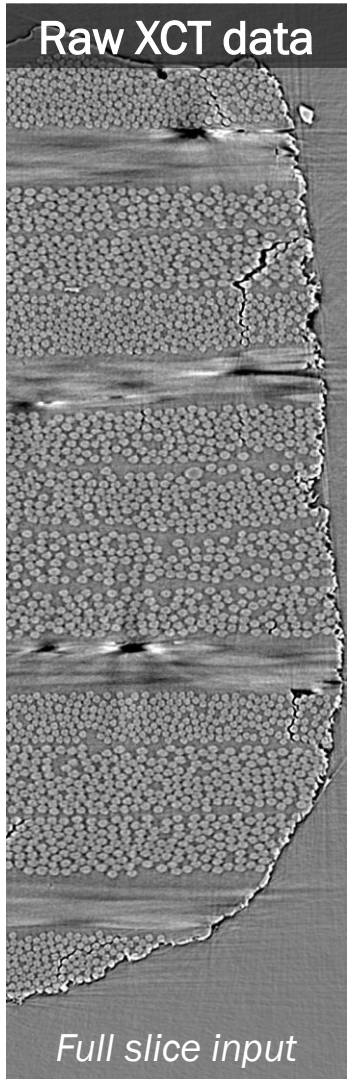



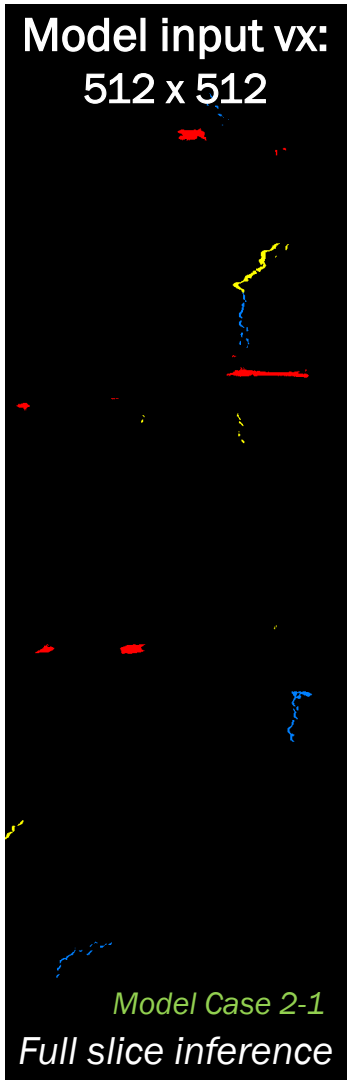

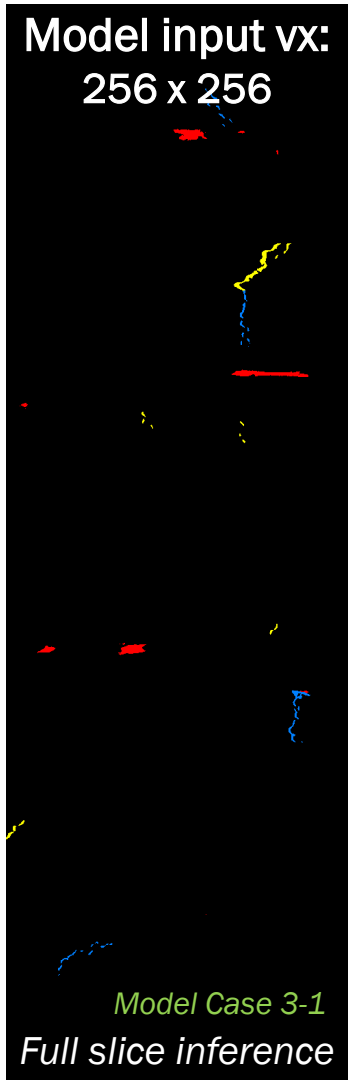



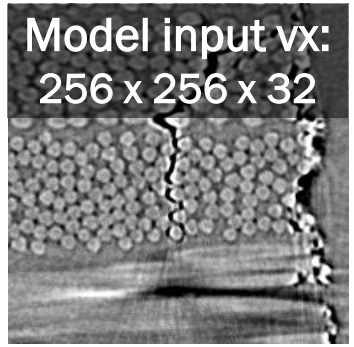

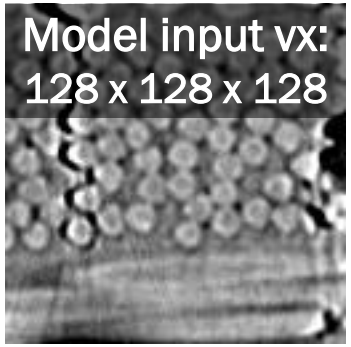

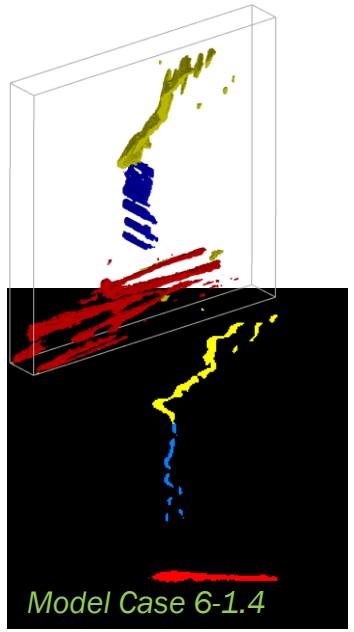

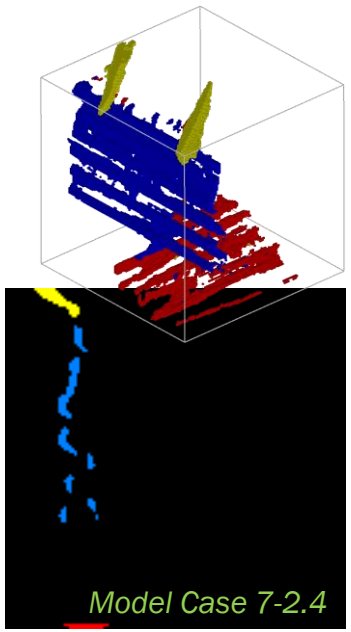

NAVAIR Public Release SPR# 2025-0376. Distribution Statement A - Approved for public release; Distribution is unlimited.

Note: 0.5 is an ideal binary threshold value

Nondeterministic Segmentation on Test Set: Effects of Model Input Dimensions (2/6)

***Test set Thin sample:** [Argmax class mean](#) of the probability distribution (generated via 32 MC samples during inference)*

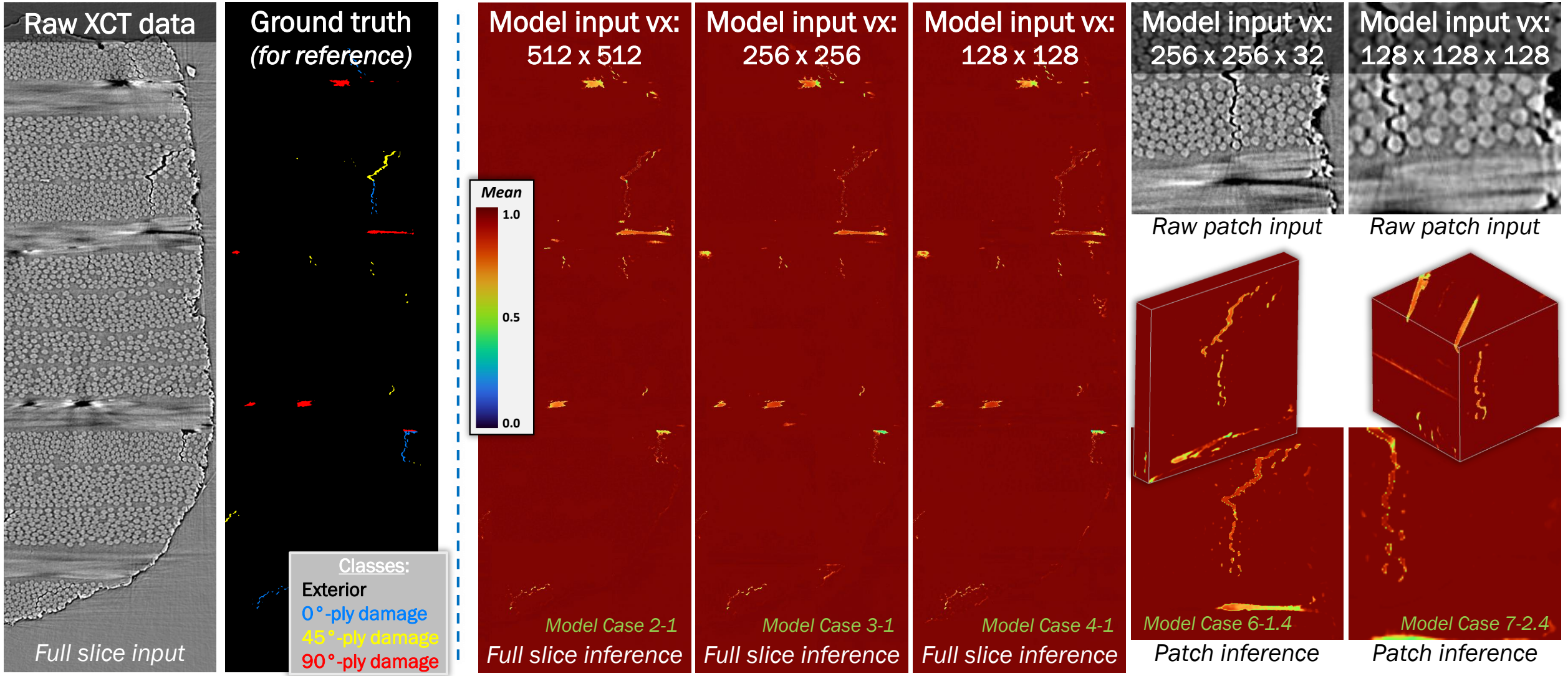

NAVAIR Public Release SPR# 2025-0376. Distribution Statement A - Approved for public release; Distribution is unlimited.

*Uncertainty refers to interquartile range

Nondeterministic Segmentation on Test Set: Effects of Model Input Dimensions (3/6)

Test set Thin sample: Argmax class uncertainty of the probability distribution (generated via 32 MC samples during inference)*

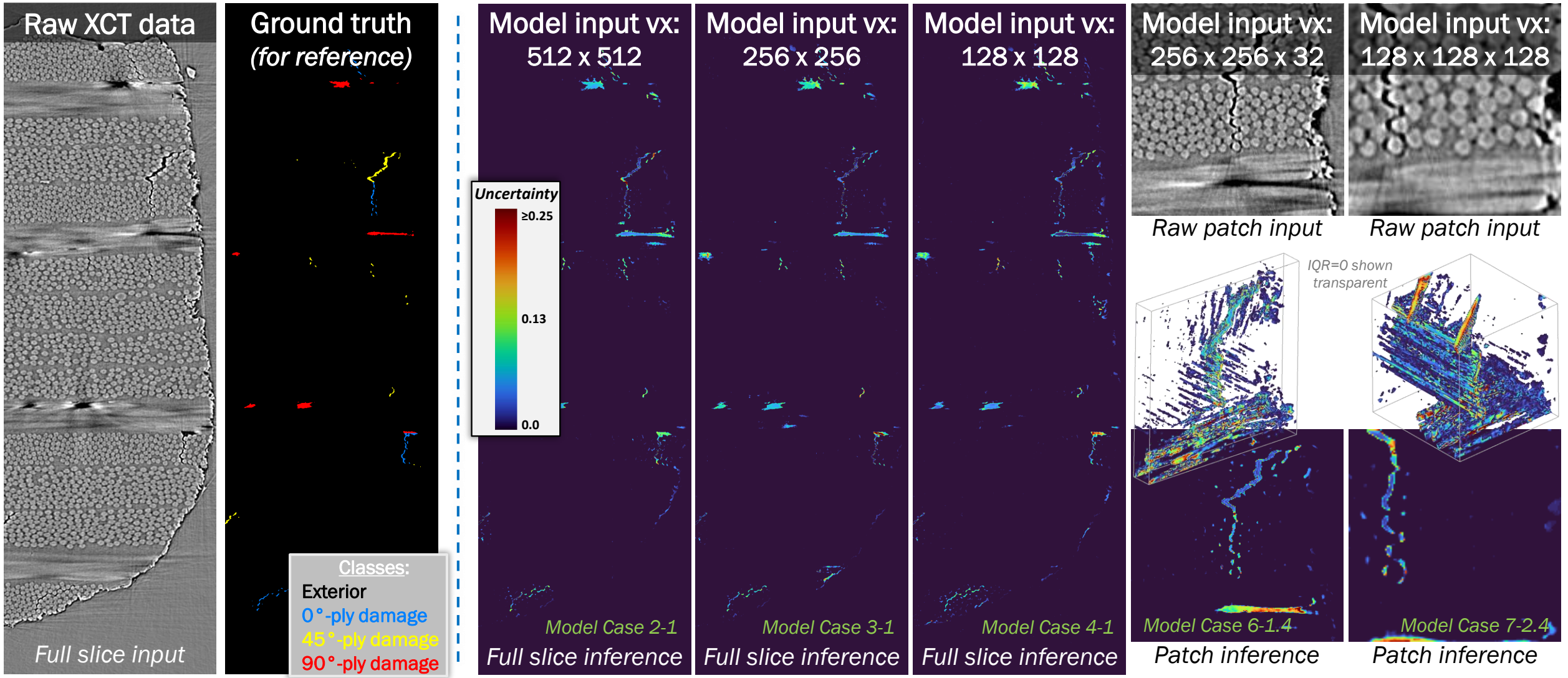

NAVAIR Public Release SPR# 2025-0376. Distribution Statement A - Approved for public release; Distribution is unlimited.

Nondeterministic Segmentation on Test Set: Effects of Model Input Dimensions (4/6)

Test set Thick sample: Argmax of the mean probability distribution (generated via 32 MC samples during inference)

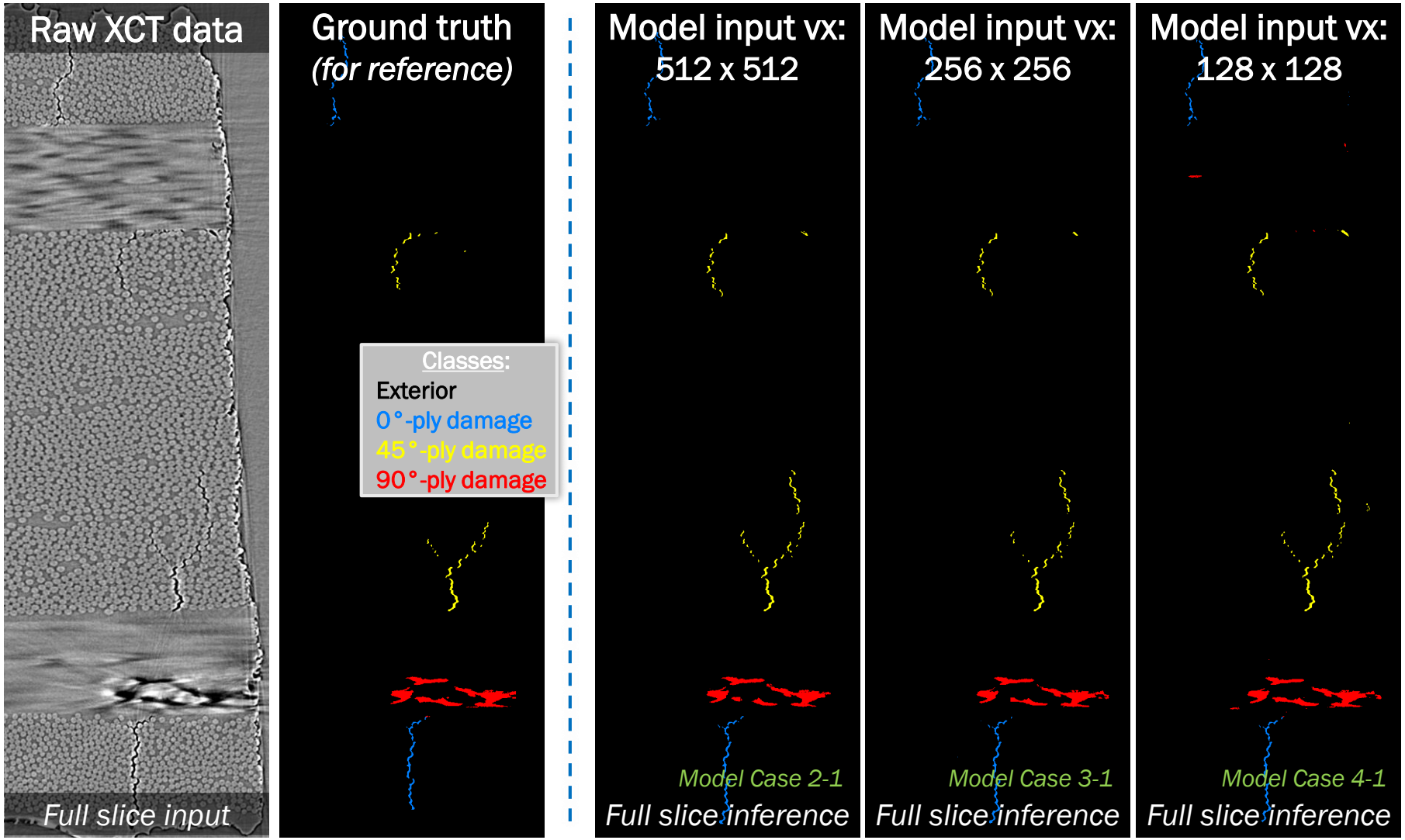

NAVAIR Public Release SPR# 2025-0376. Distribution Statement A - Approved for public release; Distribution is unlimited.

Note: 0.5 is an ideal binary threshold value

Nondeterministic Segmentation on Test Set: Effects of Model Input Dimensions (5/6)

Test set Thick sample: Argmax class mean of the probability distribution (generated via 32 MC samples during inference)

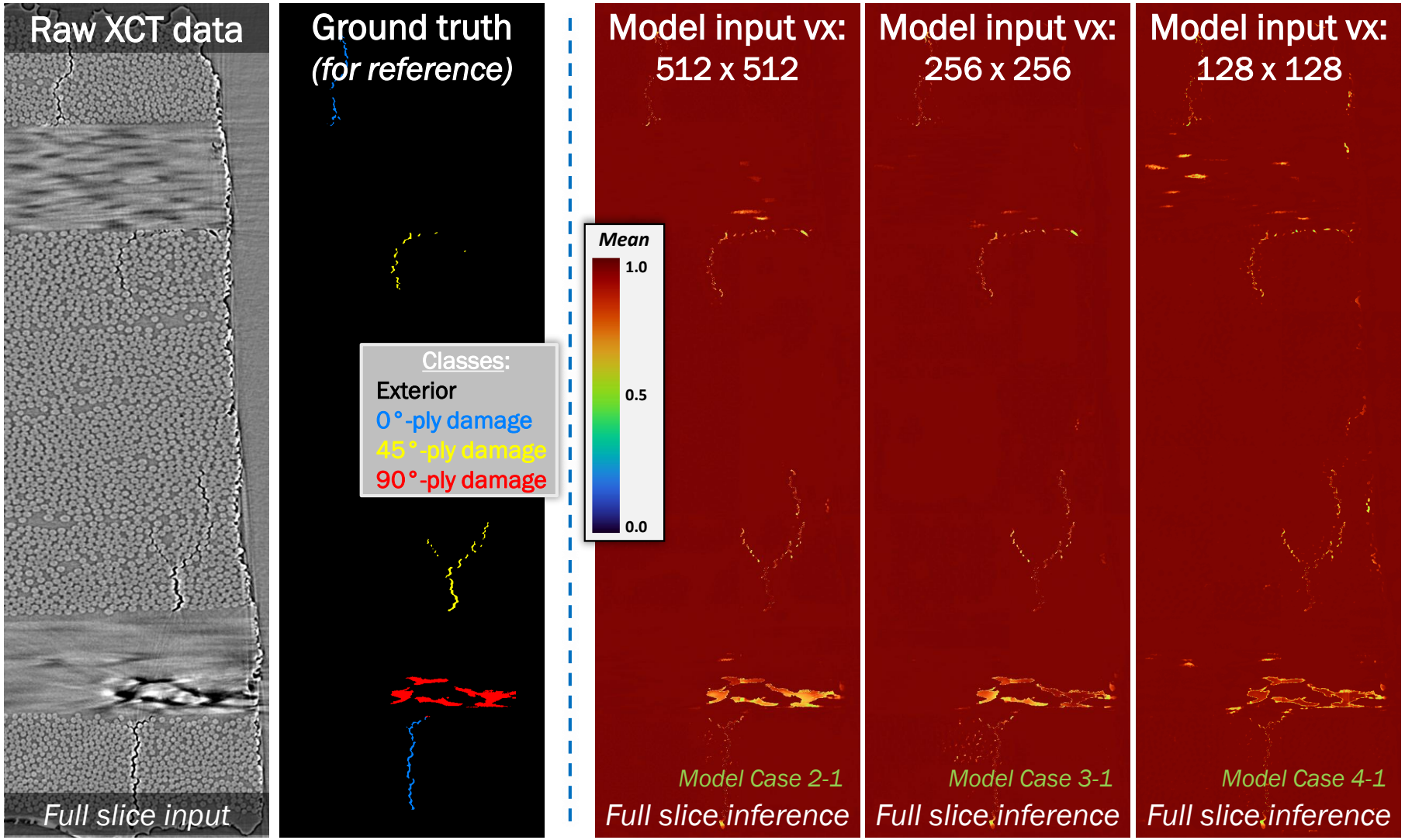

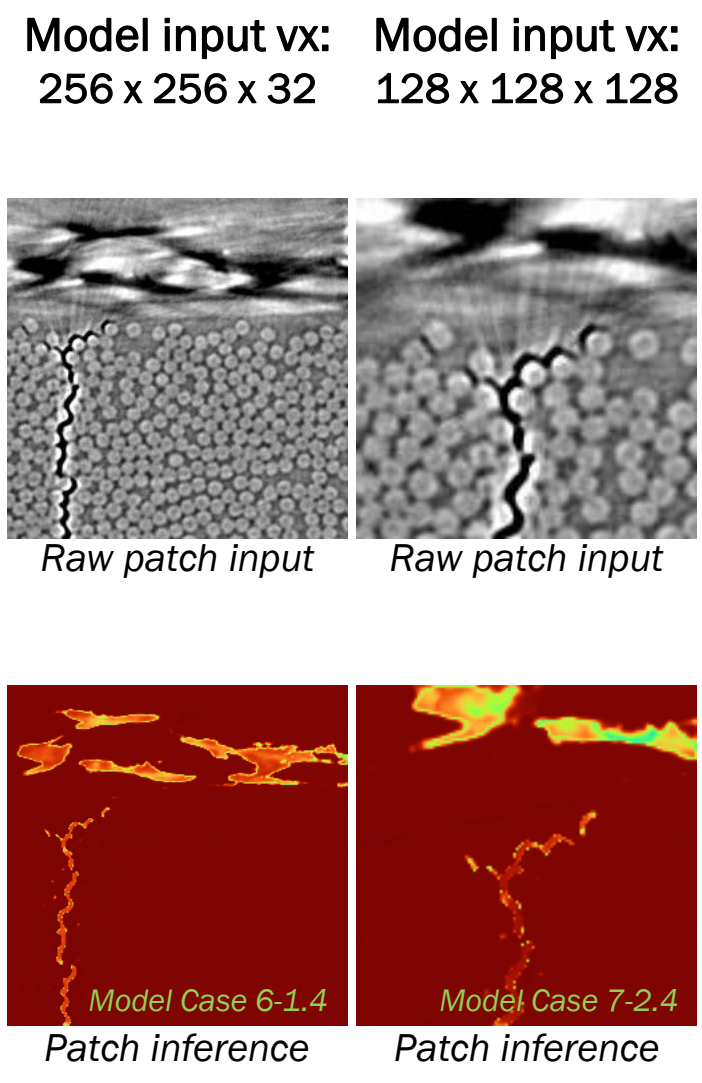

NAVAIR Public Release SPR# 2025-0376. Distribution Statement A - Approved for public release; Distribution is unlimited.

*Uncertainty refers to interquartile range

Nondeterministic Segmentation on Test Set: Effects of Model Input Dimensions (6/6)

Test set Thick sample: Argmax class uncertainty of the probability distribution (generated via 32 MC samples during inference)*

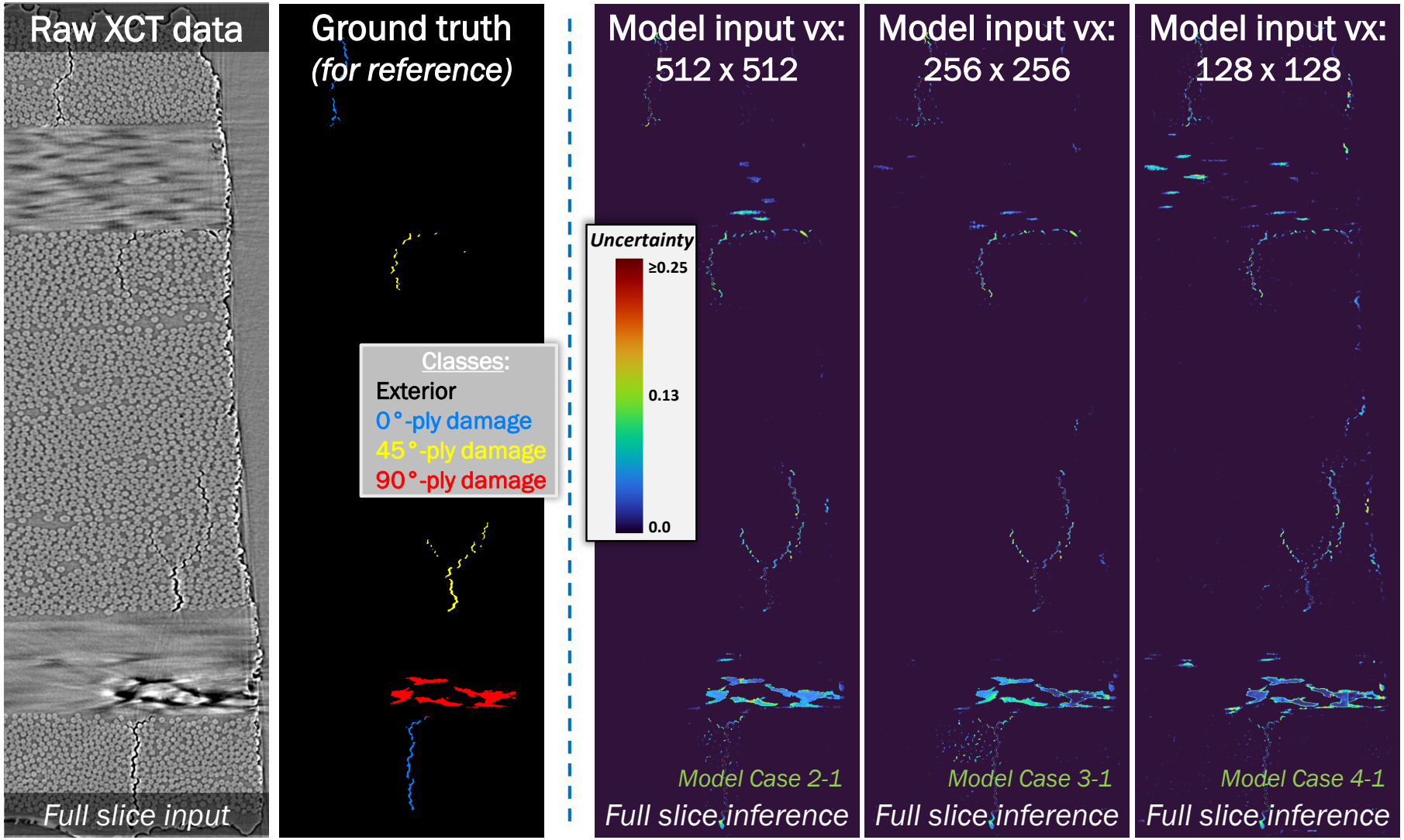

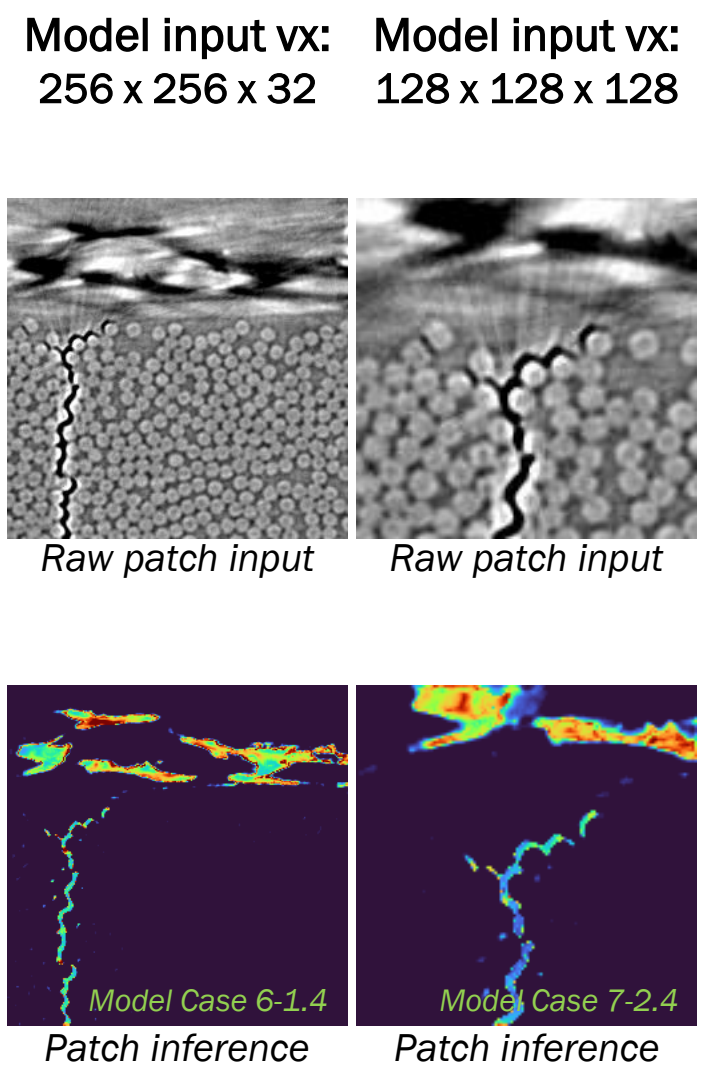

NAVAIR Public Release SPR# 2025-0376. Distribution Statement A - Approved for public release; Distribution is unlimited.

A new approach for quantifying the transverse coefficient of thermal expansion in PAN-based carbon fibres at low temperatures via X-ray Diffraction.

Jiraphant Srisuriyachot[a], Wadwan Singhapong[a], Paloma Rodriguez Santana[a], Carl Sangan[a], Chris Bowen[a], Igor P. Dolbnya[b], Richard Butler[a] and Alexander J. G. Lunt[a]

[a] Materials and Structures Research Centre, University of Bath, Bath, UK
[b] Diamond Light Source Ltd, Harwell Science and Innovation Campus, Didcot, UK

24th International Conference on Composite Materials (ICCM 24)

Baltimore, 4th -8th August 2025

Background

- Thermal expansion mismatch between fibre and matrix
  - Leads to micro-cracking resulting in tank hydrogen leakage
- Conventional thermal analysis method such as dilatometer to measure thermal expansion coefficient
  - Not accurate in the transverse direction of the fibres (5-7 micron)

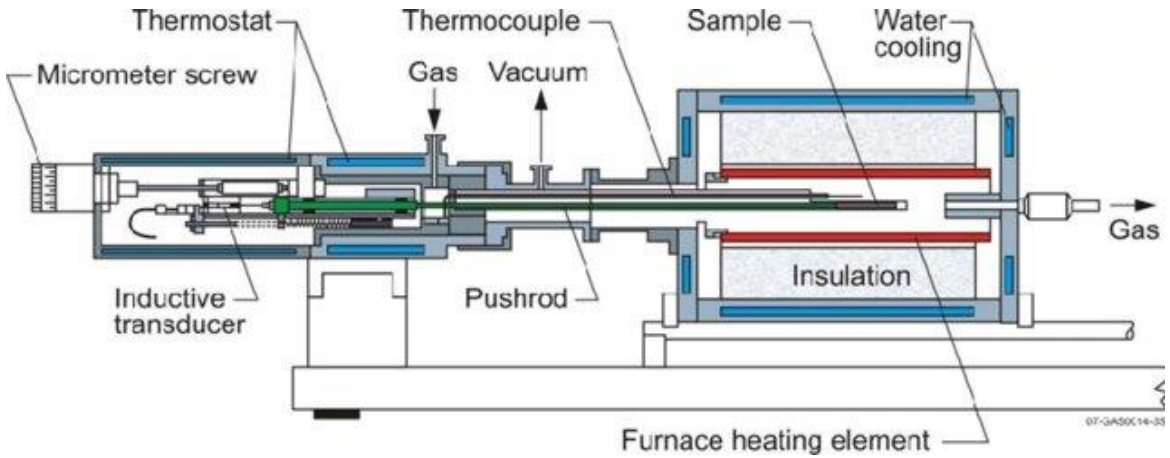

Schematic of conventional dilatometer in horizontal configuration (Joshya et al, 2008).

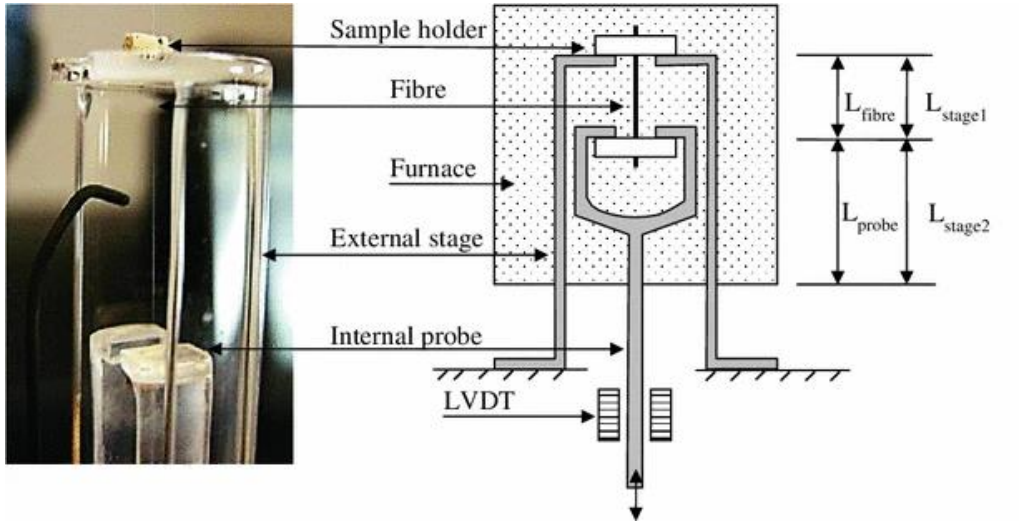

Illustration of the TMA set-up for the fibre/film sample (Yang and Thomason, 2013).

Methodology

- Synchrotron experimental setup (X-ray diffraction (XRD) and radiography)
- Dual cryostream to cool sample (open environment)
- Infrared sensors to measure temperature

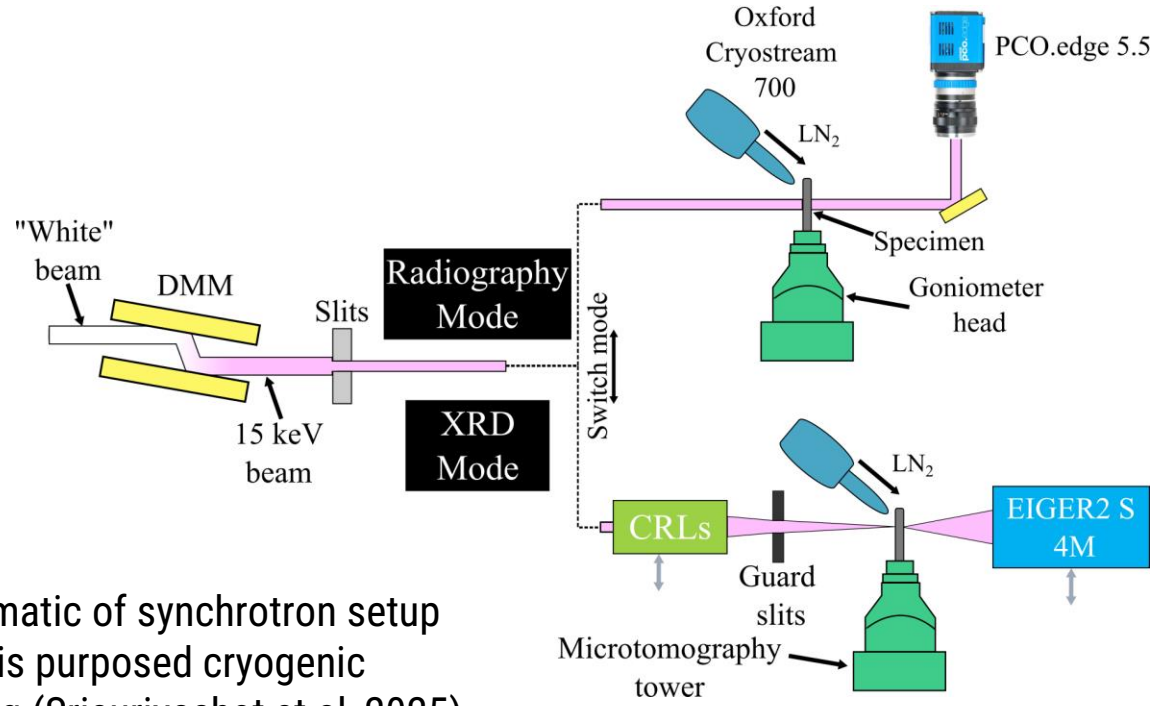

Schematic of synchrotron setup for this purposed cryogenic testing (Srisuriyachot et al, 2025).

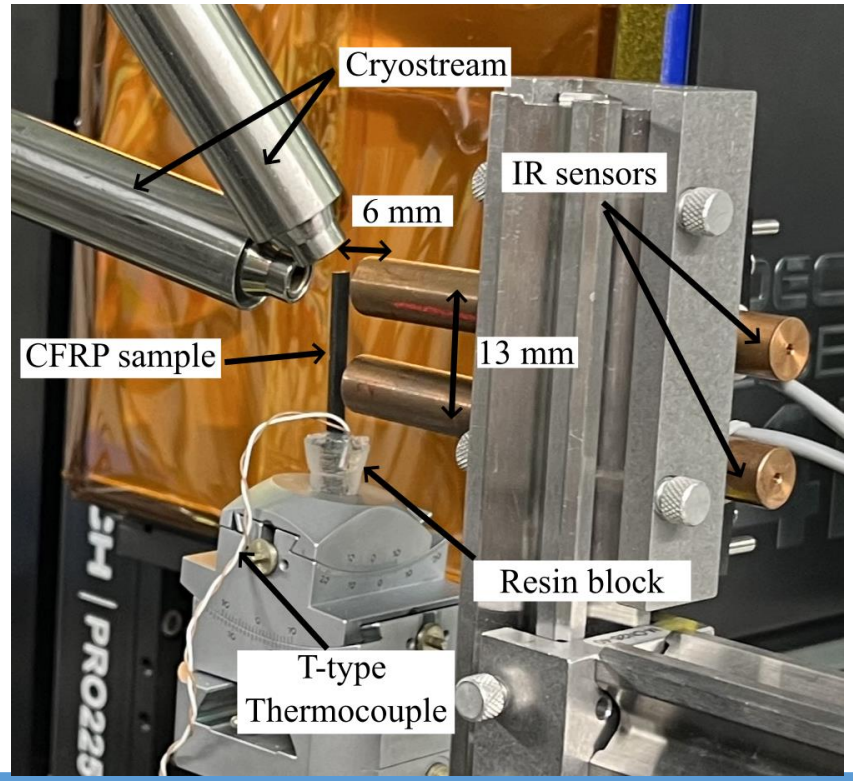

Methodology

- Example of X-ray diffraction pattern of Unidirectional (UD) and Quasi-isotropic (QI) CFRP

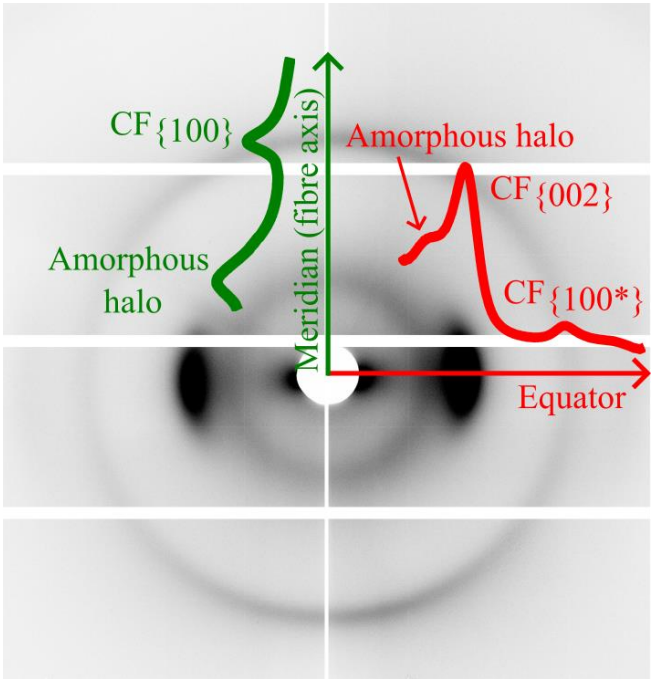

XRD pattern of UD shows the two primary PAN-based fibre lattice planes; {002} and {100}.

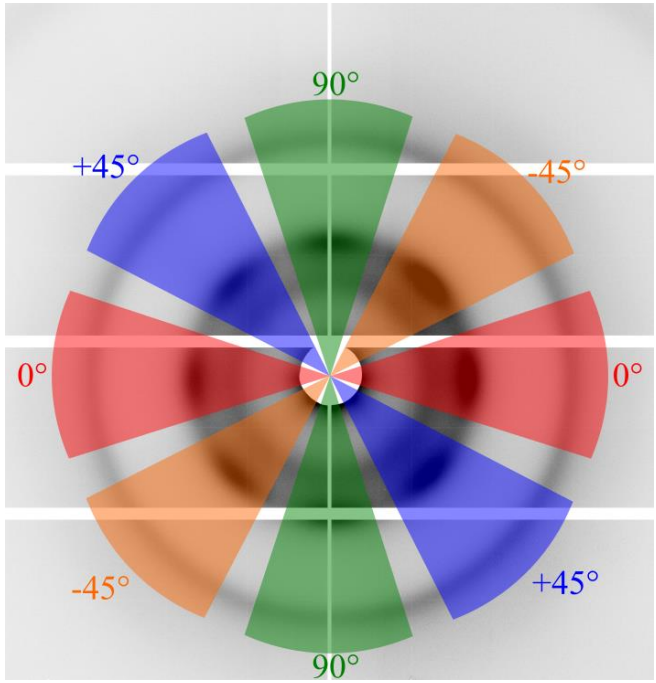

XRD pattern of QI shows the superposition of the fibre lattice planes in 0, 90 and 45/-45-degree plies.

Methodology

- Microstructure of PAN-based carbon fibres
- Measurement of the change in transverse/radial direction of fibre

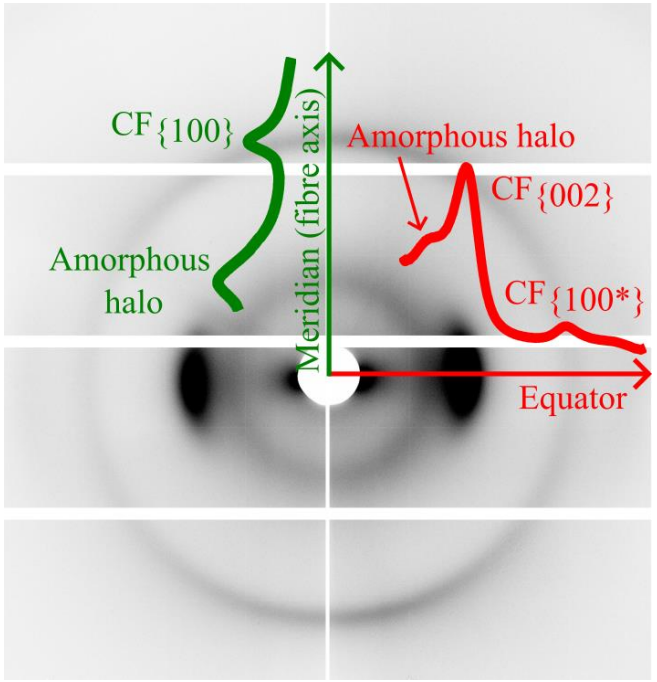

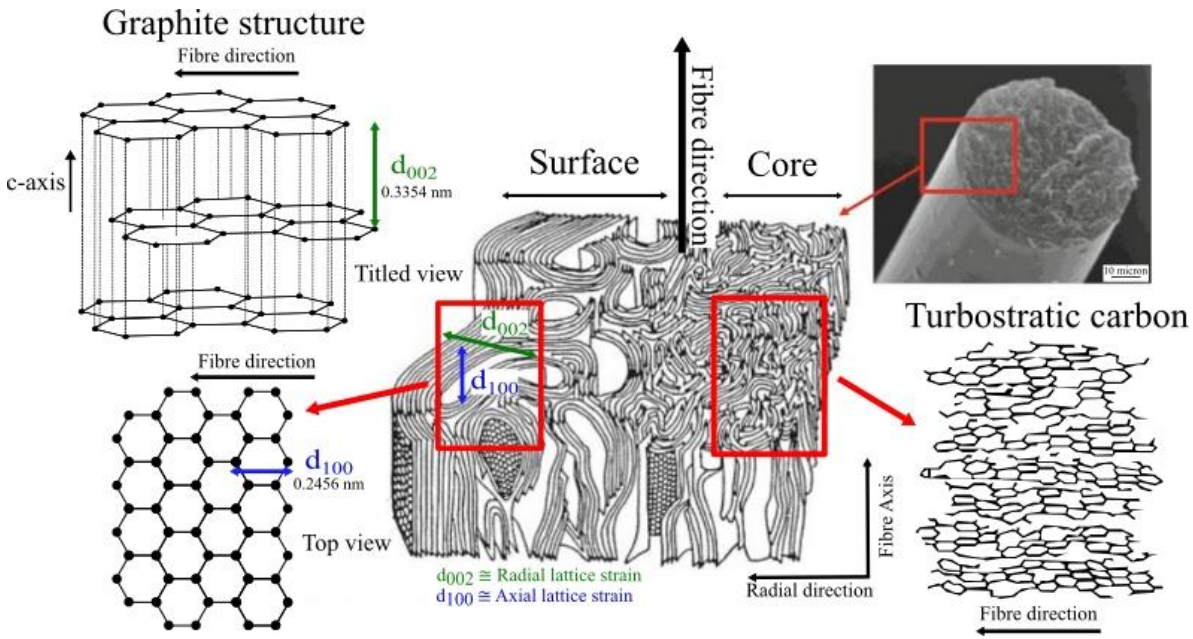

The relationship between the XRD pattern and microstructure of the PAN-based carbon fibres. Δ{002} ≈ Radial lattice strain and Δ{100} ≈ Axial lattice strain (Srisuriyachot et al., 2022).

Experimental results

- Plots of measured fibre lattice strain vs. graphite

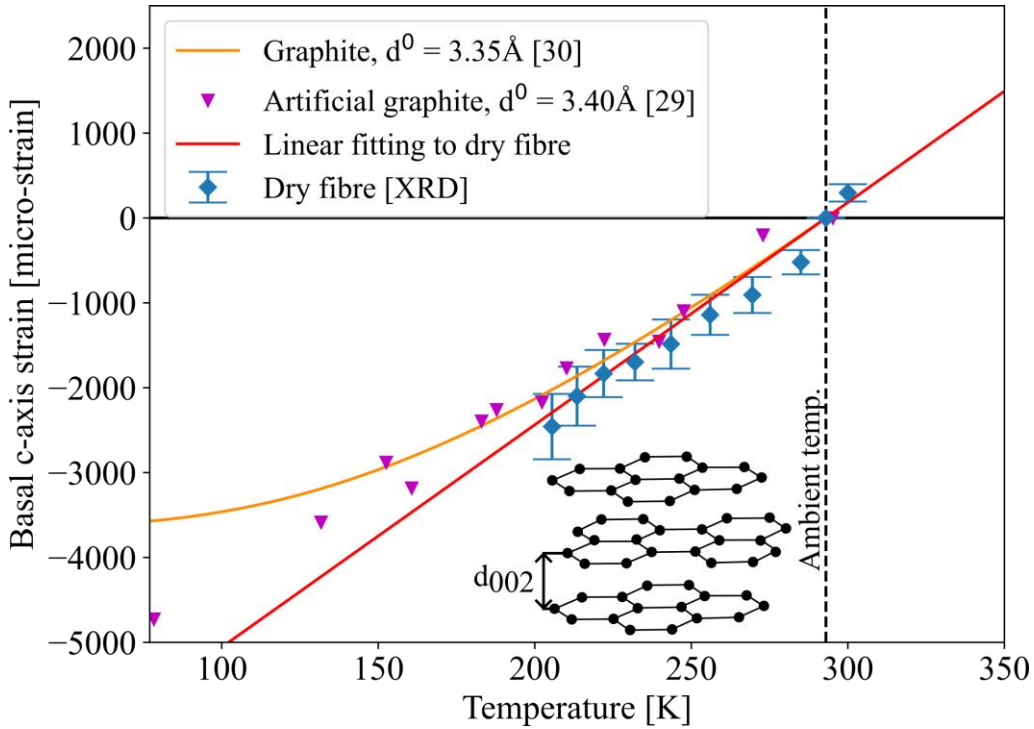

Thermal strain in dry fibre closely matches interlayer spacing changes in natural and artificial graphite up to the measured temperature.

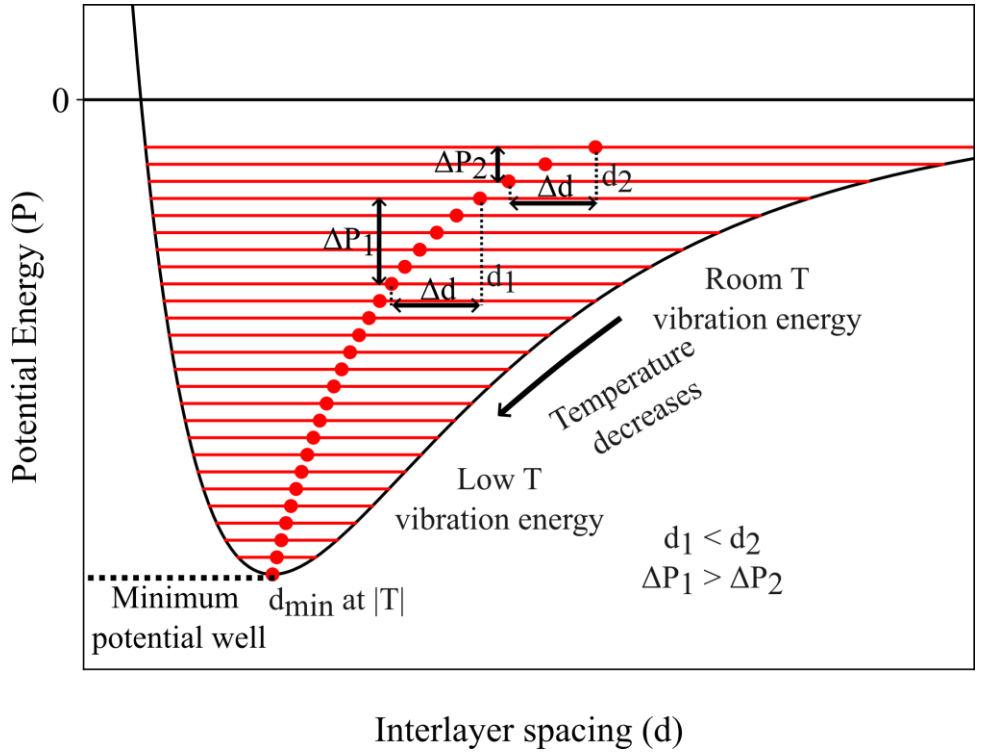

The rate of change of the lattice strain is varies depending on the initial d-spacing. A larger d-spacing will require less energy to deform the same Δd. The smaller d-spacing is starting to plateau earlier.

Experimental results

- Indirect measurement to obtain coefficient of thermal expansions from three configurations

0° composite laminate → α_{comp}^{11}

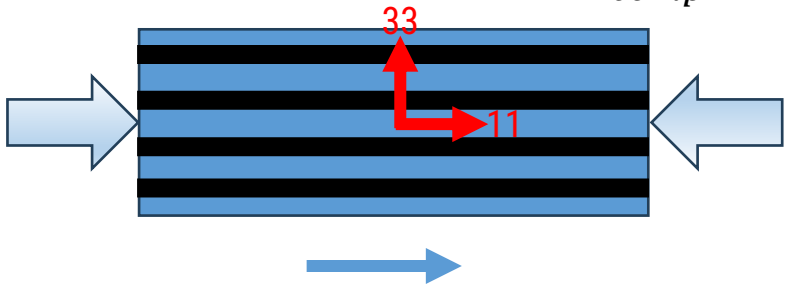

Fibre direction

90° composite laminate → α_{comp}^{22}

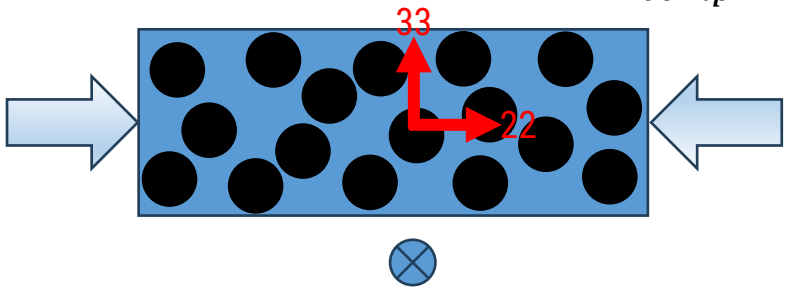

Fibre direction

Pure resin matrix → α_m



Isotropic

Experimental results

- Analytical models to workout transverse CTE of fibres

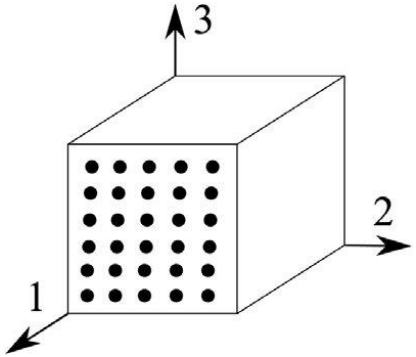

Schapery model (SH)

$$\alpha_{f_{SH}}^{22} = \frac{\alpha_{comp}^{22} - (1+\nu_m)\alpha_m V_m + \alpha_{comp}^{11}(\nu_m V_m + \nu_f^{12} V_f)}{(1-\nu_f^{12})V_f}$$

Chamberlain model (CB)

$$\alpha_{f_{CB}}^{22} = \alpha_m + \frac{(\alpha_{comp}^{22} - \alpha_m)\left[\nu_m(F-1+V_m) + \left(F+V_f\right) + (E_m/E_f^{11})(1-\nu_f^{12})(F-1+V_m)\right]}{2V_f}$$

Chamis model (CM)

$$\alpha_{f_{CM}}^{22} = \frac{\alpha_{comp}^{22} - \alpha_m(1-\sqrt{V_f})(1+V_f\nu_m\frac{E_f^{11}}{E_m})}{\sqrt{V_f}}$$

comp: composite
f: fibre
m: matrix
F: fibre packing factor

Experimental results

- Plots of measured fibre lattice strain vs. indirect measurement

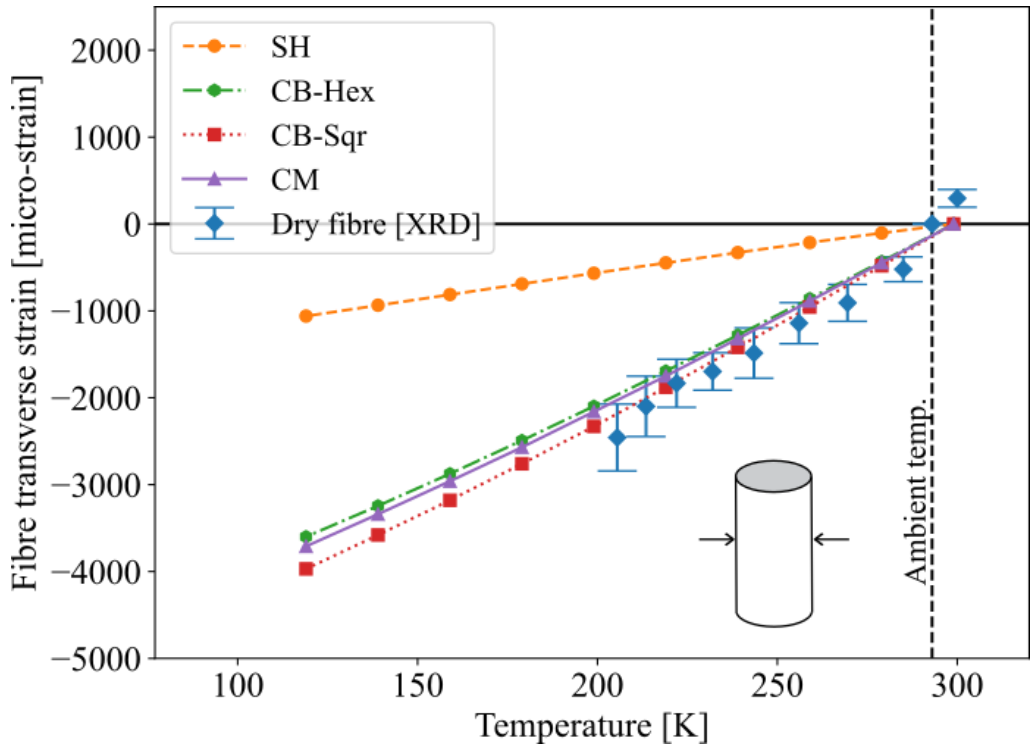

- Comparison of thermally induced dry fibre lattice strain with bulk CTE, highlighting variability due to model dependent assumptions (Gaitonde and Lowson, 1991).
- SH showed the most discrepancies but matched the reported α_f^{22} ($5.2 \times 10^{-6}\ K^{-1}$) at elevated temperature.
- This suggests macroscopic α_f^{22} $\neq$ microscopic α_f^{22} ($26.2 \times 10^{-6}\ K^{-1}$), likely due to crystalline relaxation from defects (micropores, microcracks, crimps) reducing bulk expansion to ~30% of crystallite deformation.

Experimental results

- 2D fibre lattice strain mapping
- Deconvolution of fibre lattice strain at different fibre orientation

UD laminate

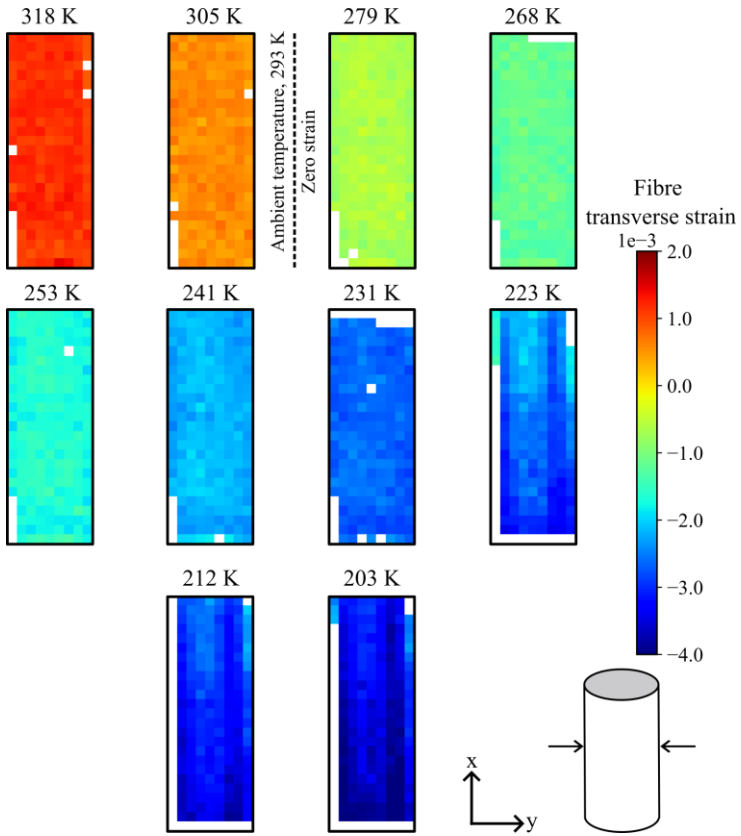

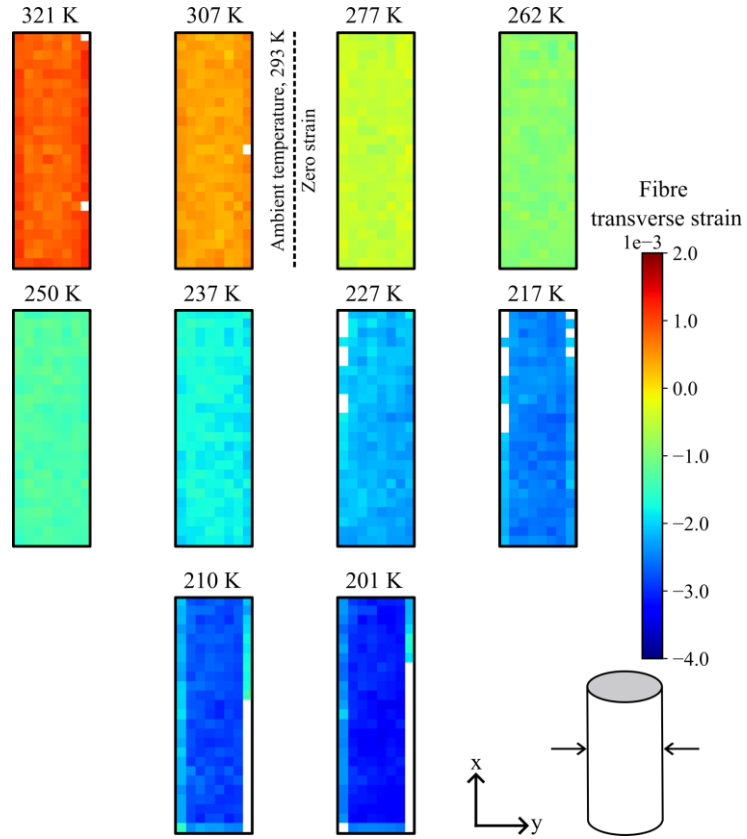

QI laminate

Experimental results

- The average lattice strain was determined and plot against each other
- Thermal induced strain: UD > QI > Dry fibre due to the existing of resin matrix and ply orientation

UD laminate

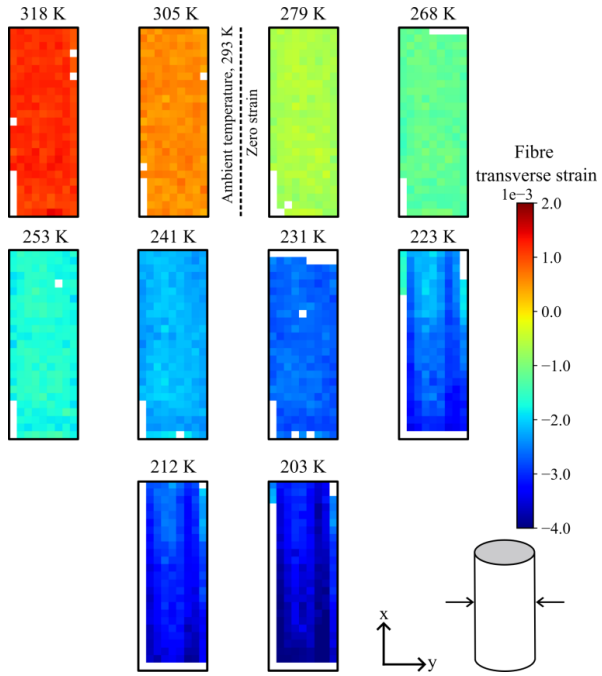

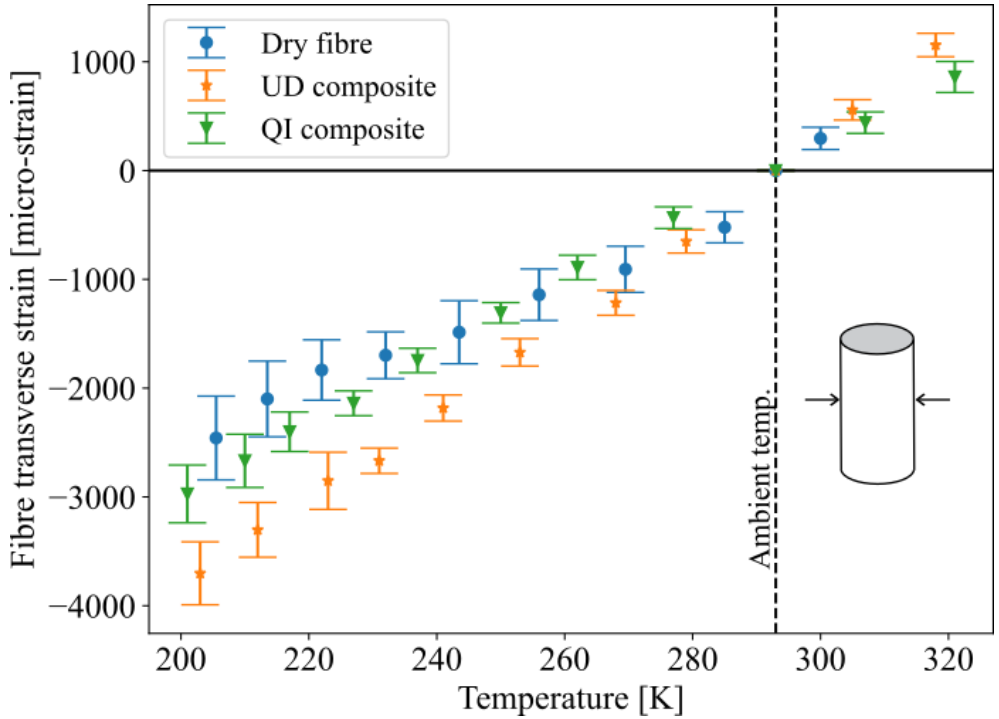

QI laminate

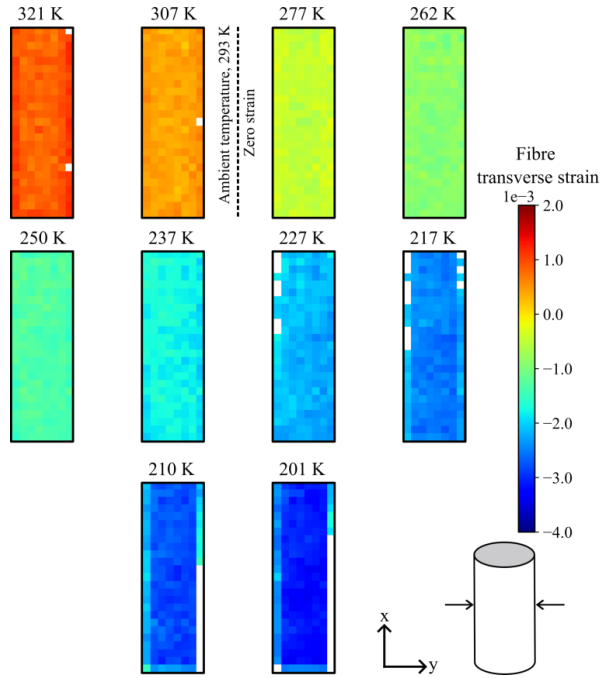

Finite element results

- Thermal induced strain in fibre compared with microscale FE model
- ~13% error between experimental and FE model at ~200 K

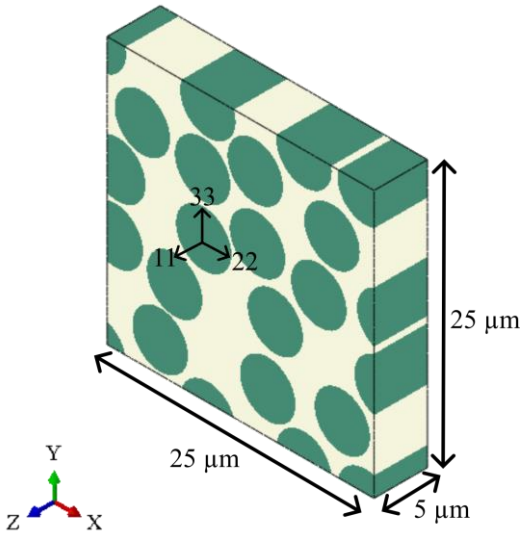

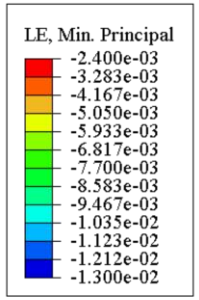



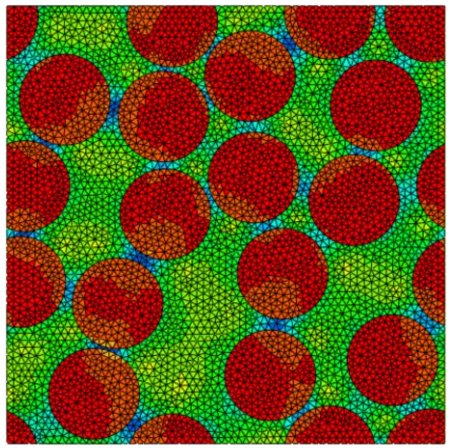

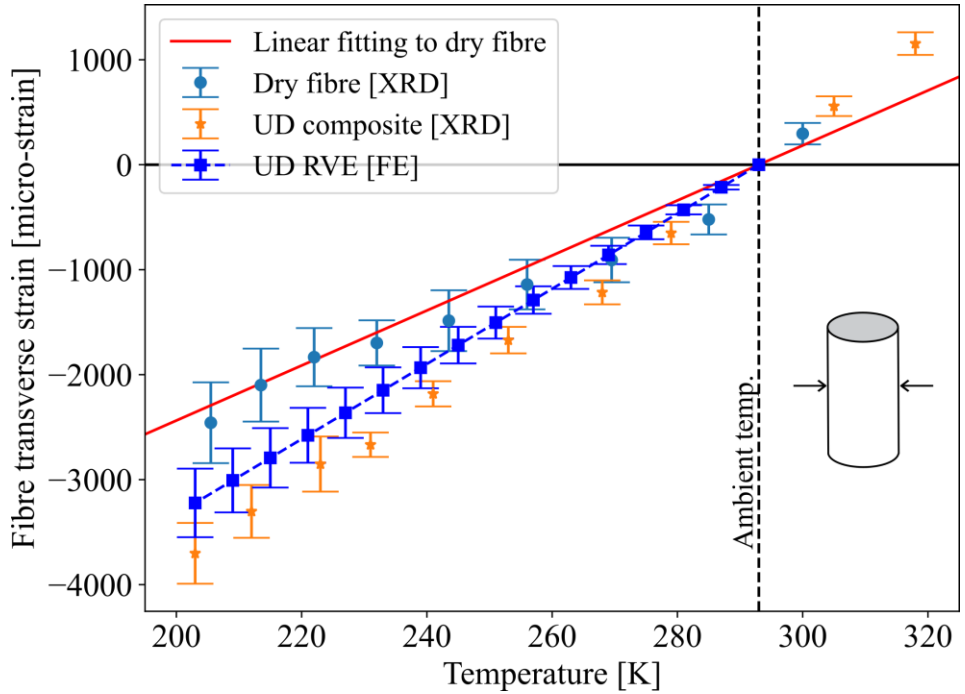

Future work

- Develop a cryostat that is compatible with a beamline in order to reach 20 K or even lower
- Different stacking and fibre volume fraction to fully understand the effect of the fibre orientation

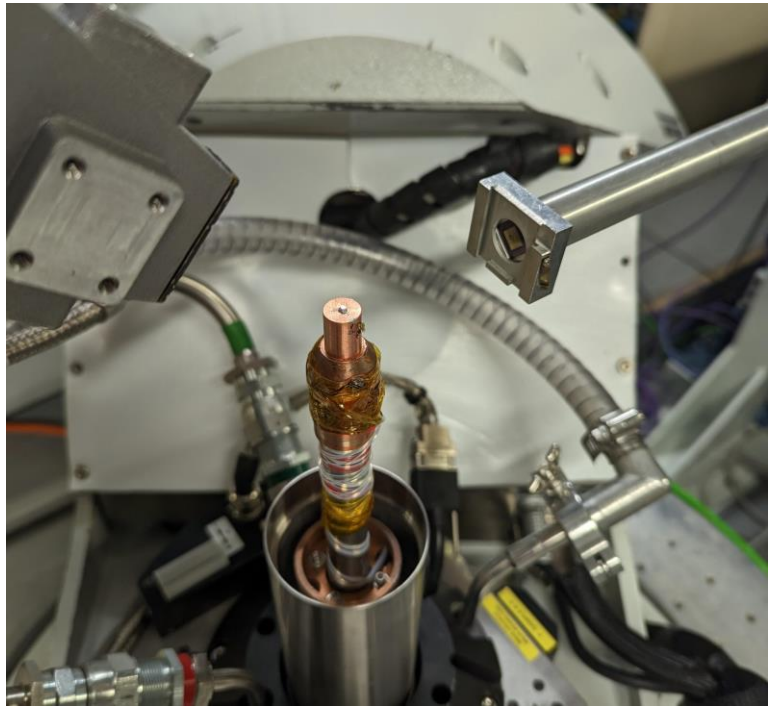

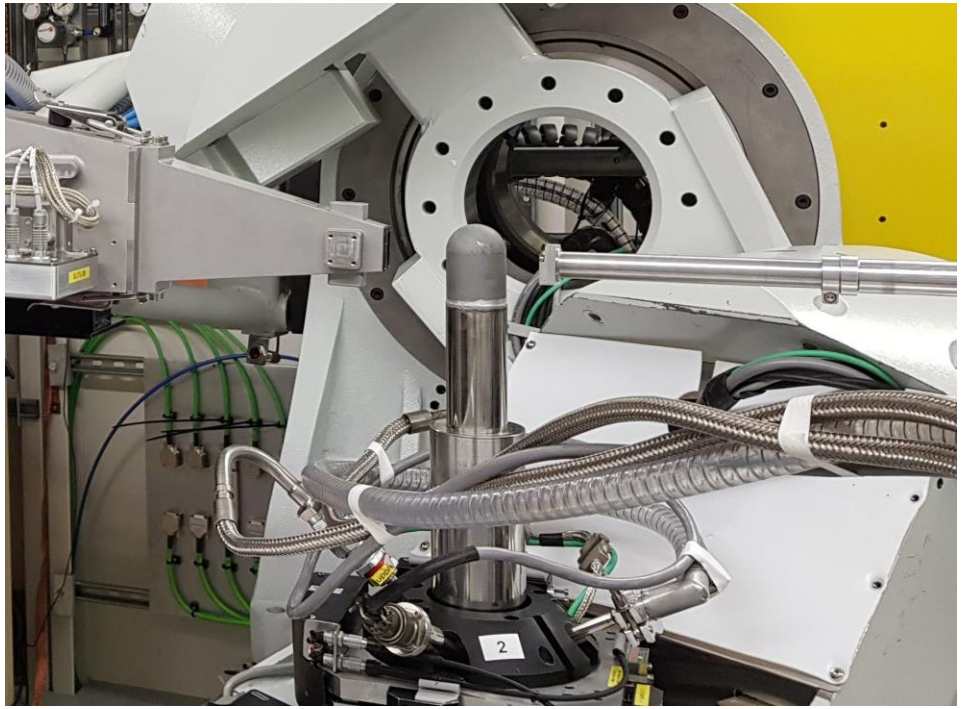

Beryllium dome, I16
Diamond Light Source, UK

Conclusion

- Measurement directly on fibre lattice strain in the transverse direction
- Fibre lattice strain ≠ Fibre strain → crystalline relaxation
- Deconvolution of fibre lattice strain at different fibre orientation
- Understanding the impact of the existing of resin and stacking sequence
- Accepted by Composites Part B: Engineering

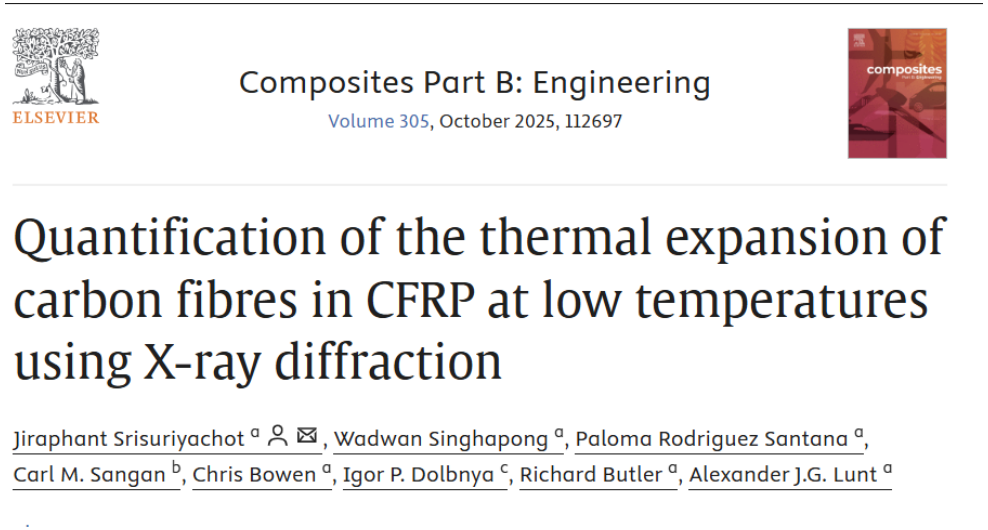

Srisuriyachot, J. *et al.* (2025) 'Quantification of the thermal expansion of carbon fibres in CFRP at low temperatures using X-ray diffraction', *Composites Part B: Engineering*, 305, p. 112697. Available at: https://doi.org/10.1016/j.compositesb.2025.112697.

Thank you for your listening

Contact detail:
Jiraphant Srisuriyachot
University of Bath
js2580@bath.ac.uk

Detection of Progressing Material Defects with FMCW Radar Signals

24th International Conference on Composite Materials
Baltimore, August 6, 2025

Florian Puch; Benedikt Neitzel; Maximilian Lang; Marton Steierlein; Felix Hellmann; Thomas Dallmann

Diese/r Präsentation/ Bericht ist durch Mitarbeiter des Fachgebietes Kunststofftechnik der TU Ilmenau erstellt. Die Verwendung, Verteilung, Zitierung und Vervielfältigung – auch auszugsweise – zum Zwecke der Weitergabe an Dritte ist nur mit vorheriger schriftlicher Zustimmung der Autoren gestattet.

Motivation



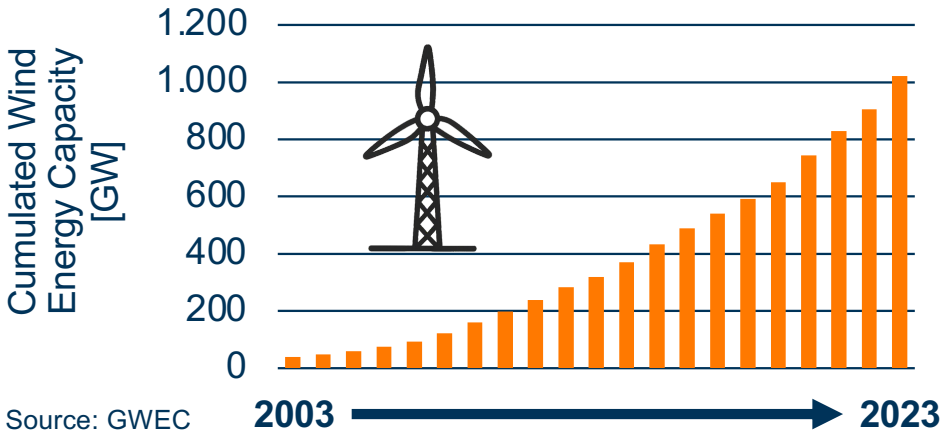

- A significant increase of wind energy capacity and increasing wind turbine blade sizes can be observed.
- As highly complex composite materials wind turbine blades are prone to a variety of defects.
- Non-destructive testing (NDT) is used for structural health monitoring (SHM) and can extend the service life of wind turbine blades

→ **This feasibility study shall explore, if radar can potentially used as NDT method for in field SHM.**

Evolution of damage in composite materials

Matrix cracks:

- Force transmission to fibers is impaired

Debonding:

- Detachment of the matrix from the fiber at the fiber-matrix interface
- Loss of adhesion, fiber cannot absorb load in this area

Delamination:

- Detachment of layers in the fiber composite component
- Complete loss of shear strength between the detached layers

Fiber breakage:

- Tearing of the fiber, can no longer absorb forces
- Accelerates all other failure mechanisms

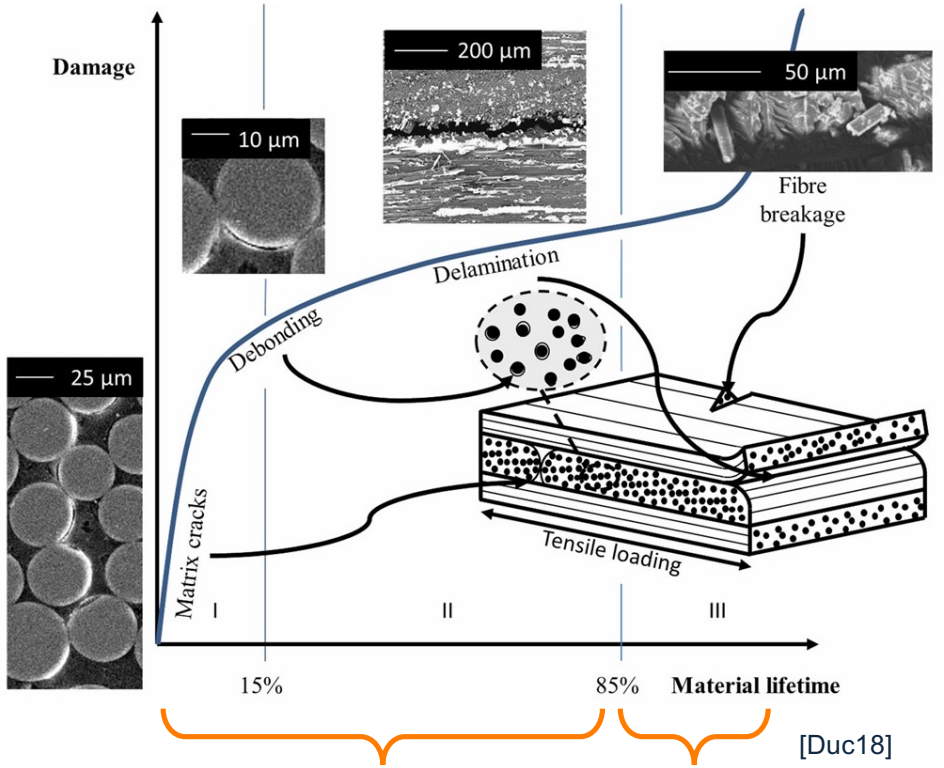

[Duc18]

KTI The SPIRIT of science TECHNISCHE UNIVERSITÄT ILMENAU

Non-destructive testing (NDT) of composite structures

Detection of internal and surface defects

- Identification of manufacturing errors and incipient damage
- After manufacturing and during operational phase (SHM)

✓ Confirmation of structural integrity

✓ Prevention of catastrophic failures

✓ Assessment of aging, fatigue and failure

✓ Condition-based maintenance reduces costs

  ✓ Minimized downtime

  ✓ Avoidance of unnecessary replacements

🧠 Challenging in-situ implementation

🧠 High data volumes need to be interpreted

🧠 Material and geometry complexity need to be accounted for

→ Extension of lifespan and reduction of waste and costs

KTI The SPIRIT of science TECHNISCHE UNIVERSITÄT ILMENAU

Non-destructive testing methods

Active or passive excitation

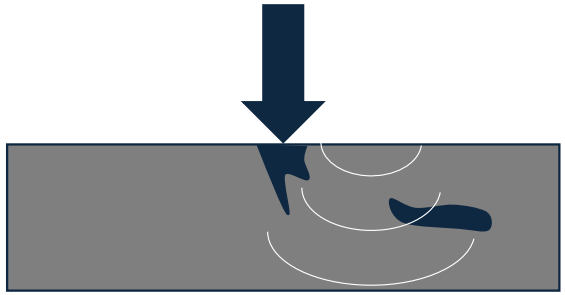

Response

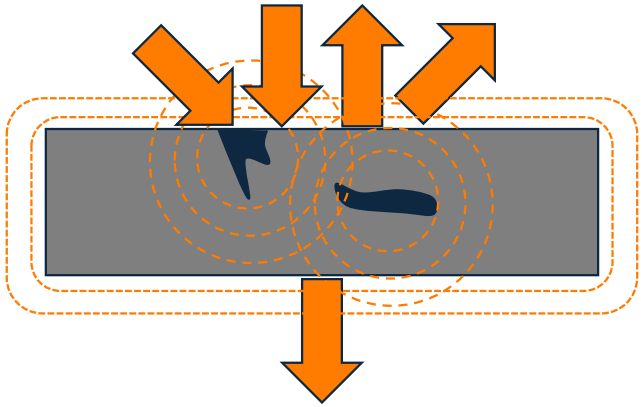

- Visual inspection
- Infrared thermography
- Magnetic particle testing
- Eddy current testing
- Acoustic emission testing
- Ultrasonic testing

Reflection / transmission

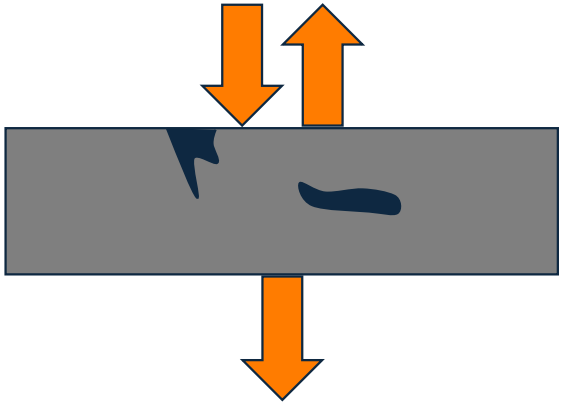

- Microwave / radar
- THz-spectroscopy
- Radiographic testing

KTI The SPIRIT of science TECHNISCHE UNIVERSITÄT ILMENAU

Overview of NDT-methods

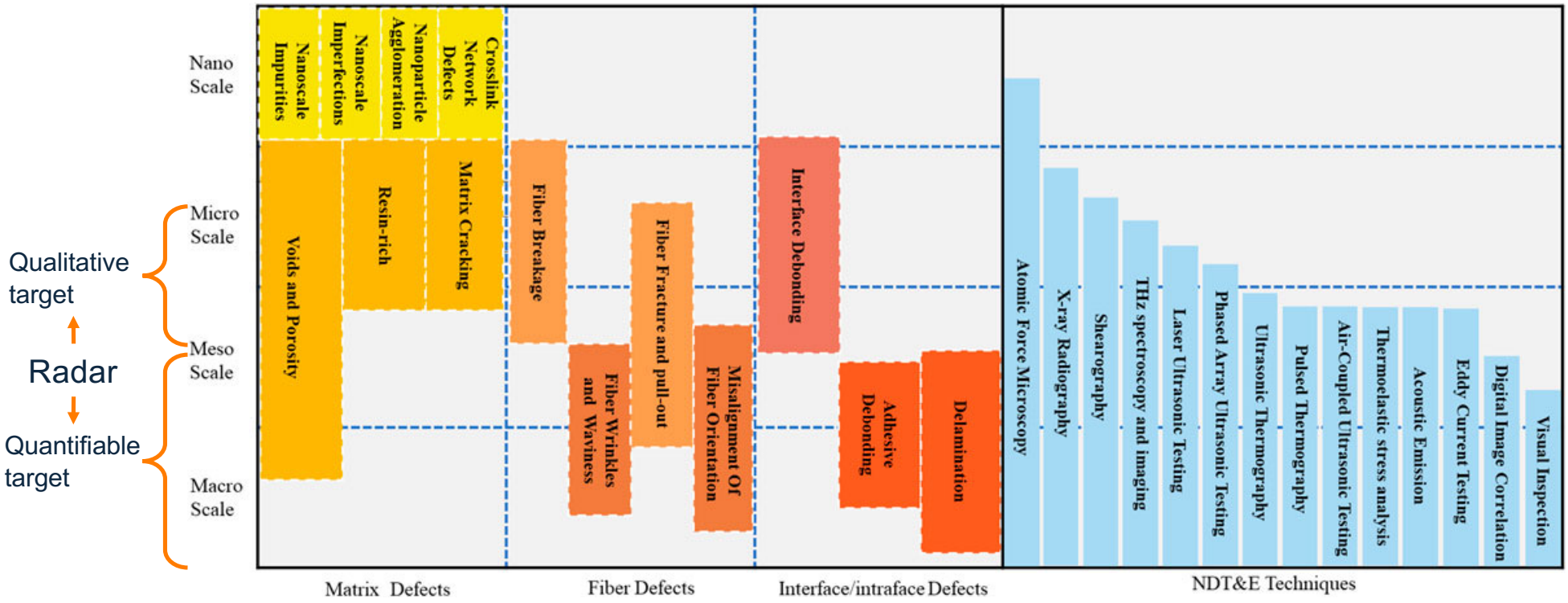

[Che22]

KTI The SPIRIT of science TECHNISCHE UNIVERSITÄT ILMENAU

Experimental setup

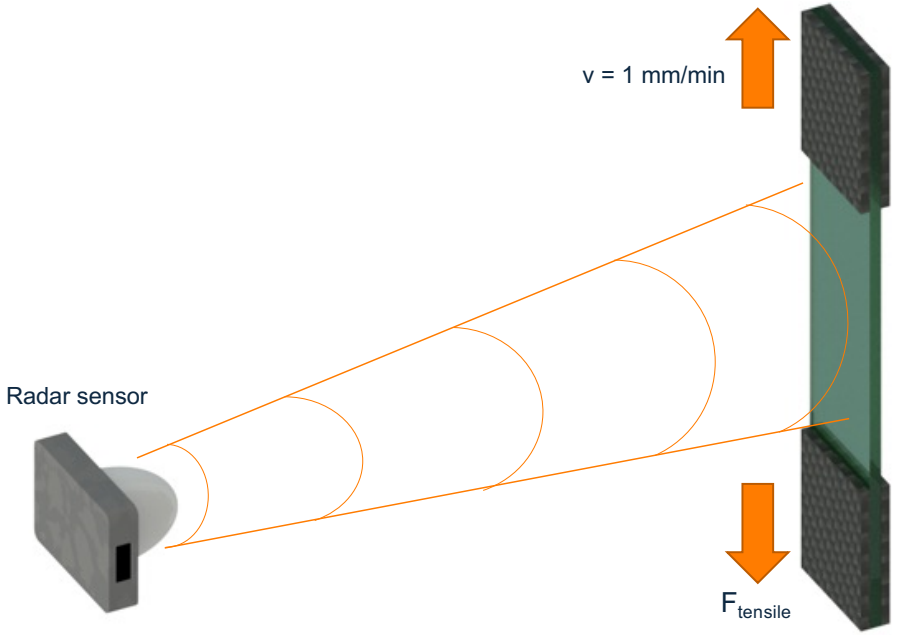

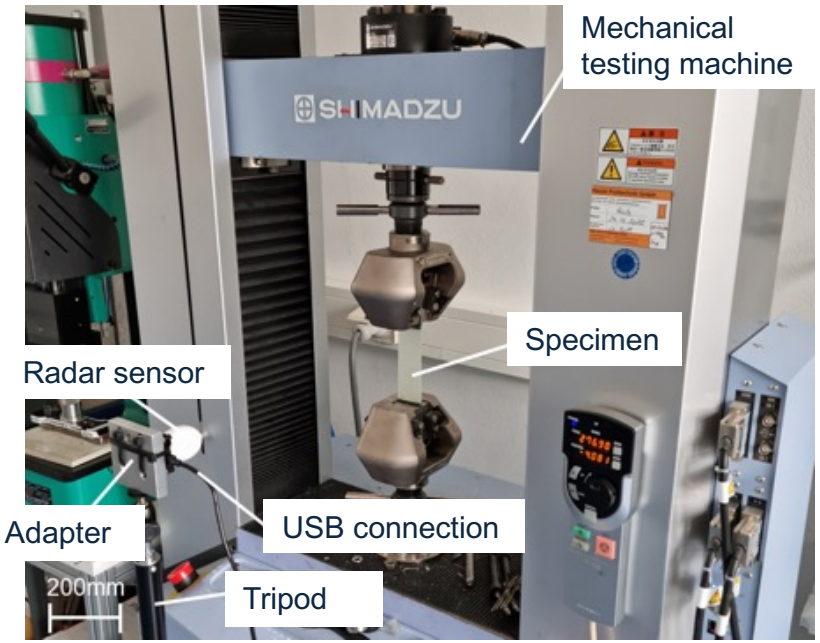

- Tensile test according to DIN EN ISO 527-4
- Change in the amplitude of the echo is observed
- Parameter settings for clear amplitude allocation
- Frequency spectrum defined as 75-85 GHz
- Bandwidth of 10 GHz

KTI The SPIRIT of science TECHNISCHE UNIVERSITÄT ILMENAU

Frequency modulated continuous wave (FCMW) radar

Radar in general:

- Electromagnetic waves in the range from 100 MHz to 100 GHz (microwave radiation)
- Transmitter sends a signal, receiver receives the echo
- Echo is analyzed to obtain information about direction, distance and relative speed to the object

FMCW radar:

- Frequency of the signal changes continuously
- Distance determination by determining the frequency difference between the transmitted and received signal

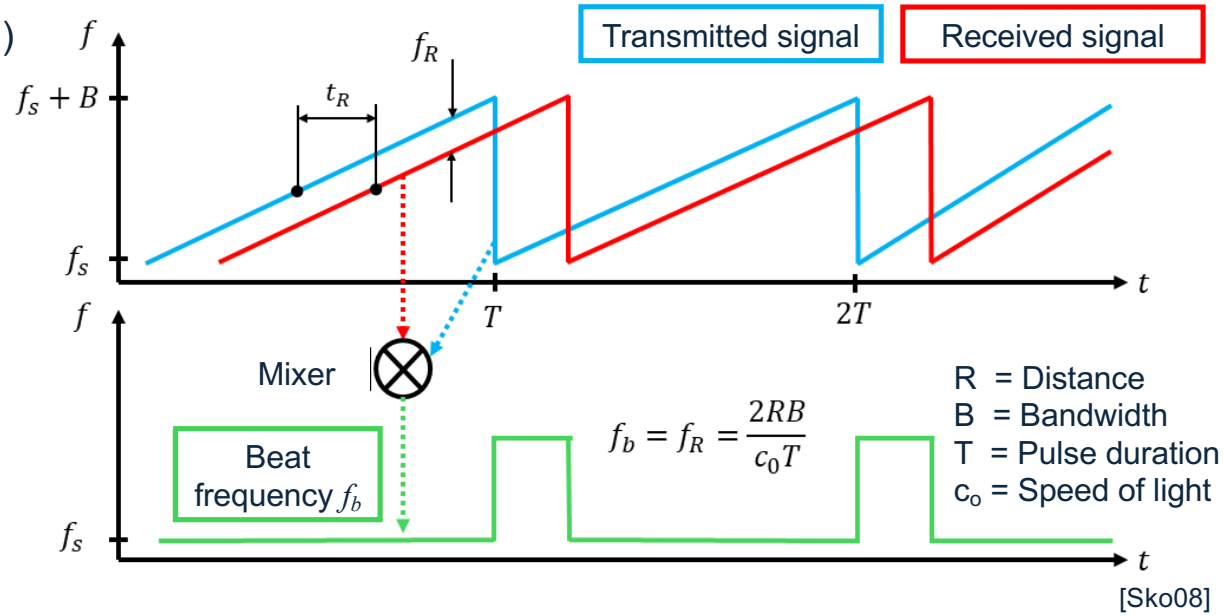

[Sko08]

KTI The SPIRIT of science TECHNISCHE UNIVERSITÄT ILMENAU

From radar measurement to result

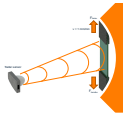
Measurement

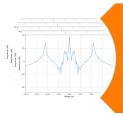
Range-diagram per measurement cycle

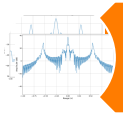
Window function and zero padding

Fast Fourier Transformation

Signal processing

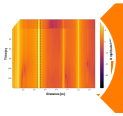
Radar diagram as function of f, t, d

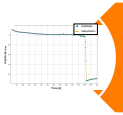
Amplitude development over time for the sample position

KTI The SPIRIT of science TECHNISCHE UNIVERSITÄT ILMENAU

Influences on the radar measurment uncertainty

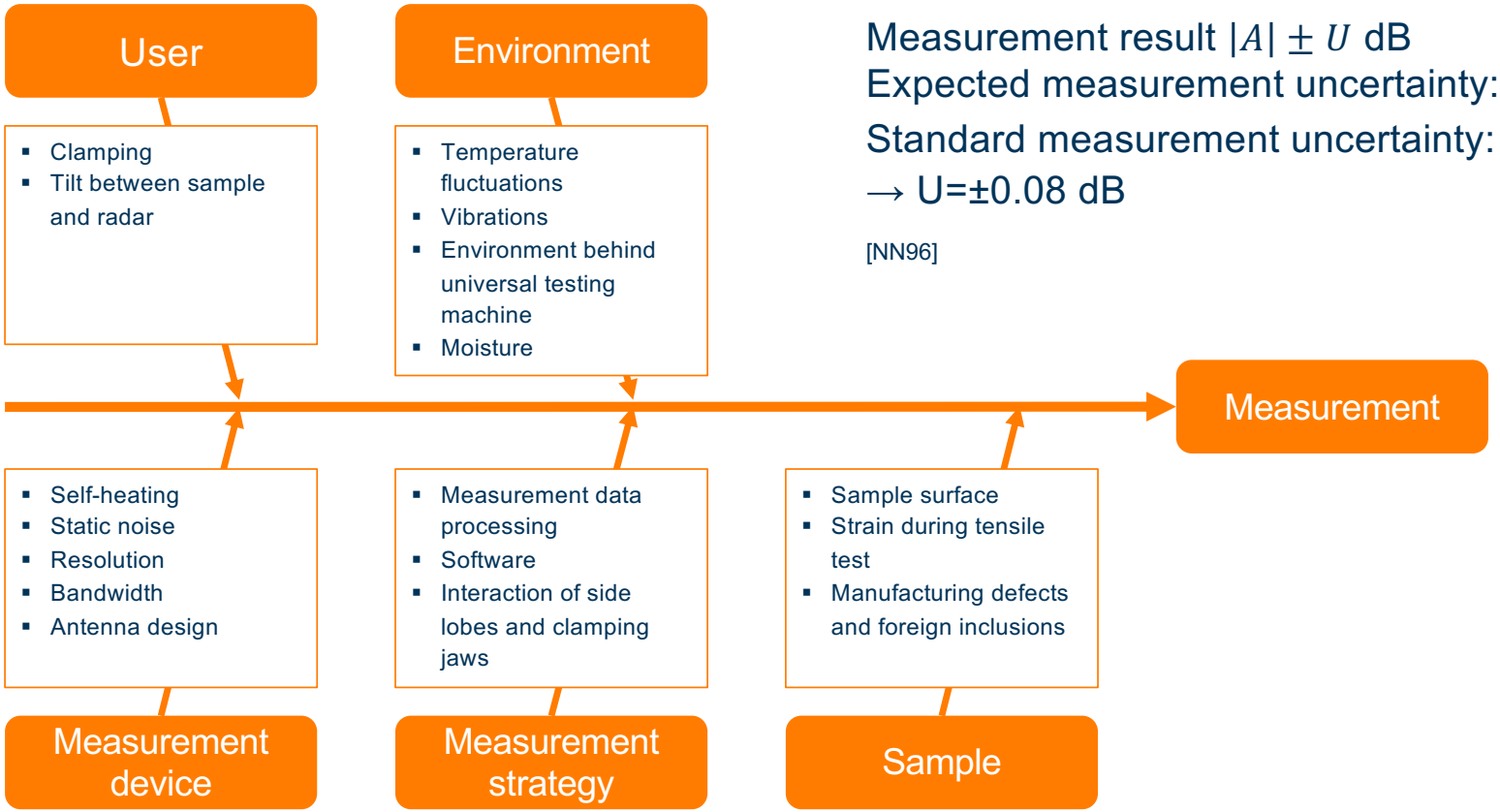

Measurement result $|A| \pm U$ dB
Expected measurement uncertainty: $U(x) = k \cdot u(x), k = 2$
Standard measurement uncertainty: $u(x) = \sqrt{\sum u(x_i)^2}$
→ U=±0.08 dB

[NN96]

Sample without defects

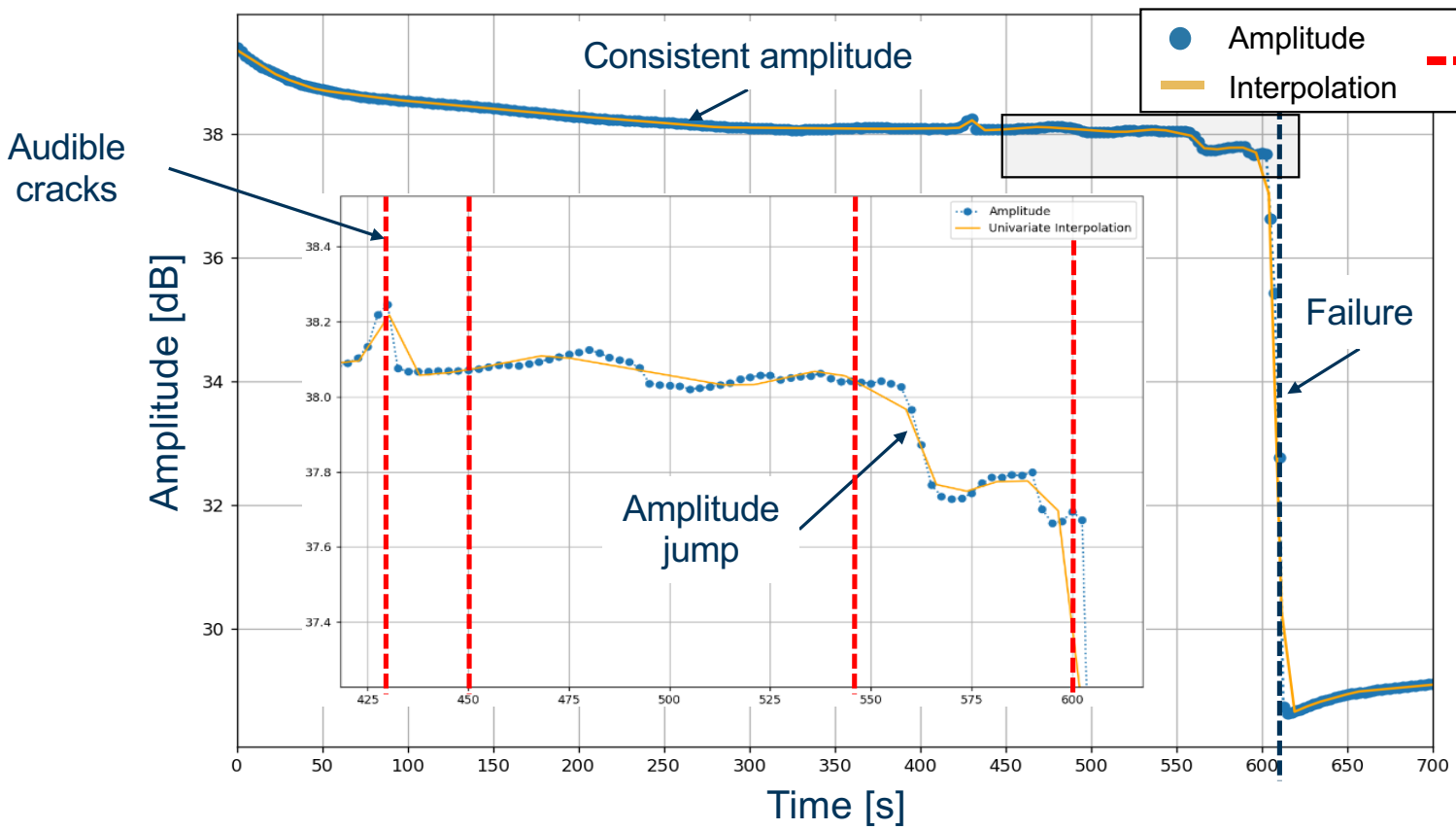

Textile fabric:
4 layersof unidirectional glass fiber fabric 440 g/m²

Epoxy system:
EPIKOTE RIMR 135 + RIMH134

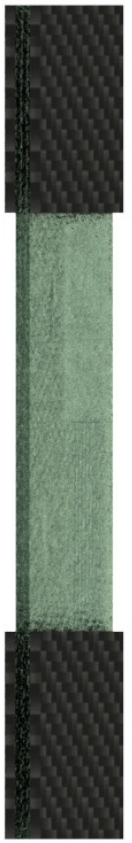

KTI The SPIRIT of science TECHNISCHE UNIVERSITÄT ILMENAU

Correlation of radar, acoustic and force signals

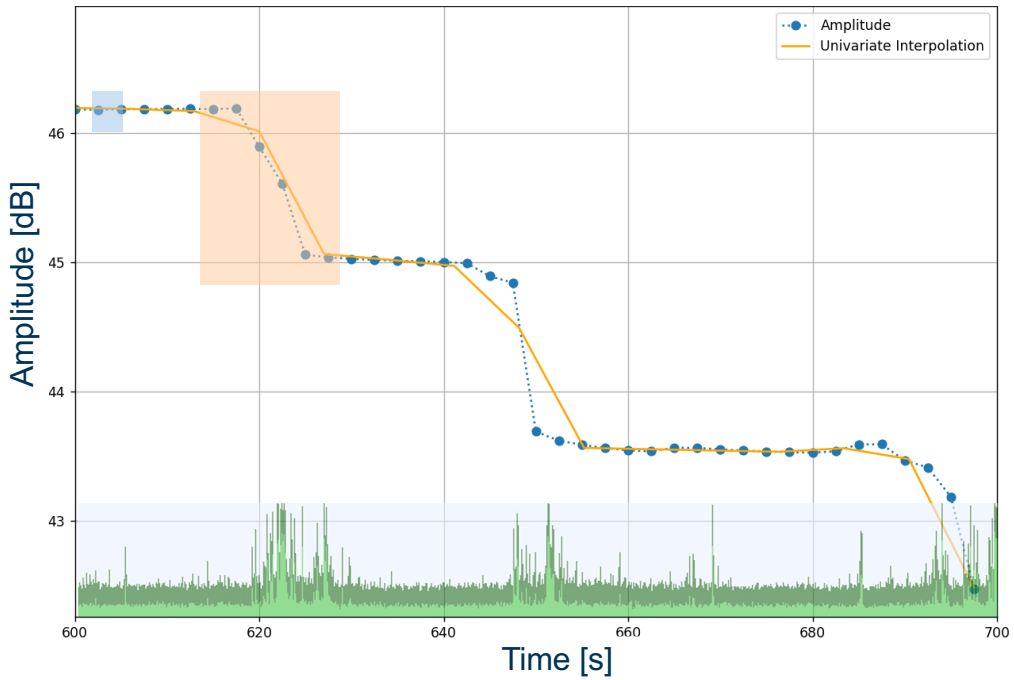

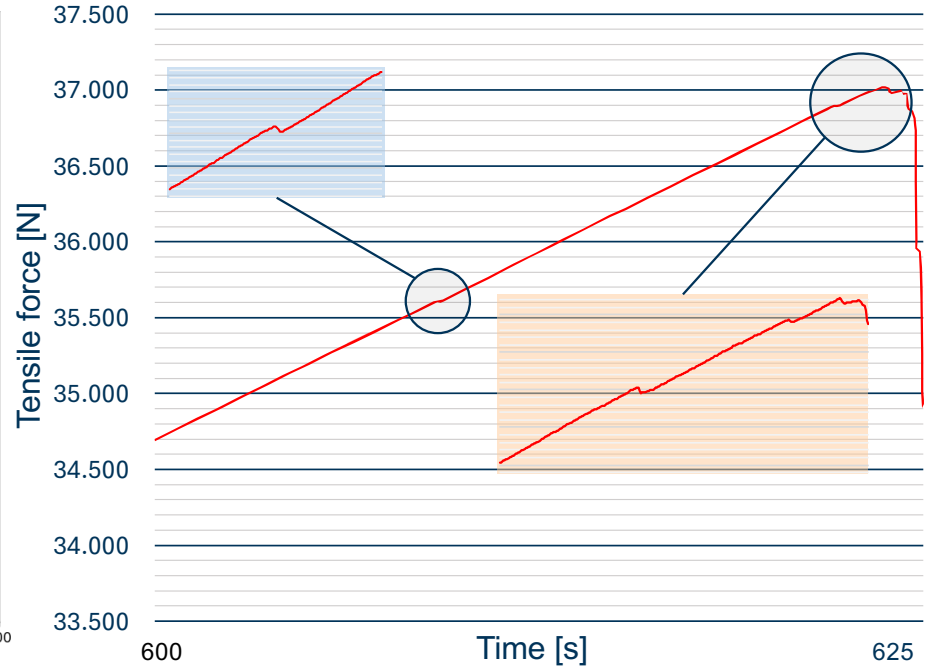

KTI The SPIRIT of science TECHNISCHE UNIVERSITÄT ILMENAU

Sample with delamination

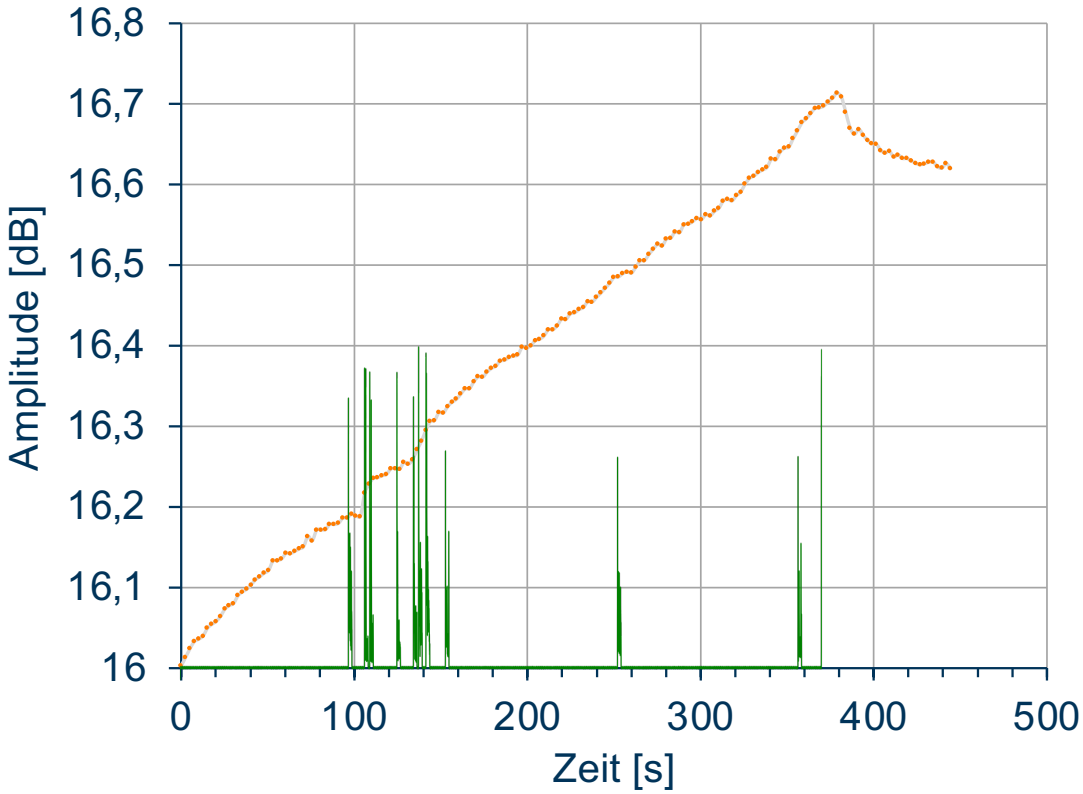

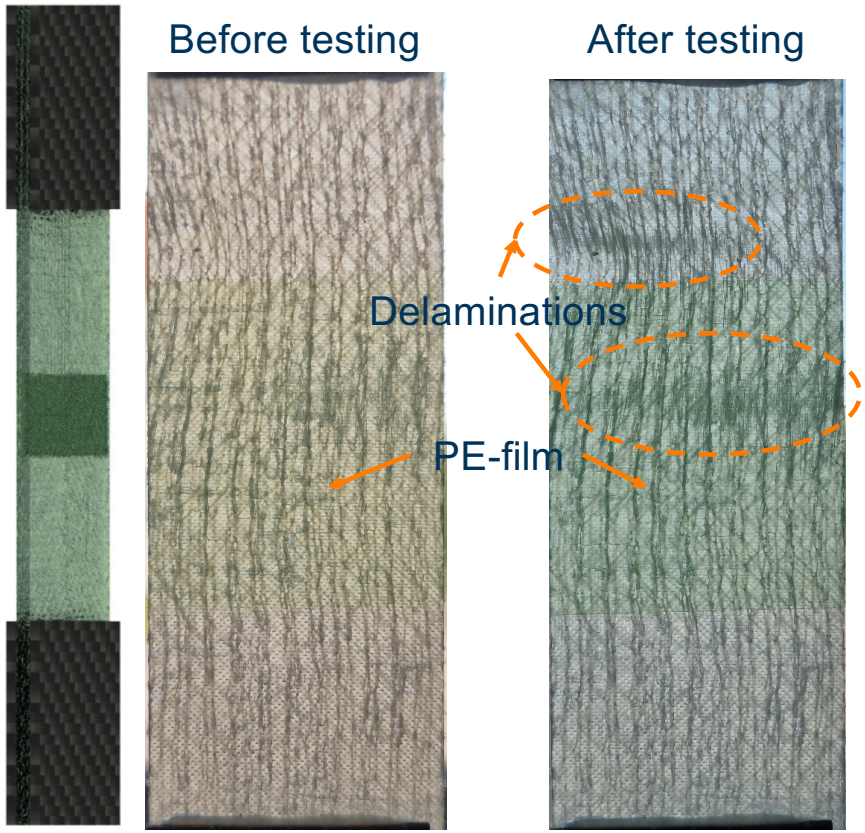

KTI The SPIRIT of science TECHNISCHE UNIVERSITÄT ILMENAU

Summary

- NDT and SHM are essential methods to detect failures and to increase service life of composite parts.
- An initial study on a contactless method using FCMW radar was presented.
- The measurement uncertainty of the presented method was determined.
- First results indicate that the measurement method using FCMW radar may be suitable to detect (larger) failures in glass fiber reinforced composite parts.
- Further investigations are necessary.

KTI The SPIRIT of science TECHNISCHE UNIVERSITÄT ILMENAU

My thanks go to…

…the audience for your attention!

…Benedikt Neitzel, Marton Steierlein, Felix Hellmann and Thomas Dallmann for the joint study!

…the organizers of the conference!

florian.puch@tu-ilmenau.de | www.tu-ilmenau.de/kti



KTI The SPIRIT of science TECHNISCHE UNIVERSITÄT ILMENAU

References

[Duc18] Duchene, P. et al.: A review of non-destructive techniques used for mechanical damage assessment in polymer composites. Journal of Materials Science 11 (2018) 53, 10.1007/s10853-018-2045-6.

[Sko08] Skolnik, M.: Radar Handbook. McGraw Hill, New York, 2008

[Che22] Chen, Jian et al. Nondestructive testing and evaluation techniques of defects in fiber-reinforced polymer composites: A review. Frontiers in Materials 9 (2022), 10.3389/fmats.2022.986645.

[GWEC] GWEC - Global Wind Report 2024, Page 148, GWEC. (2024). Installierte Windenergieleistung weltweit in den Jahren 2003 bis 2023 (kumuliert in Gigawatt), Statista GmbH, April 14, 2025, https://de.statista.com/statistik/daten/studie/158323/umfrage/installierte-windenergie-leistung-weltweit-seit-2001/

[NN96] DIN 1319-3:1996 Grundlagen der Messtechnik – Teil 3: Auswertung von Messungen einer einzelnen Messgröße; Messunsicherheit

ICCM24
AUGUST 4-8, 2025
BALTIMORE CONVENTION CENTER
BALTIMORE, MARYLAND, USA

No Technical Paper Submission for:

Callum Montgomery

University of BRISTOL

Combined *in-situ* microscopy and acoustic emission monitoring of transverse cracking in CFRP cross-ply laminates

S. Spyridonidis[1,*], G. Allegri[1], T. Laux[1], and N. Chandarana[1]

[1]Bristol Composites Institute, University of Bristol, Bristol, UK

*spyros.spyridonidis@bristol.ac.uk

bristol.ac.uk/composites

UKRI Engineering and Physical Sciences Research Council

University of BRISTOL

EPSRC Centre for Doctoral Training in Composites Science, Engineering and Manufacturing

Presentation outline

- Transverse matrix cracking in cross-ply laminates
- Experimental setup
- Results
- Conclusions and outlook

*spyros.spyridonidis@bristol.ac.uk

Transverse Cracking

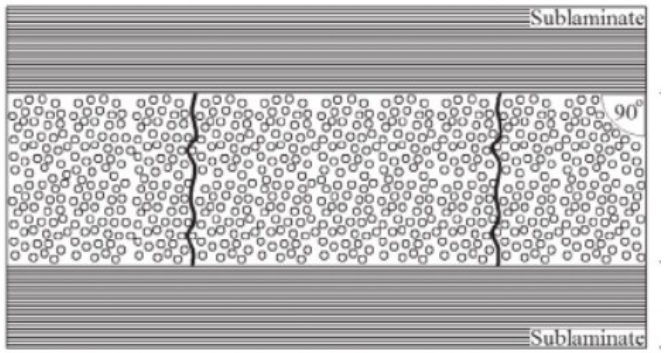

Transverse Cracks schematic (1)

- The first damage mode under most of the thermomechanical loading cases
  - Immediate sequencies in thermomechanical properties and precursor for further damage types.

Aim

Experimentally observation of the damage evolution using in-situ microscopy and acoustic emission under quasi-static loading

1. Katerelos, D., et al. (2015). "Variational models for shear modulus of symmetric and balanced laminates with cracks in 90-layer." International Journal of Solids and Structures **71.**

University of BRISTOL
Bristol Composites Institute
*spyros.spyridonidis@bristol.ac.uk

Specimen

- Tensile specimens from IM7/8552 according to ASTM D3039 Standard
- Two cross ply configurations
- Preparation for testing : Polished edge and DIC speckling

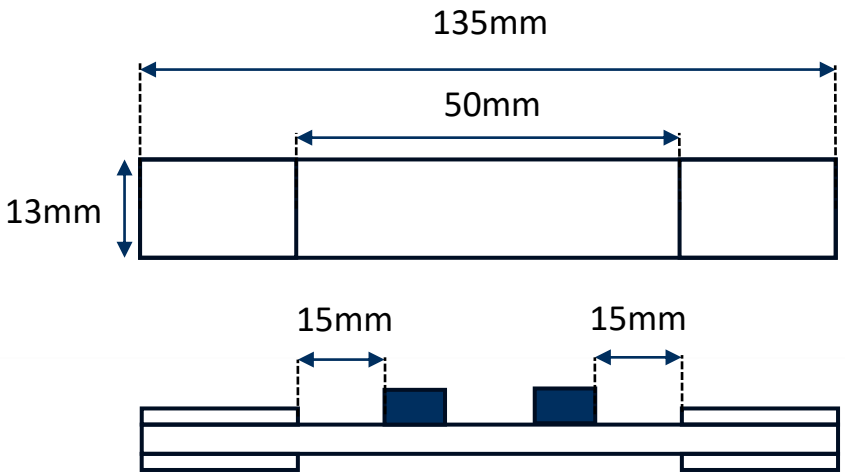

$[0_2/90_6/0]_S$

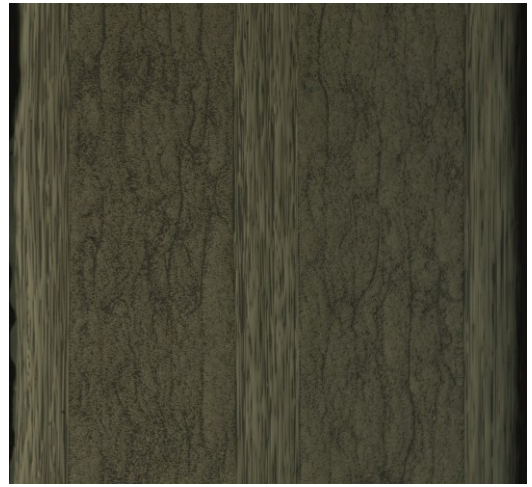

$[0_3/90_6]_S$

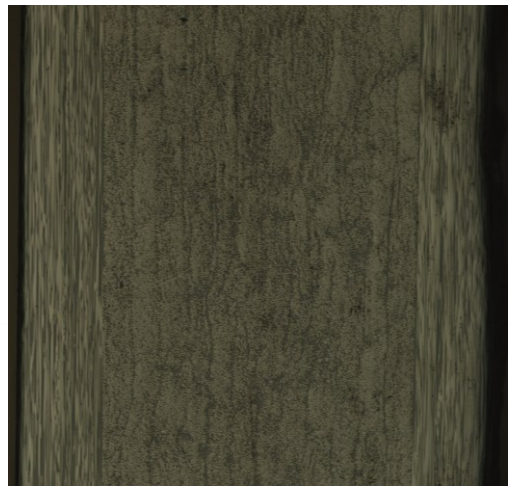

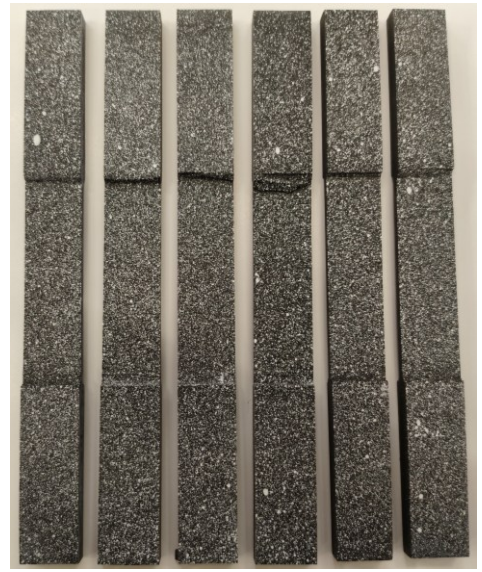

University of BRISTOL
Bristol Composites Institute
*spyros.spyridonidis@bristol.ac.uk

Specimen

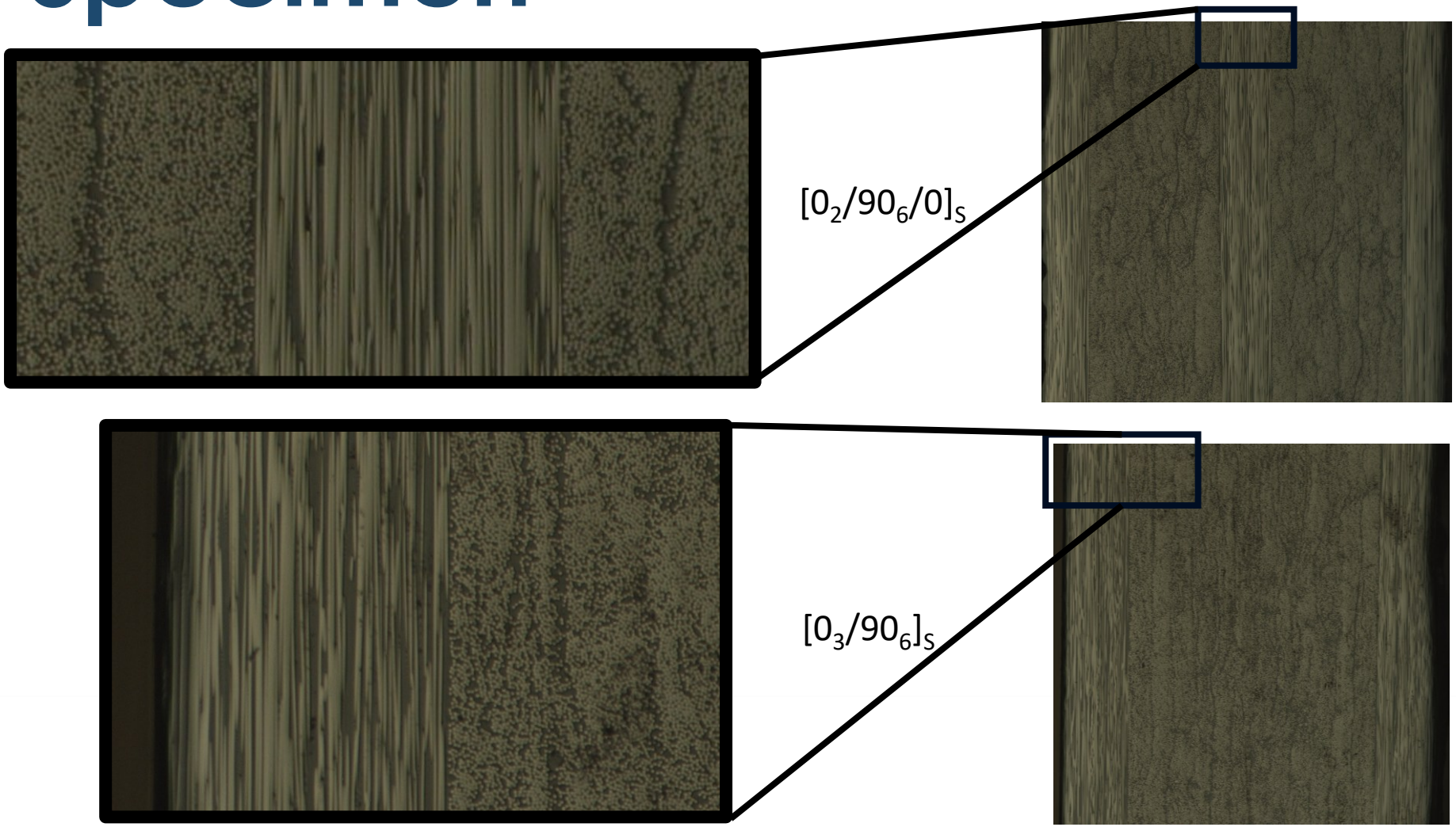



*spyros.spyridonidis@bristol.ac.uk

Experimental set-up

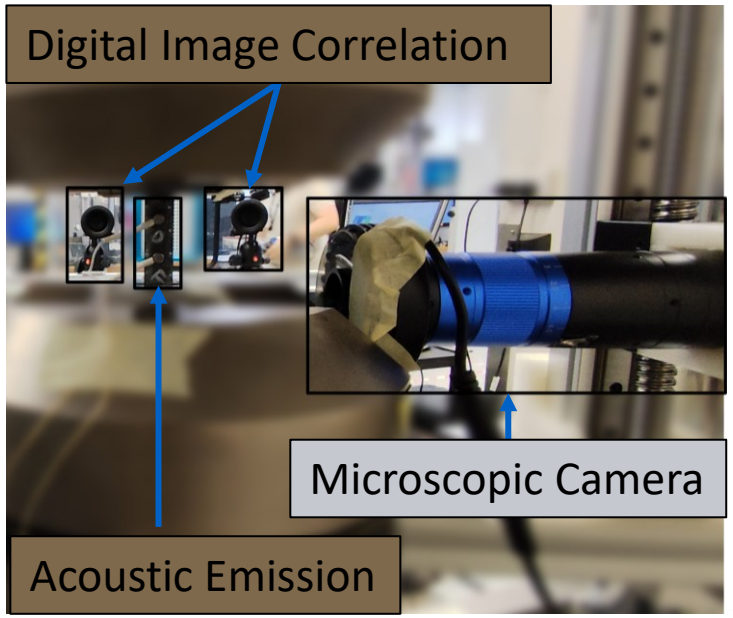

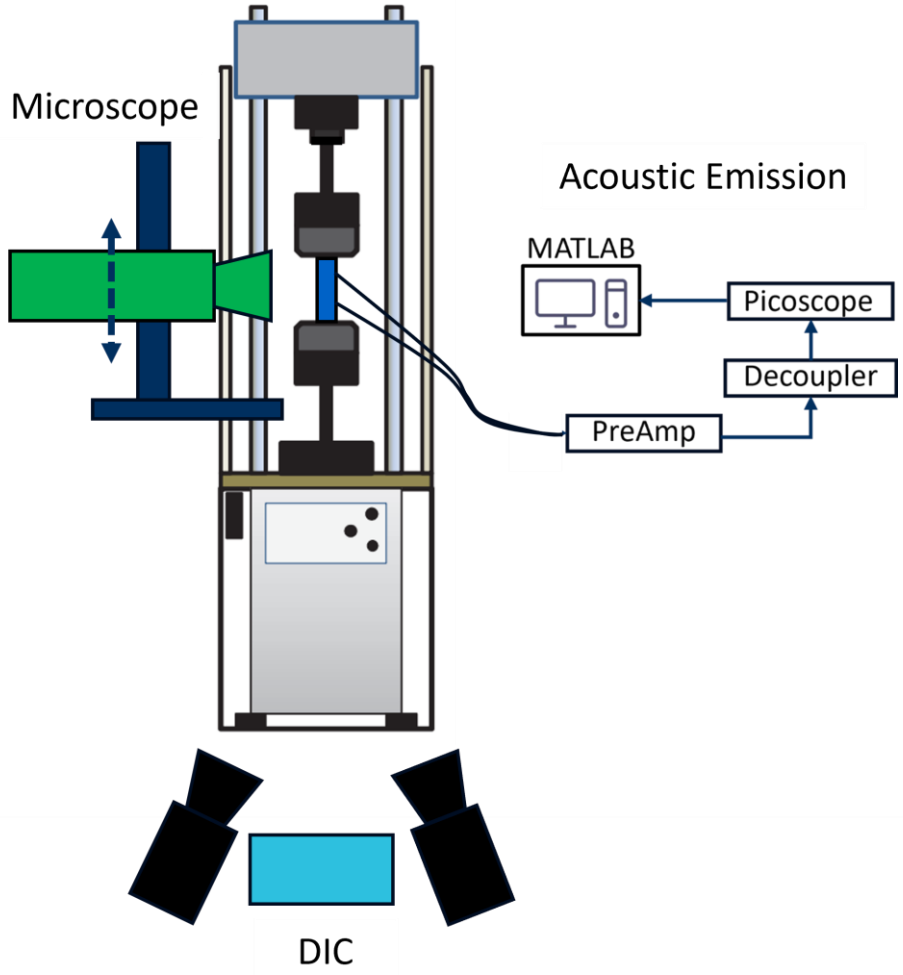

Load Profile

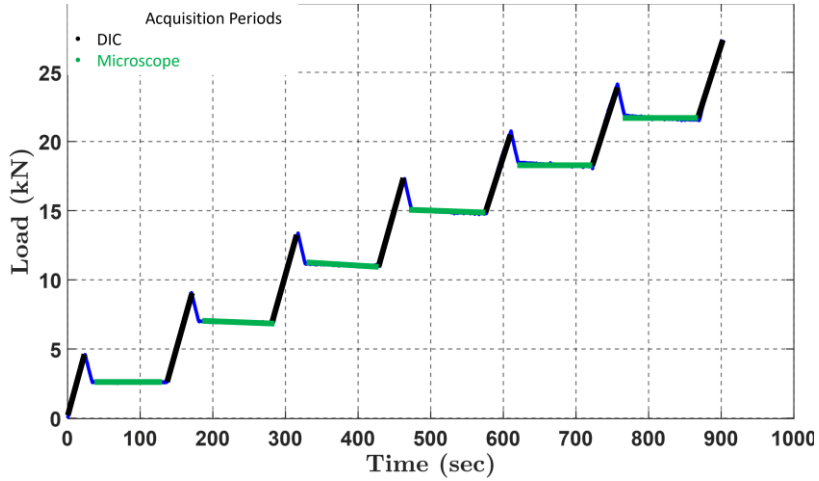

University of BRISTOL
Bristol Composites Institute
*spyros.spyridonidis@bristol.ac.uk

Image Processing for crack detection

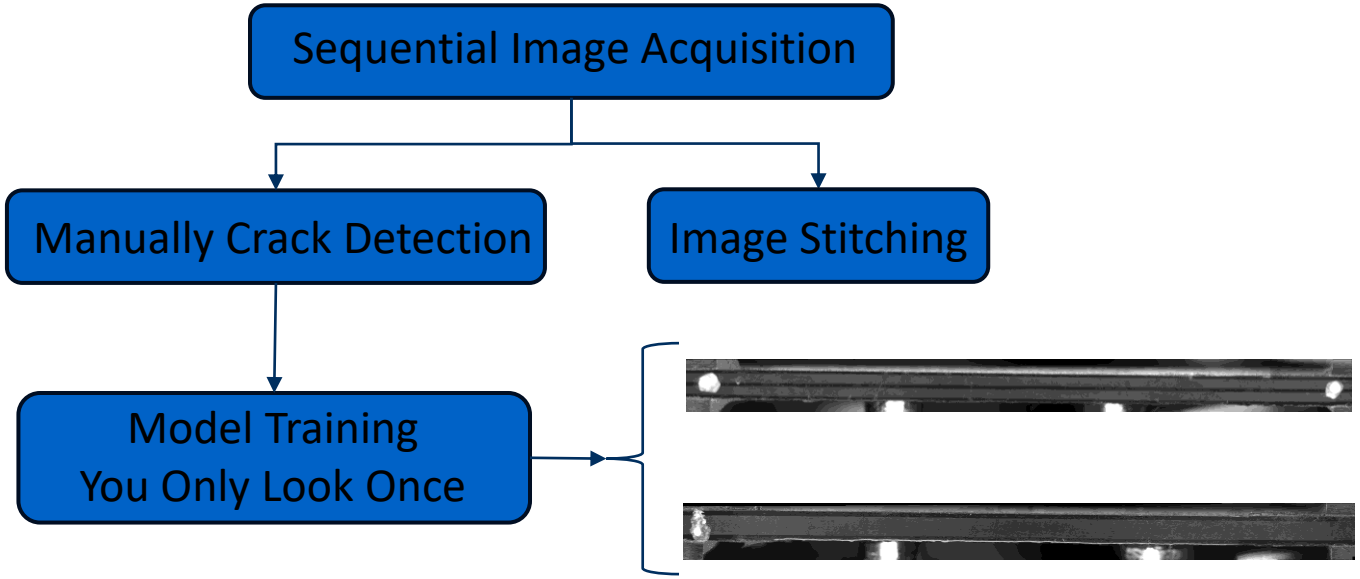

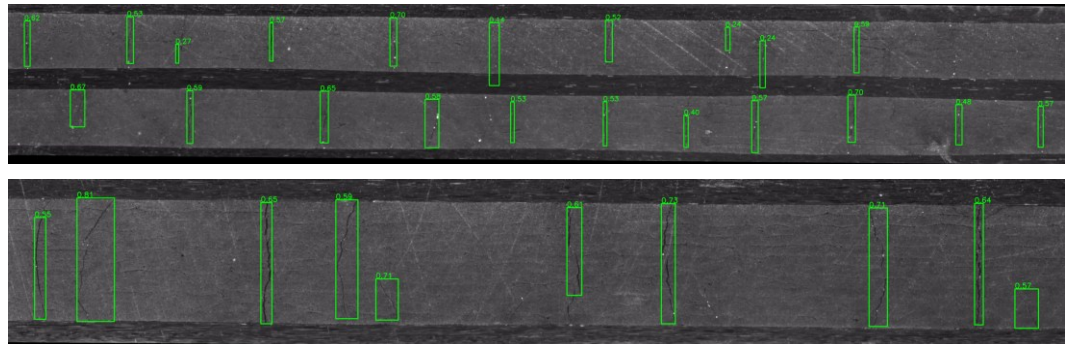

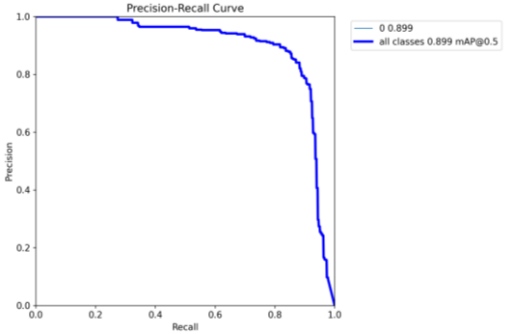

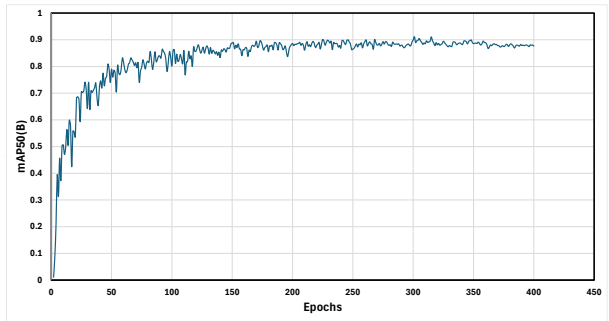

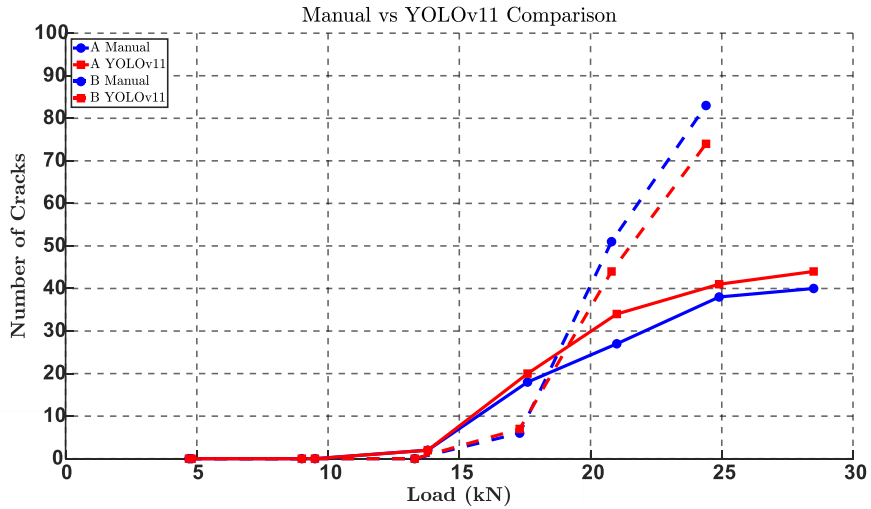

University of BRISTOL
Bristol Composites Institute
*spyros.spyridonidis@bristol.ac.uk

Results (1)

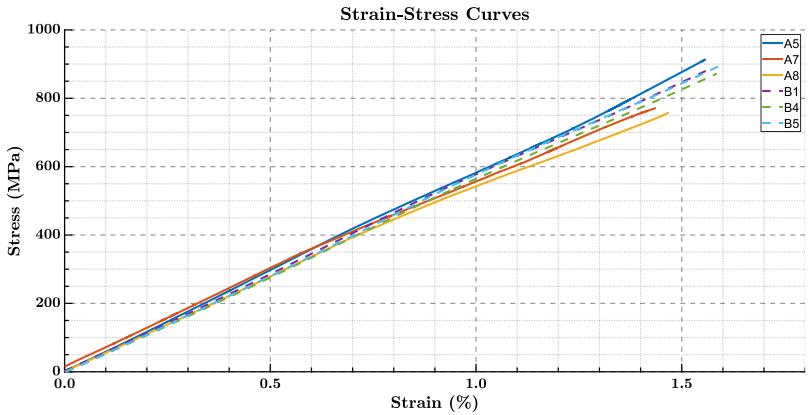

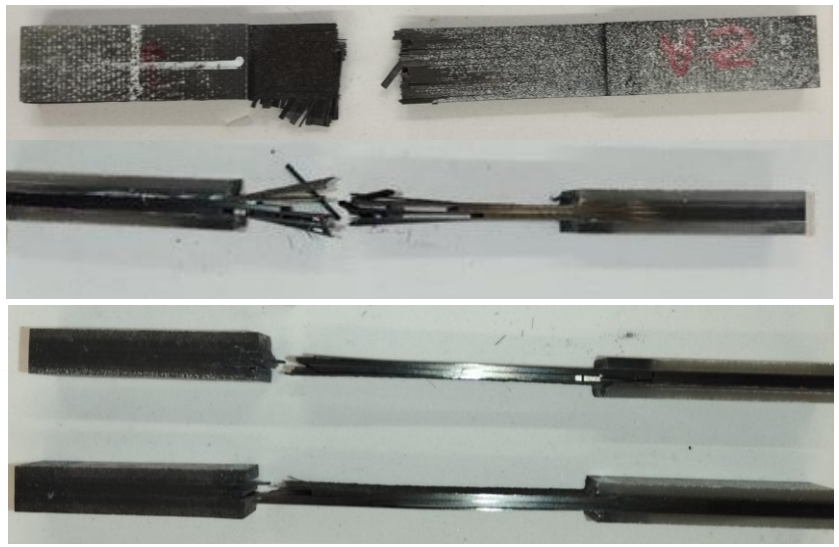

$[0_2/90_6/0]_S$

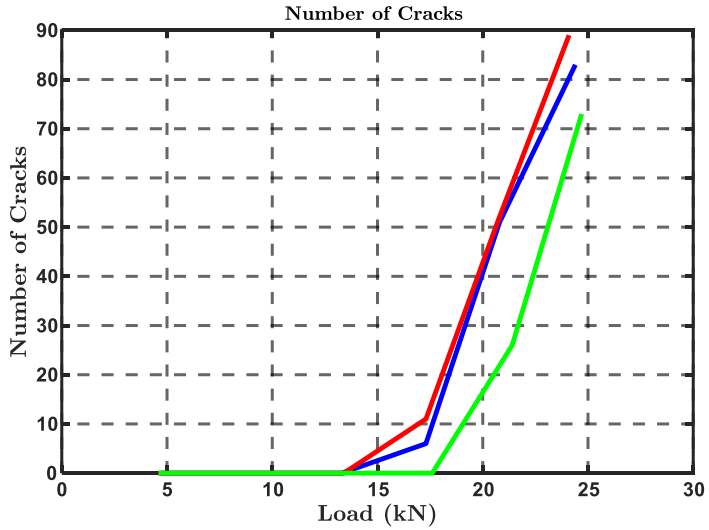

$[0_3/90_6]_S$

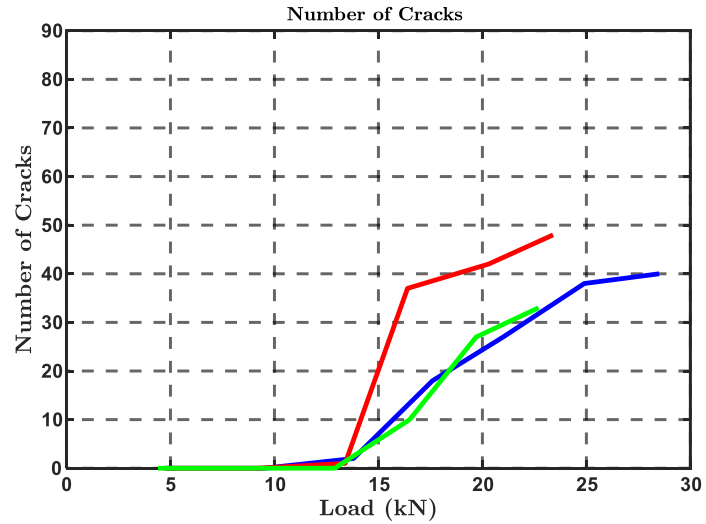

- Rapid crack increase for both lay-ups configurations
- Thin plies accumulate larger number of cracks/mm
- Both layups steep crack increase
- For blocked case the load for crack initiation is decreased
- Stohasticity of the phenomenon

University of BRISTOL
Bristol Composites Institute
*spyros.spyridonidis@bristol.ac.uk

Results (2)

Along with the formation of straight cracks, in both configurations it was observed:

- Oblique cracks
- C-shaped cracks

$[0_2/90_6/0]_S$

Load 20.8kN

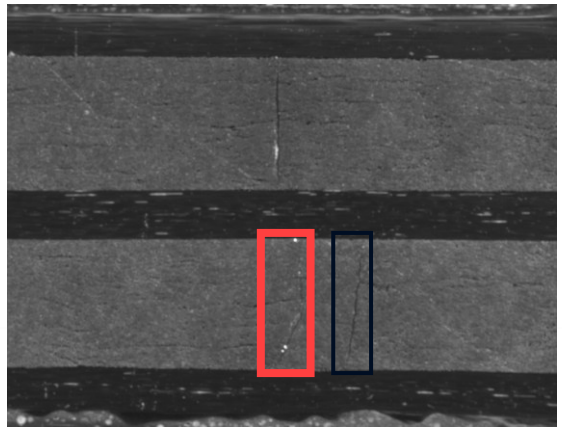

$[0_3/90_6]_S$

Load 17.6kN

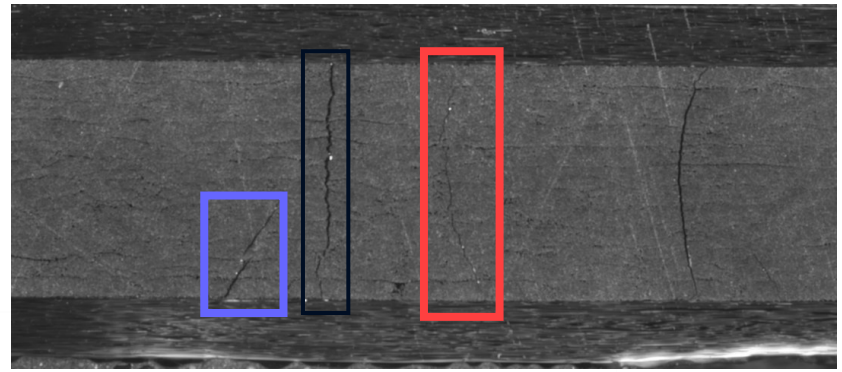

University of BRISTOL
Bristol Composites Institute
*spyros.spyridonidis@bristol.ac.uk

Results (2)

Along with the formation of straight cracks, in both configurations it was observed:

- Oblique cracks
- C-shaped cracks

$[0_2/90_6/0]_S$

Load 24.4kN
(Failure Load 27.8kN)

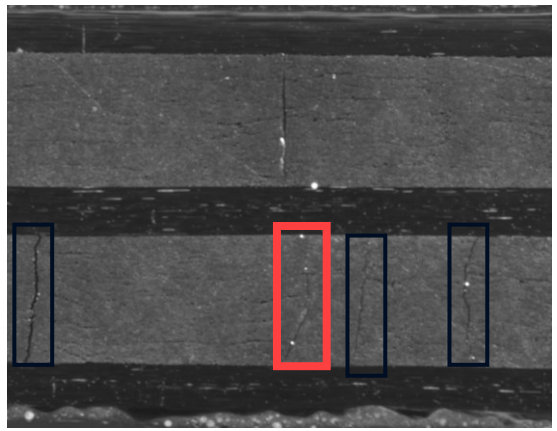

$[0_3/90_6]_S$

Load 21kN
(Failure Load 28.7kN)

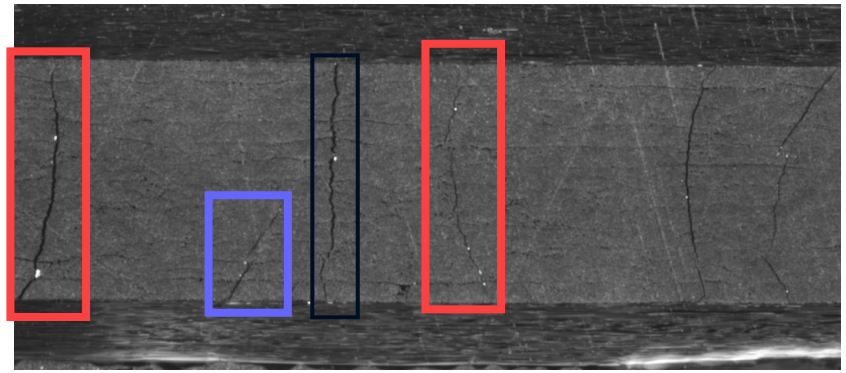

University of BRISTOL
Bristol Composites Institute
*spyros.spyridonidis@bristol.ac.uk

Results (3)

$[0_2/90_6/0]_S$

Correlation between the two experimental methods

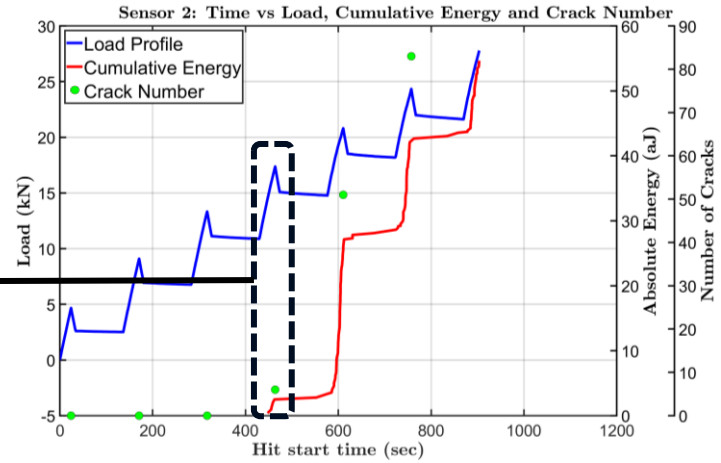

$[0_3/90_6]_S$

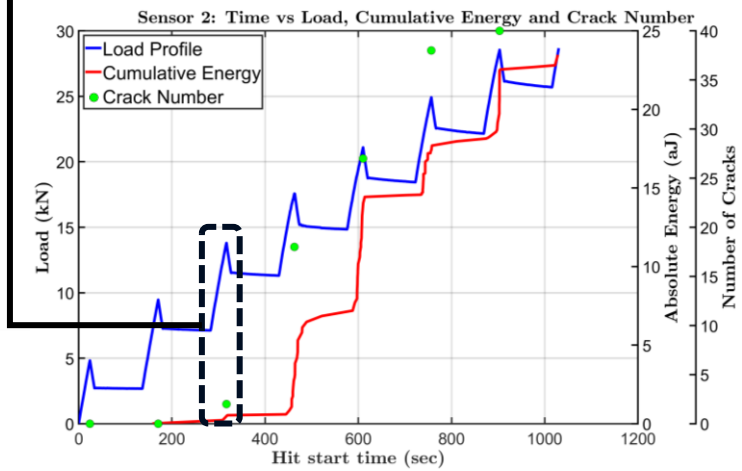

The peak frequency of the AE hits are found in a range of 50-200kHz

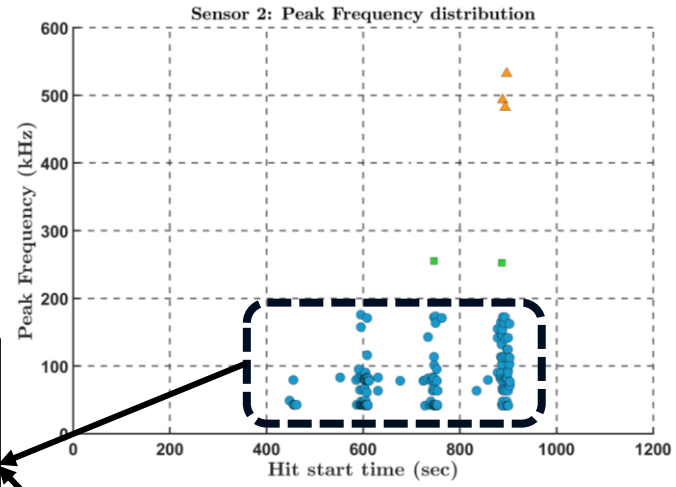

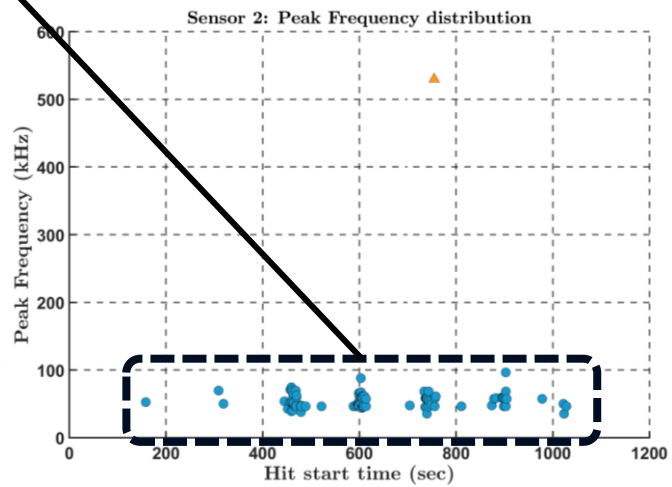

University of BRISTOL
Bristol Composites Institute
*spyros.spyridonidis@bristol.ac.uk

Conclusions and Outlook

Conclusions

- Oblique, and c-shaped cracks were observed along the formation of straight cracks, without necessary interaction of other cracks.

- The nature of nature of matrix cracking is stochastic not only in terms of spatial distribution but also regarding the number of cracks

- Matrix cracking initiation and progression was captured from both experimental techniques, using microscopy data to validate acoustic emission data

Future Work

Acoustic Emission:

- Implement a classifier with the labeled acoustic emission data from matrix cracking

Microscopy

- Training the crack detection model with a wider dataset to increase the accuracy
- Check the sensitivity of the set-up, with quasi-isotropic layup configuration.

*spyros.spyridonidis@bristol.ac.uk

Thank you for your attention!
Any questions?

Combined in-situ microscopy and acoustic emission monitoring of transverse cracking in CFRP cross-ply laminates

S. Spyridonidis[1,*], G. Allegri[1], T. Laux[1], and N. Chandarana[1]

[1]Bristol Composites Institute, University of Bristol, Bristol, UK

*spyros.spyridonidis@bristol.ac.uk

Bristol Composites Institute

bristol.ac.uk/composites

DELTA ENGINEERING

ASSESSING THE EFFECTS OF EDGE REFLECTION ON PROPAGATING ACOUSTIC WAVES IN CFRP EPOXY PANELS

Advisors:

Isabel McBrayer, Ph.D.

Benjamin Stanford, BSc.

Speakers:

Andrea Martinez, MSc.

Priyanshu Kumar, BSc.

Baltimore, August 2025.

BACKGROUND

- Non-Destructive Testing (NDT) techniques are used for assessing the manufacturing quality of complex parts and for monitoring the life cycle of installed components.
  - Minimize downtime by allowing analysis to be conducted on-site via non-destructive means.
- Non-Destructive Testing (NDT) Techniques
  - Visual Testing
    - Primarily used for detecting macroscopic irregularities.
  - Computed Tomography:
    - Captures internal attenuated X-rays and converts them into electronic signals.
    - Suitable for evaluation of micro-cracks or defects such as voids and pores..
  - Ultrasonic Testing
    - Waves interact with the material (phase-array, c-scan, air-coupled, and laser).
    - For detection of fiber misalignment, localizing porosity, and delamination [Ref. 1.0].
  - Acoustic Emissions
    - Surface vibrations are captured by AE sensor and ultimately digitalized.
    - Most effective method for internal faults and damage type detection in CFRP.
    - AE signals affected by many factors (specimen, waveguide transfer function, sensors transfer function, etc.).
    - Features such as Risetime, Frequency, Energy, and CWT have been studied as the most suitable features for analysis as they carry information about AE source type [Ref. 7.0].

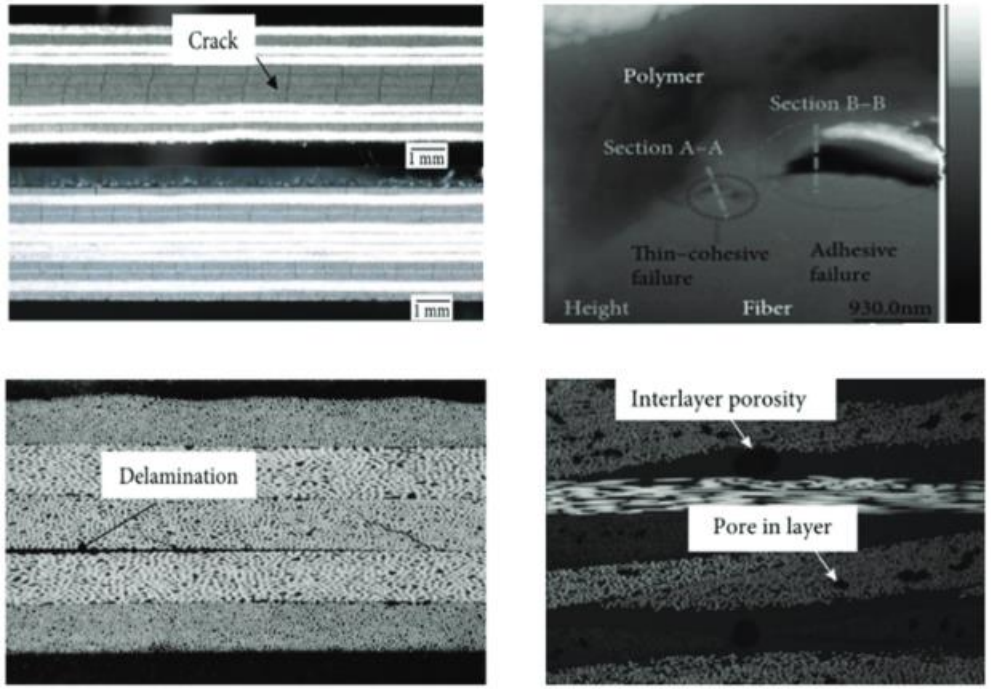

Figure 1. Common Type of Defects Analyzed in CFRP Through NDT Techniques [Ref. 1.0].

HSU-NIELSEN AE SOURCE

- Yields a consistent, replicable, burst acoustic signal if pencil lead is broken at the same angle and position each time.
- Excites a broad range of frequencies.
- Analyzed AE Features: Amplitude, Rise Time, and Energy.
  - Peak Detection Window of 200 µs.

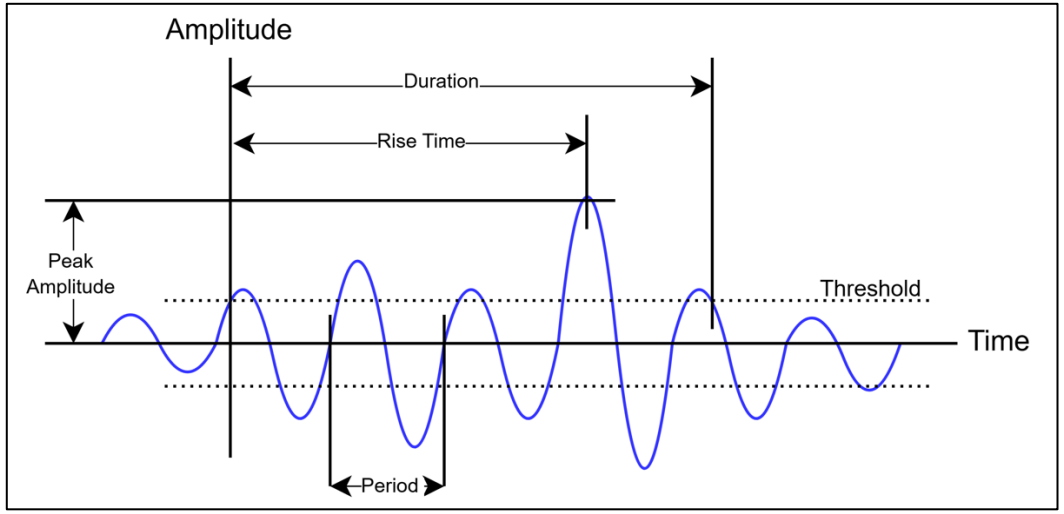

Figure 2. Acoustic Emission Features.

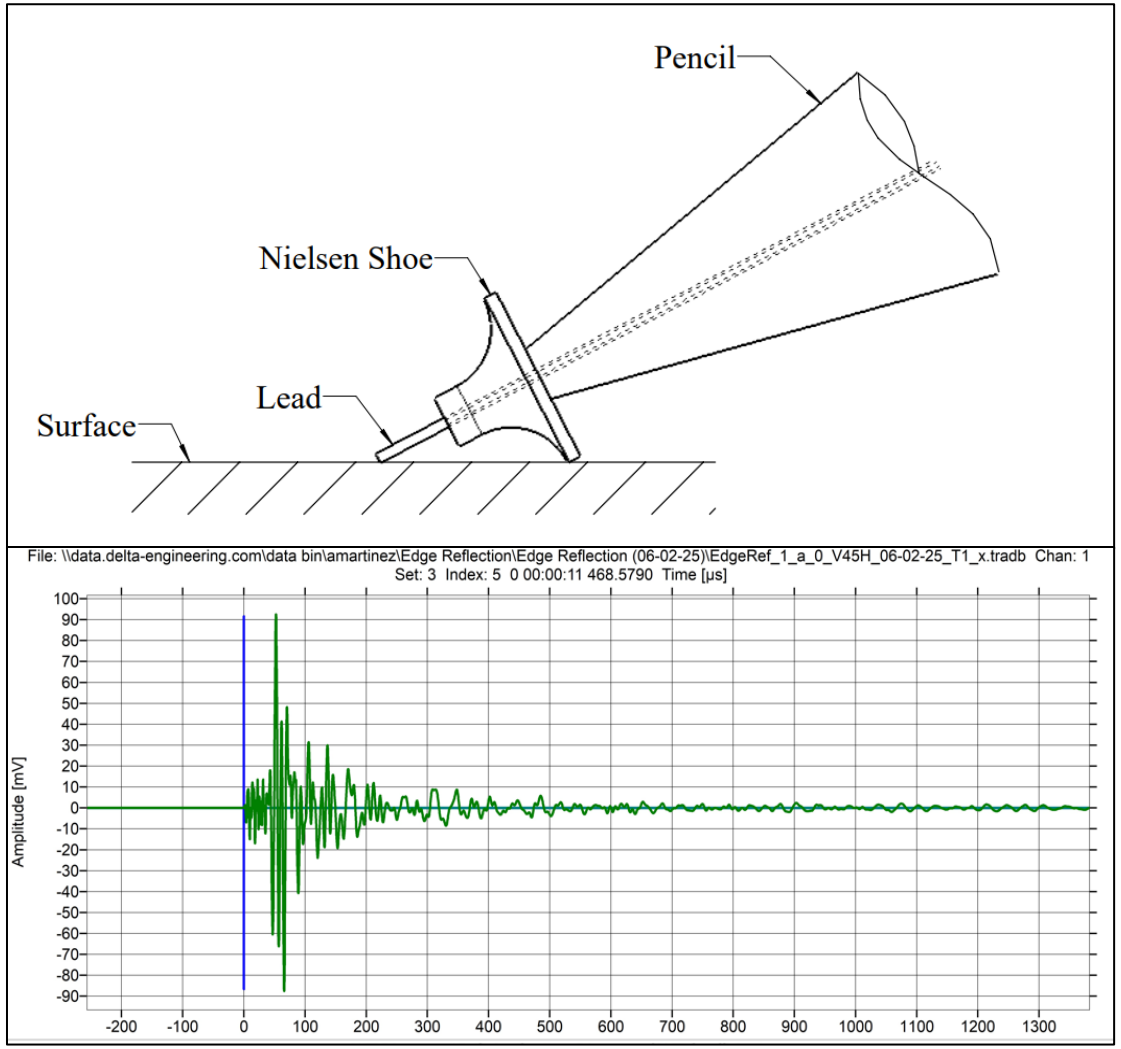

Figure 3. Hsu-Nielsen Pencil Lead Break (PLB) Technique.

TEST SETUP - OVERVIEW

- ISO Conditions: 20°C, ~1.01 MPa.
- Performed 2 sets of 30 PLBs across three panels (6 plies of 12k twill weave carbon fiber).
  - Sensors were positioned at 8.7 cm and 26.2 cm.
  - Only one sensor was used for the smallest panel.
- Tested five angles: 0°, 22.5°, 45°, 67.5°, 90° for all panels.

Large Panel

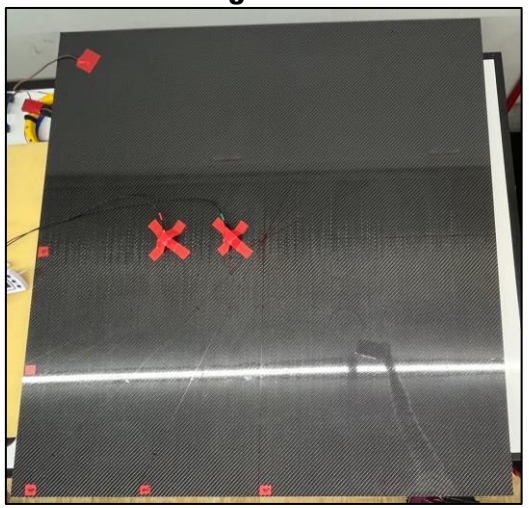

Dimensions = 122.2 cm x 122.2 cm x 4 mm.

Medium Panel

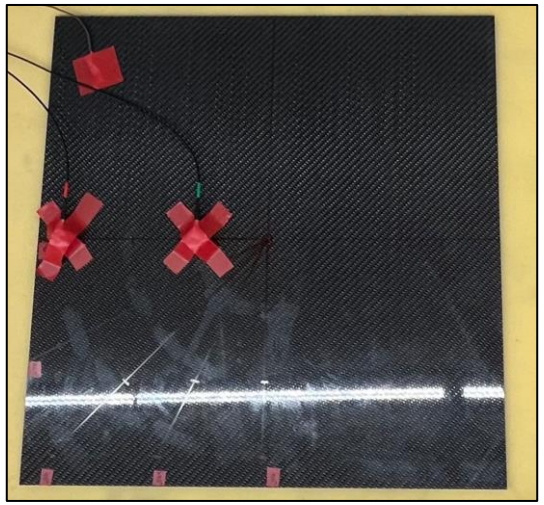

Dimensions = 58.7 cm x 58.7 cm x 4 mm.

Small Panel

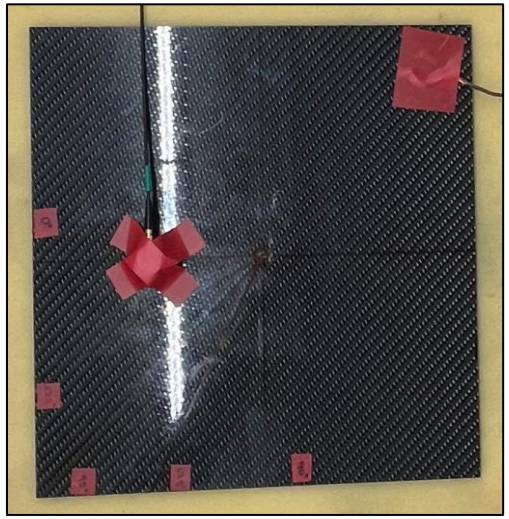

Dimensions = 34.5 cm x 34.5 cm x 4 mm.

Figure 4. Panel Geometries.

RESULTS – AMPLITUDE (0°/22.5°/45°)

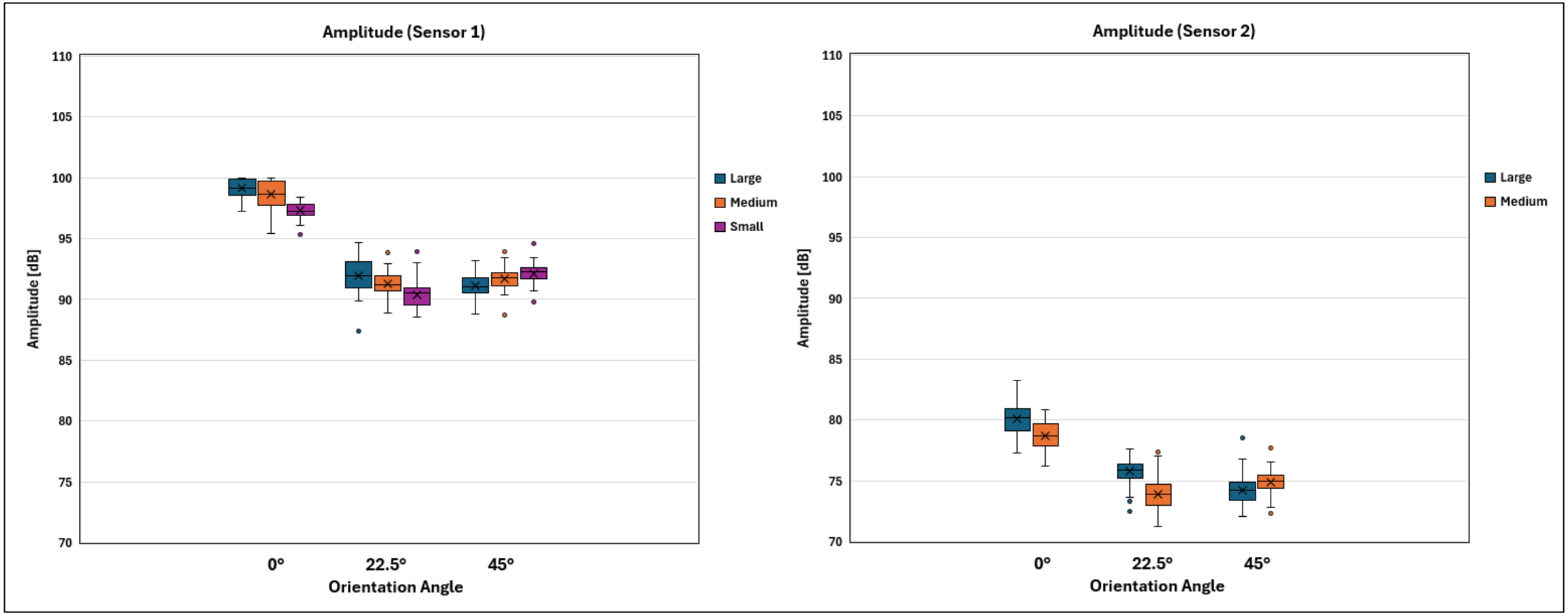

Figure 5. Amplitude Plots for 0°/22.5°/45° Orientation Angles*.

*Datasets for 67.5° and 90° are omitted for clarity. Data for 0°/90° and 22.5°/67.5° was similar.

*[Ref. 8.0, 11.0, and 12.0].

RESULTS – RISETIME (0°/22.5°/45°)

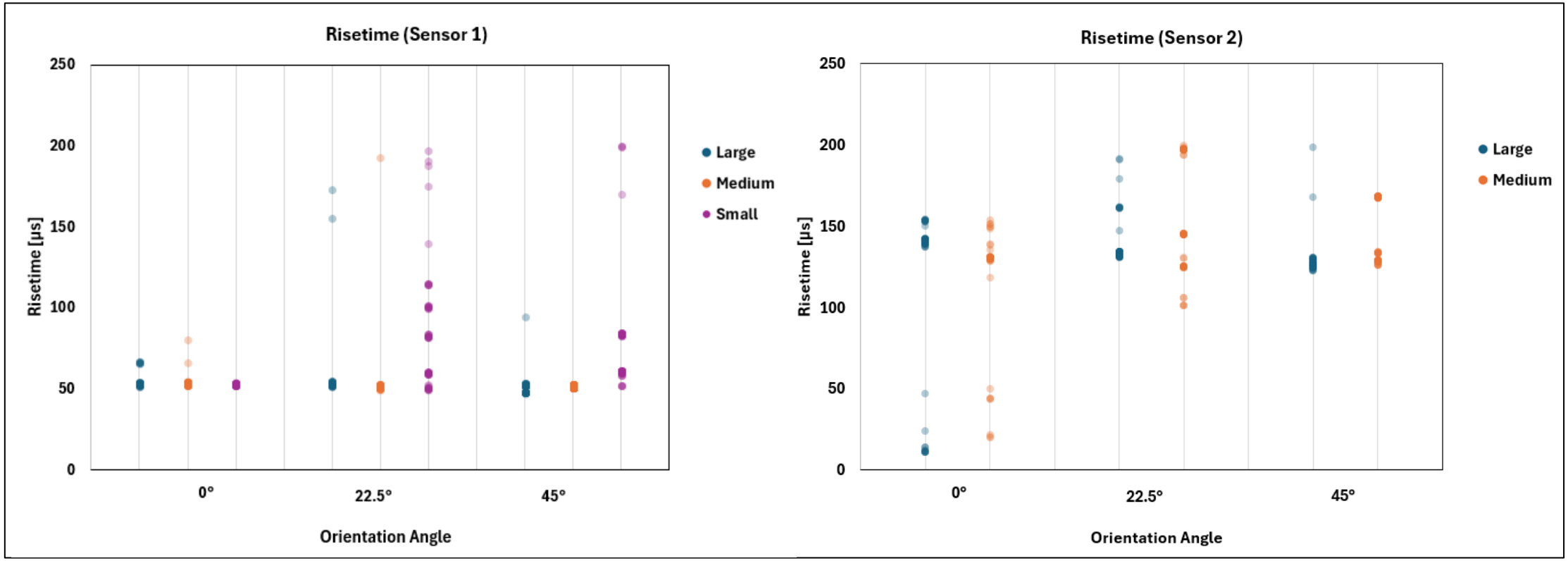

Figure 6. Risetime Plots for 0°/22.5°/45° Orientation Angles*.

*Datasets for 67.5° and 90° are omitted for clarity. Data for 0°/90° and 22.5°/67.5° was similar.

*[Ref. 7.0 and 9.0].

RESULTS – RISETIME (0°-S2-LARGE/MEDIUM PANEL)

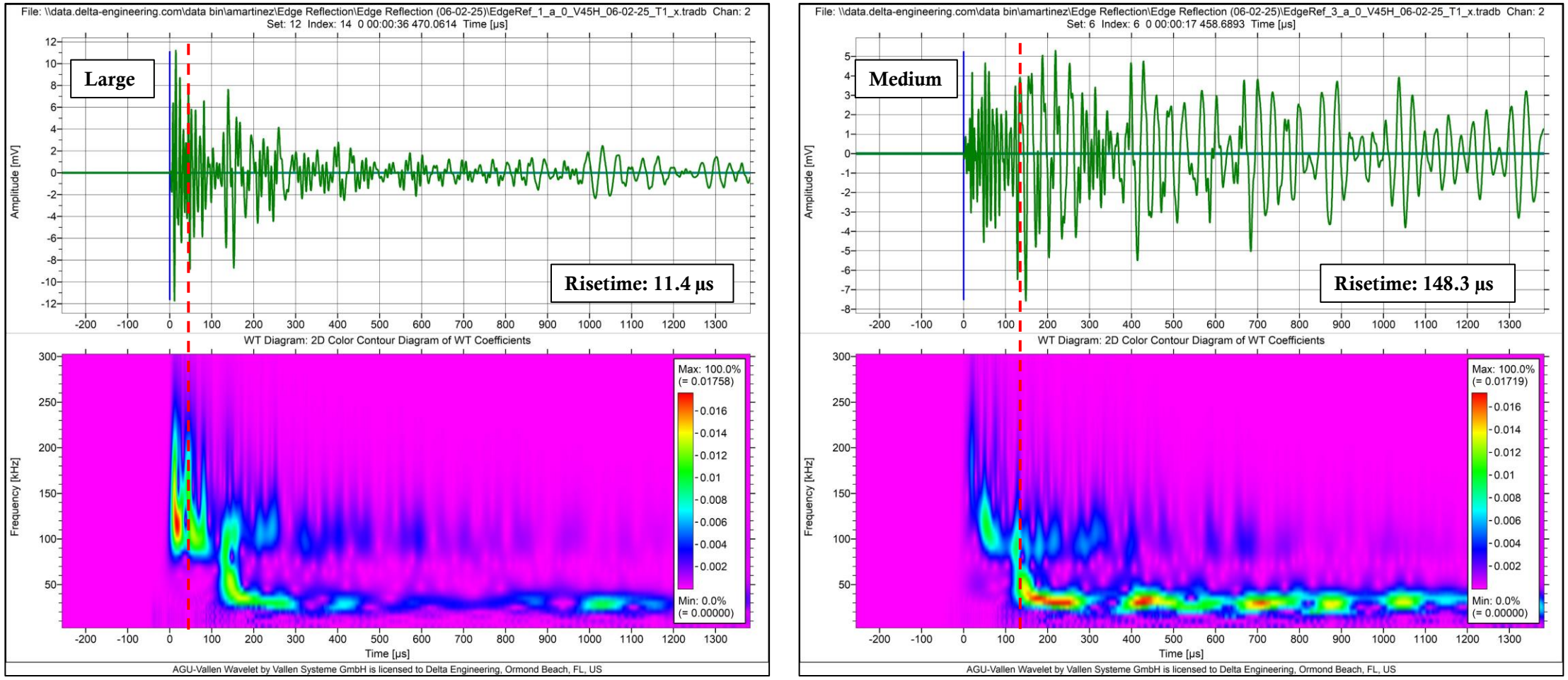

Figure 7. Waveform/Wavelet/Risetime Plots for Different Panel Sizes at Orientation Angle of 0° and Sensor Location 2.

*[Ref. 6.0].

RESULTS – RISETIME (22.5°-S1-MEDIUM/SMALL PANEL)

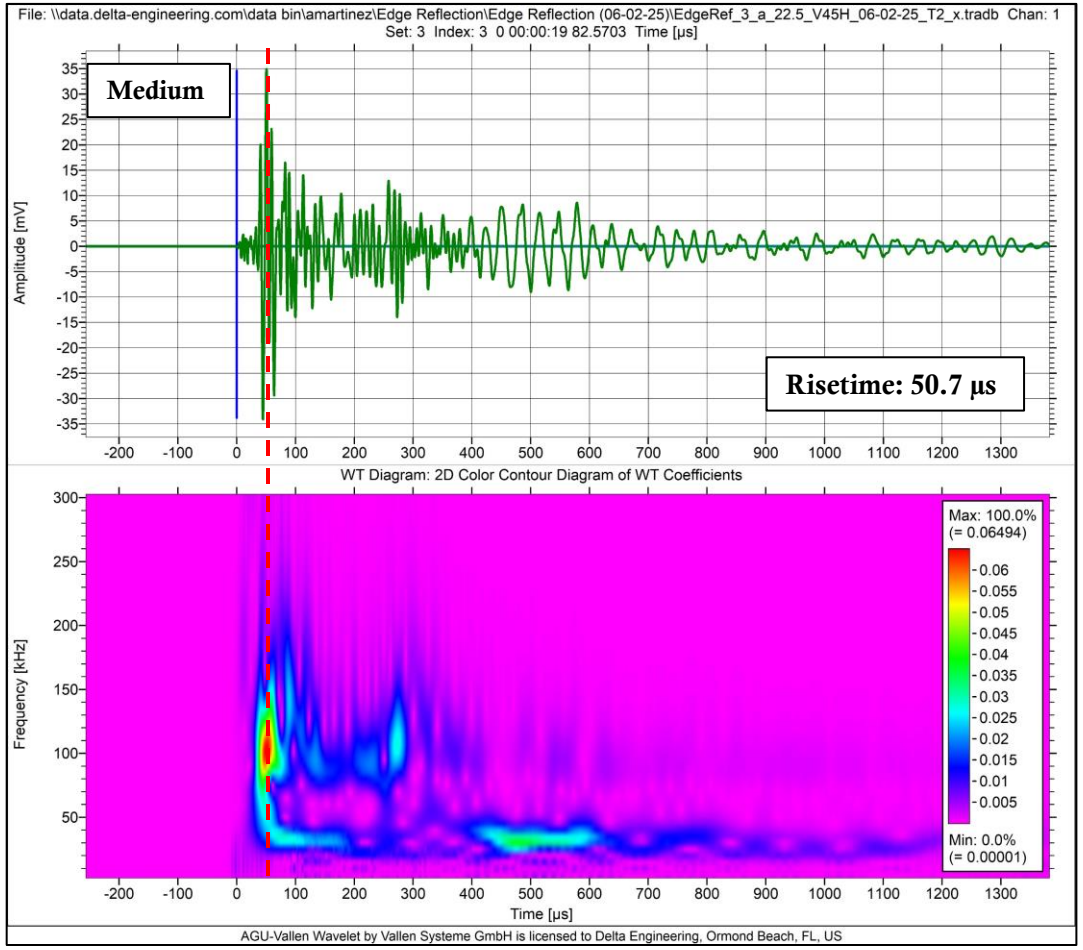

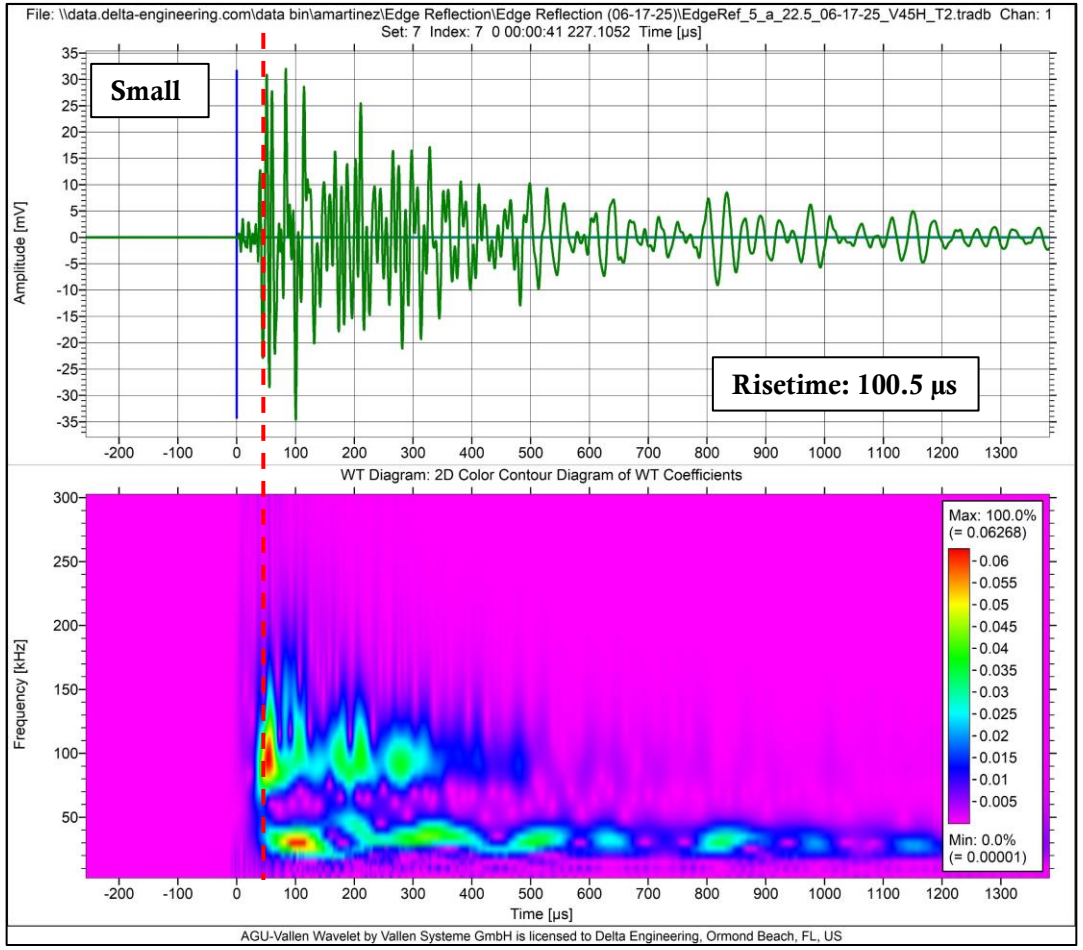

Figure 8. Waveform/Wavelet/Risetime Plots for Different Panel Sizes at Orientation Angle of 22.5° and Sensor Location 1.

RESULTS – ENERGY (0°/22.5°/45°)

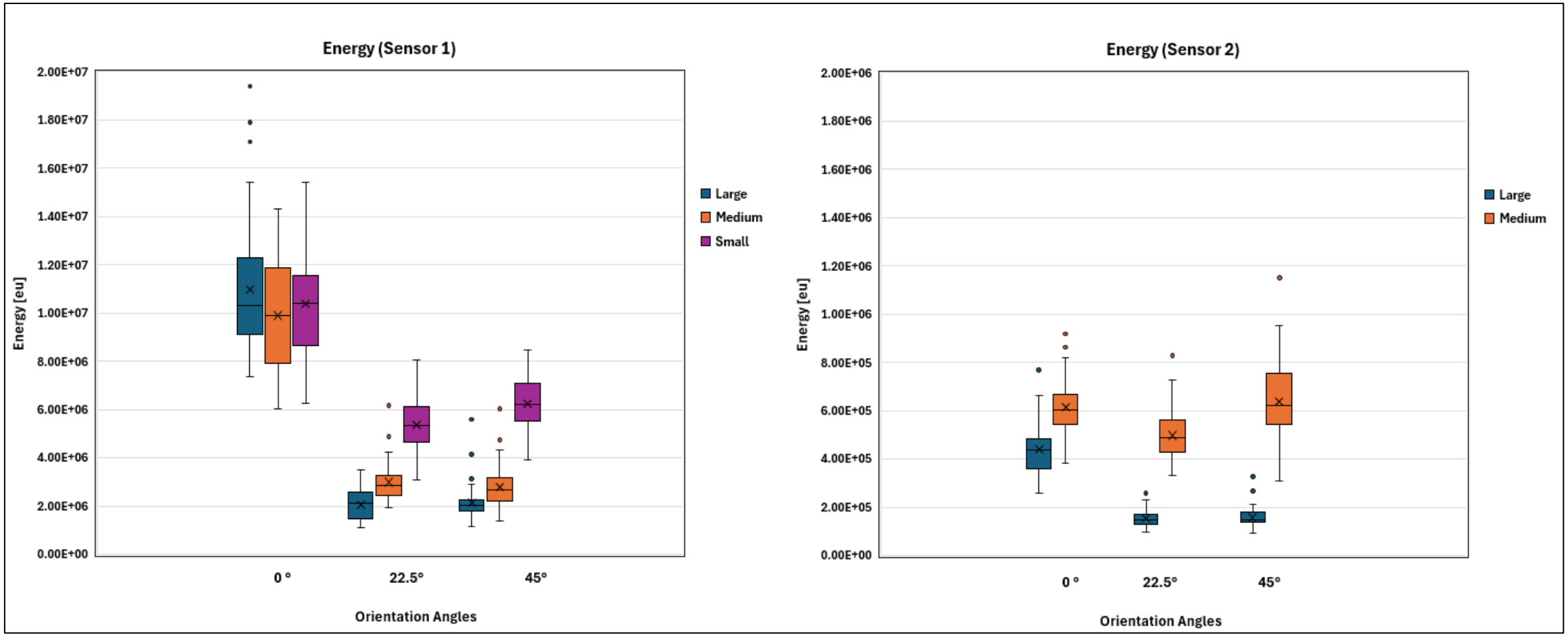

Figure 9. Energy Plots for 0°/22.5°/45° Orientation Angles.

*Datasets for 67.5° and 90° are omitted for clarity. Data for 0°/90° and 22.5°/67.5° was similar.

*[Ref. 7.0 and 9.0].

RESULTS – WAVEFORM COMPARISON (LARGE-S1-0°/22.5°/45°)

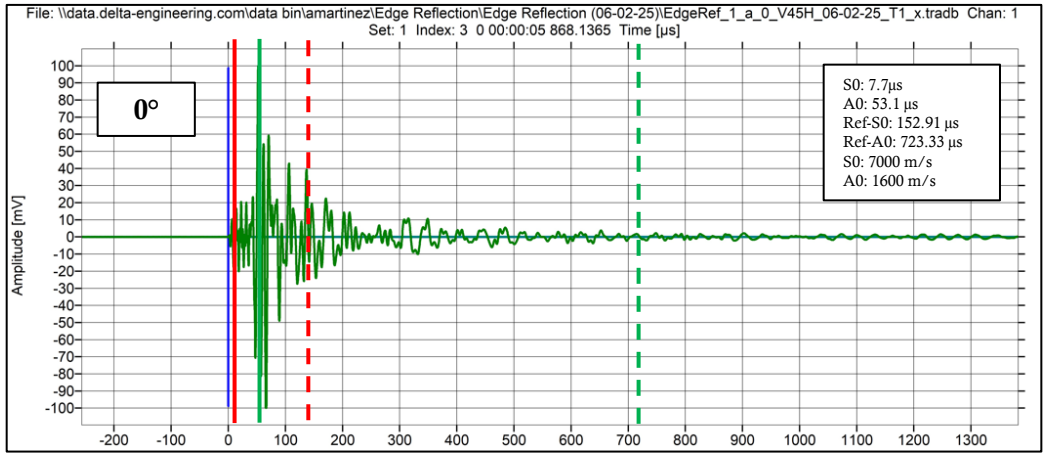

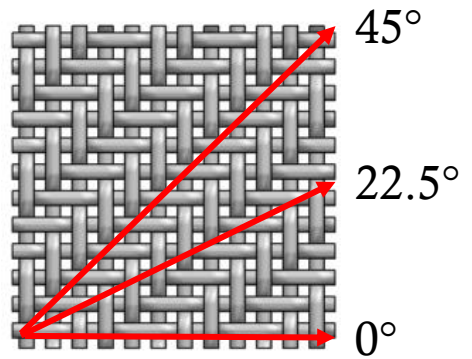

Figure 10. Twill Weave Pattern [Ref. 2.0].

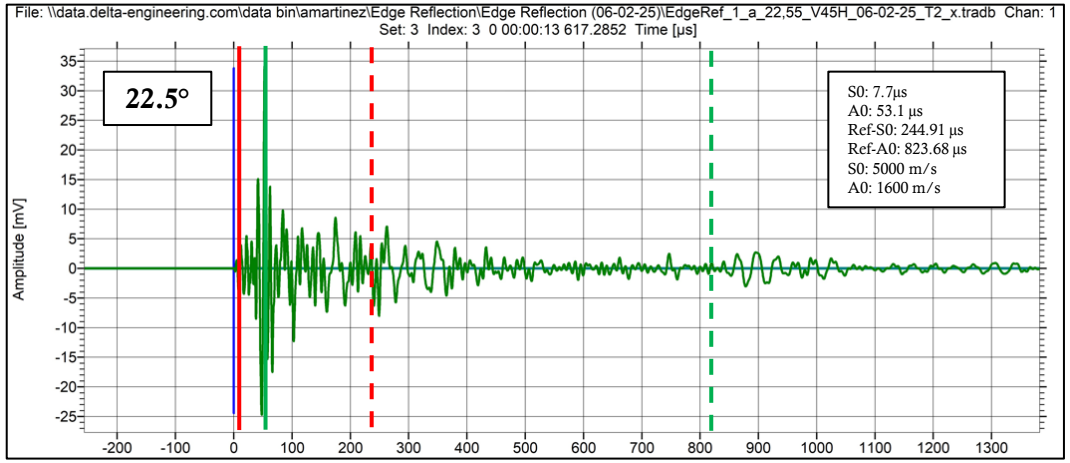

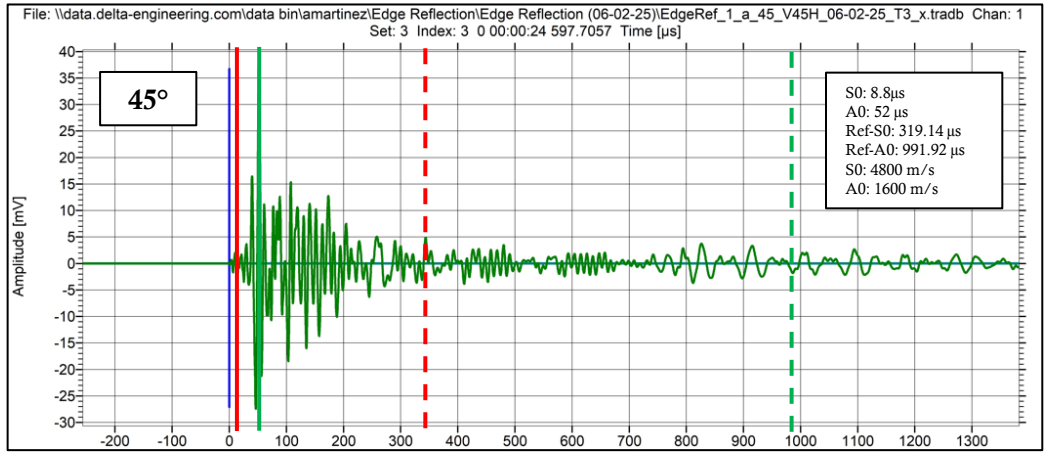

Figure 11. Large Panel Size Waveforms at Sensor Location 1 for 0°/22.5°/45° Orientation Angles.

*[Ref. 13.0].

RESULTS – WAVEFORM COMPARISON (LARGE-S1-0°/22.5°/45°)

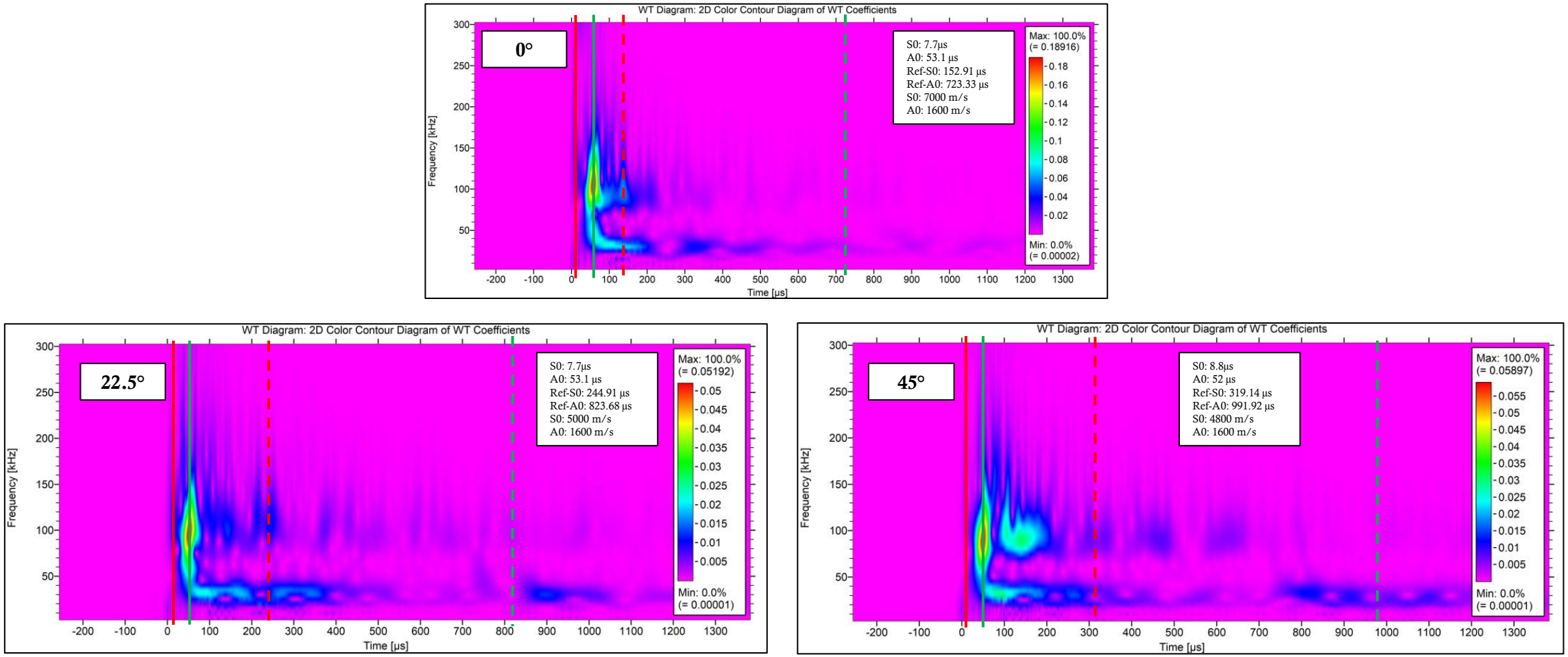

Figure 12. Large Panel Wavelet Transform at Sensor Location 1 for 0°/22.5°/45° Orientation Angles.

*[Ref. 4.0, 5.0, and 10.0].

DELTA ENGINEERING

RESULTS – WAVEFORM COMPARISON (45°-S1-LARGE/MEDIUM/SMALL)

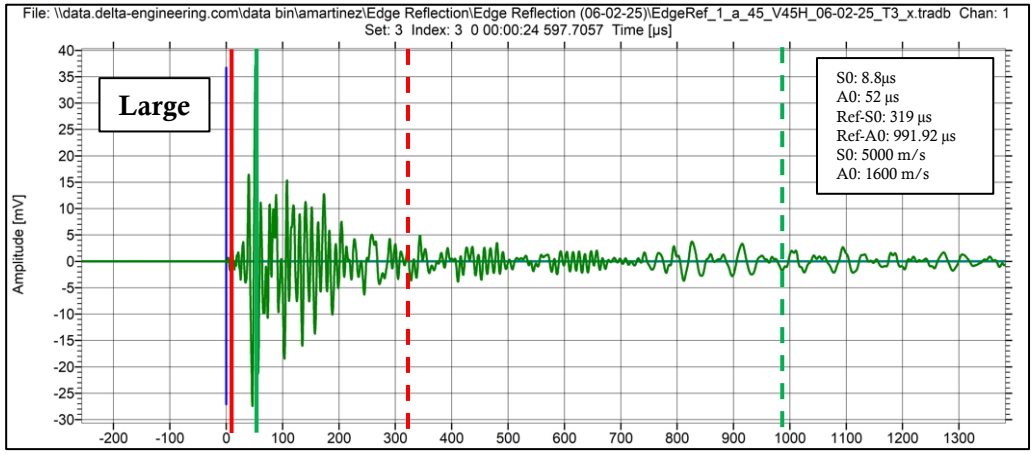

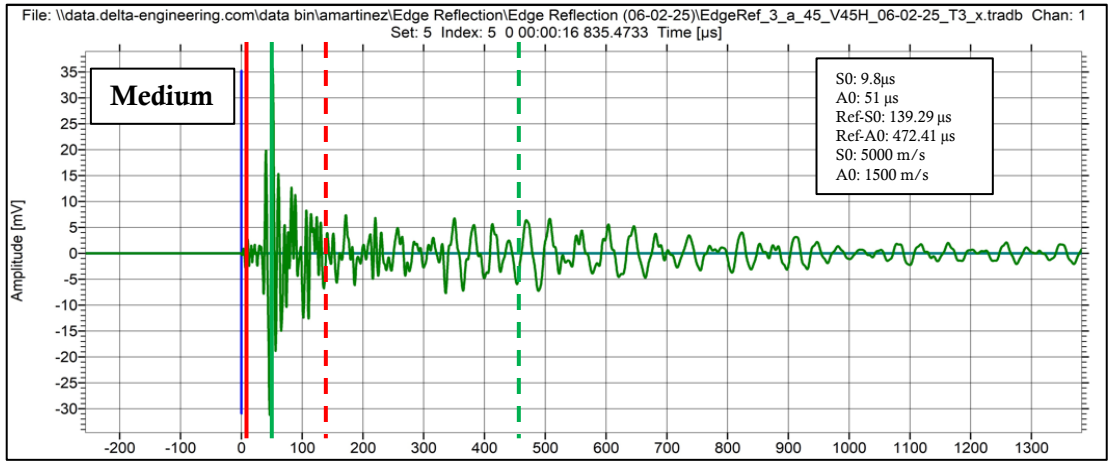

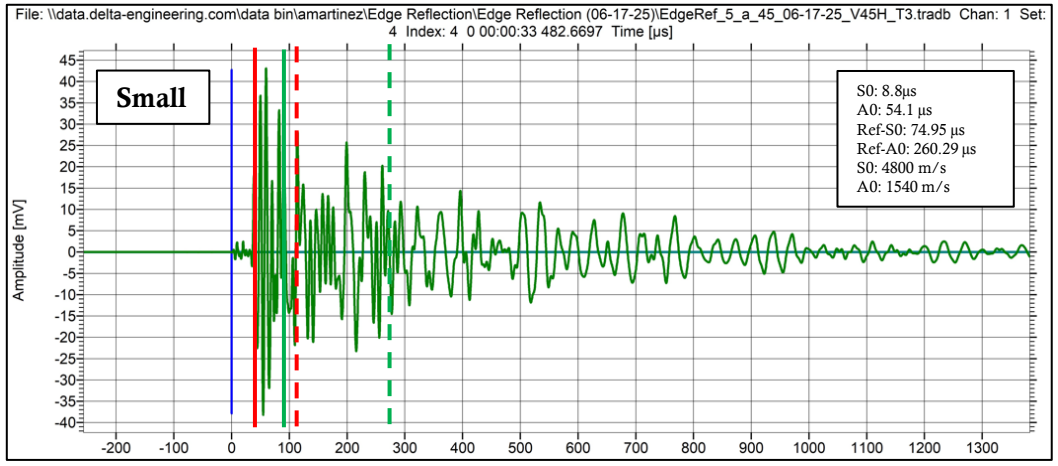

Figure 13. Waveform Plots for Sensor Location 1 at 45° Orientation Angle and Different Panel Sizes.

RESULTS – WAVEFORM COMPARISON (45°-S1-LARGE/MEDIUM/SMALL)

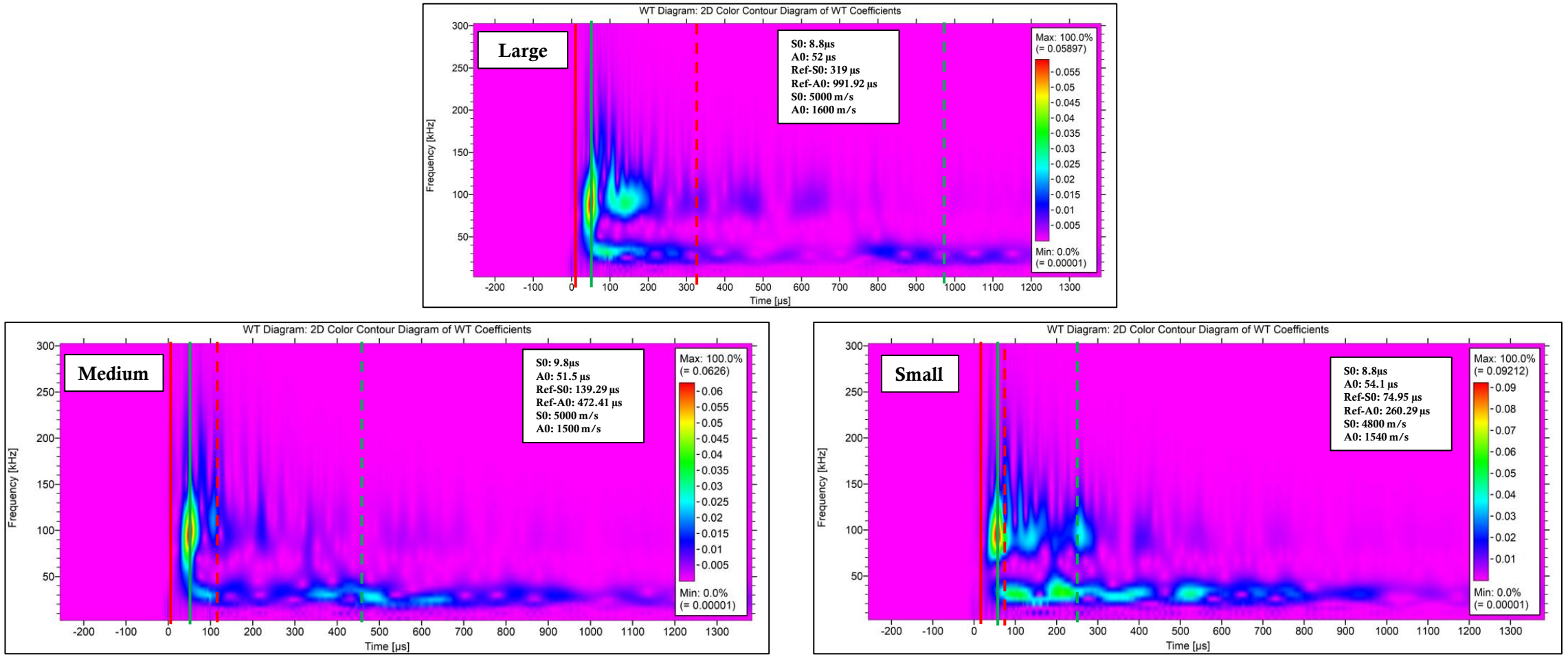

Figure 14. Wavelet Transforms for Sensor Location 1 at 45° Orientation Angle and Different Panel Sizes.

CONCLUSIONS AND RECOMMENDATIONS

CONCLUSIONS:

- The risetime is significantly affected by interference patterns between the primary waveform and the reflection.
- Amplitude was generally consistent during all tests performed for the different orientation angles and panel sizes.
- There was a large data spread for energy values at a 0° orientation angle compared to 22.5° and 45°. The highest energy magnitude was at 0° whereas the lowest magnitude was at 22.5°. The energy of a signal which is dependent on the duration and amplitude is significantly affected by reflections.
- Changes in waveform shapes indicate the presence of low and high frequency edge reflections. Interference and attenuation of a signal throughout the visualized plots can affect the AE features discussed above.
- When edge reflections are of concern, features such as energy may be better assessed for just the beginning of the signal.

RECOMMENDATIONS:

- Implementation of sensor mounts is highly recommended to keep PLB-to-Sensors and Sensor-to-Sensor distances consistent.
- Preliminary analysis of reflection arrival times is required to evaluate how risetime and energy are affected during post-processing.
- It is recommended to conduct testing on areas free from nearby bonded or fastened structure (ex. center of skin panel).

REFERENCES

[1.0] Han, S., Li, Q., Cui, Z., Xiao, P., Miao, Y., Chen, L., and Li, Y. “Non-Destructive Testing and Structural Health Monitoring Technologies for Carbon Fiber Reinforced Polymers: A Review.” *Nondestructive testing and evaluation*, Vol. 39, No. 4, 2024, pp. 725–761. https://doi.org/10.1080/10589759.2024.2324149.

[2.0] United Wire. “Five Shed Twill Weave”. *United Wire*. https://www.unitedwire.com/five-shed-twill-weave/.

[3.0] Vallen Systeme GmH. “AcqSetup-01: General AE and Transient Recorder Setup”. *Vallen Systeme*. https://www.vallen.de/products/.

[4.0] Ernst, R., Zwimpfer, F., and Dual, J. “One Sensor Acoustic Emission Localization in Plates.” *Ultrasonics*, Vol. 64, 2015, pp. 139–150. https://doi.org/10.1016/j.ultras.2015.08.010.

[5.0] Migot, A., Saaudi, A., and Giurgiutiu, V. “New Method of Impact Localization on Plate-like Structures Using Deep Learning and Wavelet Transform.” *Sensors*, Vol. 25, No. 6, 2025, p. 1926. https://doi.org/10.3390/s25061926.

[6.0] Hamstad, M. “On Lamb Modes as Function of Acoustic Emission Source Rise Time.” *J. Acoustic Emission*, Vol. 28, 2010.

[7.0] Shen, G., Li, L., Wu, Z., and Zhang, Z. “Study on the Characteristics of Acoustic Emission for Grey Cast Iron Specimens.” *e-Journal of Nondestructive Testing*, Vol. 17, No. 11, 2012.

[8.0] Csefalvay, G., and Sedlak, P. “Experimental Study on Feature Selection Using Artificial AE Sources.” *e-Journal of Nondestructive Testing*, Vol. 17, No. 11, 2012.

[9.0] Bohse, J. “Acoustic Emission Characteristics of Micro-Failure Processes in Polymer Blends and Composites.” Composites Science and Technology, Vol. 60, No. 8, 2000, pp. 1213–1226. https://doi.org/10.1016/s0266-3538(00)00060-9.

[10.0] Xiao, D., Gao, Y., Quan, D., Zhou, X., Tong, Z., Liu, X., and He, T. “A Novel Reflection Removal Method for Acoustic Emission Wave Propagation in Plate-like Structure.” Journal of Vibroengineering, Vol. 17, No. 5, 2015, pp. 2322–2337

[11.0] Aggelis, D. G., Sause, M., Packo, P., Pullin, R., Grigg, S., Kek, T., and Lai, Y.-K. “Acoustic Emission.” Detection Systems for Aerospace, 2021, pp. 175–217. https://doi.org/10.1007/978-3-030-72192-3_7.

[12.0] Pollock, A. A. “Acoustic Emission - 2.” Non-Destructive Testing, Vol. 6, No. 5, 1973, pp. 264–269. https://doi.org/10.1016/0029-1021(73)90074-1

[13.0] Wang, X., Liu, X., Tai, J., He, T., and Shan, Y. “A Novel Method of Reducing the Acoustic Emission Wave Reflected by Boundary Based on Acoustic Black Hole.” Ultrasonics, Vol. 94, 2018, pp. 292–304. https://doi.org/10.1016/j.ultras.2018.08.015.

THANK YOU FOR YOUR ATTENTION

Q & A?

EXTENDED GRATITUDE TO DELTA ENGINEERING WHO MADE THIS RESEARCH POSSIBLE.

APPLICATION OF INFRARED IMAGING TO REVEAL HIDDEN DEFECTS IN CFRP LAMINATES

Janice Dulieu-Barton, Rafeal Ruiz-Iglesias, Emily Leung and Riccardo Cappello

*Janice.barton@bristol.ac.uk

Bristol Composites Institute, School of Civil, Aerospace, and Design Engineering, University of Bristol, UK

Engineering and Physical Sciences Research Council

University of BRISTOL

Bristol Composites Institute

RESHAPING THE TESTING PYRAMID

Challenges in substructural scale testing

Complex geometry

Large size

Challenging measurement space

Multi-camera set-up

FE integration

Composite/multi-material

Multi-axial test

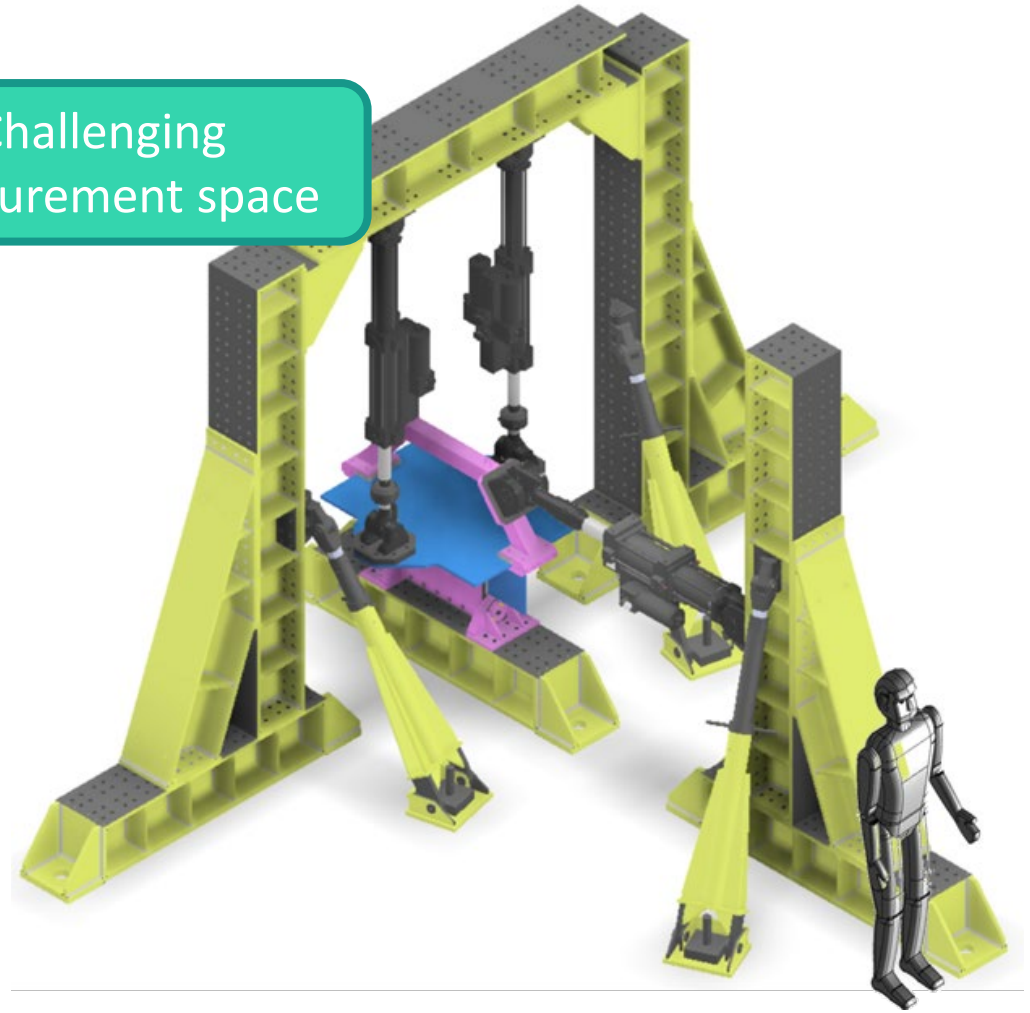

Motivation: next generation testing pyramids

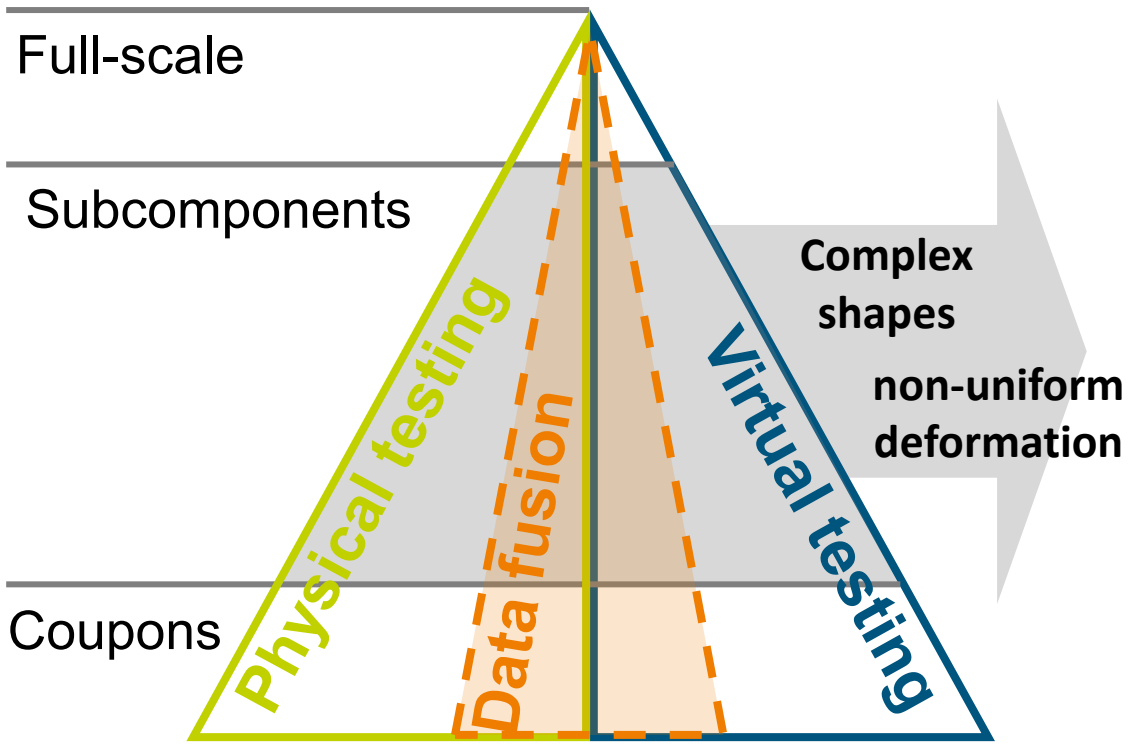

- Design & certification will increasingly rely on integrated ***physical*** and ***virtual*** testing
- Requirement for ***data fusion/correlation*** techniques to efficiently bridge the gap
- ***Multi-camera, full-field imaging*** can unlock the potential of integrated testing & modelling at subcomponent scale

DIC





IR, TSA

Thermoelastic stress analysis (TSA)

- TSA relies on the measurement of a small temperature change from a specimen subject to cyclic loading:

$$\Delta T = -T_o \frac{1}{\rho \cdot c_p}(\alpha_1 \Delta\sigma_1 + \alpha_2 \Delta\sigma_2)$$

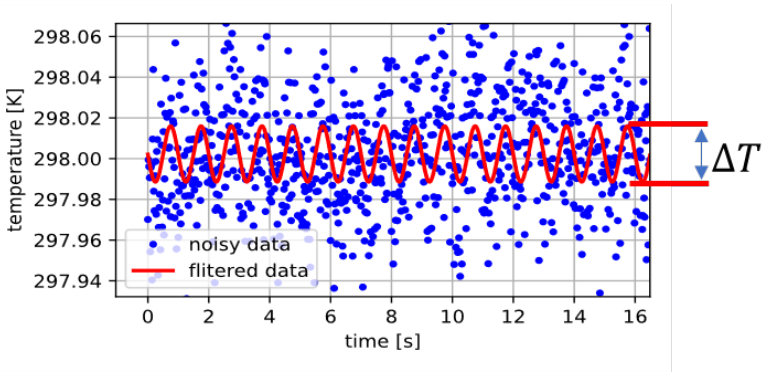

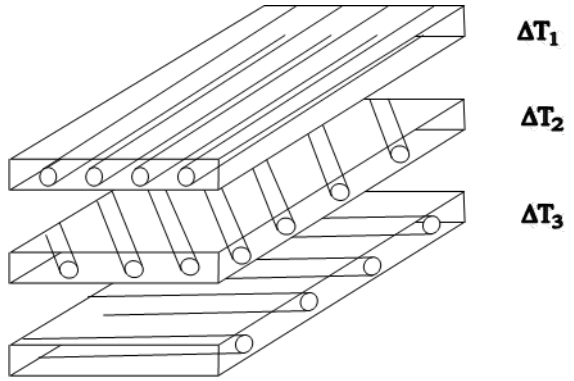

- Assumption is temperature change occurs under adiabatic conditions
- In CFRP laminates heat conduction occurs as a result of the degree of anisotropy (thermal and mechanical) and high thermal conductivity
- Increasing the strain rate (loading frequency) reduces thermal diffusion but is limited in large structural testing and high loading rate induce viscoelastic heating

Heat transfer in CFRP laminates

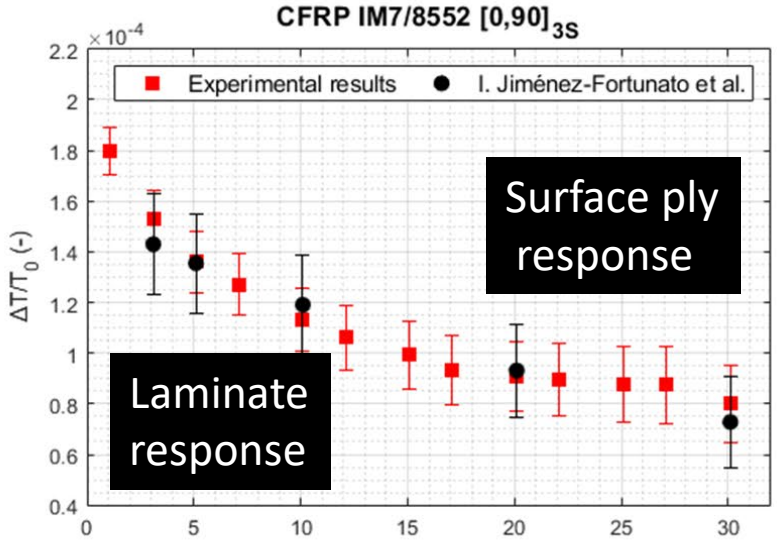

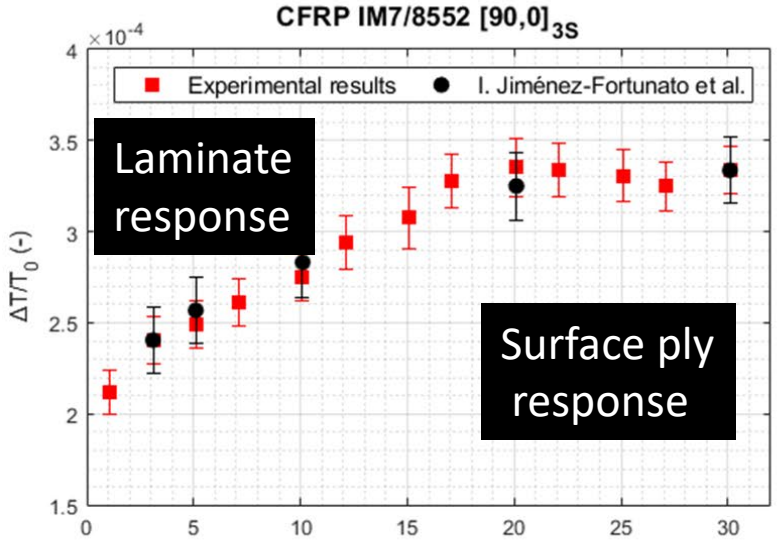

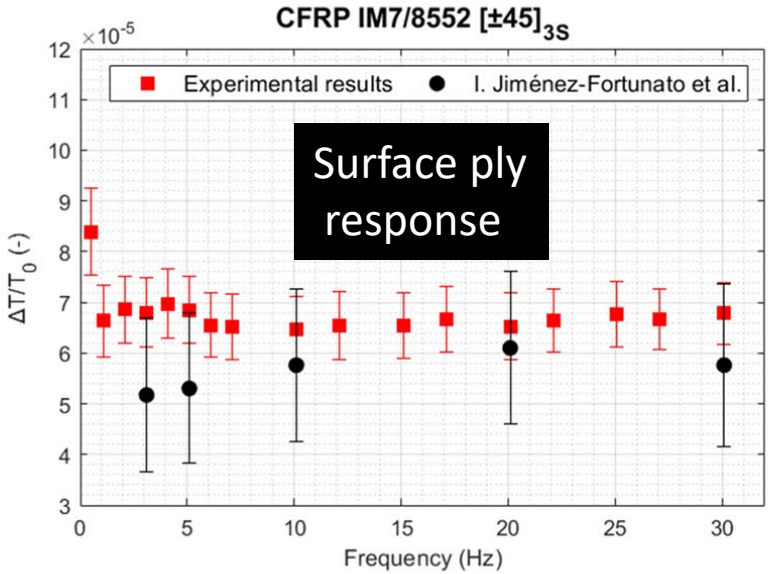

Composites: Part A 149 (2021) 106515

ELSEVIER

Contents lists available at ScienceDirect

Composites Part A

journal homepage: www.elsevier.com/locate/compositesa



Check for updates

On the source of the thermoelastic response from orthotropic fibre reinforced composite laminates

Irene Jiménez-Fortunato [a,b,*], Daniel J. Bull [a], Ole T. Thomsen [b], Janice M. Dulieu-Barton [b]

[a] School of Engineering, University of Southampton, UK
[b] Bristol Composites Institute, University of Bristol, UK

What can be done to use TSA effectively in CFRP structures

Engineering and Physical Sciences Research Council

University of BRISTOL

Bristol Composites Institute

RESHAPING THE TESTING PYRAMID

Numerical model of TSA in CFRP

Cappello, R., Pitarresi, G., Catalanotti, G.: Thermoelastic Stress Analysis for composite laminates: A numerical investigation. Compos Sci Technol. 241, 110103 (2023).https://doi.org/10.1016/J.COMPSCITECH.2023.110103

Coupled temperature-displacement analysis (Abaqus):

- Sinusoidal displacement boundary conditions.
- Inclusion of a surface resin-rich layer (RRL).
- Conduction between plies.
- Inclusion of surface paint layer

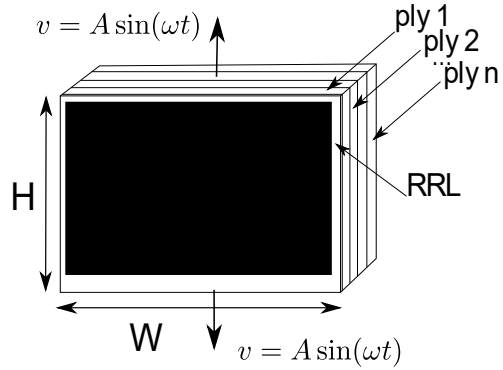

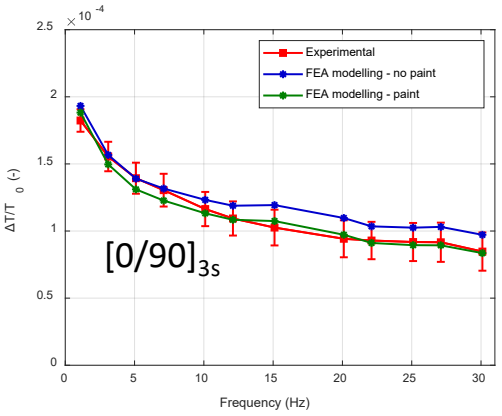

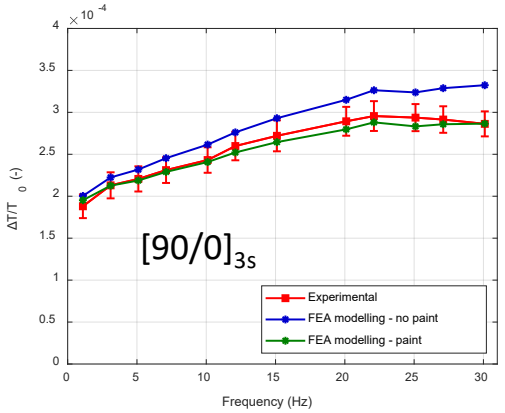

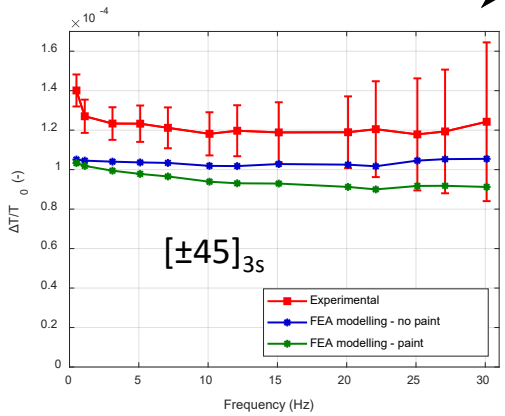

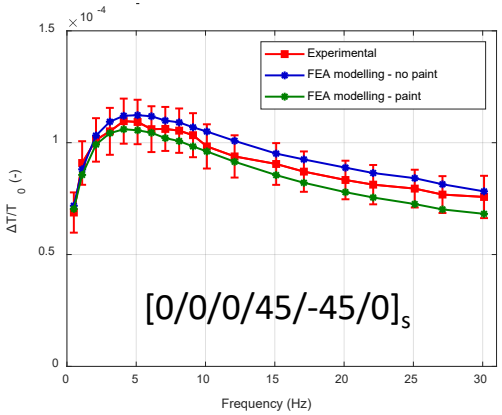

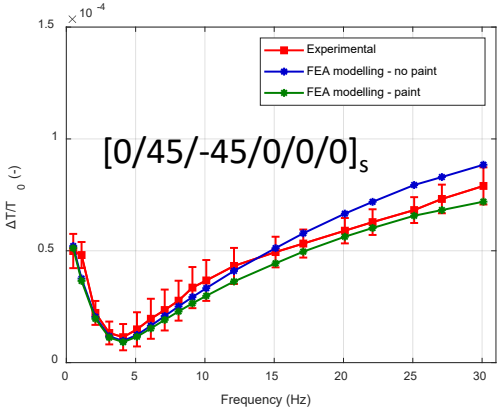

Engineering and Physical Sciences Research Council

University of BRISTOL

Bristol Composites Institute

RESHAPING THE TESTING PYRAMID

Test specimens and loading

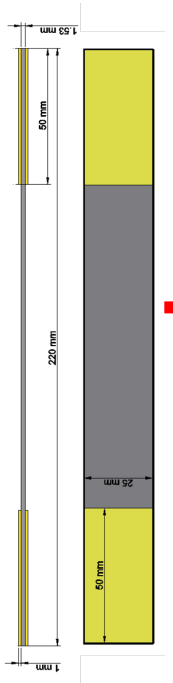

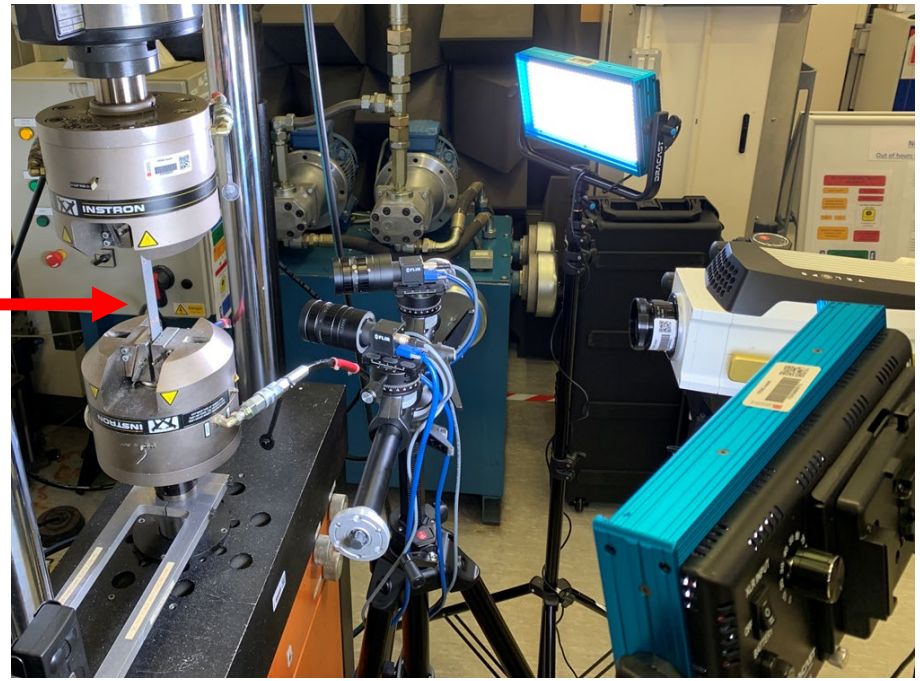

Layup	Loading scenario	FPF
$[0,90]_{3S}$	Tension Loading	541 MPa

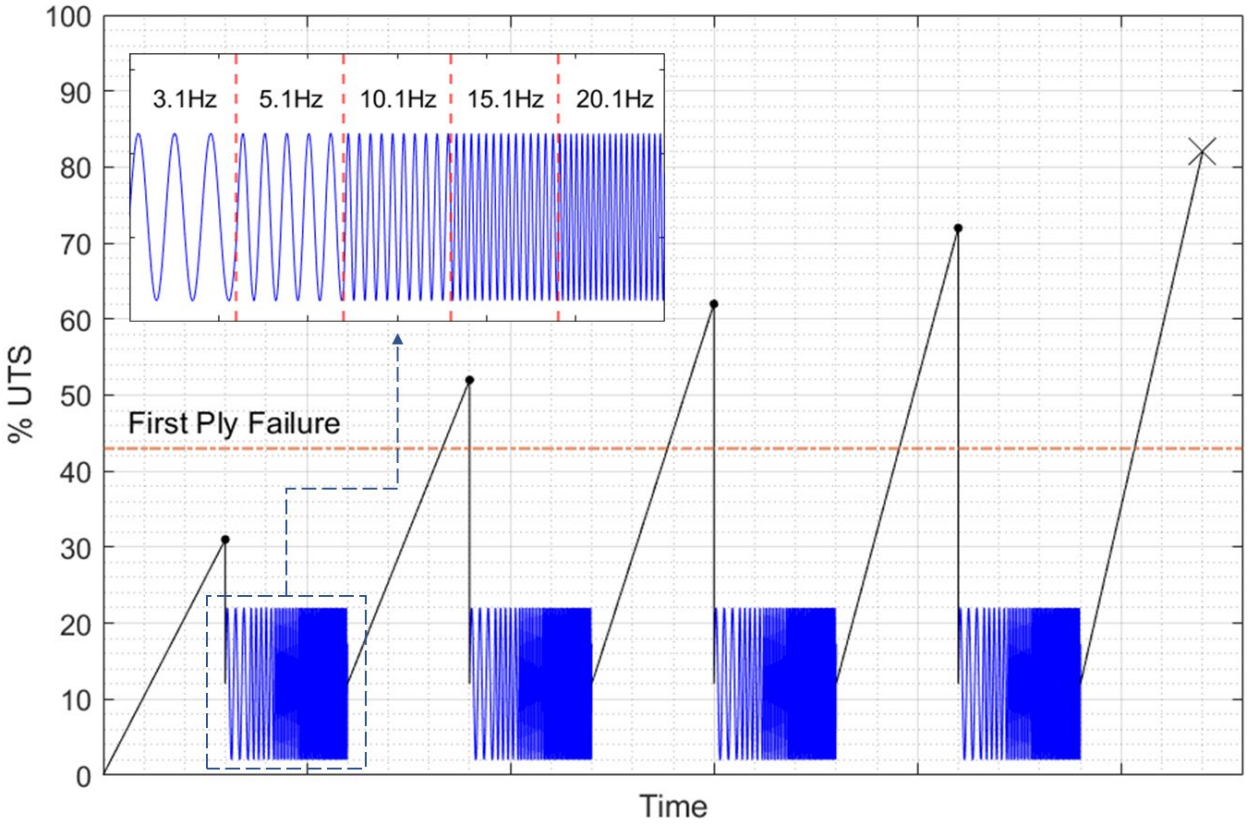

Load Ramp → **Induce damage progressively** (in tension)

Cyclic Loading → TSA and LIDIC **(Inspection)**

Damaged Laminates (59% of the UTS)

CFRP $[90,0]_{3S}$

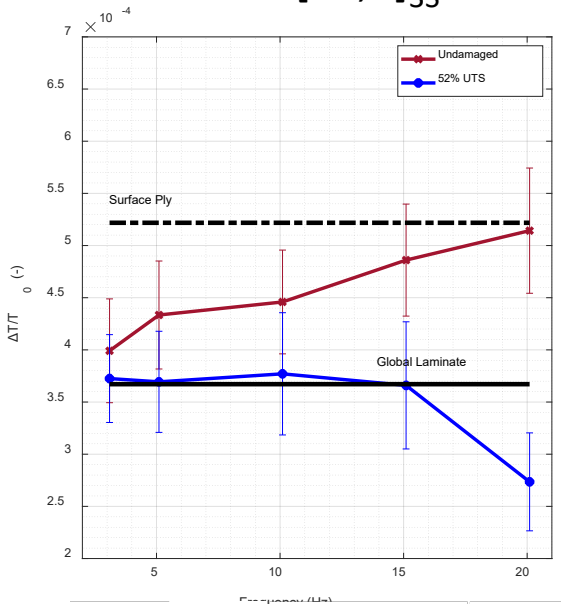

CFRP $[0,90]_{3S}$

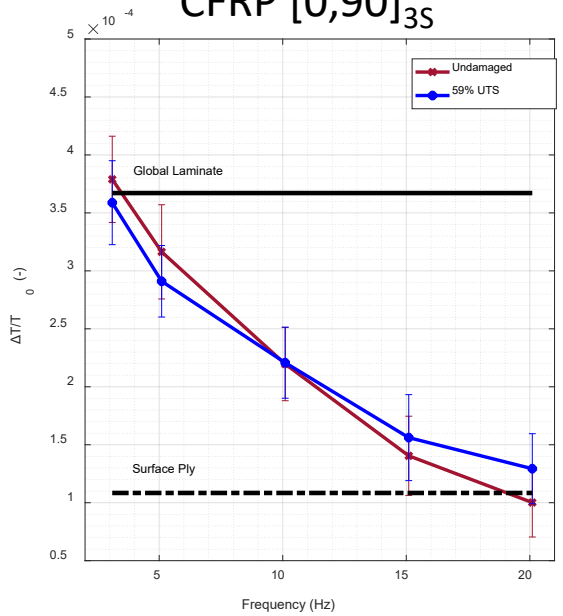

CFRP $[0,45,-45,0,0,0]_{3S}$

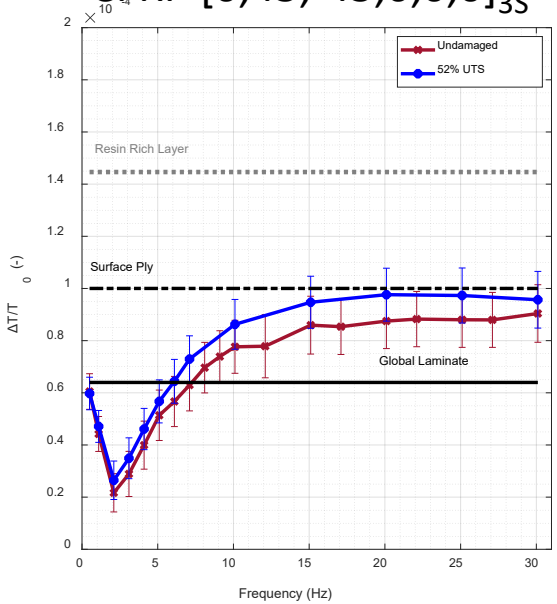

CFRP $[0,0,0,45,-45,0]_{3S}$

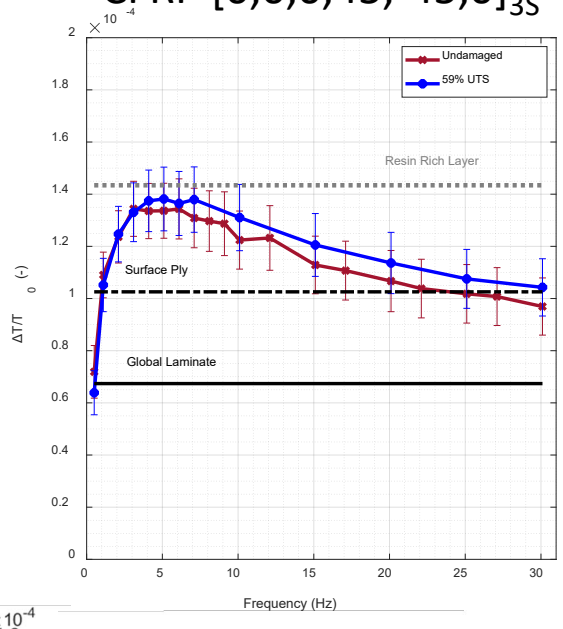

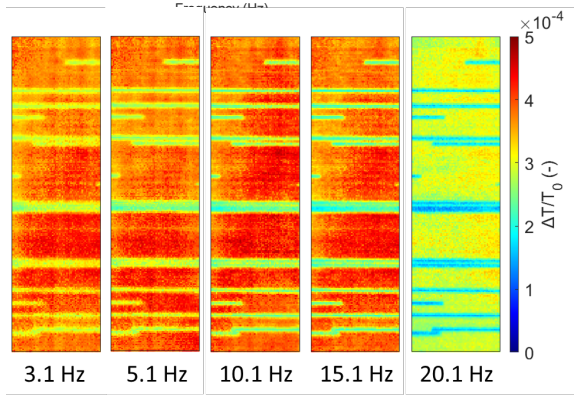

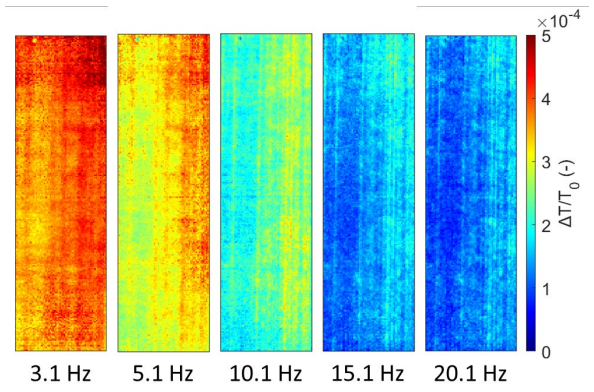

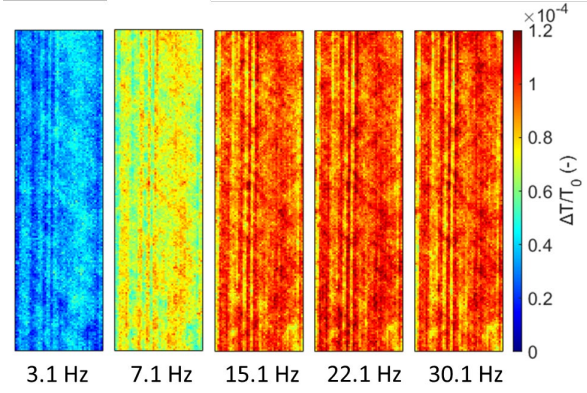

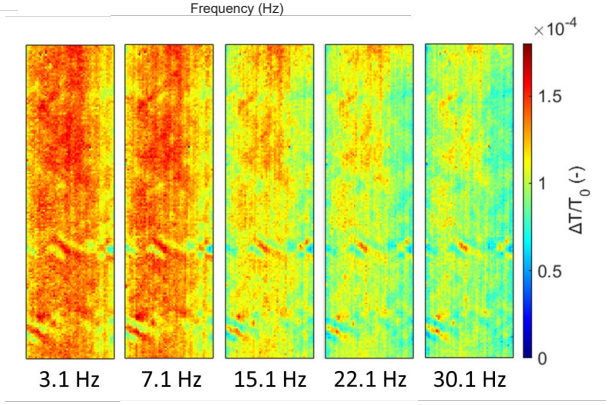

Full-field data fusion to identify subsurface damage

Opportunity to identify subsurface damage by subtracting surface ply image (DIC) from TSA image at low frequencies

TSA Raw Data



output: Images

Lock-In Algorithm

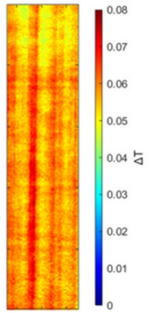

Final output: ΔT, T_0, phase

Apply Surface Ply Model to give surface ply TSA response

DIC Raw Data



output: Images

MatchID Software



output: Strains

Notch filter

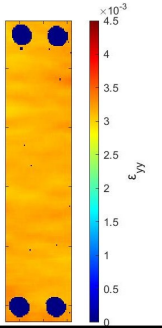

Final output: Δε, phase

Engineering and Physical Sciences Research Council

University of BRISTOL

Bristol Composites Institute

RESHAPING THE TESTING PYRAMID

Methodology 1 (M1): $(\Delta T/T_0)_{\text{TSA Low frequency}} - (\Delta T_{SP}/T_0)_{\text{DIC}}$

$[0,90]_{3S}$ $[0,45,-45,0,0,0]_{3S}$ $[0,0,0,45,-45,0]_{3S}$

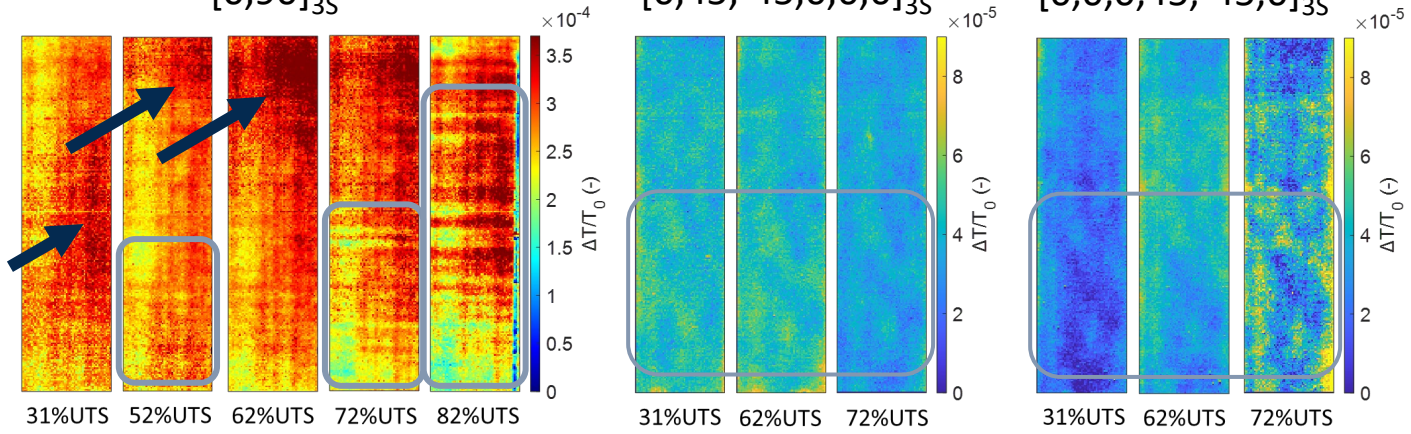

Methodology 2 (M2): $(\Delta T/T_0)_{\text{TSA Low frequency}} - (\Delta T/T_0)_{\text{TSA High frequency}}$

$[0,90]_{3S}$ $[0,45,-45,0,0,0]_{3S}$ $[0,0,0,45,-45,0]_{3S}$

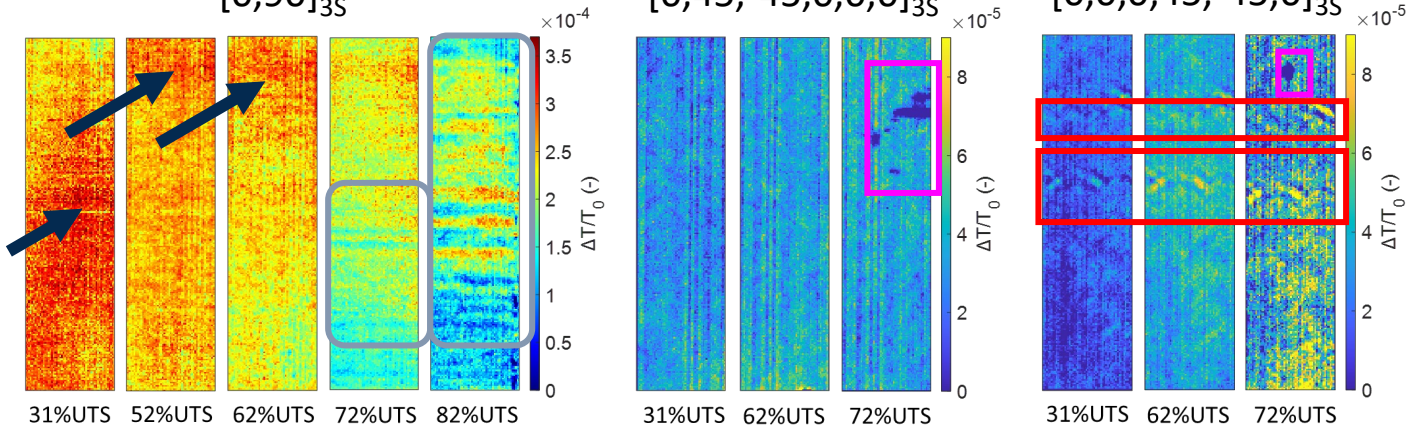

$[0,90]_{3S}$

- **After FPF → Regions of ↑$\Delta T/T_0$ change**
- **Subsurface defects start to be visible after FPF**
- **More subsurface features** are observed with **M1**
- **M2 shows a decrease of the subsurface response**

$[0,45,-45,0,0,0]_S$

- **Subsurface response (±45) is observed in M1**
- **M2 shows a similar** subsurface $\Delta T/T_0$ to M1
- **Delamination is detected using M2!**

$[0,0,0,45,-45,0]_S$

- **Subsurface response (±45) is observed in M1**
- **Wrinkles are observed**
- **Delamination is again detected using M2!**

Full-field imaging of sandwich structures (beams)

Side view of core/face sheet interface

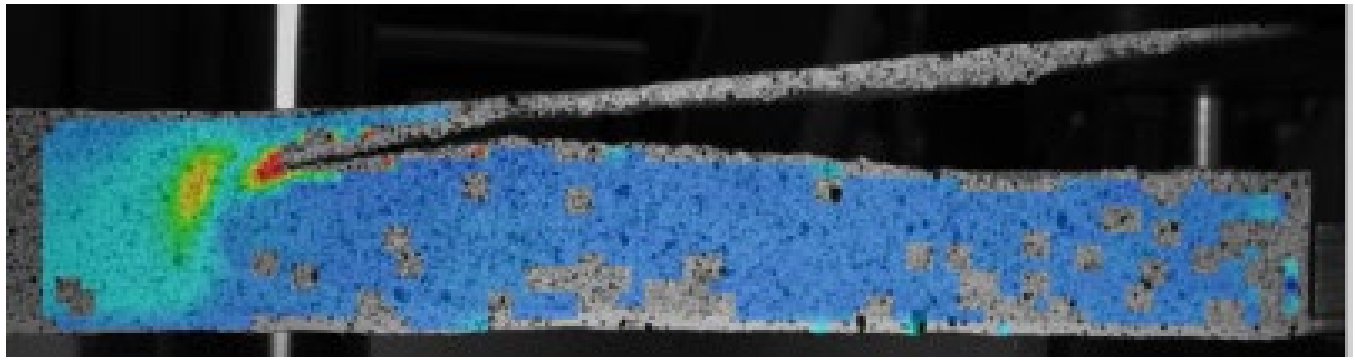

Martakos G, Andreasen J, Berggreen C, Thomsen O. Experimental investigation of interfacial crack arrest in sandwich beams subjected to fatigue loading using a novel crack arresting device. Journal of Sandwich Structures & Materials. 2019;21(2):401-421. doi:10.1177/1099636217695057

Real sandwich structures are panels - not beams where the defect is hidden under the face sheet

Face-sheet/core debonding

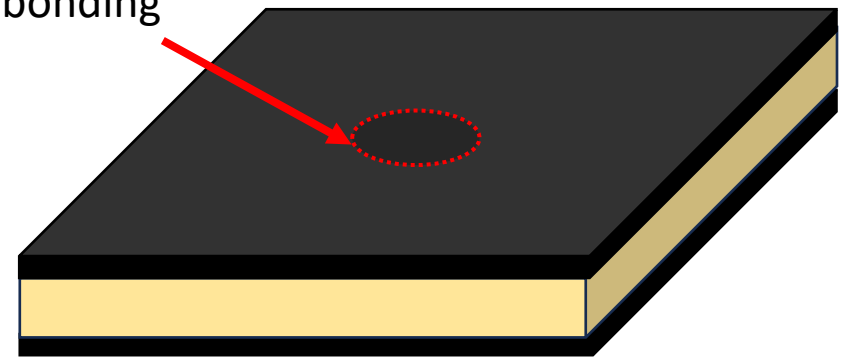

Test specimens and experiments

- Face-sheet – unidirectional CFRP
- Core - PVC
- Teflon film is used to create debonded region
- Loading: -500N ± 400 N
- Frequency: 1 - 11 Hz

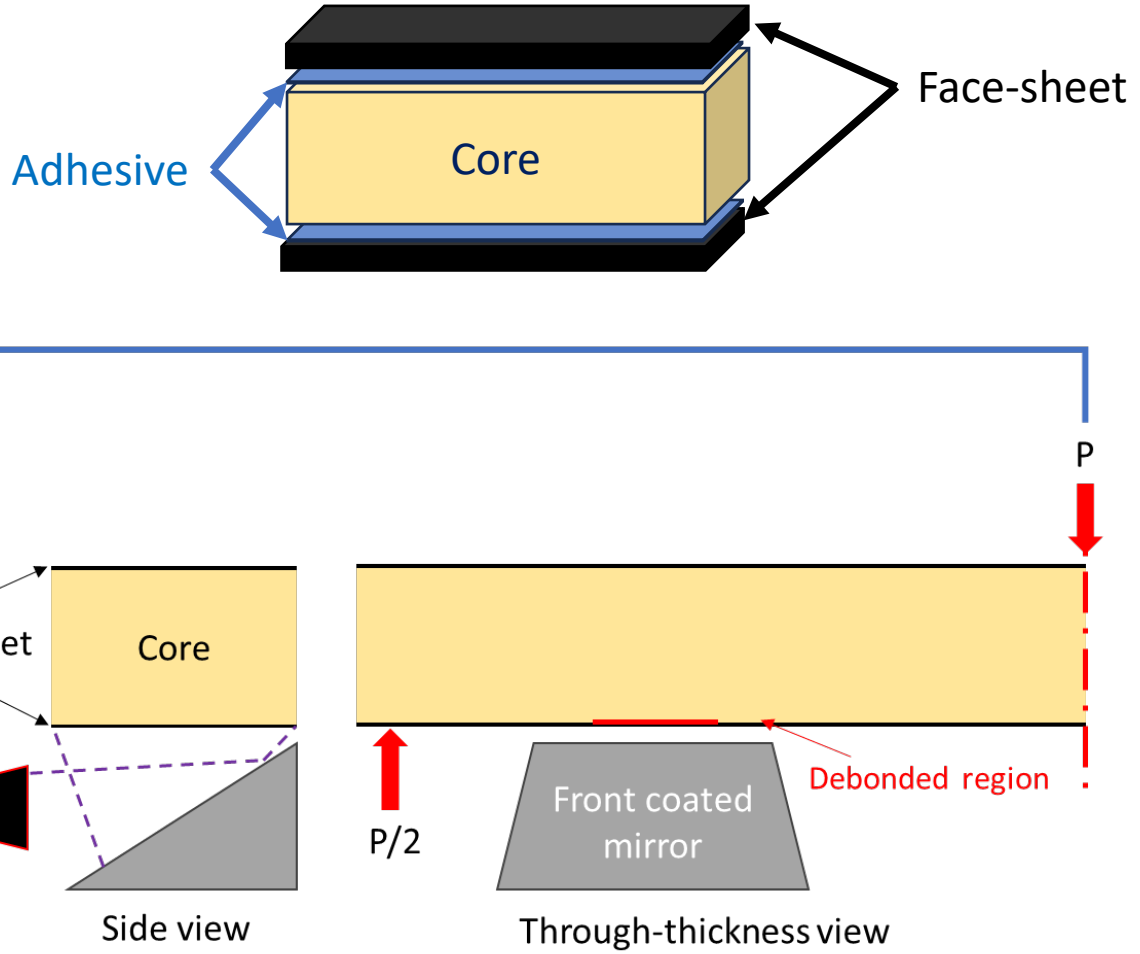

Defects identified through face sheet

Face sheet is UD – little heat transfer

- Thermal gradient is from complex 3D stress field at the debond/core interface

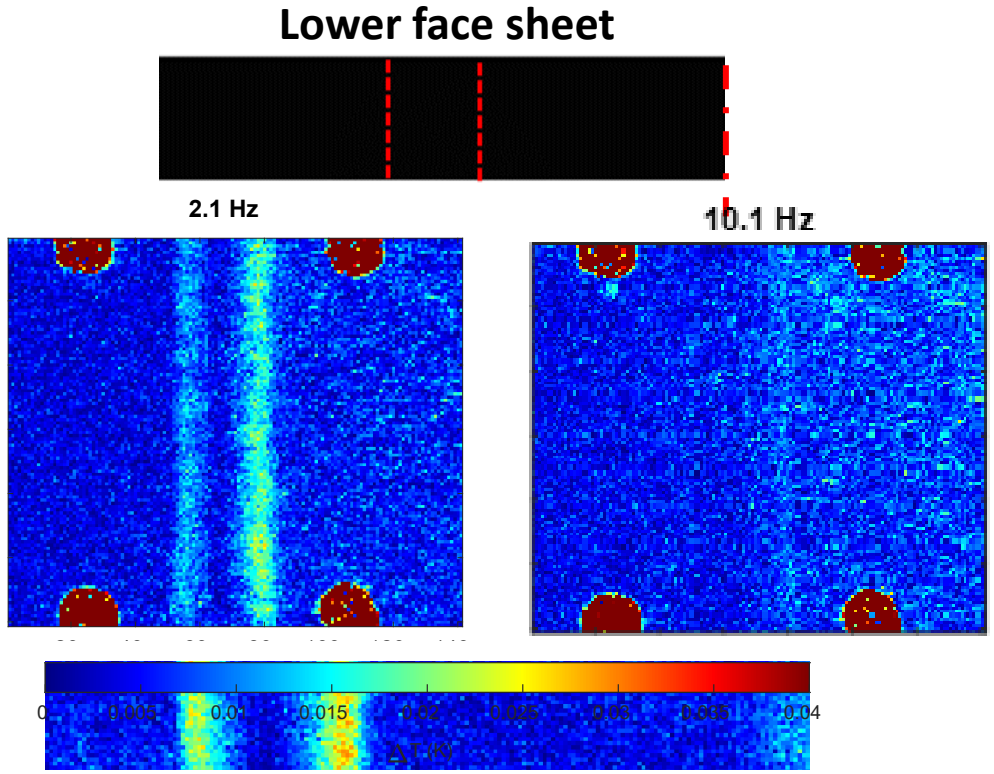

Can the response be related to the damage severity at the interface?

TSA to identify delaminations

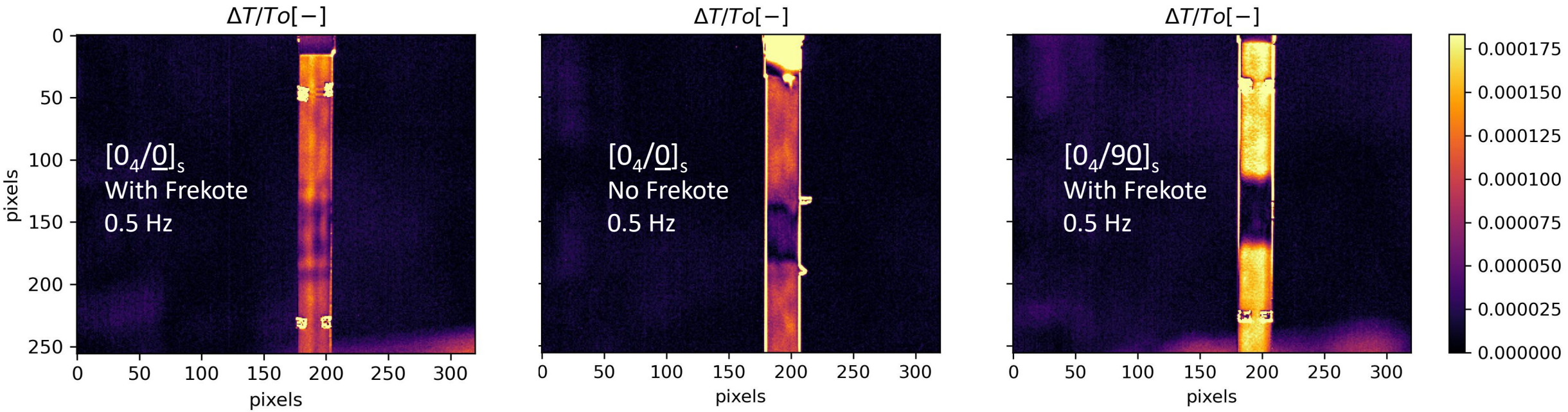

Employing low loading frequency enables identification of the subsurface defect. The heat source generated in the 90° plies aids the identification, which can be further leveraged by tuning the loading frequency to defect depth.

Progress and outlook

Showed how the non-adiabatic thermoelastic response and FFDF can be used to:

Reveal subsurface damage in

- CFRP composites
- Sandwich structures

Thermoelastic response can be modelled to help interpret non-adiabatic behaviour

Next step: apply to complex structural component

ICCM24 24TH INTERNATIONAL CONFERENCE ON COMPOSITE MATERIALS
AUG 4-8, 2025 • BALTIMORE CONVENTION CENTER • BALTIMORE, MARYLAND

COMBINING THERMOGRAPHIC AND LAMB WAVES INVESTIGATION DATA FOR THE CHARACTERISATION OF CFRP DELAMINATIONS

Lea A.C. Lecointre[1], Naoki Hosoya[2], Shin-ichi Takeda[3]
and Tomohiro Yokozeki[1]

[1]Department of Aeronautics and Astronautics, The University of Tokyo
Hongo 7-3-1, Bunkyo-ku, Tokyo 113-8654, Japan
Email: lea-lecointre@g.ecc.u-tokyo.ac.jp, web page: www.aerospace.t.u-tokyo.ac.jp/en

[2]Department of Engineering Science and Mechanics, Shibaura Institute of Technology
Toyosu 3-7-5, Koto-ku, Tokyo 135-8548, Japan
Web page: www.shibaura-it.ac.jp/en/academics/engineering_past/meo.html

[3]Aviation Technology Directorate, Japan Aerospace Exploration Agency (JAXA)
Osawa 6-13-1, Mitaka-shi, Tokyo 181-0015, Japan
Web page: www.aero.jaxa.jp/eng

Keywords: Non-destructive Testing, Ultrasonics, Thermal analysis, Delamination, Physical methods of analysis, Plates

ABSTRACT

Non-Destructive Testing (NDT) techniques have distinct advantages and limitations, making their selection highly dependent on factors such as the material being tested, the part geometry, the expected defects, or the experimental conditions. To address their limitations, researchers and industry professionals have widely explored ways to optimise existing NDT techniques. A promising direction is Data Fusion, extensively explored in Structural Health Monitoring (SHM), which combines data from multiple inspection techniques to enhance defect detection and material characterisation.

In this study, a Data Fusion methodology is implemented to combine quantitative results from InfraRed Thermographic (IRT) inspection and Lamb Waves inspection, an advanced Ultrasonic Testing (UT) technique adapted to relatively thin structures such as plates. IRT enables rapid, non-contact detection of surface and near-surface defects through heat propagation analysis. In this work, thermal diffusivities are calculated from cooling curves extracted from thermal maps. Lamb Waves are generated and measured using a fully non-contact system; their interaction with internal defects is quantified using RMS energy values, which provide insights into subsurface damage.

However, Lamb Wave propagation in anisotropic, layered composites remains challenging, with possible misdetections. Multiple CFRP samples of varying geometries and thicknesses (1.6 mm to 6.4 mm), with artificial and impact-induced delaminations, were tested. Results showed that while each method has detection limitations, their fusion offers enhanced characterisation. This is especially valuable for complex defects such as lightning-induced delaminations or deep-layer damage.

By combining IRT's surface sensitivity and Lamb Waves' subsurface reach, the fusion approach improves not only detection but also the characterisation of damage mechanisms, crucial for composite materials with complex architectures. Future work will focus on improving individual techniques, such as refining signal processing algorithms for Lamb Waves inspection, and extending the investigated dataset to a wider range of composite structures and defects.

1 INTRODUCTION

The increasing use of Carbon Fibres Reinforced Plastics (CFRP) materials in aerospace, automotive and energy sectors has led to growing demands for highly reliable and efficient Non-Destructive Testing (NDT) techniques. Due to the complex, anisotropic and layered nature of these materials, detecting and characterising internal defects such as delaminations remains a major challenge. To address this issue, industries and researchers have been widely investigating the performance of NDT methods to improve their efficiency and accuracy and obtained major advances over the last decades. For example, the introduction of X-Ray Computed Tomography (XRCT) has transformed Radiographic Testing (RT) capabilities by supplying 3D volumetric imagery methods. The development of Phased Array Ultrasonic Testing (PAUT) or non-contact systems based on guided waves revolutionised classic Ultrasonic Testing (UT) abilities [1–3].

However, the limitations inherent to each of these methods often persist, particularly as they often come from the application cases or the CFRP materials. In this context, Data Fusion has emerged as a promising approach in the field of Structural Health Monitoring (SHM). By combining data from different inspection techniques, Data Fusion aims to provide a more comprehensive and robust understanding of structural integrity. This integration can take various forms, from simple visual overlays to more advanced mathematical or statistical models that merge complementary parameters. The goal is not only to increase detection reliability, but also to enrich the interpretation of damage features by leveraging the distinct sensitivities of each technique [4–10].

This study explores the application of Data Fusion to InfraRed Thermography (IRT) and Ultrasonic Lamb Waves inspection, two NDT methods based on different physical principles. While IRT offers rapid detection of shallow discontinuities by analysing thermal response on the surface [2,11], Lamb Wave inspection enables the detection of internal defects by analysing the interaction of propagating guided ultrasonic waves with material discontinuities [12,13]. While these two techniques are particularly well-suited to thin-walled CFRP plate inspection, each of them remains subjected to physical and practical limitations when applied individually. IRT is inherently limited in depth penetration due to the thermal diffusion nature of heat propagation, and its sensitivity decreases with increasing material thickness or with defects located deep beneath the surface. Conversely, Lamb Wave inspection suffers from complex propagation behaviour in anisotropic and heterogeneous materials such as CFRPs, often leading to ambiguous or incomplete defect characterisation. Wave mode conversion, dispersion, and scattering can significantly affect signal interpretation, especially in the presence of geometrical complexity or stiffness variations [12,13].

The present work proposes a quantitative fusion approach applied to CFRP samples with known delamination features. Thermal diffusivities are extracted from IRT cooling curves, while Root Mean Square (RMS) energy values are calculated from Lamb Wave measurements to assess internal damage. The study includes a variety of sample configurations, incorporating different layups, thicknesses, and delamination types. Particular attention is paid to lightning-strike-induced delaminations, which represent a challenging case due to complex damage morphology and depth.

The paper is organised as follows: Section 2 presents the experimental samples structure and their manufacturing process, particularly the insertion of defects. Section 3 describes the experimental, data acquisition and data extraction process for the two NDT methods used in the study: IRT and UT. Section 4 details the Data Fusion methodology. The results of the study are presented and discussed in Section 5. Finally, Section 6 concludes the study and proposes directions for future work.

2 EXPERIMENTAL SAMPLES

Three types of CFRP samples were investigated in this study, as shown in Fig. 1.
The stiffened plates LW50S and LW75S are 450 × 450 mm² CF/epoxy laminates (T800S/3900-2B, autoclave-cured at 180 °C) with a quasi-isotropic 8-ply lay-up [45/0/–45/90]s. A central stiffened area (100 × 450 mm²) was created by adding eight plies with a [-45/0/45/0]s lay-up. Artificial delaminations were introduced by inserting a Teflon film between the base and stiffened zones, with widths of 50 mm and 75 mm for LW50S and LW75S, respectively.
The flat plates LW16 and LW32, also 450 × 450 mm² and made from the same CF/epoxy system, consist of 16 and 32 plies with lay-ups $[45/0/–45/90]_{2s}$ and $[45/0/–45/90]_{4s}$, respectively. LW16 contains Teflon-based delaminations of various sizes (10 to 50 mm), while LW32 includes delaminations at different depths (from 8 to 24 plies).
Finally, LS1 and LS2 are 150 × 150 mm² plates made of plain weave carbon fabric and a conductive Polyaniline/Phenol (PDPD) resin, as described in [14], with a $[0/90]_{10}$ lay-up. Artificial lightning strike tests were performed using −100 kA peak current pulses, leading to surface swelling in circular areas of about 30 mm diameter. These damaged zones are later segmented into three subregions based on thermographic imaging: a black ring, a white ring, and a grey centre.

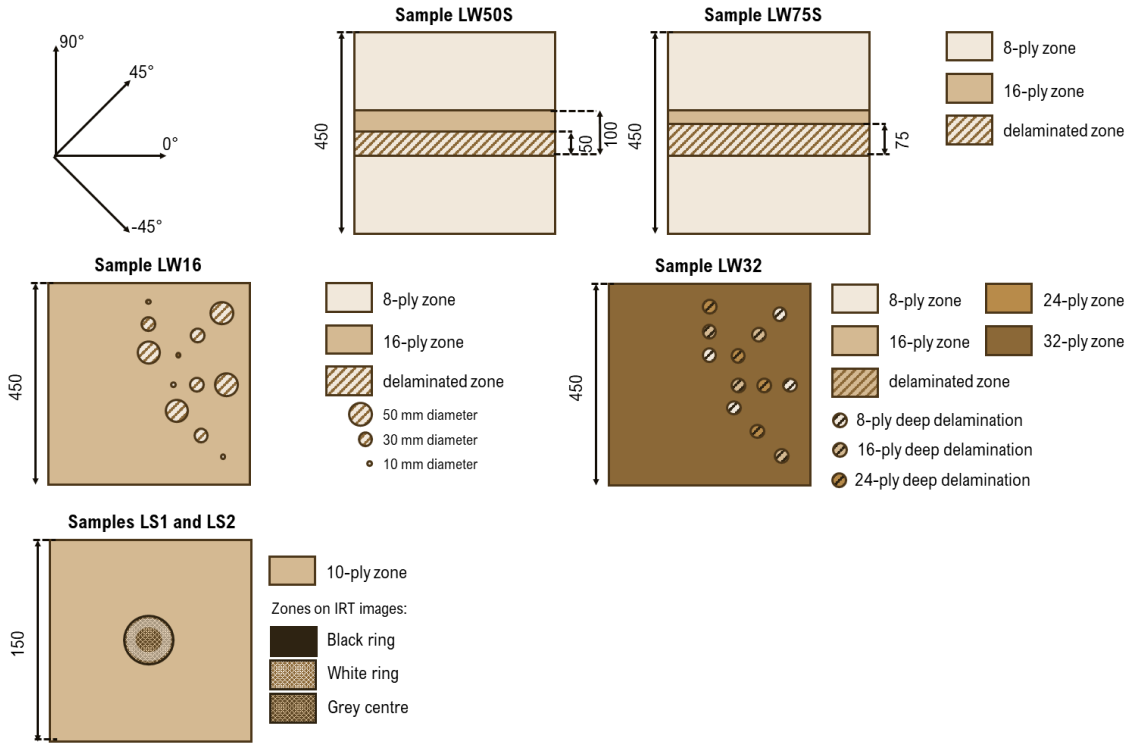

Fig. 1: Experimental samples' configuration representation (top view)

3 NON-DESTRUCTIVE TESTING

3.1 InfraRed Thermography (IRT)

3.1.1 Experimental system

The InfraRed Thermography system used in this study is the Active Pulse Thermography setup from Echotherm Thermal Wave Imaging [15]. It consists of a hood enclosing the inspected area, equipped with a high-energy flash lamp and a FLIR SC4000 infrared camera, connected via an umbilical cable to a mobile control unit containing the flash power source, a sample support, and a computer running MOSAIQ 4.2 analysis software.

For the inspection, the sample is positioned on the dedicated support and the hood is placed directly above it to ensure consistent illumination and thermal capture. Due to their large surface area, samples LW50S, LW75S, LW16 and LW32 were inspected in four successive scans (upper left, upper right, lower left, and lower right). A flash pulse of 30 ms is emitted for each scan, after which surface temperature evolution is recorded for a duration T_{shot} at 300 frames per second by the infrared camera. The acquired thermographic data are then post-processed to generate Thermographic Signal Reconstruction (TSR) cartographies.
In this study, log–log cooling curves were extracted at selected points across the sample surfaces from these TSR maps in order to estimate the thermal diffusivity α.

3.1.2 Data extraction

To evaluate the thermal behaviour of the CFRP samples, thermal diffusivity α was selected as the key parameter, as it reflects the material's ability to conduct heat relative to its capacity to store it. For each sample, log–log cooling curves were extracted from TSR cartographies at selected measurement points, allowing the determination of α based on the breaking time T_{break}, based on the relation:

$$\alpha = \frac{t^2}{\exp(T_{break})} \quad (1)$$

With t the thickness of the material and T_{break} the breaking time of the cooling curve, as shown in the Fig. 2.
The measurement points are selected for each sample depending on their configuration, in order to compare thermal behaviour in different zones such as delaminated zones and healthy zones, or zones of different thicknesses. On the stiffened samples (LW50S and LW75S), measurement points were positioned in zones of varying thickness (8-ply, 16-ply) and above the artificial delamination, with twelve and ten points respectively. For the small delamination plates (LW16 and LW32), sixteen points were selected across healthy areas and Teflon-inserted defect zones. Finally, on the lightning-strike-damaged samples (LS1 and LS2), the analysis focused on four distinct zones identified from the TSR images and represented in Fig.1: the healthy background, a peripheral "black ring", an intermediate "white ring", and a central "grey zone."
Fig. 2 shows an example of IRT results obtained from this method for LW75S sample, with a) the localisation of measurement points (different colours and shapes representing different zones of interest), b) the log-log curves extracted from each of these measurement point with an example of determination of T_{break} and c) the thermal diffusivities obtained from equation (1) using the measured T_{break}. In all cases, thermal diffusivity values were calculated with associated uncertainties, using a recording duration T_{shot} = 9.3 s and a frame rate of 300 fps. This localised quantification of α enables the identification of material heterogeneities and delamination-affected areas, offering a more informative characterisation than surface temperature mapping alone. Fig. 3 shows the thermal diffusivities calculated for all measurement points of each sample, along with a localisation of these points.

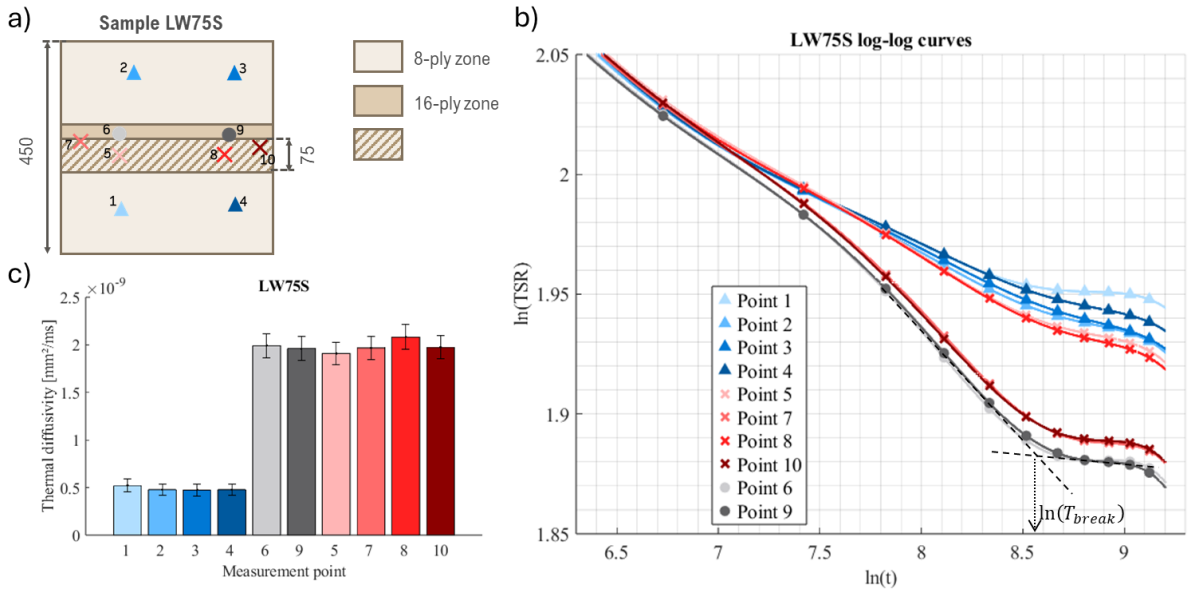

Fig. 2: IRT data obtained for sample LW75S with a) measurement points localisation, b) log-log curves with demonstration of T_{break} and c) thermal diffusivities calculated

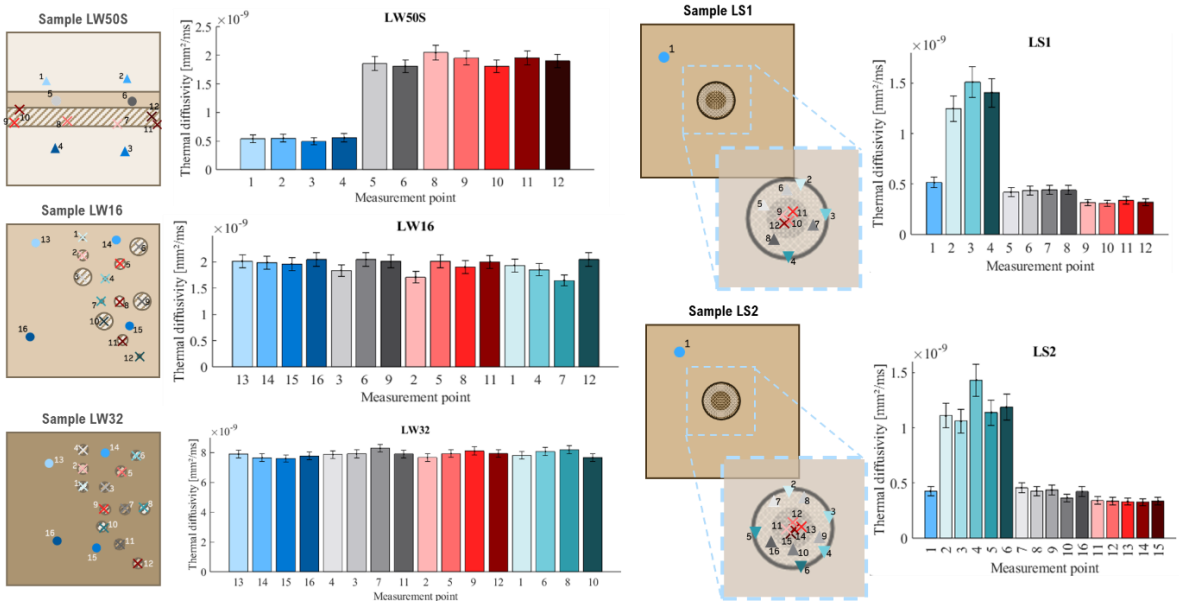

Fig.3: Results of IRT data for all experimental samples

3.2 Lamb Waves

3.2.1 Experimental system

This study uses a fully non-contact system to extract Lamb Wave propagation data from the experimental samples. The excitation is performed using a Laser Induced Plasma Shock Wave (LIPSW) setup, based on a SURELITE III-10 Nd:YAG laser (5 ns pulse, 1064 nm wavelength, 9.5 mm beam diameter, 850 mJ energy), focused through a plano-convex lens. At a standoff distance d = 10 mm from the surface, a plasma is generated and the associated shock waves, encountering the surface, are the source of Lamb Waves propagation along the experimental plate. The response is measured using a

Scanning Laser Doppler Vibrometer (SLDV). For samples LW50S, LW75S, LW16 and LW32, a Polytec PSV-500 system (He-Ne laser, 0–20 m/s velocity range) was used, while the new-generation Polytec Q-tec system was employed for LS1 and LS2. The experimental setup used in this study has been widely described in [13].

3.2.2 Data extraction

Lamb Wave propagation was measured over predefined zones on each sample using point-by-point acquisition with the SLDV system. For the stiffened samples (LW50S and LW75S), a 200 × 200 mm² central area was scanned with a 2 mm spatial step in both directions, resulting in 10,201 points, each recorded over 0.8 ms at 2.56 MHz. The resulting data formed a matrix of 10,201 columns (measurement points) by 2048 rows (time samples). For the flat plates (LW16 and LW32), the scanned area was extended to 400 × 400 mm² to cover nearly the entire surface, using the same 2 mm spatial resolution. Each point was recorded over 1.6 ms at 3.125 MHz, resulting in matrices of 40,401 points × 5000 time samples. For the lightning strike samples (LS1 and LS2), the scanned area was set to 140 × 140 mm², again with 2 mm resolution. Signals were recorded for 1 ms at 3.125 MHz, yielding matrices of 5041 columns × 3125 rows.
To quantify the signal energy at each point, the Root Mean Square (RMS) value was computed using the standard formula:

$$RMS = \sqrt{\frac{1}{n}\sum_{i=1}^{n} {S_i}^2} \tag{2}$$

Where S_i is the signal amplitude at time step i, and n is the total number of time samples.
The RMS values represent the average energy of the Lamb Wave signal at each surface point. High RMS values may indicate energy concentration due to reflections, scattering from defects, or local changes in wave amplitude, potentially linked to delaminations or thickness variations. Conversely, low RMS values suggest attenuation or limited interaction with structural features. These values are mapped across the scanned areas to generate RMS cartographies, shown in Fig. 4.

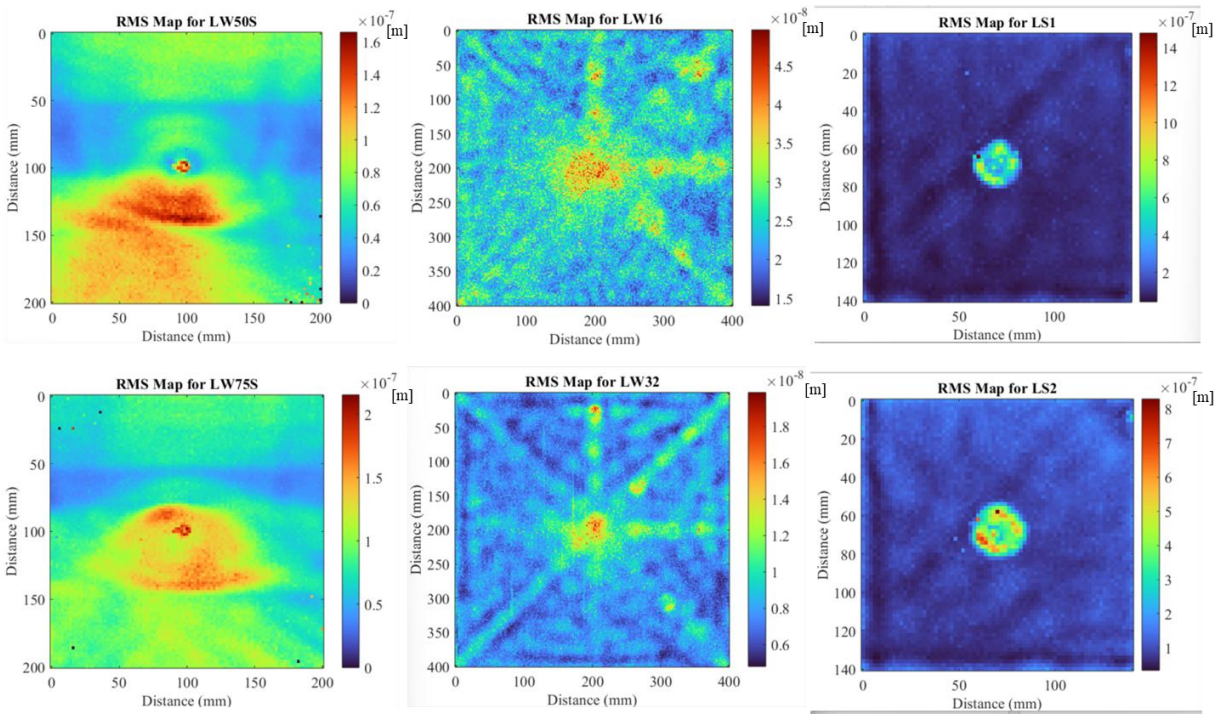

Fig. 4: RMS cartographies obtained for all experimental samples

4 DATA FUSION

Data fusion is a powerful approach for integrating multiple sources of information to enhance the reliability and interpretability of defect detection. In this study, a feature-level fusion strategy is used, inspired by similar approaches in Structural Health Monitoring (SHM) . The goal is to combine the quantitative outputs from InfraRed Thermography (thermal diffusivity α) and Lamb Wave inspection (RMS energy) to enable a richer characterisation of the inspected CFRP samples [4–10].
The method consists of plotting the thermal diffusivity values (obtained from IRT) against the RMS values (extracted from Lamb Wave measurements) in 2D scatter plots, with each point representing a measurement location on the sample. This bivariate representation allows the emergence of clusters corresponding to different zones or damage types. In contrast to a single-parameter analysis, the combined view enhances the separation between structural states that may not be distinguishable using one method alone. This is particularly useful when one modality provides ambiguous information due to physical limitations (e.g., depth sensitivity in IRT or propagation noise in Lamb Waves).
The results of the data fusion process are presented and discussed in the following section.

5 RESULTS AND DISCUSSION

The data fusion results are shown in Fig. 5 for LW50S, LW75S, LW16 and LW32, and in Fig. 6 for LS1 and LS2. In LW50S and LW75S, measurement points were grouped into three zones: i) 8-ply healthy areas, ii) 16-ply healthy areas, and iii) delaminated areas in the stiffened region.
Thermal diffusivity was calculated point-by-point from IRT data, while RMS values were averaged per zone due to the smaller acquisition area of Lamb Wave scans. Fig. 5 shows a clear separation of these three groups. Interestingly, the 8-ply zones split into two clusters depending on their position relative to the wave excitation point. This difference, captured only by Lamb Waves, illustrates that signal amplitude is influenced not only by the local structure but also by the path of propagation through the delamination.
In LW16 and LW32, 16 points were analysed across healthy and defective areas with varying defect sizes (10–50 mm) and depths (8–24 plies). As shown in Fig. 5, the fusion reveals only a weak separation between healthy and damaged zones. The Lamb Waves data show a slight drop in RMS for delaminated regions, but no clear differentiation is observed across different defect sizes or depths. This highlights a limitation of both methods when applied to small or subtle delaminations.
The damage in LS1 and LS2 exhibits a visible surface deformation and distinct thermal patterns in IRT. Based on the thermographic images, four zones were identified: healthy background, black ring, white ring, and grey centre. Using the same zone segmentation, the scatter plot in Fig. 6 shows that fusion enables a clearer distinction between zones than either method alone. For example, Lamb Waves can separate the grey centre from the healthy background, while IRT alone could not, likely due to thickness variations. Conversely, IRT captures distinct behaviour in the black ring, which is poorly resolved by Lamb Waves due to its narrow geometry and possible interference effects.
IRT provides information about surface-level heat diffusion, while Lamb Waves probe internal mechanical properties through guided wave propagation. In the stiffened and lightning-strike samples, the combination of both offers complementary insights:

(i) IRT resolves thickness variations and localised heating effects,
(ii) Lamb Waves highlight stiffness reductions due to delaminations.

In contrast, both methods struggle with small artificial delaminations, where signal changes are less pronounced and easily masked by measurement noise or geometric variability.
The apparent increase in thermal diffusivity in thicker areas, despite α being theoretically independent of thickness, is likely due to heat conduction through the metal support base. As thickness increases, thermal losses to the base decrease, leading to artificially higher α values. This phenomenon is especially visible in LW50S and LW75S and must be considered when interpreting thermal data.
In the lightning strike samples, the extreme energy conditions cause local material transformations such as carbonisation, porosity or microcracking which significantly alter both thermal and mechanical responses. This explains the high diffusivity observed in the black ring and the strong Lamb Wave scattering in the central defect.

Finally, the study demonstrates that the data fusion approach effectively compensates for the limitations of each method, providing a more nuanced picture of the internal damage, particularly in complex or multi-zone configurations.

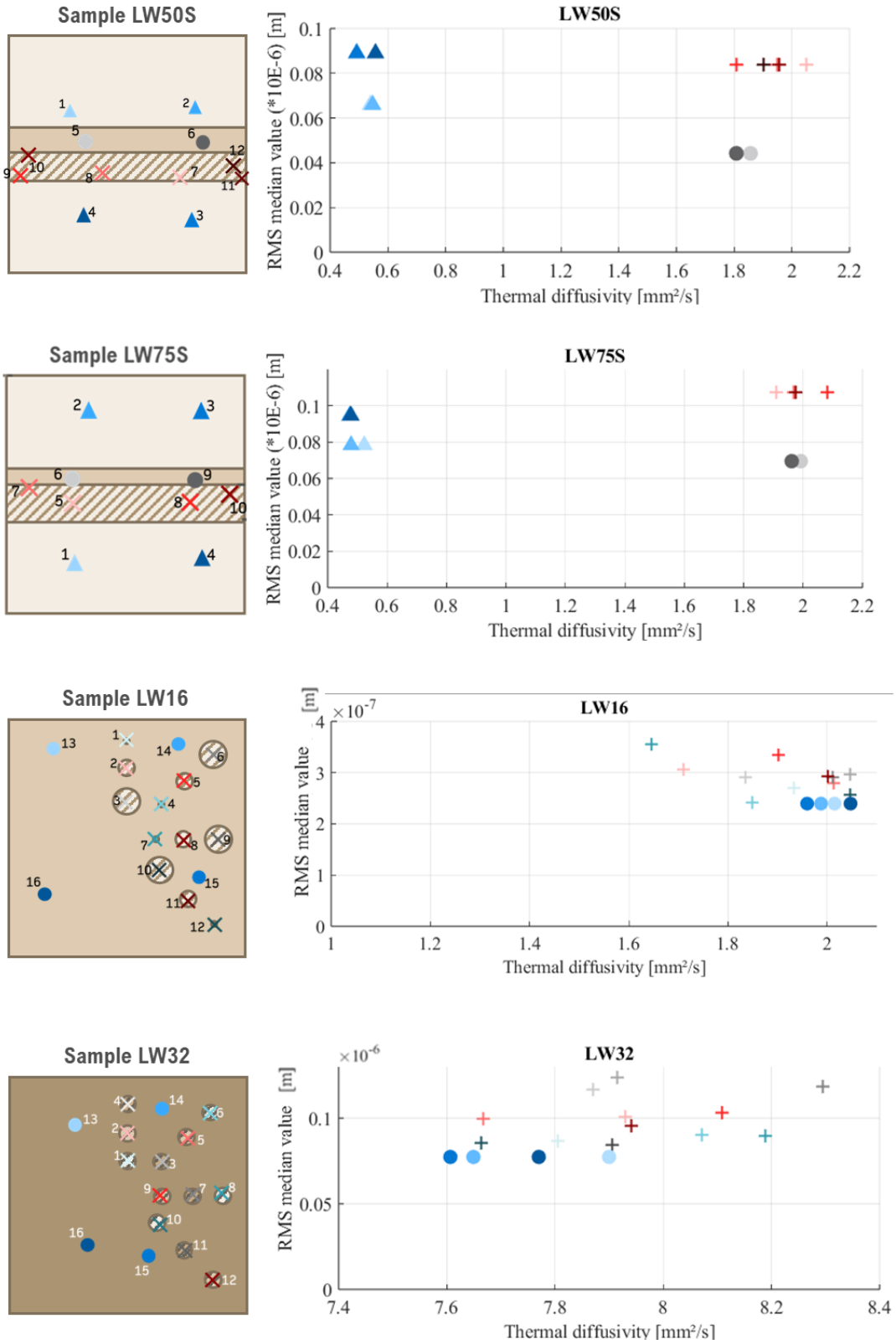

Fig. 5: Data fusion results for LW50S, LW75S, LW16 and LW32 (from top to bottom)

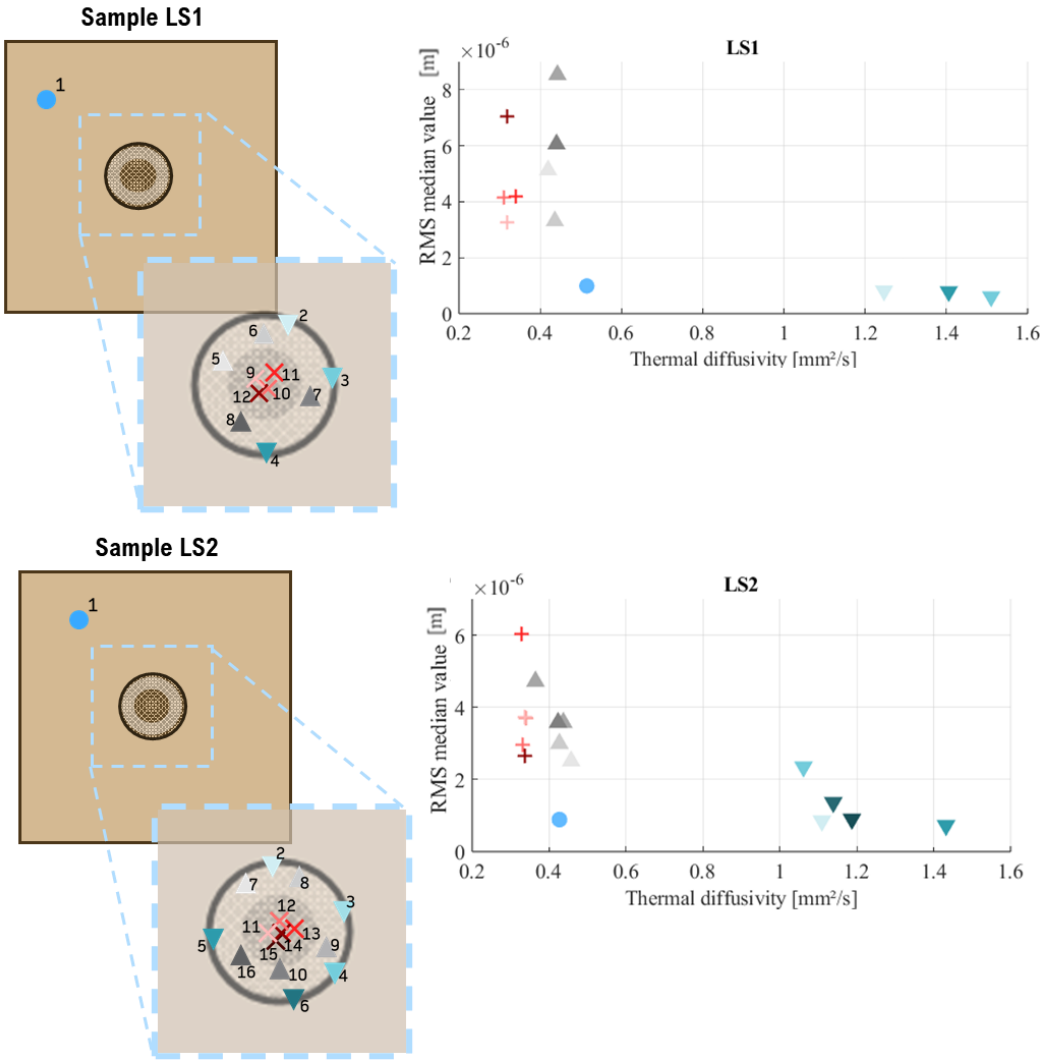

Fig. 6: Data fusion results for LS1 and LS2 (top to bottom)

6 CONCLUSION

In this study, the combination of InfraRed Thermography (IRT) and Ultrasonic Lamb Wave inspection through a data fusion approach for the characterisation of delaminations in CFRP composites has been investigated. Each technique, based on distinct physical principles, offers valuable yet partial insight into the material's condition: IRT is sensitive to surface and near-surface thermal behaviour, while Lamb Waves provide information related to internal mechanical changes. However, both face limitations when used independently, particularly in cases involving complex geometries, variable thicknesses, or subtle defect signatures.

By jointly analysing thermal diffusivity (from IRT) and RMS energy (from Lamb Waves) through feature-level fusion, the proposed method enabled a more comprehensive interpretation of damage patterns. The results demonstrated a clear benefit for samples with complex internal structures, especially stiffened panels and lightning-strike-induced damage, where single-method inspections either failed to differentiate certain zones or produced ambiguous data.

In contrast, the fusion method was less effective for small artificial delaminations, where both techniques showed limited sensitivity to variations in size or depth. These results suggest that the approach remains dependent on the physical detectability of the defect by at least one modality, and that further improvements are needed in signal acquisition and processing to enhance sensitivity to fine-scale

damage.
Beyond the immediate results, this study highlights the potential of multimodal NDT as a step towards more quantitative and integrated material characterisation. Moving beyond binary “healthy/defect” classifications, data fusion offers a promising avenue for future inspection strategies in complex composite structures, with applications in both quality control and structural health monitoring. Further work will aim to refine the methodology, explore alternative fusion strategies, and extend the study to more complex configurations and real-world defect scenarios.

ACKNOWLEDGEMENTS

The current research project has been funded by the Japan Society for the Promotion of Science under the Grant-in-Aid for Scientific Research programs (Grant No. JP22H01692). The authors acknowledge Mr. Tonegawa Shota, Mr. Mita Masakatsu and Mr. Suyama Mamoru from the Shibaura Institute of Technology for their great support in the realisation of Lamb Waves experiments, and Mr. Yu Zhou and Mr. Kamiyama Shintaro for their important expertise regarding the Lightning Strike experiments.

REFERENCES

[1] Hellier CJ, editor. Handbook of Nondestructive Evaluation [Internet]. 3rd Edition. New York: McGraw-Hill Education; 2020. Available from: https://www.accessengineeringlibrary.com/content/book/9781260441437

[2] Scott IG, Scala CM. A review of non-destructive testing of composite materials. NDT Int. 1982 Apr;15(2):75–86.

[3] Beaumont P, Soutis C. The Structural Integrity of Carbon Fiber Composites, Fifty Years of Progress and Achievement of the Science, Development, and Applications. The Structural Integrity of Carbon Fiber Composites: Fifty Years of Progress and Achievement of the Science, Development, and Applications. 2016. 1 p.

[4] Hassani S, Dackermann U, Mousavi M, Li J. A systematic review of data fusion techniques for optimized structural health monitoring. Inf Fusion. 2024 Mar;103:102136.

[5] Eleftheroglou N, Zarouchas D, Loutas T, Alderliesten R, Benedictus R. Structural health monitoring data fusion for in-situ life prognosis of composite structures. Reliab Eng Syst Saf. 2018 Oct;178:40–54.

[6] Klein L. Sensor and data fusion: A tool for information assessment and decision making: Second edition. 2012. 1 p.

[7] Gros XE, Bousigue J, Takahashi K. NDT data fusion at pixel level. NDT E Int. 1999 Jul;32(5):283–92.

[8] Shrestha R, Kim W. Non-destructive testing and evaluation of materials using active thermography and enhancement of signal to noise ratio through data fusion. Infrared Phys Technol. 2018 Nov;94:78–84.

[9] Jin X, Jiang Q, Yao S, Zhou D, Nie R, Hai J, He K. A survey of infrared and visual image fusion methods. Infrared Phys Technol. 2017 Sep;85:478–501.

[10] Wei Y, Ding L, Han Y, Luo Y, Su Z, Zhang D. Characterizing defects in materials with fusion of thermography and shearography. Measurement. 2021 Sep;182:109736.

[11] Wang Z, Pei C, Zhang Z, Chen Z. Quantitative test of delamination defects in CFRP with surface interference by laser thermography. Infrared Phys Technol. 2024 Jan;136:105046.

[12] Guo N, Cawley P. The interaction of Lamb waves with delaminations in composite laminates. J Acoust Soc Am. 1993;94(4):2240–6.

[13] Hosoya N, Mita M, Lecointre LAC, Tonegawa S, Higuchi R, Yokozeki T, Takeda S ichi. Lamb waves evaluation in CFRP plates with laser shock wave technique. Structures. 2023 Dec;58:105566.

[14] Zhou Y, Raghu SNV, Kumar V, Okada T, Yokozeki T. Simulated lightning strike investigation of CFRP comprising a novel polyaniline/phenol based electrically conductive resin matrix. Compos Sci Technol. 2021 Sep;214:108971.

[15] Echotherm Thermal Wave imaging [Internet]. Available from: https://blog.thermalwave.com/echotherm-product-sheet

ICCM24 24TH INTERNATIONAL CONFERENCE ON COMPOSITE MATERIALS
AUG 4-8, 2025 • BALTIMORE CONVENTION CENTER • BALTIMORE, MARYLAND

HIT/MISS PROBABILITY OF DETECTION FOR ARTIFICIAL DEFECTS IN DISCONTINUOUS LONG FIBER COMPOSITES VIA TRANSIENT INFRARED THERMOGRAPHY

Marco Didonè[1], Oleksandr Kravchenko[2] and Sergii Kravchenko[1]

[1] Department of Materials Engineering, The University of British Columbia
6350 Stores Rd, V7R 2M2, Vancouver, BC, Canada
Email: marco.didone@ubc.ca, web page: http://mtrl.ubc.ca

[2]Department of Mechanical & Aerospace Engineering, Old Dominion University
5115 Hampton Blvd, Norfolk, VA, USA
Email: okravche@odu.edu, web page: https://www.odu.edu/

Keywords: Discontinuous Long Fiber Composites, Non-Destructive Testing, Probability of Detection, Infrared Thermography

ABSTRACT

The inspection of discontinuous long fibre-reinforced plastic composites (DLFRPCs) presents significant challenges due to the stochastic nature of their meso-structure, particularly in detecting subsurface defects that may compromise performance in critical applications. Traditional non-destructive testing (NDT) methods struggle with the variability introduced by randomly oriented fibre strands, necessitating more advanced techniques to ensure reliable detection across varying defect depths and sizes. This study investigates the use of transient infrared thermography (T-IRT), employing halogen lamp heating, to detect subsurface voids and inclusions in DLFRPCs. T-IRT offers rapid full-field inspection and the ability to highlight thermal gradients associated with defects, making it well-suited for heterogeneous materials. Compression-molded plates (5×5 inches, 2.5 mm thick) composed of 0.25×2-inch unidirectional prepreg platelets were used. The orientation and placement of individual platelets resulted in non-uniform thermal responses, complicating defect detection and precluding the definition of a representative "sound" region. To address this, artificial defects in the form of flat-bottom holes (FBHs) were introduced at controlled depths and diameters. A pre/post scan approach was developed to calculate corrected thermal contrast at each FBH location, isolating defect-related signals from background variability. Defect detection was defined by a contrast threshold, and binary outcomes were analyzed using logistic regression within a hit/miss Probability of Detection (POD) framework. POD curves were generated to evaluate the influence of defect size on detectability. The results show that increasing defect diameter correlates with higher detection probability, as expected. However, the transition in detection is more gradual than in typical CFRP inspections, and confidence bounds are broader, attributed to the stochastic mesostructure of the DLFRPCs and associated signal variability. The pre/post scan method enabled robust contrast evaluation without relying on reference sound areas, a key contribution for defect quantification in complex materials. The findings demonstrate the feasibility of T-IRT combined with statistical POD for characterizing subsurface damage in DLFRPCs. This approach provides a foundation for optimizing inspection protocols and supports broader application of thermography in automotive and aerospace composite evaluation.

1 INTRODUCTION

Non-Destructive Testing (NDT) techniques are important for quality assurance and structural health monitoring in advanced composite materials [1]. Among these, Infrared Thermography (IRT) offers significant advantages due to its rapid, contactless inspection capability, particularly for identifying subsurface anomalies [2]. When applied in a transient mode, Transient Infrared Thermography (T-IRT), the method captures thermal diffusion responses following controlled heating, enabling the detection of internal features such as voids, delaminations, or inclusions. Discontinuous Long Fibre Reinforced Composites (DLFRPCs), such as platelet-molded carbon fibre systems, present unique challenges for NDT. Their highly stochastic mesostructure, characterized by randomly distributed and oriented fibre bundles, leads to significant variability in thermal behavior. This complicates defect detection and reduces the reliability of traditional contrast-based evaluation methods that rely on reference regions with uniform properties. To address these challenges, there is a need to quantify the detection performance of T-IRT in LDFCs using robust statistical frameworks. Probability of Detection (POD) analysis is the standard method to quantify the reliability of NDT techniques. Two common approaches exist: the continuous response method, ($\hat{a}$ vs. a) [3] ,and the binary classification method, hit/miss [4], which is used for this work.

This work presents a comprehensive POD analysis for simulated defects in compression-molded long discontinuous fibre composites inspected via T-IRT. A rigorous methodology is adopted, including the manufacturing of defect-free plates, precise machining of flat-bottom holes (FBHs) as artificial defects, execution of front-side transient thermography using halogen lamp excitation, and advanced signal processing through Thermal Signal Reconstruction (TSR) and a custom signal-to-noise ratio (SNR) classification approach. Detection reliability is quantified using a hit/miss POD framework, where a binary classification threshold is applied to matched pre- and post-drilling thermographic responses. Statistical confidence bounds are established using a logistic regression model and the delta method. The results provide new insights into the capabilities and limitations of T-IRT for inspecting LDFCs and offer practical guidance for improving defect detectability in materials with inherently random mesostructure.

2 MATERIAL SYSTEM AND PLATE MANUFACTURING

The composite plates used in this study were manufactured from XForge™ VZ TDS, a long discontinuous carbon fiber reinforced epoxy prepreg supplied by DowAksa. This material is designed for isothermal compression molding at 150°C with rapid cure cycles under 3 minutes for parts under 9.5 mm thickness. The randomly distributed platelets give rise to a highly stochastic meso-structure. Plate fabrication was carried out at Old Dominion University (ODU) under controlled conditions (see Fig. 1a). Each plate was initially molded within a 5 × 5-inch (127 × 127 mm) aluminum tool (see Fig. 1b). After curing, the plates were trimmed to final dimensions of 4 × 4 inches (101.6 × 101.6 mm) to remove edge effects and ensure dimensional uniformity. The nominal thickness of all plates was 2.5 mm, with an actual measured mean of 2.579 mm and a standard deviation s = 0.119 mm. These results confirm good geometric consistency, which is important for reliable thermographic and statistical analysis, especially considering the mold charging process is non-trivial due to the semi-preg format of the material, which requires careful manual placement. Once an optimized process was established, all subsequent plates were subjected to both IRT and UTPA prior to further processing. Only plates confirmed to be free of internal defects via UTPA were retained for testing. A total of eleven defect-free plates were selected based on these criteria. Following inspection, artificial defects were introduced in the form of Flat-Bottom Holes (FBHs), precisely machined into the back surface of each plate. These FBHs serve as controlled defect simulants with known geometries, enabling the quantification of detection capability through thermographic contrast analysis.

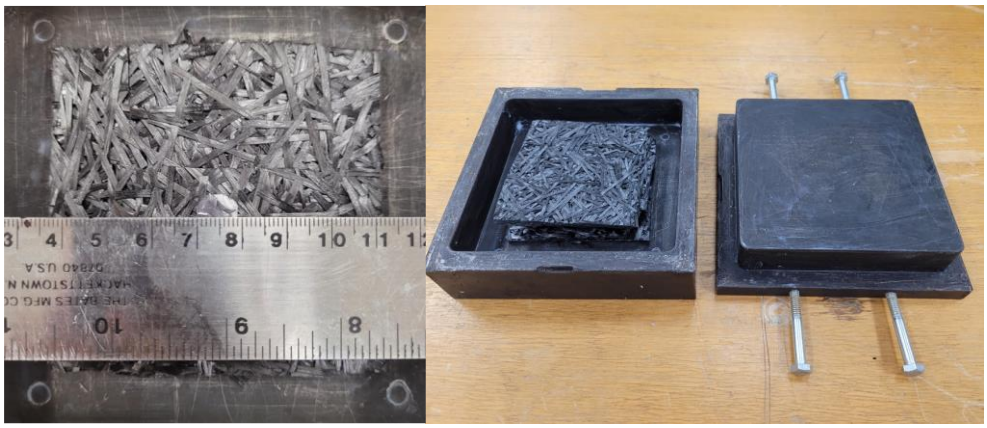

a) b)

Figure 1. a) Detail of the material after cutting b) Material placed in the 5x5 in mold.

3 DEFECT SIMULATION USING FLAT BOTTOM HOLES (FBHS)

In POD studies, artificial defects are introduced to replicate damage modes such as delaminations or voids commonly observed in impacted or poorly consolidated composites [5]. In this work, artificial defects were implemented using Flat-Bottom Holes, selected over other options such as Teflon inserts. While Teflon inserts are often used to simulate delaminations in traditional composite laminates, they proved unsuitable for DLFRPCs manufactured via hot press compression molding. During pressing, inserts tend to shift from their intended positions due to resin and fiber flow and are distorted as they become entangled within the disordered fiber bundles. This results in unpredictable geometries and locations, conditions that are incompatible with quantitative and repeatable defect detection studies.

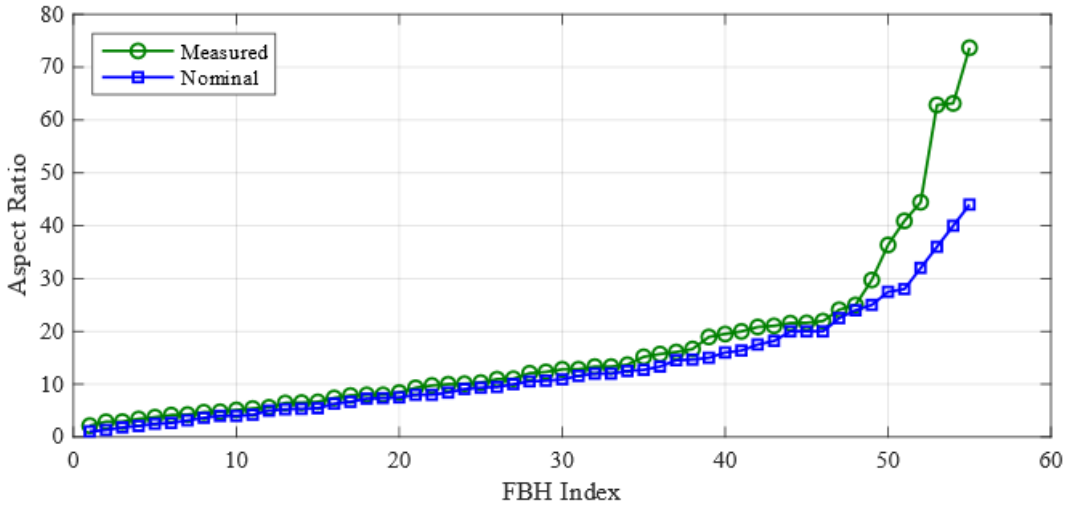

Figure 2. Flat bottom hole (FBH) index versus aspect ratio for the 55 simulated defects used in this study. This image show comparison between measured and nominal values.

In contrast, FBHs can be machined post-curing using precision CNC milling, allowing tight control over defect diameter, depth, and location. This ensures high geometric accuracy and repeatability across samples, making FBHs a reliable and reproducible defect type for thermographic POD evaluation. Due to machining tolerances inherent to the milling process, small variations in FBH depth were expected and confirmed. The

shallowest FBH in each plate (closest to the inspection surface) was designed to maintain a minimum remaining wall thickness of 0.5 mm to prevent breakthrough. Considering potential depth errors of up to ±0.3 mm from the milling setup, this safety margin was necessary. The actual measured depths of these shallowest FBHs ranged from 0.15 mm to 0.45 mm, with a mean value of 0.348 mm and a standard deviation of 0.104 mm. A total of 55 FBHs (Fig. 2) were distributed across 11 plates, consistent with the minimum recommendations outlined in MIL-HDBK-1823A and ASTM E2862. The FBH diameters range from 2 mm to 22 mm, in 2 mm increments, with five depth levels per plate. Each plate contains a unique diameter and five FBHs positioned at nominal depths of 0.5 mm, 0.8 mm, 1.1 mm, 1.5 mm, and 1.9 mm from the front (inspection) surface. This configuration covers a realistic range of subsurface defect scenarios, from easily detectable shallow defects to more challenging deeper ones that may be partially masked by backwall reflections. FBHs were drilled under constant feed and speed conditions using a precision CNC machine to minimize heat-affected zones (see Fig. 3). All dimensions were subsequently verified using a caliper. For example, Plate 001 contains FBHs ranging from 0.15 mm to 0.69 mm in depth, while Plate 011 includes defects from 0.35 mm to 1.82 mm, paired with a 22 mm diameter. Overall, the controlled and fully characterized FBH dataset developed in this study provides a rigorous foundation for assessing the detection performance of the T-IRT system and for quantifying POD in relation to defect geometry and depth.



Figure 3. Flat Bottom Hole plate design. Top: geometric design. Bottom: images of the manufacturing process (left) and the final fabricated plate (right).

4 EXPERIMENTAL SETUP FOR TRANSIENT INFRARED THERMOGRAPHY

Each plate was inspected using a Transient Infrared Thermography setup configured for front-side heating and observation. The DLFRPC material under investigation, presents unique challenges for thermographic evaluation. First, there is limited prior literature on applying IRT to such materials, and second, their inherent local fibre orientation variability introduces significant spatial non-uniformity in thermal behaviour. This makes conventional approaches in POD, where the thermal response over a defect is compared with a neighbouring sound area, unsuitable. Due to the randomness of the fibre orientation distribution (FOD), "sound" zones [6] may exhibit vastly different transient responses depending on local conductivity and heat flow patterns. This limitation is illustrated in Figure 4, which shows two distinct regions on the same plate with different thermal decay curves despite both being defect-free.

To overcome this, a differential inspection approach was implemented. Each plate was scanned twice using T-IRT: once immediately after trimming (baseline condition), and once after FBH drilling. During both

scans, all boundary and measurement conditions were kept constant, including ambient temperature, lamp intensity and position, camera distance, and sample alignment. To further minimize experimental error, four defect-free reference areas on each plate were used to calculate the average first temporal derivative of the thermal signal before and after FBH drilling. This allowed for minor residual normalization and correction, ensuring that contrast changes were attributable to the presence of the artificial defects rather than material variability or setup drift. The final evaluation of detectability was based on the ratio of thermal responses between the same area *before* and *after* - FBH drilling. This comparative metric captures local thermal contrast due to the artificial defect while compensating for the spatial variability inherent in the DLFRPCs.

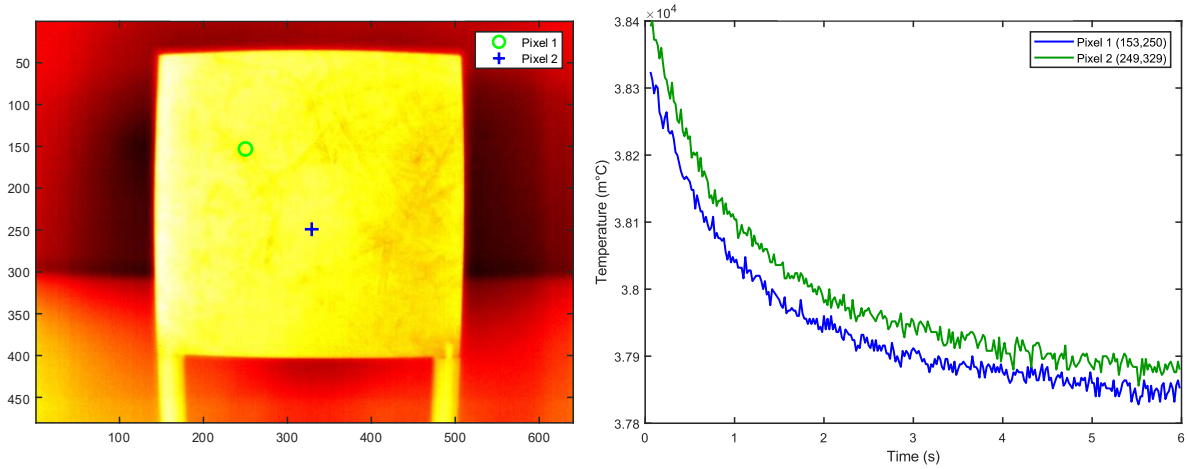

Figure 4. Left: Analyzed pixel locations. Right: Temperature profile of the analyzed pixels.

To enable reproducible and precise alignment between pre- and post-defect scans, a customized 3D-printed fixture was developed to hold the infrared (IR) camera, halogen lamps, and specimen in fixed relative positions (Fig. 5). The fixture allows the specimen to be inserted and removed while preserving a fixed geometry between all components. The plate is held in position on a height-calibrated platform to ensure repeatable distance and centering relative to the optical axis of the camera and illumination sources. The inspection was conducted in Dr. Kravchenko's laboratory at the University of British Columbia using a C-CheckIR system developed by Automation Technology (see Fig. 5). The setup included an IRS x640 NDT uncooled infrared camera equipped with a 12 mm wide lens, providing a thermal sensitivity of 75 mK and a spatial resolution of 640 × 480 pixels. For heating, two 850 W dimmable halogen lamps were used, controlled by an IRX-Box, which synchronized the entire system, including the IR-NDT Transient & Pulse Software Evaluation Module. One of the challenges in T-IRT is interpreting noisy thermal data. To create the final thermal image and improve signal-to-noise ratio and extract meaningful features such as contrast and defect depth, Thermal Signal Reconstruction (TSR) was used. This method computes temperature derivatives with respect to time and was implemented using custom MATLAB scripts based on [7,8].

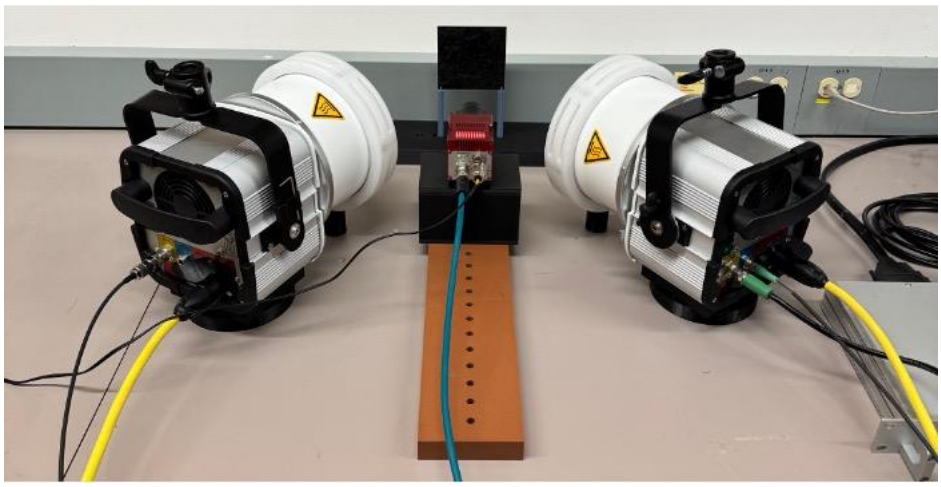

Figure 5. IRT setup

5 STATISTICAL POD ANALYSIS

In POD analysis, two main approaches are typically used: a continuous model based on response data (â vs. a), and a binary hit/miss model [5,9]. Both aim to quantify the likelihood of detecting a defect as a function of size or other damage parameters. The response-based method assumes normally distributed variability in measured signals and derives the POD curve using a cumulative distribution function above a decision threshold. Detailed derivations and assumptions are available in the referenced standards and literature [10]. In this study, the hit/miss approach was selected due to the variability in thermal signal response caused by the stochastic nature of the composite material. A defect was classified as detected when the corrected local thermal contrast exceeded a defined threshold. The resulting binary outcomes were analyzed using logistic regression, and confidence bounds were computed using the delta method. This section describes the model selection, parameter estimation, and interpretation of results based on this approach.

5.1 Hit/Miss model selection

The hit/miss analysis is a statistical method used when the inspection output is binary, meaning the result for each flaw is either a hit (detected) or a miss (not detected). This approach is especially relevant when the NDT system provides a yes/no decision instead of a continuous signal.

Ordinary linear models assume continuous and unbounded outcomes, with normally distributed residuals. However, hit/miss data are discrete and bounded between 0 and 1. For such data, the residuals follow a binomial distribution, making ordinary least squares inappropriate. Generalized Linear Models (GLMs) resolve this by using a suitable link function to transform the binary outcome into a form compatible with linear modeling.

In hit/miss analysis, a flaw is classified as detected if the signal exceeds the threshold; otherwise, it is missed. This approach is particularly robust when response measurements are not reliably quantifiable, which may occur in materials such as DLFRPCs with complex, stochastic microstructures.

Several link functions are available to model PoD as a function of flaw size a:

Logit (log-odds)
$$POD(a) = \frac{1}{1 + exp(-Xf)} \quad (1)$$

Probit (log-normal)		$POD(a) = \Phi(Xf)$	(2)
Complementary (cloglog)	log-log	$POD(a) = 1 - exp\big(-exp(Xf)\big)$	(3)
Log-log		$POD(a) = exp\big(-exp(-Xf)\big)$	(4)

Where $Xf = \beta_0 + \beta_1 \cdot \ln(a)$ is a linear function of the explanatory variable. $\Phi(\cdot)$ denotes the standard cumulative distribution function.

The choice of link function impacts the shape of the PoD curve and the estimated $a_{90/95}$. Symmetric links (logit and probit) are preferred for symmetric data, while skewed data may be better modeled with cloglog (left-skewed) or log-log (right-skewed) links. In practice, logit and probit yield similar results for well-behaved data.

To estimate the parameters of the POD model, Maximum Likelihood Estimation (MLE) was used to fit a logistic regression to the binary hit/miss data. The model relates the probability of detection to flaw size, and the log-likelihood function was optimized to determine the intercept and slope. A key performance metric is $a_{90/95}$, defined as the smallest flaw size detectable with 90% probability at 95% confidence. Confidence intervals were computed using the delta method, which propagates uncertainty from the fitted model parameters to the POD curve through partial derivatives and the variance–covariance matrix. The $a_{90/95}$ was obtained by solving for the lower 95% bound of the POD curve at 90% probability. This approach follows the procedure outlined in the ASM Handbook [10] and remains widely adopted for its efficiency and robustness. Alternative methods such as Bayesian inference or bootstrapping may be used in cases with limited data or non-ideal model assumptions.

5.2 Defect Classification and POD Curve Interpretation

To select an appropriate detection threshold ϕ_{dec} and classify defects for hit/miss POD analysis, a custom signal-to-noise ratio approach was developed. This method compares thermal contrast at the same physical location before and after FBH insertion. The objective is to isolate the defect-related signal while minimizing the impact of stochastic background variation and environmental factors (e.g., ambient temperature, lamp distance, humidity).

The local thermal contrast change at the defect site is computed as:

$$\Delta\phi = \phi_{post} - \phi_{pre}$$

where ϕ_{post} and ϕ_{pre} represent thermal contrast in the same region of interest (ROI) in the post- and pre-drilling scans, respectively. To compensate for global changes in experimental conditions, the average contrast change in unaffected reference regions $\Delta\phi_{ref}$ is subtracted:

$$\Delta\phi_{corrected} = \Delta\phi - \Delta\phi_{ref}$$

A defect is marked as detected if the corrected contrast change exceeds the detection threshold:

$$\Delta\phi_{corrected} \geq \phi_{dec}$$

A threshold $\phi_{dec} = 1.2$ was selected based on values commonly used in thermographic NDT studies (typically ranging from 1.2 to 1.5 for TSR and phase-based metrics [5,11]) and was empirically validated to balance sensitivity and false positive rate.

This approach enables robust defect classification without relying on assumptions of spatial uniformity or Gaussian noise distribution. It is particularly suitable for composites like DLFRPC, where random fiber

orientation and local mesostructure variation can compromise traditional referencing methods. By leveraging spatially aligned pre/post scan data, this method provides a consistent basis for classification under realistic noise conditions.

5.3 POD Analysis and Results

The resulting POD curve from the hit/miss classification is shown in Figure 6. The model demonstrates the expected increase in detection probability with increasing FBH size. However, the curve exhibits a relatively shallow slope and wide confidence bound, indicating variability in thermal contrast response for defects of similar size. This behaviour is attributed to the stochastic mesostructure of DLFRPCs, where local fibre orientation, platelet overlap, and resin-rich zones lead to non-uniform heat flow. These effects introduce background fluctuations that degrade defect signal repeatability and widen the statistical uncertainty of detection.

The estimated 90% detection threshold (a_{90}) was reached at an FBH ratio of approximately 22, indicating that defects of this size were detected with high probability under the current inspection conditions. However, the 90% detection at 95% statistical confidence ($a_{90/95}$) was not achieved within the tested flaw size range. This outcome highlights a key limitation in applying classical POD assumptions to random-fiber composites: material heterogeneity imposes a fundamental constraint on statistical detectability. This limitation arises not from deficiencies in the inspection method, but from inherent variability in the composite's mesostructure.

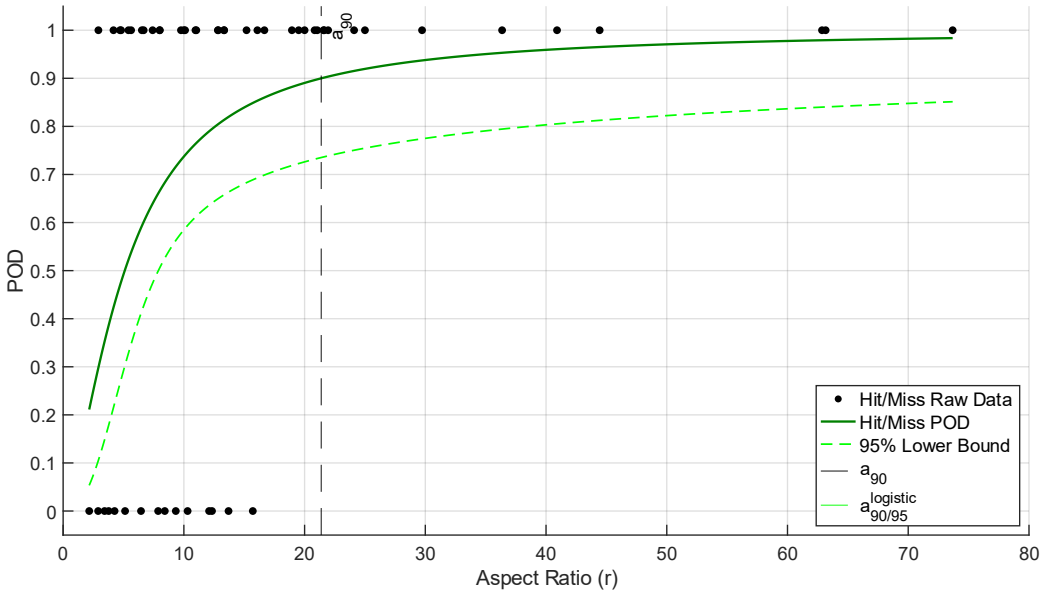

Figure 6. POD curve from the hit/miss classification.

Despite these challenges, the study demonstrates that robust thermographic POD analysis is feasible when adapted methodologies are employed. The pre/post scan approach with SNR-based classification provides a reliable framework for inspection in non-uniform composites.

6 CONCLUSIONS

A DLFRPC specimen containing 55 Flat Bottom Holes distributed across 11 plates was inspected using Transient Infrared Thermography. To address the lack of thermally uniform regions, a common limitation in randomly structured composites, a pre/post scan methodology was implemented. This approach enabled isolation of defect signals through differential thermal contrast, making it suitable for materials with significant background variability. Defect classification was performed using a custom signal-to-noise metric and hit/miss POD analysis was conducted using a detection threshold of 1.2.

The resulting POD curve exhibited a gradual increase in detection probability with flaw size, as expected. The 90% detection threshold (a_{90}) was reached at an estimated FBH aspect ratio of 22. However, the 90% detection at 95% statistical confidence ($a_{90/95}$) was not achieved within the tested range. This result highlights a key limitation when applying conventional POD models to composites with random internal architecture. In such materials, the assumption of consistent defect detectability breaks down due to the influence of local mesostructure, not shortcomings in the inspection technique itself.

"The relatively shallow slope and wide confidence intervals of the POD curve reflect the stochastic variability in thermal response caused by factors such as random fibre orientation, platelet misalignment, and non-uniform resin distribution. These features affect heat diffusion paths and result in inconsistent thermal contrast at defect sites, differing from those observed in CFRP studies [5,9,10,12].

Despite these challenges, the study demonstrates that reliable thermographic POD assessment is achievable for DLFRPCs when adapted analysis strategies are used. The integration of spatially aligned pre/post scans and contrast-based SNR metrics offers a robust framework for flaw classification in the presence of complex background noise. These findings establish a basis for developing standardized inspection protocols in stochastic composite materials.

Future improvements may include multimodal inspection strategies, such as combining thermography with ultrasonic or X-ray methods, to reduce uncertainty and improve detection confidence.

REFERENCES

[1] Bossi RH, Giurgiutiu V. Nondestructive testing of damage in aerospace composites. Polymer Composites in the Aerospace Industry, Elsevier; 2015, p. 413–48. https://doi.org/10.1016/B978-0-85709-523-7.00015-3.

[2] Elodie P. Non destructive investigation of defects in composite structures by three infrared thermographic techniques n.d.

[3] E07 Committee. Practice for Probability of Detection Analysis for Versus a Data n.d. https://doi.org/10.1520/E3023-21.

[4] E07 Committee. Practice for Probability of Detection Analysis for Hit/Miss Data. ASTM International; n.d. https://doi.org/10.1520/E2862-18.

[5] Duan Y, Servais P, Genest M, Ibarra-Castanedo C, Maldague XPV. ThermoPoD: A reliability study on active infrared thermography for the inspection of composite materials. J Mech Sci Technol 2012;26:1985–91. https://doi.org/10.1007/s12206-012-0510-8.

[6] Avdelidis NP, Gan T-H, Ibarra-Castanedo C, Maldague XPV. Infrared thermography as a nondestructive tool for materials characterisation and assessment. In: Safai M, Brown JR, editors., Orlando, Florida, United States: 2011, p. 801313. https://doi.org/10.1117/12.887403.

[7] Maldague X. Theory and practice of infrared technology for nondestructive testing. New York ; Wiley, 2001.; n.d.

[8] Ibarra-Castanedo C, Maldague X. Pulsed phase thermography reviewed. Quantitative InfraRed Thermography Journal 2004;1:47–70. https://doi.org/10.3166/qirt.1.47-70.

[9] Junyan L, Yang L, Fei W, Yang W. Study on probability of detection (POD) determination using lock-in thermography for nondestructive inspection (NDI) of CFRP composite materials. Infrared Physics & Technology 2015;71:448–56. https://doi.org/10.1016/j.infrared.2015.06.007.
[10] Berens AP. NDE Reliability Data Analysis n.d.
[11] E07 Committee. Practice for Infrared Flash Thermography of Composite Panels and Repair Patches Used in Aerospace Applications n.d. https://doi.org/10.1520/E2582-21.
[12] Kurz JH, Jüngert A, Dugan S, Dobmann G, Boller C. Reliability considerations of NDT by probability of detection (POD) determination using ultrasound phased array. Engineering Failure Analysis 2013;35:609–17. https://doi.org/10.1016/j.engfailanal.2013.06.008.

ICCM24 24TH INTERNATIONAL CONFERENCE ON COMPOSITE MATERIALS
AUG 4-8, 2025 • BALTIMORE CONVENTION CENTER • BALTIMORE, MARYLAND

DEVELOPMENT AND MANUFACTURING OF A CONFORMABLE CFRP TANK DEMONSTRATOR WITH TENSION-STRUT-REINFORCEMENT

E. Gleis[1], S. Rouaidy[1], S. Zaremba[1,2], T. Dickhut[3] and K. Drechsler[1]

[1] Chair of Carbon Composites, Technical University of Munich
Boltzmannstr. 15, 85748 Garching, Germany
Email: elisabeth.gleis@tum.de, web page: https://www.asg.ed.tum.de/en/lcc/

[2] Department of Mechanical, Automotive and Aeronautical Engineering, Munich University of Applied Sciences; Lothstraße 64, 80335 Munich, Germany
Email: swen.zaremba@hm.edu, web page: https://me.hm.edu

[3] Institute of Aeronautical Engineering, University of the Bundeswehr Munich
Willy-Messerschmitt-Straße 1, 82024 Taufkirchen, Germany
Email: tobias.dickhut@unibw.de, web page: https://www.unibw.de/aero

Keywords: Polymer-matrix composites (PMCs); Carbon fibre; Filament winding; Lay-up; Joints/joining; Mechanical testing; Optical microscopy

ABSTRACT

This study investigates the manufacturing and testing of conformable carbon fiber-reinforced polymer tanks with integrated continuous fiber-reinforced tension struts for hydrogen storage applications. Two demonstrator tanks were manufactured using 3D-printed core structures combined with wet filament winding and hand lay-up processes. While the concept demonstrated mechanical integrity under hydrostatic loading, leakage at the interface between the CFRP and aluminum boss, as well as poor laminate compaction in flat regions, revealed existing challenges. The manual forming of the strut ends was time-consuming and resulted in high variability in joint strength. These results highlight the potential of strut reinforcement while emphasizing the need for improved laminate compaction and enhanced strut–wall connection to enable practical applications of conformable composite tanks.

1 MOTIVATION AND BACKGROUND

As climate change progresses, sustainable mobility is becoming increasingly important. In the passenger car sector, battery electric vehicles (BEVs) have become the dominant form of locally emission-free mobility [1–3]. Nevertheless, some manufacturers are additionally pursuing hydrogen-powered fuel cell electric vehicles (FCEVs) to provide an alternative to BEVs [4, 5]. Due to the low production volumes, these vehicles are expensive, which represents a key barrier to broader consumer adoption [3, 6]. A cost-reduction approach is to use the same vehicle architecture for both BEVs and FCEVs. To use the skateboard platform, which is common for BEVs, in FCEVs, the hydrogen storage system must be integrated into a flat installation space in the vehicle underbody [7, 8]. Hydrogen pressure vessels on the market have a cylindrical geometry and are therefore not well suited to this installation space [7].

One approach to using the volume more efficiently for hydrogen storage is to use conformable tanks, which are adapted to the cuboid design space [7]. However, pressure vessels that deviate from a cylindrical or spherical geometry are subject to high bending forces in the vessel walls [11]. This makes it necessary to integrate reinforcing elements such as struts or ribs to counteract these forces. Several approaches for conformable composite tanks can be found in literature [7, 8, 11–13]. A major challenge is the connection of the reinforcing elements (struts, ribs, etc.) to the tank wall, as very high forces have to be transmitted in this area [11, 14].

This work presents a manufacturing process for conformable CFRP tanks with inner tension-strut reinforcement. The main aim is to investigate the feasibility of the presented concept through the development, fabrication, and testing of two tank demonstrators.

2 CONCEPT AND DESIGN

This chapter outlines the overall concept for a conformable CFRP tank with tension-strut-reinforcement, including the design of the winding core and boss elements, the integration strategy for the struts, the composite layup definition, and the materials for demonstrator manufacturing.

2.1 Manufacturing concept

The basic manufacturing concept was presented in a previous contribution at ECCM20 [15] and is briefly summarized here for completeness.

The concept consists of four main steps, as shown in Figure 1. In the first step, a winding core with integrated continuous fiber-reinforced struts is prepared. The struts, which have a thermoplastic (TP) matrix, are positioned such that both ends protrude beyond the surface of the core. In the second step, the tank wall is formed using the wet winding process. During the deposition of the impregnated fibers on the winding core, the ends of the struts pierce the rovings, resulting in a semi-finished product with an uncured composite laminate in which the end sections of the struts protrude from the outer surface of the laminate. In the third manufacturing step, the end portions of the TP-CFRP struts are formed into a flat geometry using heat. In the final step, an outer composite laminate is formed using the filament winding process to cover the reshaped ends of the struts.

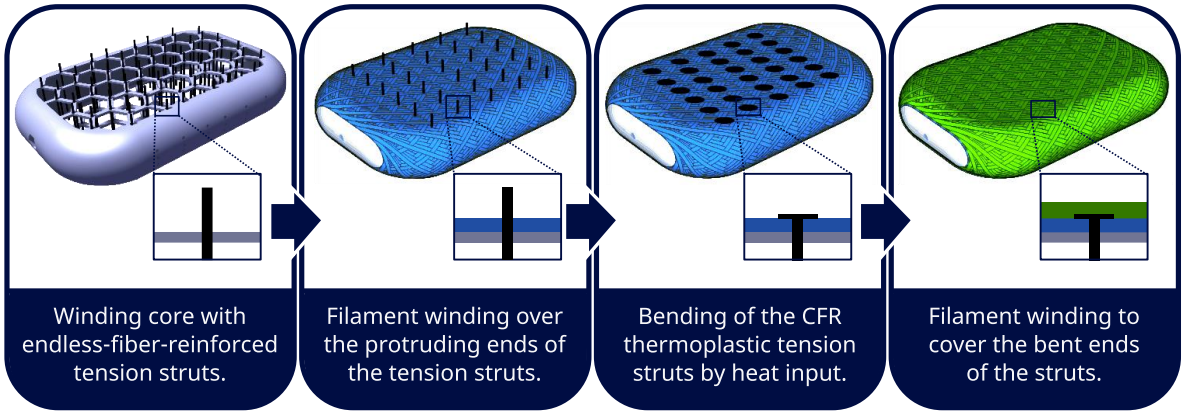

Figure 1: Overview of the manufacturing steps for the conformable CFRP tank with integrated tension struts [15].

The presented manufacturing concept demonstrates promising potential for the fabrication of conformable CFRP tanks with integrated tension struts. Compared to designs based on steel, the CFRP approach offers superior lightweight potential [14, 16]. Furthermore, the use of filament winding, a well-established process in pressure vessel manufacturing, supports scalability, as suitable equipment is already widely available in industry. An important aspect of the concept is the strut integration strategy, which is intended to allow efficient load transfer from the struts into the laminate along the fiber direction. In the configuration shown in Figure 1, a 3D-printed skeleton structure serves as a winding core. However, the concept is equally applicable to Type IV tanks, where a polymer liner with channels for the struts could fulfill this role. As such liners are currently not commercially available, the demonstrators presented in this study utilize a 3D-printed skeleton structure.

2.2 Design of winding core and boss element

The winding core for the demonstrators was designed using Catia V5 and is depicted in Figure 2. The core features a hexagonal structure, designed for 3D-printing without the need for additional support material between the hexagons. It includes holes at the intersection points for the struts, as well as

recesses to enable adhesive application during strut insertion. The core dimensions are 426 mm × 290 mm × 80 mm. The strut spacing was defined as a parameter, allowing the number of struts to be easily varied during the tank design process. Additionally, the winding core includes a recessed area for bonding the boss element, ensuring its precise positioning during assembly.

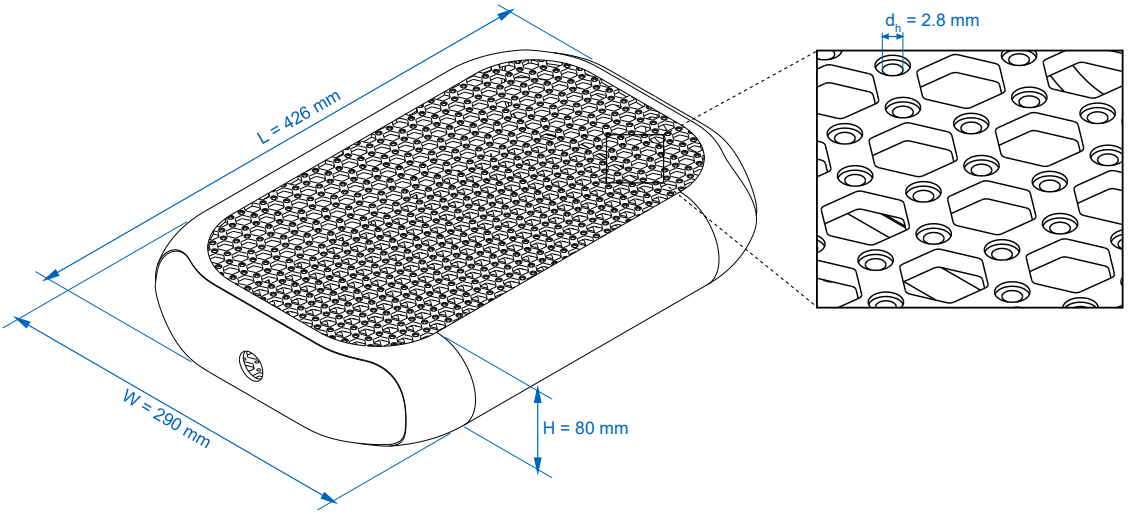

Figure 2: CAD design of the winding core.

The boss element and key dimensions are shown in Figure 3. It should be noted that the structural design of the boss was not focus of this project. Therefore, only an approximate design was created without detailed analyses, such as stiffness evaluation.

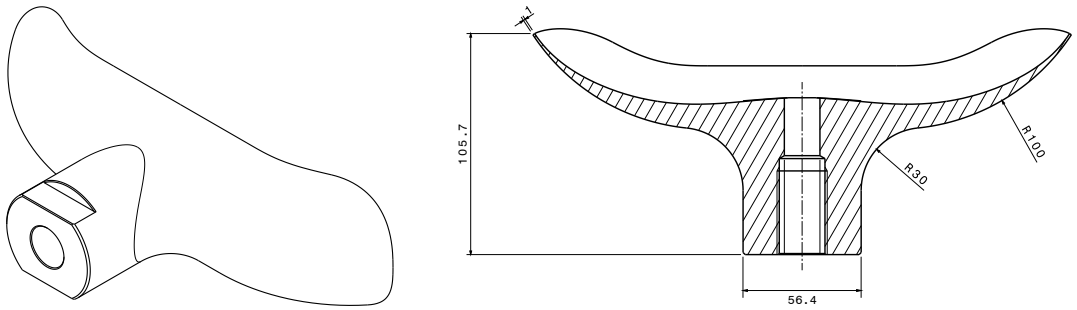

Figure 3: Boss element for conformable tank demonstrators and main dimensions in mm.

2.3 Strut integration and anchoring strategy

Comprehensive investigations to improve the strut connection were carried out. The general approach is shown in Figure 4. Parts of these investigations have been published in Gleis et al. [17]. As these investigations are not the focus of this publication, they are not discussed in further detail. From preliminary studies, a length of 4 mm for the reshaped strut end, combined with the application of thickened resin after bending of the struts was found to provide good connection strength between the struts and the tank wall.

For the building of the demonstrators, the thermal forming of the strut heads was conducted manually using a modified soldering iron. A conservative value of 1.5 kN was assumed for the transferable load between each strut and the tank wall for the definition of the strut spacing. This assumption accounts for the differing conditions during demonstrator manufacturing, which are less controlled compared to the laboratory environment during the parameter study.

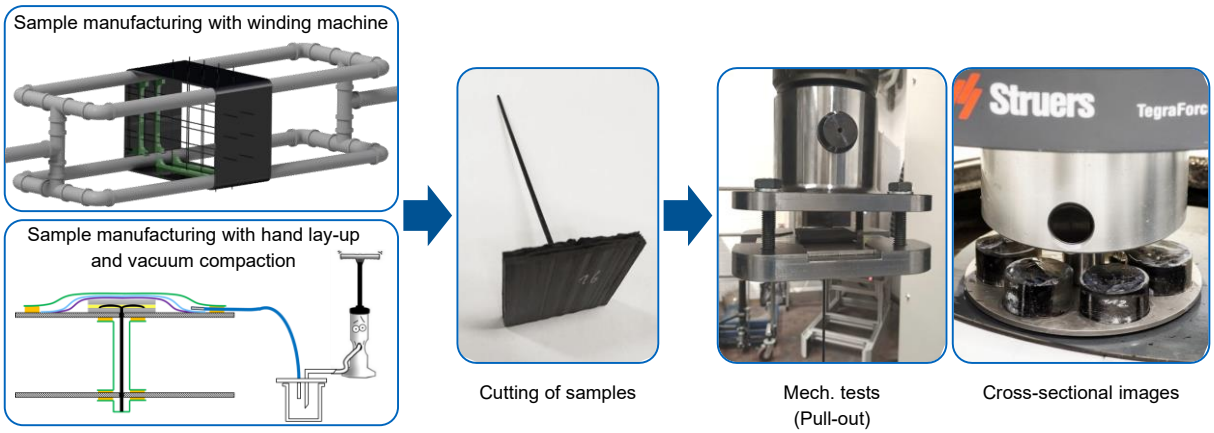

Figure 4: Approach for improving the connection between the struts and the laminate of the tank wall.

2.4 Composite layup and strut configuration

For the fabrication of the demonstrator tanks, design parameters such as the number of composite layers, the stacking sequence and the number and spacing of the struts had to be determined. It should be noted that detailed structural design was not the focus of this work. The following procedure was used as a pragmatic approach to define the key design parameters. A burst pressure of 100 bar was defined as the design target. Since the objective of the project was to investigate the strut integration concept at demonstrator level, the design parameters were selected so that the laminate of the tank wall was oversized and the strut spacing served as the critical design parameter. The aim was to ensure that during burst testing, failure would occur at the strut connection rather than in the laminate.

Strut spacing

A simplified one-eighth model of the tank was simulated in Abaqus to define a reasonable strut spacing for the demonstrator. The strut spacing was adapted in the model to achieve a maximum stress of 361 MPa in the struts in fiber direction. With the strut diameter of 2.3 mm, this corresponds to the value of 1.5 kN assumed in Section 2.3 for the pull-out strength of the strut-wall connection and resulted in a strut spacing of 12 mm in the simulation. Since the struts are arranged in a square pattern in the Abaqus model and hexagonally in the core structure of the demonstrators (due to 3D-printing constraints), the spacing was adjusted to achieve a comparable reinforcement density, resulting in 10 mm spacing distance.

Composite Layup

As current winding software cannot generate winding paths for non-rotationally symmetric geometries such as the conformable tank demonstrators, a combined approach of filament winding and hand layup was employed for the tank wall. Layers oriented at 0° and 90° were realized through circumferential winding, while ±45° layers, as well as patches on the corners and sides of the demonstrators, were applied by hand layup. A schematic illustration of the composite layup approach and the used patches is shown in Figure 5.

The number of layers was set at a total of 16, with four repetitions of the sequence 0°/90°/+45°/-45°. Before placing each 0° layer, the corners of the tank were reinforced by hand lamination, and before each 90° layer, the side patches were applied. For the 0° layers, a manufacturing aid (shown in Figure 6, right) was used to wind over the boss elements.

As described above, the aim was to over-dimension the tank wall deliberately so that failure in the burst test occurs at the strut connection and not in the laminate. To verify the selected layup, the Abaqus model mentioned above was used to simulate the tank wall with 16 layers according to the specified orientations. The maximum stress in the fiber direction and the maximum shear stress were evaluated for each layer to ensure that these values were within a non-critical range for CFRP.

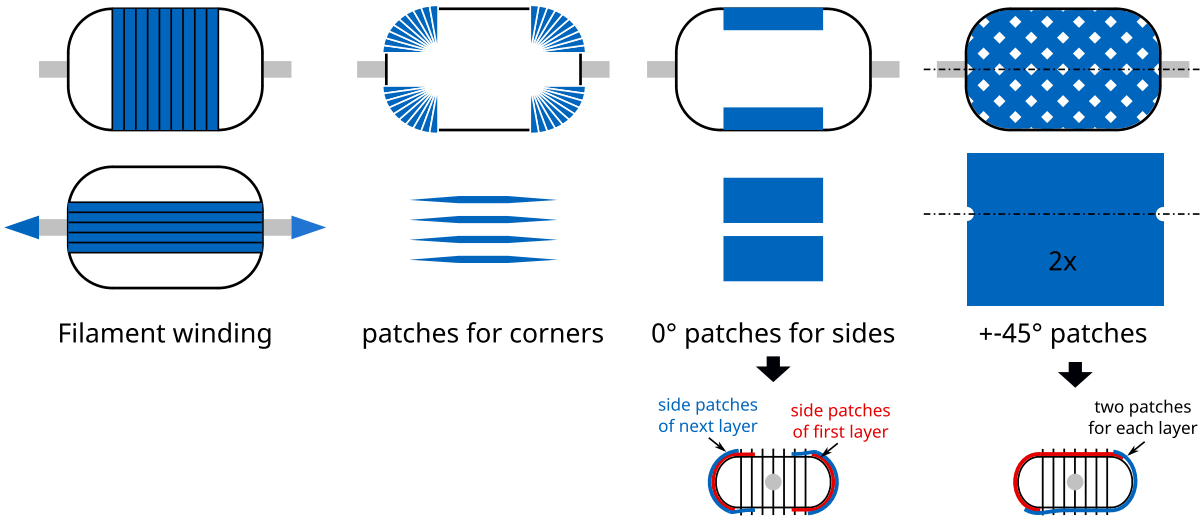

Figure 5: Schematic illustration of the layup strategy combining filament winding and hand layup for the conformable tank wall.

2.5 Materials

All the materials used for the manufacturing of the demonstrators, their specific designations, and the relevant manufacturing steps are listed in Table 1. Figure 6 shows the prepared fiber patches on the left. The conical strut caps and the 0° winding aid (middle and right) were 3D-printed using SLA resin. Two different resin systems were used for the two demonstrators, which required different 3D-printing filaments. For the demonstrator manufactured with the Araldite LY1135-1/917/960 resin system, PA6-CF was selected for the core structure due to its higher thermal resistance.

Material	Trade name	Manufacturing steps
Carbon fiber roving	Toray T700S-24K-50C	Filament winding of 90° and 0° layers
UD Non-crimp fabric (NCF)	SGL Sigratex® C U170-0/ST-E214/10g	Hand laminated edge and side patches
±45° NCF	Saertex ±45° 256 g/m²	Patches for hand laminating of ±45° layers
Struts	SGL CF/PA6 struts (prototype material)	Reinforcing strut with carbon fiber d = 2.3 mm used for both demonstrators
Resin system for 1st demonstrator	SikaBiresin® CR80/CH10	Wet winding and hand lamination of 1st demonstrator
Resin system for 2nd demonstrator	Huntsman Araldite LY1135-1/917/960-1	Wet winding and hand lamination of 2nd demonstrator
3D-printing filament PETG	Polymaker PolyLite PETG	3D-printing of core structure for first demonstrator
3D-printing filament CF-PA11	Polymaker PolyMide PA6-CF	3D-printing of core structure for second demonstrator
SLA printing resin	Anycubic standard resin	Printing of manufacturing aid for 0° layers and strut caps
Adhesive	Scotch-Weld™ DP 490	Assembly of core structure, fixation of the struts in the core structure
Thixotropic agent	Evonik AEROSIL® 380	Viscosity increase of neat resin applied after strut forming
2K Silicone	SilikonFabrik SF00 - RTV2	Implementation of silicone layer into the 2nd demonstrator as an attempt to seal it

Table 1: Materials used for the manufacturing of the demonstrator tanks.



Figure 6: Prepared fiber patches (left) and 3D-printed strut caps (middle) and manufacturing aid for 0° layers (right).

3 MANUFACTURING OF THE DEMONSTRATORS

This chapter describes the manufacturing process of the demonstrator tanks, including the preparation of the winding cores with integrated struts, the combined filament winding and hand lay-up process, the anchoring of the strut ends, and the vacuum-assisted curing procedure.

3.1 Preparation of winding cores

The core structure of the demonstrators is fabricated in four individual segments using a fused deposition modeling (FDM) process on a Prusa i3 MK3S+ printer. After printing, the segments are assembled using a 2K epoxy adhesive (Scotch-WeldTM DP 490). Two different filament materials were used for the core structures of the two demonstrators: PETG and PA6-CF. The choice was based on the requirements of the respective resin systems, which necessitate different curing temperatures. PA6-CF offers a higher heat deflection temperature, while PETG is easier to process during printing. Figure 7 shows the printing process for a single segment and the four segments prior to assembly.

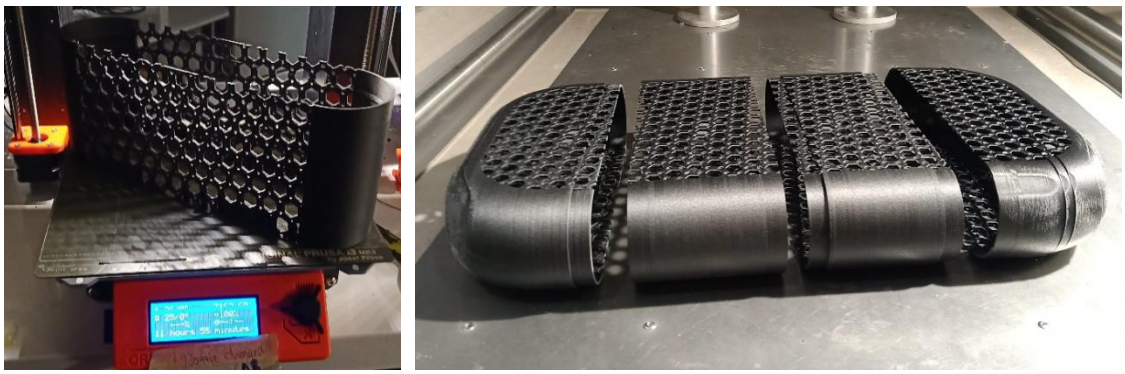

Figure 7: 3D-printing of a core segment (left) and the four segments prior to adhesive assembly (right).

The aluminum boss elements were adhesively bonded to the core structure using the aforementioned adhesive. As structural reinforcements, continuous fiber-reinforced tension struts were integrated into the conformable tank demonstrators. Prior to their insertion into the core structure, the struts were dried, cleaned with isopropanol, and trimmed to a uniform length. Each strut was individually bonded to the core structure using the DP490 adhesive, as shown in Figure 8. To facilitate piercing of the strut ends through the fiber layers during filament winding and hand lamination, conical strut caps with pointed ends were manually attached (Figure 8, right). The preparation of the core structure was very time-consuming due to the significant manual labor involved, such as the adhesive joining of 564 struts.



Figure 8: Insertion of continuous fiber-reinforced tension struts into the core structure with adhesive (left) and attachment of conical strut caps (right).

3.2 Filament winding and hand lay-up process

A total of 16 layers, consisting of four repetitions of the sequence 0°/90°/+45°/−45°, was applied. Before each 0° layer, the tank's corners were reinforced by hand lamination and before each 90° layer, the side patches were placed. After the first 0° and 90° layers, an intermediate curing step was implemented to prevent deformation of the 3D-printed core under thermal and mechanical process loads e.g. during strut forming.

For the circumferential layers in 0° and 90° direction, the wet filament winding process, shown in Figure 9, was applied. The fiber tension during winding was set to 10 N, and the winding paths were generated using CADWIND. As a workaround for the non-rotationally symmetric geometry of the conformable tank, cylindrical mandrels were modeled in CADWIND with equivalent circumferences to the core geometry in the respective 0° and 90° winding directions. The bandwidth was defined as 5.5 mm in the winding software. To enable winding in the 0° direction despite the presence of the boss element, a custom manufacturing aid was employed, as shown in Figure 9.

During winding, several practical challenges arose. In some cases, strut caps detached from the ends of the tension struts and had to be manually removed from the laminate, requiring an interruption of the winding process. Furthermore, due to the presence of the protruding strut ends, the rovings occasionally failed to deposit fully onto the surface of the mandrel and had to be manually pushed down. Winding across the boss element in the 0° direction using the manufacturing aid caused local deviations from the intended fiber alignment along the tank's longitudinal axis. Filament winding was chosen for these layers because it enables full 0° wrapping of the boss element and, compared to hand lamination, reduces the risk of layer detachment and shifting after placement.

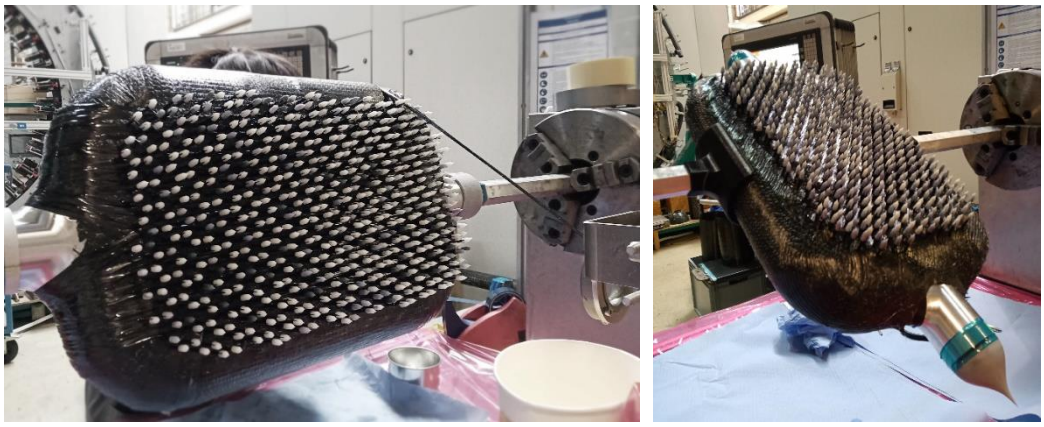

Figure 9: Wet filament winding setup for circumferential layers: 90° (left) and 0° (right). A custom manufacturing aid was used in 0° to enable fiber deposition across the boss element.

The application of the prepared fiber patches by hand lamination is shown in Figure 10. For each ±45° NCF layer, two patches were applied: one on the top and one on the bottom of the tank, overlapping

along the curved sides. A brush was used to push the ±45° NCF down onto the mandrel surface along the struts. The patches applied along the sides of the demonstrators (see Figure 10, middle) are oriented in the 0° direction and were positioned so that the strut rows adjacent to the curved sides pierced each patch alternately from the top and bottom. To cover each of the four corners of the tank, six patches (shown in Figure 6) were placed side-by-side, as illustrated on the right in Figure 10. During the layup process, several issues arose due to insufficient fixation of the fiber patches. The lack of tension complicated accurate positioning, leading to patch movement and wrinkle formation during vacuum compaction.

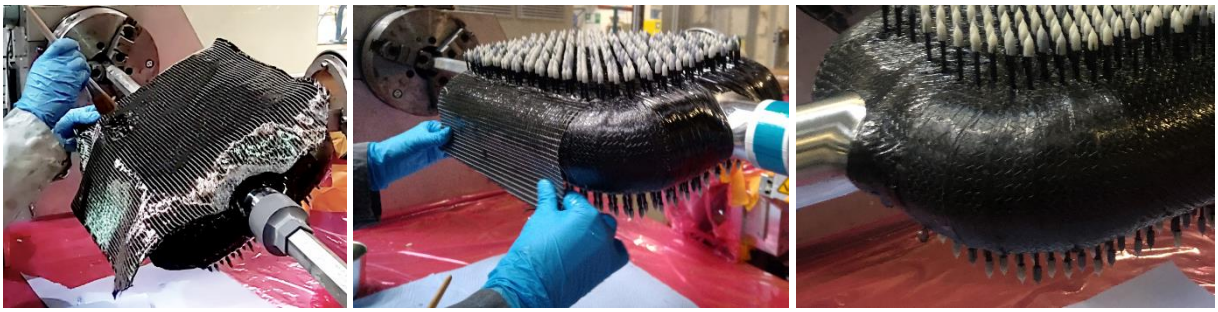

Figure 10: Hand lamination process of ±45° NCF layers (left), 0° patches along the sides (middle), and coverage of the curved shoulders (left).

3.3 Anchoring of strut ends

The thermal forming of the strut ends was performed after the 12th layer. The struts, including the caps, were first trimmed with pliers, leaving 4 mm protruding. The remaining ends were flattened directly on the uncured laminate using a soldering iron with a flat tip. The intermediate state, with some strut ends already formed and the remaining ones trimmed, is shown in Figure 11 (left). Due to the high number of struts and the limited ability to form them in parallel at this early development stage, the manual forming process was very time-consuming. Approximately four hours were required for two people to complete the thermal forming on one demonstrator. To improve the mechanical performance of the strut–laminate interface, a layer of neat epoxy resin, shown in Figure 11 (right), mixed with 4 wt-% thixotropic agent (Aerosil 380) was applied. A 90° layer was immediately wound over the area to prevent resin runoff. The remaining layers were then applied according to the defined sequence.



Figure 11: Trimmed and formed strut ends (left) and resin application with thixotropic agent (right).

3.4 Vacuum-assisted curing process

To prepare the vacuum setup, a perforated release film was stretched over the wet laminate, followed by the application of breather fabric and vacuum film. Curing was performed under a vacuum of 400 mbar (absolute pressure). Cure cycles were resin-dependent: CR80-10 was cured for 10 hours at room temperature, while Araldite LY 1135-1/917/960 was cured for 4 hours at 80°C, followed by 6 hours at 120°C. The vacuum setup and the final demonstrators after curing are shown in Figure 12.



Figure 12: Vacuum setup (left) and final demonstrators after curing (right).

4 TESTING AND EVALUATION OF THE DEMONSTRATORS

4.1 Hydrostatic burst testing and leakage analysis

Hydrostatic burst tests were conducted on both demonstrators but had to be terminated early due to premature leakage. The tank manufactured with CR80-10 resin exhibited leakage at 80 bar, while the one using Araldite LY 1135-1/917/960 showed leakage at 30 bar. A follow-up test with compressed air and leak detection spray was performed to locate the leaks. In both cases, leakage occurred at the interface between the composite structure and the boss elements (see Figure 13, right). Figure 13 (left) shows one of the demonstrators in the burst test chamber.



Figure 13: Left: Demonstrator in hydrostatic burst chamber. Middle and right: Leak detection at the composite–boss interface using compressed air and leak detection spray.

4.2 Mass and volume

The two demonstrators had masses of 5.86 kg (Demonstrator 1, CR80-10) and 6.35 kg (Demonstrator 2, Araldite 1135/917/960) and an internal volume of 7.7 L. Assuming a design pressure of 100 bar and a safety factor of 2, this corresponds to a theoretical hydrogen capacity of 32 g, resulting in a gravimetric efficiency of 0.50-0.55%. In a dissertation by Ruf [16], a gravimetric efficiency of 5.9% was reported for a conformable tension-strut-reinforced Type IV tank. However, this value is based on simulation results and does not represent a demonstrator at technical scale. The low gravimetric efficiency observed here is partly due to the deliberate overdimensioning of the tank wall and manufacturing challenges leading to a relatively low fiber volume content. This result further highlights the early development stage and low technology readiness level (TRL) of the presented concept.

4.3 Supplementary inspection of laminate and strut connections

To gain further insight into the manufacturing process and investigate the demonstrators in more detail, both tanks were cut into quarters and samples were taken for microscopy and mechanical testing of the strut connections. Cross-sectional images revealed very high porosity and low fiber volume content, especially in the flat sections where the struts are integrated. In the boss area, the composite laminate detached from the aluminum surface during cutting, confirming insufficient bonding at the interface. A neat resin layer was observed on the tank side that faced downward during curing, likely due to gravity-induced flow. The effect was more distinct in the demonstrator manufactured with the

Araldite LY1135-1/917/960 resin system, as can be seen in Figure 14, middle. A cross-sectional image, as well as cut sections from both demonstrators are shown in Figure 14.



Figure 14: Cut sections of demonstrators made with CR80-10 (left) and Araldite 1135/917/960 (middle), and a microscopy image of a strut–laminate interface (right).

Mechanical pull-out tests were performed on a total of 57 samples taken from different sections of each demonstrator to investigate the strength of the joint between the strut and the tank wall. The tests showed an average pull-out force of 1.7 kN for both tanks. However, as already observed in previous studies of the strut connection [17], the results showed considerable scatter (±0.4 kN), which is a known challenge for this concept.

5 DISCUSSION AND LESSONS LEARNED

The demonstrators provided valuable insights into the performance and manufacturability of the strut-reinforced conformable tank concept. Key aspects are summarized below.

Promising outcomes:

The integration of struts into the tank wall was successful in principle. The strut-wall connection withstood the forces expected from coupon-level testing and did not show mechanical failure during hydrostatic loading. In one of the demonstrators, no rupture occurred at 80% of the design pressure (i.e. 80 bar), indicating sufficient mechanical integrity of the strut anchorage. The test was aborted due to leakage, not structural failure.

Identified challenges:

A critical issue was leakage at the interface between the composite structure and the aluminum boss element. The lack of adhesive bonding and the mismatch in thermal expansion between aluminum and CFRP likely contributed to poor bonding, particularly during curing and cool-down of the demonstrator manufactured with the resin system Araldite 1135/917/960. Leakage occurred in both demonstrators: the one cured at 120 °C leaked at 30 bar, and the room-temperature cured one at 80 bar. This suggests that thermal effects may intensify the problem but are not the sole cause. The boss design further limited bonding strength due to the narrow contact area in the center. Local detachment of the laminate from the boss during cutting confirmed insufficient adhesion at the CFRP-boss interface.

Another major challenge was the laminate quality in the flat sections where the struts were integrated. Microscopy revealed severe porosity, attributed to inadequate compaction during winding. In filament winding, compaction relies on fiber tension combined with a convex surface. On flat surfaces, fiber tension does not result in compaction pressure. The presence of the protruding struts prevented the use of compaction rollers and intermediate vacuum consolidation steps. For future investigations, the struts could be inserted after winding to enable better compaction through suitable consolidation methods. However, inserting the struts after laminating introduces additional challenges. Besides the poor compaction, a resin layer was observed on the side of the tank that was positioned at the bottom during curing, which could in the future be prevented by rotating the tank during the curing process (compare Figure 14, middle).

The thermal forming of the strut ends was performed manually and lacked process control, resulting in significant scatter in the measured pull-out strength values. Additionally, the forming process, along

with steps such as inserting and bonding the struts to the winding core and trimming them prior to forming, proved to be highly labor-intensive and time-consuming when carried out manually.

Interpretation and concept evaluation:

From a structural standpoint, the strut-wall connection does not fully utilize the material potential. While the used PA6/CF struts have an average tensile strength of 986 MPa [17], corresponding to 4.1 kN, the strut-wall connection in the demonstrators reached only 1.7 kN on average, resulting in a connection efficiency of 41%. According to calculations by Gleis et al. [17], a 700 bar tank with 100% connection efficiency would require a strut spacing of 5.49 mm. This spacing poses significant manufacturing challenges but remains theoretically feasible given the 4 mm formed strut length used in the demonstrators. However, for the concept to achieve practical viability, the connection strength must be significantly increased. Under more controlled laboratory conditions, 2.1 kN has already been achieved, though further improvements are necessary.

From a manufacturing perspective, the current process is highly complex and involves numerous additional steps compared to the production of conventional cylindrical Type IV tanks. While some of these steps, such as strut bonding, trimming, and forming, could be automated and parallelized (e.g. using a heated press tool for simultaneous forming), the overall production effort and associated costs are high. The cost-effectiveness of these additional manufacturing steps relative to the reported 5-10% increase in volumetric efficiency for cuboid packaging spaces, as indicated by Ruf [16], needs to be further assessed.

6 SUMMARY AND OUTLOOK

This work presents the development and manufacturing of conformable CFRP tank demonstrators reinforced with continuous fiber-reinforced tension struts. While the integration of struts was successfully demonstrated, key challenges remain in improving compaction in laminate regions without curvature, as well as achieving a reliable interface between the CFRP and the aluminum boss. The two demonstrators showed leakage before burst at 30 and 80 bar, respectively. The manual and labor-intensive forming process of the strut ends shows that this approach is significantly more complex and time-consuming compared to the manufacturing of conventional cylindrical tanks. Future efforts will focus on increasing the strut-wall connection strength, enhancing compaction e.g. through a modified process sequence, and generating concepts for scalable, cost-effective production techniques.

ACKNOWLEDGEMENTS

This research work was performed within the COMET-module “Polymers4Hydrogen” (I.D. 21647053) in the framework of the COMET program of the Austrian Federal Ministry for Climate, Action, Environment, Energy, Mobility, Innovation and Technology and the Austrian Federal Ministry for Digital and Economic Affairs. The authors thank the involved partners Polymer Competence Center Leoben GmbH (PCCL, Austria), Montanuniversität Leoben (Department Polymer Engineering and Science, Chair of Chemistry of Polymeric Materials, Chair of Materials Science and Testing of Polymers), Tampere University (Department of Engineering Material Science), Peak Technology, and Faurecia for their contributions to this research work. Special thanks to Faurecia for supporting burst and leakage tests within the Polymers4Hydrogen project. Yousuf Nadeem contributed to cutting and supplementary inspection as part of his master’s thesis. Thanks to Maximilian Strobel for 3D-printing support and to Youssef Mraidi for his help with planning and manufacturing. Kalle Kind is acknowledged for feedback and proofreading. Some text was edited for clarity using AI tools (e.g. Grammarly, ChatGPT); the authors remain solely responsible for the content.

REFERENCES

[1] International Energy Agency (IEA), Ed., "Global EV Outlook 2024: Moving towards increased affordability," Paris, 2024. [Online]. Available: https://www.iea.org/reports/global-ev-outlook-2024

[2] International Energy Agency (IEA), Ed., "Global Hydrogen Review 2024," Paris, 2024. [Online]. Available: https://www.iea.org/reports/global-hydrogen-review-2024

[3] A. G. Olabi, T. Wilberforce, and M. A. Abdelkareem, "Fuel cell application in the automotive industry and future perspective," *Energy*, vol. 214, p. 118955, 2021, doi: 10.1016/j.energy.2020.118955.

[4] *BMW Group Wasserstoff-Technologie.* [Online]. Available: https://www.bmwgroup.com/de/innovation/antriebstechnologien/wasserstoff.html (accessed: Jun. 29 2025).

[5] *Ausblick auf die neue Designsprache: Hyundai enthüllt Brennstoffzellen-Konzeptfahrzeug INITIUM der BMW Group: BMW Group Wasserstoff-Technologie.* [Online]. Available: https://www.hyundai.news/de/articles/press-releases/hyundai-enthuellt-brennstoffzellen-konzeptfahrzeug-initium.html (accessed: Jun. 29 2025).

[6] D. Apostolou and S. N. Welcher, "Prospects of the hydrogen-based mobility in the private vehicle market. A social perspective in Denmark," *International Journal of Hydrogen Energy*, vol. 46, no. 9, pp. 6885–6900, 2021, doi: 10.1016/j.ijhydene.2020.11.167.

[7] M. Ruf *et al.,* "Neue Bauweisen Von Wasserstoffdruckbehältern Für Die Integration in Zukünftige Fahrzeugarchitekturen," in *PROCEEDINGS OF THE MUNICH SYMPOSIUM ON LIGHTWEIGHT DESIGN 2020/ TAGUNGSBAND*, S. Pfingstl, A. Horoschenkoff, P. Höfer, and M. Zimmermann, Eds., [S.l.]: MORGAN KAUFMANN, 2021, pp. 74–85.

[8] K. A. Öztas, K. Kunze, K. Jois, J. Sackmann, S. Zaremba, and M. G. Ruf, "A numerical approach to design a type II box-shaped pressure vessel with inner tension struts," *International Journal of Hydrogen Energy*, 2021, doi: 10.1016/j.ijhydene.2021.11.005.

[9] E. Rivard, M. Trudeau, and K. Zaghib, "Hydrogen storage for mobility: A review," *Materials*, vol. 12, no. 12, p. 1973, 2019.

[10] O. Bethoux, "Hydrogen Fuel Cell Road Vehicles: State of the Art and Perspectives," *Energies*, vol. 13, no. 21, p. 5843, 2020, doi: 10.3390/en13215843.

[11] S. M. Aceves, G. D. Berry, A. H. Weisberg, F. Espinosa-Loza, and S. A. Perfect, "Advanced Concepts for Vehicular Containment of Compressed and Cryogenic Hydrogen," in *16th World Hydrogen Energy Conference*, Lyon, France, 2006.

[12] L. Farines, F. Thiebaud, D. Perreux, "Compressed hydrogen form-fitted tank," in *ECCM15-15th European conference on composite materials*, 2012.

[13] A. Horoschenkoff, M. Huber, and A. Hupfeld, "Bauraumoptimierter Wasserstoff Tank Mit Innerer Zugverstrebung," in *Proceedings of the Munich Symposium on Lightweight Design 2020*, Berlin, Heidelberg, 2021, pp. 86–89.

[14] K. A. Öztas, R. A.J. Weerts, and M. G. Ruf, "An analytical and numerical approach to design a type I box-shaped pressure vessel with inner tension struts," *International Journal of Pressure Vessels and Piping*, vol. 192, p. 104441, 2021, doi: 10.1016/j.ijpvp.2021.104441.

[15] E. Gleis, J. Kim, S. Zaremba, and K. Drechsler, "Development of a manufacturing process for a cuboidal pressure vessel with tension struts," in *Proceedings of the 20th European Conference on Composite Materials - Composites Meet Sustainability (Vol 1-6)*, Lausanne, 2022, pp. 335–342.

[16] M. G. Ruf, *Untersuchung von neuartigen Wasserstofftankkonzepten für die Integration in zukünftige Fahrzeugarchitekturen*. München: Verlag Dr. Hut, 2023.

[17] E. Gleis, "Comprehensive parameter study and evaluation of a reinforcement concept for conformable CFRP tanks for hydrogen storage," *Zeitschrift Kunststofftechnik*, vol. 1, pp. 21–49, 2024, doi: 10.3139/O999.02072024.

ICCM24
AUG 4-8, 2025 · BALTIMORE, MARYLAND

Advanced Graphene-Enhanced Polyethylene Liners for Type IV Hydrogen Storage Tanks: Enhancing Mechanical Properties and Gas Containment

RIC2D

J Jefferson Andrew, Jabir Ubaid, WJ Cantwell, KA Khan, R Umer

Department of Aerospace Engineering, Khalifa University, Abu Dhabi, United Arab Emirates
RIC2D, Khalifa University, Abu Dhabi, United Arab Emirates

جامعة خليفة
Khalifa University

Background

Hydrogen as a clean energy carrier:

- High specific energy (~3x gasoline by weight) and environmentally friendly
- Challenges in storage due to low volumetric energy density in gaseous form

Hydrogen storage solutions:

- Commonly stored as compressed gas at 700–900 bar in composite pressure vessels
- Type IV vessels: polymer liner with carbon fiber overwrap for lightweight, strength, and gas containment

Polymer liner challenges:

- Critical barrier against hydrogen permeation.
- Subject to degradation from pressure cycles, temperature changes, and mechanical stress

Medium-Density Polyethylene (MDPE):

- Widely used liner material due to ductility, chemical resistance, and ease of fabrication
- Limitation: relatively high hydrogen permeability affecting long-term storage

Graphene Nanoplatelets (GNPs) as additives:

- High aspect ratio and impermeability create tortuous paths reducing gas diffusion
- Improve mechanical strength, stiffness, and impact resistance

Type IV Hydrogen Tank

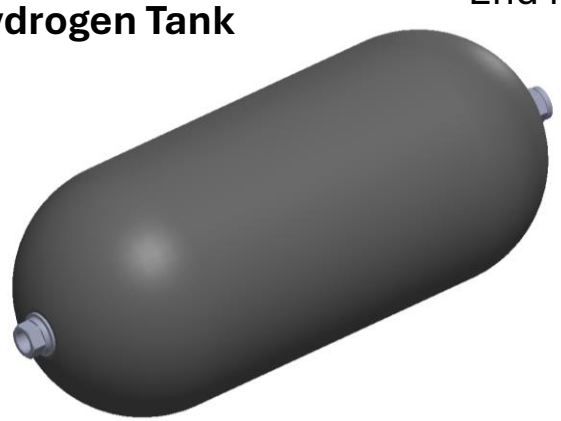

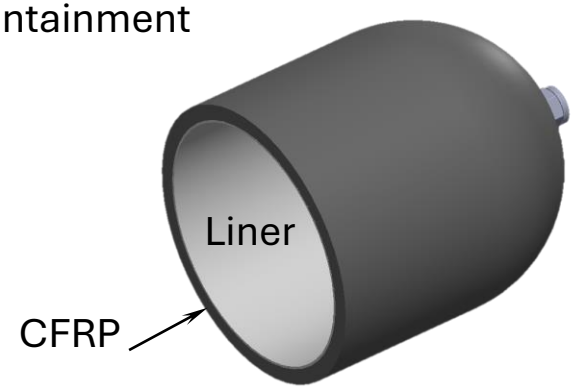

Filament winding process



Objective of the Work

To systematically investigate the effect of incorporating graphene nanoplatelets (GNPs) at 0.05–1 wt.% on medium-density polyethylene (MDPE) used as a liner material in Type IV hydrogen storage tanks.

To evaluate the impact of GNP addition on:

- Mechanical properties (tensile, flexural, and impact resistance)
- Thermal stability and crystallization behavior
- Gas barrier performance against gas permeation

To analyze the microstructure, filler dispersion, and polymer-filler interactions using advanced techniques such as Raman spectroscopy and 2D mapping.

To establish correlations between nanocomposite structure and macroscopic performance, providing guidance for optimizing liner materials in next-generation hydrogen storage systems.

Procedure

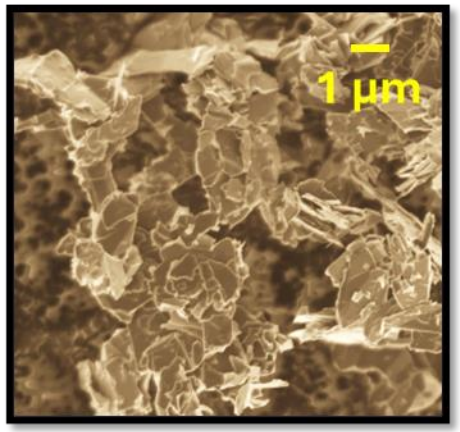

GNP

GNP + MDPE
+ Acetone

0, 0.05, 0.1,
and 0.5 wt.%

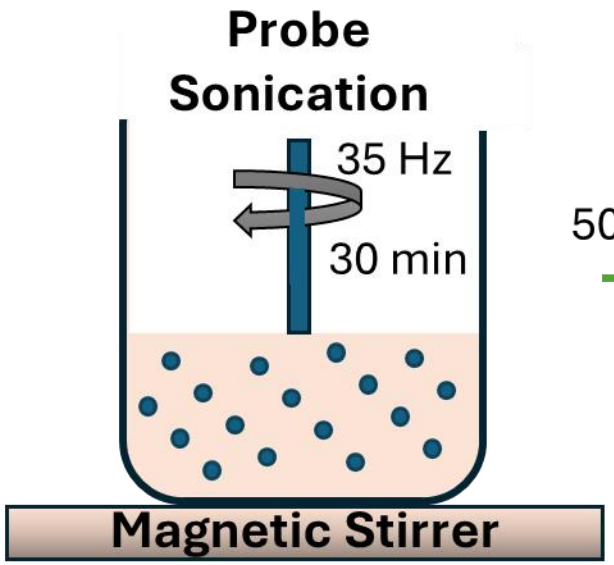

50°C

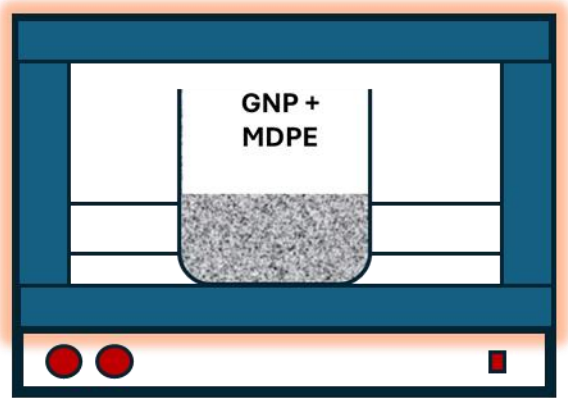

Oven

130 °C
13 Mpa 2 hrs

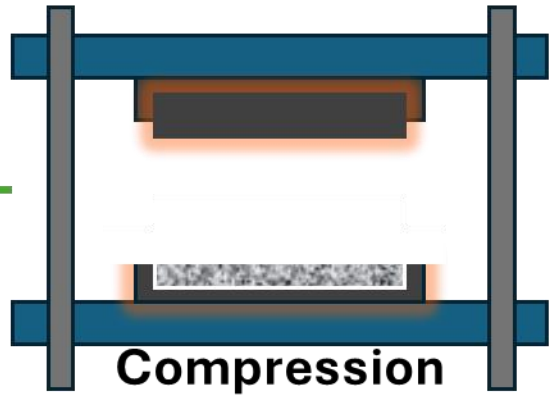

Compression
Molding

Fabricated Panels

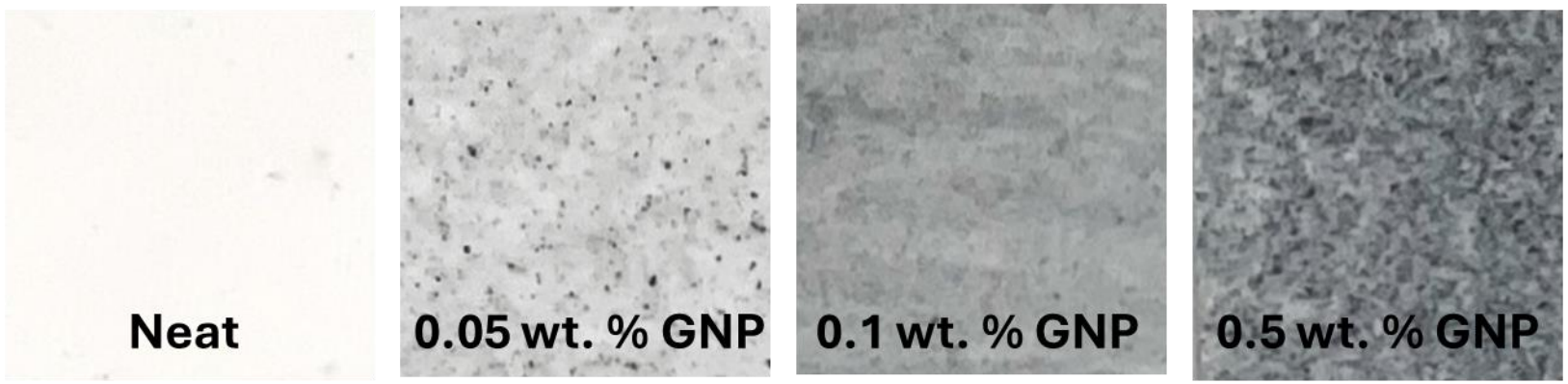

جامعة خليفة
Khalifa University

RiC2D

Raman Mapping Analysis of GNP Dispersion in MDPE Composites

Confirmation of GNP Incorporation: **G-band (1580 cm^{-1}), D-band (1350 cm^{-1}) & 2D-band (2700 cm^{-1}).**

Control Comparison: Neat MDPE shows **no graphitic peaks**, validating GNP-specific signal origin.

Final Takeaway: Optimal GNP loading **(0.05–0.1 wt.%)** ensures structural integrity and **uniform dispersion** in MDPE composites.

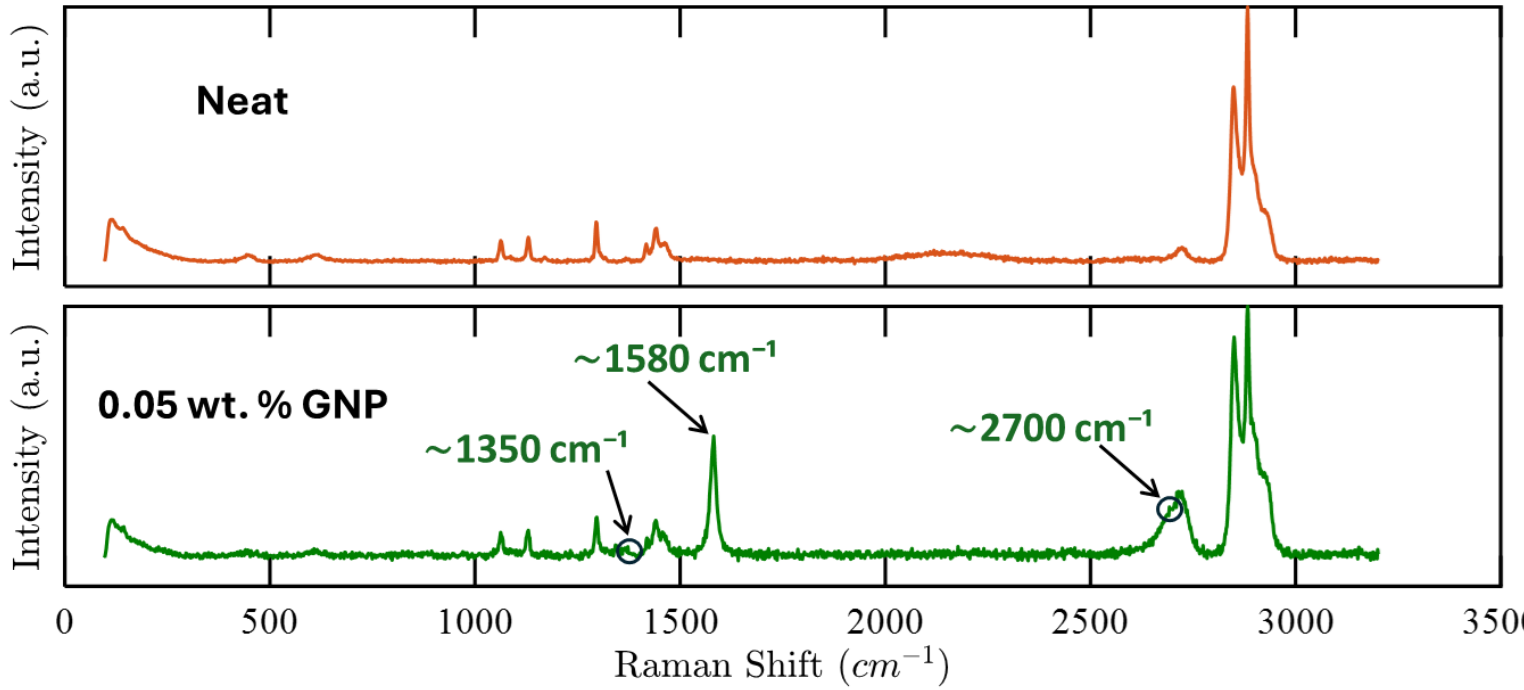

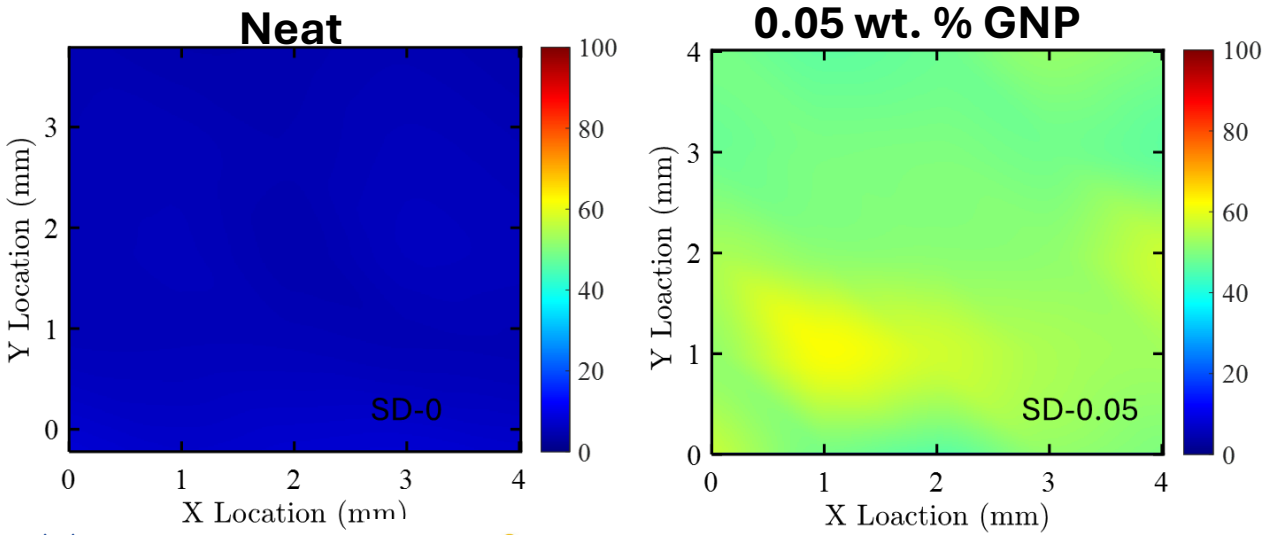

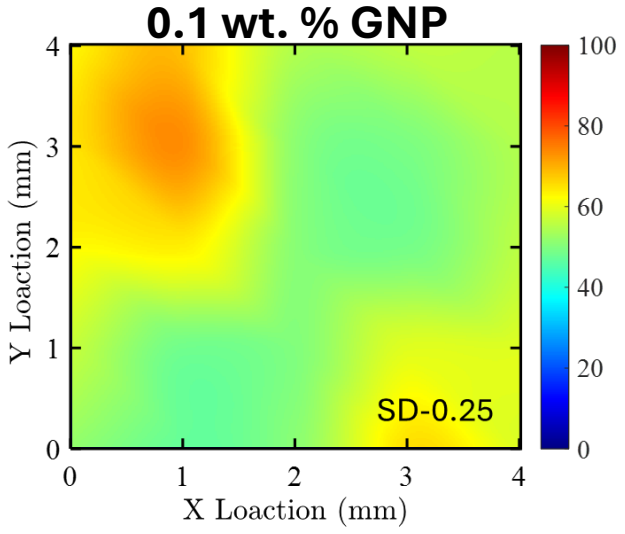

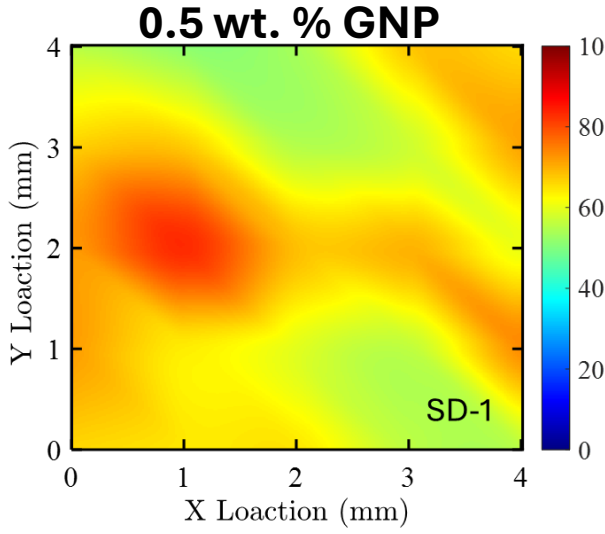

جامعة خليفة
Khalifa University

RiC2D

Quasi-Static Mechanical Properties

- **0.05 wt.% GNP** raised **tensile load by 8.1% and stiffness by 3.7% vs.** neat MDPE.
- Higher GNP content **(>0.1 wt.%)** led to **agglomeration** and reduced strength.
- **Tensile ductility fell** by **80.2%** from 114.4 mm to 22.7 mm at 0.5 wt.% GNP.
- **Flexural load** rose 23% and stiffness 19% at 0.05 wt.% GNP vs. neat MDPE.

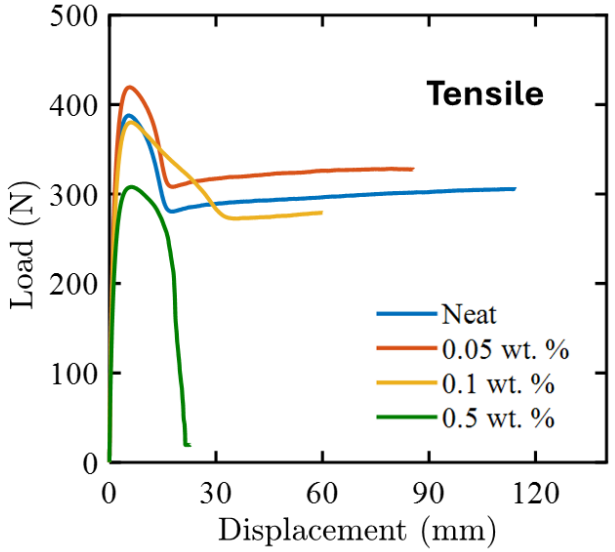

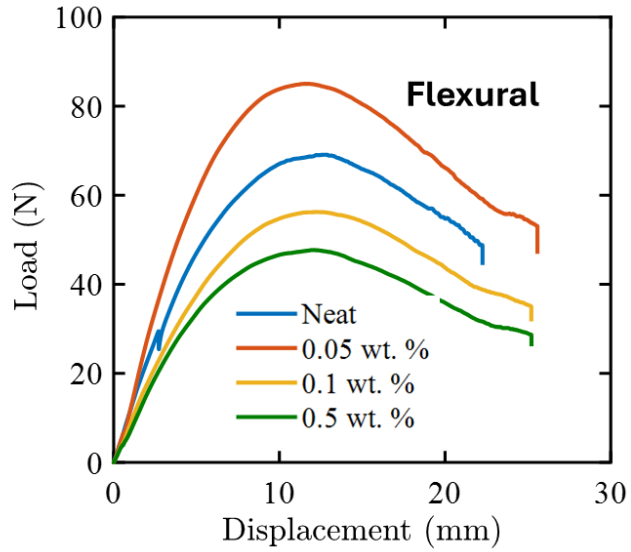

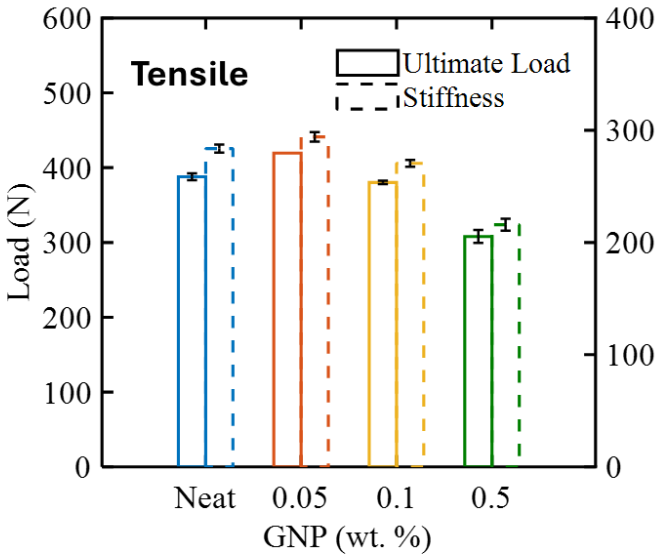

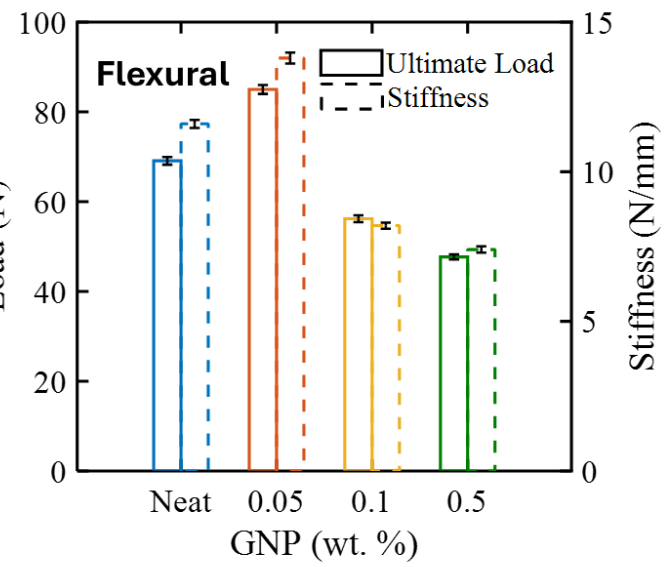

Quasi-static test	Samples Shape	Samples Dimensions (mm)	Loading Speed (mm/min)
Tension	Dog-bone	33 (gauge length) × 6.35 × 3.5	5
3-Point Flexural	Rectangular	127 ×12.7 × 3.5	5

Dynamic Energy Absorption Characteristics

- Impact trends a**lign with quasi-static results,** optimal at 0.05 wt.%.
- **Neat MDPE** absorbed **30.76 J**; GNP helps only when well dispersed.
- **0.05 wt.% GNP** improved **peak force (+5%) and energy absorption (+3.6%).**
- 0.05 wt.% GNP enhances energy dissipation mechanisms.
- **1 wt.% GNP** caused **26.5% drop** in peak force due to filler agglomeration.

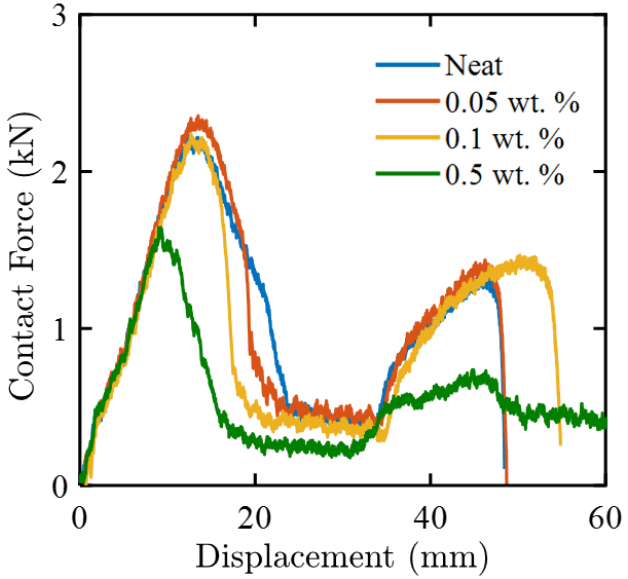

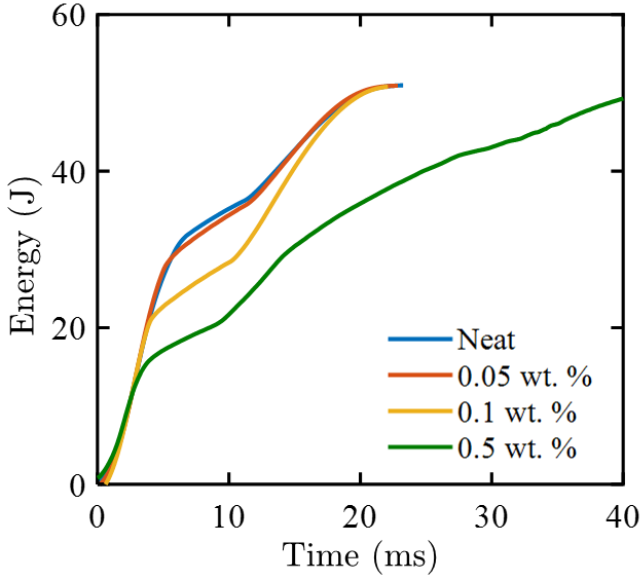

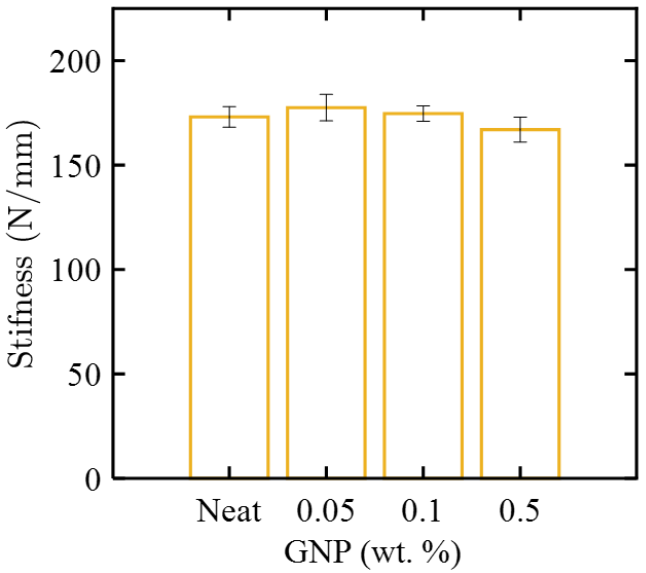

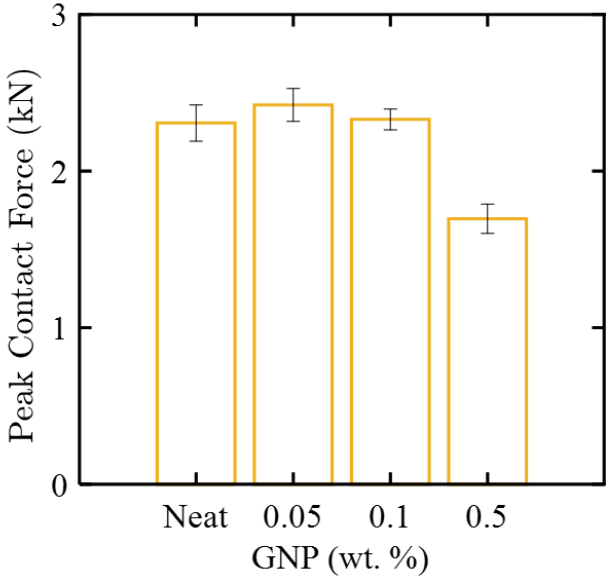

- Striker: 12.7 mm hemispherical steel
- 5.45 kg mass
- Impact energy: 50 J
- Specimen size: 60 × 60 mm^2

Thermal Analysis

- **0.05 wt.% GNP** raised melting temp **(Tm) by 1.4%;** 0.1 wt.% raised it by 3.1%.
- Tm dropped slightly at 0.5 wt.% GNP, likely due to nanoparticle agglomeration.
- Crystallization temp **(Tc)** increased from **134.4 °C to ~136.9 °C** for all GNP loads.

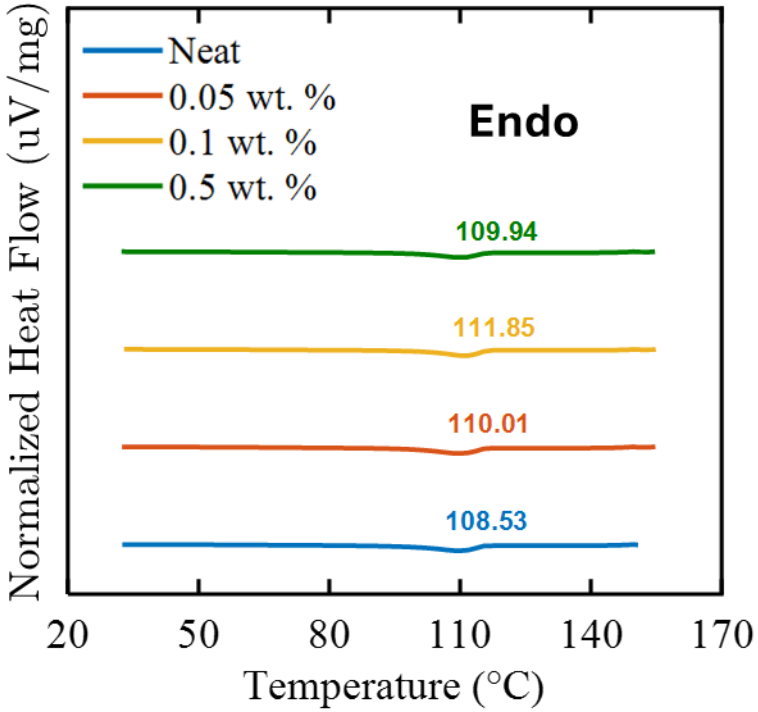

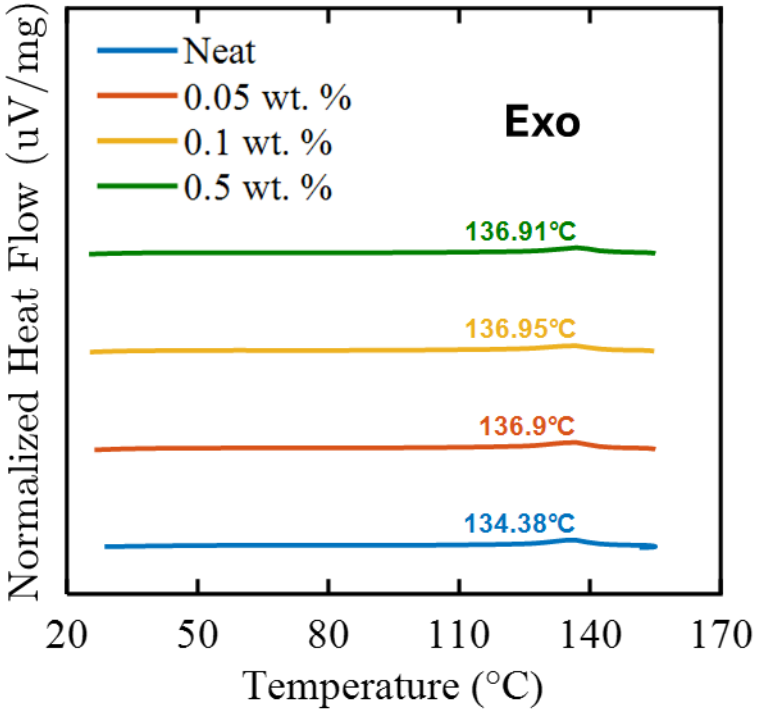

- Rise in Tc confirms GNPs act as nucleation sites during polymer cooling.
- Higher GNP loadings didn't further increase Tc, suggesting nucleation saturation.
- **Dual effect:** GNPs raise Tc via nucleation, and Tm via chain mobility restriction.
- Improved thermal transitions support **better stability** in hydrogen tank liners.

- DSC Sample mass: ~10 mg
- Heating range: 30 °C to 150 °C
- Heating/cooling rate: 10 °C/min
- Atmosphere: Nitrogen
- Cooling range: 150 °C to 30 °C

جامعة خليفة Khalifa University RiC2D

Thermomechanical Stability and Energy Dissipation Characteristics

- GNP-reinforced MDPE maintained **higher stiffness** across entire temp range.
- Loss modulus peaked ~140 MPa with GNP, 22% higher than neat MDPE (~115 MPa).
- Slightly lower tan δ (0.216 vs. 0.218) suggests restricted chain mobility.
- **GNPs enhance toughness** without sacrificing stiffness or damping.
- DMA **confirms strong GNP–matrix interaction** and good nanoparticle dispersion.
- Even 0.05 wt.% GNP **boosts thermal-mechanical stability** significantly.

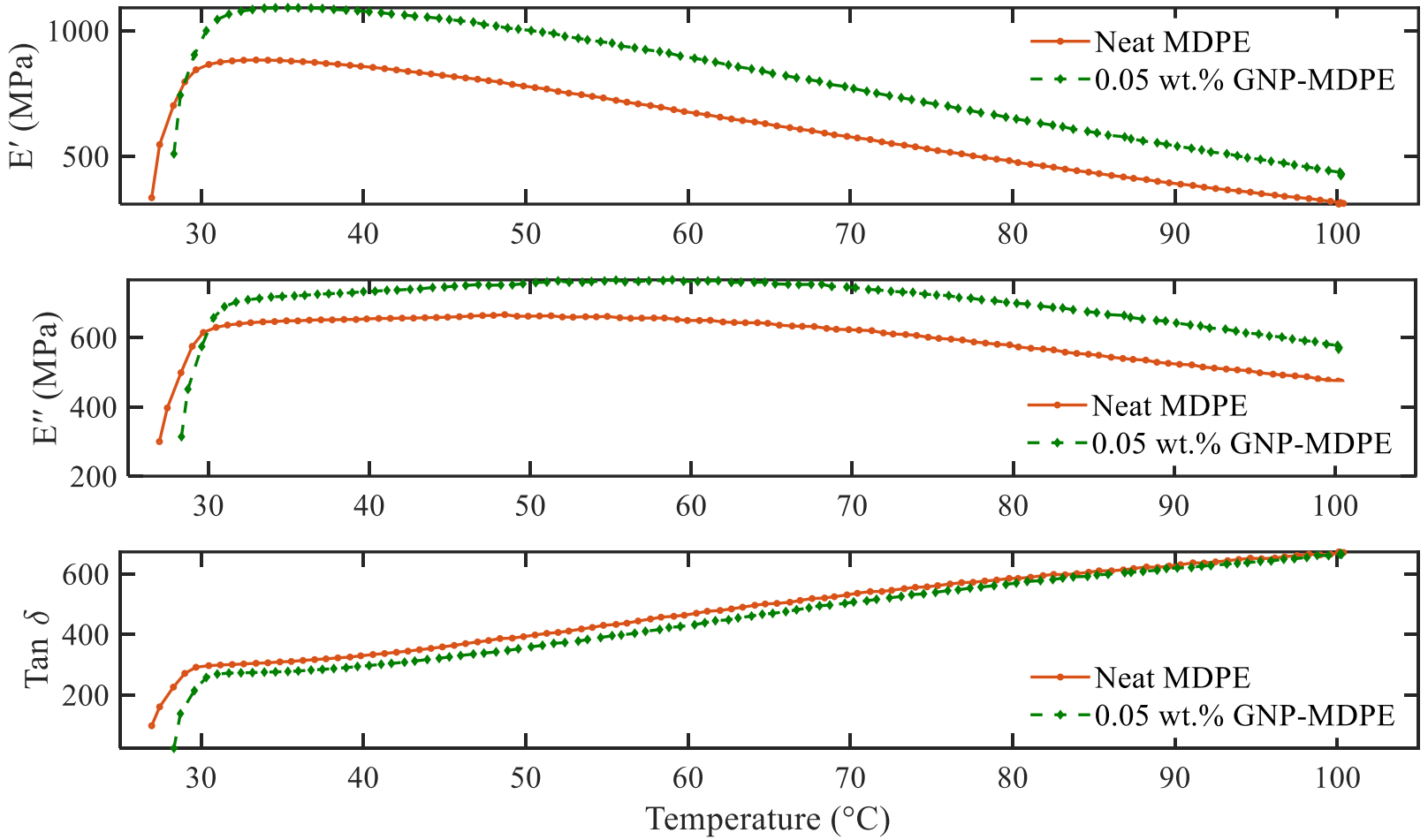

- Test mode: 3-point bending (25 mm span); Heating rate: 5 °C/min
- Specimen size: 30 × 12.5 × 3.5 mm^3; Frequency: 1 Hz
- Temperature range: –40 °C to 100 °C

Khalifa University جامعة خليفة

RiC2D

Gas Permeability test

- **0.05 wt.% GNP** significantly reduced gas permeability in MDPE sheets. GNP/MDPE showed slower pressure drop, indicating **lower gas diffusion rate**.
- GNPs create **tortuous pathways**, hindering gas molecule movement.
- Barrier effect stems from GNP's high aspect ratio and impermeability.
- Low filler loading still provides stable, **long-lasting diffusion resistance.**
- Enhanced gas resistance achieved **without sacrificing processability**.
- **Ideal for hydrogen tanks** where long-term barrier integrity is essential.

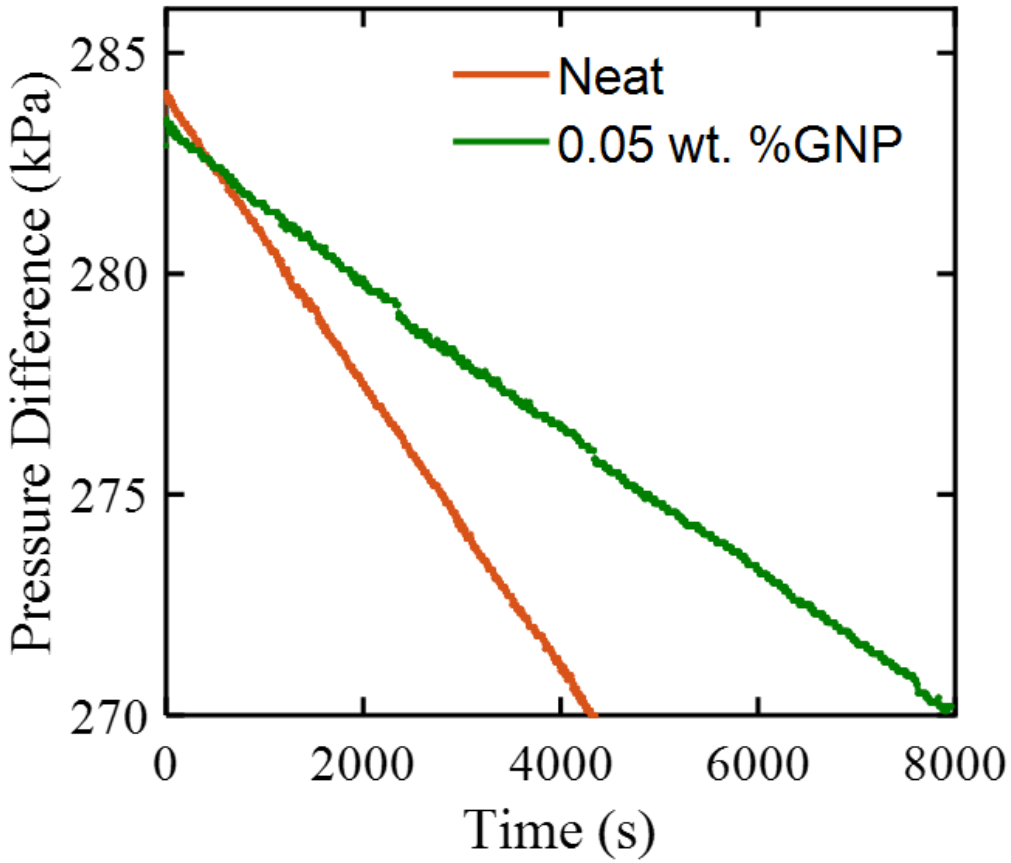

- Test gas: Helium
- Temperature: Room temperature (~25 °C)
- Pressure: Constant 10 bar
- Sample thickness: 0.5 mm

Conclusion

- The addition of GNPs significantly improved MDPE's multifunctional properties, with 0.05 wt.% identified as the optimal concentration. At this level:
  - Tensile strength and stiffness increased by 8.1% and 3.7%,
  - Flexural load and stiffness improved by 23% and 19%,
  - Low-velocity impact tests showed a 5.0% rise in peak contact force and 3.6% higher absorbed energy, indicating better dynamic load resistance.
- Raman spectroscopy and 2D mapping confirmed uniform dispersion at 0.05 wt.% (standard deviation = 0.05), while higher loadings caused agglomeration and reduced performance.
- Thermal analysis revealed: Increased melting point (from 108.5 °C to 111.9 °C)~2.5 °C rise in crystallization temperature due to nucleation
- DMA showed:15.5% increase in storage modulus21.7% increase in loss modulus, indicating improved stiffness and damping
- Helium permeability tests confirmed enhanced gas barrier performance due to well-dispersed GNPs.

These results establish low-GNP MDPE nanocomposites as strong candidates for Type IV hydrogen storage liners, combining mechanical strength, thermal stability, and impermeability.

Thank You



جامعة خليفة
Khalifa University

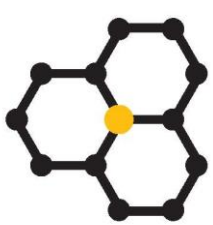

RiC2D

CMH-17
COMPOSITE MATERIALS HANDBOOK

Composite Materials Handbook (CMH-17): An Introduction and Overview

Teresa Vohsen
Wichita State University
National Institute of Aviation Research
Presenting at ICCM24 in Baltimore, MD

Outline

- What is CMH-17?
  - Organization and Operating Structure
  - Our Members and our work
  - Goals
- What does CMH-17 Offer You?
  - Upcoming releases: Vol. 2, 3, 5, 6, and 7
  - Statistics Software
  - Education, Training, and Knowledge Sharing
- How can you get involved?

What is CMH-17?

CMH-17
COMPOSITE MATERIALS HANDBOOK

- CMH-17 stands for the Composite Material Handbook, which is supported by a Composite Material Handbook *Organization*
- The Handbook itself consists of 6 volumes published by SAE, with a 7th in work on non-metallic additive manufacturing
  - The six volumes were originally MIL-HDBK-17 (Vol 1-5) and MIL-HDBK-23 (Vol 6)
  - The FAA took over management near the turn of the century and renamed the organization in 2005
- CMH-17 operates as a volunteer organization comprised of international participants from industry, government, and academia



Key Information about CMH-17

- Aviation authorities rely on CMH-17 to supplement formal guidance:
  - Strong focus on safety, certification efficiency and workforce education
  - Rich record of lessons learned and best practices

- Although funded by the FAA, handbook content is primarily written by industry and reflects priorities of both regulators and industry members:
  - In this unique organization competitors collaborate to document common engineering, manufacturing, and maintenance guidelines and protocols for complex subjects, including those applied to ensure aircraft safety and efficient product certification, which otherwise are typically kept as proprietary practice



Working with CMH-17

Our Members' Experience:

- FAA funded, chaired, and steered organization focused on safety and collaboration
- International networking with technical experts
- Collaboration across companies
- A level playing field for all membership regardless of industry segment
- Unparalleled learning opportunities with tutorials on Certification, Bonded Processes, our Statistics Software, and more

Our Organization Experiences:

- Industry consensus on content like other SDO products
- Thriving technical community of experts
- Over 20 active Working Groups and 15 active Task Groups
- Opportunities for connection, growth, and modernization based on participant feedback
- Peer-reviewed, and balloted content on industry best practices
- Biannual joint coordination meetings to deepen connections and knowledge transfer

CMH-17 Goals

CMH-17
COMPOSITE MATERIALS HANDBOOK

The handbook has three goals/purposes:

1. Provide material data
   - PMC, MMC, CMC, Sandwich Structure, and Non-Metallic AM
   - Physical and mechanical properties
   - Tied to a single material specification AND a single process specification (published elsewhere, but publicly available)
2. Describe how to generate material data
   - Material and process control
   - Test matrices and testing methodologies
   - Statistical methods
3. Describe how to use material data
   - Proven methodologies, engineering solutions, best practices, lessons learned, and case studies for the design, analysis, certification, manufacture, and field support of parts and structures made from advanced materials

- Includes significant information for aerospace applications, with benefit to other applications
- Constitutes overview of advanced composite and additive materials technology and engineering
- Volumes are continuously being updated to reflect advances in industry best practices

What's in the Handbook?

CMH-17
COMPOSITE MATERIALS HANDBOOK

Testing Procedures
Process Controls
Spacecraft Applications

Bonded Processes
Sustain-ability
Material Qualification
Design Tools
Damage Tolerance
Engine Applications
Statistical Material Data
Structural Substantiation
Support-ability
Building Block Approach
Integrated Product Teams
Analysis Methods
Case Studies
Quality and Inspection
Disbond Analysis

Active Items

WHAT DOES CMH-17 OFFER YOU?

Volume 3: PMC Materials Usage, Design, and Analysis

Revision H – planned release Oct 2025

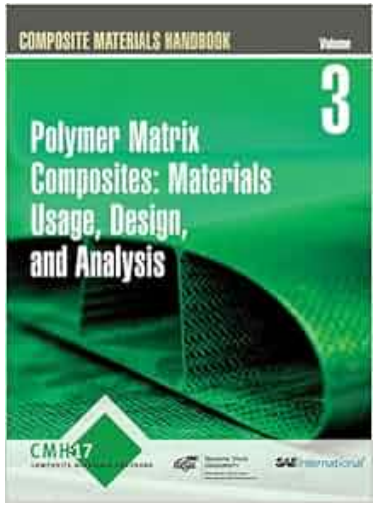

- Volume 3 provides methodologies and lessons learned for the design, analysis, manufacture, and field support of fiber-reinforced PMC structures.
- Also provides guidance on material and process specifications and procedures for utilization of the data presented in Volume 2.
- Information is an extensive compilation of the current knowledge and experiences of the engineers and scientists from industry, government, and academia who actively apply composites to products.

- Rev H has more than doubled in content (990 Rev G pages to over 2000 pages)
  - New content on Building Block Approaches, Damage Tolerance, Structural Bonding, Design, Sustainability and Supportability, Crashworthiness, Engine and Space Applications
  - The tremendous advancement could only be achieved through collaboration and buy-in from all members

Volume 5: Ceramic Matrix Composites

Revision B – planned release Dec 2025

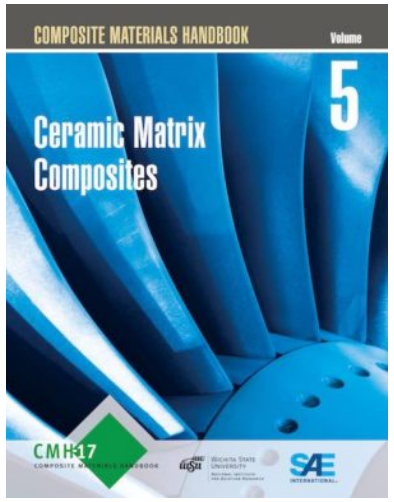

- Volume 5 contains CMC material system properties for which data meeting the specific requirements of the handbook are available.
- Also provides selected guidance on other technical topics related to SiC/SiC and Ox/Ox composites:
  - Material selection of constituents and external coatings
  - Material specifications, processing and quality control
  - Characterization, testing, and data reduction
  - Design and analysis
- Revision B has increased content by about 25% from Rev A
  - New content on Environmental Barrier Coatings, Engine Applications, new Data Sets, increased information on melt infiltrated (MI) SiC/SiC, Attachments, and Testing Methodologies.

Volume 2: PMC Material Properties

Revision J – planned release Spring 2026



- Volume 2 contains reviewed and approved material property data for polymer matrix composites.
  - Data is arranged in categories by reinforcement class and matrix class. Within a category, the data is in chronological order (based on when data was submitted).
  - Data is also divided by full data documentation (including public material specifications) and older partial documentation data
  - Volume 2 Annex contains data with export control restrictions

- Revision J will include new approved data sets

Volume 6: Structural Sandwich Composites

Revision A – planned release Spring 2027

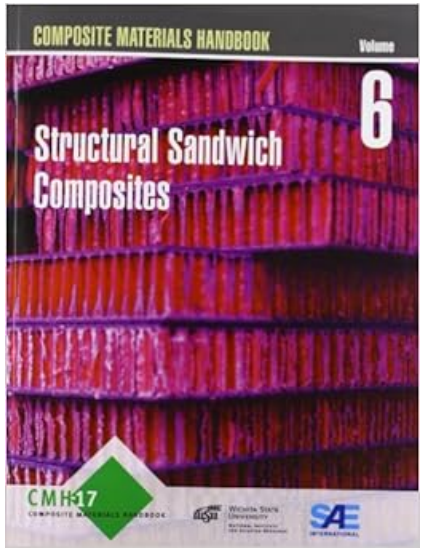

- Volume 6 provides information on the design, analysis, and fabrication of composite sandwich structures
- Includes typical design values for sandwich constituent materials (core, adhesives).
- MIL-HDBK-23 information was incorporated into initial release of Volume 6.
- Revision A will include an increased emphasis on damage tolerance and damage arrestment features as primary design considerations in structural sandwich designs.
  - Volume is being reorganized and expanded from 7 into 12 chapters
  - Will document industry best practices in a range of aircraft applications from cabin interior structures to primary structural components, covering structural design and analysis, material and process controls, manufacturing implementation and maintenance practices
  - Will provide newly developed methods for assessing damage in sandwich structures for maintenance and repair.

Volume 7: Non-Metallic Additively Manufactured Materials – planned release Fall 2026

CMH-17
COMPOSITE MATERIALS HANDBOOK

VOLUME 7
1 CMH-17 AM Introduction And Guidelines
2 Characterization Considerations
3 Evaluation of Feedstock
4 Processing and Manufacturing
5 Quality Control of Production Materials And Processes
6 Material Testing & Characterization For Submission Of Data to CMH-17
7 Property Testing of Additively Manufactured Materials
8 Statistical Methods
9 Evaluation of AM Parts
10 Element Level Testing
11 Design and Analysis
12 Maintainability And Supportability
13 Applications, Case Histories, and Lessons Learned
14 AM Property Data

Volume 7 will be a new volume covering non-metallic AM materials.

Provide knowledge necessary to efficiently design, certify, manufacture, and maintain non-metallic AM parts in aerospace applications

CMH-17 Statistics Software

CMH-17 COMPOSITE MATERIALS HANDBOOK



CMH-17 defines procedures for statistical analysis for composite testing data



Statistical methods included in CMH-17 are available in software form for purchase

Software generates A- and B-basis values and test statistics for material equivalency and acceptance testing (modified coefficient of variation (MOD CV)).

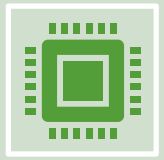

A Python based software is in development to replace the existing Excel based software

New software has finished beta testing and statistical equivalency testing

User Interface is in development

New Software and Tutorial planned for May 2026

Involvement to Influence Content Development and Learning Opportunities

CMH-17
COMPOSITE MATERIALS HANDBOOK

- Our semi-annual meetings are an excellent networking opportunity
- In attendance are subject matter experts (SMEs) from the FAA, EASA, DoD, NASA, the worldwide aerospace industry, and academia
  - Spring meetings are in person at various sites in continental US and fall meetings are virtual
  - Meetings include “all-hands” coordination sessions, a technical forum, and working and task group meetings
  - May include mini-tutorials, FAA-sponsored research reviews, panel sessions, local industry tours
  - Offer optional 6-hour tutorials during our spring in-person meetings
- We plan to aggressively increase our training offerings, both in-person and virtually, to help explain handbook content and share best practices, particularly for the newly revised volumes.
  - Will include opportunities for Q&A with organizational SME



WE'RE WORKING ON A LOT!

New Volumes, New Revisions,
New Software, New Content,
and a New Website format, **cmh17.org**

PLEASE JOIN US

Getting Involved with Us – CMH-17.org

- Attend our meetings
- Join a Working Group or Task Group
- Follow us on LinkedIn
- Join our mailing list
- Attend one of our learning opportunities

Follow us on LinkedIn!

- **There is no CMH-17 membership fee for you or your company**
  - In-person meetings have modest fee to cover meeting and food costs
  - Fees are charged for tutorials

Our Next Meeting – Fall 2025

CMH-17
COMPOSITE MATERIALS HANDBOOK

- Virtual Meeting
- Tuesday-Thursday Oct 28th-30th, Nov 4th-6th
- 4 Hours a day
- info@cmh17.org

A NOVEL SLEEVE ASSEMBLY METHOD FOR SPM MOTORS USING CFRP WITH ATYPICAL LAYUP

Kazunori Takagaki, Ichiya Takahashi, Masami Kume, Tatsuya Koyama and Hiroki Kobayashi[1]

[1] Composite & Ceramic Material Section, Materials & Processing Technology Department,
Advanced Technology R&D Center, Mitsubishi Electric Corporation
8-1-1, Tsukaguchi-Honmachi, Amagasaki City, Hyogo 661-8661, Japan
Email: Takagaki.Kazunori@ak.MitsubishiElectric.co.jp
web page: https://www.mitsubishielectric.com/en/

Keywords: Carbon fibre, Polymer-matrix composites (PMCs), Anisotropy, Mechanical properties, Laminate mechanics

ABSTRACT

Motor is one of the most important components for industry. Some of surface permanent magnet (SPM) motors have sleeves made of carbon fibre reinforced plastics (CFRPs) to prevent magnets from separating during operation. Though the CFRP sleeve is conventionally assembled by press fitting, this process is cost intensive. Therefore, this research aimed to propose a novel sleeve assembly method for the SPM motors to reduce the cost and the press-fit pressure. For the purpose, a theoretical analysis based on the classical lamination theory was carried out and the concept of 'anomalous Poisson's effect' was proposed. This is the coupling effect of an anisotropic material, inducing normal strain by shear force. The optimized layup was determined to maximize the tension in the circumferential direction after assembly. A CFRP cylinder was then fabricated to experimentally validate the theoretical result. Torsion test was carried out on the cylinder, successfully confirming the validity of the anomalous Poisson's effect. In addition, a concept was proposed to prevent interaction between the cylinder and core during assembly.

1 INTRODUCTION

Motor is one of the most important components for industry. It is a key element for electric vehicles, factory automation and so on. Since motors consume more than 40% of global electricity consumption [1], improving their performance is a crucial issue for addressing global warming as well as for cost reduction.

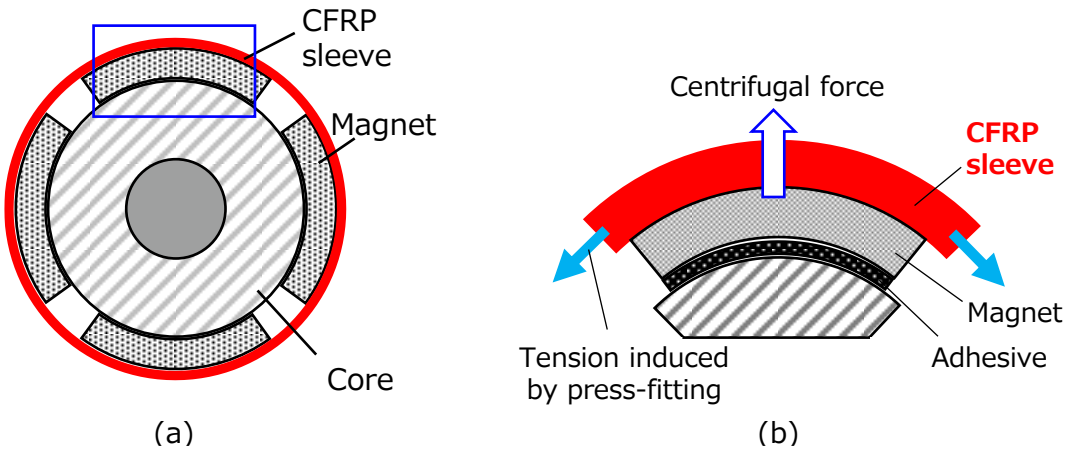

Figure 1: Schematic of rotor of SPM motor with CFRP cylinder.
(a) Cross sectional view of whole structure. (b) Enlarged view of blue line in (a).
Core and magnets are press-fitted, inducing tension in CFRP. It prevents the magnet from leaving from the core under centrifugal force.

Surface permanent magnet (SPM) motors have magnets mounted on the rotor cores and are highly efficient. Figure 1 depicts schematic of a SPM motor. SPM motors with high-speed rotation use sleeves to prevent the magnets separating from the cores under the centrifugal force. Since high strength materials are desirable for the sleeve, carbon fibre reinforce plastic (CFRP) has been adopted for some of SPM motors. A CFRP cylinder is assembled onto the core by press-fitting, making the motor manufacturing process uneconomical. This research proposes a novel sleeve assembly process with CFRP having an atypical stacking sequence to reduce the cost and the press-fit pressure.

2 CONCEPT AND THEORETICAL ANALYSIS

2.1 Basic Concept

Figure 2 illustrates the schematic of the conventional and proposed assembly processes. As shown in Figure 2 (a), the conventional method utilizes a CFRP with fibres mainly aligned in the circumferential (0°) direction. A core and magnets are press-fitted into a CFRP, inducing tension due to the change in the circumferential length of the CFRP. Meanwhile, the basic concept of the assembly process proposed in this research is to use a CFRP cylinder which expands in the radial direction when it is subjected to torsion. Torque generally do not affect diameters of cylinders made of isotropic materials (e.g., metals and polymers), and the same is true for even CFRP with a harmonic layup. The torsion-diameter coupling, however, is achieved by activating the coupling effect of an anisotropic material. Based on the analogy to the Poisson's effect, the phenomenon is called 'anomalous Poisson's effect' in this research. The middle image in Figure 2 (b) depicts the expanded CFRP under torque. After inserting the core and magnet into the expanded CFRP, the torque is released, and more preferably CFRP is twisted in the opposite direction to induce tension as shown in the bottom figure. This assembly method tightly holds the magnets in place while eliminating press-fitting process. The layup of the CFRP is discussed in the following section.

2.2 Theoretical analysis

For simplicity, CFRP with two fibre direction ($[\theta_1/\theta_2]_{2S}$) was considered in this research. Figure 3 illustrates the coordinate system used in this research. According to the classical lamination theory (CLT), resultant force is written as

$$\begin{Bmatrix} \boldsymbol{N} \\ \boldsymbol{M} \end{Bmatrix} = \begin{bmatrix} \boldsymbol{A} & \boldsymbol{B} \\ \boldsymbol{B} & \boldsymbol{D} \end{bmatrix} \begin{Bmatrix} \boldsymbol{\varepsilon}^0 \\ \boldsymbol{\kappa} \end{Bmatrix} \tag{1}$$

where $\{\boldsymbol{N}\}$ and $\{\boldsymbol{M}\}$ are force and moment resultant with three dimensions, $[\boldsymbol{A}]$, $[\boldsymbol{B}]$,and $[\boldsymbol{D}]$ are 3x3 stiffness matrices, and $\{\boldsymbol{\varepsilon}^0\}$ and $\{\boldsymbol{\kappa}\}$ are neutral plane strains and curvatures with three dimensions. For specific derivation and values, see a reference [2] for example. This research deals with symmetric laminates and therefore does not consider bending moment. Thus, $[\boldsymbol{B}]$ and $[\boldsymbol{D}]$ matrices are ignored as

$$\begin{Bmatrix} N_x \\ N_y \\ N_{xy} \end{Bmatrix} = \begin{bmatrix} A_{11} & A_{12} & A_{16} \\ A_{12} & A_{22} & A_{26} \\ A_{16} & A_{26} & A_{66} \end{bmatrix} \begin{Bmatrix} \varepsilon_x^0 \\ \varepsilon_y^0 \\ \gamma_{xy}^0 \end{Bmatrix} \tag{2}$$

where ε^0 and γ^0 are normal and shear strains at the neutral plane. The subscripts *x* and *y* represent the directions of a laminate. Assuming that only torque is applied to the cylinder, shear force N_{xy} is solely induced and eq. (2) is transformed as

$$\begin{Bmatrix} \varepsilon_x \\ \varepsilon_y \\ \gamma_{xy} \end{Bmatrix} = \begin{bmatrix} [A]^{-1}{}_{11} & [A]^{-1}{}_{12} & [A]^{-1}{}_{16} \\ [A]^{-1}{}_{12} & [A]^{-1}{}_{22} & [A]^{-1}{}_{26} \\ [A]^{-1}{}_{16} & [A]^{-1}{}_{26} & [A]^{-1}{}_{66} \end{bmatrix} \begin{Bmatrix} 0 \\ 0 \\ N_{xy} \end{Bmatrix} = \begin{Bmatrix} [A]^{-1}{}_{16} \\ [A]^{-1}{}_{26} \\ [A]^{-1}{}_{66} \end{Bmatrix} N_{xy} \tag{3}$$

where $[A]^{-1}{}_{ij}$ indicates the $[i, j]$ component of the inverse matrix of the in-plane stiffness matrix $[\boldsymbol{A}]$.

Although several failure criteria exist [3], the maximum strain theory was adopted in this research due to its simplicity. Based on the theory, the maximum allowable shear force is shown as

$$N_{xy\,\max} = \min\left(\frac{Y_1^-}{{\varepsilon_1}^1}, \frac{Y_1^+}{{\varepsilon_1}^1}, \frac{Y_2^-}{{\varepsilon_2}^1}, \frac{Y_2^+}{{\varepsilon_2}^1}, \frac{Y_{12}}{|{\gamma_{12}}^1|}, \frac{Y_1^-}{{\varepsilon_1}^2}, \frac{Y_1^+}{{\varepsilon_1}^2}, \frac{Y_2^-}{{\varepsilon_2}^2}, \frac{Y_2^+}{{\varepsilon_2}^2}, \frac{Y_{12}}{|{\gamma_{12}}^2|}\right) \quad (4)$$

where ε and γ represent the normal and shear strains induced by unit shear force $N_{xy} = 1$, and Y is the maximum allowable strain. The superscripts on the strains represent the fibre directions of the layup ($[\theta_1/\theta_2]_{2S}$), and the superscripts of Y show tension, +, and compression, -. The subscripts 1 and 2 represent fibre and transverse directions, respectively. Each value used in this research is shown in Table 1. Note that all the strains in eq. (4) are the strains in the fibre and transverse direction of each ply. From eqs. (3) and (4), the maximum strain induced by the shear force, $\varepsilon_{x\,max}$, is written as

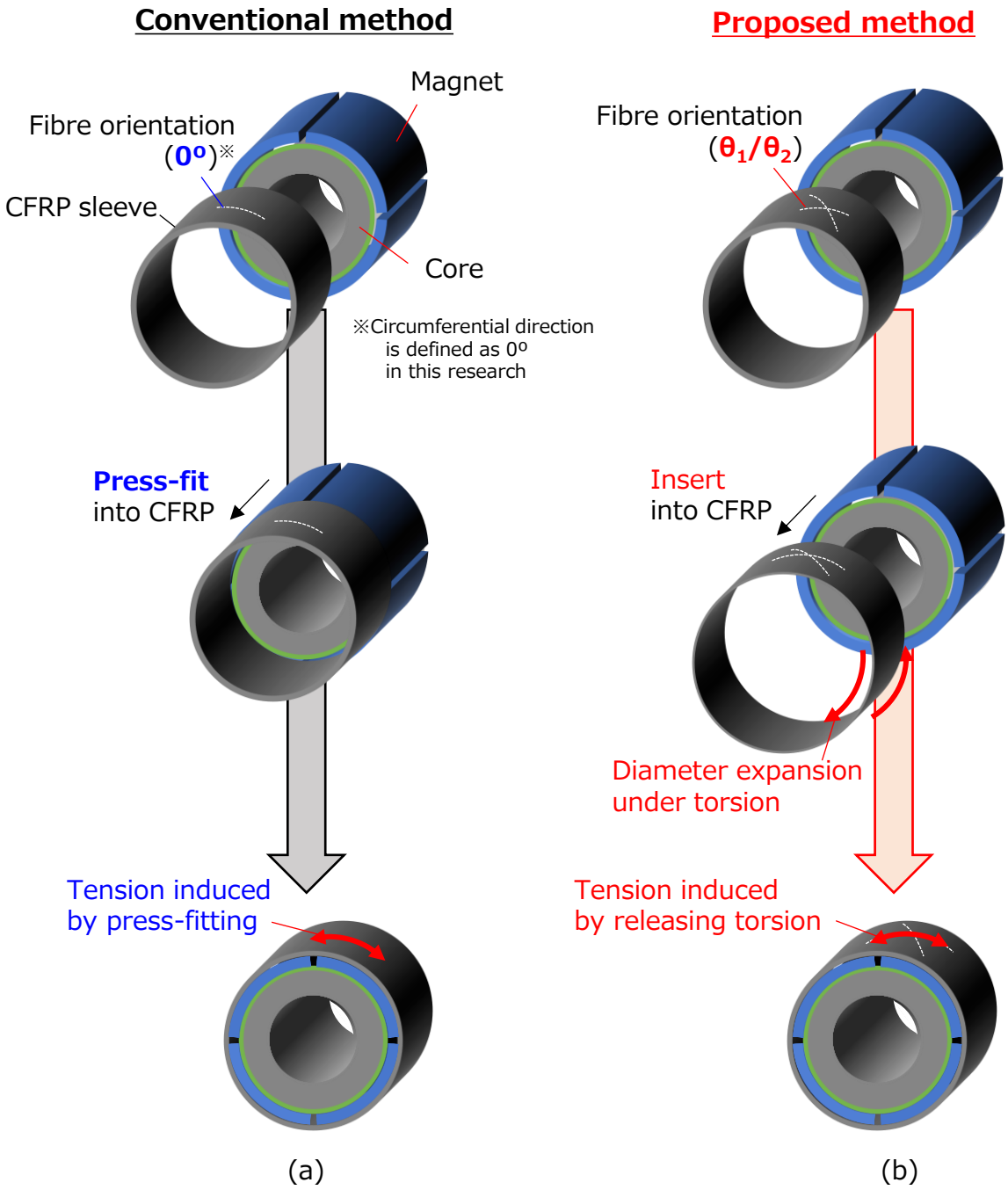

Figure 2 Assembly process of CFRP cylinder. (a) conventional press-fit method, (b) proposed method using CFRP cylinder with atypical layup.

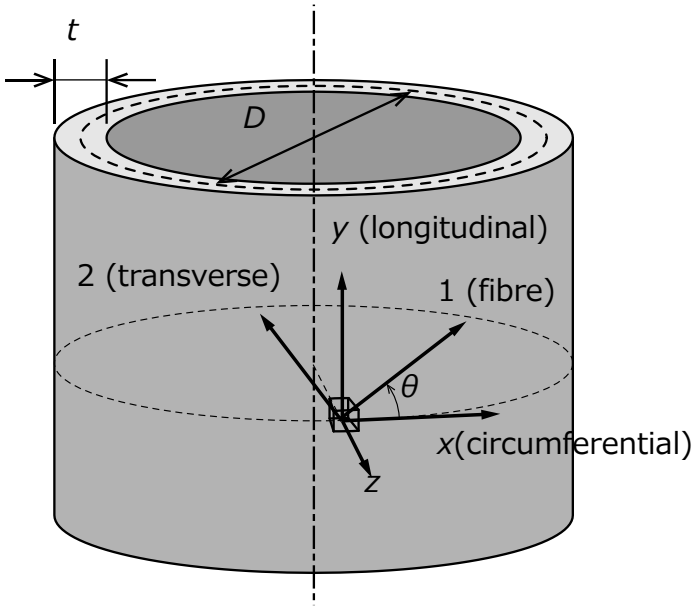

Figure 3 Coordinate system on CFRP cylinder.

$$\varepsilon_{x\,max} = [A]^{-1}{}_{16} \cdot N_{xy\,\max} \tag{5}$$

Assuming that the *x* direction corresponds to the circumferential direction of the cylinder, the maximum strain in the circumferential direction is calculated by eq. (5).

Then the tension in the circumferential direction after releasing torque is calculated, which corresponds to the bottom image in Figure 2 (b). Assuming that the forces in the longitudinal and shear direction would be negligible after releasing torque, only the circumferential force, N_x in eq. (2) exists and eq. (2) reduces to

$$\begin{Bmatrix} \varepsilon_x \\ \varepsilon_y \\ \gamma_{xy} \end{Bmatrix} = \begin{bmatrix} [A]^{-1}{}_{11} & [A]^{-1}{}_{12} & [A]^{-1}{}_{16} \\ [A]^{-1}{}_{12} & [A]^{-1}{}_{22} & [A]^{-1}{}_{26} \\ [A]^{-1}{}_{16} & [A]^{-1}{}_{26} & [A]^{-1}{}_{66} \end{bmatrix} \begin{Bmatrix} N_x \\ 0 \\ 0 \end{Bmatrix} \tag{6}$$

Assuming no gap between the expanded cylinder and the core, $\varepsilon_{x\,max}$ in eq. (5) corresponds to ε_x in eq. (6), leading to the circumferential force, N_x, after releasing torque as

$$N_x = \frac{\varepsilon_{x\,max}}{[A]^{-1}{}_{11}} = \frac{[A]^{-1}{}_{16}}{[A]^{-1}{}_{11}} \cdot N_{xy\,max} \tag{7}$$

The circumferential stress is obtained by dividing the circumferential force in eq. (7) by thickness of the cylinder, *t*, as

$$\sigma_x = \frac{N_x}{t} \tag{8}$$

Calculations were carried out for all sets of two fibre directions, θ_1 and θ_2, with 1° increments from 0° to 90°.

2.3 Analysis Results

Figure 4 shows the strain, ε_x, calculated by eq. (3) with unit shear force (i.e., N_{xy}=1). The strain, ε_x, corresponds to the circumferential strain in the cylinder case. The horizontal and vertical axes represent fibre directions, θ_1 and θ_2, respectively. The map has symmetrical contour, and several areas have high strain value above 30 με. Meanwhile, strain is not induced with harmonic layups (i.e., $\theta_2 = -\theta_1$ line in the figure), verifying the calculation.

Figure 5 (a) shows the maximum strain calculated by eq. (5). The maximum strain above 1.2% is

achievable. Note that thought the areas with strain above 1.2% matches to the high strain area in Figure 4, the maximum strain are relatively low at the high strain area at the top right and bottom left in Figure 4. This would be because different criterions in eq. (4) were applied in different areas. Figure 5 (b) shows the stress after releasing torque calculated by eq. (8). The highest stress value is above 350 MPa at the vicinity of $\theta_1 = \theta_2 = 0°$ where the fibres wound in the circumferential direction of the cylinder.

Figure 6 replots the relationship between the maximum strain (Eq. (5)) and stress after releasing torque (Eq. (8)). Each point represents a set of two fibre directions, θ_1 and θ_2. Though the maximum strain exceeds 1.2% with some layups, the stress remains relatively low, below 200 MPa. The main purpose of this research is to achieve high tension (i.e., circumferential stress) to prevent the magnets from separating from the cores. Therefore, the layup circled in red in Figure 6 was chosen for the following experiment since the highest stress is expected. Note that though the maximum strain is 0.43%, which is about one third of the highest value with another layup (above 1.2%), the diameter expands by approximately 430 μm for a cylinder with a diameter of 100 mm, for example. Since the typical fitting tolerance between a cylinder and a column is about 100 μm, 430 μm is enough for insertion.

Table 1 Material properties used for theoretical analysis.

		Unit	Value
Elastic Property	Fiber direction, E_1	GPa	156
	Transverse direction, E_2	GPa	8.87
	Shear, G_{12}	GPa	4.67
	Poisson's ratio, ν_{12}	-	0.34
Failure strain	Fiber direction/ Tension, Y_1^+	%	1.58
	Fiber direction/ Compression, Y_1^-	%	0.95
	Transverse direction/ Tension, Y_2^+	%	1.00
	Transverse direction/ Compression, Y_2^-	%	2.00
	Shear, Y_{12}	%	2.57

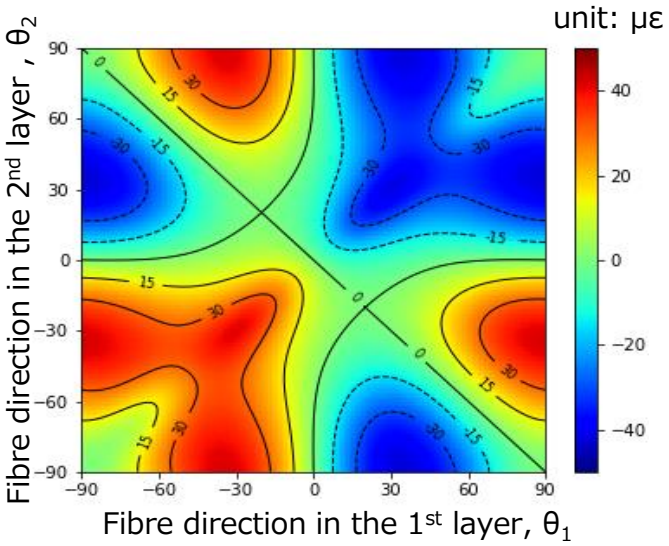

Figure 4 Circumferential strain, ε_x, induced by unit shear force (Eq. (3)).

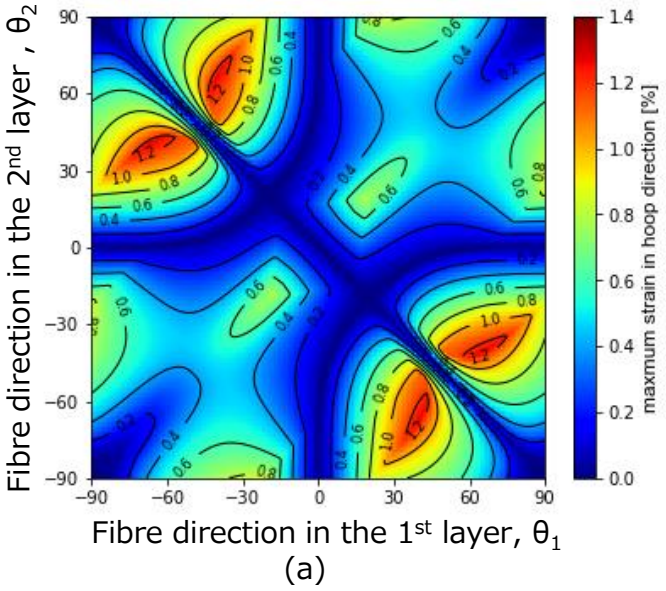

Figure 5 Maximum strain and stress. (a) strain (Eq. (5)), (b) stress (Eq. (8)).

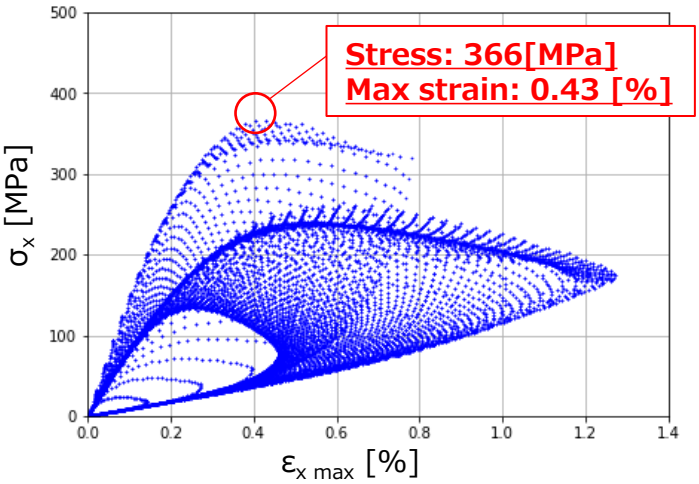

Figure 6 Maximum stress as a function of maximum strain.

3 EXPERIMENTAL VALIDATION

3.1 Materials and Method

A CFRP cylinder having the designed layup was fabricated. The manufacturing method was sheet winding using prepreg with PAN-based carbon fibre. Considering thickness and fibre direction of the laminate, prepregs were cut into rectangular shapes. The prepregs were then wound around a steel carbon mandrel. Whole the prepregs and mandrel were covered with a breather and a vacuum bagging film. The sample was vacuumed and cured in an autoclave at a gauge pressure of 0.6 MPa. The cure process included 1°C/min heating and 170°C holding for 4 hours. Shape measurement of the cured cylinder verified that the cylinder was fabricated with the designed diameter and almost perfect circle in the cross-section.

The cylinder was then mounted on a torsion testing machine. Figure 7 (a) shows a photograph of the testing machine and the mounted cylinder. Four triaxial strain gauges were attached to the specimen, with two orthogonal axes of each gauge aligned with the coordinate axes shown in Figure 3. The gauges were positioned at the longitudinal centre of the specimen, corresponding to the four cardinal directions on its cross section. Figure 7 (b) illustrates a schematic of the cross-sectional view of the test setting. Test fixtures were used to connect the cylinder and testing equipment. The fixtures and the cylinder were adhesively jointed, and the fixtures and the testing equipment were pin-connected. Torsion was applied to the cylinder at a rotational speed of 0.5 deg/min until torque dropped. Strains measured by the attached strain gauges and torque were concurrently recorded every 0.1 second.

3.2 Experimental Results and Discussion

Figure 8 shows the measured strains as a function of applied torque. Figure 8 (a) is the result of strain measured by the gauges attached in 45° direction. The four values are almost consistent, confirming that the torque was appropriately applied. The circumferential strain (Figure 8 (b)) increased almost linearly with torque. The average value of the slope was 663 με/kNm, which is well consistent with the theoretical value (743 με/kNm), experimentally proving the anomalous Poisson's effect proposed in this research. The variations of the measured strains would be caused by variations during mounting on the test equipment. Figure 8 (c) depicts the longitudinal strain. The longitudinal strains at the SG1 and SG3 have different trend from that of the SG2 and SG4, which implies a bending moment was present during mounting.

Meanwhile, the maximum torque was about 0.7 kNm, which is less than half of the expected value. Sample observation after the test revealed that the drop in torque is likely to be caused by an adhesive

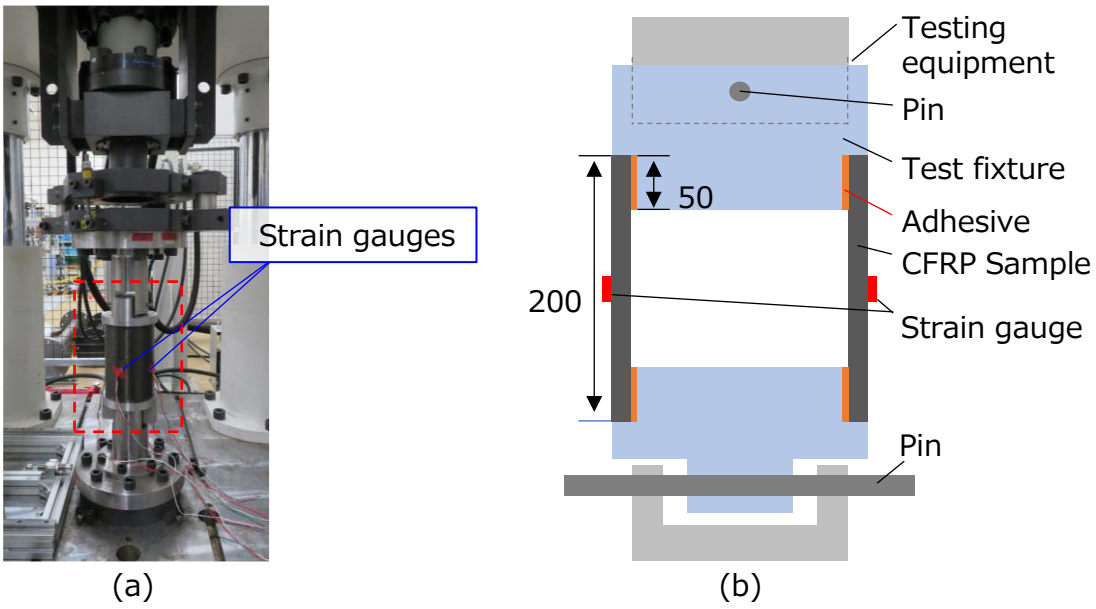

Figure 7 Test setup. (a) Photograph of setup, (b) Schematic of dotted red line in Figure (a).

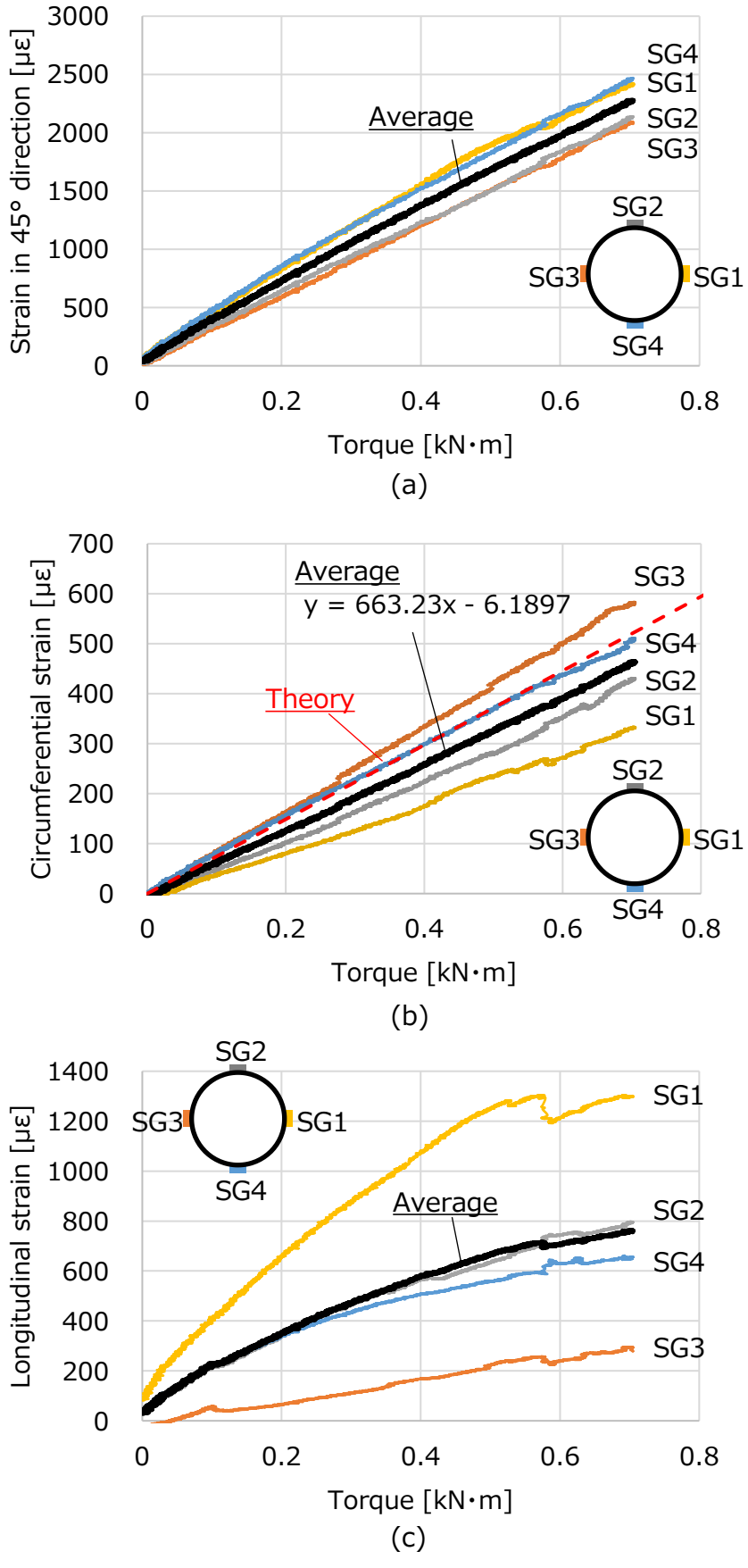

Figure 8 Measured strains as a function of torque. (a) 45°, (b) Circumferential, (c) Longitudinal.

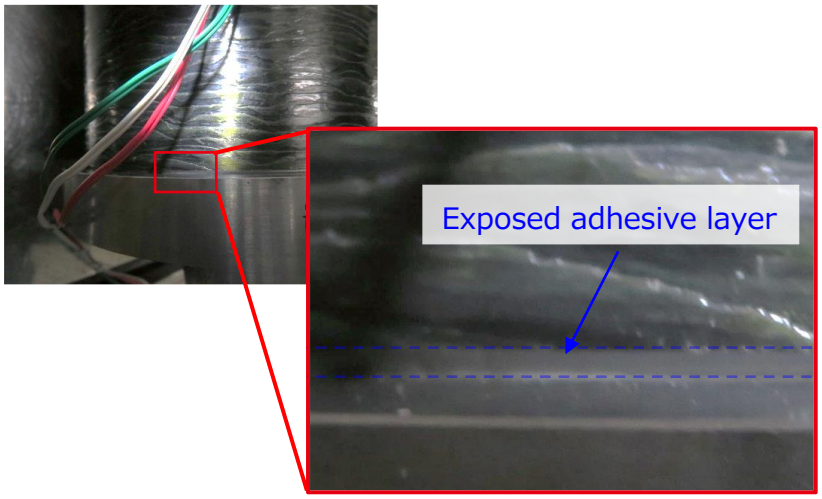

Figure 9 Photograph of edge area of CFRP cylinder after test.

failure between the test fixture and the cylinder, because no damage was observed in the cylinder (Figure 9). Though the bonding length was determined considering adhesive strength and applied torque, defects in the adhesion would have resulted in the failure. Mechanical joint is preferable to avoid process uncertainties commonly found in adhesive joints. However, with uniform cross section, the mechanically attached rigid fixture constrains deformation in the circumferential direction, preventing core insertion (Figure 10 (a)). Therefore, this research suggests a solution concept. This includes a CFRP cylinder with a tapered section where the grip fixture is attached (Figure 10 (b)). Although the attached area, similar to the uniform cross section, barely deforms, there is sufficient clearance between the core and the cylinder owing to the taper angle. Consequently, the core can be successfully inserted into the straight section of the cylinder without interaction. Future work will evaluate the validity of this proposed method.

4 CONCLUSION

This research aimed to propose a novel sleeve assembly method for SPM motors to reduce the cost and the press-fit pressure. The basic concept of the method is to use anisotropy of a CFRP and realize the ‘anomalous Poisson’s effect’. The effect induces normal strain by shear force. Theoretical analysis for the effect was carried out based on the classical lamination theory. The result led to a layup to maximize tension after the assembly while keeping enough clearance between the cylinder and core during assembly. Then a CFRP cylinder with the layup was fabricated to validate the theoretical analysis result and anomalous Poisson’s effect. Torsion test was conducted with the cylinder and the circumferential strain increased with torque, successfully confirming the anomalous Poisson’s effect. Furthermore, the strain increment with unit torque was 663 με/kNm, which is consistent with the theoretical value (743 με/kNm). Additionally, a cylinder design with a tapered section was proposed to prevent the interaction between test fixture and the core during insertion, which was an issue found in the experiment. Future work will evaluate the validity of this method.

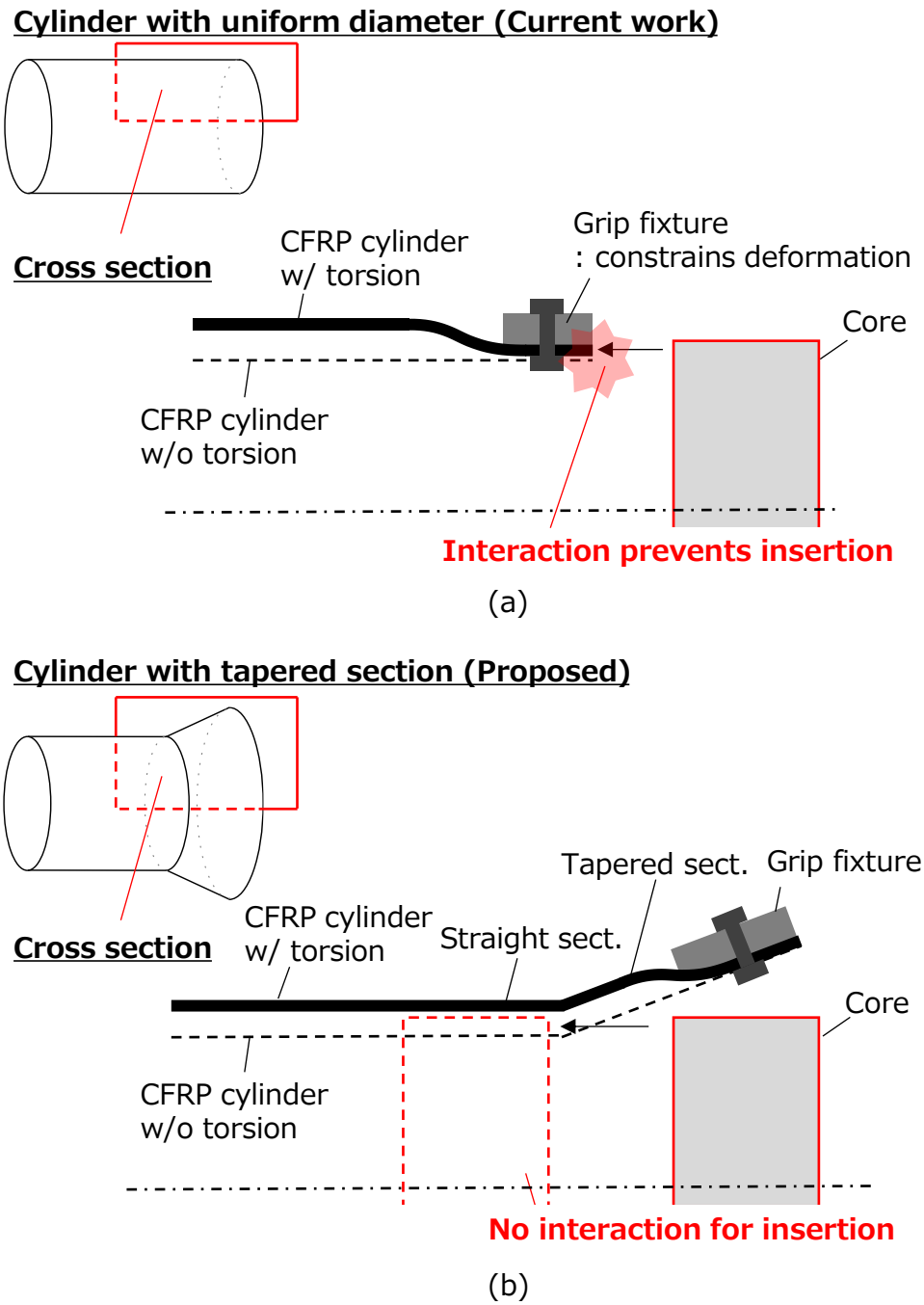

Figure 10 Schematic of assembly methods.
(a) Cylinder with uniform diameter, (b) Cylinder with tapered section.

REFERENCES

[1] P. Waide and C. U. Brunner, Energy-efficiency policy opportunities for electric motor-driven systems, *International Energy Agency Report*, 2011.

[2] R. G. Reid and R. Paskaramoorthy, An extension to classical lamination theory for use with functionally graded plates, *Composite structures*, **93**(2), 2011, pp. 639-648 (doi: 10.1016/j.compstruct.2010.08.015).

[3] M. Zako and T. Kurashiki, Introduction to Composite Materials Mechanics, Chapter 10 Strength of Composite Materials (in Japanese), *Journal of the Japan Society for Composite Materials*, **23**(4), 1997, pp. 144-150.

Singapore Institute of Manufacturing Technology

A*STAR SIMTech

Feasibility of Developing Fiber-Reinforced Polymeric Composite Couplers for Hydrogen Transmission Pipelines

Q. Wang[1], Z. A. Wu[1], Z. Su[2], P. Pitchai[2], R. Muhammad[2], A. W. M. Yek[1], H. Huang[1], W. S. Teo[1], C. Wang[1*], and A. Haris[1*]

Presenter: Dr. Andi Haris
Senior Scientist, SIMTech, A*STAR

Date: 6th Aug 2025

*Andi_Haris@simtech.a-star.edu.sg

[1] Singapore Institute of Manufacturing Technology (SIMTech), A*STAR

[2] Institute of High-performance Computing (IHPC), A*STAR

ICCM24
24TH INTERNATIONAL CONFERENCE ON COMPOSITE MATERIALS



Singapore Institute of manufacturing Technology (SIMTech), A*STAR



Almost the furthest flight to ICCM



Singapore Institute of Manufacturing Technology

(5 Cleantech Loop, #01-01, CleanTech Two Block B, Singapore 63673)

MTI MINISTRY OF TRADE AND INDUSTRY SINGAPORE

Agency for Science, Technology and Research SINGAPORE

Singapore Institute of Manufacturing Technology SIMTech

A world-class innovation partner in advanced manufacturing technologies, systems and capabilities

- Founded in 1993
- SIMTech have 400+ staff, ~90 students

Manufacturing will be Smarter, Greener and More Connected in the Future

Next-Gen Manufacturing Processes

- 4D Additive Manufacturing
- Adaptive Machining & Surface Engineering
- Hybrid & Multi-Materials Forming
- MedTech Manufacturing
- Extreme Manufacturing
- ***Advanced Polymer and Composite processing***

Industry 5.0

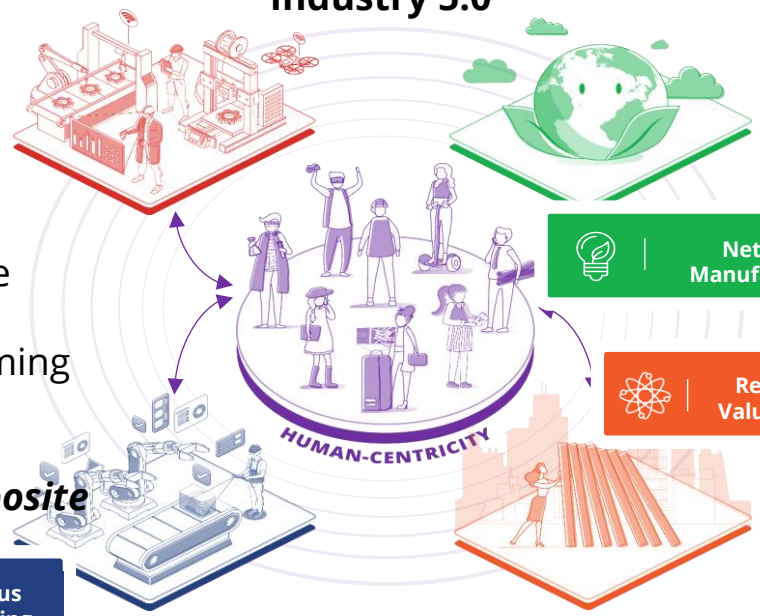

Enabling Data-Driven and Knowledge-Based Manufacturing with Workforce Augmentation Technologies

Polymer and Composite Processing Group @ SIMTech

- 01. Injection Moulding Process
- 02. Sheet Compression Moulding & Thermoforming
- 03. Extrusion and Additive Manufacturing
- 04. Lightweight Design and Process Simulation


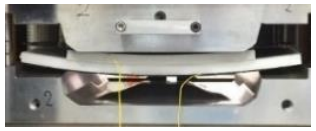

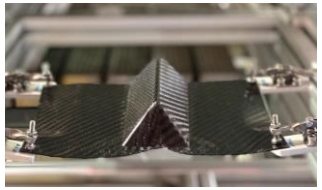

- Vacuum Forming
- 2IR Composite Thermoforming
- Compression Moulding
- In-situ consolidation
- In-situ polymerization



❑ Polymer Injection Moulding (Auburg Allrounder 570H, 200T, 2500bar, 450°C)



❑ Injection Compression Moulding (Witmann Ecopower 110, 110T, 2100bar, 350°C)



❑ High Temperature Extruder (Leistritz ZSE 27 MAXX, L/D ratio: 48, screw Diameter: 27mm, 450°C, melt pressure: 220 bar)



❑ Integrated Composite Thermoforming (320T-1.2x1.2m 125kW 2IR)



❑ Hot Press Sheet Consolidator (60T-40x40cm platen - 450°C, equipped with a water chiller)



❑ Vacuum Thermoforming (Formech HD1500, 1.5x1m,x10mm, 55kW quartz heater)



❑ Vacuum Thermoforming (CMS eidos se 1.5x1mx10mm, 75kW halogen heater)



❑ Microinjection Moulding (Babyplast, 6T, 1850bar, 75x75x70mm mould)



❑ Drying oven (Gen lab, 1.6x1.1m sheet size, 50 sheets 250°C)



❑ Composites Curing Oven (OV301 - 1070x440x500mm - 200°C)



❑ Portable Hot Bonder (Aerofom Composites AHB-380-s, 16 Amp or 32 Amp and 10 thermocouples

Background: Strategy of Hydrogen Pipeline in Singapore

Hydrogen Value-chain and Status

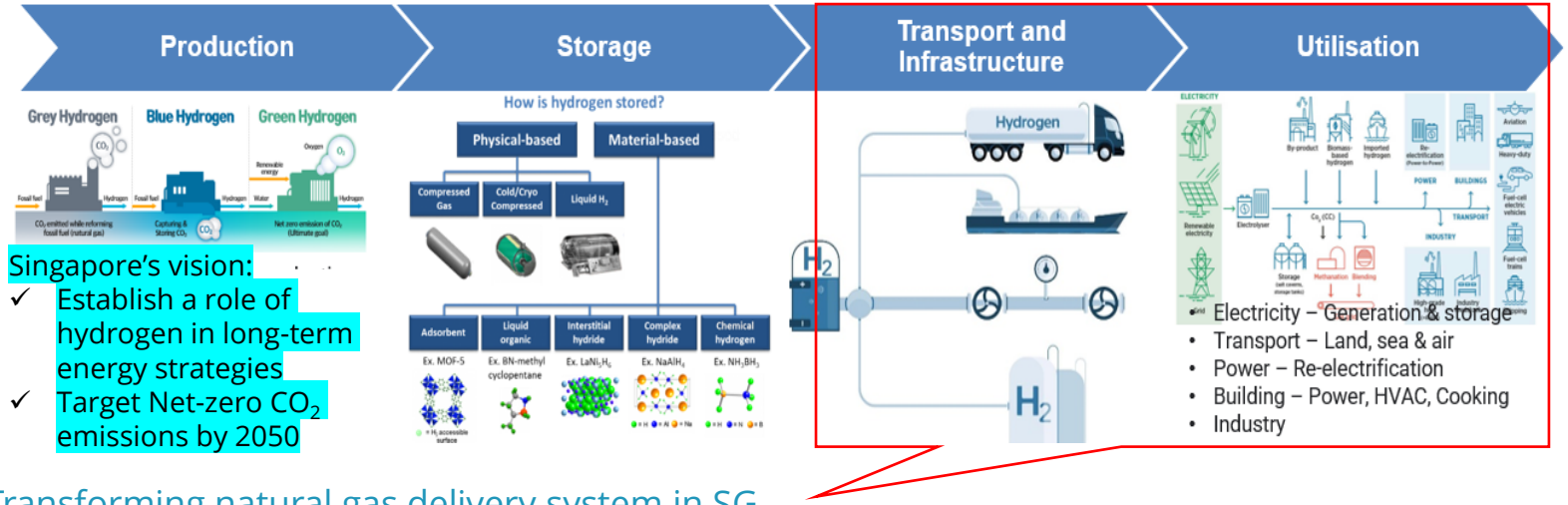

Singapore's vision:

- ✓ Establish a role of hydrogen in long-term energy strategies
- ✓ Target Net-zero CO_2 emissions by 2050

Low-Carbon Energy Research (LCER) Funding Initiative

- Directed Hydrogen Programme and Emerging Technology Grant
- Phase 1 since 2021 – S$55 Mil
- Phase 2 since 2024 – S$55 Mil

MTI Ministry of Trade and Industry Singapore
National Research Foundation Prime Minister's Office Singapore
LCER

Transforming natural gas delivery system in SG

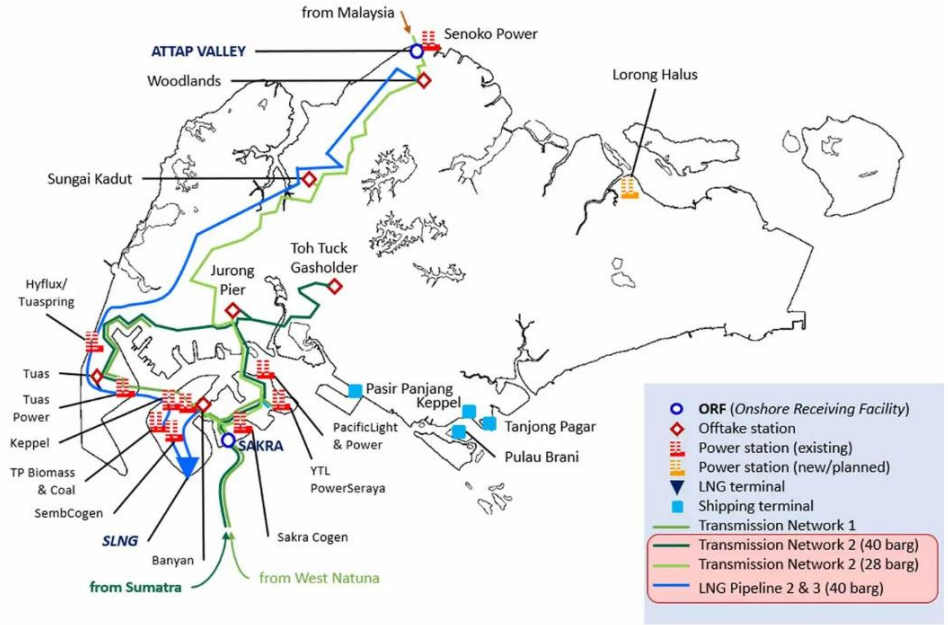

- Hydrogen transmission and receiving infrastructure is not ready in Singapore. The solution of hydrogen fuel distribution from filling stations or tanks are absent.
- Augmentation of the network such as additional pipelines and larger pipe configurations, would be required to ensure that supply can continue meeting required hydrogen energy demand of end-users.
- One possibility for rapidly expanding the hydrogen delivery infrastructure is to adapt part of the natural gas delivery.
- Both metal and fiber-reinforced composite pipelines are currently used in the gas transmission network in SG. But metal pipeline systems are not suitable for hydrogen due to hydrogen embrittlement.

Background: Review of Existing Pipeline System

Pipeline system	Applications	Materials	Operating pressure	Distribution pressure	Remarks
U.S. Natural Gas (NG) Pipeline [1]	Electric power production and split between residential and commercial uses	Carbon steel, API 5L A, B, X42 and X46	42 – 84 bar (OD 4 inch to 48 inch)	less than 17.2 bar (OD 0.5 inch to 8 inch)	
SG Town Gas (TG)	for industrial, eating houses and residential	Carbon steel X60 05 X65 grade	3 barg	0.5 barg and 0.02 barg	The pipes are internally coated with 75 micron epoxy and 2.5mm, 3-layer Polyethene coating. Welded
SG NG pipeline [2]	for power stations and industrial uses	Carbon steel for operation and PE for distribution	28 and 40 barg	3-6 barg	The Design Pressure is 50 barg and Test Pressure is 62.5 barg.
Strohm thermoplastic composite pipe (TCP)	Suitable for CO2 and Hydrogen transport	Carbon – PVDF Carbon – PA12 Fiberglass - HDPE	Failure at max 689 bar		Grades with different temp limit, 65, 80 and 121 °C.
SoluForce TCP	Hydrogen transmission	Not released	42 bar (OD 4-6 inch)		Flexible pipe system with nonmetal fitting

Current Technology for Pipe Connectivity and Limitations

Metallic coupler with mechanical joints

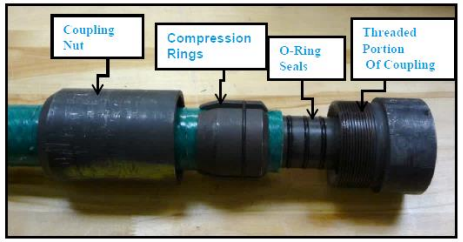

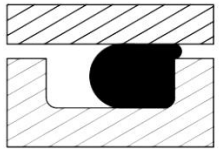

Compression of O-Ring seals



Failure of O-Ring seals

- A metallic joint with elastomer O-ring seals.
- Lack of durability in H_2.
- O-ring sealing fail during fatigue testing of the structural layer at all pressure levels for hydrogen pipes.

Polymer Electrofusion Coupler

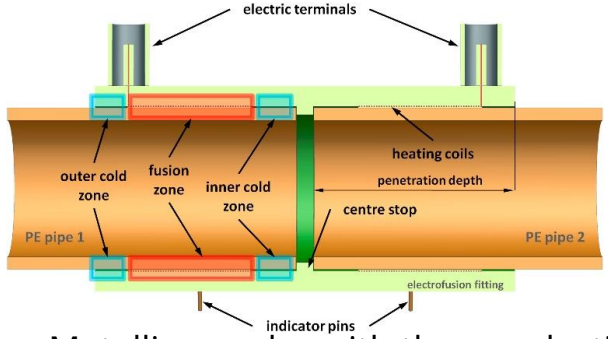



Leakage / Crack at fusion interface

- Metallic coupler with thermoplastic liner, being used in current NG and geothermal pipeline system
- Limited to a very low-pressure pipe system, energy-intensive
- Once the fusion process is completed, the joint is considered permanent and unrepairable

Growing trend of using fibre reinforced thermoplastic (FRTP) composite pipes

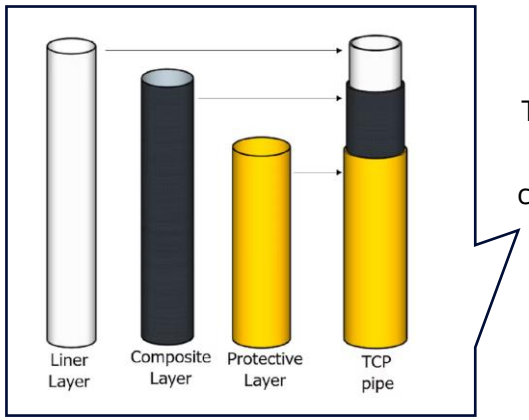



Multi-layer composite pipeline

- **Metal to FRTP pipe**
- **FRTP to FRTP pipe**

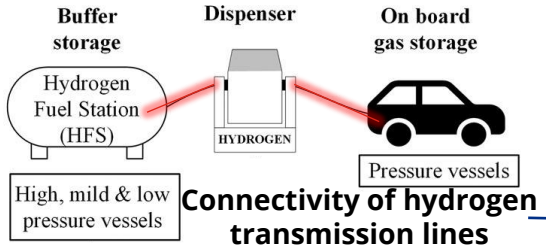

Connectivity of hydrogen transmission lines

Requirements for pipe connectivity

- Sufficient interlayer bonding
- Minimised hydrogen leakage
- Strong durability under thermocycles
- Safe, reliable and cost-effective

We want FRTP composite couplers !

- *Weldable*
- *Impermeable*
- *Energy-efficient*
- *Recyclable*
- *Durable*

FRTP Couplers: from Concept Design to Prototyping

Aims at development of a fiber reinforced thermoplastic (FRTP) composite coupler for joining metal and thermoplastic composite pipelines, synergizing robust bonding and pressure resistance

Coupler design concept

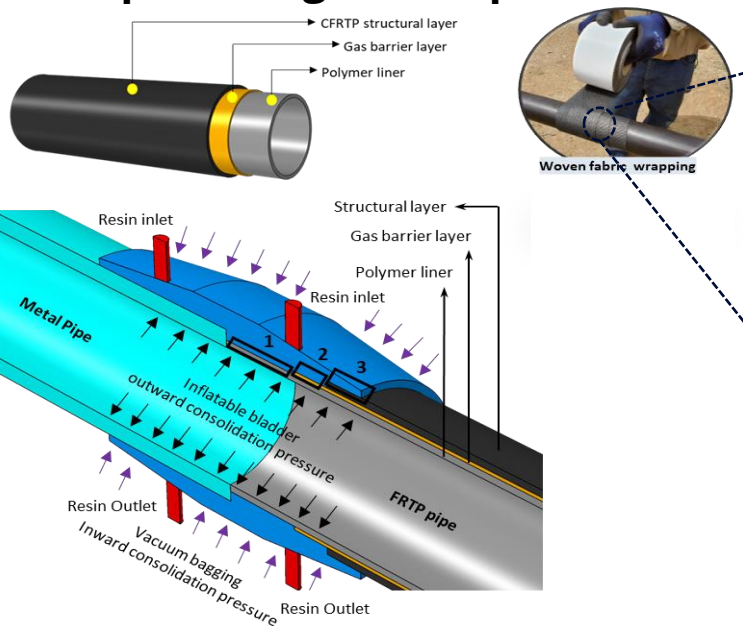

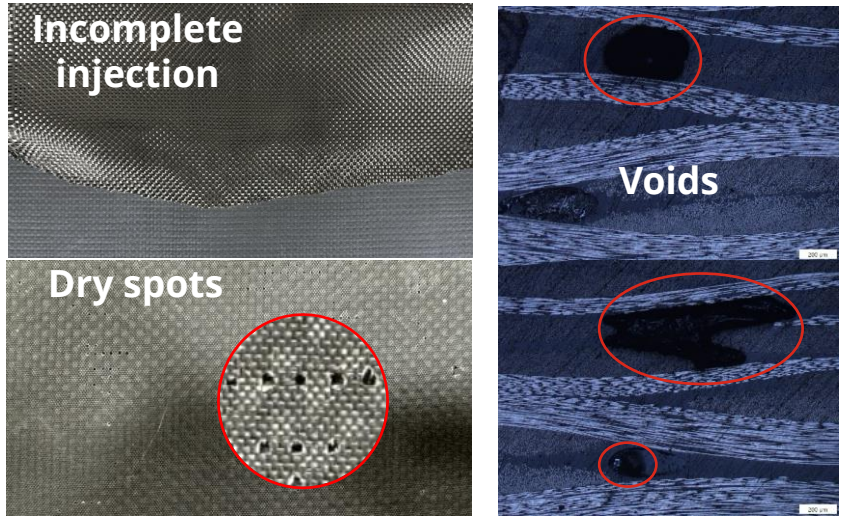

Defects in composites part fabricated by resin infusion

Research Scopes

- **In-situ polymerization technology** with infusible resins to achieve the minimised defects.
- Composite coupler formalization: tubular shape, irregular shape, etc..
- **Enhancing material compatibility regarding multiple interface bonding** between the coupler and the metal or FRTP pipelines.
- Advanced simulation techniques for **coupler layup design** and **optimization**.

Preliminary Study on Composite Coupler

❑ Composite coupler connecting carbon steel pipe and PE pipe

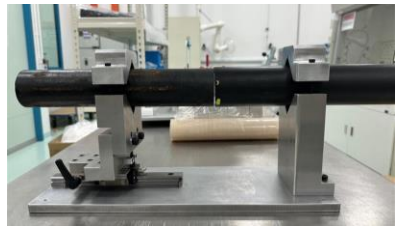

Pipe assembly fixture

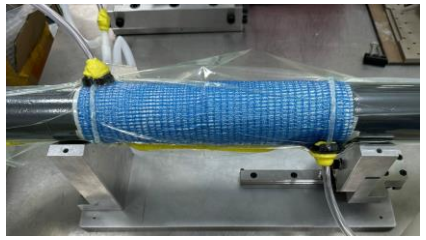

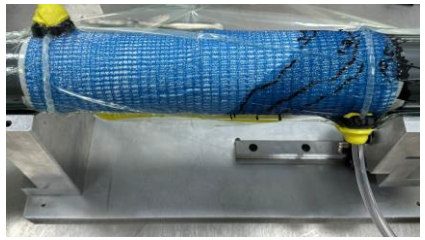

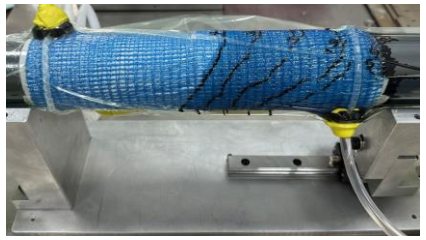

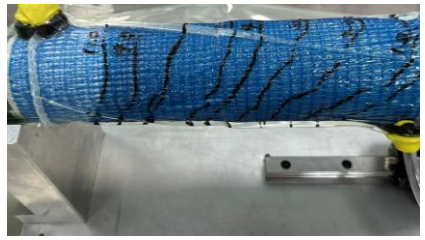



Resin infusion process of the coupler

Some difficulties identified:

- Poor resin penetration and inconsistent flow front.
- Wrinkle and distortion of fabrics after curing
- Non-uniform interface stress transfer between dissimilar materials

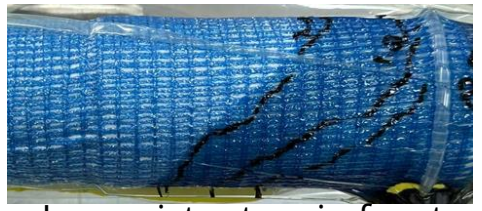

Inconsistent resin front



Fabric wrinkle

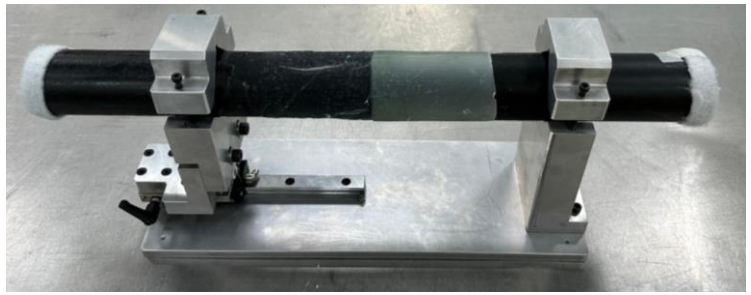

Proof-of-concept: composite coupler

Solution: It's important to develop **process monitoring system** and **physics-based process simulation model** to improve composite coupler quality.

Development of in-situ polymerization monitoring system

❑ Current solutions

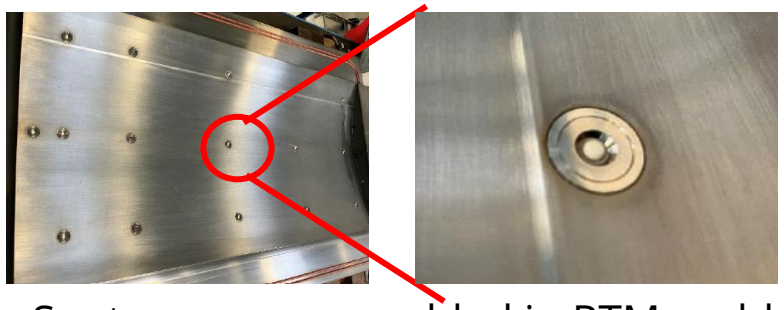

Spot sensors assembled in RTM mold [1]

- Numerous sensors are required to cover whole area, increasing tooling **complexity** and **cost**

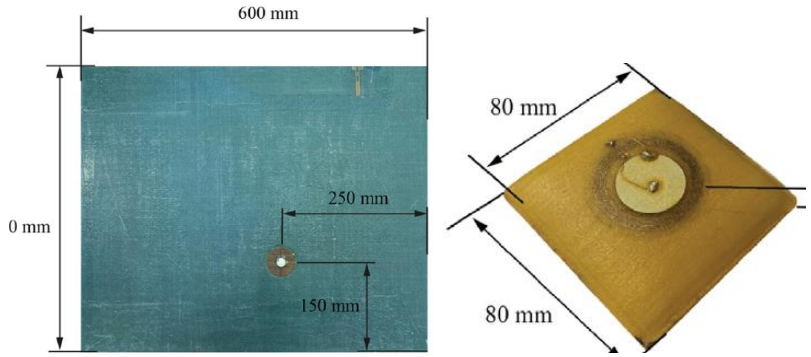

Inductively coupled sensor [2]

- Sensor **interference** with the base due to poor material compatibility, reducing structural integrity.

❑ **Distributed resistance sensor** for resin-infusion monitoring

Methodology:

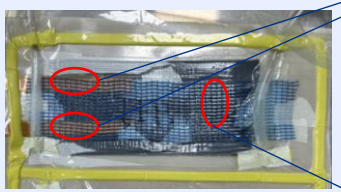

Electrodes printed on glass fiber via direct ink writing (DIW) with high conductive silver ink



Resistors printed on glass fiber via direct ink writing (DIW) with low conductive carbon ink



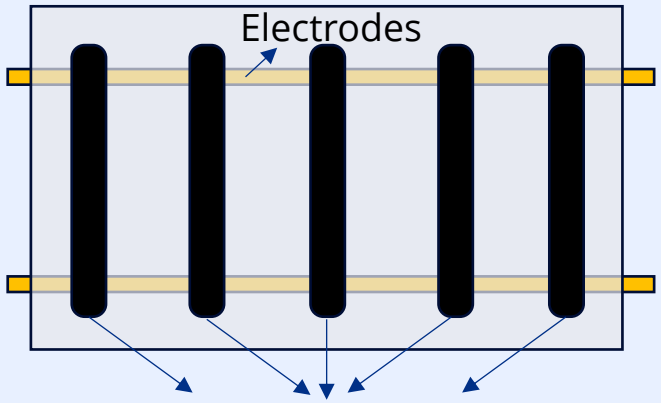

- Ultra-thin
- No foreign materials (carbon-based sensors used)
- Minimized influence on resin flow

[1] Pantelelis, Nikos, et al. "Advanced Process Monitoring and Control for CFRP RTM in Aerospace without compromises." SAMPE 2024 (2024).
[2] Chilles, James S., et al. "Monitoring cure and detecting damage in composites with inductively coupled embedded sensors." Composites Science and Technology 134 (2016): 81-88.

Development of in-situ polymerization monitoring system

❑ Resin front position captured by the distributed resistance sensor

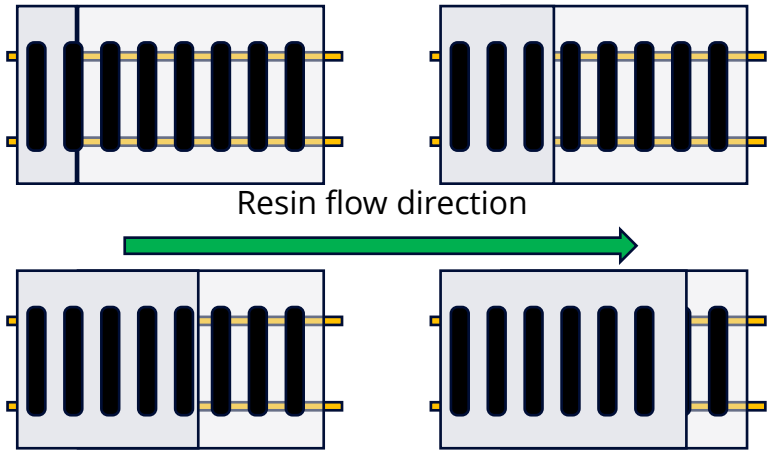

Working principle:
The resistance change when resin immerse the resistors

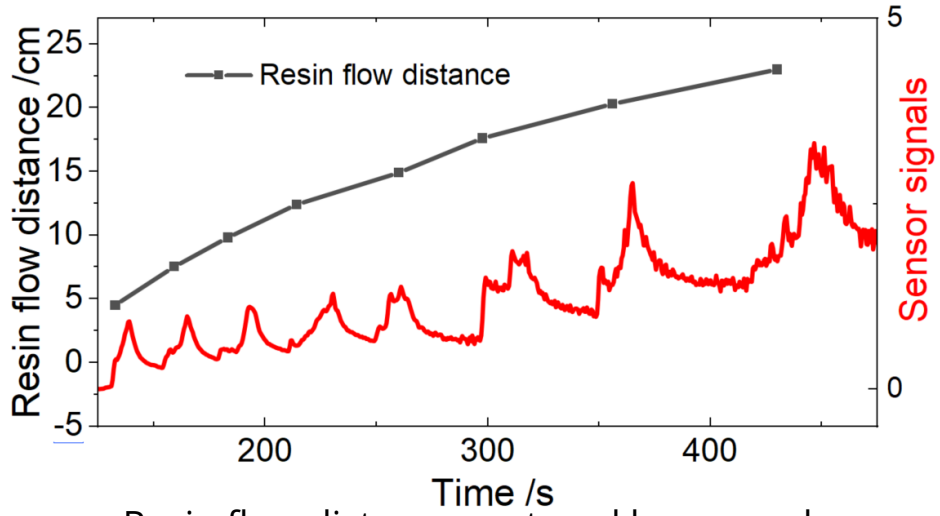

Resin flow distance captured by manual observation and distributed sensors

- Distributed resistance sensors accurately reflect the resin front positions, showing great agreement with physical flow observation.
- The resin front captured by the sensor is for the bottom layer, lagging behind that from the top layer observed. The difference is caused by uneven flow through the fabrics thickness.
- The developed sensor can be used to continuously monitor the resin front distribution.
- More effective than commercial piezoelectric and piezoresistive sensors.

Development of in-situ polymerization monitoring system

❑ Capacitance sensor for curing status monitoring

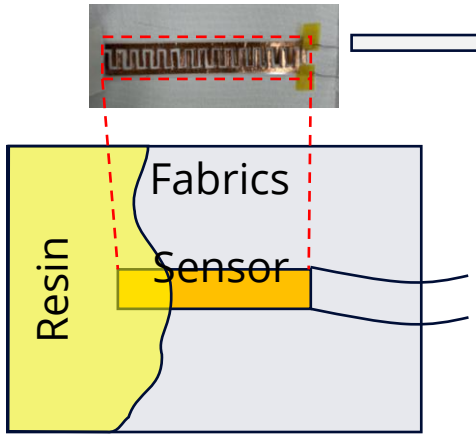

Interdigitated capacitance sensor

Embed sensors into the resin curing

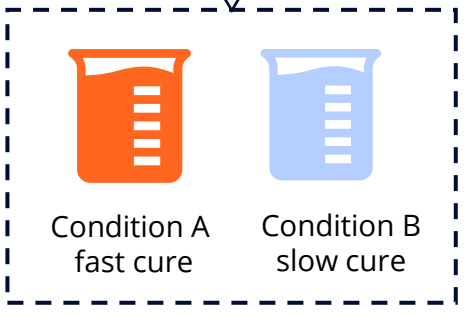

Temperature is controlled to manipulate curing speed

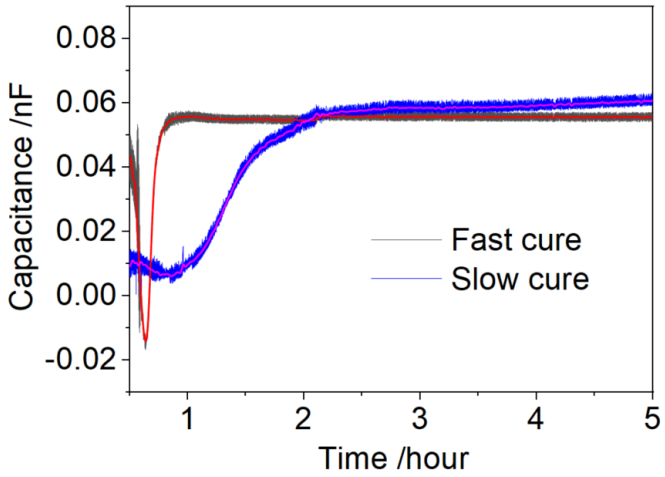

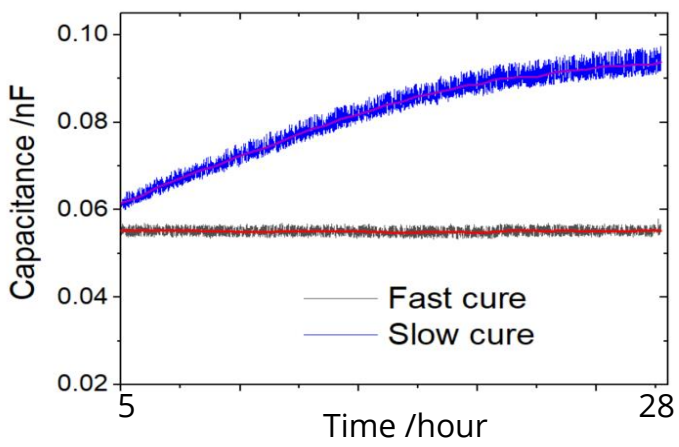

The capacitance signal of fast cure resin convergence soon, while the slow cure resin takes longer

- Two curing status were monitored, and their curing characteristics are captured by sensors
- The capacitance during the curing decrease first then increase
- Curing status can be further correlated to the capacitance signals

Infusion Process Analysis (Moldex3D)

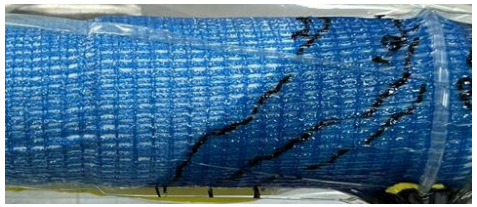

Flow complexity and the needs of process simulations

- ❑ The placement of inlet and outlet is needed to be optimised for infusion over a tubular shape. Process simulation model was hence developed.
- ❑ It is challenging to evaluate effects of fibre layup orientation, peel plies and distribution media, while a homogenous flow model lacks of accuracy.
- ❑ Flow inconsistency at top and bottom layers were captured, yet to be further validated with experiments.

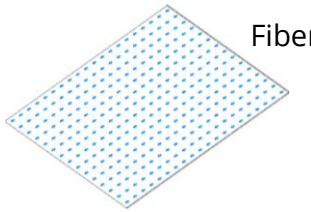

Fiber layup stacking sequence defined

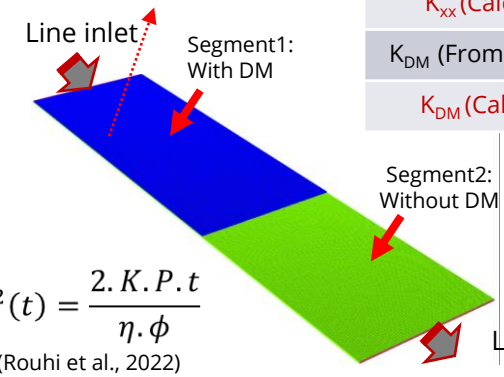

$$L^2(t) = \frac{2.K.P.t}{\eta.\phi}$$

(Rouhi et al., 2022)

Parameters	Values
K_{xx} (From Literature)	1.743×10^{-11} m^2
K_{xx} (Calculated)	1.211×10^{-10} m^2
K_{DM} (From Literature)	1.94×10^{-8} m^2
K_{DM} (Calculated)	1.038×10^{-8} m^2

Explicit numerical flow simulation models with and without distribution media (DM)

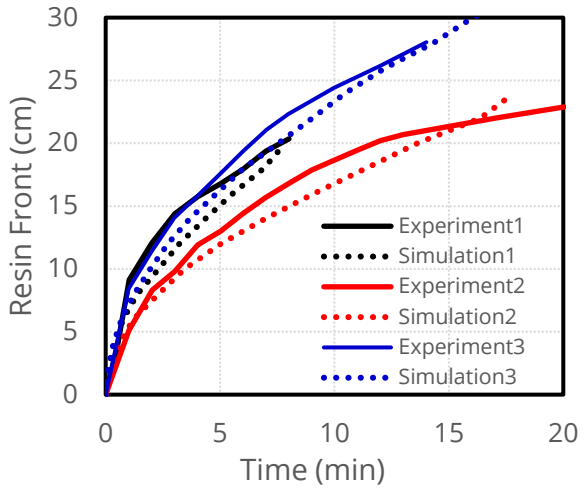

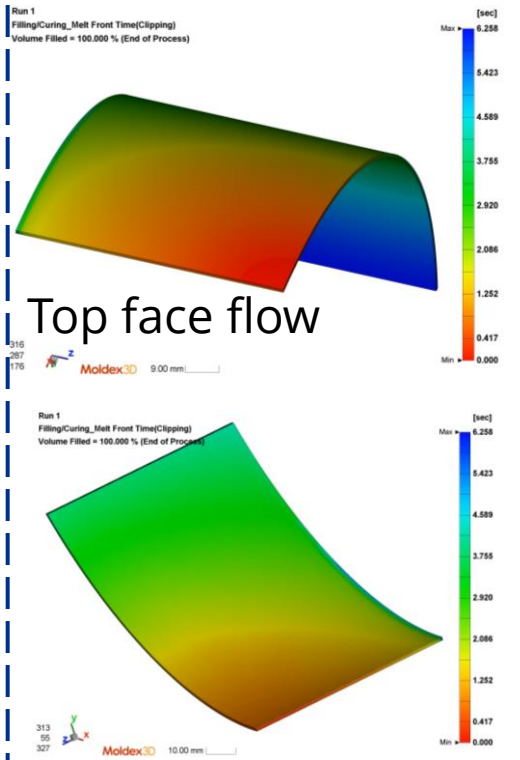

- Tubular shape model showed different flow front time between top and bottom surfaces indicated the through-thickness flow penetration

- Flat sample studies concluded that mesh sensitivity was insignificant regarding number of elements across the thickness of both the distribution media and laminates.
- We verified that back calculated permeability values ***K*** are needed instead of citing input permeability values from literatures.
- More studies are on-going to add more detailed settings regarding K values for peel ply and porosity ϕ.

Numerical Design for Composite Couplers

- Direct end-to-end joining with composite coupler
  - Adhesive bonding between the coupler and the pipes
  - Coupler with plain weave composite
- Finite-element progressive failure modelling
  - Cohesive interaction between the coupler and the pipes
  - Cohesive interaction at the two ends of the pipes

Load cases

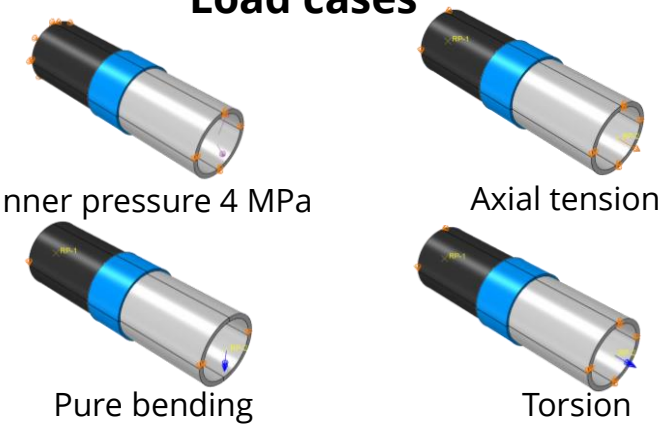

Bending and **axial tension** are identified as two critical loading cases.

- Delamination between the coupler and pipes happens in these two cases.
- Both the bonding strength and the composite lay-up need to be considered in the coupler design

Composite coupler is not easy to fail under inner pressure and torsion

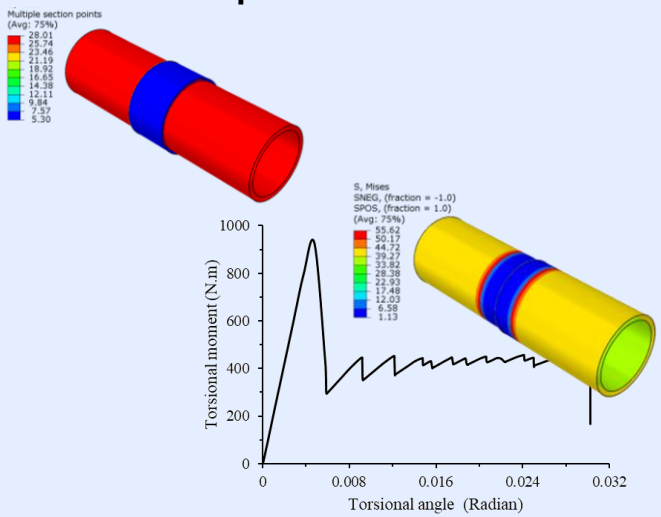

Critical Load Cases

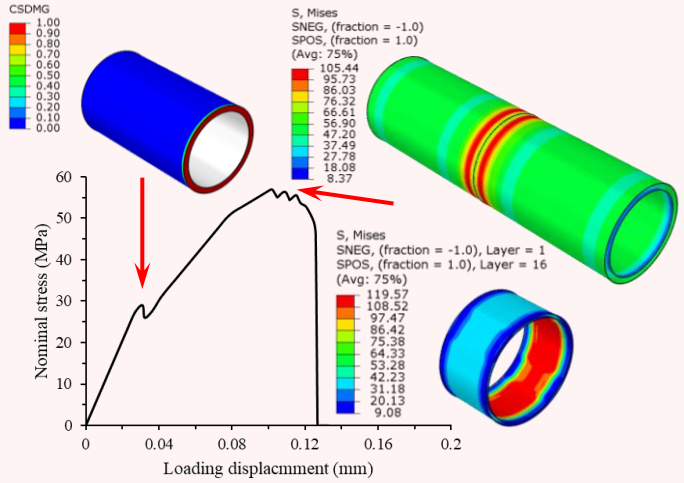

Axial tension

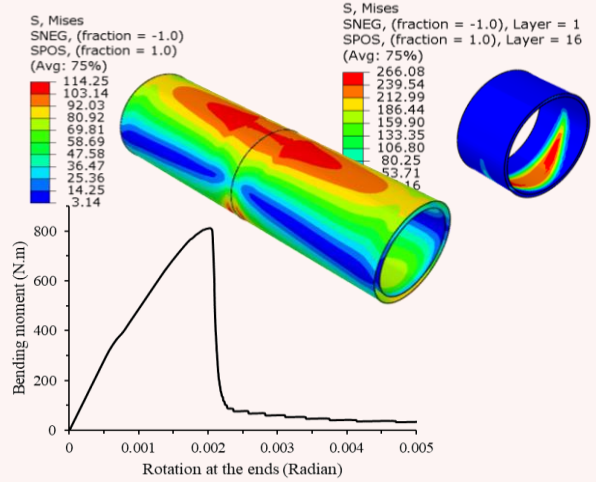

Bending

Summary And Future Work

Summary

- The development of FRTP coupler is of great significance to ensure a reliable connectivity for hydrogen transmission pipeline.
- The in-situ polymerization monitoring system was developed, including distributed resistance sensors for resin front monitoring, and a interdigitated capacitance sensor for resin polymerization monitoring.
- Critical loading cases of composite coupler were identified and process simulation models were established.

Future work:

- To develop optimal coupler structural design considering the critical loading cases.
- To improve the in-situ polymerization quality for coupler by simulation-assisted process optimization.
- To study the interface behaviour between composite coupler and heterogeneous materials.

Welcome to ICCM25 in Singapore











Singapore Institute of Manufacturing Technology
A*STAR SIMTech

THANK YOU

ASTARSG ASTAR-SG

Acknowledgement

The authors would like to acknowledge the funding support from the Agency for Science, Technology and Research and National Research Foundation of Singapore for the RIE2025 Urban Solutions and Sustainability (USS) Low-Carbon Energy Research (LCER) Phase 2 Emerging Technology Programme under Grant No. U2311D4004.

UNIVERSITY OF ILLINOIS URBANA-CHAMPAIGN

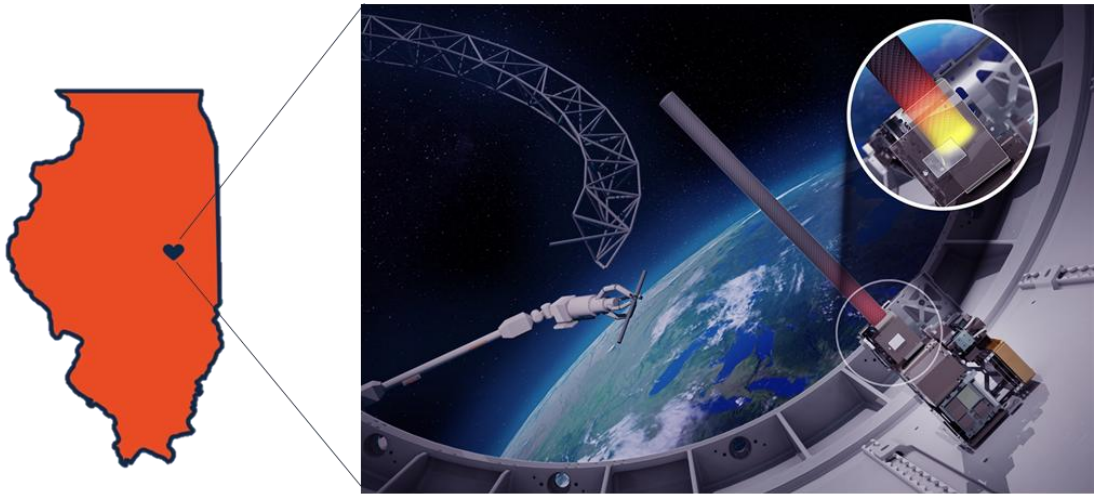

Mission 'Illinois'
Expected Launch Summer 2026

In-Space Manufacturing of High-Performance Fiber Reinforced Composites Tubes

Zheyuan Zheng, Logesh Shanmugam, Ivan Wu, Arif Abdullah, Nawaf Rasheed, Sameh Tawfick, Jeffery W. Baur

ICCM24, Baltimore, MD, August 4-8, 2025

JWBaur@Illinois.edu

Increasing Space Situational Awareness (SSA)

Current: Deployable Mesh Antenna

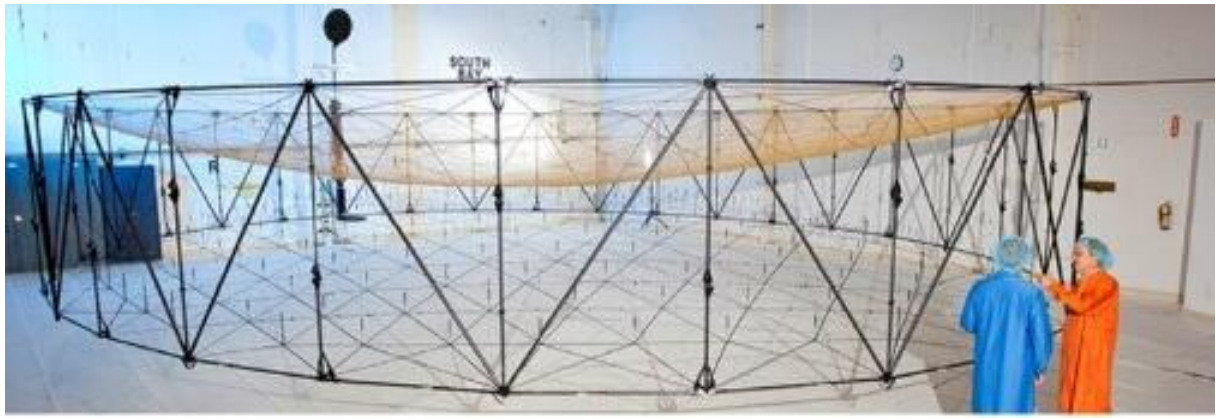

AstroMesh® deployable mesh reflector

"A review on developments of deployable membrane-based reflector antennas" M. Chandra et. al, **Adv., in Space Research**

Emerging Need

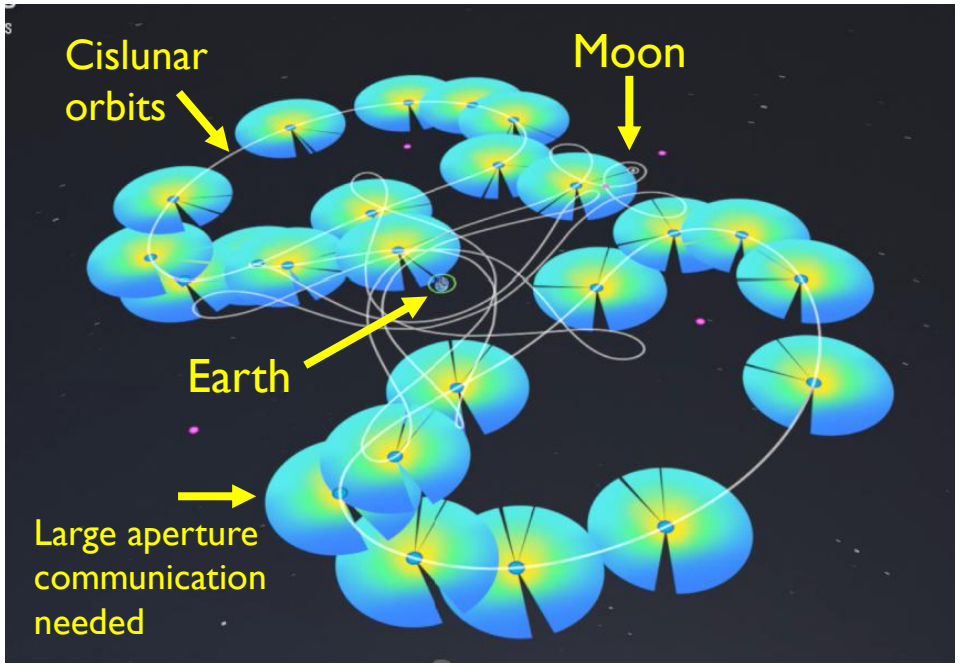

"On-Orbit Assembly and Manufacturing of Large Structures to Enable Space Situational Awareness" M. Trexler et. al, JHU, AIAA SciTech, 2023

- SSA in cislunar difficult - large volume and the chaotic orbits
- JHU study[1] - tiered RF/optical architecture, **need structures 5-10x bigger than current deployables**
- **How can we construct football stadium-sized structures in space?**

In-Space Manufacturing & Assembly of Structural Elements

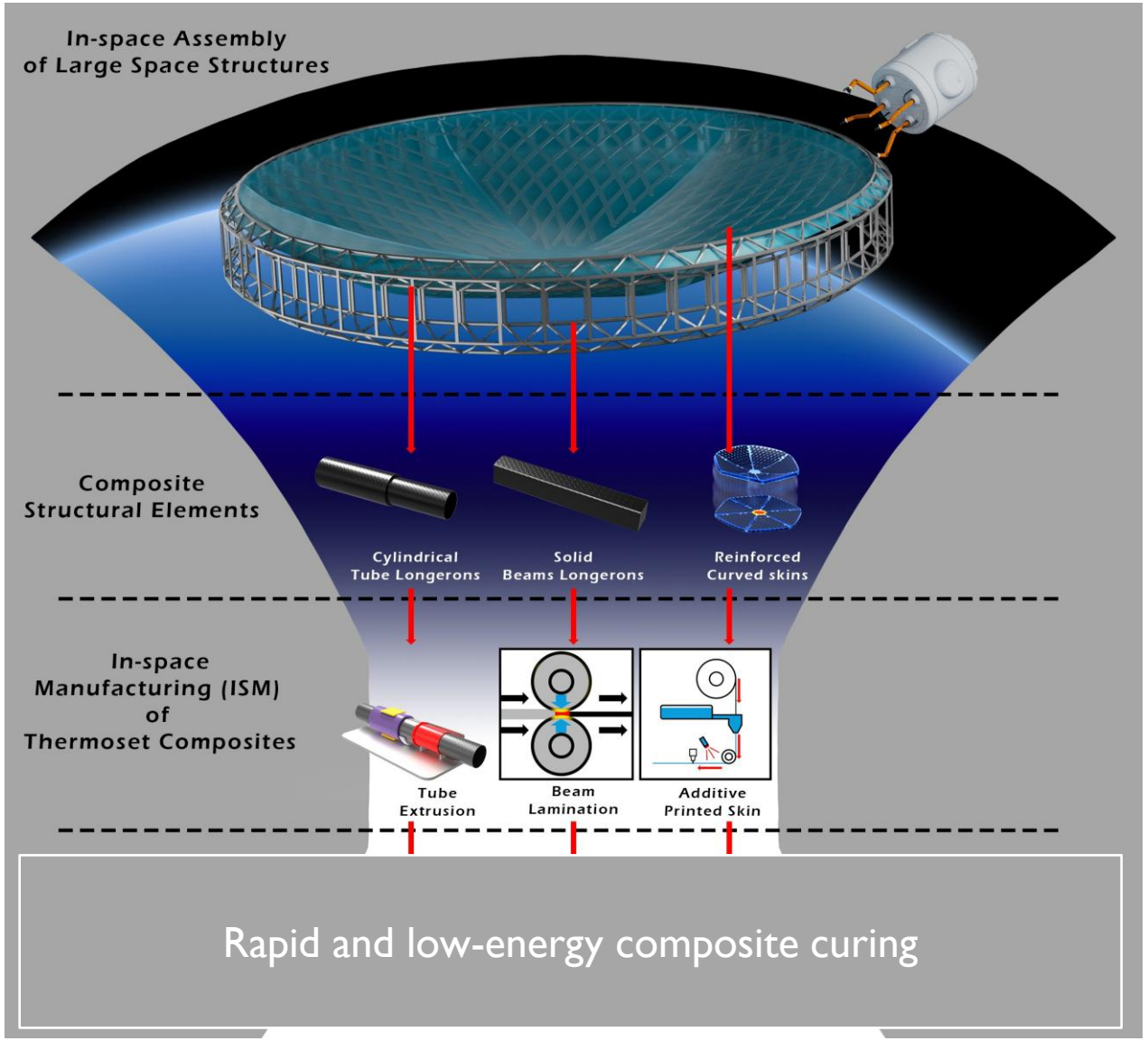

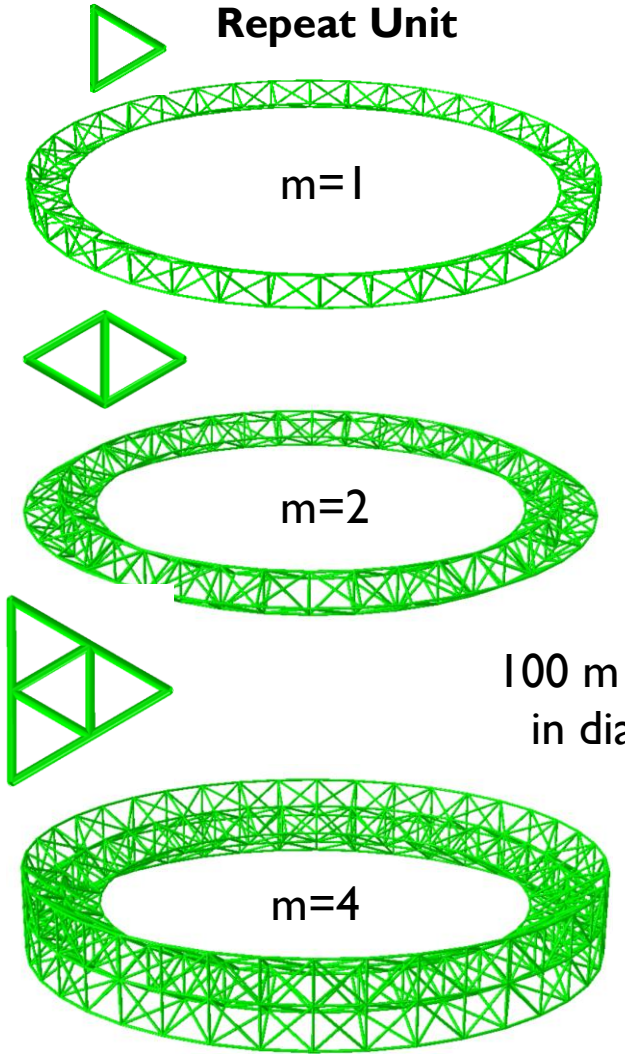

100 m to 1 km
in diameter

Courtesy: Michael Zakoworotny

Frontal Polymerization of DCPD

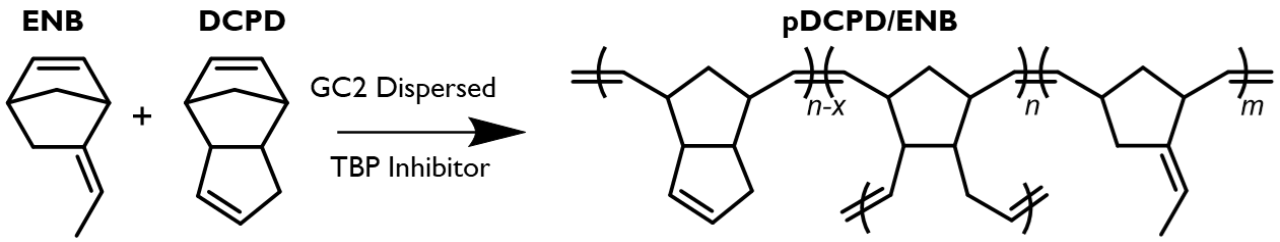



Dicyclopentadiene (DCPD)

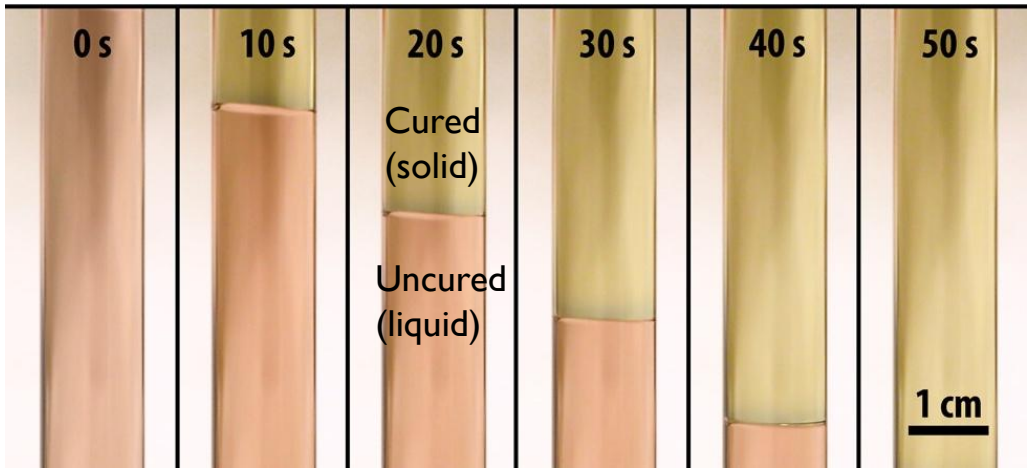



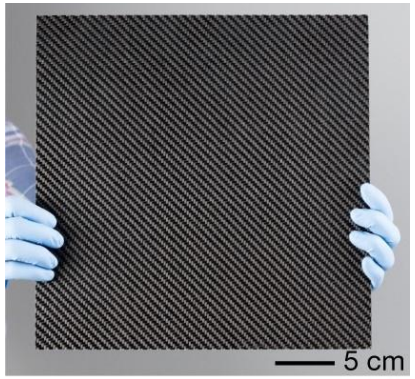

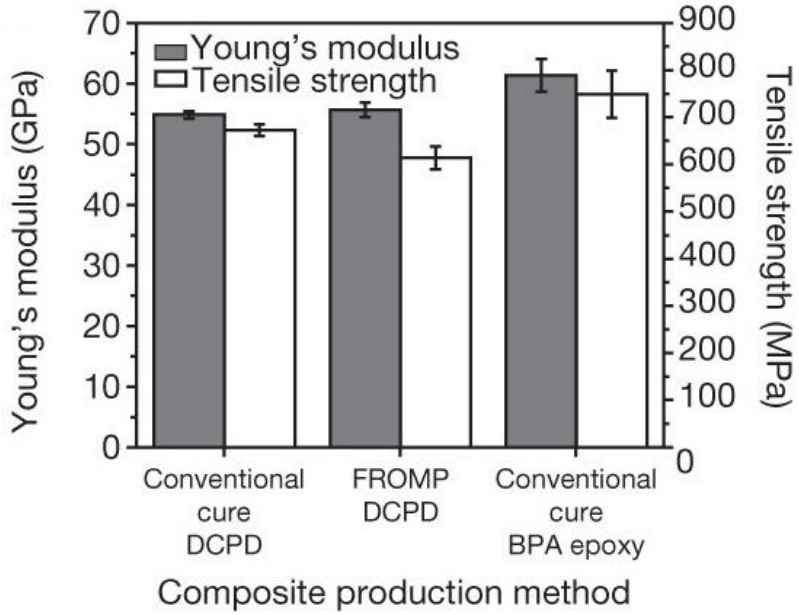

Resin Formulation: DCPD, 100ppm GC2, 1 eq TBP

"Rapid energy-efficient manufacturing of polymers and composites via frontal polymerization", Robertson, I.D., et al, *Nature,* 557(7704), 2018, 223–227.

Robertson et al., *Nature* 2018

Supplied Energy & Cycle Time per Cured Volume

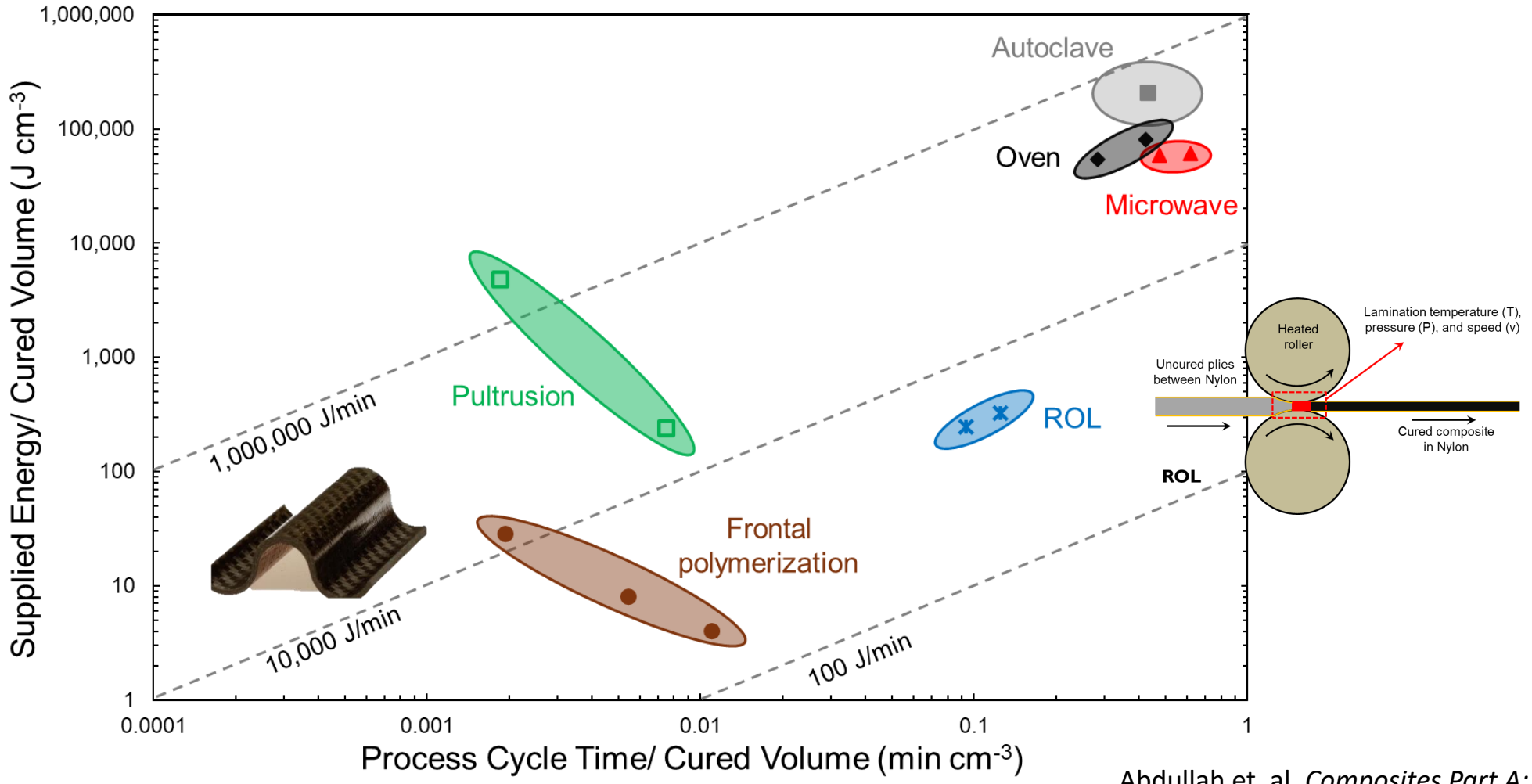

1: https://www.compositesworld.com/news/victrex-electroimpact-achieve-thermoset-afp-speeds-using-thermoplastics, https://www.compositesworld.com/news/victrex-electroimpact-achieve-thermoset-afp-speeds-using-thermoplastics
2: https://www.unicomposite.com/composite-pultrusion-the-definitive-guide/
3: Baur et al., Journal of Composite Materials, 2023

Abdullah et. al, *Composites Part A: Appl. Science and Manufacturing* (2025).

Compliant Encapsulation Prepregs for ISM

- Thermoset resin contained within sealed compliant polymer films
- Multifunctional Uses
  - Facilitates vacuum resin infusion
  - Contains low viscosity uncured resin
  - Lowers outgassing of volatiles
  - Increases resin storage life
  - Compliance enables molding/stowage
  - Thinness enables processing

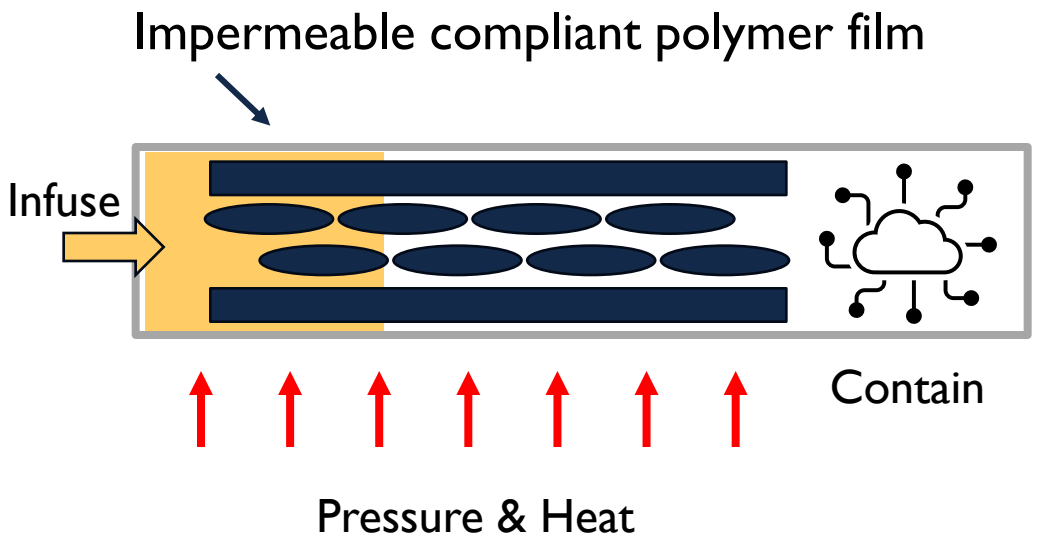

Dahlar® Bag Selection
- ETFE-Nylon, multilayer
- High Temp Capable (230°C)
- Compliant (400% max strain)
- Heat-sealable

Resin: 95/5 wt.% DCPD/ENB, 100 ppm GC2 and 1 eq. TBP.

Rapid Out-of-oven Lamination (ROL)

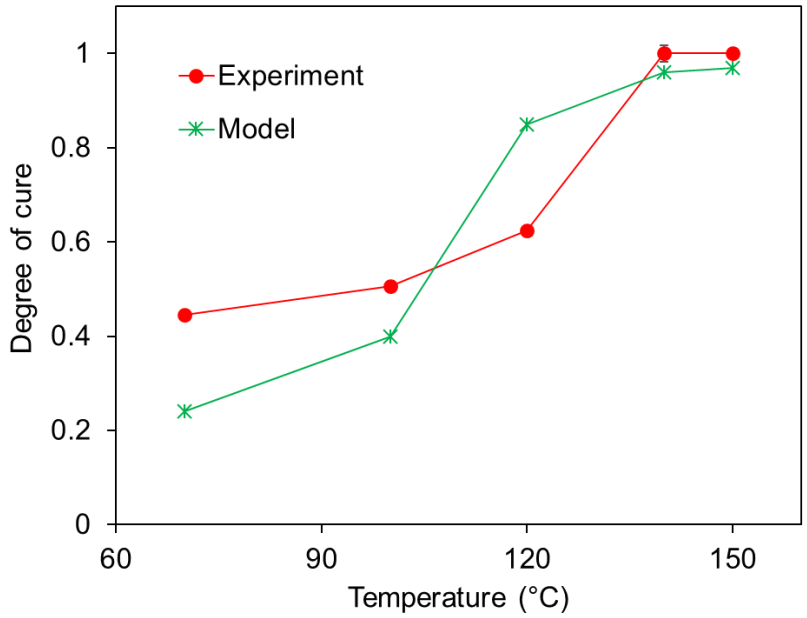

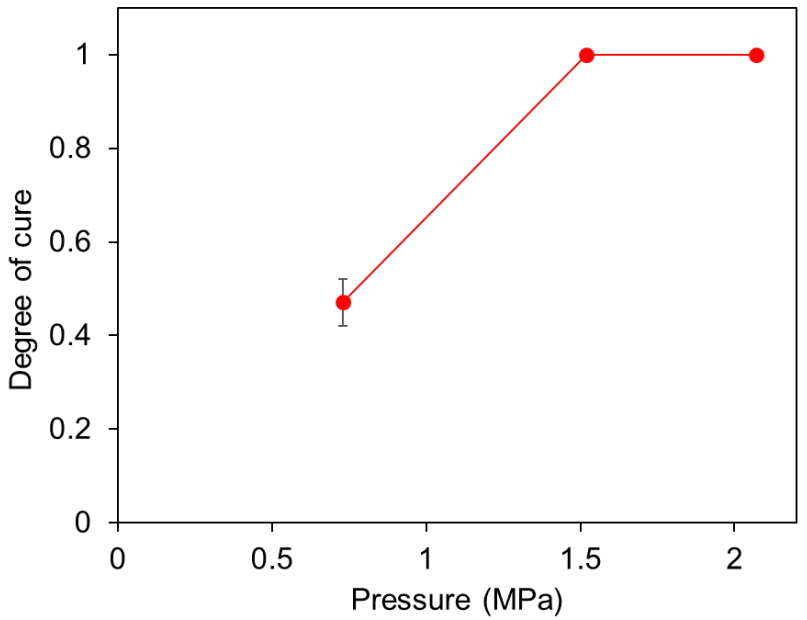

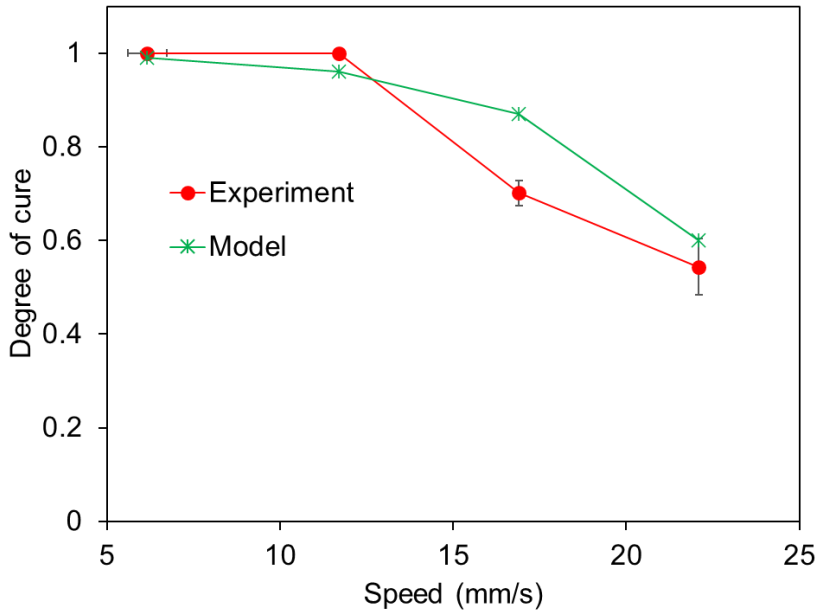

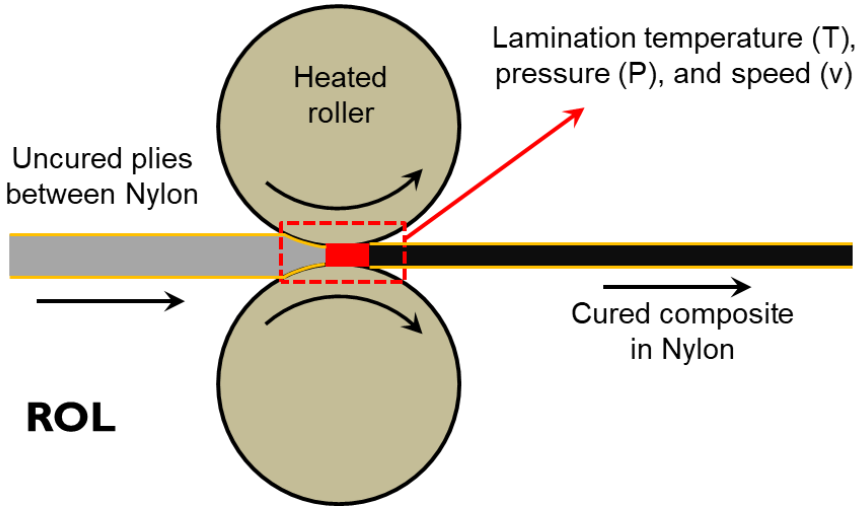

6-ply Carbon Fiber/DCPD Composite (wet lay-up):
DCPD/ENB (95/5) with 100 ppm GC2, 100 ppm TBP
6 - Unidirectional 24K Carbon Fiber Plies

Roller Conditions: (unless varied)
Speed = 11.7 mm/s, Pressure = 1.52 MPa
Temperature = 140°C

Cure: Full cure (α *>0.95*) with nominal conditions, less with higher speed, lower temperature, and less pressure

Abdullah et. al, *Composites Part A: Appl. Science and Manufacturing* (2025).

ROL Laminate Microstructure



2x2 twill weave



Unidirectional

20 mm



330 mm

CF volume ~ 60.8±1.07%

Void volume ~ 1.7±0.6%

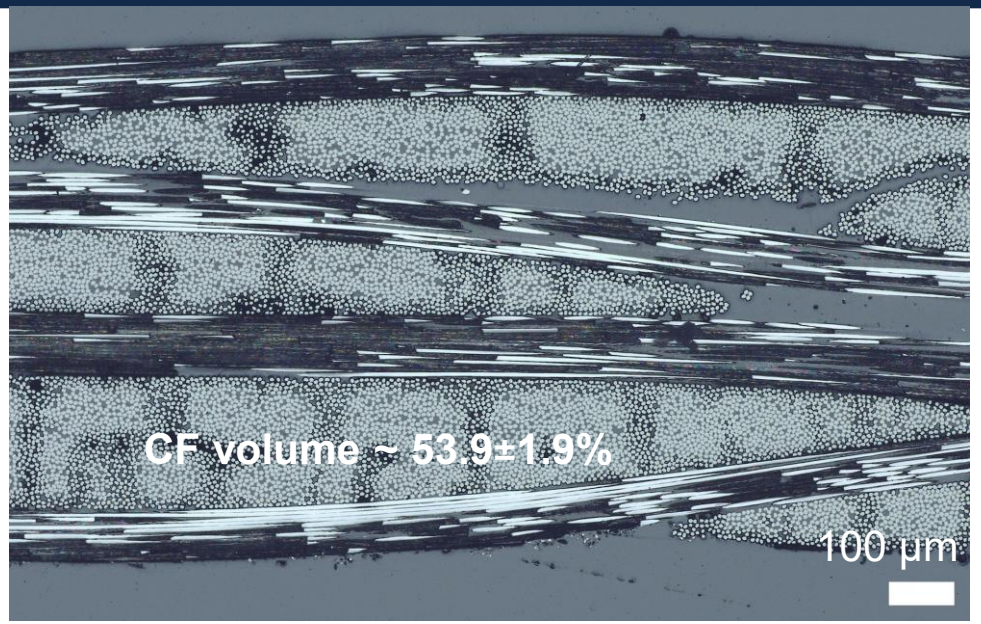

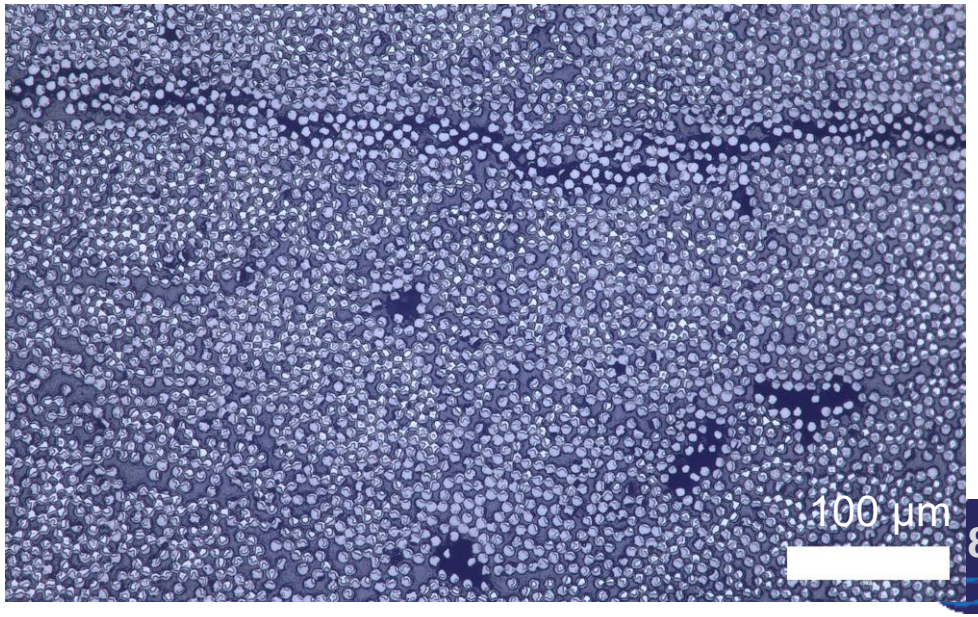

Abdullah et. al, *Composites Part A: Appl. Science and Manufacturing* (2025).

Storage Life (DSC Pan & Laminate Level)

DSC Pan

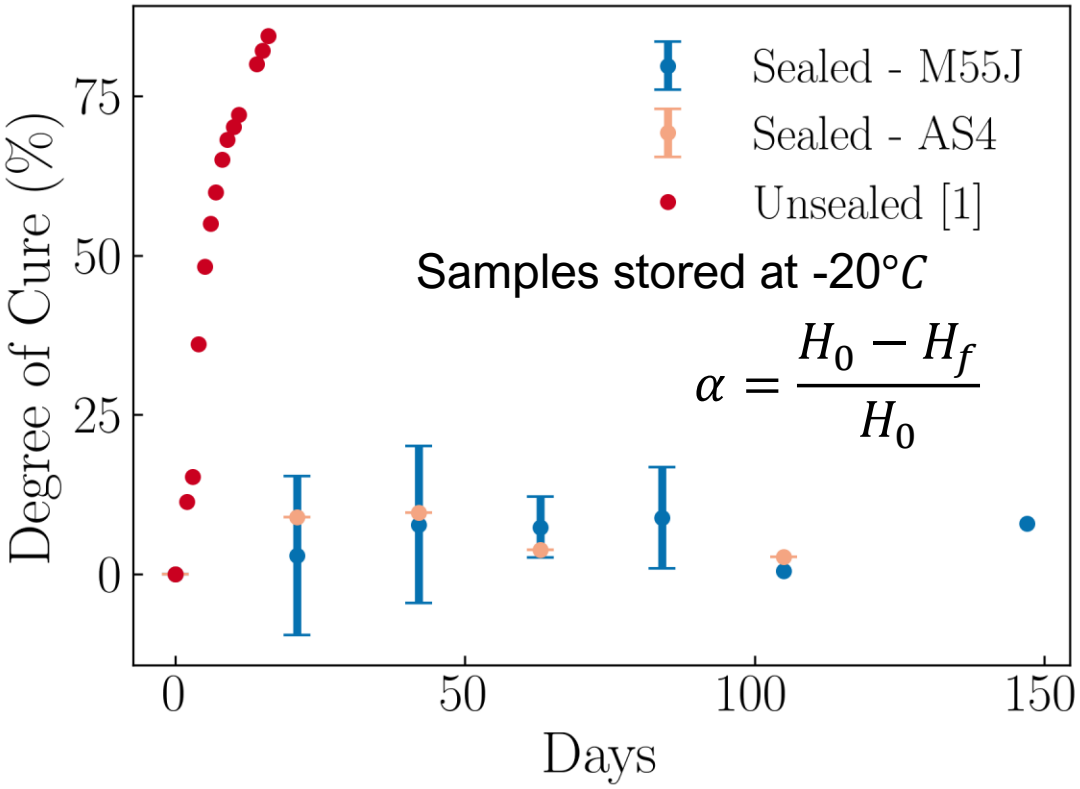

Enthalpy taken $30°C \leq T \leq 155°C$

Encapsulated Laminates

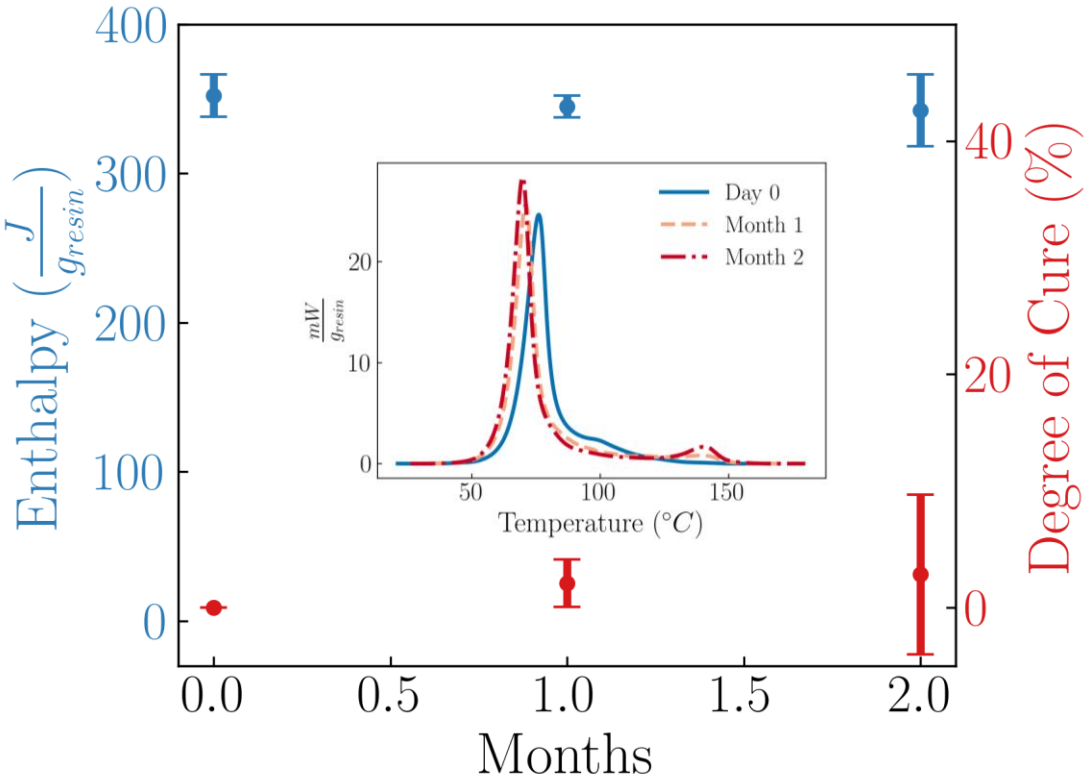

Fiber: $[0/\pm45/\pm45/0]$ with veil on both sides
Resin: 95/5 wt. DCPD/ENB, 100/100 ppm GC2/TBP

[1] Parikh, N. A. *Doctoral dissertation*, University of Illinois Urbana-Champaign, 2023.

Tubular Encapsulated Prepreg

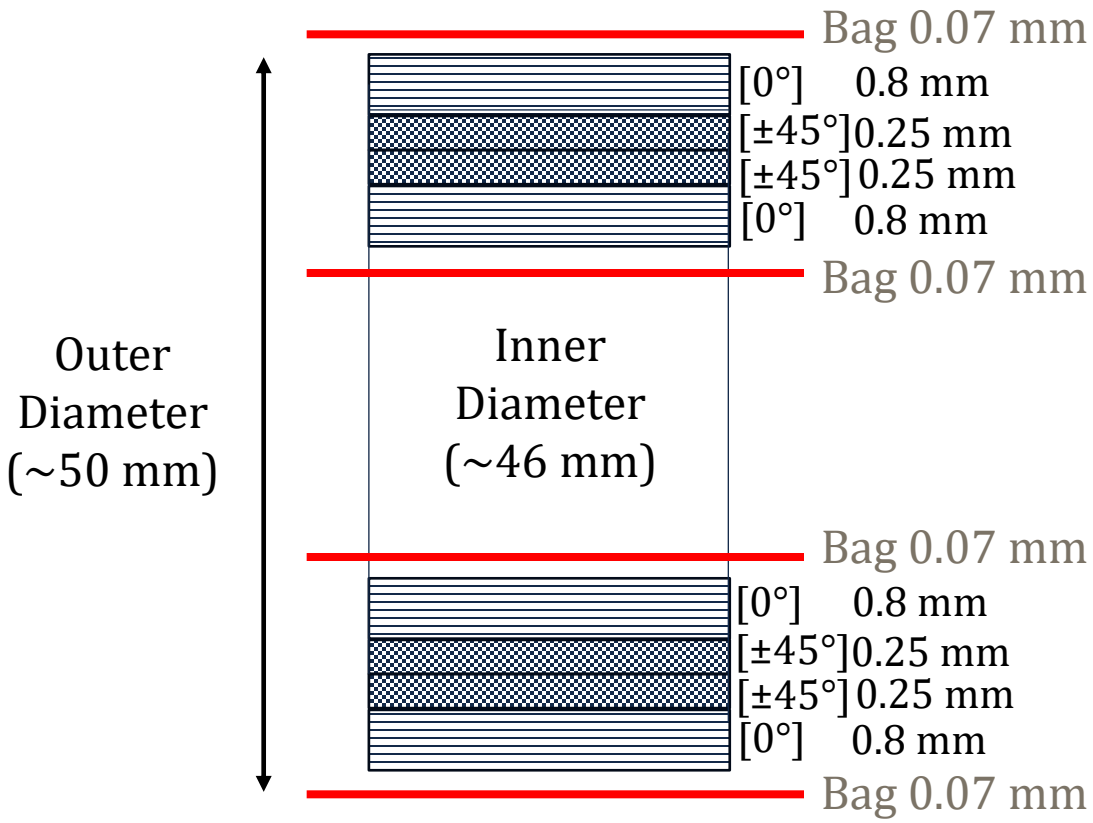

Schematic of Fiber architecture of the composite tubes



AS4 : 0° Fiber 2 cm



AS4: ± 45° Fiber 2 cm

Property	AS4
E_{f1} (GPa)	231
σ_{f1} (GPa)	2.2
E_{f2} (GPa)	13
ν_{f12}	0.3
G_{f12} (GPa)	11.3
ρ_f (kg/m^3)	1790

Note: Putting ±45° on outside aids processing/handleability

Static Cure of Wet Layup Tube

- Wet-Layup (layer by layer)

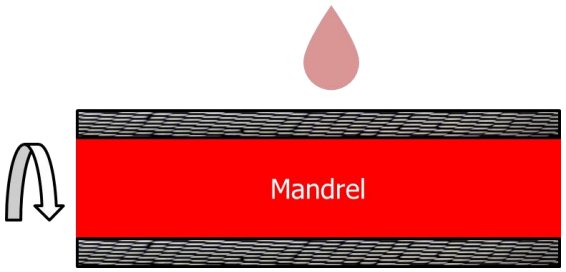

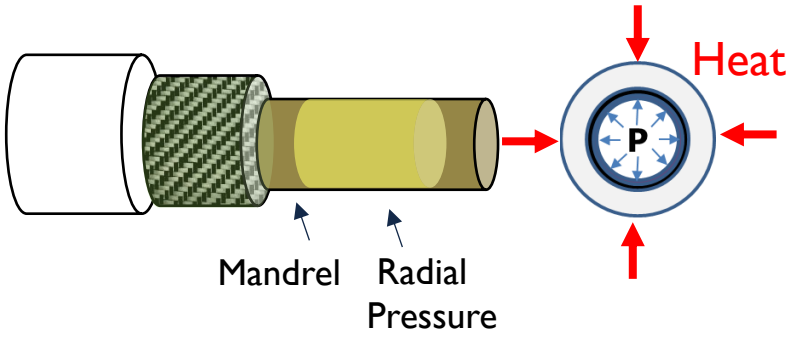

Static Bladder Molding

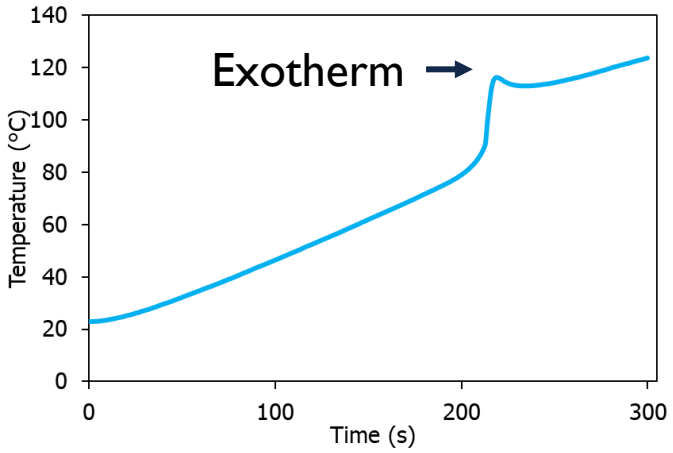



[0°,±45°,±45°,0°]

50mm



[±45°, 0°, 0°, ±45°]

50mm

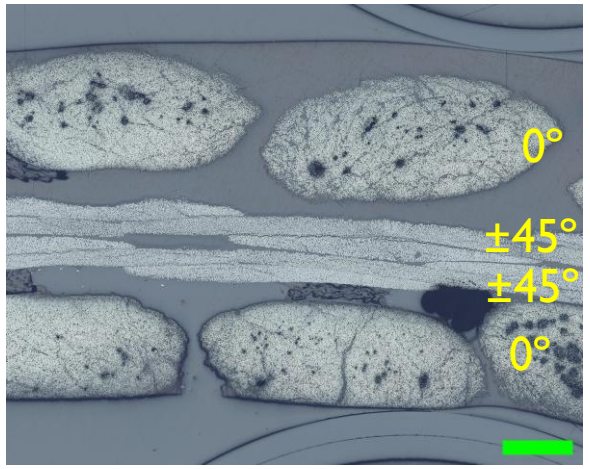

500 µm

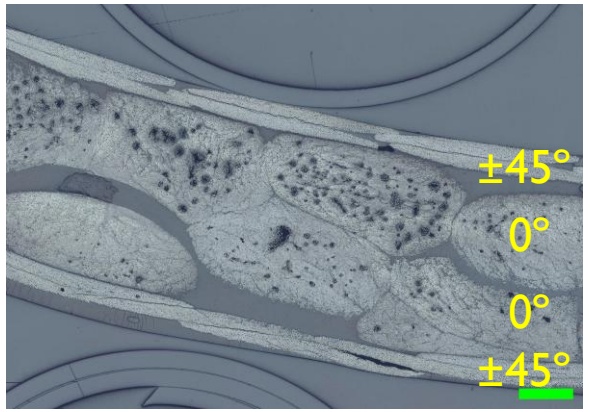

500 µm

Resin Formulation: 95/5 DCPD/ENB, 100ppm GC2, 1 eq TBP
± 45° Fiber: Braided AS4 CF Biaxial Sleeves (Fibreglast)
0° Fiber: Unidirectional AS4 CF Sleeve (Fibreglast)
Curing Condition: Cure 130°C for 3 min

Prepreg VARTM Infusion of Liquid DCPD

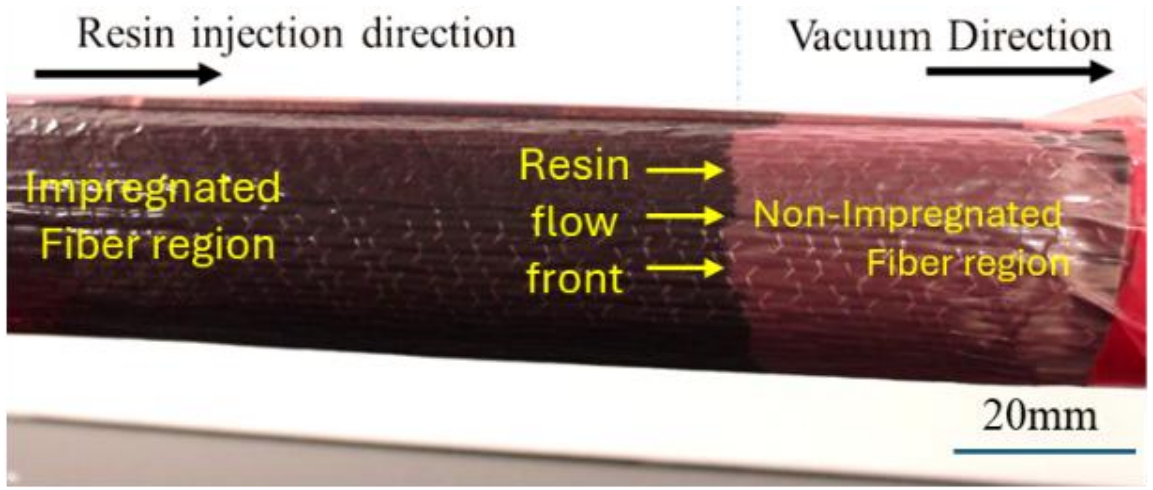

Fig. Closeup Resin Infiltration

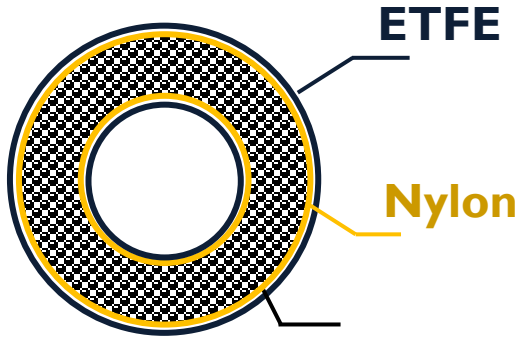

DCDP Fiber Prepreg



Rolled up Prepreg after the Infusion

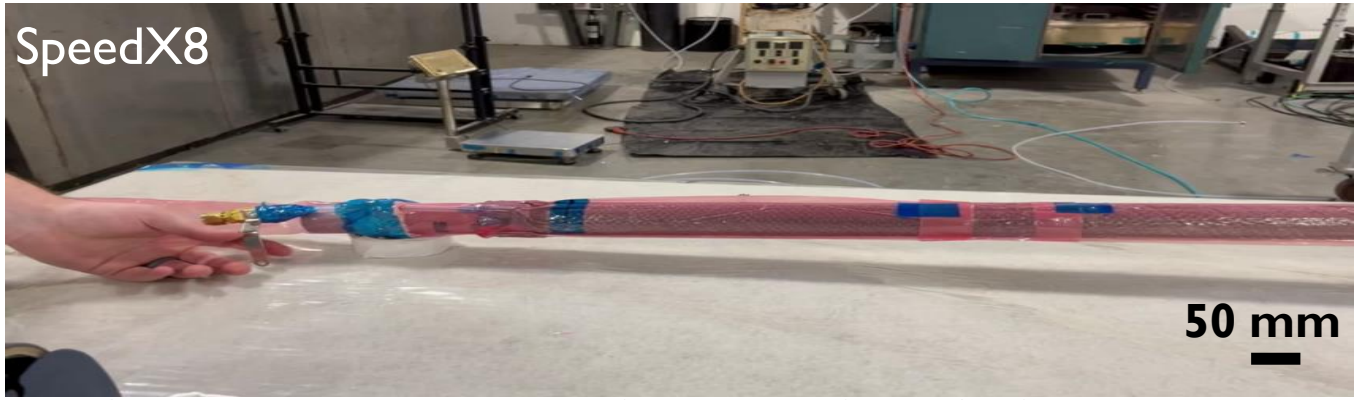

3-meter Vacuum-Assisted Resin Infusion

Carried out at Hawthorn Composites, Miamisburg, OH

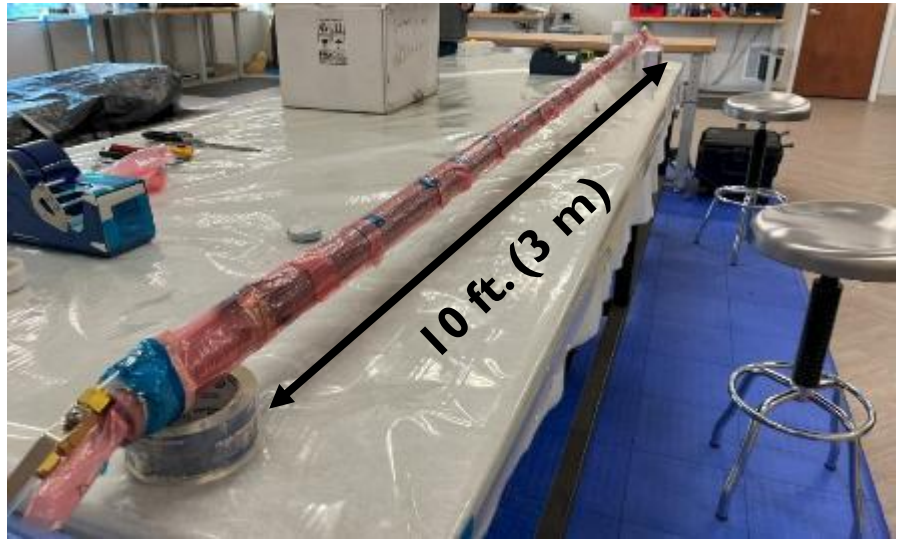

Incremental Curing Process of Longerons

Overall Process Plan



1. Compactly stowed & stable encapsulated prepreg

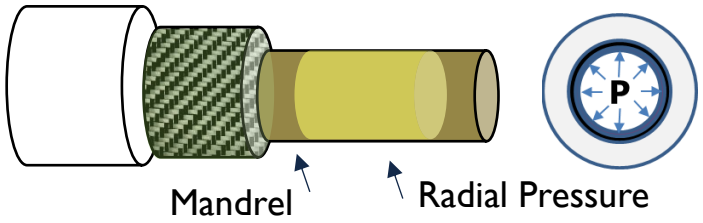

2. Initial shaping before molding

3. Apply pressure

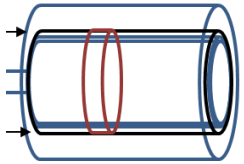

4. Heat to initiate reaction



5. Pultrude cured tube

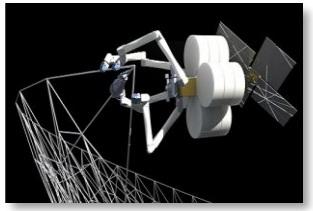

6. Cut & robotic assembly (future)

Incremental Cure Plan

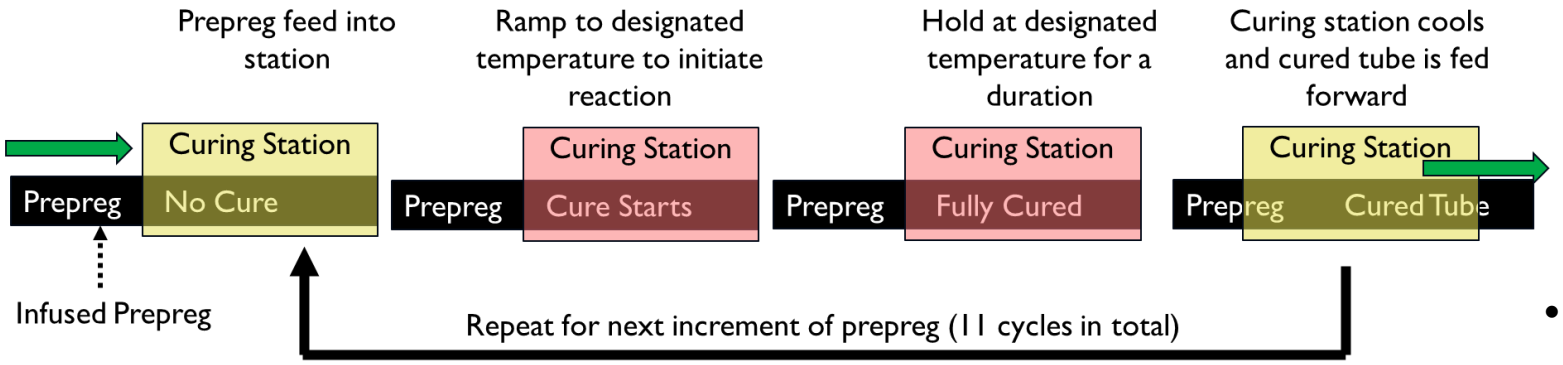

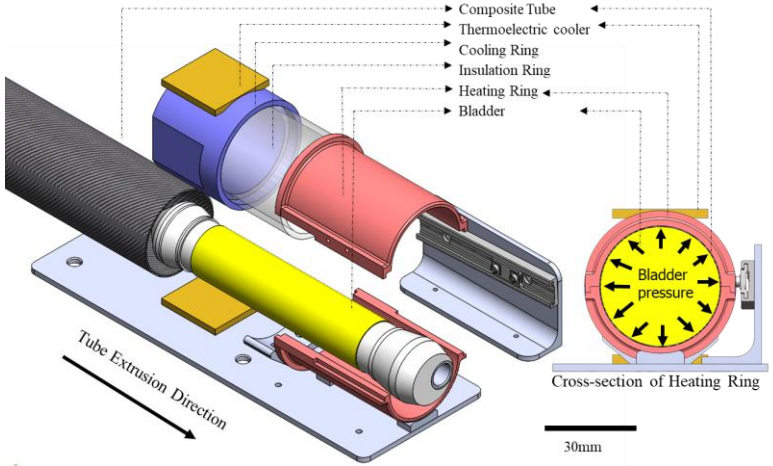

- **Cure Cycle for Each Increment**:
  - Ramp to 155°C (PID), Hold for 5 min
  - Cool Down to 40°C
  - Bladder Pressure 15 psi

Mechanical Properties of Composite Tubes

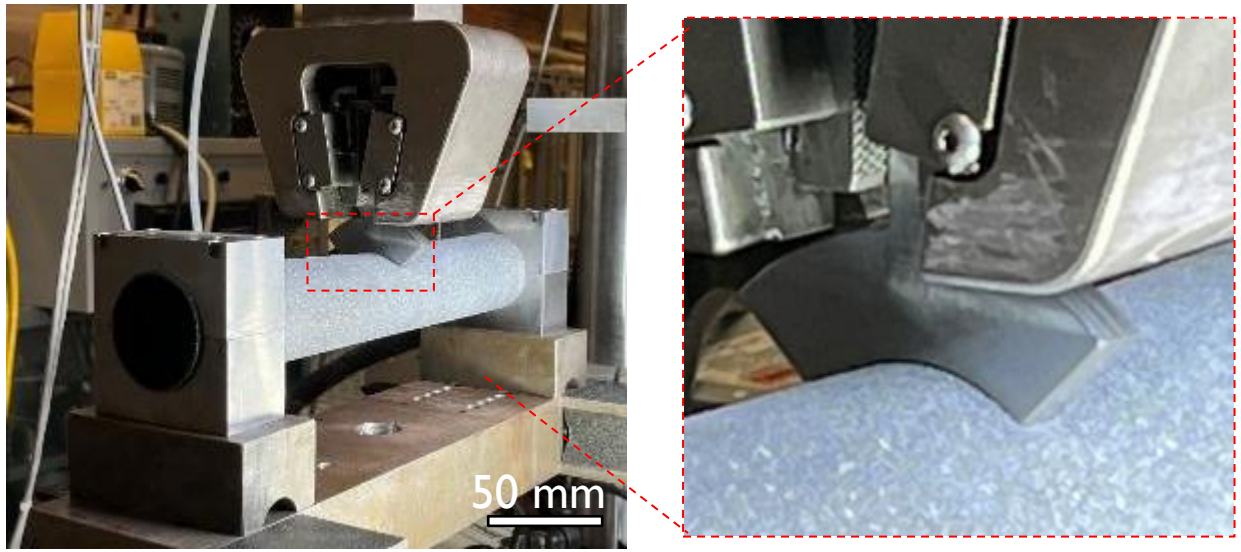

Fig. 3 Point bending Mechanical Testing

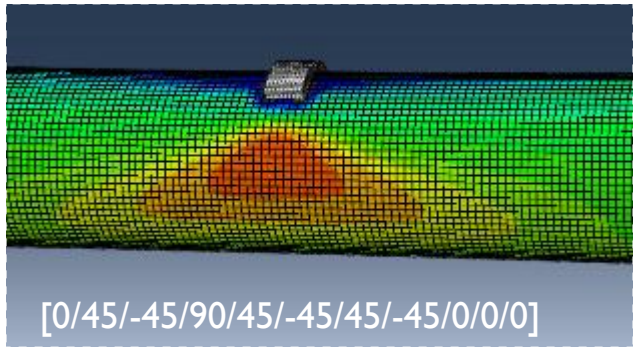

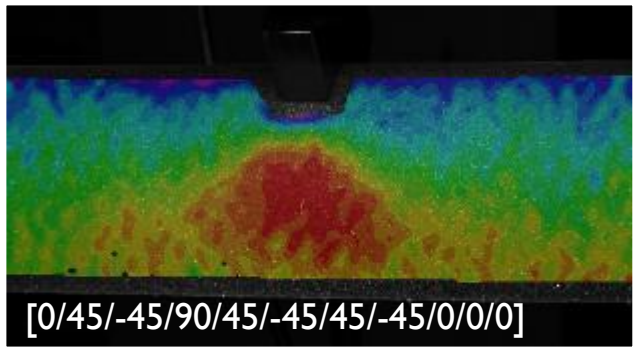

Simulation Model validated for Commercial Tube (with known properties)

Commercial Tube FVF ≈ 46% (Measured)
Simulation Model matches experimental results when assuming FVF ≈ 44%

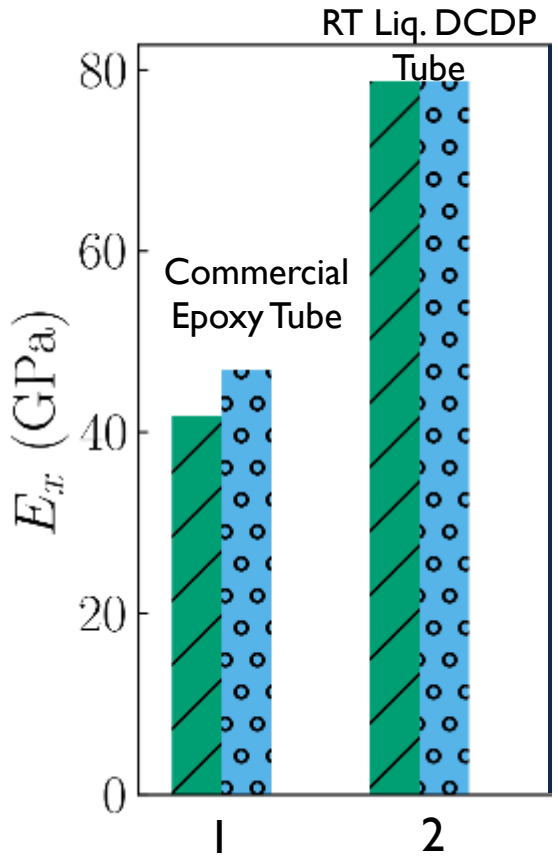

1. Commercial tube [0/45/-45/90/45/-45/45/-45/0/0/0]
2. **Static Cure Wet-layup** (AS4) $[0/\pm 45_2/0]$

Theoretical axial stiffness (AS4 fibers) = 127 GPa

3-Pt Bend Comparison: Experimental vs Model

Tube Architecture	Manufacturing Method	Load/Disp (kN/mm)
[0°,±45°,±45°,0°]	Experimental: Wet-Layup	0.84
[0°,±45°,±45°,0°]	Experimental: VARTM	1.31
FVF 40 [0°,±45°,±45°,0°]	Model	1.04
FVF 46 [0°,±45°,±45°,0°]	Model	1.18

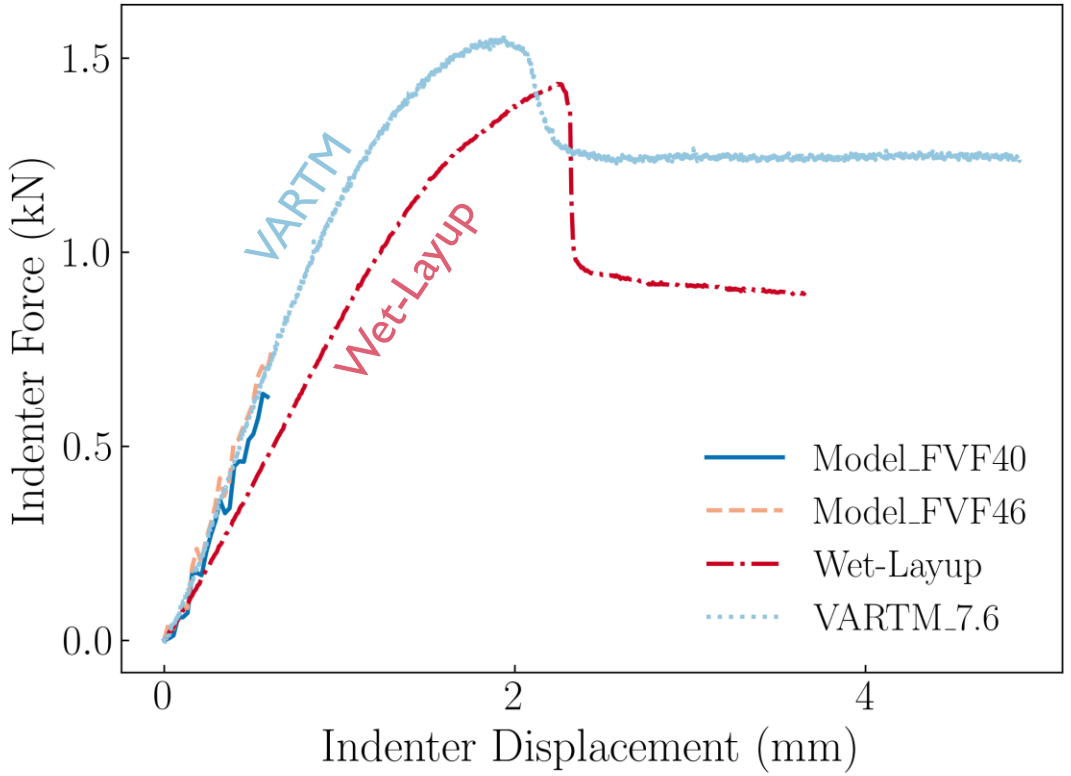

- VARTM Manufacturing methos aids improved resin distribution for the composite tubes and lower voids contributing enhanced Mechanical properties

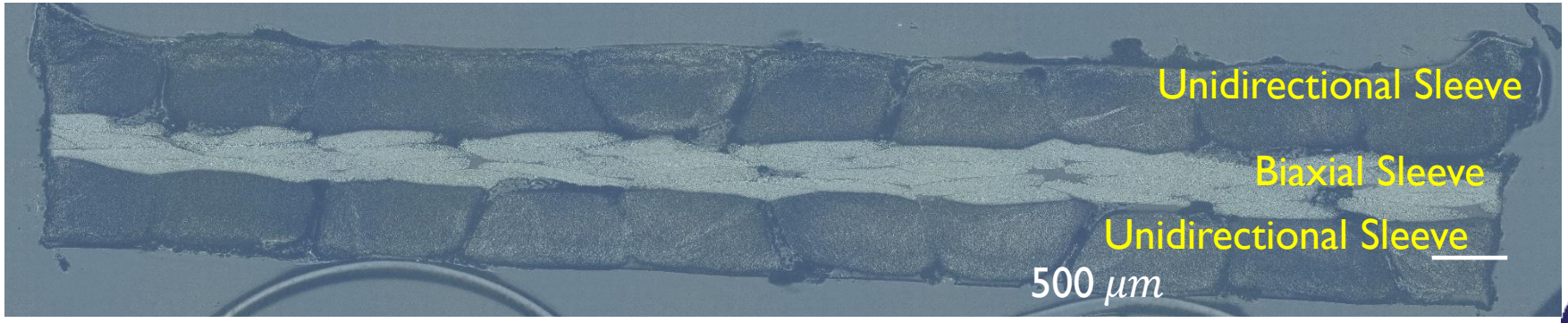

Fig. Cross-sectional of a Laminate fabricated by VARTM

Flat Laminate Tensile Tests

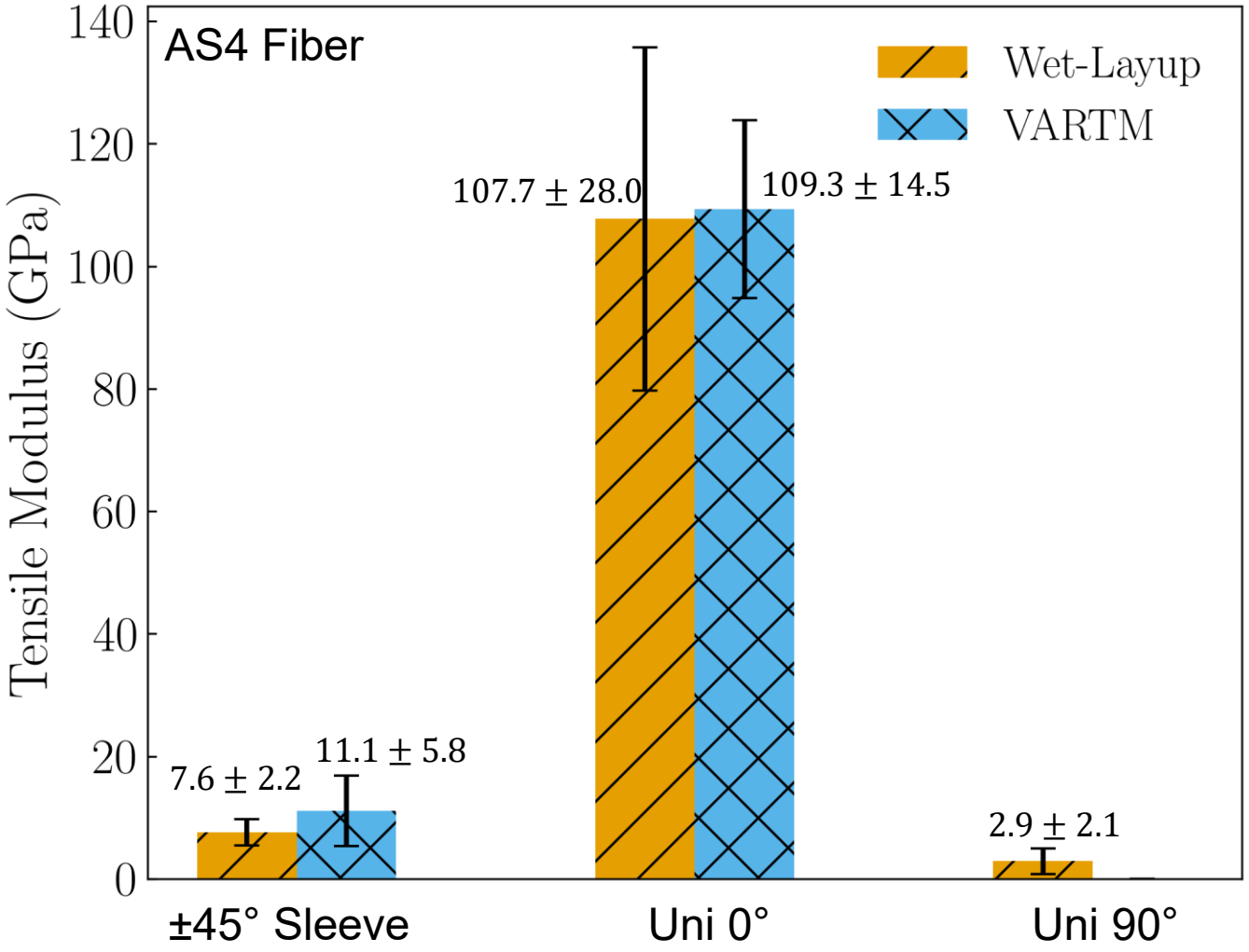

Flat Laminate Fiber Architecture	Manufacturing Method	Fiber Volume & void volume fraction
[0°,±45°,±45°,0°]	Wet-Layup	FVF: 49.2% VVF: 2.4%
[±45°, 0°, 0°,±45°]	Wet-Layup	FVF: 46.9% VVF: 2.5%
[0°,±45°,±45°,0°]	VARTM	FVF: 55% VVF: 0.5%

Properties (Theoretical): UNI

FVF = 50%→ $E_1 = 116.5GPa,$
$E_2 = 4.87\ GPa$

FVF = 40% → $E_1 = 93.6\ GPa,$
$E_2 = 4.09\ GPa$

Future Work: Mission "Illinois" Demonstration in Bishop Research Airlock on ISS in Summer 2026

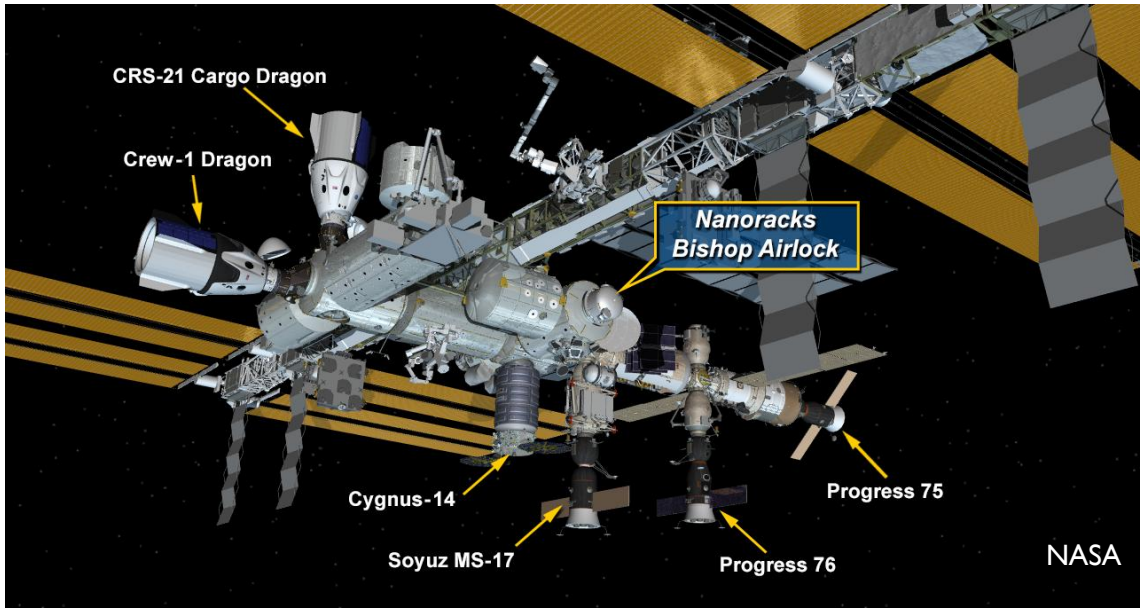

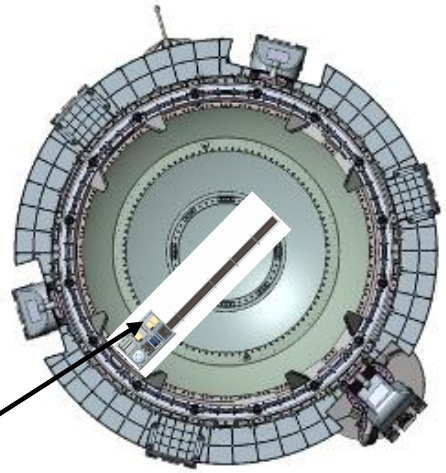

Payload



2 m Diameter SpaceWatch.Global

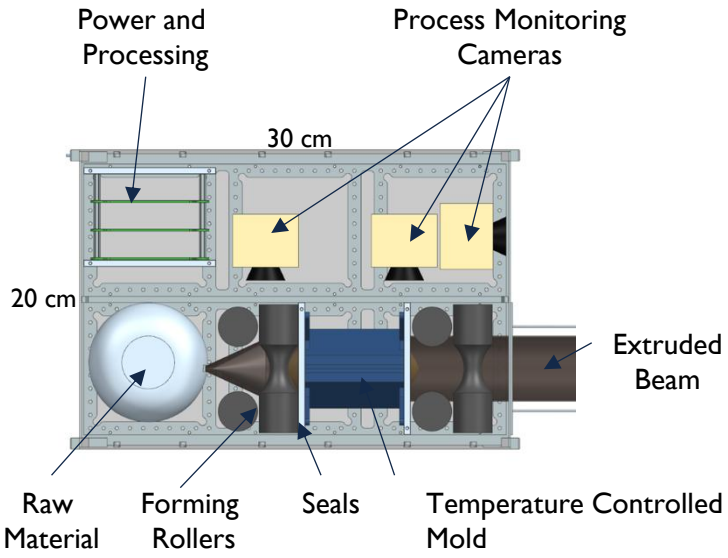

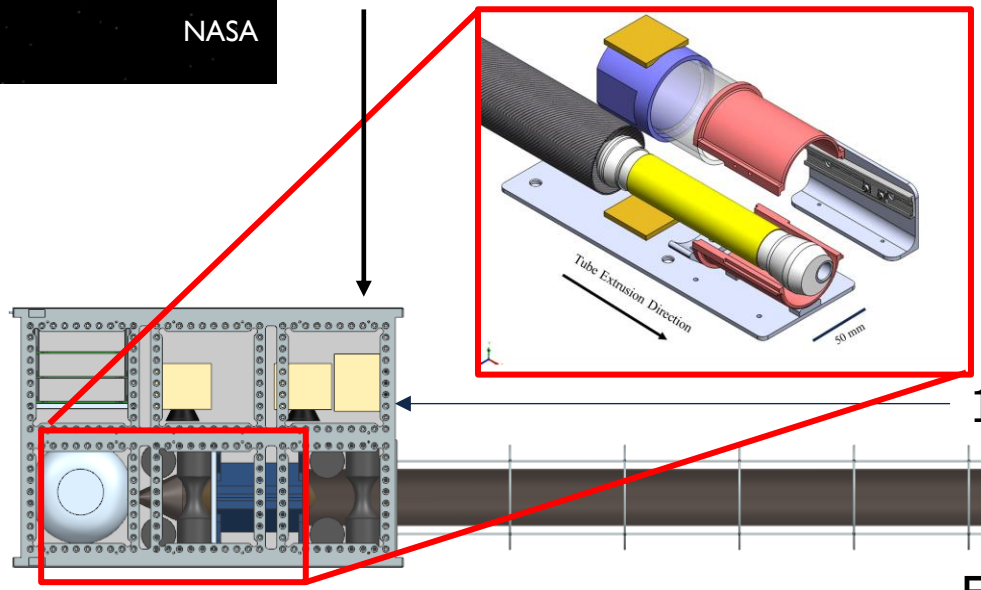

Nanoracks Launch Subcontractors:

CU Aerospace (CUA)

NearSpace Launch (NSL)

Fabricated Space Structure

Summary

- Frontal polymerized composites can enable in-space manufacturing of structural beams and tubes/longerons
  - ✓ Low processing energy
  - ✓ Rapid cure
  - ✓ Low volume and weight processing equipment
- Encapsulation of prepreg facilitates infusion, improved stability, low off-gassing, and processing
- Infusion leads to lower voids and higher flexural stiffness
- In-space manufacturing of thermoset composites is feasible

Baur Research Team Contributors

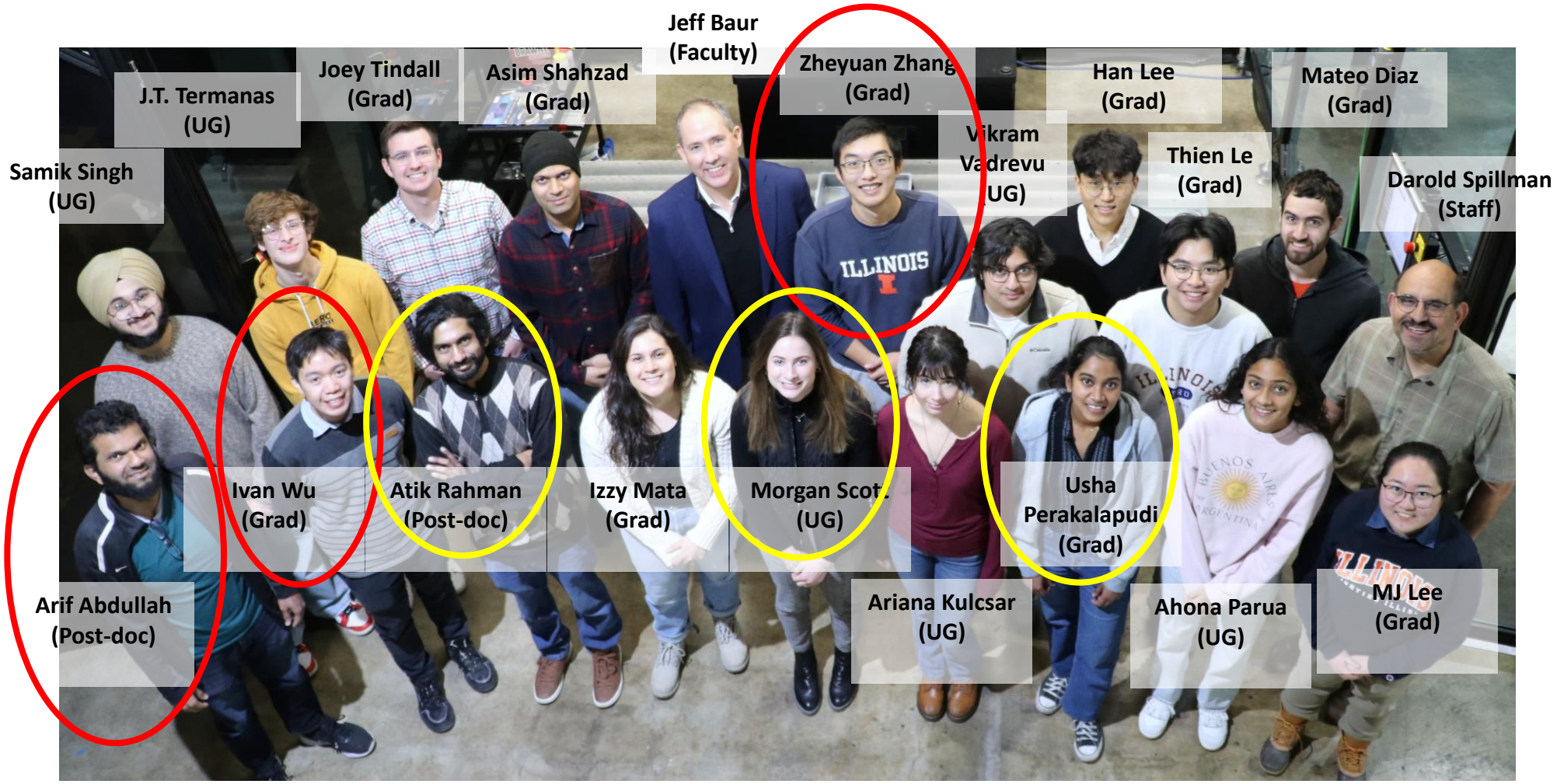



Logesh Shanmugam

Acknowledgements

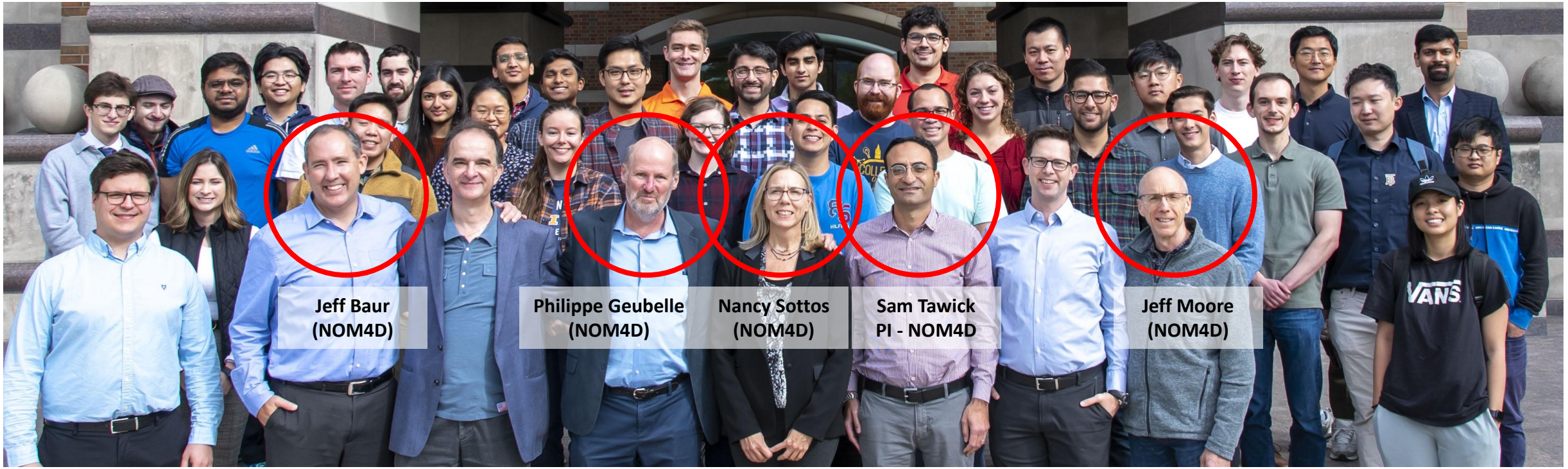

DARPA

NOM4D - Rapid Extrusion of Composite Mega-Structure for Space (REMS2)

Autonomous Materials Systems Group, Beckman Institute

Public releasable information under basic research exemption (AFOSR and DARPA/DSO sponsorship)

ILLINOIS BECKMAN INSTITUTE

ARNOLD & MABEL BECKMAN FOUNDATION

AFOSR AIR FORCE OFFICE OF SCIENTIFIC RESEARCH

Back-up Slides

Total Mass Loss of Prepreg (Flat Laminates)

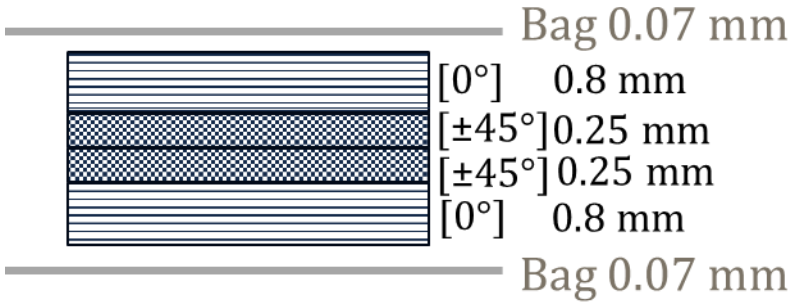

20 mins, Room temp

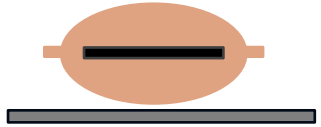

5 mins, 155°C



24 hrs., 125°C



Dahler Bag (Control) ⇔ 0.02% TML

Assuming all mass loss are due to prepreg (carbon fiber + resin) after adjusting based on control samples

ASTM E595 – Total mass loss (TML) < 1% after holding at 125°C at 24 hrs. under vacuum (10^{-5} $torr$)

Scale bars ≈ 25 mm

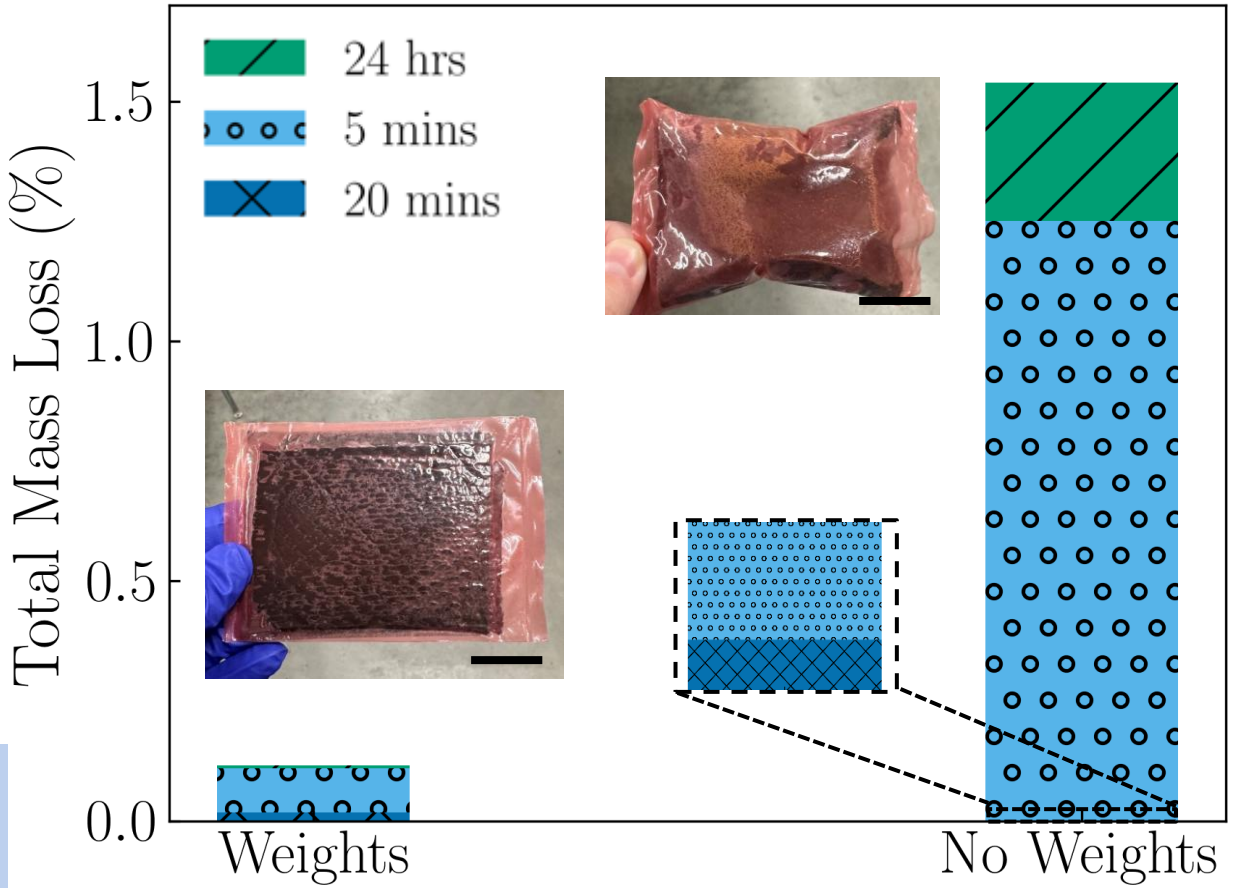

Scale precision: 0.01 mg

Longeron Dimension and Energy Consumption

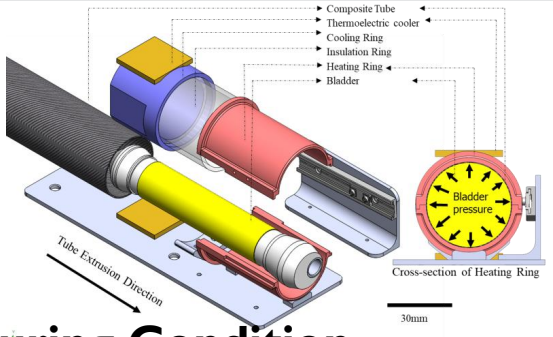

Curing Condition

Ramp to 155°C (PID), Hold for 5 min, Cool Down to 40°C, Bladder Pressure 15 psi

- Manufactured **AS4 fiber** reinforced Longeron, [0°,±45°,±45°,0°]
- Energy consumption :
- 1.95 MJ/kg*
- $2.925\ kJ/cm^3$

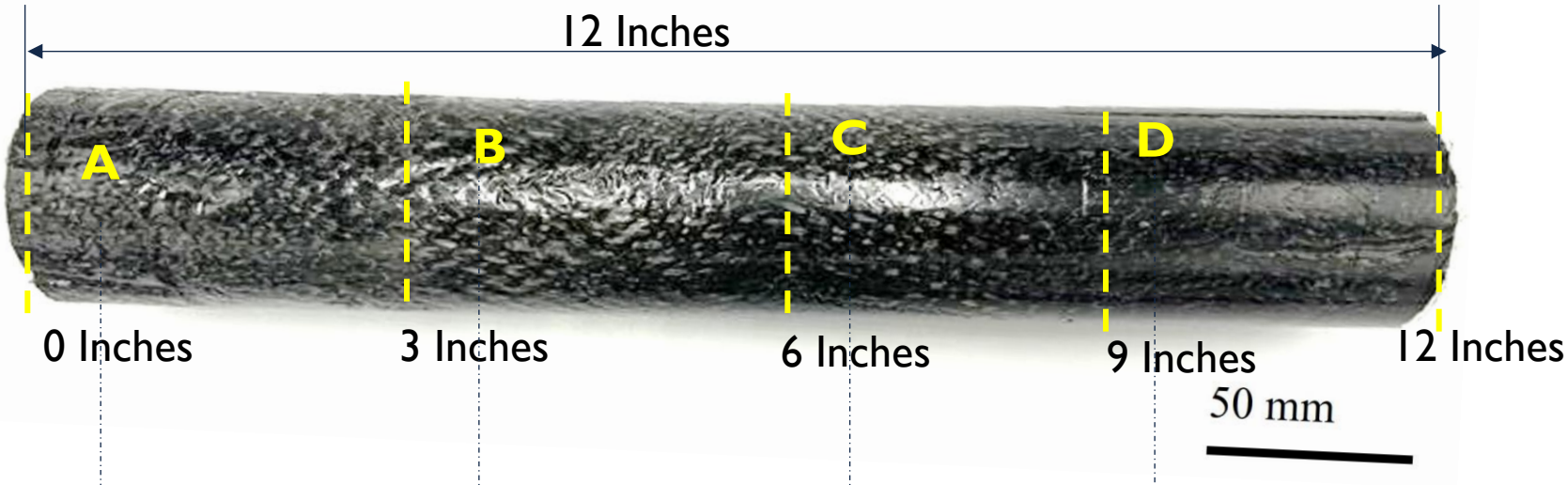

$OD = 50.42 \pm 0.14$
$ID = 45.81 \pm 0.40$
$Thickness = 2.76 \pm 0.14$

$OD = 50.21 \pm 0.17$

$OD = 49.85 \pm 0.15$

$OD = 49.11 \pm 0.24$
$ID = 43.60 \pm 0.80$
$Thickness = 3.2 \pm 0.19$

* Measured by Energy Meter

Split Disk Test

Average Hoop flexural strength = 33.8 MPa

- Tensile load is applied, with the UD fibers not taking load, since the load is applied in transvers direction
- Only fibers in ±45 takes load.

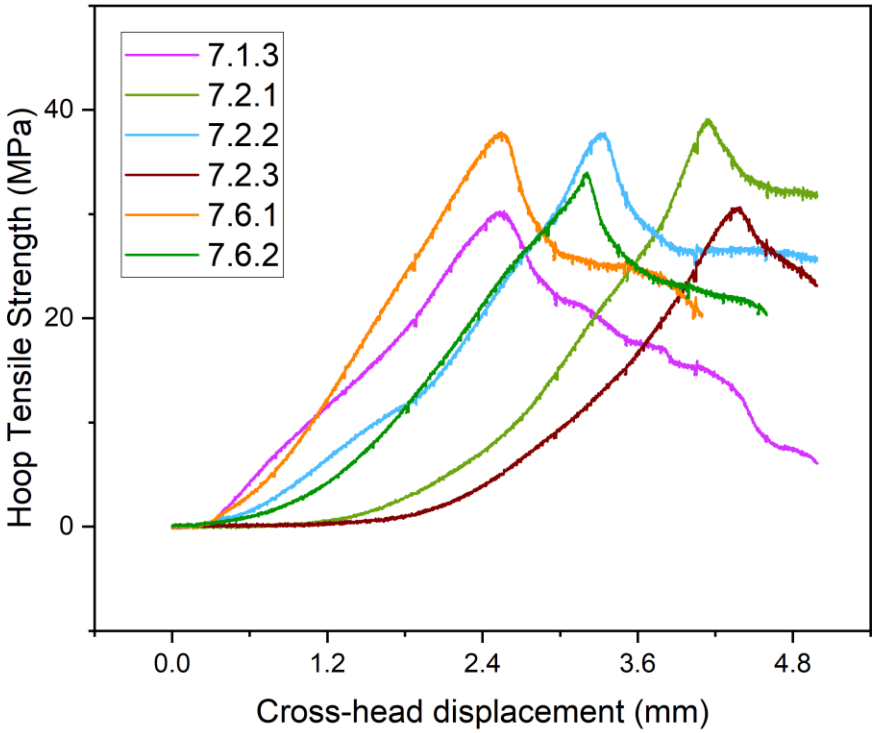

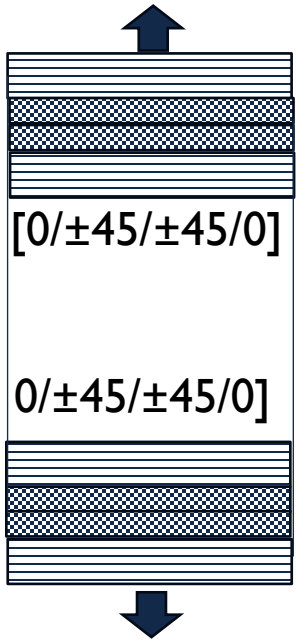

Standard - ASTM D2290 - 08 Standard Test Method for Apparent Hoop Tensile Strength of Plastic or Reinforced Plastic Pipe by Split Disk Method,

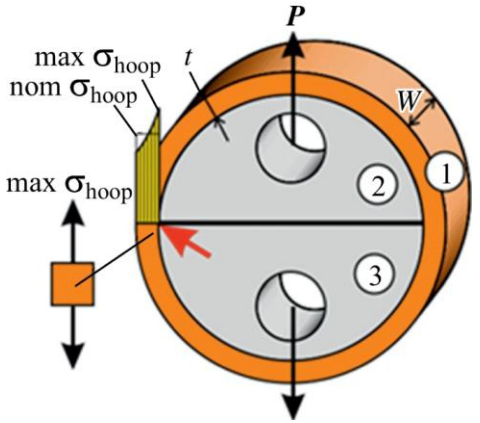

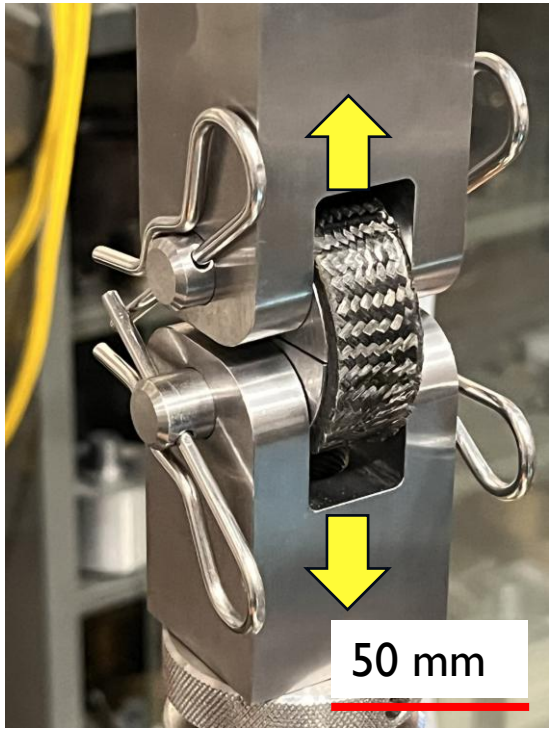



Failure Point

25 mm

Split Disk Testing by Keshat Mehra

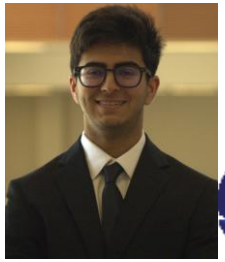

TEL AVIV UNIVERSITY

Degradation and biocompatibility of 3D-printed PLA reinforced with WS_2 nanotubes for bone scaffold applications

Ofek Golan

Department of Materials Science and Engineering,
Tel Aviv University



TEL AVIV UNIVERSITY

Research Motivation

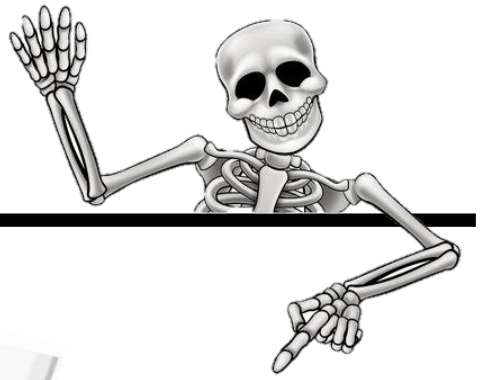

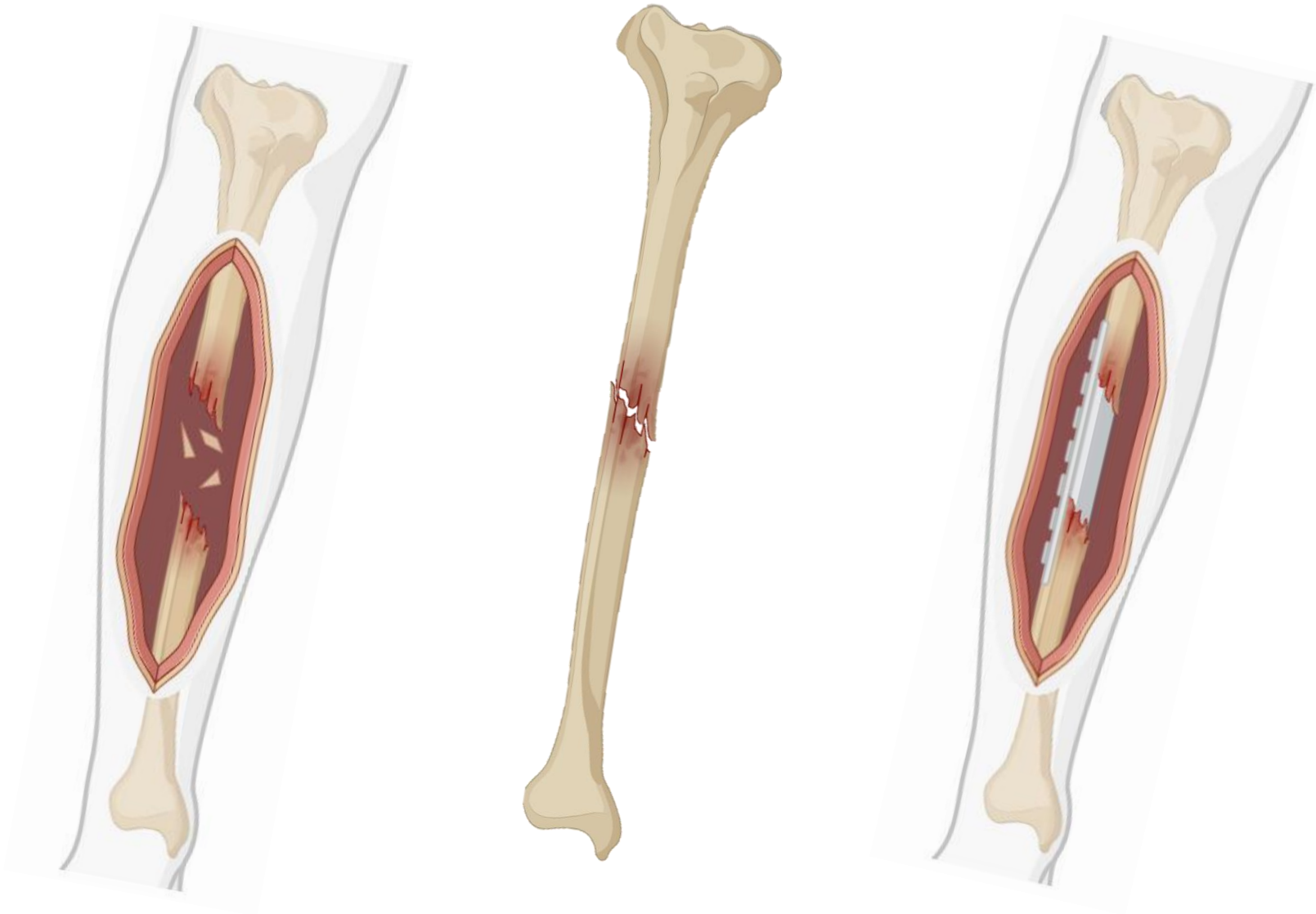

TEL AVIV UNIVERSITY

Application

- **Anchoring equipment for orthopedic implants and fractures**
- **Scaffolds in favor of a substrate for bone growth**



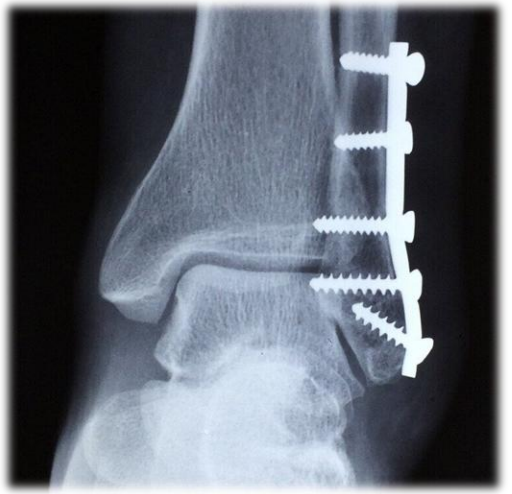

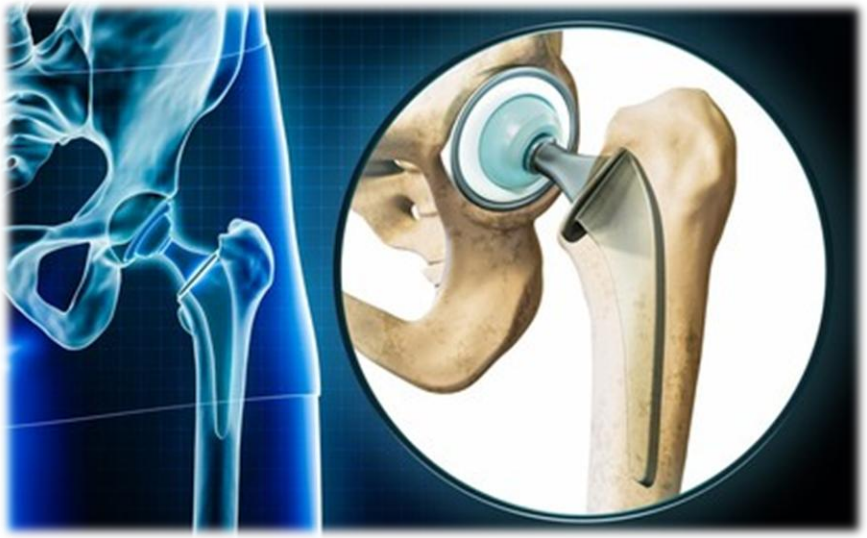

Disadvantages of today's implants

- Risk of implant rejection
- Stress shielding
- Additional surgery is required to remove them
- One size fits all

Bone Scaffold Requirements

1. Mechanical properties

Equal to or exceeding the original bone

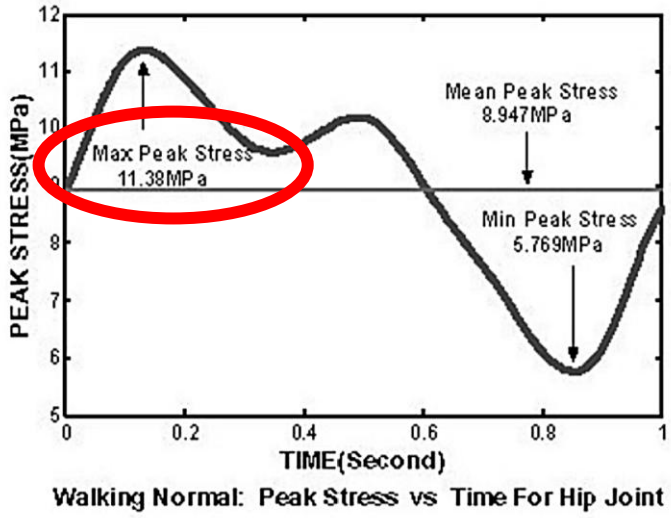

2. Degradation rate

In alignment with bone growth

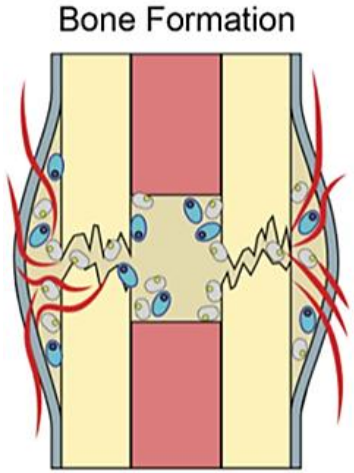

3-6 month

3. Biocompatibility



Biocompatible implants

X. S. Wang, T. Y. Wang, F. C. Jiang, and Y. X. Duan, “The hip stress level analysis for human routine activities,” *Biomed. Eng. - Appl. Basis Commun.*, vol. 17, no. 3, pp. 153–158, Jun. 2005, doi: 10.4015/S101623720500024X.

Polylactic Acid – (PLA)

- Thermoplastic
- Biodegradable
- Non-toxic
- Biocompatible
- Produce from renewable resources such as corn, sugarcane and starch

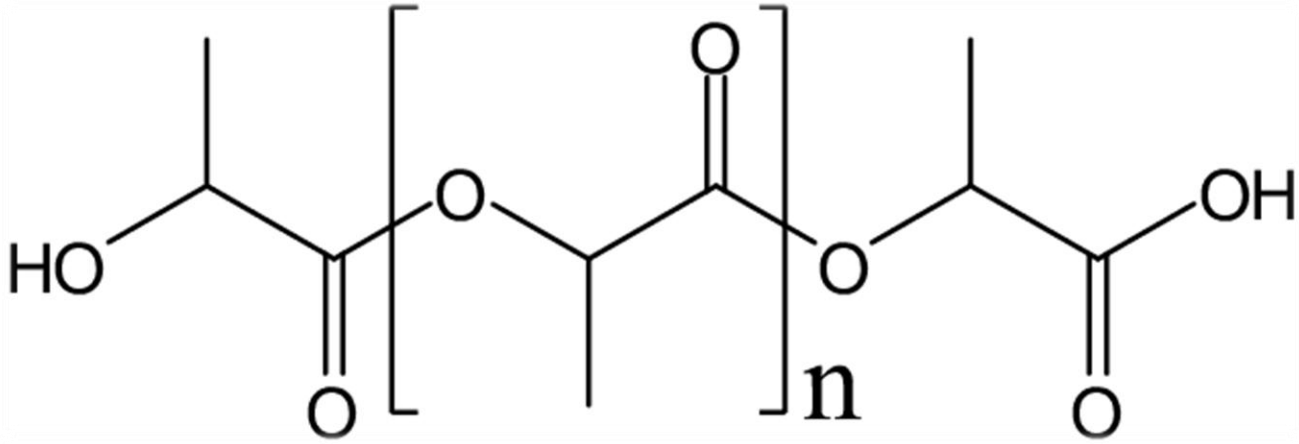



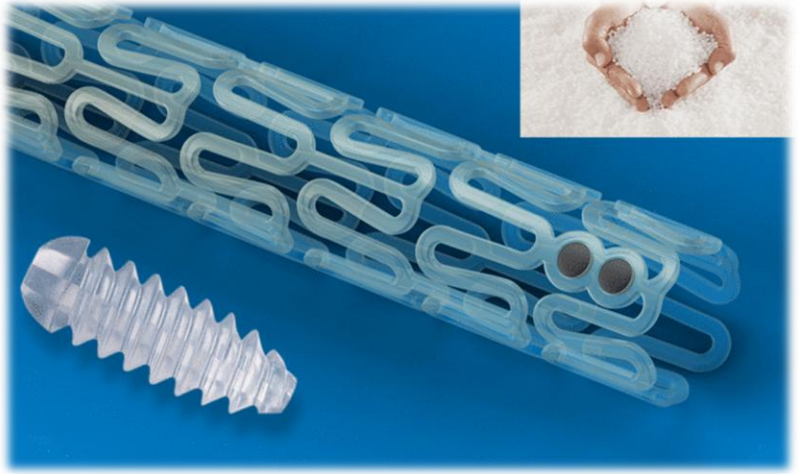

PLA Degradation Mechanism

Hydrolysis degradation

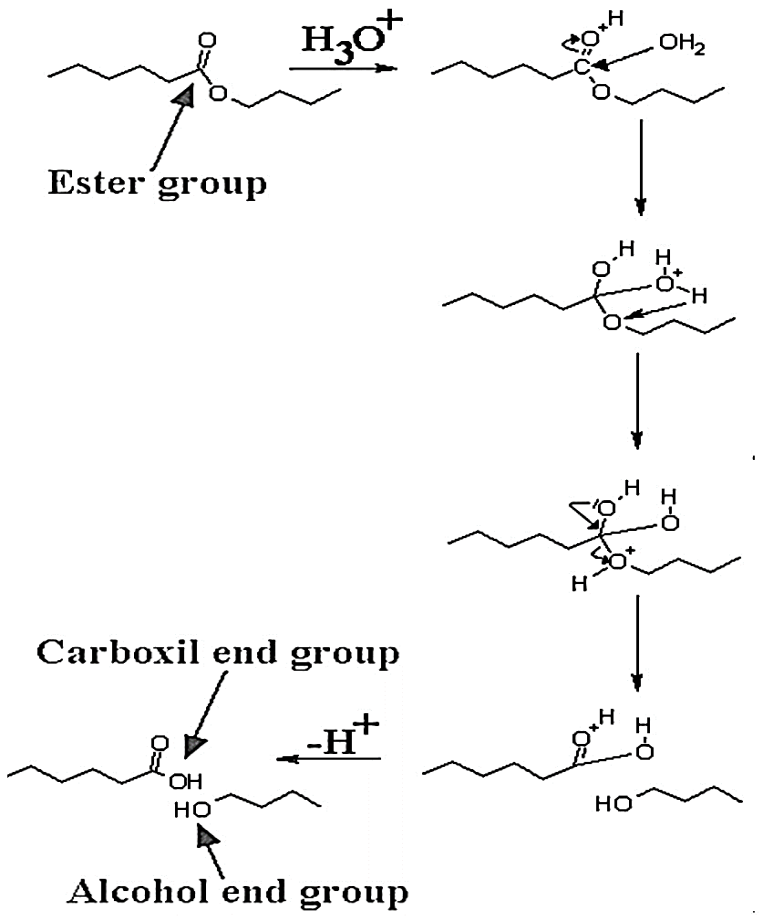

Enzymatic degradation



Vieira, A. C., Guedes, R. M., & Marques, A. T. (2009). Development of ligament tissue biodegradable devices: A Review. *Journal of Biomechanics*, *42*(15), 2421–2430. https://doi.org/10.1016/j.jbiomech.2009.07.019

Inorganic Nanotubes of WS_2

- Was synthesized and first observed by the Reshef Tenne's group in 1992
- Individual layers of the metal dichalcogenides MX_2
- Relatively possess good mechanical properties
- Non-toxic

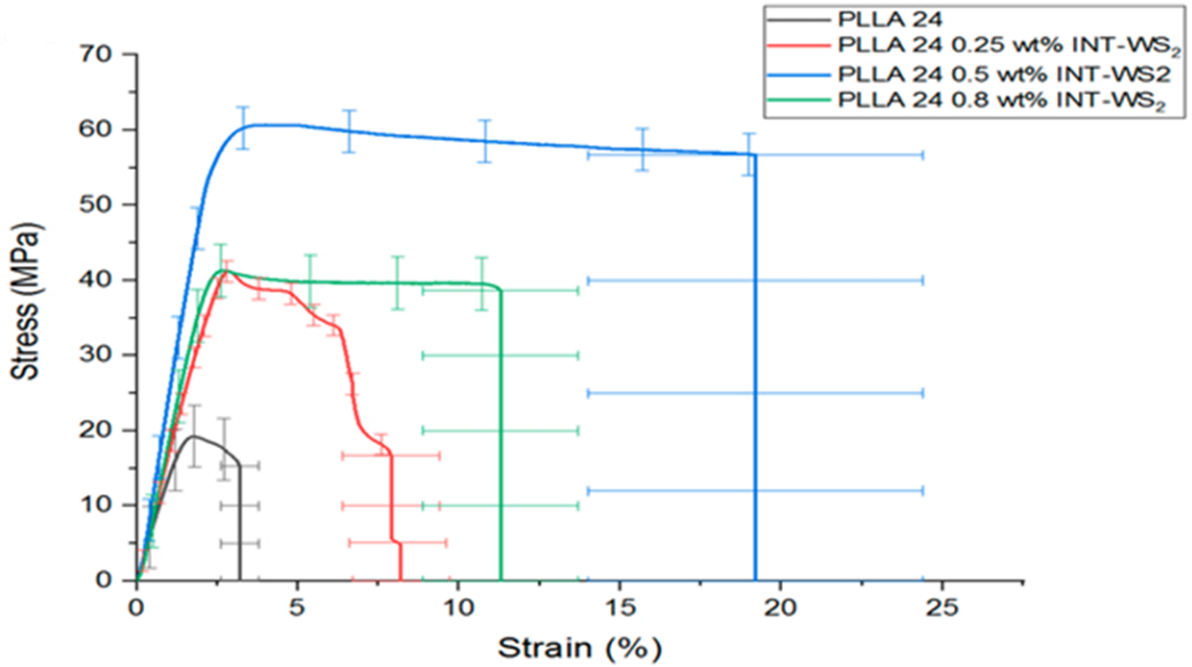

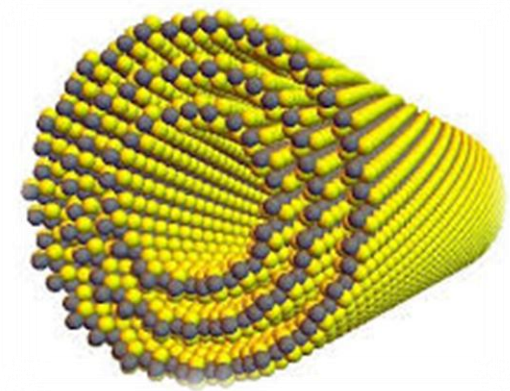

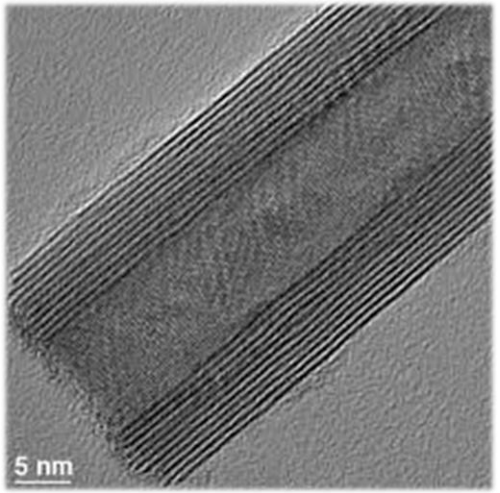

H. Shalom *et al.*, "Nanocomposite of poly(L-lactic acid) with inorganic nanotubes of WS_2," *Lubricants*, vol. 7, no. 3, 2019, doi: 10.3390/lubricants7030028.

Degradation Test Samples Preparation

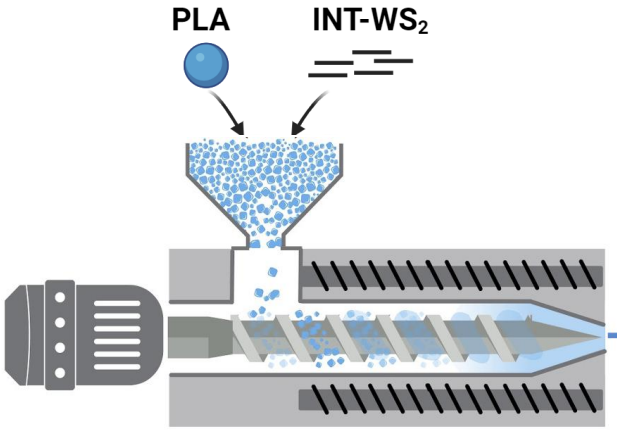

Filament manufacturing

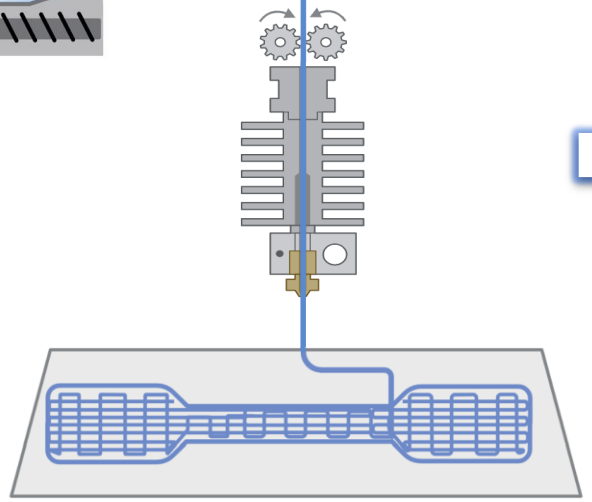

3D printing of samples

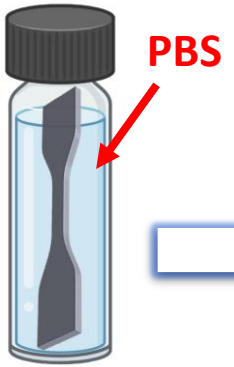

Submerging the samples in body-simulating fluid

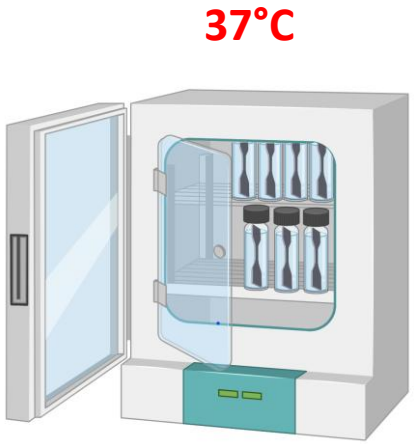

Vials kept in temperature of 37°C

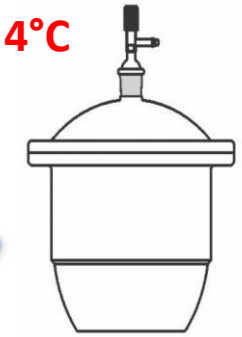

The samples were washed, dried and stored under vacuum at 4 °C

Results

TEL AVIV UNIVERSITY

Mass Change

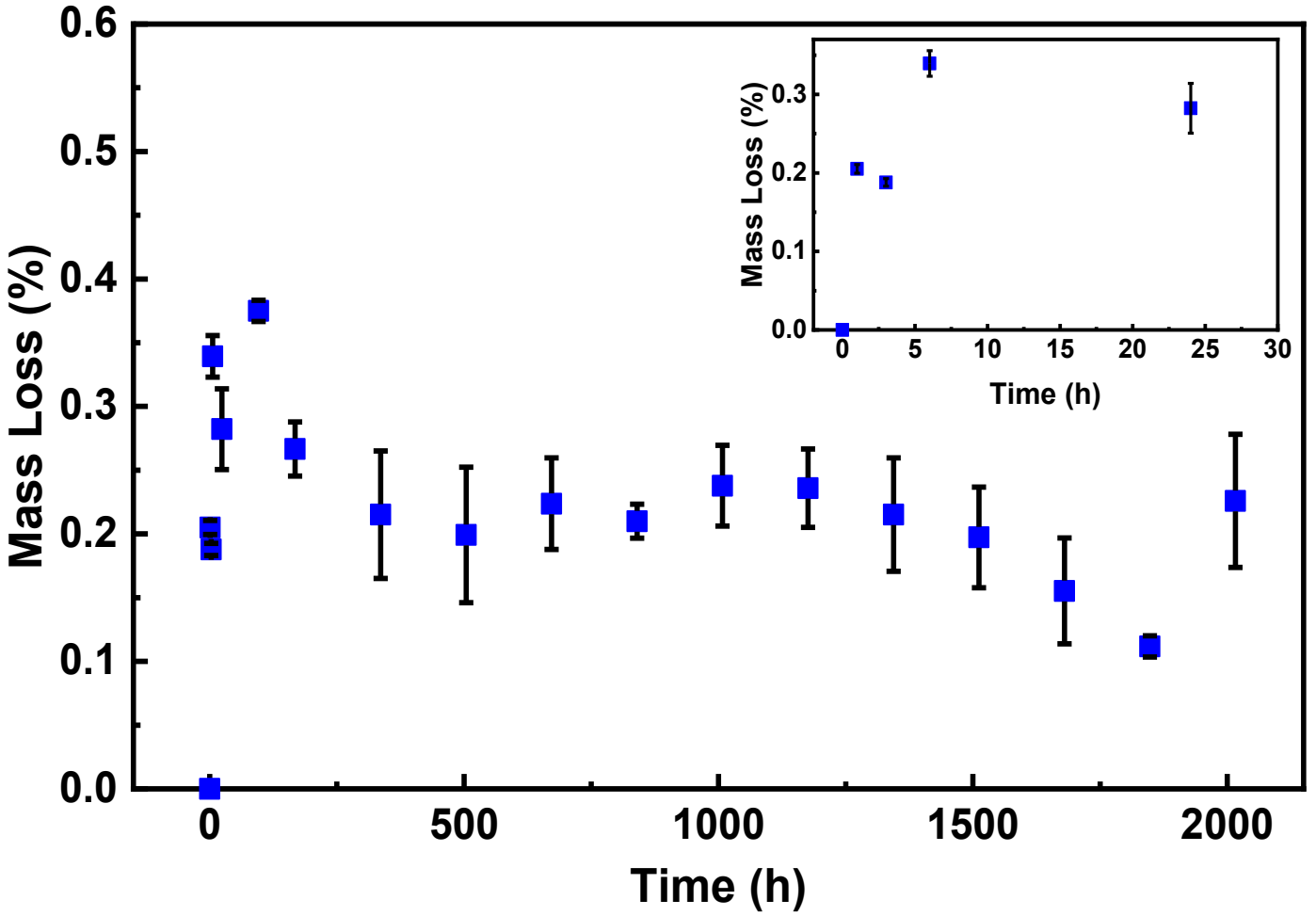

- $\boldsymbol{Mass\ Loss}\% = 100\% - \left[\frac{(m_i - m_f)}{m_i} x100\%\right]$

Mass Change

Mechanism of hydrolytic degradation

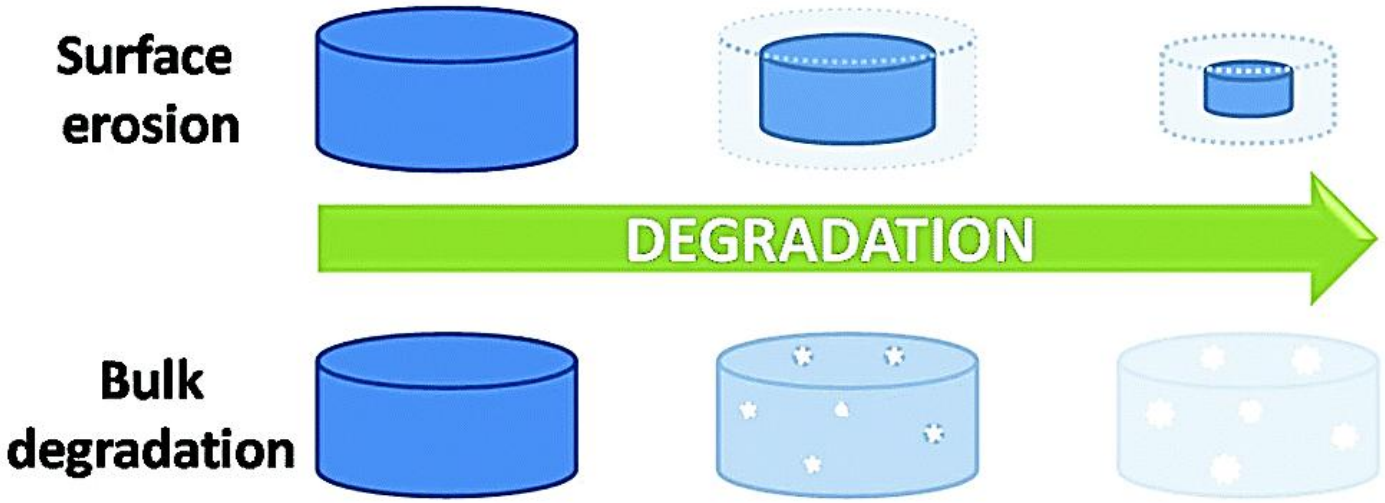



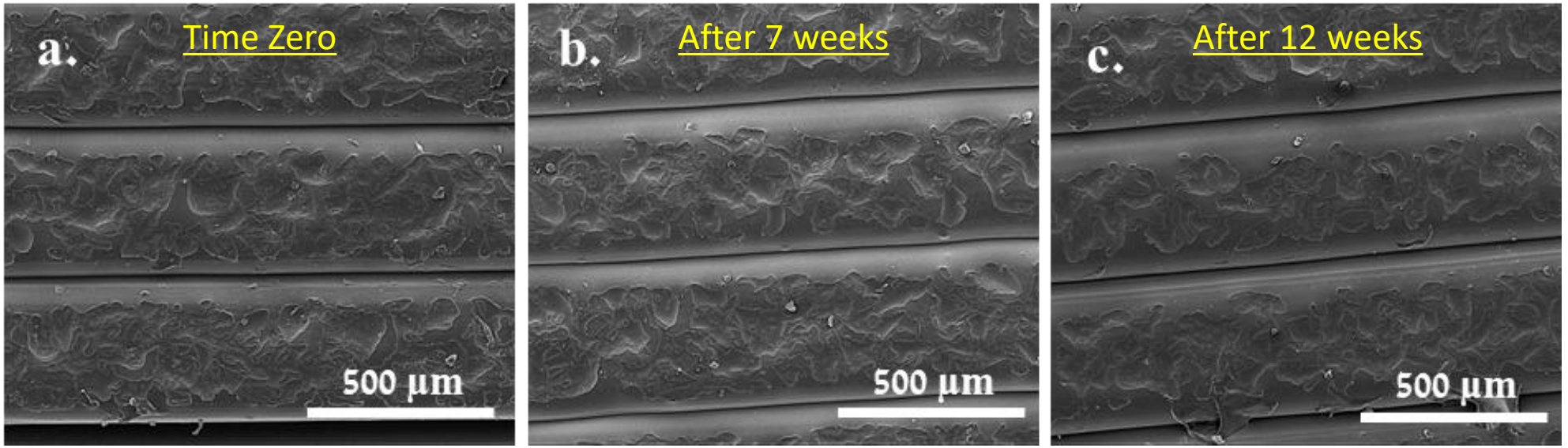

Differential Scanning Calorimeter (DSC)

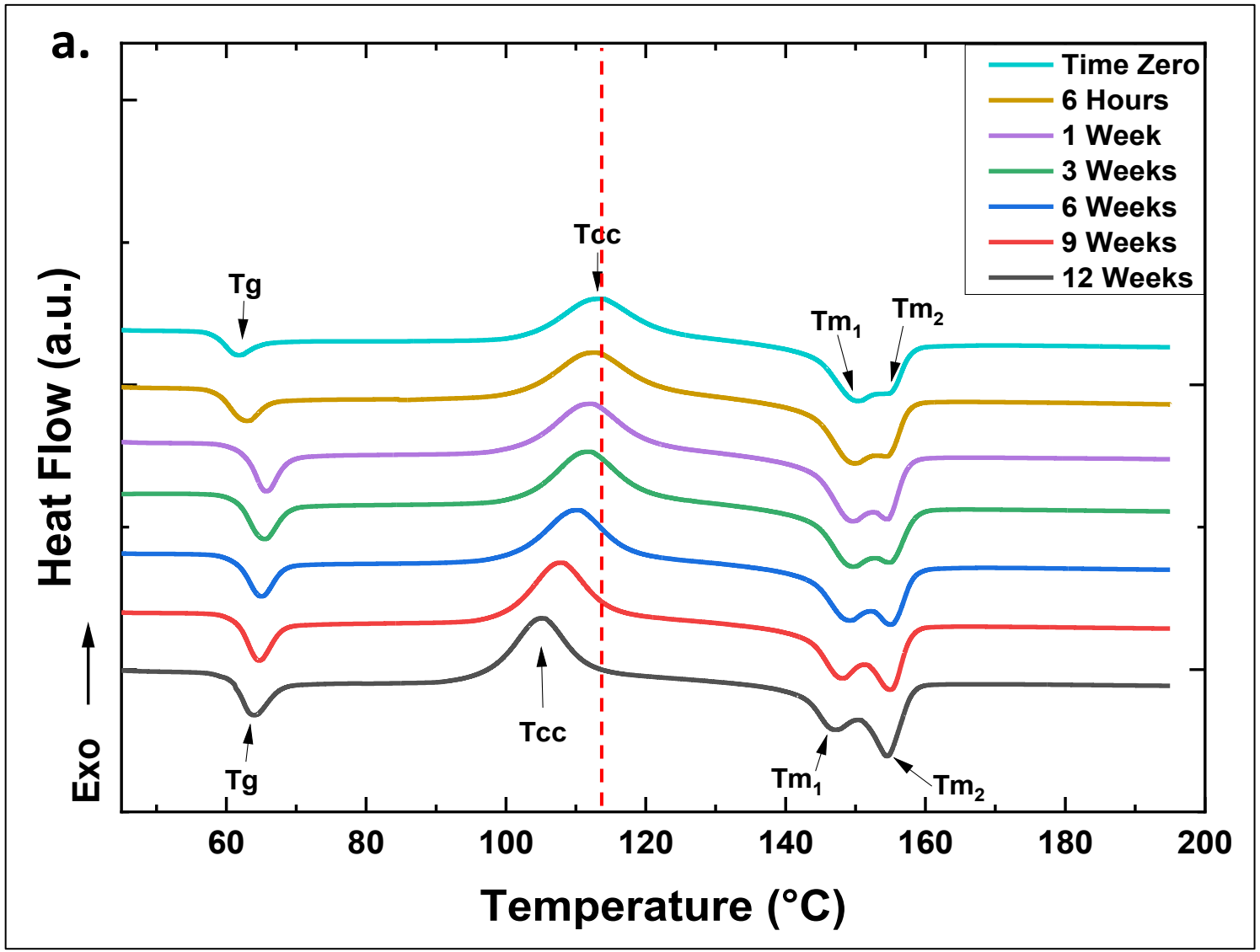

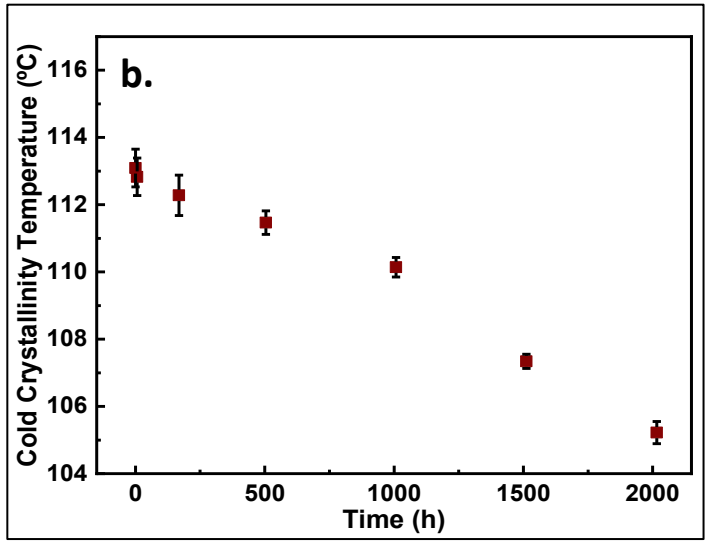

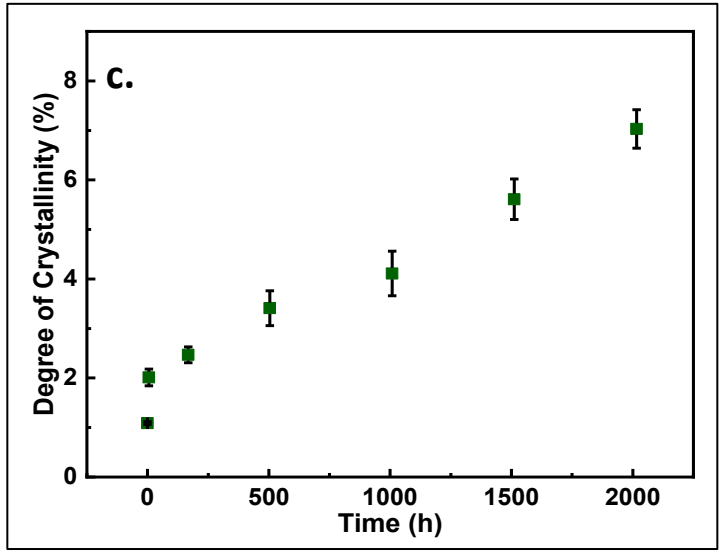

Size Exclusion Chromatography (SEC)

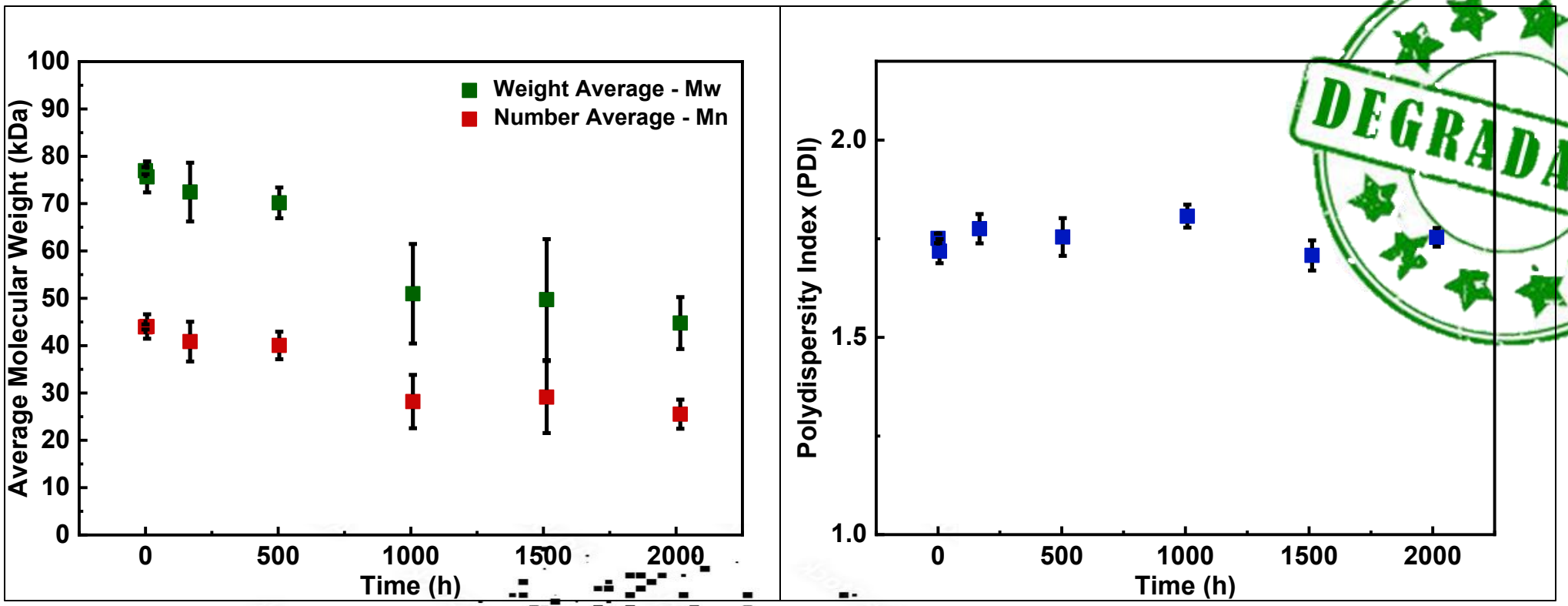

$$PDI = \frac{M_w}{M_n}$$

Mechanical Properties Tests

Micro Vickers Hardness Test

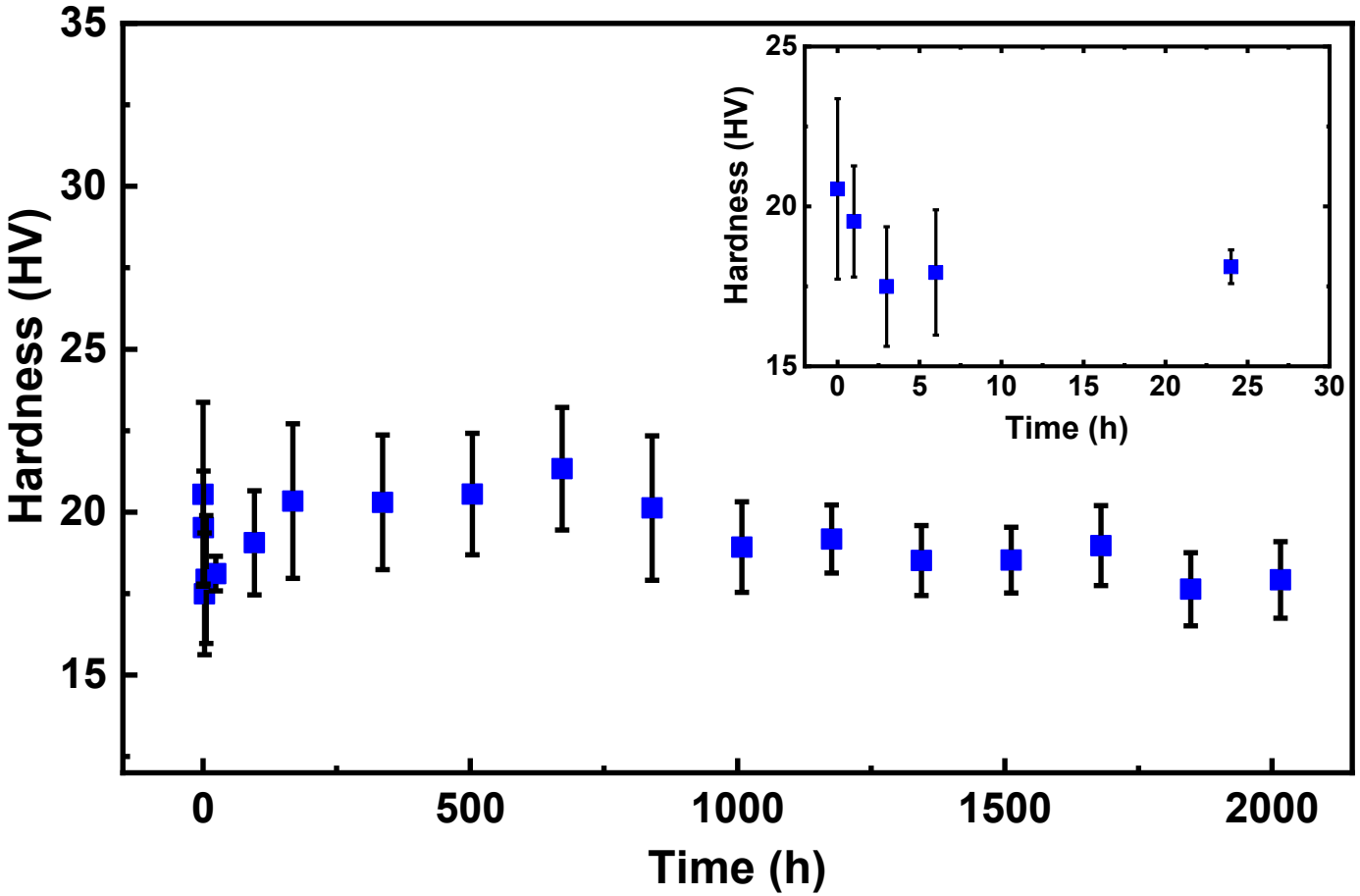

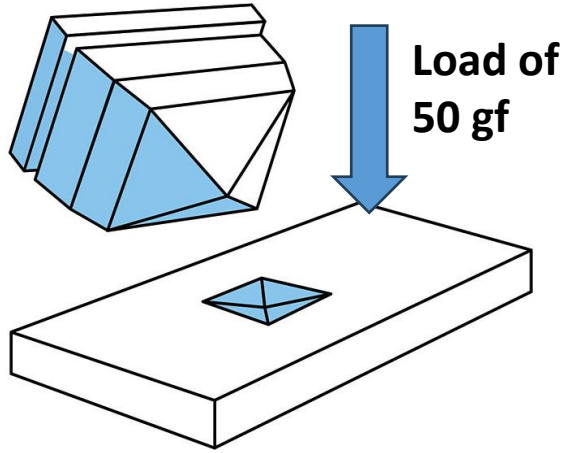

- Using relatively low loads, surface hardness properties are mostly determined

TEL AVIV UNIVERSITY

Mechanical Properties Tests

Tensile Test

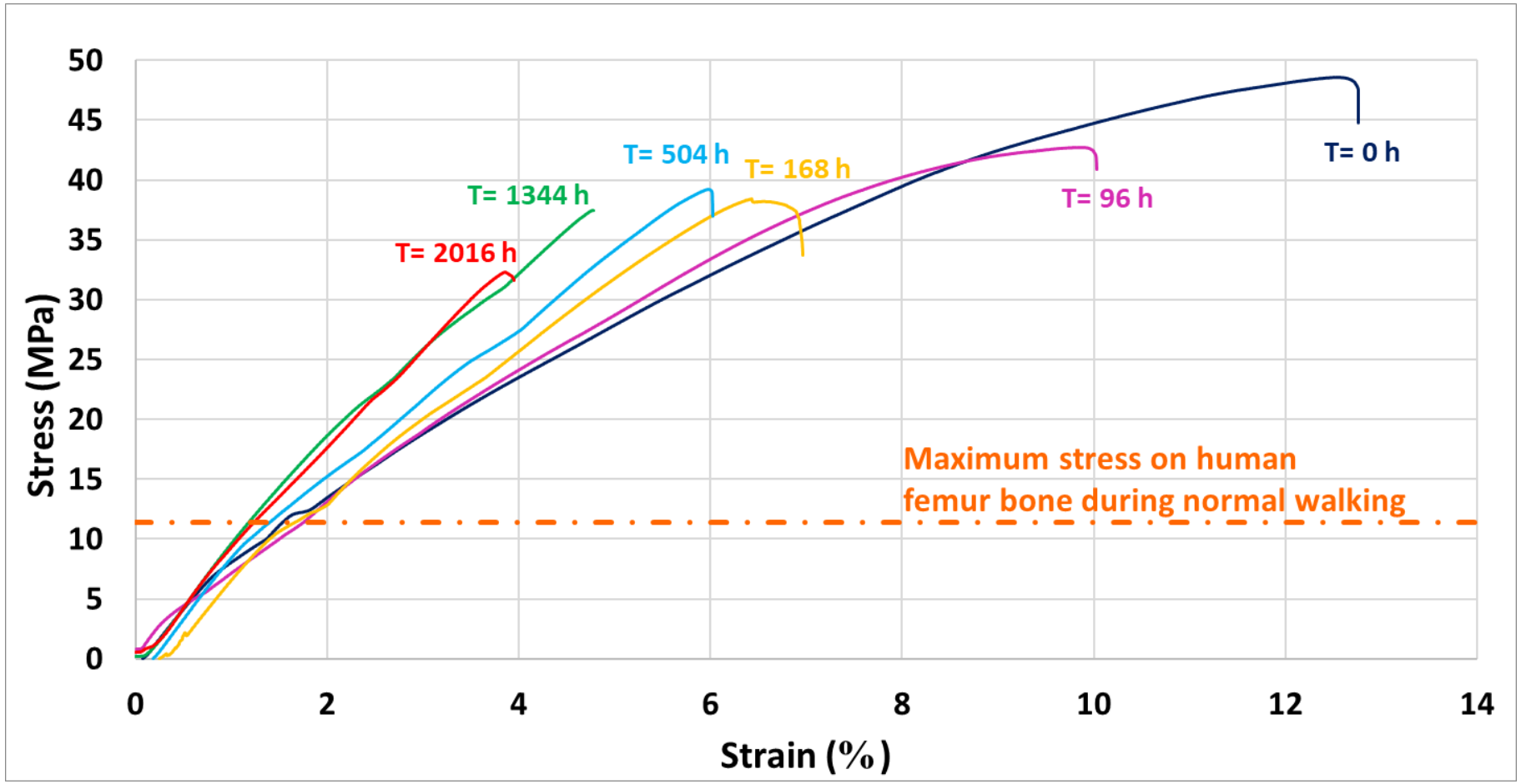

- Mostly bulk mechanical properties

TEL AVIV UNIVERSITY

Biocompatibility Test

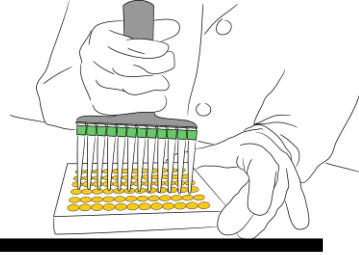

Cell viability of the filaments pre-printing

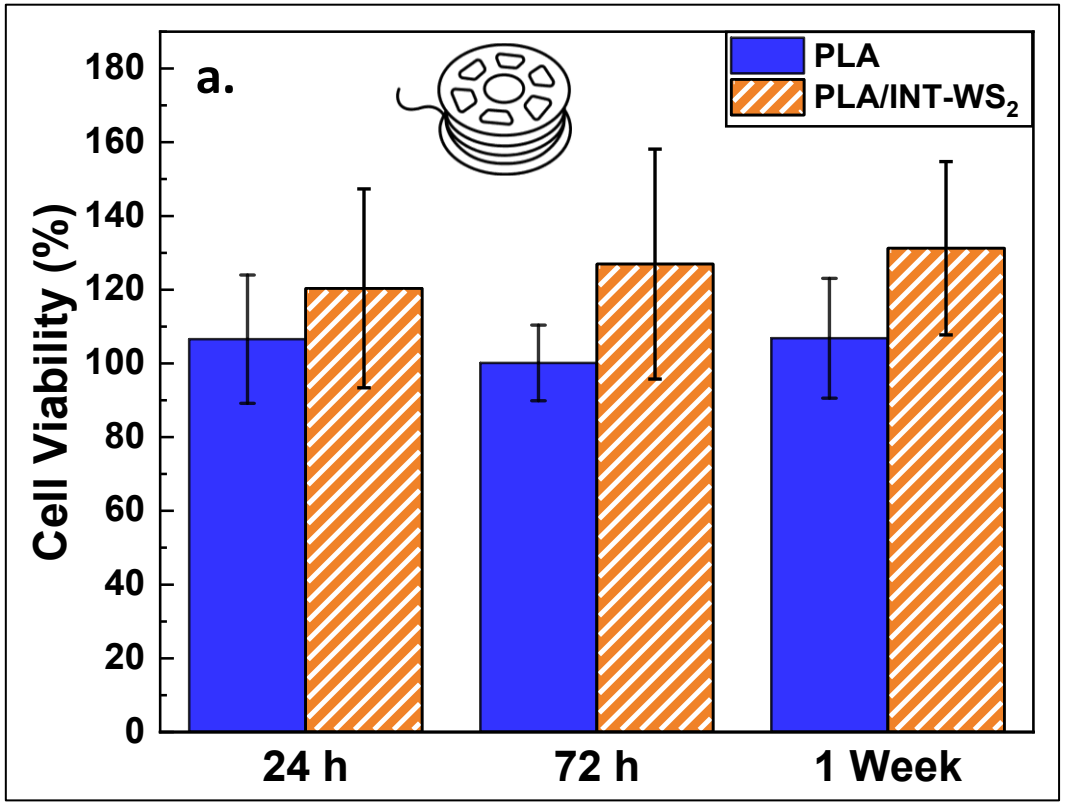

Relative metabolic activity of the cells for the 3D-printed samples

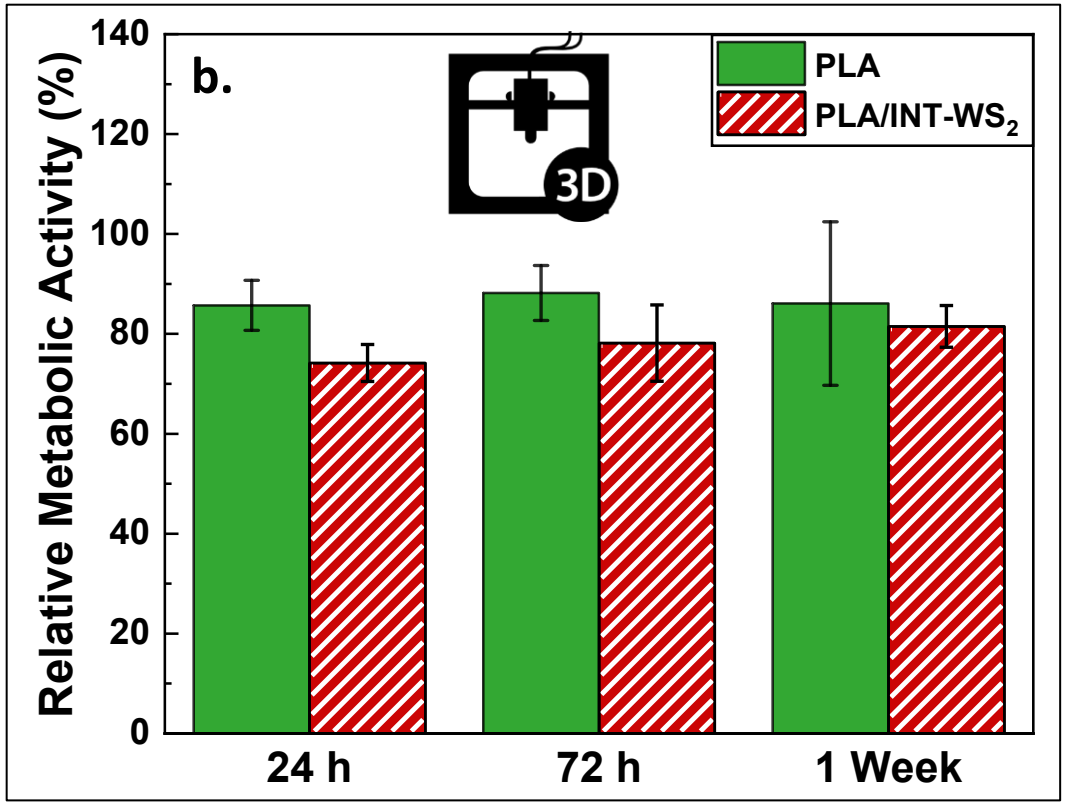

TEL AVIV UNIVERSITY

Biocompatibility Test

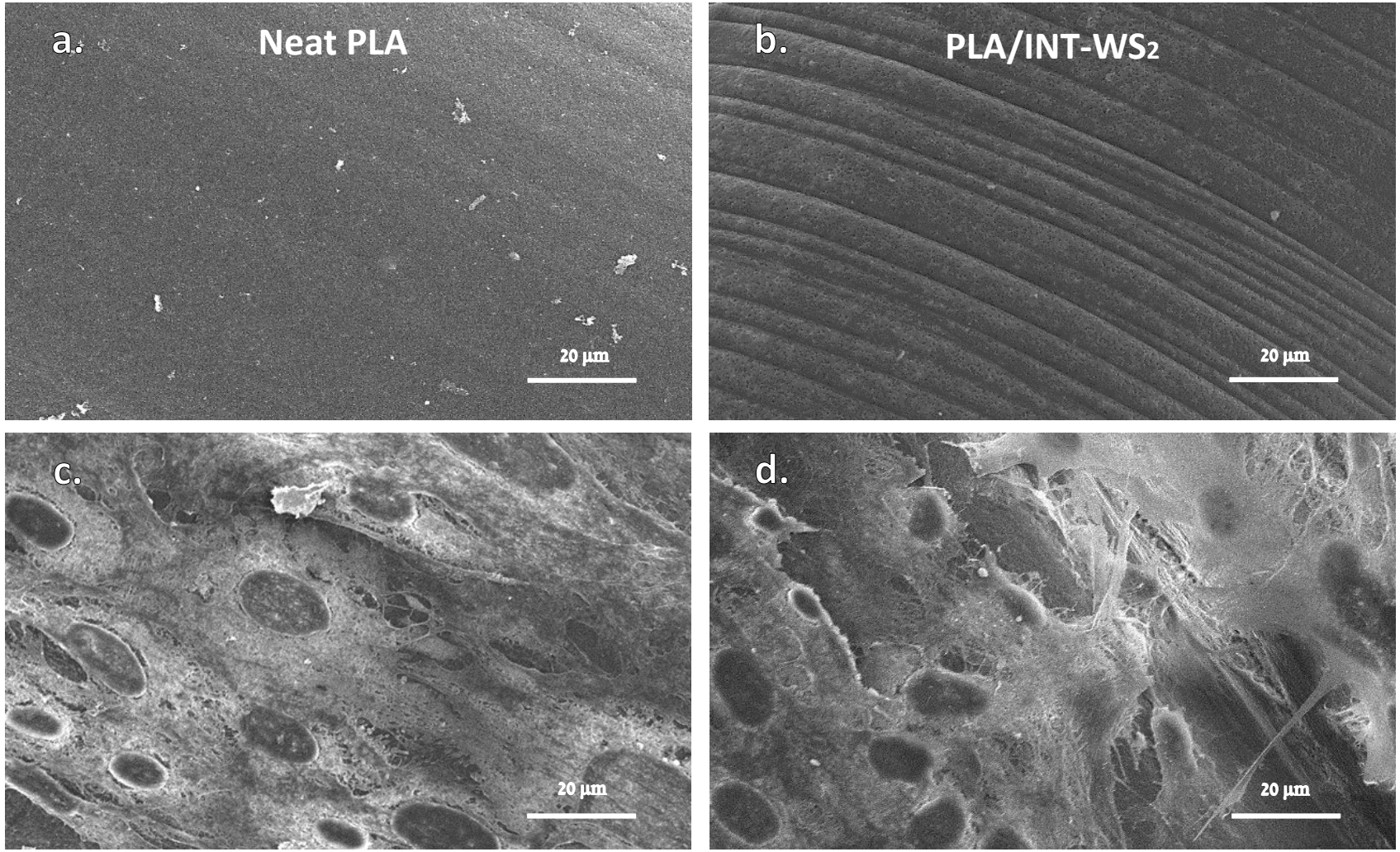

SEM images of MC3T3 cells on 3D printed samples in 20 micron bar under SE mode. a. Neat PLA and b. PLA/INT-WS_2 nanocomposite before cells siding. c. Neat PLA sample and d. PLA/INT-WS_2 after cells attachment.

Conclusions

- Tensile, thermal, and SEC analyses confirm PLA/INT-WS_2 degradation, with mass, hardness, and morphology indicates that the material underwent bulk degradation mechanism.
- Ultimate tensile strength remains 2.6 times higher than the maximum stress experienced during normal walking on a femur, after three months of degradation.
- The nanocomposite exhibits excellent biocompatibility, supporting cell growth and viability.
- Overall, the PLA/INT-WS_2 nanocomposite holds significant promise as a 3D-printed material for bone regeneration applications.

Future work

- Conduct longer-term studies to fully understand the degradation behavior of PLA/INT-WS_2 over extended periods, as bone healing can take several months to years depending on the injury.

Acknowledgements



Prof. Lihi Adler-Abramovich



Dr. Noa Lachman



Prof. Roey Amir



Francesca Netti



Noa Granada



Lin Lemesh



Dr. Salome Azoulay Ginsburg

And All of
The Noa Lachman Research Group

Composite Structures and Interfaces

TEL AVIV UNIVERSITY

Thank You

For Your Attention!

Any Questions



ICCM24
AUGUST 4-8, 2025
BALTIMORE CONVENTION CENTER
BALTIMORE, MARYLAND, USA

No Technical Paper Submission for:

Amir Hamza Nazir Ahmed Siddiqui

DEMONSTRATION OF A NOVEL HIGH PRESSURE VESSEL STRUCTURE CONSISTING OF CFRP OVERWRAPPED CYLINDER AND BELT SHAPED LOAD MEMBERS FOR FUEL CELL VEHICLES

Toshio Ogasawara [1], Ikumi Matsumoto [1], Jin Serizawa [1], Tomohiro Yokozeki [2], Akinori Yoshimura [3]

[1] Tokyo University of Agriculture and Technology
2-24-16 Naka-cho, Koganei-shi, Tokyo, Japan
Email: ogasat@cc.tuat.ac.jp, s245652s@st.go.tuat.ac.jp (presenter)

[2] The University of Tokyo
7-3-1 Hongou, Bunkyo-ku, Tokyo, Japan

[3] Nagoya University
Furo-cho, Chikusa-ku, Nagoya, Japan

Keywords: Pressure vessel, Hydrogen storage tank, CFRP, Finite element analysis

ABSTRACT

Cost reduction of CFRP hydrogen tanks is important to promote the practical use of fuel cell vehicles. In this study, in order to achieve a significant reduction in the amount of carbon fiber used, a "multi-load path structure" is proposed in which the axial and circumferential loads acting on the tank are shared by different members: CFRP overwrapped cylinder and belt shaped load members. For the purpose of technically verifying the structural concept, stress analysis, design and prototyping were carried out for a tank structure that uses two belt-shaped axial load members, and a structural strength evaluation was carried out by burst tests. As a result, it was demonstrated that it is possible to realize a tank structure that has a burst pressure almost as designed.

1 INTRODUCTION

Type-IV 70 MPa class high-pressure hydrogen tanks, in which carbon fiber is wound around a polymer liner by the filament winding (FW) method, have been applied to commercially available fuel cell vehicles (FCVs) [1, 2]. In order to expand the use of FCVs, in addition to reducing the cost and improving the productivity of hydrogen tanks, it is necessary to improve the packaging capability of the tanks to automobiles. To improve the packaging capability of the tanks, the concept of a " multiple tank module" has been proposed [3]. In the tanks made by FW method, low-angle helical winding must be applied to form the dome section, but there is a tendency for excess carbon fiber to be generated in the cylinder section. This tendency is more pronounced in small-diameter, long tanks, and simply combining the FW tanks will result in increased costs and reduced weight efficiency due to the increased amount of carbon fiber used. In order to commercialize a tank module with multiple small-diameter, long tanks, it is necessary to significantly reduce the amount of carbon fiber used.

Therefore, this study aims to achieve a significant reduction in the amount of carbon fiber used by applying a "multi-load path structure" in which the axial load and circumferential load acting on the tank are borne by different members. In this structure, the "axial load member" that bears the axial load and the "CFRP overwrapped cylinder" that bears the hoop load are manufactured separately, and then assembled into an integrated tank. It is possible to design the tank so that most of the carbon fibers reach their breaking strain at the same internal pressure when the tank bursts. Therefore, in the case of a small-diameter, long tank, it is possible to reduce the amount of carbon fiber used by more than 30 % compared to a FW tank. In addition, the axial member and cylinder have simple shapes, so productivity is also excellent. If a small-diameter, long tank with a multi-load path structure is realized, it is possible to significantly reduce the cost increase associated with connecting tanks and realize a tank structure with

excellent packaging capabilities at low cost. A similar concept to the multi-load path structure in this study was proposed in a German patent publication [4, 5], but no design considerations or technical demonstrations using tanks have been reported within the scope of the authors' investigation.

In this paper, we report on the results of stress analysis, design, and prototype fabrication of a tank structure that uses two belt-shaped axial load members, as well as the results of a structural strength evaluation conducted by a burst test, with the aim of technically demonstrating the multi-load path structure concept.

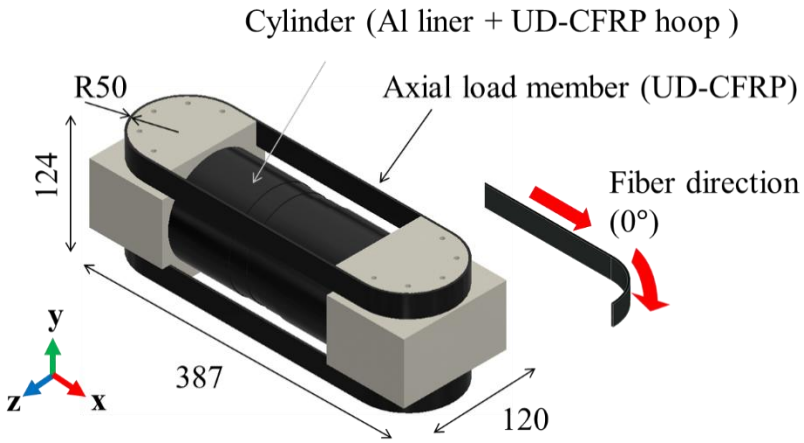

(a) Over view

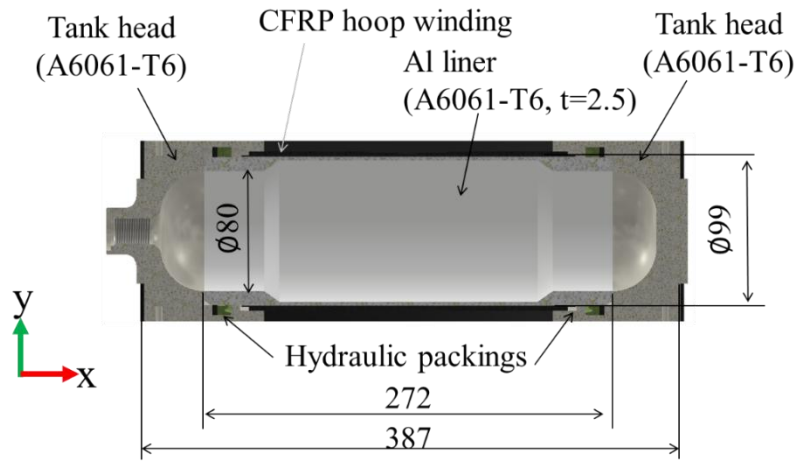

(b) Cross-sectional view

Fig. 1 Schematic drawing of a tank structure consisting of UD-CFRP axial load member and CFRP overlapped cylinder

2. STRESS ANALYSES AND DESIGN

2. 1 BASIC CONCEPT OF TANK STRUCTURE

The basic structure and cross-section of the tank used in this study are presented in Fig. 1(a) and (b). The external appearance is similar to the basic structure illustrated in the references [4, 5], but the detailed structure is significantly different. The components are an aluminum alloy (A6061-T6) liner (outer diameter φ 99 × length 272 × thickness 2.5-9.5 mm), a hoop CFRP layer (CF/Epoxy, thickness

1.6-3.6 mm), an aluminum alloy (A6061-T6) tank head, and two CFRP belt-shaped axial load members (width 25, thickness 2.4, curvature of the arc section 50 mm). The circumferential stress (hoop stress) in the cylinder due to internal pressure is mainly borne by the CFRP hoop layer overwrapped around the Al liner. The axial load acting on the cylinder is borne by two UD-CFRP belt-like axial load members. The tank head (A6061-T6) has a structure in which the dome and boss are integrated. The belt-like axial load members are made of unidirectional CFRP (CF/Epoxy) and are fitted around the top and bottom of the tank head. A high-pressure packing (NOK, Japan) is used as a water tight seal between the outer circumference of the liner and the inner circumference of the tank head.

In this structure, there is a small clearance between the axial load member and the tank head because of mechanical assembling. Therefore, even if an axial load member is applied to a Type III tank that uses a typical dome-cylinder integrated aluminum alloy liner, an axial load will also act directly on the cylinder due to the internal pressure load. In this case, since CFRP is not applied in the axial direction of the cylinder, there is a concern that the cylinder will break in the axial direction at low pressure. Therefore, it is important structural feature that the domes on both sides of the aluminum liner are eliminated, making it a cylindrical liner so that the internal pressure acts directly on the inside of the dome of the tank head.

2. 2 STRESS ANALYES OF TANK STRUCTURE

A commercial code, ABAQUS/ Standard 2023 (Dassault Systems), was used for the finite element analysis (FEA). The material of the liner and tank head was an aluminum alloy (A6061-T6), and the hoop layer and axial load members were made of unidirectional CFRP (T800/Epoxy, Mizuno Technics, Japan). The mechanical properties of the CFRP used in the analysis are shown in Table 1. The stress-strain curve of the aluminum alloy (A6061-T6) was based on literature values [6], and an elastic-plastic model according to the associated flow rule was applied.

A half model as shown in Fig. 2(a) was used for the FEA in consideration of symmetry, and an internal pressure of 100 MPa was applied to the inner wall of the tank. 10-node tetrahedral two-dimensional elements (C3D10) were used to the tank head and the dome part of the liner, and 8-node hexahedral reduced integration elements (C3D8R) were applied to the axial member, cylinder, and circular head of the liner.

Table 1 Material Properties of CFRP (T800S/Epoxy)

Properties		Values
Elastic moduli [GPa]	E_L	168.0
	$E_T = E_Z$	10.0
Shear moduli [GPa]	$G_{LT} = G_{LZ}$	6.06
	G_{TZ}	5.0
Poisson's ratio [-]	$\nu_{LT} = \nu_{LZ}$	0.31
	ν_{TZ}	0.45
Tensile strength [MPa]		3290
Failure strain [%]		1.96

2. 3 STRESS ANALYSIS RESULTS

Figures 2(a) and (b) show contour plots of the maximum principal stress in the entire tank and in the cylinder section at an internal pressure of 100 MPa, respectively. As per the design concept, it can be seen that the axial load is mainly carried by the two belt-shaped axial load members, while the circumferential load is carried by the CFRP hoop layer of the cylinder. The circumferential tensile stress is high in the central part of the cylinder, but this is because the CFRP hoop layer is thin (1.6 mm) around here. At an internal pressure of 100 MPa, the axial strain in the general part of the axial load member was 1.25 %, and the strain in the hoop direction in the cylinder CFRP layer was 1.19 %.

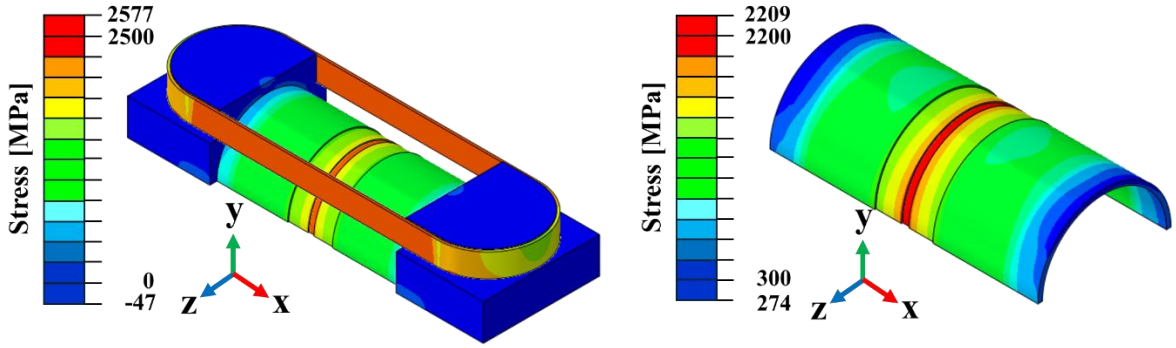

(a) Tank assembly (b) Cylinder

Fig.2 Contour plot of max principal stress at the internal pressure of 100 MPa

Fig. 3 shows the maximum principal stress distribution in the axial member when the internal pressure is 100 MPa. The axial stress in the general part of the axial member is 2083 MPa (strain 1.25 %), while the maximum principal stress around the straight line-arc boundary is 2446 MPa (strain 1.47%), which is about 17 % higher. This is because in this area, bending load is superimposed on the tensile load. In addition, watching the straight line-circular arc boundary of the axial load member in Fig. 3, the maximum principal stress is about 4% higher in the lower part (2446 MPa) than in the upper part (2351 MPa). In other words, the axial member has stress distribution in the width direction as well. Fig. 4(a) shows the distribution of the von Mises stress of the tank head when the internal pressure is 100 MPa, and Fig. 4(b) shows the deformation diagram and contour diagram of the z-direction (lateral) displacement. The z-direction displacement is about 0.12 mm larger in the lower part of the tank head compared to the upper part at the contact part of the axial member. In other words, it can be understood that the bending deformation of the tank head causes uneven load distribution on the axial member, and the tensile stress is high in the lower part of the axial member.

In the tank designed this time, it was predicted that the axial load member would break at an internal pressure lower than that of the hoop layer. In addition, based on the tensile strength of UD-CFRP (3290 MPa), it was predicted that the pressure at which the axial load member would break would be approximately 133 MPa.

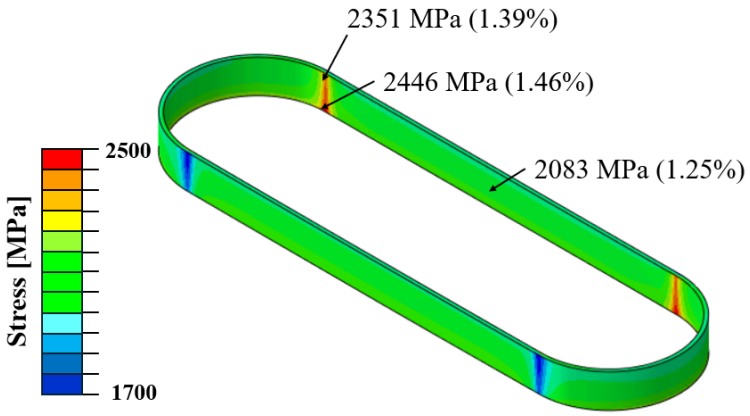

Fig.3 Contour plot of maximum principal stress of axial load member at the internal pressure of 100 MPa.

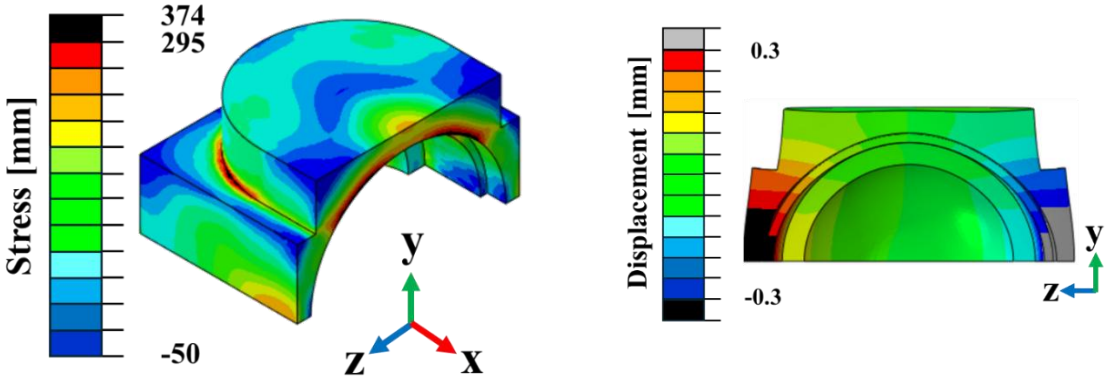

(a) Mises stress

(b) Displacement of Z direction (Magnification 20 times)

Fig.4 Contour plot of Mises stress and z-displacement of tank head at the internal pressure of 100 MPa.

Fig. 5(a) presents the longitudinal strain in the cylinder surface at internal pressures of 27 MPa, 64 MPa, and 100 MPa, respectively. Axial compressive strain appears in the cylinder at the boundary between the cylinder and the tank head. Fig. 5(b) shows the deformation diagram of the tank cross section at an internal pressure of 64 MPa. At the boundary where the longitudinal out-of-plane stiffness differs, out-of-plane bending deformation of the cylinder occurs due to the internal pressure, which can be seen to cause localized compressive strain. For the same reason, localized compressive strain is also observed at each end of the pad-up of the cylinder. Localized out-of-plane deformation also appears in the center of the cylinder, where the hoop thickness is thin, due to the difference in bending stiffness before and after it.

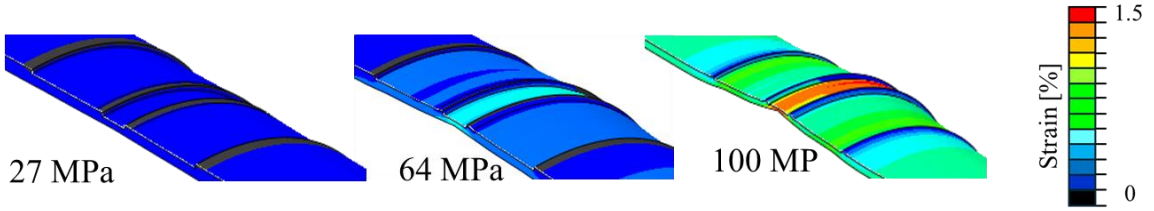

(a) Contour plot of longitudinal strain in the cylinder surface at the internal pressure of 27, 64, and 100 MPa. The deformation magnification is 20 times.

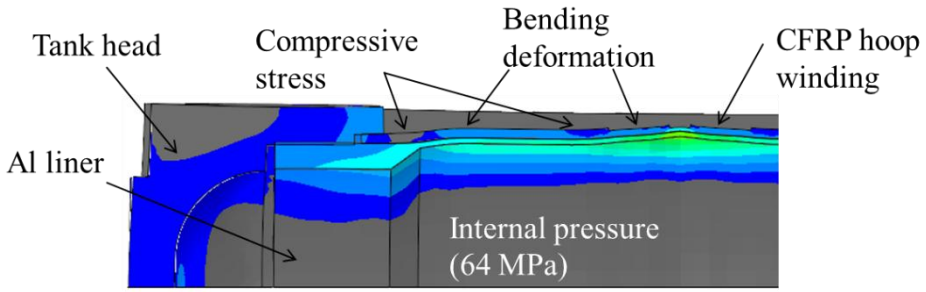

(b) Deromation showing the cross section at the internal pressure of 64 MPa.

Fig.5 Contour plot of longitudinal strain in the cylinder

3. EVALUATION OF TANK PROTOTYPES THROUGH BURST TESTS

3.1. TANK PROTOTYPE

The CFRP hoop layer was formed by wrapping CF/Epoxy Towpreg in the hoop direction around a cylindrical liner made of Al alloy (A6061-T6) using the FW method. The belt-shaped axial force member was also produced by FW forming of Towpreg. The cylinder liner and tank head were produced by machining from Al alloy (A6061-T6) blocks using an NC milling cutter. A photograph of the appearance after assembly is shown in Fig. 6.

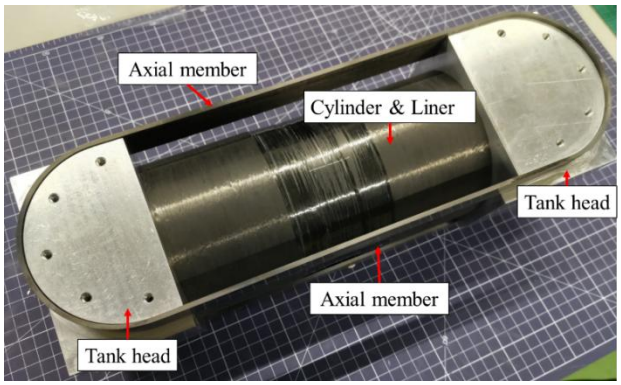

Fig.6 Photograph of a tank prototype

3.2. BURST TEST PROCEDURE

A water pressure burst test was carried out in accordance with ISO19881, with a target pressure rise rate of 0.3 MPa. Multiple strain gauges (WFCA-6-11-10LDBTB-F, Tokyo Sokki, Japan) were attached to the surfaces of the cylinder and axial load member, and strain at each part during pressurization was measured with a data logger (EDX-10, Kyowa Denki, Japan). Strain was measured in the hoop direction and axial direction of the cylinder, and in the axial direction at the center of the axial load member and above and below the straight line-arc boundary. In addition, damage and burst behavior of the tank during the test was photographed using a camera (Hero 10, GoPro, USA) installed in the chamber.

3.3. EXPERIMENTAL RESULTS AND DISCUSSIONS

Figure 7 presents the external appearance after the burst. The burst pressure was 99.8 MPa, and the fractured origin was the fiber break of the axial member. The burst pressure was about 75 % of the burst pressure (133 MPa) predicted by the FEA described above. Figure 8 shows photos captured at internal pressures of 0, 72 MPa, and 99.8 MPa from the video taken during the burst test. When the internal pressure exceeded about 50 MPa, audible sounds were heard due to the occurrence and progression of damage in the CFRP. In addition, at an internal pressure of 72 MPa, as shown in Figure 8 (b), separation between fibers (splitting) and partial fiber breakage were confirmed starting from the straight-line-arc boundary of the axial member. This coincides with the location where tensile stress concentration was confirmed in the axial load member in Figure 3. From this damage boundary, many audible sounds were heard due to the occurrence and progression of damage in the CFRP axial load member. As shown in Fig. 8(c), localized splitting and fiber breakage of the axial load member were also observed at another straight-line-arc boundary just before the rupture.

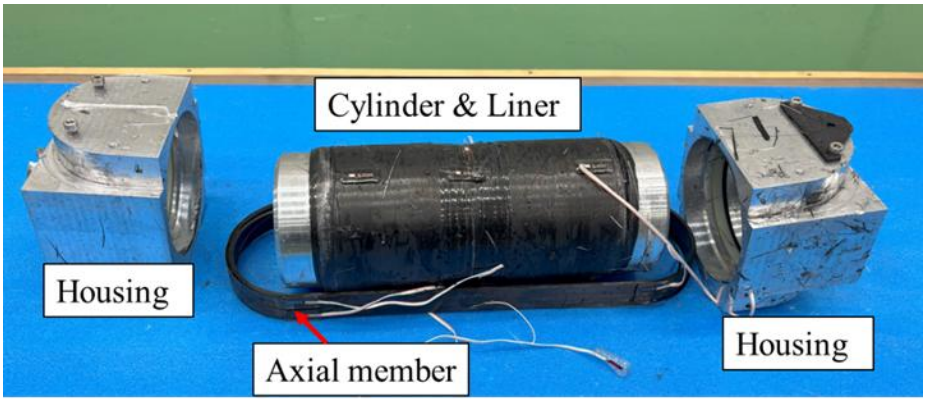

Fig.7 Photographs after burst testing (Burst pressure 99.8 MPa)

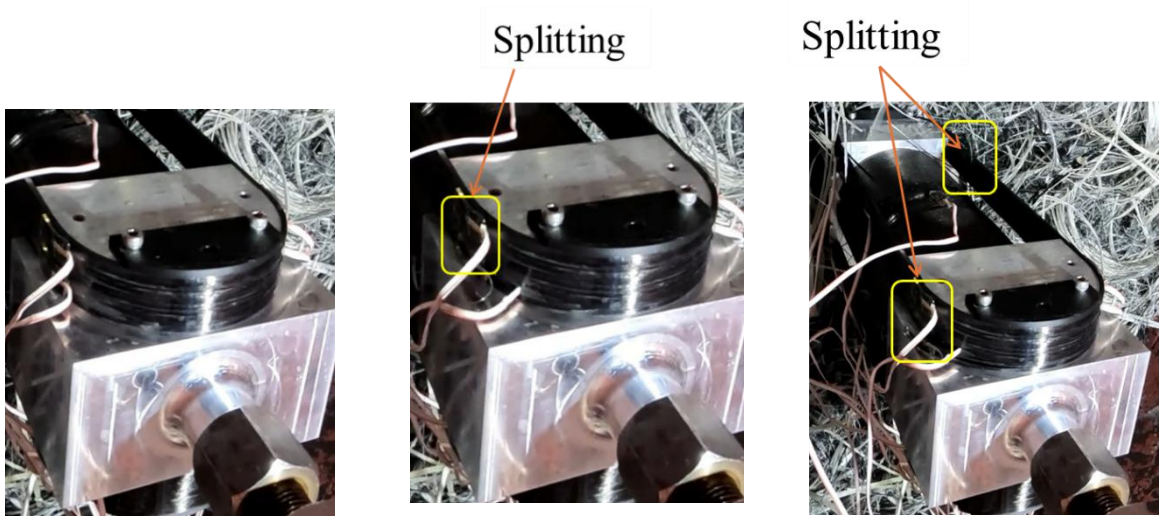

(a) 0 MPa (b) 72 MPa (c) 99.8 MPa

Fig.8 Captured images showing the splitting of axial load member.

The attachment positions of the strain gauges (#1-9) on the tank are shown in Fig. 9, and the strain measurement results for the cylinder and axial load member are presented in Fig. 10(a) and (b), respectively. The axial and hoop direction strains of the cylinder hoop layer roughly matched the FEA results. However, the experimental value for the axial strain (strain #2) at the center of the cylinder was much higher compressive strain. This is thought to be due to an error in the attachment position of the strain gauges.

Looking at the axial strain (strain #7) at the center of the axial force member shown in Fig. 10(b), a sudden increase in strain, namely “strain jumping”, can be seen at internal pressures of around 63 MPa, 72 MPa, and 91 MPa. As is clear from the images taken during the burst testing (Fig. 8(b)), local splitting and fiber breakage occurred in the axial load member at the straight-line-arc boundary when the internal pressure was 72 MPa, and this is presumed to be the cause of the strain jump in the axial load member. As mentioned above, bending deformation at the point where the axial member of the tank head is fitted causes a non-uniform stress distribution in the width direction of the axial member, as shown in Fig. 3(a) (b). As a result, in-plane and out-of-plane shear stresses occur in the axial member, and it is believed that splitting occurred due to in-plane interlaminar shear failure.

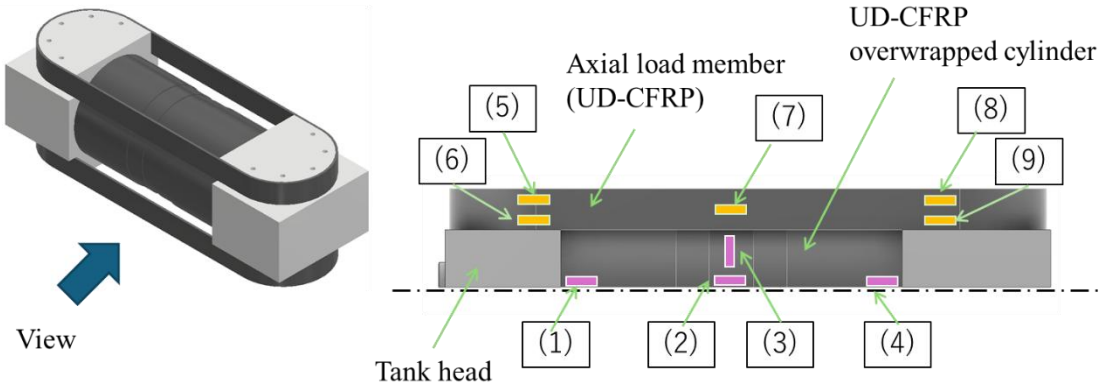

Fig. 9 Strain gauge installation position

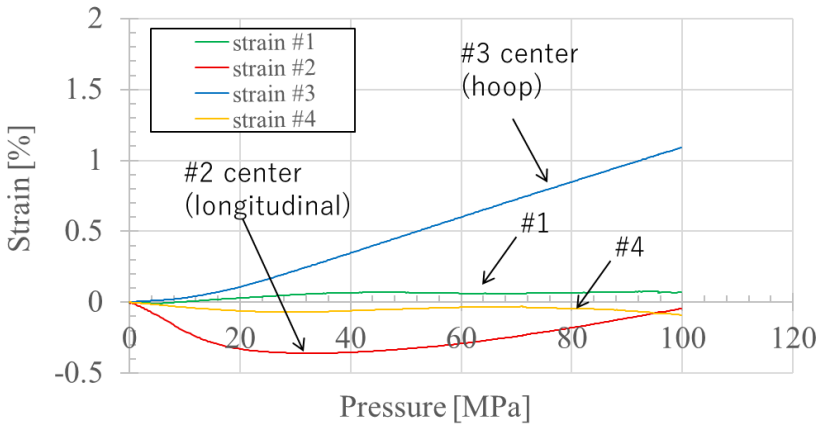

(a) Cylinder

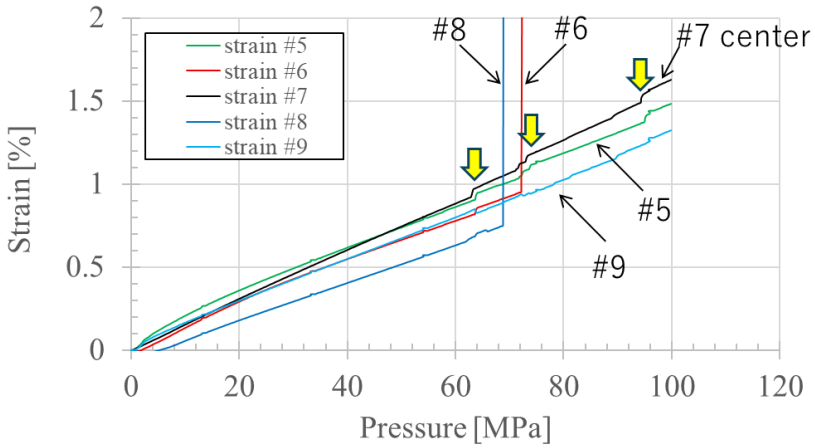

(b) Axial load member

Fig. 10 Strain versus internal pressure

The maximum strain at the time of fracture at the center of the axial member (Strain #7) was 1.63 %. This is approximately 17 % smaller than the fracture strain (1.96 %) of UD-CFRP shown in Table 1. The FEA results show that the maximum strain at the straight-arc boundary is approximately

17 % larger than the strain in the general part of the axial member. Taking these effects into account, when the strain in the general part of the axial member is 1.63 %, the strain at the straight-arc boundary is expected to be approximately 1.9 %. This is 97 % of the fracture strain (1.96 %) of CFRP, which is an appropriate value for the fracture strain of an axial member.

The above suggests that it is important to consider the prevention of splitting due to non-uniform load distribution (shear stress) in the plane and the reduction of stress concentration at the straight-arc boundary when designing axial members.

4. CONCLUSIONS

In this study, with the aim of technically verifying the multi-load path structure concept, we carried out stress analysis, design, prototyping, and evaluation of a tank structure that uses two belt-shaped axial force members and CFRP overwrapped cylinder. It was also investigated the burst behavior and the damage progressive behaviors. As a result, it was verified through analysis and experiments that it is possible to realize a tank structure with a burst pressure roughly as designed by designing a structure in which the internal tank pressure acts directly on the dome part of the tank head. Observation results during the burst test showed that localized splitting and fiber breakage occurred in the axial load members prior to the burst. It was suggested that further increases in burst pressure could be effectively achieved by making the stress acting on the axial load members uniform and by suppressing splitting of the axial load members.

ACKNOWLEDGEMENT

These results were obtained as a result of work commissioned by the New Energy and Industrial Technology Development Organization (NEDO).

REFERENCES

[1] T. Yoshida, K. Kojima, Toyota MIRAI fuel cell vehicle and progress toward a future hydrogen society, Electrochem. Soc. Interface, 24, pp. 45-49 (2015).
[2] M. Zhang, H. Lv, H. Kang, W. Zhou, C. Zhang, A literature review of failure prediction and analysis methods for composite high-pressure hydrogen storage tanks, Int. J. Hydrogen Energy, 44 [47], pp. 25777-25799 (2019).
[3] H. K. Shin and S. K. Ha, A review on the cost analysis of hydrogen gas storage tanks for fuel cell vehicles, Energies, 16 [13), 5233 (2023).
[4] E. Dahl, J.S. Becker, C. Mittelstedt and H. Schürmann, A new concept for a modular composite pressure vessel design, Compos. Part A: Applied Science and Manufacturing , 124, 105475 (2019).
[5] T. F. Druckbehälter (Inventor), Pressure vessels of simple design, Appl. DE 10 2005 006, 998 A 1; (2005). (Expired patent in Germany)
[6] M. Jin, B. Lee, J. Yoo, Y. Jo, S. Lee, Cryogenic deformation behaviour of aluminium alloy 6061-T6, Metals and Materials International, 30, pp. 1492–1504 (2024).

ICCM24
AUGUST 4-8, 2025
BALTIMORE CONVENTION CENTER
BALTIMORE, MARYLAND, USA

No Technical Paper Submission for:

John Tierney

MATERIAL BEHAVIOR OF PREPREGS IN AUTOMATED ROBOTIC SHEET-LAYUP: A COMPARATIVE STUDY

Moritz Lennartz[1], Liang Yu[1] and Thomas Gries[1]

[1]Institut für Textiltechnik der RWTH Aachen University
Otto-Blumenthal-Str. 1, 52074 Aachen, Germany
Email: moritz.lennartz@ita.rwth-aachen.de web page: https://www.ita.rwth-aachen.de

Keywords: Robotics, Prepreg, Layup, Laminates

ABSTRACT

A novel approach to the automated production of complex fiber-reinforced components, while retaining process flexibility, is robotic layup of prepreg sheets. By optimizing path planning for robot trajectory generation and employing specially developed end-effectors, the goal is to achieve error-free placement and forming of the prepreg sheets.

Research to date has focused primarily on the development of a suitable overall system consisting of one or more robots with effector tools. Initial proof-of-concept studies have already been carried out with this overall system. Nevertheless, material behavior and its interaction with the robot-based draping process and the mold geometry were often neglected. However, especially with complex, multi-curved molds, different material properties in combination with different process parameters, such as the layup sequence, lead to a very different end quality. These interactions between material, process and mold geometry must be taken into account when developing suitable robot operations.

This paper, therefore, presents a comprehensive analysis of the behavior of various prepreg materials during robotic sheet layup. The study investigates how different material properties of prepregs influence draping quality by applying different draping strategies to various complex molds. This research is the first to demonstrate the impact of material and process parameters on the fully automated, robotic layup of prepreg sheets.

The results show that various material parameters influence the quality of robot-assisted draping. However, the choice of a layup strategy for the prepreg sheets is more decisive for a good quality. An optimized draping strategy with suitable end effectors can ensure error-free forming of the prepreg sheets with almost all common prepreg materials, even on more complex molds.

1 INTRODUCTION

Fiber reinforced plastics (FRP) have undergone remarkable development in recent years and have established themselves as key materials in many industries. Their versatility, combined with increasing demands for efficiency, sustainability, and performance, has significantly enhanced their relevance. While composite parts have traditionally been used primarily in aerospace and high-performance motorsports, advancements in manufacturing technology, falling raw material prices, and improved availability have extended their application into the automotive industry, construction, and the energy sector. [1 – 3]

The excellent mechanical properties of FRPs largely depend on the fibre materials used and their precise alignment within the component (direction-dependent behavior, known as anisotropy). However, this increases manufacturing complexity, as FRPs must be built up layer by layer. The current state-of-the-art for high performance application is the prepreg process, in which a pre-impregnated textile semi-finished product is manually formed into a near-net-shape geometry and then cured into a finished component in an autoclave process. [4,5]

Forming the flexible, sticky textile layers into the desired three-dimensional shape is time-consuming, error-prone, and—due to the material's specific properties—currently only very limitedly automatable. This forming process (known as draping) requires a sensitive understanding of the material and considerable experience to avoid defects such as wrinkles and voids. Despite this, 30% of continuous

fibre-reinforced components in aerospace are manufactured through draping, with automation implemented in only 5% of those cases. [6]

Experienced and well-trained specialists can process up to 1.15 kg of material per hour. Their sensorimotor skills, cognitive flexibility, and low machine and tooling costs also enable rapid product changeovers. [7] At the same time, manual production leads to high material waste, end-product defects, and - especially in Western countries - high labor costs, making the process uneconomical. Furthermore, unattractive working conditions, which often cause health issues such as wrist or back pain and allergies, are contributing to an increasing shortage of skilled workers. [8]

A promising strategy to reduce manual processes and improve reproducibility is the automation of production. This can save up to 90% of the working time per component and increase material efficiency from around 40% to as much as 95% compared to manual production. Large companies in the aerospace and automotive industries are already using fully automated processes for manufacturing FRP components. [8, 9]

Current automation in the form of Automated Fiber Placement or Automated Tape Laying requires very high investment costs and is also limited to simple component shapes, such as shell geometries. The process also requires long set-up times, which further limits flexibility. For this reason, research has been conducted for some time into a robot-based lay-up process that takes the manual prepreg lay-up process as a model and enables prepreg lay-up and with specialized end effectors and defined trajectories. So far, the focus has been on the development of suitable hardware for draping and holding the prepreg as well as the implementation for individual component shapes. However, for an error-free robot-based prepreg layup, the material properties and different layup strategies must also be taken into account, as these have a significant influence on the layup process. [10 – 12]

For this reason, a material study is presented in which a total of four different materials were tested on four different molds. The focus of the study was to investigate the extent to which individual material properties and different draping strategies influence the quality of the final result.

2 RELATED WORK

2.1 Robot based prepreg layup

The prepreg layup is defined according to [13] as the spherical forming of planar reinforcement textiles into near-net-shape component geometries. The transformation of the textiles takes place under the influence of external forces. This forming process has a significant impact on the mechanical and optical properties of the final component. The draping result is determined by the process, the material, and the component geometry [14,15]. Various draping strategies are used to drape the textiles.

Robot-assisted draping is a promising approach for automating the prepreg layup process in the production of fiber-reinforced components. To achieve the goal of near-complete automation, an intelligent robot-assisted manufacturing system is employed, which automates the draping process, thereby ensuring consistent quality, increased productivity, and reduced labor costs. [11,12,16]

Such a system typically consists of a hybrid robot cell with multiple robot arms or a single robot arm in combination with a holding fixture. These components work closely together to grasp, position, and apply the material to a mold. Specialized end effectors are used, which form the prepreg onto the mold contour with appropriate force and precision using rollers. To avoid defects such as wrinkles or air inclusions, controlled tension during draping is required. This is achieved through the use of robots with integrated force control or a dedicated holding fixture. [11,12,16]

2.2 Draping Defects and Their Influencing Parameters

Regardless of whether a manual or robot-based draping process is used, draping effects occur during the forming of reinforcement textiles. These effects alter the fiber orientation compared to the target position and should therefore be minimized, as they—like previously mentioned—negatively impact the optical and mechanical properties of the final component [17]. A variety of draping defects are distinguished, typically classified into two-dimensional and three-dimensional defects. Two-dimensional defects include fiber undulations and gaps, while three-dimensional defects comprise wrinkles and loops. In general, the frequency and severity of draping effects correlate with the geometric

complexity of the component in automated forming processes [17,18]

The occurrence of draping defects is primarily influenced by the component geometry, the type of process, and the textile properties. Such defects are more likely to occur on component geometries featuring high aspect ratios, small radii, sharp angles, and strong curvatures. From a process perspective, draping defects are mainly promoted by relative movements between the tool and the textile, foreign particles, or excessive applied forces. However, the textile used has the most significant influence on the occurrence or prevention of draping defects. Key textile parameters include the type of textile, weave pattern, areal weight, roving material, and laminate structure. [18]

The emergence of draping defects is linked to various physical effects, with the so-called Trellis effect being predominant. The Trellis effect describes the shearing of a woven fabric. Shearing occurs when external tensile forces act on the rovings in directions other than the principal fiber orientation. As the degree of shear increases, friction between the intersecting rovings rises, requiring greater force to continue shearing. The shear force can increase until a material-specific critical shear angle is reached. Beyond this angle, the shear can no longer be accommodated within the plane of the fabric. Shearing beyond the critical angle inevitably leads to draping defects, which must be avoided. The extent of draping effects is highly dependent on the choice of textile semi-finished product and its drapability. Textiles that allow higher shear with lower shear resistance generally enable better forming quality. [18]

3 METHOD AND EXPERIMENTAL DESIGN

The aim of this study is to investigate the influence of different prepreg materials and different layup strategies on the draping quality in a robot-based sheet layup process. However, the study does not solely focus on the drapability of various materials or layup strategies; rather, it places particular emphasis on analyzing the interdependencies between process parameter, layup strategy, the geometry of the mold, and the type of textile reinforcement. Accordingly, the material study is structured using a two-stage approach.

3.1 Examination of drapability with regard to the material parameters

Initially, four materials were examined on two different mold geometries. To do this, a preliminary selection of ten commonly available prepreg materials from the market was made. From these ten materials, four were selected for testing. The selection focused on the main influencing factors, namely the type of weave, fabric weight, and weave pattern. Additionally, the materials were chosen in such a way that non-investigated factors—such as the matrix type—remained consistent across all selected materials. Table 1 presents the tested materials along with their respective parameters.

Material	Prepreg variant	Type of binding	Grammage
Nr 1	Roving	Plain weave	200 gsm
Nr. 2	Roving	Twill weave	200 gsm
Nr. 3	Roving	Twill weave	410 gsm
Nr. 4	Towpreg	Plain weave	76 gsm

Table 1: Tested Materials

The focus of this experiment was to investigate the drapability of the materials with respect to their inherent properties, without a detailed analysis of the influences from the robot's draping strategy or the mold geometry. For this reason, an ideal strategy for the robot-based draping was defined by an expert. The selected molds feature relatively simple geometries to ensure that process- and geometry-related parameters do not overshadow the textile properties. The following figure shows the two molds along with the draping strategy applied by the robot.

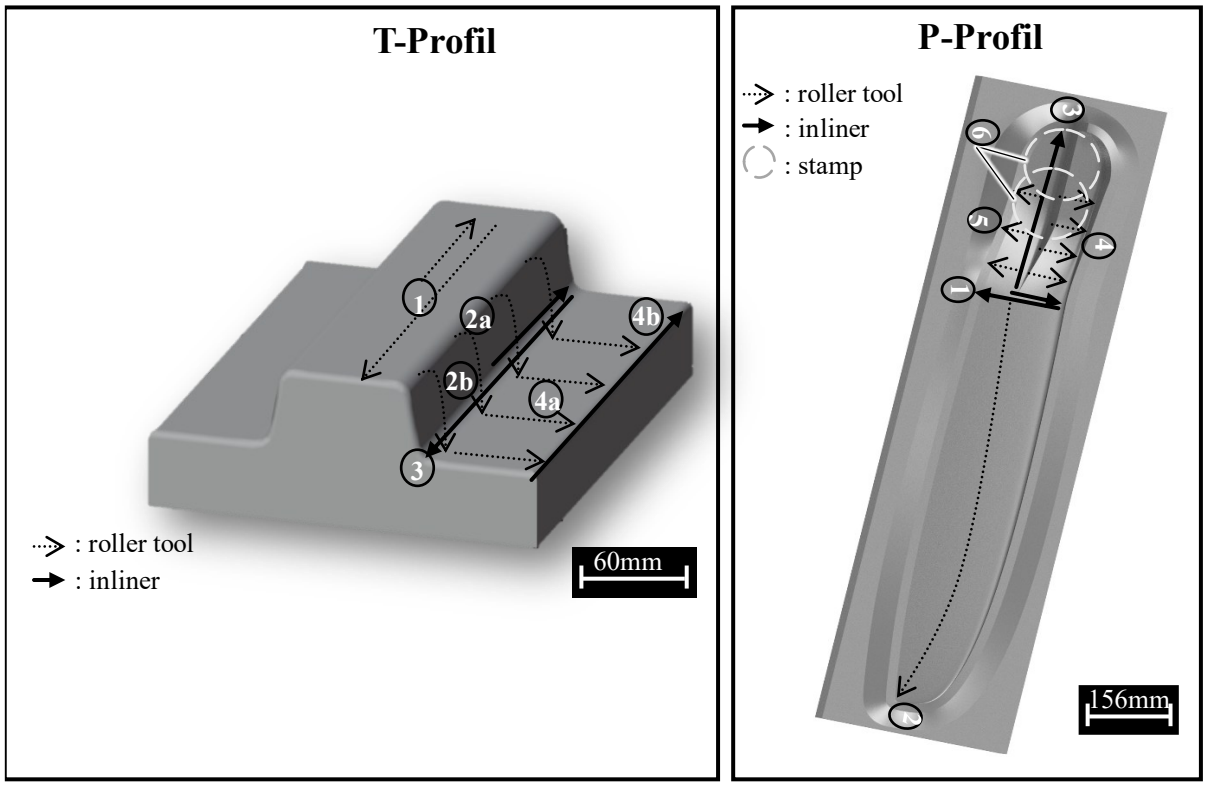

Figure 1: Used molds and corresponding trajectories

For the implementation of the draping strategies, a Universal Robot UR5e was used, featuring a payload capacity of 5 kg and a reach of 850 mm. In addition, custom-developed end effectors were employed—some designed for universal use across a wide range of geometric features, and others specifically engineered for one of the component geometries presented in this study. An integrated impedance controller was used to enable simultaneous position and force control. The initial positioning on a specific geometry element of the corresponding mold was carried out manually to ensure precise alignment. To allow for fully automated draping, an automatic tool changer was also utilized. Figure 2 shows the end effectors used as well as the complete robotic cell employed for the tests.

The evaluation of the layup quality was carried out using the method developed by Schöfer [15]. This assessment methodology enables a quantitative evaluation of quality by relating the severity of defects (Gi), the frequency and size of defects (Ai), and the distance of each defect from the component's symmetry axis (ai) to the total component area (Ages) and the maximum possible distance from the symmetry axis (amax). Based on these parameters a defect index (FI) can be calculated using the following formula, where a defect index of 0 represents perfect quality:

$$FI = 100 * \sum_{i}^{k} G_i * \left(\frac{A_i}{A_{ges}} * \left(1 - \frac{a_i}{a_{max}} \right) \right) \quad (1)$$

This method allows for a direct comparison between the individual materials. To eliminate process-related uncertainties, each trial was performed five times. In addition to the qualitative evaluation of the layup, process efficiency was also examined by measuring the cycle time.

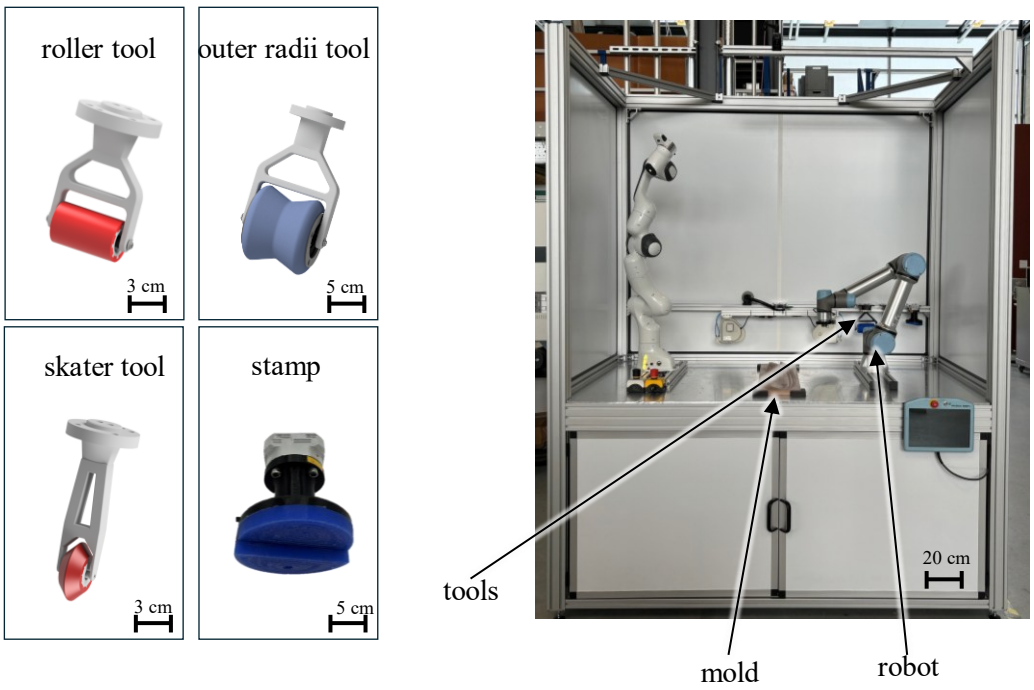

Figure 2: robot tools and used setup for the study

3.2 Investigation of drapability with respect to draping strategy and form complexity

Based on the results from the first part of the material study, the best-performing material was selected for the second part of the investigation. This material was then subjected to further testing with varying process parameters by applying different layup strategies on significantly more complex mold geometries. The two molds from the first part of the study were reused, along with two additional molds featuring considerably higher geometric complexity. The two new geometries are characterized by inward-facing corners that require very high textile shear in order to achieve a defect-free layup. However, the level of shear remains below the critical shear angle, meaning both geometries are still suitable for flawless draping.

The focus of this part of the study was to examine the extent to which different robot layup strategies and the complexity of the mold geometry influence the final layup quality. For each of the four tested geometries, three distinct layup strategies were developed by an expert and implemented by the robot in the same manner as in the first part of the study. The evaluation of quality was again performed using the Schöfer method [15]. The following Figure 3 illustrates the draping strategies applied to the four component geometries.

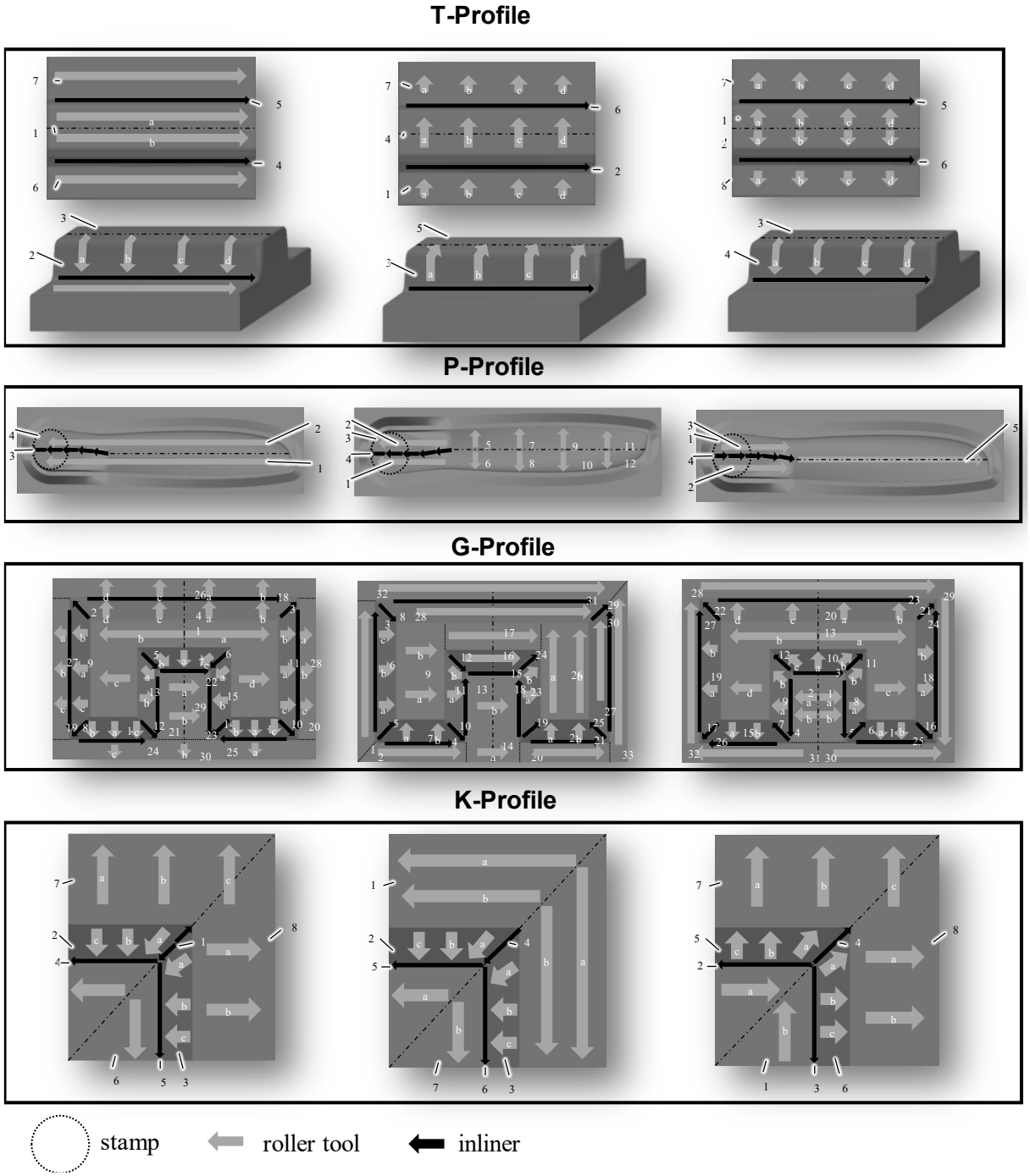

Figure 3: Layup strategies

The aim of this part of the study was to investigate the interaction between the material and various draping strategies. For this section, three identical trials were carried out for each case to eliminate process-related uncertainties.

4 EXPERIMENTAL RESULTS

The results of the study are presented below. The results are divided into several parts. Firstly, the results of the first part of the study are presented. In particular, the individual material parameters and their effects are discussed. The second part of the evaluation then examines the interactions between the material and various draping strategies.

4.1 Results of the material influence parameters on the quality of the robot-based prepreg layup

To determine the influence of material parameters, a fractional factorial experimental design was chosen, as shown in the following table. In the first test series, a roving prepreg was compared with a towpreg. Both materials feature a plain weave and have an areal weight of 200 gsm and 76 gsm, respectively. The second test series examines the influence of the weave type by comparing two roving prepregs, each with an areal weight of 200 gsm—one with a plain weave and the other with a twill weave. The third key influence parameter, the material weight, was investigated using two prepregs with a twill weave and areal weights of 200 gsm and 410 gsm.

Test series	Prepreg variant	Type of binding	Grammage
Nr 1	**Roving**	Plain weave	200 gsm
	Towpreg	Plain weave	76 gsm
Nr. 2	Roving	**Twill weave**	200 gsm
	Roving	**Plain weave**	200 gsm
Nr. 3	Roving	Twill weave	**200 gsm**
	Roving	Twill weave	**410 gsm**

Table 2: Material parameters tested in the first part of the study

First, the T-profile was draped and evaluated according to the experimental plan shown in table 2. Table 3 presents the average defect indices from all five trials. In terms of defect types, almost exclusively wrinkles occurred during the draping. No gaps or loops were observed, and fiber undulations were rare to non-existent. The table shows that neither the weave type nor the areal weight leads to a significant difference in the draping quality. Only the towpreg exhibited noticeably poorer quality.

This indicates that, for simple geometries that do not require textile shearing, the robot is able to handle and process both plain and twill weave fabrics equally well. The prepreg weight also plays a minor role in the robotic process. The end-effectors are capable of manipulating both lightweight and heavyweight prepregs. However, the towpreg cannot be processed satisfactorily by the robot. The towpreg used in this study is very tightly woven and thus extremely resistant to deformation. In addition, it allows almost no air permeability between the crossover points, of which there are very few due to the inherent characteristics of towpreg. As a result of the high inter-fiber friction and lack of permeability, the robot's end-effectors are unable to adequately conform the prepreg even to simple geometries.

According to the experimental plan from Table 2, the same tests were also carried out on the drone propeller blade shown in Figure 1. Here, similar results in draping quality were observed as with the T-profile. Wrinkles again appeared most frequently, while no gaps or loops and only minimal fiber undulations were present. The average defect index increased significantly for all four materials compared to the T-profile (see Table 2). This is due to the considerably more complex geometry. In particular, the root area of the propeller blade with its very tight radius, requires textile shearing, which the robot's end-effectors can only apply to a limited extent.

Nevertheless, even for this mold, the influence of weight and weave type on the robot-based prepreg layup remains minor. In contrast, draping using a towpreg is significantly worse than with a roving prepreg. As previously explained, this is primarily due to the weave structure and high inter-fiber friction of the towpreg material.

Material	Mean error index T-profil	Mean error index P-profil
Nr 1	0,64	4,19
Nr. 2	0,65	4,83
Nr. 3	0,0	4,28
Nr. 4	3,11	18,74

Table 3: Mean error index of the tested materials

In addition to evaluating draping quality using the Schöfer method [15], the study also analyzed where most defects occurred within the component geometries. For the T-profile, only a few defects were observed, and these could not be assigned to any specific region. Except for the towpreg, the observed defects were primarily due to process uncertainties in the robotic draping process, which could likely be eliminated through iterative process refinement.

For the propeller shape, defects—consistent with previous observations—were concentrated mainly in the root area of the blade. This is primarily due to insufficient textile shearing, which is required to conform the material to the tight radii in that region.

In summary, different material parameters have only a limited influence on the draping quality in robot-based prepreg layup when applied to simple geometries. Only the towpreg proved unsuitable for robotic draping due to its structural characteristics. However, the experiments also clearly showed that the most critical factors influencing the final draping quality are the complexity of the mold geometry and the robotic draping process itself. For this reason, the second part of the study focuses on investigating the interaction between form geometry, robotic strategy, and material behavior.

4.2 Influence of draping strategy and form complexity on robot-based prepreg layup

To investigate the interaction between the material, the robot process, and the form geometry, the molds and robot strategies described in Chapter 3.2 were used. Since the total test space with four molds, three robot strategies, and four materials would have resulted in 48 combinations that each needed to be tested at least three times, we decided to test only one material. This decision was based on previous results, which showed that material parameters have a less decisive impact on achieving good quality in robot-based draping. The chosen material was a twill weave with a weight of 200 gsm, as it is the most common material on the market and can be used in nearly all applications.

Initially, the T-profile and the propeller profile were draped again by the robot using the respective end effectors. Table 4 shows the average error index of the three identical trials for each case along with the standard deviation. Analysis of the results shows that the draping strategy has a significant influence on the final quality. Using strategies similar to those from the first part of the study (see Chapter 4.1), very good results with error indices of 0.308 and 2.584 were achieved. The two other strategies for the T-profile and the P-profile resulted in higher but still acceptable error indices. These results demonstrate that the choice of draping strategy also has a decisive impact on draping quality, even for simple form geometries. In particular, the choice of the starting point is crucial. If it is not optimally selected, there is a risk during robot-based draping that the textile can no longer adapt to the form because it is already fixed at too many points, which prevents any movement.

However, not only the choice of a suitable draping strategy is important for good draping quality. For all three strategies and both components, errors appear consistently in specific regions. As already observed in the first part of the study, errors on the propeller profile mainly occur in the complex root area (see Figure 4). For the T-profile, errors are also visible in more complex regions such as vertical surfaces and inner radii

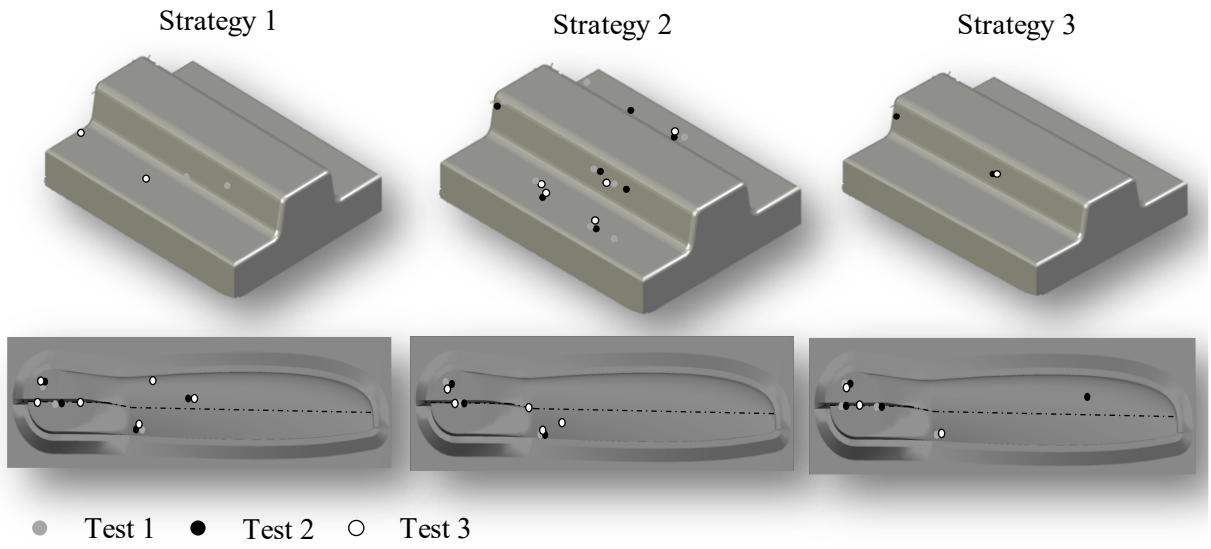

Figure 4: Regions, where erros occurred during the layup process

These two experiments have shown that, with the current draping process, less complex mold geometries can be draped with a very good result, when using an appropriate draping strategy. To analyze the interaction between draping strategy, material, and complex form geometries in more detail, the two additional shapes (see Chapter 3.2) were draped and analyzed in a subsequent step using three different strategies and one material (twill weave, 200 gsm).

With an error index ranging from 1.07 to 19.43 for the K-profile and from 7.71 to 51.154 (see Table 4), the quality for both molds is significantly lower due to the high form complexity. Furthermore, the quality, expressed by the error index, varies much more between the individual strategies for these two components than for the previously tested parts. This indicates a strong interaction between the chosen draping strategy and the form complexity. Critical influences on quality include the selection of the starting point and the sequence of the individual draping paths. It is crucial that the textile can be sheared by the end effectors for as long as possible. Additionally, strategies in which the draping movements proceed toward the outer edges of the part lead to better results than those where the movements go toward the center of the component. In the following figure the results of the three draping strategies for the k-profile are shown.

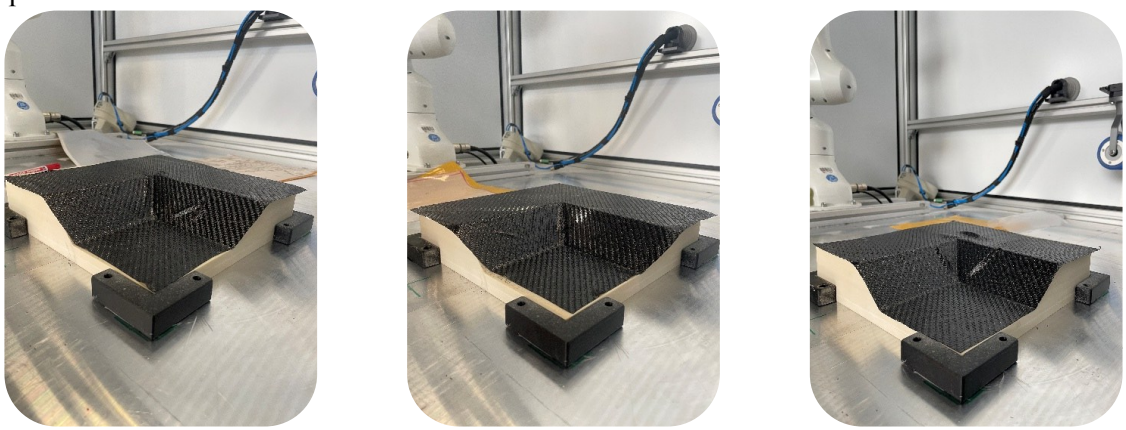

Figure 5: Draping results for the k-profile

Figure 6 assigns the errors to specific regions of the components. It is evident that the errors primarily occur where high textile shear takes place. For the K-profile, this is especially the case at the ramps, where the folds arise due to the strong shear required at the inner edge. For the G-profile, the errors are

distributed across the entire mold, but here too, it can be seen that the errors mainly occur in areas where significant textile shear occurs.

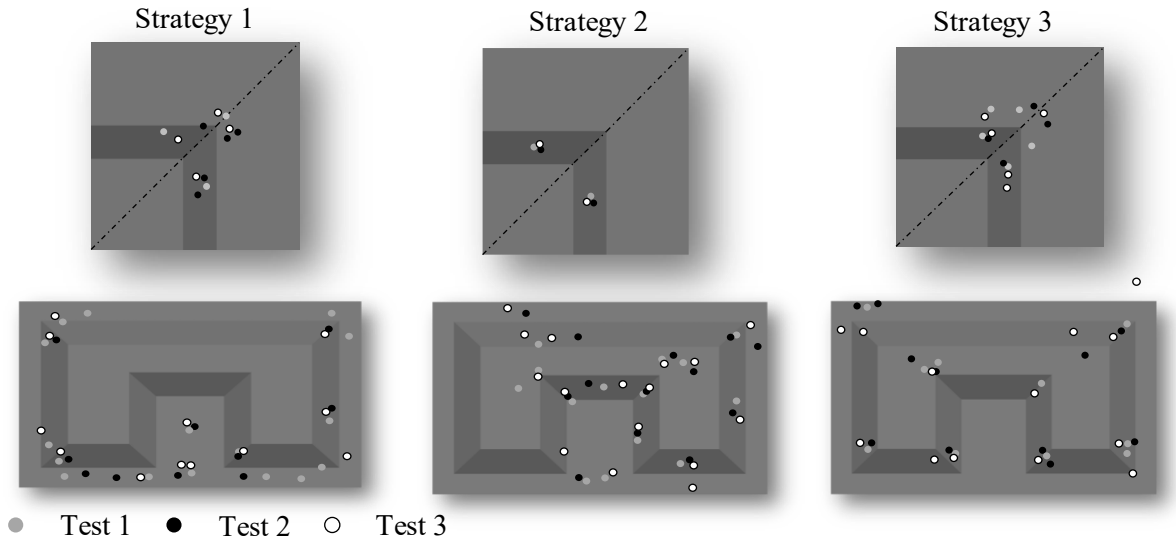

Figure 5: Regions, where erros occurred during the layup process

The experiments on the K-profile and G-profile have shown that there is a very strong interaction between the draping strategy and the form complexity. It is even more important than with simple geometries to choose the appropriate draping strategy. In particular, selecting the correct starting point, determining the proper sequence of individual draping movements, and defining the direction of these movements are crucial for achieving good results.

Test series	Mean error index	Standard deviation
T-Profil 1	1,794	1,559
T-Profil 2	4,775	0,279
T-Profil 3	0,308	0,154
P-Profil 1	7,606	8,809
P-Profil 2	5,183	1,202
P-Profil 3	2,584	0,705
G-Profil 1	51,154	1
G-Profil 2	16,066	3,729
G-Profil 3	7,707	3
K-Profil 1	12,460	11,878
K-Profil 2	4,269	2,895
K-Profil 3	19,426	5,166

Table 4: Material parameters tested in the first part of the study

5 CONCLUSION

In this study, the robot-assisted layup process of prepregs was analyzed with regard to the influence of different material parameters, the selected draping strategy, and the complexity of the part geometry. In the first part of the study, various material parameters and their impact on layup quality were evaluated. The second part focused specifically on investigating the extent to which the choice of draping strategy and the complexity of the part affect the final layup quality. A total of 40 trials were conducted

to test three material parameters on two shapes, and 36 trials were performed to evaluate three draping strategies on four different geometries.

It was found that material parameters such as weave type and areal weight have no significant impact on the quality of the final product. This indicates that all common prepreg materials can be used in a robot-based layup process.

The trials involving different draping strategies on geometries of varying complexity showed that selecting a well-suited draping strategy is crucial. In particular, the starting point and the sequence of individual draping steps must be defined with care. Furthermore, it is not only necessary for the end effectors to enable the forming of the textile, but also to actively induce textile shearing during the process so that even complex part geometries can be draped without defects.

Future research should therefore focus on the development of suitable draping strategies that can be applied to a wide range of part geometries. In this context, the analysis of manual draping motions and their abstraction and transfer to robotic processes can be especially helpful. In addition, a holding mechanism should be developed that enables targeted shearing of the prepreg during the process, thus improving the ability to prevent wrinkle formation in robotic layups.

ACKNOWLEDGEMENTS

Gefördert durch die Deutsche Forschungsgemeinschaft (DFG) im Rahmen der Exzellenzstrategie des Bundes und der Länder – EXC-2023 Internet of Production – 390621612. [Funded by the Deutsche Forschungsgemeinschaft (DFG, German Research Foundation) under Germany's Excellence Strategy – EXC-2023 Internet of Production – 390621612.]

REFERENCES

[1] J. Fleischer, R. Teti, G. Lanza, P. Mativenga, H. Möhring and A. Caggiano, Composite materials parts manufacturing, *CIRP Annals*, *67*(2), 2018, pp. 603-626 (https://doi.org/10.1016/j.cirp.2018.05.005).

[2] M. Kumar Gupta and V. Singhal, Review on materials for making lighweight vehicles, *Materials Today: Proceedings*, 56 Part 2, 2022, pp. 868-872 (https://doi.org/10.1016/j.matpr.2022.02.517.)

[3] H. Lengsfeld, F. Wolff-Fabris, J. L. Krämer, J. Lacalle and V. Altstädt, *Faserverbundwerkstoffe: Prepregs und ihre Verarbeitung,* Hanser, München, 2015

[4] C. Cherif, *Textile Werkstoffe für den Leichtbau: Techniken, Verfahren, Materialien, Eigenschaften*, Springer, Berlin, 2011

[5] M. Neitzel, P. Mitschang, U. Breuer, *Handbuch Verbundwerkstoffe: Werkstoffe, Verarbeitung, Anwendung*, Hanser, München, 2014

[6] C. Eitzinger, C. Frommel, S. Ghidoni, E. Villagrossi, System concept for human-robot collaborative draping, *SAMPE Europe (Ed.): Innovating towards perfection : SAMPE Europe Conference* Baden/Zürich, Schweitz, September 29-30 2021, Red Hook, NY : Curran Associates, Inc.

[7] J. Sloan, ATL and AFP: Defining the megatrends in composite aerostructures, *CompositeWorld,* Cincinnati, June 30 2008, Garder Business Media, Inc.

[8] H. Dammers, *Einsatzpotenziale der Mensch-Roboter-Interaktion in der Fertigung von Hochleistungsbauteilen aus faserverstärkten Kunststoffen*, RWTH Aachen University, Aachen, 2024. https://doi.org/10.18154/RWTH-2024-08021

[9] D. Jayasekara, N. Y. G. Lai, K. Wong, K. Pawar and Y Zhu, Level of automation (LOA) in aerospace composite manufacturing: Present status and future directions towards industry 4.0 *Journal of Manufacturing Systems,* 62, 2022, pp. 44-61, 10.1016/j.jmsy.2021.10.015

[10] M. P. Elkington, C. Ward, K. Potter, Automated Layup of Sheet Prepregs on Complex Moulds, *SAMPE Long Beach 2016*, United States, Mai 15 – 16 2016, International SAMPE Technical Conference 2016

[11] R. K. Malhan, A. M. Kabir, A. V. Shembekar, B. Shah, S. K. Gupta an T. Centea, Hybrid Cells for Multi-Layer Prepreg Composite Sheet Layup*, IEEE 14th International Conference on*

Automation Science and Engineering (CAS), München, August 20 - 24 2018, https://doi.org/10.1109/COASE.2018.8560586

[12] R. K. Malhan, A. V. Shembekar, A. M. Kabir, P. M. Bhatt, B. Shah, S. Zanio, S Nutt, S. K. Gupta, Automated planning for robotic layup of composite prepreg, *Robotics and Computer-Integrated Manufacturing*, vol. 67, 2021, https://doi.org/10.1016/j.rcim.2020.102020

[13] P. Ermanni, *Composite Technologien*, ETH Zürich, Zürich, 2007.

[14] H. Krieger, *Methode zur Auslegung von Gelegen mit local angepassten Fertigungsparametern für Hochleistungs-Faserverbundkunststoffe*, Shaker, Düren, 2015.

[15] S. Schöfer, *Kraftgesteuerte Materialzuführung beim Drapierprozess in der automatisierten Herstellung von Faserverbundwerkstoffen*, Shaker, Düren 2020

[16] R. K. Malhan, A. V. Shembekar, R. J. Joseph, A. M. Kabir, P. M. Bhatt, B. Shah, W. Zhao, S. Nutt and S. K. Gupta, A Smart Robotic Cell for Automating Composite Prepreg Layup, *SAMPE 2020 Virtual Series | Manufacturing Technology*, June 1 2020

[17] M. Christ, *Definition und Quantifizierung der Drapierbarkeit von multiaxialen Gelegen durch die Vermessung von Einzeleffekten*, Bremen, 2018

[18] B. Manin, *Geometriebasierte Methode zur Vorhersage der Scherwinkelverteilung in Verstärkungstextilien aus Endlosfasern nach dem Drapierprozess,* Shaker, Düren, 2023

AN INVESTIGATION OF THERMOPLASTIC TAPE-TO-TAPE BONDING USING XENON FLASH LAMP HEATING

Professor David Williams[1]

[1]Department of Mechanical Engineering, University of Bath,
Claverton Down, Bath, BA2 7AY, UK
Email : dpw40@bath.ac.uk, web page : http://www.bath.ac.uk

Keywords: Thermoplastics, Xenon flash lamp, Tape bonding, Peel strength, Welding

ABSTRACT

This research was undertaken to investigate factors affecting the tape-to-tape bond strength of thermoplastic composite tapes in the Automated Fibre Placement (AFP) process using a xenon flash lamp as the heat source. Two variants of flash lamp were studied with different spectral outputs.

The effect of exposure to the broadband output of the flash lamp on the polymer chemistry of representative thermoplastic tapes was investigated by analysing exposed tape samples. Particular focus was given to the potential for the UV wavelengths within the spectrum to photodegrade the long polymer chains into lower molecular weights, reducing their ability to form strong tape-to-tape bonds. Three spectroscopy techniques were used: Fourier-Transform Infrared Spectroscopy (FTIR); Raman Spectroscopy; and X-Ray Photoelectron Spectroscopy (XPS). The study included carbon fibre tapes with polyaryl ether ketone (CF-PAEK) and polyamide 6 (CF-PA6) matrices. From these spectroscopy studies, no clear evidence was found that exposure to flash lamp energy causes photodegradation of the polymers.

The study then investigated how the spectral output of the flash lamp affected the peel strength of the tapes through peel testing of bonded tape pairs and imaging of the peeled surfaces. Tapes were bonded (welded) by a novel process, using the flash lamp's ability to heat and apply compaction force onto the tapes simultaneously. The peeled surfaces revealed the failure mechanism of the polymer at the interface via Scanning Electron Microscopy (SEM), which in all cases showed ductile failure of discrete polymer regions and not overall brittle failure. The difference between low and high peel strengths was observed to be related to the number of discrete areas of polymer that undergo plastic deformation during the peel.

1 INTRODUCTION

Research into efficient manufacturing processes using high-temperature thermoplastic composites has been ongoing for many years ([1], [2]), but their adoption for applications in the aerospace and automotive industries has been relatively slow, in spite of their clear advantages over thermoset composites through enhanced material properties, faster manufacture and their potential to be recycled. One of the reasons for this delay in adoption has been the challenges inherent in fast, automated tape lay-up processes such as AFP or Filament Winding (FW) to achieve full, in-situ consolidation in a single manufacturing step. These fast processes typically produce partial bonding of the composite tapes, which then necessitates a secondary (slow) heating step in order to reach the desired lay-up quality. These processes also typically induce very fast cooling rates in the processed materials, which limits the level of crystallinity that can be recovered in semi-crystalline thermoplastic polymers, resulting in lower mechanical properties of the part ([2]).

There is a compelling need to understand the tape-to-tape bonding process more closely, especially when using high-power heat sources such as lasers and xenon flash lamps. With a deeper understanding of the behaviour of the thermoplastic polymers during the heating and cooling phases, it may be possible to adapt current automated manufacturing processes to achieve higher tape-to-tape bond strengths and higher quality parts. This paper investigates aspects of xenon flash lamp heating that affect the bond strength of thermoplastic tapes during AFP.

Xenon Flash Lamp Heating

The xenon flash lamp heating system consists of a xenon-filled flash lamp (a quartz glass tube with metallic electrodes), within which an energetic plasma is created in short duration pulses that emit photons from the lower ultraviolet (UV) wavelengths to the higher infrared (IR) wavelengths. The lamp is housed within a larger diameter quartz glass flow tube to allow an annular flow of deionised water to pass the lamp for cooling purposes.

The material of the lamp (or flow tube) can either be clear fused quartz (CFQ), which causes no attenuation across the spectrum, or cerium doped quartz (CDQ), which attenuates the majority of the energy within the UV spectral region. Typical spectral outputs of the CFQ and CDQ variants are shown in **Figure 1**, differing only in wavelengths below 400nm.

The flash lamp and flow tube are contained within a small, T-shaped head with a shaped reflector behind and an aperture in front of the lamp to guide the energy into a solid quartz light guide (**Figure 2**). The light guide acts to guide the diffuse flash lamp energy to the target by means of total internal reflection. The output face of the light guide can be kept as a flat surface or shaped with planar facets to create a desired heating profile ([3], [4]). The output from the light guide is thus high-energy, pulsed, broadband and diffuse.

Three pulse parameters: pulse voltage (typically 150-250V); pulse frequency (number of pulses per second – typically 60-100 Hz); and pulse duration (typically 2-5ms) are varied to modulate the average output power of the system. The maximum average power of the system used in this study was 6kW, with an instantaneous, in-pulse power of up to 85 kW. In the typical AFP usage, where the flash lamp moves on a robotic arm, pulses superimpose as the lamp passes across a moving target, resulting in an approximately constant surface temperature.

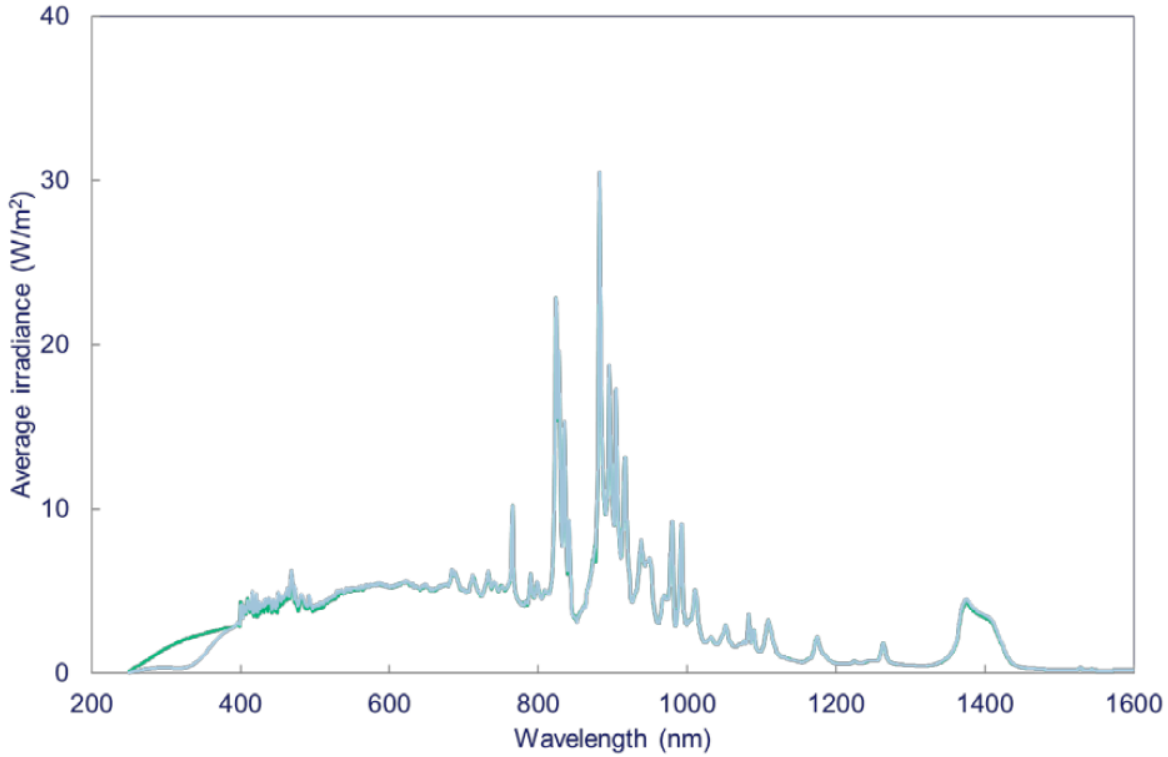

Figure 1: Spectral output of flashlamp with CFQ and CDQ flow tubes. The spectral outputs are identical above 400nm, but below 400nm most of the UV energy is removed by the CDQ case.

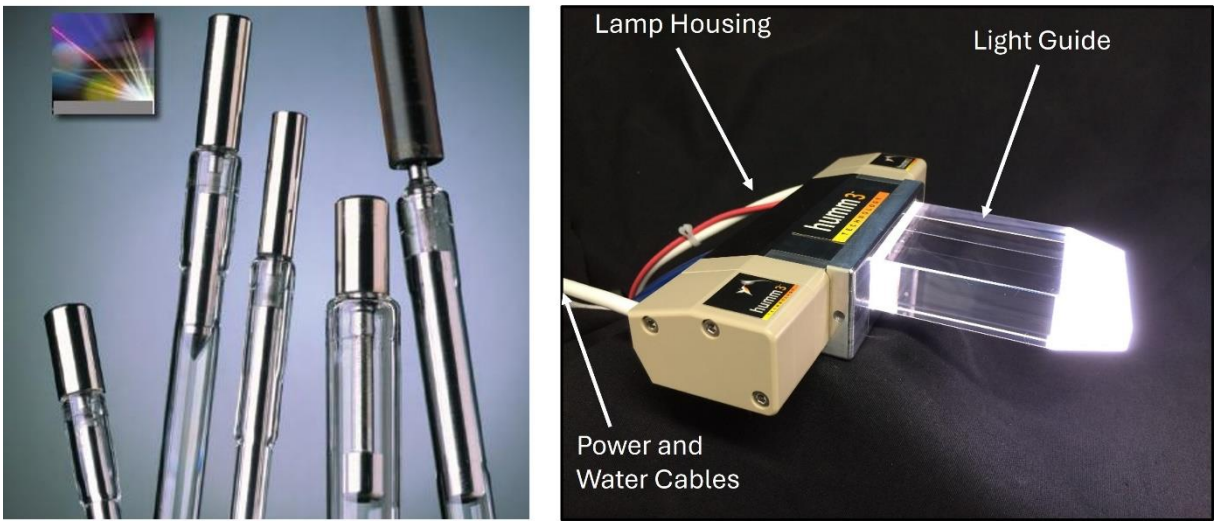

Figure 2: Image showing typical xenon flash lamps (left) and the flash lamp system head (right)

The motivation for this project arose from the results of previous unpublished work carried out at the National Composites Centre (NCC), UK, on AFP of CF-PAEK tapes using the flash lamp. The CFQ and CDQ variants of the system were compared as heat sources on a Coriolis AFP robotic system under nominally identical conditions. It was found that the CDQ variant produced tape pairs with a significantly higher bond strength than the CFQ variant, even though speed, compaction pressure and nip point temperature were matched. It was hypothesised that the additional UV content in the CFQ spectral output may have caused the lower tape-to-tape bond strengths. This motivated the current study to look for changes to the polymer surface chemistry caused by flash lamp irradiation.

It is generally well understood that polymers are sensitive to UV exposure, and can suffer degradation effects such as photooxidative aging, which may result in the breakage (scission) of polymer chains and a reduction in average molecular weight ([5]). However, the main body of literature has looked at long-term UV aging, for example by sun exposure, rather than the short exposure times (fractions of a second) typical of AFP processing.

As a result, this project has tested the hypothesis that changes to the polymer chemistry of the tape surfaces due to exposure to the broadband flash lamp radiation cause a reduction in bond strength. As a first step in this investigation, several spectroscopy techniques were deployed to look for changes to the polymer chemistry due to flash lamp exposure.

2 FLASH LAMP TAPE EXPOSURE METHOD

In the AFP process, each discrete area of the incoming tape is exposed to flash lamp energy for a short time as it passes through the heated zone, before reaching the AFP nip point and being compacted onto the substrate by the roller ([3], [4]). Under typical AFP conditions, the tapes are estimated to be within the heated zone for 0.5s to 1s, depending on the lay-up speed and dimensions of the heated zone. In order to replicate this tape exposure and investigate any changes to the tapes caused by the flash lamp heating, samples of the tape materials were exposed to flash lamp radiation on a moving linear stage without further processing. The exposure rig is shown in **Figure 3** showing the flash lamp light guide directed vertically downwards, heating the tape as it passes on the linear stage. The offset distance between light guide and tape was 20mm.

Tape surface temperatures were maintained at approximately the melting points of the polymers (220°C for PA6 and 300°C for PAEK) by modulating the tape speed at constant flash lamp pulse parameters of 175 Volts, 60 Hertz and 2 milliseconds. A thermal camera was used to monitor tape temperatures during the exposure. Tape speeds of 50mm/s were used for CF-PA6 samples and 40mm/s for CF-PAEK samples. The CFQ variant of the flash lamp system was used to create exposed tape samples for spectroscopic testing. Exposed samples were compared with unexposed (control) samples. All tapes were 1/4” wide.

Additional exposed samples were created using the same configuration but with the CDQ flash lamp variant. These samples were used in the subsequent testing of the strength of bonded tape pairs, described in section 4.

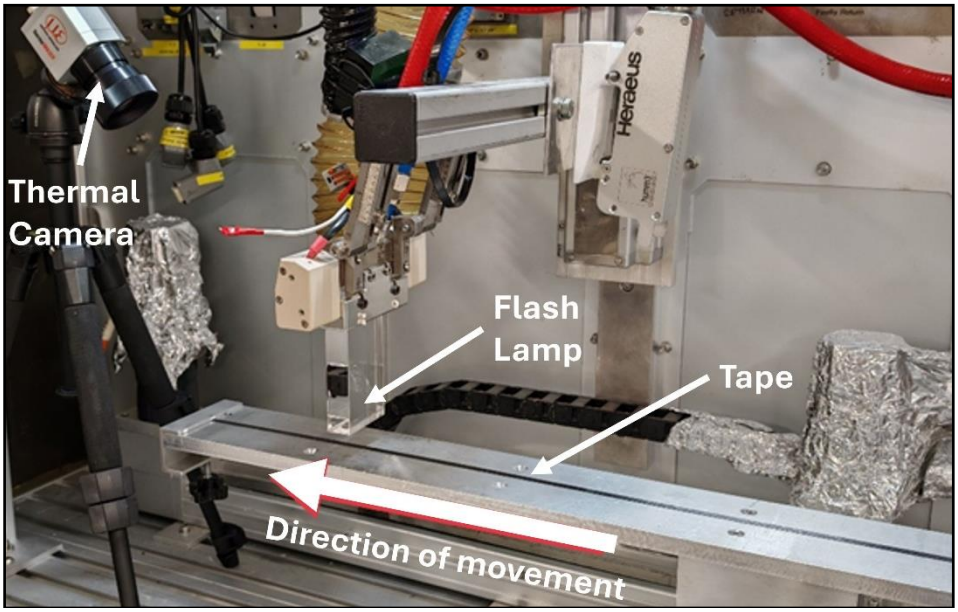

Figure 3: Flash lamp and linear stage used to expose tape samples to representative flash lamp heating

3 SPECTROSCOPY RESULTS

FTIR Spectroscopy Results

Fourier-transform infrared spectroscopy (FTIR) is a chemical analysis technique that applies infrared light to a sample to gain insights into its chemical structure. The FTIR analyses described here were conducted at the NCC. In these analyses, an attenuated total reflectance (ATR) sampling head was used attached to an Agilent Exoscan 4100 FTIR. Spectra were taken between wavenumbers of 600 cm^{-1} and 4000 cm^{-1}. For each material, the control (unexposed) and CFQ-exposed samples were compared. The tapes were held onto the ATR sampling head with a clamp and spectra were taken at three points along the surface of each tape.

Polymer chemistry changes to the tape surfaces were expected to be evidenced by changes to spectral peak positions and heights, or the appearance of additional peaks. Representative results are shown in **Figures 4** and **5**. A typical FTIR spectrum is shown in **Figure 4** for a control sample of the CF-PA6 material**.** The peaks have been annotated with their corresponding chemical bonds within the thermoplastic resin.

Figure 5 shows a comparison of nine FTIR spectra from control and CFQ samples of CF-PAEK tapes. No clear changes to peak positions, heights or numbers are observed.

It is worth noting here that carbon fibre is highly infrared absorbent across the full wavenumber range. Slight changes in the resin-to-fibre ratio on the tape surface will alter the baseline height of each graph. This effect is known as baseline drift. The slight peak height differences seen in **Figure 5** are attributed to this baseline drift rather than any chemical changes.

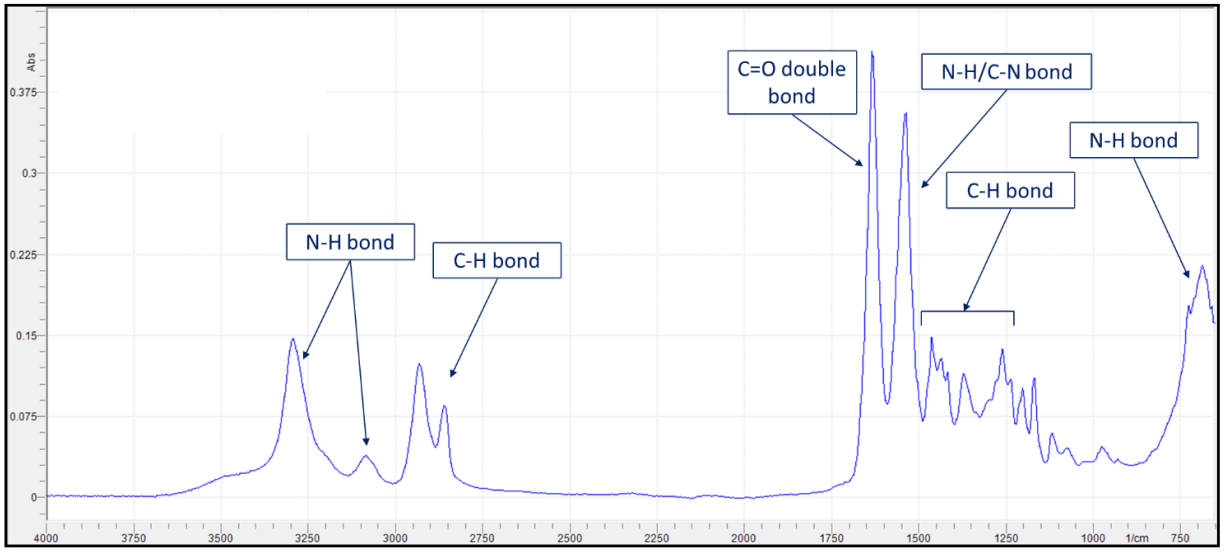

Figure 4: FTIR spectrum of unprocessed CF-PA6 tape, 650-4000cm^{-1}.

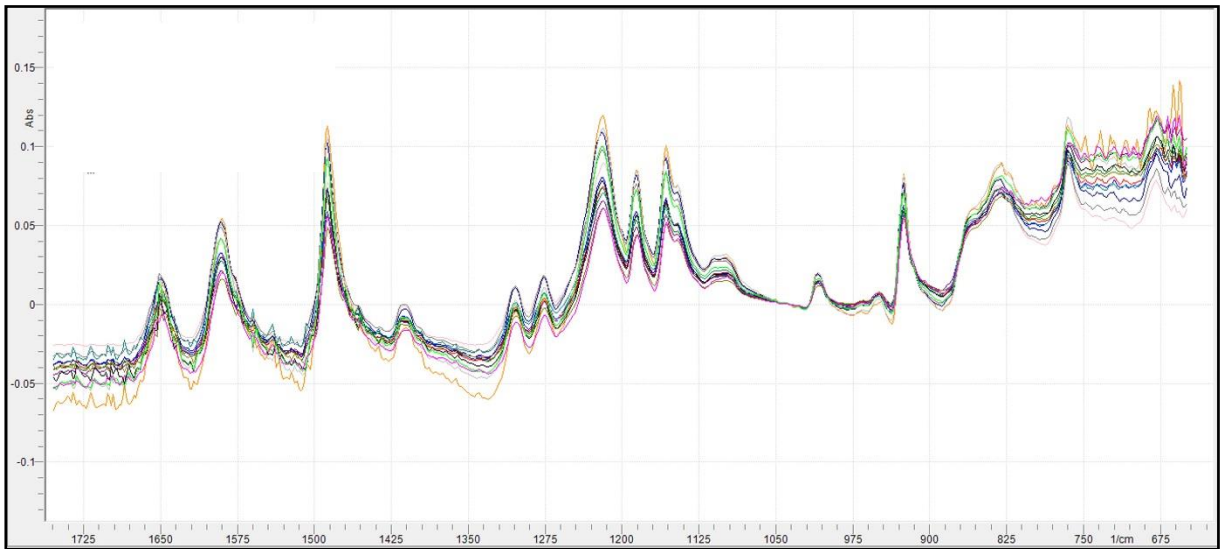

Figure 5: FTIR spectrum of control and CFQ LM-PAEK tapes, 650-1750cm^{-1}

The results shown in Figure **5** are typical of all other FTIR analyses conducted in this project. No changes to spectral peaks were observed in the case of the CF-PA6 samples. It can be concluded that no evidence of chemical degradation was observed by FTIR spectroscopy when the CF-PAEK and CF-PA6 materials were exposed to flash lamp radiation.

Raman Spectroscopy Results

Raman spectroscopy was chosen as an alternative chemical analysis technique for composite materials that typically applies high-intensity laser light to a sample to gain insights into the chemical structure. It was deployed in this project as a complementary technique to FTIR to look for evidence of chemical degradation. The Raman analysis was conducted at the University of Bristol. For all the samples tested, significant baseline drift was observed, which affected the ability to interpret results. One possible explanation of this baseline drift is the autofluorescence of exposed carbon fibres at the surface. The Raman and FTIR spectra of a control CF-PA6 tape sample are overlayed in **Figure 6**. The Raman trace is in black and the equivalent FTIR trace is in red. The peaks in the Raman trace are poorly defined and the baseline drift masks the lower intensity peaks between 1000-1750 cm^{-1}. The fluorescence

was even more pronounced for the CF-PAEK material samples tested, so that only the most intense peaks could be seen. This meant that no comparison between samples could be made as it was not possible to assess whether peak heights were changing or if new peaks were appearing.

Within the budgetary and time constraints of this project, it was not possible to improve this method. For this reason, Raman spectroscopy was discounted from the rest of the study.

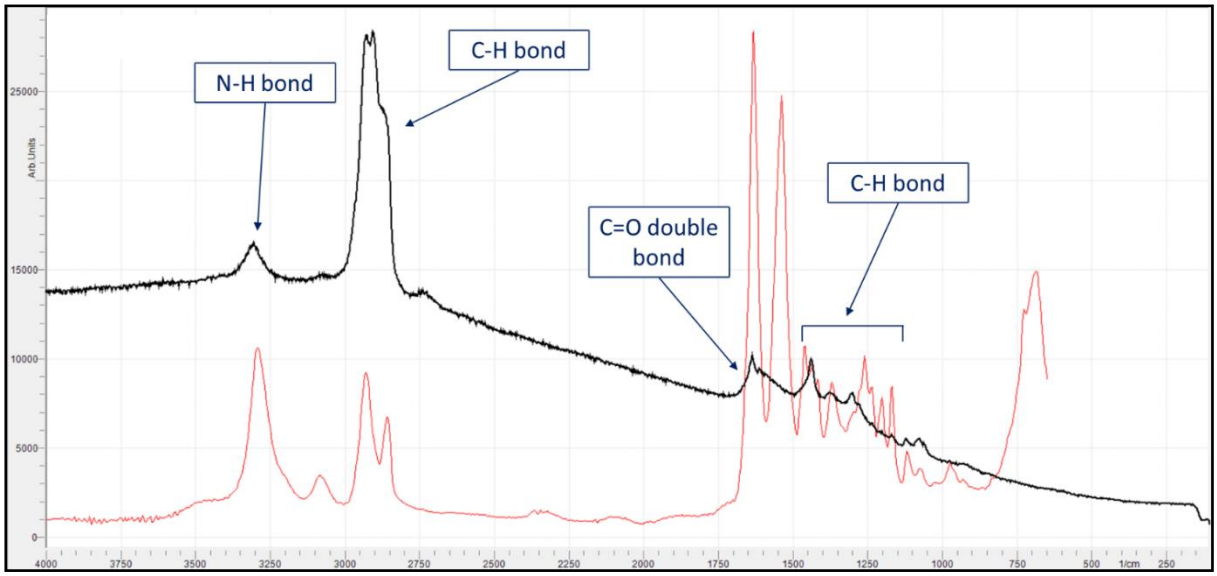

Figure 6: Black trace – Raman spectrum of control CF-PA6 tape. Red trace - FTIR spectrum of control CF-PA6 tape.

X-Ray Photoelectron Spectroscopy Tests

The results from FTIR and Raman spectroscopy did not show any clear evidence for polymer degradation of the composite sample surfaces. However, both techniques assess a relatively thick (several micron) surface layer of the material. It was thought that the high energy pulses from the xenon flash lamp may not penetrate into the material to this depth, and thus these two spectroscopy techniques may not be able to distinguish surface effects from the unaffected bulk material. As an alternative technique, X-ray photoelectron spectroscopy (XPS) was explored.

XPS is a spectroscopic technique that applies x-rays to the surface of a sample and measures the kinetic energy of the electrons that are emitted from the surface. It provides information about the chemical elements present in the sample and is a very surface-sensitive techniques that is only influenced by the top 10 nm of the material ([6]).

The XPS tests were carried out by Harwell XPS, at the EPSRC National Facility for XPS in Oxfordshire, UK. Technical details of the XPS set up and analysis are not provided here (but can be supplied by contacting the author). The samples tested were the control, CDQ and CFQ samples of each of the CF-PA6 and CF-PAEK tapes. Five repeats were carried out for each sample type, and particular interest was paid to any change in the oxygen percentage calculated, as this could be an indication of oxidative degradation of the polymer.

Composite materials are, by their nature, more difficult to assess than single material systems, especially as the ratio of resin and fibre on the surface of the material may vary with surface location and change during processing. If the ratio of resin to fibre changes, then the elemental ratios will vary. This appears to be the case for the CF-PA6 samples analysed here. As shown in

Figure **7** (left graph), the carbon percentage for the CF-PA6 tapes increased from 79.5% in the control samples to 81% for the CDQ samples and 83% for the CFQ samples. This may suggest an increase in fibre on the surface of the CDQ and CFQ samples as the carbon fibre contains solely carbon atoms compared to the polyamide resin which contains carbon, nitrogen and oxygen. A corresponding drop in nitrogen and oxygen percentage (Figure **7**, middle and right graphs) was observed. If oxidative degradation of the polymer had occurred, then an increase in the percentage of oxygen on the tape

surface would be expected. However, any increase in oxygen percentage from oxidative degradation may be masked by changes to the resin to fibre ratio. Hence it was not possible to make a firm conclusion that there was evidence of oxidative degradation. It should be noted that the standard deviation on all results (shown as black vertical bars in the figure) was large and therefore further testing would be required to determine whether these results were statistically significant.

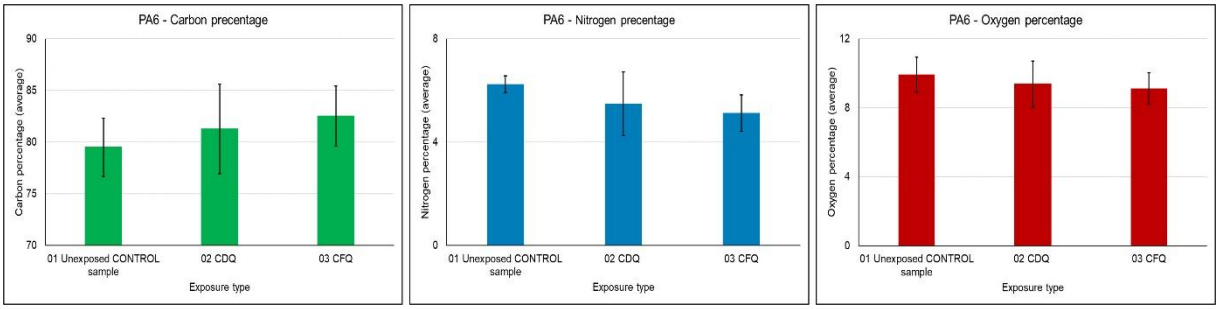

Figure 7: XPS results for the CF-PA6 samples. Carbon percentage is shown on the left, nitrogen percentage is shown in the middle and oxygen percentage is shown on the right. Each graph shows results for the control, CDQ and CFQ cases.

As with the CF-PA6 samples, there was a change in the carbon and oxygen percentage for the CF-PAEK tapes, however the opposite trend was observed. The CDQ and CFQ samples had a lower carbon percentage and higher oxygen percentage, as shown in **Figure 8**. These results are more consistent with the pattern to be expected from oxidative degradation. However, these results could also be explained by an increase in the resin to fibre ratio on the surfaces of the CDQ and CFQ samples. Again, it should be noted that the standard deviation on all these results was large and therefore further testing would be required to draw more confident conclusions.

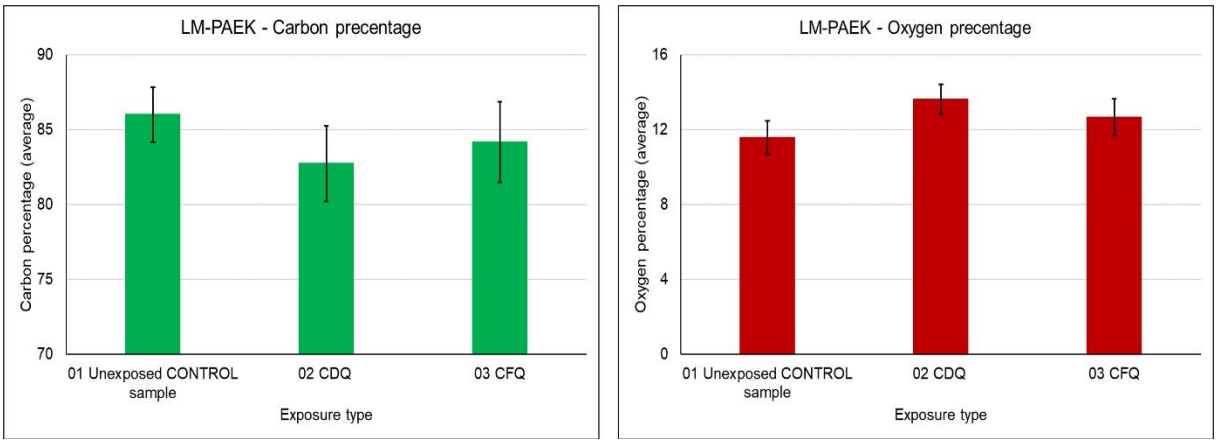

Figure 8: XPS results for the CF-PAEK samples. Carbon percentage is shown on the left and oxygen percentage is shown on the right. Each graph shows results for the control, CDQ and CFQ cases.

Conclusions from Spectroscopy

Three spectroscopy techniques, FTIR, Raman and XPS, were applied to control, CFQ-exposed and CDQ-exposed samples of CF-PA6 and CF-PAEK materials. The complementary tests did not find conclusive evidence that exposure to flash lamp radiation causes chemical degradation of the material surfaces. Of the techniques, XPS showed most promise for further work, possibly combined with similar tests on neat resin to remove the effects of the carbon fibres at the surface.

4 ALTERNATIVE FLASH LAMP TAPE BONDING METHOD

The complexity of the AFP process, with its many interacting parameters, such as compaction force, tape feed accuracy, tool temperature, first ply contact with tool, position of thermal camera and many others make repeatable tests and accurate thermal measurements difficult to achieve. Through reassessing the AFP results on thermoplastic tapes at the NCC, the results of which motivated this project, it became clear that a simpler, more laboratory-scale method of bonding tape pairs would facilitate easier assessment of the effects of single parameters on the bond strength. To this end, a new tape bonding technique was developed, and is described here for the first time, which takes advantage of the flash lamp system's unique ability to apply radiant heat and compaction pressure simultaneously. Under static conditions, it is possible to apply pressure through the quartz light guide at the same time as heating via irradiation through the light guide, creating a precise weld between tapes. The light guide itself does not heat up during the process and is therefore relatively easy to remove from the bonded tapes after processing.

The new method of tape bonding includes the following steps. The previously exposed surfaces of tape pairs are placed in contact, one on top of the other, and covered with a piece of Kapton film, before the quartz light guide is pressed onto the top surface with a known force (**Figure 9**, left). The flash lamp is then used to heat the samples for a given short duration while maintaining the compaction force, to allow the tapes to melt through their thickness and be bonded (welded) together.

In order to bond tape pairs for this project, flash lamp pulse parameters of 200 Volts, 60 Hz, and 1.5 ms, with a heating time of 1 second, were used in all cases. A compressive force of 200 N was applied by tightening a scissor-jack beneath the samples and pressing them onto the light guide of the statically mounted flash lamp head, force being measured on a set of scales beneath (**Figure 9**, right). The compressive force was maintained for 60 seconds after the heating, and a delay of 180 seconds between tests was used to allow the base plate to cool to ambient temperature between tests. Using this method, a 55mm long central section of the tape pairs was bonded (the longer dimension of the rectangular output face of the light guide). A separate project has assessed the ability of this method to bond (weld) multiple layers of thermoplastic material in one short-duration heating step, and results will be published in subsequent papers.

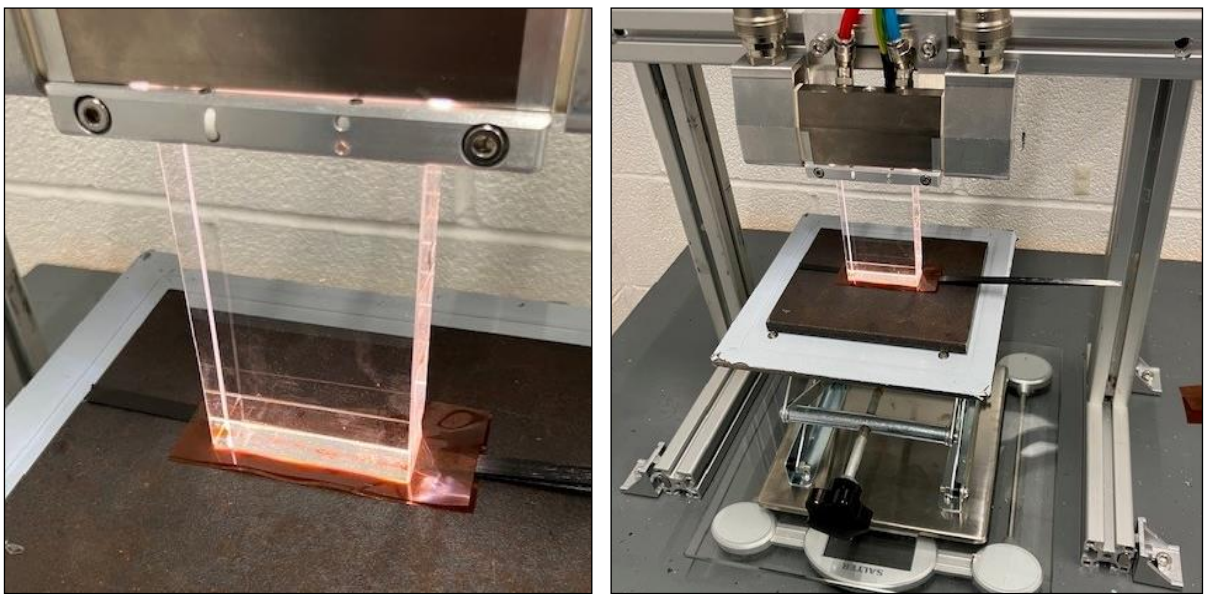

Figure 9: Xenon flash lamp system welding two CF-PAEK tapes under the quartz light guide. Left image: tape pair and Kapton film under the light guide. Right image: the scissor jack and scales.

Measuring Bond Strength of Tape Pairs

Several methods exist in the literature for measuring bond strength of welded thermoplastic interfaces. Standard tests, such as the lap shear test or double cantilever beam (DCB) test, work on thick, rigid specimens of multiple plies. These tests cannot be applied to the thin, flexible tape pairs being considered in this project. Alternatively, several different types of peel testing have been used to characterise the bonding of flexible tapes. T-peel tests, wedge peel tests and floating roller peel tests have been used in the literature ([7], [8]), however T-peel tests are prone to snapping of the tapes prior to interface failure when assessing strongly bonded samples, and wedge peel test results are complicated by the friction between the tapes and the wedge itself. The floating roller peel test ([9]), used throughout this project, provides direct measurement of the bond strength between two flexible tapes along the entire bond surface.

Figure 10 shows the floating roller peel test configuration.

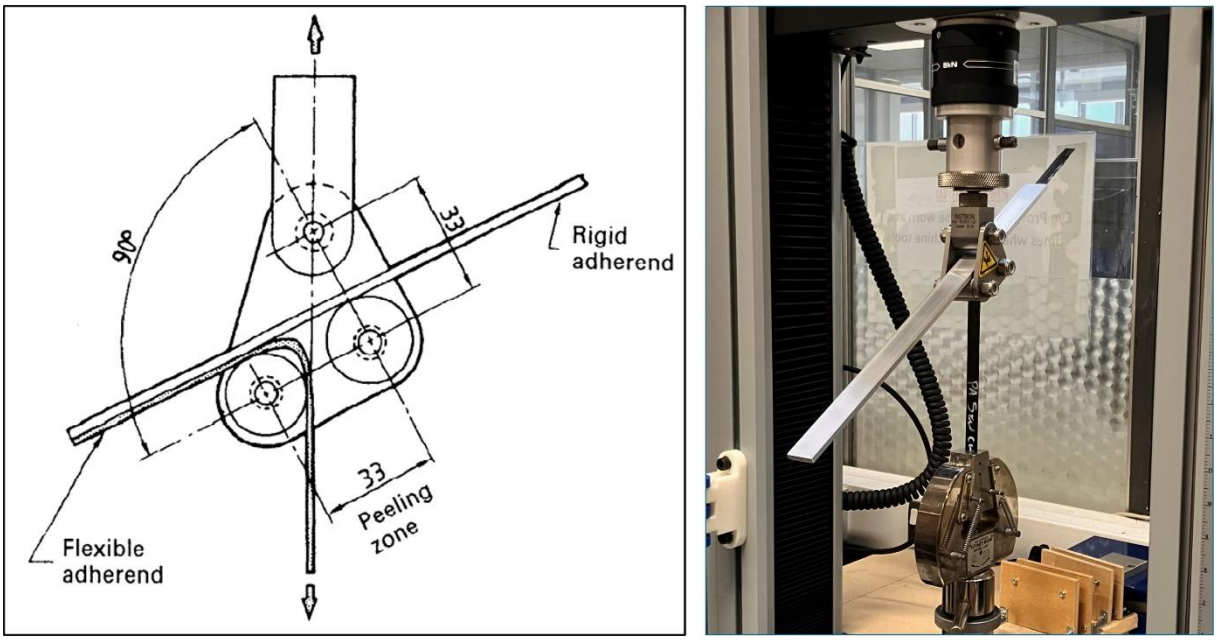

Figure 10: Floating roller peel test configuration. Left: schematic diagram from ASTM D3167−10. Right: picture of floating roller peel test in progress.

Bond Strength Results

Bonded tape pairs from the CDQ-exposed and the CFQ-exposed CF-PAEK material samples were compared with control samples that had not been exposed to flash lamp energy. A total of 10 bonded pairs were created for each category, and bond strengths were measured with the floating roller peel test.

Each tape pair was adhered to an aluminium metal backer using a strip of 3M double coated tape adhesive, 93015LE. The samples were left for at least 24 hours to allow for sufficient adhesive strength between the tape and the aluminium.

The peel tests were carried out on a Instron 5966 screw driven mechanical testing machine, fitted with a 10 kN load cell. The testing methodology was altered from that specified in D3167-10 as the length of bonded tape was only 55mm. The peel rate used was 150 mm/min.

The average force between 10 mm and 20 mm displacement was calculated for each tape pair, then the average of these values was taken over all the samples in each category to give a single number for peel strength of control, CDQ-exposed and CFQ-exposed tapes.

Figure 11 shows the results of the peel tests. The CDQ and CFQ-exposed tape samples, when bonded with the flash lamp welding method, showed a significant reduction in bond strength. There was an 86% reduction in the average force required to peel the tapes apart between the control and CDQ samples and a 98% reduction between the control and the CFQ samples. In general, these results are similar to results

from previous (unpublished) work where AFP was used to bond the tapes. Note that standard deviations, shown with vertical black bars, are high in each category, even though testing was repeated with care.

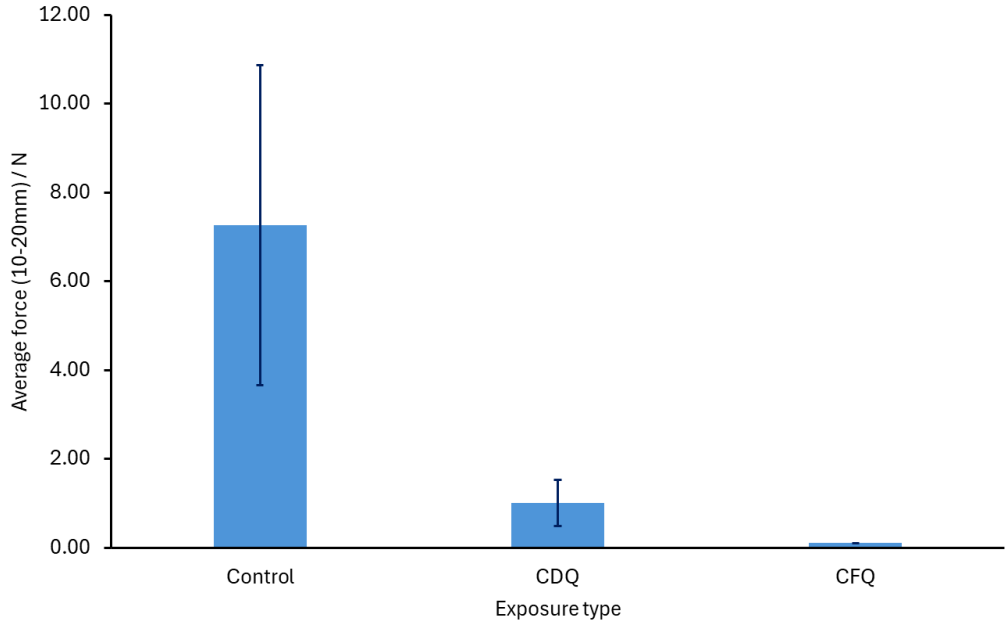

Figure 11: Peel test results from CF-PAEK control, CDQ-exposed, and CFQ-exposed tape pairs

Scanning Electron Microscopy of Peeled Surfaces

Scanning electron microscopy (SEM) images were taken of the peeled surfaces of representative tape pairs to investigate the cause of the different bond strengths seen in the peel tests described in the previous section. Images were taken on a Zeiss Evo MA25 scanning electron microscope. Tape samples were adhered to a 25mm stub using a carbon adhesive tab. The samples were positioned so that the two opposing faces of the bonded pair were next to each other with the peeled surfaces uppermost. The tape samples were coated with a 15nm layer of gold using a Quorum Q150T sputter coater. **Figure 12** shows SEMs of representative peeled surfaces for control, CDQ-exposed and CFQ-exposed samples.

The main observable difference between the control samples, which exhibited high peel strengths, and the CFQ-exposed samples, which exhibited low strengths, was the number of discrete regions of polymer that have failed in a ductile manner, seen in the top images of **Figure 12** as light-coloured ribbons of polymer projecting from the surface, but absent from the bottom images for CFQ-exposed samples. The CDQ-exposed samples exhibited some regions of ductile failure, as shown by the smaller number of ribbons of polymer in the middle image. This type of ductile failure was noted by Comer et. al. ([2]) in their study of PEEK polymer samples and attributed to plastic failure of regions of low crystallinity. The difference between low and high peel strengths was observed to be related to the number of discrete areas of polymer that undergo plastic deformation during the failure of the bond surface.

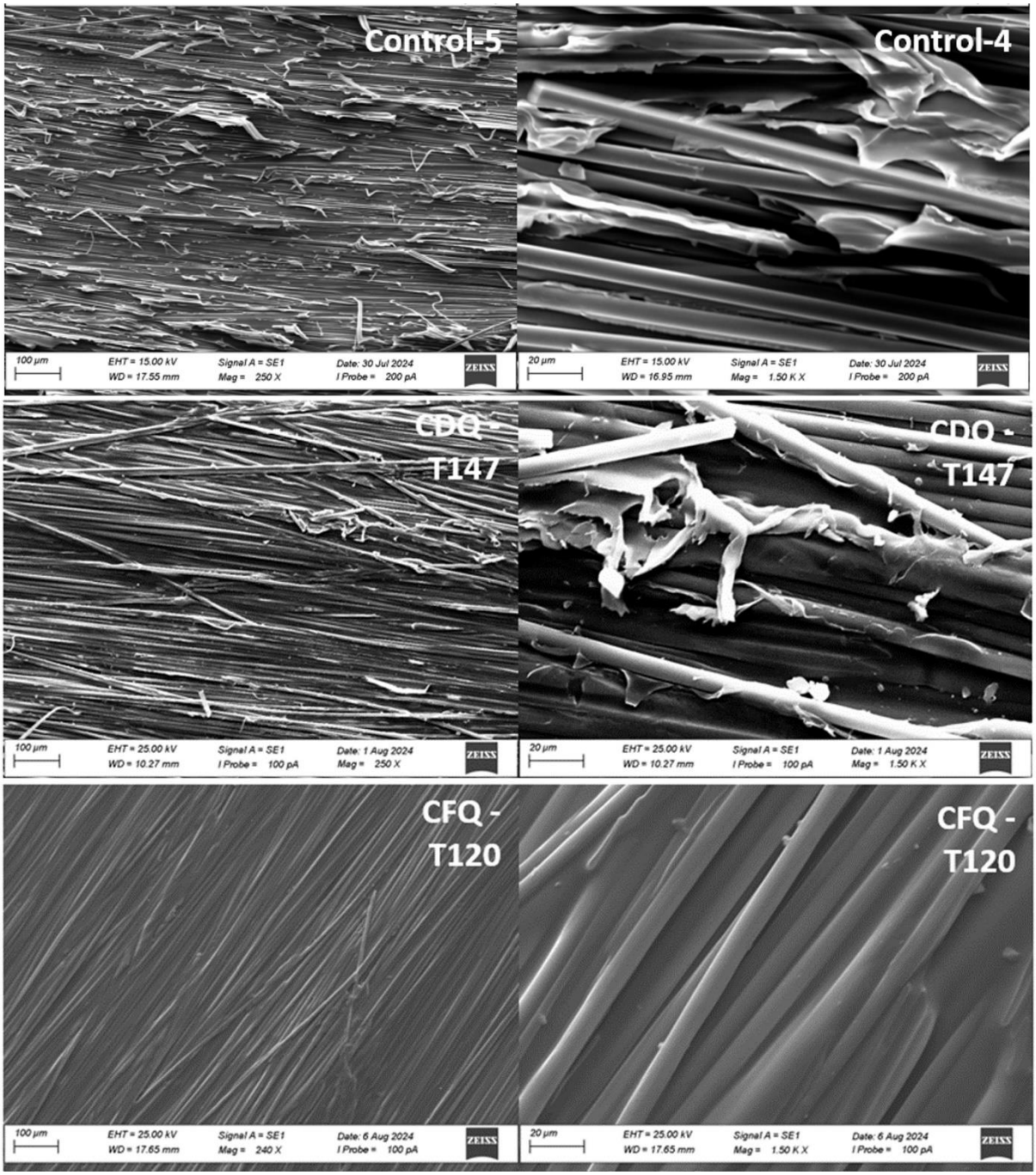

Figure 12: SEM images of peeled tape surfaces for control samples (top), CDQ-exposed samples (middle) and CFQ-exposed samples (bottom). Magnification is 250x (left) and 1500x (right).

Conclusions from Flash Lamp Bonding

Flash lamp bonding of tape pairs from control, CDQ-exposed and CFQ-exposed samples confirmed that exposure to flash lamp energy reduces bond strength. The spectroscopy analysis described in the previous section shows no clear evidence that the polymer surfaces are being chemically degraded by this short duration exposure to the flash lamp energy. An alternative explanation for this reduction in bond strength will form the subject of further work in this area.

5 DISCUSSION AND FURTHER WORK

In this project, no evidence was found that exposure to flash lamp energy caused chemical degradation to CF-PA6 and CF-PAEK tape samples. Further work will be carried out to establish which other factors, present during AFP processing, may detrimentally impact the bond strength between tapes. From the results described here, it appears that reduction in bond strength may not be caused by polymer aging due to UV exposure but by other factors associated with flash lamp heating.

ACKNOWLEDGEMENTS

The main body of this work was completed while the author was a consulting engineer at Excelitas Noblelight (formerly Heraeus Noblelight), Cambridge, UK.

The author wishes to express his gratitude to Martin Brown, Ross Kitson and colleagues at Excelitas Noblelight for supporting this work with funding, technical advice and access to the xenon flash lamp heating system.

The majority of the results shown here were generated through a project at the National Composites Centre funded by Excelitas Noblelight. The author acknowledges with thanks the important contributions of Tom Andrews and Keith Bean at the NCC to the project.

REFERENCES

[1] M. J. Donough, Shafaq, N. A. St John, A. W. Philips, B. Gangadhara Prusty, Process modelling of In-situ consolidated thermoplastic composite by automated fibre placement – A review, *Compos Part A Appl Sci Manuf*, **163**, 2022: (doi: 10.1016/j.compositesa.2022.107179).

[2] A. Comer, D. Ray, W. O. Obande, D. Jones, J. Lyons, I. Rosca, R. M. O'Higgins and M. A. McCarthy, Mechanical characterisation of carbon fibre–PEEK manufactured by laser-assisted automated-tape-placement and autoclave, *Compos Part A Appl Sci Manuf,* **69**, pp. 10-20, 2015 (doi: 10.1016/j.compositesa.2014.10.003)

[3] A. Danezis, D. P. Williams, M. Edwards, A. A. Skordos, Heat transfer modelling of flashlamp heating for automated tape placement of thermoplastic composites, *Compos Part A Appl Sci Manuf*, **145**, 202: (doi: 10.1016/j.compositesa.2021.106381).

[4] M. Brown, P. Monnot, D. P. Williams, Developments in Xenon Flashlamp Heating for Automated Fibre Placement, *Proceedings of the Fourth International Symposium on Automated Composites Manufacturing, 25th – 26th April 2019, Montreal, Canada*.

[5] V. Mylläri, T-P Ruoko, P Järvelä, The effects of UV irradiation to polyetheretherketone fibres – Characterization by different techniques, *Polymer Degradation and Stability,* **109**, 2014, pp 278-284 (doi: 10.1016/j.polymdegradstab.2014.08.003).

[6] D. Nanda Gopala Krishna, J. Philip, Review on surface-characterization applications of X-ray photoelectron spectroscopy (XPS): Recent developments and challenges, *Applied Surface Science Advances,* **12**, 2022 (doi: 10.1016/j.apsadv.2022.100332).

[7] A. Legenstein, E. Fauster, Effect of Flashlamp Heating System Parameters on the Wedge Peel Strength of Thermoplastic Carbon Fiber Tape in the Automated Tape Placement Process, *J. Manuf. Mater. Process.*, **8**, 2024, pp. 91 (doi: 10.3390/jmmp8030091).

[8] C. Zhang, Y. Duan, H. Xiao, B. Wang, Y. Ming, Y. Zhu, F. Zhang, The effects of processing parameters on the wedge peel strength of CF/PEEK laminates manufactured using a laser tape placement process, *Int J Adv Manuf Technol,* **120**, 2022, pp.7251–7262 (doi: 10.1007/s00170-022-09181-5).

[9] ASTM, *D3167−10 Standard Test Method for Floating Roller Peel Resistance of Adhesives,* 2017.

A COMPREHENSIVE APPROACH TO A DIGITAL TWIN BASED ON ASSET ADMINISTRATION SHELLS FOR A PROCESS CHAIN OF AUTOMATED TAPE LAYING AND THERMOFORMING FOR STRUCTURAL AEROSPACE COMPONENT MANUFACTURING

Fabian Röder[1], Martin Müller[1], Manuel Reif[2], Pascal Rübel[2], Valentine Domengie[1], Alexander Huf[1], Andreas Gebhard[1], Martin Ruskowski[2] and Thomas Neumeyer[1]

[1]Leibniz-Institut für Verbundwerkstoffe GmbH
Erwin-Schrödinger-Straße 58, 67663 Kaiserslautern
Email: thomas.neumeyer@leibniz-ivw.de, web page: https://www.ivw.uni-kl.de

[2]Techologie-Initiative SmartFactory KL e.V.
Trippstadter Straße 122, 67663 Kaiserslautern Germany
Email: martin.ruskowski@smartfactory.de, web page: https://smartfactory.de

Keywords: Digital Twin, Asset Administration Shell, Life Cycle Assessment, Automated Tape Laying, Thermoforming

ABSTRACT

In the aviation sector, highest demands are placed on the mechanical properties, quality and traceability of all components. Complex manufacturing processes such as Automated Tape Laying (ATL) and subsequent thermoforming imply comprehensive quality inspections to meet strict air transport safety regulations. Utilizing these processes to produce parts fulfilling the harsh requirements needs exact process control and knowledge about every aspect of the process chain. Each processing step generates huge amounts of machine not currently stored in a common, centralized form. A digital twin describing the products along the chain is created to store and transmit this data in a standardized structure and common format as a necessary requirement for overarching process control and life cycle analysis (LCA). This is achieved by means of the Asset Administration Shell (AAS), a standardized approach to implement vendor-independent digital twins and to provide an interoperable meta-model to represent relevant information. Instances of the AAS contain data for all process steps, wherein several sub-models contain general data in standardized models in combination with a self-defined model leveraging classical laminate theory (CLT). Standardized models allow taking advantage of standards beyond the boundaries of composite specific process data, such as the Product Carbon Footprint (PCF) used in the calculation of the LCA. The composite specific model retains the relevant data for composites. Due to the integration in the AAS, all data is transformed into a common shape, ensuring all data to be useable. This integration of information can be shared across processes, applications and industries. The models along the process chain are presented in this contribution, providing subject for discussion.

1 MOTIVATION

In the aviation sector, highest demands are placed on all mechanical properties, quality and traceability of all components to meet strict air transport safety regulations. As a result of this, rigorous inventory recording and tracking for all used materials, components and assemblies up to final products is mandatory. A current challenge therefore is to digitalize the documentation of these processes and test results whilst adhering to existing standards and established concepts. In addition to safety, social and governance reasons, documentation of environmental impacts has become an additional requirement. In order to precisely compute the ecological footprint of the manufacturing of structural aerospace components, processes have become the focus of data collection. At the same time, this data is an valuable asset for controlling and predicting the quality of components along the whole processing chain.

2 INTRODUCTION

To support the digitalization of aerospace manufacturing and enable precise process control, as well as continuous Life Cycle Assessment (LCA), the processes of Automated Tape Laying (ATL) and Thermoforming (TF) were digitalized. This includes the comprehensive assessment of process parameters and results, which are essential for reducing environmental impact. The rejection of defective components significantly increases the overall environmental footprint of accepted parts, making quality improvement a critical objective. To represent realistic starting points in the industry, existing software systems were not replaced, but instead new capabilities were to be added.

The solution created in the scope of this work is thus designed with a non-monolithic architecture to ensure seamless integration with existing enterprise environments. Unlike tightly coupled solutions, this approach avoids interference with established Enterprise Resource Planning (ERP), Manufacturing Execution Systems (MES), and Supply Chain Management (SCM) systems, which already manage parts of the information necessary to describe the digital twin. Instead of replacing or altering internal digital twin implementations, these are extended through the Asset Administration Shell (AAS), as defined by the Industrial Digital Twin Association (IDTA), which functions as a standardized and shareable external representation. It is utilized, because it is an industry-neutral standard with broad applicability, and has strong potential for long-term market relevance. An additional benefit as depicted in Figure 1 is the improved control over shared and published data. The external layer created by the AAS (blue) enables interoperability while maintaining strict data sovereignty. Confidential and internal company data remain fully contained within the organization's secure network (grey). The AAS merely references selected data elements that are explicitly defined for external use through control of a firewall-layer (yellow), ensuring that sensitive information is neither exposed nor transferred. Only access-controlled links to designated non-sensitive attributes are instantiated, preserving the integrity and independence of internal systems. The physical manufacturing layer (orange) and the internal layer communicate as before without experiencing change. As a result, the solution supports a high degree of system independence and facilitates structured external collaboration without compromising internal security or operational workflows.

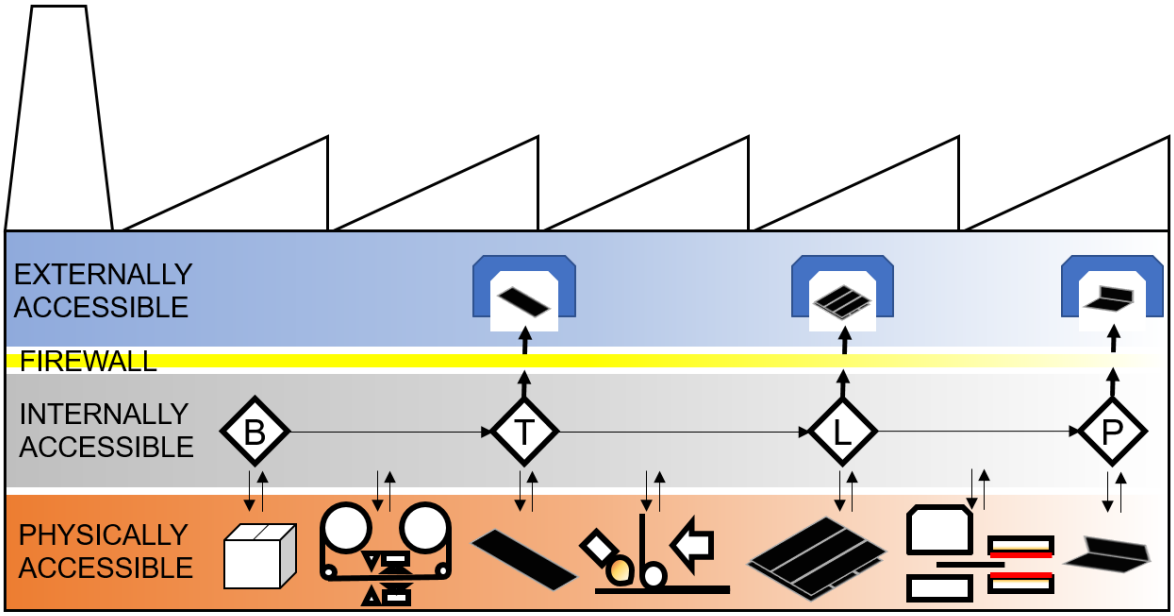

Figure 1: Representation of relationships between modelling layers in the internal and external solution as well as the physically accessible field level where data is produced and consumed for manufacturing

3 STATE OF THE ART

3.1 Life Cycle Assessment for Composite Manufacturing

One central driving aspect of the creation of the process-focused digitalization across industry is LCA, although it is closely followed by the aspect of process control. Accordingly, it is the most important subject meeting requirements and assess achievable results by the creation of the digital twin as in the European unions (EU) Battery Passport [1]. As it will likely become mandatory for a growing number of products, it is already a focus in many digitalization attempts and will remain so here.

LCA is an environmental evaluation tool for determining or predicting the potential effects associated with a product or a process that includes its entire life cycle. The conduction of LCA is standardized in DIN EN ISO 14040 (Principles and Framework) and DIN EN ISO 14044 (Requirements and Guidelines). As an iterative approach, its four phases, namely *Goal and Scope Definition*, *Life Cycle Inventory*, *Life Cycle Impact Assessment*, and *Interpretation* are interrelated and refined throughout the study. It is also a holistic approach, considering the entire life cycle of a product following a cradle-to-grave perspective, from raw material extraction to disposal and end-of-life treatment. An LCA study typically considers multiple impact categories (e.g. *Climate Change*, *Ozone Depletion*, *Human Toxicity*), whereas a Product Carbon Footprint (PCF) only assesses the climate change impact of greenhouse gas emissions. The choice of the evaluated impact categories must be documented during the *Goal and Scope Definition* phase. Incorporating multiple impact categories prevents burden shifting between environmental issues and represents a fundamental aspect of the holistic approach. During the *Life Cycle Inventory* (LCI) phase, all input and output flows relating to the unit processes of the product system under investigation are compiled and quantified. These include raw materials, energy, products (such as services, software or hardware), elementary flows (those extracted from or released into the environment) and waste. In the *Life Cycle Impact Assessment* (LCIA) phase, the results from the LCI are assigned to the different impact categories to which they contribute. A single flow can contribute to multiple impact categories.

LCA can be used as a predictive tool to estimate environmental impact under different scenarios. FERRARI ET AL. [2] applied the methodology to evaluate the environmental impacts of various production scenarios involving raw materials from different suppliers in the ceramic tile manufacturing process. In field of composites materials, raw materials account for a significant share of the environmental impact, particularly the production of carbon fibers. According to BENITEZ ET AL. [3], the impact of carbon fiber production on climate change under the conditions of the study (2019) was estimated at 69.12 kg CO_2-eq./kg, while PRENZEL ET AL. [4] reports a range from 13 to 34.1 kg CO_2-eq./kg. The wide range of results can be explained by various factors influencing the impact on climate change during carbon fiber production, such as the type of precursor used, the energy source for precursor and fiber production, the conversion rate from precursor to carbon fiber, and the geographical location of the plant [4,5]. The method applied by the LCA practitioner can additionally influence the results, for example through the choice of system boundaries, functional units or allocations [5]. Using LCA as a predictive tool enables the optimization of composite material manufacturing processes, with the dual objective of improving efficiency and minimizing environmental impacts. The rejection rate during the manufacturing process considerably influences the final LCA results, due to the high environmental cost of carbon fibers. According to LCA methodology, all material flows intended for disposal without recovery are categorized as waste flows in the LCI phase. Despite not contributing to the final product, their associated environmental burdens are included in the overall assessment.

In the context of this study, the environmental impact of the Automated Tape Laying (ATL) and thermoforming process chain is assessed with a focus on the *Climate Change* impact category. The emphasis is placed on the digitalization of manufacturing processes following a gate-to-gate approach. Transportation, use and retail, as well as end-of-life phases are out of the scope of this study. The impacts of raw materials are considered at the process level by monitoring the rejection rate, with the aim of optimizing each process step of the production chain and minimizing its environmental impact.

3.2 Digital Twins for Composite Manufacturing Processes

Whilst there have been several proposals for the definition of the term *Digital Twin*, the concept mostly is used to describe few commonalities. A digital twin is in general a virtual representation of an object or system designed not only to represent, but to reflect a physical object accurately. It spans the physicals object life cycle, updates in real time from corresponding data and provides insight into its condition and behavior.

Digital twins are mostly a concept for information provision and evaluation, which utilizes the communication capability of product systems and aggregates data from the entire product life cycle. In this way, they are a perfect fit for the continuous LCA alongside the process chain, providing current values in real time, but also quality centered process monitoring since state variables can be monitored in a central location in real time for every process and product.

Whilst the general concept of digital twins is easy to describe, fine details can make lots of differences especially considering the environment and planned usage as well as the framework and implementation. Whilst environment and usage are defined by the objective undertaken in this work, the framework to be used is subject of discussion and the implementation will be based around this decision. GIL ET AL. [6] provide a comparison and overview over different open-source digital twin frameworks, underlining the importance of AAS-based implementation as standardized solutions, whilst also pointing out the incompleteness of the frameworks.

In order to enable digital product representations that support LCA, interoperable and standardized information models are essential. The AAS plays a key role in realizing this requirement within the Industry 4.0 framework. It provides a digital representation of any physical or virtual asset, such as a machine, sensor or workpiece using an unified metamodel that allows structured data exchange across system boundaries [7].

The AAS consists of modular submodels, which cover a wide range of domains such as production planning, material properties, process capabilities, and more [8]. These submodels follow standardized structures, making data from heterogeneous systems interoperable. This makes the AAS a foundational technology for enabling cross-organizational collaboration and dynamic value chains, which are essential in modern, sustainable manufacturing scenarios [9–11].

AAS-based submodels are being successively standardized by the IDTA to ensure compatibility across industries and applications. However, in specific domains such as composite material products, standardized submodels for relevant data like material composition are not yet available. Importantly, the AAS framework supports the development of custom submodels, allowing domain-specific extensions to be added in a structured and interoperable manner [12]. This extensibility enables companies to integrate domain specific information models, still maintaining compatibility with the broader Industry 4.0 ecosystem.

3.3 The Process Chain

Since the subject of LCA and digital twins is closely related to future manufacturing of aerospace composite components, the process modelled in this work should reflect those attributes as well. Due to their specific benefits, a growing percentage of thermoplastic composites in aerospace applications can be observed in future aircrafts, used mainly in fuselage components. While many manufacturing processes are slow and costly, the thermoforming process has made it into regular production. This is due to high-rate capability, allowing the production of large panels, doors and frames [13].

Stamp forming of thermoplastic composite laminates is typically a two-step process: Fully impregnated laminates are heated in an oven to melt the matrix and to allow deformation and shearing of the laminate to fit to the later 3D-geometry. From the oven it is transferred quickly into a press, where it is stamp formed in a tool and cooled below melting point in a single step, producing the finished part within seconds. Due to the near-net-shape design of the laminate, only little machining of the part is needed, if the design of the component is optimized for thermoforming. [14, 15]

Both steps of the process – heating and thermoforming - are performed within the same equipment, a forming press with an integrated infrared oven (LZK-Uk-2600-SO, Langzauner GmbH Austria). Being equipped with a multitude of sensors, it is capable of tracking and recording all relevant processing parameters, such as pressures, positions and other states of the machine during the process. Additionally,

temperatures are monitored within the integrated infrared oven, individually controlling the 234 radiators for reproducible process conditions. Nonetheless, it also integrates a thermal camera to document temperature distribution during transfer from oven into the press during the short transfer time of approximately a second. All data is collected within an integrated process data logging system (LZ perfectDATA, Langzauner GmbH, Austria) and distributed over Message Queuing Telemetry Transport (MQTT).

To reduce the high cost and high waste of consolidated laminates, near-net-shape preforms can be manufactured in ATL with Unidirectional Reinforced Thermoplastic Tapes (UD-Tapes). A preform is a pre-consolidated laminate that is fully consolidated in the press. ATL allows load-path optimized tape placement and is suitable for high rate production of nearly flat structures such as skins and panels [16–18]. These flat tape preforms can be used as semi-finished parts for the subsequent stamp forming of three-dimensional components. Since there is a higher potential for process induced errors while placing individual tapes, there is a high demand for quality control [19,20].

The ATL machine used (F2-Compositor, ASH Automation Steeg & Hoffmeyer GmbH, Germany) is optimized for high speed deposition (up to 4 m/s) and can process UD-Tapes based on engineering as well as high performance thermoplastic polymers. To create adhesion of the individual layers, the polymer in the tape surface is molten by a hot gas torch, followed by rapid cooling under consolidation force provided by a consolidation roller. During production, it continuously and precisely measures all axis positions and temperatures, as well as material temperature and gas consumption.

It is also set up with a MQTT server with manufacturer-defined topics encompassing all aforementioned position, temperature and gas consumption data. Additionally it transmits status and further crucial process step data, thought to simplify correlation between measured data and planned program steps.

The tapes used for producing the preforms are usually commercial products supplied by different manufacturers all over the world. Therefore tapes as well as their raw materials like carbon fibers, matrices, precursors and other ingredients cannot be included explicitly into the in-house digitalized process chain. As a result, during LCA the environmental impact of tapes is computed using standardized data (e.g. datasheet or database values). However, in order to correlate information that is related to process quality, a custom built test bench is used to provide seamless quality information for every tape used in later processes [21]. The Tape-Quality-Bench (TQB) measures the precise cross section of the tested tape whilst also filming its surface using a polarization camera (VCXU-50MP, Baumer GmbH, Austria) for measuring fiber orientation close to the surface and check for defects and foreign objects.

4 CREATING THE INTERNAL SOLUTION: IIOT AND LIMS

Starting from the state as described before and an already in part created solution for a custom build Laboratory Information System (LIS), an example for the usage of a digital twin framework is created for the presented process. Here, internally developed software was combined with open-source code to create a solution that is able to be shared fully later on. The architecture and especially the workflow within this system is described to give a general overview about the internal use and capabilities and create a basis for the later following description of the externally shared AAS.

Data along the process chain is initially collected locally on the respective production machines—namely, the TQB, the F2-Compositor, and the Langzauner press—and subsequently transmitted to the internal Industrial Internet of Things (IIoT) infrastructure. To accommodate the heterogeneous nature of legacy and modern machine controls, and their varying data export capabilities, the IIoT system exposes multiple data ingestion interfaces, including MQTT brokers, Representational State Transfer Application Programming Interfaces (RESTful APIs) and Open Platform Communications Unified Architecture (OPC UA) endpoints. This multi-protocol support ensures seamless integration of both current and future manufacturing assets. All incoming data to the IIoT system must be timestamped upon ingestion. Where timestamps are not natively provided by the machines, edge devices append them, synchronized via Network Time Protocol (NTP) servers. This ensures the temporal consistency of otherwise independent data sources, which enables automated detection of stale or delayed data, and facilitates precise correlation of process data streams.

In cases where not all relevant data is natively available from the machine control, the IIoT compensates by logically integrating supplementary data sources. For example, although the F2-Compositor does not report the energy consumption of its auxiliary aggregates, this gap is filled by an external energy monitoring device (Shelly Pro 3EM, Shelly Group SE, Bulgaria), which independently measures and transmits the data via MQTT. Its measurements are published under a structured topic hierarchy, e.g., `F2Compositor/Energy/Auxiliaries`, enabling semantic classification of the data stream. Through topic-based filtering and stream parsing, the IIoT system aggregates disparate signals into unified datasets associated with logical assets. This approach ensures semantic coherence even when physical data sources are decoupled. Temporal alignment is achieved via the shared timestamping infrastructure.

While the IIoT layer provides the backbone for scalable ingestion and storage of raw process data, including sensor values, machine parameters, and energy metrics, it does not itself impose any domain-specific structure. Semantic enrichment and high-level data modeling are instead delegated to the LIS. This architectural separation ensures modularity and scalability, with the IIoT handling efficient data logistics, and the LIS capturing contextual and semantic relationships. The LIS organizes data within a hierarchical structure conceptualized as a forest, where each tree corresponds to a specific project. Root nodes are labeled with unique project identifiers, which can optionally link to external project management systems. Subordinate nodes represent physical or logical entities (e.g., materials, processes, parts) and are enriched with attributes and metadata. Each node is uniquely identified via a Universally Unique IDentifier (UUID). Nodes may be interlinked to express compositional, transformational, or inheritance-based relationships, thus capturing complex interdependencies within and between projects.

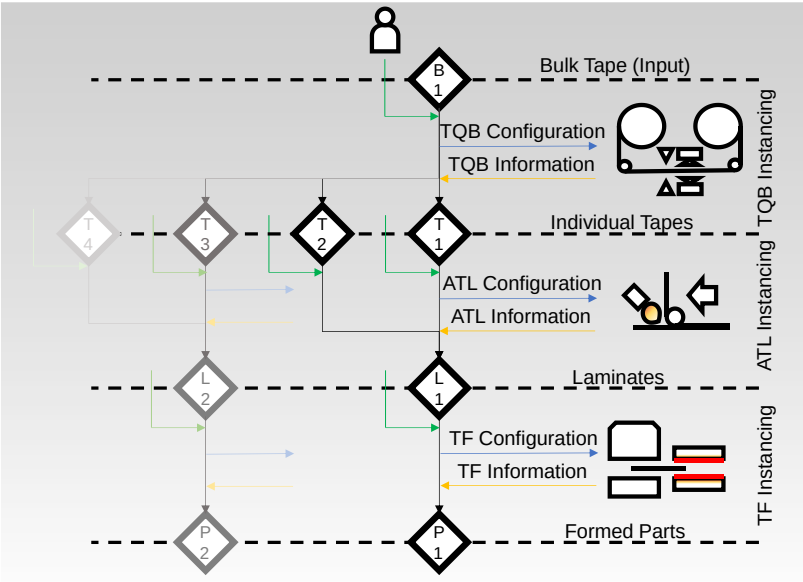

Figure 2: Representation of relationships between component instances along the manufacturing workflow in the internal solution

The manufacturing workflow, illustrated in Figure 2, begins with the thermoplastic tape, the smallest production unit. Bulk tape is initially registered in the LIS as a node containing general attributes such as type, manufacturer, mechanical properties, and nominal width as well as the PCF in form of a single numerical value. Individual spools derived from this bulk material are created as subordinate nodes. During initial quality assessment at the TQB, measured data is recorded and tagged with the associated spool's UUID, stored in the Influx time-series database of the IIoT system, resulting in a set of data which includes measured tape width and its cross-sectional height. At present, tape manufacturers do not provide machine-readable datasheets, digital product representations, or unique identifiers for individual spools. Consequently, UUIDs are generated internally by the LIS. These identifiers are physically linked to spools via QR codes, enabling consistent association between digital representations and physical items. Designed to digitally unify a set of discrete manufacturing processes

for fiber reinforced plastics, the system uses these QR codes to ensure end-to-end traceability. In addition, UUIDs serve as tags within the IIoT data streams, enabling seamless linkage between time-series data and LIS entities.

In the subsequent process step, spools are mounted on the F2-Compositor and identified via QR code scanning. This action associates the spool node with the current instance of the tape laying process and creates a new entity representing the manufactured preform. The resulting preform node automatically inherits attributes from the tape spool and is linked to process data that has been measured during its manufacturing by being linked to its parent node, which represents this manufacturing step. Users may augment these nodes with additional information such as program parameters, machine setup, manual observations, or process events, which are then available to downstream analyses. A persistent challenge in ATL processes is the correlation of process conditions with final part quality. While consolidation quality of the laminate has minimal impact, defects originating in the tape-laying step, such as wrinkled or flipped tows or foreign objects, can significantly impair quality. Although the F2-Compositor provides detailed process data, this alone has proven insufficient. Therefore, a laser line scanner (ScanCONTROL 3000-25/BL, Micro-Epsilon Messtechnik GmbH & Co. KG) is installed on the tape-laying head to capture the surface geometry of each layer. This sensor produces a continuous data stream, recorded as a time-series in the IIoT system and tagged to the corresponding laminate node in the LIS. This data can be evaluated either post-process or in real-time by subscribing to the F2-Compositor's MQTT data channels.

Finally, the laminate serves as the raw material in the thermoplastic stamp forming step. Each finished part is registered as a new node in the LIS, inheriting attributes from the laminate node and receiving its own UUID. Time-series data from this process is again captured in the Influx database. The exception is the thermal imaging data, acquired by an infrared camera. In contrast to the laser scanner, which generates continuous streams, the infrared system captures discrete images per part. These images are attached to the respective part node as singular or occasional multiple instances and are stored using MinIO (MinIO Inc., USA).

5 EXTERNAL SOLUTION: INTERFACING THROUGH AAS

The AAS is used to create external representations based on internally stored information. It is perfectly suited for this, because its modular and extensible structure allows for the integration of heterogeneously collected internal data, such as those originating from LIS, time-series databases or data processing and storage platforms, into a unified, semantically consistent model.

5.1 AAS Modeling using Standardized Submodels

AAS Structure and Infrastructure has a large degree of freedom in terms of information structure, especially in customized submodels. There are limitations of course, nesting of AAS and submodels is forbidden by the metamodel for example. In this way, the structure used in the internal implementation becomes impossible to reproduce. Instead, a new data model based on the AAS metamodel has to be created. Different implementations of the AAS can be used to achieve this easily, however there are no extensive and understandable guides for doing so yet. Also, for most cases there is currently no automated solution for checking the conformity to the metamodel or the used submodels.

In this way, defining the data structure is more difficult than it seems. Being compliant to other standards such as Concept Descriptions and SemanticIDs applies a large amount of implicit and explicit conventions, in addition to the constraints already applied by the metamodel. Handing this large amount of complexity correctly and creating fitting submodel structures is the most important aspect of the work, not only because it needs to be correct, but also because it needs to be widely applicable and understandable. In the following, an effort to structure the data created along the studied process chain is presented.

The starting point for defining the AAS from the finished part perspective is the relation between parts and resources. As stated before, nesting of AAS is not allowed. The alternative is to provide AAS with the information of either the parts containing them or alternatively the parts contained within. This is specified within the published submodel *IDTA 02011-1-1 Hierarchical Structures enabling Bills of Material*. Here, three model variants are allowed concerning the detail and way of relationship between

components. As thermoformed parts are not complete systems, the *full* type is not applicable, leaving the *one up* and *one down* modelling variants, where every component in an assembly hierarchy is linked to the ones it contains (*one down*) or the ones it is contained in (*one up*).

For our example, we define three types of AAS, representing different states of manufacturing. The first is the tapespool and instances of it, being contained within preforms, which is in turn the currently single component of a thermoformed part. Whilst fitting to our internal model closely, as the parts are used up as resources they are not components that could be recovered from the thermoformed part. However, there is the benefit of being able to export any of those three steps as AAS without the need to create a model not considered in our structure, allowing for more flexible process routes as to export every step in between. The relation is created using the inherited parent node in the internal representation at the end of the parts manufacturing process tracked in the LIS. There, an associated AAS is derived from the node, already created with the corresponding submodel for the parent node, creating a submodel entry node as well as the node defining the relationship.

The now existing AAS instance is automatically created with two more submodels containing meta-information. The first one is the *IDTA 02002-1-0 Submodel for Contact Information*. This submodel describes IVW in the form of attributes as well as a contact person. Since the presented process chain is within IVW's manufacturing department, the contact information is per default the head of the manufacturing department. The submodel element collections within Contact Information also include additional data such as an email address and telephone and fax numbers as well as typically available times of day in relation to coordinated universal time.

Similarly, general information for *IDTA 02006-3-0 Digital Nameplate for Industrial Equipment* is set for the country of origin, company logo and production date as well as address information. Additionally, depending on the type of node, the product type is set as tape, preform or part as well. Furthermore, the link to the real part is stored here. The node's UUID reflecting the marking on the real part is set as serial number.

Each AAS created in this study also incorporates the *IDTA 02023 Carbon Footprint* submodel, enabling a structured and standardized assessment of greenhouse gas emissions throughout the production process. The carbon footprint represented by the submodel encapsulates the relevant data for PCF calculation. Within the *ProductCarbonFootprint* collection, the scope and the methodology for the assessment are defined. The Submodel Element List (SML) *LifeCyclePhases* specifies the considered life cycle stages according to the ECLASS 15 value list *LifeCyclePhase*. In this study, phase *A3 - production* is selected, corresponding to a gate-to-gate approach since the internal focus is placed on the production phase of each process. The SML *PcfCalculationMethods* contain the standards applied to the calculation. In this study, the internal calculation node is aligned with the ISO 14040 and ISO 14044 standards with *Climate Change* as evaluated impact category. Quantitative results are stored as property *PcfCO2eq*, which holds the sum of greenhouse gas emissions as decimal in kilograms of CO_2-equivalent (kg CO_2-eq.). In this study, the reference unit of the product i.e. tapes, preforms, and thermoformed parts, is kilogram (kg). This layered and semantically enriched submodel structure supports transparent, traceable, and interoperable reporting of product carbon footprints.

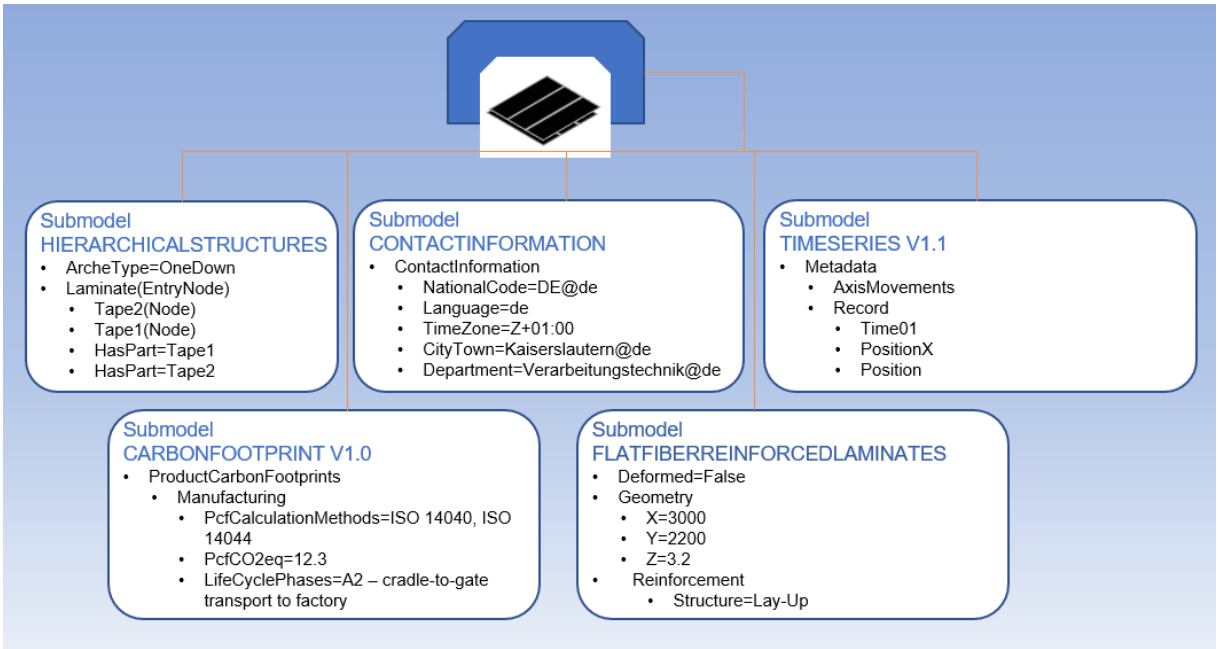

Figure 3: Representation of submodels within the external AAS-based solution as an example for the preform as used in the process chain presented here

In the calculation of the PCF, a large amount of time series data is already used and does not need to be included in the AAS. Most other data acquired for process control purposes is also time series data. Whilst it is mostly used for internal purposes, the *IDTA 02008-1-1 Time Series Data* submodel is included as well to potentially share it externally. The submodel offers many different ways to add data to it and even manipulate the data within, if used as an active model. Since the purpose and way of using the process data is not fully defined for the example yet, the data is strictly passively attached as internal data segments. This means, the selected data is saved directly within the AAS. For the proposed processes, these are width and height of the tape instance, position of the ATL axis as well as forces applied in the thermoforming process.

As the data is already included within the internal nodes representing the corresponding process steps, the data just hast to be exported to the AAS. This is also the step, where the control over process data export can be exercised. Because the data is already available as a link to influx database storage, every available data channel can be exported in the same way. Time series data corresponding to different measurement channels can be stored into individual segments of the time series submodel. The required timing information is taken directly from the Influx database in the form of Universal Coordinated Time (UTC) time stamps. Semantic data in the form of identifiers is taken from MQTT topics, including their respective data sources.

5.2 AAS Modelling of Composites and Composite Manufacturing

There are no implementations of composite-specific submodels or their processes yet. This means anybody is free to define data structures as preferred. This work uses Classical Laminate Theory (CLT) with the stacking rules for individual layers and mechanical characterization based on single layer-attributes as common ground. For this, a custom submodel *FlatFiberReinforcedLaminates*, as depicted in Figure 4 starts with the top level domain of macro-scale objects. Here, laminates and semi-finished laminates (preforms) are generally characterized as flat or deformed to conform to the needs of the thermoformed part. On the same level, the geometry of the full laminate is listed to describe strictly rectangular outlines in Cartesian notation. Here, actively calculated data for the laminates mechanical data based on the CLT calculations could be added in the future, generated from the single laminate layers. These are added as a submodel collection on this level of the model instead, integrating multiple layers as used in the stacking rules for laminate. Here, single layers are collected in a bottom to top order, named by their number of appearance within the laminate. Every single laminate is described by

their textile reinforcement structure, with lay-up as the only type used in this example. Additionally, the orientation angle of the layer is saved according to the rules of the laminate code as defined by NETTLES [22] and the height. Furthermore, the individual layers' mechanical attributes are added as an additional submodel. Here, the individual attributes as needed in the CLT are provided as properties. Further data such as areal weights and densities could be added, where available. Considering the use of thermoplastic matrices, an additional thermal submodel was set up to contain relevant thermal properties such as melting point and glass transition temperature. The original data sheet, where available is added to the layer model as well.

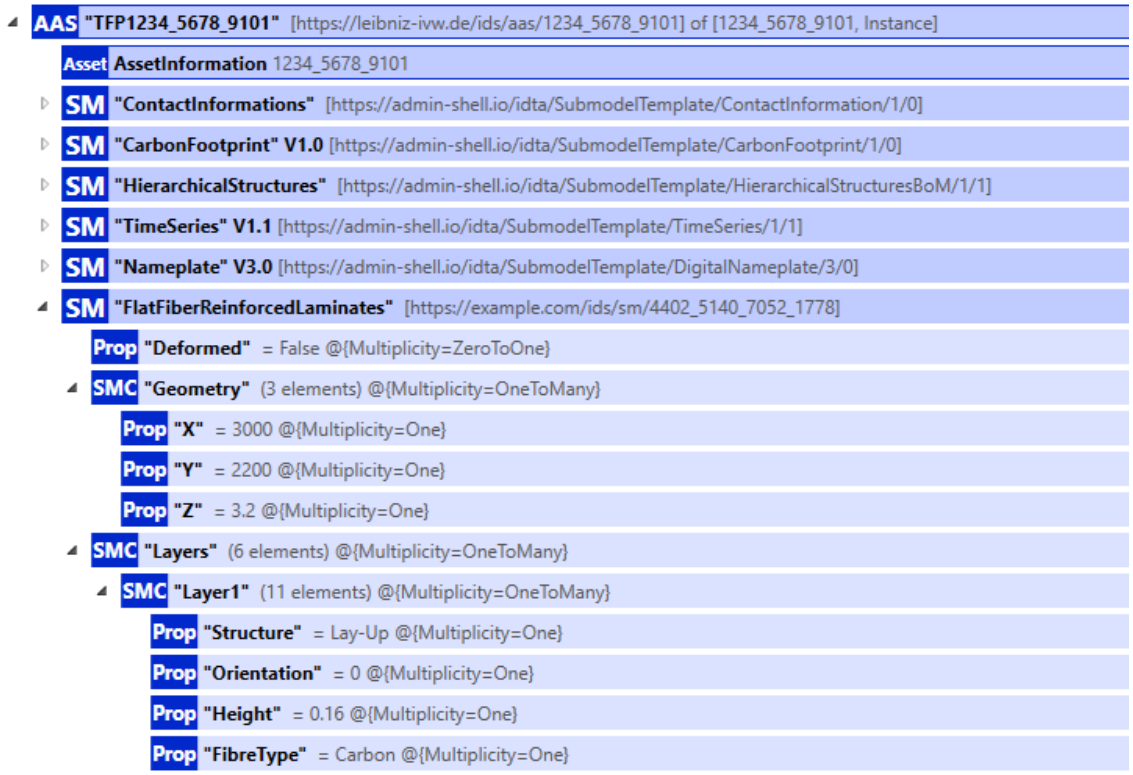

Figure 4: Depiction of an instance of a laminate shell within the AASX-Package Explorer

The presented model thus allows for the description of all states occurring within the demonstrated processing chain. Furthermore, the shared attributes between all states allows to copy or reference the submodel for process steps earlier in the process chain. In a possible next step, the matrices and fibers could be described as additional entities, resulting in a more detailed model.

6 SUMMARY AND CONCLUSION

In the presented work, digital twins for a process chain based around thermoplastic stamp forming of tape layed preforms were created. The process is a promising combination of fast production and high performance products with less emissions during the production chain compared to thermosets. For aerospace applications the process chain needs improved process control and life cycle analysis, which can be easily achieved using Digital Twin. An internal twin to collect, aggregate and store the data has been created based on a custom solution. From it, an external twin has been derived which contains the same information but in a standardized exchangeable form, using the AAS. For this external representation, different aspects of structuring data have been presented and discussed. The most basic element of the taxonomy is the representation of the tape spool, which contains only generic data, such as the manufacturer or fiber type. On the next level, tapes are aggregated into laminate layers, which in turn are aggregated into laminates, following the rules of CLT. Finally, after the thermoforming process steps, these laminates are transformed into deformed parts by adding the deformed tag.

The presented model is but an example to create such a combination of digital twins along a process chain. Through the direct integration of PCF relevant measuring devices, the groundwork for LCA has been laid. Additional feedback opportunities for linking part quality and process quality have been integrated as well. Still, the digitalized process chain lacks some components, especially to reach the goal of proper lifecycle assessment, as well as integrations into ERP, MES or SCM systems. It can however, already show the advantages of digital twins alongside a process chain in creating a clearer data structure and effectively reducing individual management effort for process data. The investigation of part quality influences across multiple process steps with data science methods can only be realized in a manner where process data is collected and managed in an automatic way, enabling this promising field of work.

Altogether, the presented work cannot represent a fully defined standard, but using standardized elements from the AAS is already a large step into the direction of a digital twin. Information as contained in the submodel for carbon footprint will likely find their way in to the product passport and will thus be enforced for businesses. As it will be a requirement to provide similar structures in the near future, we recommended to start working with the subject as soon as a standard fit for long term use has been defined. In our opinion, the AAS could be just the one that prevails, and whilst the product carbon footprint may be obligatory, additional benefits from the use of process data can be generated.

By expanding our approach down to the fiber and matrix levels as well as the machines and finally to other processes for composite manufacturing such as filament winding or sheet molding compound, we can further enhance our understanding of relevant process parameters that can be shared in standardized models. This is especially important for using LCA as a predicting tool, e.g. for selecting suitable and sustainable production techniques in the future.

7 REFERENCES

[1] V. Rizos, J. Bryhn, Implementation of circular economy approaches in the electrical and electronic equipment (EEE) sector: Barriers, enablers and policy insights, Journal of Cleaner Production 338 (2022) 130617. https://doi.org/10.1016/j.jclepro.2022.130617.

[2] A.M. Ferrari, L. Volpi, D. Settembre-Blundo, F.E. García-Muiña, Dynamic life cycle assessment (LCA) integrating life cycle inventory (LCI) and Enterprise resource planning (ERP) in an industry 4.0 environment, Journal of Cleaner Production 286 (2021) 125314. https://doi.org/10.1016/j.jclepro.2020.125314.

[3] A. Benitez, C. Wulf, A. De Palmenaer, M. Lengersdorf, T. Röding, T. Grube, M. Robinius, D. Stolten, W. Kuckshinrichs, Ecological assessment of fuel cell electric vehicles with special focus on type IV carbon fiber hydrogen tank, Journal of Cleaner Production 278 (2021) 123277. https://doi.org/10.1016/j.jclepro.2020.123277.

[4] T.M. Prenzel, A. Hohmann, T. Prescher, K. Angerer, D. Wehner, R. Ilg, T. Von Reden, K. Drechsler, S. Albrecht, Bringing Light into the Dark—Overview of Environmental Impacts of Carbon Fiber Production and Potential Levers for Reduction, Polymers 16 (2023) 12. https://doi.org/10.3390/polym16010012.

[5] H. Chen, H.P.H. Liddell, A.A. Ogale, Z.C. Miao, M.W. Ijeoma, M. Carbajales-Dale, A critical review and meta-analysis of energy demand, carbon footprint, and other environmental impacts from carbon fiber manufacturing, Resources, Conservation and Recycling 219 (2025) 108302. https://doi.org/10.1016/j.resconrec.2025.108302.

[6] S. Gil, P.H. Mikkelsen, C. Gomes, P.G. Larsen, Survey on open-source digital twin frameworks–A case study approach, Softw Pract Exp 54 (2024) 929–960. https://doi.org/10.1002/spe.3305.

[7] Details of the Asset Administration Shell, (n.d.). https://industrialdigitaltwin.org/wp-content/uploads/2022/06/DetailsOfTheAssetAdministrationShell_Part1_V3.0RC02_Final1.pdf (accessed July 7, 2025).

[8] X. Ye, S.H. Hong, W.S. Song, Y.C. Kim, X. Zhang, An Industry 4.0 Asset Administration Shell-Enabled Digital Solution for Robot-Based Manufacturing Systems, IEEE Access 9 (2021) 154448–154459. https://doi.org/10.1109/access.2021.3128580.

[9] C. Plociennik, M. Pourjafarian, A. Nazeri, W. Windholz, S. Knetsch, J. Rickert, A. Ciroth, A.D.C. Precci Lopes, T. Hagedorn, M. Vogelgesang, W. Benner, A. Gassmann, S. Bergweiler, M.

Ruskowski, L. Schebek, A. Weidenkaff, Towards a Digital Lifecycle Passport for the Circular Economy, Procedia CIRP 105 (2022) 122–127. https://doi.org/10.1016/j.procir.2022.02.021.

[10] M. Simon, S. Jungbluth, A. Farrukh, M. Volkmann, J. Hermann, M. Ruskowski, Implementation of Asset Administration Shells in a Shared Production Scenario with Gaia-X, in: 2023 IEEE 28th International Conference on Emerging Technologies and Factory Automation (ETFA), IEEE, Sinaia, Romania, 2023: pp. 1–8. https://doi.org/10.1109/etfa54631.2023.10275583.

[11] Asset Administration Shells and GAIA-X Enabled Shared Production Scenario, in: Lecture Notes in Mechanical Engineering, Springer Nature Switzerland, Cham, 2024: pp. 187–199. https://doi.org/10.1007/978-3-031-38165-2_23.

[12] S. Jungbluth, J. Hermann, W. Motsch, M. Pourjafarian, A. Sidorenko, M. Volkmann, K. Zoltner, C. Plociennik, M. Ruskowski, Dynamic Replanning using Multi-Agent Systems and Asset Administration Shells, in: 2022 IEEE 27th International Conference on Emerging Technologies and Factory Automation (ETFA), IEEE, Stuttgart, Germany, 2022. https://doi.org/10.1109/etfa52439.2022.9921716.

[13] R. Krueger, A. Bergan, Advances in Thermoplastic Composites Over Three Decades – A Literature Review, (2024).

[14] R.A. Brooks, H. Wang, Z. Ding, J. Xu, Q. Song, H. Liu, J.P. Dear, N. Li, A review on stamp forming of continuous fibre-reinforced thermoplastics, International Journal of Lightweight Materials and Manufacture 5 (2022) 411–430. https://doi.org/10.1016/j.ijlmm.2022.05.001.

[15] T.K. Slange, Rapid Manufacturing of Tailored Thermoplastic Composites by Automated Lay-up and Stamp Forming, PhD, University of Twente, 2019. https://doi.org/10.3990/1.9789036547284.

[16] A. Brasington, C. Sacco, J. Halbritter, R. Wehbe, R. Harik, Automated fiber placement: A review of history, current technologies, and future paths forward, Composites Part C: Open Access 6 (2021) 100182. https://doi.org/10.1016/j.jcomc.2021.100182.

[17] D.H.-J.A. Lukaszewicz, C. Ward, K.D. Potter, The engineering aspects of automated prepreg layup: History, present and future, Composites Part B: Engineering 43 (2012) 997–1009. https://doi.org/10.1016/j.compositesb.2011.12.003.

[18] K. Yassin, M. Hojjati, Processing of thermoplastic matrix composites through automated fiber placement and tape laying methods: A review, Journal of Thermoplastic Composite Materials 31 (2018) 1676–1725. https://doi.org/10.1177/0892705717738305.

[19] N. Yadav, R. Schledjewski, Review of in-process defect monitoring for automated tape laying, Composites Part A: Applied Science and Manufacturing 173 (2023) 107654. https://doi.org/10.1016/j.compositesa.2023.107654.

[20] V.K. Maes, K. Potter, J. Kratz, Features and defects characterisation for virtual verification and certification of composites: A review, Composites Part B: Engineering 246 (2022) 110282. https://doi.org/10.1016/j.compositesb.2022.110282.

[21] J. Mack, R. Holschuh, P. Mitschang, Qualitätsanalyse bei Bändchenhalbzeugen: Einflussgröße, Lightweight Des 7 (2014) 48–53. https://doi.org/10.1365/s35725-014-0418-6.

[22] Nettles, Allan T., Basic Mechanics of Laminated Composite Plates, Marshall Space Flight Center, Alabama, 1994.

ON LINE OPTIMISATION AND ACTIVE CONTROL OF THE CURE PROCESS OF THICK COMPOSITE LAMINATES

Konstantinos I. Tifkitsis[1,*], Michael Dreyer[2], George Maistros[3], Andreas Langenegger[2], Festus I. Anagwu[4], Andreas Winistoerfer[2], Alex A. Skordos[4]

[1]Kalero, Agias Aikaterinis & Agamemnonos 3100, Limassol, Cyprus
Email: k.tifkitsis@kaleroltd.eu, web page: https://kaleroltd.eu/

[2]Carbo-Link, Undermülistrasse 25, 8320 Fehraltorf, Switzerland
Email: langenegger@carbo-link.ch, web page: https://www.carbo-link.com/

[3]ADVISE-DETA, 34 Castle Road, Bedford, MK40 3PJ, United Kingdom
Email: gmaistros@advise-deta.com, web page: https://advise-deta.com/

[4]Centre for Materials, Cranfield University, Bedfordshire, MK43 0AL, United Kingdom
Email: a.a.skordos@cranfield.ac.uk, web page: https://www.cranfield.ac.uk/

Keywords: Composite plates, Modal analysis, Identification, Properties, Finite elements

ABSTRACT

This paper presents an active control scheme for the cure of advanced composites based on the combination of simulation with cure monitoring signals. The cure of composites is a time-intensive and energy-consuming process, often carried out under conservative conditions to satisfy process performance metrics and deal with variability. Utilisation of process simulation alongside online signals presents an opportunity to increase process efficiency, while also ensuring process robustness. An accurate cure simulation model is developed here based on detailed constitutive models, taking into consideration cure kinetics as well as the evolution of thermal properties during the cure. The development of a dielectric sensor compatible with carbon fibre reinforcement and a protocol for its calibration achieves direct and accurate measurement of the degree of cure in the curing component. This, accompanied by thermal monitoring signals, informs the simulation to predict the level of temperature overshoot online, taking into account the process history and the current state of the part. Incorporation of this information in an active control loop permits updating the thermal profile to minimise process duration, while ensuring temperature overshoot is kept below a limit. Implementation of the strategy in the curing of thick carbon fibre cable achieves a process time reduction of about 65%, demonstrating the clear cost and energy consumption benefits of the approach developed.

1 INTRODUCTION

The cure of thermosetting matrix fibre composites is a crucial stage of the manufacturing chain that plays a major role in component quality and overall manufacturing cost. In designing the cure process, manufacturers need to address often competing objectives of minimising process time, minimising tooling cost, ensuring temperature uniformity, and minimising exothermic effects, whilst satisfying constraints of adherence to process certification requirements and addressing variability challenges. Current industrial approaches address the overall problem by adopting conservative thermal profiles, usually comprising two or more isothermal segments, resulting in expensive and energy-consuming manufacturing, adversely affecting both part cost and overall sustainability.

The inefficiency of cure processing becomes more pronounced in thick parts. The exothermic character of the cure reaction, combined with the low thermal conductivity of curing composites in the thickness direction, makes temperature overshoots likely, forcing manufacturers to adopt even more conservative thermal profiles, often involving an initial long isothermal segment at low temperature to consume a significant part of the matrix reactivity under mild conditions. This increases the cost of processing significantly, often making the adoption of a composite solution for thick parts uneconomical.

Numerical optimisation methods have been put forward as a potential solution for addressing cure cost minimisation and maximisation of product quality. Optimisation approaches integrate, in their core, a method for mapping process variables (e.g., thermal profile variables, tooling properties, environmental variables) into process outcomes (maximum overshoot, process duration, cure uniformity, thermal gradients) through simulation [1] or data-based representations combined with models [2]. Optimisation schemes, such as gradient-based techniques [3], genetic algorithms [4], and neural networks [5, 6], are used to identify optimal process conditions and setups that can minimise process duration or cost, maximise quality/minimise defects, or achieve both in a multi-objective setting.

Numerical optimisation exploits regions of high sensitivity of the objectives to the design variables, often obtaining solutions that have a level of instability. In practical terms, this means processing carried out under optimal conditions can be potentially affected more by variability in the manufacturing environment and materials. The process of cure is subject to uncertainty due to variability in surface heat transfer coefficients, ambient conditions in the manufacturing environment, and the initial state of the curing matrix material [7, 8]. The utilisation of process monitoring provides a solution for resolving the uncertainty associated with composite manufacturing, with techniques based on optical, electric/dielectric, and ultrasonic sensing [9 -13] offering solutions for both the flow and cure stages of processing. In a recent development, temperature monitoring has been combined with modelling of the cure of carbon fibre composites to achieve online optimisation in an active control scheme, delivering significant simultaneous reduction in cure duration and temperature overshoot, with improvements matching those achieved using numerical optimisation, and without being affected by issues related to uncertainty [14].

The present work extends active control of cure with the utilisation of dielectric cure sensors. The method involves models for translating dielectric signals to an online estimation of degree of cure. This, alongside thermal signals and simulation of cure and its associated constitutive models, is used to predict an optimal temperature setting dynamically as the process evolves. The control scheme developed is applied to the cure of a thick carbon fibre cable to validate the development.

2 METHODS

2.1 Material characterisation

The material used is unidirectional (UD) carbon fibres prepreg with 12K tows and areal density of 385 g/m^2 with an epoxy resin mixed with hardener and accelerator (System A). The cured ply thickness of the prepreg is 0.358 mm.

Cure kinetics was characterised using differential scanning calorimetry (DSC) experiments in a DSC 250 Discovery (TA Instruments). Isothermal cure tests were carried at 120 and 110°C, following a 10°C/min ramp form ambient to the test temperature and then holding until completion of the reaction. Dynamic cure tests were performed at 2 and 10°C/min from ambient temperature to reaction completion. Isothermal heat flow signals were integrated using a horizontal baseline to calculate the degree of cure and its evolution. Integration of dynamic signals was carried out using a sigmoidal baseline. The fitting of the cure kinetics model to the experimental data to determine the values of cure kinetics parameters was performed using Solver of Microsoft Excel [15]. The evolution of the glass transition temperature as a function of the degree of was investigated using 10 samples partially cured from fully unreacted to complete reaction at 2 °C/min. The glass transition temperature of these samples was measured using the inflection point of the heat flow step at the transition in dynamic DSC tests at 10°C /min.

The evolution of specific heat capacity during the cure was measured using the DSC 250 Discovery (TA Instruments) in modulation mode. Two isothermal tests were carried out at 130 and 110°C and one dynamic at 1°C/min. In all experiments, a modulation amplitude of 1°C and modulation period of 60 s were used. Thermal conductivity in the thickness and fibre directions was measured using a Laser Flash Analyser (TA Instruments LFA Discovery 1200). Cured samples of the prepreg comprising 4 plies and 50 plies were utilised for the through thickness and fibre direction measurements. The specimen size was 10 mm × 10 mm in both cases. Prior to the measurement the specimens were sprayed with graphite to enhance optical absorption. A laser power of 1200 W was used, and measurements comprising 3 laser shots were performed in the temperature range of 20-160 °C at 40 °C intervals. The parameters of the

corresponding constitutive models for specific heat capacity and thermal conductivity through fitting to the experimental data using Solver of Microsoft Excel [15].

2.2 Manufacturing trials and process monitoring setup

A round cable with length of 2.8m consisting of wound UD prepreg plies, equivalent to 115 layers from centre to the surface consolidated by release film resulting in a diameter of 41 mm for the whole assembly was cured in an industrial oven. Two K-type thermocouples and two dielectric sensors were placed on the outer surface and in the centre of the cable. The setup of the experiment is illustrated in Figure 1.

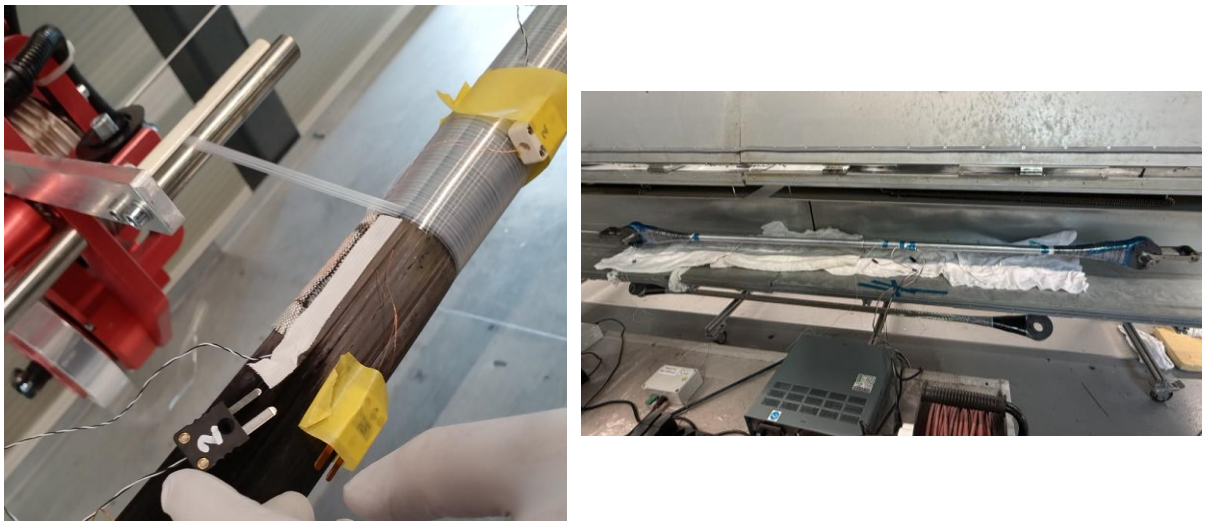

Figure 1: Trial setup: (left) wound cable with sensors and connectors; (right) curing setup.

The dielectric sensor used in the experiments is based on twisted insulated copper wires [13], which was weaved into a glass fibre cloth (Figure 2). Data acquisition for both dielectric sensors and thermocouples was carried out using a DETA-SCOPE from ADVISE-DETA [16]. Dielectric measurements were acquired in the frequency range of 1 Hz to 20 kHz. The capacitance (C) at 10 Hz was utilised to determine the degree of cure. Calibration experiments were carried out off-line using a thermal profile comprising isothermal segments at 110 and 150°C and 1°C/min ramps. Temperature signals were acquired and the cure kinetics model for the material of the study was used to calculate degree of cure (α) values to determine the coefficients b, c, and d of the calibration function:

$$\alpha = b + c\ logC + \frac{d}{T} \tag{1}$$

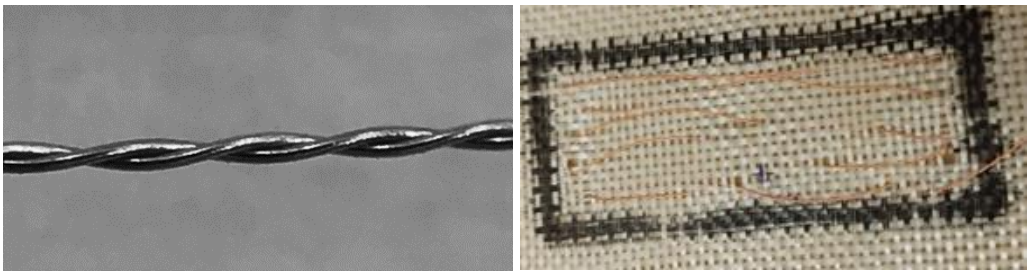

Figure 2: Sensor setup: (left) detail of sensing wire; (right) integration in woven cloth.

2.3 Cure simulation

Cure simulation was carried out using the Finite Element (FE) solver FLEXPD 7 [17]. The solver allows the definition of non-linear constitute models coupled with differential equations. The problem

solved corresponds to the representation of the cure of a circular cross-section cable in cylindrical coordinates expressed as:

$$\frac{1}{r}\frac{\partial}{\partial r}\left(K\frac{\partial T}{\partial r}\right) = \rho c_p \frac{\partial T}{\partial t} - (1-v_f)\rho_r H_{tot}\frac{d\alpha}{dt}, \qquad r \in [0, R_{cable}] \tag{2}$$

where ρ is the density of the composite, c_p is its specific heat capacity, T the temperature, α the degree of cure, K the thermal conductivity in the radial direction, v_f the fibre volume fraction, ρ_r the resin density, H_{tot} the total heat of the curing reaction, and R_{cable} the radius of the cable. The reaction rate is expressed as:

$$\frac{d\alpha}{dt} = \frac{A_1 e^{-E_1/RT}(1-\alpha)^{n_1} + A_2 e^{-E_2/RT}\alpha^m(1-\alpha)^{n_2}}{1 + e^{C_0[a-a_c-a_T T]}} \tag{3}$$

Here where m, n_1 and n_2 are reaction orders, $A_1$and A_2 are pre-exponential factors, E_1 and E_2 are activation energies and R is the universal gas constant. The denominator of Eq. 2 incorporates diffusion limitations in the cure kinetics model through a critical value of the degree of cure expressed as a function of temperature, where a_T, a_c are phenomenological parameters controlling the value of critical degree of cure as a function of temperature, and C_0 is a parameter controlling the breadth of the transition to diffusion-control. The specific heat capacity is a function of the degree of cure and temperature, implemented through the dependence of the instantaneous glass transition temperature on the degree of cure, expressed by:

$$c_p = A + \alpha G + \frac{B}{1 + e^{C_1(T_g - T + F)}} + T\left(D + \frac{H}{1 + e^{C_1(T_g - T + F)}}\right) \tag{4}$$

$$T_g = T_{go} + \frac{\lambda\alpha(T_{g\infty} - T_{go})}{1 - (1-\lambda)\alpha} \tag{5}$$

where A, B, D, F, G and H are fitting coefficients, C_1 is a parameter controlling the breadth of the glass transition, T_{go} and $T_{g\infty}$ are the glass transition temperatures of the uncured and fully cured material respectively and λ is a parameter controlling the convexity of the dependence of glass transition temperature on degree of cure. The thermal conductivity of the composite material is considered to be a linear function of temperature, with the corresponding constitutive model accounting for different conductivities in the fibre and transverse or thickness direction. In the case of the one-dimensional model of the cable, only the transverse conductivity is utilised in the solution.

Assuming uniform heating across around the cable, the heat transfer problem becomes one-dimensional in the radial direction. Symmetry implies a perfect insulation boundary condition at the cable centre. The nominal thermal profile was applied as a prescribed temperature boundary condition on the outer surface. Initial conditions are imposed at every model run following the monitored values of temperature and degree of cure at the model start, with an assumed distribution across the radial direction.

2.4 Active control scheme

The active control strategy reported in [14] was extended to incorporate cure monitoring data. A representation of the active control scheme is shown in Figure 3. The active control tool aims to determine in real time instantaneous temperatures that do not produce a high temperature overshoot while minimising the duration of the cure of the process. This is achieved by executing the simulation at every increment using existing monitoring data to define updated initial conditions.

The control system suggests a cure temperature higher than the current setpoint value, whilst considering the measured temperature and degree of cure on the cable surface and core as initial conditions in the cure simulation. The control system accepts the suggested temperature if - based on the results of the simulation - it does not produce an overshoot exceeding a predefined limit (set at 10°C here) before cure completion (Figure 4-left). If the new temperature is rejected, due to an unacceptably high overshoot (Figure 4-right), the suggested temperature is maintained at the current level and the

simulation is rerun to determine if the current temperature is acceptable. If the condition of overshoot below the limit is adhered to the temperature is maintained otherwise the temperature is lowered.

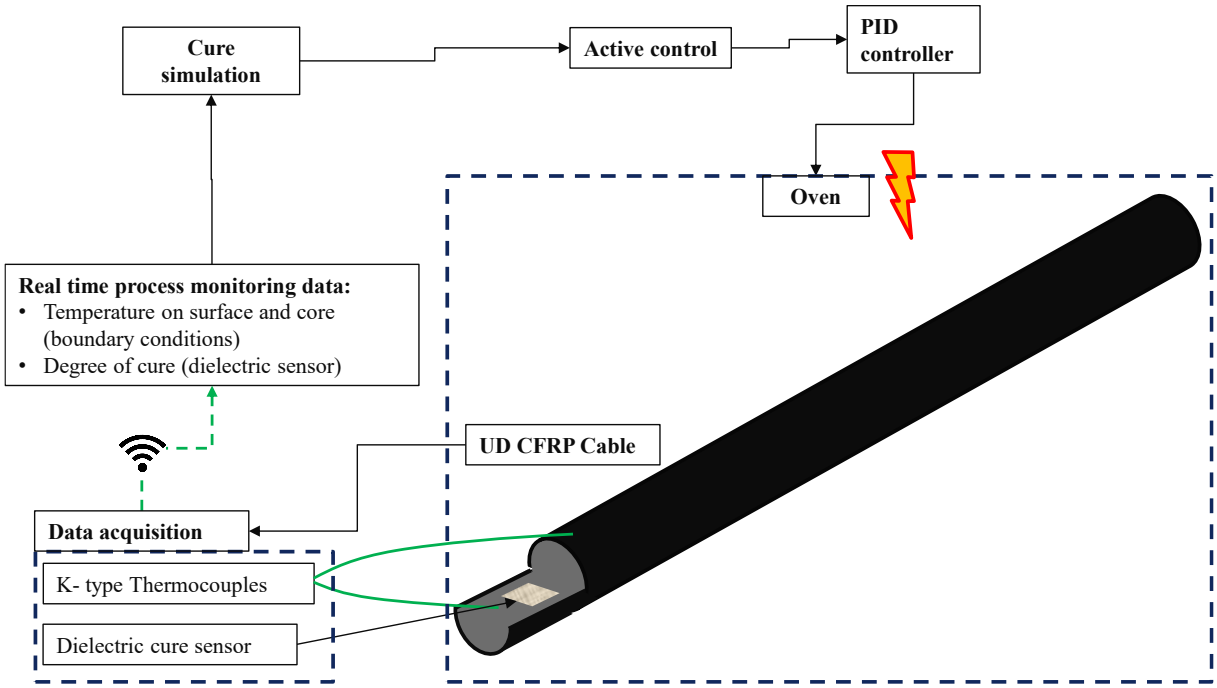

Figure 3: Integrated monitoring – modelling – control setup.

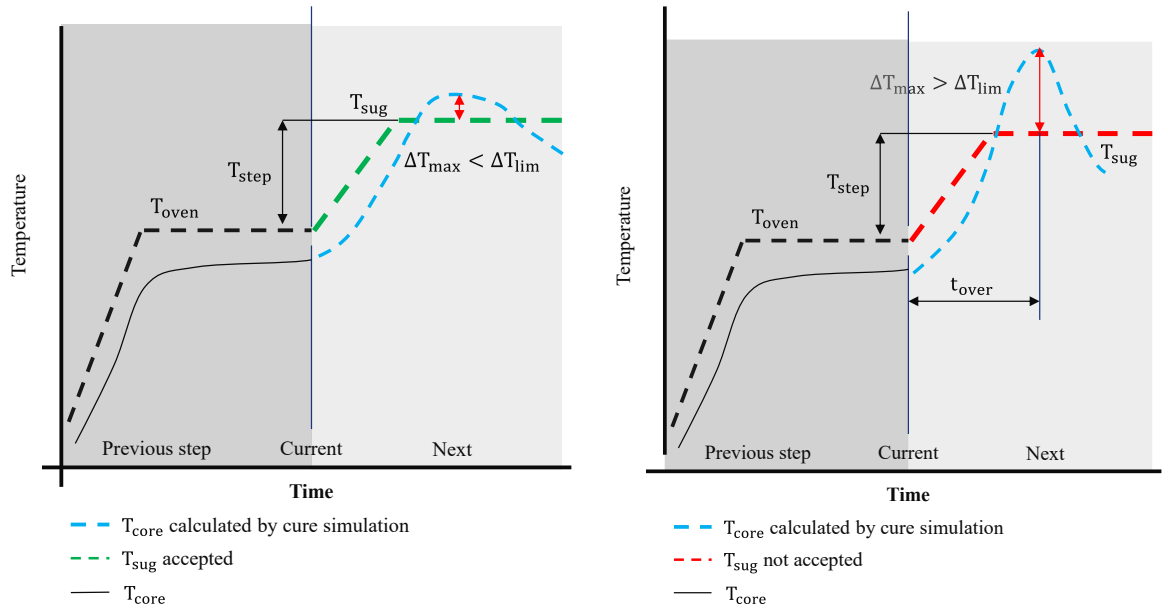

Figure 4: Examples of active control scenarios: (left) accepted increment in temperature as overshoot limit is not exceeded; (right) rejected increment due to overshoot greater than the limit occurring prior to cure completion.

3 RESULTS AND DISCUSSION

3.1 Constitutive models

Figure 5 illustrates the performed fitting of the cure kinetics model of Eq. 3. The model follows both dynamic and isothermal data closely with an average absolute error of 1.5E-5 for isothermal tests and 2.0E-4 for dynamic tests. The model reproduces successfully the autocatalytic character of the reaction at low degrees of cure and the dominance of nth reaction kinetics at high degrees of cure. The Di Benedetto equation fitting (Eq.5) matches experimental data closely with an average absolute error of 2.5°C. The fitting of Eq.4 to specific heat capacity data is presented in Figure 6-left. The model reproduces experimental data successfully including the transition region. The average error in specific heat capacity values is 0.006 J/g/°C. The linear fitting of thermal conductivity data is illustrated in Figure 6-right. As expected, the conductivity in the fibre direction is significantly greater than in the thickness/transverse direction. Overall, the constitutive models map well the evolution of properties and of reaction rate as a function of temperature and degree of cure, which provides the basis for an accurate heat transfer model of the cure.

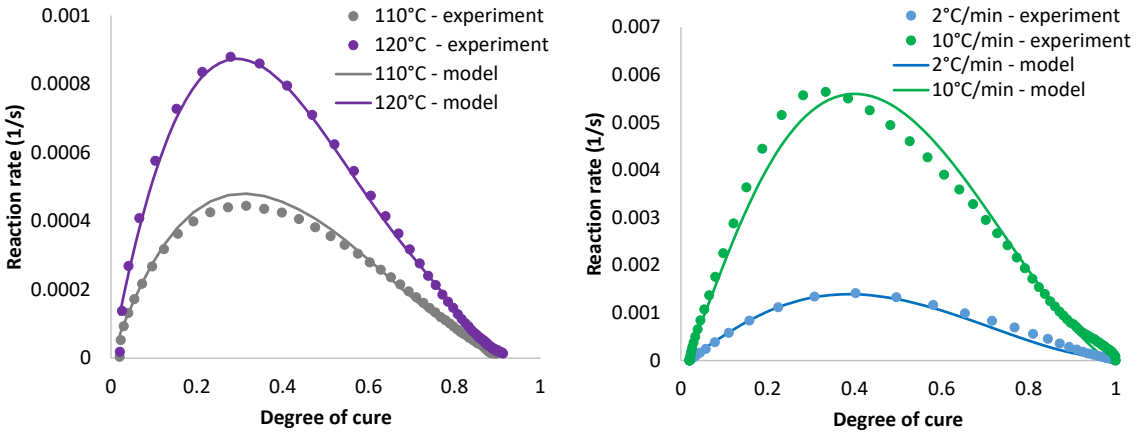

Figure 5: Cure kinetics model: (left) isothermal cure; (right) dynamic cure.

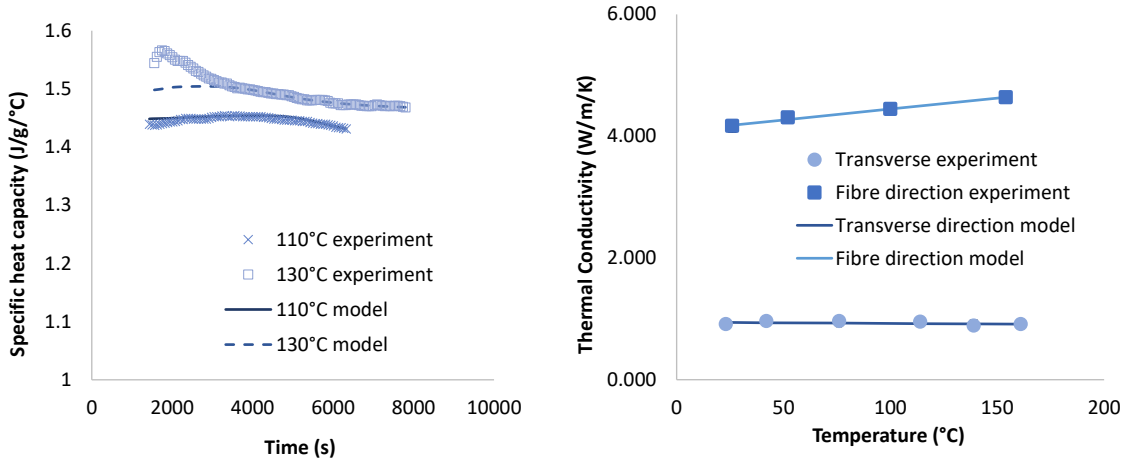

Figure 6: Constitutive models: (left) specific heat capacity; (right) thermal conductivity.

3.2 On line monitoring of the degree of cure

Figure 7 illustrates the accuracy of the use of Eq.1 for the determination of the degree of cure based on data of capacitance obtained by the dielectric sensing setup. The degree of cure based on the kinetics model reaches about 70% at the end of the first isothermal segment, progresses to about 90% at the end of the ramp, and reaches its maximum value of about 98% after 40 min at the high temperature isothermal segment. The fitting is accurate with some small deviations in the early stages of cure. The sensing data and calibration equation provide a very good direct estimate of the degree of cure even under non-isothermal conditions or when the conditions are nominally isothermal but there is significant deviation in temperature with time. The robustness of the degree of cure estimation is key for enabling its use in an active control loop.

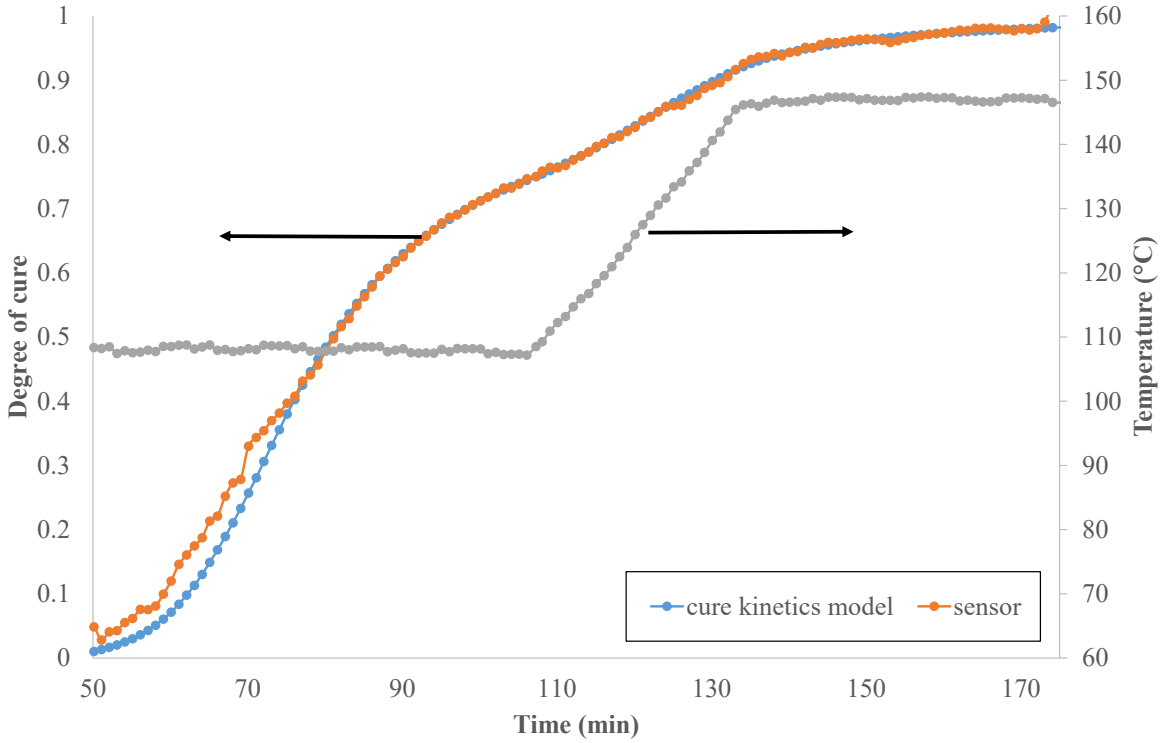

Figure 7: Validation of cure sensing functionality.

3.3 Active control trial

The results of the active control trial are illustrated in Figure 8. The degree of cure from the sensors is provided to the active control every 60 s. The initial temperature is 70°C, and the process is held at this temperature until the temperature sensors in the part approach 60°C. At this point, the active control algorithm starts increase the temperature gradually as predicted overshoots are well below the limit. This results in effective heating rate of about 1°C/min, translated to a lower but broadly uniform heating rate in the curing part. The prediction of overshoot becomes greater than the limit of 10°C when the part reaches about 90°C and the oven temperature is about 105°C. The oven temperature is stabilised at that level for about 60 min. After that time, the temperature in the part exceeds 100°C and the degree of cure reaches about 30%. At this point it is possible to increase the temperature without inducing an unacceptable overshoot, as a significant part of the reactivity of the resin has been consumed. The active control algorithm increases the temperature gradually at an average rate that approximates 1°C/min, up to about 150°C. The composite part follows at a similar rate as a result of the exothermicity of the reaction which progresses by about 50%. This is indicative of the capability of the active control system to use the heat of the curing reaction to benefit the efficiency of the process. A further 40 min at 150°C is required to complete the cure, after which colling down starts.

During the whole process, the temperature in the part is relatively uniform, with gradients kept below 10°C. The maximum overshoot observed is only 3.5°C occurring right after reaching the second isothermal segment of the profile. This shows the efficiency of the control, as the ramp stops just before an overshoot is manifested, ensuring the positive feedback of reaction exothermicity does not dominate the evolution of the thermal profile. The role of accurate sensing in this is paramount, as the strong non-linearity of exothermic effects would have easily created a risk if similar decisions for the oven temperature profile have been taken without accurate information of the state and temperature of the curing part. The degree of cure evolution is relatively uniform across the radius of the cable, with the different parts reaching the same level of cure within 10 min. The total cure time using the active control system is 2.6 h. This, compared to the 7 h duration of the nominal cure profile for the material used, represents an improvement of about 65%. This significant reduction is reflected in a corresponding improvement in both process costs and emissions. These are achieved whilst ensuring that part quality is equivalent to that obtained with the use of a conventional, slow cure profile.

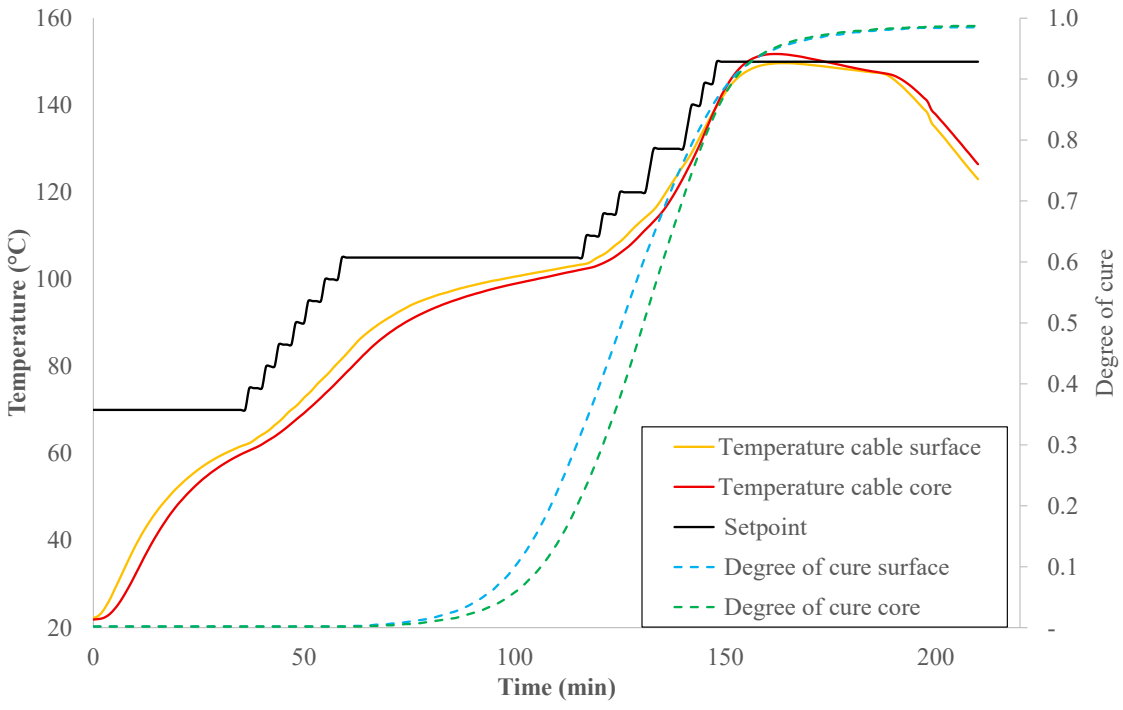

Figure 8: Demonstration of active control operation in curing of UD carbon fibre cable.

4 CONCLUSIONS

An active control strategy based on use of cure monitoring signals alongside simulation has been developed and implemented in this work. The demonstration of the system in the cure of a thick carbon fibre cable shows that the ability to inform the control algorithm with accurate thermal and cure signals allows the process to exploit the exothermicity of the curing reaction is a controlled manner. Achieving reduction in cure time by about 65%, whilst maintaining temperature uniformity and ensuring associated quality metrics are met, presents a major opportunity for decreasing costs and energy usage. This enhances the overall sustainability of composites.

ACKNOWLEDGEMENTS

Financial support by the Eureka project titled 'Hybrid sensing system for the on-line optimal process and health monitoring in composite structures' (HYPERCOMP – 644) is gratefully acknowledged.

REFERENCES

[1] K.I. Tifkitsis, T.S. Mesogitis, G. Struzziero, A.A. Skordos, Stochastic multi-objective optimisation of the cure process of thick laminates, *Composites Part A: Applied Science and Manufacturing*, **112**, 2018 pp. 383-394 (doi: 10.1016/j.jmapro.2023.01.027).

[2] R. Matsuzaki, R. Yokoyama, T. Kobara, T. Tachikawa, Multi-objective curing optimization of carbon fiber composite materials using data assimilation and localized heating, *Composites Part A: Applied Science and Manufacturing*, **119**, 2019, pp. 61-72, (doi: 10.1016/j.compositesa.2019.01.021)

[3] N. Rai, R. Pitchumani, Multi-objective optimisation of the cure of thick components, *Polymer Composites*, **18**, 1997, pp. 566-581, (doi: 10.1002/pc.10309)

[4] G. Struzziero, A.A. Skordos, Optimal cure cycles for the fabrication of thermosetting-matrix composites, *Composites Part A: Applied Science and Manufacturing*, **93**, 2017, pp. 126-136, (doi: 10.1016/j.compositesa.2016.11.014)

[5] R.L. Pagano, V.M.A. Calado, M. Bezerra de Souza, E.C. Biscaia, Proposal of an optimum cure cycle for filament winding process using a hybrid neural network - first principles model, *Polymer Composites*, **35**, 2014, pp. 1377-1387, (doi: 10.1002/pc.22790)

[6] D. Aleksendrić, C. Bellini, P. Carlone, V. Ćirović, F. Rubino, L. Sorrentino, Neural-fuzzy optimization of thick composites curing process, *Materials and Manufacturing Processes*, **34**, 2019, pp. 262-273, (doi: 10.1080/10426914.2018.1512116)

[7] T.S. Mesogitis, A.A. Skordos, A.C. Long, Stochastic simulation of the influence of cure kinetics uncertainty on composites cure, *Composites Science and Technology*, **110**, 2015, pp. 145-151, (doi: 10.1016/j.compscitech.2015.02.009)

[8] T.S. Mesogitis, A.A. Skordos, A.C. Long, Stochastic heat transfer simulation of the cure of advanced composites, *Journal of Composite Materials*, **50**, 2016, pp. 2971-2986, (doi: 10.1177/0021998315615)

[9] N. Gupta, R. Sundaram, Fiber optic sensors for monitoring flow in vacuum enhanced resin infusion technology (VERITy) process, *Composites Part A: Applied Science and Manufacturing*, **40**, 2009, pp. 1065-1070, (doi: 10.1016/j.compositesa.2009.04.022)

[10] P. Carlone, F. Rubino, V. Paradiso, F. Tucci, Multi-scale modeling and online monitoring of resin flow through dual-scale textiles in liquid composite molding processes, *The International Journal of Advanced Manufacturing Technology*, **96**, 2018, pp. 2215–2230, (doi: 10.1007/s00170-018-1703-9)

[11] E. Schmachtenberg, J. Schulte Zur Heide, J. Töpker, Application of ultrasonics for the process control of resin transfer moulding (RTM), *Polymer Testing*, **24**, 2005, pp. 330-338, (doi: 10.1016/j.polymertesting.2004.11.002)

[12] M. Danisman, G. Tuncol, A. Kaynar, E.M. Sozer, Monitoring of resin flow in the resin transfer molding (RTM) process using point-voltage sensors, *Composites Science and Technology*, **67**, 2007, pp. 367-379, (doi: 10.1016/j.compscitech.2006.09.011)

[13] K.I. Tifkitsis, A.A. Skordos, A novel dielectric sensor for process monitoring of carbon fibre composites manufacture, *Composites Part A: Applied Science and Manufacturing*, **123**, 2018, pp. 180-189, (doi: 10.1016/j.compositesa.2019.05.014)

[14] K.I. Tifkitsis, A. Winistoerfer, A.A. Skordos, Online optimisation and active control of the cure process of thick composite laminates, *Journal of Manufacturing Processes*, **87**, 2023, pp. 221-230, (doi: 10.1016/j.jmapro.2023.01.027)

[15] R. Barati, Application of Excel Solver for parameter estimation of the nonlinear Muskingum models, *KSCE Journal of Civil Engineering,* **17**, 2013, pp. 1139-1148, (doi: 10.1007/s12205-013-0037-2)

[16] DETA SCOPE – CPMS, Advise-Deta, advise-deta.com/en/pages/deta-scope-cpms

[17] FlexPDE 7®, FlexPDE Help, www.pdesolutions.com/help/index.html

ICCM24
AUGUST 4-8, 2025
BALTIMORE CONVENTION CENTER
BALTIMORE, MARYLAND, USA

No Technical Paper Submission for:

Andrew Che Swinburne

ICCM24
AUG 4-8, 2025 · BALTIMORE

Flow analysis of the capillary-driven underfill process for the use of thermally conductive epoxy composites in semiconductor packaging

Jeeeun Lee
Gyumin Sim & Seong Su Kim

Mechanical Design Lab. with Advanced Materials
Department of Mechanical Engineering, Korea Advanced Institute of Science and Technology (KAIST), Republic of Korea

Semiconductor packaging

❖ What is a semiconductor package?

The semiconductor package is a protective casing that connects the chip to the board/other chips and can help with heat dissipation

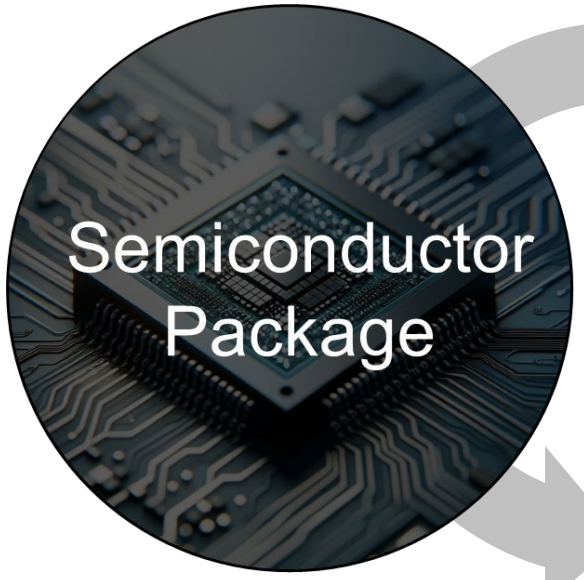

• Conventional Package



• Advanced Package

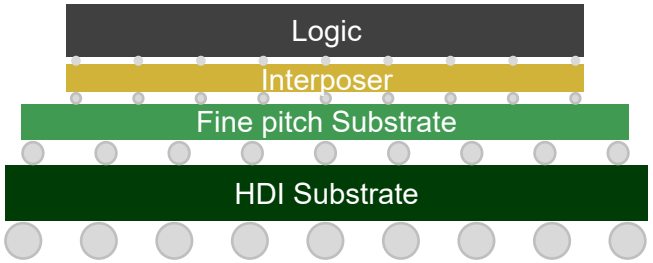

Thinner, stacked chips







Semiconductor packaging

❖ Underfill Material

➢ Composite material of epoxy and filler material that goes between the chip and substrate, improving the reliability of electrical devices.

Underfill

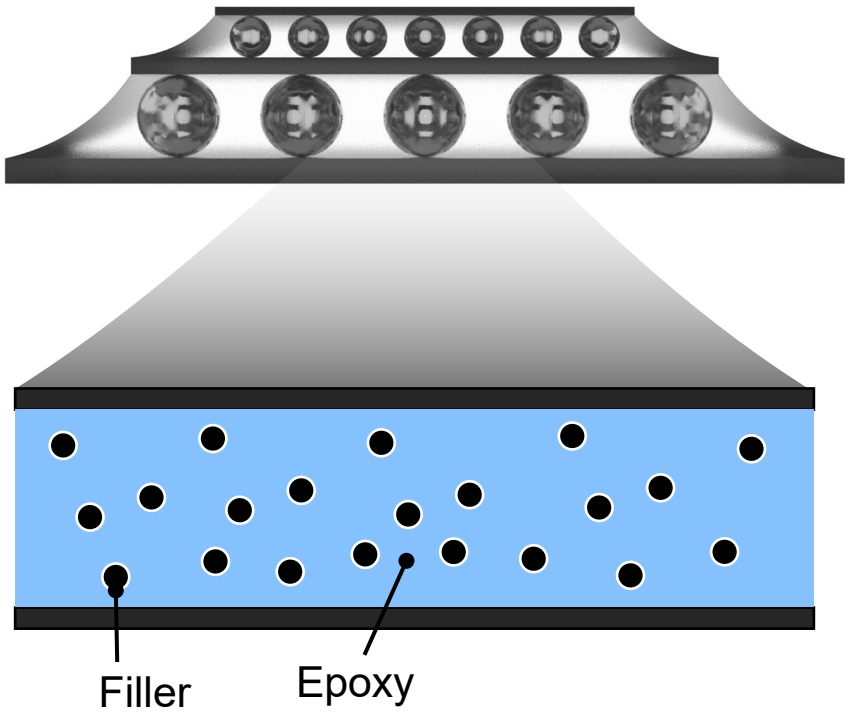

Key effect of Underfill [1]

• Mechanical Protection

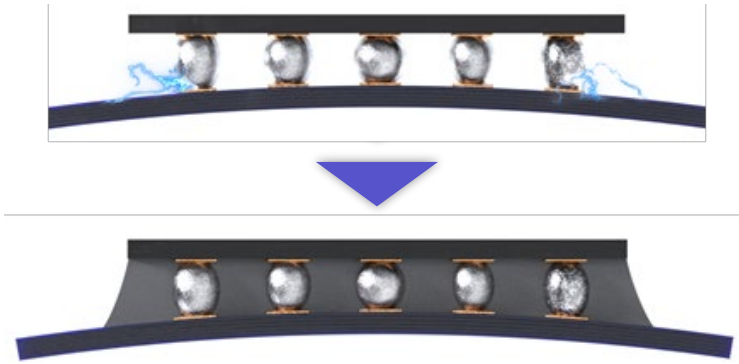

➢ Solder bump protection

➢ Stress concentration mitigation

• Heat Dissipation

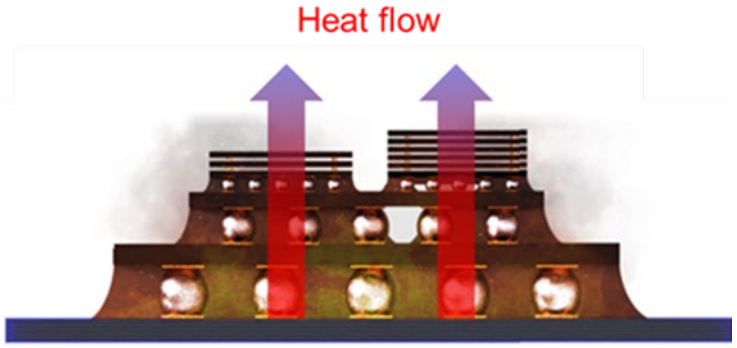

➢ Effective dissipation of heat generated by chip

Semiconductor packaging

❖ Types of Underfill Process[2,3]

No Flow Underfill

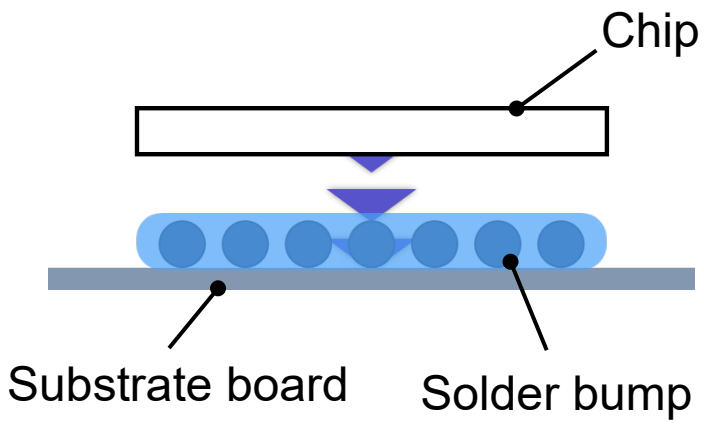

- Fast and simplified process
- High likelihood of void formation

Molded Underfill

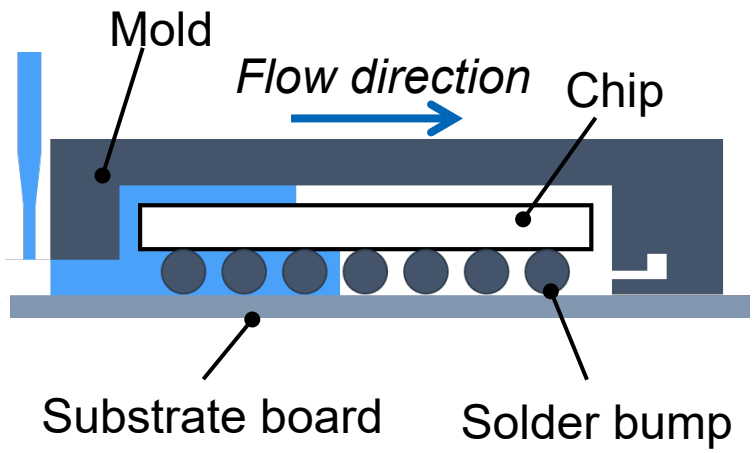

- Fast process time
- High cost
- High likelihood of void formation

Capillary Underfill

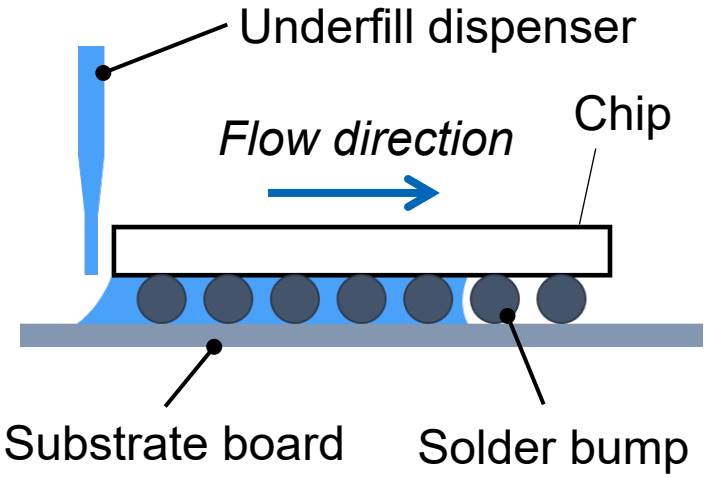

- Simplest process
- Cost-effectiveness
- Slow process time

Semiconductor packaging

Advanced technology in semiconductor packaging

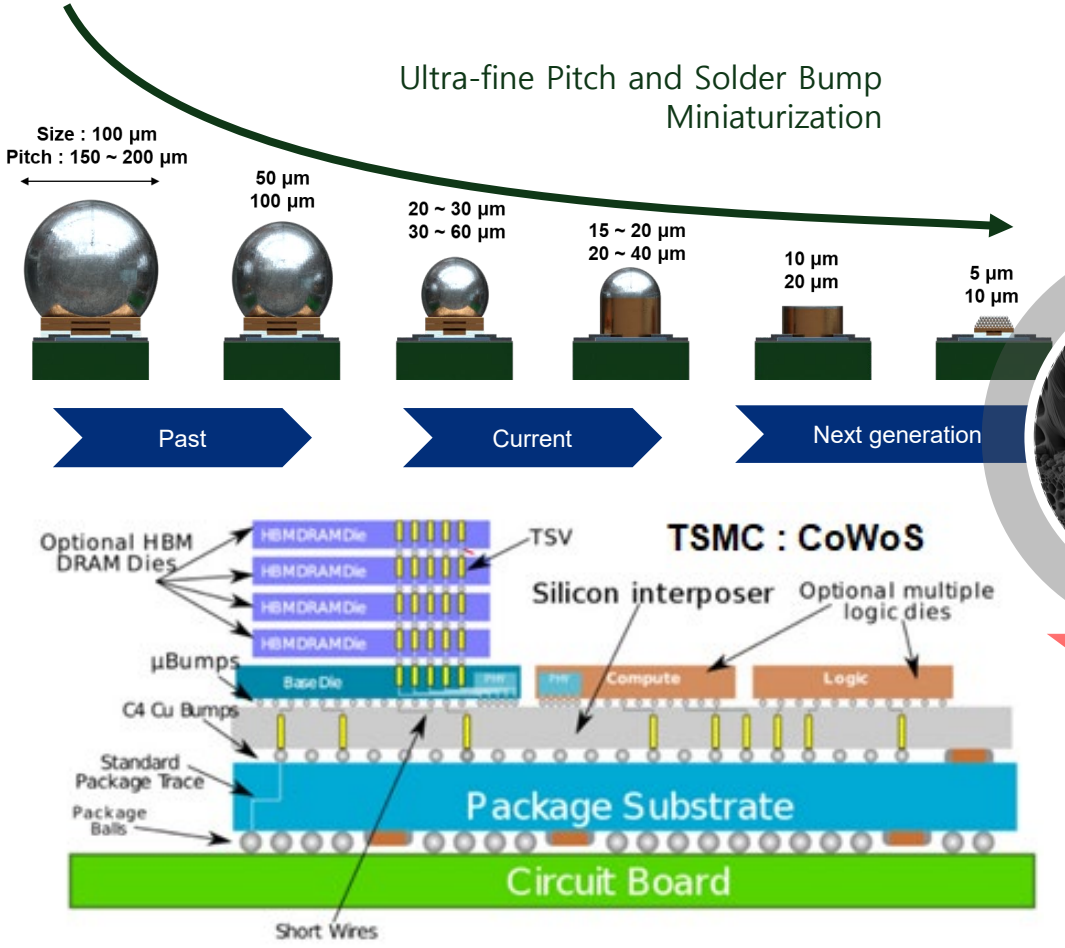

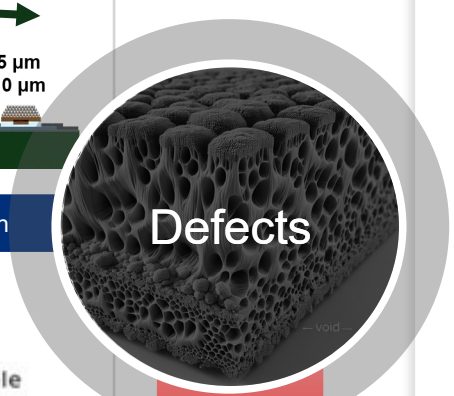

Requirements of the capillary underfill process

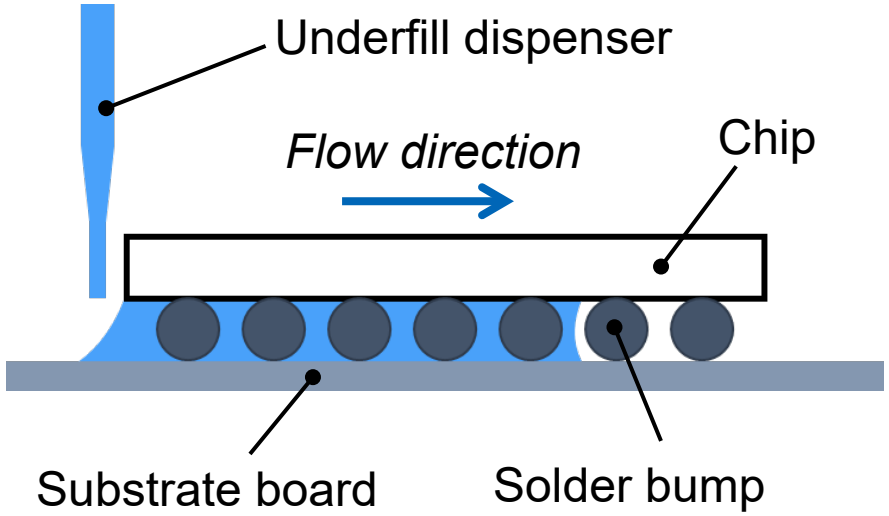



No void

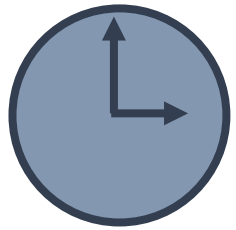

Reducing filling time

Void Formation

Micro-voids[4,5]

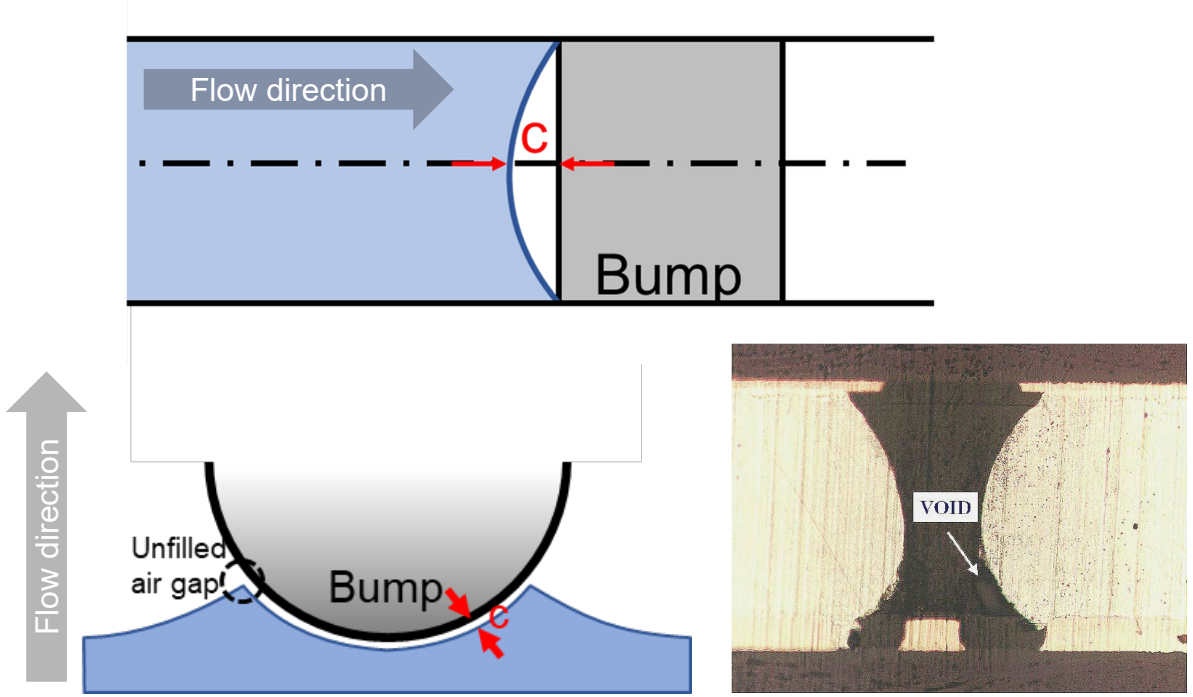

- Micro-voids formed by interaction between bumps and flow front

Macro-voids[6,7]

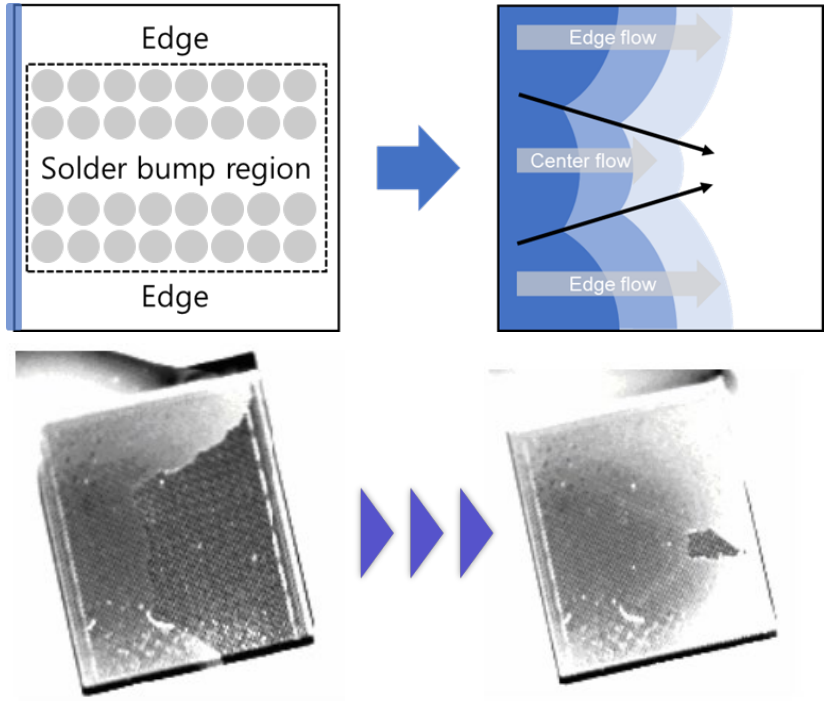

- Macro-voids formed by faster flow in the edge regions and subsequent flow front merging

Void formation

Race-tracking[7]

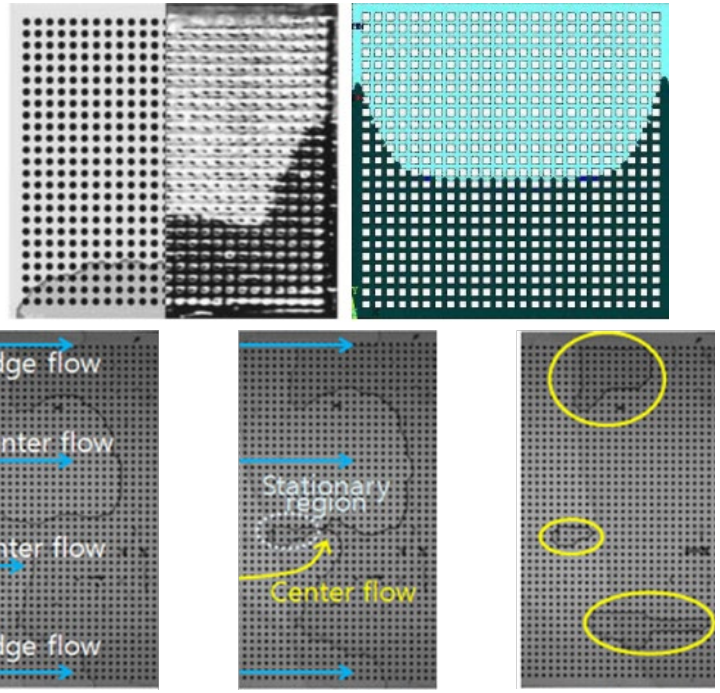

- Air entrapment due to flow difference between the edge and the center

Different dispensing types and contact angles[8]

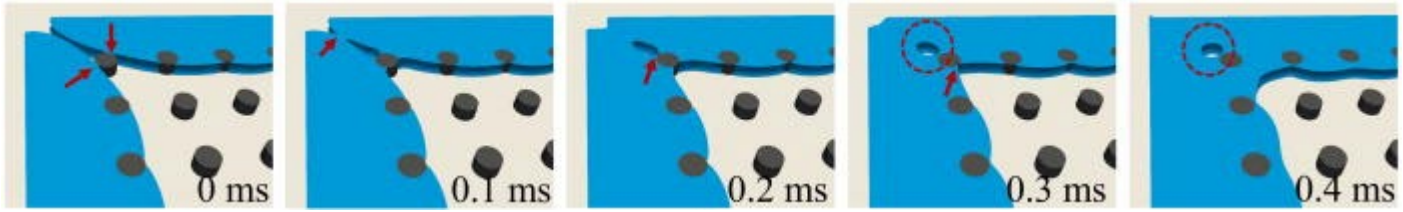

Void formation by flow front merging

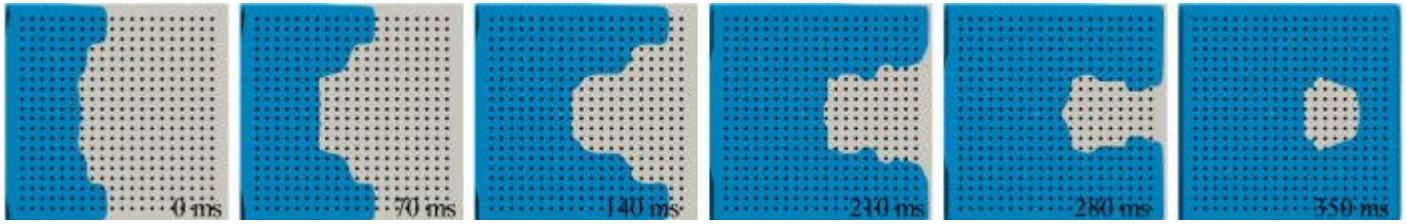

Void formation by variation in contact angles

- Void formation for different dispensing types
- Different wetting behavior (contact angles) due to flux residues

Analytic expressions of the filling time

Capillary driven flow between two plates[9]

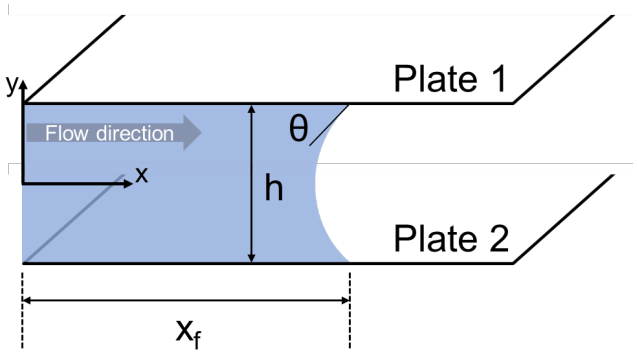

Assumptions

1. Incompressible
2. 2D fully-developed laminar
3. Gravity neglected

Plane Poiseuille flow

$$\frac{\partial p}{\partial x} = \mu \frac{\partial^2 u}{\partial y^2}$$

Young-Laplace equation for surface tension:

$$\Delta p_\sigma = \frac{2\sigma cos\theta}{h}$$

$$t_f = \frac{6\mu x_f^2}{\Delta p_\sigma h^2} = \frac{3\mu x_f^2}{h\sigma cos\theta}$$

t_f: filling time, x_f: flow distance

Capillary driven flow with solder bump[10]

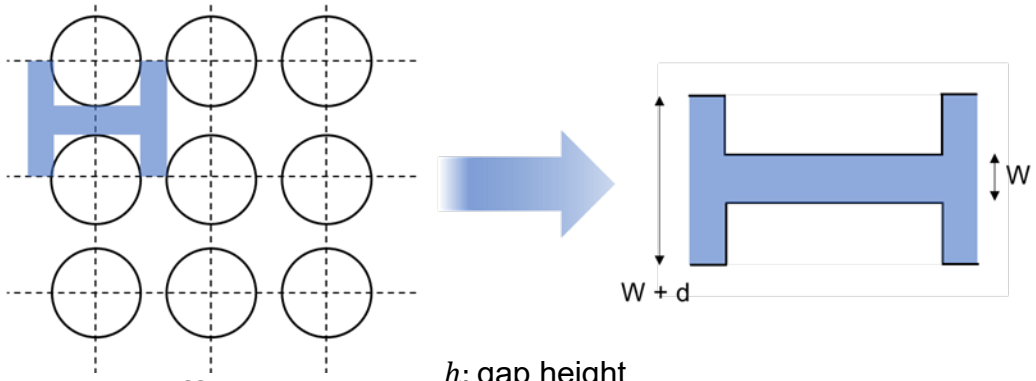

h: gap height

Pressure difference

$$\Delta p = \Delta p_\sigma - \Delta p_j$$

Δp_σ: pressure due to surface tension;

$$\Delta p_\sigma = \frac{2\sigma cos\theta}{h}$$

Δp_j : pressure loss due to solder bump;

$$\Delta p_j = 2\sigma cos\theta \left[\left(\frac{1}{h} + \frac{1}{W}\right) - \left(\frac{1}{h} + \frac{1}{W+d}\right)\right]$$

$$t_f = \frac{3\mu W(W+d)}{h\sigma cos\theta(W^2 + dW - dh)} x_f^2$$

Experiments for flow front visualization

Scale-up experiments [11,12]

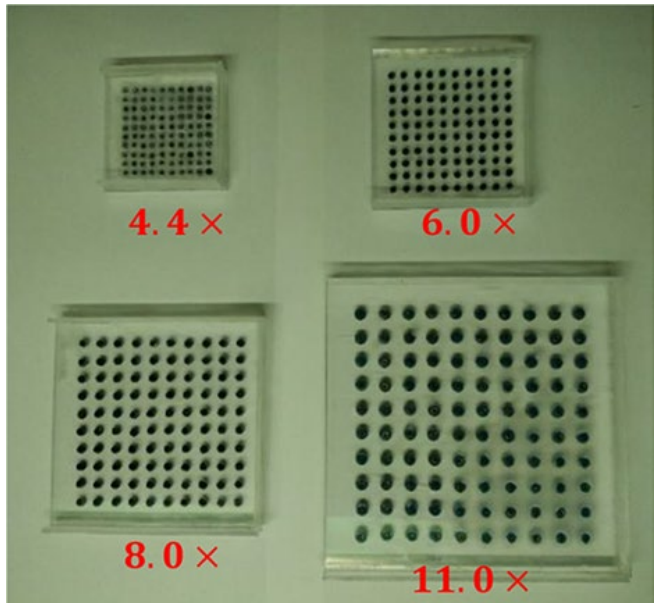

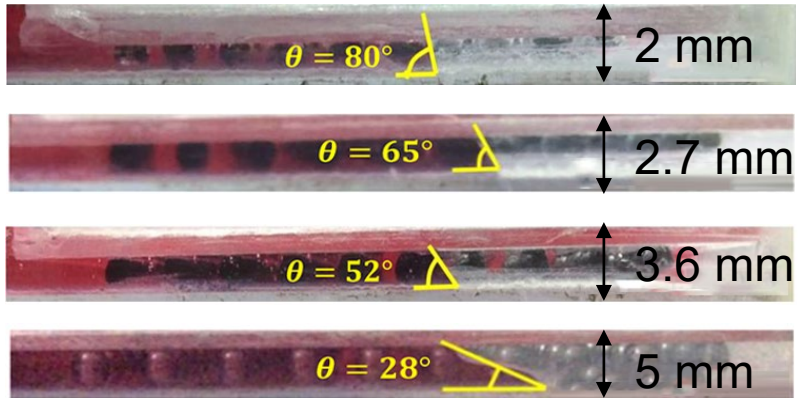

- ✓ Scale-up experiments to visualize flow front progression and calculate infiltration time
- ✓ The effects of gravity are ignored and flow similarity is not ensured

Effect of gravity[13,14]

$$h_1 < h_2 < h_3$$

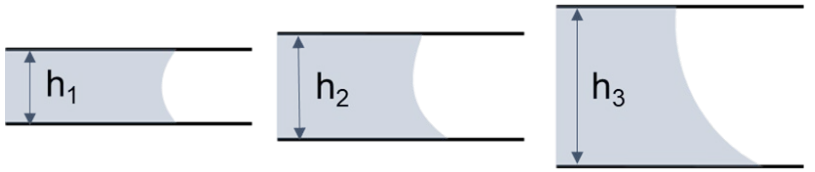

$$Bo = \frac{Gravity\ force}{Capillary\ force}$$

- ✓ The interface changes due to the effects of gravity
- ✓ The shape of the meniscus varies depending on the gap height
- ✓ **Bond number** is a key dimensionless number

Research motivation

❖ Overview

1. In the capillary underfill process, macro-voids develop due to the merging of **flow fronts advancing at different velocities**

2. Non-uniform flow between the edge and center are recognized as factors contributing to void formation, however, the **void formation mechanism has not been extensively studied**

3. Scaled-up experiments for visualizing flow and predicting infiltration time have been conducted, however, **gravity effects and flow similarity were not considered**

Research Objectives

- Investigate the void formation mechanism both numerically and experimentally
- Optimize the capillary underfill process to minimize the filling time and void formation

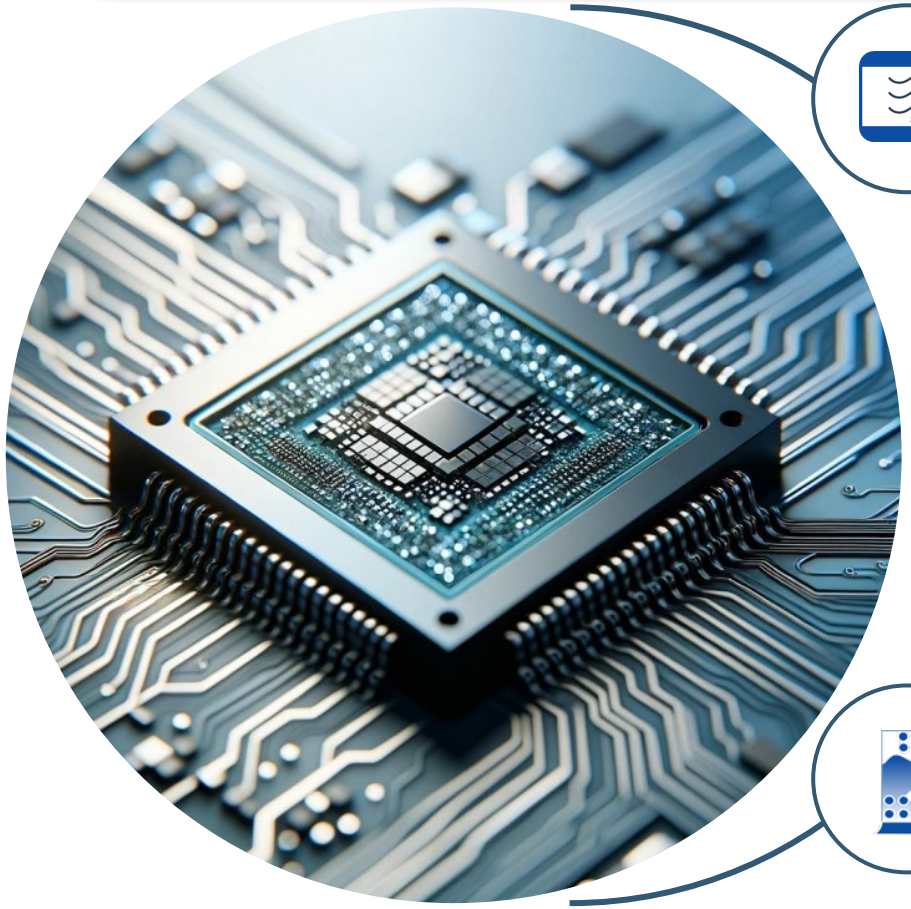

Flow simulation

- Experimental validation
- Parametric study

Experiment

- Experimental design
- Flow front measurement

Flow analysis

- Velocity difference of edge and bumps
- Void formation mechanism

MODELLING & EXPERIMENTAL SETUP

- **Numerical simulation model**
- **Experiment design**

Numerical analysis

❖ Flow simulation

▪ Boundary condition

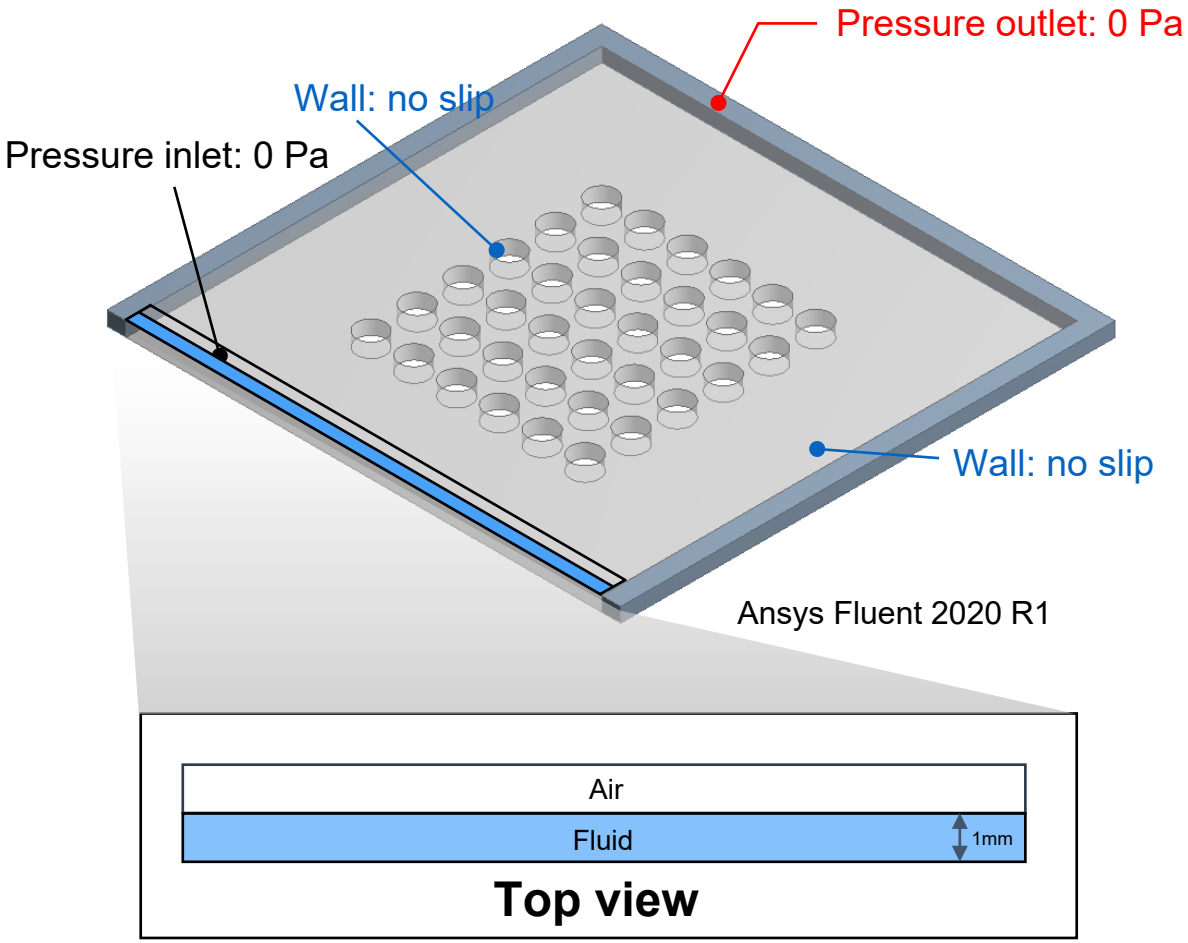

▪ Geometry

(unit: mm)

Chip size	Pitch size (W)	Bump diameter (d)	Gap height (h)
5	4.5	3	1

▪ Fluid properties (YD-114, KUKDO, Korea)

Viscosity	Density	Surface tension coefficient	Contact angle	Bump contact angle
0.6 Pa·s	1136.58 kg/m^3	0.0297 N/m	33.035°	45.939°

▪ Model

Transient flow

Multiphase flow: Volume of Fluid

Experiment design

❖ Similarity analysis

Scale up for visualization of flow

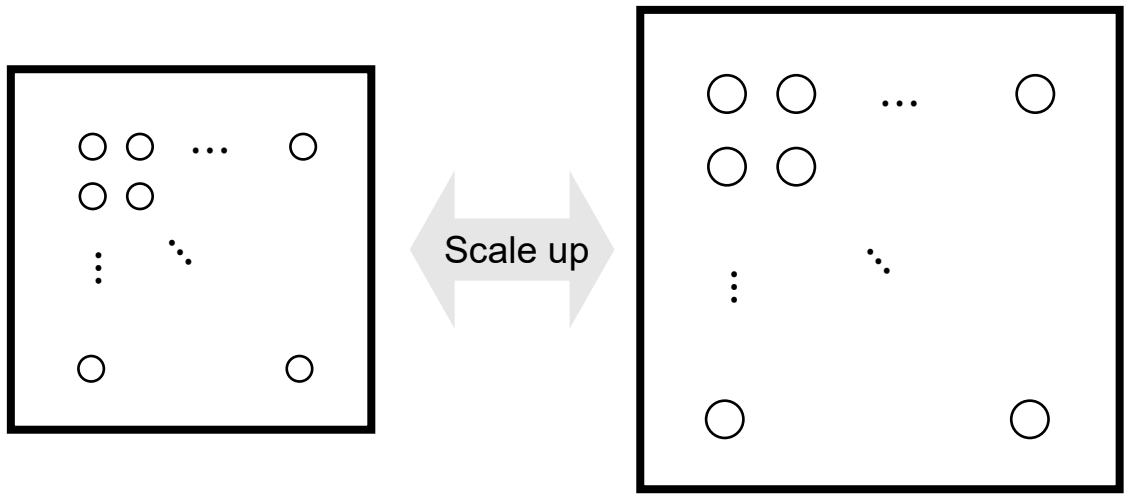

Actual chip

Scaled-up replica of chip

Chip size	Bump diameter	Bump height	Bump pitch
2.5 × 2.5	0.05	0.05	0.1

(unit: mm)

Dimensional analysis

Maintain similarity between the actual chip and scaled-up chip replica

Capillary number

$$Ca = \frac{v\mu}{\sigma}$$

Bond number

$$Bo = \frac{\rho g h^2}{\sigma}$$

μ: viscosity, ρ: density, h: gap height,
g: gravitational acceleration, σ: surface tension

Chip size	Bump diameter	Bump height	Bump pitch
5 × 5	3	1	4.5

(unit: mm)

Experiment design

❖ Effect of gravity vs capillary

Bond number[13,14]

$$Bo = \frac{Gravity\ force}{Capillary\ force} = \frac{\Delta\rho g h^2}{\sigma}$$

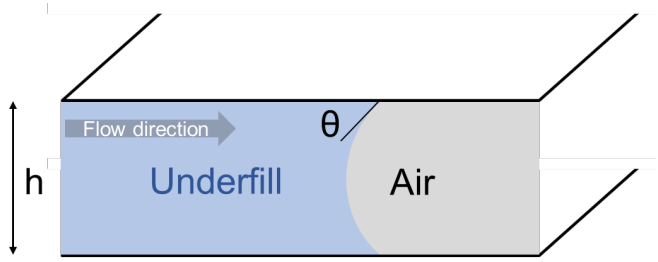

$Bo \ll 1$

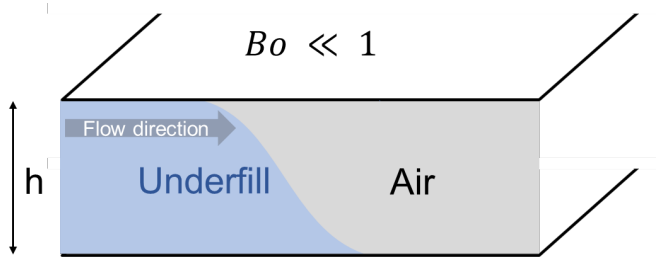

$Bo \gg 1$

Analytical model

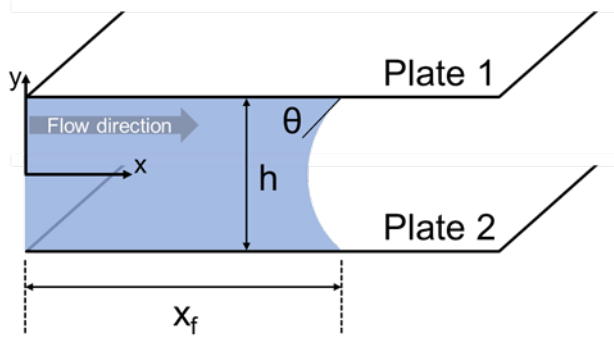

Assumptions

1. Incompressible
2. 2D fully-developed laminar
3. Gravity neglected

$$t_f = \frac{3\mu x_f^2}{h\sigma cos\theta}$$

Experiment



- Two flat plate experiments were conducted with different gap heights
- Acrylic was used for the top and bottom plates

(unit: mm)

Height (h)	1.7	1.22	1	0.9
Bond number (Bo)	1.09	0.56	0.38	0.30

Results & Discussion

❖ Two flat plate experiment

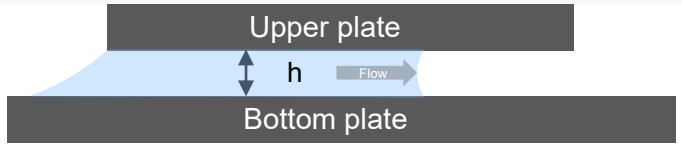

h = 1.7 mm (Bo = 1.09)

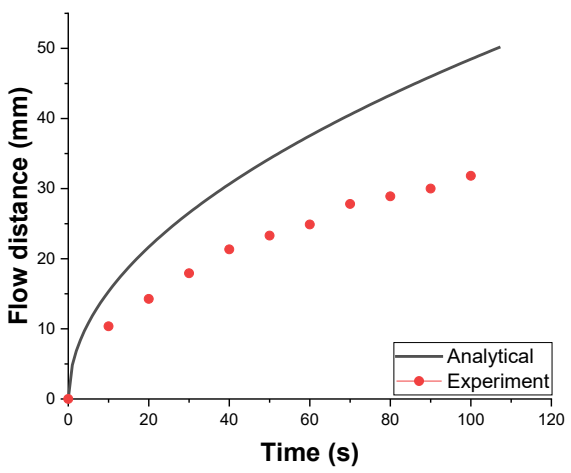

h = 1.2 mm (Bo = 0.56)

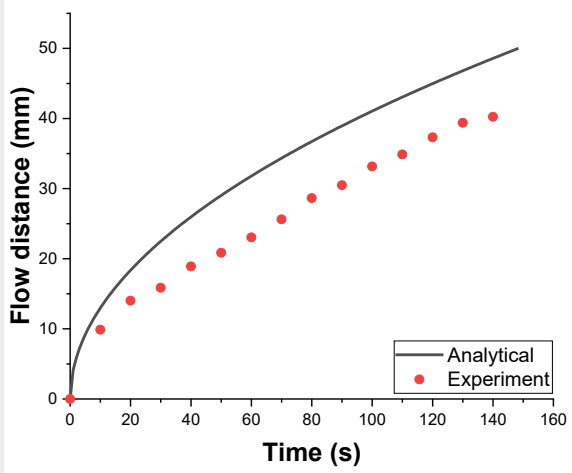

h = 1.0 mm (Bo = 0.38)

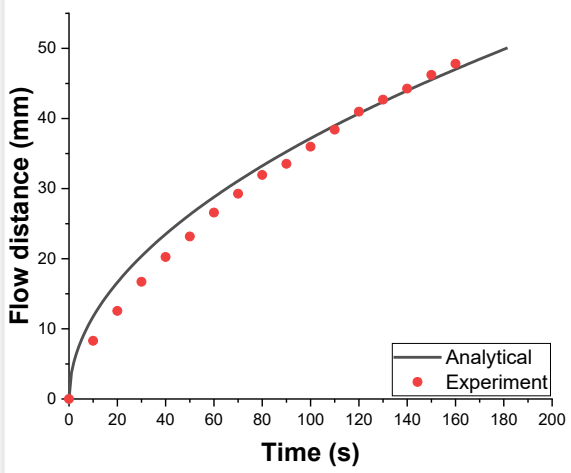

h = 0.9 mm (Bo = 0.30)

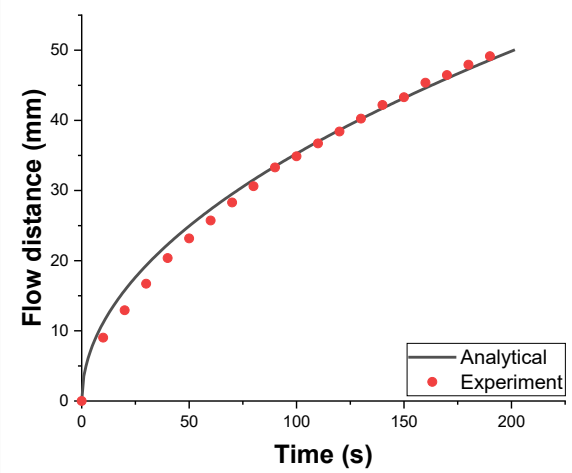

- As the gap height decreases, Bond number becomes smaller and the effect of gravity is minimized

Experiment design

❖ Experiment design

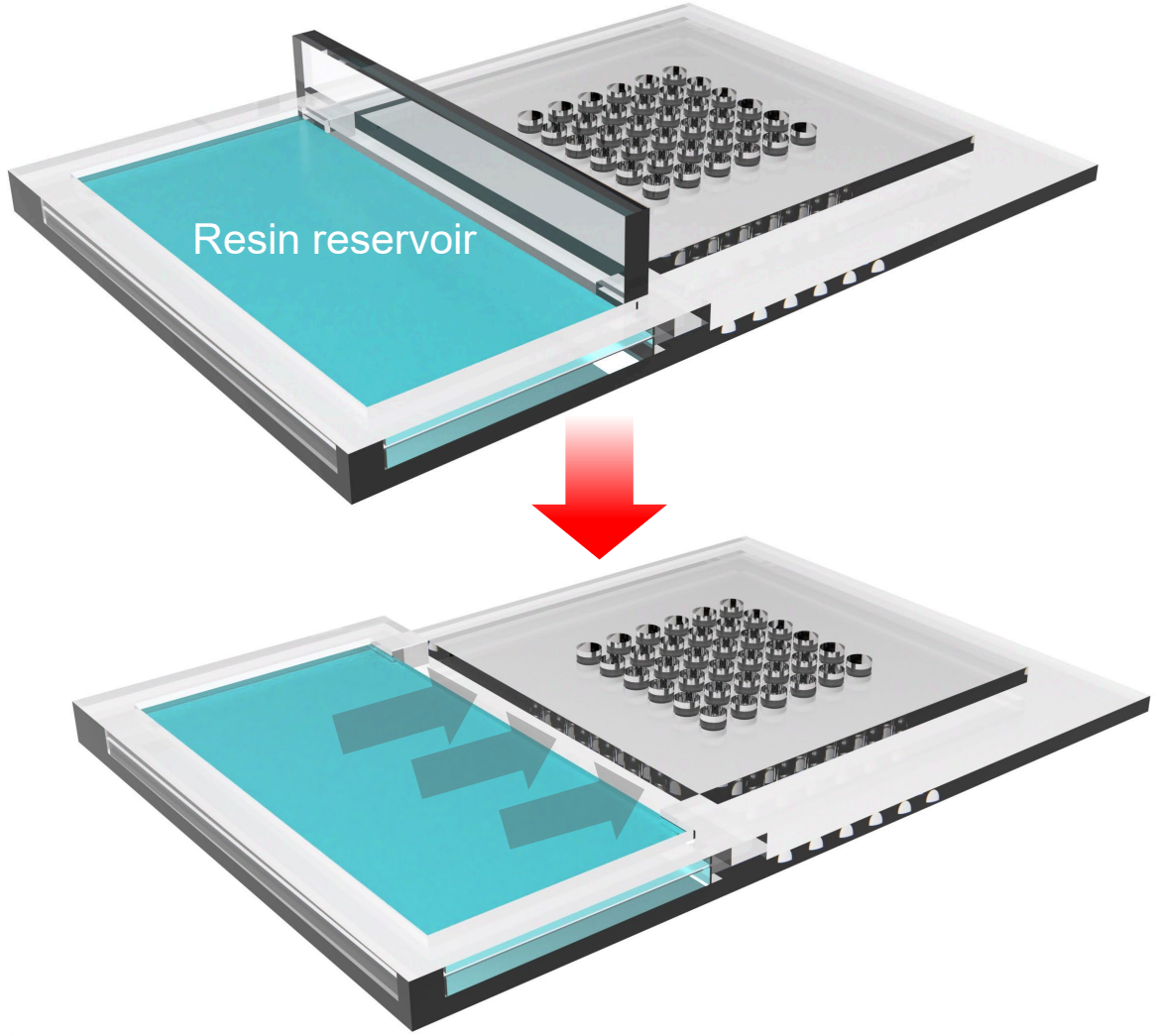

Dimensions

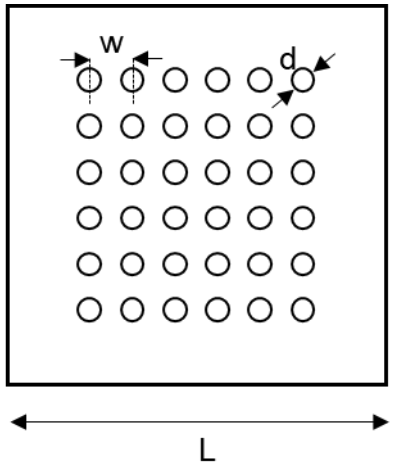

Top view

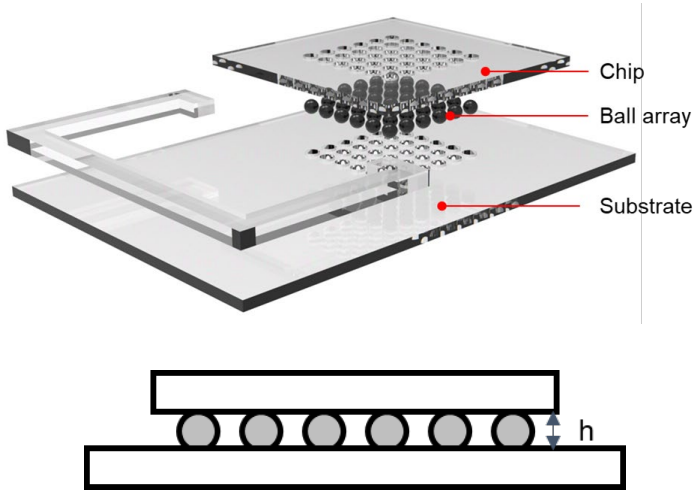

Side view

(unit: mm)

Chip size (L)	Bump pitch (w)	Diameter (d)	Height (h)
5 × 5	4.5	3	1

Materials

Chip	Substrate	Ball
Acrylic (PMMA, arystal, Korea)	Acrylic (PMMA, arystal, Korea)	Bearing steel (SUJ2)

Experiment design

❖ Experiment design for original model

Applying adhesive

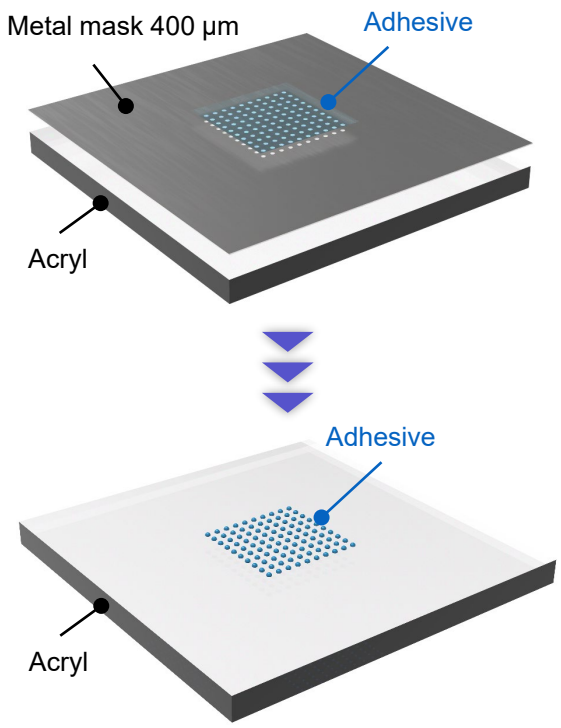

Attaching solderball

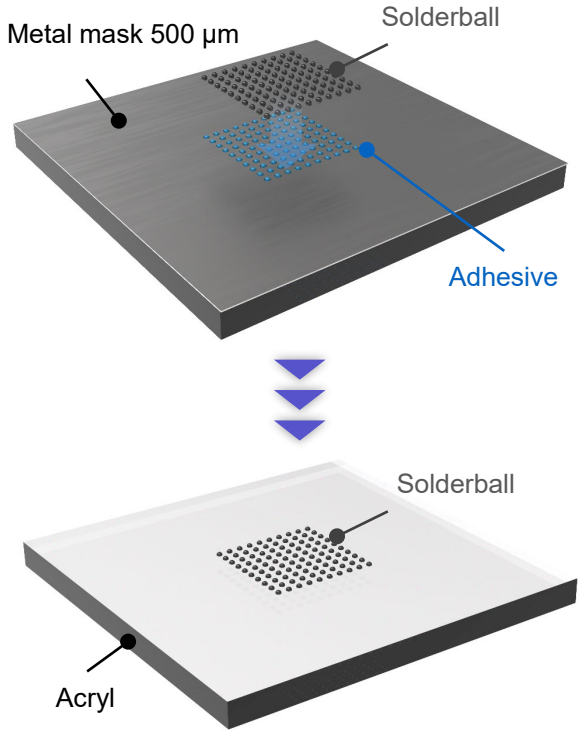

Attaching upper plate

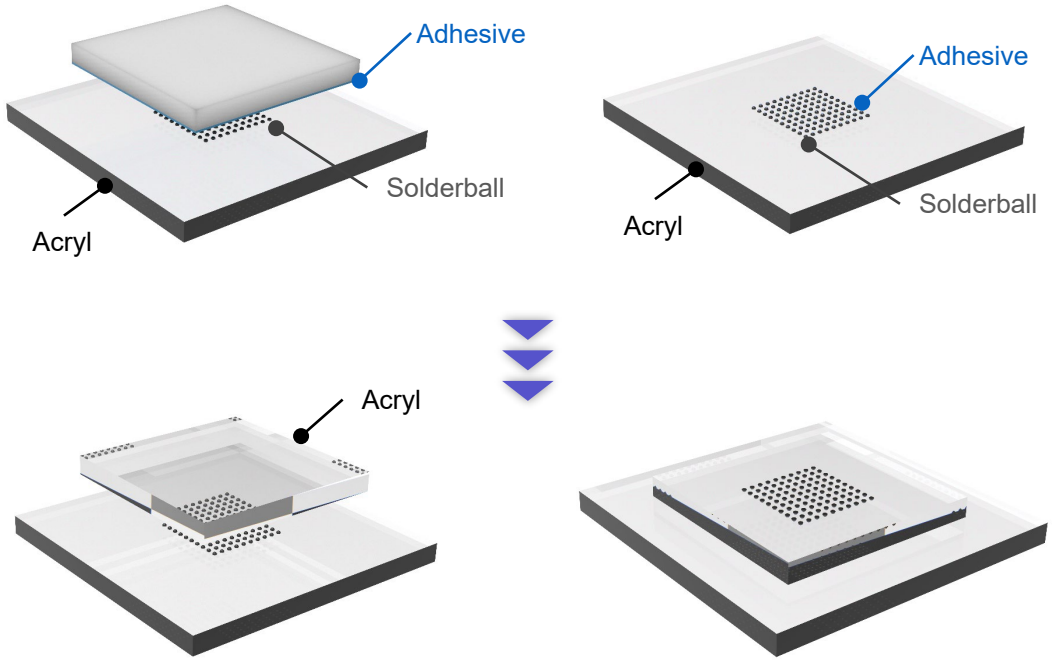

Experiment design

❖ Flow front measurement

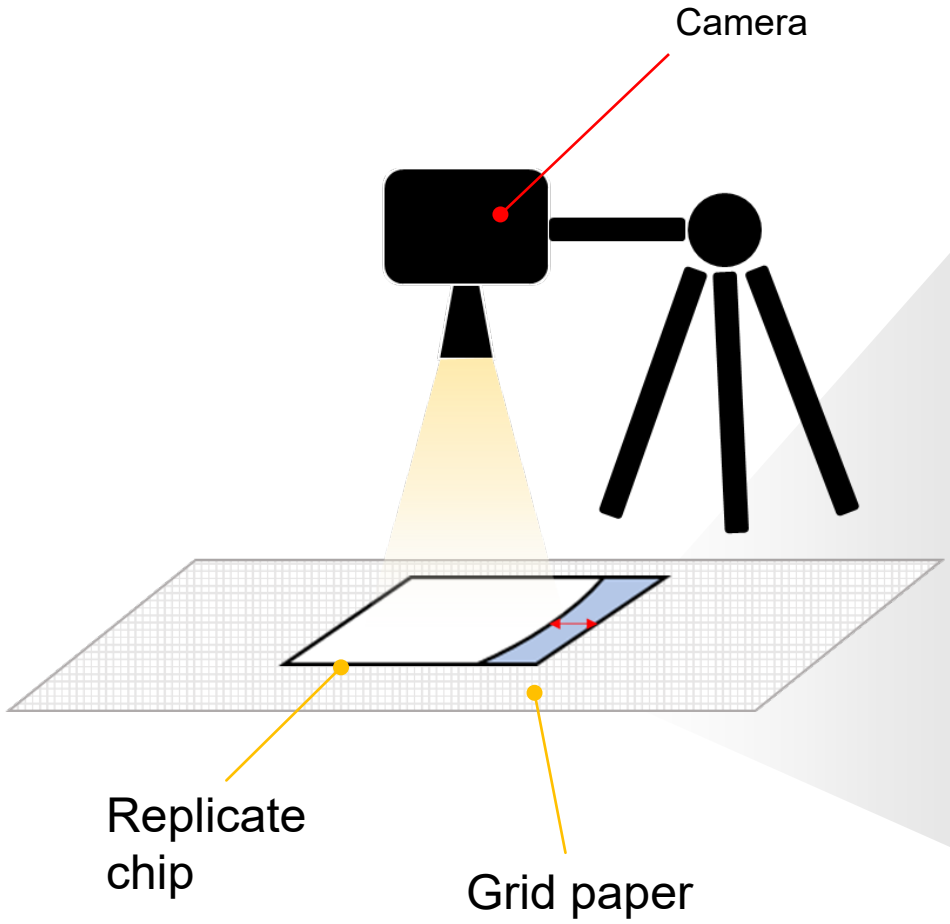

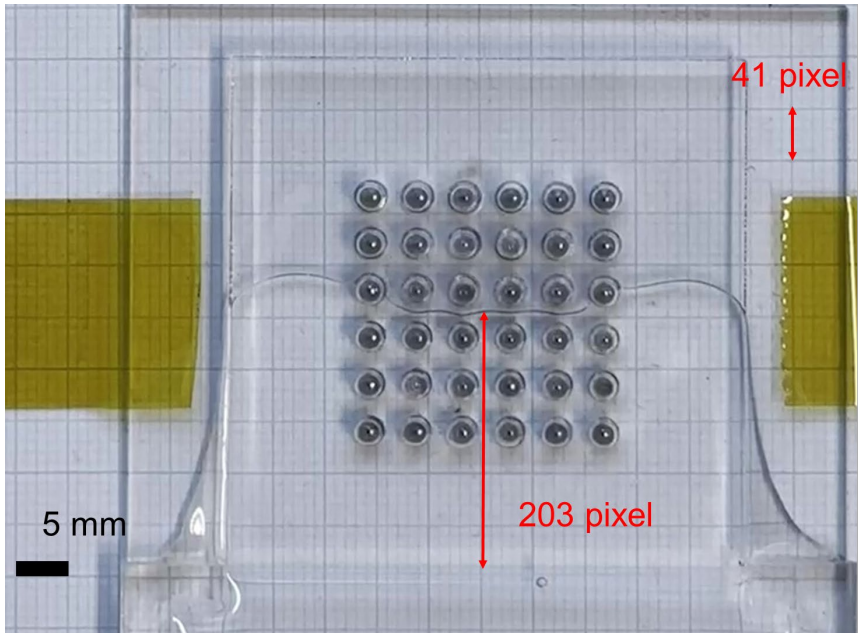

❖ Flow front measurement method

- Measurement tool: Image correlation
- 5 mm → 41 pixel
- Time step: 10 s

RESULTS & DISCUSSION

- **Simulation & experimental results**
- **Void formation mechanism**
- **Parametric study**

Experimental validation

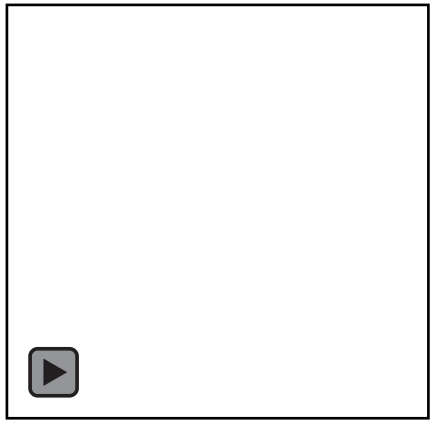

Experiment

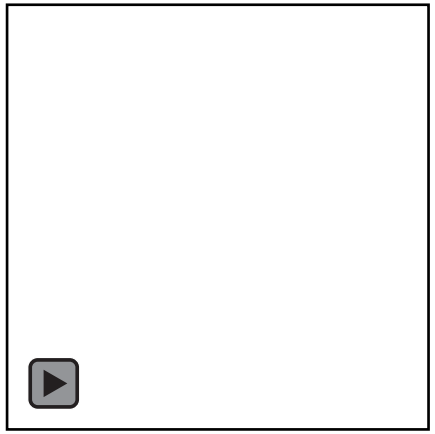

Simulation

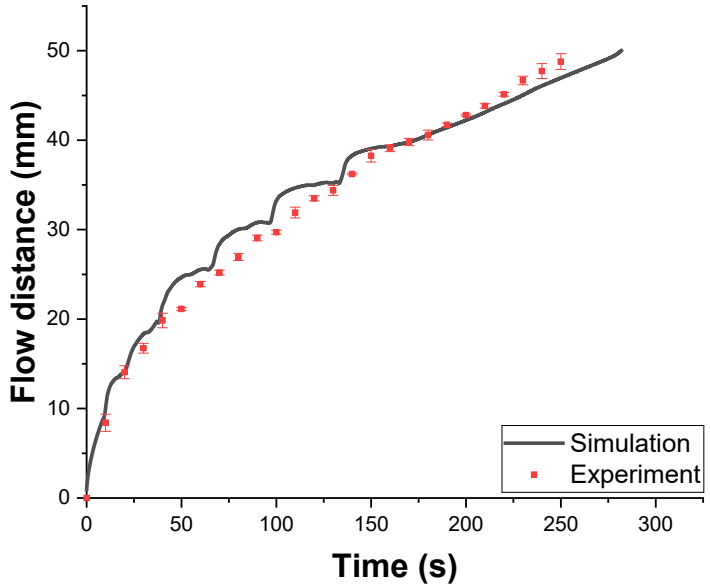

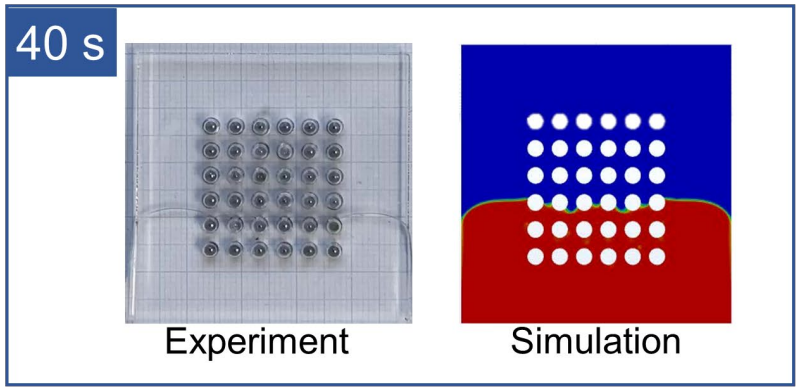

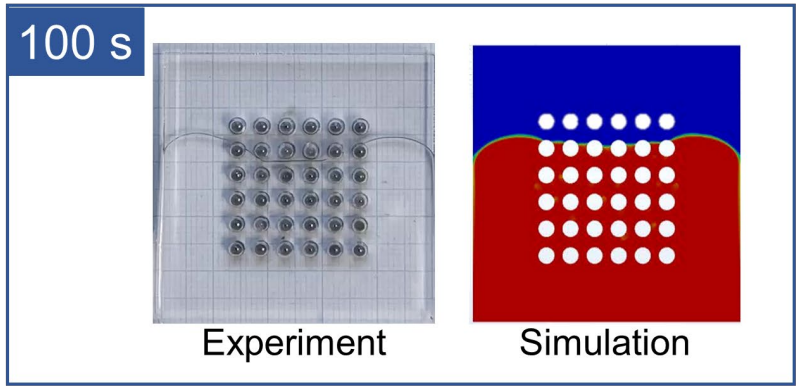

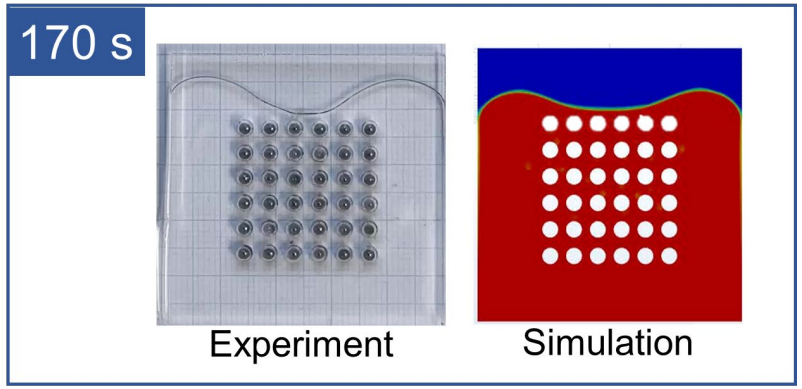

Experimental validation

❖ Scale-up model

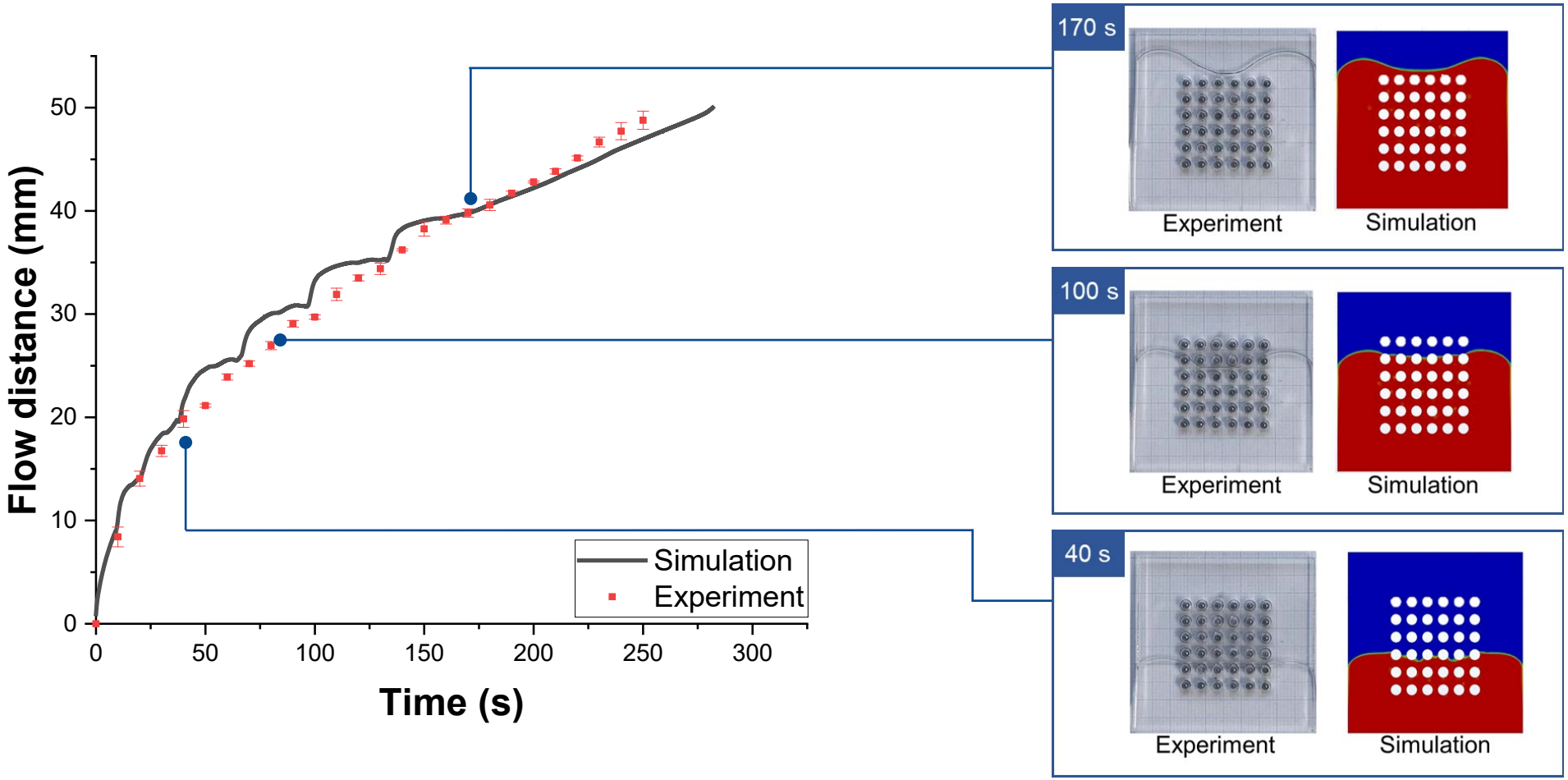

Experimental validation

❖ Original scale model

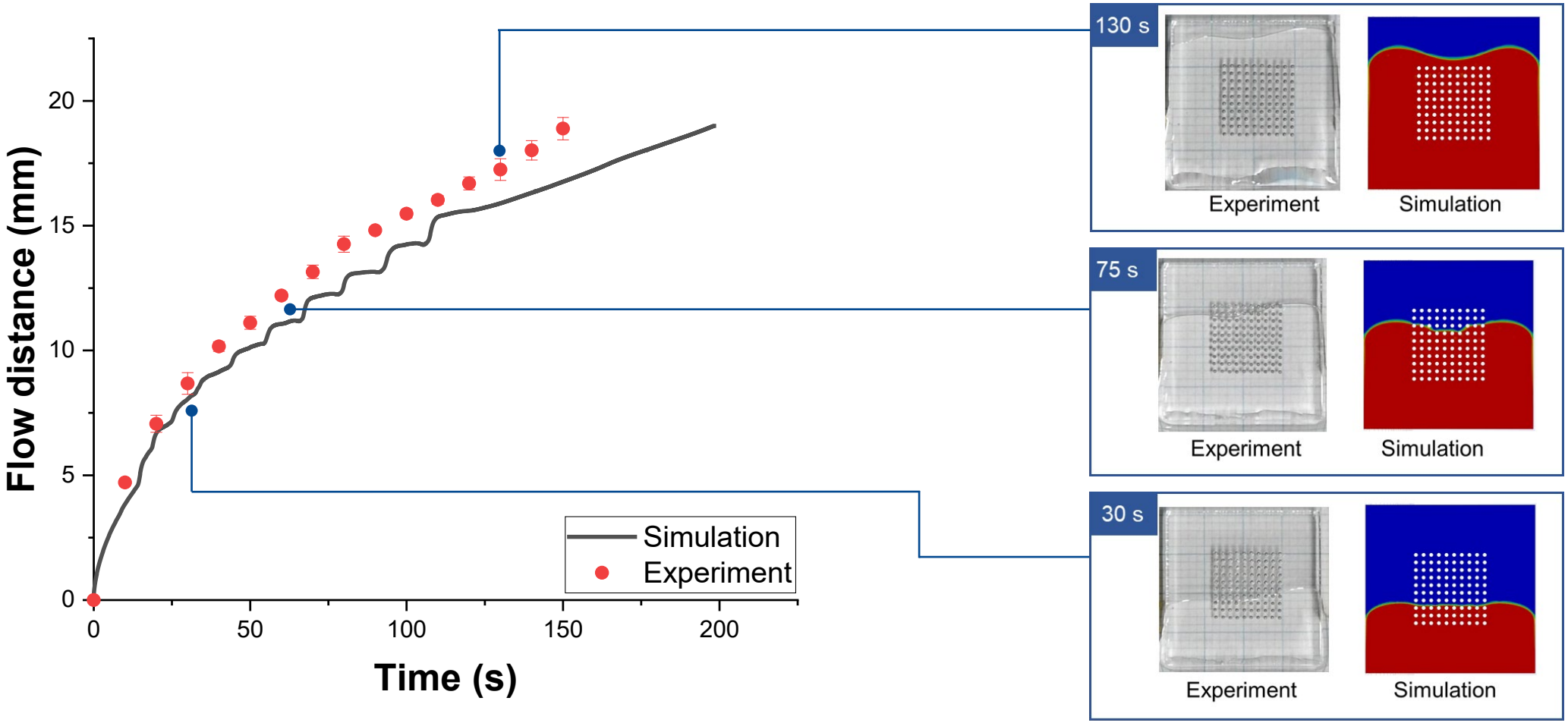

Experimental validation

❖ Flow similarity between scale-up and original scale models

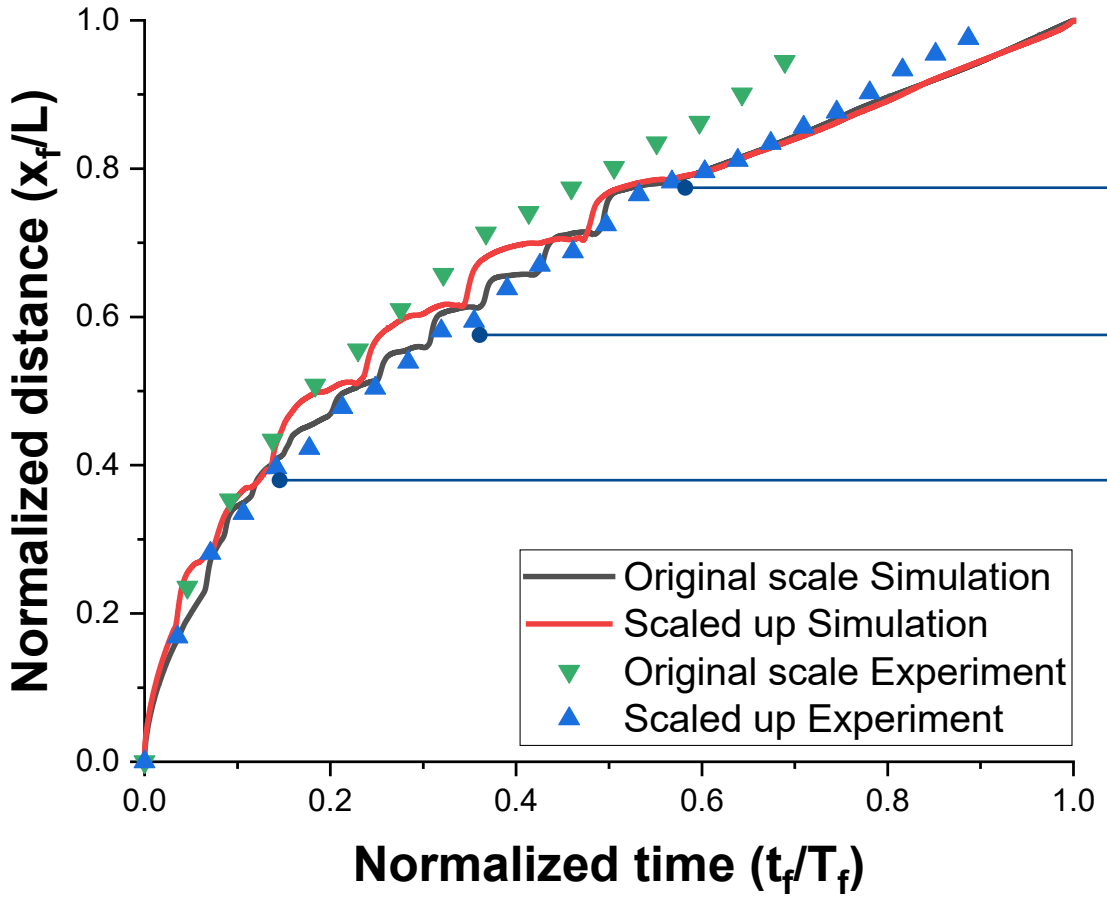

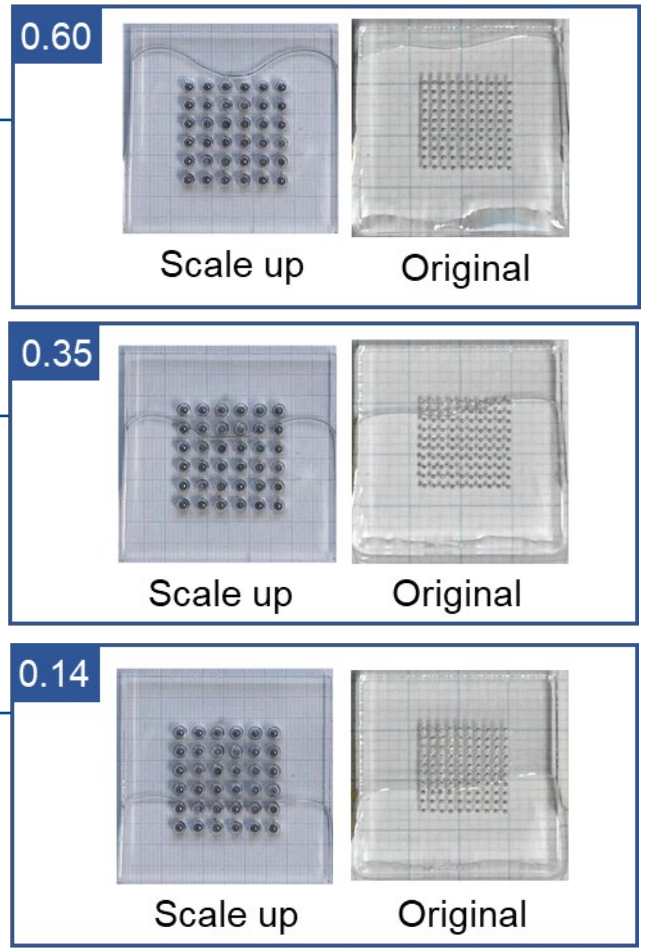

Parametric study

Representative model for parametric study

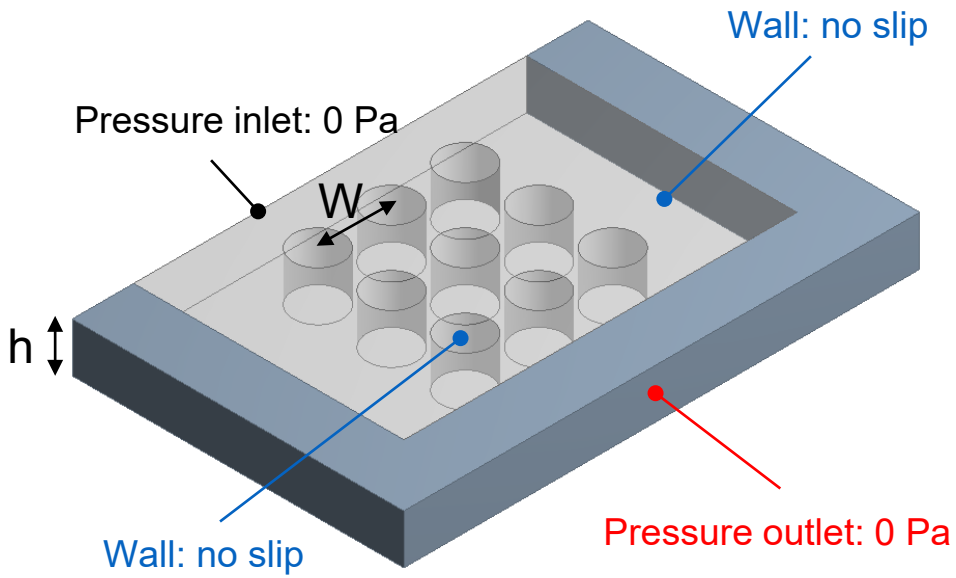

d = 80 μm

3 × 3 solderball model

(unit: μm)

Model	Bump pitch (W)	Gap height (h)
1	100	25
2		40
3		60
4	120	30
5		55
6		80
7	140	40
8		70
9		100

Parametric study

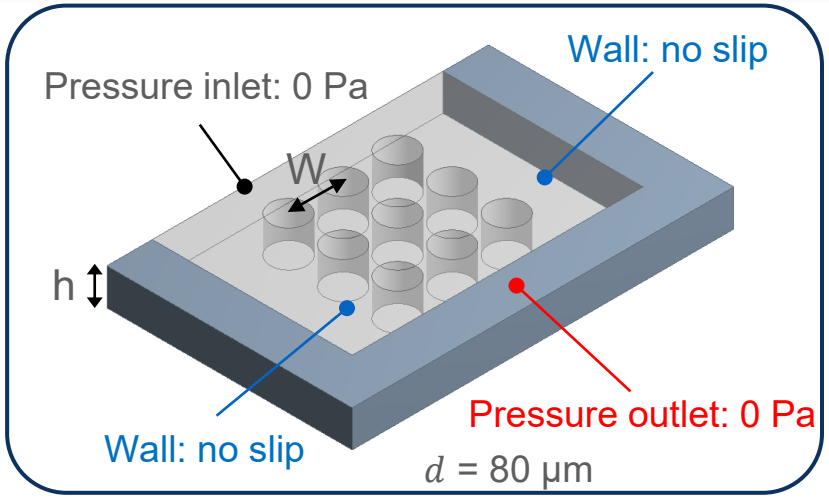

Model	Bump pitch (μm)	Gap height (μm)
1	100	25
2		40
3		60
4		30
5	120	55
6		80
7		40
8	140	70
9		100

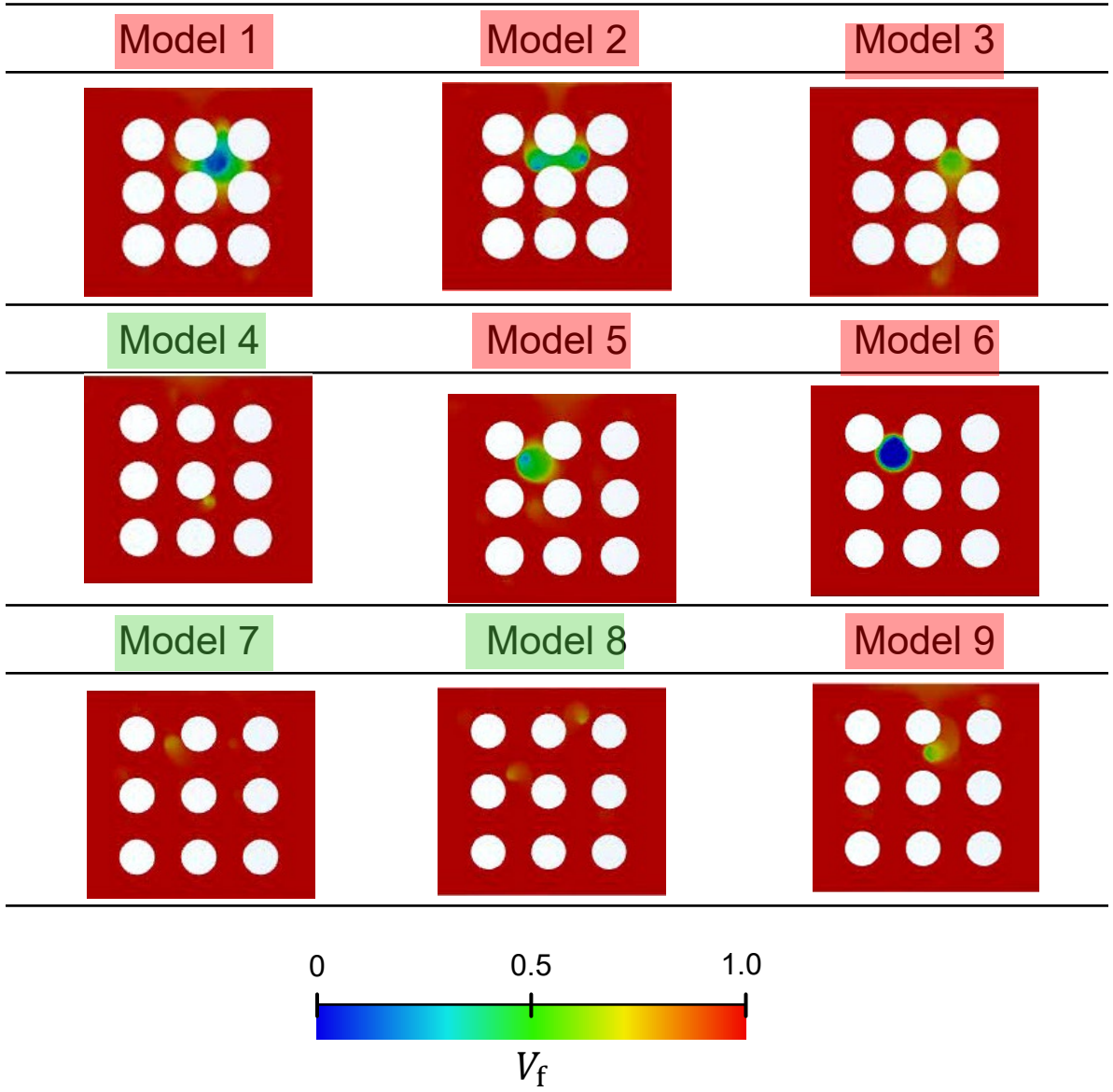

Void formation mechanism

Bump pitch effect

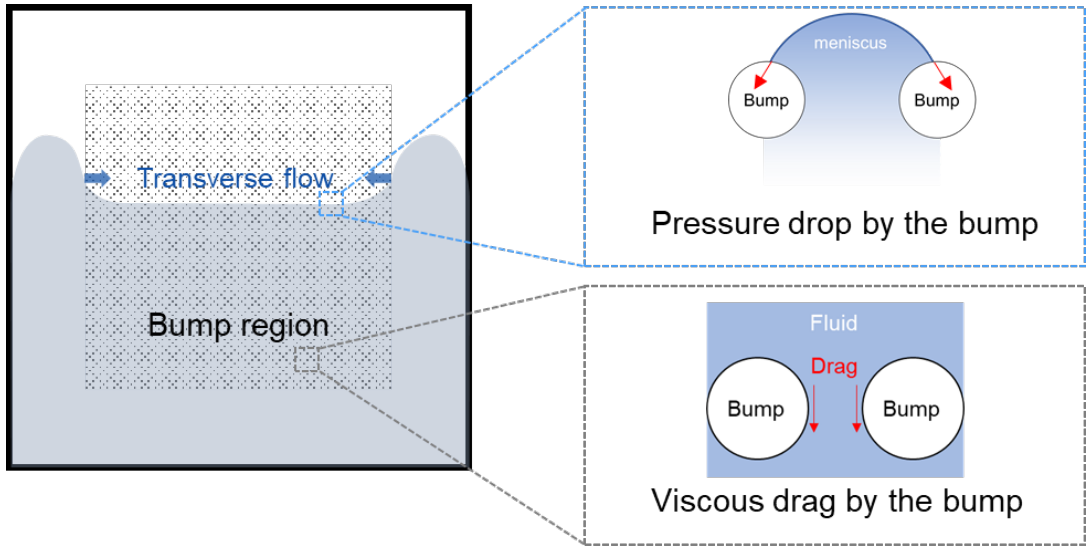

- ✓ As the bump pitch decreases, the pressure drop across the bumps and the viscous drag increase ⇒ decreased flow velocity in bump region
- ✓ Difference between the flow in the edge and bump regions increases the amount of transverse flow.

Gap height effect

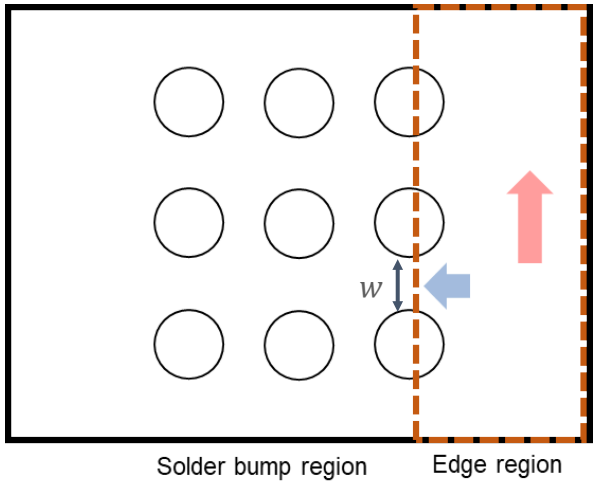

Flow direction

$$P_L = 2\sigma cos\theta \frac{1}{h}$$

Transverse flow direction

$$P_T = 2\sigma cos\theta \left(\frac{1}{h} + \frac{1}{w}\right)$$

- ✓ As the gap height becomes larger, the effect of the transverse capillary force increases.

Void formation mechanism

Flow front direction change

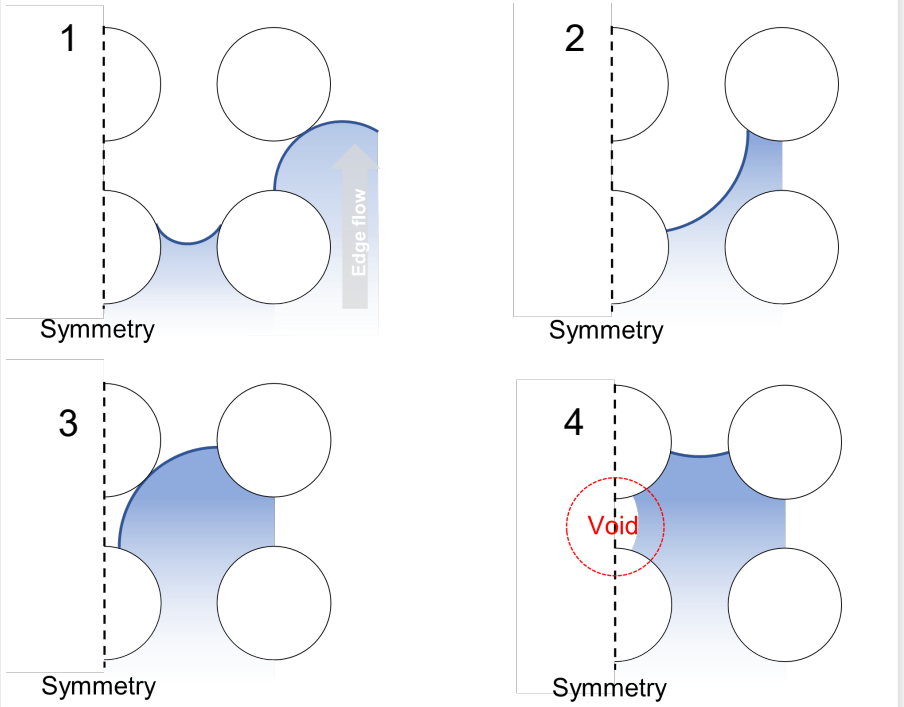

Simulation results of void formation

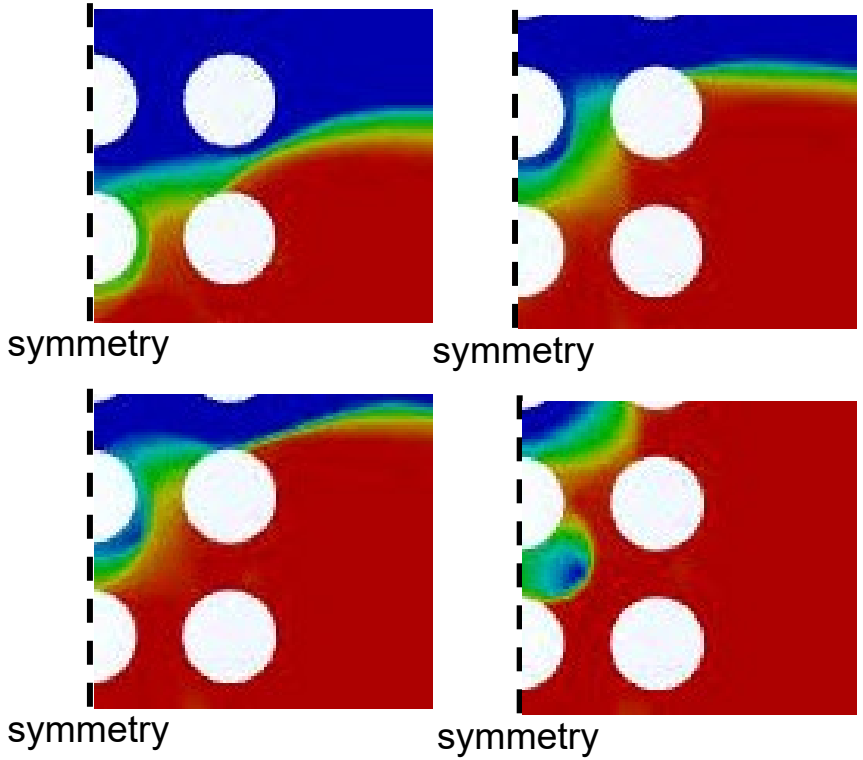

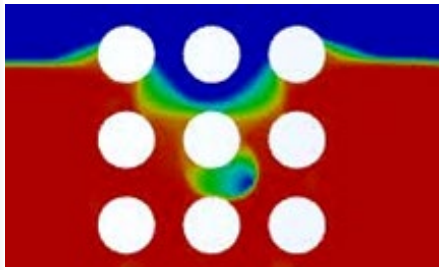

Parametric study

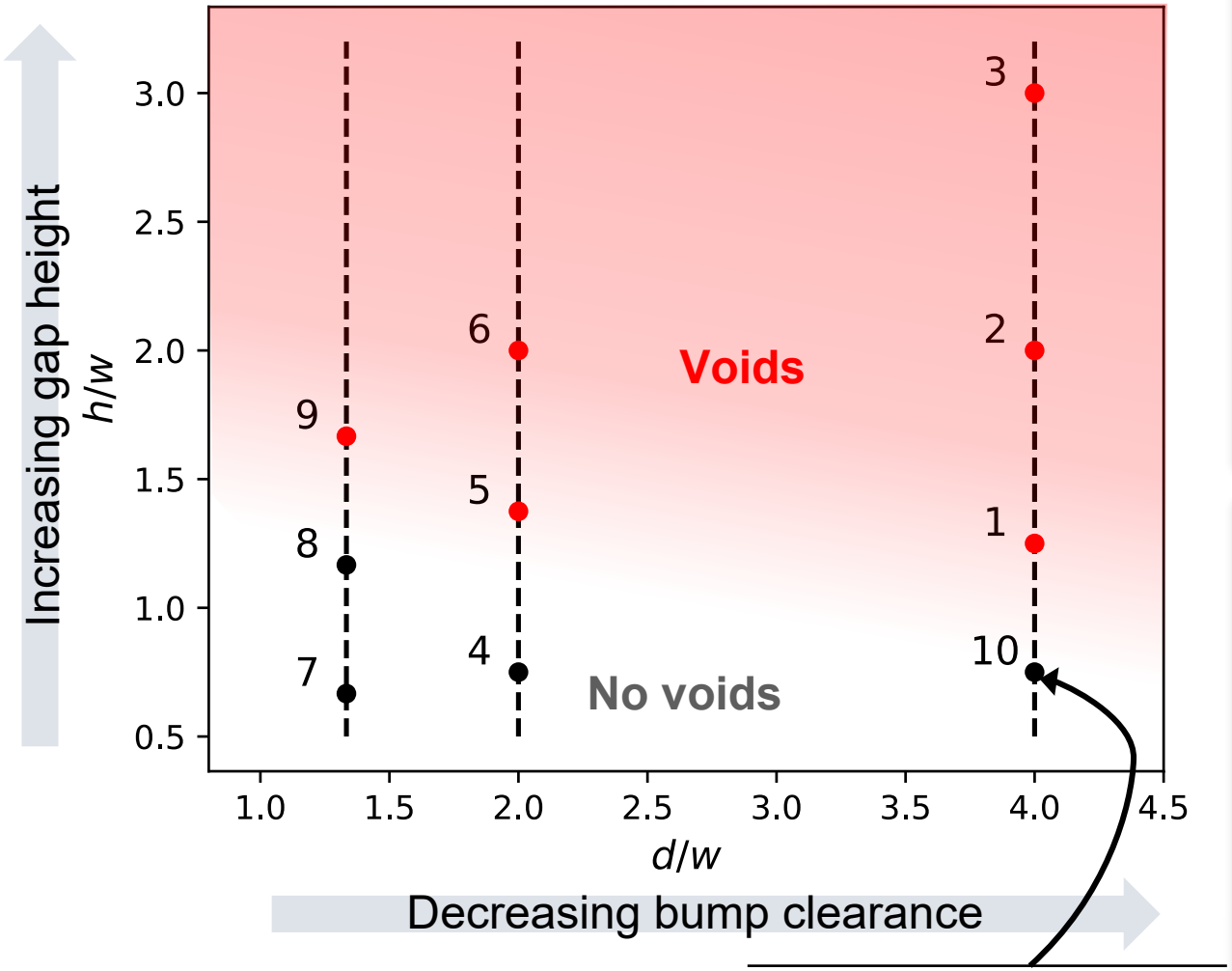

Model	Bump pitch (μm)	Gap height (μm)
10	100	15

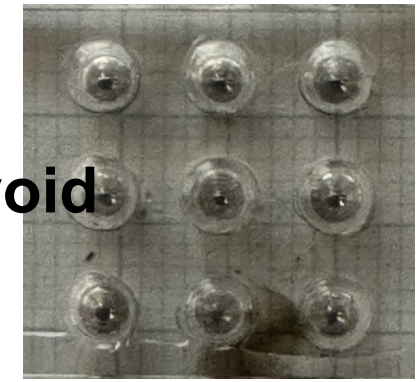

No void

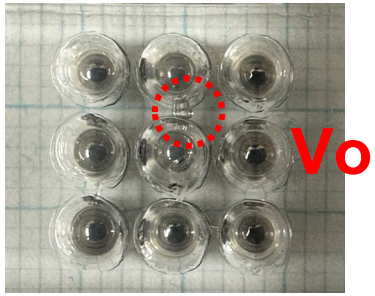

Void

Model 7 Model 3

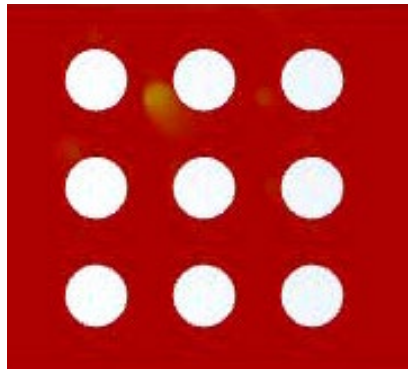

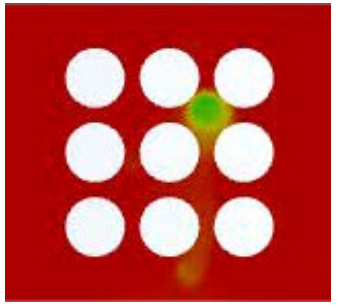

Model 7 Model 3

h: gap height, w: bump clearance, d: bump diameter

CONCLUSIONS

Conclusions

- Scaled-up test bench was constructed for improved visualization of the flip chip capillary underfill process while maintaining flow similarity
- The primary cause for void formation is air entrapment due to the velocity difference between the edge and bump regions
- Flow in the solder bump region depends on both the viscous drag and pressure drop as the flow front passes through the solder bumps
- A parametric study showed that increasing gap height and decreasing bump pitch increase the likelihood of void formation

Future work

- Extend test bench to track filler particles during filling
- Simulation of the flow of the underfill material with filler particles
- ML-driven framework to predict filling patterns for complex bump arrangements and varying fluid properties

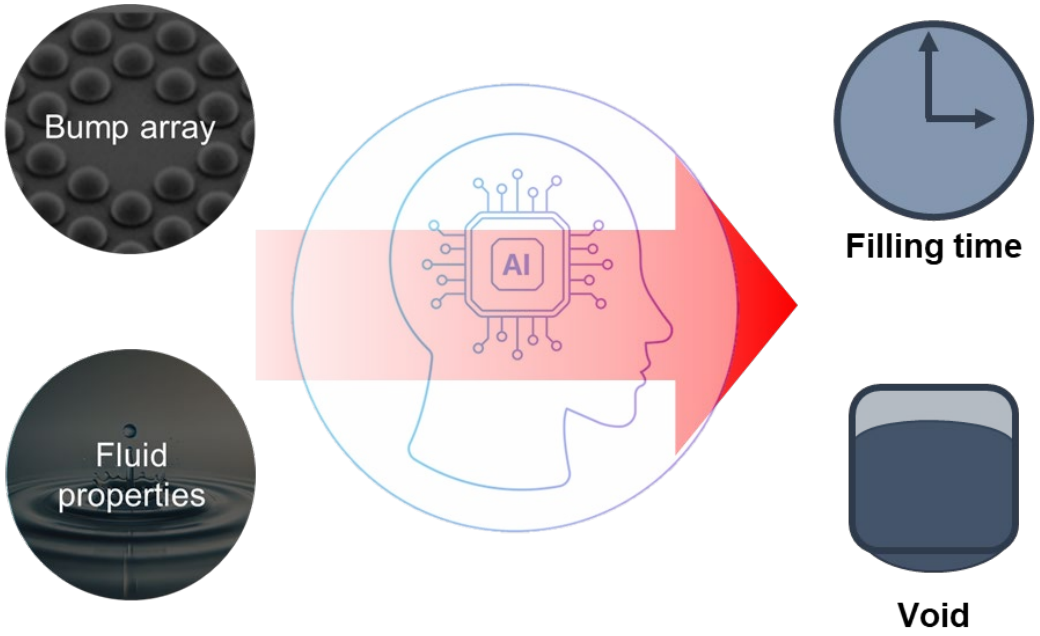

THANK YOU FOR YOUR ATTENTION

References

[1] Su et al. Journal of Electronic Materials 28 (1999) 1017-1022

[2] Ng et al. Journal of Electronic Packaging 144 (2022) 010803

[3] Wen et al. Advanced Materials 34 (2022) 2201023

[4] Ng et al. Soldering & Surface Mount Technology (2021) 112-127

[5] Peng et al. IEEE Transactions on Electronics Packaging Manufacturing 24 (2001)

[6] Wang et al. IEEE 56th Electronic Components and Technology Conference (2006)

[7] Kim et al. Journal of Mechanical Science and Technology 26 (2012) 3751-3759

[8] Wu et al. Physics of Fluids 36 (2024) 032117

[9] Edward W. Washburn, Physical Review 17 (1921) 273-283

[10] Wan et al. Microelectronics Journal 38 (2007) 67-76

[11] Ng et al. Soldering & Surface Mount Technology 29 (2017) 173-190

[12] Ng et al. Microelectronics Reliability 81 (2018) 41-63

[13] Gu et al. Journal of Petroleum Science and Engineering 40 (2003) 77-87

[14] Polzin et al. Journal of Physics D: Applied Physics 36 (2003) 3156-3167

24TH INTERNATIONAL CONFERENCE ON COMPOSITE MATERIALS (ICCM24)

UNIVERSITY OF DELAWARE
CENTER FOR COMPOSITE MATERIALS
Celebrating 50 Years

Analysis of the image-based evaluation of the permeability of carbon-carbon composites

T. Lavaggi, J. W. Gillespie Jr., P. Mulye,
C. Binetruy, S. Advani

UNIVERSITY OF DELAWARE

Project Overview

Project Goal

- Improvement of the densification process of carbon-carbon composites.

Focus of Today's Presentation

- Identification of the minimum dimensions of the statistical representative volume element of carbon-carbon composites for permeability characterization.

Outline

1. Introduction
    I. Densification process of carbon-carbon composites
    II. sRVE of carbon-carbon composites
2. Permeability of carbon-carbon composites as function of sample dimensions and inlet location
3. Image-based determination of the stochastic permeability
4. Numerical simulations for the prediction of the effective permeability
    I. Sample of 5 plies
    II. Sample of 33 plies
5. Conclusions

Outline

1. Introduction
    I. Densification process of carbon-carbon composites
    II. sRVE of carbon-carbon composites
2. Permeability of carbon-carbon composites as function of sample dimensions and inlet location
3. Image-based determination of the stochastic permeability
4. Numerical simulations for the prediction of the effective permeability
    I. Sample of 5 plies
    II. Sample of 33 plies
5. Conclusions

Densification of Carbon-Carbon Composites

Manufacturing of Carbon/Carbon Composites

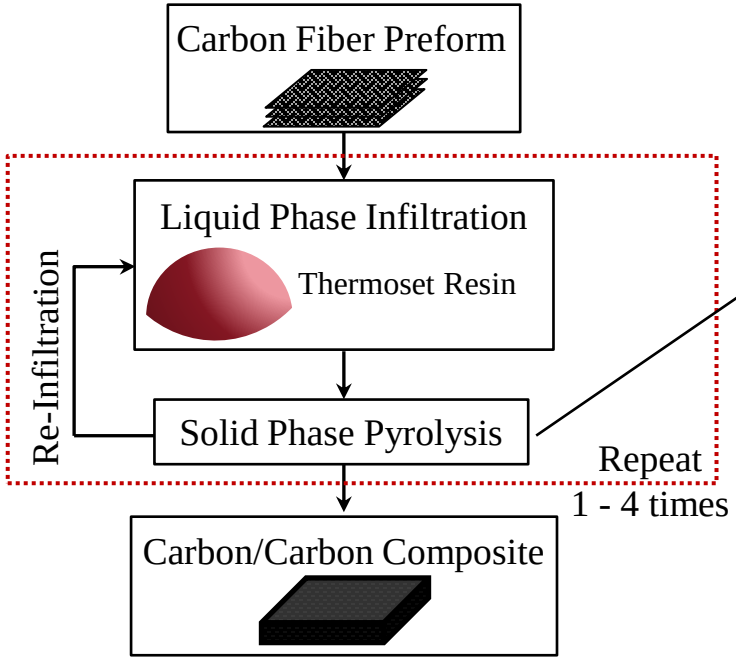

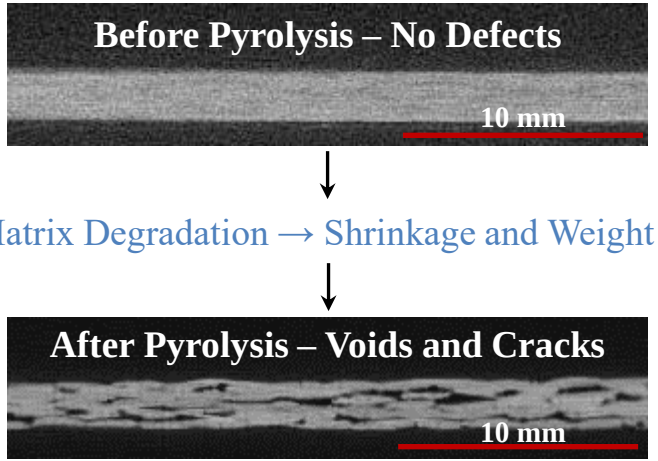

Densification Process

- Repetition Infiltration/Pyrolysis.
- Takes several months to complete.

Densification process: Muhammed et al. 2021 *J. Mater. Sci.* DOI 10.1007/s10853-021-06401-3

Improvement of Densification of Carbon-Carbon Composites

How to improve the process?

- Tailor pyrolysis schedule to control porosity development.
- Find re-infiltration parameters to reduce infiltration time.

Characterization of permeability of carbon-carbon composites (CCC)

- Key parameter for characterization of connected porosity.
- Describes how gas generated during pyrolysis evacuate porosity.
- Determines how resin permeates connected pores during re-infiltration.
- Necessary for numerical simulations to improve the densification process.

Necessary to identify the minimum size of the statistical representative volume element (sRVE)

- Macro-cracks dimensions can be comparable or larger than fabric RVE (25 mm^2).

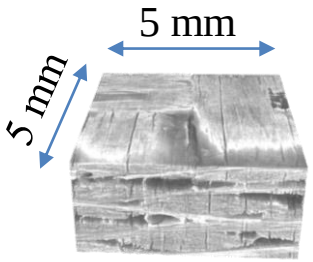

Framework for the Identification of the sRVE

Permeability Experiment



Sample of 5 plies

Measured Out-of-Plane Permeability

Minimum Size sRVE of CCC

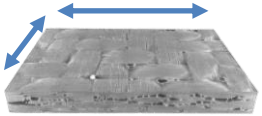

Effective Permeability

CT scan and Digital Model

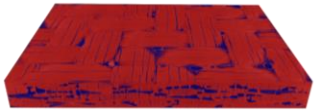

Sample of 5 plies

Red: composite blue: pores

Predicted 3D Permeability Tensor and Permeability Distribution

Numerical Simulations

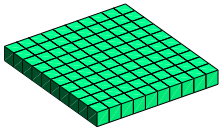

Sample of 5 plies

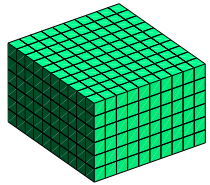

Sample of 33 plies

Outline

1. Introduction
    I. Densification process of carbon-carbon composites
    II. sRVE of carbon-carbon composites
2. Permeability of carbon-carbon composites as function of sample dimensions and inlet location
3. Image-based determination of the stochastic permeability
4. Numerical simulations for the prediction of the effective permeability
    I. Sample of 5 plies
    II. Sample of 33 plies
5. Conclusions

Permeability Experiments

Experiment Set-up

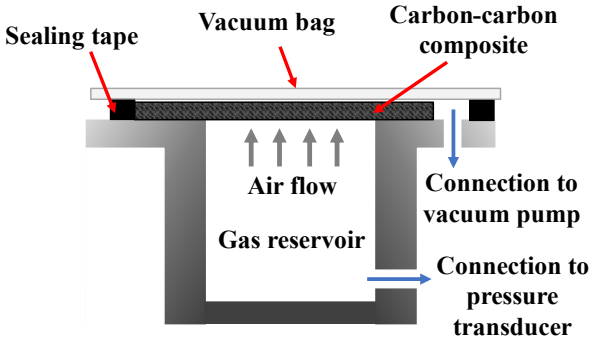

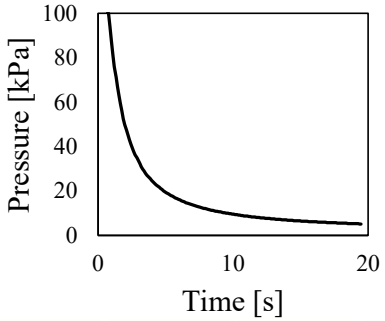

$$K = -\frac{2\mu_g L L_c}{P^2}\frac{\partial P}{\partial t}$$

Experiment Dimensions

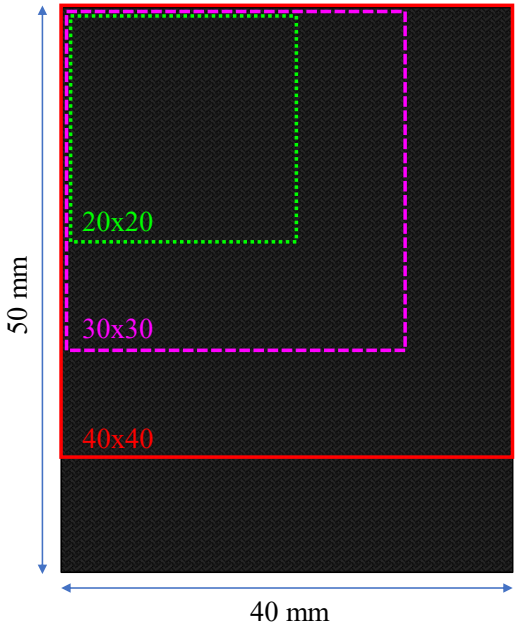

Inlet Locations

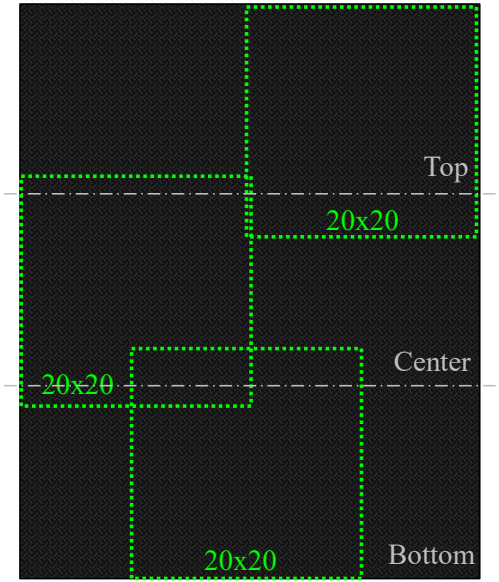

Permeability of Carbon-Carbon Composites

- Experiments are computed with same method and measuring fluids.
- Microstructure of samples between experiments does not change: variation can be attributed only to local heterogeneity.

Measured Permeability

Sample size in-plane [mm^2]	Average $\cdot 10^{-14}$ [m^2]	Standard Deviation $\cdot 10^{-14}$ [m^2]
20 x 20	5.5	1.6
30 x 30	6.0	1.0
40 x 40	5.2	0.6
40 x 50	5.0	0.1

Coefficient of Variation (Cv)

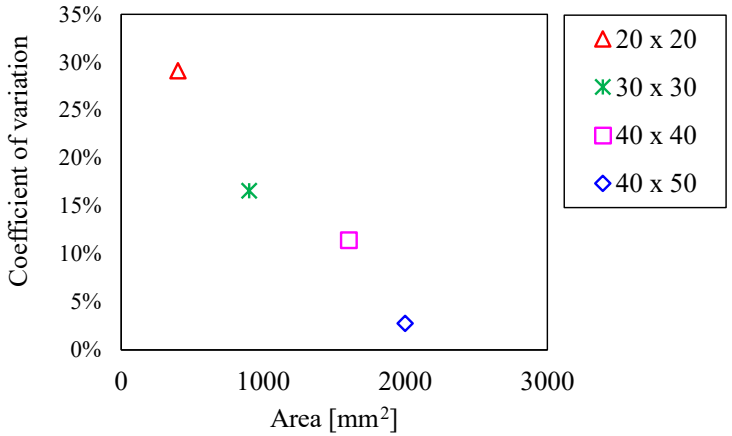

Outline

1. Introduction
    I. Densification process of carbon-carbon composites
    II. sRVE of carbon-carbon composites
2. Permeability of carbon-carbon composites as function of sample dimensions and inlet location
3. Image-based determination of the stochastic permeability
4. Numerical simulations for the prediction of the effective permeability
    I. Sample of 5 plies
    II. Sample of 33 plies
5. Conclusions

Image-Based Stokes and Stokes-Brinkman Solver PoroS

- Research software for the virtual characterization of porous materials developed at the Ecole Centrale de Nantes.
- PoroS 1.0: solves Stokes flows by finite element method (FEM) where the finite elements are the voxels (3D) or the pixels (2D) of CT images or digital twins.

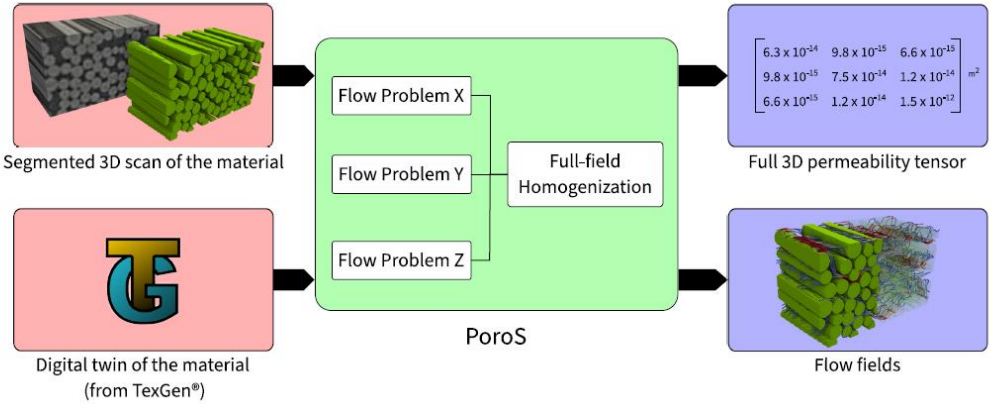

Figure: P. Mulye et al. 2024 *Materials* DOI 10.3390/ma17122873

Image-Based Predicted Permeability of Carbon-Carbon Composites



- Voxel size: 6 µm.
- Geometry divided in 70 sub-domains.

- *PoroS* used to **predict the permeability tensors** of the 70 sub-domains.
- Permeability dependent on scale of experiment even for constant microstructure of CCC.

Comparison of Experiment and Image-Based Permeability (z-dir)

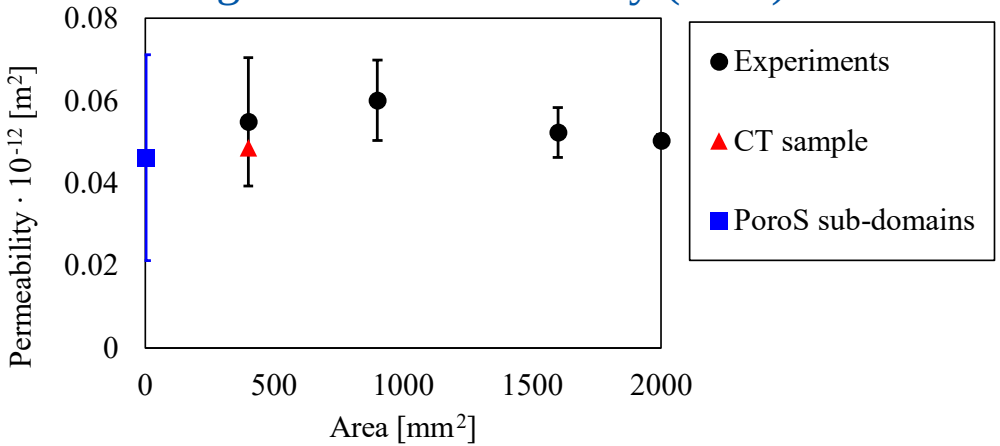

Outline

1. Introduction
    I. Densification process of carbon-carbon composites
    II. sRVE of carbon-carbon composites
2. Permeability of carbon-carbon composites as function of sample dimensions and inlet location
3. Image-based determination of the stochastic permeability
4. Numerical simulations for the prediction of the effective permeability
    I. Sample of 5 plies
    II. Sample of 33 plies
5. Conclusions

Numerical Simulations: Model Generation of Sample of 5 Plies

- Element dimensions equal to CT sub-domains dimensions.
- *Thickness* of sample of 5 plies equal to **1 sub-domain** in z-direction.
- Model in-plane dimensions increased from area of 3.5 mm^2 (1 element) to 35000 mm^2 (100 by 100 array of elements).

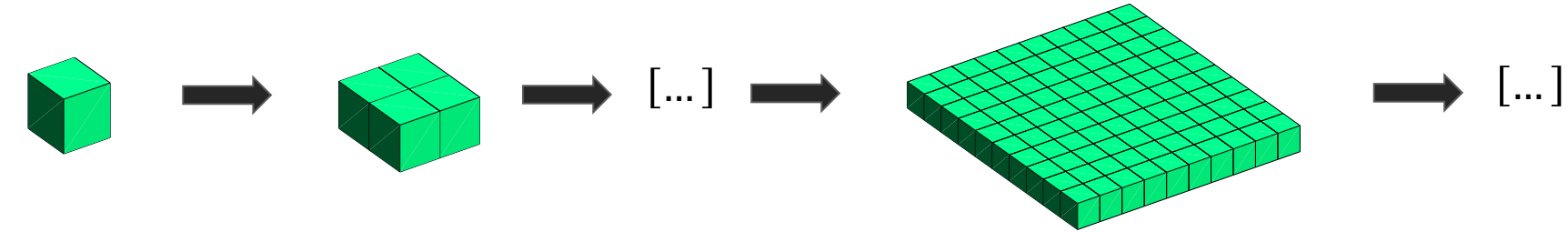

1 element 4 elements 100 elements

Numerical Simulations: Model Generation of Sample of 33 Plies

- Element dimensions equal to CT sub-domains dimensions.
- *Thickness* of sample of 33 plies equal to **6 sub-domains** in z-direction.
- Model in-plane dimensions increased from area of 3.5 mm^2 (1 element) to 35000 mm^2 (100 by 100 array of elements).

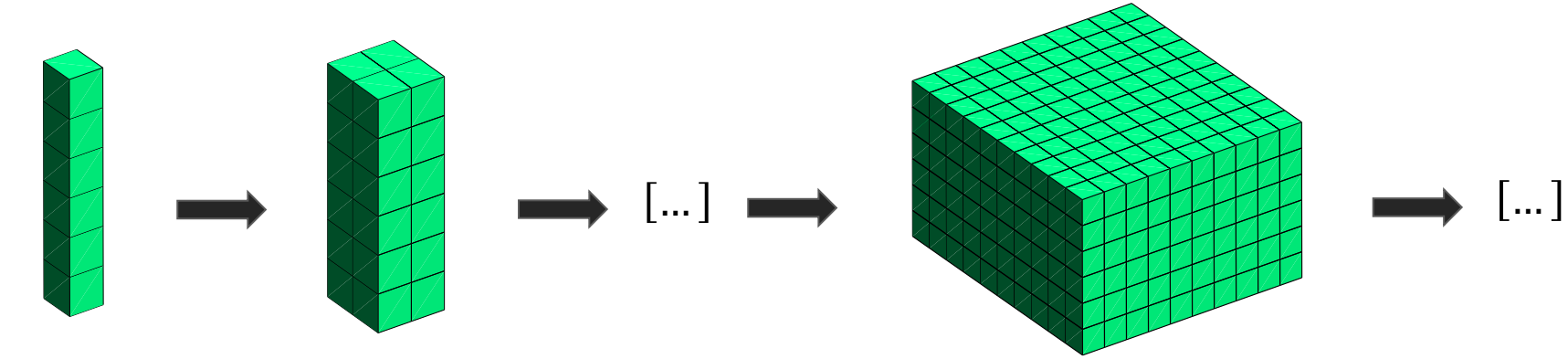

6 elements 24 elements 600 elements

Numerical Simulations: Evaluation of the Effective Permeability

Sample of 5 plies

- Flow assumed parallel for effective permeability K_{eff} in out-of-plane direction.

$$K_{eff} = \frac{1}{A}\sum_i K_i A_i$$

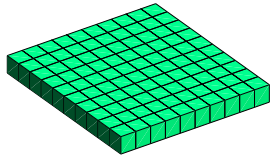

K_i: permeability of ith element.
A_i: area of ith element.
A: area of numerical model.

Sample of 33 plies

- Effective permeability K_{eff} evaluated with software Liquid Injection Molding Simulations (LIMS).

$$K_{eff} = \frac{qL\mu}{A\Delta P}$$

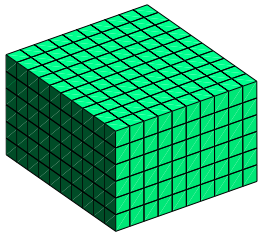

q: flowrate.
L: thickness of numerical model.
A: area of numerical model.
μ: viscosity of fluid.
ΔP: applied pressure difference.

Numerical Simulations: Liquid Injection Molding Simulations (LIMS)

- Research software developed at the Center for Composite Materials University of Delaware for the simulations of mold filling stage of liquid composite molding (LCM) processes.
- LIMS: models flow through porous media by finite element/control volume method.

Part Design/Meshing

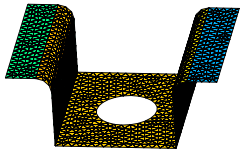

Permeability and Preform Properties

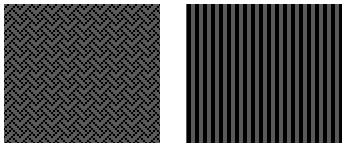

Simulation Settings

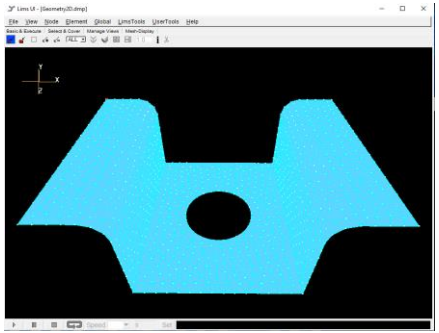

- Pressure/Flowrate
- Inlet and vent location
- Fluid properties

Running Simulation



Post-Processing Results

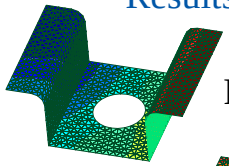

Fill Pattern

Pressure

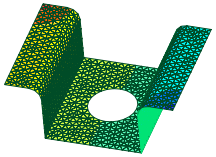

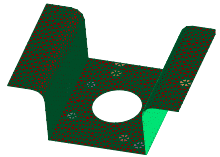

Resin Fill

Numerical Simulations: Monte Carlo Method

$$\boldsymbol{K} = \begin{pmatrix} K_{xx} & K_{xy} & K_{xz} \\ K_{xy} & K_{yy} & K_{yz} \\ K_{xz} & K_{yz} & K_{zz} \end{pmatrix}$$

Probability Density Function of K_{zz}

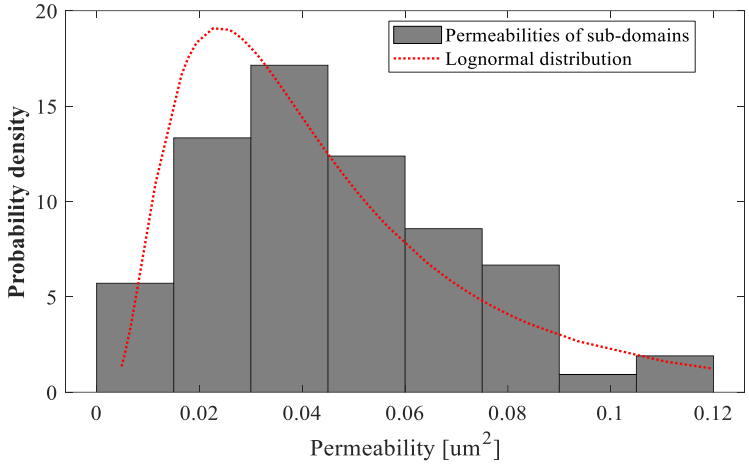

- Permeability tensors **K** of sub-domains used to generate separate probability density functions for each component of **K**.
- *Lognormal* probability functions used to **assign randomly permeability components** to elements of models of samples of 5 and 33 plies.
- 100 simulations performed on each model where the random permeability assignment is repeated each time.

Numerical Simulations: Effective Permeability of Sample of 5 Plies

- Average of simulations comparable with experiments on larger scale samples.
- Cv below 5% for model of area of 350 mm^2 (fabric RVE 25 mm^2).

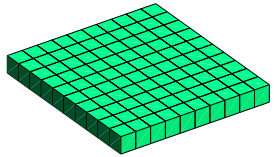

Effective Permeability

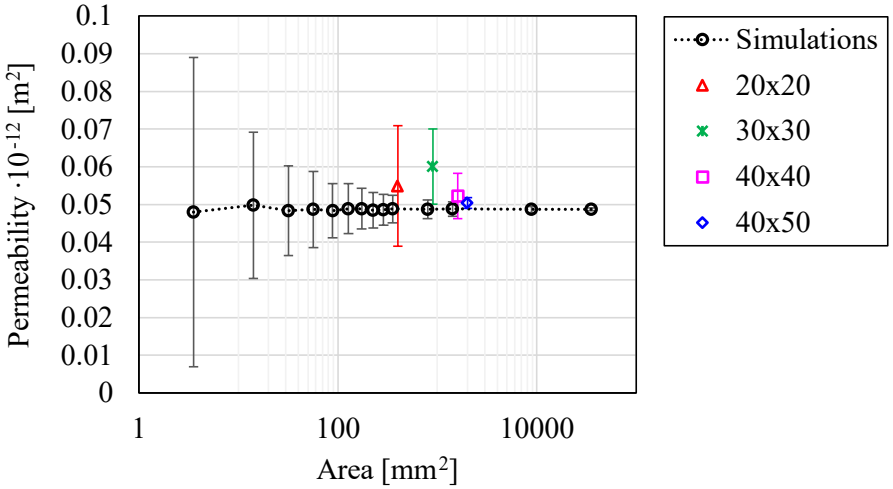

Coefficient of Variation

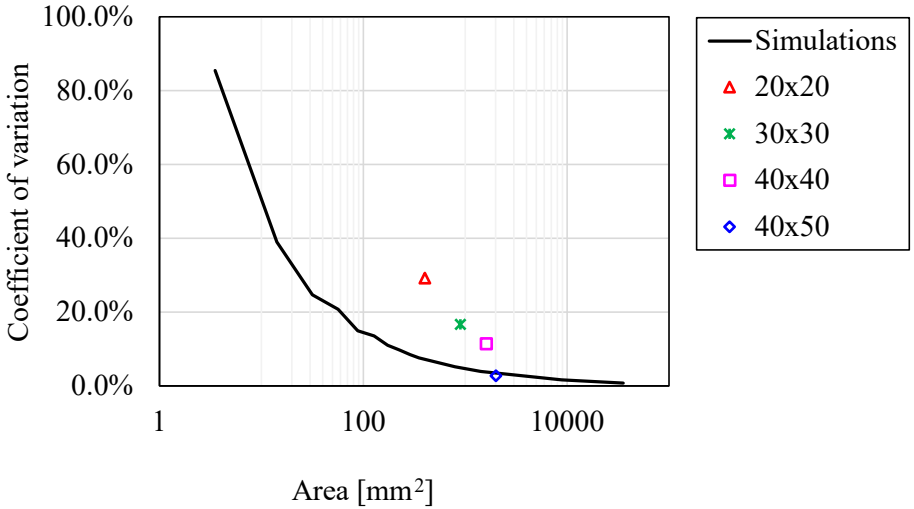

Legends: in black: simulations; colors: experiments of selected in-plane dimensions.

Numerical Simulations: Effective Permeability of Sample of 33 Plies

- Cv below 5% for model of area of 290 mm^2 (fabric RVE 25 mm^2).

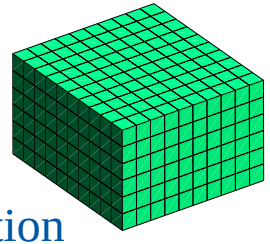

Effective Permeability

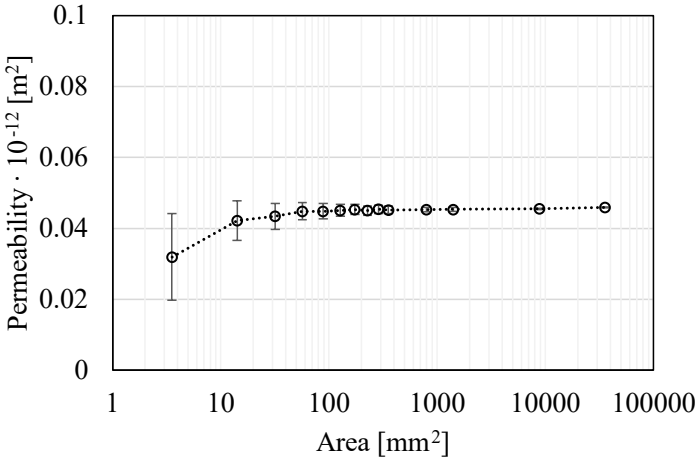

Coefficient of Variation

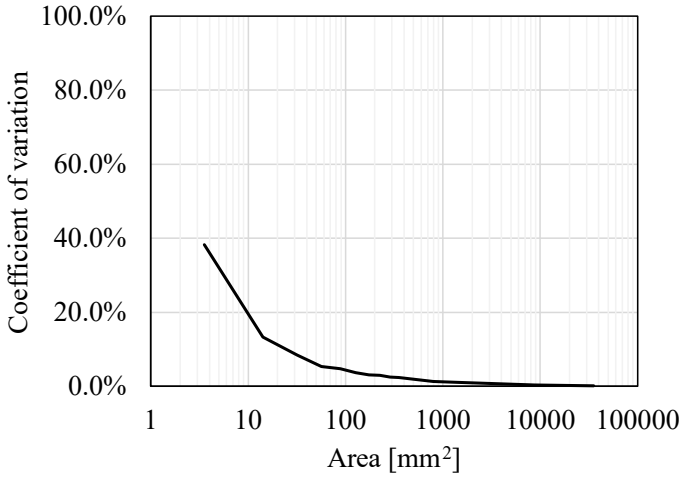

Outline

1. Introduction
    I. Densification process of carbon-carbon composites
    II. sRVE of carbon-carbon composites
2. Permeability of carbon-carbon composites as function of sample dimensions and inlet location
3. Image-based determination of the stochastic permeability
4. Numerical simulations for the prediction of the effective permeability
    I. Sample of 5 plies
    II. Sample of 33 plies
5. Conclusions

Conclusions

Permeability of CCC

Dimensions

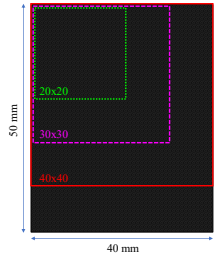

Inlet Location

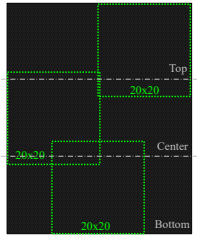

CCC Digital Model

CT scan



Permeability Distribution

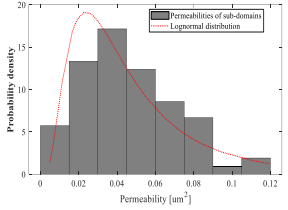

Numerical Simulations

5 Plies

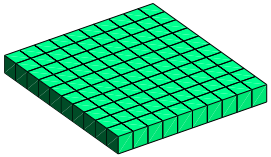

33 Plies

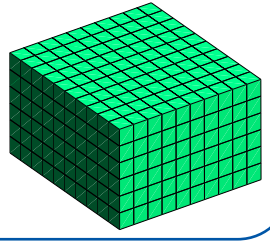

sRVE of CCC

- 5 Plies: 350 mm^2
- 33 Plies: 290 mm^2

(fabric RVE 25 mm^2)

Acknowledgements

- Research was sponsored by the Army Research Laboratory and was accomplished under Cooperative Agreement Number W911NF-18-2-0299.

- Research was supported by the University of Delaware Graduate College through the Doctoral Fellowship for Excellence.







Journal Publications

- Permeability of Carbon/Carbon Composites

"Correlation of the permeability and porosity development of carbon/carbon composites during pyrolysis"
T. Lavaggi, F. Muhammed, L. Moretti, J.W. Gillespie, S. Advani, *Composites Part A* (2024) DOI 10.1016/j.compositesa.2024.108156

"Influence of sample size on permeability of carbon-carbon composites with stochastic microstructure"
T. Lavaggi, J. W. Gillespie Jr., P. Mulye, C. Binetruy, S. Advani, *Composites Part A* (2025) DOI 10.1016/j.compositesa.2025.109126

- PoroS

"A novel finite element-based method for predicting the permeability of heterogeneous and anisotropic porous microstructure"
P. Mulye, E. Syerko, C. Binetruy, A. Leygue, *Materials* (2024) DOI 10.3390/ma17122873

- LIMS

"Desirable features in mold filling simulations for liquid composite molding processes"
P. Simacek, S. Advani, *Polymer Composites* (2004) DOI 10.1002/pc.20029

- Additional publications on Carbon/Carbon Composites

"Relating the microstructural and glass transition temperature evolution of a carbon-carbon composite precursor during pyrolysis using thermomechanical analysis" DOI 10.1002/app.54526
"Pyrolysis schedule optimization of benzoxazine-derived carbon/carbon composites through reaction rate optimization"
DOI 10.1016/j.ceramint.2023.03.121
"Influence of pyrolytic decomposition on the microstructure evolution of benzoxazine-derived carbon-carbon composites" DOI.10.1007/s10853-022-08007-9
"Influence of material and process parameters on microstructure evolution during the fabrication of carbon-carbon composites: a review" DOI 10.1007/s10853-021-06401-3

Monitoring RTM Infiltration Behavior of TFP Preforms Using Near-Net-Shaped Transparent Cavities

Cameron Welker[1], Lars Bittrich[1], Dennis Weitze[2], Sarah Schlegel[2], Luise Kärger[2], Tales Lisbôa[1], Axel Spickenheuer[1]

[1] Leibniz-Institut für Polymerforschung Dresden e. V.

[2] Institute of Vehicle System Technology, Karlsruhe Institute of Technology

Agenda

- Tailored Fiber Placement (TFP)
- Challenges in mold design for RTM injections of TFP preforms
- Additive manufactured molds for RTM infiltration
- Accuracy of 3D-printed RTM molds
- Experimental results

Properties of different materials

Normalized dense specific elastic modulus of different lightweight material

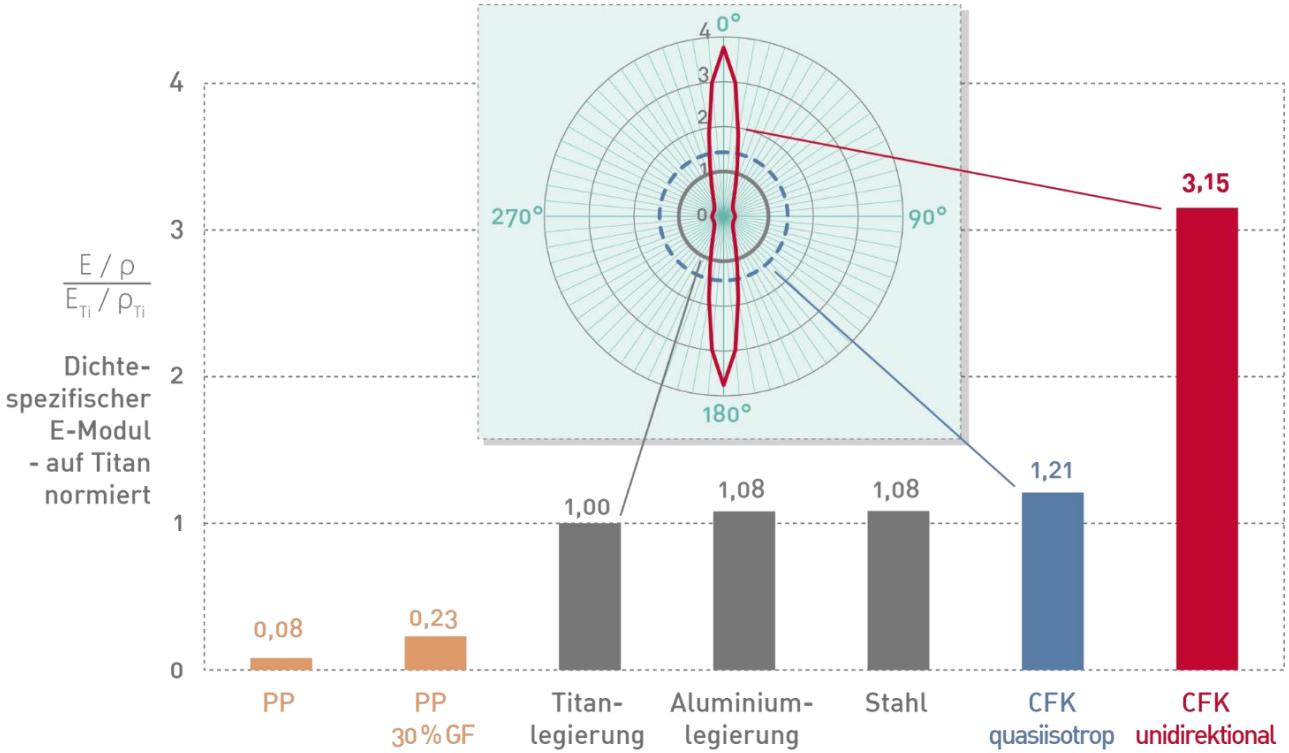

Tailored Fiber Placement (TFP)

Process characteristics

- Near-net-shape production of variable-axial textile preforms
- Almost ideal utilization of anisotropic material properties
- Placement radii up to 5 mm

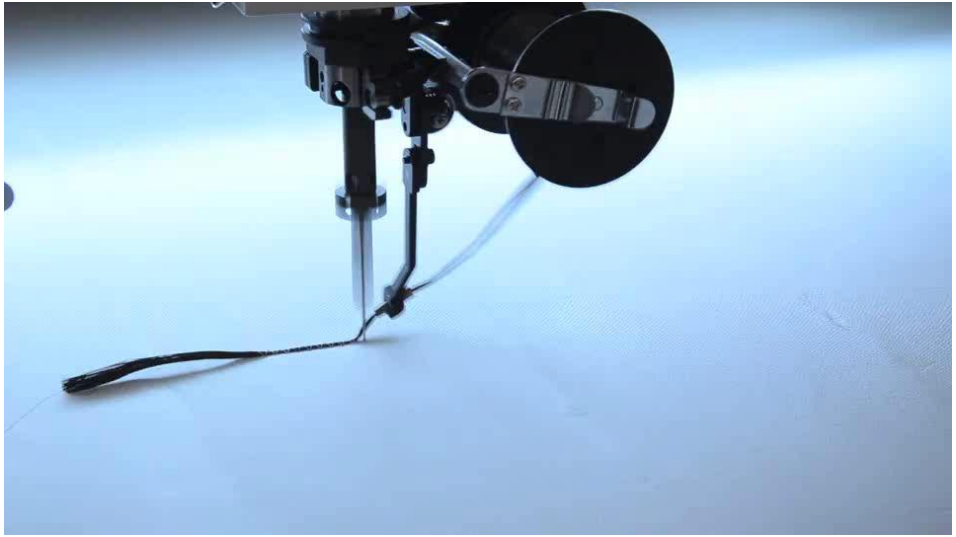

Complex infiltration behavior

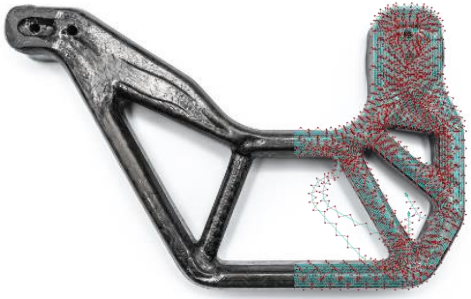

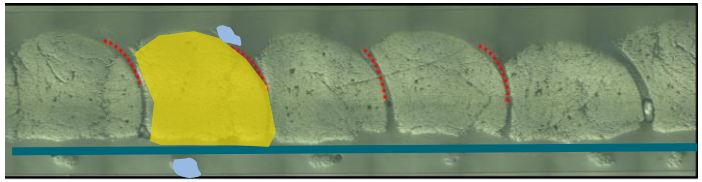

Roving Base material Stitching yarn

Tailored Fiber Placement (TFP)

Process characteristics

- Preliminary studies about measurement of in-plane permeability
- Antisymmetric stitching pattern showed higher permeability
- CFD flow simulations of the experiments for predicting resin flow

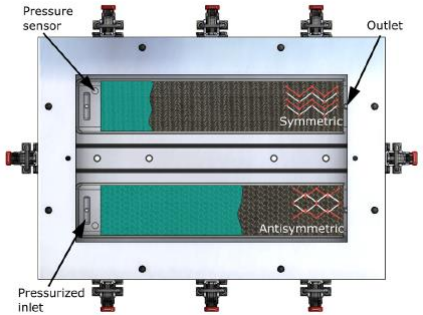

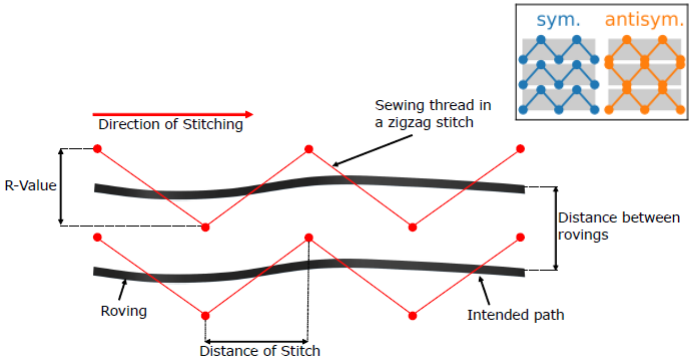

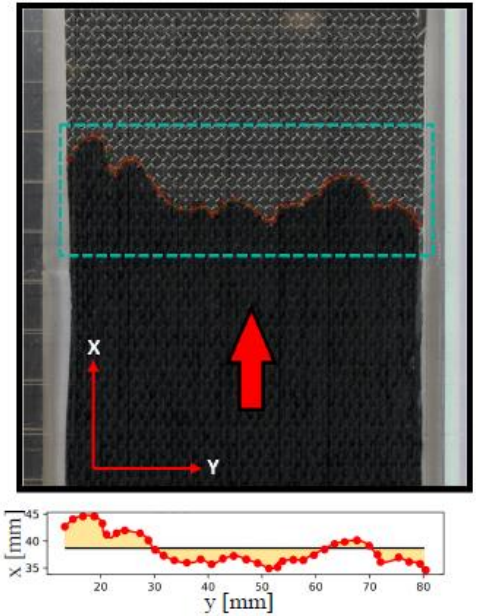

Bittrich, L.; Seuffert, J.; Dietrich, S.; Uhlig, K.; Lisboa, T.d.V.; Kärger, L.; Spickenheuer, A. On the Resin Transfer Molding (RTM) Infiltration of Fiber-Reinforced Composites Made by Tailored Fiber Placement. *Polymers* **2022**, *14*, 4873. https://doi.org/10.3390/polym14224873

Tailored Fiber Placement (TFP)

Overcoming the challenges by numerically predict resin flow

- Anisotropic material permeability needs to be evaluated by experiments
- Race-tracking needs to be avoided
- Experimental determination of out-of-plane permeability of TFP preforms is current subject of research

- ➢ Additive manufactured tools enable rapid change of cavity geometries and inlet/outlet locations
- ➢ Near-Net-Shaped cavities avoid race-tracking

(Transparent) molds for RTM injections

Comparison between different manufacturing technologies

- Complex TFP surfaces often require 3D-Milling
  - Surface Quality
  - Structural stiffness
  - Time consuming process
  - costly
- 3D-printing (Fused Deposition Modeling) technology
  - Cheap process
  - Comparatively fast
  - Not really transparent
  - Surface quality
  - Not sealed (porosity)
- 3D-printing (Stereolithography) technology
  - Transparent parts
  - Sealed structure
  - Brittle structures

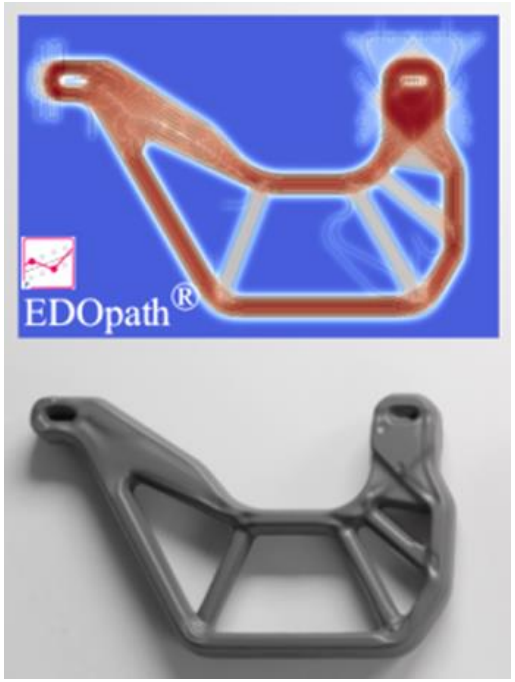

(Transparent) molds for RTM injections

3D-printed approach



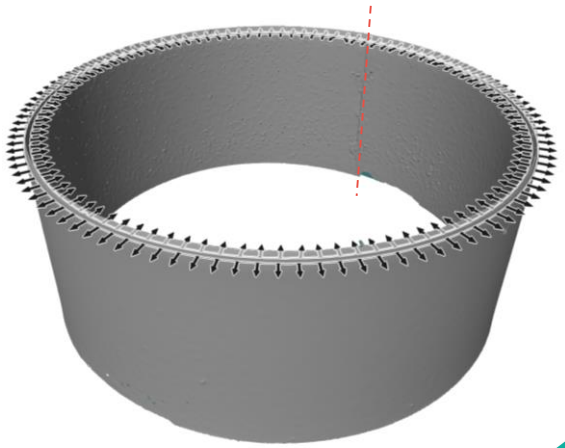

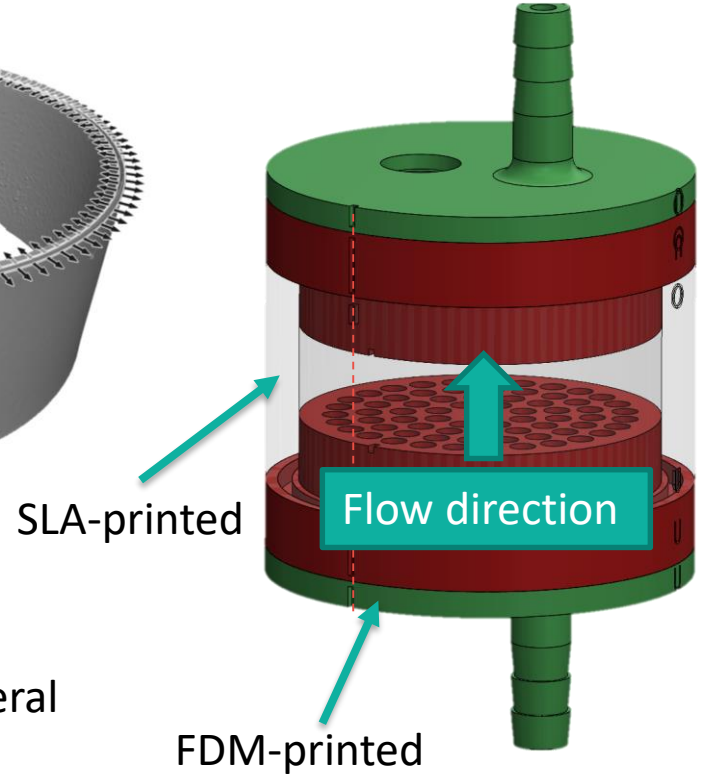

- 3D-Scan of fiber cutting tool
- Cross-section used as cavity cross section
- FDM print enables connection of various peripheral devices (pressure sensor etc.)

(Transparent) molds for RTM injections

3D-printed approach

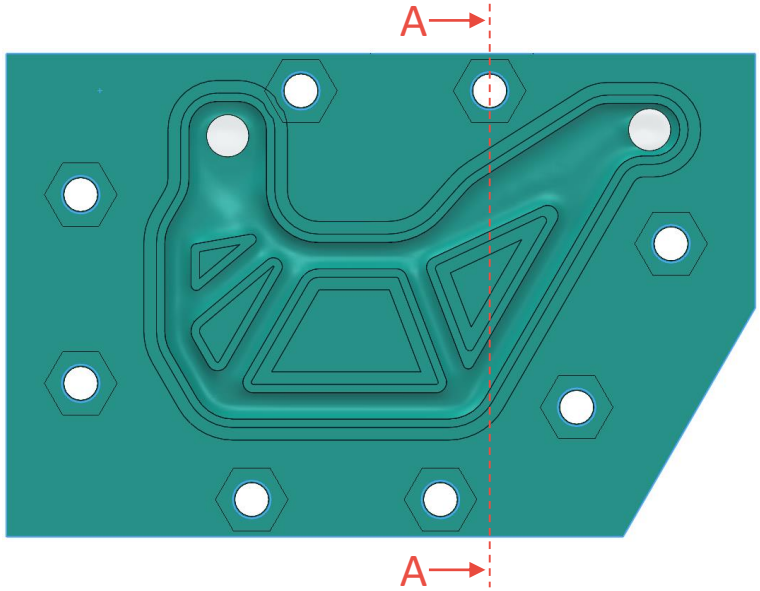

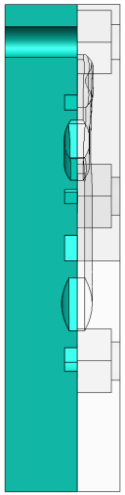

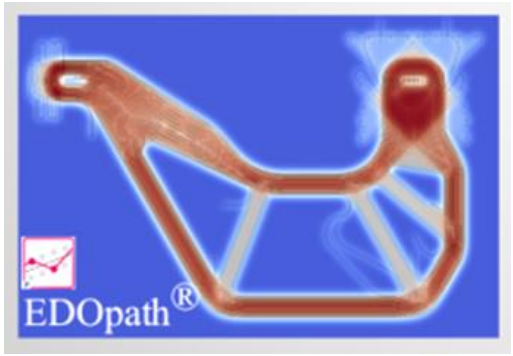

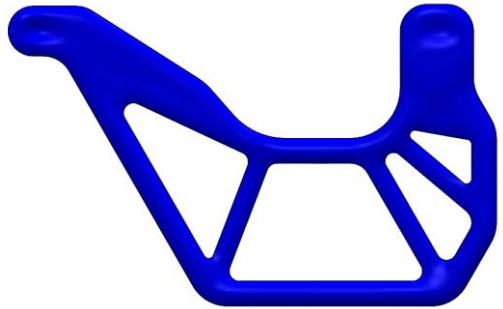

- Top part SLA printed (transparent)
- Bottom part FDM printed (non-transparent)

(Transparent) molds for RTM injections

3D-printed approach – Evaluation of accuracy

- Zeiss GOM Metrology GmbH ATOS Q, MF 170
- Deviation to CAD model by best-fit

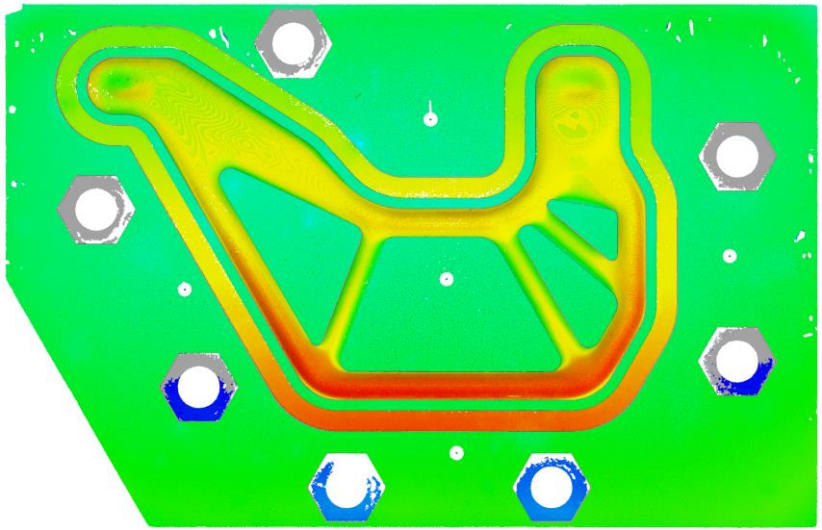

- SLA part after printing

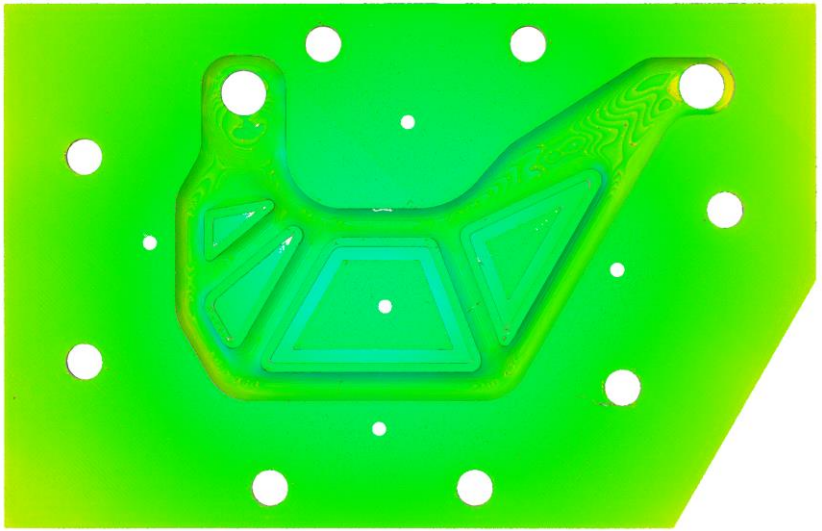

- FDM part after printing

(Transparent) molds for RTM injections

3D-printed approach

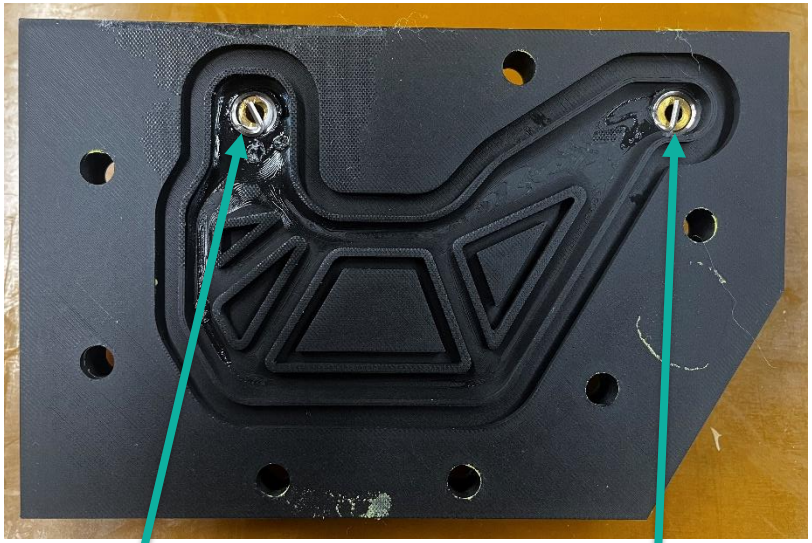

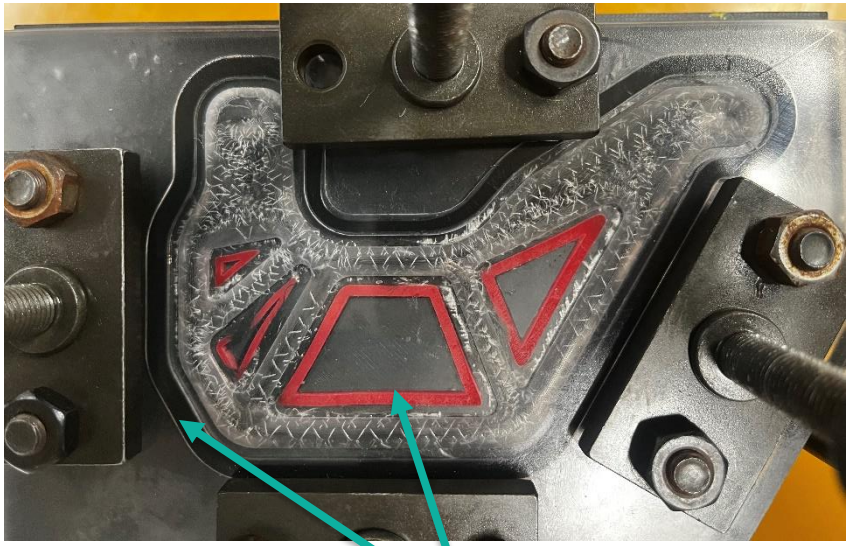

- Top and bottom part pressed together by quick release clamps

Injection experiment
simple cavity

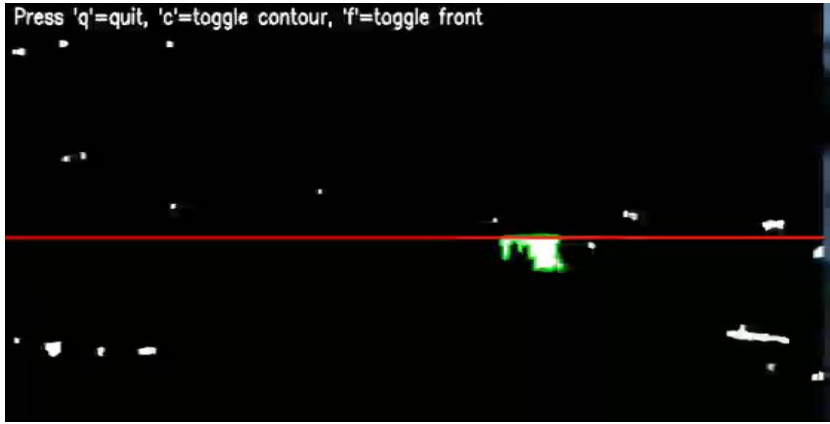

Thresholded video frame with contour detection

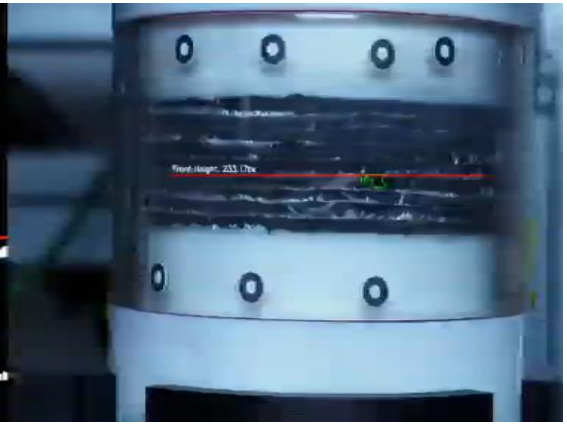

Original video frame

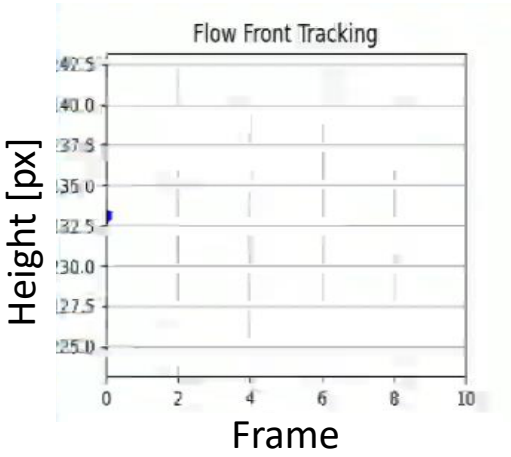

Flow front height (px) over time (frame)

- No race-tracking
- Flow front clearly visible through SLA printed cavity

Injection experiment
complex cavity



- Race tracking at borders
- Inner sealings not sufficient
- Flow front clearly visible through SLA printed cavity

Leibniz-Institut
für Polymerforschung
Dresden

Thank you for your attention!

Contact:
Cameron Welker
welker@ipfdd.de
+49 351 4658 666

Funding gratefully
acknowledged by:
DFG Deutsche Forschungsgemeinschaft
Project:
KA 4224/4-2 and SP 1646/2-2
Grant number:
415041798

Modelling and Simulating Particle Transport in Liquid Composite Moulding Processes

The 24th International Conference on Composite Materials (ICCM24)

6th August 2025, Baltimore, USA

Shanthar Rajinth

Department of Materials, The University of Manchester, United Kingdom

Center for Composite Materials, University of Delaware, USA

rajinth.shanthar@manchester.ac.uk

Supervised by

Dr. Robert Prosser, Prof. Prasad Potluri, Dr. Pavel Simacek, Prof. Suresh G. Advani, Dr. Chamil Abeykoon

Content

1 Introduction
- 1.1 RTM Process Overview
- 1.2 Particle Mixed Resin Flow

2 Methodology
- 2.1 Resin Flow Model
- 2.2 Particle Transport Models
- 2.3 Numerical Implementation
- 2.4 Particles and Permeability
- 2.5 Numerical Flow Domain

3 Results
- 3.1 Partially Coupled Model
- 3.2 Fully Coupled Model
- 3.3 Time Evolution of Particle Distribution
- 3.4 Time Evolution of Permeability
- 3.5 Influence of Particle Injection Conditions
- 3.6 Influence of Particle Size
- 3.7 Trials with Radial Flow

4 Summary and Outlook

1. Introduction

1.1. RTM Process Overview

- Resin Transfer Moulding (RTM) is a process used to manufacture Fibre Reinforced Polymers (FRP), which consists of 5 steps as shown in Fig. 1.

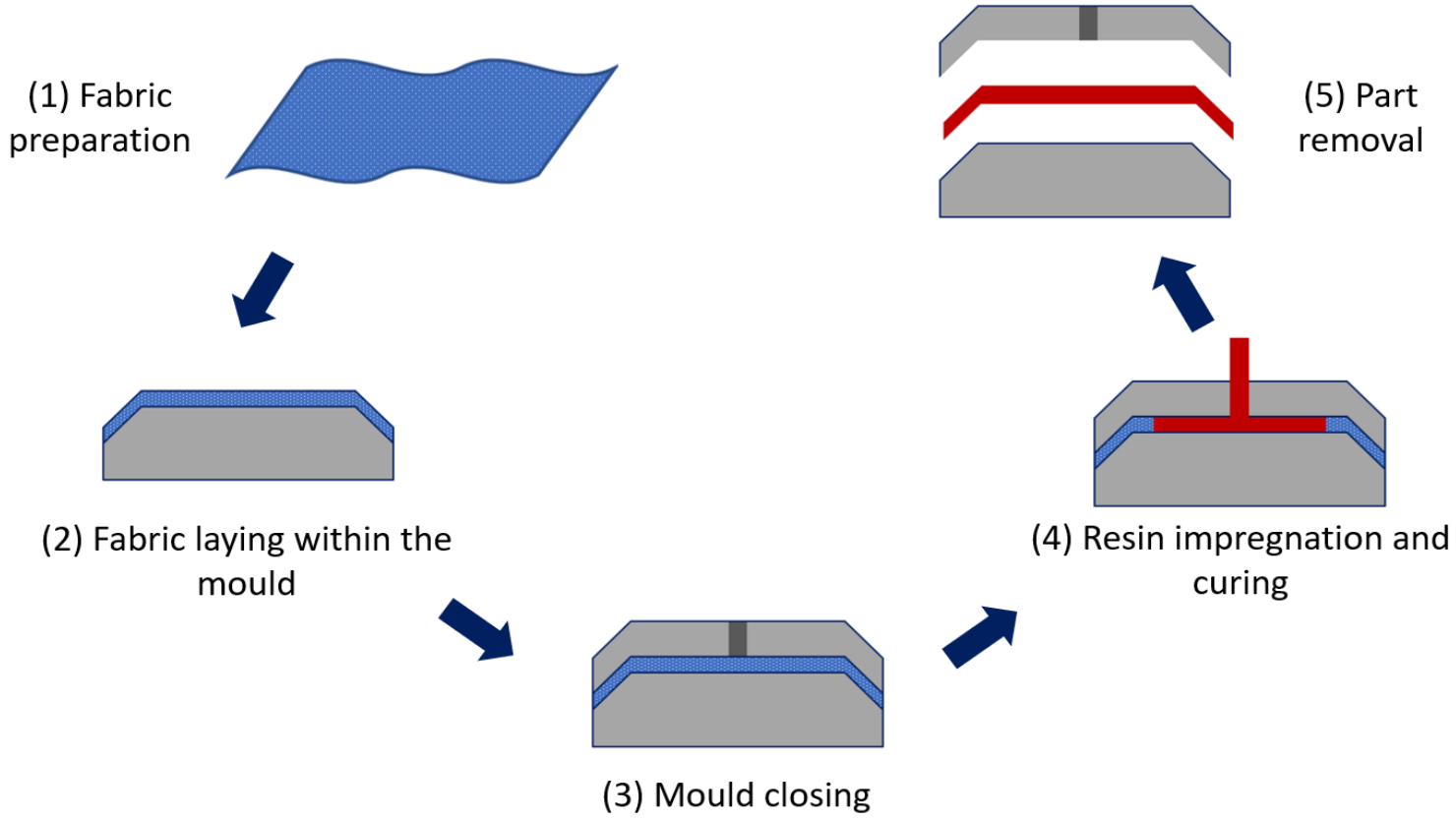

Figure 1: The Resin Transfer Moulding (RTM) process

1. Introduction

1.2. Particle Mixed Resin Flow

- Particles may be mixed with the resin to improve the properties of parts manufactured using RTM [1][2].

- The sizes of these particles can range from the micrometre scale to the nanometre scale, as shown in Fig. 2.

- Transport models and simulations can provide valuable information regarding the final particle distribution, permeability changes, and particle filtration [3].

- The presence of particles will affect the permeability of the flow channels, which in turn will affect the flow of particles [4][5].

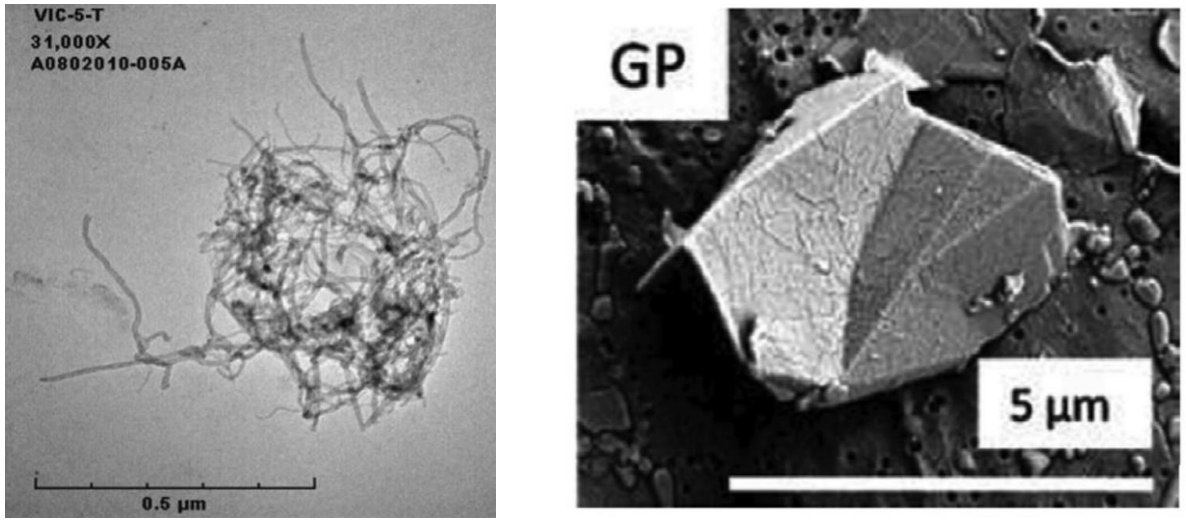

Figure 2: Different types of particles (a) Multi-Walled Carbon Nanotubes (b) Graphene Nanoplatelets [6]

2. Methodology

2.1. Resin Flow Model

- The resin flow through the reinforcement preform is modelled as a flow through a porous medium, governed by the mass conservation equation (Eq. 1) and the Darcy equation (Eq. 2).

$$\nabla \cdot \mathbf{u} = 0 \tag{1}$$

$$\mathbf{u} = -\frac{\mathbf{K}}{\mu}\nabla P \tag{2}$$

- Here, $\mathbf{u}$ is the volume-averaged resin velocity, $\mathbf{K}$ is the permeability tensor for the porous preform, μ is the resin viscosity, and P is the resin pressure.

- The above equations can be combined to obtain Eq. 3, which is then used to solve for the in-mould pressure distribution at each time step.

$$\nabla \cdot \left(\frac{\mathbf{K}}{\mu}\nabla P\right) = 0 \tag{3}$$

2. Methodology

2.2. Particle Transport Models

Partially Coupled Model

- In this approach, the preform permeability is assumed to be constant and unaffected by the presence of particles (Fig. 3a)

- After the pressure and velocity fields are solved, the particle locations are updated based on the resin flow, resulting in a passive transport.

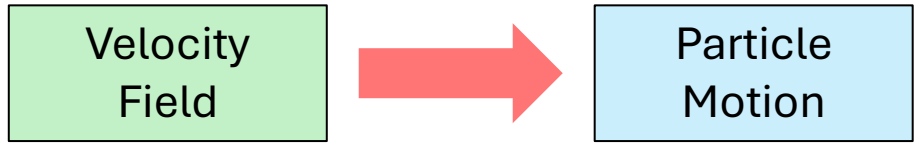

Figure 3a: Partially coupled model

Fully Coupled Model

- In this approach, the preform permeability is updated at each time step according to the presence of particles within an element (Fig. 3b)

- The new permeabilities of elements are calculated using the Gebart model by adjusting the porosity accordingly.

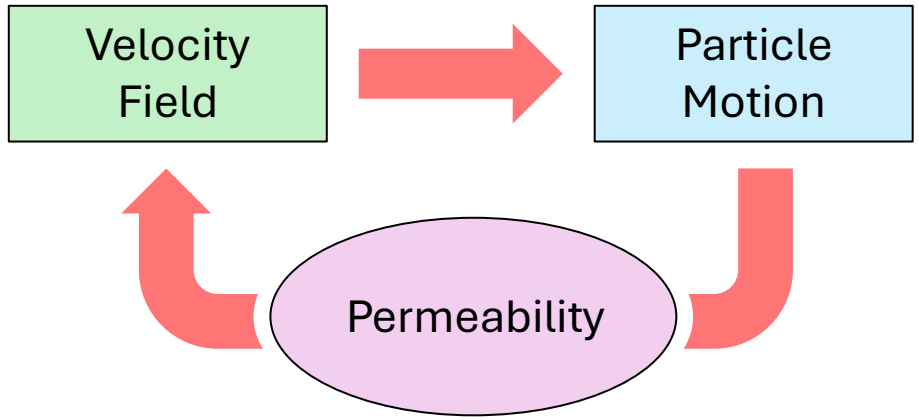

Figure 3b: Fully coupled model

2. Methodology

2.3. Numerical Implementation

- Resin pressure and velocity values are calculated using the Liquid Injection Moulding Simulation (LIMS) software developed at the University of Delaware.
- The particle transportation is implemented using a worker script that reads pressure and velocity data from LIMS and updates the particle location.
- This architecture is shown in Fig. 4 [7].
- At each time step, Eq. 3 is solved using the finite element method in LIMS.

$$\boldsymbol{\nabla} \cdot \left(\frac{\mathbf{K}}{\mu} \nabla P \right) = 0 \qquad (3)$$

- Data is communicated between LIMS and the worker script using Message Passing Interface (MPI).

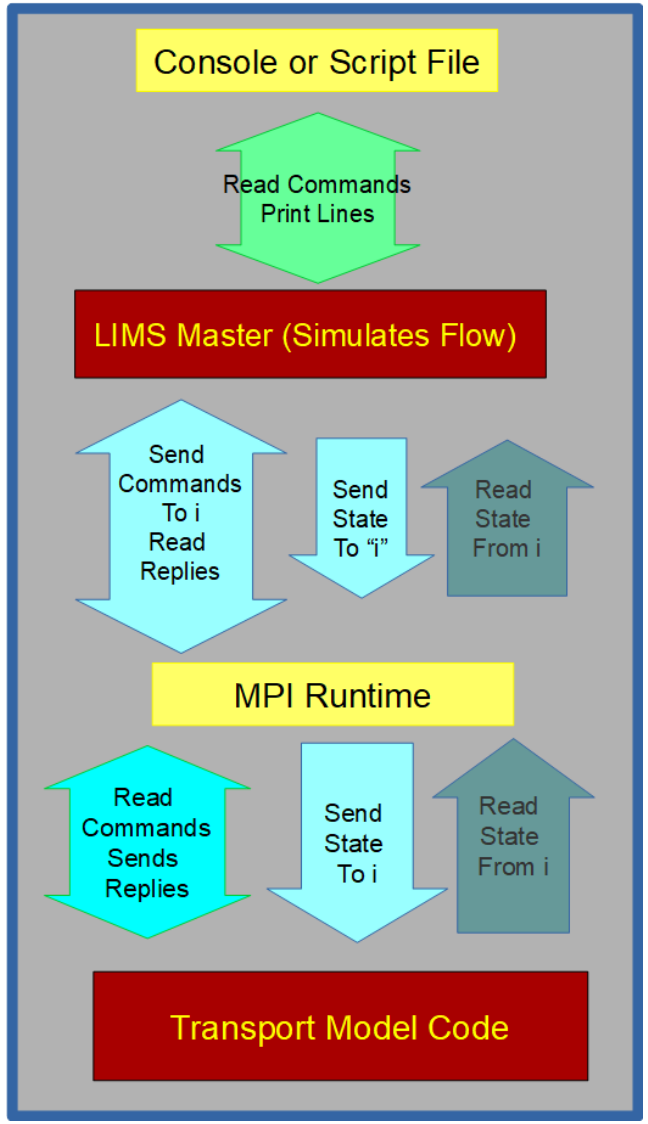

Figure 4:
Simulation software architecture [7]

2. Methodology

2.4. Particles and Permeability

- In the fully coupled model, the new permeabilities of elements are calculated using the Gebart model for transverse permeability of cylinders in quadratic arrangement, given in Eq. 4 [8].

$$K_{\perp} = \frac{16}{9\pi\sqrt{2}}\left(\sqrt{\frac{V_{fmax}}{V_f}} - 1\right)^{5/2} R^2 \qquad (4)$$

- Here, V_{fmax} is the maximum volume fraction, V_f is the volume fraction, R is the fibre radius.

- The volume fraction is updated according to the number of particles within an element, as shown in Fig. 5a.

- As more particles enter the element, the permeability gradually reduces (Fig. 5b) and becomes zero beyond the maximum fraction.

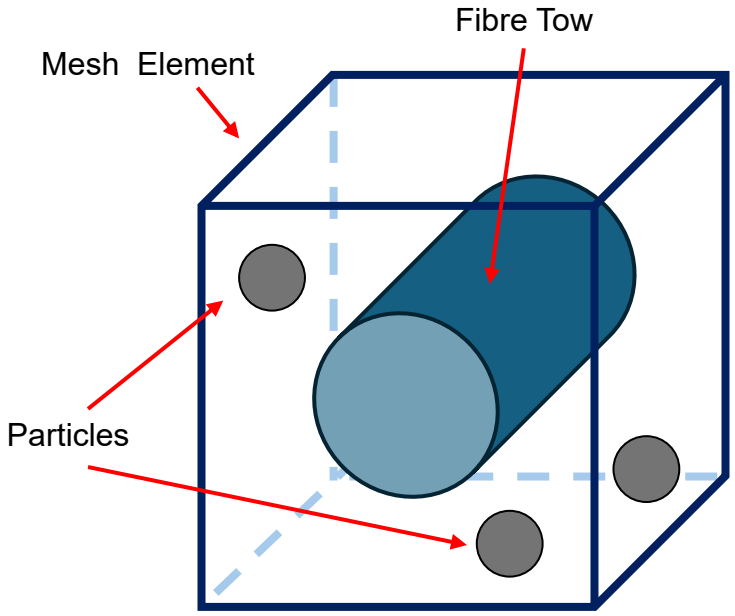

(a)

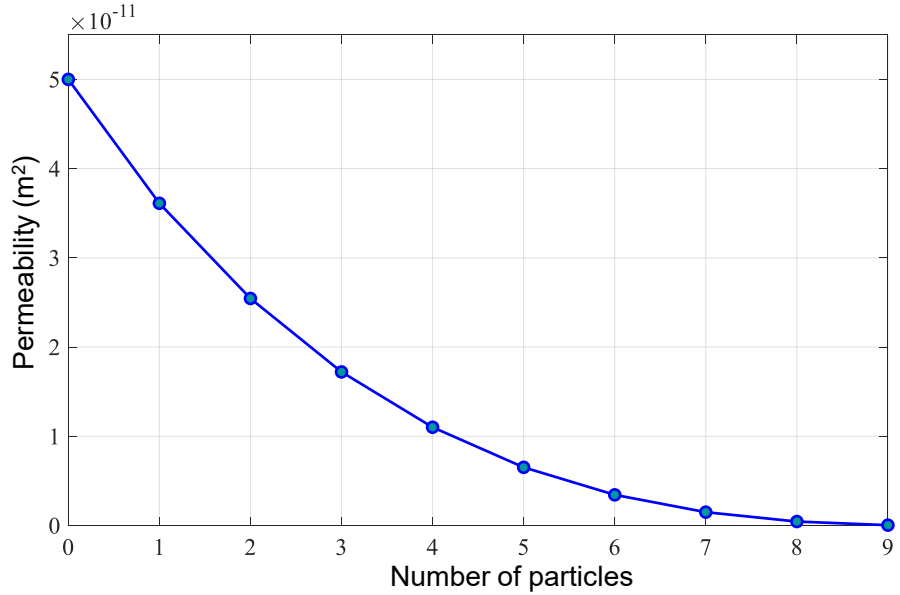

(b)

Figure 5: (a) Contents within an element (b) Variation of permeability with the number of particles within an element

2. Methodology

2.5. Numerical Flow Domain

- The numerical domain is a 10cmx30cm rectangular mould, and the resin is injected under controlled pressure from a line gate, as shown in Fig. 6.

- Particles are introduced to the system from the inlet at different concentrations and pressures, and their motion is tracked.

- The numerical parameters are given in Table 1.

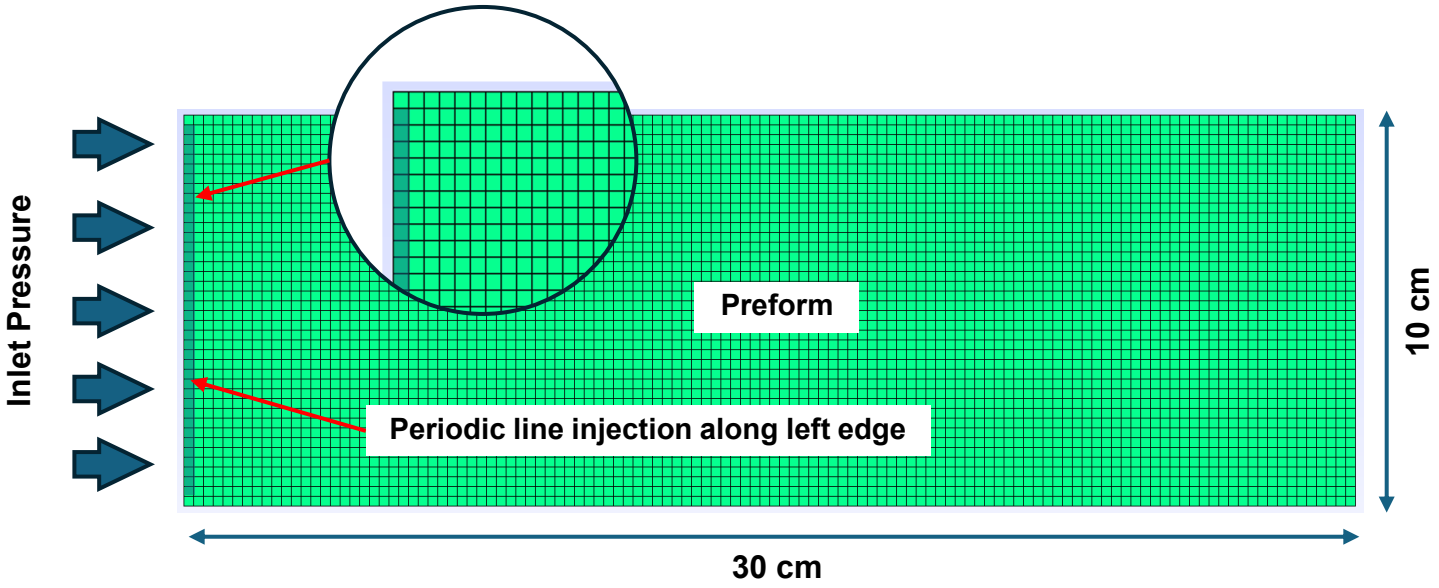

Figure 6: Numerical domain setup

Table 1: Flow simulation parameters

Parameter	Value
Preform permeability	5e-11 m^2
Resin viscosity	200 mPas
Injection pressure	25 kPa
Mould thickness	5 mm
Particle diameter	0.6 mm

3. Results

3.1. Partially Coupled Model

- During the simulation, 1710 particles were introduced into the system.
- Fig. 7a shows the path of motion of the particles.
- The particles move in straight lines due to being passively transported by the flow.
- Fig. 7b shows the distribution of the particles within the mould at fill time.
- The injection profile of the particles is preserved due to the absence of flow obstructions.

Figure 7a

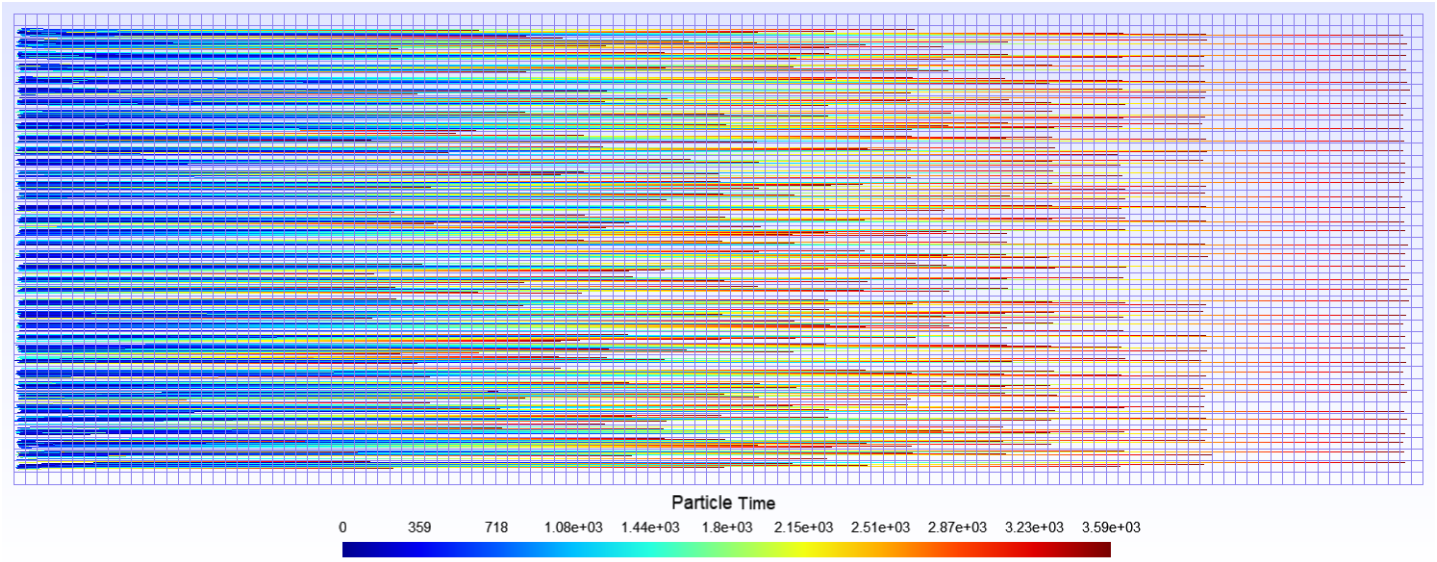

Figure 7b

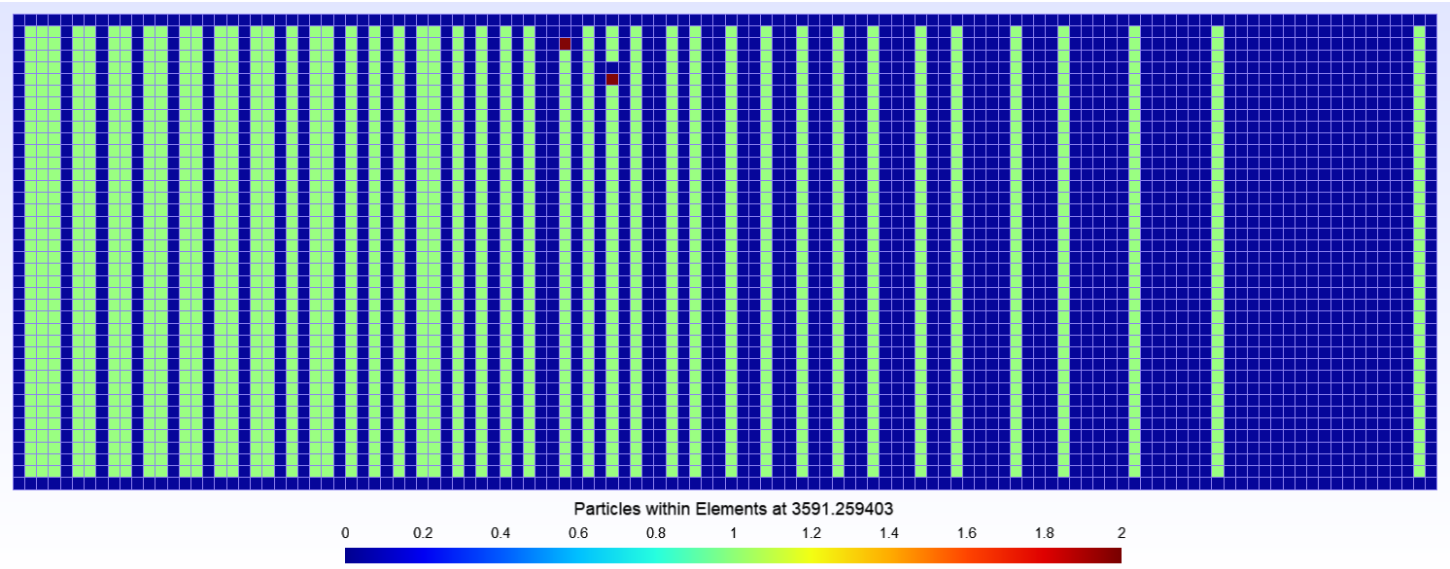

3. Results

3.2. Fully Coupled Model

- During the simulation, 2052 particles were introduced into the system.
- Fig. 8a shows the path of motion of the particles.
- Now, their flow paths are affected due to the local changes in permeability.
- Fig. 8b shows the distribution of the particles within the mould at fill time.
- Near the inlet, particles accumulate causing the permeability to reduce, leading to further accumulation.

Figure 8a

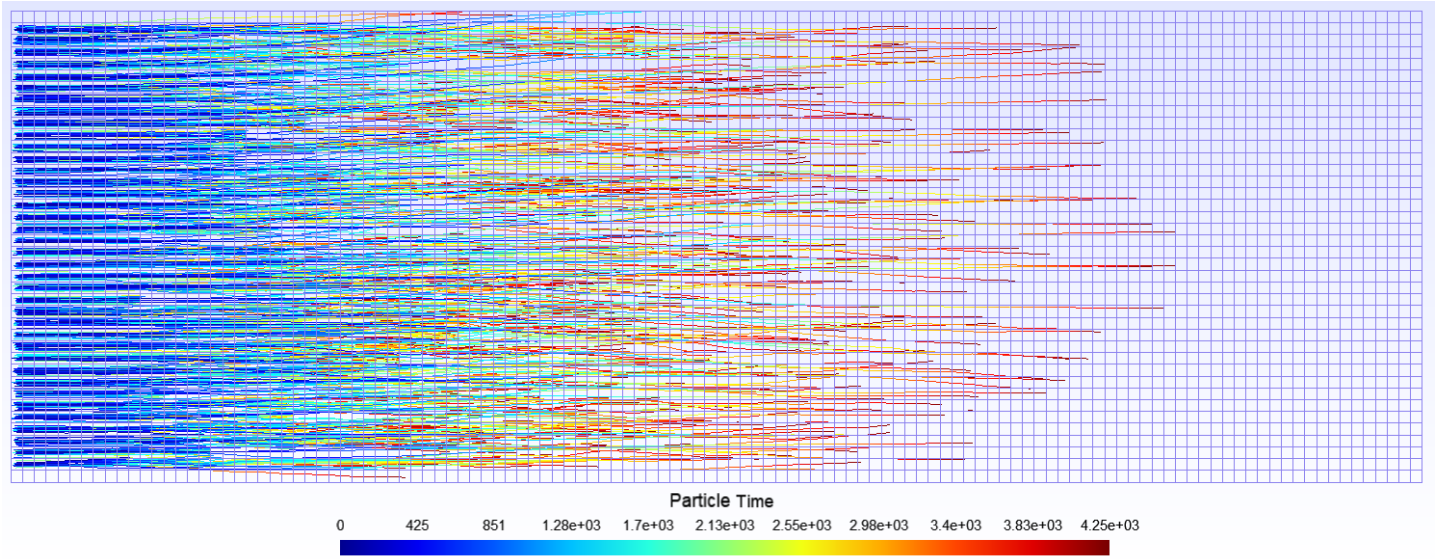

Figure 8b

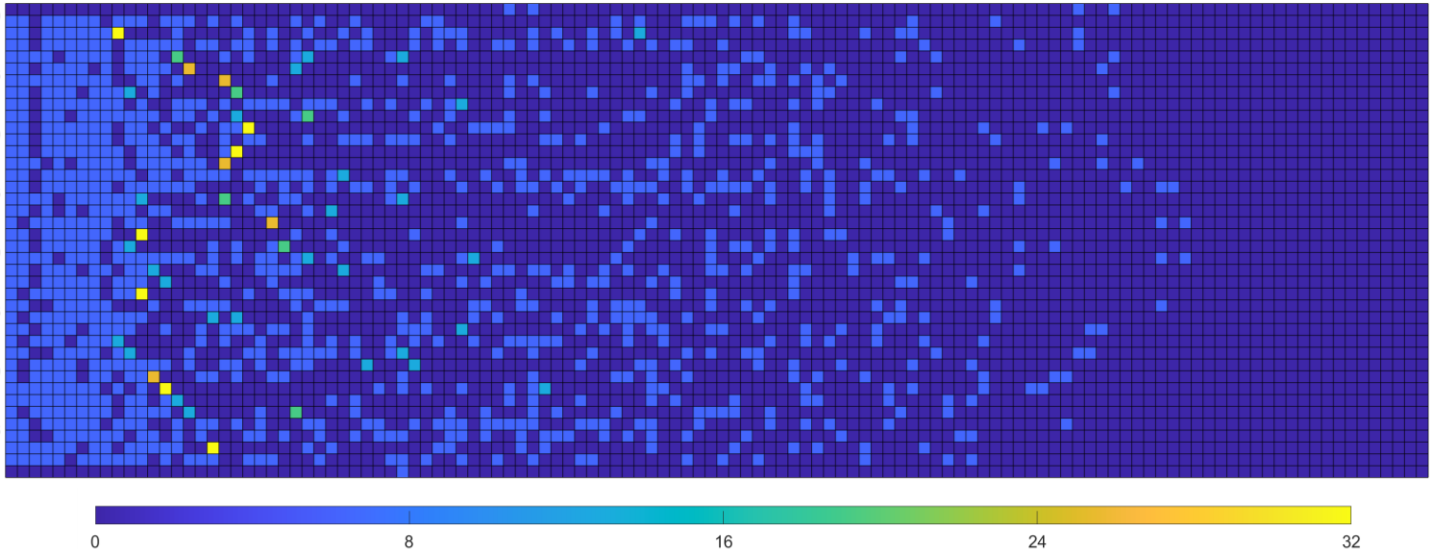

3. Results

3.3. Time Evolution of Particle Distribution

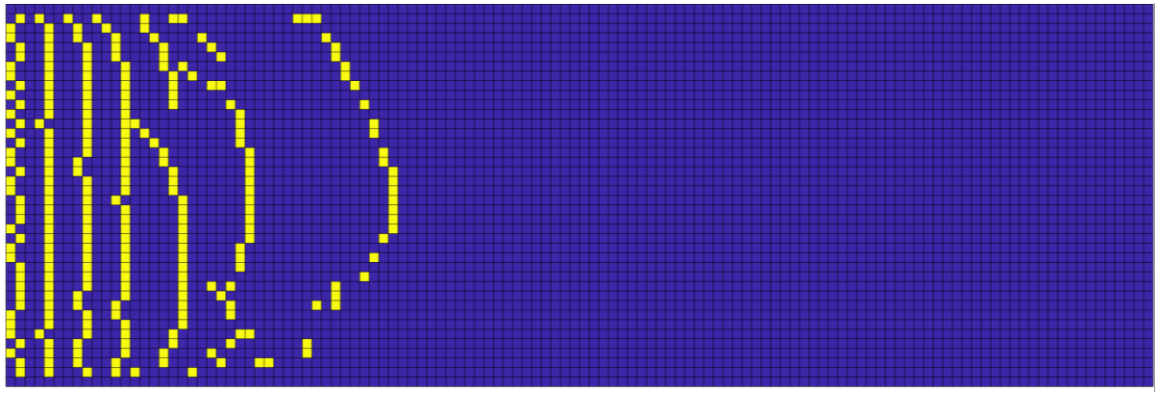

(a) t = 100 s

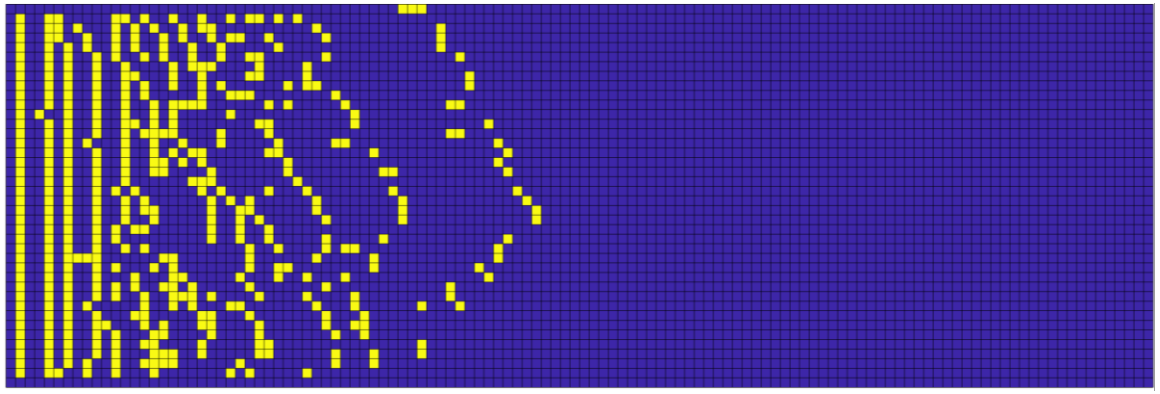

(b) t = 500 s

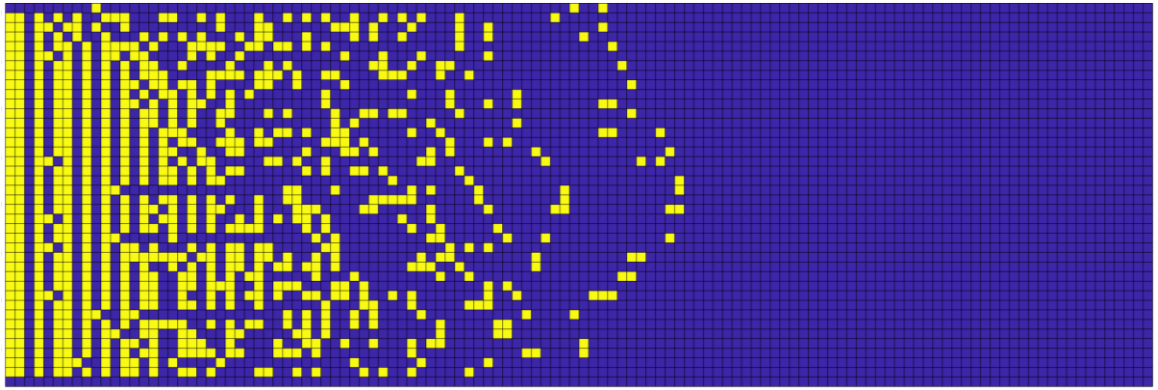

(c) t = 2000 s

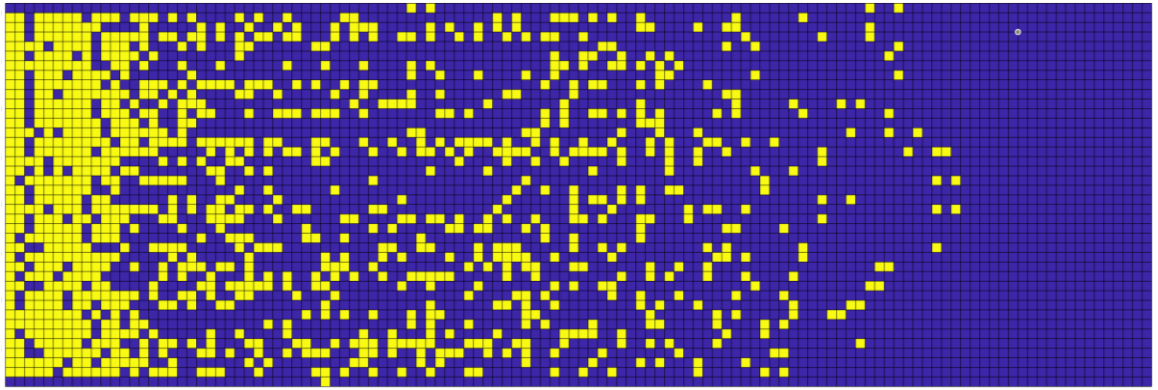

(d) Mould fill

Figure 9: Evolution of the particle distribution with time

3. Results

3.4. Time Evolution of Permeability

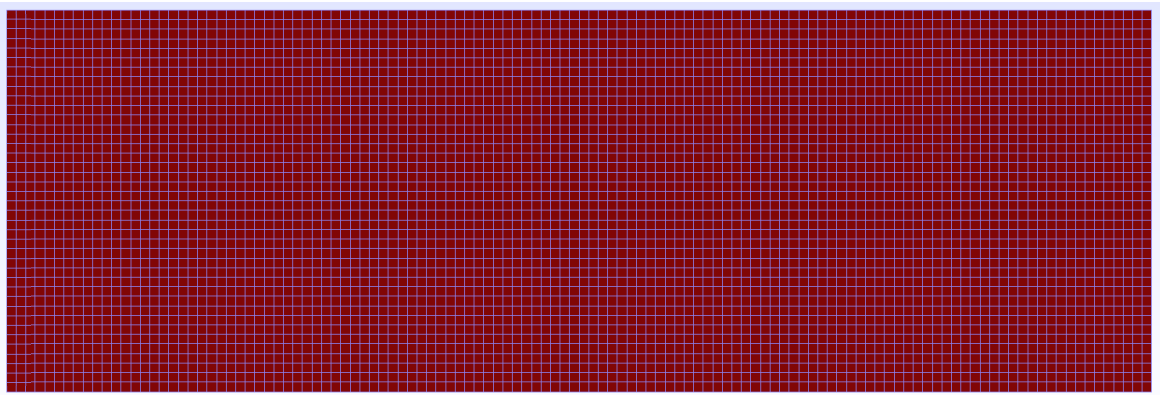

(a) t = 0 s

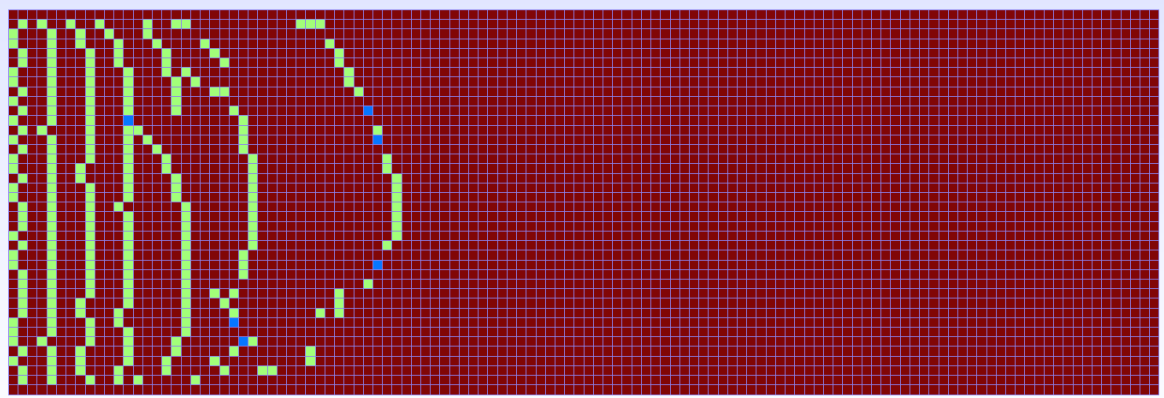

(b) t = 500 s

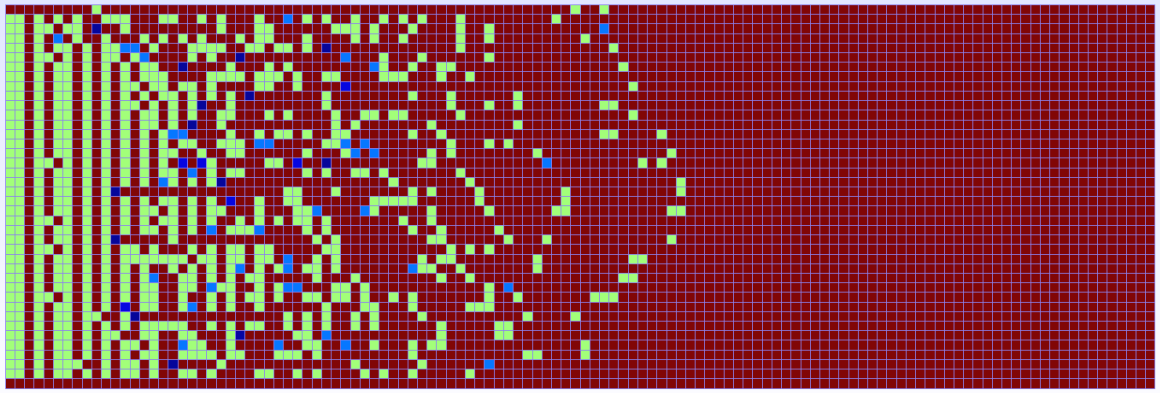

(c) t = 2000 s

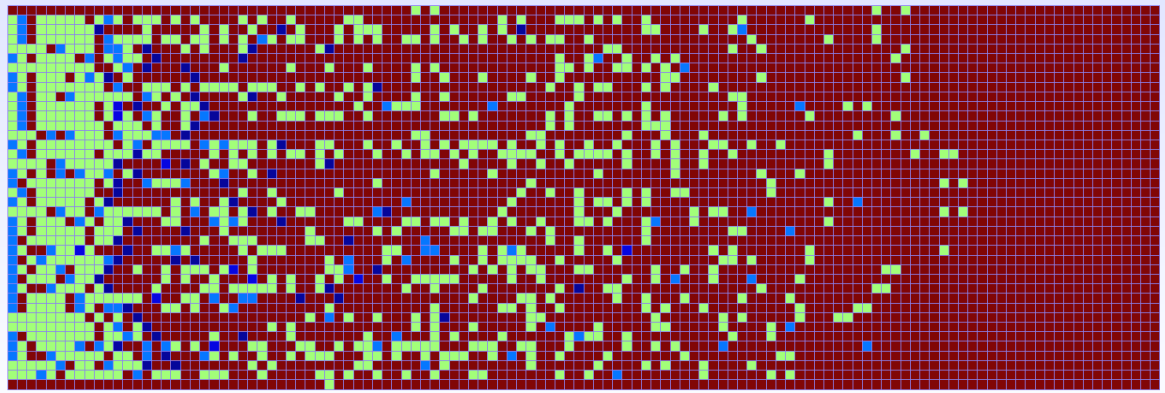

(d) t = Mould fill

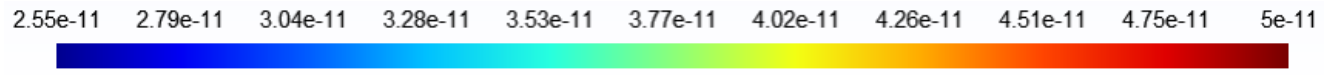

Figure 10: Evolution of the domain permeability with time

3. Results

3.5. Influence of Particle Injection Conditions – Inlet Pressure

- The effect of inlet pressure on the final distribution of particles was investigated.

- The particle inlet concentration was fixed, and the results are given in Fig. 11.

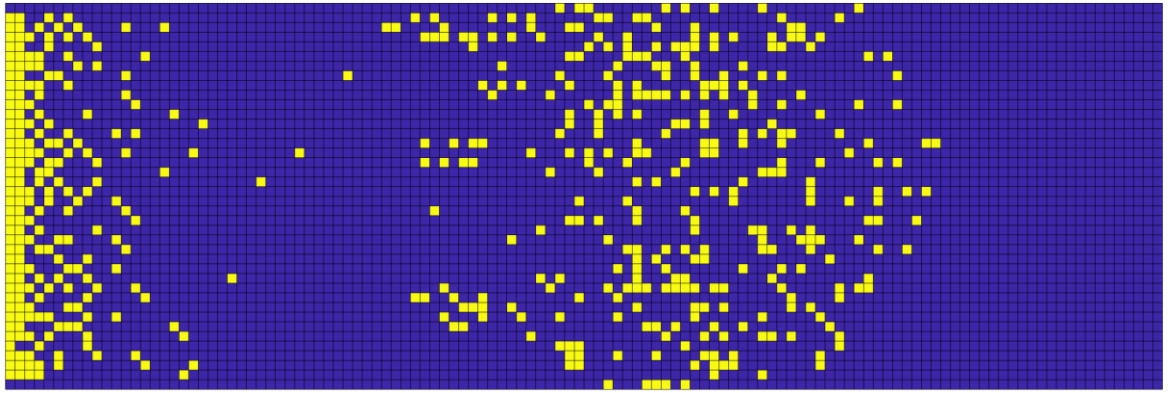

(a) 12.5 kPa inlet pressure

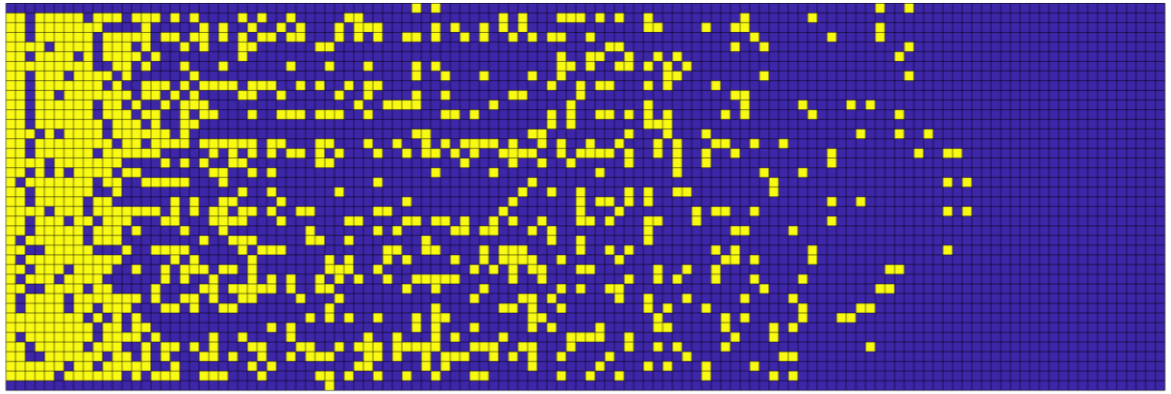

(b) 25 kPa inlet pressure

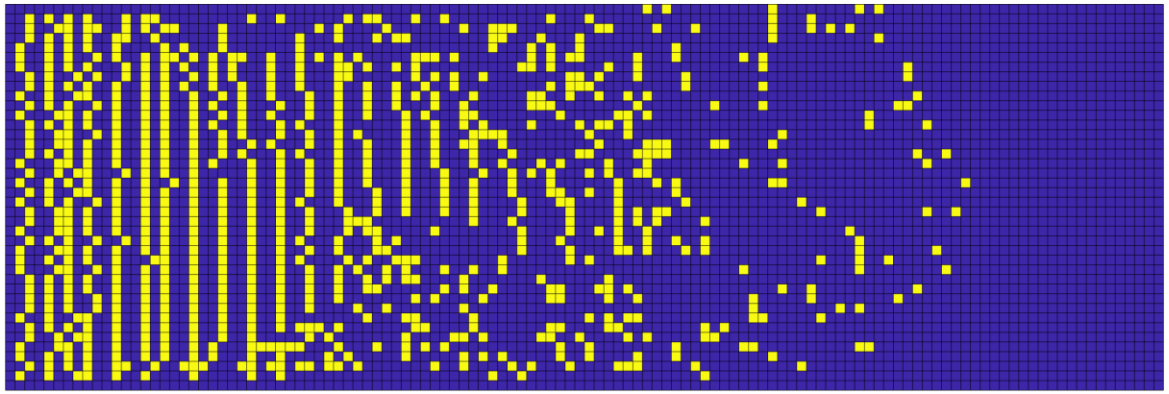

(c) 50 kPa inlet pressure

Figure 11: Variation of final particle distribution with inlet pressure

3. Results

3.5. Influence of Particle Injection Conditions – Injection Rate

- The effect of injection rate on the final distribution of particles was also investigated.
- The results are analogous to those obtained for varying inlet pressure previously, as shown in Fig. 12.

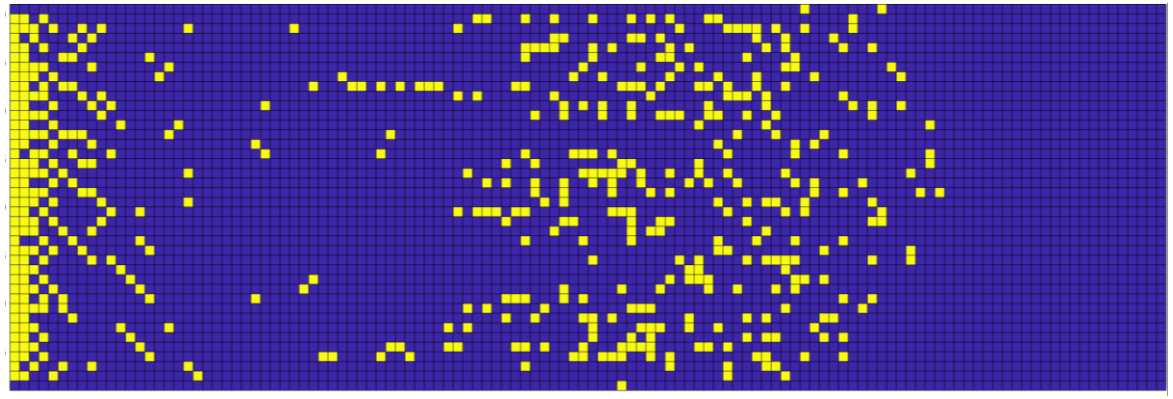

(a) 1 particle per second

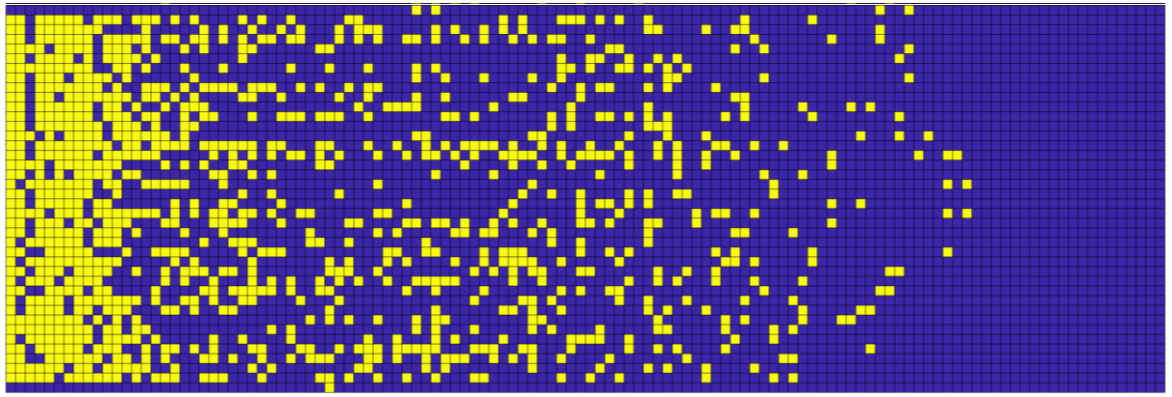

(b) 1 particle per 2 seconds

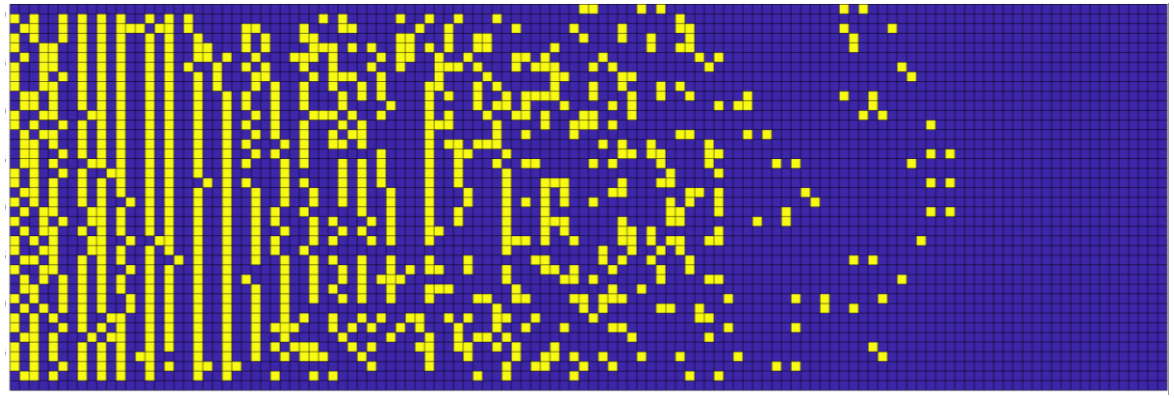

(c) 1 particle per 4 seconds

Figure 12: Variation of final particle distribution with particle injection rate

3. Results

3.6. Influence of Particle Size

- The particle size influences the rate of permeability reduction, as shown in Fig. 13.
- Larger particle sizes result in a rapid permeability reduction, leading to early particle accumulation and blockage (Fig. 13c).

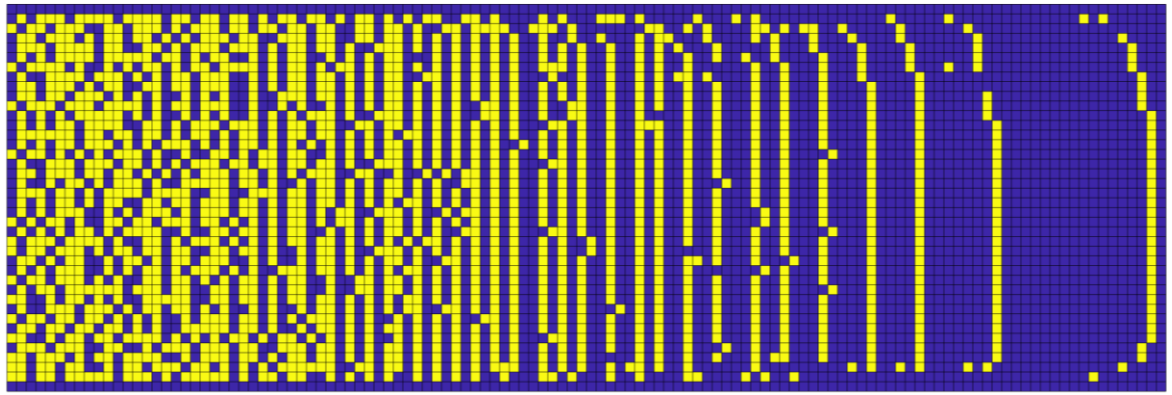

(a) r = 0.4 mm

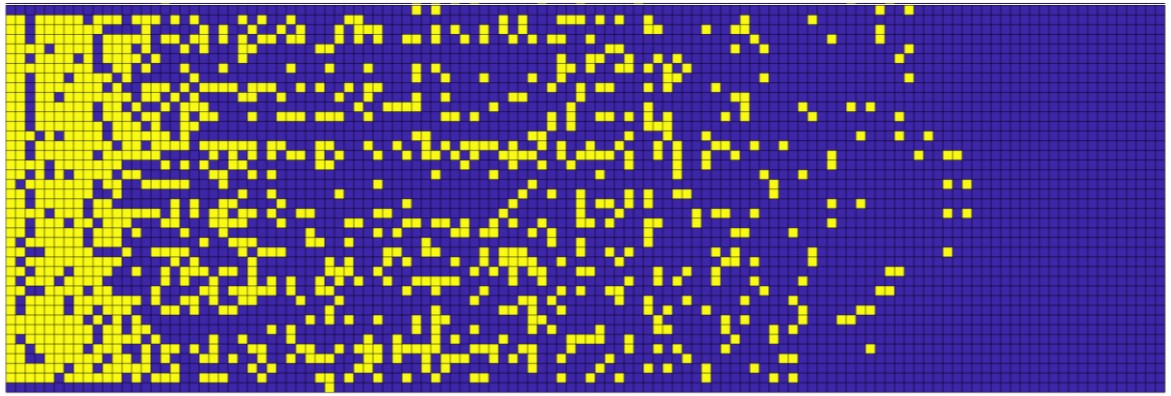

(b) r = 0.6 mm

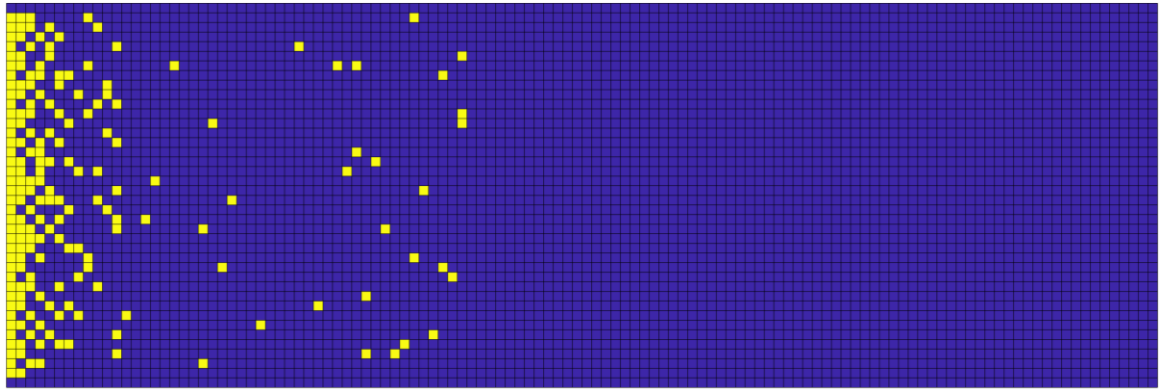

(c) r = 0.8 mm

Figure 13: Variation of final particle distribution with particle size

3. Results

3.7. Trials with Radial Flow

- Particle transport via radial flow across a 2D mould was also investigated, where particles were introduced randomly.

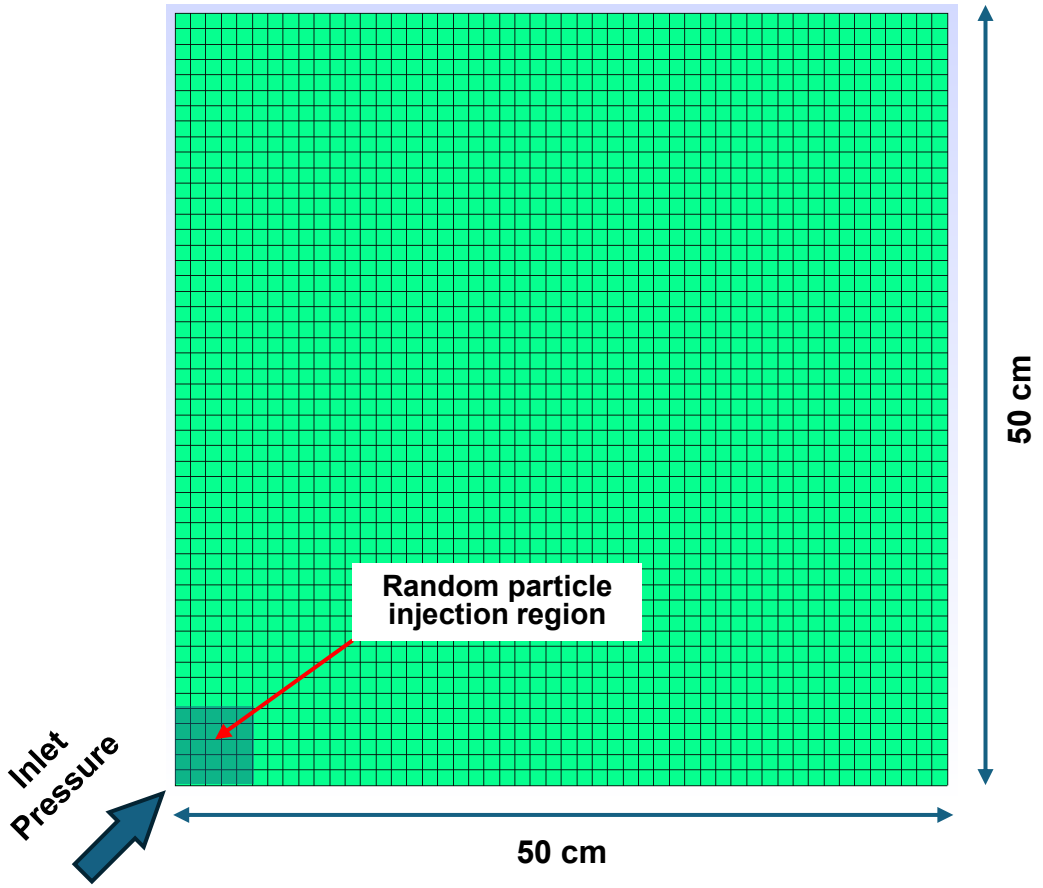

Figure 14: Radial flow geometry

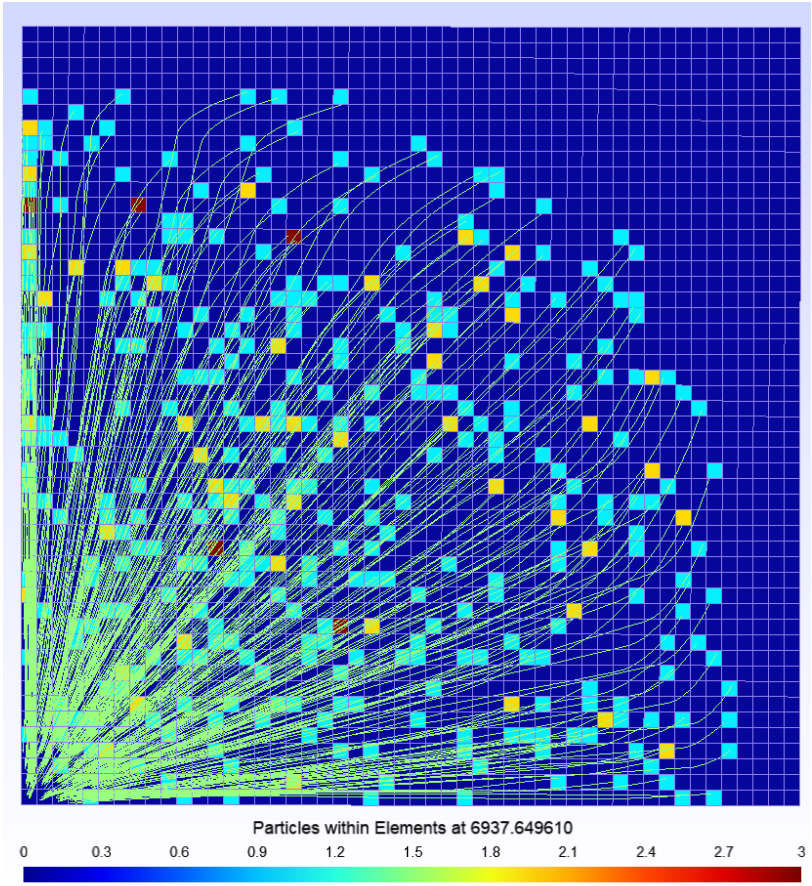

Figure 15: Particle evolution with time

3. Results

3.7. Trials with Radial Flow

- The influence of injection rate and particle size on the final particle distribution was investigated.

- Similar to the linear flow, high injection rates resulted in particle accumulation and blockages near the inlet (Fig. 16) .

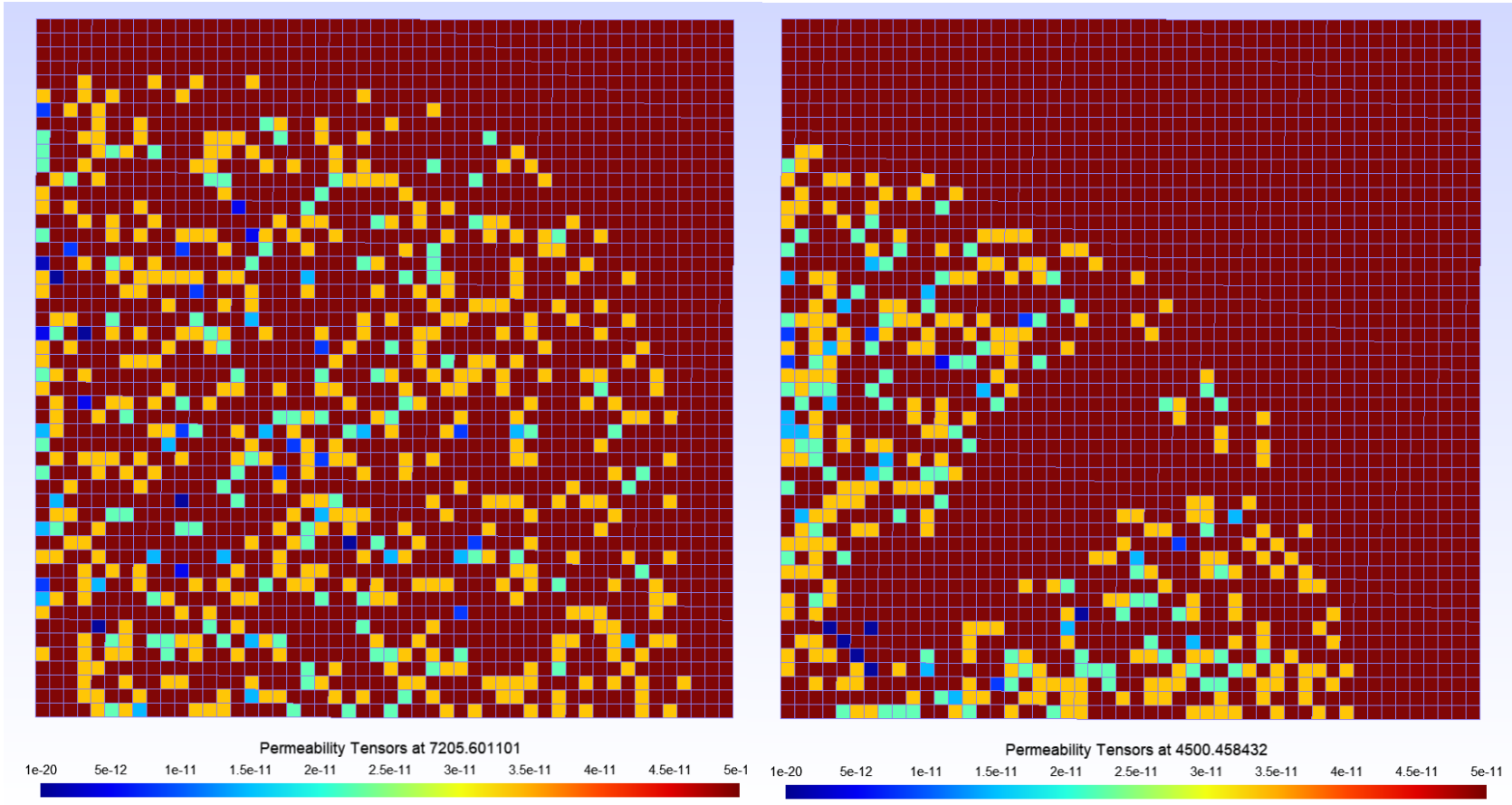

(a) 1 particle per 2 time steps

(b) 1 particle per 1 time step

Figure 16: Variation of final particle distribution with injection rate

3. Results

3.7. Trials with Radial Flow

- The influence of injection rate and particle size on the final particle distribution was investigated.
- Similar to the linear flow, high injection rates resulted in particle accumulation and blockages near the inlet (Fig. 16) .
- This was also the case for larger particle sizes (Fig. 17).

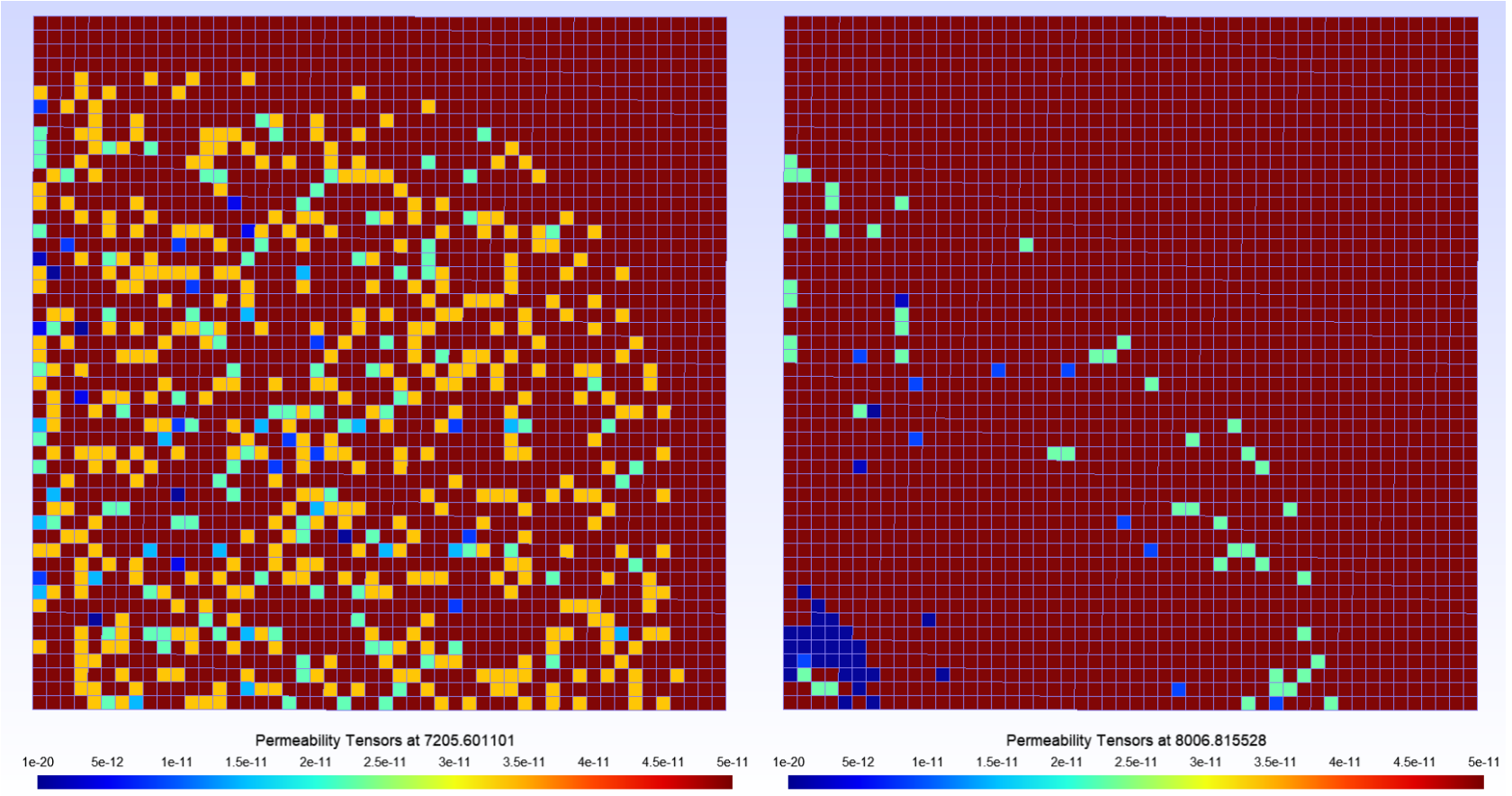

(a) r = 0.20 mm (b) r = 0.25 mm

Figure 17: Variation of final particle distribution with particle size

4. Summary and Outlook

- The transport of finite particles during resin impregnation was modelled and simulated using LIMS and MPI.
- Pressure and velocity fields are solved using LIMS, and these are used by a worker script to transport the particles.
- Updated permeabilities computed by the worker were sent back to LIMS, allowing fully coupled simulations.
- The influence of inlet pressure, injection rate, particle size and mould geometry were investigated.
- Simulating flow through further complex 3D mould geometries with varying particle sizes need to be explored.
- Particle mobility needs to be modelled and incorporated into the programme.

References

[1] J. Barroeta Robles *et al.*, 'Processing and properties of graphene-enhanced glass fibre composites using a scalable manufacturing process', *Composite Structures*, vol. 267, p. 113874, Jul. 2021, doi: 10.1016/j.compstruct.2021.113874.

[2] B. M. Louis, J. Maldonado, F. Klunker, and P. Ermanni, 'Particle distribution from in-plane resin flow in a resin transfer molding process', *Polymer Engineering & Science*, vol. 59, no. 1, pp. 22–34, 2019, doi: 10.1002/pen.24860.

[3] Y. Djebara, A. Imad, A. Saouab, and T. Kanit, 'A numerical modelling for resin transfer molding (RTM) process and effective thermal conductivity prediction of a particle–filled composite carbon–epoxy', *Journal of Composite Materials*, vol. 55, no. 1, pp. 3–15, Jan. 2021, doi: 10.1177/0021998320940035.

[4] W. R. Hwang, S. G. Advani, and S. Walsh, 'Direct simulations of particle deposition and filtration in dual-scale porous media', *Composites Part A: Applied Science and Manufacturing*, vol. 42, no. 10, pp. 1344–1352, 2011.

[5] M. Chohra, S. G. Advani, A. Gokce, and S. Yarlagadda, 'Modeling of filtration through multiple layers of dual scale fibrous porous media', *Polymer Composites*, vol. 27, no. 5, pp. 570–581, 2006, doi: 10.1002/pc.20228.

[6] C. M. Long, M. A. Nascarella, and P. A. Valberg, 'Carbon black vs. black carbon and other airborne materials containing elemental carbon: Physical and chemical distinctions', *Environmental Pollution*, vol. 181, pp. 271–286, Oct. 2013, doi: 10.1016/j.envpol.2013.06.009.

[7] P. Simacek, N. Niknafs Kermani, and S. G. Advani, 'Coupled Process Modeling of Flow and Transport Phenomena in LCM Processing', *Integr Mater Manuf Innov*, vol. 11, no. 3, pp. 363–381, Sep. 2022, doi: 10.1007/s40192-022-00268-1.

[8] B. R. Gebart, 'Permeability of Unidirectional Reinforcements for RTM', *Journal of Composite Materials*, vol. 26, no. 8, pp. 1100–1133, Aug. 1992, doi: 10.1177/002199839202600802.

Thank You

Q&A

Studies on Cut-Protective Performance of Composites Yarn Based Knitted UHMWPE Textiles in Real-world Industrial Applications

Shubham Singh,[1*] *Apurba Das,*[1] *Nandan Kumar,*[2] *& Bipin Kumar*[1]

[*]Corresponding author email**:** ttz228226@iitd.ac.in

[1]Department of Textile and Fibre Engineering, Indian Institute of Technology, Delhi, New Delhi-110016, India

[2]High Performance Textiles Pvt. Ltd., Sonipat, Haryana-131101, India

ABSTRACT

The safety of workers in hazardous environments depends on advanced protective textiles capable of withstanding various real-world challenges, especially in automotive, glass, aerospace, mining, construction, and food industries where cut hazards are prevalent. Developing flexible, high-performance protective textiles is essential to meet these needs. Ultra-high-molecular-weight polyethylene (UHMWPE) is widely utilized in cut-protective textiles for its exceptional strength and durability. This study investigates the cut-performance of stainless-steel and glass fibers reinforced UHMWPE knitted fabrics under real-world industrial conditions, focusing on the impact of varying cutting angles, outdoor environments, and thermal exposure on their cut-protective efficacy in industrial and occupational settings. Reinforcement significantly affects cut-performance, with stainless-steel reinforced UHMWPE fabric (13SU) exhibited the highest tear strength (lengthwise-313.1 N, widthwise-405.8 N) and abrasion resistance (withstanding up to 800 rubbing cycles), providing superior cut-protection with cut force of 32.43 N at a 90° cutting angle. Differential scanning calorimetry (DSC) and scanning electron microscope (SEM) characterizations revealed UHMWPE's sensitivity to thermal effects, with a significant decrease in crystallinity after exposure to radiant heat flux of 20 kW/m^2 at fabric surface, leading to diminished cut-performance. Environmental durability assessments showed degradation due to galvanic corrosion, forming ketone (C=O) and hydroxyl (O-H) polar groups that altered the UHMWPE polymer structure and reduced peak intensity, as confirmed by Fourier-transform infrared (FTIR) spectroscopy. This study would be highly beneficial for industrial employees in choosing the right cut-protective fabrics based on their specific environments and working conditions.

Highlights

- Development of stainless-steel and glass fiber reinforced UHMWPE fabrics.
- TDM-100 is integrated with radiant heater to assess cut-performance under heat.
- Reinforced UHMWPE fabrics shows higher cut-performance than 100% UHMWPE fabric.
- Cut protection is highest at 90° cutting angle.
- Glass reinforced UHMWPE fabric offers better cut-protection under heat.

Keywords: UHMWPE, cut-resistance fabric, glass fibers, stainless-steel, crystallinity, composite yarns, radiant heat exposure.

1. INTRODUCTION

Occupational safety remains a critical concern worldwide, with millions of workers facing potential hazards in industries such as manufacturing, construction, and emergency services. According to the International Labour Organization (ILO), over 317 million work-related injuries occur annually, and more than 320,000 people die, leading to significant human and economic costs. Among these, injuries from sharp objects and exposure to extreme environmental conditions are particularly common, underscoring the need for effective protective measures.[1] In response to these safety challenges, various protective clothing has been designed, such as cut-resistant gloves, bulletproof vests, stab-proof suits, and protective helmets.[2-4] These advancements are intended to help the human body better withstand or even completely avoid injuries caused by sharp objects and other hazardous impacts.[5, 6] However, traditional protective solutions such as leather garments, wire mesh steel, and steel gloves have faced several limitations, including discomfort, reduced dexterity, and inadequate protection.[7] In contrast, modern protective textiles are developed using high-performance fibers such as ultra-high-molecular-weight polyethylene (UHMWPE),[8, 9] aramids,[10-12] polyphenylene benzobisoxazole (PBO) fiber,[13, 14] as well as inorganic fibers including, glass fibers,[15, 16] carbon fibers,[17] and basalt fibers[18] exhibit excellent mechanical properties, and have proven to be an effective approach for preparing cut-/puncture resistant textile materials. These advanced materials offer superior protection without compromising on dexterity or comfort. Mayo and Wetzel[19] studied the cut-resistance properties of both inorganic and organic high-performance single fibers and attributed their effectiveness to the fibers to their isotropic and anisotropic structures.[19] Additionally, a U.S. patent titled ‘Criminology’ suggests using glass fiber as a cut-resistant material, highlighting its exceptional ability to protect against sharp objects like knives and cones.[20] In a comparative study, Tuba Alpyildiz[21] developed a double-sided knitted fabric

using yarn wrapped with Kevlar 1414 fiber, which exhibited significantly higher cut-resistance than traditional weft-knitted fabrics.[21] Javid et al.[22] developed knitted gloves using a combination of core yarns like stainless-steel filament, Kevlar filament, staple spun Kevlar, and glass filament, with sheath yarns made of 100% viscose rayon, 50/50 polyester/viscose rayon blend. Their testing revealed that gloves utilizing dual-core yarns, especially those incorporating both filament and staple spun Kevlar, demonstrated superior performance in cut, tear, puncture, and abrasion resistance properties.[22] Cut-resistance clothing is primarily produced using knitting and weaving techniques, with knitting being favored for its stretchability, flexibility, and lightweight properties.[23] Research by Flambard et al.[24] found that knitted structures made from high-performance fibers offer better energy absorption during impact, making them more effective for protective clothing than woven fabrics.[24, 25]

Numerous studies have examined the mechanical properties of high-performance single fibers under various conditions, including tension at both high and low strain rates[26, 27], torsion[28, 29], and transverse compression.[30] When cutting a single fiber under tension, the fiber likely undergoes a combination of loading modes, which may include aspects of these mechanisms along with in-plane shear.[31-36] UHMWPE fiber has a molecular weight exceeding one million[37], it demonstrates significantly higher strength and cutting resistance than other fibers, making it notably difficult to cut. This exceptional durability has led to the extensive use of UHMWPE-based knitted cut-resistant protective gear, including gloves, vests, socks, and t-shirts, across various global industries to protect workers. The cut performance of these fabrics is influenced by several factors, such as outdoor environmental conditions, cutting angles, the type of reinforcement used in the core of the UHMWPE yarn, and thermal exposure. However, the impact of these factors, particularly the influence of heat, has not been previously critically analyzed. UHMWPE fibers are especially sensitive to temperature due to their relatively low melting point, below 150 °C,[38, 39] which can significantly affect their cut performance.

In this study, cut-resistant knitted fabrics were produced on 13-gauge gloves knitting machine using UHMWPE core-spun composite yarn reinforced with stainless-steel and glass fibers. The effects of various factors, including core reinforcement (stainless-steel and glass fibers), outdoor environmental exposure (up to 90 days), different cutting angles (0°, 45°, 90°), and radiant heat exposure (heat flux density of 20 kW/m^2 at mandrel), on the mechanical and cut-resistant properties were critically analyzed. To assess the impact of radiant heat on cut performance, the cut-resistant testing instrument, a tomodynamometer, was integrated with an external radiant heat exposure lamp, enabling the cut performance evaluation of the developed

samples under controlled heat conditions. This study offers critical findings that can help employees in various industries by guiding the selection of more durable and effective cut-resistant protective gear, particularly in environments with extreme conditions such as high temperatures and outdoor exposure.

2. EXPERIMENTAL DETAILS

2.1 Materials

The commercially available high-performance yarns such as 100% UHMWPE, as well as stainless-steel and glass-reinforced UHMWPE core spun composite yarns were directly sourced from HPT Pvt Ltd in Sonipat, Haryana, India. The core spun composite yarns were produced by using ring spinning process, wherein UHMWPE fibers as sheath layer and polyester fibers as intermediate layer were wrapped out with reinforced materials such as stainless-steel and glass fibres, as shown in **Figure 1 a-c**. The inclusion of intermediate layer significantly enhances the stability of the resulting yarn, preventing the core materials from coming out. The physical properties of sourced yarns are illustrated in **Table 1**.

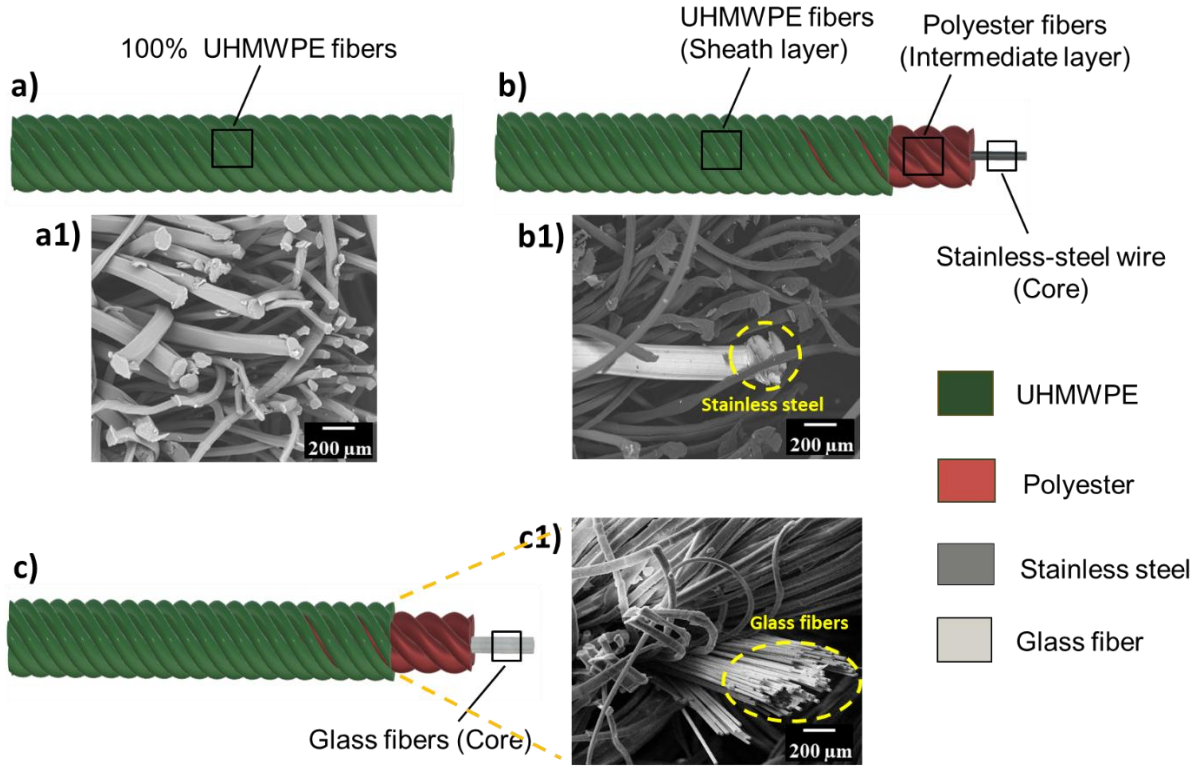

Figure 1. Schematic representation of yarn structural configuration and cross-sectional SEM images of **(a, a1)** 100% UHMWPE yarn, **(b, b1)** stainless-steel reinforced UHMWPE composite yarn, **(c, c1)** glass fiber reinforced UHMWPE composite yarn.

Table 1. Physical properties of 100% UHMWPE and core spun composite yarns

Sr. No.	Yarn type	Sheath layer		Intermediate layer		Core	
		Fiber	Fineness (Denier)	Fiber	Fineness (Denier)	Fiber	Fineness (Denier)
1	100% UHMWPE	UHMWPE	800	-	-	-	-
2	Stainless-steel/UHMWPE	UHMWPE	400	Polyester	150	Stainless-steel	200
3	Glass Fibers/UHMWPE	UHMWPE	400	Polyester	150	Glass fiber	200

Table 2. Mechanical properties of 100% UHMWPE and core spun composite yarns

Yarn specifications	100 % UHMWPE	Stainless steel/UHMWPE	Glass/UHMWPE
Linear density (tex)	89±5	90±5	90±5
Breaking load (N)	80.4	99.5	96.8
Tenacity (gf/den)	11.3	12.6	12.3
Young modulus (gf/den)	282.1	301.5	351.5
Diameter (mm)	0.82	0.85	0.85

2.2 Fabrication of cut resistance samples

The knitted cut-resistance fabrics in form of gloves were prepared on 13-gauge computerized gloves knitting machine (SHIMA SEIKI SFG-I). These glove samples are produced using the tubular knitting technology that creates a dual-layer structure, with each layer utilizing a single jersey pattern, resulting in the formation of a hollow space (pocket) between the layers (in Finger part and palm part), as shown in **Figure 2 b.** The gloves samples made from 100% UHMWPE, glass fibers-reinforced UHMWPE, and stainless-steel fibers-reinforced UHMWPE composite yarns are designated as 13U, 13GU, and 13SU, respectively. The microscopic image of the 13SU gloves is depicted in **Figure 2 d**.

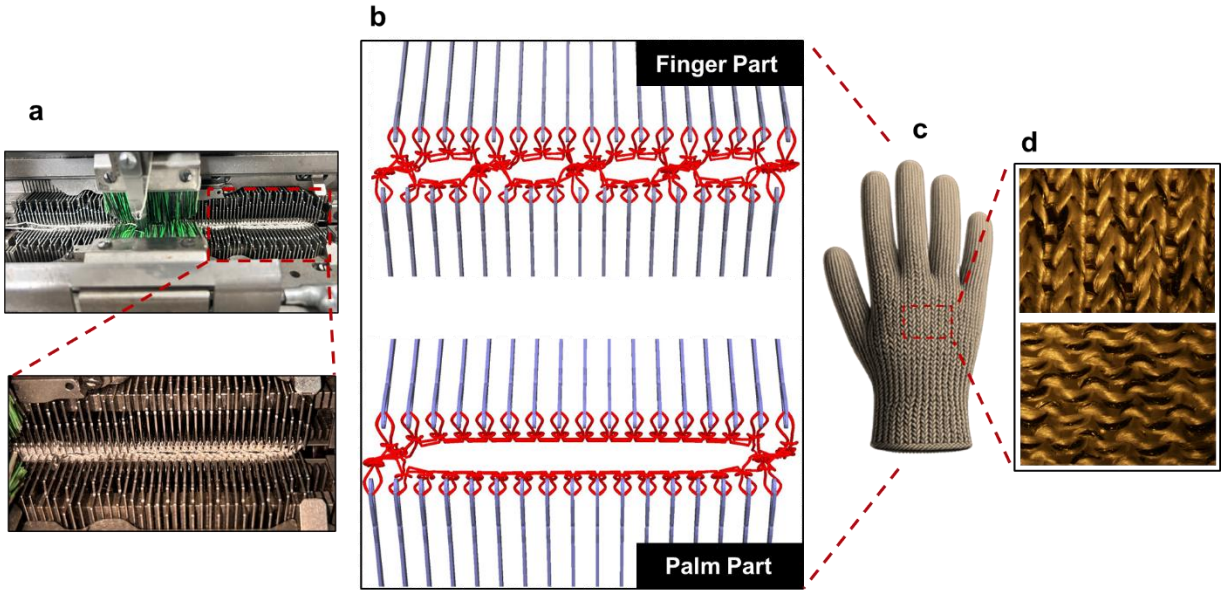

Figure 2. Fabrication of cut resistance knitted gloves: **(a)** arrangement of loops in the needle bed on gloves knitting machine; **(b)** schematic representation of loops arrangement on needle bed during formation of finger part and palm part of the glove; **(c)** developed glove samples; **(d)** microscopic image of 13SU glove sample.

2.3 Characterization and measurement techniques

The physical characteristics of the single jersey knitted fabric, such as thickness and GSM (grams per square meter), were measured following ASTM standards D177 and D3776, respectively. The mechanical properties of the 100% UHMWPE and core-spun composite UHMWPE yarns were determined according to ASTM D2256-02. The cut resistance of all samples was evaluated using a tomodynamometer (TDM-100) cut testing instrument. Before testing, the samples were conditioned for 24 hours in a controlled environment with a temperature of 20 ± 2 °C and a relative humidity of 65 ± 4% as per standard procedures.

2.3.1 Measurement of cut-resistance properties

The cut-resistance properties of all samples were measured according to standard ISO 13997 using instrument tomodynamometer (TDM-100), as shown in **Figure 3 a.** According to this test method, sample with size of 7x7 cm fixed on mandrel by mounting tape (**Figure 3 b**), and the force required for a blade to cut the samples after a sliding displacement of 20 mm at constant speed of 2.5 mm/sec is measured. Each sample were cut 15 times under varying loads, such as the cut distances ranging from 5 mm to 15 mm, 15 mm to 30 mm, and 30 mm to 50

mm. Throughout each test, the applied loads and corresponding cut distances were collected, then corrected cut through distances (CCTD) were calculated by following **Equation 1**.

$$\text{Corrected cut through distance (CCTD)} = \frac{20}{d_o} \times d \quad (1)$$

Where d_o represents the calibration cut-through distance, calculated as the average distance from five blades on a chloroprene standard sample, and d is the cut distance measured for the test sample.

Using this data, an optimal regression line fitting curve of CCTD and load (N) was plotted (**Figure 3 c**). The load corresponding to CCTD of 20 mm was considered as characteristic cut protection force.

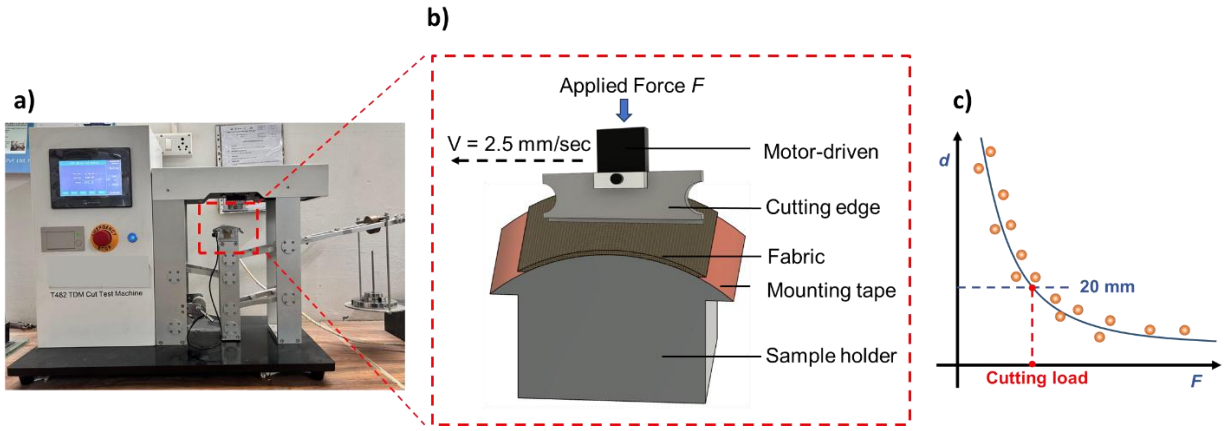

Figure 3. (a) TDM-100 cut testing instrument (b) schematic view of performing cut testing (c) plot of corrected cut through distance (CCTD) verses applied load and resulting cutting load at 20-mm CCTD.

2.3.2 Testing setup for cut performance under radiant heat exposure

The influence of radiant heat exposure on cut performance was assessed by radiant heat lamp based tomodynamometer (**Figure 4**). The heat flux was calibrated by adjusting the distance between the radiant heat lamp and the mandrel of the TDM-100. It was determined that at a distance of 28.5 cm, the heat flux density at the mandrel reached 20 kW/m². This specific heat flux was chosen based on the ISO-11612 standard, "Protective clothing – Clothing to protect against heat and flame – Minimum performance requirements," which recommends exposing protective fabrics to a radiant heat source of 20 kW/m² for a specified duration to evaluate their internal structure and shall meet at least performance Level C1. If the temperature rise within the fabric remains below a certain threshold, the material is deemed suitable for use in high-

heat environments. The heat flux from the radiant source can be adjusted depending on the intended application. After exposing the samples to radiant heat for 5 minutes, the lamp was turned off, and the cut resistance properties was measured as discussed in section **2.3.1**.

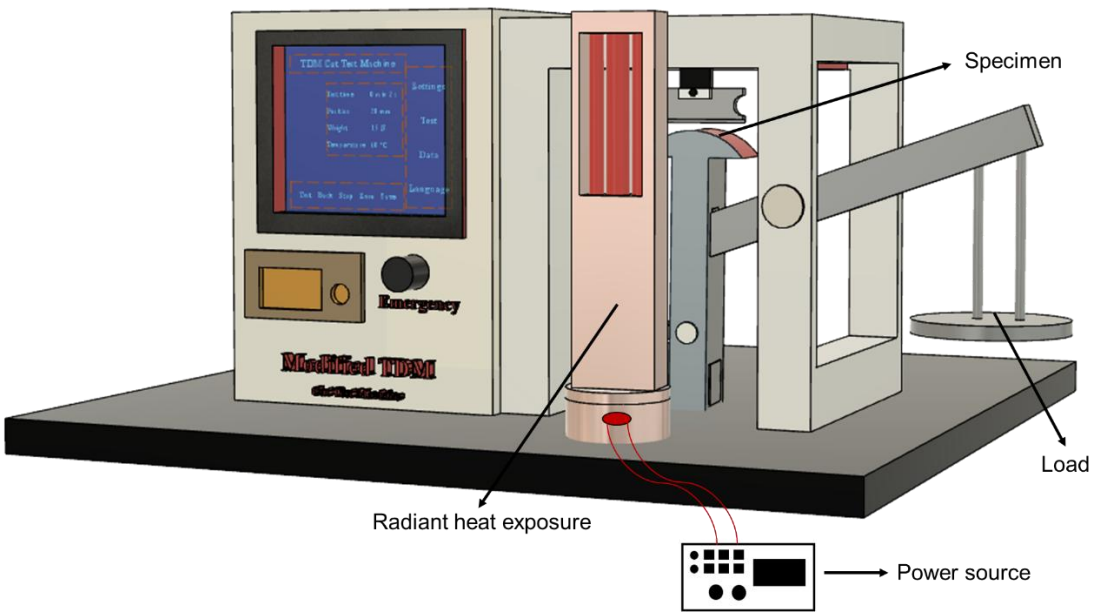

Figure 4. TDM-100 integrated with radiant heat exposure lamp.

2.3.3 Mechanical properties evaluation

The mechanical properties of all samples, including tear resistance, puncture resistance, and abrasion resistance, were evaluated according to the EN 388:2016 standard. Tear and puncture resistance tests were conducted using an electronic universal testing machine (**Supporting Figure S1**), while abrasion resistance was measured with a Martindale abrasion tester, as shown in **Supporting Figure S3**. For the tear resistance test, samples were prepared by making a 50 mm longitudinal incision on one side of 100 × 50 mm fabric strips, creating a "pants" shape (**Supporting Figure S2**). The grips of the mechanical testing frame were clamped onto the two "legs" of each sample, which were then pulled apart at a constant speed of 100 mm/min. Load-extension data were continuously recorded to determine the maximum force that the fabric could withstand before tearing. In the puncture resistance test, samples were cut into 40 mm diameter circles, and a needle was allowed to move downwards at a constant speed of 100 mm/min until it fully penetrated the fabric. The force required to achieve full penetration was recorded as the puncture load. For the abrasion resistance test, the samples with a diameter of

38 mm were cut from each fabric sample. Each sample was tested against a standard abradant fabric (180-grit, Klingspor PL31B) under a pressure of 9 kPa, and specimens were subjected to abrasion cycles until the hole formation observed.

2.3.4 Durability assessment in open environmental conditions

The durability evaluation of cut resistance fabrics under open environmental conditions is essential because these fabrics are often exposed to factors like sunlight, moisture, and temperature fluctuations in real-world use. Over time, external elements may affect mechanical and cut-resistant properties of the fabrics. This evaluation helps ensure that the fabrics maintain their protective performance over time, providing reliable safety for users. Samples of 13U, 13SU, and 13GU fabrics were exposed to outdoor conditions for 90 days, as depicted in **Figure 5**. The mechanical properties and cut performance of these fabrics were systematically assessed at 30 days intervals to analyse any changes in their durability and effectiveness throughout the exposure period.



Figure 5. Investigation of environmental effect on the performance of 13U, 13GU, and 13SU samples.

2.3.5 Thermal analysis

Differential scanning calorimetry (DSC) was done using a Q2000V24.11 Build 124 DSC analyzer, with continuous nitrogen purging throughout the process. UHMWPE/Polyester blended samples were finely granulated (3–5 mg) and sealed in aluminium pans. The samples first underwent a heating cycle from the temperature of 0 °C to 350 °C at a rate of 10°C/min.

This was followed by rapid cooling (quenching) to 0 °C, where the samples were held for 8 minutes to achieve equilibrium. The melting temperature (T_m) and crystallization temperature (T_c) were identified as the inflection point in the DSC thermograms.

2.3.6 Chemical structure analysis

Fourier Transform Infrared Spectroscopy (FTIR) was used to analyze the effects of environmental conditions on the structure of UHMWPE polymer chains and their molecular interactions. The analysis was conducted using a Nicolet iS50 spectrophotometer, equipped with an attenuated total reflectance (ATR) mode featuring a zinc selenide crystal. Spectra were recorded in the range of 4000–400 cm^{-1}, with a resolution of 4 cm^{-1}, after performing 64 scans to ensure detailed and accurate results.

2.3.7 X-ray diffraction

X-ray diffraction (XRD) analysis was performed using an XPert Pro PANalytical X-ray diffractometer to assess the crystallinity percentage and the impact of radiant heat exposure on the crystal planes within the fabric structures. The samples were scanned over a diffraction angle range of 2θ from 0° to 40°, with a scanning speed of 4°/min and a step size of 0.02°. The XRD instrument operated under conditions of 40 keV and 40 mA.

2.3.8 Surface morphology characterization

The microscopic images and surface morphology of fabric structures subjected to cut tests under radiant heat exposure and different cutting angles were examined using an optical microscope and a Zeiss EVO 18 scanning electron microscope (SEM). SEM imaging was conducted in a vacuum environment with an acceleration voltage of 20 kV.

3 RESULTS AND DISCUSSIONS

The physical characteristics of the developed samples, such as course per inch (CPI), wales per inch (WPI), stitch density, loop length, fabric thickness, and areal density were assessed and are detailed in **Table 3**. The findings indicate that after reinforcement of stainless-steel and glass fibers into the core, there was no significant increase in the areal density of any of the samples, indicating it is suitable for use in comfortable protective clothing. There are several factors that can influence the cut resistance properties, including core reinforcement, cutting angles, exposure to outdoor environmental conditions, and radiant heat exposure. These factors

have been studied in next subsection to evaluate their effects on fabric performance and durability.

Table 3. Physical characteristics of developed fabric samples

Properties	**13U**	**13GU**	**13SU**
CPI/WPI	22/15	24/16	26/15
Loop length (mm)	6.5	5.8	5.7
Stitch density (loops/inch^2)	330	384	390
Tightness factor	13.4	16.2	15.9
Areal density (g/m^2)	305 ± 5	355 ± 5	320 ± 5
Thickness (mm)	0.87	0.95	0.93

3.1 Effect of core reinforcement

3.1.1 Tear resistance properties

Tear strength of samples was determined in lengthwise and widthwise direction using ZWICK instrument with gauge length of 40 mm and at a constant speed of 100 mm/min. **Figure 6 a-c** illustrates the force-extension curves of all samples, demonstrating that as the tearing force were applied to the fabric, it increased exponentially until fabric tear. This is due to as the force increase, the yarns bunches together, which requires high force to stretch and break them. At a higher force, the curve begins to oscillate because of the fabric starts to tear one yarn at a time until at a higher force all jam up yarns ruptures at once. And it was observed from the curves that the amplitude of the oscillations in widthwise direction larger than lengthwise direction across all samples. This implies that the material in widthwise direction experiences more significant slipping or rearrangement events under stress, resulting in higher tear strength in the width-wise direction across all samples compared to lengthwise direction. (**Figure 6 d**) This phenomenon can also be attributed to the mechanics of tear propagation in weft knitted structures. When initiating a tear in the lengthwise direction of the fabric, the strain experienced in the fabric's course direction allows for greater mobility of yarn. This is attributed to higher extensibility of single jersey knitted structures in the fabric's course direction compared to the wales direction. Consequently, as the tear progresses in the lengthwise direction, the stress in

the fabric's wales direction, which is inherently less extensible, acts to restrict the mobility of the yarns. This restriction occurs because the loop in the wale or needle way has tied at the head and at the leg of the loop, resulting in minimal elongation when force is applied. As a result, a higher force is required to tear the fabric in the widthwise direction.

Figure 6 d shows that 13SU fabric highest tear strength in length wise and widthwise direction, which is 313.1 N and 405.8 N, compared to 13GU (lengthwise-224.9 N, widthwise-326.5 N) and 13U (lengthwise-212.8 N, widthwise-275.6 N) fabric, it is due to higher the tenacity (12.6 gf/den) and young modulus (301.5 gf/den) of stainless-steel reinforced yarn, as shown in **Table 2**. Basically, in a core-sheath type of yarn, the core is expected to bear the load. Moreover, slippage occurs in the composites yarn between core and sheath fibers during the breaking process and thus core material has a great contribution to the tensile load sharing. So, stronger the core material higher will be the yarn and fabric tensile strength. As a result, stainless-steel and glass fibers reinforced UHMWPE yarn shows higher tensile strength compared to 100% UHMWPE staple spun yarn.

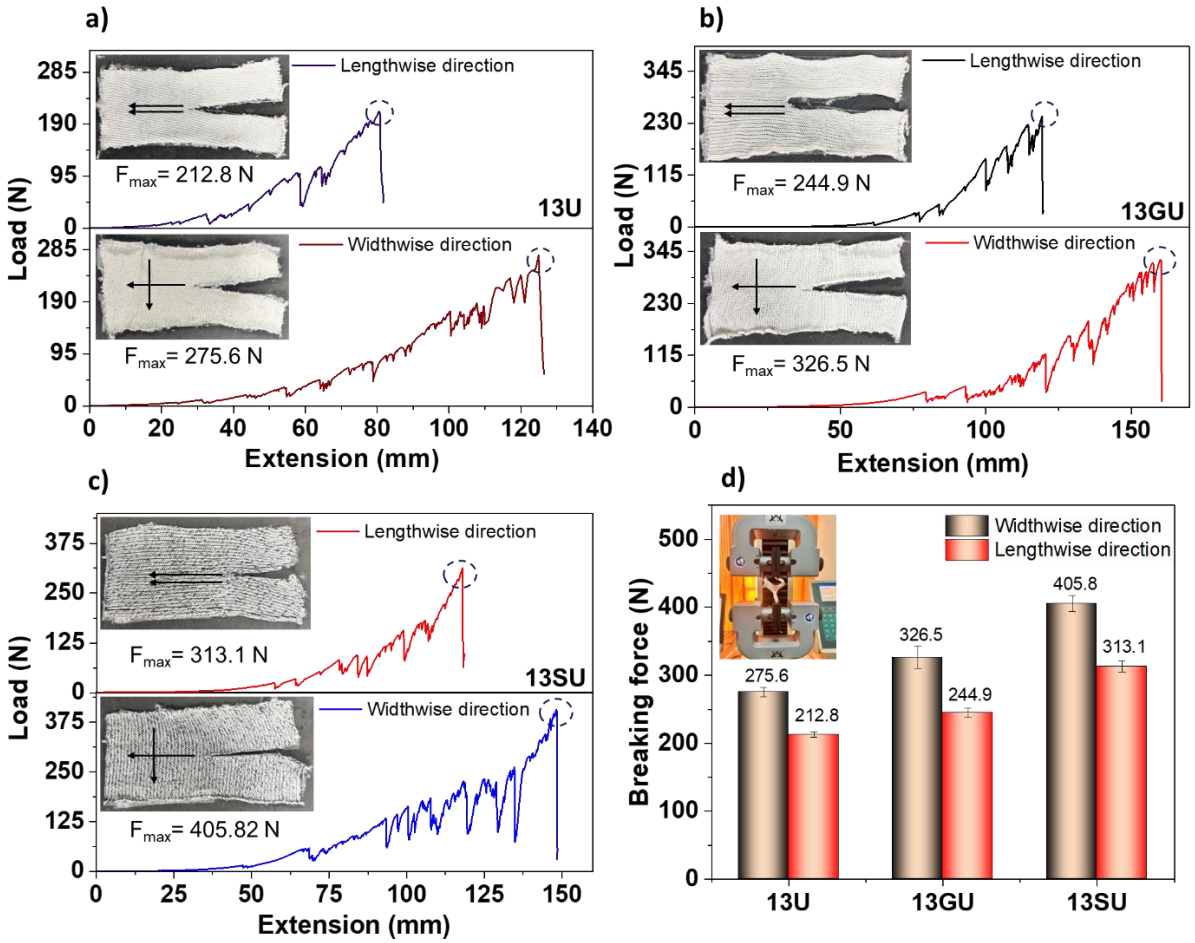

Figure 6. Load-extension curves of (a) 13U, (b) 13GU, and (c) 13SU fabrics in lengthwise and widthwise directions. (d) Comparison of breaking force required for the samples.

3.1.2 Puncture and abrasion resistance properties

All fabric samples were fixed for quasi-static puncture resistance experiments (**Figure 7 a**), and the results showed that the reinforced fabric samples (13SU and 13GU) had significant differences in their mechanical behaviour under stress compared to 13U fabric. The maximum puncture load was highest for the 13GU fabric at 111.97 N, which is 1.25 times higher than that of the 13U fabric (89.47 N), followed by 96.25 N for the 13SU fabric (**Figure 7 f**). This variation in puncture resistance is largely due to the reinforcing materials (glass fibers and stainless-steel fibers) used in the 13GU and 13SU fabrics, which significantly enhance their ability to resist puncture compared to the pure UHMWPE fabric. The presence of glass fibers in 13GU and stainless-steel in 13SU increases the energy required to penetrate the fabrics, as these reinforcements effectively distribute the stress across a larger area and absorb more energy before failure. Additionally, the 13GU fabric exhibited excellent energy dissipation

performance throughout the probe puncture phases I, II, III, and IV (**Figure 7 e**), indicating the excellent synergistic toughening properties. Friction and fiber slipping also play crucial roles in determining puncture resistance. The reinforced 13SU and 13GU fabrics create higher frictional resistance against the puncturing probe, which prevents easy fiber movement and slipping, thereby requiring more force for penetration. In contrast, the 13U fabric, lacking such reinforcements, has lower inter-fiber friction, allowing the fibers to slip more easily around the puncture point, which results in lower puncture resistance. Additionally, the strong bonding between UHMWPE fibers and the reinforcing materials in 13GU and 13SU contributes to their higher puncture resistance. Glass fibers, being stiffer and having higher hardness than stainless-steel,[40] create a rigid and well-bonded structure in 13GU, leading to the highest puncture load observed. Although stainless-steel in 13SU also enhances bonding and strength, the metal's relative flexibility compared to glass results in a slightly lower puncture load. The structural arrangement of fibers in the 13SU and 13GU fabrics, particularly the larger gaps between them, allows for more significant deformation and stretching around the puncture site before complete penetration. This is evident in the larger probe punctured openings observed in the 13GU and 13SU fabrics (**Figure 7 c-d**), whereas the 13U fabric, with smaller gaps between fibers (**Figure 7 b**), exhibits a lesser localized deformation and a pronounced "cross window" effect but with lower overall puncture resistance.

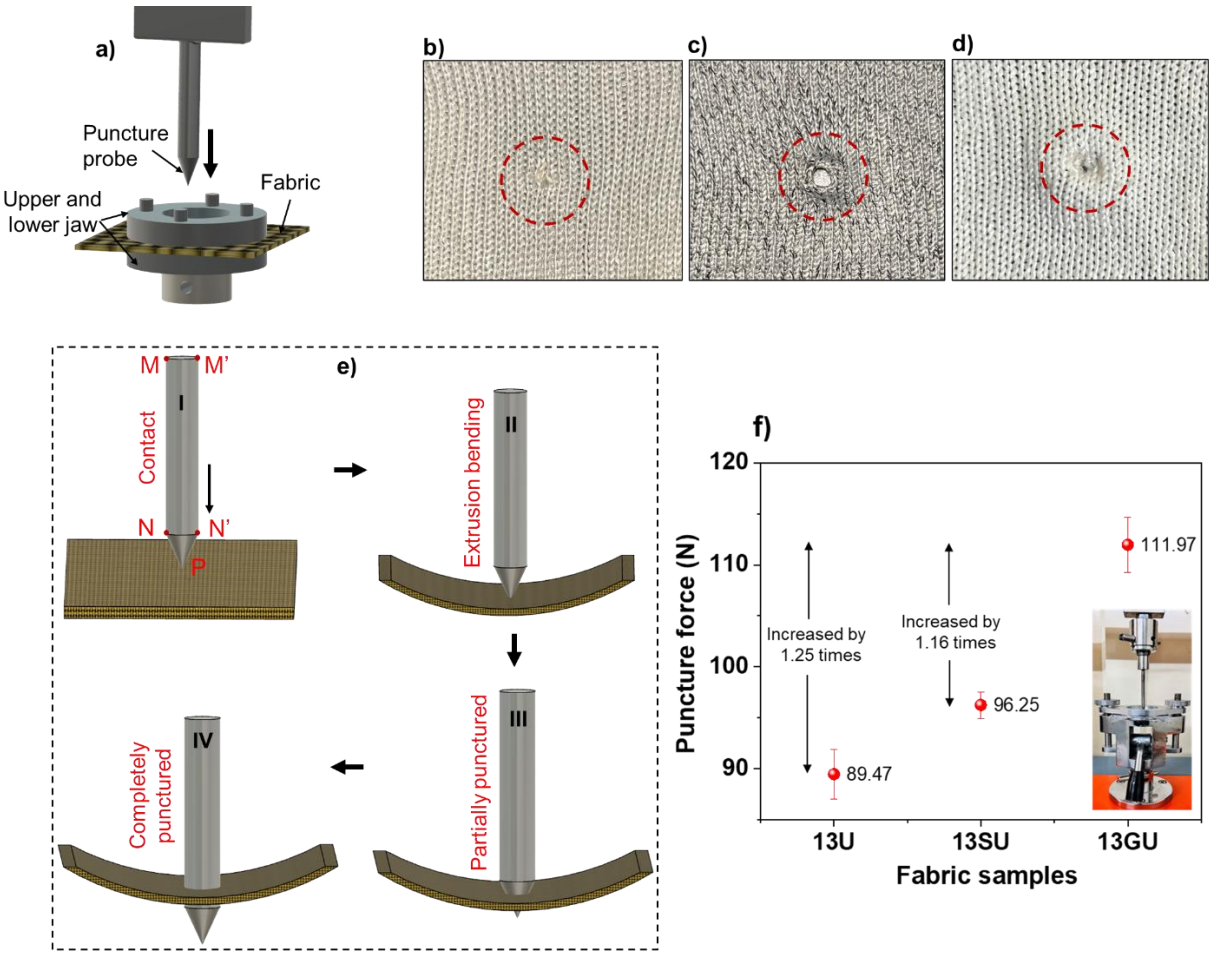

Figure 7. (a) Schematic representation of quasi-static puncture resistance test. Probe punctured deformation of (b) 13U, (c) 13SU, and (d) 13GU fabric samples. (e) Schematic diagram of the probe puncture process: **I** the puncture probe head just touched the fabric; **II** the puncture probe head started to compress the fabric; **III** the PN part of the puncture probe head pierced the fabric; **IV** the NM part of the puncture probe head entered the fabric completely. (f) Comparison of puncture force of the samples.

The abrasion resistance testing of 13U, 13SU, and 13GU fabrics was performed on Martindale abrasion tester, employing a Lissajous motion and rubbing against 180-grit Klingspor PL31B sandpaper under a pressure of 9 kPa. Abrasion resistance properties is generally influenced by factors such as, fabric thickness, GSM, tensile strength, and the type of the fibers used. The results shows that the 13SU fabric, reinforced with stainless-steel, exhibited superior abrasion resistance, with a hole forming at its surface after 800 cycles of rubbing. In contrast, the 13GU fabric, reinforced with glass fibers, showed a hole formation after 450 cycles, and the 13U fabric, composed of 100% UHMWPE, developed a hole after 350 cycles. (**Figure 8**)

The superior performance of 13SU can be attributed to the inherent properties of stainless-steel, which provide excellent resistance to abrasive forces, contributing to the fabric's high tensile strength of 804 N. The higher tensile strength enhances the fabric's ability to withstand repeated friction without significant material degradation. Additionally, 13SU recorded an extensibility of 72.3 mm/110.3 mm in lengthwise/widthwise direction before break (**Figure 10 j**), indicating a high ability to stretch under load, which plays a crucial role in its abrasion resistance. When the 13SU fabric comes into contact with the 180-grit Klingspor PL31B abrasive surface, its high extensibility allows it to deform and distribute the applied forces more evenly across the contact area. This results in a loose gripping contact with the abradant, reducing the localized stress and minimizing the damage, which in turn delays the onset of hole formation. In comparison, the 13GU fabric, while still exhibiting improved abrasion resistance over 13U, performed less favourably than 13SU due to the brittle nature of glass fibers. The tensile strength of 13GU was recorded at 569 N (lesser than 13SU), is compromised by the brittleness of glass fibers under abrasive conditions. When subjected to friction, the stiffness of the glass fibers causes a rigid response, and their brittle nature leads to breakage and dislodgement from the yarn structure, resulting in significant damage to the fabric surface and earlier hole formation. Additionally, the 13GU fabric has an extensibility of 61.6 mm/107.5 mm in the lengthwise/widthwise direction before breaking, which is lower than that of 13SU. This lower extensibility means the fabric cannot absorb and distribute abrasive forces as effectively, leading to greater damage under the same conditions. The 13U fabric, with a tensile strength of 264 N and an extensibility of 58.7 mm/99.45 mm in lengthwise/widthwise directions, exhibits the least resistance to abrasion. Its lower extensibility means that when it is subjected to frictional forces, the fabric is less able to deform and dissipate the energy generated by the abrasion. This results in a more concentrated stress on the contact area, leading to faster wear and earlier hole formation. The lack of reinforcing materials in 13U also results in a thinner fabric structure (0.835 mm) compared to 13GU (0.95 mm) and 13SU (0.93 mm), which further reduces its ability to resist abrasive forces.

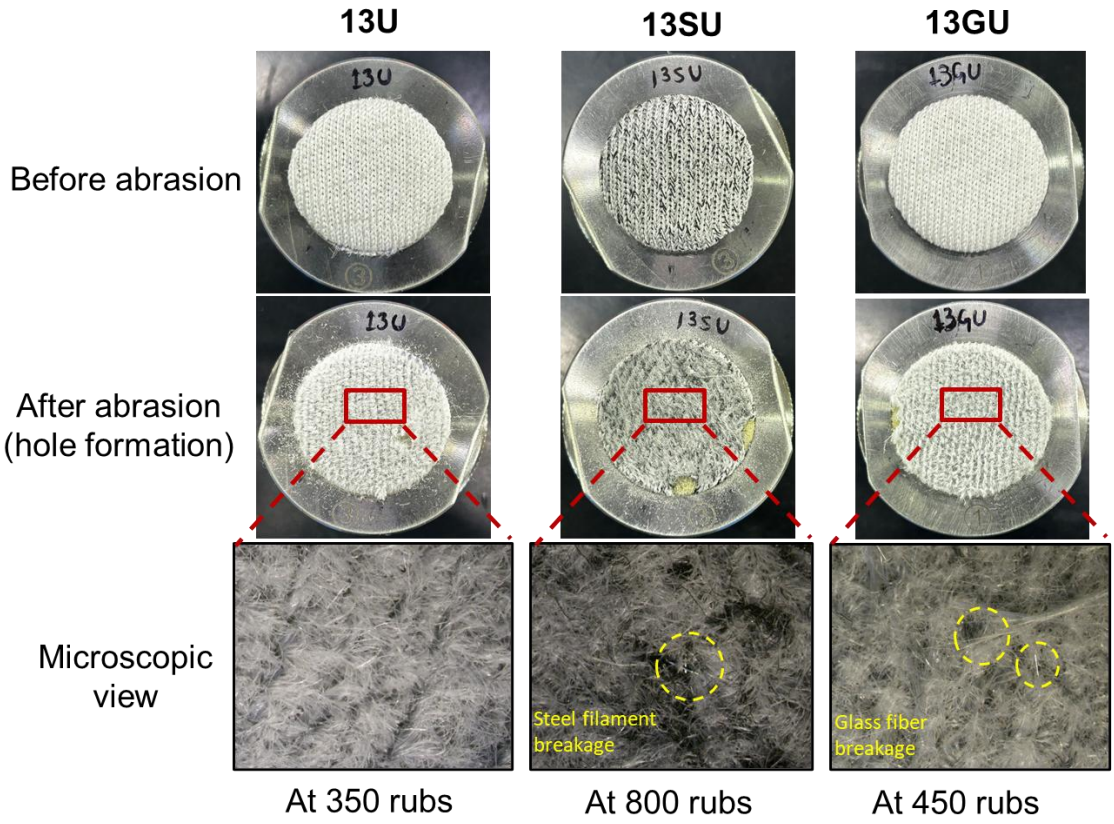

Figure 8. Optical microscopic images of the samples before and after abrasion testing until hole formation

3.1.3 Cut resistance properties

The procedure described in the **section 2.3.1** was used to evaluate the cut protection level of all fabrics. Regression curves were plotted for each sample, and the corrected cut-through distances at 20 mm were calculated from these curves to quantitatively evaluate the cut performance. As seen in **Figure 9 b-c**, the analysis revealed that cut performance of reinforced UHMWPE yarn fabrics (13SU and 13GU), was significantly superior to that of 100% UHMWPE fabrics (13U). Among the tested samples, the 13SU fabric exhibited the highest cut resistance properties, which can be thoroughly explained by XRD analysis of samples. As shown in **Figure 9 a**, the XRD peaks occurring at 21.5° and 23.9°, that are characteristic of the UHMWPE polymer. The peak intensities vary among the different fabrics, with the highest intensity observed in 13SU, followed by 13GU, and then 13U. The higher peak intensity in 13SU indicates a greater degree of crystallinity and molecular order, correlating with its superior mechanical properties and cut resistance. This increased crystallinity in 13SU, at 52.48%, can be attributed to the effective nucleating action of the stainless-steel fibers, which facilitate a more ordered alignment of polymer chains during the crystallization process. The

peak intensity in 13GU, while still higher than in 13U, reflects its relatively lower crystallinity at 51.75%, resulting in less mechanical strength compared to 13SU. The 13U fabric, with the lowest crystallinity at 48.37%, exhibits the weakest performance, as indicated by its lower peak intensity. These findings are further supported by tensile strength data, which shows that 13SU has the highest tensile strength at 804 N, followed by 13GU at 569 N, and 13U at 264 N, as discussed earlier. The enhanced tensile strength in 13SU is due to the strong interaction between the stainless-steel reinforcement and the UHMWPE fibers, enabling more effective load transfer and contributing to the material's overall mechanical strength. In comparison, glass fibers in 13GU, though beneficial, are more brittle and have a lower bonding efficiency with the UHMWPE matrix, resulting in slightly lower tensile strength.

The molecular structure of UHMWPE, primarily composed of $-CH_2-CH_2-$ units, is characterized by strong sigma (σ) bonds. However, these chains lack rigidity due to the absence of additional functional groups that could restrict chain mobility. The introduction of reinforcement materials alters this molecular structure by increasing crystallinity and improving mechanical properties. In 13SU, stainless-steel creates stronger van der Waals forces and electron cloud interactions between the polymer chains and the reinforcement material, contributing to a more stable and ordered structure that is better able to resist cutting forces. In contrast, 13GU, reinforced with glass fibers, has different interactions. Glass fibers are rigid and brittle, creating a composite with air pockets and weaker van der Waals forces compared to the metal-reinforced composite. This brittleness, along with the presence of air pockets, makes the material more susceptible to crack initiation and fracture under stress, reducing its cut resistance. During the cutting process, the behaviour of the fibers plays a crucial role. The stainless-steel in 13SU exhibits ductile cutting behaviour, deforming plastically before fracturing, which allows it to absorb more energy and resist cut-through more effectively. This ductility, combined with the strong bonding between the stainless-steel and the UHMWPE fibers, results in the highest cut resistance among the tested samples. In contrast, the lower friction coefficient of glass fibers, coupled with their brittle nature, results in a less effective resistance mechanism compared to 13SU.

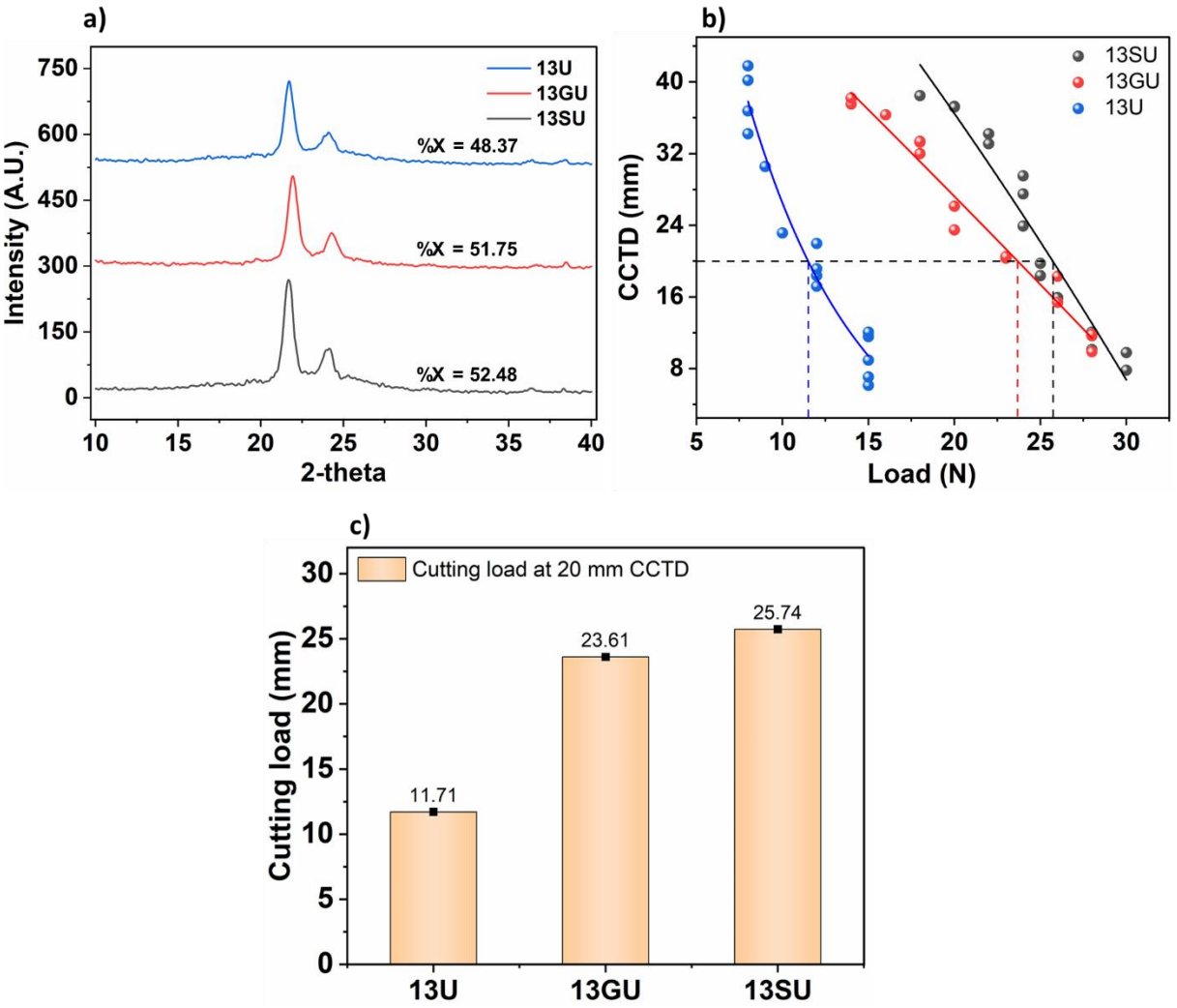

Figure 9. (a) XRD curve of fabric samples. (b) The CCTD-load data and regression line of fabric samples. (c) Comparison of cutting load at 20-mm CCTD derived from CCTD vs load curve.

3.2 Effect of cutting angles

The cut performance of all samples including 13U, 13GU, and 13SU were examined at varying angles 0°, 45°, and 90° (**Figure 10 d-f)**. At 0° (lengthwise direction), the cut forces for 13U, 13SU, and 13GU were 9.563 N, 22.609 N, and 21.784 N, respectively. At 45° (diagonal direction), the cut forces increased to 11.71 N, 25.747 N, and 23.61 N. The highest cut resistance was observed at 90° (widthwise direction), with values of 16.279 N for 13U, 32.431 N for 13SU, and 26.128 N for 13GU (**Figure 10 k**). The data indicates that the highest cut resistant values at 90° in all samples, while minimum cut resistant values occur at 0° and intermediate at 45°.

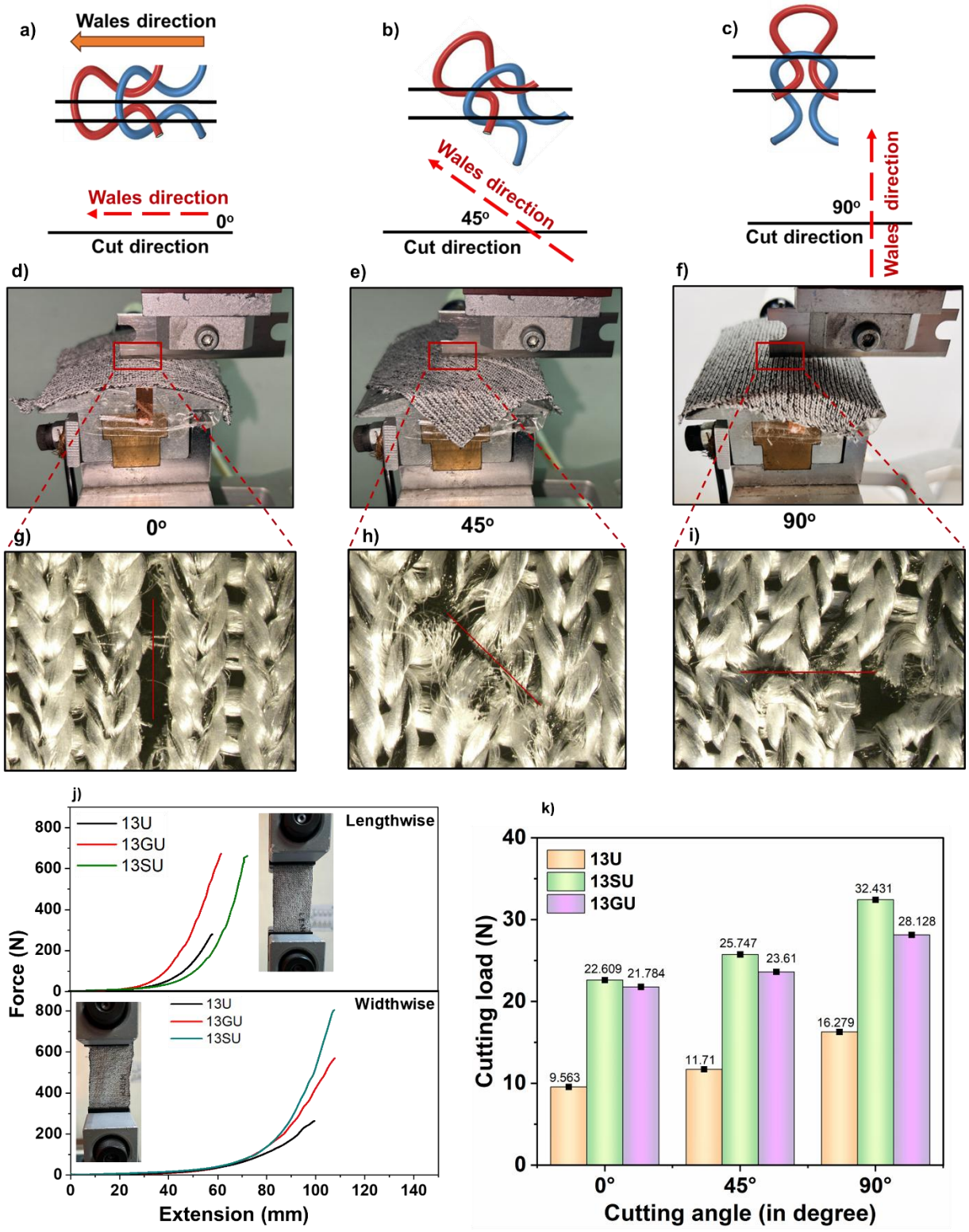

Figure 10. (a-c) Schematic representation of different cutting directions in weft plain knitted structure. (d-f) Performing cut-test on 13SU fabrics at cutting angles of 0°, 45°, and 90°. (g-i) Optical images of knit loops fractures in 13SU fabric at these cutting angles. (j) Force-extension curve of the samples in lengthwise and widthwise directions. (k) Histogram of cutting load of the samples at 0°, 45°, and 90° cutting angles.

There are several factors contribute to these observations, primarily being the extensibility of samples in both the lengthwise and widthwise directions. As shown in Force - Extension graph in **Figure 10 j**, the extensibility of 13U, 13GU, and 13SU samples in widthwise direction (99.4 mm, 107.5 mm, 110.5 mm) was higher compared to lengthwise direction (58.7 mm, 61.6 mm, 72.3 mm) because, in weft knitted fabrics the loop structure is very flexible in course direction. So, in widthwise direction, when blade moves with constant speed on fabric surface in widthwise direction (**Figure 10 f**), the fabric absorbs the mechanical energy applied by cutting force more effectively. This is due to the maximum mobility of yarns in the direction of blade movement, as shown in **Figure 10 i**. This mobility leads to an unstable contact area between the blade edge and the loops, resulting in a loose grip. Consequently, the frictional force reduced, requiring higher shear force to generate cracks in the loops. This is because of the fabric's maximal elastic potential energy in widthwise direction, which contributes to its resistant to cutting forces. In contrast, fabric's lowest extensibility in lengthwise direction, when blade moves in this direction (at 0°) (**Figure 10 d**), limits this energy absorption, and results in a better contact area with tight gripping between blade edges and loops due to lesser mobility of yarns, as shown in **Figure 10 g**. This leads to a lower shear force being sufficient to cut through the loops. The 13SU fabric, which exhibits the maximum extensibility in both the widthwise and lengthwise directions compared to 13GU and 13U, shows the highest cut performance overall, that can absorb more energy before yielding to the cutting force, contributing to its superior cut resistance. On the other hand, the extensibility of 13GU is not as high as 13SU, primarily due to the brittle nature of the glass fibers, which makes the fabric more rigid and less capable of stretching to absorb energy. This rigidity results in lower cut resistance compared to 13SU.

3.3 Effect of environmental conditions

The cut-performance of 13SU, 13GU and 13U samples was investigated by exposing them in open environment for 90 days. After a time, span of 30 days, the mechanical properties of all fabric samples are measured and reported in **Figure 11 c-f**, **Supporting Figure S4,** and **Supporting Figure S5**. The results show a progressive decrease in these properties across all samples with extended exposure to the open environment over 30, 60, and 90 days. The most significant degradation in mechanical properties was observed in the 13SU fabric, followed by 13GU and then 13U, which is due to the galvanic corrosion in 13SU, where the stainless-steel

corrodes and generates oxidative byproducts that catalyse the oxidative degradation of the UHMWPE fibers, resulting in a more rapid breakdown of UHMWPE polymer chains and a subsequent decline in mechanical properties. Additionally, due to the high thermal conductivity of stainless-steel, it efficiently absorbs and distributes heat from sunlight throughout the structure. This increased heat exposure exacerbates the thermal degradation of UHMWPE fibers, leading to further damage. The FTIR spectra of 13SU (**Figure 11 b**) reveal significant changes in the chemical structure of UHMWPE fibers over time, particularly with the emergence of new peaks at 1708 cm^{-1} and 3432 cm^{-1}, corresponding to ketone (C=O) and hydroxyl (O-H) polar groups, respectively. The intensities of these peaks increase with prolonged exposure, indicating ongoing oxidative processes that introduce these functional groups into the UHMWPE chemical structures. Environmental factors such as oxygen and UV radiation initiate free radical formation, leading to polymer chain degradation and the formation of these functional groups. Concurrently, the fundamental bands of UHMWPE, such as the C-H stretching modes at 2851 cm^{-1} and 2919 cm^{-1}, the methylene bending vibration at 1462 cm^{-1}, and the CH_2 rocking mode at 719 cm^{-1}. Over a time, by exposing the samples in open environment, the intensities of these peaks decrease, suggesting a reduction in intact methylene groups and overall degradation of the polymer backbone, further supported by the consistent decrease in the intensity of these characteristic bands, reflecting the impact of environmental exposure on the material's chemical structures. The mechanical properties of 13SU fabric, exhibit a clear decline with increased environmental exposure, consistent with the FTIR findings. Tear strength in the widthwise direction decreases from 405.8 N (non-exposed) to 391 N (30 days), 365 N (60 days), and 310 N (90 days), while in the lengthwise direction, it drops from 313.1 N (non-exposed) to 305.6 N (30 days), 287.5 N (60 days), and 245.9 N (90 days) (**Figure 11 c**). Puncture resistance performance also decreases, with the puncture load dropping from 96.25 N (non-exposed) to 92.42 N (30 days), 85.68 N (60 days), and 74.57 N (90 days). Similarly, the number of cycles to hole formation in abrasion resistance tests declines from 800 cycles (non-exposed) to 780 cycles (30 days), 750 cycles (60 days), and 700 cycles (90 days) (**Figure 11 d**). The cutting load for a 20 mm corrected cut-through distance (CCTD) shows a reduction from 25.74 N (non-exposed) to 23.37 N (30 days), 20.81 N (60 days), and 17.09 N (90 days) (**Figure 11 f**). The correlation between the FTIR spectra and mechanical properties is evident. As the FTIR spectra show increased formation of ketone and hydroxyl groups (peaks at 1708 cm^{-1} and 3432 cm^{-1}), indicating oxidation, the mechanical properties degrade. These polar group into the UHMWPE polymer disrupt the non-polar nature of UHMWPE, reducing

its hydrophobicity and weaken intermolecular forces within the UHMWPE polymer, leading to chain scission and a decrease in molecular weight, reduces its mechanical strength.

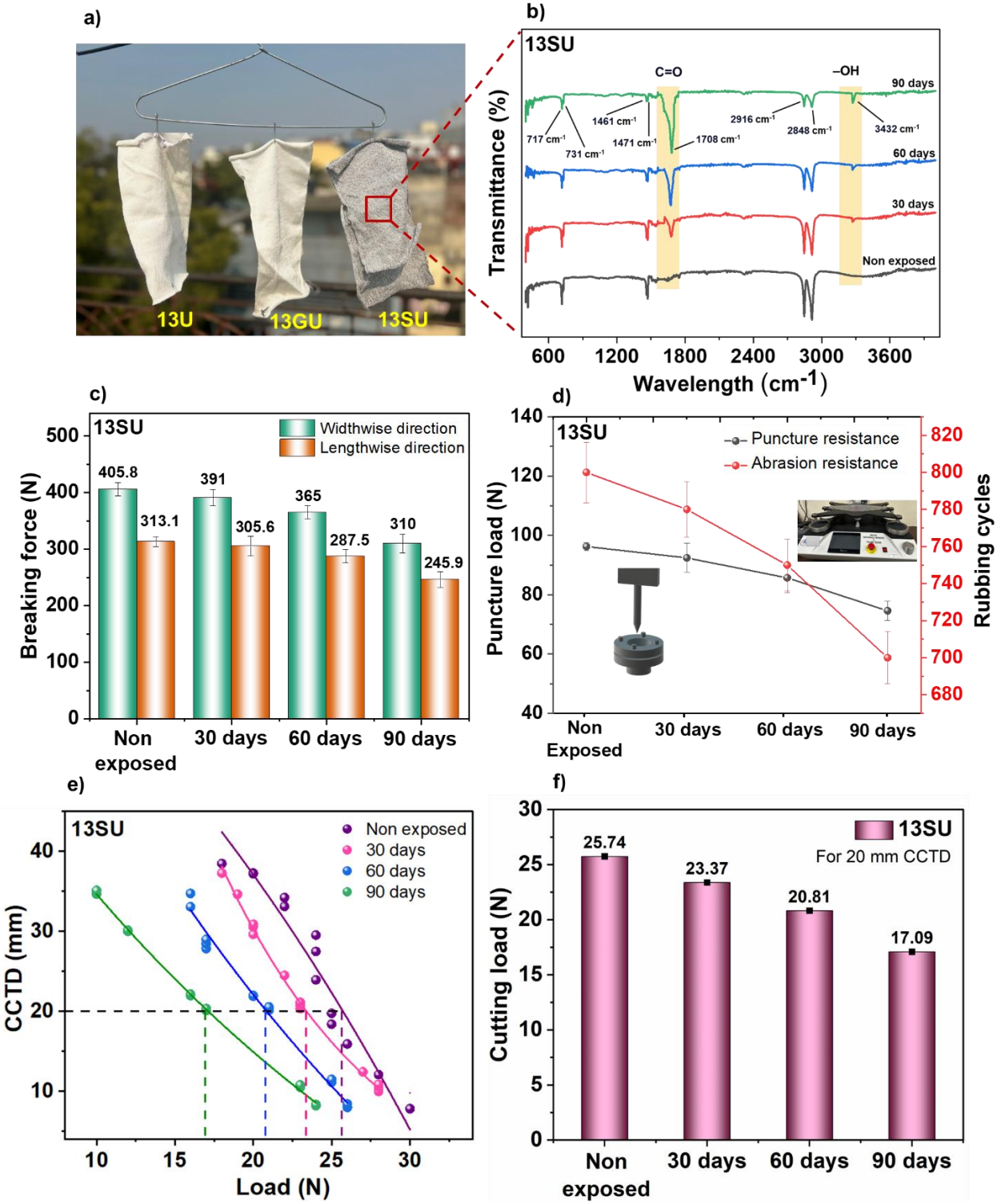

Figure 11. (a) Outdoor environmental exposure of developed samples up to 90 days. (b) FTIR analysis of non-exposed and exposed 13SU sample. Effect of outdoor environmental exposure on 13SU: (c) breaking strength, (d) puncture and abrasion resistance, (e) the CCTD vs load

data and regression line curve (f) histogram of cutting load at 20-mm CCTD, derived from CCTD vs load curve.

3.4 Effect of radiant heat exposure

XRD curves of all exposed samples at heat flux density of 20 kW/m² on the mandrel of TDM-100, as shown in **Figures 12 a-b and Supporting Figure S6**, reveals that consistent decrease in peak intensities at 21.5° and 23.9° for all samples, indicating decreased crystallinity. This decline is attributed to thermal agitation, where increased kinetic energy disrupts the ordered arrangement of polymer chains, shifting the structure from crystalline to more amorphous. DSC analysis supports this observation, showing that UHMWPE, with a melting point (T_m) of approximately 141 °C, which is significantly lower than the T_m of 230 °C for polyester, indicating UHMWPE is very sensitive to thermal effects at lower temperatures (**Figure 12 c**). Among the fabrics, 13SU shows the most significant crystallinity loss, with an 11.72% reduction. This is likely due to the high thermal conductivity of stainless-steel fibers (approximately 13 to 15 W/m·K),[41] which facilitate rapid heat transfer throughout the UHMWPE fibers, leading to elevated temperatures within the polymer structures. As the UHMWPE polymer chains are exposed to this heat, the increased molecular motion results in entropy-driven disorder, causing a breakdown of the crystalline regions. The disruption of these regions not only reduces crystallinity but also affects the overall crystal size and morphology. SEM images of 13SU (**Figure 12 e**) reveal extensive deformation and bead formation of UHMWPE fibers throughout the fabric, correlating with a substantial drop in cut resistance from 25.74 N to 18.76 N after exposure (**Figure 12 d**). While, 13GU shows better thermal stability, with only a 6.36 % reduction in crystallinity. The lower thermal conductivity of glass fibers as compared to stainless-steel fibers, helps insulate the UHMWPE fibers and minimizes the increase in entropy within the polymer, which helps in reducing the extent of degradation. SEM analysis shows only localized deformation of UHMWPE fibers and minimal structural damage in 13GU (**Figure 12 f**), consistent with a smaller decline in cut resistance from 23.6 N to 20.17 N, indicating its superior ability to maintain performance under thermal stress. The 13U fabric, composed solely of UHMWPE, shows an intermediate response, with a crystallinity reduction of about 9%. While it lacks the reinforcing fibers present in 13SU and 13GU, it still undergoes significant thermal agitation, leading to moderate degradation. SEM images of 13U (**Supporting Figure S7**) show some fiber dislocation, with a corresponding decrease in cut resistance, though less pronounced than in 13SU.

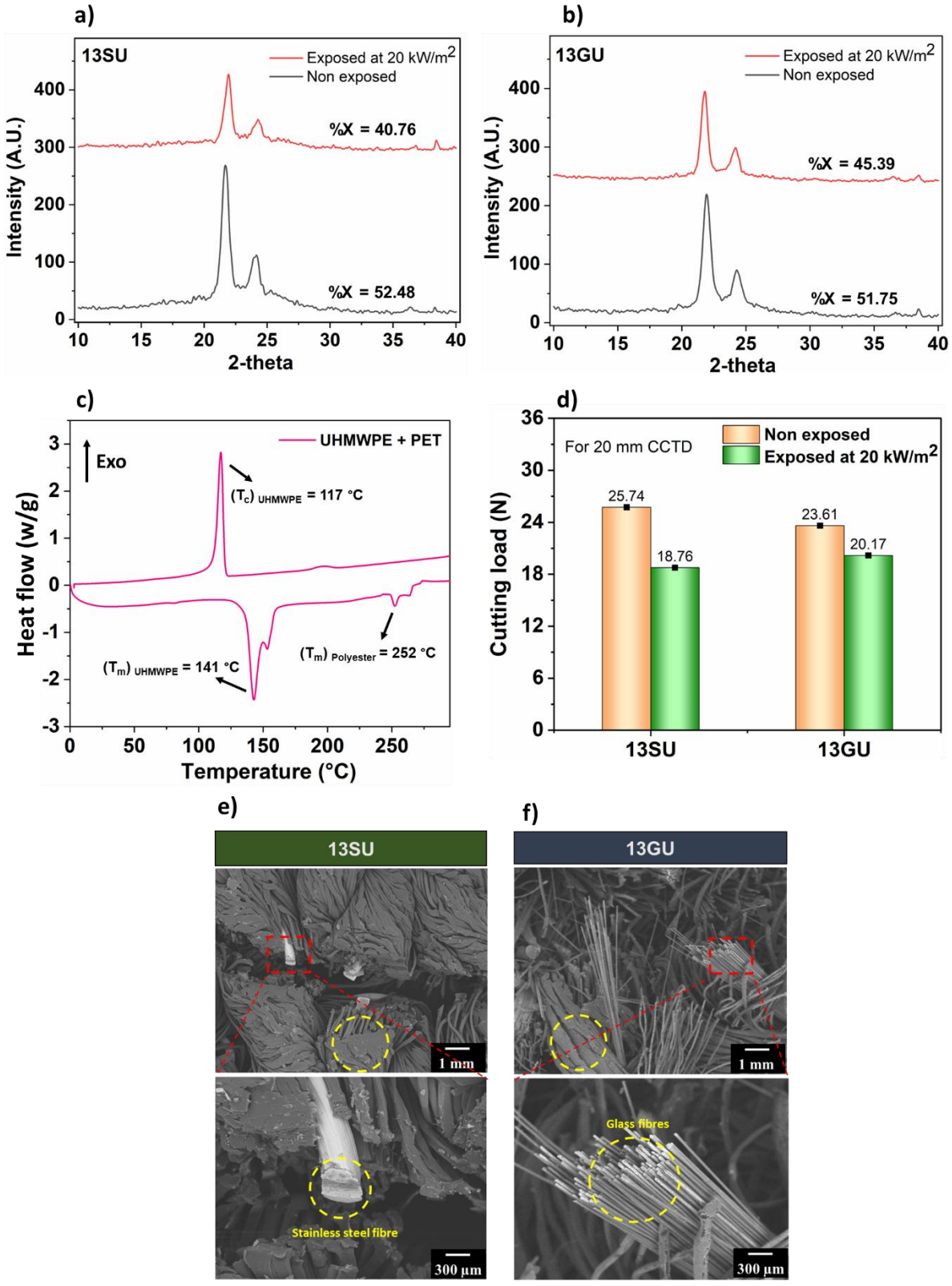

Figure 12. XRD curves of radiant heat exposed; (a) 13SU, and (b) 13GU samples. (c) DSC curves of UHMWPE/Polyester blend filaments. (d) The cutting load comparison of radiant heat

exposed and non-exposed 13SU, and 13GU samples at 20-mm CCTD. (e-f) The SEM images of radiant heat exposed 13SU, and 13GU samples.

4. CONCLUSIONS

In this study, three types of knitted fabrics (in form of gloves) were prepared, including 100% UHMWPE (13U), stainless-steel reinforced UHMWPE (13SU), and glass-reinforced UHMWPE (13GU), using a 13-gauge gloves knitting machine. The study analysed the effect of reinforcing materials, radiant heat exposure, outdoor environmental conditions, and cutting angles on the durability and cut-resistance properties of developed samples. The findings revealed that reinforcement with stainless-steel and glass fibers significantly enhanced the mechanical (tear resistance, puncture resistance, and abrasion resistance) and cut-resistance properties. The 13SU fabric, reinforced with stainless steel, exhibited the highest overall performance under normal conditions, with an increased peak intensity and crystallinity percentage of 52.48% in its crystalline structure, compared to 13GU (51.75%) and 13U (48.37%), as confirmed by XRD graphs. This enhancement is attributed to the nucleating effect of stainless-steel, which promotes a more ordered alignment of UHMWPE polymer chains, leading to improved cut-resistance properties. However, this same reinforcement also contributed to the fabric more vulnerable to environmental degradation, particularly through galvanic corrosion and oxidative degradation, which resulted in formation of ketone (C=O) and hydroxyl (O-H) polar groups, that reduced the peak intensity and altered the molecular structure of UHMWPE polymer over time (up to 90 days), as confirmed by FTIR analyses.

Radiant heat exposure further impacted the crystallinity of the UHMWPE polymer, particularly in the 13SU sample, where the high thermal conductivity of stainless-steel facilitated rapid heat transfer, leading to a significant loss in crystallinity and molecular weight. In contrast, the 13GU fabric, reinforced with glass fibers, demonstrated better thermal stability due to the lower thermal conductivity of glass, which minimized the degradation of UHMWPE's molecular structure and preserved its mechanical and cut performance. The study also found that cut resistance for all samples was highest at 90° (widthwise direction) and lowest at 0° (lengthwise direction), influenced by the fabric's extensibility, which was higher in the widthwise direction compared to the lengthwise direction. This increased extensibility allowed the fabric to absorb more energy through the loops and polymer structure, thereby contributing to its superior cut resistance at 90°cutting angle.

SUPPORTING INFORMATION

1) The detailed information about the effect of outdoor environmental exposure on 13GU and 13U sample along with XRD curves, and SEM images of radiant heat exposed 13U sample.

AUTHOR INFORMATION

Main Author and Corresponding Author 1

Shubham Singh

Mob: +919670557718

Email: shubham.official991@gmail.com ; ttz228226@textile.iitd.ac.in

Corresponding Author 2

Bipin Kumar, Ph.D.

Associate Professor

Department of Textile and Fibre Engineering

Indian Institute of Technology Delhi

Hauzkhas, New Delhi 110016

India

ORCID ID- https://orcid.org/0000-0002-9754-8210

Tel: +91-11-26597240

Mob: +91-9990240340

Fax: +91-11-26581103

Co-author 1

Apurba Das

Professor

Department of Textile and Fibre Engineering

Indian Institute of Technology Delhi

Hauzkhas, New Delhi 110016

India

Email: apurba@textile.iitd.ac.in

Co-author 2

Nandan Kumar

Managing Director

High Performance Textiles Pvt. Ltd, Sonipat, Haryana, India

Email: nandan.leeds@gmail.com

Author contributions

The manuscript was written through contributions of all authors. All authors have given approval to the final version of the manuscript.

Funding sources

This research is funded by National Technical Textiles Mission, Ministry of Textiles, Govt. of India (Project codes - RP04310G and RP04612G).

Acknowledgment

The author would like to acknowledge HPT Pvt. Ltd. Sonipat, Haryana, India for providing yarn samples, and to the Institute of Technical Textiles, Sonipat, Haryana and the CRF and NRF of Indian Institute of Technology Delhi, India for providing research facilities.

REFERENCES

(1) (ILO), I. L. O. *Safety and Health at Work: A Vision for Sustainable Prevention*; 2014.

(2) Mawkhlieng, U.; Majumdar, A.; Laha, A. A review of fibrous materials for soft body armour applications. *RSC Advances* **2020**, *10* (2), 1066-1086, 10.1039/C9RA06447H. DOI: 10.1039/C9RA06447H.

(3) Nayak, R.; Crouch, I.; Kanesalingam, S.; Ding, J.; Tan, P.; Lee, B.; Miao, M.; Ganga, D.; Wang, L. Body armor for stab and spike protection, Part 1: Scientific literature review. *Textile Research Journal* **2018**, *88* (7), 812-832. DOI: 10.1177/0040517517690623.

(4) Żyłka, E.; Irzmańska, E.; Saramak, J.; Jurczyk-Kowalska, M. Functional 3D-Printed Polymeric Materials with Metallic Reinforcement for Use in Cut-Resistant Gloves. *Materials* **2024**, *17* (1), 90.

(5) Jiang, F.; Su, T.; Fang, L.; Zhao, K.; Cong, H. Structural Design and Performance of Cut-Resistant Fabrics with Concave–Convex Arrays. *Polymers* **2024**, *16* (15), 2137.

(6) Panneke, N.; Ehrmann, A. Stab-Resistant Polymers—Recent Developments in Materials and Structures. *Polymers* **2023**, *15* (4), 983.

(7) Singh, S.; Somkuwar, V. U.; Maurya, S. K.; Garg, H.; Das, A.; Kumar, N.; Kumar, B. Temperature dependent cut-resistance properties of ultra-high molecular weight polyethylene based knitted textiles. *Journal of Applied Polymer Science* **2024**, *141* (32), e55769. DOI: https://doi.org/10.1002/app.55769.

(8) Timashev, P.; Minaev, N.; Terekhin, D.; Kuznetsov, E.; Parfenov, V.; Malinovskaya, V.; Bagratashvili, V.; Parenago, O. Structure and properties of ultra-high-molecular-weight polyethylene (UHMWPE) containing silver nanoparticles. *Russian Journal of Physical Chemistry B* **2014**, *8*, 1042-1048.

(9) Gao, Q.; Hu, J.; Yang, Y.; Wang, M.; Zhang, M.; Tang, Z.; Zhang, M.; Liu, W.; Wu, G. Fabrication of New High-Performance UHMWPE-Based Conductive Fibers in a Universal Process. *Industrial & Engineering Chemistry Research* **2019**, *58* (2), 935-943. DOI: 10.1021/acs.iecr.8b05059.

(10) Kang, T. J.; Hong, K. H.; Yoo, M. R. Preparation and properties of fumed silica/Kevlar composite fabrics for application of stab resistant material. *Fibers and Polymers* **2010**, *11*, 719-724.

(11) Mao, N. Textile materials for protective textiles. *High Performance Technical Textiles* **2019**, *22* (3), 107-157.

(12) Lin, J.; Bang, S. H.; Malakooti, M. H.; Sodano, H. A. Isolation of Aramid Nanofibers for High Strength and Toughness Polymer Nanocomposites. *ACS Applied Materials & Interfaces* **2017**, *9* (12), 11167-11175. DOI: 10.1021/acsami.7b01488.

(13) Yang, H.; Le, Y.; Zhang, R.; Zhang, J.; Wang, X.; Zhang, T.; Zhang, M. Cut-resistance of elastic high-performance composite yarn. *Textile Research Journal 0* (0), 00405175241261737. DOI: 10.1177/00405175241261737.

(14) Tamargo-Martínez, K.; Villar-Rodil, S.; Paredes, J. I.; Martínez-Alonso, A.; Tascón, J. M.; Montes-Morán, M. A. Surface characterization of PBO fibers. *Macromolecules* **2003**, *36* (23), 8662-8672.

(15) Rebouillat, S.; Steffenino, B.; Miret-Casas, A. Aramid, steel, and glass: characterization via cut performance testing, of composite knitted fabrics and their constituent yarns, with a review of the art. *Journal of Materials Science* **2010**, *45* (19), 5378-5392.

(16) Shi, X.; Zhang, R.; Ruan, K.; Ma, T.; Guo, Y.; Gu, J. Improvement of thermal conductivities and simulation model for glass fabrics reinforced epoxy laminated composites via introducing hetero-structured BNN-30@ BNNS fillers. *Journal of Materials Science & Technology* **2021**, *82*, 239-249.

(17) Chen, X.; Chu, Z.; Zhao, W.; Wu, L.; Wu, Q.; Yu, G. Buckling resistance of ultra-low-density carbon fiber curved-wall honeycomb based on stretching process. *Composite Structures* **2024**, *344*, 118322. DOI: https://doi.org/10.1016/j.compstruct.2024.118322.

(18) Mao, L.; Yu, H.; Yao, L.; Shen, Y.; Yan, X.; Ma, Y. Cut/puncture resistance and mechanisms of protective composite textiles reinforced with inorganic powder. *Materials & Design* **2024**, *237*, 112575. DOI: https://doi.org/10.1016/j.matdes.2023.112575.

(19) Mayo, J.; Wetzel, E. Cut resistance and failure of high-performance single fibers. *Textile Research Journal* **2014**, *84* (12), 1233-1246. DOI: 10.1177/0040517513517966.

(20) Goerz Jr, D. J.; Smith Jr, H. R.; Miguel-Bettencourt, K. C. Soft body armor material with enhanced puncture resistance comprising at least one continuous fabric having knit portions and integrally woven hinge portions. Google Patents: 1995.

(21) Alpyildiz, T.; Rochery, M.; Kurbak, A.; Flambard, X. Stab and cut resistance of knitted structures: a comparative study. *Textile Research Journal* **2011**, *81* (2), 205-214.

(22) Javid, M.; Bilal Qadir, M.; Jabbar, A.; Jamshaid, H. Statistical study and investigation of the cut-resistant and thermo-physiological performance of protective gloves: a new prospective. *International Journal of Occupational Safety and Ergonomics* **2024**, *30* (2), 399-411.

(23) Leong, K. H.; Ramakrishna, S.; Huang, Z.; Bibo, G. The potential of knitting for engineering composites—a review. *Composites Part A: applied science and manufacturing* **2000**, *31* (3), 197-220.
(24) Flambard, X.; Polo, J. Stab resistance of multi-layers knitted structures: comparison between para-aramid and PBO fibers. *Journal of advanced materials* **2004**, *36* (1), 30-35.
(25) Fangueiro, R.; Carvalho, R.; Silveira, D.; Ferreira, N.; Ferreira, C.; Monteiro, F.; Sampaio, S. Development of high-performance single layer weft knitted structures for cut and puncture protection. *J Textile Sci Eng* **2015**, *5* (6), 1-6.
(26) Hudspeth, M.; Nie, X.; Chen, W. Dynamic failure of Dyneema SK76 single fibers under biaxial shear/tension. *Polymer* **2012**, *53* (24), 5568-5574.
(27) Lim, J.; Zheng, J. Q.; Masters, K.; Chen, W. W. Effects of gage length, loading rates, and damage on the strength of PPTA fibers. *International Journal of Impact Engineering* **2011**, *38* (4), 219-227.
(28) Lim, J.; Chen, W. W.; Zheng, J. Q. Dynamic small strain measurements of Kevlar® 129 single fibers with a miniaturized tension Kolsky bar. *Polymer Testing* **2010**, *29* (6), 701-705.
(29) Cheng, M.; Chen, W.; Weerasooriya, T. Mechanical properties of Kevlar® KM2 single fiber. *J. Eng. Mater. Technol.* **2005**, *127* (2), 197-203.
(30) Schwartz, P.; Netravali, A.; Sembach, S. Effects of strain rate and gauge length on the failure of ultra-high strength polyethylene fibers. *Textile research journal* **1986**, *56* (8), 502-508.
(31) Cheng, M.; Chen, W.; Weerasooriya, T. Experimental investigation of the transverse mechanical properties of a single Kevlar® KM2 fiber. *International Journal of Solids and Structures* **2004**, *41* (22-23), 6215-6232.
(32) Singletary, J.; Davis, H.; Ramasubramanian, M.; Knoff, W.; Toney, M. The transverse compression of PPTA fibers Part I Single fiber transverse compression testing. *Journal of Materials Science* **2000**, *35*, 573-581.
(33) Kawabata, S. Measurement of the transverse mechanical properties of high-performance fibres. *Journal of the Textile Institute* **1990**, *81* (4), 432-447.
(34) Phoenix, S.; Skelton, J. Transverse compressive moduli and yield behavior of some orthotropic, high-modulus filaments. *Textile Research Journal* **1974**, *44* (12), 934-940.
(35) Mayo Jr, J.; Wetzel, E. Cut resistance and failure of high-performance single fibers. *Textile Research Journal* **2014**, *84* (12), 1233-1246.

(36) Chin, J.; Forster, A.; Clerici, C.; Sung, L.; Oudina, M.; Rice, K. Temperature and humidity aging of poly (p-phenylene-2, 6-benzobisoxazole) fibers: Chemical and physical characterization. *Polymer degradation and stability* **2007**, *92* (7), 1234-1246.
(37) Kelly, J. M. Ultra-high molecular weight polyethylene. *Journal of Macromolecular Science, Part C: Polymer Reviews* **2002**, *42* (3), 355-371.
(38) Rudnik, E.; Dobkowski, Z. Thermal degradation of UHMWPE. *Journal of thermal analysis* **1997**, *49*, 471-475.
(39) Goodridge, R. D.; Hague, R. J.; Tuck, C. J. An empirical study into laser sintering of ultra-high molecular weight polyethylene (UHMWPE). *Journal of Materials Processing Technology* **2010**, *210* (1), 72-80.
(40) Choudary, M. V.; Nagaraja, A.; Sai, K. O. C.; Balasubramanian, M. Characterization of laminate sandwiched with stainless steel and glass fibre. *Materials Today: Proceedings* **2020**, *22*, 847-852.
(41) Simmons, J.; Daeumer, M.; Azizi, A. Local thermal conductivity mapping of selective laser melted 316L stainless steel. In *2018 International Solid Freeform Fabrication Symposium*, 2018; University of Texas at Austin.

SINGLE CARBON AND GLASS FIBRE TENSILE PROPERTIES AND THE CORRELATION WITH THEIR GEOMETRY

Elise Van Vlierberghe[1], Sara Marie Delcourte[1], Christian Breite[1] and Yentl Swolfs[1]

[1]Department of Materials Engineering (MTM), KU Leuven
Kasteelpark Arenberg 44/bus 2450, 3001 Leuven, Belgium
Email: elise.vanvlierberghe@kuleuven.be, web page: https://www.mtm.kuleuven.be/

Keywords: Fibres, Strength, Mechanical testing

ABSTRACT

Automated single fibre tensile tests were performed on carbon and glass fibres to characterise their tensile properties and cross-section accurately. An iterative compliance correction was developed to improve the strain accuracy. The results showed no correlation between tensile properties and the fibre cross-section but a clear dependency on the gauge length, lowering strength due to a higher defect probability in longer fibres. A dataset with more than 200 tests was obtained, which can be utilised to enhance simulation inputs and support predictive models for composite design.

1 INTRODUCTION

Fibre-reinforced polymer composites (FRP) gain their mechanical performance primarily from the embedded fibres. These fibres carry most of the applied loads, thereby providing stiffness and strength to the composite parts. Accurate characterisation of these fibres is essential for understanding their role within composites and for predicting the mechanical behaviour of FRP products reliably. Classic composite simulations require properties such as the fibre diameter, the Young's modulus, the strength and the failure strain. Manufacturers provide such values, but typically only an average value and no distribution of the properties. They base their mechanical properties on impregnated bundle tests, not including the effect of fibre cross-sectional variation. In literature, fibre properties are commonly determined by single fibre tensile tests (SFTT). Those tests do allow for individual fibre cross-sectional area measurements, but care needs to be taken during handling and clamping [1, 2]. Other methods are single fibre fragmentation tests, loop tests and synchrotron radiation computed tomography on unidirectional composites [2].

Common reinforcements for FRPs are carbon and glass fibres. Given that those fibres are brittle materials influenced by the presence of manufacturing defects, they exhibit strength characteristics that are best described using probability models such as the Weibull distribution [3]. The classic Weibull distribution describes the weakest-link behaviour with a scale parameter and modulus. The scale parameter is the characteristic strength at which 63.2 % of the fibres will fail. The modulus, or shape parameter, reflects the variability in strength. A strong, reliable fibre is thus characterised by a high scale and shape parameter, respectively. The drawback of this distribution is that a large data set is required for accuracy. Several authors [2, 4] have confirmed that fewer than 100 tests introduce significant errors in the Weibull parameters.

An additional concern in SFTTs is the compliance correction. Depuydt et al.[5] and Engelbrecht-Wiggans et al. [6] have noted that the compliance correction methods suggested in the testing standards for single fibres are unable to correct the measured strain values adequately. Mesquita et al. [4] added that due to the non-linear tensile behaviour of the fibres, errors are introduced in the determination of the machine compliance. They applied an iterative compliance correction by updating the strain, which shifted the stress-strain diagram, and recalculating the compliance on the new strain range. They reported that the first iteration leads to a deviation of 11 % from the real machine compliance.

In the current study, SFTTs were performed on carbon and glass fibres to quantify their properties. Correlations between the mechanical properties and the geometry of the fibres, separated into the cross-section and the gauge length, will be analysed.

2 MATERIALS AND METHODS

2.1 Fibre types

In this study, both carbon and glass fibres were tested. The carbon fibres are T700SC-12K-50C PAN-based fibres (Toray Industries, Japan) and the glass fibres are Advantex® R25HX14 E-CR fibres (3B Fiberglass, Belgium). Table 1 summarises the properties, as specified by the manufacturer.

Table 1: Fibre properties reported in their respective data sheet.

Material	Fibre type	Diameter [µm]	Tensile modulus [GPa]	Tensile strength [MPa]	Failure strain [%]
Carbon	T700SC-12K-50C	7	230	4900	2.1
Glass	Advantex® R25HX14	17-24	81-83	2700-2800	/

2.2 Automated single fibre tensile tests

The SFTTs were performed with the ALS1500-LEX820-FDAS770 device (Dia-Stron Limited, United Kingdom). The successive stages of this test are specimen preparation, dimensional measurements and mechanical testing, while the automated loading system with vacuum suction ensures transport of the specimens. More details on the functioning of the Dia-Stron device, as well as a comparison with single fibres mounted on card frames, were described by Islam et al. [7].

The fibres were meticulously extracted from the roving by hand. To limit the adhesion between fibres due to the sizing, the roving was first divided into smaller bundles, which were further separated with a fine brush. Each fibre was mounted onto two plastic end tabs fitted into the cassette slots. The cassette serves the purpose of specimen storage and facilitates specimen preparation. The slots in the cassette were spaced at a fixed length, predefining the gauge lengths of the fibres at 4, 12 and 30 mm. Alignment of the fibres was assured by V slits in the tabs and the precise rectangularity of both the tabs and slots. The fibres were glued in the tab with UV-curing adhesive (3099, Dymax Corporation, United States) at a wavelength of 365 nm for 15 s.

The dimensional measurement of the fibre was performed with the laser scanning micrometre (LSM-500S+6200, Mitutoyo, Japan) at an accuracy of 0.3 µm. The contactless measuring device was linearly calibrated between two reference fibres measured in the scanning electron microscope: 6.8-50.8 µm for carbon and 9.0-101.3 µm for glass. Calibrating each material independently ensured limited laser-material interaction on the diameter measurement. A 3D dimensional measurement was performed with approximately one longitudinal slice per 4 mm and three rotations per slice, with each approximately 220 points per rotation.

The mechanical testing of the fibre consisted of an SFTT in the extensometer with a 20 N load cell. A cross-head strain rate of 0.15 %/s was applied according to the ASTM C1557-14 standard. A gauge force of 0.5 mN was applied, and data were sampled every 100 ms.

2.3 Determination of fibre properties

The diameter measurements were filtered to remove erroneous measurements and noise [8]. Slices with an average diameter outside a range of 0.5-1.5 times the manufacturer's diameter were considered erroneous and automatically removed. The range for filtering the slice diameter was further refined to $\mu \pm 3\sigma$, with μ the mean and σ the standard deviation. Noise was removed by discarding individual data points deviating by more than 20 % of the average slice diameter. This filtering removed 6 % of

the measurements. The cross-sectional area was obtained from the surface integral in polar coordinates of the angular data points.

The acquired force-displacement curves were corrected for compliance in line with the ASTM C1557-20 standard. The SFTT at three different gauge lengths were plotted according to

$$\frac{\Delta L}{F} = \frac{l_0}{EA} + C_s \tag{1}$$

with ΔL being the recorded crosshead displacement, F the recorded force, l_0 the fibre gauge length, E the Young's modulus, A the cross-sectional area and C_s the system compliance. Fitting a straight line through the plot of $\Delta L/F$ as a function of l_0/A allows extracting C_s at the intercept (Figure 1a). The actual elongation of the fibre Δl can then be determined by

$$\Delta l = \Delta L - C_s F \tag{2}$$

This compliance correction is then applied iteratively by replacing the ΔL in equation 1 with Δl computed in equation 2, as suggested by Mesquita et al. [4]. To ensure that the iterative method converges, outliers were removed based on an interval of 100% around the mean value of the fitted slope. The system compliances obtained are 0.024 mm/N and 0.128 mm/N for glass and carbon, respectively (Figure 1b). Using the first iteration would cause a relative error up to 154 %.

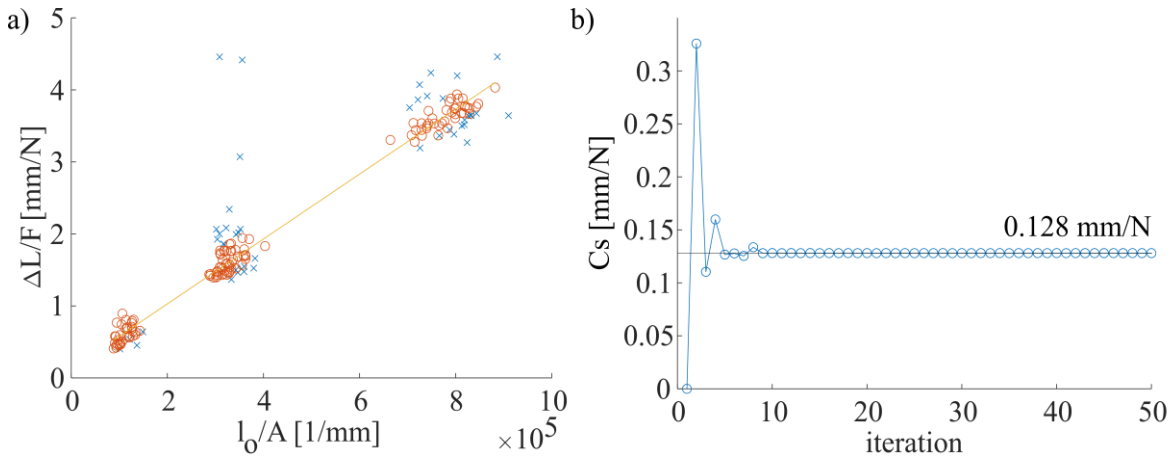

Figure 1: Carbon compliance determination: (a) final compliance curve and (b) iteration.

Stress-strain curves with a load drop were discarded from the data analysis. A load drop is defined in this study as a difference of 5 mN between successive force measurements. When such a load drop occurred before reaching 25 % of the maximum force, it was considered linked to the tab slipping in the tensile grip, and the stress-strain curve was not discarded. The modulus was determined in the range of 0.1-0.6 % strain, according to the ISO 1566-1998 standard for fibres with a nominal failure strain above 1.2 %.

3 RESULTS AND DISCUSSION

3.1 Fibre properties

From the SFTTs, the diameter, tensile modulus, ultimate tensile strength, and failure strain for both fibre types were precisely computed (Table 2). The automation ensured large datasets of approximately 200 tests, which are vital for obtaining statistically accurate parameters [4]. The average diameter of both fibre types is in line with the value provided by the manufacturer. In addition to the average diameter, the cross-sectional shape was also measured. An ellipsoidal cross-section was measured for carbon fibres, in contrast with circular glass fibres (Figure 2), consistent with observations in the literature [1]. The modulus and ultimate tensile strength were lower than the values

provided by the manufacturer. However, those properties were measured with the impregnated bundle method and are thus difficult to compare.

Table 2: Fibre properties obtained from the single fibre tensile tests with a gauge length of 12 mm (mean ± standard deviation).

Material	Number of tests	Diameter [µm]	Tensile modulus [GPa]	Ultimate tensile strength [MPa]	Failure strain [%]
Carbon	206	6.5 ± 0.3	226 ± 25	4571 ± 1092	1.75 ± 0.38
Glass	198	24.3 ± 1.4	72 ± 4	1625 ± 583	2.34 ± 0.87

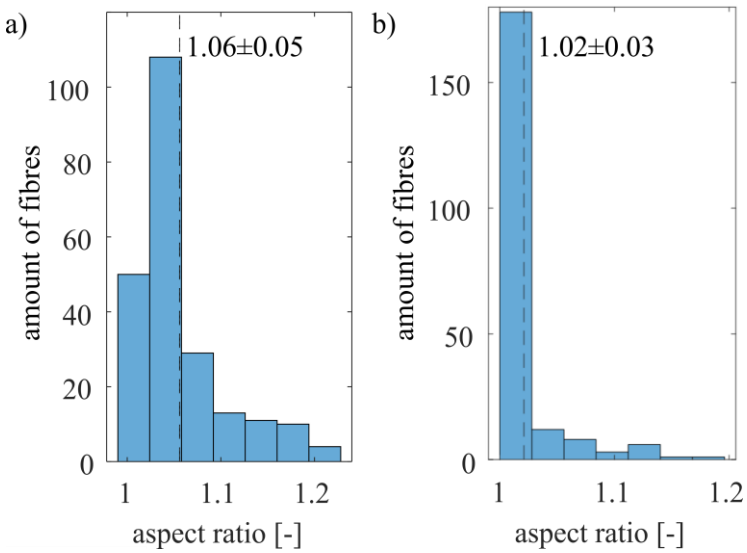

Figure 2: Aspect ratio histogram: (a) carbon and (b) glass fibres.

3.2 Correlation between tensile properties and the cross-section

The interdependence between the tensile properties and the cross-section was studied with point clouds. The relation could be observed graphically from the point cloud orientation, and the coefficient of determination R^2 provides a quantitative evaluation of the linear fit. Low R^2 indicate a limited correlation. No correlation was observed between the tensile properties and the fibre diameter or aspect ratio (Figure 3), so the results for mechanical properties are believed to be unbiased. This confirms a previous study [4], where no correlation was found between the modulus and the fibre diameter for glass and only a slight negative correlation for carbon fibres.

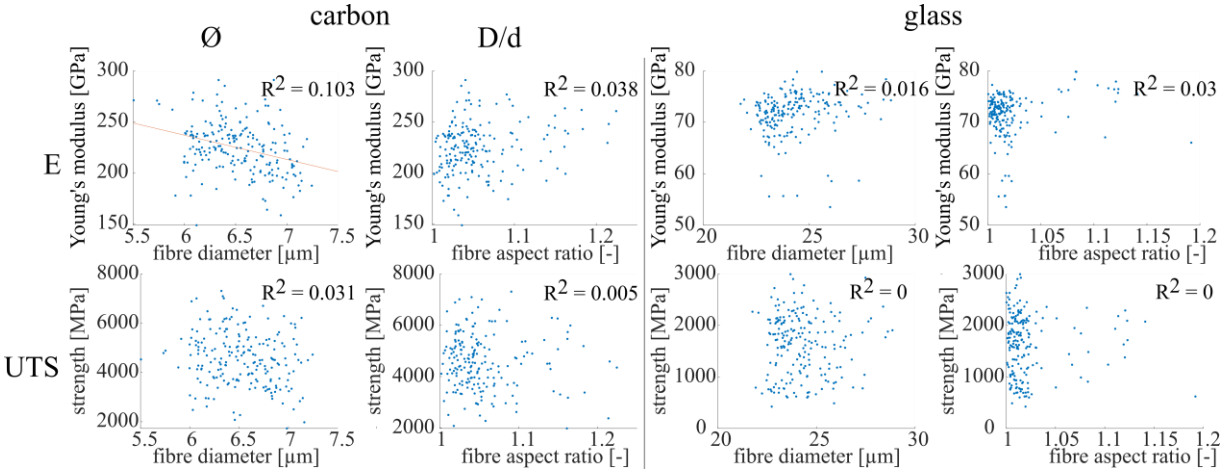

Figure 3: Point clouds indicating the correlation between tensile properties (Young's modulus and ultimate tensile strength) and the fibre cross-section (diameter and aspect ratio) for carbon and glass.

3.3 Gauge length dependency

The interdependence between the tensile properties and the fibre length was studied with the Weibull parameters (Table 3). When comparing the 30 mm fibres to the shorter ones, an obvious gauge length dependency was found, stating that there is a higher probability of finding defects in the longer fibres, resulting in a lower Weibull scale parameter (Figure 4). The Weibull modulus appeared to increase with an increasing gauge length, representing more consistent fibres with a more uniform defect distribution. By representing the strength and strain with the Weibull distribution, apparent higher values were obtained than by averaging all the tests (Table 2). Besides having a higher tensile strength, carbon fibres were observed to have a higher Weibull modulus and thus being more consistent with a more uniform flaw distribution than glass fibres. Additionally, the importance of a large data set could be confirmed as the confidence intervals reduced with an increasing number of tests.

Table 3: Weibull parameters obtained from the single fibre tensile tests (mean and 95 % confidence interval).

Material	Gauge length [mm]	Number of tests	σ_0 [MPa]	$m_{strength}$ [-]	ε_0 [%]	m_{strain} [-]
Carbon	4	55	5023 [4587, 5500]	3.1 [2.5, 3.8]	2.32 [2.14, 2.51]	3.2 [2.7, 3.9]
	12	206	4997 [4844, 5155]	4.6 [4.2, 5.1]	1.90 [1.85, 1.96]	5.1 [4.6, 5.7]
	30	60	3252 [3089, 3423]	5.2 [4.3, 6.3]	1.42 [1.34, 1.51]	4.6 [3.8, 5.4]
Glass	4	64	1591 [1454, 1740]	2.9 [2.4, 3.5]	2.60 [2.34, 2.89]	2.4 [2.0, 2.8]
	12	179	1827 [1740, 1917]	3.2 [2.8, 3.6]	2.62 [2.49, 2.75]	3.0 [2.6, 3.3]
	30	82	1208 [1107, 1319]	2.6 [2.2, 3.1]	1.48 [1.35, 1.62]	2.5 [2.2, 3.0]

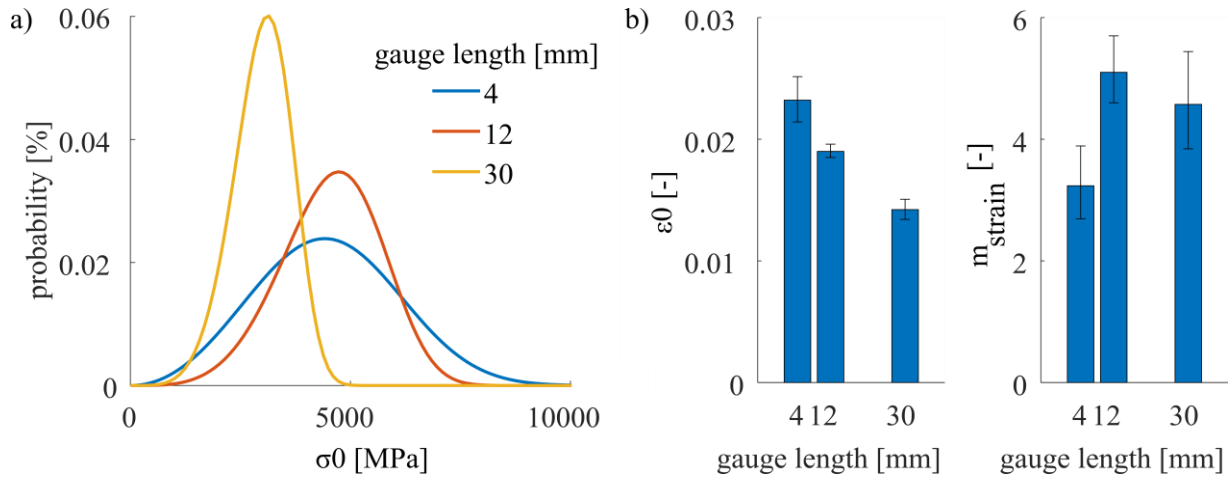

Figure 4: Weibull probability functions as a function of the gauge length for carbon fibres: (a) strength and (b) strain.

4 CONCLUSION

SFTTs were performed on carbon and glass fibres to characterise their tensile behaviour. The fibre

diameter and aspect ratio were measured longitudinally and angularly with the laser scanning micrometre. The fibre modulus, ultimate tensile strength and failure strain were extracted from the stress-strain curve. No correlation was observed between the tensile properties and fibre cross-section. A gauge length dependency was found, though, for the Weibull strength and strain, as longer fibres have a higher probability of containing critical defects.

This comprehensive study on the tensile properties of single carbon and glass fibres provides a detailed input data set for simulations and facilitates the measurement of other fibre-dependent properties. Improving predictive models based on stiffness and strength will enable the development of enhanced designs for FRP parts.

ACKNOWLEDGEMENTS

The authors wish to acknowledge Susana García Mayo for the fruitful equipment-related discussions. EVV and CB acknowledge Fonds Wetenschappelijk Onderzoek's (FWO) financial support for their PhD fellowship DELICATE (1S31625N) and postdoctoral fellowship SUBFIRE (12A0625N), respectively.

REFERENCES

[1] F. Islam, S. Joannès, S. Bucknell, Y. Leray, A. Bunsell and L. Laiarinandrasana, Investigation of tensile strength and dimensional variation of T700 carbon fibres using an improved experimental setup, *Journal of reinforced plastics and composites*, **39**, 2020, pp. 144-162 (10.1177/0731684419873712).

[2] Y. Swolfs, I. Verpoest and L. Gorbatikh, A review of input data and modelling assumptions in longitudinal strength models for unidirectional fibre-reinforced composites, *Composite Structures*, **150**, 2016, pp. 153-172 (10.1016/j.compstruct.2016.05.002).

[3] W. Weibull, A statistical distribution function of wide applicability, *Journal of applied mechanics*, 1951, pp.

[4] F. Mesquita, S. Bucknell, Y. Leray, S. V. Lomov and Y. Swolfs, Single carbon and glass fibre properties characterised using large data sets obtained through automated single fibre tensile testing, *Composites Part A: Applied Science and Manufacturing*, **145**, 2021, pp. 106389 (10.1016/j.compositesa.2021.106389).

[5] D. Depuydt, K. Hendrickx, W. Biesmans, J. Ivens and A. W. Van Vuure, Digital image correlation as a strain measurement technique for fibre tensile tests, *Composites Part A: Applied Science and Manufacturing*, **99**, 2017, pp. 76-83 (10.1016/j.compositesa.2017.03.035).

[6] A. E. Engelbrecht-Wiggans and A. L. Forster, Analysis of strain correction procedures for single fiber tensile testing, *Composites Part A: Applied Science and Manufacturing*, **167**, 2023, pp. 107411 (10.1016/j.compositesa.2022.107411).

[7] F. Islam, S. Joannès, S. Bucknell, Y. Leray, A. Bunsell and L. Laiarinandrasana, Towards accurate and efficient single fibre characterization to better assess failure strength distribution, *ECCM 18-18th European Conference on Composite Materials, Athens, Greece, 2018,* Paper pp. 7 p.

[8] S. M. Delcourte, Enkelvoudige vezeltrekproeven om het Weibull gedrag van koolstof- en glasvezel te begrijpen, *Master's thesis*, KU Leuven, 2025.

ENHANCING THE ENERGY STORAGE CAPABILITY OF LIGNIN BASED CARBON FIBRE *VIA* SURFACE MODIFICATION

Bhagya Dharmasiri[1], and Luke C. Henderson[1]

[1]Institute for Frontier Materials, Deakin University
75 Pigdons Road, Waurn Poinds, VIC 3216, Australia
Email: luke.henderson@deakin.edu.au ,

Keywords: Lignin based carbon fibre, Structural Energy, Electrochemical Surface Modification

ABSTRACT

The development of sustainable, multifunctional carbon fibre (CF) composites for structural energy storage is critical for the advancement of lightweight, energy-efficient technologies. Here, we report the surface functionalization of lignin–polyacrylonitrile (PAN) hybrid carbon fibres (LCF) with poly(o-phenylenediamine) (PoPD) via electrochemical grafting using diazonium chemistry, to enhance their electrochemical properties while preserving mechanical performance. The resulting LCF-oPD fibres exhibited a significant enhancement in energy storage behaviour, achieving a specific capacitance of 9.06 F g^{-1} at 1 mV s^{-1}, an 18-fold increase compared to unmodified LCF (0.48 F g^{-1}). Cyclic voltammetry revealed distinct redox peaks for LCF-oPD indicative of the reversible redox reaction of p-quinonediamine units, while galvanostatic charge–discharge cycling over 5000 cycles showed excellent electrochemical stability, with 100% capacitance retention and ~100% coulombic efficiency. Despite the addition of the PoPD layer, mechanical testing showed no statistically significant difference in tensile strength (LCF: 1.86 ± 0.38 GPa; LCF-oPD: 2.04 ± 0.33 GPa) or Young's modulus (LCF: 186.77 ± 14.58 GPa; LCF-oPD: 192.54 ± 17.96 GPa). Weibull analysis indicated a slight reduction in failure uniformity (shape parameter decreased from 5.82 to 5.15) but a marginal increase in scale parameter (from 2.01 GPa to 2.20 GPa), suggesting improved strength distribution. These values, although lower than those of conventional PAN-derived CFs (typically ~4 GPa strength and ~275 GPa modulus), validate the non-destructive nature of the surface modification. This work demonstrates a scalable strategy for integrating electrochemical functionality into lignin-based CFs without compromising structural integrity, advancing their potential in structural supercapacitor applications and sustainable multifunctional composites.

1 INTRODUCTION

Carbon fibre composites are used increasingly across diverse industries such as aerospace, wind energy and automotive owing to their exceptional strength-to-weight ratio[1-5]. In the automotive sector, carbon fibre reinforced polymers (CFRPs) are particularly attractive because they can significantly reduce vehicle weight by up to 60%, which directly improves fuel economy[6]. However, widespread applications of CFRPs is hindered by their high production costs, largely stemming from the price of the petroleum-based precursors like polyacrylonitrile (PAN) and mesoporous pitch, which account for over half the cost of carbon fibre manufacturing[7]. To overcome this, alternative precursors such as lignin and silk are being explored[7-9]. Lignin in particular is gaining attention due to its abundance, high carbon content, renewable nature and availability as a low-cost by-product from the paper and biofuel industries[10-13]. As industries move towards more sustainable and circular practices, developing multifunctional carbon fibres, especially those capable of energy storage has become a key priority. The world Economic Forum's "Top 10 Emerging Technologies of 2025" includes structural battery composites as a transformative innovation, highlighting the growing importance of materials that can simultaneously provide mechanical strength and store energy[14]. Achieving this requires a combination

of functional materials, sustainable feedstock and scalable manufacturing approaches, which is a significant challenge.

Lignin-derived carbon materials have been extensively explored for energy storage applications[15-19], particularly in the form of carbon nanospheres[20], nanosheets[21], and nanofibers[22]. These nanostructured forms typically offer high surface areas and can be engineered with various heteroatom dopants (e.g., N, S, O)[23] to enhance electrical conductivity, wettability, and charge storage capacity. Such materials have demonstrated promising electrochemical performance, particularly in electric double-layer capacitors (EDLCs) and pseudocapacitive systems. However, these lignin-based carbons are primarily developed for non-structural applications and often lack the mechanical integrity required for multifunctional systems. In contrast, when lignin is used as a precursor for structural carbon fibres, particularly in combination with polyacrylonitrile (PAN) to form hybrid precursors, the resulting carbon fibres are optimized for mechanical strength and stiffness [24, 25]. This necessitates processing conditions that minimize porosity and surface area, which, while beneficial for structural performance, significantly limits the fibres' ability to store charge via EDLC mechanisms. Consequently, these fibres exhibit relatively poor electrochemical capacitance when directly employed as electrodes in supercapacitor applications. Although the presence of residual oxygen-containing functional groups, such as quinones, may contribute to limited pseudocapacitive behaviour [26], the effect is typically negligible and insufficient for practical energy storage.

These limitations underscore the need for the incorporation of additional electrochemically active materials to enhance the performance of lignin-based structural carbon fibers. Surface functionalization, nanoparticle deposition, or the integration of conductive polymers and metal oxides are promising strategies to synergistically improve the electrochemical activity without compromising the structural integrity of the fibre [27-32]. Such multifunctional modifications are essential for advancing the use of lignin-based carbon fibres in structural energy storage systems.

In this work, we address this challenge by using a lignin-PAN hybrid carbon fibres as a sustainable platform for structural energy storage applications. Specifically, we functionalize the surface of these carbon fibres with the conductive polymer poly(o-phenylenediamine) via reductive diazonium chemistry through a scalable modification strategy to enhance their electrochemical activity while preserving their structural characteristics. The surface modification introduces redox-active and conductive functionalities, increasing the fibre's interfacial capacitance and enabling faradaic or pseudocapacitive charge storage behaviour. This approach not only improves energy storage performance but also maintains compatibility with standard composite manufacturing processes, making it suitable for real-world structural supercapacitor integration. Our strategy demonstrates a pathway toward high-performance, multifunctional composites that align with both sustainability and performance goals, thereby advancing the practical implementation of structural energy storage systems based on renewable carbon fibre sources

2 EXPERIMENTAL

2.1 Materials

All reagents and chemicals used in this study were purchased from Sigma-Aldrich (Australia), and were used without further purification, except for 4-nitobenzenediazonium tetrafluoroborate (NBD) which was synthesized as explained below. The resulting fibres were collected after carbonization for use in this study, prior to undergoing any surface treatment.

2.2 Synthesis of 4-nitobenzenediazonium tetrafluoroborate (NBD)

The synthesis of NBD was achieved rapidly by a one-step synthesis method, where 4-nitroaniline is reacted with nitrosonium tetrafluoroborate ($NOBF_4$) in a molar ratio of 1:1.2 in dry acetonitrile in a 2-neck round bottom flask under N_2. A typical synthesis used approximately 1 g of total reactants because of the high reactivity of aryldiazonium salts. First, 4 mL of dry acetonitrile was cooled to −40 °C using a cooling bath containing acetonitrile and liquid N_2. The required amount of $NOBF_4$ was added to cold acetonitrile in 2-neck RBF with minimum exposure to air during transfer. The solution was cooled to −40 °C while stirring. The amine was added to the solution and stirred for 30 min. The RBF was then

taken out of the cooling bath and allowed to warm to room temperature while stirring for another 30 min. The desired diazonium salt product was precipitated out of ice-cold diethyl ether. The precipitated pure product was collected by filtering at the pump and stored under N_2. Purity of the synthesized diazonium salts was determined using ^{1}H NMR and ^{19}F NMR and was consisten with literature reports[27].

2.3 Electrochemical modification of carbon fiber

Electrochemical modification of CF was carried out according to literature reports[30].The set up consisted of a standard three electrode cell with a lignin carbon fibre tow **(LCF)** as the working electrode, a platinum mesh (2.5 cm^2) as the counter electrode and a leakless Ag/AgCl reference electrode (ET069-1, eDAQ) immersed in a grafting solution consisted of 20 mM o-PD and 2 mM NBD dissolved in 4:1 deionized water:ethanol solution containing 0.6 M H_2SO_4. Electrochemical grafting procedure was carried out using potentiostatic cyclic voltammetry from −1.0 V to +1.0 V (vs Ag/AgCl) for 10 potential sweep cycles at 10 mV/s with an Autolab PGSTAT204 potentiostat. Measurements were recorded using NOVA 2.0 software. Once the electro-grafting is complete, modified CF tow **(LCF-oPD)** was washed sequentially with chloroform, dichloromethane, ethanol, and acetone to remove any physisorbed materials or excess monomers, followed by drying under reduced pressure to remove any adsorbed solvent on CF surface.

2.4 Characterization of surface chemistry and morphology

A Bruker Alpha FTIR (Bremen, Germany) equipped with a germanium crystal in the attenuated total reflectance (ATR) mode was used for FTIR spectroscopic analysis. The measurements were acquired from 600 to 4000 cm^{-1} using an average of 32 scans per measurement at a resolution of 4 cm^{-1}.
Raman spectroscopy was performed using Renishaw Raman InVia Confocal Microscope. Equipped with an Ar+ laser with an excitation wavelength of 514 nm (50 mW) and a diffraction grating of 2400 mm^{-1}. After calibrating the instrument using a silica reference, spectra were obtained between 800 and 2100 cm^{-1} with an average of 5 accumulations at an exposure time of 1 s.
SEM imaging was performed on a JEOL JSM 7800F at an electron accelerating voltage (electron high tension) of 5 kV. CF samples were mounted to an aluminium pin stub using double sided carbon tape. Imaging was performed without any conductive coating to enhance the visualization.

2.5 Characterization of electrochemical properties

Electrochemical tests were carried out using a BioLogic SP-300 electrochemical station at room temperature. Cyclic voltammetry (CV), Galvanostatic charge–discharge (GCD) and Electrochemical impedance spectroscopy (EIS) of functionalized CF (tow) electrodes were tested in a three-electrode cell set up with a leak-less Ag/AgCl reference electrode (ET069-1, eDaq) and a graphite rod counter electrode in 1 M H_2SO_4 electrolyte. EIS was performed at a frequency between 10 mHz and 100 kHz with 10 points per decade and an amplitude of 10 mV. For the SSC device, measurements were conducted in a two-electrode set up. All electrochemical data was analyzed using EC-Lab v11.42 software according to previously published reports using the following equations.
The CF electrodes were tested at 100, 50, 20, 10, 5 and 1 mV s^{-1} scan rates with an electric potential window of 0.6 V. Specific capacitance values from CV were determined using Equation 1,

$$C_{CV} = \int \frac{Idv}{m\, v\, \Delta V} \tag{1}$$

where C_{CV} (F g^{-1}) is the specific capacitance, $\int Idv$ (AV) is the area of the cyclic voltammogram corresponding to discharge processes (*i.e.,* half of total area), m (g) is the CF mass of both electrodes, v (V s^{-1}) is the scan rate, and ΔV (V) is the potential window of the CV.
GCDs were measured at different discharge current densities with an electric potential window of 0.6 V. Specific capacitance values from GCD were determined using Equation 2,

$$C_{GCD} = \left(\frac{I_D}{m}\right) \frac{t_D}{\Delta V - V_{IR}} \tag{2}$$

where C_{GCD} (F g^{-1}) is the specific capacitance, I_D (A) is the discharge current, t_d (s) is the discharge time, m (g) is the CF mass of both electrodes, and ΔV (V) is the potential window of the GCD test. Since voltage drop due to internal resistance IR (**Ω**) is inevitable in GCD tests, V_{IR} has been excluded in the calculations for more accurate results due to internal resistance. GCD tests were performed at different discharge currents densities (I_D/m) (A g^{-1}).
For electrochemical impedance spectroscopy (EIS) experiments the frequency was swept from between 10 mHz to 100 kHz with 10 points per decade and a sinus amplitude of 10 mV. EIS data was analysed and circuit Zfit (Figure S8) performed using EC-Lab v11.42 software.

2.6 Characterization of surface mechanical properties

Single filament characterization for surface modified CF was carried out on a Favimat + Robot 2 (Textechno) single fibre tester. This instrument automatically measures the linear density, diameter, tensile strength and elastic modulus of individual carbon fibre and was equipped with a 210 cN load cell. A pre-tension of 0.5 cN was applied to align the fibres before testing. Linear density of each fibre was determined via vibroscopy and then a tensile load was applied to the fibres until fibre failure. A minimum of 75 individual filaments were analyzed to provide a high degree of confidence in the results.

3 RESULTS

3.1 Surface chemistry and morphology

The electrochemical surface modification of LCF was directly translated from our previous works using pristine T300 CF that was spun using a PAN precursor [27, 30]. Aryl diazonium salts have proven highly effective in our work for forming stable covalent bonds with the carbon fibre surface, and in this case, they act as anchoring sites to facilitate the subsequent oxidative polymerisation of PoPD. The proposed electrochemical grafting mechanism and the anticipated surface chemistry of LCF-oPD are illustrated in Figure 1(a). The representative cyclic voltammogram (Figure 1(b)) clearly shows the distinct reduction of the diazonium salt and the oxidation of o-phenylenediamine, leading to the formation of radical species involved in the grafting process.
SEM has been utilized to study the unique surface topographical features on LCF surfaces before and after functionalization. As shown in Figure 1(c), the SEM image of the LCF surface displays a relatively smooth texture, in contrast to the PAN-based T300 carbon fibres, which typically exhibit striations and microgrooved surface features. Following surface modification, the SEM image of LCF-oPD (Figure 1(d)) reveals a markedly altered surface morphology, characterized by a consistent coating of polymeric material. This uniform coating represents a significant improvement compared to the same polymer applied to T300 carbon fibres, where the surface coverage was noticeably less consistent [27, 30, 33]. We previously attributed this to the heterogeneous surface chemistry of T300 CF, which likely influences local conductivity across the fibre. Four-point probe measurements indicated that the electrical conductivity of the LCF (438.62 S cm^{-1}) was lower than that of T300 CFs (884.88 S cm^{-1}); however, the more uniform surface chemistry of LCF may compensate for this by enabling more homogeneous electrochemical grafting. This could facilitate even attachment of the NBD priming layer, subsequently promoting uniform oxidative polymerization of oPD.

As shown in Figure 1(e), FTIR spectrum of LCF-oPD shows distinct peaks at 1636 cm^{-1}, 1161 cm^{-1}, 1041 cm^{-1} and 865 cm^{-1} ascribed to C=N stretching in quinoid ring, C–N stretching in benzenoid units, C–N stretching and out-of-plane bending motions of C–H of 1,2,4-trisubstituted benzene nuclei, respectively[33]. Therefore, the spectral data obtained were in good agreement with the expected structure of o-phenylenediamine. The Raman spectra of LCF and LCF-oPD reveal notable differences in the D to G band intensity ratios (I_D/I_G), which provide insights into the structural ordering of the carbon fibre surface (Figure 1(f)). For LCF-oPD, the (I_D/I_G), ratio is higher (1.04) compared to that of pristine LCF (1.00), indicating an increase in structural disorder and the presence of more amorphous carbon on the surface. This change suggests that the surface modification process, involving the oxidative polymerization of o-phenylenediamine, introduces additional defect sites and disrupts the graphitic ordering of the carbon fibre surface, consistent with the formation of a polymeric coating.

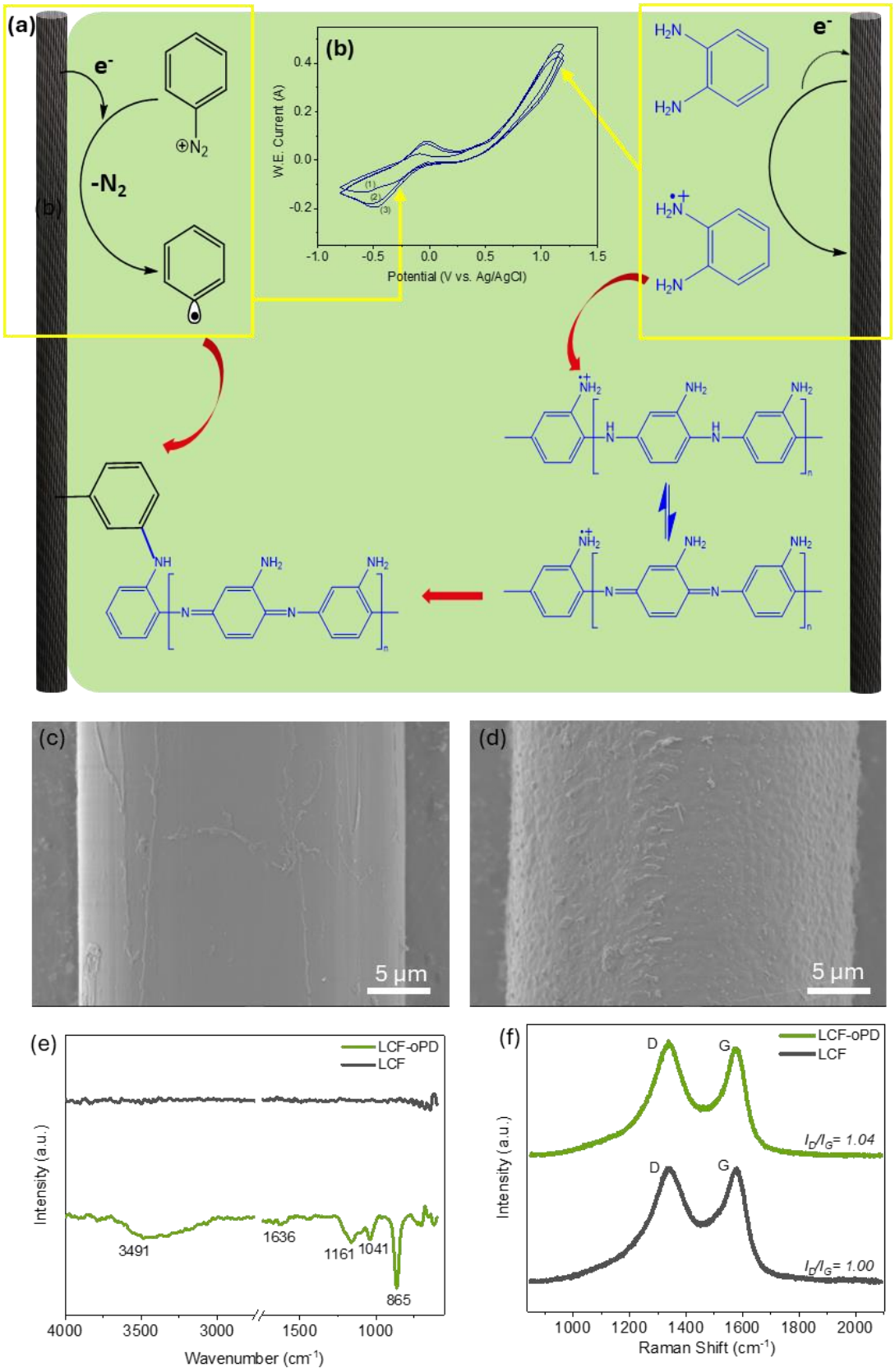

Figure 1: (a) The reaction mechanism for surface modification of LCF and expected surface chemistry on LCF-oPD, (b) a representative CV for the electrochemical surface modification with oPD (c) SEM of LCF (d) SEM of LCF-oPD (e) FTIR spectra for LCF and LCF-oPD and (f) Raman spectra for LCF and LCF-oPD

3.2 Energy storage

The electrochemical properties of LCF and LCP-oPD electrodes were explored in an aqueous electrolyte (1M H_2SO_4) to understand the electrochemical performance. Cyclic voltammetry (CV) and galvanostatic charge discharge (GCD) experiments have been conducted at different scan rates and current densities, respectively. The overall capacitance of LCF-oPD is a combination of electric double layer capacitance (EDLC) and pseudocapacitance from oPD.

Representative cyclic voltammograms (CVs) recorded at a scan rate of 20 mV s^{-1} are presented in Figure 2(a). The CV trace for LCF-oPD exhibits pronounced redox peaks characteristic of the electroactive polymer, along with a broad enclosed area indicative of enhanced charge storage capacity. Each cyclic voltammogram features a pair of redox peaks corresponding to reversible redox reaction of p-quinonediamine units accompanied by the transfer of two electrons and two protons [27]

In contrast, the CV of unmodified LCF displays a featureless, nearly linear profile with a minimal enclosed area, suggesting negligible capacitive behavior. These observations are further corroborated by the galvanostatic charge–discharge (GCD) curves shown in Figure 2(b). The GCD profile of LCF shows a steep and rapid voltage response, whereas the LCF-oPD curve demonstrates an extended, more gradual charging and discharging behavior, consistent with faradaic processes. The specific capacitance values calculated across different scan rates are summarized in Table 1 and Figure 2(c), further highlighting the superior electrochemical performance of the surface-functionalized fibres. At 1 mV/s LCF-oPD demonstrated a specific capacitance of 9.06 F/g which is a ~18x improvement compared to the capacitance of LCF which was only 0.48 F/g at the same scan rate.

Electrochemical impedance spectroscopy (EIS) analysis revealed that LCF-oPD exhibits a higher equivalent series resistance (ESR) compared to unmodified LCF. This increase is likely attributed to the introduction of the poly(o-phenylenediamine) (PoPD) layer at the fibre interface, which, despite being conductive, may introduce interfacial resistance during initial formation. To assess the long-term electrochemical stability of these electrodes, galvanostatic charge–discharge (GCD) cycling was performed over 5000 cycles. The LCF electrode initially retained 100% of its discharge capacitance; however, its performance steadily declined, retaining only 69% after 5000 cycles. In contrast, the LCF-oPD electrode exhibited a gradual increase in capacitance retention, reaching and maintaining 100% by the end of the test. This trend suggests that the PoPD layer undergoes an electrochemical conditioning process, progressively improving its performance until it reaches a stable, optimized state. Additionally, the coulombic efficiency of the LCF electrode exceeded 100%, indicative of a faster or more immediate discharge process relative to charging, possibly due to surface-related parasitic effects. In contrast, LCF-oPD maintained a consistent coulombic efficiency of approximately 100% throughout cycling, highlighting its excellent electrochemical reversibility and long-term stability.

Table 1: Specific capacitance values for LCF and LCF-oPD at different scan rates and current densities

Scan rate (mV/s)	Specific capacitance (F/g)		Current density (mA/g)	Specific capacitance (F/g)	
	LCF	LCF-oPD		LCF	LCF-oPD
50	0.06	4.85	100	0.06	6.82
20	0.08	7.01	75	0.04	7.09
10	0.10	7.52	50	0.03	7.91
5	0.14	7.86	25	0.04	9.89
1	0.48	9.06	10	0.07	2.79

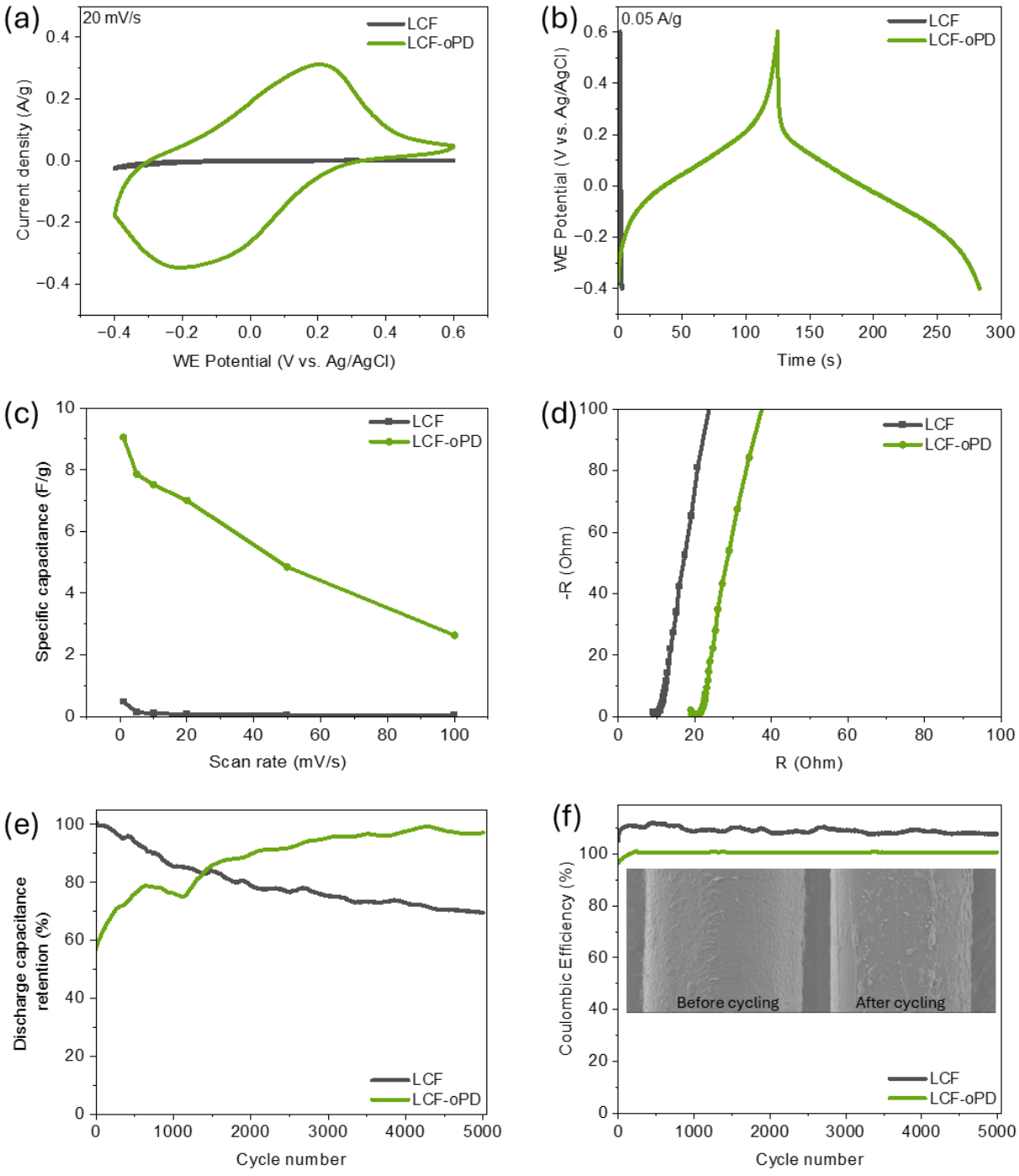

Figure 2: (a) Representative CVs of LCF and LCF-oPD done at 20 mV/s (b) Representative GCDs of LCF and LCF-oPD at 0.05 A/g (c)A graph of Specific capacitance vs the scan rate for LCF and LF-oPD (d) Nyquist plots for LCF and LCF-oPD (e) Discharge capacitance retention of LCF and LF-oPD electrodes during 5000 charge-discharge cycles (f) Coulombic efficiency of LCf and LCf-oPD during 5000 charge-dischrge cycles (inset: SEM of LCF-oPD before and after cycling)

3.3 Mechanical properties

The graph presents a comparative analysis of the tensile strength and Young's modulus of LCF and LCF-oPD samples. Although the LCF-oPD samples exhibit marginally higher mean values for both tensile strength (2.04 GPa vs. 1.86 GPa) and Young's modulus (192.54 GPa vs. 186.77 GPa) relative to the unmodified LCF, the error (typically derived from inhomogeneous distribution of flaws along the fibre) indicate that these differences are not statistically significant. This suggests that the surface modification using oPD does not detrimentally affect the mechanical integrity of the LCF, confirming the non-destructive nature of the treatment. Nonetheless, both strength and modulus values are considerably lower than those of conventional PAN-derived carbon fibers, which typically demonstrate tensile strengths around 4 GPa and moduli near 275 GPa. This further underscores the need to balance functionality and mechanical performance in modified or recycled carbon fibers.

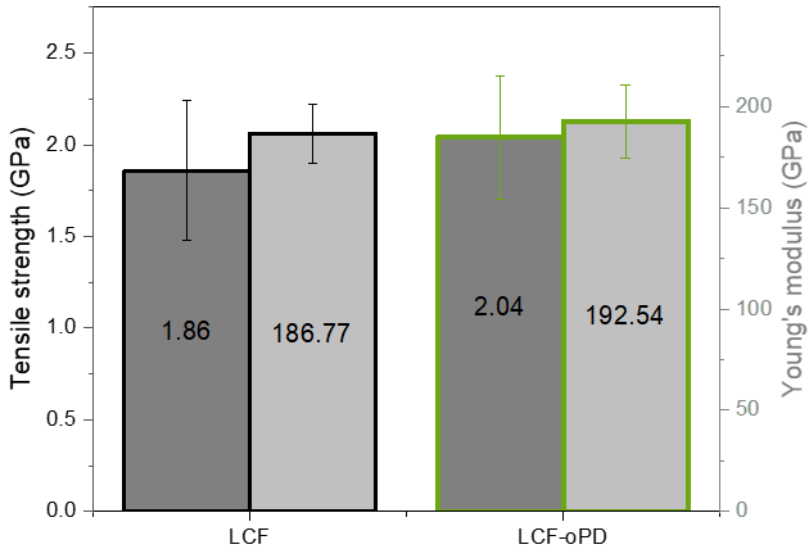

Figure 3: Comparison of tensile strength and Young's modulus of LCF and LCF-oPD

The Weibull shape parameter describes the variability of failure in a material and the scale parameter represents the strength of the fibre. A decrease in shape parameter was observed upon electrochemical functionalization of LCF with oPD (Table 2). A decrease in the shape parameter indicates more variability in terms of failure properties of the fibre, proving the fibres are slightly less consistent in terms of failure properties after surface modification. However, the Weibull scale parameter suggests an increase in the overall strength of the fibre after surface modification. Overall, the Weibull parameters suggest a less uniform failure behavior, with an increase in the overall strength after surface modification, but the average tensile strength increase is statistically insignificant.

Table 2: Mechanical properties and Weibull parameters for LCF and LCF-oPD

	Tensile strength (GPa)	Young's modulus (GPa)	Weibull shape parameter	Weibull scale parameter (GPa)
LCF	1.86 ± 0.38	186.77 ± 14.58	5.82	2.01
LCF-oPD	2.04 ± 0.33	192.54 ± 17.96	5.15	2.2

4 CONCLUSIONS

This study demonstrates the successful surface modification of lignin–PAN hybrid carbon fibers (LCF) with poly(o-phenylenediamine) (PoPD) via a scalable electrochemical diazonium grafting strategy, enabling significant enhancement of their electrochemical performance while retaining mechanical integrity. The modified LCF-oPD electrodes exhibited a substantial increase in specific

capacitance (9.06 F g^{-1} at 1 mV s^{-1}) compared to unmodified LCF (0.48 F g^{-1}) and maintained excellent cycling stability and coulombic efficiency over 5000 charge–discharge cycles. Mechanical characterization revealed no statistically significant deterioration in tensile strength or modulus following modification, confirming the non-destructive nature of the treatment.

However, the inherently lower mechanical properties of LCF (1.86 ± 0.38 GPa tensile strength, 186.77 ± 14.58 GPa modulus) compared to conventional PAN-derived CFs (~4 GPa, ~275 GPa) limit their use in high-performance structural applications. Despite this, the incorporation of multifunctionality through surface engineering makes LCF a viable candidate for structural energy storage composites, particularly where moderate mechanical demands coexist with the need for embedded energy storage. Moreover, the conductive polymer coating introduced via electrochemical grafting provides a versatile platform for further functionalization, such as the integration of MXenes or the assembly of multilayer structures with other polymers, potentially enhancing both energy storage performance and interfacial adhesion with polymer matrices. This work highlights a pathway toward sustainable, multifunctional carbon fiber composites by leveraging bio-derived precursors and advanced surface modification strategies.

ACKNOWLEDGEMENTS

The authors gratefully acknowledge Deakin University, this research was conducted with support from the Australian Research Council Industry Transformation Research Hub (IH210100023), Discovery Projects (DP180100094, DP200100090, and DP230100587), and an IM Fellowship (IM230100048). This work was also partially supported by the Office of Naval Research (N62909-22-1-2052). The authors also thank the Carbon Nexus Production Facility for providing fibers. The authors gratefully acknowledge the Deakin Electron Microscopy facility for support and assistance in this work. The authors acknowledge the facilities, and the scientific and technical assistance, of Microscopy Australia (formerly known as AMMRF) and the Australian National Fabrication Facility (ANFF).

REFERENCES

1. Zhang, S., et al., *Environmental impacts of carbon fiber production and decarbonization performance in wind turbine blades.* Journal of Environmental Management, 2024. **351**: p. 119893.
2. Fantuzzi, N., et al., *Mechanical analysis of a carbon fibre composite woven composite laminate for ultra-light applications in aeronautics.* Composites Part C: Open Access, 2024. **14**: p. 100447.
3. Semitekolos, D., et al., *Design, manufacturing, and evaluation of race and automotive prototypal components fabricated with modified carbon fibres and resin.* Polymers, 2024. **16**(14): p. 2062.
4. Dharmasiri, B., et al., *Using surface grafted poly (acrylamide) to simultaneously enhance the tensile strength, tensile modulus, and interfacial adhesion of carbon fibres in epoxy composites.* Carbon, 2022. **186**: p. 367-379.
5. Hendlmeier, A., et al., *Sizing effects on the interfacial shear strength of a carbon fibre reinforced two-component thermoplastic polymer.* Composites Part A: Applied Science and Manufacturing, 2019. **127**: p. 105622.
6. Baker, D.A. and T.G. Rials, *Recent advances in low-cost carbon fiber manufacture from lignin.* Journal of Applied Polymer Science, 2013. **130**(2): p. 713-728.
7. Zhu, J., et al., *Advances in developing cost-effective carbon fibers by coupling multiscale modeling and experiments: A critical review.* Progress in Materials Science, 2024: p. 101329.
8. Stróżyk, M.A., et al., *Decreasing the environmental impact of carbon fibre production via microwave carbonisation enabled by self-assembled nanostructured coatings.* Advanced Composites and Hybrid Materials, 2024. **7**(2): p. 39.
9. Straske, F., et al., *Carbon Fibers Made from Cellulose Acetate as a Green Polymer Precursor.* ACS Sustainable Chemistry & Engineering, 2024. **12**(15): p. 5780-5787.

10. Beaucamp, A., et al., *Sustainable lignin-based carbon fibre reinforced polyamide composites: production, characterisation and life cycle analysis.* Composites Communications, 2024. **45**: p. 101782.
11. Vaughan, M., A. Beaucamp, and M.N. Collins, *Development of high stiffness carbon fibres from lignin.* Composites Part B: Engineering, 2025. **292**: p. 112024.
12. Sazali, A.L., et al., *Lignin from oil palm biomass using deep eutectic solvent as carbon fibre precursor.* Biomass Conversion and Biorefinery, 2024. **14**(23): p. 29451-29464.
13. Kandola, B.K., et al., *Lignin-based carbon fibres: Effect of bio-polyamide on oxidative thermal stabilisation of lignin.* Journal of Materials Science & Technology, 2025. **207**: p. 191-208.
14. Doug Arent, A.M., David Parekh, *Top 10 Emerging Technologies of 2025*. 2025, World Economic Forum. p. 10-11.
15. Zhang, W., et al., *Lignin derived porous carbons: synthesis methods and supercapacitor applications.* Small Methods, 2021. **5**(11): p. 2100896.
16. Wu, X., et al., *Lignin-derived electrochemical energy materials and systems.* Biofuels, Bioproducts and Biorefining, 2020. **14**(3): p. 650-672.
17. Yi, Y., et al., *Emerging lignin-based materials in electrochemical energy systems.* Energies, 2022. **15**(24): p. 9450.
18. Jia, R., et al., *Renewable plant-derived lignin for electrochemical energy systems.* Trends in Biotechnology, 2022. **40**(12): p. 1425-1438.
19. Baloch, M. and J. Labidi, *Lignin biopolymer: The material of choice for advanced lithium-based batteries.* RSC advances, 2021. **11**(38): p. 23644-23653.
20. Cao, K.L.A., et al., *Sustainable porous hollow carbon spheres with high specific surface area derived from Kraft lignin.* Advanced Powder Technology, 2021. **32**(6): p. 2064-2073.
21. Zhang, B., et al., *Fabricating ZnO/lignin-derived flower-like carbon composite with excellent photocatalytic activity and recyclability.* Carbon, 2020. **162**: p. 256-266.
22. Svinterikos, E., I. Zuburtikudis, and M. Al-Marzouqi, *Electrospun lignin-derived carbon micro- and nanofibers: A review on precursors, properties, and applications.* ACS Sustainable Chemistry & Engineering, 2020. **8**(37): p. 13868-13893.
23. Liu, F., et al., *Nitrogen, oxygen and sulfur co-doped hierarchical porous carbons toward high-performance supercapacitors by direct pyrolysis of kraft lignin.* Carbon, 2019. **149**: p. 105-116.
24. Seydibeyoğlu, M.Ö., *A Novel Partially Biobased PAN-Lignin Blend as a Potential Carbon Fiber Precursor.* BioMed Research International, 2012. **2012**(1): p. 598324.
25. Dong, X., et al., *Polyacrylonitrile/lignin sulfonate blend fiber for low-cost carbon fiber.* Rsc Advances, 2015. **5**(53): p. 42259-42265.
26. Yang, W., et al., *Value-added utilization of lignin-derived aromatic oligomers as renewable charge-storage materials.* Industrial Crops and Products, 2021. **171**: p. 113848.
27. Dharmasiri, B., et al., *Multifunctional polymeric surface coatings of carbon fibre electrodes for enhanced energy storage performance.* Chemical Engineering Journal, 2022. **447**: p. 137560.
28. Kong, W., et al., *Polyaniline-decorated carbon fibers for enhanced mechanical and electromagnetic interference shielding performances of epoxy composites.* Materials & Design, 2022. **217**: p. 110658.
29. Dharmasiri, B., et al., *Ti3C2Tx MXene coated carbon fibre electrodes for high performance structural supercapacitors.* Chemical Engineering Journal, 2023. **476**: p. 146739.
30. Dharmasiri, B., et al., *Flexible carbon fiber based structural supercapacitor composites with solvate ionic liquid-epoxy solid electrolyte.* Chemical Engineering Journal, 2023. **455**: p. 140778.
31. Coia, P., et al., *Hierarchical Polyimide-Covalent Organic Frameworks Carbon Fiber Structures Enhancing Physical and Electrochemical Properties.* Small Structures, 2024. **5**(10): p. 2400166.
32. Coia, P., et al., *Utilization of Ti3C2Tx MXenes on carbonyl functionalized carbon fiber electrodes.* Chemical Engineering Journal, 2025: p. 160502.
33. Dharmasiri, B., et al., *Carbon reinforced carbon fibers: Using surface modification as a route to enhanced physical performance.* Composites science and technology, 2022. **218**: p. 109217.

ICCM24
AUGUST 4-8, 2025
BALTIMORE CONVENTION CENTER
BALTIMORE, MARYLAND, USA

No Technical Paper Submission for:

Colleen Murray

Funding: This work was supported by the EPSRC under Grant [number EP/W031442/2].

WEARABLE ELECTRONIC TEXTILES FOR THE DETECTION OF LONELINESS IN OLDER INDIVIDUALS

Presenter: Dr. Jingqi Liu

Line manager: Prof. Yu Shi







Smart textile & wearable

Deloneliness: £315k to UoL, £1.5M; 05/2022-0/2025

EPSRC Engineering and Physical Sciences Researcl

KING'S College LONDON

UNIVERSITY OF LEEDS

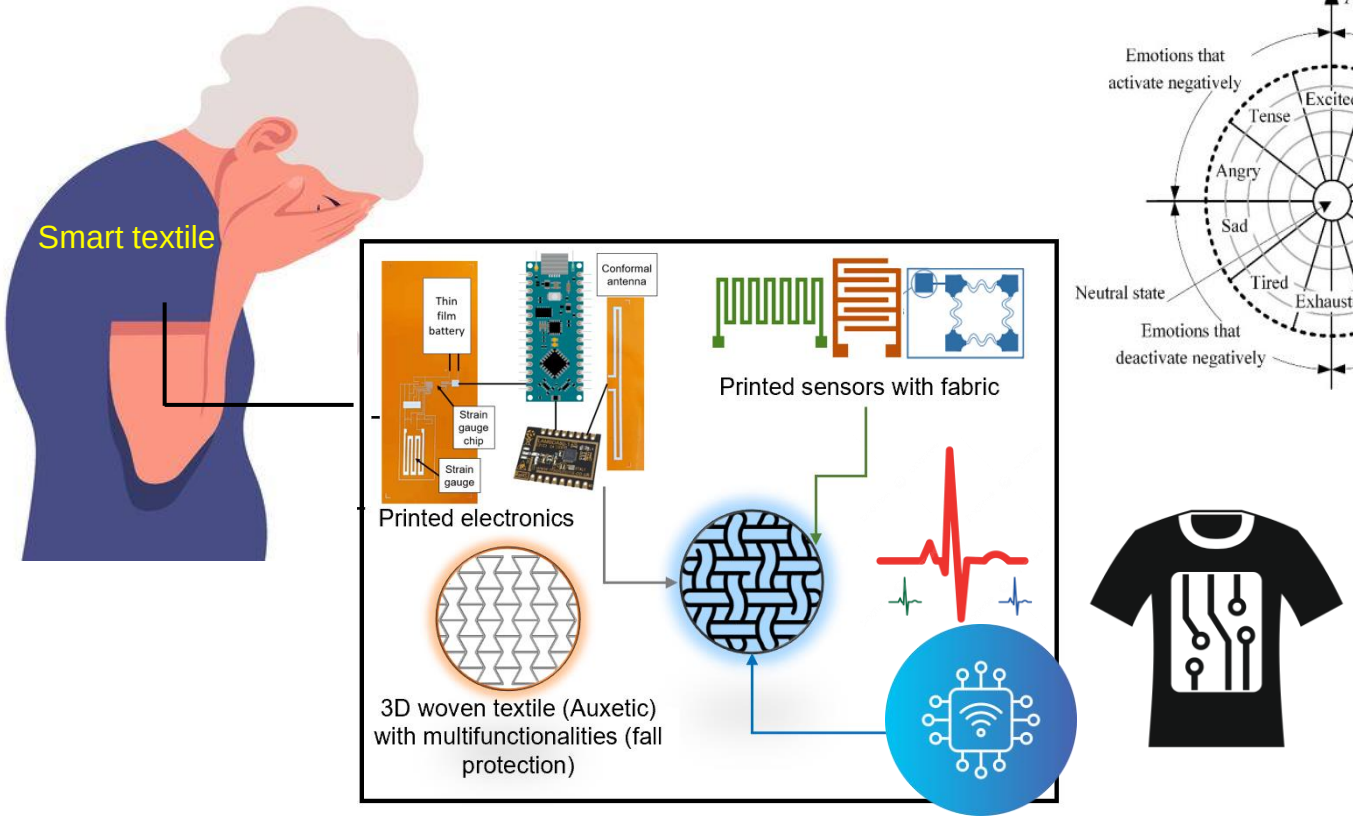

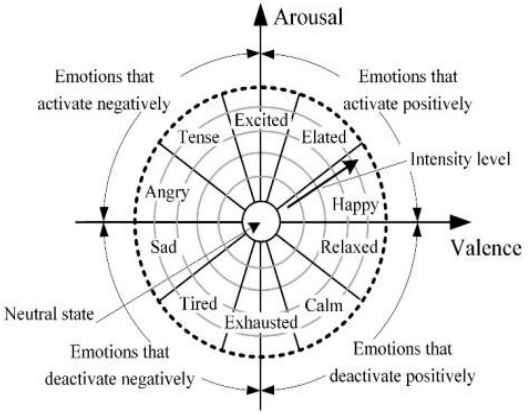

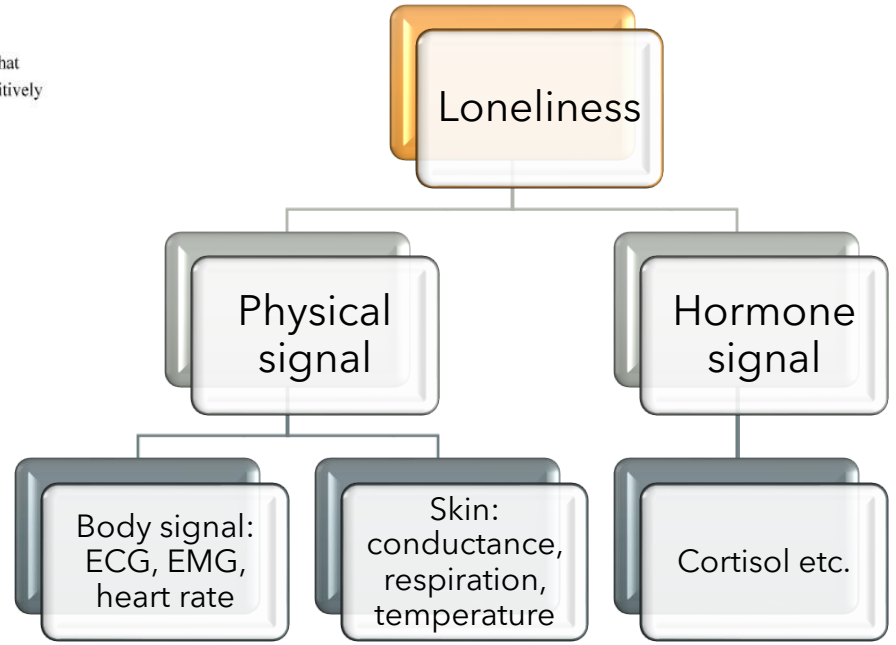

- As Age UK noted in 2018, 1.4 million older people class themselves as often lonely, and it is estimated this will rise to 2 million people over the aged of 50 by 2025;
- A report from the UK's Department for Digital, Culture, Media and Sport suggests that the wellbeing, health and productivity cost of loneliness are approximately £2.5 billion per person-year.

Background – choice of sensors

Main symptoms that need monitoring

- Increased stress and anxiety levels
- Lack of activity, sedentary lifestyle
- Lack of communication with people
- Comfort eating/drinking
- Sleep problems
- Crying

Related Physiological signals

- Heart rate
- Breathing rate
- Activity indoors/outdoors
- Cortisol levels
- Glucose levels
- Body temperature

ECG (Heart Rate)

- Stress
- Crying
- Sleep deprivation



Temperature

- Stress
- Sleep deprivation

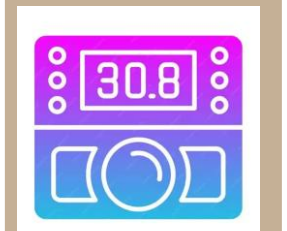

Respiration

- Walking
- Talking
- Sitting
- Relaxing
- Laughing

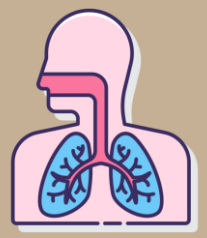

Galvanic Skin Response (GSR)

- Emotional arousal
- Stress
- Anxiety
- Depression



Cortisol

- Stress
- Sleep deprivation

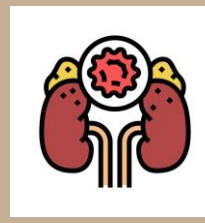

Sensors of choice for monitoring these signals

Integrated healthcare sensor – physiological signal monitoring

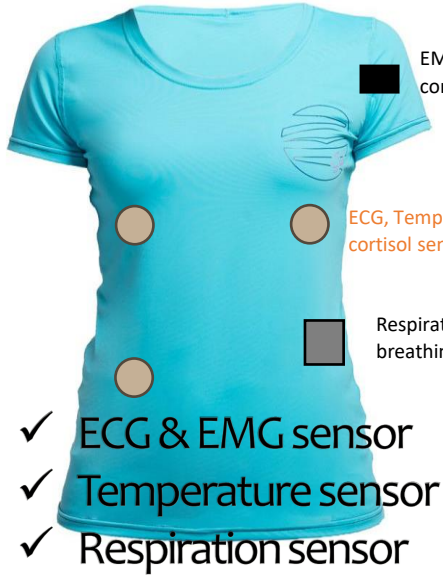

- ✓ ECG & EMG sensor
- ✓ Temperature sensor
- ✓ Respiration sensor

- ✓ Wireless data transmission
- ✓ Sensor data acquisition system

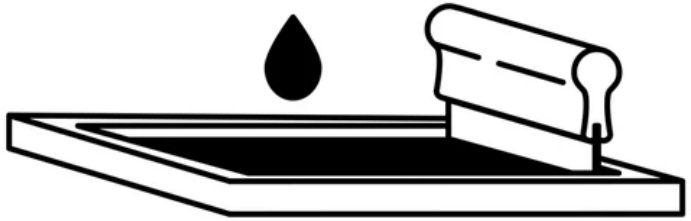

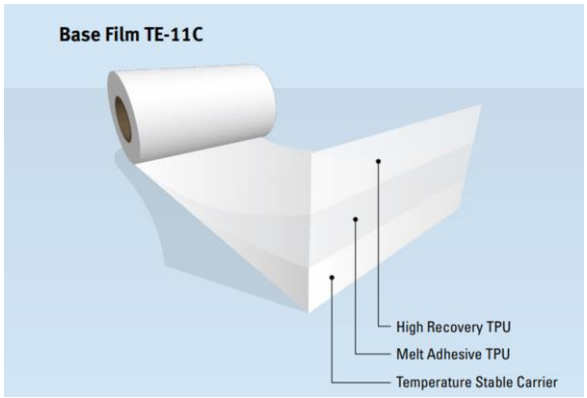

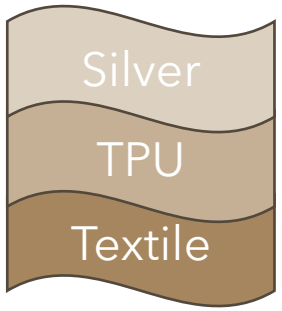

Structure of the sensor

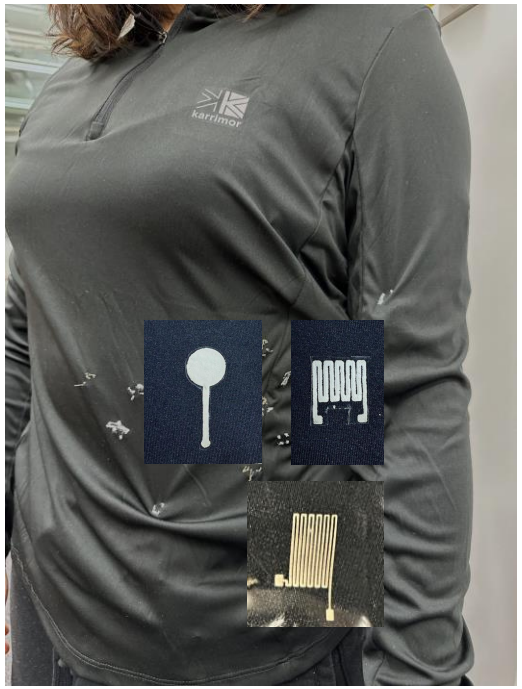

Human body temperature sensor



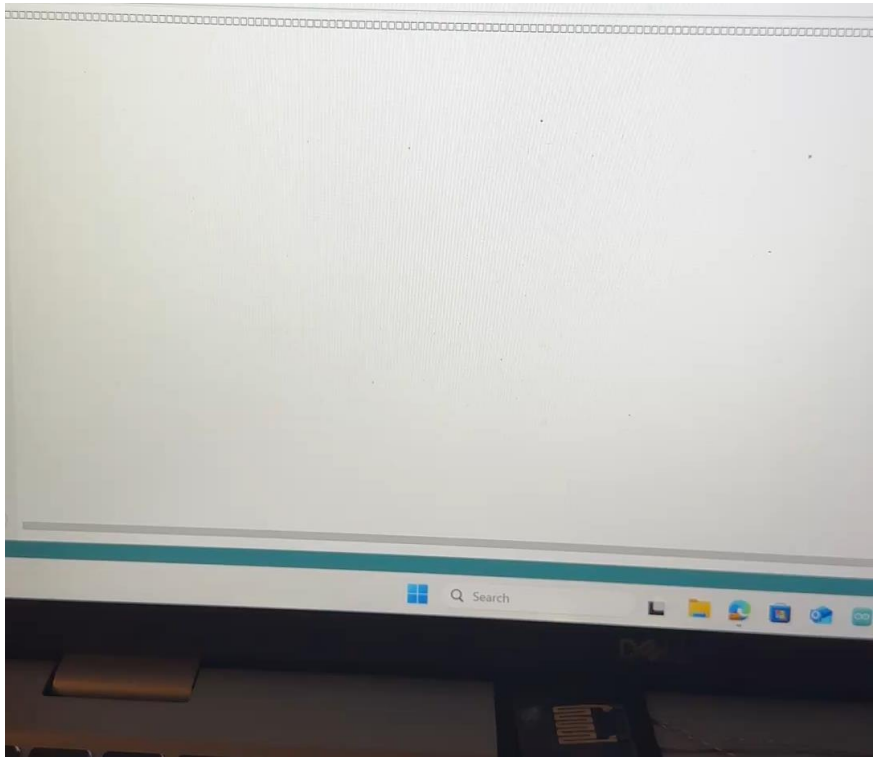

Human body temperature sensor

Smart Textile temperature sensor

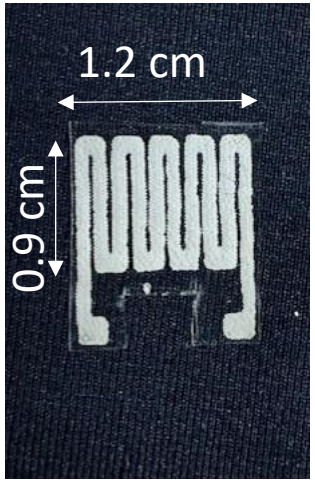

Commercial temperature sensor

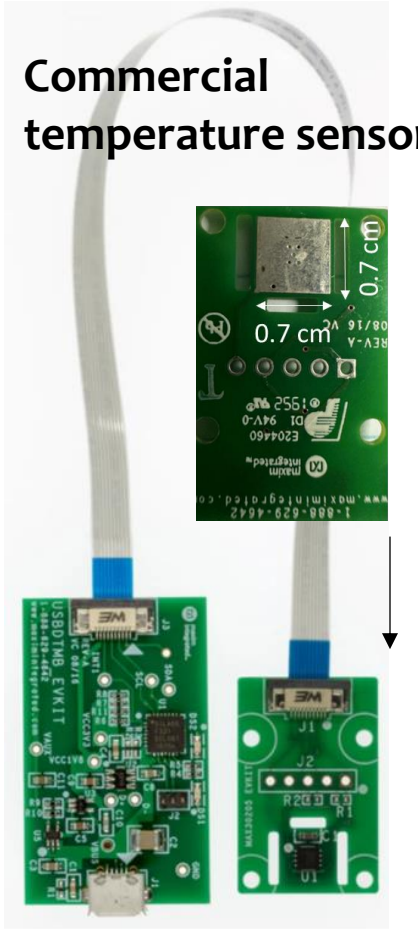

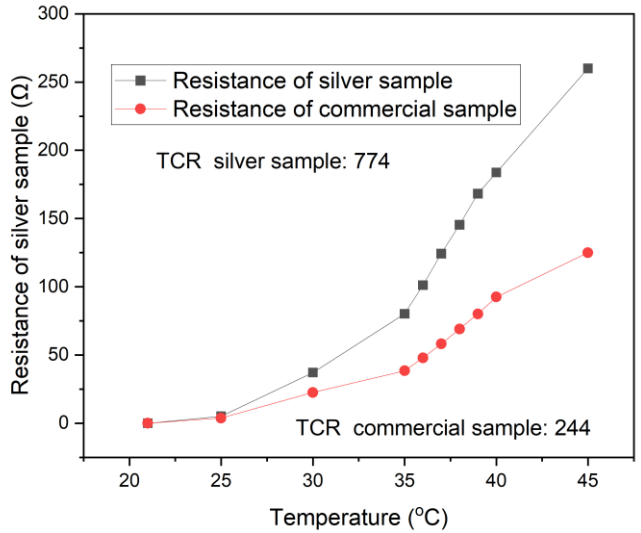

ECG sensor

Smart ECG sensor

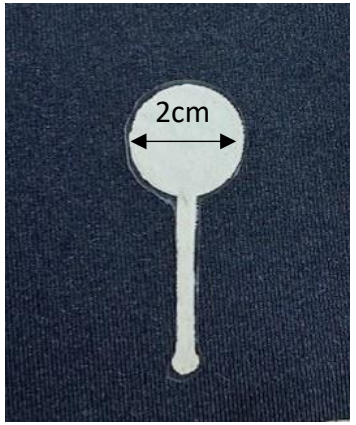

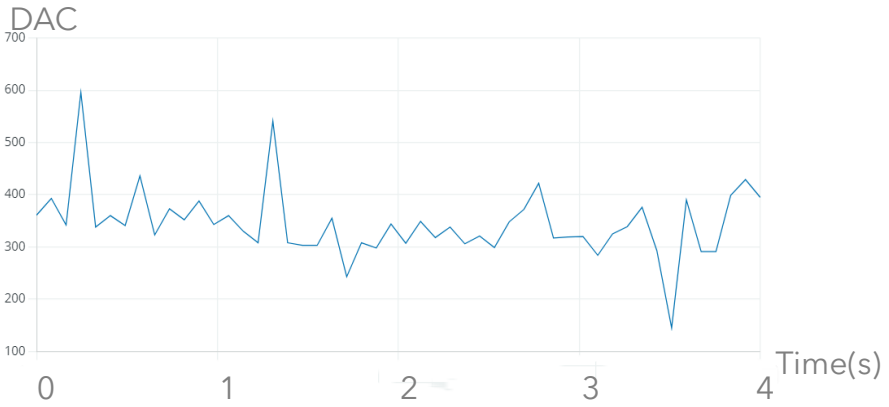

ECG value from readout circuit for textile sensor

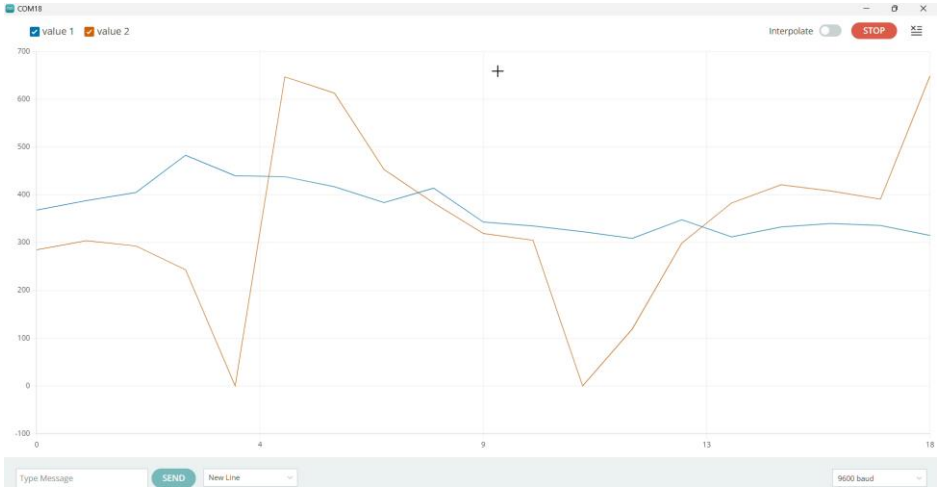

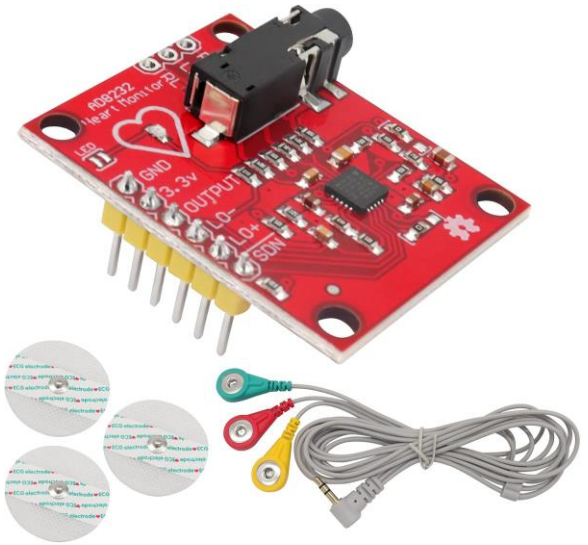

AD8233 commercial ECG sensor

Materials

- Silver nanoparticle paste
- TPU film

Fabrication method

- Screen printing

Smart Textile sensor
Commercial sensor

ECG sensor results

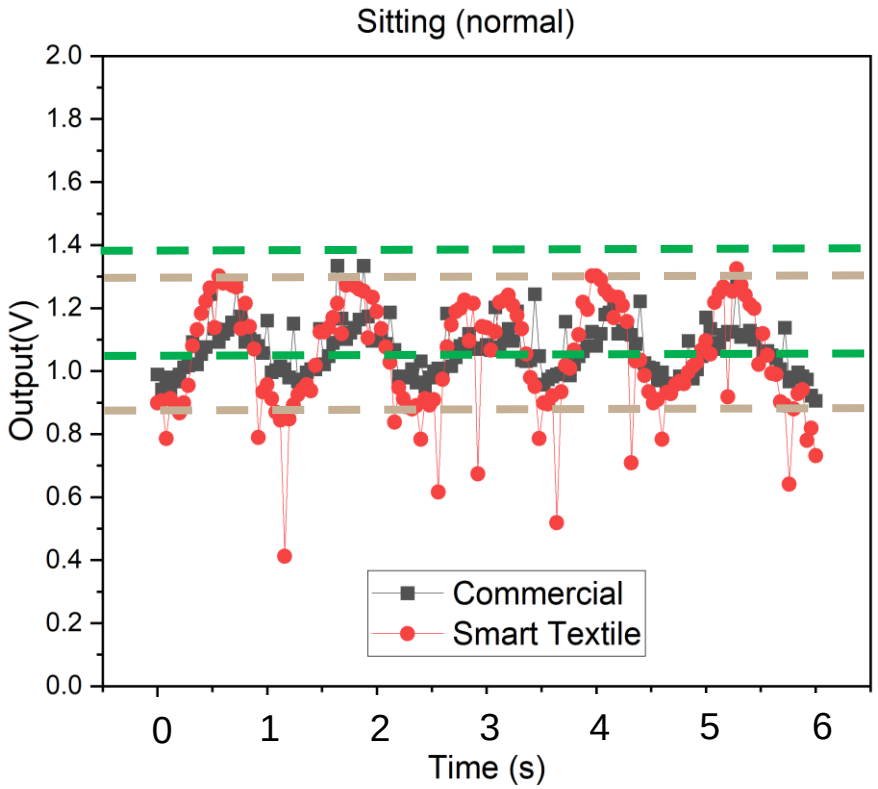

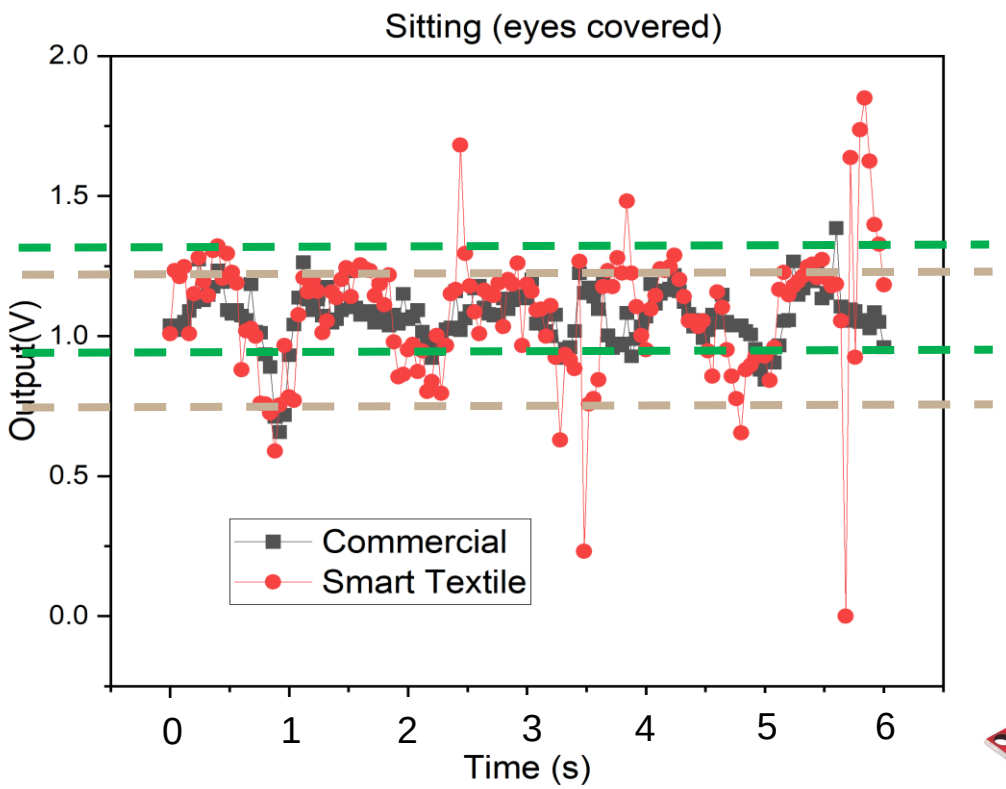



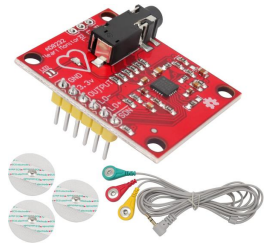

Other ECG patterns

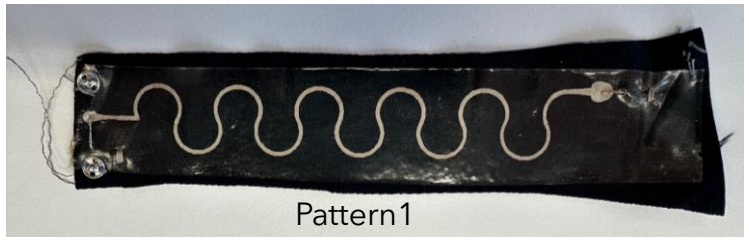

Pattern1



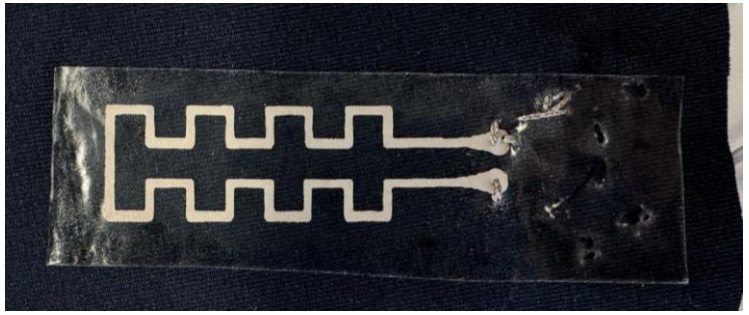

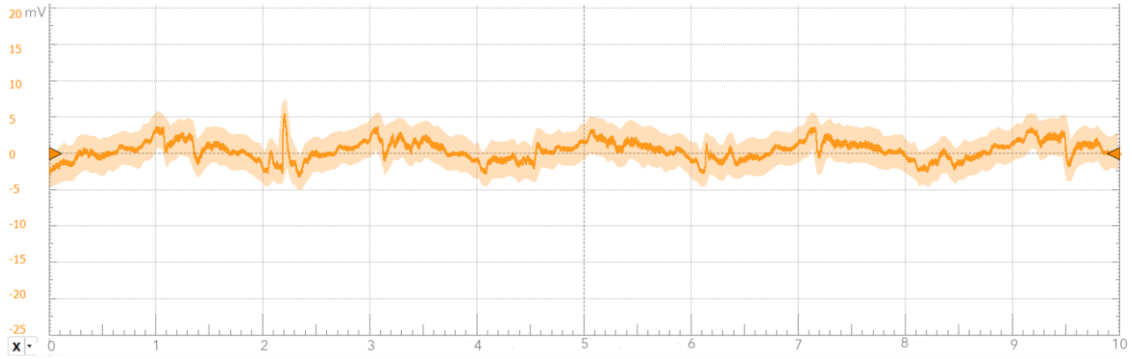

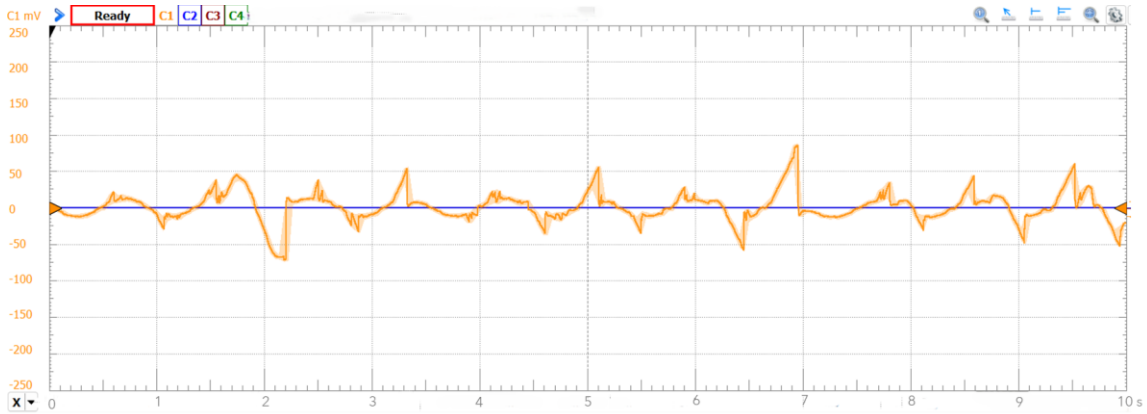

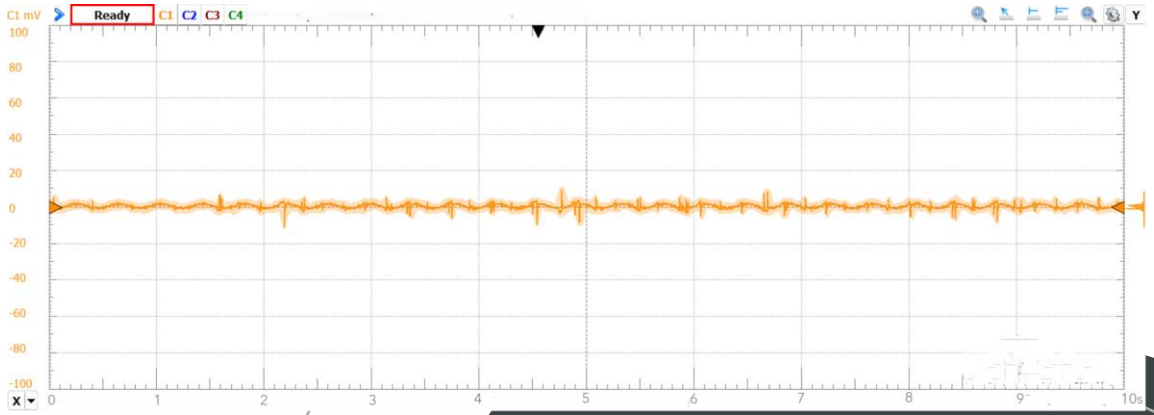

Respiratory sensor



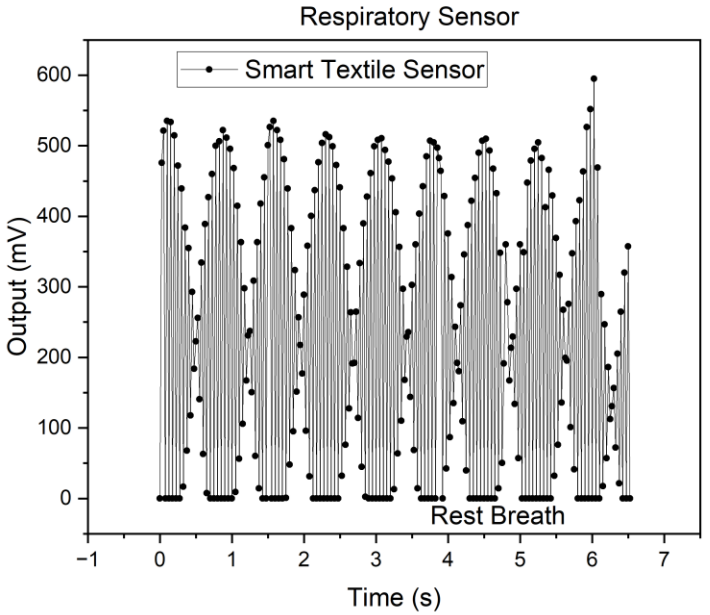

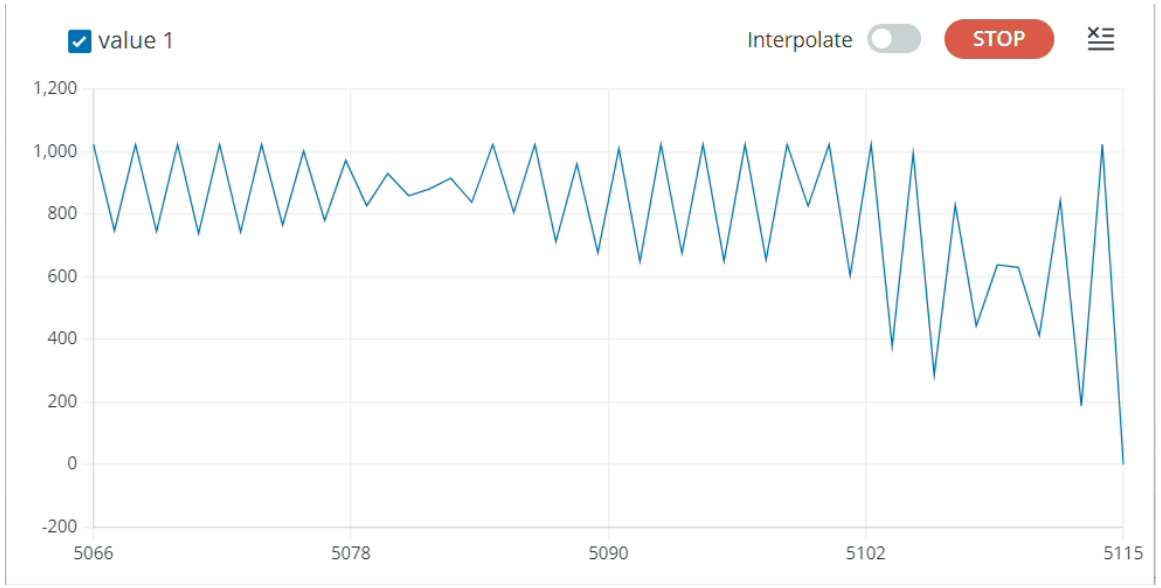

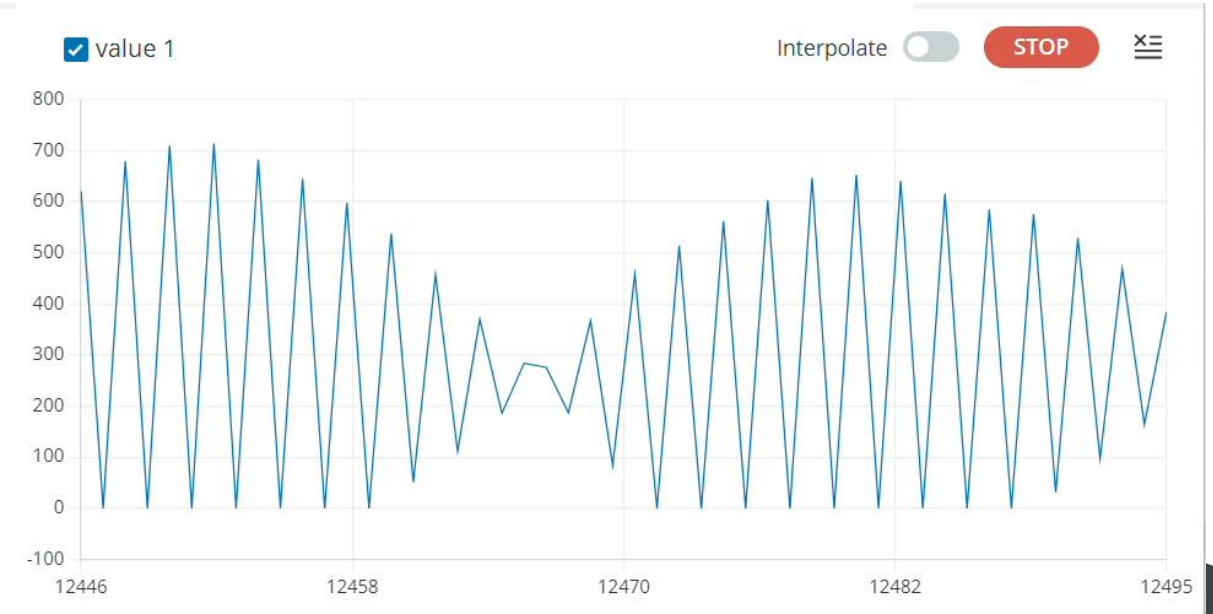

SEM image of the sensors

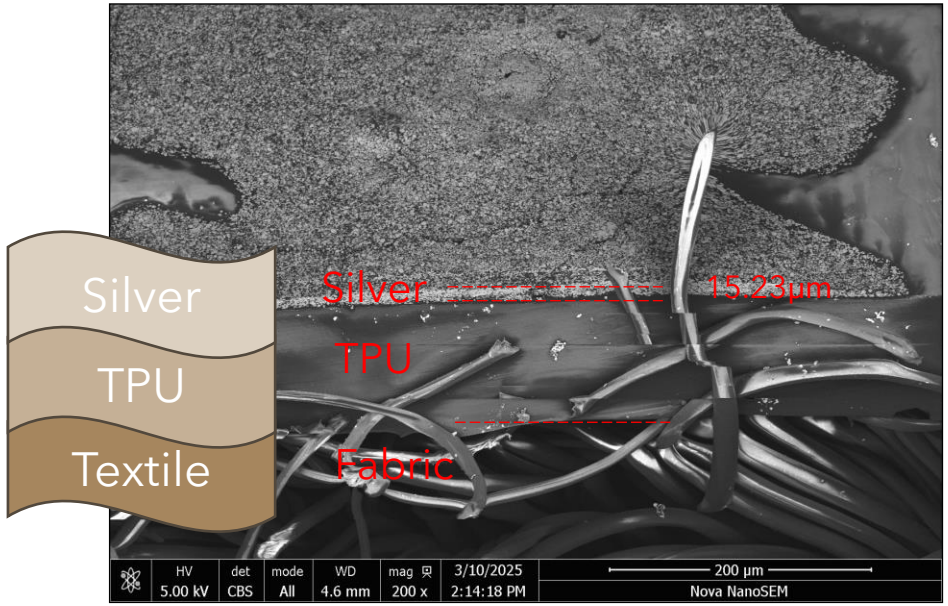

Cross-sectional view of the sensor

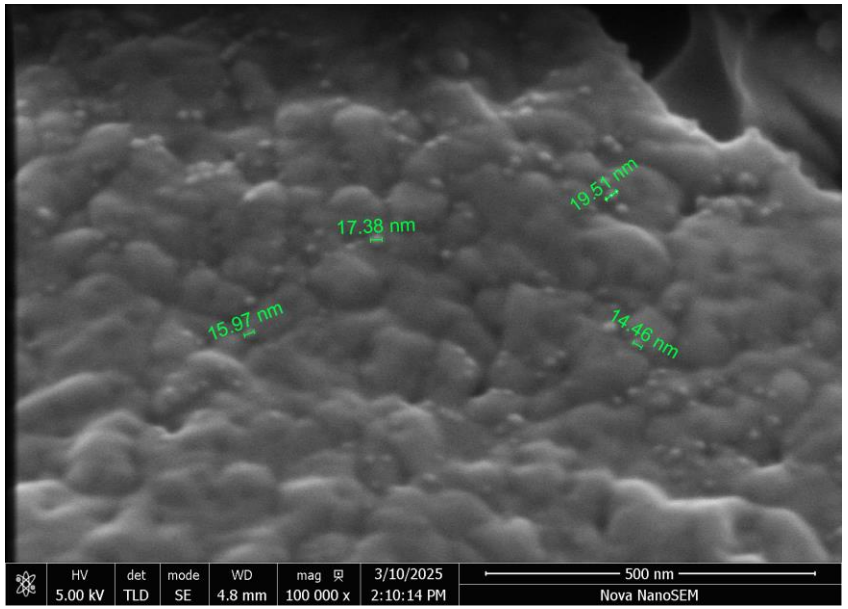

Top view of the silver nano-particles

Conclusion & Future work

- Smart textile temperature sensor compared with commercial ones
- Smart textile ECG sensor compared with commercial ones
- Different ECG pattern investigation
- Smart textile sensor investigation under different breathing rate
- Future experimental assessment on different physical movement and emotional activities

Acknowledgement

Funding: This work was supported by the EPSRC under Grant [number EP/W031442/2].



EVALUATION ON RECESSION BEHAVIORS OF B_4C CONTAINING POROUS CARBON MATERIAL AS AN ADVANCED THERMAL PROTECTION SYSTEM

Tatsuki Koshikawa[1], Yutaro Arai[1] and Yasuo Kogo[1]

[1]Department of Materials Science and Technology, Tokyo University of Science, 6-3-1, Niijuku, Katsushika-ku, Tokyo, Japan10.1007/s10853-021-05950-x
Email : 8224528@ed.tus.ac.jp, Web Page : https://www.tus.ac.jp

Keywords: Resins, Thermal properties, High temperature properties, Foams, Environmental degradation

ABSTRACT

The ablative thermal protection system (Ablator) can protect re-entry vehicles from severe aerodynamic heating during re-entry. Ablators are carbon-based materials with impregnated resin, and the decomposition of resin during re-entry prevents the temperature increase for components. Carbon monolith has been further developed as a porous carbon substrate, and it has been found that there is no significant difference in recession behaviors of carbon monoliths with or without resin. In addition, it shows superior recession behaviors to conventional porous carbons. A carbon monolith is prepared by carbonizing a porous phenolic resin (phenolic monolith) with the same structure as a carbon monolith. Since phenolic monolith is fabricated by using polymerization-induced phase separation (PIPS), it makes the addition of a second phase and the design of the structure possible. In this study, a B_4C particle dispersed carbon monolith (BCM) is prepared. The mechanical properties of them are evaluated by compression testing. The result shows mechanical properties of BCM are similar to conventional porous carbon despite the addition of a second phase. Ablation behavior is evaluated by an arc-wind tunnel test simulated for a re-entry environment. The result shows internal temperature is decreased.

1 INTRODUCTION

Ablators are well-known as one of the thermal protection systems (TPS) for re-entry vehicles and composed of carbon fibers and resin. Since the decomposition of resin (an endothermic reaction) prevents the increase of temperature for the vehicles, they protect the vehicles from aerodynamic heating during re-entry [1]. A typical example of an ablator is phenol-impregnated carbon ablator (PICA). PICA has been applied to vehicles in the Stardust mission, and the advanced version "PICA-X" has been used for the heatshield of the Space X Dragon spacecraft [2]. A notable feature of PICA is light weight because it composed of carbon felt and phenolic resin. However, it has been reported that PICA exhibits severe mechanical erosion [3].

Therefore, we have proposed to apply three-dimensional networked porous carbon (TNPC) as the substrate and prepare a porous carbon-based ablator (PCA) by impregnating TNPC with resin [4]. As a TNPC, carbon monolith has been developed and prepared by carbonizing a porous phenolic resin (phenolic monolith) with the same structure as a carbon monolith. The evaluation on carbon monolith has revealed that the carbon monolith has superior mechanical properties compared to PICA and the recession behavior has been improved by the suppression of mechanical erosion compared to PICA [5].

Since a phenolic monolith is fabricated using polymerization-induced phase separation (PIPS), the introduction of a second phase and the design of the structure are possible. A carbon monolith dispersed with ZrO_2 (ZCM) has been successfully prepared in previous studies. As the second phase, ZrO_2 was chosen owing to its low thermal conductivity (～2.5 W/m・K) and high melting point (2680 °C). It has revealed that the addition of ZrO_2 improves the recession behavior of carbon monolith and the amount of recession decreases compared to PCA. The result suggests ZCM can be applied to TPS without impregnation of resin [6]. On the other hand, the high density of ZrO_2 (~6 g/cm^3) causes the increase in weight and it makes the application to aerospace component difficult.

In response to this challenge, we have selected boron carbide (B_4C) as an alternative secondary phase. B_4C is notable for its high hardness (ranging between 38 and 44 GPa), a high melting point (2450 ℃), and a lower density (around 2.45 g/cm³) [7]. It is expected that B_4C acts as a barrier to the recession. By the oxidation of B_4C, B_2O_3 is formed and the evaporation of B_2O_3 is an endothermic process (ΔH = 322 KJ/mol, at 1250℃, 0.027 atm) and it prevents the increase of temperature for components [8]. B_4C containing carbon monolith is also expected as a candidate of advanced ablator without impregnation of resin and it will protect from severe aerodynamic heating during re-entry by the phase change of B_2O_3. Thus, we have defined this novel TPS as a "phase change shield system" (PCSS), distinguishing it from conventional ablators. The objective of this study is to develop a material process for B_4C dispersed carbon monolith (BCM) as a PCSS and evaluate the relationship between particle content, mechanical properties, thermal properties, and recession behavior under simulated re-entry conditions.

2 Experimental procedures

2.1 Fabrication of BCM

As the precursor of carbon monolith, a phenolic monolith was prepared. Then, the monomer concentration (ω, wt%) was defined as the ratio of resin and curing agent to solution by the following equation:

$$\omega = \frac{W_{resin}+W_{cure}}{W_{solution}} \tag{1}$$

$$W_{solution} = W_{resin} + W_{cure} + W_{solvent} \tag{2}$$

W_{resin}, W_{cure}, $W_{solution}$ and $W_{solvent}$ were the weight of phenolic resin, curing agent, solution, and solvent, respectively. A resol-type phenolic resin (PL2407 by Gunei Chemical, Japan), concentrated sulfuric acid, and ethylene glycol were used as resin, curing agent and solvent. These were mixed in a weight ratio of 13:1:21(hereafter as the mixed solution) in a beaker. B_4C particles (BBI10PB, particle size: 500 nm, Kojundo Chemical Laboratory Co., Ltd, Japan) were used as the particles. The mixed solution was held at 40℃ in an ambient atmosphere for 12 h to cure by using an oven (DRN320DE, ADVANTEC TOYO KAISHA, LTD. Japan). After 4 h from the beginning of curing, B_4C particles were added by 3.1, 6.1, or 9.2 vol% to mixed solution. The solution was stirred and held under a reduced pressure of about -0.08 MPa for 30 minutes using a rotary pump to remove air bubbles. After 12 h, the temperature was increased to 180℃ and held for 2 h. After that, samples were cooled to room temperature (25℃) over ~12 h. After curing, the solvent in the samples were removed in water at 80℃ for 72 h and dried in the oven at 80℃ for 72 h to obtain the B_4C dispersed phenolic monolith (hereafter denoted as BPM). BPM was carbonized at 950℃ for ~4 h in an atmospheric furnace (FT-POT-300, Fulltech) under an Ar atmosphere to obtain the B_4C particle dispersed carbon monolith (hereafter denoted as BCM). BCM with B_4C particles by 3.1, 6.1, and 9.2 vol% were defined as 3.1 BCM, 6.1 BCM and 9.2 BCM, respectively.

2.2 Basic characterization of structures for 9.2 BCM

9.2 BCM was cut into five layers as shown in Figure 1. The bottom of the beaker used during fabrication was defined as the XY plane, and the center of the XY plane in the third layer along the Z-axis was observed by scanning electron microscopy (SEM). Furthermore, the density of each layer was measured to evaluate the dispersion of particles.

2.3 Evaluation of mechanical properties for BCM

BCM was cut into rectangular blocks with size of 10×10×20 mm and 8×8×30 mm. The latter shaped continuously into a dumbbell with a cross-section of 5×8 mm in the center. The shapes of both compression test specimens are shown in Figure 2. Compression tests were conducted using a universal testing machine (model 5967, INSTRON, The U. S.), with a crosshead speed of 0.1 mm/min. The load was recorded using a 30 kN load cell, and displacement was measured using an extensometer attached to the compression jig. From these values, the Young's modulus and compression strength were evaluated.

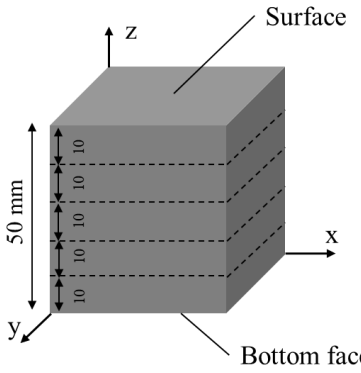

Figure 1. A schematic diagram of 9.2BCM

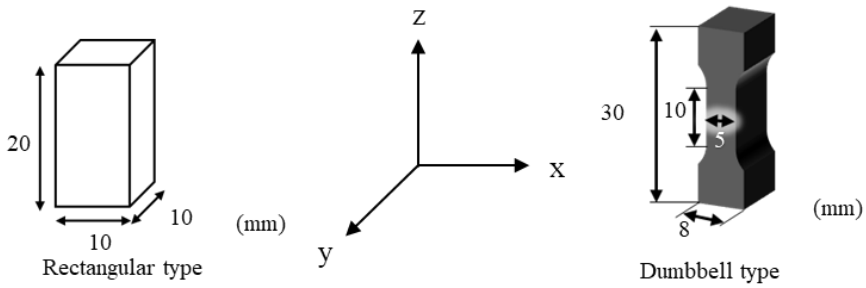

Figure 2. Shape of compression specimens

2.4 Arc-wind tunnel test

Arc-wind tunnel tests were conducted to evaluate the ablation behaviors of BCM. The tests used a 1 MW class arc heater at Japan Aerospace Exploration Agency/Institute of Space and Astronautical Science (JAXA/ISAS) in their arc-wind tunnel. In the tests, the high-enthalpy flow heated by arc heater is emitted from the nozzle into the chamber, allowing for simulated testing of atmospheric re-entry conditions. The appearance of the test specimens before and during the test in the arc heating wind tunnel were shown in Figure 3. By varying the distance between the air nozzle and the test specimen, the heat flux and dynamic pressure at stagnation point were adjusted. The size of specimens and specimen holder were exhibited in Figure 4. The specimen surface was Φ50 mm and set to bakelite holder. Nozzle distances were set at 150 mm, 100 mm, or 80 mm. The specimen surface was exposed for 30s by high enthalpy flow. The surface temperature was measured during heating by using radiation thermometer (emissivity $\varepsilon = 0.90$). The internal temperature was measured during heating and until 20 min after heating. Internal temperature was measured by inserting a type K thermocouple at 20 mm and 30 mm depth from the surface. After arc-wind tunnel test, the recession length of surface was measured by using a laser displacement sensor (LK-G155, KEYENCE CORPORATION, Japan).

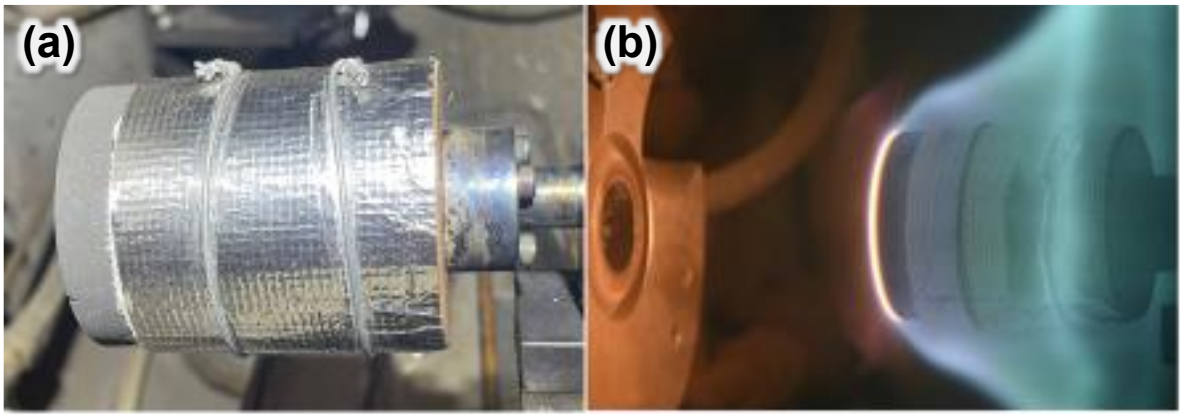

Figure 3. A typical appearance of the specimen: (a)Before test, (b)During test

Table 1. Test conditions

Test	Specimen	Nozzle distance (mm)	Exposure time (s)	Emissivity	Heat flux (MW/m^2)	Dynamic pressure (kPa)
A	3.1 BCM 6.1 BCM 9.2 BCM	150			1.92	3.09
B	3.1 BCM 6.1 BCM 9.2 BCM	100	30	0.90	3.54	10.10
C	3.1 BCM 6.1 BCM 9.2 BCM	80			6.18	20.11

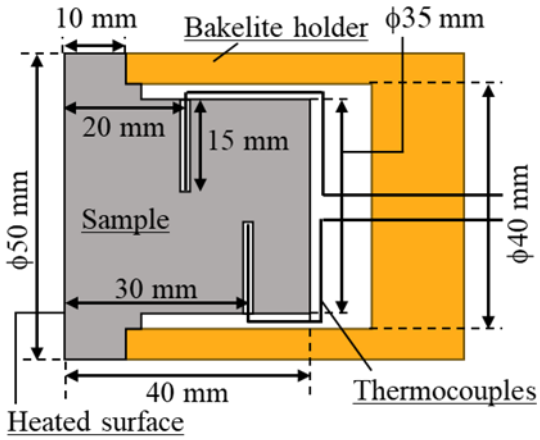

Figure 4. Cross section of arc wind tunnel specimen

3 Results and Discussion

3.1 Density of 9.2BCM

The relationship between normalized length (z) and density of 9.2 BCM and carbon monolith is shown in Figure 5. The addition of B_4C increases the density of each layer in the 9.2 BCM compared with that of the carbon monolith. Furthermore, because the relationship between normalized length (z) and density is similar for both the 9.2 BCM and the carbon monolith, the B_4C particles in the BCM are considered uniformly dispersed.

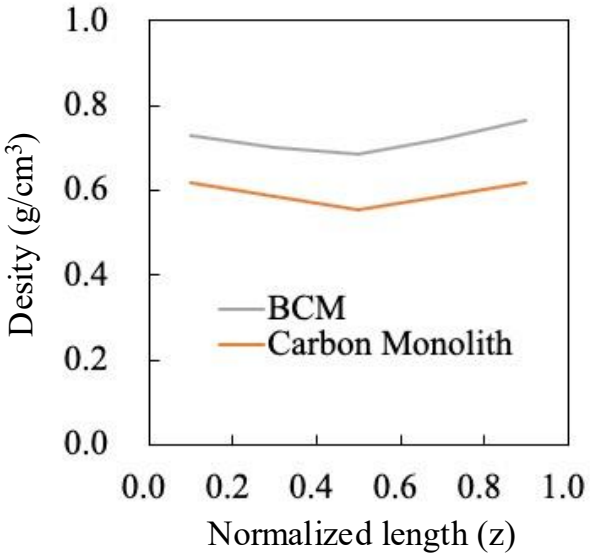

Figure 5. Relationship between normalized length (z) and density

3.2 Structural Observation

Microstructures of 9.2 BCM were presented in Figure 6. The monolith structure, which is a typical microstructure of monolith [5], is maintained even with the addition of B_4C particles. Agglomerates of B_4C approximately 2.0–3.0 μm in size were observed. However, because the monolithic structure was preserved, it was confirmed that the ZCM fabrication process can be applied to BCM.

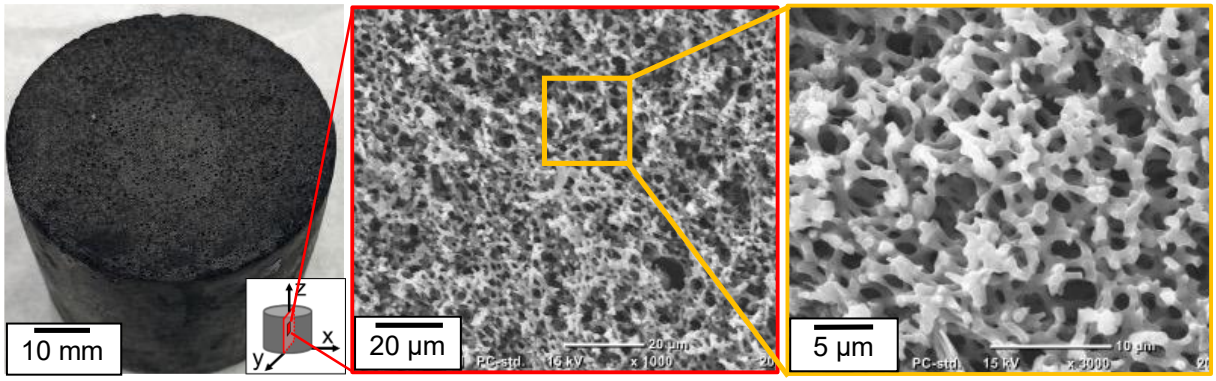

Figure 6. Typical microstructures of 9.2 BCM

3.3 Evaluation on Mechanical Properties

Young's modulus of carbon monolith, 3.1 BCM, 6.1 BCM, 9.2 BCM is 7, 3.8, 1.8 and 1.6 GPa, respectively. In addition, the compressive strength of carbon monolith, 3.1 BCM, 6.1 BCM, 9.2 BCM is ~110, ~60, ~30 and ~25MPa, respectively. These results show the compression strength and Young's modulus decrease with increase of the B_4C particles. This suggests that agglomerates influence the mechanical properties in different ways. On the other hand, the compressive strength of a conventional TNPC is ~25MPa [9] and it clearly indicates carbon monolith can maintain a certain level of compressive strength even after the addition of B_4C particles.

3.4 Arc Heating Wind Tunnel Test

The relationship between surface temperature and heat flux during tests is shown in Figure 7. In tests A and B, the carbon monolith showed a lower surface temperature than the BCM, whereas in test C this relationship was reversed. This reversal is attributed to the surface temperature in test C exceeding the melting point of B_4C, thereby causing reactions different from those occurring in tests A and B.

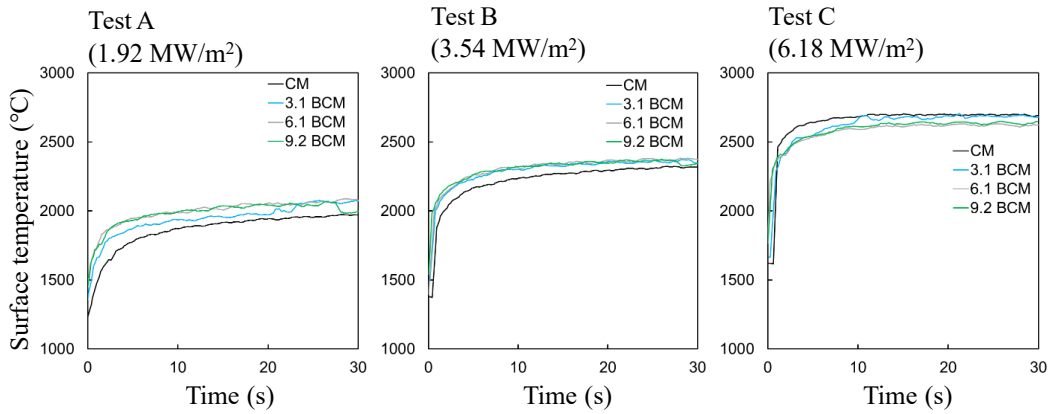

Figure 7. Temperature history of surface temperature (BCM and Carbon Monolith) [5]

The relationship between internal temperature and heat flux during tests is shown in Figure 8. At that time, the internal temperature of carbon monolith in test B could not be measured accurately because the specimen fractured. The BCM shows a lower internal temperature than the carbon monolith at every test. Moreover, the internal temperature decreases as the B_4C content increases. This can be attributed to the specific heat capacity of B_4C (1.84 J/g・K) and evaporation of B_2O_3, which is evolved by the oxidation of B_4C. The B_4C particles within the specimen absorbed heat as their temperature rose, thereby suppressing the overall temperature increase.

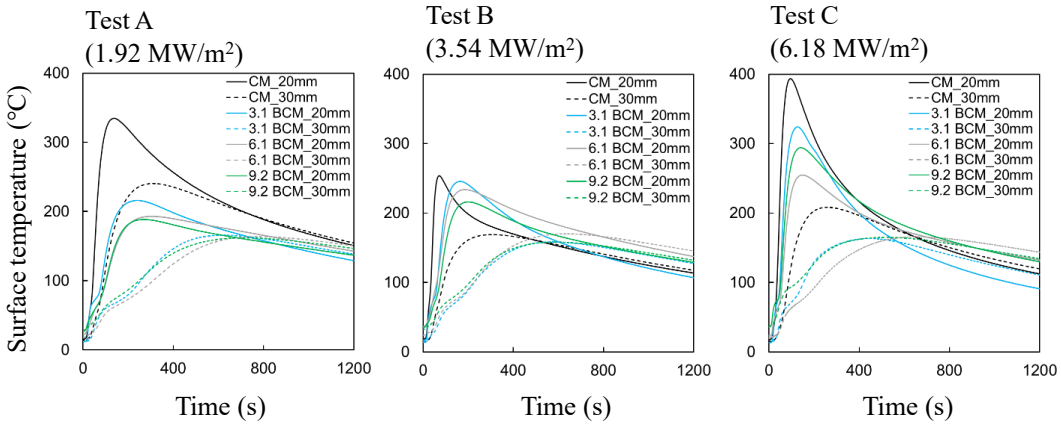

Figure 8. Temperature history of internal temperature (BCM and Carbon Monolith) [5]

4 Conclusion

BCM was fabricated by carbonizing a phenolic monolith with B_4C particles. Despite B_4C agglomerates (2–3 μm), the monolith structure was maintained. Compression tests showed that the strength decreases with the increase of B_4C content. Arc wind tunnel tests revealed lower internal temperatures for BCM than for the carbon monolith at all conditions. It was attributed to high specific heat (1.84 J / g・K) of B_4C and the evaporation B_2O_3. Thus, PCSS (in this study BCM) preserves the mechanical properties of the base monolith while providing superior thermal protection, making it a strong candidate for TPS in high-heat-flux environments.

ACKNOWLEDGEMENTS

The results of this study were derived from the arc wind tunnel tests conducted at the Institute of Space and Astronautical Science, Japan Aerospace Exploration Agency (ISAS/JAXA). The authors are grateful to Tetsuo Yoshida and Shogo Sakamoto for their assistance with these tests.

REFERENCES

[1] Sylvia M.Johnson, Thermal Protection Materials and Systems : An Overview, *Engineered Ceramics Advanced Ceramics and Ceramic Matrix Composites*, 2016, pp. 224-244

[2] Obinna Uyanna and Hamidreza Najafi, Thermal protection systems for space vehicles: A review on technology development, current challenges and future prospects, *Acta Astronautica*, **176**, 2020, pp. 341-356

[3] Jean Lachaud, Nagi Mansour, Alejandro Ceballos, Dusan Pejakovic, Luning Zhang and Jochen Marschall, Validation of a volume-averaged fiber-scale model for the oxidation of carbon-fiber preform, *42nd AIAA Thermophysics Converence*, 27-30 June 2011, Honolulu, Hawai

[4] Yuki Kubota, Toshiki Fujita, Yusei Kaneda, Ryo Inoue and Yasuo Kogo, Thermal Protection Performance of Porous Carbon Ablators with Three Different Matrices, *Journal of Spacecraft and Rockets*, **55**, 2018, pp. 1222-1229

[5] Rina Ono, Kenjiro Tsukamoto, Yutaro Arai and Yasuo Kogo, Experimental and analytical evaluation of an aerospace thermal protection system: Carbon monolith ablator, *MRS Advances*, **9**, 2024, pp. 822-829

[6] Hiroya Taniguchi, Yutaro Arai and Yasuo Kogo, Evaluation on ablation behavior of ZrO_2 nanoparticle-dispersed porous carbon composites, *Proceedings of the 21st European Conference on Composite Materials Volume 2 – Material Science*, 2024, pp. 441-448

[7] The Chemical Society of Japan, Kagaku Binran (Handbook of material data), Basic Section I, 5th Revised Edition, *Maruzen Publishing*, 2004, pp. 702-703

[8] The Chemical Society of Japan, Kagaku Binran (Handbook of material data), Basic Section II, 5th Revised Edition, *Maruzen Publishing*, 2004, pp. 251

[9] Y. Arai, Y. Daigo, E. Kojo, R. Inoue and Y. Kogo, Relationship between the microstructures and Young's modulus of 3D-networked porous carbon material, *Journal of Materials Science*, **56**, 2021, pp. 10338-10352

INTERLAMINAR FRACTURE TOUGHNESS ENHANCEMENT IN CARBON FIBER COMPOSITES VIA ASYMMETRIC FLAX FIBER HYBRIDIZATION

Abuzar Jamil[1], Dong Woo Lee[2], M. N. Prabhakar[2] and Jung-il Song[2*]

[1]Department of Smart Manufacturing Engineering, Changwon National University, Changwon-si 51140, Gyeongsangnam-do, Republic of Korea.
Email: 20217579@gs.cwnu.ac.kr, web page: http://acm.changwon.ac.kr
[2]DNA+ Research Center, Changwon National University, Changwon-si 51140, Gyeongsangnam-do, Republic of Korea.
Email: jisong@changwon.ac.kr, web page: http://acm.changwon.ac.kr

Keywords: Fracture toughness, Hybrid composite, Mechanical testing, Numerical analysis, Cellulose nanofibers

ABSTRACT

The brittle nature of the carbon fiber reinforced composites (CFRP) makes them susceptible to interlaminar fracture failures due to poor fracture toughness. This work explores the use of natural flax fiber and cellulose nanofibers to enhance the mode-I and mode-II fracture toughness of CFRP. The first part investigates the effect of asymmetric distribution of woven flax fiber in a hybrid arrangement with woven carbon fiber on the mode-I fracture toughness in comparison to CFRP. For this purpose, four different hybrid stacking sequences along with CFRP were tested using the double cantilever beam test. The critical energy release rate (G_C) evaluated exhibited a 70% increase for a one-interface carbon/flax hybrid layup. However, increasing the number of carbon/flax layers from one to four resulted in a decrease in G_C, highlighting the importance of ply placement in a hybrid arrangement for improved toughness. The experimentally evaluated G_C was used as an input in a numerical solver, which predicted the experimental response accurately. Due to the decrease in shear strength of the hybrid composite, the mode-II fracture toughness was complemented by adding cellulose nanofibers (CNFs) at the crack interface of CFRP and hybrid carbon/flax fiber reinforced composite. The CNFs were sprayed at 0.5, 0.1, and 0.2 wt% on the interface layers, resulting in an 18% and 20% increase in the mode-II fracture toughness for the CFRP and hybrid carbon/flax fiber reinforced composites, respectively. The shear strength and stiffness of the modified crack interfaces were evaluated using the cohesive zone numerical model, which showed close compliance with the experimental load-displacement plots. The fracture morphology using SEM and 3D optical microscope revealed the anchoring role of CNFs in deviating the crack path, resulting in the crack softening effect. Overall, the potential of natural fibers has been highlighted to design high-performance, lightweight, and sustainable composite structures.

1 INTRODUCTION

Carbon fiber-reinforced composites are widely used in the automotive and aerospace sectors due to their high specific strength and stiffness, enabling lightweight and fuel-efficient designs [1]. However, their brittleness and high cost limit broader application, as failures often lead to costly part replacements. To address this, hybridization with cheaper fibers like glass has been adopted, especially in interlaminar configurations where fibers are stacked layer by layer. This approach combines the strengths of different fibers while minimizing their weaknesses. Carbon/glass hybrids reduce brittleness and cost, making them popular in many applications [2]. However, growing demand for sustainable and recyclable materials calls for eco-friendly alternatives to synthetic fibers without compromising structural integrity.

Natural fibers like flax offer a promising alternative for hybridization with high-performance carbon fibers, as their specific stiffness is comparable to that of glass fibers. In hybrid composites, flax can serve as the ductile component, enhancing toughness when combined with brittle carbon fibers [3]. A common issue with CFRPs is low-velocity impact damage, which often occurs beneath the surface and remains undetectable visually. These internal damages typically develop at the fiber-matrix interface or the

interface between plies in interlaminar hybrid composites. To assess such failures, interlaminar fracture toughness tests under mode-I (opening) and mode-II (sliding) are widely employed to evaluate the toughness of composites [4].

Studies on mode-I fracture toughness for hybrid natural and synthetic fiber hybrid composites are limited in terms of taking the relevant stiffness of the beams of the double cantilever beam specimens and the utilization of asymmetric distribution of the plies to see the fracture at the natural and synthetic ply interface [5]. Moreover, the hybridization of weak natural fibers with strong carbon fibers results in a reduced shear strength, resulting in a reduction in mode-II fracture of the hybrid. For this reason, eco-friendly nano-species like cellulose nanofibers (CNFs) are adopted to offset the decrement in shear strength. But loading the CNFs at the interface so far has been in the form of interleaves that require time and extra processing steps for preparing composites with enhanced fracture toughness [6].

This work explores the effect of asymmetric hybrid placement of carbon/flax fiber composites on the mode-I fracture toughness compared to an all-carbon fiber reinforced polymer composite. Moreover, the effect of CNFs on the mode-II fracture toughness of CFRP and hybrid carbon/flax has been studied and compared with CFRP with a simple deposition method of CNFs on the interface layer. This is done to complement the decrease in shear strength due to the hybridization of flax with carbon fiber. The experimental load-displacement response has been replicated using numerical analysis, both for mode-I and mode-II fracture toughness tests. The fracture morphology of the cracked surface was observed under 3D optical microscopy and scanning electron micrographs (SEM).

2 METHODOLOGY

2.1 Materials

Plain woven CF3327-3K carbon fiber fabric was acquired from Hankuk Carbon Co., South Korea. 2-2 and Twill woven flax fiber fabric (FLAXDRYTM BL200) was supplied by EcoTechnilin, France was used as reinforcements, and Vinyl ester resin, along with cobalt naphthenate (accelerator) and methyl ethyl ketone peroxide (hardener), was supplied by CCP Composites, South Korea. was used as a matrix. The laminates were prepared by a conventional vacuum-assisted resin transfer molding (VARTM) process. A Teflon insert was used to introduce a pre-crack for the mode-I and mode-II test samples. The cellulose nanofibers were extracted from *Imperata cylindrica* grass using a hybrid chemical and mechanical treatment [7].

2.2 Experimental

The testing and specimen preparation for mode-I fracture toughness were performed as per ASTM D5528 standard using the modified beam theory. A material testing system (MTS) in a tensile mode at 3 mm/min was used to conduct the test. A double cantilever beam (DCB) test specimen was prepared, and hinges were attached using an epoxy adhesive film (Loctite EA 9695, Henkel, Korea). For the mode-II fracture toughness test, the ASTM D7905 standard was used to prepare the end-notched flexural test specimen and conduct the test. The universal testing machine (UTM) was used in a 3-point bending mode and 0.5 mm/min loading rate.

2.3 Numerical analysis

The numerical analysis was performed using ANSYS Workbench 2023 R2. For mode-I fracture toughness, a virtual crack closure technique (VCCT) was employed where the experimental G_C value was used as an input in the numerical model to simulate the experimental load-displacement behavior. For mode-II fracture toughness, a fracture energy-based cohesive zone model under pure mode-II was employed to identify the tangential contact stress (τ_{max}) and tangential contact stiffness (kt). The experimentally calculated mode-II toughness (G_{IIC}) was used directly as the critical fracture energy for tangential slip. Table 1 lists the engineering data used for the numerical analysis. A representative volume element (RVE) analysis was performed to extract the engineering data for CFRP and flax fiber reinforced polymer (FFRP).

Engineering Constants	CFRP	FFRP
ρ (g/cm^3)	1.5	1.3
$E_X = E_Y$ (GPa)	41	10
E_Z (GPa)	10	6
$\nu_{YZ} = \nu_{XZ}$	0.5	0.4
ν_{XY}	0.3	0.1
$G_{YZ} = G_{XZ}$ (GPa)	3.4	2
G_{XY} (GPa)	5	2

Table 1: Engineering Data

3 RESULTS AND DISCUSSIONS

3.1 Mode-I fracture toughness

Fig. 1 discusses the mode-I fracture toughness test. Fig. 1(a) shows the comparison of load displacement response for pure and hybrid laminates. As shown in the figure, the CFRP laminate with a peak load of 44N has the lowest load point displacement, signifying the brittle fracture. The FFRP with a peak load of 30N has a higher load point displacement, indicating its ductile nature. The hybrid laminates show a response between these two. The one interface hybrid (F/C)3/F//C/(F/C)3 exhibits the highest peak load of 50N along with the load point displacement. The peak load and the load point displacement decrease as the number of carbon/flax plies increases from one to four, showing the effect of ply asymmetry and concurrently the distribution of plies in the hybrid arrangement. The two-interface hybrid (F3C2F2//C2F2C3) exhibits a peak load at around 42N, which is like the CFRP but has higher load point displacement. For the three-interface (F2C2F3//C3F3C2), the peak load drops to 32N, which is almost like FFRP in terms of load point displacement, also. The four-interface hybrid F3C4//F4C3 exhibits similar values but lower load point displacement relevant to FFRP. Consequently, to the load displacement behaviour, Fig. 1(b) shows the critical fracture energy (G_C), which exhibits the highest value 910 J/m^2 for the one interface (F/C)3/F//C/(F/C)3 hybrid compared to 440 J/m^2 for CFRP. This is a significant improvement of 70% for the mode-I fracture toughness via hybridization. The two-interface hybrid (F3C2F2//C2F2C3) exhibits a value of 749 J/m^2, followed by the three-interface (F2C2F3//C3F3C2) hybrid at 656 J/m^2 and the four-interface hybrid F3C4//F4C3 at 430 J/m^2. The FFRP exhibits G_{IC} equivalent to 600 J/m^2 more than CFRP due to the higher load point displacement. These results indicate at the fact that a more equal asymmetric distribution of the flax plies in the beams of the DCB test specimen results in lower stiffness, causing the beams to deform more, which becomes stiff when the plies start to be grouped in other asymmetric hybrid arrangements mentioned. Fig. 1(c) shows the load displacement curves comparison of the numerical simulation model and experimental results. As exhibited, the numerical curves show close compliance in terms of predicting the peak load and the load point displacement for all the laminates, which is critical in estimating the initiation critical mode-I fracture toughness. The fracture morphology exhibited for the one interface hybrid in Fig. 1(d) shows the top view of the fractured beams, with (1) being the bottom being showing 3D optical microscopic images of the carbon ply with resin-rich region near the crack initiation point and the filament pullout indication at fiber bridging. The (2) shows the top beams' fractured surface, where the flax ply is visible underneath the resin layer on top. The texture of the opposing CFRP ply has visibly imprinted itself on the flax ply, showing mechanical interlocking effects. The SEM images taken from the side of the top flax ply show a thick resin layer on the surface of the flax ply. This shows the hydrophilicity of natural fibers, causing the resin layer to accumulate on the flax ply surface [8]. In composites, it's not an ideal

scenario as hydrophilicity leads to weak interfacial strength between the fiber and matrix, but in this case, it leads to a mechanical interlocking effect between the two different interfaces, resulting in a significant increase in the mode-I fracture toughness.

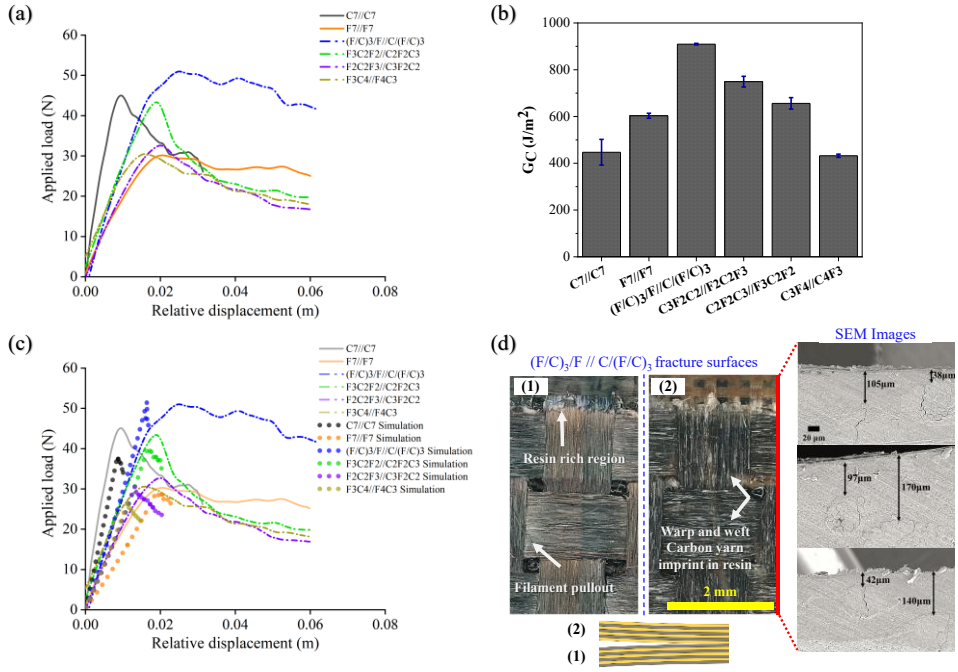

Figure 1: Mode-I fracture toughness, (a) Load displacement curves, (b) Critical fracture toughness, (c) Load displacement curves comparison, (d) fracture morphology.

3.2 Mode-II fracture toughness

Fig. 2 discusses the mode-II fracture toughness test. Fig. 1(a) shows the load displacement response of CFRP, $CFRP_{CNFs}$, hybrid, and hybrid with CNFs. From the load displacement curves, the CFRP, after reaching its peak load at around 680N, undergoes a sudden drop, which indicates the brittle fracture. The CFRP with 0.05% CNFs exhibits a peak load at around 670N, but due to the presence of CNFs, the load point displacement showed an increase compared to the CFRP. After attaining the peak load, there is no sudden drop, demonstrating the effect the CNFs have. This behaviour becomes more dominant for the CFRP with 0.1% CNFs, where the peak load reaches approximately 700N, and the crack arrest at the peak load is also more visible before the load drop. By increasing the CNFs to 0.2% the peak load reduces to around 580N, indicating the ability of the CNFs to act as an impurity at higher loading percentages, causing the crack to initiate much earlier. The reason for this behaviour is the inherent nature of the cellulose, which is derived from a natural resource, tends to be hydrophilic, resulting in reaction with matrix materials and causing the weakening of hydrogen bonding within itself. This causes a weak interfacial adhesion with the matrix, hence acting as an impurity at higher weight percentages. Similar behaviour is observed for hybrid layups [9]. In the hybrid with only flax fabric at the interface (C7/F//C7) the lowest peak load is observed at 475N, and despite no sudden load drop, the effect of placing flax fabric only at the interface was not effective. Adding 0.5 wt% of CNFs on the flax fabric at the interface (C7/F0.05% CNFs//C7) improves not only the peak load up to 500N but also enhances the crack arrest behaviour evident from the shape of the curve post peak load. A similar effect is observed for 0.1 wt% of CNFs at the hybrid interface (C7/F0.1% CNFs//C7) with a peak load at 528N, but the crack arrest post maximum load is not as dominant as the hybrid with 0.05 wt% of CNFs. Corresponding to this behaviour the G_{IIC} values are given in Fig. 2(b). The CFRP showed a G_{IIC} value of 1056 J/m^2, compared to 1045 J/m^2 for CFRP with 0.05% CNFs and 1270 J/m^2 for CFRP with 0.1% of CNFs. This shows an increase of 18% in the G_{IIC} value of CFRP with 0.1% of CNFs compared to pure CFRP. For the hybrid without CNFs, the G_{IIC} is 1006 J/m^2, which shows the decrease in shear strength of the hybrid composite. With CNFs at 0.05 wt%, the hybrid composite exhibits the highest G_{IIC}, i.e., 1295 J/m^2, while

the hybrid with 0.1 wt% of CNFs showed almost similar G_{IIC} compared to CFRP. Fig. 2(c) shows the comparison between numerical and experimental results. As shown, the cohesive zone numerical model shows close compliance to the experimental load-displacement response. In terms of the peak load, load point displacement, and the post-crack behaviour, all the attributes are correctly predicted by the numerical model for all the layups. Fig. 4(d) shows the fracture morphology under SEM for CFRP with 0.1% of CNFs and the hybrid with 0.05% CNFs. As visible from the images, the crack initiation sites showed agglomerated CNFs and fibers being pulled out from the opposing surface. This shows the anchoring role the CNFs play when loaded at their optimum amount can deviate the crack path, causing crack softening behaviour discussed from the load displacement curves. Moreover, the elongation of the crack is also due to increased fiber bridging, causing an increase in the mode-II fracture toughness.

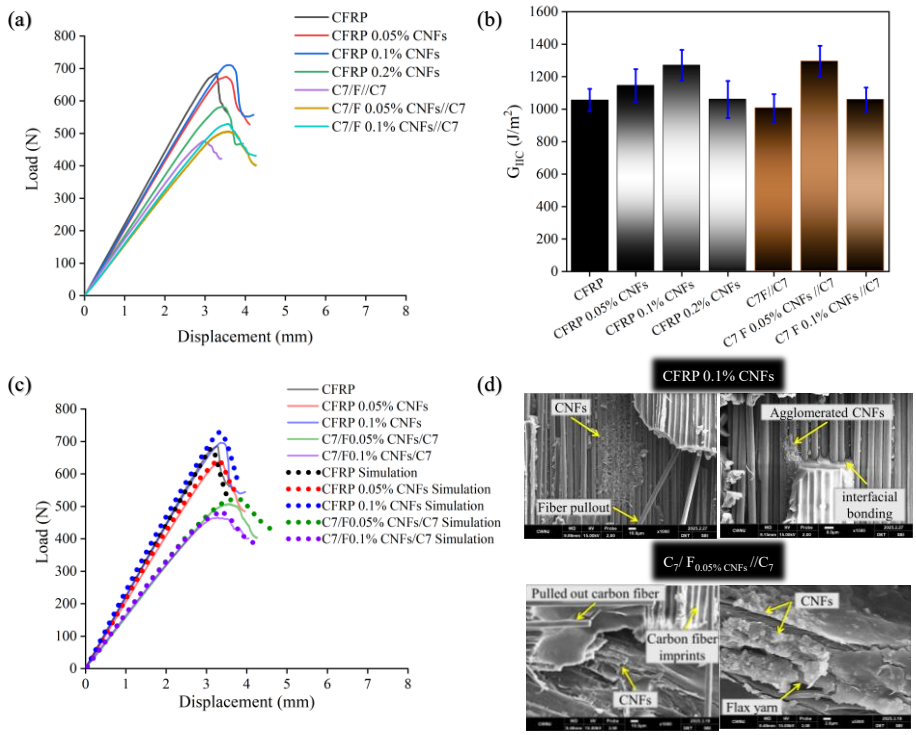

Figure 2: Mode-II fracture toughness, (a) Load displacement curves, (b) Critical fracture toughness, (c) Load displacement curves comparison, (d) fracture morphology.

4 CONCLUSIONS

In this study, the interlaminar fracture toughness of carbon fiber-reinforced polymer (CFRP) composites was significantly enhanced through two strategies: interlaminar hybridization with flax fibers for mode I and the incorporation of cellulose nanofibers (CNFs) for mode II. Under Mode-I loading, an asymmetric stacking sequence of flax and carbon fiber ($(F/C)_3/F//C/(F/C)_3$) demonstrated a 70% increase in critical energy release rate (G_{IC}) compared to conventional CFRP. For mode-II, CNFs were deposited both directly at the crack interface and via CNF-loaded flax fabrics. An 18% increase in G_{IIC} was observed for CFRP with 0.1 wt% CNFs, and a 20% increase for the hybrid with 0.05 wt% CNFs-loaded flax interface, indicating improved crack resistance during delamination. However, 0.2 wt% CNFs reduced performance due to excessive nanofiber content, resulting in impurities at the crack interface. Numerical simulations using the virtual crack closure technique for mode-I and the cohesive zone method for mode-II effectively replicated the fracture behavior, identifying the peak loads, load point displacements, and post-crack behavior. SEM and 3D microscopy confirmed increased fiber bridging due to mechanical interlocking in the case of mode-I fracture. In case of mode-II, crack deflection and matrix plasticity due to the presence of CNFs, contributing to a more stable delamination as opposed to pure CFRP and hybrid without CNFs. Overall, the study underscores the importance of ply architecture and nanofiber optimization for enhancing fracture toughness in CFRP composites.

ACKNOWLEDGEMENTS

This work was supported by the Basic Science Research Program through the National Research Foundation of Korea (NRF) funded by the Ministry of Science Education (2018R1A6A1A03024509, 2023R1A2C1006234).

REFERENCES

[1] F. Hermansson, S. Heimersson, M. Janssen, M. Svanström, Can carbon fiber composites have a lower environmental impact than fiberglass, Resour Conserv Recycl 181 (2022) 106-234. https://doi.org/10.1016/j.resconrec.2022.106234.

[2] Y. Swolfs, L. Gorbatikh, I. Verpoest, Fibre hybridisation in polymer composites: A review, Compos Part A Appl Sci Manuf 67 (2014) 181–200. https://doi.org/10.1016/j.compositesa.2014.08.027.

[3] C. Dong, Flexural properties and optimisation of hybrid composites reinforced by carbon, glass and flax fibres, Hybrid Advances 7 (2024) 100-302. https://doi.org/10.1016/j.hybadv.2024.100302.

[4] J.-S. Jeong, S.-K. Cheong, Interlaminar fracture toughness of CFRP laminates with silk fibers interleave, Journal of Mechanical Science and Technology 27 (2013) 3651–3656. https://doi.org/10.1007/s12206-013-0910-4.

[5] E.H. Saidane, D. Scida, M.-J. Pac, R. Ayad, Mode-I interlaminar fracture toughness of flax, glass and hybrid flax-glass fibre woven composites: Failure mechanism evaluation using acoustic emission analysis, Polym Test 75 (2019) 246–253. https://doi.org/10.1016/j.polymertesting.2019.02.022.

[6] G.W. Beckermann, K.L. Pickering, Mode I and Mode II interlaminar fracture toughness of composite laminates interleaved with electrospun nanofibre veils, Compos Part A Appl Sci Manuf 72 (2015) 11–21. https://doi.org/10.1016/j.compositesa.2015.01.028.

[7] R. Yu, P. M.N., J.-G. Zhai, J. Song, High-throughput extraction of cellulose nanofibers from Imperata cylindrica grass for advanced bio composites, Int J Biol Macromol 284 (2025) 111-138. https://doi.org/10.1016/j.ijbiomac.2024.138111.

[8] L. Yan, N. Chouw, K. Jayaraman, Flax fibre and its composites – A review, Compos B Eng 56 (2014) 296–317. https://doi.org/10.1016/j.compositesb.2013.08.014.

[9] B. Yang, M. Zhang, Z. Lu, J. Tan, J. Luo, S. Song, X. Ding, L. Wang, P. Lu, Q. Zhang, Comparative study of aramid nanofiber (ANF) and cellulose nanofiber (CNF), Carbohydr Polym 208 (2019) 372–381. https://doi.org/10.1016/j.carbpol.2018.12.086.

BIOINSPIRED MICRO-PATTERNED FIBRE SURFACES: ALTERNATING ADHESION ZONES FOR TOUGHER COMPOSITES

Jaime Buitrago-Osorio[1,2], Julien Bardon[1], Simon Bulou[3], David Ruch[1], Roberto Quintana[3], Carlos A. Fuentes[1,4]

[1]Structural Composites Unit, Luxembourg Institute of Science and Technology (LIST), Hautcharage, Luxembourg
[2]Department of Physics and Materials Science, University of Luxembourg, Esch-sur-Alzette, Luxembourg
[3]Plasma Process Engineering Unit, Luxembourg Institute of Science and Technology (LIST), Belval, Luxembourg
[4]Department of Materials Engineering, University of Leuven (KU Leuven), Leuven, Belgium

Email corresponding author: Carlos.Fuentes@list.lu

Keywords: Composite plates, Modal analysis, Identification, Properties, Finite elements

ABSTRACT

Nature's materials achieve exceptional fracture resistance through architectural control, as exemplified by nacre's crack-deflection mechanisms. Inspired by this principle, we engineer composite interfaces at the microscale by patterning carbon and glass fibres with alternating adhesion zones. Using a custom atmospheric pressure plasma CVD torch, we deposit spatially controlled 3-Aminopropyltriethoxysilane (APTES) coatings with 200 µm periodicity, creating regions of high and low interfacial shear strength. This approach circumvents the limitations of bulk biomimicry by directly manipulating the critical fibre-matrix interface where fracture initiates. Computational modelling reveals the transformative potential of this architecture. Finite element analysis predicts an 80% increase in debonding lengths compared to uniformly treated fibres, while retaining 95% of interfacial shear strength—effectively decoupling the classical strength-toughness trade-off. Molecular dynamics simulations further elucidate the underlying mechanism: sequential bond rupture in high-adhesion zones transitions to progressive interfacial sliding in untreated regions, enabling 40% greater energy dissipation through controlled stress redistribution. These findings align with nacre's hierarchical energy management strategy, translated here to synthetic composites. The atmospheric plasma process demonstrates significant scalability, operating at ambient conditions with fibre translation speeds exceeding 10 m/min. Experimental validation of these computational predictions through micro-droplet pull-out tests is currently underway. By establishing a direct pathway for integrating bioinspired interfaces into industrial manufacturing, this work opens new frontiers for designing damage-tolerant composites where interfacial architecture actively governs fracture behavior.

1 INTRODUCTION

Composite materials have revolutionized aerospace, automotive, and renewable energy industries through their exceptional strength-to-weight ratios. Despite these advantages, their inherent brittleness often leads to catastrophic failure under impact or fatigue loading—a critical limitation that persists across applications from wind turbine blades to aircraft structures. This vulnerability stems from inefficient energy dissipation mechanisms at the fibre-matrix interface, where stress concentrations initiate microcracks that rapidly propagate through the material.

In stark contrast, biological materials like nacre exhibit remarkable fracture resistance despite their mineral composition. Natural selection has optimized intricate architectures where staggered aragonite platelets bonded by organic layers force cracks to follow tortuous paths, dissipating energy through protein unfolding and sacrificial bond rupture. While substantial research has focused on replicating

nacre's "brick-and-mortar" structure in bulk composites, these approaches face significant scalability challenges when applied to fibre-reinforced systems.

Our research introduces a paradigm shift by directly engineering the fibre-matrix interface—the critical region governing composite fracture behavior. Rather than mimicking nacre's macroscale architecture, we translate its underlying principle of controlled crack deflection to the microscale. By creating spatially alternating zones of high and low adhesion on individual carbon and glass fibres, we force propagating cracks to repeatedly arrest and redirect, transforming brittle failure into a stable, energy-absorbing process. This strategy preserves the inherent strength of continuous fibres while introducing new toughening mechanisms at the most vulnerable interface.

Central to this innovation is atmospheric pressure plasma CVD technology, which enables solvent-free, high-speed patterning of fibre surfaces. Unlike conventional sizing or grafting methods that produce uniform coatings, our micro plasma torch creates precisely defined interfacial heterogeneities—a capability previously unattainable in composite manufacturing. The following sections detail how this bioinspired interface design fundamentally transforms composite fracture behavior.

2 MATERIALS AND METHODS

2.1 Plasma-Assisted Patterning

Carbon fibres (Toray T800S) and E-glass fibres (Owens Corning) underwent surface patterning using an in-house micro plasma torch system. The apparatus featured a precision XYZ stage with 0.1 µm positioning accuracy, coupled with a radiofrequency (RF) atmospheric plasma source operating at 20 W. A helium-ammonia gas mixture generated a stable plasma jet, while vaporized APTES precursor was introduced downstream to ensure controlled deposition.

The patterning process involved synchronized movement of fibres beneath the plasma torch with precisely timed plasma pulses. By alternating 100 ms activation and deactivation cycles while translating fibres at 5 mm/s, we achieved periodic coatings with 200 µm spacing between high-adhesion zones. This intermittent treatment created a "digital fingerprint" of alternating bond strength along each fibre's length.

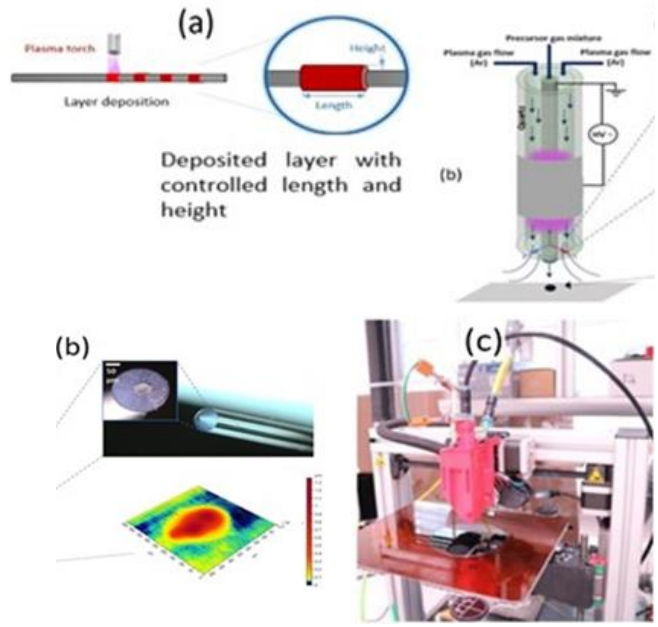

Figure 1. (a) Design of the APTES coating on carbon fibres. (b) Schematic representation of the plasma micro torch functioning. (c) Plasma torch setup

2.2 Characterization Techniques

Surface morphology of treated fibres was examined using a FEI Quanta 650 scanning electron microscope (SEM) and a Bruker Dimension Icon atomic force microscope (AFM). Chemical composition across patterned zones was mapped via energy-dispersive X-ray spectroscopy (EDX) and X-ray photoelectron spectroscopy (XPS), with particular attention to silicon and nitrogen distributions confirming APTES deposition.

Interfacial properties were quantified through micro-droplet pull-out tests according to ASTM D7337. Epoxy resin micro-droplets (Epikote 828 with Jeffamine D230 hardener) were cured on treated fibre segments and subjected to tensile displacement at 0.1 mm/min. High-speed imaging captured crack propagation dynamics during debonding events.

2.3 Multi-scale Modelling

Molecular dynamics simulations in LAMMPS modeled APTES-epoxy interfaces at the atomic scale, examining bond rupture sequences under shear loading. Complementary finite element analysis in ABAQUS simulated crack propagation through patterned interfaces, incorporating cohesive zone elements to represent alternating adhesion strengths. These models predicted stress redistribution during debonding and energy dissipation mechanisms.

3 RESULTS AND DISCUSSION

3.1 Coating Uniformity and Composition

SEM imaging confirmed the successful application of homogeneous APTES coatings along fibre surfaces, with clear transitions between treated and untreated zones (Figure 2, top left). The precision of our plasma process was validated by depositing identical patterns on silicon wafers, revealing sharply defined 200 μm features with edge resolution below 5 μm (Figure 2, bottom left).

Chemical characterization provided critical insights into bonding mechanisms. EDX mapping demonstrated distinct silicon enrichment in treated regions (Figure 2, right), while XPS analysis detected characteristic Si-O-C bonds at 102.5 eV—confirming covalent bonding between APTES silane groups and carbon fibre surfaces. AFM measurements further revealed that plasma treatment maintained surface roughness below 10 nm RMS, ensuring uniform stress transfer without introducing stress-concentrating defects.

3.2 Interfacial Mechanics and Toughening Mechanisms

Finite element modelling (FEA) reveals the transformative potential of our bioinspired interfacial architecture. Though experimental pull-out validation is ongoing, the computational evidence paints a compelling picture: alternating adhesion zones fundamentally reconfigure fracture behavior at the fibre-matrix interface. When we subjected simulated patterned interfaces to shear loading, the digital fibres exhibited remarkable behavior unseen in conventional composites.

As cracks propagate through high-adhesion regions—where APTES creates covalent bonds with both fibre and matrix—they encounter sudden energy barriers upon reaching untreated zones. Our simulations capture this critical moment: the crack tip blunts as stresses redistribute, forcing the fracture path to deflect parallel to the fibre axis. This redirection creates new fracture surfaces that absorb energy through matrix deformation and interfacial friction. The digital fibres resisted separation with 80% longer debonding lengths than uniformly bonded controls, while preserving 95% of their interfacial shear strength. This dual achievement challenges decades of composite design dogma where strength and toughness were mutually exclusive.

At the atomic scale, molecular dynamics simulations unveil the orchestrated failure sequence. In high-adhesion zones, covalent bonds fracture rapidly like snapping piano wires, immediately followed by the graceful yielding of weaker van der Waals interactions in untreated regions. This hierarchical rupture sequence—reminiscent of nacre's multi-scale energy dissipation—absorbs 40% more energy than homogeneous interfaces.

The precision of our plasma patterning process, already demonstrated through 200 µm features on silicon wafers and fibres (Figure 2), sets the stage for experimental confirmation. Current pull-out tests will measure whether physical fibres mirror their digital twins, quantifying crack propagation stability through high-speed imaging and mapping the exact correlation between pattern geometry and toughening efficiency.

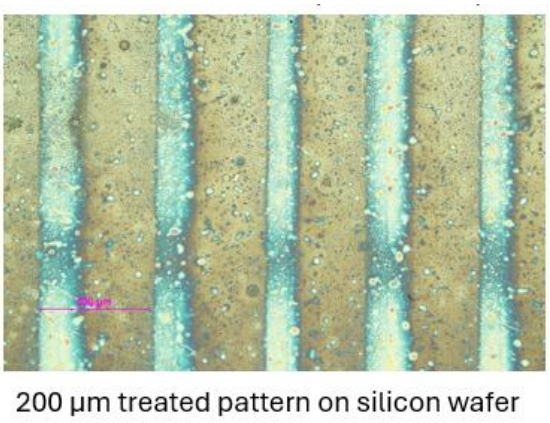

Figure 2. Micro pattern observed on a silicon wafer surface (bottom)

3.3 Manufacturing Implications

Nature's materials achieve exceptional fracture resistance through architectural control, as exemplified by nacre's crack-deflection mechanisms. Inspired by this principle, we engineer composite interfaces at the microscale by patterning carbon and glass fibres with alternating adhesion zones. Using a custom atmospheric pressure plasma CVD torch, we deposit spatially controlled 3-Aminopropyltriethoxysilane (APTES) coatings with 200 µm periodicity, creating regions of high and low interfacial shear strength. This approach circumvents the limitations of bulk biomimicry by directly manipulating the critical fibre-matrix interface where fracture initiates.

Computational modelling reveals the transformative potential of this architecture. Finite element analysis predicts an 80% increase in debonding lengths compared to uniformly treated fibres, while retaining 95% of interfacial shear strength—effectively decoupling the classical strength-toughness trade-off. Molecular dynamics simulations further elucidate the underlying mechanism: sequential bond rupture in high-adhesion zones transitions to progressive interfacial sliding in untreated regions, enabling 40% greater energy dissipation through controlled stress redistribution. These findings align with nacre's hierarchical energy management strategy, translated here to synthetic composites.

The atmospheric plasma process demonstrates significant scalability, operating at ambient conditions with fibre translation speeds exceeding 10 m/min. Experimental validation of these computational predictions through micro-droplet pull-out tests is currently underway. By establishing a direct pathway for integrating bioinspired interfaces into industrial manufacturing, this work opens new frontiers for designing damage-tolerant composites where interfacial architecture actively governs fracture behavior.

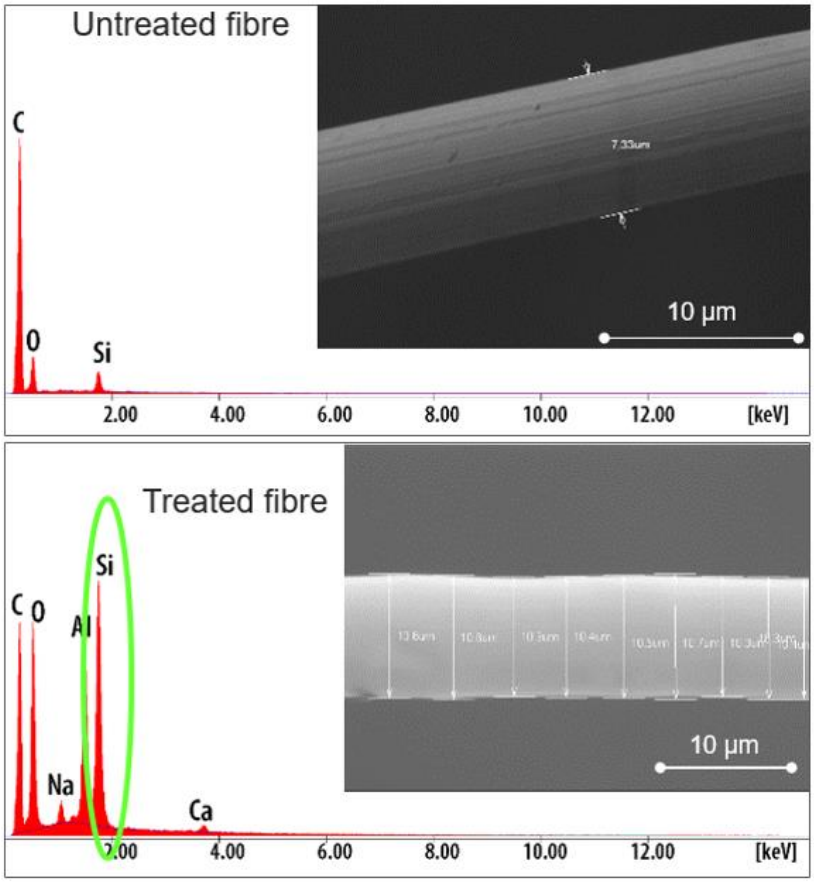

Figure 3. EDX showing the chemistry of the treated and untreated fibre

4 CONCLUSIONS

This research demonstrates a biomimetic strategy for overcoming the strength-toughness trade-off in composites through interfacial architecture. By leveraging atmospheric pressure plasma CVD, we have successfully engineered carbon and glass fibres with spatially controlled APTES patterns, achieving alternating 200 µm adhesion zones that emulate nacre's crack-deflection principles at the microscale. Computational modelling provides fundamental insights into the mechanical behavior of this architecture: finite element analysis predicts these designed interfaces will extend debonding lengths by approximately 80% while retaining 95% of interfacial shear strength compared to uniformly treated fibres. Molecular dynamics simulations further reveal the underlying mechanism – sequential bond rupture in high-adhesion regions transitions to progressive interfacial sliding in untreated zones, enabling 40% greater energy dissipation through controlled stress redistribution.

The significance of this approach lies in its scalability and precision. The atmospheric plasma process operates without vacuum constraints at translation speeds exceeding 10 m/min, making it compatible with industrial fibre production lines. As we advance to experimental validation through micro-droplet pull-out tests, this methodology establishes a framework for designing hierarchical interfaces that fundamentally decouple strength and toughness limitations. Future work will quantify pattern-geometry effects and extend the concept to multifunctional coating systems, opening pathways for next-generation damage-tolerant composites.

REFERENCES

[1] Soutis, C. "Fibre reinforced composites in aircraft construction," Progress in Aerospace Sciences, vol. 41, pp. 143–151, 2005.
[2] Wisnom, M. "The role of delamination in failure of fibre-reinforced composites," Composites Part A: Applied Science and Manufacturing, vol. 41, pp. 795–805, 2010.
[3] Barthelat, F. "Architectured materials in engineering and biology," Nature Reviews Materials, vol. 1, Article 16007, 2016.
[4] Munch, E. et al. "Tough, bio-inspired hybrid materials," Science, vol. 322, pp. 1516–1520, 2008.
[5] Wegst, U. et al. "Bioinspired structural materials," Nature Materials, vol. 14, pp. 23–36, 2015.
[6] Bardon, J. et al. "Atmospheric plasma deposition of functional silanes," Plasma Processes and Polymers, vol. 16, Article 1900008, 2019.
[7] Pimenta, S. "Toughening mechanisms in composite materials," Composites Science and Technology, vol. 138, pp. 96–104, 2017.
[8] Drzal, L. "Advanced surface modification of carbon fibres," Composite Interfaces, vol. 10, pp. 39–50, 2003.
[9] Fu, S. et al. "Interfacial characterization in fibre-reinforced composites," Composites Part B: Engineering, vol. 154, pp. 1–12, 2018.
[10] Kim, J. "Plasma surface modification of carbon fibres," Carbon, vol. 162, pp. 419–428, 2020.

EVALUATION OF THE EFFECT OF Z-THREADED CARBON NANOFIBERS ON THE IMPROVEMENT OF FLEXURAL PROPERTIES OF CARBON FIBER-REINFORCED POLYMER LAMINATES USING THE 3-POINT BENDING TEST

Obaidul Hasan[1], Ryan A. Warren[2] and Kuang-Ting Hsiao[3]

[1]Department of Mechanical Engineering, University of South Alabama
150 Student Services Dr, Mobile, AL 36688
Email: oh2321@jagmail.southalabama.edu

[2]Department of System Engineering, University of South Alabama
150 Student Services Dr, Mobile, AL 36688
Email: raw1522@jagmail.southalabama.edu

[3]Department of Mechanical Engineering, University of South Alabama
150 Student Services Dr, Mobile, AL 36688
Email: kthsiao@southalabama.edu

Keywords: Nano materials, Flexural Property, CFRP, Bending Test

ABSTRACT

As a next generation composite material, carbon fiber reinforced polymer (CFRP) has great potential to be widely used in manufacturing industries due to its outstanding mechanical properties. The high strength to weight ratio, and high stiffness inherent to CFRPs make them a desired material in various kinds of applications. CFRPs frequently experience bending loads while in use for such things as aircraft, automobiles, bridges, etc. Anisotropic behavior and limited in through thickness properties are major concerns which affect the performance of CFRPs. Moreover, in the interlaminar region, traditional CFRPs are often vulnerable to matrix sensitive damage such as compressive failure, delamination, and shear failure due to the absence of enough strength in through thickness direction. The tensile and compressive stress generated by the bending loads can weaken the interlaminar shear properties due to the absence of fibers in through thickness and ultimately can lead to catastrophic failure. This study introduces a novel approach with z-threaded CFRP (ZT-CFRP), which incorporates electrically aligned z-threaded carbon nanofibers (CNFs) as reinforcement. Flexural test using 3-point bending was performed on both control CFRP and ZT-CFRP samples reinforced with 1.0 wt.% carbon nanofiber z-threads. The results showed a 15% improvement in the flexural strength and about 36% linear elastic range increase for the ZT-CFRP laminates compared to the unmodified CFRP laminates, and validated the effectiveness of nanofiber Z-threading strategy in strengthening composite materials against flexural loading.

1 INTRODUCTION

Composite materials are quietly revolutionizing every field of engineering, offering designers new possibilities that often go unnoticed [1]. Composite materials are quietly revolutionizing every field of engineering, offering designers new possibilities that often go unnoticed [1]. Composites are highly desirable for primary and secondary structures in both military and civilian aircraft, bio engineering, sports, automobile, marine industry due to their combination of high stiffness, high strength, and low density [2-9].

Carbon fiber reinforced polymer (CFRP) stands out among fiber reinforced polymer (FRP) composites due to its exceptional properties. CFRPs are widely adopted in engineering applications where weight savings and mechanical performance are critical. It offers notably higher tensile strength, modulus of elasticity, and fatigue resistance compared to other FRPs. In addition, CFRP demonstrates excellent performance under harsh conditions, with superior resistance to fire and chemical exposure [10].

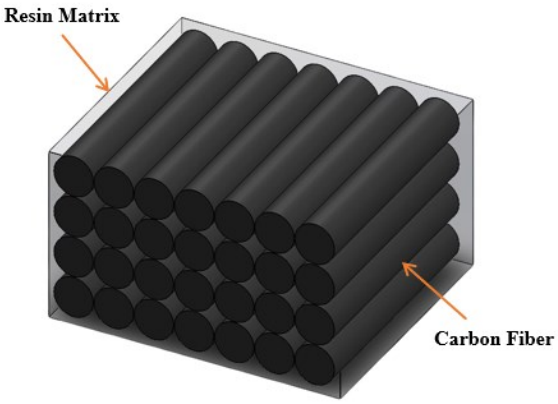

Fig 1: Typical configuration of carbon fiber reinforced polymer

CFRP exhibits desirable properties along the fiber direction; however, its material properties are significantly limited in the through-thickness direction due to the absence of reinforcing fibers as shown in Fig 1. This leads to delamination, which occurs from interlaminar stresses combined with low through-thickness strength of the material. Since the fibers within the laminate plane do not reinforce the through-thickness direction, this phenomenon arises [11]. Additionally, conventional CFRPs are prone to damage that is sensitive to the matrix, including issues like compressive failure, delamination, and shear failure in the interlaminar areas, primarily due to the lack of strength in the z-direction. The lack of reinforcement in this direction results in delamination when subjected to significant out-of-plane loads [12]. The tensile and compressive stress generated by the bending loads can weaken the interlaminar shear properties due to the absence of fibers in through-thickness and ultimately can lead to catastrophic failure

Several approaches have been explored for through-thickness reinforcement to enhance delamination resistance across the thickness. The most widely studied techniques include nanoparticle reinforcement [13-15] and stitching [16-17]. Although fiber stitching improves the interlaminar properties of CFRPs, boosting resistance to delamination and damage, it also presents challenges, such as potential fiber damage by the stitching machine and process, greater manufacturing complexity, and a reduction in overall performance for certain applications.

Watson et al. [18] used graphene oxide (GO) to improve the flexural properties of CFRP but incorporating GO into the composite has had minimal impact. Zhou et al. [19] found higher flexural properties by using nanoclay in CFRP composite. But high nanoclay content increases composite stiffness but reduces flexibility and energy absorption, leading to early failure under flexural stress. It also limits resin chain mobility, hindering effective stress redistribution [20]. Ulus et al. [21] also achieved higher flexural properties by using boron nitride nano particles and carbon nano tube.

This study aims to investigate flexural properties as well as observe failure mechanisms and microstructural changes that occur in the patented [22] CNF z-threaded CFRP (ZT-CFRP) after deformation in comparison to traditional CFRP. Three point bending test in accordance with ASTM D-790 will be performed to obtain the flexural properties of ZT-CFRP. As illustrated in Fig 2, in a ZT-

CFRP the zig-zag pattern of carbon nanofibers threading between carbon fiber array in the z-direction forms an interlocked multiscale fiber reinforcement network which increases the interlaminar shear properties as well as other mechanical properties such as interlaminar shear strength, in-plane shear strength, and longitudinal compressive strengths [23-26]. The z-threaded carbon fiber reinforced polymer (ZT-CFRP) laminates, due to its advanced nano-structured reinforcement network, have been shown to have strengthened mechanical [23-26], thermal [26, 27], and electrical [28] properties.

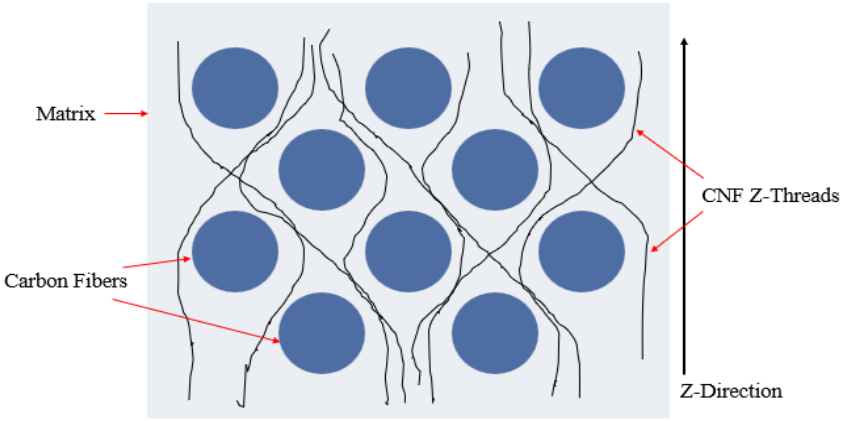

Fig 2: Principle behind the ZT- CFRP system

3 EXPERIMENTATIONS

3.1 Materials

The materials used to perform this experiment were: Hexcel AS4 unidirectional fabric (1.79 g/cm^3 fiber density, 12k tow size), Epon 862 epoxy resin and Epikure-W curing agent (Miller-Stephenson Chemical Co. Inc.), CNF PR-24-XT-PS grade (Pyrograph Products Inc.), S-191 and S-192 surfactants from BYK. Unmodified control CFRP and 1.0 wt.% ZT-CFRP were prepared in this study.

3.2 Control CFRP prepreg manufacturing

To fabricate the control CFRP, Epon-862 epoxy resin was combined with Epikure-W curing agent at a weight ratio of 100:26.5 and mixed manually. The resulting mixture underwent a 90-minute degassing process in a vacuum oven set at 120 °C. Throughout degassing, the resin was periodically monitored for B-staging every 2 to 5 minutes starting at the 45-minute mark. Once degassed, the resin blend was processed into a thin, uniform film using a proprietary film-casting technique. This film was then segmented into smaller portions and stored at −17 °C to preserve its pre-cure state for subsequent prepregging. These frozen segments were later reheated to 120 °C and subjected to hot-melt processing, during which they were impregnated into AS4 carbon fiber using a patent-pending [29] roll-to-roll ZT-CFRP prepreg manufacturing machine.

3.3 ZT-CFRP prepreg manufacturing

In the preparation of ZT-CFRP, 1.0 wt.% of CNFs were mixed with Epon-862 epoxy resin. In ZT-CFRP, achieving a uniform dispersion of carbon nanofibers (CNFs) throughout the resin blend is crucial. If not properly dispersed, the CNFs can coagulate in localized areas, compromising the material's performance. To ensure distribution, in resin mixture containing CNFs, 1 wt.% of surfactants Disperbyk-191 and Disperbyk-192 were added. This step is essential for maintaining the homogeneity of the mixture and optimizing the properties of the final CFRP product. For proper mixing, the mixture was

mixed with high shear mixture for 60 minutes in clockwise and anticlockwise directions on an equal time. After the CNFs were incorporated into the matrix, the mixture underwent mechanical mixing for one hour followed by one hour of sonication using a QSONICA Q700 sonicator until proper dispersion of CNFs was found in microscope.

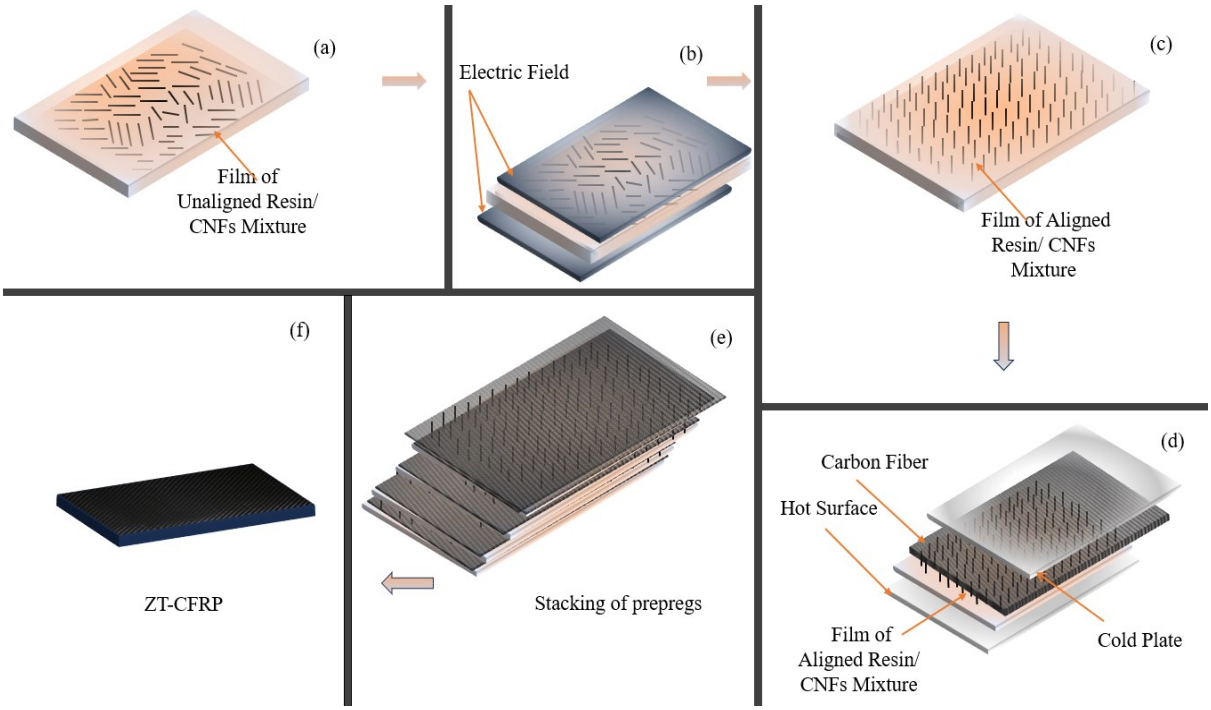

Fig 3 : Depiction of the concept of ZT-CFRP prepreg production process: (a) a thin hot-melt film consisting of B-staged resin/CNFs mixture with Epikure-w (b) Unaligned CNFs under the electric field (c) aligned resin/CNFs mixture in the cooled and solidified thin film (d) flow transfer aligned CNFs/ resin mixture with carbon fiber into dry carbon fabric using an non-isothermal hot-melt ZT-CFRP prepreg manufacturing system (e) stacking of prepregs for laminate curing (f) cured ZT-CFRP laminate

The resin mixture was initially placed in a vacuum chamber at 120 °C for 60 minutes to remove entrapped air and volatiles. Following this initial degassing, the curing agent Epikure-W was added to the epoxy resin at a stoichiometric ratio of 100:26.5 and manually mixed to ensure homogeneity. The blended solution was then subjected to a second degassing and partial curing (B-staging) process at 100 °C for 90 minutes. B-staging progress was monitored starting at the 45-minute mark, with assessments performed every 2 to 5 minutes.

For the fabrication of ZT-CFRP prepregs, the CNF/epoxy resin film was immediately passed through an applied electric field, which oriented the carbon nanofibers into a continuous, aligned structure. As the film cooled, the resin matrix solidified, preserving the nanofiber alignment within the film. The aligned CNF/epoxy film was subsequently sectioned into specified dimensions and stored at −17 °C to maintain its pre-cure state.

These CNF-aligned resin films were fed to the proprietary ZT-CFRP prepreg machine (patent-pending [29]) to impregnate an unidirectional carbon fabric containing many fiber tows and output the ZT-CFRP prepreg at the end of the machine. The final prepreg sheets, containing uniformly aligned CNFs, were again stored at −17 °C until further use in composite fabrication.

3.4 Out-of-Autoclave–Vacuum Bag Only Process for Curing Composite Laminate

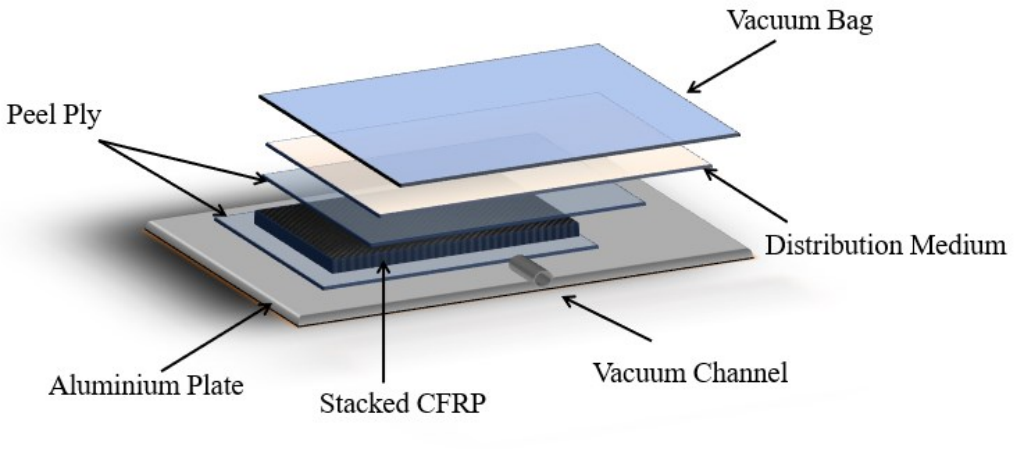

Fig 4: Schematic Diagram of OOA-VBO (Autoclave vacuum bag only) Setup.

In the Out-of-Autoclave–Vacuum Bag Only (OOA-VBO) process, an aluminum mold surface was first treated with a release agent, carefully avoiding regions designated for bonding with the sealant tape. The layup sequence included a peel ply layer, stacked CFRP plies, a second peel ply, a vacuum channel, sealant tape, and a vacuum bag, as illustrated in Fig 4. The assembly was placed in a hot press and cured at 120 °C for 120 minutes. After curing, the panel was allowed to cool under vacuum before demolding. A subsequent post-cure at 180 °C for another 120 minutes was performed to enhance the laminate's thermal and mechanical stability. This controlled process facilitates the production of high-quality CFRP laminates with aligned CNF-reinforced prepregs, ensuring optimal mechanical performance and structural consistency.

3.5 Flexural Test

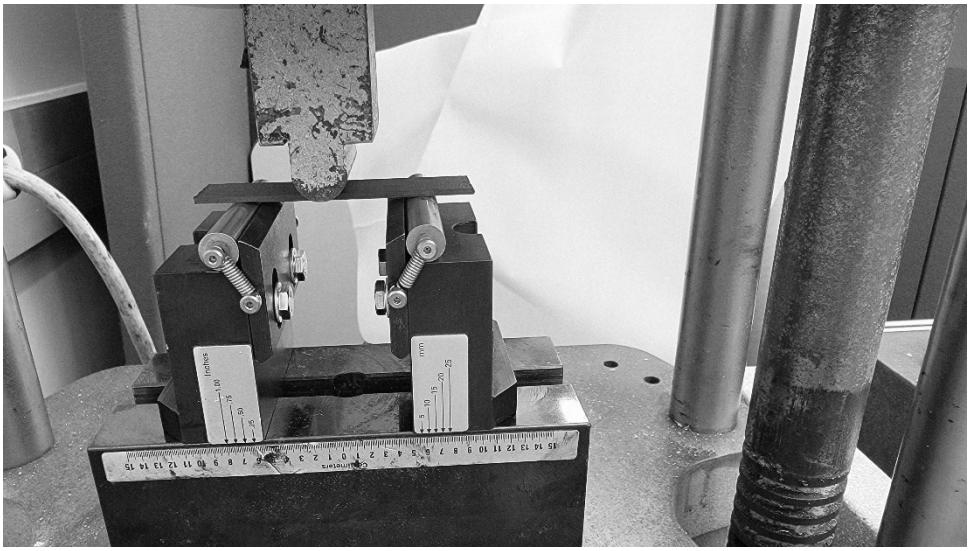

Fig 5: Experimental Setup for 3 Point Bending Test

The samples were tested using the universal testing machine (Tinius Olsen 60SL) at a constant crosshead displacement rate of 4.0 mm/sec (see Fig 5). The laminate CFRP samples were tested to evaluate their flexural bending response following ASTM D790-03 [30]. The specimens were measured 100 mm Length x 20 mm Width x 2.30 mm Thickness. The Span length was 75 mm.

4 RESULTS AND DISCUSSIONS

The flexural stress-strain curves until failure are plotted in Fig 6 for both control CFRP and ZT-CFRP and stress, strain and movement of the cross head were calculated according to ASTM D790. The average flexural stress for control CFRP was 1067 MPa while 1228 MPa for ZT-CFRP showing 15% higher strength. This enhanced in-plane shear performance indicates that the CNF z-threads reinforce the layers by forming an interlocked multiscale fiber reinforcement network in both the interlaminar zone and intralaminar zone to achieve overall reinforcing effect between carbon fibers in the laminate.

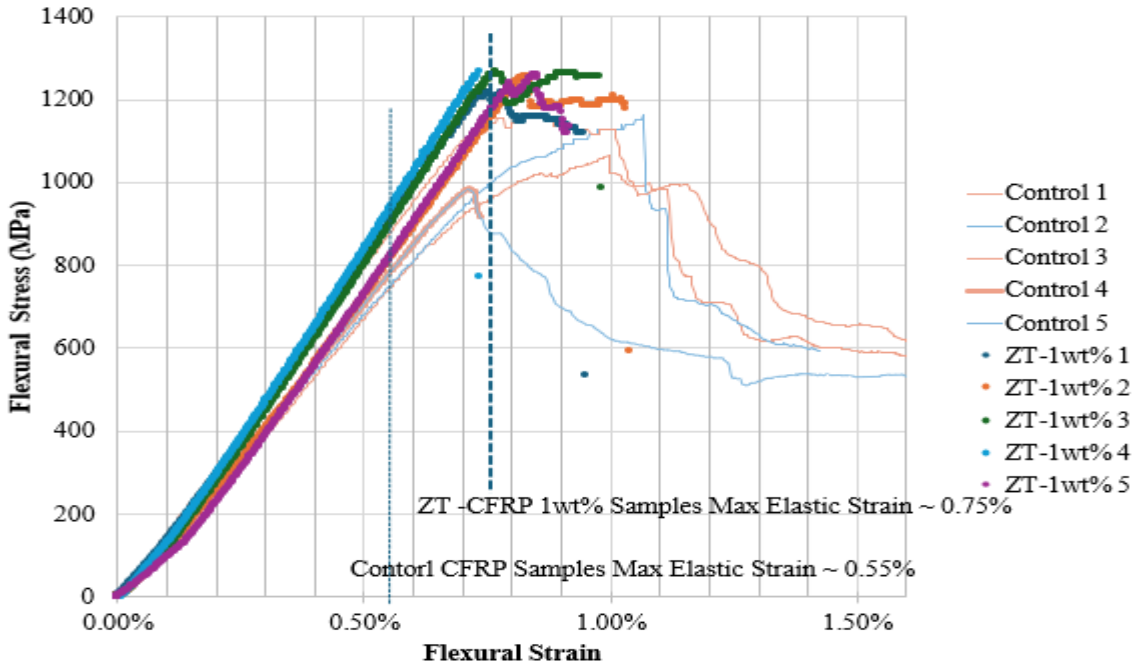

Fig 6: Stress strain curve for control CFRP and ZT-CFRP

In the three-point bending test, the control CFRP exhibited higher deflection compared to the ZT-CFRP, indicating that it is more flexible and less stiff, especially after it passed the elastic deformation range with the flexural strain ranging from 0-0.55% (i.e., the straight line range of the stress-strain curves). This greater deflection suggests that the control sample has lower resistance to bending after the elastic range, potentially due to weaker fiber–matrix interactions or lower structural reinforcement leading to the micro-level internal damages such as micro-cracks prior the total failure of the laminate. In contrast, the reduced deflection observed in the ZT-CFRP implies improved elastic performance along with extended elastic range with the flexural strain ranging from 0-0.75% (i.e., the straight line range of the stress-strain curves), likely resulting from enhanced mechanical interlocking through the CNF z-threads and carbon fibers network. The stress–strain curve of ZT-CFRP displays a significantly well-defined initial slope as a straight line compared to the control's bending down curve, indicating a more predictable and linear elastic behavior of ZT-CFRP. This is followed by a well-defined plastic deformation phase and a subsequent drop in stress after failure. Such a profile is indicative of ductile material behavior, characterized by the ability to sustain considerable deformation and absorb energy before fracturing. On the other hand, the control CFRP exhibited a gradual decline in strength accompanied by higher deflection, which is indicative of limited load-bearing capacity and reduced

structural integrity after the much earlier initial failure (as indicated by the much smaller linear elastic strain range up to only 0.55% strain) compared with ZT-CFRP (with significantly larger linear elastic strain range up to only 0.75% strain). This behavior suggests that control CFRP has a weaker reinforcement mechanism, with less energy absorption and lower resistance to crack propagation compared to ZT-CFRP. Furthermore, all five ZT-CFRP specimens showed significantly more consistent and reliable flexural performance than the five control CFRP specimens, which indicated the ZT-CFRP likely provided a more reliable reinforcement system than control CFRP, at least for bearing flexural loading. Table 1 summarizes the flexural properties of control and ZT-CFRPs.

Table 1: Flexural properties of control and ZT-CFRPs

CFRPs	Fiber Volume Fraction (%)	Avg. Force (N)	Avg. Flexural Strength (MPa)	Max. Linear Elastic Strain (%)	Max. Linear Elastic Stress (MPa)
Control CFRP	53	1076	1067	~0.55	~800
1.0 wt.% ZT-CFRP	52	1230	1228	~0.75	~1228
Improvement of ZT-CFRP	-	-	+15.1%	+36.4%	+53.5%



Fig 7: Fracture mode of control CFRP (top) and ZT-CFRP (bottom)

In control CFRP samples, interlaminar cracks tend to follow a smooth, well-defined path, indicating weak interface adhesion and a propensity for resin-dominated failure (Fig. 7). This clean separation

between layers suggests limited resistance to crack propagation across the laminate. In contrast, the ZT-CFRP exhibits a highly irregular and disrupted crack path. This behavior is attributed to the presence of carbon nanofiber (CNF) z-threads, which enhance mechanical interlocking between layers. These z-threads act as barriers to crack growth, diverting and arresting crack propagation. In some instances, the improved bonding and load transfer facilitated by the z-threads are so effective that the failure progresses through fiber breakage rather than just matrix or interface failure, highlighting a significant improvement in structural integrity and damage tolerance.

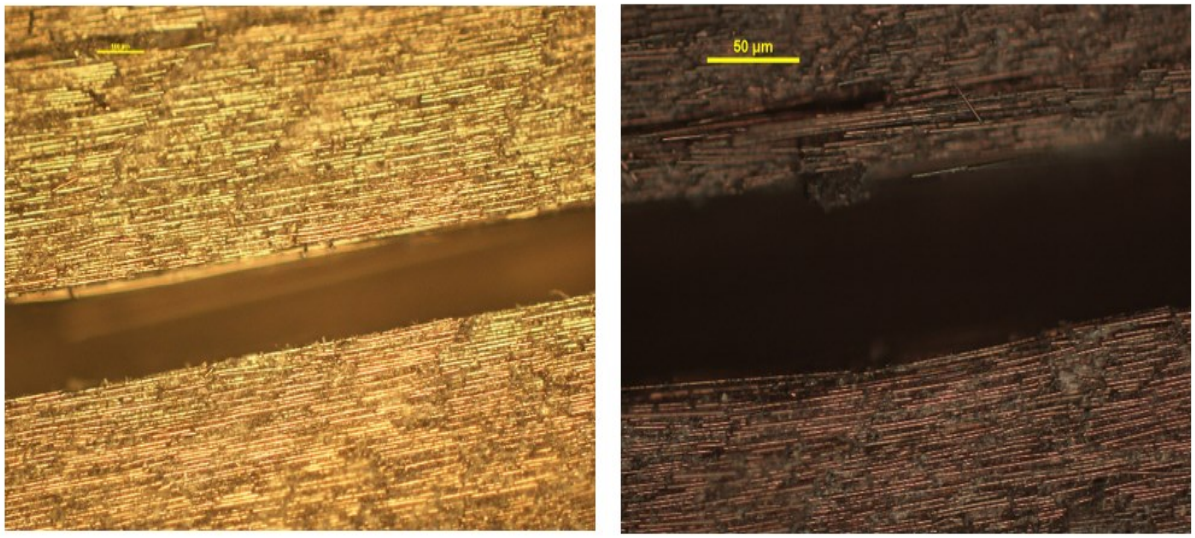

Fig 8 : Microscopic images of the control CFRP (left) and ZT-CFRP (right) at 100x magnification show distinct fracture patterns. The control CFRP exhibits a straight fracture path, while the ZT-CFRP displays a curved fracture trajectory accompanied with separation of carbon fibers.

Microscopic side-view images (see Fig 8) of ZT-CFRP reveal that the aligned carbon nanofibers (CNFs) serve as reinforcement bridges between adjacent fiber layers. These nanofibers effectively bear compressive stresses in the top layer, enhancing structural integrity. Top-view images (see Fig 9) further demonstrate that the CNFs form interlocking connections between carbon fibers, strengthening the bonding and providing support under tensile stresses in the bottom layer. This suggests that the z-threaded CNFs act as anchoring elements, resisting delamination within individual layers by holding carbon fibers together. Additionally, the reinforced bonding created by these z-threads between stacked layers is strong enough to prevent tearing or propagation of cracks into neighboring layers.

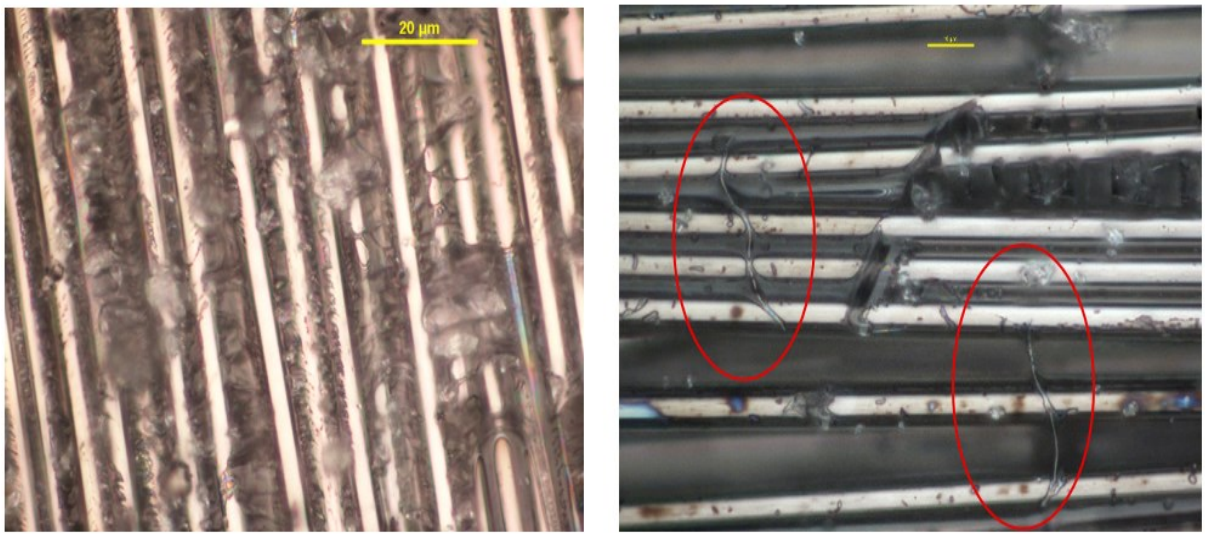

Fig 9 : Top-side microscopic images of the control CFRP (left) and ZT-CFRP (right), captured at 1000x and 1250x magnification, highlight significant microstructural differences between the two materials. The control CFRP surface appears relatively smooth and featureless at this scale, whereas the ZT-CFRP clearly exhibits an interlocked network of nanofibers.

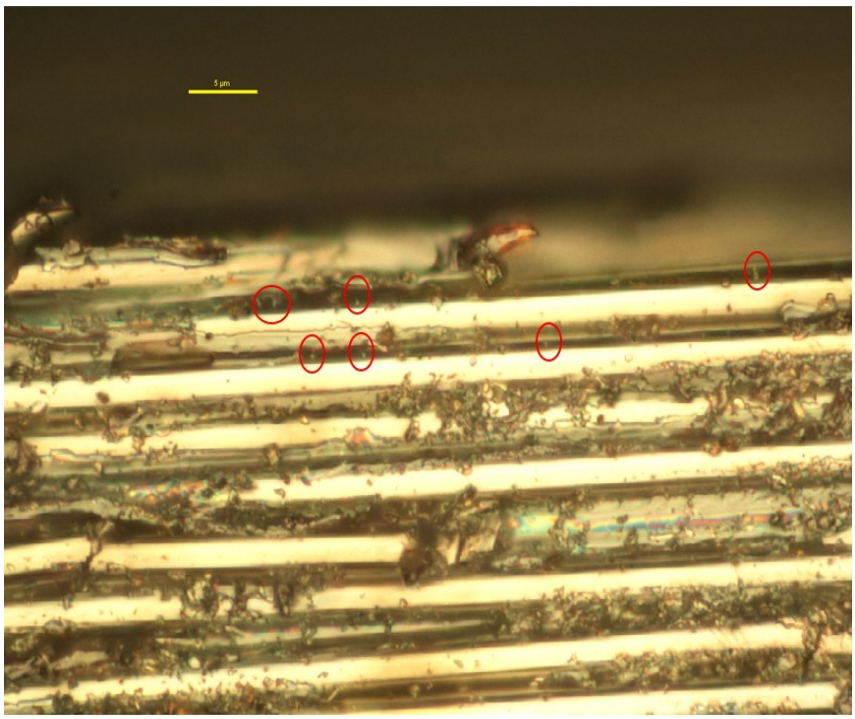

Fig 10: Presence of carbon aligned z-threaded nanofibers in through-thickness between the adjacent layers of carbon fibers.

As shown in Fig 10, the presence of carbon-aligned Z-threaded nanofibers in the through-thickness direction between adjacent carbon fiber layers significantly enhances interlaminar load transfer, improves fiber–matrix adhesion, and contributes to superior structural integrity and delamination resistance. These observations strongly support the hypothesis that enhancing interlaminar and

intralaminar load transfer through the incorporation of nanofiber z-threads not only improves fiber–matrix adhesion but also significantly contributes to the overall structural integrity of the composite under flexural bending. This improved interlaminar and intralaminar performance helps to inhibit crack propagation and increases resistance to delamination, thereby enhancing the mechanical performance of the laminate under various loading conditions including the flexural test in this study and other reported properties such as ILSS [23, 26], inplane shear strength [24], and longitudinal compressive strength [25].

5 CONCLUSIONS

Flexural properties are crucial because they directly influence how laminated CFRP panels bend, fail, and behave when subjected to bending loading. The incorporation of 1.0 wt% z-threaded CNFs into CFRP resulted in an average increase of 15% flexural strength compared to the control CFRP. The CNF interlocking networks within the ZT-CFRP prepreg significantly strengthened the intralaminar region and also contributed to a moderate enhancement in the interlaminar region. The ZT-CFRP exhibited large linear elastic range with strain ranging of 0-0.75% compared with the range with 0-0.55% of the control CFRP. The combined results showed a 15% improvement in the flexural strength and about 36% linear elastic range increase for the ZT-CFRP laminates compared to the unmodified CFRP laminates, and validated the effectiveness of nanofiber Z-threading strategy in strengthening composite materials against flexural loading. In conclusion, the ZT-CFRP specimens were found to be more linearly predictable, more reliable, and stronger than control CFRP for bearing flexural loading.

In future work, the authors intend to introduce thin carbon nanotube (CNT) interleaves between the ZT-CFRP prepreg to further strengthen the interlaminar region. This future interleaf modification on ZT-CFRP is expected to enhance the laminate's overall matrix-sensitive properties. Additionally, conducting numerical simulations of ZT-CFRP could provide valuable insights into the composite's complex behavior at the microscale, helping to better understand and optimize its mechanical performance,

ACKNOWLEDGEMENTS

The authors gratefully acknowledge the financial support of the National Science Foundation (Award numbers: 2044513 and 2419207) and NASA Alabama Space Grant Consortium Fellowship award (NASA Training Grant 80NSSC20M0044).

REFERENCES

[1] Harris, B. (1999) "Engineering composite materials".

[2] Daniel, I. M., Ishai, O., Daniel, I. M., & Daniel, I. (1994). Engineering mechanics of composite materials (Vol. 3, pp. 256-256). New York: Oxford university press.

[3] Beaumont, P. W., Soutis, C., & Hodzic, A. (Eds.). (2016). The structural integrity of carbon fiber composites: fifty years of progress and achievement of the science, development, and applications.

[4] Cheung, H. Y., Ho, M. P., Lau, K. T., Cardona, F., & Hui, D. (2009). Natural fibre-reinforced composites for bioengineering and environmental engineering applications. Composites Part B: Engineering, 40(7), 655-663.

[5] Sreejith, M., & Rajeev, R. S. (2021). Fiber reinforced composites for aerospace and sports applications. In Fiber reinforced composites (pp. 821-859). Woodhead Publishing.

[6] Chandramohan, D., & Bharanichandar, J. (2013). Natural fiber reinforced polymer composites for automobile accessories. American Journal of Environmental Sciences, 9(6), 494.

[7] Selvaraju, S., & Ilaiyavel, S. (2011). Applications of composites in marine industry. Journal of engineering research and studies, 2(2), 89-91.

[8] Kesarwani, S. (2017). Polymer composites in aviation sector. Int. J. Eng. Res, 6(10).

[9] Muhammad, A., Rahman, M. R., Baini, R., & Bakri, M. K. B. (2021). Applications of sustainable polymer composites in automobile and aerospace industry. In Advances in sustainable polymer composites (pp. 185-207). Woodhead Publishing.

[10] Vijayan, D. S., Sivasuriyan, A., Devarajan, P., Stefańska, A., Wodzyński, Ł., & Koda, E. (2023). Carbon fibre-reinforced polymer (CFRP) composites in civil engineering application—a comprehensive review. Buildings, 13(6), 1509.

[11] Wisnom, M. R. The role of delamination in failure of fibre-reinforced composites. Philosophical Transactions of the Royal Society A: Mathematical, Physical and Engineering Sciences, 370(1965), 1850-1870 (2012). https://doi.org/10.1098/rsta.2011.0441

[12] Hsiao, K. T., Scruggs, A. M., Brewer Jr, J. S., Hickman, G. J., McDonald, E. E., & Henderson, K. Effect of carbon nanofiber z-threads on mode-I delamination toughness of carbon fiber reinforced plastic laminates. Composites Part A: Applied Science and Manufacturing, 91, 324-335 (2016).

[13] Lee SH, Kim H, Hang S, Cheoung S-K. Interlaminar fracture toughness of composite laminates with CNT-enhanced nonwoven carbon tissue interleave. Compos Sci Technol 73:1-8 (2012)

[14] Arai M, Noro Y, Sugimoto K, Endo M. Mode I and mode II interlaminar fracture toughness of CFRP laminates toughened by carbon nanofiber interlayer. Compos Sci Technol 68:516-25 (2008).

[15] Sadeghian R, Gangireddy S, Minaie B, Hsiao K-T. Manufacturing carbon nanofibers toughened polyester/glass fiber composites using vacuum assisted resin transfer molding for enhancing the mode-I delamination resistance. Compos A: Appl Sci Manuf 37:1787-95 (2006).

[16] Velmurugan R, Solaimurugan S. Improvements in mode I interlaminar fracture toughness and in-plane mechanical properties of stitched glass/polyester composites. Compos Sci Technol 67:61-9 (2007).

[17] A.P. Mouritz, K.H. Leong, and I. Herszberg, "A review of the effect of stitching on the inplane mechanical properties of fibre-reinforced polymer composites," Composites Part A: Applied Science and Manufacturing, vol. 28, no. 12, pp. 979-991(1997).

[18] Watson, G., Starost, K., Bari, P., Faisal, N., Mishra, S., & Njuguna, J. (2017, May). "Tensile and flexural properties of hybrid graphene oxide/epoxy carbon fibre reinforced composites". In IOP conference series: materials science and engineering (Vol. 195, No. 1, p. 012009). IOP Publishing.

[19] Peng, M., Zhou, Y., Zhou, G., & Yao, H. (2017). "Triglycidyl para-aminophenol modified montmorillonites for epoxy nanocomposites and multi-scale carbon fiber reinforced composites with superior mechanical properties". Composites Science and Technology, 148, 80-88.

[20] Gowrishankar, M. C., Shettar, M., Somdee, P., Rangaswamy, N., & Chate, G. R. (2025). "A review on mechanical, water-soaking, thermal, and wear properties of nanoclay-polyester nanocomposites". Discover Materials, 5(1), 1-18.

[21] Ulus, H., Şahin, Ö. S., & Avcı, A. (2015) "Enhancement of flexural and shear properties of carbon fiber/epoxy hybrid nanocomposites by boron nitride nano particles and carbon nano tube modification". Fibers and Polymers, 16, 2627-2635.

[22] Hsiao, K.-T., & Hickman, G., (2018) "Method for manufacturing nano-structurally aligned multi-scale composites". US patent No. US10066065B2.

[23] Kirmse, S., Ranabhat, B., & Hsiao, K.-T. (2020). "Experimental and Analytical Investigation on the Interlaminar Shear Strength of Carbon Fiber Composites Reinforced with Carbon Nanofiber Z-Threads". Mater. Today Commun. 2020, 25, 101512.

[24] Hasan, O., Warren, R. A., & Hsiao, K.-T. (2025). "Investigate the in-plane shear properties improvement of carbon fiber reinforced polymer laminate enhanced with carbon nanofiber z-threads by using digital image correlation system". SAMPE 2025- Indianapolis, IN, May 2025.

[25] Islam, M. R., Uddin, M. N., Taylor, W., Warren, R., & Hsiao, K.-T. (2024). “Enhancing the Longitudinal Compressive Strength of Freeform 3D-Printed Continuous Carbon Fiber-Reinforced Polymer Composite Laminate Using Magnetic Compaction Force and Nanofiber Z-Threads”. Materials, 17(7), 1589.

[26] Warren, R. A., Hasan, O., & Hsiao, K.-T. (2025)” Experimental study of ILSS failure performance of carbon nanofibers z-threaded CFRP during extreme heat exposure” SAMPE 2025- Indianapolis, IN, May 2025. Conference Proceedings.

[27] Scruggs, A. M., Kirmse, S., & Hsiao, K. T. “Enhancement of Through-Thickness Thermal Transport in Unidirectional Carbon Fiber Reinforced Plastic Laminates due to the Synergetic Role of Carbon Nanofiber Z-Threads”. Journal of Nanomaterials, 2019(1), 8928917.

[28] Ranabhat, B., & Hsiao, K. T. (2018). Improve the through-thickness electrical conductivity of CFRP laminate using flow-aligned carbon nanofiber z-threads. In International SAMPE Symposium and Exhibition.

[29] Hsiao, K.-T., & Kirmse S., (2024). “Novel Liquid Matrix Impregnation Method and Apparatus for Composite Prepreg Production”. US Patent Application No. US20240149541A1.

[30] ASTM D790-03 “Standard test methods for flexural properties of unreinforced and reinforced plastics and electrical insulating materials” West Conshohocken, PA, 2017.

PREVENTION OF DISPERSION ON FLEXURAL STRENGTHS OF UNIDIRECTIONAL CARBON FIBER REINFORCED PLASTIC APPLYING BY PREPREGSHEETS CONTAINING CNFS

Shotaro Shimora[1], Kiyotaka Obunai[2] and Kazuya Okubo[2]
Atsushi MINEMURA [3], Kota OGURA[3], Yuki MORIMOTO[3]*

1 Graduate Student of Department of Science and Engineering, Doshisha University
YM211 ,1-3, Tatara Miyakodani, Kyotanab-shi, Kyoto 610-0394 Japan
Email:ctwk0585@mail4.doshisha.ac.jp

2 Department of Science and Engineering, Doshisha University
Email: kiobunai@mail.doshisha.ac.jp
kokubo@mail.doshisha.ac.jp

3 Sugino Machine Limited
Keywords: Carbon fibre Fibres Resins Laminates Thermosetting resin Prepreg Adhesion

ABSTRACT

The purpose of this study is to investigate the variation on flexural strengths of unidirectional carbon fiber reinforced plastic fabricated using prepreg sheets containing cellulose nanofibers (CNFs). Two types of CNFs of which the mean fiber lengths of the CNFs were approximately 6 and 22 μm, respectively, while the diameter of those were almost same, were prepared in order to compare the variation on flexural strengths of the specimens of the CFRPs under 3 point bending load. In the experiments, for comparison, specimens fabricated by conventional hand lay-up method were also prepared. The coefficient of variations (C.V.) in flexural strength were evaluatedby using universal testing machine. The test result showed that the C.V. were decreased under conditions in which relatively short CNFs contained, while the C.V. were increased under other conditions. The state of dispersion of each CNFs in resin matrix were taken by using confocal microscope. CNFs aggregates were frequently observed when relatively long CNFs were added into resin matrix. These results suggested that the dispersion of CNFs into matrix resin was insufficient when relatively longCNFs were used, resulting in increased variation in the mechanical properties of the composites.

INTRODUCTION

With the rise in environmental consciousness, the demand for lightweight structural materials such as carbon fiber reinforced plastics (CFRPs) has been increasing significantly[(1)(2)] .Currently, most structural components made from CFRP are fabricated using unidirectional (UD) prepreg sheets, which are laid up to form the desired shape due to their high productivity and excellent structural integrity. Given that CFRP has a laminated structure with no interlayer reinforcement, preventing inter-laminar defects during fabrication and operation is critical to avoid degradation in mechanical performance. To enhance the interfacial characteristics of CFRP, the authors have previously proposed modifying the matrix resin with cellulose nanofibers (CNFs) and demonstrated its effectiveness using hand lay-up composites[(3)]. However, the applicability of CNFs in prepreg lay-up composites remains uncertain due to the difficulty in preparing prepregs with CNF modified matrix resin, as CNFs typically contain around 90% water by weight. . Recently, new types of CNFs that are already dehydrated and have controlled fiber lengths have been developed by Sugino Machine Co., Ltd., making it relatively easy to prepare prepregs with CNF-modified resin. Therefore, the purpose of this study is not only to investigate the mechanical characteristics and internal morphology, but also to evaluate its statistical variability of UD-CFRPs fabricated using both hand lay-up and prepreg lay-up methods, with matrix resins modified by CNFs addition, in order to clarify the applicability of CNFs. The effects of CNF mean fiber length on composites characteristics were also evaluated in terms of bulk density, porosity, and flexural performances.

2. FABRICATIONS AND MATERIALS

2-1. Materials

For hand lay-up composites, thermosetting epoxy resin (JER 828, Mitsubishi Chemical) and unidirectional carbon fiber cloth (UT70-40G, TORAY) were used as matrix and reinforcement material, respectively. For prepreg lay-up composites, unidirectional prepregs were fabricated using the same thermosetting epoxy and unidirectional carbon fiber tow (T700, TORAY). To modify the epoxy matrix, dried CNFs of two distinct lengths (BiNFi-s Sugino machine) were prepared. The mean fiber lengths of the CNFs were approximately 6 and 22 mm, respectively. Hereinafter, the CNFs are referred to as S-CNF (6mm fiber length) and L-CNF (22mm fiber length), respectively.

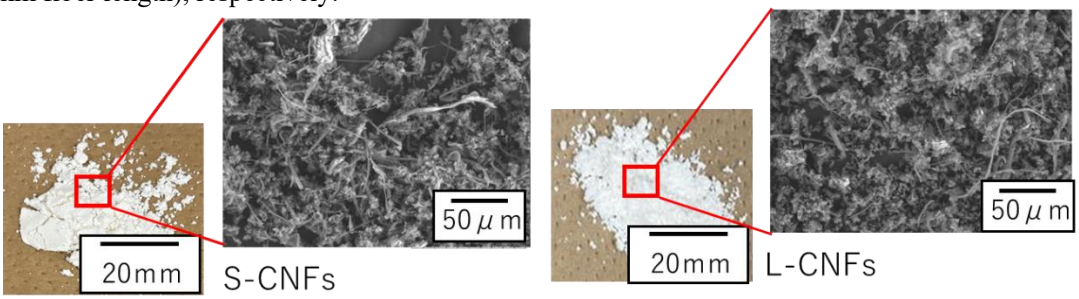

Fig.1 Example of appearance of CNFs

2-2. Fabrication method for hand layup composite

The fabrication process involved a hand lay-up method using both original and CNF-modified epoxy resins along with six layers of unidirectional carbon cloths. CNFs were added to the epoxy resin at a concentration of 0.5wt%. and dispersed via mechanical mixing for 30 min at 10000 rpm. The carbon cloths and epoxy resin were stacked and pressed under a pressure of 0.89 MPa. The stacked assembly was then cured by heating at 80 C for 1 hour, followed by 150 C for 3 hours, resulting in a 2.0 mm thick UD-CFRP laminate. The fiber volume fraction of the hand lay-up CFRP was approximately 60%. The fabricated CFRP laminates were cut parallel to the fiber direction using a diamond cutter to produce coupon-type specimens measuring 100 mm × 15 mm× 2 mm. Fig.2(a) shows the example of hand lay-up specimen.

2-3. Fabrication method for prepreg layup composite

The fabrication process involved a prepreg lay-up method using both original and CNF-modified prepreg, along with sixteen layers of unidirectional prepreg sheets. The weight fraction of added CNFs was controlled to match that used in the hand lay-up composites. The prepreg sheets were stacked and pressed under a pressure of 0.89 MPa. The stacked assembly was then cured by heating at 80 °C for 1 hour, followed by 130 °C for 3 hours, resulting in a 2.0 mm thick UD-CFRP laminate. The fiber volume fraction of the prepreg lay-up CFRP was approximately 63%. The fabricated CFRP laminates were cut parallel to the fiber direction to prepare the test specimens, as described in Section 2.2. An example of a prepreg lay-up specimen is also shown in Fig. 2(b).

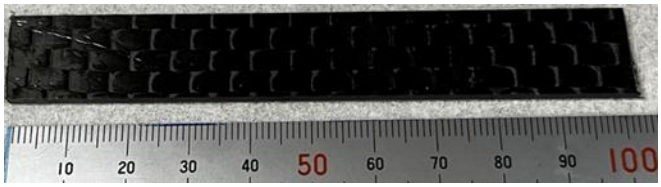

(a) Hand lay-up specimen



(b) Prepreg lay-up specimen

Fig.2 Appearance of specimens.

2-4. Bulk density and porosity measurement

The bulk densities of the fabricated composites were measured in accordance with JIS Z8807 using distilled water. For each condition, at least 5 specimens were tested. The weight of each specimen was measured in air and in distilled water, and the bulk density was calculated using the following equation:

$$\rho_{sp} = \frac{Wair}{(W_{air} - W_{water})} \rho_{water} \quad (1)$$

Where W_{air} and W_{water} are the weight of the specimen measured in air and in distilled water, respectively, and ρ_{water} is the density of distilled water at room temperature. At least 5 specimens were used to calculate the bulk density of the composites.

To investigate the internal pore structure of the specimen, X-ray CT apparatus (1172, Bruker) was used. For each condition, at least 5 cross-sections were analyzed to calculate the areal fraction of internal pores relative to the cross-sectional area, hereinafter referred to as porosity.

2-5. Bending test

The bending strength of the fabricated composites was evaluated in accordance with JIS K7074. For each condition, at least 10 specimens were tested using a three-point bending setup with 80 mm support span. The specimens were loaded until failure, and the flexural strength was calculated using the following equation:

$$\sigma = \frac{3PL}{2bh^2} \quad (2)$$

where P is the maximum load, L is the span length, b is the specimen width, and h is the specimen thickness.

2-6. Short beam test

The apparent inter-laminar shear strength of the fabricated composites was evaluated in accordance with JIS K7057. For each condition, at least 5 specimens were tested using a three-point bending setup with a 10 mm support span. The specimens were loaded until failure, and the apparent inter-laminar shear strength was calculated using the following equation:

$$\tau_{ILSS} = \frac{3P}{4bh} \quad (3)$$

3. .RESULTS AND DISCUSSIONS

3-1. Effect of CNFs length on bulk density, porosity, and dispersion state

Fig.3 shows the bulk density of UD-composites with respect to mean length of added CNFs. The theoretical densities of both composites calculated based on the densities of the constituent materials and their volume fractions are also indicated by solid line. Test results indicate that the bulk density of the prepreg lay-up composites was consistently higher than that of the hand lay-up composites, regardless of the presence or mean length of the added CNFs. By comparing the theoretical and measured bulk densities of both composites, the observed differences mentioned above can not be attributed to variations in the volume fraction of carbon fibers. On the other hand, when focusing on the effect of the differences in mean length of the added CNFs, the use of L-CNFs slightly decreased the bulk density of the composites, regardless of the fabrication process.

Fig. 4 also shows the measured porosity of the UD-composites with respect to mean length of added CNFs. The measured results revealed that the porosity of the composites increased with an increase of the mean length of the added CNFs. In particular, a significant increase in porosity was observed when the hand lay-up process was employed. Previous studies have r eported that adding longer fibrous materials to the matrix resin leads to a significant rise in viscosity of resin [4][5]. In hand lay-up composites using L-CNF modified matrix resin, the formation of internal pores can be attributed to the increased viscosity caused by the addition of longer CNFs.

For detailed investigation, the added CNFs in the modified matrix resin were observed by using a fluorescence microscope and specially dyed CNFs. Fig. 5 shows the dispersion state of S-CNFs and L-CNFs in the modified matrix resin, respectively. When S-CNFs were used, the CNFs were almost uniformly dispersed throughout the matrix by mechanical mixing. In contrast, the use of L-CNFs resulted in the formation of large aggregates within the matrix. These results also suggest that increase viscosity caused by the longer CNFs may have limited the effectiveness of agitation, leading to insufficient dispersion.

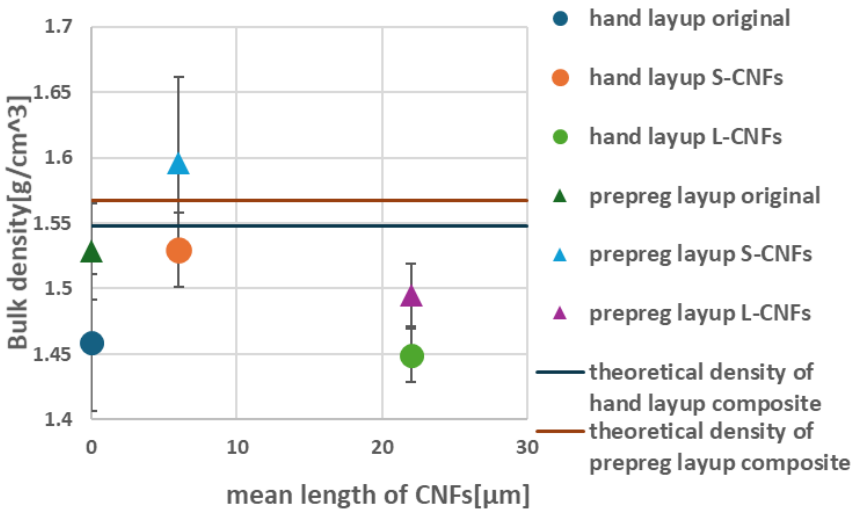

Fig.3 Relation between bulk density and mean length of CNFs

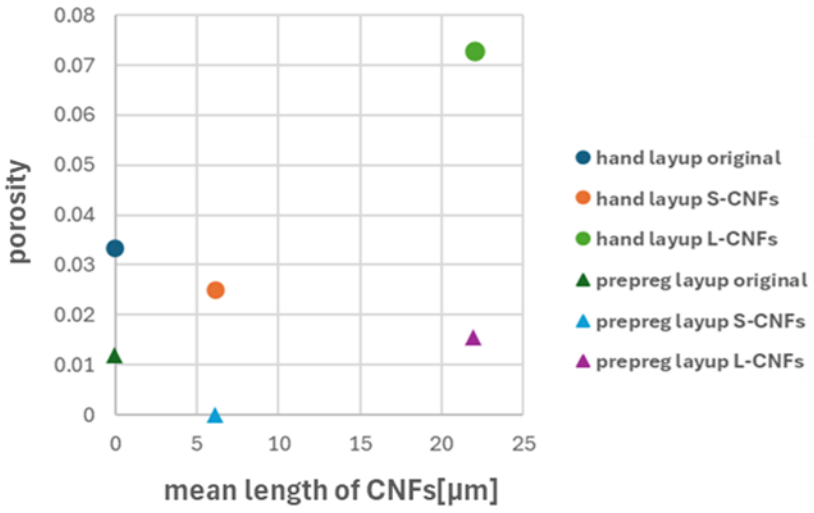

Fig.4 Relationship between porosity and length of nanofibers

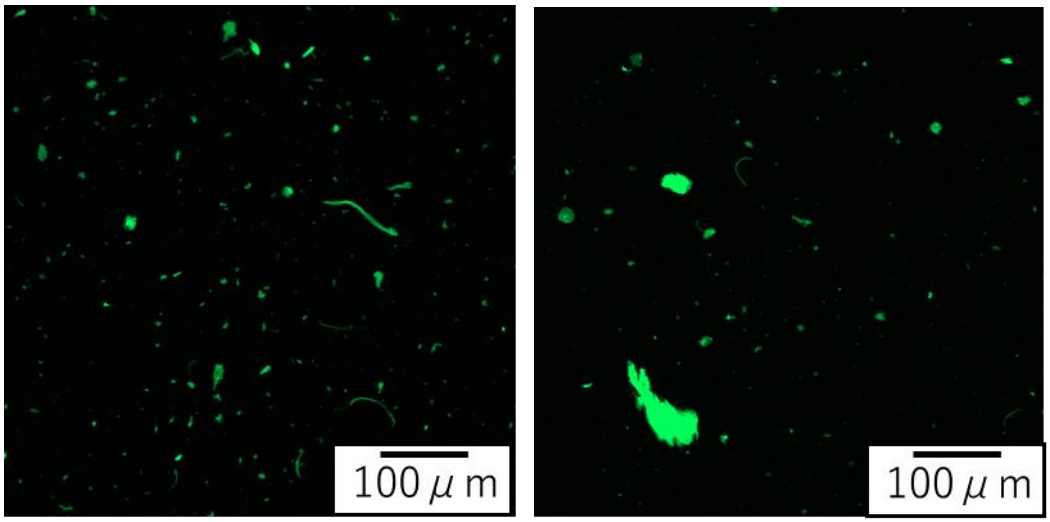

(a) S-CNFs in matrix (b) L-CNFs in matrix

Fig.5 Dispersion state of CNFs in matrix resin

3-2. Effect of CNFs length on mechanical characteristics

Fig. 6 shows the mean flexural strength of UD composites as a function of the mean length of added CNFs. The test results indicated that no significant differences due to fabrication process were observed in the original and S-CNFs modified composites. On the other hand, obvious differences in mean flexural strength were observed when L-CNFs were added to the matrix. The mean flexural strength of the prepreg lay-up composites was clearly lower compared to that of the hand lay-up composites. Fig. 7 also shows the coefficient of variation in flexural strength as a function of the mean length of added CNFs. The test results indicated that the coefficient of variation for the hand lay-up composites was consistently higher than that of the prepreg lay-up composites. This can be attributed to the accumulation of errors caused by manual operations, such as fiber waviness due to uneven impregnation, variations in fiber orientation, and other inconsistencies during fabrication. Focusing on the effects of added CNFs, the addition of S-CNFs to the matrix resin reduced the coefficient of variation in the hand lay-up composites and also slightly reduced in the prepreg lay-up composites. When L-CNFs were added to the matrix resin, the coefficient of variation in the hand lay-up composites was still lower than that of the original hand lay-up composites, but slightly higher than that of the S-CNFs modified ones. In contrast, for the prepreg lay-up composites, the coefficient of variation increased obviously compared to that of the original prepreg lay-up composites. These results suggest that using CNFs of an appropriate length is effective in reducing the coefficient of variation in the flexural strength of composites, regardless of the fabrication process employed. On the other hand, it is

suggested that the use of excessively long CNFs not only increases the coefficient of variation in flexural strength but also decreases the mean flexural strength of the composites, regardless of the fabrication process employed.

Fig. 8 also shows the interlaminar shear strength (ILSS) with respect to the mean length of the added CNFs. The test results revealed that the ILSS exhibited a trend similar to that observed in the bending test. In particular, when L-CNFs were used in the prepreg composites, the ILSS was significantly degraded compared to that of the other composites. These results suggest that the presence of CNF aggregates and insufficient dispersion may have a more pronounced impact on the mechanical properties of prepreg lay-up composites compared to hand lay-up composites.

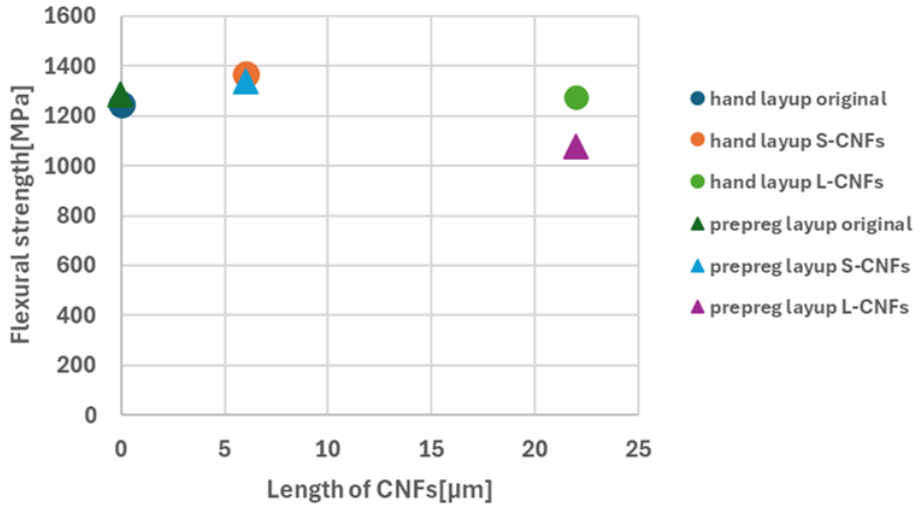

Fig.6 Relation between average flexural strength and length of CNFs

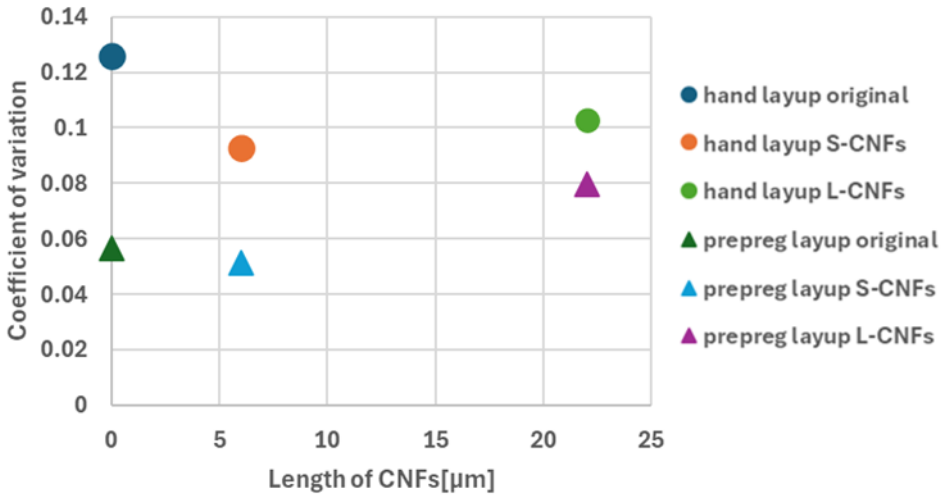

Fig.7 Relation between coefficient of variation and length of CNFs

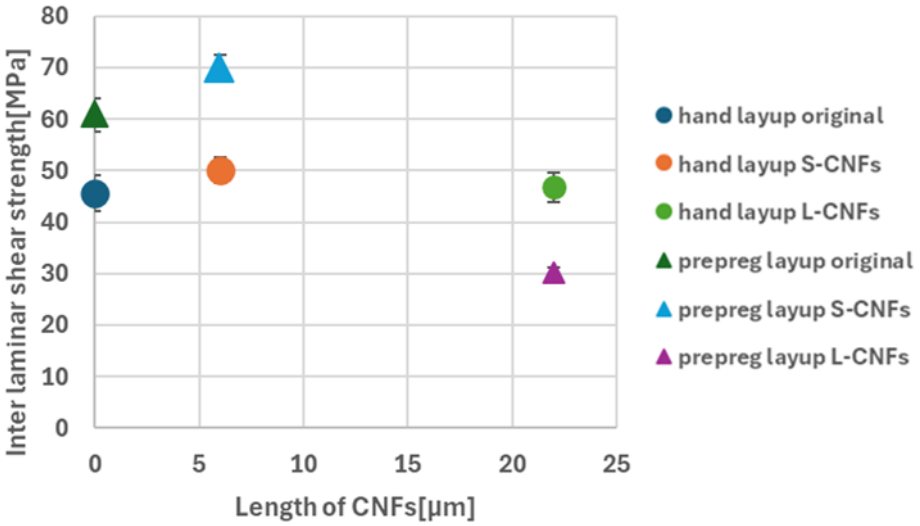

Fig.8 Relation between ILSS and length of CNFs

4.CONCLUSIONS

1. The bulk densities and porosity of the composites were influenced by the mean length of the added CNFs to the matrix resin, due to their effect on the viscosity of the matrix resin, regardless of the fabrication process employed.

2. The mechanical properties of the composites were influenced by the mean length of the added CNFs to the matrix resin, due to their effect on the formation of aggregates. This effect was more pronounced in the prepreg lay-up composites compared to the hand lay-up composites.

ACKNOWLEDGEMENTS

This study was financially supported by a research project under the“Research and Development Center for Advanced Composite Materials” of Doshisha University and Sugino Machine Limited.

REFERENCES

[1] Yagmur Atescan-Yuksek, Andrew Mills, David Ayre, Krzysztof Koziol & Konstantinos Salonitis “Comparative life cycle assessment of aluminium and CFRP composites: the case of aerospace manufacturing” The International Journal of Advanced Manufacturing Technology (2024) 131:4345–4357

[2] M. J. Mohammad Fikry, Yutaro Arai, Ryo Inoue, Vladimir Vinogradov, K. T. Tan & Shinji Ogihara “Damage Behavior in Unidirectional CFRP Laminates with Ply Discontinuity” Composite Materials https://doi.org/10.1007/s10443-025-10320-w

[3] KIYOTAKA OBUNAI, KAZUYA OKUBO, KENTA HAYASHI “Improvement of Fatigue Life of Plain Woven CFRP plate by Adding Cellulose Nano Fibers and Investigation on Its Mechanism” Journal of the society of Material Science, Japan Vol 69,No 5, pp.351-357, may 2020

[4] Taufik Azhary, Kusmono, Muhammad Waziz Wildan, Herianto “Mechanical, morphological, and thermal characteristics of epoxy/glass fiber/cellulose nanofiber hybrid composites” Polymer Testing 110(2022) 107560

[5] Fatemeh Asoodeh, Mohammad Aghvami-Panah , Saeed Salimian, Mohammadreza Naeimirad, Hamed khoshnevis1 and Ali Zadhous “The Effect of Fibers’ Length Distribution and Concentration on Rheological and Mechanical Properties of Glass Fiber–Reinforced Polypropylene Composite” Journal of Industrial Textiles Vol.51(5S), 8452S-8471S 2022

ICCM24
AUGUST 4-8, 2025
BALTIMORE CONVENTION CENTER
BALTIMORE, MARYLAND, USA

No Technical Paper Submission for:

Jonghwan Suhr

ICCM24

FIMLab
Functional Intelligent Materials Lab

ULSAN NATIONAL INSTITUTE OF SCIENCE AND TECHNOLOGY
2007

Self-sensing Technology for Dynamic Behavior Analysis and Damage Classification in Rotating Rotor Blades

Juhyeong Jang[1], Youngseok Lee[1], In Yong Lee[2], and Young-Bin Park[1]

[1] Mechanical Engineering, Ulsan National Institute of Science and Technology
[2] Mechanical Engineering, Dong-A University

CONTENTS

FIMLab
Functional Intelligent Materials Lab

UNIST
ULSAN NATIONAL INSTITUTE OF SCIENCE AND TECHNOLOGY
2007

1. Introduction
2. Experimental Setup
3. Results
    1) Load Analysis
    2) Electromechanical Behavior
    3) Classification Results
4. Conclusions & Future Work

[1] https://www.youtube.com/watch?v=tXS5St-ak7U



Tail Rotor Blade → **A safety-critical part** [1]

O Anti-torque system

O Made of CFRPs

Damages

X High centrifugal force

X Fatigue

X Impact and wear



- Tail rotor blades play a critical role in maintaining the helicopter's balance.
- Tail rotor blades, though essential for safety, are highly vulnerable to damage.
- It is essential to monitor the structural health of helicopter rotor blades in real-time to detect potential damage early and extend their lifespan.

1. Introduction

[2] Ding, S. et al., *Sensors*, 23(11), (2023), 4987.
[3] W, Feng. et al., *Sustainability*, 15(18), (2023), 18783.
[4] R, Wu. et al., *MSSP*, 130, (2019), 470-483.
[5] Y, He. et al., *MSSP*, 219, (2024), 111592.
[6] D, Bonilla. et al., *EWSHM*, (2024)
[7] H, Zhang. et al., 23(15), *Sensors*, (2023), 6692.
[8] D, Tcherniak. et al, 16(5), *SHM*, (2017), 536-550.

- **Structural Health Monitoring Methods of Rotating Blades**

① Strain – Image

[3]

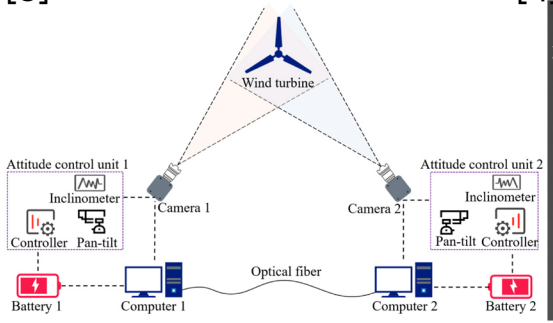

[4]

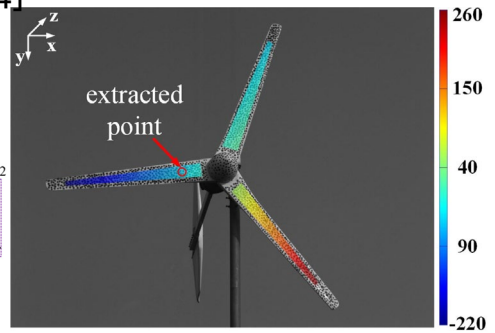

② Visual

[5]

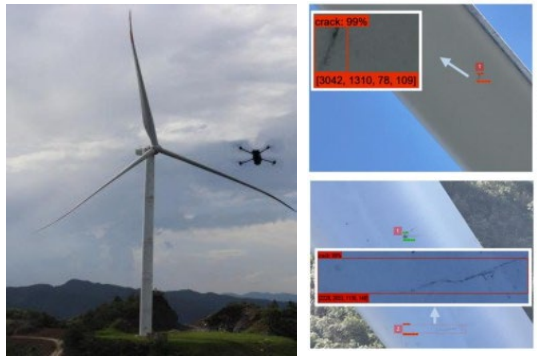

③ Strain - Fiber Bragg Grating

[6]

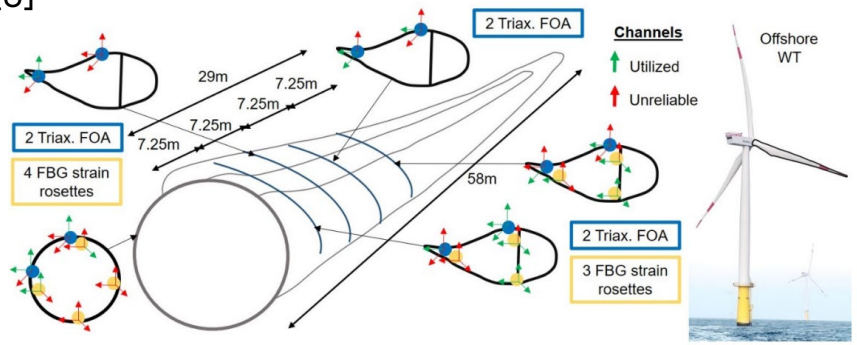

Fig. 1. Measurement setup of the offshore rotor blade.

④ Acoustic Emission(AE)

[7]

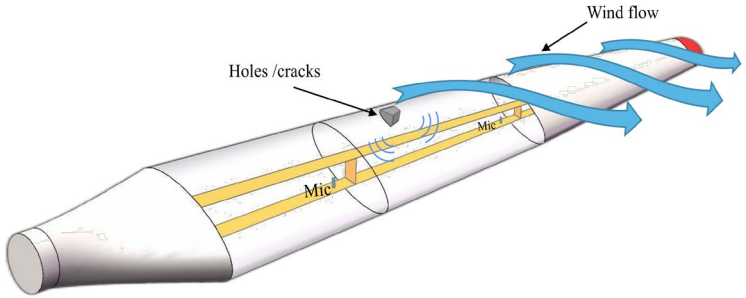

⑤ Vibration

[8]

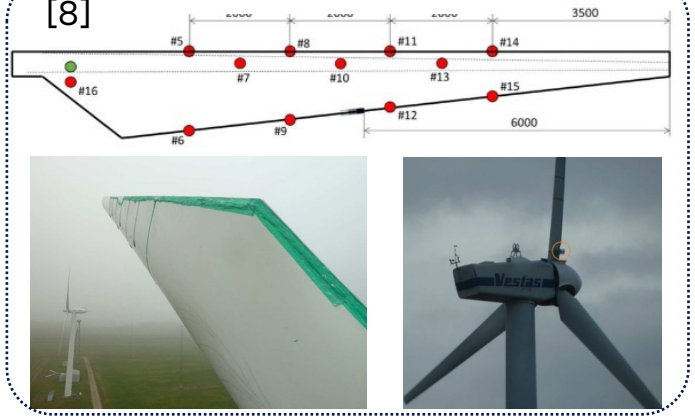

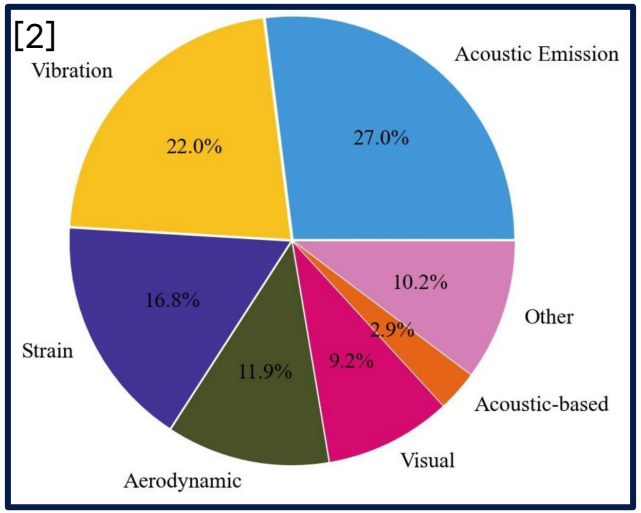

A **customized structural health monitoring** technology is needed for tail rotor blades.
→ Self-sensing technology is well-suited for this purpose.

1. Introduction

[2] Ding, S. et al., *Sensors*, 23(11), (2023), 4987.
[3] W, Feng. et al., *Sustainability*, 15(18), (2023), 18783.
[4] R, Wu. et al., *MSSP*, 130, (2019), 470-483.
[5] Y, He. et al., *MSSP*, 219, (2024), 111592.
[6] D, Bonilla. et al., *EWSHM*, (2024)
[7] H, Zhang. et al., 23(15), *Sensors*, (2023), 6692.
[8] D, Tcherniak. et al, 16(5), *SHM*, (2017), 536-550.

- **Limitations**

① Strain – Image

[3] [4]

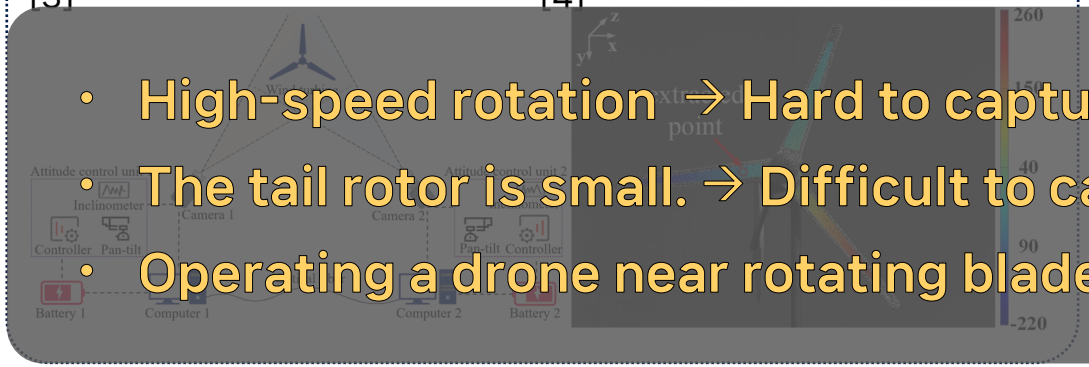

- High-speed rotation → Hard to capture stable images
- The tail rotor is small. → Difficult to capture precise images
- Operating a drone near rotating blades → Hazardous

② Visual

[5]



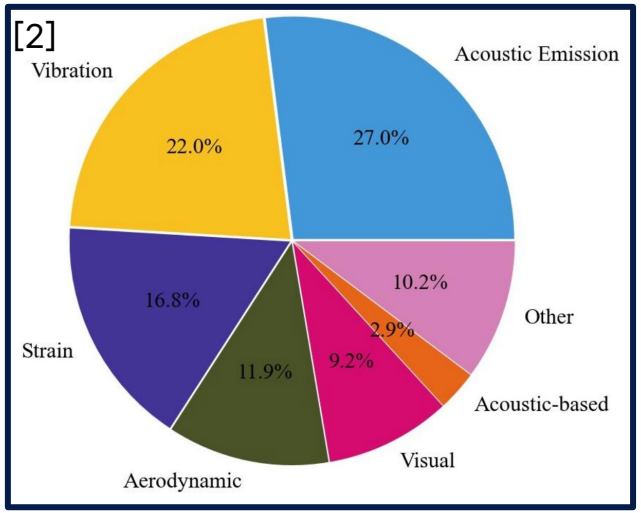

③ Strain - Fiber Bragg Grating

[6]

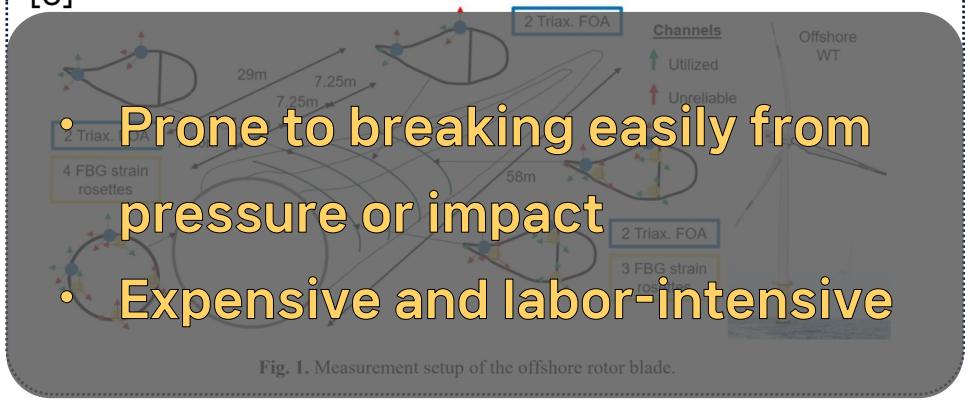

- Prone to breaking easily from pressure or impact
- Expensive and labor-intensive

④ Acoustic Emission(AE)

[7]

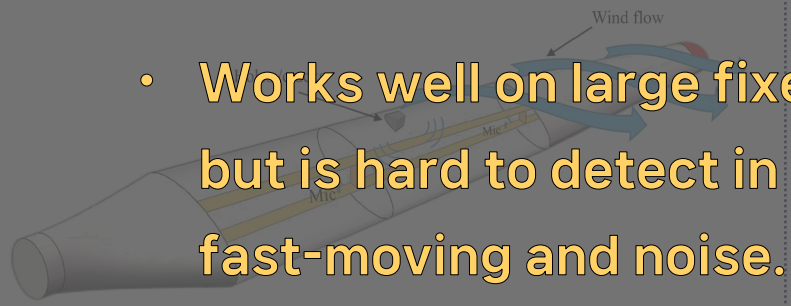

- Works well on large fixed structures, but is hard to detect in environments with fast-moving and noise.

⑤ Vibration

[8]



A **customized structural health monitoring** technology is needed for tail rotor blades.
→ Self-sensing technology is well-suited for this purpose.

[9] Todoroki, A. et al., 69(11-12), *CSTE*, (2009), 1841-1846

- **The Principle of Self-Sensing**

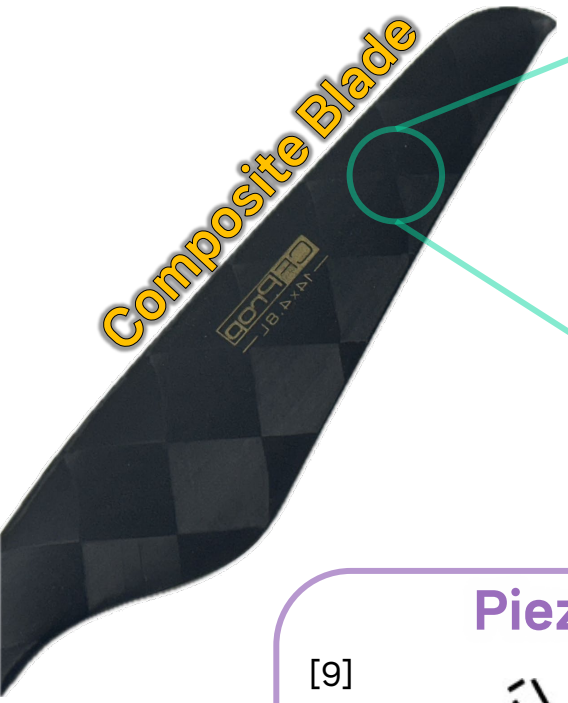

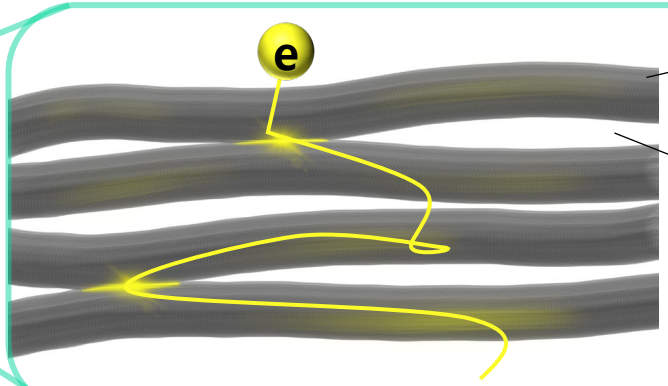

Carbon Fiber
(Conductive)
+
Resin
(Non-conductive)
=
Conductive Path

Strain Applied

Damage Occurred

Electrical Resistance Changes

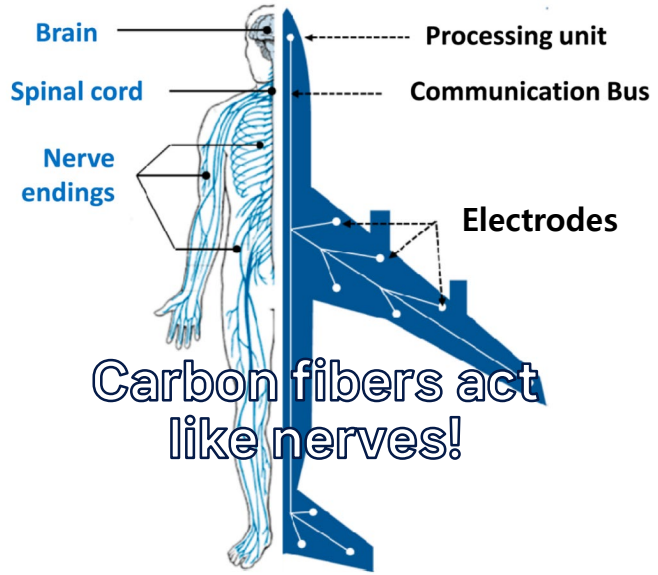

Carbon fibers act like nerves!

Piezoresistivity

[9]



< Fiber-contact separation model >

Change in the electrical resistivity of a material when mechanical strain is applied.

+

Electrical detour

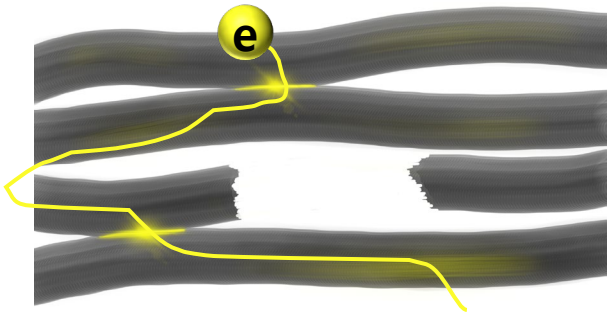

Current bypasses the damaged area, creating alternative conductive paths.

=

Advantages

- Real-time
- Intrinsic
- Wide-area coverage
- Cost-effective
- Geometry-independent

1. Introduction

[10] Oh, S.Y. et al., 281, *Int. J. Mech. Sci.*, (2024), 109511
[11] Yang, G. et al., 204, *Compos. B:*,, (2021), 108494
[12] Lee, I.Y. et al., 223, *Mater. Des.*, (2022), 111143
[13] Lee, I.Y. et al., 224, *Polym. Test.*, (2024), 111348
[14] Lee, I.Y. et al., 279, *Compos. Struct.*, (2022), 114650

- **Current Status of Self-Sensing Research**

Structural Health Monitoring

< Damage type >

[10]

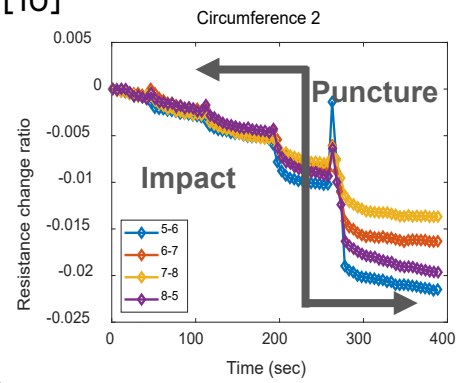

< Severity >

[11]

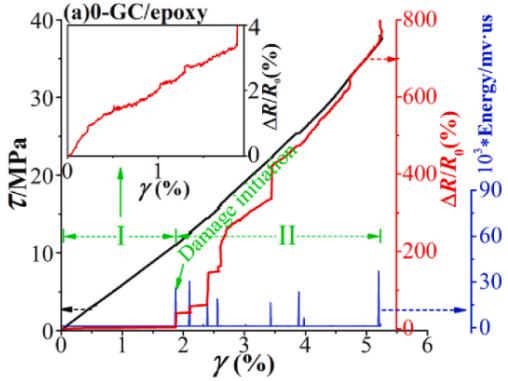

< Localization>

[12]

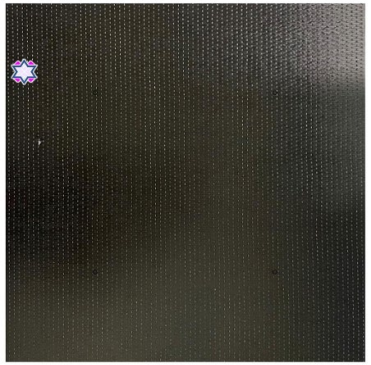

Prognostics and Health Management

< Remaining useful life >

[13]

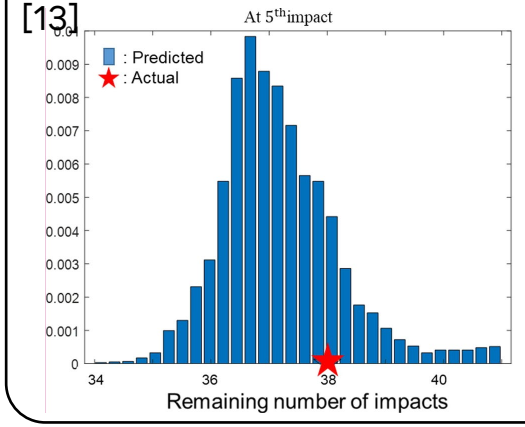

< Crack length >

[14]

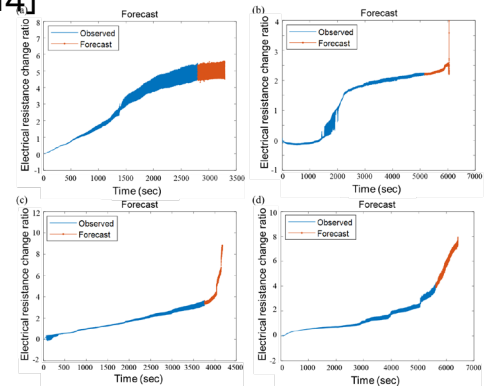

- **Current Research Gap & Research Idea**

Although CFRP is widely used in rotating structures, self-sensing has not yet been applied to rotating components.

By leveraging self-sensing signals that capture strain variations induced by rotation, this approach can be extended to real-time monitoring of rotating components.

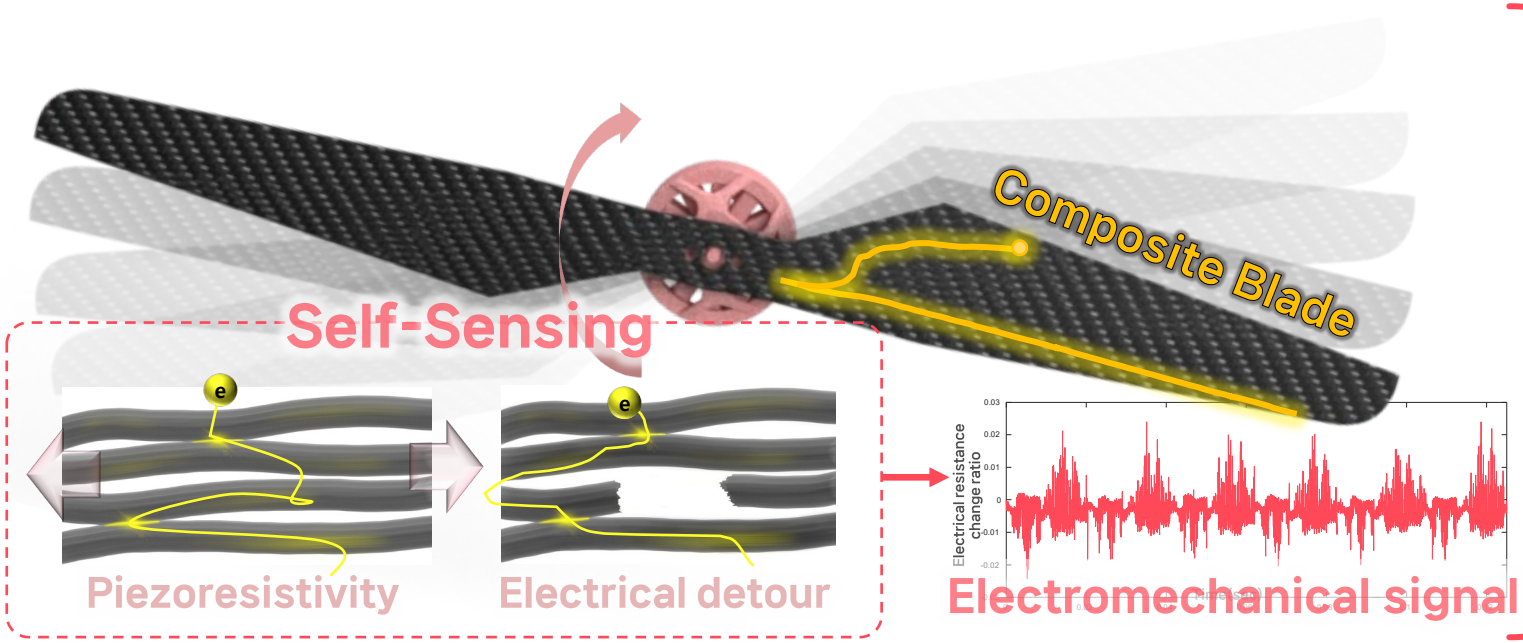

Damage Characterization

- Damage Types
- Damage Severity
- Damage Location

Research objective

✓ Analysis of the electromechanical behavior signals of rotating tail rotor blades

✓ Development of a structural health algorithm using the analyzed signals

→ Real-time in-situ structural health monitoring of rotating rotor blades using electromechanical behavior data

- **Testbed**



✓ T-MOTOR NS14*4.8 Prop

- Length: 35.56 cm
- Weight : 10.5g
- Materials : CF(T800) + Epoxy + PMI foam
- Max RPM : 8900 RPM
- Storage Temp: -10 °C ~ 50 °C
- Clockwise specimen

✓ Electrodes

- Surface was sanded with a grinder.
- Wires were attached using silver paste to minimize contact resistance.
- Electrodes are fixed with epoxy adhesive.

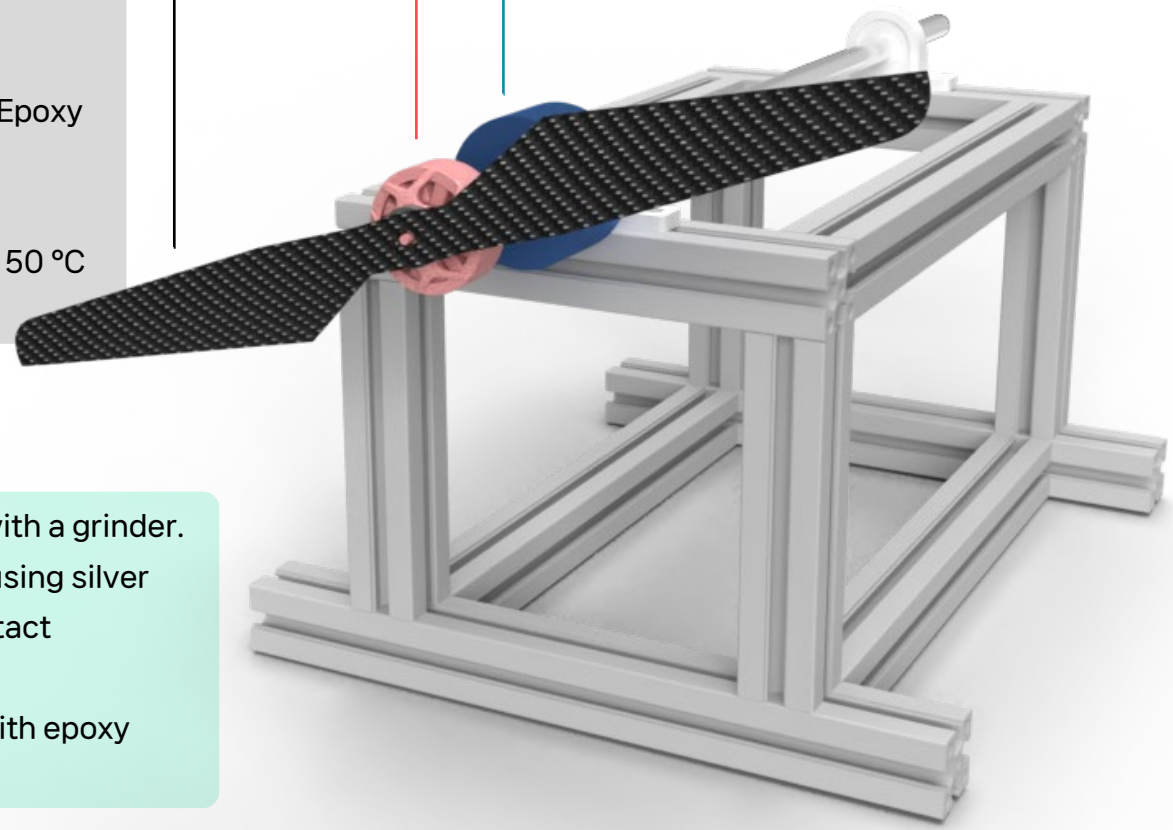

✓ SunnySky V3508 High Efficiency Brushless Motor

- Voltage: 22.2 V
- Max rotating speed: 8,436 RPM

✓ Covis CSH012-06-0506 Hollow Slip Rings 6ch

- No. of CH: 6CH
- Noise: < 0.01 Ω
- Rotating Speed: Max 600RPM
- Working Life: 60M cycles



✓ Digital Multimeter Keithley 7510

- 2 Probe measurement
- Buffer mode
- Sampling frequency: 15,220 Hz

- **Classification Pipeline**

Electrical Resistance ∝ Mechanical Strain

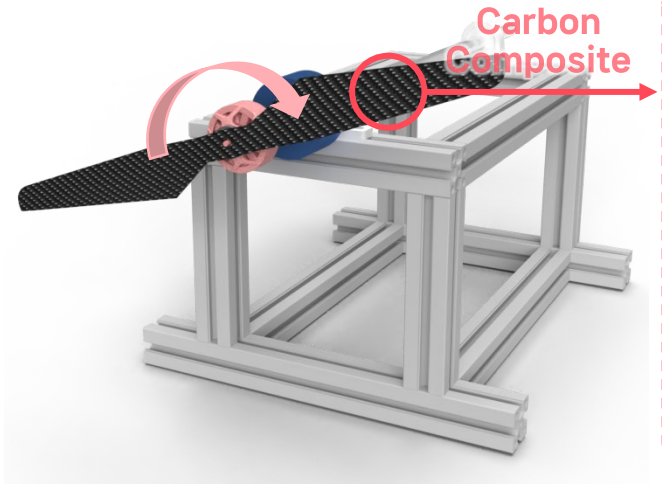

Self-sensing

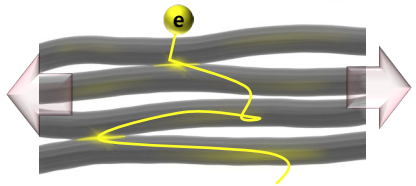

Piezoresistivity

: Change in the electrical resistivity of a material when mechanical strain is applied.

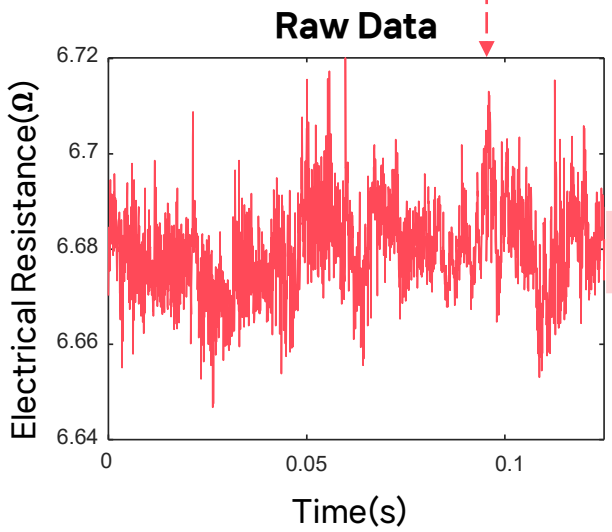

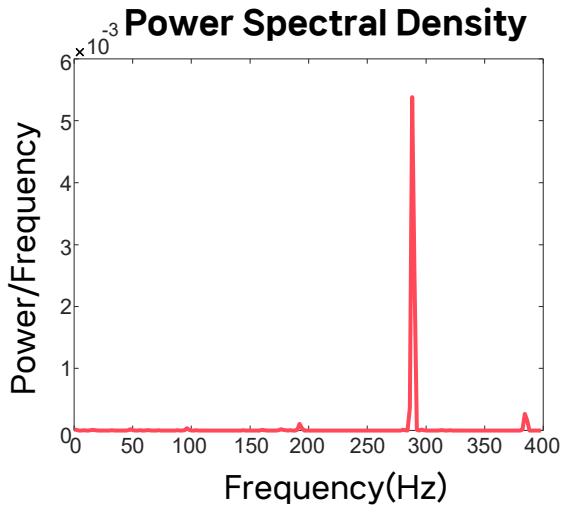

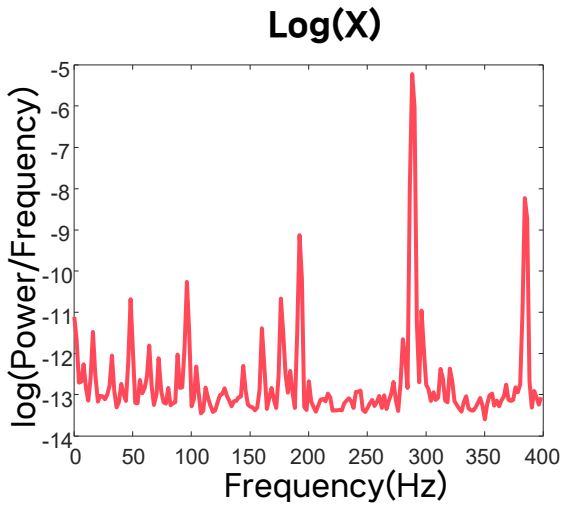

Input

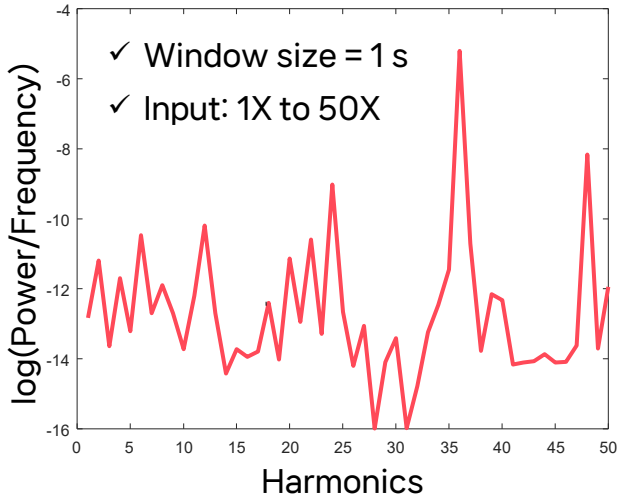

Random Forest

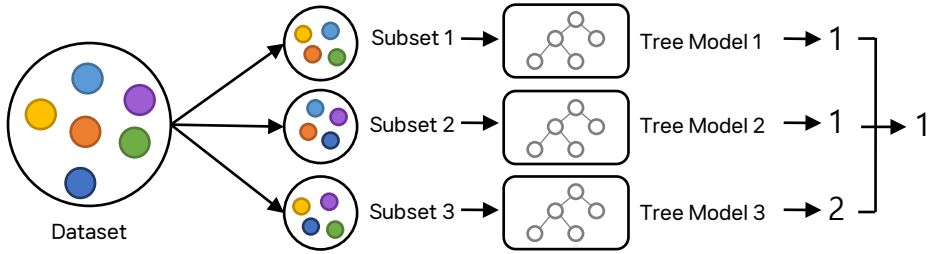

Utilizing **real-time in-situ data**
and **lightweight machine learning algorithms**
enables real-time in-situ structural health monitoring.

[15] Ogaili, A.A.F. et al., 49, *Data in Brief*, (2023), 109414
[9] Todoroki, A. et al., 69(11-12), *CSTE*, (2009), 1841-1846

- **Blade under Rotation**

Gravitational Force
Centrifugal Force
Coriolis Effect
...

Flapwise Bending

Edgewise Bending

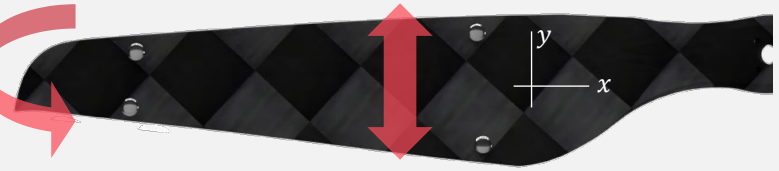

$\Delta\varepsilon_x$
$\Delta\varepsilon_y$
$\Delta\gamma_{xy}$

ΔR

Periodic Force → Periodic Mechanical Strain → Periodic Electrical Resistance

[15]

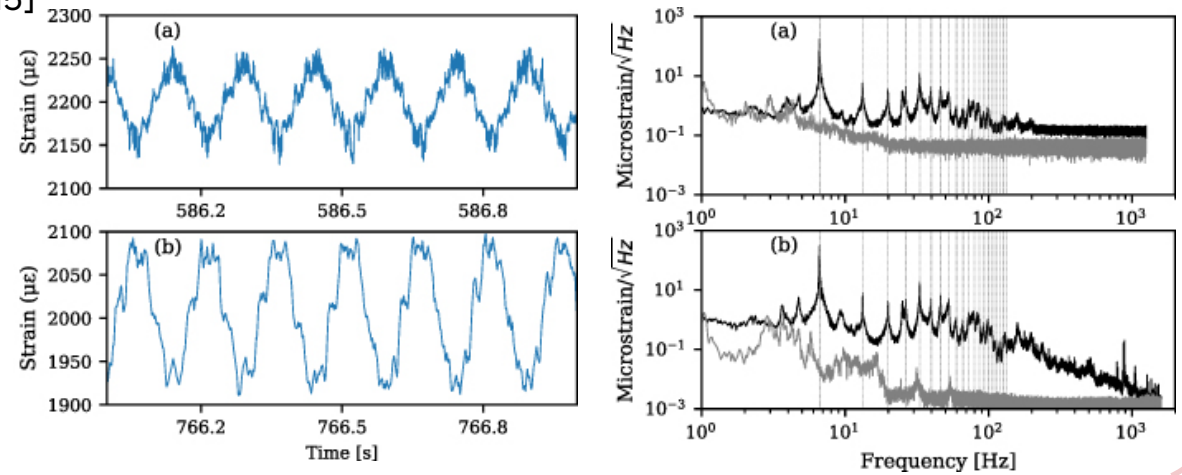

[9]

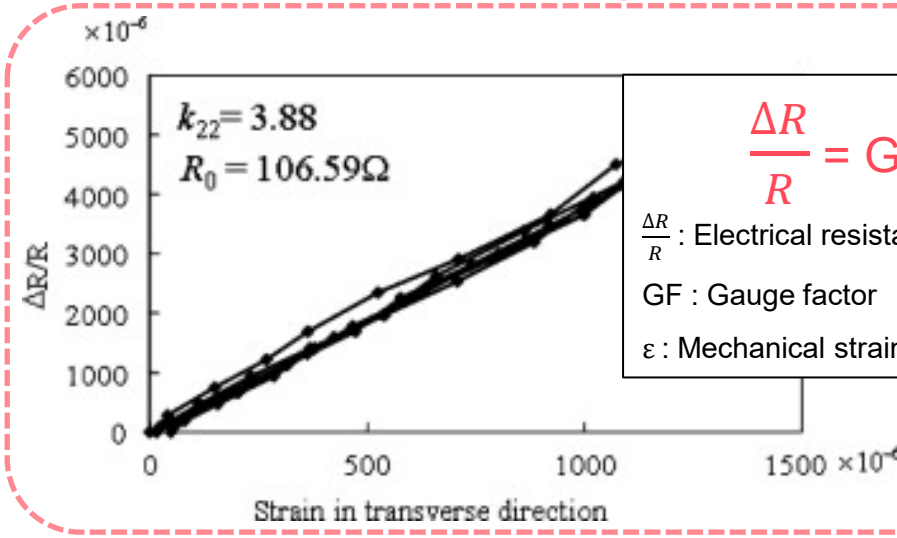

$$\frac{\Delta R}{R} = \mathrm{GF} \times \varepsilon$$

$\frac{\Delta R}{R}$: Electrical resistance change ratio

GF : Gauge factor

ε : Mechanical strain

- **Blade under Rotation**

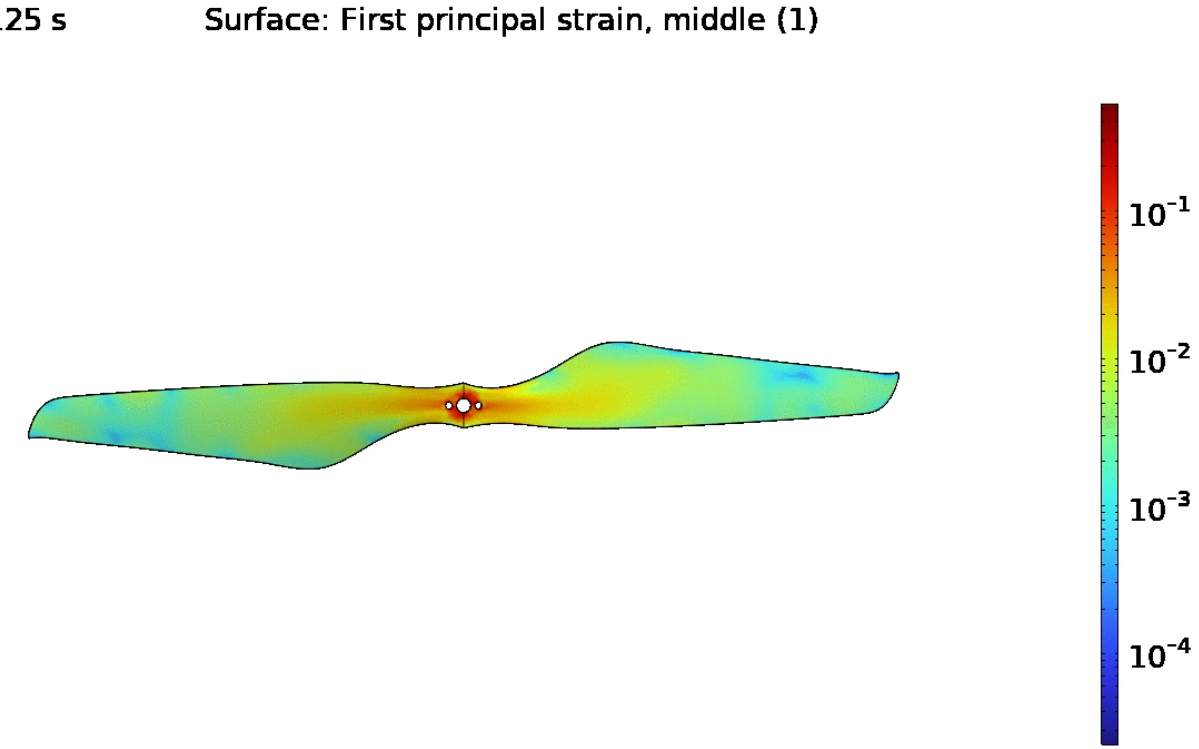

COMSOL Multiphysics
- Gravity
- Centrifugal Force
- Coriolis Effect

As the blade rotates, **gravity, centrifugal force**, and **Coriolis effect** cause strain values to differ at each position, leading to **periodic strain**.

→ **Rotational frequency-based analysis** enables evaluation of the structural state.

- **Damage Classification**

Step 1

Damage Types

Tip Fracture (T)

Crack (C)

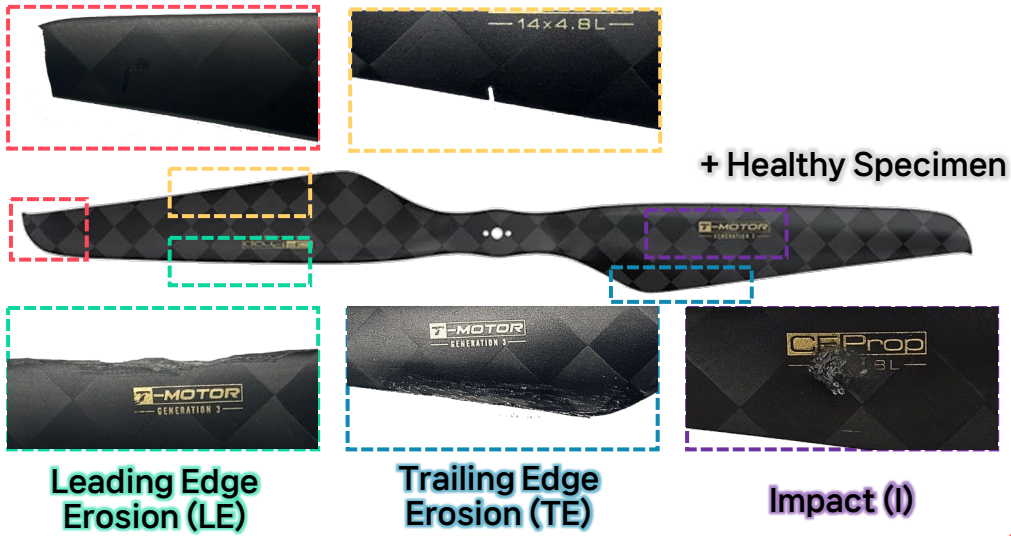

Step 2

Damage Severities

Erosion



Damage Locations

Crack

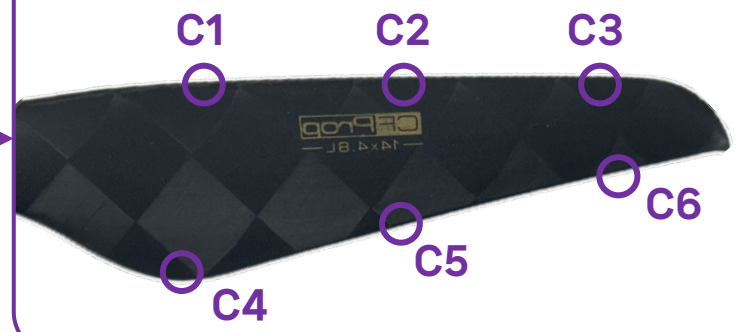

- Six damage types were first classified, followed by additional classification of severity for erosion and location for cracks.

- **Step 1. Damage Type Classification**

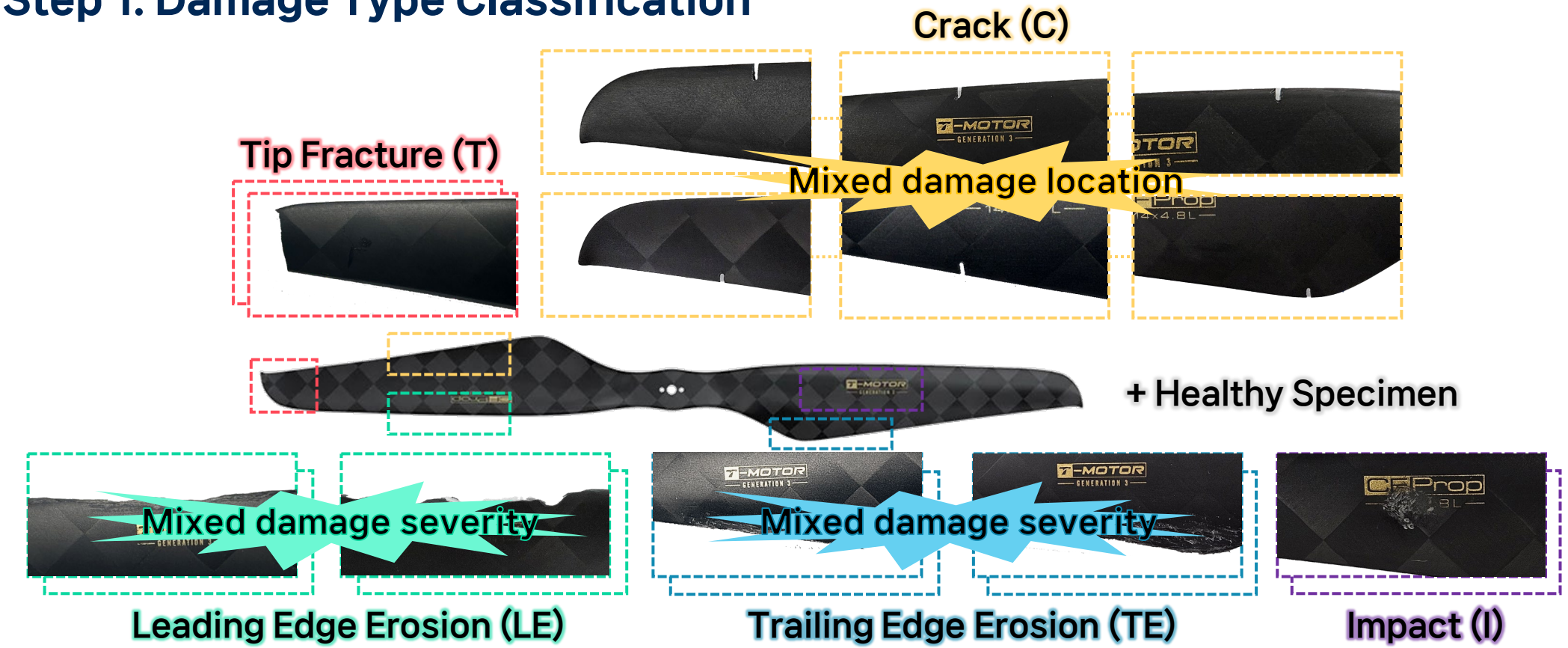

- 20 specimens with varying damage location and severity were used.

→ To extract robust damage-type information, independent of position or severity.

3. Results _ Electromechanical behavior

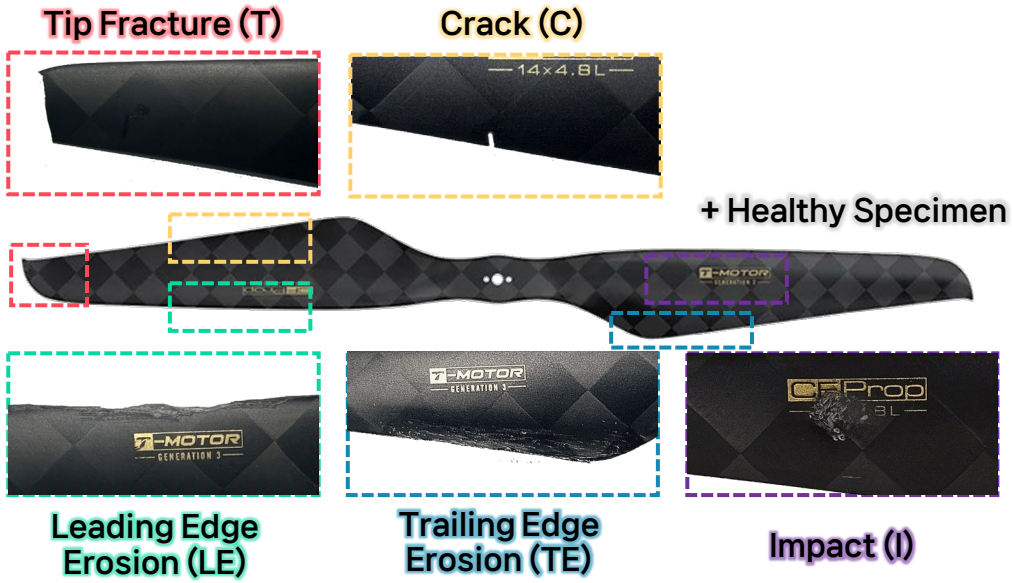

- The signal exhibits **periodicity** due to the applied periodic strain.
- If damage exists in any part, **changes in flow patterns** and **mass imbalance** cause variations in strain, which are reflected in the electrical resistance.
- **Higher-order components** arise due to structural nonlinearity, with variations depending on the type of damage.

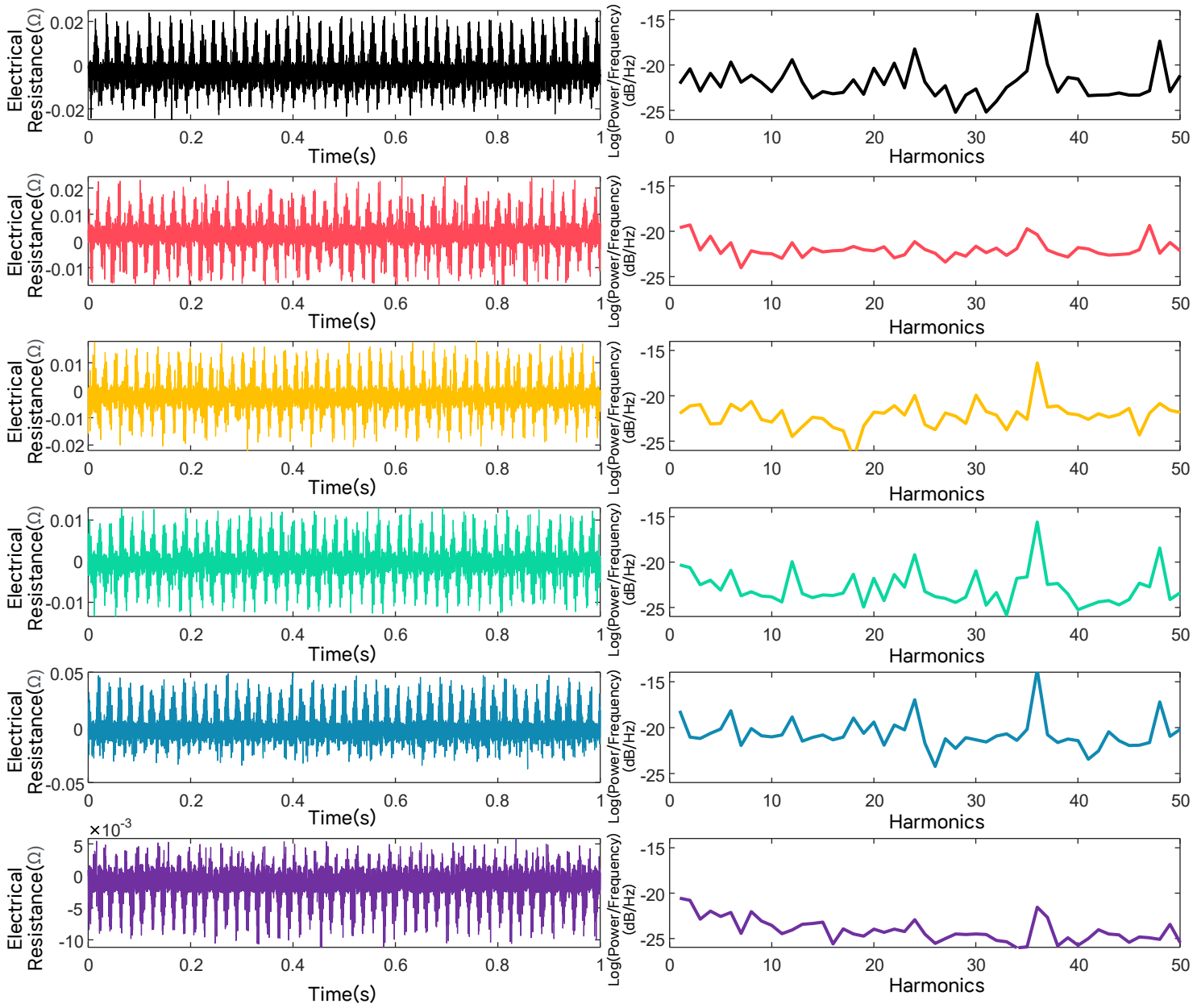

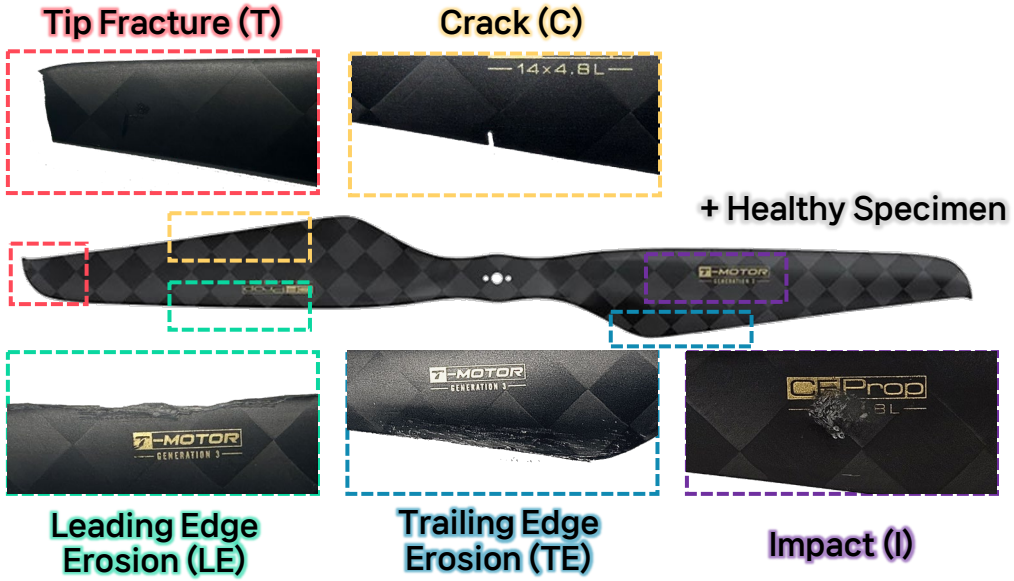

- Since the blades used in the experiment are **two-bladed**, the 2X harmonic is the most dominant in a healthy blade.
- When **damage occurs**, the proportion of the 1X harmonic increases due to imbalance.
- Each type of damage shows a distinct pattern in the magnitude and proportion of harmonics.

- **Stacked Bar Chart of Harmonics**

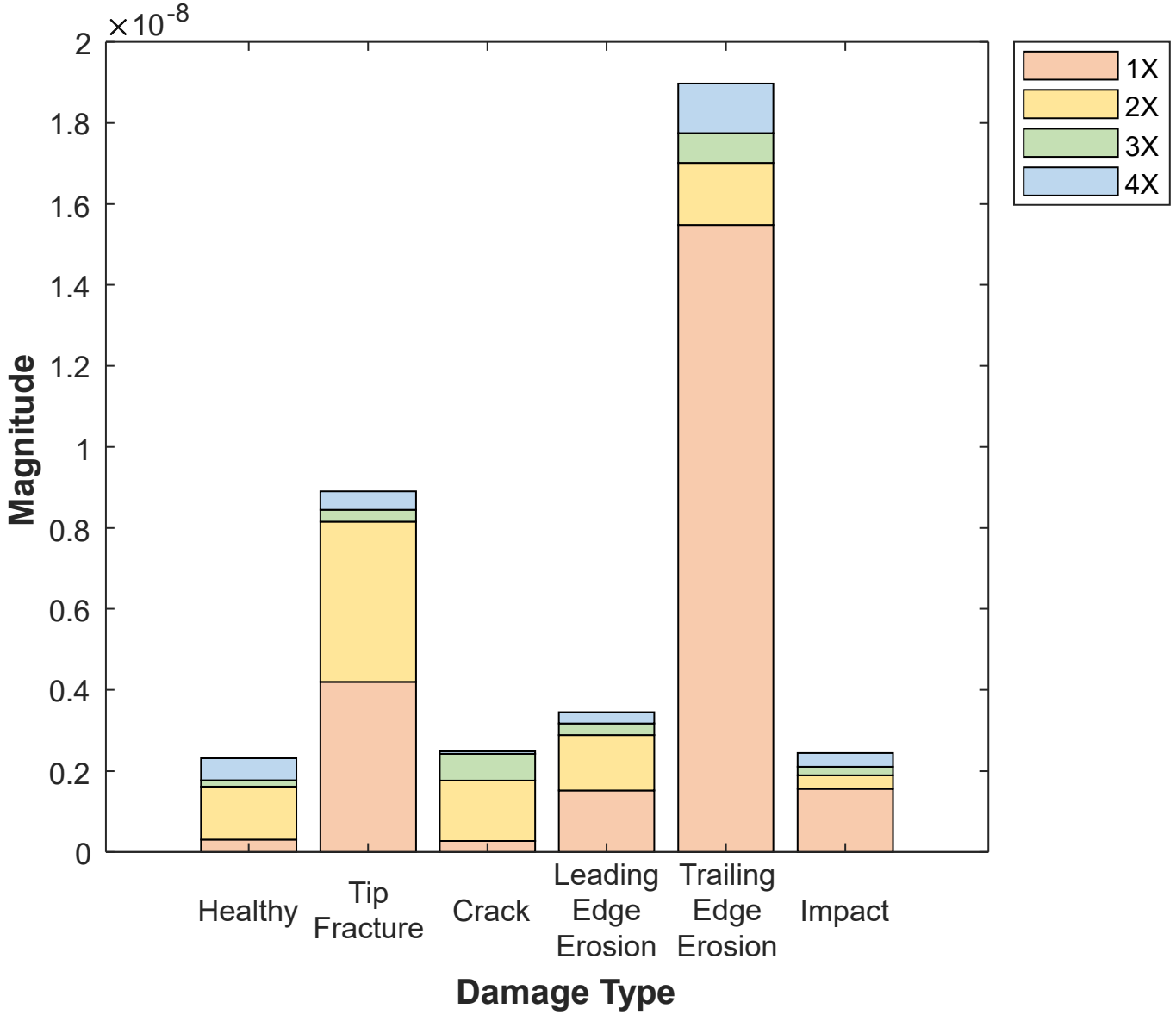

3. Results _ Classification Results

- **Step 1: Damage Type Classification**

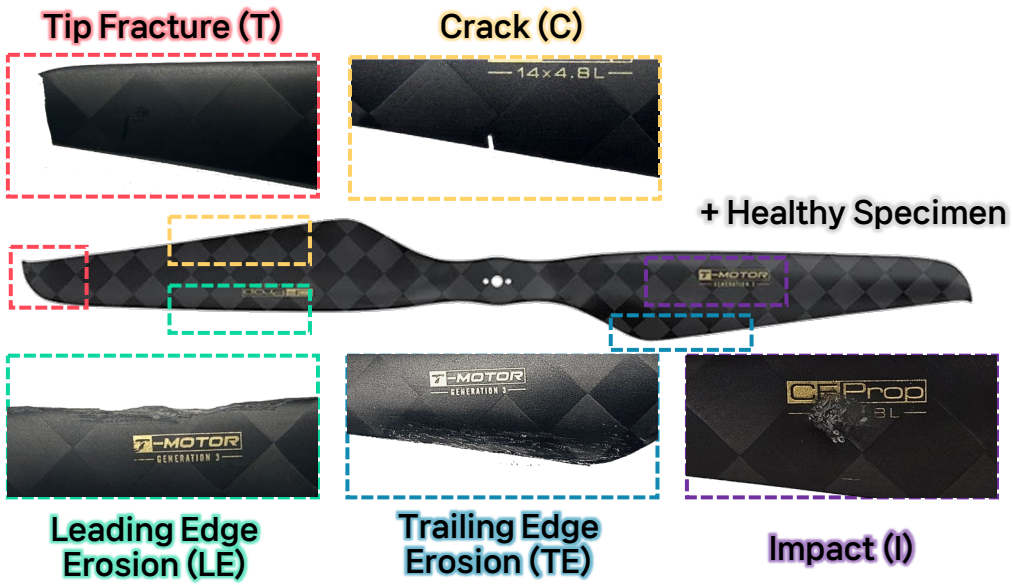

- For single RPM conditions, all damage types were classified with high accuracy.
- Even when multiple RPMs were mixed, the method maintained high accuracy, demonstrating the robustness of the signals.

< 240 RPM >

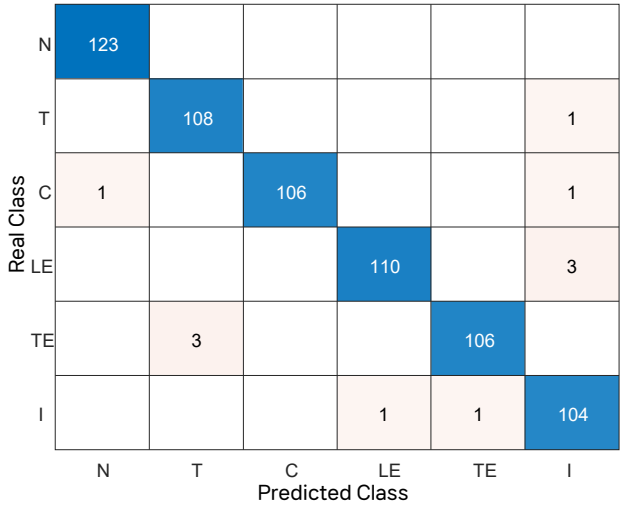

Accuracy: 98.353%

< 360 RPM >

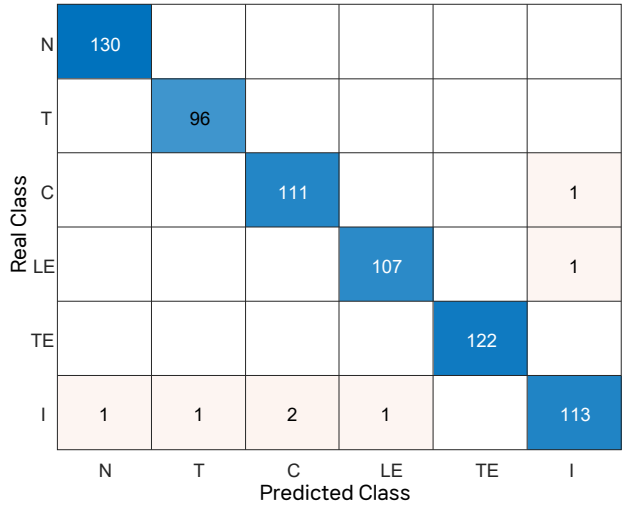

Accuracy: 98.980%

< 480 RPM >

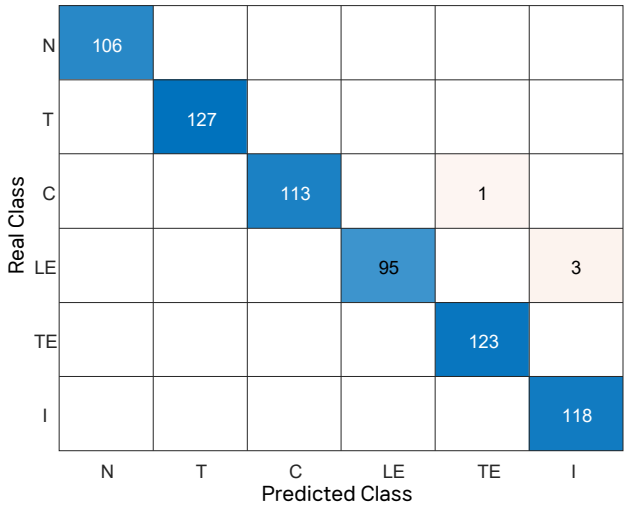

Accuracy : 99.417%

< RPM Mixed >

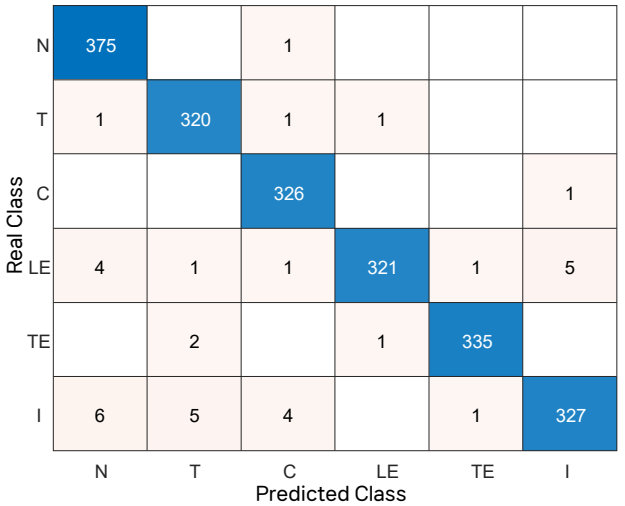

Accuracy : 98.235%

- **Step 2: Damage Severity Assessment**

	< 240 RPM >	< 360 RPM >	< 480 RPM >	< RPM Mixed >
Leading Edge Erosion (LE) Lv.1		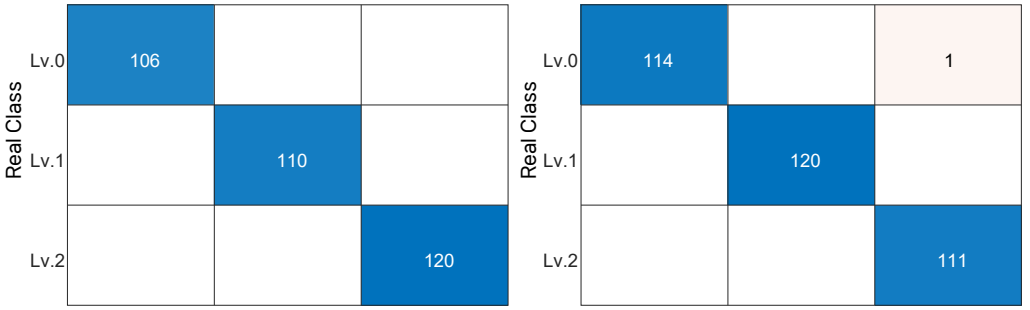	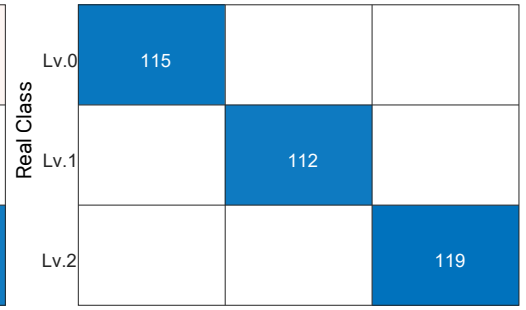	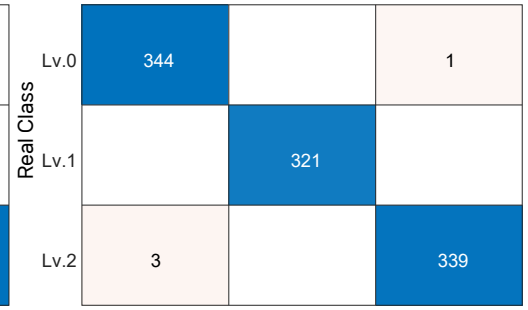
Lv.2		Accuracy: 100%	Accuracy: 99.711%	Accuracy : 100%	Accuracy : 99.603%
Trailing Edge Erosion (TE) Lv.1		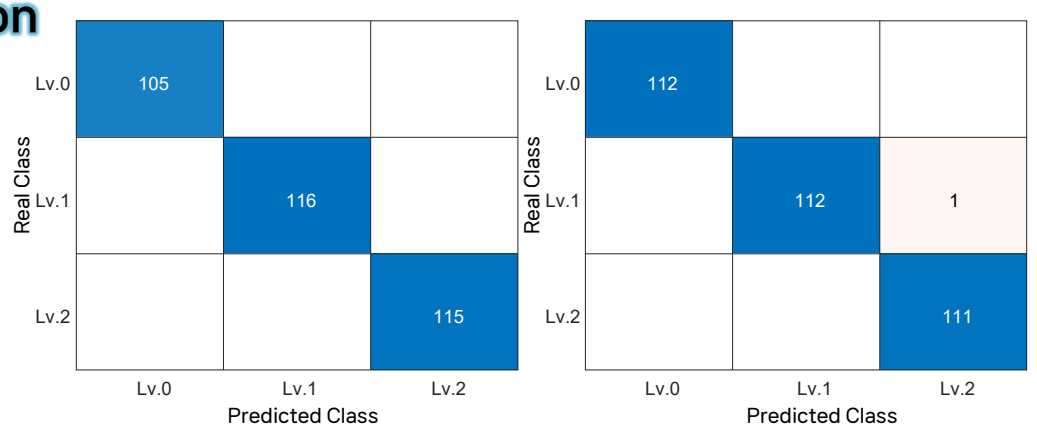	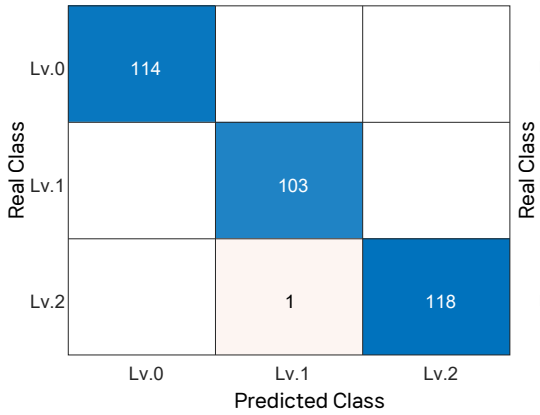	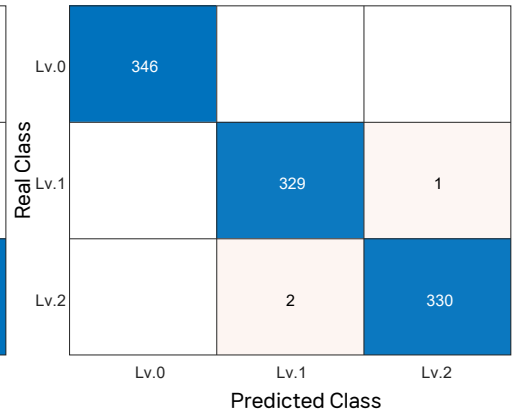
Lv.2		Accuracy: 100%	Accuracy: 99.702%	Accuracy : 99.702%	Accuracy : 99.702%

- **Step 2: Damage Localization**

Crack (C)

Leading Edge


Inner(LI)



Middle(LM)


Outer(LO)

Trailing Edge


Inner(TI)



Middle(TM)



Outer(TO)

- The high accuracy in both damage severity and localization further demonstrates the robustness of self-sensing technology.

< 240 RPM >

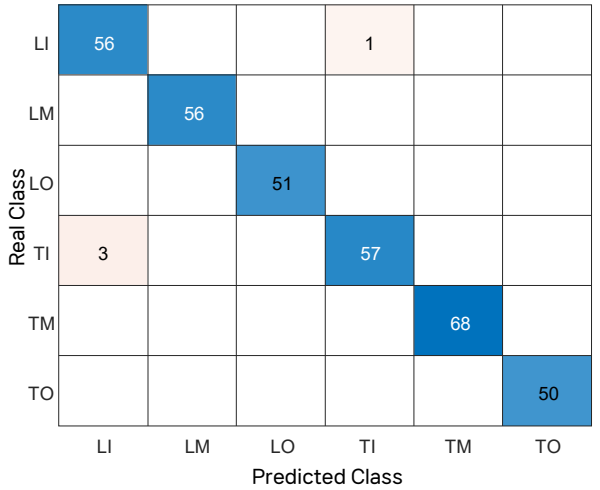

Accuracy: 98.83%

< 360 RPM >

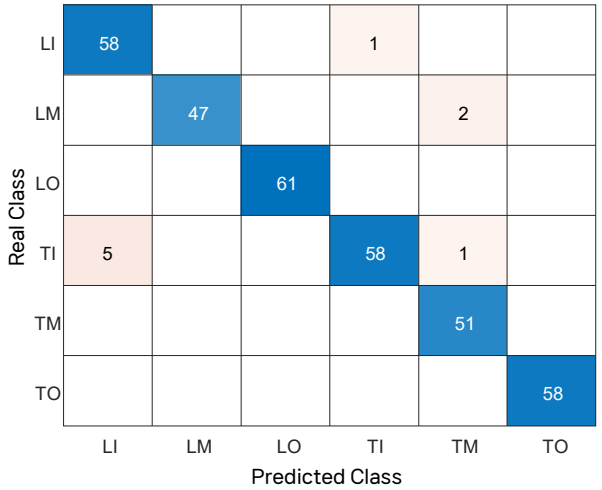

Accuracy: 97.368%

< 480 RPM >

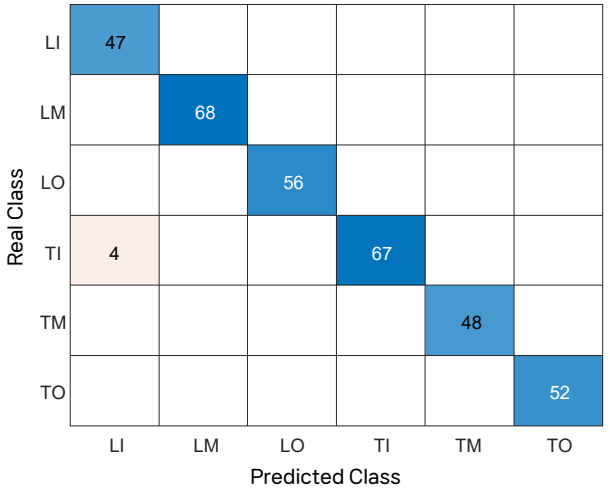

Accuracy : 98.830%

< RPM Mixed >

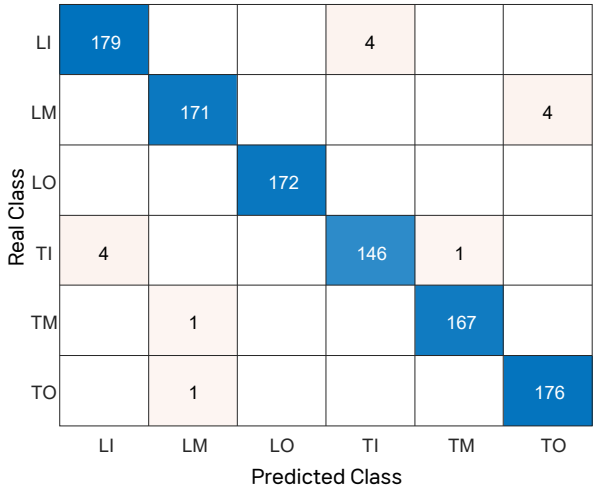

Accuracy : 98.538%

- **Importance**

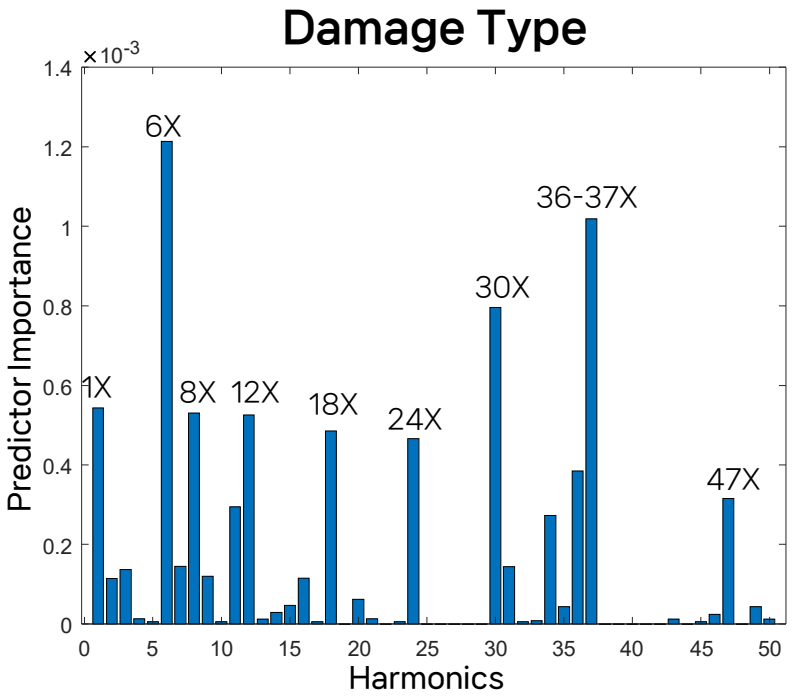

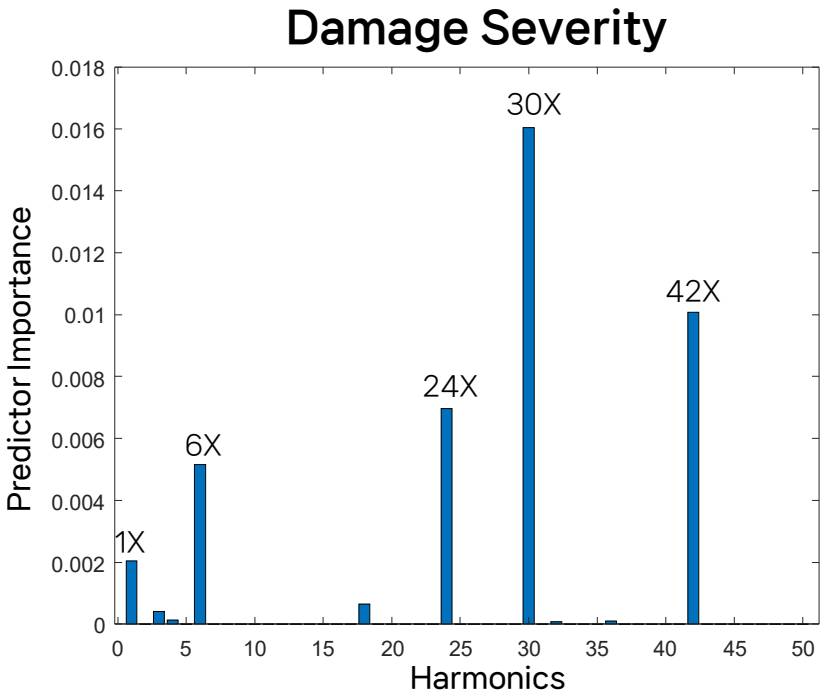

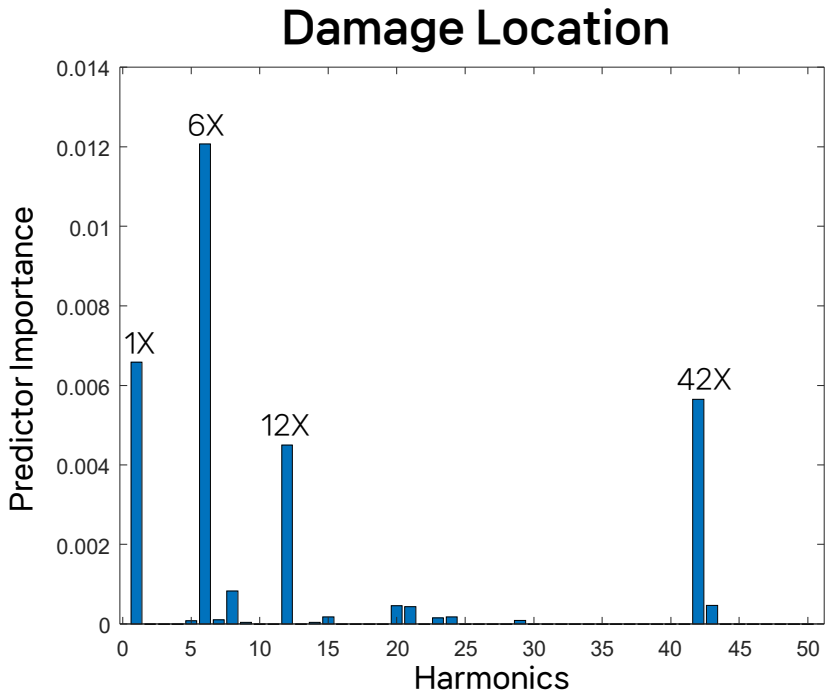

- Harmonics at multiples of six are generally found to be the most significant.
- The harmonics considered important vary depending on the classification target.
- This reveals how each type of damage affects different harmonic components.

• Conclusions

- ✓ Real-time Monitoring: The self-sensing technology successfully enabled real-time structural health monitoring of rotating rotor blades by leveraging the piezoresistive properties of CFRPs.
- ✓ High Accuracy: The approach demonstrated high classification accuracy in identifying damage types, severity levels, and locations under various rotational conditions.
- ✓ Improved Safety and Efficiency: This method offers a significant improvement over traditional systems, enhancing flight safety and reducing maintenance costs through continuous real-time monitoring.

• Future Work

- ✓ Investigation of the correlation between higher-order harmonics based on rotational frequencies and damage signatures
- ✓ Quantitative damage assessment

FIMLab
Functional Intelligent Materials Lab

UNIST
ULSAN NATIONAL INSTITUTE OF SCIENCE AND TECHNOLOGY
2007

Thank You For Listening

Juhyeong Jang (*PhD Candidate*)

Functional Intelligent Materials Lab

Department of Mechanical Engineering

Ulsan National Institute of Science and Technology (UNIST)

jurong@unist.ac.kr

Advisor: Prof. Young-Bin Park

CV

LinkedIn

ICCM24
AUGUST 4-8, 2025
BALTIMORE CONVENTION CENTER
BALTIMORE, MARYLAND, USA

No Technical Paper Submission for:

Seyda Naz Alasahin

ICCM24
AUGUST 4-8, 2025
BALTIMORE CONVENTION CENTER
BALTIMORE, MARYLAND, USA

No Technical Paper Submission for:

Mohammad Tofayel Ahmed

ICCM24
AUGUST 4-8, 2025
BALTIMORE CONVENTION CENTER
BALTIMORE, MARYLAND, USA

No Technical Paper Submission for:

Yu Shi

University of Glasgow

ICCM24

24TH INTERNATIONAL CONFERENCE ON COMPOSITE MATERIALS

MATERIALS & MANUFACTURING RESEARCH GROUP

Electrical impedance tomography for self-sensing 3D printed cellular composites

Akash Deep, Andrew McBride, S. Kumar*

ICCM24, August 4-8, 2025

*Corresponding author



University of Glasgow

Outline

- Introduction
- Background and motivation
- Objectives of the work
- Algorithmic design of cellular structures
- EIT- computational exploration
- EIT- experimental results
- Conclusions and ongoing work

University of Glasgow

Cellular structures

[1] J U Surjadi et al., *Nat. Mater.*, 2025
[2] J. Schneider et al., *Adv. Eng. Mater.*, 2024
[3] J. Schneider et al., *Mater. Horiz.*, 2025

- Achieve unprecedented properties by carefully structuring the building blocks
- Tunable mechanical/thermal/electrical properties
- Easily manufactured using 3D printing

[2]

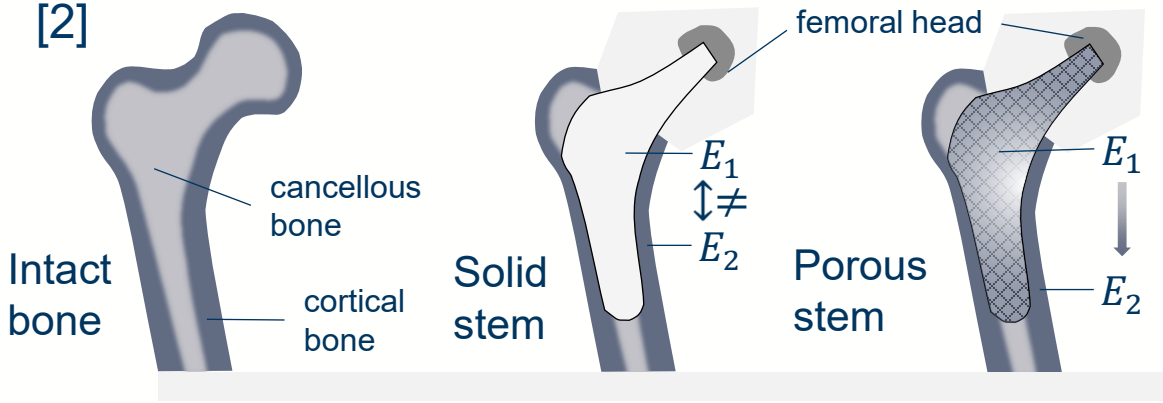

[1]

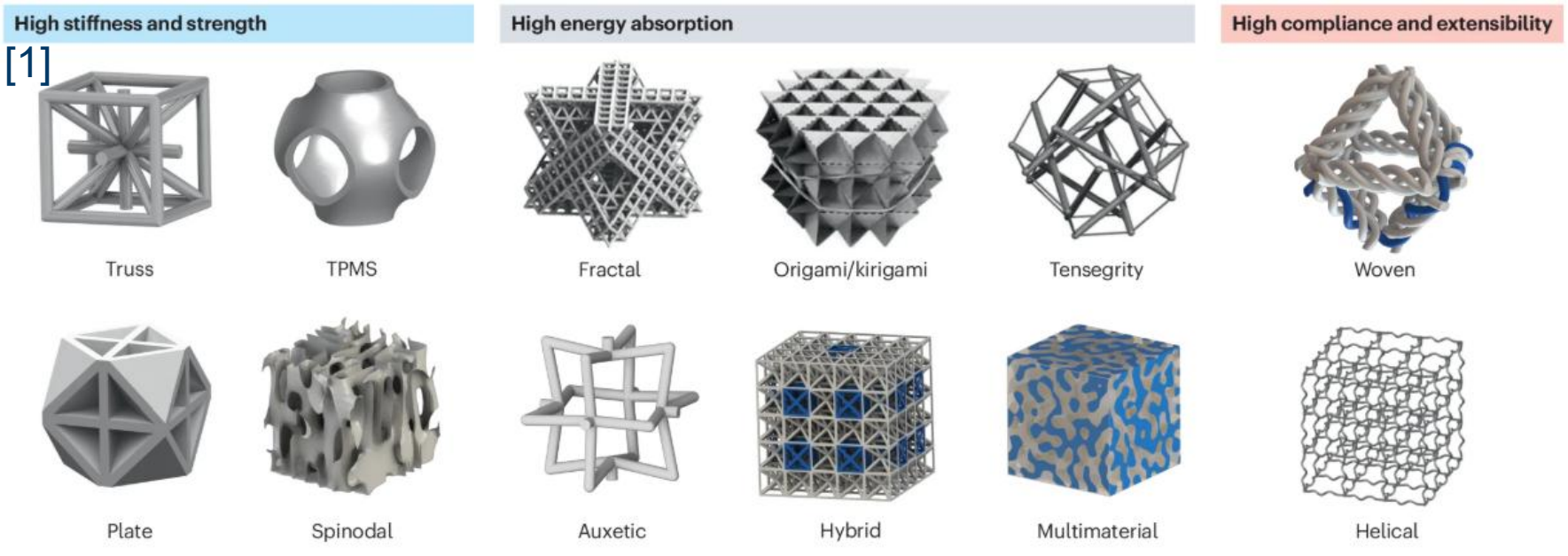

[3]

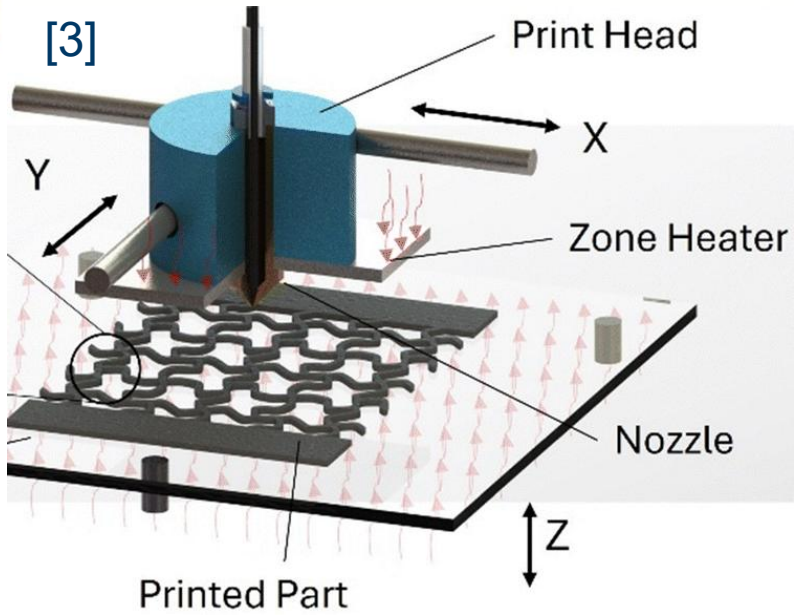

Self-sensing composites via piezoresistivity

- Polymers, when loaded with electrically conductive nanofillers like carbon nanotubes, unlock multifunctionality
- Material itself senses strain/damage via stimuli-responsive behaviour: Self-sensing

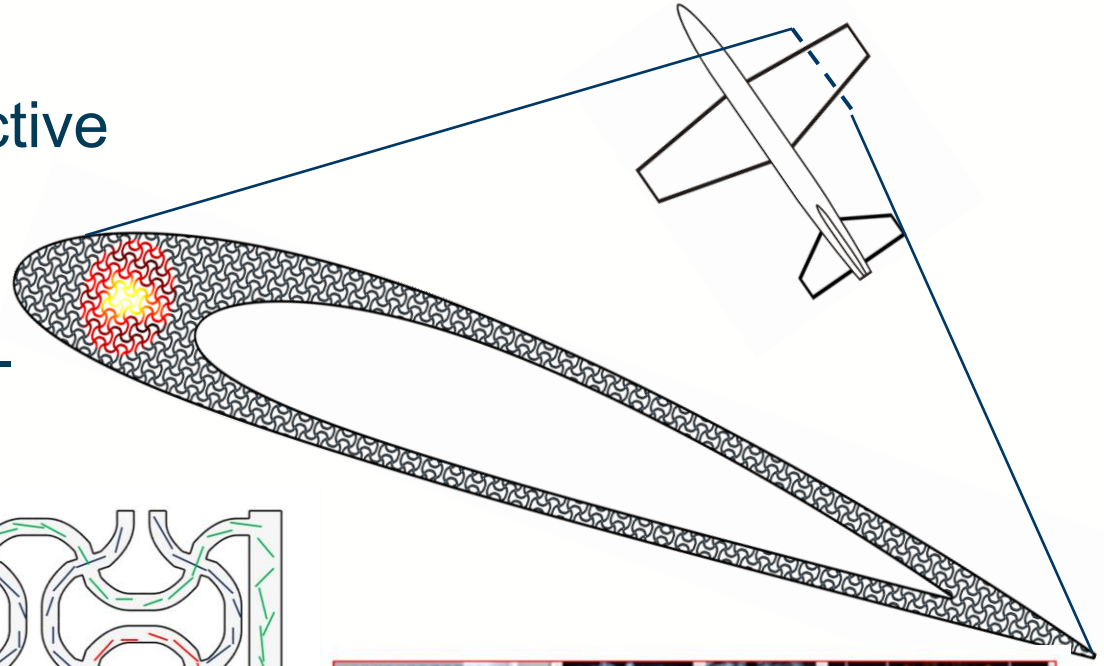

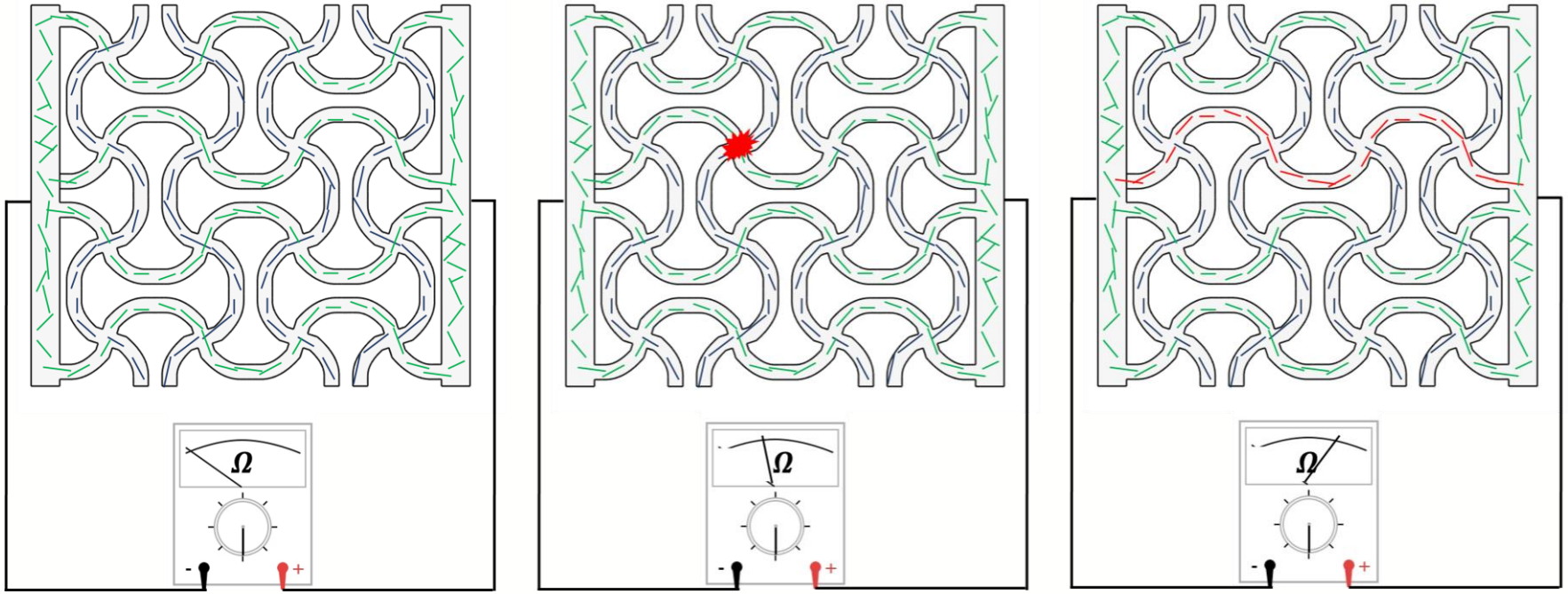



[4] P. Verma et al., *ACS Appl Mater Interfaces.*, 2022

Electrical Impedance Tomography (EIT)

- Reconstructs domain's conductivity map from boundary voltage measurements
- Inverse problem
- Models the physics of electric passage
- Soft-field tomographic method

[5]

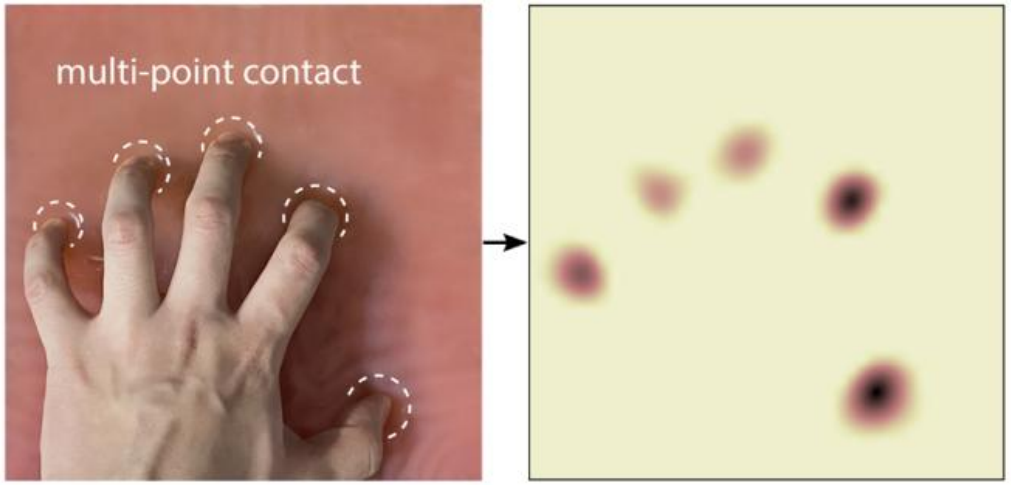

[5] K. Park et al, *Sci. Robot.*, 2022

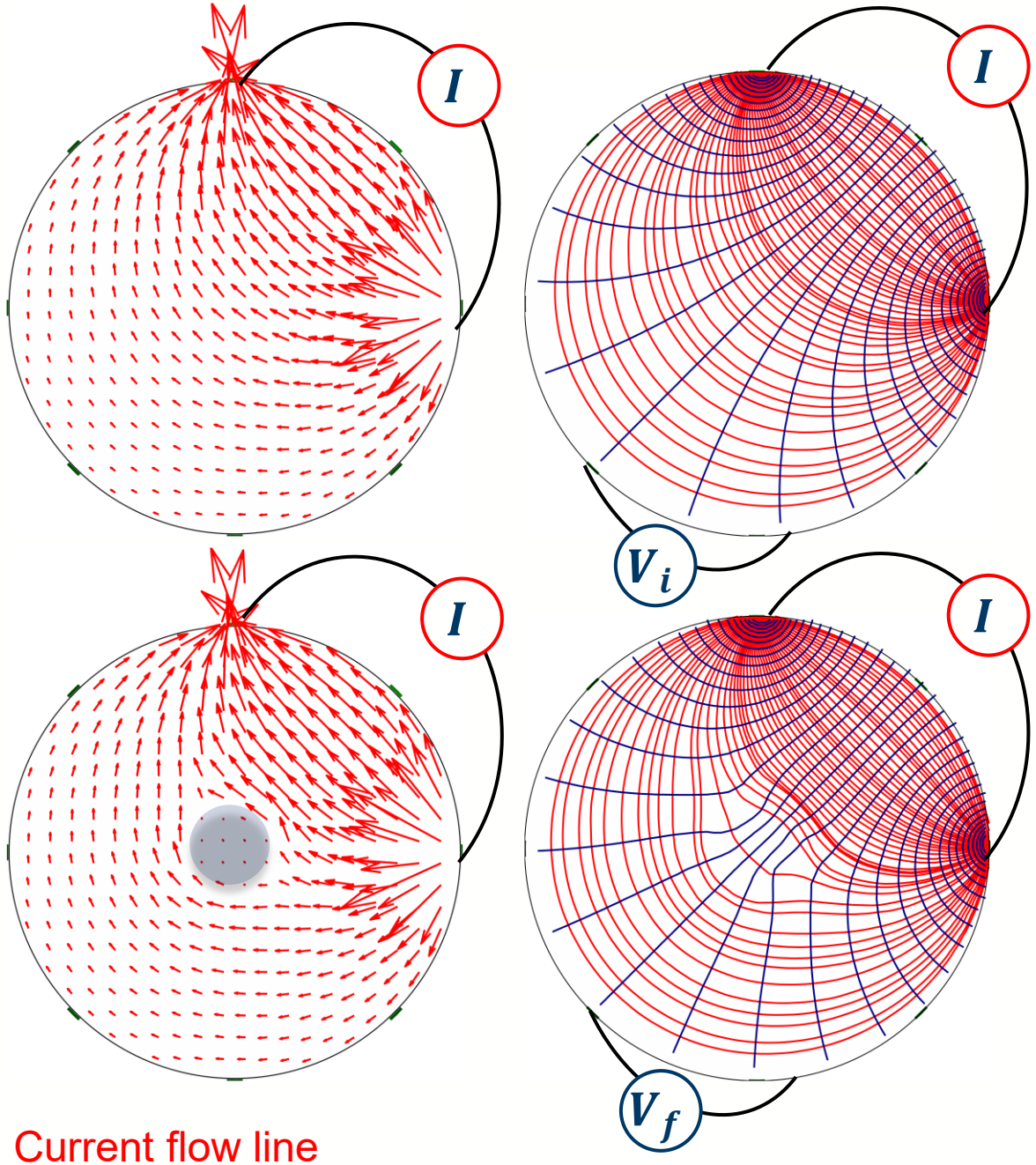

Red Line: Current flow line

Blue: Equipotential line of the resulting voltage

Objectives of the work

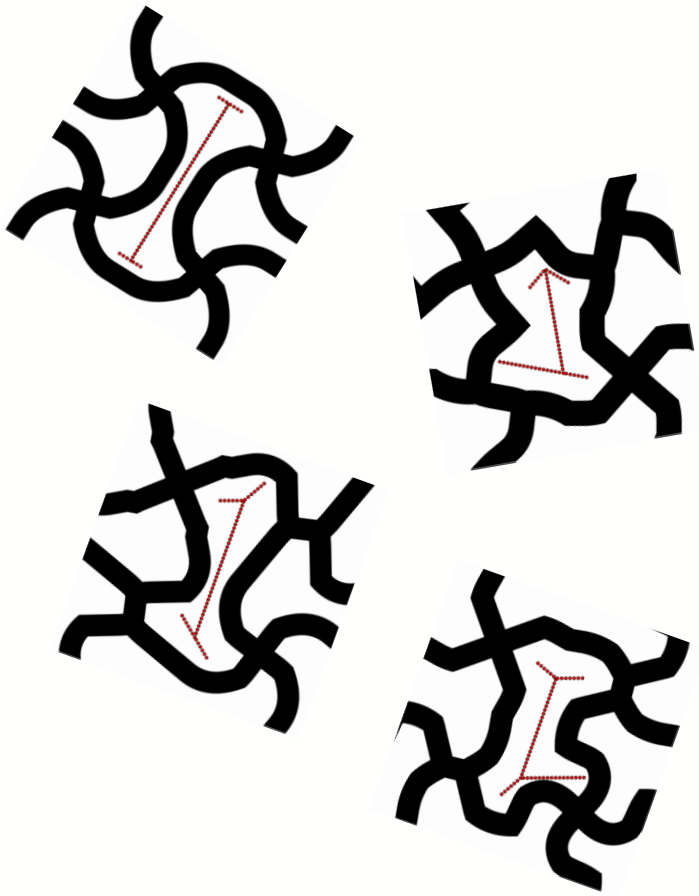

- Geometric modelling and 3D printing of cellular composites
- Improving the spatial resolution in EIT image reconstruction by programming the Jacobian via lattices
- Computational and experimental demonstration of EIT for damage detection and localisation in cellular composites

Algorithmic design of cellular structures

(a) $S = T \cup \bigcup_{k=1}^{4} B_k$



(b) $S_{i,j} = R_{\theta_{i,j}} + iT_x + jT_y$

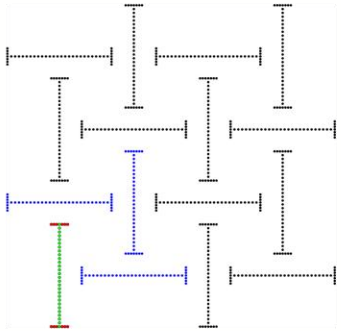

(c) $V(P) = \{ Q \in \mathbb{R}^2 \mid d(Q,P) \leq d(Q,P'), \forall P' \neq P \}$

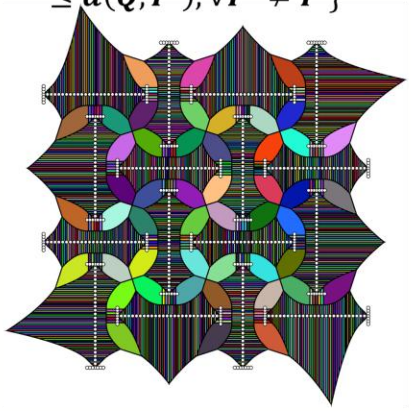

(d) $U(S_{i,j}) = \bigcup_{P \in S_{i,j}} V(P)$

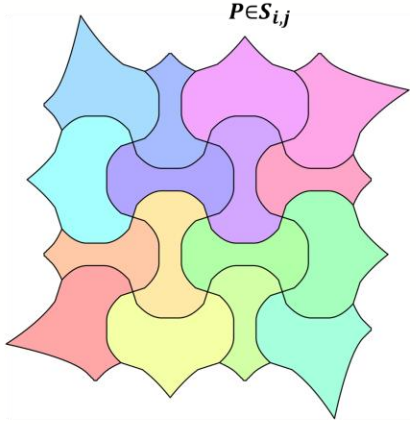

(e) $U_i' = C + \alpha(U_i - C)$

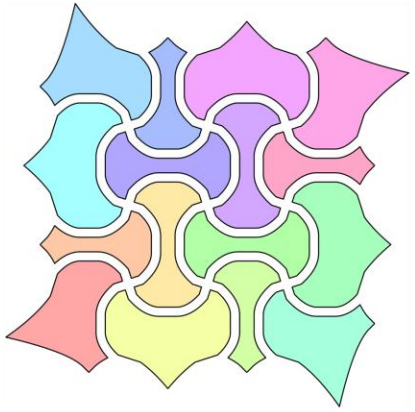

(f) $\Lambda = U_i' \setminus Q$

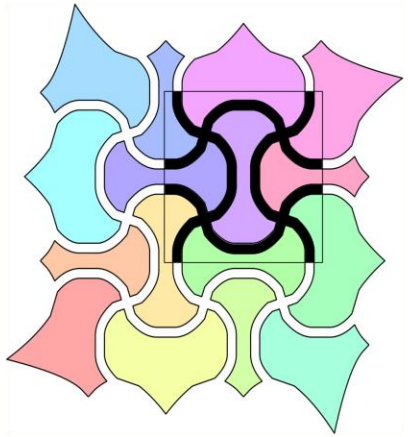

(g) $\mathcal{L} = \bigcup_{i,j} \Lambda + iL + jL$

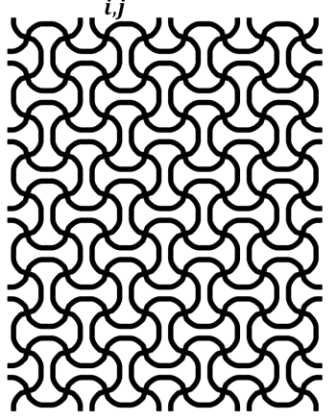

(h) $\mathcal{L}_3 = \{ (x,y,z) \mid (x,y) \in \mathcal{L}, 0 \leq z \leq h \}$

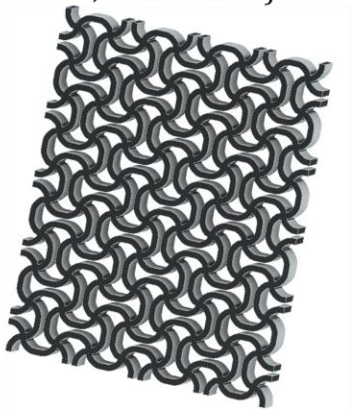

*J. Schneider et al., *Addit. Manuf.*, 2024

*J. Schneider et al., *Mater. Horiz.*, 2025



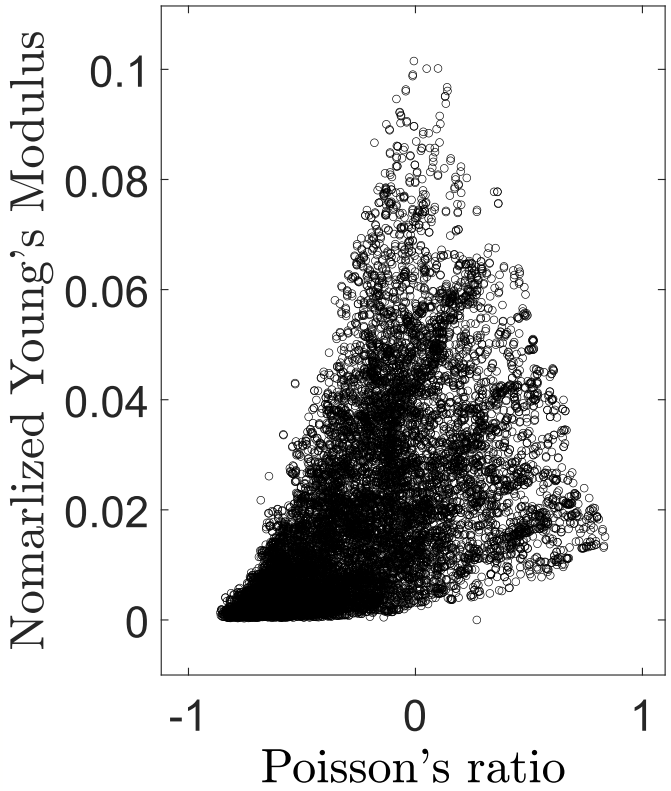

EIT- Experimental measurement schemes

- Domain lined up with electrodes
- Current injected b/w first elec pair; voltages measured between remaining pairs
- Current injection moved to next electrode pair, and voltages measured again

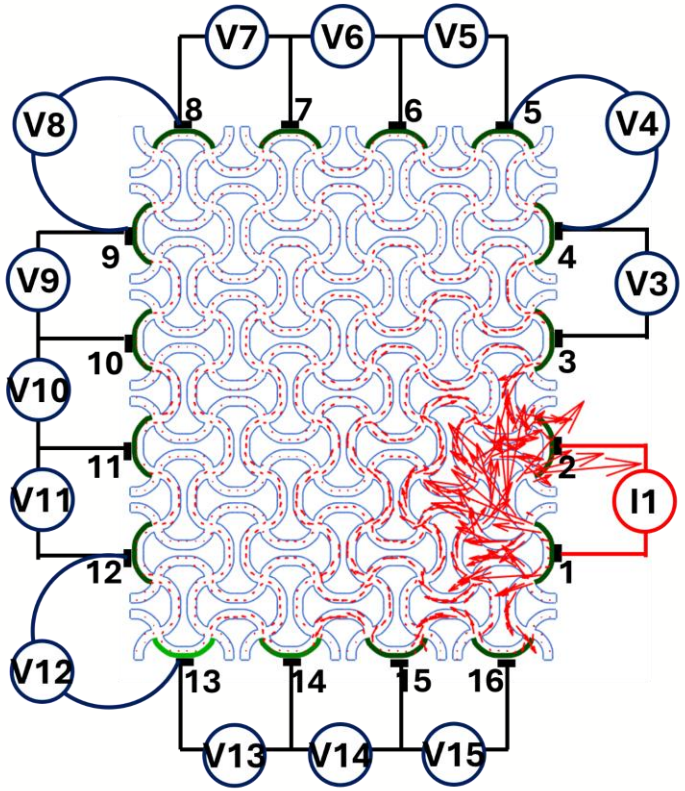

First injection

Second injection

Last injection

Forward and inverse problems in EIT

Forward Problem

- Domain conductivity ⟶ Boundary voltages (using FE)
- Simulates physics of steady-state electrical current flow

  Laplace's equation: $\nabla . \sigma \nabla \phi = 0$

  Apply complete electrode model boundary condition & charge conservation law

σ: Conductivity distribution

ϕ: Domain potential

- Jacobian, $J = \frac{\partial V}{\partial \sigma}$,

Inverse Problem

- Conductivity change: minimizes difference b/w predicted and measured boundary voltages
- Ill-poised as J is ill-conditioned
- Requires regularisation

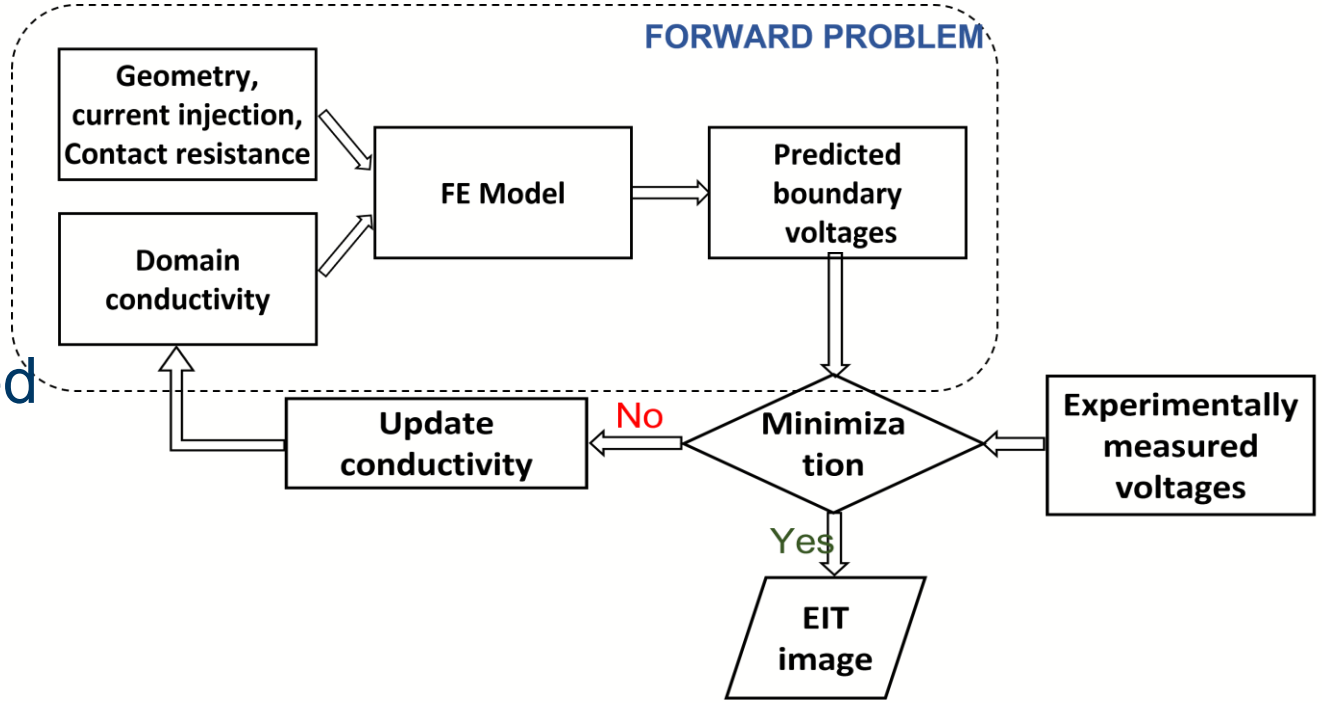

Programming Jacobian using Engineered lattice

- Existing approaches improving J include:

1. Increasing number of electrodes[6]
2. Optimising electrode placements and measurement schemes[7]

- Our approach:

Engineered lattice-based domains to improve J conditioning from within

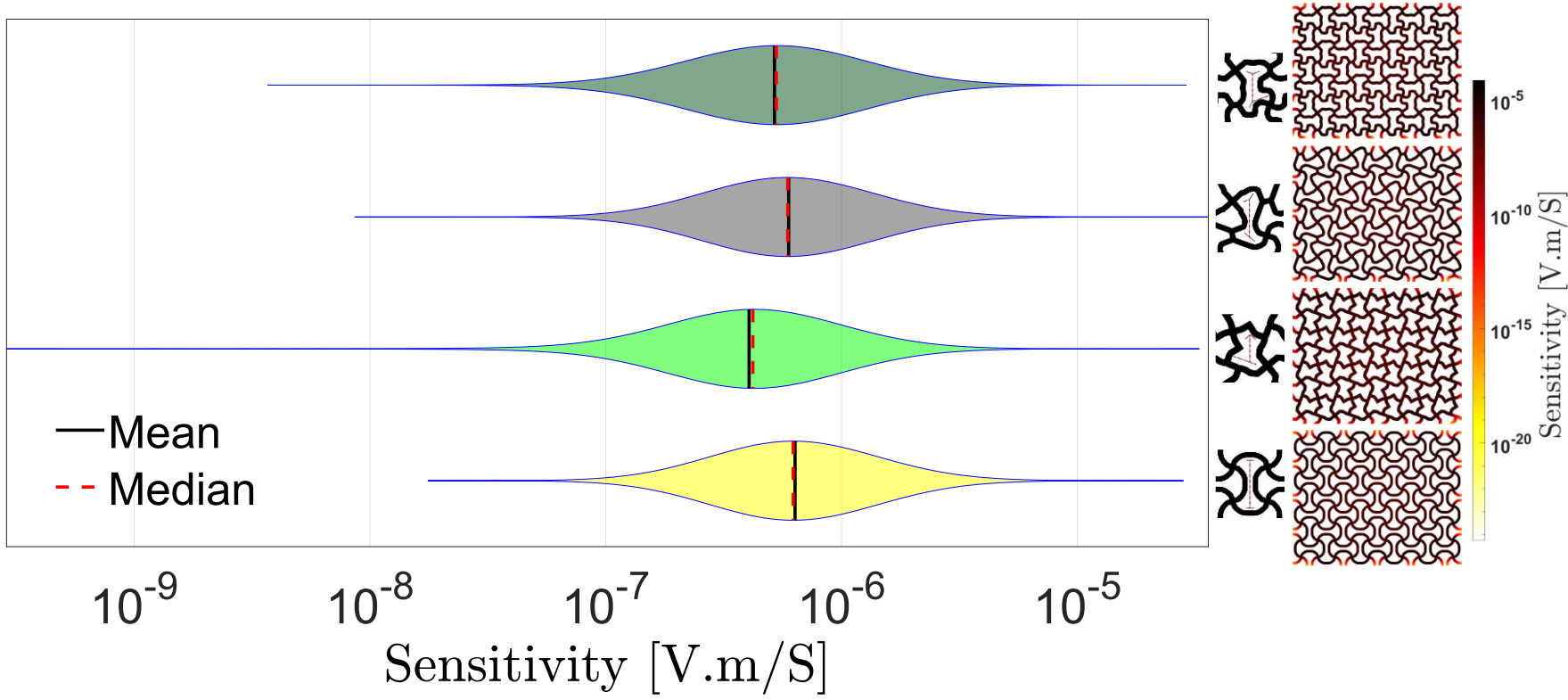

- Calculate Jacobian (J) for each lattice
- Sensitivity= $[\|j_1\|_2/N, \|j_2\|_2/N \ldots]$

where N =number of measurements

[6] M Tang et al., Physiol. Meas., 2002

[7] D Smyl et al., *IEEE Trans. Instrum. Meas., 2020*

Computational exploration

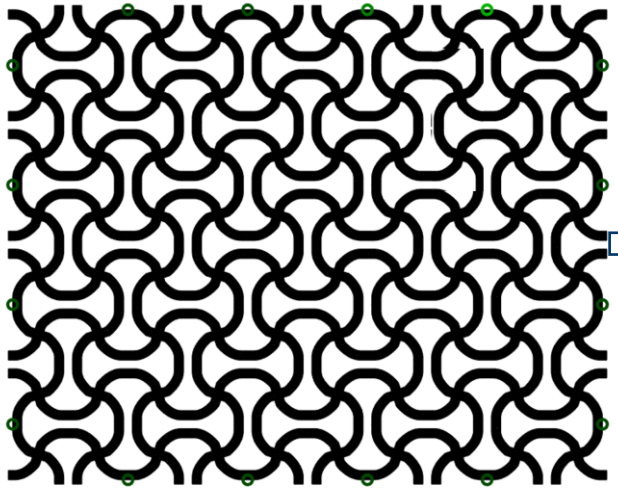

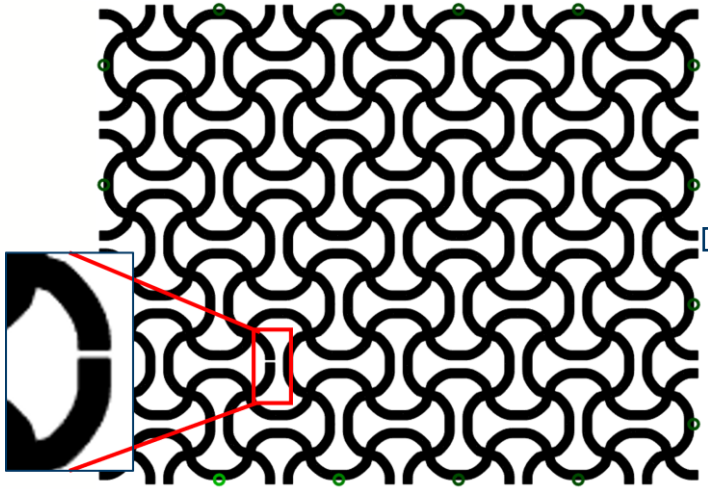

- Undamaged FE domain
- Computing V_i via forward model
- Adding noise to V_i

- Damaged FE domain
- Computing V_f via forward model
- Adding noise to V_f

$(\Delta V)_{Computaional}$

Solving Inverse problem

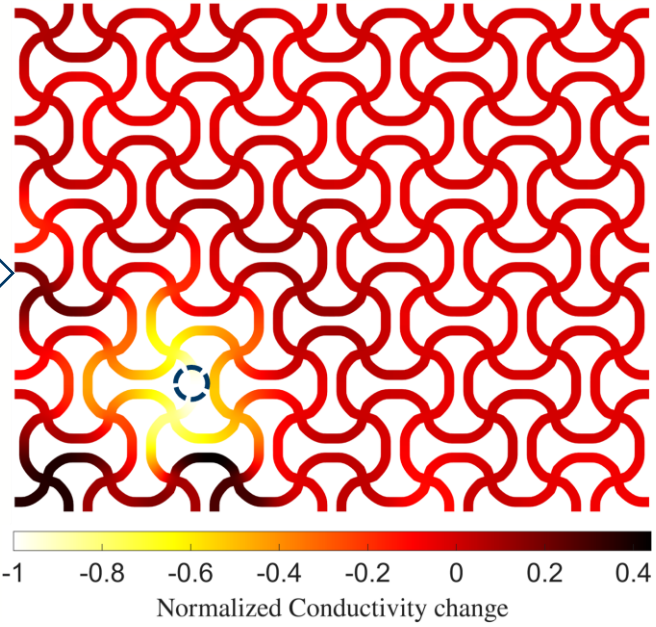

University of Glasgow

Experimental results

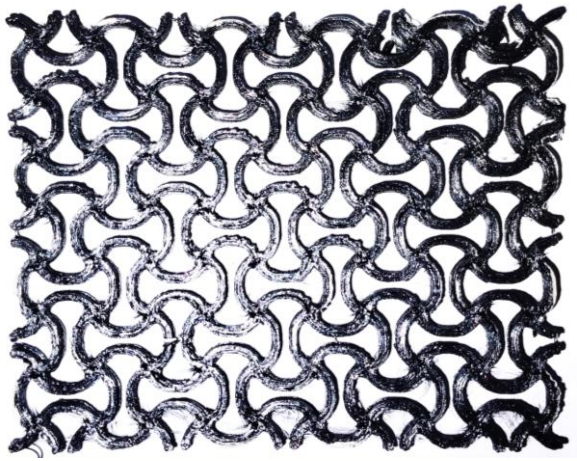

I

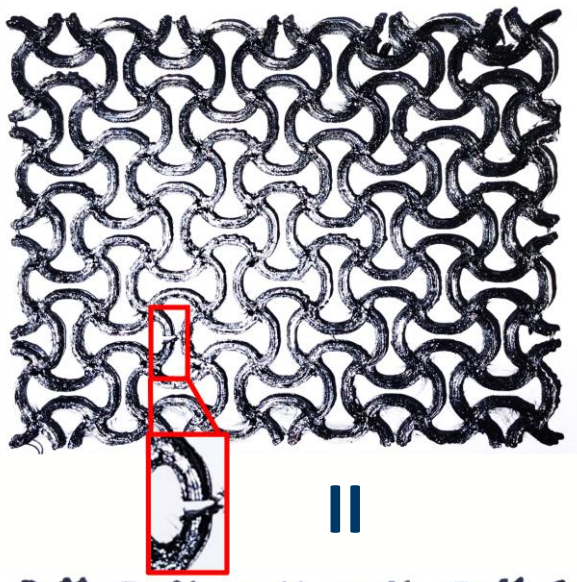

II

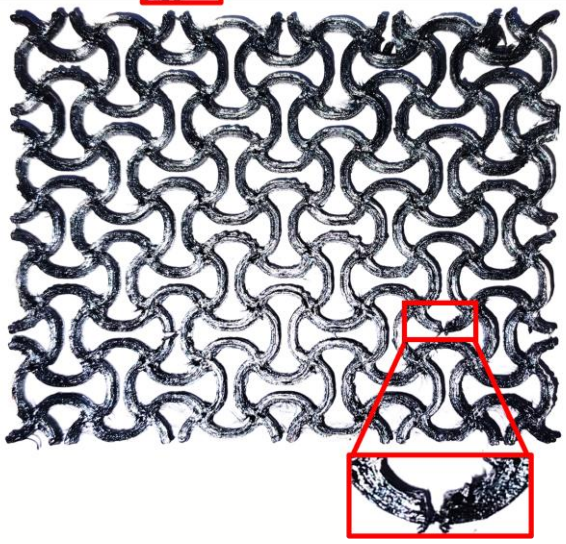

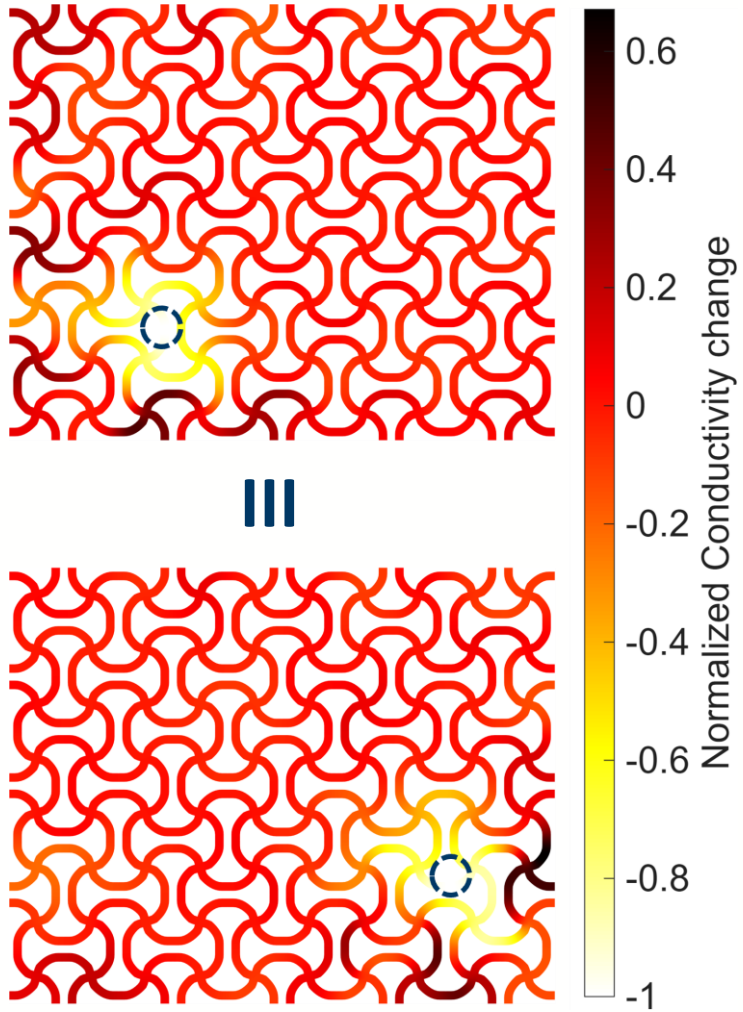

III

I: Intact PEEK/CNT cellular composite;

II: Damaged specimen at two distinct positions;

III: Corresponding EIT images

Conductivity loss overlaps with location of damage

Conclusions and ongoing work

- **Fabricated architected composite** lattice using nano-engineered PEEK-based filament via AM
- **Engineered lattice geometry** to improve conditioning of inverse problem- reducing null spaces & increasing distinguishability
- Conductivity maps show **precise detection and localisation of damage**
- Ongoing work involves ***in situ* EIT** applied to AM-based cellular composites

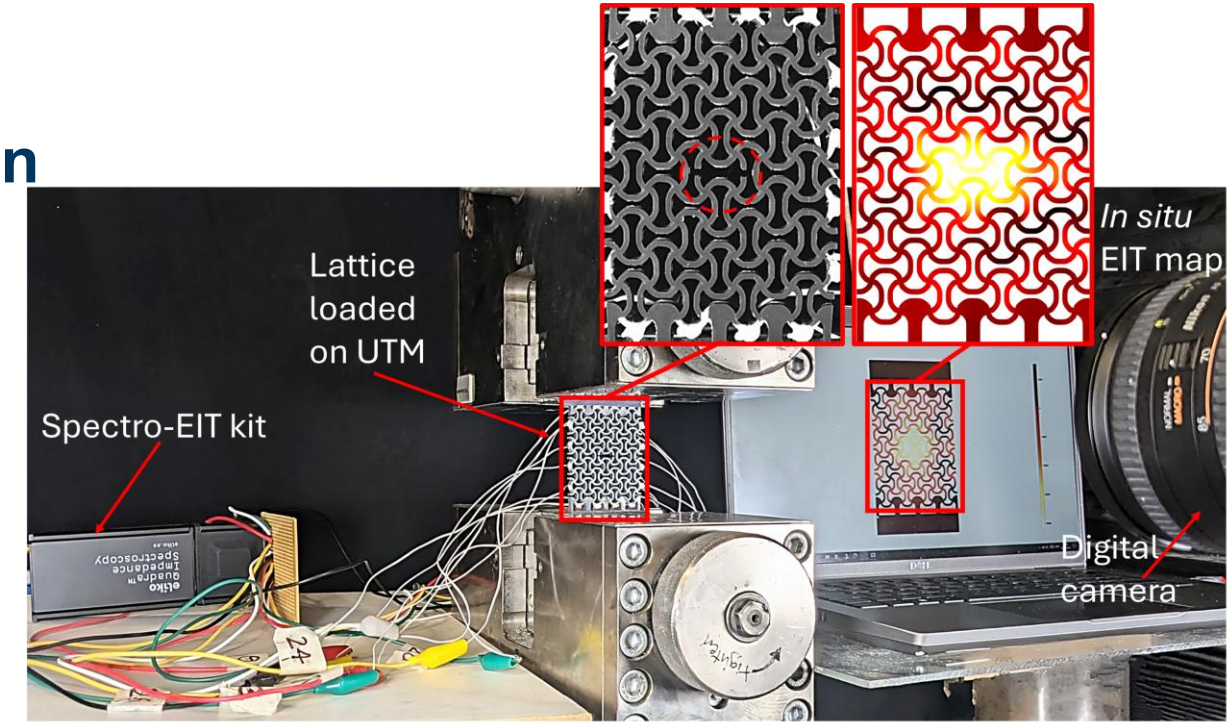

University of Glasgow

Thank you.

Contact me:
akash.deep@glasgow.ac.uk

Email

Group Website

#UofGWorldChangers

@UofGlasgow

Collaboration



Akash Deep

PhD Student,

James Watt School of Engineering



Prof Kumar Shanmugam

Professor of Composite Materials and Advanced Manufacturing



Prof Andrew McBride

Professor of Computational Mechanics

EMBEDDING OF FIBER OPTIC SENSORS UNDER INDUSTRIAL CONDITIONS AND DISTRIBUTED STRAIN SENSING IN TYPE 4 COMPOSITE PRESSURE VESSELS

B. Popiela[1], M. Schukar[2], M. Breithaupt[3], S. Günzel[4], G. W. Mair[5], K. Krebber[6], H. Seidlitz[7]

[1]Division "Safety of Gas Storage Systems", Bundesanstalt für Materialforschung und -prüfung (BAM)
Unter den Eichen 44-46, 12203 Berlin, Germany
Email: bartosz.popiela@bam.de, web page: https://bam.de

[2]Division "Fibre Optic Sensors", Bundesanstalt für Materialforschung und -prüfung (BAM)
Unter den Eichen 44-46, 12203 Berlin, Germany
Email: marcus.schukar@bam.de, web page: https://bam.de

[3]Division "Fibre Optic Sensors", Bundesanstalt für Materialforschung und -prüfung (BAM)
Unter den Eichen 44-46, 12203 Berlin, Germany
Email: mathias.breithaupt@bam.de, web page: https://bam.de

[4]Division "Safety of Gas Storage Systems", Bundesanstalt für Materialforschung und -prüfung (BAM)
Unter den Eichen 44-46, 12203 Berlin, Germany
Email: stephan.guenzel@bam.de, web page: https://bam.de

[5]Division "Safety of Gas Storage Systems", Bundesanstalt für Materialforschung und -prüfung (BAM)
Unter den Eichen 44-46, 12203 Berlin, Germany
Email: georg.mair@bam.de, web page: https://bam.de

[6]Division "Fibre Optic Sensors", Bundesanstalt für Materialforschung und -prüfung (BAM)
Unter den Eichen 44-46, 12203 Berlin, Germany
Email: katerina.krebber@bam.de, web page: https://bam.de

[7]Chair of Polymer-based Lightweight Design, BTU Cottbus-Senftenberg
Konrad-Wachsmann-Allee 13, 03046 Cottbus, Germany
Email: holger.seidlitz@b-tu.de, web page: https://www.b-tu.de/en/fg-leichtbau

Keywords: Fiber optic sensors, Composite pressure vessels, Filament winding

ABSTRACT

The number of in-operation composite pressure vessels is increasing, partly due to their attractiveness for on-board compressed gas storage and transport applications. A possible way to maintain the highest safety levels is through the structural health monitoring of the composite cylinders. Here, the use of fiber optic sensors appears to be a promising approach. However, the integration of the optical fibers into the composite structure of a pressure vessel has been shown to be challenging. In this study, insights on the embedding of optical fibers in the composite structure under industrial conditions are provided. A protection concept for the ingress and egress of the optical fibers is presented. Finally, the results from destructive slow burst tests are evaluated, showing no clear trend in the impact of the embedded optical fibers on the performance of composite pressure vessels.

1 INTRODUCTION

Composite materials play a major role in the transition toward a green economy. In the context of hydrogen technologies, composites are widely used for manufacturing composite pressure vessels,

which are used to transport and store hydrogen gas. Among the different types of pressure vessels, type 4 cylinders, consisting of a fully composite wrapped polymer liner, show the highest weight-saving potential. They are also characterized by the capability to withstand the highest working pressures [1, 2]. This makes them particularly attractive for on-board and transportation applications. However, the structural mechanical behavior of type 4 composite pressure vessels (CPVs) still needs to be better understood to precisely estimate their burst pressures and end-of-life performance.

A promising approach is the application of structural health monitoring (SHM) systems, both for the research purposes and for future applications in mass produced composite cylinders. Among other methods, such as acoustic emission or guided waves, in-situ strain monitoring with fiber optic sensors (FOS) delivers important information on the condition of the composite structure [3, 4]. FOS have been widely used for structural health monitoring of composite structures, with CPVs being one of the main applications [5-12]. However, the details of embedding optical fibers are either not described in the publications or do not correspond to industrial conditions. In practical applications, the integration of optical fibers in the composite structure proves to be challenging and time-consuming. To increase the competitiveness of FOS for the industrial applications, efficient processes for embedding optical fibers in composite cylinders need to be established. Furthermore, the FOS can be considered as a foreign body in the composite material, which can have an impact on its structural mechanical behavior.

In this study a setup for the integration of FOS in 6.8-liter type 4 CPVs was developed. The embedding of the optical fibers in the composite structure was integrated into an industrial filament winding process. The manufactured cylinders were tested in destructive slow burst tests. A comparison of the measured strains with finite element models is provided. Finally, the impact of the embedded optical fibers on the performance of the cylinders in slow burst tests (SBT) is discussed.

2 MATERIALS AND METHODS

2.1 Composite Pressure Vessels and Fiber Optic Sensors

Optical fibers were integrated into multiple composite layers of six 6.8-liter type 4 CPVs. The cylinders used, consisting of a PET liner as well as helical and hoop carbon fiber reinforced plastic (CFRP) layers, were designed for a nominal working pressure of 300 bar and test pressure PH of 450 bar. Figure 1 schematically shows the stacking sequence of the CPVs used. The helical and hoop layers with embedded FOS are marked. In total, the optical fibers were integrated into 6 of 15 CFRP layers. However, only 3 FOS were used to do so, each of which was embedded in two layers.

Three samples of wet filament wound CPV were used in the study to ensure the reproducibility of the outcomes. These samples differed in manufacturing parameters and loading history before the destructive slow burst test. However, the materials used, geometry, stacking sequence and processing time were the same. Each sample consisted of two cylinders with embedded FOS and three without optical fibers. The three samples are called Sample A, Sample B and Sample C for the sake of clarity:

1. Sample A: wound with a constant internal pressure in the liner, conditioned for 1000 hours under 450 bar and 65°C before slow burst tests;
2. Sample B: wound with an increasing internal pressure in the liner (see [13]), subjected to slow burst tests in a pristine state;
3. Sample C: wound with an increasing internal pressure in the liner, conditioned for 1000 hours under 450 bar and 65°C before slow burst tests.

Optical fibers SM1500(6.4/125)P by Fibercore were used as sensors. This optical fiber with 6.4 µm core diameter has additionally a 125 µm cladding and 155 µm polyimide coating diameter [14]. Because of the challenges in terms of handling the optical fibers, an additional protection, particularly in the ingress and egress from the CFRP, is needed [15]. Avoiding low radius bending caused by the boss geometry or other CFRP layers is of highest importance, since it could negatively influence the measurement quality, or even damage the optical fibers.

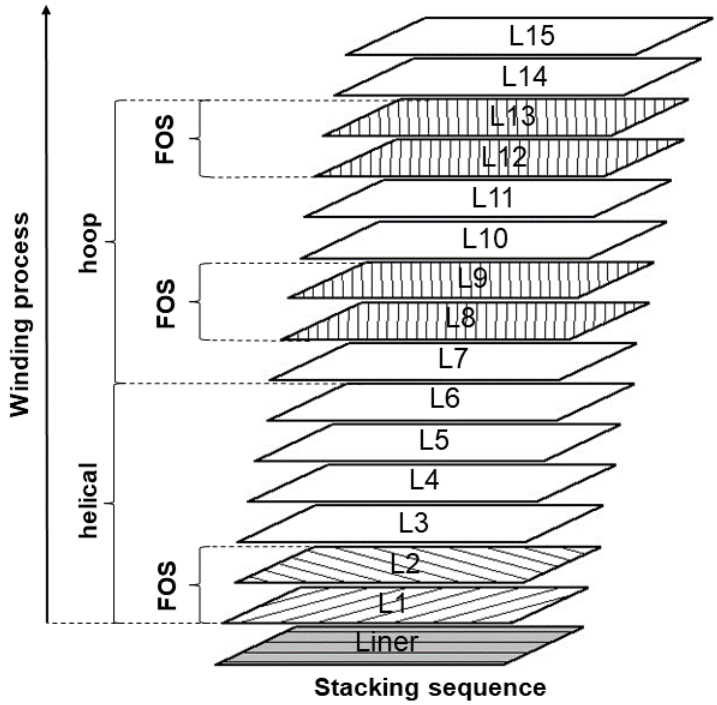

Figure 1: Stacking sequence of the used type 4 CPVs [13].

The configuration for protecting the optical fiber is shown in Figure 2. Directly behind the FC/APC plug, two protection tubes divided by a splice protection are used. The end of the 1.5 mm tube aligns with the end of the aluminum boss part or beginning of the CFRP. In the composite, only the PTFE capillary is used in the dome part, as also shown in Figure 3. It provides an additional protection in the areas in which the optical fiber leaves the fiber parallel orientation and is particularly exposed to the pressure from the winding tension of the newly wound layers.

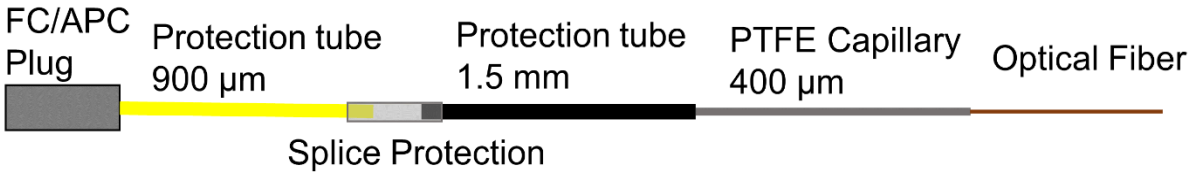

Figure 2: Concept for protection of the optical fiber at ingress and leaving carbon fiber parallel orientation.



Figure 3: Optical fibers leaving the carbon fiber parallel orientation of a hoop layer.

2.2 Finite Element Models

Finite element models were developed to discuss the strains obtained with fiber optic sensors during SBT. Since the models were extensively discussed elsewhere [13, 16], only a brief introduction based on the mentioned publications is provided at this point.

The finite element analyses were performed using ANSYS Mechanical 2023 R1. ANSYS ACP Prep/Post was used as a dedicated tool for preparing the model of the composite pressure vessel. As a basis for the geometry definition, a 3D scan of the liner was derived using Shining 3D EinScan HX. The stacking sequence of the carbon fiber reinforced layers and their nominal thickness were derived from the used type 4 6.8-liter cylinder. For the material data of the carbon fiber, resin and liner material, data sheet values and experimental data from the literature were used [17-20]. The material data for the carbon reinforced unidirectional plies was then calculated with rules of mixture according to [21] under assumption of a process typical fiber volume ratio of 60 %. A summary of the material data used can be found in Table 1 and Table 2.

Engineering constant	Abbreviation	Value	Unit
Young's Modulus in fiber direction	E_1	133500	[MPa]
Young's Modulus perpendicular to fiber direction	E_2	6380	[MPa]
Shear Modulus	G_{21}	2100	[MPa]
Poisson's ratio	ν_{21}	0.35	–
Ply thickness	t	0.45	mm

Table 1: Material data of an unidirectional CFRP ply.

Engineering constant	Abbreviation	Value	Unit
Young's Modulus	E	3600	[MPa]
Shear Modulus	G	1340	[MPa]
Poisson's ratio	ν	0.34	–
Ply thickness	t	0.40	mm

Table 2: Material data of PET liner.

The model was meshed with second order solid elements (SOLID186) with one element per composite layer. To constrain the model, displacements in x, y and z directions were suppressed at boss and the opposite dome end of the cylinder. The internal pressure loading during an SBT is applied to the whole inner surface of the cylinder. The model with the corresponding coordinate system is shown in Figure 4.

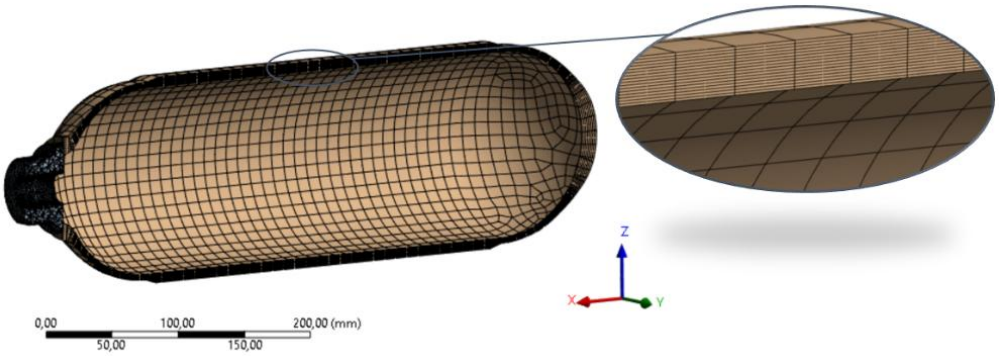

Figure 4: Finite element model used for the comparison of strains with FOS.

3 EXPERIMENTAL STUDY

3.1 Integration of Fiber Optic Sensors

For a smooth integration into the wound structure, the optical fibers for each layer were prepared on cardboard tubes in advance and placed behind the carbon fiber spools on the winding machine shafts. The length of each FOS exceeded the length of fibers used for the winding of the monitored layer by 4 m plus the distance from the cardboard tube to the wound CPV on top. The additional length was needed for ingress and egress from the CPV as well as connection to the measurement devices.

The optical fiber was led over the carbon fiber rovings and the resin bath and brought together with the carbon fiber roving directly before the pay-out eye of the winding machine. This procedure allows to avoid the contact with the epoxy resin for all parts of the sensor, which must remain flexible to later prevent damage of the optic fiber. At the same time, the optical fiber is placed onto the rotating liner together with the carbon fiber ensuring a good agreement of their winding angles. Figure 5 shows the optical fiber placed on the shaft of the winding machine and led towards the wound pressure vessel.

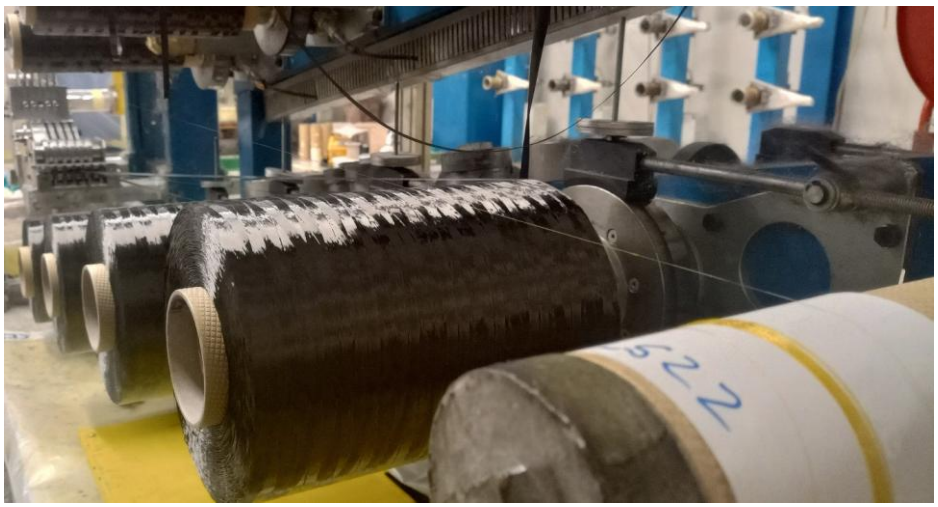

Figure 5: Optical fiber (gold in the bottom right corner) placed on the winding machine.

For ingress and egress from the CFRP, the dome part with the aluminum boss was used. Before the winding process, the boss edges were rounded to ensure a sufficient radius of all edges and to eventually avoid low radius bending of the optical fiber. The optical fiber itself was positioned in a way that ensures high bending radius, even if the optical fiber leaves the orientation of the carbon fiber roving and is particularly exposed to bending e.g., by the next carbon fiber layers (see Figure 3).

The method of integration of the FOS and the protection concept led to an excellent survival rate of the optical fibers in the project. All of the 18 embedded sensors survived the integration and could be used for strain measurements in the finished component. No adjustment of the filament winding machine was needed.

3.2 Slow Burst Tests and Strain Measurements

All 15 cylinders were destructively tested in SBT. On the one hand, the tests allowed a check of the functionality of integrated FOS by measuring the occurring strains. On the other hand, SBT are a method to assess the performance of composite pressure vessels introduced by Mair [22-25]. Therefore, an assessment of the impact of integrated optical fiber on the performance of the CPV sample is possible.

In an SBT, the pressure in a CPV is increased by 20 % of test pressure per hour, which corresponds to 1.5 bar per minute in the case of the investigated CPVs. During the tests, distributed strain measurements were performed using an ultra-high resolution optical backscatter reflectometer OBR 4600 (Luna Inc.). One measurement was performed every 5 bar, which sums up to 180 measurements up to a minimum burst pressure of 900 bar [26]. For the comparison with finite element models, an

average strain value was calculated for each measurement throughout the area of interest. For the hoop layers, two full hoop windings in the middle of the cylindrical region were considered. In case of helical windings, three sections in the cylindrical region with a length of 20 cm were defined.

4 RESULTS

4.1 Strain Distribution in Slow Burst Tests

Figure 6 shows the strains in the fiber direction in a cylinder from one specimen of Sample A subjected to an SBT. The helical winding shows significantly lower strains than the hoop windings, which was expected considering the stress distribution in a cylinder loaded with internal pressure. A good agreement between the strains measured with FOS and those calculated with finite element models can be observed. For the hoop windings a divergence of less than 10 % is present. Deviation of the material data in fiber direction can be considered as a possible cause for this behavior. The strains in the helical windings show an excellent agreement between FOS and finite element models. In general, the fiber optic sensors deliver feasible strain values and a good bonding between CFRP layers and the optical fibers can be assumed.

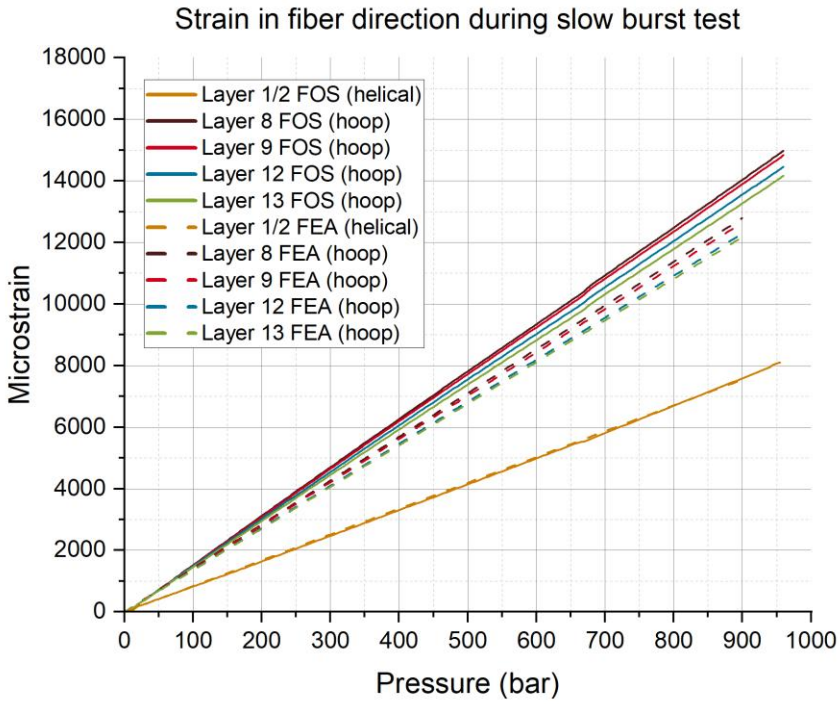

Figure 6: Strain in fiber direction during slow burst test in a CPV from sample A.

4.2 Impact of Optical Fibers on the Performance in Slow Burst Tests

No clear impact of the embedded fiber optic sensors on the behavior of the composite structure could be observed based on the post-mortem pictures of destroyed CPVs. The failure mechanisms, which were characteristic for each sample, did not vary for the CPVs with integrated fibers.

The burst pressures of all investigated cylinders are shown in Figure 7. The CPVs equipped with FOS are marked with half-filled symbols. The sample names correspond to the explanation in Section 2.1.

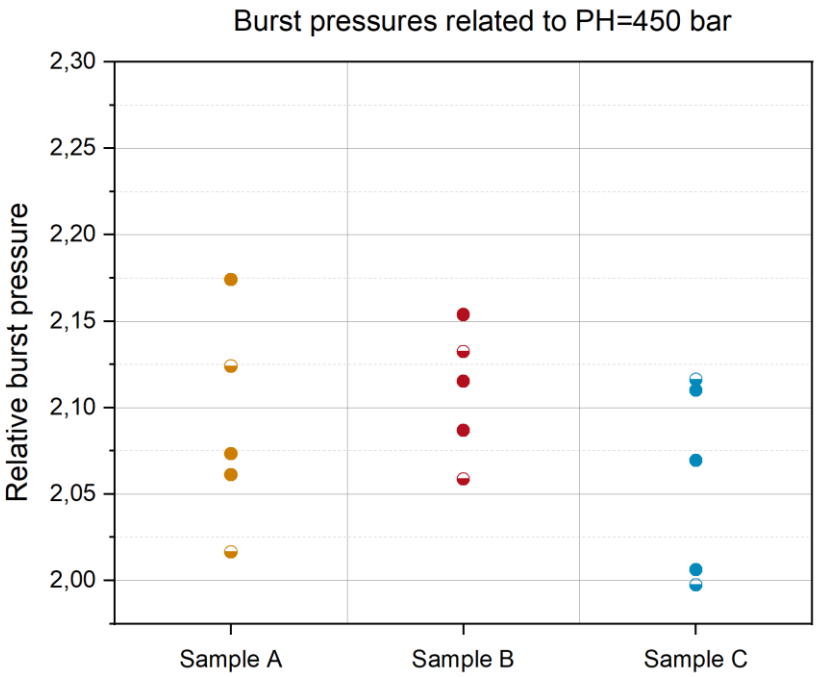

Figure 7: Relative burst pressures of all tested cylinders.

In general, the burst pressure of the CPVs with FOS are comparable with the burst pressures of the CPVs without FOS. Also, no clear trend can be observed regarding the scattering of the burst pressures. However, for each of the tested samples, the lowest burst pressure is a value obtained on a CPV with embedded optical fibers. Dixon's Q test is performed to identify if the lowest burst pressure values can be considered as outliers, which would indicate a significant impact of the integrated FOS on the mechanical behavior of the CPV. Burst pressures are arranged in increasing order and the value of Q is calculated as follows [27]:

$$Q = \frac{gap}{range} = \frac{x_1 - x_2}{x_1 - x_n} \tag{1}$$

At 95 % confidence none of the burst pressure values can be considered an outlier.

5 CONCLUSIONS

In this study optical fibers were integrated into six type 4 composite pressure vessels under industrial conditions. Three optical fibers were embedded in each composite cylinder and used for monitoring of six composite layers. No adjustments to the winding machine were needed. A protection concept for the ingress and egress of the optical fiber was developed, which resulted in an excellent survival rate of the optical fibers.

Strain measurements were performed with the integrated fiber optic sensors in slow burst tests. The obtained strain data were compared with finite element simulations showing a good agreement.

All six composite pressure vessels with embedded optical fibers and nine composite pressure vessels of the same designs were destructively tested in slow burst tests. No differences in failure mechanisms were observed within the samples. Even though a slight decrease of the mean burst pressures was observed for the cylinders with embedded fiber optic sensors, no clear trend in the influence of the embedded optical fibers on the performance of composite cylinders can be stated. An increase of the samples' size would contribute to further clarification of the influence of embedded optical fibers on the performance of the composite pressure vessels.

ACKNOWLEDGEMENTS

The authors would like to acknowledge the support of Andreas Kriegsmann, Frederek Maier and Martin Pfeifer during the performance of slow burst tests. Furthermore, the authors would like to thank Frank Basedau and Carolin Bach for their help during the integration of the optical fibers.
Bartosz Popiela gratefully acknowledges the funding from the Federal Institute for Materials Research and Testing (BAM) within the framework of Graduate School “Trustworthy Hydrogen”.

REFERENCES

[1] H. Barthelemy, M. Weber and F. Barbier, Hydrogen storage: recent improvements and industrial perspectives, *Int. J. of Hydrog. Energy*. **42(11)**, 2017, pp. 7254-7262 (doi: 10.1016/j.ijhydene.2016.03.178)

[2] E. Rivard, M. Trudeau, K. Zaghib, Hydrogen storage for mobility: a review, *Mater*., **12(12)**, 2019, 1973 (doi: 10.3390/ma12121973)

[3] D. Munzke, E. Duffner, R. Eisermann, M. Schukar, A. Schoppa, M. Szczepaniak, J. Strohhäcker, G. W. Mair, Monitoring of type IV composite pressure vessels with multilayer fully integrated optical fiber based distributed strain sensing, *Mater. Today: Proc*., **34(1)**, 2021, pp. 217-223 (doi: 10.1016/j.matpr.2020.02.872)

[4] S. Hashemi, J. Heimann, A. Charmi, J. Prager, Guided Wave Behavior in Type IV Composite Overwrapped Pressure Vessels Under Fatigue Loading, *Proceedings of the 10th European Workshop on Structural Health Monitoring (EWSHM 2024), Potsdam, Germany, June 10-13, 2024*, e-J. of Nondestruct. Test. (doi: 10.58286/29780)

[5] W. Blazejewski, A. Czulak, P. Gasior, J. Kaleta, R. Mech, SMART composite high pressure vessels with integrated Optical Fiber Sensors, *Proceedings of SPIE - The International Society for Optical Engineering*, 2010 (doi: 10.1117/12.847251)

[6] J. Degrieck, W. De Waele, P. Verleysen, Monitoring of fibre reinforced composites with embedded optical fibre Bragg sensors, with application to filament wound pressure vessels, *NDT&E Int*., **34(4)**, 2001, pp. 289-296 (doi: 10.1016/S0963-8695(00)00069-4)

[7] D.H. Kang, C.U. Kim, C.G. Kim, The embedment of fiber Bragg grating sensors into filament wound pressure tanks considering multiplexing, *NDT&E Int.*, **39(2)**, 2006, pp- 109-116 (doi: 10.1016/j.ndteint.2005.07.013)

[8] E. Saeter, K. Lasn, F. Nony, A. T. Echtermeyer, Embedded optical fibres for monitoring pressurization and impact of filament wound cylinders, *Compos. Struct.*, **210**, 2019, pp. 608-617 (doi: 10.1016/j.compstruct.2018.11.051)

[9] S.M. Klute, D.R. Metrey, N. Garg, N.A.A. Rahim, In-situ structural health monitoring of composite-overwrapped pressure vessels, *SAMPE J.*, **52(2)**, 2016, pp. 7-17

[10] E. Duffner, G. W. Mair, D. Munzke, R. Eisermann, M. Szczepaniak, M. Schukar, Lebensdauerversuche an Faserverbund-Druckbehältern überwacht mittels Schallemissionsprüfung und optischen Fasern, *22. Kolloquium Schallemission und 3. Anwenderseminar Zustandsüberwachung mit geführten Wellen Karlsruhe, Germany, 2019,* DGZfP

[11] P. Gasior, R. Rybczynski, J. Kaleta, S. Villalonga, F. Nony, C. Magnier, High Pressure Composite Vessel With Integrated Optical Fiber Sensors, *Proceedings of the ASME 2018 Pressure Vessels and Piping Conference PVP2018, Prague, Czech Republic, 2018,* ASME

[12] A. Wosniok, M. Schukar, P. Woody, M. Breithaupt, B. Wang, A. Kriegsmann, Distributed fiber optic strain sensing for structural health monitoring of 70 MPa hydrogen vessels, *Proceedings of the 10th European Workshop on Structural Health Monitoring (EWSHM 2024), June 10-13, 2024, Potsdam, Germany*, e-J. of Nondestruct. Test., (doi: 10.58286/29745)

[13] B. Popiela, S. Günzel, M. Schukar, G. W. Mair, K. Krebber, H. Seidlitz, Impact of Internal Pressure Control During Manufacturing on Residual Stresses and Safety Performance of Type 4 Pressure Vessels, *Composites Part C*, **17**, 2025, 100581 (doi: 10.1016/j.jcomc.2025.100581)

[14] Laser Components GmbH, Fibercore: Polyimide Coated SM Fiber, Olching, Germany, Data Sheet Version MD24/7, Jan. 2018.

[15] H. K. Kang, J. W. Park, C. Y. Ryu, C. S. Hong, C. G. Kim, Development of fibre optic ingress/egress methods for smart composite structures, *Smart Mater. and Struct*., **9(2)**, 2000, pp. 149-156 (doi: 10.1088/0964-1726/9/2/304)

[16] B. Popiela, S. Günzel, G. W. Mair, H. Seidlitz, Modelling of the Manufacturing Process Related Residual Stresses in Type 4 Pressure Vessels for Hydrogen Storage, *European PhD Hydrogen Conference EPHyC2024, 19-22 March 2024, Ghent, Belgium*, Hydrogen Europe Research, BE-HyFE

[17] R. Basan, Untersuchung der intralaminaren Schubeigenschaften von Faserverbundwerkstoffen mit Epoxidharzmatrix unter Berücksichtigung nichtlinearer Effekte, Ph.D. dissertation, Fakultät V - Verkehrs- und Maschinensysteme, TU Berlin, Berlin, Germany, 2011

[18] Teijin Carbon Europe GmbH, Tenax™ Filament Yarn, Data Sheet Version 1.7, Nov. 2023

[19] Olin Corporation, Olin LITESTONE® Filament Winding System: LITESTONE 3100E Epoxy Resin, LITESTONE 2106H Hardener, Technical Data Sheet.

[20] Kunststoffdreherei GmbH. Technisches Datenblatt PET, 2016

[21] H. Schürmann, *Konstruieren mit Faser-Kunststoff-Verbunden*, Vol. 2., Springer-Verlag, Berlin Heidelberg, 2007

[22] G. W. Mair, *Safety Assessment of Composite Cylinders for Gas Storage by Statistical Methods*, Springer International Publishing AG, Cham, 2017

[23] G. W. Mair, E. Duffner, A. Schoppa, M. Szczepaniak, Aspekte der Restfestigkeitsermittlung von Composite-Druckgefäßen mittels hydraulischer Prüfung, *Tech. Sicherh*., **1(9)**, 2011, pp. 50-55

[24] G. W. Mair, E. Duffner, A. Schoppa, M. Szczepaniak, Betrachtung von Grenzwerten der Restfestigkeit von Composite-Druckgefäßen, *Tech. Sicherh*., **2(11-12)**, 2012, pp. 43-50

[25] G. W. Mair, M. Hoffmann, F. Scherer, A. Schoppa, M. Szczepaniak, Slow burst testing of samples as a method for quantification of composite cylinder degradation, *Int. J. of Hydrog. Energy*, **39(35)**, 2014, pp. 20522-20530 (doi: 10.1016/j.ijhydene.2014.04.016)

[26] Transportable gas cylinders - Fully wrapped composite cylinders; German and English version prEN 12245:2022, EN Standard No. 12245:2022, August 2022 [Online]. Available: https://www.beuth.de/de/norm/din-en-12245/345513474

[27] R. B. Dean, W. J. Dixon, Simplified Statistics for Small Number of Observations, *Anal. Chem.*, **23(4)**, 1951, pp. 636-638

ICCM24
AUGUST 4-8, 2025
BALTIMORE CONVENTION CENTER
BALTIMORE, MARYLAND, USA

No Technical Paper Submission for:

Yansong Li

ICCM24 24TH INTERNATIONAL CONFERENCE ON COMPOSITE MATERIALS
AUG 4-8, 2025 • BALTIMORE CONVENTION CENTER • BALTIMORE, MARYLAND

CHARACTERISATION OF EMBEDDED CHANNEL NETWORKS IN CFRPS FOR ACTIVE COOLING

Toby R.P. Wilcox[1,2], Richard R. Trask[1,2] and Julian D. Booker[3,4] Benjamin K.S. Woods[1,2]

[1]Bristol Composites Institute (BCI), University of Bristol,
Queens Building, Univeristy Walk, BS8 1TR, Bristol
Email: toby.wilcox@bristol.ac.ukk, web page: https://www.bristol.ac.uk/composites/

[2]School of Civil, Aerospace and Design Engineering, University of Bristol,
Queens Building, Univeristy Walk, BS8 1TR, Bristol

[3]Electrical Energy Management Group (EEMG), University of Bristol,
Queens Building, Univeristy Walk, BS8 1TR, Bristol

[4]School of Electrical, Electronic and Mechanical Engineering, University of Bristol,
Queens Building, Univeristy Walk, BS8 1TR, Bristol

Keywords: Carbon Fibre-Reinforced Polymers, Thermal Properties, Thermal Analysis, Multifunctional, Active Cooling

ABSTRACT

Carbon fibre-reinforced polymers have inherently poor thermal properties, driven by their anisotropic structure and the relatively low thermal conductivity of their constituent materials, particularly the matrix phase. This makes them unfit for use in structures surrounding heat emitting components in aircraft. This low thermal performance can potentially be mitigated via active fluid cooling through embedded networks of channels within the composite structure. In order to explore the fundamental thermal management capabilities of this approach, embedded channel networks have been fabricated and thermally tested, with the performance compared against numerical results from COMSOL Multiphysics. The channel networks were manufactured within CFRP samples by embedding metallic wires along the neutral axis during prepreg hand layup up and extracting them post-cure, with fluid fittings bonded into the inlets and outlets of each channel. The samples were thermally characterised under conductive thermal loads applied via a heating mat with increasing flow rates of coolant pumped through the channels. A range of sample and channel geometries and process parameters were tested to understand their impact on thermal performance, with particular interest in the effect of channel number and diameter, flow rate, and coolant temperature. The experiments show that up to an 80% reduction in surface temperature can be achieved through active cooling, with improvements driven by increasing the flow rate and channel volume fraction. A higher number of channels within the sample is also shown to create a more uniform temperature profile, removing hot spots on the surface. Thermal modelling results were validated against the experimental results, showing good agreement.

1 INTRODUCTION

At ambient temperatures, carbon fibre-reinforced polymers exhibit excellent mechanical properties and an especially high strength-to-weight ratio that makes them ideal for use in primary structures in aircraft. A typical aerospace-grade CFRP system can be up to seven times stronger and two times stiffer than its aluminium counterpart at only two thirds the weight, with relative performance being highest when the loads are directly aligned with the fibres [1]. However, CFRPs have comparatively poor thermal properties and low maximum service temperatures which make them unsuitable for any application where they may be exposed to significantly elevated temperatures or high thermal loads. While carbon fibres themselves exhibit moderate to high thermal conductivity (5-15 W/mK for PAN-based fibres, 500-1000 W/mK for pitch-based fibres)[2-5], the much lower conductivity of the resin matrix (0.19-0.25 W/mK) [6,7] and the anisotropy of their structure means the net conductivity for a

typical CFRP layup is somewhere in the region of 4-5 W/mK in the in-plane direction and only around 1-2 W/mK in the out-of-plane direction, much lower than a typical aerospace aluminium alloy (~230 W/mK) [8-10]. This combines with glass transition temperatures typically in the range of 150-200ºC, with even lower working temperatures quoted by manufacturers due to safety factors [11]. As a result, metallics such as aluminium or magnesium alloys are still the preferred materials for aerospace structures that must withstand high levels of thermal loading, such as electric generators and gearboxes.

Several concepts have been explored to improve the thermal properties of CFRPs including fillers, coatings and crystal structure alignment [12-14]. While these passive techniques do offer some improvement in thermal conductivity, they come at the expense of increased manufacturing and materials costs, added complexity, and still do not achieve the levels of thermal conductivity needed for many real-world applications. Instead of attempting to improve the inherent thermal properties of the CFRP system, it is attractive to consider active approaches for removing heat from the structure, for example through the use of an embedded system of channels permeated by a heat transfer fluid. This technique was first inspired by biological systems that exhibit intricate microvascular networks such as leaves or the human circulatory system and was hypothesised as a means of adding multifunctionality to a structure [15,16]. Active cooling has since been determined as one such function and has been investigated both experimentally and numerically over the last 15 years by a small number of researchers [17-23]. For instance, Pety *et al* [20] achieved up to 80% cooling efficiency (proportion of heat removed over the heat applied) in composite panels with embedded channels at flow rates up to 30 ml/min, and Coppola *et al* [17] observed a 90% retention of mechanical properties in specimen subjected to 4-point bending up to 325 ºC. While the results from these studies show effective and repeatable channel fabrication, highly efficient cooling, good retention of mechanical properties, and a large scope for optimisation, the approach has not yet made it into widespread use, in part because it has never been thoroughly characterised with regards to the numerous design and process parameters that impact the effectiveness of heat removal.

This paper attempts to carry out a thorough characterisation of channel cooling performance using a broad-spectrum design of experiments, backed up by numerical analysis, to directly measure the impact of varying the key design and operating parameters within the channel network architecture. CFRP samples containing embedded channels are first manufactured with various combinations of thicknesses, channel diameters and channel pitches. The samples are then thermally tested via conduction with respect to process parameters such as flow rate, coolant fluid, and coolant fluid temperature. The results of these experiments are then discussed to analyse the effect of these parameters on cooling performance. Finally, numerical models are set up in COMSOL Multiphysics to validate against the experimental data obtained, with the models then being ready to explore a wider and more complex design space in future work.

2 METHODOLOGY

2.1 Channel fabrication

Previous work has explored numerous approaches to fabricate embedded channels within a composite, including hollow glass fibres or steel tubes, solder removal, direct ink writing, and vapourisation of sacrificial materials (VaSC) [24-31]. However, in this work, manual wire extraction (MWE) was chosen as the preferred fabrication method due to the comparative ease of the process and because there is no requirement for post-cure treatments. MWE involves embedding high tensile strength wires within the composite structure during hand layup and removing them post-cure by pulling them out manually, leaving a hollow channel of inverse shape embedded within the composite structure [32-34]. With this method, several wires could be embedded to create a network of straight and flat channels within the CFRP, each with its own inlet and outlet.

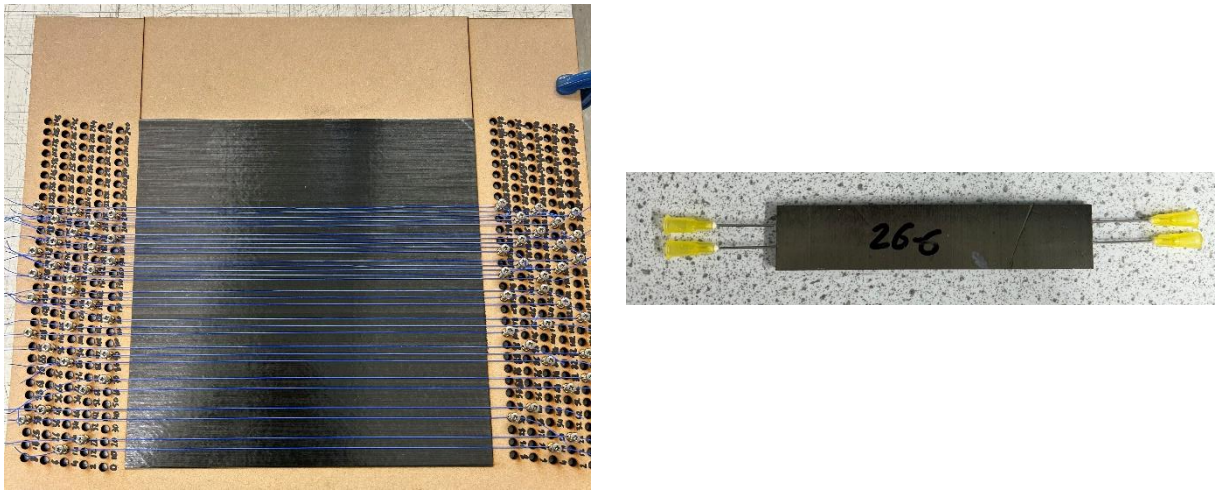

Figure 1 – a) Wire positioning jig in place over a laminate before cure b) post-cured sample with wires removed and syringe tips glued into inlet and outlet

In this work, PTFE-coated nickel-chromium (Nichrome) wires of two different diameters (0.57 mm and 0.97 mm) were used, and they were embedded at the midplane of IM7/8552 prepreg CFRP laminates during hand lay up. For both of the specimen thicknesses manufactured (2 mm and 4 mm), the ply stacking sequence was such that the wires would be entirely contained within plies orientated parallel to the channels (0º direction) to allow for the thickness of the channel to be accommodated within the layup through movement of the adjacent fibres with minimal disturbance of the off-axis plies above and below the midplane. In all cases, a large laminate (300 x 300 mm) was prepared and a series of wires (0.57 mm or 0.97 mm) at set pitches were strung across the midplane and held in place using an MDF jig with laser cut indexing holes to position screws around which the wires ends were wrapped (Figure 1a). The laminates were then cured in an autoclave under vacuum at the standard IM7/8552 cure cycle (2 ºC/min ramp up to 110 ºC, 60-minute dwell, 2 ºC/min ramp up to 180 ºC, 120-minute dwell, then cool down to ambient temperature with a vent of pressure at 60 ºC). After curing, the laminate was heated to approximately 50 ºC on a hot plate to help loosen the wires, which were manually pulled out using pliers, leaving a set of hollow channels. Finally, the large laminate was cut into smaller individual test samples (120 x 24 mm) and syringe tips (18G for 0.57 mm, 20G for 0.97 mm) were glued into the exposed channel ends using 2-part epoxy (Araldite), as shown in Figure 1b.

In order to test a large array of geometry-based parameters, laminates of thicknesses 2 mm and 4 mm were manufactured, and the wires were spaced such that the resulting collection of samples would have instances containing networks of two, three, and five evenly spaced channels. The combination of channel diameter, laminate thickness, and channel number gave rise to nine distinct sets of samples, with differing channel volume fractions, defined as the cross-sectional area of the channels in a specimen divided by its full cross-sectional area, as enumerated in Table 1.

Table 1 – Geometric parameters of samples tested

Laminate thickness [mm]	Channel diameter [mm]	Number of channels	Channel volume fraction [%]
2	0.57	2	1.08
		3	1.62
		5	2.70
4	0.57	2	0.54
		3	0.81
		5	1.35
	0.97	2	1.54
		3	2.31
		5	3.85

2.2 Thermal testing

The manufactured specimens were tested on a custom thermal conduction test rig (Figure 2). They were first placed on a silicone heater mat (from Under Control Instruments) at a set heat flux and allowed to reach steady-state temperature. The time history of the temperature distributions on the entire top surface of the specimens was tracked and captured with an IR camera (FLIR T650sc). Water at a prescribed initial temperature was then circulated through the embedded channels at a set flow rate using silicone tubing and a peristaltic pump (Watson-Marlow 503U). The water was maintained close to the desired temperature using a water bath (Grant JB Nova 12L) and was allowed to circulate around the channels until steady-state temperature was again reached. The flow rate was then increased to test the next flow condition, which was tracked with a flow meter (Omega FLR1008-D). K-type thermocouples and wet/wet pressure sensors (Omega PX26-15GV) were attached to the silicone tubing just before and after the inlet and outlet of the specimens, and the temperatures and pressures were captured using National Instruments data acquisition modules (NI 9212, NI 9219) and LabVIEW software.

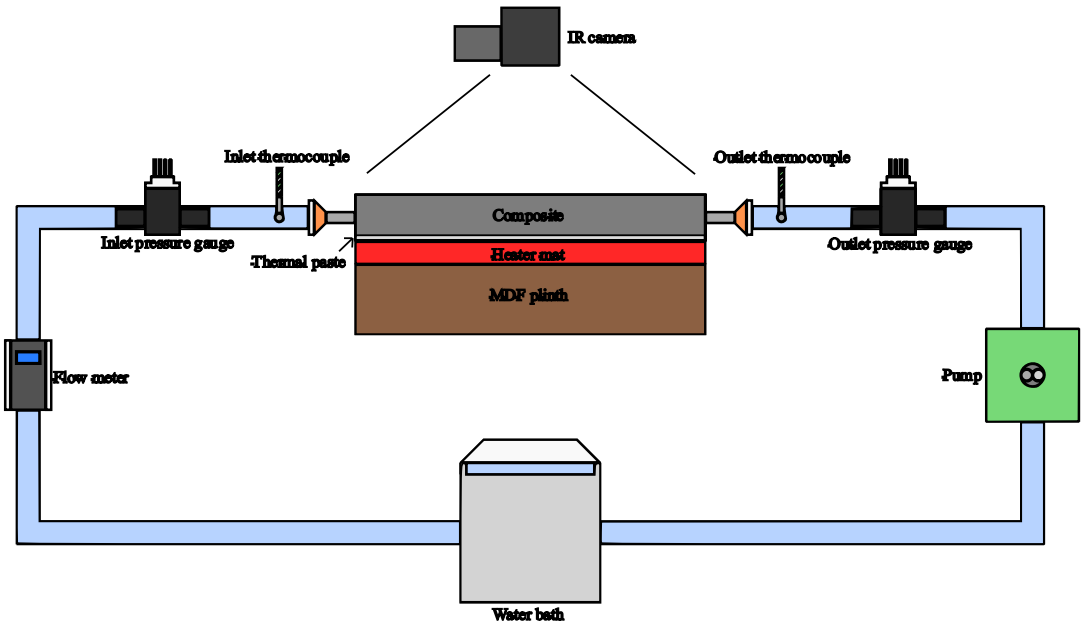

Figure 2 – Schematic of conduction test setup

Each specimen was tested at three flow rates (10, 20 and 30 ml/min) and three heat fluxes (500, 1000 and 1500 W/m^2), resulting in eighty-one separate experiments. Two sample geometries (4 mm thickness, 0.97 mm channel diameter, two and three-channels) were also chosen for further testing with higher flow rates (up to 70 ml/min), different initial water temperatures (10, 30 ^{o}C), and different coolant fluids (deionised water, mono-propylene glycol). For conciseness in this paper, the 4mm thick specimens with 0.97 mm channel diameter have been chosen as the baseline data set, with comparisons made to the other geometries.

2.3 Computational modelling

Models representing the same geometries and process parameters used in the experiments were set up in COMSOL Multiphysics using the heat transfer in solid and fluids design module. A solid body of 120 x 24 mm (4 mm and 2 mm thickness) was designed to represent the specimens with a second body of 120 x 24 x 0.5 mm was created in contact with the bottom surface of the main body to represent the heater mat. Two, three, and five-channels were then modelled with diameters 0.228 mm and 0.485 mm along the neutral axis of the main body at the desired pitches (4 mm, 6 mm, 8 mm). An example two-channel model is shown in Figure 3. The main body was assigned a custom material representing IM7/8852, with properties obtained from the material datasheet and previous experiments [35]. Built-in

material properties were used for water and silicone for the fluid channels and heater mat respectively. A full breakdown of process parameters and material properties is shown in Table 2.

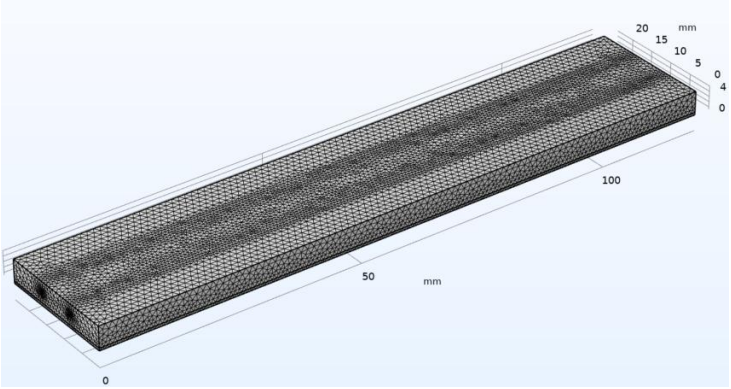

Figure 3 – Meshed COMSOL model of a two-channel specimen with 0.97 mm diameter channels

A heat source was applied to the heater mat domain to represent the desired heat flux. This was converted to raw power using Equation 1 below. External natural convection and surface-to-ambient radiation were applied to all exposed surfaces of the specimen. The channels within the specimen were grouped together and assigned a desired inlet temperature and flow rate. A global tetrahedral mesh was generated around the model, with a finer triangular mesh around the channels (548,278 total elements).

Table 2 – Parameters, model inputs and material properties for COMSOL models

Specimen Geometry	Value	Description
l	120 [mm]	Length of specimen
w	24 [mm]	Width of specimen
t	2, 4 [mm]	Thickness of specimen
r	0.285, 0.485 [mm]	Channel radius
p	4, 6, 8 [mm]	Distance between channels
Model inputs		
T_a	21-26 [°C]	Ambient temperature
T_c	14-28 [°C]	Coolant fluid inlet temperature
Q	8-33 [ml/min]	Flow rate of fluid
P	6.573-17.190 [W]	Power applied[a]
L_t	10 [mm]	Characteristic length of top surface[b]
L_s	0.984, 1.936 [mm]	Characteristic length of sides[b]
L_e	0.923, 1.714 [mm]	Characteristic length of top edges[b]
Material properties		
ρ_c	1570 [kg/m^3]	Density of IM7/8552 [35]
Cp_c	920 [kJ/kgK]	Specific heat capacity of IM7/8552 [35]
k_c	1.750 [W/mK]	Thermal conductivity of IM7/8552[c]
ϵ	0.970	Surface emissivity
ρ_w	~ 998 [kg/m^3]	Density of water[d]
Cp_w	~ 4.180 [kJ/kgK]	Specific heat capacity of water[d]
k_w	0.600 [W/mK]	Thermal conductivity of water
ρ_s	1100 [kg/m^3]	Density of heater mat (silicone rubber)
Cp_s	1.900 [kJ/kgK]	Specific heat capacity of heater mat
k_s	0.500 [W/mK]	Thermal conductivity heater mat

[a]Converted from heat flux values
[b]For external natural convection. Defined as area of surface divided by perimeter
[c]Obtained from previous, unpublished study
[d]Temperature dependent

$$P = \left(\sqrt{Q"RA}\right) * I \quad (1)$$

Where P is power, $Q"$ is heat flux, R is resistance of the heater mat, A is surface area of the specimen, and I is the current of the heater mat.

The model outputs mirrored those in the experimental test: maximum temperature of the top surface; average temperature of the top surface; and outlet temperature of the fluid. The temperature profile of the model could also be captured and directly compared to the profile from the IR images. Instead of taking generic or desired parameters (e.g. T_a=21ºC, T_c=20ºC, Q=10 ml/min) the model was set up with actual dataset specific values for ambient temperature, inlet temperature and flow rate that were captured throughout the experimental tests. This results in a model output for each individual test rather than general model results to compare against.

3 RESULTS AND DISCUSSION

During testing, the ambient temperature in the lab fluctuated depending on the outside temperature and the time of day, and this had a non-negligible effect on the temperature of the coolant fluid at the inlet to the channels, and to a lessor extent is likely to have affected the heat transferred out of the specimens. To account for the change in ambient temperature across different testing runs and datasets, the results are normalized to inlet temperature using a ratio derived from the inlet temperature and no-flow heating condition. This ratio ("effective cooling") is defined in Equation 2 below and describes the actual temperature reduction of the specimen over the maximum theoretical temperature reduction, based on the idea that the specimen temperature can approach but never be cooler than the coolant inlet temperature.

$$e_c = \left(\frac{T_{max,nf} - T_{max,Q}}{T_{max,nf} - T_{inlet}}\right) * 100 \quad (2)$$

Where e_c is the effective cooling, $T_{max,nf}$ is the maximum surface temperature of the specimen in the no-flow condition, $T_{max,Q}$ is the maximum surface temperature of the specimen for a given flow rate, and T_{inlet} is the temperature of the coolant supplied to the inlet of the channels.

The inlet and outlet temperatures could further be used to calculate a heat removal rate from the specimen, and this could then be compared to the power supplied to the specimen from the heater mat to give heat removal rate as a proportion, as shown in Equations 3 and 4.

$$q = \sum_n (Q \rho Cp \Delta T) \quad (3)$$

$$H_{\%} = \left(\frac{q}{P_m}\right) * 100 \quad (4)$$

Where q is the rate of heat removal, Q is the flow rate, ρ is coolant density, Cp is coolant specific heat capacity, ΔT is the temperature difference across the inlet and outlet of the channels, n is number of channels, $H_{\%}$ is the heat removal proportion, and P_m is the power supplied to the heater mat.

3.1 Effect of flow rate

The maximum surface temperatures and the effective cooling of two datasets are shown in Figure 4. In all samples, both the maximum and average surface temperatures decreased as flow rate increased. This began with a steep initial decrease from the no flow condition to the lowest flow rate (10 ml/min) with more marginal reductions as the flow rate was further increased. The levelling off of the effective cooling suggests that merely the presence of coolant at a minimal flow rate (10 ml/min is relatively low and easily achievable with most commercial pumps) is sufficient to cool the sample significantly. The best performing specimen geometry was observed to be the 4 mm thickness with 0.97 mm channel diameter, which exhibits up to a 116 ºC (80%) decrease in maximum surface temperature at the highest flow rate (30 ml/min), number of channels (five), and applied heat flux (1500 W/m^2). This is expected considering this configuration contains the highest channel volume fraction. However, the 4 mm, 0.57 mm specimen still exhibits a substantial surface temperature reduction (63 ºC) even at the lowest flow rate (10 ml/min), number of channels (two), and applied heat flux (500 W/m^2).

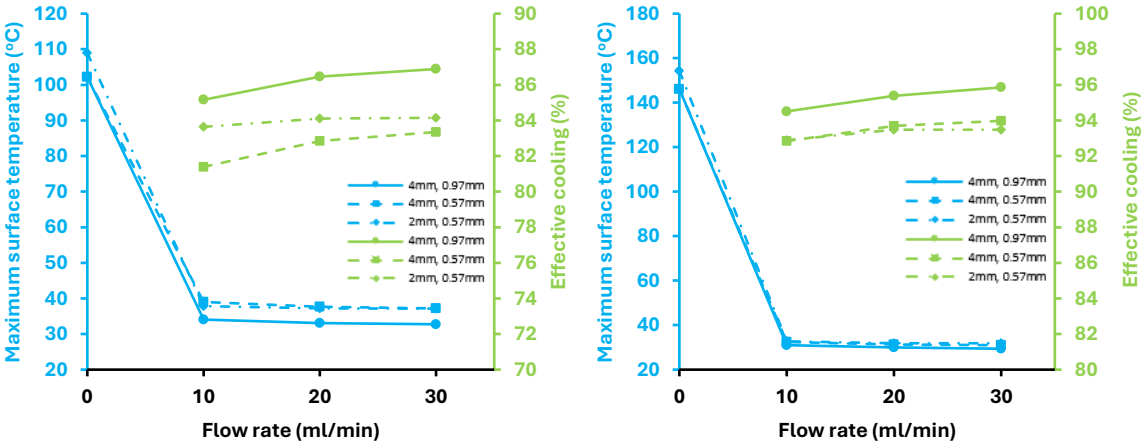

Figure 4 – Maximum surface temperature and effective cooling of specimen of all geometries and a) two-channels at 500 W/m^2 applied heat flux b) five-channels at 1500 W/m^2 applied heat flux

The temperature difference between the inlet and the outlet decreases as flow rate increases, largely due to the increased velocity in the fluid through the channel. Despite this, the heat removal proportion increases as flow rate increases, due to the fact that the increase in the flow rate outweighs the drop in temperature difference. The heat removal rates are shown in Figure 5.

Higher flow rates were tested in two and three-channel samples from the batch of specimens of 4 mm thickness and 0.97 mm channel diameter, the results of which are shown in Figure 6. Increasing the flow rate beyond 30 ml/min appears to have very little effect on further reducing the maximum surface temperature, with reductions below 0.5°C from successive flow rate increases. Increasing the flow rate above 30 ml/min does however have a significant effect on the pressure experienced across the sample (see Figure 8b in Section 3.5), leading to difficult testing conditions where the high pressure may cause leaks at the syringe/adhesive interface or in the silicone tubing. It was determined that increasing the flow rate beyond 30 ml/min is unnecessary from a cooling perspective and prohibitive from a pressure perspective, especially in the specimen containing 0.57mm diameter channels, where pressure is inherently higher to increased flow restriction.

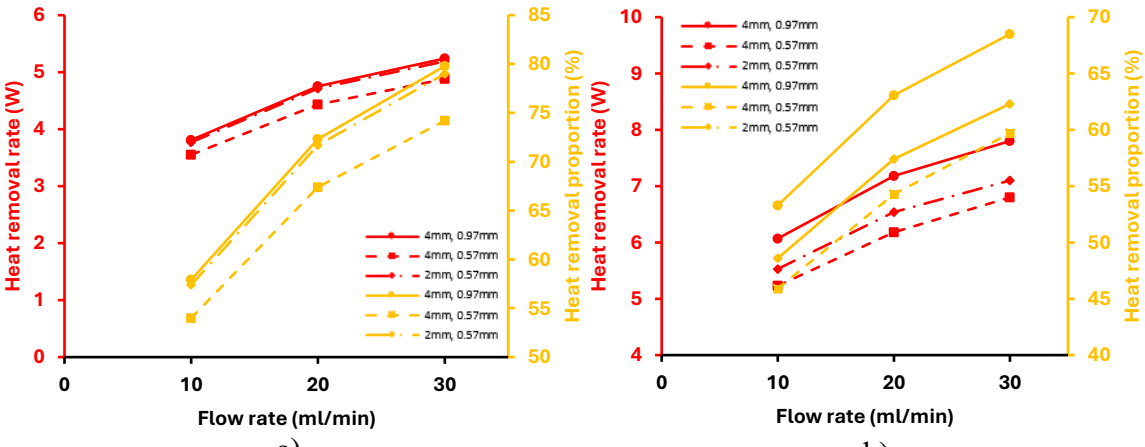

Figure 5 – Heat removal rate and heat removal proportion of specimens of all geometries and a) two-channels at 500 W/m^2 applied heat flux b) five-channels at 1500 W/m^2 applied heat flux

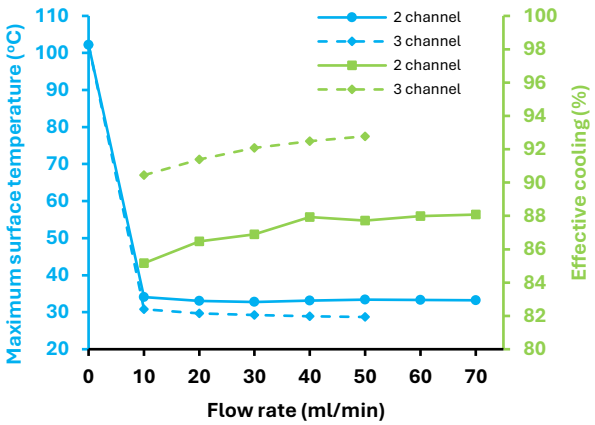

Figure 6 – Maximum surface temperature and effective cooling in a 4 mm, 0.97 mm specimen with two and three-channels at 500 W/m^2

3.2 Effect of pitch

Similar to flow rate, reducing the pitch and therefore increasing the number of channels within a sample leads to a higher reduction in maximum and average surface temperatures across all samples tested. More importantly in this case, and as seen in Table 3, having more channels in a specimen leads to a smaller difference between the maximum and average surface temperatures, giving a more uniform temperature distribution across the top surface.

An increased number of channels also leads to increased heat removal from the specimen, with a 10-12% increase from a two to a three-channel specimen and a similar gain from a three to a five-channel specimen. Using the images captured by the IR camera, the temperature profiles of specimens with the same process parameters but a different number of channels can be compared directly, as seen in Figure 7a. It is observed that there is not only a lower temperature on the surface as the number of channels increases, but also less variation in colour across the top surface. For instance, the two-channel sample clearly exhibits hotter regions either side of the channels towards the edge of the specimen. These are minimised by the three-channel specimen and completely eliminated by the five-channel specimen, leading to a more uniform temperature profile. This effect is also clearly reflected in the standard deviations of temperature across the specimens (Table 3), which have a consistent decreasing trend with increasing numbers of channels for all specimen geometries.

Table 3 – Temperature difference and standard deviation for all specimen geometries at 20 ml/min and 1000 W/m^2 applied heat flux

Specimen geometry [mm]	Number of channels	Maximum temperature [°C]	Average temperature [°C]	Temperature difference [°C]	Standard deviation [°C]
4 thickness, 0.97 diameter	2	37.48	32.32	5.16	1.66
	3	32.14	29.42	2.72	1.07
	5	28.64	27.29	1.35	0.62
4 thickness, 0.57 diameter	2	41.12	36.06	5.06	2.29
	3	36.25	32.19	4.06	1.24
	5	29.86	27.25	2.61	0.71
2 thickness, 0.57 diameter	2	42.43	34.8	7.63	2.35
	3	37.44	31.28	6.16	2.24
	5	30.01	26.65	3.51	0.85

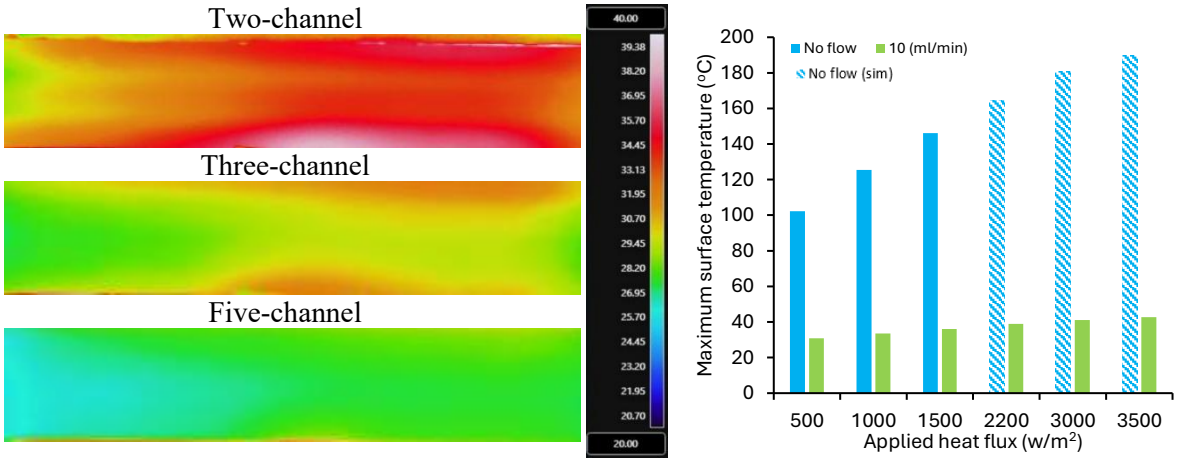

a) b)

Figure 7 – a) Surface temperature profiles of 4 mm thickness, 0.97 mm channel diameter specimens of two, three and five-channels at 20 ml/min and 1000 W/m^2 b) maximum surface temperature of a 4 mm thickness, 0.97 mm channel diameter, two-channel specimen at all heat fluxes in no-flow condition and at 10 ml/min

3.3 High heat flux

The no-flow condition can only be tested experimentally up to 1500 W/m^2 due to the temperatures on the specimen (~154 ºC on a 2 mm thickness specimen) approaching and even exceeding the maximum rated operating temperature of the heater mat (150 ºC), in addition to potential damage to the composite. As such, higher applied heat fluxes were tested in flow on conditions only, with the no-flow condition instead obtained through numerical modelling. As seen in Figure 7b, even when increasing the heat flux to 3500 W/m^2, which would result in a predicted maximum surface temperature of ~190 ºC, the presence of cooling fluid at the lowest flow rate and number of channels is still sufficient to reduce the maximum surface temperature markedly.

The higher heat fluxes were chosen based on potential applications in industry, as seen in Table 4. In all cases, the maximum surface temperature was reduced to below the maximum operating temperatures associated with these applications. This suggests that a composite structure with embedded channels could be substituted for the existing metallic casings of these components without compromising the working conditions of the component itself.

Table 4 – Application specific working temperatures and achieved cooling in a 4mm thickness, 0.97mm channel diameter, two-channel specimen

Heat flux [W/m^2]	Application	Critical temperature [ºC]	Maximum temperature no-flow [ºC]	Maximum temperature flow [ºC]	Temperature difference [ºC]
500	EV battery	55	102.81	30.79	24.21
2200	Transmission shaft	85	164.48	38.88	46.12
3000	Transmission gear	90	181.00	41.12	48.88
3500	Transmission bearing	90	189.84	42.74	47.26

3.4 Effect of coolant fluid and temperature

Deionised water and a 50:50 mixture of water and mono-propylene glycol were also tested as coolant fluids, as well as different inlet temperatures of water. As seen in the results in Figure 8a, cooling the water to below room temperature (~10 ºC) leads to an increased surface temperature reduction, with the opposite effect occurring when the water is instead heated (~30 ºC). In both these cases however, it was

challenging to maintain the target temperature, as the water would heat or cool as it left the water bath and was pumped through the tubing towards the specimen. As a result, the actual inlet temperature was on average ~16 ºC for the 10 ºC test and ~27 ºC for the 30 ºC test. Despite this, there is still a significant improvement in temperature reduction in the sample if the coolant fluid is first cooled, and this could be a significant factor if the inlet temperature can be properly maintained.

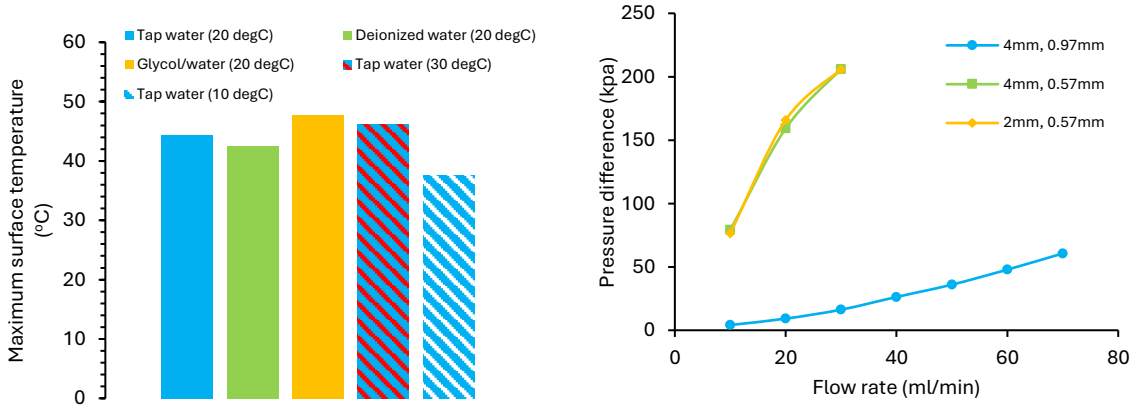

(a) (b)

Figure 8 - a) Maximum surface temperatures of a 4 mm, 0.97 mm, two-channel specimen at 1500 W/m^2 and 10 ml/min with various coolant fluids and inlet temperatures, and b) pressure differences in all two-channel specimen geometries at 500 W/m^2 at all flow rates

Changing the coolant fluid from tap water to deionised water led to a very small (~0.5 ºC) reduction in surface temperature in a specimen heated at 500 W/m^2. This was not significant enough to justify the added complexity of introducing deionised water to the cooling system. Somewhat surprisingly, the water/glycol mixture led to a higher maximum surface temperature in comparative samples. This may be due to the mixture having higher inlet temperature (~27 ºC) than the standard water (~21 ºC) due to the initial temperature of the mono-propylene glycol. Despite this disparity in inlet temperature, the glycol/water mixture still exhibits a lower effective cooling than both tap water and deionised water. However, further tests will be performed with the glycol/water mixture at inlet temperatures more in line with the other test fluids.

3.5 Pressure

The pressure difference across the specimen is a significant factor in the testing, as a high-pressure difference can lead to difficulties with the apparatus, namely lower pumping efficiency, leaks at the syringes, or bursts in the silicone tubing. The pressure differences exhibited in the specimens of all geometries are shown in Figure 8b. In general, the inlet pressure will increase as flow rate increases across all specimens. Specimens containing 0.57 mm diameter channels will exhibit up to a twenty-fold increase in inlet pressure compared to specimen containing 0.97 mm diameter channels. Generally, there is minimal change in pressure difference across a specimen as the applied heat flux increases. However, the pressure difference decreases as the number of channels increases. A comparison of applied heat flux, flow rate and number of channels is shown in Table 5.

Table 5 – Pressure difference in a 4 mm thickness, 0.97 mm channel diameter specimen at various applied heat fluxes, flow rates, and number of channels

Applied Heat flux [W/m^2]	Number of channels	Pressure difference [kpa]		
		10 [ml/min]	20 [ml/min]	30 [ml/min]
500	2	4.14	9.17	16.27
	3	3.44	9.24	16.41
	5	2.83	8.83	13.10
1000	2	4.69	9.51	16.13
	3	3.38	9.24	16.96
	5	3.86	8.76	15.58
1500	2	4.83	10.00	16.27
	3	3.31	8.96	16.20
	5	2.96	8.82	15.58

3.6 Numerical modelling

In all instances, the experimental data was compared against the predicted results from the COMSOL models. The experimental results for maximum surface temperature, average surface temperature and outlet temperature are within 10% of the same metric in COMSOL for all datasets. In general, the outlet temperature shows the most agreement with the COMSOL results (within 0.5-3.5 %) and the average surface temperature shows the least (2.5-9.5 %). A more detailed comparison for a 4 mm thickness, 0.97 mm diameter specimen with 5-channels is shown in Figure 9a.

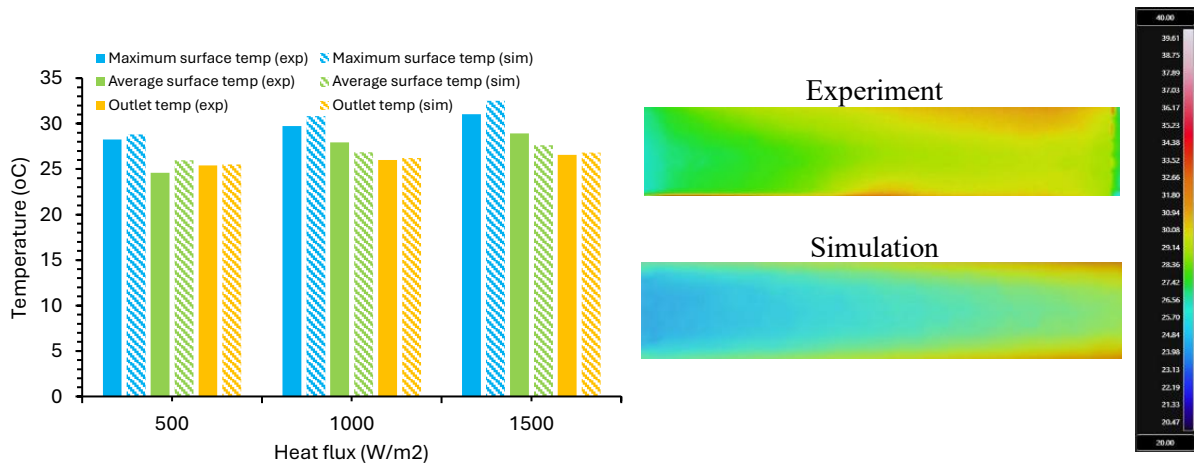

a) b)

Figure 9 – a) Experimental and simulated temperatures of a 4 mm, 0.97 mm, five-channel specimen at 1500 W/m^2 and 10 ml/min b) Experimental and simulated top surface temperature profiles of a 4 mm, 0.97 mm, five-channel specimen at 1500 W/m^2 and 10 ml/min

The COMSOL models can also be used to compare the simulated temperature profiles to those captured with the IR camera, as shown in Figure 9b. There is good visual agreement with several features, showing for instance that the specimen is hotter on the outlet side than the inlet side, as the fluid heats as it traverses the specimen.

4 CONCLUSIONS AND FUTURE WORK

This work undertook a combined experimental and numerical campaign to explore the ability of composite plates to be actively fluid cooled through the use of embedded channels. A large number of specimens were manufactured and tested to explore the impact of the key geometrical and operating parameters on the cooling performance achievable, which was considered in terms of both surface temperature reduction and heat flux.

The results show that embedded channels allow for highly effective cooling of the composite specimens even at low coolant flow rates and channel volume fractions. Higher flow rates and an increasing number of channels improve the effectiveness of this cooling, both in terms of maximum temperature reduction and in terms of temperature uniformity. Other parameters such as channel diameter and coolant fluid type play a lesser role. With the correct combination of parameters, composite systems can be successfully cooled to safe working temperatures based on application specific thermal loads, as evidenced in the high heat flux tests. However, pressure difference and inlet temperature of the fluid must be accurately regulated.

The COMSOL models have been validated against the experimental data and can now be used to explore a more complex design space with alternative channel architectures containing 2D shapes, branches and multi-layered sections. These will be designed in COMSOL to test their effectiveness and suitability before being manufactured and tested experimentally.

The existing specimens will be further tested to be fully characterised thermally, with particular attention taken to the effect of inlet temperature and coolant fluid. The specimens will also be mechanically characterised through tensile testing to determine the impact that the presence of the channels have on mechanical properties of the composite under various loading scenarios.

ACKNOWLEDGEMENTS

The author would like to acknowledge the Engineering and Physical Sciences Research Council (EPSRC) for funding this work along with sponsors at Leonardo Helicopters UK.

REFERENCES

[1] Ozkan, D., Gok, M.S., Karaoglanli, A.C. (2020). Carbon Fiber Reinforced Polymer (CFRP) Composite Materials, Their Characteristic Properties, Industrial Application Areas and Their Machinability. In: Öchsner, A., Altenbach, H. (eds) Engineering Design Applications III. Advanced Structured Materials, vol 124. Springer, Cham. https://doi.org/10.1007/978-3-030-39062-4_20

[2] Glowania, M., Lindner, D., Linke, M., Gries, T., & Heider, D. (2011). *Influence of the pitch fibre reinforcement of CFRP on the mechanical and thermal conductivity properties*.

[3] Rodrigo, O., & Bertrand, G. (2022). Radial thermal conductivity of a PAN type carbon fiber using the 3 omega method. *International Journal of Thermal Sciences*, *172*. https://doi.org/10.1016/j.ijthermalsci.2021.107321

[4] Nysten, B., Piraux, L., & Issi, J. P. (1985). Thermal conductivity of pitch-derived fibres. *Journal of Physics D: Applied Physics*, *18*(7), 1307–1310. https://doi.org/10.1088/0022-3727/18/7/016

[5] Yuan, G., Li, X., Dong, Z., Xiong, X., Rand, B., Cui, Z., Cong, Y., Zhang, J., Li, Y., Zhang, Z., & Wang, J. (n.d.). *Pitch-based ribbon-shaped carbon-fiber-reinforced one-dimensional carbon/carbon composites with ultrahigh thermal conductivity*.

[6] Wan, X., Demir, B., An, M., Walsh, T. R., & Yang, N. (2021). Thermal conductivities and mechanical properties of epoxy resin as a function of the degree of cross-linking. *International Journal of Heat and Mass Transfer*, *180*. https://doi.org/10.1016/j.ijheatmasstransfer.2021.121821

[7] Struzziero, G., Remy, B., & Skordos, A. A. (2019). Measurement of thermal conductivity of epoxy resins during cure. *Journal of Applied Polymer Science*, *136*(5). https://doi.org/10.1002/app.47015

[8] Tian, T., & Cole, K. D. (2012). Anisotropic thermal conductivity measurement of carbon-fiber/epoxy composite materials. *International Journal of Heat and Mass Transfer*, *55*(23–24), 6530–6537. https://doi.org/10.1016/j.ijheatmasstransfer.2012.06.059

[9] Pilling, M. W., Yates, B., Black, M. A., & Rsall, P. T. (1979). The thermal conductivity of carbon fibre-reinforced composites. In *JOURNAL OF MATERIALS SCIENCE* (Vol. 14).

[10] Zhang, A., & Li, Y. (2023). Thermal Conductivity of Aluminum Alloys—A Review. In *Materials* (Vol. 16, Issue 8). MDPI. https://doi.org/10.3390/ma16082972

[11] Gabrion, X., Placet, V., Trivaudey, F., & Boubakar, L. (2016). About the thermomechanical behaviour of a carbon fibre reinforced high-temperature thermoplastic composite. *Composites Part B: Engineering*, *95*, 386–394. https://doi.org/10.1016/j.compositesb.2016.03.068

[12] Burger, N., Laachachi, A., Mortazavi, B., Ferriol, M., Lutz, M., Toniazzo, V., & Ruch, D. (2015). Alignments and network of graphite fillers to improve thermal conductivity of epoxy-based composites. *International Journal of Heat and Mass Transfer*, *89*, 505–513. https://doi.org/10.1016/J.IJHEATMASSTRANSFER.2015.05.065

[13] Sweeting, R. D., & Thomson, R. S. (2004). The effect of thermal mismatch on Z-pinned laminated composite structures. *Composite Structures*, *66*(1–4), 189–195. https://doi.org/10.1016/J.COMPSTRUCT.2004.04.037

[14] Zilio, C., Righetti, G., Mancin, S., Hodot, R., Sarno, C., Pomme, V., & Truffart, B. (2018). Active and passive cooling technologies for thermal management of avionics in helicopters: Loop heat pipes and mini-Vapor Cycle System. *Thermal Science and Engineering Progress*, *5*, 107–116. https://doi.org/10.1016/j.tsep.2017.11.002

[15] Hansen, C. J., Wu, W., Toohey, K. S., Sottos, N. R., White, S. R., & Lewis, J. A. (2009). Self-healing materials with interpenetrating microvascular networks. *Advanced Materials*, *21*(41), 4143–4147. https://doi.org/10.1002/adma.200900588

[16] Norris, C. J., Meadway, G. J., O'Sullivan, M. J., Bond, I. P., & Trask, R. S. (2011). Self-healing fibre reinforced composites via a bioinspired vasculature. *Advanced Functional Materials*, *21*(19), 3624–3633. https://doi.org/10.1002/adfm.201101100

[17] Coppola, A. M., Griffin, A. S., Sottos, N. R., & White, S. R. (2015). Retention of mechanical performance of polymer matrix composites above the glass transition temperature by vascular cooling. *Composites Part A: Applied Science and Manufacturing*, *78*, 412–423. https://doi.org/10.1016/J.COMPOSITESA.2015.07.012

[18] Coppola, A. M., Thakre, P. R., Sottos, N. R., & White, S. R. (2014). Tensile properties and damage evolution in vascular 3D woven glass/epoxy composites. *Composites Part A: Applied Science and Manufacturing*, *59*, 9–17. https://doi.org/10.1016/j.compositesa.2013.12.006

[19] Pety, S. J., Tan, M. H. Y., Najafi, A. R., Barnett, P. R., Geubelle, P. H., & White, S. R. (2017). Carbon fiber composites with 2D microvascular networks for battery cooling. *International Journal of Heat and Mass Transfer*, *115*, 513–522. https://doi.org/10.1016/J.IJHEATMASSTRANSFER.2017.07.04

[20] Pety, S. J., L Chia, P. X., Carrington, S. M., & White, S. R. (2017). Active cooling of microvascular composites for battery packaging. *Smart Materials and Structures*, *26*(10), 105004. https://doi.org/10.1088/1361-665X/AA84E7

[21] Soghrati, S., Thakre, P. R., White, S. R., Sottos, N. R., & Geubelle, P. H. (2012). Computational modeling and design of actively-cooled microvascular materials. *International Journal of Heat and Mass Transfer*, *55*(19–20), 5309–5321. https://doi.org/10.1016/J.IJHEATMASSTRANSFER.2012.05.041

[22] Kozola, B. D., Shipton, L. A., Natrajan, V. K., Christensen, K. T., & White, S. R. (2010). Characterization of active cooling and flow distribution in microvascular polymers. *Journal of Intelligent Material Systems and Structures*, *21*(12), 1147–1156. https://doi.org/10.1177/1045389X10379662

[23] Phillips, D. M., Ryan Pierce, M., & Baur, J. W. (2011). Mechanical and thermal analysis of microvascular networks in structural composite panels. *Composites Part A: Applied Science and Manufacturing*, *42*(11), 1609–1619. https://doi.org/10.1016/j.compositesa.2011.07.008

[24] Bleay, S. M., Loader, C. B., Hawyes, V. J., Humberstone, L., & Curtis, P. T. (2001). *A smart repair system for polymer matrix composites*. www.elsevier.com/locate/compositesa

[25] Pierce, M. R. (2010). *MICROVASCULAR HEAT TRANSFER ANALYSIS IN CARBON FIBER COMPOSITE MATERIALS*.

[26] Trask, R. S., & Bond, I. P. (2010). Bioinspired engineering study of Plantae vascules for self-healing composite structures. *Journal of the Royal Society Interface*, *7*(47), 921–931. https://doi.org/10.1098/rsif.2009.0420

[27] Norris, C. J., Bond, I. P., & Trask, R. S. (2011). The role of embedded bioinspired vasculature on damage formation in self-healing carbon fibre reinforced composites. Composites Part A: Applied Science and Manufacturing, 42(6), 639–648. https://doi.org/10.1016/j.compositesa.2011.02.003

[28] Therriault, D., White, S. R., & Lewis, J. A. (2003). Chaotic mixing in three-dimensional microvascular networks fabricated by direct-write assembly. *Nature Materials*, *2*(4), 265–271. https://doi.org/10.1038/nmat863

[29] Toohey, K. S., Sottos, N. R., Lewis, J. A., Moore, J. S., & White, S. R. (2007). Self-healing materials with microvascular networks. *Nature Materials*, *6*(8), 581–585. https://doi.org/10.1038/nmat1934

[30] Esser-Kahn, A. P., Thakre, P. R., Dong, H., Patrick, J. F., Vlasko-Vlasov, V. K., Sottos, N. R., Moore, J. S., & White, S. R. (2011). Three-dimensional microvascular fiber-reinforced composites. *Advanced Materials*, *23*(32), 3654–3658. https://doi.org/10.1002/adma.201100933

[31] Dong, H., Esser-Kahn, A. P., Thakre, P. R., Patrick, J. F., Sottos, N. R., White, S. R., & Moore, J. S. (2012). Chemical treatment of poly(lactic acid) fibers to enhance the rate of thermal depolymerization. *ACS Applied Materials & Interfaces*, *4*(2), 503–509. https://doi.org/10.1021/am2010042

[32] McElroy, M. W., Lawrie, A., & Bond, I. P. (2015). Optimisation of an air film cooled CFRP panel with an embedded vascular network. *International Journal of Heat and Mass Transfer*, *88*, 284–296. https://doi.org/10.1016/J.IJHEATMASSTRANSFER.2015.04.071

[33] Kousourakis, A., Mouritz, A. P., & Bannister, M. K. (2006). Interlaminar properties of polymer laminates containing internal sensor cavities. *Composite Structures*, *75*(1–4), 610–618. https://doi.org/10.1016/j.compstruct.2006.04.086

[34] Kousourakis, A., Bannister, M. K., & Mouritz, A. P. (2008). Tensile and compressive properties of polymer laminates containing internal sensor cavities. *Composites Part A: Applied Science and Manufacturing*, *39*(9), 1394–1403. https://doi.org/10.1016/j.compositesa.2008.05.003

[35] Hexcel. (2015). *SAFETY DATA SHEET HexPly 8552S*.

MANUFACTURING PATTERNED CARBON FIBER CATHODES BY SUPERCRITICAL SPRAY: SIMULTANEOUS ENHANCEMENT OF ELECTROCHEMICAL AND MECHANICAL PROPERTIES OF STRUCTURAL BATTERY COMPOSITES

Farshad Bozorgmehrian[1], Mohammad Zaker Tabrizi[2], Myunghwan Jeong[3], Ehsan Hosseini[4], Dorrin Jarrahbashi[5], Homero Castaneda[6], Amir Asadi[7*]

[1]Department of Engineering Technology and Industrial Distribution, Texas A&M University, College Station, Texas 77843-3367, United States, Email: farshadbzm@tamu.edu
[2]Department of Mechanical Engineering, Texas A&M University, College Station, Texas 77843, United States Email: farhadzaker@tamu.edu
[3]Department of Materials Science and Engineering, Texas A&M University, College Station, Texas 77843-3367, United States, Email: j16mhwan@tamu.edu
[4]Department of Mechanical Engineering, Texas A&M University, College Station, Texas 77843, United States Email: ehsan.hosseini@tamu.edu
[5]Department of Mechanical Engineering, Texas A&M University, College Station, Texas 77843, United States Email: djarrahbashi@tamu.edu
[6]Department of Materials Science and Engineering, Texas A&M University, College Station, Texas 77843-3367, United States, Email: hcastaneda@tamu.edu
[7]Department of Engineering Technology and Industrial Distribution, Texas A&M University, College Station, Texas 77843-3367, United States, Email: amir.asadi@tamu.edu

Keywords: Solid-State Batteries, Structural Battery Composites, Spray Coating, Cathode Patterning

ABSTRACT

The shift toward zero-emission mobility for urban, air, and space transport requires transformative advances in structural energy storage. Carbon fiber reinforced polymer structural battery composites (CFRP-SBCs) present a compelling opportunity by integrating load bearing and energy storage capabilities. However, their practical deployment in electric aviation and e-VTOL applications is hindered by two fundamental challenges: low energy density and compromised mechanical performance. Herein, we introduce a sustainable, scalable manufacturing approach utilizing supercritical spray deposition to engineer tailorable 3D nanostructures on carbon fiber cathodes. By manipulating the amphiphilicity and droplet size of hybrid suspensions containing lithium iron phosphate (LFP) and reduced graphene oxide (rGO), distinct post-evaporation patterns, rings, domes, and disks/domes, are formed. These patterns modulate interfacial properties and electrochemical behavior, enabling the concurrent enhancement of energy density and interfacial strength, previously considered challenging. Our results show that disk/dome patterned cathodes perform better in electrochemical properties (energy density, power density, capacity) while ring patterned cathodes show higher interfacial adhesion. These results demonstrate that combining multiple patterns enables synergistic improvements in both mechanical and functional performance. This platform paves the way for the development of high-strength, high-energy-density composite systems critical to enabling future e-mobility applications.

1 INTRODUCTION

The growing demand for zero-emission vehicles for urban, air and space mobility has reignited interest in battery-powered electric mobility (e-mobility). Particularly, reshaping aviation toward a greener future by 2050 [1] will not be realized without addressing challenges in battery technology in electric flights and electric vertical take-off and landing (e-VTOL) aircrafts. Carbon fiber reinforced polymer battery composites (CFRP-SBCs), comprising polymers as electrolyte matrix and carbon fibers (CFs) as electrodes, collectors and reinforcements show a perfect synergy between structural performance and energy efficiency. However, a significant hurdle is the considerably lower energy

density (less than 40 Wh/kg in full cell configuration) [2-4] compared to the conventional batteries as well as the minimum required 400-600 Wh/kg for small-medium size planes [5], and their significantly reduced strength and stiffness (2-10 GPa modulus and ~100-200 MPa strength, 20-30% of structural CFRPs). This is arising from the inherent tradeoff between mechanical and electrochemical properties and the historical separation of batteries and structures. This is a common trait in almost all engineered materials, in which efforts to enhance multiple functions, such as energy storage and structural properties, face complexity as improvements in one compromise others. Particularly in CFRP-SBCs, two bottlenecks to achieve simultaneous high energy density and high mechanical strength are: (1) Very low ion transport in solid polymer electrolytes (10^{-6}-10^{-5} S.cm^{-1}) compared to liquid (10^{-2} S.cm^{-1}) and ceramics (10^{-5}-10^{-3} S.cm^{-1}). (2) Requirement of abundant coating of active materials on carbon fiber cathodes to reach reasonable energy density that results in weakening the interfacial adhesion with the electrolyte (and separator) that causes delamination and premature mechanical failure. Herein, we introduce scalable and green manufacturing techniques without the use of harsh solvents, wherein engineered patterns are fabricated on cathode to create tailorable microstructure for simultaneously high strength and high energy density in CFRP-SBCs.

To address the limitations of conventional lithium-ion batteries and build upon insights from prior studies demonstrating the substantial influence of nanopatterning on the mechanical robustness, thermal stability, and electrical conductivity of composites, this work explores the impact of engineered nanopatterns on LFP-rGO cathode structures. Although various fabrication techniques such as sol-gel, [6], electrophoretic deposition (EPD) [7], high-temperature reduction strategy [8], drawdown method [9], and high-energy ball milling assisted by the rheological phase method [10] have been employed to create LFP/rGO composites, these approaches do not sufficiently enable the engineering of nanoscale surface morphologies. This study, therefore, investigates optimal strategies for manipulating surface patterns to achieve desired nanoscale architectures and examines how different nanopatterns affect cathode performance. The motivation for this inquiry is rooted in evidence that tailored nanopatterns not only improve interfacial adhesion between substrates such as carbon fiber and the polymer matrix, but also significantly enhance the multifunctional performance of composites without compromising mechanical integrity [11]. By extending this concept to battery cathodes, we hypothesize that specific nanopatterning strategies can markedly improve the electrochemical performance and durability of LFP-rGO systems, offering a new pathway for advanced cathode design. This exploration specifically focuses on the influence of disk/dome and ring structures patterned on cathode surfaces within structural battery composites (SBCs), aiming to bridge the current knowledge gap in this domain. Through systematic analysis of both fabrication processes and the resulting electrochemical behavior, the study demonstrates the potential of nanoscale engineering to significantly enhance battery performance [12, 13]. These efforts are supported by the adoption of innovative fabrication techniques, notably a precision spray-deposition method, which enables controlled pattern formation and offers refined balance between power output and specific capacity, thereby embodying a rigorous approach to electrochemical tuning and optimization for LFP-rGO cathodes [11, 14-26].

Our novel, scalable and sustainable processing-manufacturing technology, in which a combination of supercritical spray technique and tailorable materials chemistry (via engineering amphiphilicity) allows creation of 3D patterns on carbon fiber-based cathodes. These patterns are combined to create desired 3D nanostructures to achieve tailorable properties. To this end, the droplet size and amphiphilicity degree of the hybrid material system contained in droplets, i.e. lithium iron phosphate (LFP) and reduced graphene oxide (RGO), are engineered based on their mass ratio and then delivered onto the carbon fibers using supercritical spray. The droplet sizes are in the range of 5 μm, as the small microscale droplets allow for faster fabrication of cathode with higher surface area that incurs higher interface with the developed electrolyte. The combination of amphiphilicity and droplet size results in three distinctive post-evaporation patterns, i.e. ring, disk, and dome. Each pattern is meticulously designed to enhance a specific functionality or property. By strategically composing these patterns with precise shape, size, and spacing, we achieve the creation of 3D nanostructured surfaces that exhibit both high energy density and exceptional mechanical strength, qualities often deemed paradoxical and unattainable with conventional manufacturing methods. The outcomes of our study are emerging key materials and a novel high-throughput manufacturing technique required for accelerated development of the next-generation multifunctional structures for battery-powered and eco-friendly mobility.

2 MATERIALS AND METHODS

Reduced graphene oxide (rGO) used in this study was sourced from ACS Material and synthesized via the N_2H_2 chemical reduction method. It appeared brownish-grey, had a thickness of approximately 1 nm, and exhibited a monolayer diameter ranging from 0.5 to 10 μm with over 90% monolayer content. Its BET surface area was measured at ~180 m^2/g, and carbon content exceeded 82 wt.%, with electrical conductivity surpassing 500 S/m. Lithium iron phosphate (LFP) from Landt International Inc. featured a particle size median (D50) of 1.302 μm, a surface area of 13.36 m^2/g, and a density of 1.14 g/cm^3. Its discharge capacity was recorded at 153 mAh/g under 0.1C at 25 °C, highlighting its electrochemical effectiveness. To fabricate composite cathodes, rGO was strategically incorporated into LFP using spray-deposition at two mass ratios: 8:1 (LFP:rGO) to produce ring-like patterns and 1:1 for dome structures. The materials were dispersed at 1.5 wt.% in dimethylformamide (DMF) and subjected to a two-step sonication process. First, LFP was sonicated at 53% amplitude for 10 minutes. Then, rGO was added and the mixture underwent an additional 20-minute sonication. The dispersion was sprayed onto acetone-cleaned aluminum substrates (19 mm diameter), which were chosen to match the dimensions required for coin cell cathodes. Each spray round was performed at 20 MPa pressure, maintaining a 15 cm distance and a 45° nozzle angle to ensure uniform coating. Pauses between rounds allowed solvent evaporation, preventing droplet agglomeration. The active material deposited was approximately 4 mg for the 8:1 sample (2.68 mg/cm^2) and 4.4 mg for the 1:1 sample (2.95 mg/cm^2). Coin cells were assembled in an argon-filled glove box using the coated cathodes, $LiPF_6$ electrolyte, lithium metal anodes, separators, spacers, and crimped stainless steel casings. Surface morphology of the deposited patterns was evaluated using a Bruker DektakXT Surface Profiler, while microstructural analysis was conducted via a Tescan FERA-3 FIB microscope. Electrochemical characterization involved cyclic voltammetry and galvanostatic charge/discharge measurements (2.0–4.25 V) using a Gamry Interface 1010E potentiostat, with CV conducted at 0.1 mV/s for 10 cycles. Specific capacities were reported based on the total mass of the LFP/rGO electrodes. We also evaluated the adhesion strength of the active material to the substrate by measuring weight loss in the tape adhesion test. The test was conducted with a 200 g for the first eight cycles, followed by 1540 g and 6540 g for the second and third eight-cycle stages, respectively.

3 RESULTS AND DISCUSSION

3.1 Cathodes Morphology

The LFP/rGO dispersion was applied to aluminum substrates/current collectors using a precision spray-deposition method. Compositions with varying LFP to rGO weight ratios were prepared and labeled as LFP/rGO-(Y:Z), where 'Y:Z' denotes the respective mass ratios. A total of 25 spray passes were performed using a 1.5 wt.% solution to deposit each formulation.

Figure 1 presents scanning electron microscopy (SEM) images of the deposited LFP/rGO ring and disk/dome patterns. These images reveal that LFP nanoparticles are predominantly encapsulated by rGO sheets and interconnected with neighboring particles following the evaporation of DMF. Figure 1a illustrates a ring-shaped pattern formed by the droplet, while Figures 1B and 1C show the material distribution at the center and periphery of the same pattern. In contrast, Figures 1E and 1F show a disk/dome pattern, where the composite material is concentrated along the outer diameter of the droplet. Compared to the dome pattern, where material is centered, the ring pattern is characterized by an empty core with materials pushed to the perimeter. These distinct morphologies arise from variations in the LFP/rGO ratio used in the spray solution.

Figure 2 provides further morphological and elemental analysis using SEM and energy-dispersive spectroscopy (EDS). Figure 2a displays a SEM image of a dried droplet from an LFP/rGO-(8:1) mixture, revealing the expected ring pattern, characterized by concentrated Fe and P signals around the droplet perimeter, with a distinct void in the center. Figures 2B and 2C, showing iron (Fe) and phosphorus (P) EDS maps, confirm this ring shape distribution. In contrast, Figures 2D, 2E, and 2F examine a droplet from an LFP/rGO-(1:1) formulation. Here, the SEM and EDS maps illustrate a diskdome morphology, marked by high material density in the center and gradual thinning toward the edges

The use of a spray-deposition approach on aluminum current collectors enables the formation of well-defined microscale patterns, ranging from rings to disks and/or domes, on the substrate surface. These patterns are dictated by the composition and amphiphilic balance of the hybrid nanoparticle suspension. Our study shows that higher rGO content, such as in the LFP/rGO-(1:1) mixture, favors disk-shaped deposits, where the droplet dries to form a dense, raised center composed of overlapping rGO-LFP clusters. In contrast, lower rGO content (e.g., LFP/rGO-(8:1)) results in ring-like patterns due to differential solvent evaporation dynamics, pushing the particles outward.

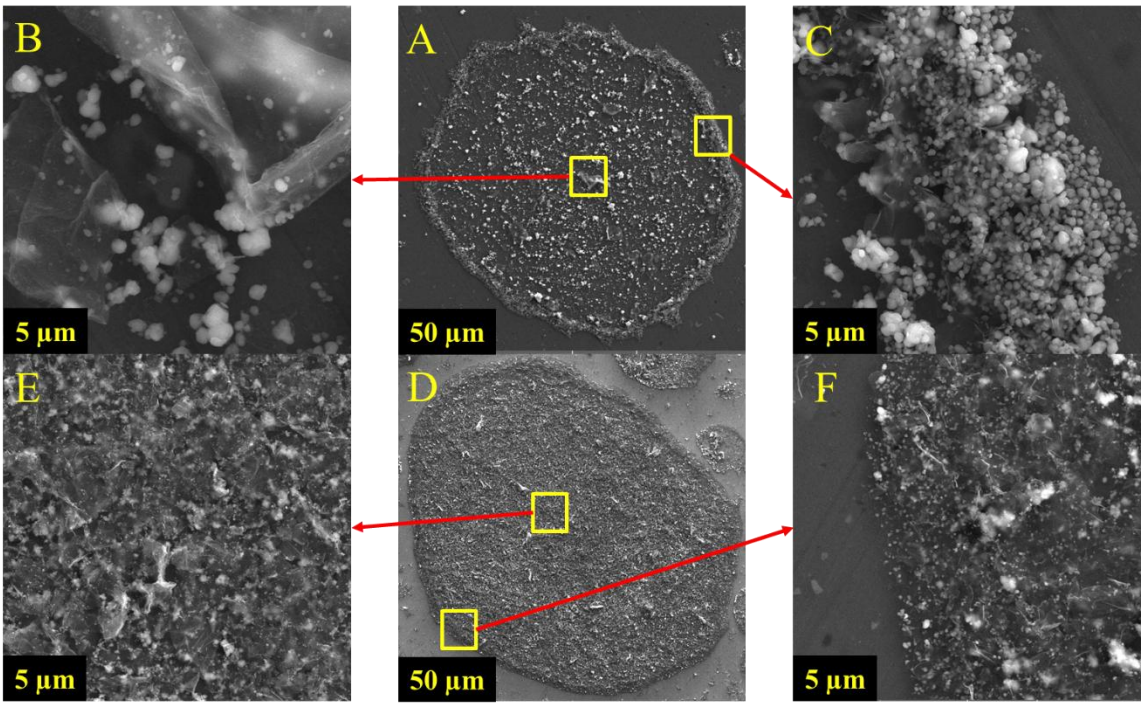

Figure 1. SEM image of LFP/rGO left after evaporation of sprayed droplets on the Al substrate/current collector cathode: A) Ring pattern (LFP/rGO-(1:1)), B) Center of the ring pattern, C) Outer diameter of ring pattern, D) Disk/Dome pattern (LFP/rGO-(8:1)), E) Outer diameter of the disk/dome pattern, F) Center of disk/dome pattern.

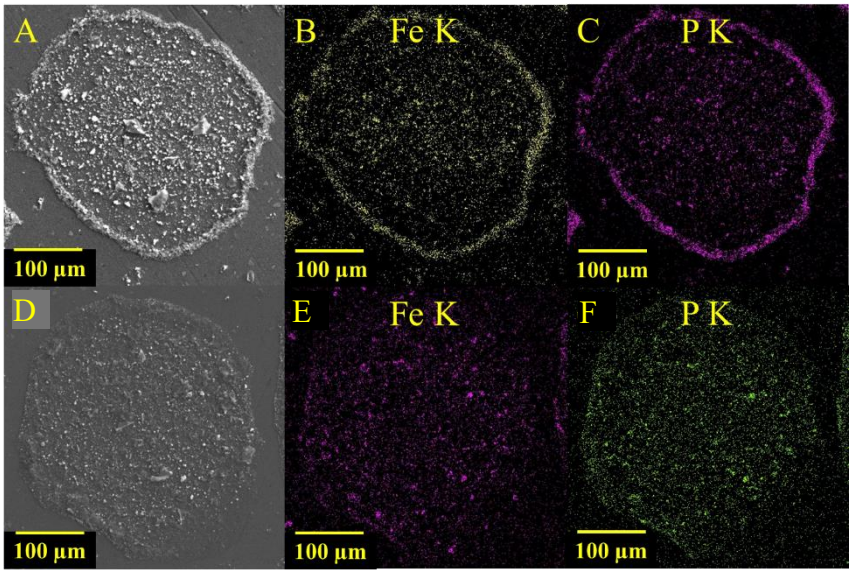

Figure 2: SEM, EDS maps and profilometry of LFP/rGO left after evaporation of sprayed droplets on Al substrate/current collector cathode A) SEM image of ring pattern (LFP/rGO-(1:1)), B, C) EDS

of ring pattern (Fe, P), D) SEM image of disk/dome pattern (LFP/rGO-(8:1)), E, F) EDS element mapping of the dome pattern (Fe, P)

3.2 Electrochemical and Mechanical Properties

The interface between the cathode and electrolyte plays a critical role in determining the electrochemical performance of lithium-ion batteries. As such, the ability to control the deposition pattern of active materials during fabrication offers a promising strategy to tailor cathode functionality. In this study, we investigated how distinct deposition patterns, namely disk and ring structures, influence the performance of LFP/rGO cathodes. Electrochemical characterization was performed using cyclic voltammetry (CV) at a scan rate of 0.1 mV/s, comparing patterned cathodes against a classic LFP formulation (LFP:PVP:Carbon Black at 93:2:5 wt.%) (Figure 4a). Both ring and disk-patterned cathodes displayed symmetrical redox peaks, indicative of good reversibility, though notable differences emerged. The disk-patterned electrodes showed sharper peaks and higher current responses than their ring counterparts, suggesting enhanced reaction kinetics and improved charge transfer efficiency. This was further supported by a smaller voltage separation between oxidation and reduction peaks, pointing to reduced polarization. While the ring pattern exhibited broader peaks and slightly lower peak currents (~80–85% of disk), its more gradual charge transfer dynamics may be advantageous under high-rate cycling, reducing parasitic losses and extending durability.

Electrochemical impedance spectroscopy (EIS) provided further insights into charge transfer behavior (Figure 4b). The charge transfer resistance (R_{ct}) of the classic LFP cathode was significantly higher (~380 Ω) compared to both patterned variants, 220 Ω for ring and 150 Ω for disk/dome, highlighting the improved conductivity introduced by rGO. When normalized to the weight of active materials, the disk/dome-patterned cathode delivered the highest specific power and energy output, approximately 486 W/kg and 44.12 kWh/kg, while the ring-patterned version followed closely with about 10% lower values. The classic LFP cathode, by contrast, exhibited significantly lower performance in all metrics (Figure 4C).

Mechanical integrity was assessed using adhesion testing (Figure 4D), which monitored residual weight loss over multiple tape-peeling iterations. Among the three designs, the ring-patterned cathode demonstrated the slowest rate of material removal, as evidenced by the smallest slope magnitude (-2.41×10^{-4} g/iteration), indicating superior adhesion. In contrast, the classic LFP cathode exhibited the fastest material loss (-8.05×10^{-4} g/iteration), suggesting weaker cohesion. This enhanced adhesion in the ring pattern is attributed to its more compact microstructure and reduced rGO content, which minimizes lubrication effects between LFP particles. Additionally, the ring geometry, with a taller and thinner outer wall, offers a larger interfacial area and improved mechanical interlocking with the electrolyte layer, further contributing to its robust adhesion performance.

Mechanical integrity was assessed using adhesion testing (Figure 4D). Interestingly, the ring-patterned cathode exhibited approximately 25% higher tangential friction force compared to the disk/dome, indicating stronger cohesion and greater resistance to delamination. This is attributed to the lower rGO content in the ring structure, as rGO tends to act as a lubricant between LFP particles. The enhanced compactness of the ring configuration results in a more mechanically robust microstructure. Tape-adhesion tests and triboindenter results corroborated these findings. Notably, the ring pattern, characterized by a thin outer wall with an average height three times greater than that of the disk/dome structure, offers a larger interfacial area and improved mechanical interlocking with the electrolyte layer.

In summary, while disk/dome-patterned cathodes deliver superior electrochemical performance in terms of peak current, specific capacity, and output power, the ring-patterned design excels in structural robustness and interfacial stability. These complementary traits suggest that combining ring and disk/dome patterns through a controlled spray-deposition process could yield a hybrid cathode architecture optimized for both performance and durability. This hybrid approach offers greater design flexibility than traditional slurry casting, enabling tailored electrode architectures for next-generation structural battery composites.

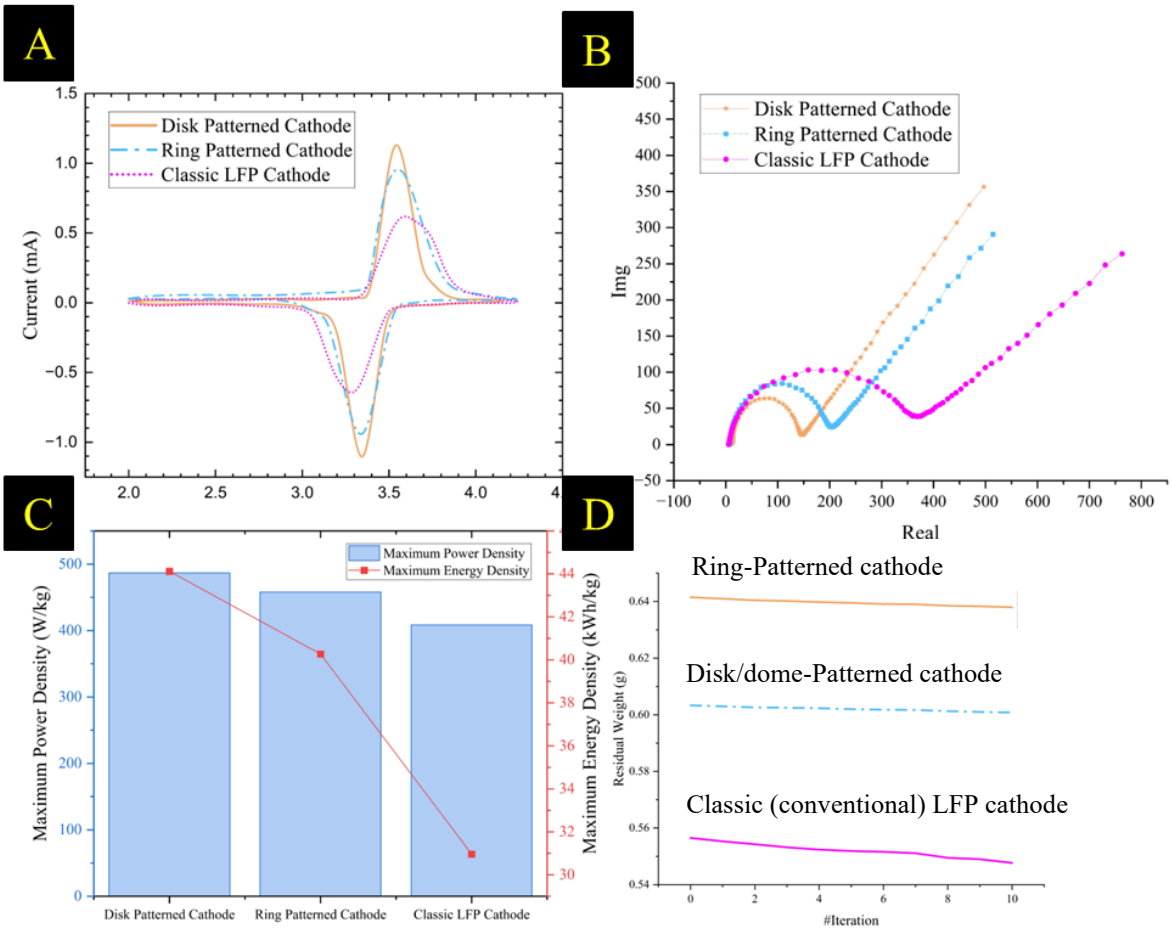

Figure 4. Electrochemical performance comparison of LFP:rGO cathodes with disk/dome and ring patterns: A) Cyclic voltammetry, B) Nyquist plot, C) Maximum power density and Energy density, and D) Adhesion mechanical test.

CONCLUSIONS

This study demonstrates that nanoscale surface patterning of active materials on cathodes, achieved through precision spray deposition, offers a powerful strategy to tailor the electrochemical and mechanical performance of lithium-ion batteries. By systematically varying the weight ratio of LFP to rGO in the spray dispersion, we produced distinct surface morphologies, disk/dome and ring patterns, that led to measurable differences in battery behavior. Electrochemical tests revealed that disk/dome-patterned cathodes deliver superior energy densities, indicating enhanced conductivity and faster charge transfer. In contrast, ring-patterned cathodes exhibit improved mechanical integrity and greater cohesion at the electrode–electrolyte interface, owing to their toroidal geometry and more compact structure.

These results highlight the trade-offs and synergies inherent in cathode design: while disk/dome patterns optimize electrochemical output, ring patterns contribute to structural durability and interfacial stability. The ability to precisely control and combine these patterns on the electrode surface introduces a novel degree of freedom in cathode engineering, offering the potential to pre-design multifunctional electrodes that achieve an optimal balance between performance and longevity. This pattern-directed strategy significantly advances the conventional two-dimensional slurry-based fabrication methods and opens new avenues for customizable, high-performance structural battery composites.

ACKNOWLEDGEMENTS

This material is based upon work supported by the National Science Foundation, Civil, Mechanical and Manufacturing Innovation (CMMI), Advanced Manufacturing, under Grants #2143286, and #2134465. The authors would like to acknowledge that the characterization part of this work was conducted at Texas A&M University Materials Characterization Core Facility, and the calculations regarding the simulation segment was performed at Supercomputer resources from Texas A&M University High Performance Computer Center (HPRC). The authors thank Dr. Liang, Humaun Kabir, and Darius Dias for their contributions to the tribology experiments.

REFERENCES

[1] E. Karadotcheva, S.N. Nguyen, E.S. Greenhalgh, M.S.P. Shaffer, A.R.J. Kucernak, P. Linde, Structural Power Performance Targets for Future Electric Aircraft, Energies 14(19) (2021) 6006.
[2] L.E. Asp, K. Bouton, D. Carlstedt, S. Duan, R. Harnden, W. Johannisson, M. Johansen, M.K.G. Johansson, G. Lindbergh, F. Liu, K. Peuvot, L.M. Schneider, J. Xu, D. Zenkert, A Structural Battery and its Multifunctional Performance, Advanced Energy and Sustainability Research 2(3) (2021) 2000093.
[3] L.E. Asp, M. Johansson, G. Lindbergh, J. Xu, D. Zenkert, Structural battery composites: a review, Functional Composites and Structures 1(4) (2019) 042001.
[4] T. Jin, G. Singer, K. Liang, Y. Yang, Structural batteries: Advances, challenges and perspectives, Materials Today 62 (2023) 151-167.
[5] V. Viswanathan, A.H. Epstein, Y.-M. Chiang, E. Takeuchi, M. Bradley, J. Langford, M. Winter, The challenges and opportunities of battery-powered flight, Nature 601(7894) (2022) 519-525.
[6] E. Suarso, A.Z. Laila, F.A. Setyawan, M. Zainuri, Z. Arifin, D. Darminto, The effect of reduced graphene oxide (Rgo) coating on electrical conductivity of lithium ferro phosphate (lfp) as an alternative cathode for li-ion battery, Materials Science Forum, Trans Tech Publ, 2019, pp. 386-391.
[7] N. Tolganbek, N. Zhalgas, Y. Kadyrov, N. Umirov, Z. Bakenov, A. Mentbayeva, Facile Deposition of the LiFePO4 Cathode by the Electrophoresis Method, ACS omega 8(8) (2023) 8045-8051.
[8] Q. Zhang, Y. Zhou, Y. Tong, Y. Chi, R. Liu, C. Dai, Z. Li, Z. Cui, Y. Liang, Y. Tan, Reduced Graphene Oxide Coating LiFePO4 Composite Cathodes for Advanced Lithium-Ion Battery Applications, International Journal of Molecular Sciences 24(24) (2023) 17549.
[9] J. Kim, S. Song, C.S. Lee, M. Lee, J. Bae, Prominent enhancement of stability under high current density of LiFePO4-based multidimensional nanocarbon composite as cathode for lithium-ion batteries, Journal of Colloid and Interface Science 650 (2023) 1958-1965.
[10] X. Wang, Z. Feng, J. Huang, W. Deng, X. Li, H. Zhang, Z. Wen, Graphene-decorated carbon-coated LiFePO4 nanospheres as a high-performance cathode material for lithium-ion batteries, Carbon 127 (2018) 149-157.
[11] O. Kaynan, E. Hosseini, M. Zakertabrizi, E. Motta De Castro, L.M. Pérez, D. Jarrahbashi, A. Asadi, Multifunctionality through Embedding Patterned Nanostructures in High-Performance Composites, Advanced Materials 35(32) (2023) 2300948.
[12] Y. Liu, X. Tao, Y. Wang, C. Jiang, C. Ma, O. Sheng, G. Lu, X.W. Lou, Self-assembled monolayers direct a LiF-rich interphase toward long-life lithium metal batteries, Science 375(6582) (2022) 739-745.
[13] X.-B. Cheng, R. Zhang, C.-Z. Zhao, Q. Zhang, Toward safe lithium metal anode in rechargeable batteries: a review, Chemical reviews 117(15) (2017) 10403-10473.
[14] X. Wu, K. Song, X. Zhang, N. Hu, L. Li, W. Li, L. Zhang, H. Zhang, Safety issues in lithium ion batteries: materials and cell design, Frontiers in Energy Research 7 (2019) 65.
[15] C.J. Bae, C.K. Erdonmez, J.W. Halloran, Y.M. Chiang, Design of battery electrodes with dual-scale porosity to minimize tortuosity and maximize performance, (2013).
[16] J. Wu, X. Zhang, Z. Ju, L. Wang, Z. Hui, K. Mayilvahanan, K.J. Takeuchi, A.C. Marschilok, A.C. West, E.S. Takeuchi, From fundamental understanding to engineering design of high-performance thick electrodes for scalable energy-storage systems, Advanced Materials 33(26) (2021) 2101275.
[17] E. Pomerantseva, F. Bonaccorso, X. Feng, Y. Cui, Y. Gogotsi, Energy storage: The future enabled by nanomaterials, Science 366(6468) (2019) eaan8285.

[18] Z. Ju, Y. Zhu, X. Zhang, D.M. Lutz, Z. Fang, K.J. Takeuchi, E.S. Takeuchi, A.C. Marschilok, G. Yu, Understanding thickness-dependent transport kinetics in nanosheet-based battery electrodes, Chemistry of Materials 32(4) (2020) 1684-1692.
[19] K.-H. Chen, M.J. Namkoong, V. Goel, C. Yang, S. Kazemiabnavi, S. Mortuza, E. Kazyak, J. Mazumder, K. Thornton, J. Sakamoto, Efficient fast-charging of lithium-ion batteries enabled by laser-patterned three-dimensional graphite anode architectures, Journal of Power Sources 471 (2020) 228475.
[20] W. Pfleging, J. Pröll, A new approach for rapid electrolyte wetting in tape cast electrodes for lithium-ion batteries, Journal of Materials Chemistry A 2(36) (2014) 14918-14926.
[21] A. Jinasena, O.S. Burheim, A.H. Strømman, A flexible model for benchmarking the energy usage of automotive lithium-ion battery cell manufacturing, Batteries 7(1) (2021) 14.
[22] Y. Kang, C. Deng, Y. Chen, X. Liu, Z. Liang, T. Li, Q. Hu, Y. Zhao, Binder-free electrodes and their application for Li-ion batteries, Nanoscale research letters 15 (2020) 1-19.
[23] O. Gerard, A. Numan, S. Krishnan, M. Khalid, R. Subramaniam, R. Kasi, A review on the recent advances in binder-free electrodes for electrochemical energy storage application, Journal of Energy Storage 50 (2022) 104283.
[24] T. Jin, Q. Han, L. Jiao, Binder-free electrodes for advanced sodium-ion batteries, Advanced Materials 32(3) (2020) 1806304.
[25] L.-I. Battery, Preparation of Tough, Binder-Free, and Self-Supporting LiFePO, Adv. Sci (2023) 2207355.
[26] J. Ji, Y. Li, W. Peng, G. Zhang, F. Zhang, X. Fan, Advanced Graphene-Based Binder-Free Electrodes for High-Performance Energy Storage, Advanced Materials 27(36) (2015) 5264-5279.

CONSIDERATION OF THE INFLUENCING VARIABLES OF PEEL PLY ON THE REACTION PROCESS OF CFRP SAMPLES UNDER LIQUID OXYGEN ENVIRONMENT AT IMPACT LOAD

M.Sc. Philipp Marin, Prof. Dr.-Ing. Tobias Dickhut

Institute of Aeronautical Engineering, Professorship for Composite Materials
and Technical Mechanics, University of the Bundeswehr Munich
Willy-Messerschmitt-Str. 1, 82024 Taufkirchen, Germany
Email: Philipp.Marin@unibw.de , web page: https://www.unibw.de/aero/aero

Keywords: Composite Material, Cryogenic Fuel Tanks, Liquid Oxygen, Impact, Influencing Variables,

ABSTRACT

Various characterization and certification processes are required for the use of carbon fibre reinforced plastics (CFRP) in the aerospace industry. This applies in particular if the material is in contact with reactive liquids. However, this poses a number of challenges, as the liquid oxygen used as an oxidizer, for example, can undergo a thermal reaction with the organic substances in the CFRP [**1**]. This highly exothermic reaction leads to a catastrophic failure of the entire launch vehicle. For this reason, it is essential to determine the compatibility of the tank materials used for the storage of liquid oxygen [**2**]. Several compatibility tests carried out at *University of the Bundeswehr Munich* have shown that the results obtained are sometimes subject to extreme fluctuations, which can lead to inconsistent statements about material compatibility. The influencing variables that affect the reaction process are partly unknown and are not taken into account in the standard. Based on the known problem, a newly developed test rig was set up at the *University of the Bundeswehr Munich*. The influence of the use of peel ply on the compatibility results was explicitly investigated. As a result of the stripping process, rough ridges and irregularities remain on the surface. The roughness of the component surface, caused by cavities, indentations, and surface irregularities, along with local dry spots, leads to increased reactivity of the sample in a liquid oxygen environment. As part of a series of tests to determine the influencing variables on the reaction process of carbon fibre-reinforced plastics in liquid oxygen, it was demonstrated on the test bench at the *University of the Bundeswehr Munich* that the chemical reactivity of the samples increases when using peel ply.

1 INTRODUCTION

The majority of reusable launch vehicles currently in use and those planned for the future are designed for operation with liquid propellants, using liquid oxygen (LOX) as the oxidizing agent. The state of the art to date comprises metallic tank structures that are used in current generations of launch vehicles. These structures account for over 60 % of the dry mass of a launch vehicle [**3**]. To increase the payload capacity, it is essential to reduce the dry mass. By using carbon fiber reinforced plastics (CFRP), weight savings of up to 40 % could be achieved [**3**].

However, the compatibility of CFRP materials with the LOX oxidizing agent used is a critical factor. A material is considered compatible if it does not react with LOX or potential ignition sources under the expected pressure and temperature conditions [**4**]. The avoidance of ignition events is therefore essential for the selection of suitable materials for LOX contact applications. Ignition can occur if a sufficiently high amount of energy is applied locally to the surface exposed to the LOX like shown in Figure 1 for a CFRP test Sample.



Figure 1 Exemplary reaction of a CFRP sample in liquid oxygen, in which an impact pulse of 98 J is transmitted into the sample via a Striker Pin and recorded at 240 FPS using a slow-motion camera

The compatibility of a material for use under cryogenic LOX conditions is assessed using standardized test methods. The relevant test standards include ASTM G86-17 [**5**], ASTM D2512-95 [**6**] and ISO 21010 [**7**]. Common to all methods is the transfer of kinetic energy into the material sample, which leads to an exothermic reaction with LOX in the event of incompatibility. According to ASTM G86, a material is considered compatible if no reaction occurs after 20 tests or at most one reaction after 60 tests.

A comparison of the test results according to different standards shows some considerable deviations in the assessment of LOX compatibility. The reasons for this have not yet been conclusively clarified. Although the oxidation and ignition mechanism itself is well described [4], there is a lack of reliable explanations for the random nature of the reactions and the deviations between the standards. A deeper understanding of these mechanisms is required to ensure reproducible and reliable test results for future material certifications.

The need for research therefore lies in the investigation of the reaction mechanisms of CFRP materials in contact with LOX and the identification of relevant influencing variables - particularly with regard to test stand design, sample preparation and surface properties. Experimental investigations were carried out at the *University of the Bundeswehr Munich* to analyze the influence of the sample surface on the reaction behavior. The surface topography was specifically varied by using different peel ply fabrics during laminate production. The aim is not only to determine the general influence of the surface roughness on the reaction behavior, but also to identify the causes of increased reactions.

2 STATE OF THE ART

Liquid-propellant rocket engines are widely used in modern spaceflight. With the emergence of the "New Space" movement and the development of new European launch vehicles (e.g., *Ariane 6*, *HyImpulse*, *Rocketfactory Augsburg*, *Isar Aerospace*), the demand for improved cryogenic tank systems has significantly increased. To reduce structural weight and maximize payload capacity, advanced lightweight composite materials are being integrated into launch vehicle architectures—both for primary and secondary propellant tanks. These tank structures can account for up to 60% of a launch vehicle's dry mass [3].

Future launch systems require a high propellant mass fraction to ensure performance and cost-efficiency. Due to their high strength-to-weight ratio, fiber-reinforced polymers (FRPs) are well-suited for achieving these objectives. Liquid oxygen (LOX), serving as the oxidizer in most modern vehicles such as *Ariane 6* and *Falcon 9*, is a key driver in material selection for cryogenic tanks. While CFRP-based LOX tanks offer considerable weight savings, their use introduces challenges due to potential chemical reactivity with LOX. For a material to be considered LOX-compatible, it must withstand all forms of combustible or hazardous reactions under operating conditions [10].

Material compatibility is typically assessed through a set of standardized test methods, including:

- ASTM D2512: Standard Test Method for Compatibility of Materials with Liquid Oxygen [6]
- ASTM G86-17: Determination of Mechanical Impact Sensitivity in LOX and Pressurized Oxygen Environments [5]
- ISO 21010: Compatibility of Gases and Materials in Cryogenic Containers [7]
- NASA-STD-6001: Material Flammability, Offgassing, Odor, and Compatibility Requirements [8]

At the *University of the Bundeswehr Munich*, investigations focused specifically on the influence of surface topography on reaction behavior. Prior research by *Gerzeski* [4] demonstrated that mechanical impact alone is not the sole ignition driver; surface-induced friction plays a significant role. *Gerzeski* proposed a probabilistic model combining Hertzian fracture theory and kinetic friction mechanisms to describe the transition from mechanical failure to heat generation. His findings suggest that surface irregularities, such as those introduced by peel ply usage, can result in local frictional heating, increasing the likelihood of ignition. This mechanism aligns with the so-called “hot spot” theory, widely cited in the literature as the primary cause of polymer reactivity in LOX environments. *Hongyu* et al. [9] reported that localized energy input from friction or impact can decompose polymer chains, releasing reactive hydrogen and hydroxide ions that violently react with LOX, leading to ignition or explosion. Similarly, *Li* et al. [3] describe thermal decomposition of the epoxy matrix as the key trigger for LOX reactivity, again emphasizing the role of temperature-induced hot spots.

Currie et. al [11], the addition of silicon carbide was shown to significantly increase reaction sensitivity in impact LOX tests. Its abrasive nature promotes local heating at the material surface, intensifying both reaction frequency and severity.

Similar investigations were conducted by *Duo* et al. [12], who provided a detailed analysis of the energy transfer process between the striker pin and the specimen surface. Their findings indicate that a significant portion of the mechanical impact energy is converted into heat, with localized temperature increases of several hundred degrees Celsius observed. The quality of the contact interface between the striker and the specimen, as well as the precise impact location, were identified as key factors influencing the test outcomes. According to *Duo* et al. [12], approximately 25% of the kinetic energy is dissipated through friction, while the remainder is transformed into internal energy. This frictional heating can raise local temperatures beyond the decomposition threshold of the epoxy matrix. As a result, highly reactive hydroxyl radicals are generated, which subsequently react with the surrounding liquid oxygen, potentially triggering an exothermic event.

The current study aims to investigate the formation of surface hot spots on CFRP specimens, focusing on resin-rich microstructures caused by different peel ply treatments during laminate fabrication.

3 STANDARDIZED TESTING METHODOLOGY AND EXPERIMENTAL SETUP

As part of the conducted experimental series to determine the influencing factors of auxiliary materials on the reaction behavior of CFRP specimens in liquid oxygen under impact loading, tests were carried out according to ASTM G86-17. The standardized procedure involves dropping a defined mass from a specified height onto a striker pin positioned directly on the specimen. The goal is to apply an impact energy of 98 J to the sample, derived from a 9.1 kg drop mass released from a height of 1.1 m. During the test, the specimen is placed in a test cup filled with liquid oxygen. Material incompatibility with LOX is identified based on the following observable criteria [5]:

1. Audible explosion
2. Flash (visually or electronically detected)
3. Signs of combustion, such as visible charring
4. Significant discoloration due to ignition
5. Measurable increases in temperature or pressure during testing

According to ASTM G86, a material is considered compatible if none of these reactions occur in 20 tests or if no more than one reaction is observed in 60 tests. The test specimens used are circular CFRP flat samples with a diameter of 17.5 mm and a thickness of approximately 2 mm. The ASTM G86 [5]

standard also requires the test setup to be kept as clean and contaminant-free as possible. Accordingly, the testing at the *University of the Bundeswehr Munich* is performed, exceeding standard requirements, in a cleanroom environment. The test cup, striker pin, and CFRP samples are thoroughly cleaned prior to each run. During testing, the fall time is measured to verify compliance with the expected energy input. The measured fall time must not deviate by more than ±3% from the calculated target.

In the context of this scientific investigation, the focus was not on a standard qualification test of the material but rather on identifying the influence of the peel ply treatment on the reaction behavior. For this reason, deviations from the standard procedure, specifically in terms of impact energy and number of trials, were intentionally introduced. These modifications are explained in greater detail in **Chapter 4**.

The LOX impact test facility developed at the *University of the Bundeswehr Munich* is illustrated in the following figure.

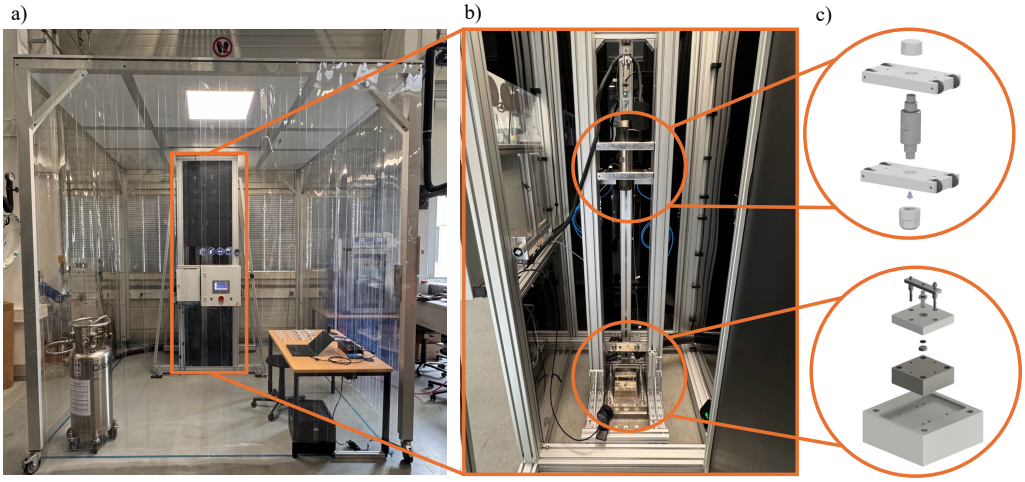

Figure 2 Test facility at the *University of the Bundeswehr Munich* for determining the LOX compatibility of CFRP specimens. a) External view of the test setup inside the cleanroom. b) Close-up of the test device where the drop weight impacts the striker. c) Technical illustration of the individual components of the test rig, consisting of the drop weight and the test chamber containing the specimen immersed in liquid oxygen

To ensure cleanliness during testing and minimize external influences on the experimental procedure, the test bench is located in a cleanroom certified according to ISO 14644 providing an air quality rating of ISO 8.The test facility at the *University of the Bundeswehr Munich* features a modular design that enables LOX compatibility testing across various energy levels. Both the drop height and the drop mass can be flexibly adjusted. Advanced sensor technology allows not only visual and acoustic monitoring of the test but also extended analytical evaluation of the reaction behavior. A fully automated pneumatic adjustment unit enables single-operator testing. Key parameters such as drop mass, fall time, and rebound height are displayed and logged via the integrated HMI system.

The test bench is enclosed in a completely darkened housing, which allows detection of even the smallest reaction events on the specimen. In addition, protective side panels shield the operator from any fragments ejected during specimen failure. To enhance safety and maintain cleanliness within the test chamber, a specialized CFPR vacuum extraction system is employed. This unit removes combustion gases and airborne debris, thereby minimizing contamination and maintaining optimal testing conditions.

4 PREPARATION OF TEST SPECIMENS AND SETUP OF LOX IMPACT TESTING

As part of the experimental campaign to investigate influencing factors on the reaction behavior of CFRP specimens under impact loading in liquid oxygen, a total of five laminate panels were manufactured. Each panel yielded 80 circular test specimens. The only variable among the panels was the type of auxiliary material (peel ply) used during fabrication. All specimens were cured

simultaneously in the same autoclave cycle.

It is well documented in the literature that surface condition can significantly influence test outcomes, as it affects frictional behavior during mechanical loading. Increased friction leads to localized temperature rises, resulting in so-called “hot spots” that promote the thermal decomposition of the epoxy matrix and may trigger a chain reaction with liquid oxygen. However, it remains unclear whether a generally rough surface is sufficient to increase reactivity, or whether the degree of surface roughness also plays a measurable role. A further question is whether surface features introduced by peel ply treatments alter the contact area between the striker and the specimen, thereby affecting the energy transmitted per unit area.

4.1 Fabrication of CFRP Test Samples

To investigate this, specimens with different frictional characteristics were prepared while all other material and process variables remained constant. The aim of the study is to evaluate the influence of surface roughness generated by different peel ply materials on the reactivity of CFRP samples. The results are compared to a reference specimen, referred to as the base plate (GP), produced without peel ply and featuring a smooth surface. **Table 1** lists the fabricated plates together with their designations, the achieved surface-roughness values, and the measured fiber volume content (FVC).

Specimen ID	Peel-Plie	FVC [%]	Ra [µm]	Rz [µm]
GP	none	66,69	0,28	1,95
AB68L-1	Peel ply 68 gsm	65,67	8,91	56,76
AB90L-2	Peel ply 90 gsm	66,97	12,80	78,57
AB100K-4	Peel ply 100 gsm	66,42	9,59	63,9
BLB- 5	Bleeder Lease	68,67	9,0	56,89

Table 1 Overview of the fabricated plates, including their designations, achieved surface roughness values, and measured fiber volume content (FVC).

For this test, all panels were made from Hexply 8552 prepreg with a symmetric 0/90 Orientation. In total 16 Layers were used to obtain a plate thickness of approximately 2 mm. During the laying process, an intermediate vacuum was drawn every 5 layers to achieve the best possible quality. To determine the surface roughness a 3D laser scanning microscope was used. The fiber volume fraction of the CFRP specimens was determined by a loss-on-ignition analysis, in which the polymer matrix was completely removed by pyrolytic burn-off in a muffle furnace.

Figure 3 shows the surface of the fabricated specimens, which differ only in the peel ply used.

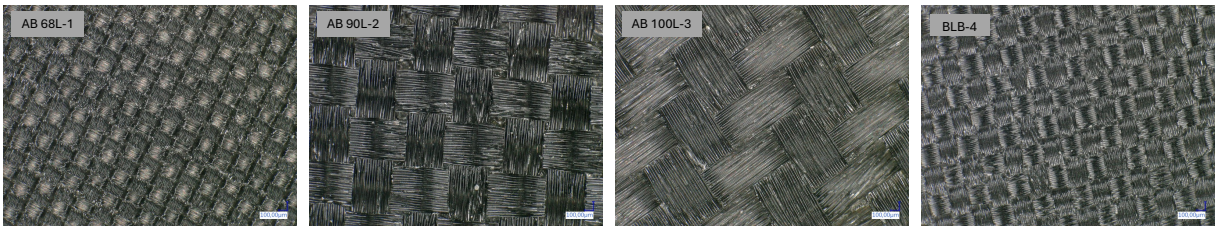

Figure 3 comparison of the surface structures of the manufactured test specimens. The texture of the respective peel ply is transferred to the specimen surface upon its removal. The pictures were taken with a digital microscope VH-ZST from Keyence with a dual zoom lens. All images were taken with the ZS 20 lens at a magnification of 100

The analysis of the surface topographies recorded after removal of the peel ply reveals pronounced differences between the specimens. Firstly, peel plies with different weave architectures were used,

resulting in variations in the spacing between warp and weft yarns. Secondly, the number of binding points per unit area differs among the samples. A detailed examination of the surfaces and their correlation with the LOX results is presented in **Chapter 5**. **Table 2** summarizes the auxiliary materials employed and their relevant properties.

Peel Ply [g/m^2]	Weave pattern	Fineness [dtex]	Material	Properties
Peel-Plie 68 g/qm	plain weave	Warp yarns 44 Weft yarns 78	PA 6.6	Finely textured, rough surface
Peel-Plie 90 g/qm	plain weave	Warp & weft 235	PA 6.6	Finely textured, rough surface
Peel-Plie 100 g/qm	2/2 twill	Warp & weft 235	PA 6.6	Finely textured, rough surface
Bleeder Lease B 62 g/qm	plain weave	-	Nylon	Coated with silicone release,

Table 2 Summary of the release fabrics used for the tests to determine the influencing factors on the reaction process under impact loading in a liquid oxygen environment

4.2 Surface Characterization:

To quantify surface roughness, selected specimens were analyzed using a confocal 3D laser scanning microscope (Keyence VK-X series). These measurements provided both qualitative surface images and quantitative roughness data. An example result is shown in **Figure 4**.

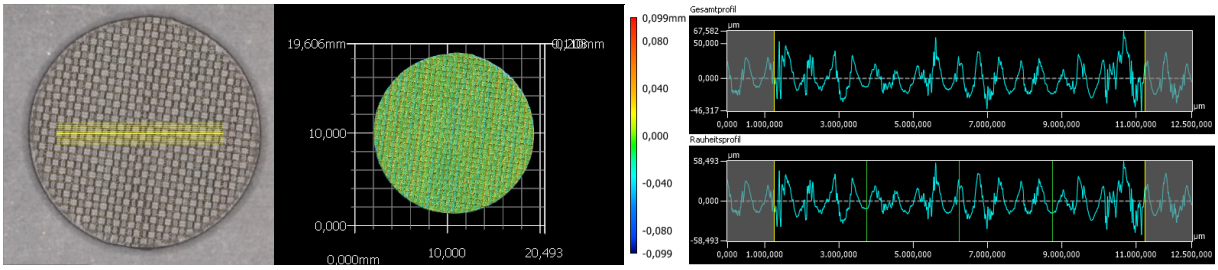

Figure 4 Representation of the analysis of a specimen labeled AB90L-2. Both the raw image of the specimen and the recorded depth profile are shown. The surface roughness was measured along the yellow marking on the specimen. The analysis of the overall profile on the right side of the figure shows the height differences on the surface of the profile.

In addition to roughness values, the contact area between the striker and the specimen must also be assessed to evaluate the relationship between peel ply surface and material reactivity: The results of these investigations are summarized in **Chapter 5**.

In addition to the characterization of surface roughness parameters, further investigations were carried out regarding the peak density (***Spd***), reduced peak height (***Spk***), and peak material volume (***vpm***). An evaluation of these parameters is presented in **Figure 5.**

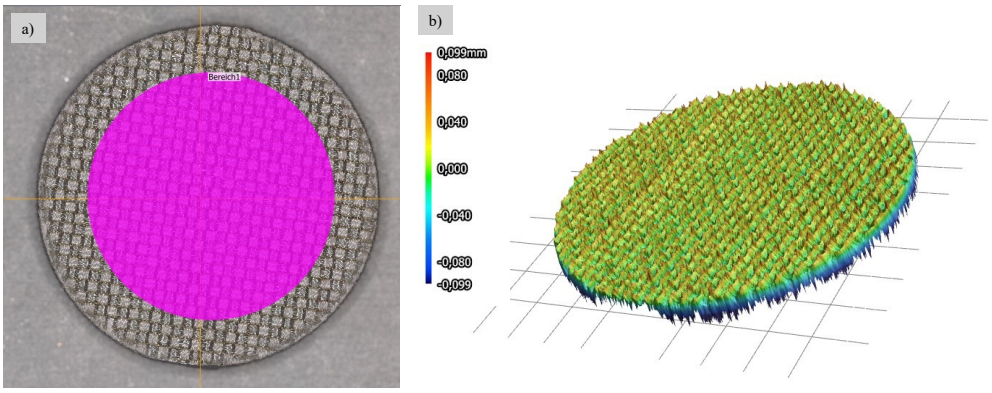

Figure 5 Analysis of the sample surface with respect to the number of peaks, peak height, and peak material volume. The peaks, consisting of matrix material, are formed by the weave structure of the peel ply and appear on the surface after the removal of the release fabric. This could affect the reactivity of the material regarding the LOX-compatiblity

The Spd (peak density) parameter describes the number of surface summits per unit area. A higher Spd value indicates a greater number of potential contact points with interacting surfaces, which can be relevant for tribological performance or adhesion behavior. The Spk (reduced peak height) parameter refers to the average height of the surface peaks above the core material surface and provides information about the prominence of surface asperities. In contrast, the Vpm (peak material volume) parameter quantifies the material volume present at a specified bearing area of p %. Beyond this, Vpm is also used to derive volumetric characteristics of the surface, including the size of the core area, the volume of reduced peaks, and the volume of reduced valleys, thereby contributing to a more detailed assessment of the functional surface profile.

To determine a significant influence between the generated rough surface and the reaction behaviour in liquid oxygen, additional parameters beyond the roughness values must be evaluated. Particular attention must be paid to the area on which the striker rests prior to impact. Reducing this contact area increases the energy input per unit area under otherwise identical conditions. Consequently, more energy is transferred into the specimen as the resin-rich peaks are indented. The causal relationship is discussed in greater detail in Chapter 5.

4.3 Test procedure

After waterjet cutting, the specimens were cleaned with isopropanol and placed in a desiccator for 48 hours. Subsequently, they were conditioned for an additional 72 hours in a controlled climate chamber to eliminate any environmental influences, particularly humidity, that could affect reactivity.

Prior to each test series, the entire test chamber and surrounding area are thoroughly cleaned. Test cups and striker pins are cleaned in an ultrasonic bath after every ten tests. Before reuse, striker pins are also cleaned with isopropanol and degassed in an oven. After cooling, they are ready for operation.

To prepare for testing, the striker pins and specimen cups are precooled in a liquid nitrogen bath. The specimens themselves are cooled in liquid oxygen immediately before testing. Once all test components have reached the required temperature, they are placed into the test chamber, which is then filled with liquid oxygen.

To determine the influencing factors on the reaction process, various energy levels must be tested, deviating from the standard procedure. The aim is to identify an energy level at which approximately 50% of the samples react. This allows for the detection of significant external changes in reactivity. In the context of this test series, the following energy levels were examined.

Energieniveu [J]	Eingestellte Fallhöhe [m]
22,3	0,250
30	0,336
40	0,448
56,3	0,631

Table 3 Overview of the investigated energy levels used in the experimental study. The energy level is derived from a 9.1 kg drop weight with varying drop heights.

For each energy level, ten samples from a single sample plate were tested. In addition to the reaction itself, the intensity of the reaction is also recorded.

5 EXPERIMENTAL RESULTS AND DISCUSSION

During the experiments, it was observed that, in addition to the number of reactions, differences in their intensity could also be identified. These variations influence, among other factors, the damage pattern of the specimen and the resulting chain reaction. The following figure illustrates the differences between various reactions and their respective intensities

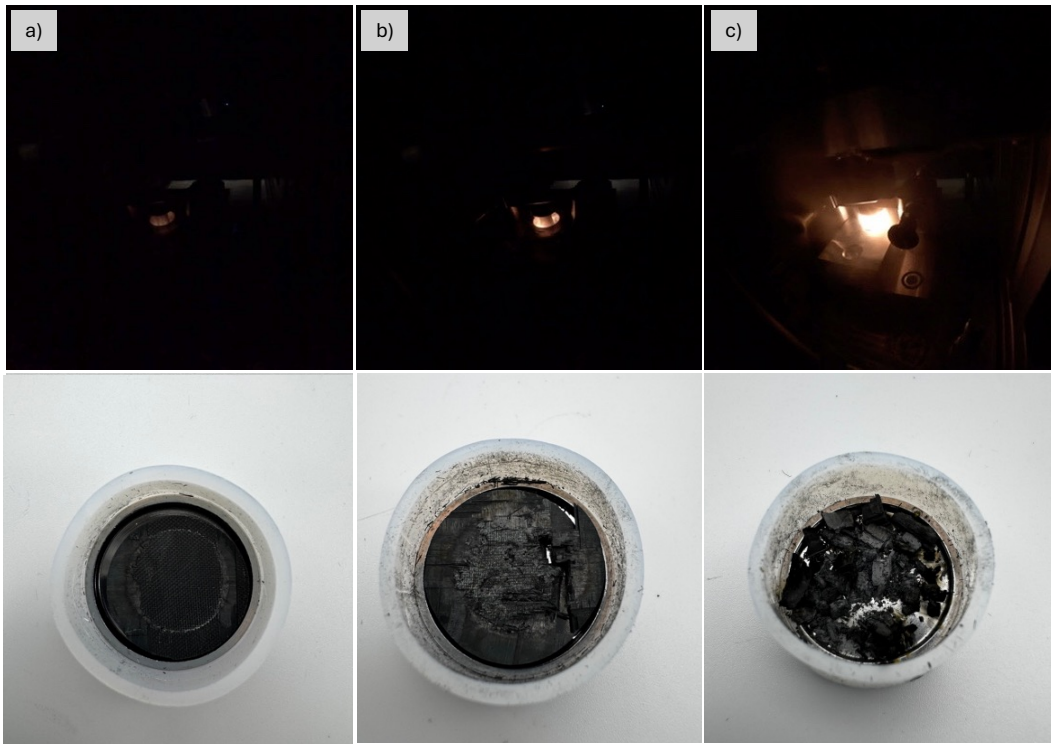

Figure 6 Comparison of reaction intensity based on the light emission and the damage pattern of the specimen. For this purpose, three different specimens were examined under identical energy conditions of 56,3 Joule: a) AB68-L reaction of very low intensity b) AB100-L low intensity reaction c) AB90-L High intensity reaction

The recorded damage pattern not only quantifies the number of reactions but also provides insight into their intensity, allowing a more differentiated assessment of the various peel-ply fabrics. Figure 6 clearly demonstrates that different peel plies, and the resultant surface characteristics, significantly influence reaction intensity. At an impact energy of 56.3 J, specimens prepared with the finest peel ply exhibited the lowest reaction intensity.

This finding must now be correlated with the number of reactions observed at the respective energy levels and with the measured surface properties of the individual specimen series. **Table 4** summarises all detected reactions across the tested energy levels together with the corresponding surface parameters of each series.

Sample	FVC [%]	Ra [µm]	Rz [µm]	Spd [1/mm²]	spk	vmp	Number of reactions for different Energy levels			
							22 [J]	30 [J]	40 [J]	56 [J]
AB68L-1	65,67	8,91	56,76	489,28	11,91	0,59	0	0	2	7
AB90L-2	66,97	12,8	78,57	448,52	22,71	1,1	1	2	9	10
AB100K-4	66,42	9,59	63,9	592,48	18,61	0,85	0	1	7	8
BLB-5	68,67	9	56,89	503,85	12,95	0,65	0	2	6	9
GP-8	66,69	0,28	1,95	-	-	-	0	0	0	0

Table 4 Representation of the identified reactions across various energy levels. In addition, the characteristic surface properties of each tested specimen plate are summarised. The table also includes the determined FVC values.

The experimental evaluation revealed that untreated base plates without peel ply produced the best results: no reaction was detected at any of the investigated energy levels. In contrast, the use of peel ply drastically altered the reaction behaviour, and all coated panels exhibited substantially more reactions. Among the peel plies tested, both the number and the intensity of reactions varied.

The 68 gsm peel ply yielded the most favourable results, with markedly lower reaction intensity. Surface roughness parameters as well as the reduced peak height and peak material volume recorded the lowest values. Although the number of surface asperities is lower than for the 100 gsm peel ply or the very fine Bleeder Lees fabric, which implies a higher induced energy per unit area, the considerably flatter asperities mean that less material must be compressed and destroyed before the striker contacts the remaining surface. Consequently, no significant difference between the BLB-5 and AB68-L specimens was observed, as their characteristic surface features differ only marginally.

The reaction behaviour of specimens with the AB100-K peel ply is particularly noteworthy. Despite a much higher asperity density compared with the other specimens, no significant difference in the number of reactions relative to BLB-5 was detected. Nevertheless, the AB100-K samples reacted far more intensely. This may be attributed to the taller asperities remaining on the surface, which permit a greater exothermic conversion of reactive material. This effect is also evident in the striker damage pattern depicted in **Figure 7**.

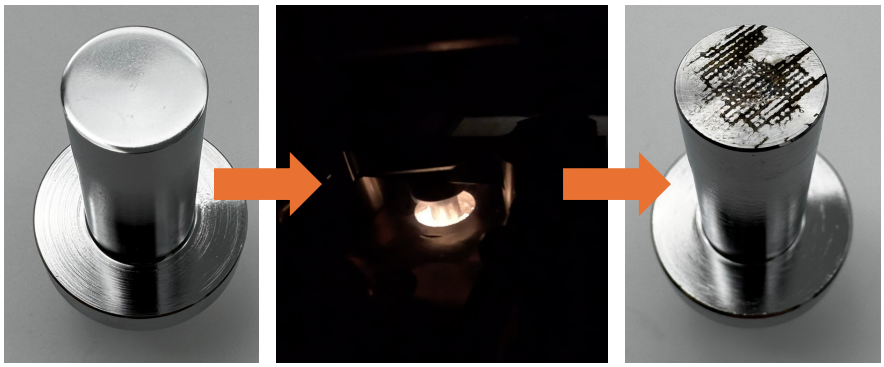

Figure 7 Surface alteration of the striker pin after an impact test at 56.3 joules for specimen material AB100-K. The specimen surface was imprinted onto the pin due to the impact. Areas of the striker that reacted with the liquid oxygen are clearly visible.

Although no substantial increase in the number of reactions was detected compared with the BLB experiments, the reaction intensity was markedly higher. As illustrated in **Figure 7**, this is reflected in the residual surface of the striker pin, onto which the specimen's surface profile is imprinted. Particular attention must be paid to the combustion pattern on the pin. While a uniformly distributed circular

reaction pattern is typically observed, the present results clearly indicate that the material reacted primarily along the protruding volumetric features of the specimen surface. Hence, the height of the residual asperities and thus the surface relief, constitutes a decisive factor, a conclusion that likewise applies to the AB90-L series.

The reaction behaviour of the AB90-L specimens is even more pronounced. Both the number and the intensity of reactions exceed those of all other series. Notably, AB90-L was the only plate to react at an impact energy of 22.3 J. This specimen exhibits the highest surface roughness and the lowest asperity density, resulting in the greatest induced energy per unit area. In addition, both asperity height and volume are maximised relative to the other specimens, so that a larger amount of reactive matrix material first comes into contact with the striker-pin during impact. This configuration accounts for the considerably stronger reactions observed. Sufficient material is present in the form of raised regions that are compressed and destroyed by the rapid impulse, thereby generating hot-spot zones that initiate and amplify exothermic reactions.

Furthermore, friction must be considered. *Gerzeski* [4] demonstrated that, despite a central impact and a fixed striker, relative movement of the pin is possible. The characteristically rough surfaces of the specimens augment such frictional effects, thereby promoting additional reaction events.

6 SUMMARY AND FUTURE WORK

The experiments conducted to determine the influence of surface characteristics generated by different peel-ply fabrics have clearly shown that increased surface roughness significantly affects compatibility performance. Compared with a smooth reference surface of the same material, a marked rise in both reaction frequency and reaction intensity was observed. The key findings are summarised in the diagram below.

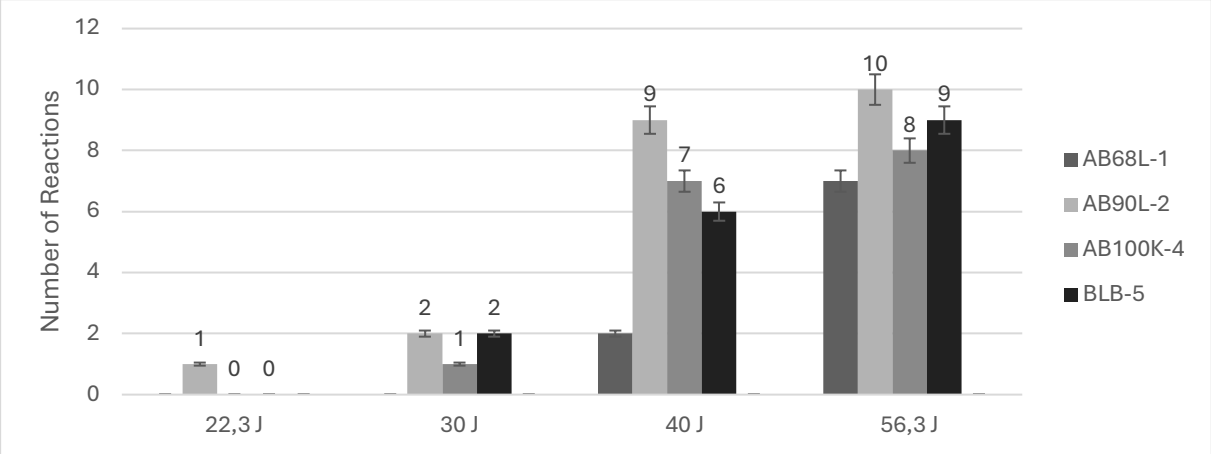

Figure 8 Comparison of compatibility results for various test specimens differing in the applied peel-ply material and, consequently, in their characteristic surface roughness properties. The results were benchmarked against the untreated base plate without peel ply, which exhibited no reaction at any of the tested energy levels. a 5% deviation of the results was assumed, which is shown in the bar chart

The results demonstrate that not only the contrast between a smooth base plate and a peel-ply surface is relevant but the specific choice of peel ply itself also exerts a decisive influence. As asperity height and the associated volume of the residual surface protrusions increase, reaction intensity rises. Variations in surface-roughness parameters and in the characteristic asperity features, such as asperity density, height, and volume, clearly deteriorated compatibility, as evidenced by the early response of specimen AB90-L at 22.3 J.

These findings underline that the surface quality of test specimens is of critical importance. The surface configuration ultimately present in the finished component can significantly affect certification with respect to liquid-oxygen (LOX) compatibility. It is therefore essential to specify precisely whether a peel-ply surface is required and, if its use cannot be avoided, to what extent subsequent surface

finishing is feasible.

Future work should focus on a detailed characterisation of the residual surface features resulting from the peel ply. Further experimental work should include specimens with post-processed surfaces to assess how surface reworking affects compatibility results compared to both the original test series and the untreated base plate. In addition, a substantial increase in the number of specimens per experimental series is recommended to enhance statistical significance.

REFERENCES

[1] Hongyu, W.; Cong, P.; Shichao, L.: Improvement of the liquid oxygen compatibility of epoxy via the addition of surface-modified boehmite; Journal of applied polymer science 2018, APP.46918

[2] Bechel, V.; Kim, R.Y.; Tudela, M.A.:
LOX Impact compatibility testing considerations for polymer matrix composites
49th AIAA/ASME/ASCE/AHS/ASC Structures, Structural Dynamics, and Materials Conference, 2008, Schaumburg, IL

[3] Li, S.; Cui, Y; Jinrui, Y.: Liquid oxygen compatibility of epoxy matrix and carbon fiber reinforced epoxy composite. Composites Part A, Elsevier 2022, S. 154

[4] Gerzeski, R.: Improving the D 2512 LOX compatibility of composites by using thermally conductive graphite fibers. Air Force Research Laboratory, 2005

[5] ASTM G86-17, Standard Test Mehtod for Determining Ignition Sensitivity of Materials to Mechanical Impact in Ambient Liquid Oxygen and Pressurized Liquid and Gaseous Oxygen Environments, ASTM International, United States, 2017

[6] ASTM D2512-95: Standard Test Method for Compatibility of Materials with Liquid Oxygen (Impact Sensitivity Threshold and Pass-Fail Techniques), ASTM International, United States, 2017

[7] ISO 21010:2017-12 Kryo-Behälter - Verträglichkeit von Gas/Werkstoffen

[8] NASA STD-6001 Flammability, Odor, Offgassing and compatibility Requirements and test procedures for materials in environments that support combustion

[9] Hongyu, W.; Cong, P.; Shichao, L.: Improvement of the liquid oxygen compatibility of epoxy via the addition of surface-modified boehmite; Journal of applied polymer science , 2018

[10] Graf, N.A.; Hudgins, R.J.; McBain, M.: Oxygen compatibility testing of composites materials. NASA conference Paper, Lockheed Martin Space Systems Company, 2000

[11] Currie, J. L., Irani, R. S., Sanders, J.: Factors Affecting the Impact Sensitivity of Solid Polymer Materials in Contact with Liquid Oxygen, Flammability and Sensitivity of Materials in Oxygen-Enriched Atmospheres: Third Volume, ASTM STP 986, American Society for Testing and Materials, Philadelphia, 1988, pp. 233-247.

[12] Duo, C.; Juanzi, L.; Yuhuan, Y.: A review of the polymer for cryogenic application: Methods, Mechanisms and Perspectives. Polymers, 13 2020, Seite 320

ICCM24
AUGUST 4-8, 2025
BALTIMORE CONVENTION CENTER
BALTIMORE, MARYLAND, USA

No Technical Paper Submission for:

Serafin Sanchez-Carmona

University of Southern Queensland

ICCM24
24TH INTERNATIONAL CONFERENCE ON COMPOSITE MATERIALS

Centre for Future Materials

Effect of simulated hygrothermal ageing on the interfacial shear strength of carbon/epoxy composites

Abdullah Iftikhar, Zaneta Senselova, Allan Manalo, Wahid Ferdous, Mazhar Peerzada, Hannah Seligmann, Kate Nguyen, Brahim Benmokrane

Hosted by: UNIVERSITY OF DELAWARE CENTER FOR COMPOSITE MATERIALS Celebrating 50 Years · ARCTOS

Sponsors: University of BRISTOL · Bristol Composites Institute · NATIONAL COMPOSITES CENTRE · Anton Paar · ACM Australian Composites Manufacturing CRC · FAMU-FSU College of Engineering · INSTRON

Introduction

- The global use of FRP composites in civil engineering and construction is rapidly rising because of:
  - Corrosion resistance
  - High strength-to-weight ratio
  - High stiffness-to-weight ratio



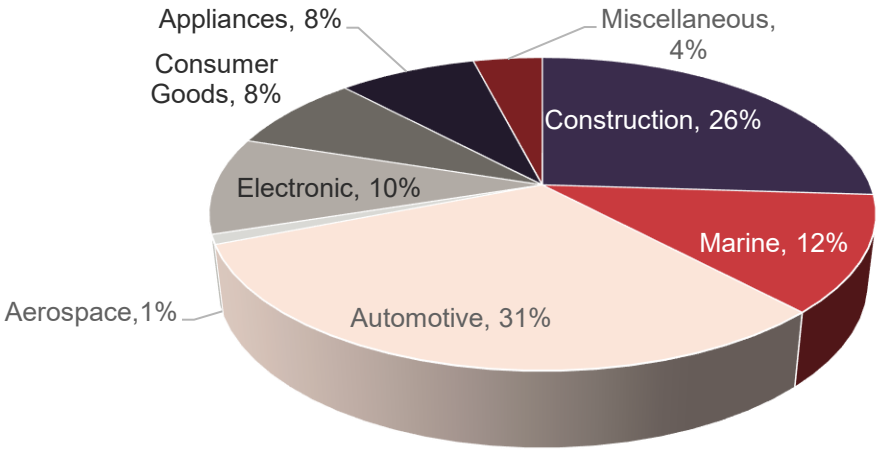

FRP Market Share by Application

https://doi.org/10.3390/fib10030027
https://doi.org/10.1016/j.compositesb.2022.110463

Introduction

- Exposure to different Environments
  - High Temperature
  - High Humidity

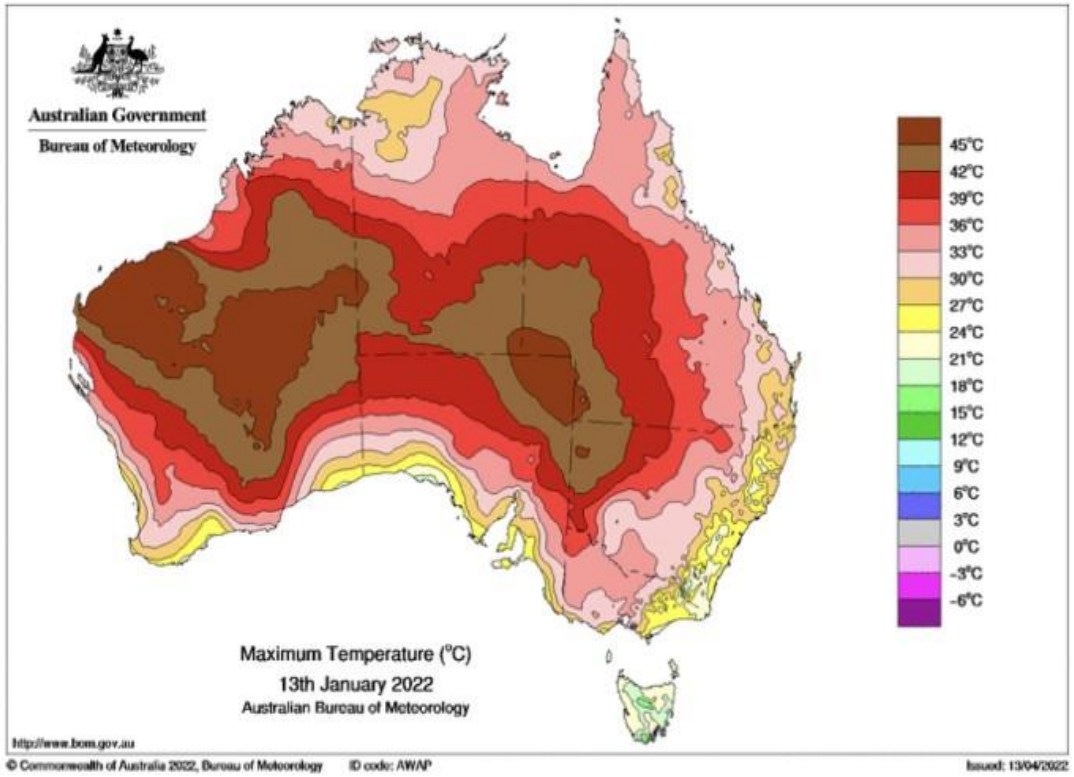

- Degradation in FRP composites can be due to either:
  - Resin Degradation
  - Fiber breakage
  - Interphase damage

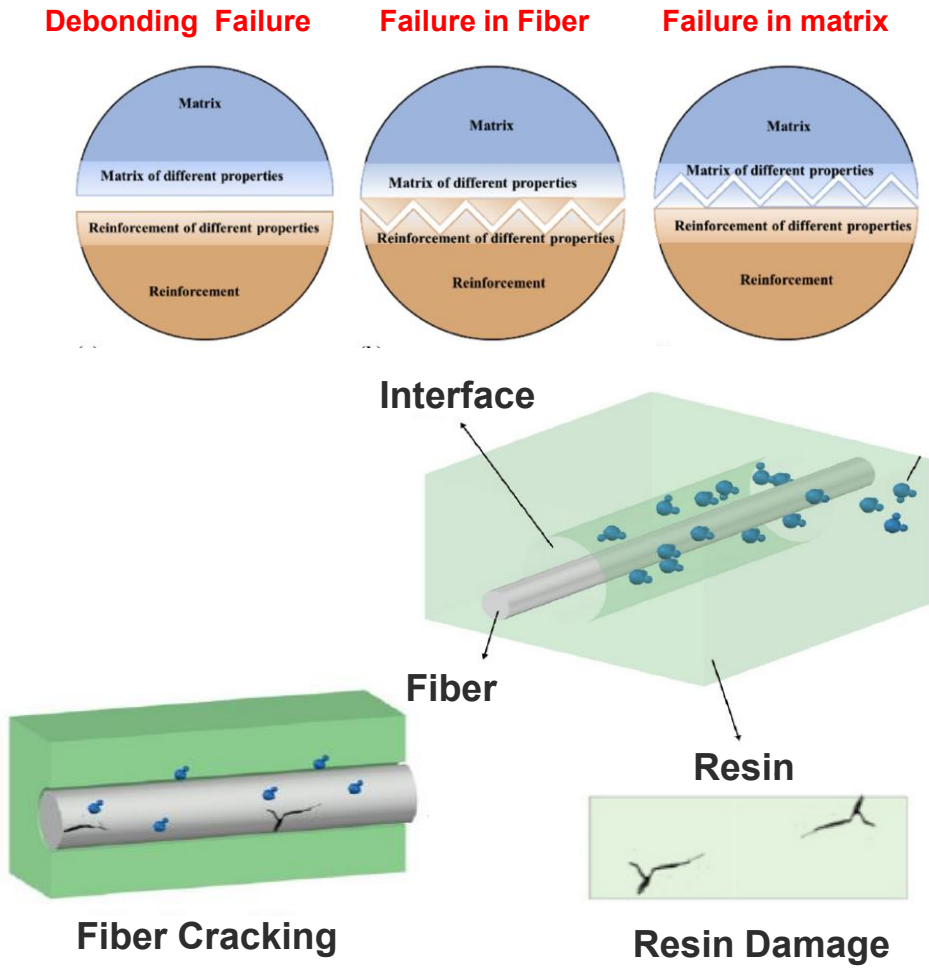

Methodology

Single Yarn Composites

Fibers

Carbon
68 Tex
Epoxy sizing

Resins

Carbon/Epoxy

DGEBA Epoxy

Mould Preparation







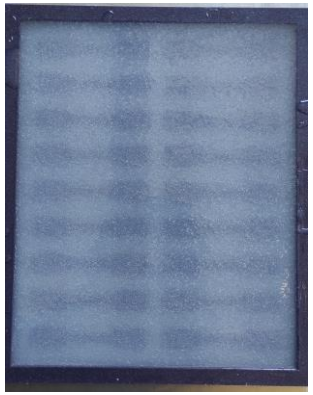



Resin Samples





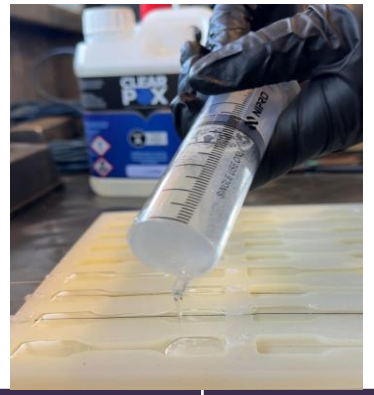





Resin Type	Units	Resin	Hardener	Curing Time	Curing Temperature
Epoxy	Parts by weight	100	25	24 hrs	Room temperature
				16 hrs	50oC

UniSQ

ICCM24
24TH INTERNATIONAL CONFERENCE ON COMPOSITE MATERIALS

Testing

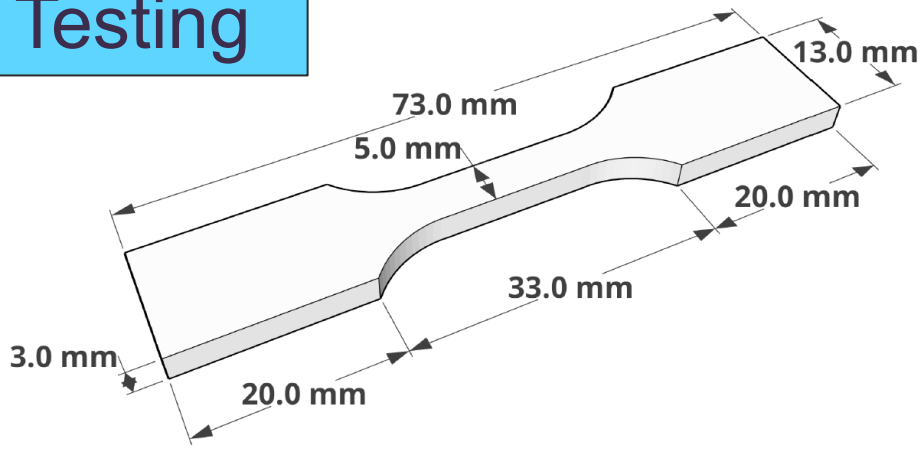

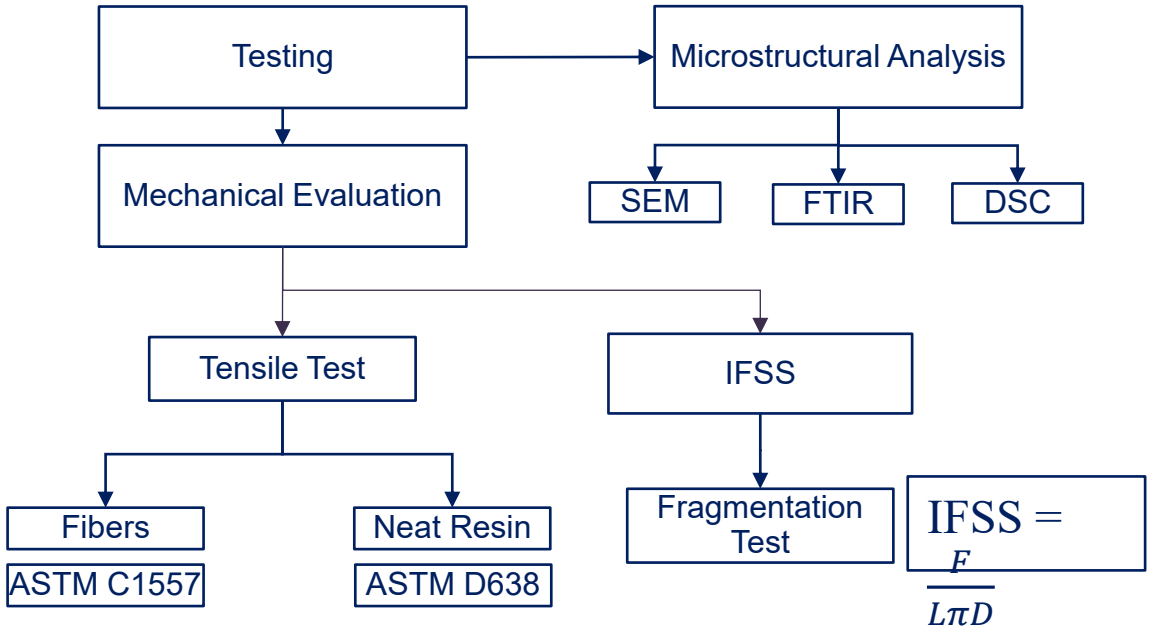

Hygrothermal Exposure

Parameters:

Temperature 60 C
Humidity 98%
1000hr, 2000hr, 3000hr



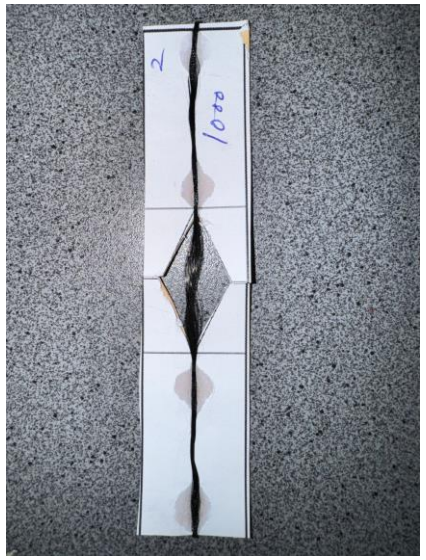

Fibre yarn for tensile test

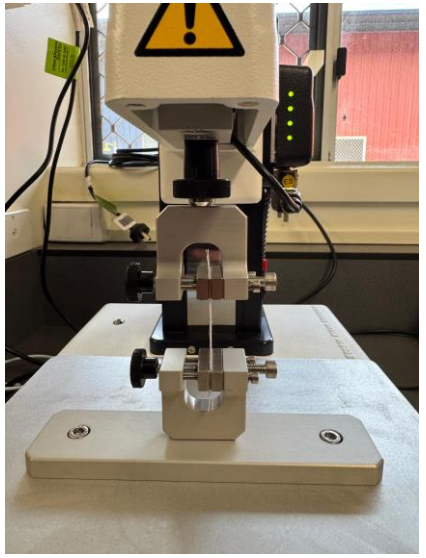

Fibre tester (1KN)

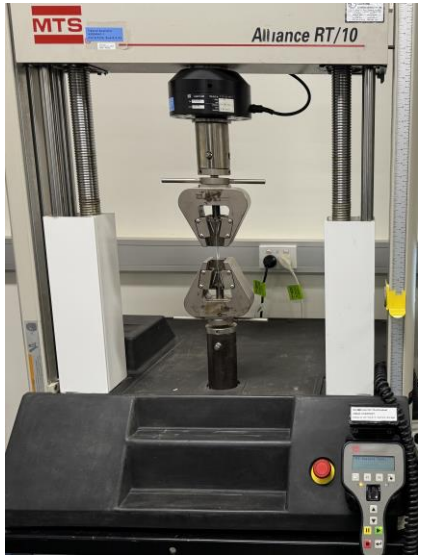

MTS (10KN load cell)

UniSQ

This content is protected and may not be shared, uploaded, or distributed

ICCM24

Differential scanning calorimetry

Degree of Cure:

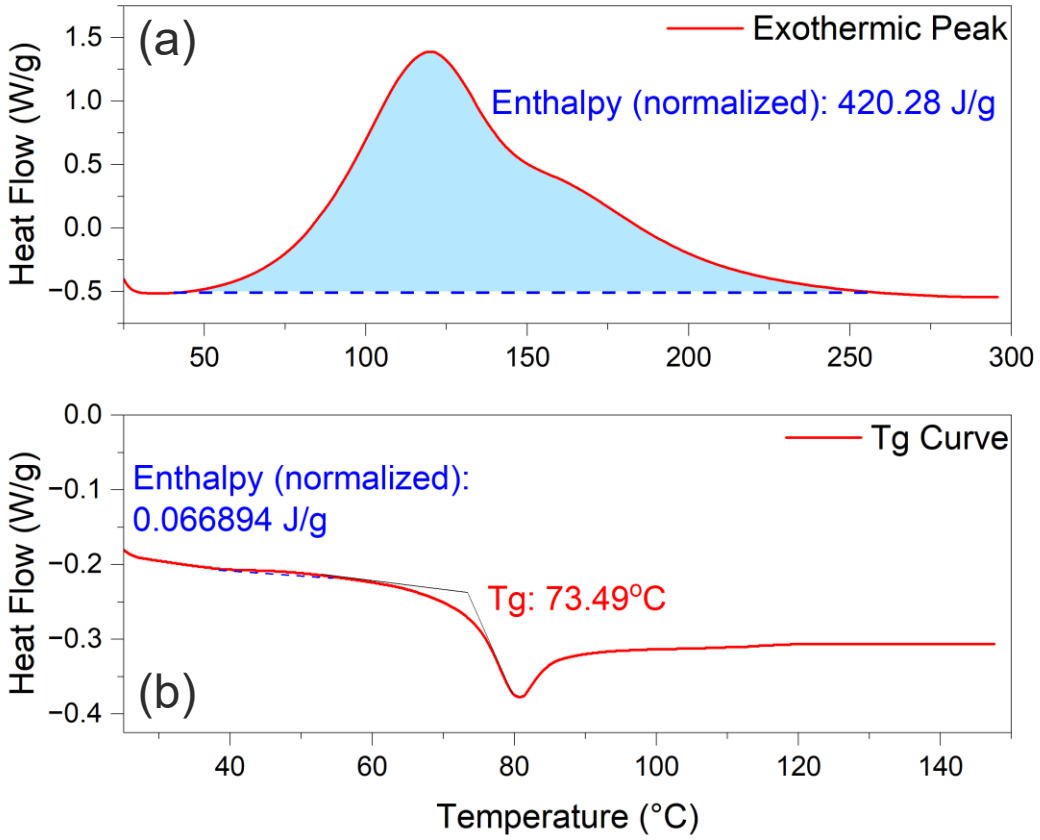

(a) Uncured (b) Fully Cured

Glass Transition Temp:

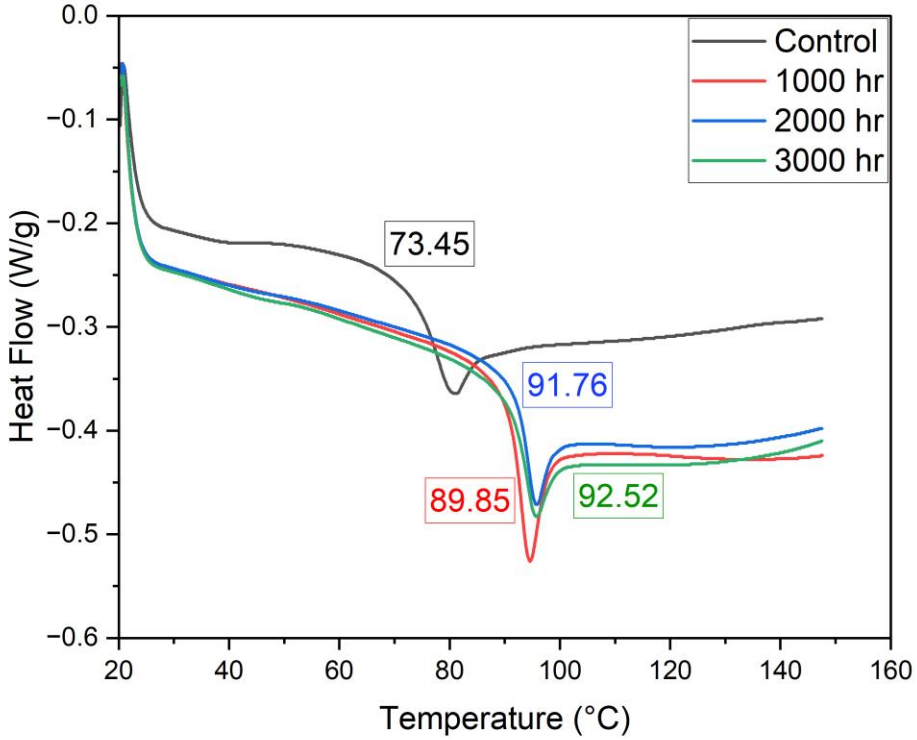

Tg after Hygrothermal Exposure

UniSQ

This content is protected and may not be shared, uploaded, or distributed

ICCM24
24TH INTERNATIONAL CONFERENCE ON COMPOSITE MATERIALS

FTIR Analysis

W. No	Peaks
3390	O-H
2920	C-H
1608	C=C
1504	C=C
1234	C-O-C
1033	C-O-C

FTIR Spectra

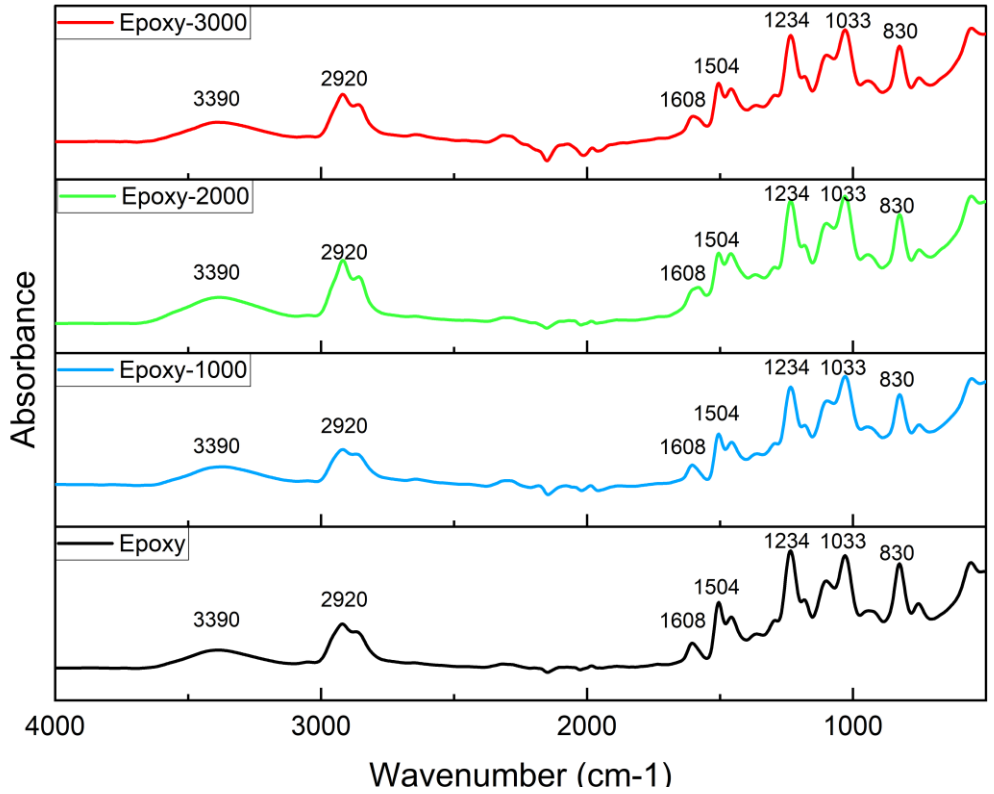

O-H & C-H Peaks

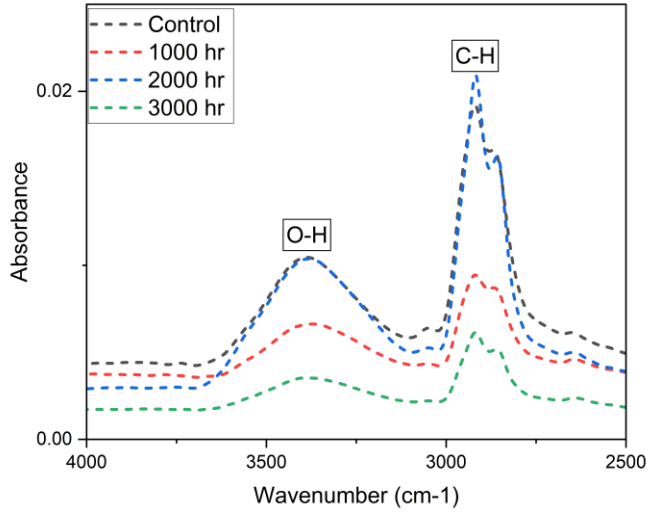

Area under O-H & C-H Peaks

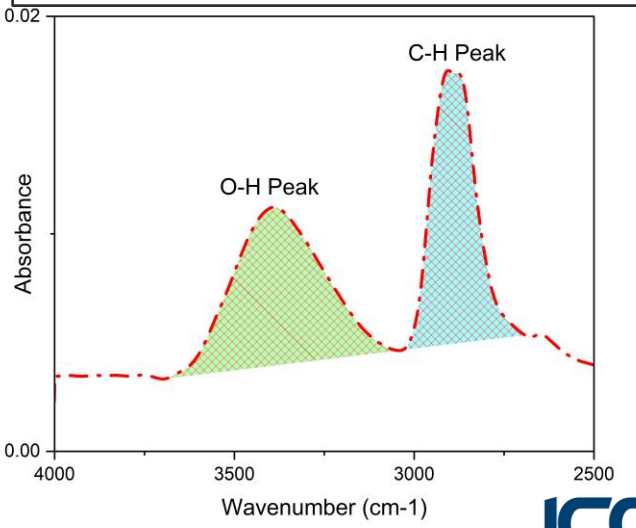

O-H/C-H ratio			
Control	1000 hr	2000 hr	3000 hr
0.835	1.02	1.05	1.15

UniSQ

This content is protected and may not be shared, uploaded, or distributed

ICCM24

Strength retention

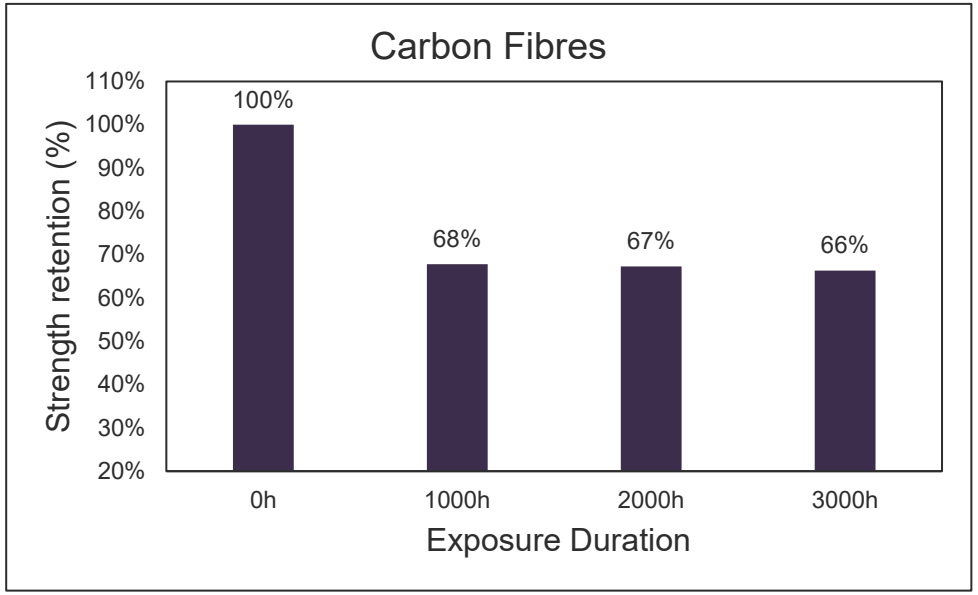

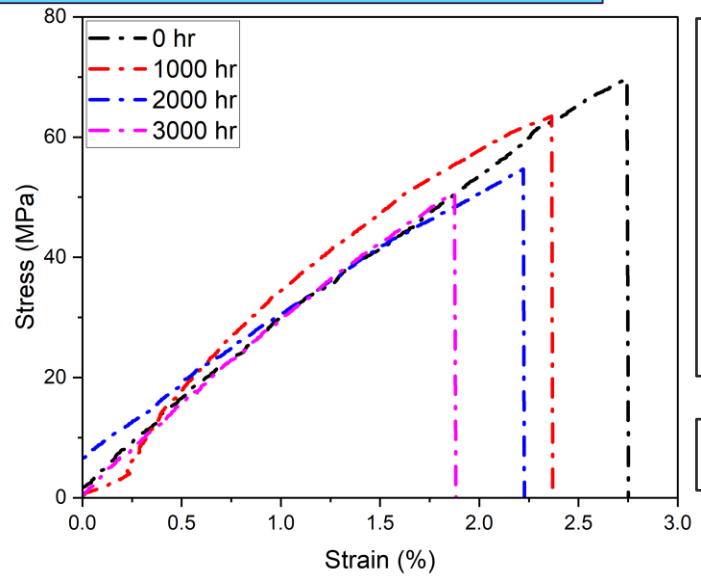

Damage Percentage

- Fibres: 34%
- Resin: 23%
- Interface: 7%

Modulus increased 12%

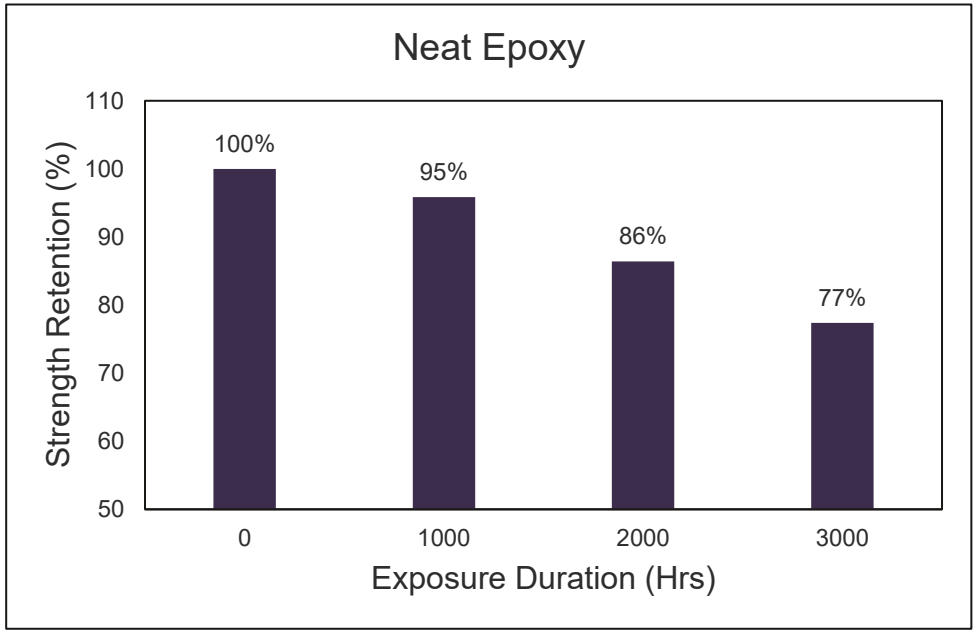

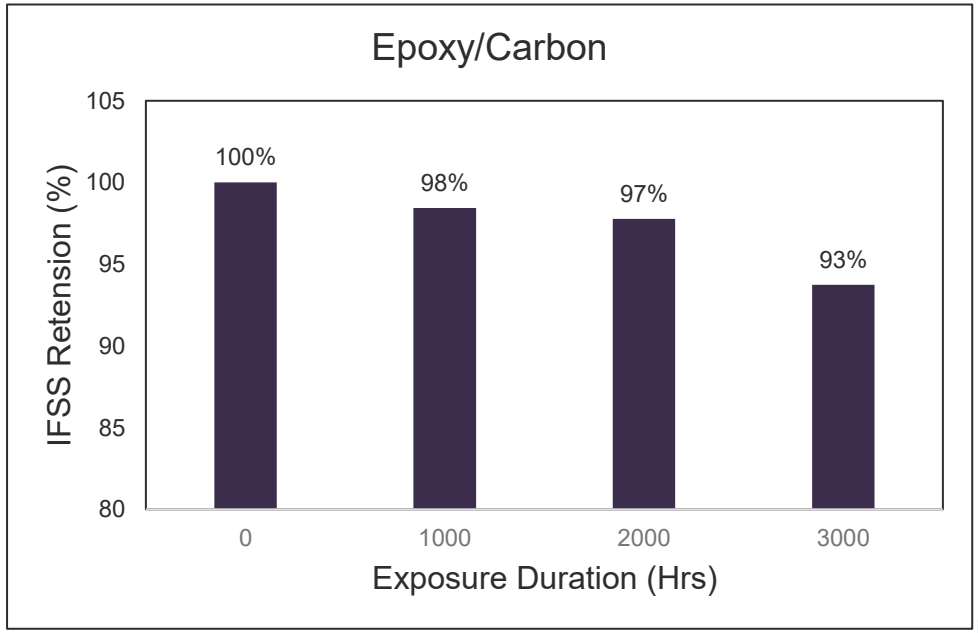

This content is protected and may not be shared, uploaded, or distributed

SEM

Unexposed

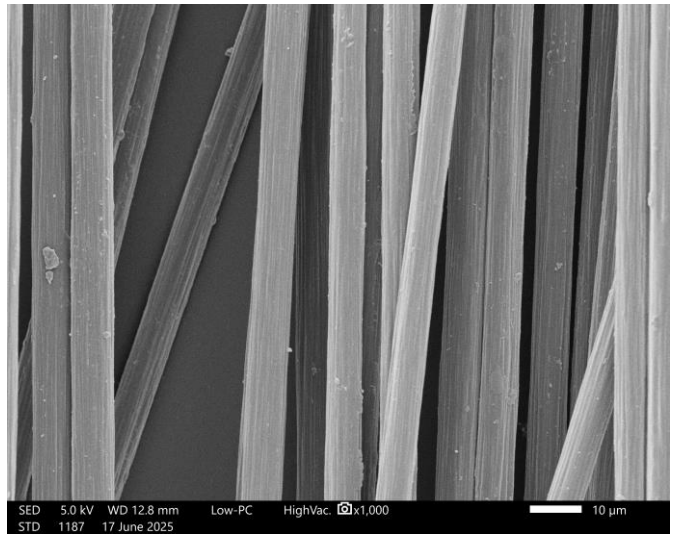

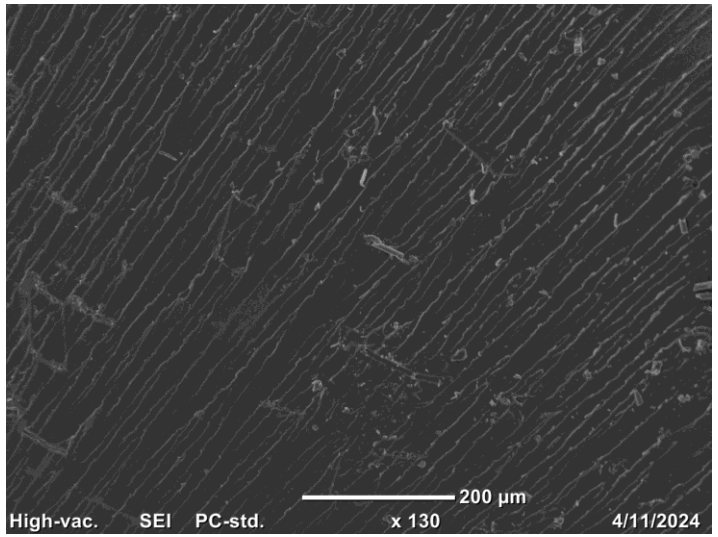

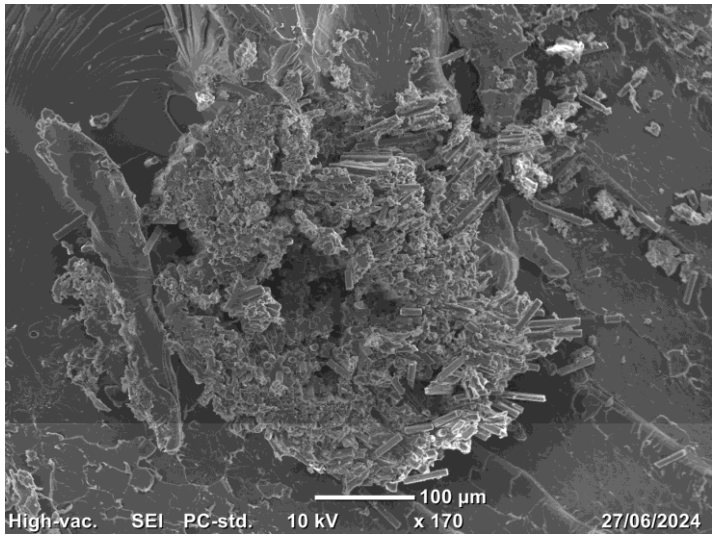

After 3000 hrs

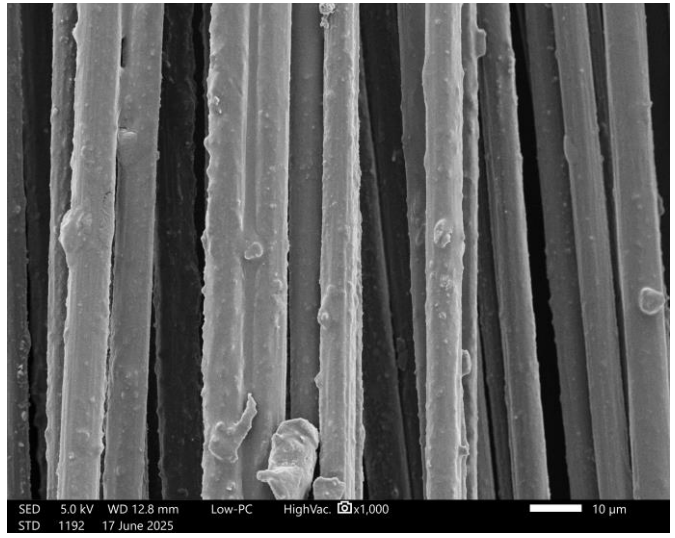

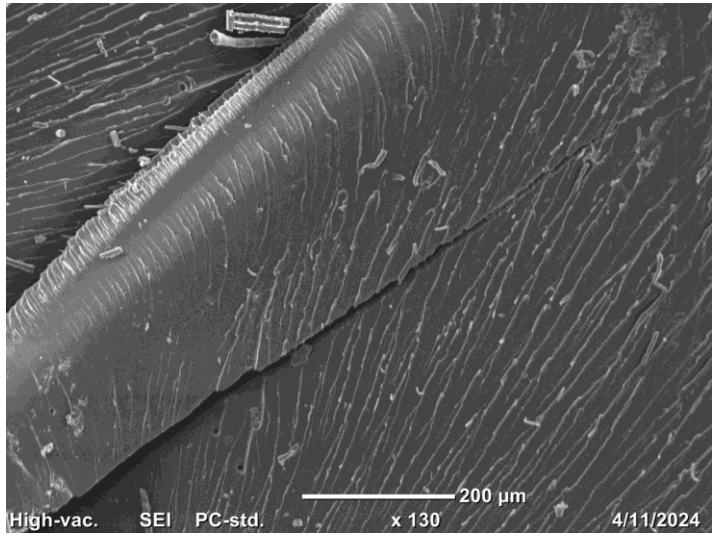

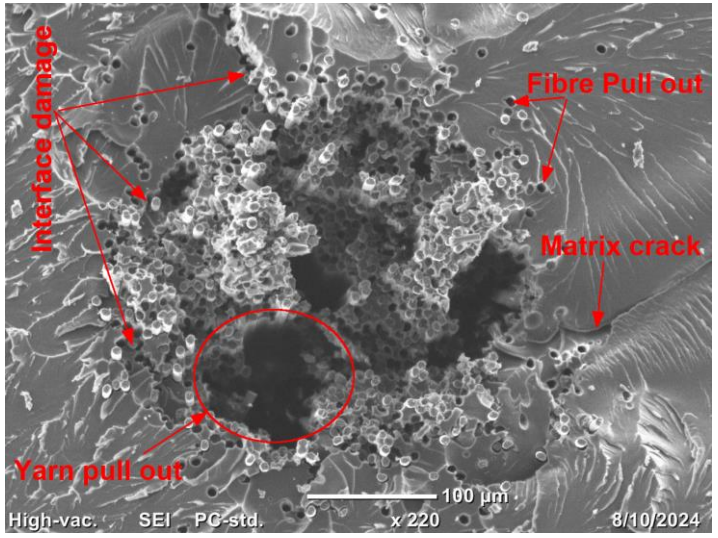

UniSQ

This content is protected and may not be shared, uploaded, or distributed

ICCM24
24TH INTERNATIONAL CONFERENCE ON COMPOSITE MATERIALS

Conclusions

- After 3000 hours of exposure, the glass transition temperature (Tg) of the epoxy resin showed an increase of up to 26%, likely as a result of enhanced cross-linking within the polymer chains.
- FTIR analysis indicated chemical degradation of the epoxy network through hydrolysis mechanisms, evidenced by the formation of additional hydroxyl groups.
- The tensile strength of both fibre yarns and resin was notably reduced following exposure, primarily due to degradation of the sizing layer on the fibres and the combined effects of plasticization and hydrolysis within the resin matrix.
- The interfacial strength was also reduced because of the damage at the fibre-matrix interface.
- A reduction in interfacial strength was also observed, attributed to degradation at the fibre–matrix interface.
- All three constituents—fibre, resin, and interface—experienced degradation; however, the resin was the most severely affected. Although unembedded fibres exhibited a greater reduction in tensile strength, this does not directly translate to composite performance, as the surrounding resin matrix in the composite structure partially shields the fibres.

This content is protected and may not be shared, uploaded, or distributed

Thank You

This content is protected and may not be shared, uploaded, or distributed

University of Southern Queensland

Degradation mechanism of Bio-epoxy based Composites under Hygrothermal Ageing

Zaneta Senselova, Allan Manalo, Abdullah Iftikhar, Omar AlAjarmeh, Kiru Pasuparhy, Kate Nguyen, Brahim Benmokrane



Overview

- Introduction
- Materials and Methods
- Results and Discussion
- Conclusion

Introduction

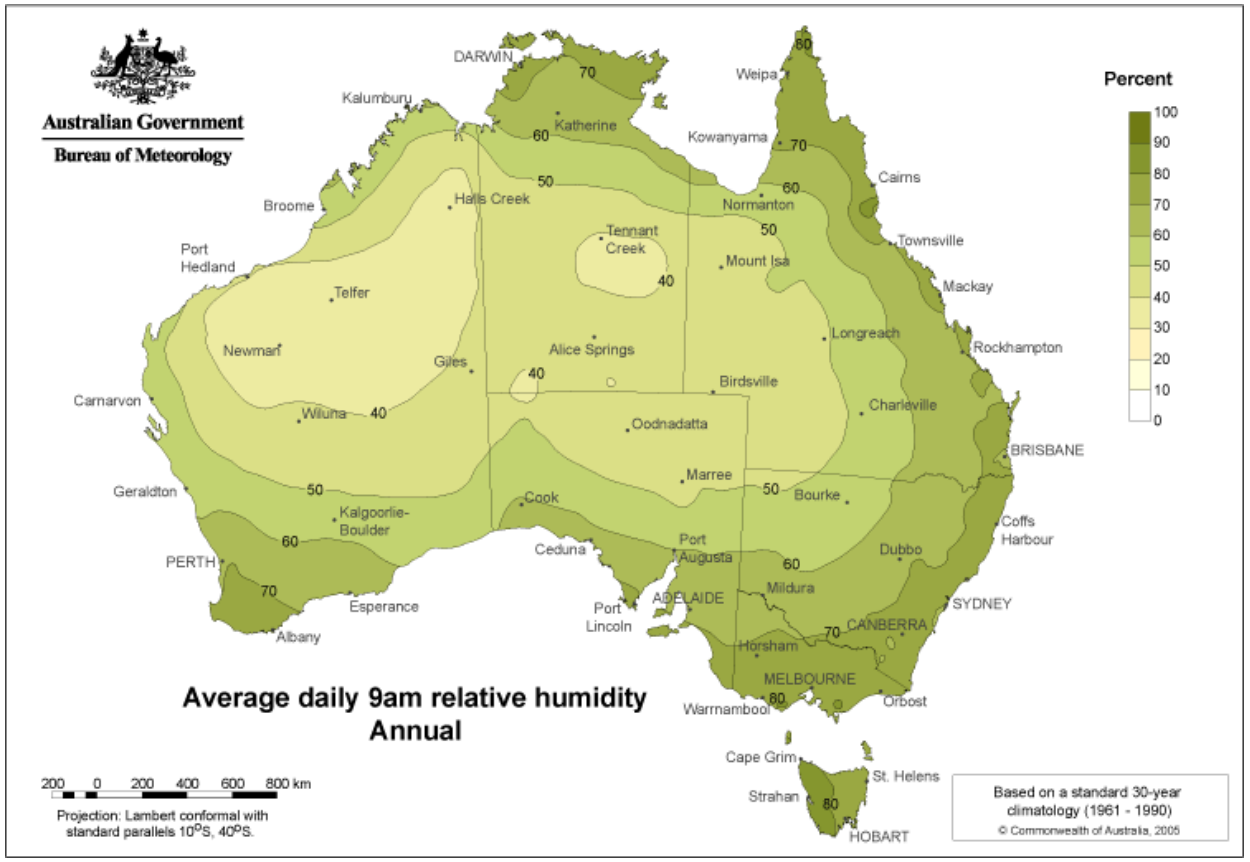

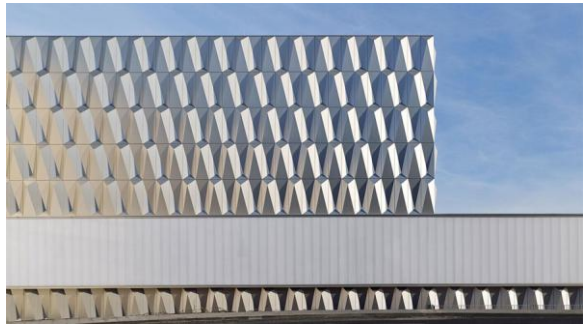



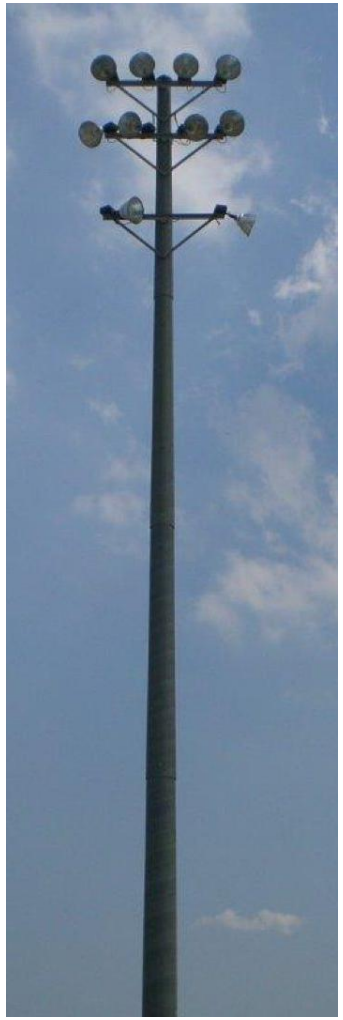

- 85% of Australia‘s population lives near the coast
- High average relative humidity + elevated in-service temperature
- Composite structures are becoming widely used in Australian infrastructure

Materials and methods

BYOXY by Change climate



Glass

Carbon



- 100% Bio-Based
- Non-Toxic & BPA-Free
- Low VOC Emissions

Preparation of specimens





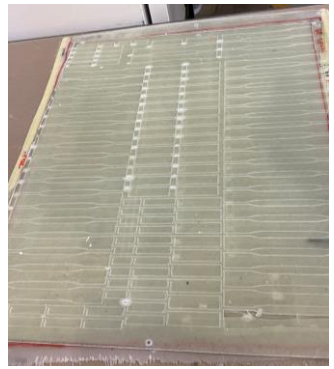

Conditioning

Duration
- 42 days
- 83 days
- 125 days

Temperature
- 23°C (RT)
- 40°C
- 60°C



Characterisation

Degree of Cure

$$DoC\ (\%) = \left[1 - \left(\frac{\Delta H_r}{\Delta H_t}\right)\right] \times 100$$

Constituent content of composite materials

Composite	DoC (%)		Percentage of fibres	Percentage of resin
Glass+bio-epoxy	99.999		67%	33%
Carbon+bio-epoxy	99.991		66%	34%

UniSQ

Results and discussion

Effect on Physical Properties

Change of colour

- discolouration and yellowing

	42 days (1000 hrs)	83 days (2000 hrs)	125 days (3000 hrs)
RT (23°C)			
40°C			
60°C			

	42 days (1000 hrs)	83 days (2000 hrs)	125 days (3000 hrs)
RT (23°C)			
40°C			
60°C			

Water absorption

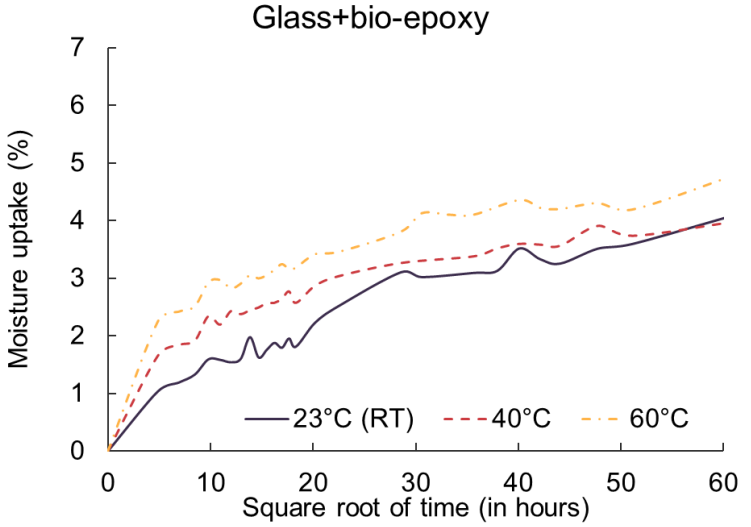

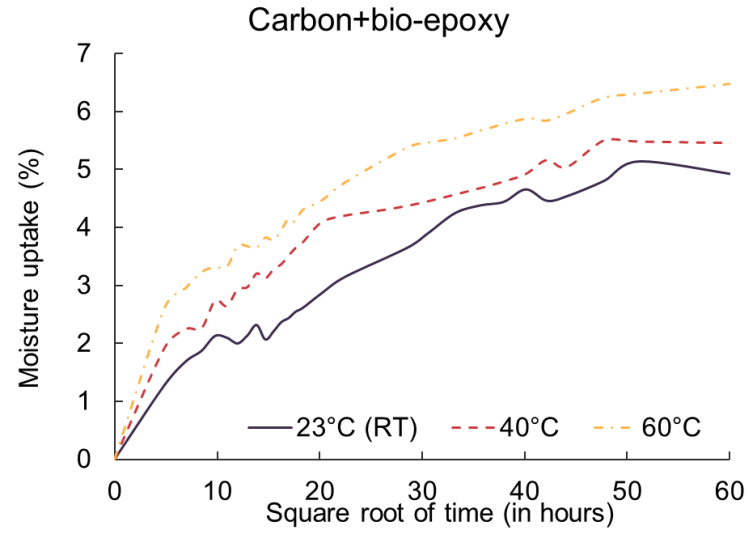

UniSQ

Results and discussion

Effect on Thermomechanical Properties

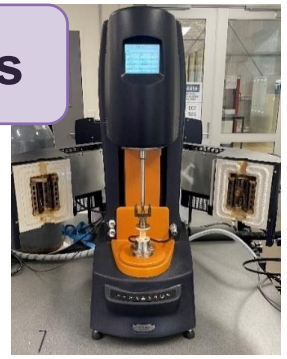

Glass transistion temperature t_g

- Significant reduction – up to 50%
- The largest Tg drop occurred after 83 days at 40°C

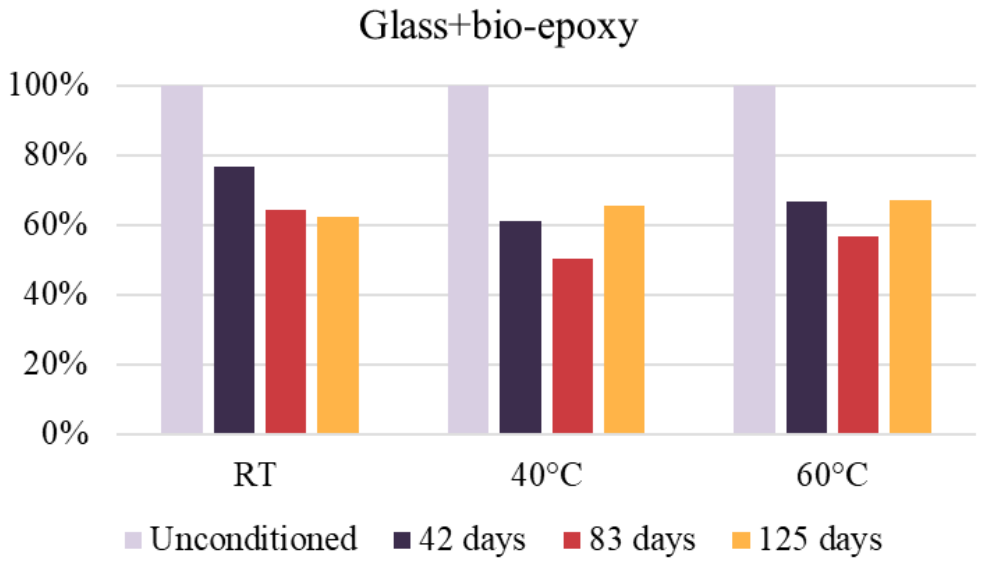

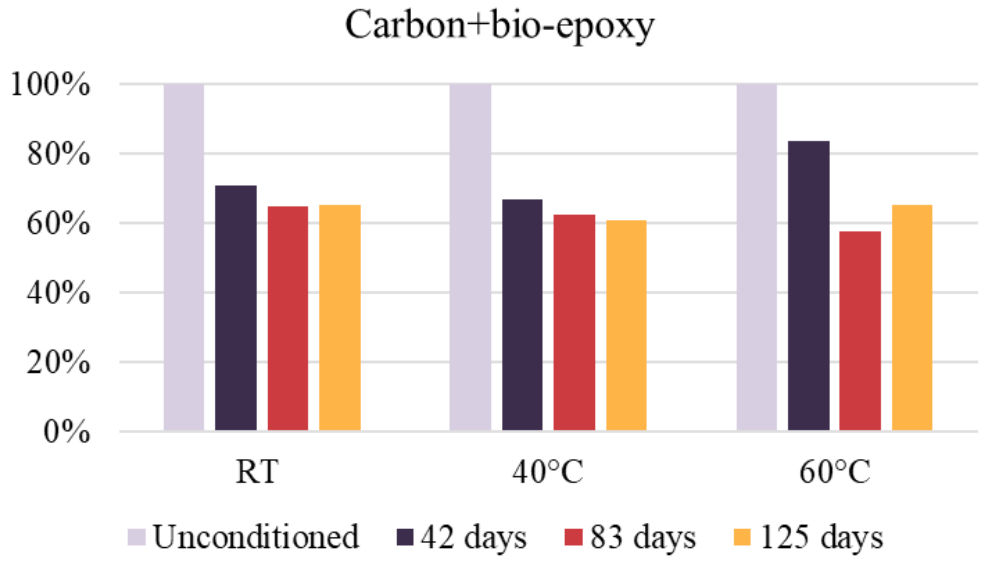

Conditioning	Control	RT	40°C	60°C
42 days	62.05	47.58	37.99	41.48
83 days	62.05	39.90	31.18	35.11
125 days	62.05	38.74	40.62	41.61

Conditioning	Control	RT	40°C	60°C
42 days	65.07	46.08	43.57	54.34
83 days	65.07	42.15	40.53	37.63
125 days	65.07	42.35	39.58	42.53

Results and discussion

Effect on Chemical Properties



Fourier Transform Infrared (FTIR) Spectroscopy

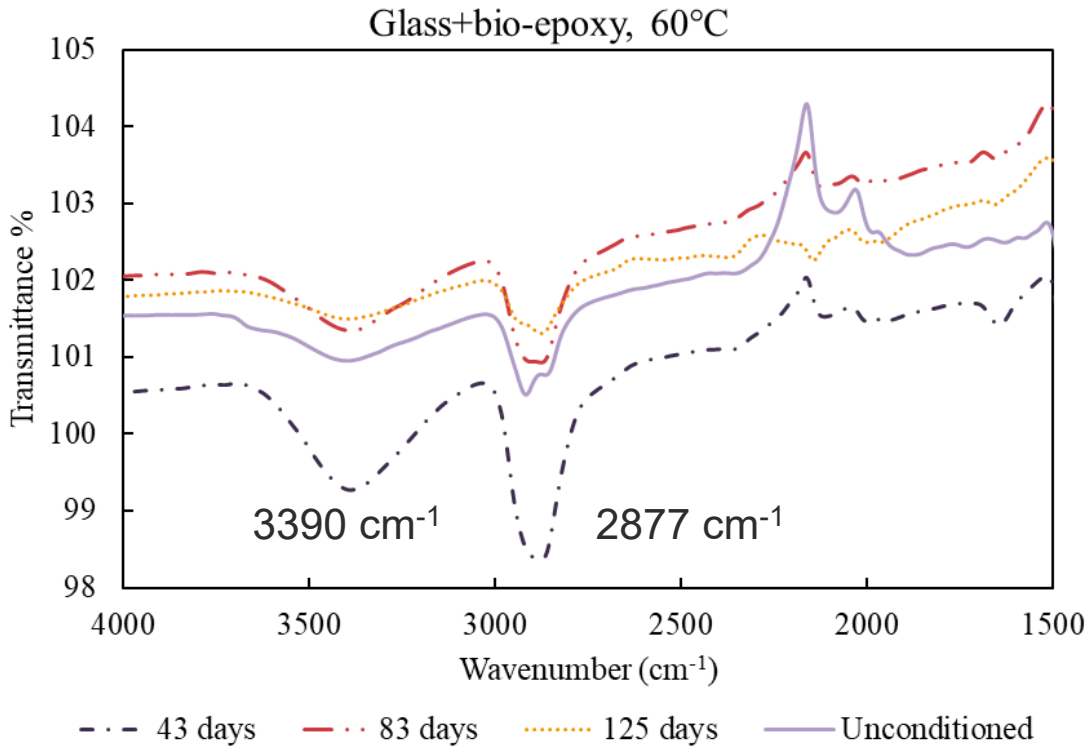

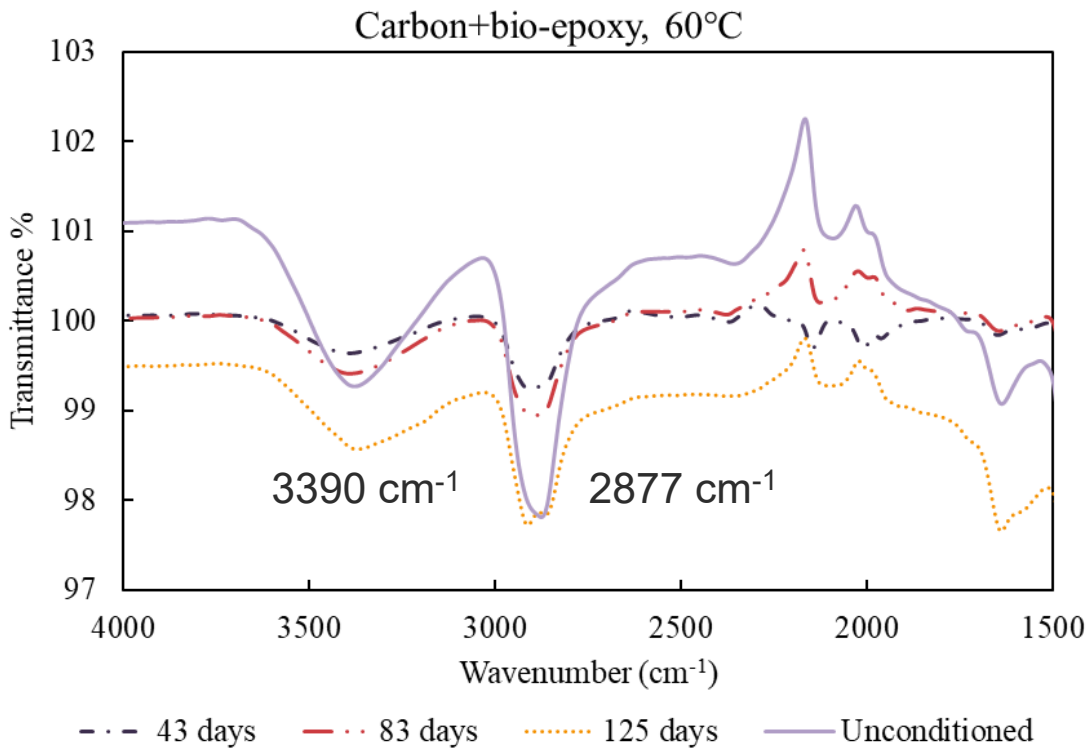

- 3390 cm^{-1} O-H stretching
- 2877 cm^{-1} C-H stretching
- Increasing O-H/C-H area ratio over time confirms the formation of hydroxyl groups, indicating hydrolysis

Results and discussion

Effect on Mechanical Properties

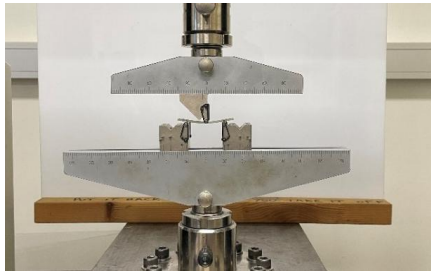

Interlaminar Shear Strength (ILSS)

- Temporary improvement at 83 days – linked to crosslinking or moisture equilibrium
- Progressive degradation due to hydrolysis and matrix damage

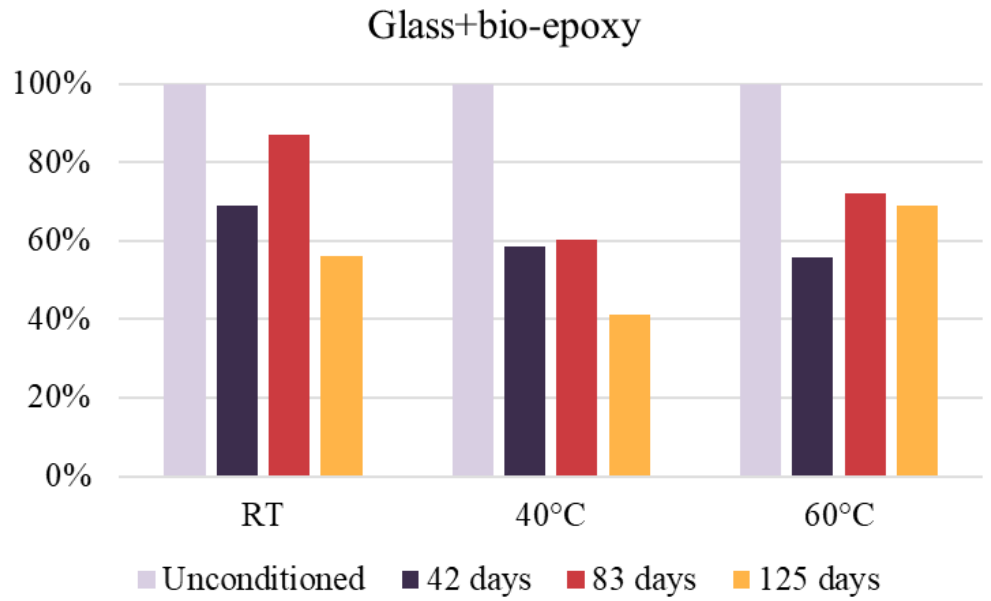

Conditioning	Control	RT	40°C	60°C
42 days	23.36	16.16	13.7	13.05
83 days	23.36	20.33	14.1	16.87
125 days	23.36	13.12	9.63	16.09

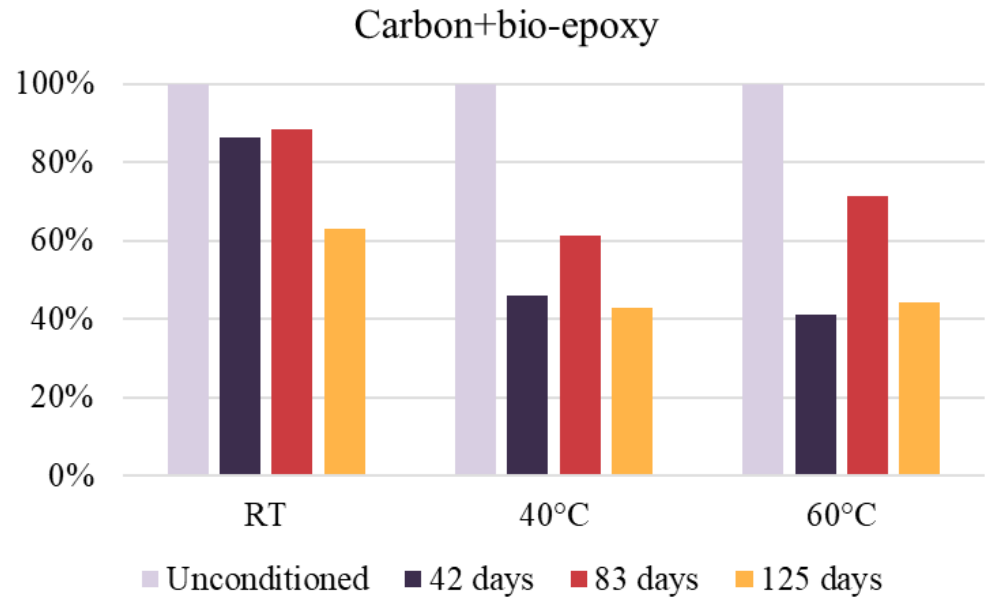

Conditioning	Control	RT	40°C	60°C
42 days	37.51	32.35	17.21	15.40
83 days	37.51	33.10	22.95	26.71
125 days	37.51	23.59	16.10	16.62

Results and discussion

Effect on Microstructural Properties

Microstructure observation

GFRP	42 days (1000 hrs)	83 days (2000 hrs)	125 days (3000 hrs)
RT (23°C)			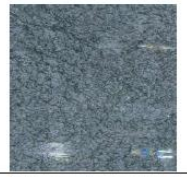
40°C			
60°C			

CFRP	42 days (1000 hrs)	83 days (2000 hrs)	125 days (3000 hrs)
RT (23°C)			
40°C			
60°C			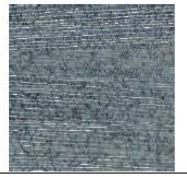

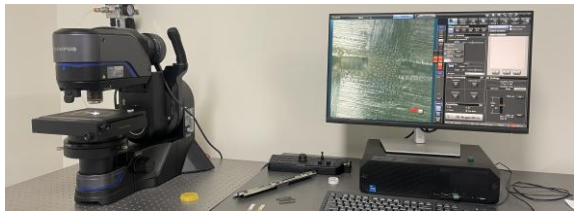



Delamination

Resin degradation

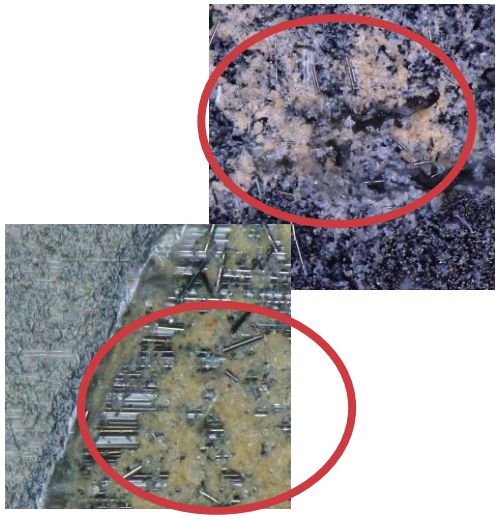

Yellowing

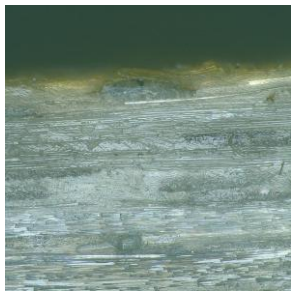



Resin rich areas

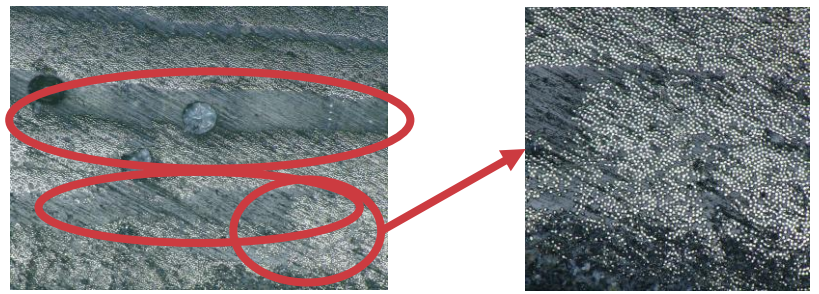

UniSQ

Conclusion

- CFRP absorbed more moisture (up to 6.5%) than GFRP composites (4.5%), but has minimal colour change. Yellowing was observed for GFRP composites.
- Tg of bio-epoxy can be severely affected by hygrothermal environment (up to 50% reduction).
- Hygrothermal environment can cause hydrolysis in bio-epoxy based composites
- ILSS can be enhanced with exposure to hygrothermal environemnt (up to 40%) possibly due to crosslinking or thermal relaxation.

University of Southern Queensland

Thank you for your attention

unisq.edu.au

CRICOS: QLD 00244B, NSW 02225M TEQSA: PRV12081

This content is protected and may not be shared, uploaded, or distributed

SYSTEMATICALLY ADAPTING PROCESSABILITY AND FLAME RETARDANCY OF EPOXY GLASS FIBER REINFORCED COMPOSITES FOR RAILWAY APPLICATIONS

Sruthi Sunder*[1], Leonard Hieke*[1], Rodrigo Q. Albuquerque[1] and Holger Ruckdäschel[1]

[1]Department of Polymer Engineering, University of Bayreuth
Universitätstrasse 30, 95447, Bayreuth, Germany
Email: sruthi.sunder@uni-bayreuth.de, web page: www.polymer-engineering.de
* These authors contributed equally to the paper

Keywords: Machine learning, Flame retardancy, Glass fiber composites, Epoxy resins

ABSTRACT

Epoxy glass fiber composites offer significant weight reductions for railway applications, reducing fuel consumption by 12–14%. However, the intrinsic flammability of the epoxy matrix poses challenges in achieving HL-2 fire classification under DIN EN 45545. This study addresses this limitation by systematically identifying and optimizing phosphorus-based flame retardants (FRs) compatible with vacuum infusion. An initial pool of 14 FR additives, including both solid (e.g., ammonium polyphosphate variants) and liquid (e.g., triethyl phosphate esters (TEP)) was screened in a Bisphenol F epoxy resin preloaded with 10 wt% resorcinol bis(diphenyl phosphate) (RDP). To reduce experimental effort, a batch active learning (B-AL) approach using Gaussian process regression (GPR) was applied to select 18 formulations for thermal and rheological characterization. Simultaneous thermal analysis (STA) parameters were used as surrogates for fire behavior in cone calorimetry, while pot life and storage stability were assessed to ensure processability. Surrogate models trained on STA and processability data achieved moderate predictive performance (R^2 = 0.4–0.6). Permutation importance was used to rank the FRs, identifying silane-coated APP (APPIII), melamine-coated APP (APPIV), TEP, and DOPOI as the most influential additives. These FRs were used in a secondary design space to generate 16 randomized formulations for transfer into woven glass fiber composites. Cone calorimeter tests conducted on top- and bottom-face exposures revealed increased filtration effects with higher solid FR content. The best balance between reduction in maximum average rate of heat emission (MARHE) from 155 kW/m^2 in the reference composite to 110 kW/m^2 and standard deviation in the MARHE values were found for the resin formulation containing 9% w/w of the liquid TEP with 1% APP and 10% RDP. Further optimization is required to satisfy railway norms. This machine learning-guided framework demonstrates a scalable route to optimize FR combinations that balance fire safety and processability.

1 INTRODUCTION

Lightweight fiber-reinforced composites are vital for the railway industry, offering corresponding fuel-efficiency improvements of 12–14 % which is a compelling driver for sustainability and reduced operating costs. However, these systems, particularly epoxy (EP)–glass fiber reinforced composites (GFRCs), pose significant fire-safety challenges due to the intrinsic flammability of the EP matrix, which fails critical safety thresholds required for passenger rail applications. Materials used in railway applications must comply with DIN EN 45545-2 [1], which outlines various parameters, most notably maximum average rate of heat emission (MARHE). For Hazard Level HL-2 compliance, the MARHE limit is 90 kW/m^2, while more stringent HL-3 applications demand values $\leq$ 60 kW/m^2. Meeting EN 45545-2 using phosphorus-based flame retardants (FRs) is one approach since they act synergistically in both the gas phase—by releasing radicals that suppress flame propagation—and the condensed phase, by promoting char formation to shield the polymer. For instance, aluminium diethyl phosphinate is a well-established flame retardant for epoxies operating via this dual mechanism [2–5]. Combinatorial systems like ammonium polyphosphate (APP) or intumescent blends have demonstrated

the potential to reduce peak heat release rate (pHRR) [6–9], and thus, MARHE values [10]. The relatively low viscosity (300-2000 mPa.s) required for vacuum infusion or resin transfer molding (RTM) processing, combined with the need to avoid filtration effects [11–13], constrains FR selection to additives that maintain processability.

While full-scale cone calorimetry (EN ISO 5660-1[14]) remains the gold standard for MARHE measurements, proxy screening via simultaneous thermal analysis (STA) using parameters like thermal decomposition onset and char yield can be indicative of fire performance ahead of composite fabrication [15]. For example (Figure 1), in differential scanning calorimetry (DSC), a left-shift in the heat energy of the first peak (Q1), or a decrease in intensity of the heat energy of the second peak (Q2) correspond to a decrease of pHRR and thus, MARHE values. Similarly, the, adjusted heat enthalpy of the first thermal event (ΔH_{1adj}) in thermogravimetric analysis (TGA) also represents a decrease in the pHRR. These correlations were generated using logistic regression combined with a least absolute shrinkage and selection operator (LASSO) model for a Bisphenol F Diglycidyl Ether (DGEBF)-diethyl toluene diamine system by Binder et al. [15]. Although modified contexts may result in modified correlation strengths between STA and cone parameters, it is assumed that these correlations can be exploited to screen FR additives for transfer to composites.

Comprehensive experimental screening becomes resource-intensive given the combinatorial nature of FR systems. Krebs [16] investigated how to boost the flame-retardant performance of a high-temperature epoxy resin for both aerospace and railway applications. Screening synergistic mixtures of AlPi with zinc stannate (ZnSt), and two inorganic silicate additives, guided by Bayesian optimization (BO) via Gaussian process regression (GPR) helped simultaneously minimize a hybrid target with total smoke production (TSP) and MARHE. When transferred to GFRCs via prepregs, the BO-optimized formulation nearly satisfied a HL-2 classification. Modelling with both linear and nonlinear regressors showed that a Random Forest algorithm best captured the complex, nonlinear relationships between FR content and performance. Storage stability estimations over months for iterative machine learning (ML) experiments are time consuming; accelerated aging of resin formulations at temperatures > 25°C can be used to estimate storage stability based on differences in the initial glass transition temperature T_{g0} over shorter time periods [17].

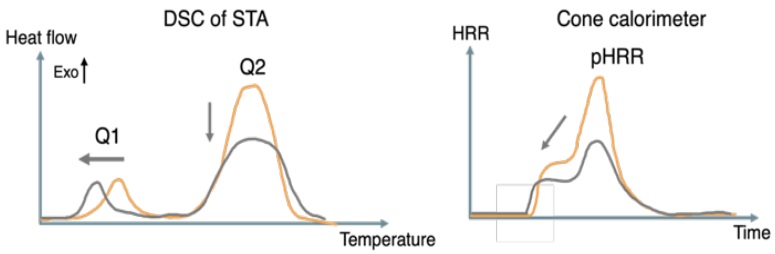

Figure 1: Correlations between heat flow in DSC measurements and pHRR measurements

The use of active learning (AL) using batch experiments (B-AL) with GPR also enables efficient exploration across the formulation space beyond BO [18–20]. This study builds upon these foundations by screening 14 phosphorus-based FR additives (gas- and condensed-phase) in a DGEBF resin containing 10 % w/w resorcinol bis(diphenyl phosphate)) (RDP). Processability via shear viscosity, and storage tests, targeting vacuum infusion compatibility. STA-informed B-AL/GPR models are used to gather data for training surrogate models for FR selection. Selected FRs based on feature importance estimations are transferred into 100 g/m² glass fiber composites via vacuum infusion across 16 randomized design trials, guided by BO. This approach integrates fire safety, processing constraints, and machine-learning-based surrogate modelling to enable accelerated material development in compliance with EN 45545 for weight-efficient and safe composite components.

2 MATERIALS AND METHODS

An overview of the methods used in this investigation is shown in Figure 2. B-AL is used as the exploratory phase to eventually reduce the number of features (FRs) for future exploitative Bayesian optimisation experiments.

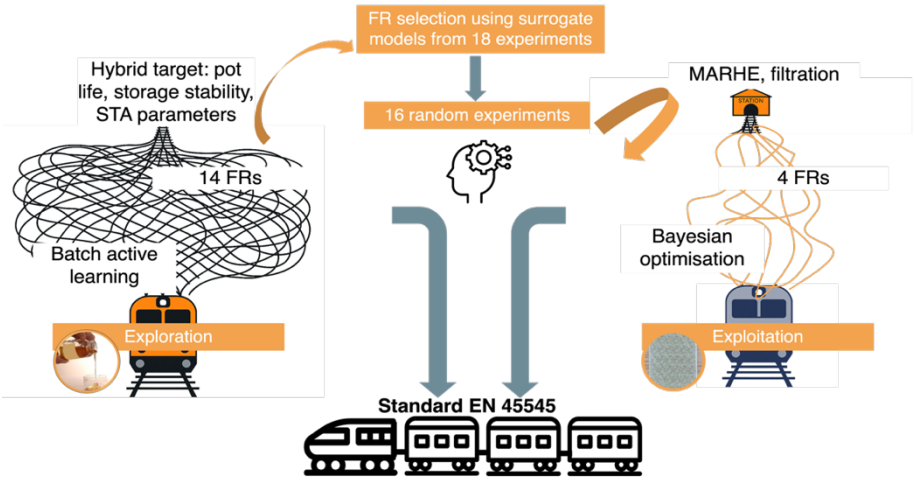

Figure 2: Overview of the methodology in the investigation

2.1 Resin preparation

A DGEBF resin system (Polyphlox 3721, Struktol GmbH) with an epoxy equivalent weight (EEW) of 235 g/Eq and a dynamic viscosity of 3000 mPa.s at room temperature containing 10% w/w of a RDP liquid FR was reacted with an IPDA-PACM hardener with an amine hydrogen equivalent weight (AHEW) of 47.6 g/Eq. DGEBF and IPDA were combined and dispersed by hand in the stochiometric ratio of 100:22 based on the following equation:

$$\text{Resin} - \text{hardener ratio} = \left[\frac{100 \times (\text{AHEW}_{\text{IPDA-PACM}})}{(\text{EEW}_{\text{DGEBF}})}\right] \quad (1)$$

2.1 Flame retardants and glass fibers

Table 1 summarizes the various FR additives used within the study for feature selection screening. RDP is already mixed at a fixed proportion within the DGEBF resin. The halogenated flame retardant PropCP is considered for a comparison with the non-halogenated FRs and not intended for transfer to the composite. DOPOI is considered as an alternative liquid FR for transfer to the composite after feature importance determination from the existing 14 initial FRs. The particle size distribution of the 50% fraction of the FRs is reported as d_{50} in µm.

Chemical formulation	Commercial name	Supplier	Coating	d_{50} µm	Abbrev.	Form	P %
Resorcinol bis(diphenyl) phosphate	-	Struktol	-	-	RDP	Liquid	20
Ammonium polyphosphate	Polyphlox 3721 Comp. B		-	5	APPI	Solid	32
	FR CROS 484	Budenheim	-	20	APPII		

Ammonium polyphosphate	FR CROS 486	Budenheim	Silane	20	APPIII	Solid	32
	FR CROS C30		Melamine	7	APPIV		
	FR CROS 584		-	18	APPV		
	FR CROS 585			18	APPVI		
Intumescent mixture with APP	FR CROS 638			12	APPVII		24
Melamine polyphosphate	FR CROS 513			8	MPP		13
Aluminium diethyl phosphinate	EXOLIT OP 935	Clariant		10	DEPALI		22
	EXOLIT OP 1230			20	DEPALI I		
Triethyl phosphate	Luvogard HF P70	Lehvoss		-	TEP	Liquid	18
2-Propanol, 1-chloro-, phosphate (3:1)	Fyrol PCF	ICL		-	ProCP		10
Zinc hydroxystannate	Flamtard H	William Blythe		5	ZHS	Solid	0
Inorganic silicate	Flamtard V100			5	Insi		
6H-Dibenz [c,e] [1,2] oxaphosphorin-6-propanoic acid, butyl ester, 6-oxide	Sacoflam 47201	Krems Chem		-	DOPOI	Liquid	20

Table 1: Database of FRs with varying physical forms, P content and chemical formulations for feature importance determination via B-AL trials

The variation in the fraction of the 14 FRs used for AL trials across 18 experiments is given in the heatmap in Figure 3. Aerospace textile satin woven glass fibers (GFs) (9111-FK144 from Valmiera glass) with an areal weight of ~ 105 g/m^2 coated with a silane/volan finish were used for vacuum infusion.

3 METHODS

3.1 Active learning via batch experiments for FR selection

A library of fourteen phosphorus-based flame retardants (14 features) was initially gathered (Table 1), to evaluate their relative importance with respect to STA-derived thermal metrics, pot life, and storage stability to be determined. To minimize the number of physical trials, batch active learning employing a Gaussian process regression surrogate model was implemented: the first five formulations were sampled from a constrained virtual design space of 10,000 candidates via Gaussian sampling. The total FR loading was maintained $\leq$ 10 w/w, which including RDP was $\leq$ 20 w/w. In total, 18 experimental formulations, with 5 initial experiments and subsequently 3 per round were ultimately evaluated, and

permutation-based feature-importance analysis was applied to these results to identify the most influential additives.

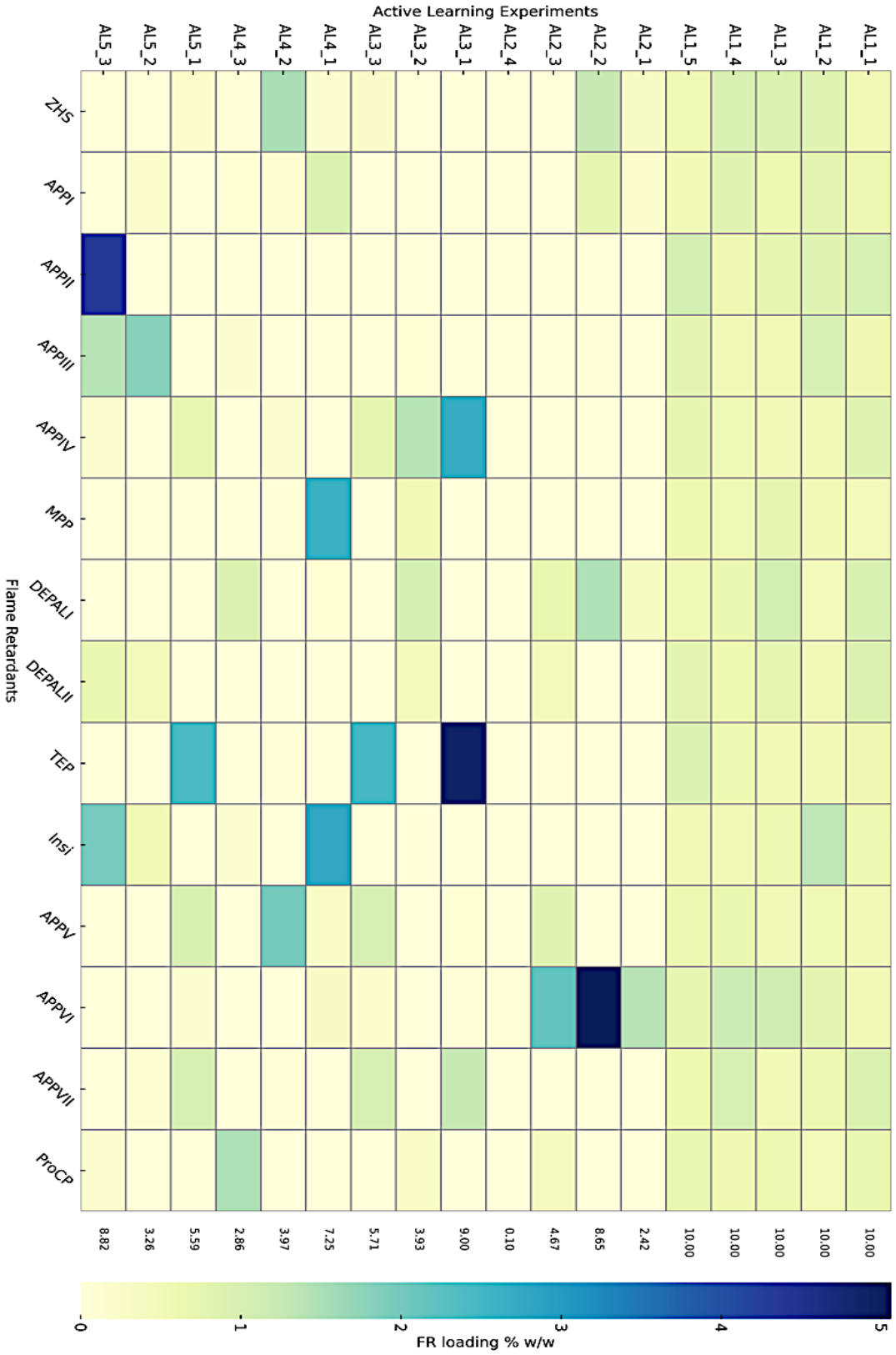

Figure 3: FR loadings in w/w for the 18 experiments based on B-AL

A hybrid target function containing 12 sub-targets was defined as:

$$\text{fFR1} = 0.25[(\text{Pot Life}) - (|T_{g0}|) + (\text{Positive parameters}) - (\text{Negative parameters})] \quad (2)$$

Here, the relevance of the positive and negative parameters is explained in Table 2. The STA parameters were each weighted based on the LASSO coefficients derived from the study by Binder et al.[15].

Influence on fire performance	Impact on pHRR	STA parameters
Positive influence on fire performance	Negative (increase in parameters implies a decrease in pHRR)	Initial sample mass, mass residue of the second peak in DSC, **heat energy of the first curing peak in DSC**, temperature at 50 % conversion of the first peak in TGA, temperature at 50 % conversion of the second peak, **adjusted heat enthalpy of the first peak in DSC**
Negative influence on fire performance	Positive (increase in parameters implies an increase in pHRR)	Total heat value in DSC**, heat energy of the second curing peak in DSC**, temperature of the second peak in DSC, heat flow of the first curing peak in DSC

Table 2: STA parameters positively and negatively influencing fire performance

3.2 Pot life

The influence of the FR additive combinations as additives for the DGEBF systems on pot life was measured using an Anton Paar Rheometer (MCR 301). The rheological properties of the resins were then evaluated at an isothermal sweep at 50 ºC for 120 mins using a parallel plate (PP25) with a gap between parallel plates of 1 mm. The pot life in mins was determined as the time at which the resin reached a complex viscosity of 2000 mPa.s. A constant strain of 0.1% was used, with a maximum torque of 140 mN/m.

3.3 Storage stability

For the storage stability measurements, the DGEBF resin was not reacted with the hardener but directly combined with the FR additives and dispersed by hand. The resins were tested in a DSC1 from Mettler Toledo (USA) directly after preparation (Day 0). A sample mass of 5-10 mg, with a temperature range of -25 ºC to 250 ºC at a ramp rate of 10 K/min was used for each measurement. A constant flow of synthetic air at 50 mL/min was maintained. The samples were subsequently stored in a Memmert ULE 400 convection oven at 50 ºC for 7 days after which a DSC measurement was performed. A benchmark of $\boldsymbol{\Delta T_{g0}} \leq 10$ ºC was used to determine the storage stability of the resins. $\boldsymbol{\Delta T_{g0}}$ was calculated using the following equation:

$$\Delta T_{g0} = T_{g0}^{Day7} - T_{g0}^{Day1} \quad (2)$$

3.4 Simultaneous thermal analysis (STA)

For STA measurements, the FRs were dispersed into the resin-hardener mixture by hand mixing and cured overnight by film casting on a glass plate at 25 °C. Subsequently, the cured resin was comminuted in a cryomill at ~ 19,000 rpm using a 200 µm sieve. Samples with a mass of ~ 10 mg were tested simultaneously for DSC and TGA parameters in a Netzsch STA 449 F3 Jupiter using a temperature range from 25 °C to 800 °C with a ramp rate of 7.5 K/min. The various parameters mentioned in section 3.1 were then extracted.

3.5 Vacuum infusion and cone calorimetry

The resin formulations were preheated to 50 °C and infused into ~ 32 layers of the GFs stacked by hand under vacuum of 0 mbar. The infused GFs, with a target fiber volume content of 50 ± 5 % were cured overnight at room temperature and subsequently cut to size (100 mm x 100 mm x 3 mm) for cone calorimeter tests. The top and bottom faces of the samples were labelled. The samples were tested in a horizontal orientation – with one sample with the top face exposed to the cone heater, and with another with the bottom face exposed, under an external heat flux of 35 kWm^{-2} and 25 mm from the cone heater following ISO 5660-1 norms. The MARHE values and the standard deviation between the top and bottom face exposures from the cone tests was calculated to determine the presence of filtration effects.

4 RESULTS AND DISCUSSION

4.1 Pot life and storage stability

Figure 4 (a) reveals that the pot life values for all 18 formulations converge within a narrow range (±10 min), suggesting a consistent impact of FR incorporation on resin rheology. No anomalous gelation behavior was observed, indicating thermal stability of the curing system under the evaluated formulations. Despite the high dimensionality of the features and targets within the AL experiments, a gradual increase in the value of the hybrid function is visible in Figure 4 (b).

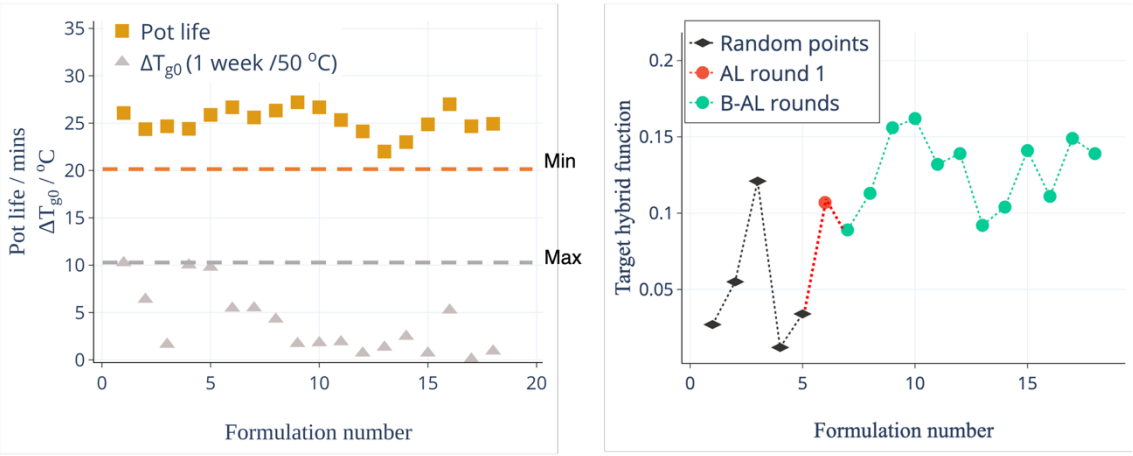

Figure 4: Variation of pot life and ΔT_{g0} for the resin formulations (a) and progress in the hybrid target across the 18 experiments (b) – Random, AL points

4.2 Training surrogate models for feature selection

The 14 input features (FR compositions) were scaled using None, MinMax, Standardisation and Robust scalers and either unpre-processed or pre-processed with techniques such as polynomial features of degree 2 (Poly2), first 5 principal components (PCA5) etc. The 12 sub-targets (see equation 2) from the 18 experiments via B-AL, the data were used as individual targets. The data from each sub-target was split into training test sets, to train 7 surrogate models – linear, random forest regression, gradient boosting regression (GBR), support vector regression (SVR), k-nearest neighbour (KNN), decision tree

(DT) and LASSO model. A five-fold cross-validation was employed for each surrogate model pipeline, ensuring that each of the 18 data points was held out once. The best pipelines of these 140 pipelines determined by those which predicted individual parameters with the highest cross validation (CV) R^2 values, lowest CV mean square error (MSE) and lowest CV mean absolute error (MAE) (Table 2) relative to the data, were selected to determine feature importance using permutation importance.

Target property (highlighted in table 2)	Pre-processing	Scaler	Surrogate model	CV R^2	CV MSE	CV MAE
Heat energy of the first curing peak	PCA	Standard	Linear	0.6320	0.0032	0.04805
Adjusted heat enthalpy of the first curing peak	PCA	None	Linear	0.5883	0.0004	0.01656
Heat energy of the second curing peak	Poly2	Robust	LASSO	0.4869	0.4298	0.5446

Table 3: Best pipelines based on 140 combinations of data preprocessing, scaling and training of 7 surrogate models

Thereby, the top ranked FRs based on feature importance were silane coated APP (APPIII), melamine coated APP (APPIV), proCP and TEP. Since proCP is halogenated, it was eliminated at this stage based on REACH regulations. While this 18-point AL dataset enabled proof-of-concept surrogate modelling, the moderate R^2 values indicate that additional rounds are required to fully capture nonlinear FR interactions. Future work will integrate high-throughput thermal screening to expand the design space. The high permutation importance of APPIII and APPIV is promising due to their known condensed-phase char-promoting behavior, while TEPs gas-phase radical-quenching action supports its intermediate ranking. DOPOI was selected as an additional liquid FR for 16 randomised trials in vacuum infusion. For this purpose, a second constrained virtual design space of 10,000 candidates via Gaussian sampling was generated with these 4 selected FRs, and 16 randomised trials were generated for vacuum infusion experiments and subsequent cone calorimeter tests.

4.3 Fire performance and filtration effects of the composites (under construction)

The pareto plot between TSP and MARHE of the randomized samples are shown in Figure 5. Sample number 14 was invalidated due to technical errors during cone calorimeter operation and showed the highest error in MARHE (±85 kW/m^2). Sample 13 containing a combination of 9% w/w of TEP with 1% w/w of APP simultaneously showed one of the lowest MARHE values and filtration effects. Although Sample 5, containing 5% w/w APPIII, 2% APPIV and 2% TEP showed the lowest MARHE values of all valid samples with significant intumescent behavior during fire testing, the difference from the top face (MARHE ~ 70 kW/m^2) and bottom face was ~ 30%. Thus, it can be hypothesized that although a potential synergistic effect is present in sample 5 with primarily condensed phase action from the APP leading to a HL-2 classification when the top face is exposed to a fire, the higher solid content present in the resin causes a gradient effect and reduces FR penetration and thus, fire performance towards the bottom of the composite. Compared to the composite without FRs, all samples containing at least 2% w/w of some combination of FRs improved the MARHE values, with the best formulation (sample 5) producing a ~ 30% reduction in MARHE.

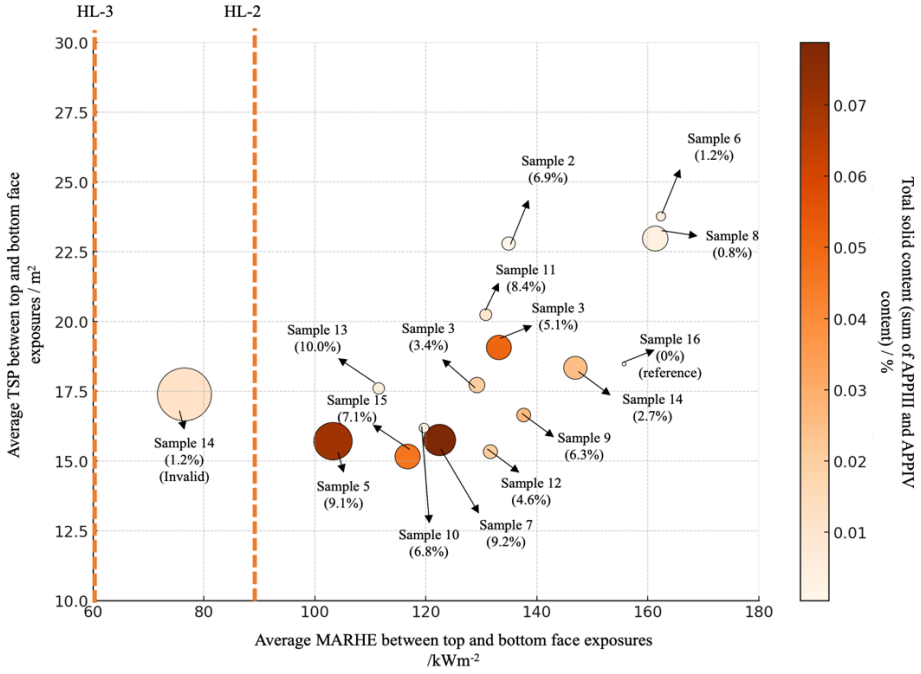

Figure 5: Pareto plot between average TSP and MARHE for the 16 samples showing solid content and filtration effects. Larger data points represent higher uncertainty in MARHE indicating higher filtration effects. All FR percentages are in addition to 10% w/w RDP content in the resin

5 CONCLUSION AND OUTLOOK

In this study, a systematic, ML-guided approach was used to identify and optimize P-based FRs as additives for EP GFRCs. From an initial pool of 14 candidate FRs, a B-AL framework using Gaussian-process surrogate models were used to efficiently screen formulations. By leveraging simultaneous thermal analysis (STA) parameters as rapid proxies for cone-calorimetry performance, we reduced the experimental burden completing 18 guided trials while still capturing feature importance. Coated APP formulations dominated the feature ranking, followed by a halogenated liquid FR and a TEP liquid FR.

16 randomized vacuum-infused composite specimens containing 4 selected FRs were fabricated and characterized via cone calorimetry under both top- and bottom-face exposures. Using only random trials, the MARHE values could be reduced by ~30%, close to the HL-2 standard for railway applications. Although successful as a proof of concept, expanding the AL dataset will help capture nonlinear synergistic effects among multiple FRs. Validation under shear rates representative of injection molding ($\approx 10\ s^{-1}$) and scale-up trials in RTM will ensure further industrial applicability. Further improvement of the FR content in the resin is also required, potentially via Bayesian optimization rounds to balance filtration effects with MARHE values until a HL-2 classification is possible.

ACKNOWLEDGEMENTS

This study was funded by AIF Project GmbH via the Zentrale Innovationsprogramm Mittelstand (ZIM) (project number: KK5120807EB4). The authors would like to acknowledge Dr. Hauke Lengsfeld for his contribution to the project.

REFERENCES

[1] Railway applications - Fire protection on railway vehicles - Part 2: Requirements for fire behaviour of materials and components; German version EN 45545-2:2020+A1:2023 2023, (doi: 10.31030/3490950).

[2] M. J. Rozo, S. Sunder, H. Ruckdaeschel, B. Schartel, Unveiling Aluminum Diethyl Phosphinate Dual Identity: Transfer from Epoxy Resins to Glass Fiber-Reinforced Composites, *Polymer Composites,* 2024, (doi: 10.1002/pc.29911).

[3] U. Braun, B. Schartel, Flame Retardancy Mechanisms of Aluminium Phosphinate in Combination with Melamine Cyanurate in Glass-Fibre-Reinforced Poly(1,4-butylene terephthalate), *Macro Materials & Engineering,* **293,** 2008, pp. 206–217 (doi: 10.1002/mame.200700330).

[4] S. Brehme, B. Schartel, J. Goebbels, O. Fischer, D. Pospiech, Y. Bykov, M. Döring, Phosphorus polyester versus aluminium phosphinate in poly (butylene terephthalate)(PBT): flame retardancy performance and mechanisms, *Polymer Degradation and Stability,* **96,** 2011, pp. 875–884 (doi: 10.1016/j.polymdegradstab.2011.01.035).

[5] A. R. Horrocks, G. Smart, S. Hörold, W. Wanzke, E. Schlosser, J. Williams, The combined effects of zinc stannate and aluminium diethyl phosphinate on the burning behaviour of glass fibre-reinforced, high temperature polyamide (HTPA), *Polymer degradation and stability*, **104,** 2014, pp. 95–103 (doi: 10.1016/j.polymdegradstab.2014.03.027).

[6] M. Rajaei, D.-Y. Wang, D. Bhattacharyya, Combined effects of ammonium polyphosphate and talc on the fire and mechanical properties of epoxy/glass fabric composites, Composites Part B: Engineering, **113,** 2017, pp. 381–390 (doi: 10.1016/j.compositesb.2017.01.039).

[7] S. Sunder, M. J. Rozo, S. Inasu, D. Meinel, B. Schartel, H. Ruckdäschel, Effect of Ammonium Polyphosphate/Silicate Content on the Postfire Mechanics of Epoxy Glass-Fiber Composites Using Facile Chocolate Bar-Inspired Structures, *Fire and Materials*, **49,** 2025, pp. 329–346 (doi: 10.1002/fam.3280).

[8] S. Sunder, M. Jauregui Rozo, S. Inasu, B. Schartel, H. Ruckdäschel, Investigating the changing dynamics of processing, temperature-based mechanics, and flame retardancy in the transfer of ammonium polyphosphate/inorganic silicate flame retardants from epoxy resins to glass fiber composites, *Journal of Applied Polymer Science*, 2024, e55988 (doi: 10.1002/app.55988).

[9] Z.-B. Shao, J. Zhang, R.-K. Jian, C.-C. Sun, X.-L. Li, D.-Y. Wang, A strategy to construct multifunctional ammonium polyphosphate for epoxy resin with simultaneously high fire safety and mechanical properties, *Composites Part A: Applied Science and Manufacturing,* **149**, 2021, p. 106529 (doi: 10.1016/j.compositesa.2021.106529).

[10] D. Chen, Y. Zhang, J. He, X. Li, Making polycarbonate flame retardant: Flame retardant selection and calorimetric analyses, *Polymer Testing,* **117**, 2023, p. 107876 (doi: 10.1016/j.polymertesting.2022.107876) .

[11] A. Toldy, B. Szolnoki, G. Marosi, Flame retardancy of fibre-reinforced epoxy resin composites for aerospace applications, *Polymer degradation and stability*, **96**, 2011, pp. 371–376 (doi: 10.1016/j.polymdegradstab.2010.03.021).

[12] A. Hindersmann, Confusion about infusion: An overview of infusion processes, *Composites Part A: Applied Science and Manufacturing*, **126**, 2019, p. 105583 (doi: 10.1016/j.compositesa.2019.105583).

[13] S. H. Yum, W. I. Lee, S. M. Kim, Particle filtration and distribution during the liquid composite molding process for manufacturing particles containing composite materials, *Composites Part A: Applied Science and Manufacturing,* **90**, 2016, pp. 330–339 (doi: 10.1016/j.compositesa.2016.07.016).

[14] Reaction-to-fire tests ± Heat release, smoke production and mass loss rate ± Part 1: Heat release (cone calorimeter method) ISO/FDIS 5660-1

[15] S. Binder, A. Kühn, Prognose Der Ergebnisse von Brandprüfungen Mittels Methoden Des Maschinellen Lernens Auf Basis von Kalorimetrischen Messungen, PhD Thesis, FH Münster, 2023.

[16] N. Krebs, Co-Synergists for Smoke Suppression and Optimization of Flame-Retardant Properties Via Bayesian Optimization of a High-Tg Epoxy Prepreg System, University of Bayreuth, Department of Polymer Engineering, 2024.

[17] S. Ciutacu, P. Budrugeac, I. Niculae, Accelerated thermal aging of glass-reinforced epoxy resin under oxygen pressure, *Polymer degradation and stability*, **31**,1991, pp. 365–372 (doi: /10.1016/0141-3910(91)90044-R).

[18] S. M. Pai, K. A. Shah, S. Sunder, R. Q. Albuquerque, C. Brütting, H. Ruckdäschel, Machine learning applied to the design and optimization of polymeric materials: A review, *Next Materials*, **7**, 2025, p. 100449 (doi: 10.1016/j.nxmate.2024.100449).
[19] J. Xu, T. Luo, Unlocking enhanced thermal conductivity in polymer blends through active learning, *Computational Materials,* **10**, 2024, p. 74 (doi: 10.1038/s41524-024-01261-2).
[20] H. Zhou, Y. Fang, H. Gao, Using Active Learning for the Computational Design of Polymer Molecular Weight Distributions, *ACS Engineering*, **4**, 2024, 231–240 (doi: 10.1021/acsengineeringau.3c00056).

Effect of Hygroscopic Aging on the Transverse Damage Behavior of Fiber-Reinforced Composites: A Computational Micromechanics Study

K V Vaishakh[1], N K Parambil[2], Vikas Srivastava[1]

1 School of Engineering, Brown University

2 Center for Composite Materials, University of Delaware

ICCM24, 6th August 2025

BROWN
School of Engineering

Introduction

- FRP composite: heterogeneous phase of fiber and polymeric matrix
- Application: Aerospace, Marine, and Wind turbine blades
- Exposure to extreme environments

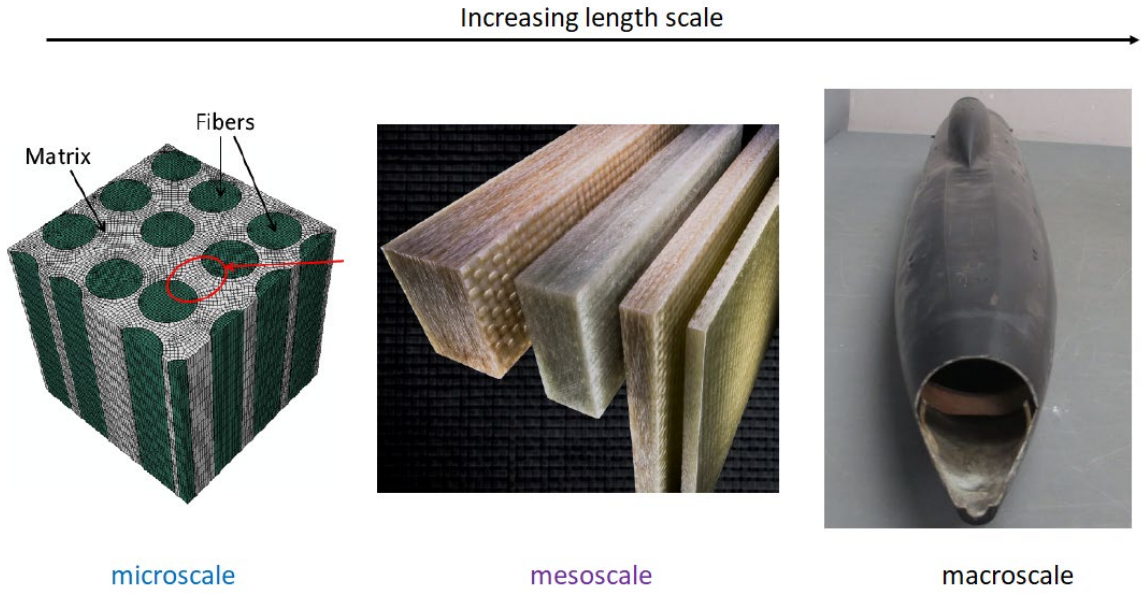

Hygrothermal exposure

- Synergetic effects of water and temperature
- No effect on fiber
- Matrix undergoes chemical and physical changes
- Mechanical properties of composite deteriorate

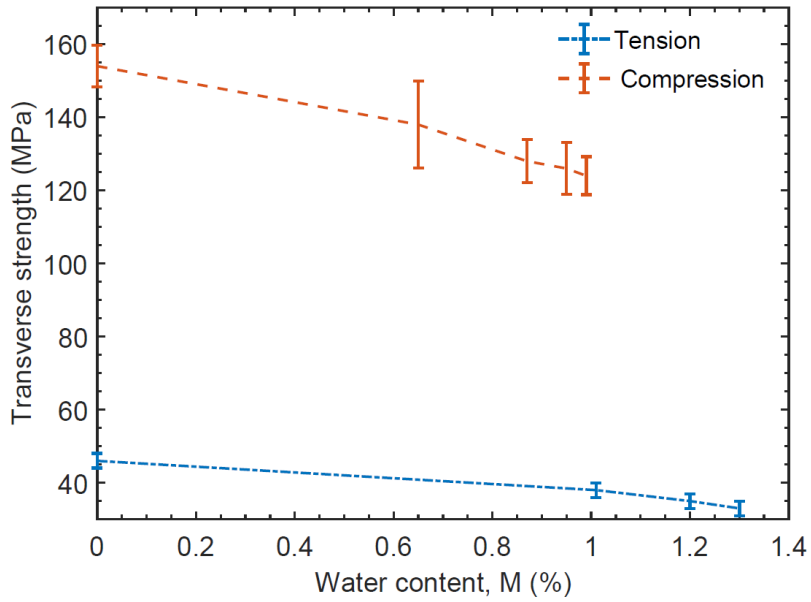

BROWN
School of Engineering

[1] Tual et al (2015) Compos. A

Background

- Material: Carbon/Epoxy unidirectional laminates
- Tests: Diffusion at various temp
- Void characterization: micro-CT scan.

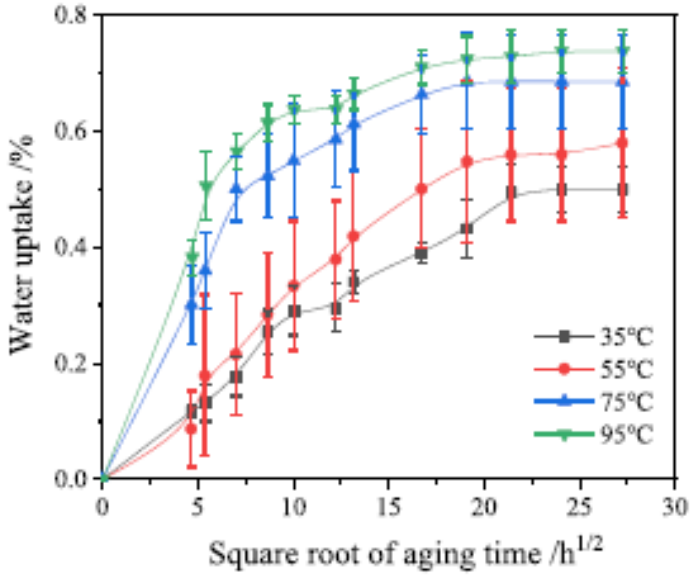

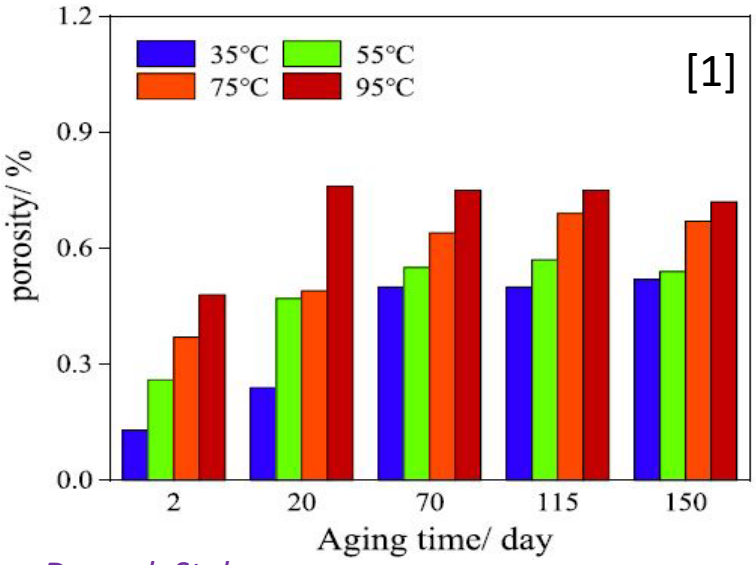

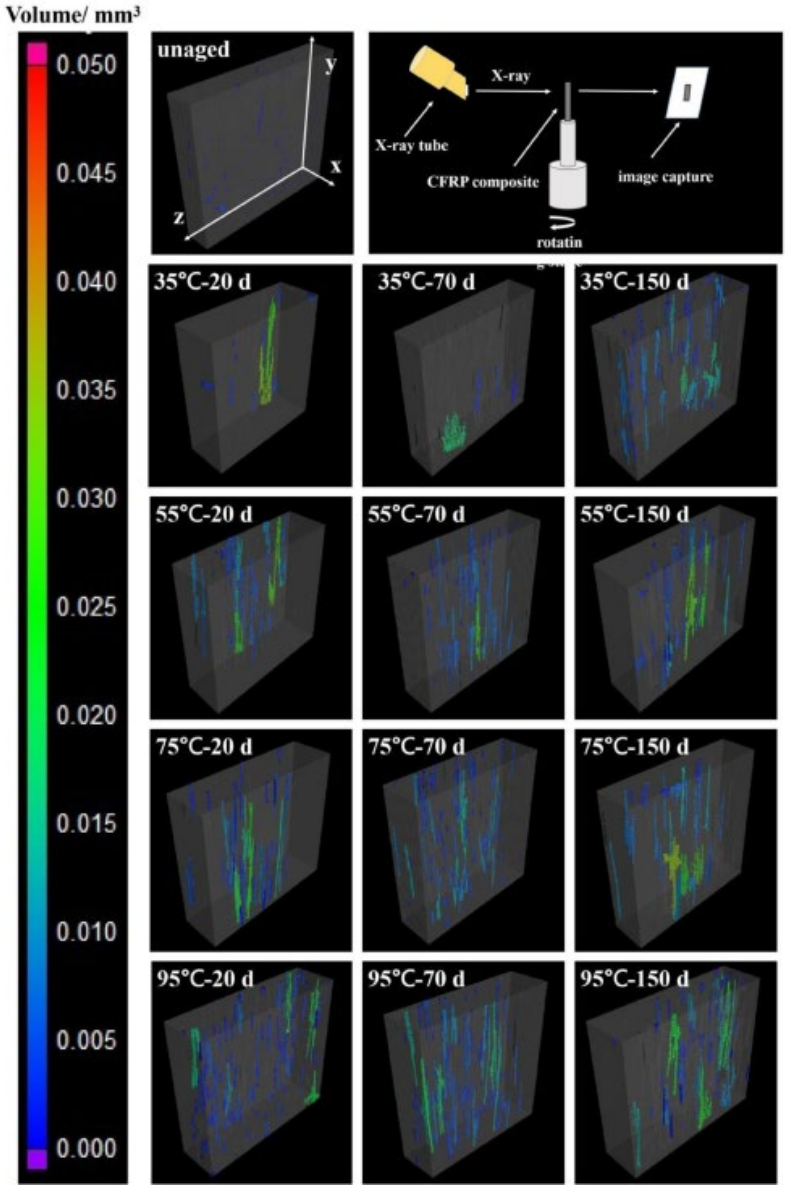

- Unaged: no pores (voids)
- With water ingress porosity increases
- Void formation along the fiber at the interface

BROWN
School of Engineering

[1] Zhuang et al (2022) Polym. Degrad. Stab.

Background

- Atomistic analysis of the hygrothermal effect on carbon fiber epoxy interface.
- Water molecules drastically deteriorate the integrity of the carbon fiber/epoxy interface.
- Elevated temperature level further degrades the interfacial mechanical response.

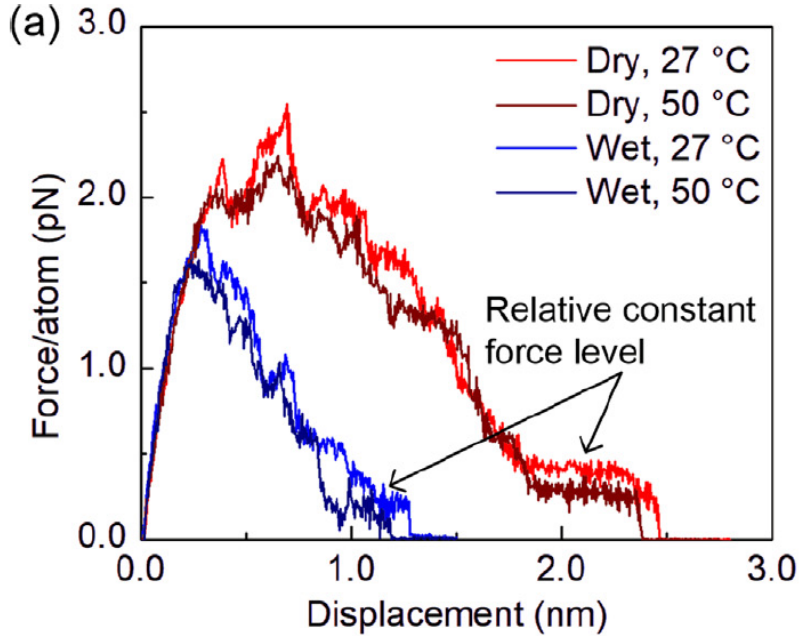

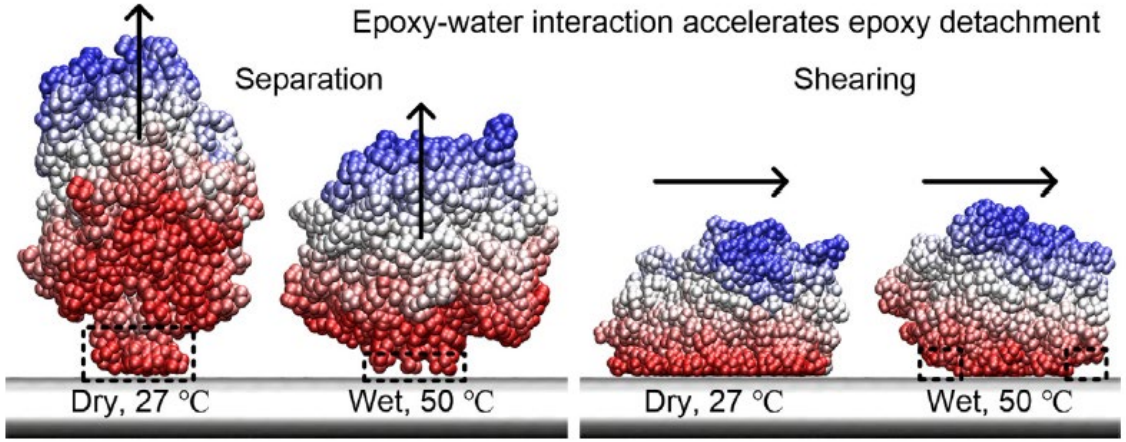

BROWN
School of Engineering

Tam et al (2019) Constr Build Mater.

Motivation and Objective

- Many studies on the influence of void on mechanical properties
- Either inter-fiber voids or matrix voids
- How process-induced voids influence the water ingress in the specimen

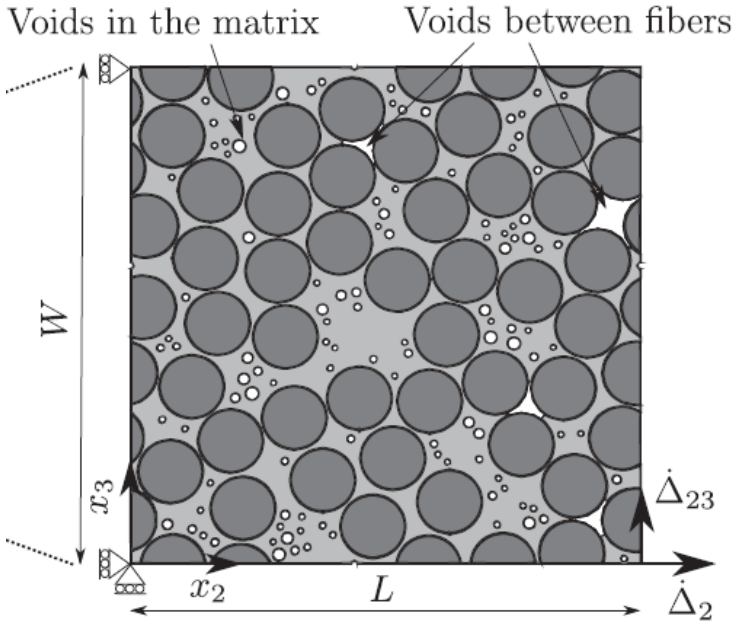

Void types [1]

Objective

- Systematic study of interface voids
- Develop a correlation: Moisture-induced porosity with water content in the specimen

BROWN
School of Engineering

[1] Vajari et al (2014) Compos. Sci. Techno.

FE geometry and Modeling details

Composite: Fiber, matrix, fiber/matrix interface, void (pore)

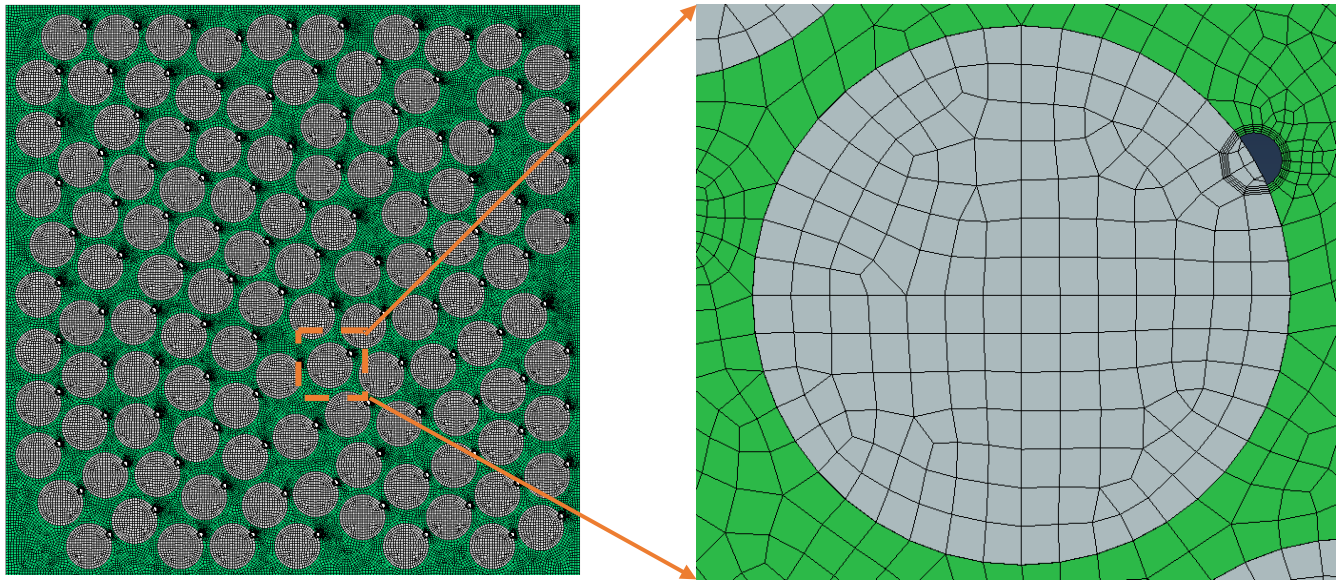

RVE FE mesh

- Fiber vol fraction (v_f) is maintained at 0.56
- Periodic boundary condition (PBC) is applied at the boundaries
- RVE loading: a tensile strain of 1%
- Post processing: homogenized stress-strain curve

Parameters considered in the study:

1. Porosity (p in %) through r_v= [0, 0.1, 0.3, 0.6, 0.9]
2. Location of the pore (Θ) = [0^0, 15^0, 30^0, 45^0, 60^0, 90^0]
3. Relative position of pore = [interface, matrix]

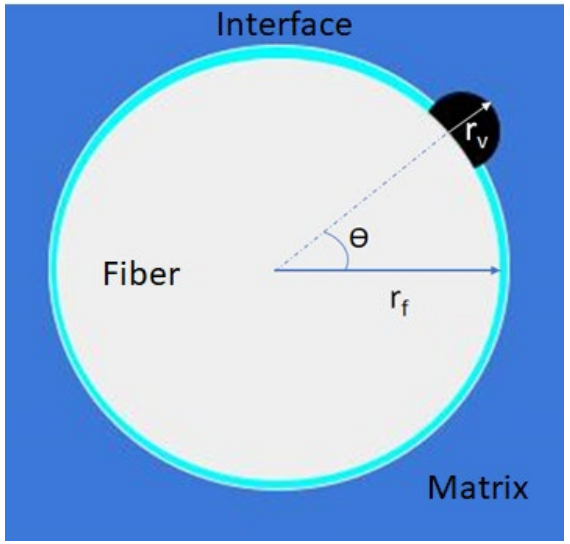

$$r_v = \sqrt{\frac{2p}{v_f}}\, r_f$$

BROWN
School of Engineering

Material model

Fiber: elastic material

Matrix: elasto-plastic

- Matrix: pressure-dependent yielding [1]

$$\Phi(\boldsymbol{\sigma}, \sigma_{c,} \sigma_{t,}) = 6J_2 + 2I_1 (\sigma_c - \sigma_t) - 2\sigma_c \sigma_t$$

- Hardening law: saturation hardening: $\sigma = \sigma_y + (\sigma_s - \sigma_y) * \tanh \frac{H\epsilon^p}{(\sigma_s - \sigma_y)}$

Dry and wet material properties of epoxy matrix

Condition	E (GPa)	σ_{yt} (MPa)	σ_{st} (MPa)	H_t (MPa)	σ_{yc} (MPa)	σ_{sc} (MPa)	H_c (MPa)
Dry	3.10	45	83	6500	66	126	6500
Wet	2.99	27	64	6500	40	104	6500

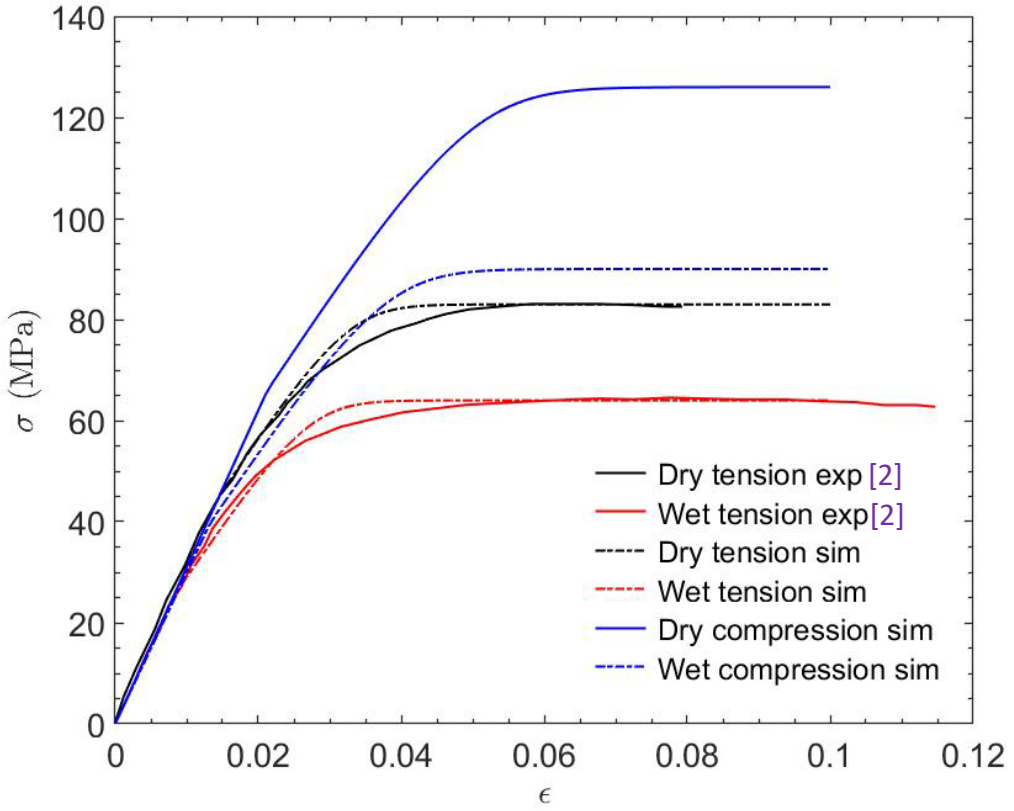

Matrix material (epoxy) response

BROWN School of Engineering

[1] Melro et al (2013) IJSS

[2] Dezulier et al (2022) Compos. B

Material model

Fiber/matrix interface:

- Cohesive interface with mixed-mode damage evolution

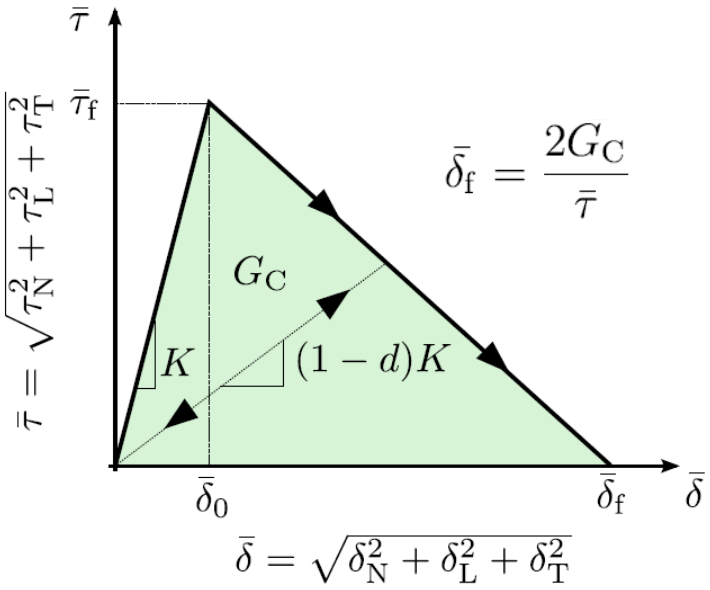

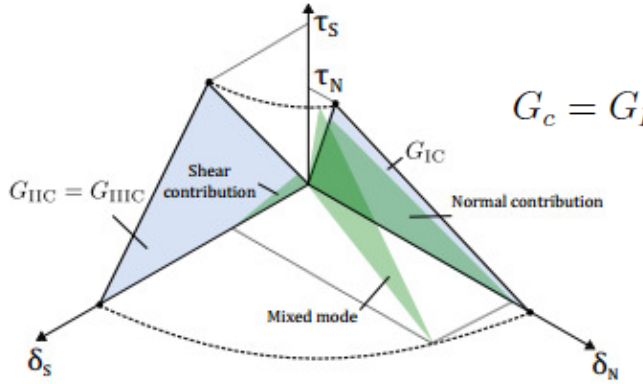

$$G_c = G_{Ic} + (G_{IIc} - G_{Ic}) \left(\frac{G_s}{G_t} \right)^m$$

Interface properties [1, 2]

Property Description	Value
Stiffness	
K_c (N/mm^3)	10^8
Maximum strength	
σ_n^0 (MPa)	54
τ_T^0 (MPa)	81 ($1.5\sigma_n^0$)
τ_L^0 (MPa)	81 ($1.5\sigma_n^0$)
Critical energy release rate	
G_{Ic} (N/mm)	0.002
G_{IIc} (N/mm)	0.1
G_{IIIc} (N/mm)	0.1
$G_s = G_{IIc} + G_{IIIc}$	
$G_t = G_{Ic} + G_{IIc}$	
Parameter in the BK law, m	1.45

[1] Naya et al (2017) Compos. A

[2] Hyde et al (2020) Compos. B

Effect of porosity on strength

Effect of size

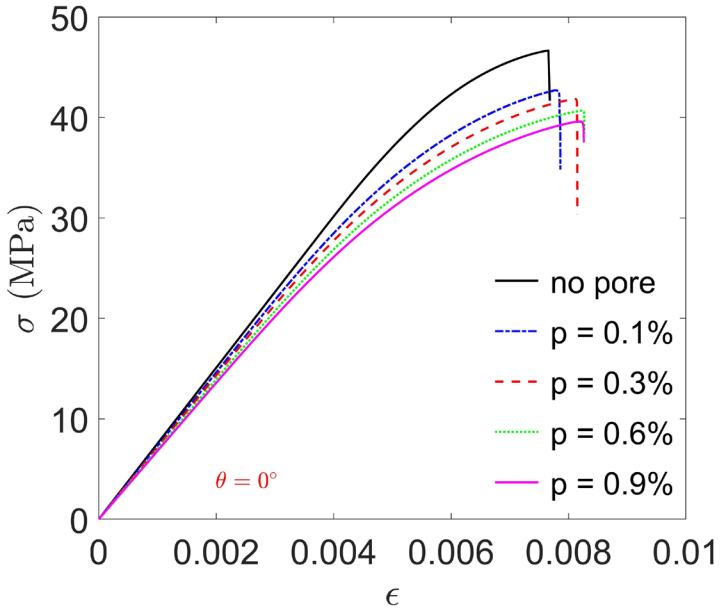

Effect of orientation

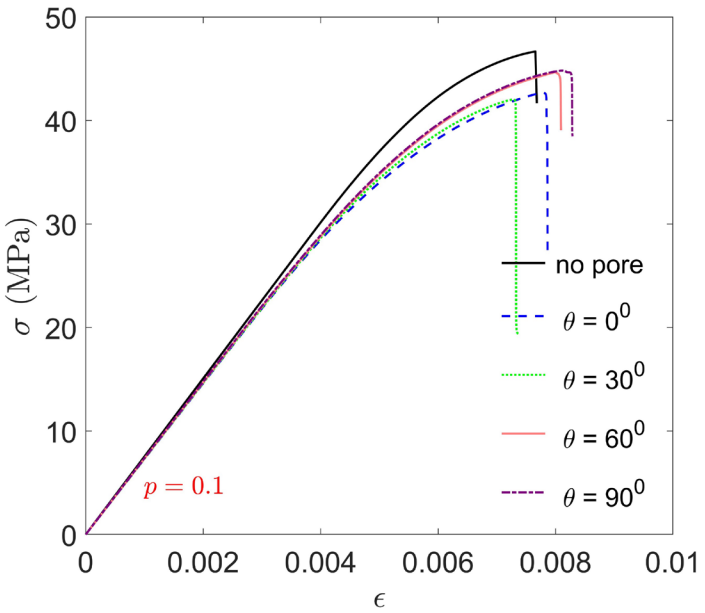

Effect of position

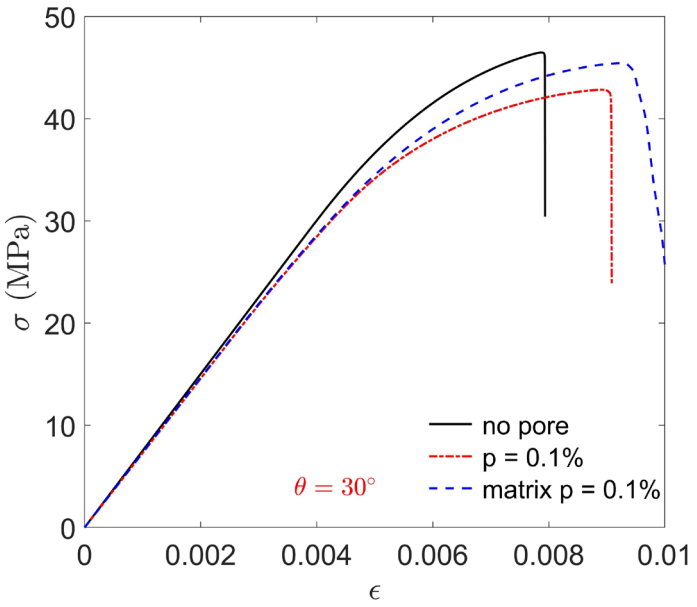

- Unexposed: no pores (voids)
- As porosity increases strength of the specimen decreases
- As θ ⬆ strength ➡ no pore strength
- Matrix porosity has a marginal effect on the strength.

BROWN
School of Engineering

Contours of stress and plastic strain

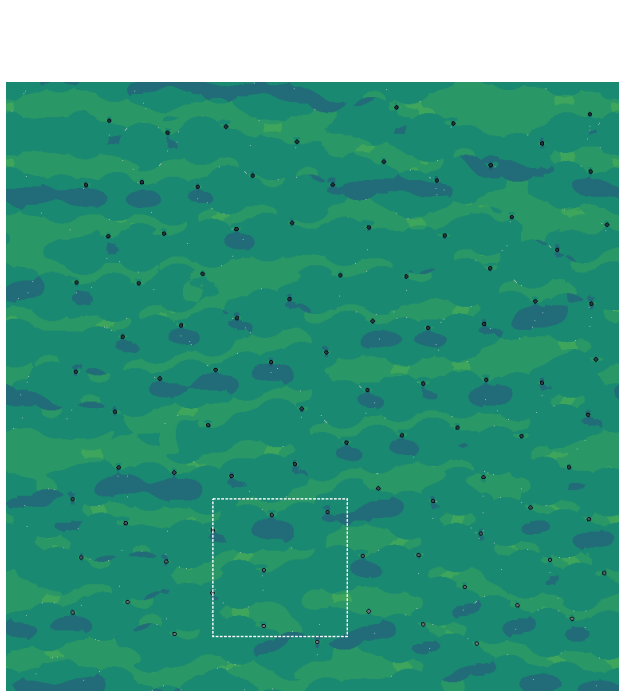

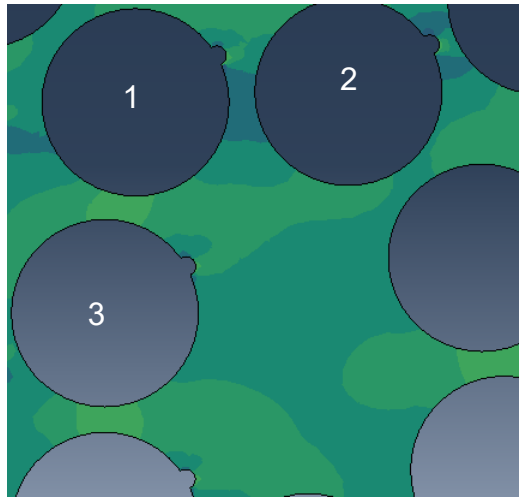

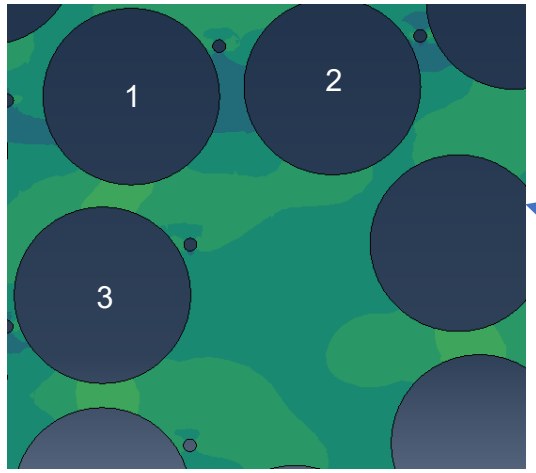

Interface-void

Matrix-void

σ_{11} (MPa)

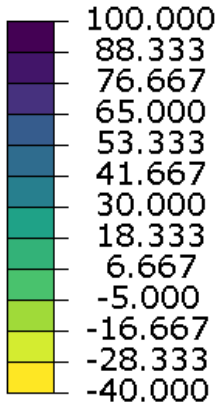

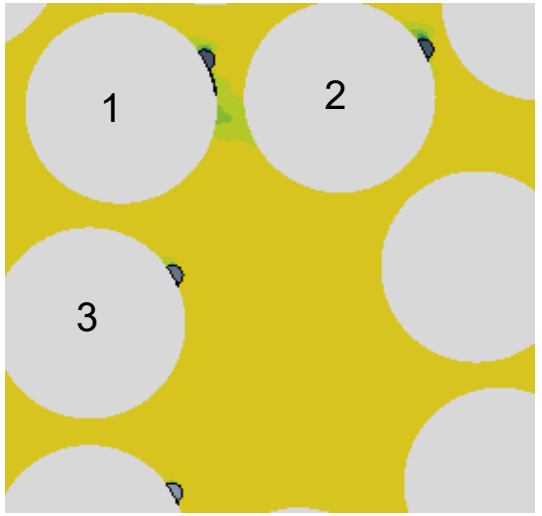

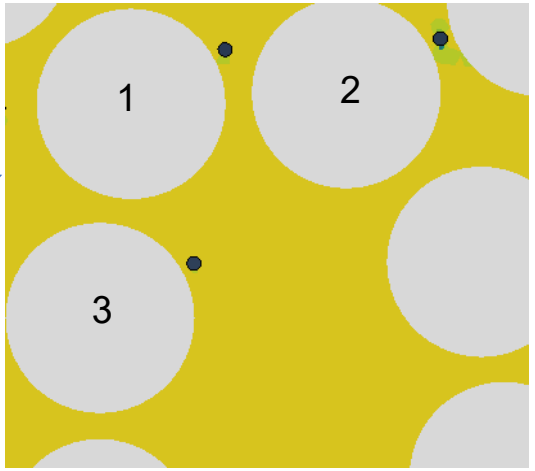

$\bar{\epsilon}_{pl}$

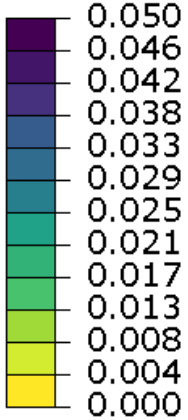

- Interface void: High stress concentration and intense plastic strain
- Matrix void: Near-void contours differ

BROWN
School of Engineering

Void-moisture relationship

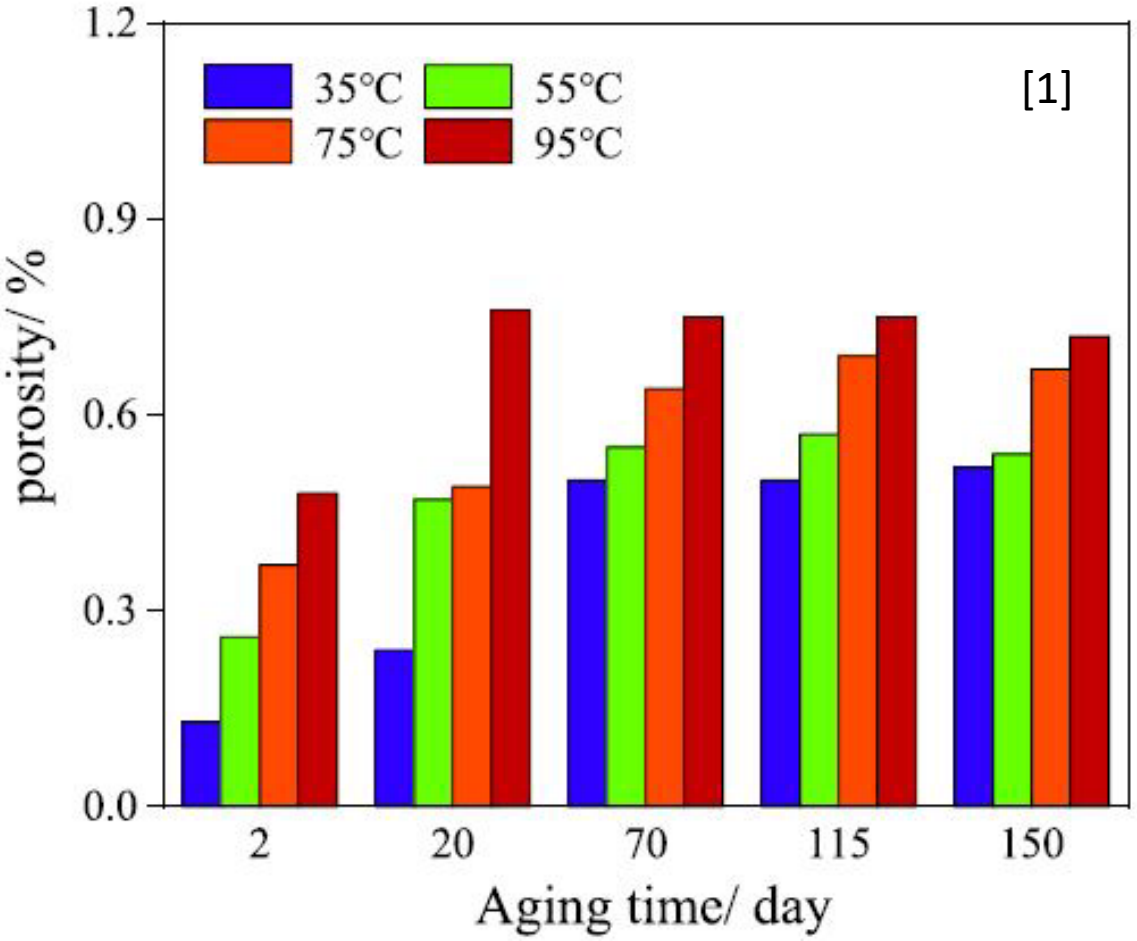

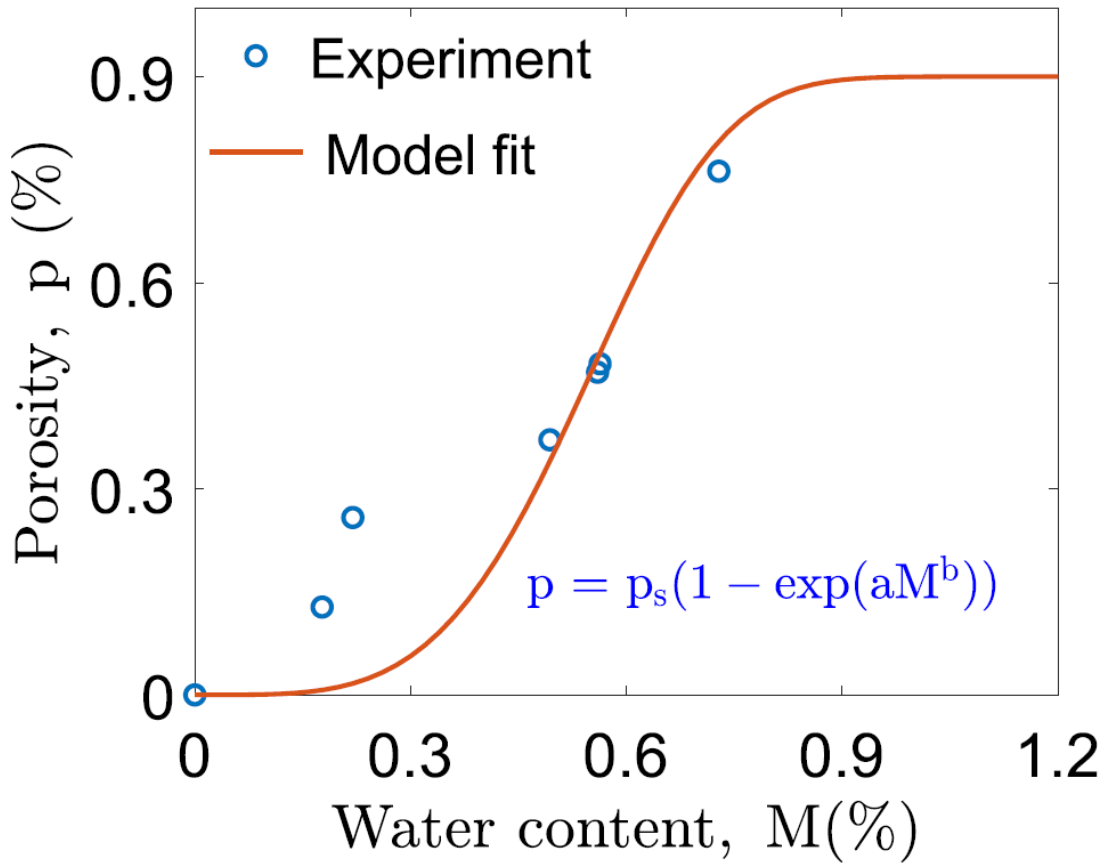

BROWN
School of Engineering

[1] Zhuang et al (2022) Polym. Degrad. Stab.

Strength prediction and comparison

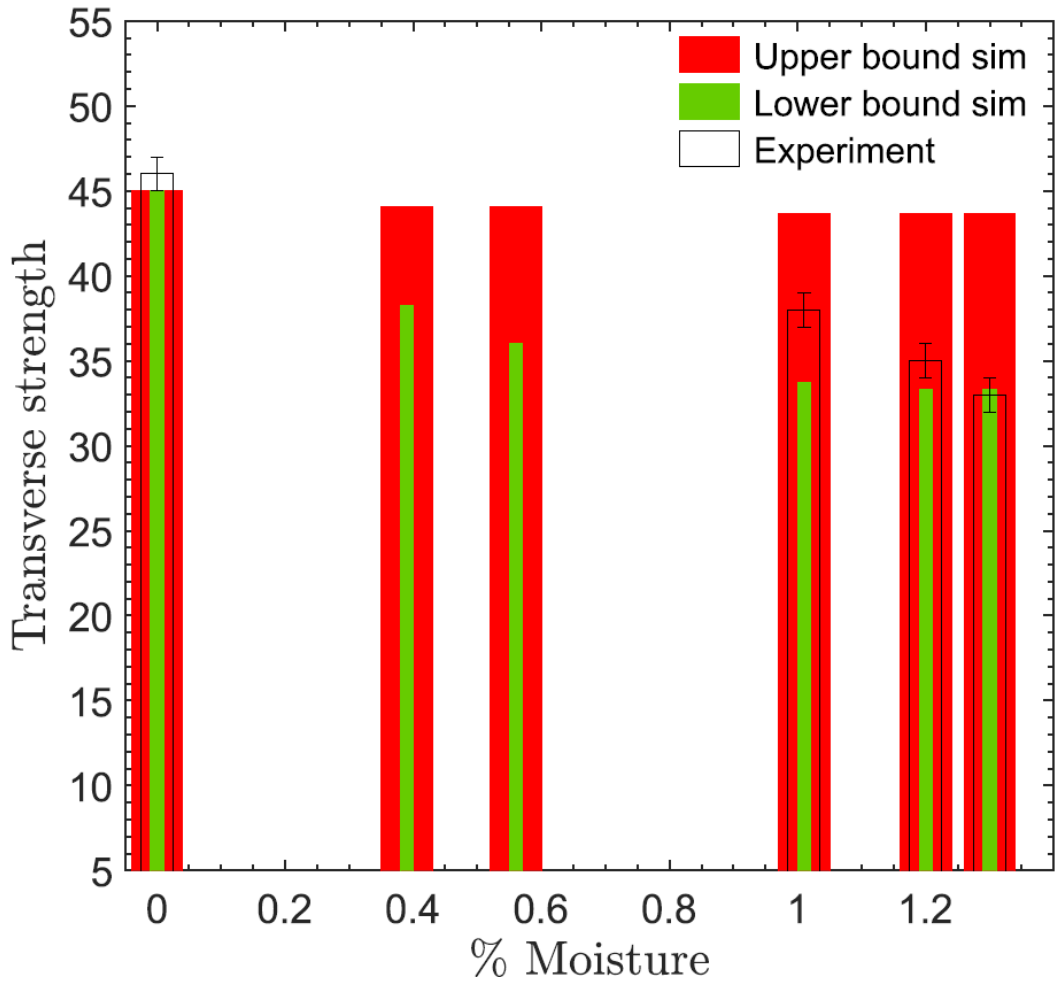

- Experimental result are within the lower and upper bounds predicted by simulations

BROWN
School of Engineering

Different approach: Probabilistic interface properties

- Strength of porous RVE: lower and upper bound
- Each interface: a probabilistic strength values (σ^0_x)
- Based on percentage reduction of lower and upper bound the

$$\sigma^0_{min} \leq \sigma^0_x \leq \sigma^0_{max}$$

- Distribution: Random and Softmin

Softmin distribution $$p(x_i) = \frac{\exp(-x_i)}{\sum_j \exp(-x_j)}$$

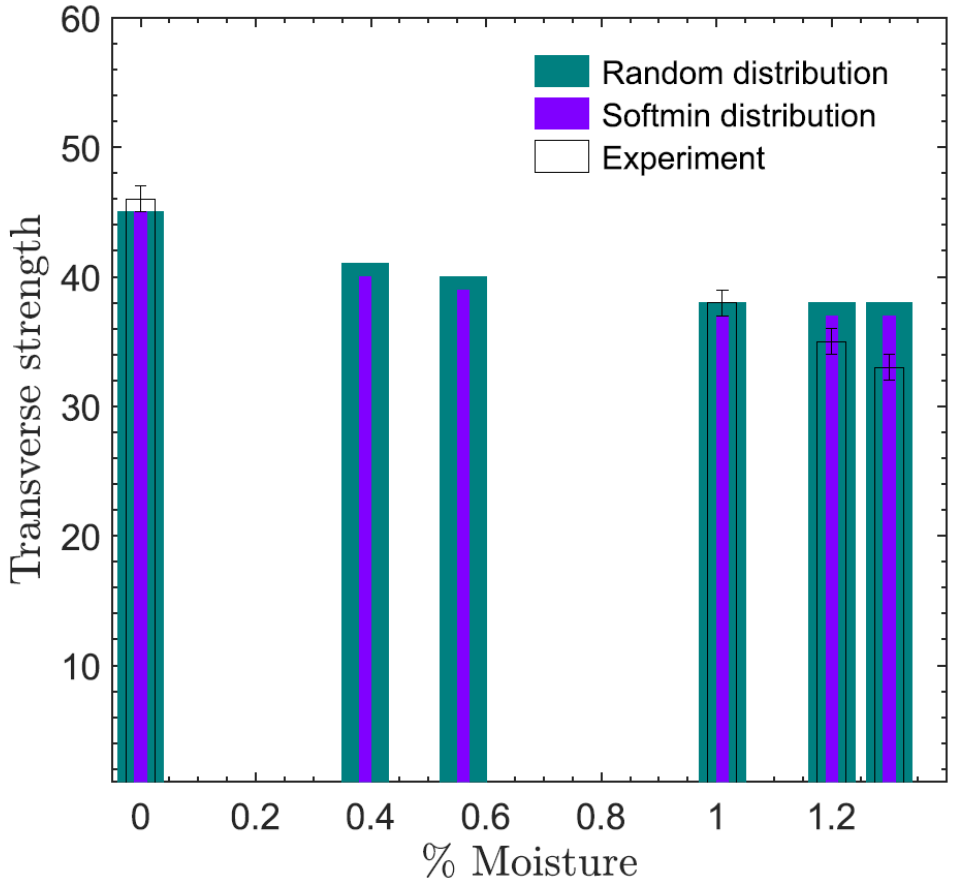

BROWN
School of Engineering

Conclusions and future direction

- Interface void substantially influence the stress and strain distribution within the specimen
- Porosity of as small as 0.1% resulted in 15% reduction in strength
- Strength seems to depend on pore size, its orientation and location. The maximum impact is when void is at the interface and aligned along the loading direction ($\theta = 0^0$)
- A different probability-based approach to overcome the modeling complexity

Future work

- Coupled diffusion damage model for the interface and matrix material (polymer)
- Meso-scale modeling to predict the toughness of aged laminates

Funding: DOD Office of Naval Research



Thank you!

ICCM24
AUGUST 4-8, 2025
BALTIMORE CONVENTION CENTER
BALTIMORE, MARYLAND, USA

No Technical Paper Submission for:

Dazhi Jiang

Characterization of Fiber Reinforced Thermoplastic Composites Fabricated by Composites-Based Additive Manufacturing CBAM Technology

Gavin Stoker, Won Gyo Seo, Devin Young, Juhyeong Lee

Advisor: Prof. Dae Han Sung

ICCM 2025 Conference

August 6th, 2025

UtahState University

FICAM Functional Intelligent Composites & Advanced Manufacturing

00 Outline

1. Introduction and Motivation
2. Manufacturing
3. Mechanical Testing
4. UAM Application
5. Conclusion
6. Future Work & Acknowledgements

01 Introduction and Motivation

- **Additive manufacturing of composites**
  - **Less wasted material**
  - **Recyclable materials**
  - **Faster manufacturing process**
  - **More consistent results**
  - **High-volume manufacture**
  - **Complex geometries**

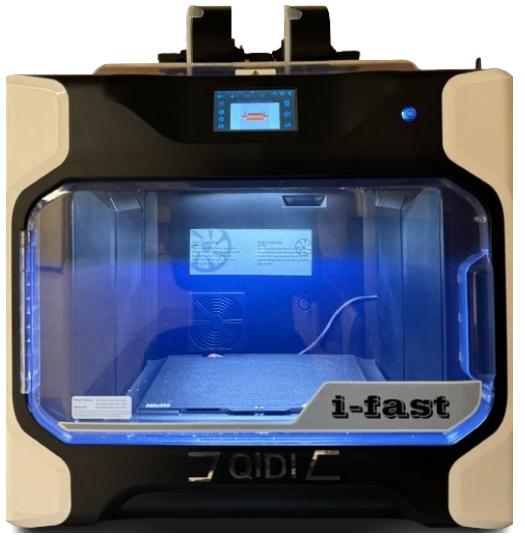

QIDI i-fast dual extruder 3D printer



Impossible Objects CBAM2 printer

01 Introduction and Motivation

Extrusion-Based Additive Manufacturing Methods

- Fused Deposition Molding (FDM)
- Large-Scale Additive Manufacturing (LSAM)
- Big Area Additive Manufacturing (BAAM)

Limitations and Drawbacks

- Slow
- Limited material selection
- Restricted Volume Fraction
- Short Fiber reinforcement only
- Weak interlayer bonding properties



BAAM
https://doi.org/10.2172/1434289

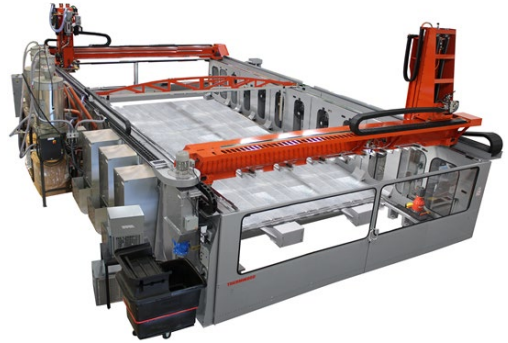

LSAM 1540
https://www.thermwood.com/images/2017_site/machines/lsam



PEEK-300 FDM
https://www.creatbot.com

Composites-Based Manufacturing (CBAM)

- New composites technology
- Requires investigation and comparison with existing methods (FDM)

01 Introduction and Motivation

Manufacturing Procedure of CBAM

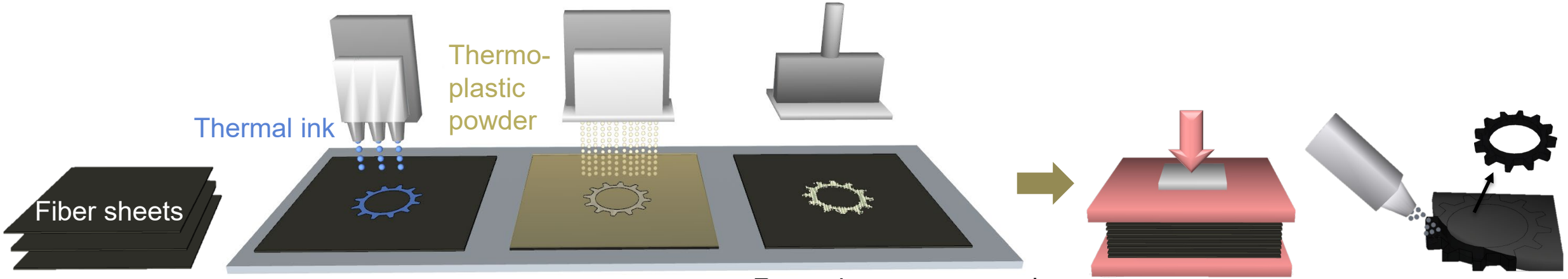

Feeding raw fiber sheets

Depositing thermal ink onto sheet based on CAD slice pattern

Applying thermal-plastic powder onto the sheet

Removing excess powder and retaining the adhered powder in the shape of the printed design

Hot-pressing → Sand blasting

Composite-Based Additive Manufacturing (CBAM) → **Post-processing**

02 Manufacturing

All units are in mm

ASTM D3039

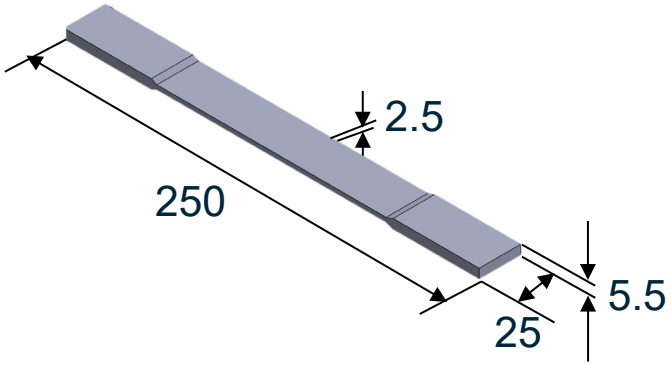

Tensile test coupon

ASTM D7264

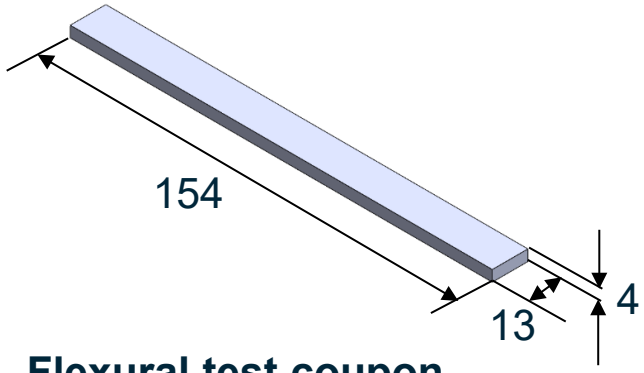

Flexural test coupon

ASTM D695 Ø12.7

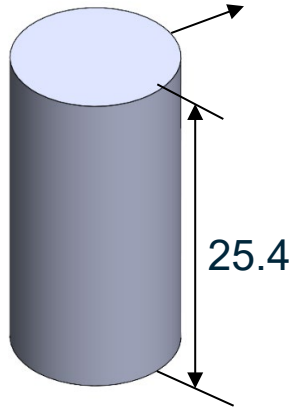

Compression test coupon

Tension

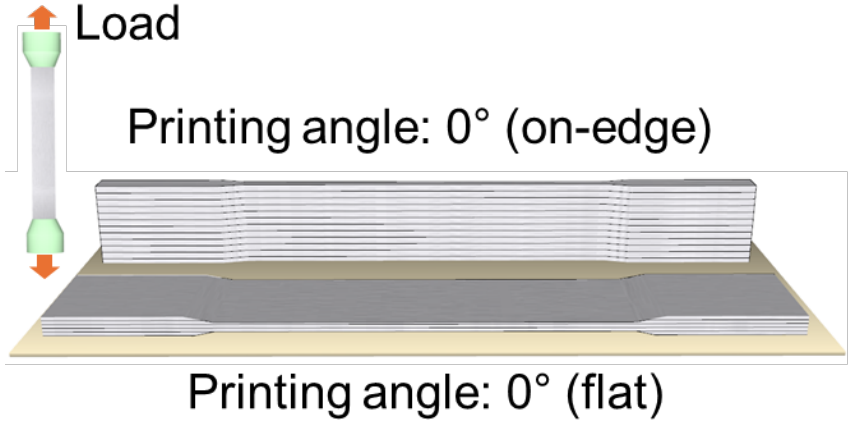

Flexural

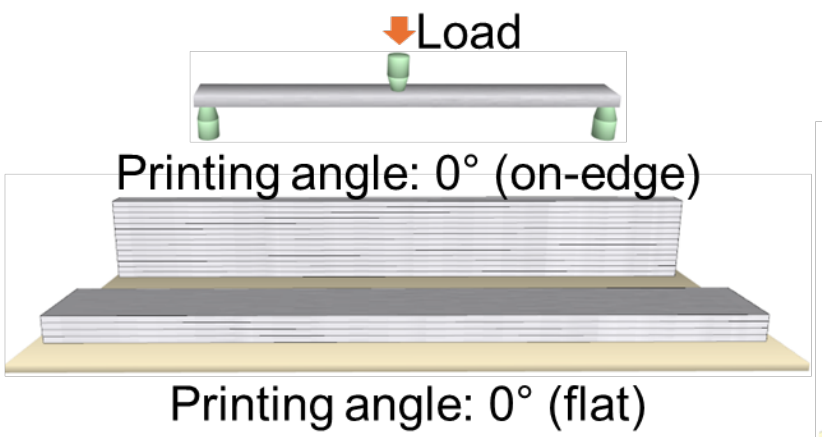

Compression

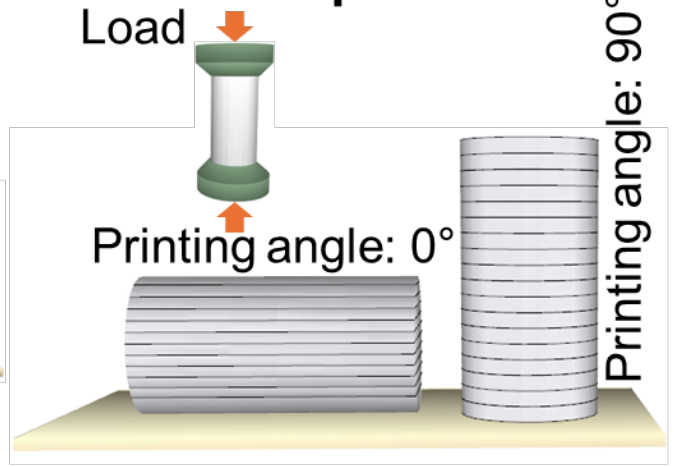

02 Manufacturing

CBAM

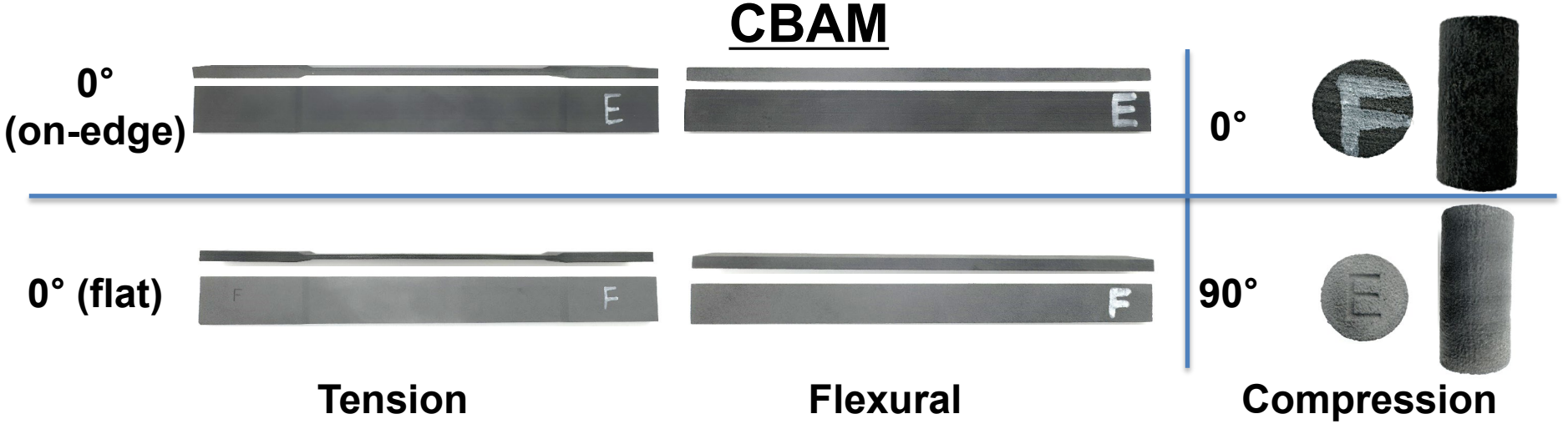

FDM



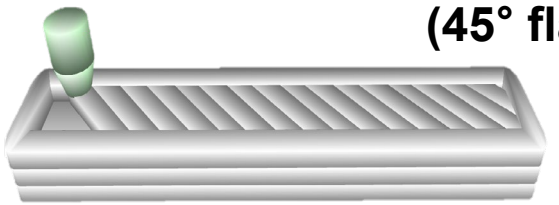

02 Manufacturing

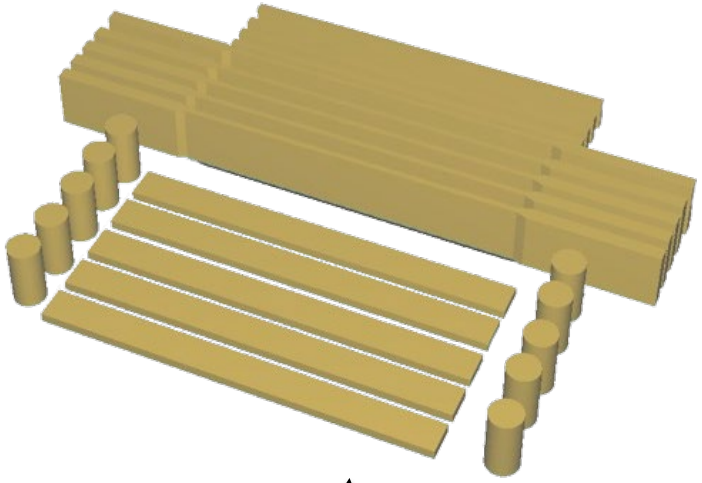

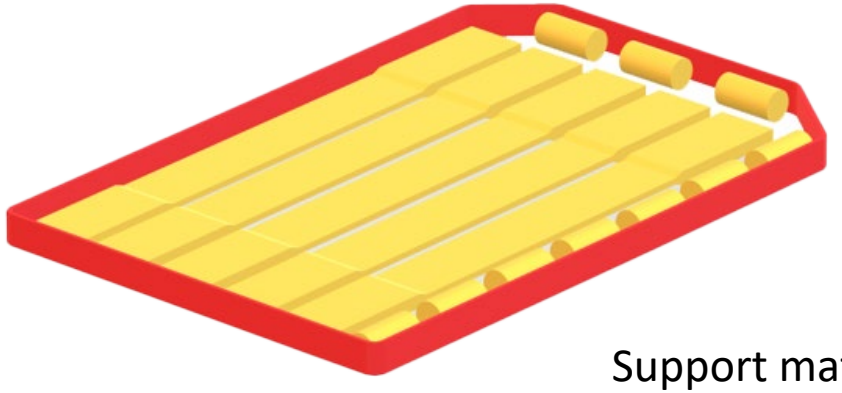

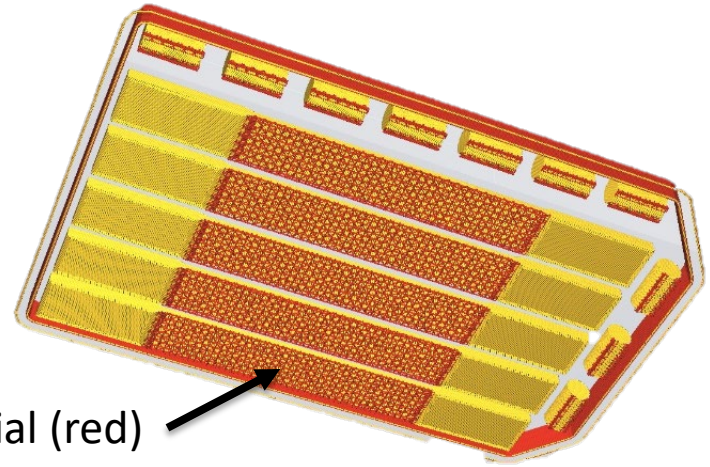

Support material (red)

QIDI i-fast dual extruder 3D printer

CBAM achieves higher part density using z-axis stacking at no additional time cost

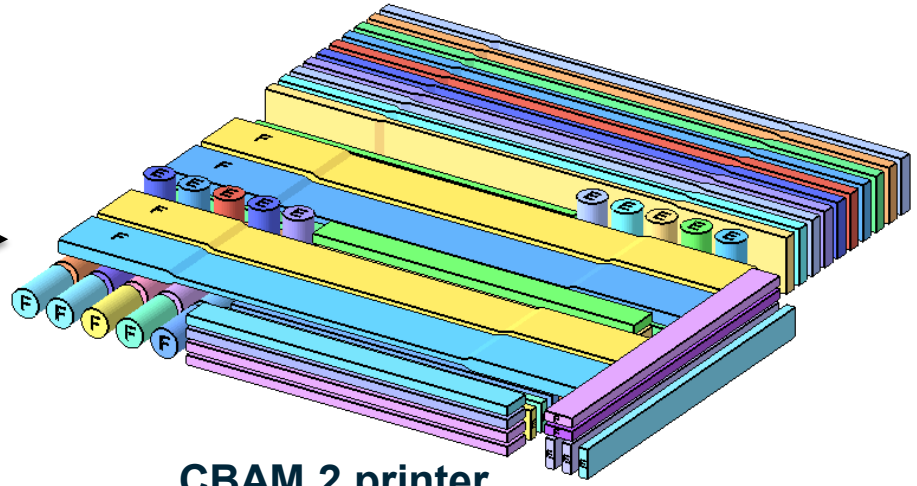

CBAM 2 printer



02 Manufacturing

X-ray Micro-Computed Tomography (μ-CT) Pore Size Distribution

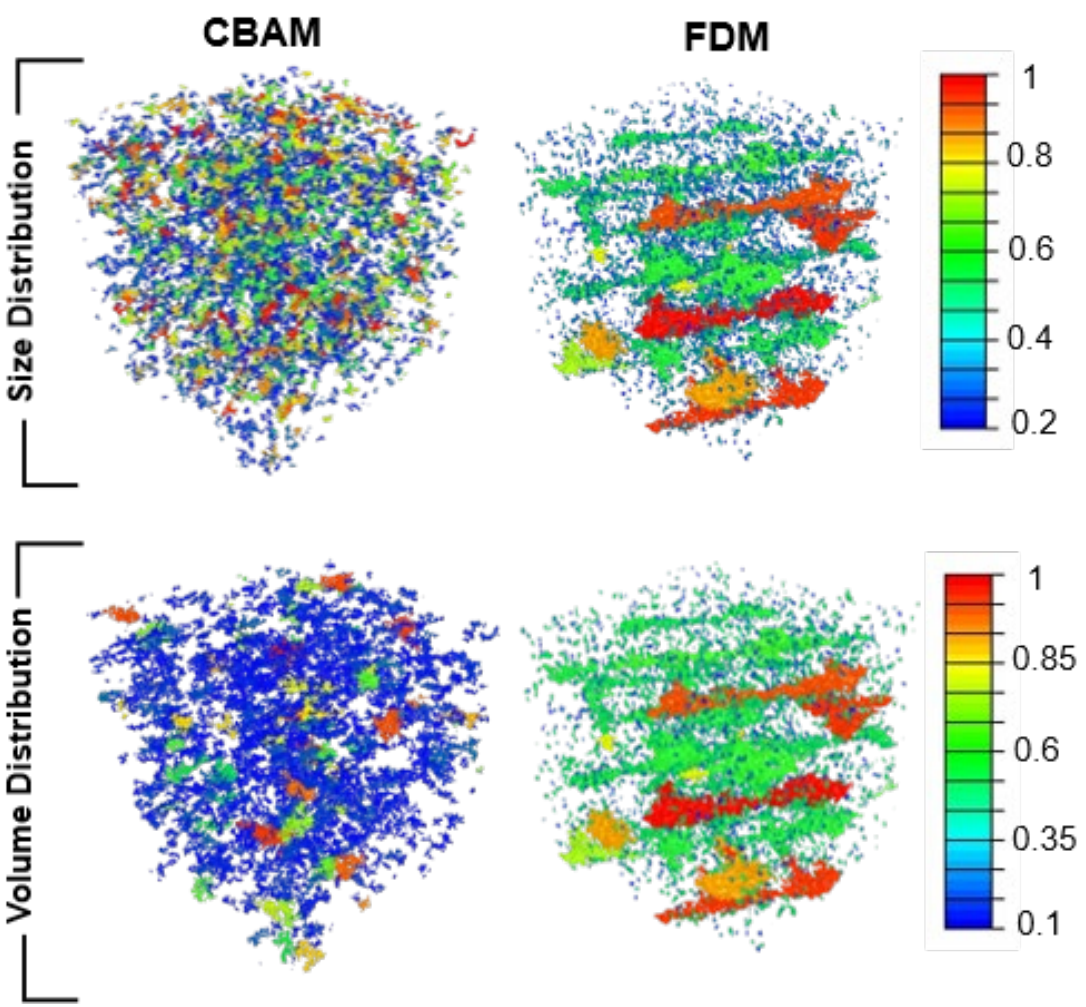

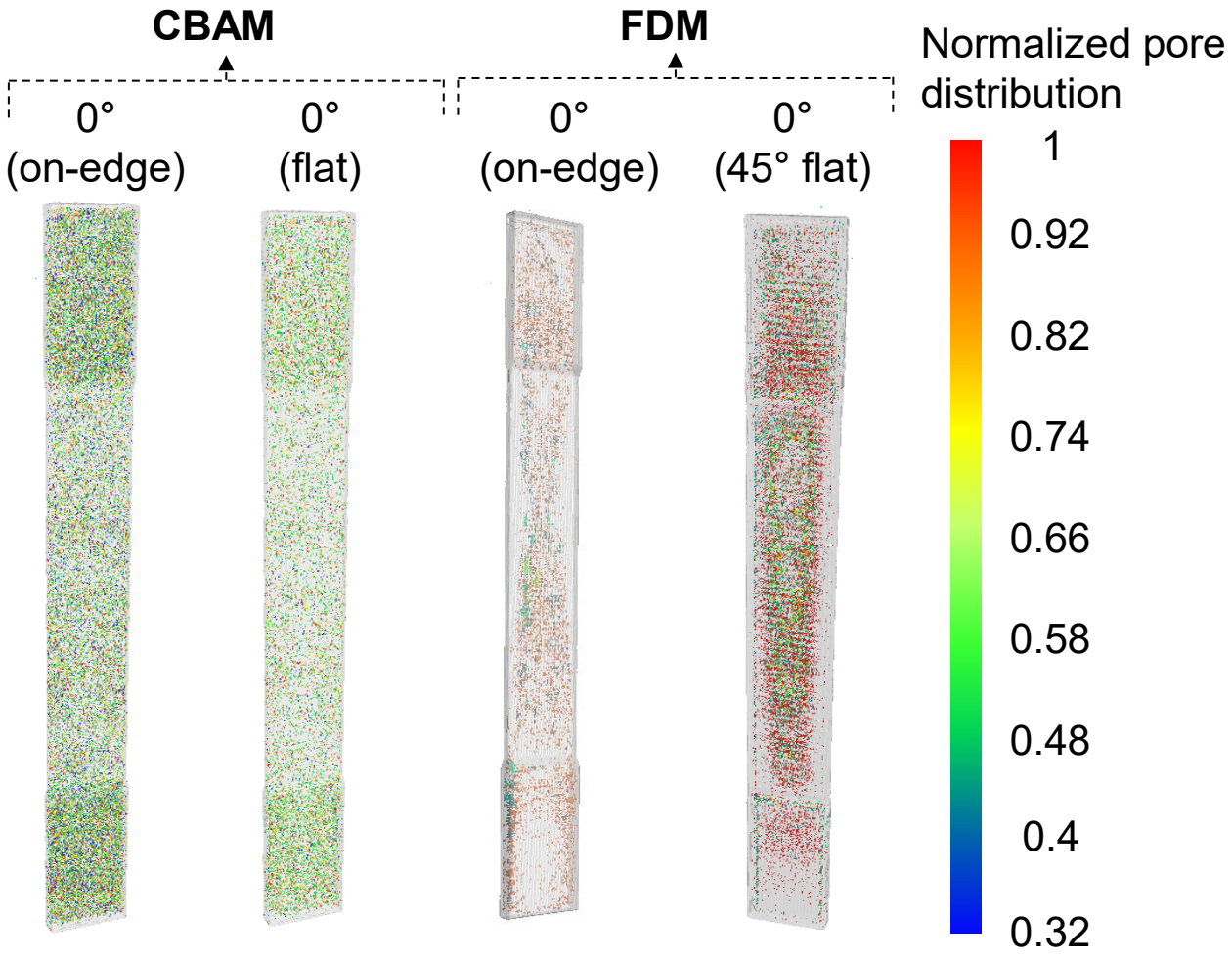

02 Manufacturing

Void Comparison

CBAM

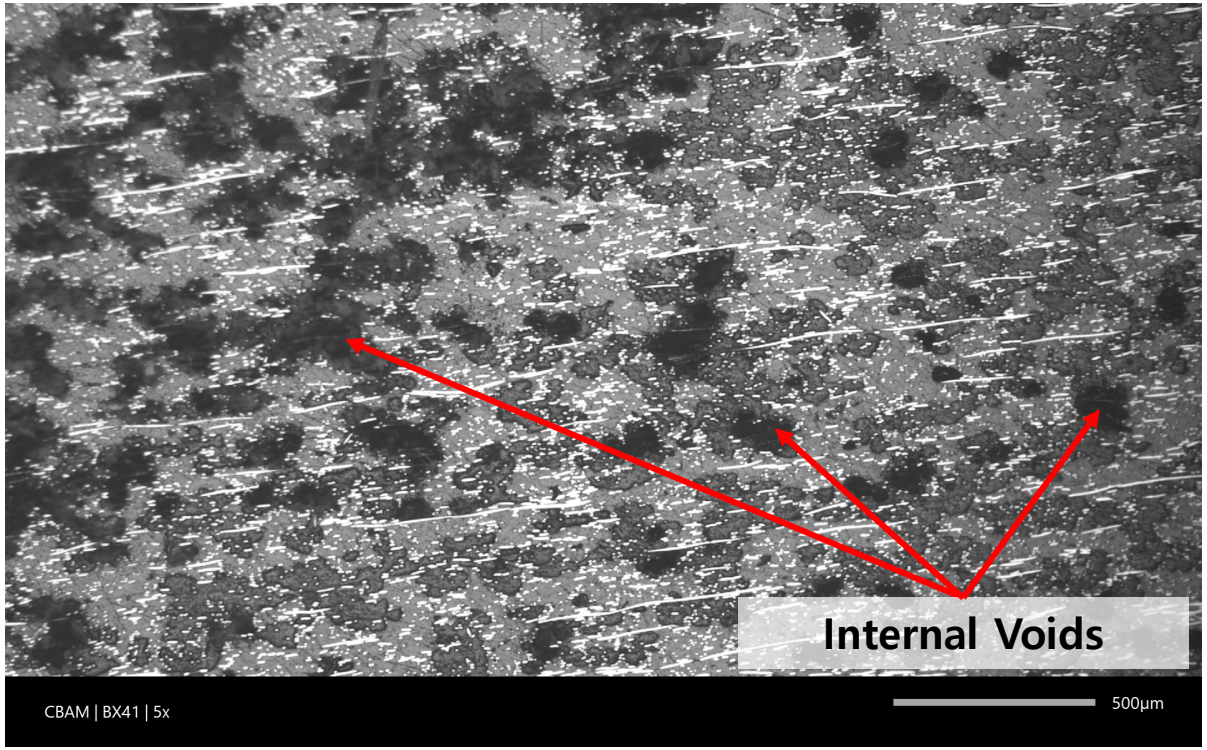

FDM

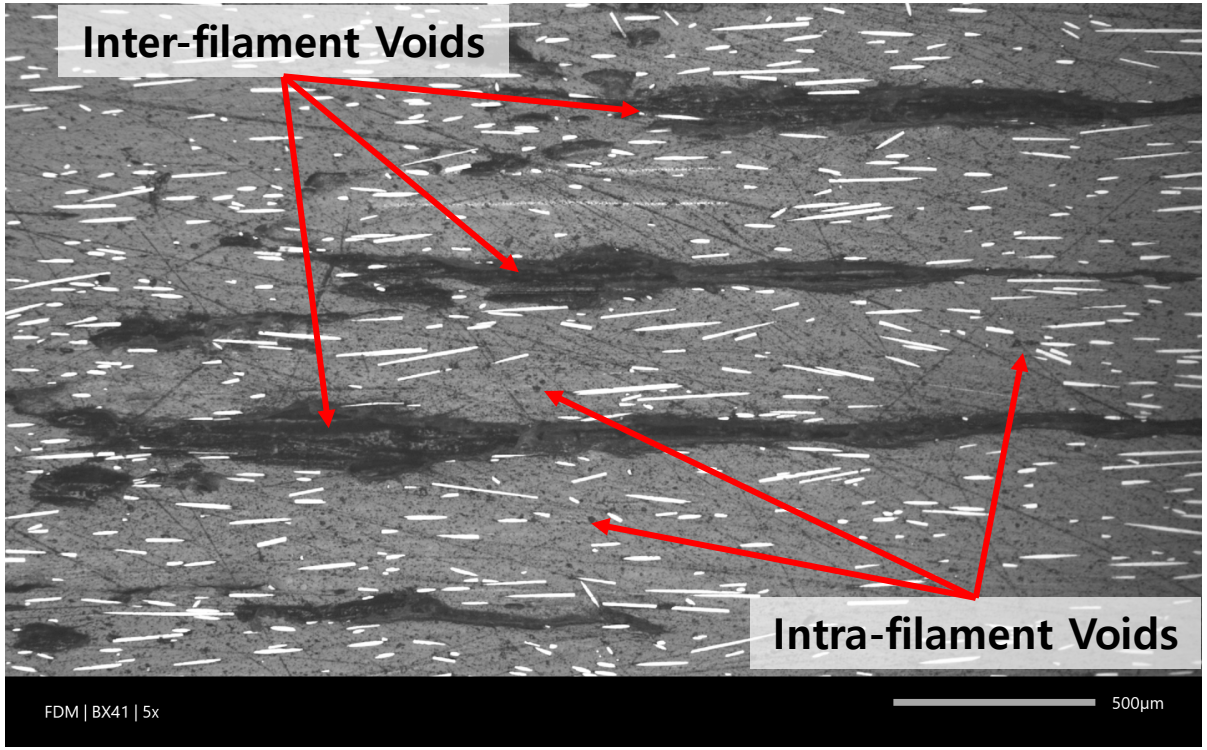

CBAM has larger density of medium-sized voids but has fibers pass through them

FDM has smaller internal voids, but also has large-volume inter-filament voids that can become fracture planes

03 Mechanical Testing

Tensile Coupon Test Results

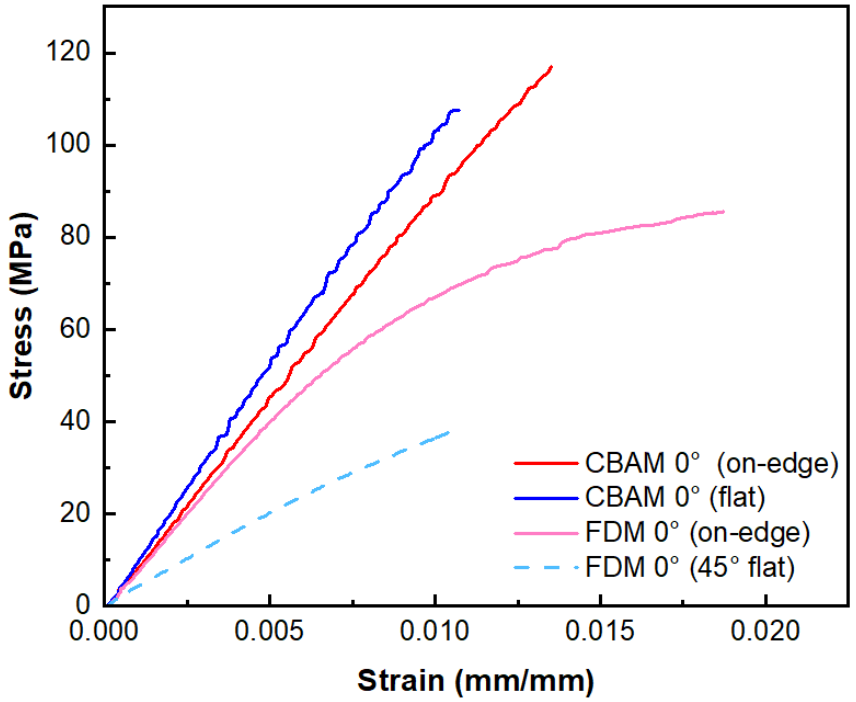

0° (on-edge)

Before test
(Ultrasonic C-scan)

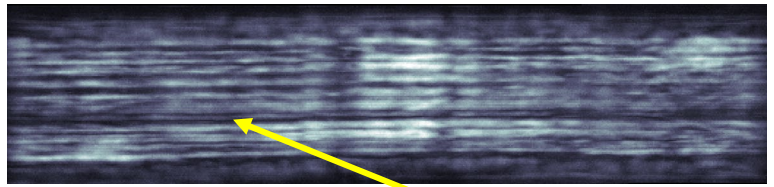

After test

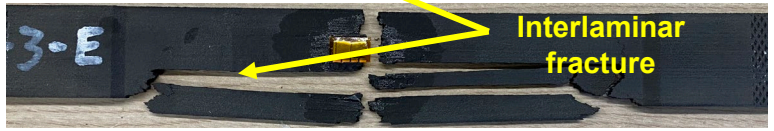

0° (flat)

Before test
(Ultrasonic C-scan)

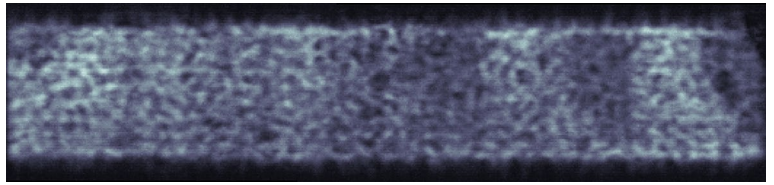

After test

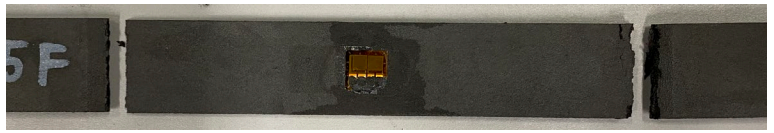

CBAM

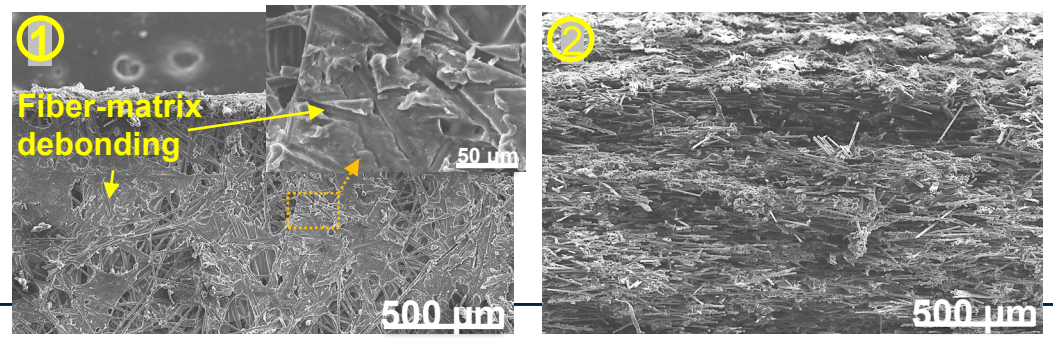

FDM

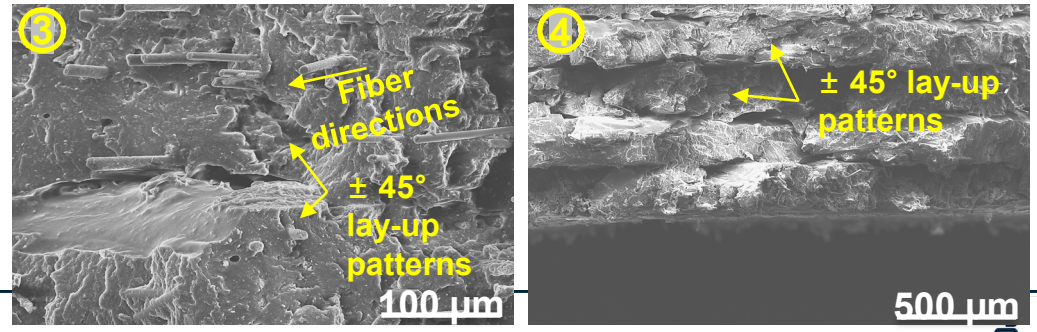

04 Mechanical Testing

Compression Coupon Test Results

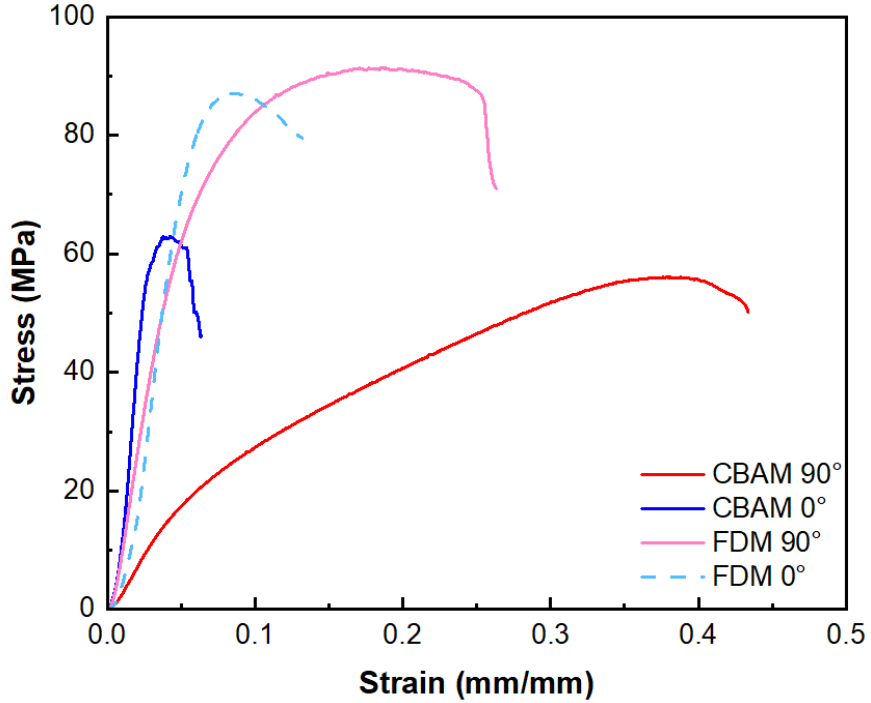

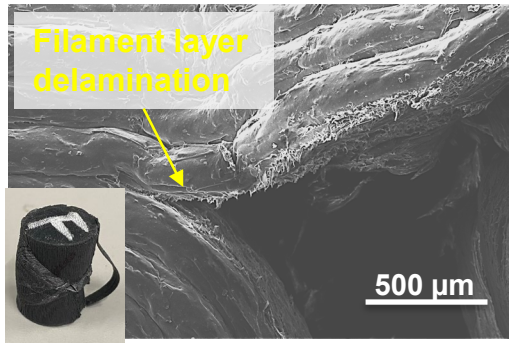

Shear (45°) failure

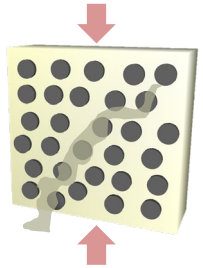

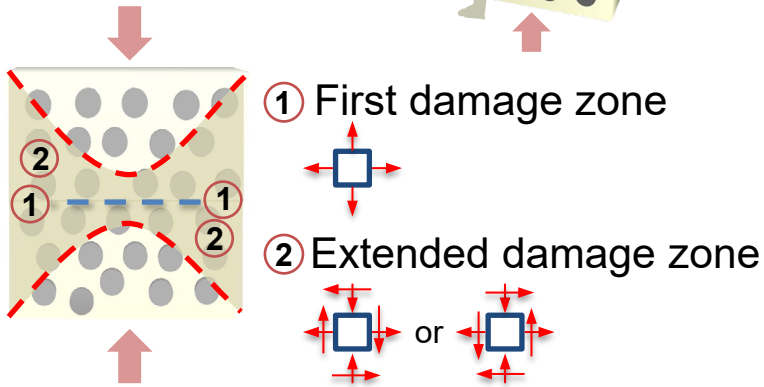

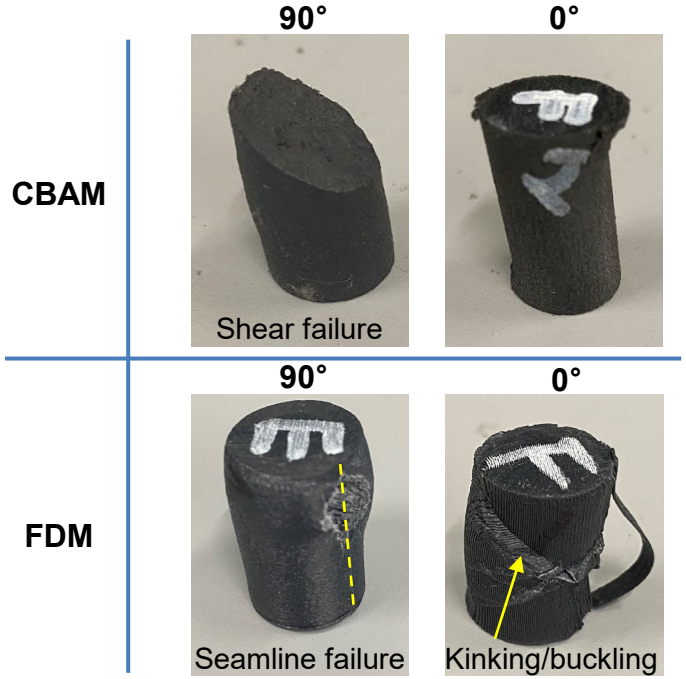

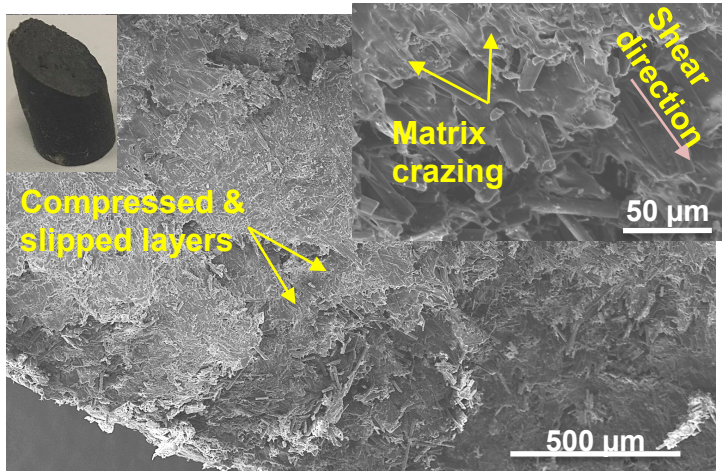

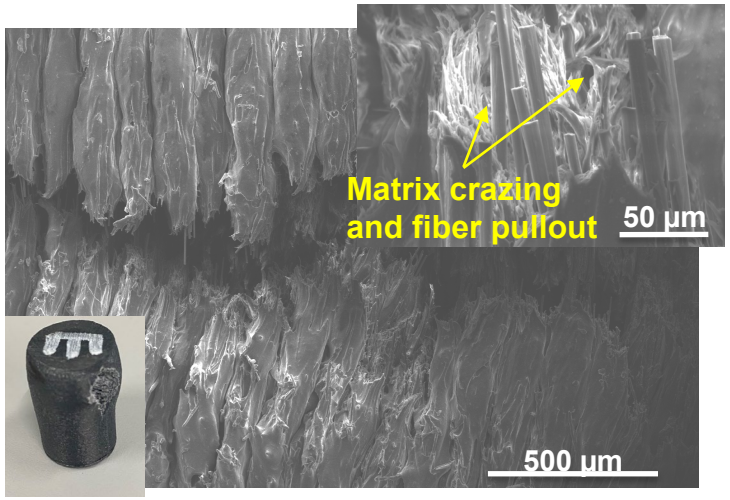

04 Mechanical Testing

Flexural Test Results

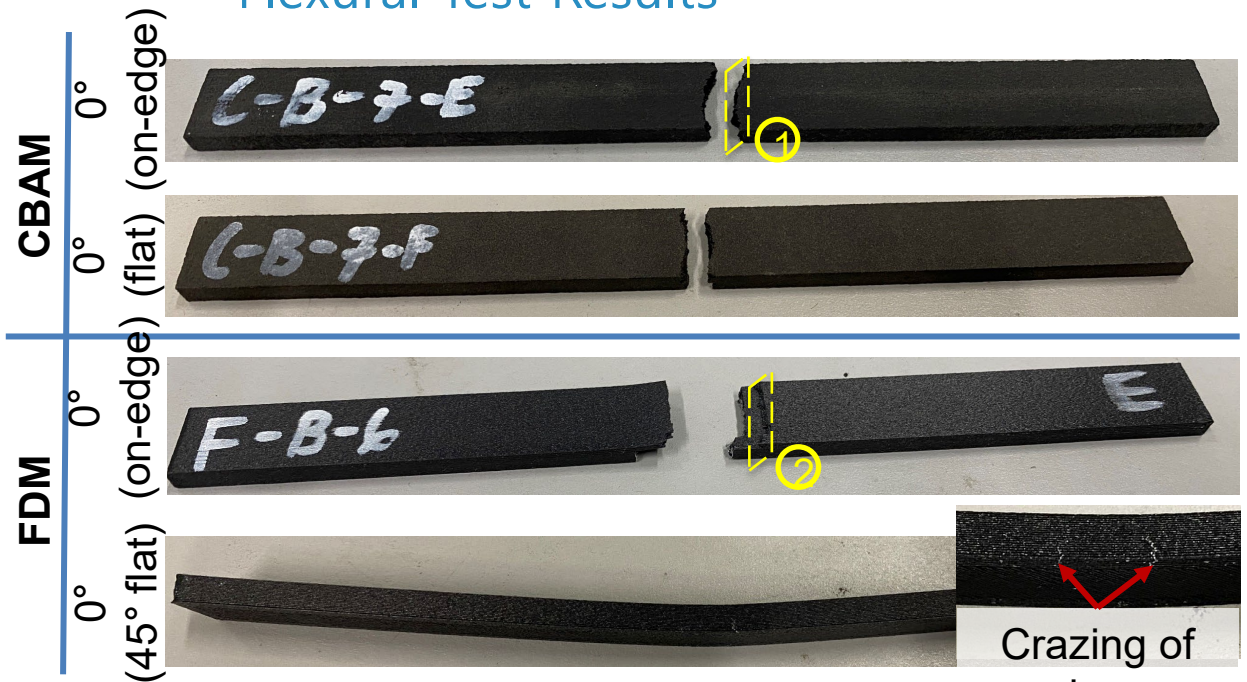

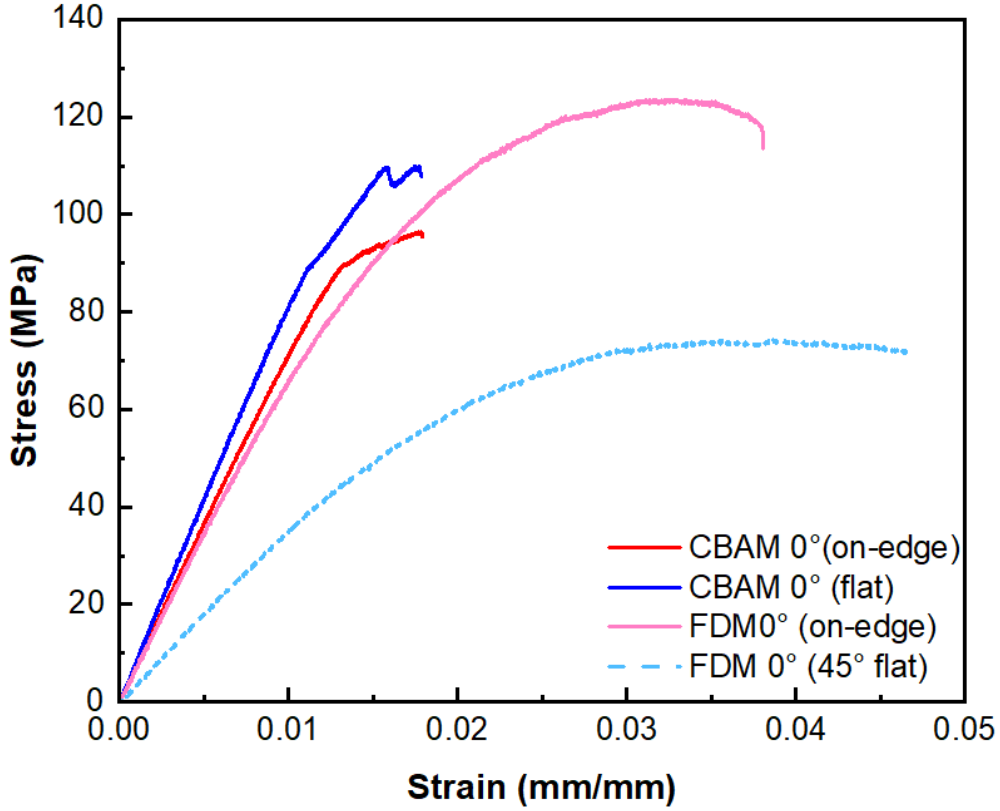

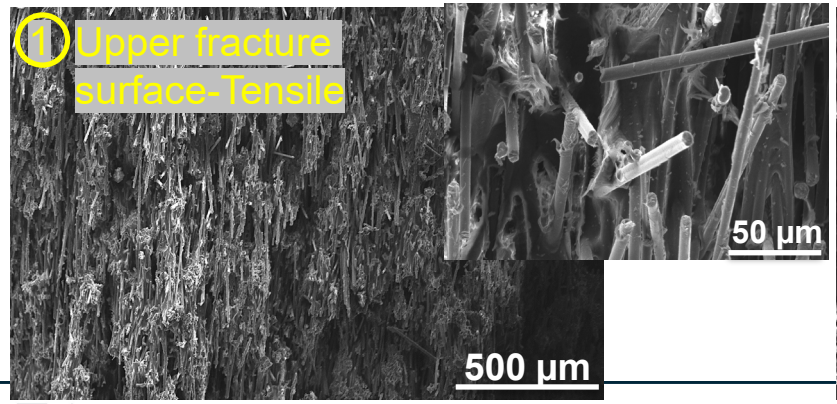

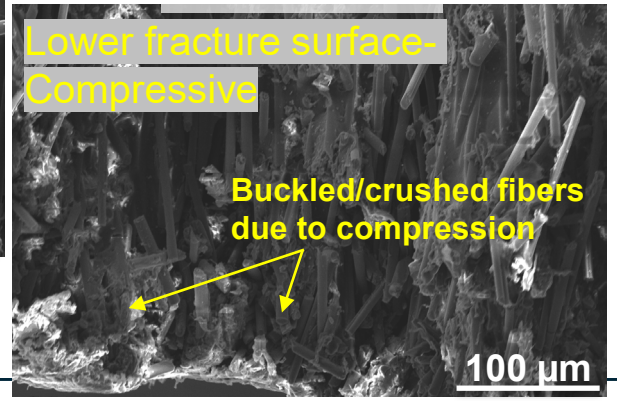

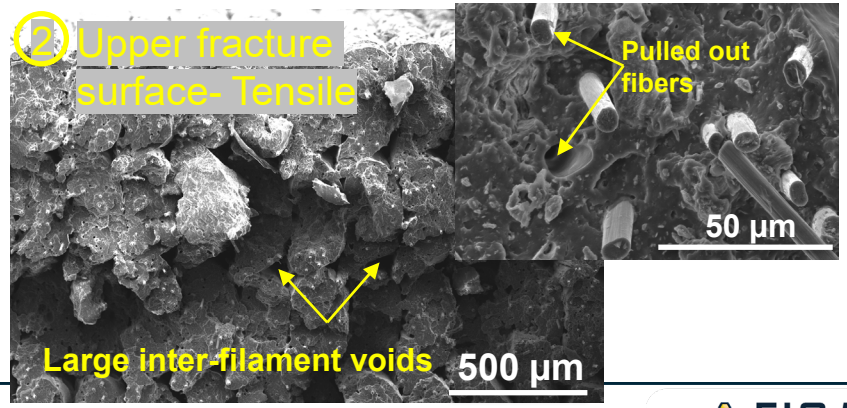

05 UAM Application

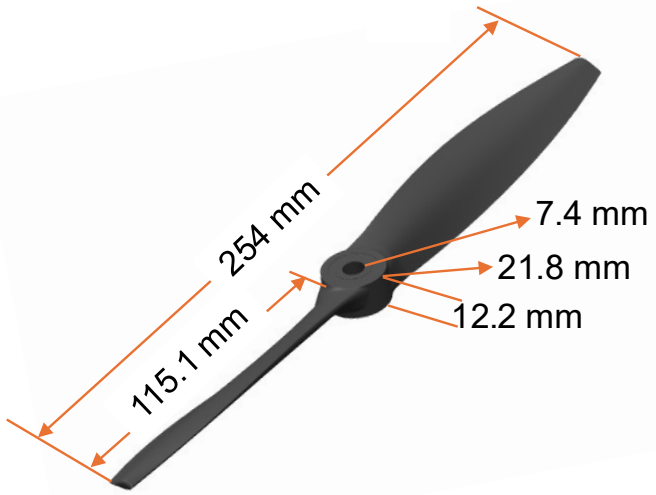

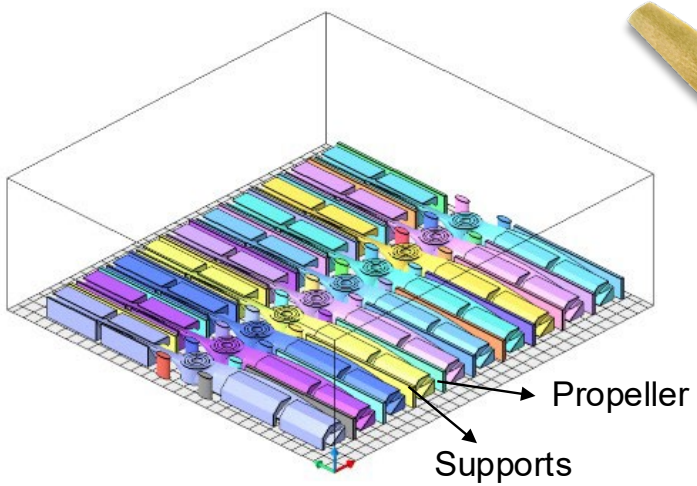

CBAM printed propeller



Geometric comparison

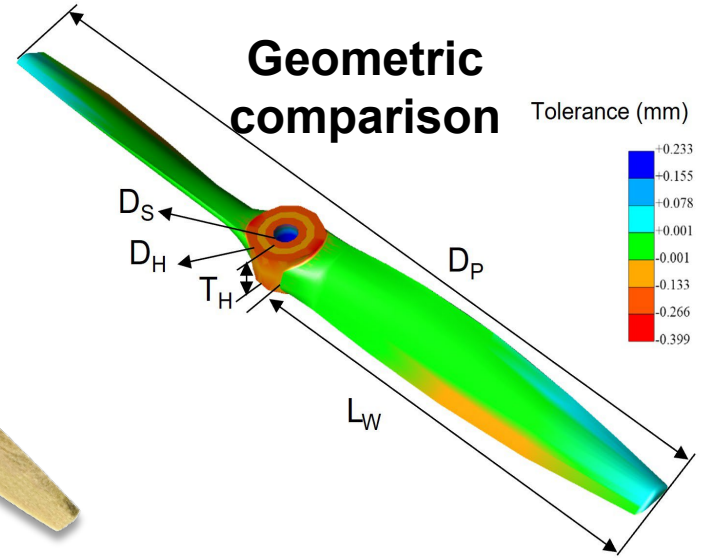

Geometry	Unit	2-blade		
		CAD	Actual	Offset (%)
Propeller volume	cm^3	16.76	16.67	0.5
Propeller diameter (D_P)	mm	254	254.1	0.04
Hub diameter (D_H)	mm	21.84	21.7	0.6
Hub thickness (T_H)	mm	12.2	11.8	3.3
Shaft diameter (D_S)	mm	7.37	6.9	6.4
Wing length (L_W)	mm	115.1	115.5	0.3

- Investigation to determine UAM suitability
- Printed propeller to compare with purchased
- 10 GF / PA-12 CBAM printed propellers
- Average dimensional deviations within 1mm
- ~3 hours print time compared to 35 hours FDM

06 Conclusion

- **Manufacture of CBAM to compare with FDM**
  - CBAM prints faster than FDM
  - CBAM allows for higher part density per build
  - CBAM process is more compatible with in-line assembly processes
- **Internal structure characterizations**
  - FDM contains a high amount of large inter-filament voids
  - CBAM contains a larger number of small voids
- **Testing results**
  - CBAM performs better than FDM in tensile stress due to higher fiber volume fraction and longer fibers
  - FDM performs better in compression due to the more randomly-aligned fibers
  - CBAM shows a strong dependence on printing direction, especially for compression
- **Shows promise in aerospace and automotive applications**
  - CBAM shows promise in applications requiring high performance parts
  - CBAM bridges the gap between low-volume FDM custom parts and High-volume traditional processes

06 Acknowledgements

- This research was financially supported by Hyundai Motor Group – Hyundai NGV, and Utah State University Office of Research
- Dr. Dae Han Sung, Dr. Juhyeong Lee, Samiul Alam from Utah State University, and Dr. Devin Young (Weber State University – Miller Advanced Research and Solution (MARS) Center)
- The authors acknowledge Impossible Objects and Brett Davis for providing the material supply and Dolphitech NDT device.

EFFECT OF FIBER VOLUME FRACTION AND MATERIAL HOMOGENEITY ON THE MECHANICAL PERFORMANCE OF RECYCLED WOVEN THERMOPLASTIC COMPOSITES

[1]F.F. Visser, [2]V. Marinosci, [3]M. van Drongelen, [1]R.A. Akkerman

[1]Production technology, Department of Engineering Technology, University of Twente
Horst Building, nr. 20 P.O. Box 217 7500 AE Enschede The Netherlands
Email: f.f.visser@utwente.nl , web page: https://www.utwente.nl/en/et/

[2]ThermoPlasticcompositeResearchCenter, TPRC,
Palatijn 15, 7521 PN Enschede, The Netherlands
Email: vanessa.marinosci@tprc.nl, web page: https://tprc.nl/

[3]Trinseo,
4542 NH, Terneuzen, The Netherlands
Email: mvandrongelen@trinseo.com, web page: https://www.trinseo.com/

Keywords: Recycling; Thermoplastic composites; mixing; homogeneity

ABSTRACT

This study investigates the effect of fiber volume fraction (FVF) and material homogeneity on the mechanical performance of recycled woven thermoplastic composites. Recycling thermoplastic composites (TPCs) offers advantages over thermoset composites by enabling complete material recycling through melting and reshaping. The research utilized shredded 8-ply Toray Cetex 1100 C/PPS 5 harness satin woven composite mixed with neat PPS polymer at various ratios to achieve target FVFs of 16%, 20%, 25%, and 50%.

Processing was conducted using an internal mixer followed by compression molding into plates. Microstructural characterization was performed using optical microscopy and image analysis to quantify fiber volume fraction distribution and fiber bundle size. Samples were mechanically tested under tensile loading conditions.

Results demonstrate that dilution and mixing significantly improve fiber dispersion compared to unmixed material. The 50% FVF unmixed sample exhibited high stiffness but poor strength and ductility due to large undispersed fiber bundles. Lower FVF samples (16-25%) showed improved dispersion and mechanical performance, though with varying degrees of scatter. The 20% FVF sample demonstrated optimal balance of properties with good dispersion and reduced bundle sizes.

Image analysis successfully correlated microstructural features with mechanical performance, revealing that bundle size distribution and local FVF variations are critical factors affecting material strength. The study provides insights for optimizing recycling processes of aerospace-grade thermoplastic composites.

1 INTRODUCTION

The composites market has seen significant growth [1], with a corresponding increase in production and end-of-life waste. While thermoset-based composites are recycled on a small scale, focusing only on fiber recovery, thermoplastic-based composites (TPCs) offer a more comprehensive recycling solution. The thermoplastic polymer matrix allows for recycling the entire material through melting and reshaping, eliminating the need to separate fibers from the matrix.

A recycling approach for TPCs that has shown potential is schematically shown in Figure 1 [2]. The first step consists of mechanical recycling, by shredding the composite into flakes having a processable size (10 mm to 20 mm). Afterwards, the material can be diluted with additional polymer to facilitate compounding and then molding.

In the resulting discontinuous fiber reinforced recycled compound, significant attention is given to the fiber length, as it is an important factor influencing mechanical performance [3]. However, additional factors need to be considered, as they also contribute to the mechanical performance, such as fiber orientation and homogeneity of the fiber distribution.

A homogeneous distribution of the fibers in the polymer matrix is a critical factor in ensuring a high and consistent performance of both virgin and recycled composites. For short-fiber composites, homogeneity can be achieved relatively easily as standard mixing methods mix well but cause fiber breakage. For long fiber composites, heterogeneity is more pronounced, particularly when dealing with aerospace grade TPCs as the input material to be recycled has an initial high fiber volume fraction. Additionally, during the mixing process, the composite flake or tape structure needs to be disentangled to create a homogeneous material. A solution is to reduce the fiber fraction by incorporating additional polymer matrix during the mixing step [2]. This step is essential for distributing fibers evenly, significantly improving the uniformity of the final composite material.

In the recycling process the optimal final fiber volume fraction is not well defined at this point in time. In general, for virgin composites, it is well known that with low fiber volume fractions there is little reinforcement to ensure high mechanical performance. On the other hand, with high fiber volume fractions a drop in the material strength was observed when dealing with discontinuous fibers [4], [5]. This result suggests that other factors are limiting the performance at high fiber volume fraction. This indicates that more aspects need to be considered when recycling aerospace-grade composites, as they are characterized by a high fiber volume fraction, up to 60%.

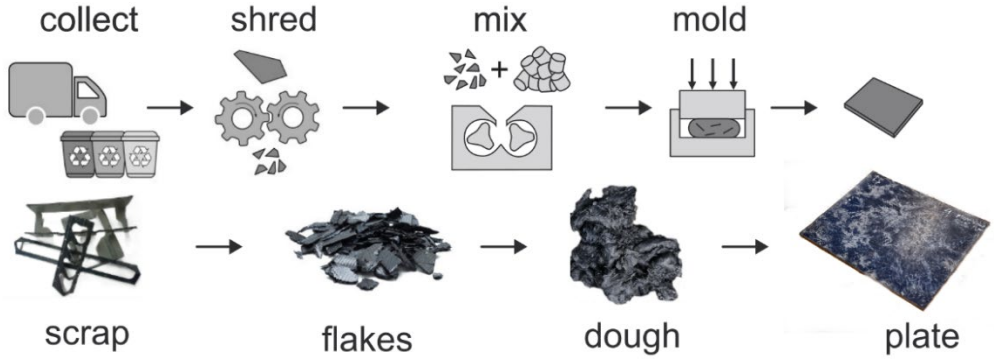

Figure 1: Thermoplastic scrap processing cycle

2 METHODOLODY

2.1 MATERIALS & PROCESSING

The current study aims to investigate the recyclability of unidirectional and woven TPCs, understanding the effect of morphology of the recycled compound on the mechanical performance. The two components used in processing are shredded 8 ply thick consolidated laminates of Toray Cetex 1100 C/PPS 5 harness satin woven composite and for the matrix material Celanese Fortron 214 PPS is added.

Using an internal mixer, a Brabender Plastograph EC Plus W50 EHT measuring mixer, C/PPS scrap was compounded with different fractions of neat PPS as described in Table 1. All samples were processed for 5 minutes at 320°C and 5 RPM rotational speed, and a fill fraction of 0.7, occupying 35 ml of the available 50ml chamber. To create 50 grams of compounded composite material. Except for the undiluted scrap material of 50% FVF, which is intractable in the mixer and thus is compression molded as is.

Subsequently, these were compression molded at 50 bars of pressure into plates of dimensions 125 × 125 x 2 mm. Figure 2 shows the specimen layout. Each plate contains nine tensile specimens conforming to ISO 527-2-12A dimensions and was used for 16 micrographs. The tensile specimens were milled out of the plates.

Target FVF [%]	Fiber wt%	Mix time [min]	Additional polymer [wt%]
16	20	5	65%
20	25	5	56%
25	31	5	46%
50	57	0	0%

Table 1: Mixing parameters operated in the internal mixer.

For the microstructural characterization, the material in between the tensile bars was embedded in epoxy for polishing. For each imaging plane two areas (A and B as indicated in Figure 2) were imaged on a Keyence vhx-7000 optical microscope. Each image spans 5.4 x 2.1 mm at a resolution of 0.3 µm, resulting in 16 micrographs and an imaged area of 181.44 mm^2 per plate.

Tensile testing was performed in an Instron universal testing machine. Mechanical tests were performed at 23°C degrees and a constant crosshead displacement resulting in an engineering strain rate of $\dot{\varepsilon} = 10^{-3}$. The strain was measured using an Instron AVE2 video extensometer with a gauge length of 20 mm.

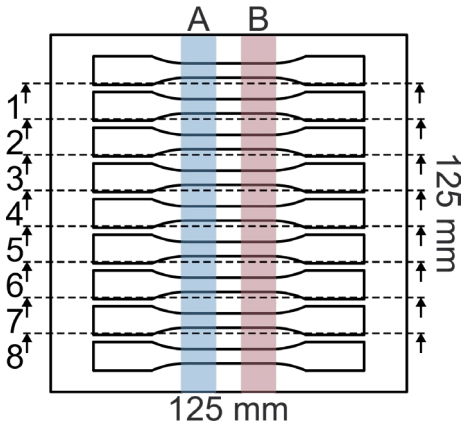

Figure 2: Specimen dimensions and microscopy section planes

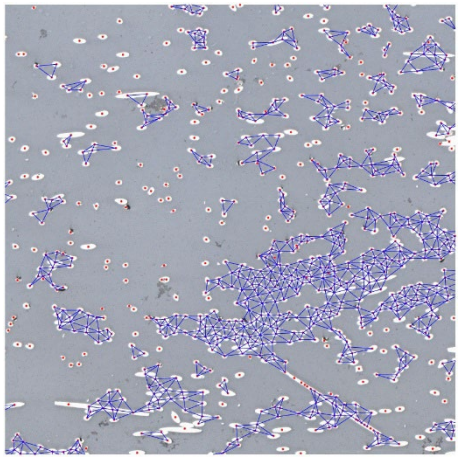

Figure 3: Example of the bundle triangulation of the 20% sample in location A-2

2.1 IMAGE PROCESSING & ANALYSIS

Image analysis of the fiber dispersion starts with identifying the locations of the fibers, subsequently the distribution is analyzed. As a first step, the image is binarized using the distinct peaks that are present in the image histogram. Each peak represents one of three components of the image, the mounting epoxy, the matrix material, and the fibers. A binary mask is constructed by taking the luminosity value in the middle of these peaks as the boundary. This binary map is used as the first check of the FVF by comparing the number of pixels assigned to the matrix and the fibers.

Second, the binary mask of the fiber locations is used to analyze the local fiber volume fraction. This method is based on analyzing the local fiber volume fraction compared to the mean fiber volume fraction. These steps are used to calculate the Intensity of segregation (IoS), as is used in analyzing mixtures in chemistry [6], [7]. However, on a pixel level the volume fraction is binary, therefore an averaging step is used at different cell sizes to get the local fiber volume fraction. The variance of the fiber volume fraction of the sample is divided by the variance of the fiber volume fraction before mixing. As 16 micrographs are analyzed per sample the IoS is calculated per micrograph and then averaged to get one IoS value for the sample. The spread of the IoS values within the sample can be used to show the bandwidth of the IoS.

Third, the fiber centers are analyzed using the MATLAB regionprops function, with the fiber centers a triangulation of the fiber centers is constructed. Then any links in the triangulation longer than three times the average fiber diameter are removed and any resulting links that are lines and do not form a

triangle are removed. The resulting triangulation corresponds to the bundles present in the composite. An example part of the triangulation is shown in figure 3. This process is analogous to the image analysis by Vincent et al [8].

3 RESULTS

The results are treated in the following order: first, the microstructure is discussed, then the image analysis results are treated, concluding with the mechanical results.

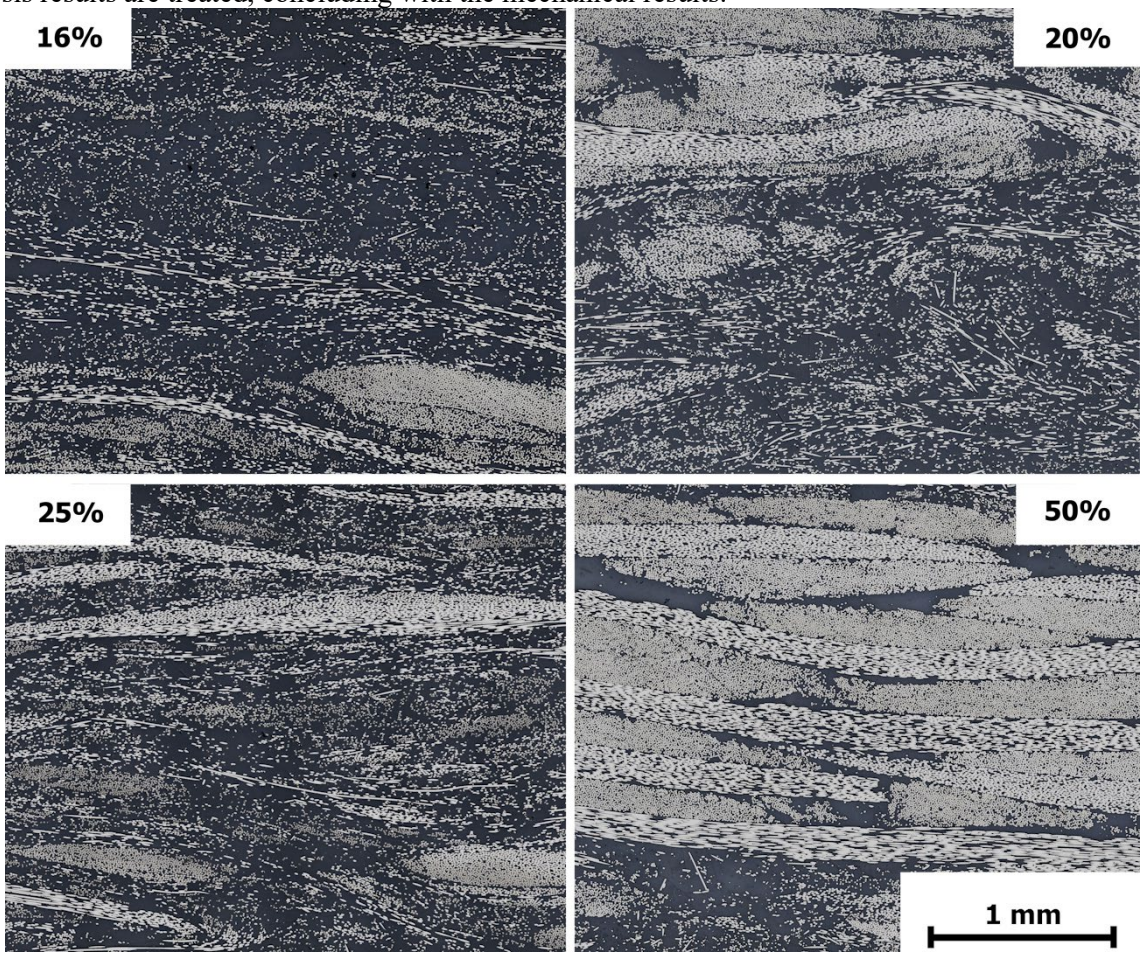

Figure 4: Cropped cross sections from the A-2 plane of all the samples having a global fiber volume fraction of (a) 16%, (b) 20%, (c) 25%, (d) 50%.

3.2 Microstructure

Figure 4 shows example cross sections of the plate specimens from plane 2 and location A as indicated in Figure 2. A first observation from the micrographs is that no voids could be found, indicating good consolidation. Second, the microstructure differs significantly. In Figure 4a of the 16% FVF specimen, both well dispersed fibers that have almost equal spacing to their neighbors exist, as well as the presence of a large undispersed fiber bundle originating from the 3K bundles present in the woven scrap material. A similar structure can be seen in the example of the 20% FVF sample, as well as undispersed bundles and dispersed individual fibers, a matrix-rich area is present in between two fiber bundles. By contrast the example of the 25% FVF sample shows only dispersed fibers and smaller fiber bundles. Lastly the unmixed 50% FVF specimen in Figure 4d shows stacks of fiber bundles with small resin rich areas and surprisingly small areas of dispersed fibers. Concluding, the microstructures of these materials show different characteristics depending on the fiber volume fraction. However, only qualitative information can be gathered directly from micrographs.

3.2 Image analysis

To validate the approach for thresholding the average volume fraction of each of the 16 micrographs per specimen is compared to the average volume fraction as is targeted through the compounding mixture.

Figure 5a shows the correlation between the input target FVF of the compounding process and the measured fiber volume fraction in the image analysis. First it is evident that the two measures of the fiber volume fraction agree quite well. Second, the lowest and highest FVF mixtures have a significantly higher spread in the fiber volume fraction.

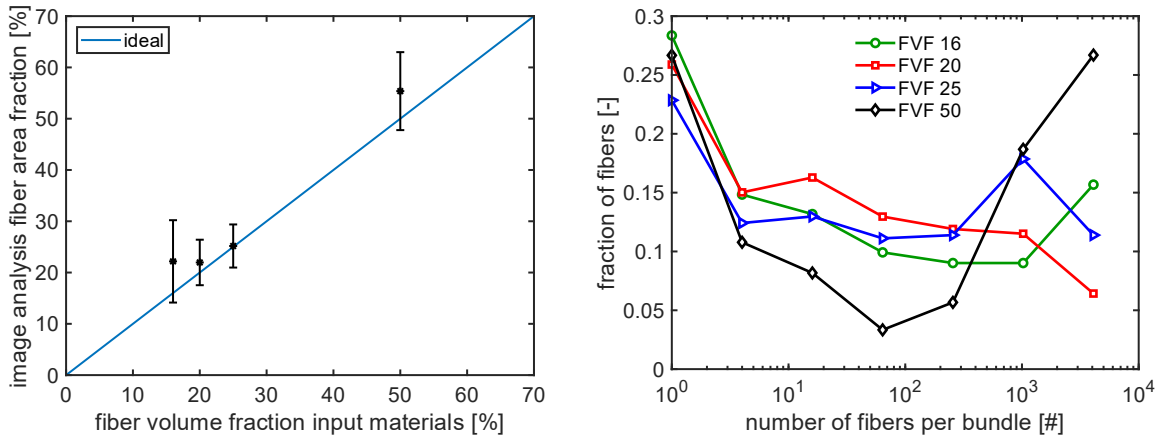

Figure 5: (left) Relation of the fiber volume fraction from the input materials to the fiber volume fraction from the micrographs. (right) Distribution of the fibers present in the volume over the bundle size that contains them.

Figure 5b shows the distribution of the bundle sizes that the present fibers are contained within. It is evident that the dilution and mixing step result in a large change in the microstructure. This is well reflected in the change in the bundle size distribution from the 50% FVF sample compared to the mixed and diluted samples. Between the three diluted samples, the 16% FVF sample shows the largest remaining portion of large bundles. While the reduced bundle size of the 20% FVF samples indicates a good dispersion of the initial bundles.

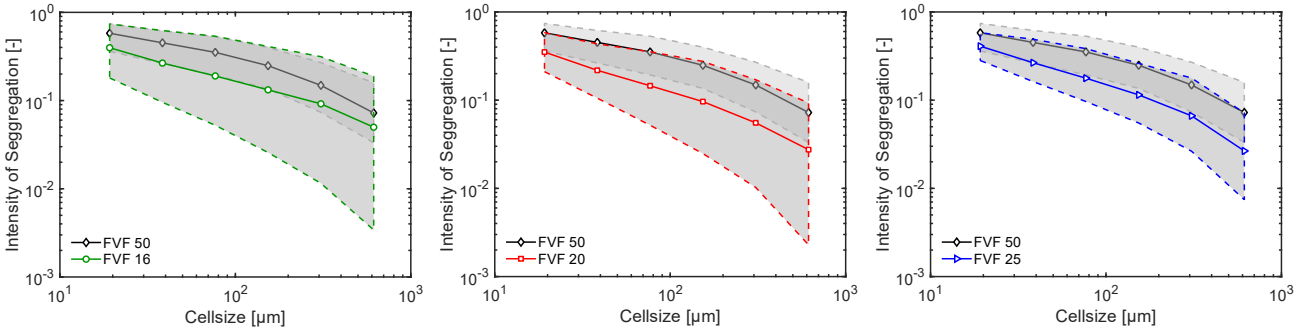

Figure 6: IoS of the three mixed samples compared to the IoS of the unmixed 50% FVF samples (black) as a function of the averaging cell size. The areas contained by dashed lines indicate the bandwidth of the IoS.

The IoS of the three mixed samples are shown in Figure 6 and compared to the IoS of the unmixed sample. The value of the intensity of segregation relates to the variance of the fiber volume fraction. The 16% FVF sample shows an average IoS that is lower than the 50% FVF sample indicating some dispersion. But the bandwidth includes the whole range indicating that there are micrographs that have a similar variance in volume fraction as the unmixed 50% sample. All the way up to a low value of FVF. The 20% FVF sample has a lower average IoS and the maximum IoS is close to the mean of the unmixed 50% sample. Similarly, the 25% sample has a low average IoS and similar maximum values of IoS. However, the bandwidth is much lower.

Next to the fiber volume fraction, the fiber orientation in a specimen relates directly to the strength and stiffness of the material. After mixing the material is large in volume and during compression molding the height is reduced from 30mm to 2mm, meaning it is reasonable to assume a 2D random fiber orientation. However, it is good to check this assumption. By using the identified ellipses traced by the fibers in the cross sections the orientation in 3D can be determined. From these orientations an average orientation tensor can be constructed. The resulting tensors aligned with expectations for a 2D random case, showing diagonal components of 0.5 in the long directions of the plates. Only the 25% FVF sample showed a slight preferential orientation of 0.57 in the tensile direction and 0.34 perpendicular to it and 0.08 for the out of plane component.

3.3 Mechanical results

Aside from the fiber volume fraction and the fiber orientation, the fiber length is also of influence. It should be noted that only 50% FVF was not processed in the mixer and thus did not undergo a step where significant fiber attrition can occur. For these kind of fiber loadings and this type of mixer it has been reported that the weight average length is typically reduced to or below 500µm [9]. Therefore, the 50% FVF specimen has a significant advantage in fiber length compared to the other three samples.

Figure 7 shows the tensile curves for the different samples created. The scatter in results is evident from all the tensile curves. The bundle size distribution results are reflected in the large difference in performance between the mixed and diluted samples and the unmixed 50% FVF sample. The unmixed 50% FVF material has high stiffness but very poor strength and ductility. The 16% FVF sample that showed a spread in local FVF values from the image analysis and large remaining bundles also has a large spread in mechanical performance. So, the extremes of the samples show a correlation with the fiber bundle distribution and the local volume fraction.

The middle ground occupied by the FVF 20% and 25% samples show more subtle differences. The FVF 20% sample shows a large scatter in stiffness but a smaller scatter in strength, and most interesting two groups of failure strains. The FVF 25% by contrast, has a narrow distribution in stiffness but a large scatter in strength, but also shows the highest strength values of all specimens.

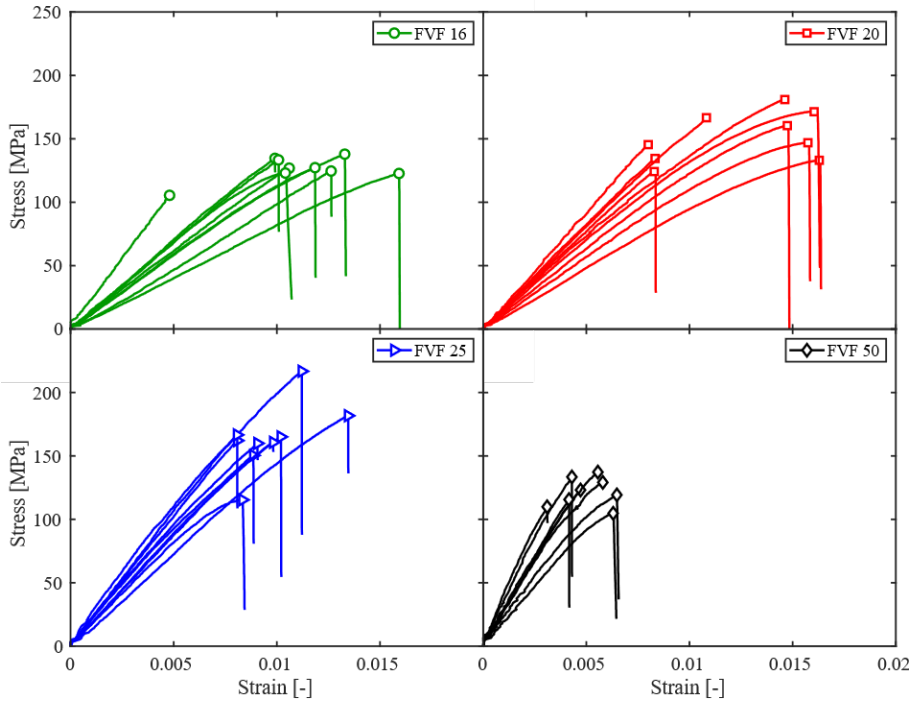

Figure 7: Tensile results of the reprocessed scrap materials

In conclusion, the performance of the material shows no trivial relationship between the fiber volume fraction and the resulting strength. However, at the high fiber volume fraction the performance is the worst even though that sample also has the highest fiber length, but the low homogeneity is likely inhibiting performance.

9 CONCLUSIONS

Using the current image analysis techniques, it is shown that the fiber volume fraction can be calculated quite accurately. Second, the bundle size distribution of the microstructure can provide a first indication towards the expected strength of the material. Interestingly, the sample with a high-volume fraction and the longest fiber length does not show the best performance. The benefits of dispersing and diluting woven composite scrap became evident in mechanical testing. Significant improvements in performance can be achieved by decreasing the fiber volume fraction and higher homogeneity could play a part in this relation.

ACKNOWLEDGEMENTS

This research forms part of the research programme of DPI, project #860t21, Recycling of thermoplastic composites. DPI, P.O. Box 902, 5600 AX Eindhoven, the Netherlands.

REFERENCES

[1] D. E. Witten and V. Mathes, “Der europäische Markt für Faserverstärkte Kunststoffe / Composites 2021,” 2022.
[2] G. Vincent, “Recycling of thermoplastic composite laminates: the role of processing,” PhD, University of Twente, Enschede, The Netherlands, 2019. Accessed: Oct. 12, 2022. [Online]. Available: http://purl.org/utwente/doi/10.3990/1.9789036548526
[3] D. E. Sommer, S. G. Kravchenko, W. B. Avery, and R. B. Pipes, “Mechanisms of notch insensitivity in long-fiber discontinuous, prepreg platelet compression molded composites,” *Composites Part A: Applied Science and Manufacturing*, vol. 162, p. 107133, Nov. 2022, doi: 10.1016/j.compositesa.2022.107133.
[4] J. L. Thomason, “The influence of fibre length and concentration on the properties of glass fibre reinforced polypropylene. 6. The properties of injection moulded long fibre PP at high fibre content,” *Composites Part A: Applied Science and Manufacturing*, vol. 36, no. 7, pp. 995–1003, July 2005, doi: 10.1016/j.compositesa.2004.11.004.
[5] M. Park, J. H. Park, B. J. Yang, J. Cho, S. Y. Kim, and I. Jung, “Enhanced interfacial, electrical, and flexural properties of polyphenylene sulfide composites filled with carbon fibers modified by electrophoretic surface deposition of multi-walled carbon nanotubes,” *Composites Part A: Applied Science and Manufacturing*, vol. 109, pp. 124–130, June 2018, doi: 10.1016/j.compositesa.2018.03.005.
[6] P. V. Danckwerts, “The definition and measurement of some characteristics of mixtures,” *Appl. sci. Res.*, vol. 3, no. 4, pp. 279–296, July 1952, doi: 10.1007/bf03184936.
[7] A. Kukukova, J. Aubin, and S. M. Kresta, “A new definition of mixing and segregation: Three dimensions of a key process variable,” *Chemical Engineering Research and Design*, vol. 87, no. 4, pp. 633–647, Apr. 2009, doi: 10.1016/j.cherd.2009.01.001.
[8] G. A. Vincent, T. A. de Bruijn, S. Wijskamp, M. I. A. Rasheed, M. van Drongelen, and R. Akkerman, “Characterisation and improvement of the quality of mixing of recycled thermoplastic composites,” *Composites Part C: Open Access*, vol. 4, p. 100108, Mar. 2021, doi: 10.1016/j.jcomc.2021.100108.
[9] B. Fisa, “Mechanical degradation of glass fibers during compounding with polypropylene,” *Polymer Composites*, vol. 6, no. 4, pp. 232–241, Oct. 1985, doi: 10.1002/pc.750060408.

IN-LINE PLASMA MODIFIED CARBON FIBRE FOR ENHANCED THERMOPLASTIC TAPE MANUFACTURING – REPURPOSING HARD TO RECYCLE WASTE IN NEW ZEALAND

M. Pitto[1,2], P. Hubert[3,4], H. Fiedler[5], CJR. Verbeek[1,2], TD. Allen[1,2], S. Bickerton[1,2]

[1]Centre for Advanced Materials Manufacturing and Design, The University of Auckland
[2]Department of Mechanical and Mechatronics Engineering, The University of Auckland
Auckland, Newmarket 1023, New Zealand
Email: mpit768@aucklanduni.ac.nz, web page: https://profiles.auckland.ac.nz/mpit768
Email: johan.verbeek@auckland.ac.nz, web page: https://profiles.auckland.ac.nz/johan-verbeek
Email: tom.allen@auckland.ac.nz, web page: https://profiles.auckland.ac.nz/tom-allen
Email: s.bickerton@auckland.ac.nz, web page: https://profiles.auckland.ac.nz/s-bickerton

[3]Department Structures and Composite Materials Laboratory, McGill University
[4]CREPEC – Research Center for High Performance Polymer and Composite Systems
Montreal, Quebec, Canada
Email: pascal.hubert@mcgill.ca, web page: https://www.mcgill.ca/composite/members/pascal-hubert

[5]National Isotope Centre, GNS Science
Lower Hutt, 5010, New Zealand
Email: h.fiedler@gns.cri.nz, web page: https://www.gns.cri.nz/about-us/staff-search/holger-fiedler/

Keywords: Surface treatment, Recycling, Plasma diagnostics, Composites processing

ABSTRACT

To meet increasing legislative demand for a circular plastics economy, novel technology is needed to produce high-performing composites from waste polymers. Introduced processes must be low-cost and environmentally friendly to be future proof. In this paper, a novel slot-channel melt impregnation tool was used to produce continuous carbon fibre (CF)-reinforced thermoplastic tapes with fewer processing steps than state-of-the-art powder and commingling processes. Process applicability was tested for polyamide 6 (PA6), PA6 blended with polypropylene (PP), and waste film linear low-density polyethylene (LLDPE) containing PA6. For the first time, an atmospheric pressure plasma jet with air carrier gas was applied in-line to enhance the melt impregnated tapes. The slot-channel melt impregnation process operated more consistently with the active in-line plasma surface treatment as a result of improved fibre alignment and cohesion by pneumatic spreading. The slot-channel melt impregnator produced tapes with high degrees of impregnation for all matrix systems, irrespective of the reinforcement treatment. Compression moulded PA6 and PA6/PP (50:50 wt.%) matrix composite short beam strength significantly benefited from CF plasma surface treatment, increasing by 45.2% and 89.8%, respectively. The 36% increase of O/C elemental composition on the CF surface did not enhance PA6/LLDPE (20:80 wt.%) composite performance because the dominant dispersive matrix is incompatible with the polar fibre surface. The present work introduces a viable thermoplastic tape manufacturing process that can effectively impregnate dry fibres with as-received and shredded waste polymers. This process is especially promising because it significantly enhances tapes made with a PA6/PP matrix, a common hard-to-recycle blend that is currently not repurposed in New Zealand.

1 INTRODUCTION

Polymeric waste is poorly utilised in New Zealand. Out of the estimated 45,000 tonnes of plastic collected for recycling annually, up to 90% are exported [1]. While large quantities of engineering thermoplastic such as nylon are available for reuse in municipal and post-industrial waste, they are usually considered as hard to recycle by council recycling schemes [2]. Consequently, clean recovery of polyamides is currently under prioritised, leading to potential contamination and phase separation of

waste thermoplastic with non-compatible polymers [3]. Such incompatibilities reduce the matrix strength [4] and compatibilisation between the fibre surface and multiple matrix constituents [5]. Despite the aforementioned concerns, technology to produce fibre-reinforced thermoplastic composites with matrices containing waste polymer must be developed to meet the demand for a circular plastics economy. An appropriate issue to address is that 39% of plastics in Europe were converted to packaging in 2020 [6], necessitating processes that re-use polymeric film blends. This work investigates the feasibility of producing carbon fibre (CF)-reinforced thermoplastics constituting a blended polyamide 6 (PA6) matrix. Mixtures of PA6 with polypropylene (PP) or polyethylene (PE) are commonly found in hard-to-recycle packaging films.

Enhanced bonding between the incompatible CF-reinforcement and the blended matrix, without the use of wet chemical treatments, is of primary interest to align with the environmental motivations of this project. This paper instead presents a continuous air plasma functionalisation process to rapidly modify the CF surface for interface enhancement, similar to other works in the literature [7, 8, 9, 10]. Two novel contributions are presented in this work. Firstly, the integration of in-line plasma treatment with a novel slot-channel melt impregnation process is studied. Secondly, the process is used to elucidate the influence of plasma surface treatment on tape matrices constituting (i) PA6, (ii) PA6/PP made from virgin constituents to emulate the waste mixture, and (iii) waste PA6/PE film. Overall, issues encountered when processing continuous fibre-reinforced composites from hard-to-recycle waste polymers are demonstrated, and the performance enhancement by rapid in-line plasma modification is shown using the short beam strength test.

2 METHODOLOGY

2.1 Materials

Commercial high-strength, standard modulus polyacrylonitrile-based CFs were supplied unsized by Hyosung (Tansome H2550, Republic of Korea) as continuous 12K tows (tex = 800 $g.km^{-1}$, filament diameter = 7 μm, tensile modulus = 250 GPa, tensile strength = 5516 MPa, elongation = 2.2%, untwisted). Unsized CFs were utilised in this work to remove the complexity of size burn-off and degradation during surface treatment [11]. The virgin PA6 matrix used in this work was Ultramid B3S (BASF GmbH, Germany). Before compounding or melt impregnation, the hygroscopic PA6 was dried at 92ºC for 24 h. The virgin polymer blend matrix, emulating a hard-to-recycle waste blend, admixed MOPLEN HP400N PP (LyondellBasell, USA) to the PA6. Waste polymer films were sourced from an Auckland, New Zealand-based recycling facility.

2.2 Continuous plasma surface treatment

The pulsed DC plasma source utilised in this continuous treatment was a Tantec-X PLX (Denmark) atmospheric pressure plasma jet (APPJ) with an excitation frequency, power, and flow rate range of ~40.4 kHz, 416 W and 1400-2500$L.h^{-1}$, respectively. Figure 1 depicts the experimental setup for in-line plasma treatment. The fibre tow was let-off (2) from a bobbin and aligned with the plasma treatment zone (6). Vertically offset nitride-hardened 5 mm steel pins spread and tension the tow (5). The line-speed of 0.83 $m.min^{-1}$, yielding a good degree of impregnation, was controlled by a belt pulling unit prior to take-up on a winder. The working gas flow rate and fibre-nozzle distance used for tape manufacturing were 2200 $L.h^{-1}$, and 10 mm, respectively. The selection of these parameters is elucidated in Section 3.1 by optical emission spectroscopy (OES) and high-speed imaging.

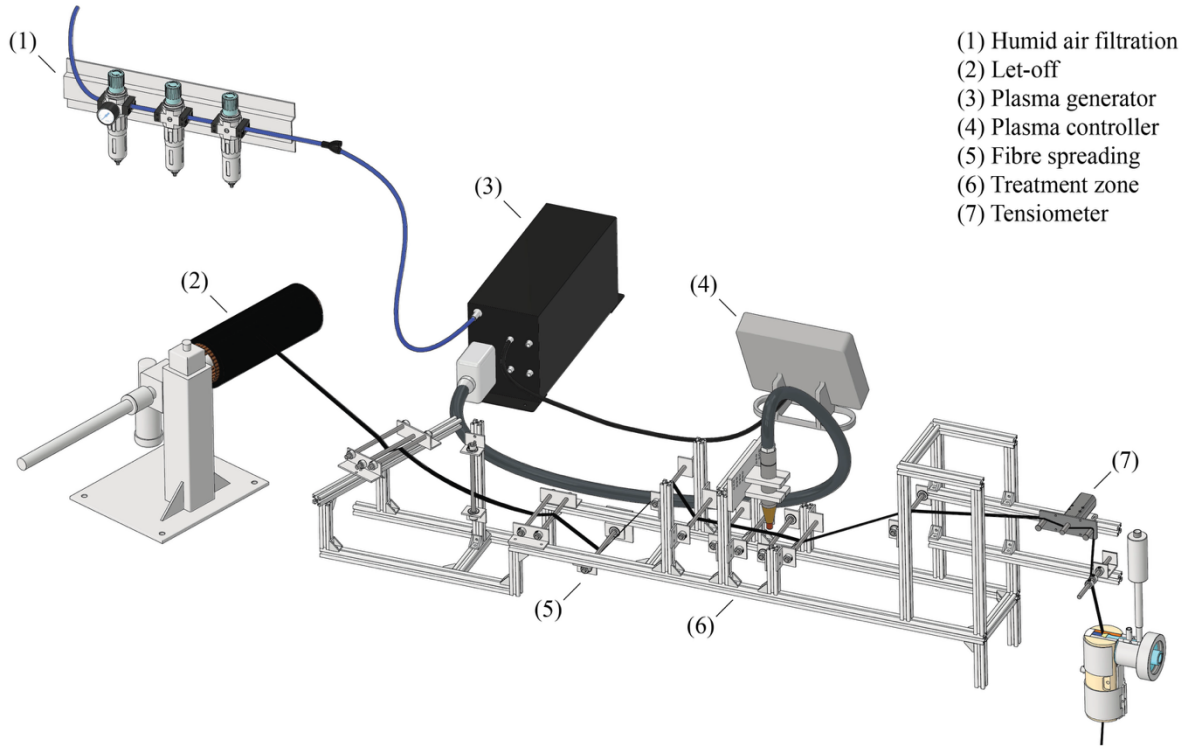

Figure 1: Continuous APPJ treatment setup schematic to modify the CF surface in-line prior to melt impregnation.

2.3 Optical emission spectroscopy

OES was applied to inspect spatial and working gas flow rate trends of reactive species in the air plasma discharge. The optical emission spectrographs were acquired on an EPP2000 portable spectrometer (Stellarnet, USA) by targeting a fibre optic cable mounted to a three-axis micro-positioning table. Spatial emission variation was measured along the APPJ system line of axial symmetry with coordinates centred at the nozzle exit. Measurements were acquired for distances from 2 to 12.5 mm and working gas flow rates between 1400 and 2200 $L.h^{-1}$.

2.4 High-speed imaging

A VEO 410L (Phantom, USA) global shutter and mono sensor, high-speed camera equipped with a 105 mm Micro-NIKKOR (Nikon, Japan) lens was used to capture the plasma discharge at the nozzle exit. An exposure time, frame rate, aperture and exposure index of 490 µs, 2000 fps, f/4 and 6400, respectively, were used to capture diffuse and filamentary discharge frames for nozzle-fibre distances between 6 and 12 mm.

2.5 X-Ray Photoelectron Spectroscopy

Functionality of the CF tow top surface was assessed by X-ray photoelectron spectroscopy (XPS). Samples were stuck on vacuum safe sticky tape immediately after plasma treatment to be placed in the XPS vacuum chamber, pumped down within 4 hours of the plasma treatment, and measured within 72 hours. The XPS measurements were acquired on an Axis Ultra (Kratos analytical, USA) using monochromatic Al Kα X-rays with a power of 124 W. The survey and high-resolution scan pass energy was 160 and 20 eV, respectively. Elemental composition was calculated from the survey spectrum.

2.6 Polymer processing

The virgin polymer blend was melt-blended in a corotating twin screw extruder (Brabender, GER) with a diameter and length-to-diameter ratio of 20 mm and 40, respectively. Blends were extruded at a screw speed of 60 rpm and a downstream temperature profile of 190 – 200 – 210 – 220 – 230 – 240ºC. Waste polymer film was shredded into flakes. The flakes were dried and directly used in the melt impregnation process. Filamentary extrusion to pelletise the waste polymer was avoided to minimise degradation and processing costs.

2.7 Differential scanning calorimetry

Polymer constituent mixtures were characterised by differential scanning calorimetry (Netzsch, DSC300 Caliris classic, Germany). All samples were annealed at 275 ºC, and subsequent melting endotherms were measured between -25 and 275ºC at a heating rate of 10ºC.min^{-1} in a nitrogen atmosphere.

2.8 Melt impregnation process

The impregnation die utilised in this work had a wavey geometry with a slot channel through which the fibre and polymer passed, as depicted in Figure 2a with a three-dimensional view in Figure 2b. The process is analogous to pin-driven impregnation in a melt chamber. Its difference lies in the small channel cross-section that develops elevated melt pressure. The impregnator was baselined on a non-vented 19/20 single-screw extruder (Brabender, Germany) that was flood-fed with dry PA6, PA6/PP, and shredded waste film. Samples made from as-received or plasma surface-treated reinforcement are identified as CF and pCF, respectively. After melt impregnation, the out-of-tool tape passed over two hot pins at 270ºC (Figure 3) in order to post-consolidate and smoothen the tape surfaces.

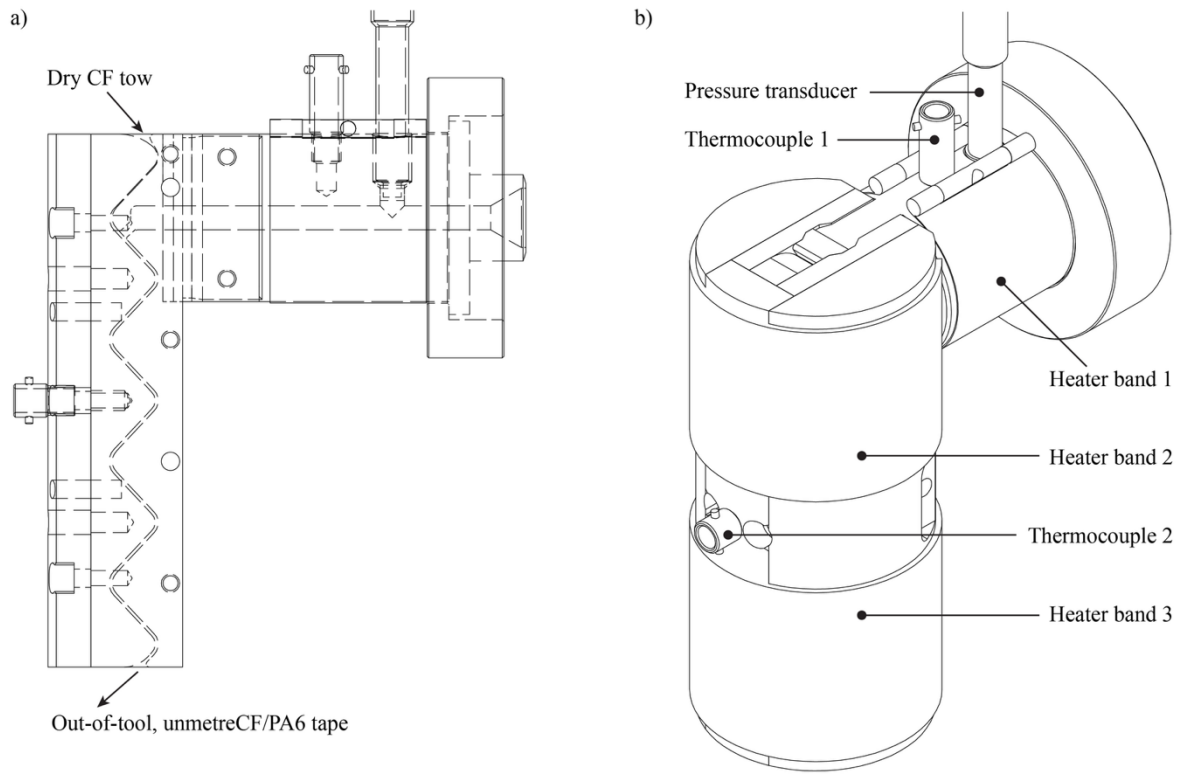

Figure 2: (a) Schematic of the wavy slot channel cross-head thermoplastic melt impregnator. The skeleton drawing omits the thermal conductor jackets and the heater bands over the slot for clarity. Image (b) illustrates the assembled tool including heater bands and instrumentation.

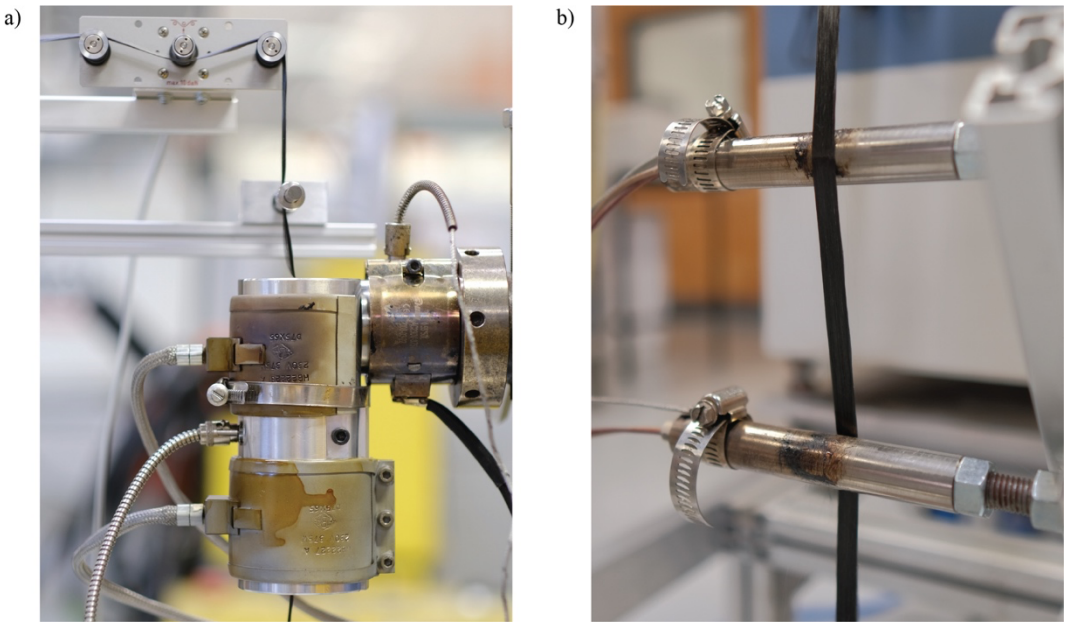

Figure 3: Images of (a) the instrumented cross-head melt impregnator and (b) the out-of-tool tape passing over two hot pins below the melt impregnator.

2.9 Cross-sectional microscopy

Tape quality was qualitatively inspected by microscopy. Out-of-tool and hot-pin post-consolidated tapes were mounted in SpeciFix-40 (Struers, Denmark), polished to a finish of 0.05 µm and ultrasonically cleaned to remove contamination from pores. Cross-sectional micrographs were acquired on a DSX1000 (Olympus, Japan) digital microscope.

2.10 Mechanical characterization

After drying for 24 hours, the tapes were stacked in a 3 mm thick compression mould to produce samples for short beam strength testing according to ASTM D2344. The compression moulding temperature and compaction pressure were 280ºC and 16 bar, respectively. The pre-heating and compression cycle times were 8 and 2 min, respectively. A 10-minute water cooling cycle reduced the mould temperature to 40 ºC. The diamond-cut unidirectional laminates (18 mm x 6 mm x 3 mm) were environmentally conditioned prior to testing at room temperature and 50% relative humidity. At least five specimens were tested for each sample.

3 RESULTS AND DISCUSSIONS

3.1 Plasma characteristics and carbon fibre surface modification

APPJs have a higher spatial heterogeneity compared to plasma devices with tubular or parallel plate electric field configurations. The spatial heterogeneity is presented in Figure 4 using OES data, where the maximum emission intensity of atomic oxygen exponentially decays with increasing distance from the nozzle exit. Critically, the emission intensity is more sensitive to position than the working gas flow rate.

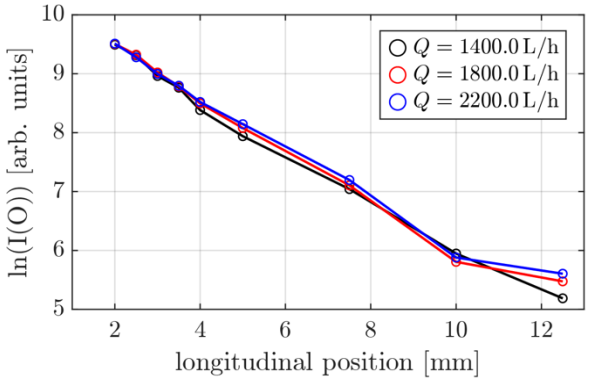

Figure 4: Optical emission spectroscopy logarithmic maximum emission intensity of the 777 nm atomic oxygen band for varying working gas flow rate. The longitudinal measurement point along the APPJ centre line was measured with respect to the nozzle exit.

Since emission intensity is proportional to species density, the logarithmic decay from Figure 4 suggests that the CF tow should pass through the APPJ treatment zone with a minimum nozzle-fibre distance for maximum exposure. However, the electrical conductivity of CFs disallows small nozzle-fibre distances. This is due to a transition from diffuse to filamentary plasma discharge when moving the fibre tow surface closer to the nozzle exit. Figure 5 illustrates the discharge mode transition behaviour for a fixed working gas flow rate of 1800 $L.h^{-1}$ at nozzle-fibre distances between 6 and 12 mm. It shows that distances beyond 10 mm yield diffuse plasma for the fixed flow rate. However, we have previously shown that the working gas flow rate also governs the discharge mode [12].

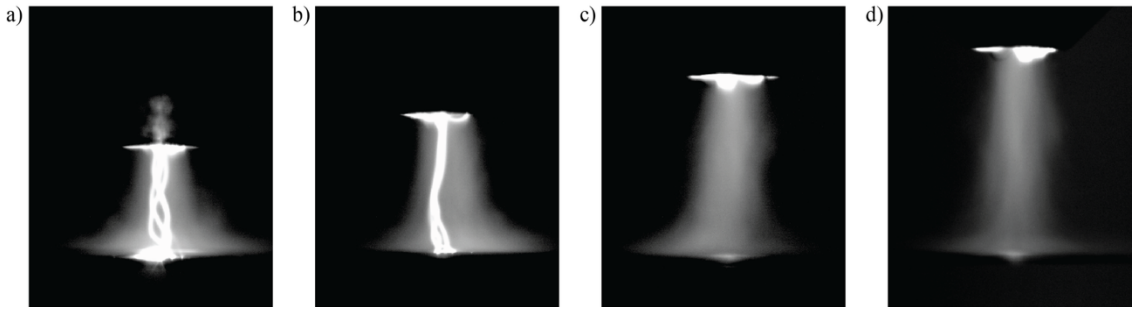

Figure 5: High speed camera frames of the APPJ interacting with the CF tow. The nozzle fibre distances for images (a) – (d) are 6, 8, 10, and 12 mm, respectively.

Fibre surface functionality after plasma treatment at a fixed distance and a fixed working gas flow rate is also a function of residence time [12]. Since the in-line plasma treatment residence time in this work is governed by the overall melt impregnation line speed, for the sake of brevity, surface functionality for varying line-speed is not presented. Instead, we show the as-received and plasma-treated CF surface functionality measured by XPS in Figure 6, where the line-speed, working gas flow rate and nozzle-fibre distance were 0.83 $m.min^{-1}$, 2200 $L.h^{-1}$, and 10 mm, respectively. Visually inspecting the C 1s band in Figure 6a gives the impression that the C-OH, C-O-C and C=O concentrations have increased after surface treatment. The O 1s peak in Figure 6b gives further evidence for an increase in R-O-R and -OH functionality. However, a similar increase in =O functionality is not observed, indicating that the C=O peak fitting of the C 1s peak may be subject to fitting error. Overall, the survey spectra reveal an O/C increase of 36%.

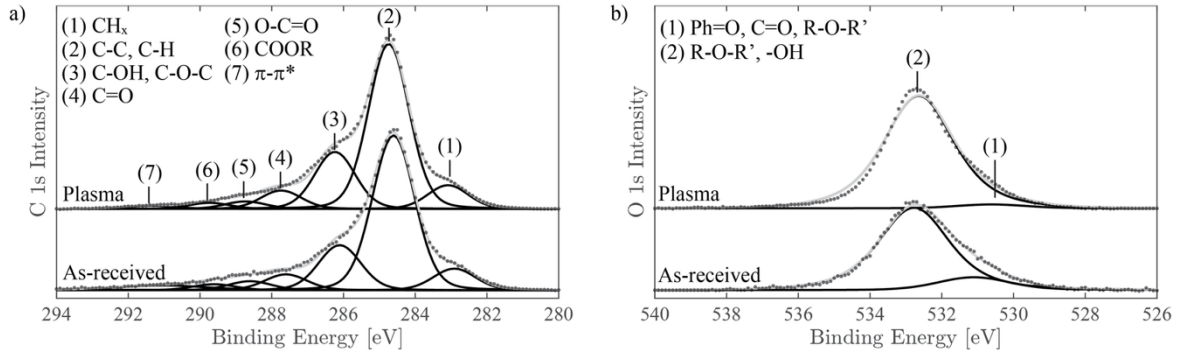

Figure 6: High-resolution XPS spectra of the (a) C 1s and the (b) O 1s band before and after plasma surface treatment. The line speed, working gas flow rate and nozzle-fibre distance were 0.83 m.min^{-1}, 2200 L.h^{-1}, and 10 mm, respectively.

3.2 Polymer mixture characterisation

DSC was used to detect the waste film composition. Table 1 summarises the peak melting temperatures of the various phases in each sample. The neat PA6 melting curve has a single peak at 220ºC with a heat of fusion of 61.54 J.g^{-1}. Blending PA6 with PP adds a peak at 163ºC with a heat of fusion of 50.73 J.g^{-1}. This confirms the 50:50 ratio in the blend, as the PA6 heat of fusion has been reduced by 52%. The waste film exhibits a similar PA6 melting peak at 220ºC with a heat of fusion of 12.06 J.g^{-1}. Assuming that it has an equivalent heat of fusion as the neat PA6 Ultramid B3s, the PA6 mass fraction in the hard-to-recycle film is approximately 20%. Most of the hard-to-recycle film is linear low-density polyethylene (LLDPE), as ascertained from the low-temperature melt peak at 128.9ºC [13].

Table 1: PA6, PA6/PP and waste film DSC data

Sample	Peak temperature 1 [ºC]	Peak temperature 2 [ºC]	Peak area 1 [J.g^{-1}]	Peak area 2 [J.g^{-1}]	PA6 mass fraction
PA6	-	220	-	61.54	1
PA6/PP	163	220	50.73	29.44	0.48
Waste film	128.9	218	98.58	12.06	0.2

3.3 In-situ plasma treatment for enhanced melt impregnation

Subtle separation of fibres from the unsized CF tow (Figure 7a) can lead to pronounced fibre misalignment and eventual failure of the tape manufacturing process. Fibres entering the viscous melt in the impregnator tend to wash out, necessitating careful control of the fibre alignment in the dry tow. It was found that the tow was firmly bundled when the in-line plasma treatment was active (Figure 7b). This led to diminished fibre washout and eliminated spontaneous process failure. Improved tow cohesion and uniform alignment by plasma treatment are explained by the pneumatic spreading effect of the dry air flowing through the nozzle.

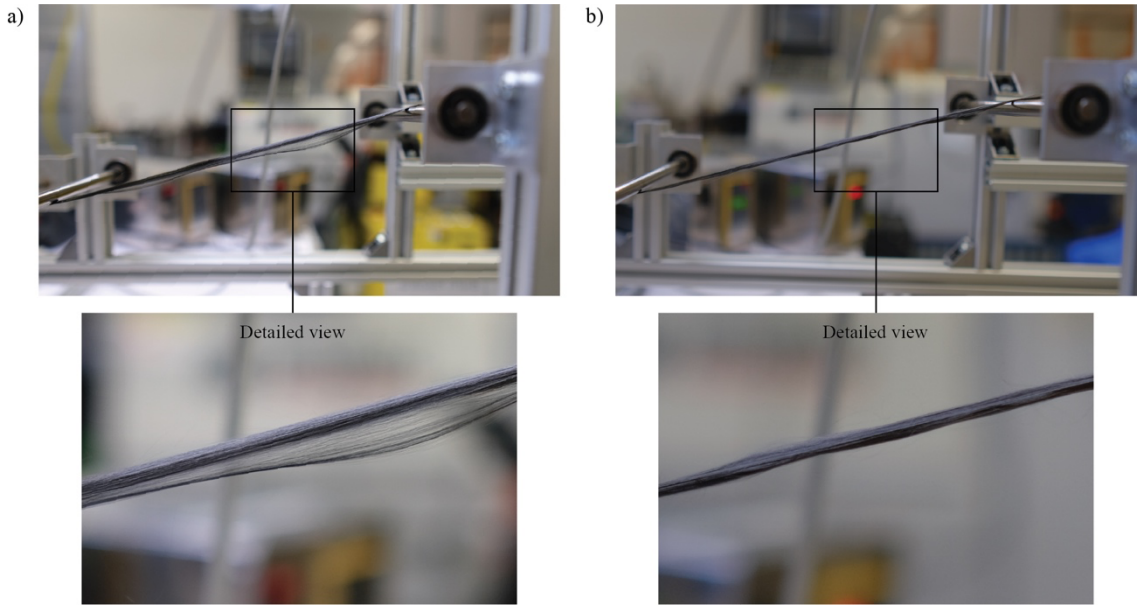

Figure 7: Images of the dry (a) as-received and (b) in-situ plasma surface treated CF tow passing between guiding pins leading to the melt impregnator.

3.4 Melt impregnated carbon fibre tape properties

After melt impregnation and hot-pin post-consolidation, at a fixed speed, the tape quality for the three matrix systems was assessed by cross-sectional microscopy, depicted in Figure 8. The tape dimensions changed for the various matrices. PA6 tapes (Figures 8a and 8b) were around 4.8 mm wide. PA6/PP (Figures 8c and 8d) and PA6/LLDPE (Figures 8e and 8f) tapes were wider, with widths of approximately 6.3 and 6.2 mm, respectively. Plasma surface treating the CF appears to have had an effect on the PA6/PP tape, where the width increased to approximately 7.3 mm. Overall, these results suggest that the plasma surface treatment has little effect on the tape dimensions.

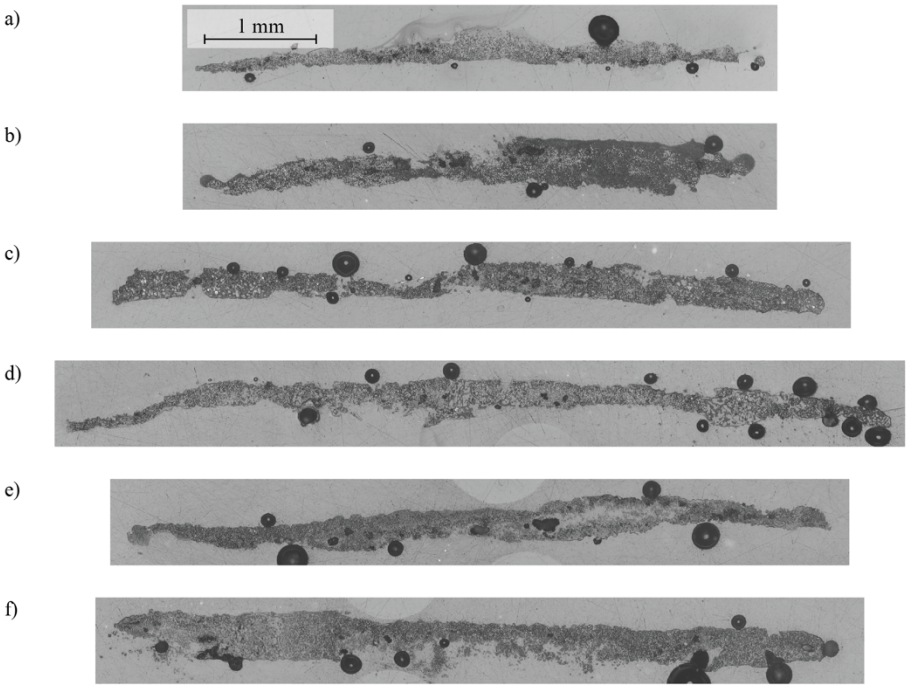

Figure 8: Cross-sectional micrographs of composite tapes constituting (a) CF/PA6, (b) pCF/PA6, (c) CF/PA6/PP, (d) pCF/PA6/PP, (e) CF/rPA6/rLLDPE, and (f) pCF/rPA6/rLLDPE.

Blended polymeric matrices can shape intricate morphologies that strongly govern the composite performance [14]. Micro-scale cross-sectional images of fibre-reinforced PA6/PP and PA6/LLDPE tapes are illustrated in Figures 9a and 9b, respectively. Evidently, the PA6/PP composite, with a 50:50 wt.%, exhibits a co-continuous morphology. The heterogeneous dispersion is especially visible in resin-rich areas. Composites made from the waste film had a mixture ratio disparity (Section 3.1). Hence, it is expected that the LLDPE would form a continuous matrix phase with dispersed PA6 particles. However, the presence of PA6 particles is not easily observed in Figure 9b. It may be that the shredded PA6/LLDPE film did not melt-blend effectively in the single screw extruder, leading to distinct phases at a larger scale. The PA6-LLDPE mixture quality during extrusion and its effect on composite performance must be assessed in future work.

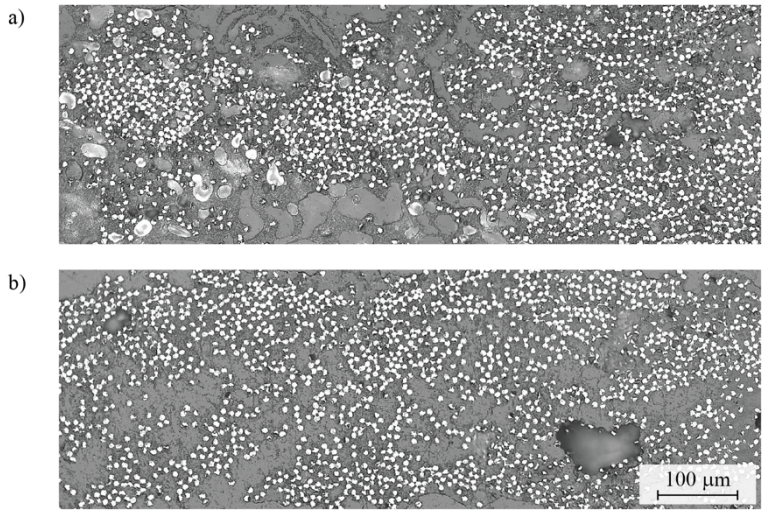

Figure 9: Cross-sectional micrographs of composite tapes constituting (a) CF/PA6/PP and (b) CF/PA6/LLDPE.

The cross-sectional images show that the melt impregnation die can produce high-quality tapes with PA6, PA6/PP, and PA6/LLDPE matrices. Compared to state-of-the-art powder and commingling impregnation processes, the introduced melt impregnator minimises intermediate processing steps, such as powderisation, powder dispersion, or filament drawing. The introduced process is also solvent-free. Everything considered, the plasma-enhanced melt impregnation process minimises environmental harm and processing complexity while facilitating the use of hard-to-recycle polymeric blends, as demonstrated with PA6/PP and PA6/LLDPE. It is a viable process to directly impregnate dry fibres with shredded waste polymer and easily integrates in-line fibre treatment.

3.5 Composite properties

Short beam strength of unidirectional fibre-reinforced samples is plotted in Figure 10. Plasma surface treating the CF statistically significantly increased the short beam strength for composites with PA6 and the PA6/PP matrices. For the first time, we show that in-line plasma surface treating CF increased the mean PA6 and PA6/PP matrix composite short beam strength by 45.2% and 89.8%, respectively. Importantly, the PA6/PP matrix composite made from as-received fibre failed by inelastic deformation (Figure 11). Plasma surface treating CF changed the composite failure to be caused by inelastic deformation and interlaminar shear. Plasma treatment had no effect on composites made from the hard-to-recycle film. These composites also had a significantly lower short beam strength compared to the PA6 and the PA6/PP matrix composites.

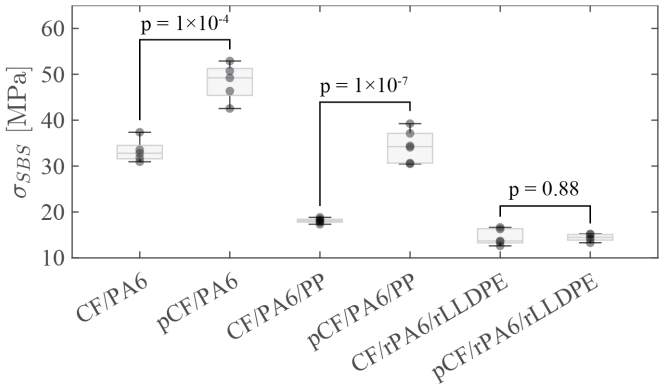

Figure 10: Short beam strength boxplots of unidirectional CF-reinforced (a) PA6, (b) PA6/PP, and (c) recycled PA6/LLDPE. The two-sample t-test statistical significance is indicated between as-received and plasma surface treated CF samples for the three matrix systems.

The short beam strength curves in Figure 11 show that plasma surface treating the CF significantly stiffened the PA6/PP matrix composite and altered the failure mode to inelastic and interlaminar shear. This can be explained by enhanced bonding between the functionalised pCF surface and PA6, constituting 50% of the matrix. Co-continuous PP in the matrix continues to bond poorly to the incompatible PA6 and the functionalised pCF. Composites made from the hard-to-recycle polymer failed inelastically. Plasma treatment had no statistically significant beneficial effect on these composites, suggesting that a higher PA6 content is needed for enhanced bonding with the polar pCF surface. This highlights that the surface functionality must be tailored to suit the polymeric matrix. In the case of PA6/LLDPE waste, the polar PA6 blended with dispersive LLDPE must be compatibilised, for instance, using maleic anhydride [15] or by plasma modifying the bulk polymer blend in a reactive extrusion process [4]. When both matrix constituents are polar, the interface can benefit from a 36% increase in O/C ratio on the CF surface (Section 3.1). Moreover, even if pCF-PA6 bonding is enhanced in the PA6/LLDPE (20:80 wt.%) composite, the small dispersed PA6 content in the LLDPE phase with a seven times lower Young's modulus leads to poor load transfer to the pCF and PA6. The combination of weak interfacial bonding and poor load transfer led to comparatively weak PA6/LLDPE matrix composite performance.

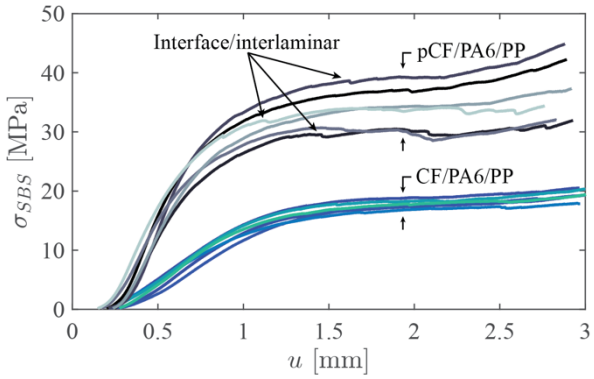

Figure 11: Short beam strength curves for as-received and plasma surface treated unidirectional CF-reinforced PA6/PP composite.

4 CONCLUSIONS

This paper presents two important contributions. Firstly, a novel slot-channel melt impregnation tool was used to produce CF-reinforced tapes from hard-to-recycle polymer blends found in the New Zealand waste stream. Namely, PA6/PP (50:50 wt.%), which was produced from virgin polymer, and

PA6/LLDPE (20:80 wt.%) waste film. Secondly, for the first time, an APPJ treatment was integrated to surface treat CF immediately prior to melt impregnation. During tape production, the in-line plasma treatment enhanced fibre alignment and cohesion in the tow by pneumatic spreading below the jet. As a result, process failures by fibre washout in the melt impregnator channel, which occasionally occurred with as-received fibre, were eliminated. This work demonstrated that increasing the CF surface O/C ratio by 36% leads to significantly enhanced fibre-matrix bonding in compression moulded composites made from melt-impregnated tapes containing primarily PA6. The CF surface treatment increased the mean PA6 and PA6/PP matrix composite short beam strength by 45.2% and 89.8%, respectively. The small PA6 content in the PA6/LLDPE matrix hindered significant composite performance enhancement by polar fibre functionalisation. Consequently, the dry air plasma surface treatment is not compatible with all matrix systems. Specifically, the dry air plasma-modified CF surface is highly compatible with the polar PA6 but remains incompatible with dispersive LLDPE. Hence, a compatibilisation process of the blend is needed for improved composite performance when the dispersive matrix constituent is dominant. Overall, the introduced slot-channel melt impregnation process effectively produces fibre-reinforced hard-to-recycle polymer tapes while minimising additional processing steps that are needed in powder or commingling impregnation. Plasma surface modifying the reinforcement effectively strengthened interfacial adhesion with polar matrix constituents.

ACKNOWLEDGEMENTS

This work was supported by the New Zealand Ministry of Business, Innovation and Employment (No. UOAX2212) and the New Zealand Synchrotron Group. The corresponding author received support from the University of Auckland Doctoral Scholarship.

REFERENCES

[1] Office of the Prime Minister's Chief Science Advisor. Rethinking Plastics in Aotearoa New Zealand, 2021 [online]: https://www.pmcsa.ac.nz/topics/rethinking-plastics/

[2] Royal Society of New Zealand, Plastics in the Environment: Te Ao Hurihuri – The Changing World, Royal Society of New Zealand, 2021 [online]: https://www.royalsociety.org.nz/what-we-do/our-expert-advice/all-expert-advice-papers/plastics-in-the-environment-evidence-summary/

[3] Gall, Markus, Freudenthaler, Paul J, Fisher, Joerg, Lang, Reinhold W, "Characterization of Composition and Structure–Property Relationships of Commercial Post-Consumer Polyethylene and Polypropylene Recyclates," *Polymers,* no. 10, pp. 1574, 2021.

[4] Ashraf, Jesna, Bertin, Maicon, Verbeek, Casparus Johannes Reinhard, "Plasma-induced reactive compatibilization of polypropylene/polyamide 6 blends," *ACS Applied Polymer Materials,* vol 7, pp. 641-653, 2025

[5] Xanthos, M, Narth, KA, "Product design with glass fiber reinforced polymer blends, with potential applications in recycling," *Polymer Composites,* vol. 19, issue 6, pp. 768-780, 2004

[6] Plastics Europe, 2023. Plastics – the fast Facts 2023. *Plastics Europe* [online]: https://plasticseurope.org/knowledge-hub/plastics-the-fast-facts-2023/

[7] Ho, Kingsley KC, Adam F. Lee, Steven Lamoriniere, and Alexander Bismarck, "Continuous atmospheric plasma fluorination of carbon fibres," *Composites Part A: Applied Science and Manufacturing,* vol. 39, no. 2, pp. 364-373, 2008.

[8] Xie, Jianfei, Danwei Xin, Hongyan Cao, Cuntao Wang, Yi Zhao, Lan Yao, Feng Ji, and Yiping Qiu, "Improving carbon fiber adhesion to polyimide with atmospheric pressure plasma treatment," *Surface and coatings technology,* vol. 206, no. 2-3, pp. 191-201, 2011.

[9] Xiao, Jianqi, Xuejun Zhang, Zehua Zhao, Jie Liu, Qiufei Chen, and Xiaoxu Wang, "Rapid and continuous atmospheric plasma surface modification of PAN-based carbon fibers," *ACS omega,* vol. 7, no. 13, pp. 10963-10969, 2022.

[10] Moosburger-Will, Judith, et al., "Methyltrimethoxysilane plasma polymerization coating of carbon fiber surfaces," *Surface & Coatings Technology,* vol. 311, pp. 223-230, 2017.

[11] Pitto, Maximilian, Fiedler, Holger, Kim, Nam Kyeun, Verbeek, Casparus Johannes Reinhard, Allen, Tom David, Bickerton, Simon, "Carbon fibre surface modification by plasma for enhanced polymeric composite performance: A review," *Composites Part A,* vol. 180, 2024.

[12] Pitto, Maximilian, Fiedler, Holger, Verbeek, Casparus Johannes Reinhard, Allen, Tom David, Bickerton, Simon, "High-power air plasma diagnostics by optical emission spectroscopy for subsecond continuous carbon fibre surface treatment," *Composites Part A,* vol. 193, 2025.

[13] Camargo, Mariangela, Forte, Maria Madalena Camargo, Wolf, Carlos Rodolfo, "Linear low density polyethylene thermal fractions by DSC technique," *International Journal of Polymer Analysis and Characterization*, vol. 13, pp. 49-65, 2007.

[14] Trongsatikul, Tatiya, Chaiwong, Saowapa, "In situ fibre-reinforced composite films of poly(lactic acid)/low-density polyethylene blends: effects of composition on morphology, transport and mechanical properties," *Polymer International*, vol. 66, pp. 1419-1683, 2017.

[15] Cao, Jiandong, Liu, Hailiang, Chen, Qinjia, Bai, Yangxiao, "Enhancing the interfacial properties of polyethylene-based carbon fiber composites through low-temperature thermally reduced graphene," *Fibers and Polymers*, vol. 24, pp. 4823-4830, 2024.

PROGRESSIVE FAILURE MODELING OF 3D-PRINTED CONTINUOUS CARBON FIBER NYLON COMPOSITE LAMINATES

Siavash Sattar[1], Thienan Le[2], Oleksandr G. Kravchenko[2], Hamid Eisazadeh[3]

[1]Engineering Department, Randolph College
2500 Rivermont Ave, Lynchburg, VA 24503, US
Email: siavashesin@gmail.com

[2]Department of Mechanical and Aerospace Engineering, Old Dominion University
Hampton Boulevard, Norfolk, VA 23529, US

[3]College of Engineering and Technology, Western Carolina University
1 University Drive, Cullowhee, NC 28723, US

ABSTRACT

Fused Filament Fabrication (FFF) using fiber-reinforced thermoplastics is a promising technology for producing fiber-reinforced composite parts with complex geometries, offering structural-grade mechanical behavior along with lightweight properties and recyclability. This study investigates the tensile and failure behavior of composites printed using a dual-nozzle FFF system. Short carbon fiber (SCF)-reinforced nylon was combined with continuous carbon fiber (CCF) nylon layers to produce a hybrid configuration. Various CCF stacking sequences of FFF composite laminates were examined to investigate their impact on the overall mechanical behavior. A finite-element progressive failure (PFA) model was developed using a continuum damage approach. This allowed the prediction of the failure mode in SCF/CCF-reinforced FFF composite and capture various failure modes in the hybrid material system, enabling an understanding of the material's failure behavior. The simulation results were validated using experimental tensile testing for various stacking sequences. The proposed computational approach can be used as a predictive design tool for the mechanical behavior of hybrid fiber-reinforced composites fabricated via FFF.

Keywords: Fiber reinforced composites; Additive manufacturing; Continuum damage mechanics; Progressive failure modeling

1 INTRODUCTION

Advanced carbon fiber–reinforced composites are increasingly adopted in aerospace and other structural applications for their high specific strength and stiffness [1], [2]. Recent additive manufacturing techniques, such as fused filament fabrication (FFF), now enable the fabrication of hybrid composite laminates that combine continuous carbon fiber (CCF) with a short carbon fiber (SCF) reinforced nylon matrix within a single printed part [3]. In this approach, a thermoplastic matrix filament (commercially known as Onyx, containing dispersed short carbon fibers) is interleaved with layers of continuous carbon fiber, resulting in a multi-material laminate structure [3], [4]. Dual-nozzle 3D printers (e.g., Markforged Mark Two) deposit the SCF/ nylon material and embed CCF in specified layers, allowing tailored fiber orientations and placement throughout the part [3]. This hybrid architecture aims to leverage the ease of printing and the toughness of short-fiber nylon material, while harnessing the high load-carrying capability of continuous fiber reinforcement. The resulting printed laminates can achieve structural-grade performance in lightweight designs, with the continuous fibers bearing primary loads and the short-fiber thermoplastic providing matrix support and geometric complexity.

Although the FFF process offers structural and manufacturing advantages, the mechanical response of such hybrid laminates is governed by the complex interaction of multiple constituents and orientations [5]. The presence of two distinct reinforcing forms (continuous fiber layers vs. short-fiber matrix layers) creates multiple potential damage mechanisms that can interact. In matrix-dominated

regions (the SCF/nylon layers and off-axis plies), the material may experience matrix cracking and fiber–matrix interfacial debonding, whereas in fiber-dominated CCF layers, tensile loading can cause abrupt fiber bundle fracture when their strength is exceeded [1]. At the same time, the weak interfaces between dissimilar layers are susceptible to delamination. Experiments on 3D-printed CCF/SCF laminates under flexural and tensile loading indeed reveal a combination of these failure modes. For instance, Barber et al. observed extensive interlayer cracking (delamination) between printed layers at failure, occurring at both homogeneous SCF–SCF interfaces and at the heterogeneous SCF–CCF boundaries, with the SCF–CCF interfaces showing the most severe splitting [3]. Capturing the location and mechanism by which each of these damage modes initiates is crucial for understanding the progressive failure of the hybrid composite.

The mechanical behavior of 3D-printed hybrid composites is primarily governed by their anisotropic, heterogeneous architecture, which combines continuous fiber-dominated layers with more compliant short fiber-filled thermoplastic regions [6]. A clear understanding of how layer orientation, material morphology, and interface design influence the structure–property relationships in these hybrid laminates is essential for advancing their use in structural applications. Under service loads, these hybrid laminates inevitably accumulate damage in multiple modes – e.g., matrix cracking, fiber fracture, fiber/matrix debonding, and inter-layer delamination – all of which progressively degrade the structure's stiffness and strength [1]. Furthermore, phenomenological failure theories (e.g., Tsai–Wu, Hashin) have been developed for composites, achieving reasonable predictions of initial failure to some extent. However, these criteria provide only a static snapshot of failure onset and do not describe how damage propagates. As a result, traditional single-mode or empirical failure models often fail to predict the ultimate strength of hybrid composites when multiple damage mechanisms interact. This limitation motivates the use of a progressive failure analysis (PFA) approach that can track damage initiation and propagation across all relevant modes. While recent studies have explored the mechanical performance of such systems experimentally [1], modeling efforts that quantitatively capture progressive damage and failure evolution in these multi-material, printed architectures remain limited. Existing modeling efforts often rely on simplified elastic assumptions or empirical failure criteria [7], [8], [9], which limits their ability to capture the progressive damage processes that emerge in layered hybrid architectures. More advanced approaches incorporating cohesive zone modeling and continuum damage mechanics (CDMs) have been proposed for conventionally manufactured composites [1], [10], [11], but their extension to printed hybrid composites remains scarce. This study addresses that gap by presenting a progressive failure framework that applies CDMs to simulate multi-mode failure evolution in 3D-printed CF–SCF laminates with varying stacking sequences.

In this study, a finite element-based PFA framework was developed to predict the failure behavior of a hybrid 3D-printed composite laminate reinforced with both short and continuous carbon fibers. The framework incorporates a CDM model for individual plies, featuring cohesive zone elements between layers to simulate interfacial interactions. The hybrid architecture, comprising layers of unidirectional continuous fibers and ±45° short fiber-reinforced plies, introduces complex failure interactions due to differences in fiber length, orientation, and reinforcement scale. The CDM-based approach enables a unified simulation of interacting failure modes. The model emphasizes the role of anisotropic material behavior introduced by the layered deposition process and varying fiber orientations. By tracking damage initiation and evolution at the ply level, the framework captures the onset and progression of failure, providing insights into the underlying failure mechanisms. This CDM-based PFA framework demonstrates its effectiveness in predicting the stress–strain response and failure mode of hybrid printed composites, supporting its applicability for performance-driven virtual testing of additively manufactured composite structures.

2 MATERIAL AND PROCESSING

The composite system investigated in this study consists of a dual-material configuration: a SCF reinforced nylon filament, known commercially as Onyx, and nylon reinforced with CCF. Onyx contained ~30% by weight and serves as the semi-structural material matrix. Though it contains discontinuous carbon fibers for enhanced stiffness and strength, the primary reinforcement is derived from CCF layers.

Fabrication was carried out using a Markforged Mark Two 3D printer, which utilizes FFF. The printer has two independent nozzles integrated into a shared print head, one dedicated to extruding the Onyx matrix and the other to laying CCF along predefined paths. During printing, the Onyx filament is heated and deposited layer by layer to form the structural base. CCF tows are then embedded within specific layers at programmed orientations to reinforce the part. The higher temperature of the extruded Onyx results in localized reheating of the underlying layers, promoting interlayer adhesion.

Dog-bone specimens were designed in Autodesk Inventor, sliced in Eiger.io, and fabricated using a hybrid 3D printing process with Onyx as the matrix material and CCF as reinforcement. Each specimen consists of six embedded CCF layers arranged in one of the following configurations: $[0]_6$, $[90]_6$, $[0/90/0]_6$, and $[60/120/0]_6$. The CCF layers are separated by two-layer SCF interleaf regions with a [+45/−45] raster orientation, which serve to enhance interlaminar bonding and enable more effective load transfer between plies. Additionally, the top and bottom surfaces of the specimen consist of four SCF layers, $[+45/-45]_2$, providing structural symmetry and improved surface quality. This architecture yields a multilayered composite with a hierarchical structure that promotes damage dispersion and load redistribution, as further analyzed. The stacking configurations and print orientations of the tested specimens are summarized in Table 1. Fig. 1 illustrates the composite architecture and internal structure. A schematic of the laminate illustrates the stacked configuration of CCF and SCF layers, while microscopic imaging of a representative sample reveals the layered morphology and typical porosity features throughout the laminate. The magnified image of the SCF interleaf reveals void clustering along raster boundaries—features that may impact interfacial strength.

Drying was performed in a closed oven at 70 °C (below the glass transition temperature of nylon), with samples covered in release film to prevent sticking. Moisture removal from the nylon matrix improves stress distribution and increases mechanical strength by mitigating plasticization effects.

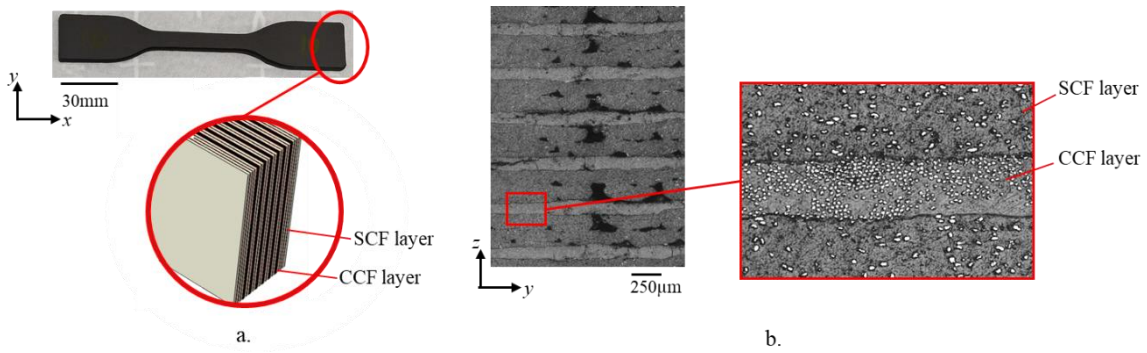

Fig. 1 (a) Geometry and layered architecture of the 3D-printed composite specimen. (b) Cross-sectional microstructure

Table 1. Layered Architecture of Hybrid CCF and SCF Laminates

Sample ID	CCF Orientation	SCF Orientation	SCF Layering Structure
S1	$[0]_6$	[+45/–45]	2 SCF layers between CCFs; outer SCF layers: $[+45/–45]_2$
S2	$[90]_6$	[+45/–45]	Same as above
S3	$[0/90/0]_s$	[+45/–45]	Same as above
S4	$[60/120/0]_s$	[+45/–45]	Same as above

3 EXPERIMENTAL CHARACTERIZATION METHODS

3.1 Mechanical Testing

Tensile testing of dog-bone samples was conducted using an MTS Systems. The samples were tested

with a crosshead rate at 1 mm/min until failure occurred. The MTS machine used for tensile testing is equipped with TestWorks4 software. Tensile tests were conducted on each sample with different layer print orientations. After the failure, the stress-strain curves are obtained from each test run.

3.2 SEM Analysis

Microscopic analysis, using scanning electron microscopy (SEM), was employed to investigate the fracture surface morphology of the post-mortem tensile samples. Representative sections of each sample type were used for microstructural analysis. Before imaging, the samples were sputter-coated with a thin layer of Au to enhance surface conductivity and image quality under the SEM. High-resolution SEM images were acquired to examine fracture surfaces and identify failure mechanisms.

4 MODELING PROCEDURE

A finite element analysis (FEA) was used to simulate the tensile behavior of 3D-printed samples. FEA simulation was performed using the Abaqus Implicit commercial software. The model accounted for the material with the printed stacking of SCF and CCF reinforcement. Finite element domains were assigned coordinate systems for every printed layer with a specified material orientation to represent the orientation during printing. CDM was used to model the homogenized material behavior of SCF and CCF layers, assuming transverse isotropy. Cohesive interfaces were implemented to model interactions between the layers by defining the bonding behavior.

4.1 Virtual Sample Modeling Generation

A custom Python-based script was developed and integrated with Abaqus to automate the generation of FEA models for 3D-printed composites. A virtual specimen of 3D printed material is modeled as a continuum in (x, y, z) space (Fig. 2). The stacking structure is generated with specified stacking sequences, ply orientations, thicknesses, material properties, mesh configurations, and cohesive interfaces. The geometry of the laminated composite was defined based on user inputs for the number of stackings, ply orientations, and thicknesses. Each layer was meshed with assigned element orientations using a discrete field. The meshing resolution was controlled using input parameters for element size, allowing accurate modeling of the laminated structure. Sub-domains were assigned local coordinate systems $(1,2)$ to represent individual stacking orientation (Fig 2b). Cohesive interfaces were implemented between each layer to simulate interlaminar bonding. Traction-separation laws were assigned to model the interaction and failure behavior at the interfaces. Cohesive tie constraints were defined to link the cohesive layers with adjacent plies, enabling the simulation of delamination and interfacial failure under tensile loading. Boundary conditions were applied to replicate tensile testing, including displacement and fixed constraints. CDM was implemented to capture progressive damage and failure behavior in the plies.

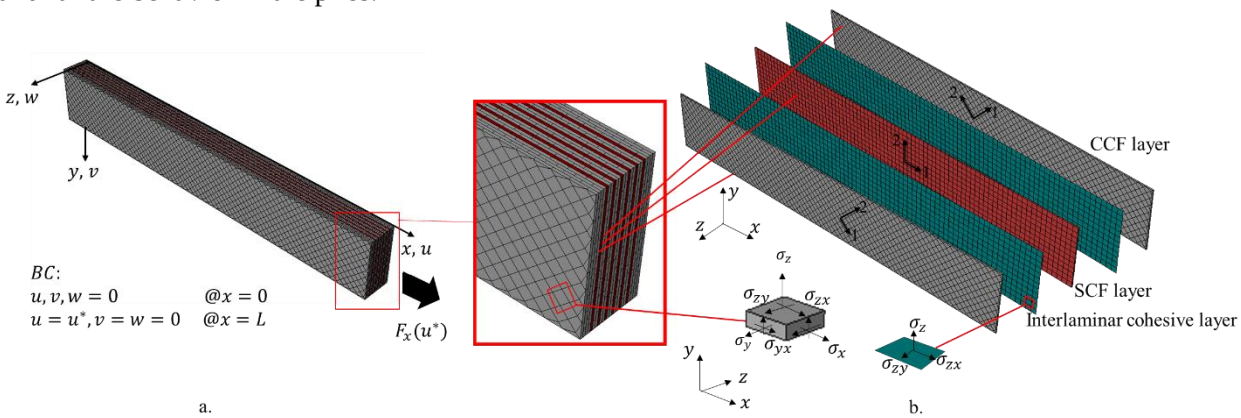

Figure 2 a. Generated morphology of virtual 3D printed sample b. The orientation of the stacking

4.2 Constitutive Properties and Damage Modeling for Bundles

A continuum damage model was employed to describe the failure modes in the longitudinal and transverse planes of the 3D-printed materials. A user material (UMAT) FORTRAN subroutine for Abaqus standard implicit was used to simulate the damage initiation and propagation in the printing direction and transverse plane. The longitudinal damage, d_1, considers stiffness degradation in the direction of the freeze-casting, while the transverse damage index, d_2, reflects the degradation of the material stiffness in the transverse direction to the printing direction. The material constitutive relationship followed the transversely isotropic behavior, as shown in Eq. 1.

$$\begin{bmatrix}\sigma_{11}\\ \sigma_{22}\\ \sigma_{33}\\ \sigma_{12}\\ \sigma_{13}\\ \sigma_{23}\end{bmatrix}=\begin{bmatrix}C_{11} & C_{12} & C_{13} & 0 & 0 & 0\\ C_{12} & C_{22} & C_{23} & 0 & 0 & 0\\ C_{13} & C_{23} & C_{33} & 0 & 0 & 0\\ 0 & 0 & 0 & C_{44} & 0 & 0\\ 0 & 0 & 0 & 0 & C_{55} & 0\\ 0 & 0 & 0 & 0 & 0 & C_{66}\end{bmatrix}\times\begin{bmatrix}\varepsilon_{11}\\ \varepsilon_{22}\\ \varepsilon_{33}\\ \gamma_{12}\\ \gamma_{13}\\ \gamma_{23}\end{bmatrix} \quad (1)$$

where C_{ij} is the damaged stiffness matrix depending on the undamaged stiffness components (C_{ij}^0) and damage variables in principal directions (d_{i}). The damage stiffness components were defined by Eq. 2.

$$\begin{aligned} &C_{11}=(1-d_1)C_{11}^0;\ C_{12}=(1-d_1)(1-d_2)C_{12}^0\ ; \quad (2)\\ &C_{13}=(1-d_1)(1-d_2)C_{13}^0\ ;\ C_{22}=(1-d_2)C_{22}^0;\\ &C_{23}=(1-d_2)C_{23}^0\ ;\ C_{33}=(1-d_2)C_{33}^0\ ;\ C_{44}=(1-d_1)(1-d_2)C_{44}^0\ ;\\ &C_{55}=(1-d_1)(1-d_2)C_{55}^0\ ;\ C_{66}=(1-d_2)C_{66}^0 \end{aligned}$$

Eq. 3 shows the damage initiation criteria, f_1, in the printing direction when the corresponding criterion reaches one. Hill's anisotropic failure criterion, f_2, was used to define the damage initiation in the transverse plane (Eq. 4).

$$f_1=\sqrt{\frac{\sigma_{11}^2}{\sigma_{11}^{f,t}\sigma_{11}^{f,c}}+\sigma_{11}\times\left(\frac{1}{\sigma_{11}^{f,t}}-\frac{1}{\sigma_{11}^{f,c}}\right)} \quad (3)$$

$$f_2=\sqrt{\left(\frac{1}{\sigma_{22}^{f,c^2}}-\frac{1}{2\sigma_{11}^{f,c^2}}\right)(\sigma_{22}-\sigma_{33})^2+\frac{1}{\sigma_{23}^{f\ 2}}\sigma_{23}^2} \quad (4)$$

where $\sigma_{\mathrm{ii}}^{f,t}$ and $\sigma_{\mathrm{ii}}^{f,c}$ are the failure stresses in the principal directions in tension and compression, respectively. The damage variables (d_1 and d_2), evolves from 0 to 1, where 0 represents the undamaged material, and one corresponds to the fully damaged state (E. 5).

$$d_i=1-\frac{\sigma_{\mathrm{ii}}^f}{C_{\mathrm{ii}}f_{\mathrm{i}}}\exp\left(\frac{\sigma_{\mathrm{ii}}^f\left(\sigma_{\mathrm{ii}}^f/C_{\mathrm{ii}}-f_{\mathrm{i}}\right)l^*}{G_c}\right),i=1,2 \quad (5)$$

where, l^* is the characteristic element length associated with the material and G_c is the fracture energy in the lamellar direction. Material constitutive properties for CCF and SCF stacking are represented in Tables 2-3 and are derived using micromechanical models as described in Appendix A.1 and A.2. The assigned transverse tensile strength for the CCF layers reflects the influence of the ductile SCF matrix in which the continuous carbon fibers are embedded. While this value is higher than typical for thermoset-based unidirectional laminates, it is consistent with prior observations in layered

discontinuous fiber composite (LDFC) systems, where matrix ductility and constrained damage propagation contribute to enhanced transverse performance [12], [13].

Table 2. Stiffness and strength properties for 3D printed CCF layers

Material property	Value
Longitudinal modulus, $\boldsymbol{E_{11}(MPa)}$	60,000
Transverse modulus, $\boldsymbol{E_{22}}$, $\boldsymbol{E_{33}(MPa)}$	5,000
Shear modulus, $\boldsymbol{G_{12}}$, $\boldsymbol{G_{13}(MPa)}$	3,000
Shear modulus, $\boldsymbol{G_{23}(MPa)}$	1,000
Poisson's ratios,$\boldsymbol{\nu_{12}}$, $\boldsymbol{\nu_{13}}$	0.29
Longitudinal tensile strength,$\boldsymbol{F_{1t}(MPa)}$	100
Transverse tensile strength,$\boldsymbol{F_{2t}(MPa)}$	200
Fracture energy $\boldsymbol{G_c[kJ/m^2]}$	8

Table 3. Stiffness and strength properties for 3D printed SCF layers

Material property	Value
Longitudinal modulus, $\boldsymbol{E_{11}(MPa)}$	5,000
Transverse modulus, $\boldsymbol{E_{22}}$, $\boldsymbol{E_{33}(MPa)}$	1,800
Shear modulus, $\boldsymbol{G_{12}}$, $\boldsymbol{G_{13}(MPa)}$	2,000
Shear modulus, $\boldsymbol{G_{23}(MPa)}$	690
Poisson's ratios,$\boldsymbol{\nu_{12}}$, $\boldsymbol{\nu_{13}}$	0.38
Longitudinal tensile strength,$\boldsymbol{F_{1t}(MPa)}$	100
Transverse tensile strength,$\boldsymbol{F_{2t}(MPa)}$	50
Fracture energy $\boldsymbol{G_c[kJ/m^2]}$	4

The CDM with transversely isotropic damage for 3D printed stacking combined with a cohesive zone modeling (CZM) at the interfaces between printed stacking to capture debonding using a traction separation law. Eq. 6 shows the constitutive equation of traction separation, where interlaminar σ_{ij} stress, δ_j is the relative separation between the elements, d is the damage variable, and $k_i^0 = 730 \times 10^6\, {MPa}/{mm}$ is the initial stiffness.

$$\begin{bmatrix}\sigma_{13}\\ \sigma_{23}\\ \sigma_{33}\end{bmatrix}=\begin{bmatrix}(1-d)k_1^0 & 0 & 0\\ 0 & (1-d)k_2^0 & 0\\ 0 & 0 & (1-d)k_3^0\end{bmatrix}\begin{bmatrix}\delta_1\\ \delta_2\\ \delta_3\end{bmatrix} \quad (6)$$

The failure initiation criterion of the delamination between the printed layers is given by Eq. 7 where $N_{max} = 40\ MPa$ and $S_{max} = T_{max} = 60\ MPa$ represent the normal and shear cohesive strengths, respectively.

$$(\frac{\sigma_{33}}{N_{max}})^2 + (\frac{\sigma_{13}}{S_{max}})^2 + (\frac{\sigma_{23}}{T_{max}})^2 = 1 \quad (7)$$

The propagation of the delamination is defined by a linear fracture mechanism of power law through Eq. 8 [14].

$$\frac{G_I}{G_{IC}} + \frac{G_{II}}{G_{IIC}} + \frac{G_{III}}{G_{IIIC}} = 1 \quad (8)$$

where G_I, G_{II}, G_{III} are the work done by the tractions and their corresponding displacements in the normal and shear directions, and $G_{IC}, G_{IIC}, G_{IIIC}$ are the critical strain energy release rates corresponding to the fracture modes, where $G_{IC} = 1\ ^{kJ}/_{m^2}, G_{IIC} = G_{IIIC} = 2\ ^{kJ}/_{m^2}$.

5 NUMERICAL AND EXPERIMENTAL RESULTS

5.1 Comparison of Experimental and Numerical Modeling Predictions

Figure 3 shows the stress–strain behavior of 3D-printed composite laminates consisting of CCF/LCF layers. Four different CCF stacking sequences, [0], [0/90/0], [60/120/0], and [90], are examined under uniaxial tensile loading, with both experimental results and simulation data presented for comparison. Figure 4 compares the average UTS of hybrid 3D-printed laminates. Experimental results are shown with error bars representing standard deviation, while red markers indicate predictions from simulations. The [0] CCF laminate exhibits the highest stiffness and strength, as the fiber alignment is parallel to the loading direction, and the ±45° SCF layers provide additional shear resistance without significantly compromising axial load transfer. The [90] CCF laminate, with fibers oriented transverse to the loading direction, exhibits the lowest tensile strength and stiffness, as the load is primarily borne by the ±45° SCF layers, which have lower axial modulus compared to the CCF interlayers. The $[0/90/0]_s$ and $[60/120/0]_s$ laminates demonstrate intermediate strengths, governed by the presence of off-axis CCF layers that reduce axial stiffness, while the alternating ±45° SCF layers enhance damage tolerance and redistribute local stress. The simulation results, based on continuum damage mechanics, align well with the experimental data, capturing the variation in stiffness, peak strength, and strain at failure across stacking sequences. These findings confirm the role of CCF layup design and the synergy between reinforcement and matrix orientations in determining the strength of additively manufactured composite laminates.

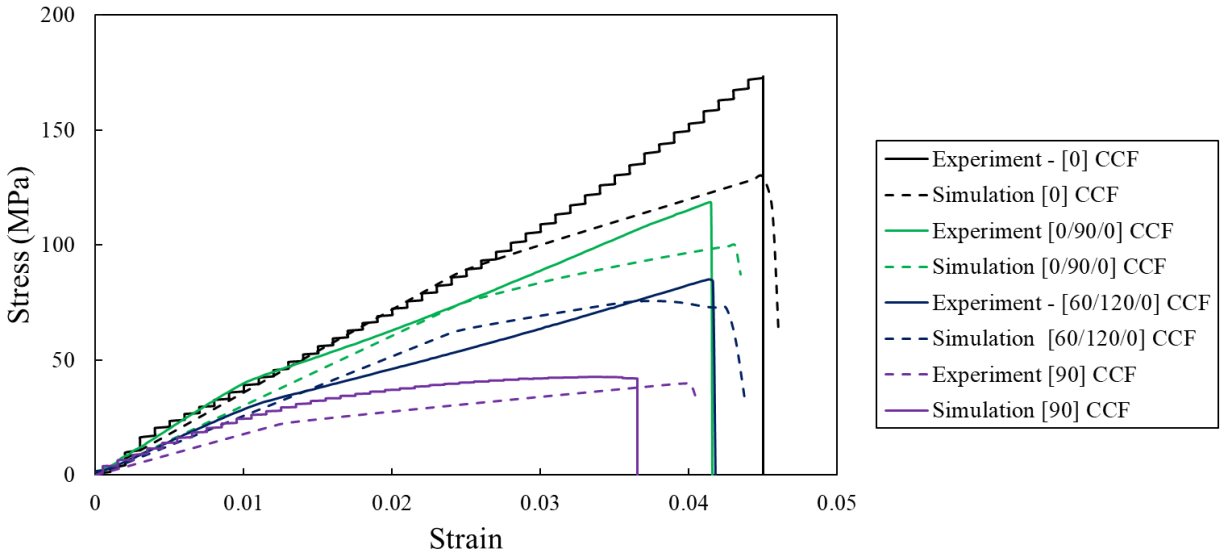

Figure 3. Stress–strain curves from experimental tests and finite element simulations for hybrid 3D-printed polymer composite laminates with different CCF stacking

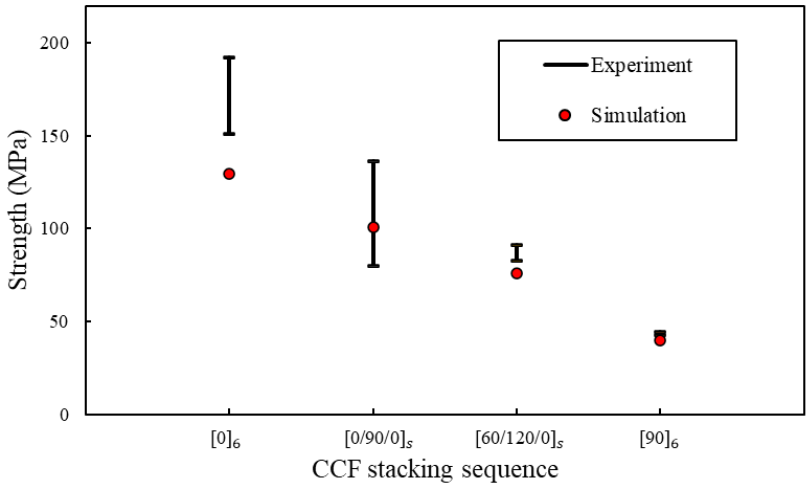

Figure 4. Comparison of experimental and simulation results for the ultimate tensile strength of hybrid 3D-printed polymer composite laminates with different CCF stacking.

5.2 Damage Propagation

Failure in the hybrid 3D-printed polymer composite laminate arises from the complex interplay of multiple damage mechanisms, including fiber/matrix debonding, matrix cracking, interstacking delamination, and fiber pull-out. The damage is spatially distributed throughout the composite volume, reflecting the heterogeneous nature of the printed architecture and interfaces. Initiation and propagation occur concurrently at multiple sites, driven by the tailored stacking sequence and directional deposition of both continuous and short fibers. This architecture introduces intrinsic structural redundancy, allowing for local load redistribution after damage initiates. As a result, the laminate exhibits multi-site failure behavior.

The fracture surfaces observed in the SEM images (Fig 5) reveal mix-mode failure mechanisms within the 3D-printed composite laminate composed of CCF and SCF matrix stacking. Figures a. and b. shows the fracture surface of $[0]_6$ CCF stacking sample (200×) and highlights failure in the continuous fiber region, where long, aligned fibers exhibit pull-out and interfacial debonding. This suggests that failure was dominated by fiber–matrix interface separation. Fig. 5b (350×) shows the fracture surface of the SCF stacking region, characterized by a rough short fiber pull-out and matrix cracking.

Figures c. and d. shows the fracture surface of $[90]_6$ CCF stacking sample. Long-aligned fibers protrude from the matrix, indicating a dominant fiber pull-out mechanism. The gaps between the matrix and fibers suggest interfacial debonding between the CF and the surrounding polymer. Figure d shows the visible gaps between the stacking point and interlaminar delamination and interstacking shearing. Figures e. and f. show the fracture surface of $[60/120/0]_s$ CCF stacking sample. Figure F's upper stacking displays SCF stacking with rough, polymer-rich morphology, randomly oriented broken fibers, and matrix cracking. The central region includes a distinct, aligned bundle of CF, indicating fiber pullout and matrix fiber debonding.

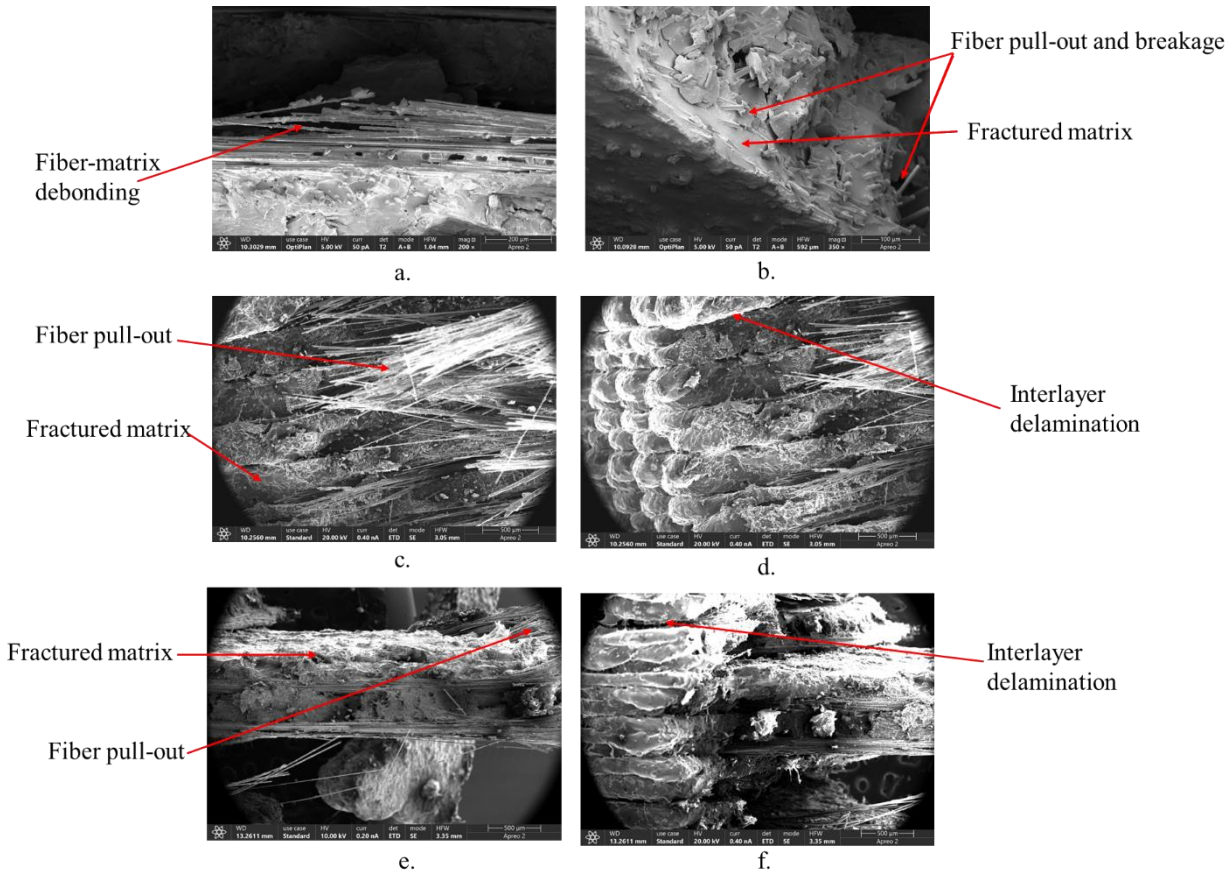

Figure 5. SEM images of fracture surfaces in hybrid 3D-printed polymer composite laminates with continuous carbon fiber (CCF) interstacking: (a) and (b) correspond to the $[0]_6$ stacking, (c) and (d) to the $[90]_6$ stacking, and (e) and (f) to the $[60/120/0]_s$ stacking configuration.

Figure 6 illustrates the cumulative relative frequency distributions of the damage variables in the simulations. The figure highlights distinct damage indices in the fiber direction (d_1) and the transverse direction (d_2), revealing the directionality and progression of failure at peak stress. The 0° CCF stacking exhibits concentrated and localized damage in the fiber direction (d_1), which can be attributed to the fiber breakage under axial tensile loading. This confirms that the stacking is the primary load-bearing component, effectively resisting tensile stress until failure initiation. Transverse damage (d_2) in these stackings remains limited and confined, suggesting strong out-of-plane stability and minimal matrix cracking attributed to the alignment and stiffness of the continuous fibers. In contrast, this configuration's SCF stacking displays more widespread and diffused damage patterns. The d_1 field in the SCF stacking shows scattered failure. The d_2 damage in these regions is more prominent and spatially extended, indicating matrix-dominated transverse cracking and reduced out-of-plane resistance.

In the $[90]_6$ CCF sample, the layers are oriented perpendicular to the loading direction, resulting in negligible or delayed fiber-aligned damage. Consequently, they do not significantly contribute to axial load bearing. Instead, transverse damage becomes dominant, manifesting as matrix cracking. The simulation results also show the dominant d_2 damage for CCF and SCF stacking.

The $[0/90/0]_s$ interstacking CCF laminate**,** the 90° CCF, and the SCF stacking dominate the transverse damage (d_2) field. This pattern reflects the matrix-dominated failure behavior of the 90° plies, which contribute minimally to axial strength. The SCF stacking further exhibits extensive transverse matrix cracking due to shear-induced stresses. In the $[60/120/0]_s$ CCF laminate, the d_2 field shows localized transverse damage in the 60° and 120° CCF stacking. The SCF stacking exhibits widespread

transverse damage, as seen in extended matrix cracking and interfacial failure under combined transverse and shear loading.

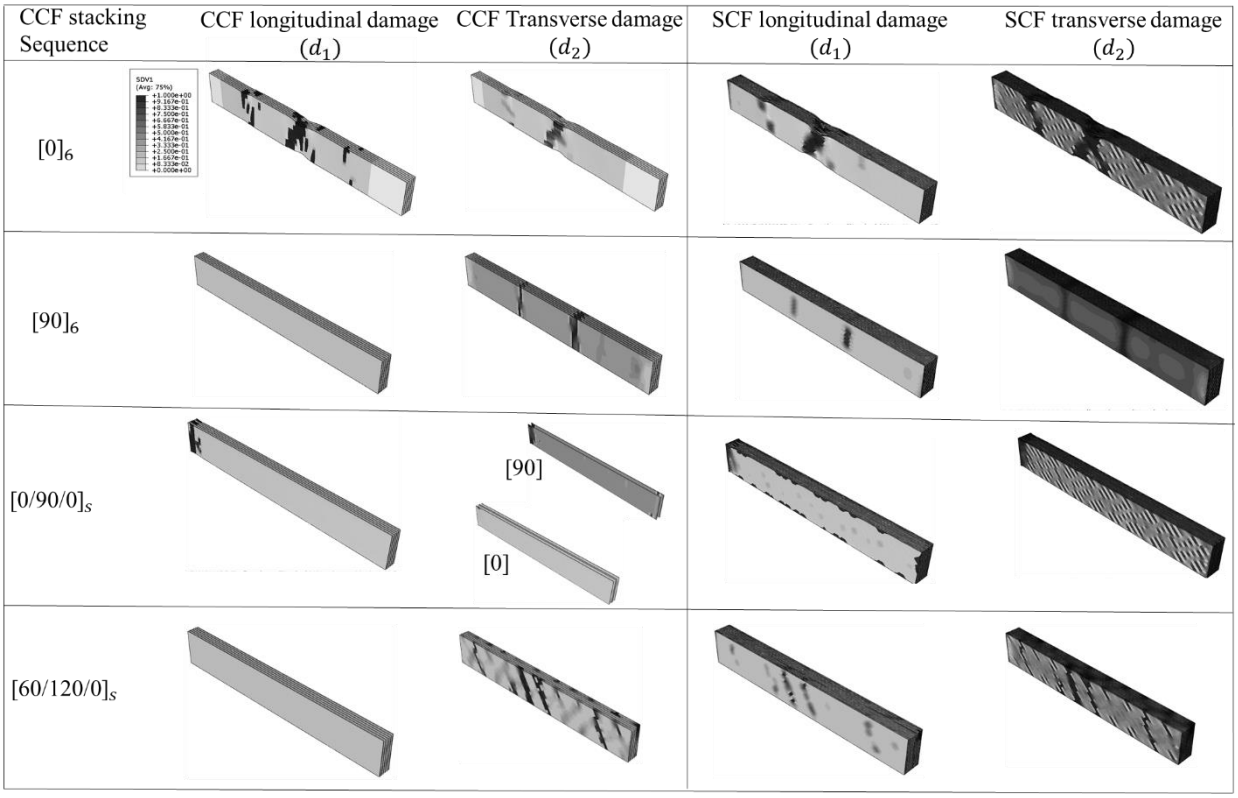

Figure 6. This is an example of a figure.FE simulation results showing fiber-direction (d_1) and transverse (d_2) damage distributions in 3D-printed laminates with various CCF stacking configurations

6 CONCLUSIONS

This study developed and validated a progressive failure modeling framework for 3D-printed hybrid composite laminates composed of CCF and SCF-nylon to predict mechanical behavior and failure evolution. Various stacking sequences were fabricated to investigate the influence of fiber orientation and hybrid architecture on mechanical performance. The finite element model, based on CDM, captured intralaminar damage mechanisms, such as fiber fracture and matrix cracking, as well as interlaminar delamination through cohesive interface modeling. The model showed close agreement with experimental tensile results, not only in terms of ultimate tensile strength and stiffness but also in spatial damage distribution, except for the [0]° CCF configuration, where the prediction underestimates the strength due to limitations in calibrating the longitudinal tensile strength and fiber-dominated failure parameters. Results revealed that stacking configurations with off-axis CCF layers and SCF interleaves led to higher accumulation of transverse and shear-driven damage, while unidirectional fiber alignments promoted fiber-dominated failure. While further calibration of principal material properties is warranted, this modeling framework enables the predictive analysis of printed composites with variable fiber orientations and material interactions, supporting virtual design optimization in advanced engineering applications.

APPENDIX A

A.1 Constitutive Properties of CCF

The printed CCF stackings are modeled as a unidirectional composite of continuous carbon fibers embedded in the SCF matrix. The fibers are assumed to be perfectly aligned in the 1-direction (longitudinal), and the composite is treated as anisotropic.

The fiber volume fraction is V_f= 0.4. The constituent properties used in the calculations are:
- Carbon fiber: $E_f =$ 190 GPa, $G_f = 20$ GPa, $\nu_f = 0.2$
- SCF matrix: $E_m =$ 1.8 GPa, $G_m = 0.7$ GPa, $\nu_m = 0.42$
Longitudinal modulus (: E_{11}) is calculated using the Rule of Mixtures:

$$E_{11} = V_f \times E_f + (1 - V_f) \times E_m \quad \text{(A-1)}$$

To account for imperfections and practical limitations, a conservative value of E_{11} = 60,000 MPa is assigned.

Transverse modulus (E_{22} = E_{33}) is estimated using the Inverse Rule of Mixtures:

$$1/E_{22} = V_f/E_f + (1 - V_f)/E_m \quad \text{(A-2)}$$

Shear moduli (G_{12} = G_{13}):

$$1/G_{12} = V_f/G_f + (1 - V_f)/G_m \quad \text{(A-3)}$$

Transverse shear modulus (G_{23}) is matrix-dominated: $G_{23} \approx G_m$= 1,000 MPa
Poisson's Ratios:

$$\nu_{12} = V_f \times \nu_f + (1 - V_f) \times \nu_m \quad \text{(A-4)}$$

$\nu_{13} = \nu_{12}$ (assumed symmetry)
Longitudinal tensile strength (F_{1t}):

$$F_{1t} = V_f \times \sigma_f + (1 - V_f) \times \sigma_m \quad \text{(A-5)}$$

($\sigma_f = 2000MPa, \sigma_m = 80MPa$)

A.1 Constitutive Properties of SCF Layers

Fibers in these layers are assumed to be partially aligned due to the extrusion process, and the resulting material is treated as anisotropic.

The effective elastic modulus is calculated using the Halpin–Tsai equation:

$$E_c = E_m \times [(1 + \xi \times \eta \times V_f)/(1 - \eta \times V_f)] \quad \text{(A-6)}$$

where

$$\eta = (\frac{E_f}{E_m} - 1)/(\frac{E_f}{E_m} + \xi) \quad \text{(A-7)}$$

(ξ = 2)

Tensile strength is estimated using a modified Rule of Mixtures:

$$\sigma_c = \eta_0 \times \beta \times V_f \times \sigma_f + (1 - V_f) \times \sigma_m \quad \text{(A-8)}$$

η_0 = 0.4 (orientation efficiency), β = 0.6 (length efficiency)

REFERENCES

[1] Y. Liu *et al.*, "Characterization of progressive damage behaviour and failure mechanism of carbon fiber reinforced composite laminates," *Sci. Rep.*, vol. 15, no. 1, p. 13791, Apr. 2025, doi: 10.1038/s41598-025-98774-7.

[2] G. Marabello, C. Borsellino, and G. Di Bella, "Carbon Fiber 3D Printing: Technologies and Performance—A Brief Review," *Materials*, vol. 16, no. 23, p. 7311, Nov. 2023, doi: 10.3390/ma16237311.

[3] J. Barber, P. Revolinsky, J. Bhagatji, D. Pedrazzoli, S. Kravchenko, and O. Kravchenko, "Polymorphism and Mechanical Behavior in Hot-Pressed 3D-Printed Polyamide Composite: Effects of Pressure and Temperature," *Polymers*, vol. 17, no. 7, p. 922, Mar. 2025, doi: 10.3390/polym17070922.

[4] J. Barber, P. Revolinsky, E. Spinelli, V. C. Jamora, H. Eisazadeh, and O. G. Kravchenko, "Investigation of high temperature compaction on fracture toughness of 3D printed carbon fiber polyamide composites," *Prog. Addit. Manuf.*, vol. 9, no. 4, pp. 1119–1134, Aug. 2024, doi: 10.1007/s40964-023-00507-7.

[5] Y. Chen and L. Ye, "Path-Dependent Progressive Failure Analysis for 3D-Printed Continuous Carbon Fibre Reinforced Composites," *Chin. J. Mech. Eng.*, vol. 37, no. 1, p. 72, Jul. 2024, doi: 10.1186/s10033-024-01054-0.

[6] H. Zheng *et al.*, "3D Printing Continuous Fiber Reinforced Polymers: A Review of Material Selection, Process, and Mechanics-Function Integration for Targeted Applications," *Polymers*, vol. 17, no. 12, Art. no. 12, Jan. 2025, doi: 10.3390/polym17121601.

[7] E. Polyzos, D. Van Hemelrijck, and L. Pyl, "Numerical modelling of the elastic properties of 3D-printed specimens of thermoplastic matrix reinforced with continuous fibres," *Compos. Part B Eng.*, vol. 211, p. 108671, Apr. 2021, doi: 10.1016/j.compositesb.2021.108671.

[8] S. Bhandari, R. A. Lopez-Anido, L. Wang, and D. J. Gardner, "Elasto-Plastic Finite Element Modeling of Short Carbon Fiber Reinforced 3D Printed Acrylonitrile Butadiene Styrene Composites," *JOM*, vol. 72, no. 1, pp. 475–484, Jan. 2020, doi: 10.1007/s11837-019-03895-w.

[9] M. Rahman, J. C. Liggett, K. Grella, B. Gagnon, and A. Membreno, "Validation of a finite element method for simulation of components produced by continuous carbon fiber reinforced additive manufacturing," *Int. J. Comput. Methods Eng. Sci. Mech.*, vol. 23, no. 2, pp. 182–192, 2022, doi: 10.1080/15502287.2021.1946620.

[10] S. Sattar, B. B. Laredo, S. G. Kravchenko, and O. G. Kravchenko, "Effect of platelet length and stochastic morphology on flexural behavior of prepreg platelet molded composites," *Polym. Compos.*, vol. 44, no. 4, pp. 2122–2137, 2023, doi: 10.1002/pc.27230.

[11] P. Shabani, L. Li, J. Laliberte, G. Qi, D. Rapking, and D. Mollenhauer, "High-fidelity simulation of low-velocity impact damage in fiber-reinforced composite laminates using integrated discrete and continuum damage models," *Compos. Struct.*, vol. 313, p. 116910, Jun. 2023, doi: 10.1016/j.compstruct.2023.116910.

[12] S. Sattar, B. Beltran Laredo, D. Pedrazzoli, M. Zhang, S. G. Kravchenko, and O. G. Kravchenko, "Mechanical behavior of long discontinuous glass fiber nylon composite produced by in-situ polymerization," *Compos. Part Appl. Sci. Manuf.*, vol. 154, p. 106779, Mar. 2022, doi: 10.1016/j.compositesa.2021.106779.

[13] S. Sattar *et al.*, "Influence of Flow-Induced Polymorphism and Fiber Morphology on Mechanical Behavior in Long Discontinuous Glass Fiber Polyamide Composites," *Compos. Part Appl. Sci. Manuf.*, vol. 185, p. 108353, Oct. 2024, doi: 10.1016/j.compositesa.2024.108353.

[14] J. D. Whitcomb, *Analysis of Instability-related Growth of a Through-width Delamination*. National Aeronautics and Space Administration, Langley Research Center, 1984.

ICCM24 24TH INTERNATIONAL CONFERENCE ON COMPOSITE MATERIALS
AUG 4-8, 2025 • BALTIMORE CONVENTION CENTER • BALTIMORE, MARYLAND

INFLUENCE OF SPECIMEN GEOMETRY AND UD PLY LAYUP ON THERMOPLASTIC WELDED DOUBLE-NOTCHED TENSION TEST SPECIMEN BY USE OF MECHANICAL AND VIRTUAL TESTING

S. Hamedinger[1], R. Hinterhölzl[1], M. Tiefenthaler[2], G. Wallner[2] and S. Becker[3]

[1]Lightweight Design and Composite Materials, University of Applied Sciences Upper Austria
Stelzhamerstraße 23, 4600 Wels, Austria
Email: sebastian.hamedinger@fh-wels.at, roland.hinterhoelzl@fh-wels.at,
web page: https://fh-ooe.at/en

[2]Institute of Polymeric Materials and Testing, Johannes Kepler University Linz,
Altenberger Straße 69, 4040 Linz, Austria
Email: martin.tiefenthaler@jku.at, gernot.wallner@jku.at,
Web Page: https://www.jku.at/en/institute-of-polymeric-materials-and-testing/

[3]FACC Operations GmbH,
Fischerstrasse 9, 4910 Ried im Innkreis, Austria
Email: s.becker@facc.com, Web Page: https://www.facc.com/

Keywords: Thermoplastic resin, Mechanical testing, Finite element analysis (FEA), Laminates

ABSTRACT

Thermoplastic composites can play a key role in developing future forms of transportation due to their high mechanical performance as well as their wide range of automatable joining and manufacturing methods. Thermoplastic welding techniques like induction and resistance welding provide flexible joining methods for many applications such as skin-stringer joints in an aircraft fuselage. With various welding processes existing, finding a suitable testing method to compare these processes would be beneficial. This paper shows the sensitivity of an ASTM D3165 based testing method (designated as double-notched tension test in this paper) especially to notch depth, as well as the three different laminate layups. It highlights the challenges to sample preparation and result interpretation, as well as the suitability of the testing method for the comparison of different welding techniques. Virtual testing is performed with a continuum damage finite element model, which is capable of mapping inter and intra-laminar failure, as well as failure of the welding zone itself to gain insight into the mechanical behavior of the tested sample.

1 INTRODUCTION

Upcoming urban and advanced air mobility (UAM & AAM), as well as new generation single aisle aircraft raise the need to evolve established materials and processes to enable manufacturers to satisfy the rising demand for all types of aircraft. Global commercial aircraft OEM forecast that traffic will more than double in the next two decades, requiring more than 40,000 aircraft deliveries, depending on high-rate capable production technologies. The Multi-Functional Fuselage Demonstrator (MFFD) developed and manufactured as part of the Clean Sky 2 Program with 14 project participants shows the application of over 40 airframe production technologies, highlighting dustless joining with thermoplastic welding methods. [1]

Manufacturing targets of electric vertical take-off and landing vehicle (eVTOL) OEM have been constantly adapted over the last years [2] and are highly depending on regulatory requirements, which are widely still work in progress like in the “Innovate28” plan of the Federal Aviation Administration (FAA). Nevertheless, when successfully regulated, that type of aircraft is capable of further improving urban transportation [3], since it offers a safer, quieter, more economic aircraft, compared to common vertical take-off and landing vehicles such as helicopters. [4]

Essential for the application of this material class is the understanding and consideration of various factors, like material behavior and testing, process-specific characteristics or numerical simulation methods. This paper addresses the applicability of a specific testing method (ASTM D3165) for thermoplastic welded joints as well as its numerical analysis with finite element (FE) simulation to find out if it's suitable for the quantitative comparison of different adherend architectures and welding procedures.

2 TEST DESCRIPTION

The test selected to compare different welding techniques is based on the ASTM D3165 - "Standard Test Method for Strength Properties of Adhesives in Shear by Tension Loading of Single-Lap-Joint Laminated Assemblies" [5] and further designated as double-notched tension test (DNT) within this paper. The schematical test setup can be seen in Figure 1. There are several sound reasons for choosing that specific testing method. Firstly, the geometrically induced secondary bending is reduced, compared to the commonly used single lap shear test, since the specimen is providing a higher bending stiffness outside the shear zone due to increased specimen thickness. Also edge effects showing up in joining and manufacturing processes, for instance during induction welding, can be reduced. Examples would include no excess matrix material which would normally squeeze out at the overlap edges of a single lap shear test (Kupski et. al [6] considered the induced skew for adhesively bonded single lap joints) or increased current densities near the edge [7,8] when joining with induction welding. Further, the steps of the test procedure show low complexity, which enables an efficient execution of test campaigns on common universal testing machines.

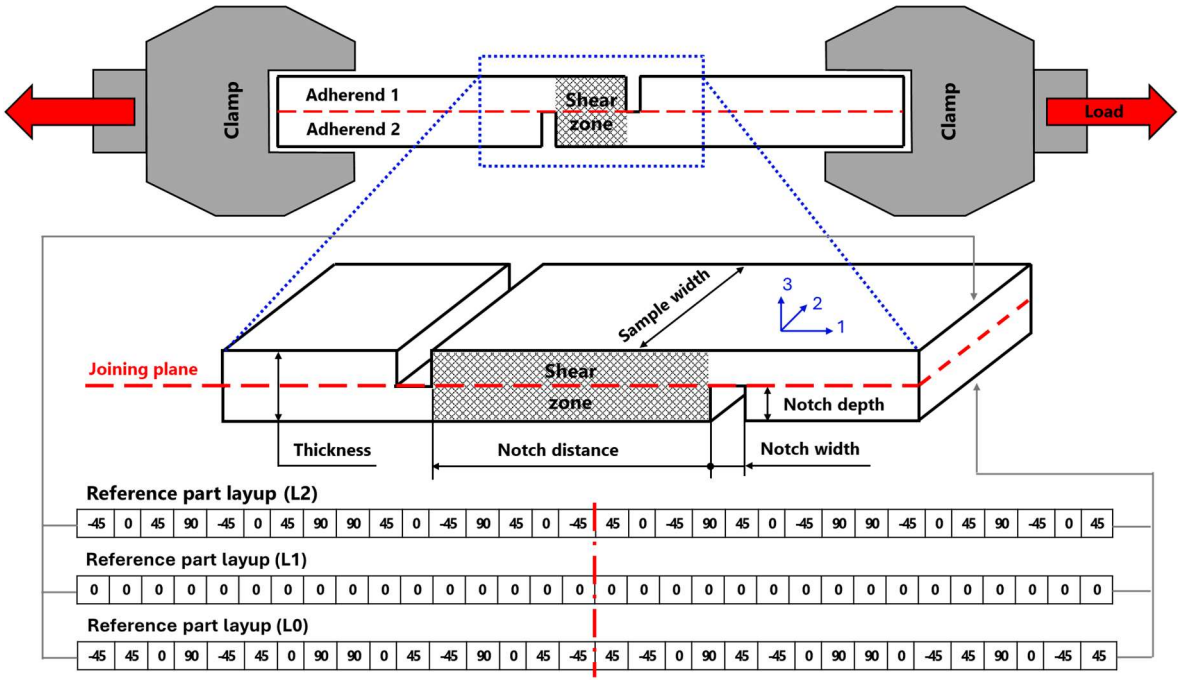

Figure 1: Schematical test setup and layup description.

The load is applied with a displacement rate of 1.27 mm/min via clamps to the specimen, where the load is transferred to the shear zone through a combination of shear and peel forces, resulting in a multiaxial stress state of the specimen. This scenario reflects critical, as well as relevant loading conditions when thinking of welded, thin-walled composite shell components.

3 SPECIMEN DESCRIPTION

The material used in this research is Toray® Cetex® TC1225, a unidirectional carbon fiber reinforced semi-crystalline low melt polyaryletherketone (PAEK) Tape from Toray Advanced Composites (TAC), the Netherlands. Considering future component manufacturing, the UD tape material is processed to laminate plates in a hot press, previous the actual joining procedure. This way, the material is experiencing the pressure and temperature it would receive in an actual manufacturing process like thermoforming. That's reasonable since the high process temperatures around 400°C can lead to degradation of the thermoplastic matrix material, which stayed well below 5% within this research.

After the hot press consolidation, the manufactured composite laminate plates are co-consolidated in an autoclave according to the processing guidelines for TC1225 LMPAEK composites from TAC, providing sample plates, from which the actual specimen are manufactured by milling. The specimens tested have a total length of 175 mm, a sample width of 25 mm and a notch distance of 12.7 mm. The notch depth as well as the thickness of the laminate varied over the specimen.

4 NUMERICAL SIMULATION

This study employs the finite element analysis software *Abaqus/Explicit* to perform dynamic structural simulations of the Double-Notched Tension (DNT) test. The numerical model is designed to replicate the experimental setup with high fidelity, enabling detailed investigation of damage initiation and progression within the composite structure. The following sections describe the modeling approach, material definitions, boundary conditions, and contact formulations used in the simulation framework.

4.1 Material Parameter

Due to the limited availability of material-specific parameters, the simulation model was based on data from the literature corresponding to a similar material system—an unidirectional carbon fiber-reinforced high-performance thermoplastic polymer. The material parameters used in the simulations are summarized in Table 1.

Material parameter		Value
E_1	[MPa]	138300
$E_{2,\,3}$	[MPa]	10400
$\nu_{12,\,13}$	–	0.316
ν_{23}	–	0.487
$G_{12,\,13}$	[MPa]	5190
G_{23}	[MPa]	3500*
X_T	[MPa]	2350
X_C	[MPa]	1621
Y_T	[MPa]	87
Y_C	[MPa]	273
$S_{12,5\%}$	[MPa]	90
S_{13}	[MPa]	90
S_{23}	[MPa]	90
G_{Ic}	[kJ/m^2]	0.7
G_{IIc}	[kJ/m^2]	1.45
η_{BK}	–	2.9
ζ_{1+}	[kJ/m^2]	125
ζ_{1-}	[kJ/m^2]	61
ζ_{2+}	[kJ/m^2]	1.12
ζ_{2-}	[kJ/m^2]	18.3

* $G_{23} = E_3 / (2 * (1 + \nu_{23}))$

Table 1: Material parameter for numerical simulation. [9, 10, 11]

4.2 Modelling Technique

An explicit finite element model was developed employing continuum shell elements to represent the composite plies. Interply and welding zone behavior were incorporated using a general cohesive contact formulation. Each individual ply was discretized with a single element through its thickness, and the built-in Hashin continuum damage model in Abaqus was utilized to simulate energy-based matrix and fiber damage, as well as ply failure.

The interply and welding zones were modeled using general contact with defined contact pairs, each assigned cohesive properties to capture energy-based cohesive damage and failure mechanisms. Load application was implemented by coupling the specimen's end surfaces to a reference point via tie constraints, where boundary conditions were imposed. A steadily increasing velocity was applied at the reference point to introduce the quasistatic displacement speed of the testing machine. Figure 2 shows a schematical representation of the FE Model.

A mesh convergence study was performed to validate the accuracy of the explicit dynamic structural simulations conducted in Abaqus/Explicit. The model was discretized using the SC8R elements. Several mesh densities were evaluated, focusing on key response parameters such as stress distribution and nodal displacements. Convergence was observed with a mesh consisting of approximately 438,000 elements and 897,000 nodes, beyond which further refinement produced negligible changes in the results. This mesh configuration was therefore adopted for all subsequent analyses to ensure computational efficiency without compromising accuracy.

To find out how valid the resulting simulation outcomes of this modelling technique are, the test shown in [11] was simulated with the modelling technique and simulation data described and shown above. The resulting failure load of the simulation is well withing the test range shown in [11].

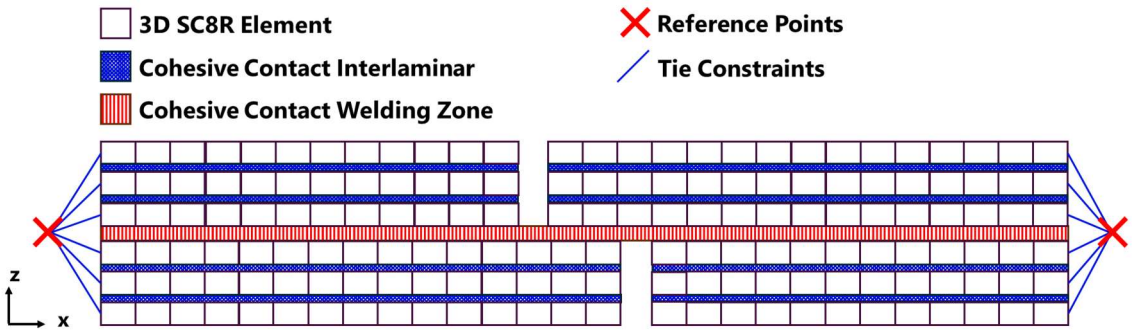

Figure 2: Schematical representation of FE model.

4.3 Virtual Testing of Notch Depth Variation

To investigate the impact of different parameters, a virtual testing is performed. Specifically, a variation of the notch depth for three different Layups is presented within this paper.

During the research it was found that the notches, which are milled in the double-notched tension specimens, are one of the most challenging topics in the manufacturing process of the test samples. For that reason, the effect of possible deviations in the depth of the notches was investigated by virtual testing. In more detail, the notch depth varied from ± 2 plies around the welding plane, which would result in a total amount of possible configurations of $2^5 = 32$ for two notches. That number was reduced to 15 when accounting for symmetries. The simulated configurations can be seen in Figure 2, where the notch-overlap u is introduced in Equation 1 as the difference between the total of the notch depths d_1 and d_2 and the laminate thickness T, where all values are discrete with increments of the ply thickness t. A positive notch-overlap indicates the number of milled-through plies, whereas a negative notch-overlap shows the number of continuous plies, which do not get machined at all.

$$u = (d_1 + d_2) - T$$
$$d_1,\ d_2,\ T \in \{n \cdot t \mid n \in \mathbb{N}^0\} \tag{1}$$

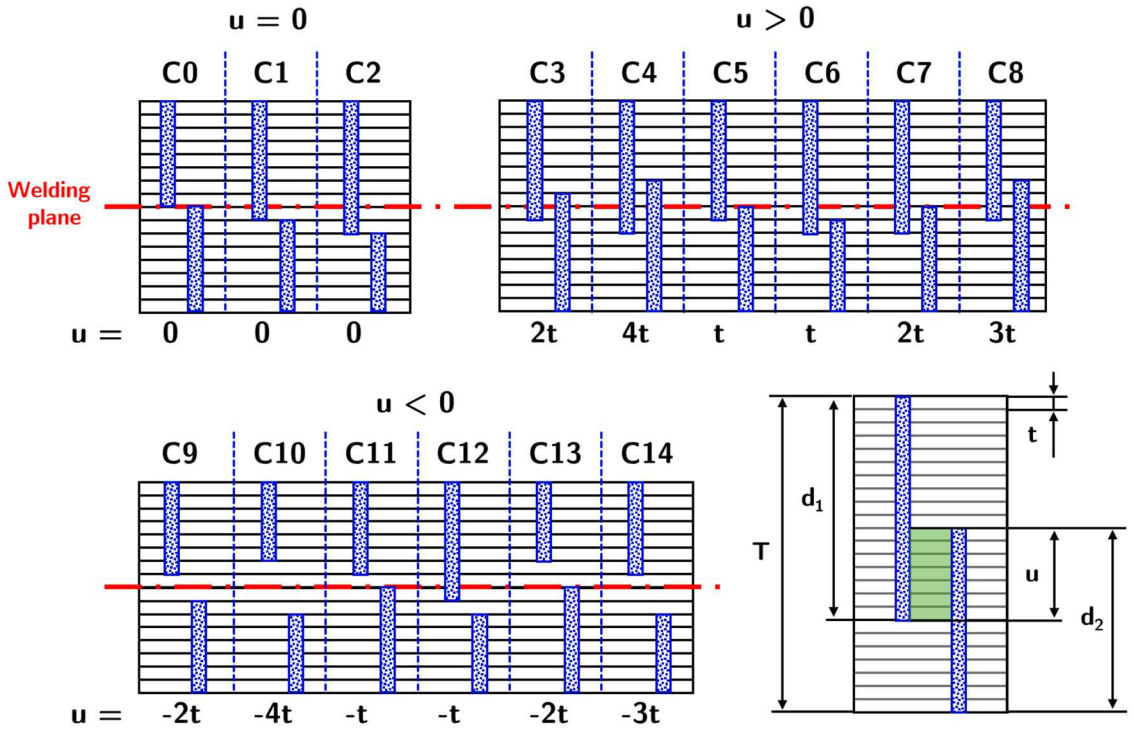

Figure 2: Virtual tested notch depth configurations.

5 RESULTS

The results of the virtual testing of the notch depth variation can be seen in Figure 3. For comparison, the resulting failure loads of the respective simulations have been normalized about configuration 0 of layup 0. The graph shows that some laminate configurations are more sensitive to the introduced notch overlap than others. For laminate 1 the notch overlap has a high impact on the resulting failure load, where laminate 0 shows to be less sensitive.

L2 has, similar like L0, a quad based symmetric layup. They differ by the quad sequence -(-45/45/0/90) for L0 and (-45/0/45/90) for L2. Compared to L0 the simulation results show higher values for L2, when the 0° ply near the welding zone is still intact. Once that ply gets separated, the laminate performs worse than L0. This behavior is most likely due to the fact that of all plies in the quasi-isotropic laminate, the 0° plies are delivering the highest proportion to the laminate's bending stiffness. Once they are damaged, the bending stiffness drops dramatically and the flexural deformation is increased, which reduces the load transmission through shear and increases bending and peel stresses.

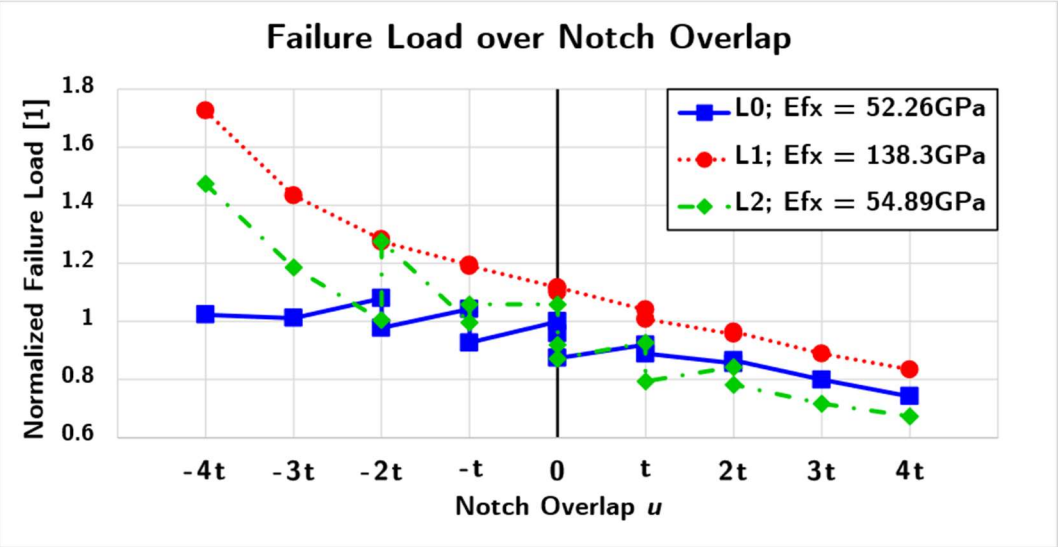

Figure 3: Virtual testing failure load results over notch overlap *u*.

The normalized results for the mechanical testing can be seen in Figure 4. The test value highlighted with a circle in Figure 4 serves as the reference for the normalization of the test data. It is related to the simulation value and multiplied by the baseline used for the normalization of the simulation data.

The results of the mechanical testing are indicating a dependence of the resulting failure load to the introduced notch depth machined in the samples. Further L1 is showing significant higher failure load values than L0 and L2.

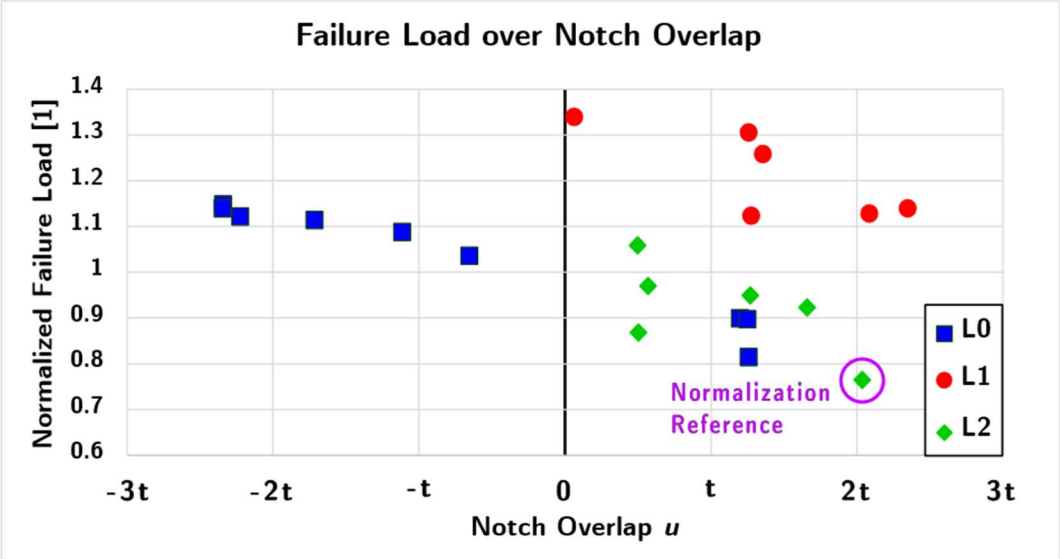

Figure 4: Mechanical testing failure load results over notch overlap *u*.

Figure 5 shows the results of the mechanical (MT) and virtual testing (VT). Simulation as well as mechanical testing results show both a tendency of decreasing failure load with increasing notch overlap.The simulation and the tested samples show good agreement for L0 and L2. For L1 the simulation shows an underestimation compared to the failure laod of the mechanical tests.

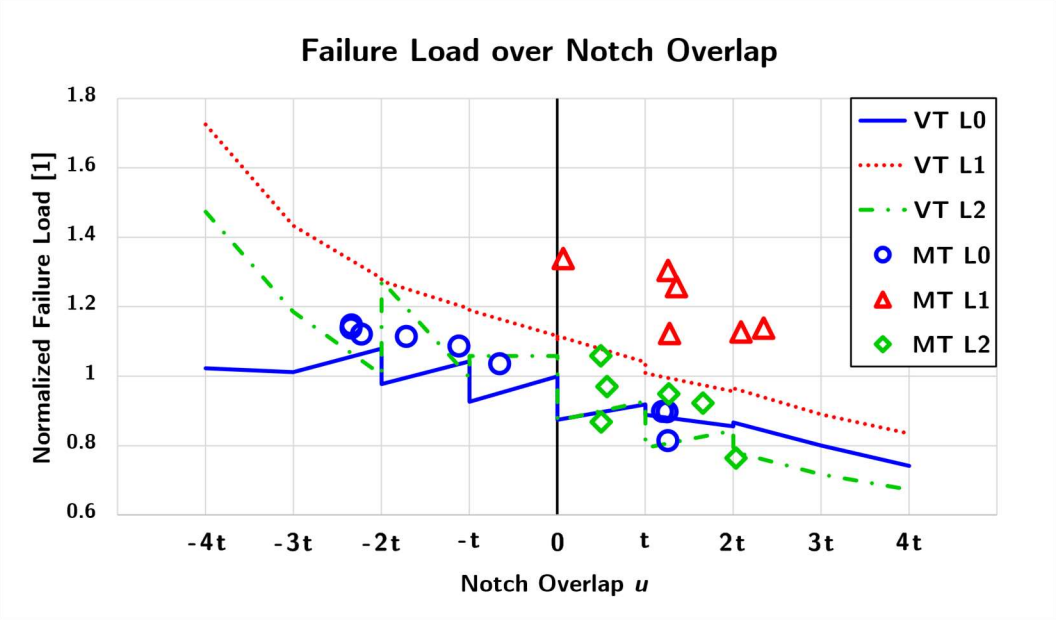

Figure 5: Comparison of virtual and mechanical testing: failure load result over notch overlap u.

6 CONCLUSIONS

The results of the mechanical and virtual testing strongly indicate a dependency of the failure load on the notch depths of the double-notched tension test specimens, which also prove to be layup dependent. This dependency is further influenced by the laminate layup, with a major effect observed when 0°-plies are cut.

For accurate and reliable results, it is crucial to precisely determine the notch depths prior to mechanical testing to ensure all plies are correctly machined.

In scenarios, where intact, continuous plies are still present (configurations with a negative notch overlap parameter u), the test primarily measures the tensile strength of the intact plies rather than the weld performance, leading to questionable conclusions regarding the weld's integrity. Therefore, test configurations with intact continuous plies are not recommended.

While the present study focuses on the influence of the notch overlap parameter u, it is important to acknowledge that the actual position of the overlap can also play a significant role in the resulting failure load, particularly depending on the laminate layup and the position of the 0°-plies. In certain configurations, the notch overlap may be less critical, still delivering usable results for comparison. Further investigations are necessary to comprehensively understand the influence of the notch overlap's position. The notch centroid is proposed as a useful parameter for identifying the actual overlap position, offering the possibility for a more detailed insight, than the current overlap parameter alone.

The double-notched tension test demonstrates potential as a comparative method for evaluating welded laminates, provided that high precision and low tolerance are guaranteed during notch manufacturing. The acceptable tolerance is, however, dependent on the laminate layup and the position of the 0°-plies within. It must be noted that this test method exhibits high sensitivity to relatively small deviations in notch depth, indicating a lack of robustness. Consequently, the applicability of the double-notched tension test requires detailed evaluation for each specific case to ensure its suitability and the reliability of the obtained results.

ACKNOWLEDGEMENTS

The Austrian Research Promotion Agency (FFG) is gratefully acknowledged for funding this research in the OOE2022 – Future Mobility Program (Project AdiosRivet; Grant No.901697).

REFERENCES

[1] Clean Aviation, *Clean Sky 2 Achievement Report 2014 - 2024*, Clean Aviation Joint Undertaking, Belgium, 2025 pp. 36-37.

[2] A. Joshi, A. Roy, V. Tiwari, *eVTOLs – The New 'Vertical' for the Composite Industry : 2025 Edition* [White paper], Composights by Stratview Research, 2025.

[3] J. Holden and N. Goel, *Fast-Forward to a Future of On-Demand Urban Air Transportation* [White paper], UBER Elevate, 2016.

[4] L.A. Garrow, B.J. German, C.E. Leonard. Urban air mobility: A comprehensive review and comparative analysis with autonomous and electric ground transportation for informing future research. *Transportation Research Part C: Emerging Technologies*, **132** : 103377, 2021, (https://doi.org/10.1016/j.trc.2021.103377).

[5] ASTM Standard D3165 – 00, Standard Test Method for Strength Properties of Adhesives in Shear by Tension Loading of Single-Lap-Joint Laminated Assemblies, *ASTM International*, 2000.

[6] J. Kupski, S. Teixeira de Freitas, D. Zarouchas, P.P. Camanho, R. Benedictus. Composite layup effect in the failure mechanism of single lap bonded joints. *Composite Structures*, **217**, 2019, pp. 14-26 (https://doi.org/10.4121/uuid:8a51631a-a18e-4737-9757-6d325d8733c0).

[7] T.J. Ahmed, D. Stavrov, H.E.N. Bersee, A. Beukers. Induction welding of thermoplastic composites–an overview. *Composites Part A: Applied Science and Manufacturing*, **37**, issue 10, 2006, pp. 1638-1651 (https://doi.org/10.1016/j.compositesa.2005.10.009).

[8] D. Barazanchy, J. Pandher, M. Van Tooren. The edge-effect in thermoplastic induction welding, *Proceedings of of AIAA scitech 2021 forum, virtual, January 11-15 & 19-21, 2021,* American Institute of Aeronautics and Astronautics, 2021, pp. 1890.

[9] S.T. Pinho, P. Robinson, L. Iannucci. Fracture toughness of the tensile and compressive fibre failure modes in laminated composites, *Composites Science and Technology*, **66**, issue 13, 2006, pp. 2069–2079 (https://doi.org/10.1016/j.compscitech.2005.12.023)

[10] G. Catalanotti, J. Xavier, P.P. Camanho. Measurement of the compressive crack resistance curve of composites using the size effect law. *Composites Part A: Applied Science and Manufacturing*, **56**, 2014, pp. 300-307.

[11] B.H.A.H. Tijs, M.H.J. Doldersum, A. Turon, J.E.A. Waleson, C. Bisagni. Experimental and numerical evaluation of conduction welded thermoplastic composite joints, *Composite Structures*, **281**, issue 1, 2022, 114964 (https://doi.org/10.1016/j.compstruct.2021.114964)

Effects of Fiber Type and Cooling Rate on the Crystallization Behaviour of Low-Melt PAEK Thermoplastic Composites

K.Gordnian[1], A.Forghani[1], D.Howell[2], A.McKee[1], M.Roy[1], T.Ytre-Eide [3], G.Fernlund[1], A.Chadwick[4], T.Wiedmann[4], H.Voggenreiter[4], and A. Poursartip[1,3]

[1]Convergent Manufacturing Technologies, Vancouver, BC, Canada
[2]Toray Advanced Composites, Morgan Hill, CA, USA
[3]Composites Research Network, Department of Materials Engineering, The University of British Columbia, Vancouver, BC, Canada
[4]German Aerospace Centre (DLR), Stuttgart, Germany

August 2025, Baltimore, MD

Physics-Based Process Simulation

- Physics-based modelling is founded on our understanding of causality of events
- The phenomena of interest are modelled using mathematical representations
- In Process Simulation, a physics-based model needs to include representations of:
  - **Material**
  - **Shape**
  - **Tooling**
  - **Equipment**
  - **Process**
- The more complex the system, the more useful process simulation becomes!
- Process simulation should be used at all stages of the lifecycle of a product, even before building the equipment and tooling

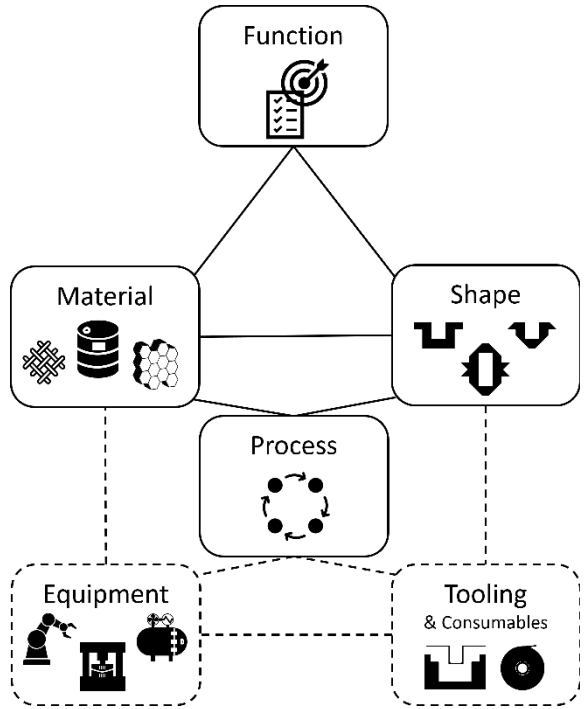

Source: https://compositeskn.org/KPC/A208

Process Simulation Workflow

Different Analysis Types and Outcomes

Composites Process Modelling

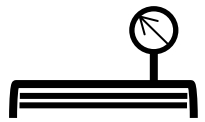

Gas Formation & Transport

- Porosity

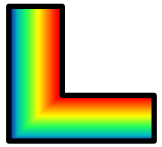

Thermal + Phase Transformation

- Thermal Lags
- Thermal Gradients
- Cure (Exotherm)
- Melt/Crystallization (Endo/Exo)

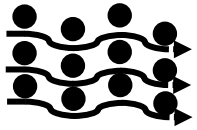

Flow-Compaction

- Interface, gaps, thickness changes
- V_f variation
- Porosity
- Wrinkling

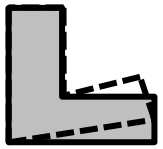

Stress-Deformation

- Spring-in
- Warpage
- Residual Stress

Importance of Crystallization/Melt Kinetics

- Degree of crystallinity: Key state variable for all downstream material models in thermoplastic composites process simulation.
- Thermoplastic composites continuously undergo crystallization and melting during manufacturing processes.
- Cooling rate significantly impacts the degree of crystallinity in the final composite part.
- Unlike thermoset cure kinetics, thermoplastic crystallization kinetics can be influenced by the fiber type.

Importance of Crystallization/Melt Kinetics

- Toray Cetex® TC1225 LM-PAEK composites:
  - Lower processing temperatures due to reduced melt temperature.
  - High service temperatures comparable to PEEK and PEKK due to similar glass transition temperatures.

- TC1225 UD tapes available with various fibers, notably T700G and T1100G.

- Study objectives:
  - Investigate cooling rate and fiber type (T700G, T1100G) effects on crystallization behaviour.
  - Develop crystallization/melt kinetics models for accurate process simulations.

Materials and Methodology

- Case Study Materials:
  - Toray Cetex® TC1225 LM-PAEK UD tape, two fibre types:
    - T1100G
    - T700G
  - $T_g = 147\ ℃\ (297\ °F)$
  - $T_m^0 = 305\ ℃\ (581\ °F)$
  - Processing temperature: $340 - 385\ ℃\ (644 - 725\ °F)$
  - Resin mass fraction: 34%

- Differential Scanning Calorimetry (DSC) tests (Using a PerkinElmer DSC 8500 machine):
  - Dynamic melt crystallization tests (1 CPM – 250 CPM)
  - Isothermal melt crystallization tests
  - Dynamic melting tests (1 CPM – 250 CPM)

Experimental Results:TC1100G-Effect of Cooling Rate

Dynamic Melt Crystallization

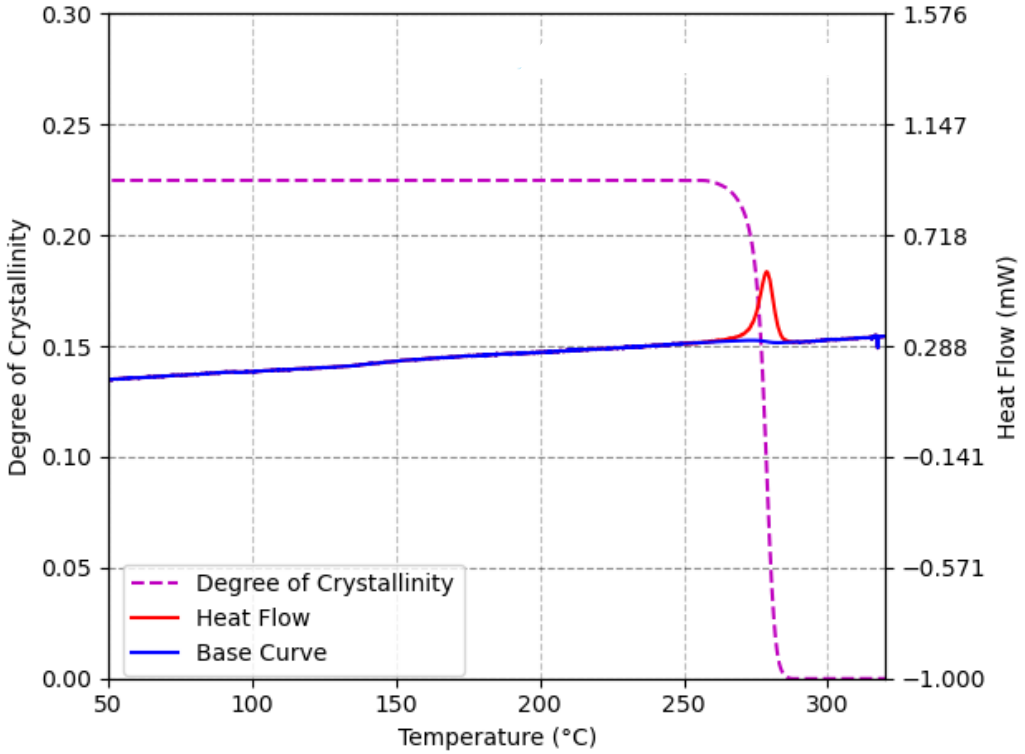

Cooling at 1 ℃/min

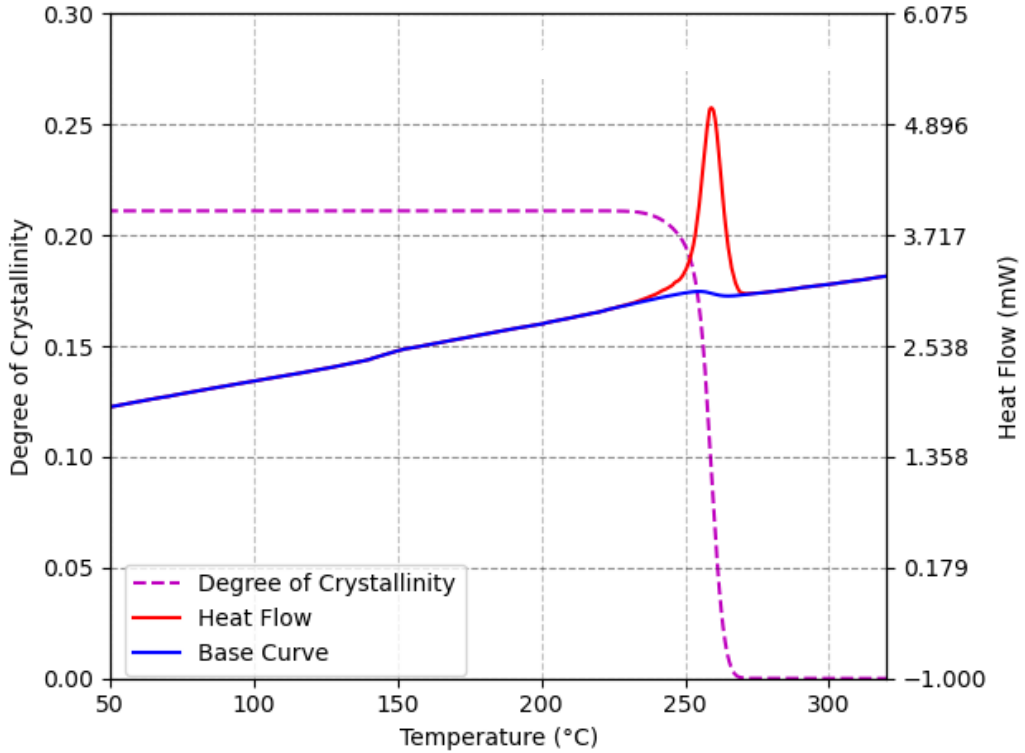

Cooling at 10 ℃/min

Experimental Results:TC1100G-Effect of Cooling Rate

Dynamic Melt Crystallization

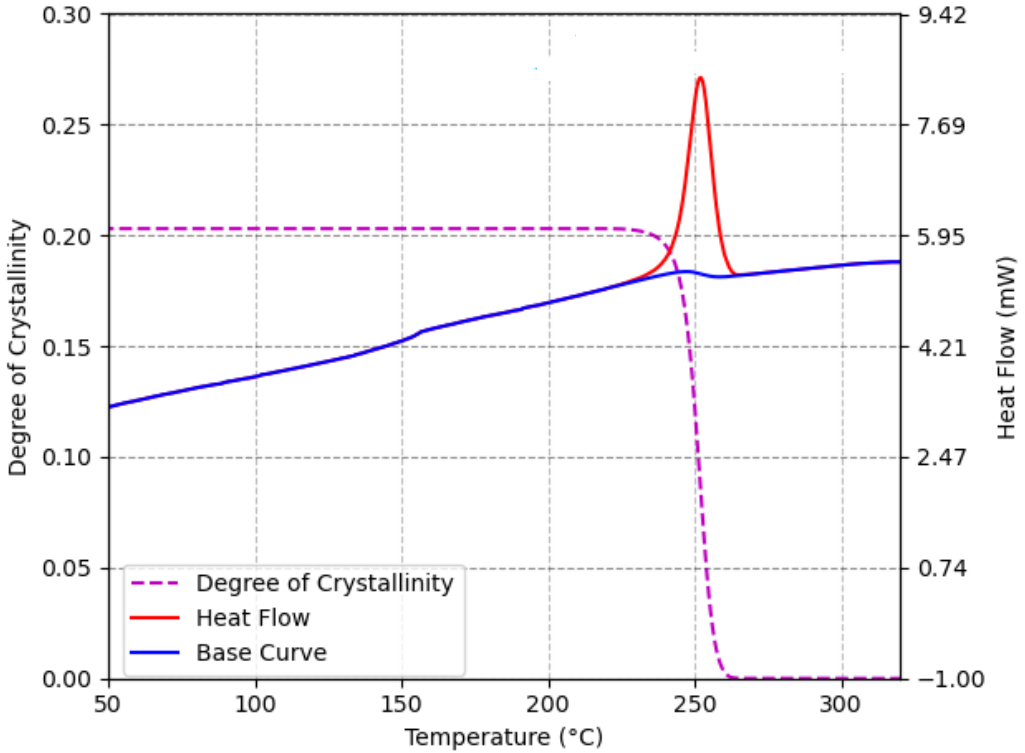

Cooling at 20 ℃/min

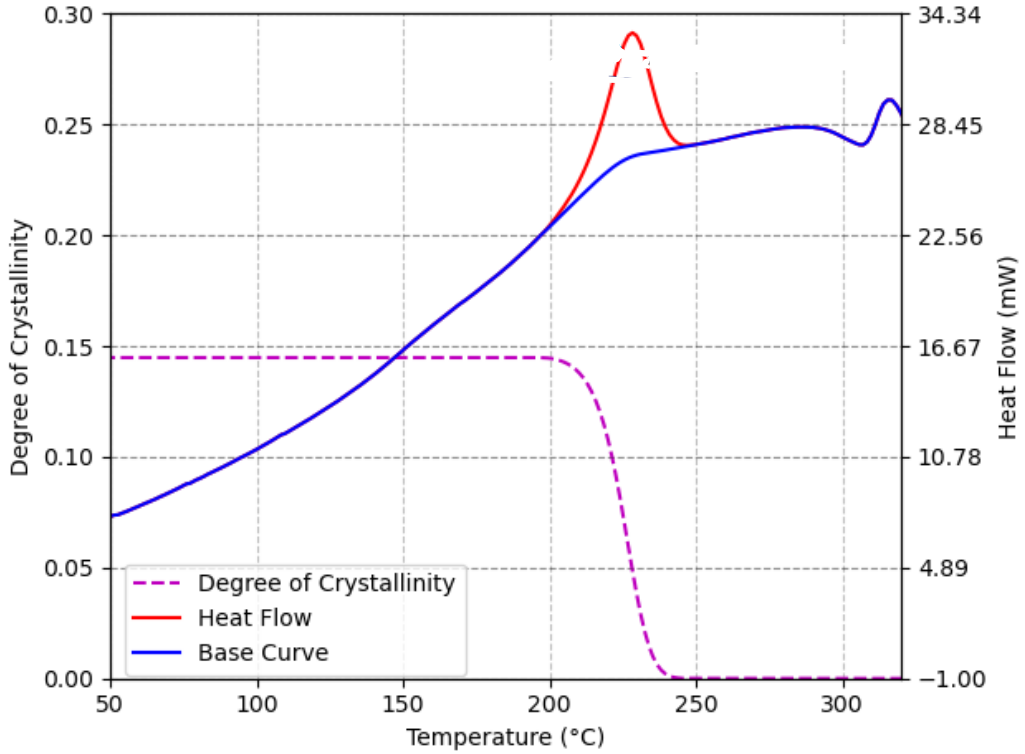

Cooling at 90 ℃/min

Effect of Cooling Rate on Crystallization

- Experimental Observations:
  - Increasing the cooling rate shifts crystallization initiation to lower temperatures.
  - Completion of crystallization also occurs at lower temperatures as cooling rate increases.

- Impact on Degree of Crystallinity:
  - Higher cooling rates lead to a decrease in the final degree of crystallinity.
  - Reduced crystallinity can influence mechanical and thermal performance of the composite.

Experimental Results:TC1100G

Isothermal Melt Crystallization

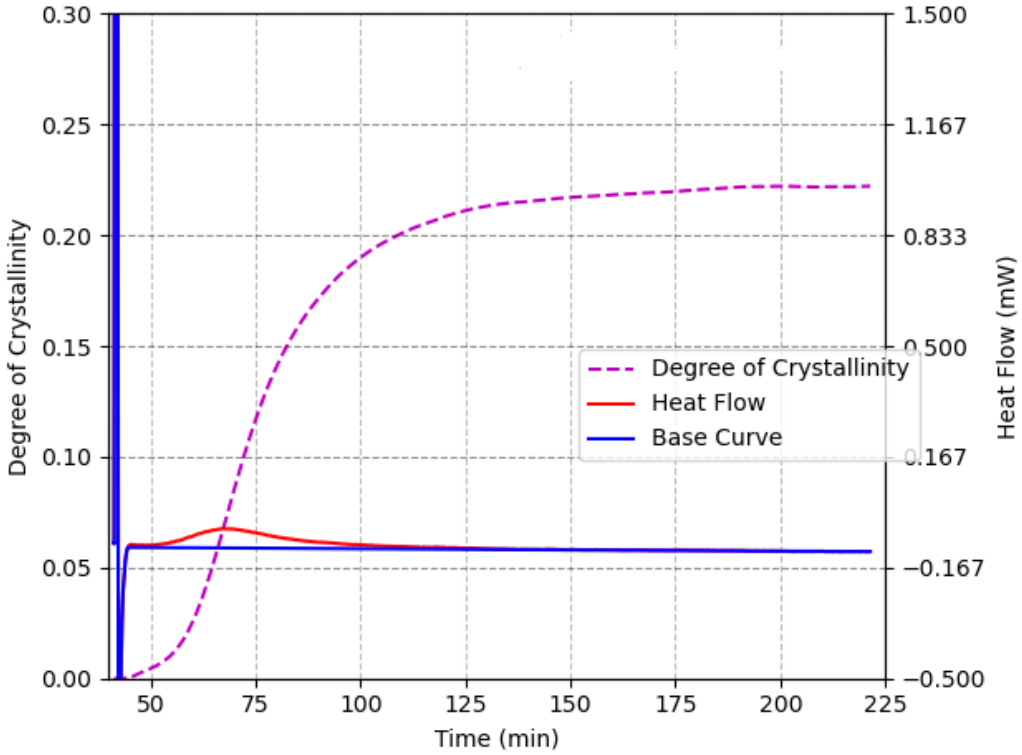

Isothermal at 290 ℃

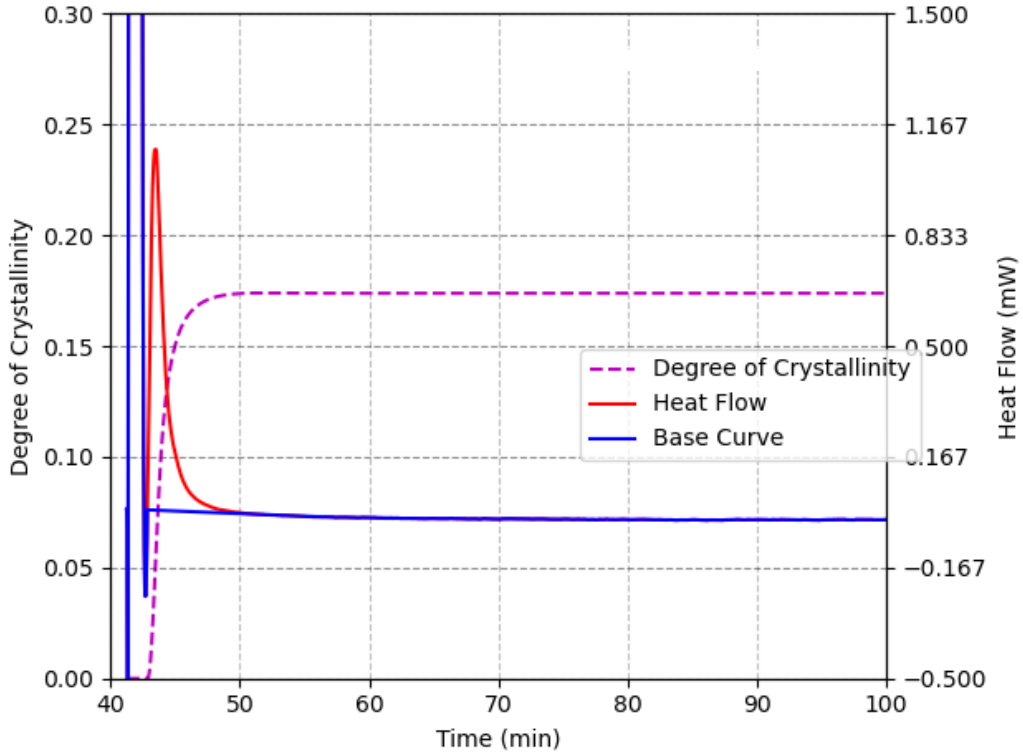

Isothermal at 265 ℃

Experimental Results:TC1100G

Dynamic Melting

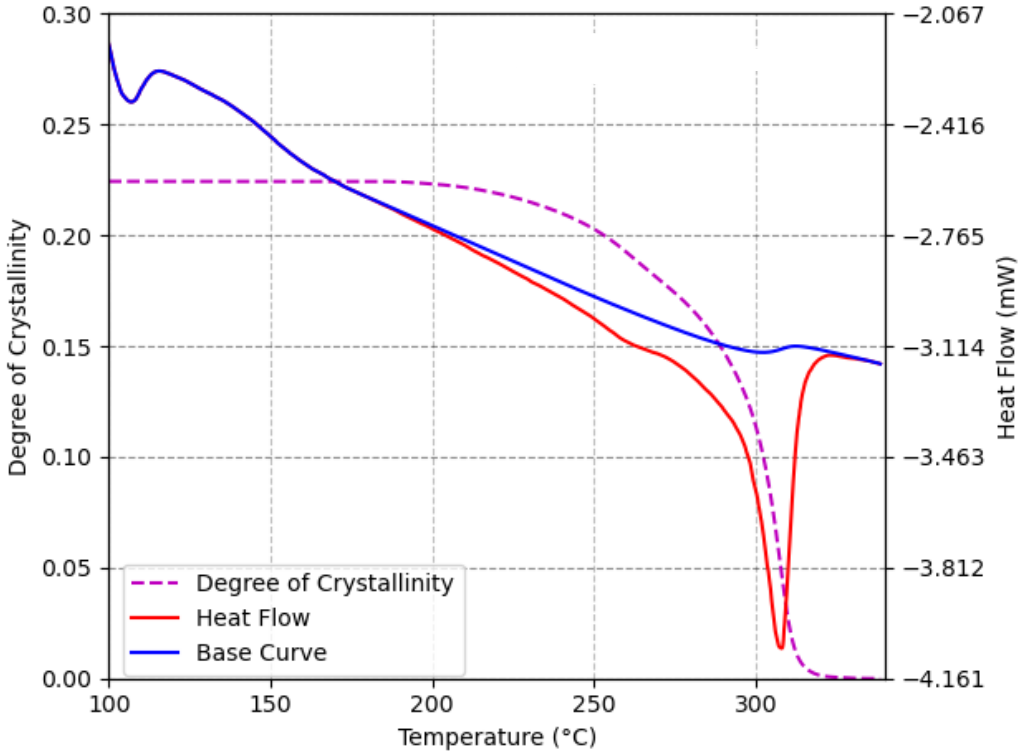

Heating at 10 ℃/min

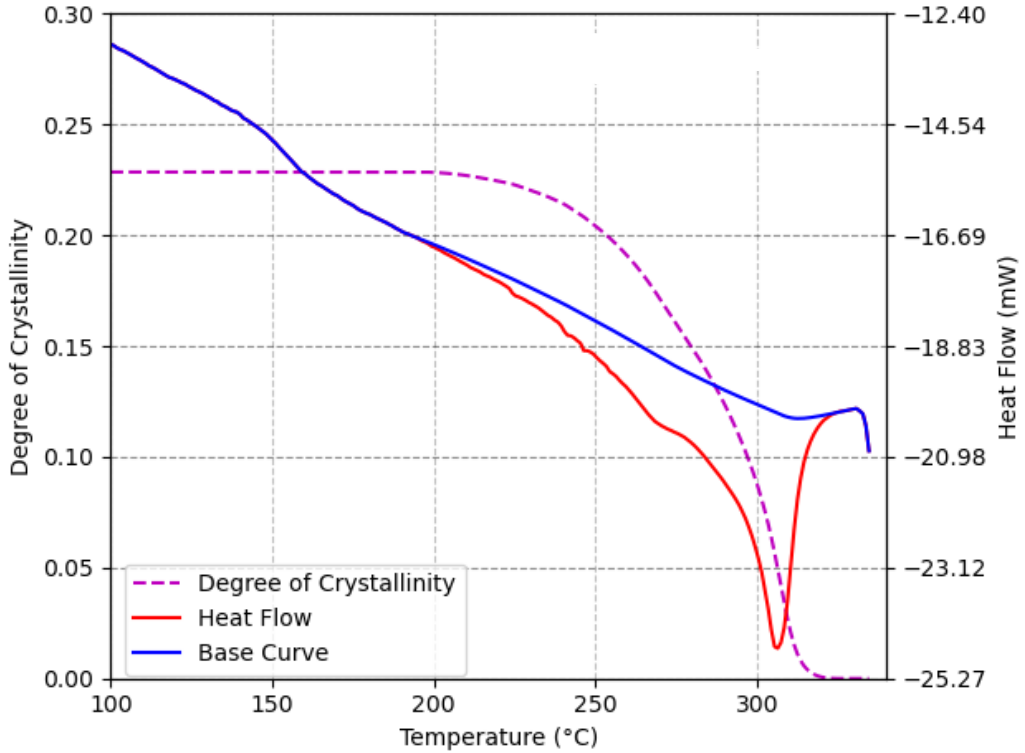

Heating at 60 ℃/min

Experimental Results: Effect of Fibre Type

Low Cooling Rate (5°C/min)

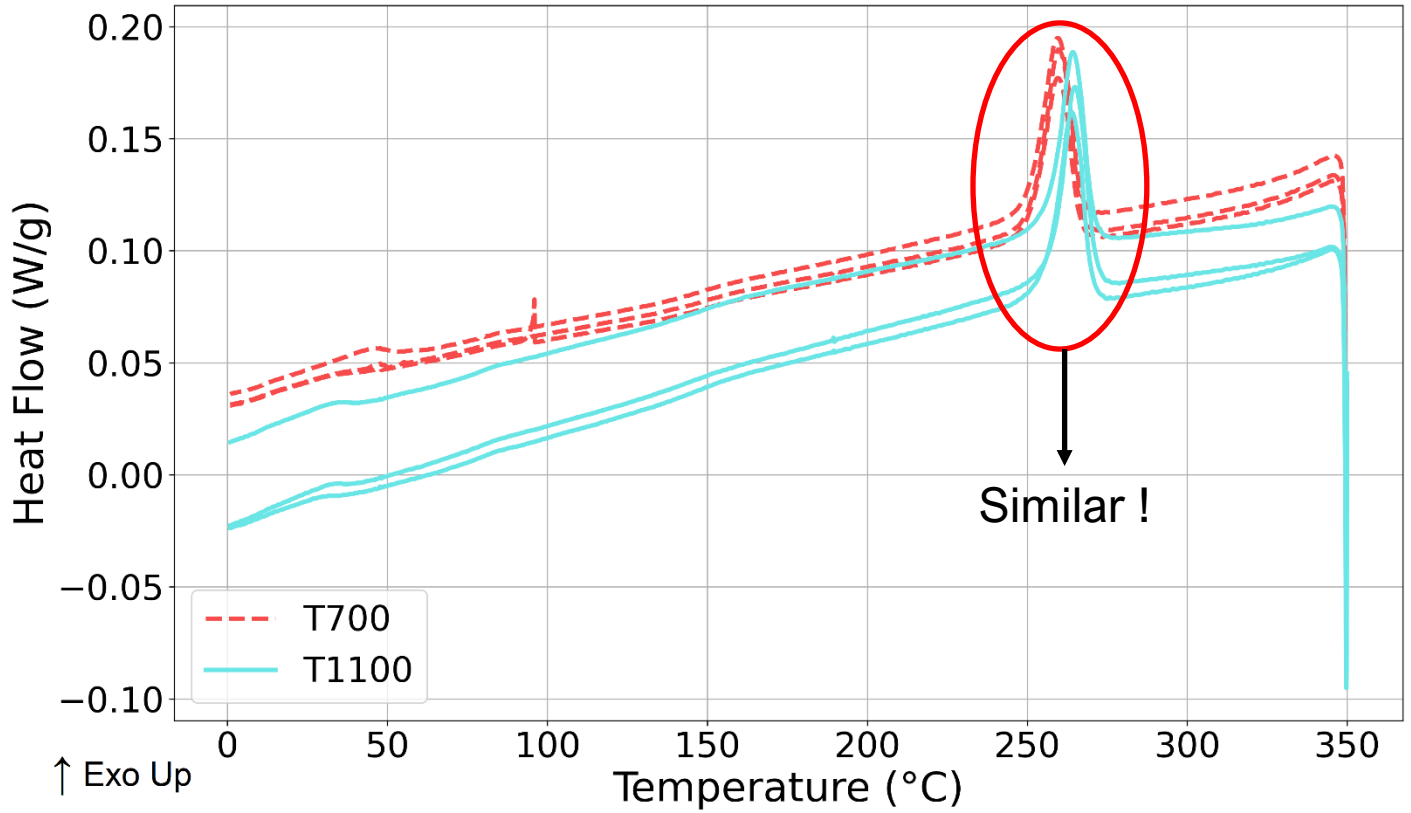

Understanding and Modeling the Effect of Fiber Type on the Crystallization Kinetics of a Thermoplastic Matrix Composite
Tristan Wiedmann, MASc Thesis, Institute of Aircraft Design, University of Stuttgart, August 2024

Experimental Results: Effect of Fibre Type

Low Cooling Rate (90°C/min)

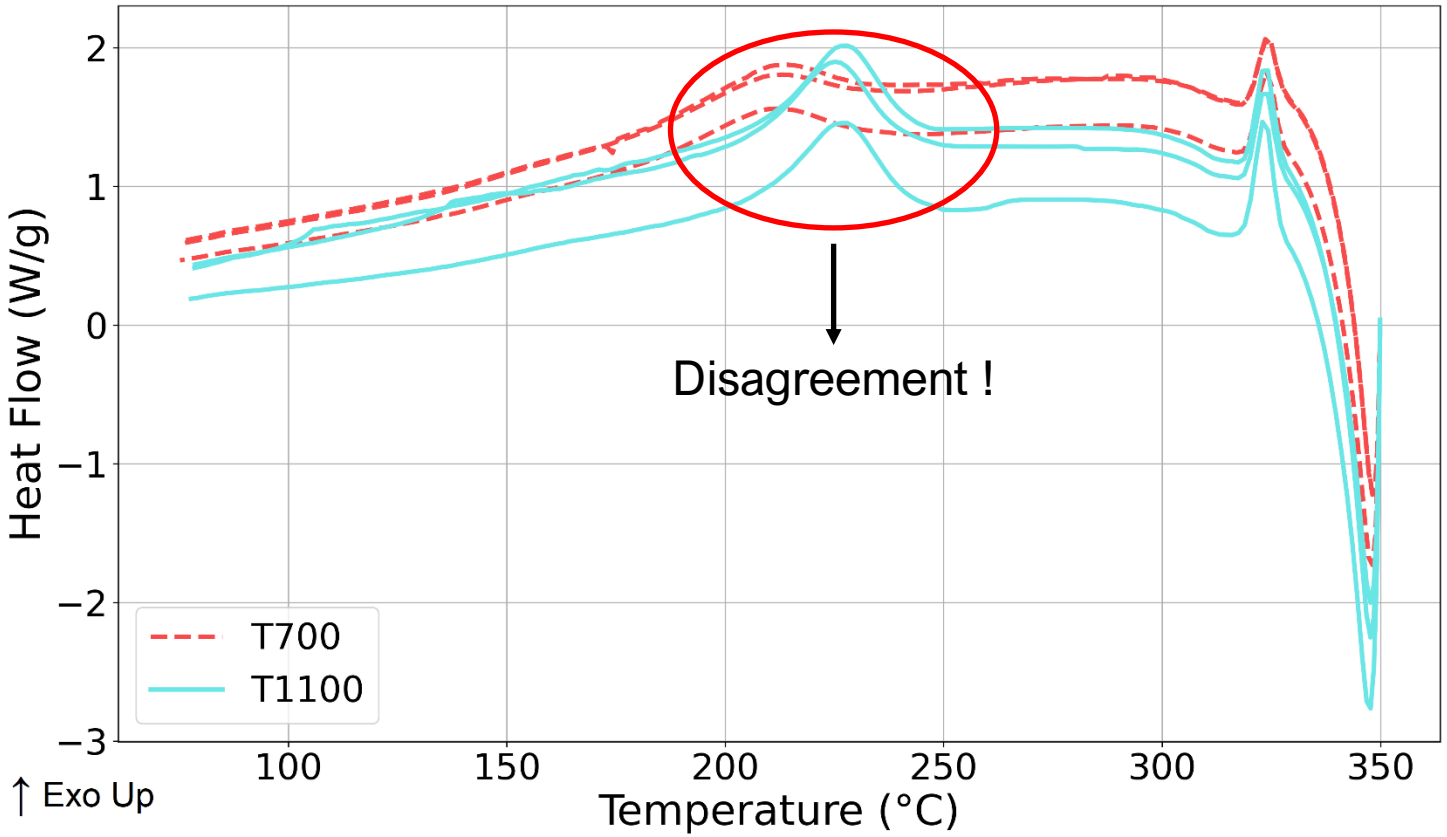

Understanding and Modeling the Effect of Fiber Type on the Crystallization Kinetics of a Thermoplastic Matrix Composite
Tristan Wiedmann, MASc Thesis, Institute of Aircraft Design, University of Stuttgart, August 2024

Experimental Results: Effect of Fibre Type

Temperature at Maximum Crystallization Rate:

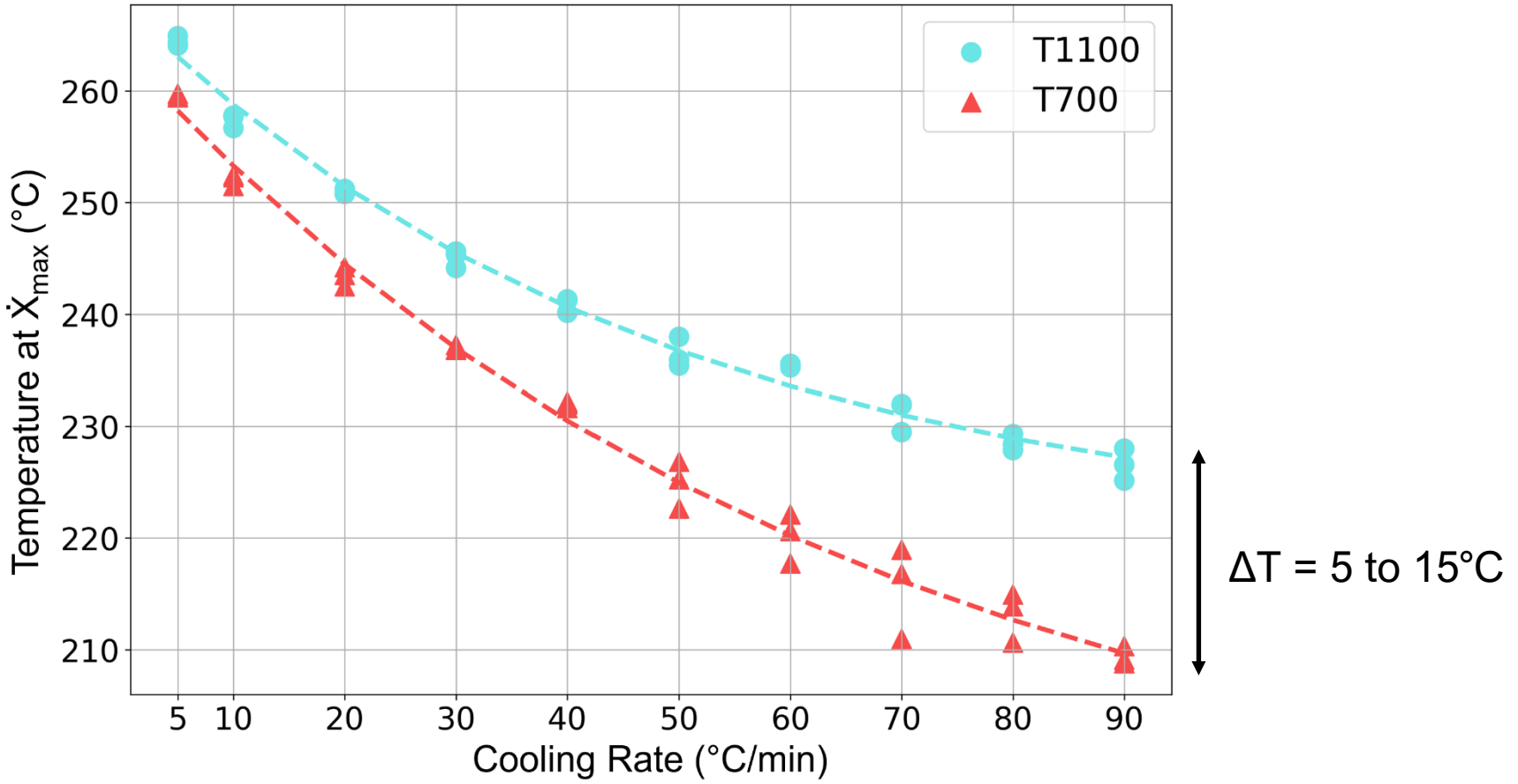

Understanding and Modeling the Effect of Fiber Type on the Crystallization Kinetics of a Thermoplastic Matrix Composite
Tristan Wiedmann, MASc Thesis, Institute of Aircraft Design, University of Stuttgart, August 2024

Crystallization-Melt Kinetics

- Most of the works in the literature consider isothermal or non-isothermal crystallization, separately, while in reality, cycles are combined
- Most crystallization kinetics models in the literature do not account for the induction time
- There are very few works which consider melt kinetics models

- We believe that state-of-the-art crystallization/melt kinetics models for thermoplastics must include:
  - Rate type (differential form): suitable for an arbitrary temperature cycle
  - Induction time
  - Accurate representation of melt kinetics

Crystallization Kinetics

Iso-conversional Crystallization Data – T1100G Fibre

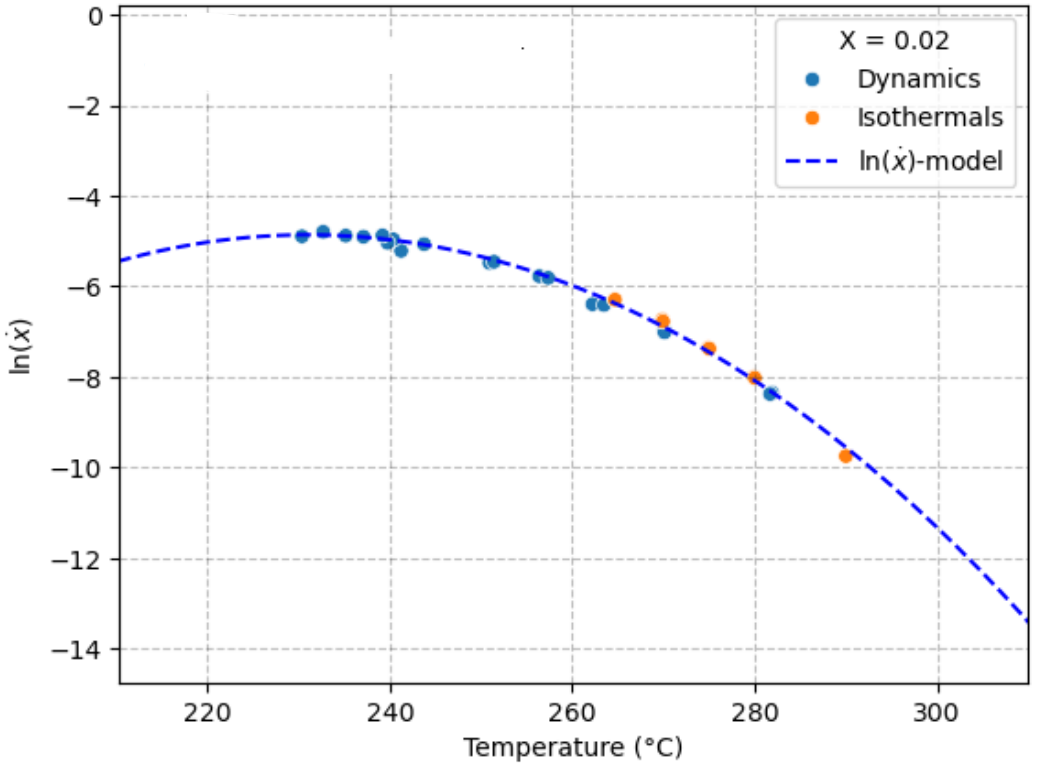

$X = 0.02$

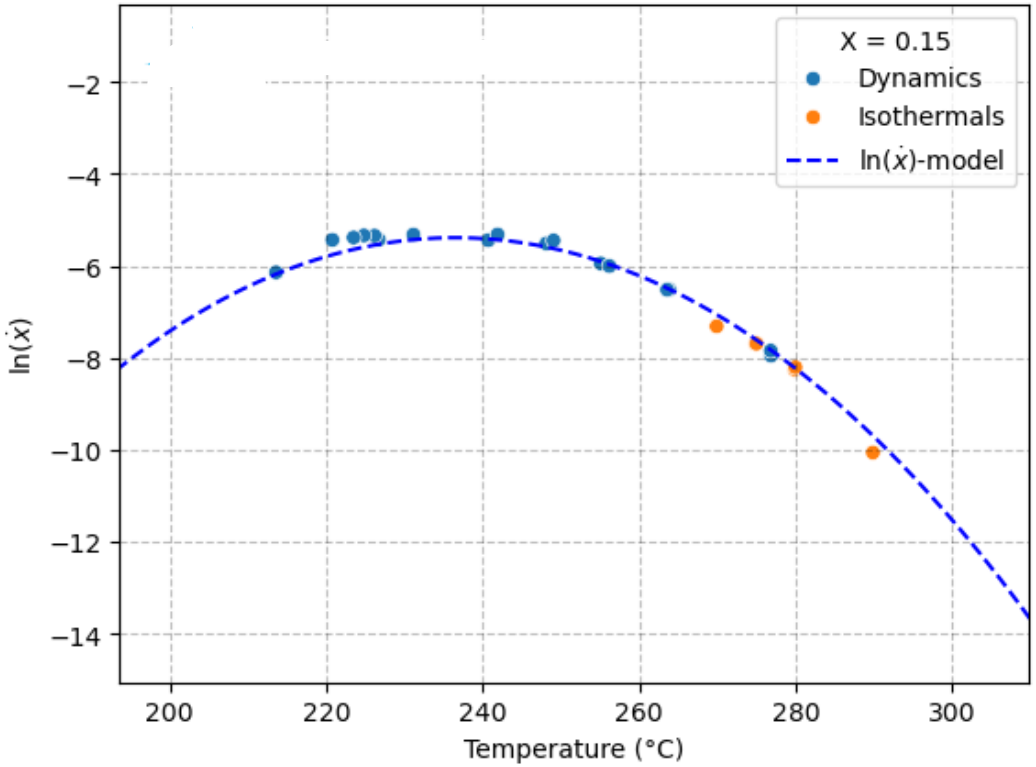

$X = 0.15$

Crystallization Kinetics Model

- No significant difference in crystallization mechanisms in isothermal and non-isothermal crystallization.

$$\frac{dX}{dt} = K(T)f(X)$$

- Two competing mechanisms in crystallization:

$$(T_m^0 - T) \nearrow \Rightarrow \frac{dX}{dt} \nearrow \qquad (T - T_g) \searrow \Rightarrow \frac{dX}{dt} \searrow$$

$$K(T) = K_0 e^{\frac{-E_g}{R(T-T_g)}} e^{\frac{-E_m}{R(T_m^0-T)}}$$

- There is an “induction time” model to capture the induction time or incubation period.

Crystallization and thermo-viscoelastic modelling of polymer composites
Kamyar Gordnian, PhD Thesis, The University of British Columbia, 2017

Crystallization Kinetics-Predictions- T1100G Fibre

Dynamic Melt Crystallization

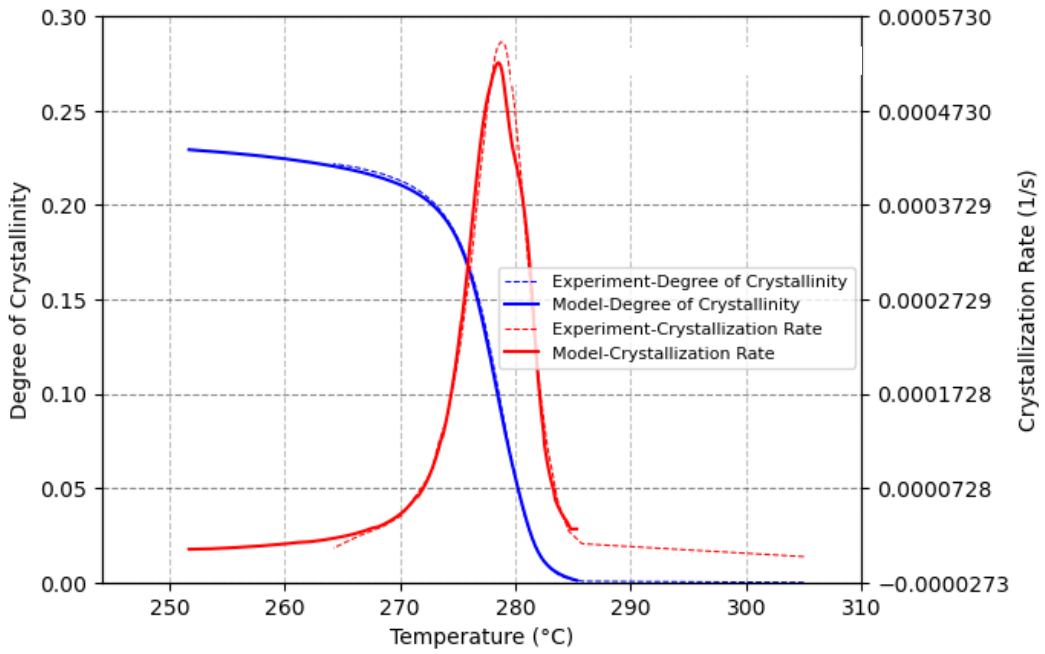

Cooling at 1 ℃/min

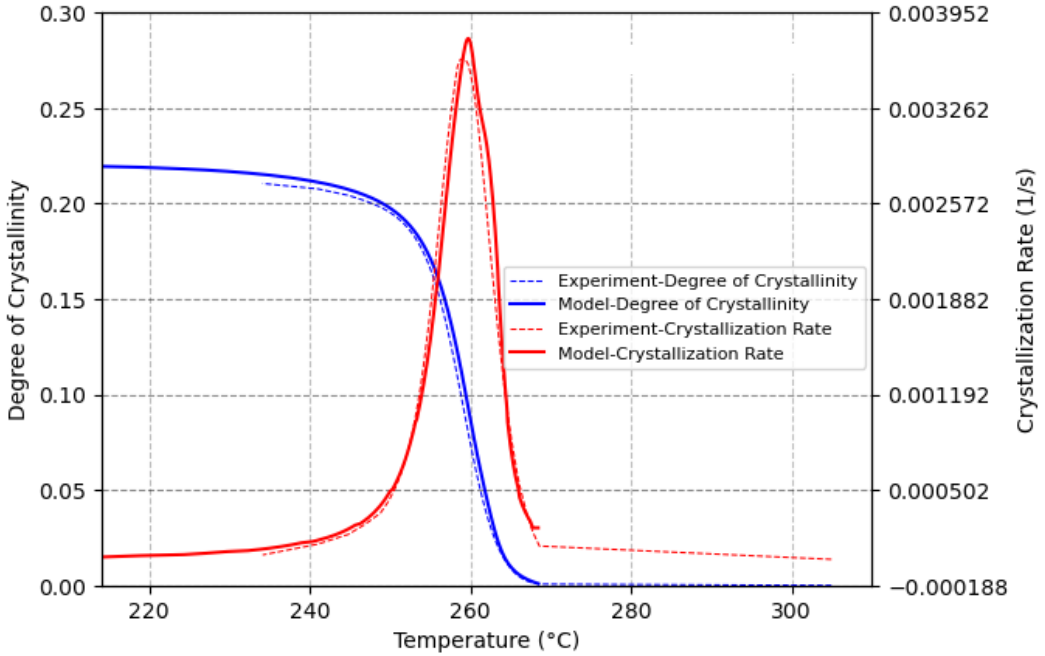

Cooling at 10 ℃/min

Crystallization Kinetics-Predictions- T1100G Fibre

Dynamic Melt Crystallization

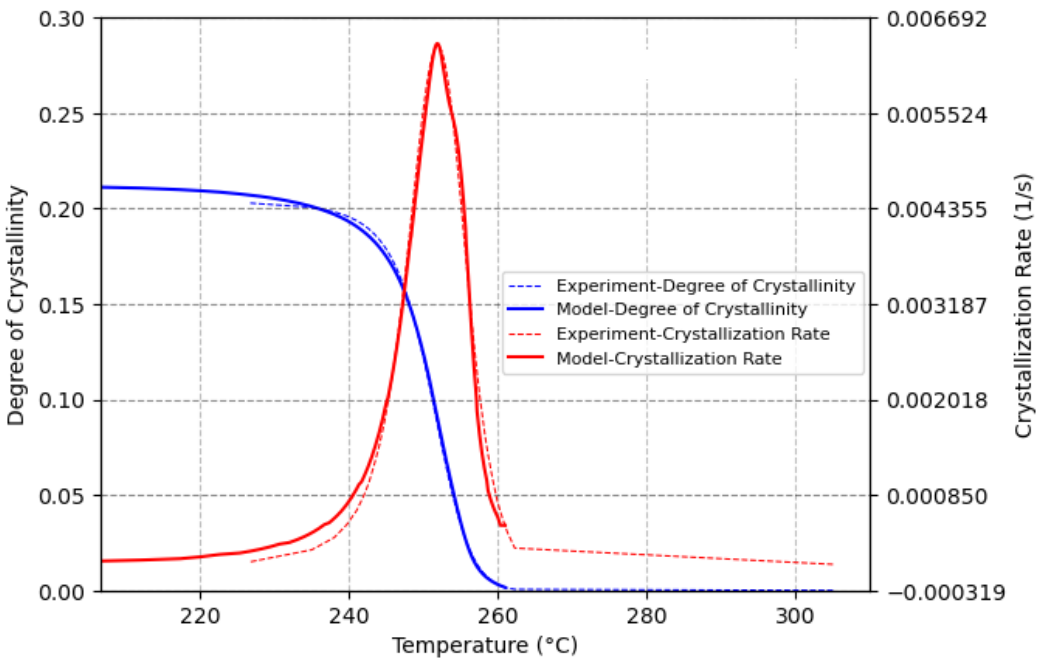

Cooling at 20 ℃/min

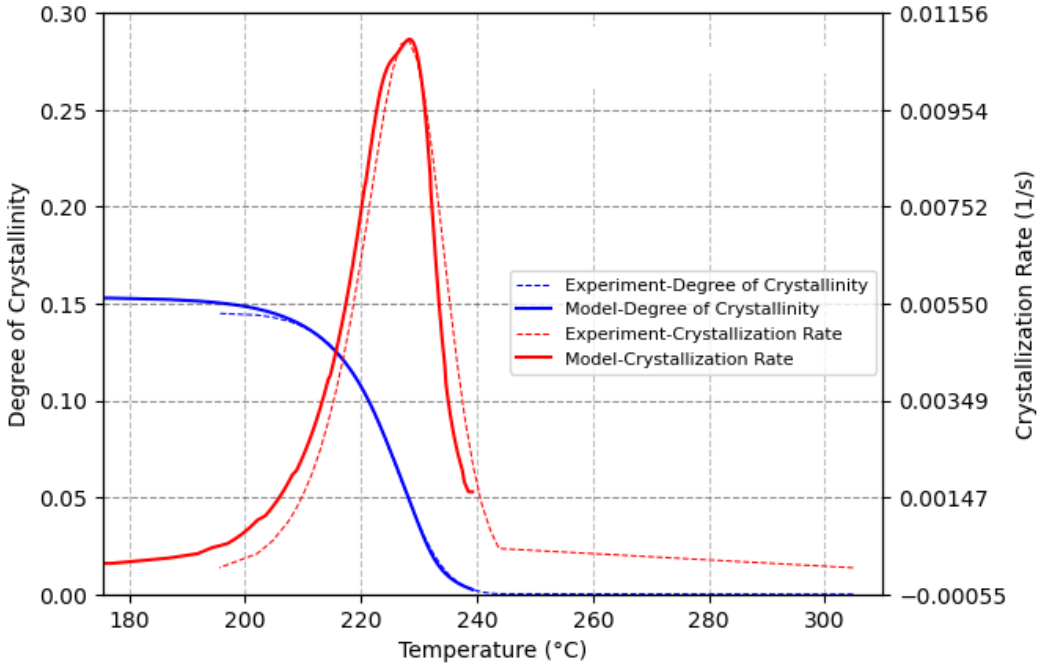

Cooling at 90 ℃/min

Melt Kinetics Model

- Master melt curve and crystallization kinetics model used for prediction of crystallinity during melting and crystallization

- Crystallization/Recrystallization Increment

$$\Delta X_c = \begin{cases} \dfrac{dX_c}{dt}\Delta t & X < X_{max} \\ 0 & X = X_{max} \end{cases}$$

- Melting Increment

$$\Delta X_m = \begin{cases} \left(\dfrac{dX}{dT}\right)_{\text{master}} \Delta T & \dot{T} > 0 \\ 0 & \dot{T} \leq 0 \end{cases}$$

- Updating X

$$\Delta X = \Delta X_c + \Delta X_m$$
$$X^n = X^{n-1} + \Delta X$$

(Gordnian, 2017)

Crystallization and thermo-viscoelastic modelling of polymer composites
Kamyar Gordnian, PhD Thesis, The University of British Columbia, 2017

Melt Kinetics-Predictions- T1100G Fibre

Dynamic Melting

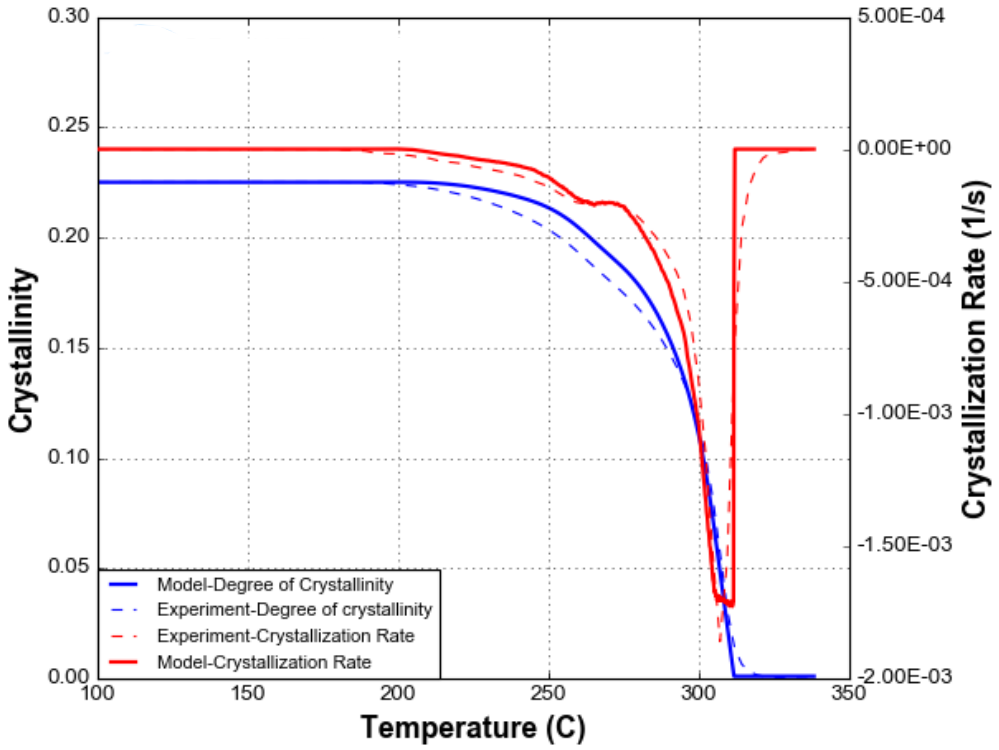

Heating at 10 ℃/min

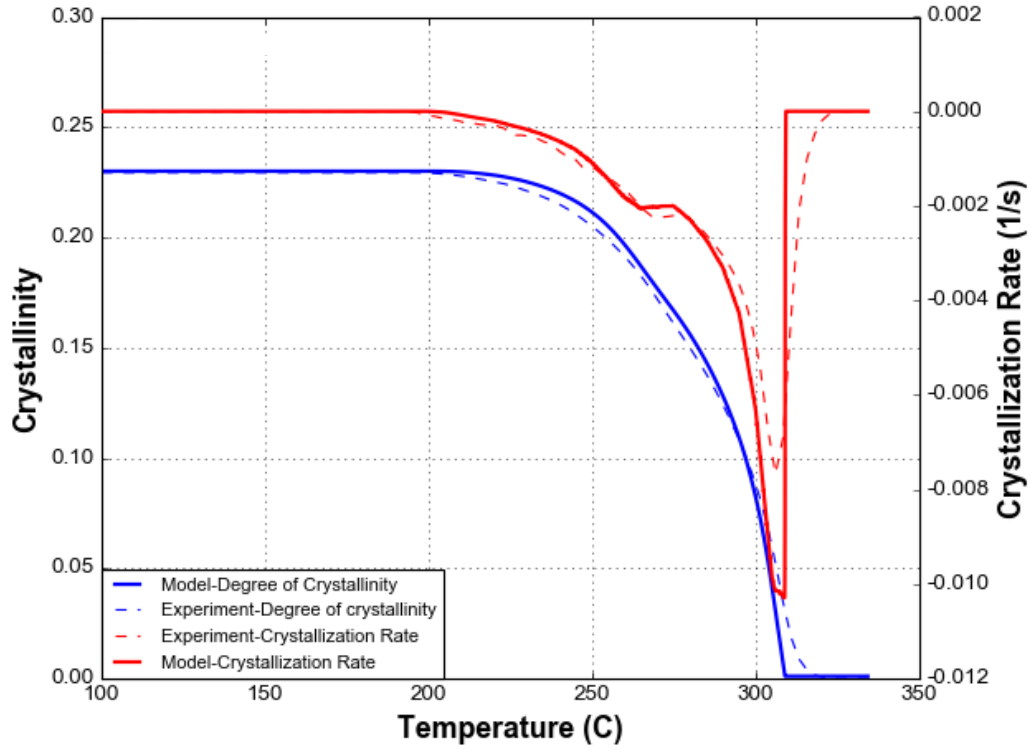

Heating at 60 ℃/min

Model Predictions-Effect of Cooling/Heating Rate- T1100G Fibre

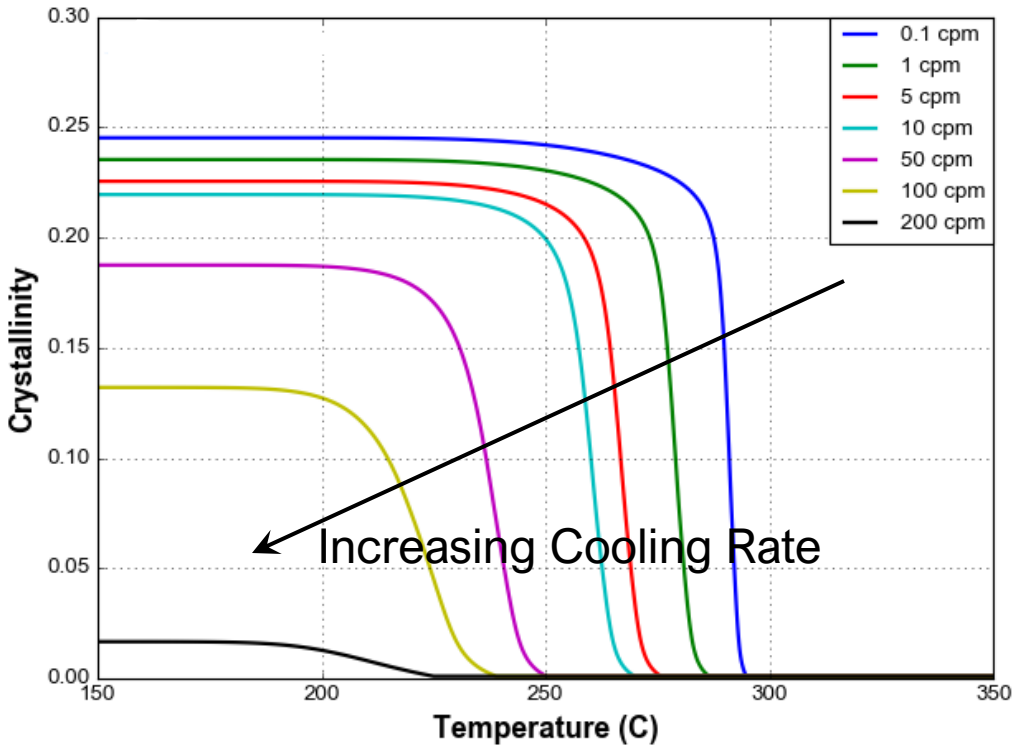

Crystallization

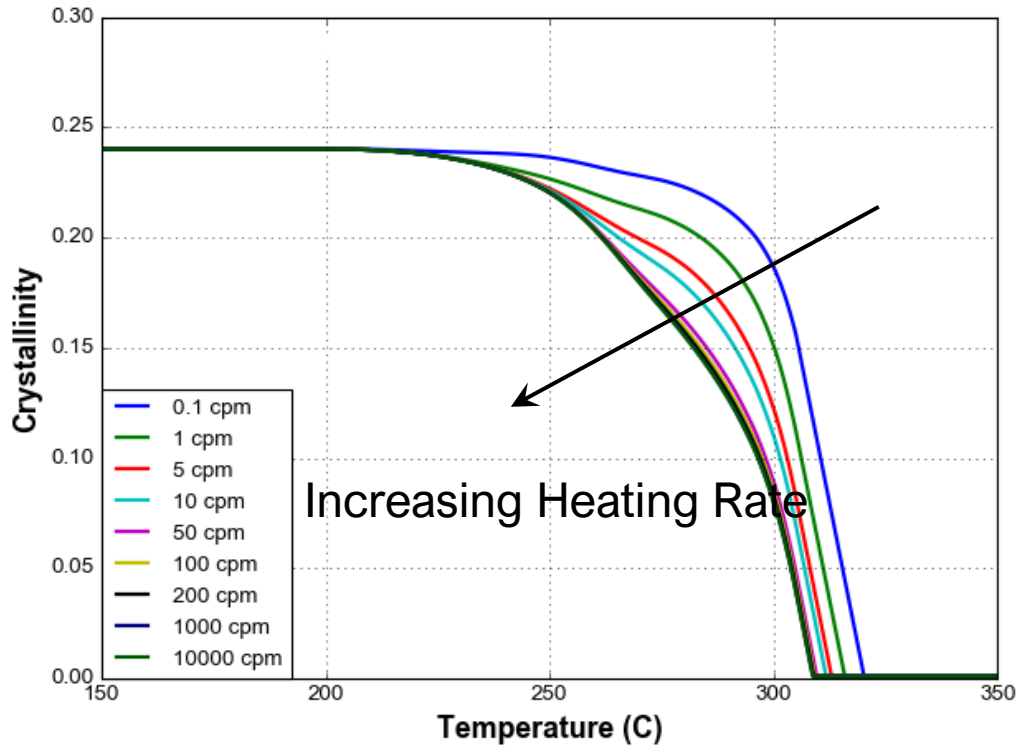

Melting

Model: Effect of Fibre Type

Can one material model predict the crystallization kinetics of CF/LM-PAEK for another fiber type?

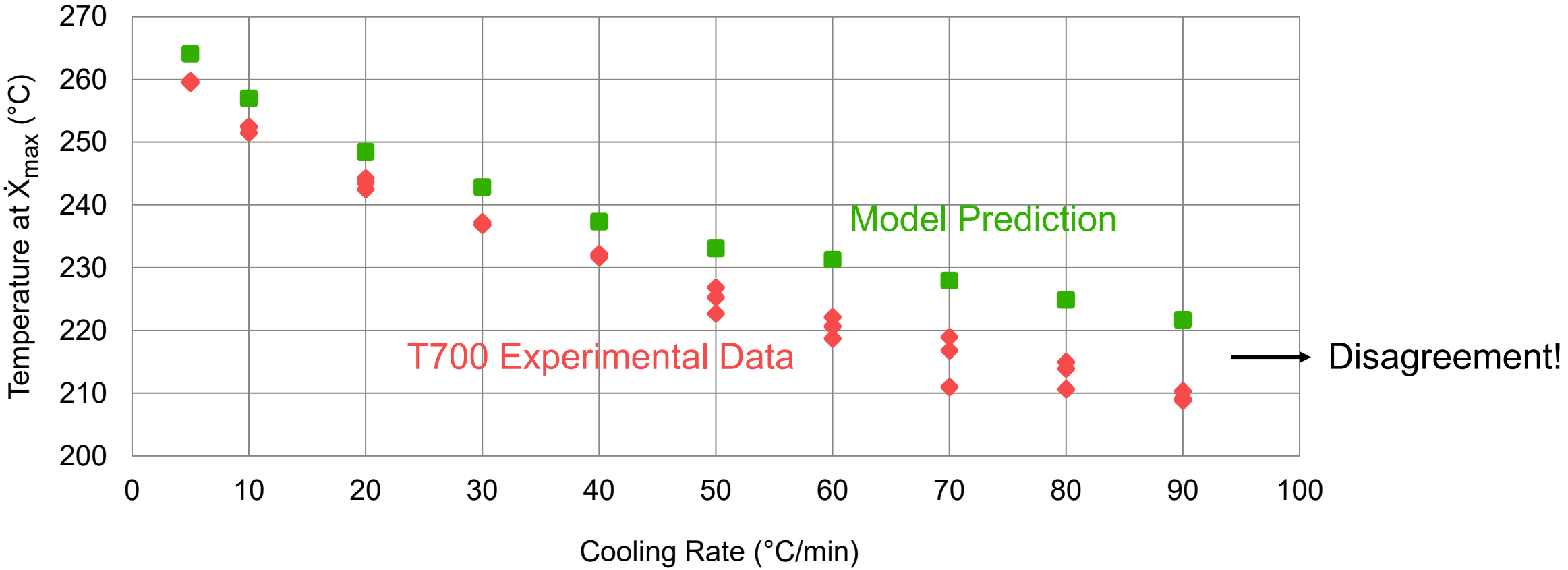

Understanding and Modeling the Effect of Fiber Type on the Crystallization Kinetics of a Thermoplastic Matrix Composite
Tristan Wiedmann, MASc Thesis, Institute of Aircraft Design, University of Stuttgart, August 2024

Summary and Conclusions

- Toray Cetex® TC1225 LM-PAEK/T1100G UD tape and Toray Cetex® TC1225 LM-PAEK/T700G UD tape were characterized for crystallization and melt kinetics
- Increasing the cooling rate shifts crystallization initiation to lower temperatures.
- Higher cooling rates lead to a decrease in the final degree of crystallinity.
- Fiber type affects both the induction time and the crystallization behavior. A complete crystallization kinetics characterization is required for each fiber type.

References

- Crystallization and thermo-viscoelastic modelling of polymer composites, Kamyar Gordnian, PhD Thesis, The University of British Columbia, 2017

- Understanding and Modeling the Effect of Fiber Type on the Crystallization Kinetics of a Thermoplastic Matrix Composite, Tristan Wiedmann, MASc Thesis, Institute of Aircraft Design, University of Stuttgart, August 2024

- Gordnian K, Mussali A, Forghani A, McKee A, Lane M, Howell D, Fernlund G, Poursartip A. Prediction of Process-Induced Deformations of Semi-Crystalline Thermoplastic Composites, SAMPE 2024 Conference, Long Beach, CA, May 2024

Thank You!

ICCM24
AUGUST 4-8, 2025
BALTIMORE CONVENTION CENTER
BALTIMORE, MARYLAND, USA

No Technical Paper Submission for:

Burcu Saner Okan

ICCM24
AUGUST 4-8, 2025
BALTIMORE CONVENTION CENTER
BALTIMORE, MARYLAND, USA

No Technical Paper Submission for:

Paul Davidson

Cooling-rate Independent PEEK Composites via OATMEAL for High-Rate Processing

Dr. Tyler Hudson (NASA Langley)
Dr. Mehran Tehrani (UCSD)
John Hopkins (NASA Langley)
Skylar Kindred (UCSD)
Libang Wang (UCSD)

Presentation by Joseph Kirchhoff (UT-Austin)

The University of Texas at Austin
Walker Department of Mechanical Engineering
Cockrell School of Engineering

ODEN INSTITUTE FOR COMPUTATIONAL ENGINEERING & SCIENCES

UC San Diego
JACOBS SCHOOL OF ENGINEERING

NASA

Thermoplastic Composite Manufacturing: Need for Speed





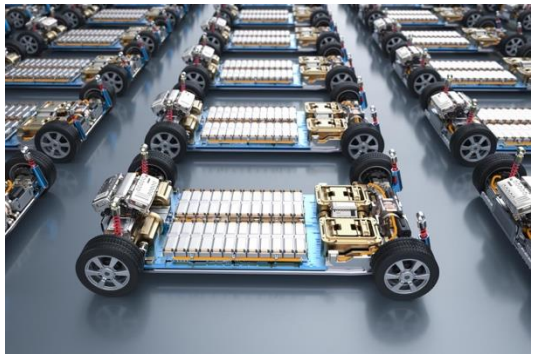

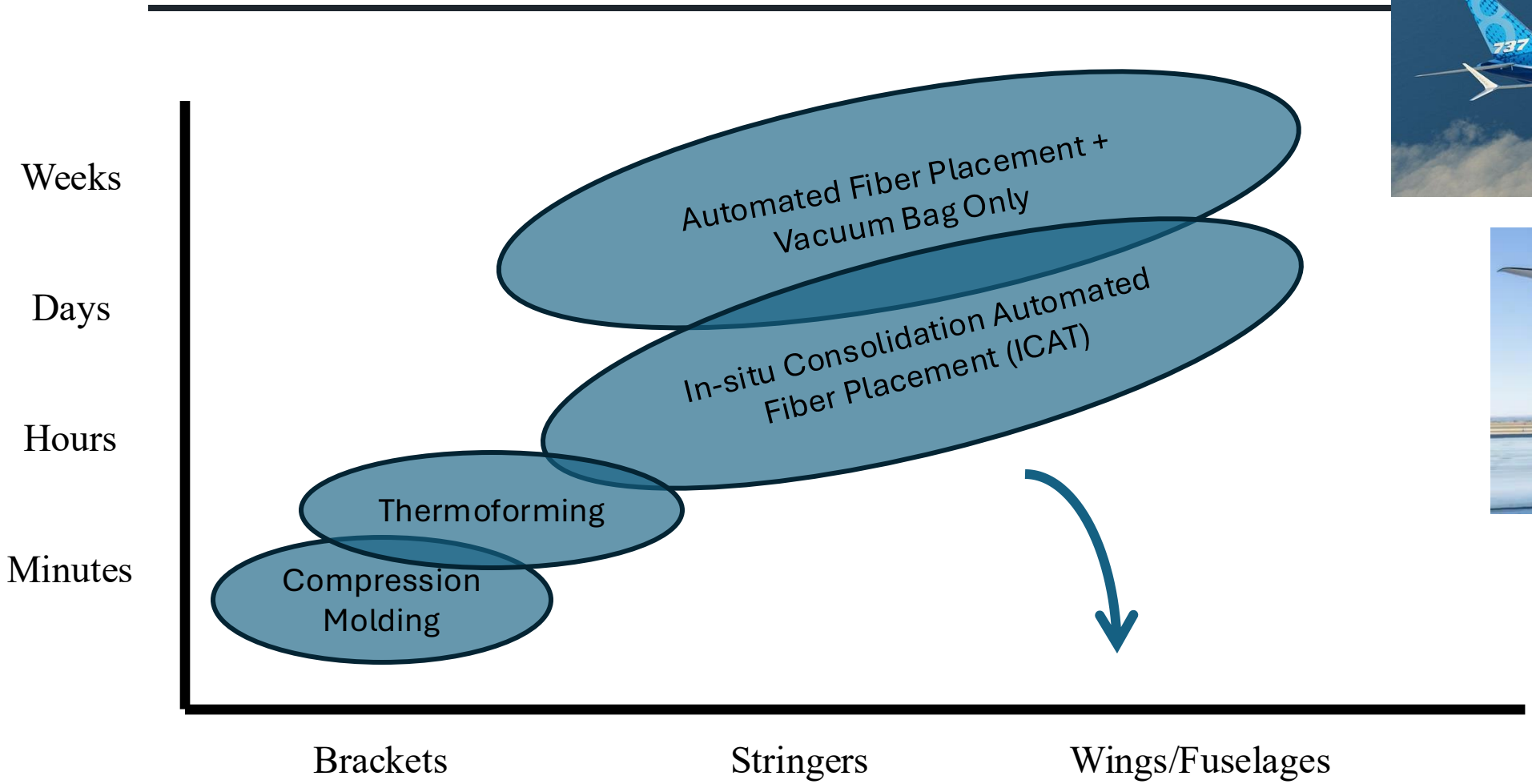

High Cooling Rates in AFP: Increased Voids and Reduced Primary Crystallization

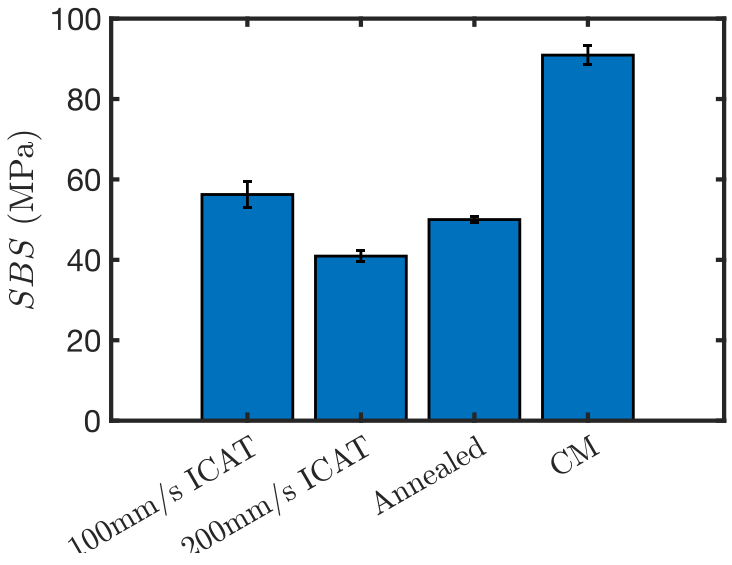

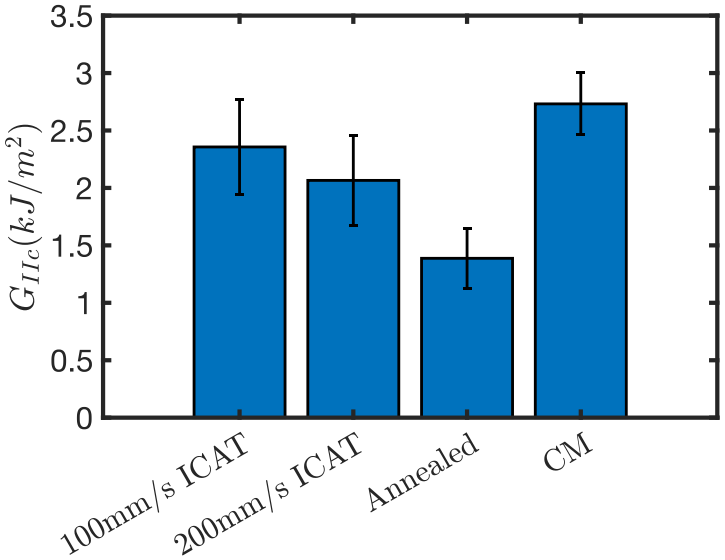

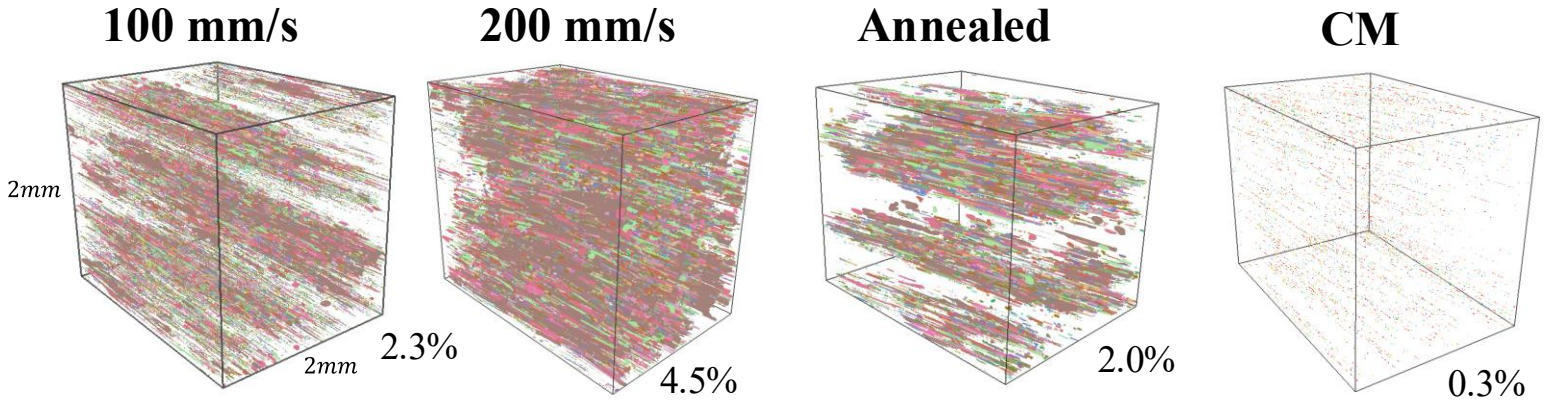

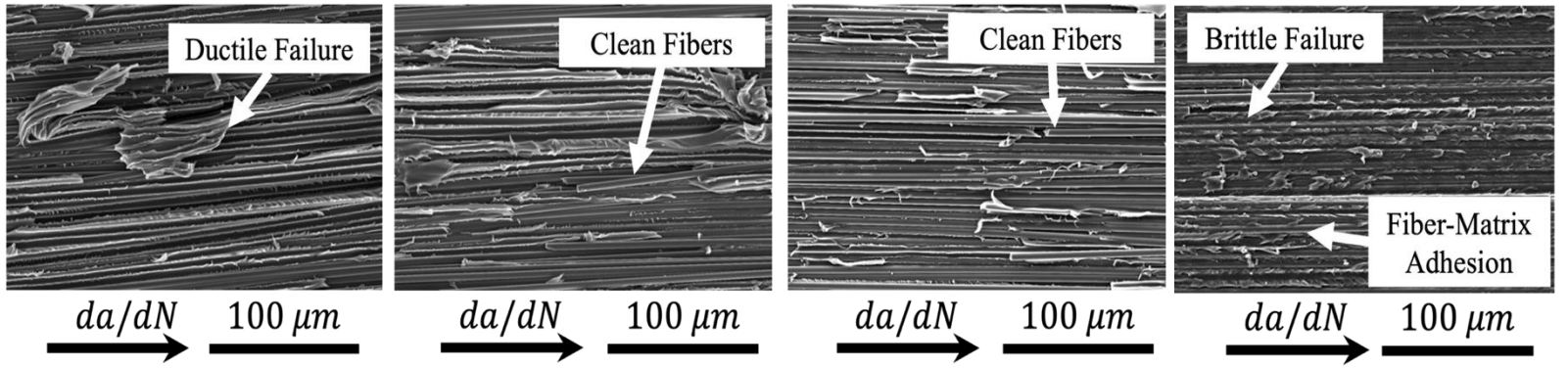

Kirchhoff, Joseph G. and Heathman, Nathaniel T. and Yap, Timothy and Koirala, Pratik and Hudson, Tyler and Tehrani, Mehran, **Interlaminar Bonding in Thermoplastic Composites: A Comparative Analysis of Laser Afp and Post-Processing**. Available at SSRN: https://ssrn.com/abstract=4955051

Fusion Bonding in Thermoplastic Composites

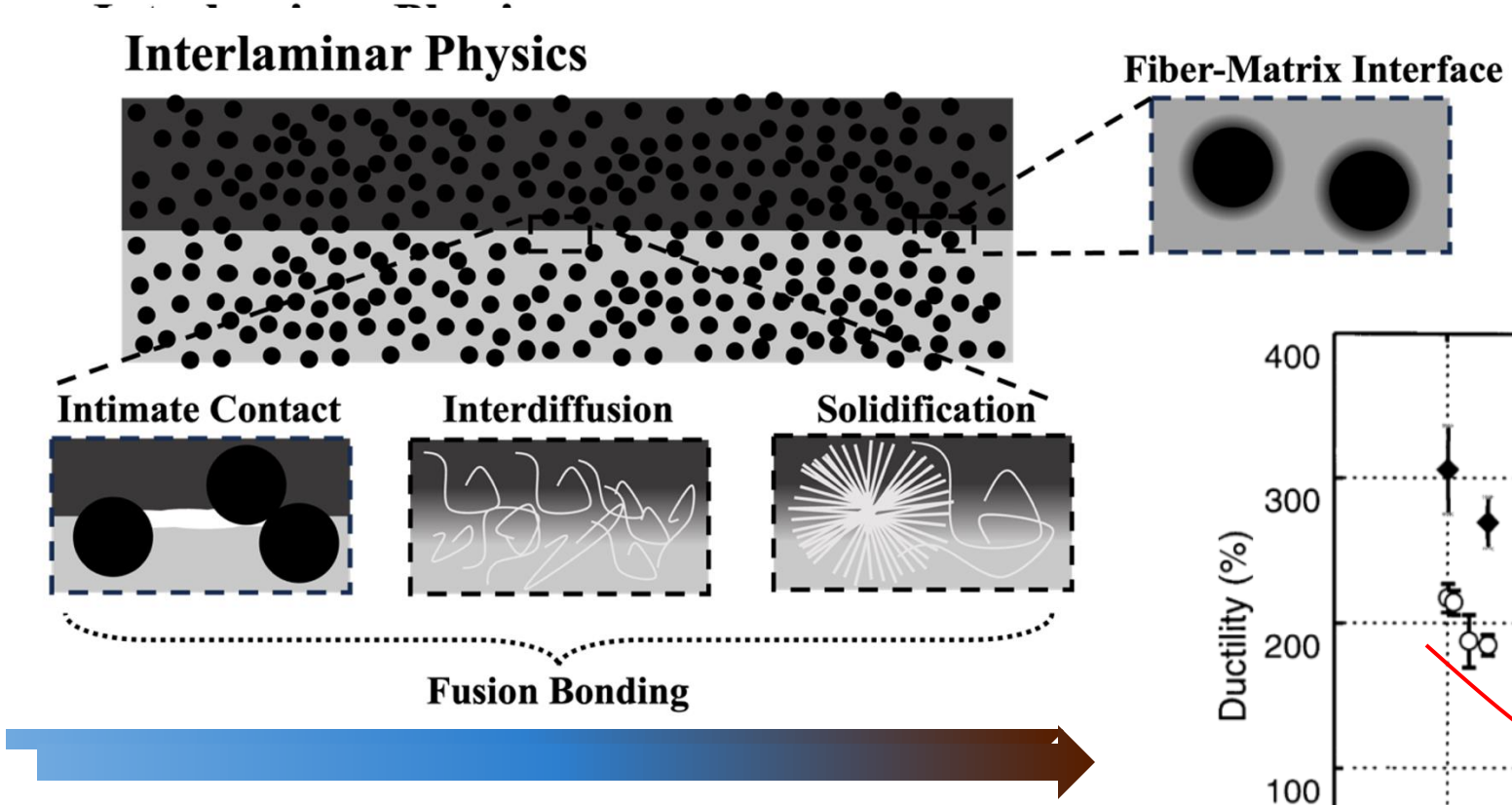

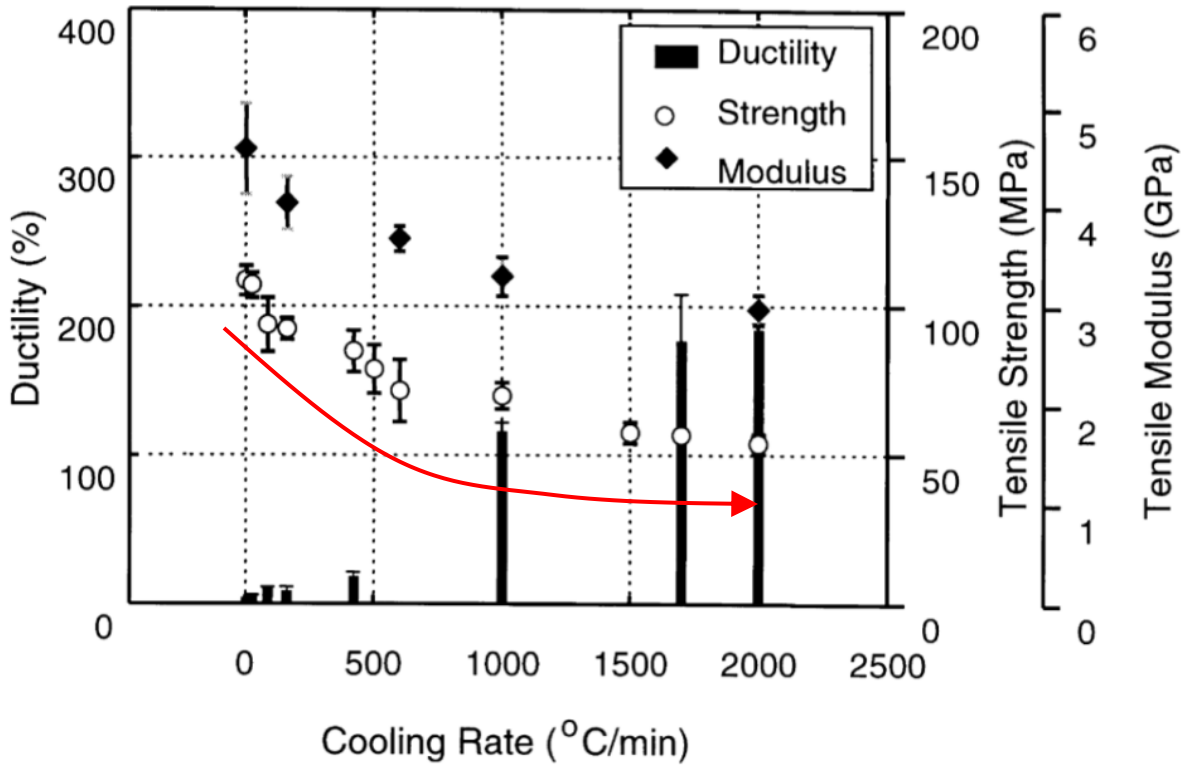

Gao and Kim, Composites A, 2000.

Crystallinity in Thermoplastics Actually Inhibits Interdiffusion

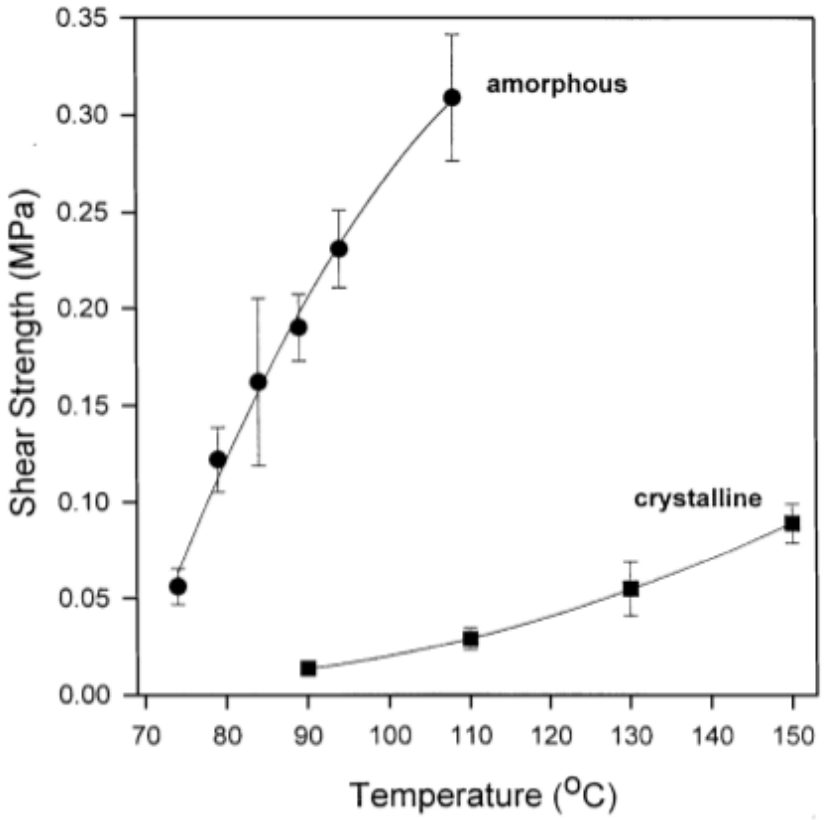

Fig. 2. Shear strength as a function of healing temperature at amorphous/amorphous and crystalline/crystalline PET ($M_0 = 15\,000$) interfaces. Healing time is 30 min.

Boiko et al., **Healing of interfaces of amorphous and semi-crystalline polyethylene terephthalate in the vicinity of the glass transition temperature**, Polymer (2001)

How can we leverage amorphous bonding for high-speed manufacturing?

Exploring Amorphous Bonding:
A Preliminary Investigation


The University of Texas at Austin
Walker Department
of Mechanical Engineering
Cockrell School of Engineering



UC San Diego
JACOBS SCHOOL OF ENGINEERING

Two-Step Experimental Plan

Materials

- Low Melt PAEK™ (LM-PAEK), with 55% fiber volume fraction, supplied by Toray (TC1125)
- Polyetherimide (PEI, Ultem 1000), supplied from piezopvdf as a neat polymer 5-micron film

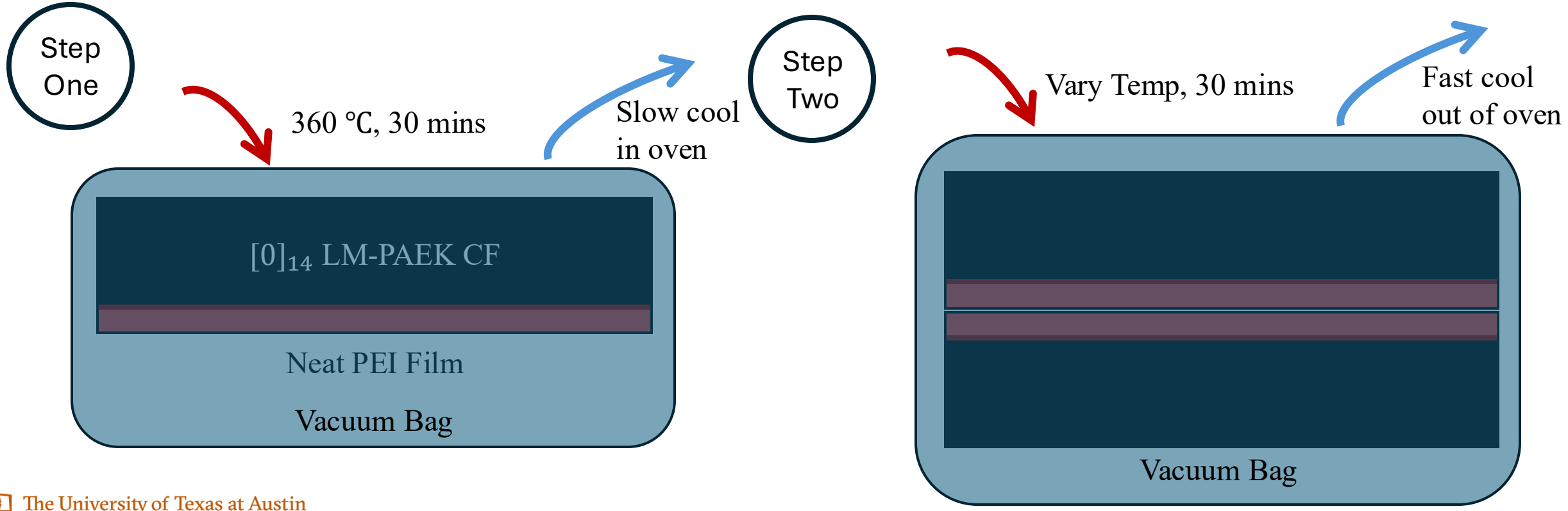

Both Steps Were Done in a Vacuum Bag Only Setting

PEI Thickness (μm)	Step Two Temperature (℃) – 30 mins
5	230
10	280
15	360
20	

*Melt Temperature of LM-PAEK (305 ℃)

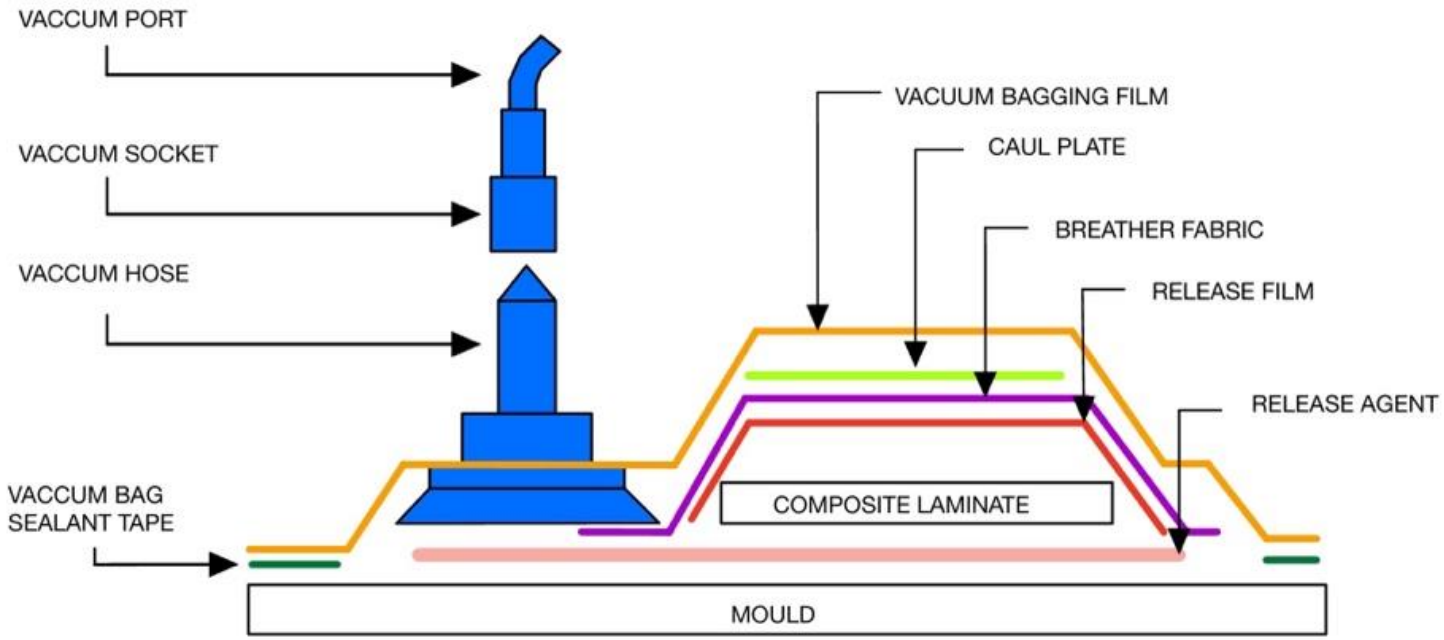

All bagging materials supplied by Airtech

Amorphous Bonding: Unlocking Processing Below Melt Point

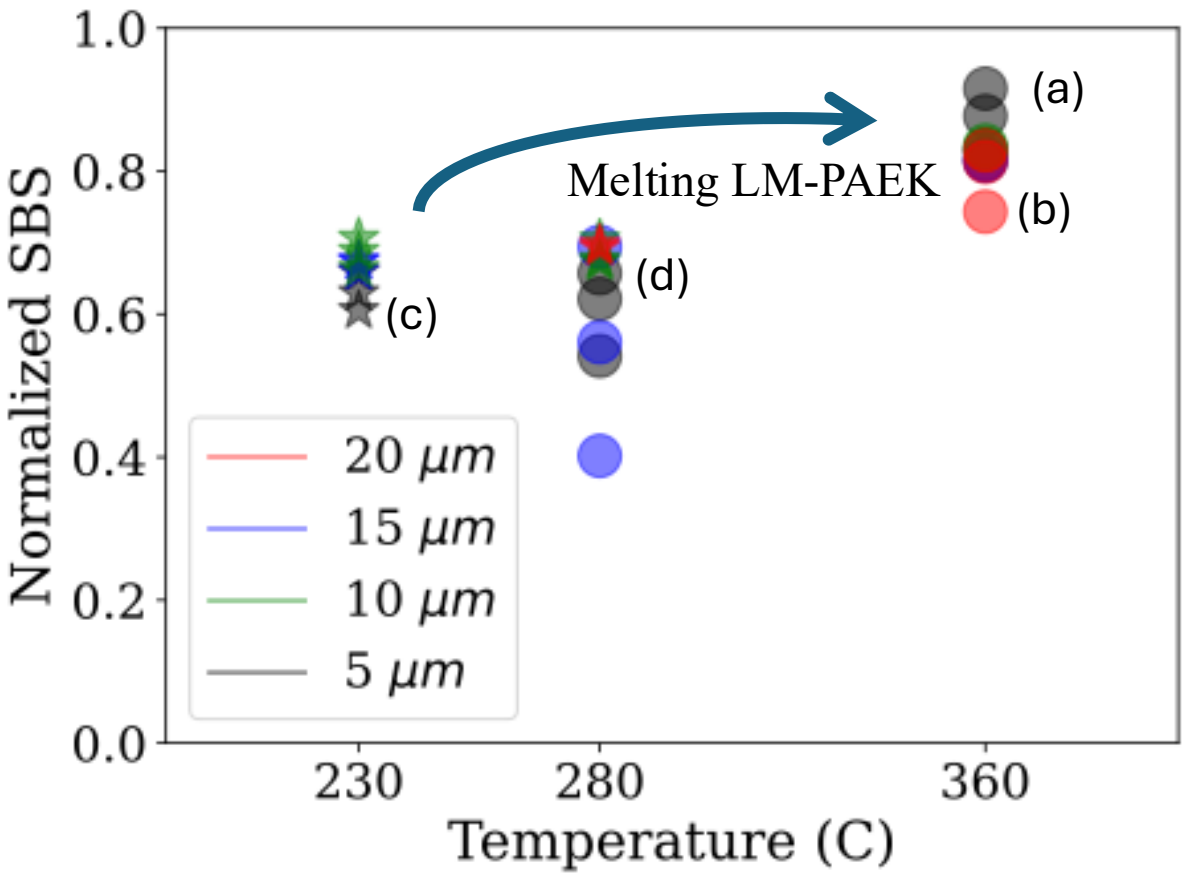

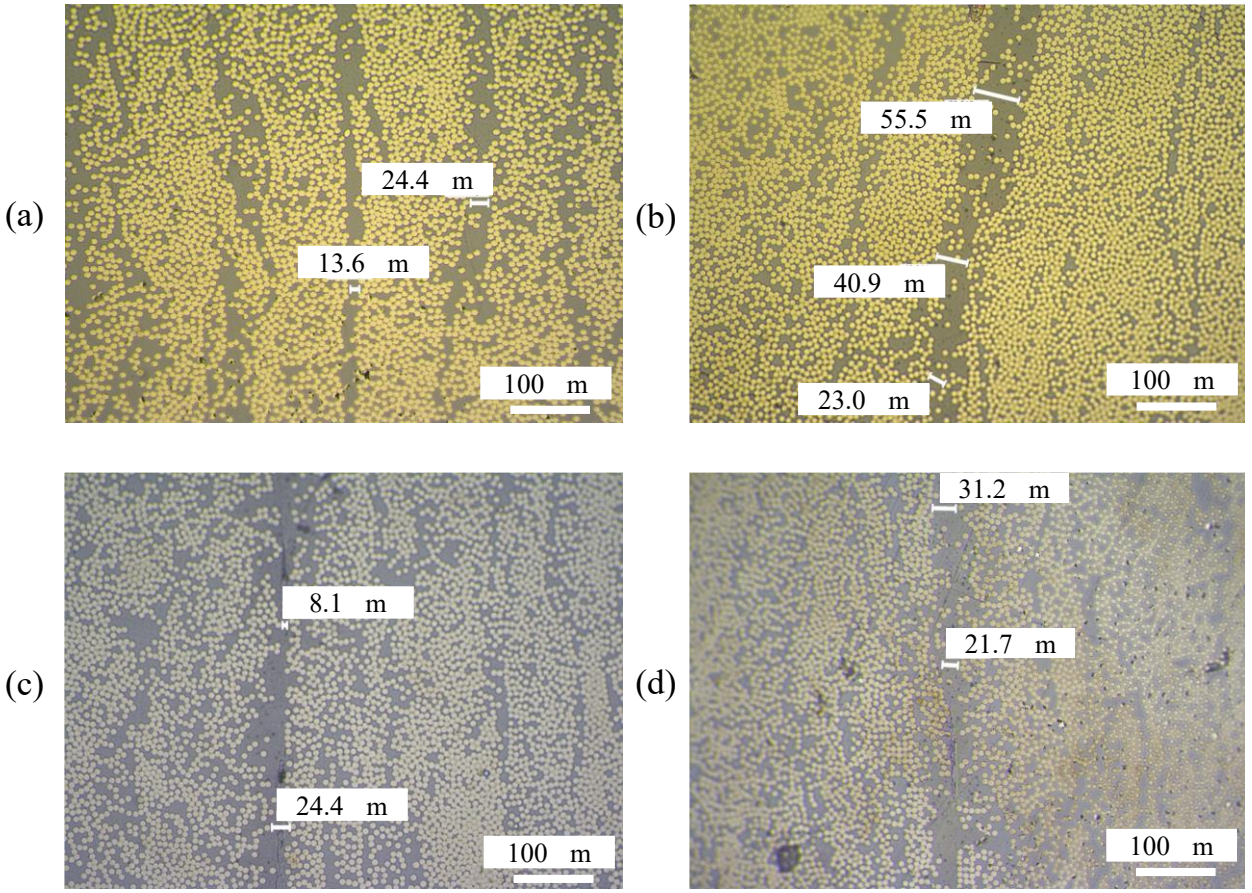

SBS normalized in respect to National Institute for Aviation Research (NIAR). (2020, February 21). *CAM-RP-2019-036 Rev NC*. Wichita State University.

PEI-PEEK Tape + Laser Ablation (OATMEAL)

The University of Texas at Austin
Walker Department of Mechanical Engineering
Cockrell School of Engineering

ODEN INSTITUTE FOR COMPUTATIONAL ENGINEERING & SCIENCES

UC San Diego
JACOBS SCHOOL OF ENGINEERING

NASA

OATMEAL is Engineered to be Cooling-rate Agnostic

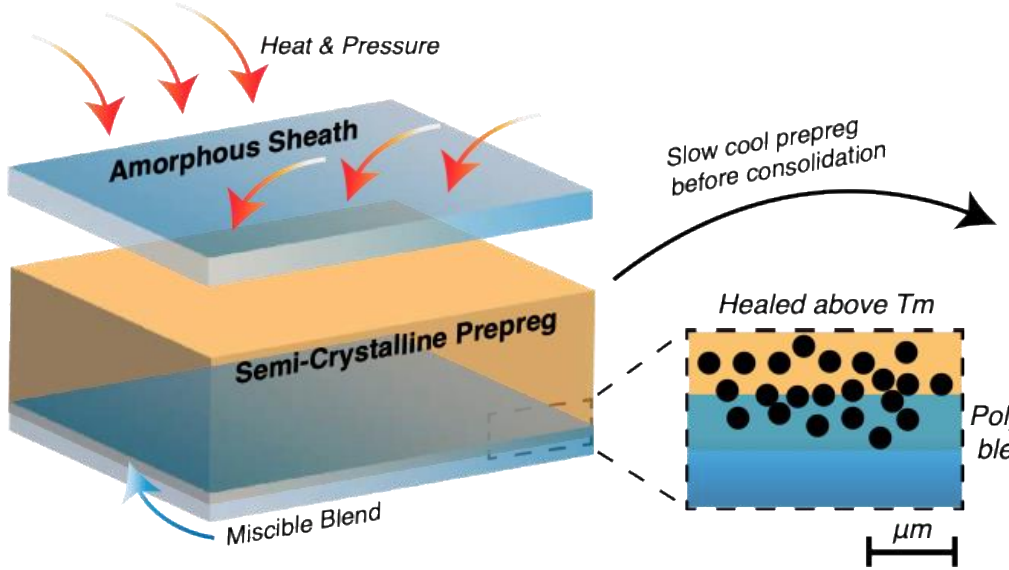

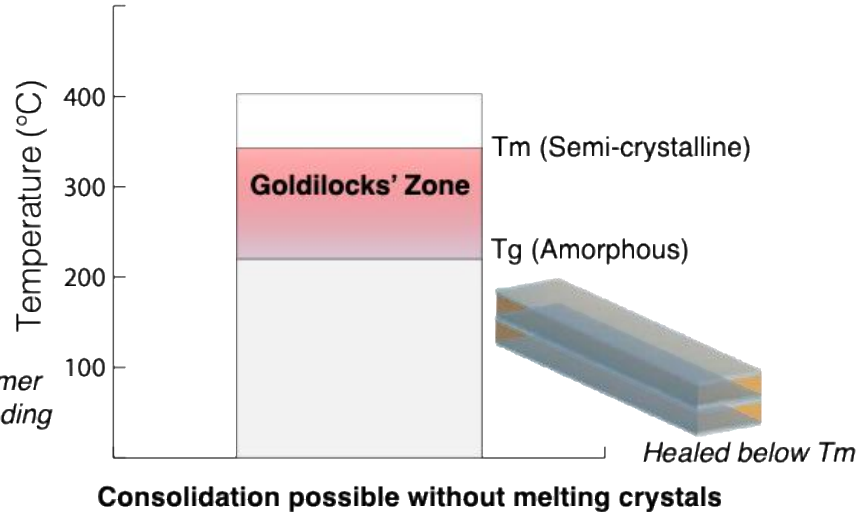

Consolidation possible without melting crystals

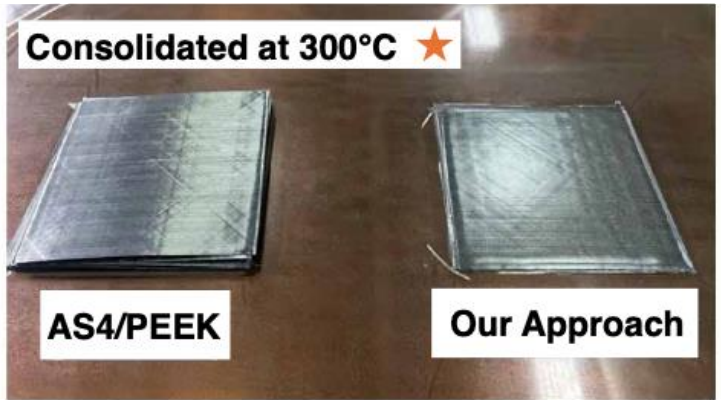

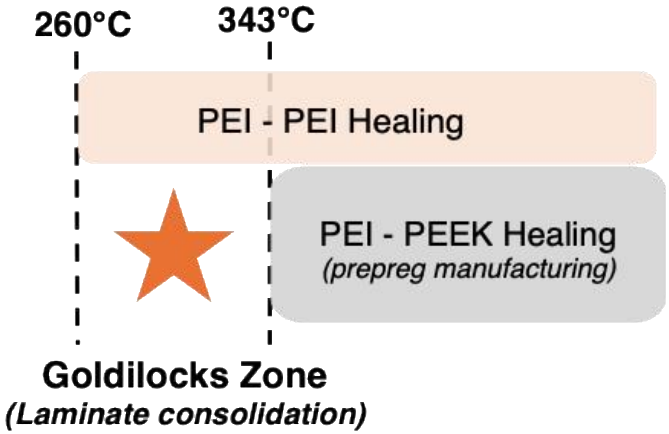

The added amorphous polymer enables sub-melt consolidation (without losing crystalline history)

Why OATMEAL?

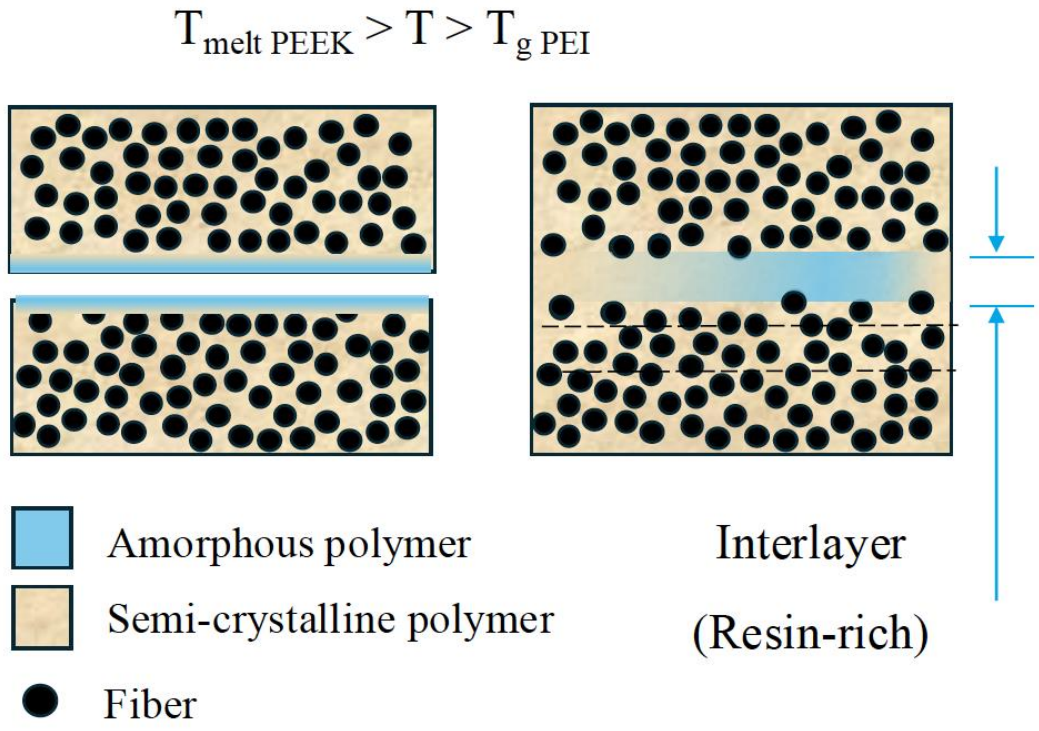
$T_{melt\ PEEK} > T > T_{g\ PEI}$
Amorphous polymer
Semi-crystalline polymer
Fiber
Interlayer
(Resin-rich)

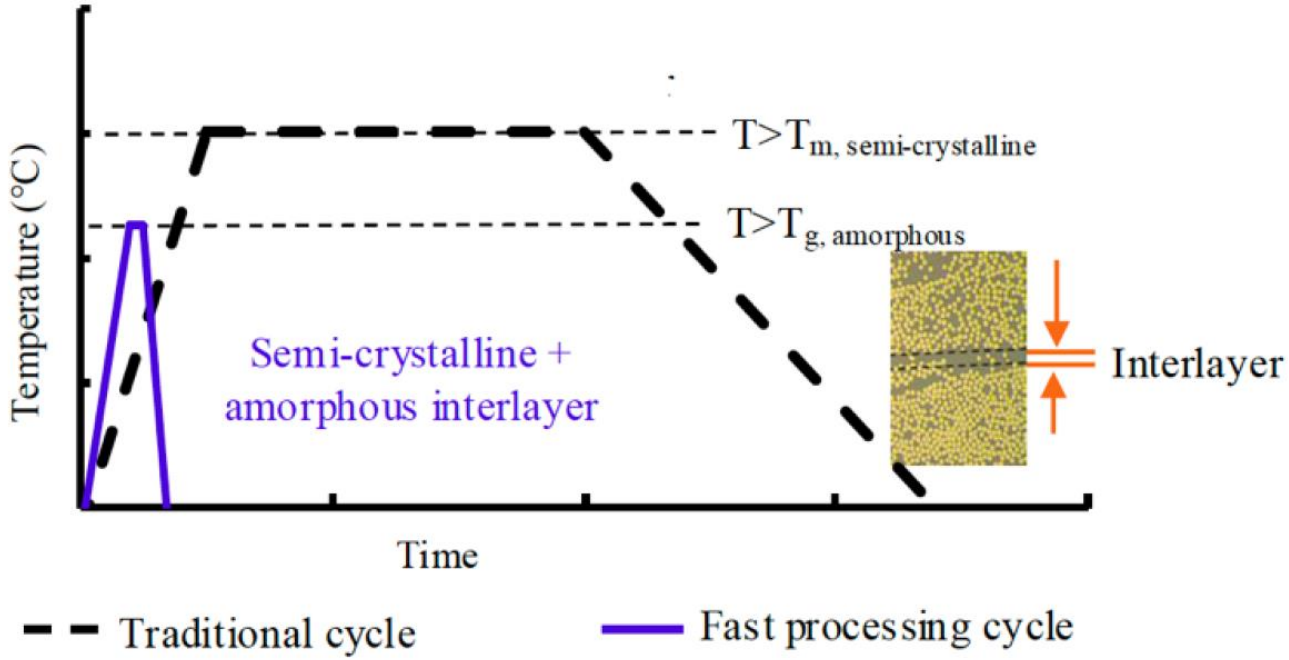
Temperature (°C)
$T>T_{m,\ semi\text{-}crystalline}$
$T>T_{g,\ amorphous}$
Semi-crystalline + amorphous interlayer
Interlayer
Time
Traditional cycle
Fast processing cycle

Laser Ablate Excess PEI to Improve Performance

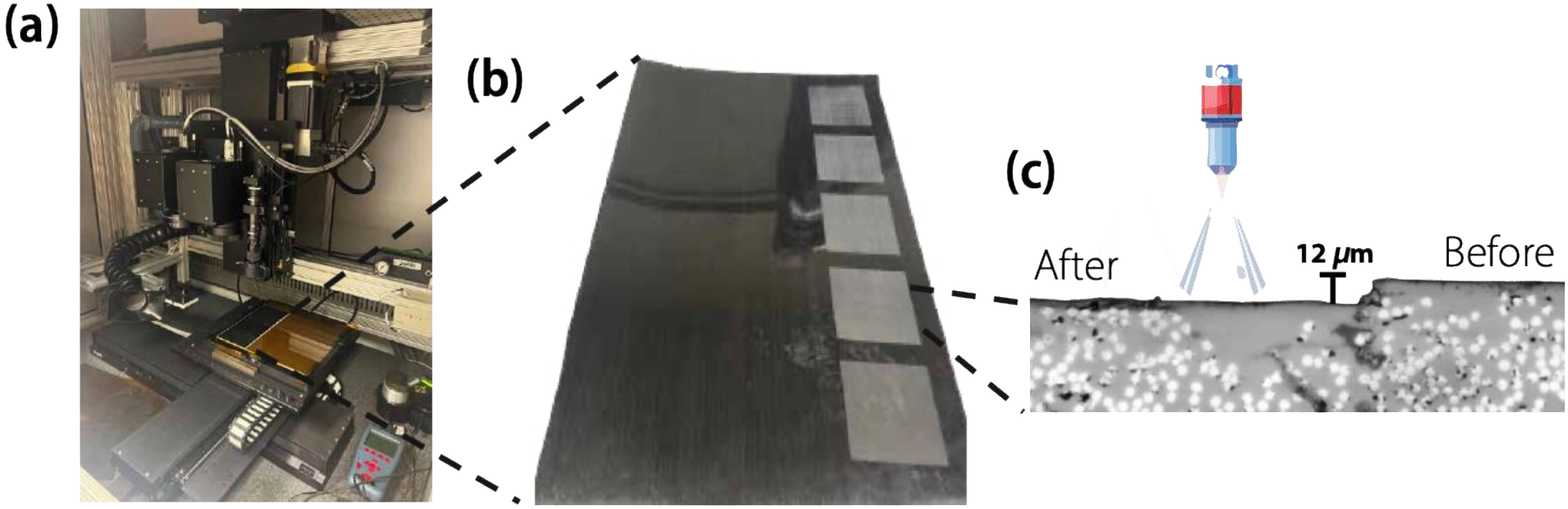

Performance improves after laser ablation

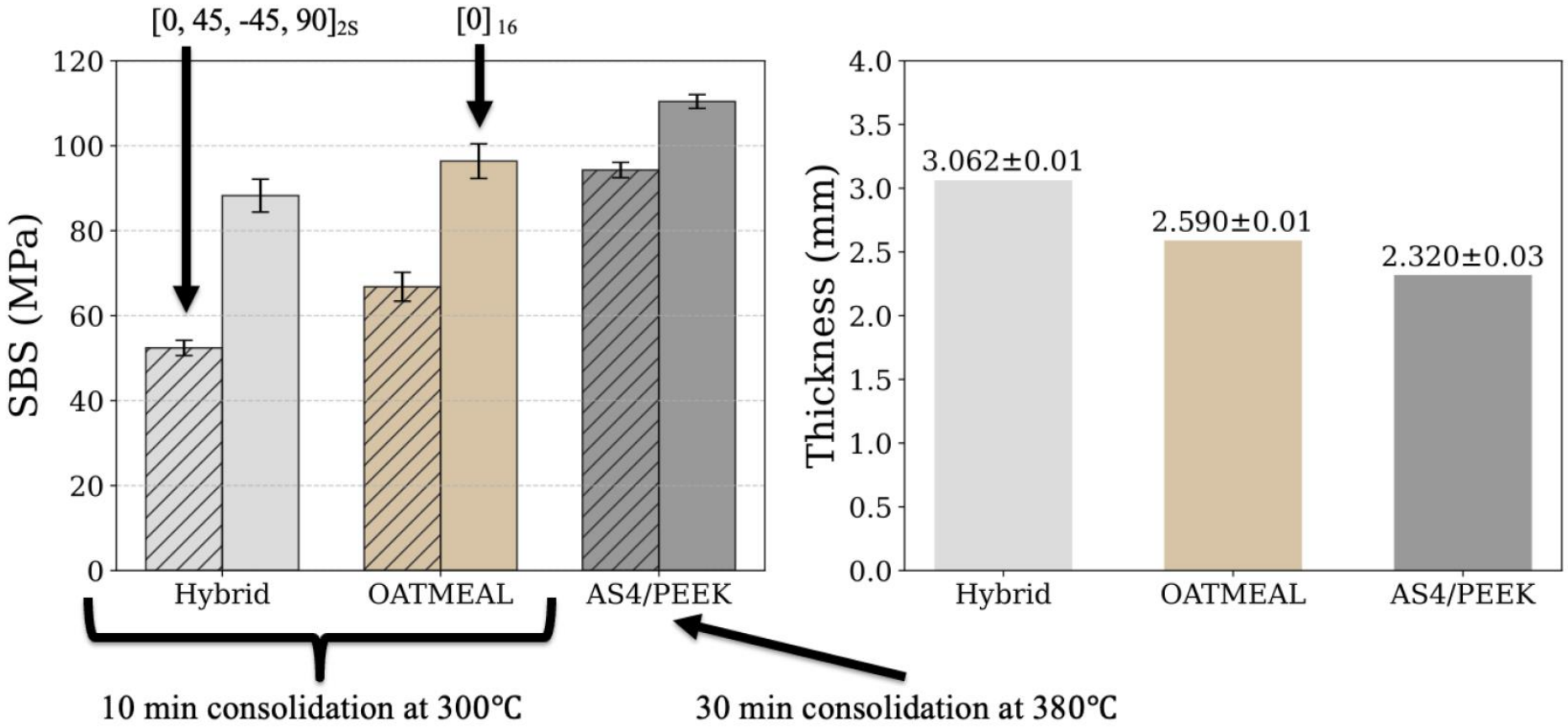

Crystallinity Measurements

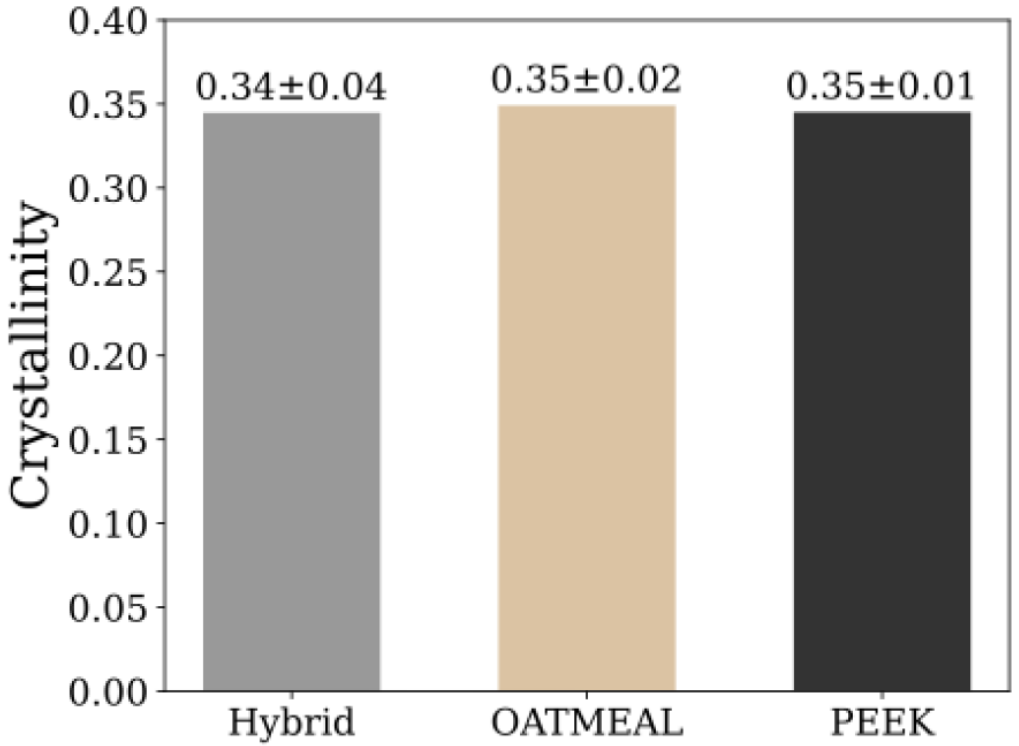

AFM-IR Shows Us that PEI Interdiffuses ~25-30 Microns

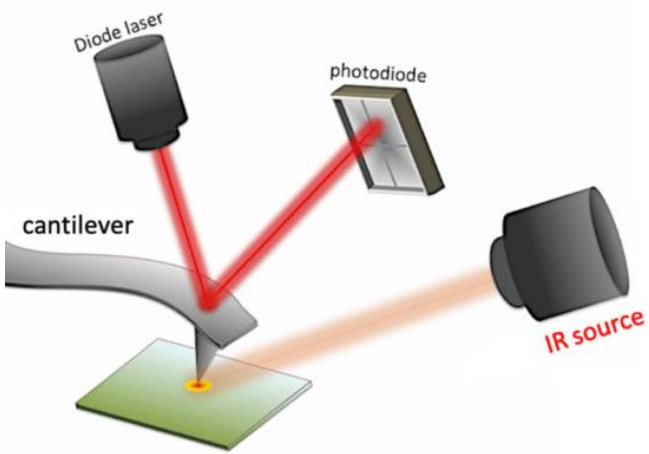

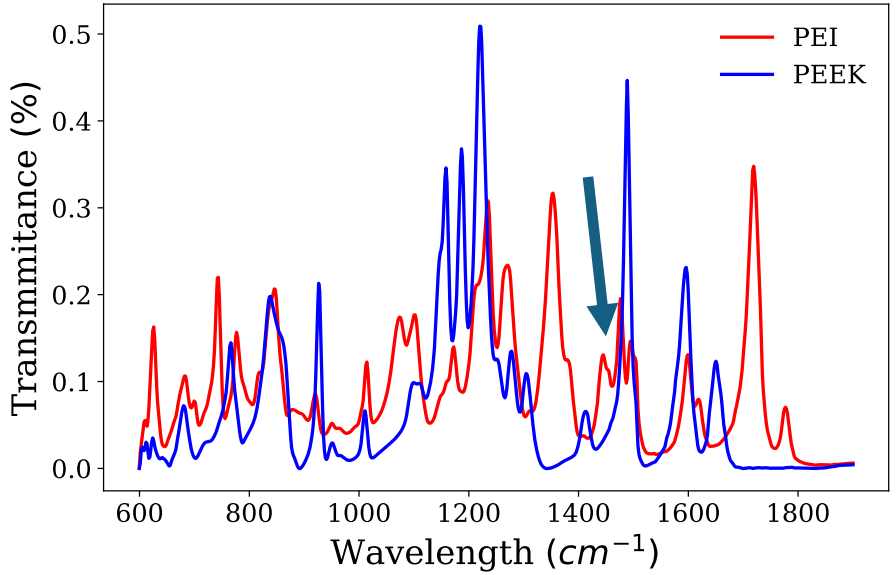

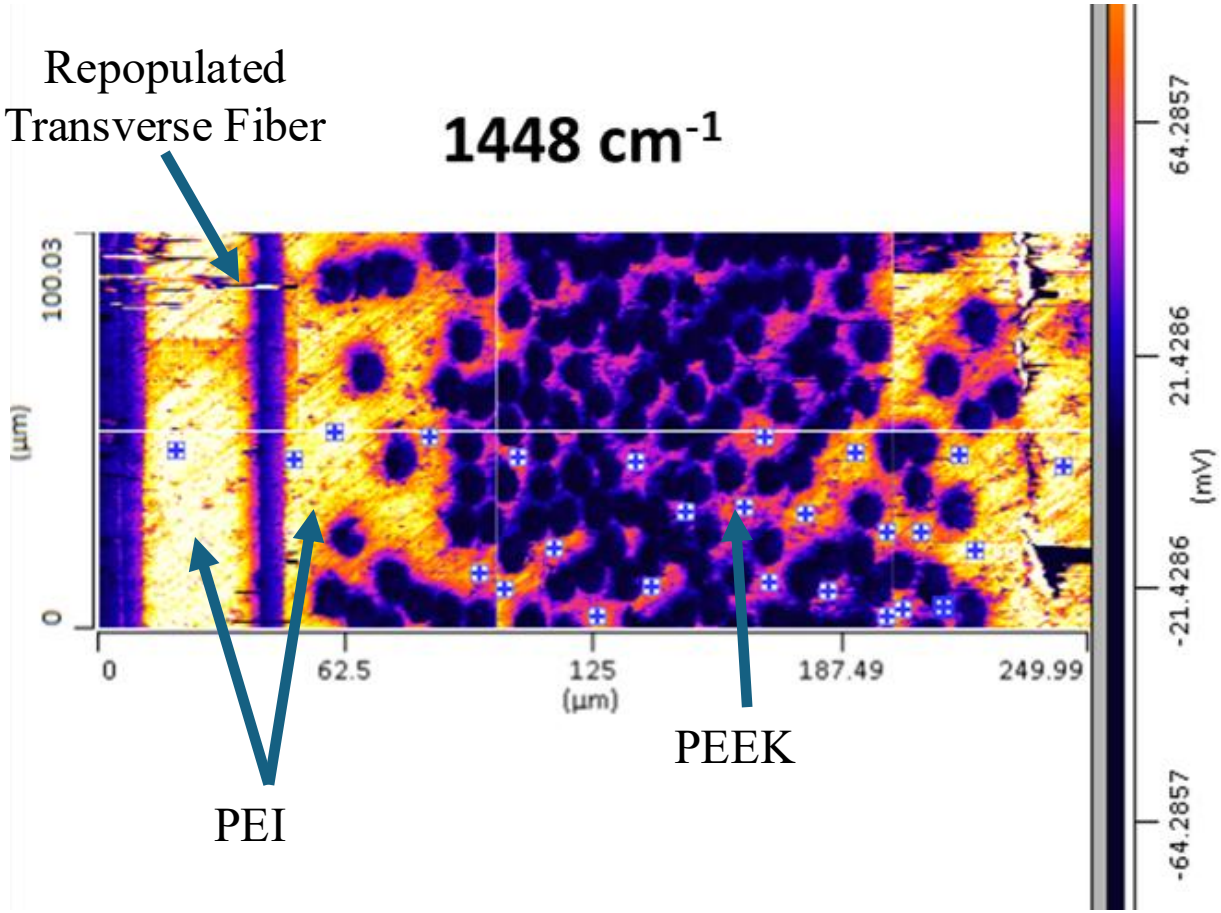

Schematic from: Mathurin et al., "Advanced Infrared Nanospectroscopy Using Photothermal Induced Resonance Technique, AFMIR: New Approach Using Tapping Mode" (2020)



Joseph Kirchhoff

Jgkirchhoff.github.io
(personal webpage)

The University of Texas at Austin
Walker Department
of Mechanical Engineering
Cockrell School of Engineering

NASA NSTGRO #80NSSC22K1203

(ONR) grant #N00014-24-1-2178

(AFOSR) # FA9550-21-1-0066

Recent Publications:

1) "In situ consolidation of carbon fiber PAEK via laser-assisted automated fiber placement", Heathman et al., Composites Part B (2023)
2) "Resin percolation and intimate contact in fast processing of thermoplastic composites", Kirchhoff et al., Composite Part A (2024)
3) "Interlaminar Bonding in Thermoplastic Composites: A Comparative Analysis of Laser AFP and Post-Processing", Kirchhoff et al., SSRN (2024)
4) "Experimental Evaluation of the In-Situ Consolidation Automated Fiber Placement of Polyaryletherketone Composites", Grimsley, Hudson et al., Thermoplastics Composites Conference (2024)
5) "Feasibility of Amorphous Bonding in Thermoplastic Composites and the Resulting Interlaminar Residual Stresses", Kirchhoff, Hudson, Tehrani, SAMPE (2025)

ICCM24
AUGUST 4-8, 2025
BALTIMORE CONVENTION CENTER
BALTIMORE, MARYLAND, USA

No Technical Paper Submission for:

Ahmed Hassen

ICCM24
AUGUST 4-8, 2025
BALTIMORE CONVENTION CENTER
BALTIMORE, MARYLAND, USA

No Technical Paper Submission for:

Adam Sawicki

ICCM24
AUGUST 4-8, 2025
BALTIMORE CONVENTION CENTER
BALTIMORE, MARYLAND, USA

No Technical Paper Submission for:

Michelle Johnson

Structural Fire Response of Polymer Composites

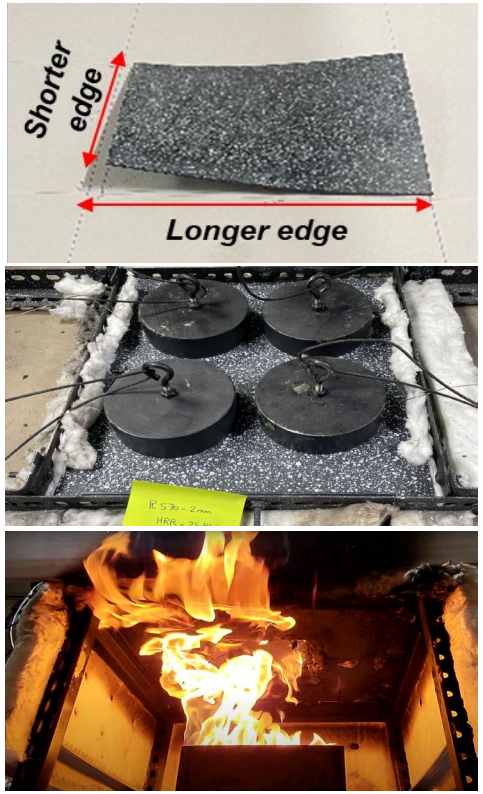

Plate-scale testing

Scott W. Case, PhD
Reynolds Metals Professor
Associate Department Head for Undergraduate Studies
Via Department of Civil and Environmental Engineering
Virginia Tech

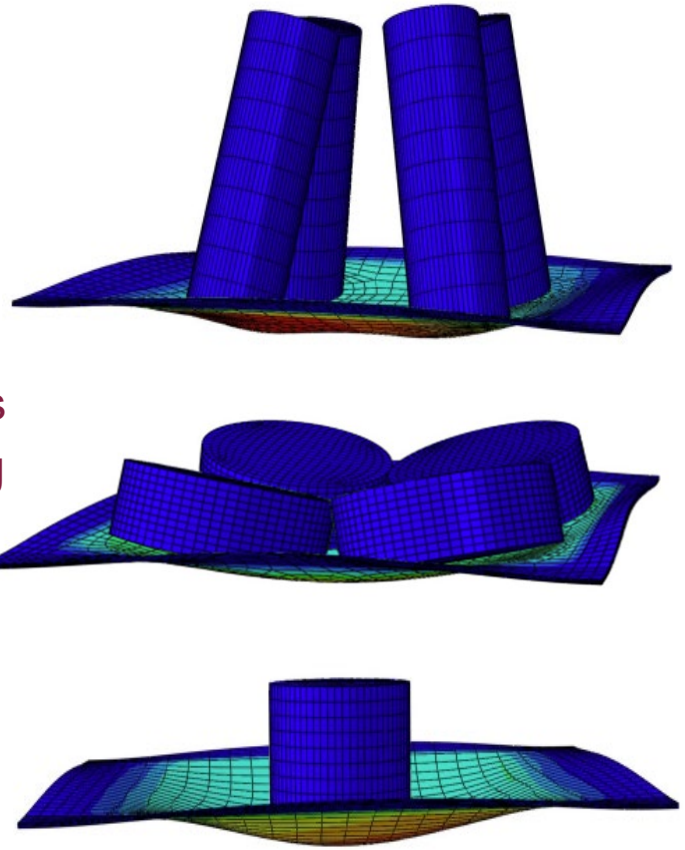

ICCM24
24TH INTERNATIONAL CONFERENCE ON COMPOSITE MATERIALS

August 4-8, 2025

Motivation: How did I get into this business?



Buckling of laminate

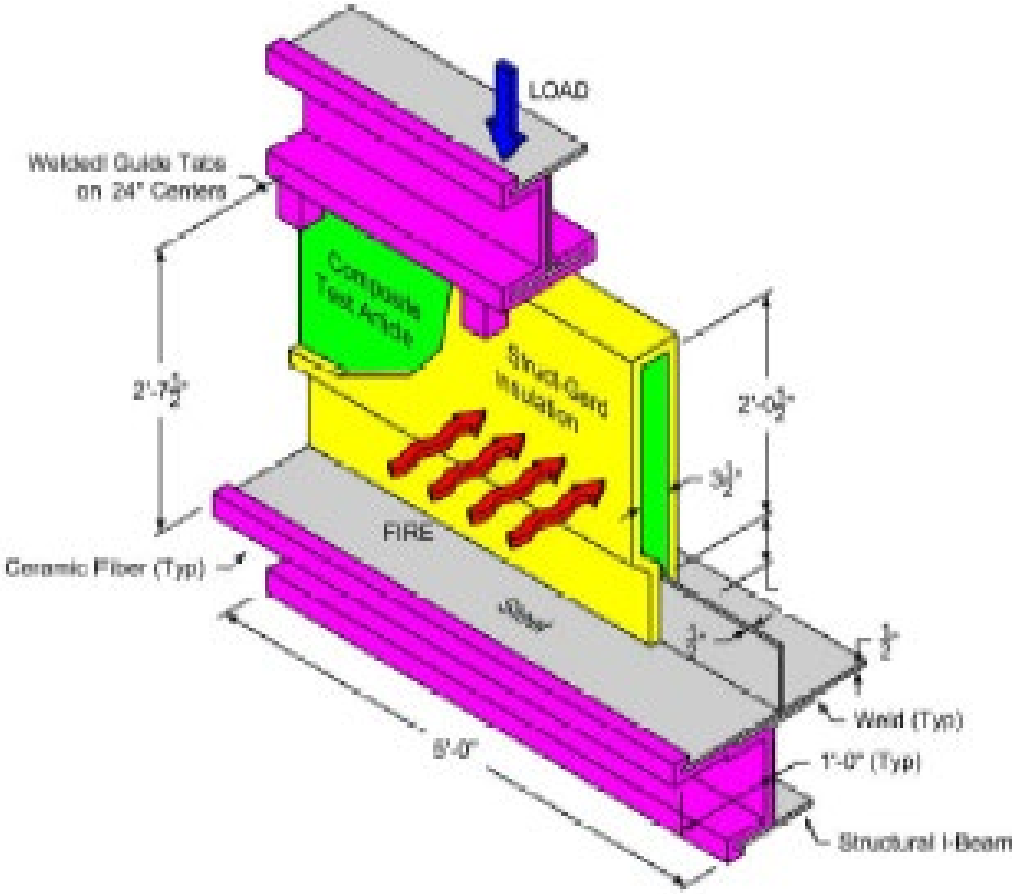

Articles from tests conducted at Southwest Research Institute - Summer 2002

Presentation Overview

- Framework for analysis of failure of composites subjected to combined fire and mechanical loading
- Micromechanics of failure
  - Compression controlled failures
  - Tension controlled failures
- Laminate-level response
- New measurement techniques
- Integration with numerical tools
- Ongoing applications
- Conclusions
- Acknowledgements

Framework for Analysis

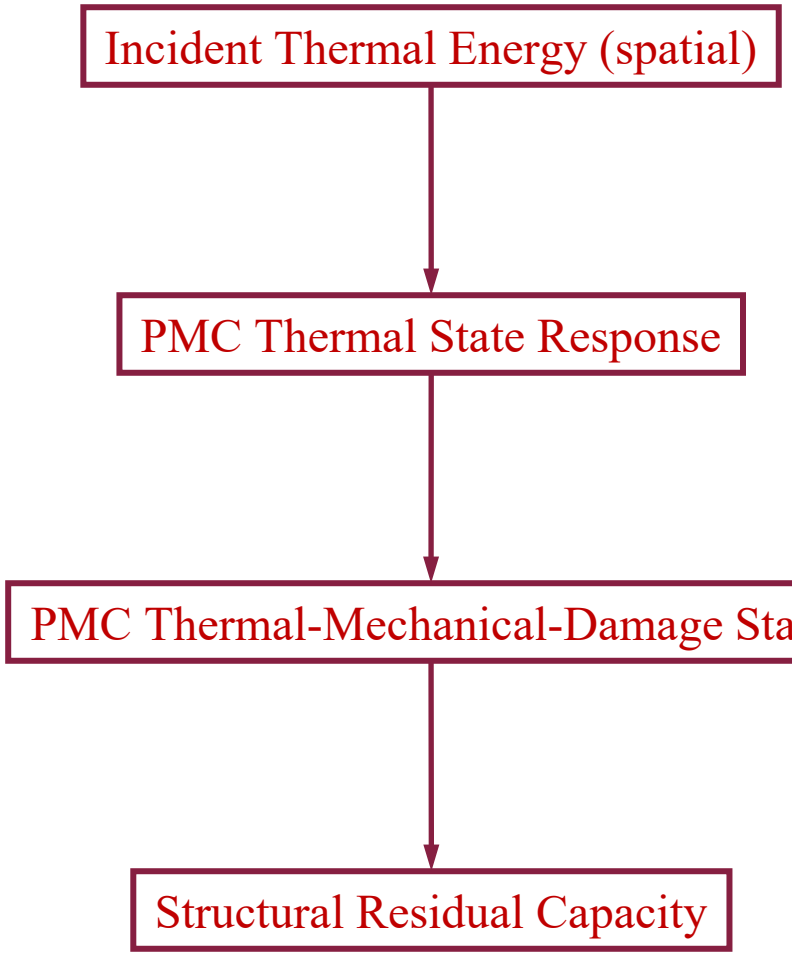

$q''(x,y,z,t)$

- Property evolution (decomposition)
- Intumesence
- Delamination
- Volatile evolution

- $E_{ij}(T,t)$ - *creep*
- $X_{ij}(T,t)$ - *creep rupture*

Limit state

- Local failures
- Global buckling
- Local buckling (delamination)
- Deflection

Viscoelastic Characterization: E-glass/Vinyl Ester

$[\pm 45]_{2s}$ Laminate
Vetrotex 324/Derakane 510A-40

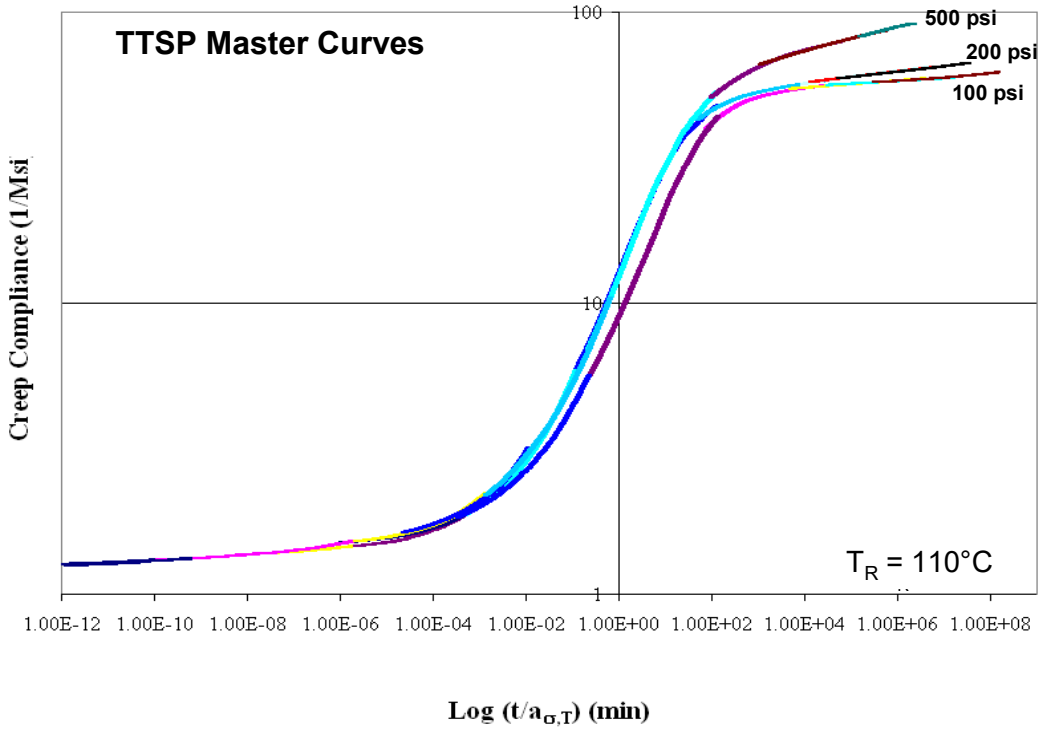

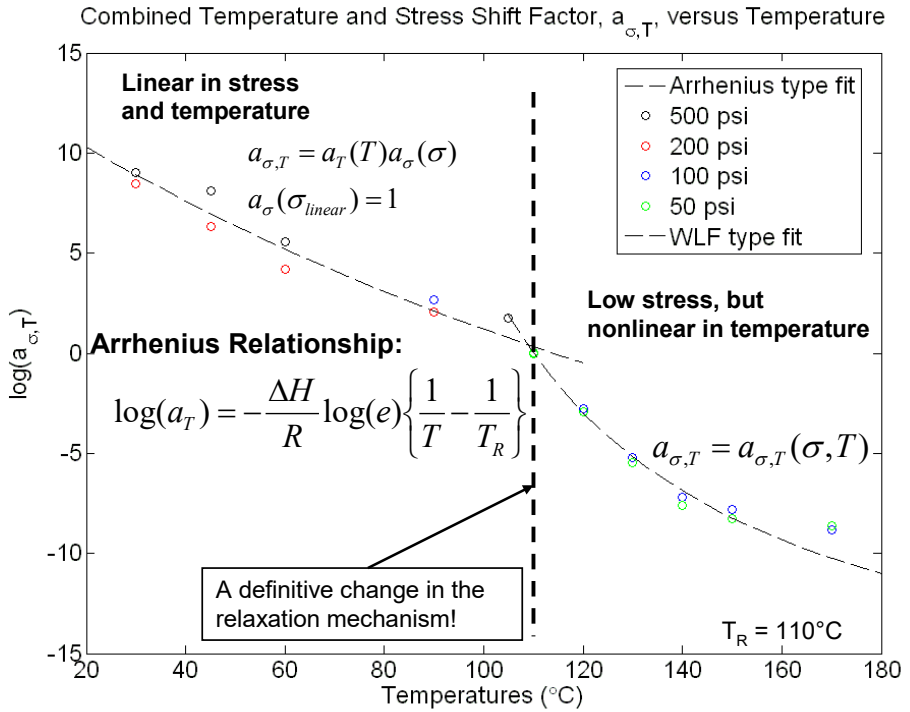

Creep and recovery data (30° to 170°C & 0.05 to 4 ksi) modeled using Zapas/Crissman visco-plastic model describing creep response to a wide range of temperature & loads

Observations of High Temperature Compression Failures

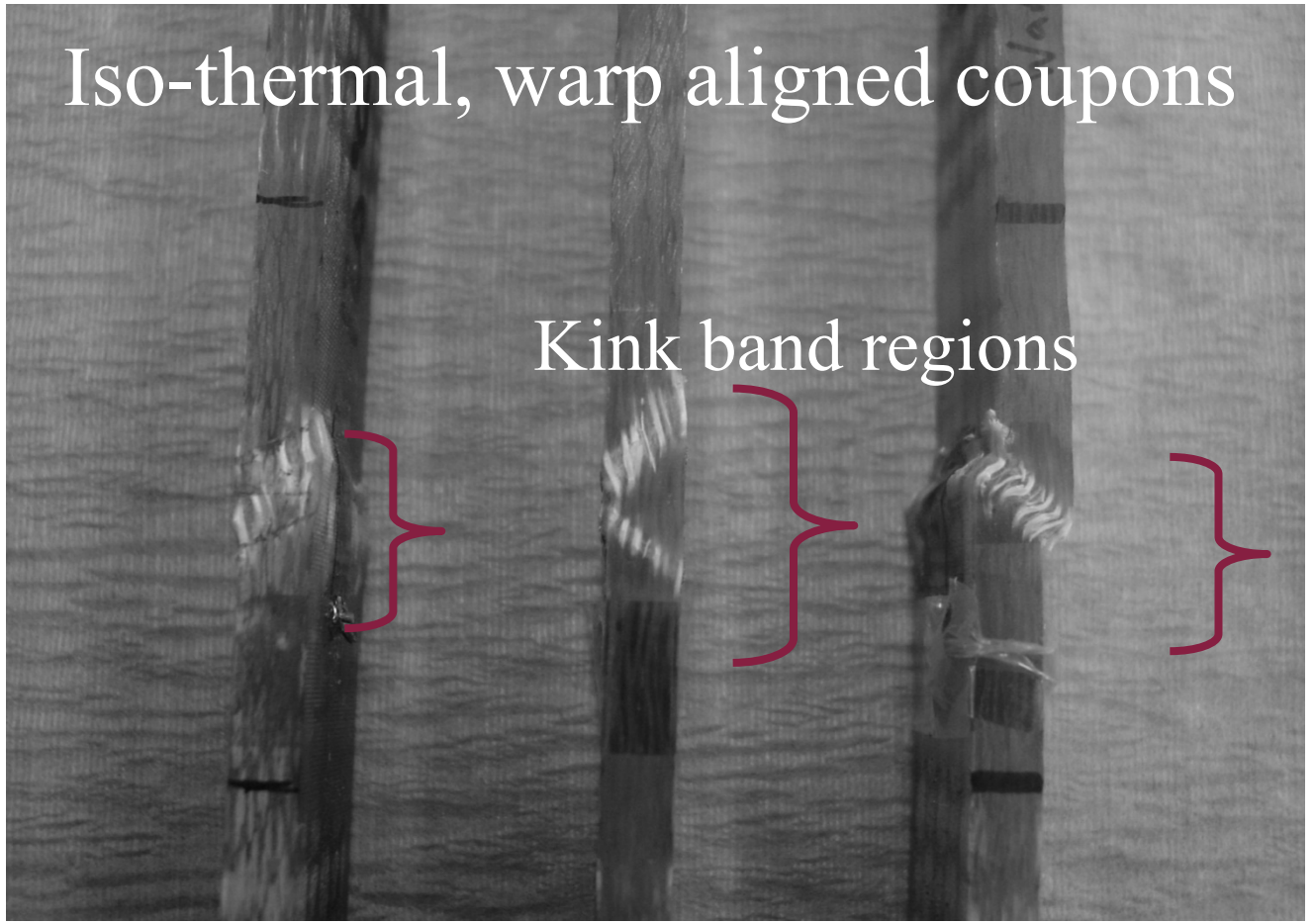

Vetrotex 324/Derakane 510A-40

Compression Mechanics

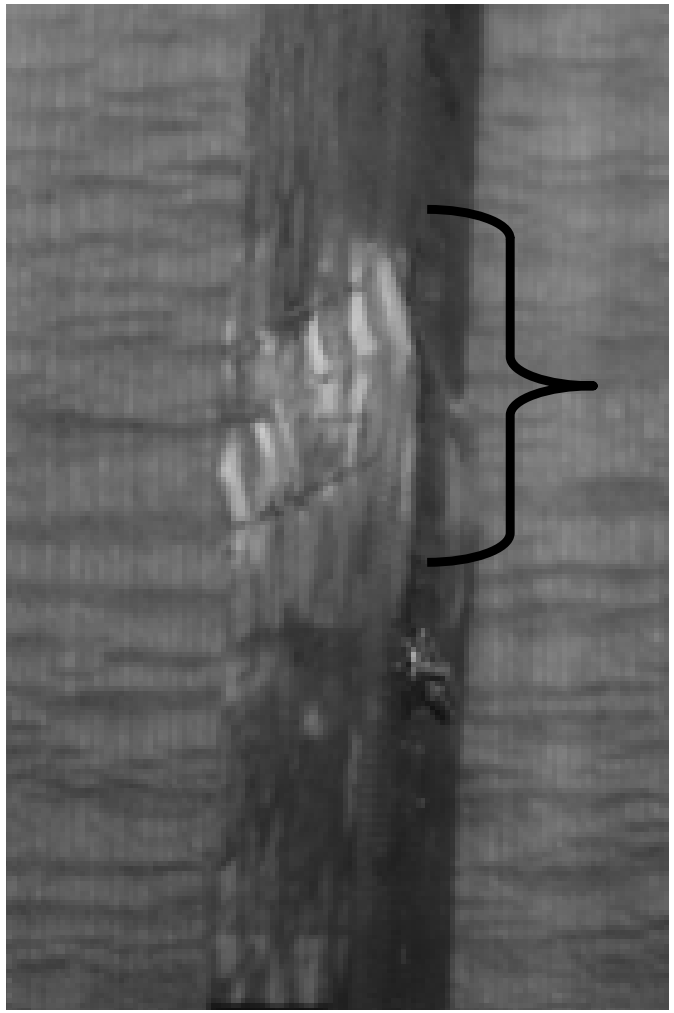

Use Budiansky & Fleck compression strength model, assuming a Ramberg-Osgood shear stress-strain relation

$$\frac{\gamma}{\gamma_y} = \frac{\tau}{\tau_y} + \left(\frac{3}{7}\right)\left(\frac{\tau}{\tau_y}\right)^n$$

Compression strength modified as a function of temperature and time

$$X_c(T,t) = G(T,t)\left[1 + n(T)\left(\frac{3}{7}\right)^{\frac{1}{n(T)}}\left(\frac{\bar{\varphi}}{\gamma_y(T)\left(n(T)-1\right)}\right)^{\frac{n(T)-1}{n(T)}}\right]^{-1}$$

Compression Mechanics

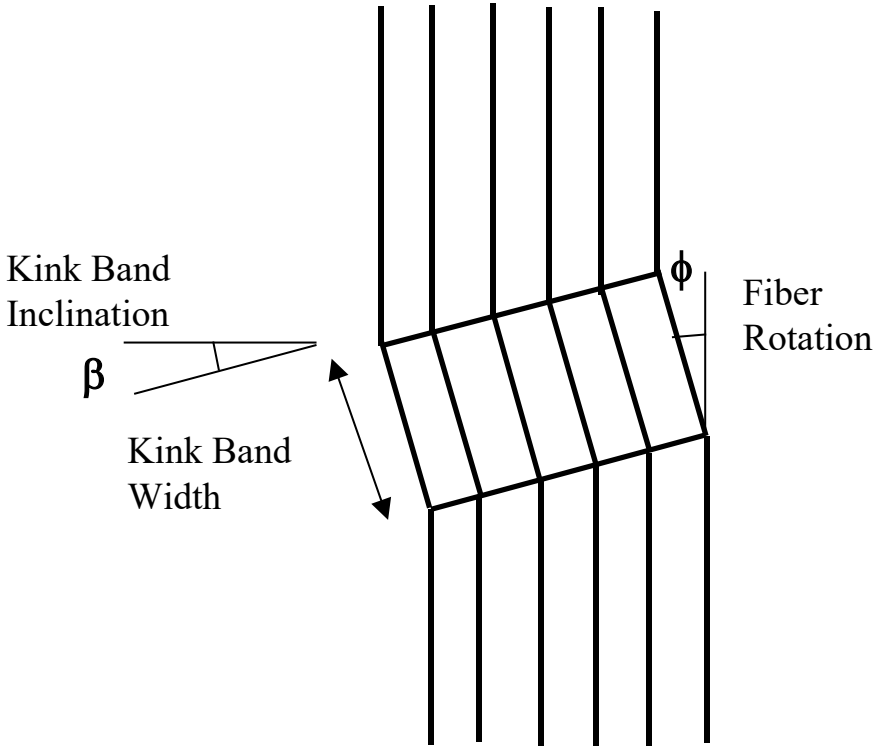

Use Budiansky & Fleck compression strength model, assuming a Ramberg-Osgood shear stress-strain relation

$$\frac{\gamma}{\gamma_y} = \frac{\tau}{\tau_y} + \left(\frac{3}{7}\right)\left(\frac{\tau}{\tau_y}\right)^n$$

Compression strength modified as a function of temperature and time

$$X_c(T,t) = G(T,t)\left[1 + n(T)\left(\frac{3}{7}\right)^{\frac{1}{n(T)}}\left(\frac{\bar{\varphi}}{\gamma_y(T)\left(n(T)-1\right)}\right)^{\frac{n(T)-1}{n(T)}}\right]^{-1}$$

Isothermal Compression Creep Rupture

Shift factors from shear creep compliance used to collapse compression creep rupture data

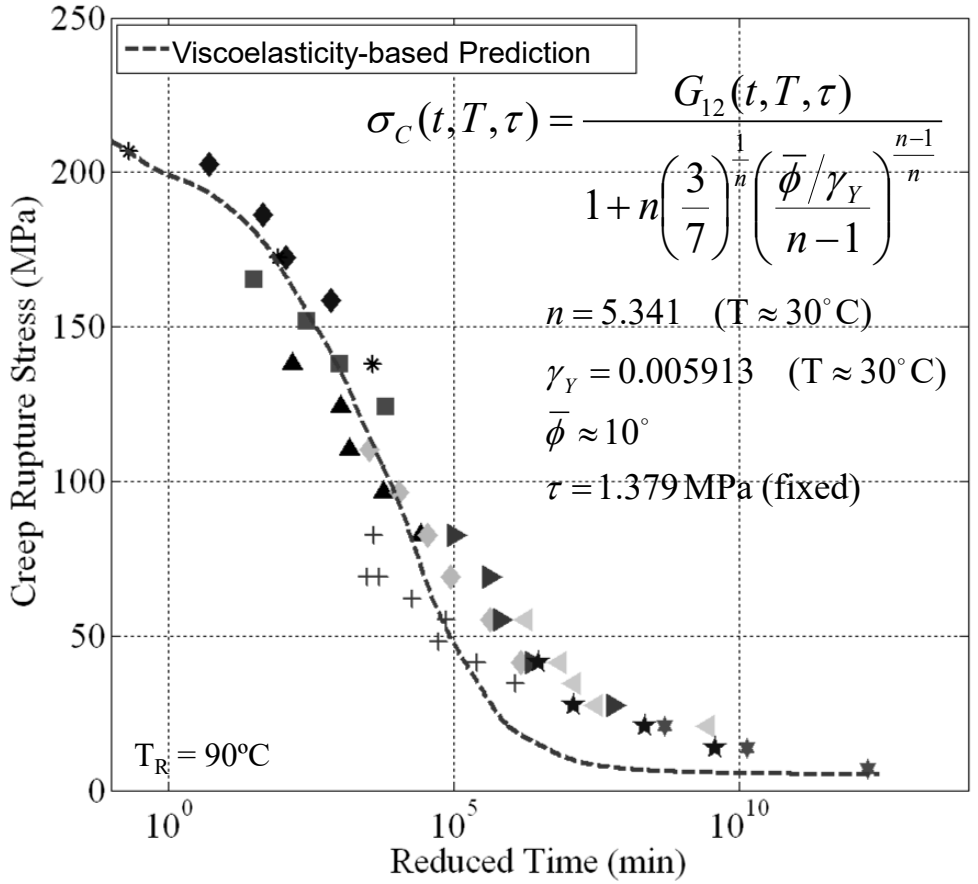

$$X_C(\xi) = \frac{G_{12}(\xi)}{1+n\left(\frac{3}{7}\right)^{\frac{1}{n}}\left(\frac{\bar{\phi}/\gamma_Y}{n-1}\right)^{\frac{n-1}{n}}}$$

$$n = 5.3 \quad (T \approx 30^\circ C)$$

$$\gamma_Y = 0.59\% \quad (T \approx 30^\circ C)$$

$$\bar{\phi} \approx 10^\circ$$

Warp $[0°]_{10}$ and Weft $[90°]_{10}$ coupons of Vetrotex 324/Derakane 510A - 40

Key Conclusion: Temperature-dependent compression strength and time-dependent compression creep rupture are both manifestations of the same viscoelastic behavior of composite

Temperature Effects on E-Glass Tensile Strength

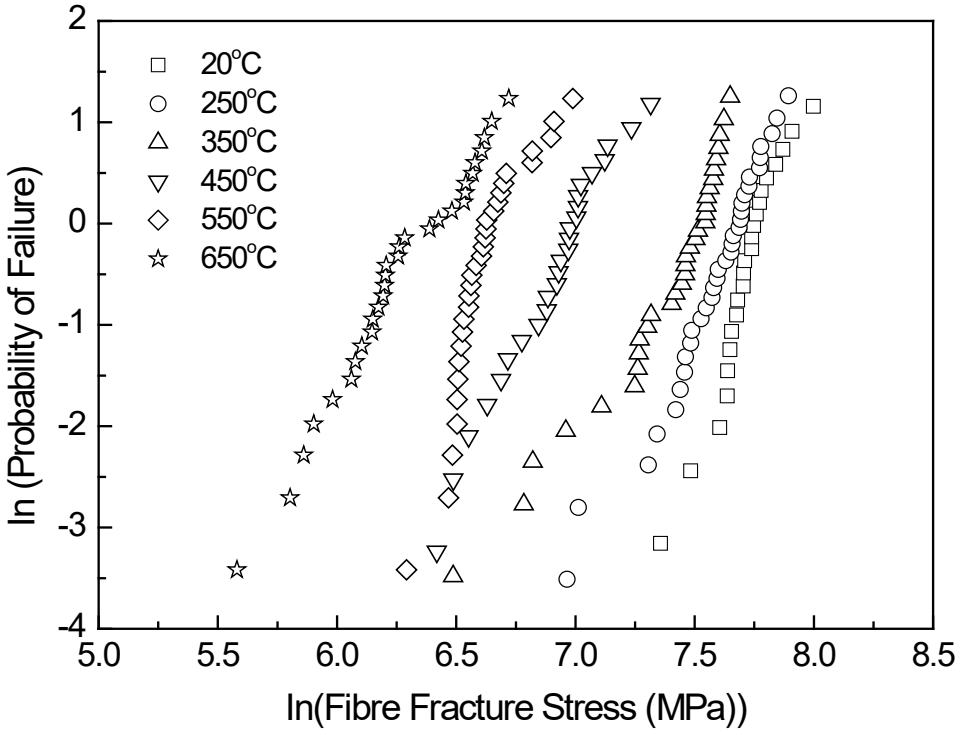

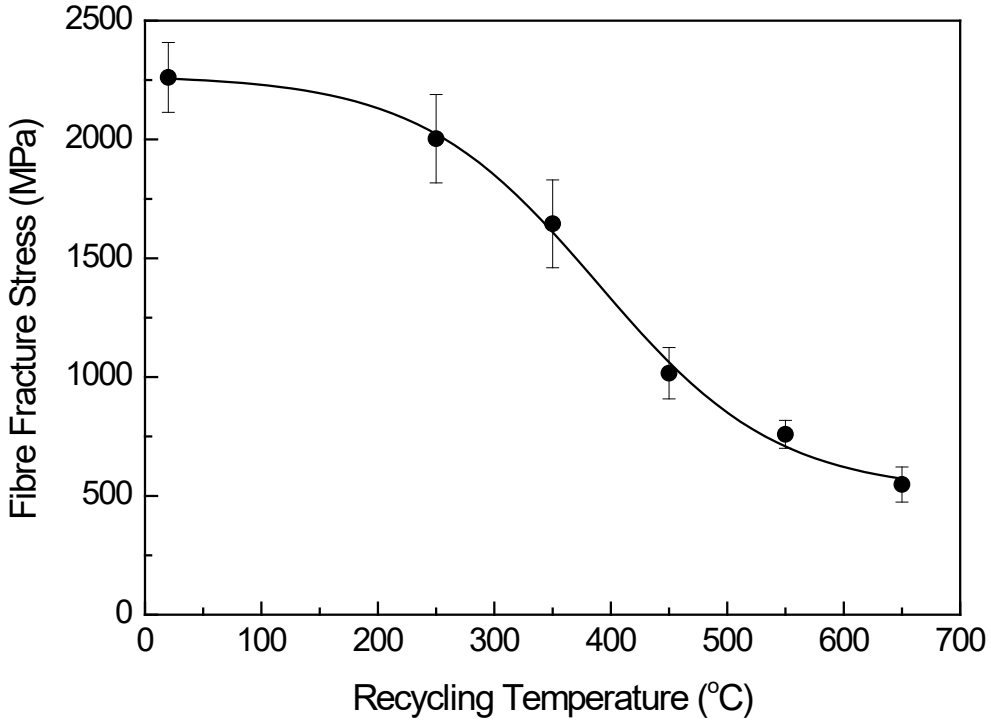

Not only applies to fire, but also thermal recyling

Temperature Effects on E-Glass Tensile Strength

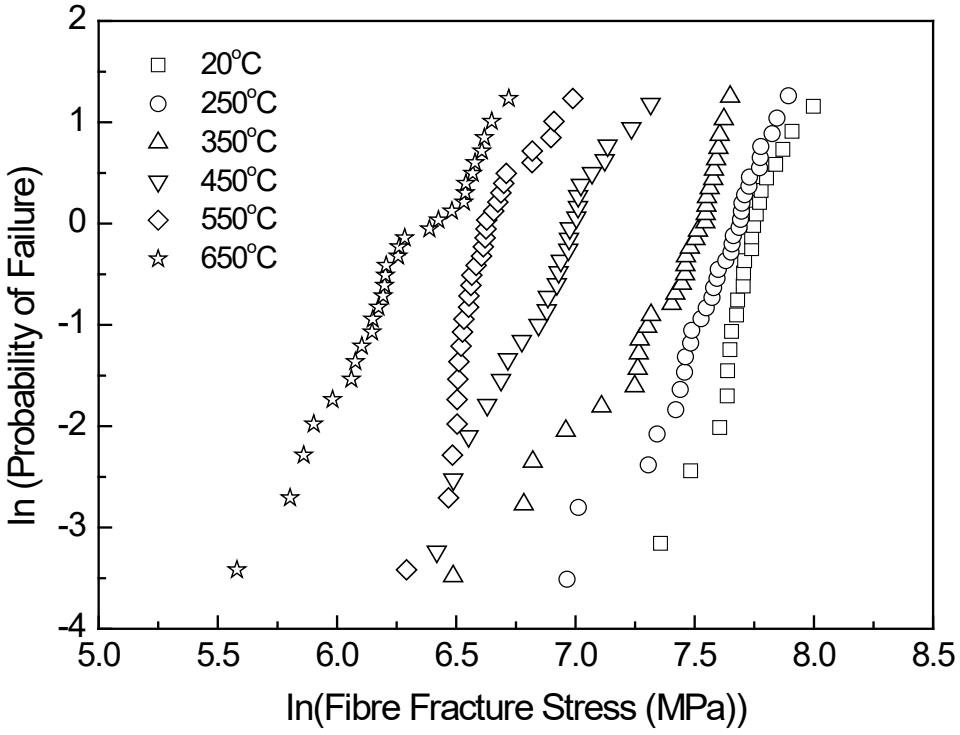

No exposure

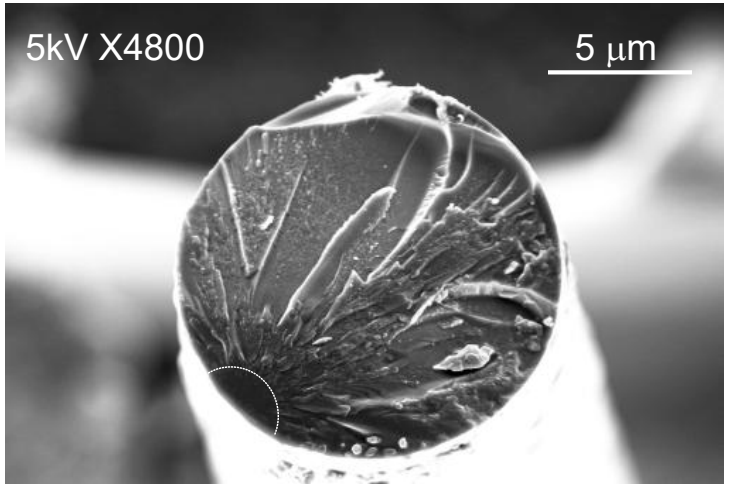

450°C exposure

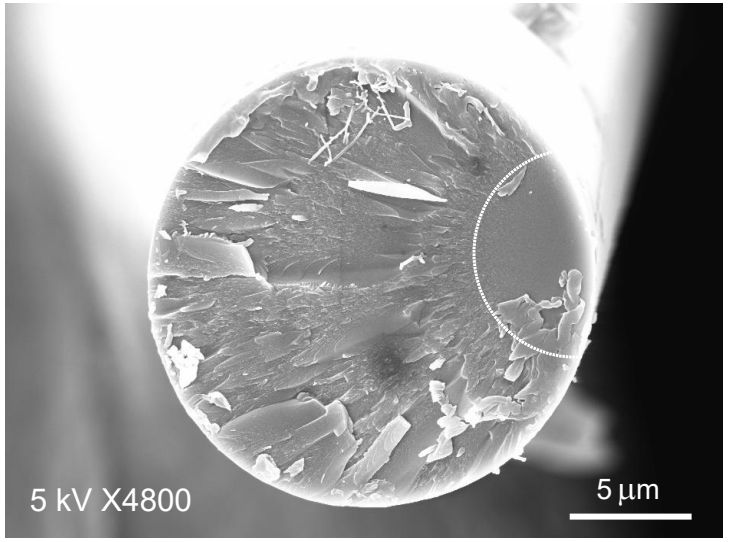

Temperature Effects on E-Glass Tensile Strength

Are Flaws Growing or is Bulk Toughness Decreasing?

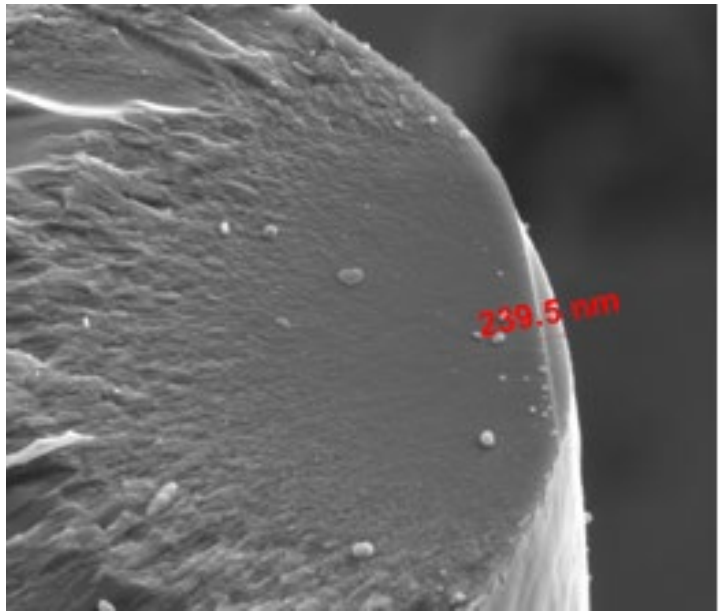

Fracture surface of glass fiber containing straight FIB milled notch (239.5 nm deep)

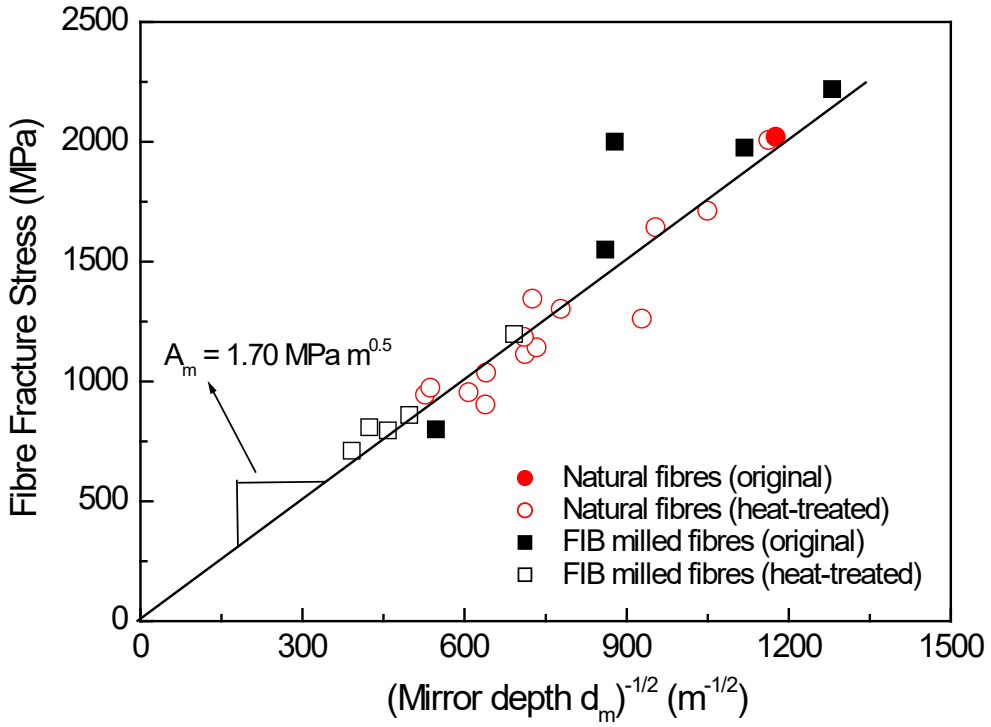

Temperature Effects on E-Glass Tensile Strength

Are Flaws Growing or is Bulk Toughness Decreasing?

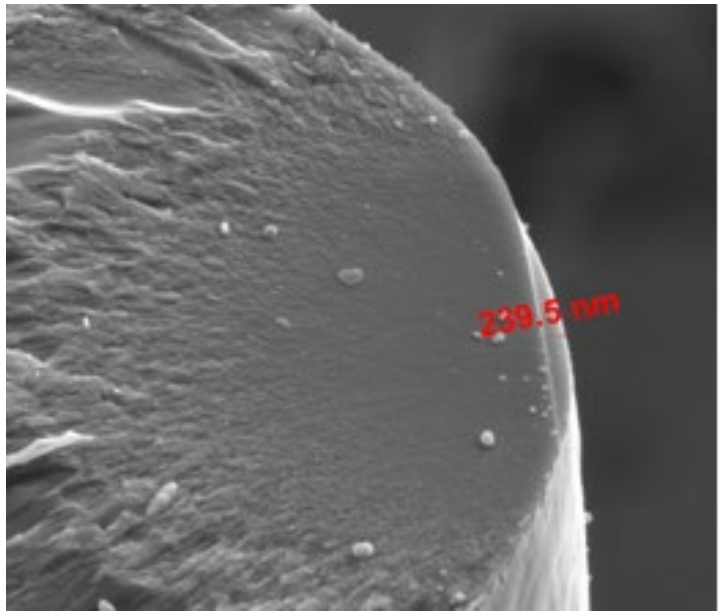

Fracture surface of glass fiber containing straight FIB milled notch (239.5 nm deep)

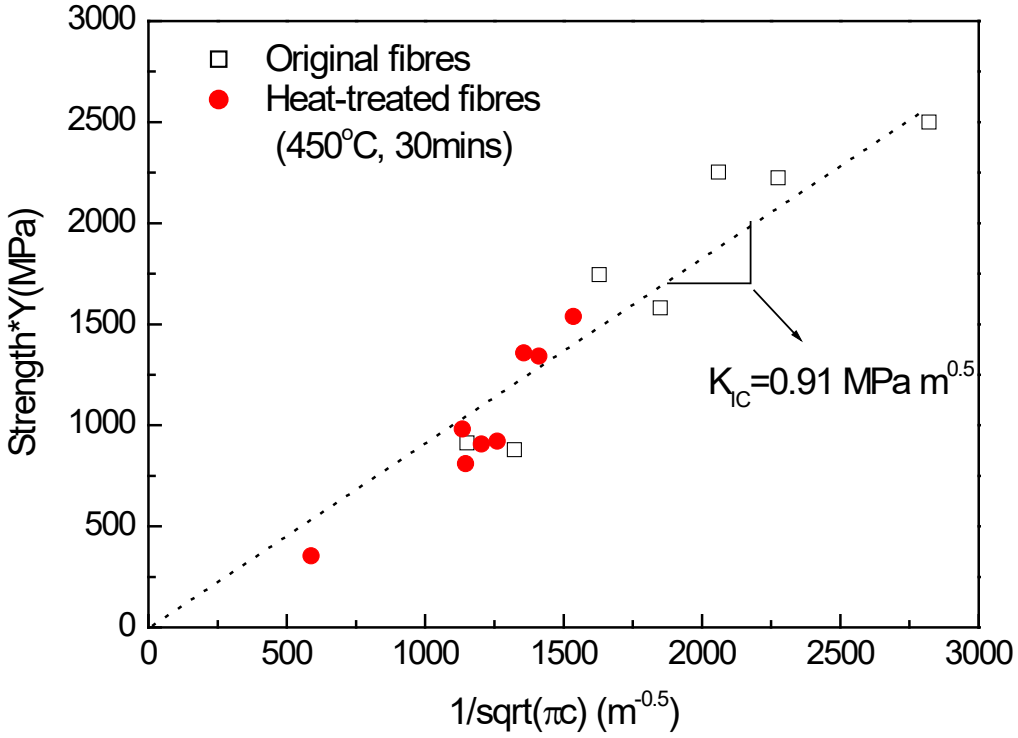

Sustained Compression Load & One-sided Heat Flux Exposure

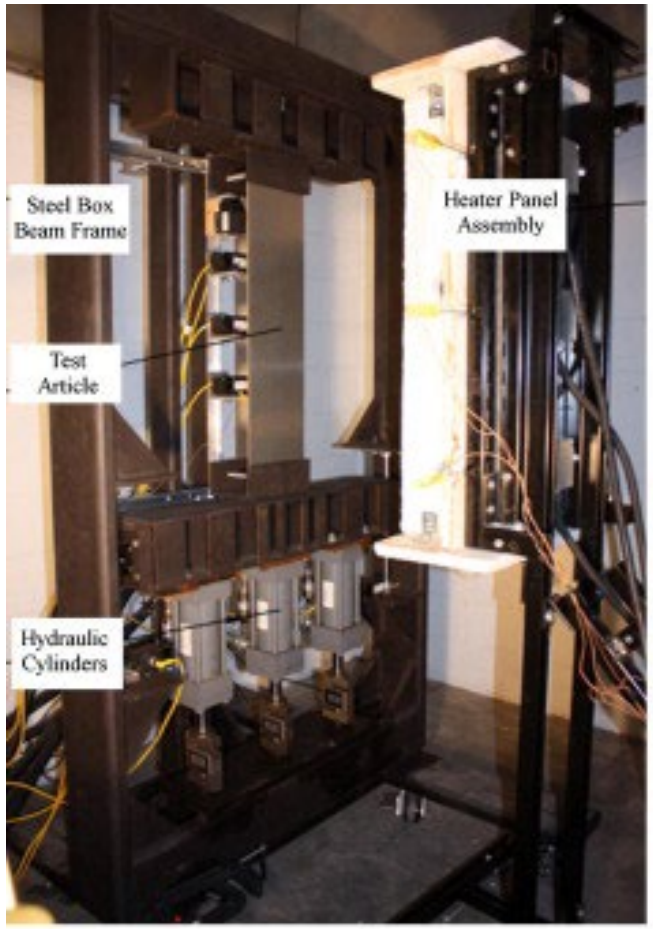

(a)

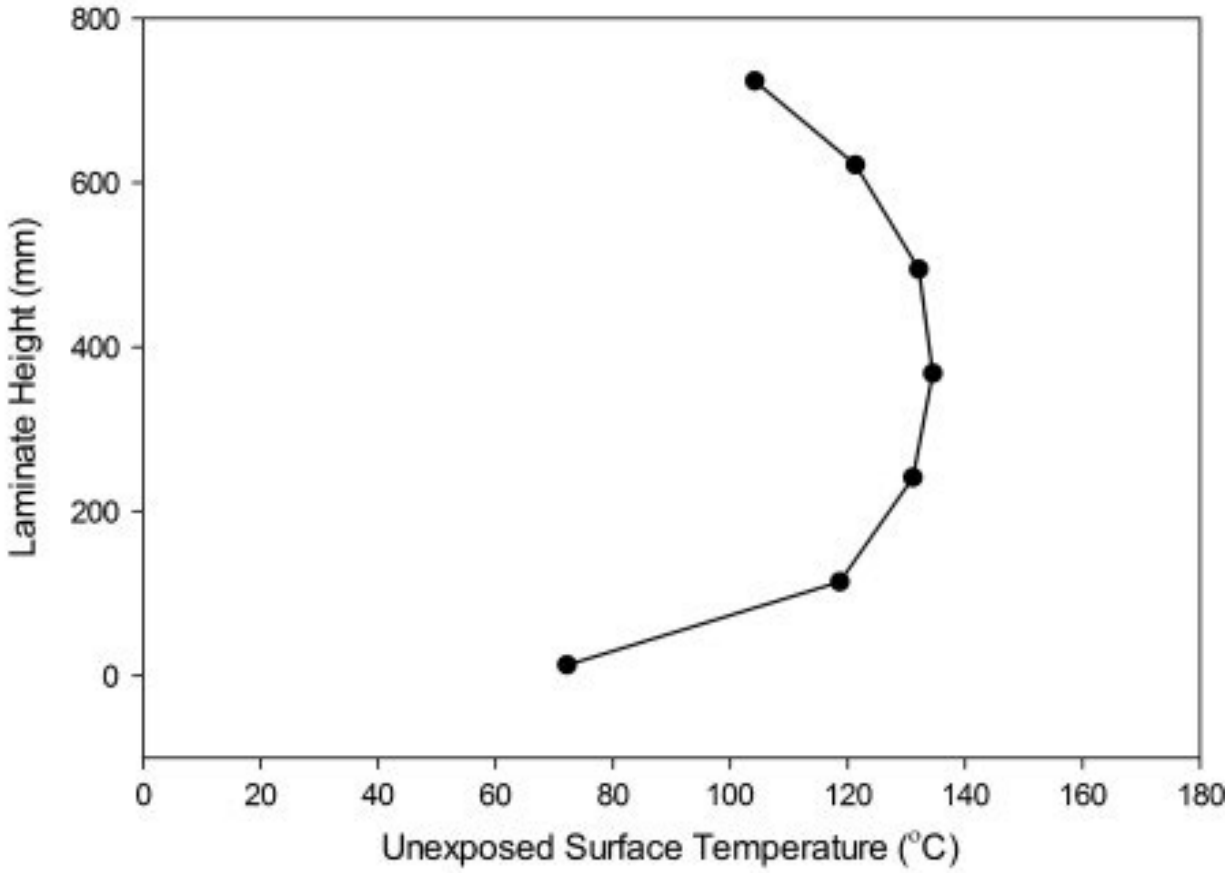

(b)

Sustained Compression Load & One-sided Heat Flux Exposure

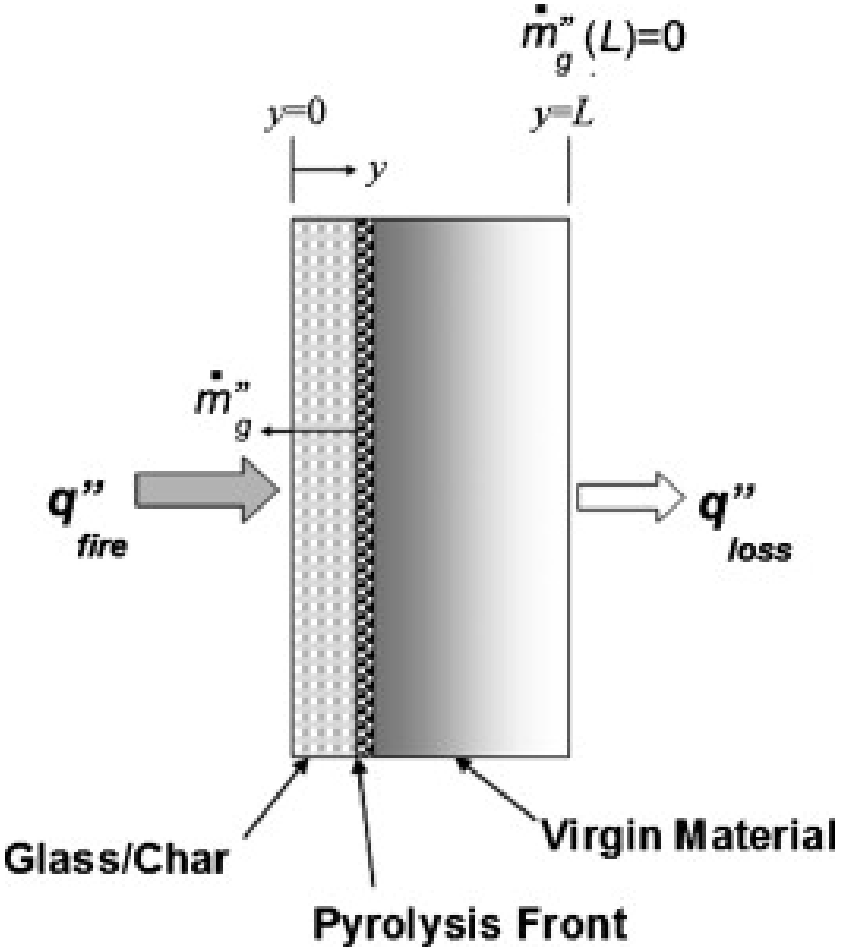

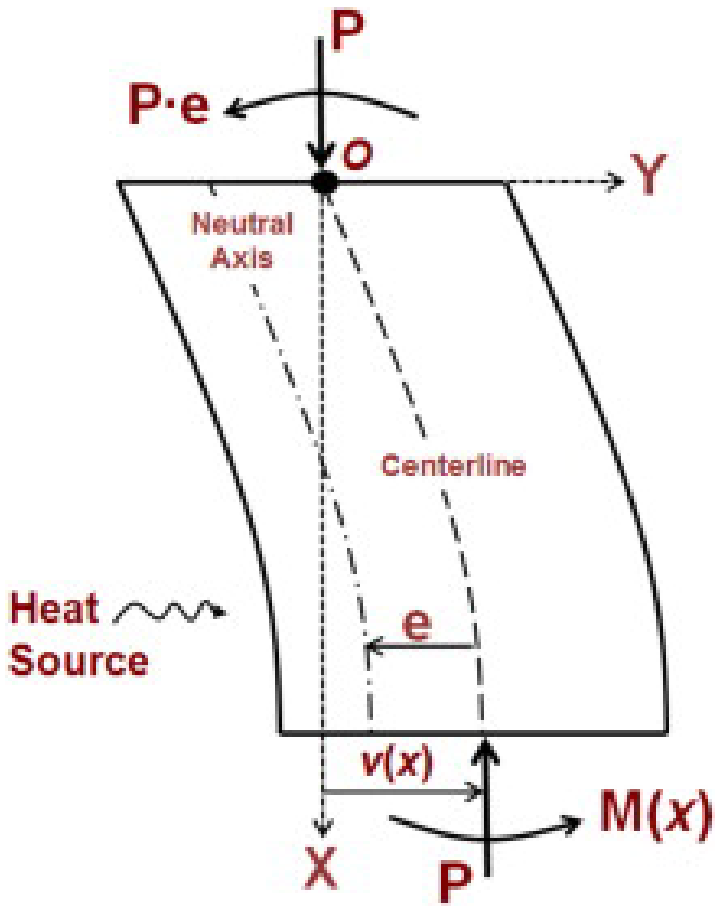

$$(EI)_{eq}\frac{d^2\theta(x)}{dx^2}+P\theta(x)=\left(M^{T}_{x,\theta}+Pe_0\right)\left(\frac{8-8K}{L^2}x-\frac{4-4K}{L}\right)$$

Simple Mechanics Model to Predict the Response

Sustained Compression Load & One-sided Heat Flux Exposure

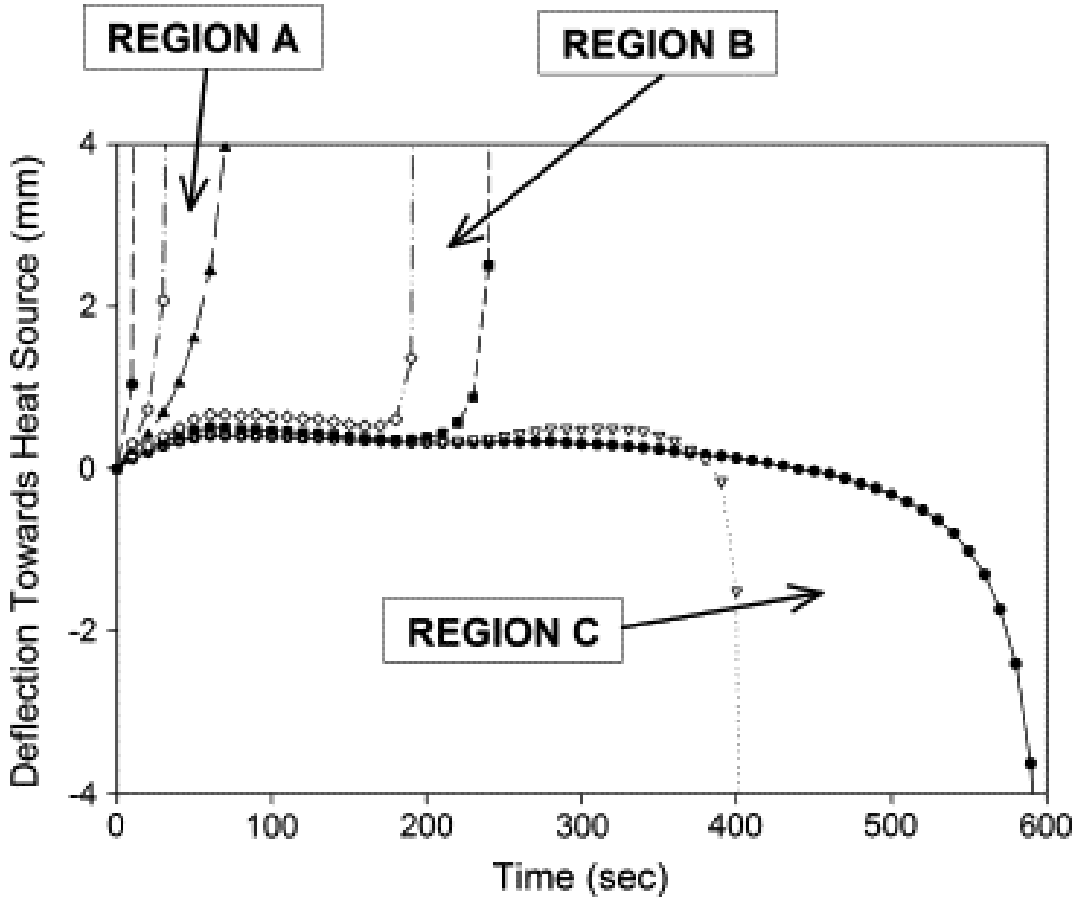

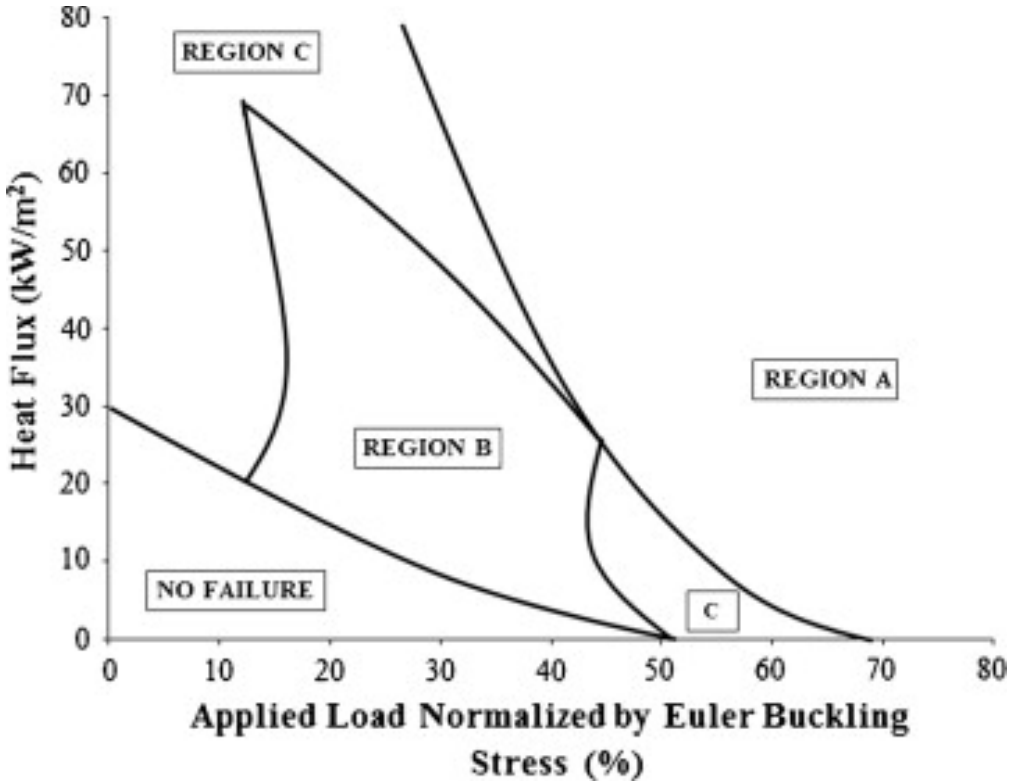

Simple Mechanics Model to Predict the Response

Coupled Viscoelastic, Thermomechanical Model

- Combine partial differential equations representing
  - Viscoelastic mechanical constitutive equation, using rule of mixtures for char and virgin material
  - Decomposition reaction equation (solid mass)
  - Heat transfer equation (temperature)
  - Gas diffusion equation (gas pressure)
- Solve using finite element method in Abaqus
  - Constitutive behavior in UMAT
  - Heat transfer and decomposition in UMATHT1
  - Gas diffusion in UMATHT2 (with pressure, rather than temperature as the variable)
  - Overlay elements used: UMAT and UMATHT1 applied to first layer; UMATHT2 applied to second layer
  - State variables and common blocks

Validation: Experimental Data from RMIT

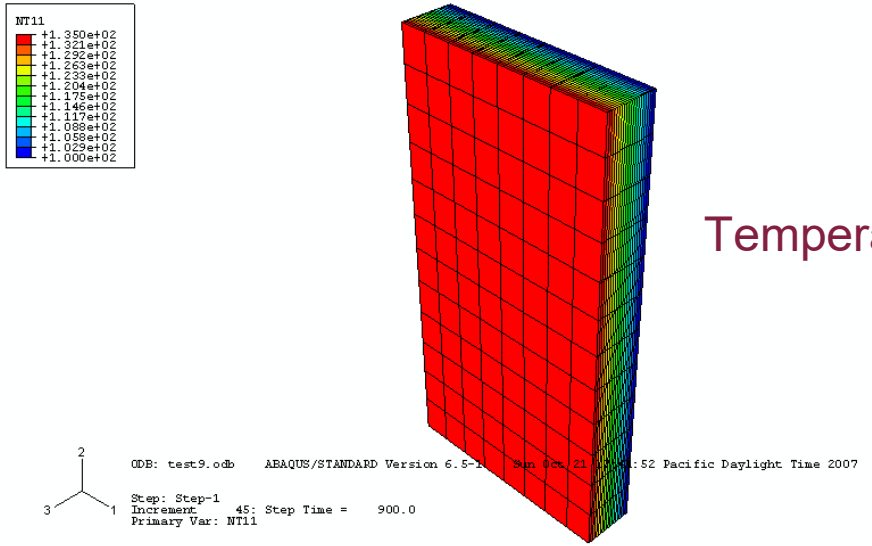

Temperature

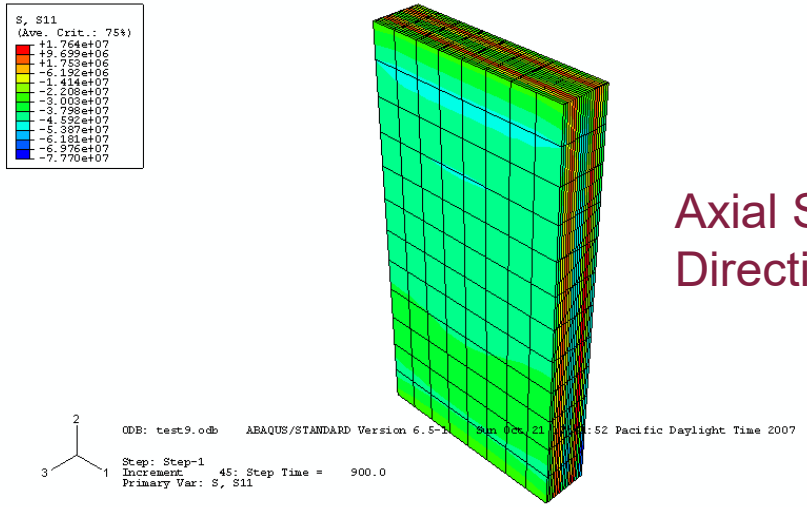

Axial Stress in Fiber Direction

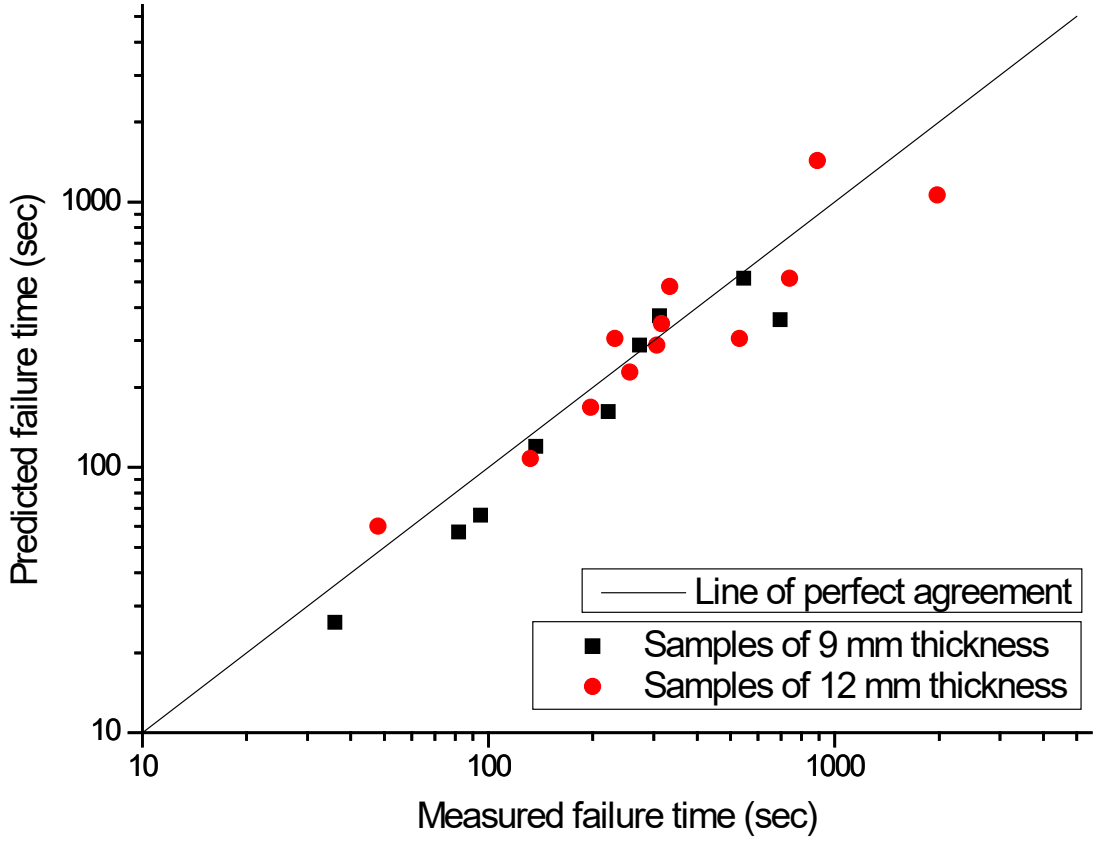

Comparison of the predicted and experimental failure times (compression controlled failure)

Measurement Improvement: TDIC

- Heat flux of 10kW/m^2 (minimal decomposition of front skin)
- No insulation of specimens on back surface to allow for field measurements.
- DIC average on back face recorded for each test.
- Non-uniform heat flux observed due to different densities of balsa
- Delamination of front skin ‘cools’ back face.

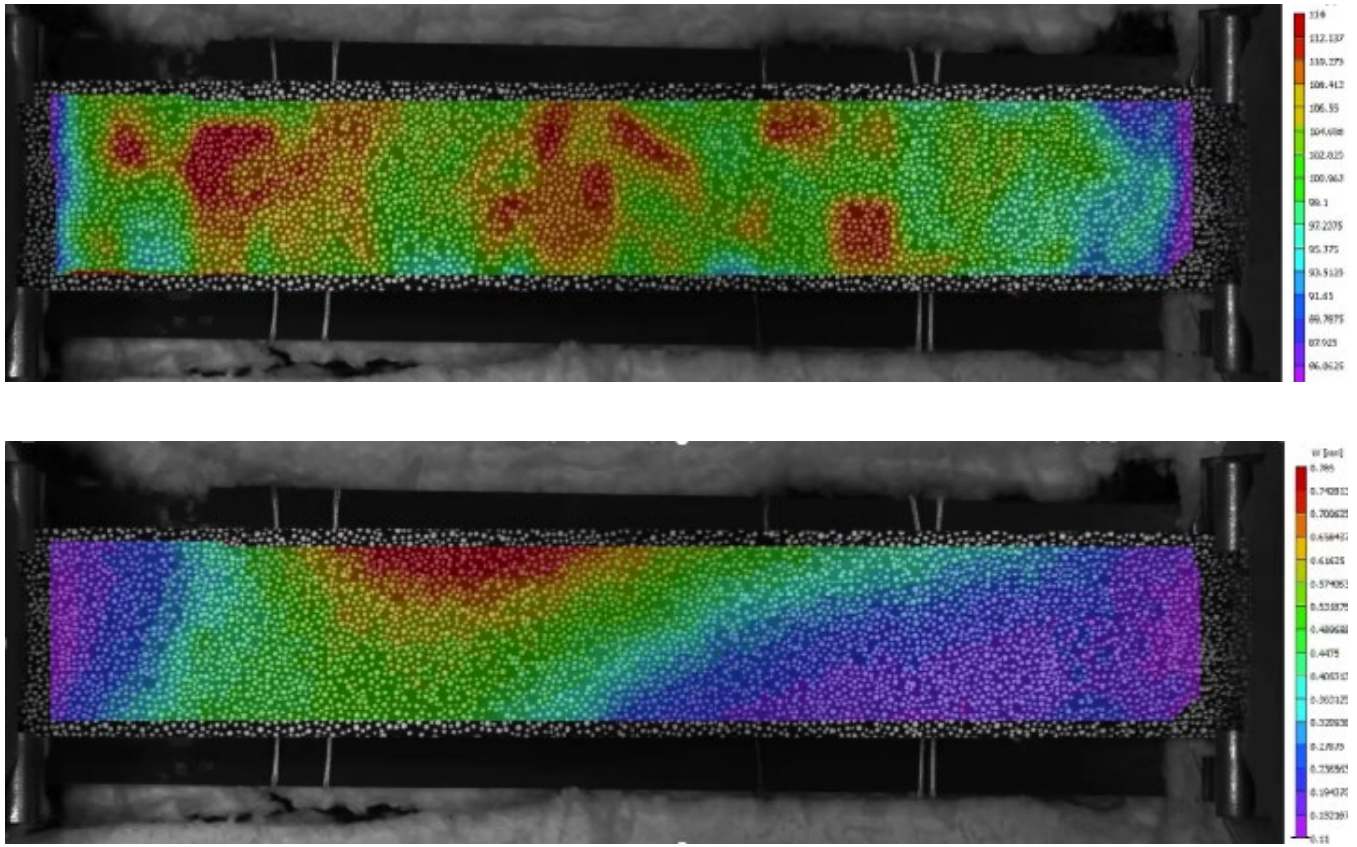

Thermoplastic Battery Enclosures for Electric Vehicles

Lithium-Ion Batteries in Electric Vehicles (EVs)

EVs have attracted substantial interest due to greater efficiency and potential reduced emissions of CO_2.

Challenge: Limited lithium-ion battery capacity

- Larger number of lithium-ion batteries
  - Increase in weight
  - Risk of fire and explosion

Metal-intensive Battery Pack

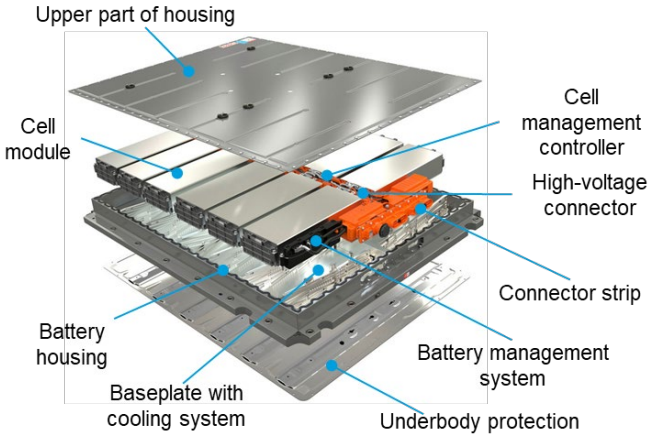

Volkswagen. (2019). Key components for a new era – the battery system.



Solution?

Replace metallic battery packs with **intumescent thermoplastic polymer-based** composite systems

- Reduced weight
- Improved fire protection
- Lower thermal conductivity

RESEARCH PLAN

Selected Materials

Flame-retardant polypropylene (FR-PP) composites with 30% glass fiber-reinforcement **with controlled characteristics**

- Fiber length
- Flame retardancy

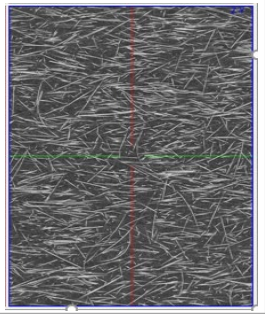

Injection-molded with random fiber length & orientation distribution

Material Characterization

- Thermogravimetric Analysis; TGA
- Thickness expansion
- Thermal Conductivity
- Specific Heat
- Dynamic Mechanical Analysis; DMA

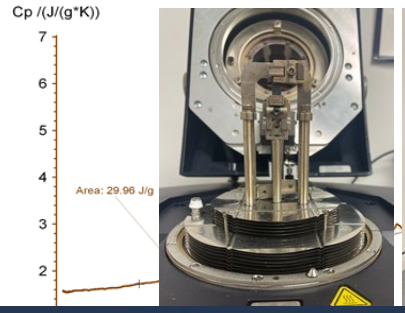



Plate Responses to Fire & Mechanical Loads

- Custom Set-up
- Inverse Heat Transfer; IHT
- IR Temperature Measurements
- DIC Deformations
- Thermocouple Measurements

Simulations

IHT or Fire Dynamics Simulator (FDS) for Thermal Loading

Abaqus for Coupled Thermomechanical Modeling

- Thickness expansion via Effective Thermal Conductivity
- Viscoelasticity via Prony Series & User TRS Subroutine
- Thermomechanical Contact Simulation

Validation

- Unexposed Temperature
- Deflection

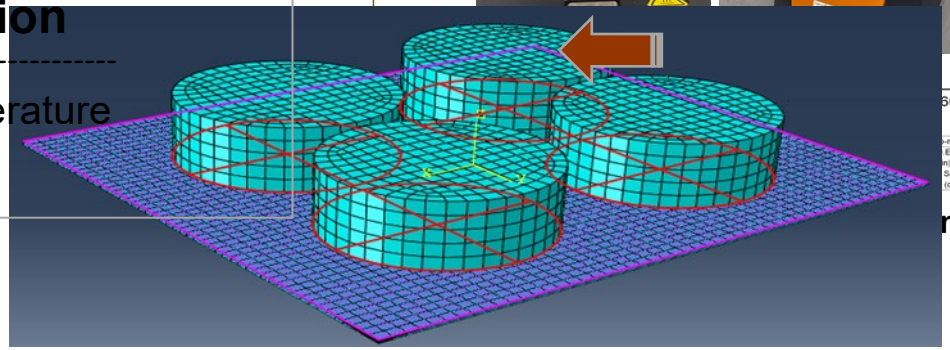

EXPERIMENTAL SETUP

OVERALL GOAL: To predict the coupled thermomechanical behavior of thermoplastic composites for newly manufactured battery pack systems.



Joel, M. EV Battery Types - A Simple Guide. How Does an Electric Vehicle Battery Work? 2024

Lithium-ion battery on top of each plastic module exerts an approximately total gravity weight of 1.1 kN/m^2

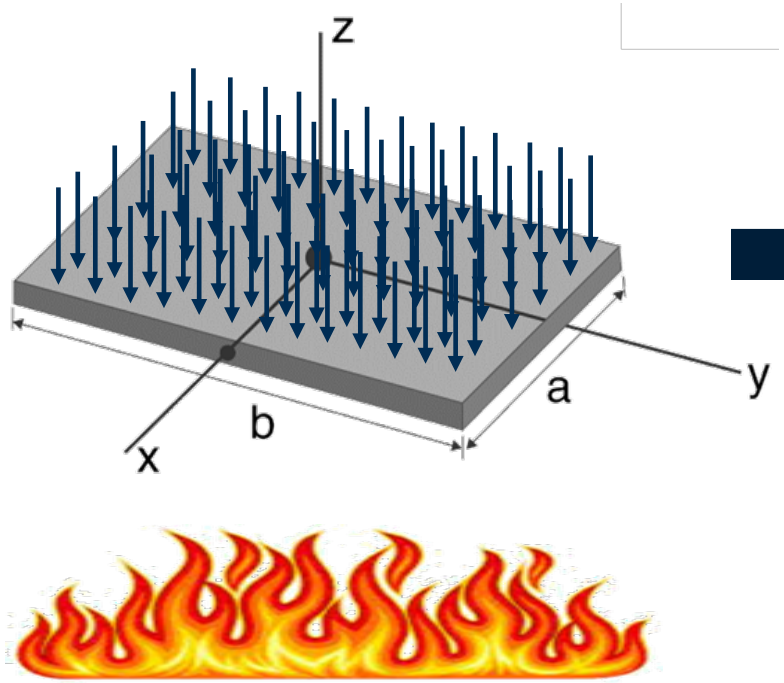

External fire or thermal runaway convective and radiative heat source

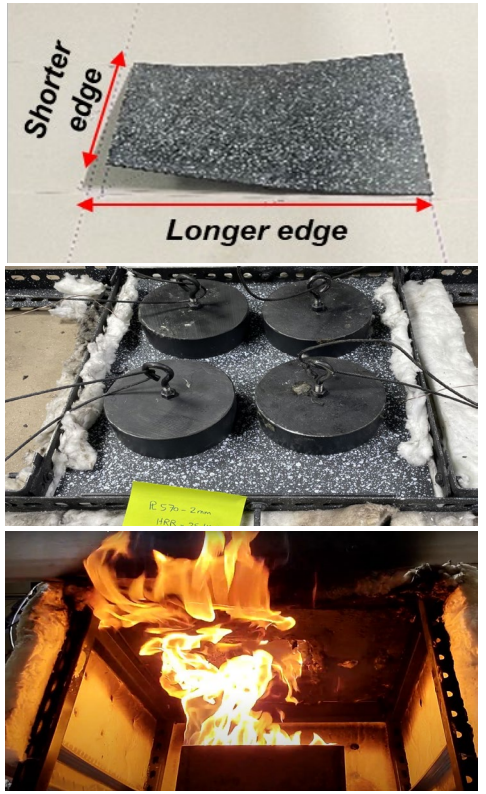

Plate-scale testing

SAND-BURNER EXPOSURE

Mechanical Loading & Fire

Weight of battery enclosure ≈ 90 N uniformly distributed over the area of the plate.

Initial tests: Four equal 22.5 N and 50 mm diameter steel cylinders weights.

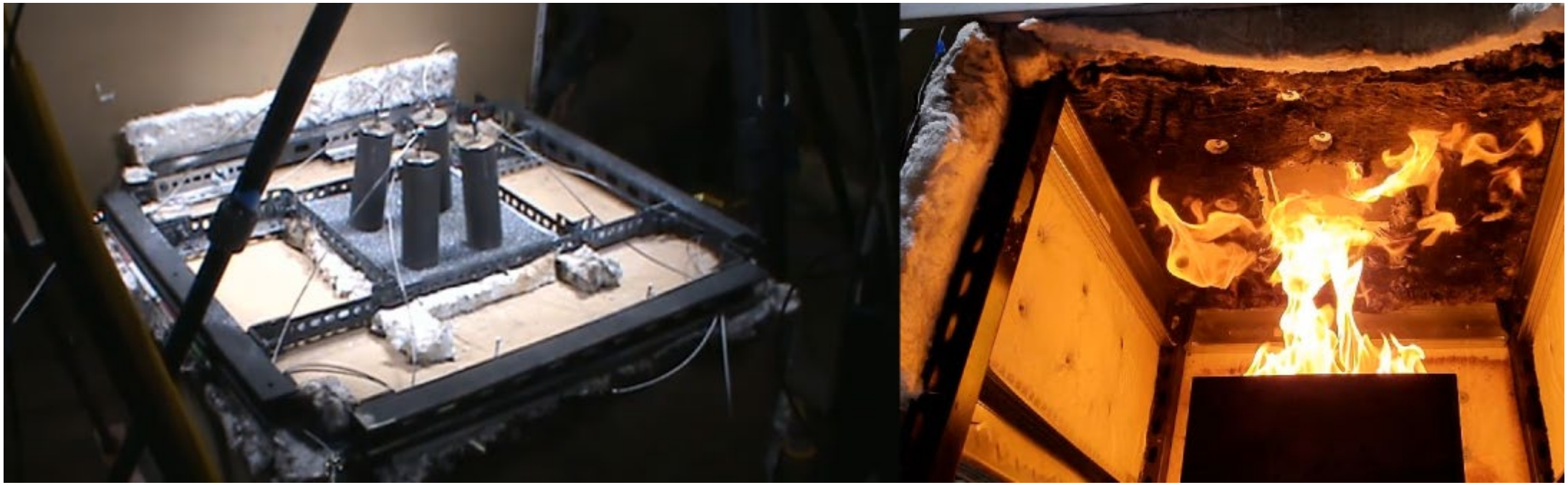

TDIC Measurements of Temperature and Displacement

TDIC Measurements

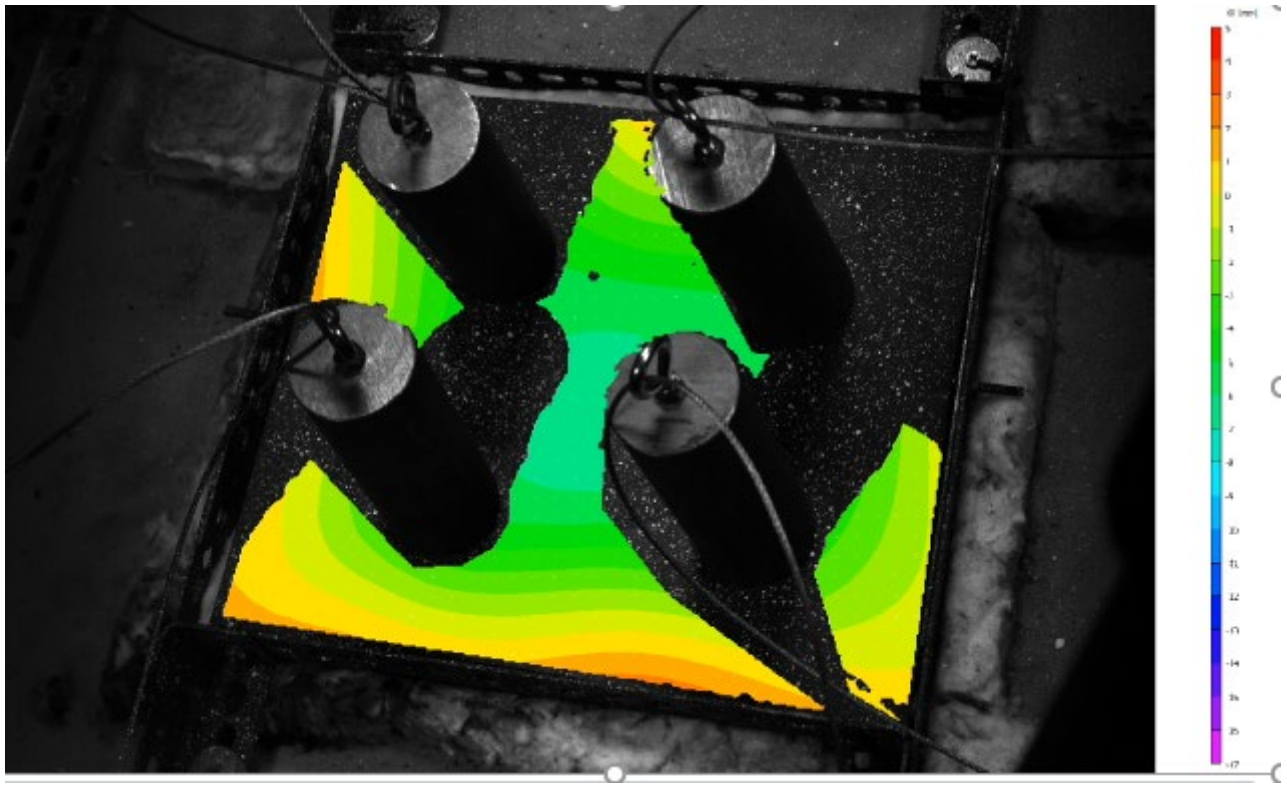

Out-of-Plane Displacement

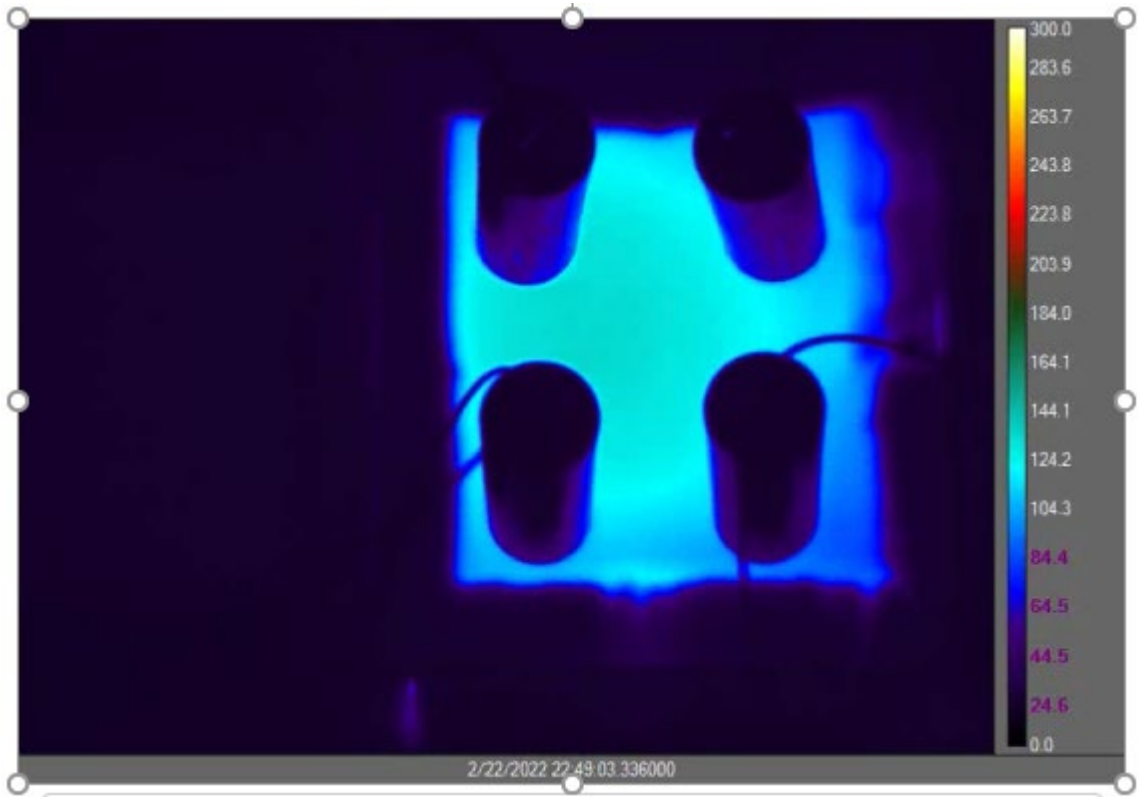

Temperature

THERMOMECHANICAL MODELING

Loaded Plates

Subjected to one-sided external fire and various mechanical loading scenarios

4 × 50 mm diameter weights

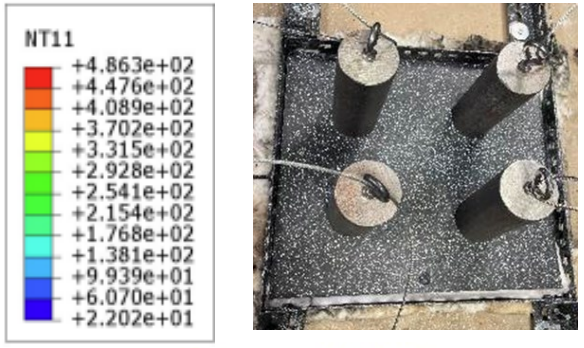

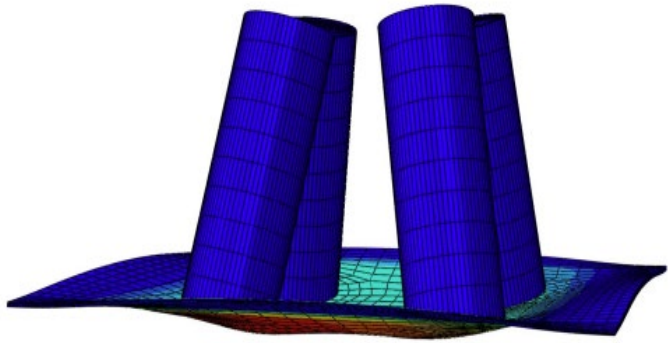

4 × 100 mm diameter weights

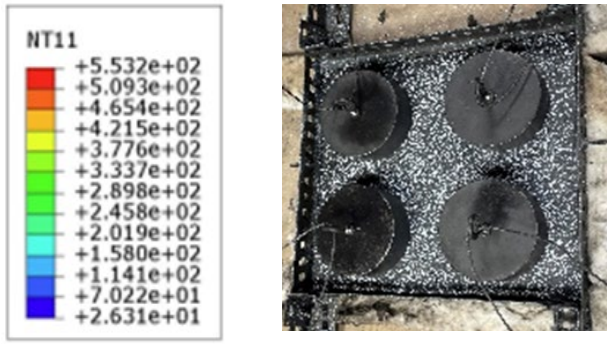

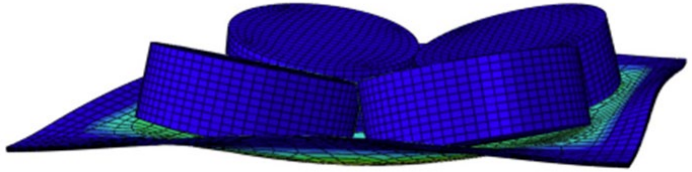

1 × 75 mm diameter weights

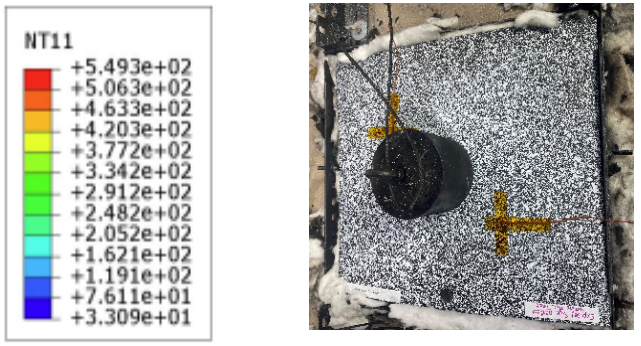

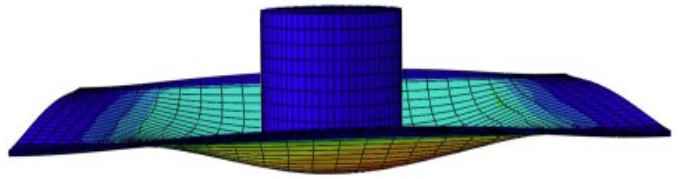

Conclusions

- Developed a framework for analysis of failure of composites subjected to combined fire and mechanical loading
- Examined micromechanics of failure using combination of experiments and analysis
  - Shift factors indicate that viscoelasticity controls compression failure (same shift factors for shear creep compliance and compression creep rupture data)
  - Good success in using Budiansky-Fleck type compression model to predict failures
  - Fiber tensile strength changes with temperature in E-glass fibers linked to surface flaw growth
- Relatively simple laminate-level mechanics models can explain key features of laminate out-of-plane deformation during simulated fires
- Integration of material models with numerical tools allows use to predict the failure of E-glass/vinyl ester laminates in a wide range of configurations and size scales
- New measurement techniques such as TDIC have promise in leading to greater understanding of the underlying behavior and validation of modeling tools
- Currently applying to long and short fiber thermoplastic composites for electric vehicle applications

Questions?









http://www.ivanmorozov.com/virginia-tech/campus

Acknowledgements

- Sponsors: ONR, Global Engineering and Materials, SABIC
- Collaborators
  - J. Bausano, S. Boyd, Z. Zhang, P. Summers, N. Cholewa, J. Hodges, C. Rippe, M. Farhadi, I. Khadakkar
  - H. Halverson, J. Lesko, B. Lattimer, J. Lua, A. Mouritz, S. Feih, G. Gibson, B. Aidi, H. Goossens, F. Chang, L. Chen

References

- S.E. Boyd, J.J. Lesko, and S.W. Case, “The Thermo-Viscoelastic, Viscoplastic Characterization of Vetrotex 324/Derakane 510A-40 Through Tg,” *Journal of Engineering Materials and Technology*, 128, October 2006, pp. 586-594.
- S.E. Boyd, J.V. Bausano, S.W. Case, and J.J. Lesko, “Compression Creep Rupture Behavior of a Glass/Vinyl Ester Composite Subject to Isothermal and One-sided Heat Flux Conditions,” *Composites Part A: Applied Science and Manufacturing*, **38**, 2007, pp. 1462–1472.
- S. Feih, Z. Mathys, A.G. Gibson, and A.P. Mouritz, Modelling the compression strength of polymer laminates in fire. Composites Part A, 2007. 38(11): p. 2354-2365.
- Z. Zhang, S. Case, J. Lua, “A model and finite element implementation for the thermo-mechanical analysis of polymer composites exposed to fire,” ICCM 17, 2009, pp. 27-31.
- S. Feih, A.P. Mouritz, S.W. Case, “Determining the mechanism controlling glass fibre strength loss during thermal recycling of waste composites,” *Composites Part A: Applied Science and Manufacturing*, **76,** 2015, pp. 255–261.
- P.T. Summers, B.Y. Lattimer, S.W. Case, S. Feih, “Sensitivity of thermo-structural model for composite laminates in fire,” *Composites Part A: Applied Science and Manufacturing*, **43**(5), 2012, pp. 783–792.
- N. Cholewa, P.T. Summers, S. Feih, A.P Mouritz, B.Y. Lattimer, S.W. Case, “A Technique for Coupled Thermo-Mechanical Response Measurement using 3-D Infrared Thermography Digital Image Correlation (TDIC),” *Experimental Mechanics*, **56**, 2016, pp. 145-164.
- M. Farhadi, B.Y. Lattimer, S.W. Case, “Fire Performance of Short and Long Glass Fiber Polypropylene Composites for Electric Vehicle Battery Enclosures,” American Society for Composites Thirty-Eight Technical Conference, 2023.
- M. Farhadi, I. Khadakkar, H. Goossens, B.Y. Lattimer, S.W. Case, “Fire Performance of Intumescent Thermoplastics in EV Battery Packs Under Varying Fire Exposures,” Society of Plastics Engineers (SPE) ANTEC 2025 Conference
- M. Farhadi, B. Aidi, H. Goossens, L. Chen, F. Chang, B. Lattimer, S. Case, “Experimental Response of Intumescent Fiber-reinforced Glass Fiber Filled Polypropylene Thermoplastic Battery Enclosure Materials to External Fire and Mechanical Loading,” submitted to *Composites Part B*, June 2025.

ICCM24
AUGUST 4-8, 2025
BALTIMORE CONVENTION CENTER
BALTIMORE, MARYLAND, USA

No Technical Paper Submission for:

Kyriaki Kalaitzidou

ACCELERATING AIRFRAME DEVELOPMENT TASKS

ICCM24
BALTIMORE, MD
4 AUGUST 2025

C. Q. Rousseau
Sr. Tech Fellow

J. F. Mullen
Structures Chief Engineer

D. B. Bush
Sr. Staff Engineer

LOCKHEED MARTIN

DISTRIBUTION STATEMENT A: Approved for public release; distribution is unlimited.

©2025 Lockheed Martin Corporation. All Rights Reserved

Abstract

- ***Lockheed Martin has a clear mandate from gov't customers to accelerate the air vehicle development timeline relative to what industry has traditionally done.***
- ***The airframe, though higher TRL/MRL than most systems on new platforms, is the most time-consuming component to develop.***
- ***Digital transformation into model-based engineering is intended to be a major contributor to compressing development timelines.***
- ***Airframe development involves a myriad of individual processes that are hard to standardize/digitize, hindering significant schedule advancement.***

Objectives

- ***Examine various engineering processes for inefficiencies, bottlenecks, and potential for improvement.***
- ***Suggest ways to overcome inertia in process standardization, digitization, and airframe development timeline compression.***

©2025 Lockheed Martin Corporation. All Rights Reserved

Outline

- ***Airframe Development Process***
- ***Airframe Development Timelines***
- ***Digital Transformation Concepts***
- ***LM Aero Structures DTX Realities***
- ***Proposed Process Changes***
- ***Summary***

©2025 Lockheed Martin Corporation. All Rights Reserved

LOCKHEED MARTIN

Airframe Development Process

Business Development & F&BO | Production | SCM | Sustainment

Concurrent Engineering

Conceptual Design

- Material Selection
- Structural Arrangement
- MDIO



Preliminary Design (Phase 1)

- Tools and Methods

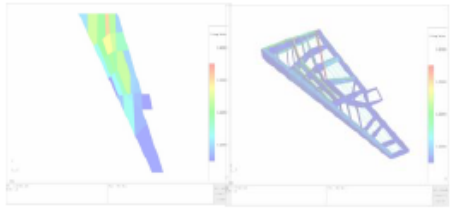

Detailed Design (Phase 2)

- Topology Optimization
- Design for X
- Advanced Analysis Tools
- Low-Cost Structures
- Additive Manufacturing

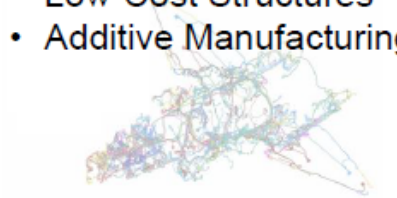

Production Design (Phase 3)

- Simulation Based Verification (SBV)

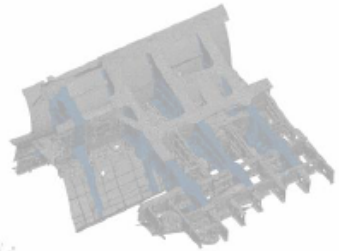

Concurrent Engineering

LoB/Programs Chief Engineers | Eng. Functions (AVE/SEIT/CS) | Quality | IT/Aero DX & 1LMX | Mod/Retrofit (Upgrade)

1st flight, IOC, mod/sustainment, etc

While every development program is different, and all have unique aspects, the basic process has not changed in 80+ years.

©2025 Lockheed Martin Corporation. All Rights Reserved

Significant Manual Effort Reprocessing & Aligning Multiple Inputs
No Standards for Data Exchange
Underutilized Feedback Loops

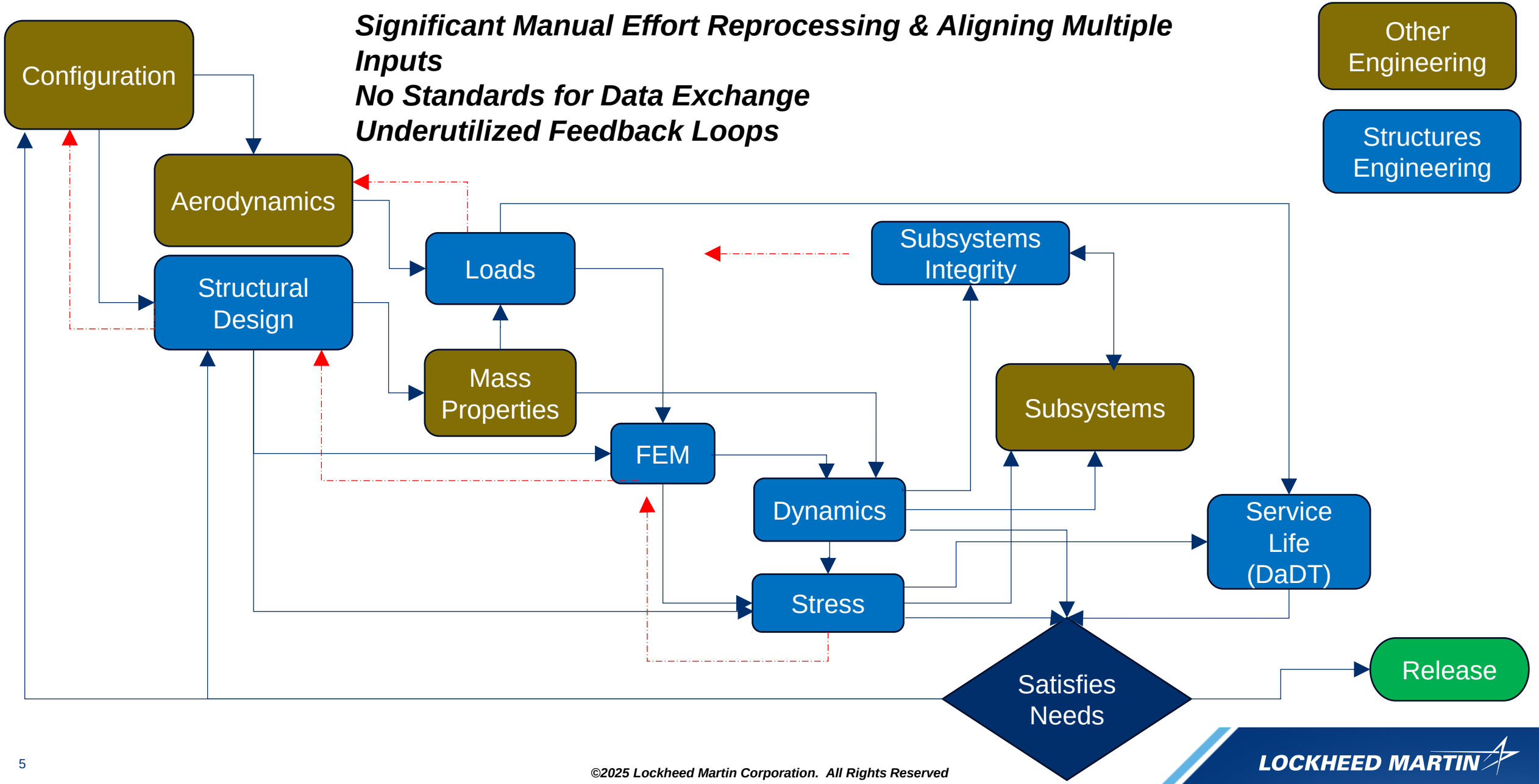

©2025 Lockheed Martin Corporation. All Rights Reserved

Outline

- ***Airframe Development Process***
- ***Airframe Development Timelines***
- ***Digital Transformation Concepts***
- ***LM Aero Structures DTX Realities***
- ***Proposed Process Changes***
- ***Summary***

©2025 Lockheed Martin Corporation. All Rights Reserved

LOCKHEED MARTIN

Airframe Development Timelines

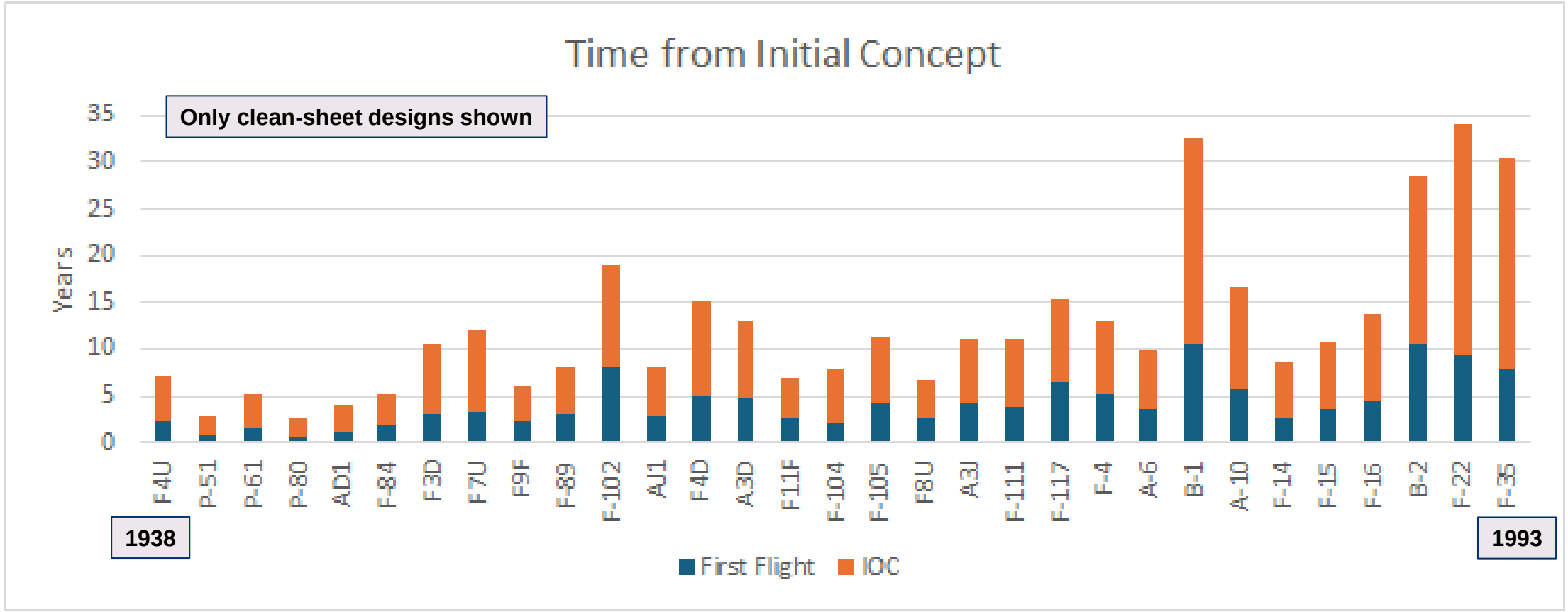

- *1st flight generally X- or Y-variant.*
- *B1A cancelled, B1B IOC shown.*
- *B2, F22, and F35 redesigned before IOC.*
- *F22 avionics further delayed IOC.*
- *Recent IOC timelines affected by extensive mission/vehicle system flight test requirements.*

Industry needs shorter timelines for both 1st flight as well as production aircraft IOC. Cannot fully redesign Y-variant for production.

©2025 Lockheed Martin Corporation. All Rights Reserved

Airframe Development Timelines

Sources of timeline expansion over last 80 years:

- ***Additional requirements (DaDT, ballistic tolerance, crash, lightning strike, stealth)***
- ***Advanced design/mfg concepts (Titanium, composites, bonded joints, hot structures, complex systems interfaces)***
- ***Advanced methods/tools (3D part models, detailed FEMs, complex loads, structural optimization)***
- ***Staff inexperience (many now only do 1 or 2 development programs in career)***
- ***Ill-defined/non-standard workflows, data mining limitations, over-engineering and re-processing***

Sub-Task	U-2	C-130A->J	F-111	C-5	F-16A->F	F-117	F-22	F-35 A-C
1st Flight Year	1955	1955	1964	1968	1974	1981	1997	2006/08/09/10
Drawings	Paper	Paper	Paper	Paper	Paper->Catia	CADAM?	Catia	Catia
Load Cases		50->400		250	150->1400		90k	44k/55k/41k

- ***Data hand-offs between and within engineering teams must be standardized and digitized.***
- ***Systems Engineering Best Practices must be followed.***

©2025 Lockheed Martin Corporation. All Rights Reserved

Outline

- ***Airframe Development Process***
- ***Airframe Development Timelines***
- ***Digital Transformation Concepts***
- ***LM Aero Structures DTX Realities***
- ***Proposed Process Changes***
- ***Summary***

©2025 Lockheed Martin Corporation. All Rights Reserved

LOCKHEED MARTIN

Digital Transformation Concepts

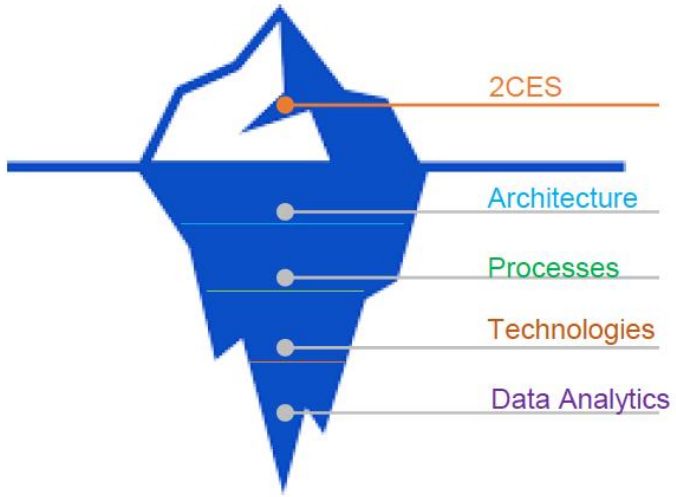

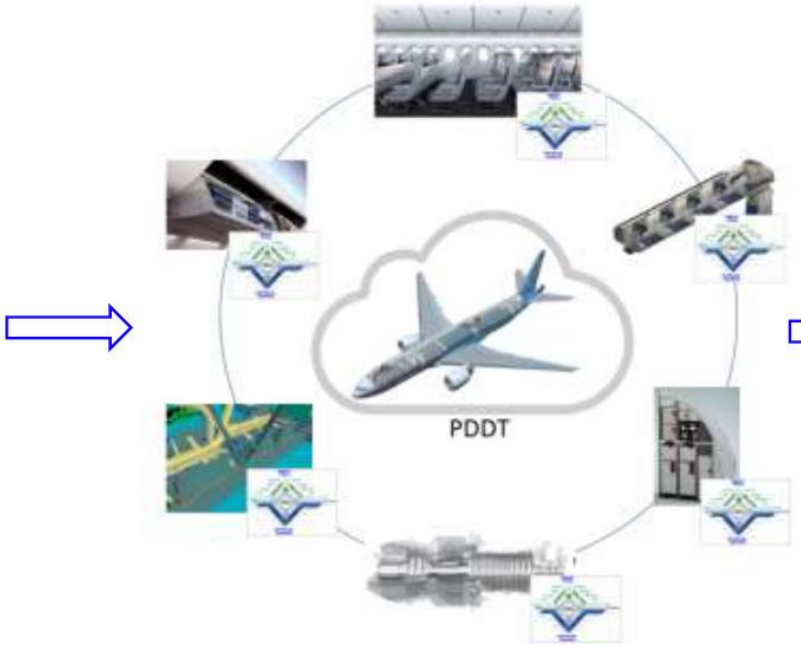

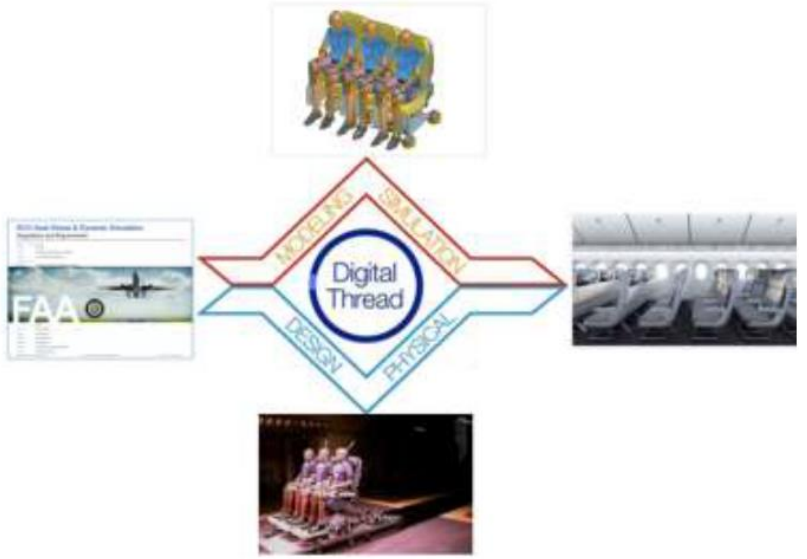

2nd Century Enterprise Systems (2CES) Enabler:
- Common Architecture
- Methods, Processes and Tools
- Technologies and Innovations
- Data and Data Analytics

Product Development Digital Twins (PDDT):
- Airframe structure
- System Engineering
- Payloads and Interiors
- Propulsion Engineering
- Test and Certification
- Production system

Smarter Seat Certification Digital Twins:
- Structural Integrity
- Passenger Safety

3rd-Parties and S/W vendors only view the design process in general terms. Real issues/roadblocks are at the detail-level.

©2025 Lockheed Martin Corporation. All Rights Reserved

Outline

- ***Airframe Development Process***
- ***Airframe Development Timelines***
- ***Digital Transformation Concepts***
- ***LM Aero Structures DTX Realities***
- ***Proposed Process Changes***
- ***Summary***

©2025 Lockheed Martin Corporation. All Rights Reserved

LOCKHEED MARTIN

Lockheed Martin Aeronautics High Level Data Architecture

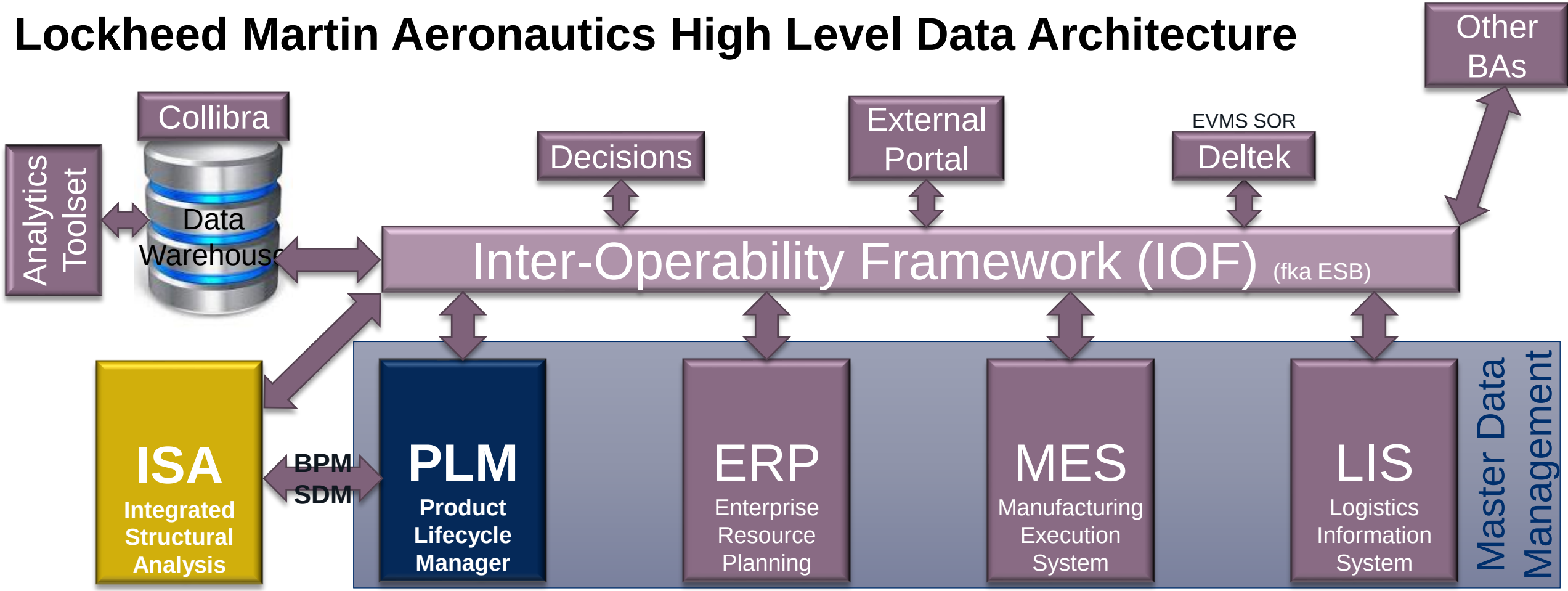

System of Record (SOR) for:
- Proprietary Tools/Processes
- Large Analysis Only Data

COTS PLM suppliers don't recognize need for separate ISA

System of Record (SOR) for:
- Product Definition (E/M/S/An BOM)
- Mod Kit Config
- Tech Data
- Mfg Eng Plans
- Change Mgmt
- Program Baseline

System of Record (SOR) for:
- Part Instance
- Contracts
- Supplier QA
- Finance
- As-Delivered BOM
- Demand Planning

System of Record (SOR) for:
- As-Built (S/N & Batch/Lot)
- Prod QA
- Shop Work Orders

System of Record (SOR) for:
- Fleet Mgmt
- Basing
- Fleet Performance
- Allowable Configuration
- Part Instance History
- As-Maintained BOM

©2025 Lockheed Martin Corporation. All Rights Reserved

- *Process Capture & Automation*
- *Reusable, Repeatable, Reliable, Releasable*
- *Knowledge Continuity*

ICAT

CATDM

- *Graphics Driven Interface*
- *Structural Analysis Products Database*
- *Force Structural Management*

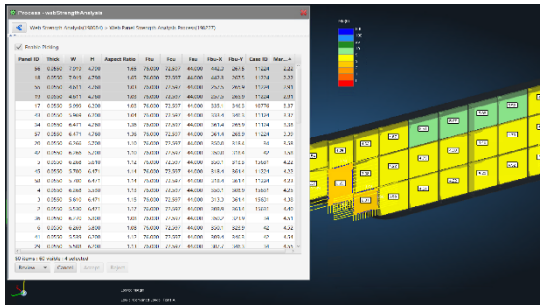

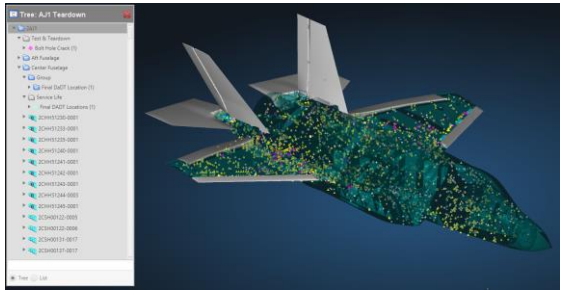

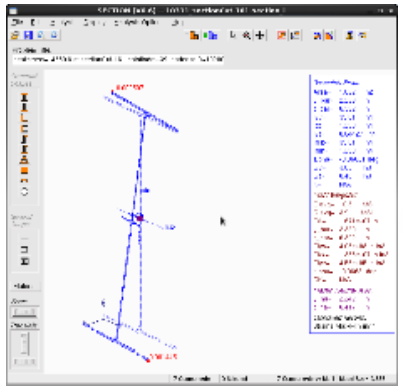

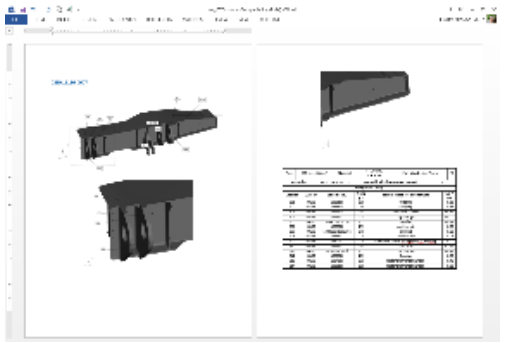

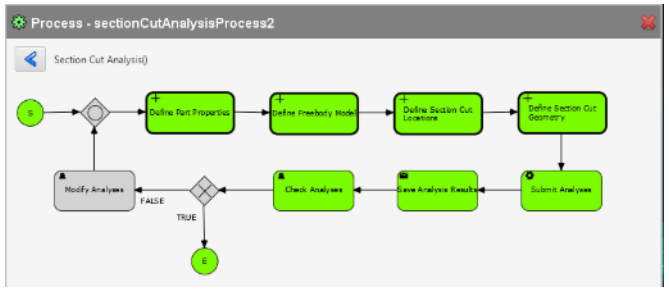



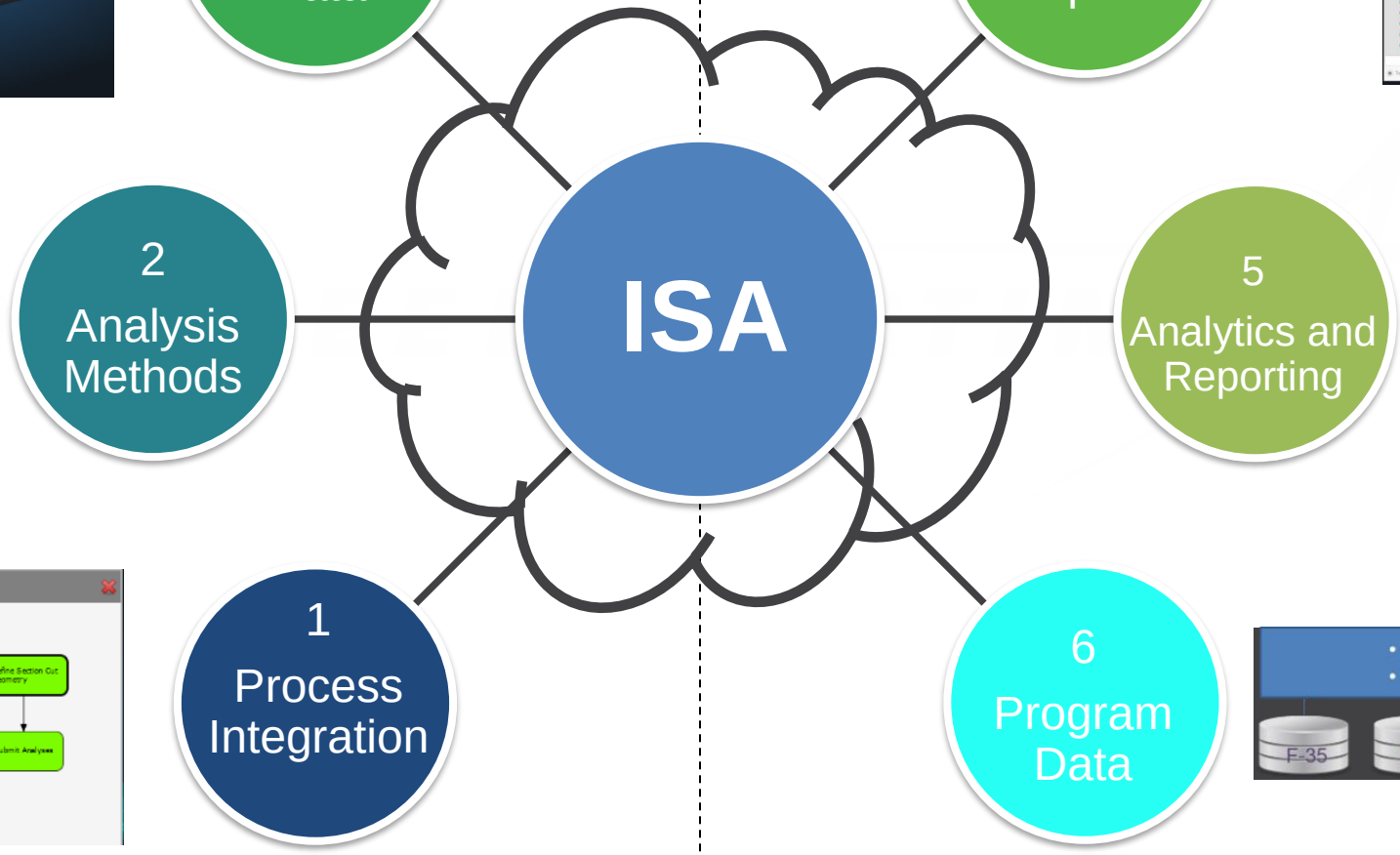

©2025 Lockheed Martin Corporation. All Rights Reserved

What is CATDM?

- ***The Common Analysis Toolset and Data Manager***
- ***Collects Design, Production, And Maintenance Data***
  - *Increases engineering and documentation efficiency*
  - *Displays on a 3D Model generated for visualization purposes only*
  - *Currently used for structural data only*
  - *Used by F-16, F-22, F-35, and some ADP Programs*
- ***Intelligent Database***
  - *TVE Cognizant Data*
  - *LM can use to amalgamate data from many sources for quick access*
- ***Customizable***
  - *Users define all aspects of data from fields to permissions*

- *Support data to drive decision making throughout lifecycle*

As Built

Stress Analysis
- *Production Defects*
- *Stress Margins*
- *Part Life Summaries and Equations*

As Maintained

Sustainment
- *Inspection Intervals*
- *Damage Reports*
- *Aircraft Conditional Inspection Findings*
- *Structural Defects*
- *Crack Growth Analyses*

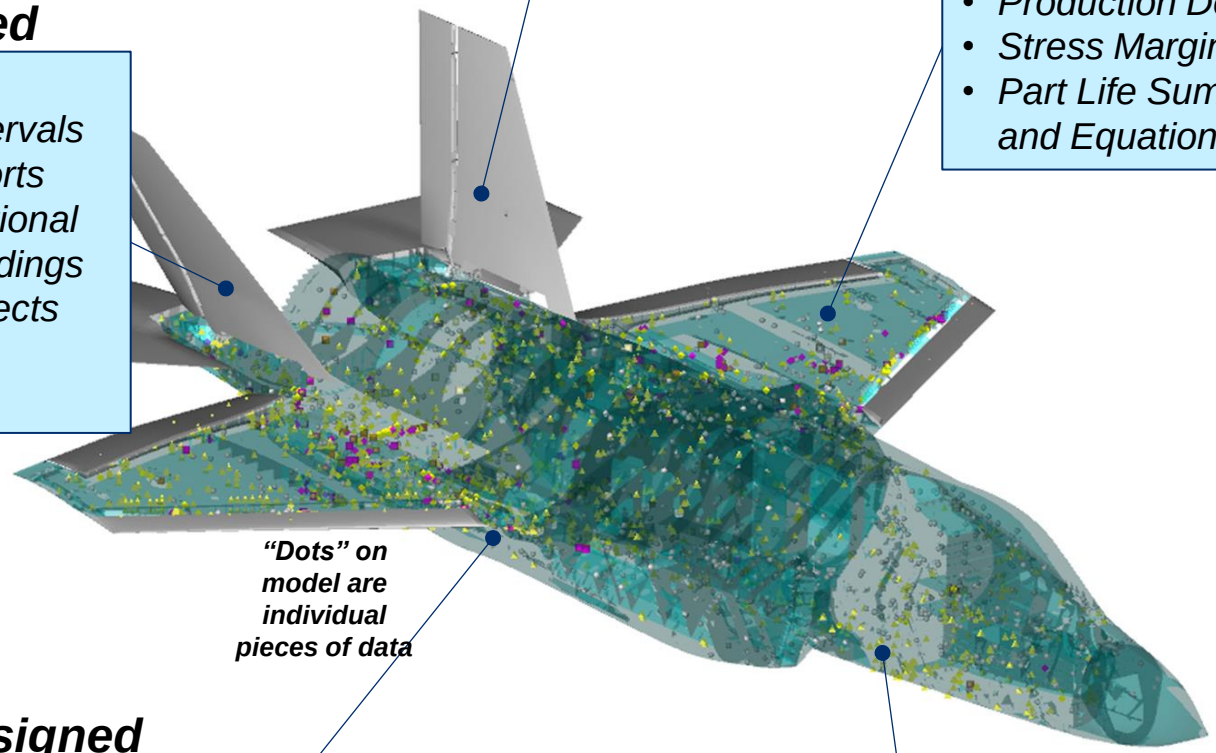

"Dots" on model are individual pieces of data

As Designed

Loads and Dynamics
- *Strength Summary and Operating Restrictions (SSOR)*
- *Static Load Conditions*

Damage Resolution
- *Maintenance Requirement Board Models*
- *Depot/Field Support Data*
- *Damage Evaluation Tables*

©2025 Lockheed Martin Corporation. All Rights Reserved

What is ICAT?

- ***The Integrated Common Analysis Toolset***
- ***Cloud-Based Analysis Library***
  - *Non-program-specific analyses promotes common methodology*
- ***Automated Standard Processes***
  - *ICAT's automated analyses increase efficiency*
- ***Provides Means for Integration of Program Specific Processes***
  - *Custom-developed methods from a single traceable and controlled source consistent across users and partners*
- ***Contains Analysis Data***
  - *ICAT contains documented analysis methodologies from SME's using validated tools and the analysis data needed to perform them*

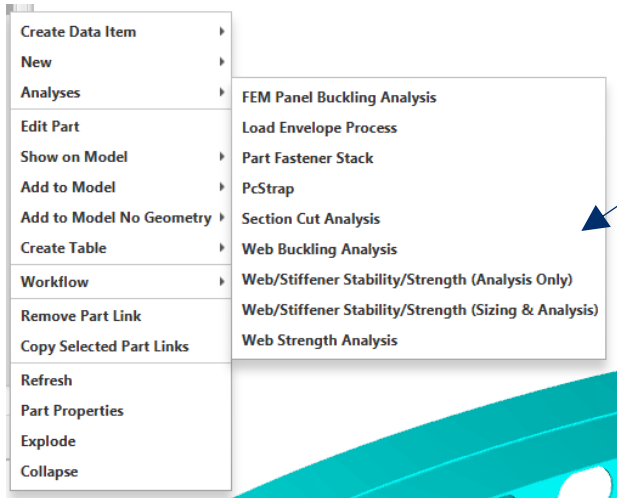

ICAT

February 2025 Analysis Library

- *Web/Stiffener Strength and Stability Sizing*
- *Joint Fastener Loads*
- *F-35 IMAT Stress Equation Derivation*
- *Service Life Risk Analysis*
- *Bolted Joint Margins*
- *Flange Analysis*

Future Work

- *XVE*
- *Common Individual Aircraft Tracking (IAT)*

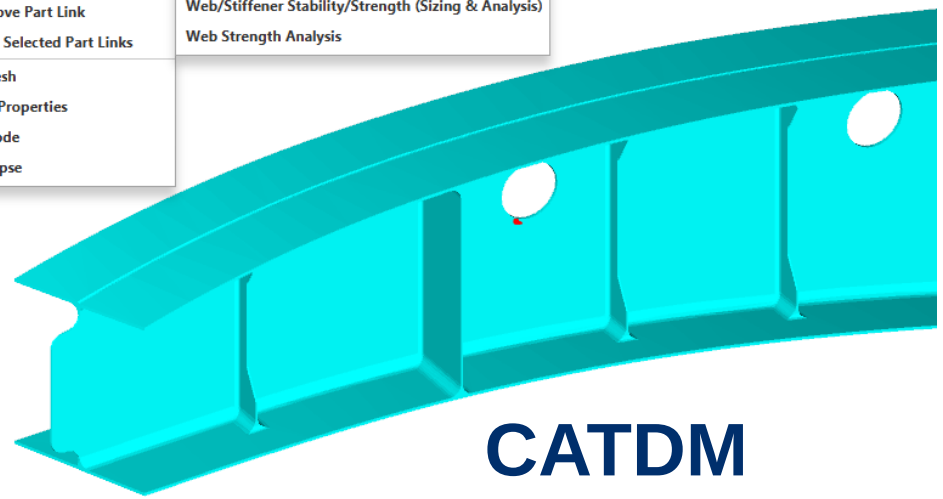

CATDM

©2025 Lockheed Martin Corporation. All Rights Reserved

ICAT Analysis Example – Web/Stiffener Strength/Stability Analysis

- ***ICAT uses Business Process Modeling Notation (BPMN), a visual language for modeling business processes***
- ***Each Structured Process implements a SME-developed, E&T approved workflow with defined inputs/outputs used to accomplish an overall analysis task***
- ***Standardized workflow enables Agile development of the process, guides individual analysts from beginning to end, and gives opportunities for analyst and lead review of both input data and results***

Structured Process

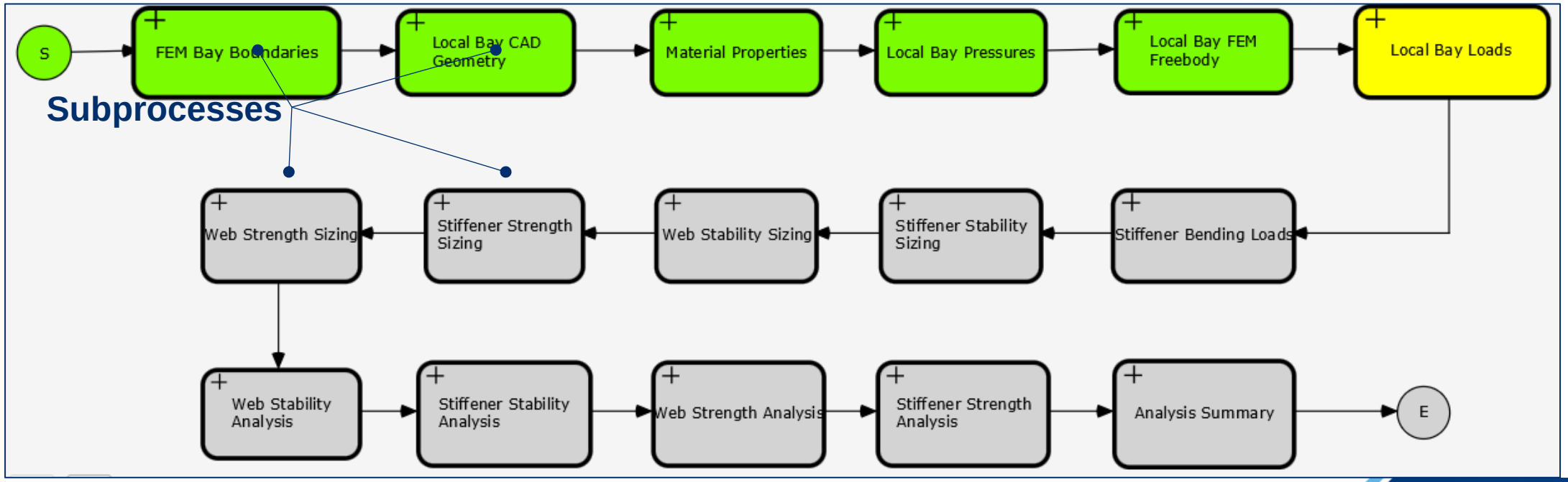

©2025 Lockheed Martin Corporation. All Rights Reserved

LOCKHEED MARTIN

Status – Structural Analysis Digital Transformation

ICAT

- ***Web & Stiffener Sizing & Analysis – Deployed***
  –Limited Adoption in ADP – Increase planned with Flange Analysis
- ***Flange Sizing & Analysis – Ready to Deploy***
  –Planned Adoption in ADP Q2 2025 – UAT Complete
- ***Fastener Loads – Deployed***
  –Adopted - In General Use in ADP
- ***Bolted Joint Margins – Deployed***
  –Limited Adoption in ADP – Increase planned with Flange Analysis
- ***Individual Aircraft Tracking Process - Ready to Deploy***

CATDM

- ***CATDM External Web Application***
  –A fast, lightweight web portal to CATDM
  –Automatic report creation based on CATDM Data
  –Input forms for corrosion data – directly from depot

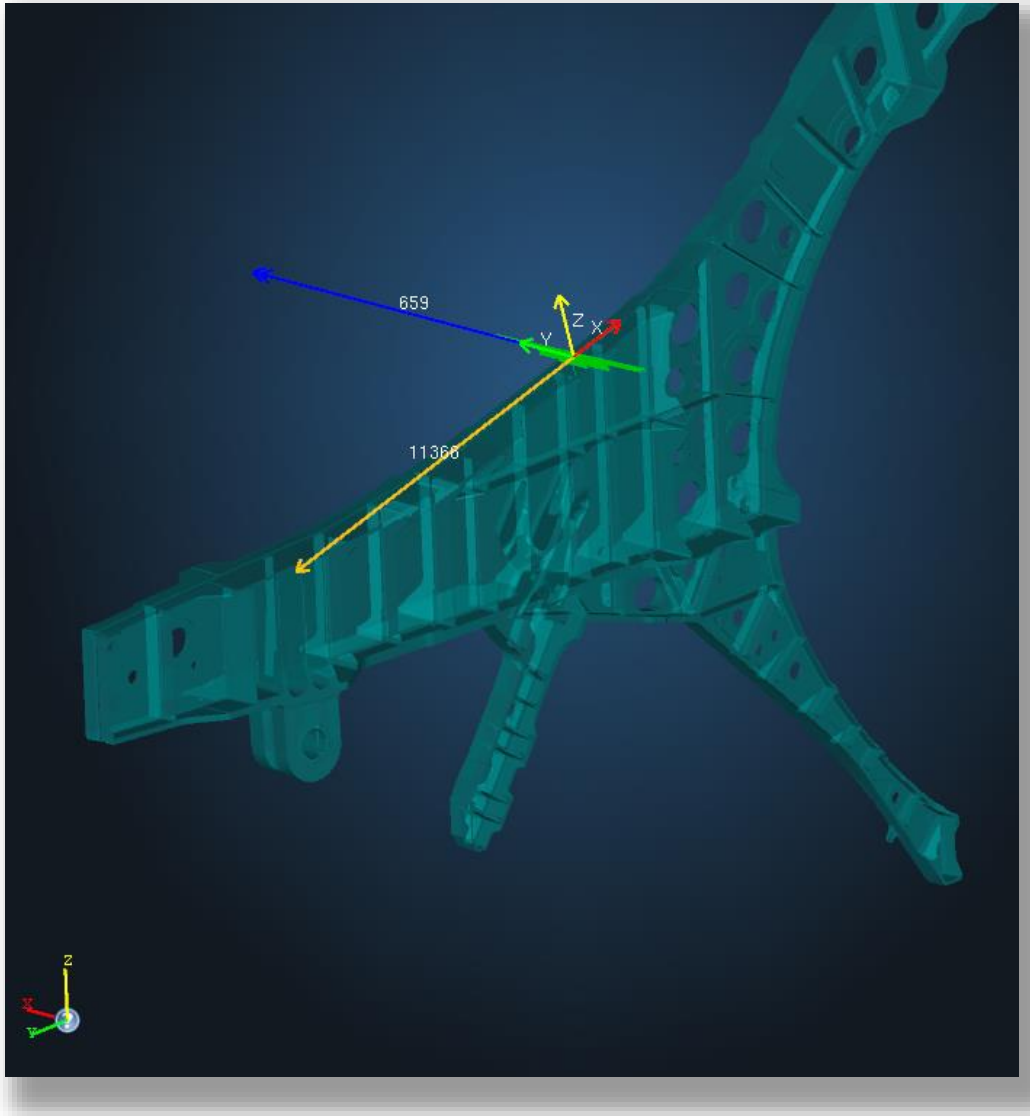

©2025 Lockheed Martin Corporation. All Rights Reserved

Outline

- ***Airframe Development Process***
- ***Airframe Development Timelines***
- ***Digital Transformation Concepts***
- ***LM Aero Structures DTX Realities***
- ***Proposed Process Changes***
- ***Summary***

©2025 Lockheed Martin Corporation. All Rights Reserved

LOCKHEED MARTIN

Proposed Process Changes

- ***Aero needs to re-tool its structures conceptual design approach, both with guidelines and staffing (maybe not tool automation?)… get this right and fewer disruptive major downstream changes will be required.***
  - *Get the right SME's involved at the right times.*
  - *Lay out the major airframe structure ("big bones") efficiently, then accommodate various systems (not the other way around).*
- ***Cross-team communications need to be greatly improved.***
  - *Feedback loops need to be standardized and digitized.*
  - *Hand-offs between Aero-&-Loads, Mass-Properties-&-Loads/Dynamics, Loads-&-FEM, etc. are too slow because of the need for translation into the format the receiving team needs.*
- ***Too much detail goes into AVFEM too early. FEM team needs better pre-design guidelines.***
  - *CAD surfaces for AVFEM meshing, material data from PLM and IDAT to FEM, fastener hangpoints & metadata all need to be standardized and streamlined.*
  - *Layout phase and maybe BTP FEM's do not need sprung skins, 2.5D flanges, DFEMs, etc.*

©2025 Lockheed Martin Corporation. All Rights Reserved

Proposed Process Changes

- ***ICAT stress Digital Transformation tools are more mature than those for other analysis disciplines, but analysts need to be trained to minimize – rather than maximize – efforts.***
  - *Limit amount of detail and load cases in finite element models to only what is required for a given phase of development.*
  - *Ignore tertiary details and non-critical parts prior to BTP phase but properly set the big-bones arrangement at Conceptual Design Review (CoDR).*
  - *Agree on a limited number of loads updates and schedule the rest of the analysis tasks around these deadlines.*
- ***SLA input into pre-design, layout, and BTP phases needs to be streamlined/simplified and new guidelines for limited life vehicles developed.***
  - *SLA is unnecessary for certain classes of vehicles and for limited life prototypes.*
  - *SLA should be greatly simplified in all development phases through BTP. Post-BTP SLA can and should be more detailed for manned aircraft fleets with complex service life spectra.*

©2025 Lockheed Martin Corporation. All Rights Reserved

Outline

- ***Airframe Development Process***
- ***Airframe Development Timelines***
- ***Digital Transformation Concepts***
- ***LM Aero Structures DTX Realities***
- ***Proposed Process Changes***
- ***Summary***

©2025 Lockheed Martin Corporation. All Rights Reserved

LOCKHEED MARTIN

Summary

- ***Airframe development is a complex, iterative process with many inter- and intra-discipline data handoffs.***
- ***Timelines for airframe development have generally increased over time due to additional requirements, advanced design and manufacturing concepts, and a combination of more advanced tools being used by less experienced engineers.***
- ***Digital transformation efforts, particularly in stress and service life analysis, have demonstrated the value of standardized workflows in reducing analysis spans but have not been widely adopted.***

Recommendations

- ***Modify structures conceptual design approach to optimize major airframe structure before accommodating various systems components.***
- ***Improve cross-team communications with standard digital data handoffs in accordance with a program milestone-based schedule.***
- ***Define appropriate amount of detail required in finite element models based on phase of program and ensure Design & Extremal Loads processes align with required FEM inputs.***
- ***Develop training to emphasize the appropriate level of detail of analysis at each phase of a program and minimize analysis effort needed to achieve program requirements.***

©2025 Lockheed Martin Corporation. All Rights Reserved


LOCKHEED MARTIN

ICCM24

24TH INTERNATIONAL CONFERENCE ON COMPOSITE MATERIALS

Rapid Manufacturing Pathways for High-Performance Thermoplastic Composites

Mehran Tehrani

Associate Professor

Callaway Golf Endowed Chair

Structural and Materials Engineering

Advanced Composites & Aerospace Structures

August 07, 2025

UC San Diego

Outline

- Introduction to thermoplastic composites and their manufacturing
- In-situ consolidation of thermoplastic composites (TPC)
- Engineered pathways for post-consolidation of TPCs
- Energy-efficient Aerospace-grade Laminates = OATMEAL

Introduction

Matrix: Thermoplastics vs Thermosets

Thermoplastics
Reversible melting

Thermosets
Irreversible curing
(heat or UV activated)

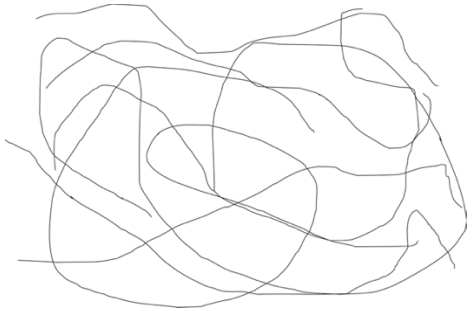



More viscous

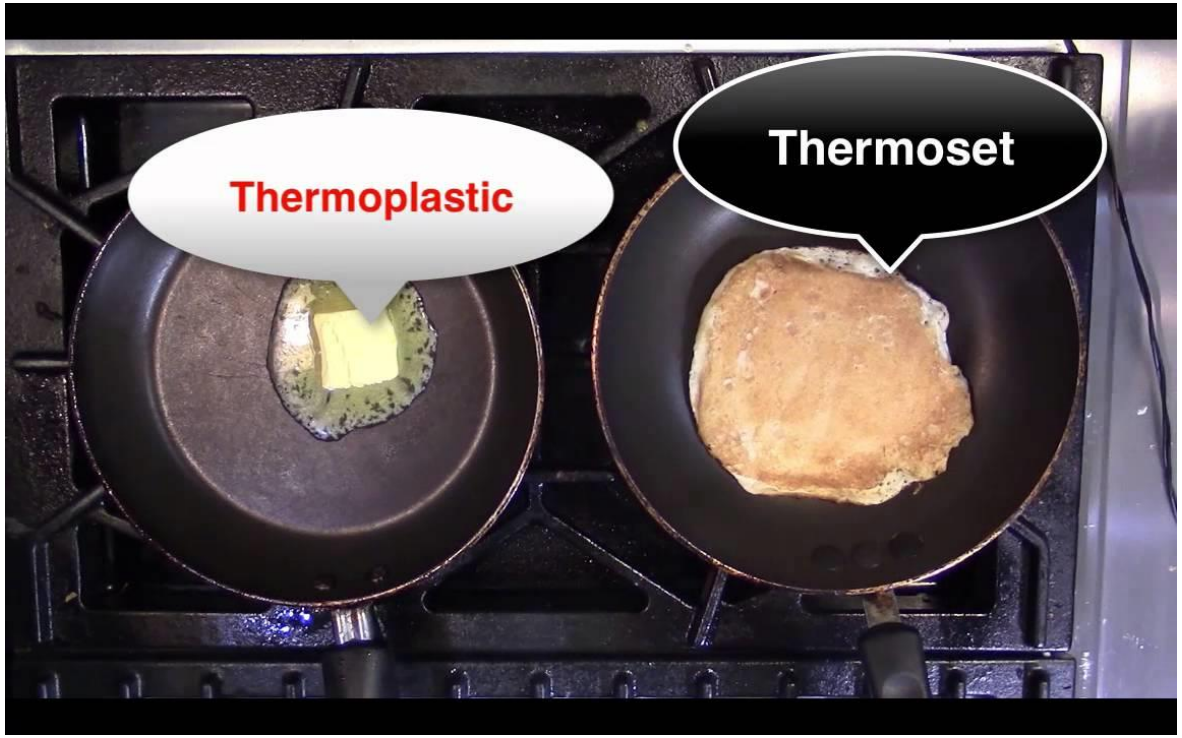

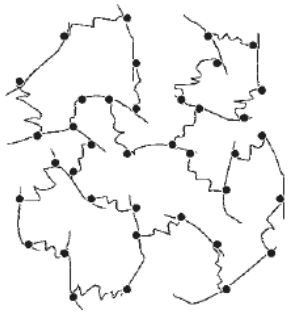



Less viscous

These properties affect processing

Images are from the internet.

Additive Manufacturing of TPCs

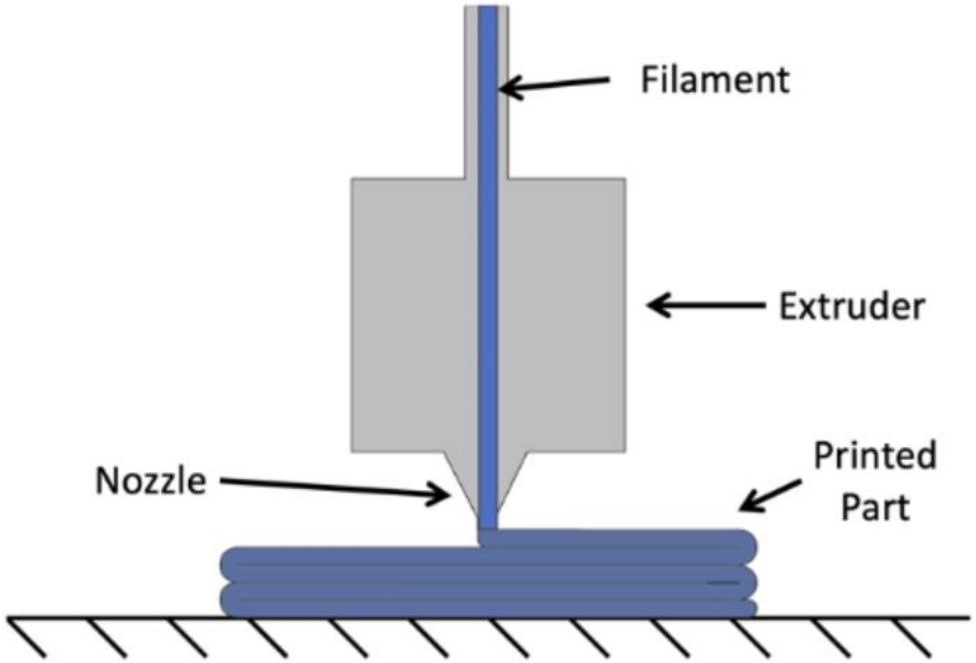

Material Extrusion (ME)

Fused Filament Fabrication (FFF)

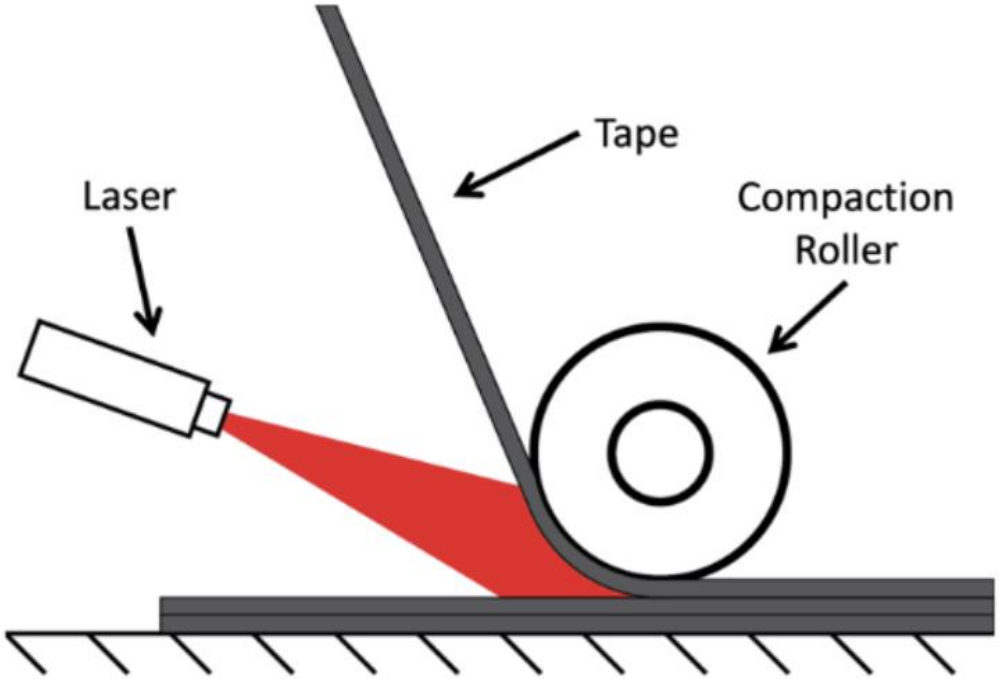

Directed Energy Deposition (DED)

Laser-Assisted Automated Fiber Placement (AFP)

Advanced Manufacturing of Thermoplastic Composites



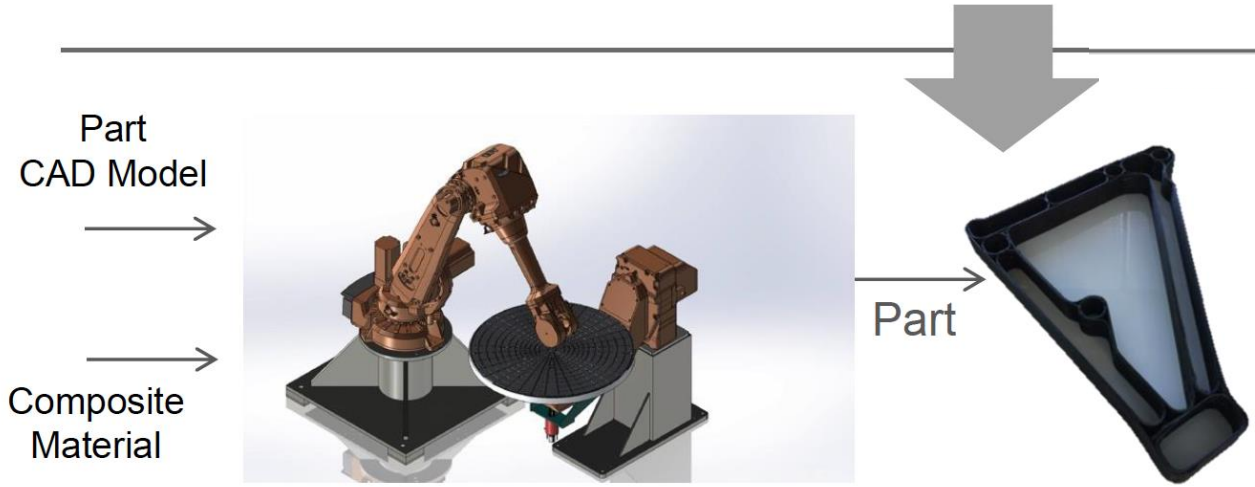



Out of Autoclave and Rapid Manufacturing

Fast Rate Assembly and Quality Control

UC San Diego
JACOBS SCHOOL OF ENGINEERING

Courtesy of Arevo Inc.

Semi-Crystalline Thermoplastic Super-Polymers

PAEKs: superior thermo-mechanical and chemical properties, Max Service Temp. 260°C (500°F)

- PEEK
- PEKK
- LM-PAEK
- PEK





ketone (R-CO-R) and ether groups (R-O-R)

Source: Arkema

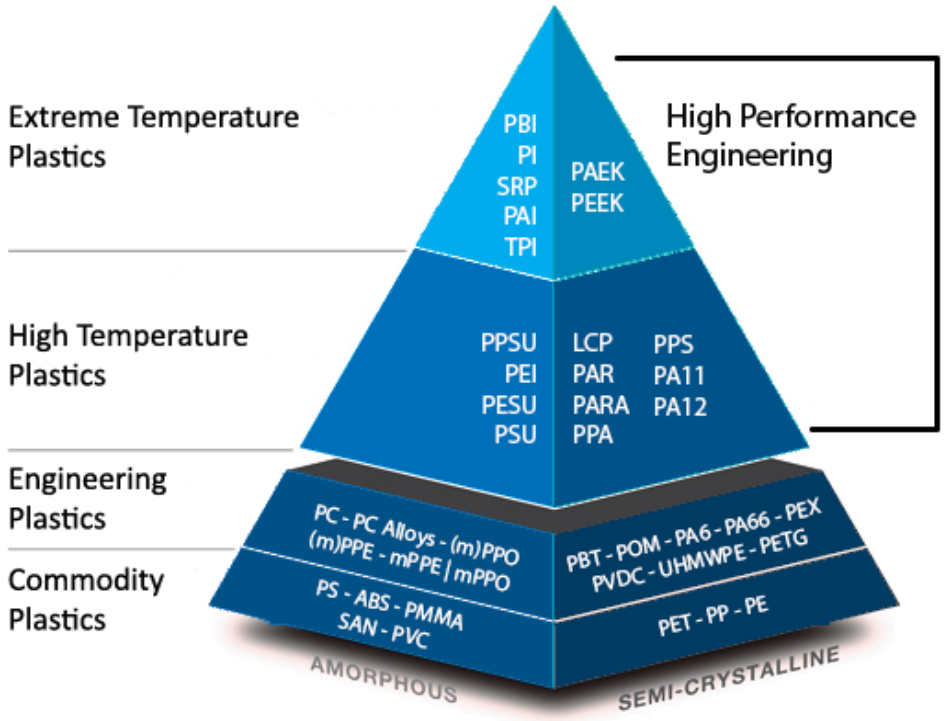

Source: Polymers.com

Thermoplastic Composites: Impact damage resistant, weldable (no fasteners or adhesives), easily repairable, fast-rate processing, potentially recyclable.

In-situ consolidation of Thermoplastic Composites

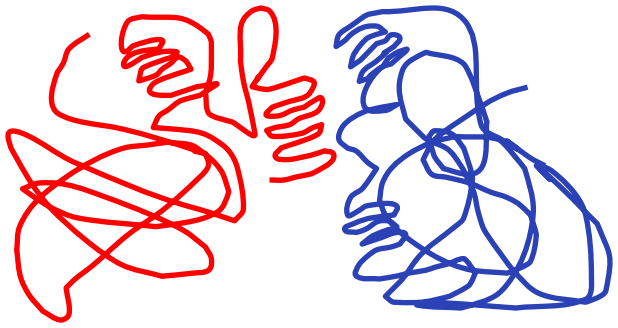

In-House Laser-AFP Test Bed

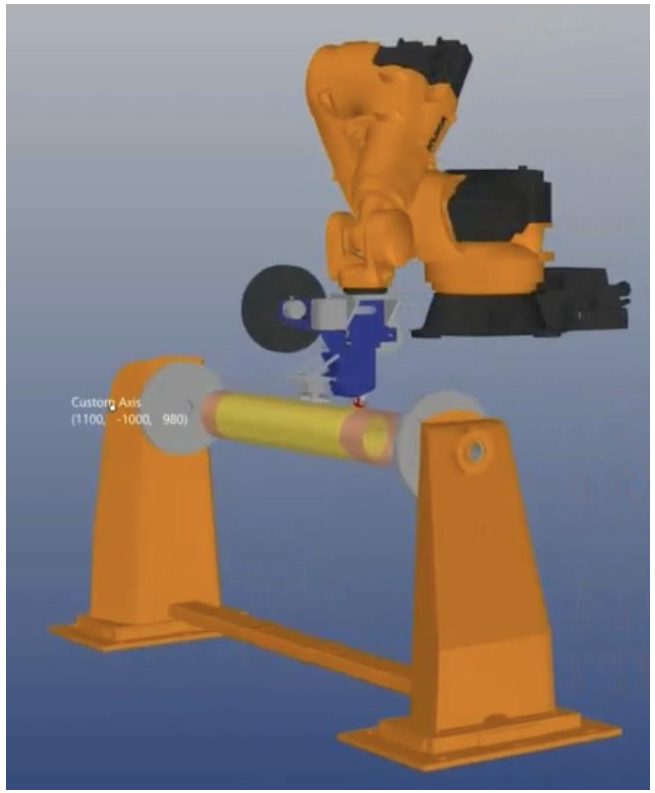

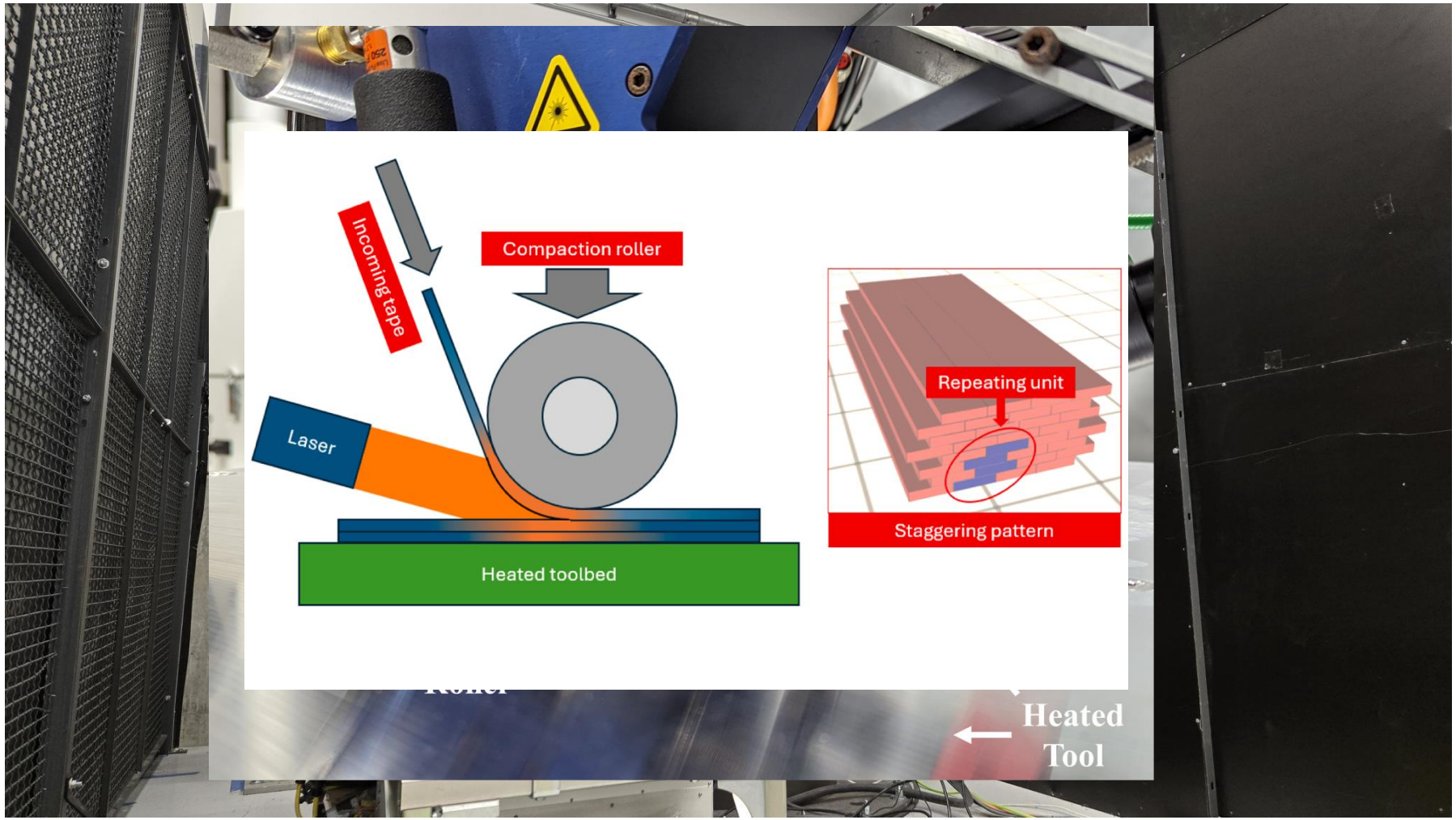

Bonding Physics

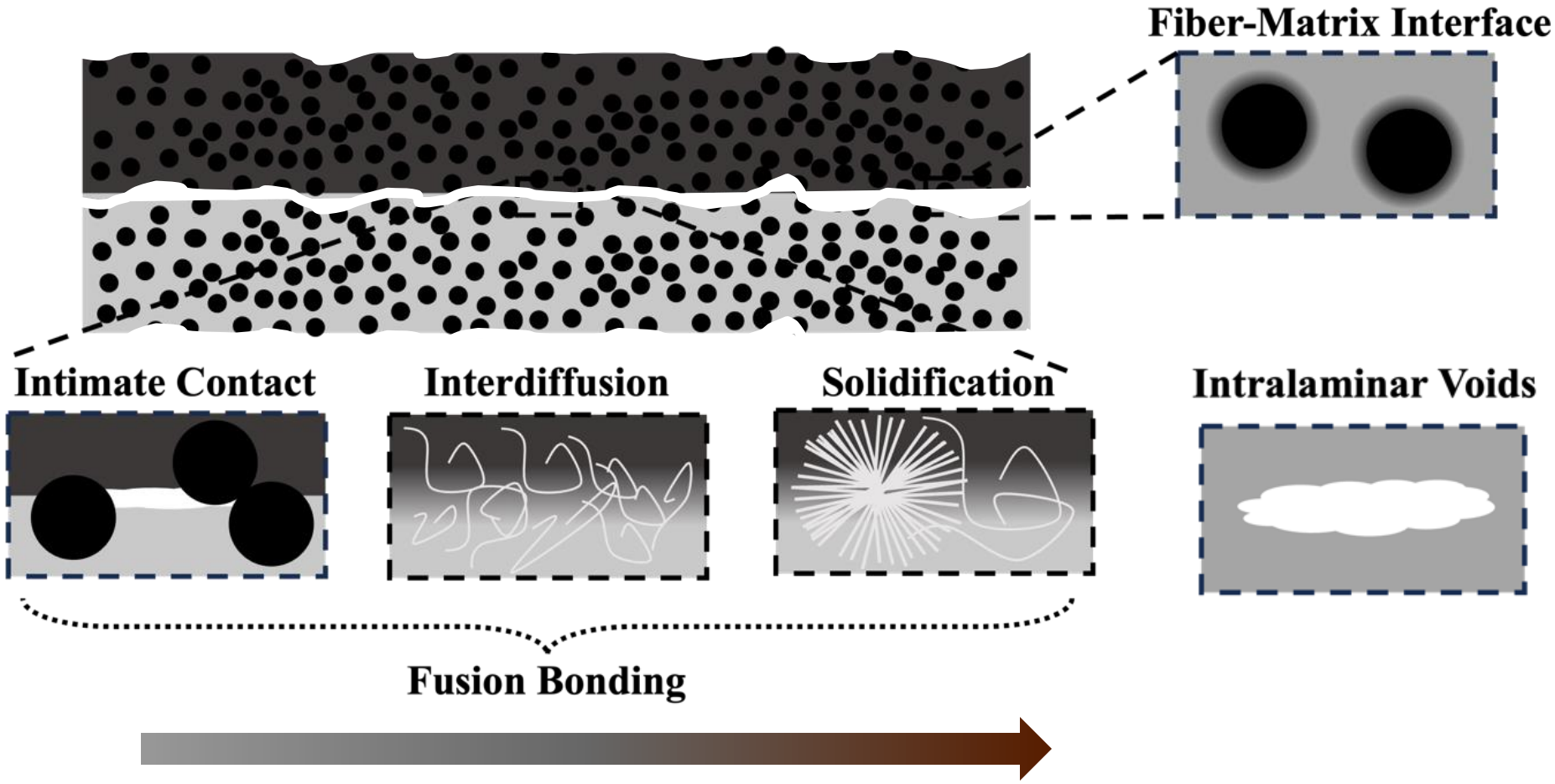

Kirchhoff, …, Tehrani, Composites Part B 294 (2025) 112156

Modelling the AFP Process

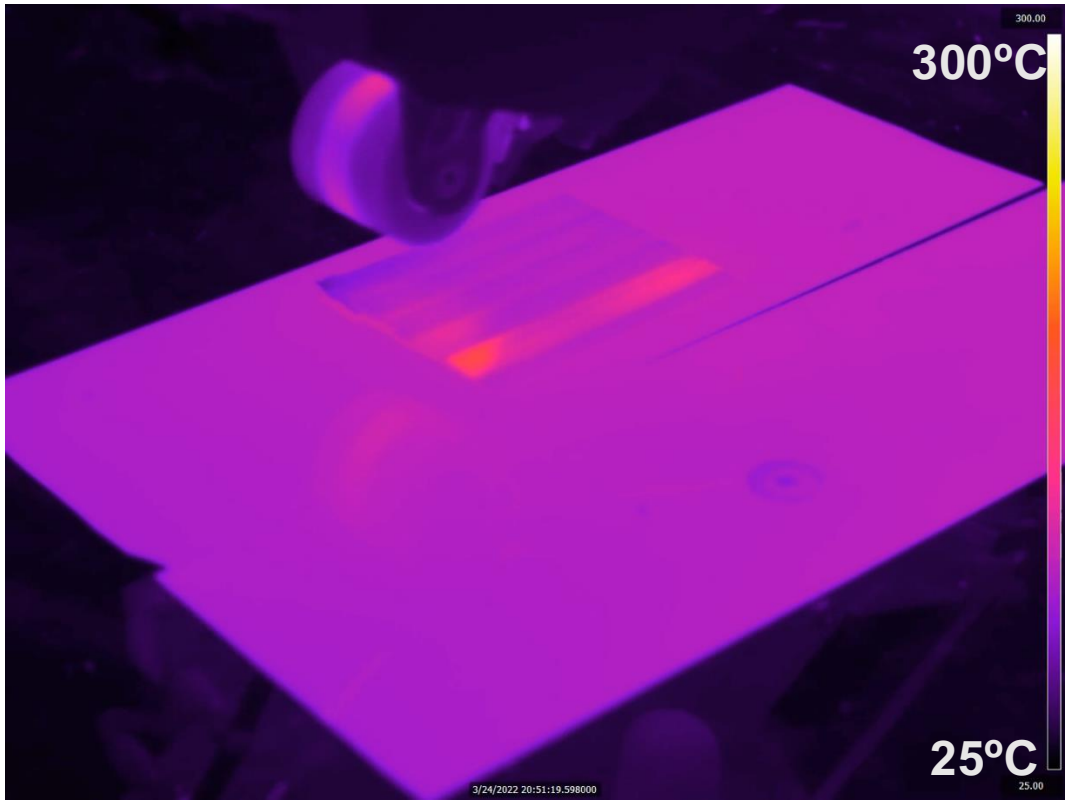

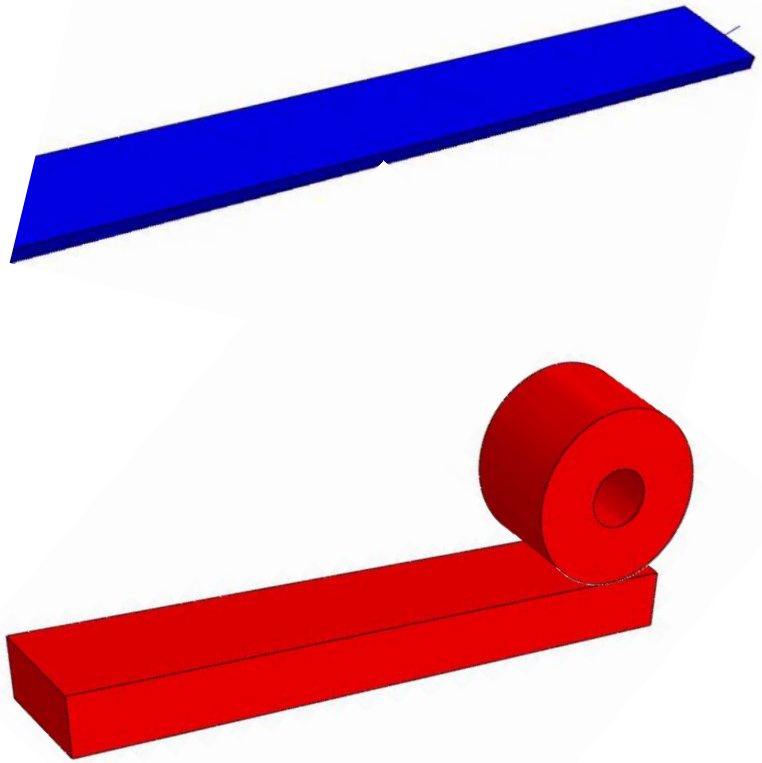

Heathman, …, Tehrani, Composites Part B 249 (2023) 110405

Modelling the AFP Process: 50 mm/s

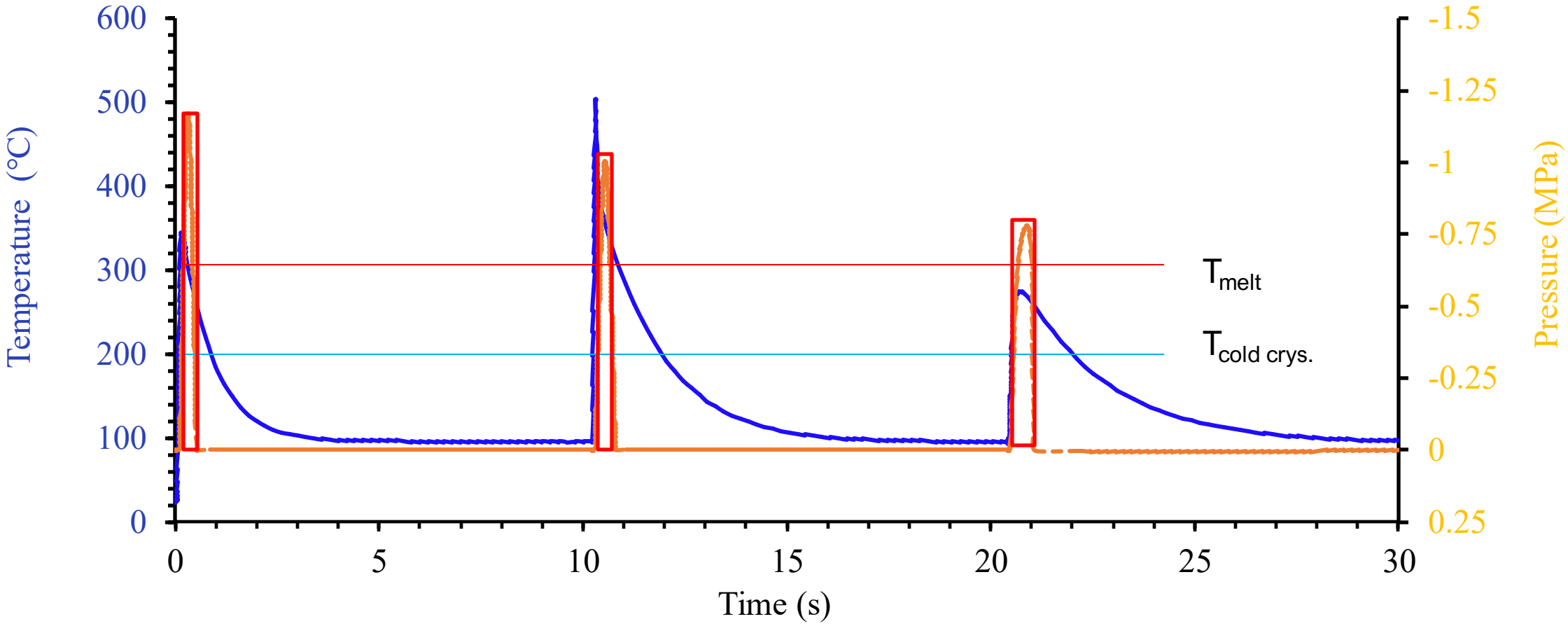

Cooling rates of >10,000 ºC/min – Repetitive heating results in cold-crystalization

UC San Diego
JACOBS SCHOOL OF ENGINEERING

Heathman, …, Tehrani, Composites Part B 249 (2023) 110405

Interlaminar Properties: Degree of Consolidation

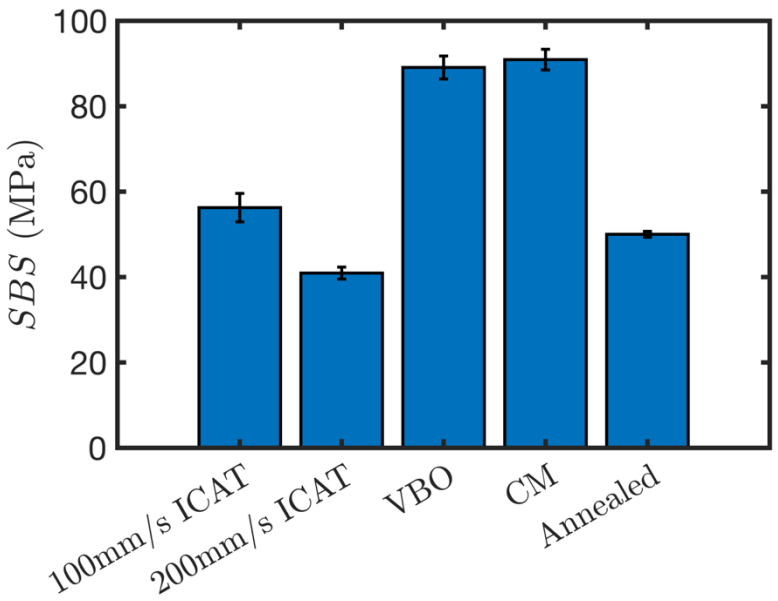

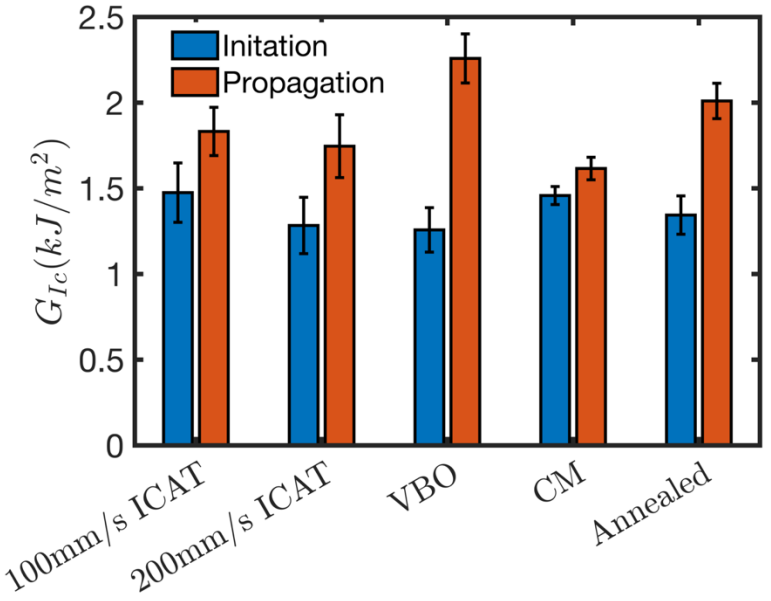

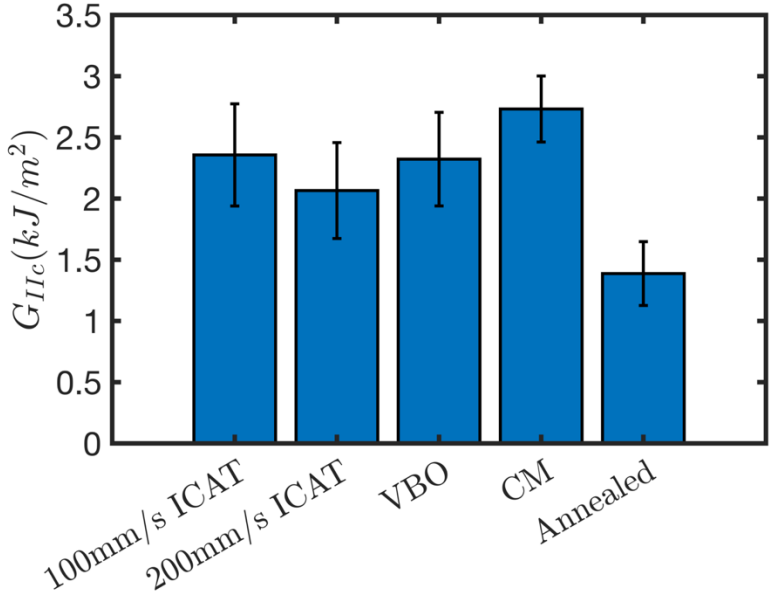

ICAT: in-situ consolidation
VBO: Fast AFP + vacuum bag only oven processing
CM: Fast AFP + compression molding
Annealed: Fast AFP + annealing @210°C

UC San Diego
JACOBS SCHOOL OF ENGINEERING

Kirchhoff, …, Tehrani, Composites Part B 294 (2025) 112156

Intra-Laminar Properties

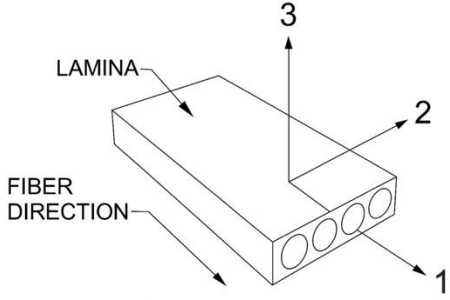

E_1	Young's modulus in the fiber direction
E_2	Young's modulus in the transverse direction
F_1^c	compressive strength in the fiber direction
F_1^t	tensile strength in the fiber direction
F_2^c	compressive strengthin the transverse direction

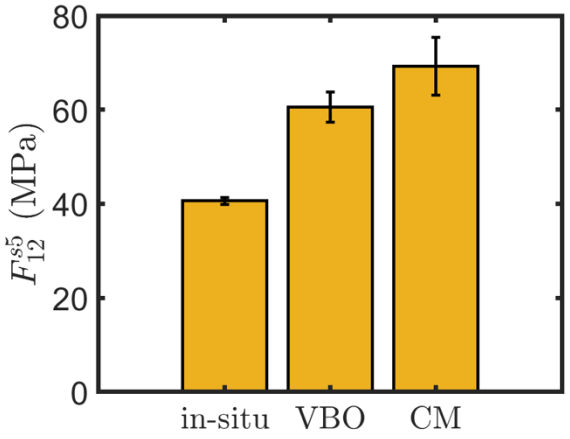

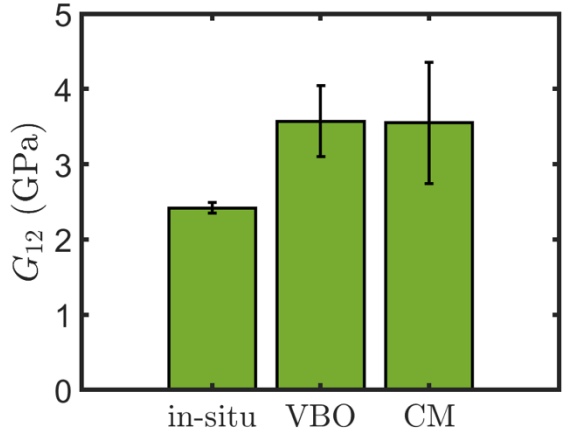

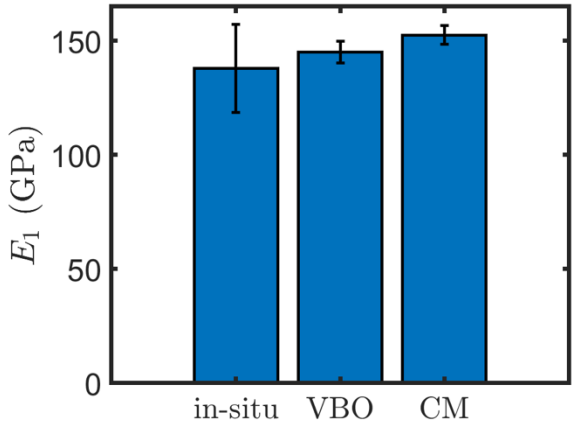

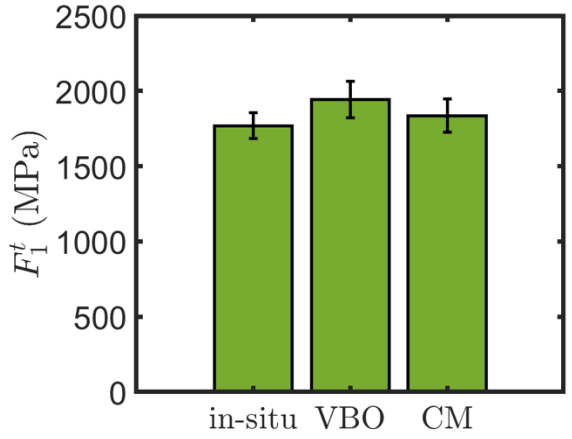

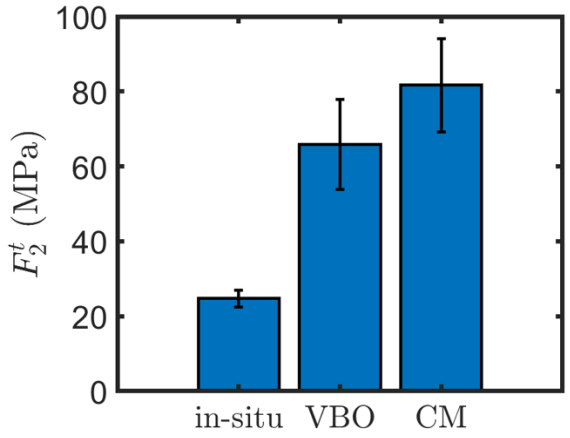

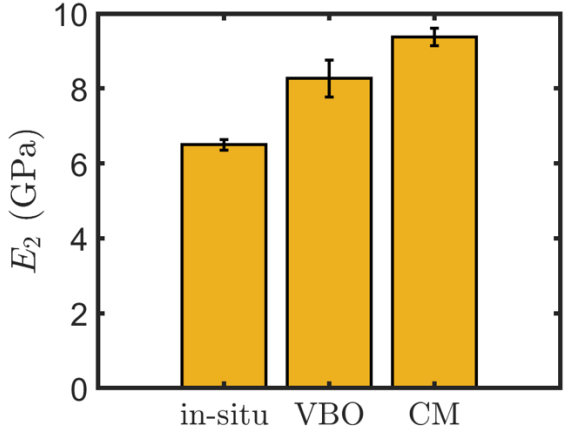

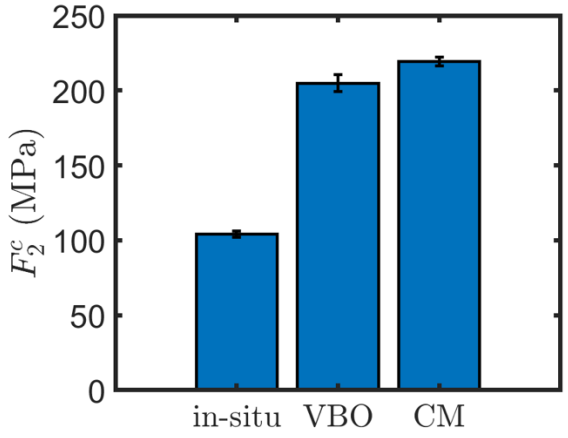

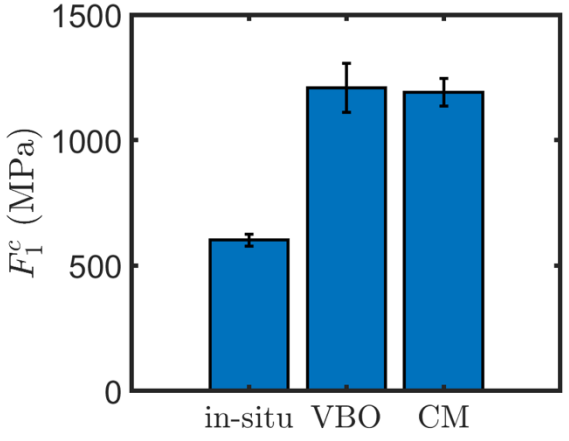

F_2^t	tensile strengthin the transverse direction
$F_{12}^{s0.2}$	in-plane shear strength at offset strain of 0.2 %
F_{12}^{s5}	in-plane shear strength at offset strain of 5 %
G_{12}	in-plane shear modulus

UC San Diego
JACOBS SCHOOL OF ENGINEERING

Yap, …, Tehrani, Composites: Part A 188 (2025) 108525

Differences in Structure

- Fiber-polymr interfaces
- Cracks
- Interlaminar and intralaminar voids
- Waviness
- Crystallinity
- Resin rich regions

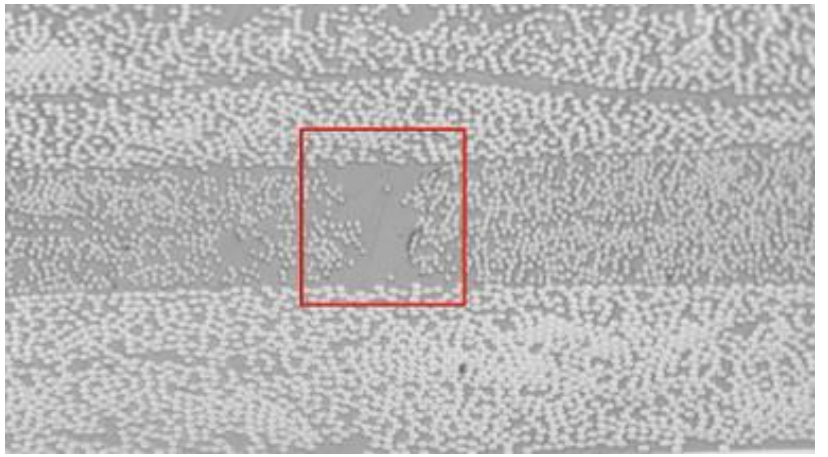

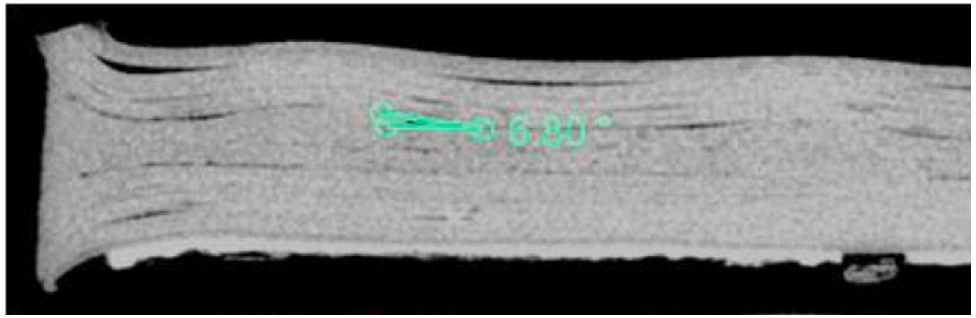

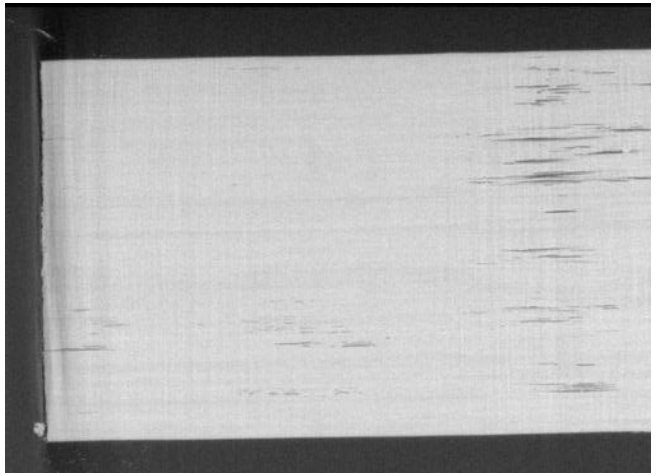

Koirala, …, Tehrani, Composites Part B 299 (2025) 112444
Kirchhoff, …, Tehrani, Composites Part B 294 (2025) 112156
Yap, …, Tehrani, Composites: Part A 188 (2025) 108525

Engineered Pathways for Post-consolidation of TPCs

Intentional Gaps and Delaminations

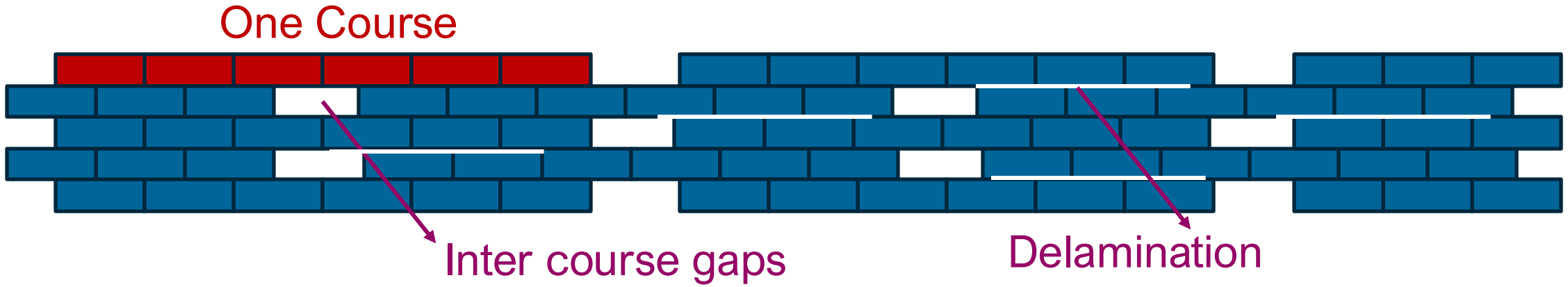



Lightly bonded, fast AFP with intentional gaps

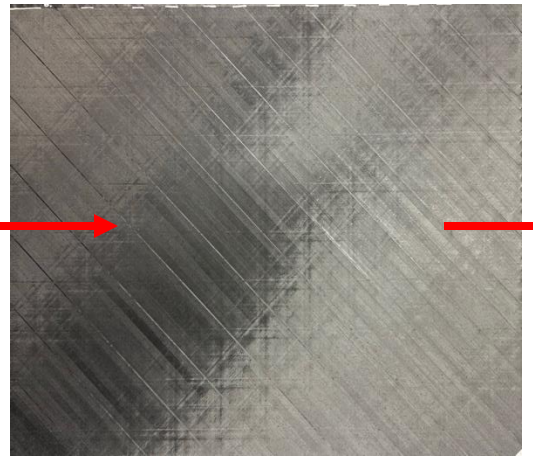

Part made by AFP

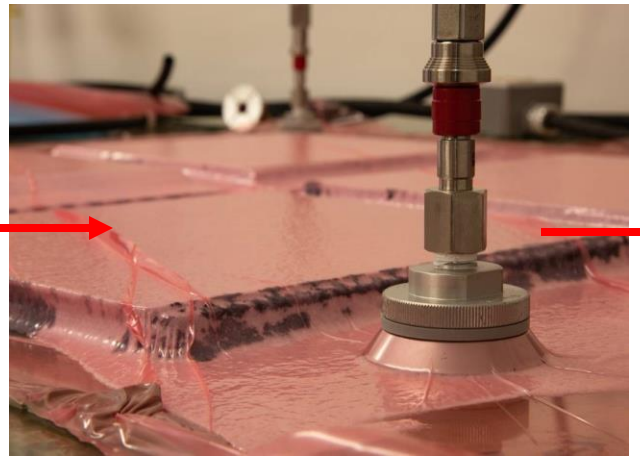

Vacuum bagging oven processing

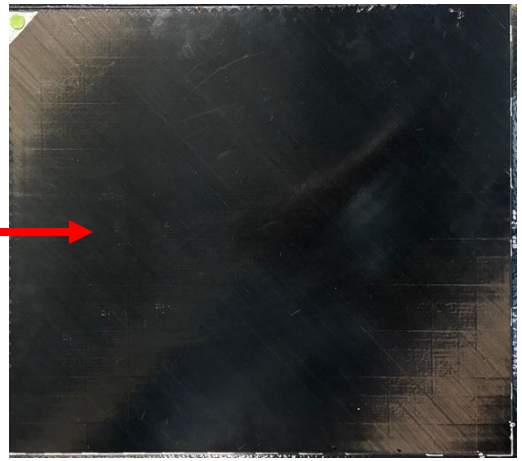

Final Part with low void content and high SBS

Source: CORIOLIS

Optimization Procedure

A. Long VBO (Reference)

B. Short VBO #1

C. Short VBO #2

D. Short VBO #3:

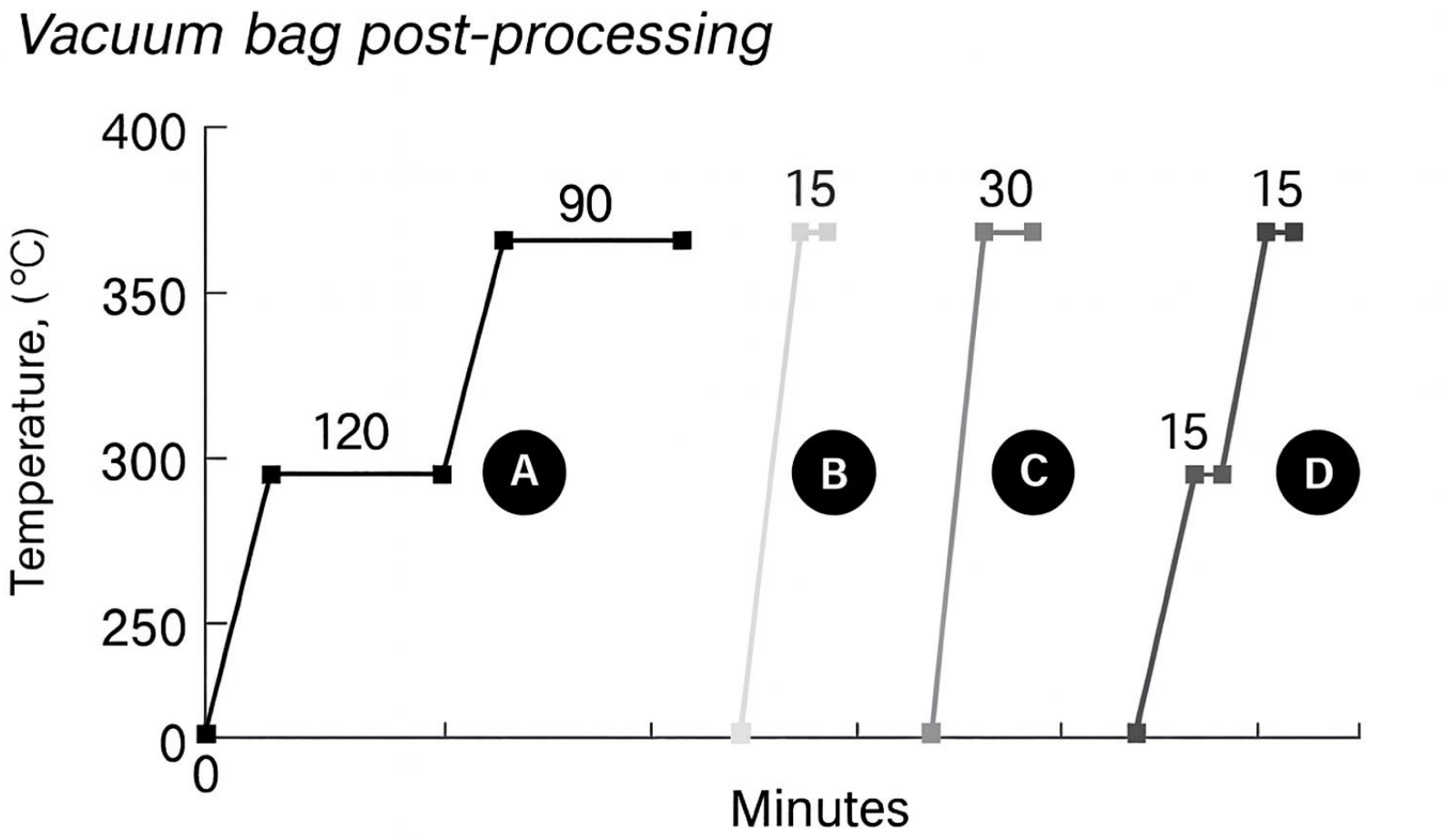

UC San Diego
JACOBS SCHOOL OF ENGINEERING

X-Sectional Microscopy: VBO w/ Engineered Gaps

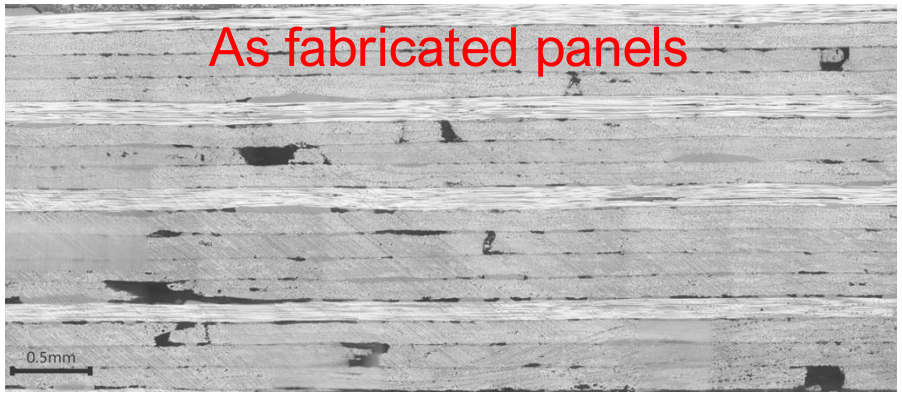



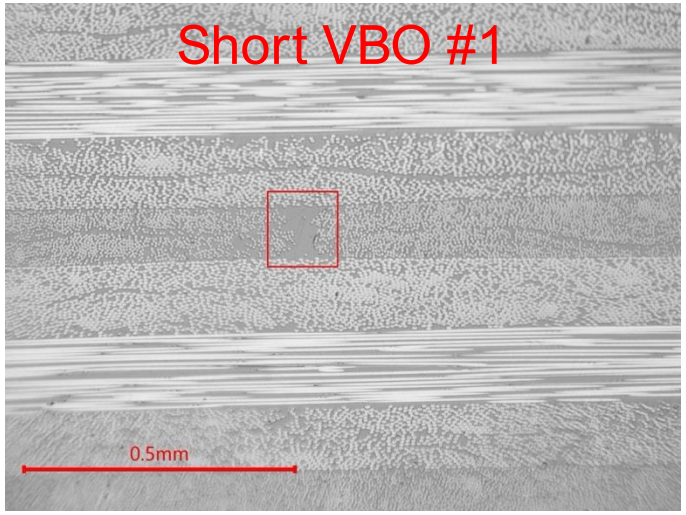

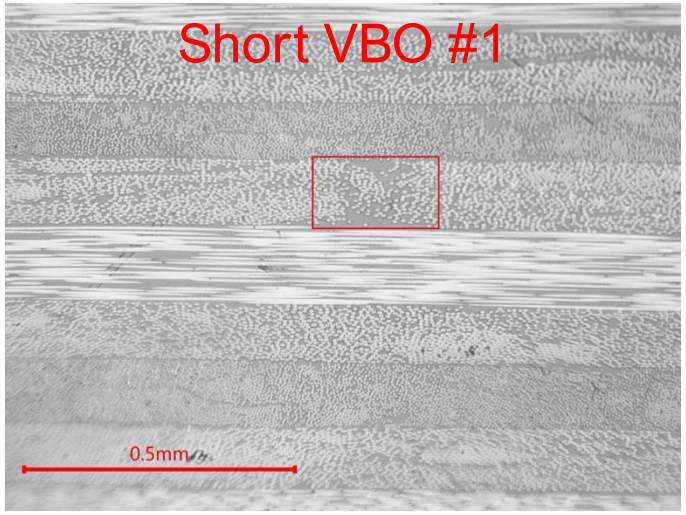

X-Sectional Microscopy: VBO w/ Engineered Overlaps

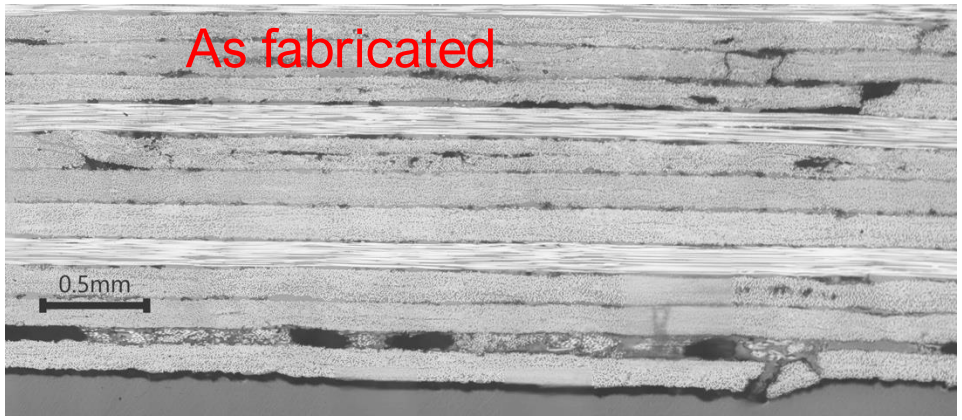

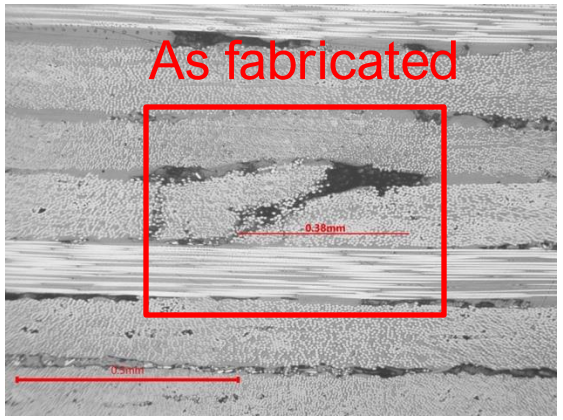

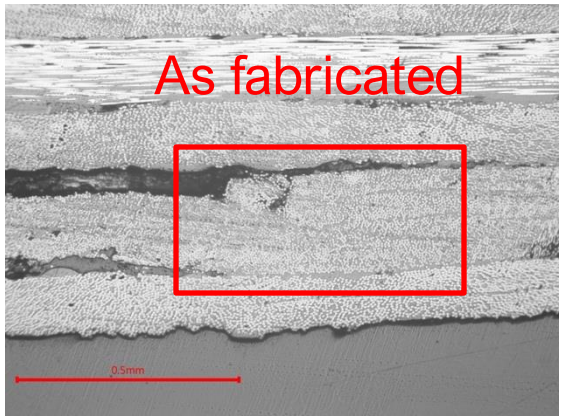



C-Scans

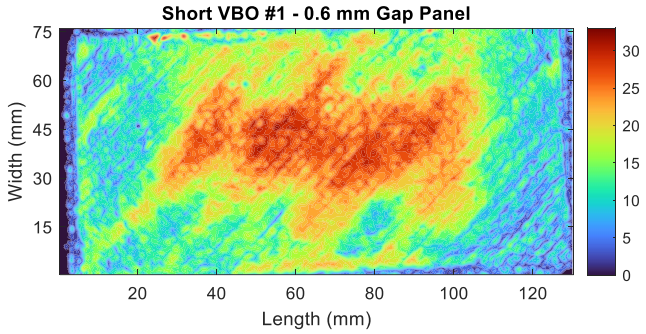

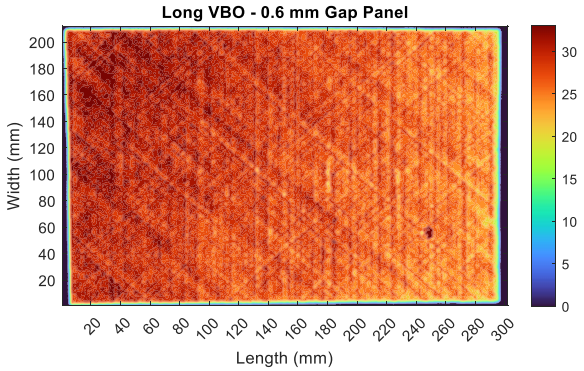

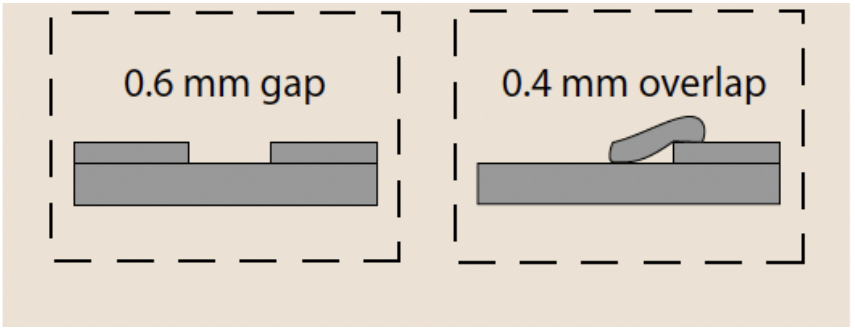

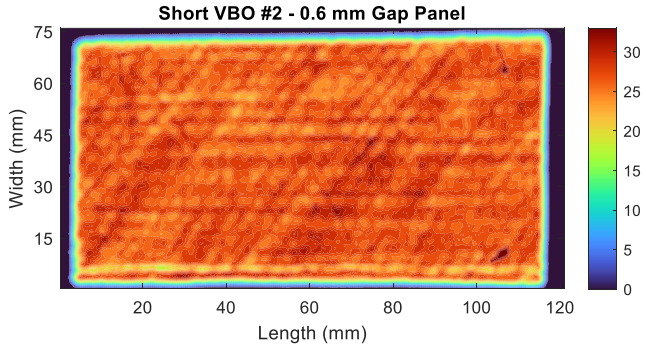

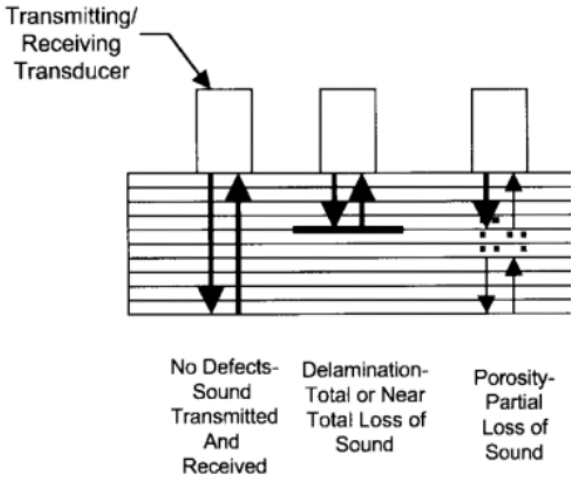

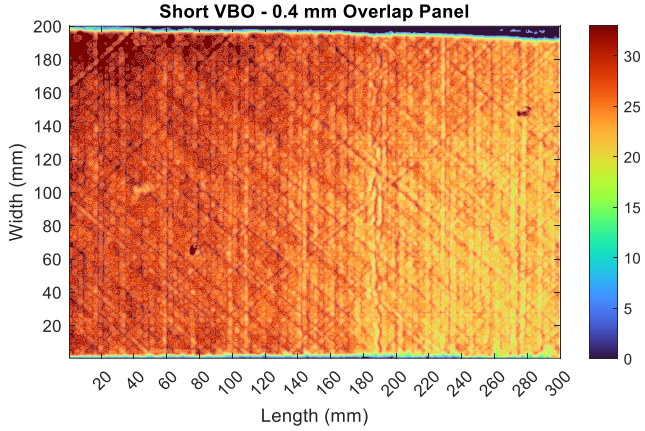

UC San Diego
JACOBS SCHOOL OF ENGINEERING

Interlaminar Bonding Strength

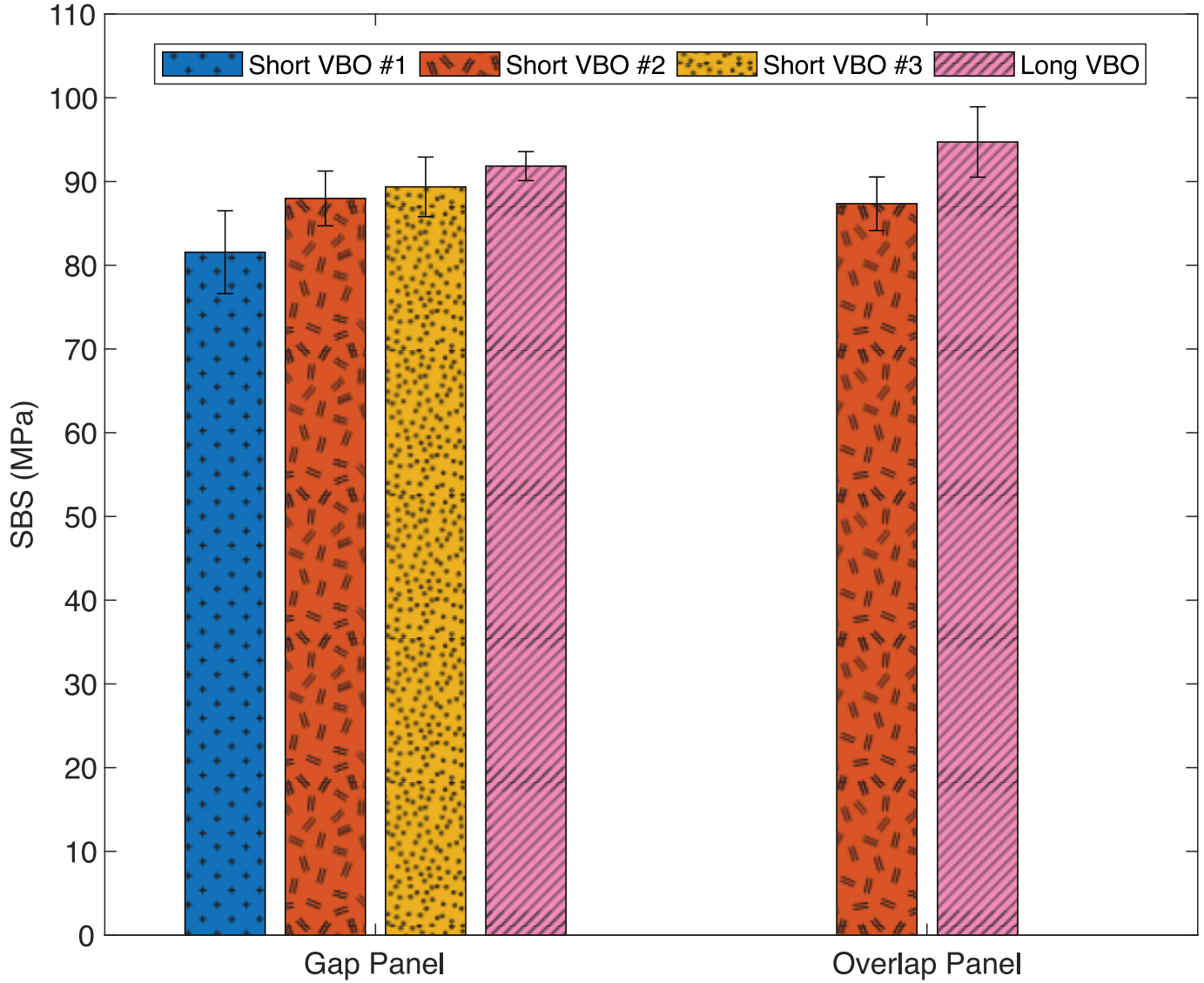

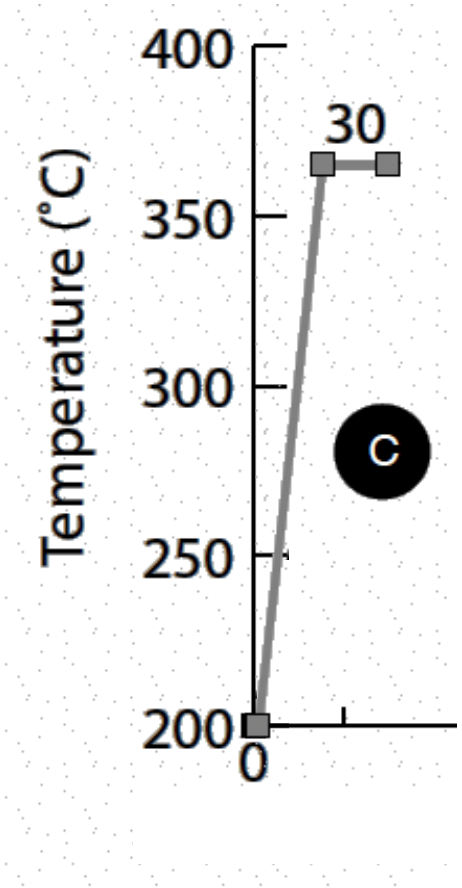

UC San Diego
JACOBS SCHOOL OF ENGINEERING

Out-of-autoclave Amorphous/Crystalline Thermoplastic Materials for Energy-efficient Aerospace-grade Laminates (OATMEAL)

UC San Diego
JACOBS SCHOOL OF ENGINEERING

What is OATMEAL?

Out-of-autoclave **A**morphous/semicrystalline **T**hermoplastic **M**aterial for **E**nergy-efficient **A**erospace-grade **L**aminates.

	Tg (℃)	Tm (℃)	Tensile Modulus (GPa)
PEI	220	--	3.4
PEEK	143	343	3.8

Welding Times

	280 ℃ (s)	320 ℃ (s)	340 ℃ (s)	420 ℃ (s)
PEI	17,155	< 1	--	--
PEEK	NP	NP	592	<1

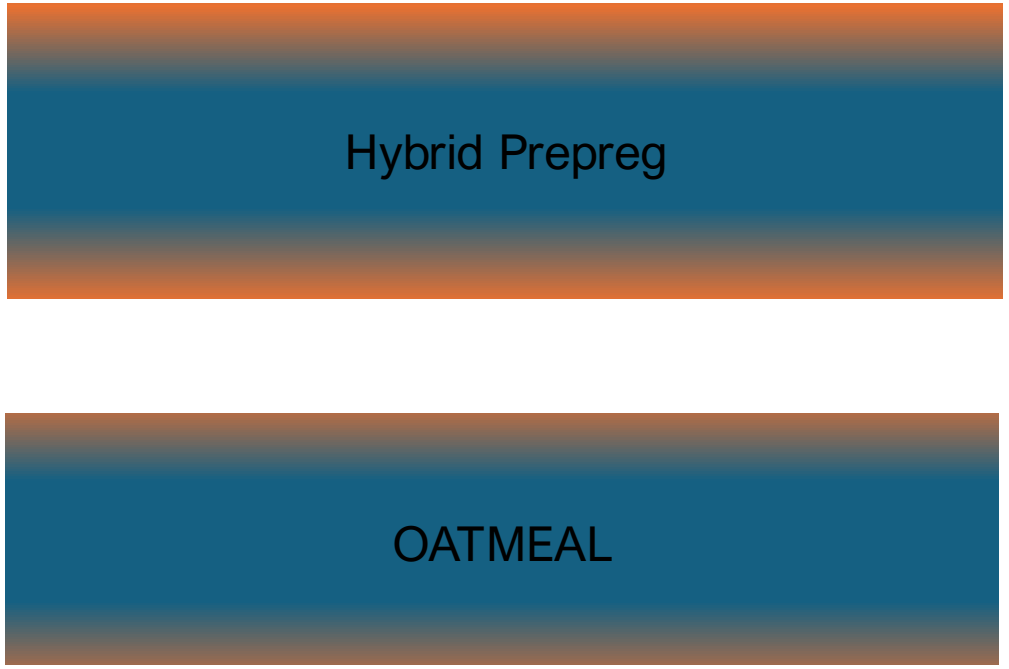

UC San Diego
JACOBS SCHOOL OF ENGINEERING

J. Barroeta Robles, M. Dubé, P. Hubert, A. Yousefpour, "Healing study of poly (ether-imide) and poly ether ether ketone using resin flow across a porous interface", Composites Part A: Applied Science and Manufacturing (2024)

Why OATMEAL?

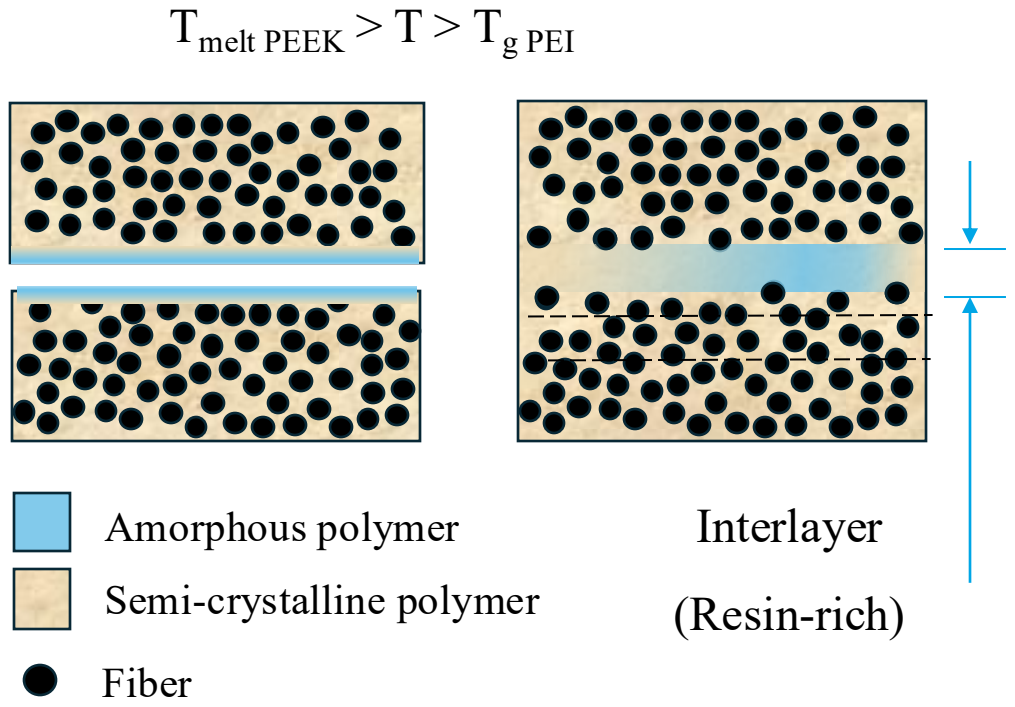
$T_{melt\ PEEK} > T > T_{g\ PEI}$
Amorphous polymer
Semi-crystalline polymer
Fiber
Interlayer
(Resin-rich)

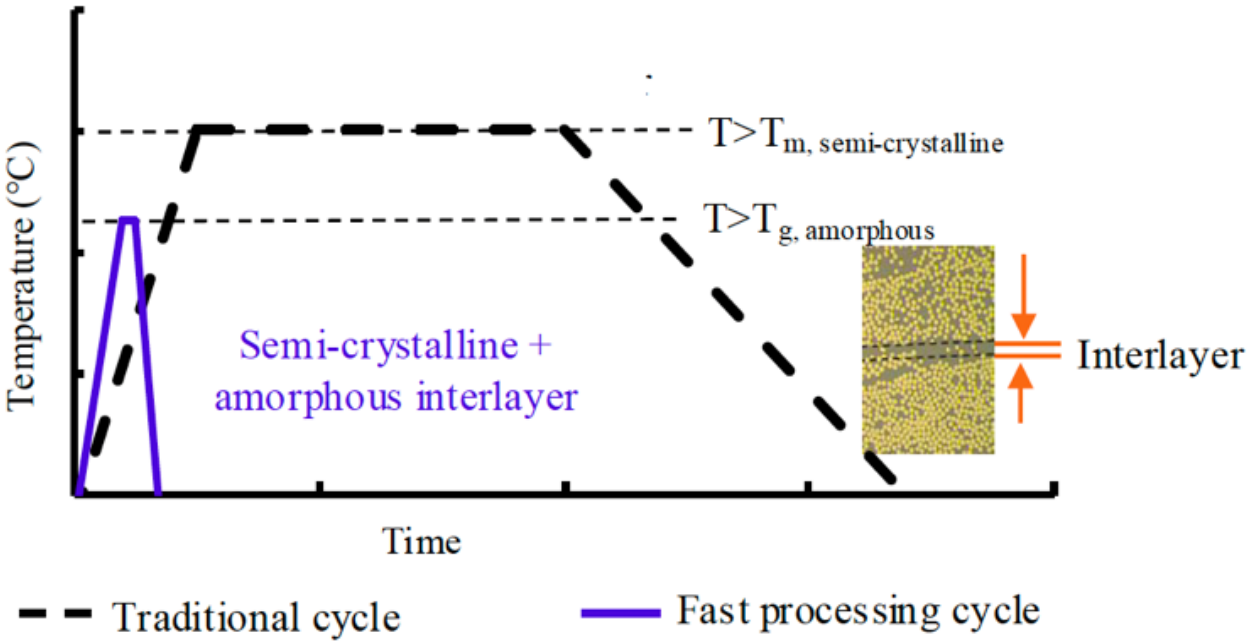
Temperature (°C)
$T>T_{m,\ semi\text{-}crystalline}$
$T>T_{g,\ amorphous}$
Semi-crystalline + amorphous interlayer
Interlayer
Time
Traditional cycle
Fast processing cycle

Cooling-rate Agnostic Material

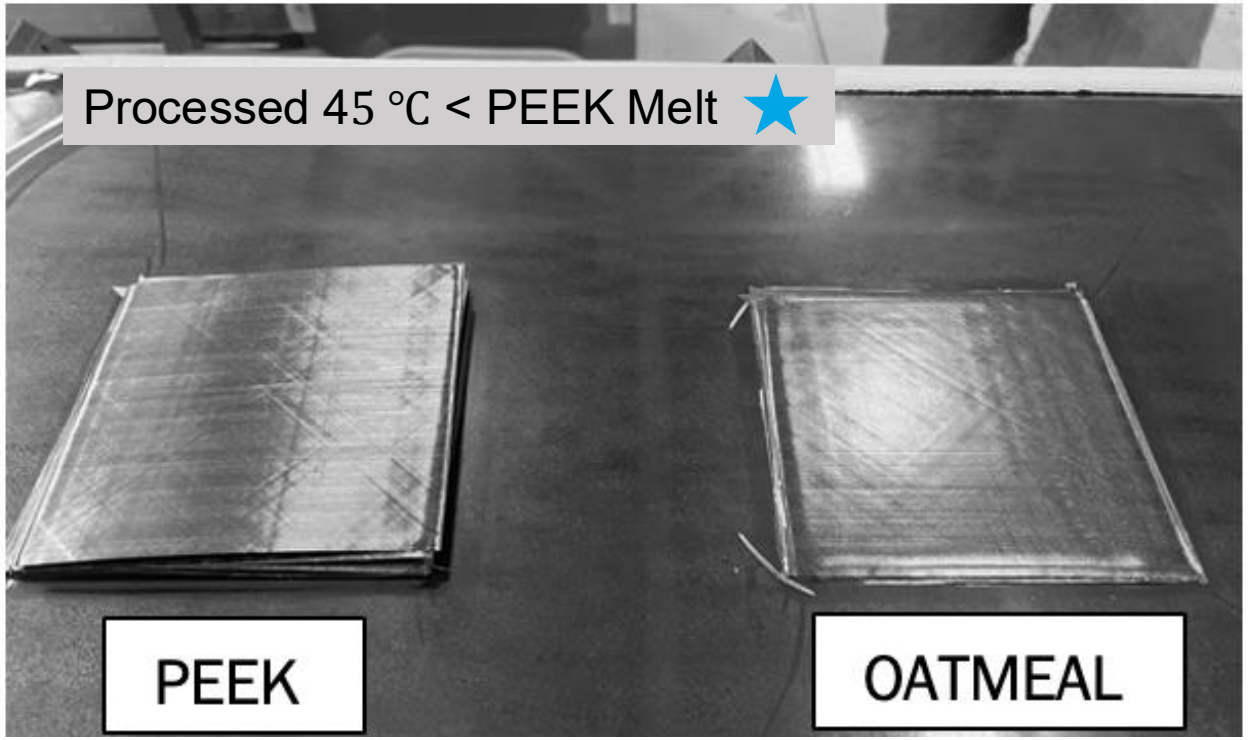

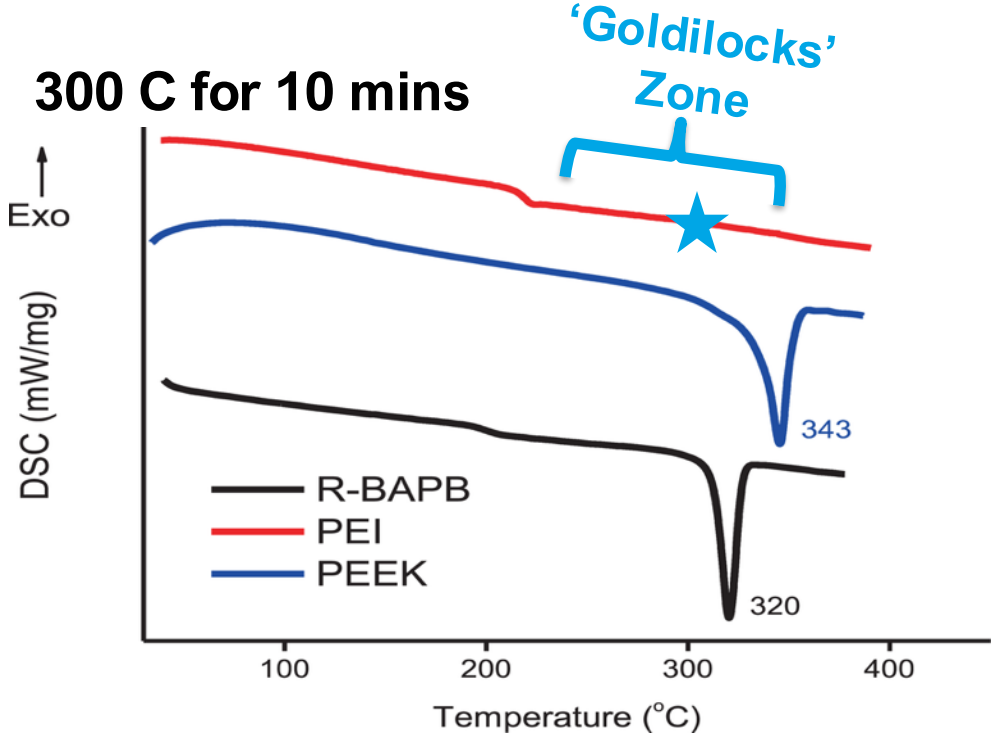

UC San Diego
JACOBS SCHOOL OF ENGINEERING

Thickness and SBS

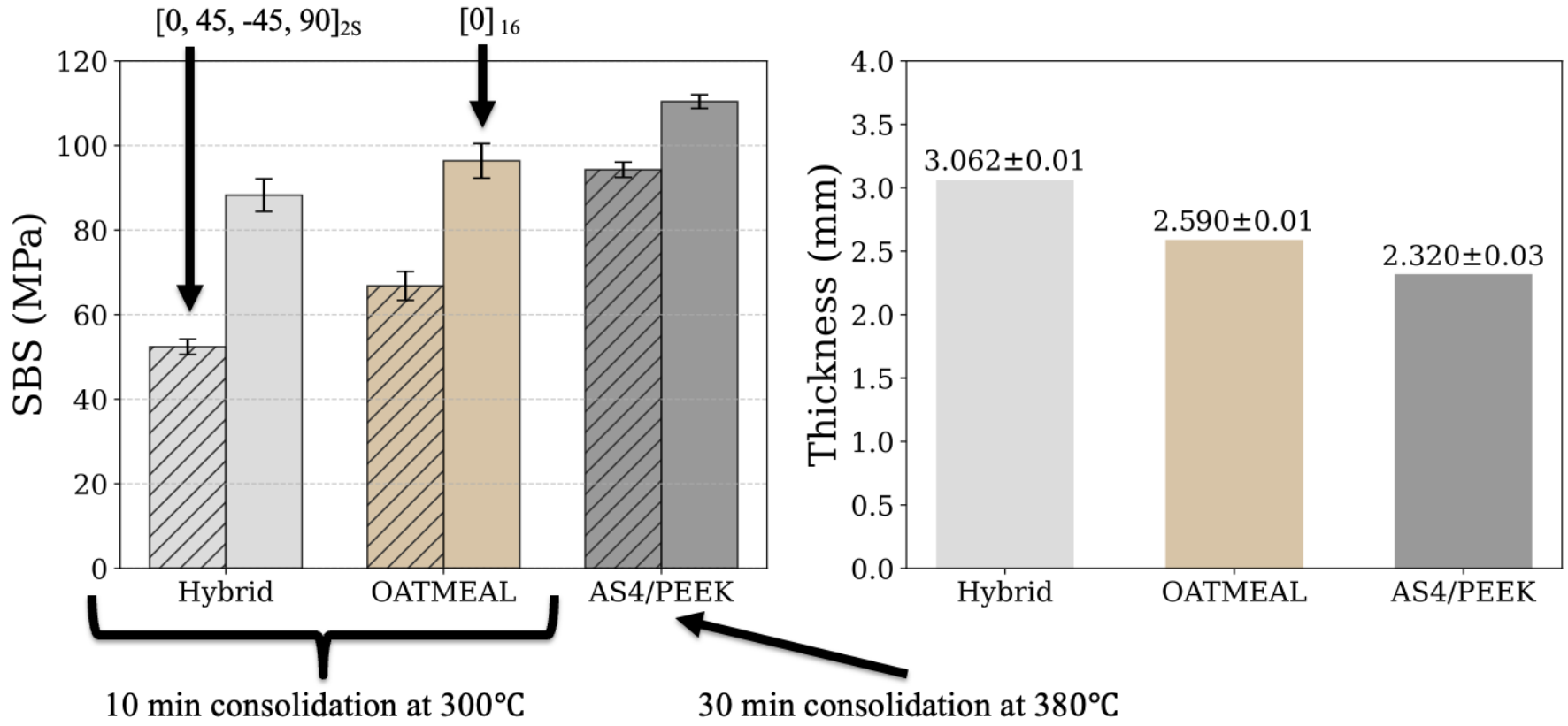

Crystallinity Measurements

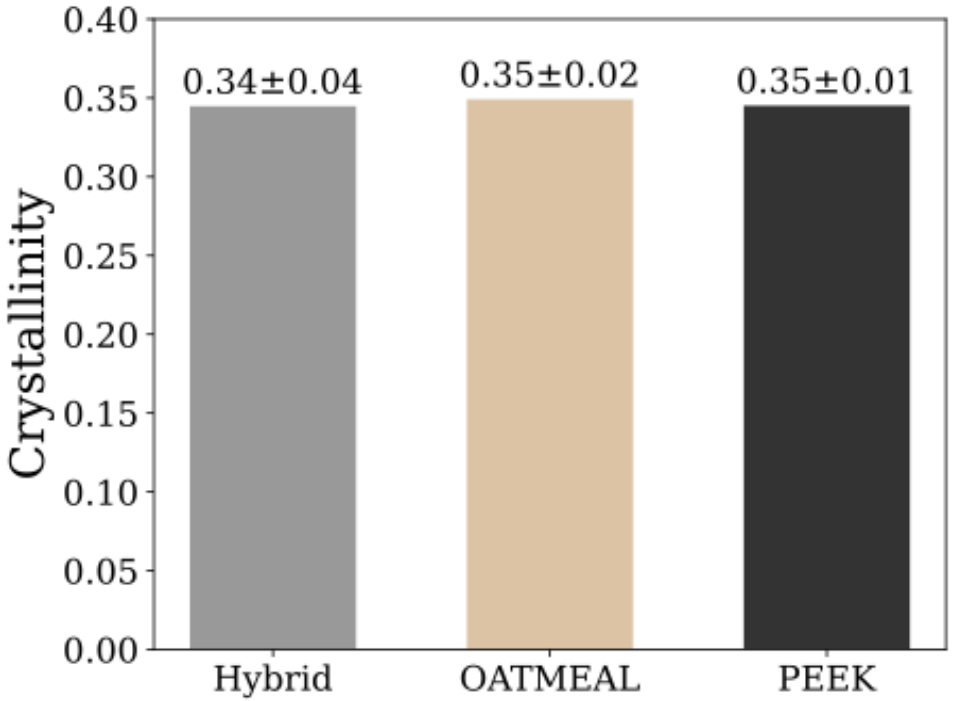



FROM WASTE TO CIRCULARITY: VITRIMERIZATION IN THERMOSET COMPOSITES

V. Ambrogi[1], M. Agizza[1], M. Salzano de Luna[1], G. Filippone[1]

[1]Department of Chemical, Materials and Production Engineering, University of Naples Federico II, Piazzale Tecchio, 80, 80131 Naples, Italy
Email: ambrogi@unina.it, web page: https://www.polyfun.unina.it/

Keywords: Vitrimerization, Thermoset Composite Reprocessing, Dynamic Covalent Bonds, Mechanochemical activation

ABSTRACT

The demand for thermoset composites is growing rapidly, driven by urbanization, expanding infrastructure, the push for lightweight and fuel-efficient vehicles, and the increasing use of wind energy systems. This growth is largely due to the excellent mechanical strength, chemical resistance, and low maintenance requirements of thermoset composites.
However, these materials are difficult to recycle. Their tightly crosslinked, three-dimensional covalent structures make them thermally stable but non-meltable, which severely limits conventional recycling options. Current methods, such as pyrolysis and solvolysis, break down the polymer matrix to recover the reinforcing fibers, but they typically destroy the resin in the process. Fully recycling both the resin and fibers remains a major challenge. As a result, there is a growing push to develop more sustainable, circular approaches to composite recycling,an urgent need for the future of advanced materials.
One promising solution is vitrimer chemistry. Vitrimers belong to a class of materials known as Covalent Adaptable Networks (CANs), which rely on thermally activated exchange reactions. In vitrimers, a dynamic covalent bond is broken only when a new one is formed, keeping the network intact. These bonds become increasingly dynamic at higher temperatures, allowing the material to soften without losing structural integrity.This unique behavior enables vitrimers to be reshaped, self-heal, and even recycled in a closed-loop process, all while maintaining high performance.
In this work, we explore the practical application of vitrimer technology and highlight its potential to address one of the biggest challenges in the field: designing high-performance composites that support a circular economy.

VITRIMER CHEMISTRY IN THERMOSET COMPOSITES

Thermosetting composites are a class of high-performance materials formed by reinforcing a thermosetting polymer matrix with fibers, fillers, or other strengthening agents [1]. Unlike thermoplastics, thermosetting polymers undergo an irreversible curing process, typically initiated by heat, radiation, or chemical additives, resulting in a rigid, crosslinked molecular structure. This crosslinking imparts excellent mechanical strength, chemical resistance, dimensional stability, and thermal performance, making thermosetting composites ideal for demanding structural and functional applications. Common thermosetting resins include epoxy, polyester, vinyl ester, and phenolic systems, which are frequently combined with reinforcing materials such as glass, carbon, or aramid fibers. These composites are widely used in industries ranging from aerospace and automotive to wind turbines, and marine engineering, where lightweight yet durable materials are essential.

Despite their advantages, thermoset composites pose a major challenge: they cannot be reprocessed after curing due to their permanent covalent crosslinking of the matrices. This limits recycling options to mechanical, thermal, or chemical recovery methods (Figure 1), all of which are energy-intensive and often degrade the material quality [2,3].

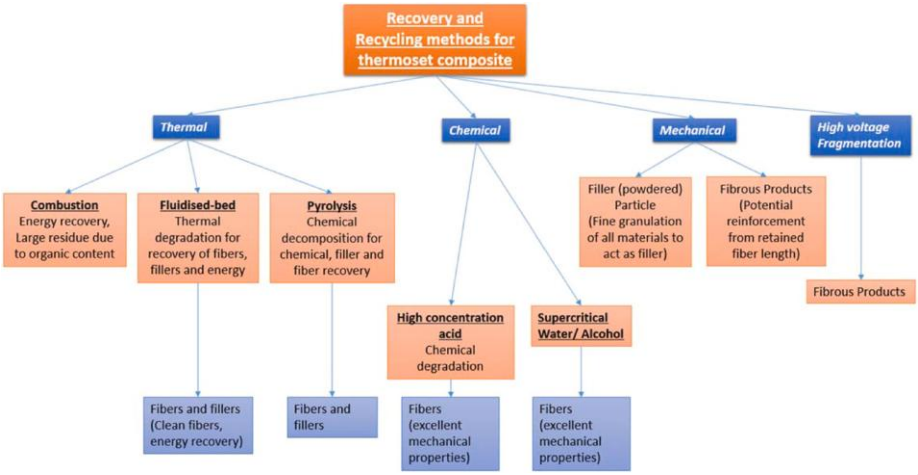

Figure 1: Traditional methods used to recycle polymer composites. Adapted from ref. [3]

To address this issue, emerging research focuses on Covalent Adaptable Networks (CANs). CANs offer the mechanical strength of thermosets along with the reprocessability and reshaping capabilities of thermoplastics. This is achieved through the incorporation into the networks of covalent bonds, which undergo reversible chemical reactions in response to external stimuli such as heat or UV light. These chemical exchanges allow the polymer network to rearrange, maintaining its overall structure and function while altering the connectivity between chains. As a result, CANs behave like traditional thermosets at low temperatures, but above a certain threshold, the dynamic bond exchange enables chain mobility and flow. Additionally, these reversible bonds allow the material to self-heal by temporarily increasing chain mobility without compromising structural integrity or mechanical properties [4-6].

Typically, bond exchange within CANs occurs through one of two mechanisms [7]: a dissociative mechanism, where crosslinks break apart into reactive fragments before reforming, or an associative mechanism, where a reactive group within the network directly replaces an existing bond through substitution (Figure 2). The associative pathway is central to the function of vitrimers, a newer class of CANs that exhibit dynamic behavior while maintaining network integrity, offering significant advantages for high-performance applications. Introduced by Prof. Leibler in 2011 [8], vitrimers have brought new challenges and misconceptions regarding their design and functionality.

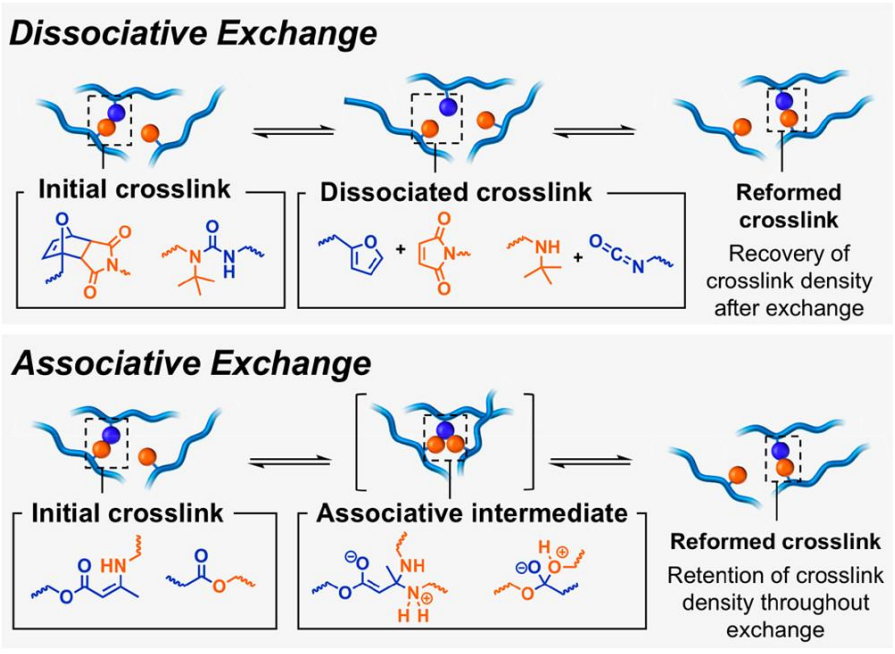

Figure 2: Schematic representation of dissociative and associative bond exchange mechanisms

governing CANs. Adapted from ref. [7]

The term vitrimers originates from their characteristic viscosity–temperature relationship, which parallels that of vitreous silica. These materials exhibit a continuous decrease in viscosity with increasing temperature, following an Arrhenius-type dependence at elevated temperatures. This behavior facilitates dynamic processes such as thermoforming, autonomous self-healing, and closed-loop recyclability through bond exchange reactions, motivating the growing interest in these systems especially in terms of sustainability in different industrial fields, including composites [9,10]. Because of this, there's growing interest in designing and developing thermoset composites using vitrimer technology. Research is now focusing on several key challenges, one of the most important being how fillers affect the movement of polymer chains, known as molecular mobility. Molecular mobility plays a major role in how the material behaves under stress (its viscoelastic properties) and how well it can be reshaped or repaired. While fillers can improve the material's strength and durability, they might also make the polymer chains less flexible. If that happens, the material's ability to rearrange its bonds—which is crucial for self-healing and reprocessing—can be reduced.

Understanding how different fillers interact with the polymer network is therefore essential for developing high-performance, recyclable vitrimer-based composites. Moreover, practical considerations related to manufacturing and scalability must be taken into account. These include the workability of the reactive mixture, its compatibility with existing processing technologies (e.g., molding, extrusion, or hot pressing), and the ability to achieve consistent and reliable performance in the final product. Parameters such as curing conditions, pot life, viscosity, and integration with reinforcement materials must be optimized for large-scale production.

Due to these stringent requirements, the range of thermosetting chemistries suitable for vitrimer formulations is currently limited. Only a few polymer platforms, those that offer a favorable balance between dynamic network behavior, filler compatibility, and processability, are considered viable for real-world applications. This limitation is illustrated in Figure 3, which outlines the most used matrix systems for vitrimer composite development.

.

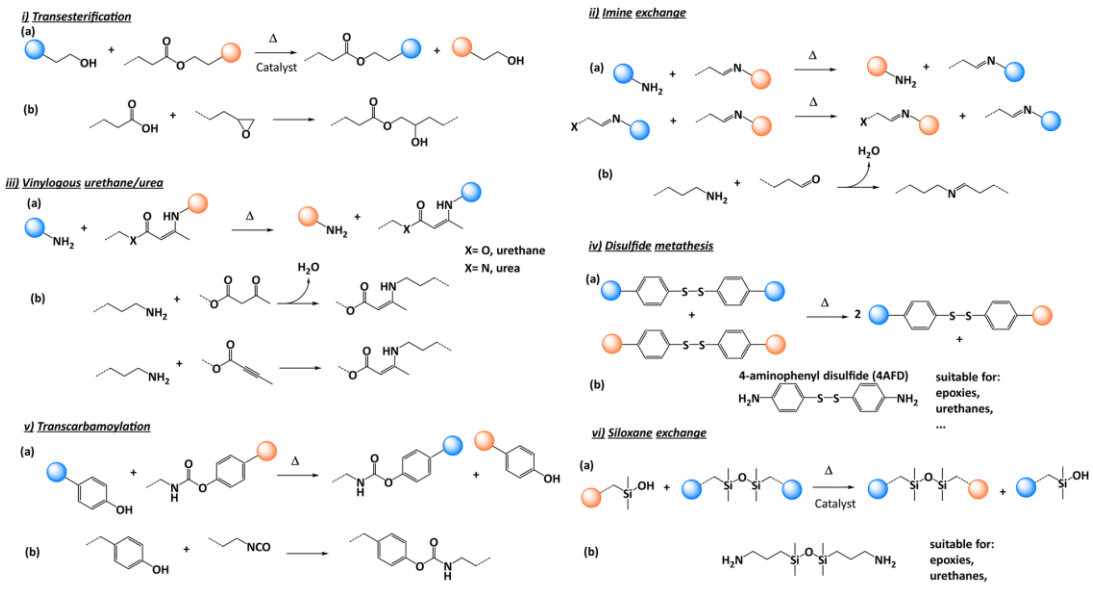

Figure 3: Vitrimer chemistry for thermoset composites. Adapted from ref. ref. [11]

In transesterification-based vitrimers (Figure 3a), epoxy reacts to form exchangeable ester linkages bearing a β-hydroxy group. This chemistry allows for tunable exchange kinetics by adjusting the type and amount of catalyst, offering control over activation energy and processing conditions. However, under off-stoichiometric conditions, careful regulation of network formation is required to prevent the

formation of non-dynamic ether linkages, which can create rigid clusters and compromise vitrimer adaptability. Imine-based vitrimers (Figure 3b) offer robust and dynamic bond exchange via free-amine or imine metathesis, with high bond stability and minimal side reactions. Their advantages include simple synthesis, tunable properties, and excellent mechanical performance, though careful water management is required during formation to prevent internal defects that may be detrimental. Vinylogous urethane-based vitrimers (Figure 3c) enable catalyst-free dynamic exchange via Michael addition or iminium intermediates, offering fast relaxation times and good stability comparable to epoxy/acid systems. Advantages include hydrolysis resistance, water-compatible synthesis, and tunable exchange through external catalysts. However, challenges include managing water release during formation and ensuring long-term stability of free amines to prevent oxidative degradation. Disulfide-based vitrimers (Figure 3d) offer catalyst-free exchange via a [2+1] radical-mediated mechanism at moderate temperatures, making them easy to implement with accessible precursors and widely used in formulations like epoxy and rubber. However, their dynamic properties can degrade over time due to thiol oxidation in air and the thermal sensitivity of the S–S bond. Transcarbamoylation (Figure 3e) enables dynamic exchange in both aliphatic and aromatic polyurethanes, with aromatic structures allowing catalyst-free reactions between phenols and urethanes. Siloxane bonds, known for their high chemical and thermal stability, are common in materials like silicone rubber and glass (Figure 3f), making them attractive for dynamic materials. While traditional silyl ethers exchange slowly, recent advances using a base catalyst have enabled much faster siloxane bond exchanges, offering promising applications in composites with readily available commercial precursors. Carbon nanotubes, graphene, glass fibers or inorganic powders, such as silica (SiO_2) or alumina (Al_2O_3) are used as reinforcement fillers for vitrimeric composites [11,12].

A growing body of literature highlights the versatility of vitrimeric composites, demonstrating their applicability across diverse technological domains. In particular, they have emerged as promising candidates in the field of smart electronics, where their dynamic properties can be leveraged for advanced functionality. In their work, N.J. Van Zee et al. [13] developed conductive thermoset composites by dispersing less than 10 wt.% multiwalled carbon nanotubes (MWCNTs) into a polyimine-based vitrimer, obtained by thermally curing terephthalaldehyde, diethylenetriamine, and tris(2-aminoethyl)amine. These composites combined dynamic covalent bond exchange with the electrical conductivity and mechanical reinforcement of MWCNTs. Remarkably, they maintained stable conductivity after multiple deformation and healing cycles, making them potential candidates for recyclable flexible electronics.

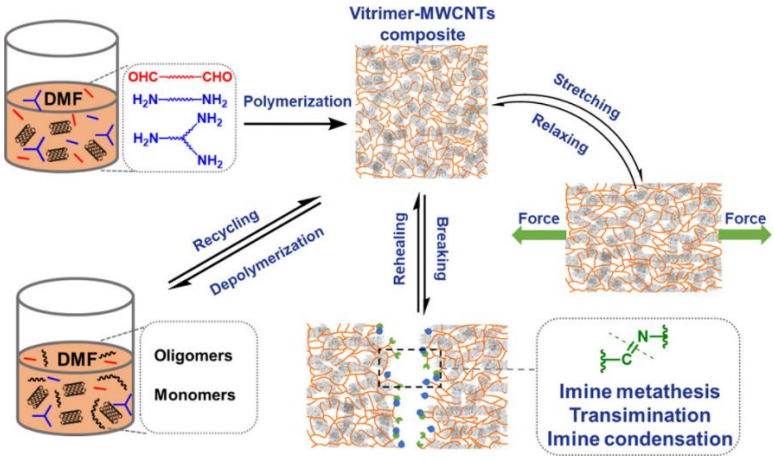

Figure 4: Polyimine-MWCNTs vitrimer composites for flexible electronics. Adapted from ref. [13]

Glass fibre-reinforced vitrimer composites have been developed using both epoxy and vinylogous urethane matrices. Prepreg sheets prepared and consolidated via hot pressing or resin transfer molding (RTM) resulted in dense multilayer composites with improved mechanical properties. Despite high fibre

volume fractions (>50 vol%), these composites retained weldability through dynamic covalent chemistries such as transesterification and amine exchange, enabling adhesive-free joining. The mechanical performance matched that of conventional glass fibre/epoxy systems, highlighting the potential of vitrimer-based prepregs for structural applications, particularly in aerospace where large or complex geometries are required.

An alternative approach is based on the conversion of permanently cured systems into exchangeable thermoset composites. This is achieved by mechanically grinding the cured resin, then treating it with a dynamic exchange catalyst and reinforcing filler under elevated temperature and pressure. The resulting material is a fully crosslinked composite that retains structural integrity while offering improved thermomechanical performance and the ability to undergo thermal reprocessing.

In their work, A. R. de Luzuriaga and his colleagues optimized a fabrication method for fibre-reinforced vitrimer composites involving hot-pressing woven carbon fibres with vitrimer powders derived from mechanically ground, cured DGEBA-based matrices [14]. The formation of the composite material occurred through exchange transesterification reactions within the hot-pressed powder, using a one-minute dry process, faster than conventional liquid-state thermoset processing. The resulting composites retained thermoformability and reprocessability, expanding their manufacturing potential and highlighting the importance of vitrimer particle size in promoting effective healing and full recovery of mechanical properties.

A notable study explored the vitrimerization of thermoset polymers using hydroxyl-rich cellulose nanocrystals (CNCs) as fillers for the fabrication of vitrimeric epoxy-based nanocomposites [15]. The process relied on the use of planetary ball milling to grind the crosslinked resin and mix it with CNCs (Figure 5).

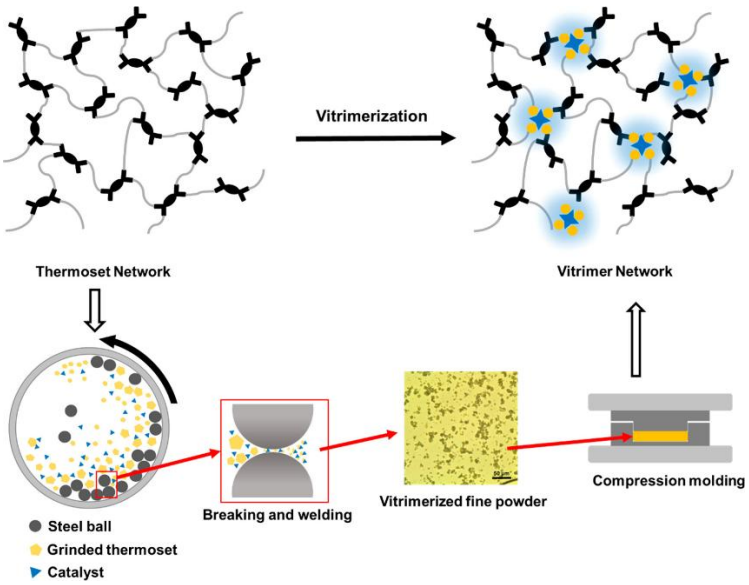

Figure 5: Catalyst-free vitrimerization based on transesterification of a thermoset resin into a vitrimeric composite through the use o planetary ball milling technique. Adapted from ref. [15]

Interestingly, the abundant hydroxyl groups on CNCs facilitate dynamic transesterification at the polymer interface, initiating mechanochemical activation and network reconfiguration thus effectively converting the rigid, irreversible network into a vitrimer composite structure. The authors demonstrated that incorporating CNCs as a source of external hydroxyl groups significantly enhanced the rate of exchange reactions and improved the thermomechanical performance of the resulting epoxy vitrimer. Beyond improving recyclability, the bio-based CNCs also contributed to mechanical self-healing and enhanced material recovery. This method offers a sustainable route for upcycling both thermoset and lignocellulosic wastes into functional vitrimer materials, making it a promising strategy for scalable, industrial applications.

In this work, a case study on the development of vitrimeric composites by modifying epoxy resins with cellulosic fibers is also discussed. The study aims at generating reliable and reproducible data on

the reprocessability of epoxy-based thermosetting resins and at elucidating the influence of key experimental parameters on both material performance and process optimization. The study begins with the preparation of a well-defined epoxy/anhydride system, which is thermally cured to form a crosslinked network representative of conventional thermoset matrices. To simulate an end-of-life treatment scenario, the cured resin is subsequently subjected to ball milling, a mechanochemical technique that reduces the material to fine powder without the use of solvents, in line with sustainable processing approaches.

The milled resin powder is then combined with a predetermined amount of hydroxyl-rich natural fibers, selected for their ability to promote dynamic transesterification reactions due to the presence of –OH functional groups. The reprocessability of the resulting formulations is systematically investigated by varying processing parameters, namely temperature, pressure, and time, during hot pressing. These parameters are chosen based on their relevance to vitrimeric bond exchange kinetics and their practical applicability in scalable manufacturing settings.

An initial qualitative assessment is conducted by evaluating the morphological homogeneity and structural integrity of the reprocessed specimens. Subsequently, a quantitative evaluation is performed by determining a global mechanical quality index, which serves as a comprehensive indicator of the physical performance and cohesion of the vitrimeric composites post-reprocessing.

This methodology aims to establish a robust experimental framework for the assessment of post-consumer thermoset waste treatment and its conversion into reprocessable composite systems. The findings are expected to contribute to the broader effort of integrating circular economy principles into the lifecycle of high-performance polymeric materials by enabling the recovery and reuse of crosslinked thermosets and reinforcing fibers.

The overarching goal of this work is to explore and validate the feasibility of producing recyclable thermoset materials with high added value. By combining renewable feedstocks with dynamic covalent chemistry and environmentally friendly processing, the activity contributes to advancing sustainable practices in the field of polymer science and composite materials. Ultimately, it aims to broaden the scope of circular strategies for thermosets, integrating waste valorization and recyclability into the design of advanced functional materials.

REFERENCES

[1] D. Ratna, in *Recent Advances and Applications of Thermoset Resins (Ed. D. Ratna),* Elsevier, 2nd edn, 2022, pp. 371–418

[2] R. Morales Ibarra, Recycling of thermosets and their composites. *In: Thermosets*. Elsevier, 2018. pp. 639-666;

[3] S. Utekar, V.K. Suriya, N. More, A. Rao, Comprehensive study of recycling of thermosetting polymer composites–Driving force, challenges and methods. *Composites Part B: Engineering*, 2021, 207, pp. 108596

[4] M.A. Lucherelli, A. Duval, L. Avérous. Biobased vitrimers: Towards sustainable and adaptable performing polymer materials. *Progress in Polymer Science*, 2022, 127, pp. 1015155

[5] D.B. Tiz, D. Benedetto, F.A. Vicente, A. Kroflič, and B. Likozar, Lignin-based covalent adaptable network polymers─ when bio-based thermosets meet recyclable by design. *ACS Sustainable Chemistry & Engineering*, 2023, 11(38), pp. 13836-13867.

[6] A. Marotta, F. Scherillo, G. Filippone, M. Salzano de Luna, and V. Ambrogi, (2025). Self-healing Coatings Based on Epoxy Vitrimers. *Macromolecular Materials and Engineering*, pp. 2500005.

[7] G.M. Scheutz, J.J. Lessard, M.B. Sims, and B.S. Sumerlin, Adaptable crosslinks in polymeric materials: resolving the intersection of thermoplastics and thermosets. *Journal of the American Chemical Society*, 2019, 141(41), pp. 16181-16196.

[8] D. Montarnal, M. Capelot, F. Tournilhac, and L. Leibler, Silica-like malleable materials from permanent organic networks. *Science*, 2011, 334(6058), pp. 965-968.

[9] Yue, L., Bonab, V. S., Yuan, D., Patel, A., Karimkhani, V., & Manas-Zloczower, I.. Vitrimerization: A novel concept to reprocess and recycle thermoset waste via dynamic chemistry. Global Challenges, 2019, 3(7), pp. 1800076

[10] N.J. Van Zee, R. Nicolaÿ Vitrimer chemistry and applications. *Macromolecular Engineering: From Precise Synthesis to Macroscopic Materials and Applications*. 2022, 7, pp. 1-38.

[11] V. Schenk, K. Labastie, M. Destarac, P. Olivier, and M. Guerre, Vitrimer composites: current status and future challenges. *Materials Advances,* M. 2022, 3(22), 8012-8029.

[12] N.J. Van Zee, N. Renaud, Vitrimer chemistry and applications. *Macromolecular Engineering: From Precise Synthesis to Macroscopic Materials and Applications*, 2022, pp. 1-38.

[13] J. Zhang, Z. Lei, S. Luo, Y. Jin, L. Qiu, and W. Zhang, W. Malleable and recyclable conductive MWCNT-vitrimer composite for flexible electronics. *ACS Applied Nano Materials*, 2020, 3(5), 4845-4850.

[14] A. R. de Luzuriaga, R. Martin, N. Markaide, A. Rekondo, G. Caban˜ero, J. Rodr´ıguez and I. Odriozola, Epoxy resin with exchangeable disulfide crosslinks to obtain reprocessable, repairable and recyclable fiber-reinforced thermoset composites. *Materials Horizons*, 2016, 3(3), 241-247.

[15] L. Yue, H. Guo, A. Kennedy, A. Patel, X. Gong, T. Ju, and I. Manas-Zloczower, I., Vitrimerization: converting thermoset polymers into vitrimers. *ACS Macro Letters*, 2020, 9(6), 836-842.

ICCM24
AUGUST 4-8, 2025
BALTIMORE CONVENTION CENTER
BALTIMORE, MARYLAND, USA

No Technical Paper Submission for:

Roger Ghanem

ICCM24 24TH INTERNATIONAL CONFERENCE ON COMPOSITE MATERIALS
AUG 4-8, 2025 • BALTIMORE CONVENTION CENTER • BALTIMORE, MARYLAND

INNOVATIVE SUSTAINABLE COMPOSITES FOR LIGHTER AND FLAME RETARDANT ELECTRIC VEHICLE PARTS TO BOOST CLIMATE BENEFITS

Suman Kumar Ghosh[1,2], Kehinde Olonisakin[1,2], Arturo Rodriguez-Uribe[1,2], Amar K. Mohanty[1,2], Manjusri Misra[1,2*]

[1]Bioproducts Discovery and Development Centre, Department of Plant Agriculture, University of Guelph, Crop Science Building, Guelph, Ontario N1G 2W1, Canada

[2]College of Engineering, Thornborough Building, University of Guelph, Guelph, N1G 2W1, Ontario, Canada

Authors Email: sghosh07@uoguelph.ca, kolonisa@uoguelph.ca, rarturo@uoguelph.ca, mohanty@uoguelph.ca, mmisra@uoguelph.ca, web page: https://www.uoguelph.ca

***Presenting Author**: Manjusri Misra, Email: mmisra@uoguelph.ca*

Keywords: Sustainable composites, Polyamide, Biocarbon, Reduced flammability, EV parts

ABSTRACT

This study investigated novel, lightweight, and sustainable flame-retardant biocomposites of polyamide 6 (PA6) and waste-derived biocarbon for electric vehicle (EV) parts to address EV challenges and promote sustainable waste management. Agricultural wheat straw and mixed paper-plastic wastes underwent pyrolysis at 600 °C, and the resulting biocarbons were employed as reinforcements at 20 and 30 wt% loading in the PA 6 matrix through melt extrusion. The mechanical and flammability characteristics of these biocarbon-loaded PA 6 composites were compared with those of 20 wt% polyurethane-treated recycled carbon fiber (PurCF) reinforced polyamide 6,6 (PA6,6) composites developed by Olonisakin et al. [1]. The morphological analysis revealed that biocarbon particles showed significant adherence and integration within the polyamide matrix, although oriented randomly, indicating a robust interfacial bond between the biocarbon particles and the polyamide matrix. The incorporation of biocarbon effectively improved the mechanical performance of the corresponding biocomposites. The heat distortion temperature (HDT) of neat PA increased from 120.8 °C to 182.4 °C and 186.3 °C with the addition of 30 wt% WSB and PPB, respectively. The inclusion of biocarbon into neat PA 6 increased the overall flame duration of composites during the vertical burning test, except for 20PPB, achieving a UL-94 V-2 rating. During the horizontal burning test, all samples demonstrated a linear burning rate of 0 mm/min, which can be attributed to the intumescent behaviour of biocarbon composites. The PA 6,6 composites exhibited higher mechanical properties compared to PA 6 composites, but inferior flame retardancy compared to PA 6 composites. The developed lightweight, sustainable PA 6 biocomposites with reduced flammability and boosted mechanical, rheological and thermal performance could potentially be applied to develop EV parts.

1 INTRODUCTION

The rapid rise in the automotive sector, particularly in electric vehicles (EVs), has intensified the need for lightweight, robust, non-flammable, and environmentally friendly materials to enhance fuel efficiency and mitigate greenhouse gas emissions. Polymer composites have garnered considerable attention among innovative materials due to their beneficial characteristics [2]. Polyamide 6 (PA6) is a prevalent engineering thermoplastic in the automobile industry, recognised for its remarkable tensile

properties, chemical resistance, and heat stability [3]. To improve its characteristics or alleviate its drawbacks, many fillers have been included in polyamide, either alone or in combination. Glass and carbon-based mineral fillers are commonly employed for their exceptional thermal stability and ability to endure the high processing temperatures of PA 6, which may exceed 290 °C [3]. However, these fillers often pose difficulties, as they may be costly, unwieldy, or environmentally detrimental. Advanced fillers such as carbon fibre, carbon nanotubes, and graphene possess great density and are significantly expensive due to their complex and costly production methods. Meanwhile, materials like talc, nanoclay, and glass fibre offer a cost-effective alternative, but they are characterised by their notably high densities. The aforementioned fillers are also unsustainable due to their derivation from petroleum-based materials or the exhaustion of natural resources. The performance of PA6 can be further improved by integrating appropriate fillers or reinforcements. The primary utilisation of petroleum-derived fillers prompts environmental and economic issues, requiring a transition to renewable and bio-based substitutes [4–6].

Biomass-derived biocarbon or biochar, a carbon-rich material generated via pyrolysis of renewable biomass sources like agricultural residues, forestry by-products, or organic waste, has been recognised as a potential reinforcement in polyamide composites. Biocarbon reduces reliance on fossil resources and offers a sustainable approach to waste management [7]. The unique properties of low density render it an appealing filler material for the development of eco-friendly composites [8]. Moreover, it is generally more cost-effective than nearly all carbon-based fillers and exhibits a lower density, which ranges from 1.34 to 1.96 g/cm^3 [8]. Biocarbon is a highly complex material. The characteristics, especially the surface chemistry, may vary considerably depending on the initial chemical composition and the processing conditions. The proportions and types of functionalities can vary significantly and are largely dependent on the pyrolysis temperature [9]. As a result of its polar characteristics, biocarbon exhibits a significant affinity for polymers of similar polarity, such as PA 6. Researchers examined various biomass-derived biocarbon sources, such as wood, miscanthus, corn cob and lignin, as sustainable reinforcing fillers for PA6 [3,5,9].

The conversion of biomass and waste materials into valuable products reduces environmental impacts and increases economic value [10]. Canada's annual production of wheat straw is estimated at 21 million tonnes [11]. Kalak indicated that approximately 360 million tonnes of biomass, specifically straw, are utilised worldwide. The applications include the pulp and paper industry, furniture and building materials, agriculture for animal feed and bedding, and the energy sector. The accessibility, affordability, and renewable nature of wheat straw make it a valuable resource for biocarbon production [12]. Research indicates that biochar derived from wheat straw can serve as a fertiliser for sustainable agricultural practices and in thermal energy storage applications. Compared to wheat straw, plastics are among the most widely used materials in various applications on a daily basis. The volume of plastic waste has significantly increased in recent years [13]. The pyrolysis of mixed plastic-paper waste into biocarbon for polymers has the potential to mitigate various environmental challenges and play a substantial role in advancing the circular economy. Biocarbon derived from waste demonstrates greater stability compared to raw biomass or waste, thereby presenting considerable potential as a reinforcing filler for sustainable polymer composites. There is a notable deficiency in research regarding the utilisation of both wheat straw and plastic-paper waste pyrolysed biocarbon in sustainable polymer composite applications, indicating a necessity for further investigation.

The primary aim of this research work is to develop waste-derived biocarbon reinforced PA6 sustainable composites with reduced flammability for automotive applications, especially for EV parts. The wheat straw and mixed paper-plastic waste were subjected to pyrolysis at a constant temperature of 600 °C, followed by ball milling for 2 hours before integration into the polymer matrix. For the first time, PA6 sustainable composites containing 20 and 30 wt% of this biocarbon were assessed in terms of physico-mechanical, thermal, rheological, and flame-retardant properties. Finally, the mechanical and flammability properties of PA6 biocomposites were compared with those of 20 wt% polyurethane-treated recycled carbon fiber (PurCF) reinforced polyamide 6,6 (PA6,6) composites developed by Olonisakin et al. [1].

2 EXPERIMENTAL, RESULTS AND DISCUSSION

2.1 Materials

Polyamide 6 (PA6): Ultramid B27E was provided by BASF. This particular grade of PA 6 has been identified by a density of 1.12–1.15 g/cm^3, melting point of 220 °C and melt flow index: MFI $_{(250\ °C,\ 2.16\ kg)}$ of 38 g/10 min. The plastic and paper waste, having approximately 20w/80w composition, was collected from the University of Guelph, Canada campus. The wheat straw was purchased from Salem Creek Farms, 2408 Concession 4, Teeswater, Canada.

2.2 Pyrolysis of wheat straw and paper-plastic waste

The pyrolysis process of wheat straw and paper-plastic waste was performed by employing a laboratory-scale pyrolysis reactor at 600 °C to produce biocarbon. All the raw waste and biomass materials were dried for at least 24 hours prior to the pyrolysis process to get a moisture content of less than 5%. To conduct the pyrolysis process, a Carbolite GLO 10/11-1G front-loading retort furnace (UK) configured in a horizontal orientation was used. About 1000 g of each raw material was put into the furnace using a steel vessel, subsequently, the atmosphere was rendered inert by flushing with nitrogen gas. A heating rate of 7.5 °C/min was utilized to attain the target performing temperature of 600 °C, upheld for a residence duration of 1 hour prior to cooling the furnace to ambient temperature for biocarbon removal for all three cases. The biocarbons were subsequently subjected to ball milling at a rotational speed of 200 rpm for 2 hours for each biocarbon sample. The overall yield of the wheat straw and paper-plastic biocarbon was 34 and 24.4%, respectively. The above-mentioned two biocarbons are designated as WSB and PPB, respectively.

2.3 Processing of PA 6 sustainable biocomposites

In order to prevent void formation and hydrolysis during the melt-extrusion process, the biocarbon and PA 6 were dried before to the processing step. Melt-extrusion was performed to make neat PA 6 and its sustainable biocomposites in a DSM Micro Xplore 15cc, Netherlands twin-screw micro-compounder for a duration of two minutes at a temperature of 250 degrees Celsius and a rotor speed of one hundred revolutions per minute. For the purpose of producing tensile dumbbell-shaped, flexural bars, and impact bars specimens in accordance with the parameters of ASTM standards, the molten polymer was first collected in a transfer device and then injected into an injection moulding machine, Micro 12cc, Netherlands. The temperature of the machine was set to 30 degrees Celsius. Prior to the testing, each sample was conditioned for a period of forty-eight hours at a humidity level of fifty percent at room temperature. Sustainable composites with both 20 and 30 wt% of each biocarbon were fabricated and designated as shown in Table 1.

Sample designation	PA 6 (wt%)	Paint char (wt%)	Wheat straw biocarbon (wt%)	Paper-plastic biocarbon (wt%)
PA6	100	0	0	0
20WSB	80	0	20	0
20PPB	80	0	0	20
30WSB	70	0	30	0
30PPB	70	0	0	30

Table 1: Compositions for PA 6 composites containing 20 and 30 wt% biocarbon

2.4 Characterizations

Using the FEI Quanta FEG 250 machine and an accelerating voltage of 20 kV, scanning electron microscopy (SEM) was used to examine the biocarbon dispersion in the PA6 matrix. The Denton Desk

V TSC sputter coater was used to gold sputter the broken surface of impact samples, with a 90-second coating period. Using the Melt Flow Indexer Qualitest 2000A in accordance with ASTM D1238, the MFI of the clean PA 6 and all sustainable composites was calculated at 250 oC with a constant load of 2.16 kg [14]. The MD-300S Densitometer (Alfa Mirage, Japan) was used to quantify the density of each specimen. In accordance with ASTM D638-14 for the tensile test at a speed of 50 mm/min for neat PA 6 and 5 mm/min for sustainable composites, and ASTM D790-10 for the flexural testing at a rate of 14 mm/min, the mechanical analysis was carried out using an Instron Universal Testing Machine (3382, MA, USA) [15,16]. Using a 2.75 J impact pendulum and the Zwick/Roell Hit25P (Ulm, Germany), the Izod notched impact test was conducted in accordance with ASTM D256 standard (test method A) [17]. Using the Q800 dynamic mechanical analyzer (DMA), the heat deflection temperature (HDT) was measured in accordance with the technical note from TA Instruments (DE, USA). Samples loaded in the three-point clamp of the instrument were heated to 250 °C with a heating rate of 2 °C/min under a force of 0.455 MPa until a deflection of 250 µm was achieved. For the composite of 20 wt% PurCF loaded PA 6,6 (PurCF20) used here to compare the results with PA 6 composites, a force of 1.8 MPa was used to measure the HDT value [1]. The flame-retardant properties of neat polyamide and its sustainable biocomposites were tested in accordance with ASTM D635-22 [34]. The vertical flammability test was performed in accordance with ASTM D3801-20a for five specimens of comparable lengths [18]. The classification of the samples was established based on the observed after-flame and after-glow durations, as well as dripping and cotton ignition during the testing process [19].

2.5 Results and discussion

2.5.1 Density and melt flow index (MFI)

Because they have such a large impact on the vehicle's total weight and fuel efficiency, low-density polymers and composites are ideal for use in automobiles [1]. The measured density of neat PA 6 and its sustainable biocomposites with two different types of biocarbon are provided in Table 2. Virgin PA 6 exhibited a density of 1.105 g/cm^3. The addition of 20 and 30 wt% of biocarbon increased the density of the resultant PA 6 composites. The density of 20 wt% PurCF-filled PA 6,6 composites was found to be higher compared to PA 6 composites with 20 wt% biocarbon but lower than those with 30 wt% biocarbon [1]. The preferred MFI of composite materials for the injection molding process should be greater than 10 g/min to achieve better processability and thereby cost and output efficiencies. **Table 2** also provides the MFI of neat PA 6 and all sustainable composites loaded with 20 and 30 wt% biocarbon, as well as PA 6,6 composite (PurCF20). It can be seen that neat PA 6 exhibited an MFI of 39.6 g/10 min, which decreased with the incorporation of carbonaceous filler such as biocarbon particles in the neat PA matrix. The incorporation of biocarbon raised the viscosity of the melt due to PA 6 chain tangling and the high aspect ratio of biocarbon promotes strong adhesion between the carbonaceous fillers and the PA matrix phase. The PPB composites exhibited a higher MFI value compared to that of the WSB composites. The reduction of the MFI of polyamide with biocarbon inclusion was extensively studied and reported in the literature [5,9]. The PA 6,6 composites exhibited higher MFI compared to PA 6 composites owing to the high MFI value of neat PA 6,6 [1].

Sample designation	Density (g/cm^3)	MFI (g/10 min)
PA 6	1.105±0.003	39.6±1.2
20WSB	1.154±0.001	21.0±0.53
20PPB	1.150±0.002	27.46±0.50
30WSB	1.197±0.005	13.7±0.41
30PPB	1.191±0.001	17.8±0.72
20rCF	1.18 ± 0.003	106.38±1.24

Table 2: Density and MFI of neat PA 6, PA 6 biocomposites and PA 6,6 composites

2.5.2 Morphological analysis

The biocarbon dispersion in the neat polyamide matrix was investigated by SEM analysis of the impact-fractured composite samples. Figure 1(a) and (b) represent the SEM images of impact fracture surfaces of PA 6 sustainable biocomposites loaded with 20 wt% of wheat straw and paper-plastic biocarbon, respectively, whereas the surface morphology of 30 wt% biocarbon-filled composites is represented in Figure 1(c) and (d). Several biocarbon particles identified on the fracture surface of all composites were noted, showing no signs of dislodgement or significant pullouts. The biocarbon particles demonstrated significant adherence and integration within the polyamide matrix, indicating effective interfacial adhesion. The platelet-shaped WSB and PPB particles are uniformly distributed within the polyamide matrix, although they exhibit a random orientation at both 20 and 30 wt% filler loading. The surface properties of biocarbon particles improved interfacial interactions with polar PA 6 chains.

2.5.3 Mechanical properties

The effect of carbonaceous filler types and concentration in PA 6 on the mechanical properties, HDT and flame retardancy was investigated and the obtained results are depicted in Figure 2. The mechanical, HDT and flammability properties of 20 wt% PurCF loaded PA 6,6 composites were also provided in Figure 2 for comparison [1]. The variation of tensile strength and modulus for polyamide composites loaded with 20 and 30 wt% biocarbon as well as PA 6,6 composites, is shown in Figure 2(a). Virgin PA 6 possessed a tensile strength and tensile modulus of 73 MPa and 2693 MPa, respectively. The incorporation of 20 wt% biocarbon enhanced tensile strength, particularly tensile modulus, relative to unmodified polyamide, and these attributes were further augmented by 30 wt% char and biocarbon-reinforced composites. This phenomenon is ascribed to the stiffening effect of high modulus filler particles, which are typically more rigid than the polymer matrix. A 34.3% and 36.8% increase in tensile modulus was achieved for the PA 6 composites using 30 wt% wheat straw and paper-plastic biocarbon, respectively, in comparison to the pure polymer. The flexural strength and flexural modulus of PA 6 were markedly enhanced with biocarbon loading, as illustrated in Figure 2(b). Both the flexural strength and modulus consistently exhibited greater values for 30 wt% biocarbon composites in comparison to those with 20 wt% filler loading. The rapid and effective transmission of stress from the polyamide to the char and biocarbon in tension mode, coupled with the confinement of the PA molecular chains by the biocarbon in compression mode, resulted in a significant improvement in flexural characteristics [5]. From both Figure 2(a) and (b), it was noted that 20 wt% PurCF-reinforced PA 6,6 composites demonstrated remarkably high tensile and flexural strength, as well as moduli, in comparison to PA 6 composites. This can be attributed to the fundamental characteristics of carbon fibre, including its stiffness, high strength, and modulus [1]. The variation in the notched impact strength of neat PA 6 and its sustainable biocarbon, as well as PA 6,6 composites, is provided in Figure 2(c). An impact strength of 57.9 J/m was achieved for neat PA 6, which decreased continually with filler loading. With 20 wt% of carbonaceous filler loading, the impact strength of neat polyamide was reduced to 35.6 and 33.7 J/m for WSB and PPB, respectively. The incorporation of reinforcing fillers significantly reduces the ductility of the composite material blend. The impact strength was further decreased with 30 wt% filler concentration in the polyamide matrix. The presence of invasive biocarbon particles may create vulnerabilities within the matrix, thus promoting crack propagation [20]. The PurCF20 composite exhibited an impact strength of 38 J/m, that is slightly higher than that for 20 wt% biocarbon-loaded PA 6 composites [1].

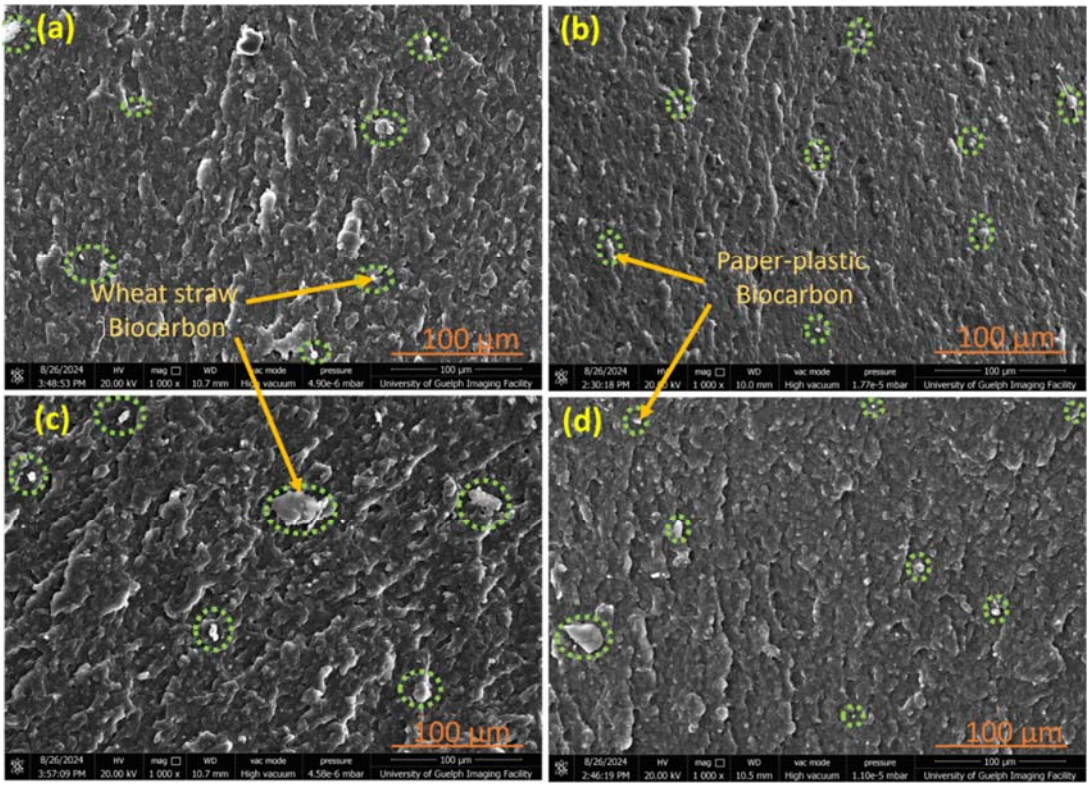

Figure 1: SEM micrographs of PA 6 biocomposites filled with (a) 20 wt% wheat straw biocarbon, (b) 20 wt% paper-plastic biocarbon, (c) 30 wt% wheat straw biocarbon and (d) 30 wt% paper-plastic biocarbon.

2.5.4 Heat deflection temperature (HDT)

HDT is a critical attribute of engineering thermoplastics, particularly in the automotive sector, as it establishes temperature thresholds for material processing [3]. HDT reflects a material's resistance to heat under a specified load. The HDT of virgin polyamide 6 composites and PA 6,6 composite (PurCF20) are plotted in Figure 2(c). The HDT value of neat PA 6 was 121 ºC, which was markedly enhanced by the incorporation of 20 wt% char and biocarbon in the matrix phase. When the biocarbon concentration in the PA matrix was increased from 20 to 30 wt%, the HDT of the corresponding composites increased further. The HDT of neat PA increased to 182.4 °C and 186.3 °C with 30 wt% WSB and PPB loading. The thermally stable biocarbon particles restricted the movement of polyamide chains, limiting the composite deformation by raising the temperature required to deform the composite materials [5]. Hence, HDT improved significantly for biocarbon composites. The higher carbonaceous content of WSB and PPB compared to PCB contributed to the greater HDT value of the corresponding composites, attributed to the boosted stiffness and rigidity of the filler particles of denser structure. The PA 6,6 composite with 20 wt% PurCF exhibited a higher HDT value of 242.9 °C measured at a force of 1.8 MPa [1].

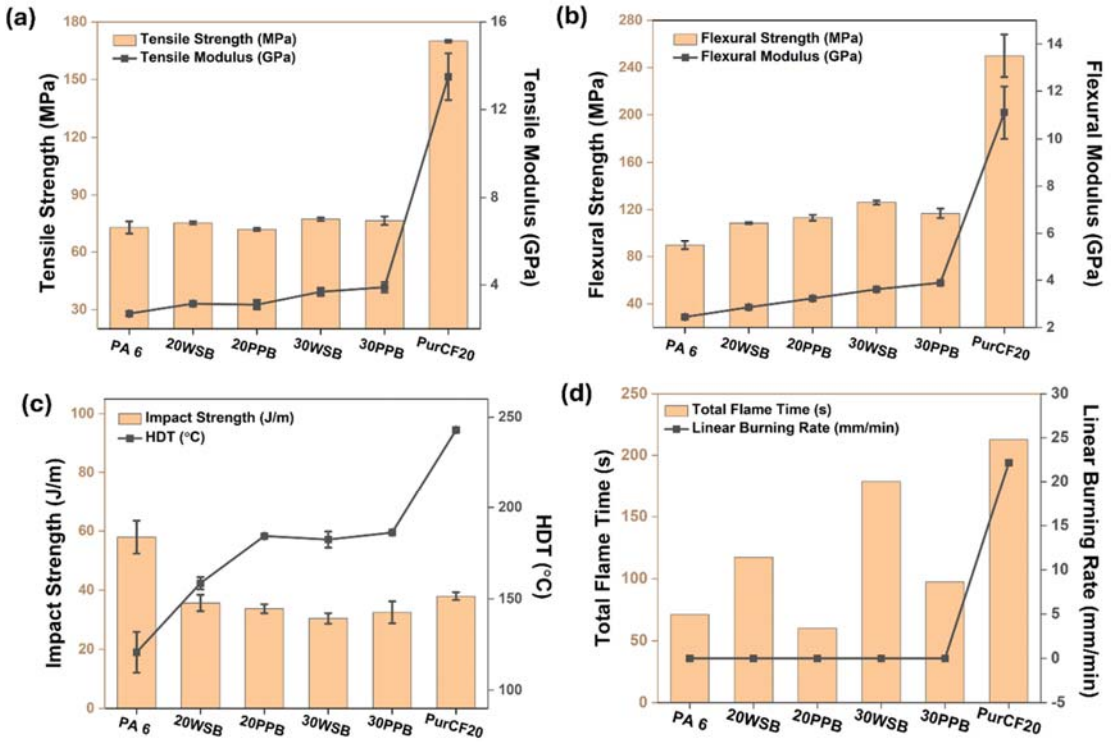

Figure 2: (a) Tensile strength and modulus, (b) flexural strength and modulus, (c) impact strength and HDT, and (d) flammability behavior in the UL-94 vertical (total flame time) and horizontal burning (linear burning rate) tests of PA 6 composites and PA 6,6 composite [1].

2.5.5 Flammability characteristics

A critical characteristic of materials utilised in the automotive sector, particularly in electric vehicle components, is their flame resistance. For these applications, the materials must demonstrate minimum flammability to the highest degree feasible [21]. The UL-94 vertical and horizontal flammability tests are among the most used methods employed to assess the flame retardancy of polymer composites. The reaction of pure PA 6 and biocarbon-infused composites to flame exposure was documented as total flame duration for five samples in the vertical test and linear burning rate in the horizontal experiment. The outcomes for PA 6 composites and PurCF PA 6,6 sustainable composites are illustrated in Figure 2(d). The incorporation of 20 wt% WSB biocarbon particles into the PA 6 matrix extended the total flame duration to 117.4 seconds. The 20PPB composite demonstrated a flame time of 59.9 seconds, which is less than that of neat polyamide. The PA 6,6 composites demonstrated a total flame duration of 212.8 seconds, surpassing that of PA 6 composites. All composites demonstrated a UL-94 V-2 classification in the vertical test. The improved fire retardancy of paper-plastic biocarbon-loaded composites is due to the emergence of a more efficient protective carbon layer resulting from the more ordered and crystalline carbon structure of PPB particles. In the horizontal burning test, both the pure polymer and composites exhibited a burning rate of 0 mm/min and were categorised as HB, as illustrated in Figure 2(d). None of the samples exceeded the 25 mm reference point, and the flame extinguished. The thermally stable carbon structure of the filler and the little nitrogen content in the filler particles resulted in intumescent behaviour when positioned horizontally. Muir et al. investigated and reported the diminished flame retardancy of recycled PA 6 infused with lignin biocarbon pyrolysed at various temperatures [22]. The PurCF20 composites showed a linear burning rate of 22.16 mm/min in the horizontal flammability test [1]. Therefore, biocarbon-loaded PA 6 composites exhibited higher flame retardancy compared to PurCF-loaded PA 6,6 composites owing to the formation of more effective char layers by biocarbon particles than carbon fibers.

3 CONCLUSIONS

This research investigated the effect of wheat straw and mixed paper-plastics derived biocarbon on the characteristics and performance of PA 6 sustainable composites intended for automotive applications, especially in EVs. The impact of 20 and 30 wt% biocarbon (pyrolyzed at 600 °C) concentration on the thermomechanical, rheological, and flammability qualities of PA biocomposites was assessed and compared with 20 wt% polyurethane-treated CF-loaded PA 6,6 composites published by Olonisakin et al. [1]. The addition of biocarbon significantly improved tensile/flexural strength and moduli in comparison to neat PA 6. The HDT increased to 186 ºC for 30PPB composites and consistently remained higher for all biocarbon composites than the neat polyamide. The integration of biocarbon extended the overall flaming duration of biocomposites to neat polyamide in the vertical burning test. Although the 20PPB composite demonstrated a shorter flame duration compared to neat PA 6, all composites, along with neat polyamide, were categorized as V-2, demonstrating dripping and ignition of cotton. In the horizontal burning test, all samples exhibited a linear burning rate of 0 mm/min, attributed to the intumescent behavior of char and biocarbon composites. The PA 6,6 exhibited higher mechanical properties compared to PA 6 composites, but inferior flame retardancy compared to PA 6 composites.

ACKNOWLEDGEMENTS

This study was financially supported by (i) the Ontario Ministry of Agriculture, Food and Rural Affairs (OMAFRA)/University of Guelph – Bioeconomy for Industrial Uses Research Program (Project No. 100038); (ii) the Natural Sciences and Engineering Research Council of Canada (NSERC), Canada Research Chair (CRC) program (Project No. 460788); the NSERC Discovery Grants (Project No. 401111); (iii) the Ontario Ministry of Colleges and Universities (MCU), Ontario, Canada Research Fund –Research Excellency, ORF- RE11-003 (Project No. 056185) and (iv) Agriculture and Agri-Food Canada (AAFC) and Bio industrial Innovation Canada (BIC) (Project No. 056369).

REFERENCES

[1] K. Olonisakin, A. Rodriguez-Uribe, T. Wang, A.K. Mohanty, M. Thimmanagari, M. Misra, Engineered advanced light-weight sustainable composites from surface modified recycled carbon fiber reinforced polyamide 6,6 for metallic part alternative in automotive, *Composites Part B: Engineering,* **300**, 2025, p. 112375 (doi: 10.1016/j.compositesb.2025.112375).

[2] A. Beaucamp, M. Muddasar, M. Culebras, M.N. Collins, Sustainable lignin-based carbon fibre reinforced polyamide composites: Production, characterisation and life cycle analysis, *Composites Communications,* **45**, 2024, pp. 101782 (doi: 10.1016/j.coco.2023.101782).

[3] E.O. Ogunsona, M. Misra, A.K. Mohanty, Impact of interfacial adhesion on the microstructure and property variations of biocarbons reinforced nylon 6 biocomposites, *Composites Part A Applied Science and Manufacturing,* **98**, 2017, pp. 32–44 (doi: 10.1016/j.compositesa.2017.03.011).

[4] E.O. Ogunsona, A. Codou, M. Misra, A.K. Mohanty, A critical review on the fabrication processes and performance of polyamide biocomposites from a biofiller perspective, *Materials Today Sustainability*, **5,** 2019, p. 100014 (doi: 10.1016/j.mtsust.2019.100014).

[5] E.O. Ogunsona, A. Codou, M. Misra, A.K. Mohanty, Thermally Stable Pyrolytic Biocarbon as an Effective and Sustainable Reinforcing Filler for Polyamide Bio-composites Fabrication, *Journal of Polymers and the Environment,* **26**, 2018, pp. 3574–3589 (doi: 10.1007/s10924-018-1232-5).

[6] R. Yadav, M. Singh, D. Shekhawat, S.Y. Lee, S.J. Park, The role of fillers to enhance the mechanical, thermal, and wear characteristics of polymer composite materials: A review, *Composites Part A Applied Science and Manufacturing,* **175**, 2023, p. 107775 (doi: 10.1016/j.compositesa.2023.107775).

[7] S.Y. Foong, R.K. Liew, Y. Yang, Y.W. Cheng, P.N.Y. Yek, W.A. Wan Mahari, X.Y. Lee, C.S. Han, D.-V.N. Vo, Q. Van Le, M. Aghbashlo, M. Tabatabaei, C. Sonne, W. Peng, S.S. Lam,

Valorization of biomass waste to engineered activated biochar by microwave pyrolysis: Progress, challenges, and future directions, *Chemical Engineering Journal*, **389**, 2020, p. 124401 (doi: 10.1016/j.cej.2020.124401).

[8] C.E. Brewer, V.J. Chuang, C.A. Masiello, H. Gonnermann, X. Gao, B. Dugan, L.E. Driver, P. Panzacchi, K. Zygourakis, C.A. Davies, New approaches to measuring biochar density and porosity, *Biomass and Bioenergy*, **66**, 2014, pp. 176–185 (doi: 10.1016/j.biombioe.2014.03.059).

[9] Z.B. Varsally, N. Tripathi, H. Weldekidan, A. Rodriguez-Uribe, O. Das, A.K. Mohanty, M. Misra, A sustainable approach for developing biocarbon from lignin and its utilization in recycled ocean nylon based biocomposites, *Composites Part C: Open Access*, 12, 2023, p. 100376 (doi: 10.1016/j.jcomc.2023.100376).

[10] S.S. Siwal, Q. Zhang, N. Devi, A.K. Saini, V. Saini, B. Pareek, S. Gaidukovs, V.K. Thakur, Recovery processes of sustainable energy using different biomass and wastes, *Renewable and Sustainable Energy Reviews*, **150**, 2021, p. 111483 (doi: 10.1016/j.rser.2021.111483).

[11] D.S. Bajwa, S. Adhikari, J. Shojaeiarani, S.G. Bajwa, P. Pandey, S.R. Shanmugam, Characterization of bio-carbon and ligno-cellulosic fiber reinforced bio-composites with compatibilizer. *Construction and Building Materials*, **204**, 2019, pp. 193–202 (doi: 10.1016/j.conbuildmat.2019.01.068).

[12] J. Miedzianowska-Masłowska, M. Masłowski, M. Delekta, K. Strzelec, Waste management of straw to manufacture biochar: An alternative reinforcing filler for natural rubber biocomposites, *Industrial Crops and Products*, **222**, 2024, p. 119629. (doi: 10.1016/j.indcrop.2024.119629).

[13] R. Blanchard, T.H. Mekonnen, Valorization of plastic waste via chemical activation and carbonization into activated carbon for functional material applications, *RSC Applied Polymers*, **2**, 2024, pp. 557–582 (doi: 10.1039/d4lp00016a).

[14] ASTM D1238, Standard Test Method For Melt Flow Rates of Thermoplastics by Extrusion Plastometer, ASTM International, West Conshohocken, PA, 2020. ASTM Standard D1238-20.

[15] ASTM D638, Standard Test Method For Tensile Properties of Plastics, ASTM International, West Conshohocken, PA, 2022.

[16] ASTM D790, Standard Test Methods For Flexural Properties of Unreinforced and Reinforced Plastics and Electrical Insulating Materials, ASTM International, West Conshohocken, PA, 2017.

[17] ASTM D256, Standard Test Methods For Determining the Izod Pendulum Impact Resistance of Plastics, ASTM International, West Conshohocken, PA, 2018.

[18] ASTM D635. Standard Test Method for Rate of Burning and/or Extent and Time of Burning of Plastics in a Horizontal Position. 2022.

[19] ASTM D3801. Standard Test Method for Measuring the Comparative Burning Characteristics of Solid Plastics in a Vertical Position. 2020.

[20] Z. Yang, H. Peng, W. Wang, T. Liu, Crystallization behavior of poly(ε-caprolactone)/layered double hydroxide nanocomposites, *Journal of Applied Polymer Science,* **116**, 2010, pp. 2658–2667 (doi: 10.1002/app).

[21] E.N. Kalali, W. Guo, X. Wang, W. Xing, L. Song, Y. Hu, Effect of metal-based nanoparticles decorated graphene hybrids on flammability of epoxy nanocomposites, *Composites Part A Applied Science and Manufacturing,* **129**, 2020, p. 105694 (doi; 10.1016/j.compositesa.2019.105694).

[22] V. Muir, N. Tripathi, A. Rodriguez-Uribe, A.K. Mohanty, M. Misra, Sustainable biocomposites from pyrolyzed lignin and recycled nylon 6 with enhanced flame retardant behavior: Studies on manufacturing and quality performance evaluation, *SPE Polymers,* **5**, 2024, pp. 277–292 (doi: 10.1002/pls2.10123).

ICCM24
AUGUST 4-8, 2025
BALTIMORE CONVENTION CENTER
BALTIMORE, MARYLAND, USA

No Technical Paper Submission for:

Pavana Prabhakar

ICCM24
AUGUST 4-8, 2025
BALTIMORE CONVENTION CENTER
BALTIMORE, MARYLAND, USA

No Technical Paper Submission for:

Omar El Arwadi

ICCM24
AUGUST 4-8, 2025
BALTIMORE CONVENTION CENTER
BALTIMORE, MARYLAND, USA

No Technical Paper Submission for:

Kaiyue Deng

ICCM24
AUGUST 4-8, 2025
BALTIMORE CONVENTION CENTER
BALTIMORE, MARYLAND, USA

No Technical Paper Submission for:

Md Habib Ullah Khan

OLD DOMINION UNIVERSITY

Enhanced Structural Performance of Additively Manufactured 2D-lattice Sandwich with Tailored Fiber Orientation using Hot Powder Bed Compaction

Jimesh D. Bhagatji, Oleksandr G. Kravchenko

Department of Mechanical and Aerospace Engineering,
Old Dominion University, Norfolk, VA 23529, US

COMPOSITES MODELING AND MANUFACTURING GROUP

ICCM24

Overview

- Introduction
- HPBC process overview
- Material, LSS design and characterization tests
- Progressive damage modeling
- Results and analysis
- Conclusion

Additive manufacturing and flexible consolidation process

Material extrusion (MEX) process

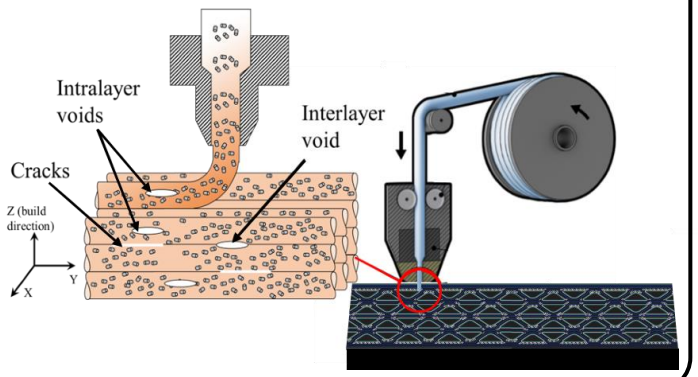

- Co-printed skin and truss core
- Trussed aligned fiber
- Doesn't required mold
- Poor consolidation

Hot powder bed compaction LSS consolidation under hydrostatic compaction

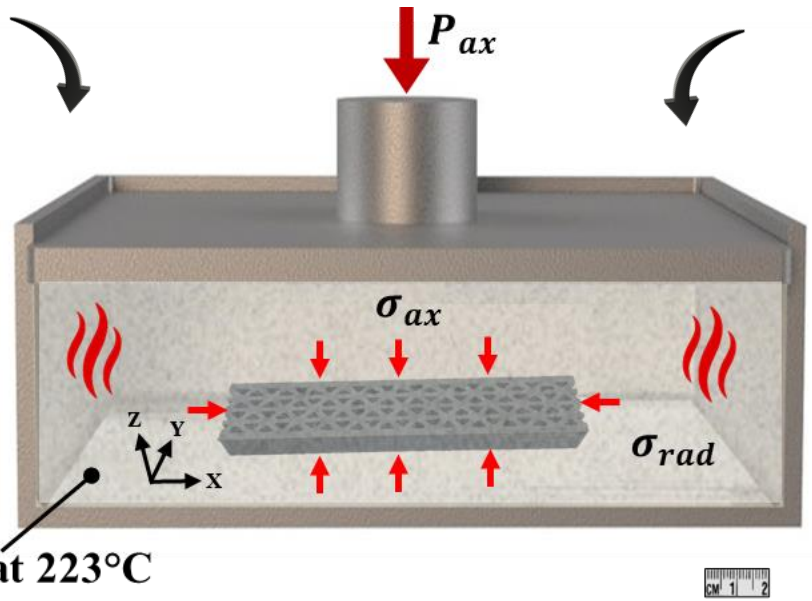

Compression molding or Autoclave curved

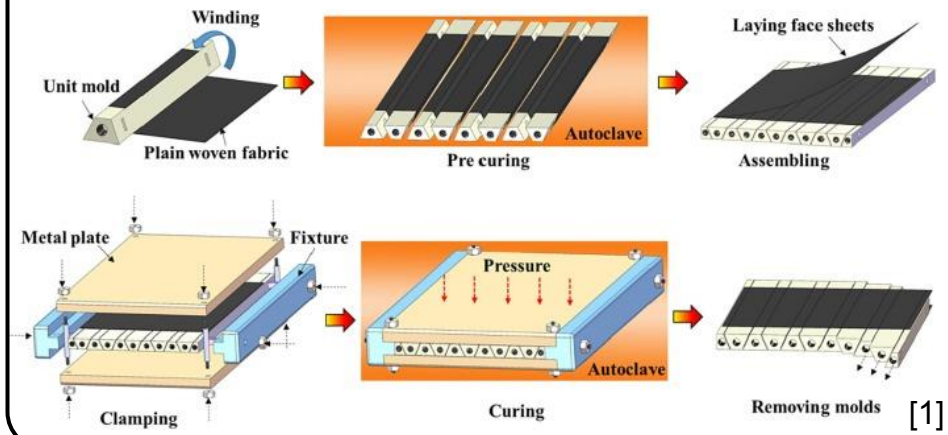

[1]

- Good consolidation
- Multi-step process
- Required multi-assembly mold

- **HPBC provides the synergy between traditional compression molding (good for consolidation but required for specific mold) and MEX process (doesn't required mold but poor consolidation)**

ICCM24

[1] Li, Xinyu, et al. "Failure Mechanisms of Fluted-Core Sandwich Composite Panels under Uniaxial Compression." Composite Structures, vol. 303, Jan. 2023

Hot powder bed compaction process

- **Powder Densification Stage:** Fine talc powder serves as a flexible medium, compacted under 1-2 tons (~500 kPa axial pressure) of load for 10 minutes.
- **Heating Stage:** Mold was heated in a convection oven to 223°C (endset of PA6 melt enthalpy) 140 minutes.
- **Consolidation of MEX part during cool-down:** During cooling, continuous compressive force was maintained, allowing molten matrix flow and void closure, improving part consolidation.
- This process supports complex geometries from subtractive manufacturing, MEX topology-optimized parts, and lattice sandwich structures.

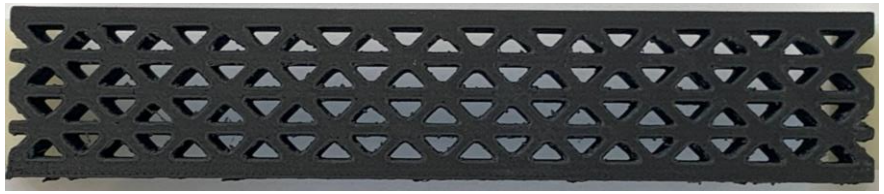

MEX lattice structure

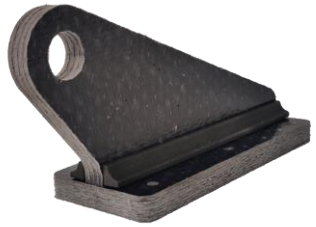

Subtractive manufacturing



MEX topologically optimized rocker

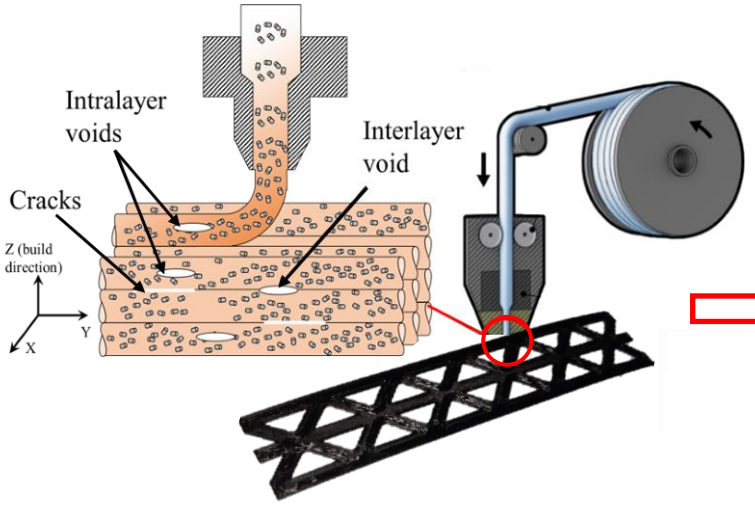

Material extrusion (MEX)

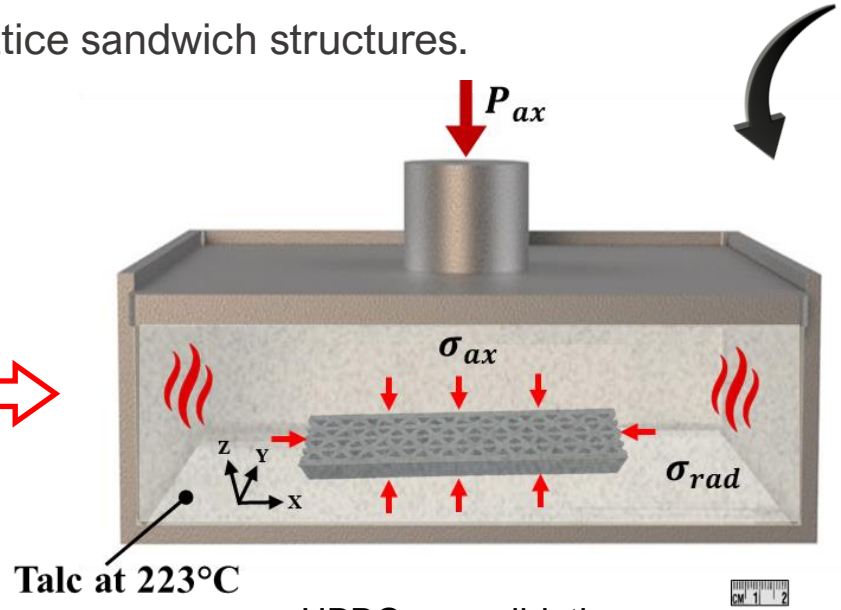

HPBC consolidation

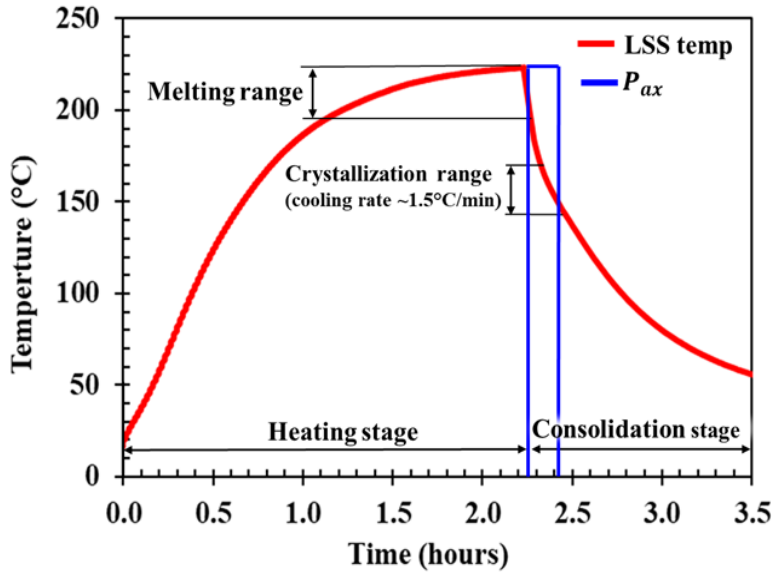

Material and mechanical characterization test

- Material: Fiber reinforced nylon (PA6)
  - SCF: 10.5% fiber volume fraction
  - LCF: 45% fiber volume fraction
- Microscopy analysis
  - Void distribution analysis
- Mechanical Test:
  - Tensile coupon test
  - Sandwich structure 3PB test
- DSC Analysis
  - Crystallinity fraction
  - Enthalpy of melting

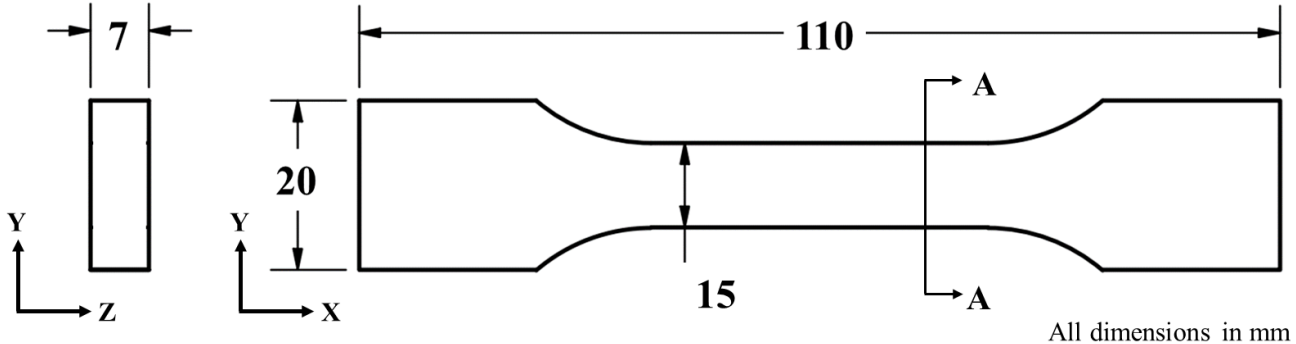

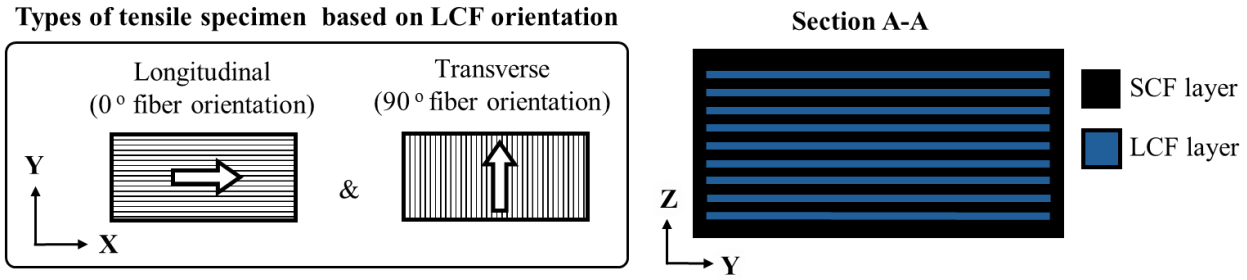

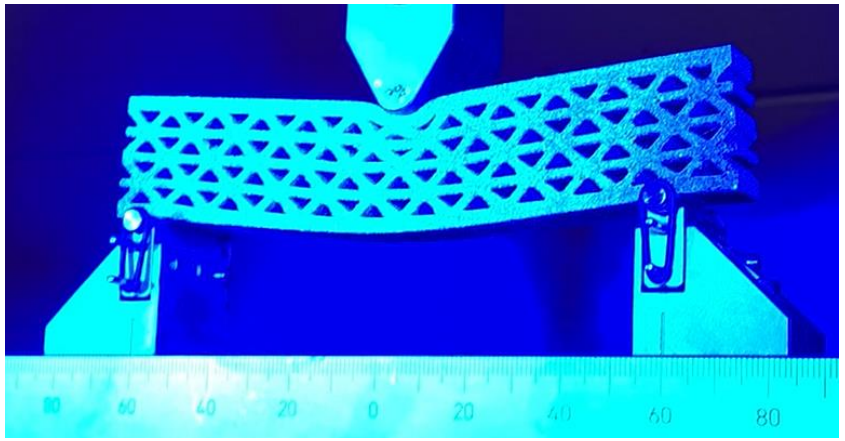

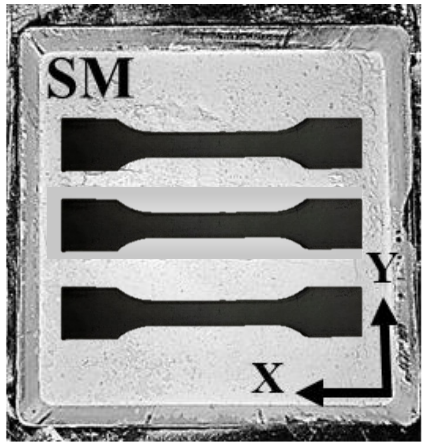

2D-LSS design

- Two truss core configuration with same beam height, core density and LCF volume fraction
  - Nr = 4 → 4-row core with 2.2 mm trusses with 1 LCF tow per truss
  - Nr = 2 → 2-row core with 4.4 mm trusses with 2 LCF tow per truss
- Both configurations had 2 LCF tows in top and bottom skins
- Same A/l_t ratio ensured constant axial rigidity of trusses across designs.
- The design ensured that structure performance differences between pre- and post-HPBC LSS resulted solely from material and microstructural changes, not geometry variations.

	Pristine (mm)		HPBC (mm)	
	$N_r = 4$	$N_r = 2$	$N_r = 4$	$N_r = 2$
h	28.4	28.4	28.25	29.35
b	15	15	12.28	12.36
t_1	6	12	5.92	11.89
t_2	12	24	12.21	24.37
t_h	2.2	4.4	2.75	5.63
t_s	2.2	2.2	2.19	2.19
s	144	144	146.13	146.23
A/l_t	3.89	3.89	4.03	4.14
I_{33}/l_t^2 (mm²)	0.18	0.37	0.3	0.65

Lattice structure geometry

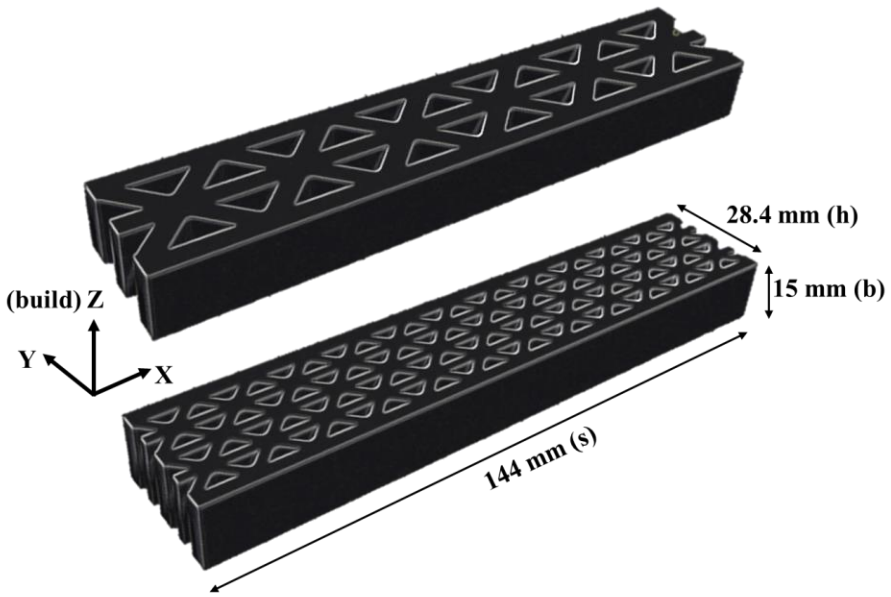

Tailored fiber orientation in truss direction

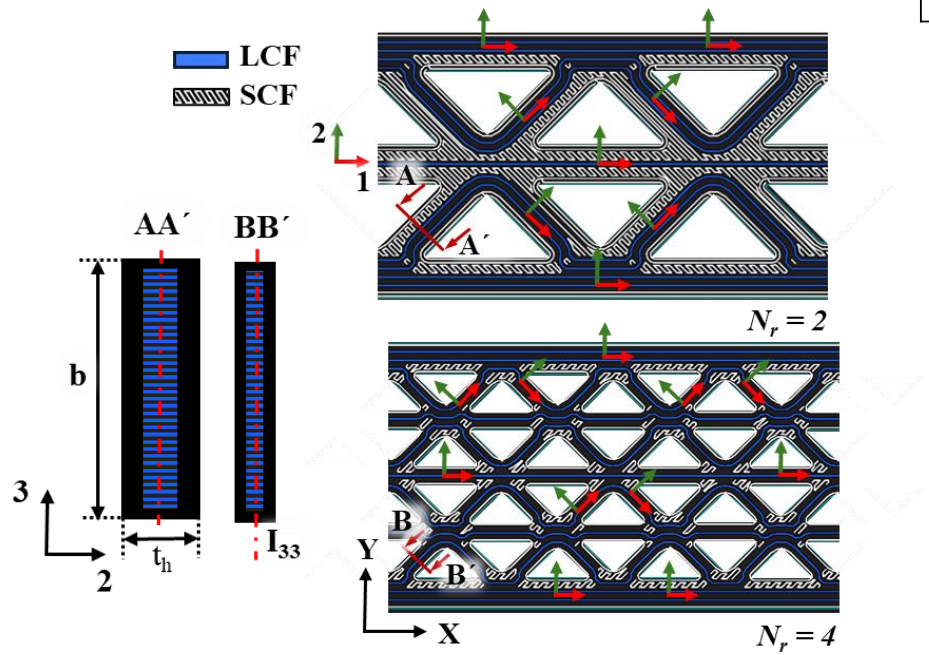

Parametric geometry of LSS

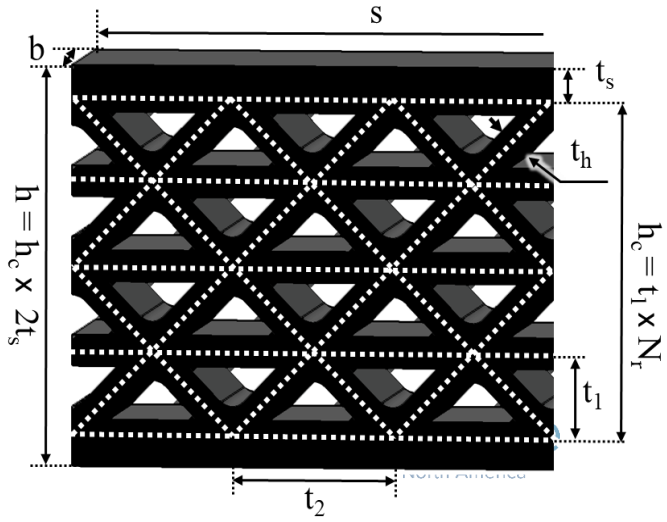

Effective homogenized post-HPBC SCF and LCF properties

- A microstructure-based finite element approach using Digimat-FE was used to anisotropic homogenize the SCF layer properties.
- Microscopy analysis was used to determine a void fraction of 3.1% and a fiber length distribution of 0.098 ± 0.014 mm.
- During the MEX process, short fibers tend to align in the direction of material deposition due to shear-induced flow, resulting in a non-random fiber orientation distribution (FOD).
- Homogenized anisotropic LCF layer properties were predicted using a hybrid micromechanical model considering contributions from both continuous and highly aligned long discontinuous fibers with weight average of 0.5:0.5.

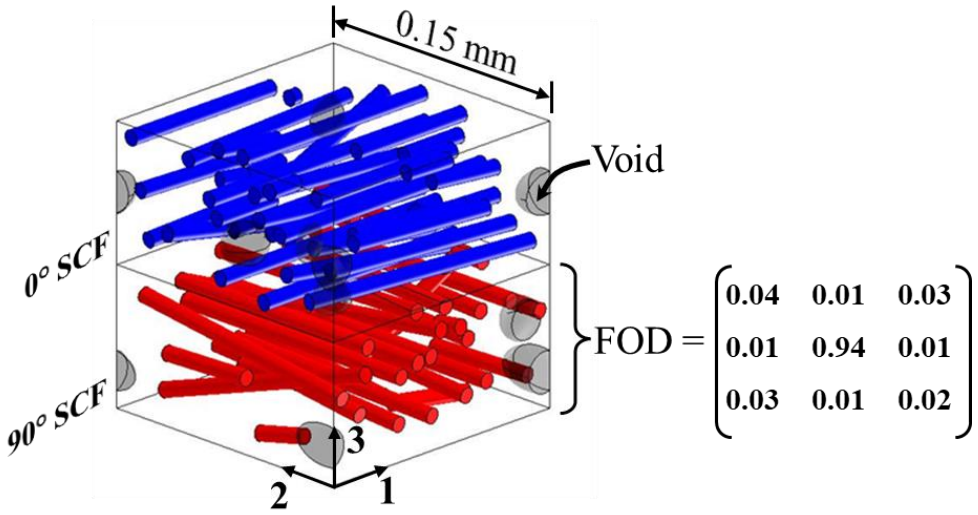

$$FOD = \begin{pmatrix} 0.04 & 0.01 & 0.03 \\ 0.01 & 0.94 & 0.01 \\ 0.03 & 0.01 & 0.02 \end{pmatrix}$$

Modified Halpin–Tsai model

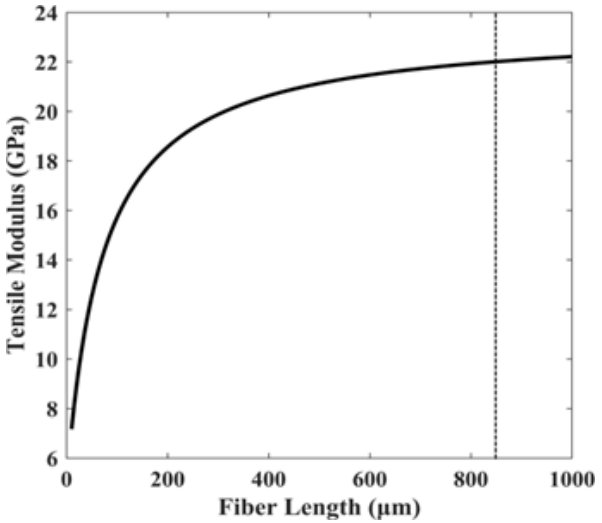

Table 1: Homogenized stiffness and strength properties		
Material property	SCF	LCF
Longitudinal modulus , E_{11} (GPa)	6.41	86
Transverse modulus, E_{22} (GPa)	6.41	5.1
Through-thickness modulus, E_{33} (GPa)	3.11	5.1
In-plane shear modulus, G_{12} , G_{13} (GPa)	0.88	3.2
Out-of-plane shear modulus, G_{23} (GPa)	0.78	960
In-plane poisson's ratios, ν_{12} , ν_{13}	0.28	0.25
Out-of-plane poisson's ratios,ν_{23}	0.33	0.38
Longitudinal tensile strength, σ_{1t}(MPa)	110	1150
Longitudinal compressive strength, σ_{1c} (MPa)	230	1900
Transverse tensile strength, σ_{2t} (MPa)	110	80
Transverse compressive strength, σ_{2c} (MPa)	230	180
Transverse shear strength, τ_{12} (MPa)	80	150
Fracture energy in fiber, G_{11} (kJ/m^2)	6	12
Fracture energy in matrix, G_{22} (kJ/m^2)	2	4
Viscosity regularization in fiber, ηf	0.001	0.001
Viscosity regularization in fiber, ηm	0.001	0.001

FEA modeling of tensile coupons and LSS components

- A homogenized LCF layer was sandwiched between two [+45°/–45°] oriented homogenized SCF layers.
- The LCF layer were aligned in the truss direction to capture actual fiber orientation during MEX deposition.
- Anisotropic linear elastic material was assigned at roller contact regions to avoid damage due to stress concentrations.
- The sandwich structure was meshed with finer elements (0.3 mm × 0.3 mm) in the central 48 mm region and coarser mesh (0.3 mm × 0.6 mm) elsewhere, with 0.125 mm thickness through all layers.

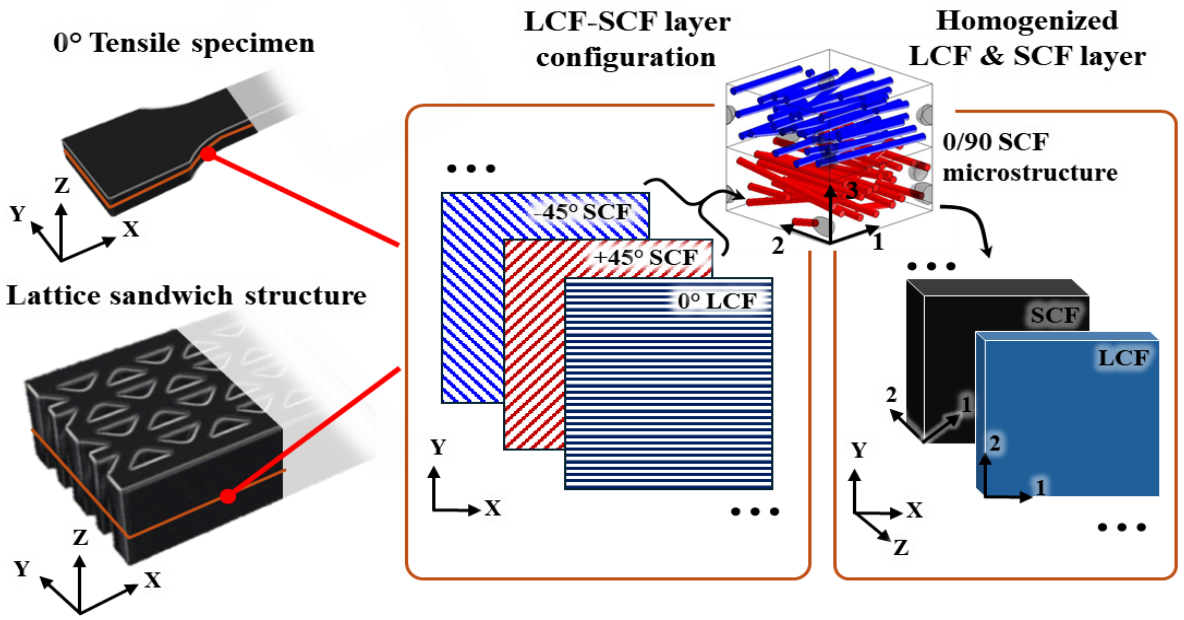

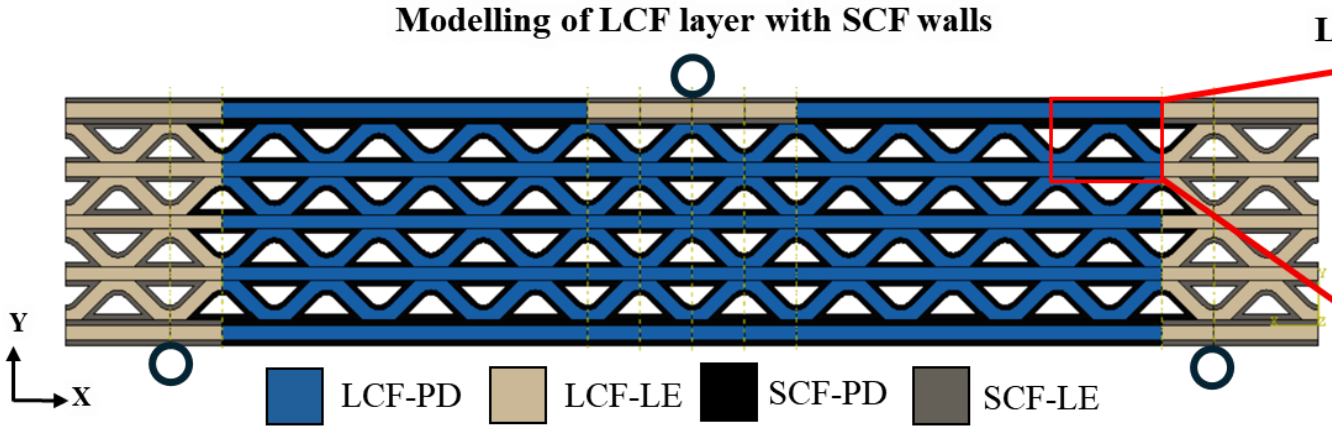

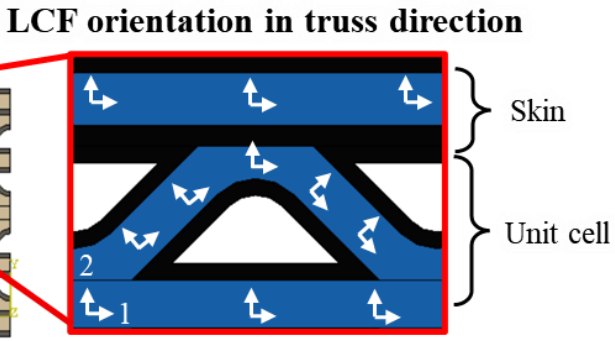

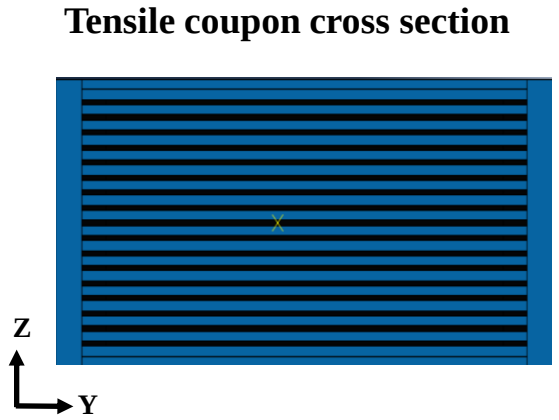

Continuum damage mechanics model

- A strain-based CDM model was implemented in ABAQUS using UMAT subroutine.
- The framework captured nonlinear fiber and matrix damage progression, enabling accurate prediction of stiffness degradation and damage progression
- HPBC-treated dogbone specimens exhibited the following properties:
  - Elastic modulus: 25.5 ± 0.61 GPa (longitudinal), 6.93 ± 0.22 GPa (transverse)
  - Tensile strength: 285.66 ± 4.83 MPa (longitudinal), 101.69 ± 1.43 MPa (transverse)

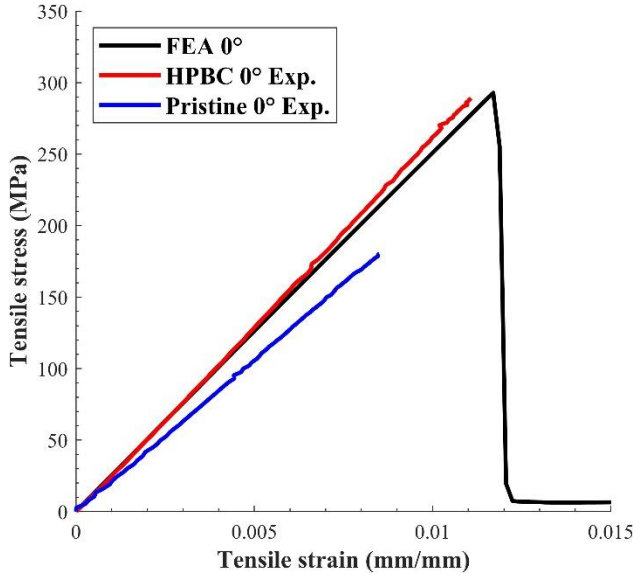

$$f_1^2 = \frac{(\epsilon_{11})^2}{\epsilon_{11}^{ft}\epsilon_{11}^{fc}} + \left(\frac{\epsilon_{11}}{\epsilon_{11}^{ft}} - \frac{\epsilon_{11}}{\epsilon_{11}^{fc}}\right)$$

$$f_2^2 = \frac{(\epsilon_{22})^2}{\epsilon_{22}^{ft}\epsilon_{22}^{fc}} + \left(\frac{\epsilon_{22}}{\epsilon_{22}^{ft}} - \frac{\epsilon_{22}}{\epsilon_{22}^{fc}}\right) + \left(\frac{\epsilon_{12}}{\epsilon_{12}^{f}}\right)^2 \qquad f_3^2 = \left(\frac{\sigma_{33}}{F_{3z}}\right)^2 + \left(\frac{\sigma_{13}}{F_{sz}}\right)^2 + \left(\frac{\sigma_{23}}{F_{sz}}\right)^2$$

$$d_i = 1 - \frac{\epsilon_{ii}^{ft}}{f_i} e^{\left(\frac{C_{ii}\epsilon_{ii}^{ft}\left(\epsilon_{ii}^{ft} - f_i\right) \times l_c}{G_i}\right)};\ i = 1, 2$$

$$d_3 = \begin{cases} 0, & f_3 < 1 \\ 0.95, & f_3 \geq 1 \end{cases}$$

$$\sigma_{ij} = \begin{bmatrix} (1-d_1)\,C_{11}^0 & (1-d_1)(1-d_2)C_{12}^0 & (1-d_1)C_{13}^0 & 0 & 0 & 0 \\ & (1-d_2)C_{22}^0 & (1-d_2)(1-d_3)C_{23}^0 & 0 & 0 & 0 \\ & & (1-d_3)C_{33}^0 & 0 & 0 & 0 \\ & & & (1-d_1)(1-d_2)C_{44}^0 & 0 & 0 \\ & & sym. & & (1-d_3)C_{55}^0 & 0 \\ & & & & & (1-d_3)C_{66}^0 \end{bmatrix} \times \varepsilon_{ij}$$

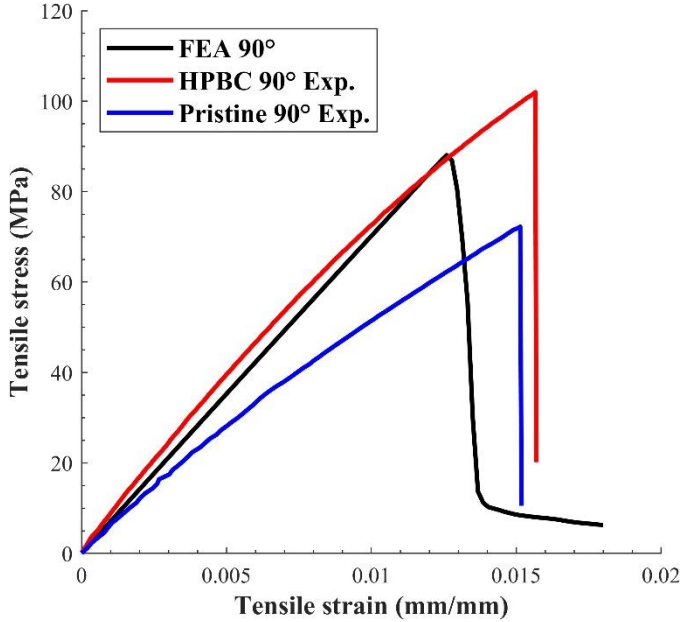

Microscopic analysis of post-HPBC sandwich beam

- The improved microstructure exhibited void content less than 2.3% and improved consolidation, with consistent shrinkage for both HPBC-treated LSS. A 17.8% reduction in width (Z-direction) and 26.4% increase in truss thickness were observed.

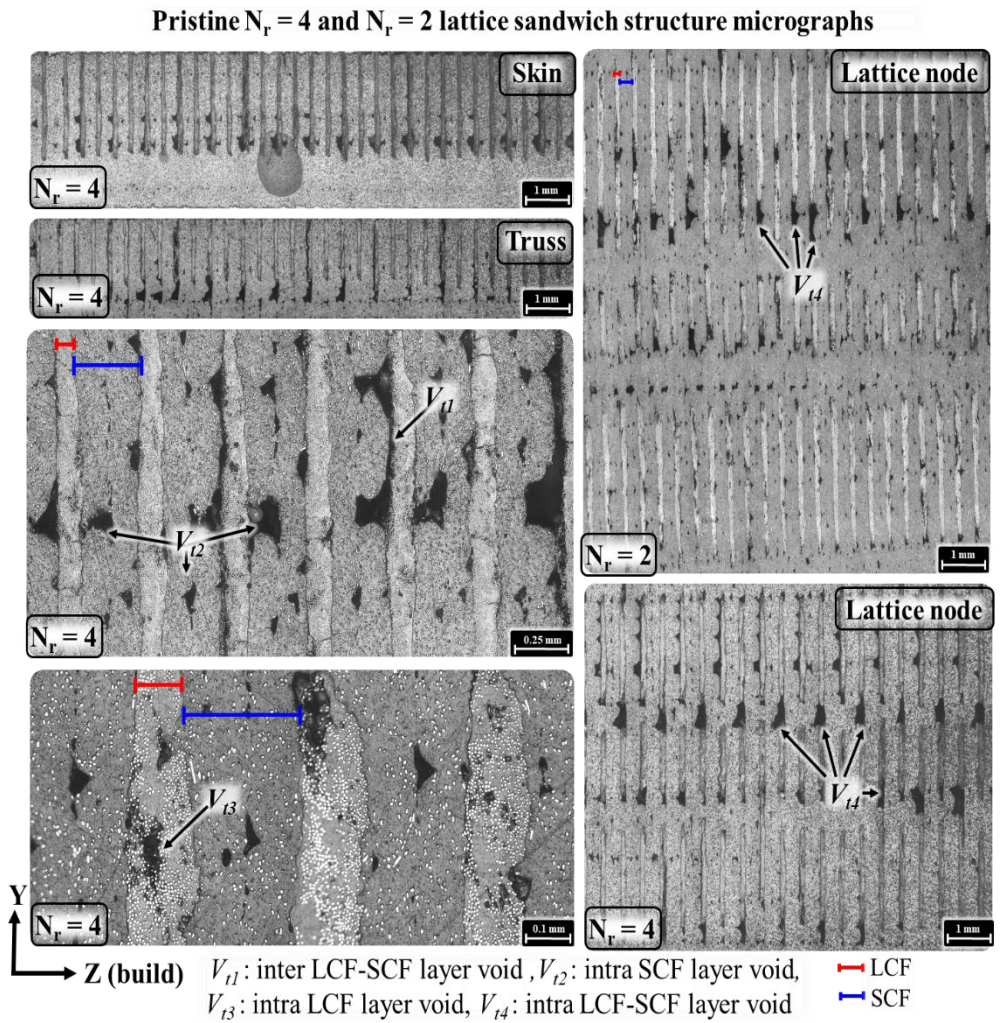

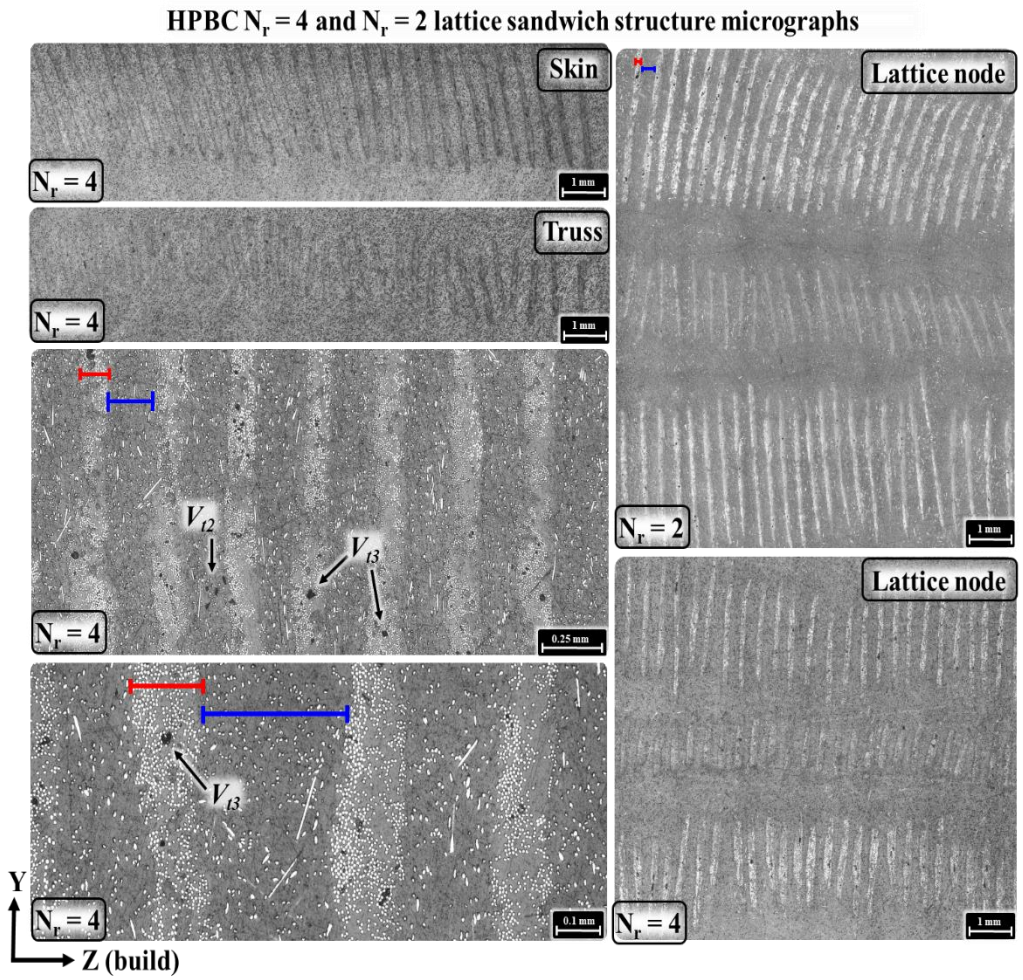

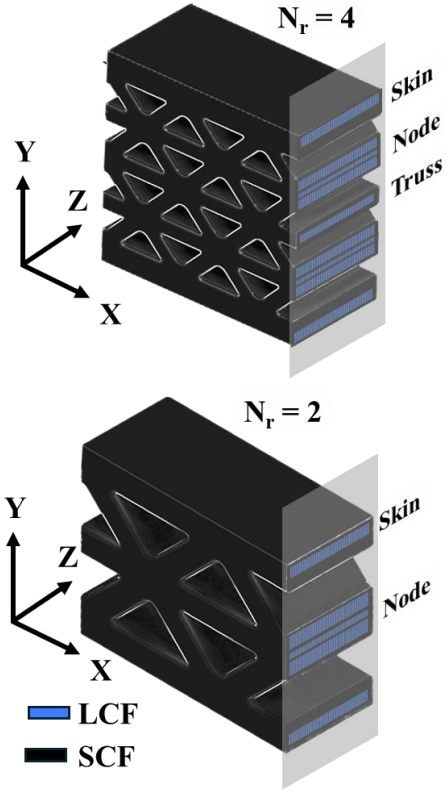

Failure analysis of LSS with DIC Y- displacement

- DIC full-field displacement analysis revealed failure modes including localized skin yielding and truss buckling in LSS.
- Higher I_{33}/I_{t^2} ratio in the Nr = 2 configuration provided higher critical truss buckling load, increasing skin yielding load
- Pristine failure initiated at the tensile-side skin, propagating through the core along weak LCF–SCF interface voids.
- HPBC-treated samples showed only localized skin yielding and no truss deformation in Nr = 4 and Nr = 2.
- Performance improvements were mainly due to microstructural changes like better interlayer fusion and void reduction, not phase transformation or crystallinity fraction (HPBC :27.67 ± 1.33% ; Pristine: 33.49 ± 0.18 %), as confirmed by the DSC results.

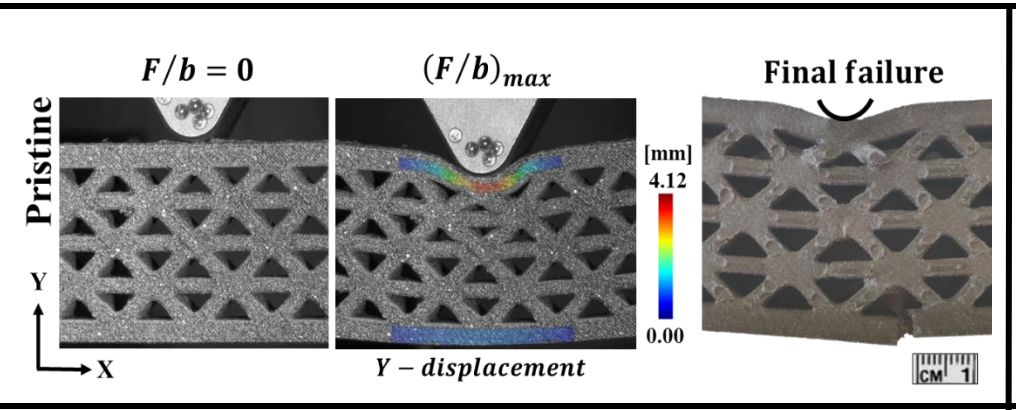

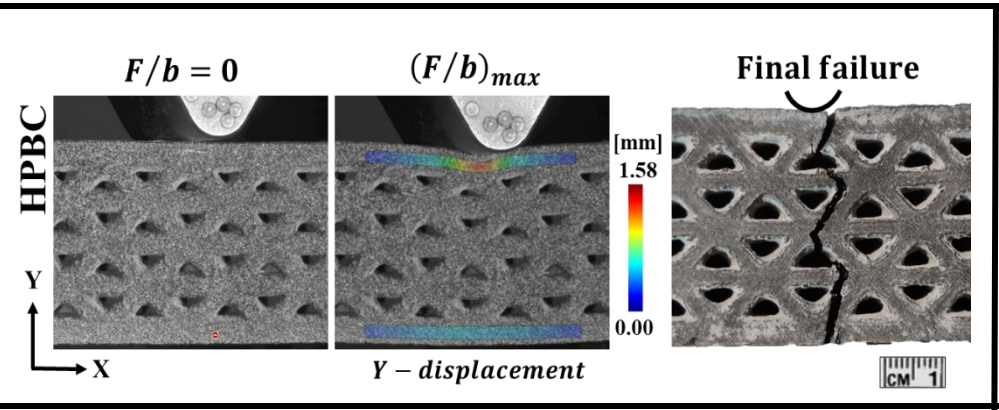

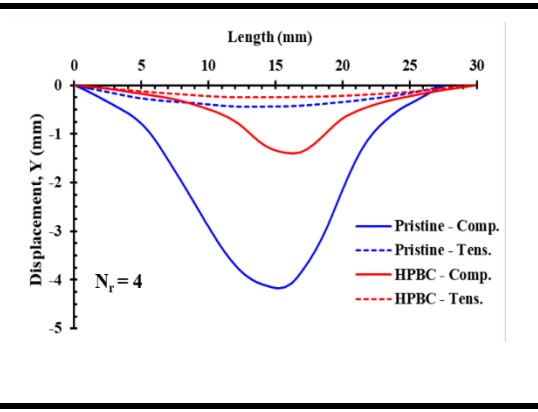

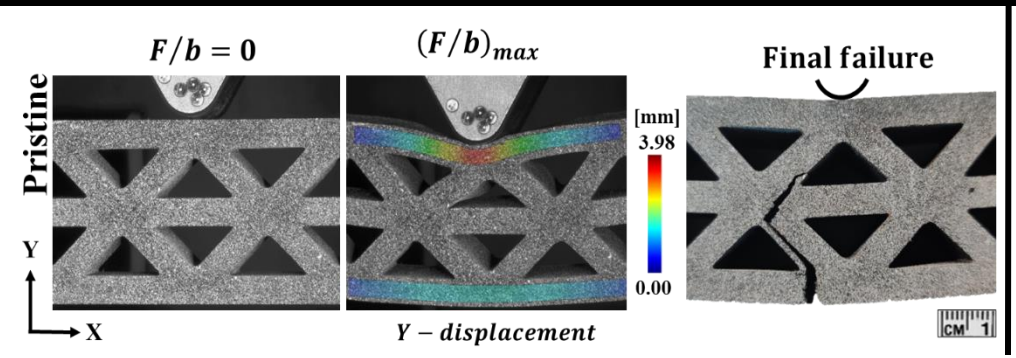

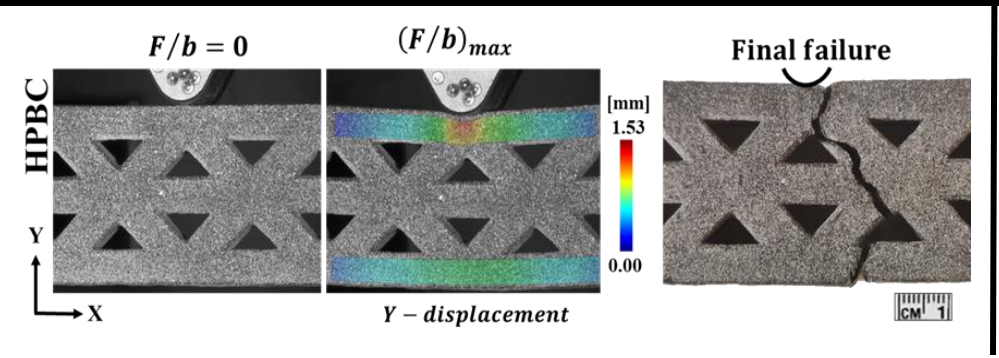

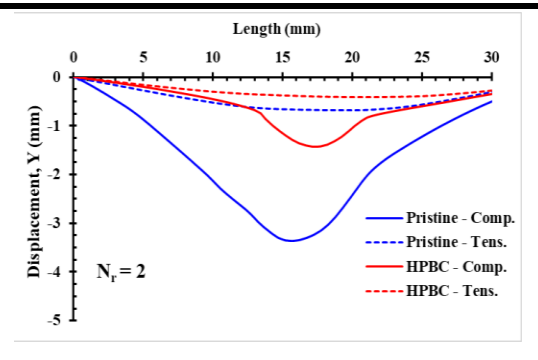

Test results and progressive damage analysis of LSS

- Both pristine LSS configurations showed similar unit width stiffness (~111.6 ± 4.4 N/mm²); however, N_r = 2 exhibited 425.1 N/mm, 30% higher strength compared to N_r = 2
- Post-HPBC, stiffness improved by 122% for both configurations;
  - Strength of N_r = 2 increased by 86%, while N_r = 4 showed a 154% stiffness gain
- The FEA predicted a stiffness of 265.3 N/mm² and strength of 689.8 N/mm.
- Crack initiation at the tension-side skin and progression into the core, was demonstrated through fiber direction stress (σ_{11}) evolution during damage propagation.

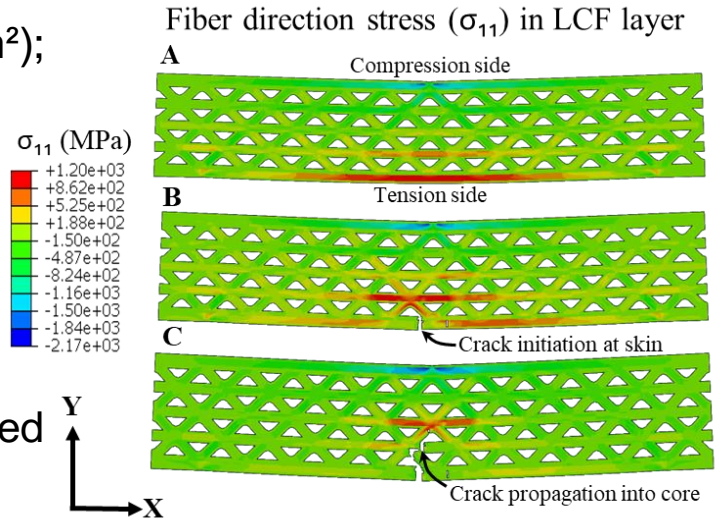

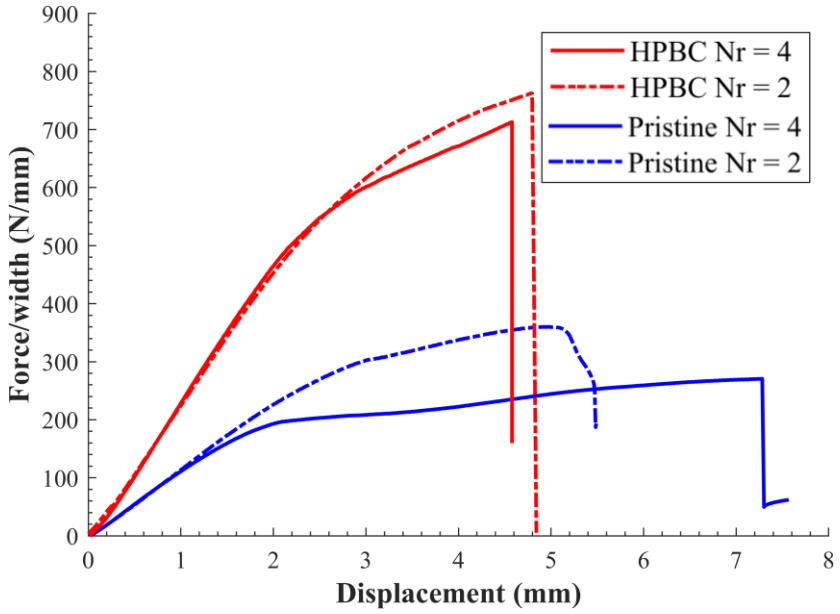

Extensive crack propagation in simulation and experiment



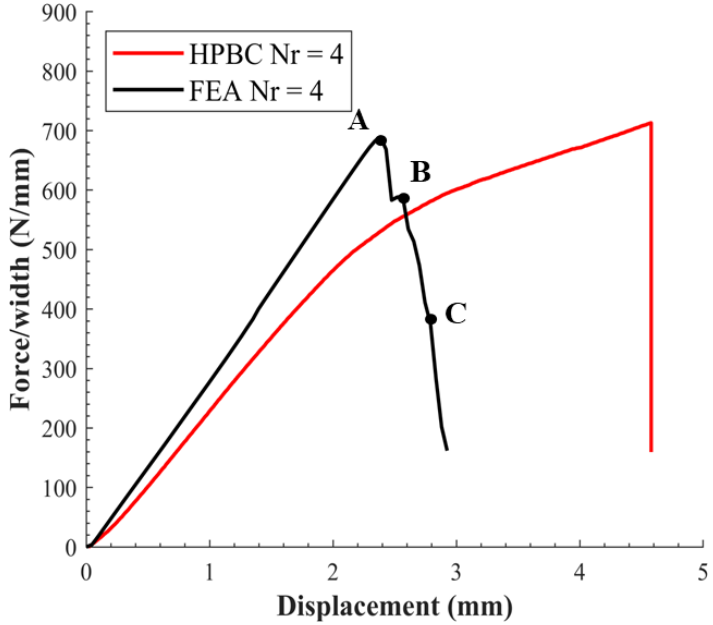

Conclusion

- HPBC process **improved LSS strength** by 154% and **stiffness** by 119%, without the need for rigid tooling.
- Tailored LCF–SCF reinforcement enabled **effective consolidation** in two complex cores geometry, reducing voids below 2.3%.
- DIC analysis showed failure shifted from **truss-induced skin yielding (pristine)** to **skin failure (HPBC)** post HPBC process.
- **Meso-scale CDM-based FEA approach** closely predicted stiffness, strength, and crack progression.
- A consistent **17.8% Z-direction shrinkage** was observed, enabling predictable geometry control during design.
- Combining HPBC with MEX offers a scalable, cost-efficient route for **fabricating complex, high-performance composites**.

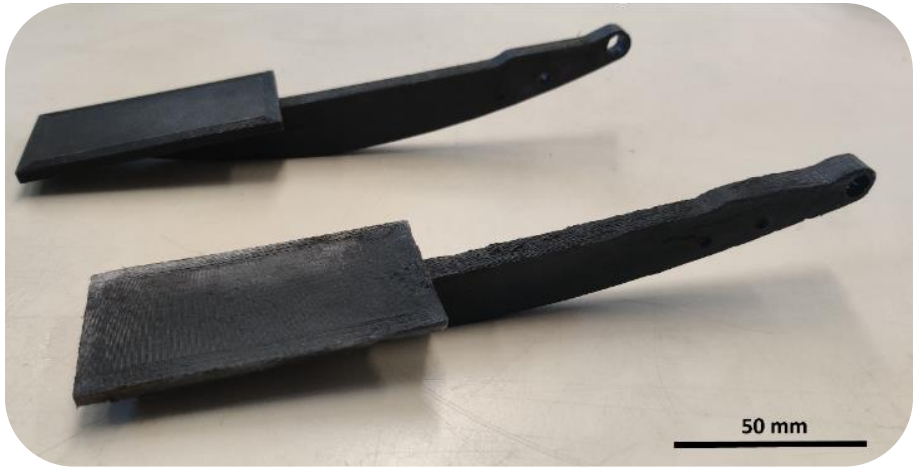





Thank You

(Question, suggestion and comments)

ICCM24
AUGUST 4-8, 2025
BALTIMORE CONVENTION CENTER
BALTIMORE, MARYLAND, USA

No Technical Paper Submission for:

Zizhao Peng

OAK RIDGE National Laboratory

Effect of Process Parameters on Thermal Conductivity and Temperature History in Extrusion-Deposition Additive Manufacturing

Eonyeon Jo

Bredesen Center, University of Tennessee, Knoxville, TN

Felipe Poblete, Britt Helten, Soydan Ozcan, Uday Vaidya and Seokpum Kim

ORNL is managed by UT-Battelle LLC for the US Department of Energy

U.S. DEPARTMENT OF ENERGY

Research sponsored by the U.S. Department of Energy, Office of Energy Efficiency and Renewable Energy, Industrial Technologies Program, under contract DE-AC05-00OR22725 with UT-Battelle, LLC.

Extrusion-based large-format additive manufacturing (LFAM)

- Advantages of extrusion-based LFAM
  - **High deposition rate:** up to 86 kg per hour using the thermoplastic extrusion process.
  - **Processability**: facilitates the manufacturing of large-scale structures efficiently.
  - **Cost reduction**: significantly lowers tooling costs.
  - **Enhanced properties**: offers superior thermal and mechanical properties with diverse options of engineering plastics and reinforcements.

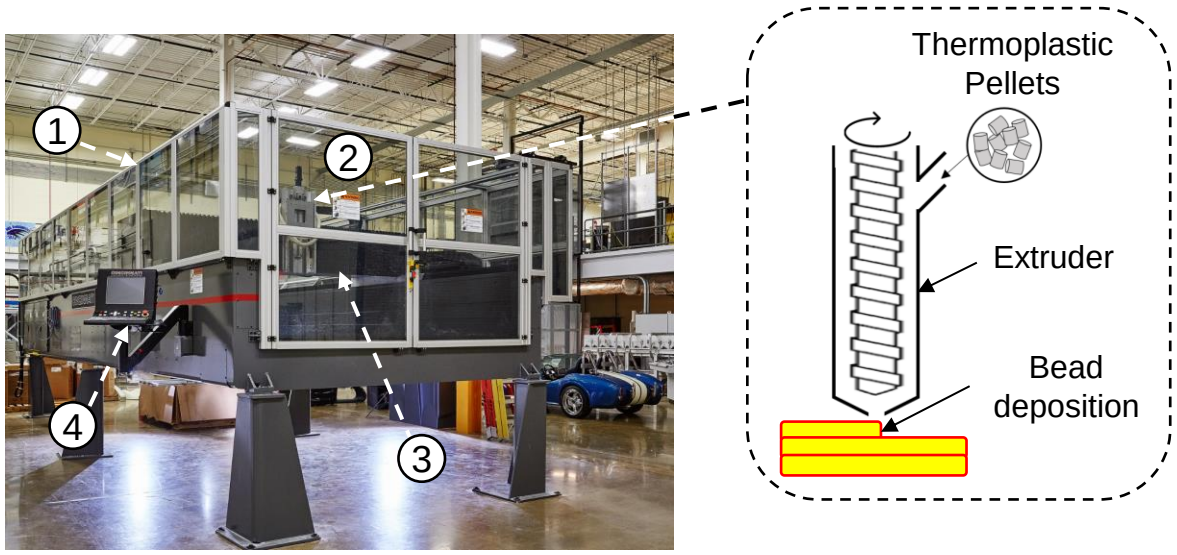

BAAM system; 1) Printing chamber (6m length x 2.5m width x 1.8m height), 2) Single screw polymer extrusion deposition head, 3) Gantry system, and 4) Control station[1]



Ingersoll – MasterPrint 3x by UMaine (30.5m length x 18.3m width x 3m height)[2]

[1]A. A. Hassen, et.al., "The Durability of Large-Scale Additive Manufacturing Composite Molds," in *CAMX 2016*, 2016.

[2]https://composites.umaine.edu/facilities/additive-manufacturing/

Applications of extrusion-based LFAM

Electric vehicle, “Olli” (Local Motors)[1]





Marine, “A boat - 3Dirigo” (UMaine)[2]

Aerospace, “trim-and-drill tool for aircraft component” (ORNL)[3]





3D-printed House with bio-based materials (UMaine)[4]

[1]Kirsten K., “Meet Olli 2.0, a 3D-printed autonomous shuttle,” 2021.
[2] UMaine news, “World Records related to largest 3D printer,” 2019.
[3]Office of Technology Transitions, “3D printed tool for building aircraft achieves Guinness World Records Title,” 2016.
[4]Joan F., et al., “Research report: R1 Global Impact – Local Relevance,” University of Maine: Orono, ME, USA, 2023.

Challenges and key factors in extrusion-based LFAM

- Challenges
  - **Structural stability**: risk of failure or warpage.
  - **Skilled labor dependence**: heavily rely on the experience of skilled operators.
  - **Manufacturing variances**: variability in material, geometry, process parameters, toolpath.
  - **Anisotropic material behavior**: material properties highly dependent on the toolpath.



Warpage in a printed structure

- Key factors
  - **Temperature history:** the structural stability and defect are determined by temperature.
  - **Layer deposition time (layer time)**: the total time required for a layer to be deposited.



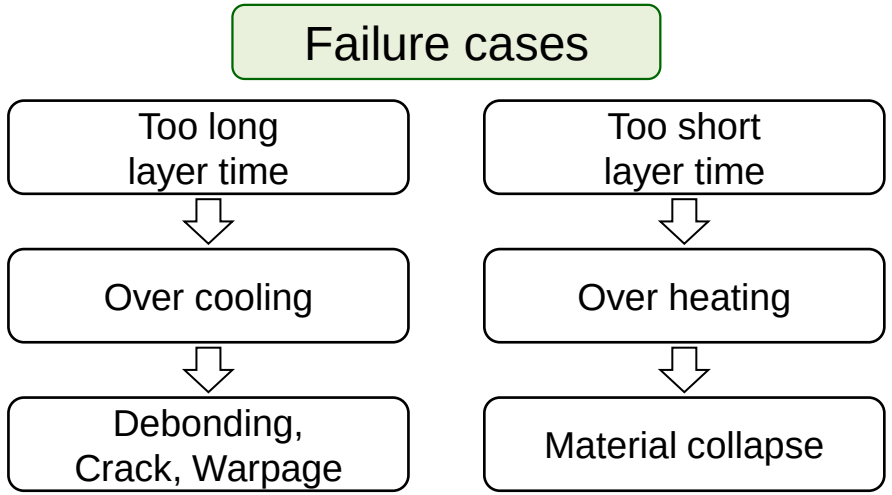

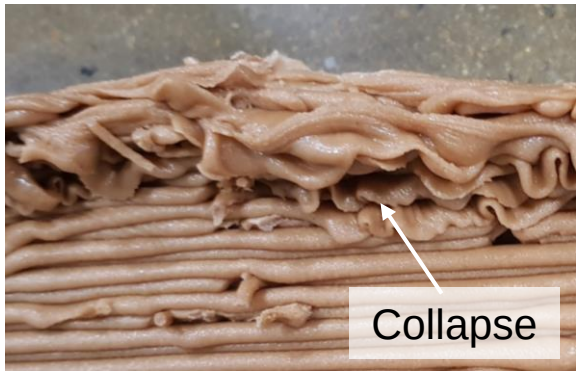

[1] L. J. Love, et al., "Utility of Big Area Additive Manufacturing (BAAM) for the rapid manufacturing of customized electric vehicles," Technical report, Oak Ridge National Laboratory, 2015.

Objectives and material

- Objectives:
  - Objective 1: Evaluating the effect of bead overlap distance on thermal conductivity.
  - Objective 2: Evaluating the effect of bead geometry on temperature history during the manufacturing.
  - Objective 3: Sensitivity analysis of thermal conductivity, heat capacity and thermal expansion coefficient on temperate and deformation history.
- Material:
  - Wood flour reinforced amorphous polylactic acid (compound of NatureWorks aPLA 3D700 and American Wood Flours 100 mesh Norther Yellow Pine)

Objective1
Effect of bead overlap distance on thermal conductivity

Objective 2
Effect of bead geometry on thermal history

Objective 3
Sensitivity analysis of properties on temperature & deformation history



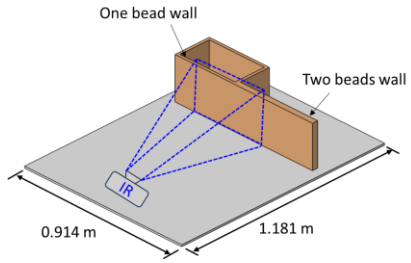

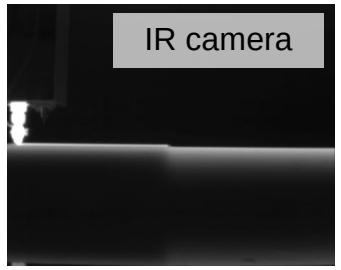

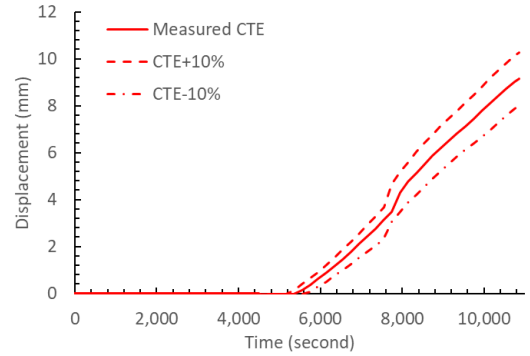

Objective 1:
Evaluating the effect of bead overlap distance on thermal conductivity.

Specimen fabrication

- Base line specimen is manufactured using compression molding at 180 °C and 50 bar.

- Box print with simple raster pattern using different bead overlap distance.
  - 6 steps of overlap: 5%, 8%, 10%, 11% and 14%

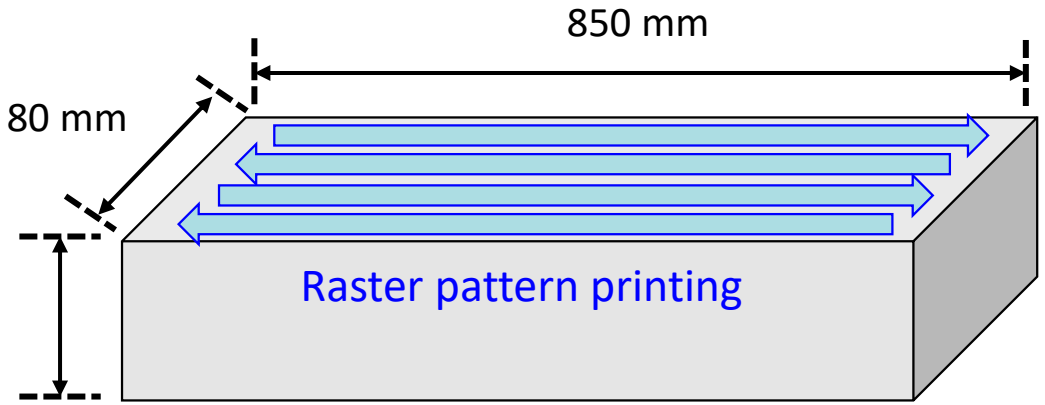

Box print geometry print

- Thermal conductivity measurement in anisotropic direction (x, y, z – direction)
  - Printing direction is defined as x-direction

Sample geometry:

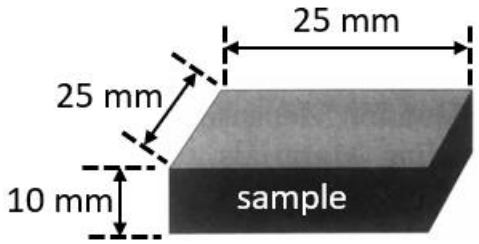

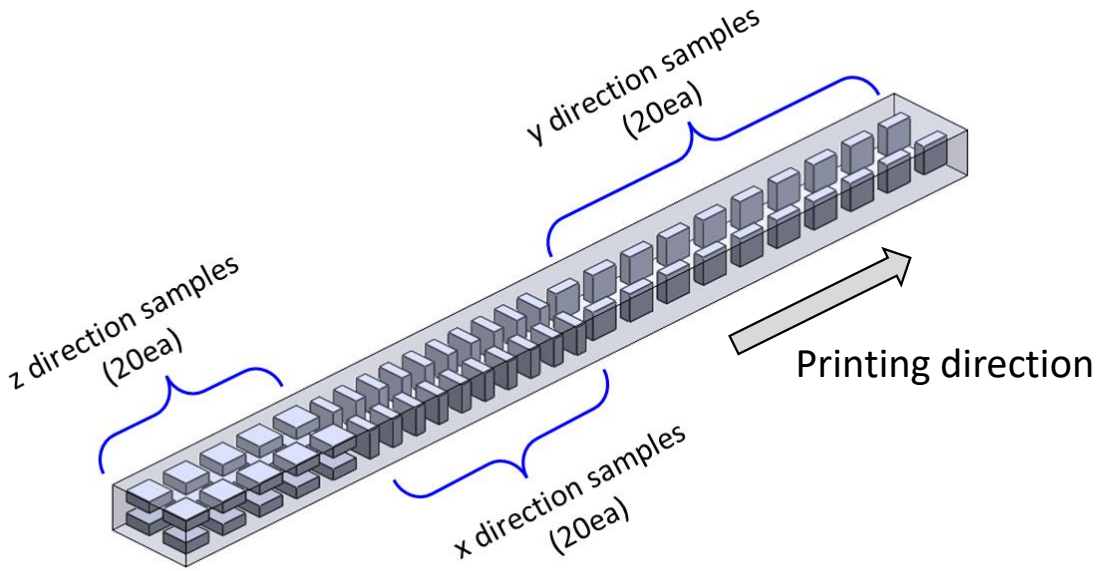

Prepared specimen for thermal conductivity measurement

- Baseline specimen

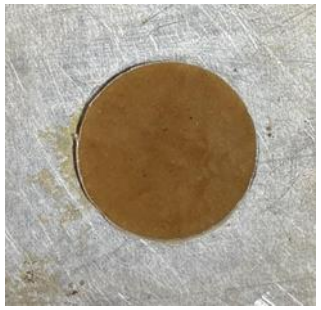

- Specimens with different overlap distance in x, y, z direction.

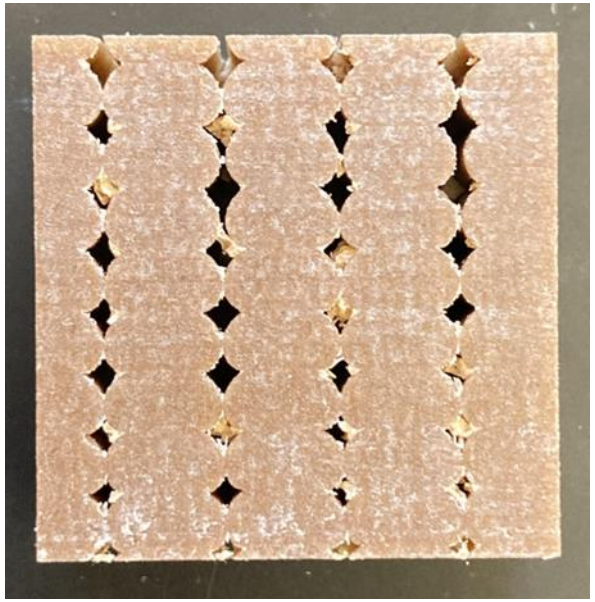

5% overlap – x direction



5% overlap – z direction



14% overlap – x direction



14% overlap – z direction

Heat capacity and thermal conductivity measurement

- Differential scanning calorimetry (DSC)
  - Specific heat, glass transition temperature
- Transient plane source (TPS)
  - Thermal conductivity



DSC

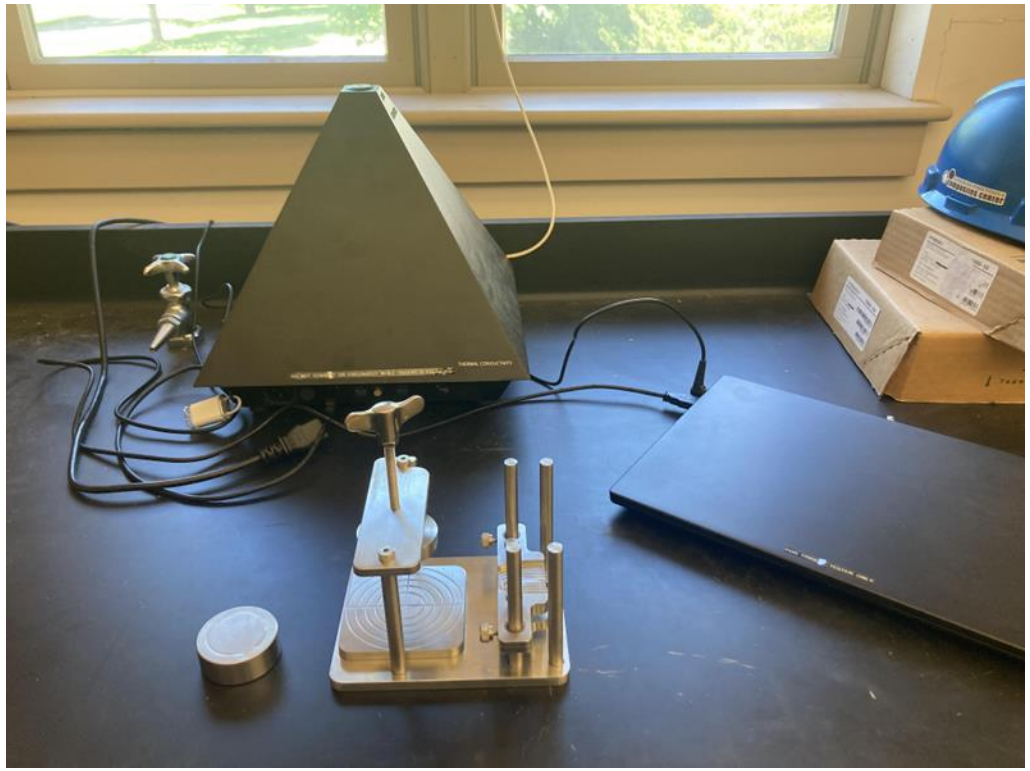

TPS

TPS test set up

- TPS test conditions
  - 6 mm sensor
  - Test time: 40 seconds
  - Power: 0.02 W

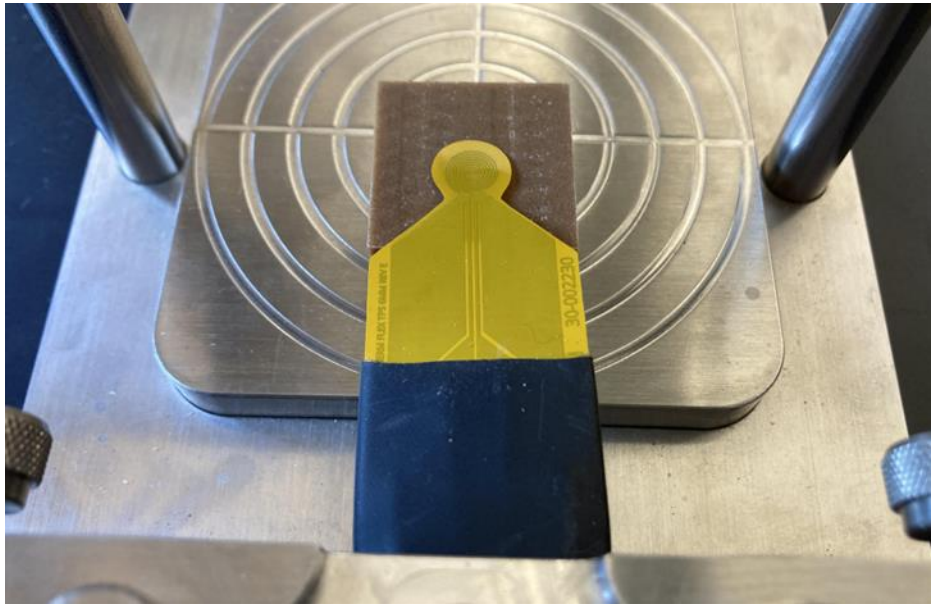

6 mm sensor

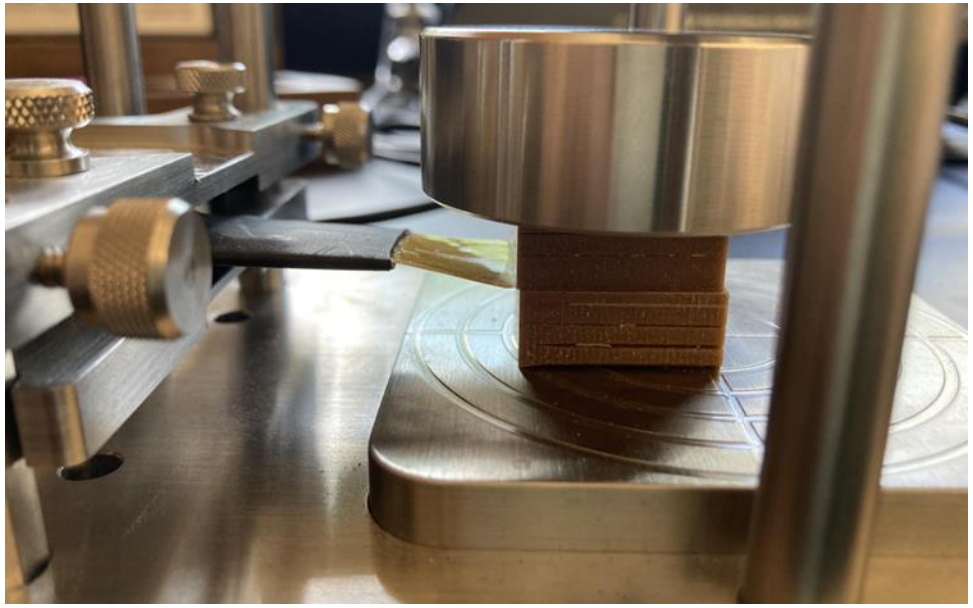

Sensor installation

TPS test results

- Thermal conductivity $(\kappa, W/mK)$

$$\kappa = \alpha \cdot \rho \cdot C_p$$

α: diffusivity (m^2/s), ρ: density (kg/m^3)

C_p: specific heat (J/kgK)

- Specific heat: 1,350 J/kgK (@ 25 ℃)

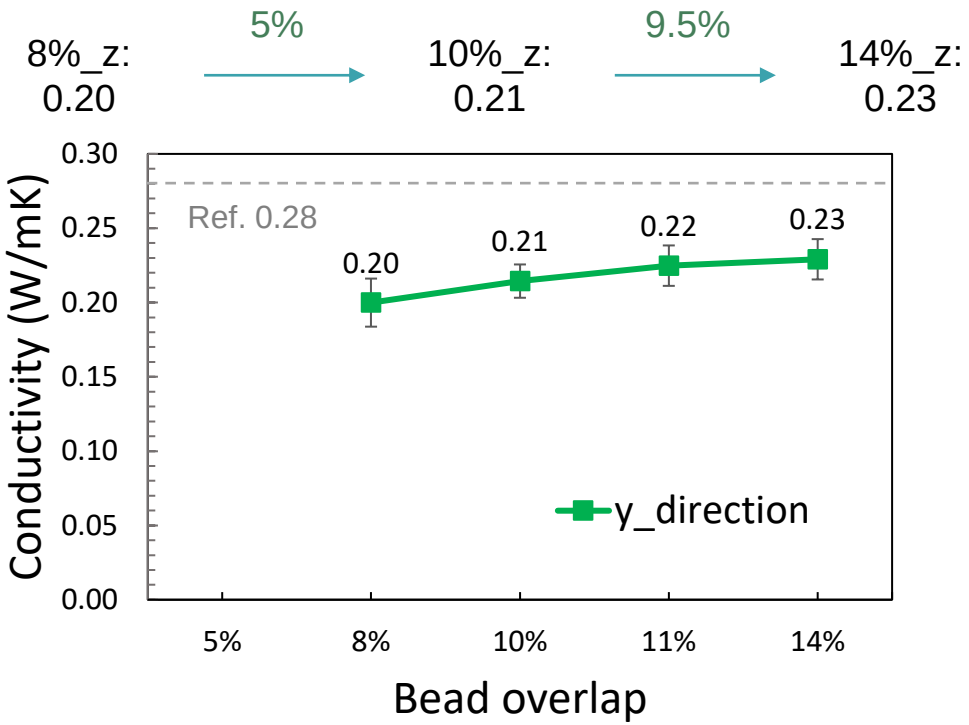

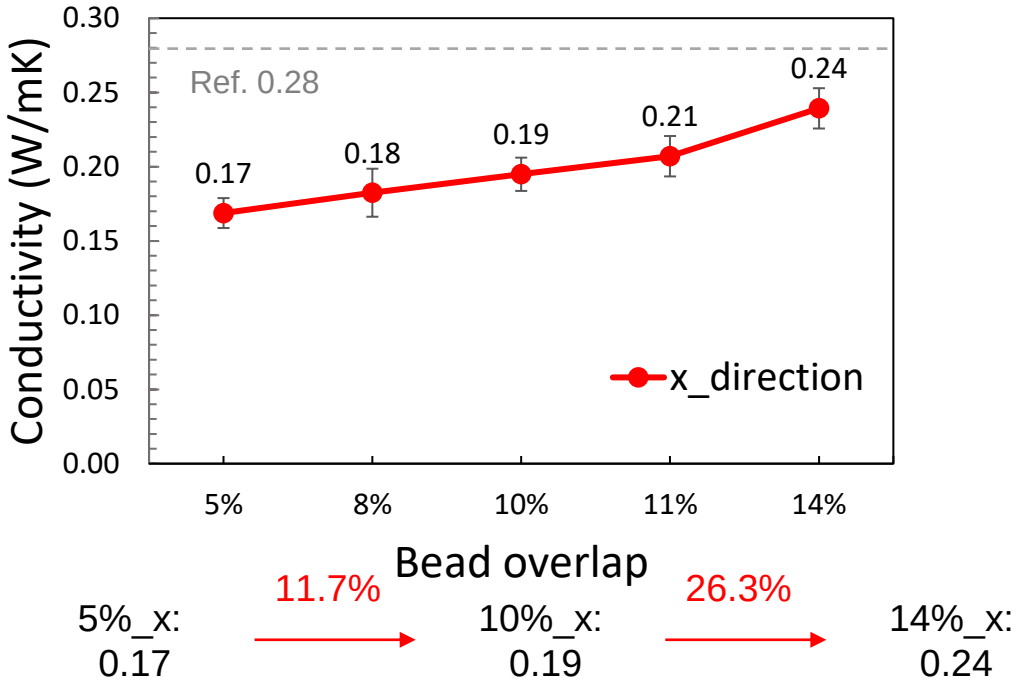

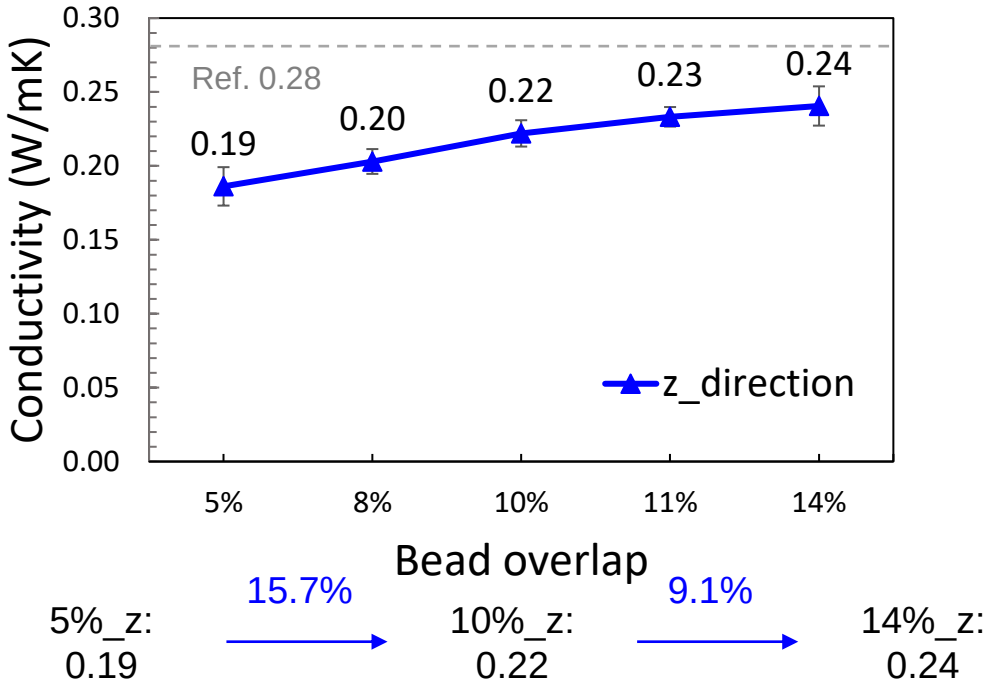

Objective 2:
Evaluating the effect of bead geometry on temperature history during the manufacturing.

Temperature measurement during P-shape print

- Geometry: Multi-beads wall geometry with 60 layers
  - Half (one bead) : Half (two beads)
- Temperature measurement using an Infrared (IR) camera
  - IR camera: FLIR Boson, FOV: 0.4m x 0.32m
- Bead geometries:

Bead geometry	Nozzle Diameter (mm)	Width (mm)	Height (mm)
# 1	4	6	1.5
# 2	6	9	2.25
# 3	10	15	3.75

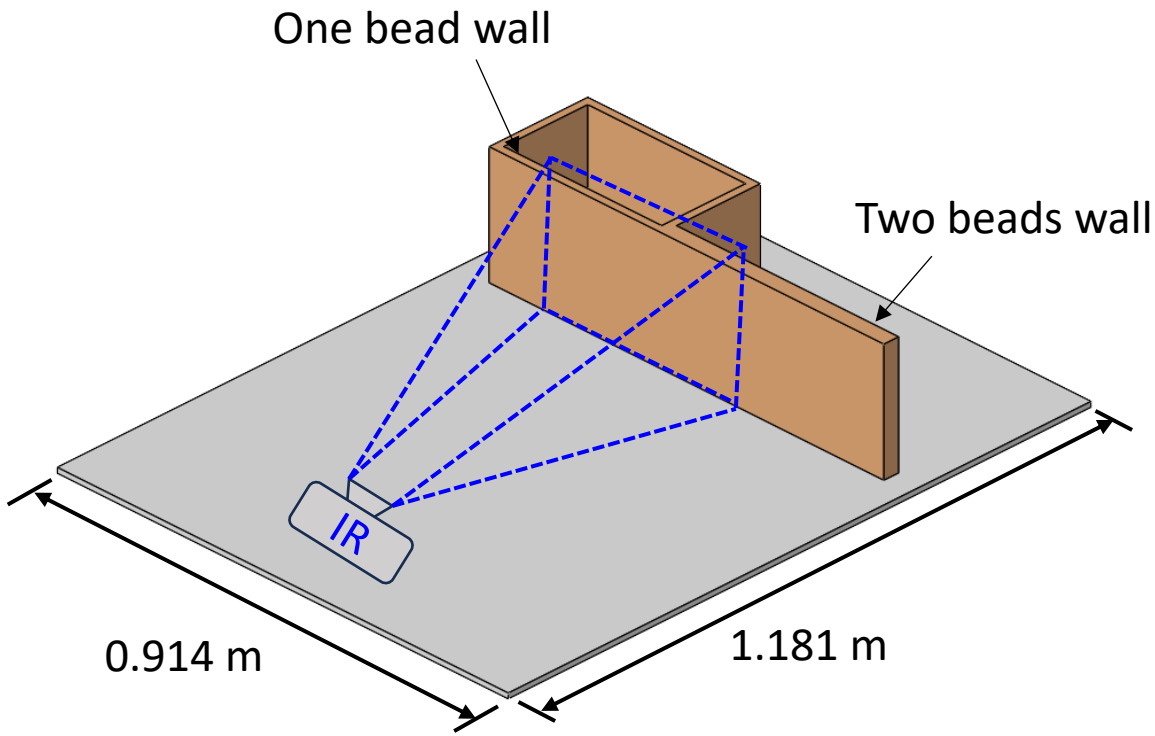

P-shape print geometries

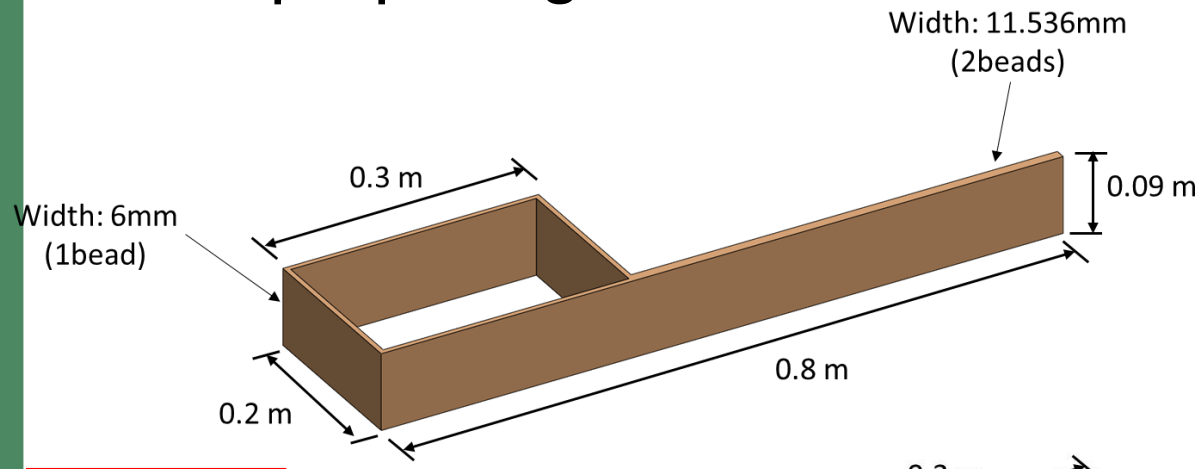

Case 1

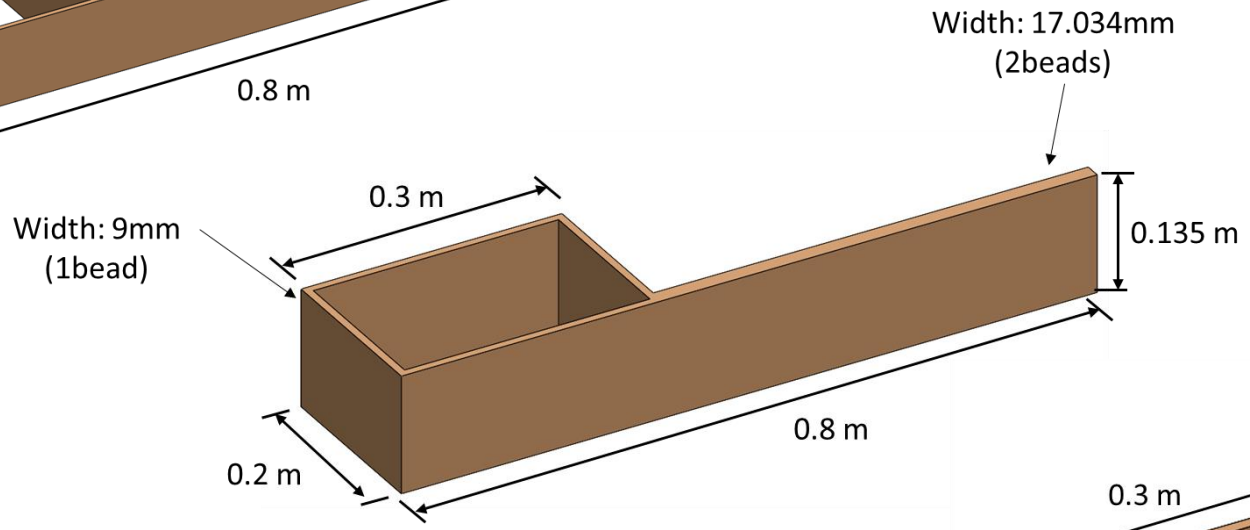

Case 2

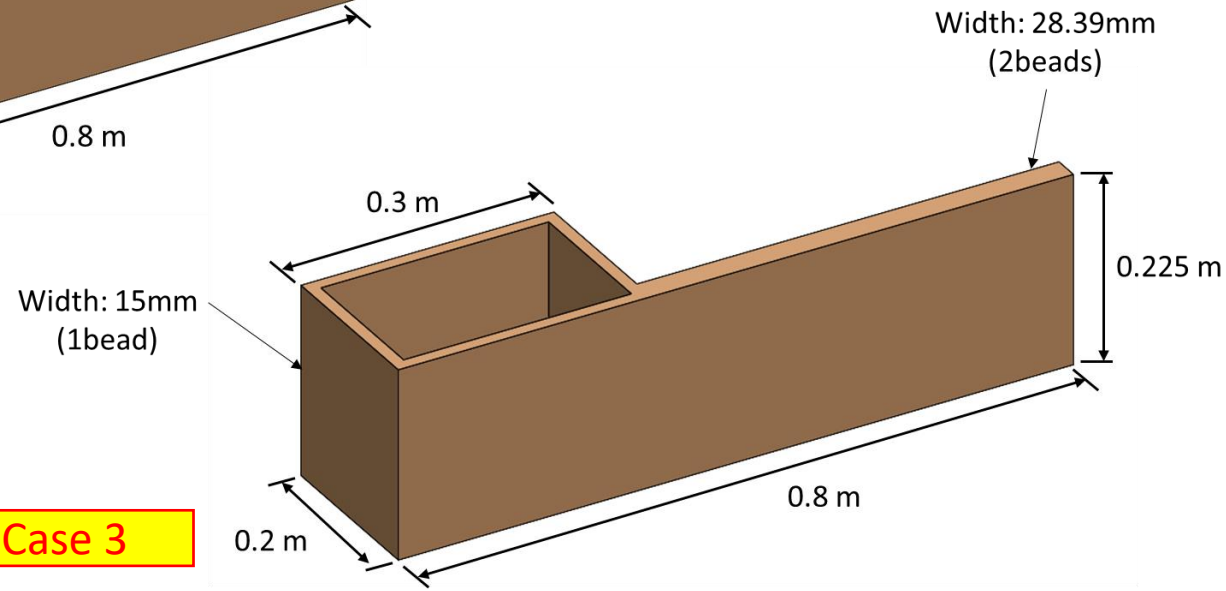

Case 3

AM printing with Juggerbot 3D (Tradesman Series P3-44)

- Used material: Wood fiber reinforced PLA (20 wt. %)
- Print speed: 1350, 848, and 425 mm/min
- Extrusion temperature: 165 ˚C
- Layer time: 90, 140, and 240 seconds



Juggerbot3D – Tradesman Series P33-44

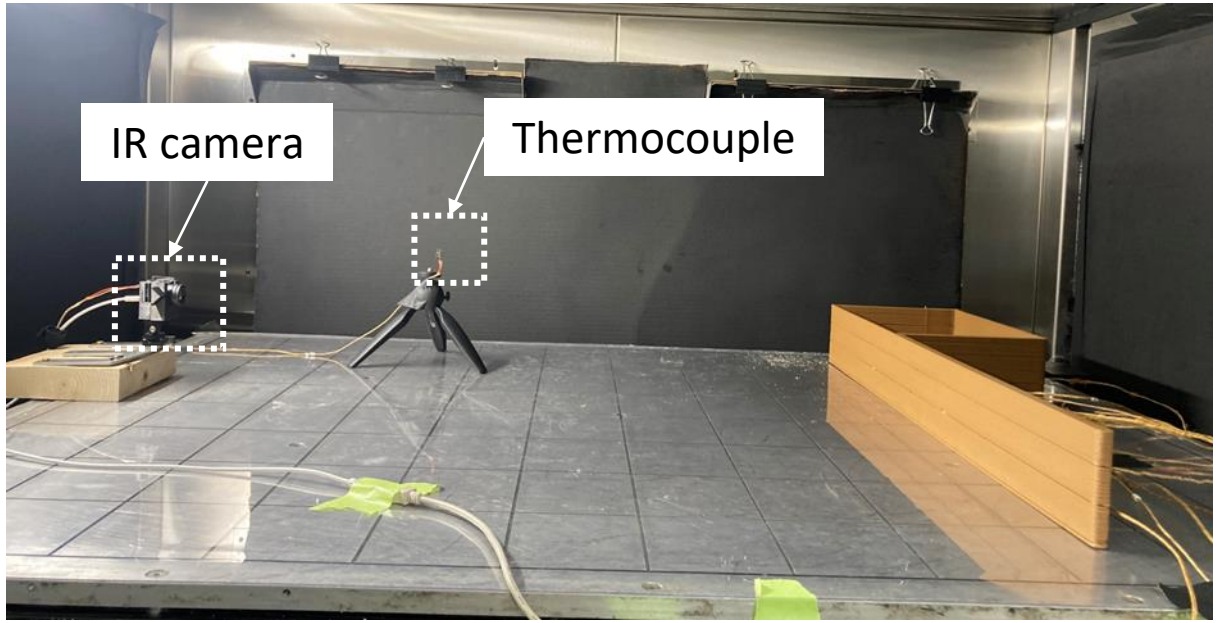

Experimental setup

Transient heat transfer model using finite element analysis (FEA)

- Element activation
  - Activate elements when a tool path passes through the elements (tool path from Gcode).
  - Update boundary conditions (activate elements in extrusion temperature).

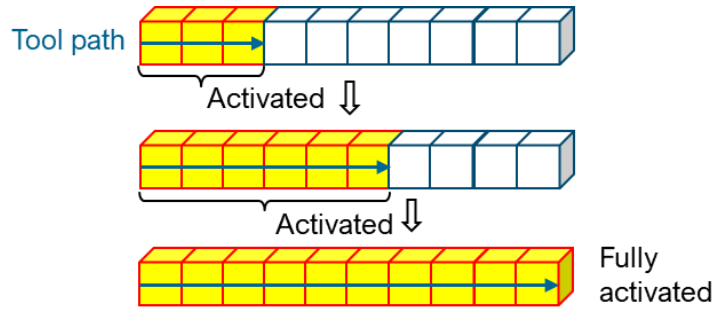

- Anisotropic thermal properties with printing direction
  - The fiber in the extruded substance is aligned with the tool path.
  - The principal direction (x-direction) is chosen as the print direction (z-direction = stacking direction).

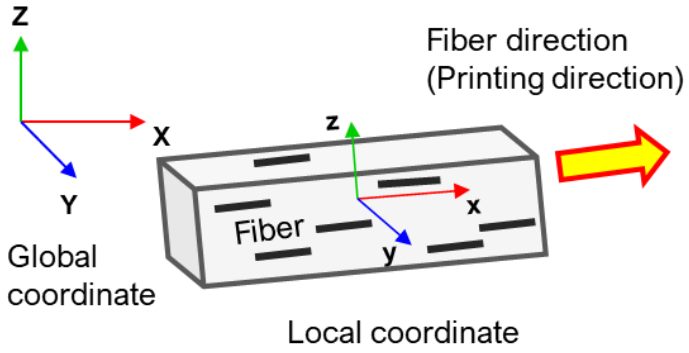

- Layer height (number)
  - The element has the same height (number) as the real print to simulate the layer-by-layer stacking procedure.

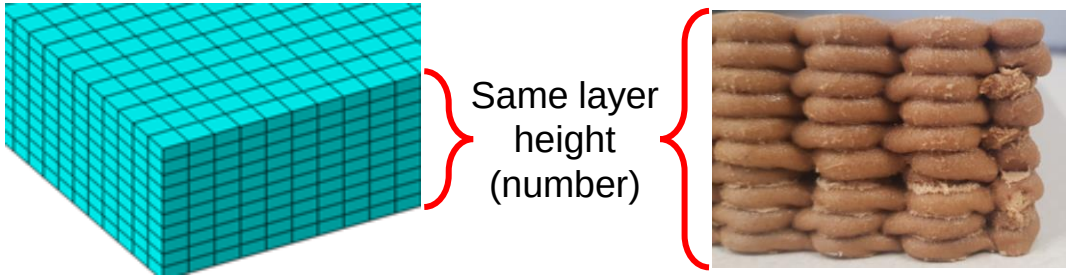

FEA heat transfer model

- Temperature prediction for the P-shaped print
  - Temperature history is predicted over the entire process.
  - Temperature field is displayed as color maps, with hot areas in red and cold areas in blue.
- Material properties: Wood flour reinforced polylactic acid (WFPLA, 20wt.%)
  - **Density**: 1,240 kg/m^3, **Specific heat**: 1,476 $J/kg{\cdot}K$, **Conductivity** (x, y, z): 0.198, 0.186, 0.159 $W/m{\cdot}K$

Boundary conditions

- Extrusion temp. = 130°C
- Base temp. = 28°C
- Ambient air temp. = 28°C

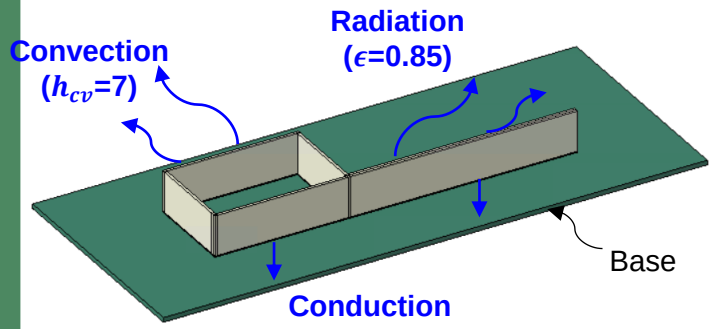

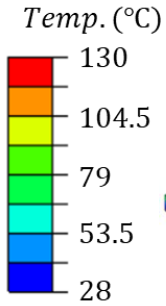

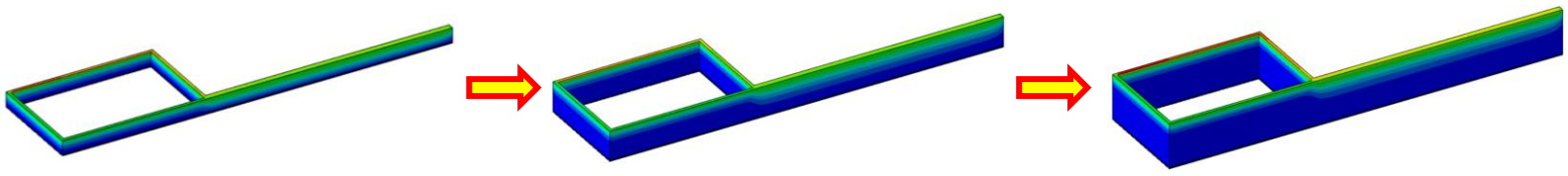

t = 1,800s (Layer 20) t = 3,780s (Layer 40) t = 5,780s (Layer 60)

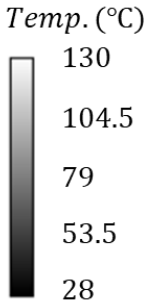

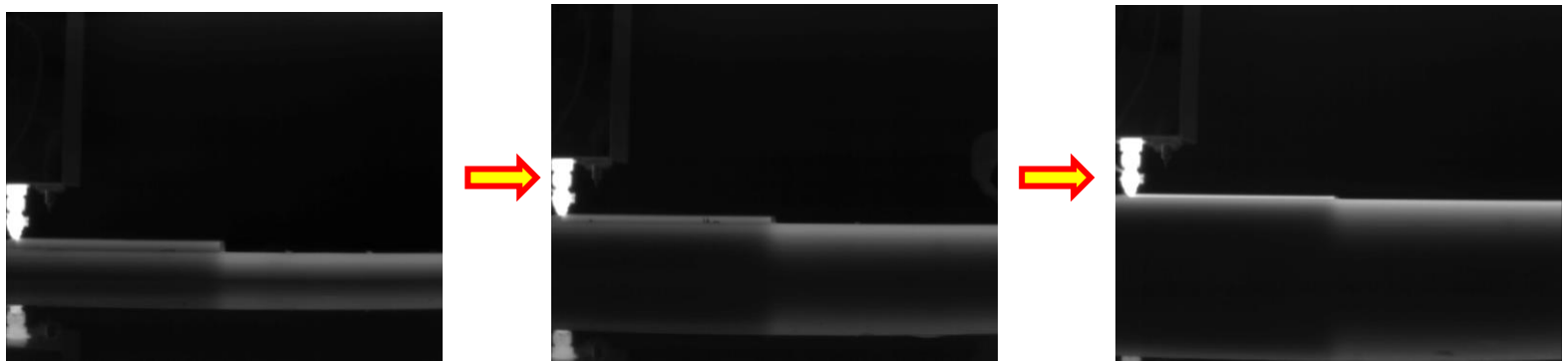

Simulation parameter calibration

1. Deposition temperature calibration
   - Extruded material experiences rapid cooling and the simulation model lacks the ability to simulate this accurately.
   - By comparing the temperature at the center of wall position when the layer deposition process is finished, the deposition temperature is calibrated.

2. Convection coefficient calibration
   - By comparing the temperature profiles, the convection coefficient is calibrated.

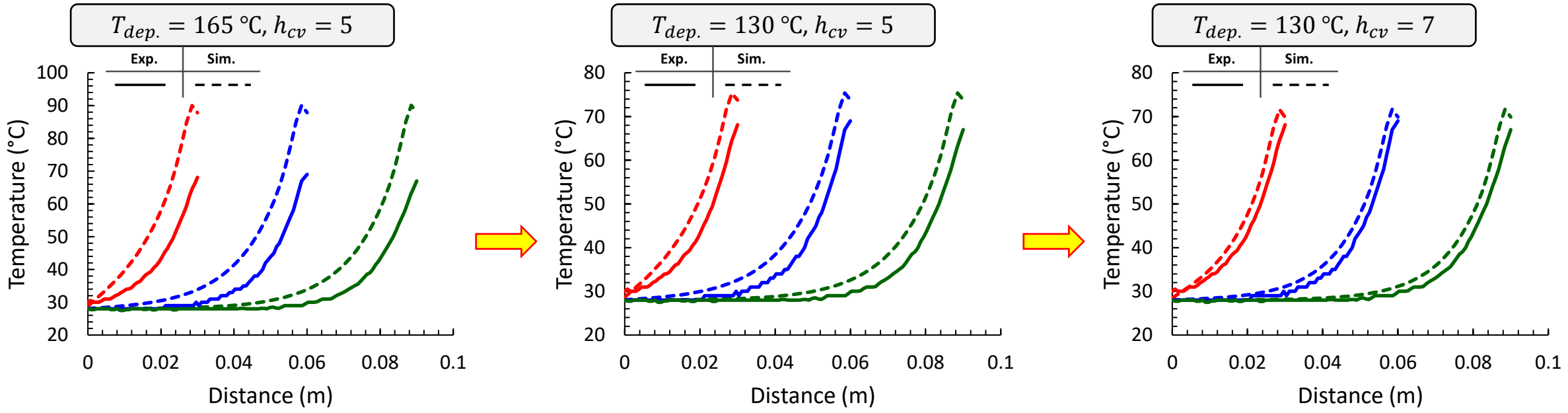

Results: P-shape print case 1

- Case 1
  - # of thermal images: 5,140
  - Layer time: 90s → theoretical printing time for 60 layers: 5,400s
  - Overall printing time with IR camera (printing + thermocouple installation): 5,763s
    - Installation time (1st and 2nd): 177s and 200s
    - Printing time: 5,386s

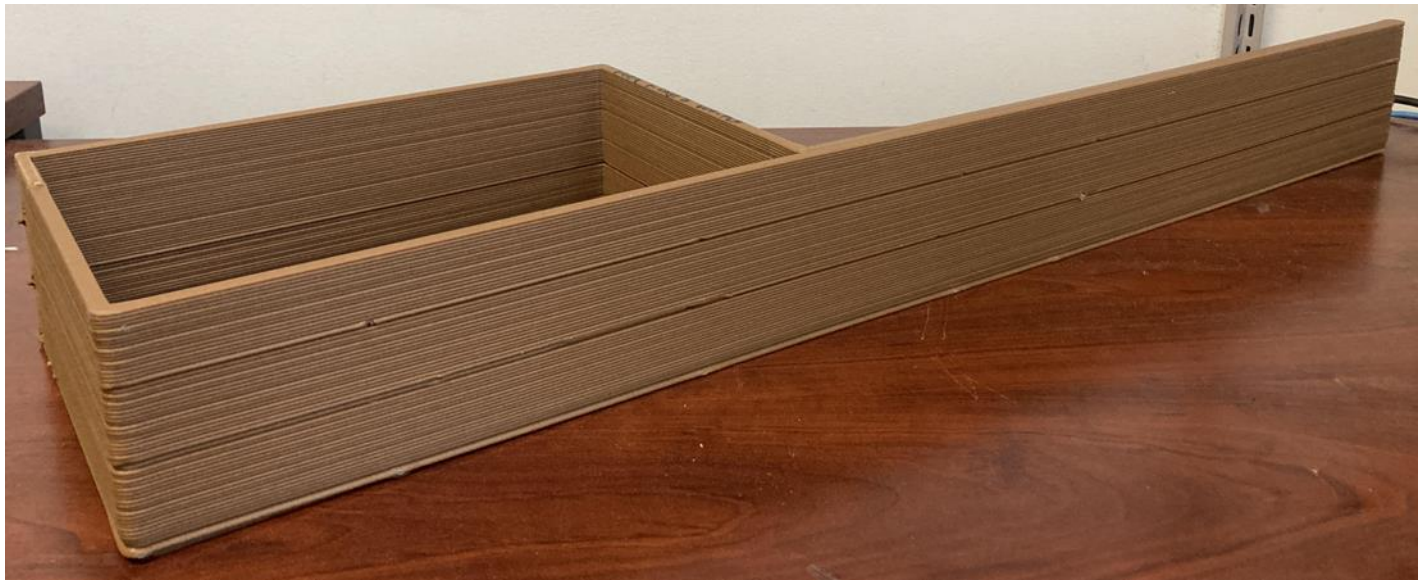

Comparison of IR thermal data with simulation _Case 1

- Boundary conditions:
  - Deposition temperature: 130 °C
  - Boundary temperature: 28 °C
  - Convection coefficient: 7
  - Emissivity: 0.85

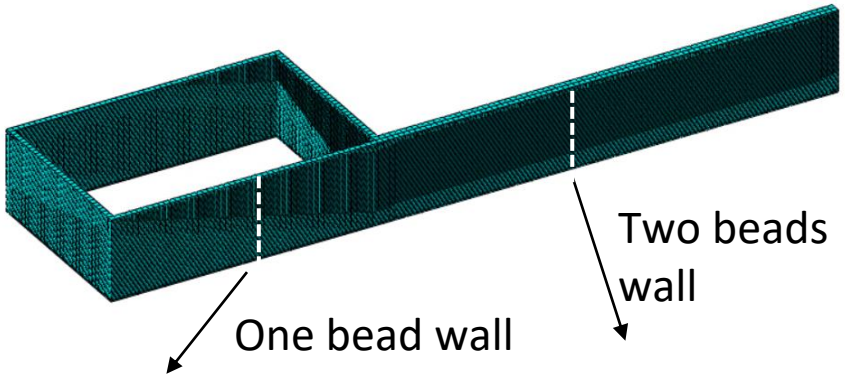

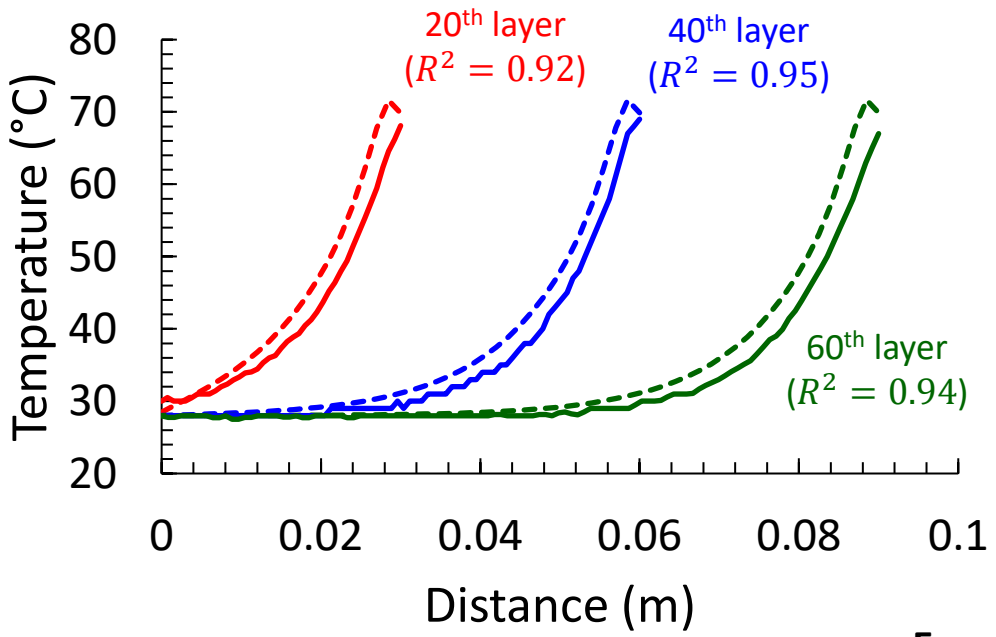

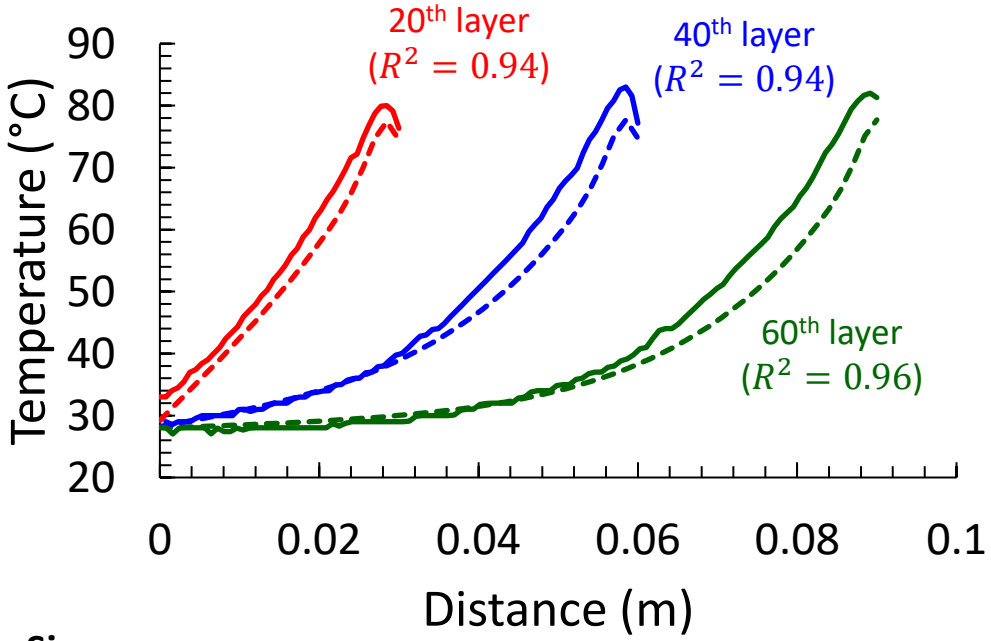

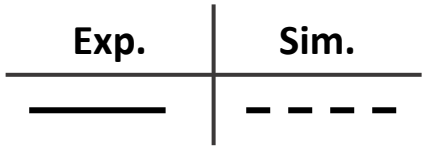

Results: P-shape print case 2

- Case 2
  - # of thermal images: 7,606
  - Layer time: 120s (1~15th) & 140s → theoretical printing time for 60 layers: 8,100s
  - Overall printing time with IR camera (printing + thermocouple installation): 8,764s
    - Installation time (1st and 2nd): 402s and 197s
    - Printing time: 8,165s

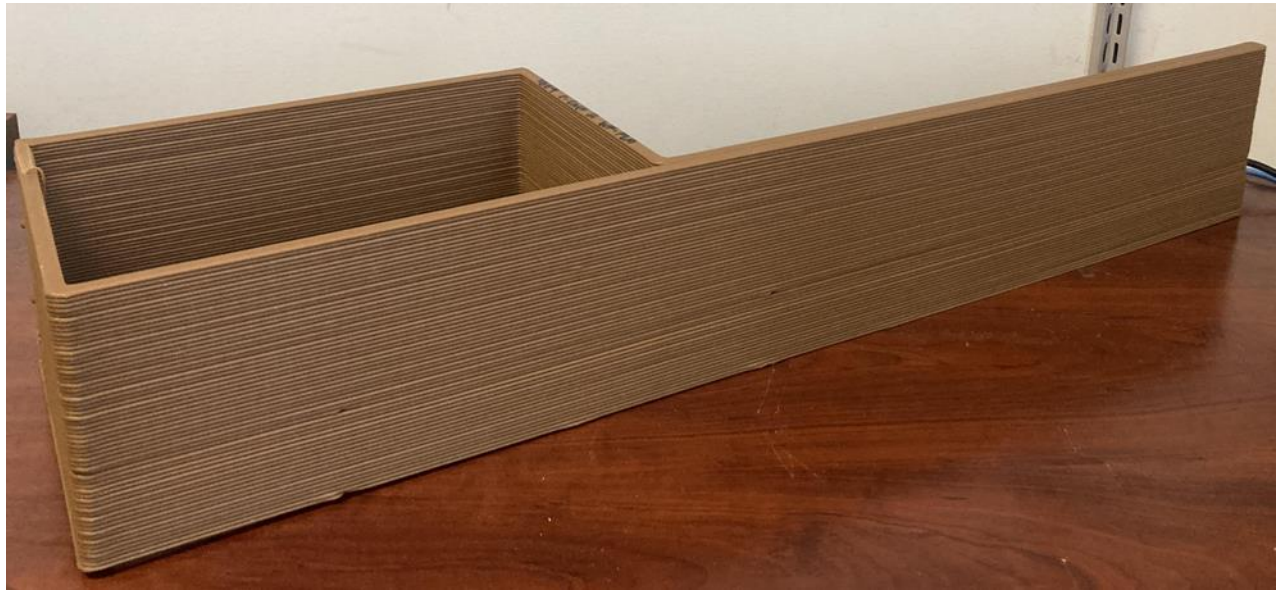

Comparison of IR thermal data with simulation _Case 2

- Boundary conditions:
  - Deposition temperature: 130 °C
  - Boundary temperature: 28 °C
  - Convection coefficient: 7
  - Emissivity: 0.85

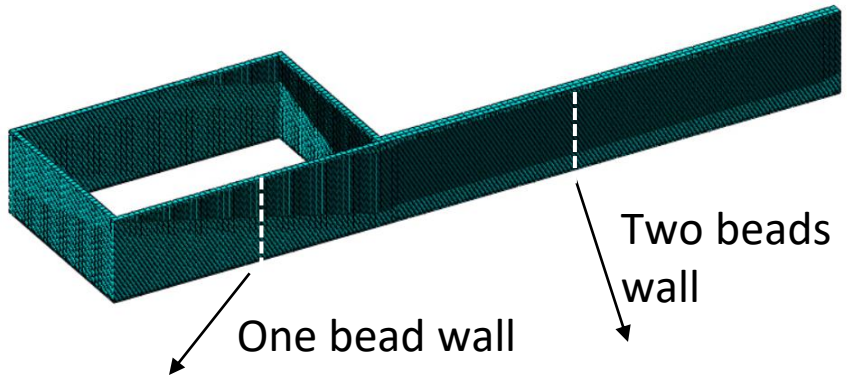

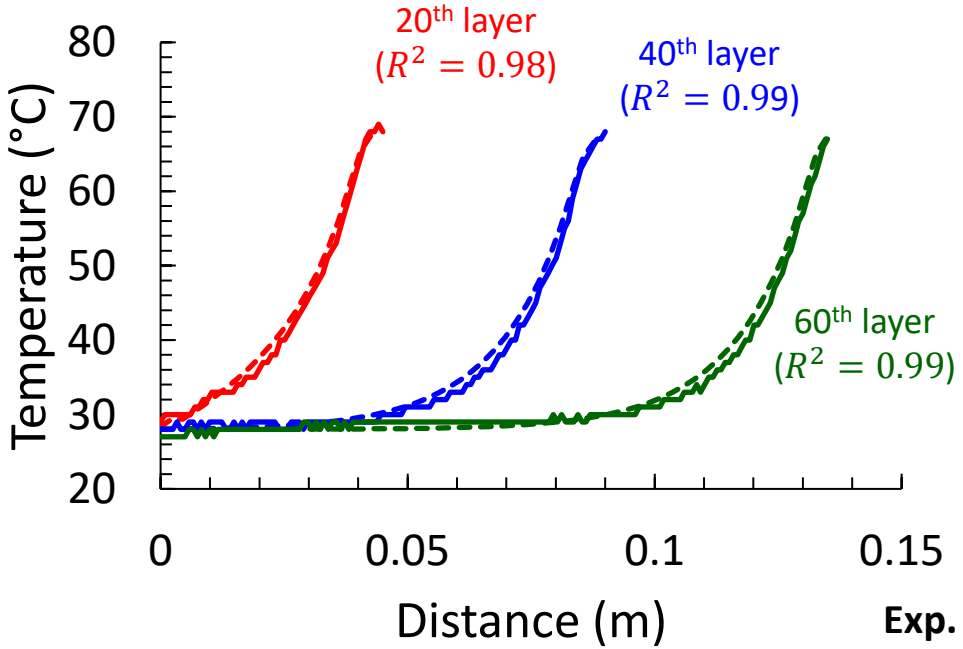

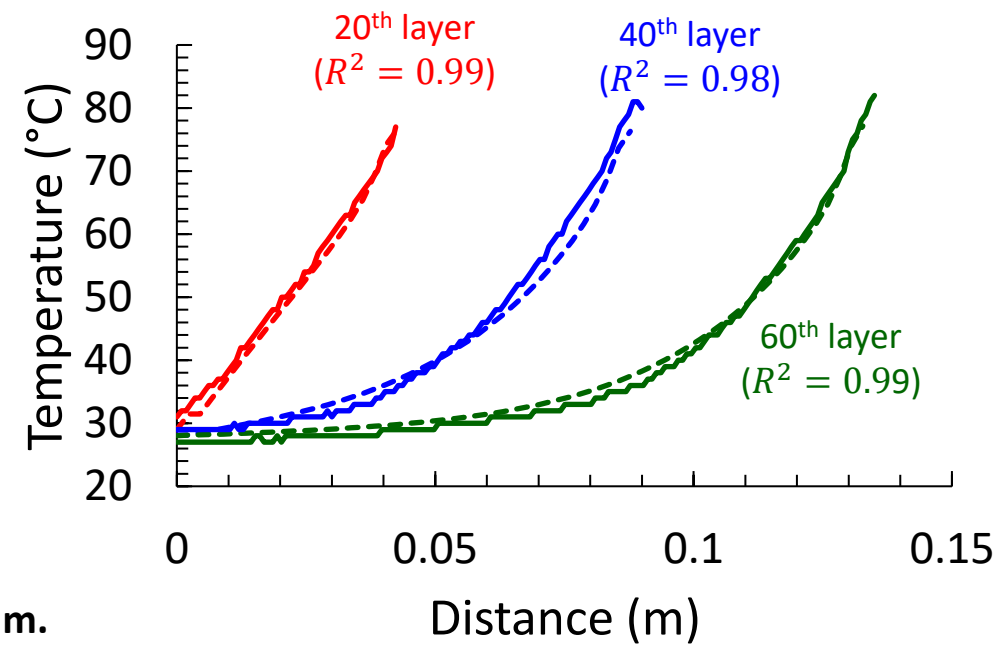

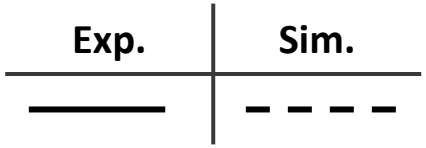

Results: P-shape print case 3

- Case 3
  - # of thermal images: 14,771
  - Layer time: 275s→ theoretical printing time for 60 layers: 16,500s
  - Overall printing time with IR camera (printing + thermocouple installation): 16,868s
    - Installation time (1st and 2nd): 225s and 170s
    - Printing time: 16,473s

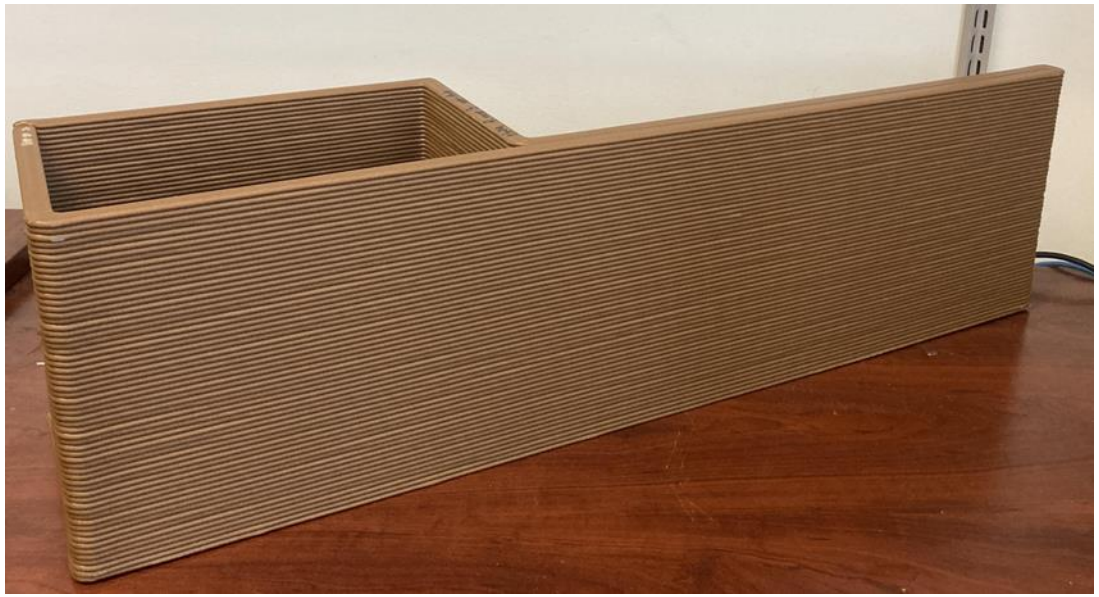

Comparison of IR thermal data with simulation _Case 3

- Boundary conditions:
  - Deposition temperature: 130 °C
  - Boundary temperature: 28 °C
  - Convection coefficient: 7
  - Emissivity: 0.85

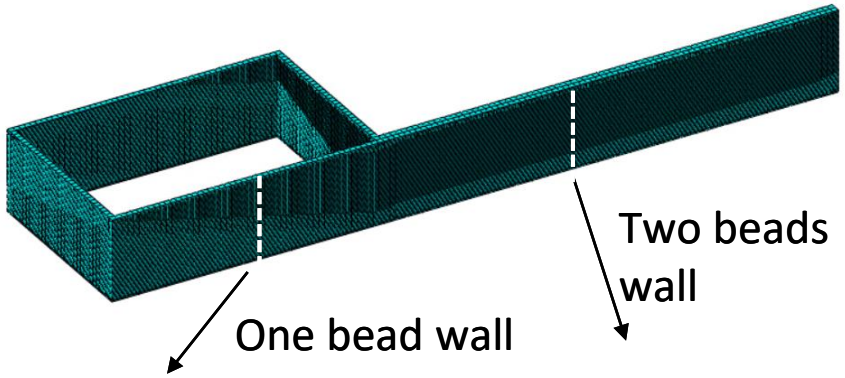

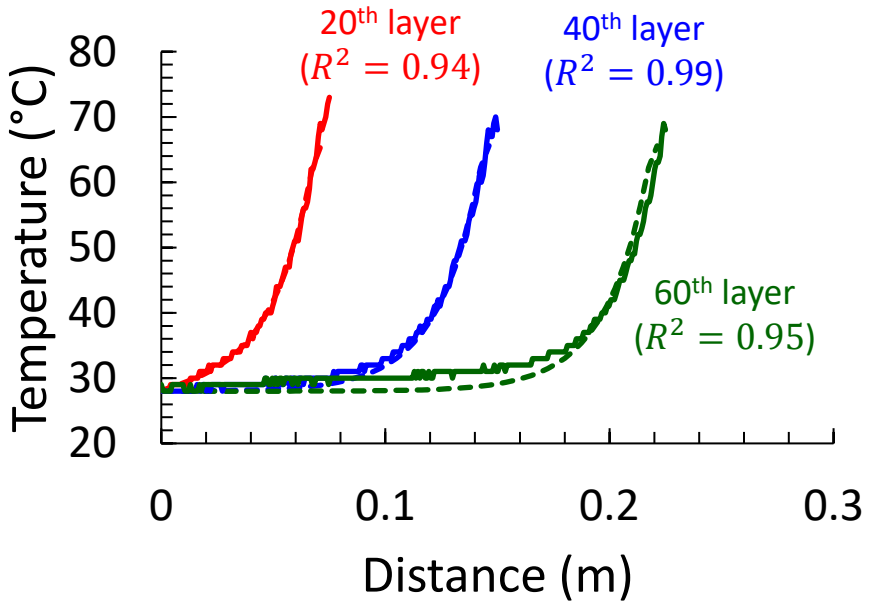

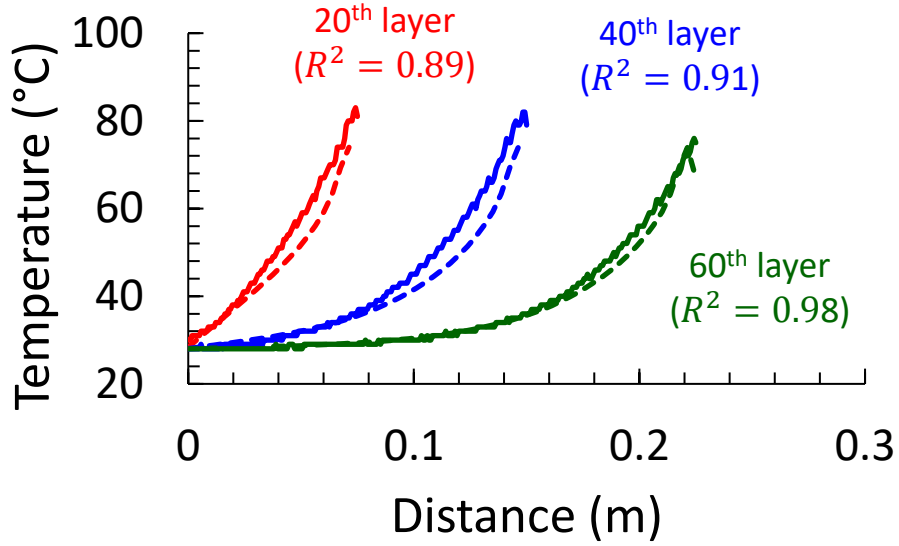

Exp.	Sim.
———	- - - -

Objective 3:
Sensitivity analysis of thermal conductivity, heat capacity and thermal expansion coefficient on temperature and deformation history

Temperature and deformation measurement during wall print

- Experimental set up
  - Temperature measurement using an IR camera
  - Displace measurement using Linear Variable Differential Transformer (LVDT)
  - Wall dimensions (L x W x H, m): 1.36 x 0.0153 x 0.3
  - Bead geometry (W x H, mm): 7.65 x 2.54



Experimental set up

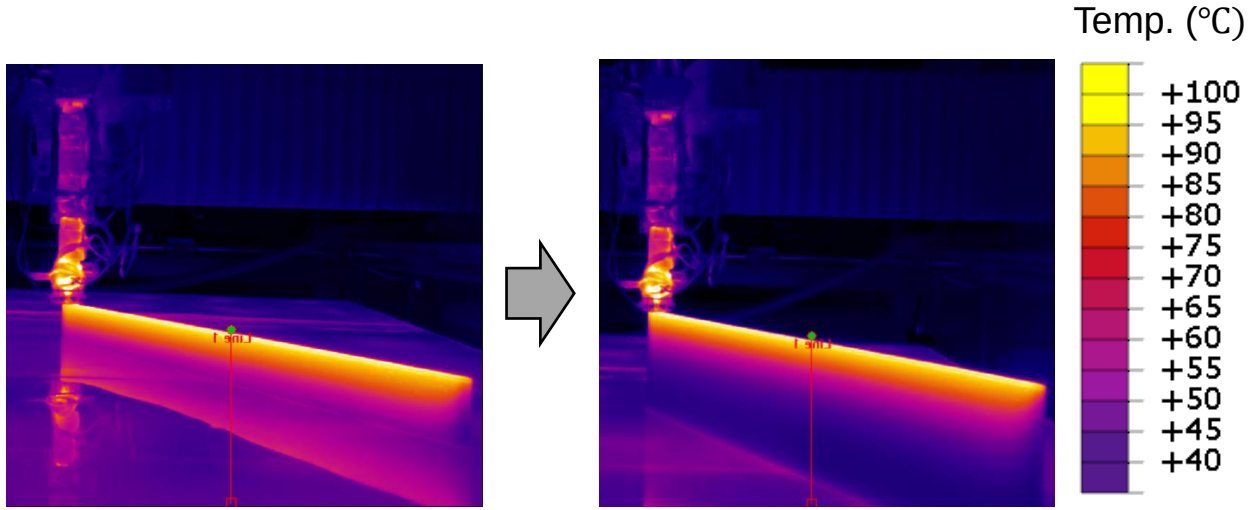

IR image of 3D printing process (Temperature measure)



Warpage measurement with LVDT

Simulation model for temperature and deformation prediction

- Sequentially coupled thermomechanical model
  - Step 1 (thermal simulation): transient heat transfer analysis is conducted to obtain the temperature field data by using the heat transfer element (e.g., DC3D8).
  - Step 2 (structural simulation): Sequentially, the mechanical analysis is conducted to obtain the stress/deformation field based on the previously predicted temperature data by using the structural element (e.g., C3D8).
- Boundary conditions

Step 1: Thermal simulation

- Deposition temperature (T_{dep}) = 210 °C
- Base temperature (T_{base}) = 50 °C
- Air temperature (T_{air}) = 30 °C

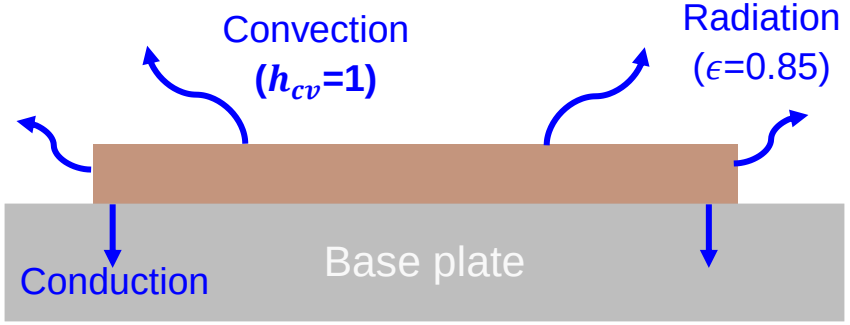

Step 2: Structural simulation

- Gravity for whole model (9.81 m/s^2)
- Base plate is fixed.

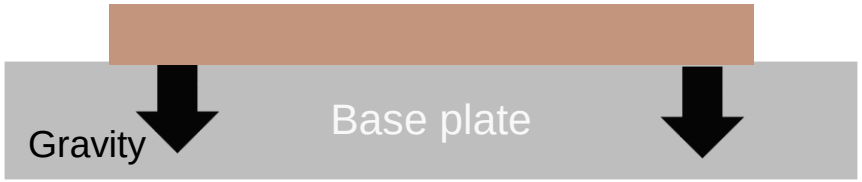

Results of temperature prediction

- Temperature at the center of the wall was recoded and compared those from experiments and simulation model.
  - Total print time (10,800 seconds) was divided in 5 intervals.
  - Each time interval the temperature from basement to surface was measured.

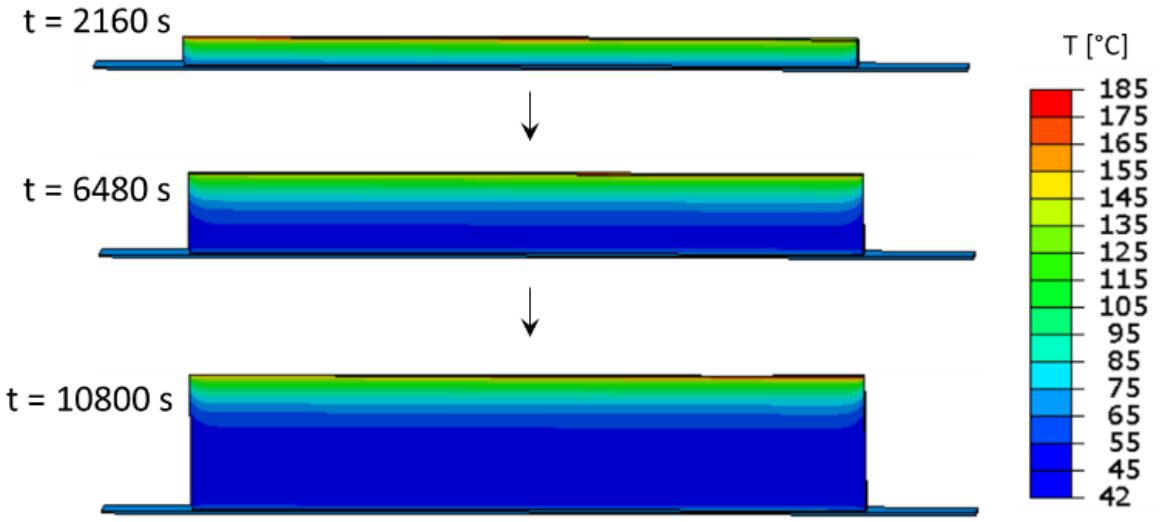

Temperature field at different time interval

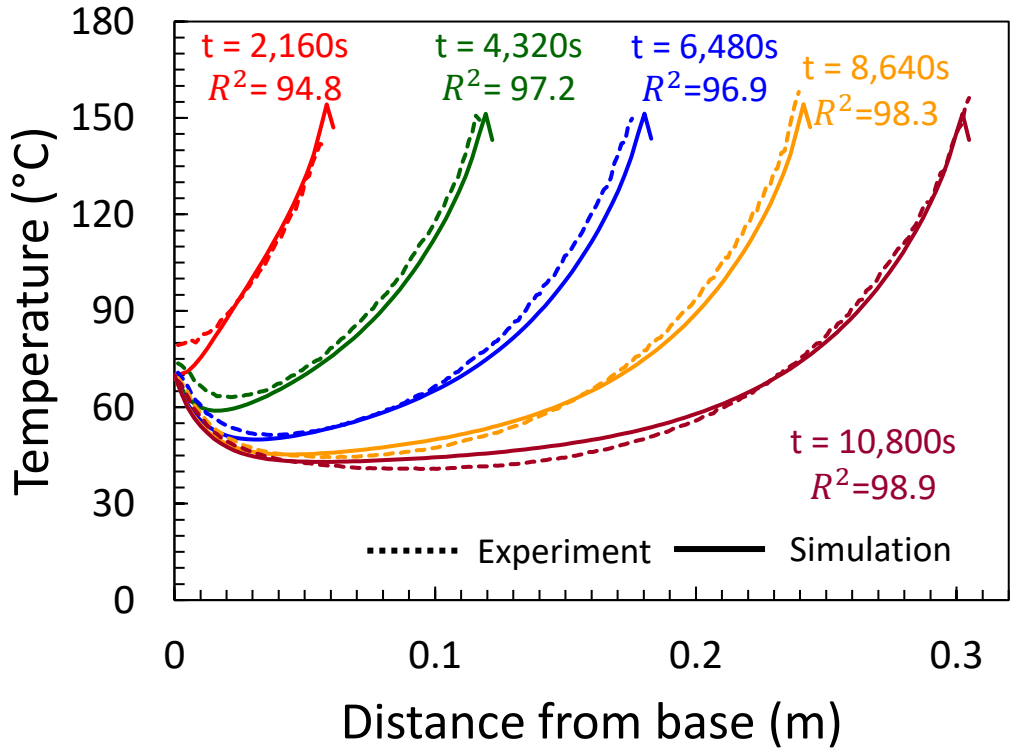

Comparison of temperature profile from experiments with those from simulation model.

Results of deformation prediction

- Deformations at the left and right corner was measured and compared those from experiments and simulation model.
  - The deformation is recorded during the whole printing process
  - In experiments, the length of left and right were different, so the deformation was unsymmetric.

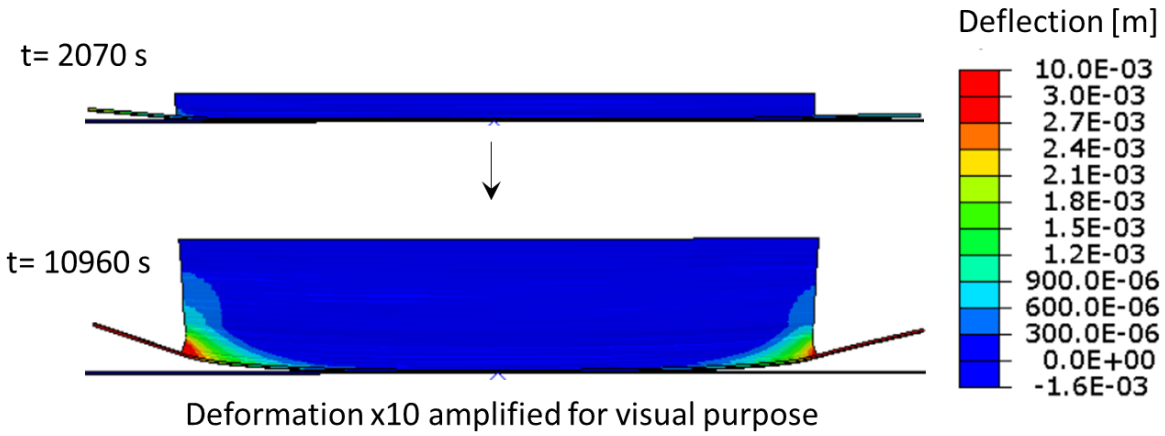

Deformation field at different time interval

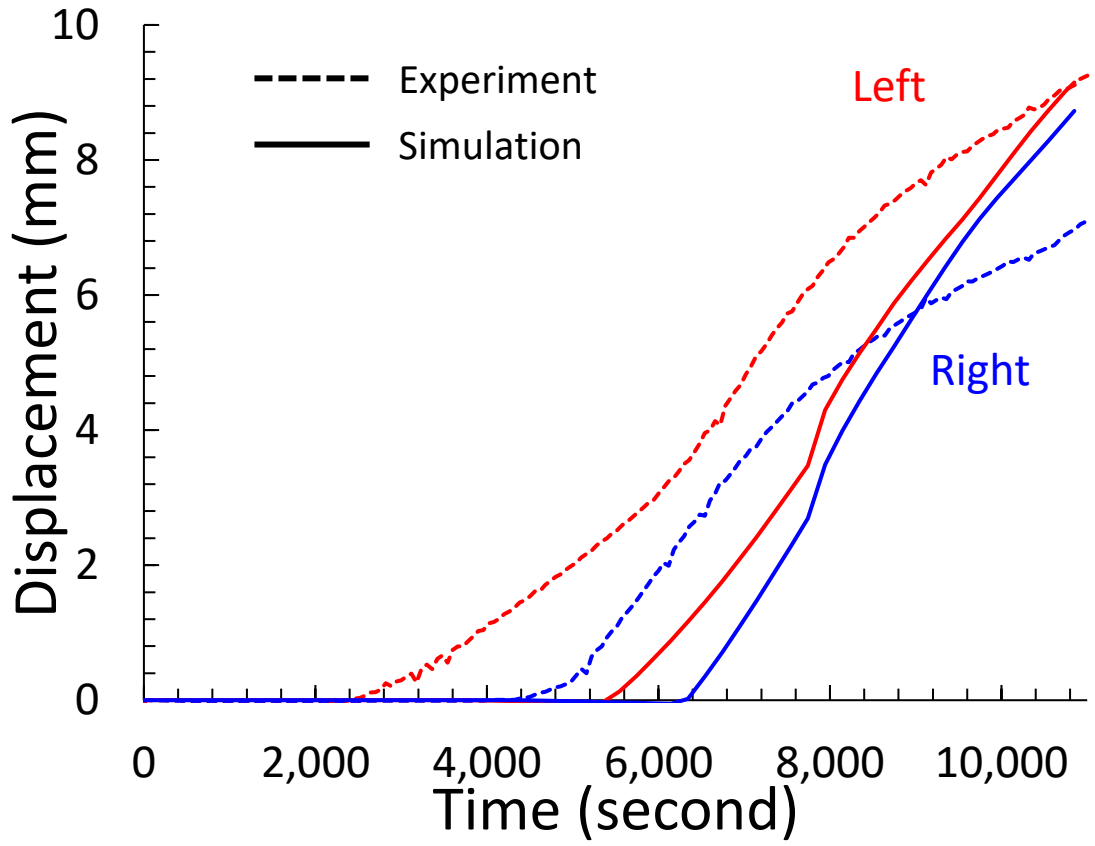

Sensitivity test of thermal conductivity on temperature history

- Thermal conductivity was increased and decreased by 10%.

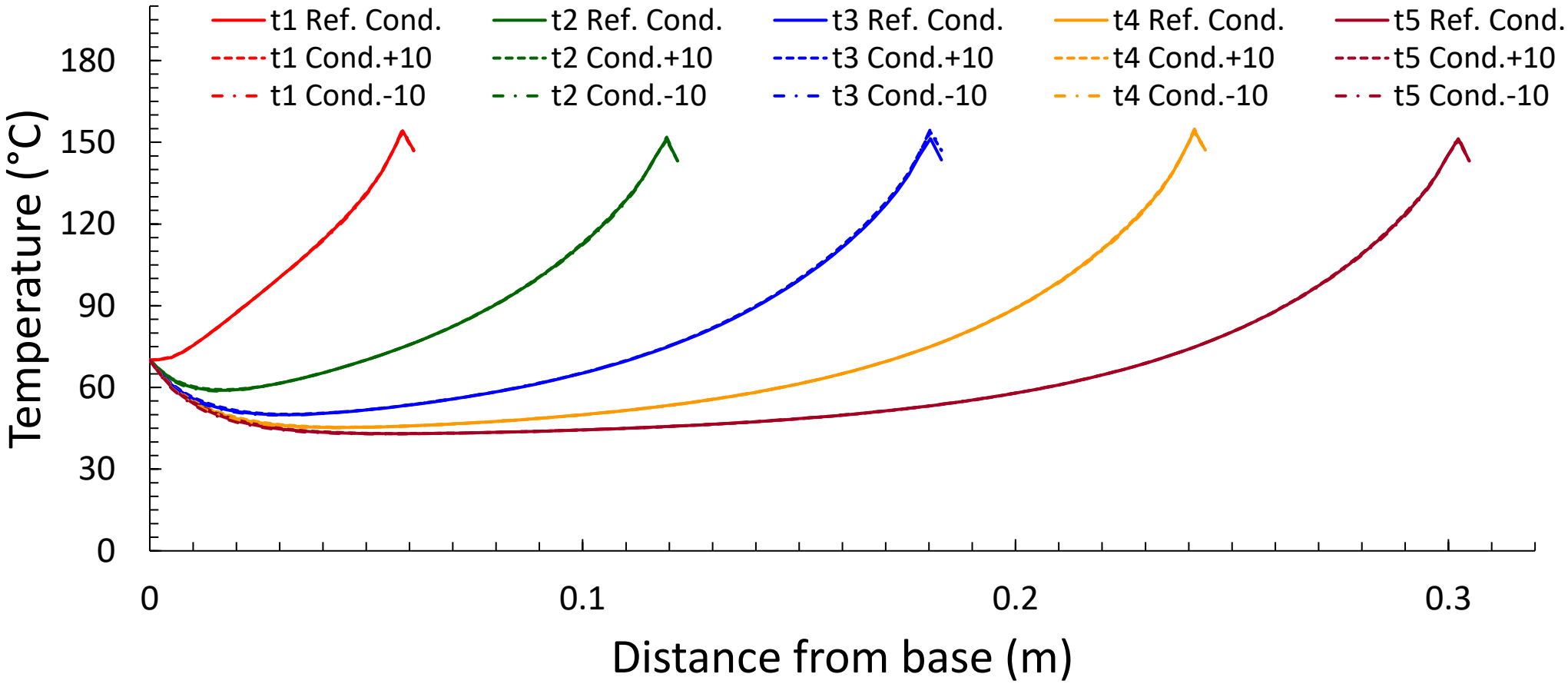

Sensitivity test of heat capacity on temperature history

- Heat capacity was increased and decreased by 10%.

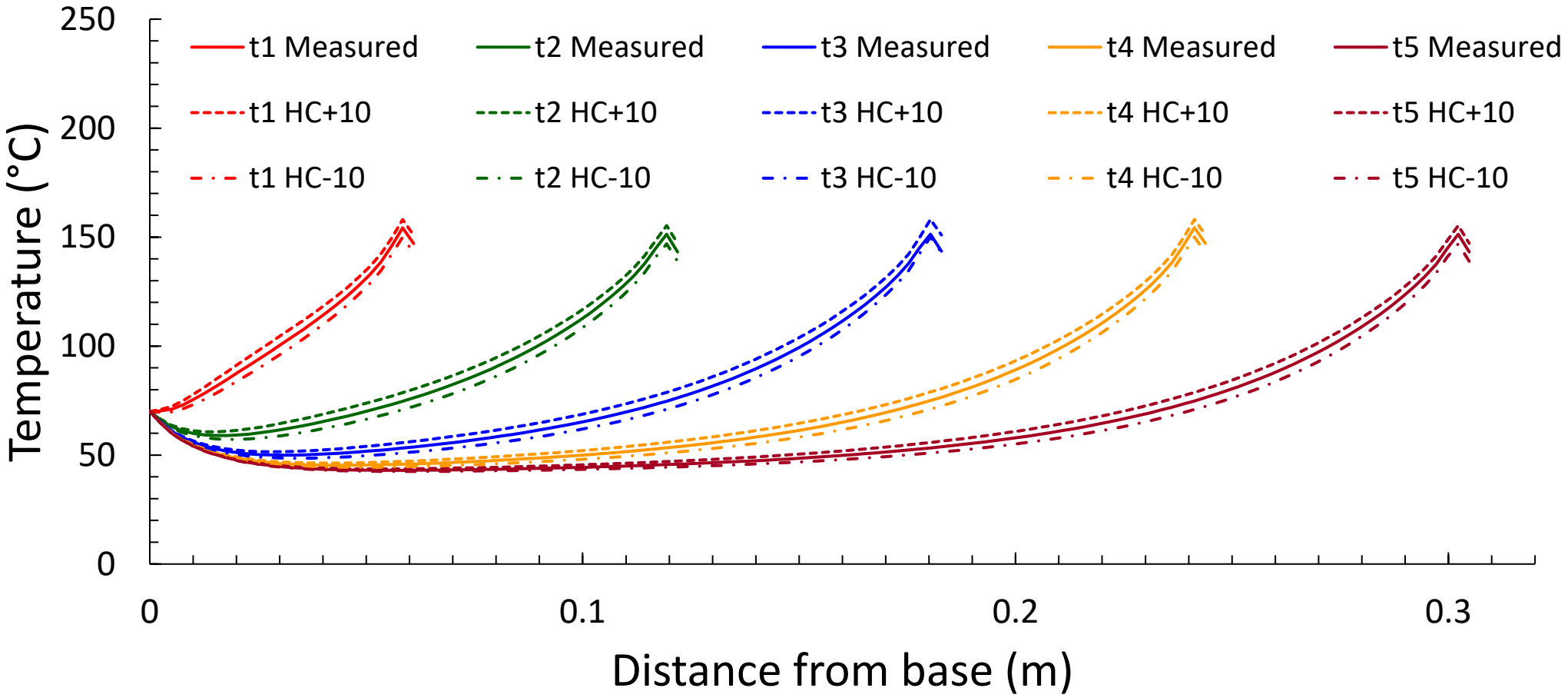

Sensitivity test of thermal expansion on deformation history

- Coefficient of thermal expansion was increased and decreased by 10%.

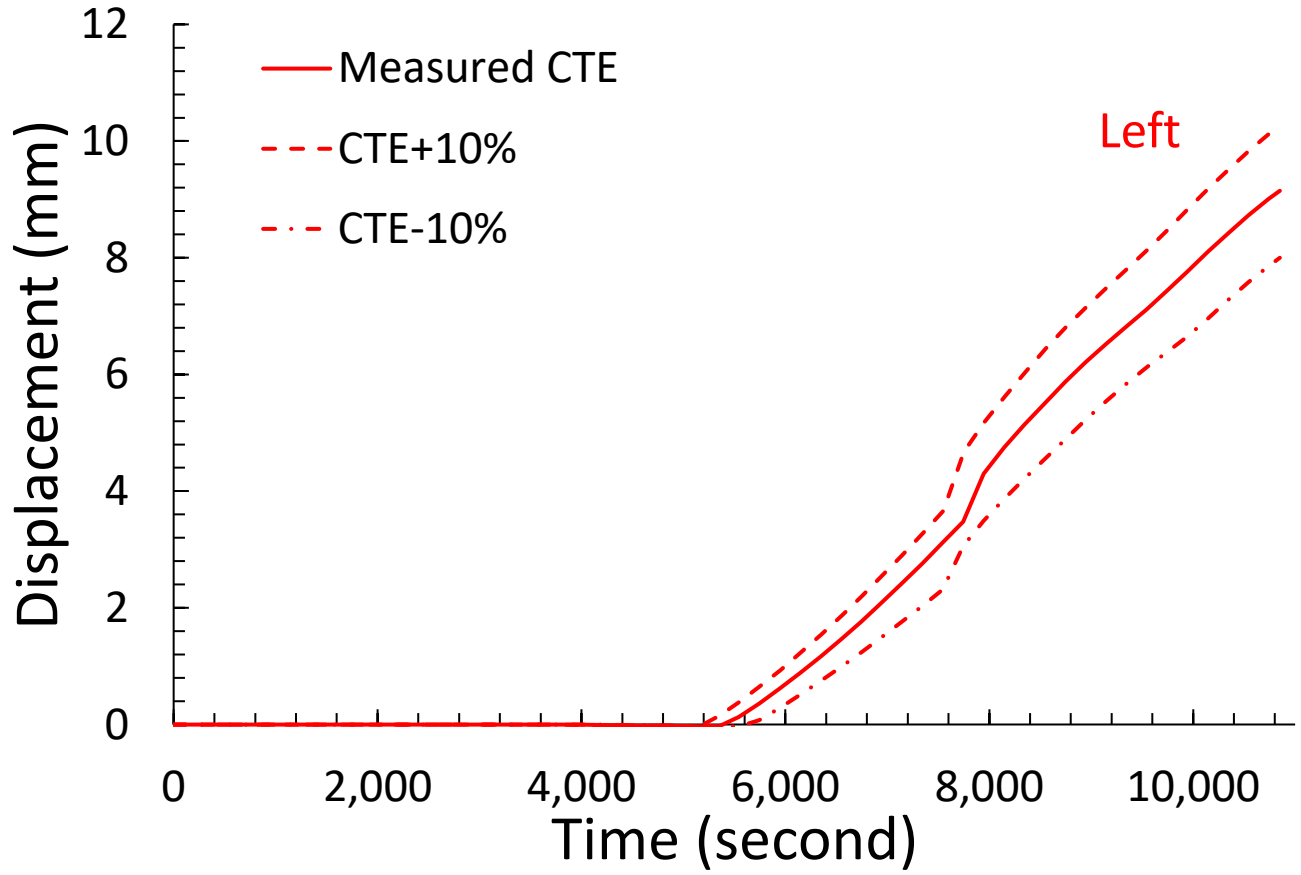

Summary & Conclusion

- Effect of bead overlap distance on thermal conductivity was evaluated
  - Specimens were manufactured with varying overlap distances.
  - Thermal conductivity increased as the bead overlap distance increased, indicating greater contact surface area between beads.
- Effect of bead geometry on thermal history was investigated
  - P-shaped structures were printed with different bead geometries.
  - The cooling rate decreased with the increase in bead size due to the greater thermal mass. However, the transient heat transfer model accurately predicted the temperature history regardless of the bead geometry.
- Sensitivity analysis of thermal conductivity, heat capacity, and thermal expansion on temperature and deformation history was conducted.
  - Thermal conductivity and heat capacity have minimal effect on the thermal history.
  - In contrast, thermal expansion has a comparatively greater impact on the final deformation.

Other developments of simulation

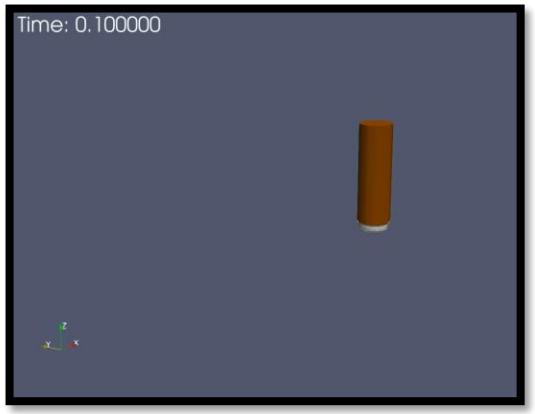

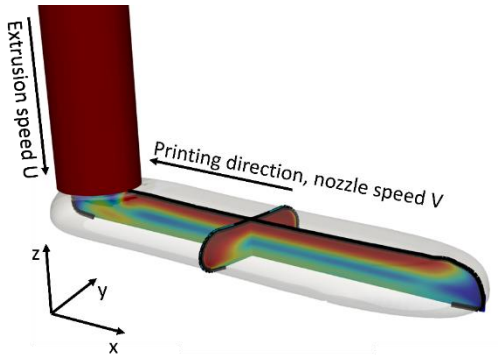

Extrusion deposition additive manufacturing

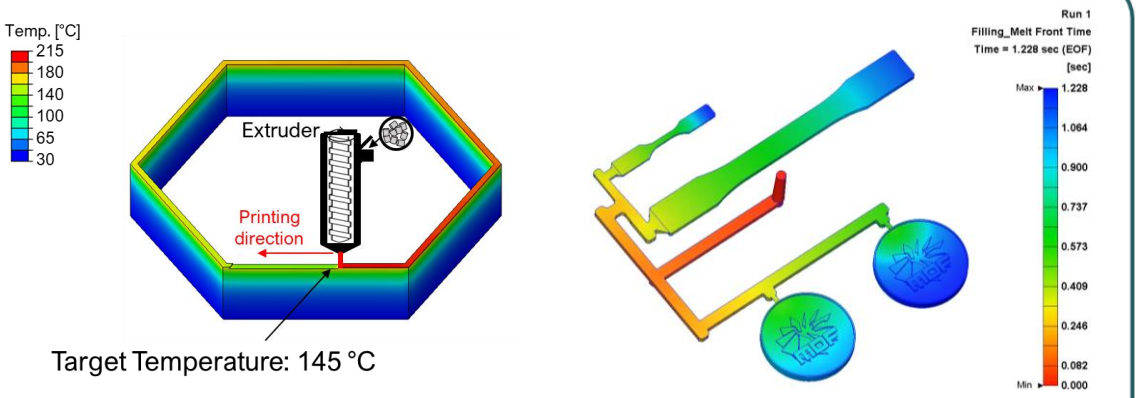

Process parameters optimizations

Manufacturing Process → Characterization (Mechanical) → Part Performance Evaluation → Process and Performance Optimization → In-situ Process Monitoring and Process Control

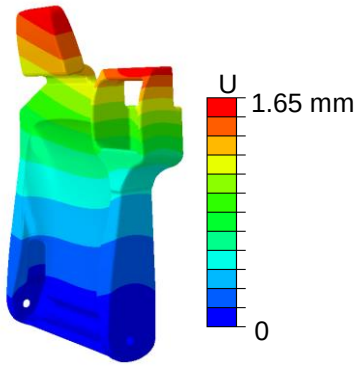

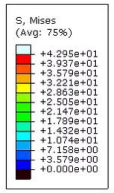

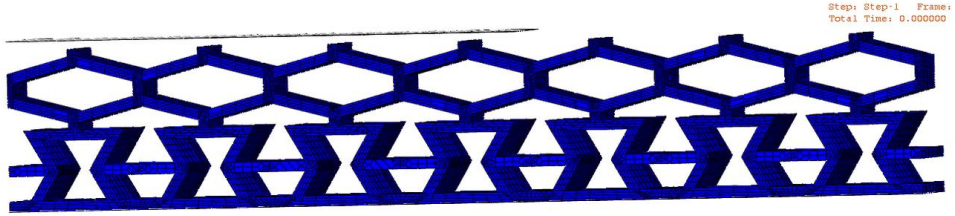

Performance simulations

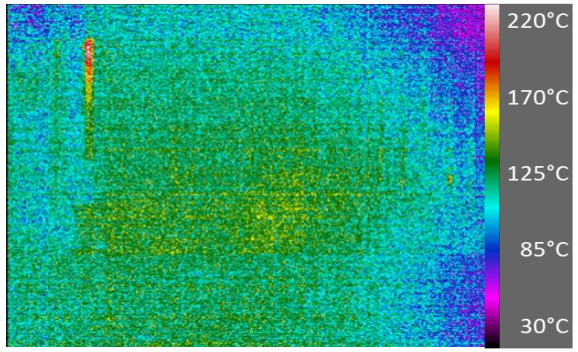

Process monitoring and real time process control

Thank you!

Development of vertical wind turbine blades using 4D printing of composites

Emad Fakhimi and Suong Van Hoa

Concordia Center for Composites

Department of Mechanical, Industrial and Aerospace Engineering

Concordia University

Montreal, Quebec, Canada

Emad.fakhimi@gmail.com; hoasuon@encs.concordia.ca

Abstract:

This paper presents the procedure to make vertical wind turbine blades using the technique of 4D printing of composites (4DPC). The blade is made using carbon/epoxy composite materials with fiber volume fraction of about 60%. Even though the blade has a 3D shape with curvatures, it is made using only a flat mold. The procedure can provide time and cost savings due to the fact that molds of complex curvature are not necessary. At the same time, the material is strong, stiff, and light giving further savings in weight and subsequent benefits in handling. Testing on wind turbines with original aluminum blades and with composite blades shows that the wind turbines with composite blades run at higher speeds. Also, wind turbine with composite blades gives higher efficiency than wind turbines with original aluminum blades.

Introduction:

Wind turbines are one source of generators of green energy. The majority of wind turbines are horizontal axis type, with very long blades and can generate a large amount of energy. Another type of wind turbine is the vertical axis wind turbine. These are smaller wind turbines. They are usually located on the roof of buildings. The amount of energy they generate is small but may be sufficient for energy needs in a small building. The global vertical axis wind turbine (VAWT) market size accounted for USD $12.9 billion in 2022, and is projected to achieve a market size of USD $17.7 billion by 2032 growing at a CAGR of 3.2% from 2023 to 2032. According to research conducted by the National Renewable Energy Lab ((NREL) in the U.S., VAWTs provide more yearly energy per unit area than horizontal axis wind turbines (HAWT) [1].

One example of the vertical axis wind turbine is shown in Figure 1. This wind turbine is of RX-SV2 turbine from R & X Technology company in Nantong, China. The company specifications mention it exhibits a nominal power output of 200 Watts, a wheel diameter measuring 48 cm, and a weight of 15 kg. It utilizes 2 sets of aluminum blades, with each set comprising 5 individual segments. The segments are assembled around a vertical axis, facilitated by horizontal arms. It can be observed that the blades are configured with a backward twist to reach higher performance and harvest more energy. These blades may be made by roll forming, or hydraulic pressing techniques. Either of these techniques requires a mold.



Figure 1: One example of the vertical axis wind turbine

Technique of 4D printing of composites:

4D Printing of Composites (4DPC) is a technique of composite manufacturing that does not require a mold of complex geometry. It only requires a flat mold. As such it is also called Moldless Composite Manufacturing. The technique was conceived in 2017 [2]. To manufacture a structure with curved geometry, first, a stack of soft composite prepregs (such as carbon/epoxy) is laid on top of a flat mold. The deposition can be done either by hand (for simple lay-ups) or by the use of an automated fiber placement machine (AFP) for either simple or more complex lay-ups. The AFP machine does manufacturing in an additive fashion. In principle, it is similar to a 3D printer, except that it is much larger, and it can deposit strips containing continuous fibers embedded in a polymer matrix. It can deposit strips of fiber-reinforced polymers in different directions. The lay-up sequence of the different layers in the stack is of critical importance. Rather than the usual symmetric lay-up sequences that have been used in most of the composite community, un-symmetric lay-ups are used. In the soft state of the prepregs, there is no interaction between the layers due to the difference in their fiber orientations. However, after these prepreg layers are heated to the cure temperature, the resin hardens and the layers become stiff. During the cooling process from cure temperature to room temperature, the difference in coefficients of thermal expansion between the layers along the different directions creates interaction between them. This interaction gives rise to the change in shape from flat to curved.

The 4DPC technique has been used to develop pieces with S shape [2], leaf springs [3], omega stiffeners [4], corrugated core for flexible aircraft wings [5], and conical shells (figure 2) [6]. The same concept of 4DPC is also used for the development of manufacturing of blades of the vertical axis wind turbine.

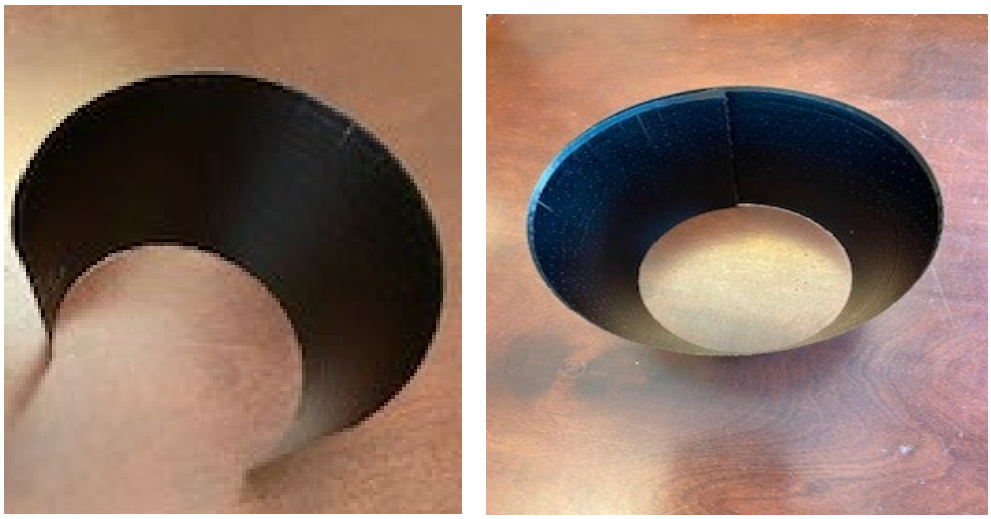

Figure 2: Conical shells made using the 4DPC technique. Left: Partial shell. Right: Complete shell [6].

Procedure to manufacture the blades of the vertical wind turbine using 4DPC:

Most of the structures presented in references [2-6] are of the forward type of problem. In the forward type of problem, some lay-up sequence is proposed, and the resulting structure is obtained. The procedure to make the blades for the vertical wind turbine follows a reverse type of problem. In the reverse type of problem, a structure with a certain shape and configuration is desired. The problem is to find the flat lay-up sequence such that when the stack of prepregs is cured and cooled to room temperature, the desired shape and configuration is obtained. This procedure consists of the following steps:

Step 1: Determination of the configuration of the existing (or desired) structure.

Step 2: Propose some lay-up sequence.

Step 3: Determination of the configuration of the structure resulting from the proposed lay-up sequence. At the initial stage, this can be a trial-and-error approach. After some experience, the trial-and-error process can be minimized.

Step 4: A final configuration that fits the most to the desired configuration is obtained.

Details of the above steps for the development of the blades of the vertical axis wind turbine using 4DPC are presented below.

Step 1: Determination of the configuration of the existing (or desired) structure

The two blades of the existing commercial wind turbine as shown in figure 1 consist of two similar blades. Each blade consists of 5 segments. Each segment is a curved piece. Figure 3 shows the 6 segments disassembled from the wind turbine. The focus of the work is to develop the procedure of manufacturing of one segment using 4DPC. Once this is accomplished, the other segments can be made the same way. They will then be assembled to make up the blade.

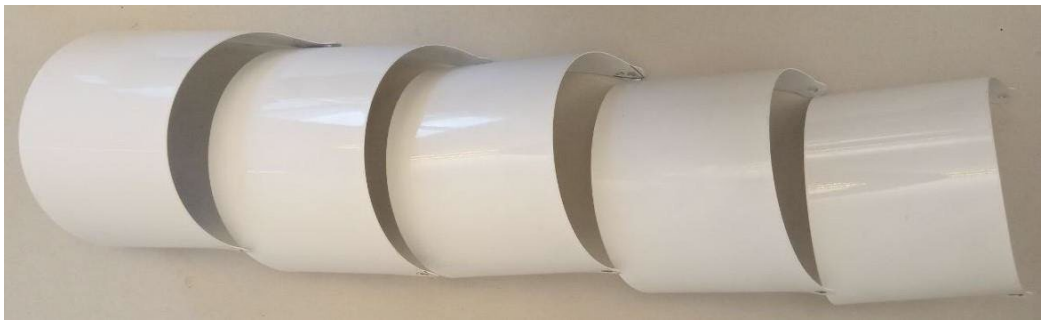

Figure 3: One segment of the blade in commercial wind turbine.

The overall dimensions of the segment is shown in figure 4.

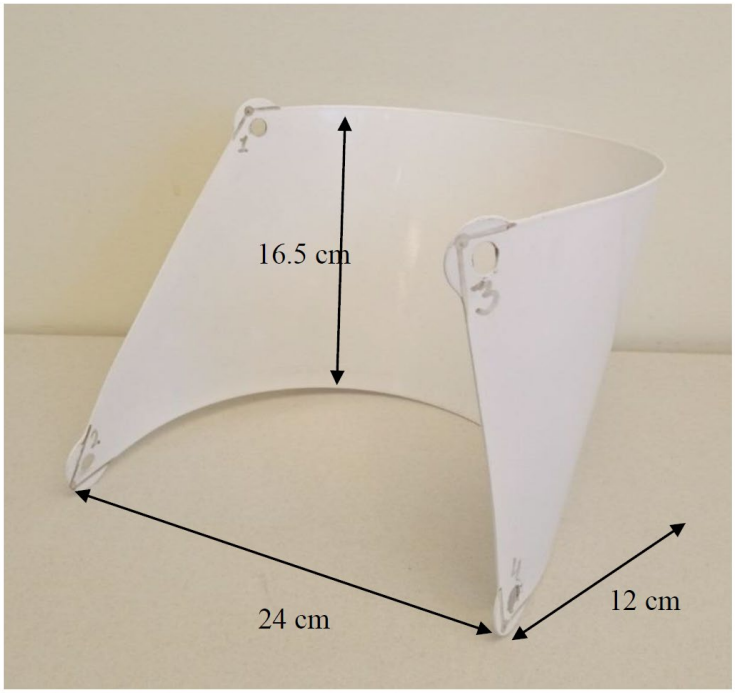

Figure 4: Overall dimensions of a segment

Detailed configuration of one segment was obtained by scanning the segment using a laser projection machine as shown in figure 5.

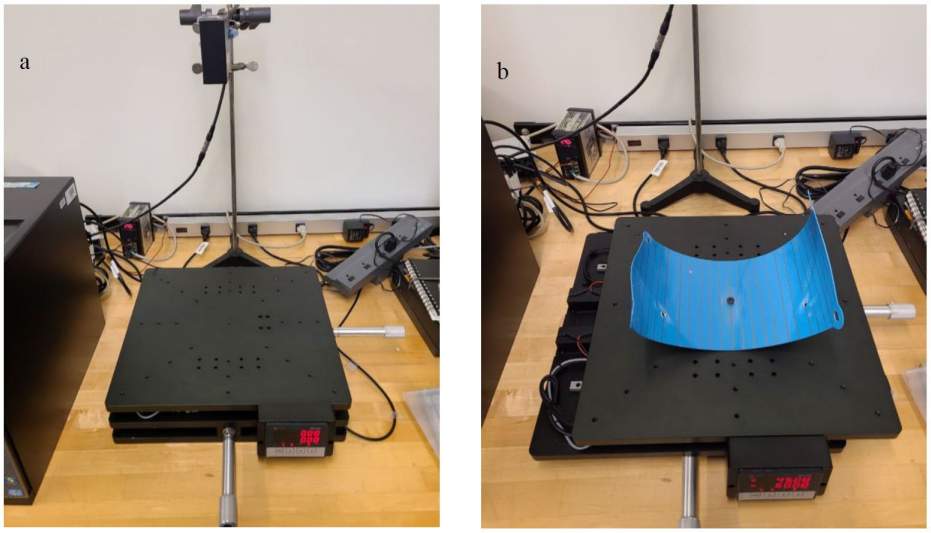

Figure 5: A segment in the laser projection machine. (a) Laser projection machine with laser mounted on top. (b) Segment on the base of the machine.

By adjusting the two probes on the right and front of the segment, the coordinates of various points on the surface can be measured, allowing for the complete generation of the surface of the segment. Two hundred points were measured. A sample of the data of 16 points is shown in Table 1.

Table 1: Sample of the data for 16 points from coordinate measurements.

No.	x (mm)	y (mm)	z (mm)	No.	x (mm)	y (mm)	z (mm)
1	0	220	0	**121**	75.4	206.6	100
10	97.1	170.5	0	**130**	152.5	114.7	100
20	109.6	51.1	0	**140**	111.3	1.9	100
30	12.5	-19.3	0	**150**	5.15	-22.5	100
61	38.6	216.6	50	**181**	116.9	186.4	160
70	130.2	139.5	50	**190**	173	80.4	160
80	109.3	21.3	50	**200**	109.3	-21.3	160
90	8.9	-21.2	50	**210**	0.4	-23	160

The data collected were processed using the surface fitting tool in MATLAB software. This generates equation (1). The linear dimensions are in meter, and the angle is in radians.

$$x = 0.12\ sin[\theta + 3.5\ z] + 0.1\ sin[3.5\ z]$$

$$y = 0.12\ cos[\theta + 3.5\ z] + 0.1\ cos[3.5\ z] \qquad (1)$$

Where z is the coordinate along the vertical direction, and θ is the polar coordinate in the horizontal plane. x and y are the coordinates in a plane parallel to the horizontal plane at elevation z. These are in meters.

The nature of the surface can be revealed by examining a few points using equation (1).

At z = 0 (the base plane), one has:

$$x = 0.12\ sin[\theta] \qquad y = 0.12\ cos[\theta] + 0.1 \qquad (2)$$

Equation (2) represents that of a circle with radius of 0.12 m (120 mm) with center located at O_b (0, 100 mm) in the base horizontal x, y plane, as shown in figure 6. The axes are x_1 (parallel with x) and y_1(coinciding with y). Note that the points at the base plane of the blade only occupy a portion of the circle with origin at O_b in the figure .

At z = 10mm (0.01 m) in equation (1) one has:

$$x = 0.12\ sin[\theta + 0.035] + 0.1\ sin[0.035] \quad y = 0.12\ cos[\theta + 0.035] + 0.1\ cos[0.035] \quad \text{or}$$

$$x = 0.12\ sin[\theta + 0.035] + 0.0035 \qquad y = 0.12\ cos[\theta + 0.035] + 0.1 \qquad (3)$$

Equation (3) represents that of a circle with radius 120 mm with the origin at O_2 (3.5 mm, 100 mm). To keep the same boundary points as for the case of z = 0 mm, the coordinate axes are x_2, y_2 (rotated 0.035 radians (2.0°)) relative to the x, y axes. .

At z = 20 mm (0.02 m), in equation (1) one has:

$$x = 0.12\ sin[\theta + 0.07] + 0.1\ sin[0.07] \qquad y = 0.12\ cos[\theta + 0.07] + 0.1\ cos[0.07] \quad \text{or}$$

$$x = 120\ sin[\theta + 0.07] + 0.007 \qquad y = 0.12\ cos[\theta + 0.07] + 0.1 \qquad (4)$$

Equation (4) represents that of a circle with radius 120 mm with the origin at O_3 (7.0 mm, 100 mm). Again, to keep the same boundary points as in the case z 0, the coordinate axes are x_3 , y_3 (rotated 0.07 radians (4.0°)) relative to the x, y axes.

At z = 165 mm (0.165 m), in equation (1) one has:

$$x = 0.12\ sin[\theta + 0.5775] + 0.1\ sin[0.5775] \quad y = 0.12\ cos[\theta + 0.5775] + 0.1\ cos[0.5775]$$

or

$$x = 0.12\ sin[\theta + 0.5775] + 0.055 \qquad y = 0.12\ cos[\theta + 0.5775] + 0.084 \qquad (5).$$

Equation (5) represents that of a circle with radius 120 mm with the origin at O_t (55mm, 84 mm). The coordinate axes are x_t, y_t (rotated 0.5775 radians (33.1°)) relative to the x, y axes. Note that z = 165 mm is at the top of the segment (subscript t). This circle is shown in figure 6.

It can be seen that even the radius of curvature of the blade remains the same as z changes, there is a shift in the center of the circle (mainly in the x direction). In order to keep the same boundary points in all cases, there is also a rotation of the axes. As such point A_b in the bottom plane moves to point A_t on the top plane (Note that figure 6 does not show the change in

elevation of the top circle). At the same time, point B_b moves to point B_t. The circular portion A_bB_b changes to A_t B_t. The rotation does not present a twist.

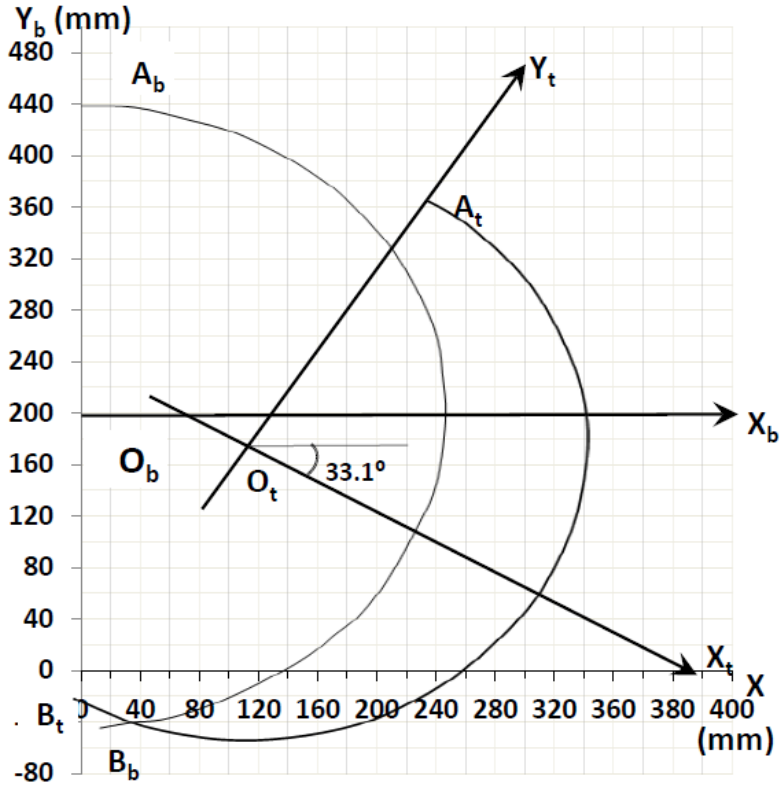

Figure 6: Curved lines connecting nodes 1 to 300 (z = 0 mm, bottom) and nodes 181 to 210 (z = 165 mm, top). Node numbers are shown in figure 7.

Using MATLAB, the whole surface of the blade as given by equation (1) is plotted and shown in figure 7.

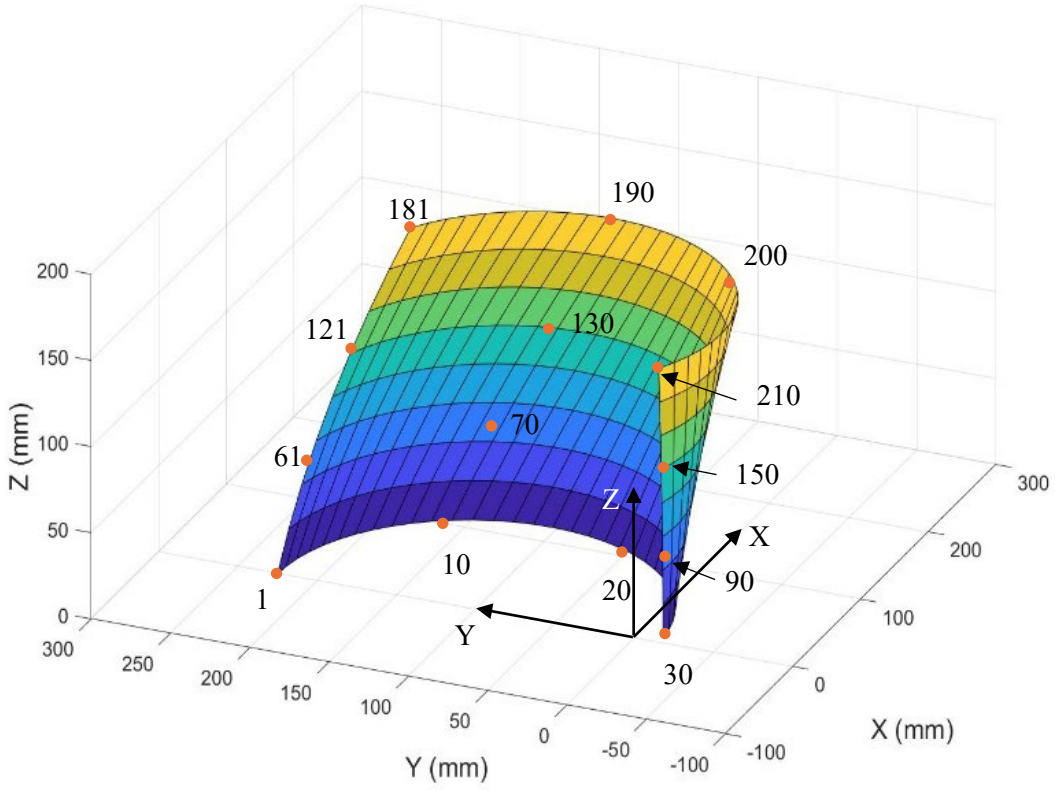

Figure 7: Plot of equation (1)

From the analysis of principal curvatures shows that the points can be classified into two groups (the edge group and the central region). The principal curvatures of these two groups are shown in Table 2.

Table 2: Principal curvatures for two regions

	K_1 (m^{-1})	K_2 (m^{-1})
Left edge (nodes 1, 61, 121, 181)	9.5	1.07
Right edge (nodes 30, 90, 150, 210)	9.3	1.10
Central region (nodes 10, 20, 70, 80, 130, 140, 190, 200)	8.2	0.52

Table 2 shows that there is a large difference between the values of K_1 and K_2. The small curvature of K_2 indicates that the structure is practically flat along this direction. As such, at any

point on the surface of the segment, cylindrical curvature exists. This means that there is no twist.

The above observations are used as guidelines for the determination of the lay-up sequence to make the segment structure using 4D printing of composites. The curvature of the central region (8.2 m^{-1}) is used as the main focus. In the following, a number of trial laminate sequences will be examined. Laminate theory will be used to determine the curvature from these laminates. The lay-up sequence yielding the closest value of curvature to 8.2 m^{-1} will be selected.

Step 2: Determination of the lay-up sequence:

The material used is carbon/epoxy prepreg (1409-D) supplied from Rockwest composites. The curing cycle is shown in figure 8.

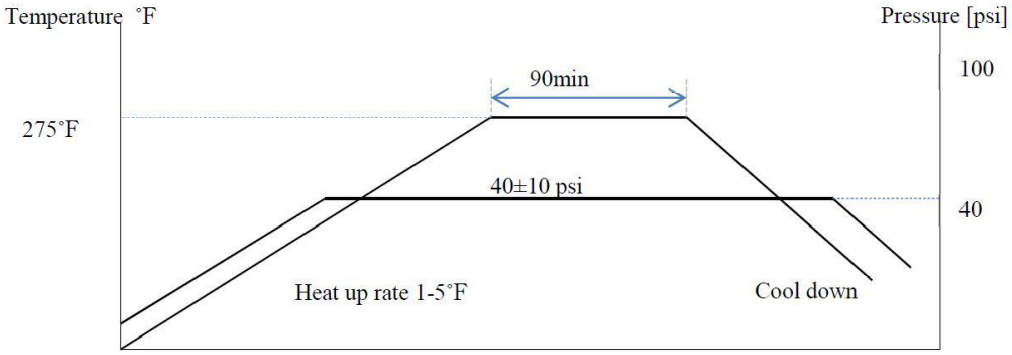

Figure 8: Curing cycle for carbon/epoxy from Rockwest Composites

The material properties are shown in Table 3. These values were measured at the Concordia Center for Composites laboratories. The other properties are taken from reference [8] as: shear modulus G_{12} = 4.4 GPa, and coefficient of thermal expansion α_1 = - 0.018 x 10^{-6}/°C.

Table 3: Material properties

E_1 (GPa)	120.2
E_2 (GPa)	7.4
ν_{12}	0.219
α_2 (10^{-6}/°C)	33.33
Thickness of one ply (h) (mm)	0.165

The curvatures are calculated using laminate theory as described in reference [2]. A Matlab program was developed for this [9]. Table 4 shows the curvatures of the different laminates.

Table 4: Curvatures of different laminates

Laminate sequence	**K_1 (m^{-1})**	**R_1(mm)**
[0/90]	11,4	74.6
[0/90_2]	9.2	92.6

[0/90$_3$]	9.1	110
[0/90$_4$]	7.8	128

Table 2 shows that the curvatures in the segment vary from 8.2 m^{-1} to 9.5 m^{-1} from the central region to the edges. From Table 4, both laminates with lay-up sequences [0/90$_2$] and [0/90$_3$] provide curvatures that fit within this window. For light weight consideration, laminates with lay-up sequence [0/90$_2$] was selected.

Step 3: Procedure to lay-up the surface of the segment:

The flat blank, which is a development of the curved segment into a flat panel, is shown in figure 9.

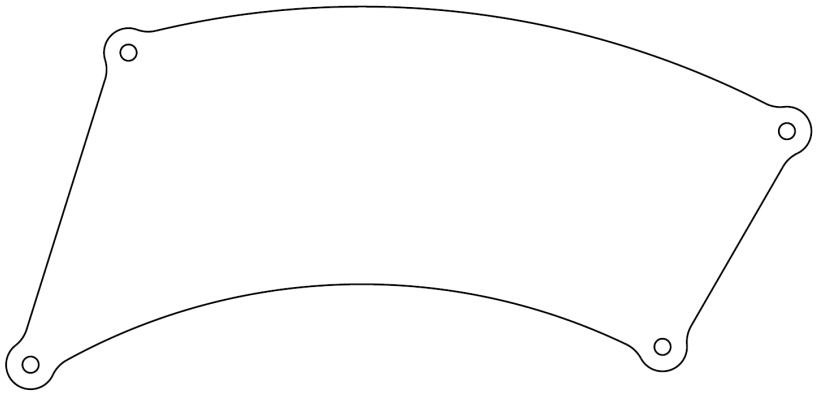

Figure 9: Flat blank as developed from the curved segment.

It was shown in the above section that as one moves along the x direction, it is necessary to rotate the x,y axes a few degrees in order to conform to the surface of the segment. In order to maintain the same radius of curvature, the same lay up sequence of [0/90$_3$] needs to be maintained. In order to address the rotation, from a 4DPC point of view, the flat is divided into four sections. The lay up sequence is rotated a few degrees as one moves from segment 1 to segment 2 etc. Figure 10 shows the lay-up sequence after the rotation. Figure 11 shows the detailed dimensions of the sections.

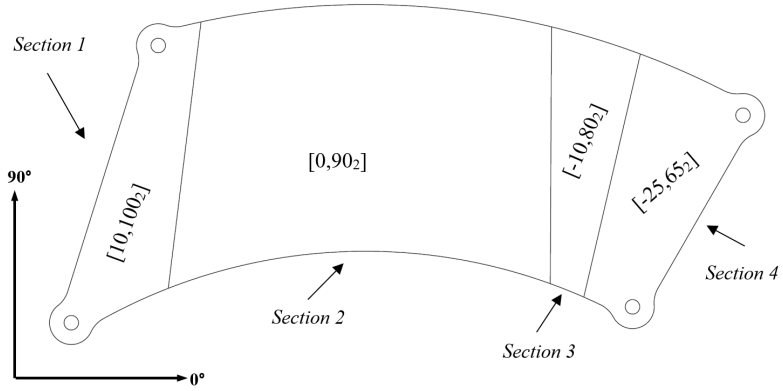

Figure 10: Lay-up sequence in the four regions of the segment

Using the above procedure, the composite segment was matched up with the aluminum segment from the commercial wind turbine. Figure 11 shows the two pieces together (blue piece is aluminum). It can be seen that the two pieces match together fairly well for the majority of the surfaces. There is a slight mismatch at the left edge.

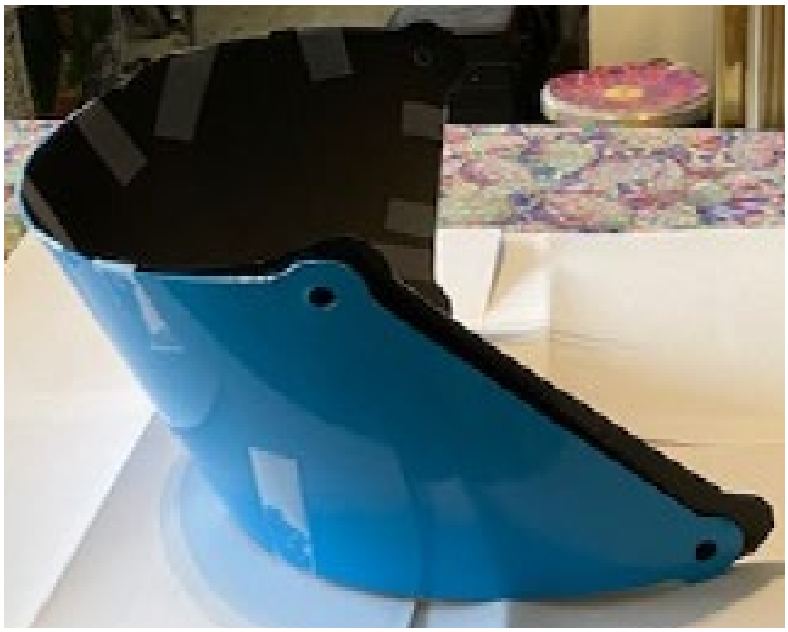

Figure 11: Comparison between the manufactured piece and the real segment.

After manufacturing all the segments, they were assembled to the central pole of the vertical axis wind turbine alongside with the aluminum blades. The final assembly of the wind turbine can be seen in figure 12.

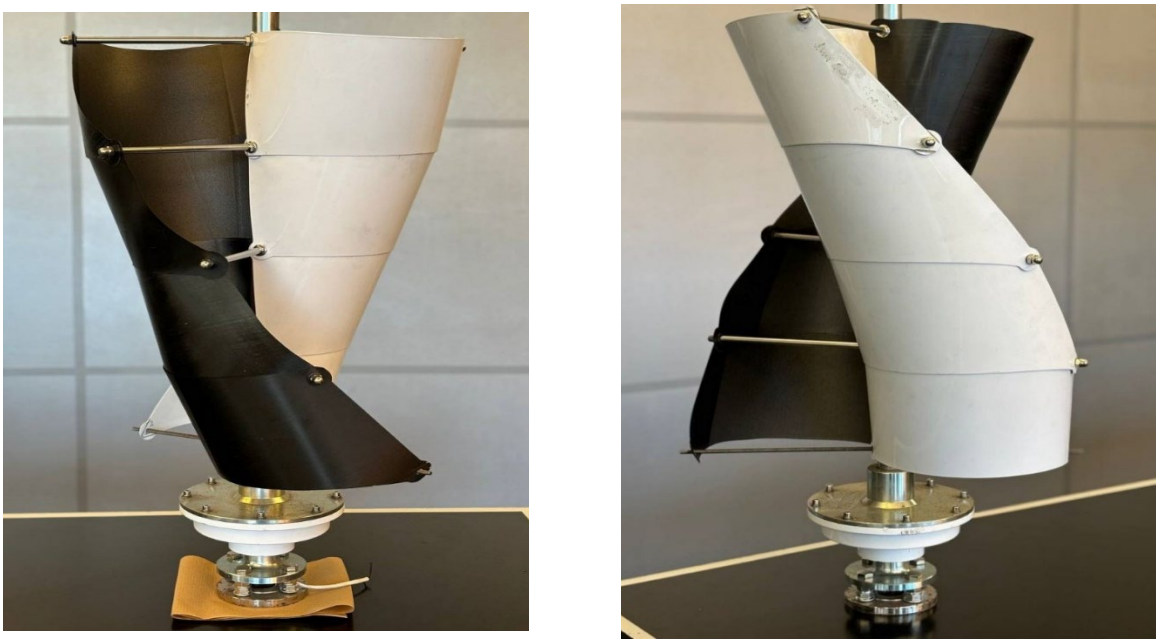

Figure 12- The final assembly of the vertical axis wind turbine blades.

Conclusion

It was shown that it is possible to make wind turbine blades for vertical axis wind turbines using the technique of 4D Printing of Composites (4DPC). The segments of the blades made have similar shape as the aluminum segment of the original design. The new method is a moldless way of manufacturing, which provides savings in cost and time. The use of composite materials offers light weight which can improve efficiency of operation.

References:

1. Acumen researchandconsulting.com /vertical-axis-wind-turbine-market.
2. Hoa Suong Van, “Factors affecting the properties of composites made by 4D printing”, Advanced Manufacturing: Polymers and Composites Science, 2017, 3, 1-9.
3. Suong Van Hoa, “Development of composite springs using 4D printing method”, Composite structures, 210, 2019, pp. 869-876.
4. Suong V. Hoa, Bhargavi Reddy, Daniel Rosca, “Development of omega stiffeners using 4D printing of composites”, Composite Structures, 272, 2021, 114264.
5. Suong Hoa, Marjan Abdali, Anick Jasmin, Daniel Radeschi, Victor Prats, Hadi Faour, Backer Kobaissi, “ Development of a new flexible wing concept of Unmanned Aerial Vehicles using corrugated core made by 4D printing of composites”, Composite Structures, 290, 2022, 115444.
6. Suong Van Hoa and Mahmoud Fereidouni, “Conical shells made using 4D printing of composites”, Composites, Part A, Applied Science and Manufacturing, Vol. 178, March 2024, 107971.
7. Toponogov VA. Differential geometry of curves and surfaces. Springer; 2006.
8. Hyer M.W. “Stress analysis of fiber reinforced composite materials+, Destech Publications, 2009.
9. Hoa Suong Van, “4D printing of composites”, De Gruyter, 2025.

ICCM24
AUGUST 4-8, 2025
BALTIMORE CONVENTION CENTER
BALTIMORE, MARYLAND, USA

No Technical Paper Submission for:

Madhura Limaye

Korea Aerospace University

2024 International Conference on Composites Materials

3D-Printed stealth honeycomb conductive nanoparticles-filled PEEK thermoplastic resin curve patch composite for enhanced RCS reduction

***Jaewon Shim[1], Hanjun Seo[1], Kwangsik Choi[2], and Youngwoo Nam[1, 3†]**

[1]Graduate School of Aerospace and Mechanical Engineering, Korea Aerospace University
[2]Materials & Processes Team, Korea Aerospace Industies, Ltd.
[3]Department of Smart Drone Engineering, Korea Aerospace University

August 7, 2025

MCML
MULTIFUNCTIONAL COMPOSITES & MANUFACTURING LABORATORY

Table of Contents

I. Introduction

II. Materials and methods

III. Design and fabrication

IV. Results and discussion

V. Conclusions

I. Introduction

Background

❖ *3D-Printing based RAS (Radar Absorbing Structure)*

- FDM (Fused Deposition Modeling) 3D-Printed EM wave absorbing metastructure

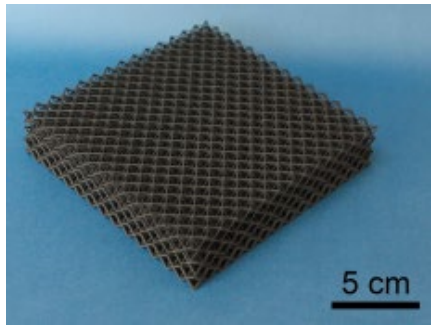

< Octet truss based metastructure[1] >

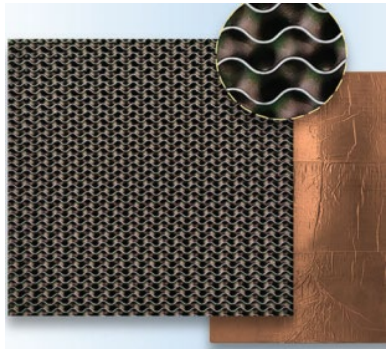

< Gyroid based metastructure[2] >

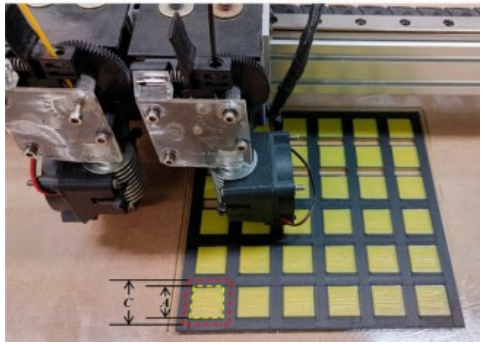

< Dual-nozzle frequency-selective composites [3] >

- Conventionally fabricated composite RAS

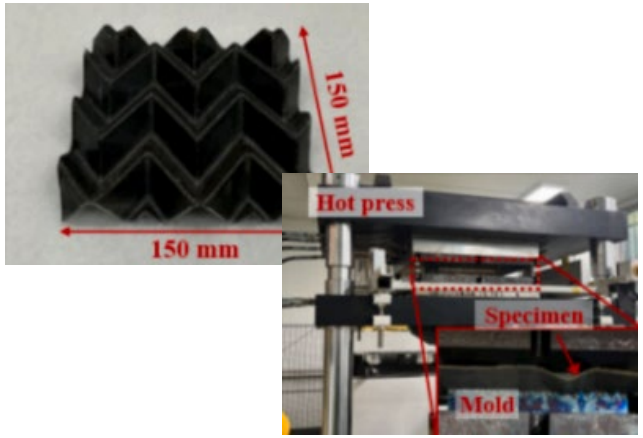

< Hot-press molding processes[4]>



< Autoclave curing processes[5] >

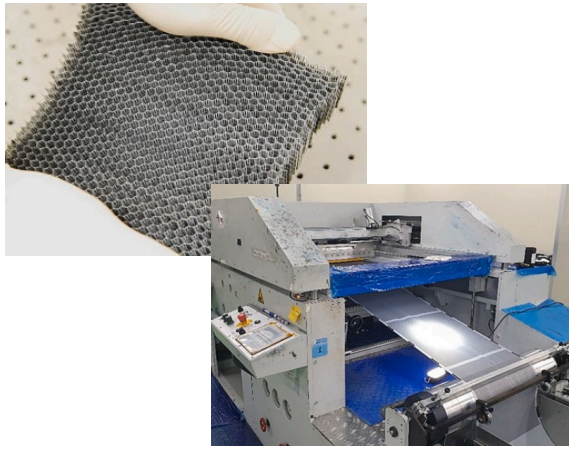

< Pattern printing processes[6] >

[1] D.D.Lim et al. Broadband mechanical metamaterial absorber enabled by fused filament fabrication 3D printing, Additive Manufacturing 55 (2022) 102856
[2] Q. An et al. A Novel Ultra-Wideband Electromagnetic-Wave-Absorbing Metastructure Inspired by Bionic Gyroid Structures, Adv. Mater. 2023, 35, 2300659
[3] J.Y.Cho et al. Fusedly Deposited Frequency-Selective Composites Fabricated by a Dual-Nozzle 3D Printing as Microwave Filter, Polymers 2024, 16, 786
[4] W.H.Jang et al. High-temperature corrugated-core radar stealth Ni-plated glass/ bismaleimide sandwich composites, Composite Structures 365 (2025) 119185
[5] W.H.Choi et al. Broadband microwave-absorbing honeycomb structure with novel design concept, Composites Part B 83 (2015) 14-20
[6] S.M.Baek et al. A lightweight, flexible, and polarization-insensitive microwave absorbing honeycomb core using conductive losses in printed periodic pattern, Composites Part A 180 (2024) 108089

Background

❖ *Application of 3D-Printed RAS*

- 3D-Printing for ABDR (Aircraft Battle Damage Repair)





< Replaceable 3D-Printed polymeric hatch for Gripen by Saab[7] >

- 3D-Printing patch for RCS reduction





< Application of 3D-Printed patch for RCS reduction[8] >

[7] https://3dprintingindustry.com/news/saab-trials-3d-printing-to-repair-battle-damaged-gripen-fighter-aircraft-187974
[8] https://www.twz.com/29218/these-images-of-an-f-22-raptors-crumbling-radar-absorbent-skin-are-fascinating

Background

MCML
MULTIFUNCTIONAL COMPOSITES & MANUFACTURING LABORATORY

❖ *Limitation of conventional thermoplastic for 3D-printing*

- Amorphous
  - Impact toughness
  - Dimensional stability
  - Optical transparency
  - Low heat resistance
  - Solvent sensitivity
  - Stress-cranking

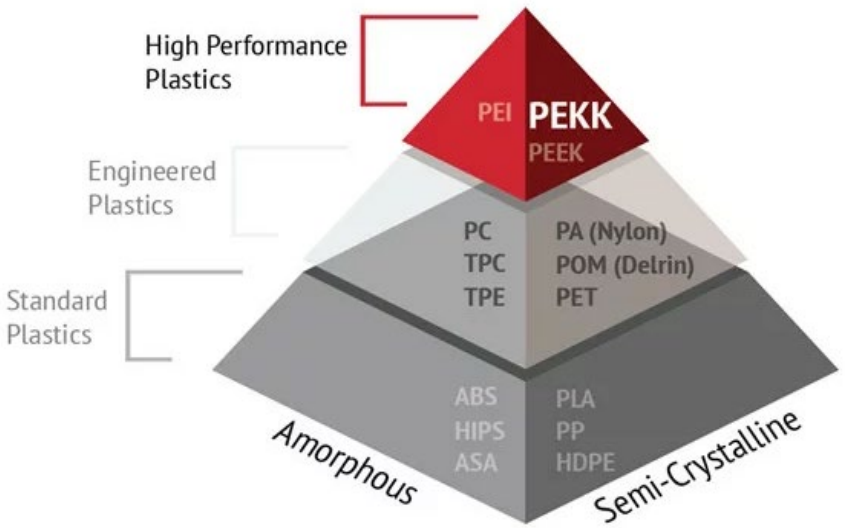

- Semi-Crystalline
  - High heat resistance
  - Chemical resistance
  - Good Fatigue strength
  - High shrinkage and warpage
  - Process complexity

Material	Tensile Strength, Yield (MPa)	Tensile Modulus (GPa)	Flexural Strength (MPa)	Flexural Modulus (GPa)	Izod Impact (kJ/m^2)	Glass Transition Temp (℃)	Moisture Content	Printing Temp (℃)	Chemical Resistance
PEEK (Polyetheretherketone)	85 – 95	3.6 - 4.0	100 - 120	3.8 - 4.0	7	143	0.02	360 - 420	Excellent
Ultem 1010 (Polyetherimide)	81	2.77	144	2.82	21	215	0.02	365 - 395	Excellent
PA66 (Polyamide, Nylon)	60 - 80	2.5 - 3.2	100 - 120	2.5 - 3.0	6 - 9	70	2.5	260 - 290	Poor
PC (Polycarbonate)	55 - 65	2.25	90	2.15	8 -12	143	0.3	260 - 300	Moderate
PLA (Polylactic Acid)	50 - 70	3.0 - 3.6	80 - 100	3.5 - 110	2 - 5	60	0.4	190 - 220	Poor
ABS (Acrylonitrile-Butadiene-Styrene)	40 - 50	2.2 - 4.4	80 - 100	2.0 - 2.3	15 - 25	105	0.4	230 - 260	Poor

Literature survey (1/2)

3D printed Carbon Black/Polylactic acid composites for microwave absorption

[9] Chengtao Sum et al. Design of functionally gradient metastructure with ultra-broadband and strong absorption, Composites Part B, 280, 2024, 111484

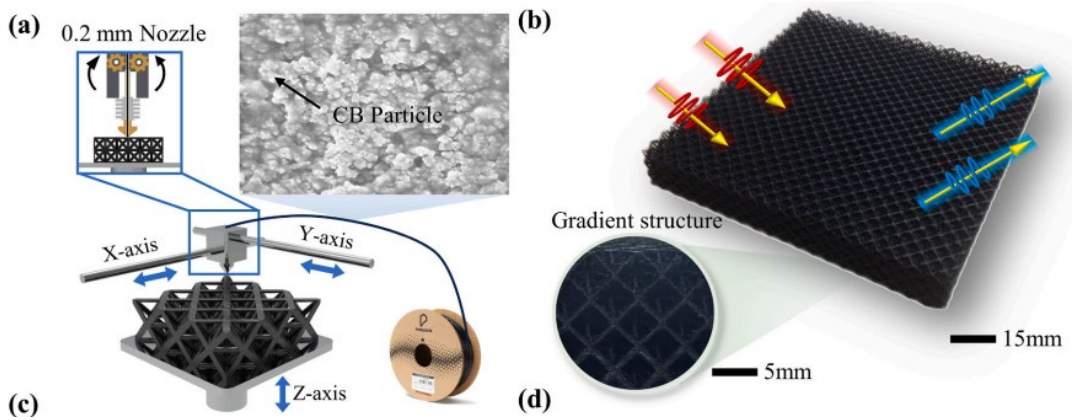

< PLA/CB filament based gradient meta strudture >

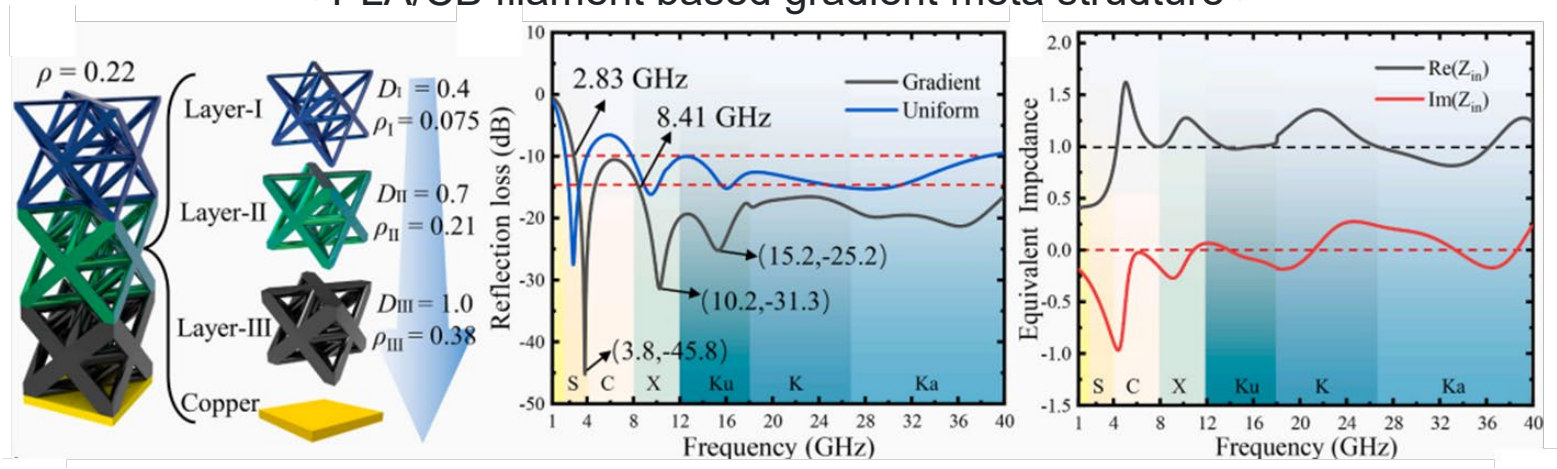

< Design of gradient metastructure and EM wave absorbing performance >

Literature survey (1/2)

Effect of annealing on mechanical and electrical properties of 3D printing PEEK/CNT nanocomposites

[10] Xin Ye et al. Effect of annealing and carbon nanotube infill on the mechanical and electrical properties of additively manufactured polyether-ether-ketone nanocomposites via fused filament fabrication, Additive Manufacturing, 59, (2022), 103188

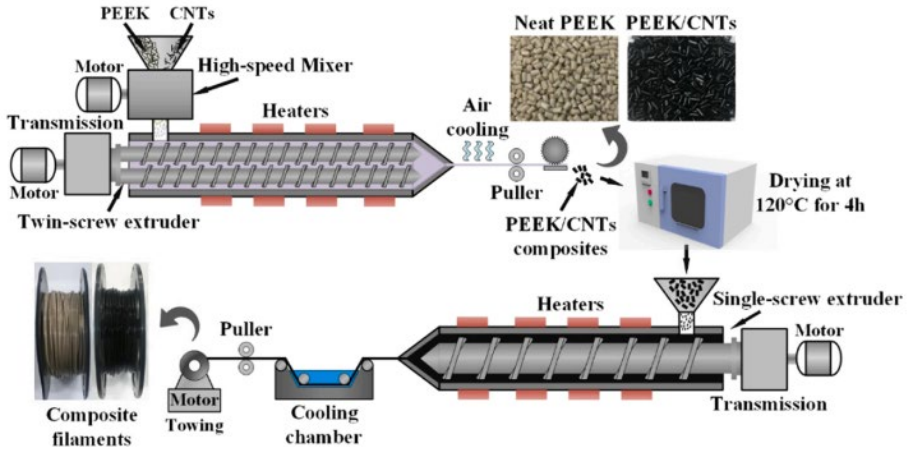

< Preparation process of PEEK/CNT composite filaments >

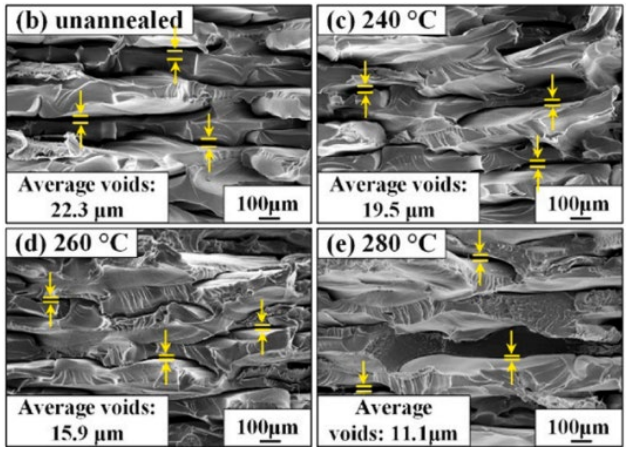

< Effect of annealing treatment on the interfacial voids >

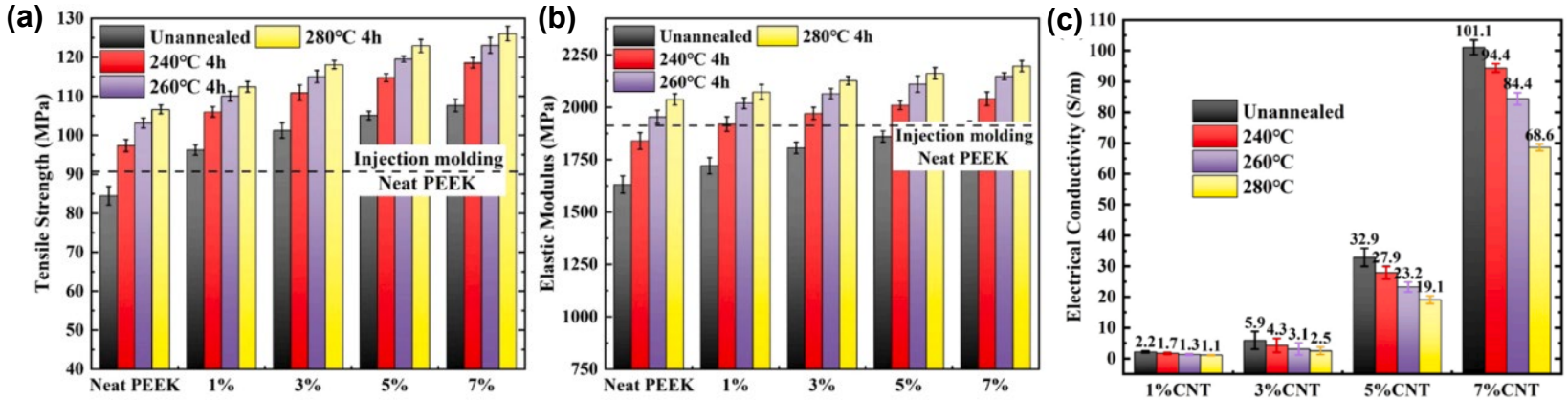

< Effect of annealing treatment on (a) tensile strength, (b) elastic modulus (c) electrical conductivity>

Research highlights

MCML
MULTIFUNCTIONAL COMPOSITES & MANUFACTURING LABORATORY

Manufacturing

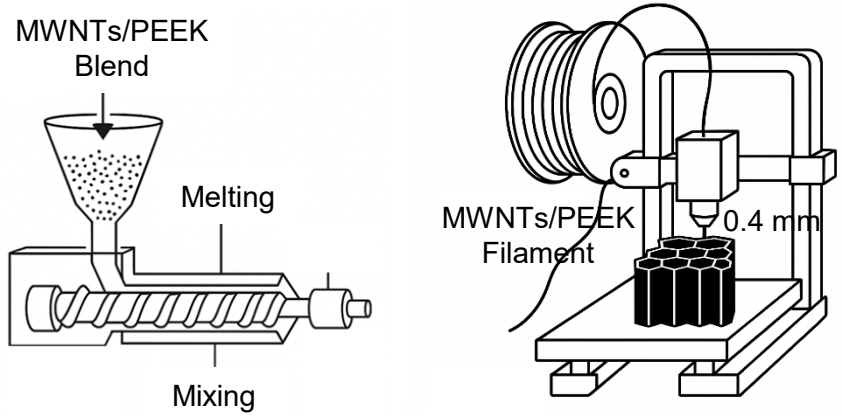

Design

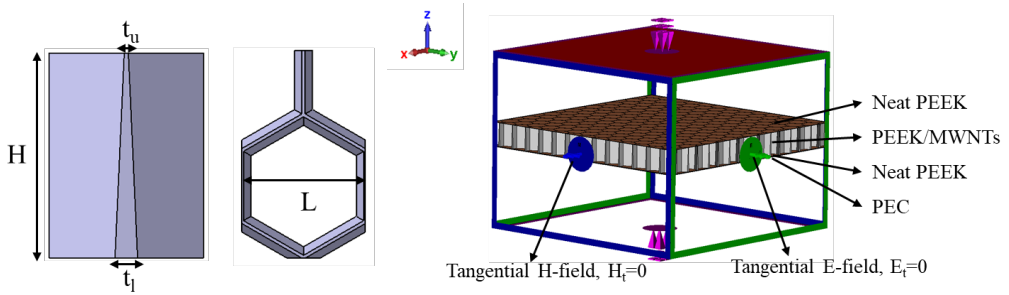

Measurement

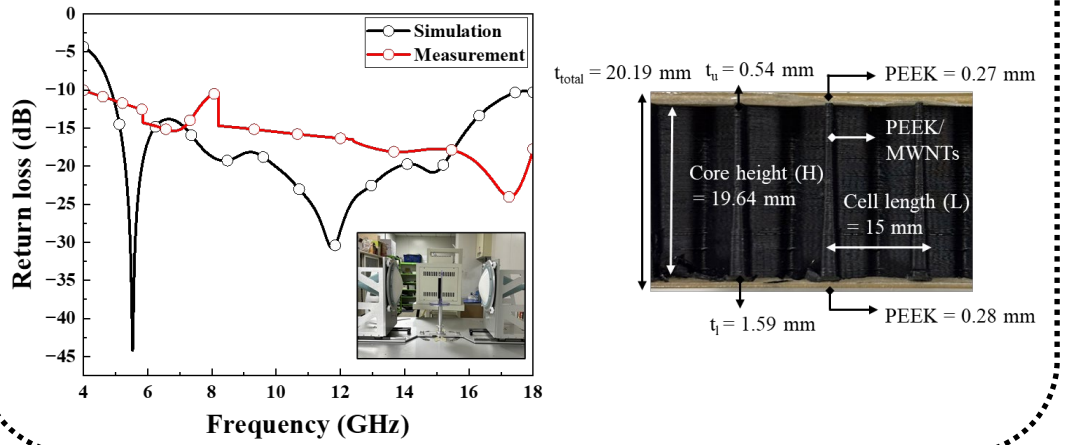

Mechanical behavior analysis

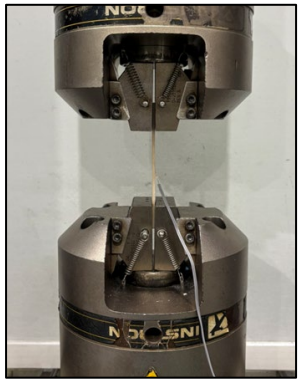

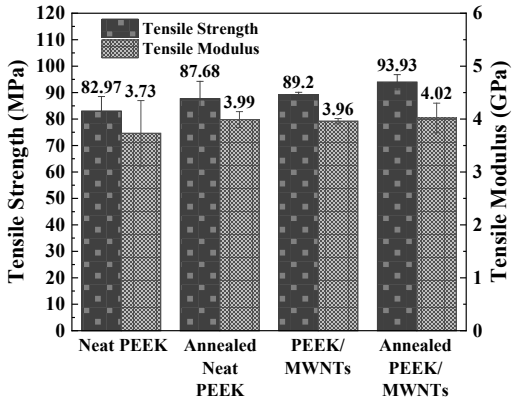

II. Materials and methods

Material preparation

- PEEK

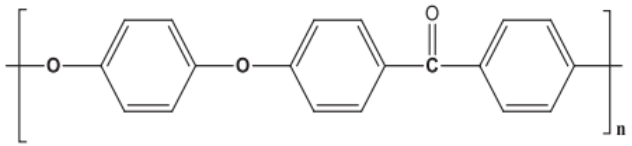



- Superior mechanical properties and toughness
- Above 450 °C, primary thermal decomposition occurs this must be taken into account during filament fabrication
- Chemical, thermal resistance

Name	Glass transition temperature (°C)	Melting temperature (°C)	Deposition temperature (°C)	Crystallinity (%)	Tensile strength (MPa)	Young Modulus (GPa)
PEEK	144	340	450	30	100	3.7-4.0

< Chemical structure, thermal and tensile properties of neat PEEK[11] >

- Multi-Walled Carbon Nanotubes

- Increase dielectric loss properties
- Increase mechanical properties
- Aggregation due to van der Waals forces
- Viscosity control

Name	Average diameter (㎚)	Length (㎛)
MWNTs	15-25	5-15

< Dimensional specifications of Multi-Walled Carbon Nanotubes[12] >

[11] Anouar El Magri et al An overview on the influence of process parameters through the characteristic of 3D-printed PEEK and parts, High Performance Polymers, 2021, 1–19
[12] Shandong Dazhan Nano Materials, GT-304 Technical Data Sheet

Material preparation

❖ *PEEK based filament extrude process*

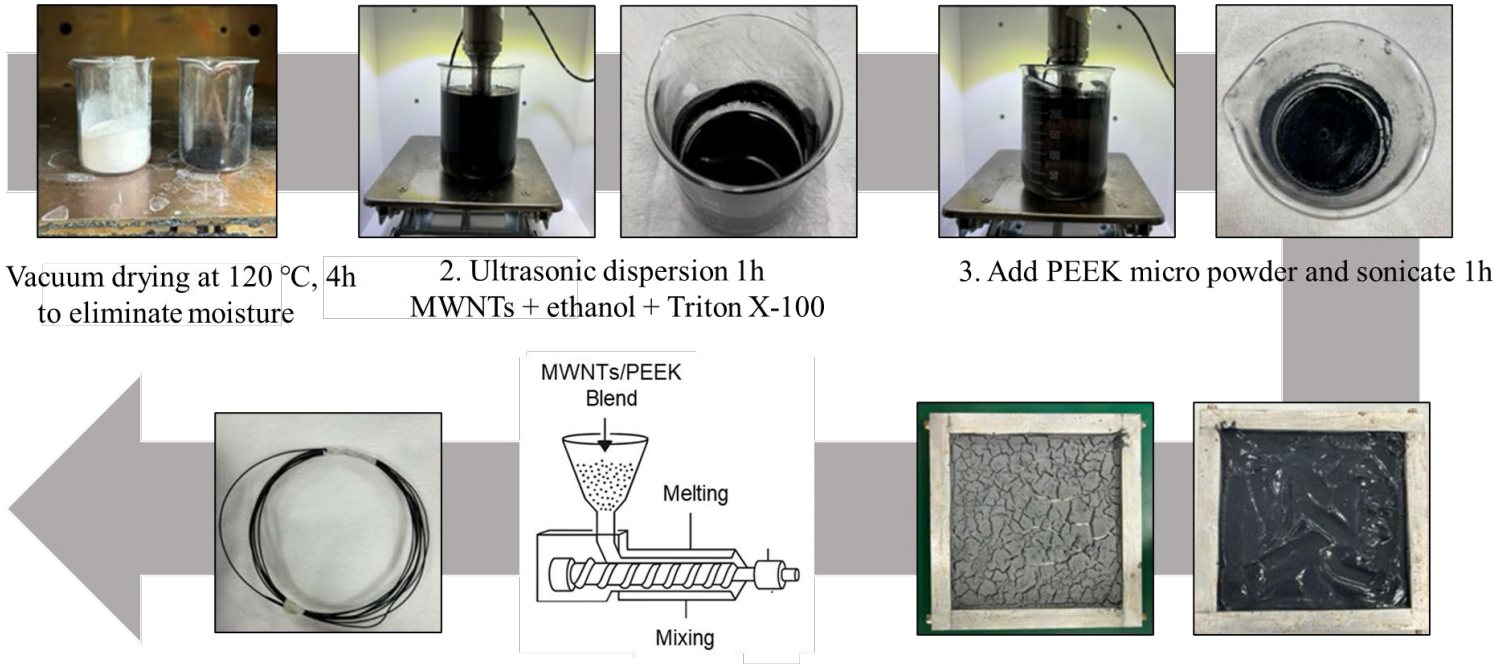

< MWNTs dispersion and extrude process >

(a)

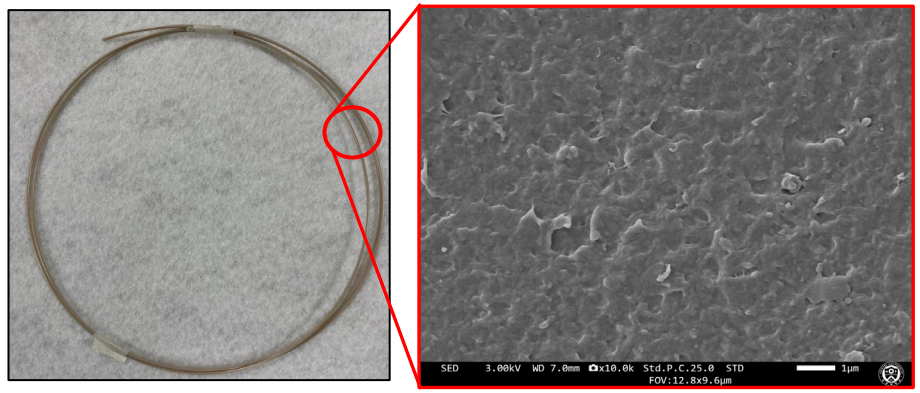

(b)

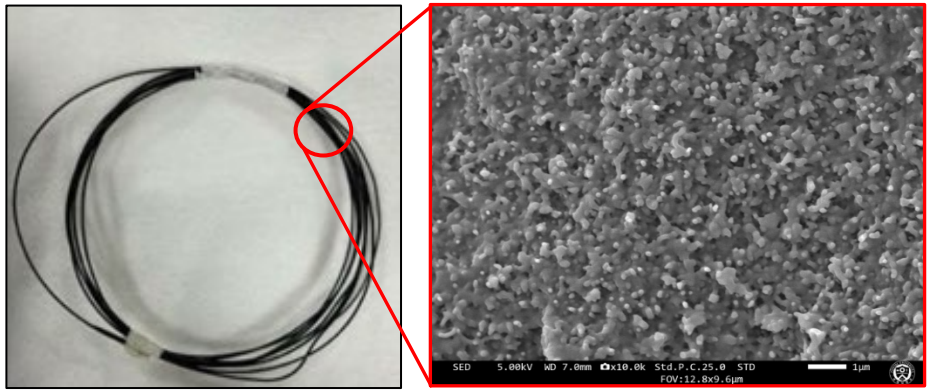

< SEM images of (a) Neat PEEK, (b) PEEK/MWNTs 12 wt% >

Material preparation

❖ *Electromagnetic properties of PEEK/MWNTs nanocomposites*

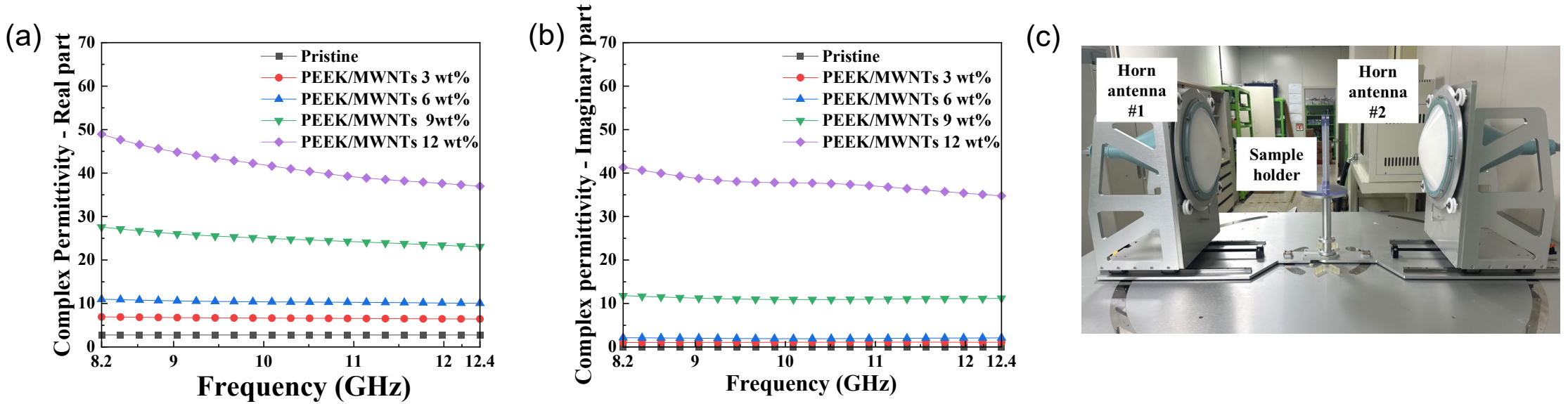

< Complex permittivity of PEEK/MWNTs (a) real part, (b) imaginary part and (c) free space measurement system >

@ 10 GHz	Neat PEEK	PEEK/ MWNTs 3 wt%	PEEK/ MWNTs 6 wt%	PEEK/ MWNTs 9 wt%	PEEK/ MWNTs 12 wt%
Complex permittivity	2.70 - j0.03	6.85 – j1.30	12.77 – j2.67	22.43 – j9.58	29.64 – j38.13
Complex permeability	0.96 – j0.01	0.98 - j0.01	0.98 – j0.01	0.95 – j0.02	0.97 – j0.01

< Complex permittivity and permeability of PEEK/MWNTs at 10 GHz >

Methods

❖ *Multilayer radar-absorbing structure*

- General formulation of multilayer absorber

✓ Optimizing multilayer absorber is a process of minimizing the magnitude of the reflection coefficient

✓ It is achieved when the impedance of the absorber is matched to the closet value with Z_0, 377Ω

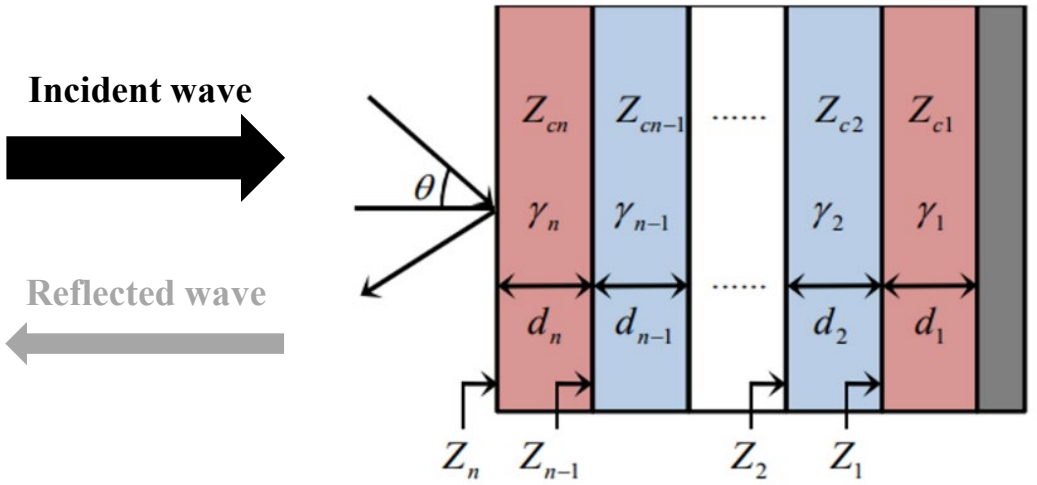

- Input impedance of i-th layer

$$Z_{i+1} = Z_{ci}\frac{Z_{i-1} + Z_{ci}\tanh(\gamma_i d_i)}{Z_{ci} + Z_{i-1}\tanh(\gamma_i d_i)}$$

- Reflection coefficient

$$\Gamma = \frac{Z_{i+1} - Z_0}{Z_{i+1} + Z_0}$$

Z_i = Input impedance of i-th layer

Z_{i-1} = Input impedance of i-1th layer

Z_{ci} = Characteristic impedance of i-th layer

γ_i = Wave number of i-th layer

d_i = Thickness of i-th layer

III. Design and fabrication

Design

❖ *Design of tapered honeycomb core radar absorbing structure*

- Design parameter of tapered honeycomb core

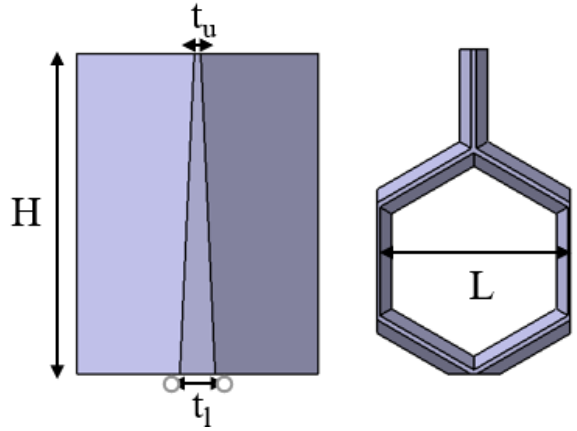

Design parameter:
H: Height
t_u : Upper thickness
t_l : Lower thickness
L: Cell length

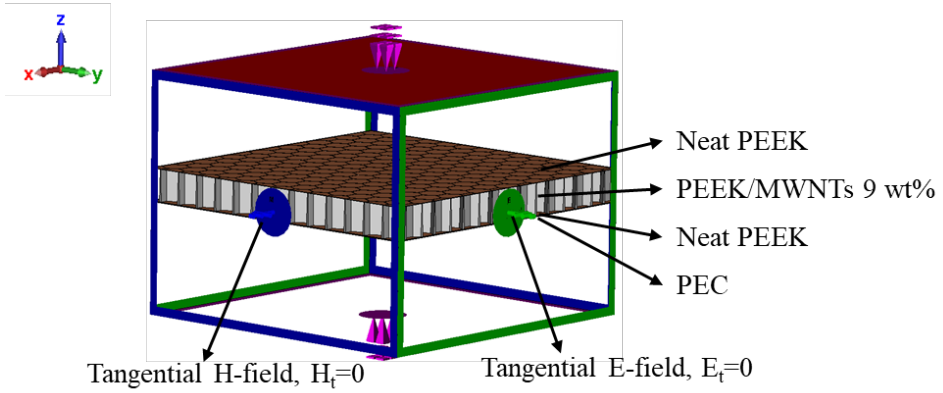

< (a) Design parameters of tapered honeycomb core, (b) simulation model of the tapered honeycomb core sandwich composites >

- Parameteric study of thickness gradient honeycomb core

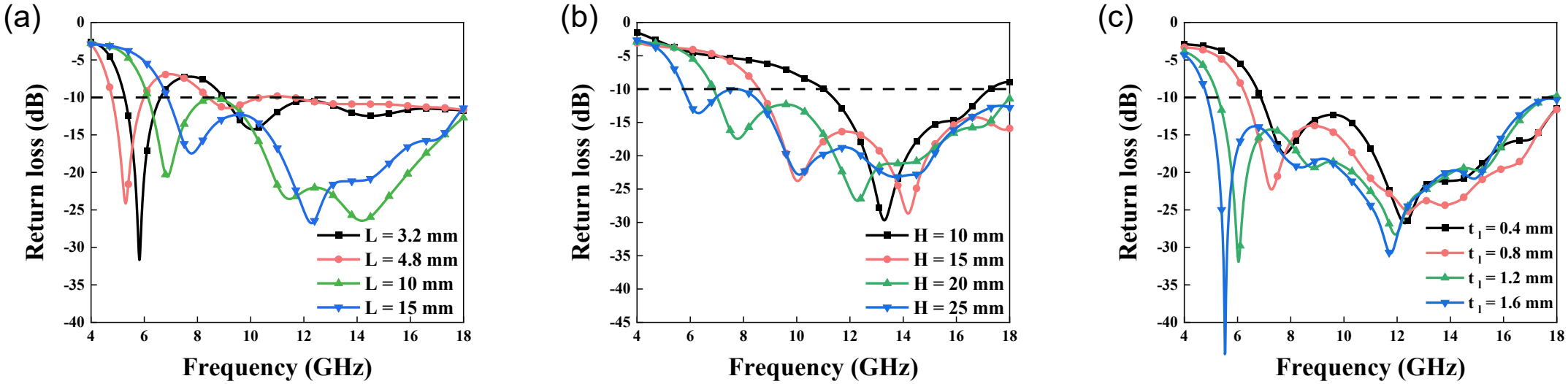

< Return loss simulation results of the tapered honeycomb core (a) cell length, (b) height, (c) lower thickness >

Design

❖ *Electromagnatic characteristic of designed radar absorbing structure*

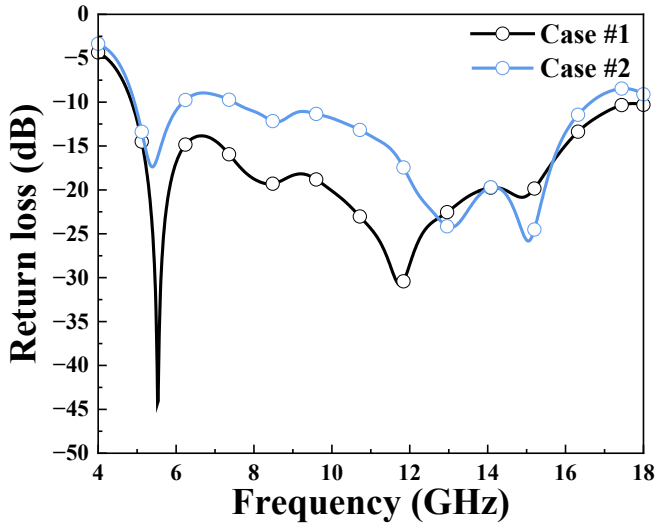

< Return loss of honeycomb core sandwich structure with PEC >

(a) Case #1

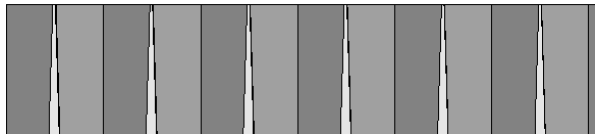

(b) Case #2

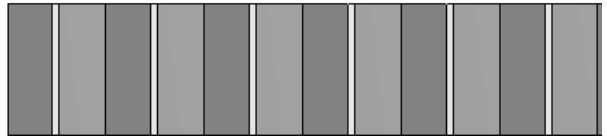

Parameter	L (mm)	H (mm)	t_u (mm)	t_l (mm)
Case #1	15	20	0.4	1.6
Case #2	15	20	1	1

< Return loss of honeycomb core sandwich structure with PEC >

(a)

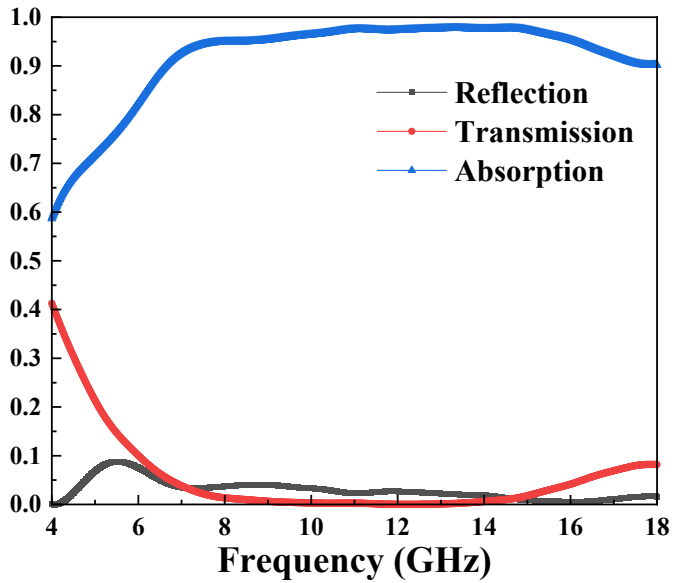

(b)

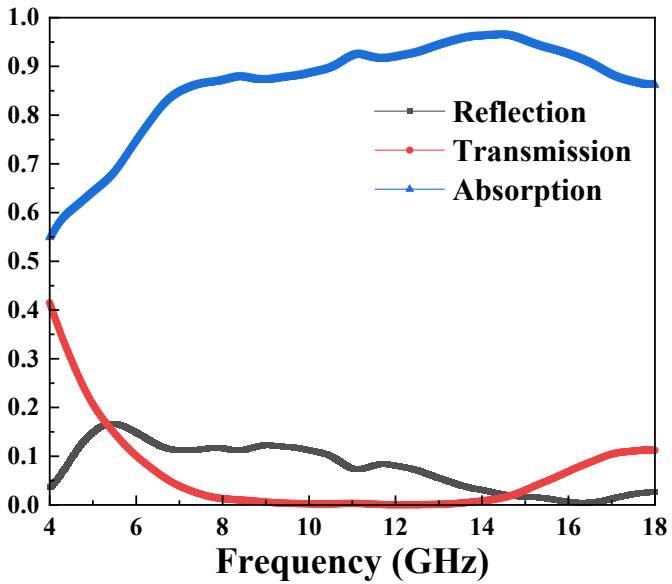

$$Absorption = 1 - Reflection - Transmission = 1 - |S_{11}|^2 - |S_{21}|^2$$

< Electromagnatic characteristic of tapered honeycomb core (a) Case #1, (b) Case #2 >

Fabrication

❖ *FDM 3D-Printing parameter of MWNTs dispersed PEEK*

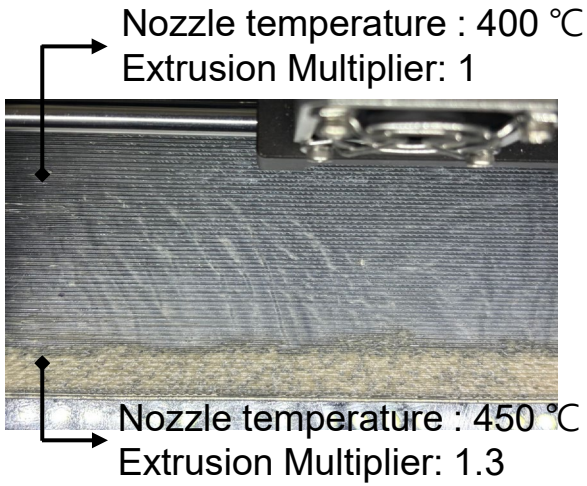

< Different printing result with nozzle temperature and Extrusion Multiplier>

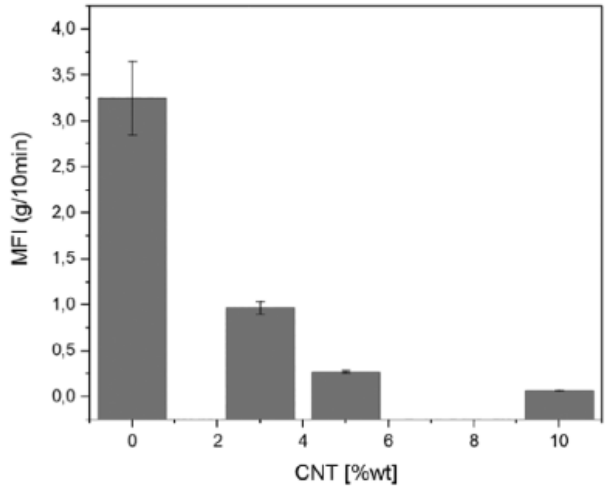

< Melt Flow Index(MFI) of PEEK/CNT at 400 ℃ [13] >

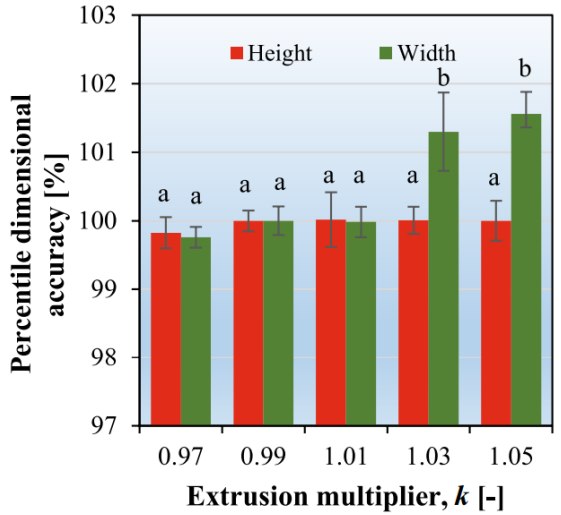

< Percentile dimensional accuracy as a function of extrusion multiplier [14] >

Printing parameters	PEEK	PEEK/MWNTs
Nozzle temperature	400 ℃	450 ℃
Extrusion Multiplier	1	1.3
Chamber temperature	70 ℃	70 ℃
Printing speed	20 mm/s	20 mm/s
Layer thickness	10 mm	10 mm
Nozzle diameter	0.4 mm	0.4 mm

< Major printing parameter of PEEK based filaments >

[13] Marianna Rinaldi et al. Fused filament fabrication ofpolyetheretherketone/multiwalled carbonnanotube nanocomposites: the effect ofthermally conductive nanometric filler on theprintability and related properties, *Polym Int*, 2021; 70: 1080 – 1089
[14] László Lendvai et al. Experimental study on the efect of flament-extrusion rate on the structural, mechanical and thermal properties of material extrusion 3D-printed polylactic acid (PLA) products, Progress in Additive Manufacturing (2025) 10:619–629

IV. Results and discussion

Results and discussion

❖ *Return loss of 3D-Printed tapered honeycomb core RAS*

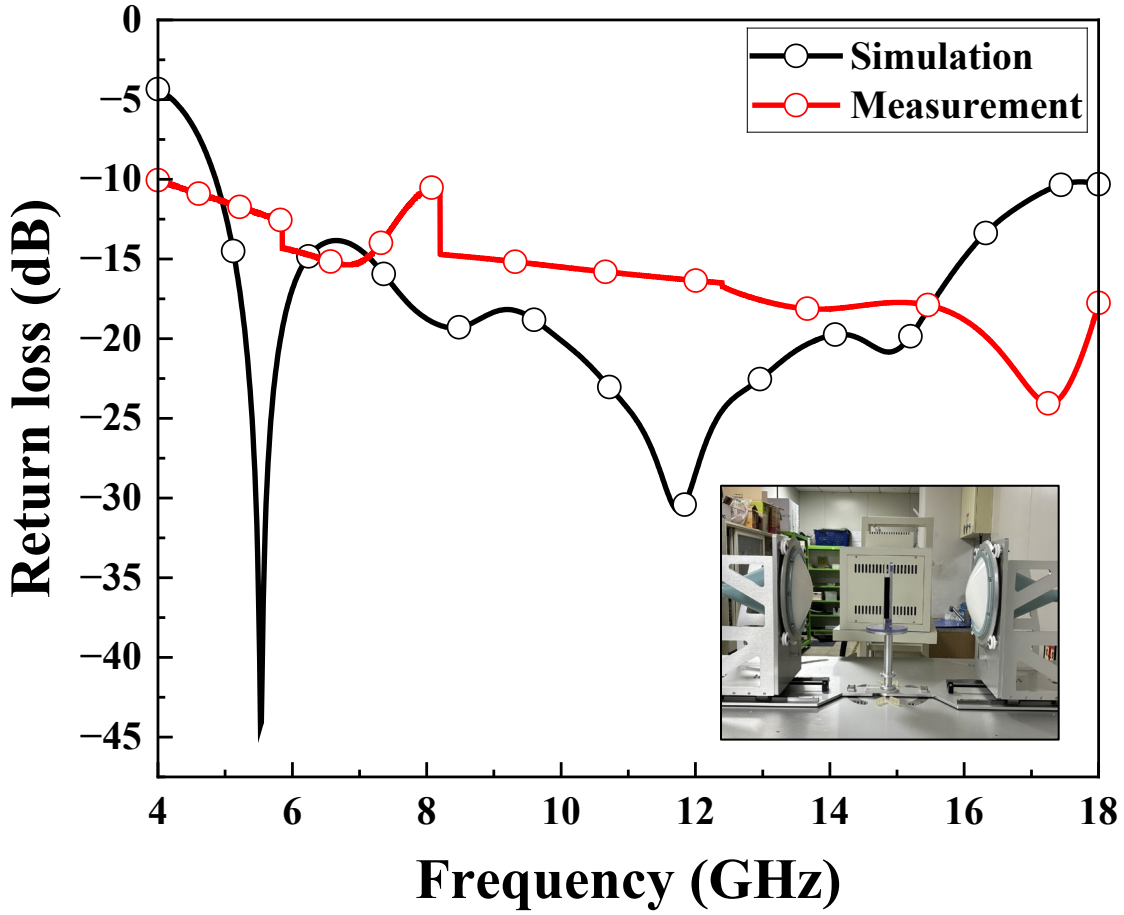

< Comparison of simulation results and printed RAS >

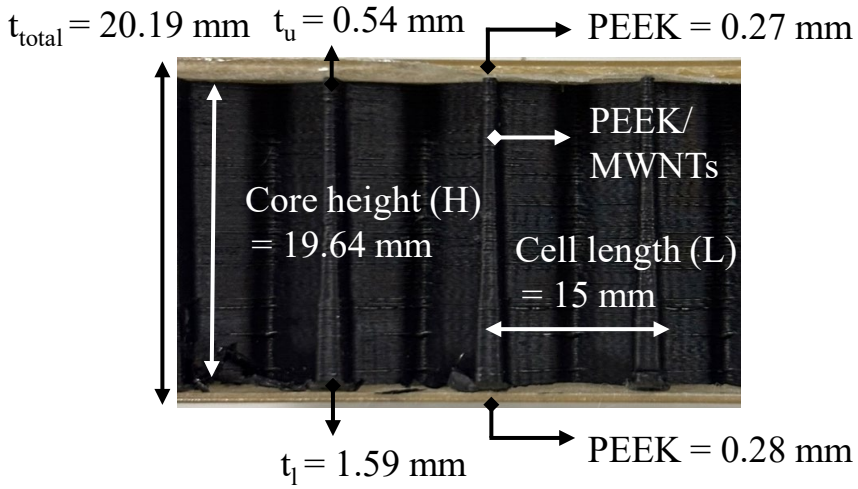

< Dimension of 3D-Printed RAS >

Parameter	t_{total} (mm)	L (mm)	H (mm)	t_u (mm)	t_l (mm)
Designed	20.6	15	20	0.4	1.6
3D-Printed	20.19	14.8	19.64	0.54	1.59

< Comparison of designed dimension and 3D-Printed dimension >

Results and discussion

❖ *Mechanical properties of PEEK/MWNTs nanocomposites*

- The annealing process was conducted at 260°C for 4 hours in a vacuum oven, followed by a cooling rate 1°C/min

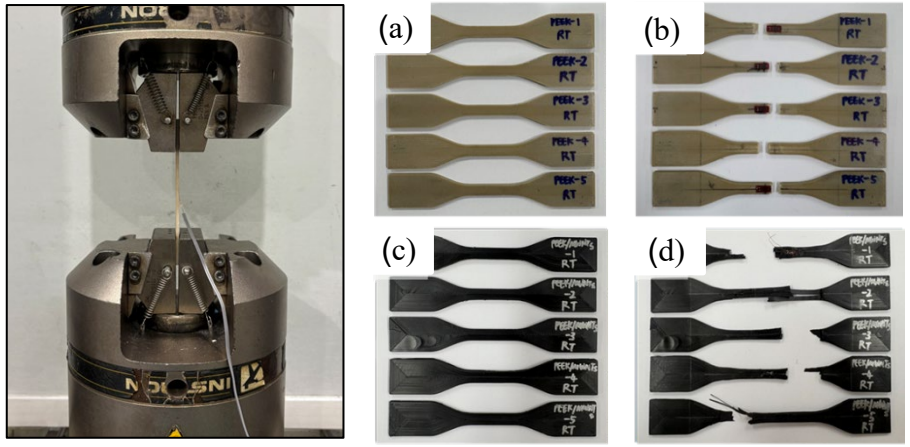

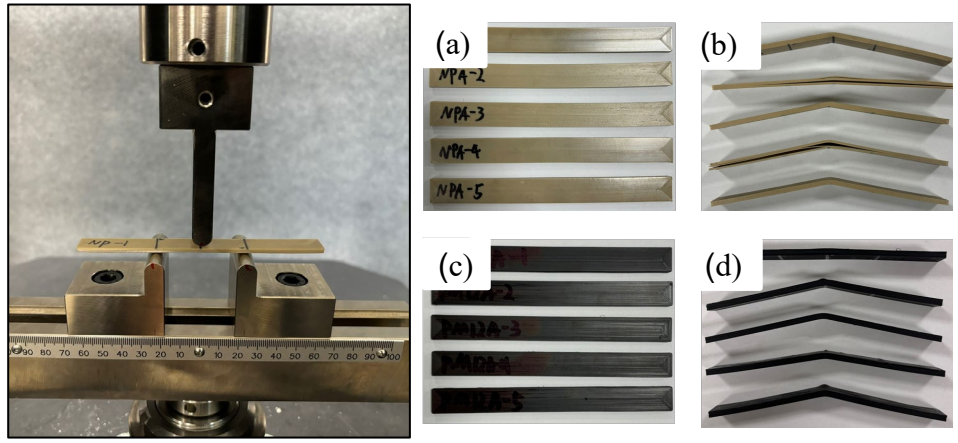

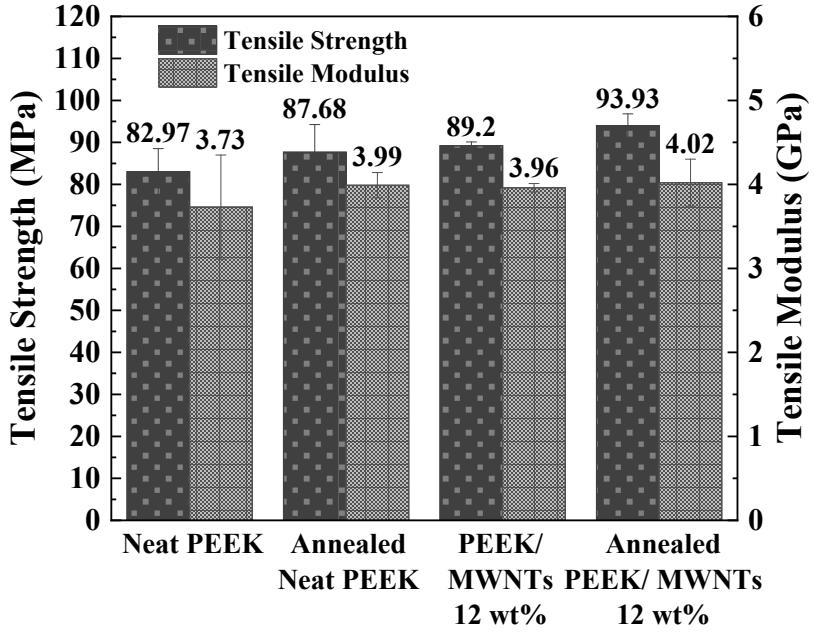

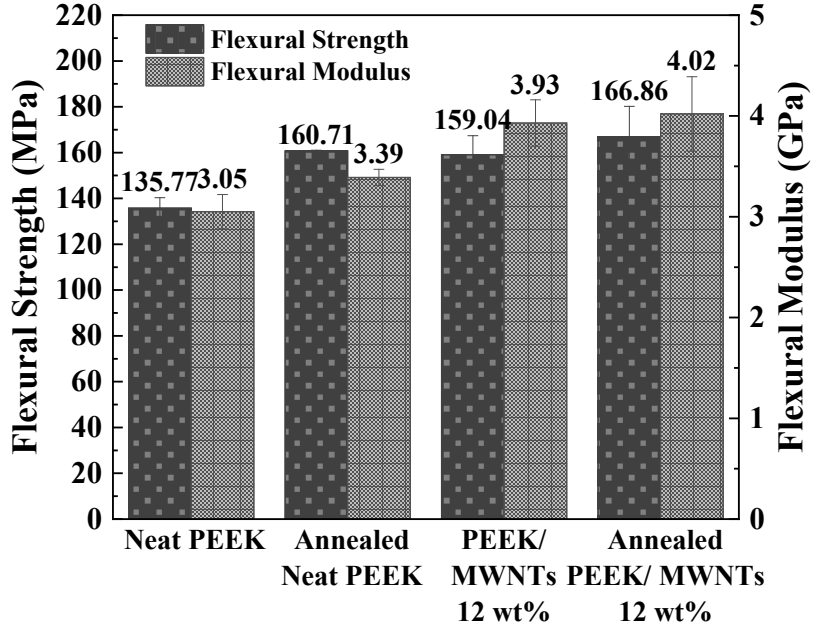

Results and discussion

❖ *Crystallinity of PEEK/MWNTs nanocomposites*

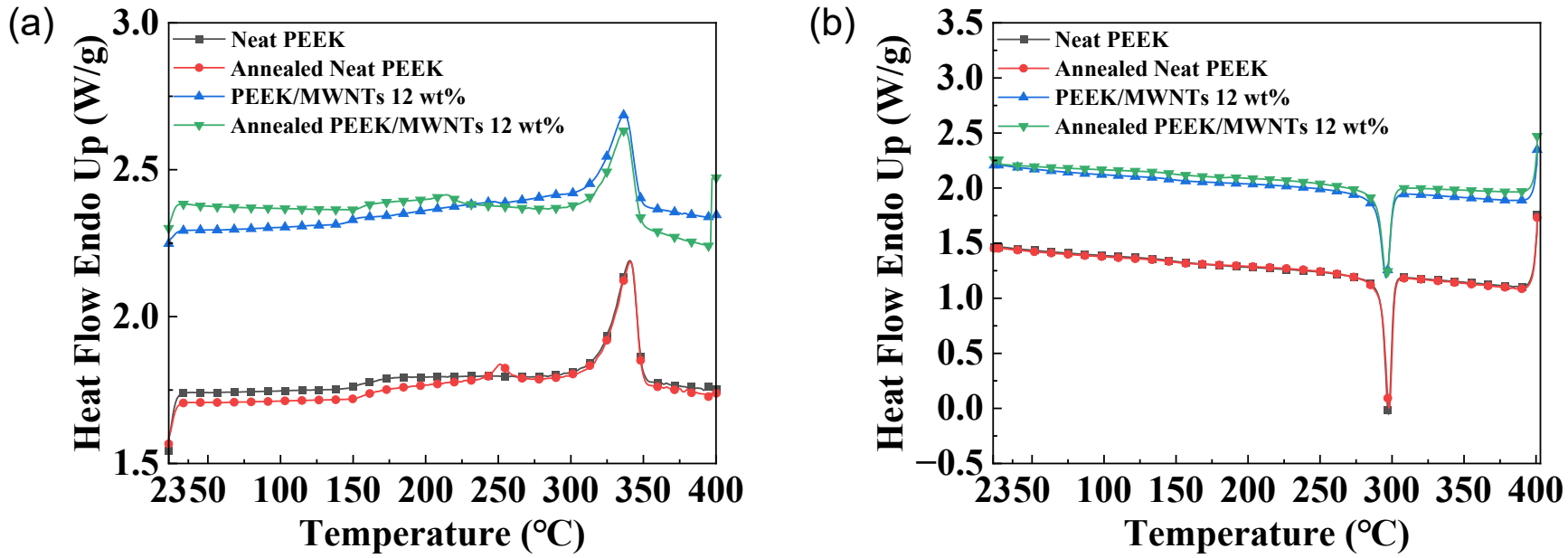

< DSC anlysis results (a) heating cycle, (b) cooling cycle >

Material	H_m	H_f	$(1-V_{MWNTs})$	X_c (%)
Neat PEEK	39.07	130	1	30.05
Annealed Neat PEEK	43.20	130	1	33.23
PEEK/MWNTs 12 wt%	31.74	130	0.912	26.87
Annealed PEEK/MWNTs 12 wt%	35.44	130	0.912	29.89

< The crystallization behavior of the PEEK and PEEK/MWNTs composites >

V. Conclusions

Conclusions

MCML
MULTIFUNCTIONAL COMPOSITES & MANUFACTURING LABORATORY

- In this study, electromagnetic wave absorbing PEEK/MWNTs nanocomposites filament were developed for for radar absorbing structure
- Extrusion and FDM printing parameters were studied to extrude dimensionally consistent filaments and printed parts
- The thickness gradient tapered honeycomb core was designed and printed, and this structure significantly reduced surface reflection and enhanced broadband EM absorption
- MWNTs increased the tensile and flexural strength of PEEK and a 260 ℃ annealing process raised crystallinity, further improving mechanical performance
- In future work, we will compare the mechanical behavior of tapered honeycomb and uniform honeycomb core at the same density

MCML
MULTIFUNCTIONAL COMPOSITES & MANUFACTURING LABORATORY

Thank you for your attention

Acknowledgement

This research was conducted with support from the 2024 Korea Aerospace Industries, Ltd. (KAI) integrated in-house R&D project (KZZ90114B).

Korea Aerospace University

KAI 한국항공우주산업㈜ KOREA AEROSPACE INDUSTRIES, LTD.

Presenter jwshim@kau.kr
Professor ywnam@kau.ac.kr
Web page mcml.kau.ac.kr

ARREST AND COMPARTMENTALISATION OF UNSTABLE COMPRESSIVE FAILURE IN CARBON-FIBRE REINFORCED POLYMER LAMINATES USING A PLY-DISCONTINUITY FEATURE

Bruno P. Santos[1], Emile S. Greenhalgh[2] and Silvestre T. Pinho[3]

[1]Department of Aeronautics, Imperial College London
South Kensington Campus, London, SW7 2AZ, United Kingdom
Email: b.santos22@imperial.ac.uk, web page: http://www.nextcomp.ac.uk

[2]Department of Aeronautics, Imperial College London
South Kensington Campus, London, SW7 2AZ, United Kingdom
Email: e.greenhalgh@imperial.ac.uk, web page: http://www.nextcomp.ac.uk

[3]Department of Aeronautics, Imperial College London
South Kensington Campus, London, SW7 2AZ, United Kingdom
Email: silvestre.pinho@imperial.ac.uk, web page: http://www.nextcomp.ac.uk

Keywords: Carbon fibre, Damage tolerance, Directional orientation, Fractography, Mechanical testing

ABSTRACT

Crack-arrest strategies are central to damage-tolerant structural design, particularly in large-scale components. By halting crack propagation and compartmentalising damage, such features prevent catastrophic failure, extend service life, and enable more flexible, cost-effective, and safer design approaches. This study developed a ply-discontinuity based feature to arrest unstable cracks in multidirectional Carbon-Fibre Reinforced Polymer (CFRP) laminates under compressive loading. The method targets the arrest of unstable kink-band propagation by replacing 0° plies with off-axis ones. This reconfiguration promotes fracture energy reflection and dissipation, while altering failure mechanisms. enabling the laminate to arrest high-velocity cracks (~1 km/s) and improve ultimate failure strain. Validation was performed using IM7/8552 CFRP elements incorporating off-axis ply regions with additional local reinforcement to preserve longitudinal stiffness. Two different crack-arrest element configurations were tested. These configurations differed from one another by the off-axis ply orientations used to replace 0° plies (±30° and ±45°). Mechanical performance was monitored via strain gauges and digital image correlation. Post-failure analysis employed C-scans, radiography imaging, and scanning electron microscopy to characterise damage evolution and arrest mechanisms. Both lay-up configurations successfully arrested crack propagation and significantly increased strain capacity. Enhancements in ultimate failure strain reached up to 38% for ±30° elements and up to 100% for ±45° elements. Repeated tests confirmed result reproducibility. These findings demonstrate the potential of ply-discontinuity features for improving damage tolerance in composite structures and provide insight into their underlying failure-arrest mechanisms.

1 INTRODUCTION

Compressive performance, particularly in the presence of in-service damage, remains a key limitation in composite structural design. Compressive strength of Fibre-Reinforced Polymers (FRPs) is significantly inferior to their tensile performance, generally corresponding to 60-70% of latter [1]. Factors such as high sensitivity to manufacture defects and a complex combination of failure modes are the main responsible for this discrepancy [2-3]. Additionally, if compressive failure initiates in a component, there are no means to arrest such fracture. As a result, composite structures are typically designed under a 'no-damage-growth' philosophy. Transitioning to a 'damage-growth tolerance'

approach, where controlled crack propagation is permissible, would unlock the full structural potential of composites.

Central to this philosophy are crack-arrest strategies, which aim to contain unstable failure, compartmentalise damage and extend service life. Such features are well-established in other engineering fields. In compressed-gas transmission pipelines, ribs are used to contain long tensile cracks in metallic pipes [4,5]. Similarly, in aircraft fuselages tear straps are used to stop tear propagation in the composite skin [6]. Nevertheless, little to no research has addressed compressive crack-arrest in fibrous composite laminates.

By developing an unstable crack-arrest feature for CFRP compression, this research aspires to pave the way to fail-safe design in large composite structures. Such feature enables the design of components that remain operational following initial unstable fracture. Thus, it enhances safety and allows lighter and more permissible structural designs. These benefits are particularly critical in applications where failure has life-threatening consequences, such as in aircraft wing roots. Figure 1 exemplifies how such a feature would be able to avoid structural collapse in a damaged wing root.

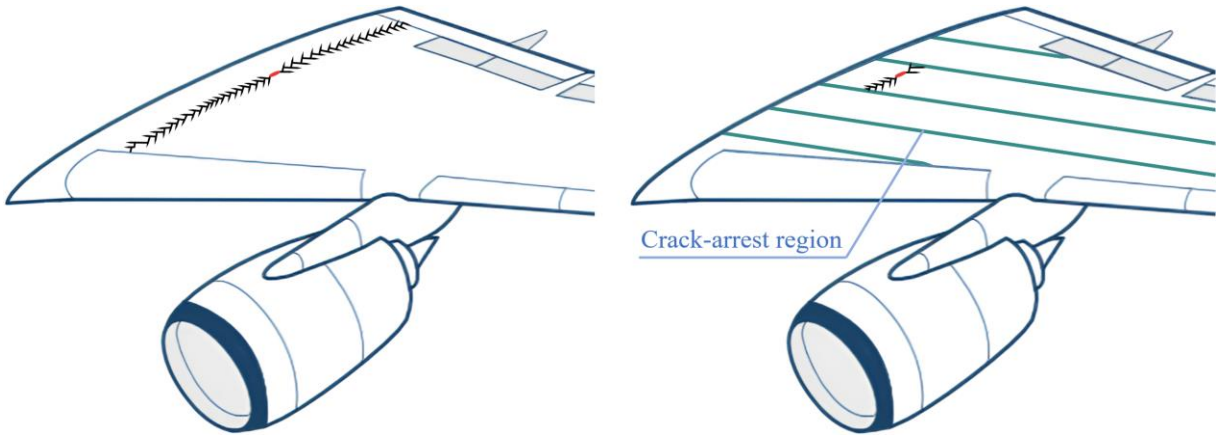

(a) (b)

Figure 1: Representation of compressive-crack compartmentalisation on a damaged aeroplane wing. (a) Crack propagation from the damaged region without crack arrest mechanisms, unrestrictedly expanding across the wing's chord and causing catastrophic failure. (b) Failure compartmentalisation by periodic crack-arrest bands, allowing the wing to remain in service.

2 FEATURE CONCEPT

Unstable compressive crack propagation in CFRPs can reach speeds approaching 1 km/s [7]. This rapid growth is driven by the propagation of out-of-plane kink-bands, which then facilitate the formation of secondary fracture types [8]. Due to the high energy involved, arresting crack growth requires mechanisms that dissipate or deflect associated fracture energy. Thus, a ply-discontinuity-based feature was developed. This feature exploits the fact that kink-bands typically occurs in 0° plies and propagate perpendicular to the loading direction. Thus, by locally replacing these plies with off-axis ones, it may be possible to divert or even arrest an unstable compressive fracture. Additionally, lay-ups dominated by 0° plies ("hard lay-ups") show lower translaminar toughness than off-axis-only ("soft lay-ups") configurations. Hence, introducing ply discontinuities creates regions of higher toughness, enhancing crack containment and resistance to propagation.

Importantly, the developed feature uses only existing, certified aerospace materials. This simplifies certification and facilitates integration into current aerospace structures. Furthermore, using a single composite type also eases recycling and end-of-life material handling.

3 MATERIALS AND METHODS

To validate this concept, test elements were designed and manufactured using IM7/8552 carbon-fibre reinforced epoxy. Additional reinforcement layers were introduced in soft lay-up regions, to maintain longitudinal stiffness across the width of the panel. A U-notch (10 mm length and 5 mm diameter) was designed to induce unstable failure around -3100 με. This value was chosen for being slightly above the -2500με design limit load typically used in aerospace industry [9]. Sandwich configuration, with aluminium honeycomb core and CFRP skins, was employed to prevent global buckling during testing (Figure 2).

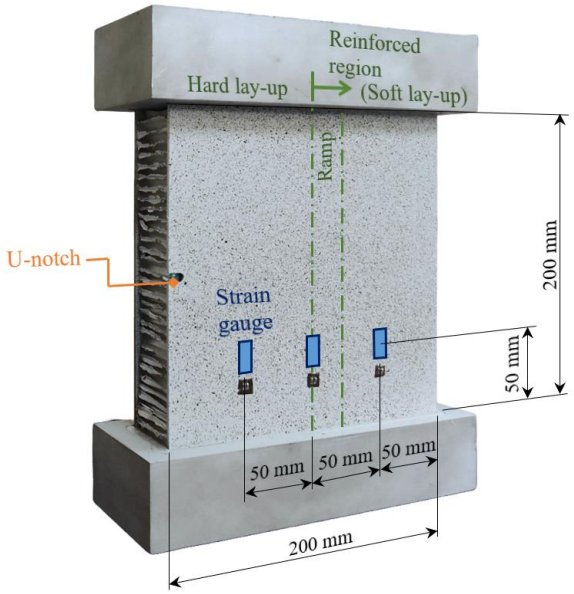

Figure 2: Compression test element geometry. Being the interest region, the frontal skin is divided in soft and hard lay-ups, and equipped with a notch to induce failure initiation. The rear skin is composed only by the hard lay-up and does not possess a notch.

The 200×200 mm element gauge area represents only a small fraction of a full-scale structure's overall dimensions. Therefore, even the loss of the entire 200mm section would not represent a significant reduction in the complete structure's load-bearing capacity. Thus, the most reliable indicator of a given element's performance is not their load capacity but their strain tolerance. This tolerance represents the structure's capability of being deformed before collapsing.

To control test variables, specific constraints were applied during the definition of the skins' lay-ups. Since the hard lay-up is multidirectional, while 0° layers were replaced by off-axis ones, the remaining plies were maintained continuous to conserve element integrity. Both lay-ups were designed as symmetrical, eliminating compression-bending coupling effects. Finally, additional plies were added to the soft lay-up to match stiffness across the element width. To minimise undesired stress concentration, the lay-up transition was implemented gradually, forming a 'ramp' profile. The front skin, identified as the primary surface of interest, was the only one containing the arrest feature.

Two different lay-up configurations were tested, differentiated by distinct off-axis ply angles (±30° and ±45°) replacing the 0° oriented plies. For each configuration two identical Crack-Arrest (CA) elements were tested, as well as a suitable baseline. This sought to ensure the reproducibility of the crack-arrest behaviour. The baselines consisted in panels without arrest feature, in which the entirety of the frontal skin was composed by the hard lay-up.

Lower longitudinal stiffness of 45° plies, when compared to 30° ones, implicated in a higher number of additional soft lay-up plies. The ±30° feature configuration had 19 and 33 plies in its hard and soft regions, respectively. Meanwhile, panels with the ±45° feature configuration had 19 and 55 plies in their hard and soft lay-ups.

The elements were tested in a 250-tonne screw-driven compression test machine under displacement control. Mechanical behaviour during tests was assessed using strain gauges and digital

image correlation, while post-failure analysis was performed through C-scans, radiography imaging, and optical and scanning electron microscopy to better understand failure initiation and arrest mechanisms.

4 RESULTS

As expected, both baseline elements suffered abrupt failures that propagated across the entire width of their notched skins. These fractures lead to the collapse of the baseline elements, with almost complete loss of load-bearing capability. The failure of the crack-arrest elements, however, was successfully stopped upon reaching the beginning of the arrest region. Following this initial failure, additional strain was endured by the elements, progressively causing smaller failure steps. Ultimate failure was achieved when the crack front reached the opposite end of the frontal skin width. Figure 3 represents the test behaviour of both baseline elements, as well as one element of each crack-arrest feature configuration. The remaining elements showed similar results to those represented, attesting to the reproducibility of these results.

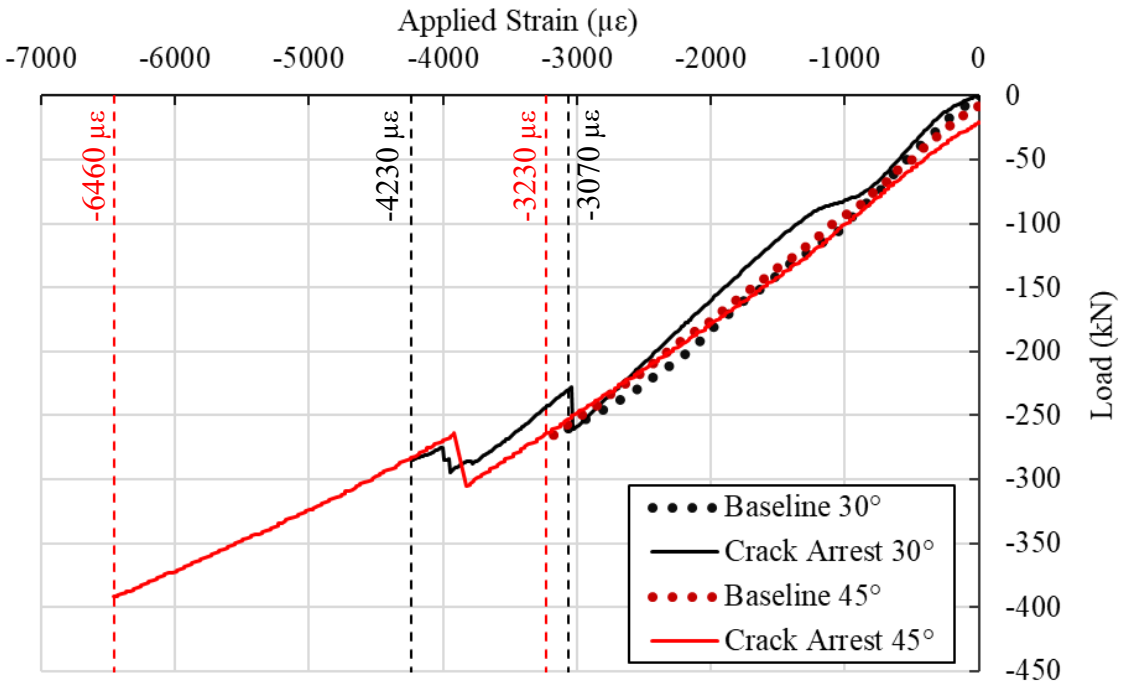

Figure 3: Evolution of applied strain for both crack-arrest configurations, as well as their respective baselines. Both configurations were successful in stopping failure propagation and increasing ultimate failure strain. Notably, the 45° configuration was able to double the strain to failure of is baseline.

It is possible to observe that both feature configurations showed elastic behaviour compatible with their respective baselines before initial failure. Additionally, the baselines failed near -3100 με strain, as per the notch design.

For the feature lay-up using ±30° off-axis plies, baseline failure happened at -3070 με, while that of the CA element started at -2980 με. The chart still portrays its subsequent growth steps, up to the ultimate failure at -4230 με. This represents a 38% increase in ultimate failure strain. Repeating the test with an identical element, similar behaviour was observed, resulting in an ultimate failure strain increase of 33%. It is notable that, although possessing the same stiffness as the baseline, the CA elements presented ultimate strains to failure one third higher than it.

Meanwhile, for the feature lay-up using ±45° off-axis plies, the baseline panel failed at -3230 με. CA failure started at -3800 με, being subsequently arrested, and final panel collapse happened at -6460 με. This constitutes a 100% increase in ultimate failure strain, with results from a repeat test showing an 85% strain increase. Hence, this configuration is capable of nearly doubling its baseline performance.

Radiographies and C-scans were employed to visualise subsurface damage in each element. The radiography images presented in Fig. 4 allow visualisation of the main failure path and secondary fractures for representative elements.

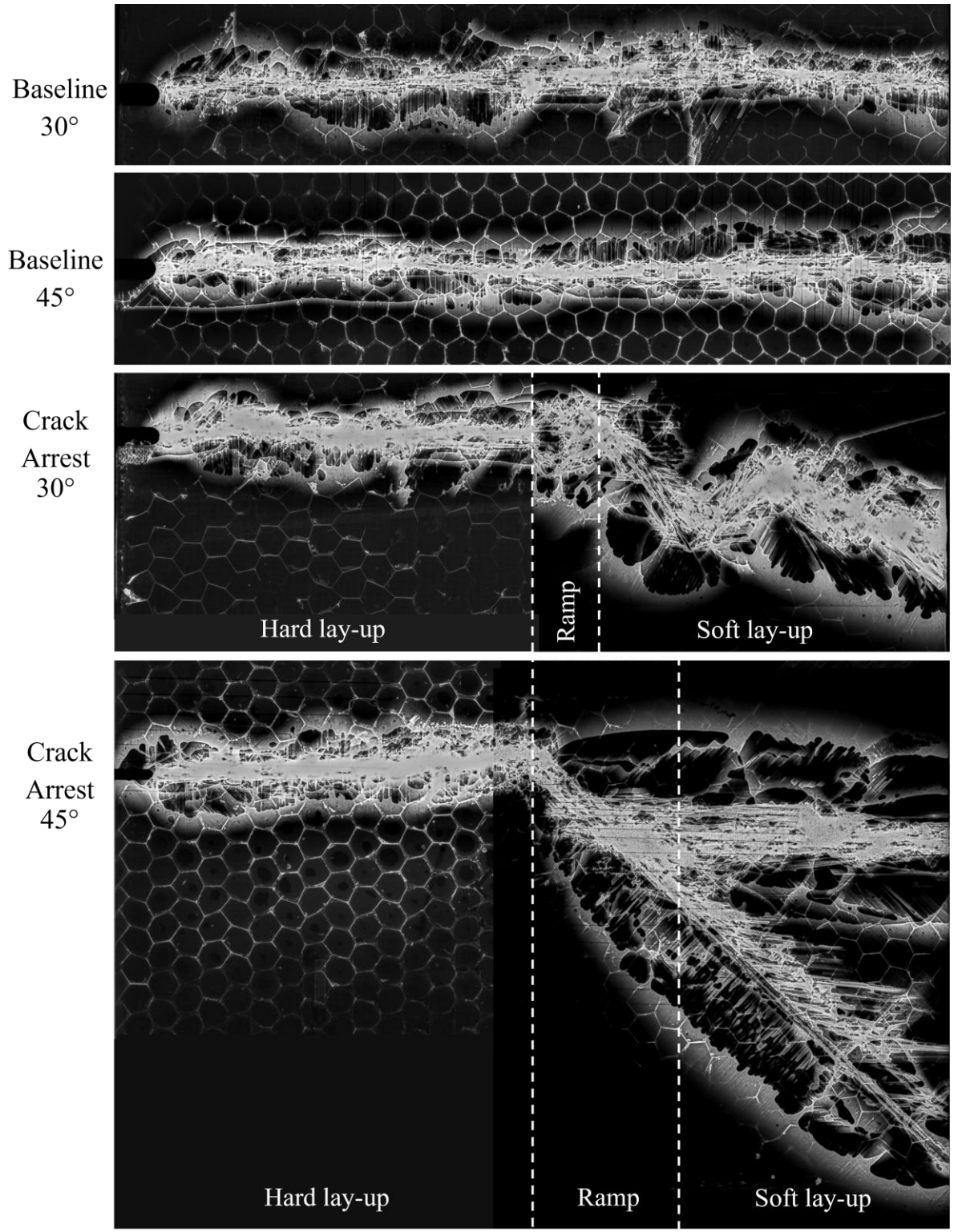

Figure 4: Radiographies of fracture regions for the different test elements, portraying the change in failure path caused by ply-discontinuity. Differences in delamination area surrounding fracture are also visible.

Both baselines behaved in a similar manner, with fracture showing a tendency of propagating perpendicular to loading direction. The same behaviour appears in the hard lay-up regions of the CA elements. However, the soft lay-up regions exhibit a modified failure path, with fracture propagating in oblique directions. Moreover, in the ±45° CA element, fracture propagation was split into two main failure paths after the initial arrest. Significantly higher amounts of delamination are also observable in the soft lay-ups, when compared to their hard counterparts.

5 DISCUSSION

Both versions of the developed feature were successful in compartmentalising unstable failure growth. However, the increase in ultimate failure strain provided by the ±45° plies was significantly higher than that of the ±30° plies. This configuration nearly doubled strain tolerance, even withstanding higher loads than its baseline despite significant panel section loss.

It is important to consider, however, the additional weight penalty inherent to this configuration. The usage of a ply direction with lower longitudinal stiffness results in a higher thickness in the soft lay-up section. Nevertheless, in real work conditions such penalty could be mitigated by adjusting the frequency and width of periodic crack-arrest bands. Moreover, this concept introduces the possibility of fail-safe design, creating thinner panels and achieving weight reduction for the overall structure.

Analysing the fracture properties in Fig. 4, a better understanding of the mechanisms responsible for the feature's success becomes possible. It is notable that, as seen in the baseline, initial fracture in the CA elements grew perpendicular to load application direction. Similar fracture morphology was also observed between these failures, consistent with the baseline's suitability as comparison. Nevertheless, following the initial arrest, the subsequent failure in the CA elements presented significant changes in both growth direction and fracture morphology. These behavioural changes hint as to the effects of the of ply replacement in obstructing the kink-band propagation.

The concepts key component is the removal of fibres that would enable kink-band to propagate in its preferential growth direction. Upon reaching a geometric discontinuity in lay-up, a fraction of the dynamic fracture energy is reflected, reducing its momentum. Beyond that, in the absence of 0° plies to allow perpendicular growth, fracture is forced to seek alternative routes. This increases the length of the failure path, resulting in higher energy dispersion and posing an obstacle to failure growth.

Together with the more tortuous failure path caused by crack deflection, the increase in secondary damage surfaces contributes to energy dissipation. These factors also hint to the reasons behind the higher performance of the ±45° feature configuration. By further redirecting the fracture's path and successfully splitting its growth into two main fronts, this lay-up potentializes energy dissipation. Similarly, this behaviour results in a significantly higher amount of secondary fracture surfaces, hampering crack growth.

6 CONCLUSIONS

A crack-arrest concept for CFRPs under compression was developed and experimentally validated. The feature successfully arrested unstable kink-band propagation, significantly delaying ultimate failure and enhancing the strain tolerance of the tested elements. Two configurations of the feature were tested, using off-axis angles of ±30° and ±45°. Their performances were compared to suitable baselines and to one another.

The feature operates by locally introducing fibre orientation discontinuities, which deflect the crack and create longer, more tortuous failure paths. This results in increased kink-band energy dissipation. Additionally, the soft lay-up experiences more secondary damage, aiding energy dissipation and enhancing crack arrest.

The ±30° feature demonstrated a one-third increase in ultimate failure strain, relative to its baseline. Meanwhile, the ±45° feature was able to nearly double its baseline's strain tolerance. When compared to one another, the ±45° feature was evaluated as the most promising, displaying larger amounts of secondary fracture and longer failure paths. Therefore, despite possessing a larger weight penalty, its significant increase in ultimate strain represents a promising route for fail-safe design.

Future work will focus on reducing the weight penalty associated to the crack-arrest feature. For that purpose, the minimum arrest band width necessary to stop failure propagation will be defined.

Additionally, a study of weight penalty reduction by reinserting stiffer plies into the soft lay-up will be performed.

ACKNOWLEDGEMENTS

The authors kindly acknowledge the funding for this research provided by UK Engineering and Physical Sciences Research Council (EPSRC) programme Grant EP/T011653/1, Next Generation Fibre-Reinforced Composites (NextCOMP): a Full-Scale Redesign for Compression a collaboration between Imperial College London and the University of Bristol. For the purpose of open access, the authors have applied a Creative Commons Attribution (CC BY) license to any author accepted manuscript version arising.

REFERENCES

[1] Q. Sun et al. “Experimental and computational analysis of failure mechanisms in unidirectional carbon fiber reinforced polymer laminates under longitudinal compression loading”. In: *Composite Structures* 203 (2018), pp. 335–348 (see p. 1).
[2] S. Nunna, A.R. Ravindran, J. Mroszczok, C. Creighton and R.J. Varley. A review of the structural factors which control compression in carbon fibres and their composites, *Composite Structures*, 303, p.116293, 2023.
[3] C.V. Opelt, G.M. Cândido and M.C. Rezende. Compressive failure of fiber reinforced polymer composites – A fractographic study of the compression failure modes, *Materials Today Communications*, 15, pp.218-227, 2018.
[4] B.M. Albaghdadi and A.O. Cherniavsky. Possibility of using ribs to protect pipelines from the long crack propagation, Bulletin of the South Ural State University. Ser. Mechanical Engineering Industry, 16(3), pp.15-20, 2016.
[5] X.K. Zhu. State-of-the-art review of fracture control technology for modern and vintage gas transmission pipelines, Engineering Fracture Mechanics, 148, pp.260-280, 2015.
[6] A. Velicki and D.C. Jegley. PRSEUS structural concept development, In 52nd Aerospace Sciences Meeting, p. 0259, 2014.
[7] J. Ankersen et al. Dynamic fracture in CFRP panels under compressive loading. Proceedings of the 15th European Conference on Composite Materials. 2012.
[8] E.S. Greenhalgh. Failure analysis and fractography of polymer composites. Elsevier, pp.117-126, 2009.
[9] E.S. Greenhalgh. Technical Evaluation of DAMOCLES; Damage Management of Composite Structures for Cost-Effective Life-Extensive Service, Technical Report QinetiQ/FST/TR023421, 2002.

INTEGRATION OF FUZZY CARBON OVERBRAIDS INTO STRUCTURAL MEMBERS FOR IMPROVED COMPRESSIVE PERFORMANCE

Iheoma Chigoziri Nwuzor, Laura Rhian Pickard, Bohao Zhang, Xiaodong Xu, Nicolas Darras, Ian Lee, Kawthar Alkateb, Curtis Wong, Darren Lo, Giuliano Allegri, Michael R Wisnom, & Richard S Trask

Bristol Composites Institute, University of Bristol

Laura.Pickard@Bristol.ac.uk

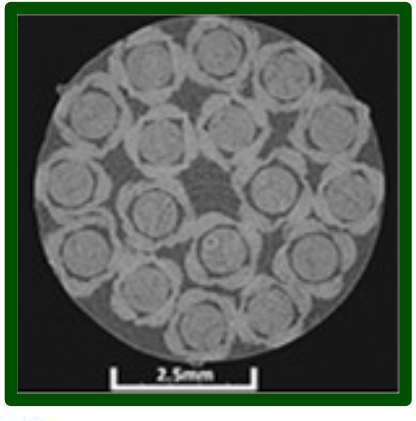

Next COMP
Next Generation Fibre-Reinforced Composites

IMPERIAL

The Composites Centre

University of BRISTOL
Bristol Composites Institute

UK Research and Innovation

Engineering and Physical Sciences Research Council

NEXT GENERATION FIBRE-REINFORCED COMPOSITES

A full scale redesign for compression

NextCOMP takes inspiration from the hierarchical structure of natural materials

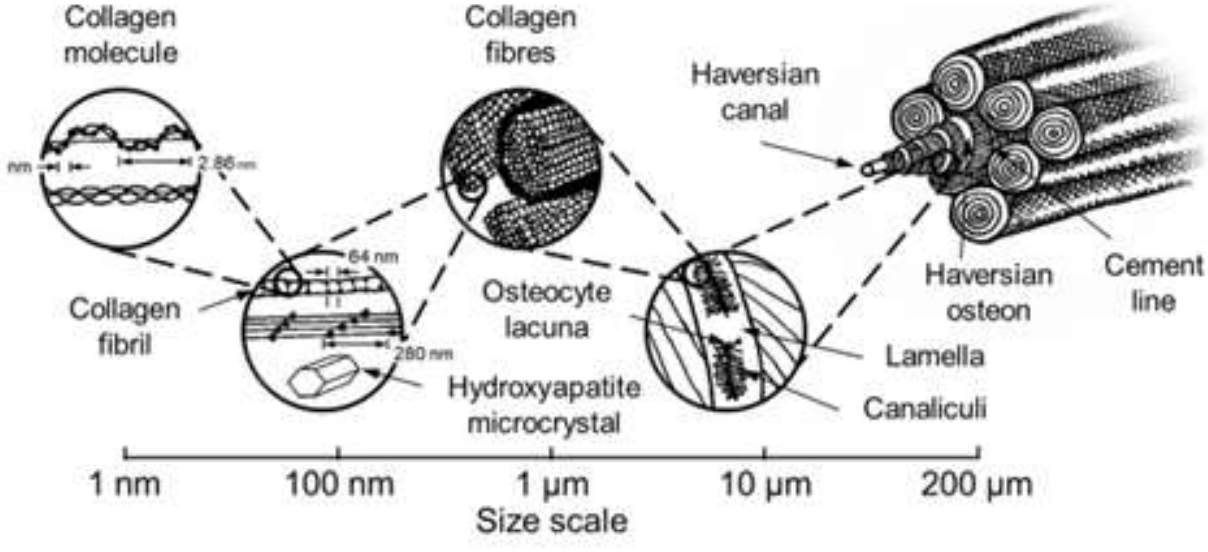

Illustration of the structure of human compact bone, a biological, hierarchical composite. Adapted from R. Lakes, "Materials with structural hierarchy," Nature, vol. 361, no. 6412, pp. 511–515, Feb. 1993, doi: 10.1038/361511a0.

IMPERIAL

NextCOMP

University of BRISTOL
Bristol Composites Institute

HIERARCHICAL COMPOSITES

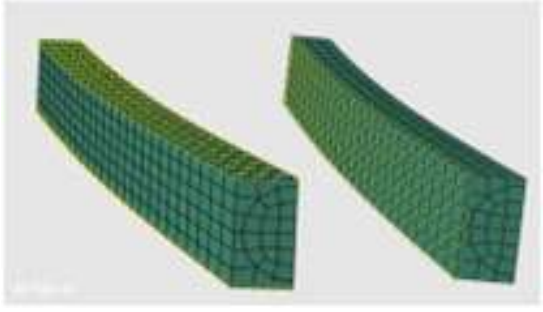

Mechanistic modelling

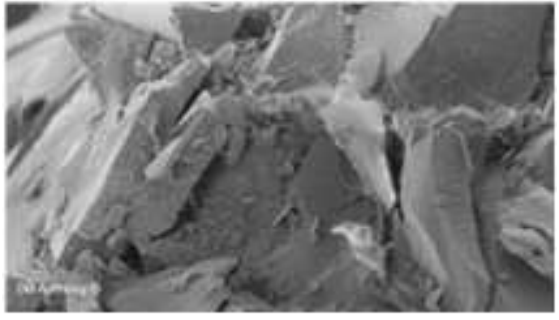

Resin systems

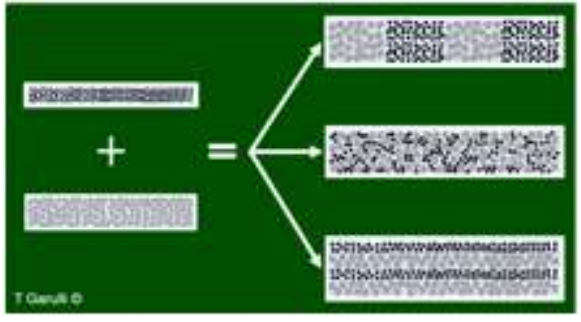

Ply level systems



In-Situ mechanistic studies

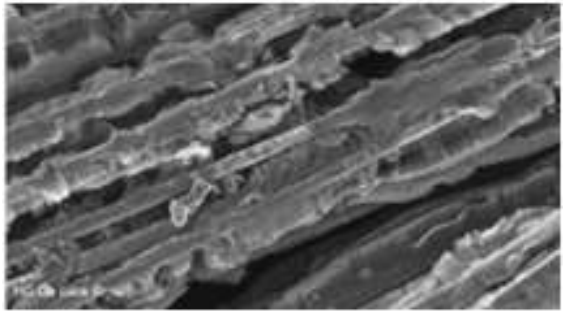

Fibre platforms



Bundle systems

HIERARCHICAL APPROACH: BUNDLE SYSTEMS

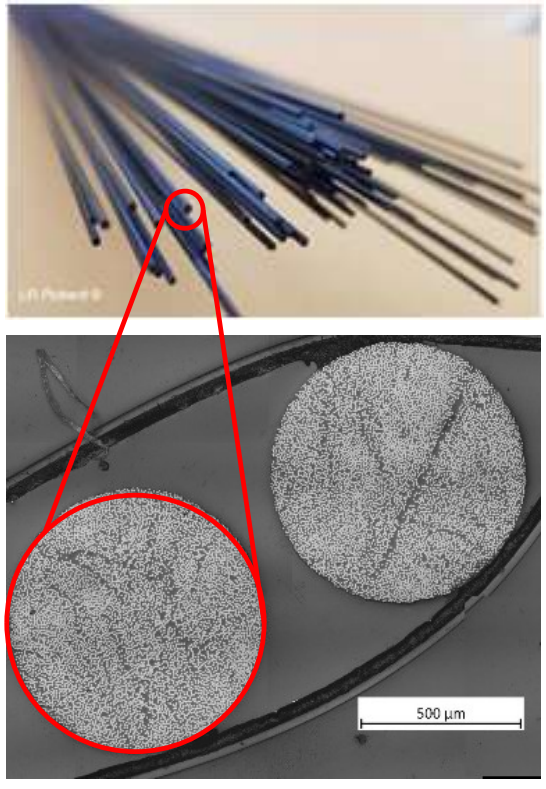



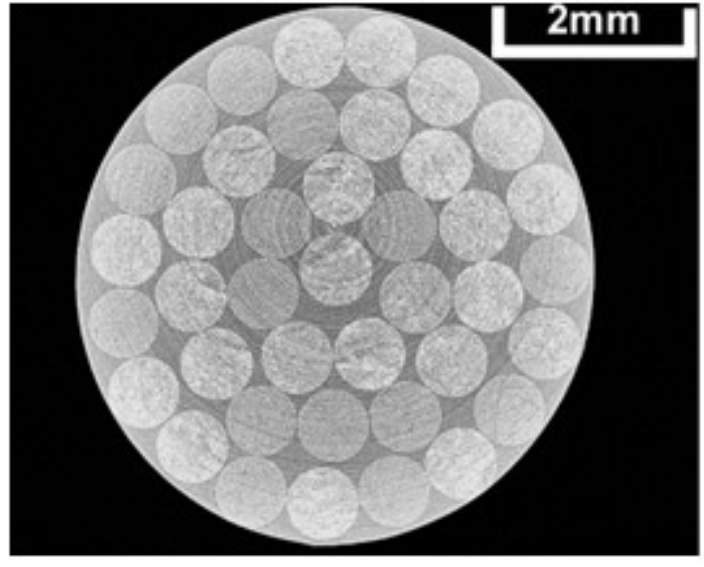

Top left: pultruded carbon fibre-epoxy rods. Bottom left: Microscope image of rod cross sections. Top right: Strut. Bottom right: X-ray CT slice showing cross section of strut.

CYLINDRICAL STRUCT MANUFACTURE



Church lane bridge over A4174, Google maps

- Initial trial used flexible mould with outer constraint
- Moved to fixed multi-part mould for geometrical regularity
- Resin heated and injected at $5x10^5$Pa
- Porosity below limit of detection in Nikon XTH-320 X-ray CT scanner

- Optimisation of packing
- Material hybridisation

- Tested in buckling

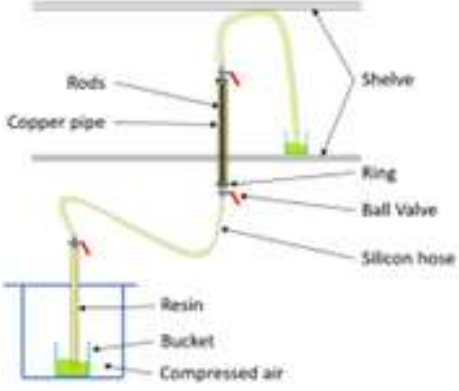

Manufacturing approach with flexible mould



Fixed geometry multi part mould

OVERWINDING AND OVERBRAIDING

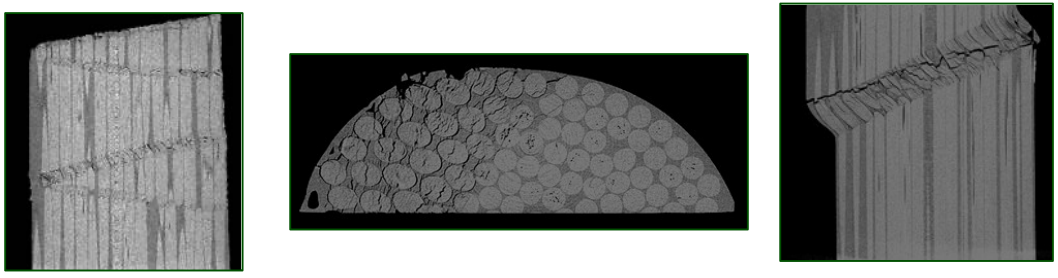

Samples from Potter et al 2000,CT scans L R Pickard. Following compression after impact tests. Overwound strut (left) exhibited greater compressive strength than without overwind (centre, right)

- Can we apply this in a hierarchical manner?
  - Overbraid individual rods
  - Constrain kink band formation at rod level



Herzog microbraider with 8 tows PBO 273dtex overbraiding pultruded rod.

Expected Effect of Overbraiding Rods

- Model 'halo' of shear support around rod based on fit to data

$$\sigma_{shear} = G_1(1 - e^{-G_2\varepsilon})$$

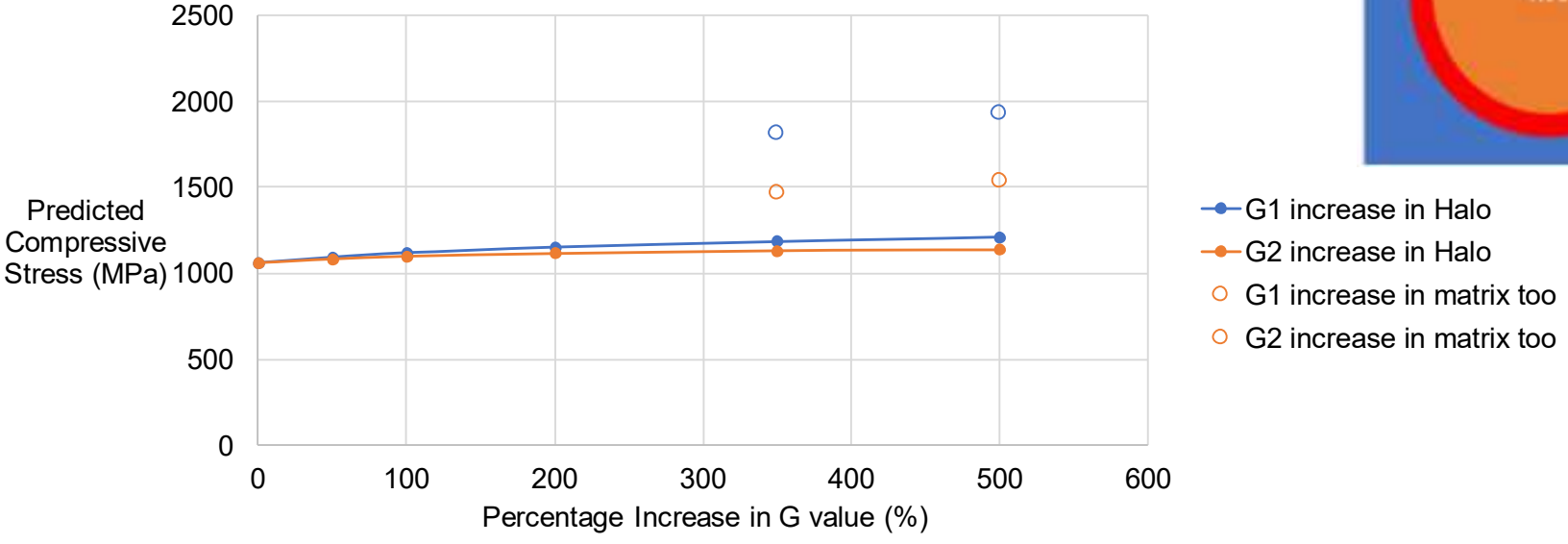

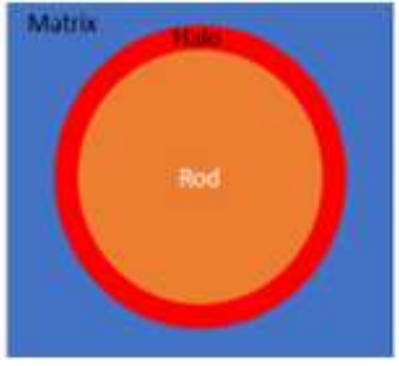

- How can we create this extended zone of shear support?

Fuzzy Carbon Overbraids

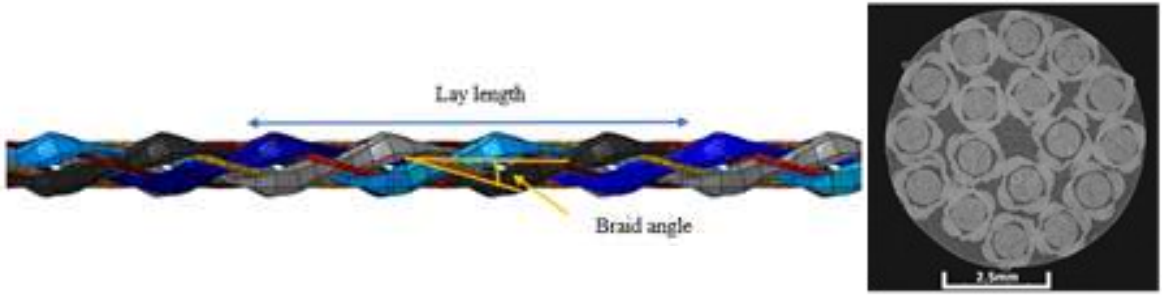

Left: diagram illustrating lay length.

Right: X-ray CT scan of Strut consisting of pultruded rods with fuzzy carbon overbraids, image I. Nwuzor

- Short lay length with brittle fibres-> fuzzy effect
- Fuzzy carbon-> shear support in wide region around rod
  - Plain vs overbraided rods
  - Different lay lengths

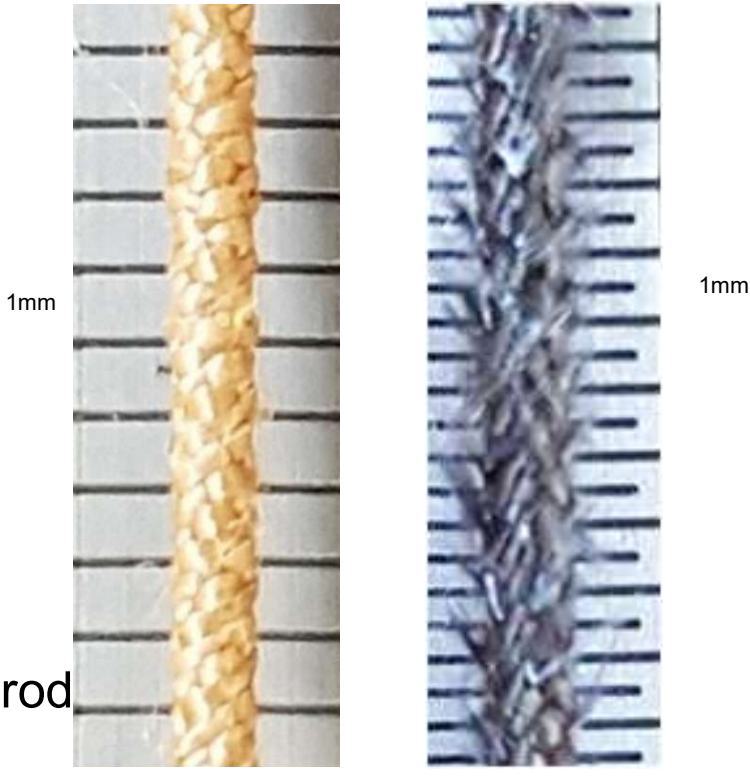

Rods overbraided with Zylon (left) and fuzzy Carbon

L. R. Pickard, G. Allegri, and M. R. Wisnom, *ECCM20.*, 2022
DOI: 10.5075/epfl-298799_978-2-9701614-0-0

TESTING AND ANALYSIS

- Strut trimmed to 300mm
- 3 strain gauges around centre at 120 degree spacing
- X-ray CT imaging
- Strut tested in eccentric buckling at 3mm/min

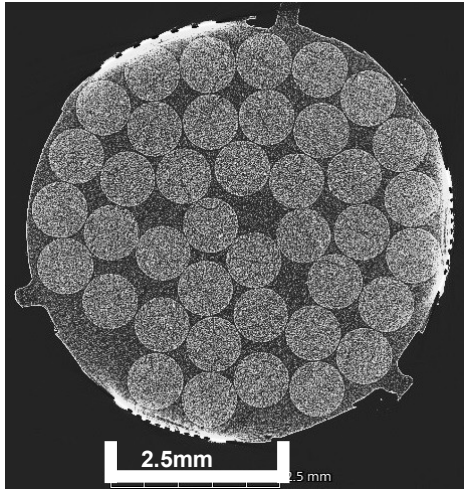

X-ray CT cross section of strut showing strain gauges

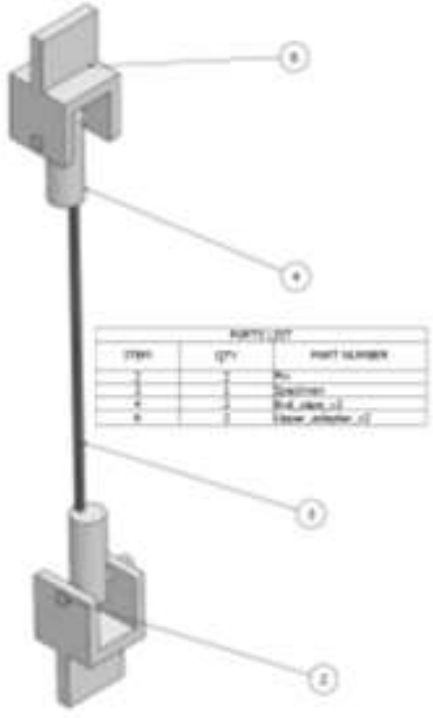

TESTING AND ANALYSIS

- Strut trimmed to 300mm
- 3 strain gauges around centre at 120 degree spacing
- X-ray CT imaging
- Strut tested in eccentric buckling at 3mm/min

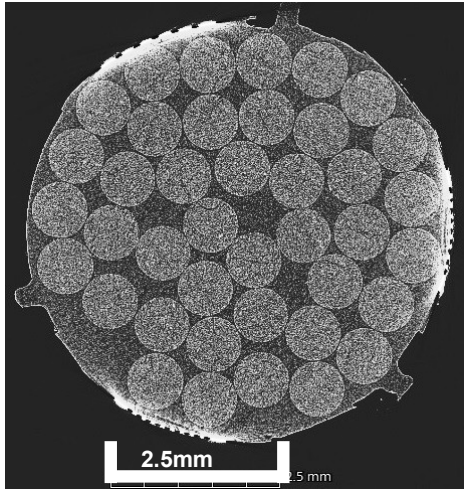

X-ray CT cross section of strut showing strain gauges



TESTING AND ANALYSIS

- Strut trimmed to 300mm
- 3 strain gauges around centre at 120 degree spacing
- X-ray CT imaging
- Strut tested in eccentric buckling at 3mm/min

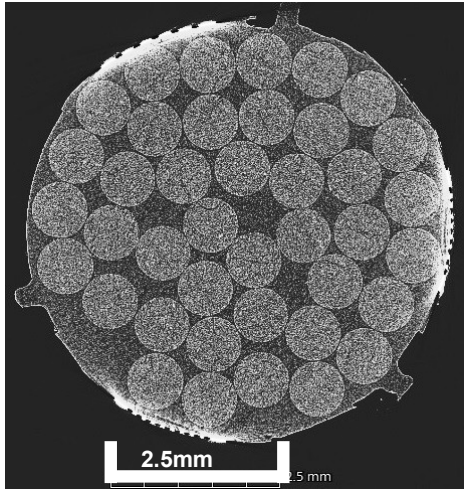

X-ray CT cross section of strut showing strain gauges



FRACTOGRAPHY EXAMPLES

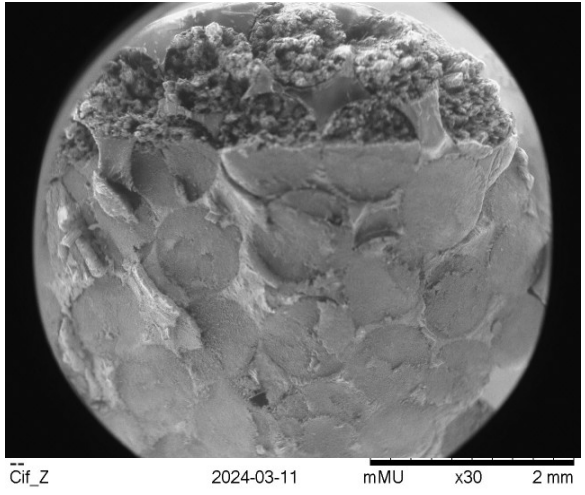

Failure surface of strut with plain rods, no overbraids

FRACTOGRAPHY EXAMPLES

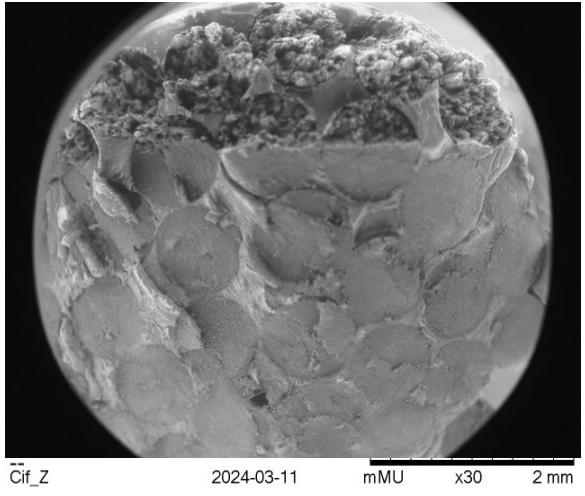

Failure surface of strut with plain rods, no overbraids

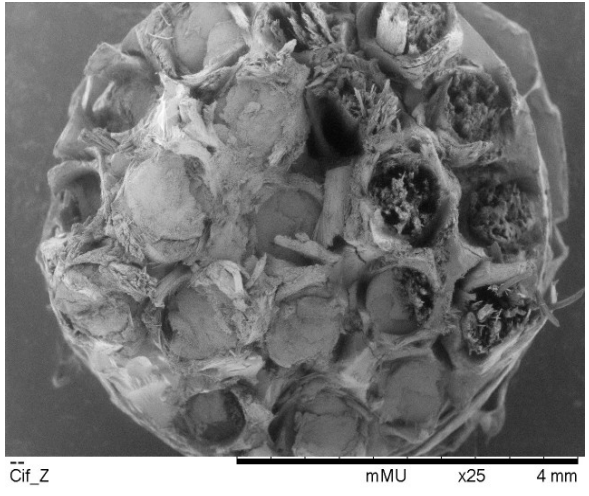

Failure surface of strut with 6mm lay length overbraids

FRACTOGRAPHY EXAMPLES

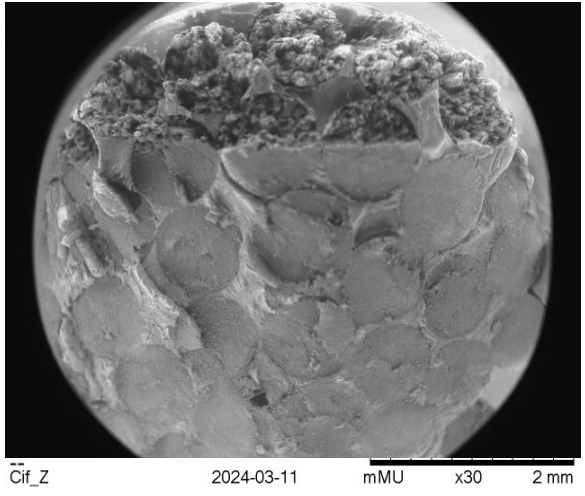

Failure surface of strut with plain rods, no overbraids

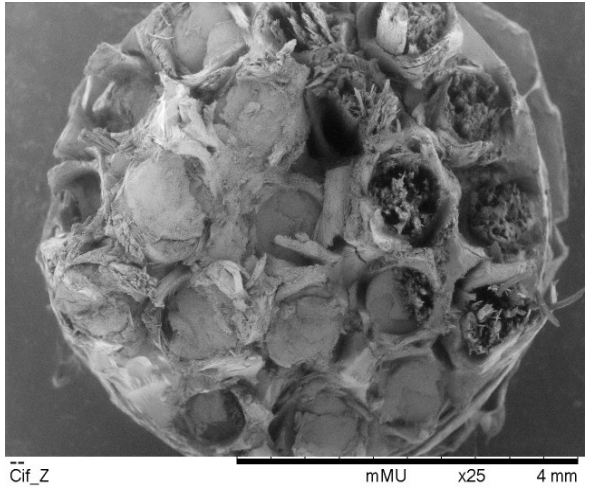

Failure surface of strut with 6mm lay length overbraids

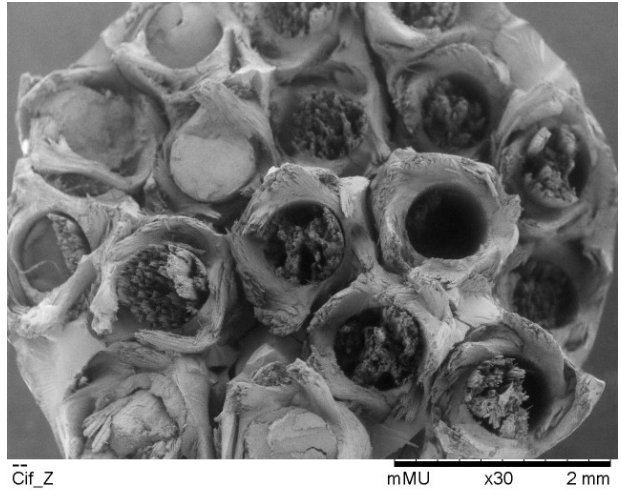

Failure surface of strut with 2.5mm lay length overbraids (fuzzy)

FRACTOGRAPHY EXAMPLES



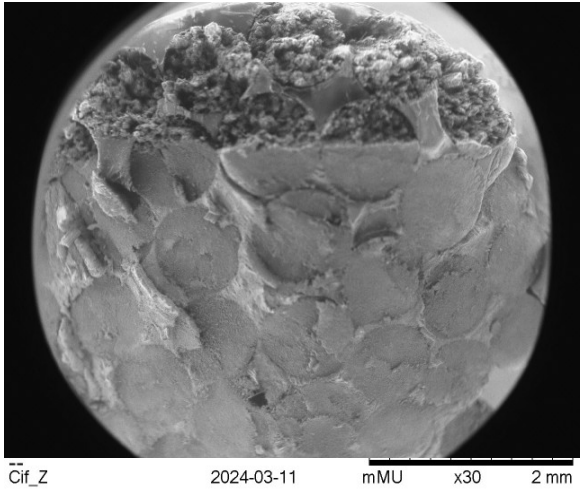

Failure surface of strut with plain rods, no overbraids

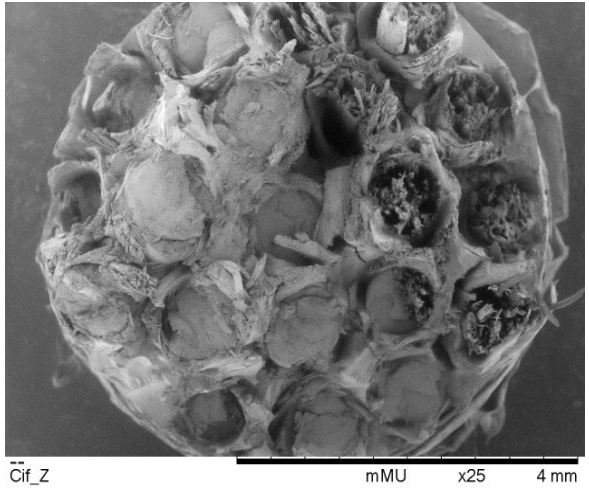

Failure surface of strut with 6mm lay length overbraids

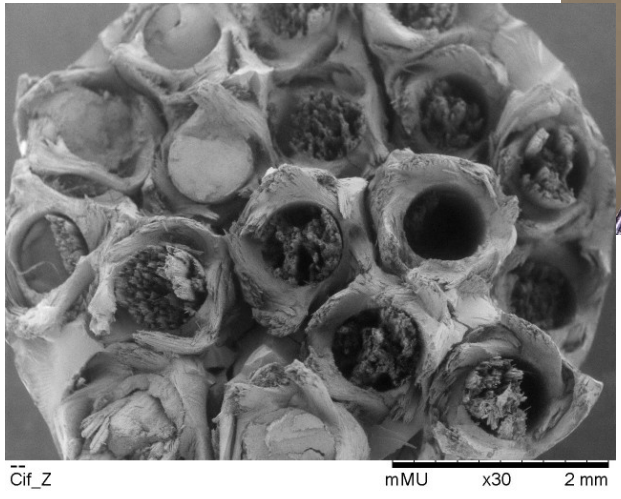

Failure surface of strut with 2.5mm lay length overbraids (fuzzy)

KEY RESULTS

- Struts with 0.8mm diameter rods manufactured and tested in buckling:
  - Plain rods, no overbraids
  - 8 x 1k T300 carbon fibre overbraids of lay length:
    - 2.5mm, fuzzy carbon
    - 4mm
    - 6mm
- Struts with 2.5mm lay length overbraids failed in **tension**, all others in **compression**
  - Indicates improved performance in compression with fuzzy carbon overbraid
- Hybridised carbon/aramid overbraids can improve packing while keeping ‘fuzzy carbon’ aspect
- 4x 1 T300 carbon fibre and 4x aramid initial trials carried out
  - Both tensile and compressive failure seen

IMPERIAL

Next COMP

University of BRISTOL
Bristol Composites Institute

SUMMARY

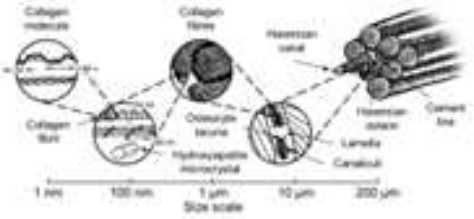

- Hierarchical, biomimetic composite structures offer a new design space
- Struts made with pultruded rod elements are suitable for use in a variety of applications



- Overbraiding rods with carbon creates a ‘fuzzy’ effect at low lay length due to partial breakage
  - Increase fibre-resin contact region
  - Shear support of fibre
  - Initial results indicate change in failure mode under buckling
    - Increased performance under compression

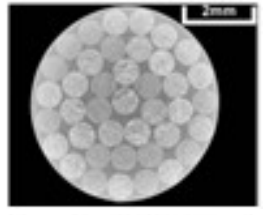

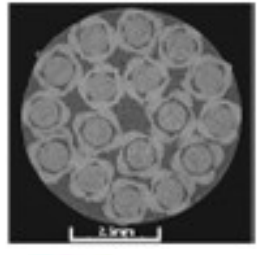

IMPERIAL

Next COMP

University of BRISTOL
Bristol Composites Institute



Next COMP
Next Generation
Fibre-Reinforced Composites

https://nextcomp.ac.uk

I would like to acknowledge funding which supported this work from the UK Research and Innovation - EPSRC Programme Grant; Next Generation Fibre-Reinforced Composites: A Full Scale Redesign for Compression (EP/T011653/1)

A collaboration between Imperial College London and University of Bristol

IMPERIAL

University of BRISTOL
Bristol Composites Institute

Compression behavior of unidirectional carbon fiber/filler reinforced plastics

Masahito Ueda[1], Ryuji Nishi[1], Naruki Ichihara[1] and Kohei Yamada[2]

[1] Nihon University, Japan

[2] Industrial Technology Center of Fukui Prefecture, Japan

NU CST 100TH 1920 » 2020

Background : axial compressive strength of UD CFRP

- Current status of tensile vs compressive strength of unidirectional carbon fiber reinforced plastics (UD CFRP).

T300
- Fiber ・・・ Tensile strength 3,530 MPa
- UD CFRP (V_f = 0.6) ・・・ Tensile strength 1,860 MPa (≈3530×0.6, Rule of mixture)
  Compressive strength 1,470 Mpa

T1000
- Fiber ・・・ Tensile strength 6,370 MPa
- UD CFRP (V_f = 0.6) ・・・ Tensile strength 3,040 MPa (≈6370×0.6, Rule of mixture)
  Compressive strength 1,570 MPa

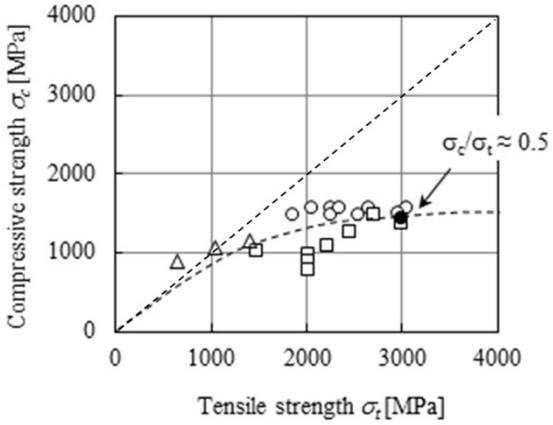

Tensile and compressive strength of UD CFRP [1)]

Toray
□ M35J
M30G
M30S
M40
M40J
M46J
M50J
M55J
M60J

Toray
○ T300
T300J
T400H
T600S
T700G
T700S
T800H
T800S
T1000G

Nippon Graphite Fiber
△ XN-05
XN-10
XN-15

Toray
● T800S/2592

Lower compressive strength than tensile strength

UD CFRP shows unbalanced mechanical property

1) M. Ueda et. al., Composites Part A, 67 (2014), 96-101.

Background : prediction of axial compressive strength

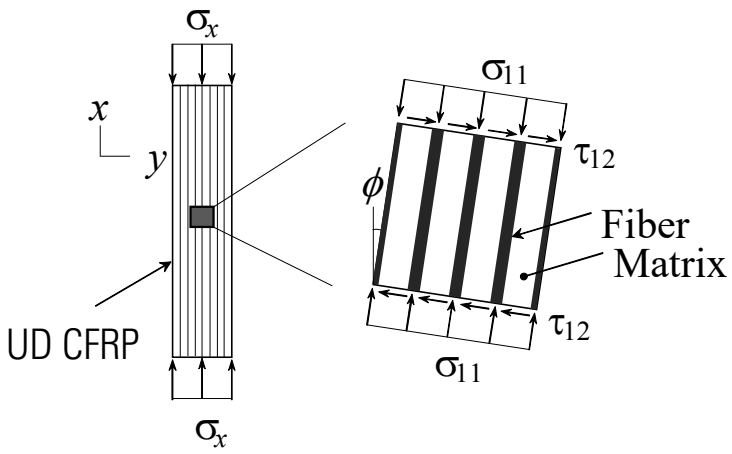

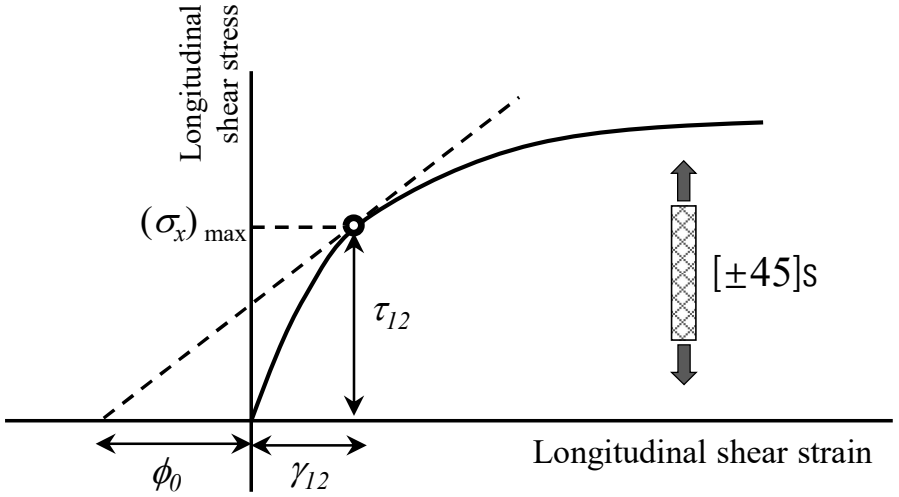

- Axial compressive stress of a UD CFRP is expressed as [2,3]

$$\sigma_x \approx \frac{\tau_{12}}{(\phi_0 + \gamma_{12})}$$

τ_{12}, γ_{12} : Longitudinal shear stress and strain
ϕ_0 : Fiber misalignment angle

- Maximum σ_x indicates a compressive strength.

- Longitudinal shear stress-strain relation of a UD CFRP and the determination of compressive strength [4]

Compressive strength is determined by
- fiber misalignment (ϕ_0)
- shear stress-strain relation (τ_{12}-γ_{12})

2) M.R. Wisnom, Composites, 21, (1990), 403-407.
3) B. Budiansky, N.A. Fleck, J Mech Phys Solids, 41, (1993), 183-211.
4) I.M. Daniel, et. al., Composites Part B, 27, (1996), 543-552.

Background : prediction of axial compressive strength

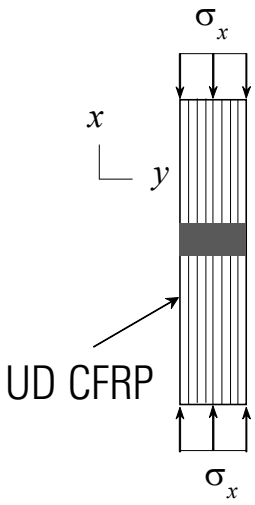

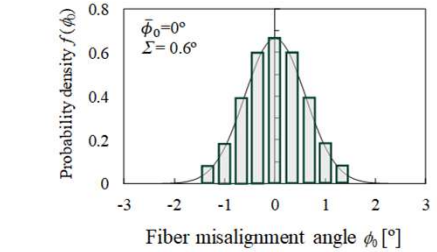

Fiber misalignment angle distribution

Grouping of fibers based on the misalignment angle

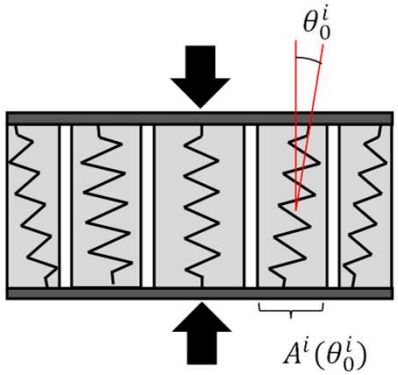

$$\bar{\sigma}_x = \sum_i \sigma_x^i A^i$$

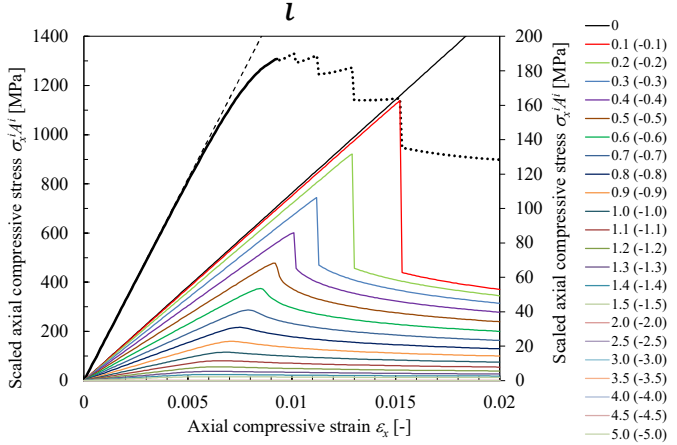

The contribution of each fiber group to the load bearing was calculated and summed based on the area ratio A^i. [5)]

Compressive strength is determined by

- fiber misalignment and the distribution (mean angle ϕ_0 and the standard deviation Σ)
- shear stress-strain relation (τ_{12}-γ_{12})

5) M. Ueda et. al., Composites Part A, 175, (2023), 107821.

Objectives : Toward improved axial compressive strength

What is already clear from previous researches

- Compressive strength could be increased by

  improving shear-stress-strain relation without degrading fiber misalignment and distribution.

Objectives

- Improved axial compressive strength of UD CFRP

Contents

- Epoxy matrix was modified by three types of fillers: improving shear-stress-strain relation.
- UD CFRP was fabricated based on prepreg-autoclave molding method.
- Fiber misalignment distribution was measured by X-ray CT imaging: to ensure that the fibers are not misaligned.
- Compression tests were performed, and the compressive strength was evaluated.

Materials and Methods

- Materials

  Carbon fiber : MR50R-12M, Mitsubishi Chemical
  Epoxy resin : Bisphenol A epoxy resin (130deg cure)
  Filler : 1 (Nanoscale filler), 2.0wt%
  2 (Sub-micron scale filler), 1.5wt%
  3 (Nanoscale filler), 0.2wt%

  *Weight fraction was the ratio to the epoxy resin.
  *Weight fraction of fillers was determined based on the viscosity suitable for prepreg production.

- Prepreg : Thin-ply prepreg technique (t =0.04mm)

⇨ Four types of unidirectional prepreg sheets were fabricated with fiber volume fraction Vf = 60%.

ID	Carbon fiber	Epoxy resin	Filler	Filler content
CFRP	MR50R-12M	Bisphenol A epoxy	None	-
CFRP_1			1	2.0wt%
CFRP_2			2	1.5wt%
CFRP_3			3	0.2wt%

Materials and Methods

- Fabrication technique

  Autoclave molding



UD CFRP laminate



Compression test specimen

- Specimen configuration

  Rectangular coupon : Overall dimension 140×12×2 mm
  (ASTM D6641) Gage section 12×12.7mm
  End tabs : The same CFRP

- Compression test

  Loading type : Combined loading (ASTM D6641)
  Loading speed : 1.3 mm/min

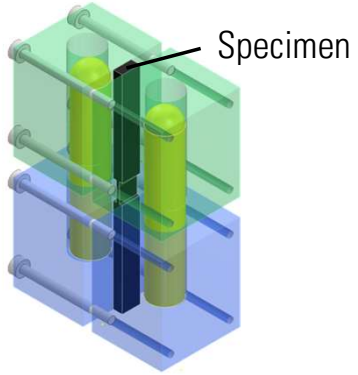

Schematic image of compression test jig

Materials and Methods

- Measurement of fiber misalignment distribution
  - A X-ray CT system : TDM1601-II, Yamato Scientific, Japan
  - The fiber misalignment angle was quantitatively calculated using the structure tensor analysis technique [6].

    [Step 1] Cross-section of UD CFRP photographed using X-ray CT system

    [Step 2] Distinguishing carbon fibers from epoxy in the cross-section (threshold processing)

    [Step 3] Structure tensor analysis and calculation of misalignment angles

[Step 1]

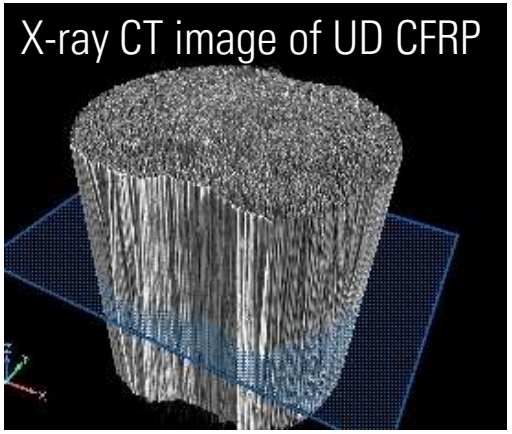

[Step 2]

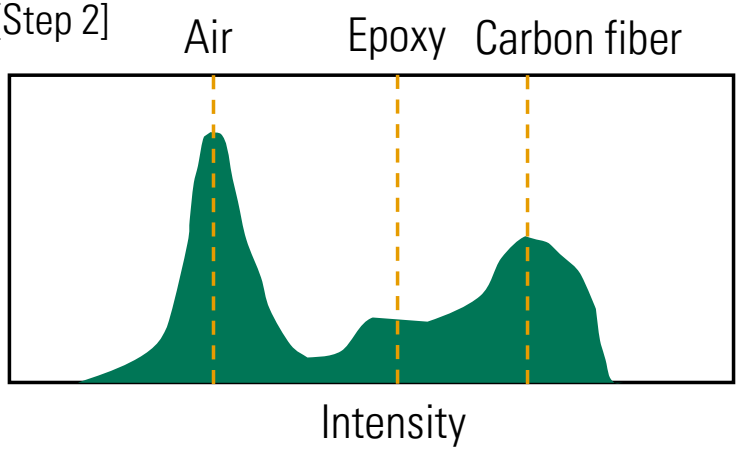

6) N, Mikkelsen LP, et. al., Compos Appl Sci Manuf, 149 (2021), 106541

Materials and Methods

- Measurement of fiber misalignment distribution
  - A X-ray CT system : TDM1601-II, Yamato Scientific, Japan
  - The fiber misalignment angle was quantitatively calculated using the structure tensor analysis technique [6].

[Step 1] Cross-section of UD CFRP photographed using X-ray CT system

[Step 2] Distinguishing carbon fibers from epoxy in the cross-section (threshold processing)

[Step 3] Structure tensor analysis and calculation of misalignment angles

[Step 3]

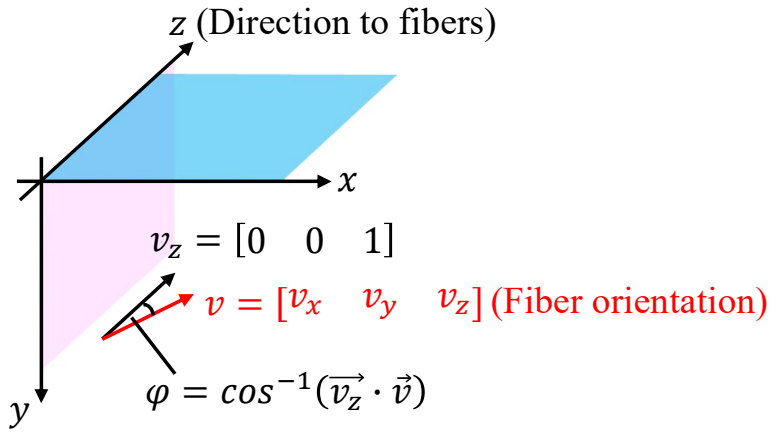

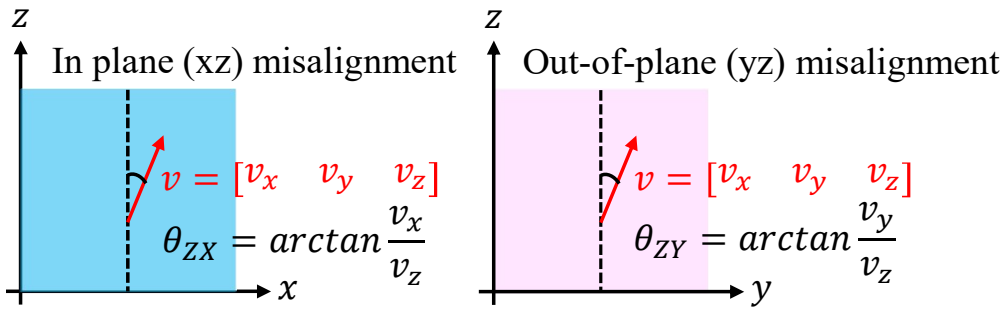

6) N, Mikkelsen LP, et. al., Compos Appl Sci Manuf, 149 (2021), 106541

Results : Fiber misalignment angle distribution

- Fiber misalignment angle of CFRP_1

  Fiber alignment was not disturbed by the inclusion of filler.

  (Note: The average angle is meaningless because it depends on the angle error of the sample cut-out and the placement of sample in the CT scanner).

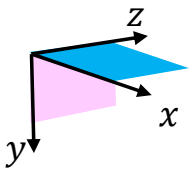

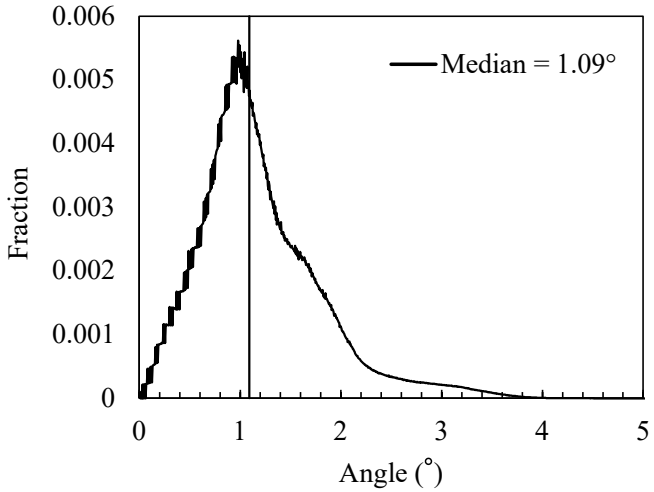

(a) Misalignment angle from axial direction (z axis)

Standard deviation ± 0.88°

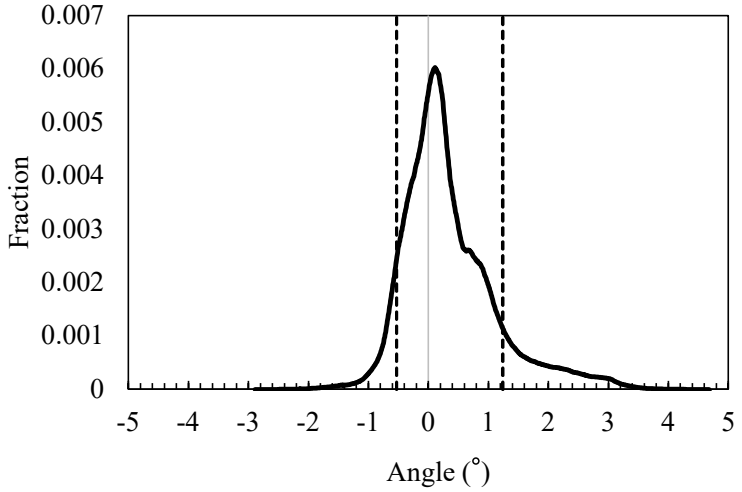

(b) In-plane (xz) misalignment

Standard deviation ± 0.66°

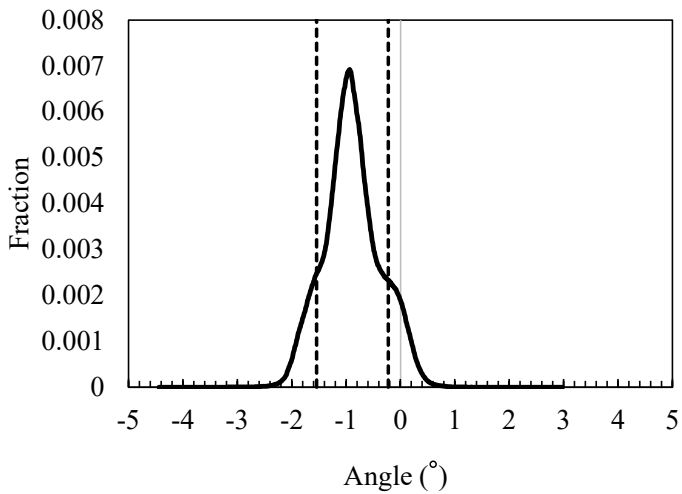

(c) Out-of-plane (yz) misalignment

Distribution of fiber misalignment angle

Results : Failure modes

- Compression stress-stroke

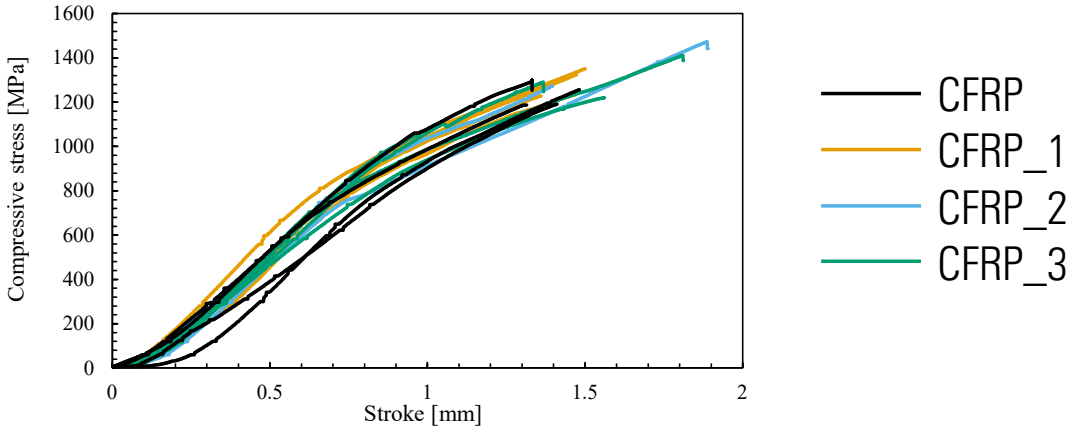

- Failure modes

  Kink band failure followed by splitting

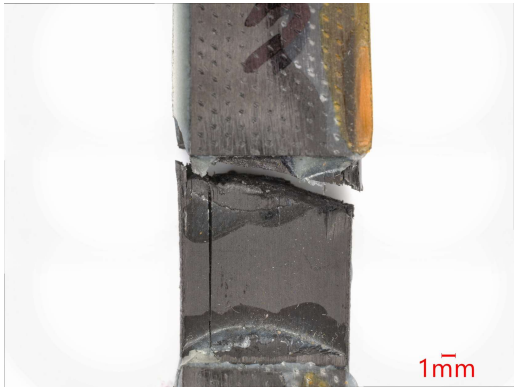

CFRP



CFRP_1

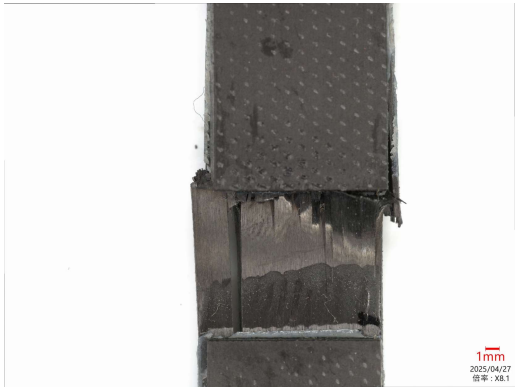

CFRP_2

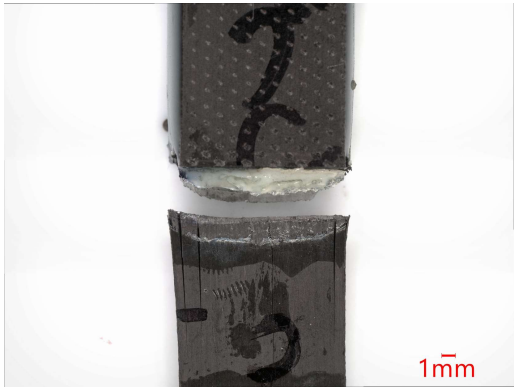

CFRP_3

Results : Compressive strength

- Compressive strength improvement rate relative to CFRP without filler reinforcement.
  CFRP_1 ：4.1%
  CFRP_2 ：11%
  CFRP_3 ：0.9%
- Reinforcement of epoxy resin with fillers improved the compressive strength under conditions where fiber alignment was not degraded.
- The improvement effect varies depending on the type of filler.

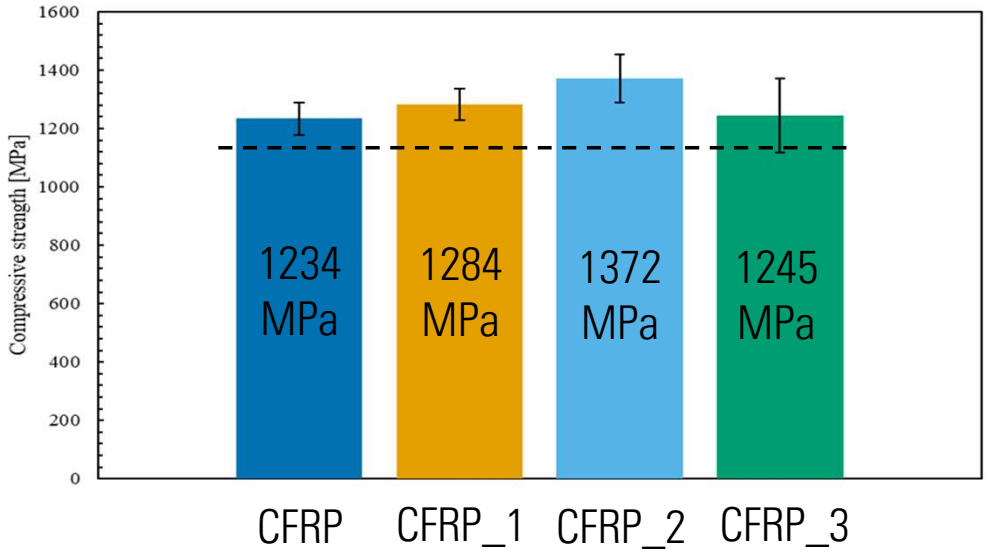

Conclusions

- Four types of unidirectional carbon fiber/filler reinforced plastic were fabricated using a prepreg-autoclave molding method.
- Compressive strength was improved by reinforcing the matrix with filler, provided that the fillers did not degrade the fiber alignment and the distribution.
- The effect of fillers on the axial compressive strength varied depending on the filler type.

Free app for Compressive strength estimation

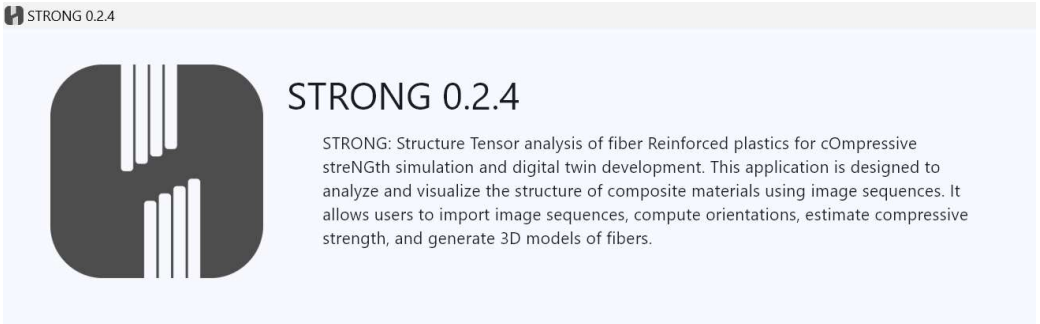

https://github.com/Naruki-Ichihara/strong/releases/tag/v0.2.4

Questions and comments

ueda.masahito@nihon-u.ac.jp

RAMAN SPECTROSCOPIC AND FIB-SEM INSIGHTS INTO COMPRESSIVE FRAGMENTATION OF HIGH MODULUS CARBON FIBRES MODEL COMPOSITES

Cameron G. Woodgate[1], Christopher P. Jones[2], Richard S. Trask[3], Milo S.P. Shaffer[4], Stephen J. Eichhorn[5]

[1]Bristol Composites Institute, School of Civil, Aerospace and Design Engineering
University of Bristol, University Walk, Bristol, BS8 1TR, UK.
Department of Materials and Department of Chemistry, Imperial College London,
South Kensington Campus, London, SW7 2AZ, UK.
Email: c.woodgate@imperial.ac.uk

[2]Interface Analysis Centre, School of Physics, H. H. Wills Physics Laboratory
University of Bristol, Bristol, BS8 1TL, UK.
Email: cj0810@bristol.ac.uk

[3]Bristol Composites Institute, School of Civil, Aerospace and Design Engineering
University of Bristol, University Walk, Bristol, BS8 1TR, UK.
Email: R.S.Trask@bristol.ac.uk

[4]Department of Materials and Department of Chemistry, Imperial College London,
South Kensington Campus, London, SW7 2AZ, UK.
Email: m.shaffer@imperial.ac.uk

[5]Bristol Composites Institute, School of Civil, Aerospace and Design Engineering
University of Bristol, University Walk, Bristol, BS8 1TR, UK.
Email: s.j.eichhorn@bristol.ac.uk

Keywords: Carbon fibre, Debonding, Fragmentation, Electron Microscopy

ABSTRACT

Compressive failure in unidirectional carbon fibre reinforced polymers remains a critical limitation in structural design. This study integrates findings from previous Raman spectroscopy analysis and a novel focused ion beam scanning electron microscopy (FIB-SEM) methodology to investigate fundamental micromechanical failure in high-modulus (HM) polyacrylonitrile carbon fibres under compressive loading. FIB-SEM offers high-resolution 3D imaging of fibre break geometries. The combination of Raman spectroscopy and FIB-SEM confirms shear-type fragmentation and interfacial debonding mechanisms previously predicted through Raman analysis, enabling a deeper understanding of compressive failure processes in Carbon Fibre Reinforced Plastics (CFRPs). To enable FIB-SEM imaging of model composite samples, careful sample preparation is required, following specific steps to allow imaging to be carried out.

1 INTRODUCTION

The compressive properties of unidirectional carbon fibre reinforced polymer composites (CFRPs) are widely recognised as inferior to their tensile performance [1], often forming a critical limitation in structural applications. Improving compression strength and reliability requires a detailed understanding of the failure mechanisms associated with each constituent material. While matrix shear yielding is commonly implicated in compression failure, the role of the fibre–matrix interface and fibre fragmentation, particularly in high-modulus (HM) fibres—is also thought to be dominant [1].

Direct mechanical testing of individual fibres in compression remains challenging due to their small scale and high aspect ratio [2]. Raman spectroscopy offers an indirect yet effective technique to probe

micromechanical and interfacial responses in carbon fibres subjected to compressive loading. The method enables spatially resolved stress mapping at sub-micron resolutions (0.5–2 μm), by detecting changes in atomic vibrational frequencies induced by deformation [3].

Previous studies have utilised Raman spectroscopy to monitor the evolution of local stress states in fragmenting HM fibres, tracking deformation across individual fibre segments [4,5]. Coupling Raman mapping with optical microscopy allows predictions regarding fibre fragmentation geometry and interfacial behaviour and how they evolve with increasing deformation [4]. To validate key predictions, an advanced imaging technique, focused ion beam scanning electron microscopy (FIB-SEM) has been employed. FIB-SEM enables nanometre-scale serial sectioning and imaging, allowing for high-resolution 3D reconstruction of fibre failure geometries. FIB-SEM is widely used in many fields for transmission electron microscope (TEM) foil preparation and preparation of specimens for micromechanical testing, including micropillar compression of carbon fibres [5,6].

In this work, FIB-SEM was applied to single fibre model composites previously characterised by Raman spectroscopy. This novel integrated approach enables the identification and high-resolution 3D reconstruction of fibre failure geometries, including shear-type fractures and interfacial debonding; offering direct validation of micromechanical predictions [4]. The combination of quantitative Raman stress mapping with high-resolution FIB-SEM imaging provides a robust framework for understanding compressive failure in HM carbon fibres.

To enable features of interest to be located and imaged with high resolution SEM, careful sample preparation methodology is required. The following discussion will focus on how samples are prepared, with some initial data to demonstrate the feasibility of the technique.

2 METHODOLOGY

Model composites were prepared by embedding a single fibre near the surface of an epoxy prism, then fragmented in uniaxial compression. Key features identified during *in situ* Raman stress mapping were located by introducing surface landmarks, allowing serial block face imaging via FIB-SEM, to explore the local microstructure in 3D at high resolution (~10 nm).

2.1 SAMPLE PREPARATION

Model composite samples used here, were prepared as described elsewhere [4,7,8]. Samples were short, 2-5 mm, single carbon fibres (Toray M46J and M55J) embedded in epoxy prisms (Huntsman LY5052 and Aradur 5052CH) forming single fibre model composites. Model composite samples were fabricated and subjected to uniaxial compression with *in situ* Raman spectroscopic measurements to measure stress. Samples discussed here were imaged in their post-fibre failure, relaxed states. Fibres in imaged samples were encapsulated ~10-30 μm below the surface of epoxy, verified with laser scanning confocal microscopy. Post-deformation, the samples were imaged using optical microscopy to identify features of interest and measure their positions along the fibres relative to local surface features. This step was essential as the fibre cannot be observed using SEM without removing the encapsulating layer surrounding the feature.

Fibre locations were marked by scratching the epoxy surface with a needle to indicate the general positions of interest. To aid fibre identification using SEM, a Parallel Bar 100 Mesh TEM grid (Agar Scientific Ltd) was adhered to the epoxy surface using polyvinyl chloride based adhesive tape, as shown in Figure 1. Optical microscopy (Euromex bScope® metallurgical microscope coupled with a VC.3040 UHD-4K camera) was used to map the features of interest relative to the TEM grid.

A conductive gold coating was sputtered onto the sample surface, with the TEM grid in place, to improve surface conductivity for SEM imaging. Multiple coatings were applied to ensure adequate conductivity. After removing the TEM grid, thin additional coatings were added to ensure the entire surface was coated but the original pattern was not hidden. The TEM grid served as a mask to create a pattern, providing clear reference lines visible in SEM.

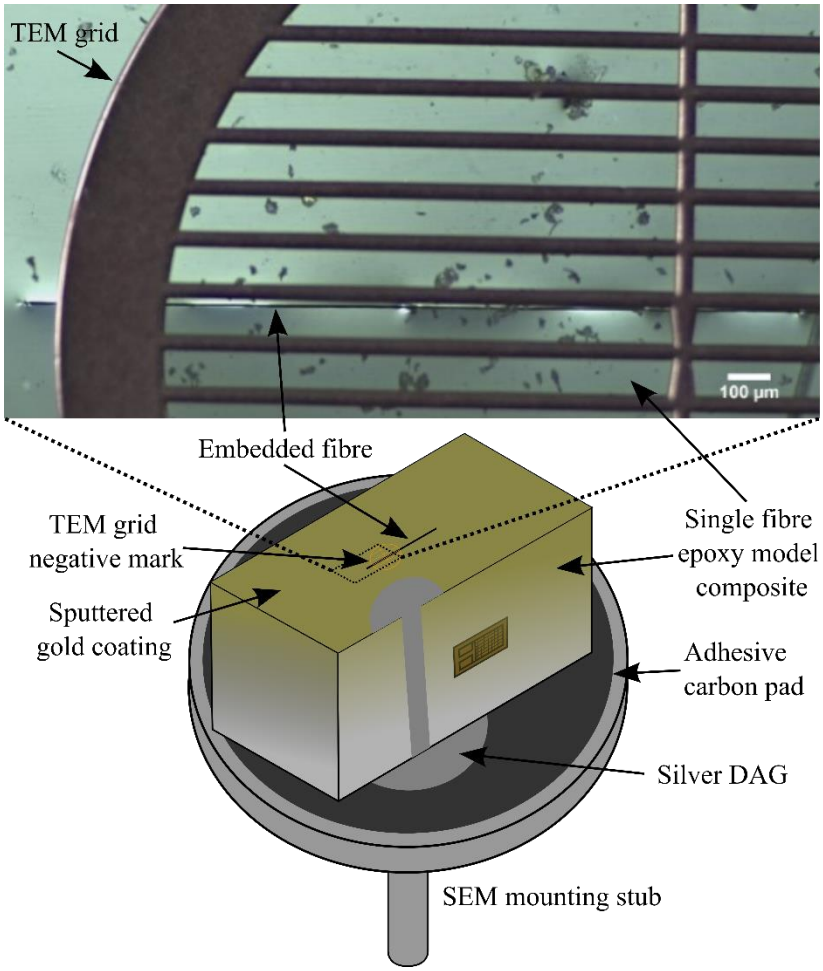

Figure 1. FIB-SEM sample preparation showing: (top) a polarised light optical microscope image of a TEM grid adhered to the surface of an epoxy prism model composite, used to locate the fibre during FIB-SEM analysis. A broken fibre is visible beneath the grid, with contrast enhanced by polarisation. A schematic illustrating the sample setup for analysing fibre features (bottom).

The samples were mounted on an SEM stub using a carbon pad, with silver electrodag paint applied from the pad to the surface of the epoxy prisms, creating a conductive bridge between the prism surface and the stub, addressing charging issues encountered when locating the sample and imaging fibre features, as epoxy is non-conductive.

2.2 FIB-SEM SECTIONING

The system used was a Thermo Fisher Scientific Helios 5 Hydra CX with multiple ion plasma FIB (PFIB) source gases available; gaseous O_2 was used here. The PFIB column had an ion beam current range of 1.5 pA to 2.5 µA with an acceleration voltage range of 500 V – 30 kV. SEM components included a FEG electron source with 350 V – 30 kV acceleration voltage, with an in-lens SE/BSE detector and Everhart-Thornley SE detectors.

Gold-coated model composite samples on SEM stubs were mounted onto the FIB-SEM stage for position of interest (POI) preparation, milling, and imaging. A process was developed to accurately locate previously identified features of interest, such as fibre breaks, utilising optical microscopy identified fibre positioning relative to surface features, e.g., the fibre ends, surface marks and the TEM grid pattern.

The first step involved determining the fibre's position, depth, and alignment. The sample was brought to the correct working distance to focus both the imaging electron beam and the milling ion

beam, with the eucentric position confirmed. During milling, the stage was tilted so the ion beam was perpendicular to the surface, while the electron beam was angled at 52° to the surface.

An oxygen (O_2) plasma was used as the ion source, effectively milling both epoxy and carbon fibres, enabling the production of high-quality polished milled sections, suitable for high-resolution imaging with minimised voxel size due to thinner slice thickness. Plasma focused ion beam (PFIB) allows higher beam currents and faster milling rates with smaller probe sizes than typical gallium FIB sources [9]. Furthermore, use of PFIB avoids implantation of ions, which commonly occurs in epoxy when using a gallium or xenon source [10].

Plasma ion beam conditions of 45 nA and 1.9 µA at 30 kV were employed to mill the epoxy gradually, preventing widespread surface damage observed at currents exceeding 1.9 µA. High power densities (>26 nA at 30 kV) were observed to cause the gold coating to flake off, damaging the sample surface.

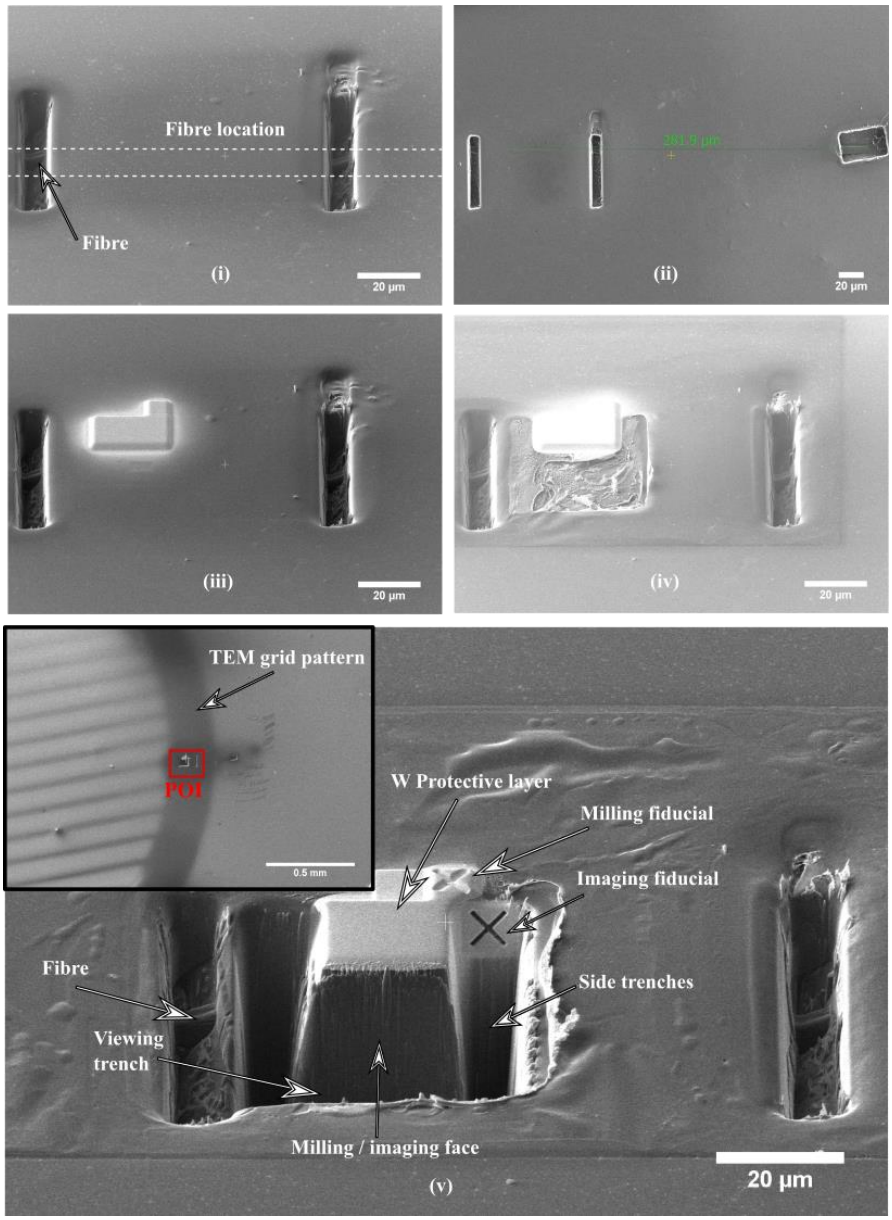

Figure 2. FIB-SEM area preparation procedure shown using representative SEM images: (i) Milled trenches exposing the fibre, (ii) measurement of the distance from the fibre end to the feature of interest, (iii) tungsten protective layer deposited over the POI, (iv) initial milling of the viewing and side trenches, and (v) the POI location on the TEM grid pattern (inset) with the final region of interest (ROI) prepared for polishing and sectioning.

Using the ion beam column's reduced-area imaging mode under these conditions, trenches were selectively etched into the epoxy approximately 50 μm away from a fibre fracture to avoid disturbing the feature of interest. Careful monitoring with both the electron and ion imaging beams ensured the trenches were milled until the fibre was exposed. The same process was repeated on the opposite side of the POI, exposing the fibre on both sides. The stage was then aligned relative to the beam using these two exposed sections, as shown in Figure 2i.

A fibre end was typically located first using the same method, providing a positional reference for identifying the feature (Figure 2ii). Once the fibre was located and the POI identified from prior measurements, a thin (<1 μm) tungsten (W) protective layer was deposited over the epoxy surface at the POI location.

The W deposition was performed by introducing an organometal precursor gas ($W(CO)_6$) via an inserted needle over the POI. The ion beam locally decomposes the gas, depositing metallic W in place [11]. A typical W protective layer is shown in Figure 2iii, which protects the POI from accidental damage, increasing local conductivity, and enhancing the surface finish of the milled face during sectioning.

The viewing and side trenches were milled to a depth well below the fibre. For instance, for a fibre at a 20 μm depth below the surface, a trench of approximately 50 μm around the POI was milled (Figure 2iv, v). Optimal fibre depths for high-quality, resolved sectioning images ranged from 10–30 μm. Beyond 30 μm, the sectioning time exceeded 12 hours with a lower imaging resolution. Fibre depths greater than 50 μm are experimentally impractical due to poor image quality and long processing times.

Imaging and milling fiducials, such as cross marks (Figure 2v), were milled into the epoxy, preferably on W-coated sections to maximise contrast. The fiducials were essential for Thermo Fisher Auto Slice-and-View sectioning, allowing automatic positional adjustments.

2.3 AUTOMATIC SLICE-AND-VIEW SECTIONING

To section the prepared POI, Thermo Fisher Scientific's Auto Slice & View 5 software was used. The programme sets milling and imaging parameters, and automatically adjusts the stage position using fiducial markers to account for the focal plane movement as material is removed. By adjusting the milling depth, slice thickness, and imaging parameters, the voxel size and processing time can be controlled. Generally, a minimum voxel size is typically desired with a reasonable processing time of under 15 hours.

The slice-and-view process removed a layer of the POI with a polishing mill pass, followed by SEM imaging, and was repeated for the set milling thickness. Autofocus was applied with each frame for optimal image quality. The output was a stack of SEM images collected imaged with the SEM's Everhart-Thornley detector (ETD), with a field emission gun electron source at 5 kV with a working distance of 4.1 mm.

2.4 IMAGE SEGEMENTATION

To analyse and process SEM image stacks obtained from FIB-SEM milling, ImageJ (Fiji, ver. 2.16.0) and Dragonfly 3D World version 2024.1 (Object Research Systems ORS Inc, Montreal, Canada, build 1601) were used for image segmentation. The segmentation process, outlined in Figure 3, began by selecting a wide field of view (FOV) of 30-50 μm to account for potential uncertainty in break feature locations within the region of interest (ROI). After image collection, image pre-treatment was required to refine the stack, cropping to remove excess background. ImageJ pre-treatment then focused on maximizing the contrast between the fibre, voids, and the matrix. A Gaussian blur filter with a standard deviation value (sigma value) of 2-3 was applied to reduce noise and improve contrast without sacrificing fine details, aiding effective ROI segmentation [12].

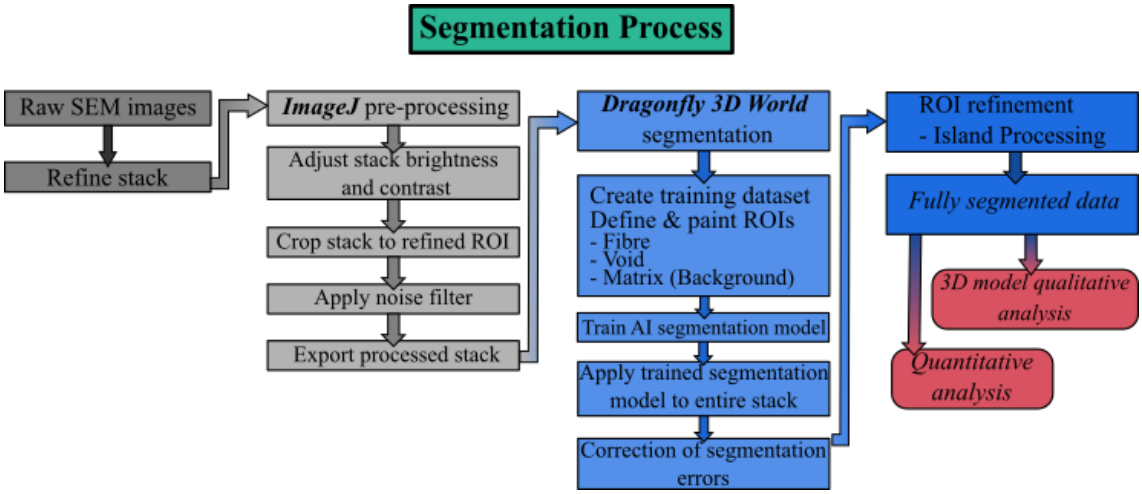

Figure 3. Flowchart for the image processing steps for FIB-SEM data segmentation.

The cropped and ImageJ-treated stacks were imported into Dragonfly, where inbuilt AI-assisted automatic segmentation models were used to process stacks of images (typically 400-700 images). A U-Net-based deep learning architecture, designed to analyse visual imagery, was trained to segment the stack. U-Net is particularly effective at handling noisy images and artifacts [13]. The model was trained by annotating 5-10 example images, defining the regions of interest (ROIs) as the fibre, void, and matrix (background). Once trained, the model can segment the entire stack, with manual review and corrections made as necessary. The accuracy of automatic segmentation improves with higher contrast between the phases, fibre, matrix and void. The fully segmented stack was then visually analysed in 3D, allowing for detailed observations of fibre breaks that may not be visible in the 2D stack. Quantitative measurements of fibre features, debond lengths, and alignment were also made using Dragonfly's analysis tools.

3 RESULTS AND DISCUSSION

The experimental methodology developed to study carbon fibre compressive fragmentation is appropriate for both finding and imaging features in high resolution. Post-processing of the produced image stacks produces 3D reconstructions of the fibre break geometries and internal structures, as illustrated in Figure 4.

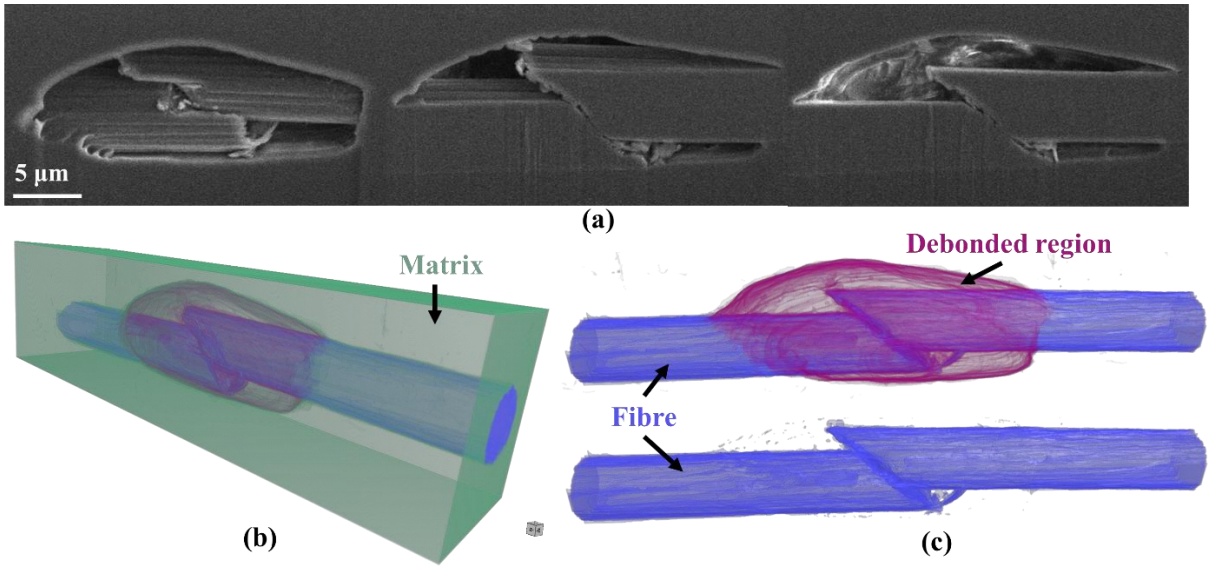

Figure 4. FIB-SEM results from a fragmented M55J sample, showing (a) SEM micrographs taken at various stages across sectioning, with (b) and (c) resulting segmented 3D models produced in Dragonfly, where (b) is an orthographic projection of the 3 segmented phases and (c) is a plan view of the fibre with (top) and without (bottom) the debonded region.

Figure 4 depicts a segmented M55J fibre which has undergone compressive failure resulting in a shear-type fibre break geometry, with the crack at approximately 47° to the fibres longitudinal axis, as previously predicted [4]. The sample experienced an initial fibre failure at a matrix strain (ε_m) of 0.5 % (peak fibre stress ~ 2.2 GPa) and was deformed until a ε_m of 1.25 %. The resulting 3D ROI models at two different viewing orientations are shown at the top of the figure, with and without the purple 'void' regions which depicts where debonding has occurred surrounding the break. This region is representative of voiding around the fibre. The fibre region is represented as a blue ROI, superimposed onto the example SEM images shown in Figure 4. The matrix is also segmented and has a ROI superimposed onto the SEM frames for clarity but is excluded in the figures.

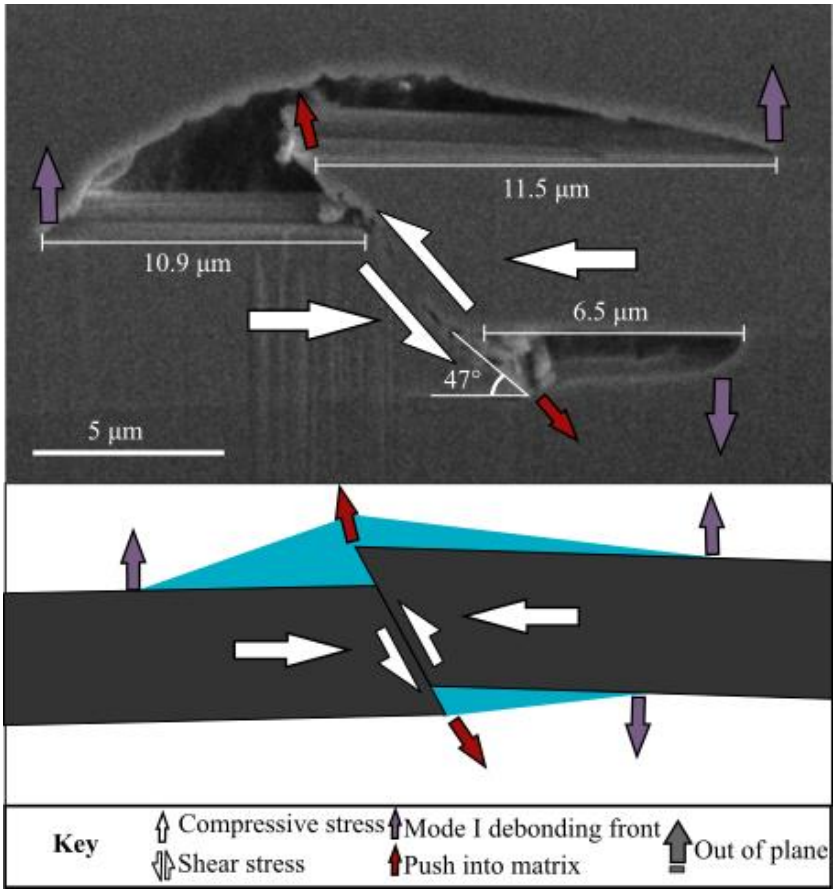

Figure 5. Observed debonding behaviour depicting fibre movements resulting in interfacial debonding observed via FIB-SEM (image (2) in Fig. 7.5), with a schematic of the mechanism predicted based on Raman stress mapping measurements (see reference [4]).

When compared to the predictions of HM fibre failure from Raman mapping data made in a previous study [4] the post-failure geometry of the fibre imaged in Figure 4 is visually similar. In Figure 5, the fibre movement prediction arrows have been overlayed to demonstrate how the fibre is predicted to have moved post-failure, pushing up into the matrix. The mode I push-off, or 'peeling', interfacial mode I debonding is evident, due to the debonded lengths on each of the fragment ends, as illustrated. The volume of the void region was 570.5 μm^3 (measured in Dragonfly) with debonded regions surrounding the break, as marked on the image in Figure 5.

4 CONCLUSIONS

The use of FIB-SEM can produce high quality 3D information regarding the geometries and internal structures of high modulus carbon fibre model composite breaks. The FIB-SEM imaging technique was developed specifically for the single-fibre model composite samples used previously with *in situ* Raman mapping under compressive loading. Key sample preparation steps have been refined, including marking positions of interest, sectioning, and image segmentation. Predictions made in previous reported work regarding interfacial debonding mechanisms, such as the "push-off" or "peeling" mode I debonding, have been validated using this approach.

Compared to other *in situ* imaging techniques, such as optical microscopy (limited resolution) or synchrotron X-ray holotomography (limited accessibility), FIB-SEM offers relative ease of access and simplicity, with higher imaging resolution, and the ability to select small specific regions of interest. Combined with Raman spectroscopy stress mapping, these complementary methodologies can contribute to a comprehensive understanding of model composite micromechanics.

ACKNOWLEDGEMENTS

The authors kindly acknowledge the funding for this research provided by UK Engineering and Physical Sciences Research Council (EPSRC) programme Grant EP/T011653/1, Next Generation Fibre-Reinforced Composites (NextCOMP): a Full Scale Redesign for Compression a collaboration between Imperial College London and the University of Bristol. For the purpose of open access, the authors have applied a Creative Commons Attribution (CC BY) license to any author accepted manuscript version arising. Supporting data can be requested from the corresponding author but may be subject to confidentiality obligations.

The authors also acknowledge the Interface Analysis Centre (IAC), University of Bristol, for the use of FIB-SEM capabilities, as well as the Dragonfly software (Object Research Systems (ORS) Inc.) for the free, non-commercial, academic licence used in analysis.

REFERENCES

[1] N. Oya, D.J. Johnson, Longitudinal compressive behaviour and microstructure of PAN-based carbon fibres, Carbon N. Y. 39 (2001) 635–645. https://doi.org/10.1016/S0008-6223(00)00147-0.

[2] S. Nunna, A.R. Ravindran, J. Mroszczok, C. Creighton, R.J. Varley, A review of the structural factors which control compression in carbon fibres and their composites, Compos. Struct. 303 (2023) 116293. https://doi.org/10.1016/j.compstruct.2022.116293.

[3] S. Narayanan, L.S. Schadler, Assessment of strains along fiber surface features in graphite/epoxy composites loaded in compression, Compos. Sci. Technol. 59 (1999) 1589–1596. https://doi.org/10.1016/S0266-3538(99)00020-2.

[4] C.G. Woodgate, R.S. Trask, M.S.P. Shaffer, S.J. Eichhorn, Raman spectroscopic stress mapping of single high modulus carbon fibre composite fragmentation in compression, Compos. Sci. Technol. 255 (2024) 110721. https://doi.org/10.1016/j.compscitech.2024.110721.

[5] D. Tomus, H.P. Ng, In situ lift-out dedicated techniques using FIB-SEM system for TEM specimen preparation, Micron 44 (2013) 115–119. https://doi.org/10.1016/j.micron.2012.05.006.

[6] T.S. Guruprasad, V. Keryvin, G. Kermouche, Y. Marthouret, S. Sao-Joao, Compressive behaviour of carbon fibres micropillars by in situ SEM nanocompression, Compos. Part A Appl. Sci. Manuf. 173 (2023) 107699. https://doi.org/10.1016/j.compositesa.2023.107699.

[7] C.G. Woodgate, R.S. Trask, M.S.P. Shaffer, S.J. Eichhorn, Compressive Characterisation of Single Carbon Fibres and Their Composite Interfaces Via in Situ Raman Spectroscopy, ICCM Int. Conf. Compos. Mater. (2023).

[8] C.G. Woodgate, R.S. Trask, M.S.P. Shaffer, S.J. Eichhorn, Probing compressive behaviour and failure in single fibre carbon fibre composites: in-depth analysis using in situ Raman spectroscopy, ECCM Eur. Conf. Compos. Mater. 8 (2024) 1–8. https://doi.org/10.60691/yj56-np80.

[9] C. Berger, M. Dumoux, T. Glen, N.B. y. Yee, J.M. Mitchels, Z. Patáková, M.C. Darrow, J.H. Naismith, M. Grange, Plasma FIB milling for the determination of structures in situ, Nat. Commun. 14 (2023) 1–12. https://doi.org/10.1038/s41467-023-36372-9.

[10] W. Possart, J.J. Kochumalayil, A. Meiser, F. Soldera, Focused ion beam irradiation: Morphological and chemical evolution in epoxy polymers, Surf. Interface Anal. 41 (2009) 931–940. https://doi.org/10.1002/sia.3121.

[11] K. Sloyan, H. Melkonyan, H. Apostoleris, M.S. Dahlem, M. Chiesa, A. Al Ghaferi, A review of focused ion beam applications in optical fibers, Nanotechnology 32 (2021) 472004. https://doi.org/10.1088/1361-6528/ac1d75.

[12] S. Upadhyay, A. George Smith, D. Vandepitte, S. V. Lomov, Y. Swolfs, M. Mehdikhani, Deep-learning versus greyscale segmentation of voids in X-ray computed tomography images

of filament-wound composites, Compos. Part A Appl. Sci. Manuf. 177 (2024) 107937. https://doi.org/10.1016/j.compositesa.2023.107937.

[13] P. Galvez-Hernandez, K. Gaska, J. Kratz, Phase segmentation of uncured prepreg X-Ray CT micrographs, Compos. Part A Appl. Sci. Manuf. 149 (2021) 106527. https://doi.org/10.1016/j.compositesa.2021.106527.

ICCM24 24TH INTERNATIONAL CONFERENCE ON COMPOSITE MATERIALS
AUG 4-8, 2025 • BALTIMORE CONVENTION CENTER • BALTIMORE, MARYLAND

METHODOLOGY FOR GENERATING AND VALIDATING MICROMODELS TO PREDICT FIBER-DIRECTION COMPRESSIVE FAILURE IN CFRPS

G. Seon[1], S. Ghaffari[1], B. Shonkwiler[1] and A. Makeev[1]

[1] Department of Mechanical and Aerospace Engineering, University of Texas at Arlington, Arlington, Texas, U.S.A.
seon@uta.edu

ABSTRACT

Carbon fiber-reinforced polymer composites (CFRPs) enable lightweight, strong, and durable structures for a wide range of engineering applications, including aerospace, automotive, biomedical, and civil systems. To accelerate material development and reduce certification costs, there is increasing reliance on modeling within Integrated Computational Materials Engineering (ICME) frameworks. In recent years, micromodels have shown promise in predicting material allowables for structural quantification. However, the complex failure mechanisms of CFRPs—particularly fiber-direction compressive failure—continue to present challenges, especially when bridging microscale behavior with macroscale performance. Fiber-direction compressive failure, typically governed by fiber kinking due to initial fiber misalignment and shear instability, is a key limiting factor in the design of primary CFRP aircraft structures. While Representative Volume Element (RVE) models have advanced the understanding of fiber kinking, they often rely on idealized assumptions—such as uniaxial sine-wave misalignment—that do not capture the inherently random nature of CFRP microstructures and fiber architecture. Furthermore, experimental validation at the microscale remains limited.

To address these limitations, this work presents a novel computer graphics–based methodology for generating densely packed 3D micromodels with realistic, randomly distributed fibers and local 3D misalignments using the open-source software Blender. The generated models are first used in RVE simulations to investigate the effect of random misalignment on compressive strength. Comparisons with conventional RVEs using uniform and uniaxial misalignment highlight the limitations of oversimplified assumptions and underscore the importance of statistically representative geometries.

A thin four-point bend notched test specimen is also introduced as a proposed path toward experimental validation of micromodels for predicting fiber kinking. The specimen is designed to promote localized kinking and enable direct comparison with simulation results. The numerical model includes a homogenized global FE model and a locally embedded fiber-segmented micromodel to capture fiber kinking in the notch region.

1 INTRODUCTION

Carbon Fiber-Reinforced Polymer composites (CFRPs) enable lightweight, strong, and durable structures for a wide of range engineering applications, including aerospace, automotive, biomedical, and civil industries. To accelerate and reduce the cost of material design and qualification, as well as structural design, certification, and sustainment of advanced CFRPs parts, there has been a growing demand for greater reliance on modeling. In particular, recent years have seen significant progress in the development of micromodels for predicting material allowables that can be used for structural quantification. The advancement of such multiscale modeling capabilities has the potential to significantly improve the efficiency and effectiveness of composite part design within the framework of Integrated Computational Materials Engineering (ICME) [1-3]. However, the complex failure mechanisms of CFRPs continue to pose significant challenges to modeling efforts, particularly when bridging the gap between microscale behavior and macroscale performance.

A key critical challenge is the development and validation of micromodels for predicting fiber-direction compressive failure. The fiber-direction compressive strength of unidirectional CFRPs is significantly lower than the tensile strength, with experimental data typically reporting a 30-40% reduction for intermediate modulus (IM) carbon fiber material systems [4-5]. This reduction is a limiting factor in the design of primary composite aircraft structures. Fiber-direction compressive failure in CFRPs is generally governed by the formation of fiber kinking, which can involve multiple interacting microscale mechanisms such as matrix yielding, fiber-matrix debonding, and fiber fracture.

Micromechanical finite element (FE) models, often based on Representative Volume Elements (RVEs), have been instrumental in improving the understanding of fiber kinking by incorporating explicit microstructural features such as fiber distribution and misalignment [6-9]. These models have proven valuable for estimating the compressive strength based on constituent properties [8–10]. However, most existing micromodels rely on idealized representations of fiber architecture, often assuming uniform, uniaxial sine-wave fiber misalignment to initiate shear instability and formation of fiber kinking. These simplifications neglect the inherent stochastic nature of fiber misalignment that arises from manufacturing variability, limiting their predictive capability.

The synthetic generation of realistic micromodels with highly packed non-intersecting fibers with spatially varying, random 3D misalignment presents significant geometric and meshing challenges. To address this challenge, this work introduces a new methodology that leverages Blender —an open-source computer graphics software—to rapidly generate densely packed three-dimensional (3D) fiber distributions with stochastic misalignment and high fiber counts. The approach is fully automated using Python scripting and relies on Blender's rigid body simulation engine, allowing the user to specify key input parameters and apply custom constraints to control the final fiber architecture. The resulting fiber network geometry is imported into Abaqus CAE for meshing and analysis. Example of 3D models are presented to quantify the effect of misalignment randomness on the fiber compressive strength and are benchmarked against conventional micromodels with idealized uniaxial misalignment.

Beyond model generation, validation of the micromodels remains an important and unresolved issue. The strong sensitivity of the predicted fiber-direction compressive strength to geometric assumptions in the micromodels, as demonstrated in this work, reinforces the need for experimental verification. Recent validation efforts have employed in situ testing combined with ultra-high-resolution imaging techniques such as synchrotron X-ray computed tomography (CT) [10,11]. While these techniques offer valuable insight into damage mechanisms and may support model generation and validation, their reliance on very small specimens may raise concerns about the representativeness of observed failure modes. In addition, the high cost and limited availability of synchrotron facilities limit their broader accessibility.

To provide a more accessible validation pathway, this study considers a thin four-point bend notched specimen configuration. The test setup is designed to promote initiation and stable growth of localized fiber kinking while avoiding global buckling and can be implemented using a standard universal testing machine. The thickness of the specimen is reduced to one ply—approximately 180 microns—allowing the use of an embedded fiber-segmented micromodel that spans the entire width of the specimen and captures the full region where fiber kinking develops. A coarser, homogenized global finite element model is used to apply boundary conditions consistent with the experimental setup onto the embedded micromodel. This configuration enables direct comparison between experimental observations and numerical predictions, offering a promising route for verifying micromechanical simulations and advancing predictive capabilities for fiber-direction compressive strength.

2 MICROMODELS WITH IDEALIZED FIBER MISALIGNEMENT

In this section, two-dimensional and three micromodels with idealized initial fiber misalignment are used to highlight some of the key challenges and limitations of micromodels for prediction of fiber kinking and fiber-direction compressive strength in CFRPs.

2.1 Finite Element Models

An idealized fiber misalignment is introduced in the FE models using a cosine function with a half-wavelength L and an initial misalignment angle ϕ_0 as illustrated in Figure 1 and defined by Equations (1) & (2).

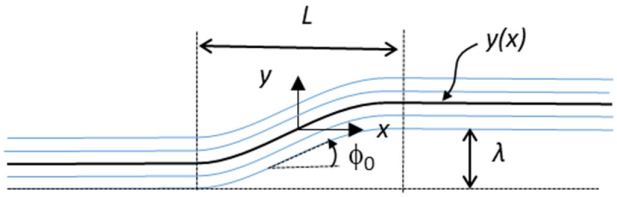

Figure 1: Idealized fiber misalignment.

$$\begin{aligned} y &= -\frac{\lambda}{2} && for\ x \le -\frac{L}{2} \\ y &= -\frac{\lambda}{2} cos\left(\frac{\pi}{L}\left(x + \frac{L}{2}\right)\right) && for\ -\frac{L}{2} < x < \frac{L}{2} \\ y &= \frac{\lambda}{2} && for\ x \ge \frac{L}{2} \end{aligned} \tag{1}$$

Here, λ is the amplitude of the misalignment curve, defined as:

$$\lambda = \frac{2L}{\pi} tan(\phi_0) \tag{2}$$

The two-dimensional FE micromodel considered in this study is shown in Figure 2. The model consists of a rectangular fiber-segmented domain with dimensions L_{tot} x H analyzed using the Abaqus finite element software. A uniform fiber misalignment is imposed perpendicular to the loading direction by shifting the Y-coordinates of all nodes according to the cosine function described above. The model is partitioned into N fiber segments and $N + 1$ matrix segments. A fiber diameter of 5 µm, representative of IM7 carbon fibers, is used to define the height of the fiber partitions while the matrix partition height is selected such that the fiber regions occupy a target area fraction of $V_f = 60\%$.

The model uses 2D plane strain quadrilateral elements (CPE4), with a unit thickness assumed in the out-of-plane direction. Abaqus built-in cohesive contact is used to model the mechanical interaction at the fiber–matrix interfaces. Boundary conditions include a fixed constraint in the axial (X) direction on one end of the model, with loading applied at the opposite end via a reference point and coupling constraints on the axial degree of freedom. A pinned condition is applied to the bottom-left corner node to prevent rigid body translation in the Y direction. Depending on the model dimensions, the total number of degrees of freedom ranged from approximately 50,000 to 150,000. The total model length selected was $L_{tot} = 200$ µm, with a nominal misalignment half wavelength of L=150 µm.

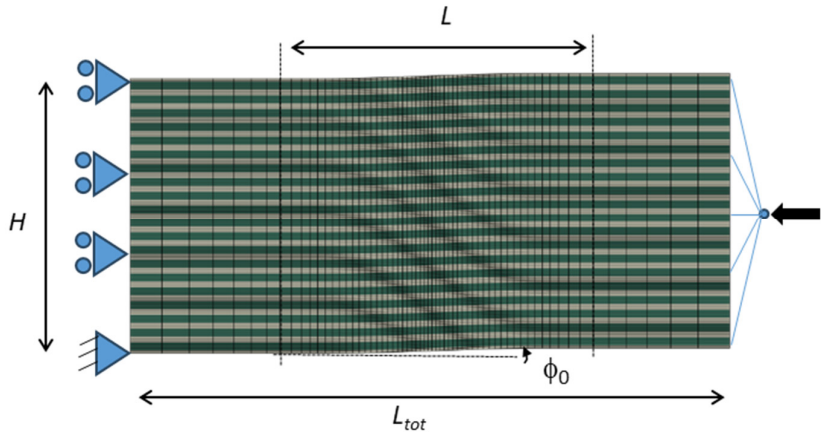

Figure 2: 2D FE micromodel

The three-dimensional FE model with idealized fiber misalignment is similar to the 2D model but incorporates a random distribution of cylindrical fibers within a $H \times W \times L_{tot}$ prismatic block of matrix, as shown in Figure 3. The model is generated by sweeping a 2D fiber-segmented cross-sectional mesh profile created using a modified Random Search Algorithm, enabling the generation of highly packed representative volume elements (RVEs). A fiber volume fraction of Vf = 60% is used in this study.

Similar to the 2D model, a uniaxial initial fiber misalignment is introduced in the 3D FE model by shifting (morphing) the mesh nodes along the transverse Z-direction. The mesh consists primarily of 8-node reduced-integration brick elements (C3D8R), with a smaller number of 6-node wedge elements (C3D6), resulting in a total degree of freedom count between 1.5 and 2.5 million. The nominal cross-sectional area of the 3D model is 50×50 μm^2, containing a total of 77 fibers. The mesh is generated using the Abaqus CAE Python scripting interface, with a minimum clearance of 0.25 μm imposed between fibers and with model boundaries to alleviate meshing difficulties and reduce excessive mesh refinements. A mesh refinement study determined that discretizing the fiber diameter with 16 elements along the circumference (element size ≈ 0.98 μm) and 120 elements along the length in the axial loading direction (element size ≈ 1.6 μm) was sufficient to achieve convergence of the peak load within 2%.

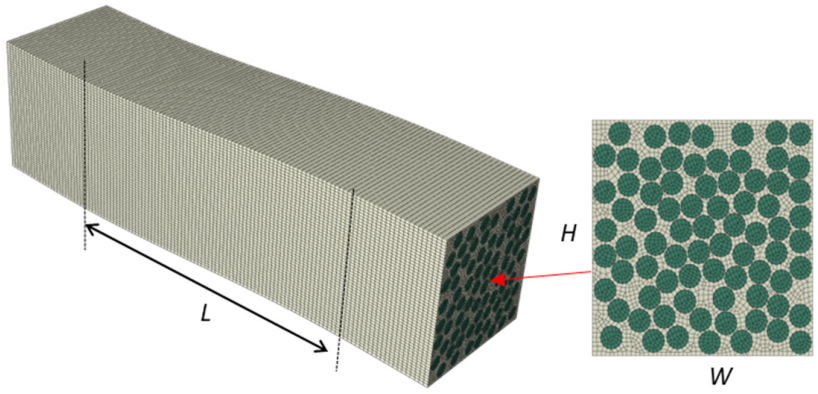

Figure 3: 3D FE micromodel.

The IM7/8552 carbon fiber/epoxy matrix material system is selected in this study due to its widespread use in aerospace applications and the broad availability of material property data. A linear elastic orthotropic material model is used for the IM7 fiber material and the local fiber orientation within the segmented fiber regions in the mesh is assigned using Abaqus tools for surface-based discrete

orientation definition, allowing the material principal directions to follow both the initial misalignment geometry and its deformation during loading. The analysis accounts for nonlinear geometry effects. For the 8552 epoxy matrix, a nonlinear plasticity-based material model is adopted, using the extended Drucker–Prager formulation available in Abaqus material models library for modeling concrete damage plasticity. The fiber–matrix interface is modeled using a cohesive contact formulation, including a bilinear traction–separation law with a quadratic damage initiation criterion and a mixed-mode, energy-based Benzeggagh–Kenane (BK) law for damage evolution. The material properties used for the IM7/8552 system are obtained from the literature [6,12].

2.2 Analysis Results

Under compressive loading, shear stresses develop in regions of fiber misalignment, leading to local fiber rotation and a further increase in matrix shear stresses as well as matrix/fiber interfacial stresses. As compressive loading continues to increase, this results in matrix yielding and/or interfacial debonding, ultimately leading to the formation of a kink band, as illustrated in Figure 4 for a 2D model.

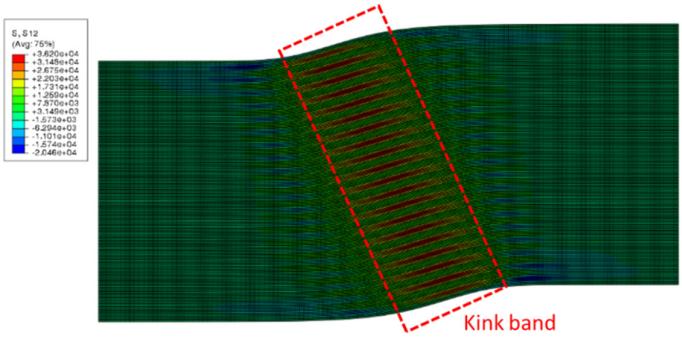

Figure 4. Kink band formation in a 2D micromodel with uniform sine curve fiber misalignment under compressive loading.

To capture the snap-back instability associated with kink band formation, the Abaqus Riks implicit solver is used for the analysis of the 2D model. Figure 5 shows an example of typical load-displacement response (normalized into a stress-strain response) with snap-back instability obtained in the 2D model with the Riks solver for an initial misalignment angle of 2 degrees.

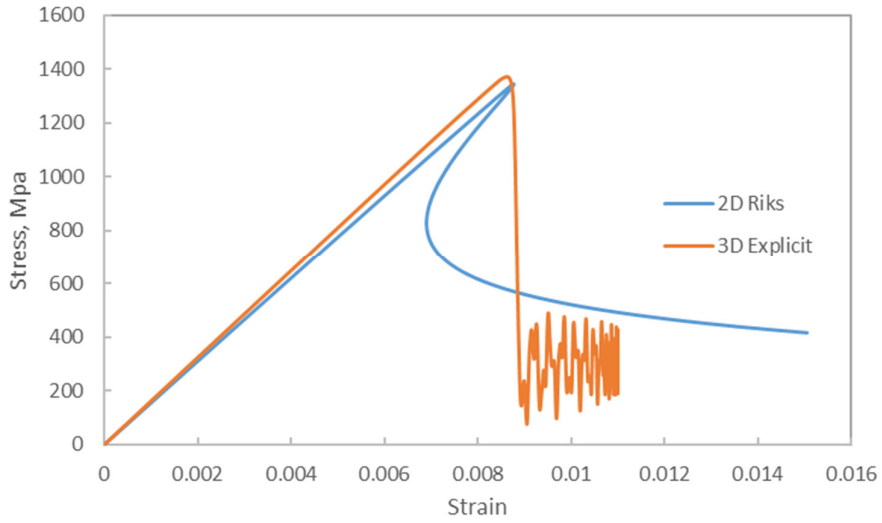

Figure 5: Typical load–displacement response for 2D (Riks) and 3D (Explicit) models showing snap-back instability.

For the 3D model, analysis is performed using the explicit dynamic solver under an applied displacement and quasi-static loading conditions. The use of mass scaling enables a computationally efficient simulation, with total simulation times ranging from 2 to 4 hours on a 60-core machine for the 3D models considered in this study, which contain between 1.5 and 3 million degrees of freedom. For comparison, an analysis of a 3D model with 1.5 million degrees of freedom required approximately 12 hours to reach the peak load using the Riks implicit solver on the same machine. It is worth noting that while the explicit solver can accurately capture the peak load prior to instability, it cannot resolve the post-peak response due to the onset of dynamic effects and loss of equilibrium. Figure 6a shows the development of plastic strain in the confined matrix regions between fibers in the area of misalignment just before instability, and Figure 6b illustrates the progression of interfacial damage. For the IM7/8552 material properties used in this study, the instability is initiated by matrix yielding, which occurs prior to full fiber–matrix debonding. Lower interfacial shear strength properties may lead to an instability mechanism dominated by interfacial debonding.

The typical load–displacement response for a 3D model analyzed with the explicit solver is compared to that of a 2D model analyzed using the implicit *Riks* solver in Figure 5.

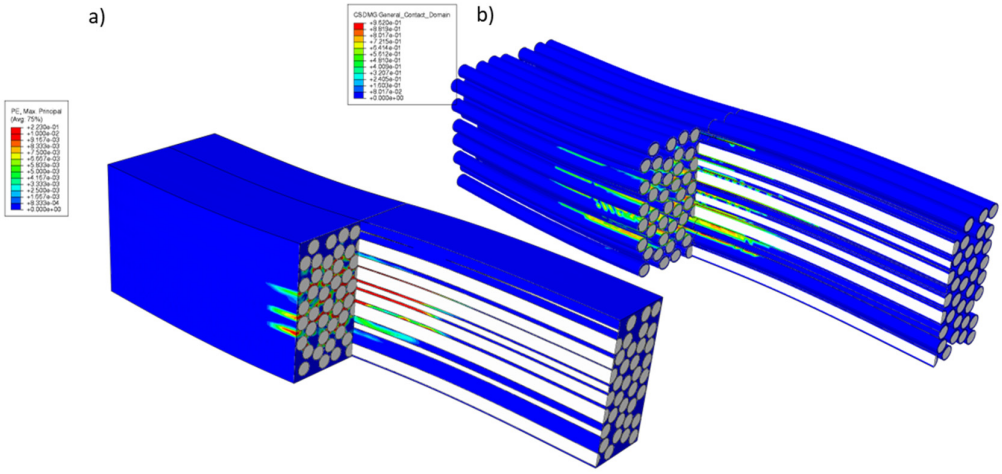

Figure 6: (a) Plastic strain localization and (b) interfacial damage near fiber misalignment prior to instability in the 3D model.

As documented in the literature, the compressive strength predicted by the typical micromodels presented above is highly sensitive to a range of parameters. These include material input properties—such as the matrix yield strength and interfacial shear strength—as well as geometric characteristics, such as the initial fiber misalignment angle and the wavelength of the sine function used to represent the misalignment. Additional challenges arise from the sensitivity of the results to model size and boundary conditions. The dependence on geometry, model size and boundary conditions particularly complicates the development of a robust model for prediction of the fiber-direction compressive strength.

For illustration purposes, the effects of some selected parameters on the load-displacement obtained with the 2D model using the Riks solver are presented in Figures 7 and 8 below.

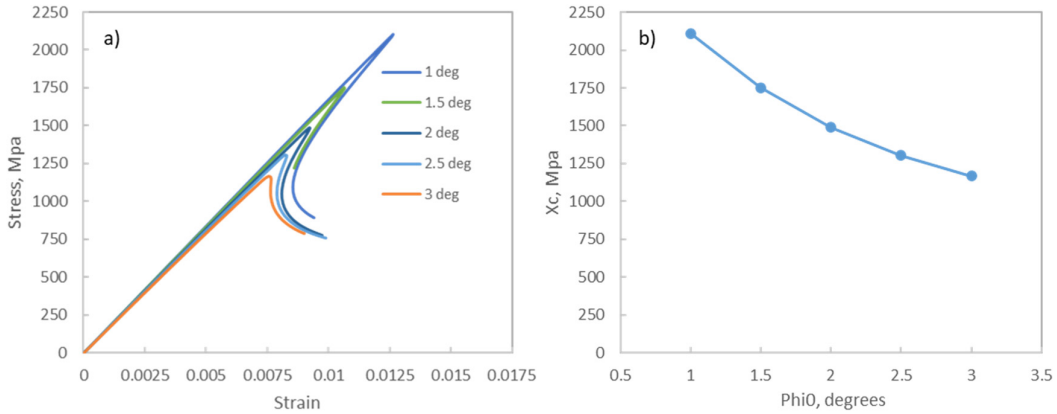

Figure 7: Effect of the misalignment angle in the 2D model: a) stress-strain response and b) compressive strength as a function of misalignment angle Φ_0.

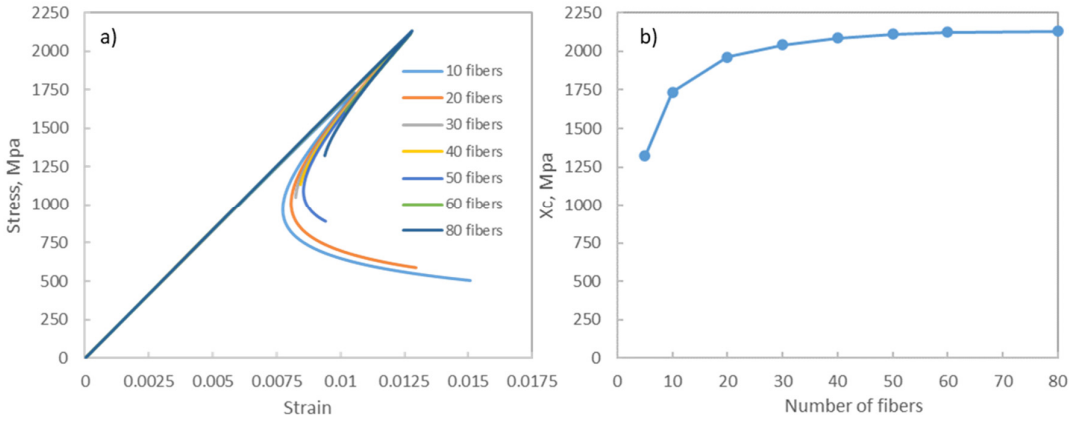

Figure 8: Effect of number of fibers in the 2D model: a) stress-strain response and b) compressive strength as a function of the number of fibers (*H* dimension in Figure 2).

Figure 7 shows the effect of the initial misalignment angle Φ_0 on the compressive strength, calculated as the peak load divided by the cross-sectional area. In these models, the number of fibers—corresponding to the height dimension *H* in Figure 2—was set to 50. As shown, the compressive strength is highly sensitive to small misalignment angles in the range of 1° to 3°, and it decreases as the misalignment increases, which is a well-known behavior. For reference, a 0° compressive strength X_c of 1540 MPa is reported for IM7/8552 in the Hexcel datasheet [13], which corresponds to a misalignment angle of approximately 1.8° in the model.

Figure 8 illustrates the effect of the number of fibers (i.e., the model height *H*) on the compressive response. As shown, the compressive strength increases with the number of fibers and appears to converge for values above 60 fibers. In these simulations, a misalignment angle of 1° was used.

Similar dependencies are observed using the 3D micromodel presented in Figure 3.

3 MICROMODELS WITH RANDOM FIBER MISALIGNEMENT

The results presented above underscore the strong sensitivity of the compressive strength predicted using micromodels to the geometric characteristics of the fiber misalignment introduced. In these models, the misalignment is idealized as uniform and uniaxial—an assumption that does not accurately reflect the inherently stochastic nature of fiber misalignment observed in real composite materials. Moreover, the common implementation approach, which involves uniformly shifting the entire volume—including both fibers and matrix—according to a prescribed misalignment function, may undermine the validity of applying periodic boundary conditions. Periodic boundary conditions are often used to reduce mesh size sensitivity and ensure representative behavior in the homogenization of RVE results.

3.1 Model Generation

One of the reasons simplified misalignment is typically adopted in micromodels is that generating highly packed representative cells with a stochastic distribution of non-intersecting fibers and spatially varying 3D misalignment poses a significant geometric and meshing challenge. To address this, a novel method based on a computer graphics modeling engine is proposed in this work. The method uses open-source computer graphics software Blender to construct complex and realistic fiber architectures.

The overall workflow for the method is outlined in Figure 9.

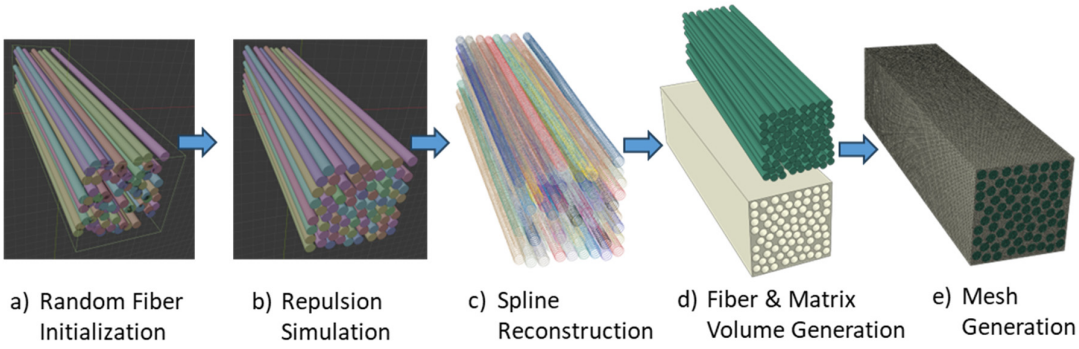

Figure 9: Workflow for generating realistic 3D fiber architectures in FE micromodels using Blender.

The process begins by creating a Blender scene that includes N randomly positioned fibers confined within a container box (Figure 9a). The container is typically modeled as a rectangular prism to facilitate the application of periodic boundary conditions in the FE model, but other shapes, such as a cylinder, can also be used. The number of fibers N is selected such that the total fiber volume matches a target volume fraction V_f relative to the container volume. Individual fibers may be randomly selected from a pre-defined collection with varying geometric characteristics, such as differences in diameter and local misalignment (undulation with wavelength smaller than the length of the container). Random rotations along all three Euler angles can also be applied to further randomize the initial positioning and include global fiber misalignment. Each fiber is modeled as a cylindrical mesh with user-defined discretization in the axial and radial directions.

The initial fiber distribution is generated using an emitter plane and Blender's hair particle system modifier. At this stage, many fibers typically intersect, as illustrated in Figure 9a. If no intersections are present, which may occur for very low fiber volume fraction, the Repulsion Simulation step b) can be skipped and the process can continue at step c). Otherwise, to remove intersections and achieve a tightly packed configuration, Blender's rigid body physics simulation engine is used.

Each fiber is assigned an active rigid body model with collision detection enabled, while the container is defined as a passive rigid body, also with collision enabled. Gravity is disabled in the simulation, and Blender's default repulsion force field is applied to all active rigid bodies (fibers). This force is proportional to the overlapping volume between intersecting objects. This setup causes overlapping fibers to repel one another at the start of the simulation, triggering collisions with neighboring fibers and the container walls. The system then evolves toward an equilibrium state in which no fibers intersect either each other or the container boundaries (Figure 9b). Surface friction and damping may be introduced to control the time needed to reach equilibrium. The final distribution and orientation of the fibers may exhibit stochastic behavior due to the combined influence of the repulsion force model, collision dynamics, and multi-body interactions. While evaluation of this stochastic behavior is beyond the scope of the present work, it is identified as a subject of future investigation.

Once equilibrium is reached, the simulation is baked, and the vertex coordinates of each fiber mesh are extracted. These coordinates are imported into Abaqus CAE, where they are used to reconstruct each fiber geometry via a series of spline profiles extruded along the fiber axis (Figure 8c). A lofted surface is generated from the spline sections and capped to create solid fiber volumes. The fiber volumes are then used to cut into a prismatic matrix block using Abaqus CAE's native Boolean operations, resulting in the final fiber and matrix volume geometry (Figure 9d).

Meshing of the fiber and matrix domains is then carried out using Abaqus CAE's meshing tools (Figure 9e). The fibers can typically be meshed using a sweep technique, enabling the generation of high-quality hexahedral or hex-dominated elements. For the matrix, sweep or bottom-up meshing strategies may be feasible when the fiber paths are relatively straight or when the fiber volume fraction is low. However, in the general case—particularly when dealing with random 3D fiber misalignment and high fiber volume fractions—free tetrahedral meshing is required to ensure successful mesh generation.

The entire process is automated by leveraging Blender and Abaqus CAE respective Python interfaces. It is worth noting that the Blender simulation is typically very fast. In this work, the 3D random positioning problem involving up to 800 fibers was resolved in under one minute.

Figures 10 and 11 present examples of fiber distributions generated with a 60% fiber volume fraction and approximately 500 fibers. Figure 10 illustrates a case in which a small degree of global fiber misalignment was introduced by allowing fiber rotation during the collision simulation. Figure 10a shows the initial fiber distribution in the Blender scene, while Figure 10b shows the final configuration after the repulsion-based collision simulation. Figure 10c provides a 3D view of the final distribution.

In the front view shown in Figure 10b, darker regions correspond to misaligned fibers. Clustering of these fibers appears in two distinct regions, suggesting a possible underlying stochastic behavior associated with the collision physics and multi-body dynamics of the packing process.

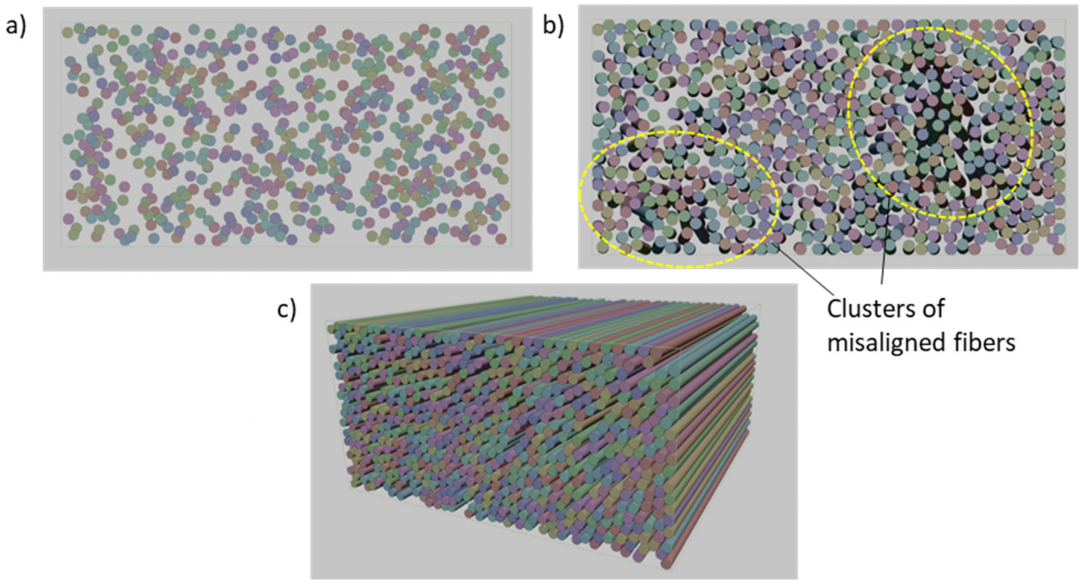

Figure 10: Example of 3D fiber distribution with global misalignment: a) initial distribution (2D view), b) final distribution in 2D view, and c) final distribution in 3D view.

Figure 11 presents an example of a fiber distribution in which a few individual fibers exhibit large global misalignment angles approaching 45°. This configuration is intended to mimic observations from CT scans of carbon/epoxy specimens where significant fiber misalignment occurred at ply interfaces due to the manufacturing process. The initial and final fiber distributions in the Blender model are shown in Figures 11a and 11b, respectively. Figure 11c shows CT data highlighting individual fibers with large misalignment angles.

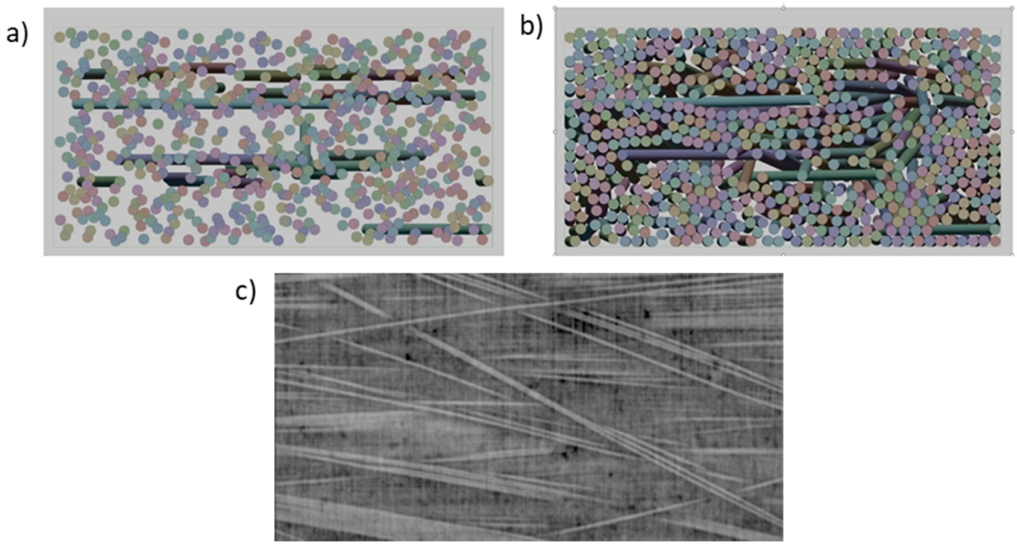

Figure 11: Example of simulated fiber distribution with large global misalignment angles: a) initial distribution, b) final distribution and c) similar fiber distribution observed in CT data.

Rigid body constraints can be applied to individual fibers to provide additional control over their final distribution. In the example shown in Figure 12, identical fibers with initial uniaxial sine-curve misalignment along the Z-axis, defined by Equation 1, are used in the repulsion-based simulation. Rigid body constraints are introduced to restrict fiber motion to translations along the Y and Z directions during the simulation, with no rotations allowed. This results in a random, non-intersecting fiber distribution with uniform uniaxial fiber misalignment, similar to the configuration shown in Figure 3. However, a key distinction is that the matrix block in Figure 12 remains a regular, undeformed rectangular prism, whereas in Figure 3, the matrix geometry is morphed to follow the fiber paths. Maintaining a prismatic matrix block in this case would enable straightforward and unambiguous application of periodic boundary conditions.

In Figure 13, the same rigid body constraints are applied, and the same fiber geometry with sine-curve misalignment is used. However, each fiber is randomly sampled from a collection of fibers that have been pre-rotated (randomly) about the X-axis. This introduces variation in the orientation of the local misalignment plane, resulting in a non-intersecting fiber distribution with randomly oriented sine-curve misalignment, as shown in Figure 13.

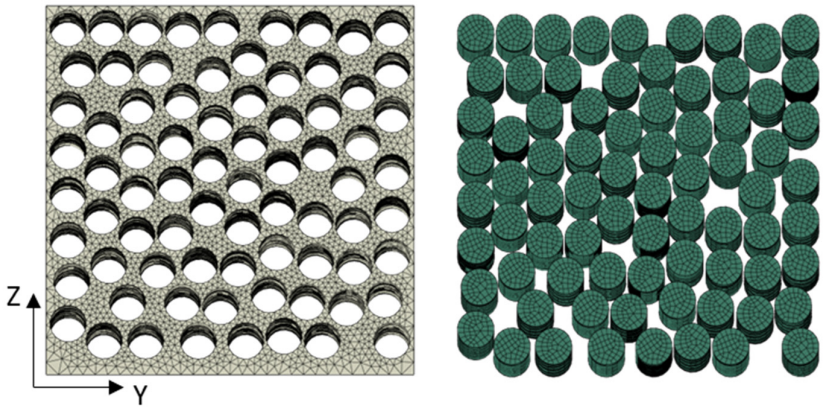

Figure 12: Random distribution of fibers with uniform uniaxial sine-curve misalignment.

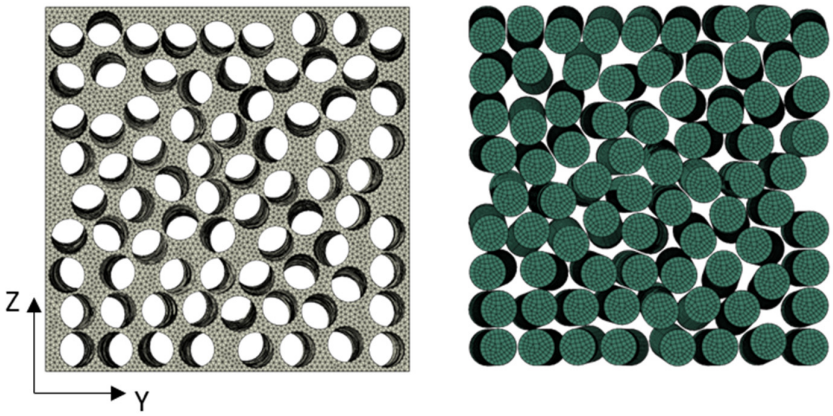

Figure 13: Random fiber distribution with sine-curve misalignment randomly rotated about the X-axis.

3.2 Analysis Results

Analysis results are presented and compared for the four 3D micromodels listed in Table 1, which outlines the key features of each configuration. All models incorporate local fiber misalignment using the sine curve function defined in Equation 1, centered at mid-length $L_{tot}/2$, with parameters $L = 150$ μm and $\Phi_0 = 1°$. Each model contains 77 fibers, corresponding to a fiber volume fraction of 60%.

The primary differences among the models lie in the orientation of the misalignment plane along the X-axis (uniaxial vs. randomly rotated) and the method used to introduce the misalignment, which affects the external geometry of the matrix volume. Model 1 uses the traditional "morphing" approach discussed in Section 2, where the mesh is deformed to follow the uniaxial sine curve. Models 2 through 4 are generated using the Blender-based approach described above, which allows for maintaining an undeformed prismatic or cylindrical matrix block. The orientation of the misalignment plane is uniaxial in Models 1 and 2 (along the XZ plane) and randomly rotated along the X axis in Models 3 and 4. Additionally, Model 4 features a cylindrical cross section, unlike the rectangular cross sections used in Models 1–3. All models use similar boundary conditions to those shown in Figure 2, and the simulations are performed using the explicit solver under quasi-static compressive displacement loading in the X direction.

	Model 1	Model 2	Model 3	Model 4
Matrix Cross Section	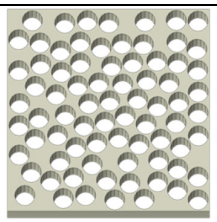	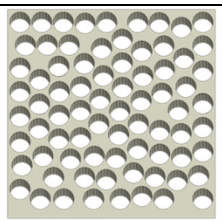	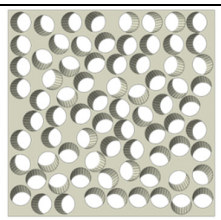	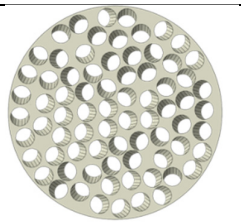
Iso View	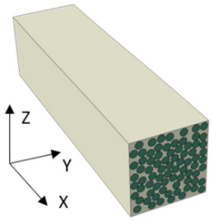	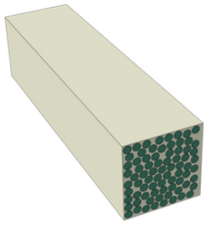	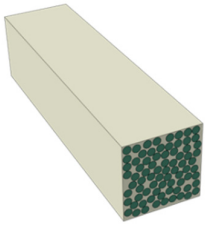	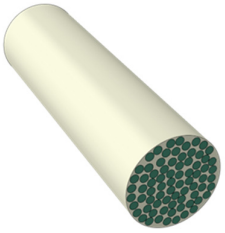
Features	- Uniform fiber misalignment in XZ plane - Rectangular cross section - Mesh morphed to misalignment sine curve in XZ plane	- Uniform fiber misalignment in XZ plane - Rectangular cross section - Prismatic mesh aligned along X	- Random rotation of fiber misalignment plane along X - Circular cross section - Prismatic mesh aligned along X	- Random rotation of fiber misalignment plane along X - Circular cross section - Cylindrical mesh aligned along X

Table 1: 3D micromodel configurations with varying misalignment orientation and matrix geometry.

The stress-strain response (normalized load-displacement response) for the four configurations is plotted and compared in Figure 14. The respective compressive strength values are listed in Table 2.

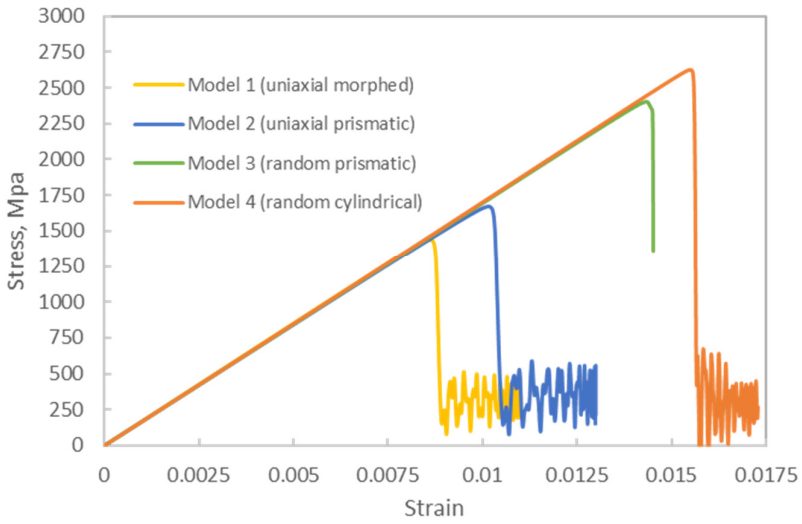

Figure 14: Effect of number of fibers on the compressive strength in the 2D model.

	Model 1	Model 2	Model 3	Model 4
X_c [MPa]	1440	1672	2404	2627

Table 2: Compressive strength values for the four 3D micromodel configurations.

A significant variation in compressive strength is observed across the different configurations, with an 80% increase between the lowest value of 1440 MPa for Model 1 and the highest value of 2627 MPa for Model 4. The substantial increase in average compressive strength observed in Models 3 and 4, compared to Models 1 and 2, can be physically justified: the random orientation of fiber misalignment delays the early development of shear stress along a preferred direction. In contrast, Models 1 and 2—with their uniaxial misalignment—promote early localization of matrix shear along the XZ plane. In Models 3 and 4, a global direction of matrix shearing eventually becomes dominant under continued compressive loading, ultimately leading to instability. Figure 15 illustrates the global shearing deformation observed in Model 3 just prior to failure, characterized by a combination of torsion about the X-axis and bending in the XZ plane.

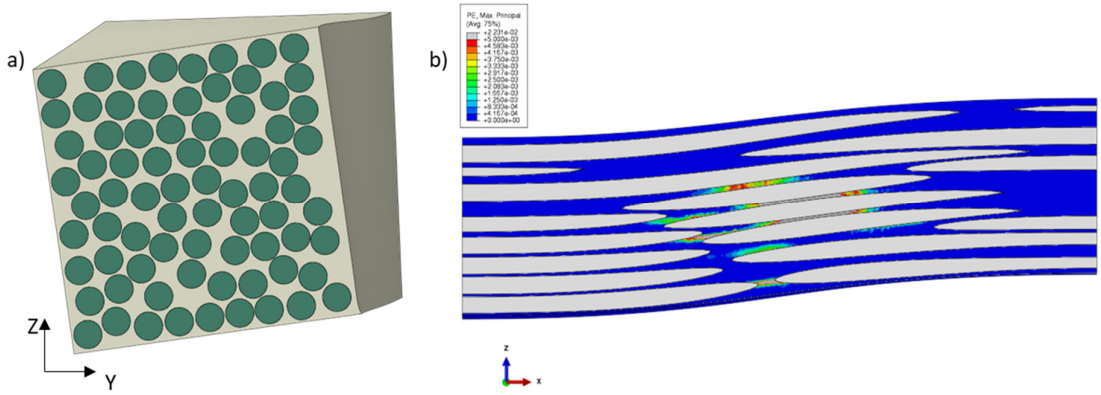

Figure 15: a) Combined torsion and bending deformation and b) development of plastic strains prior to failure in Model 3 (deformation scale is multiplied by 2).

The differences in peak load between Models 1 and 2, and between Models 3 and 4, are also notable, highlighting the influence of the cell geometry on the predicted compressive strength. This sensitivity remains a challenge for predicting the fiber-direction compressive strength of CFRPs using micromechanics modeling. Ideally, micromodel predictions using representative volume elements (RVEs) should be independent of model size and shape. Ongoing work includes the implementation of periodic boundary conditions to evaluate whether such an approach can mitigate these model dependencies.

4 THIN FOUR-POINT BEND NOTCHED SPECIMEN

The results presented in the previous sections highlight the need for direct experimental validation of micromodels for predicting fiber-direction compressive strength. To support this need, a thin four-point bend notched specimen configuration is considered. The configuration is designed to facilitate localized kinking in the notch region while avoiding global buckling. The thickness of the specimen is reduced to the minimum (one ply, or about 180 microns thick), allowing for the use of an embedded fiber-segmented micromodel directly in the notched region. This enables direct comparison between simulation and experimental results.

The test setup is illustrated in Figure 17 and includes a Plexiglas fixture that enables the observation of failure and full-field strain monitoring using the Digital Image Correlation (DIC) technique, while also preventing global buckling. Figure 17a shows an example of the DIC-measured axial strain distribution prior to failure initiation, and Figure 17b shows the out-of-plane kink band failure that developed from the notch, as visible in post-test CT data. The load-displacement responses obtained for six one-ply thick IM7/8852 specimens are shown in Figure 18. A load drop in the load-displacement response was associated with the initial kinking failure at the tip of the notch. After initiation, the kink band continued to grow in a stable manner along the transverse direction.

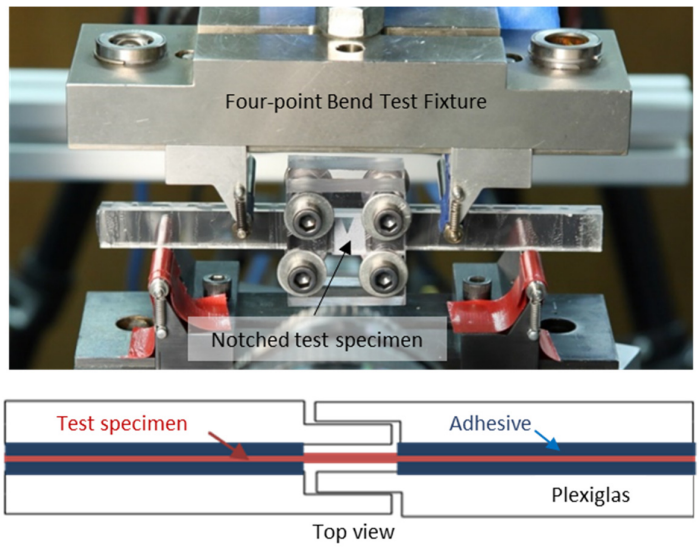

Figure 16. Four-point bend test setup.

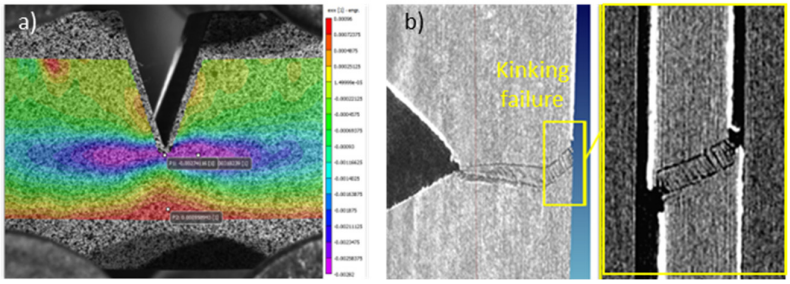

Figure 17. a) Example of DIC-measured axial strain field prior to failure initiation, and b) out-of-plane kinking failure visible in CT data.

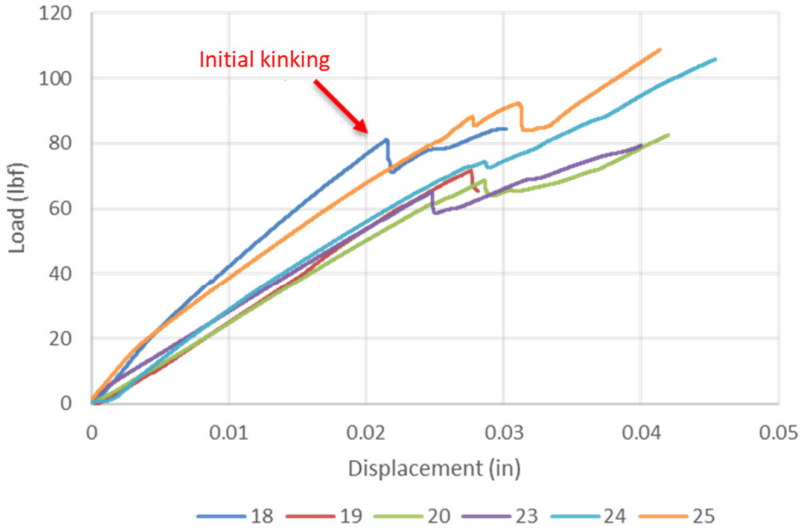

Figure 18. Load-displacement results for six IM7/8552 notched specimens.

The finite element model developed for comparison with experimental data is shown in Figure 19. A coarser homogenized global FE model is used to impose boundary conditions representative of the experiment, while the entire notch region where kinking develops is modeled using an embedded fiber-segmented local micromodel. This approach eliminates the ambiguities commonly associated with RVE size and boundary condition assumptions. Analysis and comparison with experimental data are ongoing at the time of writing.

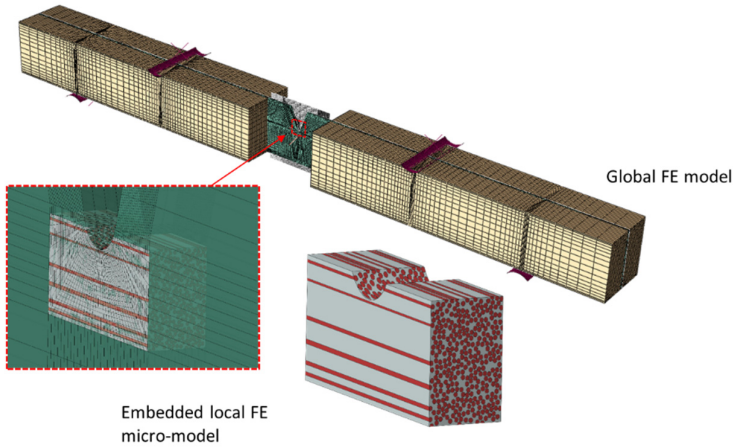

Figure 19. Embedded local and global Abaqus FE model for the Thin Four-Point Bend Specimen.

6 CONCLUSIONS

This work introduced a novel methodology for generating realistic 3D micromodels of CFRPs with random fiber misalignment for predicting fiber-direction compressive failure. A key contribution is the introduction of a computer graphics-based modeling framework using the open-source software Blender that enables the efficient creation of densely packed fiber architectures with spatially varying, stochastic misalignment. This approach addresses the limitations of conventional micromodels based on uniaxial sine-wave misalignment, which do not capture the true variability of fiber architectures in CFRPs and may lead to overly conservative strength predictions. It is also worth mentioning that the misalignment amplitude in such idealized micromodels is typically a calibrated parameter, further limiting their predictive capability.

Finite element simulations showed that both the orientation of fiber misalignment and the geometry of the representative domain can have a significant influence on the predicted compressive strength. Models incorporating randomly rotated misalignment planes led to delayed shear localization and a substantial increase in predicted strength—by as much as 80%—compared to conventional micromodels models with uniaxial misalignment. These results underscore the importance of accurately representing fiber architecture variability to enhance the reliability of micromechanical predictions.

To address the critical challenge of experimental validation, a thin four-point bend notched specimen was proposed. This configuration promotes localized kink band development while preventing global buckling. The small thickness of the specimen enables the use of a high-fidelity embedded fiber-segmented micromodel directly in the notched region for micromechanics-based simulation of fiber kinking. Preliminary test results confirmed the specimen's suitability for studying fiber-direction compressive failure through fiber kinking, laying the groundwork for direct validation.

Future work will focus on implementing periodic boundary conditions to reduce size and boundary effects and on validation using the proposed specimen configuration.

ACKNOWLEDGEMENTS

This research was partially funded by the U.S. Government under Agreement No. W911W6-17-2-0002. Such support is gratefully acknowledged. The U.S. Government technical monitor is Mahendra Bhagwat. The views and conclusions contained in this document are those of the authors and should not be interpreted as representing the official policies, either expressed or implied, of the U.S. Government.

REFERENCES

[1] Su, X. and Wagner, D., (2019) Integrated Computational Materials Engineering Development of Carbon Fiber Composites for Lightweight Vehicles (No. EE0006867). Ford Motor Company, Detroit, MI (United States)

[2] Hearley, B.L., Arnold, S.M., Shah, S.P. and Maiaru, M. (2024) Automation of the ICME Workflow Incorporating Material Digital Twins at Different Length Scales Within a Robust Information Management System (No. NASA/TM-20240010796). *National Aeronautics and Space Administration*.

[3] Arnold, S.M., Holland, F.A., Bednarcyk, B.A. and Pineda, E.J. (2015) Combining material and model pedigree is foundational to making ICME a reality. *Integrating Materials and Manufacturing Innovation*, 4, pp. 37-62.

[4] Kaddour AS, Hinton MJ, Smith PA, Li S. (2013) Mechanical properties and details of composite laminates for the test cases used in the third world-wide failure exercise. *Journal of Composite Materials*, 47, pp. 2427-42

[5] Soutis, C. (1991). Measurement of the static compressive strength of carbon-fibre/epoxy laminates. *Composites Science and Technology*, 42(4), pp.373-392.

[6] Naya, F., Herráez, M., Lopes, C.S., González, C., Van der Veen, S. and Pons, F. (2017) Computational micromechanics of fiber kinking in unidirectional FRP under different environmental conditions. *Composites Science and Technology*, 144, pp.26-35.

[7] Sun, Q., Guo, H., Zhou, G., Meng, Z., Chen, Z., Kang, H., Keten, S. and Su, X (2018) Experimental and computational analysis of failure mechanisms in unidirectional carbon fiber reinforced polymer laminates under longitudinal compression loading. *Composite Structures*, 203, pp.335-348.

[8] Varandas, L.F., Catalanotti, G., Melro, A.R., Tavares, R.P. and Falzon, B.G. (2020). Micromechanical modelling of the longitudinal compressive and tensile failure of unidirectional composites: The effect of fibre misalignment introduced via a stochastic process. *International Journal of Solids and Structures*, 203, pp.157-176.

[9] Chen, J., Wan, L., Nelms, K., Allegri, G. and Yang, D., 2024. Failure analysis of unidirectional CFRP composites with the coupled effects of initial fibre waviness and voids under longitudinal compression. *Composite Structures*, 347, p.118451.

[10] Takahashi, T., Todoroki, A., Kawamura, C., Higuchi, R., Sugiyama, T., Miyanaga, T., Hattori, K., Ueda, M., Yokozeki, T. and Honda, M. (2022) Unidirectional CFRP kinking under uniaxial compression modeled using synchrotron radiation computed tomography imaging. *Composite Structures*, 289, p.115458.

[11] Srisuriyachot, J., Bénézech, J., Couégnat, G., McNair, S.A., Maierhofer, T., Butler, R. and Lunt, A.J. (2023) Synchrotron micro-CT in kink-band formation of UD-CFRP laminates with microdefects. *Composites Part B: Engineering*, 266, p.111038.

[12] Arteiro, A., Catalanotti, G., Melro, A. R., Linde P., and Camanho, P. (2014) Micro-mechanical analysis of the in situ effect in polymer composite laminates. *Composite Structures*, 116, pp. 827-840.

[13] Hexcel Corporation. (2016a). HexPly®8552 Mid-Toughened, High Strength, Damage-Resistant, Structural Epoxy Matrix. Product Data Sheet. Accessed at https://www.hexcel.com/user _ area/content _ media/raw/HexPly _ 8552 _ us _ DataSheet.pdf on July 8, 2025.

Novel Computational Approach Towards the Investigation of Microstructural Instabilities for Composite Materials

Mark Flores[1], Daniele Pelessone[1], Antonio Deleo[1], Sean Phenisee[1], Marco Salviato[2]
[1]ES3, [1]University of Washington

Microstructural Instabilities

Kink Band

- **Mechanism:** Localized, abrupt bending or rotation of crystallographic planes within a material under compression or bending.
- **Known for:** Buckling
- **Relevancy:** Structural Design



Shear Band

- **Mechanism:** Narrow, planar regions of intense, highly localized plastic deformation that propagate through a material.
- **Known for:** Collapse, Crushing, Post/Pre-Buckle Response
- **Relevancy:** Ballistic Impacts, High-Strain Rate Deformation, Tension-Compression Fatigue

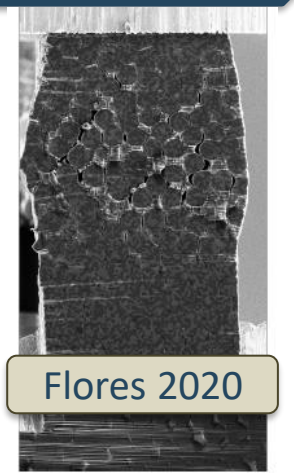

Slope Bands

- **Mechanism:** Potential precursors that leads to other instabilities (Cohesive in Nature)
- **Known for:** Bridging, Brooming, (Avalanches/Land slides/Ice Faults)
- **Relevancy:** Early warning detection, Interlaminar Shear Strength.



Fracture

- **Mechanism:** The ultimate consequence of accumulated damage required to understand preceding instabilities.
- **Known for:** Failure Behavior, Material Separation
- **Relevancy:** Component Failure, Design Limit

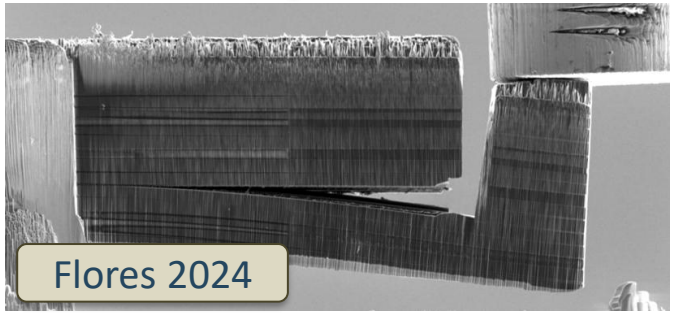

ES3 Proprietary Data. All Rights Reserved.

Assumptions on how Kink Bands Form

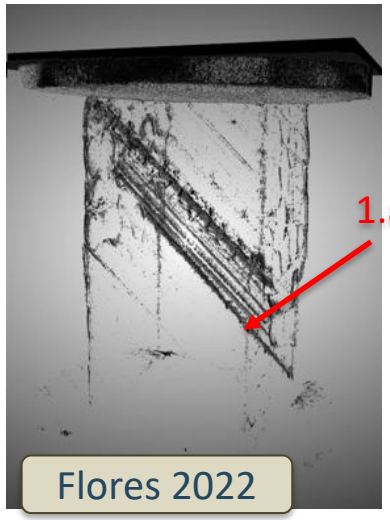

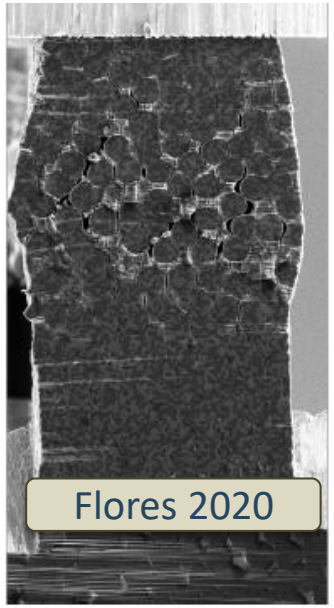

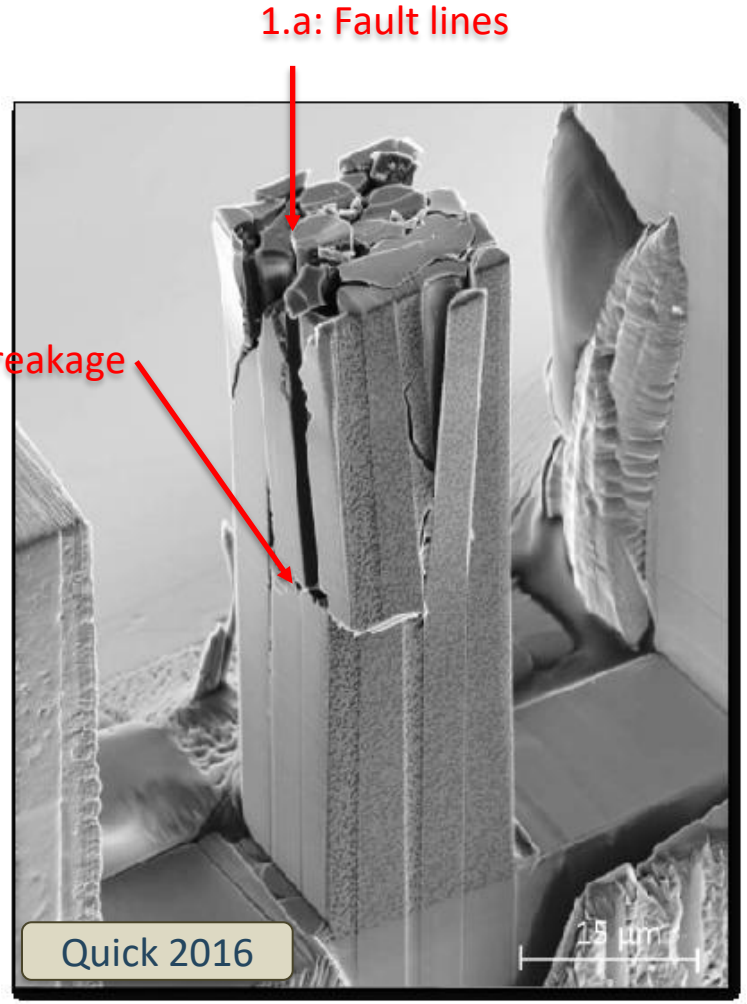

1. Fiber/Matrix Debonds
   a. Creating Fault Lines (aka slope bands)
2. Matrix cracks initiation and propagation
   a. Parallel crack growth as a relationship of fiber distribution
   b. Buckling/Collapse
3. Fibers incapable of holding load
   a. Distributive damage networks leaves fibers exposed to stress concentration
   b. Distributive damage networks enables fibers to deform

ES3 Proprietary Data. All Rights Reserved.

Where are we in the Multiscale Paradigm?

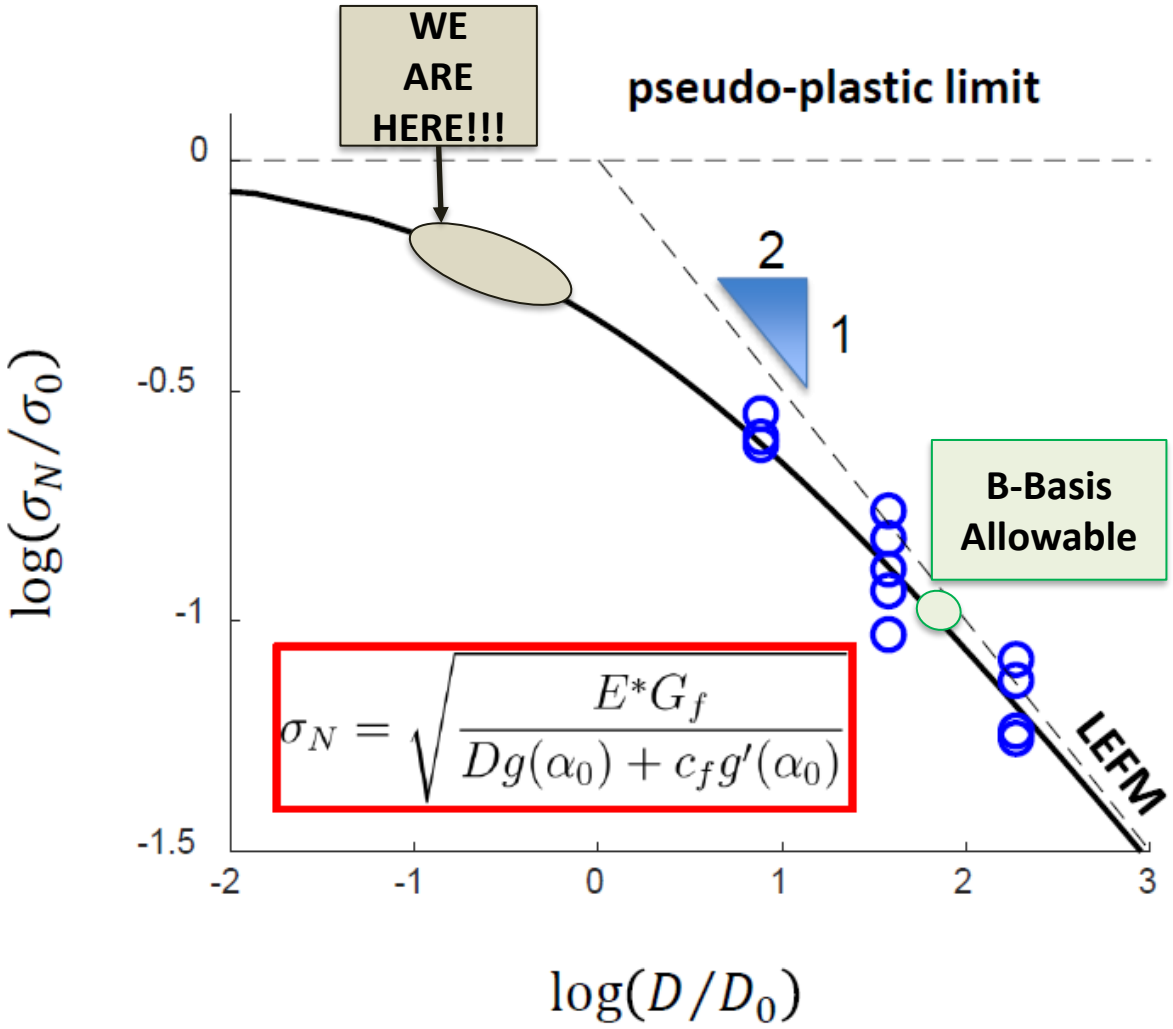

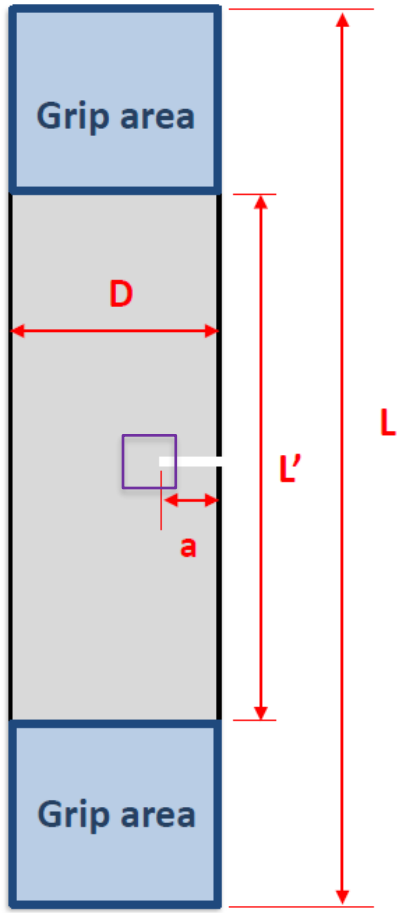

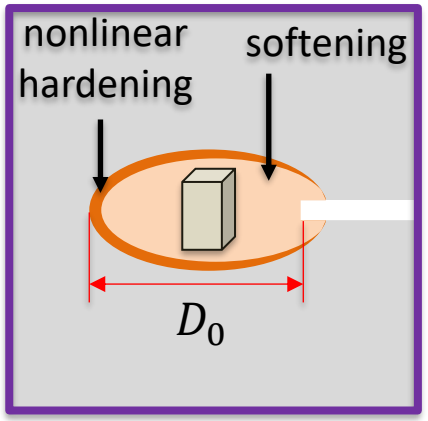

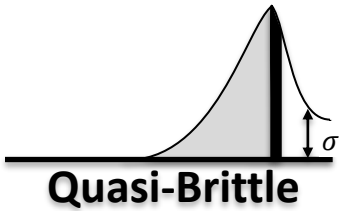

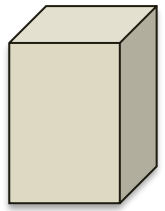

Type	D_0 (um)	D (um)
SEL Type 2	800	
Kink Band		~ 20
Shear Band		< 75
Slope Band		< 75
Micro Fracture		~ 125
Ply thickness		~133
Fiber Diameter		~5.2

ES3 Proprietary Data. All Rights Reserved.

Design Consideration for Model Development

Revisit Basic Truths

- **Fracture Process Zone for Matrix Cracks Only:**
  - The effective length is 800 um
- **Ply Dimensions:** 125 – 150 um
- **Number of Plies:** 5 – 6 plies
- **Unit Cell:** 125 um x 125 um x 125 um
- **Fibers per Unit Cell:** 150 – 200 fibers
- **Total Fibers of FPZ:** >1,000 fibers
- **Behavior:** Quasi-Brittle -> Pseudo-Ductile
- **Probabilistic Framework:** Statistical vs Energetic

- How do we model **>1,000 fibers** in an efficient way?
- Many of the micromechanical experiments have over **75 fibers**
- How can we solve these problems in the comfort of your laptop?
- Calibrate properties FOR ALL mechanisms

DM4C Framework

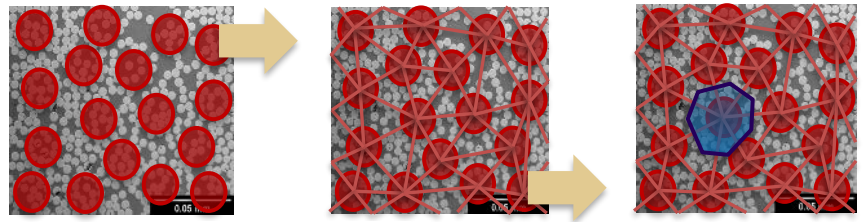

3D View of 3 Fibers resulting a tetrahedron

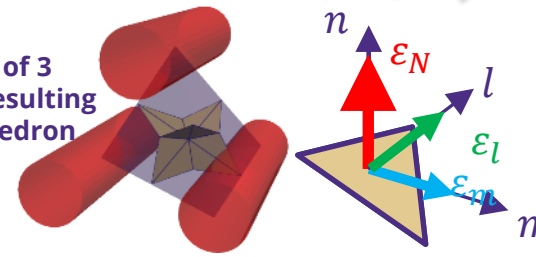

Kinematic relations between nodes provide a strain vector to each facet

Constitutive Laws

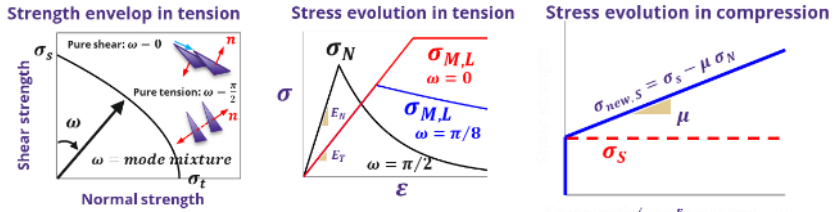

L_0, Initial Length



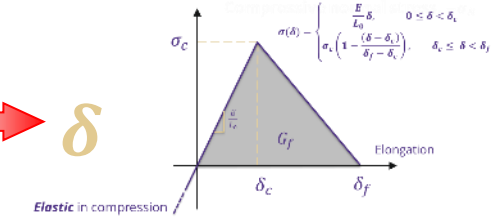

ES3 Proprietary Data. All Rights Reserved.

Calibration Elastic Properties

CMH-17 Properties	Tension	Compression
Fiber Volume Fraction, %	68.50	
Void Fraction, %	1.69	
Axial Modulus, E_{11}, MPa	164000	137000
Transverse Modulus, E_{22}, MPa	8980	8690
Shear Modulus, G_{12}	5010	
Shear Modulus, G_{23}	3800	
Poisson's Ratio, ν_{12}	0.32	
Poisson's Ratio, ν_{23}	-	
Axial Strength, X, MPa	2905	1569
Transverse Strength, Y, MPa	78.9	248
Shear Strength, S_{12}, MPa	57.9	99.4
Axial Strain, ε_{11}, %	1.61	1.28
Transverse Strain, ε_{22}, %	-	3.12
Fracture Process Zone, c_f, mm	.770	

Material STL DFM	
Density	1.8 g/cm3
YoungsModulus	276.0 Gpa
PoissonsRatio	0.3
TensileStrength	2905 MPa
FractureEnergy	438.8 N/m

Material MTRX Dm2	
NormalModulus	63120 MPa
Alpha	0.25
Beta	0.12
TensileStrength	78.9 MPa
TensileCharacteristicLength	0.77 mm
SofteningExponent	0.2
ShearStrengthRatio	1.26
PlasticPlateauExponent	0.0
PlasticSofteningStrength	0.12
PlasticSofteningFailure	0.003
InitialFriction	0.36
AsymptoticFriction	0.36

ES3 Proprietary Data. All Rights Reserved.

Calibrating Microstructural In/Elastic Properties

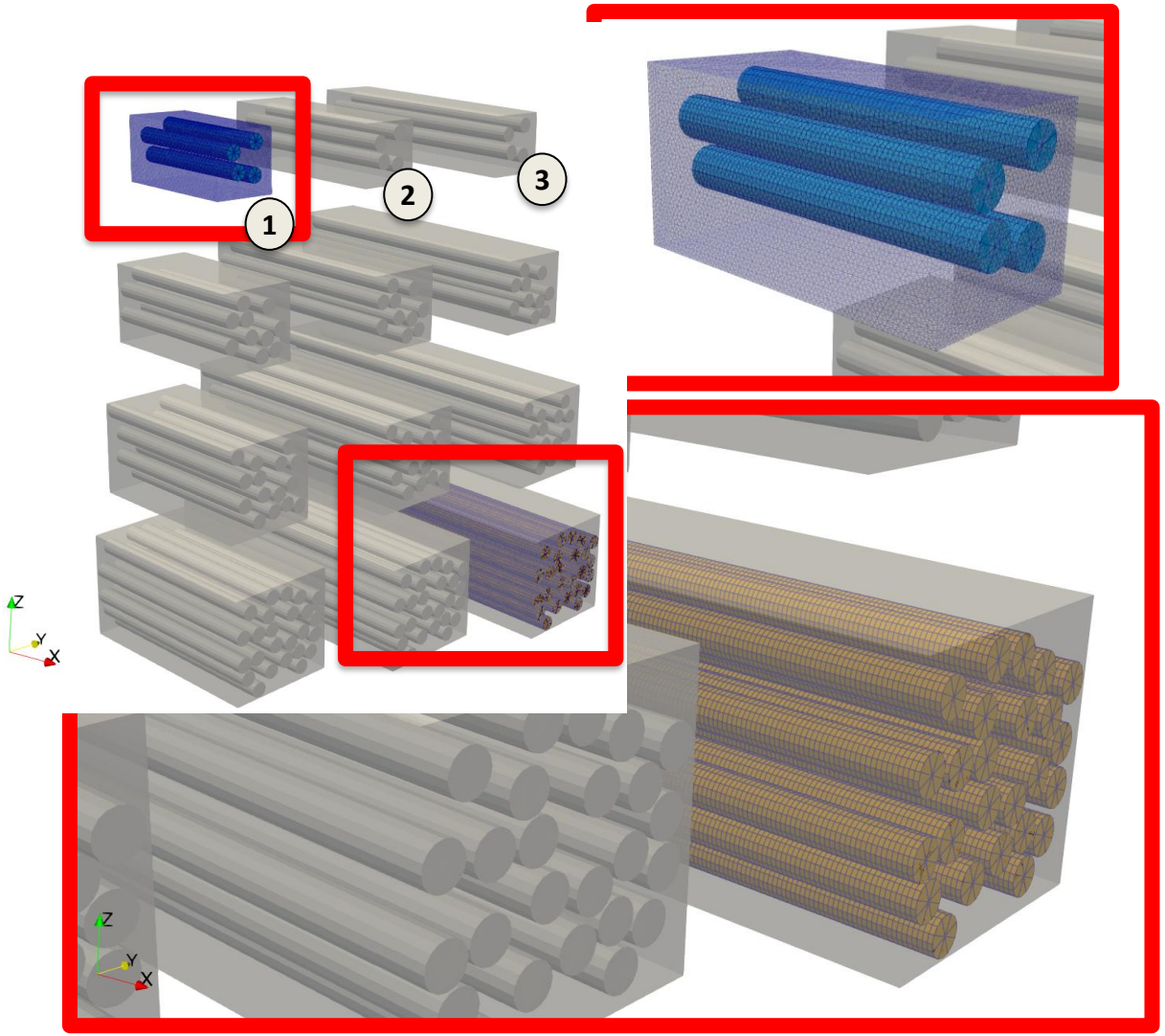

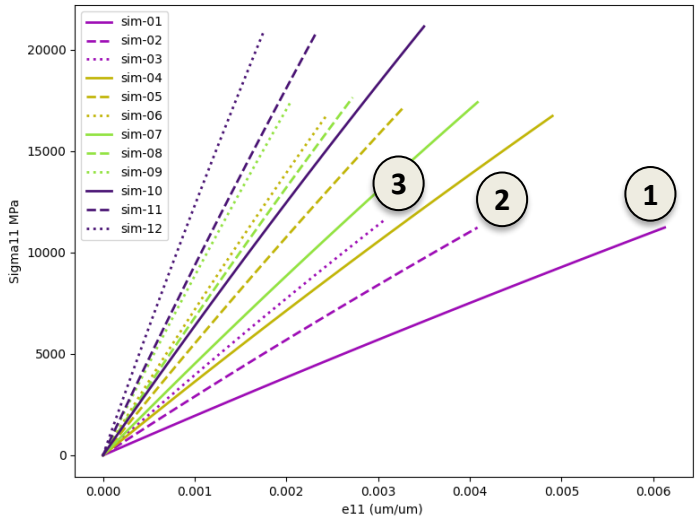

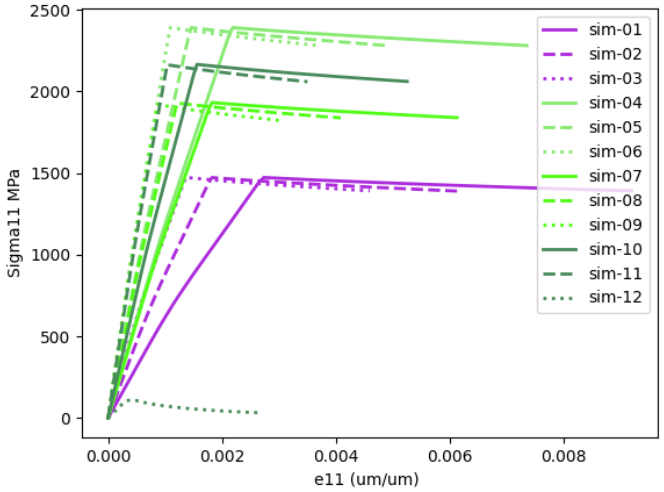

ES3 Proprietary Data. All Rights Reserved.

Calibrating Microstructural Fracture Energy

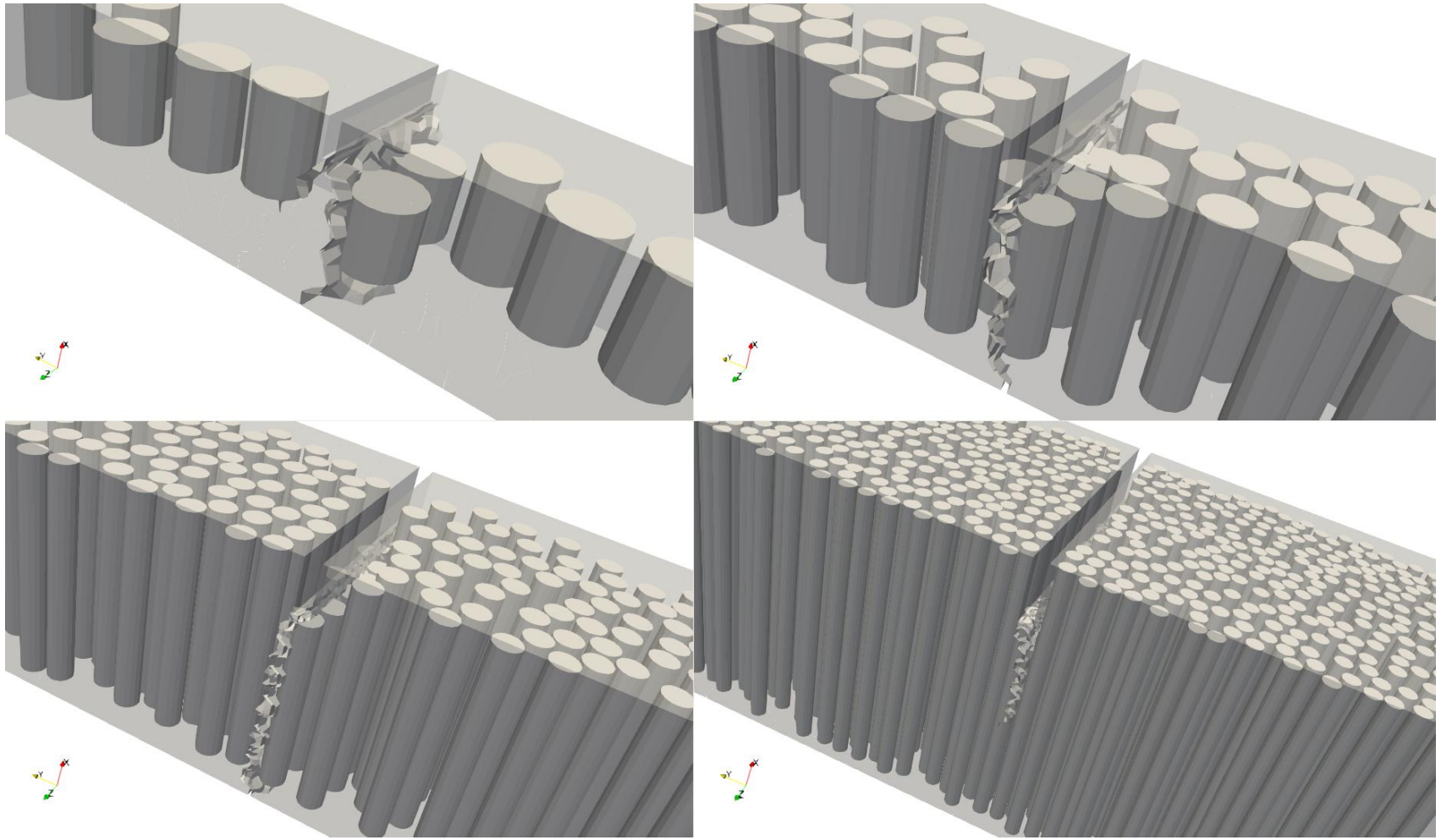

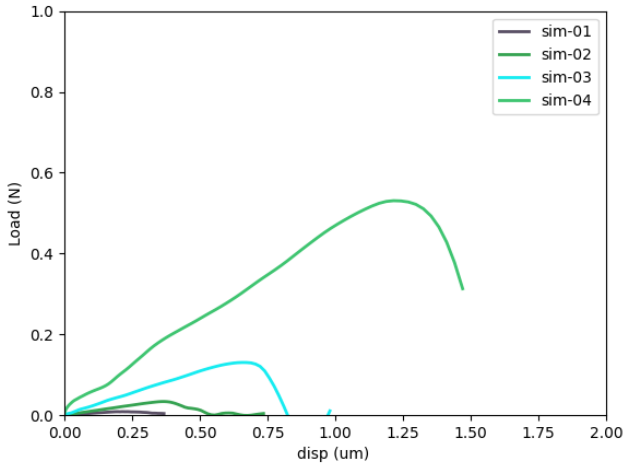

ES3 Proprietary Data. All Rights Reserved.

Slope Instabilities

Approach

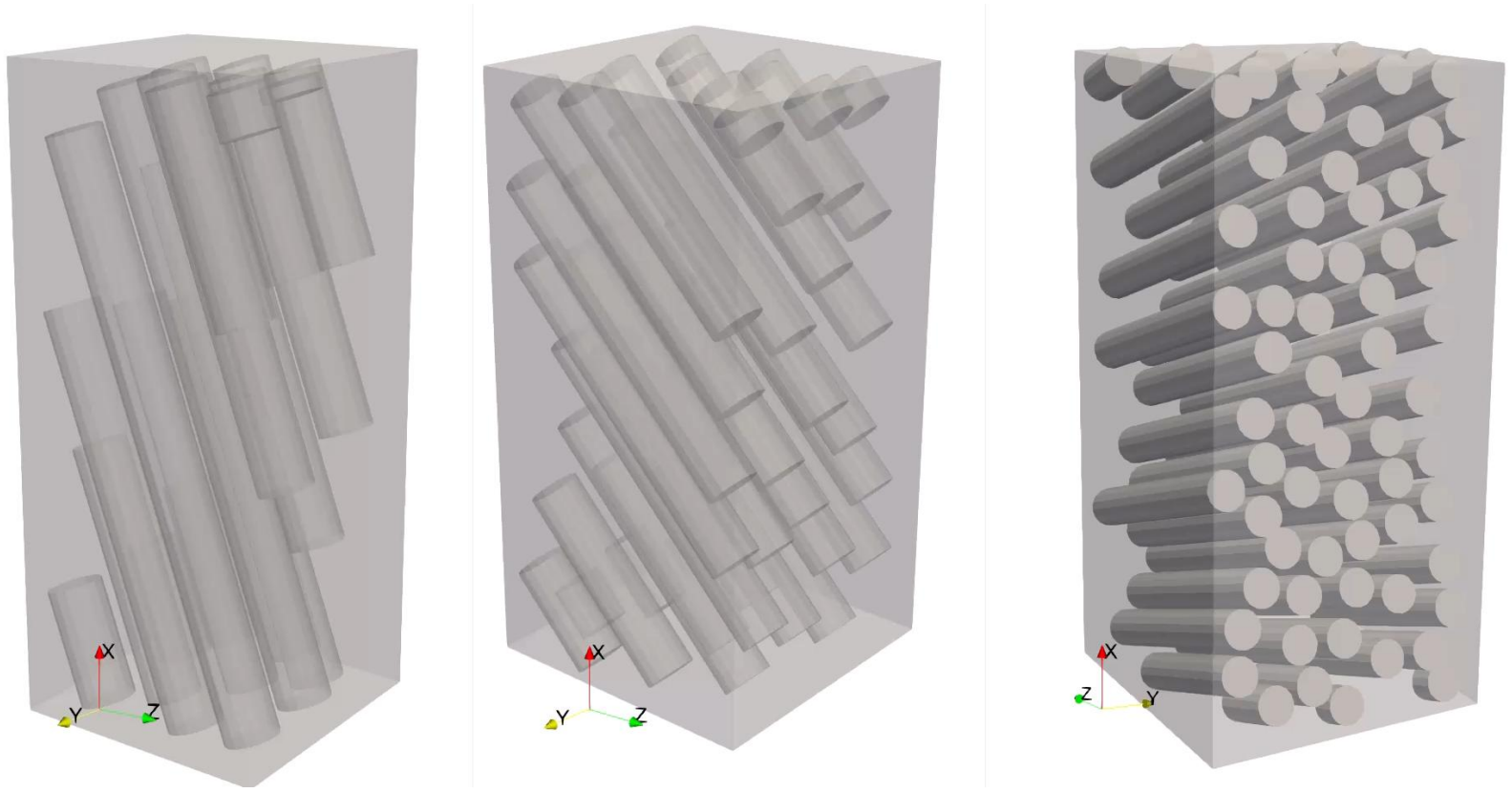

Resources

- HP Zbook, 8 GB RAM
- Simulation Time: 360 minutes
- No Calibration

Key Findings

- Captured Slope Bands from offset angled fiber studies (20˚, 45˚,and 70˚specimens)
- Captured Shear Bands
- Damage formation is nearly identical to the experiment

Reference

Keynote: Flores M etal (2024) In-situ X-ray nCT Experiment Showing Slope Instabilities In PMC Microstructures, MSORVAE

ES3 Proprietary Data. All Rights Reserved.

Slope Instabilities

Approach

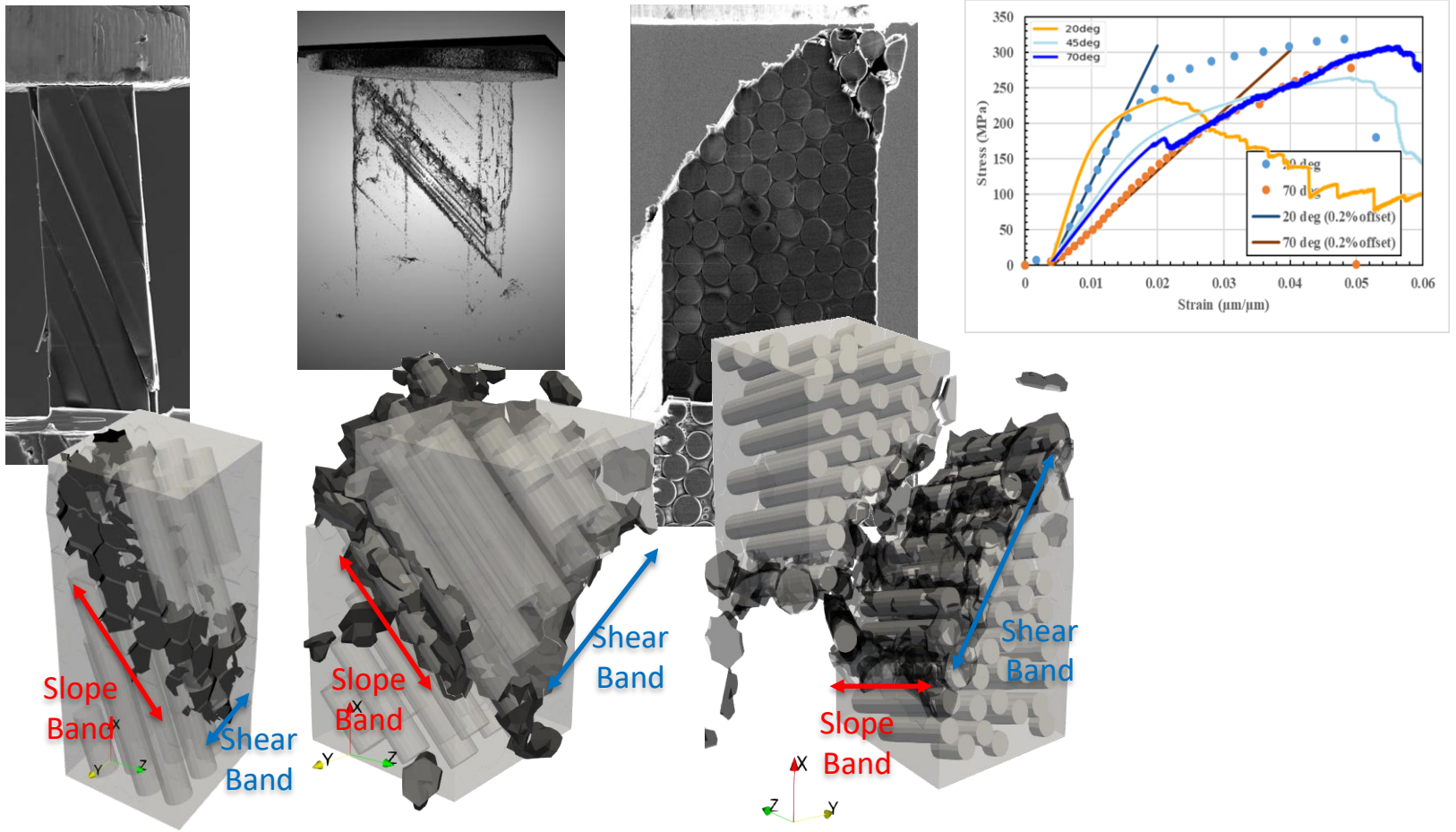

Resources

- HP Zbook, 8 GB RAM
- Simulation Time: 360 minutes
- No Calibration

Key Findings

- Captured Slope Bands from offset angled fiber studies (20˚, 45˚,and 70˚specimens)
- Captured Shear Bands
- Damage formation is nearly identical to the experiment

Reference

Keynote: Flores M etal (2024) In-situ X-ray nCT Experiment Showing Slope Instabilities In PMC Microstructures, MSORVAE

ES3 Proprietary Data. All Rights Reserved.

Shear Bands

Resources

- HP Zbook, 8 GB RAM
- Simulation Time: 60 minutes
- No Calibration

Key Findings

- Captured parallel crack formations
- Captured shear bands
- Crack formations are nearly identical to the experiment

Reference

Flores M, etel, “Experimental Analysis of PMC Microstructures Under Transverse Compression Loading,” Composites Part A: Applied Science and Manufacturing, V156, May 2022, 106859

Approach

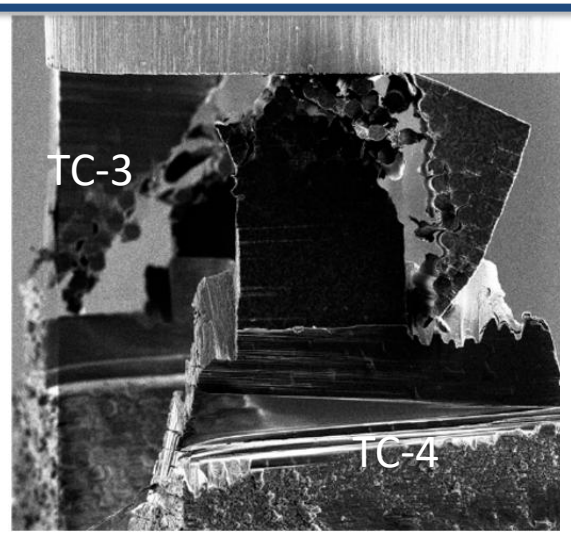

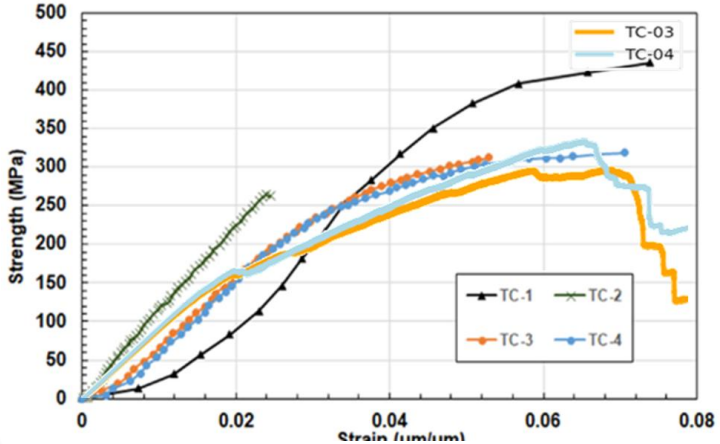

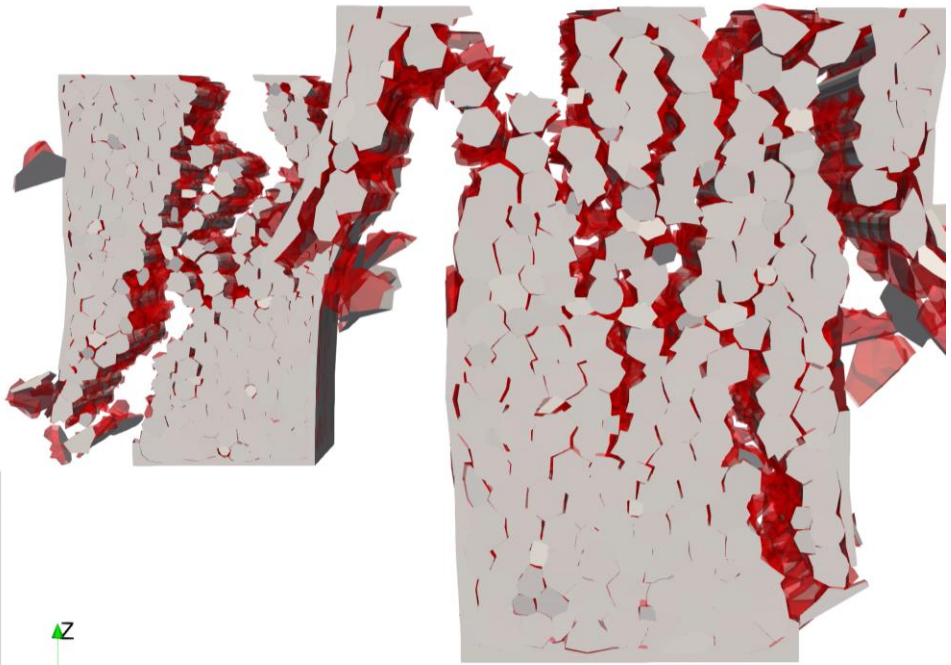

ES3 Proprietary Data. All Rights Reserved.

Kink Bands

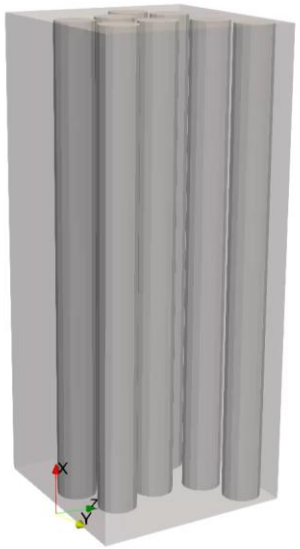

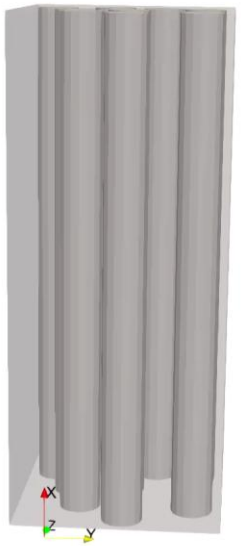

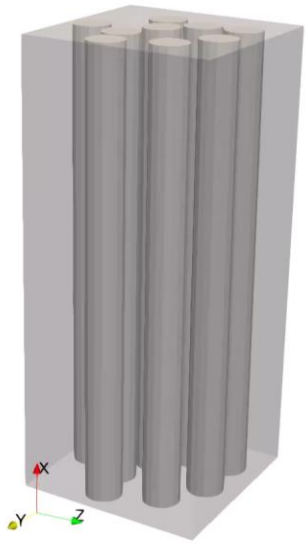



	Dimension	Stress (GPa)	Strain (%)	Modulus (GPa)
Results: TC Quick et al: Microscale Testing (IM7/5250-4)				
FP-1	20x13x50 um	1.18	2.8	41.6
FP-2	19x13x65 um	1.72	2.1	81.0
Results: Lu et al: Micro and Meso Tests (IM7/thermoset)				
Micro	18x15x53 um	1.98	1.04	190
Macro	6.25x3.17x108 mm	0.95	1.33	71
Results: Flores et al: DM4C Simulations (IM7/977-3)				
Micro	**25x25x60 um**	**1.5-1.9**	**1.9-2.1**	**86.9-104.1**

Resources

- HP Zbook, 8 GB RAM
- Simulation Time: 90 minutes
- No Calibration

Key Findings

- Captured precursors to the Kink bands (i.e. slope bands, and shear bands).
- Due to not modeling the edge fibers, model did not capture fiber breakage

Reference

Quick T etal, " Compression Testing of Micro-scale Unidirectional Polymer Matrix Composites," Conference Proceedings of the Society of Experimental Mechanics Series, (2016)

ES3 Proprietary Data. All Rights Reserved.

Mode I Fracture Using a DCB

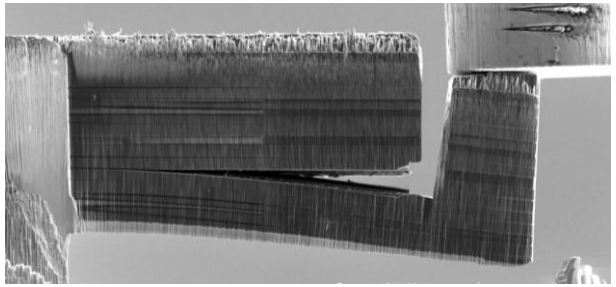

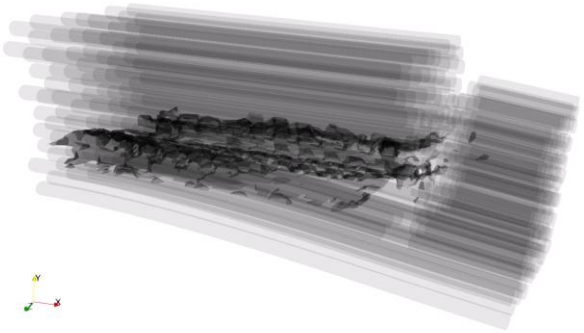

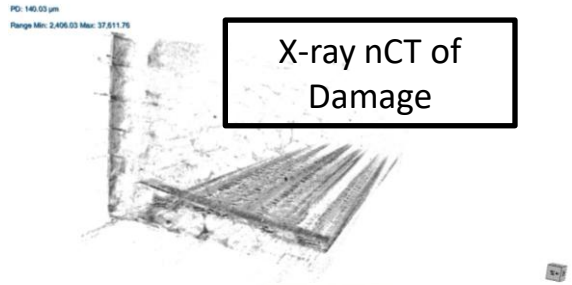

X-ray nCT of Damage

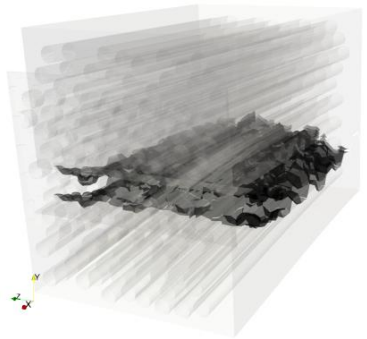

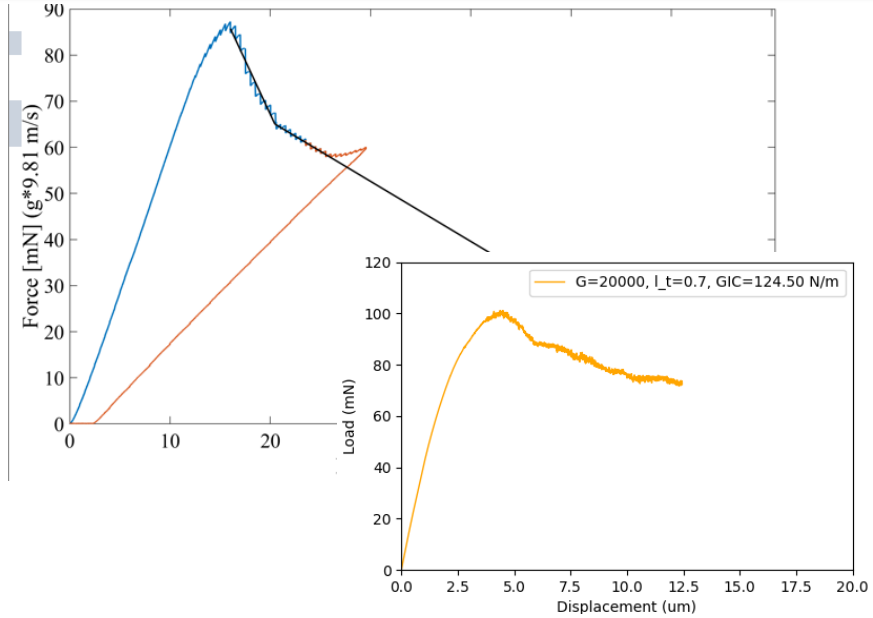

Resources

- HP Zbook, 8 GB RAM
- Simulation Time: 30-45 minutes
- No Calibration

Key Findings

- Captured Mode I fracture behavior
- Load response requires some improvement
- Captured behavior, but stiffnesses are different

Reference

Flores M etal (2024) In-situ X-ray nCT Experiment Showing Slope Instabilities in PMC Microstructures, Microscopy Society of the Ohio River Valley Annual Meeting

ES3 Proprietary Data. All Rights Reserved.

Summary

Kink Band

- **Captured:** Localized, abrupt bending or rotation of crystallographic planes within a material under compression or bending.
- **Known for:** Buckling
- **Missing/Needs Work:** Capture fiber breakage better by including edge fibers



Shear Band

- **Captured:** Narrow, planar regions of intense, highly localized plastic deformation that propagate through a material.
- **Known for:** Collapse
- **Next Steps:** High-Strain Rate Deformation



Slope Bands

- **Captured:** Precursors that contributed to the shear band and the kink band
- **Known for:** Fault Lines seen in kink bands.
- **Next Steps:** Thermal/Moisture

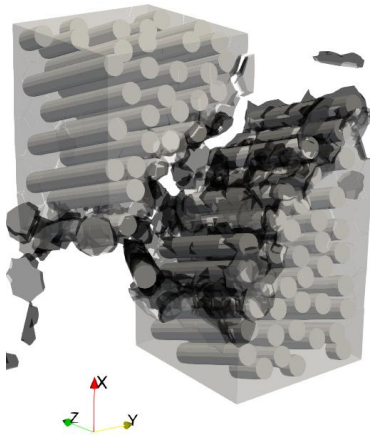

Fracture

- **Captured:** Accumulated damage required to understand preceding instabilities.
- **Known for:** Failure Behavior, Material Separation
- **Next Steps:** Development of an Energy-Centric Calibration study for DM4C

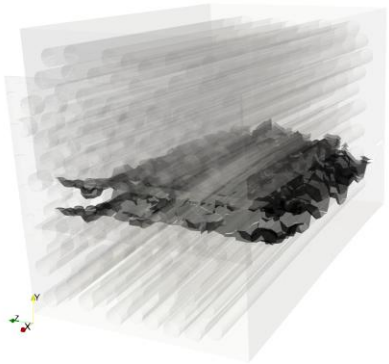

ES3 Proprietary Data. All Rights Reserved.

Future Work

DM2 Model

- **DM2:** Develop a simple tetrahedral mesh to evaluate the same microstructures by explicitly modeling the fiber.
- **Relevancy:** Evaluating CMC performance under extreme environments.

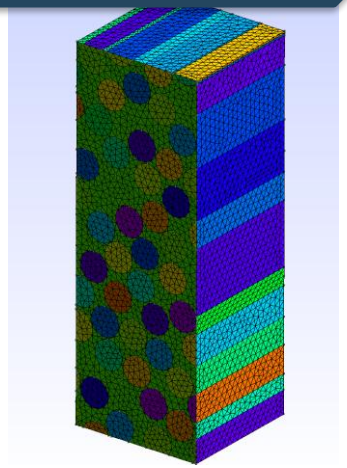

Expansion of DM4C

- **Edge Fibers:** Create Timoshenko beams that can go on the edges.

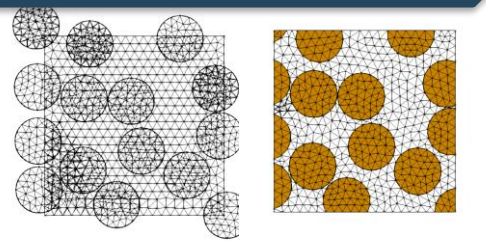

- **Relevancy:** Help aid in the prediction of fiber breakage in micromodels.

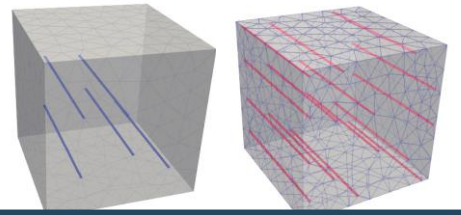

Autocalibration

- **Autocalibration:** Develop systematic tools that can perform the calibration for you internal to DM4C as a priori condition.
  - Material Properties
  - Geometrical Representation of the Fiber
- **Relevancy:** Input become substantial simpler and requires little effort to start modeling using our toolsets.

Implicit Solver

- **Elastic Analysis:** Substantial improvement in the performance of the simulation.
  - Elastic Analysis can take anywhere between 5 and 15 minutes for a single problem.
- **Relevancy:** Calibration, Optimization Problems, Multi-Physics parameter identification

ES3 Proprietary Data. All Rights Reserved.

ICCM24 24TH INTERNATIONAL CONFERENCE ON COMPOSITE MATERIALS
AUG 4-8, 2025 • BALTIMORE CONVENTION CENTER • BALTIMORE, MARYLAND

A NEW TEST FOR THE MECHANICAL CHARACTERISATION OF COMPOSITE PULTRUDE RODS UNDER COMPRESSION

G. Quino[1,2], C. Zhao[1], B. Zhang[2], P. Robinson[1], and R. S. Trask[2]

[1]Department of Aeronautics, Imperial College London
Exhibition road, SW7 2AZ, London, United Kingdom
Email: g.quino-quispe@imperial.ac.uk, web page: https://www.imperial.ac.uk/aeronautics/

[2]Bristol Composites Institute, University of Bristol
University walk, BS8 1TR, Bristol, United Kingdom
web page: www.bristol.ac.uk/composites

Keywords: CFRP; test method; compression; 4-point bending; pultrusion; DIC

ABSTRACT

Traditional direct compression tests on pultruded rods typically generate stress concentrations around the gripping regions, preventing accurate measurement of the true compressive strength. This paper introduces the 'cradle test', a novel experimental methodology designed to better characterise the compression performance of such materials. The setup consists of a polymeric beam that 'cradles' a pultruded rod, which is adhesively bonded to the beam. The method produced consistent failure within the gauge length and clear evidence of compression-dominated failure modes. A complementary technique based on full-field digital image correlation (DIC) strain measurements was also developed to obtain the complete strain *vs*. stress response. The approach is extendable to the characterisation of other materials.

1 INTRODUCTION

Composite pultruded rods can be key in the manufacture of components and structures with enhanced compression performance, as they typically exhibit reduced fibre misalignment [1]. However, measuring their compressive behaviour is challenging. Traditional compression testing methods, such as direct compression, often fail to produce consistent failure within the gauge length [2], [3].

We propose the 'cradle test' as a new method for characterising the mechanical response of fibre composite pultruded rods under uniaxial compression [4], [5]. The test gradually generates compression on the pultruded rod by applying four-point bending on a polymeric beam to which the rod is bonded to.

In the following sections a summary of the experimental methodology and some key results will be presented. Further details on the experimental methodology, data processing and results can be found in the full journal article published by the authors [4].

2 EXPERIMENTAL

2.1 Materials and specimen design

The material system characterised in this study was a commercially available carbon fibre/epoxy pultruded rod with a diameter of 0.8 mm. The fibre volume fraction was within the range of 49-55%, measured from micrographic images of the rods' cross sections. Tensile experiments on these rods showed that their elastic modulus was 134.1±4.5 GPa. This modulus value will later serve as validation of the results.

Figure 1a shows a schematic of the cradle test specimen assembly. The design of the specimen was conducted with a combination of analytical and FEA computational tools, such that: (i) The cradle

behaves linear and does not fail before the rod; (ii) buckling is prevented; (iii) rod bending is reduced; and (iv) strains on the cradle are measurable. The cradle test beams were fabricated from 15 mm thick polycarbonate (PC) plates. Load and supports spans were selected as $L = 120$ mm and $D = 60$ mm, respectively. The final dimensions of the cradle that met the design requirements are shown in Figure 1b.

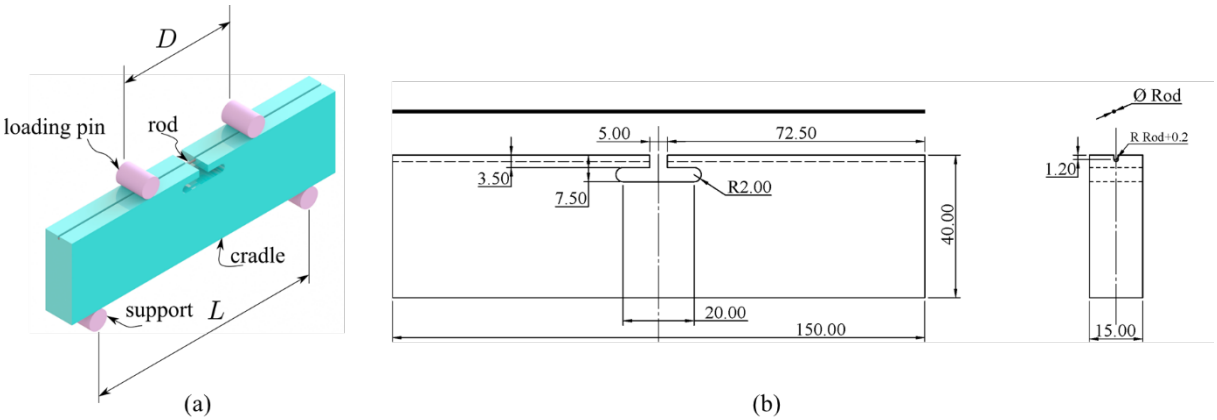

Figure 2: Cradle test design: (a) Schematic, and (b) Dimensions of the cradle test assembly.

2.2 Experimental setup

The setup, shown in Figure 2, included two cameras to image the speckled surfaces of the cradle (camera 1) and the pultruded rod (camera 2). Speckle patterns were carefully prepared to enhance the accuracy of DIC [6]. For the cradle, the 'tattoo speckle' pattern was used to provide optimal speckle sizes for the specific optical setup [7]. The experiment was conducted under displacement control at 0.18 mm/min, ensuring quasi-static loading of the specimen.

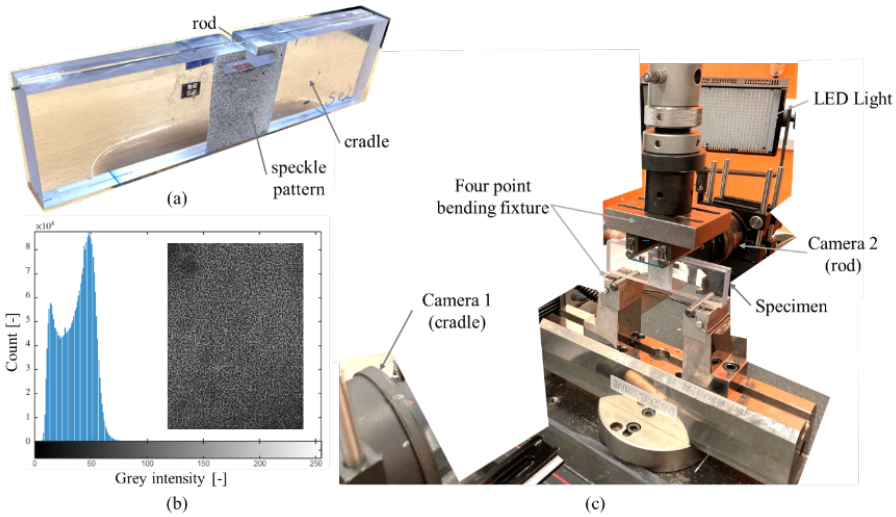

Figure 2: Prepared specimen and the loading rig and acquisition setup.

2.3 Data reduction method

By prescribing force equilibrium in the x-direction in the free body diagram shown in Figure 3, the resultant force across the cradle's midplane is equal to the absolute value of the compressive force on the pultruded rod F^r. FEA simulations demonstrated that the horizontal component of the reaction forces on the loading and supporting pins had negligible influence; therefore, they were excluded from the analysis. The compressive force acting on the rod can therefore be calculated by assuming plane stress, elasticity, and the integration of the DIC strain field of the cradle along the midplane path as shown in

equation (1).

$$F^r \approx -b \int_0^h \frac{E}{1-\nu^2} \varepsilon_{xx}^c(y) + \frac{\nu E}{1-\nu^2} \varepsilon_{yy}^c(y) dy, \quad (1)$$

where $\varepsilon_{xx}^c(y)$, and $\varepsilon_{yy}^c(y)$, are the x-, and y-strain components on the surface of the cradle along the midplane path; b is the width of the cradle (15 mm), and h is the length of the midplane path. The strain history of the rod ε^r was obtained using DIC on the images acquired by camera 2. Finally, F^r and ε^r were combined to produce the strain vs. stress curves. Figure 4 summarises the data reduction process.

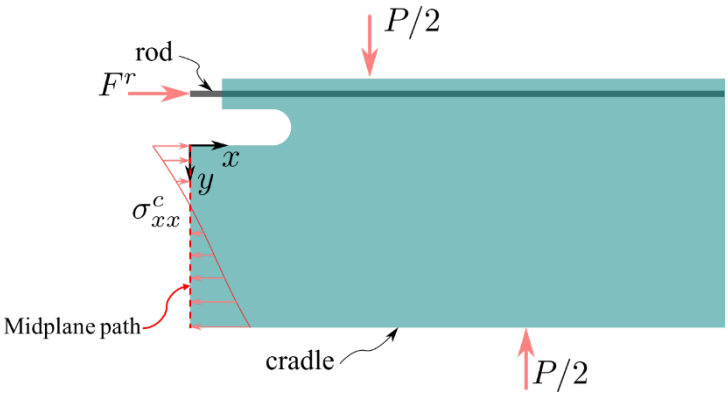

Figure 3: Free body diagram of half of the specimen.

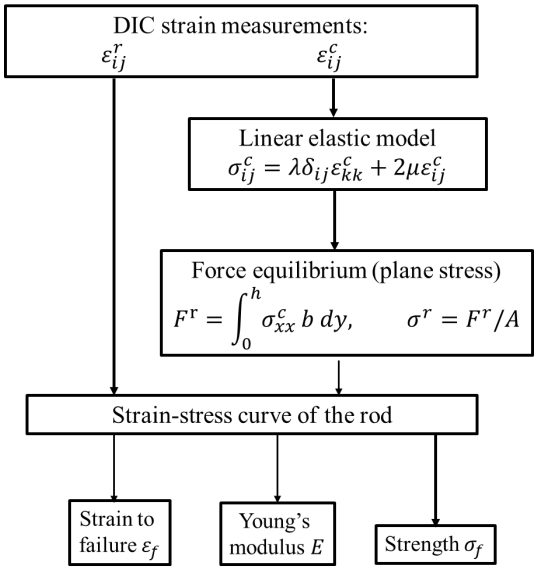

Figure 4: Flow chart of the data reduction process.

4 RESULTS

A typical displacement *vs*. load curves, and DIC strain fields measured in the experiment are shown in Figure 4a. Compression failure, away from the gripping region was consistently obtained across experiments (Figure 4b). From all tests, the DIC reconstructed strain *vs*. stress curves are shown in Figure 5. The average of the obtained elastic moduli was E=133.0 ± 11.3 GPa, close to the 134.1 ± 4.5 GPa measured from uniaxial tensile tests, validating the experiment and methodology. The average strain to failure was 1.16 ± 0.13%. The SEM images shown in Figure 6 showed fibre kink bands, a characteristic feature of compression failure.

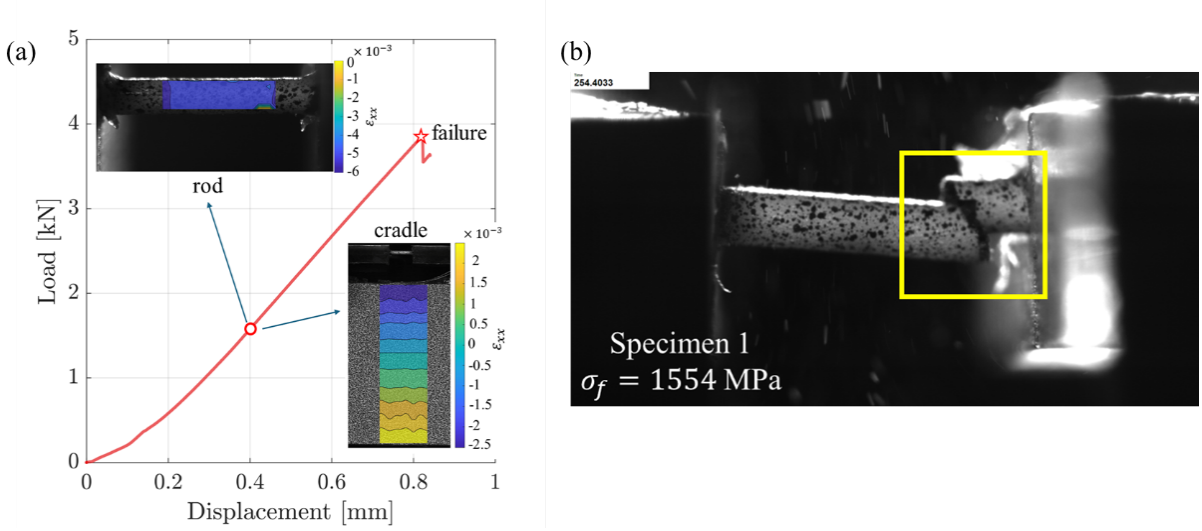

Figure 4: Data from a typical test: (a) Displacement-load curve and strain maps; and (b) pultruded rods failure mode.

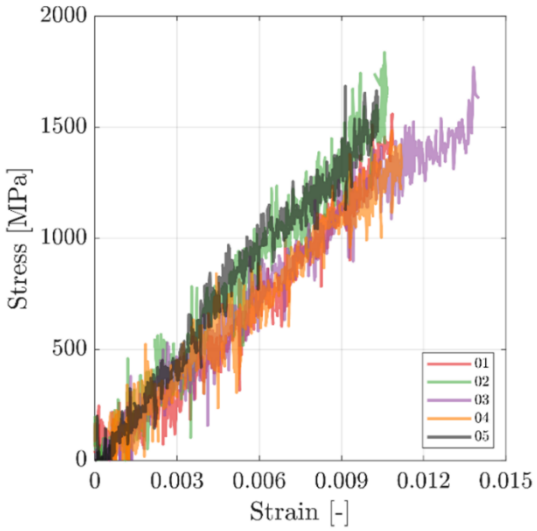

Figure 5: Strain-stress curves of all specimens

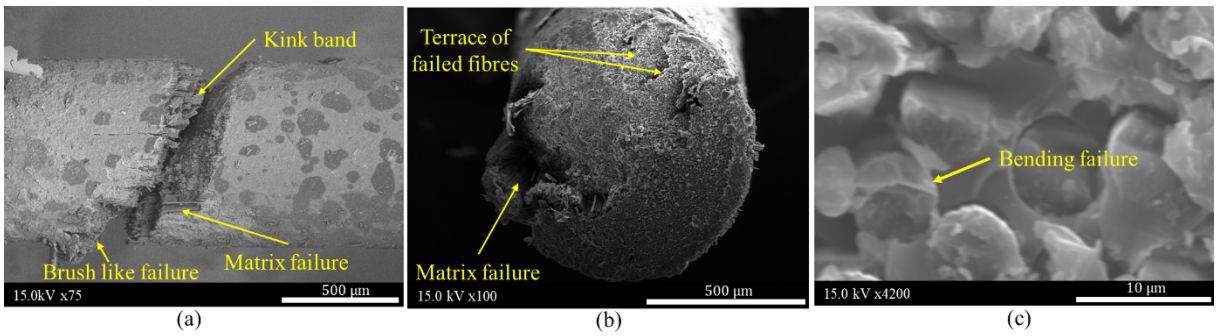

Figure 6: SEM micrography images: a) Full image of a failed specimen, b) Failure surface of another representative sample, and c) Individual failed fibres showing bending failure.

5 CONCLUSIONS

In this work, we presented and validated the ‘cradle test’, a novel methodology for characterising the compressive mechanical behaviour of pultruded rods. The main conclusions are:

- The new method simplifies specimen preparation and test setup and ensures compressive failure within the gauge length.
- The methodology can reconstruct the compressive strain vs. stress curves.
- The failure planes were located far from the bond region, suggesting mitigation of stress concentrations at gripping zones.

Further work is required to reduce the noise in the reconstructed stress, coming from the integration of the DIC strain field. The method will be used to rank various new material systems produced by pultrusion.

ACKNOWLEDGEMENTS

The authors kindly acknowledge the funding for this research provided by UK Engineering and Physical Sciences Research Council (EPSRC) programme Grant EP/T011653/1, Next Generation Fibre-Reinforced Composites (NextCOMP): a Full-Scale Redesign for Compression a collaboration between Imperial College London and the University of Bristol.

For the purpose of open access, the authors have applied a Creative Commons Attribution (CC BY) license to any author accepted manuscript version arising. Supporting data can be requested from the corresponding author but may be subject to confidentiality obligations or all underlying data to support the conclusions are provided within the manuscript or supplementary information.

REFERENCES

[1] N. Jeppesen, L. P. Mikkelsen, A. B. Dahl, A. N. Christensen, and V. A. Dahl, "Quantifying effects of manufacturing methods on fiber orientation in unidirectional composites using structure tensor analysis," *Compos Part A Appl Sci Manuf*, vol. 149, p. 106541, Oct. 2021, doi: 10.1016/j.compositesa.2021.106541.

[2] C. Soutis, "Compression testing of pultruded carbon fibre-epoxy cylindrical rods," *J Mater Sci*, vol. 34, pp. 3441–3446, 2000, [Online]. Available: https://link.springer.com/article/10.1023%2FA%3A1004832606677

[3] S. R. Vankar, A. N. Kaore, and C. S. Yerramalli, "Methodology for testing the compressive strength of pultruded composites," *Journal of Reinforced Plastics and Composites*, vol. 42, no. 11–12, pp. 544–557, Jun. 2023, doi: 10.1177/07316844221133293.

[4] C. Zhao, G. Quino, B. Zhang, P. Robinson, and R. S. Trask, "The cradle test: A new experiment to characterise the compression response of pultruded rods," *Compos Part A Appl Sci Manuf*, vol. 197, p. 109054, Oct. 2025, doi: 10.1016/j.compositesa.2025.109054.

[5] G. Quino, P. Robinson, and R. S. Trask, "Design of a bending experiment for mechanical characterisation of pultruded rods under compression," *Proceedings of the 20th European Conference on Composite Materials*, vol. Vol 3-Char, pp. 167–172, 2022, doi: 10.5075/epfl-298799_978-2-9701614-0-0.

[6] G. Quino, "Impact damage analysis of composite structures using digital image correlation," in *Non-destructive Testing of Impact Damage in Fiber-Reinforced Polymer Composites*, Elsevier, 2024, pp. 69–86. doi: 10.1016/B978-0-443-14120-1.00003-0.

[7] G. Quino *et al.*, "Speckle patterns for DIC in challenging scenarios: rapid application and impact endurance," *Meas Sci Technol*, vol. 32, no. 1, p. 015203, Jan. 2021, doi: 10.1088/1361-6501/abaae8.

THE EXPERIMENTAL INVESTIGATION OF THE COMPRESSIVE PERFORMANCE OF PULTRUDED ROD COMPOSITE STRUTS

B. Zhang[1], L.R. Pickard[1], I.C. Nwuzor[1], N.ST. Darras[1], M.R. Wisnom[1], G. Allegri[1], G. Quino[2], P. Robinson[2] and R.S. Trask[1]

[1]Bristol Composites Institute, Department of Aerospace Engineering, University of Bristol, Bristol BS8 1TR UK
Email: bohao.zhang@bristol.ac.uk, web page: www.bristol.ac.uk/composites

[2]The Composite Centre, Department of Aeronautics, Imperial College London, London SW7 2AZ UK
web page: www.imperial.ac.uk/composites-centre

Keywords: Pultruded composite struts, Eccentric buckling test, Compressive performance

ABSTRACT

Pultruded carbon fibre/epoxy composites possess high fibre alignment. However, the characterisation of the compression performance of these materials in axial compression loading is sensitive to the factors such as specimen end preparation, loading misalignment and localised non-uniform loading. End fittings have been used to prevent the premature failure of these materials in axial compression test but this induced high complexity of the preparation process. In this study, we developed aneccentric buckling test methodology to investigate the compressive performance of pultruded carbon fibre/epoxy composites. The test results showed that the elastic modulus (85.5 ± 1.3 GPa) and flexural modulus (87.3 ± 3.0 GPa) were consistent with the value measured from tensile test at 88 GPa. A compressive failure strain at failure at -0.0134 ± 0.0007 was measured, which is higher compared with the reported values in literature for carbon fibre/epoxy pultruded rods. This shows that the eccentric buckling test is suitable for measuring the compressive failure strain of carbon fibre/epoxy pultruded rods.

1 INTRODUCTION

Carbon fibre/epoxy composites have been widely used in engineering applications due to their excellent mechanical performance. However, the material exhibits relatively weak compressive performance, partially due to fibre misalignment and waviness [1]. Pultruded carbon fibre/epoxy composites have been developed [2], with the applied pulling force in the pultrusion process to improve the fibre alignment of the resulting composites. Greater compressive performance is therefore expected.

Works have been conducted to characterise the compressive performance of the pultruded composites using the direct compression test method [3-6]. For example, carbon fibre/epoxy pultruded rods of 1.7 mm in diameter were bonded with metallic cylindrical holders and then loaded against upper and lower metal platens in compression until failure [3]. The results showed that stress concentration at the junction of gauge length and cylindrical holders was observed, and that the presence of voids and fibre misalignment resulted in reduced compressive strength. In another study, 6 mm diameter carbon fibre-polyester pultruded rods were snugly fitted into metallic end pieces and then tested in direct compression [4]. Test results showed that failure occurred at low compressive strain and reduced strength was measured, possibly due to stress concentration near specimen gauge section and specimen misalignment during mounting. Collars have been used to laterally support specimens upon compression. In summary, the direct compression test for pultruded rod composites requires extensive experience and skills on specimen preparation, endcap design and specimen mounting, to prevent incorrect load induction, stress concentration, buckling instability, and specimen end crushing and booming due to gripping and specimen misalignment [2].

Alternatively, some of the authors of the current work have developed a ‘cradle’ test method using 4-point bending [7]. Easycomposite Carbon fibre/epoxy pultruded rods of 0.8 mm in diameter have been

tested and a compressive failure strain of -0.0116 has been reported. However, the test method may not be suitable for large diameter pultruded rods due to the complex design of the cradle.

We have developed an eccentric buckling test methodology to investigate the compressive performance of 6 mm diameter pultruded carbon fibre/epoxy composites. Compressive failure strain was measured and compared with published data measured from other test methods. This method provides an alternative way to measure the compression behaviour of circular pultruded composite rods.

2 EXPERIMENTAL INVESTIGATION

2.1 Materials

In this study, Easycomposite pultruded carbon fibre/epoxy (ECPRs) of 6 mm in diameter, purchased from Easycomposite, UK, were used in the development of this test method. The manufacturer's datasheet indicates an elastic modulus of 28-40 GPa [8] for the rod material but a much higher value of 132 GPa has been reported for 0.8 mm diameter ECPRs [7]. Tensile tests were therefore conducted to measure the elastic modulus of the ECPR strut specimens in this study.

2.2 Specimen preparation

The as-received ECPR struts of 6 mm in diameter and 1 meter long were cut into 300 mm long (i.e. an aspect ratio of 50:1 was used). Sections of the material were cast in epoxy resin and the polished cross section was examined under microscope.

Figure 1a shows the specimen dimensions. The ECPR struts were then marked with three longitudinal lines separated by 120° on the circumferential surface at the mid-span location. Three uniaxial strain gauges were subsequently bonded longitudinally at the marked lines. A line corresponding to one of the strain gauge positions was also marked close to each end of the stut to help align the end caps.

The ECPR struts with the strain gauges were CT-scanned (Zeiss Xradia 5200, DE) to determine the actual enclosed angles between strain gauges and to measure the diameter of the struts. After this, the ECPR struts were bonded with endcaps using an epoxy resin adhesive (3M DP490, UK). The endcap, shown in Figure 1b, is designed so that the strut axis is offset by 7 mm from the loading pin centre to promote bending. During bonding, the marked lines at each end of the ECPR strut was aligned with the engraved mark on the endcaps. This ensured that one strain gauge was aligned with the nominal position of the maximum compression stress in the strut upon testing. The curing of the adhesive followed the resin manufacturer's recommendation.

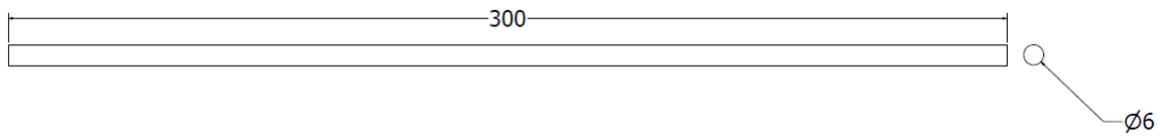

(a)

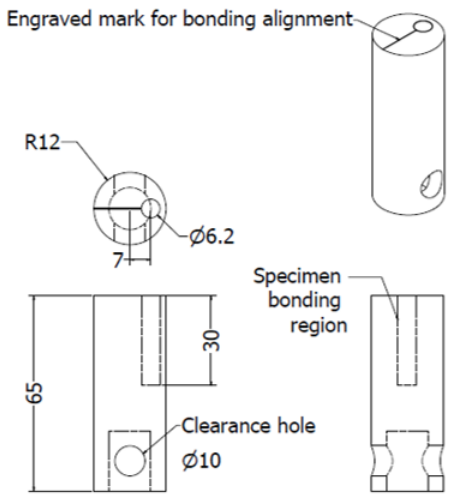

(b)

Figure 1: (a) ECPR strut dimension (mm) and (b) endcap design (mm).

The centre zone of 40 mm length of each ECPR strut was painted in white using an acrylic spray paint. Once fully dried, black speckles were applied onto the paint for strain measurement with digital image correlation (DIC).

2.3 Eccentric buckling tests

Eccentric buckling tests were conducted on an Instron 1341 test machine fitted with a 5 kN axial loadcell. Figure 2 shows the test setup. The specimen was mounted onto the test machine using pins inserted through the clearance holes in the endcaps and the fixture. The mounting ensured that the strut was pin-ended and would buckle in the yz plane. Spacers were used to ensure there was no eccentricity of loading in the x-direction. The specimen was loaded in displacement-control at a constant crosshead speed of 3 mm/min until failure.

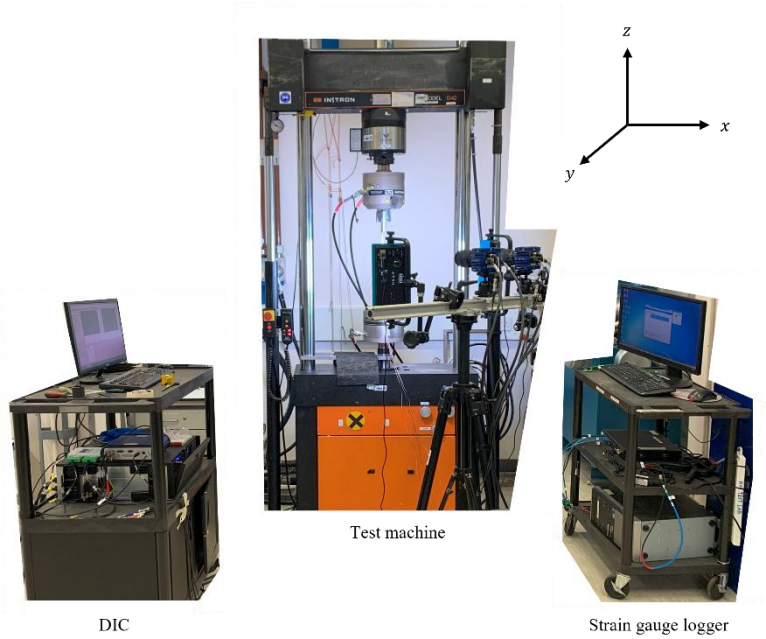

Figure 2: The eccentric buckling test setup.

Stereo DIC with two 16 mega-pixel cameras (LaVision, DE) and external LED light arrays were used to capture the full-field strain development to capture the strain development in the central zone of the strut viewed in the y-direction. The pixel size was 0.0055 mm. The captured images were processed using Davis (LaVision, DE) with a subset size of 31 pixels and a step size of 15 pixels. The bonded strain gauges were connected to the strain gauge logger for strain measurement.

Load (F) was measured from the test machine and strains were recorded by both the bonded strain gauges and the DIC, at a constant sampling rate of 1 Hz.

2.4 Data reduction

The applied stress (σ) was calculated using the equation (1)

$$\sigma = \frac{F}{A} \tag{1}$$

where A is the cross-sectional area of the strut at the mid-span position.

The critical buckling stress (σ_b) is given by

$$\sigma_b = \frac{\pi^2 EI}{L^2} \tag{2}$$

where E is elastic modulus, I is the second moment of area and L is the length between the loading pin hole centres of the endcaps.

The strain in the strut at the mid-length position can be considered as the superposition of the axial strain (longitudinal strain acting at the centroid) and the bending strain which varies linearly over the cross-section. The axial and bending strains can be determined from the three strain gauge measurements.

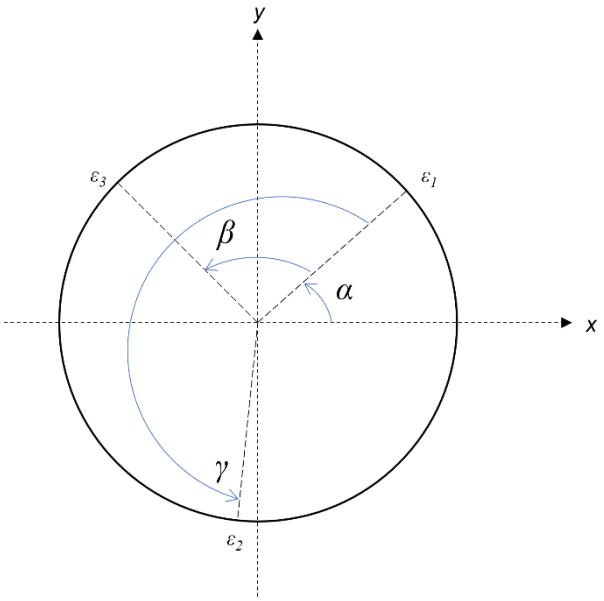

Figure 3: The schematic diagram of the calculation of axial strain and compressive strain from the three strain gauge measurements.

At the mid-span cross section of an ECPR strut specimen, three direct strains (ε_1, ε_2, and ε_3) are measured at the strain gauge locations as shown in Figure 3. Assuming linear elasticity and that buckling and bending occur about the x-axis, the neutral axis (zero bending strain) lies along the x-axis. The

maximum tensile and compressive strains, occur at the top and bottom surfaces intersecting the y-axis. The axial strain can be derived from a set of three sine wave equations related with the direct strain recorded at the three strain gauges locations. For bending about the x-axis the following equations can be established

$$\varepsilon_1 = A\sin\alpha + C$$
$$\varepsilon_2 = A\sin(\alpha + \gamma) + C \quad (3)$$
$$\varepsilon_3 = A\sin(\alpha + \beta) + C$$

where A is the magnitude of the bending strain at $y = \pm R$ (the radius of the circular cross-section), α is the unknown enclosed angle of the first strain gauge and the x-axis, β and γ are the enclosed angles between the first strain gauge and the second and third strain gauges respectively measured from CT-scan, and C is the axial strain.

From the equation set (3), and the CT-measured values of β and γ, the axial strain and the location and value of the maximum bending strain component can be determined.

The bending stress (σ_{bend}), assuming a linear elastic response, is given by the question (4)

$$\sigma_{bend} = \frac{32F(\delta + e)}{\pi D^3} \quad (4)$$

where δ is the deflection measured from DIC, e is the initial eccentricity of the load, and D is the strut diameter.

Axial modulus (E) can be determined from the applied axial stress – axial strain plot and the flexural modulus (E_f) can be derived from the bending stress – bending strain plot. These were used to compare with the elastic modulus measured from the tensile tests to validate the proposed test methodology.

3 RESULTS AND DISCUSSION

3.1 Mechanical performance of pultruded struts

Figure 4 shows the applied axial stress – axial strain responses of a typical ECPR strut specimen subjected to eccentric buckling. The dotted line is the critical buckling stress and the axial strain is calculated from the set of the three sine wave equations assuming a linear response. It can be seen that the specimen failed before reaching the critical buckling stress, as expected. The axial modulus, taken from the slope of the initial linear region at axial strains from 0 to -0.0001, is 86 GPa. This is consistent with the elastic modulus of 88 GPa measured in the tensile test but is significantly lower than the published value of 132 GPa for 0.8 mm diameter ECPR measured from the cradle test [7].

The inserted DIC images in Figure 4 shows that the specimen exhibited variation from compressive strain to tensile strain over the strut diameter. However, unexpected bands of compressive strain and tensile strain across the strut diameter have been developed. These may be due to the poor speckle quality and need further investigation. The maximum compressive strain measured from strain gauge was -0.0135. However, initial failure was observed to be by fibre breakage on the tensile side of the strut. Further investigation into the occurrence of such tensile failure via an interrupted test will be conducted.

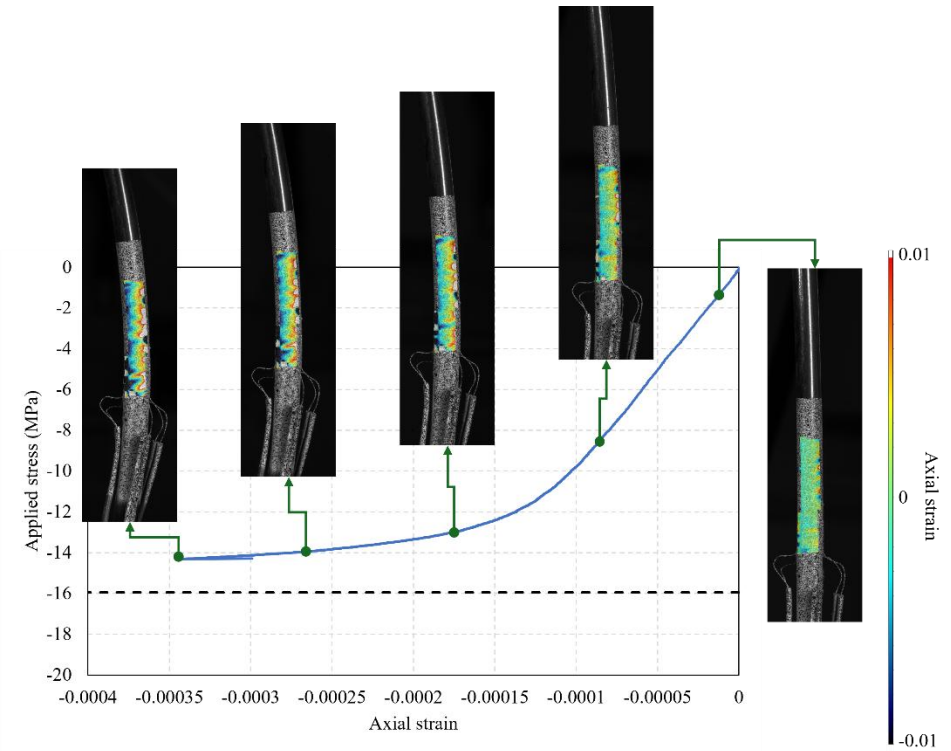

Figure 4: The applied stress – axial strain curve of a typical ECPR strut specimen subjected to eccentric buckling, with the inserted DIC images to show the compression-tension transition.

Figure 5 shows the bending stress – bending strain response of the same ECPR strut specimen at the compression side. The figure shows that a linear response of the material is observed, with the flexural modulus measured as 84 GPa. This is consistent with the axial modulus determined from the applied axial stress – axial strain plot.

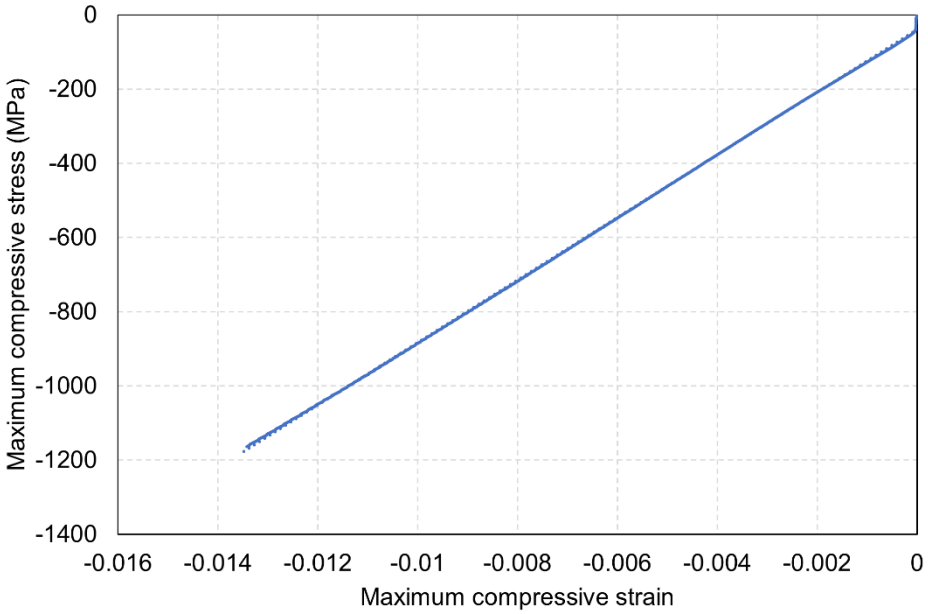

Figure 5: The bending stress-strain plot of the typical ECPR strut specimen.

Table 1 summarises, for a set of 5 repeated tests, the average axial and flexural moduli, the average measured compressive failure strain from the strain gauge close to the peak compression position and

the average compressive failure strain calculated as the maximum determined from the three strain readings and locations of all three strain gauges. (Standard deviation values are given in brackets.) It shows that the axial modulus is consistent with the value measured separately from a tensile test at 88 GPa, and that the flexural modulus shows very good agreement with the axial modulus, as expected. The compressive failure strain, is significantly higher than the failure strain values reported in literatures, although these are for other pultruded carbon fibre/epoxy materials. For example, *Soutis* reported the compressive strain at -0.0092 of 4 mm diameter T300/828 pultruded rods [9] and *Vankar et al* measured the compressive strain of 6.5 mm diameter pultruded rods at -0.0036 [10]. The high compressive failure strain may be partially due to the strain gradient in a bending test [11]. The average compressive failure strain calculated from the set of the three sine wave equations is slightly higher than the average measured compressive failure strain determined from the strain gauge located on the compressive side of the strut, but this is as expected if the strain gauge is not perfectly positioned with the maximum compressive strain location.

Average elastic modulus [GPa]	Average flexural modulus [GPa]	Average measured compressive strain [S]	Average calculated compressive strain [S]
85.5 (1.3)	87.3 (3.0)	-0.0134 (0.0007)	-0.0145 (0.0010)

Table 1: The average mechanical properties of ECPR strut specimens subjected to eccentric buckling test.

3.2 Microscope examination

Figure 6 shows the microscope image of the cross-section of an ECPR strut specimen. It can be seen that fibre clusters, resin-rich region and voids were formed during the pultrusion process.

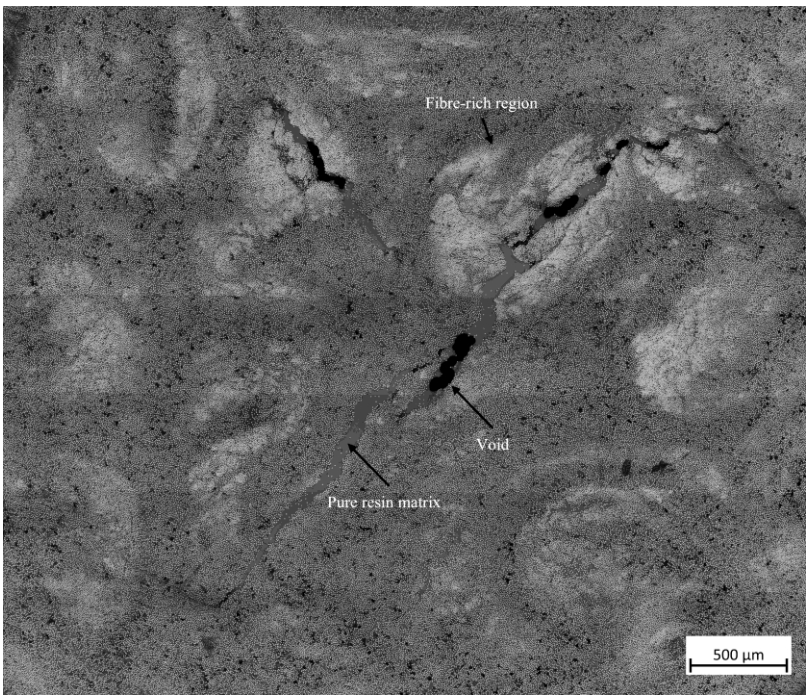

Figure 6: The microscope images of a ECPR specimen to indicate the fibre-rich region, neat resin region and voids. (20× magnification).

4 CONCLUSIONS

We have proposed an eccentric buckling test methodology to investigate the compressive

performance of large diameter pultruded carbon fibre/epoxy composites. ECPR struts of 6 mm in diameter were tested. The test results have shown that the axial modulus (85.5 ± 1.3 GPa) and flexural modulus (87.3 ± 3.0 GPa) were in good agreement with the value of 88 GPa measured in a tensile test. A compressive failure strain at failure of -0.0134 ± 0.0007 was measured, which is higher than values reported in the literature for other carbon fibre pultruded rods.

The next step of this study is to investigate the compressive performance of hierarchical pultruded rod epoxy composite struts developed within the NextCOMP research project.

ACKNOWLEDGEMENTS

The authors kindly acknowledge the funding for this research provided by UK Engineering and Physical Sciences Research Council (EPSRC) programme Grant EP/T011653/1, Next Generation Fibre-Reinforced Composites (NextCOMP): a Full Scale Redesign for Compression a collaboration between Imperial College London and the University of Bristol. Supporting data can be requested from the corresponding author but may be subject to confidentiality obligations.

For the purpose of open access, the authors has applied a Creative Commons Attribution (CC BY) license to any author accepted manuscript version arising.

REFERENCES

[1] B. Budiansky, N.A. Fleck, Compressive failure of fibre composites, *Journal of the Mechanics and Physics of Solids*, **41**, 1993, pp. 183-211 (doi: https://doi.org/10.1016/0022-5096(93)90068-Q).

[2] A. Vedernikov, A. Safonov, F. Tucci, P. Carlone and I. Akhatov, Pultruded materials and structures: A review, *Journal of Composite Materials*, 54, 2020, pp. 4081-117 (https://doi.org/10.1177/0021998320922894).

[3] C. Creighton and T. Clyne, The compressive strength of highly-aligned carbon-fibre/epoxy composites produced by pultrusion, *Composites science and technology*, **60**, 2000, pp. 525-533 (doi: https://doi.org/10.1016/S0266-3538(99)00153-0).

[4] M. Piggott and B. Harris, Compression strength of carbon, glass and Kevlar-49 fibre reinforced polyester resins, *Journal of materials science*, **15**, 1980, pp. 2523-2538 (doi: https://doi.org/10.1007/BF00550757).

[5] M. Saha, R. Prabhakaran and W. Waters, Compressive properties of pultruded composites, *Mechanics of composite materials*, **36**, 2000, pp. 469-474 (doi: https://doi.org/10.1023/A:1006706616386).

[6] A. Clarke, M.R. Wisnom and K. Potter, A comparison of the mechanical properties of Graphlite unidirectional carbon rod with conventional prepreg, *Plastics, Rubber and Composites Processing and Applications*, **26**, 1997, pp. 447-450.

[7] C. Zhao, G. Quino, B. Zhang, P. Robinson and R.S. Trask, The cradle test: A new experiment to characterise the compression response of pultruded rods, *Composites Part A: Applied Science and Manufacturing*, **197**, 2025, pp. 109054 (doi: https://doi.org/10.1016/j.compositesa.2025.109054).

[8] Easycomposites 6 mm Pultruded Carbon Fibre Rod Technical Datasheet. (https://www.easycomposites.co.uk/6mm-carbon-fibre-rod) [access date: 30 June 2025].

[9] C. Soutis, Compression testing of pultruded carbon fibre-epoxy cylindrical rods, *Journal of materials science*, **35**, 2000, pp. 3441-3446 (doi: https://doi.org/10.1023/A:1004832606677).

[10] S.R. Vankar, A.N. Kaore and C.S. Yerramalli, Methodology for testing the compressive strength of pultruded composites, *Journal of Reinforced Plastics and Composites*, **42**, 2023, pp. 544-557 (doi: https://doi.org/10.1177/07316844221133293).

[11] X. Wu and M.R. Wisnom, Compressive failure strain of unidirectional carbon fibre composites from bending tests, *Composite Structures*, **304**, 2023, pp. 116467 (doi: https://doi.org/10.1016/j.compstruct.2022.116467).

PERFORATION AND PENETRATION MECHANICS OF COMPOSITES: THEORY, EXPERIMENT AND FINITE ELEMENT ANALYSIS

Bazle Z. (Gama) Haque[1]

[1]Senior Structural Aerospace Engineer, Mclaurin Aerospace, Jacobs JETS II Contract
NASA Johnson Space Center, 2101 NASA Pkwy, B13-230, Houston, TX 77058, USA
Email: bazle.z.haque@nasa.gov, bzhaque@udel.edu

Keywords: Perforation, Penetration, Thick-section Composites, Plain-Weave S-2 Glass/SC15, Punch-Shear, Punch-Crush, MAT162, LS-DYNA

ABSTRACT

Transverse impact of right circular cylinder (RCC) projectiles on finite-thickness thick and thin composite laminates are of great importance in understanding the mechanics and physics of lightweight protection materials. The fundamental objective is to optimize the deceleration of the impactor as a function of energy dissipating materials damage mechanisms in space and time following the conservation of energy and momentum.

Quasi-static punch shear test (QS-PST) experimental methodology had been developed by the author in quantifying the energy dissipating quasi-static perforation and penetration damage mechanisms of 1 to 24 layers (L) of plain weave (PW) 24 oz/yd^2 S-2 Glass/SC-15 composites. Ballistic limit experiments had been conducted on 24L and 32L thick laminates and then sectioned in understanding the ballistic damage mechanisms. It had been identified that the ballistic damage mechanisms can be simulated by the QS-PST experiments. By conducting QS-PST experiments as a function of punch diameter to support diameter ratio (SPR) and superimposing the experimental load-displacements, an envelope penetration curve had been constructed to represent 70% of the ballistic energy. A quasi-static model of ballistic penetration has been developed which also utilizes the maximum force from QS-PST experiment at SPR = 0 aka QS-Indentation (QSI) experiment and using a dynamic increase factor DIF = 1.1 yields 100% of the ballistic energy.

Finite element analysis of ballistic experiments for 11L, 24L, and 32L PW S-2 Glass/SC15 composites had been performed using rate dependent progressive composite damage model MAT162 in LS-DYNA in determining the time history of penetration resistance force and projectile dynamics. MAT162 progressive composite damage model has been proven to capture the ballistic damage mechanisms and had been validated for several composite materials.

The validated FE models are then used to simulate the ballistic limit analysis of very thick to thin e.g., 88L, 66L, 44L, 32L, 24L, 12L, 8L, 4L, & 2L PW S-2 Glass/SC15 composite laminates. From these simulations, three phases of ballistic penetration had been identified, i.e., (i) Penetration or P-phase, (ii) Transition or T-phase, and (iii) Perforation or F-phase. Calculating the through-thickness longitudinal wave velocity it has been postulated that the end of P-phase is complete when the shock wave reflects from the rear face of the target and meets the penetration font.

The classic penetration resistance test had been modified in understanding the P-phase of ballistic penetration and is termed as Depth of Penetration (DoP) test. An energy based theoretical model for the DoP experiments had been developed in calculating the characteristic time of DoP, impact contact force and projectile dynamics. A threshold velocity of penetration V_{TH} has been defined when the projectile will cease to penetrate the target. During the ballistic penetration and perforation of a finite thickness target, when the projectile velocity reduces to V_{TH}, the projectile continues to deform the remaining target and predominantly fails under tension-shear damage mechanism which is termed as the perforation or F-phase.

The relative thickness of a composite laminate has been defined based on the different phases of ballistic penetration. A thin laminate is defined as a laminate which only shows the perforation or F-phase (1L to 10L of PW S-2 Glass/SC15). An intermediate thickness laminate is defined which shows

both the transition or T-phase and perforation or F-phase of ballistic penetration (10L to 30L of PW S-2 Glass/SC15). A thick section composite laminate is defined where all three penetration phases are present, i.e., P-phase, T-phase, and F-phase (.GT. 30L of PW S-2 Glass/SC15).

Phoenix and Porwal (2003) have developed a 2D membrane theory which has been used to validate FE models for orthotropic composite materials in calculating the deformation cone/kink wave and bending wave velocities.

While the energy dissipating perforation damage mechanisms can be represented by QS-PST experiments, the penetration phase or P-phase damage mechanisms have been investigated by modifying the QSI experiments. The quasi-static indentation (QSI) strength $\mathrm{X_{QSI}}$ have been identified as a vital experiment in relative ranking of composite materials.

DoP experiments, QSI experiments, QS-PST experiments, ballistic limit experiments presented in this paper can quantify the energy dissipating penetration and perforation damage mechanisms. Theoretical models and LS-DYNA MAT162 computational analysis have provided insight in to the penetration and perforation of composites.

1 PERFORATION MECHANICS OF THIN-SECTION COMPOSITES

Transverse impact of a right circular cylinder (RCC) projectile on a 2D isotropic membrane is a good example of perforation (Phoenix & Porwal (P&P), 2003, [1]); in which, the thickness t_m of the membrane is considered much smaller than the diameter $D_P = 2r_p$ of the projectile, i.e., $t_m/D_P \ll 1$. For constant impact velocity V_P on a 2D membrane (Fig. 1), the axial/implosion membrane strain $\tilde{\varepsilon}_t(\tilde{r})$ can be expressed in terms of 1D implosion strain ε_0 and 1D cone/kink wave velocity $c_{k,0}$ in the material coordinate system as: $\tilde{\varepsilon}_t(\tilde{r}) = \varepsilon_0(r_s/\tilde{r}) \approx \alpha_0^2(r_s/\tilde{r}), r_k < \tilde{r} < r_s$, where $\alpha_0 = c_{k,0}/a_0 \approx \sqrt{\varepsilon_0} \approx \left(V_P/a_0\sqrt{2}\right)^{2/3}$. The membrane strain in the cone wave region can be expressed as: $\varepsilon_t(r) \approx \alpha^2(r_k/r), r_p < r < r_s, \alpha = c_k/a_0$, where c_k is the 2D cone/kink wave velocity in materials coordinate system. Determining $\varepsilon_t(r_p)$ and equating to the fracture strain of the material one can determine the perforation velocity of the membrane. A summary of 1D fiber theory and 2D membrane theory can be found in Ref. Haque et al., 2017 [2] and is presented in Appendix A.

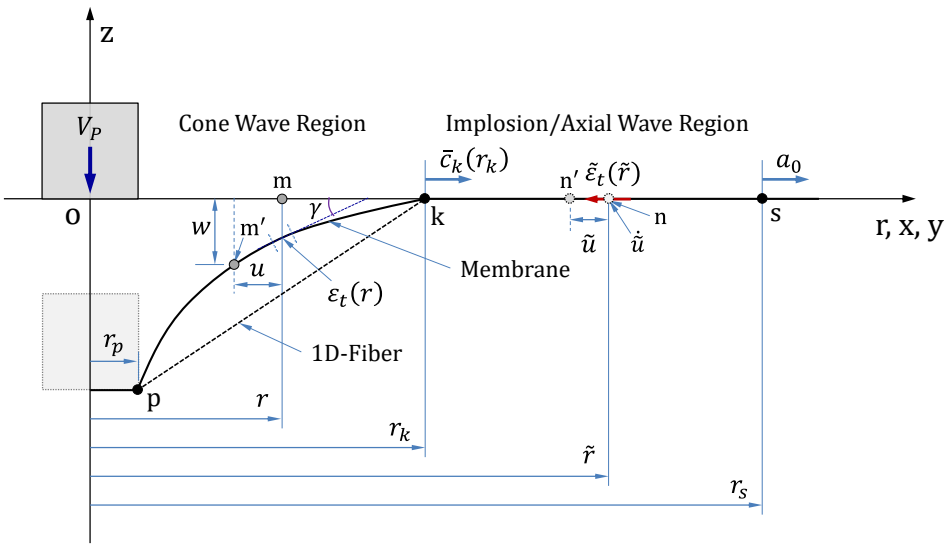

Figure 1: Nomenclature for Phoenix and Porwal (P&P, 2003) [1] 2-D Membrane Theory for Isotropic Materials. 1D axial/implosion wave velocity, $a_0 = \sqrt{E/\rho}$. Haque et al., 2017 [2].

In case of orthotropic thin-composite laminates, the use of 2D membrane theory is inadequate and thus finite element models have been developed and validated in computing the cone wave velocities (c_k) for ultra-high molecular weight polyethylene (UHMWPE) soft-ballistic sub-laminates (SBSL) [2].

Thin-composite laminates have high in-plane and shear moduli and under transverse impact exhibits cone wave propagation superimposed on out-off-plane bending waves. In this study, cone

wave velocity and bending wave velocities have been computationally determined for plain-weave (PW) S-2 Glass/SC15 (814 g/m^2, 24 oz/yd^2, 5×5 tows/in, 0.6 mm per one layer 1L) composites subjected to transverse impact velocity less the perforation velocities in the thickness range 1.20 mm (2L) $< H_C <$ 4.80 mm (8L). In Ref. Gama & Gillespie, 2017 [3]; materials and modeling parameters of a progressive composite damage model MAT162 in LS-DYNA has been validated with ballistic experiments and will be used in this paper (Appendix B). A tension-shear damage equation in MAT162 uses a new punch-shear strength (SFS=X_3^{PSS}) in simulating the perforation failure of a thin-section composite laminate.

Finite element models of 2L, 4L, 6L, & 8L laminates of dimensions 974mm x 974mm have been developed with finer mesh (0.53mm~3.7mm) in the central 178mm x 178mm region with 3 through-thickness elements for every 2 layers (3 TTE/ 2L) with free boundary condition (BC). A 50cal RCC steel projectile of is used for all impact analyses (Fig. 2).

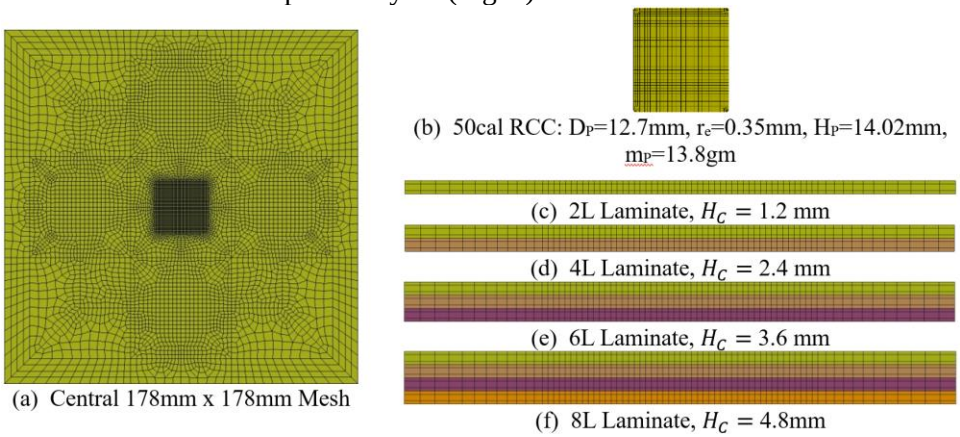

Figure 2: Finite Element Models for Perforation Mechanics Study.

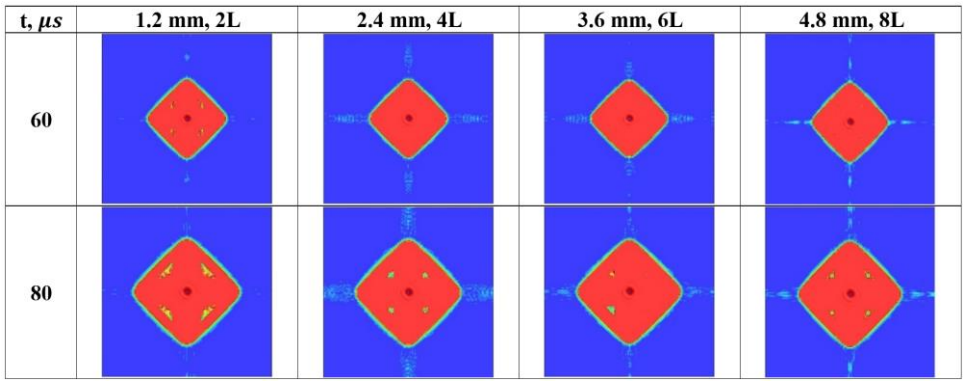

Figure 3: Cone/Kink Wave Propagation in Thin-Section Composites. Haque & Haque, 2025 [4].

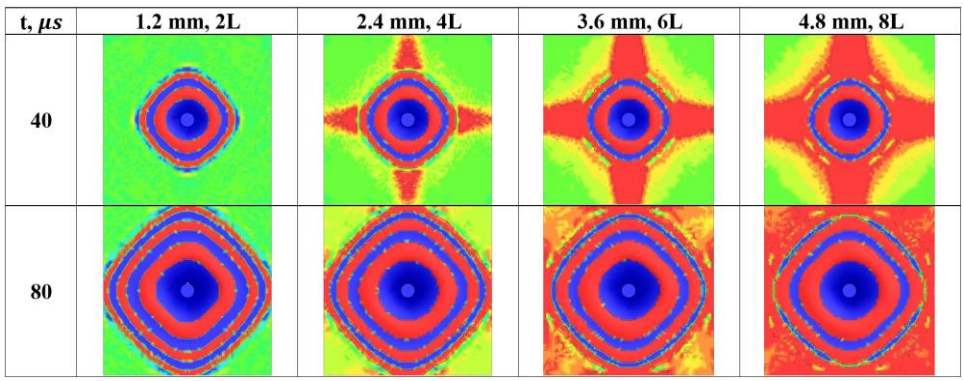

Figure 4: Bending Wave Propagation in Thin-Section Composites. Haque & Haque, 2025 [4].

Propagation of cone/kink wave and bending wave are presented in Figs. 3 & 4 from which the time history of cone/kink waves and bending waves have been calculated and an exponential model has been used to calculate the regression parameters (Fig. 5).

$$\bar{c}_k(t) = \bar{c}_{k\infty} + [\bar{c}_{k\infty} - \bar{c}_k(0)]\exp(-t/\tau_k) \quad (1a)$$

$$c_B(t) = c_{B\infty} + [c_{B\infty} - c_B(0)]\exp(-t/\tau_B) \quad (1b)$$

Where, $\bar{c}_{k\infty} = 260 - 7.5H_C$, $\bar{c}_{k\infty}$ is in m/s, H_C is in mm, $\tau_k = 42.2\ \mu s$, $\bar{c}_{k\infty} - \bar{c}_k(0) = 212.4$ m/s, $c_{B\infty} = 290$ m/s, $c_{B\infty} - c_B(0) = 505$ m/s, and $\tau_B = 28.6\ \mu s$. Eq. (1a) can be integrated to determine the $r_k(t) = r_p + \int_0^t \bar{c}_k(t)dt$. Eq. (1) is essential in writing integral momentum and energy equations and will be presented elsewhere. Perforation mechanics and ballistics of PW S-2 Glass/SC15 thin-section composites are presented in Fig. 6.

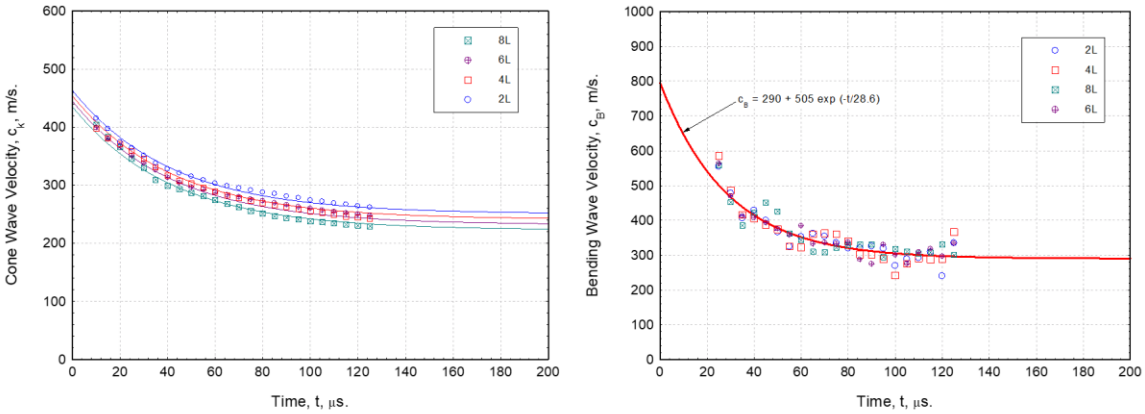

(a) Cone/kink wave velocity (b) Bending Wave velocity

Figure 5: Variation of Cone/Kink and Bending Wave Velocity. Haque & Haque, 2025 [4].

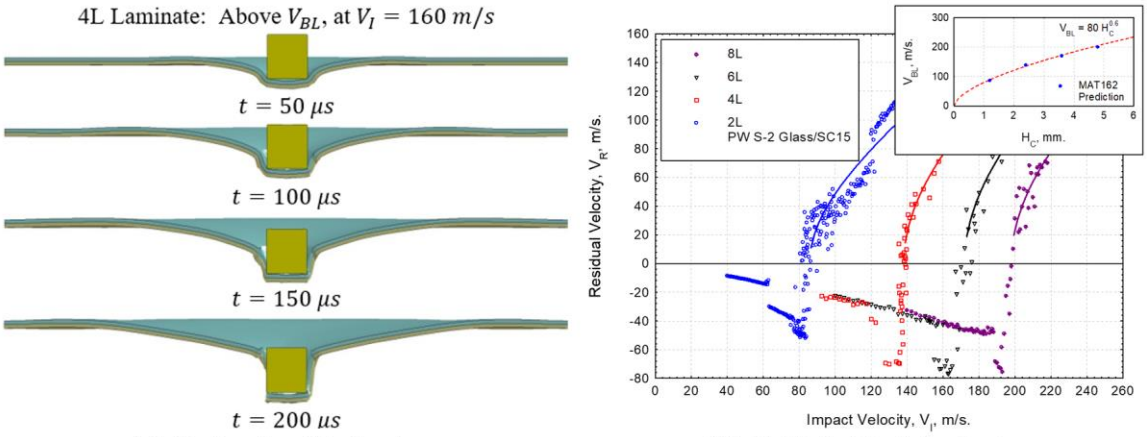

(a) Perforation Mechanics (b) Ballistic Limit Analysis

Figure 6: Perforation Mechanics and Ballistics of Thin Laminates. Haque & Haque, 2025 [4]

LS-DYNA stochastic simulations have been performed on square laminates (178mm x 178mm, all edges perfectly clamped BC) in predicting the residual velocity V_R as a function of impact velocity V_I (Fig. 6b) and Haque-Gillespie (H-G, 2015) [5] ballistic equation Eq. (2) is used to determine the ballistic limit velocity V_{BL} and model parameters, i.e., H-G jump velocity V_T, Lambert [6] parameter β^*, and H-G scaling parameter ζ (Table 1). Perforation V_{BL} as a function of H_C shows a power-law behavior $V_{BL} = 80H_C^{0.6}$ (Fig. 6b). Further discussion on perforation mechanics and ballistics will be presented elsewhere.

$$V_R = [V_T^2 + \beta^*(\zeta V_I^2 - V_{BL}^2)]^{1/2} \quad (2)$$

No. of Layers	Thickness, H_C, mm	V_T, m/s	β^*	ζ	V_{BL}, m/s
2L	1.20	4.64	0.895	0.999	85.9
4L	2.40	11.42	0.887	0.999	138.5
6L	3.60	20.80	0.829	0.956	169.6
8L	4.80	30.73	0.669	0.982	199.6

Table 1: 2L-8L Residual Velocity Plots with Ballistic Limits.

2 BALLISTIC PERFORATION AND PENETRATION DAMAGE MECHANISMS

In Ref. Gama & Gillespie, 2017 [3], ballistic experiments with a 101.6mm circular support span and perfectly clamped BC have been conducted on 22L (H_C=13.2mm) and 33L (H_C=19.8mm) with 50cal RCC and 50cal FSP projectiles, respectively (Fig. 7). The ballistic damage modes & mechanisms identified are: (i) deep penetration on the impact side, (ii) plug formation under the projectile, (iii) interlaminar delamination, (iv) tension-shear perforation damage in a thin delaminated rear-portion of the laminate. In order to understand these energy dissipating ballistic damage mechanisms, the author has developed a series of quasi-static (QS) and ballistic experimental methodologies; i.e., (a) QS punch-shear test (QS-PST), (b) QS indentation (QSI) or QS punch-crush test (QS-PCT), (c) ballistic perforation test, and (d) depth of penetration (DoP) test.

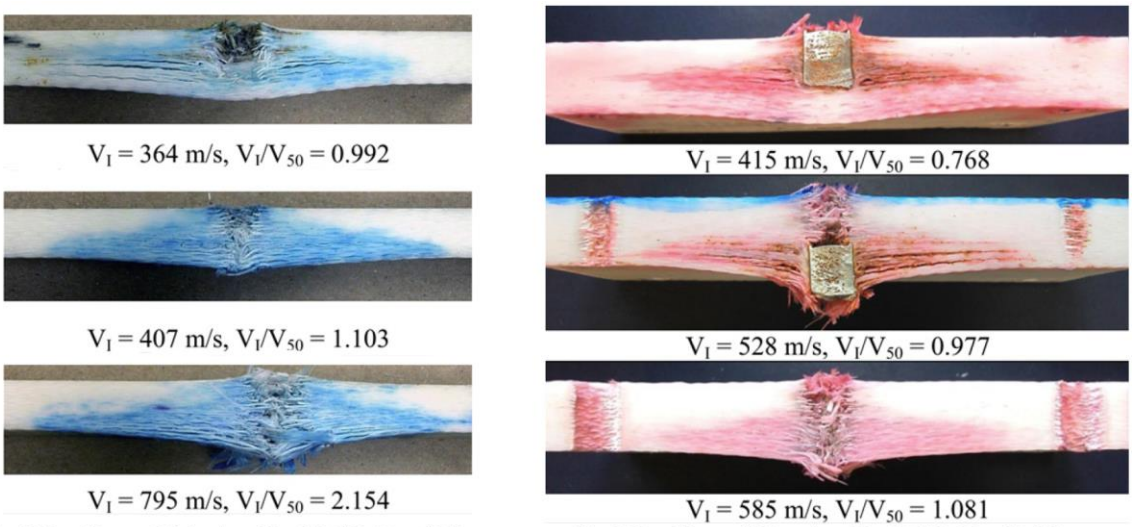

(a) 22L: V_{50} = 367 m/s. 50cal RCC: D_P=12.7mm, r_e=0.35mm, H_P=14.02mm, m_P=13.8gm

(b) 33L: V_{50} = 540 m/s. 50cal FSP: D_P=12.57mm, H_P=14.88mm, m_P=13.5gm

Figure 7: Ballistic Damage Mechanisms. Gama & Gillespie, 2017 [3].

3 QS-PST AND QSI EXPERIMENTAL METHODOLOGY

To quantify the energy dissipating ballistic damage mechanisms, a QS punch-shear test (QS-PST) experimental methodology (Fig. 8) has been developed by the author where a perfectly clamped laminate is subjected to transverse loading of a RCC punch (D_P) while varying the support span to punch diameter ratio (SPR=D_S/D_P) [7]. It has been shown that the ballistic damage mechanisms can be simulated and quantified by varying the SPR in the range 1.2 < SPR < 8 under load-unload-reload experimental methodology [8]. A punch-shear based penetration model of ballistic impact has been developed in Ref. [8] which can predict 97% of ballistic limit energy (Fig. 9). Punch-shear strength (X_3^{PSS}) of a composite has been defined by the author as:

$$X_3^{PSS} = \lim_{SPR \to 1} F_P^{max} / \pi D_P H_C \quad (3)$$

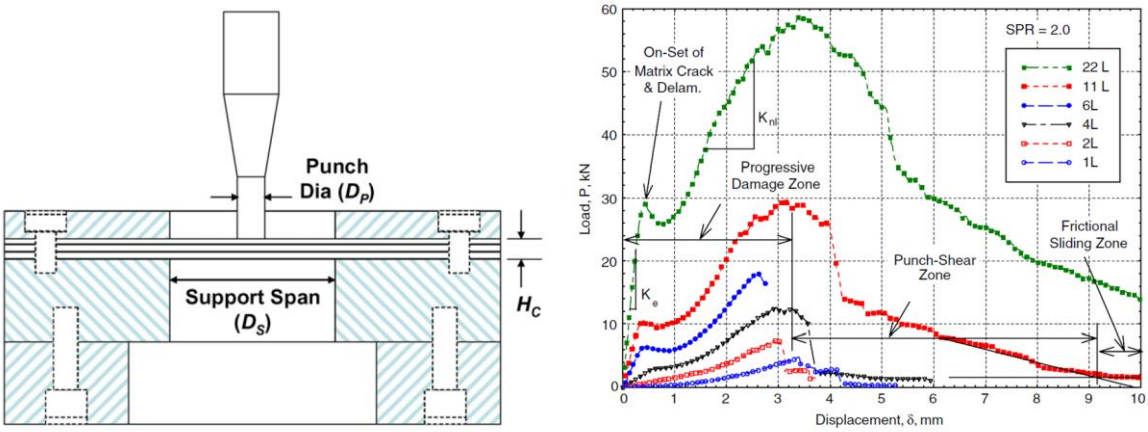

(a) QS-PST Experimental Setup (b) Quantification of QS-PST Energy Dissipation

Figure 8: Quasi-Static Punch Shear Test (QS-PST) Experimental Methodology. Ref. [7].

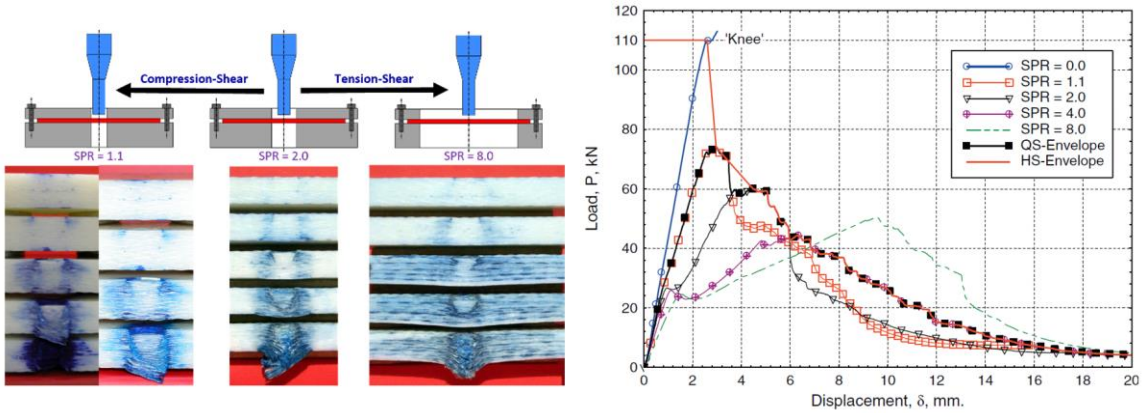

(a) QS-PST Damage Progression vs SPR (b) Concept of QS-Envelope & HS-Envelope

Figure 9: A QS Punch-Shear based Model of Ballistic Penetration. Gama & Gillespie, 2008 [8].

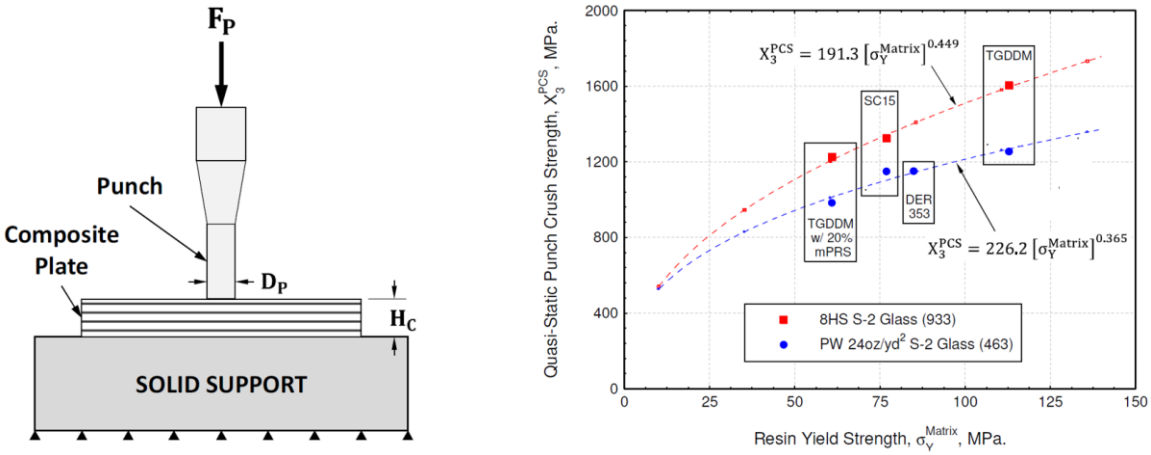

(a) QS-PCT/QSI Experimental Setup (b) X3PCS vs. Resin Yield Strength. Fig. 5b Ref. [9].

Figure 10: QS Punch-Crush Test (QS-PCT) or QS Indentation (QSI) Experiment. Refs. [7-9].

A quasi-static punch-crush test (QS-PCT, SPR=0) or quasi-static indentation (QSI) experimental methodology has been developed by the author in Refs. [7-9].

$$X_3^{PCS} = 4F_P^{\max}/\pi D_P^2 \tag{4}$$

Punch crush-strength (X_3^{PCS}) is defined by Eq. (4) which is a function of composite fiber volume fraction (FVF) and resin yield strength (Fig. 5, Ref. [9]). X_3^{PCS} is used in MAT162 as parameter SFC

to model this important damage mechanisms; and defines the threshold velocity of penetration in the depth of penetration (DoP) analysis methodology.

4 PENETRATION MECHANICS OF THICK-SECTION COMPOSITES

In addition to 2L, 4L, 6L, & 8L perforation simulations; and 11L, 22L, & 33L ballistic simulations in Ref. [3]; additional high velocity impact simulations on 44L to 88L (H_C = 26.4mm to 52.8mm) composite laminates (Fig. 11) using experimentally determined MAT162 parameters SFS = X_3^{PSS} & SFC = X_3^{PCS} are computationally determined softening [7] and rate parameters [3] (Table B1, Appendix B). Based on the observations of the 88L penetration simulations, Haque & Gillespie, 2014 [10] have identified four phases of ballistic penetration (Fig. 12), i.e., (i) Penetration or P-Phase (0 to 30 μs), (ii) Transition or T-Phase (30 to 60 μs), (iii) Perforation of F-Phase (60 to 140 μs), & (iv) Retraction or R-Phase (140 to 300 μs).

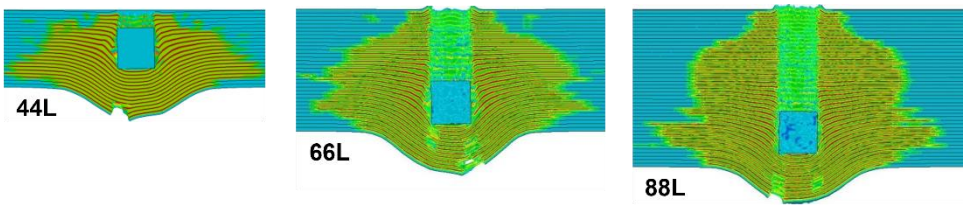

Figure 11: Penetration of 44L to 88L Thick-Section Composites.

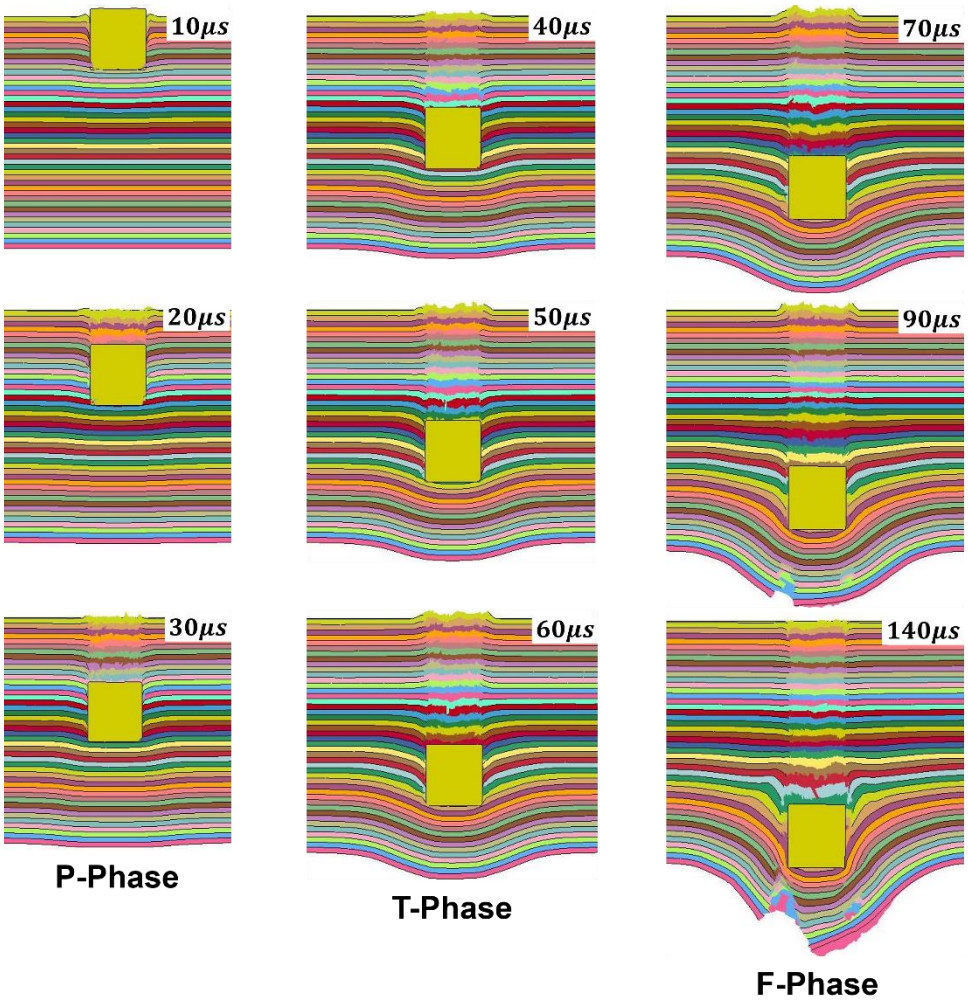

Figure 12: Ballistic Penetration or P-Phase (0 to 30 μs), Transition or T-Phase (30 to 60 μs), and Perforation or F-Phase (60 to 140 μs). Haque & Gillespie, 2014 [10].

The P-Phase represents deep penetration and ejection of crushed particles under the projectile, initiation of delamination, and with near zero particle velocity of the surrounding laminate; which can be characterized by DoP experiments. During the T-Phase, significant particle velocity in the laminate is observed with delamination growth in the laminate with continued deep penetration. The end of T-Phase and beginning of F-Phase is when the penetration ceases, and the material ahead of the projectile attains the same velocity as the projectile. During F-Phase, the remaining laminate perforates under tension-shear. A thick-section laminate is defined which shows all three phase of penetration, while an intermediate-thickness laminate is defined which shows the T-phase and F-phase. A thin-section laminate is defined which only shows the F-Phase. While thick-section and intermediate-thickness laminates can be characterized by high velocity ballistic limit (HVBL) experiments, the thin-section laminates can be also be characterized by high velocity ballistic perforation (HVBP) experiments.

5 DEPTH OF PENETRATION (DOP) EXPERIMENTAL METHODOLOGY

In a DoP experiment (Fig. 13), a finite-thickness target is clamped on a rigid 'solid support' using another rigid 'cover plate.' Upon the impact of a RCC projectile on the target at an impact velocity V_I, the projectile penetrates, compresses, and crushes the composite under the projectile, the crushed particles eject through the penetration cavity around the projectile in a direction opposite to the projectile motion, and finally the projectile stops inside the target at a penetration depth of d_P; which is plotted as a function of V_I and is also known as classic penetration-resistance test. The author has developed [12] an energy based DoP model (Eq. 5) where the experimental data provides two DoP parameters: (i) V_{TH} – the threshold velocity of penetration, and (ii) τ_{DoP} – the characteristic time of DoP

$$d_P = \tau_{DoP}(V_I - V_{TH}) \tag{5}$$

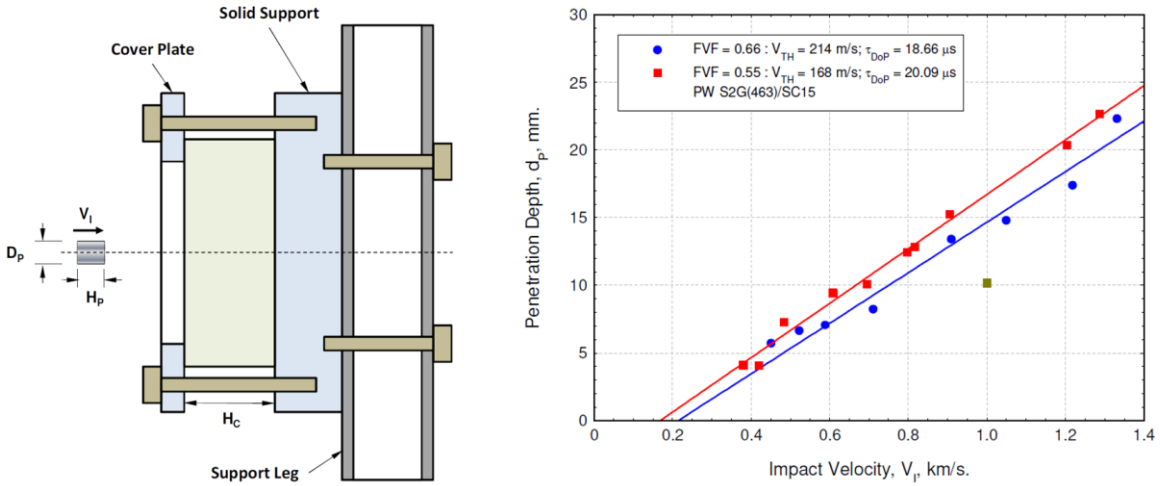

(a) DoP Experimental Setup (b) PW S-2 Glass (463)/SC15 (814 g/m^2, 24 oz/yd^2) [9]

Figure 13: DoP Experimental Methodology.

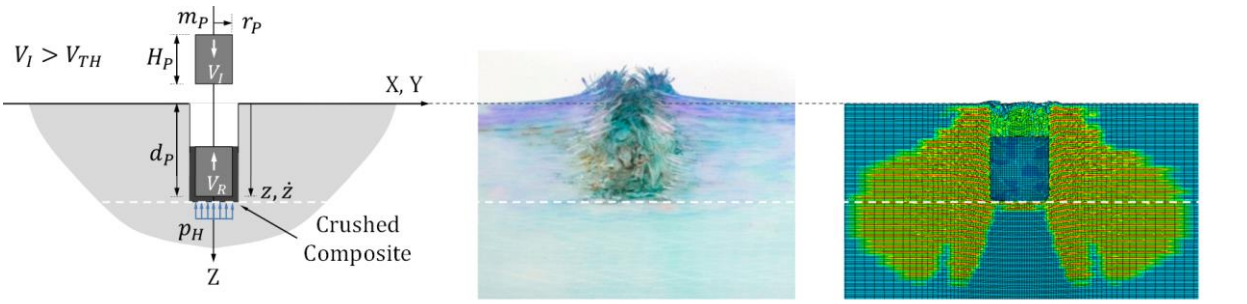

(a) Nomenclature (b) DoP Damage, PW S-2 Glass/SC15 (c) LS-DYNA MAT162 Prediction

Figure 14: DoP Experimental, Theoretical, and Computational Modeling Methodology.

From the energy based DoP model (Fig. 14a), the projectile instantaneous rigid body velocity $\dot{z}(t)$ (Eq. 6a), the hydrodynamic pressure $p_H(t)$ of the crushed particles under the projectile (Eq. 6b) and the penetration resistance force $F(t)$ on the projectile (Eq. 6c) can be derived.

$$\dot{z}(t) = V_I \exp(-t/\tau_{DoP}) \quad (5a)$$

$$p_H(t) = (\rho_P H_P/\tau_{DoP})V_I \exp(-t/\tau_{DoP}) \quad (5b)$$

$$F_P(t) = (m_P/\tau_{DoP})V_I \exp(-t/\tau_{DoP}) \quad (5c)$$

Punch-crush and punch-shear are two unique damage mechanisms of the DoP experiments on thick-section composites (Fig. 14b). While punch crush of composites occurs under the projectile, the punch shear occurs along the edge of the projectile. Micromechanical punch crush damage mechanisms are (i) matrix crack, (ii) fiber fracture, (iii) fiber-matrix debonding (iv) hydrodynamic crush of both matrix and fibers; and the micromechanical punch shear damage mechanisms are (a) matrix crack, (b) matrix tension-shear, (c) fiber-matrix debonding, and (d) mode II dominated fiber fracture.

6 SUMMARY

This paper presents the fundamental understanding of the perforation and penetration mechanics of very thick to thin composite laminates developed by the author over the last two decades. In addition, new results on the cone/kink wave and bending wave propagation on thin-section composites have been presented along with stochastic ballistic limit predictions using rate dependent progressive composite damage model MAT162 in LS-DYNA. Two experimental methods for punch-shear & punch-crush developed by the author are also presented. New results of deep penetration of thick-sections composite have been presented and used to define three phases of ballistic penetration, i.e., Penetration (P-), Transition (T-), and Perforation (F-) phases. DoP experimental, theoretical, and computational models developed by the author has also been presented. The methodologies developed here will further be extended to develop an unified theory of ballistic penetration and perforation of composite laminates and left as future work.

ACKNOWLEDGEMENTS

The author gratefully acknowledges the funding for the conference attendance provided by Les Hall at McLaurin Aerospace. The research work on wave propagation in thin composite laminate conducted by Showvik Z. Haque is also gratefully acknowledged.

REFERENCES

[1] Phoenix, S. L., and Porwal, P. K. A new membrane model for the ballistic impact response and V50 performance of multi-ply fibrous systems. International Journal of Solids and Structures, Vol 40, pp 6723-6765, 2003.

[2] Haque, B. Z. (Gama), Ali, M. A., Gillespie Jr., J. W. Modeling transverse impact on UHMWPE soft ballistic sub-laminate. Journal of Thermoplastic Composite Materials. 2017;30(11):1441-1483.

[3] Gama, B. A., and Gillespie Jr., J. W. Finite element modeling of impact, damage evolution and penetration of thick-section composites. International Journal of Impact Engineering. 2011;38:181-197.

[4] Haque, S. Z., and Haque, B. Z. (Gama). Perforation mechanics of thin-section composites. Manuscript under preparation, 2025.

[5] Haque, B. Z. (Gama), Gillespie, J. W. A new penetration equation for ballistic limit analysis. Journal of Thermoplastic Composite Materials. 2015;28(7):950-972.

[6] Lambert, J. P. MD: Ballistic Research Laboratory, Aberdeen Proving Ground; 1978. ARBRL-MR-02828.

[7] Xiao, J. R., Gama, B. A., and Gillespie, J. W. Progressive damage and delamination in plain weave S-2 glass/SC-15 composites under quasi-static punch-shear loading. Composite Structures. 2007; 78:182-196.

[8] Gama, B. A., and Gillespie, J. W. Punch shear-based penetration model of ballistic impact of thick-section composites. Composite Structures. 2008; 86:356-369.

[9] (Gama) Haque, B. Z., Kubota, M., and Gillespie Jr. J. W. Depth of penetration experiments of S-2 glass/epoxy composites: A new Experimental Methodology in determining the rate dependent dynamic crush strength of composites. Composites Part B: Engineering. 2022;238:109917.

[10] (Gama) Haque, B. Z., Gillespie Jr., J. W. Penetration and Perforation of Composite Structures. Mechanical Engineering Research Journal. Dept. of Mech. Engg., Chittagong Univ. of Engg. & Tech, (CUET). 2013;9:37-42. [https://www.cuet.ac.bd/merj/files/MERJ-Vol-9,%202013,%20page%2037-42.pdf]

[11] Meyer, C. S., Catugas, I. G., Gillespie Jr. J. W., and (Gama) Haque, B. Z. Investigation of normal, lateral, and oblique impact of microscale projectiles into unidirectional glass/epoxy composites. Defence Technology. 2022;18(11):1960-1978.

[12] (Gama) Haque, B. Z., Gillespie Jr., J. W. Depth of penetration of Dyneema® HB26 hard ballistic laminates. Journal of Thermoplastic Composite Materials. 2023;36(4):1361-1381.

APPENDIX A: THEORY OF TRANSVERSE IMPACT ON FIBERS AND MEMBRANE

Theories of constant velocity transverse impact on 1D-fiber had been developed between 1945 to 1960 by Rakhmatulin and Smith. Following these classic theories, Phoenix and Porwal (P&P, 2003) has developed an axi-symmetric membrane theory for constant velocity transverse impact on an isotropic elastic membrane with a cylindrical projectile. The well-known Smith (1958, 1960) equations considers constant velocity transverse impact on a 1D isotropic fiber. Upon the impact of a projectile with impact velocity V_P, an implosion or axial strain wave of amplitude ε_0 propagates along the fiber between points 'p' and 's' with an axial wave speed of $a_0 = \sqrt{E/\rho}$ followed by a transverse cone wave with a constant cone wave front velocity, $\bar{c}_{k,0}$, at point 'k' with respect to the laboratory frame of coordinate, and forms a constant cone angle γ with the fiber axis at the projectile root at point 'p'. Smith's equations for the explosion strain ε_0, the cone wave front velocity $\bar{c}_{k,0}$ in laboratory frame of coordinates, the cone wave front velocity $c_{k,0}$ in material coordinates, and the cone root angle γ as a function of constant impact velocity V_P are given by:

$$V_P = a_0\sqrt{\varepsilon_0(1+\varepsilon_0) - \left[\sqrt{\varepsilon_0(1+\varepsilon_0)} - \varepsilon_0\right]^2} \tag{1a}$$

$$\bar{c}_{k,0} = a_0\left[\sqrt{\varepsilon_0(1+\varepsilon_0)} - \varepsilon_0\right] \tag{1b}$$

$$\frac{c_{k,0}}{a_0} = \sqrt{\frac{\varepsilon_0}{(1+\varepsilon_0)}} = \alpha_0 \tag{1c}$$

$$\sin\gamma = \frac{V_P}{a_0\sqrt{\varepsilon_0(1+\varepsilon_0)}} \tag{1d}$$

In order to express $\varepsilon_0 = \varepsilon_0(V_P, a_0)$, Eq. (1a) have been simplified to:

$$\varepsilon_0 \approx \left(\frac{V_P}{a_0\sqrt{2}}\right)^{4/3} \tag{1e}$$

Equation (1e) can noe be used to evaluate the other Eqs. (1b), (1c) & (1d). Phoenix & Porwal (2003) developed a 2D-membrane theory for isotropic materials where the cone wave velocity starts at 1D value (Eq. 1b & 1c), increases non-linearly with time and essentially forms a plateau. P&P (2003) provided analytical solutions for cone wave velocity $\bar{c}_k$ in laboratory frame of coordinates, and membrane strain $\varepsilon_t(r)$ as follows:

$$\bar{c}_k = c_k + \dot{u}_k = a_0\left\{\alpha + \frac{\alpha^2\left[\ln\alpha - \ln\left\{1 - \frac{r_p}{r_k}(1-\alpha)\right\} - 1\right]}{1 + \frac{(1-\alpha)(r_k - r_p)}{\alpha r_k}}\right\} \tag{2a}$$

$$\varepsilon_t(r) \approx \varepsilon_t(r_k)\frac{r_k}{r} \approx \alpha^2\frac{r_k}{r} \qquad r_p < r < r_s \tag{2b}$$

Where, c_k is the kink wave velocity in materials coordinate system, $\dot{u}_k = \dot{\tilde{u}}_k$ is the particle velocity at the kink point 'k', $\alpha = c_k/a_0$, r_p is the radius of the projectile, r_k is the location of the cone wave front at point 'k', and r_s is the location of the implosion wave front at point 's'. The value of α can be determined iteratively using the following formula as described in P&P (2003).

$$\alpha_{n+1} \approx \alpha_0\left(\frac{r_p}{r_k}\right)^{\frac{1}{3}}\frac{\left\{\frac{1}{\alpha_n}\left(\frac{r_k}{r_p}-1\right)\right\}^{\frac{1}{3}}}{\left\{\ln\left[1+\frac{1}{\alpha_n}\left(\frac{r_k}{r_p}-1\right)\right]\right\}^{\frac{1}{3}}} \tag{3}$$

Where $n = 0,1,2,\cdots$, and $\alpha_0 = c_{k,0}/a_0$. P&P (2003) showed that only two iterations provides quite accurate result, i.e., $\alpha \approx \alpha_2$. Once the value of α can be determined using Eqs. (3), (1c) & (1e); then Eqs. (2a) and (2b) can be evaluated. Eq. (2a) has been further reduced for 1D case in P&P (2003) to:

$$\bar{c}_{k,0} = c_{k,0} + \dot{u}_{k,0} = \alpha_0 a_0(1 - \alpha_0 + \alpha_0^2) \tag{4}$$

Eq. (4) provides a slightly smaller value of $\bar{c}_{k,0}$ as compared to Eq. (1b). P&P, 2003, showed that the cone/kink wave velocity for the 2D membrane, c_k, is equal to $c_{k,0}$ at $r_k = r_p$, increases to a maximum at around $r_k = 2r_p$, then reduces to a plateau value (higher than $c_{k,0}$) for $r_k \gg 2r_p$ for a constant value of ε_0. It is also important to mention that the 2D membrane cone/kink wave speed increases with the increase in ε_0, that is with impact speed V_P. In Ref. [8], it has been shown that for isotropic 1D fiber and 2D membrane, a finite element model can capture the theoretical physics of deformation with good correlations. We will use these 1D and 2D equations to verify the finite element models of transverse impact on thin-section composite plates.

APPENDIX B: MAT162 INPUT PROPERTIES & PARAMETERS FOR PW S-2 GLASS/SC15 COMPOSITES

MID	RO, kg/m³	EA, GPa	EB, GPa	EC, GPa	PRBA	PRCA	PRCB
162	1850.00	27.50	27.50	11.80	0.11	0.18	0.18
GAB, GPa	**GBC, GPa**	**GCA, GPa**					
2.90	2.14	2.14					
SAT, MPa	**SAC, MPa**	**SBT, MPa**	**SBC, MPa**	**SCT, MPa**	**SFC, MPa**	**SFS, MPa**	**SAB, MPa**
604.00	291.00	604.00	291.00	58.00	850.00	300.00	75.00
SBC, MPa	**SCA, MPa**	**SFFC**	**PHIC**	**E_LIMT**	**S_DELM**		
58.00	58.00	0.300	10	0.200	1.200		
OMGMX	**ECRSH**	**EEXPN**	**CRATE1**	**AM1**			
0.999	0.001	4.500	0.030	2.00			
AM2	**AM3**	**AM4**	**CRATE2**	**CRATE3**	**CRATE4**		
2.00	0.50	0.20	0.000	0.030	0.030		

Table B1. MAT162 Input Properties and Parameters for S-2 Glass/SC15 Composite [3]

FINITE ELEMENT MODELING OF THE THERMO-OXIDATION GRADIENTS IN ORGANIC MATRIX COMPOSITES

Juan P. Márquez Costa[1], E. Monteiro[1] and X. Colin[1]

[1] PIMM, Arts et Métiers Institute of Technology, CNRS – UMR 8006, CNAM
151 boulevard de l'Hôpital, F-75013 Paris, France
Email: juan-pablo.marquez_costa@ensam.eu, eric.monteiro@ensam.eu, xavier.colin@ensam.eu, web page: https://pimm.artsetmetiers.fr

Keywords: Polymer-matrix composites (PMCs), Environmental degradation, Interface/interphase, Finite element analysis (FEA)

ABSTRACT

This work outlines the development of a finite element-based numerical tool designed to simulate the thermal aging behavior of epoxy-diamine matrix composites reinforced with continuous fibers under thermal exposition to temperatures below their glass transition temperature (T_g). The approach begins with homogenization technique using a representative elementary volume (REV) that include the fibers, surrounding matrix and interfacial zones around the fibers. Periodic boundary conditions in oxygen (O_2) concentration are applied to numerically determine the effective components of the diffusion tensor for a unidirectional composite. The thermo-oxidation degradation model incorporates a strong coupling between the anisotropic diffusion of O_2 and its consumption by the chemical reaction with the epoxy matrix. The stabilizing effect of carbon fibers in mitigating this degradation is also taken into account. This framework enables the estimation of oxidation gradients across the thickness of the composite sample along its principal directions. The thickness of the oxidized layer (TOL) is calculated from O_2 consummation gradients as recently done for samples of neat epoxy resin. In order to check the robustness of the model and the proposed criterion of TOL detection, the numerical TOL values are compared to experimental measures from literature. The originality of this work lies in the assessment of anisotropic oxidation gradients in composites, particularly by accounting for the crucial role of the fiber-matrix interface and the associated interfacial diffusion in the homogenization calculation.

1 INTRODUCTION

1.1 Thermo-oxidative degradation scenario in Polymer Matrix Composites

Carbon/epoxy composites are widely used in the design of structural parts in the aeronautics sector due to their excellent specific properties. However, their exposure to high temperatures represents a crucial issue to be considered during the design and certification phases of structures. Among the identified risks, thermo-oxidative aging of the matrix plays a particularly decisive role [1]. This phenomenon leads to the formation of an oxidized layer on the surface, causing localized embrittlement and stress and strain gradients likely to cause a catastrophic cracking scenario. Fig. 1 shows the degradation scenario in a thick sample of neat resin by thermo-oxidation. In a first step (between 0 and t_l), the O_2 is consumed while it tries to diffuse in the thickness direction. In a second step (at t_F), the stress and strain fields induced on the surface allow the initiation of a crack, then its propagation in the embrittled zone. Eventually (at t_{2l}), oxidation can cross the oxidized layer/intact core interface to finally progress into the core of the composite, following a progressive damage scenario, and lead to its premature failure [2].

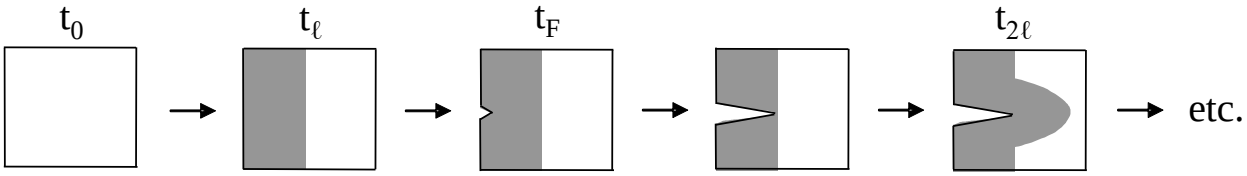

Figure 1. Scenario of crack propagation within a neat resin sample [2].

In the case of a unidirectional (UD) composite reinforced with continuous fibers, the degradation scenario depends on the anisotropy of the composite. The anisotropic oxidation gradients, due to the presence of fibers and interfaces, will lead to heterogeneity of stress and strain fields inducing crack initiation and propagation in the thickness of the oxidized layer (TOL), as shown schematically in Fig. 2:

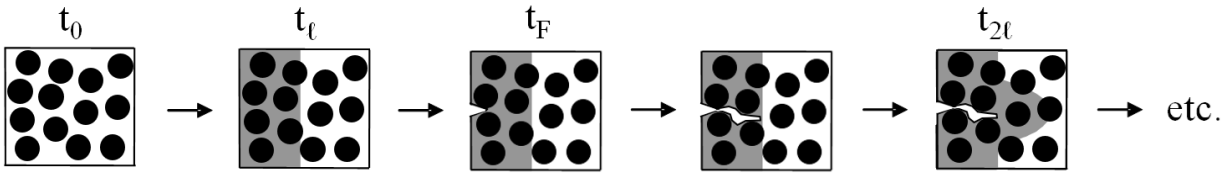

Figure 2. Scenario of crack propagation within a composite sample. View of a section perpendicular to the longitudinal direction of the fibers

In order to address this complex issue, knowledge of the link between the evolution of the TOL and the degradation of the thermomechanical properties of interest of the composites is essential, before focusing on the critical conditions of crack initiation. For this, the numerical simulation of oxidation gradients proves to be a relevant tool for predicting the value of the TOL. Recent work [3] has shown the robustness of a model developed under finite elements and based on an O_2 balance equation, coupling the diffusion of O_2 and its consumption by the chemical reaction, to predict the TOL in neat resin samples.

Concerning the prediction of oxidation kinetics, it is necessary to consider the anisotropic properties induced by the specific structure of the composites, in particular the anisotropic diffusion of O_2. In order to propose a relevant model adapted to composites reinforced by continuous fibers, the following question arises: should a specific behavior of the fiber/matrix interface be considered, in particular through interfacial diffusive and reactive terms, to faithfully describe the oxidation gradients of the composites? To answer this question, the article will aim to achieve two objectives. Firstly, it will be a question of: (i) proposing a kinetic model of thermo-oxidation of carbon fiber/epoxy-diamine matrix composites, and secondly: (ii) linking the evolution of the oxidation gradients to that of the TOL in each of the main directions of the composite (1 – fiber direction, 2 – transverse direction and 3 – out-of-plane direction). Thus, the article will be divided into two main parts. First, Section 2 will outline the numerical calculation code developed for composites. Then, Section 3 will compare the numerical simulations of this code with experimental data, in particular with TOL measurements. This last section will conclude on the key role of the fiber/matrix interface. Finally, after a conclusion, perspectives, aimed at predicting the evolution of the thermomechanical properties of interest of composites in the aeronautical field, will be drawn up.

2 MODELING OF OXIDATION GRADIENTS

2.1 Time-dependent kinetics of thermo-oxidative aging

Numerical simulation of oxidation gradients proves to be a relevant tool to predict the evolution of TOL. Recent work [3] has proposed a first numerical calculation code developed under finite elements to simulate the evolution of the oxygen (O_2) concentration in the thickness of neat resin samples. This code is based on the coupling of the two main mechanisms: (i) the diffusion of O_2 and (ii) its

consumption by the chemical reaction. In the case of unidirectional diffusion (e.g. along the thickness of the sample), this equation (Eq. 1) is written:

$$\frac{\partial C(x,t)}{\partial t} = D\frac{\partial^2 C(x,t)}{\partial^2 x} - r(C(x,t)) \quad (1)$$

C(x,t) being the local O_2 concentration, *D* the O_2 diffusion coefficient, *x* the thickness coordinate, and *t* the time. $r(C)$ represents the rate of chemical consumption of O_2, the analytical expression of which was determined by carrying out a kinetic analysis of the so-called "closed loop" oxidation reaction. This expression was generalized to the entire family of epoxy-diamine networks [4]:

$$r(C) = 2r_0\frac{\beta C}{1+\beta C}\left(1-\frac{\beta C}{2(1+\beta C)}\right)\left(\frac{1}{1+be^{-Kt}}\right)^2 \quad (2)$$

With $\beta = \frac{k_6 k_2}{k_5 k_3 [PH]}$, $r_0 = \frac{k_3^2[PH]^2}{4k_6}$, and $K = 2(r_0 k_{1b})^{1/2}\left(\frac{\beta C}{1+\beta C}\right)^{1/2}$, three parameters which are expressed as a function of the elementary rate constants of the oxidation reaction.

The integration with respect to time of $r(C)$ allows direct access to the O_2 consumption gradients:

$$Q(C) = \int r(C)dt \quad (3)$$

On the basis of this quantity representative of the oxidation kinetics, a criterion for estimating the TOL for epoxy-diamine networks exposed to temperatures on either side of their T_g has been validated [3]. This criterion compares the normalised O_2 consumption to the maximal amplitude, as shown in Figure 3 for an epoxy/DDS exposed at 200°C in air:

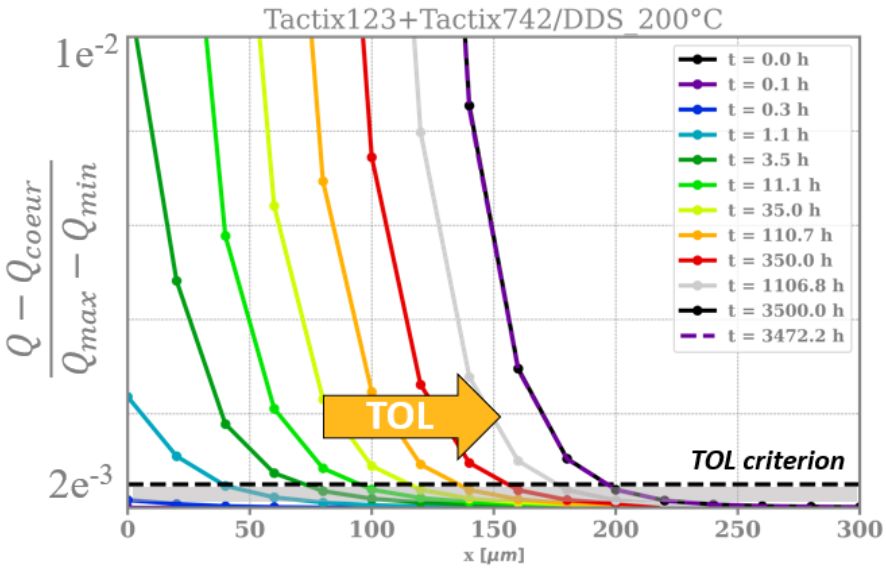

Figure 3. Normalized oxidation gradients in air at 200°C for an epoxy/DDS. Application of the oxidation criterion to estimate the TOL.

The extension of the previous model to epoxy/carbon composites involves the generalization of Eq. 1 in the 3D domain, considering the anisotropy of the composite. For this, we define the coordinate vector $\boldsymbol{x} = [x, y, z]$ corresponding to the three orthonormal directions in space. The diffusion/reaction coupling is therefore described according to the following equation (Eq. 4):

$$\frac{dC(\boldsymbol{x},t)}{dt} = \boldsymbol{\nabla} \cdot (\boldsymbol{D}(\boldsymbol{x}) \cdot \boldsymbol{\nabla C}(\boldsymbol{x},\boldsymbol{t})) + r_{UD}(C(\boldsymbol{x},t)) \quad \text{(Eq. 4)}$$

$\boldsymbol{D}$ being the effective anisotropic diffusion tensor (of order 2) and $\boldsymbol{\nabla C}(\boldsymbol{x},t)$ the O_2 concentration gradient. $r_{UD}(C(\boldsymbol{x},t))$ is the homogenized reactive term in the elementary ply of the UD composite. It is assumed that fibers can chemically play a role in oxidation kinetics, leading to a non-negligible mitigation effect. To consider it, $r_{UD}(C(\boldsymbol{x},t))$ can be written as follows to include the stabilizing effect of carbon in the vicinity of the fiber:

$$r_{UD}(C) = 2r_0 \frac{\beta^* C}{1+\beta^* C}\left(\frac{1-\varphi}{1+\varphi/2} - \frac{(1-\varphi)^2}{2}\frac{\beta^* C}{1+\beta^* C}\right)\left(\frac{1}{1+be^{-K^* t}}\right)^2 \quad \text{(Eq. 5)}$$

With $\beta^* = \frac{\beta}{1+\varphi/2}$ and $K^* = k_3[PH]\left(\frac{k_{1b}}{k_6}\right)^{\frac{1}{2}}(1-\varphi)^{\frac{1}{2}}\left(\frac{\beta^* C}{1+\beta^* C}\right)^{\frac{1}{2}}$.

$\varphi = \frac{k_C[Carb]}{k_3[PH]}$ is the efficiency of stabilization by carbon which, according to reference [5], would be of the order of 10^{-2} to 10^{-1} for certain carbon/epoxy composites. Note that, in the absence of carbon fiber ($\varphi = 0$), we find the reactive term of the neat resin (Eq. 2).

Since the reactive term $r_{UD}(C(\boldsymbol{x},t))$ is described at the UD composite scale, it is also valid at the homogenized ply scale. The following section describes the method for homogenizing the components of the effective D tensor (homogenized at the UD ply scale) using a representative elementary volume (REV) of the composite microstructure (fiber/interface/matrix) and periodic boundary conditions (PBCs) in O_2 concentration.

2.2 Effective O_2 diffusion based on a homogenization approach

Periodic boundary conditions (PBCs) are commonly used for representative elementary volumes (REVs) to simulate an infinite and repetitive microstructure of the material. The definition of PBCs ensures that the solution obtained for the REV represents the global behavior of the reinforced composite material. In the case of thermo-oxidation, the boundary conditions must ensure the continuity of the field variable (i.e. C) and its flux (q_C) on the opposite faces of the REV [6]. For this, PBCs must accurately capture the behavior of the composite at the macroscopic scale while resolving the interactions at the REV scale, in particular for the diffusive term affecting the fibers, matrix, and interfaces.

To apply PBCs in C, it is necessary to define a series of equations such that the difference of C between 2 paired nodes is imposed and equal to the macroscopic gradient of C $\boldsymbol{\nabla C}$. As an example, considering the direction d (*e.g.*, x, y, z) of the REV domain, the equation for paired nodes i and j on opposite faces A and B and distanced Δl_d is:

$$C_{j_{|B}} - C_{i_{|A}} = \nabla_d C \, \Delta l_d = \Delta C \quad (6)$$

With $C_{i_{|A}}$ and $C_{j_{|B}}$ the concentrations at nodes i and j, and $\nabla_d C = \Delta C / \Delta l_d$ the imposed concentration gradient, giving rise to a concentration difference ΔC across the distance between opposite faces Δl_d of the REV in the d direction. The PBCs impose a flow periodicity such that:

$$\boldsymbol{q_C}(\boldsymbol{x})_{|\boldsymbol{B}} = \boldsymbol{q_C}(\boldsymbol{x})_{|\boldsymbol{A}} = -\boldsymbol{D}\frac{\Delta C}{\Delta l_d} \quad (7)$$

The calculation of the three main components (D_{xx}, D_{yy}, D_{zz}) of the tensor $\boldsymbol{D}$ requires the performance of 3 calculations by imposing the concentration gradient between each pair of opposite surfaces according to the x, y and z directions. For each direction d, we can write:

$$D_{dd} = \frac{\langle q_{c_d} \rangle}{\Delta C / \Delta l_d} \quad (8)$$

$\langle q_{c_d} \rangle$ representing the mean flux within the whole REV volume. The three diffusion components are equivalent to D_{11}, D_{22}, D_{33} in the three principal directions of the UD composite. Table 1 gives the values of the diffusion coefficients of the constituents used for the calculation of the $\boldsymbol{D}$ tensor for two different composites exposed to a temperature of 180°C in air: (a) a simplified epoxy/carbon composite (without fiber/matrix interface) with a fiber volume ratio of $V_f = 0.65$, and (b) an idealized composite (with fiber/matrix interface) with an interphase thickness $h^{interface} = 0.15\ \mu m$. It is important to point out that this is a completely realistic interphase thickness, roughly corresponding to the average value of interphase thicknesses reported in the literature for thermosetting matrix composites. The calculations were carried out with Abaqus software. Table 2 shows a synthesis of the results obtained numerically and compared to several analytical laws proposed in the literature [7].

Constituent	**Carbon fibre (IM7)**	**Matrice époxy (ACE)**	**Interface**
D [m^2/s]	0	$2.3\ 10^{-12}$	$2.3\ 10^{-9}$
Source	Estimated	[3,5]	Estimated*

Table 1. Diffusion coefficients of the different constituents.
*The fiber/matrix interphase is assumed to be in a rubbery state.

***(a)* Composite fibre/matrice**					
$\nabla_x C$		$\nabla_y C$		$\nabla_z C$	
q_{c_x}	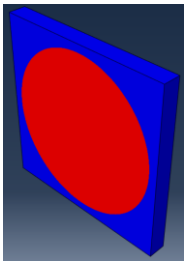	q_{c_y}	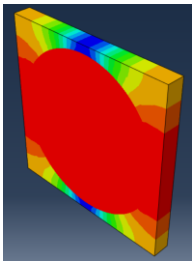	q_{c_z}	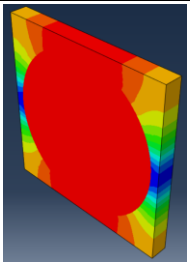
D_{xx}	$2.3\ 10^{-12}$	D_{yy}	$1.21\ 10^{-12}$	D_{zz}	$1.21\ 10^{-12}$
Analytical [7]					
D_{xx}	$2.3\ 10^{-12}$	D_{yy}	$1.22\ 10^{-12}$	D_{zz}	$1.22\ 10^{-12}$

***(b)* Composite fibre/interface/matrice**					
$\nabla_x C$		$\nabla_y C$		$\nabla_z C$	
q_{c_x}	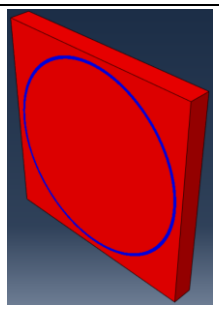	q_{c_y}	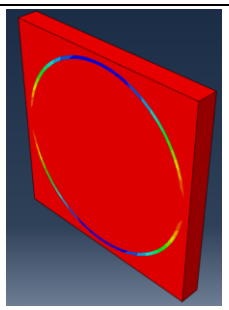	q_{c_z}	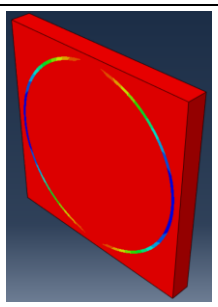
D_{xx}	$2.88\ 10^{-10}$	D_{yy}	$3.77\ 10^{-11}$	D_{zz}	$3.77\ 10^{-11}$

Table 2. Results of diffusion coefficients [m^2/s] from calculations in the REV with PBCs.

The results obtained clearly highlight the significant effect of the interface on the effective diffusion coefficient, particularly in the longitudinal direction. As often reported in the literature, the fiber/matrix interface of an epoxy matrix composite would be in a rubbery state at the exposure temperature of the composite. Consequently, the oxidation kinetics of the composites described by Eq. 2 must consider this influence of the interface. The following section presents a comparison of numerical simulations of oxidation gradients as well as a confrontation with the TOLs measured experimentally in literature studies.

3 NUMERICAL RESULTS AND COMPARISON WITH EXPERIMENTAL TESTS

Solving the 3D problem presented in Section 2.1 gives access to the evolution of the O_2 concentration gradient $C(\boldsymbol{x}, t)$ in the three directions of the composite frame. Simulations in air at 180°C for an epoxy/carbon composite of type 977-2/IM7 were carried out for the two composites whose effective diffusion tensor was calculated in Section 2.2: (a) a fiber/matrix composite and (b) a fiber/interface/matrix composite. For each composite, 3 configurations are simulated in order to highlight the oxidation kinetics in each direction: (i) 1 – fiber direction, (ii) 2 – direction transverse to the fibers and (iii) 3 – out-of-plane direction to the fibers.

A criterion was defined for the calculation of the TOL in each direction, as already proposed for neat resin samples [3]. In the case of UD composites, the O_2 consumption gradients ($Q(\boldsymbol{x}, t)$) are calculated by integrating over time $r_{UD}(C)$, given by Eq. 5. Thus, it is possible to estimate the evolution of the TOL for each of the studied directions (1, 2 and 3). Figure 4 shows the evolution of the TOL for the two types of composites studied: (a) with perfect fiber/matrix interface (i.e. no interface in the modeling) and (b) with idealized fiber/matrix interface (*i.e.*, modeled interphase and assumed to be in a rubbery state). These results were compared with experimental measurements [2], highlighting: (i) the anisotropy of the thermo-oxidation problem of UD composites and (ii) the importance of considering, in the proposed model, the predominant effect of the interphase on the evolution of the TOL, particularly in the longitudinal direction (1 – fiber direction).

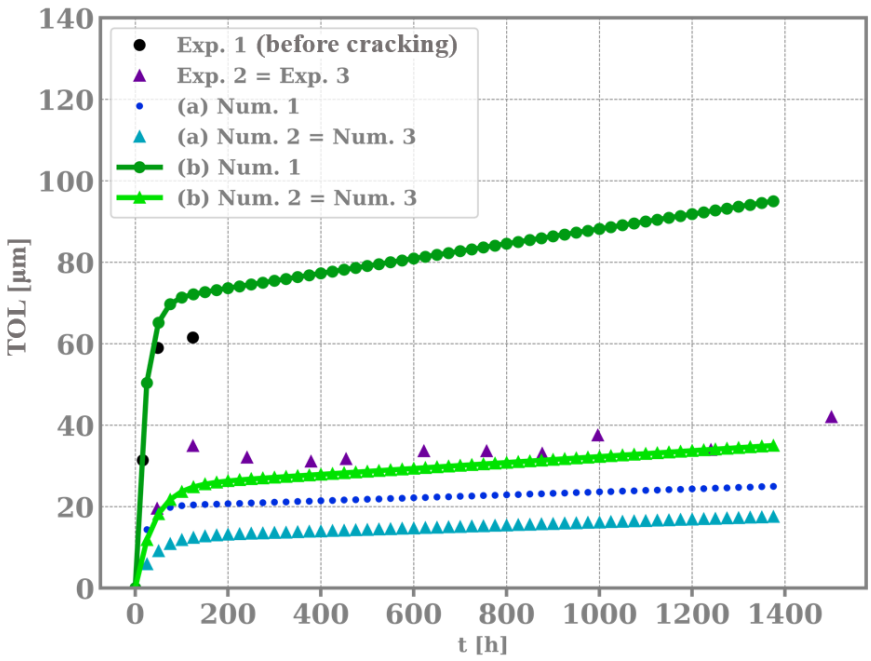

Figure 4. Comparison of experimental TOLs (black circles and purple triangles for directions 1, 2 and 3 which are denoted Exp. 1, Exp. 2 = Exp. 3, respectively) to numerical simulations for: (a) fiber/matrix composite (Num. 1 and Num. 2 = Num. 3) and (b) fiber/interface/matrix composite (Num. 1 and Num. 2 = Num. 3).

4 CONCLUSIONS AND PERSPECTIVES

A FEM-based model considering the specificities of the diffusion/reaction behavior of UD composites was proposed to describe their thermo-oxidation gradients: the stabilizing effect of carbon fiber and the anisotropic diffusion of O_2 accentuated by a fiber/matrix interphase, assumed in the rubbery state. The reactive term describing the oxidation kinetics at the UD scale has been adapted from neat resin kinetics in order to include a mitigation effect on the oxidation rate induced by the presence of fibers. Diffusion tensor homogenization calculations clearly show the significant effect of the interphase, which was numerically represented by a finite interface at the REV scale. The faster O_2 diffusion in the interphase results in an increase of the effective diffusion coefficient at the UD scale of the order of $< 10^1$ in the transverse directions 2 and 3, and of $> 10^2$ in the longitudinal direction to the fibers 1, directly impacting the TOL values. The comparison of numerical simulations with experimental data allowed to discuss and verify the hypotheses of the literature [2,6] on the non-negligible effect of the interphase, particularly in direction 1.

Future work will focus on other key aspects aimed at completing the general approach to predicting lifetime of composite under thermal aging:

(i) the experimental validation of the kinetic evolution laws of physicochemical properties (*e.g.*, r_{UD}, $\boldsymbol{D}$),

(ii) the evolution of thermomechanical properties of interest for the aeronautical field (*i.e.*, T_g and elastic properties) and,

(iii) the integration of these laws into the calculation code to access the gradients of stresses and deformations induced by oxidation, to predict the initiation, then the propagation of cracks in composites.

These steps are necessary to further investigate the coupling between damage and oxidation through a generalized approach in order to predict the lifespan of composite parts based on accurate material thermo-chemo-mechanical degradation criteria.

REFERENCES

[1] T.K. Tsotsis, S.M. Lee, Long-term thermo-oxidative aging in composite materials: Experimental methods, *Composites Science and Technology*, 32(11), 1998, pp. 1115-1135 (doi: 10.1016/S0266-3538(97)00123-1).

[2] X. Colin, A. Mavel, C. Marais, J. Verdu, Interaction between cracking and oxidation in organic matrix composites, *Journal of Composite Materials*, **39(15)**, 2005, pp. 1371-1389 (doi: 10.1177/0021998305050430).

[3] J.P. Marquez Costa, X. Colin, Finite element modelling of the oxidation gradients of epoxy-diamine matrices below and above their glass transition temperature, *Polymer Degradation and Stability*, **234**, 2025, pp. 111194 (doi: 10.1016/j.polymdegradstab.2025.111194).

[4] X. Colin, F. Essatbi, J. Delozanne, G. Moreau, A new analytical model for predicting the thermal oxidation kinetics of composite organic matrices. Application to diamine cross-linked epoxy, *Polymer Degradation and Stability*, **186**, 2021, pp. 109513 (doi: 10.1016/j.polymdegradstab.2021.109513).

[5] X. Colin, C. Marais, J. Verdu, Kinetic modelling of the stabilizing effect of carbon fibres on thermal ageing of thermoset matrix composites, *Composites Science and Technology*, **65**, 2005, pp. 117-127 (doi: 10.1016/j.compscitech.2004.06.009).

[6] K.V. Pochiraju, G.P. Tandon, G.A., Schoeppner, Evolution of stress and deformations in high-temperature polymer matrix composites during thermo-oxidative aging, *Mechanics of Time-Dependent Materials*, 12(1), 2008, pp. 45-68 (doi: 10.1007/s11043-007-9042-5).

[7] T. Peret, A. Clement, S. Freour, F. Jacquemin, Homogenization of Fickian and non-Fickian water diffusion in composites reinforced by hydrophobic long fibers: Application to the determination of transverse diffusivity, *Composite Structures*, **226**, 2019, pp. 111191 (doi: 10.1016/j.compstruct.2019.111191).

Numerical Analysis of Viscoelastic Creep and Transverse Cracking in Fiber-reinforced Composites

[a]Yamato Hoshikawa, [a]Kazuki Ryuzono,
[b]Yoshiaki Kawagoe, [a]Tomonaga Okabe

[a] Graduate school of Engineering, Tohoku University
[b] The University of Tokyo

This presentation has been accepted for publication in the "International journal of damage mechanics".
Doi: https://doi.org/10.1177/10567895241302543



International Journal of Damage Mechanics

Impact Factor: 3.9 / 5-Year Impact Factor: 3.6

Restricted access | Research article | First published online December 30, 2024

Finite element modeling of viscoelastic creep behavior and transverse cracking in fiber-reinforced com

Yamato Hoshikawa, Kazuki Ryuzono, [...], and Tomonaga Okabe +2 View all authors and affiliations

OnlineFirst | https://doi.org/10.1177/10567895241302543

Contents | Get access | Cite article | Share options | Information, rights and permissions | M

Abstract

Fiber-reinforced composites are essential in the aerospace industry, highlighting the need for an in-depth understanding of their durability. This study introduces a novel approach that integrates viscoelasticity and damage evolution based on continuum damage mechanics, employing finite element analysis. The method utilizes an anisotropic viscoelastic constitutive law to examine creep behavior under constant stress, decomposing stresses into equilibrium and non-equilibrium components. Moreover, it integrates a transverse crack damage variable associated with crack density. After solving stiffness equations, a detailed analysis of transverse crack propagation is conducted. This technique was applied to creep tests on carbon fiber-reinforced plastics and 3D woven ceramic matrix composites, resulting in strain and crack density profiles. The numerical simulations successfully reproduced experimental outcomes. The developed method offers a comprehensive tool for analyzing transverse crack propagation under viscoelastic creep conditions through finite element analysis, significantly enhancing design considerations by incorporating aspects of long-term durability.

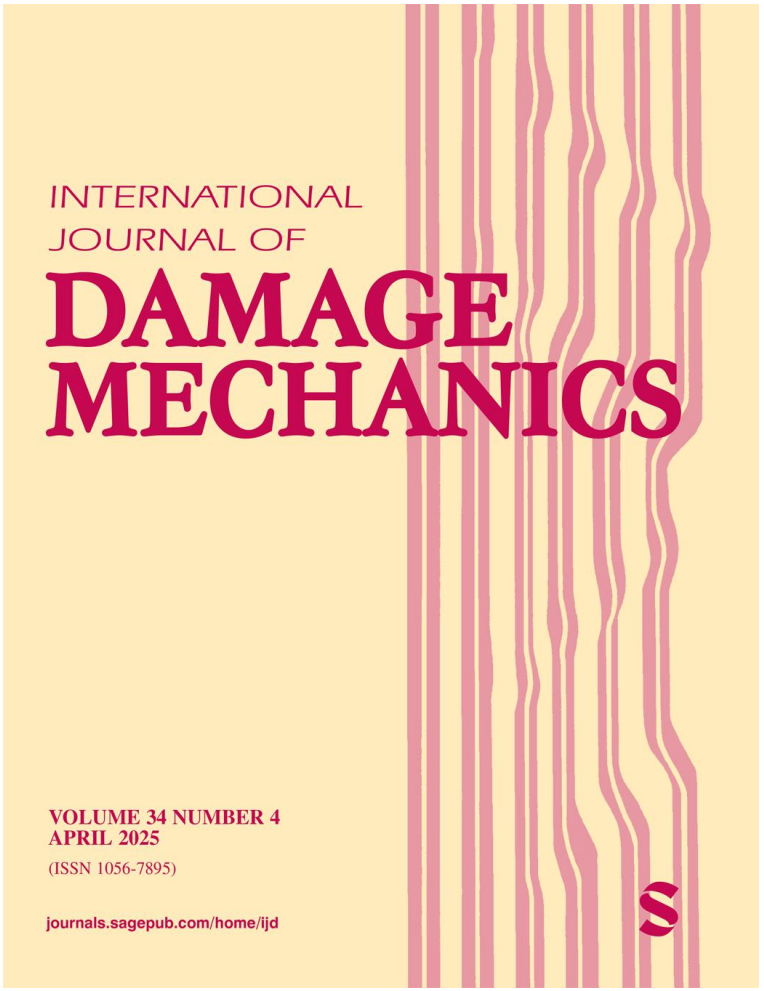

Background

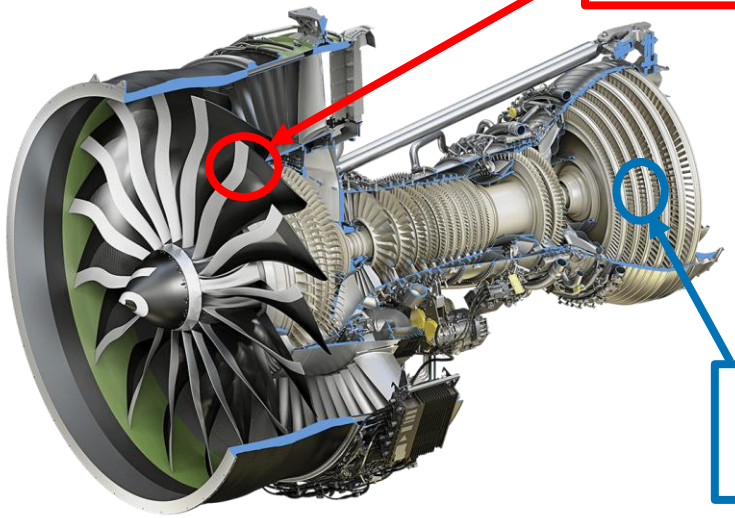

CFRP fan blades

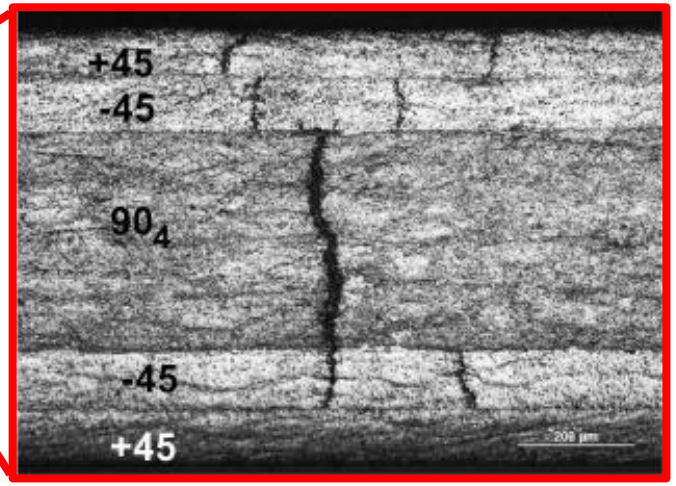

CFRP laminate[2].

Turbine blades crafted by CMCs

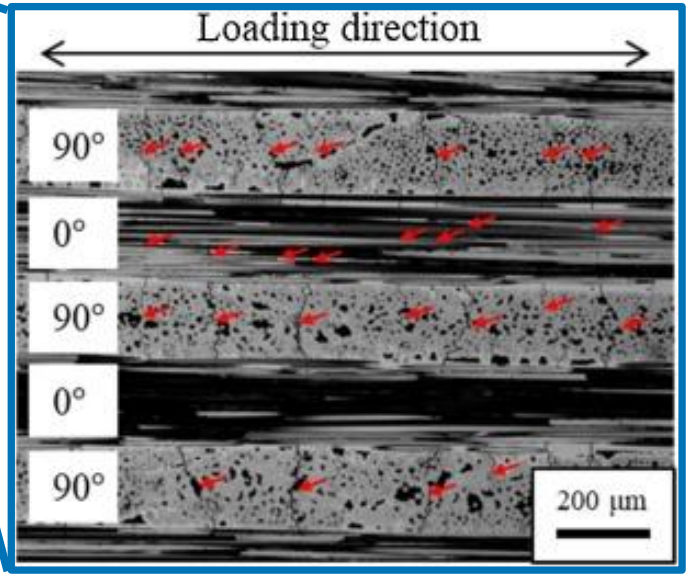

Creep tests cause the transverse cracks in CMCs [3].

Applications of PMCs and CMCs in GE9X [1]

1. High bypassing (larger size)
   - ➢CFRP fan blades/case
2. Improvement in combustion efficiency
   - ➢CMC turbine blades

Time-dependent damage

[1] https://www.geaviation.com/commercial/engines/ge9x-commercial-aircraft-engine
[2] Asadi et al., *Compos. B Eng.*, 2011.
[3] Ikarashi Y. et al., *Journal of the European Ceramic Society*, 2020.

Objective

Previous studies : theoretical model

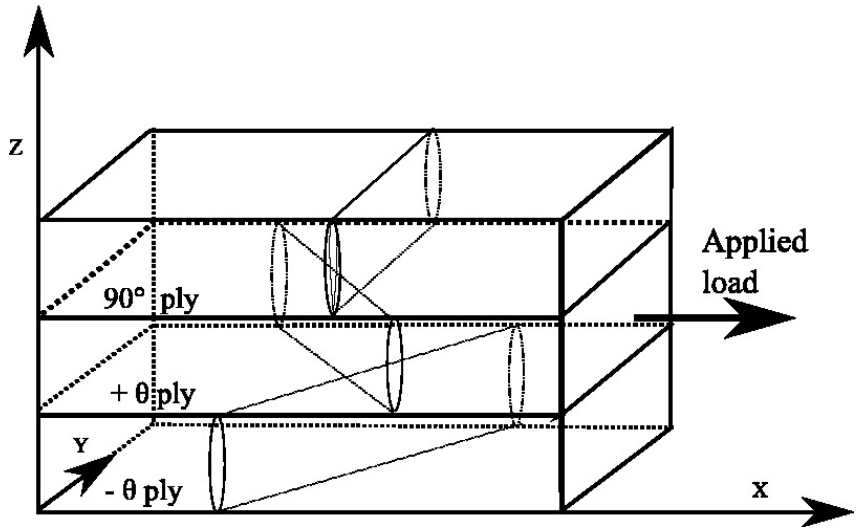

Theoretical model [1]

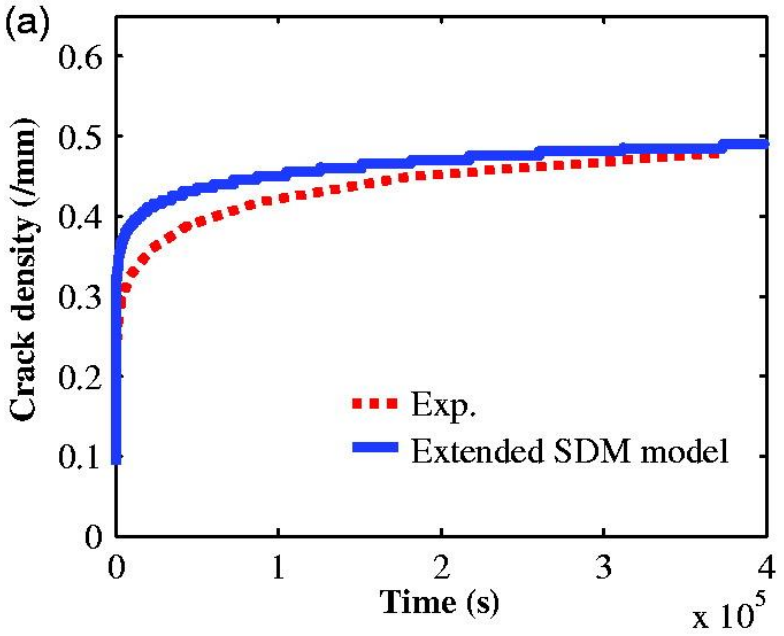

Transverse cracking under creep tests [1].

✓ Transverse cracking density enables quantitative evaluation of damage [1,2,3]

➢ The long-term durability of components can be evaluated by finite element method (FEM).

[1] Berton T. et al., *International Journal of Damage Mechanics,* 2016.
[2] Ogi and Takao, *Advanced Composite Materials,* 2001.
[3] Ikarashi Y. et al., *Journal of the European Ceramic Society*, 2020.

Our works

FEM modeling of creep deformation and transverse cracking

Efforts in this presentation

(1) Anisotropic viscoelastic constitutive law

➢ Different viscoelasticity in fiber direction/transverse.

(2) Transverse crack damage model

➢ Crack density - Damage variable relationship.

➢ Time-dependent damage propagation.

(3)Validation

➢Transverse crack propagation during creep testing behavior during creep tests.

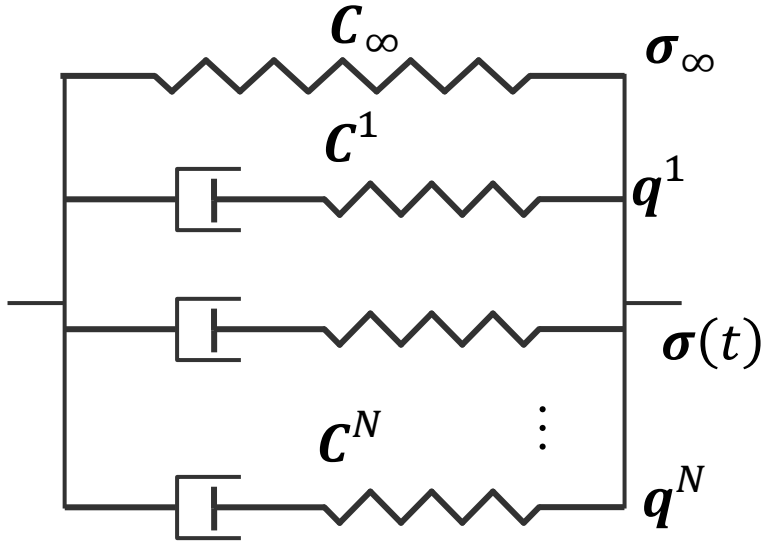

Genialized Maxwell model

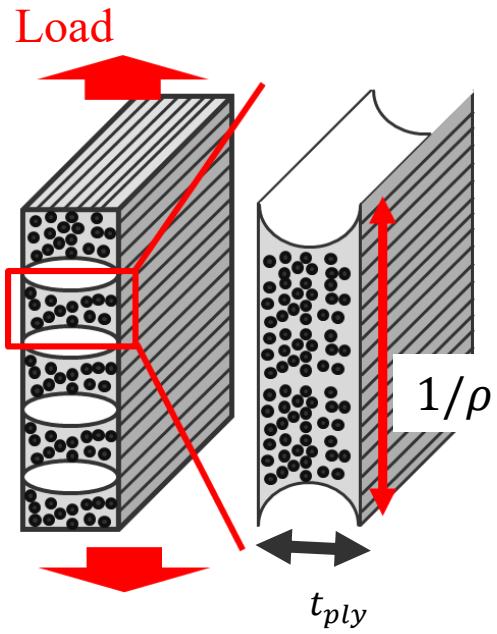

Transverse crack damage model

An isotropic viscoelasticity

Generalized Maxwell model

➢Linear spring + damper

✓Voigt notation:

$$\sigma_i(t) = \sum_{j=1}^{6} C_{ij}(t)\varepsilon_j(0) + \sum_{j=1}^{6} \int_0^t C_{ij}(t-\tau)\frac{\partial \varepsilon_j(\tau)}{\partial \tau} d\tau \quad (1)$$

$$C_{ij}(t) = C_{ij}^0 - \sum_{k=1}^{N} C_{ij}^k \left(1 - e^{-\frac{t}{\alpha_T T_k}}\right) \quad (2)$$

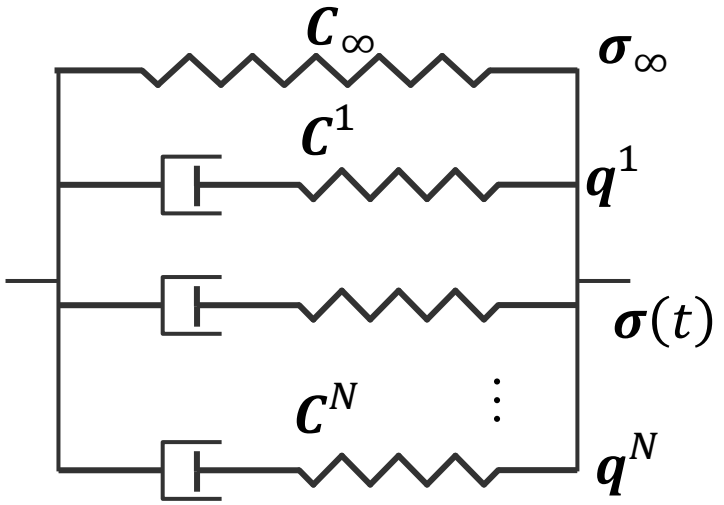

Generalized Maxwell model

Discretization

$$\sigma_i(t) = \sum_{j=1}^{6} C_{ij}^0(t)\varepsilon_j(0) - \sum_{k=1}^{N}\sum_{j=1}^{6} q_{ij}^k \quad (3)$$

Static component

Non-equibulium component

C_{ij}^0:initial stiffness

C_{ij}^k: relaxation stiffness

$$q_{ij}^k(t_{n+1}) = e^{-\frac{\Delta t}{\alpha_T T_k}} q_{ij}^k(t_n) + C_{ij}^k \varepsilon(t_{n+\theta}) \left(1 - e^{-\frac{\Delta t}{\alpha_T T_k}}\right) \quad (4)$$

Transverse cracking (1)

Crack density-damage variable[1] :

Crack density ρ:

➢Number of cracks/length of observed area

Damage model [1] :

➢Damage variables d_{ii} associated with ρ

$$d_{ii} = \frac{2\rho}{\beta_{ii}} \tanh \frac{\beta_{ii}}{2\rho}$$

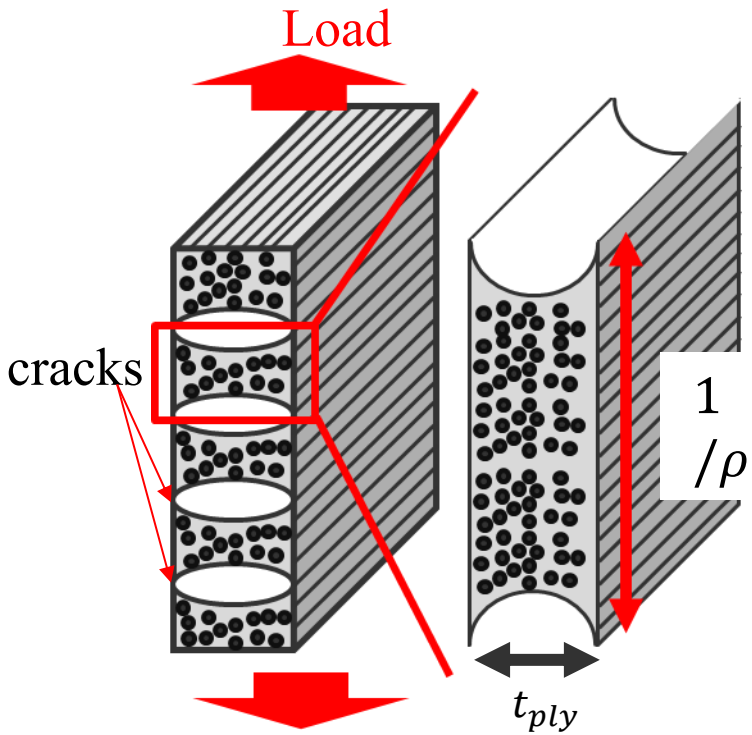

Representative volume elements RVEs [1]

Continuous damage model [2]:

➢ Applied to elastic compliance $\boldsymbol{S}^0$ [2], relaxation elasticity $\boldsymbol{C}^k$

$$S_{ii}^0 = (1 - d_{ii})^{-1} S_{ii,ini}^0$$
$$C_{ii}^k = (1 - d_{ii}) C_{ii,ini}^k$$

β_{ii}:Material constants
S_{ii}^0: Elastic compliance

[1] S. Onodera et al., *International Journal of Damage Mechanics*, 2022.
[2] C. Lopes, P. Camanho, Z. G¨urdal, et al., *Compos Sci Technol*, 2009.

Transverse cracking (2)

Transverse crack propagation :

➢ Energy-stress criteria with time development [1]

Energy criterion

$$G(\rho) \geq G_C$$

G : Energy release rate
G_c: Fracture toughness

➢ The energy release rate assumes that cracks occur at equal intervals.

$$G(\rho) = \frac{U\left(\frac{\rho}{2}\right) - 2U(\rho)}{A_{tr}}$$

U :Strain energy
A_{tr} :Cross-sectional area

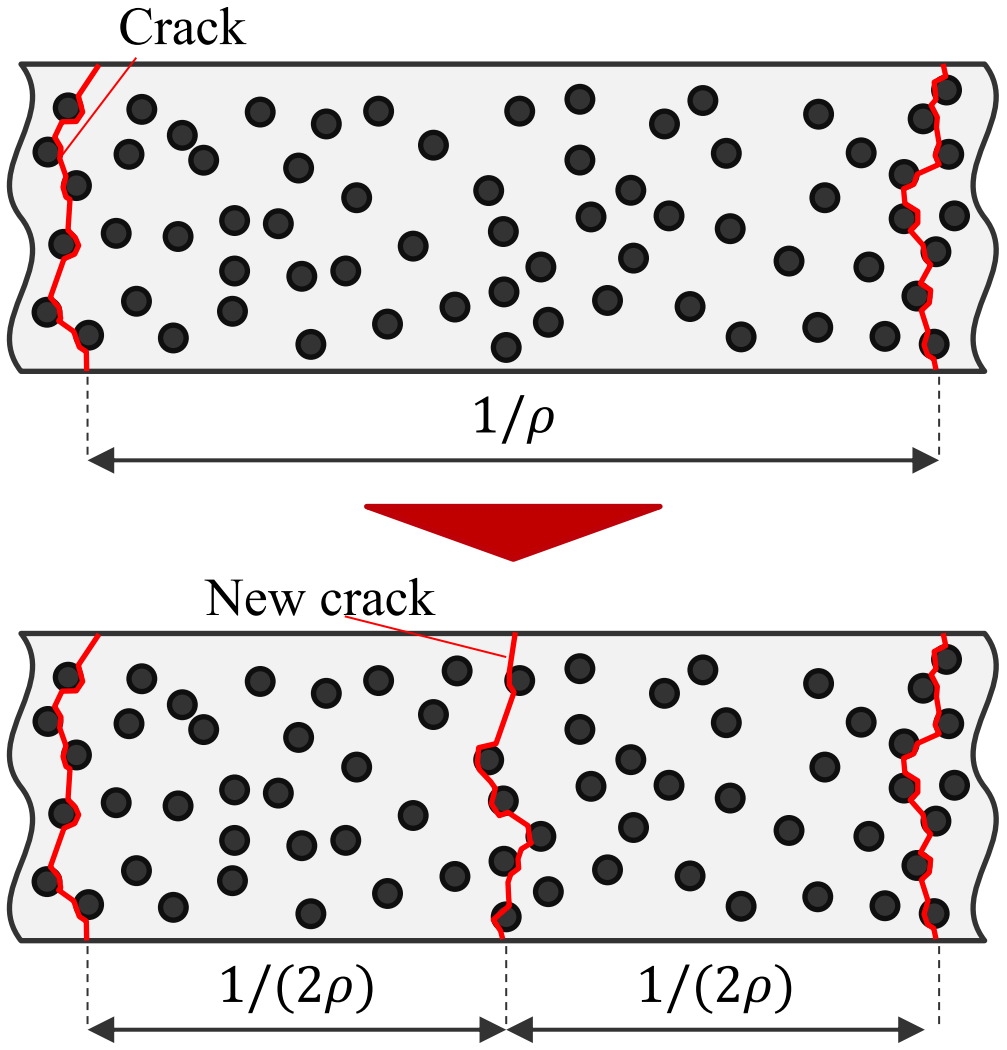

Time dependence of the fracture toughness [2]

$$G_C(t') = \frac{G_C^0}{2}\left(1 + \exp\left(-\frac{t'}{10^4}\right)\right)^{0.807}$$

G_C^0: Initial value

t': Accumulated time after creep initiation

[1] S. Onodera et al., *International Journal of Damage Mechanics*, 2022.
[2] T. Berton et al., *Compos Struct.* 2018.

Transverse cracking (3)

Transverse crack propagation :

➢ Energy-stress criteria with time development [1]

Stress-criterion

➢ Judging damage onset

$$\left(\frac{\sigma_{22}(\rho)}{\sigma_{22C}}\right)^2+\left(\alpha\frac{\sigma_{44}(\rho)}{\sigma_{22C}}\right)^2+\left(\beta\frac{\sigma_{55}(\rho)}{\sigma_{22C}}\right)^2\geq 1 \quad (12)$$

※$\alpha=\beta=1$

Intralaminar strength time dependence

➢Intralaminar strength loss during creep testing

$$\sigma_{22C}(t')=k_d\sigma_{22C}^0+(1-k_d)\left(\exp\left(-\frac{t'}{T_d}\right)\right)^m \quad (13)$$

When both energy and stress criteria are satisfied
➢Crack propagation

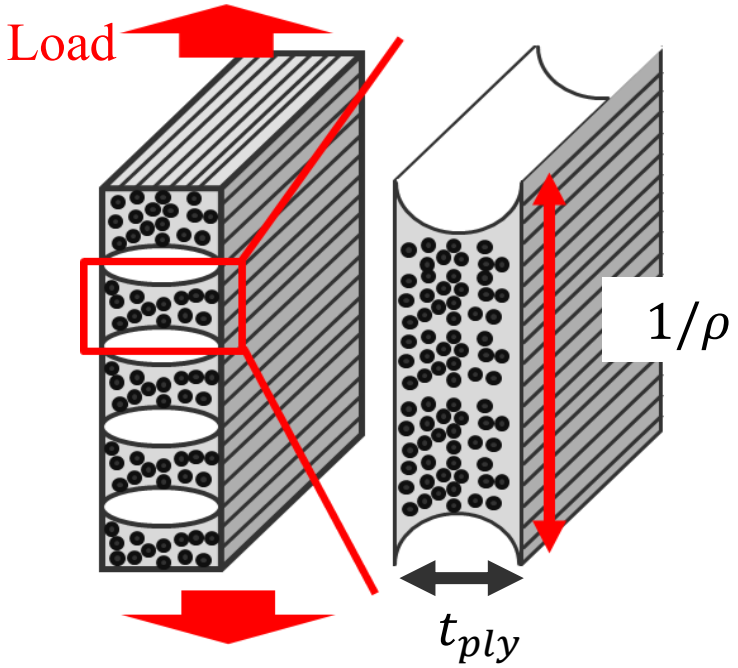

RVE [1]

σ_{22C}: Intralaminar strength
k_d
m
T_d
} Fitting parameters

[1] S. Onodera et al., *International Journal of Damage Mechanics*, 2022.
[2] T. Berton et al., *Compos Struct.* 2018.

Transverse cracking (4): Flowchart

Numerical procedure :

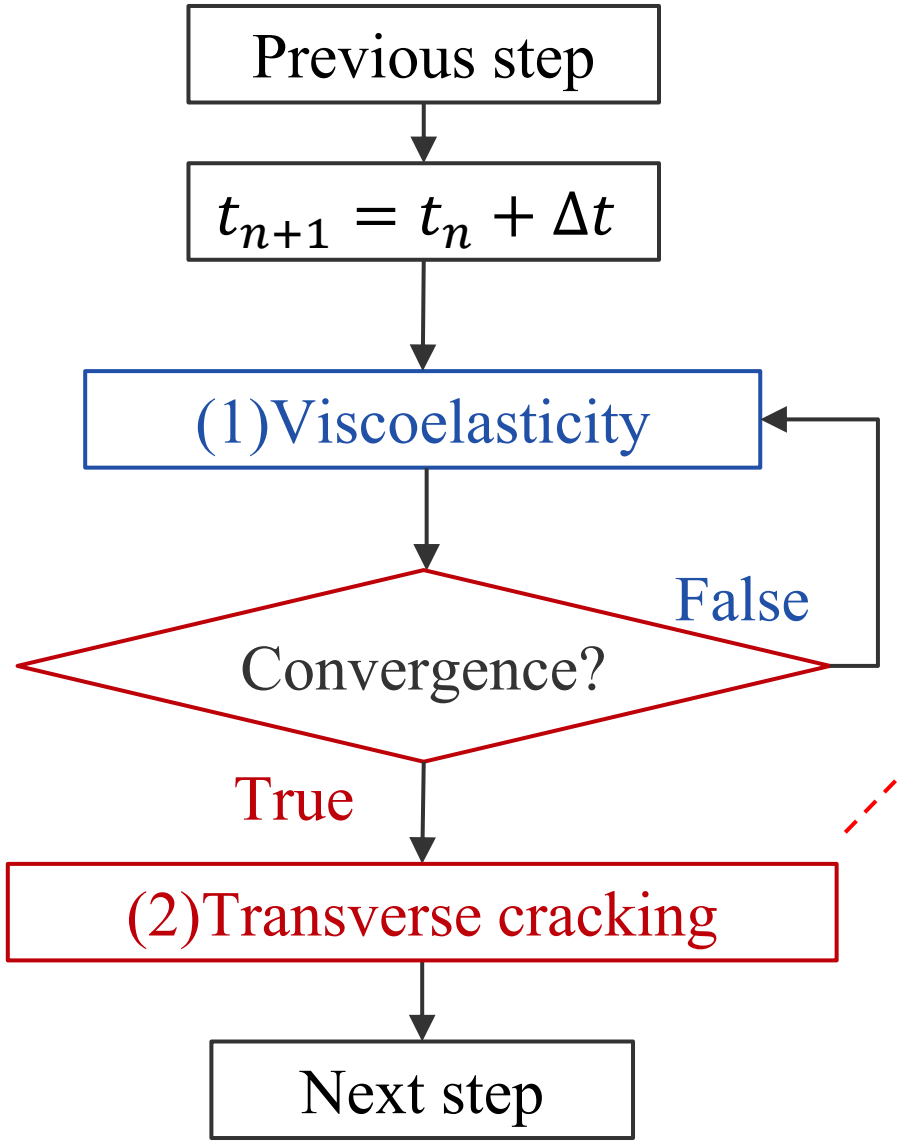

Transverse cracking :

➢ Evaluate the crack density of each element.

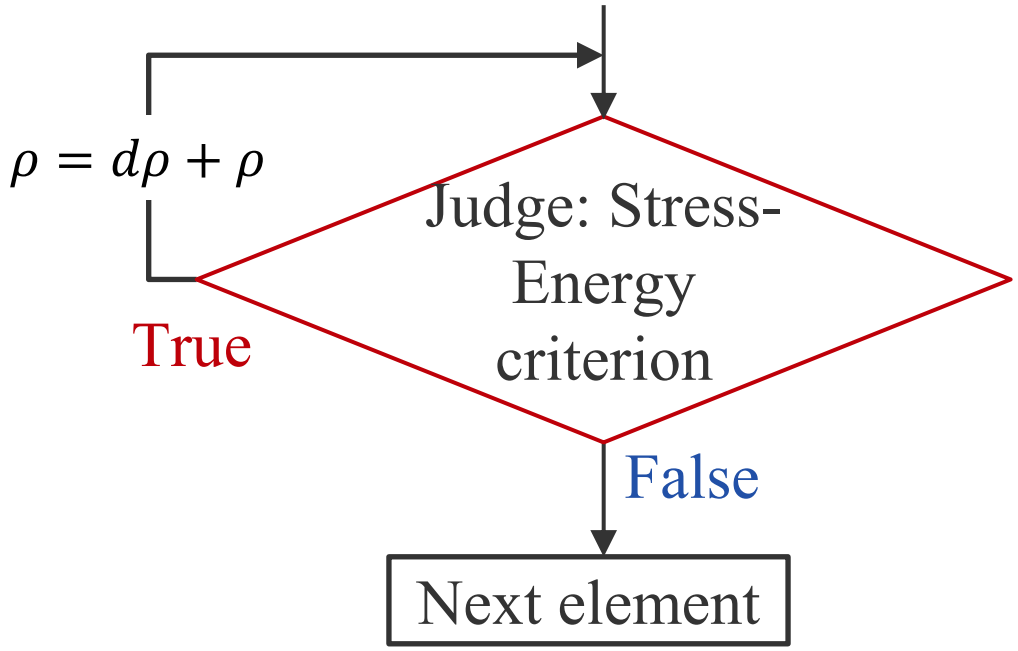

Viscoelasticity: implicit

Transverse cracking: explicit.

Validation analysis: CFRP(T800H/#3631)

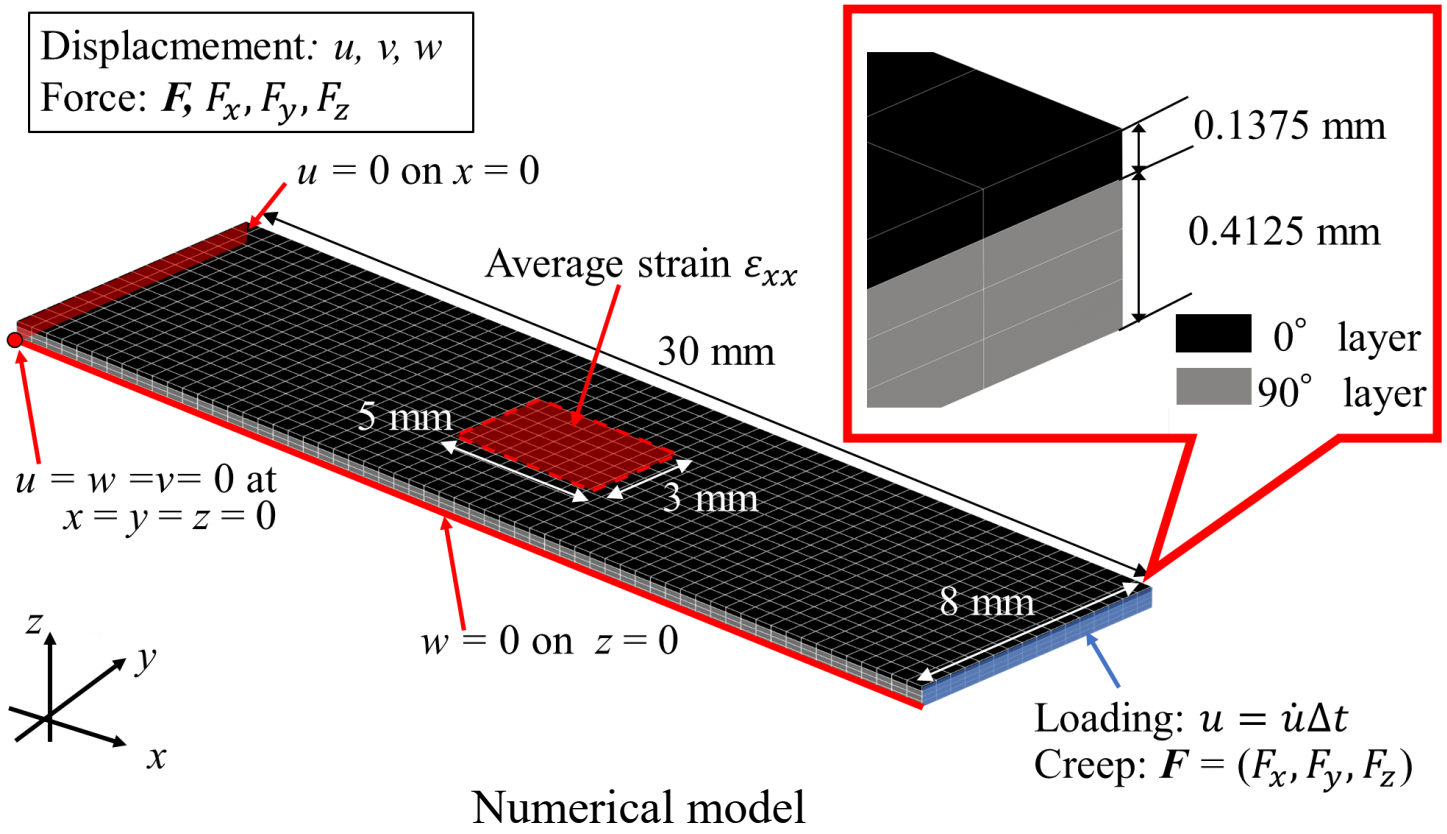

Numerical model

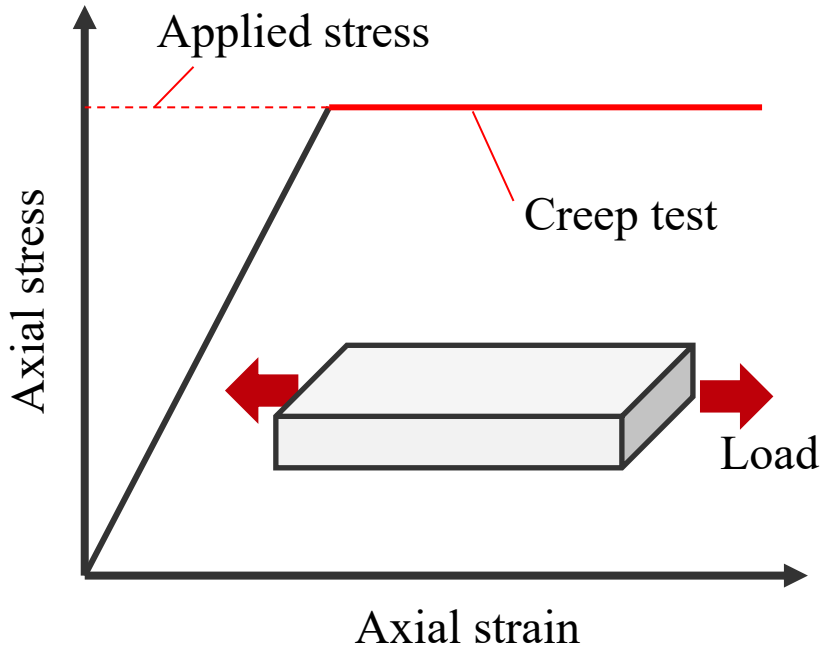

- ✓ CFRP-Cross-ply laminate ($[0/90_3]_s$)
- ✓ Viscoelasticity : Applied in the transverse direction to the fiber
- ✓ Applied stress : 510 MPa, 530 MPa

- ✓ Strain-history : Element average of model center.
- ✓ Transverse crack density : Average value of 90° layer elements

[1] Ogi and Takao, *Advanced Composite Materials,* 2001.

Validation analysis: CFRP(T800H/#3631)

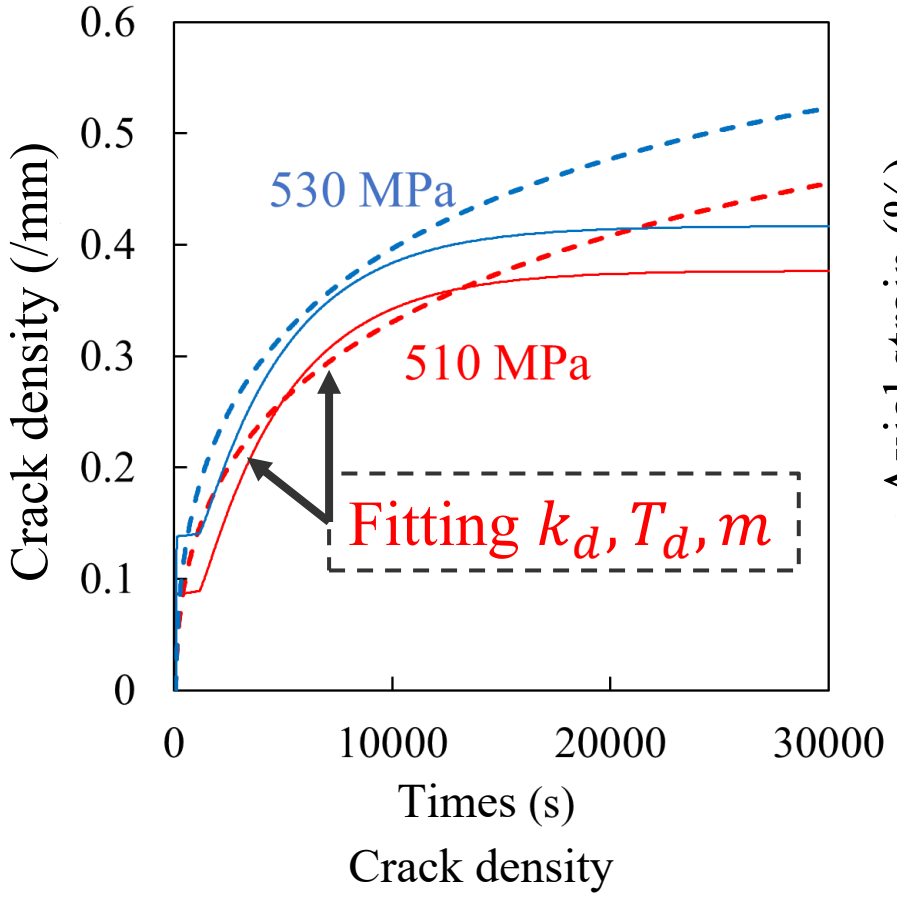

Crack density

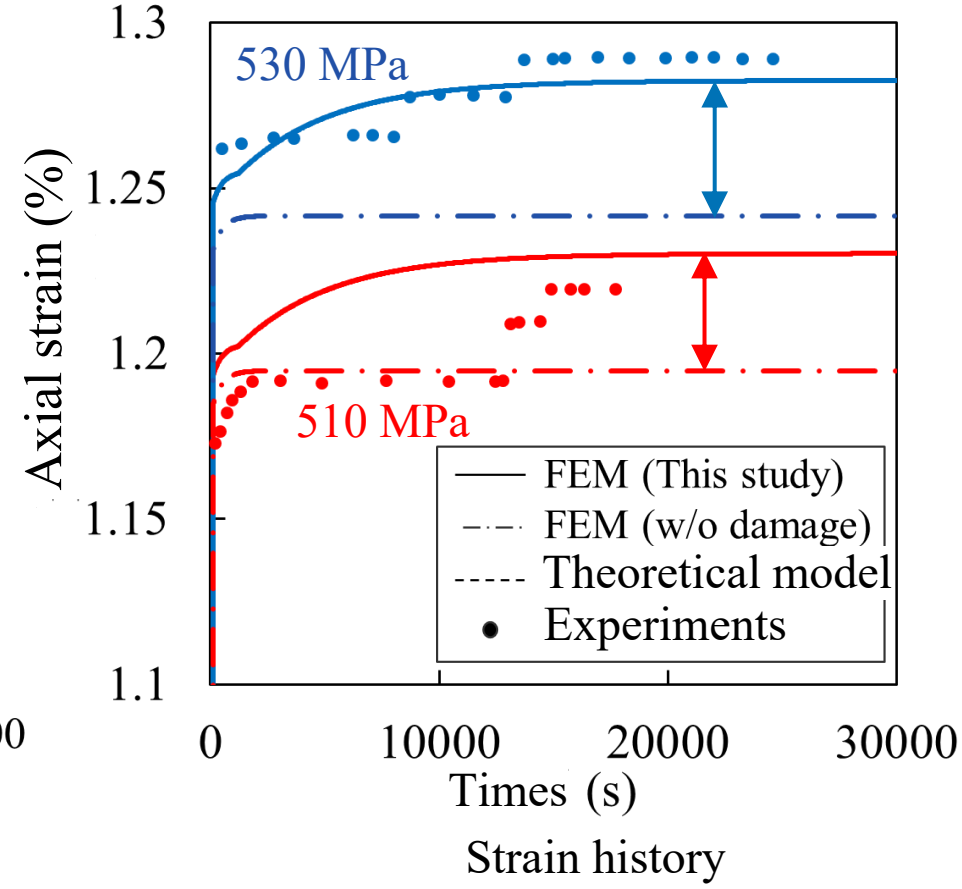

Strain history

- ✓ Determine stress criterion parameters k_d, T_d, and m using crack density history [1].
  - ➢ Good reproduction of strain history of test results
- ✓ Only viscoelasticity model deviates from experimental results
  - ➢ Contribution of time-dependent damage is significant.

[1] Ogi and Takao, *Advanced Composite Materials,* 2001.

Validation analysis: CMC

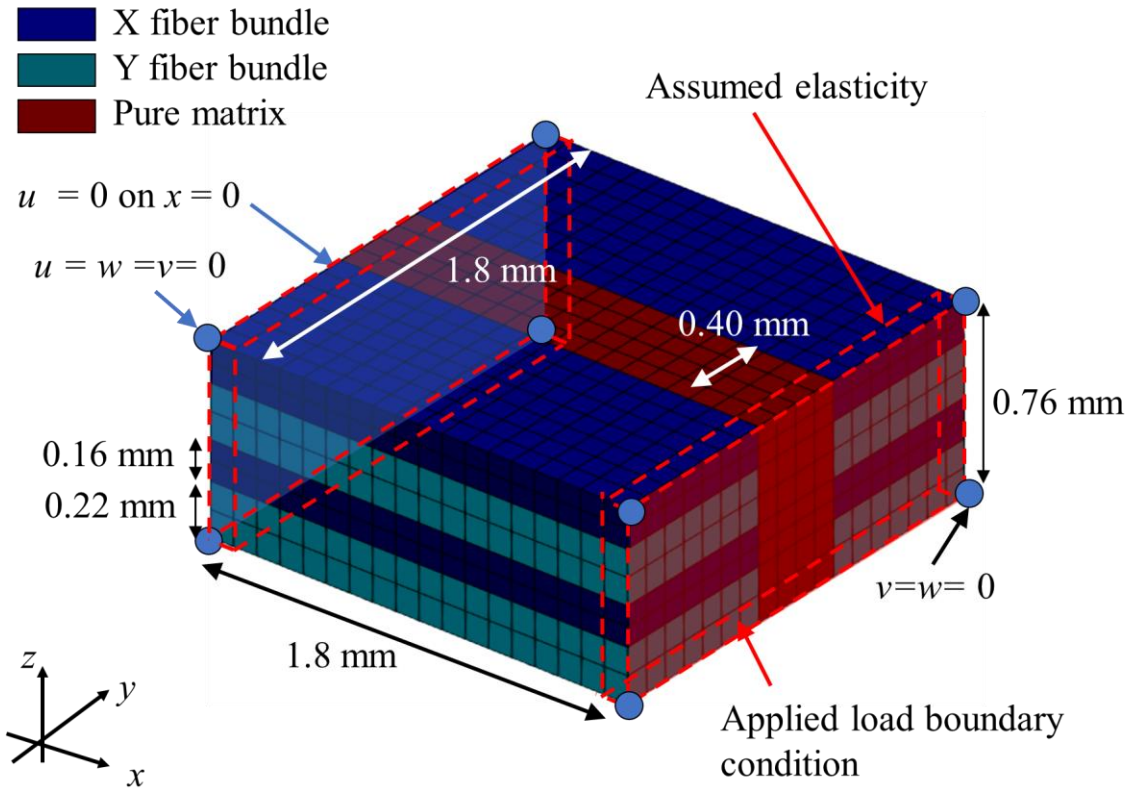

Numerical model

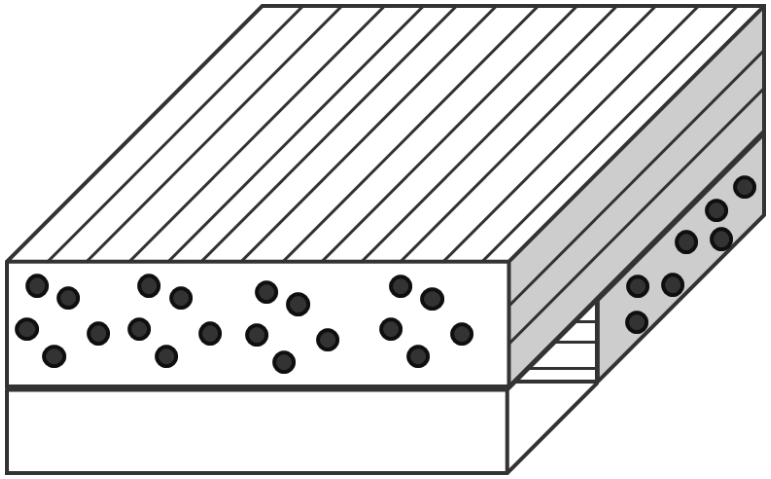

CMC mosaic model [1]

- ✓ Orthogonal woven fabric of CMC [1]
- ✓ Mosaic model consisting of X, Y fiber bundles, pure matrix [1]
- ✓ Viscoelasticity : Applied in fiber direction
- ✓ Strain history : Calculated from unit cell model load direction displacement
- ✓ Crack density : Elements average of Y fiber bundle

[1] Ikarashi Y. et al., *Journal of the European Ceramic Society*, 2020.

Validation analysis: CMC

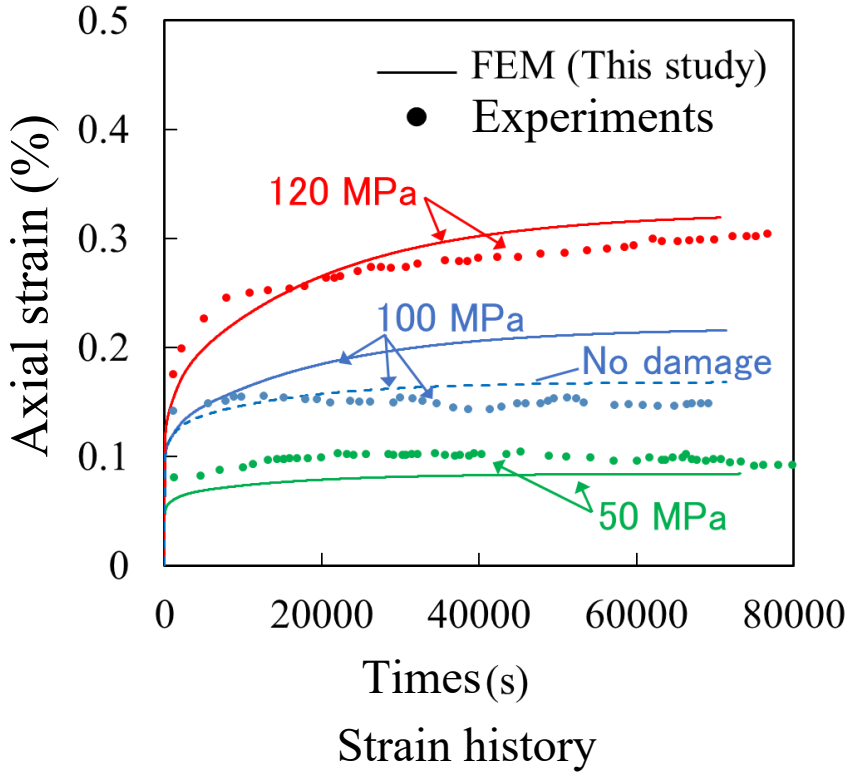

Strain history

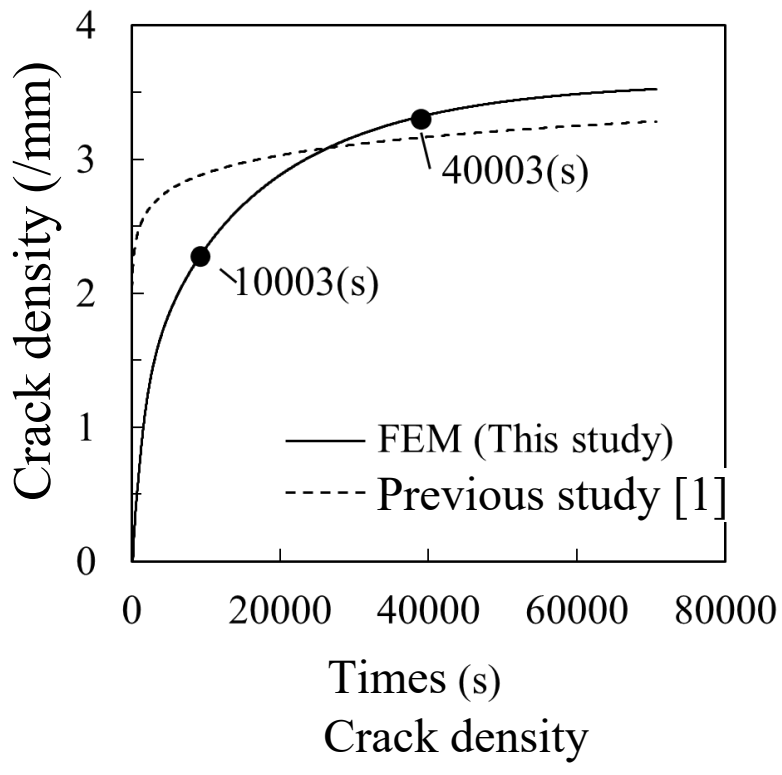

Crack density

- ✓ Consistent with the crack estimation curve in previous study [1] (w/o time dependency damage , k_d=1)
- ➢ Damage to fiber bundle Y is accelerated by relaxation of fiber bundle X.
- ✓ Load strain history at 100 MPa deviates from experiment
- ➢ Consistent with experimental results when assuming no damage

[1] Ikarashi Y. et al., *Journal of the European Ceramic Society*, 2020.

Validation analysis: CMC

➢ Strain/damage distribution plotted at 120 MPa, creep test 40003 (s) elapsed

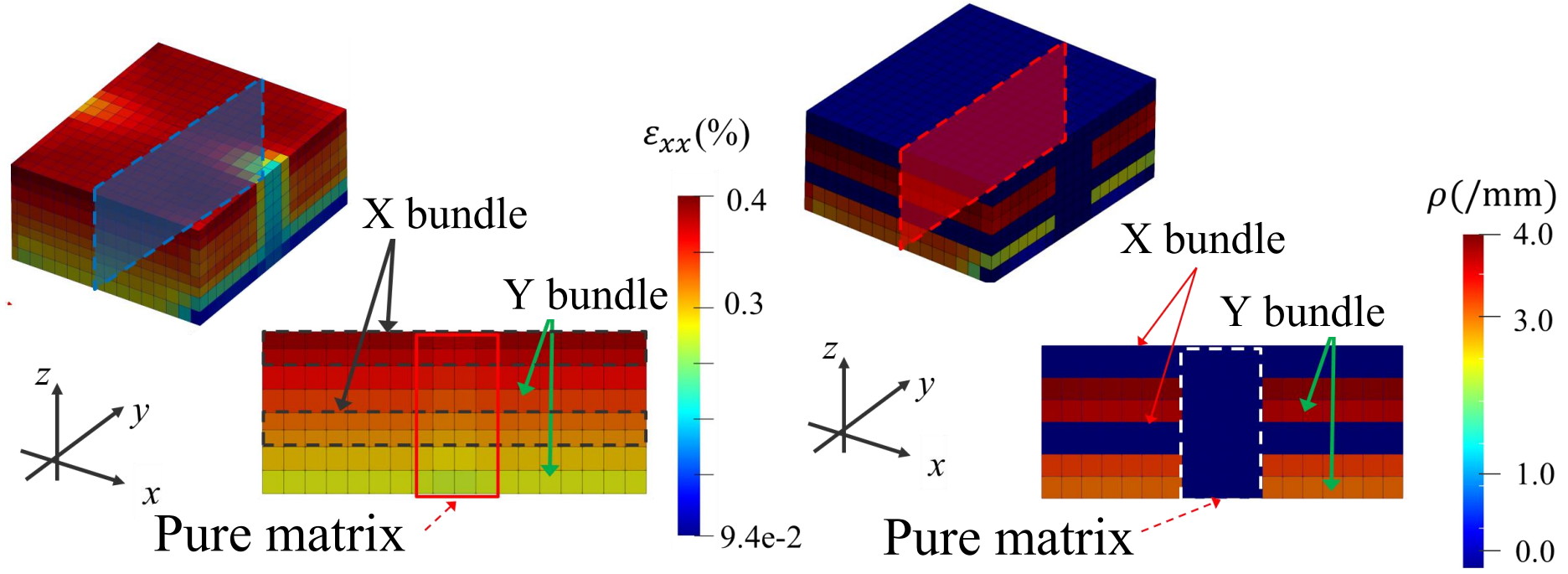

Longitudinal strain

Damage distribution

✓ Stronger strain and damage distribution occurs in fiber bundle Y surrounded by fiber bundle X.

➢Damage to fiber bundle Y increases due to stress relaxation caused by the viscoelasticity of fiber bundle X.

➢Creep damage mechanism of fabric CMC at the microscale is reproduced.

Summary

Development of a Quantitative Evaluation Method for Transverse Cracks in Fiber-Reinforced Composites Using FEM

- Anisotropic viscoelastic constitutive laws and a time-dependent transverse crack propagation model were implemented into the FEM.
- The method was validated through creep tests of CFRP and CMC, showing good agreement in both crack density and creep deformation.
- This study enables damage evaluation of 90° plies under creep loading using crack density.

➢Combined with fiber-direction damage and delamination models, it supports long-term durability assessment.

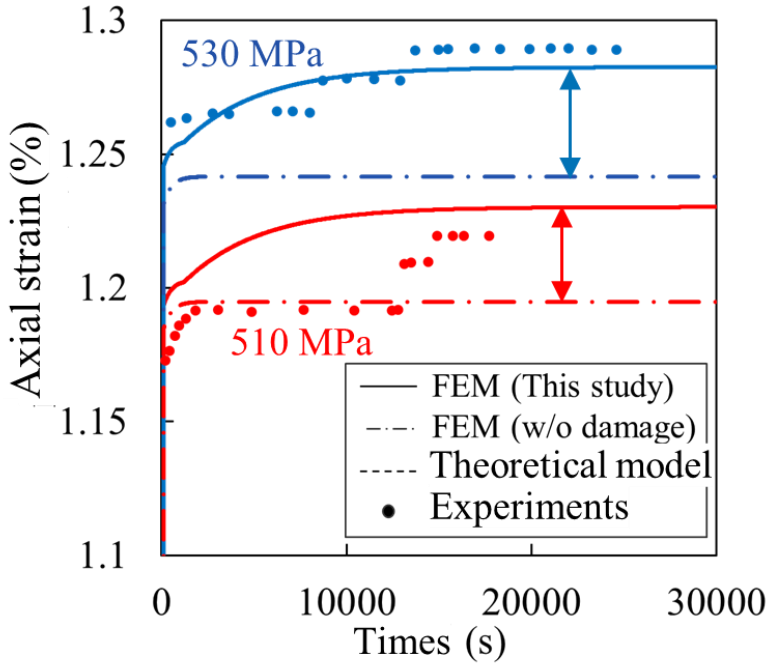

Strain history

ICCM24
24TH INTERNATIONAL CONFERENCE ON COMPOSITE MATERIALS
AUG 4-8, 2025 • BALTIMORE CONVENTION CENTER • BALTIMORE, MARYLAND

Characterization of highly filled thermosetting composite for the numerical prediction of residual stresses development during the production process of solid surface sanitary products



Joana Malheiro[1], Paulo Antunes[1], Helena Rocha[1], Manuel Grancha[2], Nuno Marques[2,3], Andreia Antunes[2,3]

[1]PIEP, [2]ROCA Group, [3]SANITANA





Contents

Introduction
Objectives
Numerical approach
- Workflow

Composite properties characterization
Numerical model
- Production cycle
- Boundary Conditions, Assumptions and Mesh

Numerical results
- Curing
- Residual stresses

Conclusions

Introduction

- Traditionally, sanitary ware and kitchen counter tops are produced with ceramics and stone.

- Nowadays, solid surface composites are used as substitutes
  - thermoset resins filled with high percentage of mineral particles

- These thermoset resins are highly reactive, which makes the process control difficult due to the high temperature generated by the exothermic curing reaction. This intrinsic characteristic of the composite can lead to the development of residual stresses an strains, which should be minimized to assure an optimal structural behaviour of the products.

Objectives

- Predict stresses originated by the production process.
- Optimize the production process focusing on the stresses developed.

Numerical Approach

Composite:
- ≈27% of Thermoset resin (polyester based)
- ≈73% of mineral Fillers (particles)

Workflow

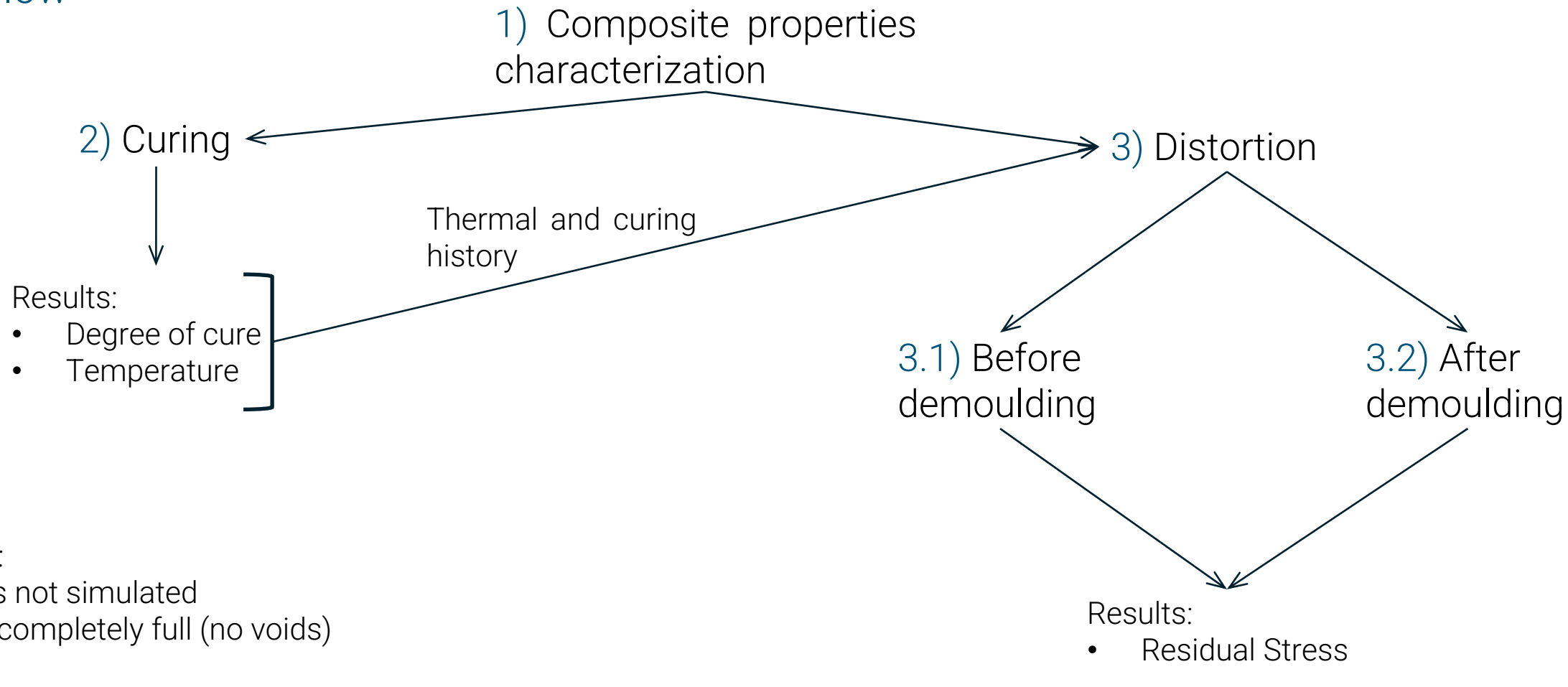

Assumptions:
- Casting is not simulated
- Mould is completely full (no voids)

Composite properties characterization

Thermal Conductivity

- MDSC (ASTM E1952)
- Isothermal runs (between 0°C and 90°C)
- Calibration material: polystyrene
- Specimen completely cured (with different thicknesses)
- λ = f(T)

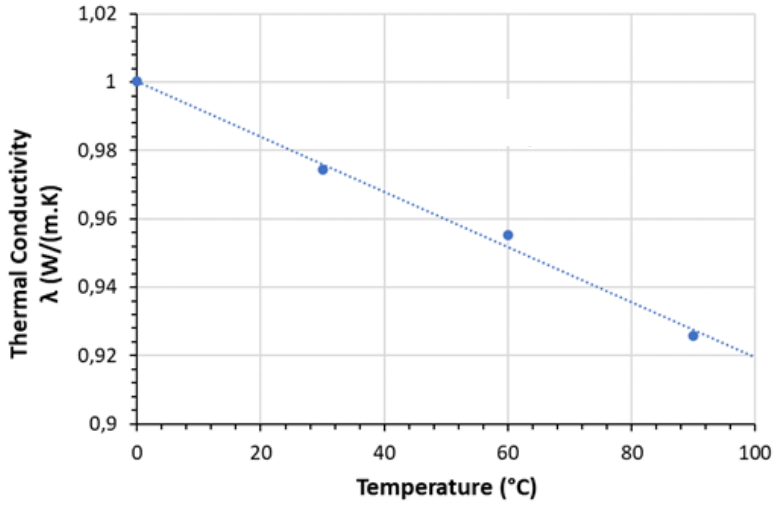

Specific Heat

- DSC (ISO 11357-4)
- Dynamic runs (from -50°C to 220°C at 10°C/min): blank, synthetic sapphire and material
- Specimen uncured (no catalyst) and completely cured
- Cp = f (T)

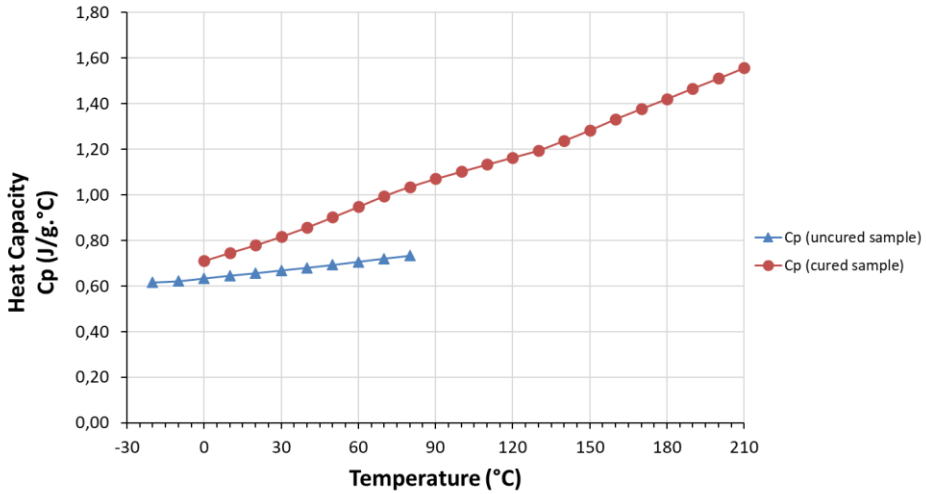

Composite properties characterization

Curing Kinetics and Enthalpy

- DSC
- Dynamic runs (between -50°C and 250°C at different heating rates 5, 10, 20 and 30°C/min.)
- Specimen uncured
- Enthalpy = constant
- Friedman method (differential isoconversional method):

$$ln\left(\frac{d\alpha}{dt}\right)_{\alpha} = ln\left(k(T).f(\alpha)\right) = \ln\left(A_{\alpha}.f(\alpha)\right) - \frac{E_{a\,\alpha}}{RT_{\alpha}}$$

  - Model free (reaction model, f(α), unnecessary)
  - Accounts for activation energy (Ea) dependency on conversion

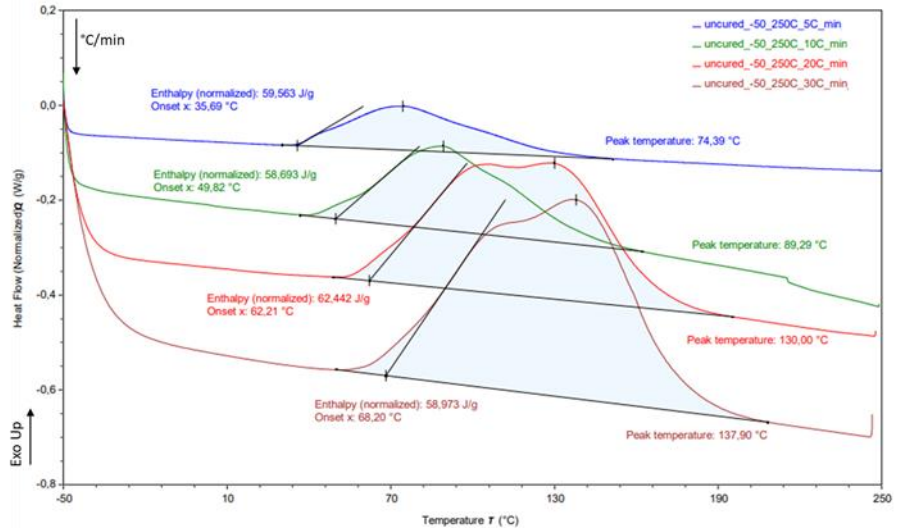

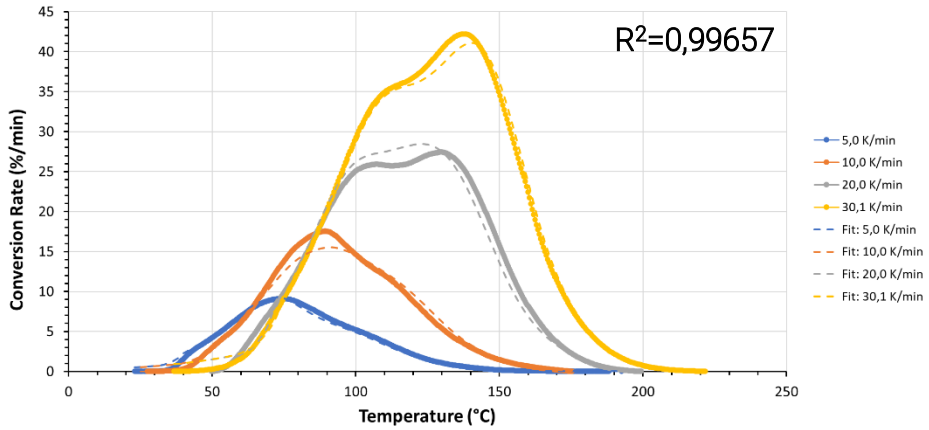

Composite properties characterization

Glass Transition temperatures

- DSC
- For Tg_0 and Tg_∞: dynamic runs (between -90°C and 250°C at different heating rates)
- For Tg_α: Isothermal run (60°C for different periods of time) followed by dynamic run (between -50°C and 250°C at 5° C/min)
- Specimen uncured (no catalyst), partially cured and cured
- Tg = f(α)

$$\frac{T_g - T_{g0}}{T_{g\infty} - T_{g0}} = \frac{\lambda\alpha}{1-(1-\lambda)\alpha}$$

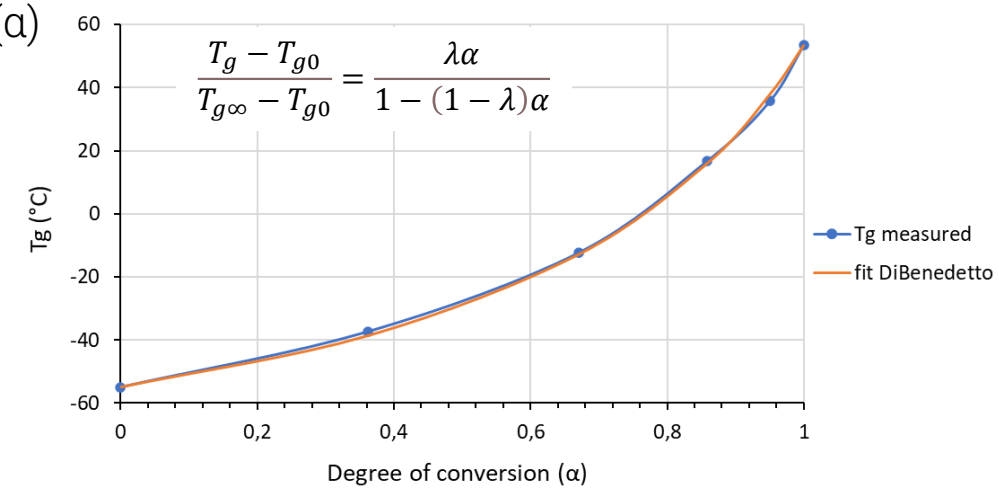

Degree of cure at gelation

- Oscillatory Rheometer (parallel plates) + DSC
- Isothermal runs (between 25°C and 60°C) + Conversion curves
- Specimen uncured
- Criteria: G' and G'' crossover point and tan(δ) = 1
- α at gel point

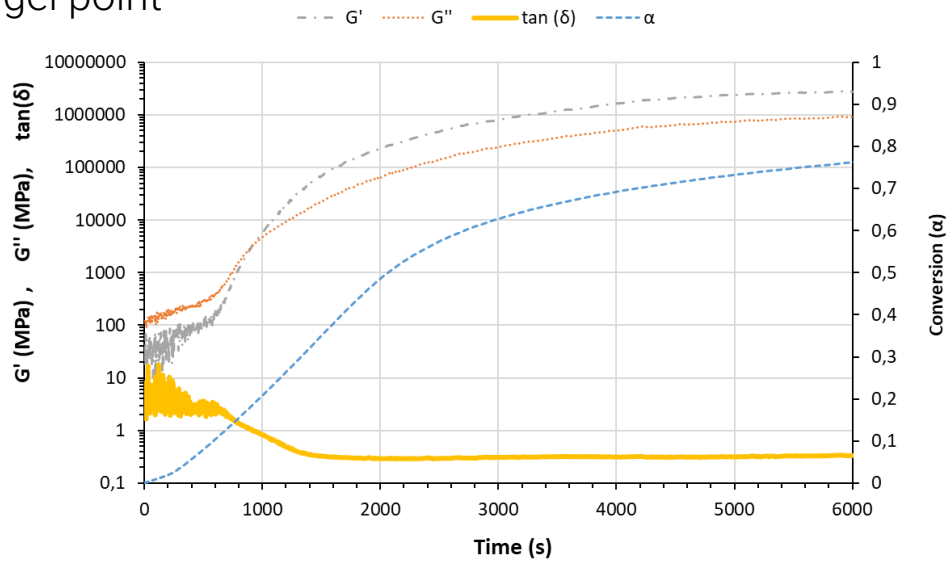

Composite properties characterization

Time – Temperature – Transformation (TTT) Diagram

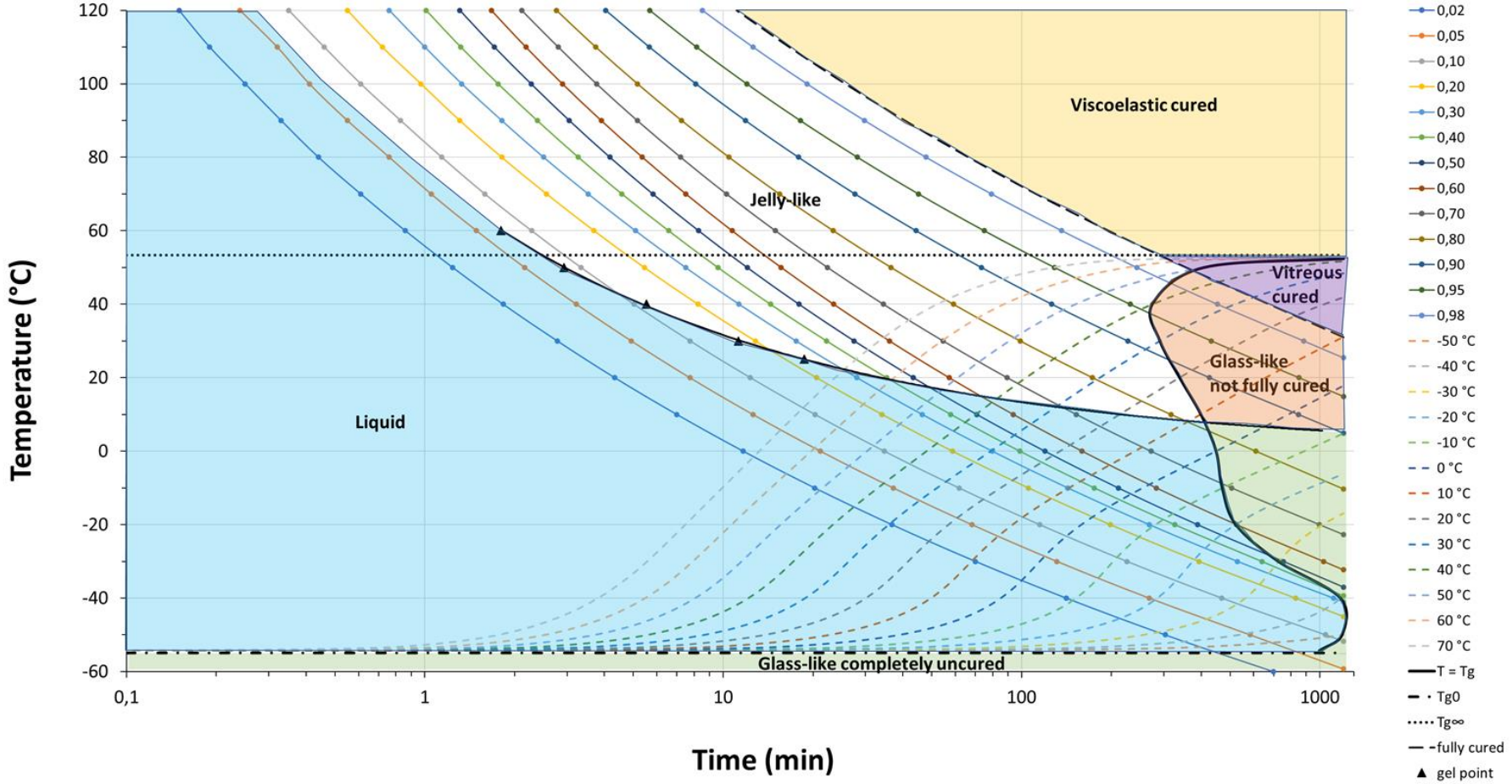

Composite properties characterization

Chemical Shrinkage (CCS)

- Oscillatory Rheometer (parallel plates) + DSC
- Quasi-static isothermal runs (between 25°C and 60°C with 0.0N axial force) + Conversion curves
- Specimen uncured
- ε_V = constant

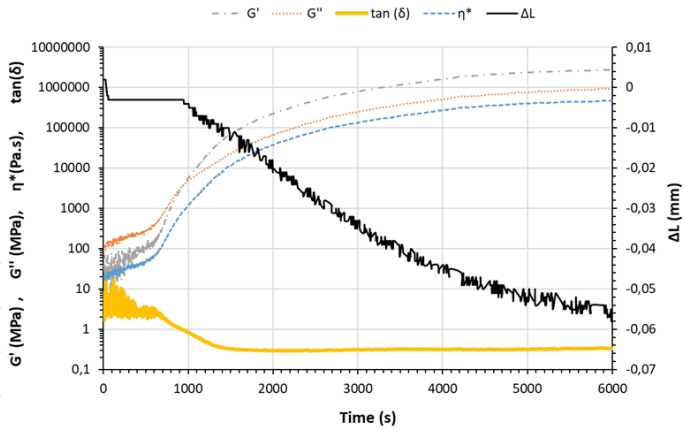

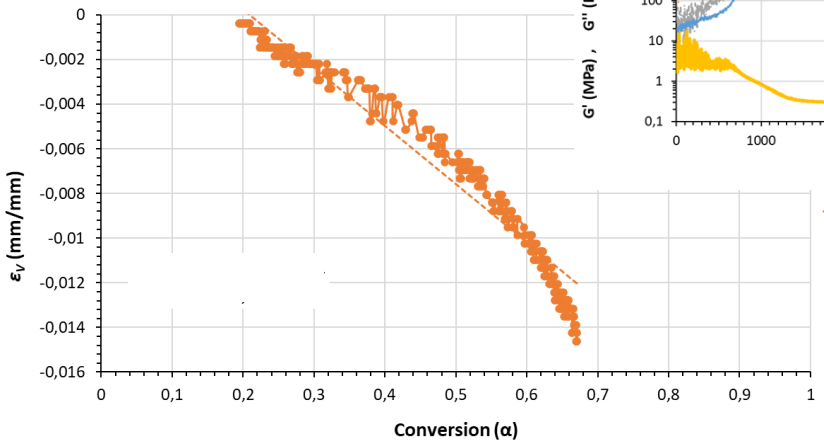

$$+\frac{1}{3}\left(\frac{h-h_0}{h_0}\right)\Big]^3 - 1$$

Thermal Expansion (CTE)

- DMA
- Quasi-static compression mode, dynamic runs (between -10°C and 120°C at 1°C/min, with 0.0N axial force)
- Specimen completely cured
- CTE =

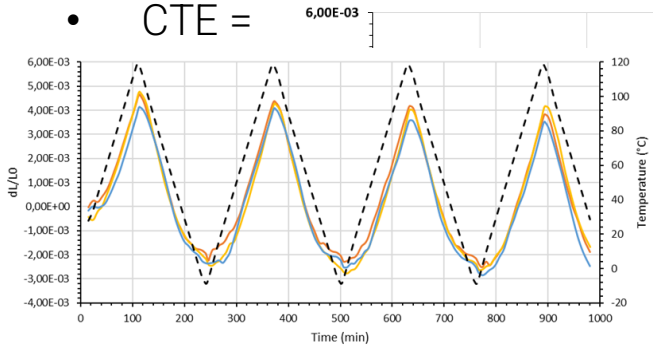

Composite properties characterization

Tensile properties

- Tensile test (ASTM D5083) + strain gauge
- Specimen completely cured
- Young Modulus, Poisson coefficient, tensile strength = f(T)

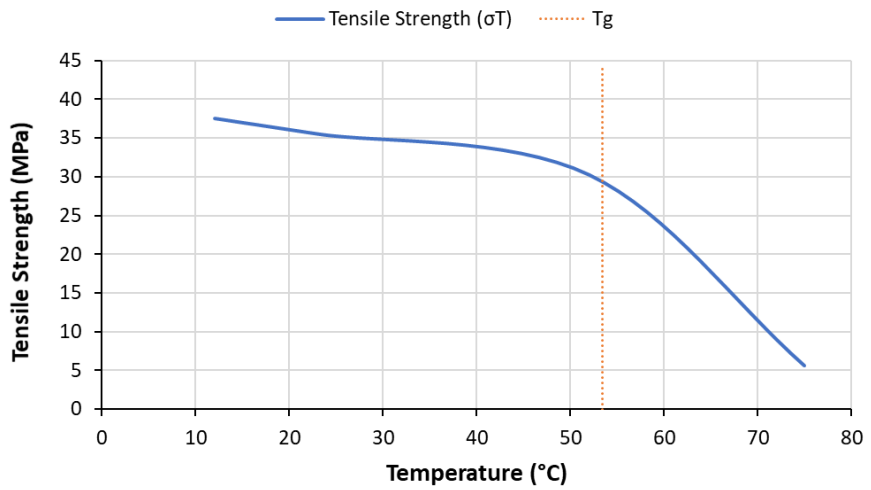

Compression properties

- Compression test (ISO 604)
- Specimen completely cured
- Compression strength = f(T)

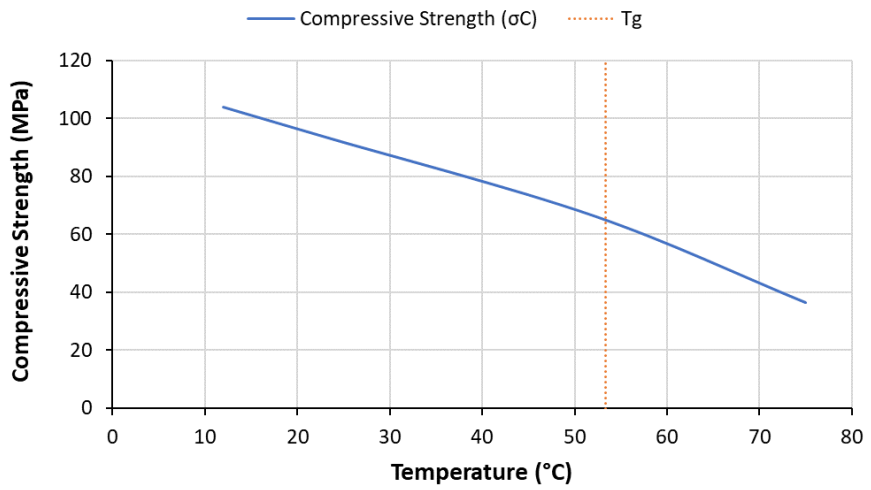

NOTE:

- Standard for sanitary appliances EN 249 requires successive thermal shock cycles of 12°C and 75°C.

Numerical Model

Production cycle

- General production cycle:
  - Casting at room temperature (1)
  - First curing stage (with controlled temperature), up to gel point (before demoulding) (2)
  - Demoulding (3)
    - after 41 min, with rotation of the part and placed on wood like racks
  - Second curing stage with or without post-curing (after demoulding) (4 and/or 5)
- First and second curing stages are varied for optimization

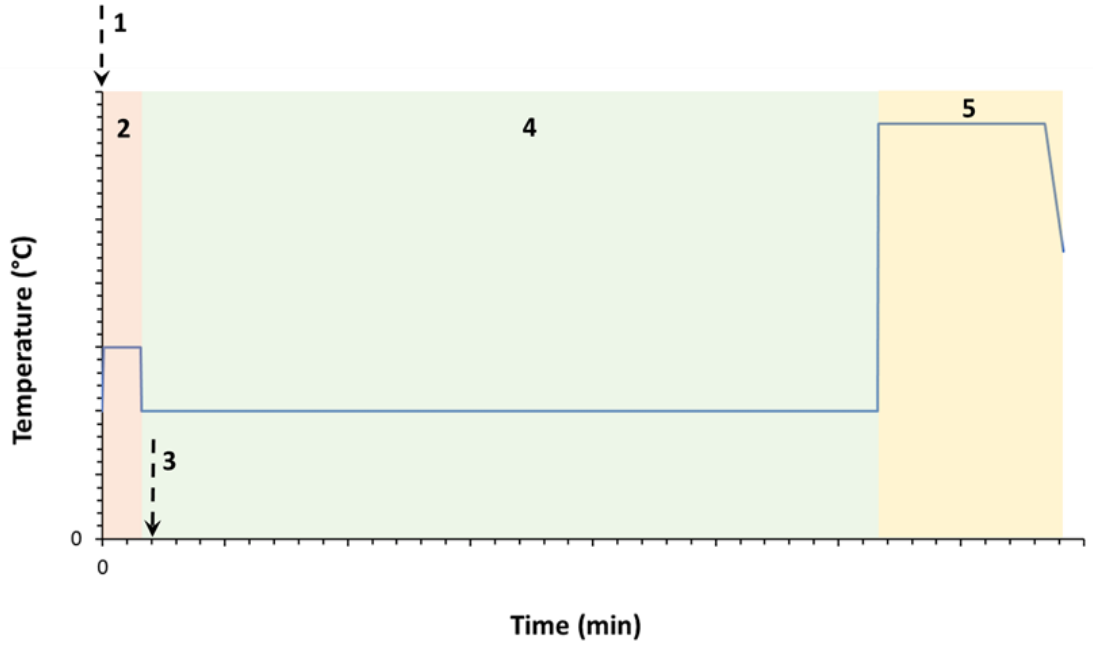

Numerical Model

Boundary Conditions, Assumptions and Mesh

- Cavity of mould completely filled (no voids)
- Initial degree of cure: ≈ 0
- Convection coefficient: 10 W/m^{2}K (free convection of air with velocity ≈ 0 m/s, applied to all surfaces of mould and part exposed to air)
- Thermal condition at Interface: variation of HTC (W/m^{2}K) with temperature:

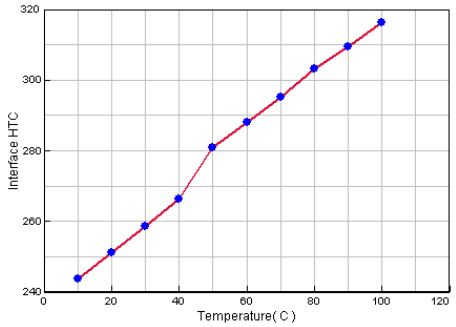

- Temperature cycle applied on surfaces exposed to air

- Initial temperature: 20°C (mould) and 30°C (composite)
- Demoulding at 41 min
- Rotation of the part
- Convection through wood board: 2.5 W/m^{2}K
- Before demoulding Locking condition: contact interface between mould and composite
- After demoulding Locking condition: isostactic (rigid body motion locked)
- Effect of gravity: 9.81 m/s^2

Mesh

- Solid tetra elements
- Part (element size): ≈ 1.5 - 3 mm
- Mould (element size): ≈ 5 mm

Numerical Results

- The location of the maximum residual stress is independent of the production cycle:

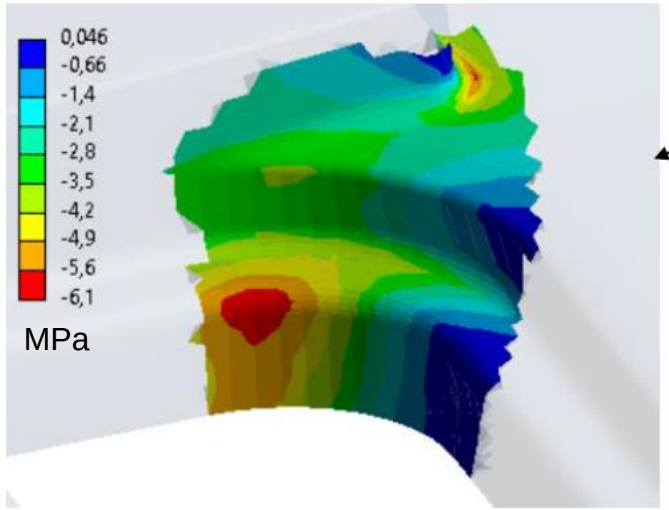

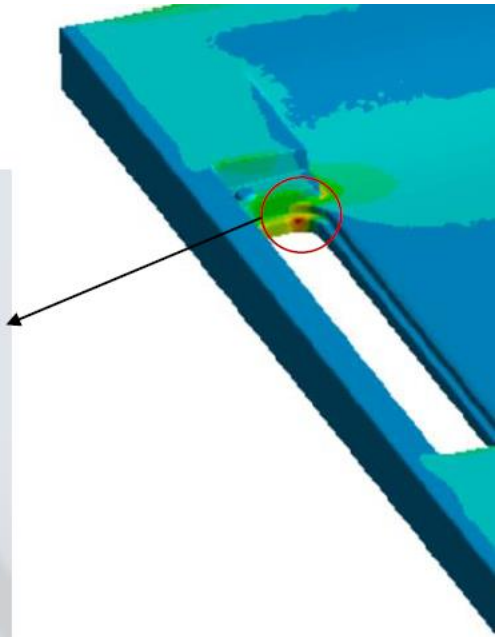

- Monitoring points:

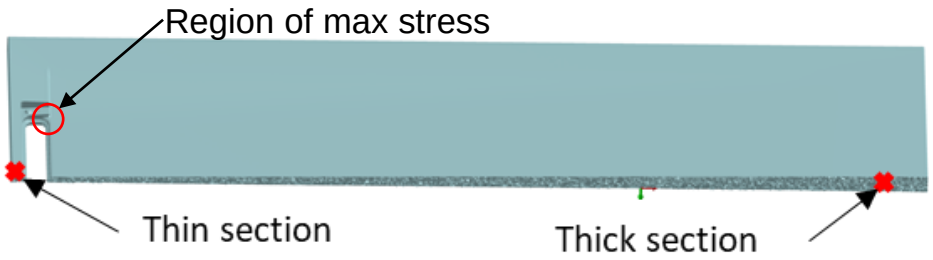

Numerical Results

Scenario: isothermal at 25°C

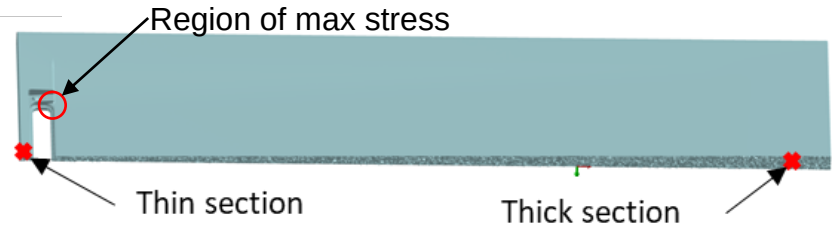

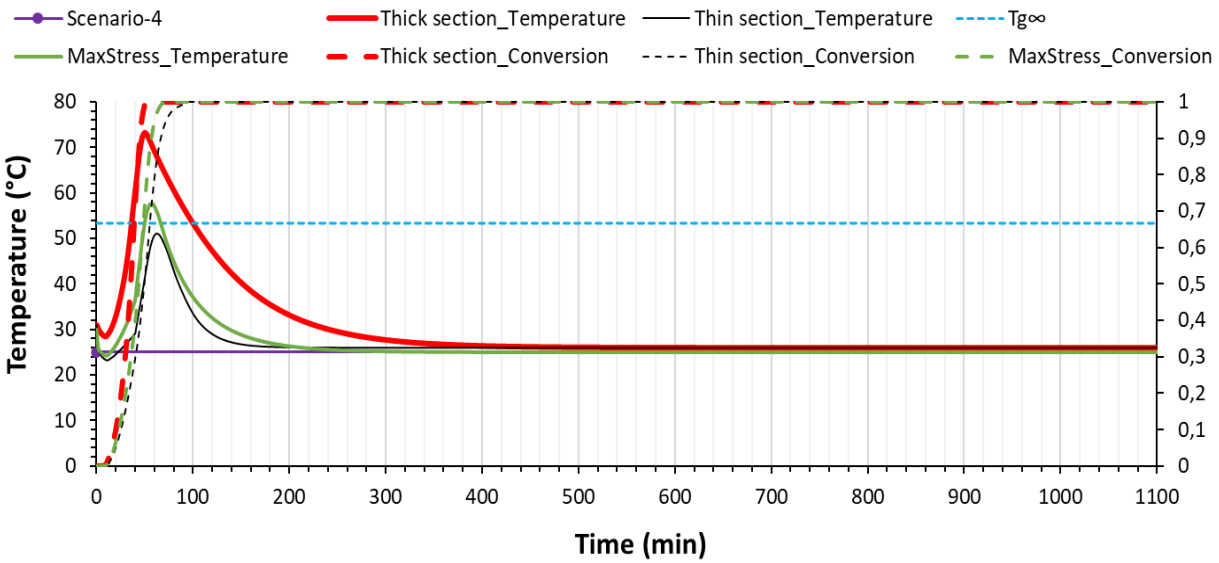

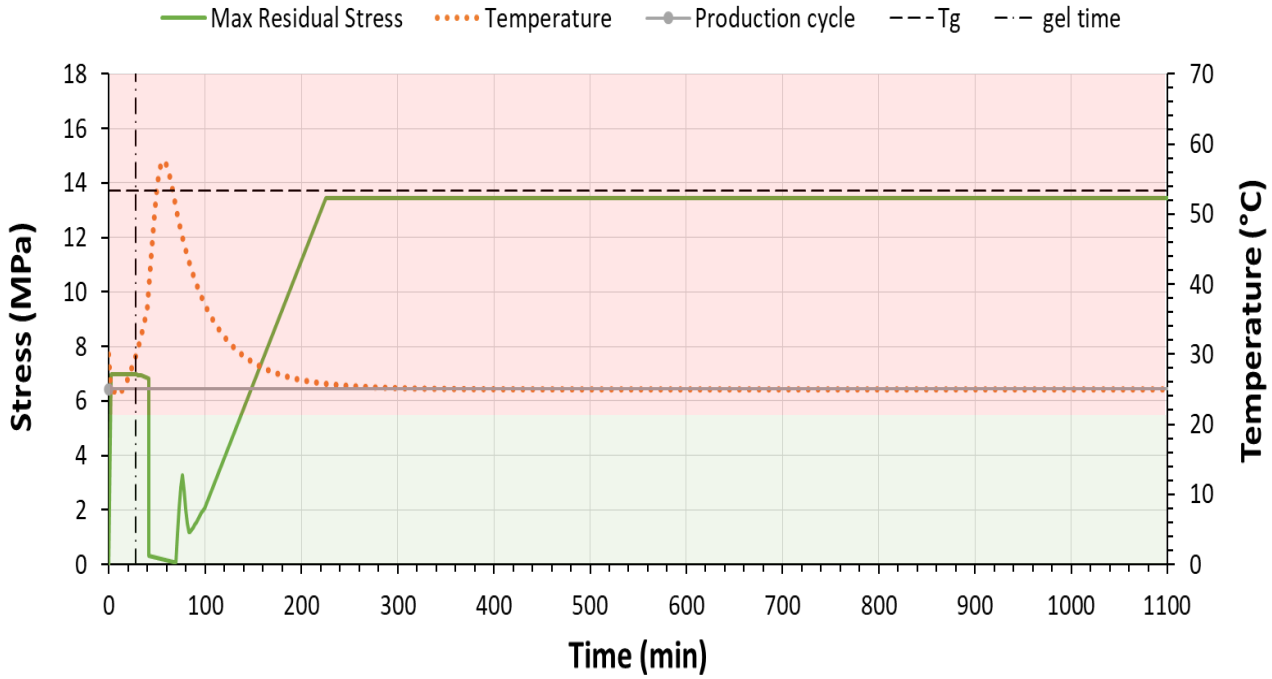

- Fully cured
- Thin section does not reach Tg_{∞}
- High residual maximum stress

Numerical Results

Scenario: isothermal at 25°C with initial heating at 35°C

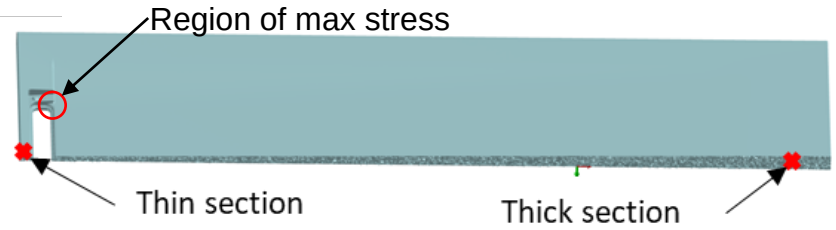

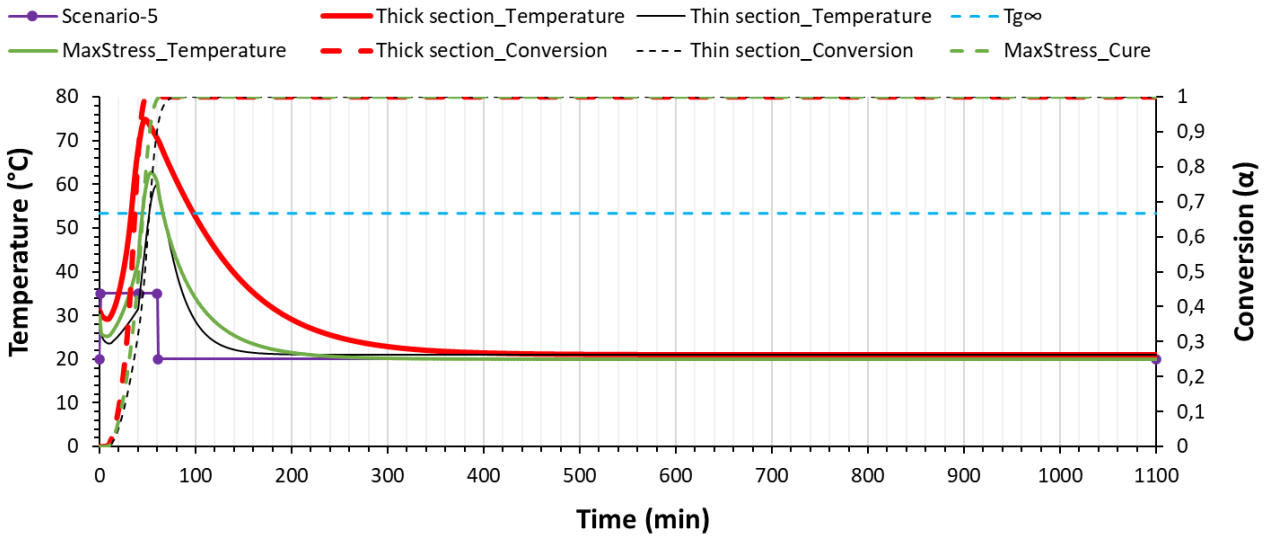

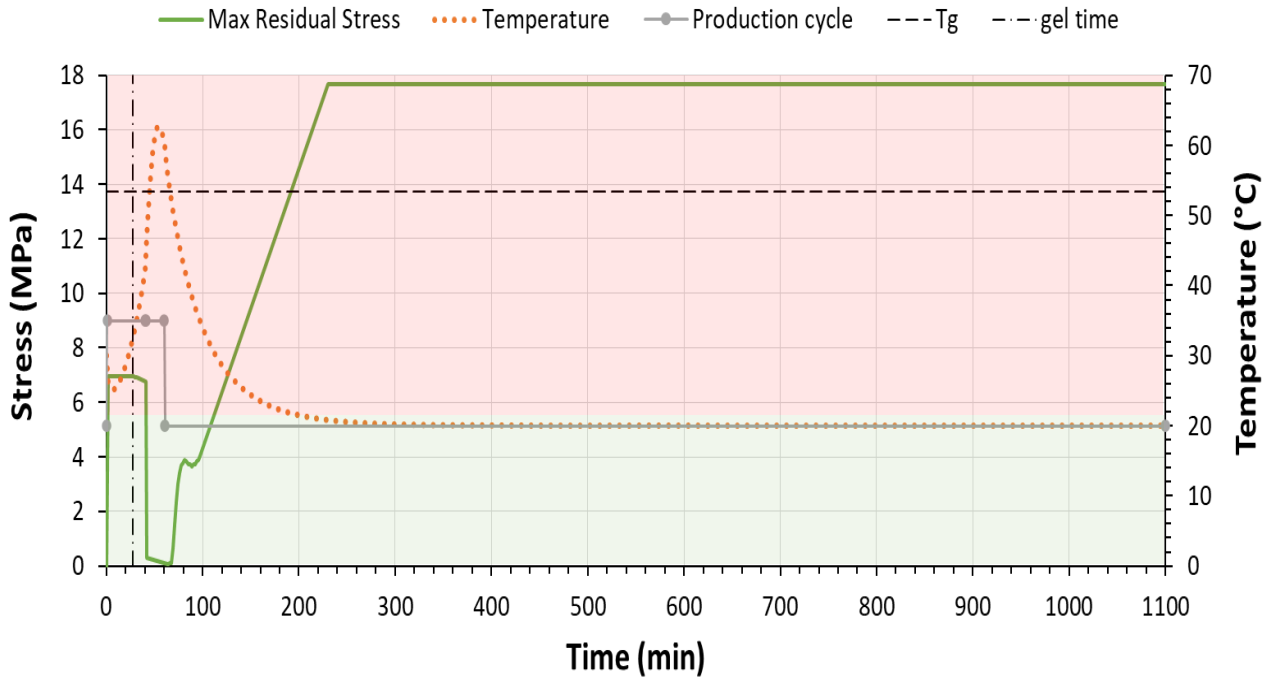

- Fully cured
- Whole part reach Tg_{∞}
- High residual maximum stress
- Initial heating does not improve residual stress

Numerical Results

Scenario: isothermal at 25°C with post-cure

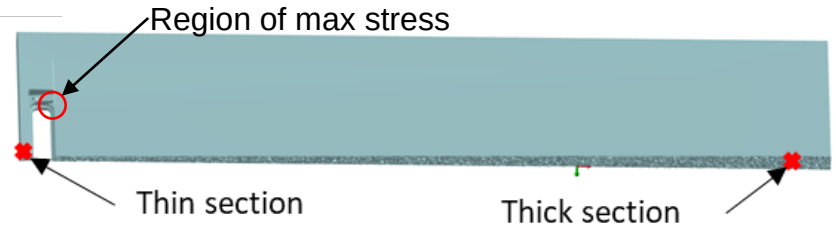

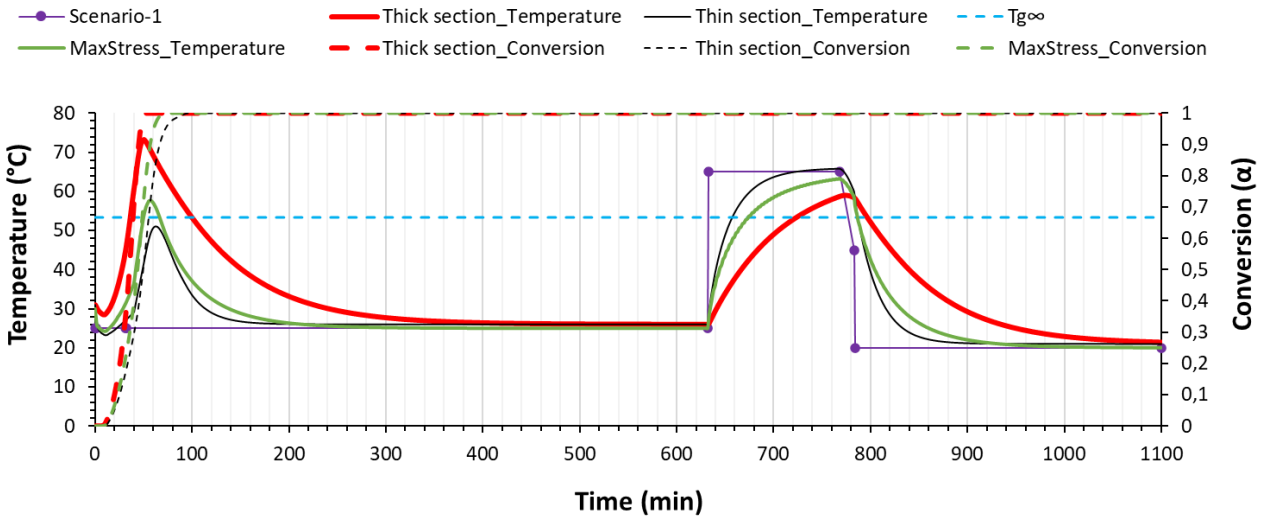

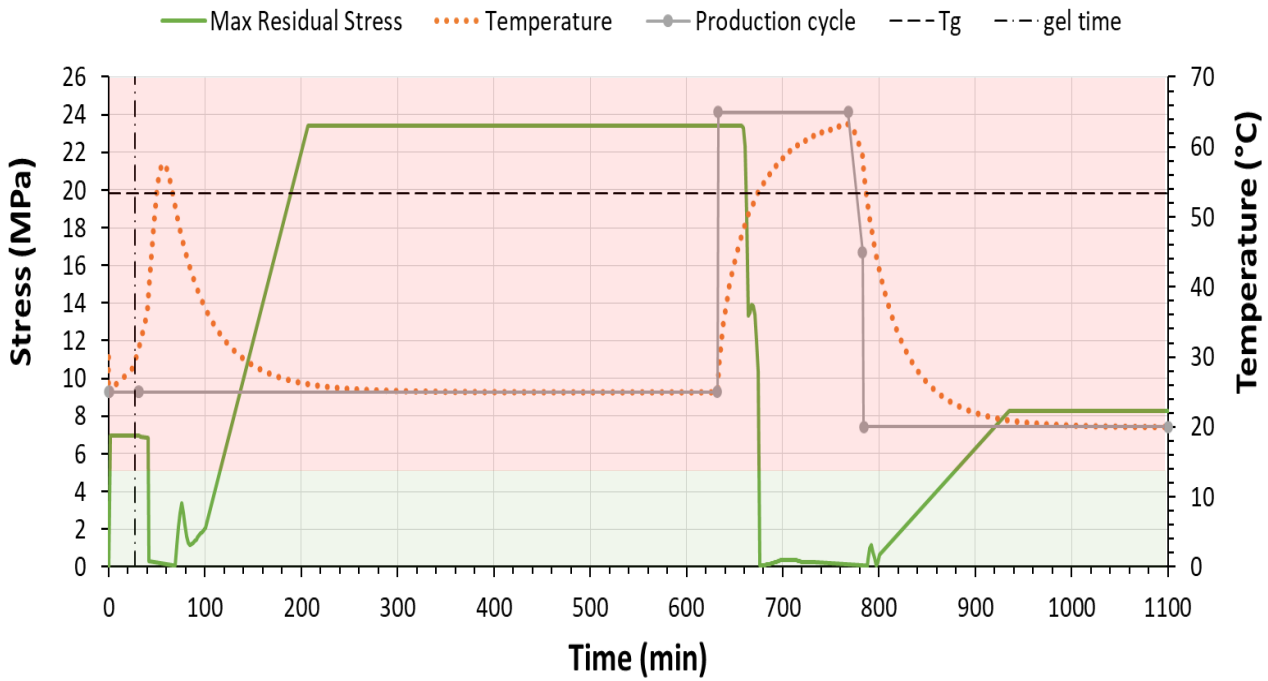

- Fully cured
- Thin section does not reach Tg_{∞} (before post-cure)
- High residual maximum stress
- Post-curing improve residual stress (but not enough)

Numerical Results

Scenario: with post-cure, without resting period

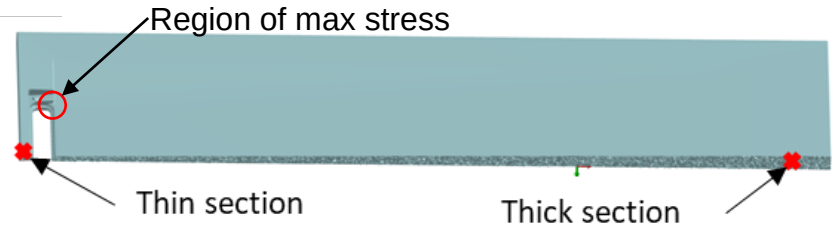

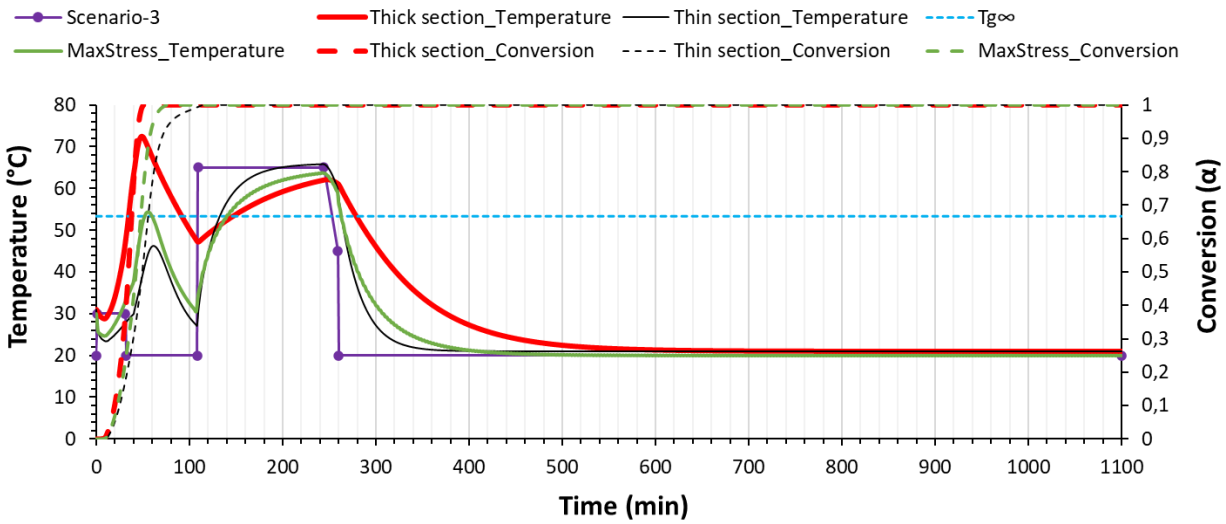

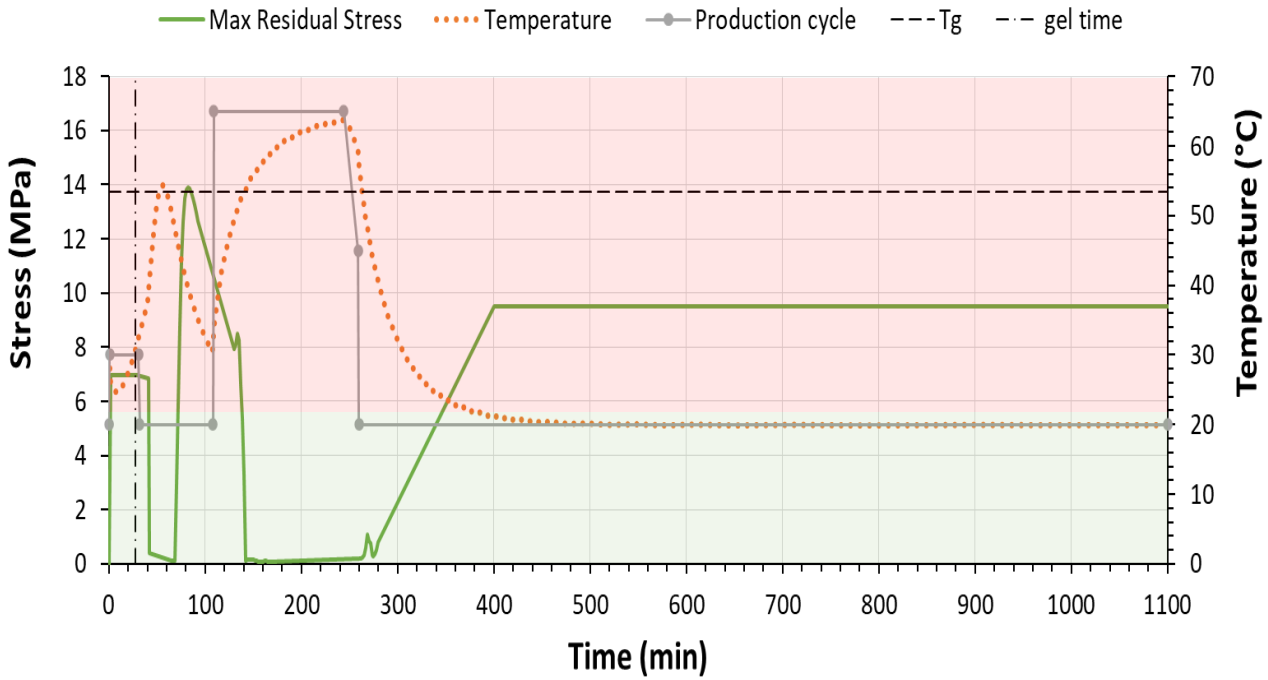

- Fully cured
- Thin section does not reach Tg_{∞} (before post-cure)
- High residual maximum stress
- Eliminating resting period does not improve residual stress

Numerical Results

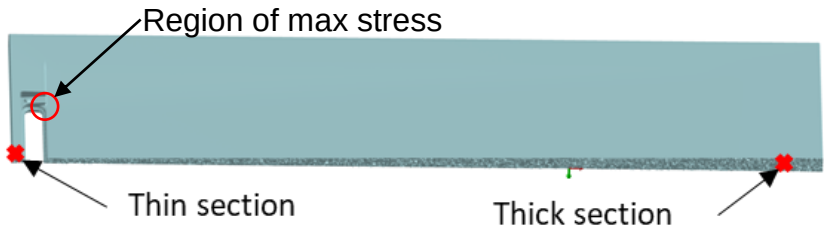

Scenario: with post-cure (extended cooling), without resting period

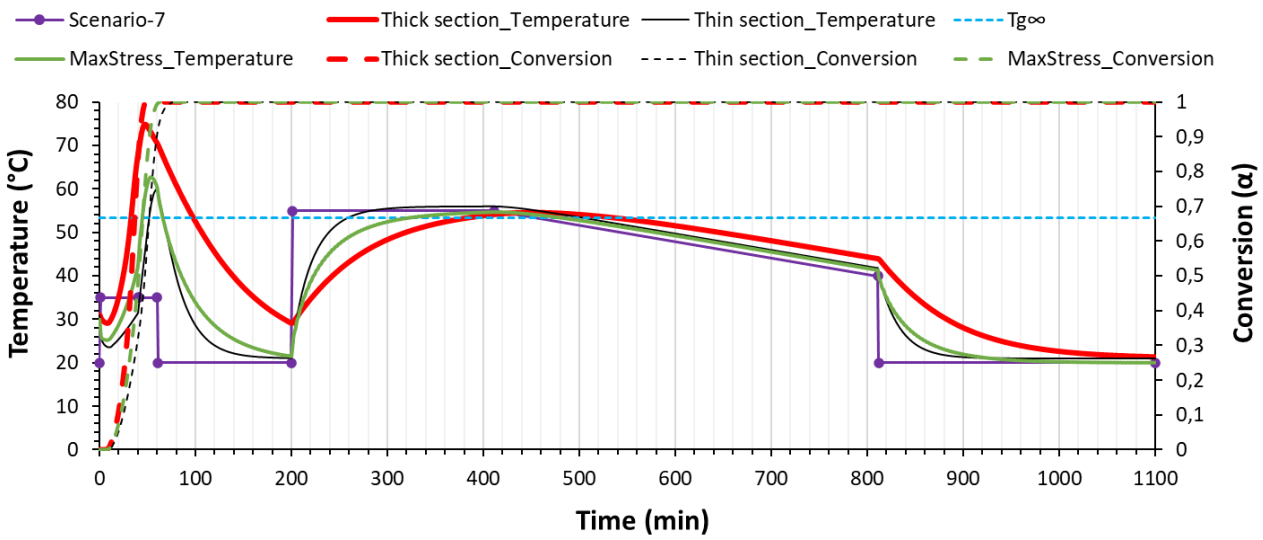

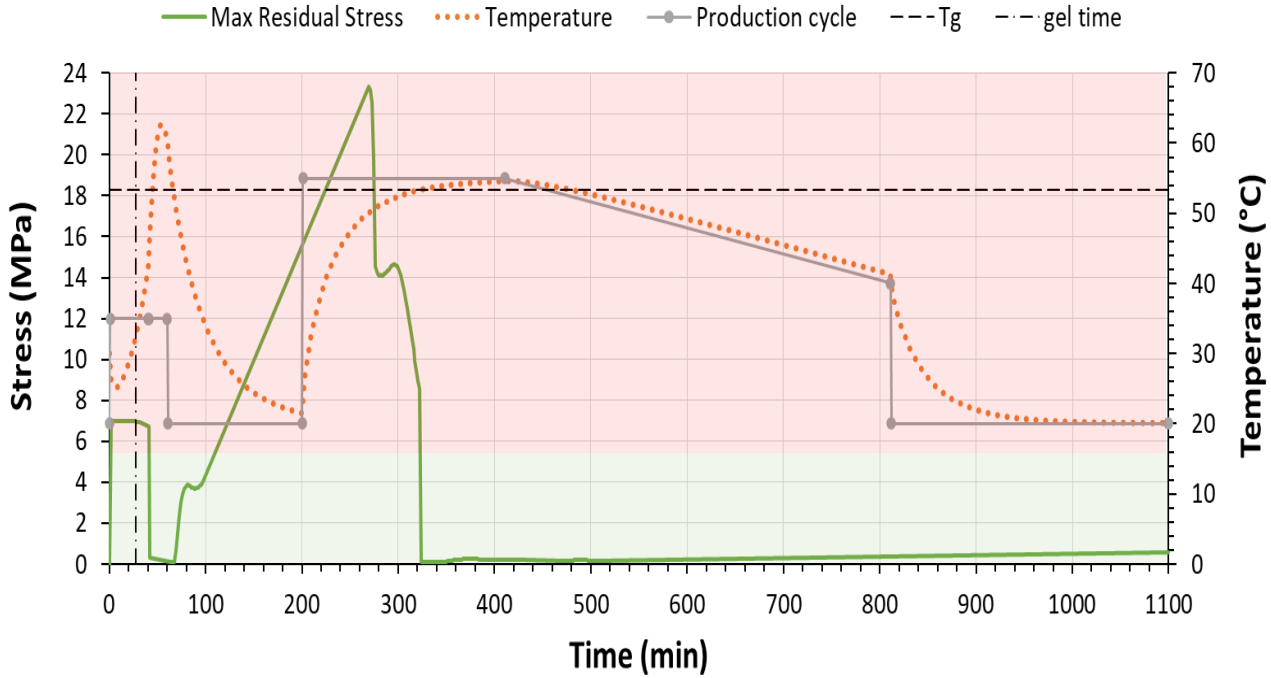

- Fully cured
- Whole part reach Tg_{∞}
- Low residual maximum stress
- Extended cooling improves residual stress

Numerical Results

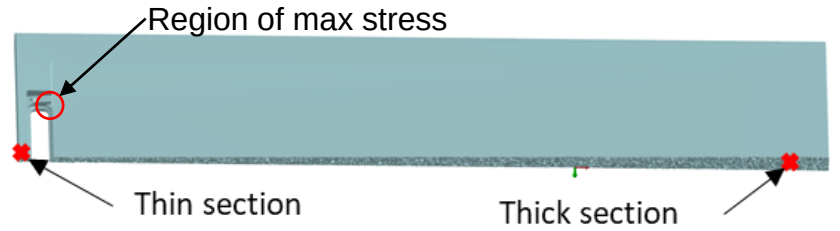

Scenario: cooling control with high initial temperature (>Tg_∞)

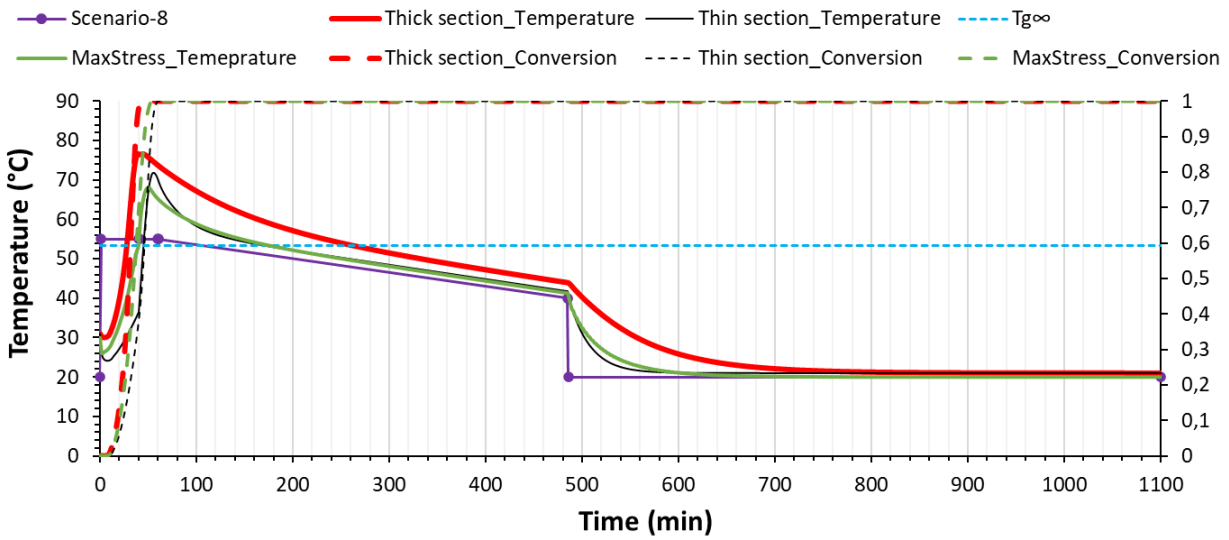

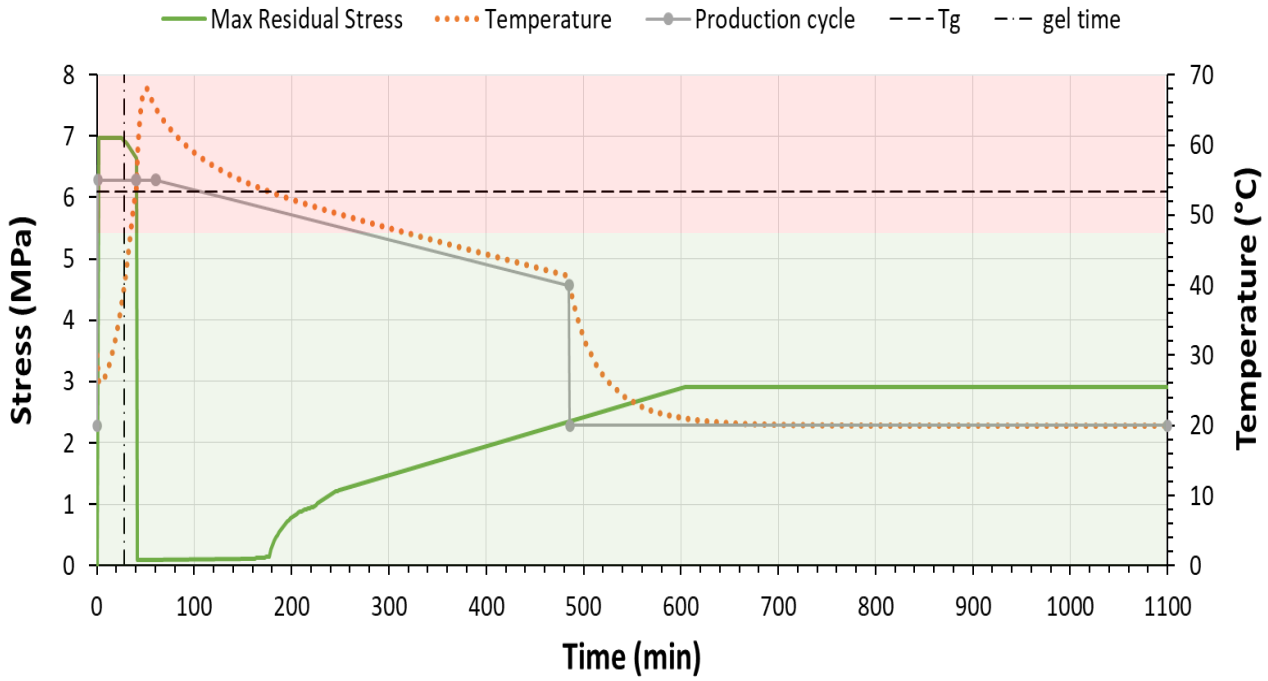

- Fully cured
- Whole part reach Tg_∞
- Low residual maximum stress

Numerical Results

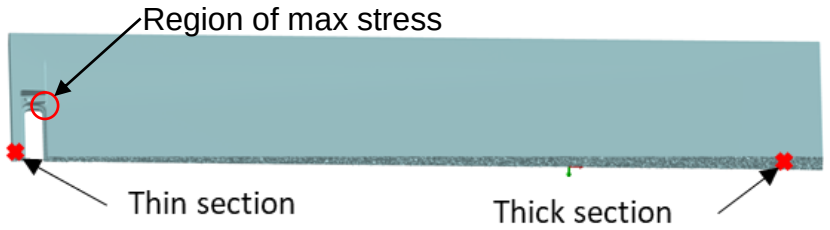

Scenario: with post-cure (cooling control), with low initial temperature (25°C)

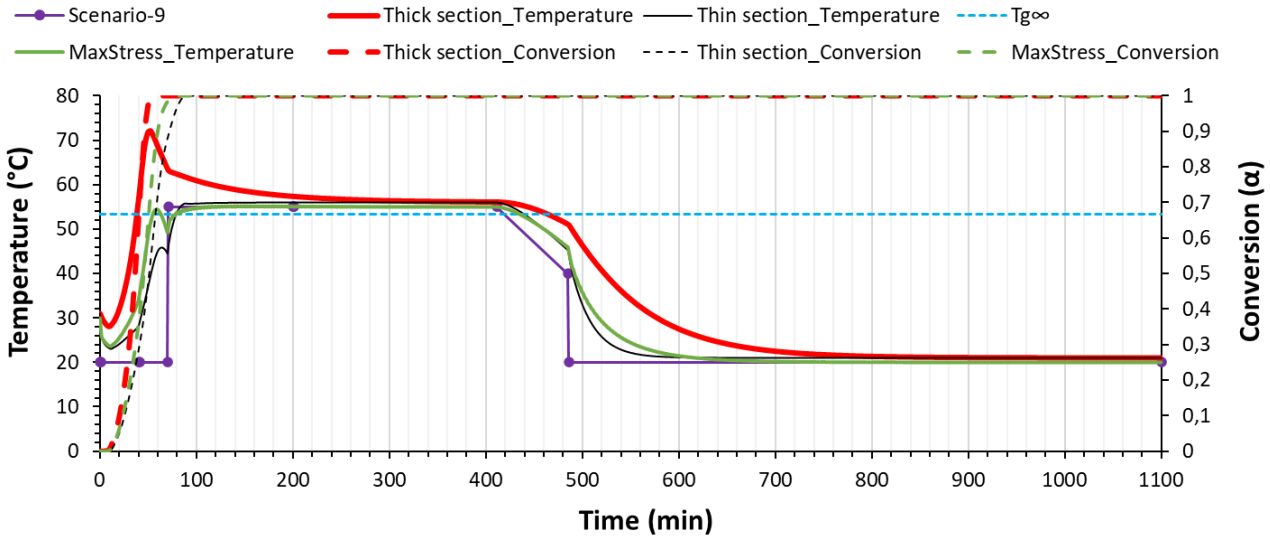

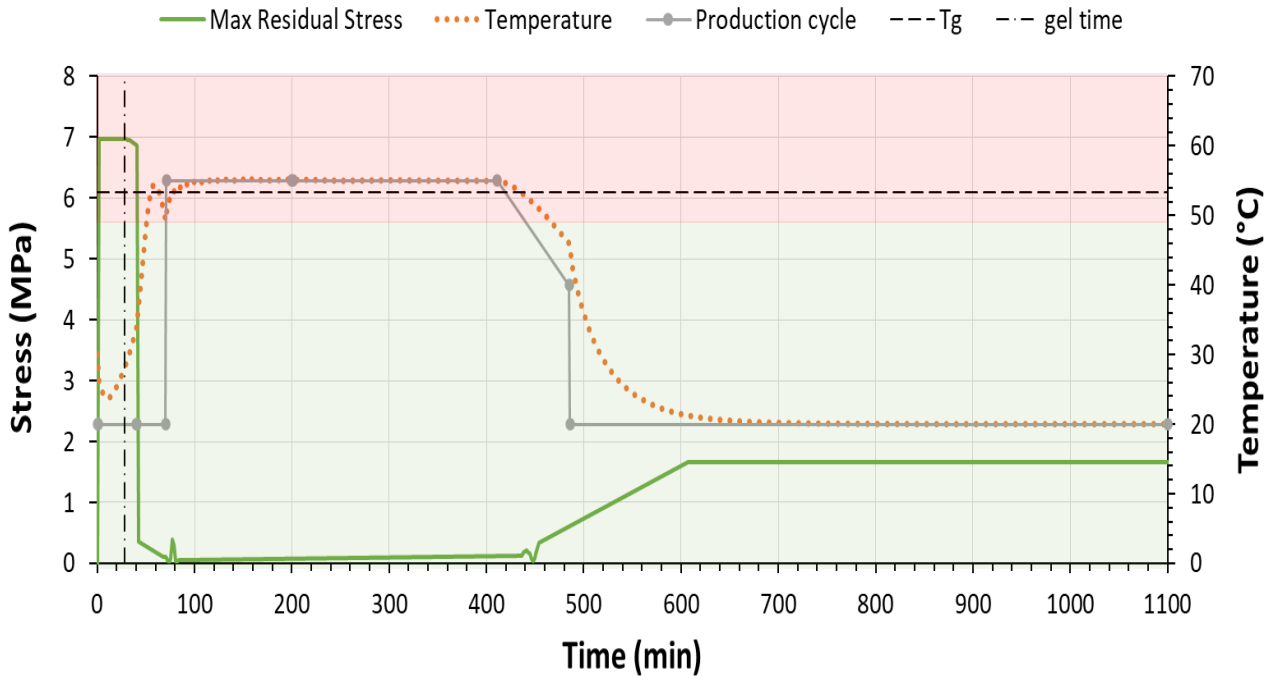

- Fully cured
- Thin section does not reach Tg_{∞} (before post-cure)
- Low residual maximum stress

Conclusions

- Independently on the production cycle, cure is completed within 60 min, due to the heat generated by the exothermic curing reaction.
- The Tg_{∞} is only guaranteed if heating is added to the production cycle
- The magnitude of the maximum residual stress depends considerably on the thermal conditions of the production cycle.
- Post-cure, resting period and/or initial heating can be eliminated from the production cycle if:
  - Cooling is controlled
  - The Tg_{∞} is reached in the whole part



Thank you!

Questions?

(351) 253 510 075

joana.malheiro@piep.pt

www.piep.pt

PIEP - Pólo de Inovação em Engenharia de Polímeros,
Universidade do Minho, Campus de Azurém, Edifício 15
4800-058 Guimarães, Portugal

Follow us

VACUUM ASSISTED TECHNIQUES FOR IMPROVED REPAIR PERFORMANCE IN LEGACY FIBRE-REINFORCED COMPOSITES

James A. Quinn, Nick Orde, Calum J.A. Taylor, Darshana Rathnayaka Mudiyanseladge, Jasotharan Sriharan, Dilum Fernando and Edward D. McCarthy

School of Engineering, Institute for Materials and Processes
& Institute for Infrastructure and Environment,
The University of Edinburgh, UK

Keywords: Polymer-matrix composites (PMCs), Mechanical properties, Mechanical testing, Lay-up (manual/automated), Resin transfer moulding (RTM)

ABSTRACT

Some large fibre reinforced polymer (FRP) marine structures—such as the U.K.'s mine countermeasures vessels—were designed decades ago. Of these early designs, some entered production, and have been in regular service for many years. When compared to modern FRP structures, the sparsity of literature available for legacy structures means they often constitute an asset maintenance dilemma. In these contexts, certain repair variables are often fixed according to the original design and are not possible to change easily. Examples could include the materials used in the repair and laminate structure. This paper presents a study aimed at improving the effectiveness of repairs on these legacy marine FRPs by using vacuum assistance to produce higher quality repairs, without changing the materials used in, or the design of, the repairs. First, the relationship between consolidation pressure applied to a wet lay-up repair and the repair's performance, was investigated. Thereafter, a vacuum-assisted resin infusion process replaced the wet lay-up, to demonstrate further improvements in repair performance. Both of these improvements are based on the repair procedures, and are readily implementable within the asset maintenance programs of in-service legacy marine FRP structures. Extending the life of these structures by means of improved repair practices like these would mitigate their environmental impact by reducing unnecessary structure downtime and premature decommissioning, especially where end-of-life disposal processes are limited and environmentally harmful.

1 INTRODUCTION

Fibre Reinforced Polymer (FRP) composites have been widely adopted across a range of applications, with marine structures among the earliest large-scale implementations. Notably, the United Kingdom's mine countermeasures vessels (MCMVs), introduced in the latter half of the twentieth century, represent significant examples of early FRP structural use. These vessels—many of which remain in service—pose a number of challenges with respect to maintenance. For example, the original materials and lay-up configurations are typically fixed, limiting how current repair techniques may be enhanced or adapted.

The broader field of FRP repair has advanced considerably in recent decades, particularly with respect to aerospace applications, where the drive for high performance has led to increasingly sophisticated repair methodologies [1]. Within the marine domain, however, repairs are often carried out under less controlled conditions, and the dominant technique—manual wet lay-up—remains heavily dependent on operator experience. This introduces variability in the quality of repairs, particularly in relation to void content, resin distribution, and fibre alignment, all of which can significantly influence structural performance [2]. In the context of legacy marine composites, there remains a clear need for repair strategies that are both robust and compatible with existing material systems.

Scarf repair continues to be the preferred method for repairing damage on composite structures in the marine industry, primarily due to its capacity to recover in-plane load-bearing capacity when appropriately executed [3]. There are a number of different factors that affect the quality of scarf repair,

and in the following section brief accounts of parameters such as taper angle, surface preparation, and ply sequencing are provided.

The scarf or taper angle θ_{SC} is defined as the angle between the surface of the repaired laminate and the inclined plane of the bond line formed between the original material and the repair patch. Mathematically, the scarf angle is expressed in degrees, though it is commonly referenced via the taper ratio—defined as the length of the taper divided by the thickness of the laminate. Composite repair handbooks often recommend a tapered slope between 20:1 and 50:1 [4][5] although practically on ships this is not always possible and ratios of 12:1 are considered acceptable with $\theta sc < 5°$ [3]. Optimisation studies on how taper angle affects peak stresses on 8 ply thick fibre composite, have been done by Bendemra and Compston [8], with taper angles ranging from 3°to 12°. They found peak stresses increased exponentially with scarf angle, with a greater stress increase from a scarf angle of going from 8° to 12° than with an increase from 3° to 5°. A study by Ahn and Springer [5] found that increasing the scarf angle from 0.5° to 2.5° decreased the failure load although only minimally concluding scarf angle becomes increasingly relevant at larger taper angles.

To ensure a good quality bond between the old fibres and the new, surface contaminants should be reduced to a minimum. This is recommended to be achieved with the use of a solvent, often acetone [3]. Sanding is recommended to roughen up the surface abrading it and improving bond strength. Ahn and Springer [5] tested how failure load varies on a scarf repair with different grit numbers on a diamond sander. It was found that changing the grit number had a negligible effect on failure load concluding that a grit of 100 would be reasonable for scarf repair.

There are two ply sequencing techniques used in scarf repair. The first technique is to lay the smallest patch down first and increase in size towards the repair surface. The second is to start with the largest patch and decrease in size. Among marine FRP operators, The National Maritime Centre, have reported the former method produces a relatively weak resin rich layer at the surface of the repair and recommend the latter technique of placing the largest ply first [6]. Additionally, the former technique has been reported to produce weaker points of increased stress at the end of each ply, where cracks would often propagate from [3].

Adding additional layers of laminate to the repair surface, overlapping at the edge of the repair to bond to the original material has been found by Ahn and Springer [5] to increase failure load, for example, the addition of two external plies increased failure load by approximately 50%. Similar results were reported by Myhre and Beck [7]. Research into the effect of the over-ply lap length (i.e., how far the external ply extends over the repair region) was done by Bendemra and Compston [8], concluding that peak peel stress was significantly reduced by inclusion of over-plies, and identifying a critical lap length of 5 mm.

Recent work has highlighted the potential for process-level improvements—rather than material substitution—to deliver tangible gains in repair quality. In particular, vacuum-assisted techniques have shown promise in improving consolidation and reducing void formation in manually applied repairs. These approaches are especially attractive in the context of legacy FRP structures, where the scope for altering material or geometric parameters is limited.

This paper presents an investigation into the potential for improving repair performance in legacy FRP marine structures by refining the repair process itself. The study first examines the influence of consolidation pressure in traditional wet lay-up repairs and subsequently explores the application of a vacuum-assisted resin infusion method. Both approaches were designed to be compatible with the constraints typical of legacy vessel maintenance, requiring no change to material systems or laminate design. The findings contribute to ongoing efforts to support the long-term serviceability of FRP marine assets, while aligning with broader objectives around sustainability and responsible lifecycle management in composite structures.

2 METHODOLOGIES

2.1 Manufacturing original laminates

The material system and manufacturing methods were selected to represent that of typical marine composite structures. Crystic 701PAX isophthalic polyester resin and (2% by volume) Butanox M50 methyl ethyl ketone peroxide crosslinking initiator, were combined and subsequently impregnated by

hand into the reinforcing fibres. The reinforcement was Scott & Fyfe "Polyform WR" 800 g m−2 plain woven glass mat. For all original (reference and pre-repair) laminates the lay-up recipe was $[0_8]_T$. The curing cycle was 24 h at room temperature (20°C) in a closed mould process with no additional environmental control or post-curing steps.

2.2 Scarf repair design

To evaluate different repair methods, a single-sided surface-to-midplane scarf repair was designed (Fig. 1). This simulates a typical repair process that is often followed for damage that extends not further than the laminate midplane. For this type of damage, the repair is usually conducted exclusively from one side of the structure. Herein, material was removed from one surface of the laminate in a stepped pattern until the laminate midplane was reached. Thereafter, the stepped patterns were graded to create scarf angles of 5°. Dry fibre plies of the same reinforcement were cut to match the quantity and dimensions of the removed plies. These repair plies were laid up monolithically according to the direction of the parent laminate. For wet lay-up cases, the repair plies were impregnated by hand using brushes and rollers, in a ply-by-ply manner. For vacuum infusion methods, repair plies were laid up dry, and resin injected into the scarf repair zone using the parent laminate as a mould base. In all cases, one additional surface ply was applied with over-ply areas bonded to the surface of the original laminate on each side of the repair.

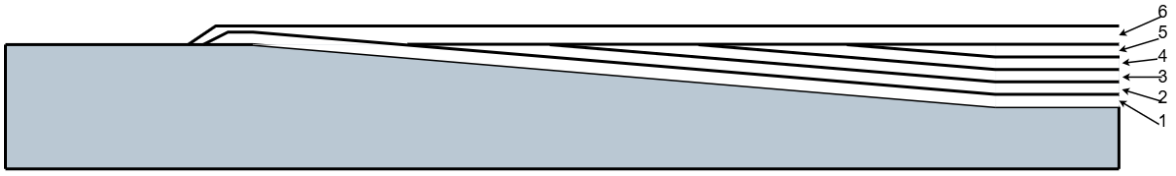

Figure. 1: Ply arrangement in laminate repair patch.

2.3 Improved repair part 1: consolidation pressure

In initial investigations, repair plies were exclusively impregnated by manual wet lay-up. Four original laminates were manufactured according to Section 2.1: one reference laminate and four test case laminates. The test case laminates were scarfed and repaired according to Section 2.2. All scarf repairs were cured for 24 h at room temperature (20°C) in a closed-mould process using a Radius 70T platen press machine with no additional environmental control or post-curing steps. To investigate the influence of pressure applied during consolidation, each scarf repair was cured at a unique value of consolidation pressure. The four values of consolidation pressure were 0 kPa, 100 kPa, 300 kPa, and 600 kPa.

2.4 Improved repair part 2: impregnation method

In a subsequent investigation, repair plies were impregnated by two methods: 1) manual wet lay-up and 2) vacuum resin infusion. Two original laminates were manufactured according to Section 2.1. Both laminates were scarfed according to Section 2.3. The first laminate was repaired in a wet lay-up process at 1 bar of applied pressure, whilst the second laminate was repaired using vacuum resin infusion to wet out the repair plies. Both scarf repairs were cured for 24 h at room temperature (20°C) with no additional environmental control or post-curing steps.

2.5 Data acquisition

2.5.2 Flexure

Five specimens per case were tested in accordance with BS EN ISO 14125 [9]. Specimens were loaded in crosshead displacement-controlled flexure at a constant rate of 4.5 mm min^{-1}, using an Instron 3369 with a 10 kN load cell and Wyoming Test Fixtures Four-Point Flexure Test Fixture (Fig. 2a). An MTS AVX04 video extensometer package was used to capture specimen central displacement data at a sampling rate of 10.02 ± 0.02 Hz. Average specimen widths and thicknesses were calculated from vernier calliper measurements taken at three locations, before a speckle pattern was applied to the central

20 mm of the specimen side (through thickness) facing the camera. Specimens were placed centrally on the (5 mm diameter) support rollers with the loading axis being normal to the long edge of the specimen. Tests were concluded at ultimate failure of the specimens, defined as an instantaneous stress drop exceeding 50% of the preceding measured value.

The nominal flexural stress observed in the specimen outer surface at specimen mid-span, is denoted σ_f and is defined in Equation 1 where P is the load measured, L is the specimen span (defined in the standard as (16.5×h), b is the specimen width, h is the specimen thickness. Flexural strain in the specimen outer surface at specimen mid-span, is denoted ε_f , and is defined in Equation 2 where: s is the deflection of the mid-span of the specimen under load, h is the specimen thickness, L is the specimen span (defined in the standard as 16.5h). Flexural strength, σ_{fM}, is defined as the first local maximum flexural stress observed. Flexural modulus, E_f , is defined as the initial slope of the flexural stress-strain curve, for the region $0.05\% \leq \varepsilon_f \leq 0.25\%$ (Equation 3) where ΔF is the difference in loads corresponding to deflections s'' and s', Δs is the difference in mid-span deflections (s'' and s') corresponding to flexural strains 0.25% and 0.05%, respectively.

$$\sigma_f = {PL}/{bh^2} \tag{1}$$

$$\varepsilon_f = {4.7\mathrm{sh}}/{L^2} \tag{2}$$

$$E_f = \frac{0.21L^3}{bh^3}\left(\frac{\Delta F}{\Delta s}\right) \tag{3}$$

2.5.1 In-plane shear

Five specimens per case were tested in accordance with ASTM D3518 [10]. Specimens were loaded in crosshead displacement-controlled tension at a constant rate of 2 mm min^{-1} using an MTS Criterion C45.305 (Fig. 2b) fitted with a 250 kN load cell and hydraulic wedge grips. An MTS AVX04 video extensometer package was used to capture strain data at a sampling rate of 10.02 ± 0.02 Hz. Average specimen widths and thicknesses were calculated from vernier calliper measurements taken at three locations, before a speckle pattern was applied to 50 mm of the central gauge region. Specimens were clamped in the crosshead grips with 100 kPa clamping pressure applied evenly to the entire grip region. The loading axis was parallel to the long edge of the ± 45° specimen. Tests were concluded at ultimate failure of the specimens, defined as an instantaneous stress drop exceeding 90% of the preceding measured value.

In-plane shear stress observed within the gauge region—parallel to the xy plane—is denoted τ_{xy}, and is defined in Equation 4, where P_x is the load measured and A is the original specimen cross-sectional area, as measured before the test. Shear strain observed—in the direction of the loading axis—is denoted γ_{xy}, and is defined in Equation 5, where Δl_x is the linear displacement of two targeted observation zones within the specimen gauge region, l_x is the original linear separation of the two target observation zones, as measured before the test. In plane shear strength, τ_{xyM}, is defined as the shear stress observed at γ_{xy} = 5.0%. In plane shear modulus—in the direction of the loading axis—, G_{xy}, is defined as the initial slope of the shear stress-strain curve, for the region $0.05\% \leq \gamma_{xy} \leq 0.25\%$ (Equation 6), where τ''_{xy} is the stress measured at γ_{xy} = 0.25%, τ'_{xy} is the stress measured at γ_{xy} = 0.05%, γ'_{xy} = 0.05%, γ''_{xy} = 0.25%.

$$\tau_{xy} = {P_x}/{2A} \tag{4}$$

$$\gamma_{xy} = {\Delta l_x}/{l_x} \tag{5}$$

$$G_{xy} = \frac{\tau''_{xy} - \tau'_{xy}}{\gamma''_{xy} - \gamma'_{xy}} \tag{6}$$

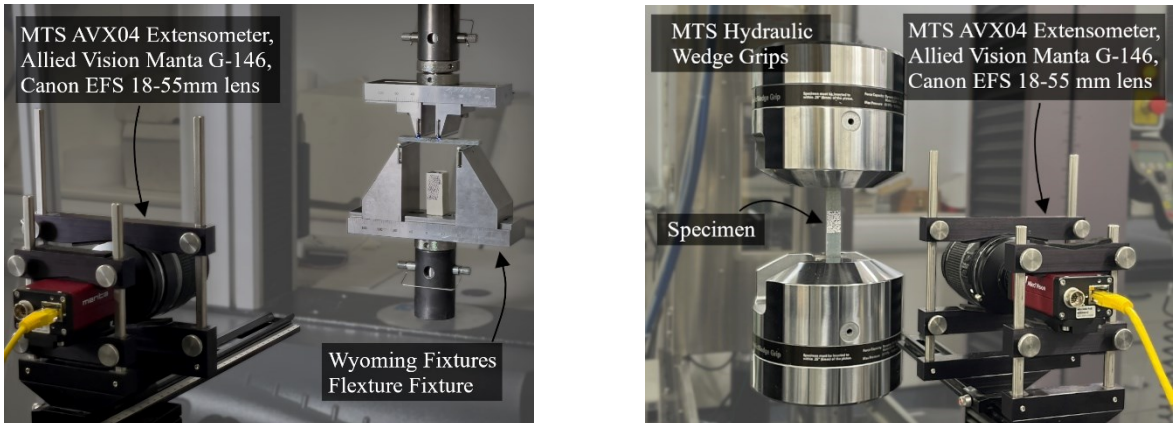

(a) (b)

Figure. 2. Standardized experimental test setups: (a) flexure, (b) in-plane shear.

2.5.3 Density and fibre volume fraction

Density determination was completed using an Ohaus Adventurer AX324 analytical balance paired with an Ohaus density determination kit, which exploits Archimedes' principle by comparison of dry mass, A, to that observed when the specimen is submerged in a known liquid, B—shown in Equation 7, where ρ_C is the density of the specimen, ρ_O is the density of the liquid—in this case, distilled water; 0.998 g cm^{-3} at 20°C—and ρ_L is the air density (0.0012 g cm^{-3}). For each test case, five extractions of approximately 100 mm^2 were cut from random locations in the respective plates using a diamond bladed wet saw. Specimen conditioning before and after submersion was completed in a Prolan environmental chamber in accordance with ISO 185 291:2008 [11]. FVFs, V_r were measured through a pyrolysis/burn-off approach—as specified in ASTM D3171-22 Method I [12]—using a Nabertherm L15/11 muffle furnace and Haldenwanger porcelain crucibles with lids. The expression shown in Equation 8 was used to calculate the FVF where Mr is the mass of reinforcement remaining in the crucible at completion of the pyrolysis. One additional crucible containing traveller fibres verified that fibre mass-loss through the pyrolysis process was negligible. The pyrolysis cycle was determined using thermal degradation data acquired from Thermogravimetric Analysis of the same cured isophthalic polyester resin (2% hardener). The pyrolysis cycle began with a chamber ramp rate of 10°C min^{-1} from ambient temperature to a maximum temperature of 600°C. This maximum temperature was sustained for 6 hours to ensure full burn-off of all the resin in the samples. Thereafter, the furnace chamber underwent a passive cooldown to return to the ambient temperature.

$$\rho_c = \frac{A}{A-B}(\rho_O - \rho_L) + \rho_L \tag{7}$$

$$V_r = 100\, M_r\, \frac{\rho_c}{\rho_L} \tag{8}$$

3 RESULTS AND DISCUSSION

3.1 Improved repair part 1: consolidation pressure

The flexural strengths of repaired specimens are plotted against repair consolidation pressure in Fig. 3a. Increased flexural strengths were observed for specimens with repairs cured under higher consolidation pressures. Non-linear fits were applied to the mean values from each set to infer the relationship between repair cure consolidation pressure and flexural strength within the empirical range. It is suggested that the presence of the scarf repair redistributes the internal stresses under load, and that the extra surface plies in the repair zones contributed to improved compression-under-flexure responses compared to the reference cases. Similar observations were drawn from the flexural stiffness data in Fig. 3b. Most repaired specimens exhibited higher flexural moduli compared to the reference specimens.

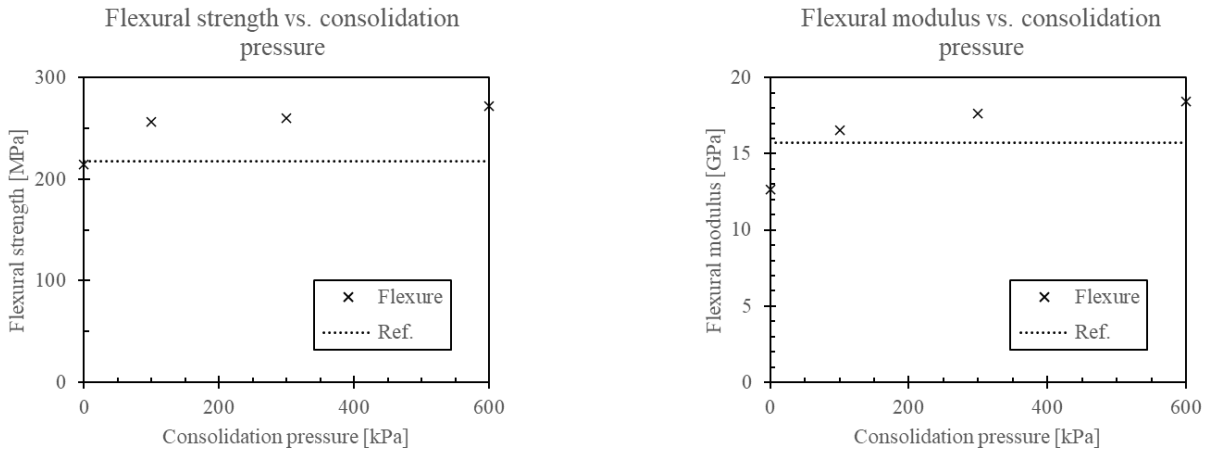

(a) (b)

Figure 3: Flexural properties of repaired specimens vs. consolidation pressure: (a) strengths, (b) moduli.

Similarly, the in-plane shear strengths of repaired specimens were compared to their reference specimen counterparts in Fig. 4a. Again, increased consolidation pressures were correlated with increased in-plane shear performance. Similar observations can be made about the in-plane shear moduli in Fig. 4b, which increased marginally as a function of increased consolidation pressure. However, the standard deviations of each test case are large relative to the respective means. Consequently, it is suggested that a minimum threshold repair consolidation pressure is required to ensure appropriate

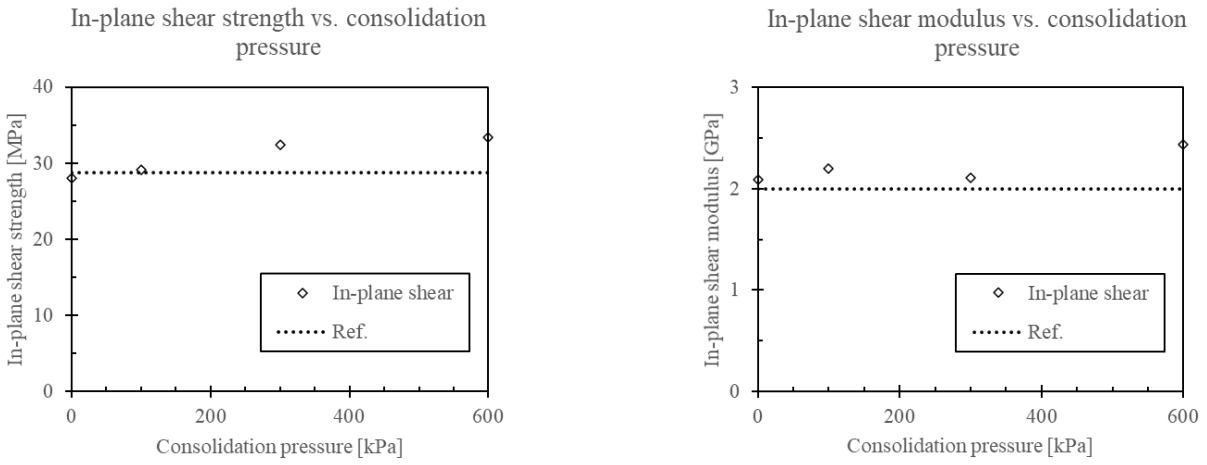

(a) (b)

Figure 4: In-plane shear properties of repaired specimens vs. consolidation pressure: (a) strengths, (b) moduli.

bonding of the repair patch, however, once this threshold has been achieved, additional applied pressure may not significantly improve the in-plane shear properties of the repaired laminates. It is reasoned that since in-plane shear properties are dominated by interlaminar fracture, these damage mechanisms are not easy to treat with applied pressure alone. Furthermore, this scarf repair approach generated plies that were not in-plane with the applied load, and thereby, geometrical effects could have complicated the experimental data interpretation.

The influence of FVF on FRP mechanical properties is well documented, e.g., Refs [13-14], therefore this observation is intuitive. Higher consolidation pressures had the effect of increasing FVF through reductions in void content and increased expulsion of excess resin from the moulds. One method to control for fluctuations in FVFs, is to consider specific properties, i.e., properties divided by densities, on the basis that the specimen density implies information about the specimen volume fractions. Considering the specific flexural properties in Table 1, repairs consolidated under higher pressures performed better, implying that these improvements were not solely driven by enhanced FVFs.

Table 1: Mean specimen flexural properties as measured during part 1 of the study.

Category	$\overline{\rho}$ [g cm^{-3}]	$\overline{V_r}$ [%]	$\overline{E_{fSP}}$ [kNm kg^{-1}]	$\overline{\sigma_{fMSP}}$ [kNm kg^{-1}]
Ref.	1.72 ± 0.01	39.4 ± 0.4	9.14E+03 ± 179.1	126.3 ± 05.2
0	1.68 ± 0.01	36.4 ± 0.6	7.55E+03 ± 443.8	127.5 ± 17.1
1	1.68 ± 0.01	36.4 ± 0.5	9.86E+03 ± 397.9	152.5 ± 07.3
3	1.73 ± 0.01	40.3 ± 0.9	1.02E+04 ± 291.9	150.6 ± 06.2
6	1.74 ± 0.02	40.1 ± 1.4	1.06E+04 ± 292.3	156.3 ± 11.5

Similarly in Table 2, improvements in specific in-plane shear strengths are correlated with higher consolidation pressures. Since the repairs all fail at the repair line it follows that increased consolidation pressures would improve the quality of that repair bond through void reduction, thereby increasing the energy required to induce and propagate interlaminar cracks.

Table 2: Mean specimen in-plane shear properties as measured during part 1 of the study.

Category	$\overline{\rho}$ [g cm^{-3}]	$\overline{V_r}$ [%]	$\overline{G_{12SP}}$ [kNm kg^{-1}]	$\overline{\tau_{12\,SP}}$ [kNm kg^{-1}]
Ref.	1.72 ± 0.01	39.4 ± 0.4	1161.3 ± 49.9	16.7 ± 0.5
0	1.68 ± 0.01	36.4 ± 0.6	648 ± 70.2	16.7 ± 0.3
1	1.68 ± 0.01	36.4 ± 0.5	1311.8 ± 53.5	17.3 ± 0.2
3	1.73 ± 0.01	40.3 ± 0.9	1217.0 ± 47.9	18.7 ± 0.3
6	1.74 ± 0.02	40.1 ± 1.4	1398.2 ± 65.6	19.2 ± 0.3

3.1 Improved repair part 2: impregnation method

Table 3 shows the mean flexural properties of the reference and repaired specimens. The reference specimens naturally showed the highest mean flexural strength, whilst wet lay-up repaired specimens were restored to 91.3% of the mean reference strength, and VARTM repaired specimens were restored to only 62.1% of the mean reference strength. Both repair methods resulted in consistent flexural moduli (20.0 - 21.3 GPa), indicating that the repair method mainly influenced strength rather than stiffness.

Table 4 shows the mean in-plane shear properties of the reference and repaired specimens. The reference specimens again showed highest mean shear strength, establishing a baseline for evaluating repair performance. The specimens repaired by wet lay-up were restored to 91.7% of reference shear strength and 69.5% of the reference shear modulus. The VARTM repaired specimens were restored to 83.9% of the reference shear strength 66.3% of the reference shear modulus. For both repair methods strength recovery was better than modulus recovery, indicating that whilst repair method changed the energy required to initiate and propagate failure, the resulting material had consistent elastic behaviour.

Table 3: Mean specimen flexural properties as measured during part 2 of the study.

Category	$\overline{\rho}$ [g cm^{-3}]	$\overline{V_r}$ [%]	$\overline{E_f}$ [GPa]	$\overline{\sigma_{fM}}$ [MPa]
Ref.	1.75 ± 0.01	39.8 ± 0.6	20.1 ± 1.2	327 ± 30.2
Wet Lay-up	1.74 ± 0.02	39.6 ± 2.0	21.3 ± 0.5	289 ± 15.3
VARTM	1.77 ± 0.03	39.3 ± 2.0	20.8 ± 1.6	212 ± 16.4

The mean specific flexural strengths (Fig. 5a) follow similar trends: the reference laminate achieved the highest specific strength, with 88% restoration of mean specific flexural strength for specimens repaired by wet lay-up and 64% restoration of mean specific flexural strength for specimens repaired by VARTM. Although a marginal increase can be seen in the mean specific flexural moduli of specimens repaired by wet lay-up compared to VARTM (Fig. 5b), there is considerable overlap of the datapoints after accounting for the standard deviations of each set. Further analysis via t-test revealed no statistical significance ($p > 0.05$) in the mean flexural moduli data.

Table 4: Mean specimen in-plane shear properties as measured during part 2 of the study.

Category	$\overline{\rho}$ [g cm^{-3}]	$\overline{V_r}$ [%]	$\overline{G_{12}}$ [GPa]	$\overline{\tau_{12M}}$ [MPa]
Ref.	1.75 ± 0.01	39.8 ± 0.6	4.0 ± 0.3	40.9 ± 3.7
Wet Lay-up	1.74 ± 0.02	39.6 ± 2.0	2.8 ± 0.2	37.5 ± 4.1
VARTM	1.77 ± 0.03	39.3 ± 2.0	2.7 ± 0.2	34.3 ± 3.4

Fig. 6a shows the mean specific in-plane shear strengths, which follow similar trends to their flexural strength counterparts. The wet lay-up repairs restored an average of 92% of the mean reference specific in-plane shear strength, whilst the VARTM repairs restored an average of 81% of the reference mean specific in-plane shear strength. For specific in-plane shear modulus (Fig. 6b), wet lay-up again out-performed VARTM in terms of performance restoration, however, neither method was able to match the specific in-plane shear modulus of the reference case. Despite the numerical differences between repair methods no statistical differences exists between repair methods for shear stress ($p = 0.078$) or modulus ($p=0.086$) indicating from a practical perspective, both methods offer statistically equivalent in-plane shear performance.

The similarities between flexural and in-plane shear performances in part 2 of this study implies that wet lay-up repairs out-perform VARTM repairs in terms of strength, whilst marginal difference can be detected in terms of stiffness.

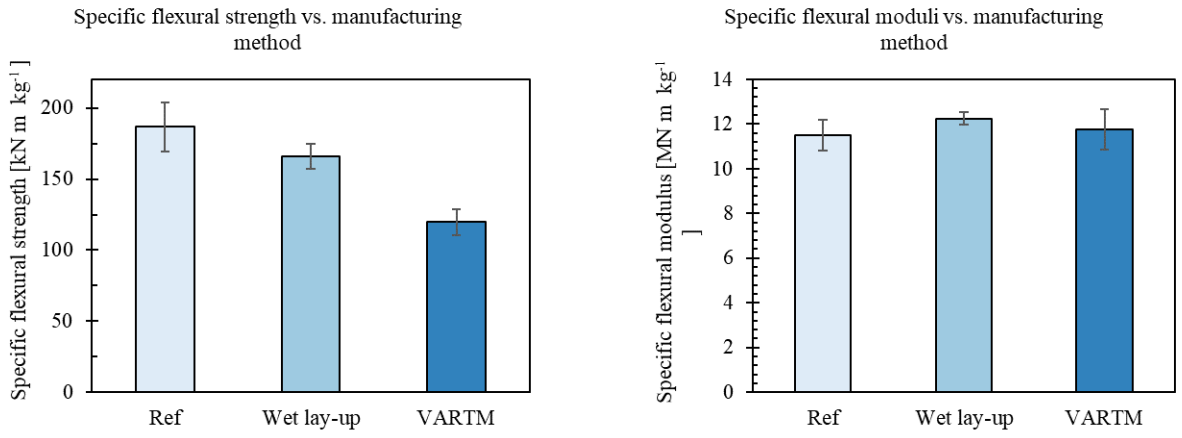

(a) (b)

Figure 5: Flexural properties of repaired specimens vs. manufacturing method: (a) strengths, (b) moduli.

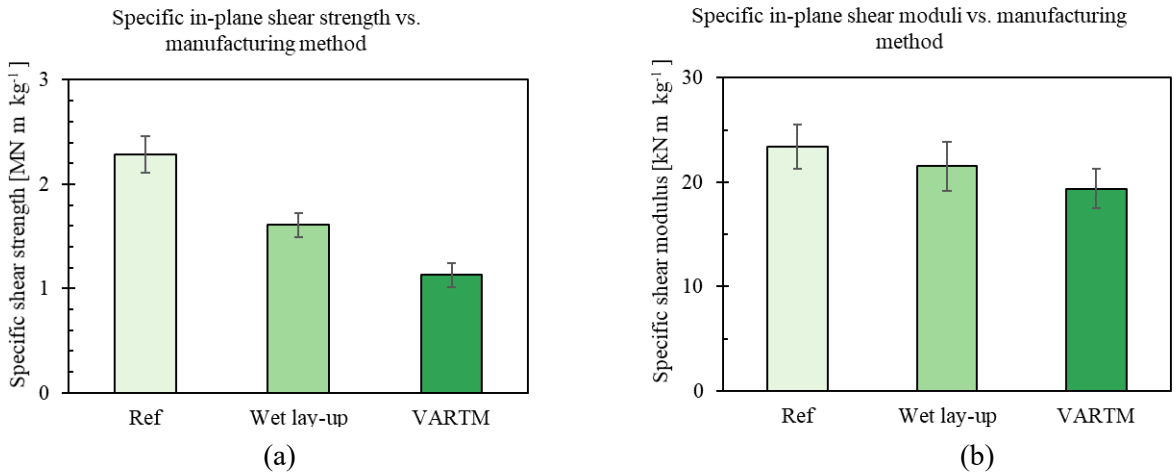

Figure 6: In-plane shear properties of repaired specimens vs. manufacturing method: (a) strengths, (b) moduli.

9 CONCLUSIONS

In this paper, repair strategies for legacy fibre-reinforced polymer (FRP) marine composites, were investigated. Focus was given to process-driven improvements that do not require changes to material systems. Two approaches were considered: 1. Increasing consolidation pressure during wet lay-up repairs, and 2. Using vacuum-assisted resin infusion (VARTM) as an alternative impregnation method. Repairs cured under higher consolidation pressures resulted in increased flexural and in-plane shear strengths. These gains were partially attributed to higher fibre volume fractions, but improvements in specific strength properties indicated enhanced load transfer and bonding quality too. In the latter part of the study, VARTM repairs resulted in specimens with comparable flexural and in-plane shear strengths to the traditional wet lay-up method. Similarly, no statistically significant differences in flexural or in-plane shear stiffnesses, were detected. Overall, the findings indicate that both increased consolidation pressures and vacuum-driven impregnation methods have potential to improve the mechanical performance of repaired specimens. Beyond the structural performances, the optimization of these techniques can support broader sustainability goals (reducing unnecessary or premature disposal) by extending the useful lives of in-service assets.

ACKNOWLEDGEMENTS

The authors would like to thank John Blackford for his valuable technical assistance and insightful advice throughout this project. His suggestions for improved methods and his support in guiding the team contributed substantially to the successful completion of this work.

REFERENCES

[1] T. Khan, F. Hafeez and R. Umer, *Repair of Aerospace Composite Structures Using Liquid Thermoplastic Resin*, Polymers, 15, 1377, 2023 (doi: 10.3390/polym15061377).

[2] D. Ferrandez-Pastrana, J. Costa, V. Marco and L. Gil, *Marine Application of Fiber Reinforced Composites: A Review*. Journal of Marine Science and Engineering, 8(1), 26, 2020 (doi: 10.3390/jmse8010026).

[3] A.P. Mouritz, R.S. Trask, A.J. Russell, Ship Structure Repairs, Composites, Vol 21, ASM Handbook, Editors D.B. Miracle, Steven L. Donaldson, ASM International, 2001, p 899–905 (doi: 10.31399/asm.hb.v21.a0003454).

[4] K.B. Armstrong, L.G. Bevan, and W.F. Cole II. Care and Repair of Advanced Composites, 2nd Edition, SAE International, Warrendale, 2005.

[5] S.H. Ahn and G.S. Springer. Repair of Composite Laminates. Technical report, U.S. Department of Transportation, Washington, D.C., 2000.

[6] National Maritime Center. Navigation and Vessel Inspection Circular No. 8-87, Change 1. CH-1 to NVIC 8-87, Notes on Design, Construction, Inspection and Repair of Fiber Reinforced Plastic (FRP) Vessels, Technical report, National Maritime Center, Arlington, 1993.

[7] S. H. Myhre and C. E. Beck. Repair Concepts for Advanced Composite Structures, Journal of Aircraft, 16(10), 2012, (doi: 10.2514/3.58595).

[8] H. Bendemra, P. Compston and P.J. Crothers, Optimisation study of tapered scarf and stepped-lap joints in composite repair patches, Composite Structures, 130, 2015, (doi: 10.1016/j.compstruct.2015.04.016).

[9] ISO, BS EN ISO 14125:1998+A1:2011 Fibre-reinforced plastic composites — Determination of flexural properties, BSI Electronic Catalogue, 1998.

[10] ASTM International, ASTM D3518/D3518M-18 Standard Test Method for In-Plane Shear Response of Polymer Matrix Composite Materials by Tensile Test of a ±45◦ Laminate, ASTM Compass, 2018.

[11] ISO, BS EN ISO 291:2008 Plastics — Standard atmospheres for conditioning and testing, BSI Electronic Catalogue, 2008.

[12] ASTM International, D3171-22 Standard Test Methods for Constituent Content of Composite Materials, ASTM Compass, vol. 97, 2022

[13] E.J. Barbero. *Prediction of Compression Strength of Unidirectional Polymer Matrix Composites*. Journal of Composite Materials. 32(5):483-502, 1998 (doi:10.1177/002199839803200504).

[14] M.R. Wisnom. *The Relationship between Tensile and Flexural Strength of Unidirectional Composites*. Journal of Composite Materials, 26(8):1173-1180. 1992, (doi:10.1177/002199839202600805).

ICCM24
AUGUST 4-8, 2025
BALTIMORE CONVENTION CENTER
BALTIMORE, MARYLAND, USA

No Technical Paper Submission for:

Sushrisangita Sahoo

ENHANCING THE MECHANICAL AND THERMAL PROPERTIES OF RECYCLED EVOH FILMS WITH NANO- SILICA INCORPORATION

Kowsar Rezvanian [1], Vijaya Rangari[1]*

[1] Department of Material science and Engineering, College of Engineering, Tuskegee University, Tuskegee, AL 36088, USA; krezvanian8358@tuskegee.edu

*Correspondence: vrangari@tuskegee.edu

Keywords: Recycling, STRAP, EVOH film, Composite, SiO_2 nanoparticles.

ABSTRACT

This study investigates the reinforcement of poly(ethylene-co-vinyl alcohol) (EVOH) films—recycled through the STRAP (Solvent-Targeted Recovery and Precipitation) process with SiO_2 nanoparticles at varying concentrations (0.1, 0.25, and 0.5 wt.%). EVOH was selectively dissolved in dimethyl sulfoxide (DMSO), and SiO_2 NPs was dispersed before precipitation of the pellets. The recovered EVOH composites were extruded into blown films and characterized for mechanical, thermal, and structural properties. FTIR analysis confirmed the incorporation of SiO_2 through Si–O–Si bonding, while SEM imaging revealed dispersion quality at different loadings. Thermal (TGA, DSC) and mechanical (tensile) tests demonstrated that the 0.1 wt.% SiO_2 sample offered the most significant improvements, with an elastic modulus of 0.25 GPa and a maximum tensile stress of 11.71 MPa. Higher loadings (0.25 and 0.5 wt.%) resulted in decreased performance, likely due to nanoparticle agglomeration disrupting polymer continuity. DSC results showed that the 0.1 wt.% addition increased melting and crystallization temperatures, indicating enhanced thermal resistance, while higher loadings had the opposite effect. XRD analysis further supported these findings. A broad peak at $2\theta \approx 23°$ confirmed the amorphous nature of SiO_2 grafted to the recycled EVOH matrix. Relative crystallinity increased with 0.1 wt.% SiO_2 but declined at higher concentrations due to poor dispersion and aggregation. Therefore, low concentrations of nano-SiO_2 significantly enhanced the mechanical strength, thermal stability, and crystallinity of recycled EVOH films. These findings demonstrate the potential of nanoparticle-assisted upcycling to improve the performance of barrier polymers recovered from multilayer packaging waste.

1 INTRODUCTION

The growing accumulation of packaging waste has led to widespread interest in recycling strategies. However, materials recovered through these processes often suffer from inadequate thermal and mechanical performance, which restricts their reuse in demanding applications. One promising solution is the incorporation of nanoscale additives, which can significantly improve the functional properties of recycled polymers. Nanoparticles are particularly effective due to their high surface area, which facilitates stronger interactions at the interface between polymer chains and filler particles. These interactions can enhance properties such as strength, thermal resistance, and durability in polymer nanocomposites [1]. Silicon dioxide (SiO_2) is a frequently applied inorganic nanoparticle known for its three-dimensional framework of SiO_4 units. It exists both in naturally occurring crystalline structures—like quartz and in synthetic, non-crystalline (amorphous) forms [2]. Owing to its strong chemical resistance, heat tolerance, and mechanical strength, SiO_2 serves as a valuable additive in polymer matrices, helping to enhance durability and barrier efficiency in composite materials such as films and coatings [1,2]. In particular, amorphous SiO_2 has been recognized as a biocompatible material, making it suitable for use in food-grade and pharmaceutical applications without known adverse health effects [3]. This research focuses on the use of nano-SiO_2 as an additive in recycled ethylene vinyl alcohol (EVOH) films obtained through a selective dissolution process. The study examines the influence of different SiO_2 loadings (0.1, 0.25, and 0.5 w/w%) on the films' chemical, mechanical, and thermal properties, aiming to enhance the performance of recycled EVOH for practical reuse.

2 MATERIALS AND METHODS

EVOH pellets containing 48 mol% ethylene (grade G176B) were supplied by Kuraray Co., Ltd., Houston, TX. Amorphous silicon dioxide (SiO_2) nanoparticles and dimethyl sulfoxide (DMSO), 99.5%, were supplied by Sigma-Aldrich (St. Louis, MO), with DMSO serving as the solvent for dissolving the EVOH. Structural properties of the samples were analyzed from the X-ray Diffraction (XRD) pattern. The XRD pattern of all the samples were recorded using Rigaku Smartlab with a Cu Kα source (λ=1.5406 Å) in the 2θ range of 10–80°, scanning rate of 1°/min and step size of 0.01. A Labtech Ultra Micro Film Blowing Line (model LUMF- 150) single-screw extrusion extruder was utilized to produce films. The films' mechanical properties were examined through tensile tests conducted with a Zwick Roell Z2.5 universal testing machine. The testing followed the ASTM D882- 10 standard, using a 20 N ceramic load cell, and five samples from each batch were tested to ensure consistent results. The Fourier transform infrared (FTIR) spectra of the polymer films were obtained using a Shimadzu IRTracer- 100 spectro photometer in transmittance mode over wavelengths ranging from 500 to 4000 cm−1 at a resolution of 4 cm−1. Thermogravimetric analysis (TGA) was carried out in a TA Q 500TGA. PSPW (15 mg) samples were heated from 30°C to 600°C at a heating rate of 10°C/min under a nitrogen atmosphere.

The recycling process began by dissolving EVOH films in DMSO at a 1:10 weight-to-volume ratio. Silica nanoparticles were then added to the solution and dispersed using 10 minutes of sonication to ensure uniform distribution. Precipitation was carried out using distilled water as an antisolvent, after which the recovered EVOH pellets were thoroughly washed three times with distilled water to remove residual DMSO. The resulting material was extruded into films with a thickness of 0.03 mm and subjected to mechanical and thermal characterization. Techniques such as Fourier-transform infrared spectroscopy (FTIR), thermogravimetric analysis (TGA), differential scanning calorimetry (DSC), and scanning electron microscopy (SEM) confirmed the effective incorporation of SiO_2 NPs into the EVOH matrix.

3 RESULTS AND DISCUSSION

FTIR spectra (Fig. 1a) of neat EVOH and EVOH films incorporated with varying concentrations of SiO_2 nanoparticles (0.1, 0.25, and 0.5 w/w%), compared with pure SiO_2 nanoparticles. The characteristic Si–O–Si stretching vibration around 1100 cm^{-1} confirms the successful incorporation of silica into the polymer matrix. Progressive shifts and intensity changes in the spectra indicate increasing interaction between EVOH and SiO_2 with higher nanoparticle loading.

Thermal analysis (Fig. 1b-d) revealed that the incorporation of nano-SiO_2 significantly improved the thermal stability of recycled EVOH films, particularly at low concentrations. The addition of 0.1 w/w% nano-SiO_2 increased the melting and crystallization temperature, indicating enhanced thermal resistance and molecular ordering. In contrast, a higher concentration of 0.5 w/w% led to a decrease in both transition temperatures, likely due to nanoparticle agglomeration that disrupted the polymer's crystalline structure. These trends are consistent with prior findings on SiO_2 based nanocomposites [7]. Therefore, the addition of SiO_2 NPs, particularly at low concentrations, effectively enhanced the mechanical and thermal properties of recycled EVOH films. These results highlight the potential of SiO_2 NPs to improve the performance of recycled polymeric materials, offering a sustainable approach to high performance film production. The mechanical performance of EVOH/SiO_2 nanocomposites (Fig. 1c) varied significantly with SiO_2 content. The 0.1 w/w% SiO_2 sample exhibited the best reinforcement, showing a 177.78% increase in elastic modulus and an 88.87% improvement in Fmax, indicating excellent nanoparticle dispersion and strong interaction with the polymer matrix. At 0.25%, both modulus and Fmax dropped sharply to 33.33% and 34.83% improvement, respectively, likely due to poor dispersion and disruption of polymer continuity. With 0.5% SiO_2, a partial recovery was observed possibly due to the rigid filler effect, although dispersion remained suboptimal. Therefore, the 0.1% concentration demonstrated the most favorable mechanical enhancement. The reduction in mechanical properties at higher concentrations might be attributed to the inadequate formation of intermolecular hydrogen bonds, as reported by Voon et al. (2012), and nanoparticle aggregation, which disrupts the uniform distribution of nanoparticles within the polymer matrix [4-6].

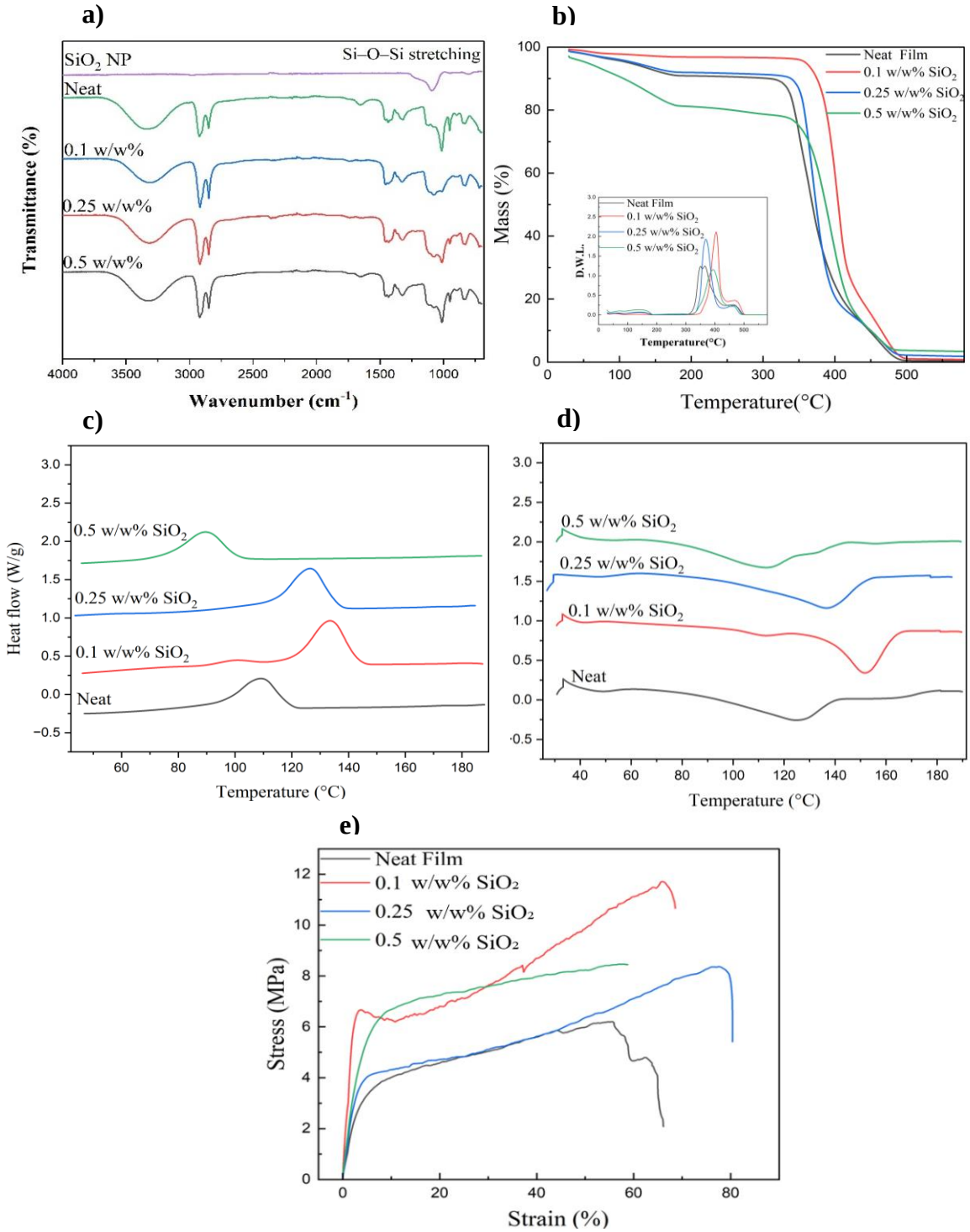

Figure 1: Impact of nano SiO2 on EVOH polymer properties: **a)** FTIR spectra **b)** TGA analysis, **c)** DSC crystallization analysis, **d)** DSC melting analysis, and **e)** Tensile test analysis.

The crystalline structure of SiO_2 nanoparticles and the changes in the crystalline structures of EVOH after incorporating SiO_2 NPs and their relative crystallinity (%) were obtained using XRD [8]. Due to the addition of the nanoparticles inside the polymer structure, some alterations of the matrix and molecular packaging crystalline structure can be found. For packaging, nanomaterials added inside this structure affect crystallinity, barrier properties, mechanical performance, and among others [9,10]. The XRD pattern of SiO_2 nanoparticles (Fig. 2a) displays a broad, prominent peak characteristic of

amorphous silica, consistent with the findings of Sun et al. (2017), who observed a similar peak around 2θ = 23°, confirming the amorphous nature of SiO_2 NPs used in alite–calcium sulfoaluminate (CSA) cement-based nanocomposites [11].

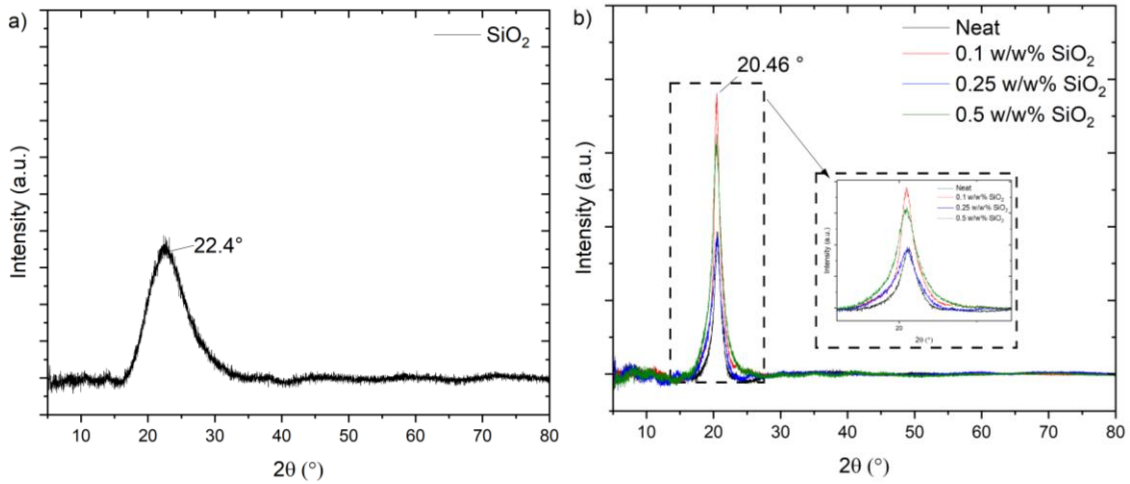

Figure 2: Diffractograms of the **a)** SiO_2 and **b)** EVOH films and their nanocomposite films, varying SiO_2 percentage (0.1, 0.25, and 0.5%).

In Fig. 2b, a distinct diffraction peak appears at approximately 2θ = 20–21° in both neat EVOH and nanocomposite films containing SiO_2 NPs, corresponding to the semi-crystalline structure of EVOH. Notably, the addition of SiO_2 nanoparticles did not introduce new peaks or cause significant peak shifts, suggesting that the crystalline structure of EVOH remains largely unchanged. The relative crystallinity, 2θ values, peak area, and full width at half maximum (FWHM) obtained through peak deconvolution are summarized in Table 1.

Table 1: Relative Crystallinity (%) obtained from XRD diffractograms for SiO_2/EVOH composite films(0.1, 0.25, and 0.5wt/wt%), area under the peak, and Full width at half maximum (FWHM) obtained by deconvolution of diffractograms.

Samples	Relative Crystallinity (%)	2θ degree	The area under the peak	Full width at half maximum (FWHM)
SiO_2	15.91	----	----	----
Neat	5.98	20.60	0.50	1.36
0.1 w/w% SiO_2	14.81	20.54	0.94	1.40
0.25 w/w% SiO_2	7.49	20.43	0.70	1.96
0.5 w/w % SiO_2	10.95	20.47	1.20	2.10

From the values presented in Table 1, relative crystallinity (%) increased when added 0.1 %. Increasing the percentage of SiO_2 nanoparticles for 0.25 and 0.5 w/w.%, a reduction of relative crystallinity was found. Wang et al. (2018) reported that there was an increase in the crystallinity of the PHBV-containing rice husk SiO_2 nanoparticles. However, exceeding 3 wt.% of nanoparticles, a reduction of the crystallinity was verified. Firstly, the increase can be associated with the anisotropic nucleation of the SiO_2 NPs. However, from its limit, this value can decrease due to the agglomeration of these nanoparticles into the polymer matrix [12]. Besides, the interaction between hydroxyl groups of the EVOH and SiO_2 nanoparticles could have created hydrogen bonds, thus forming a large amount of EVOH crystals around the SiO_2 nanostructures [13,14]. the nucleating action of the SiO_2 nanoparticles for 0.1 w/w.% inside the EVOH polymer matrix can create a tortuous pathway for the gases, increasing the barrier property of the food packaging [15].

4 CONCLUSIONS

Based on the comprehensive analysis of FTIR, tensile, thermal, and XRD data, it can be concluded that incorporating low concentrations of nano-SiO_2, particularly at 0.1 w/w%, significantly enhances the performance of recycled EVOH films. FTIR confirmed the successful interaction between SiO_2 and the EVOH matrix through Si–O–Si vibrational bands, with increasing interaction at higher loadings. However, the mechanical and thermal evaluations revealed that 0.1 w/w% SiO_2 yielded the highest improvements in modulus, Fmax, and thermal transitions, attributed to uniform dispersion and strong interfacial bonding. XRD results further supported this by showing increased relative crystallinity at 0.1 w/w%, likely due to the nucleating effect of well-dispersed nanoparticles. Higher concentrations (0.25–0.5 w/w%) led to nanoparticle agglomeration, decreased crystallinity, and diminished mechanical and thermal benefits. Overall, the 0.1 w/w% SiO_2 NPs concentration presents an optimal balance of improved mechanical strength, thermal stability, and crystallinity without compromising structural integrity, offering a sustainable solution for upcycling EVOH-based packaging waste.

ACKNOWLEDGEMENTS

The authors would like to acknowledge the financial support from NSF- CREST #1735971 and NSF-EFMA # 2132093

REFERENCES

[1] Mallakpour, S., & Naghdi, M. (2018). Polymer/SiO_2 nanocomposites: Production and applications. *Progress in Materials Science, 97*, 409–447. https://doi.org/10.1016/j.pmatsci.2018.04.002

[2] Martin, K. R. (2007). The chemistry of silica and its potential health benefits. *The Journal of Nutrition, Health & Aging, 11*(2), 94.

[3] Gazzano, E., Ghiazza, M., Polimeni, M., Bolis, V., Fenoglio, I., Attanasio, A., ... & Ghigo, D. (2012). Physicochemical determinants in the cellular responses to nanostructured amorphous silicas. *Toxicological Sciences, 128*(1), 158–170. https://doi.org/10.1093/toxsci/kfs145

[4] Voon, H. C., Bhat, R., Easa, A. M., Liong, M. T., & Karim, A. A. (2012). Effect of addition of halloysite nanoclay and SiO_2 nanoparticles on barrier and mechanical properties of bovine gelatin films. *Food and Bioprocess Technology, 5*(5), 1766–1774. https://doi.org/10.1007/s11947-010-0461-y

[5] Shahabi-Ghahfarrokhi, I., Khodaiyan, F., & Mousavi, M. (2015). Preparation of UV-protective kefiran/nano-ZnO nanocomposites: Physical and mechanical properties. *International Journal of Biological Macromolecules, 72*, 41–46. https://doi.org/10.1016/j.ijbiomac.2014.07.047

[6] Hassannia-Kolaee, M., Khodaiyan, F., Pourahmad, R., & Shahabi-Ghahfarrokhi, I. (2016). Development of ecofriendly bionanocomposite: Whey protein isolate/pullulan films with nano-SiO_2. *International Journal of Biological Macromolecules, 86*, 139–144. https://doi.org/10.1016/j.ijbiomac.2016.01.032

[7] Yang, M., & Xia, Y. (2017). Preparation and characterization of nano-SiO_2 reinforced alginate-based nanocomposite films (II). *Journal of Applied Polymer Science, 134*(38), 45286. https://doi.org/10.1002/app.45286

[8] da Costa, T. B., Camani, P. H., Ferreira, R. R., Barbosa, R. F. S., & dos Santos Rosa, D. (2025). Enhancing corn starch hydrogels for effective sorption of potentially toxic metals: The role of amylose and amylopectin content. *Journal of Polymers and the Environment, 33*(3), 1615–1635. https://doi.org/10.1007/s10924-025-03495-7

[9] Abutalib, M. M., & Rajeh, A. (2021). Enhanced structural, electrical, mechanical properties and antibacterial activity of Cs/PEO doped mixed nanoparticles (Ag/TiO_2) for food packaging applications. *Polymer Testing, 93*, 107013. https://doi.org/10.1016/j.polymertesting.2020.107013

[10] Deshmukh, R. K., Kumar, L., & Gaikwad, K. K. (2023). Halloysite nanotubes for food packaging application: A review. *Applied Clay Science, 234*, 106856. https://doi.org/10.1016/j.clay.2023.106856

[11] Sun, J., Xu, Z., Li, W., & Shen, X. (2017). Effect of nano-SiO_2 on the early hydration of alite-sulphoaluminate cement. *Nanomaterials, 7*(5), 102. https://doi.org/10.3390/nano7050102

[12] Wang, L., Guo, Y., Chen, Y., Chen, T., Zhu, S., Zhang, T., & Liu, S. (2018). Enhanced mechanical and water absorption properties of rice husk-derived nano-SiO_2 reinforced PHBV composites. *Polymers, 10*(9), 1022. https://doi.org/10.3390/polym10091022

[13] Hedayati, F., Moshiri-Gomchi, N., Assaran-Ghomi, M., Sabahi, S., Bahri-Laleh, N., Mehdipour-Ataei, S., Mokhtari-Aliabad, J., & Mirmohammadi, S. A. (2020). Preparation and properties of enhanced nanocomposites based on PLA/PC blends reinforced with silica nanoparticles. *Polymers for Advanced Technologies, 31*(3), 566–573. https://doi.org/10.1002/pat.4797

[14] Soliman, T. S., Vshivkov, S. A., & Elkalashy, S. I. (2020). Structural, thermal, and linear optical properties of SiO_2 nanoparticles dispersed in polyvinyl alcohol nanocomposite films. *Polymer Composites, 41*(8), 3340–3350. https://doi.org/10.1002/pc.25623

[15] Jafarzadeh, S., & Jafari, S. M. (2021). Impact of metal nanoparticles on the mechanical, barrier, optical and thermal properties of biodegradable food packaging materials. *Critical Reviews in Food Science and Nutrition, 61*(16), 2640–2658. https://doi.org/10.1080/10408398.2020.1783200

ICCM24
AUGUST 4-8, 2025
BALTIMORE CONVENTION CENTER
BALTIMORE, MARYLAND, USA

No Technical Paper Submission for:

Chundu Tamang

ICCM24
AUGUST 4-8, 2025
BALTIMORE CONVENTION CENTER
BALTIMORE, MARYLAND, USA

No Technical Paper Submission for:

Martina Salzano de Luna

ICCM24
AUGUST 4-8, 2025
BALTIMORE CONVENTION CENTER
BALTIMORE, MARYLAND, USA

No Technical Paper Submission for:

Monis Kazmi

COST-EFFECTIVENESS OF STRUCTURAL HEALTH MONITORING ON THE LIFECYCLE OF COMPOSITE AEROSPACE ELEMENTS

Pietro Ballarin[1], Giuseppe Sala[1], Marco Macchi[2], Irene Roda[2], Andrea Baldi[3], Alessandro Airoldi[1]

[1]Department of Aerospace Science and Technology, Politecnico di Milano, Via La Masa 34, Milan 20156, Italy
Email: pietro.ballarin@polimi.it, web page: https://www.polimi.it/

[2]Department of Management, Economics, and Industrial Engineering, Politecnico di Milano, Via Lambruschini 4/B, Milan 20156, Italy
Email: marco.macchi@polimi.it, web page: https://www.polimi.it/

[3]Leonardo S.p.A., Helicopters Division, Via Giovanni Agusta 520, Cascina Costa di Samarate 21017, Italy
Email: andrea.baldi01@leonardo.com, web page: https://www.leonardo.com/it/

Keywords: mechanical testing; process monitoring; autoclave; cure; damage tolerance

ABSTRACT

Structural Health Monitoring Systems (SHMS) enable real-time monitoring of composite aeronautical structures, offering the potential to reduce maintenance efforts. However, their overall impact on the lifecycle remains uncertain. This study presents a methodology to assess the economic impact of SHMS, structured in four steps: (i) identification of SHMS applications, (ii) assessment of SHMS performance, (iii) integration of SHMS into the lifecycle, (iv) evaluation of the resulting economic impact. The methodology is applied to two distinct lifecycle stages of a composite rotorcraft blade: the Beginning of Life (BOL), which involves the development of a new sensorized component, and the Middle of Life (MOL), which focuses on its operational use and maintenance. In the BOL phase, results indicate that SHMS can offer economic advantages if they enable a reduction in the number of curing cycles below a certain threshold. In the MOL phase, while SHMS reduce manpower needs, these savings are offset by higher spare parts costs and longer repair times. The findings highlight the importance of considering both technical performance and cost implications when integrating SHMS into aerospace applications.

NOMENCLATURE

$\ldots^{as\ is}$	Superscript referring to the scenario “as is”
$\ldots^{SHMS}$	Superscript referring to the scenario “with SHMS”
$C_{acq\ sys}$	Cost of the acquisition system for the scenario “as is”
c_{blade}	Cost of the blade to the customer
$C_{cur\ cycle\ def}$	Cost to define the curing cycle
C_{energy}	Cost of energy for the autoclave
CF	Cash flow per year
C_{FBG}	Cost of 1 FBG sensor
$C_{FBG\ sys}$	Cost of the interrogation system for FBG sensors
c_{fuel}	Cost of fuel per hour consumed by the helicopter
C_g	Cost of 1 strain gauge
$C_{lab\ act}$	Cost to perform laboratory activities
C_m	Cost of the material to produce one blade

$C_{test\ lab}$	Cost to perform laboratory tests
C_{th}	Cost of 1 thermocouple
$K_{partition}$	Partition coefficient
L_{eng}	Labour rate of engineers
L_{pilots}	Labour rate of pilots
$L_{tr\ wo}$	Labour rate of trained workers
n_{auto}	Number of autoclave cycles
n_b	Number of rotor blades
n_{FBG}	Number of FBG sensors embedded in one blade
n_g	Number of strain gauges applied on one blade
n_{test}	Number of laboratory blade tests
n_{th}	Number of thermocouples embedded in one blade
R	Revenue loss
r	Discount rate
t_{auto}	Time to perform one autoclave cycle
t_{depot}	Time needed by the helicopter to reach the depot
t_{DI}	Time to perform detailed inspection
t_{eng}	Time needed by the engineers to assess the quality of the acquired data
t_{GVI}	Time to perform general visual inspection
$t_{mount\ blade}$	Time to mount one blade on the rotor hub
t_{repair}	Time to repair one blade
t_{test}	Time to perform one test on the blade
$t_{tr\ wo}$	Time needed by the trained workers to laminate, prepare the vacuum bag and demould the blade

1 INTRODUCTION

Maintenance is a critical activity for ensuring safety in the aviation sector; however, it requires substantial resources in terms of manpower, spare parts, and downtime. In commercial aviation, maintenance can represent up to 28% of total operational costs [1]. At present, maintenance activities rely on Non-Destructive Testing (NDT) techniques such as tapping, ultrasound, and radiography. While these methods are effective, they are restricted to localized inspections, must be performed while the aircraft is on the ground, and often necessitate disassembly of components for access. In comparison, Structural Health Monitoring Systems (SHMS) offer continuous, in-situ monitoring capabilities and allow for the inspection of larger areas than conventional NDT. The use of SHMS in aerospace structures has been extensively explored. For instance, [2] evaluated the performance of a fiber Bragg grating (FBG)-based SHMS on a stiffened metallic helicopter panel under different crack lengths. In [3], a strain-based SHMS was employed to detect damage in a helicopter rotor blade, while [4] used convolutional neural networks to identify damage in composite wings. Although these studies demonstrate clear benefits—particularly in improving safety and enabling condition-based maintenance—the economic impact of SHMS over the lifecycle of monitored structures remains uncertain. In [1], the deployment of Piezoelectric Wafer Active Sensors on a commercial aircraft fuselage was found to offer no economic advantage, as maintenance savings were offset by increased fuel consumption from the added SHMS weight. In [5], replacing A-check and C-check inspections with piezoelectric sensors affected aircraft performance, making SHMS economically impractical. Conversely, [6] indicated potential cost savings when SHMS replaced DVI and GVI using ultrasonic and FBG sensors on an Airbus A320. In [7], SHMS enabled greater allowable design limits and mass reduction for damage-tolerant composite structures, though no benefits were observed for structures designed against instability. To date, most existing research has focused on fixed-wing aircraft [1, 5–10], and, to the best of the authors' knowledge, no studies have assessed the economic implications

of SHMS applied to helicopter structural elements. Moreover, current literature primarily addresses the operational phase, often overlooking the possible impacts of SHMS on the production and development stages.

This study evaluates the economic impact of an optical fiber–based SHMS applied to composite rotorcraft blades. The SHMS performance was assessed using a finite element model of the blade, allowing simulation of multiple damage scenarios used to train an artificial neural network (ANN)–based damage detection algorithm. Both the Beginning of Life (BOL)—which corresponds to production—and the Middle of Life (MOL)—which concerns usage—were examined. The IDEF0 formalism was used to define key processes, inputs, outputs, resources, and constraints, thus forming the foundation for the cost model. Two scenarios were compared using the Life Cycle Cost (LCC) methodology: the current configuration without SHMS ("as-is" scenario) and an alternative configuration with blades equipped with FBG sensors ("with SHMS").

This paper is organized as follows: Section 2 presents the scenarios and associated cost models, including the methodology used to derive them across the BOL and MOL phases. Section 3 describes the cost model implementation, providing a parametric analysis for BOL and a Probabilistic Damage Tolerance Analysis for MOL. Section 4 concludes with the main findings of the study.

2 DEVELOPMENT OF THE COST MODEL

The lifecycle of any product can typically be divided into three main stages: (i) BOL, during which the component is manufactured and introduced to the market; (ii) MOL, during which the component is used and maintained by the customer to perform its intended operational functions; and (iii) End of Life (EOL), when the component is decommissioned and disposed of. This study focuses on the first two stages of the lifecycle: BOL and MOL. To evaluate the economic impact of SHMS on the rotorcraft lifecycle, the following methodology was adopted: (i) identification of the SHMS application; (ii) assessment of SHMS performance; (iii) integration of SHMS into the lifecycle; and (iv) evaluation of the economic impact. Based on this procedure, a composite rotorcraft blade instrumented with FBG sensors was selected as the reference structural element. The choice of FBG sensors is justified by their immunity to electromagnetic interference and their ability to be embedded within the composite laminate with minimal invasiveness [11].

The following subsections provide further details on each step of the proposed methodology.

2.1 Beginning Of Life

With regard to step (ii) of the procedure for assessing the economic impact of SHMS, the performance of the SHMS was not evaluated in this work, as doing so would have required an extensive experimental campaign. Instead, this section focuses on step (iii), which concerns the integration of SHMS into the rotorcraft lifecycle.

At the BOL stage, two applications of SHMS were considered in relation to the laboratory activities required for developing a new composite blade: the definition of the curing cycle and the execution of laboratory tests. The first application relates to the optimization of the curing cycle, in which the evolution of pressure and temperature over time is determined. The second involves laboratory testing to verify the structural integrity of the blade during the initial certification phase.

Currently, defining the appropriate curing cycle for composite elements requires several iterations, since the polymerization of thermoset composites is an exothermic process, and the internal temperature distribution often deviates from the one imposed by the autoclave. Temperature measurements are typically obtained by embedding thermocouples in the laminate, and the curing cycle is repeated and adjusted until the desired thermal conditions are achieved. In the "with SHMS" scenario, SHMS is assumed to be employed during curing by acquiring the internal temperature field via embedded FBG sensors, replacing conventional thermocouples. The superior accuracy of FBG measurements is expected to provide a more precise representation of the temperature distribution, potentially reducing the number of required curing cycles.

After defining the curing parameters, the next phase involves mechanical testing to evaluate the blade's performance. This is traditionally done by applying static and fatigue loads and measuring strain with strain gauges. In the "with SHMS" scenario, the strain gauges are replaced by FBG sensors

to provide more accurate strain measurements, potentially reducing the number of required tests. The total cost of laboratory activities for developing a new composite blade is therefore divided into two components: the cost of defining the curing cycle $C_{cur\ cycle\ def}$ and the cost of conducting mechanical tests $C_{test\ lab}$ as expressed in Eq. 1.

$$C_{lab\ act} = C_{cur\ cycle\ def} + C_{test\ lab} \tag{1}$$

The process related to the laboratory activities, modeled using the IDEF0 formalism, is illustrated in Figure 1. The IDEF0 formalism is designed to map complex processes with the aim of highlighting the following elements: (i) Activities, represented by rectangular boxes; (ii) Inputs, indicated by arrows entering from the left side of each activity; (iii) Outputs, indicated by arrows exiting from the right side; (iv) Constraints, represented by arrows entering from the top; (v) Resources, represented by arrows entering from the bottom;

The cost models were developed based on the inputs and resources required for each activity within the process. A color-coding convention was adopted to distinguish between the two scenarios: activities specific to the "as-is" scenario are shown in red, those belonging to the "with SHMS" scenario are shown in green, and activities common to both scenarios are depicted in black.

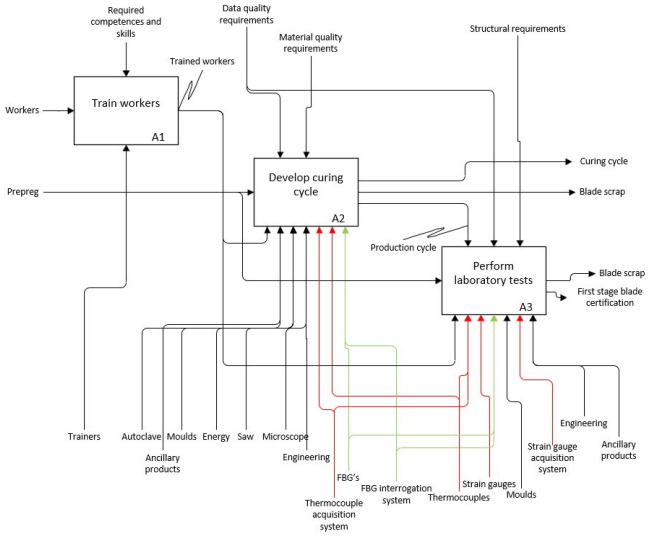

Figure 1: IDEF0 model of the process of the laboratory activities necessary to develop a new composite blade

Following the IDEF0 diagram, for the scenario "as is", the following Eq. 2 representing the cost model for the development of the curing cycle can be obtained.

$$C^{as\ is}_{cur\ cycle\ def} = \left(C_m + L_{tr\ wo} t_{tr\ wo} + n_{th} C_{th} + C_{energy} t_{auto} + L_{eng} t_{eng}\right) n^{as\ is}_{auto} + C_{acq\ sys} \frac{t_{auto} n^{as\ is}_{auto}}{t_{auto} n^{as\ is}_{auto} + t_{test} n^{as\ is}_{test}} \tag{2}$$

While, considering the scenario "with SHMS", the following Eq. 3 can be written.

$$C^{SHMS}_{cur\ cycle\ def} = \left(C_m + L_{tr\ wo} t_{tr\ wo} + n_{FBG} C_{FBG} + C_{energy} t_{auto} + L_{eng} t_{eng}\right) n^{SHMS}_{auto} + C_{FBG\ sys} \frac{t_{auto} n^{SHMS}_{auto}}{t_{auto} n^{SHMS}_{auto} + t_{test} n^{SHMS}_{test}} \tag{3}$$

The final terms in Eq. 2 and Eq. 3 represent the cost allocation for the acquisition system in the "as-is" scenario and the interrogation system in the "with SHMS" scenario, respectively. Both equations are linearly dependent on the number of autoclave cycles required to determine the optimal curing parameters. Additionally, it can be noted that in Eq. 2, the cost associated with thermocouples is replaced in Eq. 3 by the cost of FBG sensors.

With regard to the laboratory testing activities required to complete the initial phase of blade certification, the cost models for the "as-is" and "with SHMS" scenarios are presented in Eq. 4 and Eq. 5, respectively.

$$C_{test\ lab}^{as\ is} = \left(C_m + L_{tr\ wo}t_{tr\ wo} + n_g C_g + C_{energy}t_{auto} + L_{eng}t_{eng}\right) n_{test}^{as\ is} + C_{acq\ sys}\frac{t_{test}n_{test}^{as\ is}}{t_{auto}n_{auto}^{as\ is} + t_{test}n_{test}^{as\ is}} \quad (4)$$

$$C_{test\ lab}^{SHMS} = \left(C_m + L_{tr\ wo}t_{tr\ wo} + n_{FBG}C_{FBG} + C_{energy}t_{auto} + L_{eng}t_{eng}\right) n_{auto}^{SHMS} + C_{FBG\ sys}\frac{t_{test}n_{test}^{SHMS}}{t_{auto}n_{auto}^{SHMS} + t_{test}n_{test}^{SHMS}} \quad (5)$$

The final term in Eq. 4 and Eq. 5 represents the cost allocation for the acquisition system in the "as-is" scenario and the interrogation system in the "with SHMS" scenario, respectively. Both equations are linearly dependent on the number of blades tested. Furthermore, it can be noted that the cost of strain gauges in Eq. 4, corresponding to the "as-is" scenario, is replaced by the cost of FBG sensors in Eq. 5, corresponding to the "with SHMS" scenario.

2.2 Middle Of Life

In accordance with step (ii) of the proposed procedure for assessing the economic impact of SHMS, the performance of the SHMS was evaluated using a finite element (FE) model, experimentally validated and representing a portion of the rotorcraft blade—specifically, the blade root. Damage was assumed to occur exclusively within the adhesive layer that bonds the central core to the surrounding antitorsional layer. Various damage sizes, ranging from 3 mm to 30 mm, were analyzed and distributed across the adhesive surface. In the FE model, damage was simulated by removing the elements enclosed within a sphere, the center of which was located on the surface of the adhesive layer. An example of a 30 mm damage scenario is shown in Figure 2a. As illustrated, two coordinate systems were employed to define damage locations: a curvilinear coordinate system along the blade's length and a cross-sectional coordinate system. Damage was distributed at 10 equally spaced positions along the curvilinear coordinate, and for each position, four evenly spaced locations were selected across the cross section. This yielded a total of 40 damage locations. For each of these 40 locations, the following damage sizes were considered: 3, 6, 9, 12, 15, 18, 21, 24, and 30 mm—resulting in a total of 360 distinct damage scenarios.

The analyses served as input for training an ANN–based algorithm designed to detect the presence of damage. Strain measurements were extracted from selected elements within the FE model. Specifically, six virtual optical fiber lines were defined, each containing ten virtual FBGs, resulting in a total of 60 virtual FBGs. These were positioned inside the antitorsional layer, at a distance of 0.25 mm from the adhesive interface. To simulate realistic measurement conditions, Gaussian noise with a standard deviation of 4% was added to the sampled strain values during the training, validation, and testing phases of the ANN.

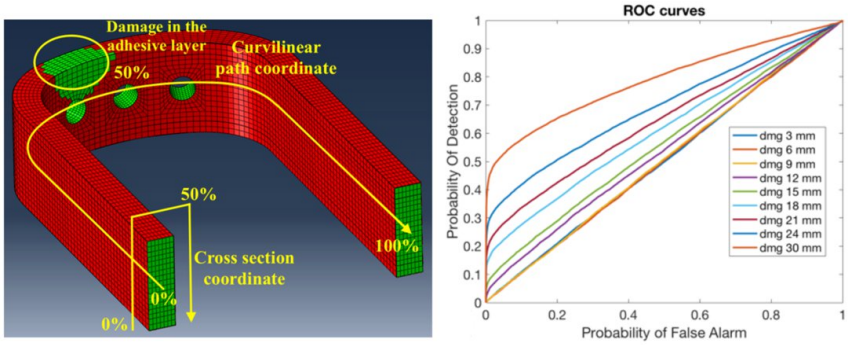

a) b)

Figure 2: a) FE model of the blade root, the central core is colored green while the adhesive layer connecting the central core to the antitorsional layer is colored red; b) Receiver Operating Characteristic curve obtained for a Gaussian noise of 4%.

A pattern recognition ANN architecture was adopted, consisting of three hidden layers with ten neurons per layer. The network's output was a scalar value between 0 and 1. A blade was classified as damaged if the ANN output exceeded a predefined threshold; otherwise, it was considered undamaged. The damage detection performance of the SHMS was quantified in terms of Probability of Detection (POD) and Probability of False Alarm (PFA), as shown in Figure 2b for a 4% Gaussian noise level. Receiver Operating Characteristic (ROC) curves were generated by varying the classification threshold from 0 to 1. POD was calculated as the ratio of correctly identified damaged blades to the total number of damaged blades, while PFA represented the ratio of undamaged blades falsely classified as damaged to the total number of undamaged blades evaluated.

Step (iii) of the proposed methodology, concerning the integration of the SHMS into the rotorcraft's lifecycle, is addressed below. In both the "as-is" and "with SHMS" scenarios, helicopter downtime was considered to result in revenue loss. It was assumed that the helicopter was owned by a leasing company renting aircraft to external operators.

For the "as-is" scenario—based on practical experience in the aerospace sector—the blade was assumed to undergo two types of inspections: General Visual Inspection (GVI), performed every 50 flight hours (FH) without removing the blade from the rotor hub, and Detailed Inspection (DI), carried out using a tap hammer every 1200 FH, requiring blade removal. The annual cash flow associated with the "as-is" scenario is expressed in Equation 6.

$$CF^{as\ is} = \sum_{i=1}^{n\ travels} 2At_{depot}K_{partition} + \sum_{i=1}^{n\ blade\ mount-sched} 2Bt_{mount\ blade} + \sum_{i=1}^{n\ blade\ mount-unsch} \frac{2}{n_b}Ct_{mount\ blade} + \sum_{i=1}^{n\ GVI} Bt_{GVI} + \sum_{i=1}^{n\ DI} Bt_{DI} + \sum_{i=1}^{n\ repairs} Ct_{repair}^{as\ is} + \sum_{i=1}^{n\ spare\ parts} c_{blade}^{as\ is} \quad (6)$$

Where the coefficients A, B, and C were defined by the Eq. 7, Eq. 8, and Eq. 9, respectively.

$$A = \left(L_{pilots} + c_{fuel} + R\right) \quad (7)$$

$$B = \left(L_{tr\ wo} + RK_{partition}\right) \quad (8)$$

$$C = \left(L_{tr\ wo} + R\right) \quad (9)$$

Several cost elements were taken into account in Eq. 6, including travel to the maintenance

depot, blade removal from the rotor hub, performance of GVI and DI inspections, blade repair, and blade replacement. A distinction was also made between scheduled and unscheduled maintenance activities. For scheduled activities, a partition coefficient $K_{partition}$ was introduced to allocate the helicopter's revenue loss R specifically to blade-related maintenance. This reflects the fact that, during scheduled downtime, multiple maintenance tasks are typically performed concurrently across different aircraft systems. Therefore, only a portion of the total revenue loss can be attributed to rotor blade maintenance. In contrast, for unscheduled activities caused specifically by the rotor blades, this partitioning is not applicable. Since these events occur outside of the planned maintenance schedule, they do not allow for simultaneous work on other components. As a result, the full revenue loss R is attributed solely to the rotor blade issue. Consequently, unscheduled activities are significantly more costly than scheduled ones. In the "with SHMS" scenario, the GVI was assumed to be carried out identically to the "as-is" scenario. However, the SHMS was intended to progressively replace the DI. During the initial years of the blade's lifecycle, the DI interval was extended to 2400 FH, supported by additional automatic inspections enabled by the SHMS. In later years, once confidence in the SHMS's performance had grown, it was assumed that the system would fully replace DI activities, achieving a fully Condition-Based Maintenance (CBM) approach.

It is important to note that SHMS data were assumed to be retrieved at regular intervals by a ground-based operator. However, if the SHMS issued an alert and no damage was identified during the GVI, the helicopter was assumed to return to the depot for a DI using the same procedures as in the "as-is" scenario.

The annual cash flow for the "with SHMS" scenario is described by Equation 10.

$$\begin{aligned} CF^{SHMS} = & \sum_{i=1}^{n\ travels-sched} 2At_{depot}K_{partition} + \sum_{i=1}^{n\ travels-unsch} 2At_{depot} \\ & + \sum_{i=1}^{n\ blade\ mount-sched} 2Bt_{mount\ blade} + \sum_{i=1}^{n\ blade\ mount-unsch} \frac{2}{n_b}Ct_{mount\ blade} + \sum_{i=1}^{n\ GVI-sched} Bt_{GVI} \\ & + \sum_{i=1}^{n\ GVI-unsch} \frac{1}{n_b}Ct_{GVI} + \sum_{i=1}^{n\ DI-sched} Bt_{DI} + \sum_{i=1}^{n\ DI-unsch} \frac{1}{n_b}Ct_{DI} + \sum_{i=1}^{n\ repairs} Ct_{repair}^{SHMS} \\ & + \sum_{i=1}^{n\ spare\ parts} c_{blade}^{SHMS} \end{aligned} \tag{10}$$

It is worth noting that different costs were assumed for both the blade and the repair time compared to the "as-is" scenario. Additionally, unlike in the "as-is" case, the travel activity in the "with SHMS" scenario was considered unscheduled, as an SHMS-triggered alarm could prompt the helicopter to return to the depot for a DI.

The Net Present Value (NPV), shown in Equation 11, was selected as the performance indicator to compare the two scenarios. This metric enables the discounting of all cash flows occurring throughout the helicopter's operational lifecycle.

$$NPV = \sum_{t} \frac{CF(t)}{(1+r)^{t}} \tag{11}$$

The two scenarios—"as-is" and "with SHMS"—were compared under the same Probability of Failure (POF) for the blade, as determined through a Probabilistic Damage Tolerance Analysis [13]. According to [14], in offshore operations, a helicopter is expected to experience one main rotor impact every 1000 FH. Assuming an average usage of 500 FH per year over a 30-year lifespan, a total of 15 impacts are anticipated throughout the helicopter's lifecycle. These impacts were randomly distributed

in the lifecycle simulation. Impact energies were modeled based on the "medium energy" distribution described in [15]. Blade degradation following an impact was assumed to follow the behavior described in [16], where helicopter blades were subjected to steel sphere impacts at varying energy levels, and data were provided for residual indentation and skin-foam disbonding area. The residual strength of the blade after an impact was estimated by calculating the ratio between the cross-sectional area affected by indentation and the original cross-sectional area. A schematic representation of the blade's strength degradation is shown in Figure 3a.

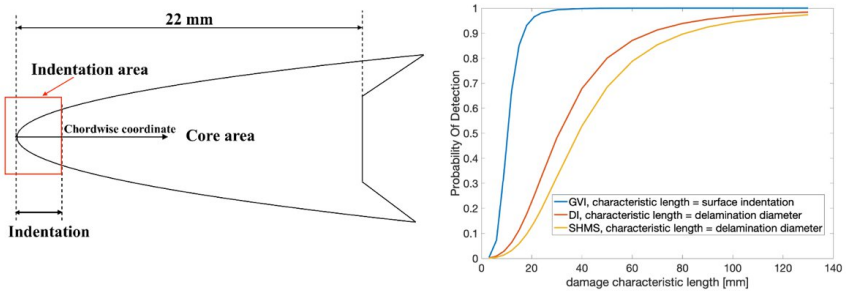

Figure 3: a) Schematic representation of the blade strength degratation function of the residual indentation; b) POD curves corresponding to the GVI, DI, obtained from [17], and SHMS, the latter calculated considering a threshold such to reach a PFA of 0.12% from the ROC curves presented in Figure 2b.

Accordingly, the following Eq. 12 was used to compute the ratio between the initial strength and the strength after an impact.

$$strength\ ratio\ = 1 - 1.5\frac{indentation\ area}{core\ area} \tag{12}$$

A coefficient of 1.5 was introduced to account for stress concentration effects. The indentation area was calculated by approximating the shape of the cross section near the leading edge with a square root function, resulting in Eq. 13. This equation expresses the indentation area as a function of the indentation depth.

$$indentation\ area\ = 2.89 \times indentation^{1.5} \tag{13}$$

Figure 3b shows the performance of GVI, DI, and SHMS in terms of the POD as a function of damage size. It is important to note that, while damage size for DI and SHMS refers to the delamination size, for GVI it corresponds to the surface indentation. The POD curves for GVI and DI were obtained from [17], while the performance of SHMS was previously derived using the FE model of the blade root. These SHMS results were assumed to be representative of the entire blade length. Assuming the total blade length is 7.5 times longer than the portion analyzed in the FE model, the number of FBG sensors was scaled proportionally. As a result, a total of 450 FBG sensors was considered for one blade.

In the Probabilistic Damage Tolerance Analysis, the load exceedance probability per FH was calculated based on [18]. The initial blade strength ratio was set to 2, representing the ratio between the failure load and the limit load. The blade's lifecycle was simulated on an hourly basis using a MATLAB script, averaging results across 30000 simulated scenarios. At each hour, the code checks whether it is time to perform an inspection. Accordingly, the inspection intervals for GVI, DI, and SHMS (the latter only for the "with SHMS" scenario) were defined as input parameters.

The cost model described by Eqs. 6–11 was implemented in the same script, which aggregates yearly cash flows across the lifecycle and ultimately calculates the NPV.

3 RESULTS

In this section, the final step (iv) of the procedure for assessing the economic impact of SHMS was completed. Table 1 presents selected values of the variables used in this study to evaluate the economic impact.

Variable	Value	Source
$C_{acq\ sys}$	13000 €	[19]
$c_{blade}^{as\ is}$	40000 €	DAER-lab
C_{energy}	10.6 €/h	[20]
C_{FBG}	90 €	DAER-lab
$C_{FBG\ sys}$	20000 €	[21]
c_{fuel}	272.64 €/h	[22, 23]
C_g	1 €	DAER-lab
C_m	1307 €	[20] and DAER-lab
C_{th}	10 €	[24]
$K_{partition}$	0.1	DAER-lab
L_{eng}	42 €/h	DAER-lab
L_{pilots}	48.2 €/h	[25]
$L_{tr\ wo}$	28 €/h	[26]
n_b	4	DAER-lab
n_{FBG}	450	DAER-lab
R	6560.6 €/h	[27]
r	8%	[28]
t_{auto}	8 h	DAER-lab
t_{depot}	0.5 h	DAER-lab
t_{DI}	15 h	DAER-lab
t_{eng}	0.0167 h	DAER-lab
t_{GVI}	0.652 h	DAER-lab
$t_{mount\ blade}$	0.5 h	DAER-lab
$t_{repair}^{as\ is}$	8 h	DAER-lab
$t_{tr\ wo}$	25 h	DAER-lab

Table 1: values and sources of the variables assumed in this study.

3.1 Beginning Of Life

The results related to the BOL analysis highlighted the presence of break-even points, beyond which one of the two scenarios becomes more economically advantageous than the other.

In terms of curing cycle development, it was found that if the number of cycles required to identify the optimal curing parameters is significantly reduced—thanks to the improved temperature field quality provided by FBG sensors—an economic benefit can be achieved. In this case, the “with SHMS” scenario becomes more favourable. For example, as shown in Figure 4a, if the number of curing cycles decreases from 26 in the “as is” scenario to fewer than 19 when using 10 FBG sensors (the “with SHMS” scenario), then the “with SHMS” scenario becomes more economically viable.

A similar trend was observed in relation to the laboratory tests required during the initial stage of blade certification. Here too, break-even points exist beyond which one scenario becomes more advantageous than the other. Specifically, if the number of tested blades can be sufficiently reduced—thanks to the improved strain field data from FBG sensors—an economic benefit is achieved under the “with SHMS” scenario. For instance, as shown in Figure 4b, if the number of tested blades decreases

from 22 in the "as is" scenario to fewer than 18 in the "with SHMS" scenario using 10 FBG sensors, the latter becomes the more cost-effective option.

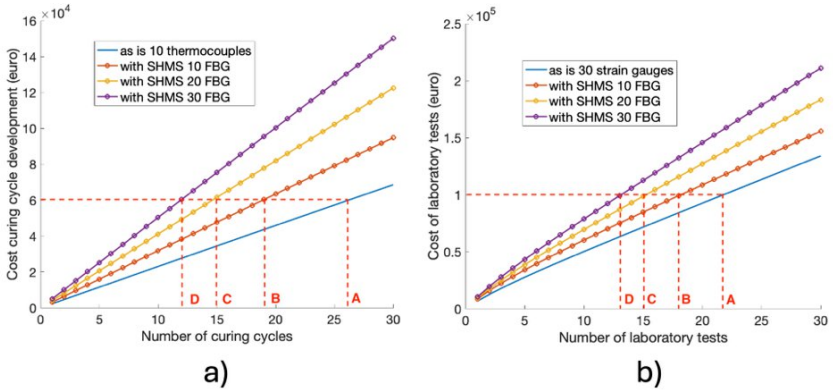

Figure 4: a) Cost of the curing cycle development versus the number of curing cycles performed, with sensitivity analysis on the number of FBG sensors embedded in the blade; b) Cost of laboratory tests versus the number of laboratory tests, with sensitivity analysis on the the number of FBG sensors embedded in the blade.

3.2 Middle Of Life

The results related to the MOL phase indicated that, in the "with SHMS" scenario, it was possible to extend the DI interval up to 2400 FH, provided that automatic inspections using SHMS were performed every 1070 FH. This extension maintained the same POF for the blade as in the original scenario. For this reason, the comparison between the two scenarios was conducted assuming an automatic inspection interval of 1070 FH for the SHMS. As shown in Figure 5, this condition is represented by the green vertical dashed line. Comparing the two scenarios at this inspection interval reveals a negative economic impact associated with the SHMS over the helicopter's lifecycle.

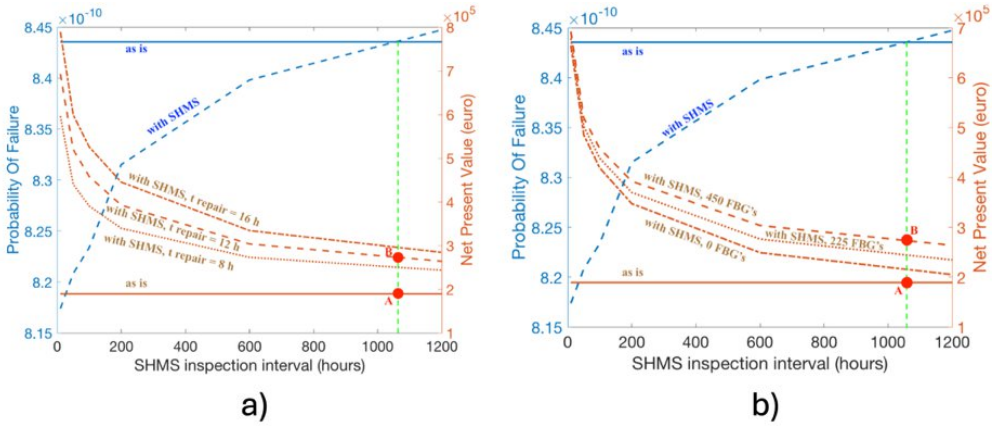

Figure 5: a) POF and NPV function of the inspection interval of the SHMS, with sensitivity analysis on the repairing time of the sensorized blade; b) POF and NPV function of the inspection interval of the SHMS, with sensitivity analysis on the number of FBG sensors charged to the customer.

Specifically, as illustrated in Figure 5, points A and B correspond to the "as is" and "with SHMS" scenarios, respectively. The NPV for the "as is" scenario is €1.89×10^5, while the NPV for the "with SHMS" scenario is €2.726×10^5. This indicates that maintenance in the "with SHMS" scenario is more expensive than in the "as is" scenario.

One of the main reasons for this outcome is the high number of unscheduled maintenance activities triggered by SHMS alarms, which makes it difficult to coordinate maintenance operations and consequently increases helicopter downtime. In fact, an analysis of the NPV breakdown shows that the use of SHMS led to a reduction in the effort required for DI, decreasing from 22% in the "as is"

scenario to 6% in the "with SHMS" scenario. However, this saving was offset by increased costs related to spare parts and repair operations.

It is also worth noting the findings from the sensitivity analyses shown in Figures 5a and 5b. These results indicate that even when assuming the same repair time of 8 hours for both standard and sensorized blades, the "as is" scenario remains the more cost-effective option. Furthermore, even under the assumption that the cost of the FBG sensors is not passed on to the customer—as illustrated in Figure 5b—the "as is" scenario continues to be the more economically favourable choice.

4 CONCLUSIONS

In this work, the economic impact of an FBG-based SHMS was investigated from two perspectives: BOL and MOL. The assessment followed the LCC methodology, which involves comparing different alternatives. In this study, two scenarios were evaluated: the current baseline scenario ("as is") and the scenario incorporating SHMS ("with SHMS").

Several key conclusions can be drawn from the analysis. First, a methodology to assess the economic impact of SHMS was developed and applied to the case of a rotorcraft composite blade. Although tailored to this specific application, the methodology can be generalized and adapted to other composite structural components. Second, at the BOL stage, SHMS implementation was shown to have a positive economic impact when a sufficient number of autoclave cycles are saved during the definition of curing parameters. Third, for the MOL stage, the use of SHMS on the composite rotorcraft blade resulted in a negative economic outcome. The savings achieved through automated scheduled inspections using SHMS were offset by the higher costs of spare parts and increased complexity of repair operations. To make SHMS economically viable, they should be applied to structural components that are difficult to access during maintenance. In such cases, the full potential of SHMS to reduce maintenance burden and downtime can be more effectively leveraged.

Future work should aim to quantify the actual reduction in the number of curing cycles and laboratory tests, made possible by the improved quality of temperature and strain field measurements obtained through FBG sensors.

REFERENCES

[1] Dong, T., & Kim, N. H. (2018). Cost-effectiveness of structural health monitoring in fuselage maintenance of the civil aviation industry. Aerospace, 5(3), 87.

[2] Sbarufatti, C., Manes, A., & Giglio, M. (2013). Performance optimization of a diagnostic system based upon a simulated strain field for fatigue damage characterization. Mechanical Systems and Signal Processing, 40(2), 667-690.

[3] Serafini, J., Bernardini, G., Porcelli, R., & Masarati, P. (2019). In-flight health monitoring of helicopter blades via differential analysis. Aerospace Science and Technology, 88, 436-443.

[4] Lin, M., Guo, S., He, S., Li, W., & Yang, D. (2022). Structure health monitoring of a composite wing based on flight load and strain data using deep learning method.Composite Structures,286, 115305.

[5] Cusati, V., Corcione, S., & Memmolo, V. (2021). Impact of structural health monitoring on aircraft operating costs by multidisciplinary analysis.Sensors,21(20), 6938.

[6] Büchter, K. D., Sebastia Saez, C., & Steinweg, D. (2022). Modeling of an aircraft structural health monitoring sensor network for operational impact assessment.Structural Health Monitoring,21(1), 208-224.

[7] Dienel, C. P., Meyer, H., Werwer, M., & Willberg, C. (2019). Estimation of airframe weight reduction by integration of piezoelectric and guided wave–based structural health monitoring.Structural Health Monitoring,18(5-6), 1778-1788.

[8] Cusati, V., Corcione, S., & Memmolo, V. (2022). Potential benefit of structural health monitoring system on civil jet aircraft.Sensors,22(19), 7316.

[9] Steinweg, D. M., Hornung, M., & Bauhaus Luftfahrt eV, W. (2019).Methods evaluating the impact of structural health monitoring on aircraft lifecycle costs. Bonn, Germany: Deutsche Gesellschaft für Luft-und Raumfahrt-Lilienthal-Oberth eV.

[10] Boller, C. (2014). Implementation Strategies for SHM in Civil and Military Applications.Structural Health Monitoring of Military Vehicles; Suleman, A., Ed.; STO-EN-AVT-220. STO Educational Notes.
[11] Sala, G., Di Landro, L., Airoldi, A., & Bettini, P. (2015). Fibre optics health monitoring for aeronautical applications.Meccanica,50, 2547-2567.
[12] Bottasso, L. M., Sala, G., Bettini, P., Tagliabue, P., Corbani, F., Platini, E., Guerra, A., Anelli, A. (2018). Rugged Fiber Optics Monitoring System for Helicopter Rotor Blades. In44th European Rotorcraft Forum (ERF 2018)(pp. 965-980). Curran Associates.
[13] Palmberg, B., Blom, A. F., & Eggwertz, S. (1987). Probabilistic damage tolerance analysis of aircraft structures. InProbabilistic fracture mechanics and reliability(pp. 47-130). Dordrecht: Springer Netherlands.
[14] Weber, S., Lone, M., & Cooke, A. (2019). Recent experiences of helicopter main rotor blade damage.Journal of the American Helicopter Society,64(3), 1-5.
[15] Kan, H. P. (1998).ENHANCED RELIABILITY PREDICTION METHODOLOGY FOR IMPACT DAMAGED COMPOSITE STRUCTURES(No. DOT/FAA/AR-97/79).
[16] Tawk, I., Aubry, J., Navarro, P., Ferrero, J. F., Marguet, S., Rivallant, S., ... & Rauch, P. (2012). Study of impact on helicopter blade.Engineering Failure Analysis,24, 38-45.
[17] Huang, C., & Lin, K. (2005, April). A method for reliability assessment of aircraft structures subject to accidental damage. In46th AIAA/ASME/ASCE/AHS/ASC Structures, Structural Dynamics and Materials Conference(p. 1830).
[18] Chen, X., Ren, H., Bil, C., & Cai, J. (2014). Repair tolerance analysis for composite structures using probabilistic methodologies.Journal of Aircraft,51(6), 1997-2004.
[19] Cost of acquisition system. Accessed on 10th of July 2023. Url: https://b2bstore.hbm.com/myHBM/app/displayApp/(cpgnum=1&layout=7.01-16_153_6_9_70_34_65_73_134_6&uiarea=6&citem=CC58514E6AD90F12E1000000AC1099340017A47744441EE1B2B08ED8335B1888&carea=CC58514E6AD90F12E1000000AC109934&rdb=0&cpgsize=0)/.do?rf=y.
[20] Morse, L., Cartabia, L., & Mallardo, V. (2022). Reliability-based bottom-up manufacturing cost optimisation for composite aircraft structures.Structural and Multidisciplinary Optimization,65(5), 159.
[21] Cost of interrogation system. Accessed on 10th of July 2023. Url: https://b2bstore.hbm.com/myHBM/app/displayApp/(cpgnum=1&layout=7.01-16_153_6_9_70_34_65_73_134_6&uiarea=6&citem=319DCC4F1E60564AE1000000AC109A0CA01D4895C9E81EE79BC34A9F7F62510B&carea=319DCC4F1E60564AE1000000AC109A0C&xcm=hbm_b2boccasionalcrm&rdb=0&cpgsize=0)/.do?rf=y
[22] Cost of fuel. Accessed on 23rd of July, 2023. Url: https://jet-a1-fuel.com/price/italy.
[23] Fuel consumption. Accessed on 22nd of July, 2023. url: http://c.eqcdn.com/_a15f1bfe5225ae94a025b%204998691df71/%20ergrpinc/db/61/472/spec_sheet/AW139+Spec+Sheet_09_16_2016.pdf.
[24] Cost of thermocouples. Accessed on 10th of July,2023. Url: https://www.ersa-shop.de/de/product_info.php?info=p1912_themoelement-k-type.html&gad=1&gclid=EAIaIQobChMIyZ3T4q-DgAMVqItoCR2UhACiEAQYDSABEgL8D_D_BwE.
[25] Labour rate helicopter pilots. Accessed on 25th of October, 2023. url: https://ca.indeed.com/q-helicopter-pilot-jobs.html.
[26] Labour rate aircraft maintenance technicians. Accessed on 25th of October, 2023. url: https://www. indeed.com/career/aircraft-maintenance-technician/salaries.
[27] Annual revenue. Accessed on 22nd of July, 2023. url: https : / / www . statista . com / statistics /629751/babcock-international-annual-revenues/.
[28] Discount rate. Accessed on 16th of July, 2023. url: https://valueinvesting.io/BAB.L/valuation/wacc.

PERFORMANCE IMPROVEMENT OF TYPE-4 HYDROGEN PRESSURE VESSEL USING PROGRESSIVE PLY FAILURE MECHANISM

Akash Kumar Burolia[1], Rajeev Kumar Verma[1] and Swati Neogi[1]

[1]Department of Chemical Engineering, Indian Institute of Technology Kharagpur
P.O. Paschim Medinipur, West Bengal-721302, India

Email: akashburolia@gmail.com , web page: https://www.iitkgp.ac.in/department/CH/faculty/ch-swati
Email: rajeev0iitkgp@gmail.com , web page: https://www.iitkgp.ac.in/department/CH/faculty/ch-swati
Email: swati@che.iitkgp.ac.in , web page: https://www.iitkgp.ac.in/department/CH/faculty/ch-swati

Keywords: Hydrogen storage, Type-4 pressure vessel, genetic algorithm, classical laminate theory (CLT), Failure theories

ABSTRACT

This study presents an analytical and optimization-based approach to enhance the burst performance of type-4 hydrogen pressure vessels. An analytical model using Classical Laminate Theory (CLT) was developed and validated against experimental and finite element data (FEA) from Sharma et al. (2023), showing strong agreement with less than 1% error compared to FEA and 8.3% deviation from experimental burst pressure. Among various failure theories, Hashin criterion accurately predicted matrix dominated failure in the cylindrical section, consistent with experimental observations. To improve structural performance, a Progressive Ply Failure (PPF) strategy was first applied by replacing the first failed plies, resulting in a 16.28% increase in burst pressure. However, to achieve optimal stacking efficiency, a Genetic Algorithm (GA) was employed. Through iterative evolution using tournament selection, the GA achieved a 28.89% improvement in burst pressure compared to the reference model using Hashin failure. This combined approach of analytical modeling, failure prediction, and evolutionary optimization provides a reliable and scalable method for designing high-performance hydrogen storage vessels, supporting the advancement of safe and efficient clean energy systems.

1. INTRODUCTION

Compressed hydrogen is an emerging energy carrier for sustainable and clean energy systems, specifically for fuel cell vehicles (FCVs). The major challenge in hydrogen adoption is the safe and efficient hydrogen storage for onboard and stationary automobile applications. Moreover, hydrogen gas have high diffusivity (6.1×10^{-5} m^2/s at NTP), reactivity, wide flammability range (4 - 74 % v/v in air) and low volumetric storage density (0.089 kg/m^3) at atmospheric condition which resist the commercialization of FCVs [1]. Therefore, hydrogen gas needs to be compressed and stored in pressure vessels at higher pressure up to 100 MPa, to improve the volumetric storage density.

There are four types of pressure vessels categories based on their material of construction as shown in Figure 1 (A). Type-1 is a traditional metallic pressure vessel with an operating pressure of ≤ 20 MPa. These vessels are highly prone to hydrogen embrittlement and their strength-to-weight ratio is very low. Type-2 pressure vessels are upgraded with hoop winding over a metallic liner/vessel, these vessels can hold the operating pressure up to ≤ 30 MPa. Type-3 is hybrid pressure vessels with fully overwrapped with hoop and helical layers over a metallic liner, these vessels have operating pressure up to ≤ 50 MPa. Type-4 is lightest among all the pressure vessels due to their material of construction, these vessels are fully overwrapped on a high hydrogen gas barrier polymeric liner. Type-4 pressure vessels have higher operating pressure up to 100 MPa, offers higher volumetric storage density and protected from hydrogen embrittlement. However, the major challenge in type-4 composite pressure vessels is the design of the composite structure because composite is the main strength contributor whereas the liner is a non-load

sharing component which is used to hold the hydrogen gas under allowable permeation rate and providing mandrel for filament winding [2], [3]. Composite structure of the pressure is composed of many hoop (90^0 angle layer) and helical layers (other than 90^0 angle layer) arranged in a specific order to achieve the desirable burst performance of the pressure vessels as shown in Figure 1 (B). These layers can be arranged in several ways to achieve the desired burst performance. The structural integrity and burst performance of Type-IV vessels are highly dependent on the stacking sequence of the composite layers. An optimized laminate design not only improves safety and reliability but also enhances material efficiency and reduces cost.

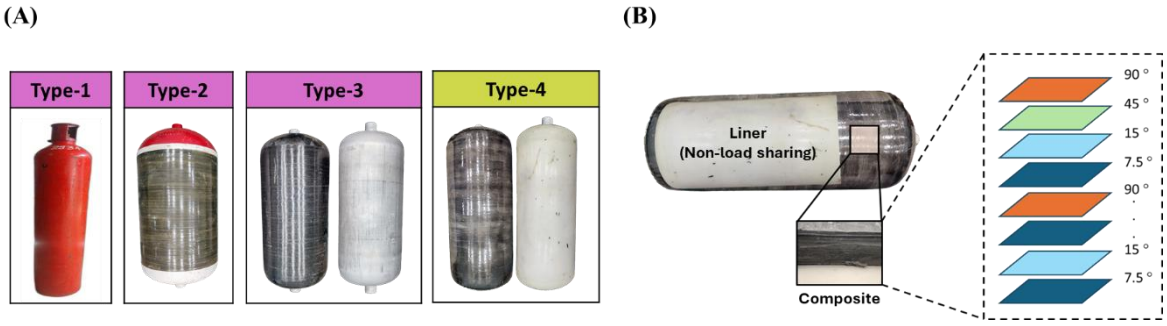

Figure 1: (A) Types of pressure vessel and (B) cross-sectional view of composite in type-4.

Several studies have been reported on the performance improvement of composites. Leh et al. developed a simulation platform to predict the burst pressure of type-4 pressure vessels using progressive failure mechanism. However, model was based conventional approach [4]. Nebe et al. investigate the burst pressure of composite pressure vessel based on first ply failure mechanism and found 67 % difference in experimental and model prediction [5]. Chang et al. worked on experimental validation of progressive ply failure using acoustic emission AMS3 (AE) system. However, his work does not involve any specific optimization technique [6]. The literature found that the progressive failure is a powerful approach for preliminary investigation of burst pressure and design. However, for fast and reliable designing of pressure vessel required a robust optimization technique to optimize the vessel design specifically layer sequence.

Alcantar et al. worked on optimization of type-4 pressure vessels using genetic algorithms and simulated annealing. the study reported 11.2 % improvement in design performance [7]. Fanding et al. integrated an artificial neural network with a finite element model to predict the first performance, and the model was accurate up to 2% of error [8].

Based on extensive literature, designing of composite pressure vessel with an optimum winding sequence for better performance is the major challenge. To address this challenge, this study integrates an analytical model based on Classical Laminate Theory (CLT) with failure criteria and optimization algorithms to improve vessel performance. The model is validated against experimental and finite element burst pressure data. A Progressive ply failure (PPF) approach is initially applied to iteratively enhance the layer sequence. However, due to its limitations, a Genetic Algorithm (GA) is introduced to perform a global optimization of the stacking sequence under mechanical and manufacturing constraints. This research aims to demonstrate the effectiveness of combining analytical modeling, failure analysis, and evolutionary optimization in designing high-performance Type-IV pressure vessels that meet stringent safety standards, such as ISO 11119-3. The findings provide a framework for systematic laminate optimization and support the advancement of safer, lighter, and more efficient hydrogen storage systems.

2. MATERIALS AND METHOD

2.1. MATERIALS

T700SC-12k carbon fiber manufactured by Toray, Japan and Araldite LY556 with hardener XY54 manufactured by Huntsman were used for the manufacturing of the type-4 pressure vessels. The composite properties were calculated by using micromechanics, measured properties are listed in Table 1 [9]. The fiber volume fraction of the composite material was 30 v/v%, measured by using muffle furnace by heating the small coupon of the composite at 600 ^{0}C temperature.

Table 1: Carbon-epoxy composite material specifications.

Properties	Symbol/unit	Carbon fiber (T700SC)	Epoxy resin Araldite LY 556 Hardener XY 54	Composite
Longitudinal modulus	E_{11} (MPa)	230000	3450	71415
Transverse modulus	E_{22} (MPa)	17000	3450	6123
In-plane shear modulus	G_{12} (MPa)	900	1280	2414
Out of plane shear modulus	G_{23} (MPa)	4600	1280	1383
Major Poisson's ratio	v_{12}	0.2	0.35	0.305
Minor Poisson's ratio	v_{23}	0.25	0.35	0.555
Longitudinal Tensile strength	X_{11}^{t} (MPa)	4900	90	1470
Transverse tensile strength	X_{22}^{t} (MPa)	-	90	88.5
In-plane shear strength	X_{12} (MPa)	600	50	118
Out of plane shear strength	X_{23} (MPa)	600	50	98
Density	ρ (kg/m^3)	1800	1150	1345

2.2. METHODS

In this study, the type-4 pressure vessel design parameters were taken from Sharma et al. [9], for modelling and validation. The type-4 vessel has 29 layers $[7.5_7/15_6/25_4/35_1/45_1/90_{10}]$ with an experimental burst pressure of 81.9 MPa. Figure 2 shows the flowchart to predict the burst pressure of type-4 pressure and the approaches to improve the burst performance. The burst performance of the pressure vessel was predicted by an analytical model of the type-4 pressure vessel using Classical Laminate Theory (CLT) in MATLAB 2024. CLT is an analytical framework to predict the mechanical behaviour of the composite laminate under in-plane loading. CLT enables the determination of in-plane stresses, strains, and deformations in a laminate composed of multiple orthotropic laminae stacked at various orientations. The analytical model was developed based on the following assumptions: 1) each lamina behaves as a linear elastic orthotropic material, 2) Kirchhoff hypothesis, and 3) Perfect bonding [10].

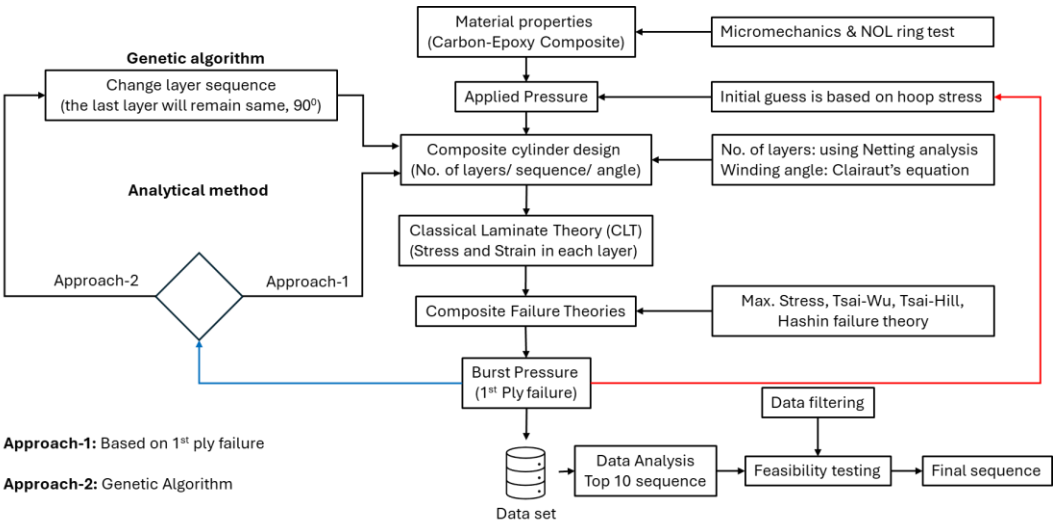

Figure 2: Flowchart for burst pressure prediction and performance improvement strategies.

The fundamental equation of CLT is given by the equation (1). This equation is used to express in-plane strain and curvature at any location of the composite [11].

$$\begin{bmatrix} N_x \\ N_y \\ N_{xy} \\ M_x \\ M_y \\ M_{xy} \end{bmatrix} = \begin{bmatrix} A_{11} & A_{12} & A_{16} & B_{11} & B_{12} & B_{16} \\ A_{12} & A_{22} & A_{26} & B_{12} & B_{22} & B_{26} \\ A_{16} & A_{26} & A_{66} & B_{16} & B_{26} & B_{66} \\ B_{11} & B_{12} & B_{16} & D_{11} & D_{12} & D_{16} \\ B_{12} & B_{22} & B_{26} & D_{12} & D_{22} & D_{26} \\ B_{16} & B_{26} & B_{66} & D_{16} & D_{26} & D_{66} \end{bmatrix} \begin{bmatrix} \varepsilon_x^0 \\ \varepsilon_y^0 \\ \gamma_{xy}^0 \\ k_x \\ k_y \\ k_{xy} \end{bmatrix} \quad (1)$$

$$A_{ij} = \sum_{k=1}^{n} \left[\left(\overline{Q}_{ij}\right)\right]_k (h_k - h_{k-1});\ B_{ij} = \frac{1}{2}\sum_{k=1}^{n} \left[\left(\overline{Q}_{ij}\right)\right]_k ({h^2}_k - {h^2}_{k-1});$$

$$D_{ij} = \frac{1}{3}\sum_{k=1}^{n} \left[\left(\overline{Q}_{ij}\right)\right]_k ({h^3}_k - {h^3}_{k-1}) \quad (2)$$

$$\begin{bmatrix} \varepsilon^0 \\ k \end{bmatrix} = \begin{bmatrix} A_1 & B_1 \\ B_1 & D_1 \end{bmatrix} \begin{bmatrix} N \\ M \end{bmatrix} \quad (3)$$

Where [A], [B] and [D] are extensional, coupling and bending stiffness matrix, respectively. These stiffness matrices are a function of the transformed reduced stiffness matrix $[\overline{Q}]$ and the total number of layers n, where h represents the thickness of each layer. Finally, the stress-strain on each layer is calculated by using equation (4). Where z is total thickness of the composite.

$$\begin{bmatrix} \sigma_x \\ \sigma_y \\ \tau_{xy} \end{bmatrix} = [\overline{Q}] \begin{bmatrix} \varepsilon_{x0} \\ \varepsilon_{y0} \\ \gamma_{xy0} \end{bmatrix} + z[\overline{Q}] \begin{bmatrix} k_x \\ k_y \\ k_{xy} \end{bmatrix} \quad (4)$$

$$\begin{bmatrix} \varepsilon_x \\ \varepsilon_y \\ \gamma_{xy} \end{bmatrix} = \begin{bmatrix} \varepsilon_{x0} \\ \varepsilon_{y0} \\ \gamma_{xy0} \end{bmatrix} + z \begin{bmatrix} k_x \\ k_y \\ k_{xy} \end{bmatrix} \quad (5)$$

Once the stress and strain in the composite are calculated, then failure theories can be implemented to find the burst pressure of the composite. However, conventional isotropic failure criteria are inadequate for the anisotropic and heterogeneous nature of fiber-reinforced composites. Therefore, Maximum stress, Tsai Wu, Tsai Hill, and Hashin failure criteria were used to predict he failure. Each criterion has a different approach in defining how and when failure occurs in a composite lamina [12], [13].

Maximum stress failure criteria: is a noninteractive, simplest and conservative failure theory that assumes failure when any individual stress component in the local lamina coordinate system exceed its corresponding ultimate strength limit as given by equation (6).

$$-(\sigma_1^c)_{ult} < \sigma_1 < \left(\sigma_1^T\right)_{ult};\ -(\sigma_2^c)_{ult} < \sigma_2 < \left(\sigma_2^T\right)_{ult};\ -(\tau_{12}^c)_{ult} < \tau_{12} < \left(\tau_2^T\right)_{ult} \quad (6)$$

Tsai Wu failure criteria: is an interactive theory which includes linear and quadratic terms to account for different strength in tension and compression. This theory assumes the failure of composite when the left side terms of equation (7) is less than 1. This criterion considers tension-compression asymmetry and stress interactions, making it more accurate but computationally intensive.

$$(F_2 + F_3)\sigma_1^2 + (F_1 + F_3)\sigma_2^2 + (F_1 + F_2)\sigma_3^2 - 2F_3\sigma_1\sigma_2 - 2F_2\sigma_1\,\sigma_3 - 2F_1\sigma_2\,\sigma_3 + 2F_4\tau_{23}^2 + 2F_5\tau_{13}^2 + 2F_6\tau_{12}^2 < 1 \quad (7)$$

$$F_1 = \frac{1}{2}\left(\frac{2}{\left[(\sigma_2^T)_{ult}\right]^2} - \frac{1}{\left[(\sigma_1^T)_{ult}\right]^2}\right);\ F_2 = \frac{1}{2}\left(\frac{2}{\left[(\sigma_2^T)_{ult}\right]^2}\right);\ F_3 = \frac{1}{2}\left(\frac{2}{\left[(\sigma_1^T)_{ult}\right]^2}\right);\ F_6 = \frac{1}{2}\left(\frac{2}{[(\tau_{12})_{ult}]^2}\right) \quad (8)$$

Tsai Hill failure criteria: is an interactive with stress component. The theory is based on von Mises distortion energy theory, which predicts the failure when left side term of equation (9) is less than 1.

$$H_1\sigma_1 + H_2\sigma_2 + H_6\tau_{12} + H_{11}\sigma_1^2 + H_{22}\sigma_2^2 + H_{66}\tau_{12}^2 + 2H_{12}\sigma_1\sigma_2 < 1 \quad (9)$$

$$H_1 = \frac{1}{(\sigma_1^T)_{ult}} - \frac{1}{(\sigma_1^C)_{ult}};\ H_2 = \frac{1}{(\sigma_2^T)_{ult}} - \frac{1}{(\sigma_2^C)_{ult}};\ H_{11} = \frac{1}{(\sigma_1^T)_{ult}(\sigma_1^C)_{ult}};\ H_{22} = \frac{1}{(\sigma_2^T)_{ult}(\sigma_2^C)_{ult}};\ H_{66} = \frac{1}{[(\tau_{12})_{ult}]^2};\ H_6 = 0 \quad (10)$$

Hashin failure criteria: distinguish between different failure modes such as fiber tension, fiber compression, matrix tension and matrix compression given by equation (11). Mostly used for progressive damage model and finite element simulation.

$$\left(\frac{\sigma_1}{(\sigma_1^T)_{ult}}\right)^2 \geq 1\ ;\ \left(\frac{\sigma_1}{(\sigma_1^C)_{ult}}\right)^2 \geq 1 \quad (11)$$

$$\left(\frac{\sigma_1}{(\sigma_1^T)_{ult}}\right)^2 + \left(\frac{\tau_{12}}{(\tau_{12}^T)_{ult}}\right) \geq 1\ ;\ \left(\frac{\sigma_2}{2(\sigma_2^C)_{ult}}\right)^2 + \left(\frac{\tau_{12}}{(\tau_{12}^T)_{ult}}\right) \geq 1 \quad (12)$$

2.2.1. APPROACH-1: PROGRESSIVE PLY FAILURE

Composite is an anisotropic material in which the failure initiates from the weakest lamina and progresses through the entire laminate in a random manner. 1st play failure in the progressive ply failure (PPF) mechanism identifies the onset of the damage in the laminate. This method provides a more realistic prediction of initial damage than global failure criteria, especially in pressure vessels where localized stress concentrations may cause early damage initiation. In this approach, FPF is calculated by using failure criteria and replacing that ply orientation with another angle to investigate the role of sequence. This method is a conventional and time-consuming method to find the best burst performance. However, this strategy is integrated with a genetic algorithm to automate the process to optimize the sequence based on targeted burst pressure. However, the FPF method helps to identify the weakest ply, its angle, and position [6], [11], [14].

2.2.2. APPROACH-2: GENETIC ALGORITHM

The stacking sequence of composite laminates plays a crucial role in determining the mechanical performance and burst pressure of Type-4 hydrogen pressure vessels. Due to the combinatorial nature of stacking possibilities, Genetic Algorithm (GA) was employed to efficiently explore the design space. In this approach, each chromosome (ply) encodes a candidate layer sequence, with fiber orientations represented as discrete values $[7.5_7/15_6/25_4/35_1/45_1/90_{10}]$. The algorithm iteratively evolves the population through selection, crossover, and mutation operations, guided by a fitness function based on performance metrics such as burst pressure and compliance with failure criteria. To assess its fitness value, an objective function is utilized. If the convergence criterion is not met, the algorithm applies genetic operators again to produce a new generation. This process repeats for multiple generations until either the convergence criterion is satisfied, or the maximum number of generations is reached. Figure 3 illustrates the flowchart of the proposed genetic algorithm (GA). This approach provides a robust and flexible framework for the design optimization of composite pressure vessels. At last, the top 10 data sets were selected for data processing, in which the pressure vessel dome geometry is designed in ANSYS to identify the uneven dome geometry at the corresponding layer sequence [15], [16], [17].

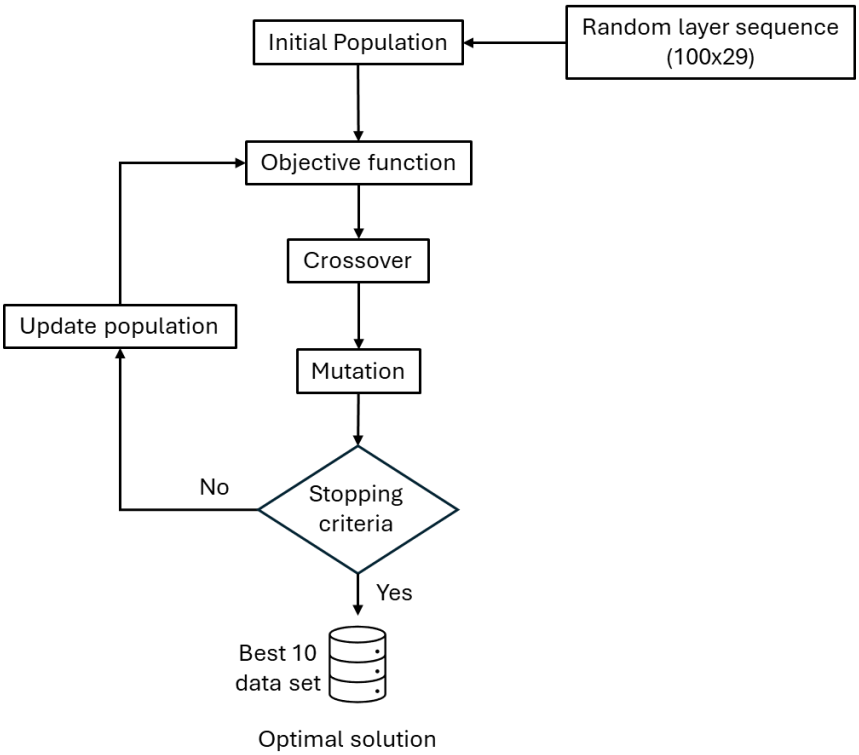

Figure 3: Flowchart for the genetic algorithm for composite sequence optimization.

3. RESULTS AND DISCUSSION

In this section, the analytical CLT model of a type-4 hydrogen pressure vessel is validated with the experimental burst pressure and finite element analysis provided by reference. The validated model is incorporated with the first ply failure strategy, followed by a genetic algorithm to improve the performance of the type-4 hydrogen pressure vessel by optimizing the layer sequence.

3.1. MODEL VALIDATION

Figure 4 (A) depicts the comparison of the analytical CLT model with the finite element and experimental burst pressure of a type-4 pressure vessel. The analysis shows that the model follows the Hashin matrix failure, which is also reported in the reference design. The burst pressure predicted by the analytical model is 75.61 MPa compared to finite element (75.3 MPa) and experimental (81.9 MPa) [9]. The model shows a good agreement with failure theory, with an error of less than 1 % with finite element and 8.3 % with experimental burst pressure. The model is also designed using finite element analysis in ANSYS to identify the safe and unsafe model of the failure. Figure 4 (B) and (C) shows that the failure of the type-4 pressure vessel lies in the cylindrical section, which corresponds to a safe failure model. Moreover, the investigation found that the Hashin failure is more realistic to predict the burst pressure due to its distinct nature in the failure model. However, the other failure theories are over-predicted, such as maximum stress due to no interaction with stress components.

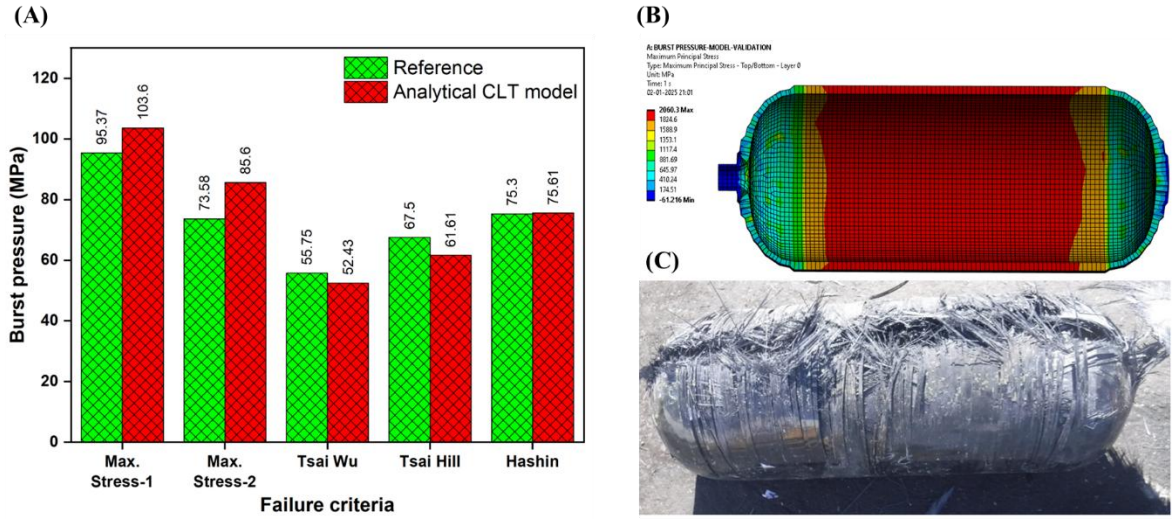

Figure 4: (A) comparison for failure criteria for analytical CLT with reference, (B) failure mode using finite element and (C) experimental burst tested type-4 pressure vessel.

3.2. APPROACH-1: PROGRESSIVE PLY FAILURE

The Figure 5 represents the theoretical burst pressure for different stacking sequences**,** changed by replacing the orientation of the first ply failure. Their corresponding values are given in Table 2. In this approach, the ply that fails first was replaced by the ply that fails last or has a different orientation, because that ply has taken the most stress till the end of the complete composite failure. The analysis shows the burst performance has been improved by 16.28 % compared to the finite element in reference for stack-2. After stack -2, it is observed that the maximum stress failure is significantly reduced which is even below the nominal burst pressure (2 time of operating pressure) as per ISO 11119-3. Therefore, the stack-3 to 5 is considered for the applicable layer sequence.

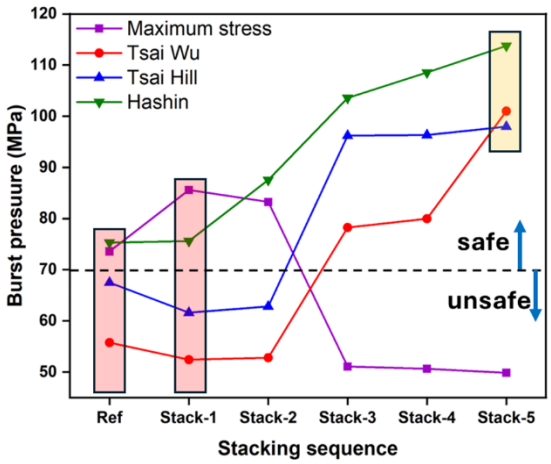

Figure 5: Bust performance improvement by PPF mechanism.

Table 2: Comparison of burst performance for different stacking sequences based on PPF.

	Stacking sequence [$90_{10}/45_1/35_1/25_4/15_6/7.5_7$]	**Max. stress**	**Tsai Wu**	**Tsai Hill**	**Hashin (matrix failure)**	**Experimental burst test**
	Reference	73.58	55.75	67.5	75.3	81.9
1	Stacking -1	85.60	52.43	61.61	75.61	
2	Stacking -2	83.27	52.81	62.82	87.56	
3	Stacking-3	51.1	78.25	96.20	103.58	
4	Stacking-4	50.64	79.97	96.34	108.57	
5	Stacking-5	49.85	101.01	97.98	113.76	

This strategy is complex, time-consuming, and fails to provide the optimum layer sequence for best performance. Therefore, the PPF is integrated with a genetic algorithm to optimize the sequence.

3.3. APPROACH-2: GENETIC ALGORITHM (GA)

In GA, the first 10 layers were fixed as they are important to generate the symmetry of the dome with the cylindrical shape, and the last layer was also fixed with 90^0 orientation because that layer helps to hold the helical layer and avoid its slippage. Since,18 layers left for implementing the GA, those layers were considered as genes of the system.

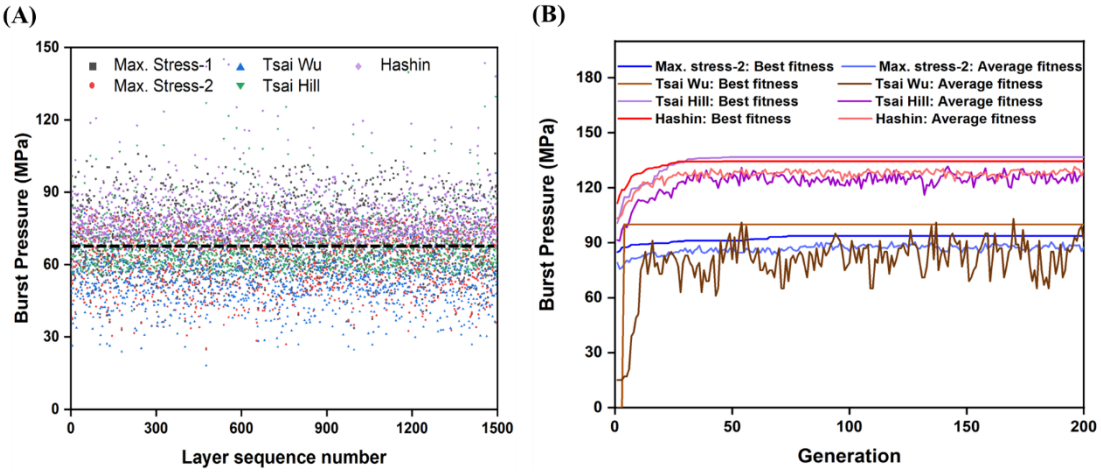

Figure 6: (A) initial population using brute force technique and (B) fitness profile for different failure criteria.

Firstly, an initial population was created using brute force technique in which random combinations are generated with all plies keeping the total number of layers the same as 29. Figure 6 (A) shows the initial population representing the theoretical burst pressure at different failure criteria. In the initial population, 100 data set points called chromosomes were filtered, which have the lowest possible burst pressure of 70 MPa under any failure criteria to meet the ISO 11119-3. These chromosomes are evaluated using a fitness function that quantifies their burst performance based on objectives function. Tournament selection technique was employed to choose the parent solution based on their fitness as shown in Figure 6 (B) **.** Now, the genes of the parents were crossover to generate a new population with different genes. To maintain diversity and avoid premature convergence, random mutations were introduced with a constraint that the new population/sequence cannot create any sequence that has more than two orientations simultaneously. This constraint helps to avoid the nonuniformity in the cylindrical shape. The best performing chromosomes were retained using elitism, and the population is iteratively evolved over successive generations. This process continues until a burst pressure approaches constant value with an convergence of 10^{-3} as shown in Figure 6 (B) . Where the average burst pressure approaches steady state after 100 generations. After the completion of the process, the optimum layer sequence is identified which have lowest possible burst pressure of 70 MPa So that the actual type-4 with optimum winding sequence should not have burst pressure less than safety factor. Table 3 listed burst pressure at the optimum layer sequence compared with progressive ply failure and reference data.

The analysis found the GA has improved the burst performance by 28.89 % compared to reference holding Hashin failure criteria.

Table 3: Comparison of burst performance.

Failure Theory	Burst pressure (MPa)					Burst performance Improvement (%)
	Experimental	Reference	Analytical CLT model	Approach-1: PPF	Approach-2: GA	
Max Stress 1	**81.9**	95.37	103.02	98.64	101.41	+ 6.33
Max Stress 2		73.58	85.6	83.27	83.25	+ 13.14
Tsai-Wu		55.75	52.43	52.81	82.89	+ 48.68
Tsai-Hill		67.5	61.61	62.82	87.24	+ 29.24
Hashin		**75.3**	**75.61**	**87.56**	**97.05**	**+ 28.89**

4. CONCLUSION

An analytical CLT model for a Type-IV hydrogen pressure vessel was validated against experimental and finite element results, showing excellent agreement within 1% of FEA and 8.3% of experimental data. The Hashin failure criterion accurately captured matrix-dominated failure in the cylindrical section, aligning with the observed failure modes. A progressive ply failure (PPF) approach provided up to 16.28% improvement in burst pressure but was limited in efficiency. To overcome this, a Genetic Algorithm (GA) was integrated, optimizing the stacking sequence while maintaining structural constraints. The GA-based method achieved a 28.89% improvement in burst pressure compared to the reference design using Hashin failure. This study demonstrates that combining analytical modeling, FPF theory, and evolutionary optimization effectively enhances the structural performance of Type-IV composite pressure vessels.

ACKNOWLEDGEMENTS

This work is supported and funded by the Technology Mission Division (Energy, Water & all Others), Department of Science & Technology, Ministry of Science & Technology and Government of India under the project Integrated Clean-Energy Material Acceleration Platform (IC-MAP) on Bioenergy & H_2, Project reference number: DST/TMD/IC-MAP/2K20/02(C).

REFERENCES

[1] D. Mori and K. Hirose, "Recent challenges of hydrogen storage technologies for fuel cell vehicles," *Int. J. Hydrogen Energy*, vol. 34, no. 10, pp. 4569–4574, 2009, doi: 10.1016/j.ijhydene.2008.07.115.

[2] P. Sharma, A. K. Burolia, A. Mandal, and S. Neogi, "Commercially available resources for physical hydrogen storage and distribution," in *Towards Hydrogen Infrastructure: Advances and Challenges in Preparing for the Hydrogen Economy*, Elsevier, 2023, pp. 225–256. doi: 10.1016/B978-0-323-95553-9.00010-8.

[3] J. Bellosta von Colbe *et al.*, "Application of hydrides in hydrogen storage and compression: Achievements, outlook and perspectives," *Int. J. Hydrogen Energy*, vol. 44, no. 15, pp. 7780–7808, 2019, doi: 10.1016/j.ijhydene.2019.01.104.

[4] D. Leh, P. Saffré, P. Francescato, R. Arrieux, and S. Villalonga, "A progressive failure analysis of a 700-bar type IV hydrogen composite pressure vessel," *Int. J. Hydrogen Energy*, vol. 40, no. 38, pp. 13206–13214, 2015, doi: 10.1016/j.ijhydene.2015.05.061.

[5] M. Nebe, T. J. Asijee, C. Braun, J. M. J. F. van Campen, and F. Walther, "Experimental and analytical analysis on the stacking sequence of composite pressure vessels," *Compos. Struct.*, vol. 247, p. 112429, 2020, doi: 10.1016/j.compstruct.2020.112429.

[6] R. R. Chang, "Experimental and theoretical analyses of first-ply failure of laminated composite

pressure vessels," *Compos. Struct.*, vol. 49, no. 2, pp. 237–243, 2000, doi: 10.1016/S0263-8223(99)00133-6.

[7] V. Alcántar, S. M. Aceves, E. Ledesma, S. Ledesma, and E. Aguilera, "Optimization of Type 4 composite pressure vessels using genetic algorithms and simulated annealing," *Int. J. Hydrogen Energy*, vol. 42, no. 24, pp. 15770–15781, 2017, doi: 10.1016/j.ijhydene.2017.03.032.

[8] F. D. Li *et al.*, "Optimal design of thin-layered composites for type IV vessels: Finite element analysis enhanced by ANN," *Thin-Walled Struct.*, vol. 187, Jun. 2023, doi: 10.1016/j.tws.2023.110752.

[9] P. Sharma, A. K. Burolia, N. C. Adak, J. Daiya, H. H. Sardar, and S. Neogi, "Effect of tension on liner buckling and performance of a type-4 cylinder for storage of compressed gases with experimental validation," *Thin-Walled Struct.*, vol. 189, Aug. 2023, doi: 10.1016/j.tws.2023.110928.

[10] S. Adali, E. B. Summers, and V. E. Verijenko, "Optimisation of laminated cylindrical pressure vessels under strength criterion," *Compos. Struct.*, vol. 25, no. 1–4, pp. 305–312, 1993, doi: 10.1016/0263-8223(93)90177-R.

[11] T. Y. Kam, Y. W. Liu, and F. T. Lee, "First-ply failure strength of laminated composite pressure vessels," *Compos. Struct.*, vol. 38, no. 1–4, pp. 65–70, 1997, doi: 10.1016/S0263-8223(97)00042-1.

[12] L. Wang, C. Zheng, S. Wei, and Z. Wei, "Micromechanics-based progressive failure analysis of carbon fiber/epoxy composite vessel under combined internal pressure and thermomechanical loading," *Compos. Part B Eng.*, vol. 89, pp. 77–84, 2016, doi: 10.1016/j.compositesb.2015.11.018.

[13] Z. Hu *et al.*, "Investigation on failure behaviors of 70 MPa Type IV carbon fiber overwound hydrogen storage vessels," *Compos. Struct.*, vol. 259, no. November 2020, pp. 1–11, 2021, doi: 10.1016/j.compstruct.2020.113387.

[14] S. Lin, L. Yang, H. Xu, X. Jia, X. Yang, and L. Zu, "Progressive damage analysis for multiscale modelling of composite pressure vessels based on Puck failure criterion," *Compos. Struct.*, vol. 255, no. September 2020, p. 113046, 2021, doi: 10.1016/j.compstruct.2020.113046.

[15] M. H. Hajmohammad, A. Tabatabaeian, A. R. Ghasemi, and F. Taheri-Behrooz, "A novel detailed analytical approach for determining the optimal design of FRP pressure vessels subjected to hydrostatic loading: Analytical model with experimental validation," *Compos. Part B Eng.*, vol. 183, no. December 2019, 2020, doi: 10.1016/j.compositesb.2019.107732.

[16] P. F. Liu, J. K. Chu, S. J. Hou, P. Xu, and J. Y. Zheng, "Numerical simulation and optimal design for composite high-pressure hydrogen storage vessel: A review," *Renew. Sustain. Energy Rev.*, vol. 16, no. 4, pp. 1817–1827, 2012, doi: 10.1016/j.rser.2012.01.006.

[17] C. U. Kim, C. S. Hong, C. G. Kim, and J. Y. Kim, "Optimal design of filament wound type 3 tanks under internal pressure using a modified genetic algorithm," *Compos. Struct.*, vol. 71, no. 1, pp. 16–25, 2005, doi: 10.1016/j.compstruct.2004.09.006.

[1] D. Mori and K. Hirose, "Recent challenges of hydrogen storage technologies for fuel cell vehicles," *Int. J. Hydrogen Energy*, vol. 34, no. 10, pp. 4569–4574, 2009, doi: 10.1016/j.ijhydene.2008.07.115.

[2] P. Sharma, A. K. Burolia, A. Mandal, and S. Neogi, "Commercially available resources for physical hydrogen storage and distribution," in *Towards Hydrogen Infrastructure: Advances and Challenges in Preparing for the Hydrogen Economy*, Elsevier, 2023, pp. 225–256. doi: 10.1016/B978-0-323-95553-9.00010-8.

[3] J. Bellosta von Colbe *et al.*, "Application of hydrides in hydrogen storage and compression: Achievements, outlook and perspectives," *Int. J. Hydrogen Energy*, vol. 44, no. 15, pp. 7780–7808, 2019, doi: 10.1016/j.ijhydene.2019.01.104.

[4] D. Leh, P. Saffré, P. Francescato, R. Arrieux, and S. Villalonga, "A progressive failure analysis of a 700-bar type IV hydrogen composite pressure vessel," *Int. J. Hydrogen Energy*, vol. 40, no. 38, pp. 13206–13214, 2015, doi: 10.1016/j.ijhydene.2015.05.061.

[5] M. Nebe, T. J. Asijee, C. Braun, J. M. J. F. van Campen, and F. Walther, "Experimental and analytical analysis on the stacking sequence of composite pressure vessels," *Compos. Struct.*, vol. 247, p. 112429, 2020, doi: 10.1016/j.compstruct.2020.112429.

[6] R. R. Chang, "Experimental and theoretical analyses of first-ply failure of laminated composite pressure vessels," *Compos. Struct.*, vol. 49, no. 2, pp. 237–243, 2000, doi: 10.1016/S0263-8223(99)00133-6.

[7] V. Alcántar, S. M. Aceves, E. Ledesma, S. Ledesma, and E. Aguilera, "Optimization of Type 4 composite pressure vessels using genetic algorithms and simulated annealing," *Int. J. Hydrogen Energy*, vol. 42, no. 24, pp. 15770–15781, 2017, doi: 10.1016/j.ijhydene.2017.03.032.

[8] F. D. Li *et al.*, "Optimal design of thin-layered composites for type IV vessels: Finite element analysis enhanced by ANN," *Thin-Walled Struct.*, vol. 187, Jun. 2023, doi: 10.1016/j.tws.2023.110752.

[9] P. Sharma, A. K. Burolia, N. C. Adak, J. Daiya, H. H. Sardar, and S. Neogi, "Effect of tension on liner buckling and performance of a type-4 cylinder for storage of compressed gases with experimental validation," *Thin-Walled Struct.*, vol. 189, Aug. 2023, doi: 10.1016/j.tws.2023.110928.

[10] S. Adali, E. B. Summers, and V. E. Verijenko, "Optimisation of laminated cylindrical pressure vessels under strength criterion," *Compos. Struct.*, vol. 25, no. 1–4, pp. 305–312, 1993, doi: 10.1016/0263-8223(93)90177-R.

[11] T. Y. Kam, Y. W. Liu, and F. T. Lee, "First-ply failure strength of laminated composite pressure vessels," *Compos. Struct.*, vol. 38, no. 1–4, pp. 65–70, 1997, doi: 10.1016/S0263-8223(97)00042-1.

[12] L. Wang, C. Zheng, S. Wei, and Z. Wei, "Micromechanics-based progressive failure analysis of carbon fiber/epoxy composite vessel under combined internal pressure and thermomechanical loading," *Compos. Part B Eng.*, vol. 89, pp. 77–84, 2016, doi: 10.1016/j.compositesb.2015.11.018.

[13] Z. Hu *et al.*, "Investigation on failure behaviors of 70 MPa Type IV carbon fiber overwound hydrogen storage vessels," *Compos. Struct.*, vol. 259, no. November 2020, pp. 1–11, 2021, doi: 10.1016/j.compstruct.2020.113387.

[14] S. Lin, L. Yang, H. Xu, X. Jia, X. Yang, and L. Zu, "Progressive damage analysis for multiscale modelling of composite pressure vessels based on Puck failure criterion," *Compos. Struct.*, vol. 255, no. September 2020, p. 113046, 2021, doi: 10.1016/j.compstruct.2020.113046.

[15] M. H. Hajmohammad, A. Tabatabaeian, A. R. Ghasemi, and F. Taheri-Behrooz, "A novel detailed analytical approach for determining the optimal design of FRP pressure vessels subjected to hydrostatic loading: Analytical model with experimental validation," *Compos. Part B Eng.*, vol. 183, no. December 2019, 2020, doi: 10.1016/j.compositesb.2019.107732.

[16] P. F. Liu, J. K. Chu, S. J. Hou, P. Xu, and J. Y. Zheng, "Numerical simulation and optimal design for composite high-pressure hydrogen storage vessel: A review," *Renew. Sustain. Energy Rev.*, vol. 16, no. 4, pp. 1817–1827, 2012, doi: 10.1016/j.rser.2012.01.006.

[17] C. U. Kim, C. S. Hong, C. G. Kim, and J. Y. Kim, "Optimal design of filament wound type 3 tanks under internal pressure using a modified genetic algorithm," *Compos. Struct.*, vol. 71, no. 1, pp. 16–25, 2005, doi: 10.1016/j.compstruct.2004.09.006.

Determination of recycled carbon fiber strength distribution using fiber bundle tensile test

Yoshiki SUGIMOTO[1], Yusuke IMAI[1] and Masaki HOJO[2]

[1]Department of Multi-Material research Institute, Advanced Industrial Science and Technology (AIST)
4-205, Sakurazaka, Moriyama-ku, Nagoya, Aichi 463-8560, JAPAN
Email: y.sugimoto@aist.go.jp, web page: https://www.aist.go.jp/

[2]Kinki Polytechnic College
3-1-1, Kishinooka-cho, Kishiwada, Osaka 596-0817, JAPAN
Email: Hojo.Masaki@jeed.go.jp, web page: https://www3.jeed.go.jp/osaka/college/index.html

Keywords: Carbon fiber, Strength distribution, Recycle, Properties

ABSTRACT

In this study, we investigated the improvement in carbon fiber (CF) bundle tensile tests. To effectively evaluate the mechanical properties of CF using the fiber bundle tensile test, measurement system compliance correction considering nonlinear behavior and Weibull analysis using curve fitting were conducted. Weibull parameters were extracted by fitting the stress-strain curves, while considering the effect of the kinetic friction force. The obtained parameters from the fiber bundle tensile test correspond to those from the single fiber tensile test. This method was also applied to the recycled CF bundles. It was found that the recycled CF bundles have orientation distributions and tends to overestimate their strength. However, it was found that this method is suitable for screening of the recycle CF bundles.

1 INTRODUCTION

Carbon fibers (CFs) have high tensile strength and high tensile modulus reinforcement fibers and are used in various field, such as in aerospace and sports gears. The demand of CFs is increasing, and the reuse and recycling of CFs are necessary to meet the increasing demand [1, 2]. The main stream of matrix polymers for CF composites are mostly thermoset resins, such as epoxy resin, and the CFs are recovered from these composites by removing the matrix resin. Several methods are used to recover CFs from their matrix polymers; however, these methods tend to degrade the mechanical properties of the recycle CFs (rCFs) and their composites [3-5]. Therefore, it is very important to evaluate the mechanical properties of the rCF.

Single fiber tensile tests are commonly carried out to evaluate the mechanical properties of rCF [6]. The strength of CFs is usually follows Weibull distribution, and a large number of tests are needed to estimate the distribution. rCFs can have a wider strength distribution compared to the virgin CFs, owing to various damages suffered during their history of usage, and recovery processes. In addition, the damage stage of the rCFs during the recovery process is not uniform, even in the same batch rCFs. Therefore, a considerably greater number, typically hundreds, of tests is necessary to accurately evaluate the strength distribution of rCFs, which is time-consuming and laborious. Addition to this, recently continuous rCFs can be obtained from hydrogen pressure tanks and efficient evaluation methods for such continuous rCF are urgent.

To overcome these issues, the fiber bundle tensile test is considered an effective method to obtain the fiber strength distribution [7-13] with smaller numbers of tests. In this method, fiber bundle stress-strain curves are obtained experimentally, and the Weibull parameters, which express the fiber strength distribution, are derived from the stress-strain curves. To effectively evaluate the fiber strength distribution, precise strain measurements should be obtained. The strain can be obtained by using the measurement system compliance correction [7, 10] and an extensometer [8, 9, 10, 13]. Recently, digital image correlation analysis has been applied as a novel non-contact strain measurement method [12].

The advantages of the fiber bundle test methods are accepted, and they are applied to measure the strength distribution of various fibers, such as CFs [7, 8, 11, 13], silicon carbide fibers [12], and glass

fibers [9]. However, these methods are only applicable to fiber bundle specimens with well-defined bundle shapes, restricted fiber numbers, and lengths. In case of rCFs, it is difficult to prepare the required bundle specimen for the bundle test as the rCFs usually have a limited length of several tens of millimeters or less. Therefore, it is important to develop an improved test method that can effectively measure the strain of shorter and thinner bundles.

In this study, we investigated the effectiveness of the measurement system compliance correction method and the calculation method of Weibull parameters for the tensile test of CF bundles using specimens of different gauge lengths. The Weibull parameters were calculated considering the effect of kinetic friction between the fibers. In addition, the validity of the fiber bundle tensile test was examined by comparing the obtained Weibull parameters with those of the single fiber tensile tests. This test method was also applied to the rCF bundles and revealed the issues.

2 EXPERIMENTAL

2.1 Materials

Virgin CF bundles with a width of 7 mm (T700S, Toray Ind.) and recycled CF bundles (Carbon Fiber recycle Industry co. ltd.) were used in this study.

The CF bundles were not impregnated with polymers to effectively evaluate the fiber strength distribution. The bundle consisted of 12,000 fibers and was coated with a sizing agent for convergence. The sizing agent was not removed to avoid disruption of the fiber orientation.

The recycled CF bundles were obtained from aerospace parts by a pyrosis method. The orientation of the recycled CF bundles was slightly disordered, so they were combed to align the fiber orientation. The thickness of the recycled CF bundles was below 0.15 mm. The cross-sectional area of the bundle was calculated by dividing the bundle liner density by the bundle density. The bundle liner density was obtained by measuring the bundle weight of the 300 mm length bundle, and a bundle density of 1.8 g/cm^3 in the catalogue data was used for this calculation.

2.2 Fiber bundle tensile test

A schematic illustration for preparation of the fiber bundle tensile test specimen is shown in Fig. 1. Specimens that have both ends of the bundle tabbed are prepared as follows. First, a cardboard with a thickness of 0.5 mm was cut into pieces as tabs (20 mm × 60 mm) and spacers (5 mm × 6 mm). Then, the spacers were fixed on the tab, and an epoxy adhesive was painted on the tab. The CF bundle was placed on the adhesive with application of tension in order to keep the bundle straight, epoxy adhesive was painted over the bundle, and covered with another tab. In this study, the distance between the tabs was defined as the gauge length. In order to conduct the system elongation, virgin CF bundle tensile test specimens with gauge lengths of 10, 50, 75, and 100 mm were fabricated. Test specimens with gauge length of 50 mm were prepared for rCF.

Tensile tests of the fiber bundles were conducted using a universal testing machine (AG-Xplus 10 kN, Shimadzu Corp.) attached to a 5 kN load cell. A pneumatic flat grip attached to the universal joint was employed. The apparent strain rate, which is obtained by dividing the cross-head speed by the gauge length, was 1 %/min. The alignment of the test system is essential for achieving uniform loading to the bundle. Therefore, the alignment of the grips was adjusted by gripping the metal plate. The alignment of the specimen was carried out by suspending a string with a load to the lower tab and adjusting the string axis and tensile axis. To ensure the alignment of the specimens, the pretention of 5 N was applied to the specimens before the test.

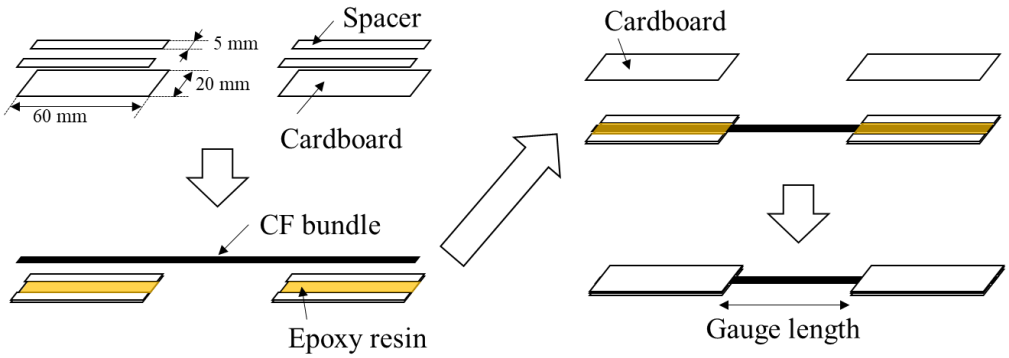

Figure 1 Schematic illustration of the preparation of the specimen.

2.3 Single fiber tensile test

Single fiber tensile test specimens with a gauge length of 10 mm were prepared by fixing a single CF to the paper templat. The specimen was placed on a tensile test machine (EZ-SX, Shimadzu Corp.) attached to a 10 N load cell. After scissoring both sides of the paper template, the tensile tests were conducted with a cross-head speed of 1 mm/min.

3 RESULTS AND DISCUSSION

3.1 Load-displacement curves of fiber bundle tensile test

Load-displacement curves of the fiber bundle tensile tests with different gauge lengths specimens are presented in Fig. 2. Progressive failures were observed in specimens with gauge lengths above 50 mm. This may be due to the difference in compliance between the fiber bundle and the measurement system. While the compliance of the bundle is proportional to the fiber length and inversely proportional to the number of fibers in the bundle, that of the measurement system is almost constant. The compliance of the bundle decreases with a decrease in the gauge length. Therefore, if the fibers in the bundle broke partially, the compliance of the bundle remained at a small value. This indicates that the applied load remained almost constant, and resulted in an unstable brittle failure of the bundle. Further, it was observed that the peak load increased with a decrease in the gauge length, except for the specimen with a gauge length of 10 mm

Fig. 3 shows the pictures of the specimens before and after the fiber bundle tensile tests. The specimens with a gauge length longer than 50 mm were dense and straight before and during tensile tests, but expanded forms after the test, reflecting the undulation of fibers after fracture. In contrast, the fibers of the specimen with a gauge length of 10 mm showed almost limited winding after the tests and were substantially ruptured. These results correspond to the different load-displacement curves in Fig. 2.

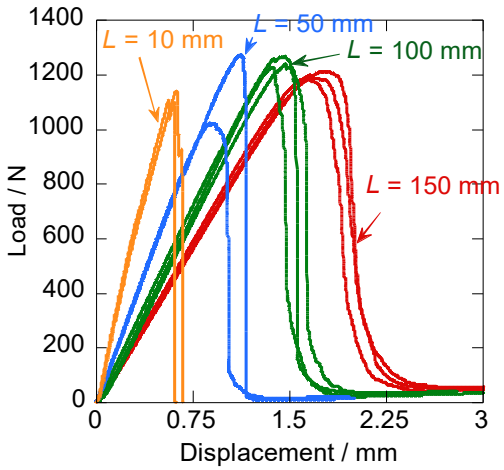

Figure 2 Load -displacement curves of fiber bundle tensile tests with different gauge lengths.

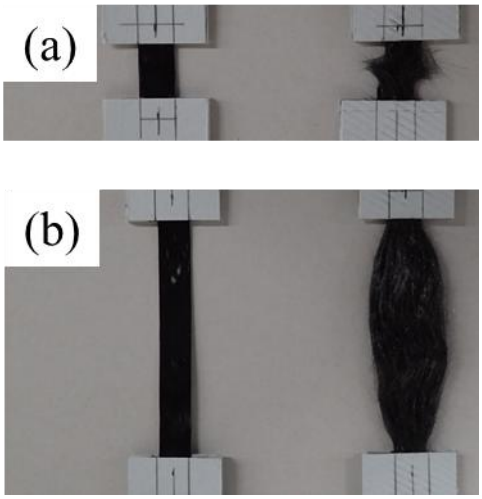

Figure 3 Pictures of the fiber bundle specimens with a gauge length of (a) 1 cm and (b) 5 cm. The specimen on the left is before the test and the specimen on the right is after the test.

3.2 Correction of measurement system elongation

Total elongation, ΔL_{total}, is the sum of the fiber bundle elongation, ΔL_{fiber}, and the measurement system elongation, ΔL_{system}, and the following equation is established[16].

$$\Delta L_{\text{total}} = \Delta L_{\text{fiber}} + \Delta L_{\text{system}} = L_{\text{fiber}} \frac{P}{SE} + \alpha \cdot \Delta L_{\text{system}} \tag{1}$$

where P is tensile load, E is fiber tensile modulus, S is cross section area of the fiber bundle, L_{fiber} is gauge length and α is shape factor which is governed by the shape of the tab and the fiber bundle as follows:

$$\alpha = \sqrt{\frac{w_0(W - w_0) \cdot \ln\left(\frac{W}{w_1}\right)}{w_1(W - w_1) \cdot \ln\left(\frac{W}{w_0}\right)}} \tag{2}$$

where W is adhesive width and w_1 is recycled CF bundle width and w_0 is virgin CF width which is used for measurement of system elongation. When $w_0 = w_1$, $\alpha = 1$.

Thus, the measurement system elongation at load P can be obtained from the slope of the plot of ΔL_{total} against the gauge length. Fig. 4(a) shows the relationship between ΔL_{total} and L_{fiber} at two loads of 250 N and 500 N. As shown in Fig. 4(a) the plots are on linear lines, and the system elongation can be obtained from the intercept of the lines.

Since the measured load was quite large in the current tests, the stress-strain relationship of the epoxy adhesive, which was used for fixing the tabs, was nonlinear. Hence, the measurement system elongation also exhibited nonlinear behavior. To evaluate the load dependence of the measurement system elongation, the measurement system elongation was calculated for various loads up to 1100 N with 50 N increments. The measurement system elongation of a fiber bundle with a width of 7 mm is represented in Fig. 4(b) with red symbols. From Fig. 4(b), it was confirmed that the measurement system elongation exhibited nonlinear behavior. By fitting the measurement system elongation with a quadratic function, $\Delta L_{\mathrm{system}} = 2.31 \times 10^{-8} P^2 + 2.63 \times 10^{-4} P + 3.06 \times 10^{-2}$ was obtained as the equation of the measurement system elongation for the 7 mm width fiber bundle.

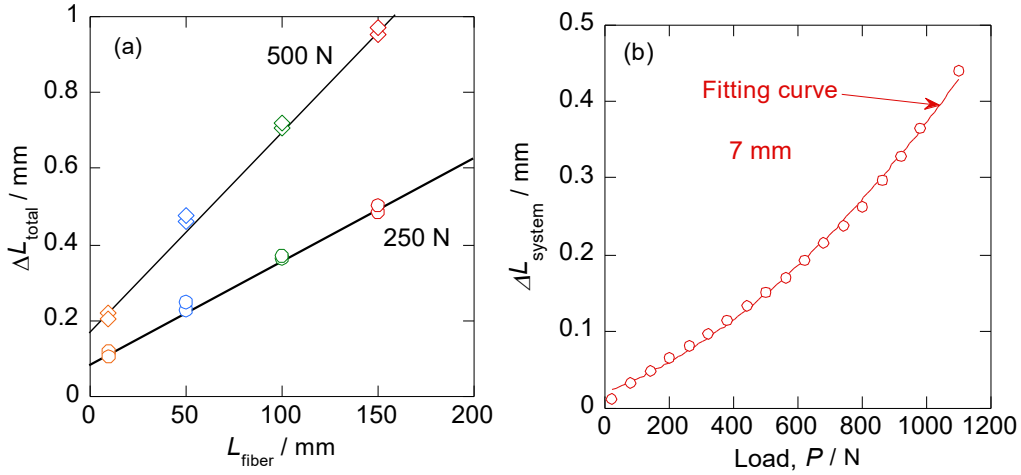

Figure 4 (a) Plots of total elongation, $\Delta L_{\mathrm{total}}$, versus gauge length, L_{fiber}, and (b) plots of measurement system elongation, $\Delta L_{\mathrm{system}}$ versus load, P.

3.3 Stress-strain curves for virgin CF fiber bundle tensile test

The stress-strain curves for the 7 mm width virgin CF bundles are shown in Fig. 5. Here, the bundle fiber strain was calculated using gauge length and bundle elongation which was obtained by subtracting the elongation of the measurement system from the total elongation. The bundle stress was calculated by dividing the load by the initial bundle cross-sectional area. In all the specimens, except for the specimens with a gauge length of 10 mm, the initial slope in the small strain region was consistent, which indicated that system elongation correction was performed properly. The deviation of the specimens with gauge length of 10 mm considered to be due to the misalignment. Even if the shift between upper and lower tabs is the same, the tilt angle of the bundle from the loading direction becomes larger for shorter gauge length. Thus, higher test accuracy of equipment and specimen placement is required to effectively experiment with the short gauge length specimens.

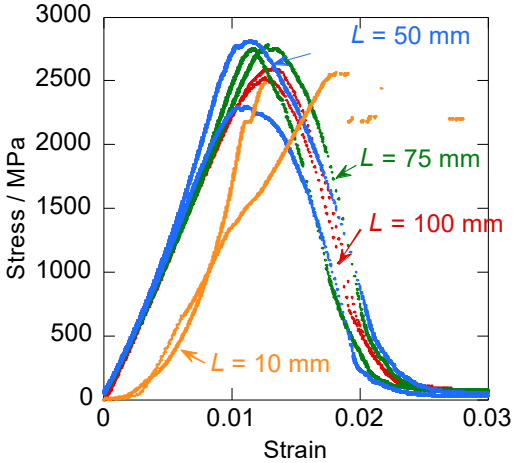

Figure 5 Stress-strain curves of virgin CF bundles with different gauge lengths.

3.4 Weibull parameters obtained from fiber bundle tensile test

Assuming that the fiber bundle is pulled simultaneously without sagging and its strength follows Weibull distribution, its stress, $\sigma_{\mathrm{measured}}$, can be expressed as follows [16].

$$\sigma_{\mathrm{measured}} = E\varepsilon \cdot \exp\left(-\frac{L_{\mathrm{fiber}}}{L_0}\left[\frac{E\varepsilon}{\sigma_0}\right]^m\right) + T\left\{1 - \exp\left(-\frac{L_{\mathrm{fiber}}}{L_0}\left[\frac{E\varepsilon}{\sigma_0}\right]^m\right)\right\} \quad (3)$$

where m is Weibull shape parameter, σ_0 is Weibull scale parameter, ε is strain of the fiber bundle, E is tensile modulus of the bundle, T is friction force between fibers in the bundle, L_{fiber} is gauge length, and L_0 is reference length (1m). E, m, σ_0, and T can be obtained by fitting stress-strain curves with equation (3).

The measured stress-strain curves for gauge lengths of 50 – 100 mm were fitted by equation (3) using generalized reduced gradient method [15] and fitting parameters were obtained. Fig. 6 shows the fitting results for the gauge length of 550 mm. It was confirmed that the whole region of the stress-strain curved was successfully fitted by the equation (3) considering the kinetic friction.

To evaluate the validity of the fiber bundle tests, the Weibull parameters obtained by the fiber bundle tests were compared to those obtained by the single fiber tensile tests. The Weibull parameters obtained by the CF bundle tensile tests corresponded moderately to those obtained by the single fiber tensile tests. Therefore, fiber bundle testing using compliance correction can be considered as a valid test method for evaluating the mechanical properties of fibers.

Figure 6 also shows the stress-strain curves from the tensile test of the rCF bundle. In this case, the rCFs originally had a tensile modulus of 230 GPa; however, the modulus of the fiber bundle was found to be low, at 51 GPa. This indicates that some fibers are not connected between the tabs. Although the rCF strength can change, the rCF tensile modulus is typically maintained. Thus, we assumed that the tensile modulus of the rCFs remained unchanged, and we obtained the rCF Weibull parameters by fitting a modified theoretical equation that included a parameter indicating the initial rCF break fraction. As a result, the Weibull parameters of the fiber were obtained: a scale parameter of 2.7 GPa and a shape parameter of 6.8. This value is in accordance with the tensile strength of virgin fiber bundles, indicating that the recycling process properly maintains fiber strength. However, this result also indicates that fibers may break during specimen fabrication (or the recycling process), so special care may be needed to obtain reliable results.

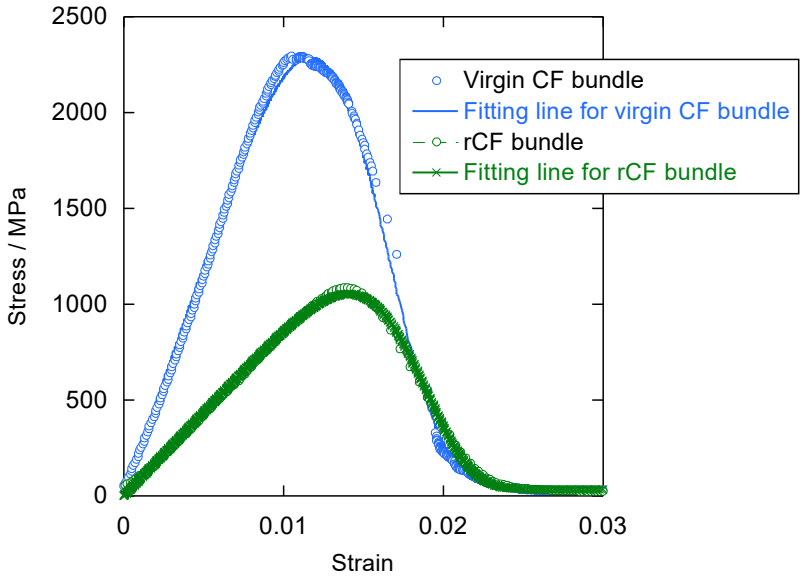

Figure 6 Stress-strain curves of virgin CF and recycled CF bundles.

4 CONCLUTIONS

In this study, fiber bundle tensile tests were conducted to evaluate the tensile strength of CF and rCF bundle. The dependence of the measurement system elongation on the fiber width was investigated. By using equation considering the effect of kinetic friction in the theoretical bundle stress-strain relationship, the Weibull parameters and kinetic friction were evaluated. The obtained Weibull parameters obtained from the fiber bundle tensile test roughly corresponded with those obtained from the single fiber tensile tests, and the validity of the fiber bundle tensile tests was confirmed. For the specimens with a short gauge length, the test was difficult due to the misalignment of the specimen from loading axis.

Even though rCF bundle seem perfectly continuous fibers, they contained discontinuous fibers. Even in such case the strength distribution could be evaluated supposing the tensile modulus. Although this method has some point such as preparation of the specimens that need to be overcome, this method can be considered as an effective method to evaluate the tensile strength of recycled CFs.

ACKNOWLEDGEMENTS

This paper is based on results obtained from a project commissioned by the New Energy and Industrial Technology Development Organization (NEDO).

REFERENCES

[1] Zhang J, Chevali VS, Wang H and Wang CH. Current status of carbon fibre and carbon fibre composites recycling. *Composits, Part B* **193**(2020)

[2] Verma S, Balasubramaniam B, and Gupta RK. Recycling, reclamation and re-manufactureing of carbon fibes. *Curr. Opin. Green Sustainable Chem*.**13**(2018)86-90.

[3] Sun H, Guo G, M SA, Xu W, Zhang Q, Zhu JH, Xing F. Recycling of carbon fibers from carbon fiber reinforced polymer using electrochemical method. *Composite, Part A* **78**(2015):10-17.

[4] Ma C, Sanchez-Rodriguez D Kamo T. Influence of thermal treatment on the properties of carbon fiber reinforced plastics under various conditions. *Polym. Degrad. Stab*. **178**(2020):109199.

[5] Cai GB, Wada M, Ohsawa I, Kitaoka S, and Takahashi J. Tensile properties of recycled carbon fibers subjected to superheated steam treatment under various conditions. *Composite, Part B***133**(2020), 105869.

[6] ISO 11566:1996 Carbon fibre - Determination of the tensile properties of single-filament specimens-.

[7] Chi Z, Cho TW, and Determination of single fibre strength distribution from bundle testings. *J. Mater. Sci.* **19**(1984)3319-3324.

[8] Calard V and Lamon J, Failure of fiber bundles, *Compos. Sci. Technol.* **64** (2004) 701-710.

[9] R'Mili M, Moevus M, and Godin N. Statistical fracture of E-glass fibres using a bundle tensile test and acoustic emission monitoring. *Compos. Scie. Technol.* **68**(2008)1800-1808.

[10] ISO 22459:2020 Fine ceramics (advanced ceramics, advanced technical ceramics) — Reinforcement of ceramic composites — Determination of distribution of tensile strength and tensile strain to failure of filaments within a multifilament tow at ambient temperature

[11] Zhou Y, Wang Y, Zia Y, and Jeelani S. Tensile behavior of carbon fiber bundles at different strain rate, *Mater. Lett.* **64**(2010) 246-248.

[12] Callaway EB and Zok FW. Strength of ceramic fiber bundles: Theory and practice. *J. Am. Ceram. Soc.* **100**(2017)5306-5317.

[13] Boulanghien M, R'Mili M, Bernhart G, Berthet F, and Soudais Y. Mechanical Characterization of Carbon fibres Recycled by steam Thermolysis: A statical Approach. *Adv. Mater. Sci. Eng.* (2018)8630232.

[14] Naito K, Tanaka Y, Yang JM, and Kagawa Y. Tensile Properties of ultrahigh strength PAN-based, ultrahigh modulus pitch-based and high ductility pitch-based carbon fibers, *Carbon***46**(2008)189-195.

[15] Lasdon LS, Waren AD, Jain A, and Ratner M. Design and testing of a generalized reduced gradient code for nonlinear programming. *ACM T Math. Softw.*, **4** (1) (1978), pp. 34-50

[16] Sugimoto Y, Imai Y, Hojo M *et al.* Determination of Carbon Fiber Strength Distribution Using Bundle Fiber Tensile Test: Correction of Measurement System Elongation and Kinetic Friction Between Fibers in the Fiber Bundle. *J. Mater. Res.* **36**, 961–969 (2021). https://doi.org/10.1557/s43578-020-00043-y

ICCM24
AUGUST 4-8, 2025
BALTIMORE CONVENTION CENTER
BALTIMORE, MARYLAND, USA

No Technical Paper Submission for:

Behrad Koohbor

ICCM24
24TH INTERNATIONAL CONFERENCE ON COMPOSITE MATERIALS

Impact of Stacking Sequence and Thickness on Composite Strength

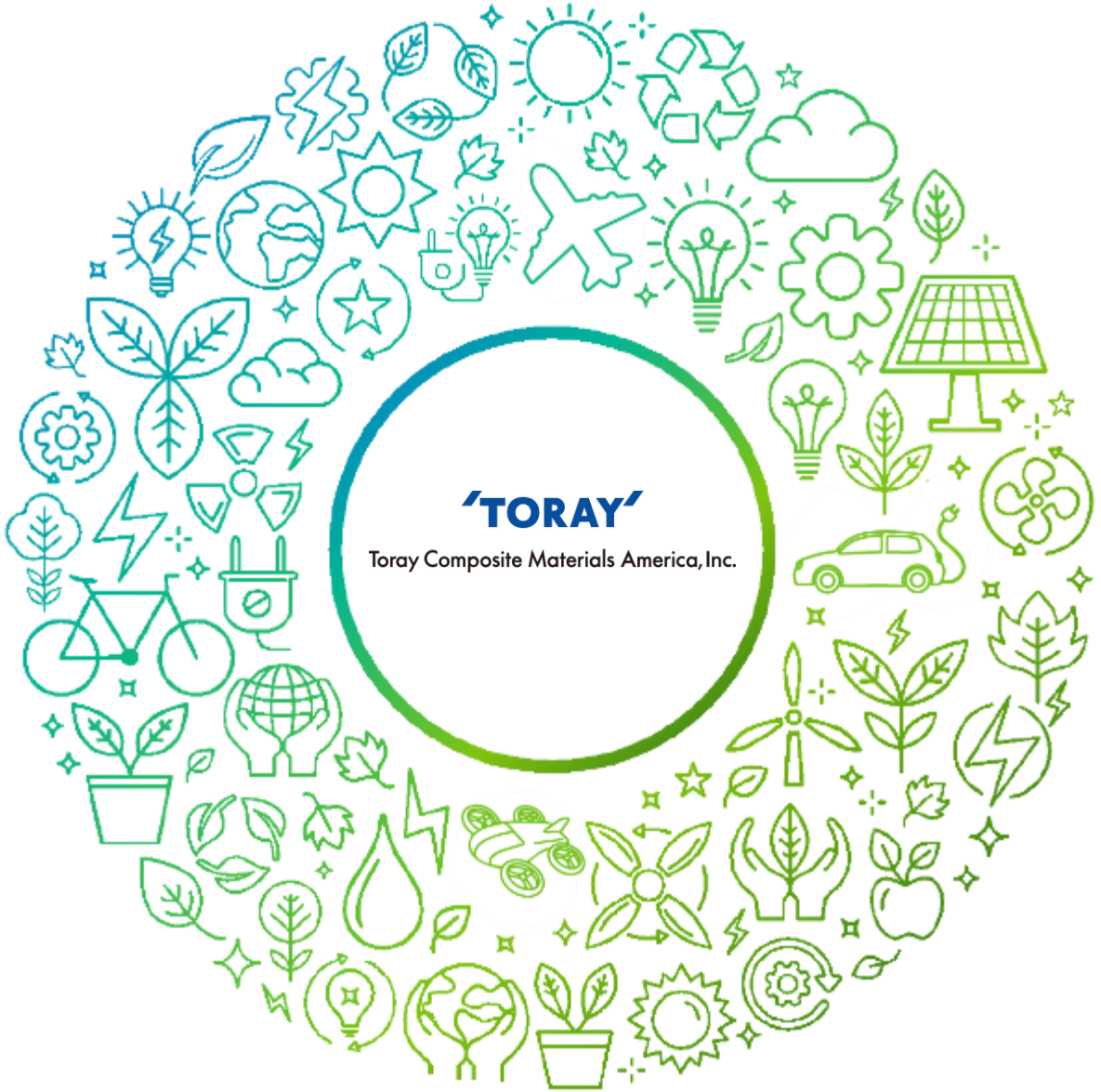

Toray Composite Materials America
Composite Materials Research Laboratory

Don Lee and Joseph McDonald
August 6, 2025

24th International Conference on Composite Materials,
Baltimore, USA

TORAY COMPOSITE MATERIALS US CAPABILITIES

Producer of Precursor, Carbon Fiber, and Prepreg Materials



LEGEND

- Prepreg
- Carbon Fiber Precursor
- Carbon Fiber Carbonization
- Sales Office

Toray World – Composites Division



Copyright © 2025 Toray Composite Materials America, Inc. |

T1100G/3960 Toughened Aerospace-Grade Prepreg

- Next-Gen 350°F (177°C) system for primary aerospace structure
- NCAMP (National Center for Advanced Materials Performance) qualified*
- Excellent balance of CAI and OHC
- Long out life, extremely long freezer life
- Available in AFP tape/hand layup prepreg, unidirectional/plain-weave, FAW UD = 70/145/192 g/m^2
- Flexible cure by autoclave, Out-Of-Autoclave/Vacuum Bag Only, press cure capabilities
- High-fidelity modeling and simulation support available (COMPRO/RAVEN)

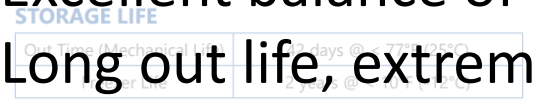
STORAGE LIFE

Out Time (Mechanical Use)	10 days @ 77°F/25°C	
Freezer Life	12 months @ -0°F (-18°C)	

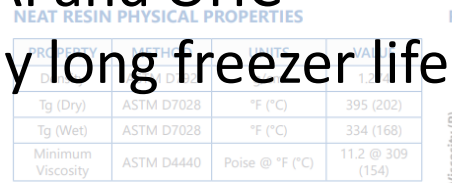
NEAT RESIN PHYSICAL PROPERTIES

Tg (Dry)	ASTM D7028	°F (°C)	395 (202)
Tg (Wet)	ASTM D7028	°F (°C)	334 (168)
Minimum Viscosity	ASTM D4440	Poise @ °F (°C)	11.2 @ 309 (154)

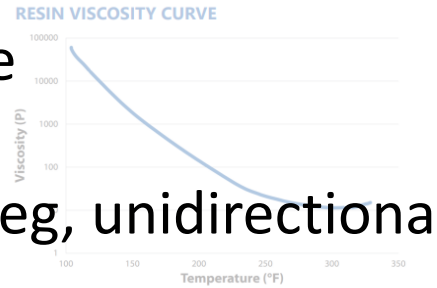

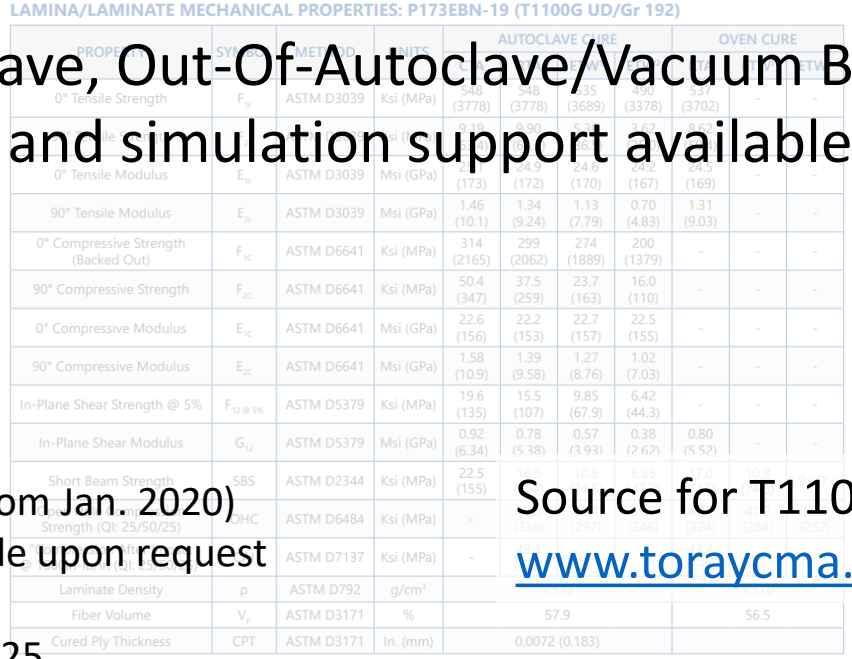
LAMINA/LAMINATE MECHANICAL PROPERTIES: P173EBN-19 (T1100G UD/Gr 192)

PROPERTY	SYMBOL	METHOD	UNITS	AUTOCLAVE CURE				OVEN CURE		
				CTA	RTA	ETW¹	ETW²	CTA	RTA	ETW¹
0° Tensile Strength	F_{1t}	ASTM D3039	Ksi (MPa)	548 (3778)	548 (3778)	535 (3689)	490 (3378)	537 (3702)	-	-
90° Tensile Strength	F_{2t}	ASTM D3039	Ksi (MPa)	9.10 (62.7)	8.90 (61.4)	8.60 (59.3)	7.80 (53.8)	8.50 (58.6)	-	-
0° Tensile Modulus	E_{1t}	ASTM D3039	Msi (GPa)	25.0 (173)	24.9 (172)	24.6 (170)	24.2 (167)	24.5 (169)	-	-
90° Tensile Modulus	E_{2t}	ASTM D3039	Msi (GPa)	1.46 (10.1)	1.34 (9.24)	1.13 (7.79)	0.70 (4.83)	1.31 (9.03)	-	-
0° Compressive Strength (Backed Out)	F_{1c}	ASTM D6641	Ksi (MPa)	314 (2165)	299 (2062)	274 (1889)	200 (1379)	-	-	-
90° Compressive Strength	F_{2c}	ASTM D6641	Ksi (MPa)	50.4 (347)	37.5 (259)	23.7 (163)	16.0 (110)	-	-	-
0° Compressive Modulus	E_{1c}	ASTM D6641	Msi (GPa)	22.6 (156)	22.2 (153)	22.7 (157)	22.5 (155)	-	-	-
90° Compressive Modulus	E_{2c}	ASTM D6641	Msi (GPa)	1.58 (10.9)	1.39 (9.58)	1.27 (8.76)	1.02 (7.03)	-	-	-
In-Plane Shear Strength @ 5%	$F_{12@5\%}$	ASTM D5379	Ksi (MPa)	19.6 (135)	15.5 (107)	9.85 (67.9)	6.42 (44.3)	-	-	-
In-Plane Shear Modulus	G_{12}	ASTM D5379	Msi (GPa)	0.92 (6.34)	0.78 (5.38)	0.57 (3.93)	0.38 (2.62)	0.80 (5.52)	-	-
Short Beam Strength	SBS	ASTM D2344	Ksi (MPa)	22.5 (155)	22.5 (155)	10.8 (74.5)	6.85 (47.2)	22.0 (152)	-	-
Open Hole Compressive Strength (QI: 25/50/25)	OHC	ASTM D6484	Ksi (MPa)	-	[36] (248)	[34] (234)	[32] (220)	[34] (234)	[32] (220)	[32] (220)
Open Hole Tensile Strength (QI: 25/50/25)	OHT	ASTM D7137	Ksi (MPa)	-	[36] (248)	[34] (234)	[32] (220)	[34] (234)	[32] (220)	[32] (220)
Laminate Density	ρ	ASTM D792	g/cm^3	1.520						
Fiber Volume	V_f	ASTM D3171	%	57.9				56.5		
Cured Ply Thickness	CPT	ASTM D3171	In. (mm)	0.0072 (0.183)						

Notes:
CTA: -65°F/-54°C, as-received
RTA: 72°F/22°C, as-received
ETW1: 180°F/82°C, equilibrium conditioned
ETW2: 250°F/121°C, equilibrium conditioned

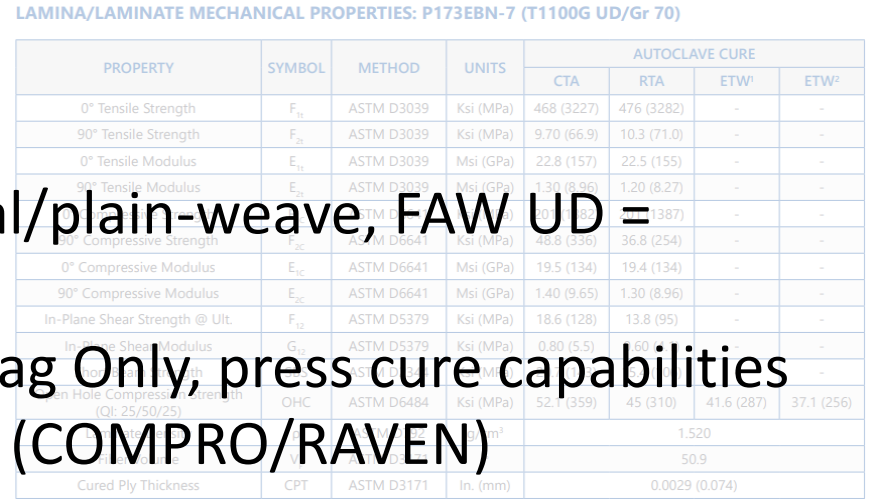
LAMINA/LAMINATE MECHANICAL PROPERTIES: P173EBN-7 (T1100G UD/Gr 70)

PROPERTY	SYMBOL	METHOD	UNITS	AUTOCLAVE CURE			
				CTA	RTA	ETW¹	ETW²
0° Tensile Strength	F_{1t}	ASTM D3039	Ksi (MPa)	468 (3227)	476 (3282)	-	-
90° Tensile Strength	F_{2t}	ASTM D3039	Ksi (MPa)	9.70 (66.9)	10.3 (71.0)	-	-
0° Tensile Modulus	E_{1t}	ASTM D3039	Msi (GPa)	22.8 (157)	22.5 (155)	-	-
90° Tensile Modulus	E_{2t}	ASTM D3039	Msi (GPa)	1.30 (8.96)	1.20 (8.27)	-	-
0° Compressive Strength	F_{1c}	ASTM D6641	Ksi (MPa)	201 (1387)	201 (1387)	-	-
90° Compressive Strength	F_{2c}	ASTM D6641	Ksi (MPa)	48.8 (336)	36.8 (254)	-	-
0° Compressive Modulus	E_{1c}	ASTM D6641	Msi (GPa)	19.5 (134)	19.4 (134)	-	-
90° Compressive Modulus	E_{2c}	ASTM D6641	Msi (GPa)	1.40 (9.65)	1.30 (8.96)	-	-
In-Plane Shear Strength @ Ult.	F_{12}	ASTM D5379	Ksi (MPa)	18.6 (128)	13.8 (95)	-	-
In-Plane Shear Modulus	G_{12}	ASTM D5379	Ksi (MPa)	0.80 (5.5)	0.60 (4.1)	-	-
Open Hole Compressive Strength (QI: 25/50/25)	OHC	ASTM D6484	Ksi (MPa)	52.1 (359)	45 (310)	41.6 (287)	37.1 (256)
Laminate Density	ρ	ASTM D792	g/cm^3	1.520			
Fiber Volume	V_f	ASTM D3171	%	50.9			
Cured Ply Thickness	CPT	ASTM D3171	In. (mm)	0.0029 (0.074)			

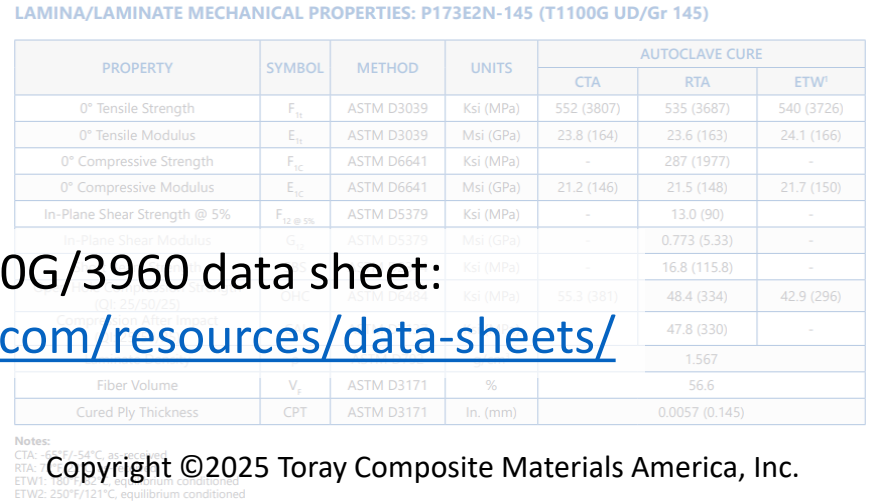
LAMINA/LAMINATE MECHANICAL PROPERTIES: P173E2N-145 (T1100G UD/Gr 145)

PROPERTY	SYMBOL	METHOD	UNITS	AUTOCLAVE CURE		
				CTA	RTA	ETW¹
0° Tensile Strength	F_{1t}	ASTM D3039	Ksi (MPa)	552 (3807)	535 (3687)	540 (3726)
0° Tensile Modulus	E_{1t}	ASTM D3039	Msi (GPa)	23.8 (164)	23.6 (163)	24.1 (166)
0° Compressive Strength	F_{1c}	ASTM D6641	Ksi (MPa)	-	287 (1977)	-
0° Compressive Modulus	E_{1c}	ASTM D6641	Msi (GPa)	21.2 (146)	21.5 (148)	21.7 (150)
In-Plane Shear Strength @ 5%	$F_{12@5\%}$	ASTM D5379	Ksi (MPa)	-	13.0 (90)	-
In-Plane Shear Modulus	G_{12}	ASTM D5379	Msi (GPa)	-	0.773 (5.33)	-
Short Beam Strength	SBS	ASTM D2344	Ksi (MPa)	-	16.8 (115.8)	-
Open Hole Compressive Strength (QI: 25/50/25)	OHC	ASTM D6484	Ksi (MPa)	55.3 (381)	48.4 (334)	42.9 (296)
Open Hole Tensile Strength (QI: 25/50/25)	OHT	ASTM D7137	Ksi (MPa)	-	47.8 (330)	-
Laminate Density	ρ	ASTM D792	g/cm^3	1.567		
Fiber Volume	V_f	ASTM D3171	%	56.6		
Cured Ply Thickness	CPT	ASTM D3171	In. (mm)	0.0057 (0.145)		

Notes:
CTA: -65°F/-54°C, as-received
RTA: 72°F/22°C, as-received
ETW1: 180°F/82°C, equilibrium conditioned
ETW2: 250°F/121°C, equilibrium conditioned

*NCAMP qualification (5-yr program from Jan. 2020)
UD: **Complete**, NCAMP reports available upon request
AFP slit tape: **Complete**
PW: **On track** for completion end of 2025

Source for T1100G/3960 data sheet:
www.toraycma.com/resources/data-sheets/

Copyright ©2025 Toray Composite Materials America, Inc.

Understanding the Quad Layup: Historical and Current Practice

"Quad Layup" Quasi-Isotropic, Balanced & Symmetric, π/4 increments, [25/50/25]

	1950s	1960s	1970s	1980s	1990s	Post 2000	Present Study
Enabling Factors	"Glass Reinforced Plastic" emerged as structural materials Glass fiber Owens-Corning: 1930s -	Stiffness optimization for matching metal replacements Boron fiber Hughes Aircraft: 1960s - Carbon fiber UC, Toray: 1960s -	Failure prediction models Strength optimization (esp. notched strength)		Damage tolerance (Delamination resistance & impact tolerance) Automated manufacturing		At Toray CMA, Quad layups (OHT/OHC, UNT/UNC, …) are either [45/90/-45/0]*n*S (*n* = 1, 2, 3) or [-45/0/45/90]*n*S (*n* = 1, 2, 3)
Technical Focus	CLT developed Classical plate and shell theory to handle layered anisotropic materials	Formal adoption of CLT "Pseudo-isotropic"	Experimental validation and implementation "Quasi-isotropic"		Shift to smoother angular transition	Established with FAA certification standards Rise of AFP	Thickness effect & stacking sequence effect
Notched Strength Consideration			AFWAL & NASA Langley on OHT/OHC [0/(±45)/90]S, [(±60)/0]S	• NASA Langley Workshop (1981) [45/0/-45/90]nS OHC • Boeing BSS7260 (1982) • SACMA SRM 3-88 (1988) • Hercules E23004DT06005 (1990) • MIL-HDBK-17 (now CMH-17) on OHT/OHC testing but no specific layup	ASTM D5766 OHT (1995) ASTM D6484 OHC (1999)	ASTM D6742 FHT/FHC (2002) ASTM D8066 UNC (2017)	Focus on OHT + OHC, UNT/UNC, 0TS, 0CS, etc.
Layup Studied*		Unidirectional π/3 QI (e.g., [(±60)/0]S)	[0/(±45)/90]nS: 9 [(±45)/0/90]nS: 1 [0/90/(±45)]nS: 4 [90/0/(±45)]nS: - [90/(±45)/0]nS: 1 [(±45)/90/0]nS: - [45/0/90/-45]nS: - [45/90/0/-45]nS: - [0/45/90/-45]nS: 1 [90/45/0/-45]nS: - [45/0/-45/90]nS: 1 [45/90/-45/0]nS: -	[0/(±45)/90]nS: 14 [(±45)/0/90]nS: 4 [0/90/(±45)]nS: 5 [90/0/(±45)]nS: - [90/(±45)/0]nS: 2 [(±45)/90/0]nS: - [45/0/90/-45]nS: - [45/90/0/-45]nS: - [0/45/90/-45]nS: 4 [90/45/0/-45]nS: - [45/0/-45/90]nS: 3 [45/90/-45/0]nS: 2	[0/(±45)/90]nS: 8 [(±45)/0/90]nS: 8 [0/90/(±45)]nS: 3 [90/0/(±45)]nS: 3 [90/(±45)/0]nS: 3 [(±45)/90/0]nS: 2 [45/0/90/-45]nS: 1 [45/90/0/-45]nS: 1 [0/45/90/-45]nS: 7 [90/45/0/-45]nS: 1 [45/0/-45/90]nS: 9 [45/90/-45/0]nS: 6		Comparison of quad layups with different ply orderings and counts [-45/0/45/90]*n*S vs. [-45/90/45/0]*n*S Effect of *n* Broader stacking sequence effects

*ASTM-recommended QI (D5766, D6484, …)

"Typically a $[45_i/-45_i/0_j/90_k]ns$ tape should be selected such that a minimum of 5 % of the fibers lay in each of the four principal orientations"

Copyright ©2025 Toray Composite Materials America, Inc.

Industry Adoption of Quad Layup: Observations across Test Campaigns

Midplane Ply	Layup	Ply Count	Material	UNT	OHT	FHT	UNC	OHC	FHC
0°	[45/90/-45/0]S	8	UD2	-	Customer A	Customer A	-	-	-
	[45/90/-45/0]2S	16	UD1						
			UD1						
			UD4						
			UD2	-	Customer D	-	-	Customer D	-
			UD2	-	-	-	-	Customer A	-
	[45/90/-45/0]3S	24	UD1						
			UD4						
			UD2	-	-	-	-	Customer D	-
90°	[45/0/-45/90]S	8	UD2	-	Customer E	-	-	Customer E	-
	[45/0/-45/90]2S	16	UD1						
			UD1						
			UD1						
			UD2	Customer G	Customer G	Customer G	Customer G	-	-
	[45/0/-45/90]3S	24	UD1						
			UD2	-	-	-	-	Customer G	Customer G

*FAW = 190 g/m^2 for all materials above

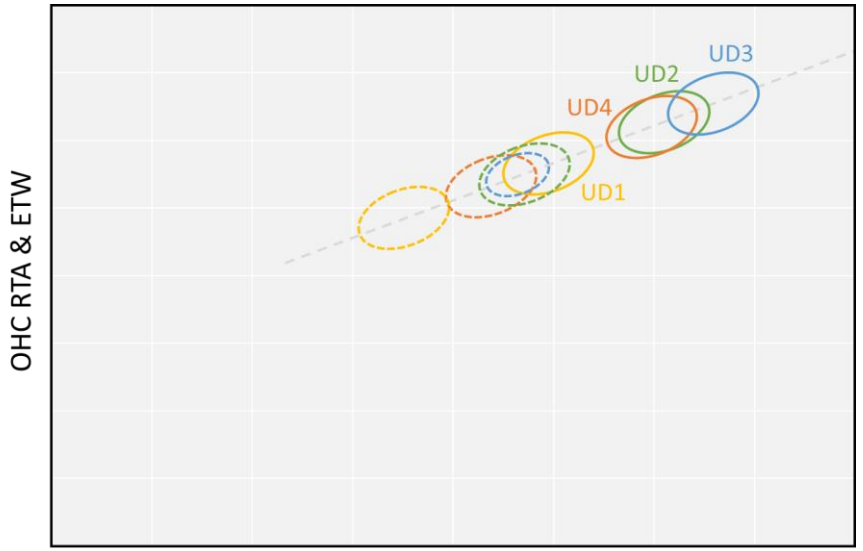

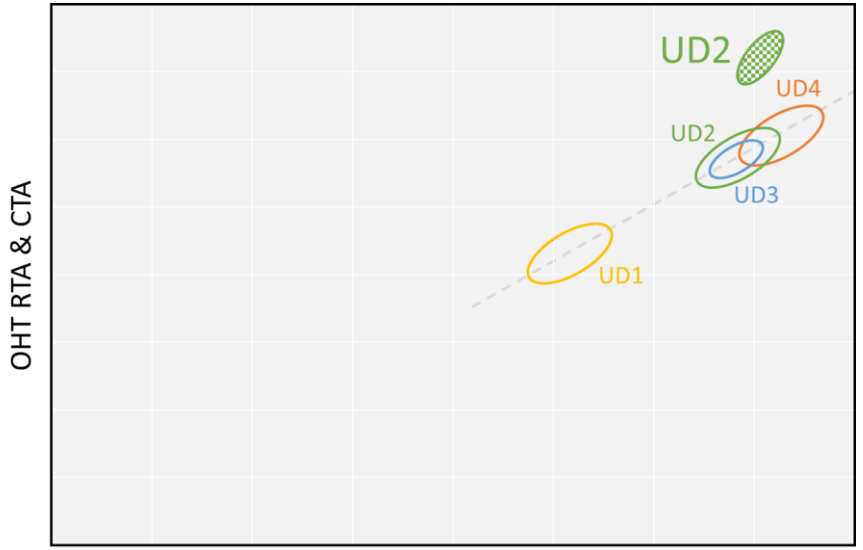

Copyright ©2025 Toray Composite Materials America, Inc.

Phased Test Campaign Overview

Project Goals and Motivation

- Understand how stacking sequence and thickness influence mechanical performance
- Aim at demystifying variability across reported data
- Support customer design decisions by clarifying expected performance ranges
- Recommend optimized test layups in order to broaden and secure design space

Phase 1.

- Review historical data to identify *Thickness Effect* and *Stacking Sequence Effect* from Toray's material DB
- Test 0° Tension and Quad OHT/OHC, T1100G/3960, FAW = 190 g/m^2 (CPT = 7.2 mil, 0.18 mm) — Published in ASME SSDM 2024

*Fiber Areal Weight *Cured Ply Thickness

Phase 2.

- Test UD/Quad Compression, Quad UNT/UNC, T1100G/3960, FAW = 190 g/m^2 — Published in ICCM 2025
- Test 0° Tension, Quad OHT, CLC, T1100G/3960, FAW = 70 g/m^2 (CPT = 3 mil, 0.076 mm) — To be published in ASC 2025
- Expand test matrix to varied thicknesses by ply count control — TBD

Phase 3.

- Test Quad OHT with varied stacking sequences, T1100G/3960, FAW = 190 g/m^2 — TBD
- Test Quad OHT hybridized with other materials, T1100G/3960, FAW = 190 g/m^2 — TBD
- Test Soft/Hard OHT with varied stacking sequences, T1100G/3960, FAW = 190 g/m^2 — TBD

Copyright ©2025 Toray Composite Materials America, Inc.

Test Matrix Overview: Phases 1 & 2

Tension	Test Method	Layup	Test Condition	
TS UD	ASTM D3039 0.5" x 10" (15 x 250 mm)	[0]2 [0]4 [0]6 (NCAMP) [0]8 [0]12 [0]16	RTA CTA -75°F ETW 180°F	Phase 1
TS Quad	ASTM D3039 0.5" x 10" (15 x 250 mm)	[45/90/-45/0]S [45/90/-45/0]2S [45/90/-45/0]3S [45/90/-45/0]4S	RTA	
		[-45/0/45/90]S [-45/0/45/90]2S [-45/0/45/90]3S [-45/0/45/90]4S	RTA	
UNT	ASTM D5766 1.5" x 12" (38 x 300 mm)	[45/90/-45/0]S [45/90/-45/0]2S [45/90/-45/0]3S ~~[45/90/-45/0]4S~~	RTA	Phase 2
		[-45/0/45/90]S [-45/0/45/90]2S (NCAMP) [-45/0/45/90]3S ~~[-45/0/45/90]4S~~	RTA	
OHT	ASTM D5766 1.5" x 12" (38 x 300 mm)	[45/90/-45/0]S [45/90/-45/0]2S [45/90/-45/0]3S [45/90/-45/0]4S	RTA CTA -75°F	Phase 1
		[-45/0/45/90]S [-45/0/45/90]2S (NCAMP) [-45/0/45/90]3S [-45/0/45/90]4S	RTA CTA -75°F	

Planned due to UNT Limitations

Compression	Test Method	Layup	Test Condition	
CLC UD	ASTM D6641 0.5" x 5.5" (12 x 140 mm)	[0]4 [0]6 [0]8 [0]14 (NCAMP) [0]16 [0]20	RTA	Phase 2
CLC Quad	ASTM D6641 0.5" x 5.5" (12 x 140 mm)	[45/90/-45/0]S [45/90/-45/0]2S [45/90/-45/0]3S [45/90/-45/0]4S	RTA	
		[-45/0/45/90]S [-45/0/45/90]2S (NCAMP) [-45/0/45/90]3S [-45/0/45/90]4S	RTA	
UNC	ASTM D8066 1.5" x 12" (38 x 300 mm)	[45/90/-45/0]S [45/90/-45/0]2S [45/90/-45/0]3S [45/90/-45/0]4S	RTA	
		[-45/0/45/90]S [-45/0/45/90]2S (NCAMP) [-45/0/45/90]3S [-45/0/45/90]4S	RTA	
OHC	ASTM D6484 1.5" x 12" (38 x 300 mm)	[45/90/-45/0]S [45/90/-45/0]2S [45/90/-45/0]3S [45/90/-45/0]4S	RTA ETW 180°F	Phase 1
		[-45/0/45/90]S [-45/0/45/90]2S [-45/0/45/90]3S (NCAMP) [-45/0/45/90]4S	RTA ETW 180°F	

Copyright ©2025 Toray Composite Materials America, Inc.

Phase 1 Results: UD Tension, RTA CTA & ETW

Phase 1.

- Test 0° Tension and QI OHT/OHC, T1100G/3960, FAW = 190 g/m^2 (CPT = 7.2 mil, 0.18 mm)

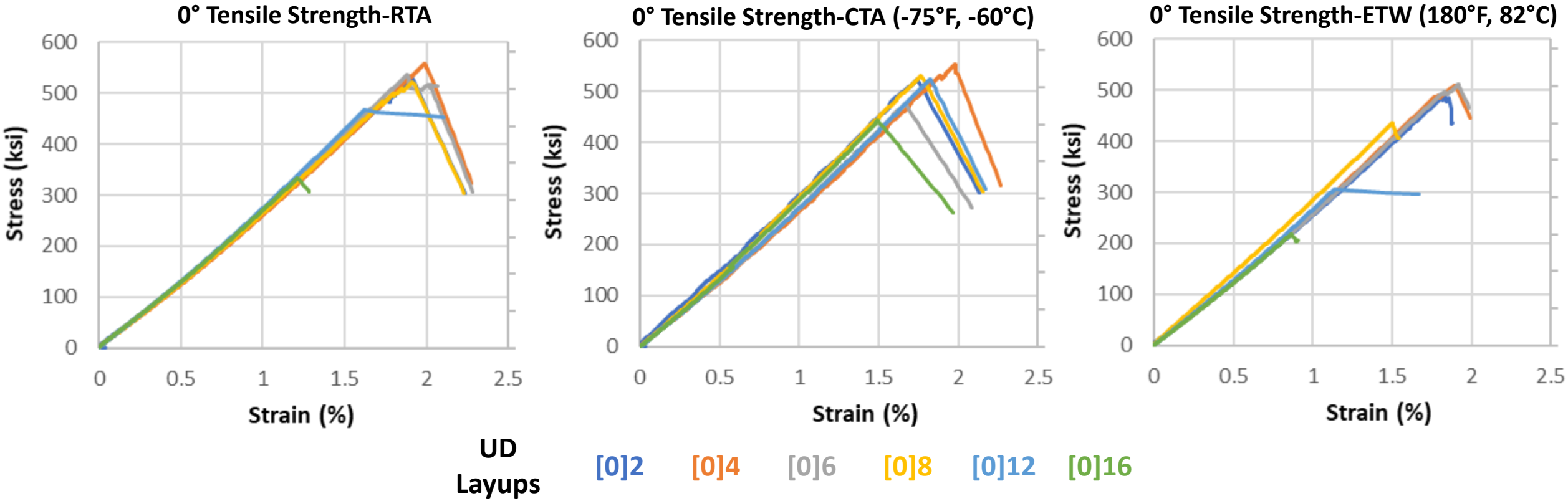

Copyright ©2025 Toray Composite Materials America, Inc.

Phase 1 Results: Quad Notched Strengths

Phase 1.

- Test 0° Tension and QI OHT/OHC, T1100G/3960, FAW = 190 g/m^2 (CPT = 7.2 mil, 0.18 mm)

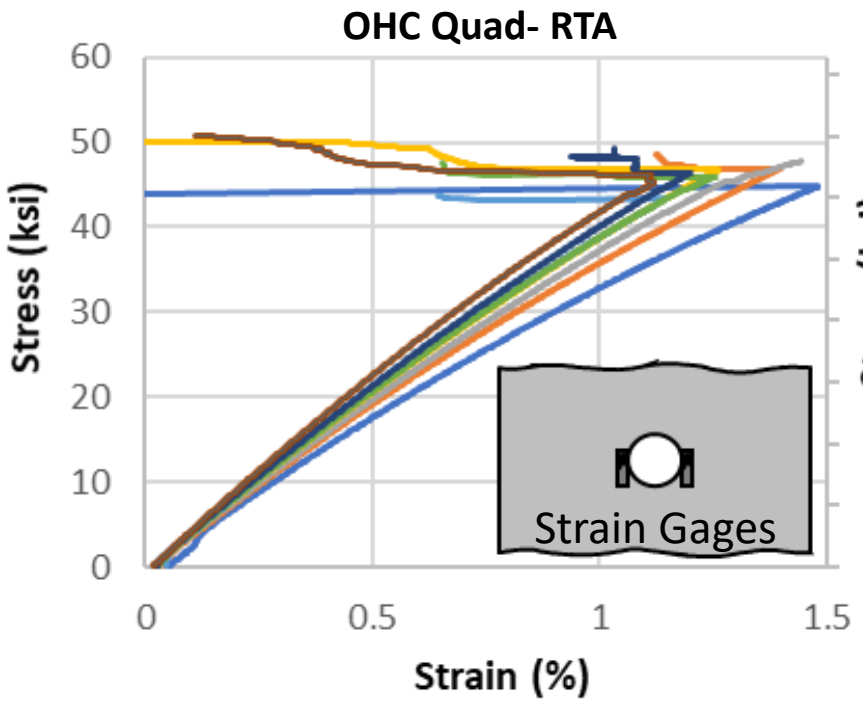

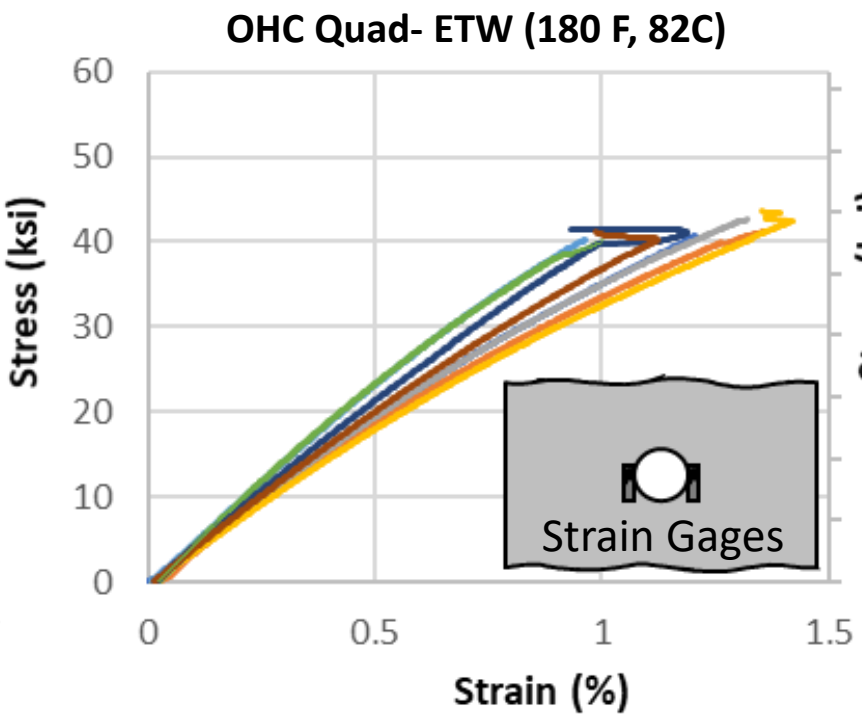

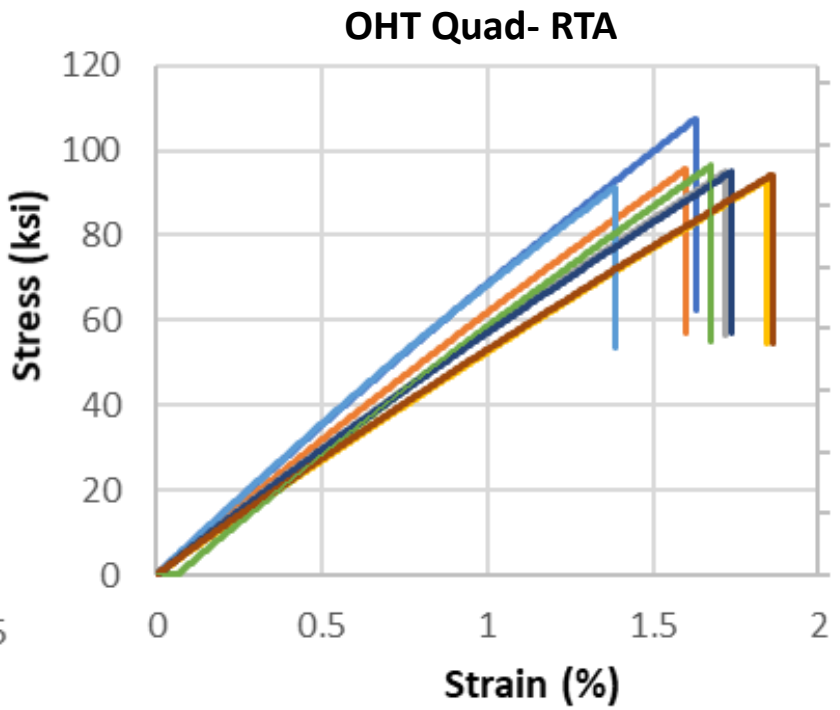

Quad Layups

[45/90/-45/0]S [45/90/-45/0]2S [45/90/-45/0]3S [45/90/-45/0]4S [-45/0/45/90]S [-45/0/45/90]2S [-45/0/45/90]3S [-45/0/45/90]4S

Notes:

- OHC Coupon Strain measured 0.85 mm from hole edge Grid size = 1.2 x 0.6 mm
- OHT Strain computed from test frame's displacement

Copyright ©2025 Toray Composite Materials America, Inc.

Phase 2 Results: UD and Quad Compression

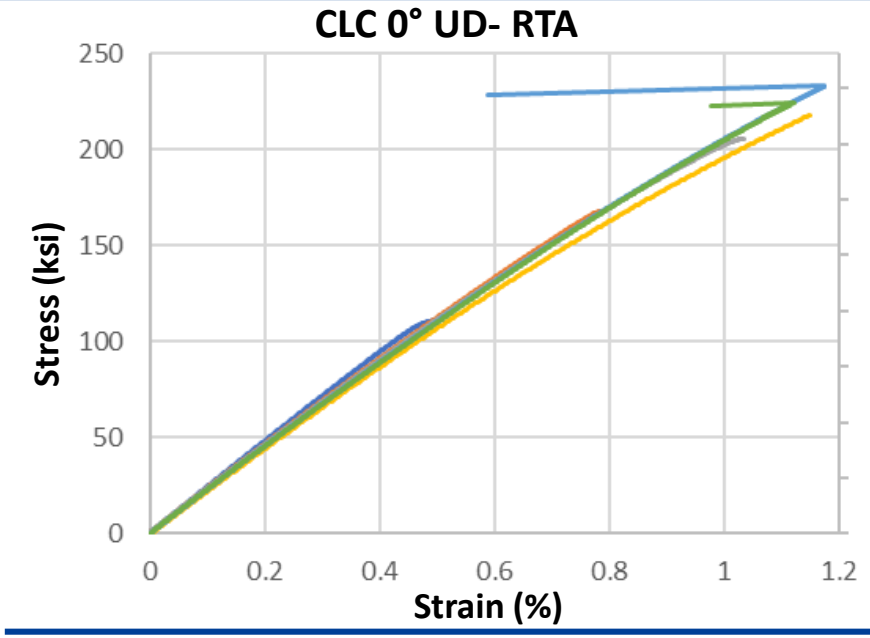

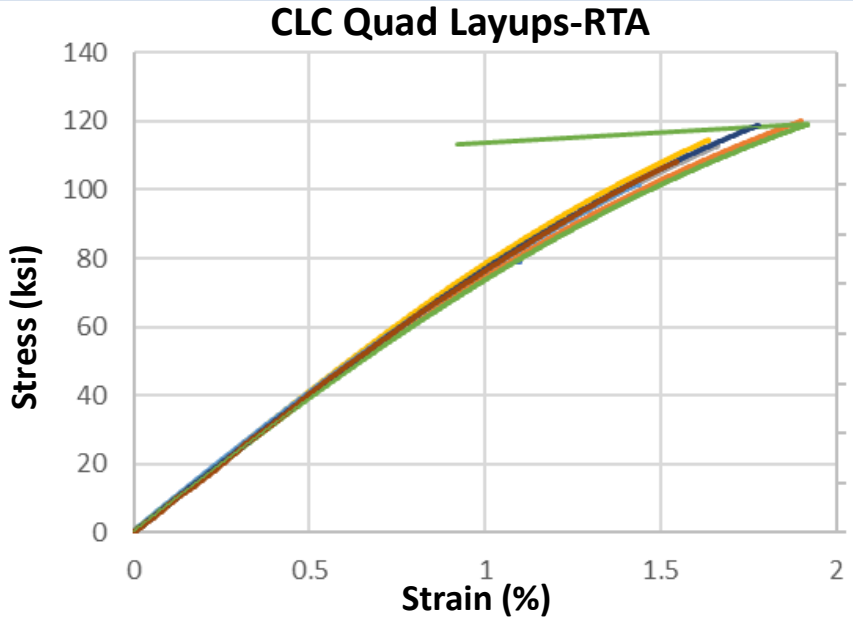

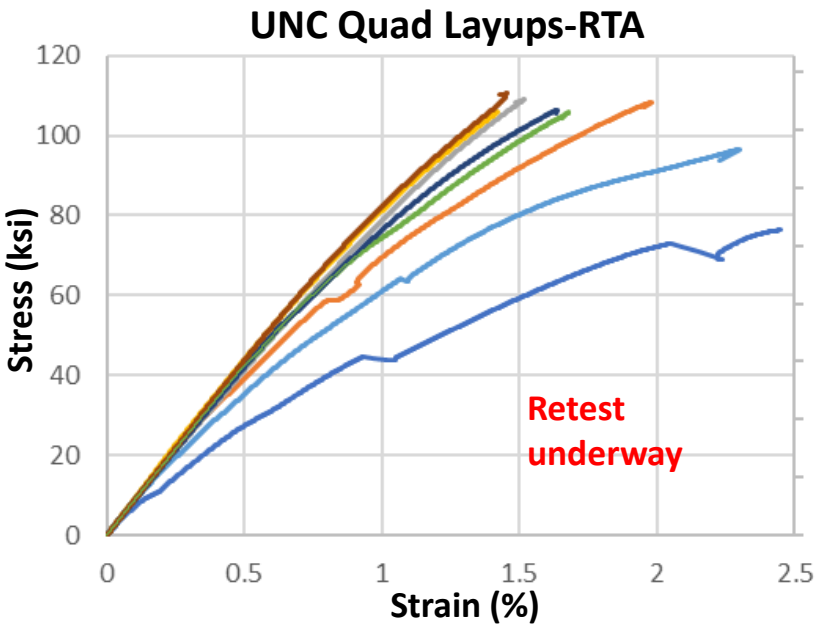

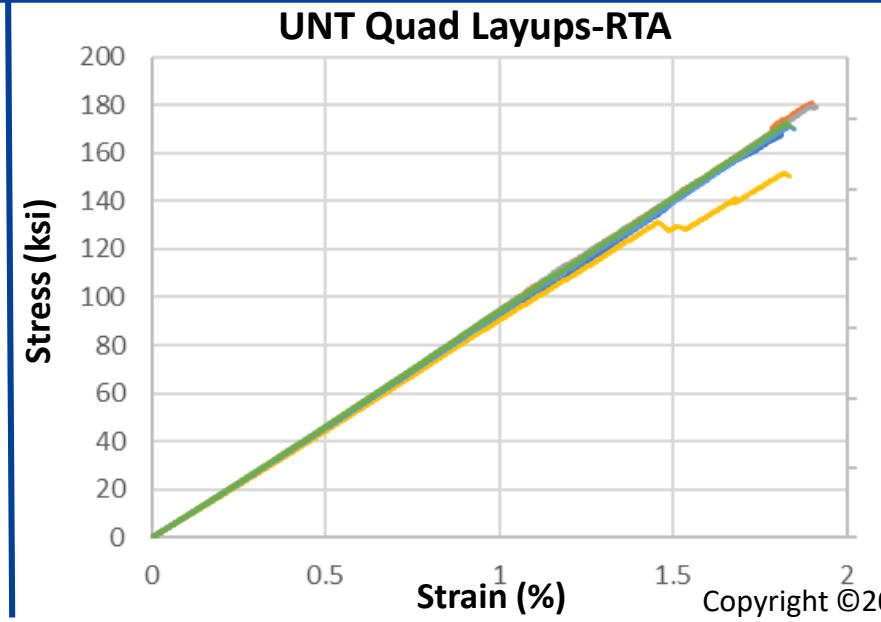

Compressive Strength UD Layups

[0]4	[0]6
[0]8	[0]14
[0]16	[0]20

Compressive Strength Quad Layups

[45/90/-45/0]S	[-45/0/45/90]S
[45/90/-45/0]2S	[-45/0/45/90]2S
[45/90/-45/0]3S	[-45/0/45/90]3S
[45/90/-45/0]4S	[-45/0/45/90]4S

Copyright ©2025 Toray Composite Materials America, Inc.

Phases 1 & 2: Strength vs. Ply Count For Quad Layups

Test (Method)	Width & Length	Gage Section
UNT (ASTM D8066)	1.5" x 12“ (38 x 305 mm)	8” (203 mm)
OHT (ASTM D8066)	1.5" x 12“ (38 x 305 mm)	8” (203 mm)
UNC (ASTM D8066)	1.5" x 12“ (38 x 305 mm)	4” (100mm)
OHC (ASTM D6486)	1.5" x 12“ (38 x 305 mm)	4” (100mm)
CLC (ASTM D6641)	0.5" x 5.5“ (12.7 x 140 mm)	0.5” (12.7 mm)

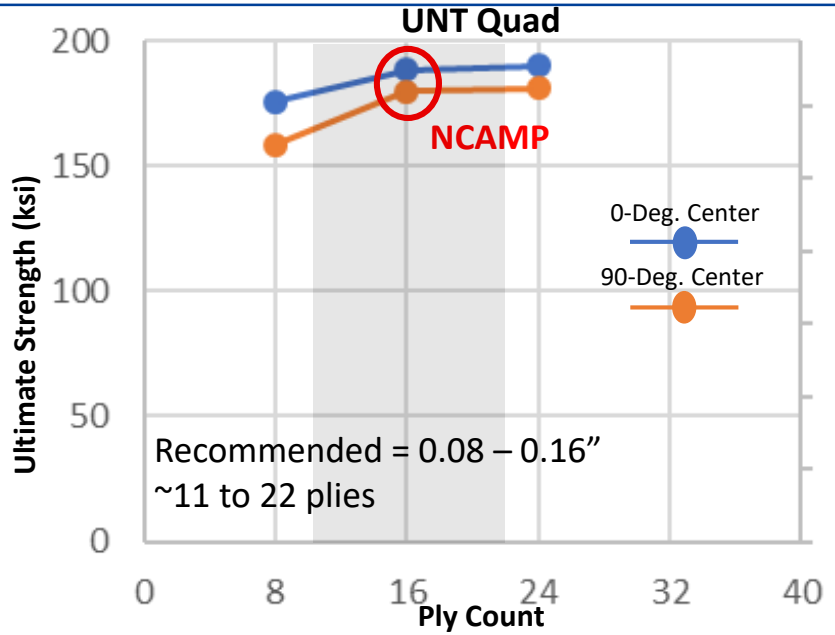

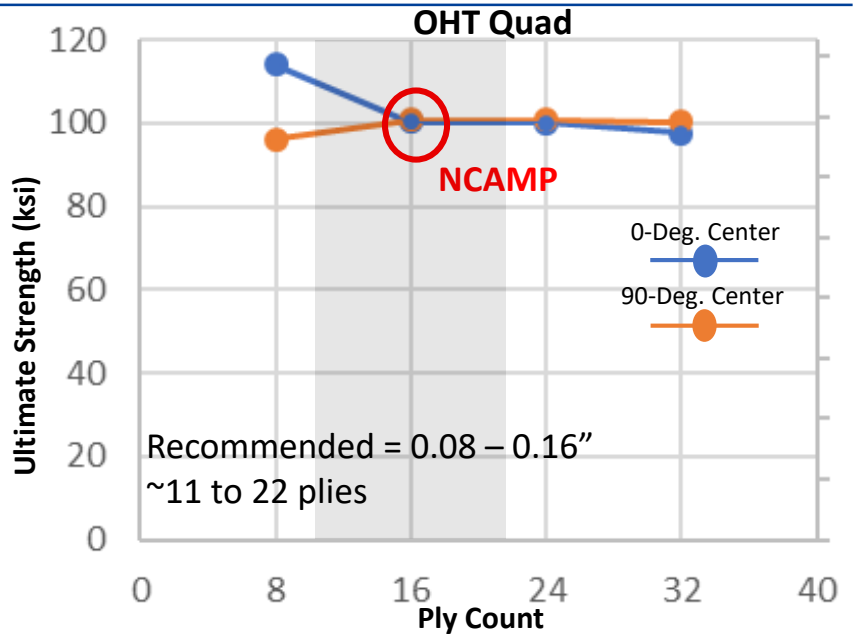

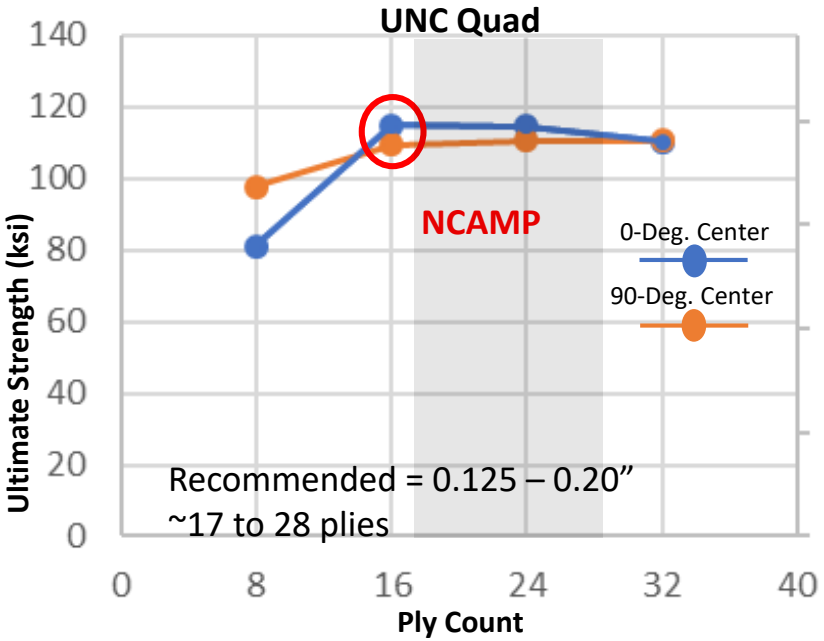

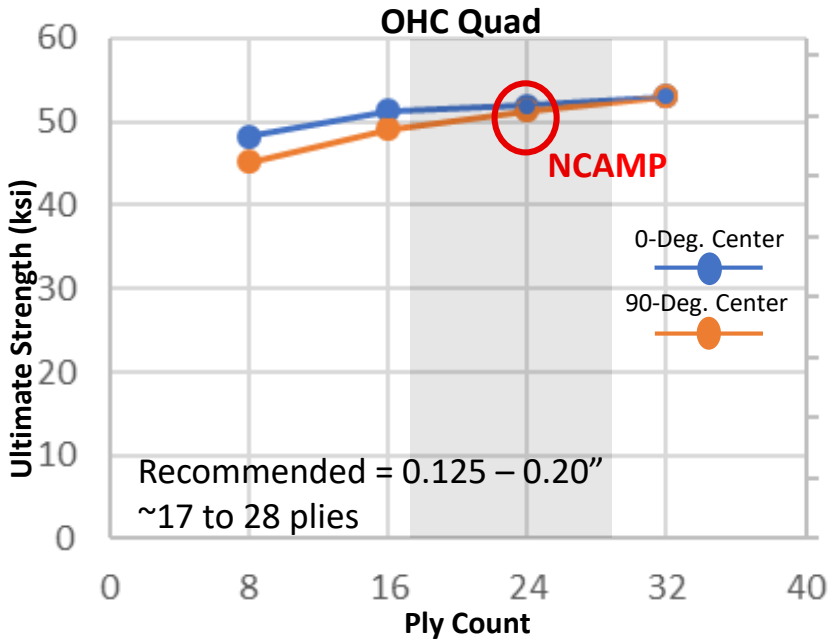

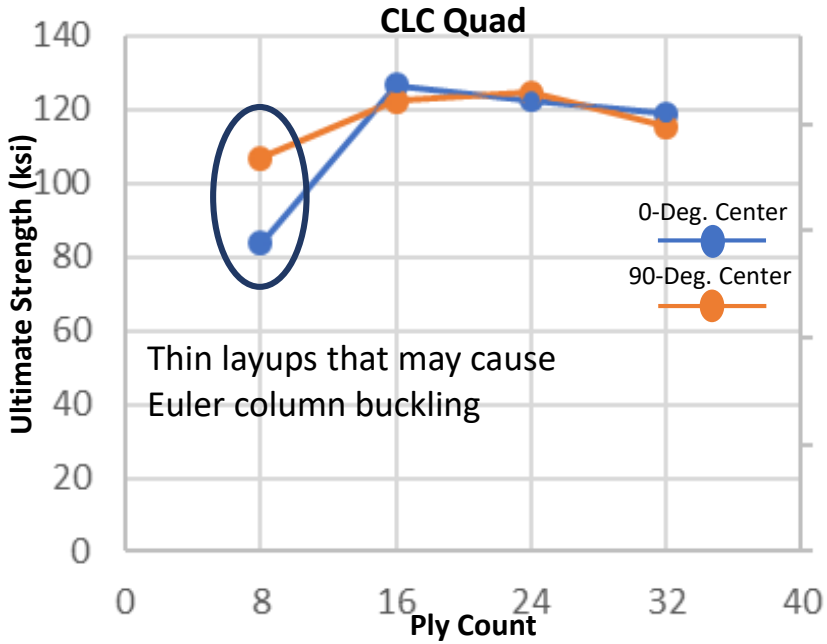

Phases 1 & 2: Strength vs. Ply Count- UD Tests

Test (Method)	Width & Length	Gage Section
0° TS (ASTM D8066)	1.5" x 12“ (38 x 305 mm)	8” (203 mm)
CLC (ASTM D6641)	0.5" x 5.5“ (12.7 x 140 mm)	0.5” (12.7 mm)

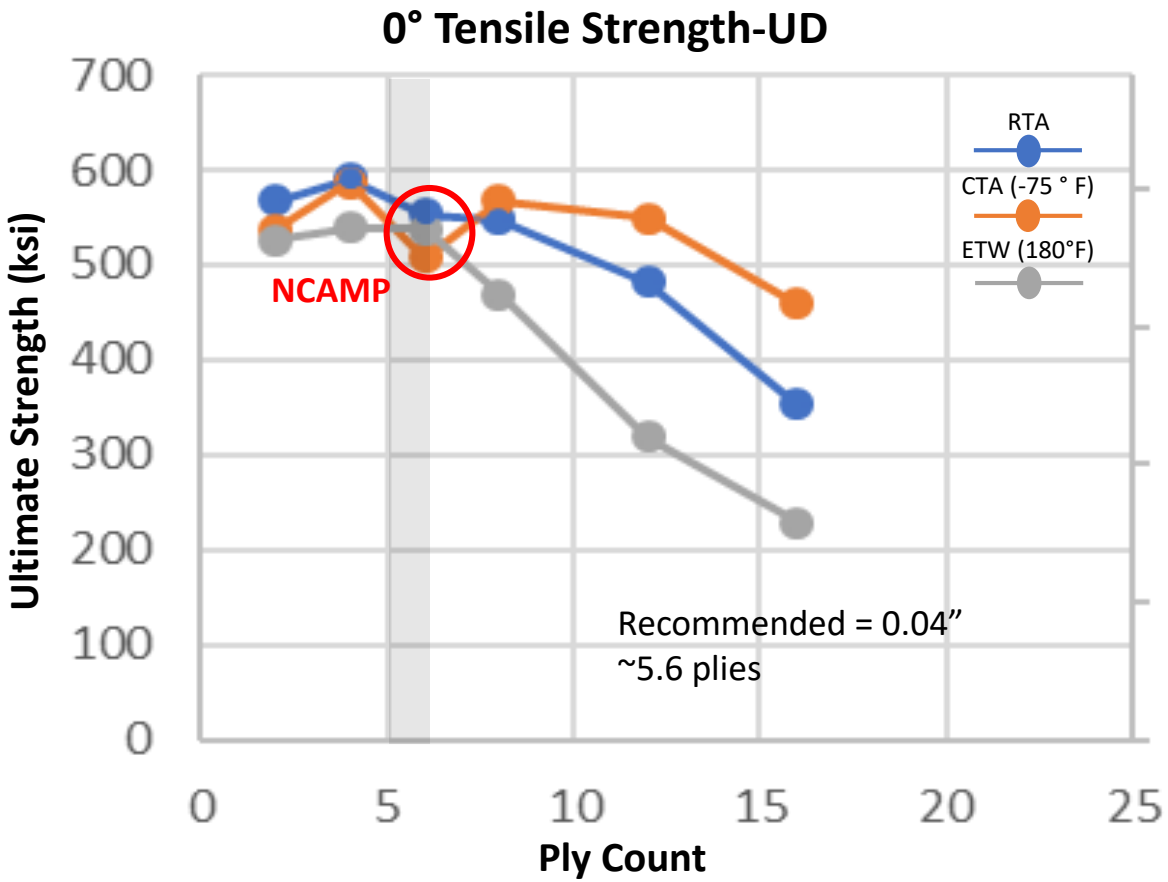

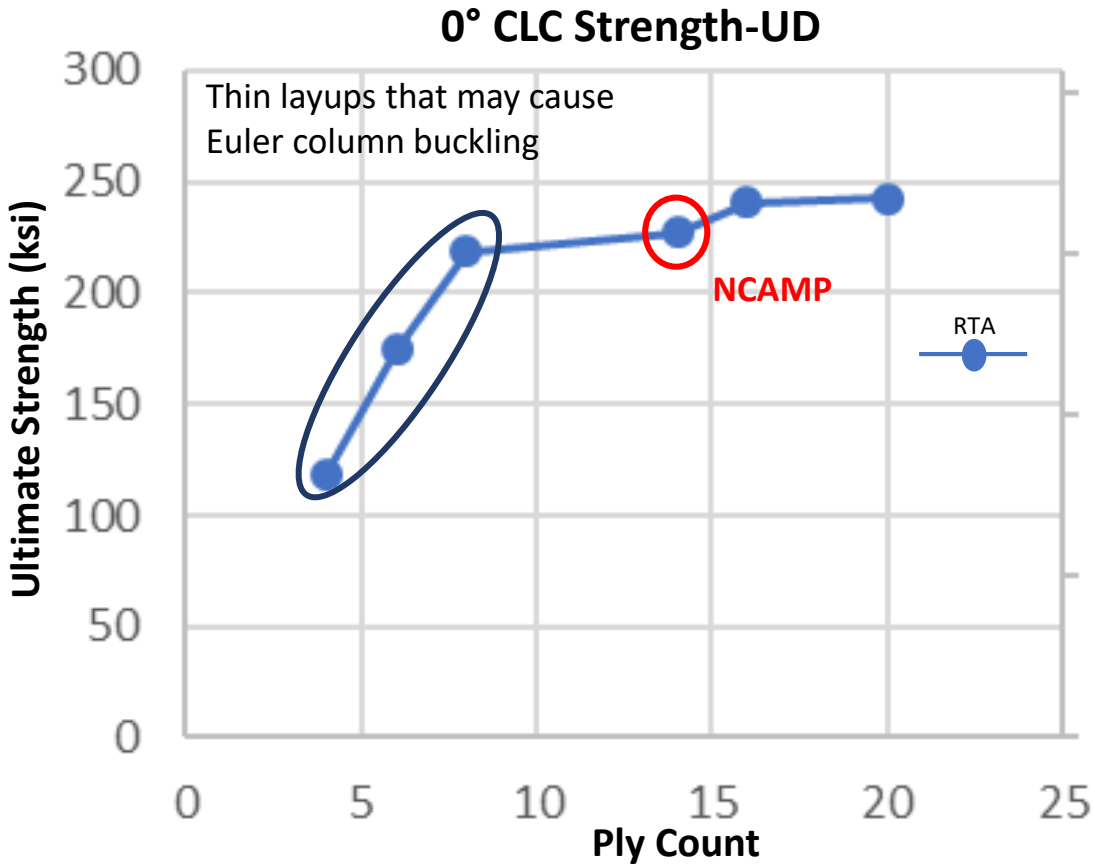

Copyright ©2025 Toray Composite Materials America, Inc.

Compressive Strengths Summary & Comparison

CLC 0° UD RTA	CLC RTA Quad-0°	CLC RTA Quad-90°	UNC RTA Quad-0°	UNC RTA Quad-90°	OHC RTA Quad-0°	OHC RTA Quad-90°	OHC ETW Quad-0°	OHC ETW Quad-90°

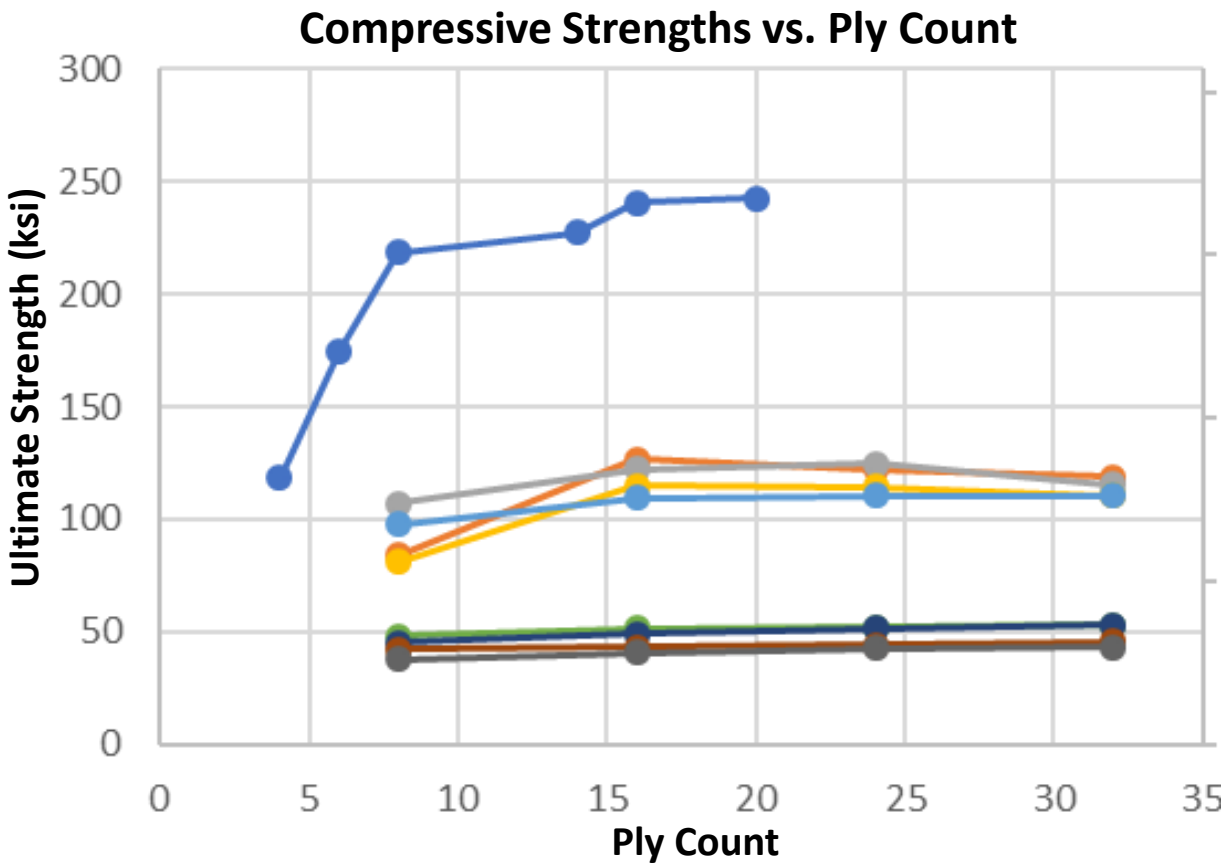

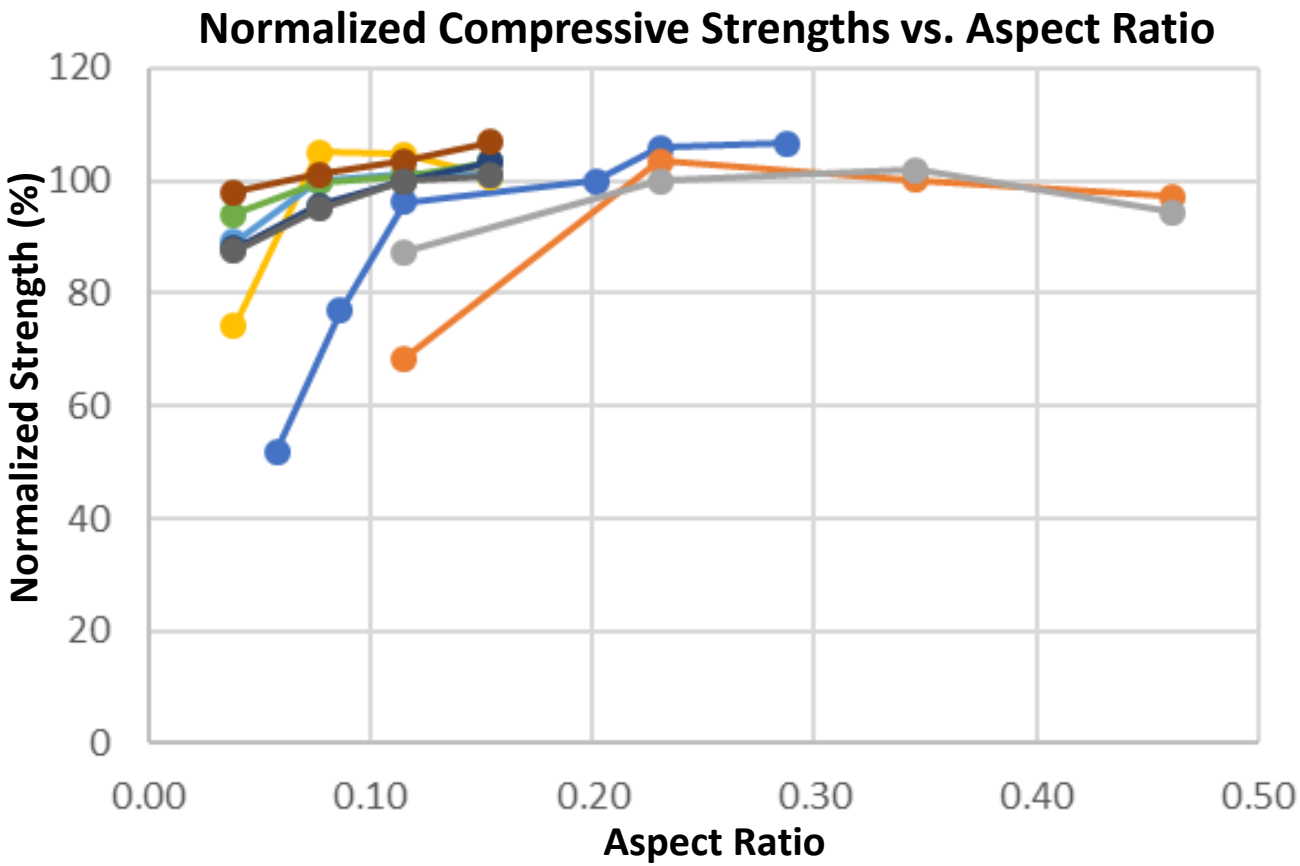

Copyright ©2025 Toray Composite Materials America, Inc.

Tensile Strengths Summary & Comparison

0° UD RTA	0° UD CTA	0° UD ETW	UNT RTA Quad-0°	UNT RTA Quad-90°	OHT RTA Quad-0°	OHT RTA Quad-90°	OHT CTA Quad-0°	OHT CTA Quad-90°

Tensile Strengths vs. Ply Count

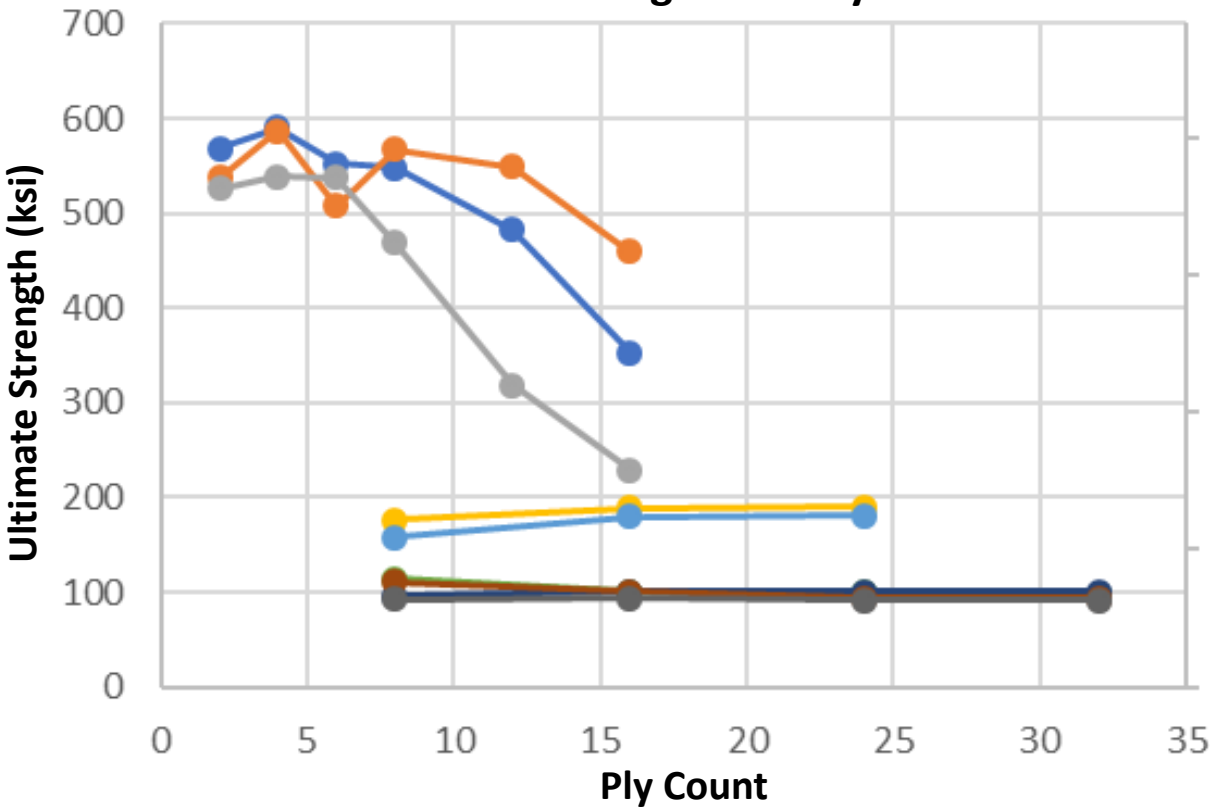

Normalized Tensile Strengths vs. Aspect Ratio

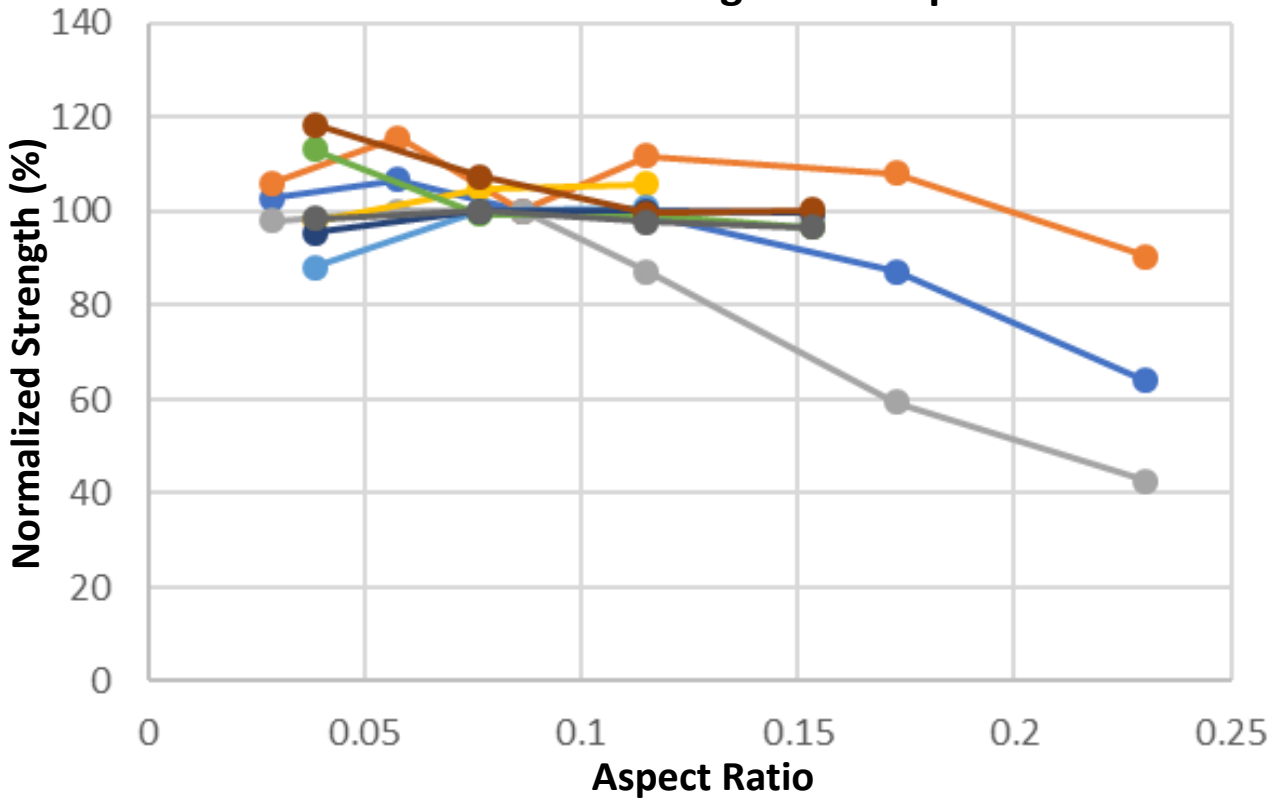

Copyright ©2025 Toray Composite Materials America, Inc.

Summary and Design Implications-Thickness Effects

Unidirectional Thickness effects

- Tensile strength (including 0°TS, OHT, UNT) tends to decrease with increasing thickness
- Compressive strength (including 0°CS, OHC, UNC) tends to increase with increasing thickness

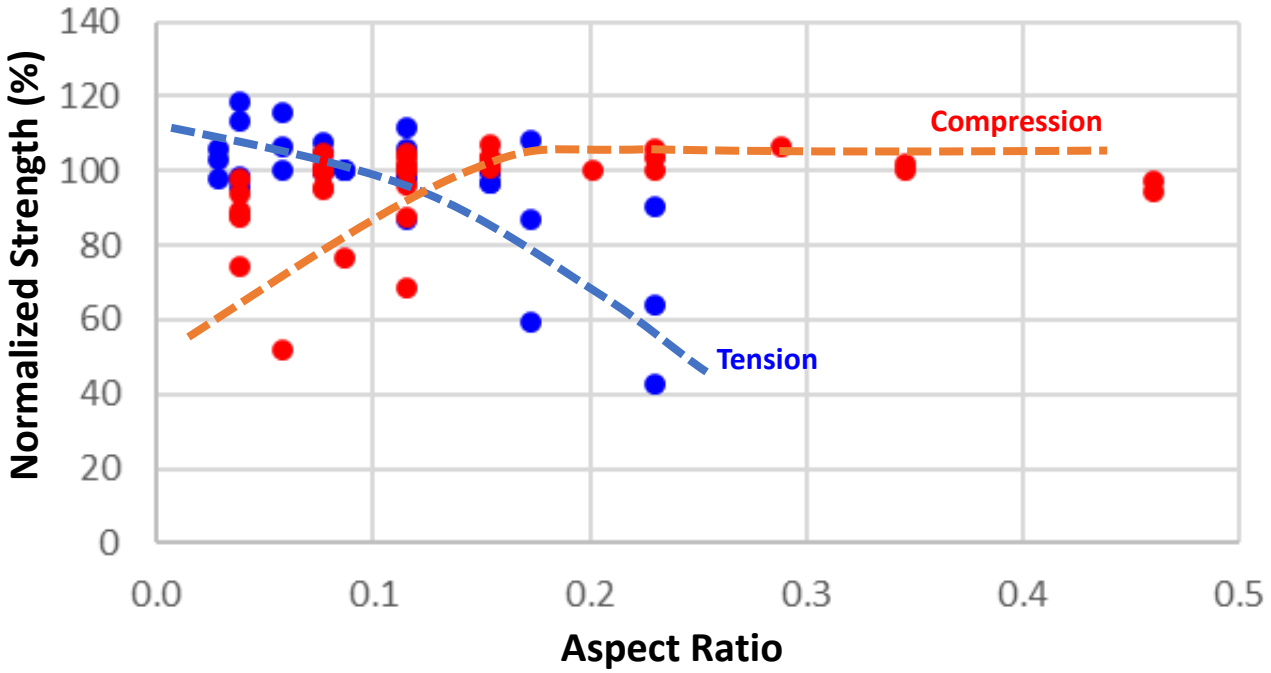

UNT/UNC, OHT/OHC Quad Layup Thickness Effects

- High scatter at ply count = 8, becomes more consistent as ply count increases
- Outliers in thin layups deserve further replication
  - Observed ~10% increase for 8-ply OHT depending on center orientation

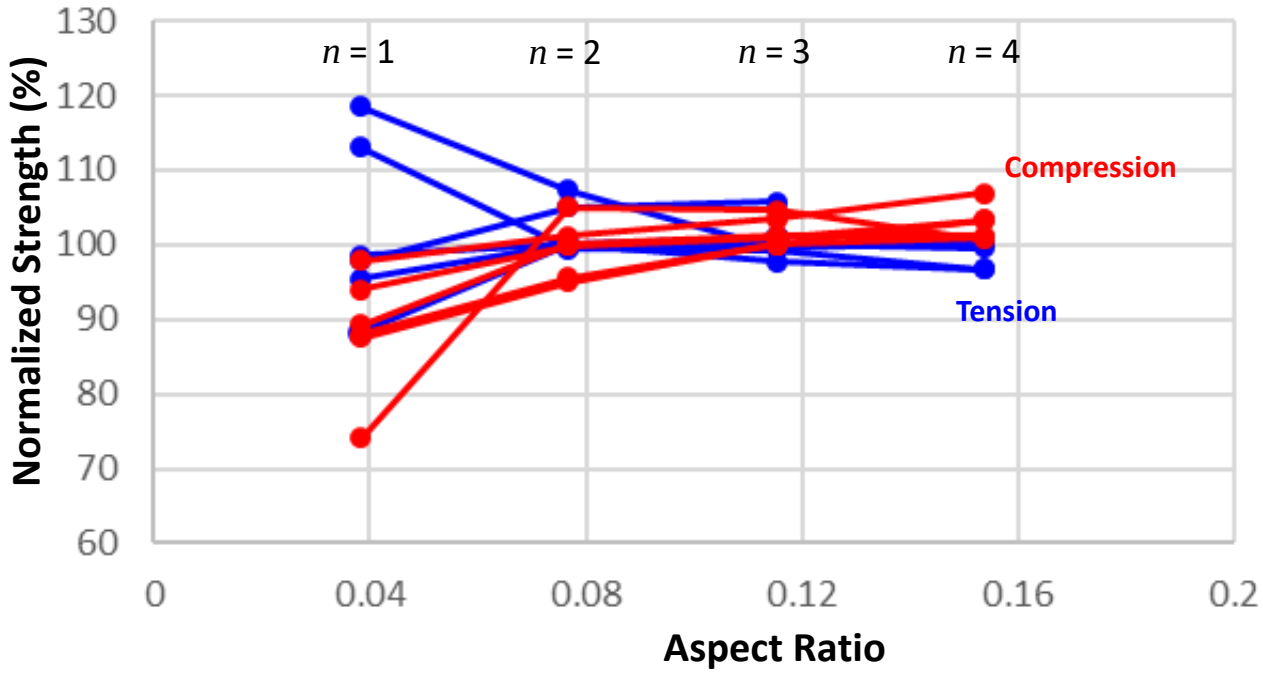

Copyright ©2025 Toray Composite Materials America, Inc.

Summary and Design Implications-Quad Layup Choices

Stacking sequence effect in quad layup

- Quad layups with 0° in the midplane performs better, especially in tension

- Differences diminish as ply count increases
- Strength variability higher at low ply counts – stabilizes with thickness

Design implications

- Thin layups should avoid relying solely on 0° strength, thicker laminates show more reliable compression performance

- A shared *thick* panel for OHT/OHC, UNT/UNC, FHT/FHC streamlines layup, reduces lab workload, and minimizes potential confusion in lab workflows

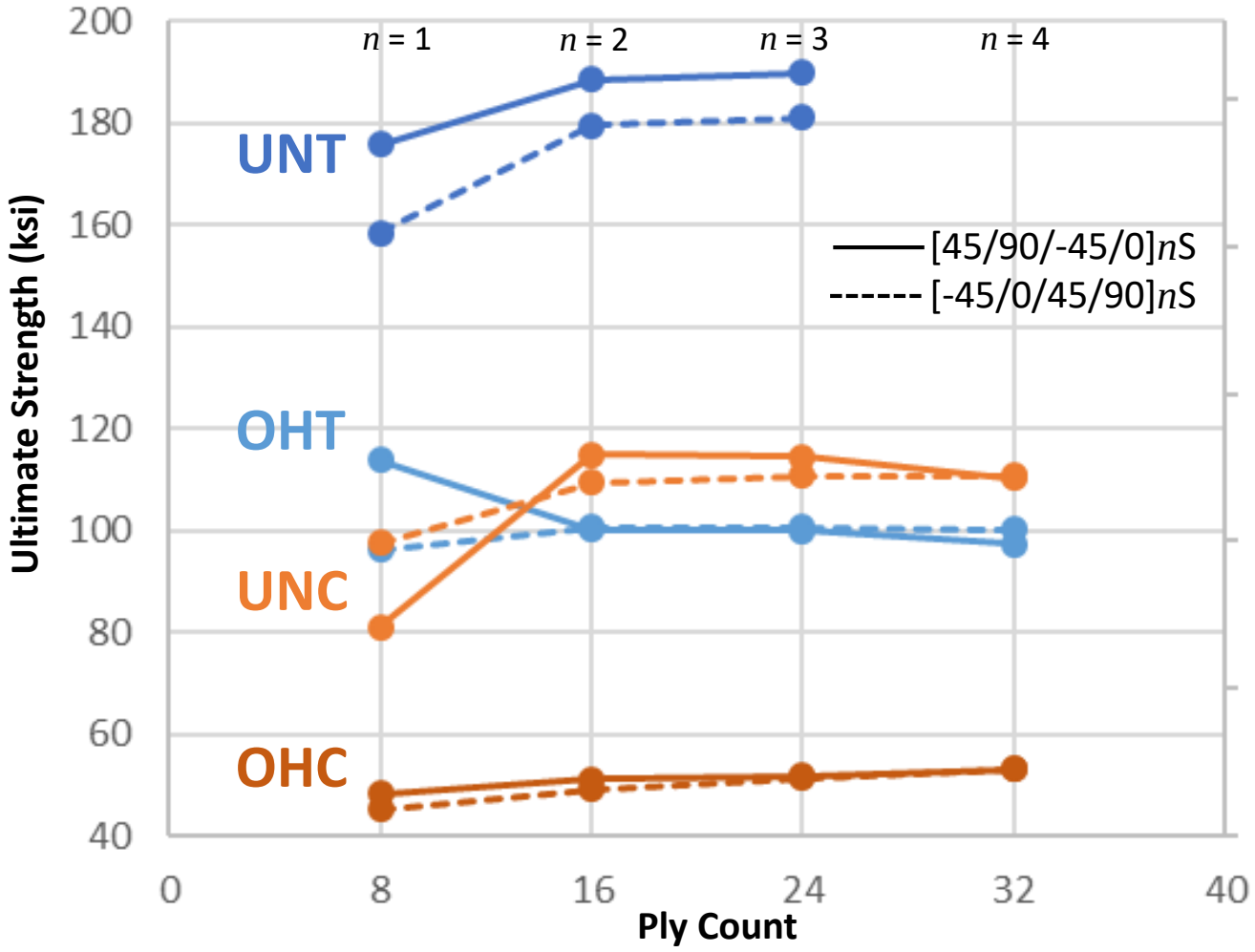

Copyright ©2025 Toray Composite Materials America, Inc.

Conclusions (and Recommendations for Designers & Test Engineers)

- Quad layup stacking sequence significantly influences strength, particularly in thin laminates
- 0° plies in the midplane enhance tensile and compressive strength, with larger effects at low ply counts
- Thickness impacts both performance and variability – strength stabilizes with increased thickness
- High OHT outliers are repeatable and valid, warranting further targeted testing
- Future work: Expand test matrix with varied FAW and hybridized systems

Don Lee, Ph.D.
Principal Research Scientist
CMRL, Toray CMA (Tacoma, WA)
Don.Lee@toraycma.com

Joseph McDonald
Research Scientist
CMRL, Toray CMA (Tacoma, WA)
Joseph.McDonald@toraycma.com

Copyright ©2025 Toray Composite Materials America, Inc.

References

1. ASTM STP , Vol. 452 (1968) through Vol. 1330 (1998) 31 volumes, 739 technical reports
2. G. Nehls, “Toray and Bell collaborate on new NCAMP design allowable dataset for 3960 prepreg system,” CompositesWorld, May 25, 2022. Accessed: Sep. 15, 2024. [Online]. Available: https://www.compositesworld.com/news/toray-and-bell-collaborate-on-new-ncamp-design-allowable-dataset-for-3960-prepreg-system
3. J. McDonald, D. Lee, and I. Taketa, “Impact of Stacking Sequence and Size Effects on Open Hole Compressive Performance,” presented at the the ASME 2024 Aerospace Structures, Structural Dynamics, and Materials Conference, Renton, Washington, Jun. 2024. doi: https://doi.org/10.1115/SSDM2024-120908.
4. “T1100G-Technical-Data-Sheet-1.pdf.pdf.”
5. ASTM D5766/D5766M − 23: Standard Test Method for Open-Hole Tensile Strength of Polymer Matrix Composite Laminates, D5766, Sep. 01, 2023. doi: 10.1520/D5766_D5766M-23.
6. ASTM D6484/6484M-23 Standard Test Method for Open-Hole Compressive Strength of Polymer Matrix Composite Laminates1, D6484, Oct. 2023. doi: 10.1520/D6484_D6484M-23.
7. ASTM D8066/D8066M − 23: Unnotched Compression Testing of Polymer Matrix Composite Laminates, ASTM D8066, May 01, 2023. doi: 10.1520/D8066_D8066M-23.
8. ASTM D3039/D3039M − 17:Standard Test Method for Tensile Properties of Polymer Matrix Composite Materials, D3039. doi: 10.1520/D3039_D3039M-17.
9. ASTM D6641/D6641M- 23: Standard Test Method for Compressive Properties of Polymer Matrix Composite Materials Using a Combined Loading Compression (CLC) Test Fixture, ASTM D6641, Dec. 06, 2023. doi: 10.1520/D6641_D6641M-16E02.

Copyright ©2025 Toray Composite Materials America, Inc.

ICCM24 24TH INTERNATIONAL CONFERENCE ON COMPOSITE MATERIALS
AUG 4-8, 2025 • BALTIMORE CONVENTION CENTER • BALTIMORE, MARYLAND

QUANTITATIVE EVALUATION AND COMPARISON OF TERAHERTZ AND ULTRASONIC TESTING OF GLASS-FIBER REINFORCED PLASTICS

Praveen Kumar Allu[1], Jens Schuster[1*], Raphael Hussung[2], Joachim Jonuscheit[2]
[1]: Institut für Kunststofftechnik Westpfalz - IKW, University of Applied Sciences Kaiserslautern, Germany
[2]: Fraunhofer-Institut for Techno- und Wirtschaftsmathematik - ITWM, Rheinland-Pfälzische Technische Universität, Germany
* Corresponding author: jens.schuster@hs-kl.de

Keywords: Terahertz, Ultrasonics, Nondestructive testing, Glass fiber reinforced plastics, Signal/noise ratio

ABSTRACT

Composite materials are essential in aerospace and automotive structures, yet their safety-critical use demands reliable nondestructive testing (NDT). Ultrasonic inspection is well suited for carbon-fiber-reinforced plastics (CFRP) but struggles with glass-fiber composites (GFRP) and structural foams because scattering and attenuation mask defect echoes. Terahertz testing, which uses electromagnetic waves between 0.1 and 1 THz and needs no coupling medium, overcomes these limits for non-conductive materials. Ultrasound and terahertz are therefore complementary. This paper evaluates the best choice depending on frequency, defect size and depth.

This study quantitatively compares signal-to-noise ratios (SNR) delivered by focused ultrasonic transducers (1, 2.25, 5 MHz) and continuous-wave terahertz probes (100, 150, 300 GHz). Two specimens were prepared: a 50 mm pultruded GFRP block with blind holes 2.5 - 8 mm at nine depths, and a 15 mm expanded-polypropylene foam slab with 2-12 mm holes at two depths. Water-coupled pulse-echo C-scans and matching terahertz scans were recorded with 300 µm steps. The signal-to-noise ratio was defined as the maximum defect amplitude divided by the maximum surrounding echo.

Ultrasonic testing detected most GFRP defects to 35 mm with the 2.25 MHz probe. 5 MHz resolved 2 mm holes but only to a depth of 15 mm, while 1 MHz penetrated the full block yet with blurred indications at higher depths. Terahertz produced higher SNR overall. 100 GHz was optimal for GFRP, imaging an 8 mm hole at 40 mm, whereas 300 GHz yielded the clearest foam images. The foam could not be inspected ultrasonically.

The signal-to-noise ratio increases with flaw size and drops with depth and frequency. Its optimum shifts deeper as frequency falls. Terahertz is besides the more expensive computer tomography the only effective method for closed-cell foams. For GFRP, 2.25 MHz ultrasound remains the most versatile for defects larger than 6 mm for ultrasonic testing, while terahertz offers superior signal-to-noise ratios. Combining both techniques maximizes defect detectability for non-carbon composite components.

1 INTRODUCTION AND OBJECTIVES

Composite materials are gaining increasing importance in the aerospace and automotive industries due to their advantages in weight, stiffness and strength. Because of high safety requirements in the use of these materials in primary and secondary aircraft structures, composite materials demand sophisticated nondestructive testing methods, such as ultrasonic inspection, radiography or thermography. Ultrasonic testing in particular provides excellent results for the detection of a broad variety of defects and has proven to be a reliable inspection tool in recent years and is used to inspect primary and secondary aircraft structures made of carbon fiber reinforced plastics [1, 2]. However, the range of materials has expanded considerably in recent years, meaning that glass fiber-reinforced composites and foams must also be tested non-destructively. Ultrasonic testing is very problematic with these materials due to the high scattering and attenuation.

Instead, terahertz testing can be used. It is a comparatively new NDT method that works very similarly to ultrasonic testing. Instead of mechanical sound waves, electromagnetic waves in a frequency range of 0.1 to 1 THz are used for testing. The advantage of terahertz testing is that no coupling medium needs to be used. A major

disadvantage for general use is the exclusion of testing electrically conductive materials such as metals or carbon fiber-reinforced plastics. Terahertz technology is therefore particularly suitable for testing nonconductive materials such as foams or glass fiber-reinforced plastics [2]. Both materials are difficult to test with ultrasound. However, both materials are used for demanding parts for aerospace and maritime applications (Fig. 1 & 2).



Figure 1: Sailplane made out of GFRP [3]

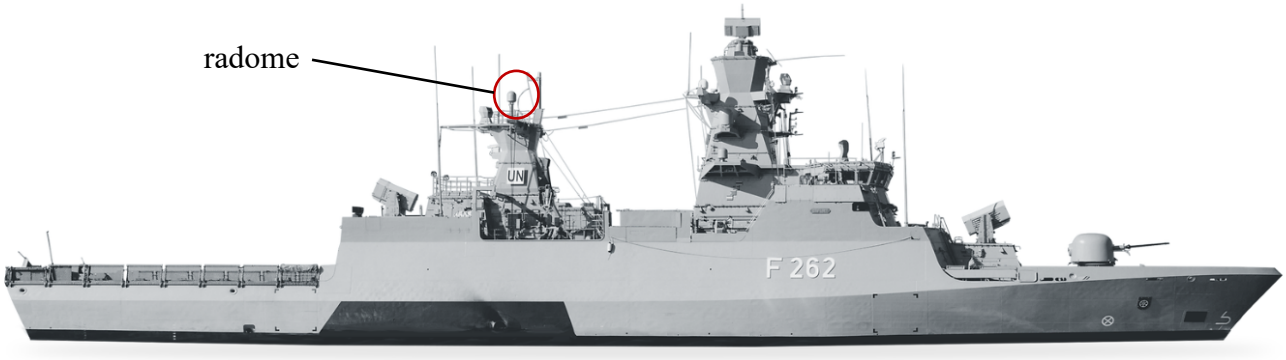

Figure 2: Foam based radome of a German corvette [4]

Thus, terahertz testing should not be seen as a competitive process, but rather as a powerful complement to ultrasound testing [5]. Of course, there are materials, such as GFRP, where both methods can be used. In this case, it is interesting to know which method produces the higher signal-to-noise ratio during detection depending on the test frequency, defect size and defect depth, if this is possible at all. An early comparison was done by J. Dong, et.al. in terms of a qualitative evaluation [6]. The investigation presented here focusses on a quantitative comparison of the measured signal-to-noise ratios in order to obtain the optimal test method and testing frequency.

2 EQUIPMENT AND TEST PIECES

2.1 ULTRASONIC FACILITY

The research and development described was conducted at the Institut für Kunststofftechnik Westpfalz (IKW) located on the campus of the University of Applied Sciences Kaiserslautern. The institute´s state-of-the-art ultrasonic system was manufactured by the company Hillger in Germany and operates in a frequency range from 0.1 up to 30 MHz in a fully digitized way (Fig. 3). Ultrasound can be applied water- and air-coupled. However, in this study only water coupling was used. The Hilgus-software package allows the realization of through-transmission tests and A-, B-, C-, D-, and F-scans, which e.g. allows the evaluation of frequency shift based on real-time Fast-Fourier-Transformation (FFT). In addition, full-waveform-scans can be performed allowing post-scanning gate-settings. In total, besides a trigger gate two evaluation gates can be set. Three scanning systems can be connected to the ultrasonic control unit:

- Four axes system for shell-like parts (40 x 60 x 80 cm) and short rotational parts
- Two axes system for rotational parts (length 120 cm, diameter 15 cm)
- Two axes system for through-transmission air-coupled ultrasonic testing.

in-house construction of the Fraunhofer-Institut for Techno- und Wirtschaftsmathematik (ITWM) with which tests for the generation of A-, B- and C-scans in the frequency range from 70 GHz to 500 GHz 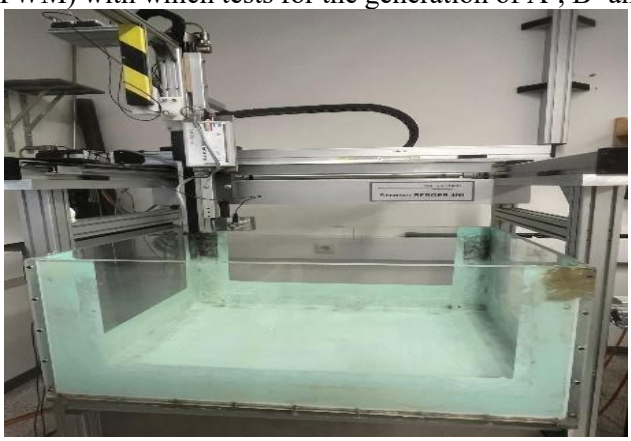

Figure 3: Ultrasonic scanner with immersion tank

Three focused transducers from Olympus NDT - Panametrics with center frequencies of 5 MHz, 2.25 MHz and 1 MHz were used for the ultrasonic tests (Fig. 4, Table 1).



Figure 4: 1 MHz, 2.25 MHz, and 5 MHz transducer

Transducer name	Frequency f [MHz]	Diameter of active element D [inch]	Focal length F [mm]	Near field length N [mm]	Bundle diameter b [mm]
V394	1	1.125	96.5	137	5.25
V304	2.25	1	76.2	244	2.07
V309	5	0.5	50.8	136	1.24

Table 1: Transducer properties

2.2 TERAHERTZ FACILITY

The terahertz test facility is an in-house construction of the Fraunhofer-Institut for Techno- und Wirtschaftsmathematik (ITWM) with which tests for the generation of A-, B- and C-scans in the frequency range

from 70 GHz to 500 GHz are possible (Fig. 5). The depth information is generated by the FMCW principle. Three probes with 100 GHz, 150 GHz and 300 GHZ were used for the measurements undertaken (Fig. 6).

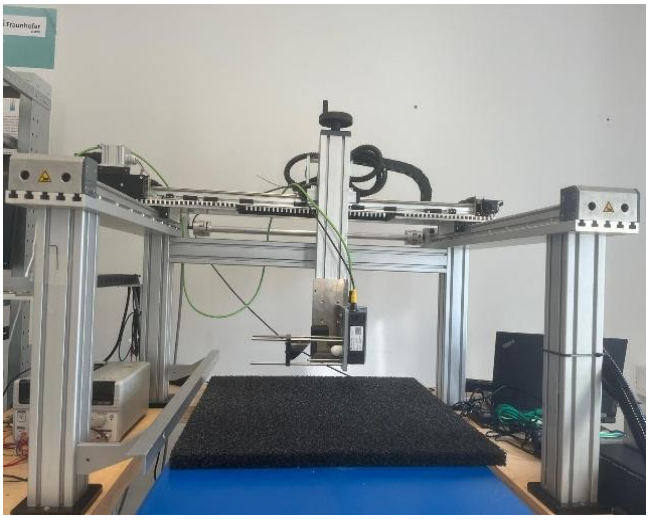

Figure 5: Terahertz facility



Figure 6: Terahertz probe

2.3 SAMPLES

Two test pieces were used. The first one was a pultruded glass fiber reinforced block (GFRP-block) with a thickness of 50 mm in which blind holes with diameters of 2.5 mm, 4 mm, 6 mm and 8 mm were drilled at nine different depths (5 mm, 10 mm, 15 mm, 20 mm, 25 mm, 30 mm, 35 mm, 40 mm, and 45 mm as shown in Fig. 7a. The speed of sound of this GFRP was determined to be 2.350 m/s. The second sample was an EP-foam panel (density 170 kg/m^3) with a thickness of 15 mm and blind holes (diameter 2 mm, 3 mm, 4 mm, 5 mm, 6 mm, 7 mm, 8 mm, 9 mm, 10 mm and 12mm) and depths of 2.5 and 5 mm) in two different depths (2.5 mm and 5 mm) as depicted in Fig. 7b.

a) 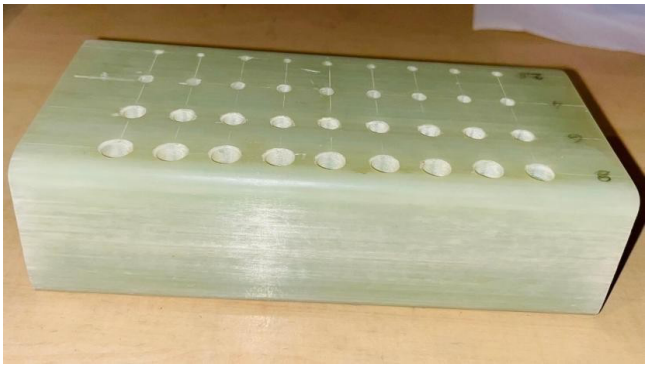

b) 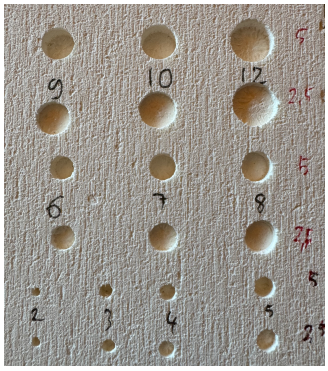

Figure 7: Samples, a) GFRP-sample, b) EP-foam sample

3 EXPERIMENTAL

Ultrasonic testing of the GFRP-sample was done in pulse-echo with gates with a width of 4 µm starting at 2 µm behind the front surface echo and one gate set around the back surface echo resulting in ten C-scans for each transducer. The measurements were performed from the rear side of the sample. Because only four gates can be evaluated during one test, three measurement runs were required. The use of an auxiliary reflector did not work due to the thickness of the part and the associated attenuation of the ultrasound. The focal points were placed into

that depth were the gates were set. The C-scan were quantitatively evaluated with a custom-made program named Oculus.

The same approach was used for the foam sample but with gate lengths set around the expected defect echoes. The increment was chosen in both scanning directions to 300 µm. The foam part clamped to a stainless steel plate to avoid floating.

The terahertz tests of the GFRP-sample were performed accordingly to the ultrasonic C-scans with the focal point set in the area of interest. The foam part was inspected by means of an auxiliary reflector (steel plate) which was placed 10 mm below the rear sides of the samples. Also here, the increment was chosen in both scanning directions to 300 µm. All A-scans were stored as a full-waveform scan. Similar to the ultrasonic C-scans, the THz-C-scans of the GFRP-sample were quantitatively evaluated with features programmed into the scanning program.

4 RESULTS

It turned out that with ultrasonic testing, it was not possible to detect any defects in the foam sample. Exemplary C-scans of the GFRP-sample are shown for the blind hole defects in a depth of 15 mm (Figure 8). With the 2.25 MHz probe, most defects could be detected up to a depth of 35 mm. With the 5 MHz probe, only defects up to a depth of 15 mm could be detected. After that, the attenuation of the material was too great due to the scattering of the glass fibers. Interestingly, it was even possible to generate a backwall echo with the 1 MHz probe. However, with this probe it was only possible to image defects up to a depth of 20 mm.

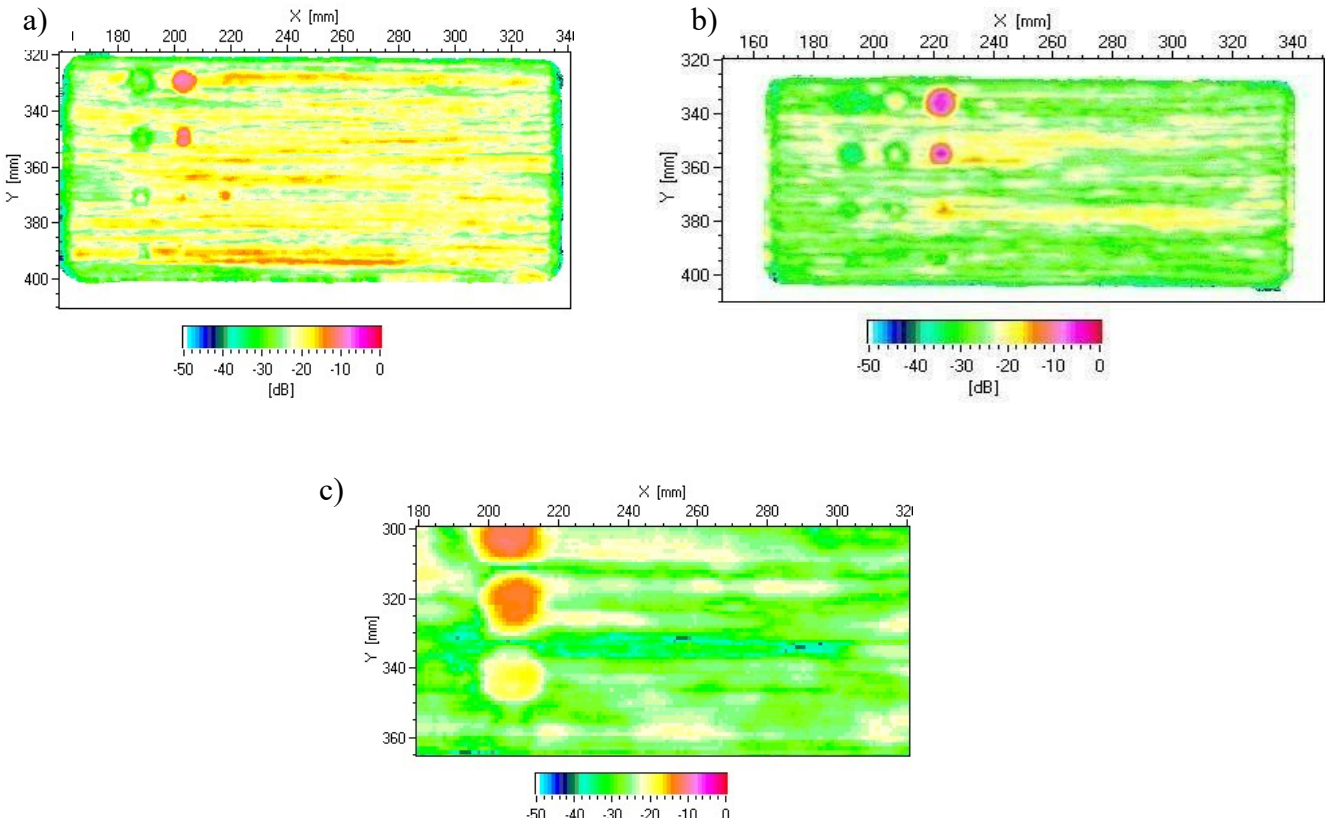

Fig. 8: C-scans of the GFRP-samples with gate set between 10 and 14 µm, a) 5 MHz, b) 2.25 MHz, c) 1 MHz

The high-lying defects (5 mm depth) could not be detected in any case because the spurs from the front surface echo covered the defect echoes. The signal-to-noise ratio decreased with increasing depth and decreasing defect size. Due to the shorter wavelength of the 5 MHz transducer in comparison to the 2.25 MHz transducer (470 µm to 0,97 µm) the 2 mm defects could be found. Furthermore, it can be noticed that the 1 MHz transducer enlarges the defects significantly.

The results of the terahertz-measurements are exemplary shown in Fig. 9 and Fig. 10. It turned out that the 300 GHz probe was not suitable to inspect the GFRP-sample. In turn, it showed the best results for the thinner foam sample.

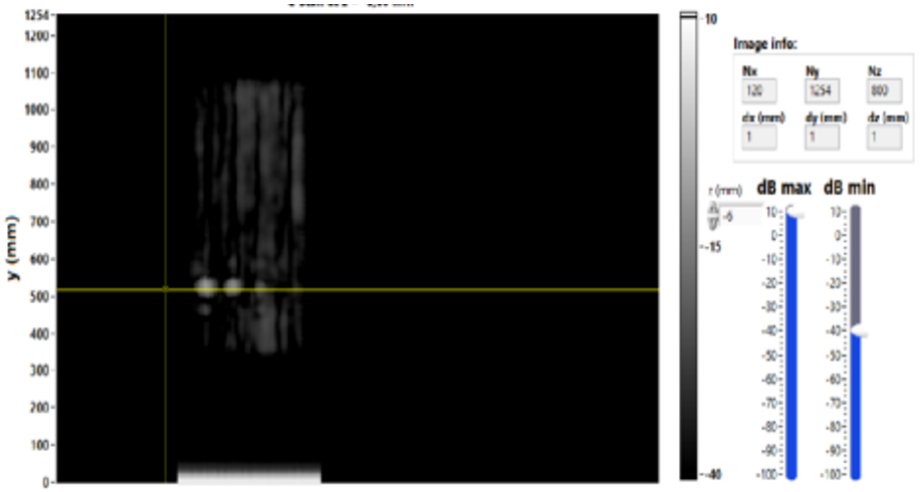

Fig. 9: THz-C-scan of the GFRP-samples with 100 GHz and a depth of 15 mm

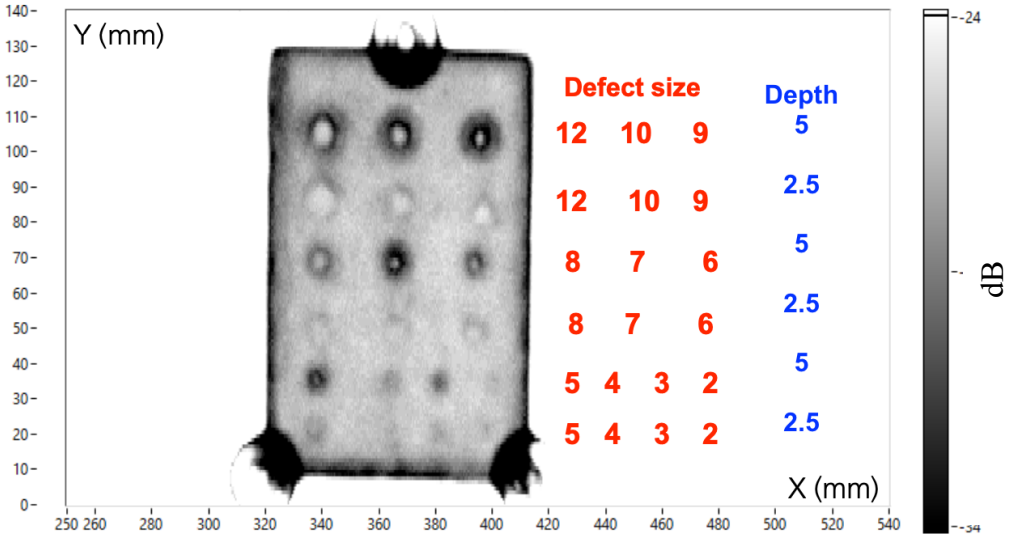

Fig. 10: THz-C-scan of the GFRP-samples with 300 GHz and a depth of 15 mm

5 EVALUATION

5.1 FUNDAMENTALS

The signal/noise ratio determines how much the echo amplitude of an indication differs from that of the flawless vicinity. In order to quantify the signal/noise ratio of an indication, four different approaches can be realized:

a. maximum indication amplitude versus maximum ambient echo
b. maximum indication amplitude versus average ambient echo
c. average indication amplitude versus maximum ambient echo
d. average indication amplitude versus average ambient echo,

where the ambient can be understood as that part of the sample not including any defects. Here, the maximum indication amplitude versus maximum ambient echo in the vicinity of the defect was used for the analysis of the

signal/noise ratio. This procedure is also consistent with the optical assessment strategy of an UT-operator to identify an indication by looking at the highest difference between indication and ambient echo amplitudes (sharpest contrast). Parameters significantly influencing the signal/noise ratio are as follows:

- depths of defect
- defect size
- transducer frequency (UT and THz)
- focal length
- bundle diameter (focal point diameter)
- active element diameter
- inspection strategy (kind of echo, position of focal point)

Focal length, focal point diameter, active element diameter and frequency are transducer properties and cannot be chosen freely [1]. The influence of the remaining four parameters was analyzed by keeping two of them constant and considering the effect of variations of the two others on the signal/noise ratio.

5.2 INFLUENCE OF DEFECT SIZE

First, the dependency of the defect size was evaluated for two different depths (10 and 25 mm). The result of this evaluation can be seen in Fig. 11 and 12.

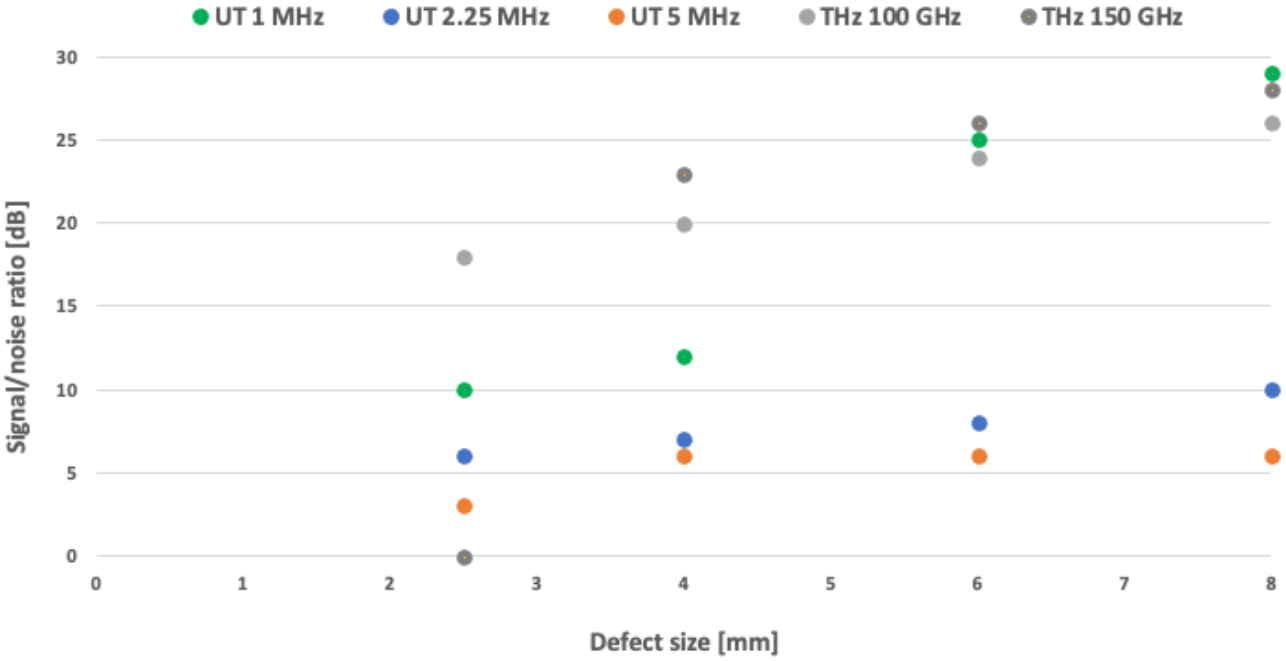

Fig. 11: Dependency of the defect size on the signal/noise-ratio (depth 10 mm)

The evaluation of the signal-to-noise ratios for the various defect sizes at a defect depth of 10 mm shows that all defects are easily detectable (Fig. 11). With ultrasound, the signal-to-noise ratios decrease with the frequency and increase with the flaw size. This is also the case with terahertz testing. Terahertz testing enables the detection of defects with a higher signal-to-noise ratio.

The result is very similar for the defects at a depth of 25 mm (half the sample thickness). The signal-to-noise ratios for ultrasonic testing are higher than for a defect depth of 10 mm, which can be explained by the surface echo that has been completely attenuated at this depth reducing the ambient noise. The signal-to-noise ratio of the 100 GHz terahertz test is again the highest. At a depth of 40 mm, only the 8 mm defect could be visualized at 2.25 MHz with ultrasound and with the 100 GHz terahertz probe with signal-to-noise ratios of just above two digits.

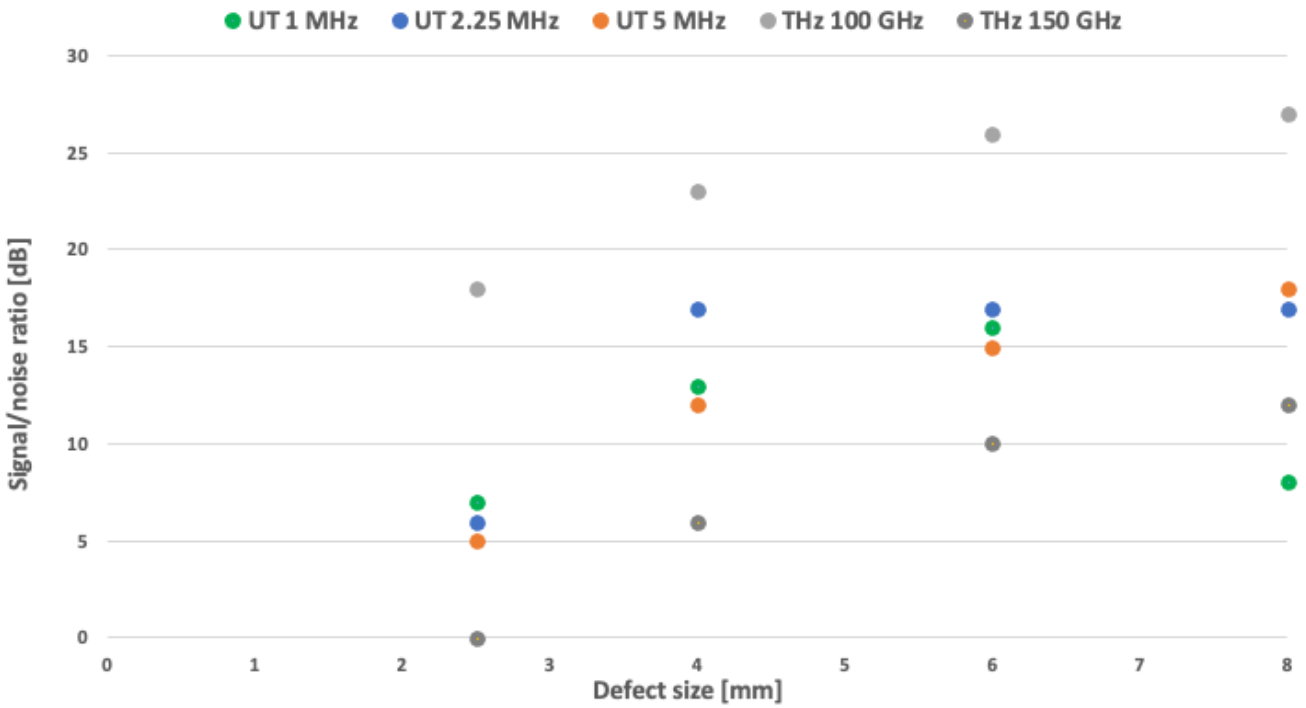

Fig. 12: Dependency of the defect size on the signal/noise-ratio (depth 25 mm)

5.3 INFLUENCE OF DEFECT DEPTH

First, the dependency of the defect depth was evaluated for a defect diameter of 8 because this defect is sufficiently large to be detected in all cases. The result of this evaluation can be seen in Fig. 13.

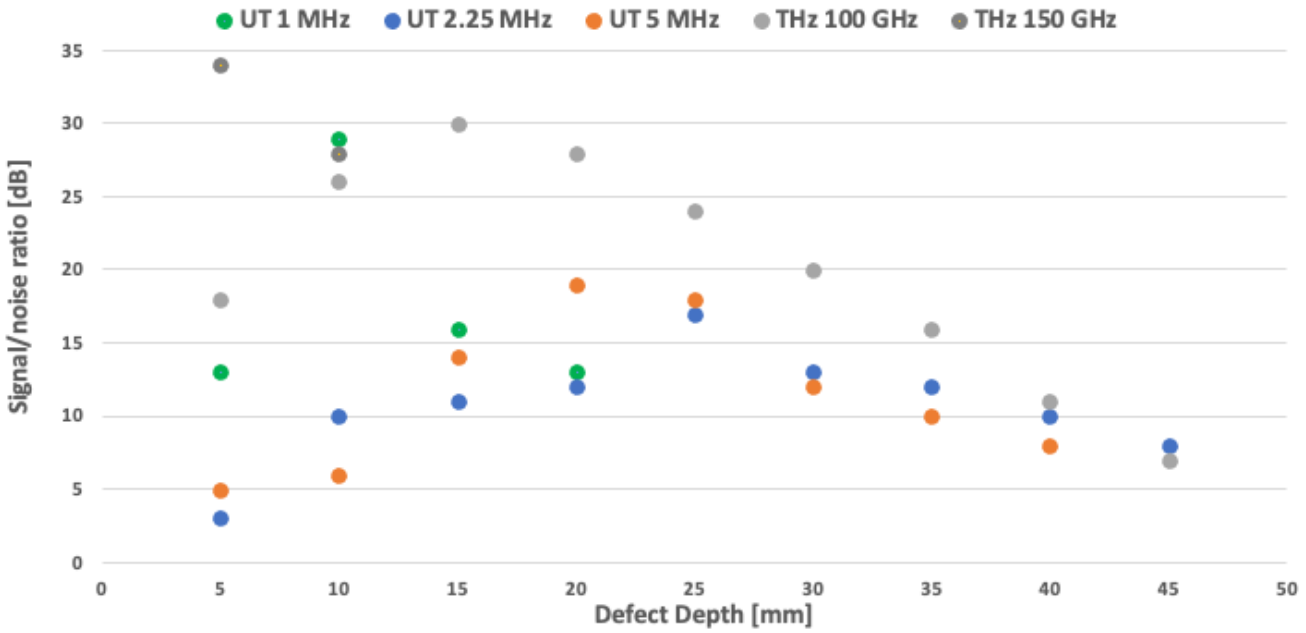

Fig. 13: Dependency of the defect depth on the signal/noise-ratio (8 mm defect)

Figure 13 clearly shows that there is an optimum for each test frequency and method. As the test frequency decreases, this optimum signal-to-noise ratio shifts towards greater defect depths. It has to be pointed out once

again that it was possible to penetrate the part under inspection with the 1 MHz probe. However, due to the focus point widening, the fault indications merged into one another, so that the indications were not evaluated.

5.4 EVALUATION OF THE FOAM SAMPLE

The evaluation of the foam sample shows a difference for the depth of the errors in this auxiliary reflector measurement. The double passing of the walls of the defect perpendicular to the beam path caused a significant attenuation of the defect in the deeper defects. This resulted in a greater signal-to-noise ratio of up to 10 dB in the defect display itself for defect sizes above 5 mm. The small defects located higher up (depth 2.5 mm) were only found with a low signal-to-noise ratio of 3 - 4 dB.

6 CONCLUSIONS

The signal/noise ratio is significantly influenced by seven parameters, which are not independent of each other. Thus, it seems to be difficult to choose the optimal transducer providing the highest detectability of defects possible whereas the defects have certain size for a given material situation. However, the minimum defect size to be detected in Airbus CFRP-aircraft components is about 6 mm in diameter according to AITM-standards. This study dealt also with smaller defects to show the limits of certain test frequencies and yielded that the 2.25 MHz ultrasonic transducer provides the highest signal/noise ratio for ultrasonic testing deeper positioned defects as depicted in Fig. 13.

The evaluation of the foam sample shows a difference for higher defects are better found with the 5 MHz probe. A very good alternative here is terahertz testing, which has a much greater selectivity of defects and defect-free areas. In addition, terahertz testing is the only NDT method besides the more expensive computer tomography with which foams can be tested in a meaningful way.

REFERENCES

[1] J. Schuster, C. Bauer and K. Friedrich, Influences on signal/noise ratio during ultrasonic inspection of composites, *NDT & E International,* **26**, 5, 1993, pp. 255 - 260

[2] J. Schuster, “Correlation of transducer frequency and signal/noise ratio of thin-walled filament wound CFRP-tubes inspected by ultrasonics”, Proceedings The 19th International Conference on Composite Materials – ICCM19, Edinburgh, Great Britain (2009)

[3] https://www.facebook.com/photo.php?fbid=1142116424581002&id=100063479645095&set=a.468820808577237 (June 2025)

[4] https://www.bundeswehr.de/de/ausruestung-technik-bundeswehr/seesysteme-bundeswehr/korvette-k130 (June 2025)

[5] F. Friedrich, K.H. May, B. Baccouche, C. Matheis, M. Bauer, J. Jonuscheit, M. Morr, D. Denman, J. Bramble and N. Savage, Terahertz radome inspection, *Photonics*, **5**, 1, 2018, p.p 1 - 10

[6] J. Dong, B. Kim, A. Locquet, P. McKeon, N. Declercq and D.S. Citrin, Nondestructive evaluation of forced delamination in glass fiber reinforced composites by terahertz and ultrasonic waves, *Composites Part B*, **79**, 2015, pp. 667 - 675

ICCM24
AUGUST 4-8, 2025
BALTIMORE CONVENTION CENTER
BALTIMORE, MARYLAND, USA

No Technical Paper Submission for:

Hatice Sas

FOSSIC
Flexible-photonic Optical Strain Sensing In Composites

The Effect of Optical Fibre Cross-Sectional Shape and Microstructure on Out-of-Plane Strain Sensitivity in Flexible Photonic Sensors

Robin Hartley[a], Pawel Maniewski[b], Bruno Moog[b], Mathew Whitaker[b], Martynas Beresna[b], James Kratz[a], Janice Dulieu-Barton[a], Christopher Holmes[b]

[a]*University of Bristol*

[b]*University of Southampton*

University of Southampton | University of Bristol | Prifysgol Wrecsam Wrexham University | Warwick The University of Warwick | University of Hertfordshire UH | The University of Nottingham

Background and motivation

FBG in standard fibre

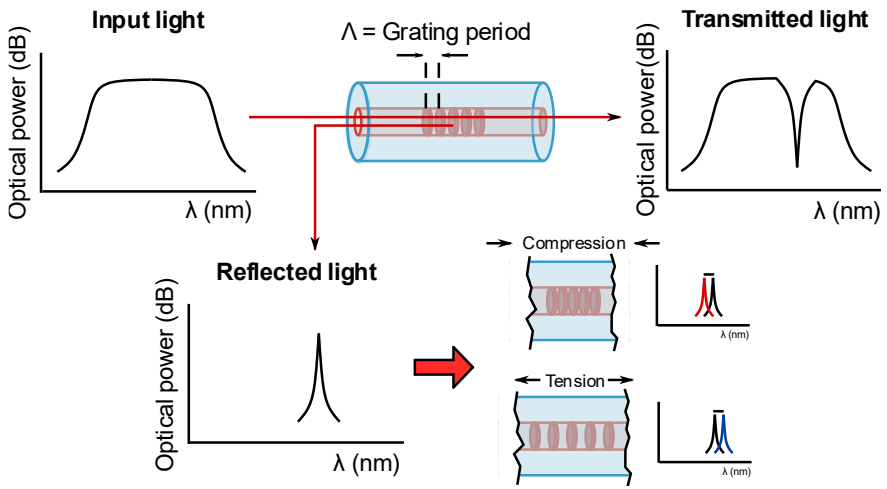

FBG in polarisation maintaining fibre

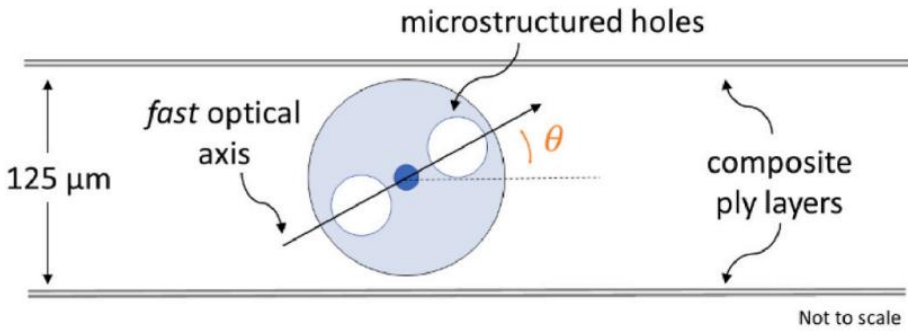

Motivation

- CFRP strain monitoring often uses FBGs in standard circular fibre.
- These detect in-plane strain well, but not through-thickness strains critical in delamination, matrix cracking.
- Polarisation-maintaining fibres can detect out of plane strains through birefringent response, but…
- Circular geometry twists, making direction of strain ambiguous - $\boldsymbol{\theta = ?}$.

Objective

- Create orientation-stable, birefringent sensors that can resolve in-plane and out-of-plane strains.
- Enabling comprehensive 3D strain mapping during both manufacturing and in-service use of CFRPs.

Prior Work: 3D Strain Sensing - FHD planar chips

Approach: Uses a strain–optic matrix (K-matrix) derived from first principles of the photoelastic effect.
Formulation: Based on spectral shifts in TE and TM polarisations of two orthogonal waveguides:

Limitations:
- Chip-based fabrication is not scalable for long sensor lengths.
- Difficult to integrate into continuous optical fibre networks.
- Coupling to fibre and embedding chips remain complex and fragile.

$$\frac{\Delta\lambda_i}{\lambda_i} = \sum_j K_{ij}\varepsilon_j$$

Where:
- $\frac{\Delta\lambda_i}{\lambda_i}$: Normalized wavelength shift in mode i (e.g., TE or TM).
- K_{ij}: Elements of the strain–optic sensitivity matrix (based on waveguide orientation and photoelastic constants).
- ε_j : Strain components ε_x, ε_y, ε_z

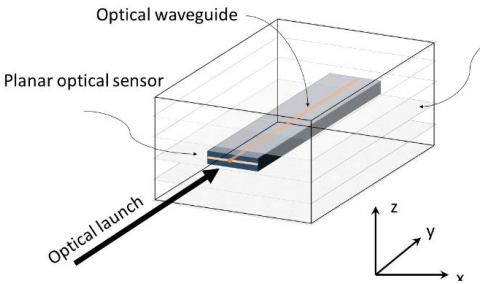

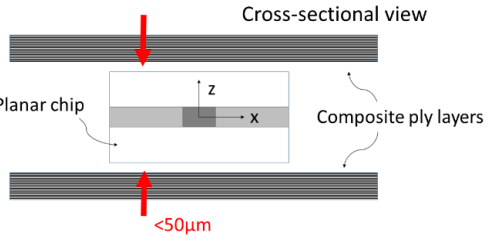

CFRP tensile tests: measured strain comparison

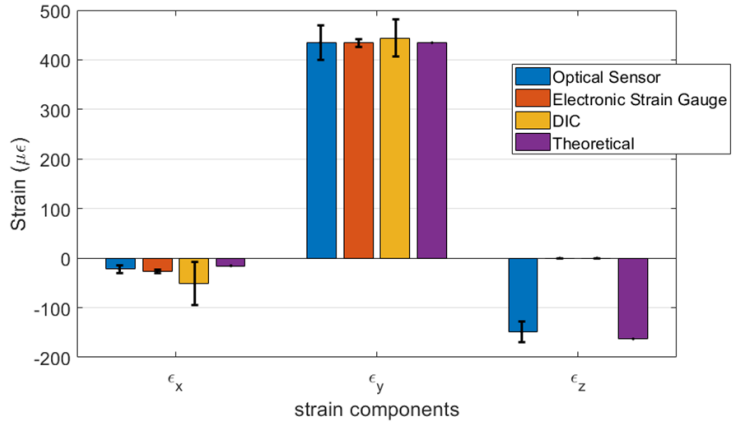

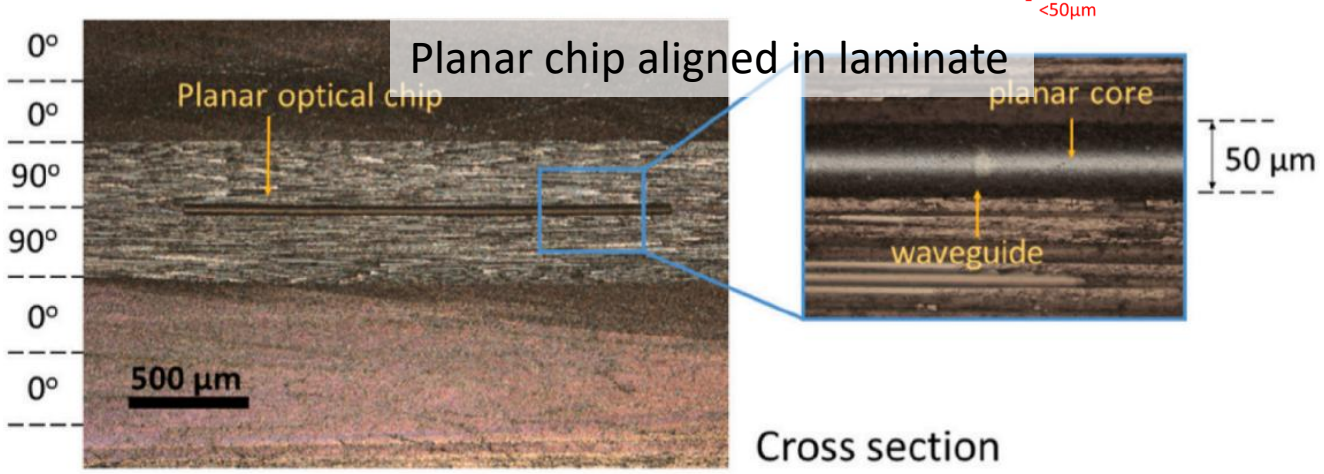

C. Holmes, M. Godfrey, D. J. Bull, J. Dulieu Barton, *Opt. Lasers Eng.*, 2020, 133, 106111

Sensor fabrication – Flat fibres

Key innovations – enable scalability and integration

Laser powder deposition of waveguides

- Precise placement of doped silica cores on flat preforms
- Avoids the need for traditional MCVD or lithographic patterning.
- Flexible core design: refractive index, geometry, and number of cores can be tuned.

Rectangular Preform Design & Stack-and-Draw

- Rectangular in cross-section → high aspect ratio final fibre.
- Compatible with standard fibre draw towers → scalable production.

Incorporation of Internal Microstructure

- Microstructures such as air channels can be embedded → tune birefringence

Femtosecond Laser Post-Processing

- Enables fine-tuning of waveguide paths or inscription of Bragg gratings.
- Multi-core patterning or localised index modifications.

Laser powder deposition

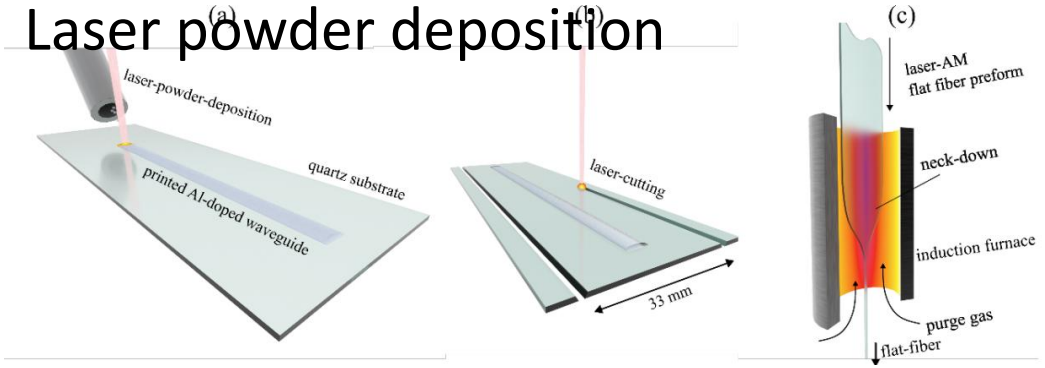

Stack and draw

P. Maniewski, B. Moog, M. Whittaker, *Proc. of SPIE,* Vol. 13356 1335606-1

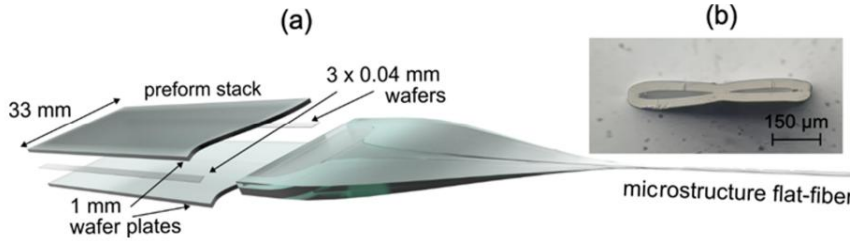

Femtosecond laser writing

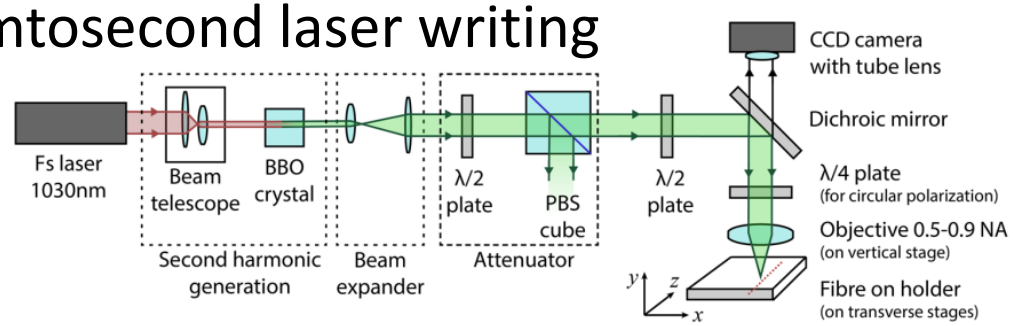

T. Lee, P. Maniewski, M. Whittaker, B. Moog, M. Beresna, C. Holmes, *Proc. of SPIE,* Vol. 13639 136396V-4

Sensor optimisation

What determines sensitivity?:

- "The degree to which the birefringence of the waveguide changes in response to through thickness strains"
- Birefringence governed by principal strains ($\epsilon_{33} - \epsilon_{22}$)

$$B = n_2 - n_3 = \frac{n_0^3}{2}(p_{11} - p_{12})(\epsilon_{33} - \epsilon_{22})$$

- Create parameterised model – vary h, t, w, and δx to vary geometry
- FEA – model fibre under 5 bar hydrostatic pressure (proxy for out of plane strain)
- Centre of fibre cross-section ($x, y = (0,0)$) ideal for waveguide placement
  - High birefringence
  - Spatially suitable

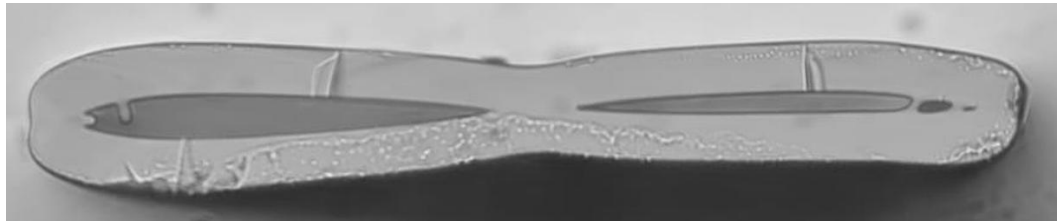

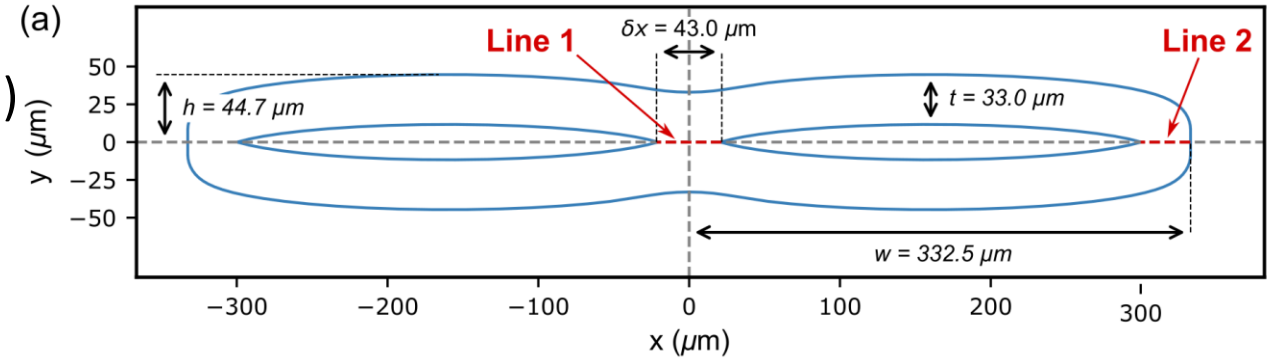

Result from 5 bar hydrostatic pressure FEA: $(\epsilon_{33} - \epsilon_{22})$

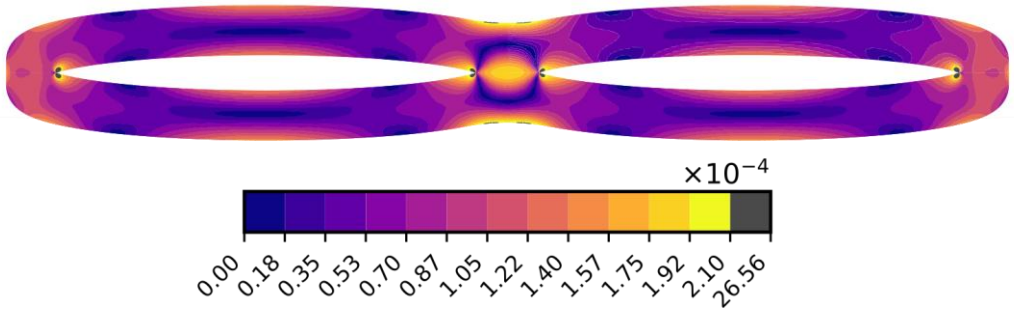

Parametric study: sensitivity to geometry

Objective:

Quantify how sensitive birefringence is to variations in each geometric parameter.

Statistical method:

- All input parameters and the birefringence response are normalized [0, 1]
- A linear regression model is fitted:

$$Normalised\ Birefringence = \sum_i (Coefficient_i \times Normalised\ Parameter_i)$$

- Regression coefficients indicate **relative sensitivity**:
  - Larger absolute values = stronger influence
  - Positive vs negative = direction of effect

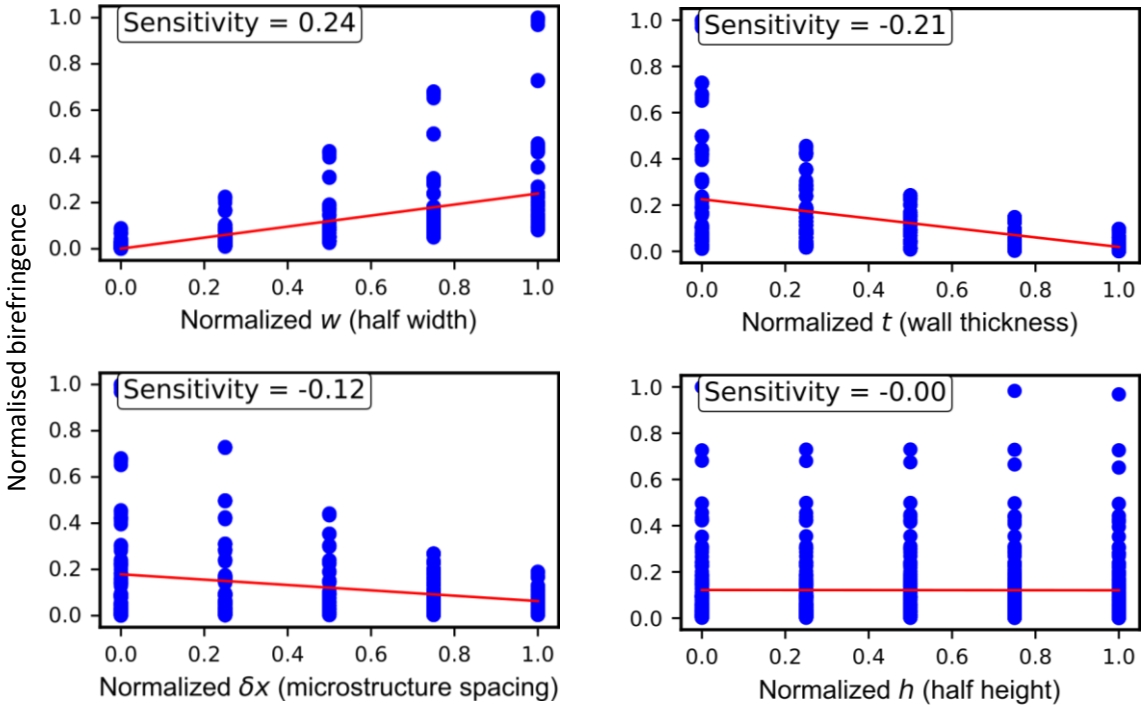

Key takeaway: Sensitivity is enhanced in high aspect ratio, thin-walled sensors

Integration into composite materials

Hot press: Easy fibre optic egress – rapid sensor development.

- Applications:
  - Cure monitoring and producing integrated sensor laminates
- 100 kN Test Machine
  - Displacement and load-control modes.
  - Compression grips for attaching tooling.
- Heated Tooling
  - Cavity dimensions: **84 mm × 140 mm × 10 mm** (W × L × D).
  - Embedded thermocouple slots positioned 0.5 mm below surface.
  - Small egress holes for thermocouples and optical fibres.
- Watlow EZ-Zone PID Temp Control
  - 2 tool embedded control thermocouples for PID feedback.
  - Data logging for up to 8 laminate thermocouples
- Fibre Optic Interrogation
  - SmartFibre FBG sensors (standard FBG strain sensors).
  - µHARFF FBG sensors (pressure-sensitive Fabry–Pérot type).

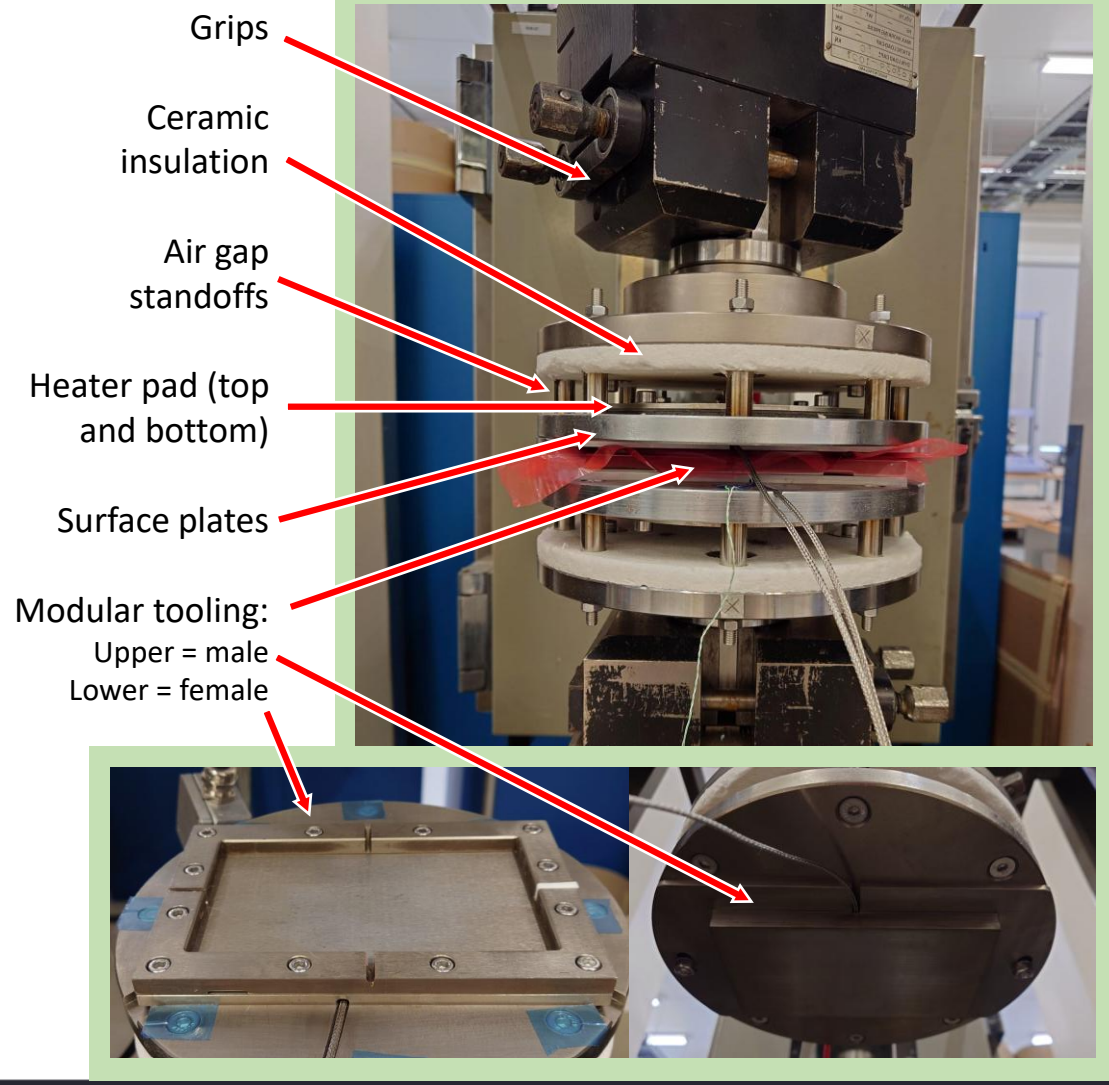

3D-PRINTED CORE REINFORCED WITH UNIDIRECTIONAL TAILORED FIBER PLACEMENT AND BRAIDED STRUCTURES FOR USE IN CUSTOM-MADE COMPOSITE KNEE ORTHOSES

Marcin Barburski[1], Jakub Szary[1], David Ranz[2]

[1]Institute of Architecture of Textiles, Faculty of Material Technologies and Textile Design, Lodz University of Technology, Zeromskiego 116, 90-543 Lodz, Poland
Email: marcin.barburski@p.lodz.pl, web page: https://p.lodz.pl/

[2]Department of Design and Manufacture Engineering, University of Zaragoza, C/María de Luna, 50018 Zaragoza, Spain
Email: dranz@unizar.es, web page: https://www.unizar.es/

Keywords: Composite, Additive manufacturing, Tailored fibre placement, Knee orthosis, Finite elements

ABSTRACT

A custom-made approach to medical devices is crucial for delivering effective therapy and enhancing quality of life. However, producing devices tailored to individual needs presents unique challenges that differ significantly from mass production. These challenges include precise measurement, specialized modeling and design, and customized tooling.

In this study, we present CAD and FEM modeling, used to create custom knee orthoses. Research indicates that 3D-printed cores can be strengthened by adding an outer layer made from various textile structures, such as braids, knits, and woven fabrics [1, 2]. Additionally, UD fibers can be effectively integrated into composites through tailored fiber placement techniques [3].

For our application, the composite structure was built using an individually designed, 3D-printed core based on a 3D scan of a human leg, embroidered unidirectional (UD) glass fibers, and a braided carbon fiber tube, all infused with epoxy resin via the infusion method [4]. Tensile tests were conducted for each textile structure orientation to model the FEM of the composite knee brace.

Our research demonstrates that the new composite can be successfully used in custom-made orthoses, with specific strength comparable to the aluminum alloy commonly used in knee braces. Additionally, the successful development of an FEM model, which allows for the analysis of various reinforcement configurations within a quasi-elastic range, was validated through tensile test of the composite.

1 INTRODUCTION

A custom-made approach to medical devices plays a crucial role in delivering effective therapy and improving patients' quality of life. This is especially important for knee orthoses, which must address not only the biomechanical requirements of the user but also their unique anatomy. In recent years, additive manufacturing and composite technologies have attracted increasing attention as they enable the production of personalized medical devices with optimized mechanical properties.

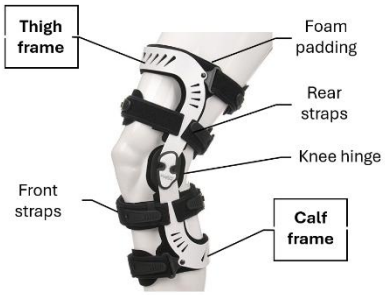

Figure 1: Main components of a knee orthosis [1].

However, the design and manufacturing of custom-made orthoses pose numerous challenges that distinguish them from mass production. These challenges include the need for precise anatomical measurements, the development of individualized CAD models, strength analysis using finite element methods (FEM), and the selection of appropriate textile structures and technologies for their integration with the composite matrix.

Previous research indicates that reinforcing 3D-printed cores with textile structures—such as braids, knits, and woven fabrics—can significantly improve their mechanical properties [2, 3]. Moreover, precise techniques like tailored fiber placement allow unidirectional (UD) fibers to be integrated into composites in a way that maximizes their potential [4].

The aim of this study was to develop and investigate the properties of a novel composite knee orthosis structure, which incorporates an individually designed, 3D-printed core, tailored fiber placement UD glass fibers, and a braided carbon fiber sleeve, all used to build the frame of the orthosis. Mechanical tests and FEM analysis were carried out to evaluate the potential of this innovative construction for orthotic applications.

2 MATERIALS

2.1 Unidirectional glass fiber (UGF)

The unidirectional (UD) reinforcement was fabricated using tailored fiber placement (TFP) technology on a ZSK JCZA 0109-550 embroidery machine (Figure 1). Three layers of E-glass roving (density $\rho = 2.54$ g/cm³, linear density 600 tex, silane-sized, supplied by Krosglass S.A.) were stitched onto a 280 × 280 mm polyester substrate with an areal density of 50 g/m². Non-load-bearing threads were used for stitching: polyester 2 × 10 tex and polyamide 11 tex on the top side. The glass fibers were arranged at a density of 42 rovings per centimeter, with a stitch length of 4 mm. The total areal weight of the UD reinforcement was determined to be 2 755 g/m², comprising 2 520 g/m² from the glass fibers, 120 g/m² from the polyester threads at the bottom, and 65 g/m² from the polyamide threads at the top.

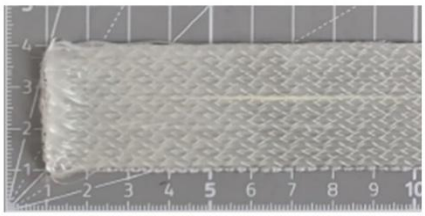

Figure 1: Unidirectional E-glass textile reinforcements produced by tailored fiber placement (UGF).

2.2 Braided carbon fiber (BCF)

A 2×2 biaxial braided sleeve, shown in Figure 2, was manufactured from carbon fiber using 12K GRAFIL 34-700 rovings (density $\rho = 1.8$ g/cm³, linear density 800 tex) by Eurocarbon B.V. (reference D144/11). The fabric exhibited an areal weight of 665 ±10 g/m² and was braided at an angle of ±30°, with a pick density of 20 picks per decimeter. For preparation, the braided tube was slit lengthwise and its edges were reinforced with tape to prevent fraying.



Figure 2: ±30° 2×2 biaxial braided carbon fiber sleeve (BCF).

2.3 Multi-layered composite (MLC)

Two types of textile reinforcements, UGF and BCF, were positioned on a 3D-printed (3DP) core and infused with resin under vacuum conditions. For the UGF layer, a strip measuring 30 × 250 mm was applied, while the BCF reinforcement used a smaller-diameter braided sleeve (Eurocarbon B.V., D-048-14, with an areal weight of 665 g/m² at a ±30° braid angle). Figure 3 presents a cross-sectional view illustrating the dimensions and stacking sequence of the composite structure.

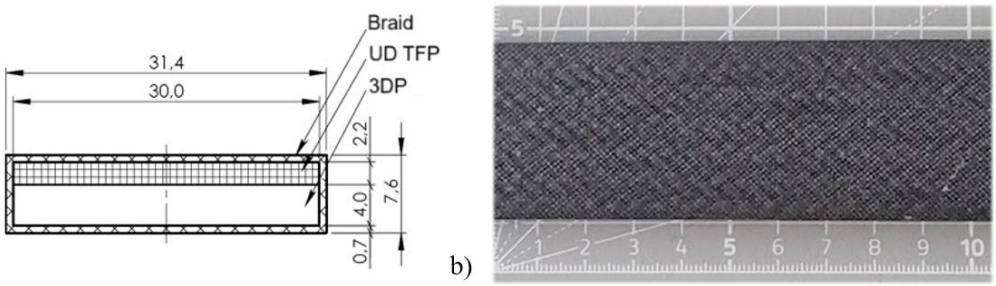

Figure 3: Structure and dimensions of the Multi-Layered Composite (MLC).

The core was manufactured by powder bed fusion using an HP Jet Fusion 3D 4200 printer, employing Multi Jet Fusion (MJF) technology. PA12 powder served as the build material, processed with an 80/20 ratio of recycled to fresh powder. The layer thickness was set to 0.08 mm, and the balanced printing mode achieved a speed of 4 115 cm³/h with solid infill. Components were spaced with a 5 mm gap, resulting in a packing density of 8.98%. The printed cores were oriented along the X-axis, and the final material density was measured at 1.01 g/cm³. Following the printing process, the cores underwent cleaning via sandblasting.

2.4 Composite preparations

The textile layers were arranged on a flat glass plate layered with peel-ply, infusion mesh, and a vacuum bag. Resin feed and evacuation points were set on opposite edges of the fabric assembly. For the MLC configuration, the resin inlet was located at the start of the core and the outlet at its far end. The infusion process employed a mixture of HAVEL Composite LH145 epoxy resin combined with HAVEL Composite H135 hardener at a 100:35 weight ratio. Following resin impregnation, the composites were cured at 25 °C for at least 24 hours before being shaped and oriented for testing, with final cutting performed by water jetting.

3 METHODS

3.1 Tensile test

Tensile testing was performed following ISO 527-4 [6], with data analysis based on ISO 527-1 [7]. The tests utilized an INSTRON universal testing machine (Model 8982), operating at a crosshead speed of 1 mm/min. Five specimens from each configuration were tested until failure. Strain measurements were obtained using a 50 mm gauge-length extensometer. For UGF and MLC samples, the specimens measured 2.2 × 25 × 250 mm, and the initial distance between grips was set at 150 mm. To reduce stress concentrations during testing, end tabs made of epoxy-impregnated carbon fiber twill were bonded to these samples. In the case of BCF specimens, due to the geometric constraints of the flattened braided sleeve, the dimensions were adjusted to 25 × 150 mm, and end tabs were omitted.

3.2 Finite Element Analysis (FEA) of MLC

The FEA of the MLC was performed using ANSYS APDL. A model was developed to accurately represent the mechanical behavior of the composite under tensile loading conditions. Key parameters were used to determine the stiffness matrix and to analyze the influence of different materials on the modulus of the MLC.

In the FEA model, one end of the specimen was fully fixed in all degrees of freedom to represent the stationary grip of the tensile testing machine. The opposite end was subjected to a displacement along the loading axis (Z-axis) corresponding to the maximum experimental strain. A quasi-static analysis was performed up to the elastic range identified in the experimental results.

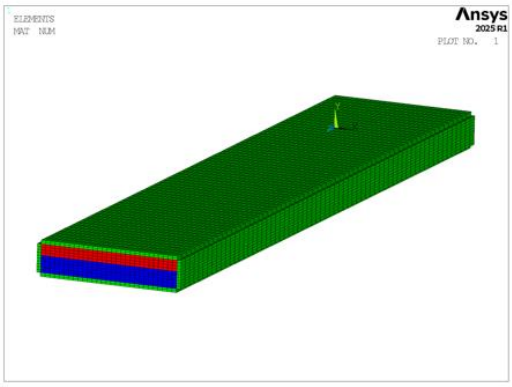

Figure 4: Finite element analysis (FEA) model of Multi-Layered Composite (MLC).

The geometry of the MLC, presented in Figure 4 was defined by specifying the number of layers, their orientations, and thicknesses. A finite element mesh was generated using SOLID185 elements for the 3DP core and SHELL181 elements for the UGF and BCF reinforcements. Material properties were assigned to each layer, taking into account orthotropic elastic behavior.

4 RESULTS AND DISSCUSION

4.1 Tensile tests of composite layers

Tensile tests were performed on the UGF and BCF structures. The resulting tensile stress–strain curves are shown in Figure 5, while Table 1 provides a summary of their corresponding mechanical properties.

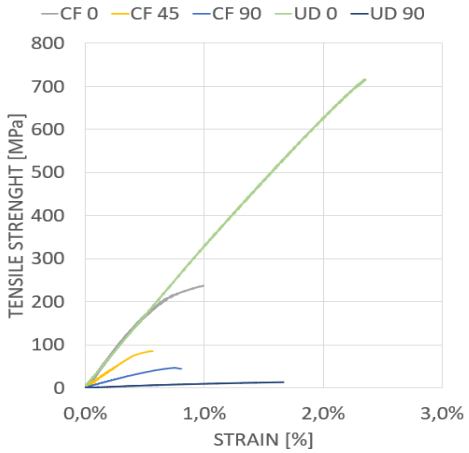

Figure 5: Tensile stress-strain curves of composite layers.

Parameter	UGF 00	UGF 90	BCF 00	BCF 45	BCF 90
Tensile strength σ_m [MPa]	730 ±44	12 ±1,5	219 ±16	64 ±5	39 ±2
Tensile strain ε_m [%]	2.3 ±0,2	1.3 ±0,2	0.8 ±0,1	0.4 ±0,1	0.8 ±0.1
Tensile modulus E_t [MPa]	32 860 ±485	5 870 ±450	35 880 ±1 570	18 950 ±1 430	7 060 ±240

Table 1: Tensile parameters of composite layers.

Significant differences in tensile strength were observed between the two structures. The UGF fabrics demonstrated approximately three times higher tensile strength in the 0° orientation compared to the

BCF braided structures, although the braided samples showed a tensile modulus about 8% higher. In the tested samples, only a single reinforcement layer was used, which had a substantial impact on the measured tensile properties.

It is important to note that in typical braided structures, fibers form a continuous pattern, whereas in rectangular tensile samples, fibers are cut, disrupting their continuity. During tensile loading, fibers can stretch and reorient along the applied force direction, particularly if they were initially set at an angle. This behavior affects the measured tensile strength and strain, meaning these parameters may not accurately represent the tensile strength of the braided structures. Moreover, research indicates that the initial modulus values for samples oriented at 0° and 90° are similar, suggesting comparable moduli in both directions despite differences in tensile strength [8].

4.2 Tensile tests of MLC

The MLC was fabricated using a 3D-printed core combined with two types of textile reinforcements, which were impregnated with epoxy resin. Tensile tests were then carried out on the prepared samples. Table 2 summarizes the key parameters of the MLC. Additionally, the accompanying graph highlights the Initial Linear Line (ILL), representing the elastic region of the MLC; here, ILL+ indicates the upper bound and ILL- the lower bound of the modulus.

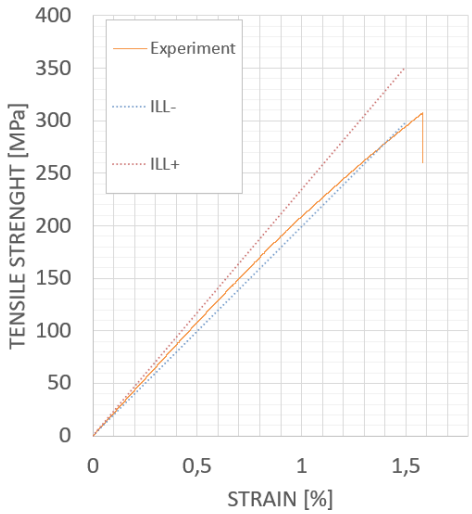

Figure 6: Tensile stress-strain curves of the MLC.

Parameter	MLC
Tensile strength σ_m [MPa]	302 ±13
Tensile strain ε_m [%]	1.5 ±0.1
Tensile modulus E_t [MPa]	21 700 ±1 800

Table 2: Tensile parameters of the MLC.

The stress–strain response of the MLC displayed quasi-elastic behavior, with a slight reduction in slope detected between approximately 0.4% and 0.6% strain, as marked by the ILL. This reduction indicated a decrease in structural stiffness, although the composite still maintained its ability to bear loads. The carbon fiber layer was the first to fail, accompanied by the characteristic sound of carbon fiber fracture, which was evident in the graph as a further slope reduction around 1% strain. This abrupt failure of the carbon layer also led to the destruction of the 3D-printed core at a strain of about 1.5%. Following the failure of the BCF layer, the UGF reinforcement continued to support the load until it ultimately fractured, corresponding to the final drop in the stress–strain curve. The samples obtained after tensile and flexural testing are shown in Figure 7.

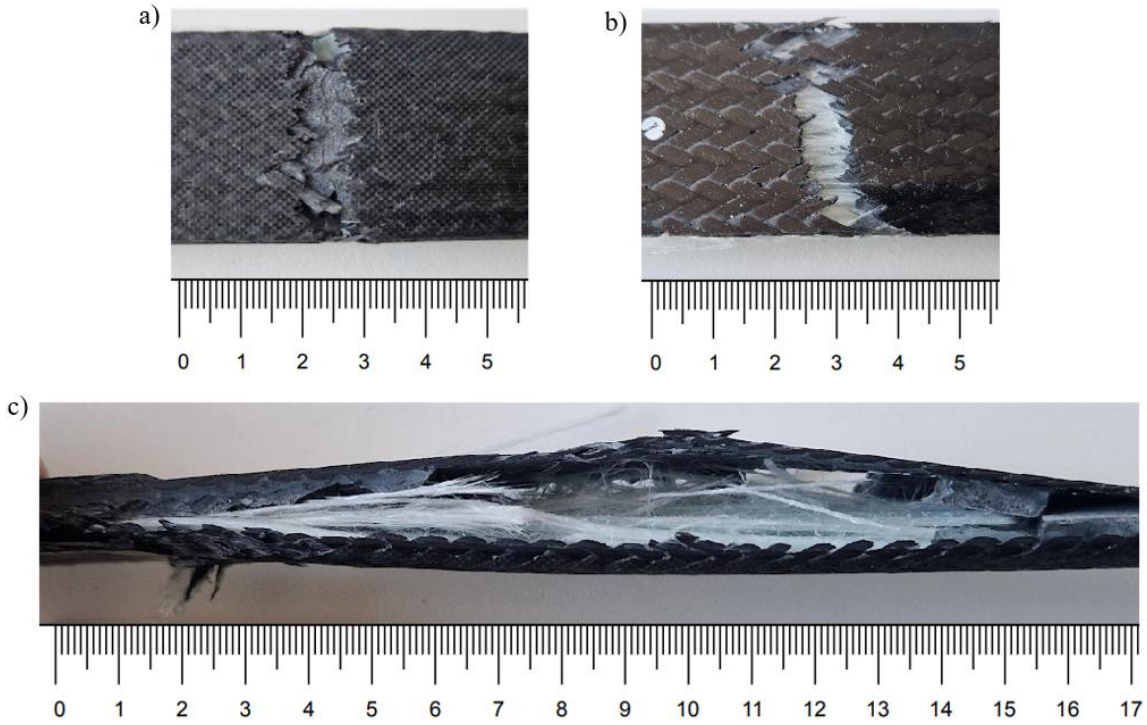

Figure 7: Samples after tensile test. a) bottom view b) top view c) side view.

Figure 8 shows the specific strength and specific modulus of different materials, calculated as the ratio of the respective material property to its density. The MLC was assessed relative to the EN AW 6061 T6 aluminum alloy, commonly used in knee brace manufacturing, as well as the PA12 material produced using powder bed fusion technology [1, 8].

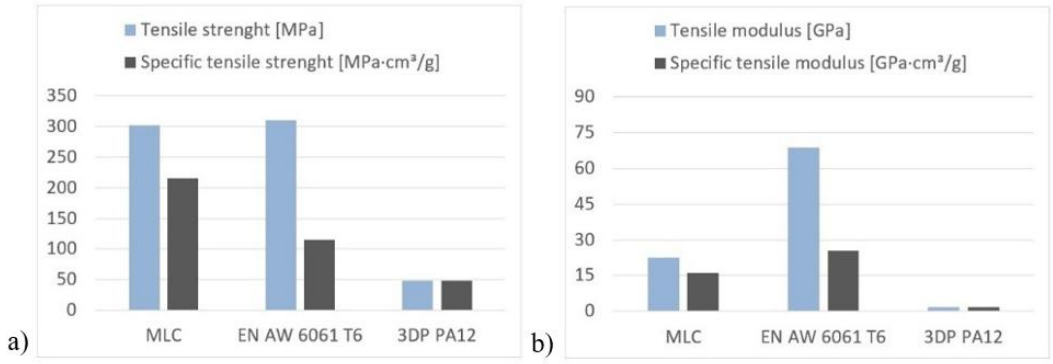

Figure 8: Comparison of the (a) specific strength and (b) specific modulus of various materials.

It is important to highlight that these parameters describe the materials as homogeneous structures and are intended solely for comparative purposes and assessing the potential of the new composite. While both aluminum and the MLC demonstrated the highest tensile strength, the MLC achieved a superior specific tensile strength, enhancing its effectiveness in applications where a high strength-to-weight ratio is essential. In terms of tensile modulus, the aluminum alloy showed a value approximately three times greater than that of the MLC. However, the stiffness of the composite could be increased by enlarging its cross-sectional area through the addition of extra FRC layers. When comparing specific modulus, the gap between aluminum and the MLC narrowed considerably to around 60%. The 3DP material displayed the lowest values across all parameters. Given that aluminum production requires expensive, single-use tooling, and that 3DP alone offers limited strength and stiffness, the MLC presents a promising solution for manufacturing custom-made components.

4.3 Finite Element Analysis (FEA) of MLC

The MLC was manufactured using a 3DP core with two types of textile reinforcements and infused with an epoxy resin. The samples underwent tensile testing, and the results were compared with the finite element model predictions, as presented in Figure 8 and summarized in Table 3.

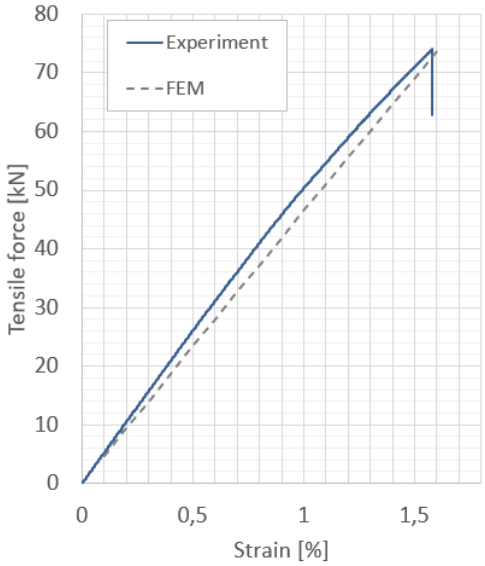

Figure 9: Comparison of experimental and FEM tensile force–strain curves for the MLC.

Parameter	Experiment	FEM +30°/-30° Model	Error
Elastic modulus [MPa]	21 670 ±1 780	19 500	10%

Table 3: Comparison of tensile test results with FEM model.

The FEM simulations demonstrated a good correlation with the experimental results, showing only a 10% deviation in the elastic modulus, which confirms the reliability of the numerical model for predicting the behavior of various material configurations.

UD Configurations	Elastic modulus [MPa]	Difference vs. MLC
3DP/BCF/UD Carbon fiber	39 800	+104 %
3DP/BCF/UD Aramid	26 200	+34,4 %
3DP/BCF/UD Flax	15 900	-18,5 %

Table 4: Comparison of elastic moduli of different TFP UD reinforcements.

The analysis indicates that incorporating unidirectional carbon fibers could potentially double the modulus of the composite, significantly enhancing stiffness, while substituting flax fibers leads to a modest 18.5% reduction in modulus. This highlights the possibility of tailoring mechanical properties to specific applications and suggests that natural fibers like flax offer a promising, eco-friendly alternative for other applications.

5 CONCLUSIONS

This study demonstrated that the hybrid MLC composite, combining a 3D-printed core with tailored textile reinforcements, offers promising potential for use in personalized knee orthoses. The composite exhibited tensile strength comparable to aluminum while achieving approximately twice the specific tensile strength, indicating an excellent strength-to-weight ratio essential for lightweight medical

devices. Although the MLC's elastic modulus was three times lower than that of aluminum, the difference in specific modulus was significantly reduced, highlighting its suitability for applications requiring high stiffness-to-density performance.

Finite element simulations showed good agreement with experimental data, deviating by only 10% in elastic modulus, thereby validating the numerical model for predicting various material configurations. Furthermore, the analysis confirmed that incorporating carbon fibers as unidirectional layers could substantially increase the modulus, whereas using flax fibers resulted in only a moderate reduction of 18.5%, offering an environmentally friendly alternative. Overall, the presented approach enables the development of customized, high-performance orthopedic devices that can be tailored to individual anatomical and mechanical requirements.

ACKNOWLEDGEMENTS

The research was carried out within the Ministry of Science and Higher Education project number DWD/5/0365/2021 "Doktorat wdrożeniowy V".

The authors acknowledge the project "Sustainable Industrial Design of Textile Structures for Composites," which is funded by the European Union. Grant Agreement no. 101079009 Call: HORIZON-WIDERA-2021-ACCESS-03/Twinning. Acronym: SustDesignTex.

REFERENCES

[1] Follow Force; https://qmedinfo.pl/pl/oferta/konczyna-dolna/staw-kolanowy/item/486-follow-orteza-stawu-kolanowego-z-regulacja-zakresu-ruchomosci; 07.2025
[2] Szary J, Barburski M, Świniarski J. Mechanical properties of textile-reinforced composites with 3D printed core, Fibres & Textiles in Eastern Europe. 2023; 10.2478/ftee-2023-0034
[3] Poniecka A, Barburski M, Ranz D, Cuartero J, Miralbes R. Comparison of Mechanical Properties of Composites Reinforced with Technical Embroidery, UD and Woven Fabric Made of Flax Fibers. Materials. 2022 Oct 25;15(21):7469.
[4] Szary J., Barburski M., Mechanical Comparison and Practical Application of Composites with a 3D Printed Core and Textile Reinforcement, In: Conference Book of International Conference Innovatex 2023, p. 28-34, 22-24 November 2023.
[5] Szary J., Barburski M. Orteza stawu kolanowego, UPRP Patent pending PL442096A1, filled 26.08.2022 and issued 04.03.2024.
[6] ISO 527-4:2021 - Plastics - Determination of tensile properties - Part 4: Test conditions for isotropic and orthotropic fibre-reinforced plastic composites.
[7] ISO 527-1:2019 - Plastics - Determination of tensile properties - Part 1: General principles.
[8] Cichosz J, Wehrkamp-Richter T, Koerber H, et al (2016) Failure and damage characterization of (±30°) biaxial braided composites under multiaxial stress states. Compos Part Appl Sci Manuf 90:748–759. https://doi.org/10.1016/j.compositesa.2016.08.002.
[9] Aluminum 6061-T6 datasheet, https://www.matweb.com/; 07.2025

Challenges and recommendations for longitudinal tensile testing of unidirectional composites based on a round-robin programme

Babak Fazlali, Christian Breite, Gergely Czél, Bodo Fiedler, Dennis Gibhardt, Masaki Hojo, Hannes Koerber, Rajnish Kumar, María Luisa Velasco, Ian McEnteggart, Lars P. Mikkelsen, Federico Paris, Ichiro Taketa, Michael R. Wisnom, Yentl Swolfs



07-08-2025

KU LEUVEN

Composite Materials Group

The challenges of tensile testing composites

Stress concentrations

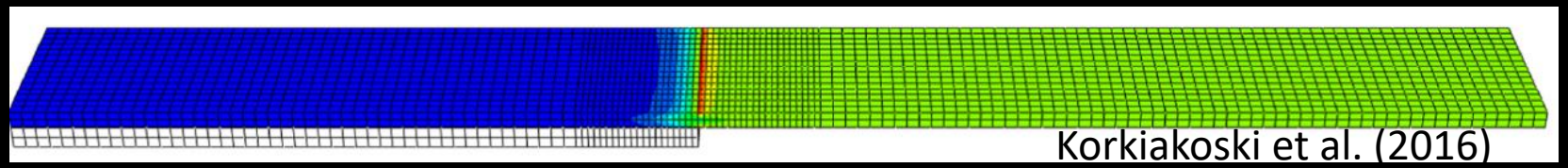
Korkiakoski et al. (2016)

Failure near the grips/tabs


De Paiva et al. (2006)

Difficult to detect failure location


Portnov et al. (2006)

6 specimen designs and 7 labs

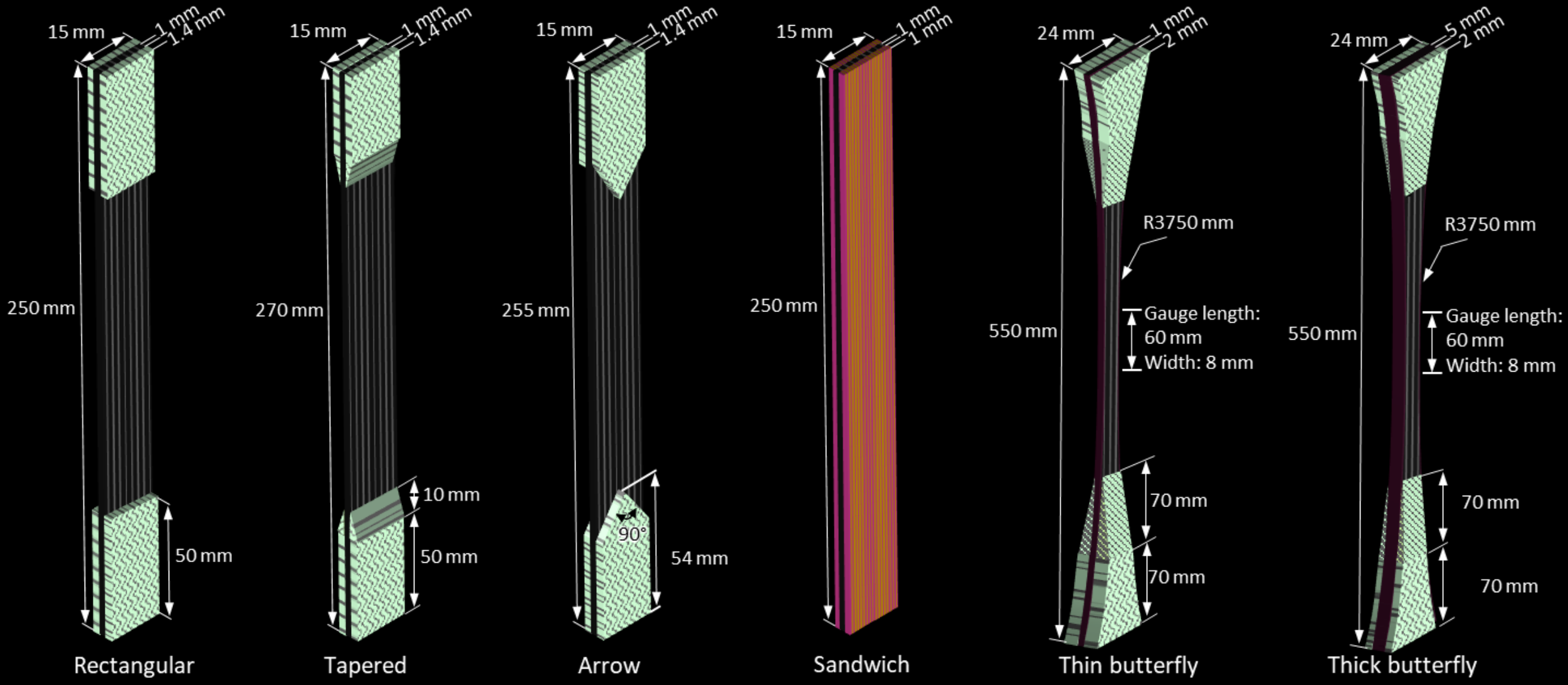

Minor differences in modulus between labs

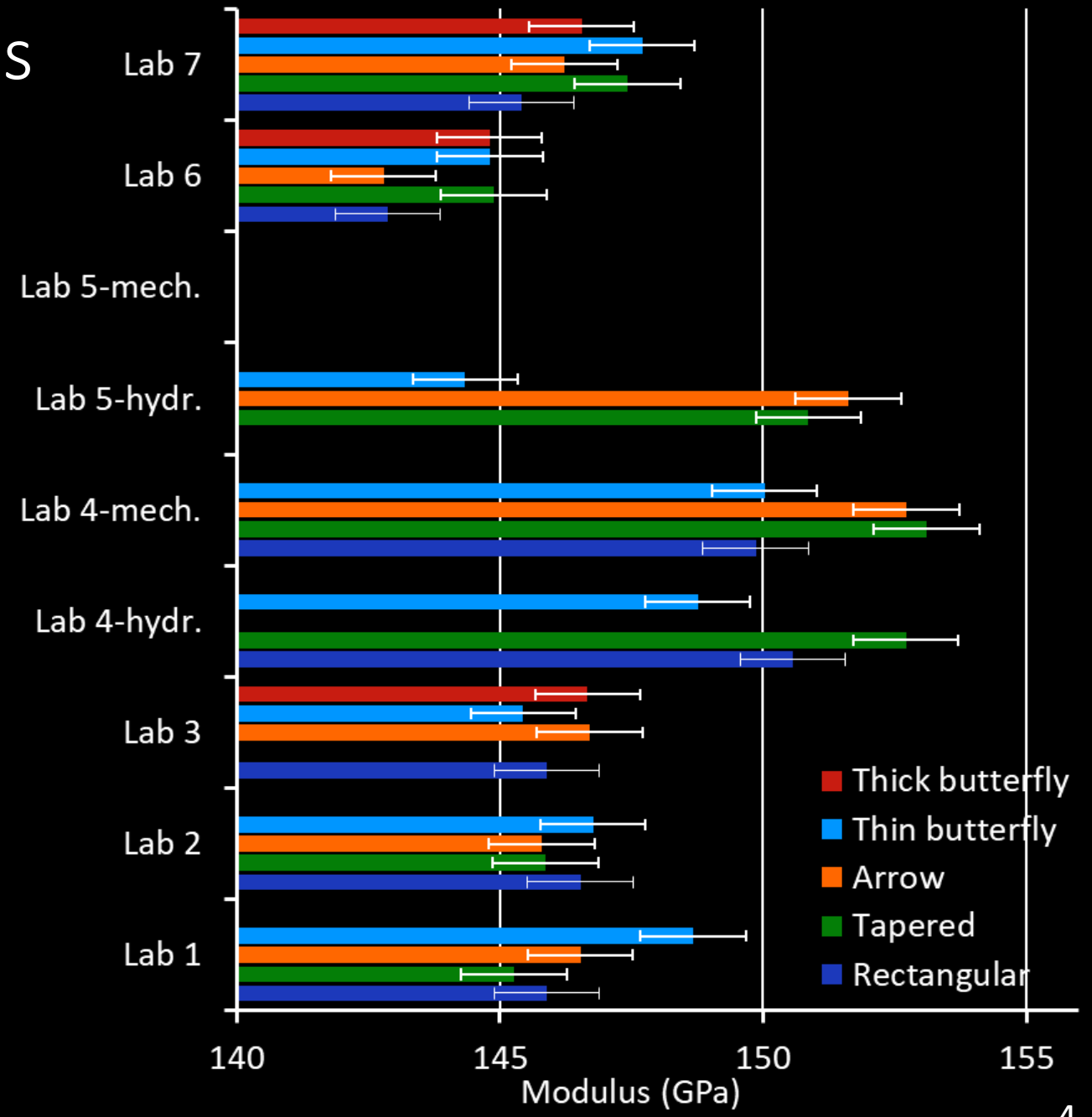

Minor differences in strength and failure strain

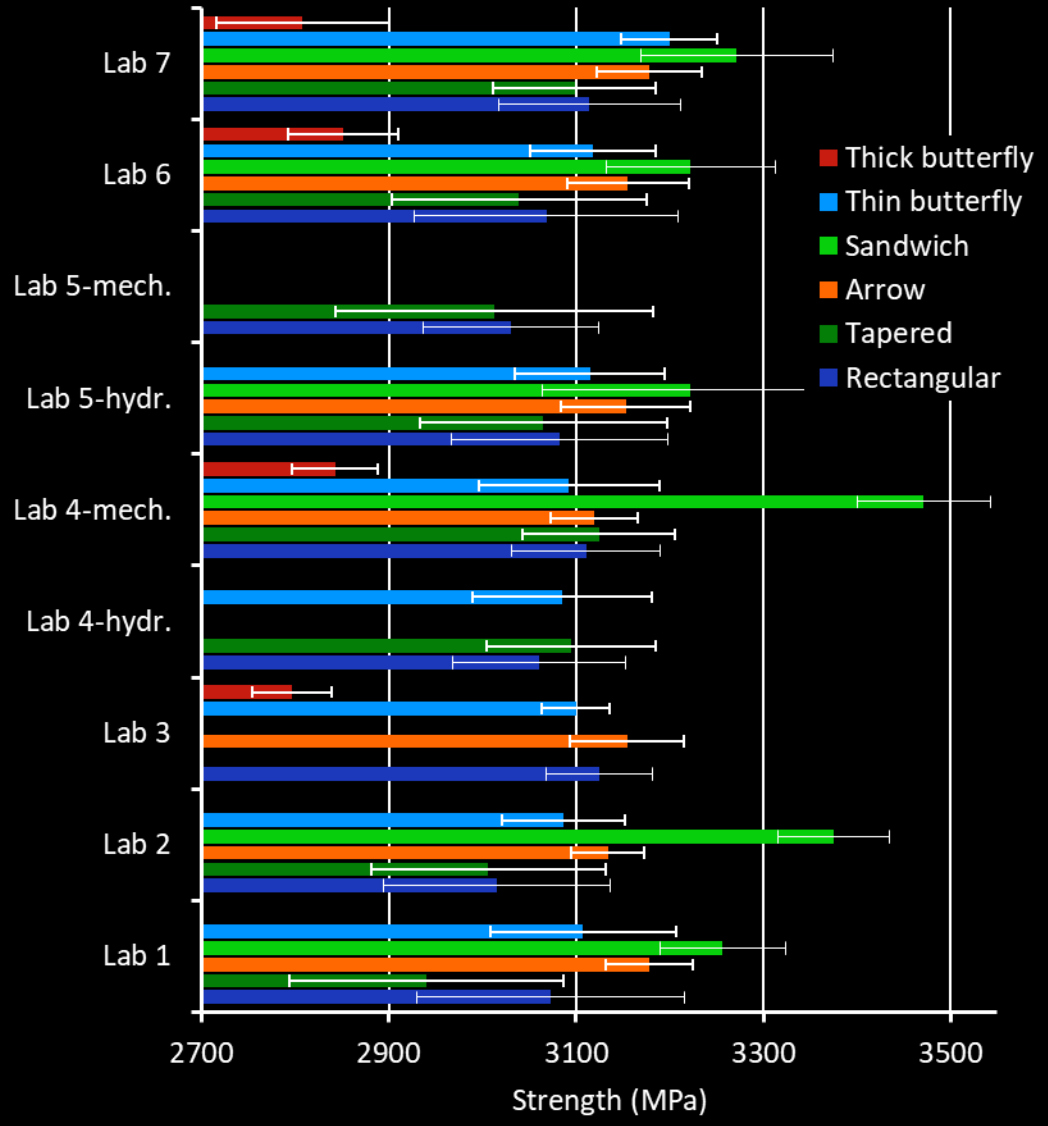

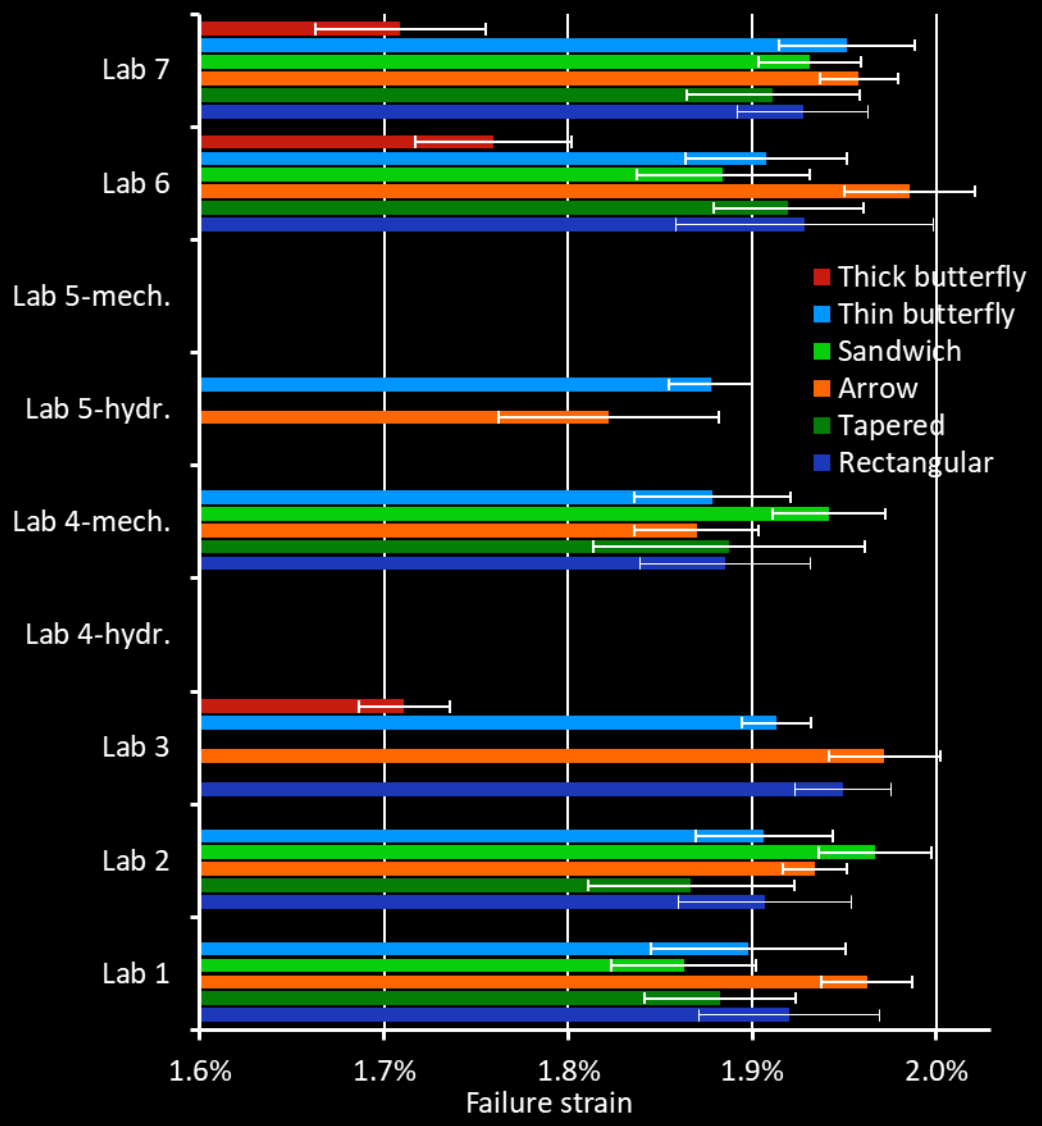

Some differences in measured strength

Continuous tabs: mainly due to inaccuracy in stress back-calculation

Thick butterfly: premature splitting + size effect (3-5.5%)

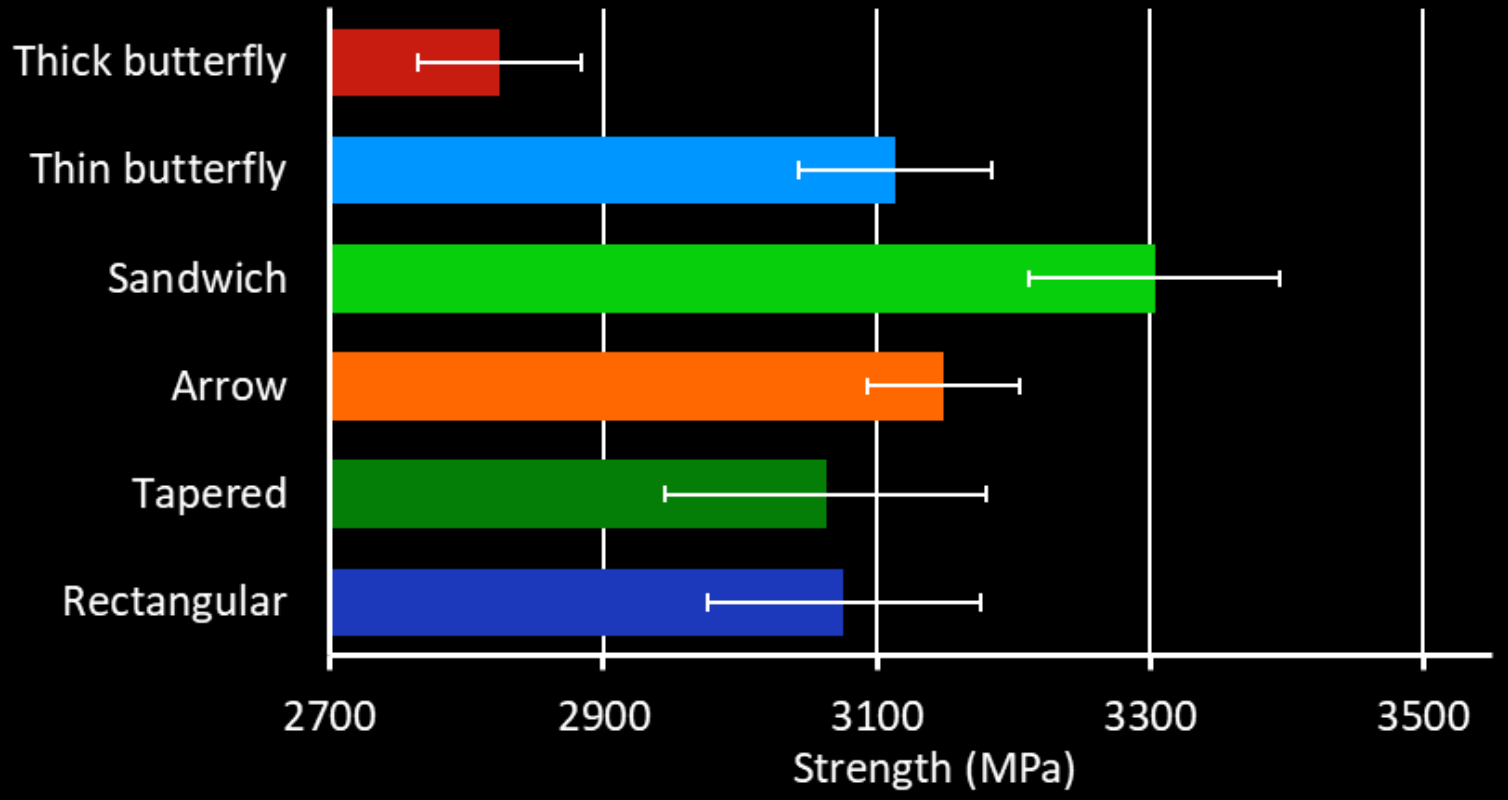

Very consistent failure strain values

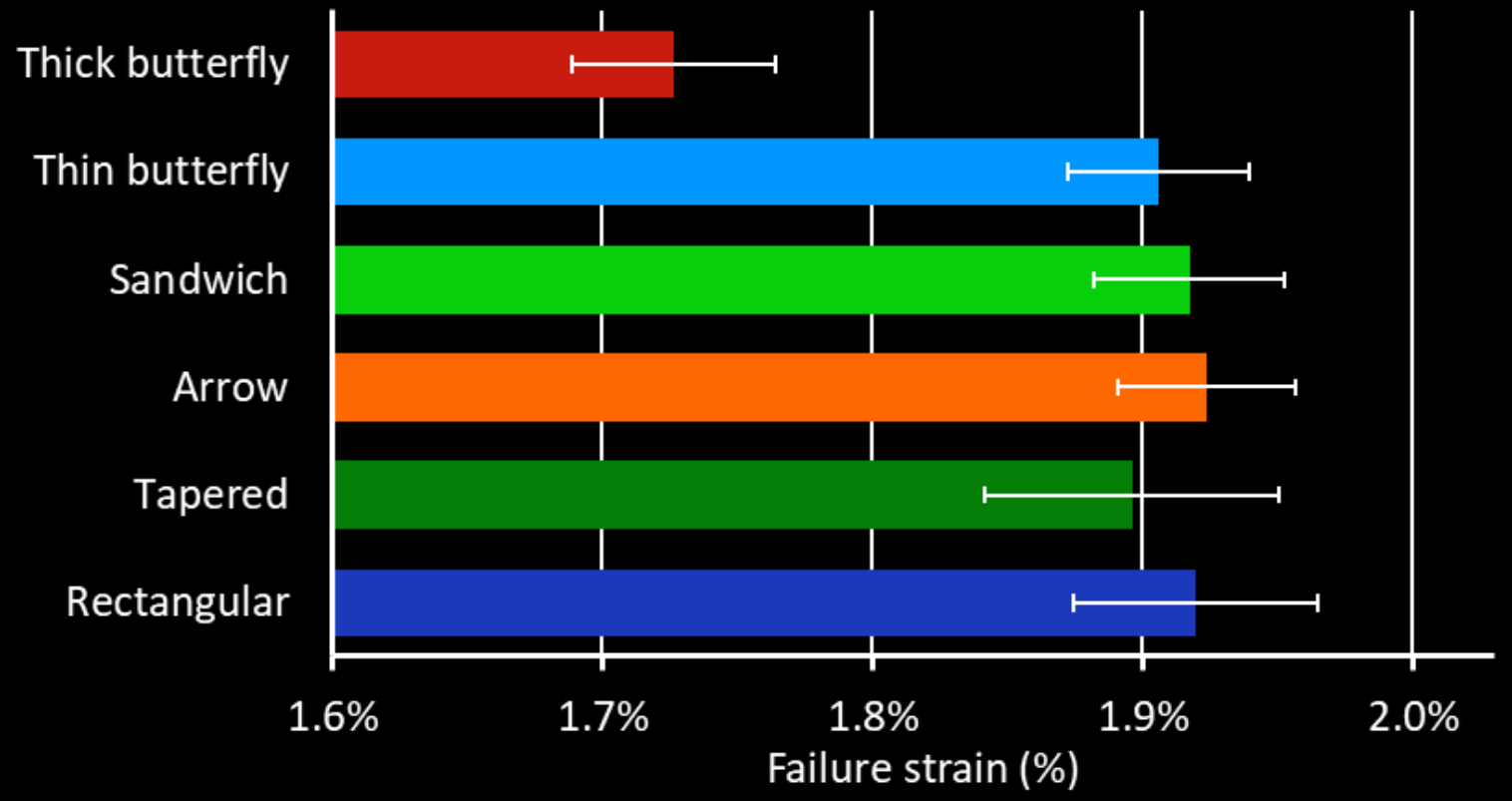

Diamond disk or water jet cutting?

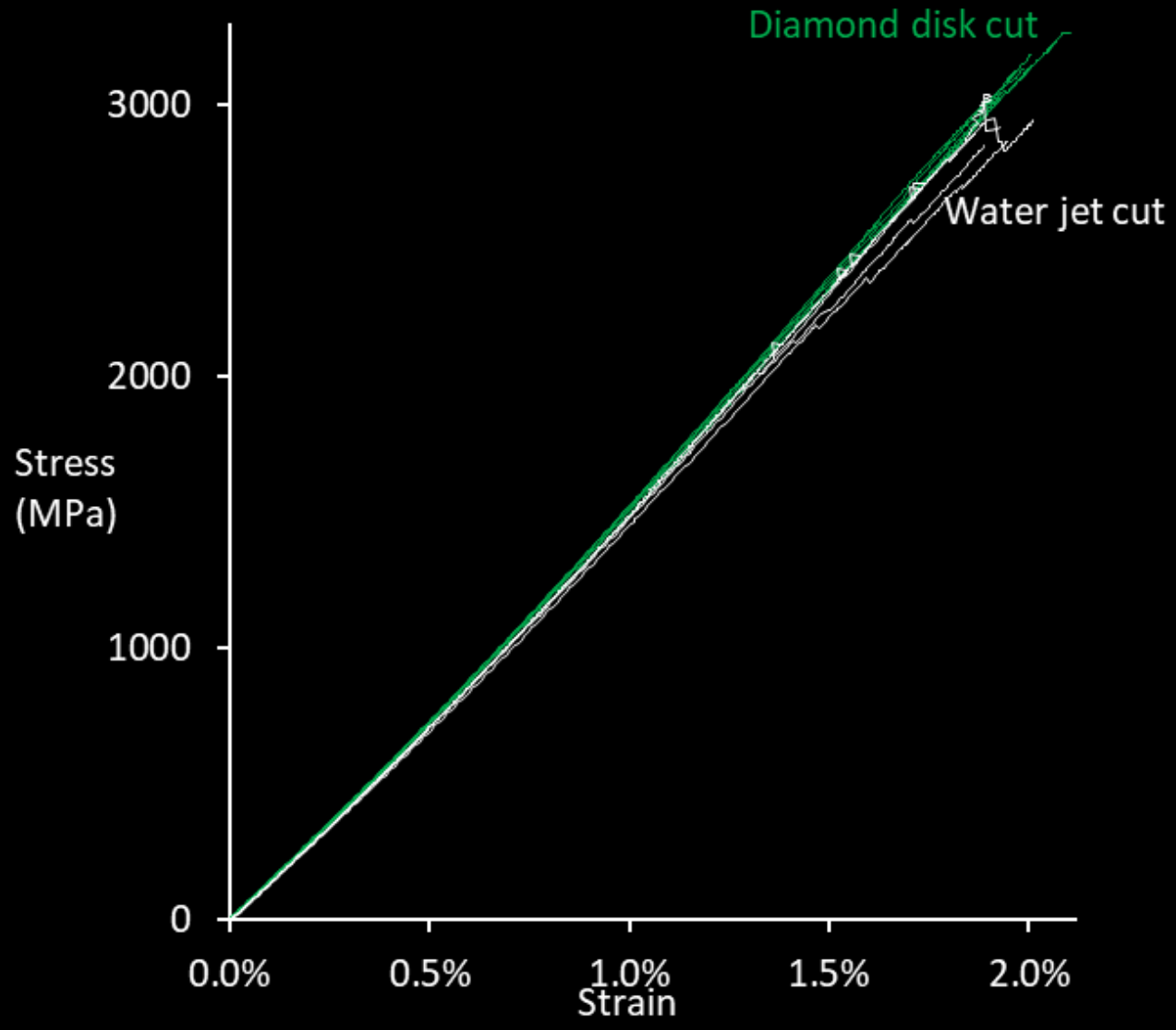

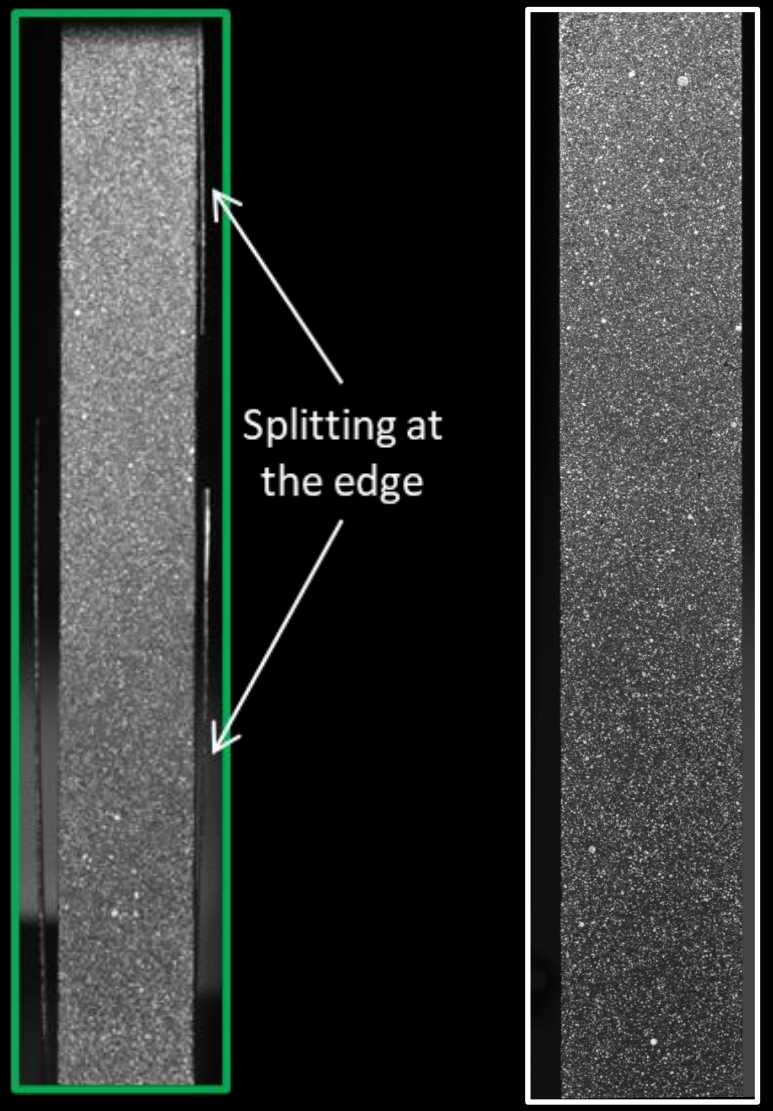

Don’t apply too much gripping force

Enough to avoid slippage, but no more!

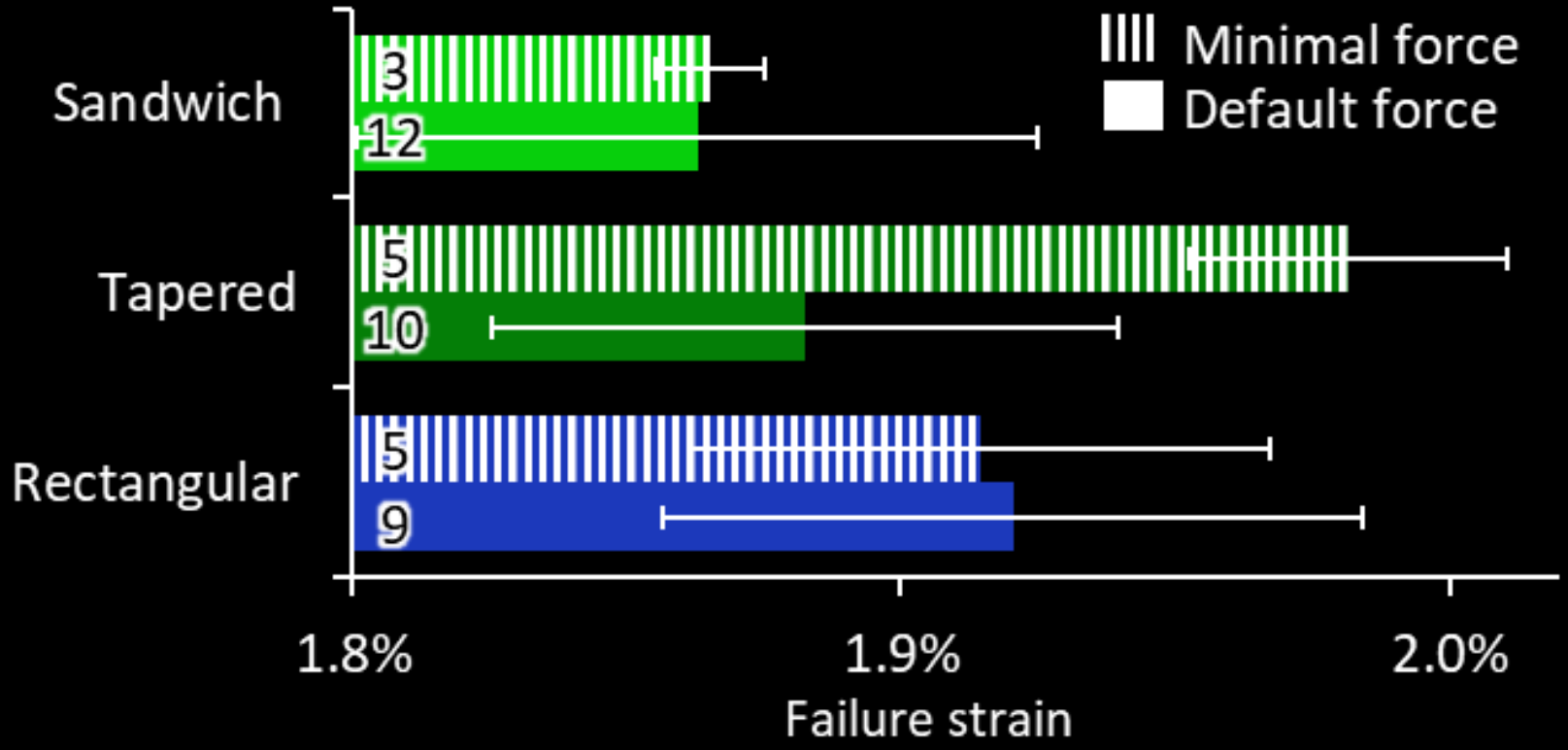

Detecting the failure location

Observing postmortem = impossible

Two solutions:

- Continuous tabs
- High-speed imaging at 10 Mfps

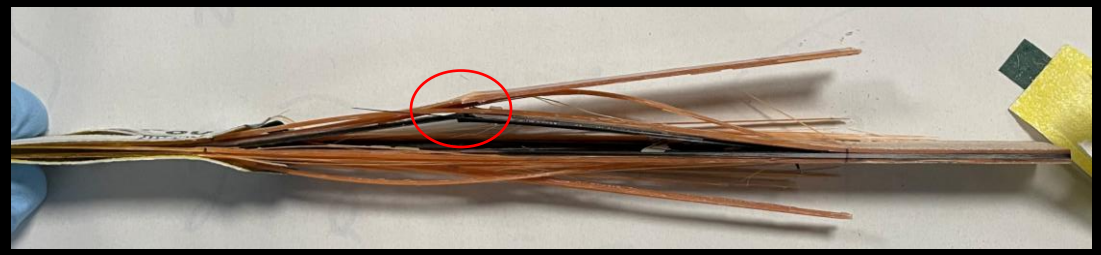



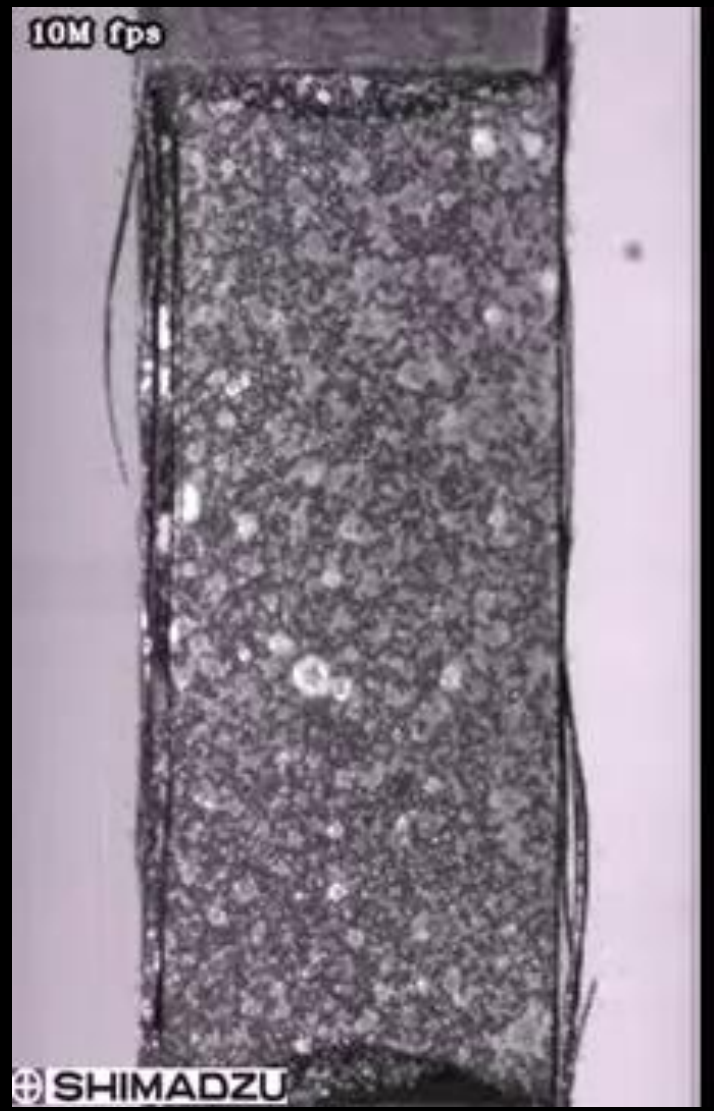

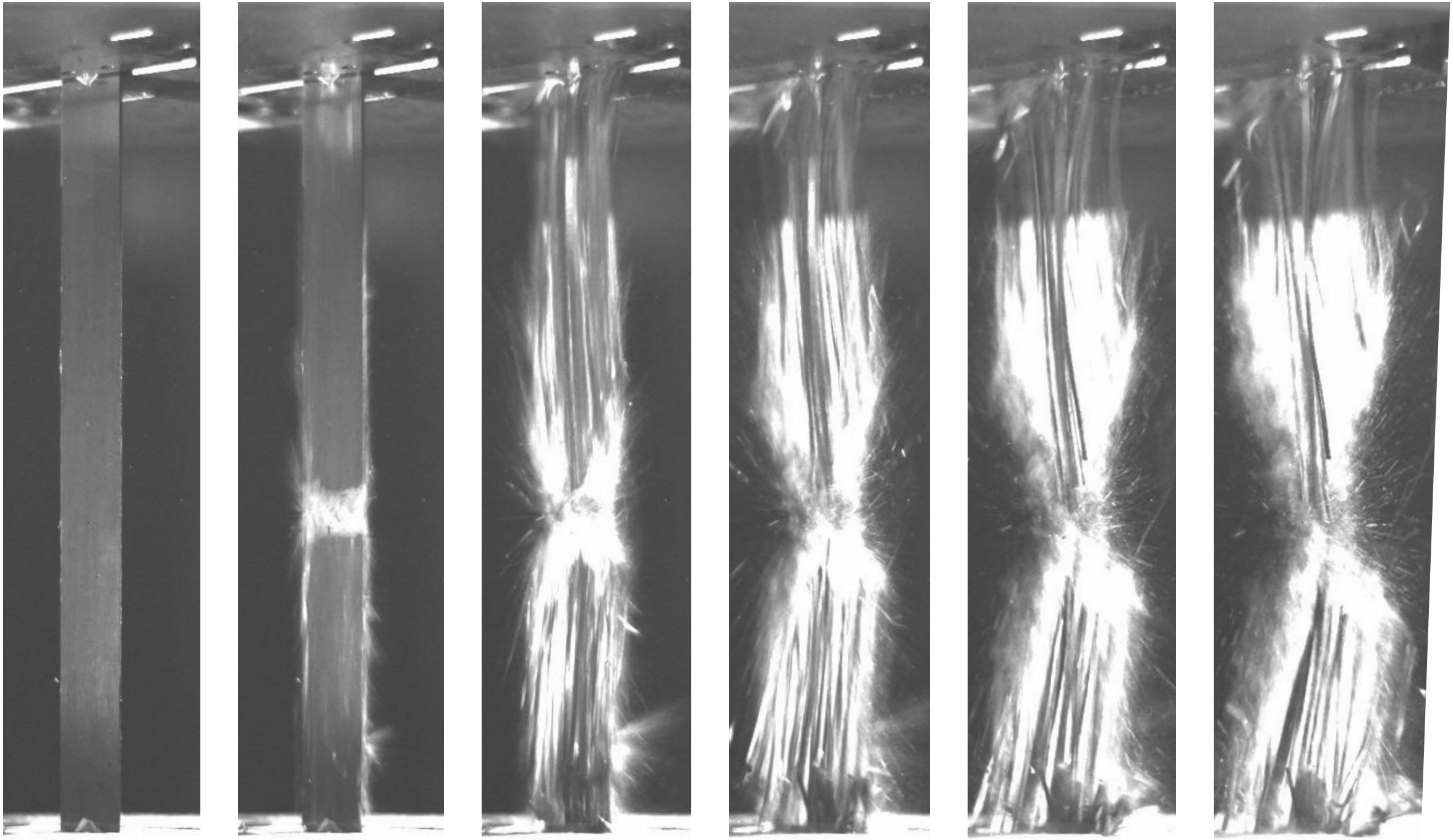

Reference +0.1 ms +0.2 ms +0.3 ms +0.4 ms +0.5 ms

Recommendations

Lab-to-lab variations larger than design-to-design variations

➔ Reliably measurements possible, if:

- Very well aligned fibres, plies, and cutting
- High-quality edge

Non-standardised designs: high failure strain and strength

Standardised designs: almost as good

Sandwich coupons: great for failure strain

Thick butterfly specimens underperformed, but different purpose

Recommendations

Determine failure location: 1000 fps camera or faster

Non-contact strain measurements methods preferred

Discard specimens with significant load drops (>3% of tensile strength)

Desired outcome:
Minor modifications to test standards

Final notes

All data available: https://zenodo.org/records/12771361



A request from all benchmark exercises and round-robins:

Appreciate us

Challenges and recommendations for longitudinal tensile testing of unidirectional composites based on a round-robin programme

Babak Fazlali, Christian Breite, Gergely Czél, Bodo Fiedler, Dennis Gibhardt, Masaki Hojo, Hannes Koerber, Rajnish Kumar, María Luisa Velasco, Ian McEnteggart, Lars P. Mikkelsen, Federico Paris, Ichiro Taketa, Michael R. Wisnom, Yentl Swolfs



07-08-2025

KU LEUVEN

Composite Materials Group

ADVANCED CHARACTERIZATION OF POLYMERS AND COMPOSITE MATERIALS USING AXIAL-TORSIONAL DYNAMIC MECHANICAL ANALYSIS

José Alberto Rodríguez Agudo[1], Matthias Ruf[3], Dominik Fauser[3], Christopher Giehl[1], Jan Haeberle[1], Jörg Läuger[1], Abhishek Shetty[2], Holger Steeb[3], Gunther Arnold[1]

[1]*Anton Paar Germany GmbH, Ostfildern, Germany;*

[2]*Anton Paar USA Inc, Ashland, United States*

[3]*Institute of Applied Mechanics, Chair of Continuum Mechanics, University of Stuttgart, Germany*

Gunther.Arnold@anton-paar.com

AXIAL-TORSIONAL DMA

- Originally, functionality and application scope of DMA and rheometer clearly separated
- Modern high-end rheometers are able to combine a rotational and a linear motor in a single device

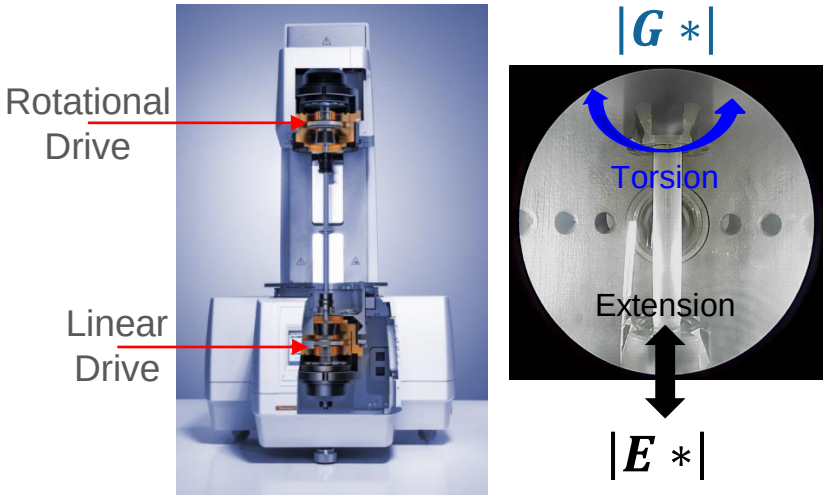

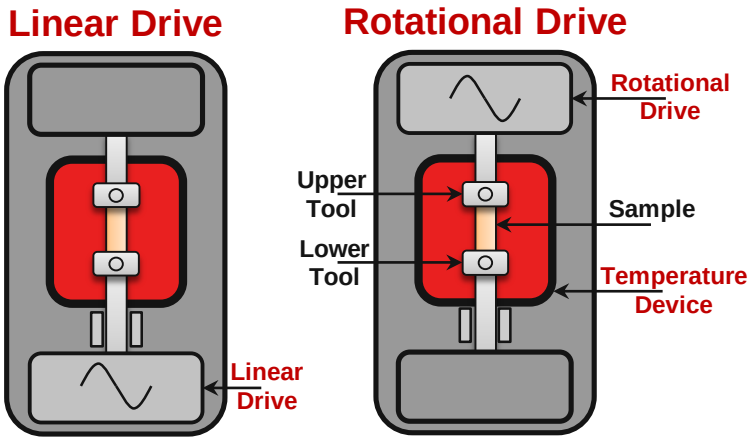

- All DMA working modes in one device
- Combine **torsional/extensional measurements** on viscoelastic solids

AXIAL-TORSIONAL DMA

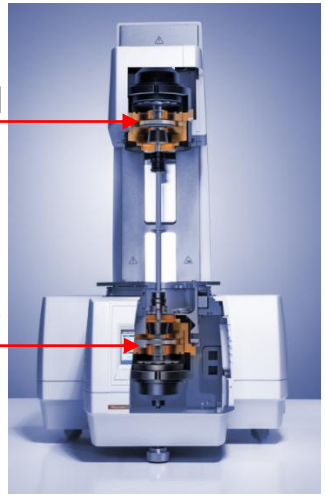

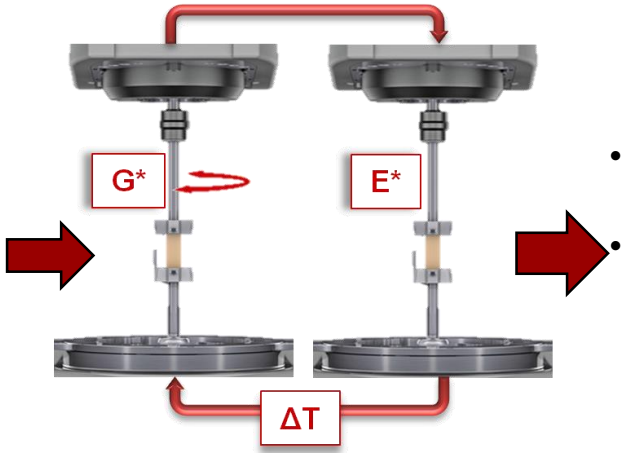

We add one more direction to the characterization of the linear viscoelastic behavior in a single experiment!

- $|G*|$ and $|E*|$ obtained **on the same specimen** in **one single measurement** and under **same conditions**
- **In accordance to Tschoegl protocol[1]**
- For isotropic samples → Indirect measurement of the complex Poisson‘s ratio

$$\nu = -\frac{\varepsilon_{trans}}{\varepsilon_{axial}} \qquad \upsilon^*(\omega, T) = \frac{E^*(\omega, T)}{2 \cdot G^*(\omega, T)} - 1$$

- Measurements on **cylindrical specimens** (No **warping torsion effects[2,3,4,5]**)

*1. Tschoegl et al. 2002
*2. Szabó 2013
*3. Dessi et al. 2016
*4. Diani and Gilormini 2017
*5. Dessi et al. 2021

POISSION´S RATIO

EXAMPLE: POLYMETHYL METHACRYLATE

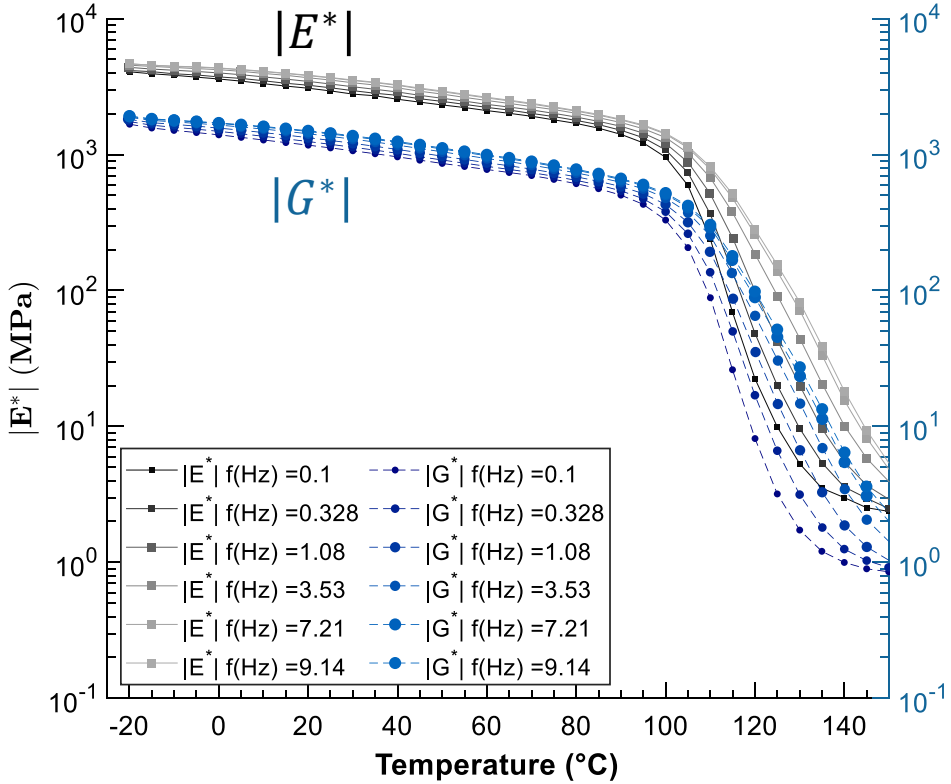

$$\boldsymbol{\upsilon}^*(\omega,T) = \frac{E^*(\omega,T)}{2\cdot G^*(\omega,T)} - \mathbf{1}$$

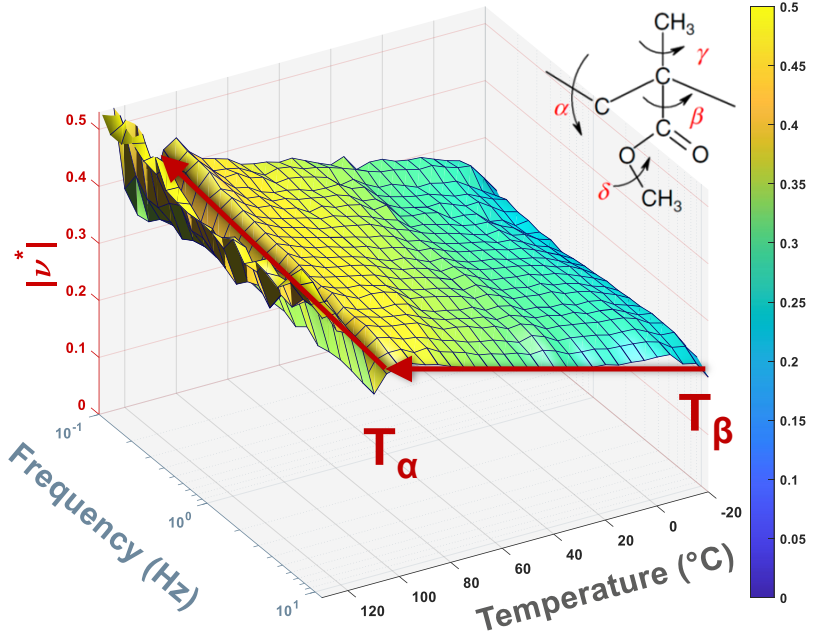

*6. J.R Agudo et al., 2023, *J. Rheol.*

POISSION´S RATIO

COMPARISON OF DIFFERENT POLYMERS

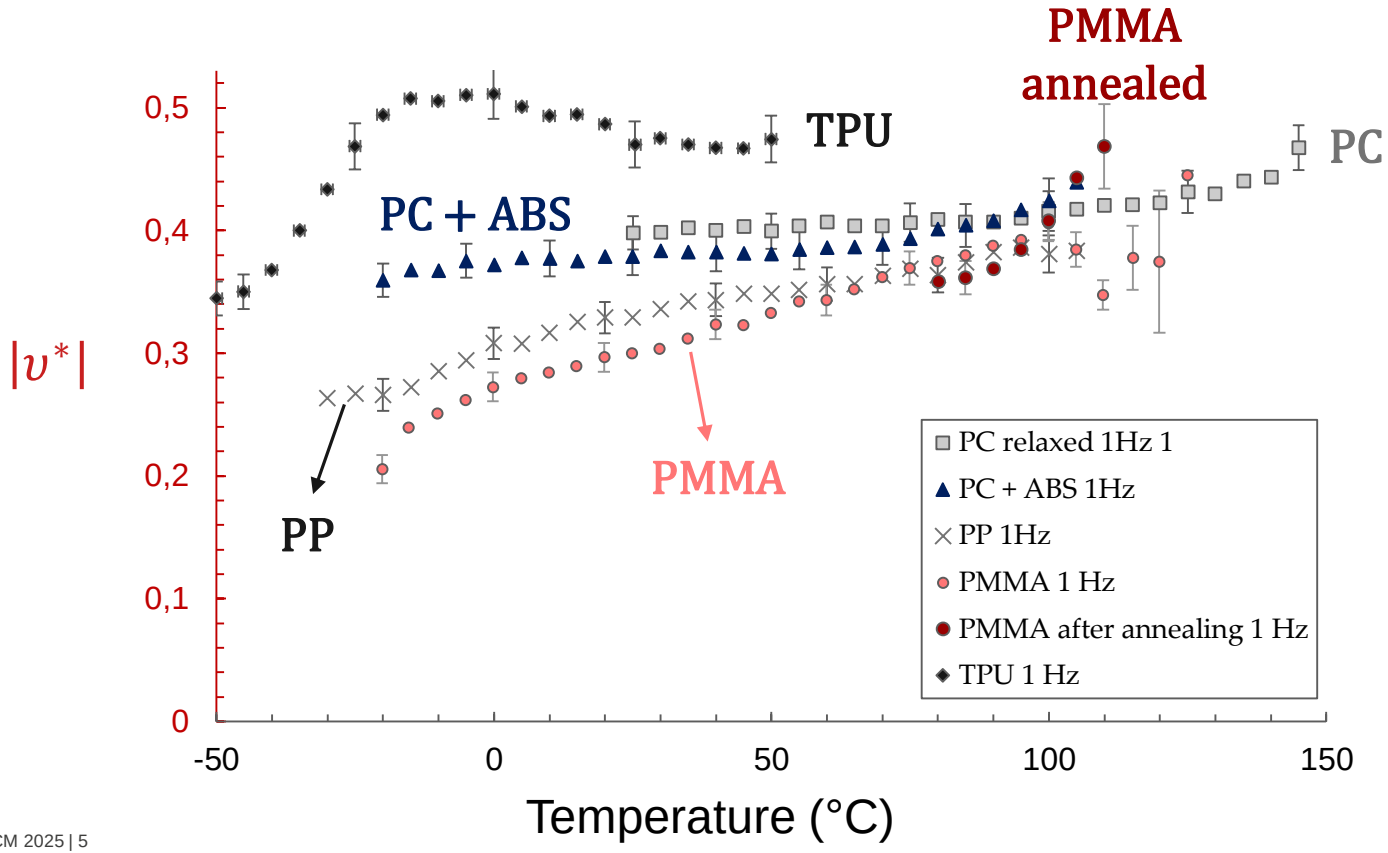

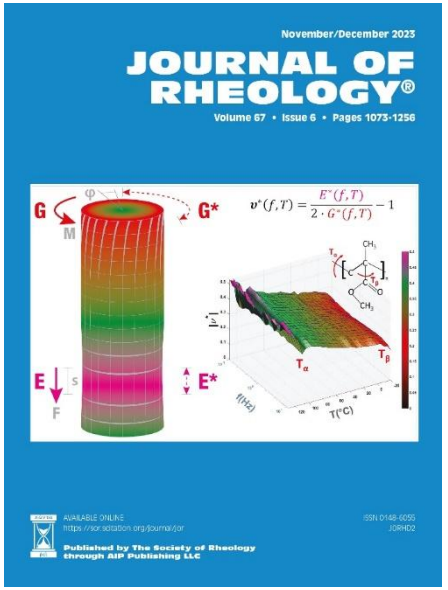

*6. J.R Agudo et al., 2023, *J. Rheol.*

AXIAL-TORSIONAL DMA

ANISOTROPIC MATERIALS

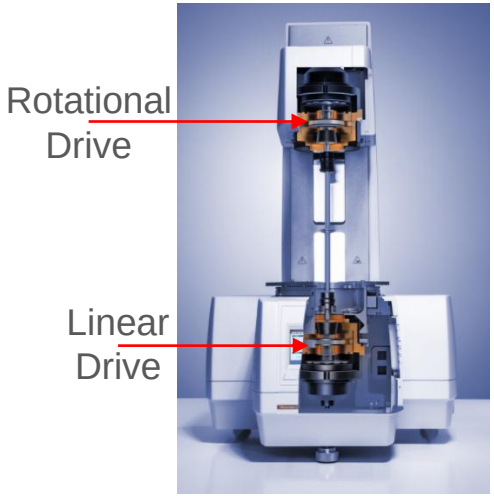

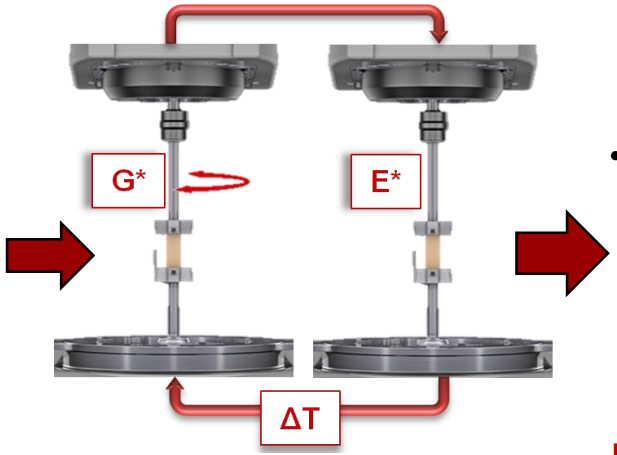

- $|G*|$ and $|E*|$ obtained **on the same specimen** in **one single measurement** and under **same conditions**
- Concept of single Poisson‘s ratio not valid anymore

For anisotropic samples

Extra information about viscoelastic anisotropy of the sample?

AXIAL-TORSIONAL DMA

POLYPROPYLENE / GLASS FIBER REINFORCED POLYPROPYLENE

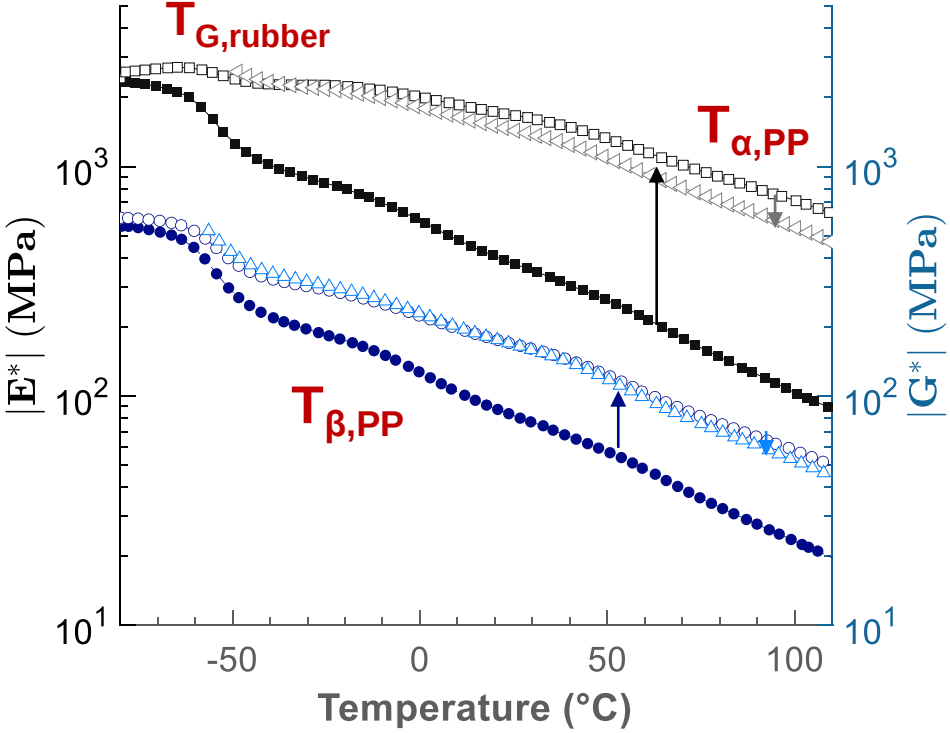

Blend of isotactic PP and ethylene/1-olefin copolymer rubber

Polypropylene blend matrix (PP)

Polypropylene
25% glass fiber (PP-GF)

Recycled Polypropylene
25% glass filler (PP-GF-R)

E* by a factor of 7
G* by a factor of 2.4
E* by a factor of 30%
G* by a factor of 7%

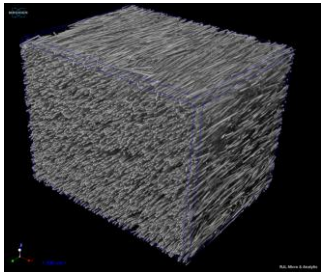

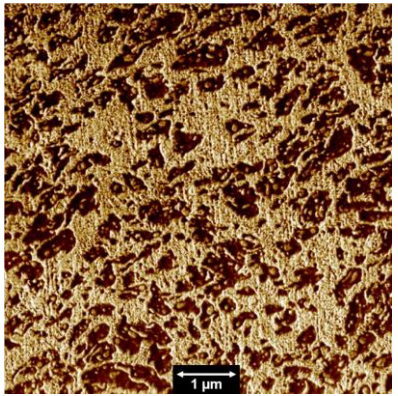

AXIAL-TORSIONAL DMA

POLYPROPYLENE / GLASS FIBER REINFORCED POLYPROPYLENE

$$\zeta = tan\delta_G / tan\delta_E ?$$

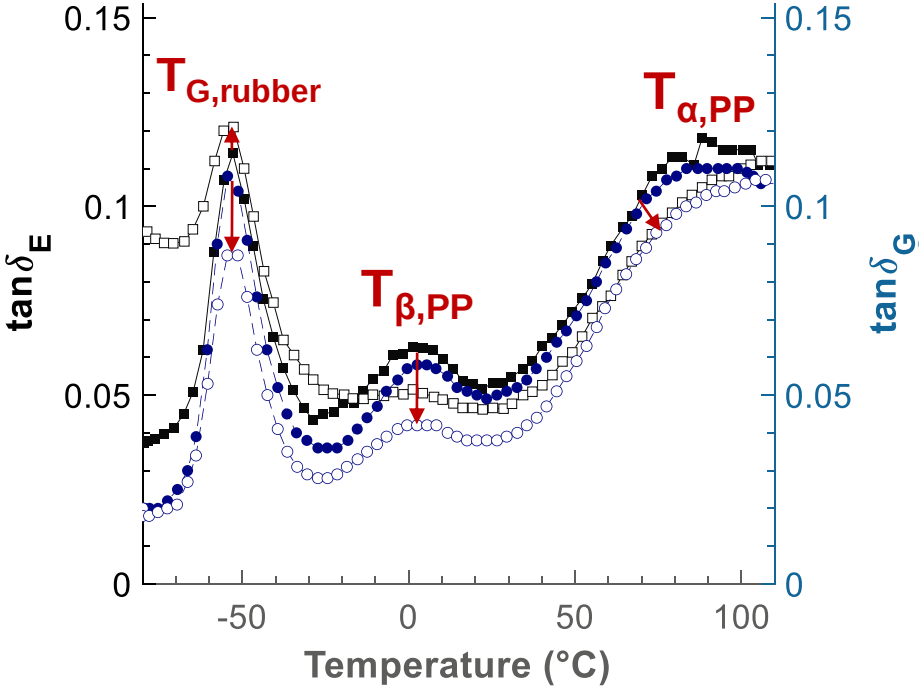

Blend of isotactic PP and ethylene/1-olefin copolymer rubber

Polypropylene blend matrix (PP)

Polypropylene
Glass Filled PP-GF (25%)

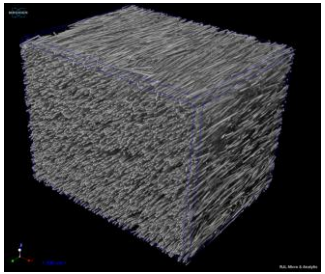

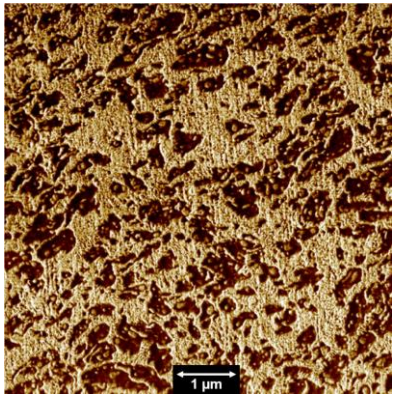

AXIAL-TORSIONAL DMA

POLYPROPYLENE / GLASS FIBER REINFORCED POLYPROPYLENE

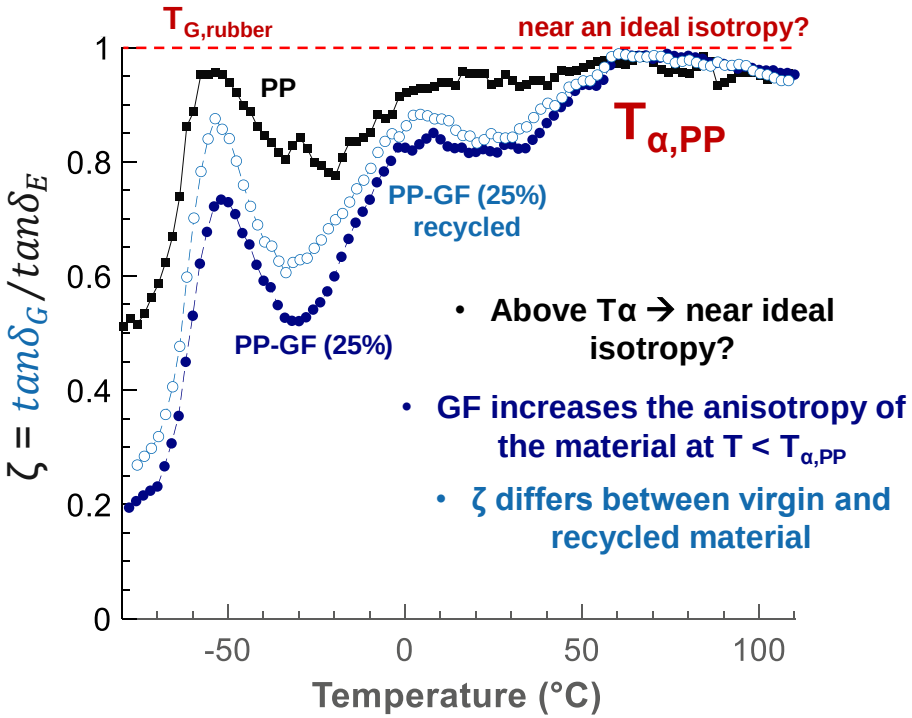

Hypothesis → ζ may behave as a dynamic macroscopic fingerprint unique to each anisotropic structure?

STRUCTURE ANALYSIS

MICRO X-RAY COMPUTED TOMOGRAPHY (MXRCT)

Matthias Ruf, Dominik Fauser and Prof. Steeb: Institute of Applied Mechanics (CE), University of Stuttgart

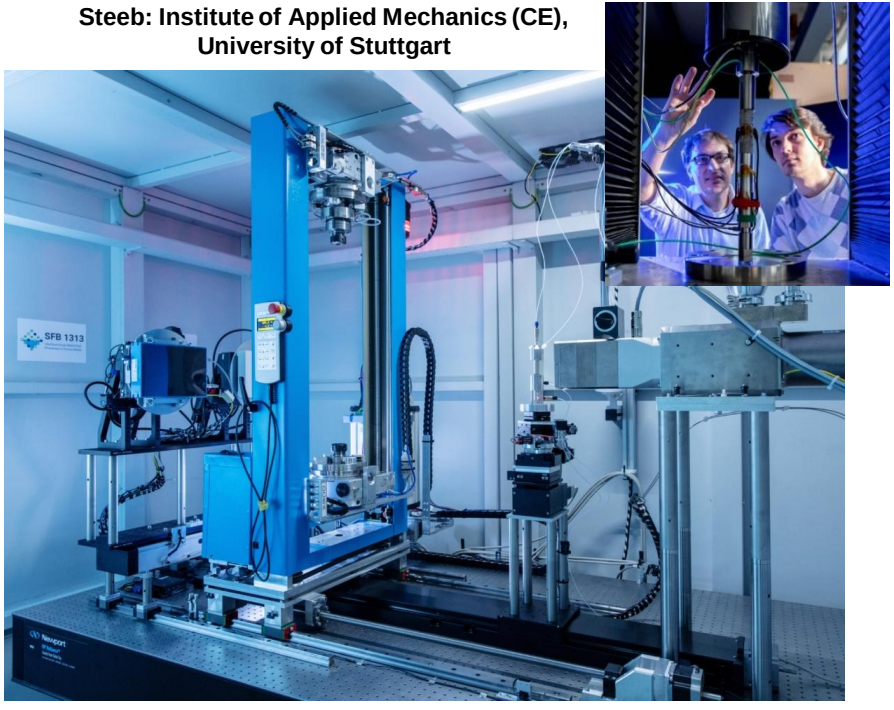

1x1x1 mm³ sub-volume

Evaluated fibers ~ 8000

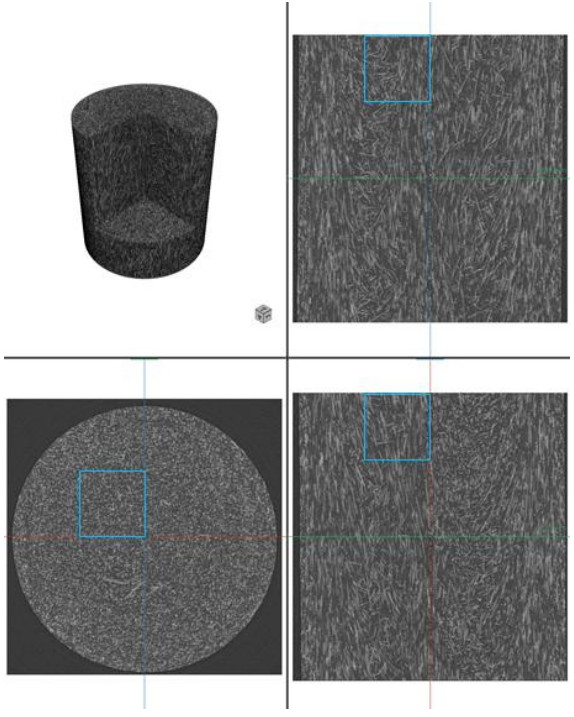

STRUCTURE ANALYSIS

MICRO X-RAY COMPUTED TOMOGRAPHY (MXRCT)

Anton Paar

University of Stuttgart
Institute of Applied Mechanics (MIB)

Polypropylene and glass fiber reinforced Polypropylene

- Location of fiber regions with the use of a machine learning tool called “Insegt Fibre” - (*7 Emerson et al. 2019)
- Tracking of the fibers by the tool “OpenFiberSeg” - *(*8 Sosa-Rey et al. 2022)*
  - Fiber length (L_f)
  - Fiber orientation (deviation angle θ and azimuth angle Φ)

Polypropylene 25% glass fiber (PP-GF)

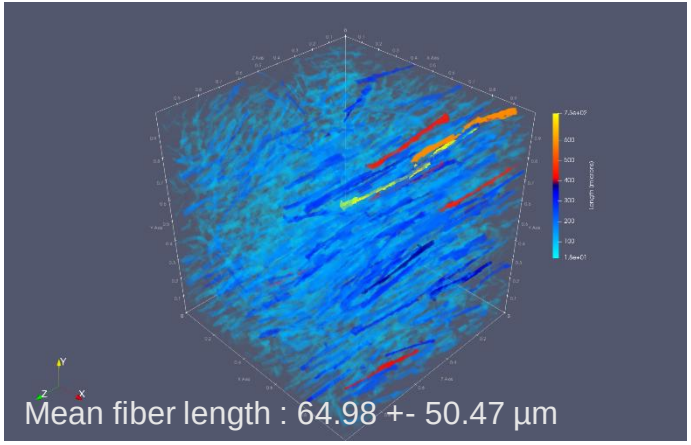

Recycled Polypropylene 25% glass filler

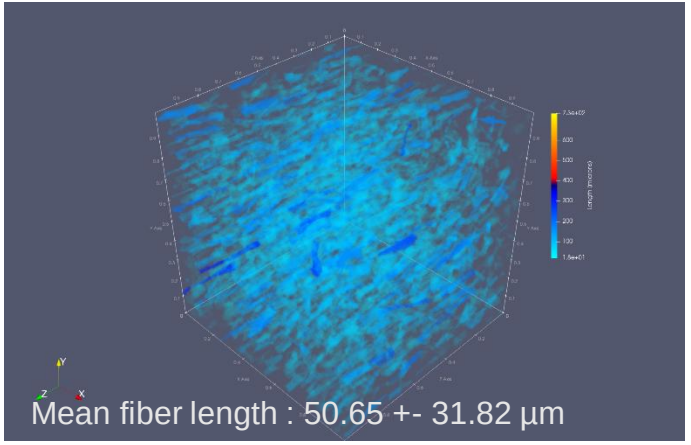

STRUCTURE ANALYSIS

MICRO X-RAY COMPUTED TOMOGRAPHY (MXRCT)

Anton Paar

University of Stuttgart
Institute of Applied Mechanics (MIB)

Polypropylene and glass fiber reinforced Polypropylene

Polypropylene 25% glass fiber

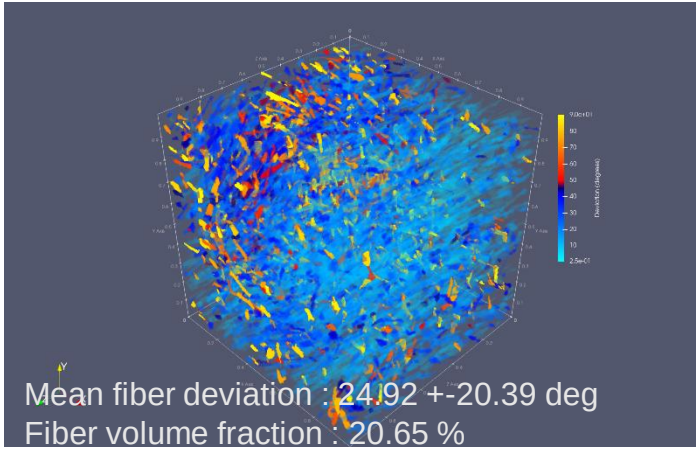

Recycled Polypropylene 25% glass filler

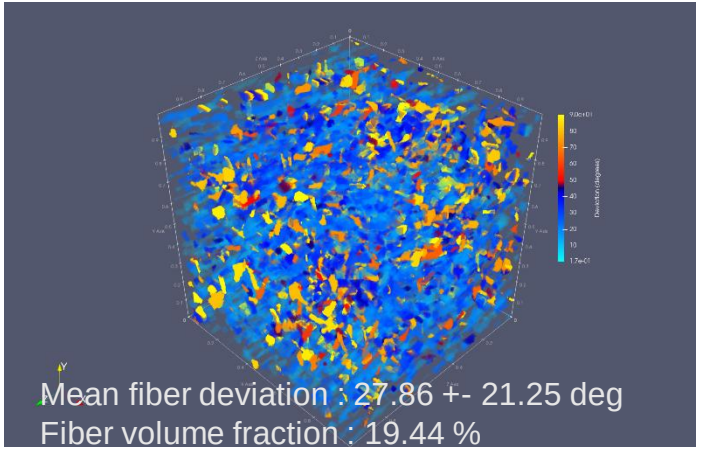

µXRCT characterization reveals a statistically significant difference in both the mean fiber length and the mean fiber orientation!

RESULT ANISOTROPIC MATERIAL I

POLYPROPYLENE / GLASS FIBER REINFORCED POLYPROPYLENE

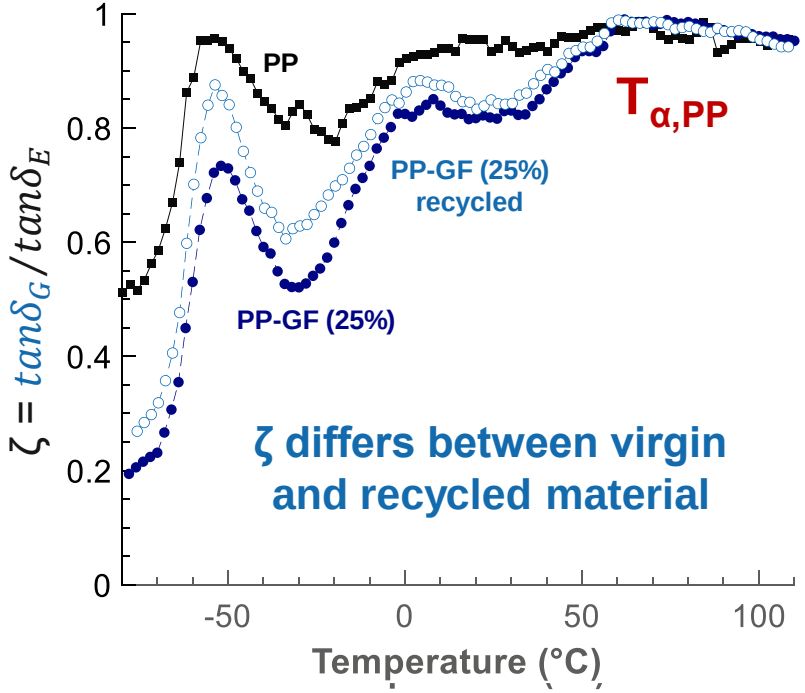

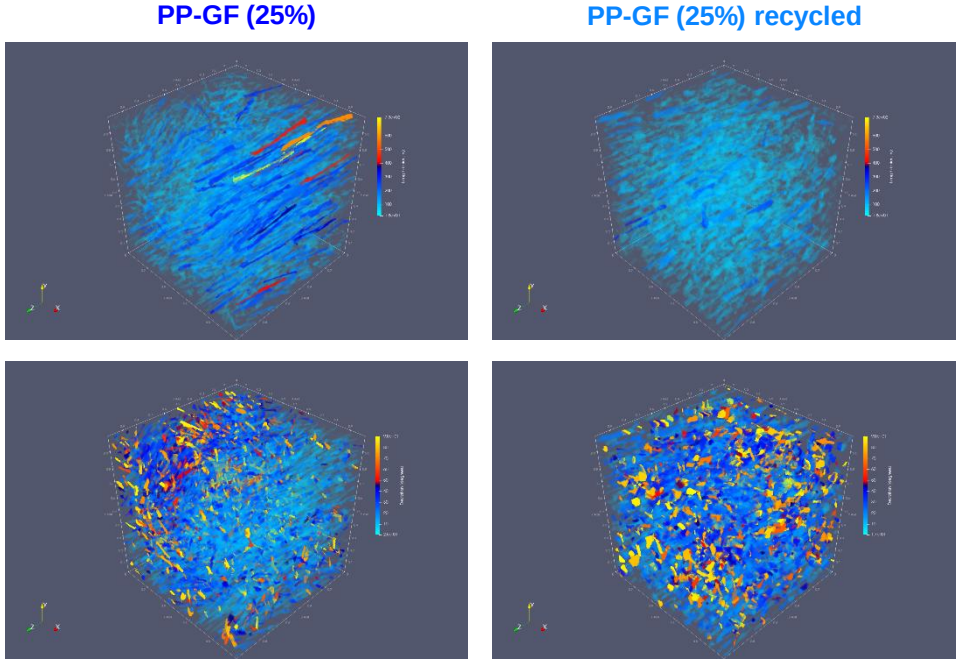

FURTHER RESULTS

POLYKETONE AND CARBON FIBER REINFORCED POLYKETONE

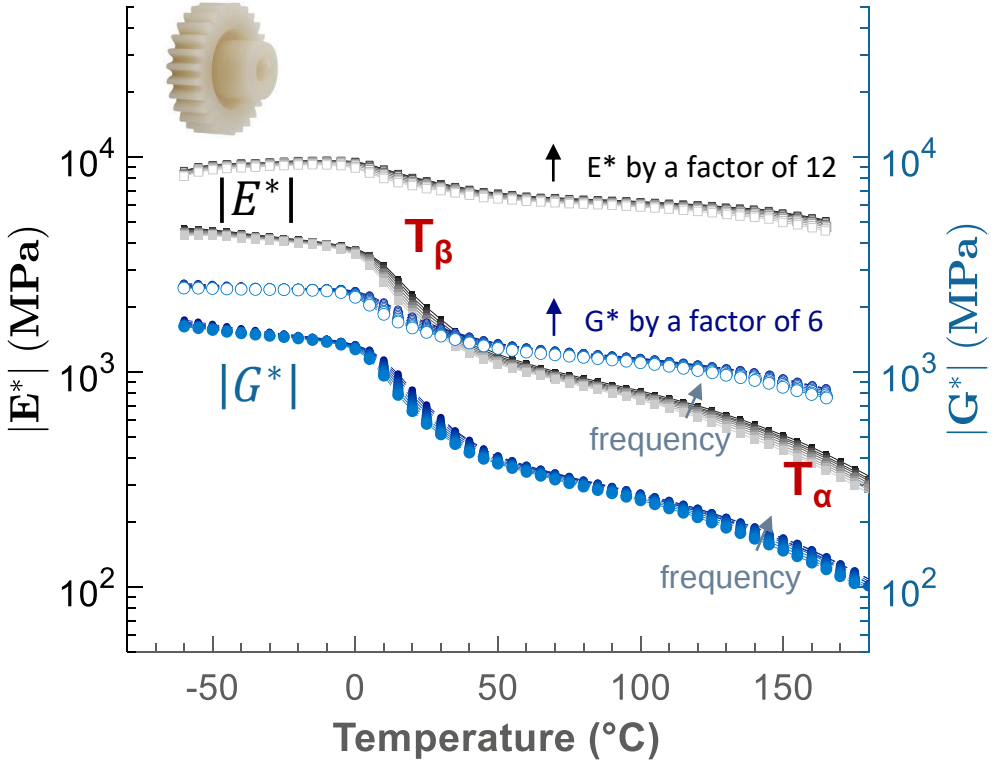

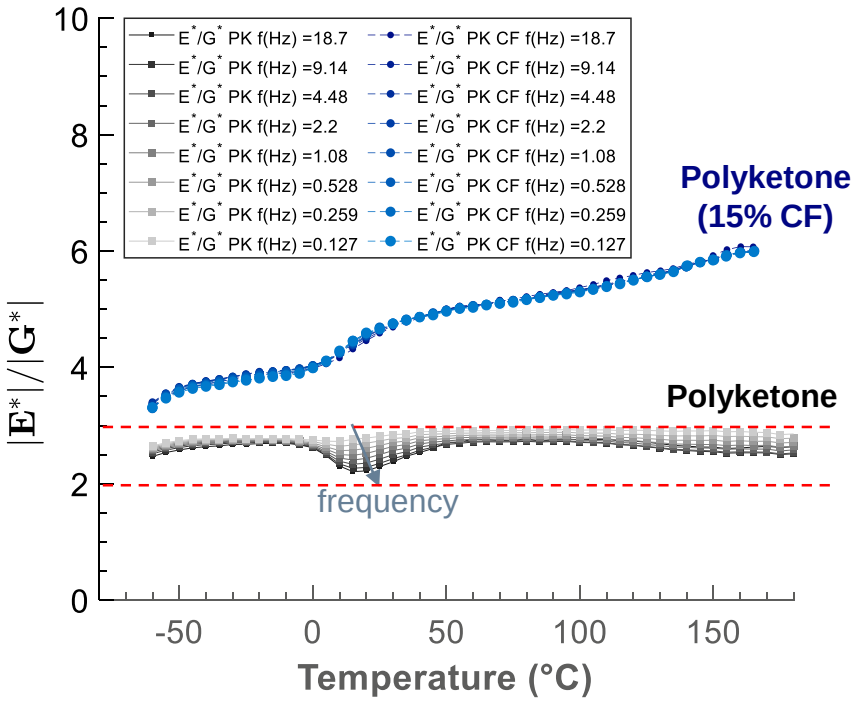

FURTHER RESULTS

POLYKETONE AND CARBON FIBER REINFORCED POLYKETONE

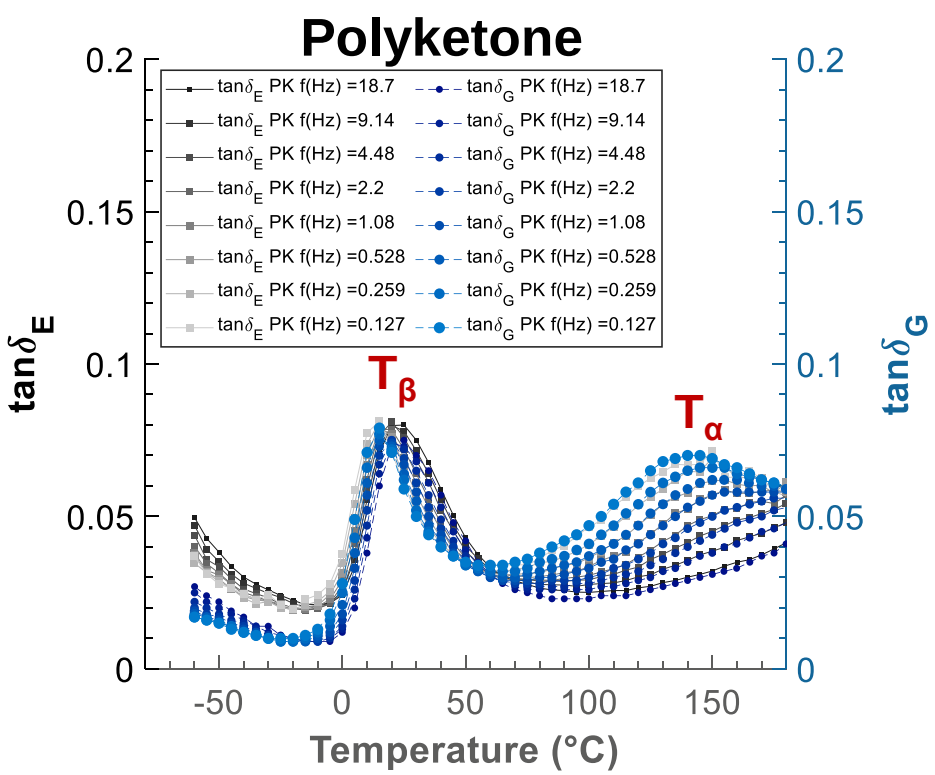

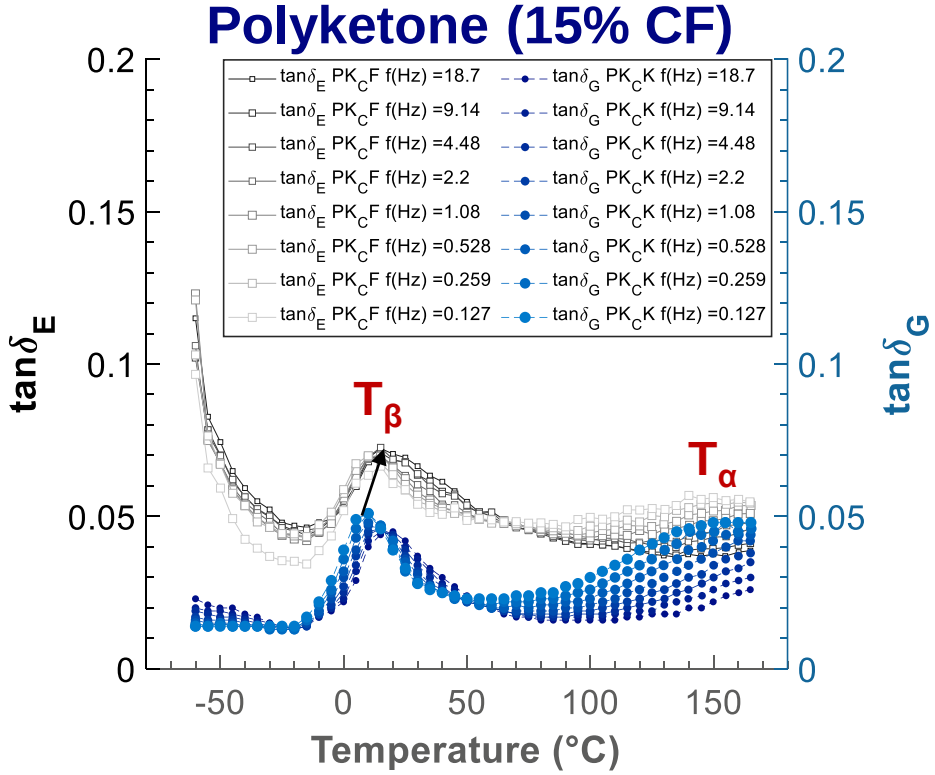

FURTHER RESULTS

POLYKETONE AND CARBON FIBER REINFORCED POLYKETONE

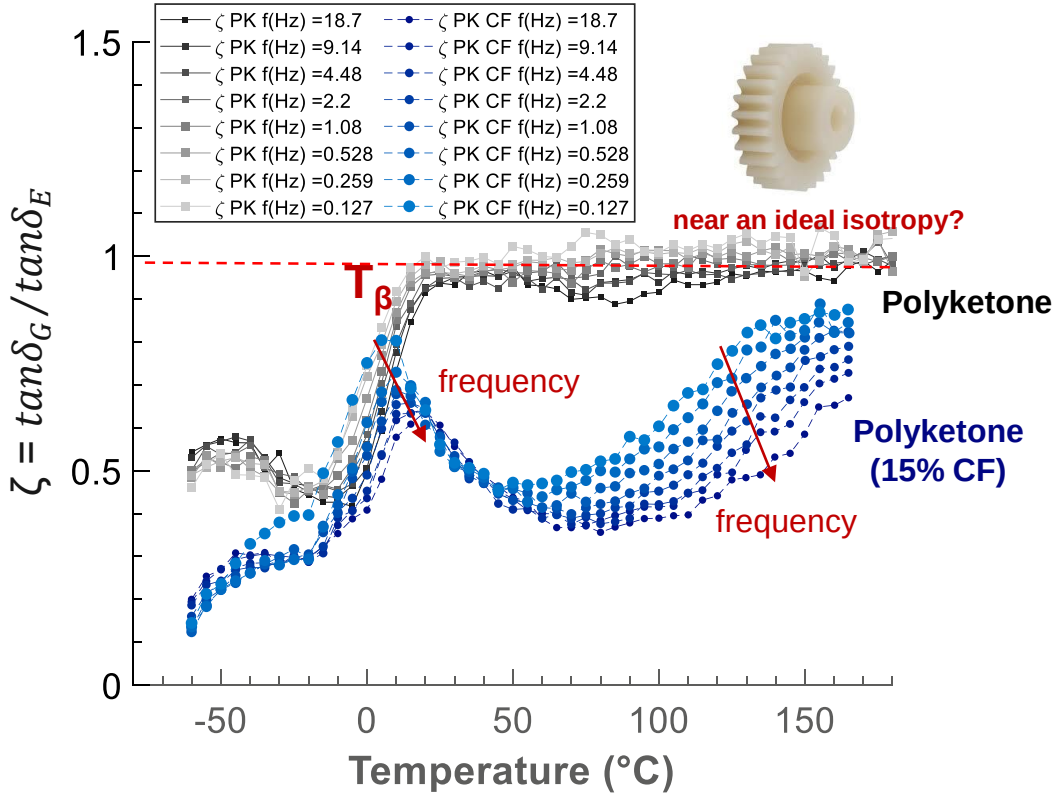

ζ → **dynamic fingerprint** unique for each material?

→ Distinguish anisotropic structures and its dependency on temperature and frequency

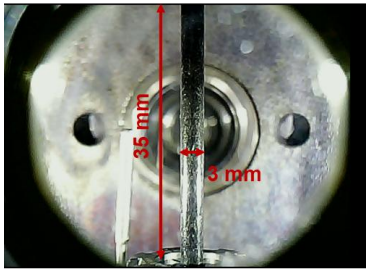

SUMMARY

- Use of measurements with rotational and axial drive enable determination of $|G^*|$ and $|E^*|$ on the same specimen under the same conditions and in one single experiment
- For homogeneous and isotropic samples → Complex Poisson's ratio, $|\upsilon^*|$
- For anisotropic materials, information of the material in longitudinal and torsional direction can be determined ($E', E'', tan\delta_E, G', G'', tan\delta_T$) →$|E^*|/|G^*|$= function(T,f)
- Results with µXRCT indicated differences in average fiber size and fiber alignment and hence a different level of anisotropy - as predicted by ζ = $tan\delta_G/tan\delta_E$
- ζ = $tan\delta_G/tan\delta_E$ could be a new dynamic fingerprint unique for each material
  - Distinguish anisotropic structures and its dependency on temperature and frequency → Significant time saving compared to other conventional methods



THANK YOU FOR YOUR ATTENTION

Dr. Gunther Arnold
Product Manager MCR 702e MultiDrive
Rheometry and Dynamic Mechanical Analysis

gunther.arnold@anton-paar.com

REFERENCES

1. Tschoegl, N.W, Knaus, W.G & Emri, I.(2002) Poisson's ratio in linear viscoelasticity – A critical review. Mechanics of Time-Dependent Mater, 6, 3-51.
2. Szabó, I., "Höhere technische Mechanik: nach Vorlesungen," Springer-Verlag (2013).
3. Dessi, C. et al. (2016) Analysis of dynamic mechanical response in torsion. Journal of Rheology, 60, 275-287
4. Diani, J., Gilormini, P. (2017). On necessary precautions when measuring solid polymer linear viscoelasticity with dynamic analysis in torsion. Polymer Testing, 63, 275-280.
5. Dessi, C., Coppola, S.& Vlassopoulos, D. (2021). Dynamic mechanical analysis with torsional rectangular geometry: A critical assessment of constrained warping models. Journal of Rheology, 65, 325-335.
6. Rodriguez Agudo, J.A. et al. (2023). Characterization of the temperature and frequency dependency of the complex Poisson's ratio using a novel combined torsional-axial rheometer. Journal of Rheology, 67, 1221-1250.
7. Emerson M et al. (2019). Insegt fibre: A user-friendly software for indivifual fibre segmentation. Proceedings of 22nd International Conference on Composite Materials
8. Sosa-Rey Facundo et al. (2022). Openfiberseg: Open-source segmentation of individual fibers and porosity in tomographic scans of additively manufactured short fiber reinforced composites. Composites Science and Technology. 226, 109497

MatchID
Metrology beyond colors

ICCM24
24TH INTERNATIONAL CONFERENCE ON COMPOSITE MATERIALS

4-8 August 2025
Baltimore, MD, USA

Identification of the through-thickness orthotropic stiffness components of thick filament-wounded composite tubes in an industrial context

Authors

Dr. Pascal Lava,

Dr. Amar Peshave,

Prof. Fabrice Pierron

Industry collaborators

Dr. Erick Montes de Oca Valle

Dr. Irene Jimenez Fortunato,

Magma Global, UK

Presenter

Dr Isabella M. Jacobsen

Composites tubes, pipes and pressure vessels

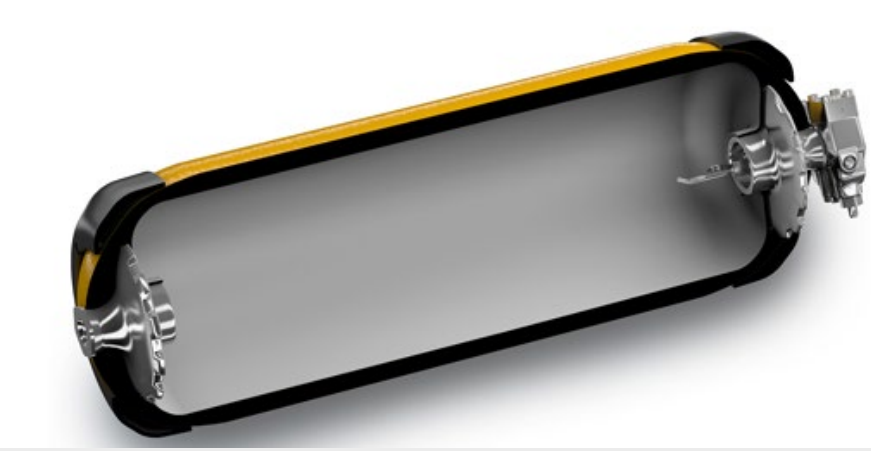

https://www.cf-composites.toray/

https://cstoptimum.com/
Hydrogen storage



Hydrocarbon, water, gas

magma
A TechnipFMC Company



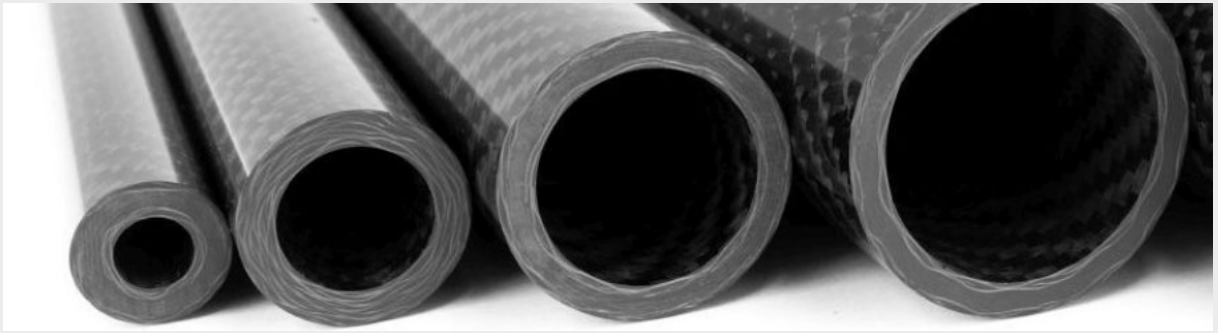

https://www.carbon-composite.com/

Through-thickness properties

- Material Testing 1.0*
  - Statically determinate
  - Strain gauges
- Time consuming
- Effect of curvature?

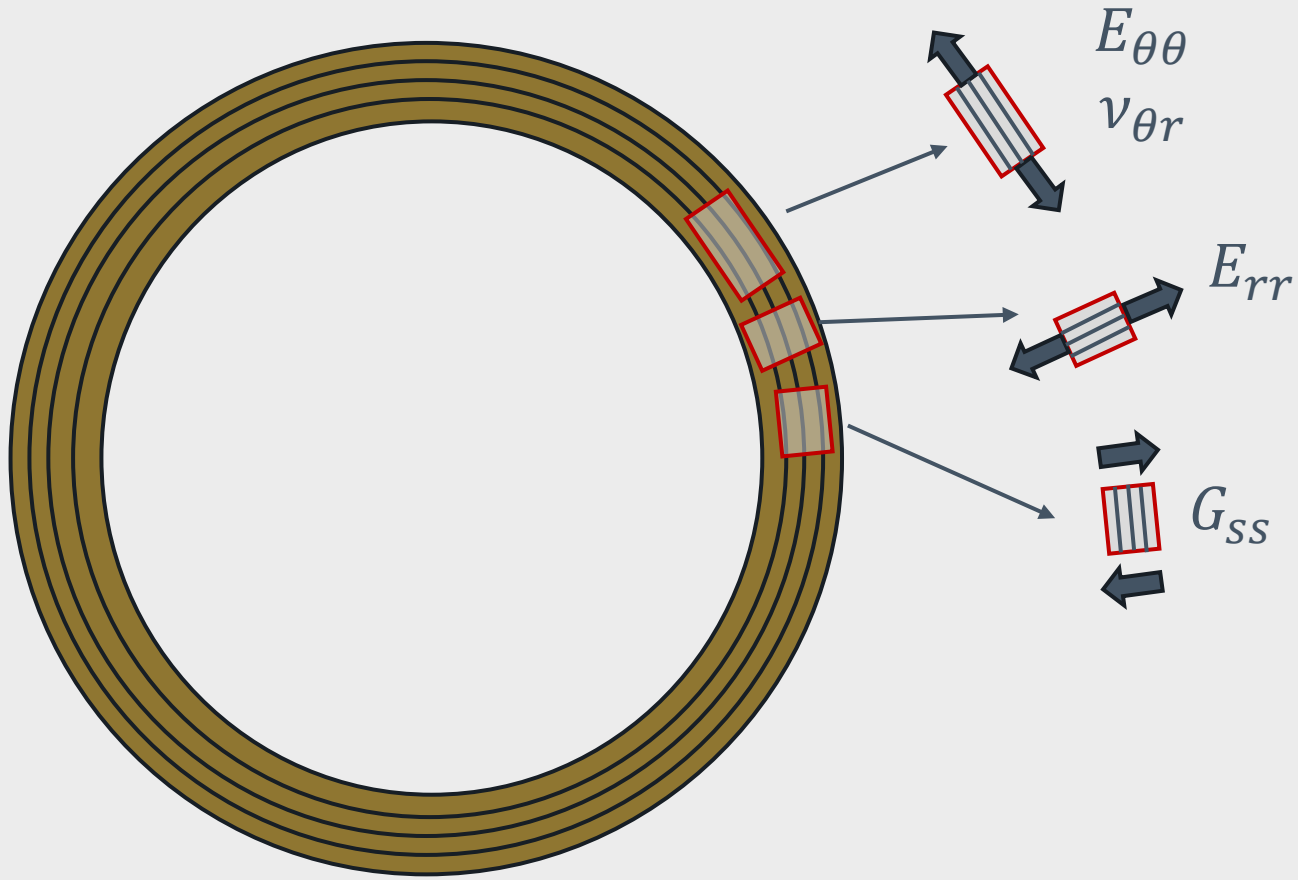

*Pierron, F., & Grédiac, M. (2021). Towards Material Testing 2.0. A review of test design for identification of constitutive parameters from full-field measurements. *Strain, 57(1), e12370.*

Material Testing 2.0

Heterogeneous test

Digital Image Correlation

Inverse identification

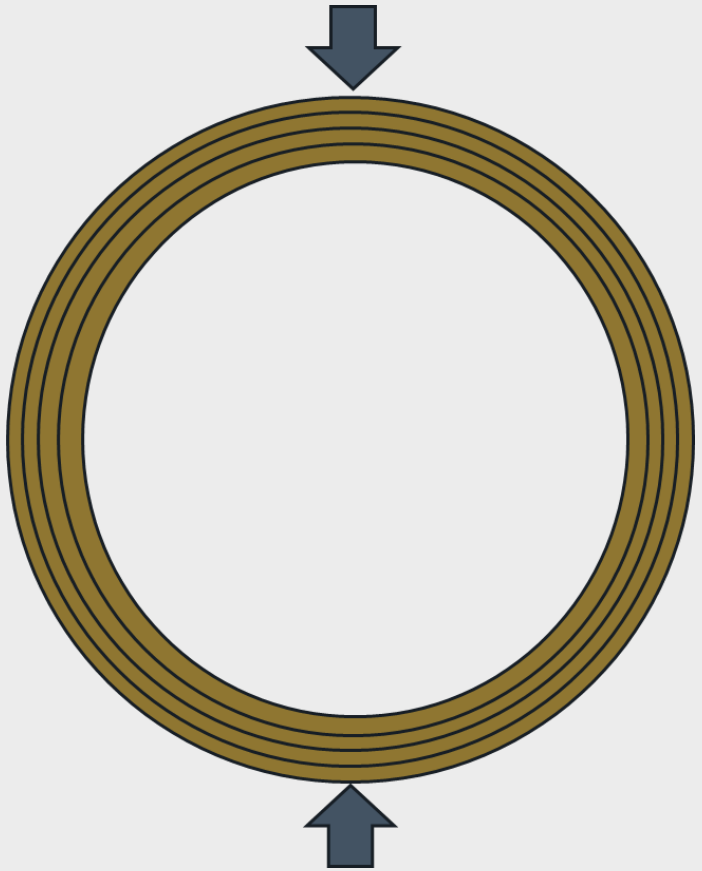

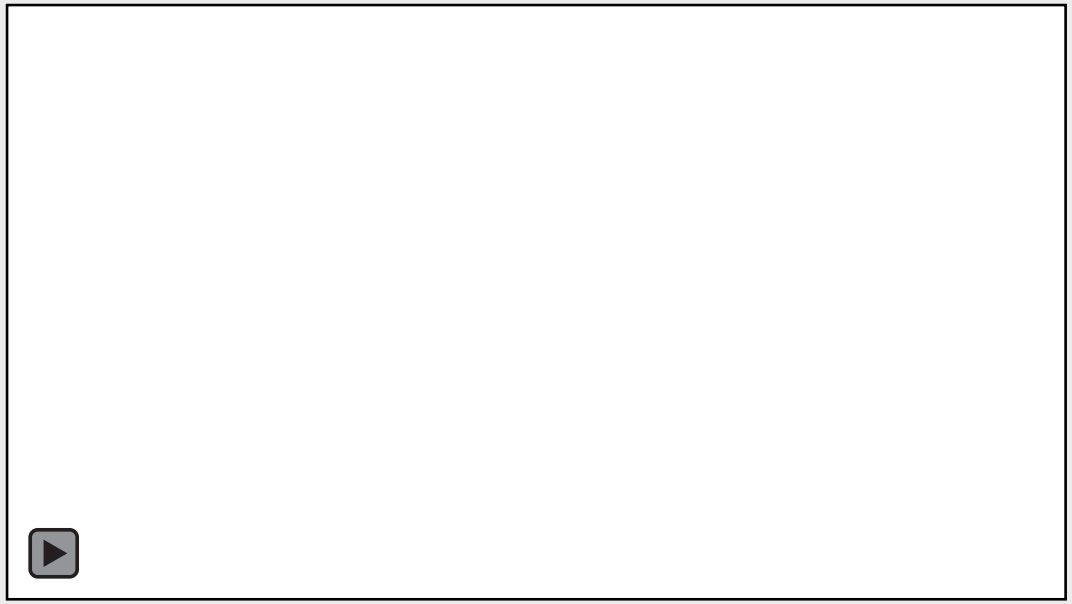

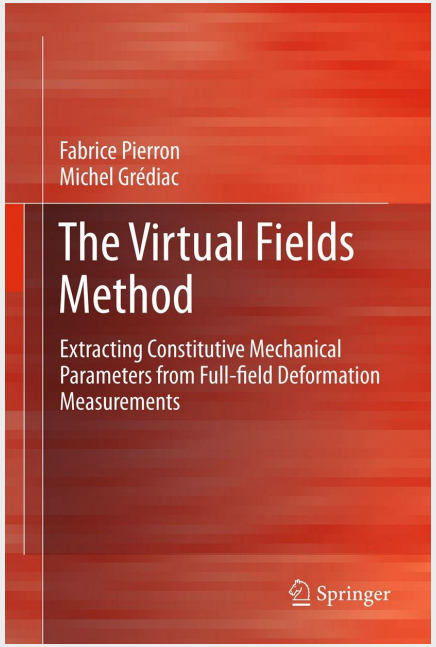

Pierron, F. (2023). Material Testing 2.0: A brief review. *Strain, 59(3), e12434.*

Finite Element Model Updating

Strain

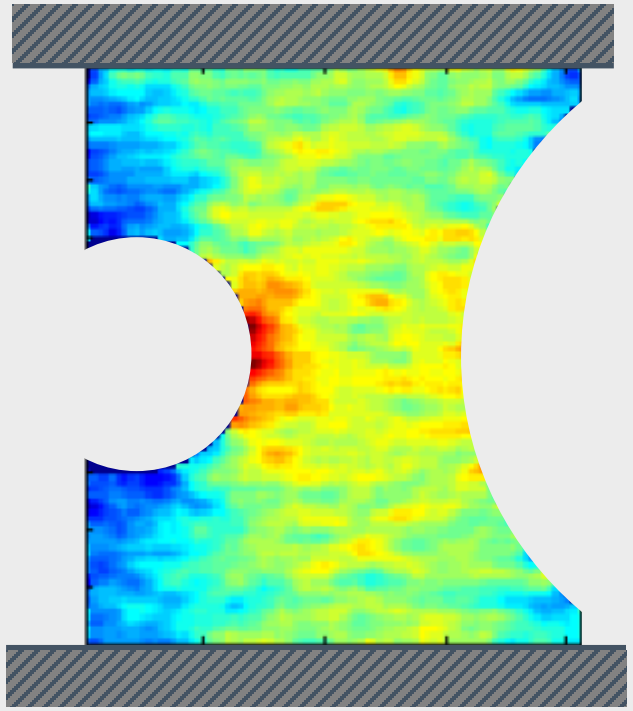

F

Strain



F

FE model (principle of virtual work (PVW))

Initial material parameters

‘Statically admissible’ (obeys the rules of mechanics).

Cost function

$$\Phi = \left\{ \; - \; \right\}^2$$

$$\Phi \to 0$$

Final material parameters

The Virtual Fields Method

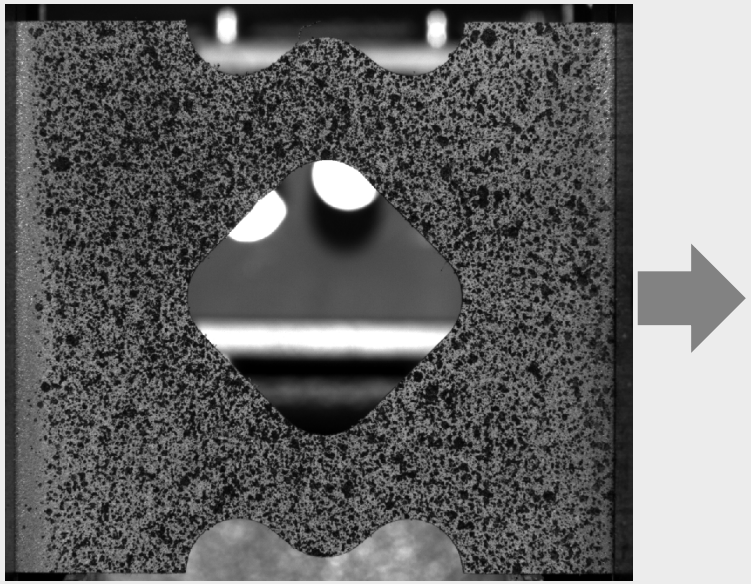

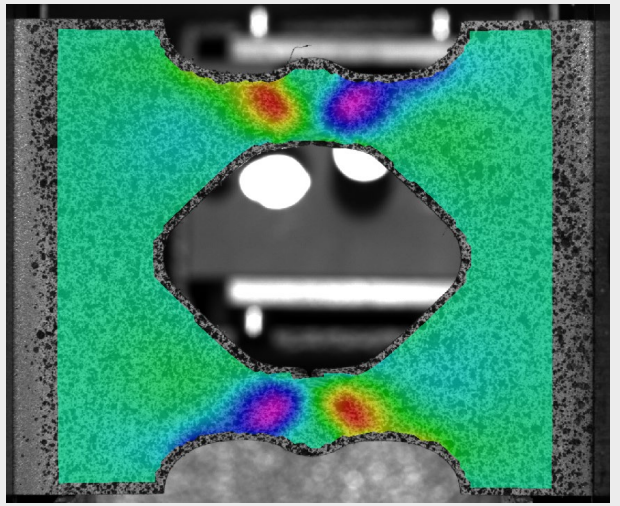

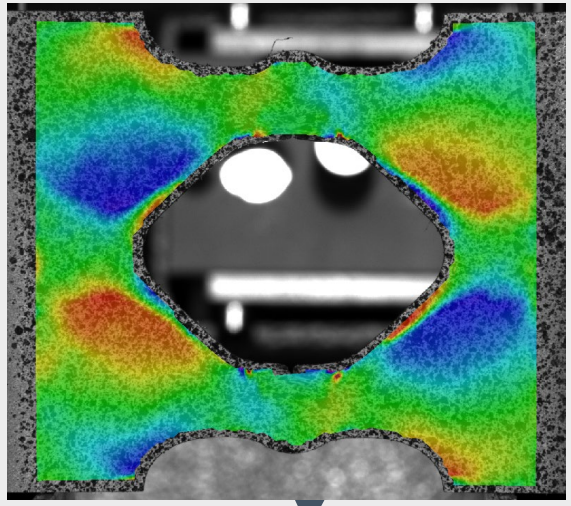

Initial material parameters

Strain

Stress

No

Statically admissible (PVW)?

Yes

Final material parameters

In the literature…

- Thick glass/epoxy ring from tube, 90° (hoop)

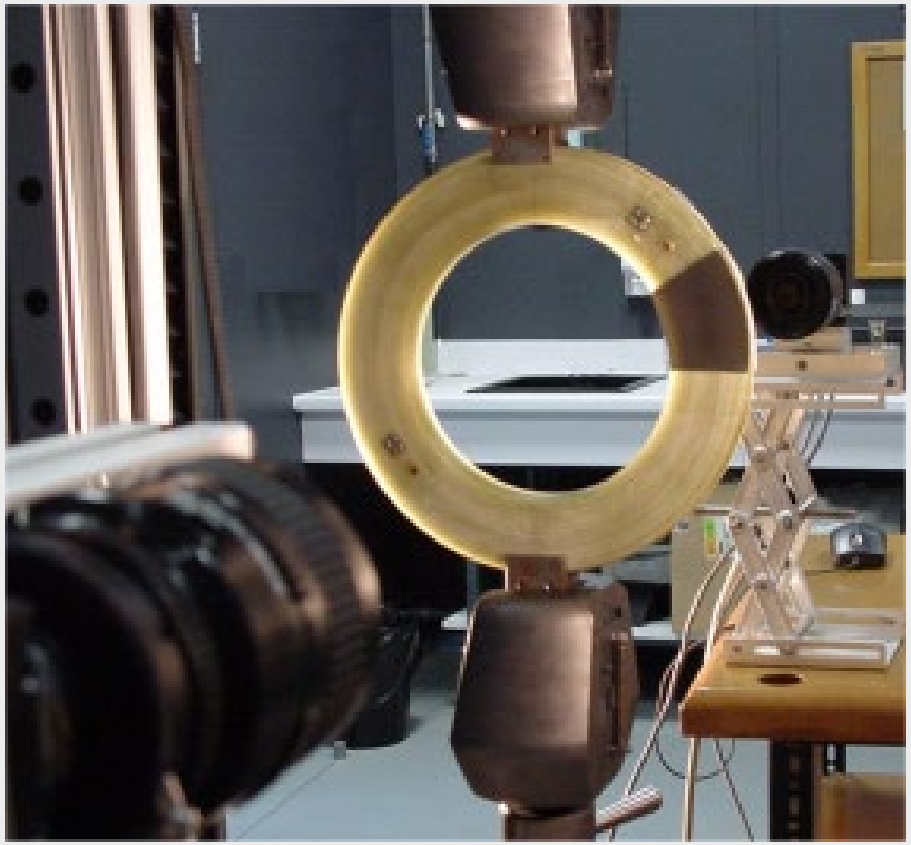

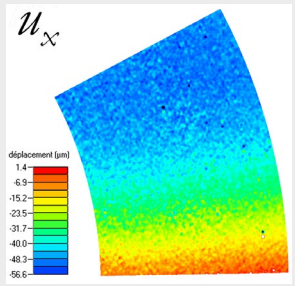

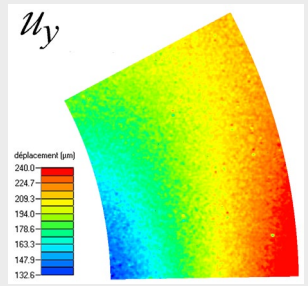

	Q_{rr}	$Q_{\theta\theta}$	$Q_{r\theta}$	Q_{ss}
Reference (GPa)	10	40	3	4
Identified (GPa)	11.4	45.4	2.62	6.78
CV(%) – 9 tests	29	10	29	4

Moulart, R., Avril, S., & Pierron, F. (2006). Identification of the through-thickness rigidities of a thick laminated composite tube. *Composites Part A, 37(2), 326-336.*

Context and present contribution

- MatchID's VFM module
- Extend to cylindrical material coordinates
- New choice of virtual fields
- Verify on synthetic data
- Validate on experiments

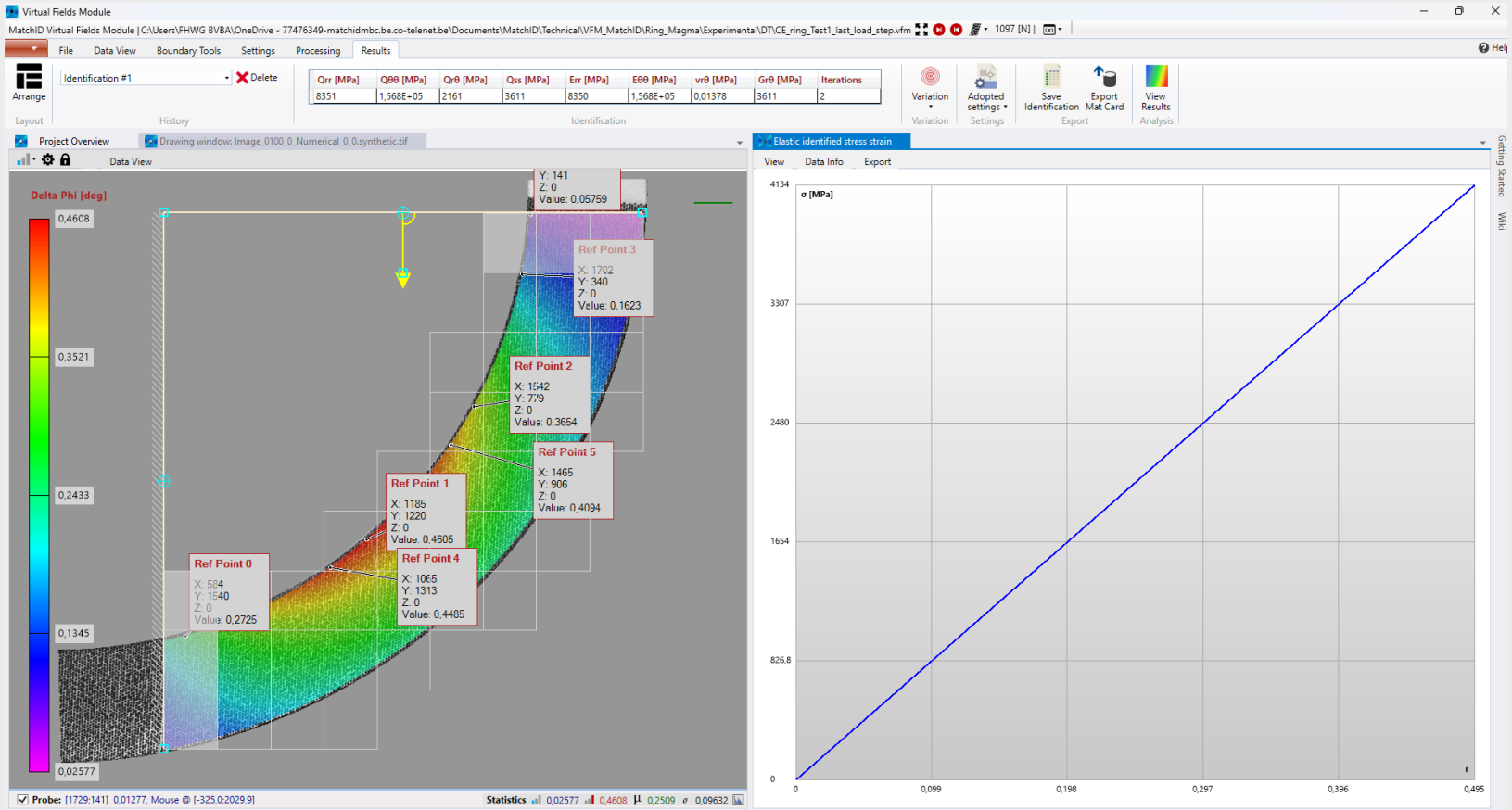

Virtual fields selection

- Manually-defined[1]
  - 😊 Ease of programming
  - 😞 Suboptimal, boundary condition dependent
- Noise optimized[2]
  - Piecewise expansion[3], in cylindrical coordinate systems[4]
  - 😊 Maximum likelihood solution
  - 😞 Complex programming, sensitive to outliers, limited to elasticity
- Sensitivity-based[5]
  - 😊 Piecewise expansion, based on stress sensitivities
  - 😞 Highly flexible, very efficient
  - Require more stress computations

First time application to elasticity problems

[1] Pierron, F., Zhavoronok, S., & Grédiac, M. (2000). *Int. J. of Sol. and Struct., 37(32), 4437-4453.*

[2] Avril, S., Grédiac, M., & Pierron, F. (2004). *Computational Mechanics, 34(6), 439-452.*

[3] Toussaint, E., Grédiac, M., & Pierron, F. (2006). *Int. J. of Mech. Sci., 48(3), 256-264.*

[4] Moulart, R., Avril, S., & Pierron, F. (2006). *Composites Part A, 37(2), 326-336.*

Test specimen

- Test specimen
  - Carbon/epoxy ring cut from tube, hoop-wound
- Experimental setup



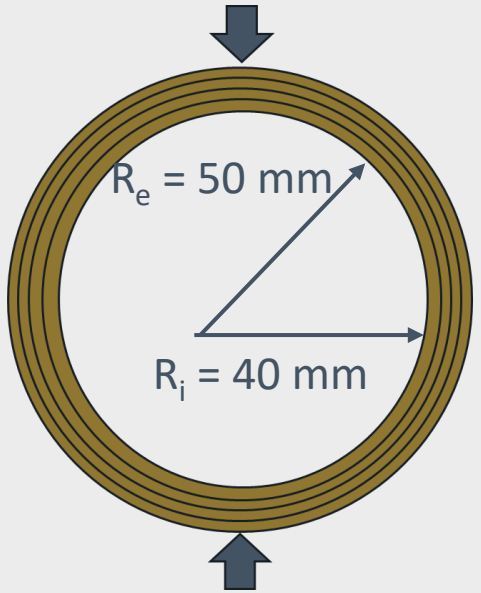

Thickness: 5 mm

- Blue LEDs
- PointGrey 5 Mpx cameras(2448 x 2048)
- Fujinon 50 mm XA series
- In-house built compression fixture

Images

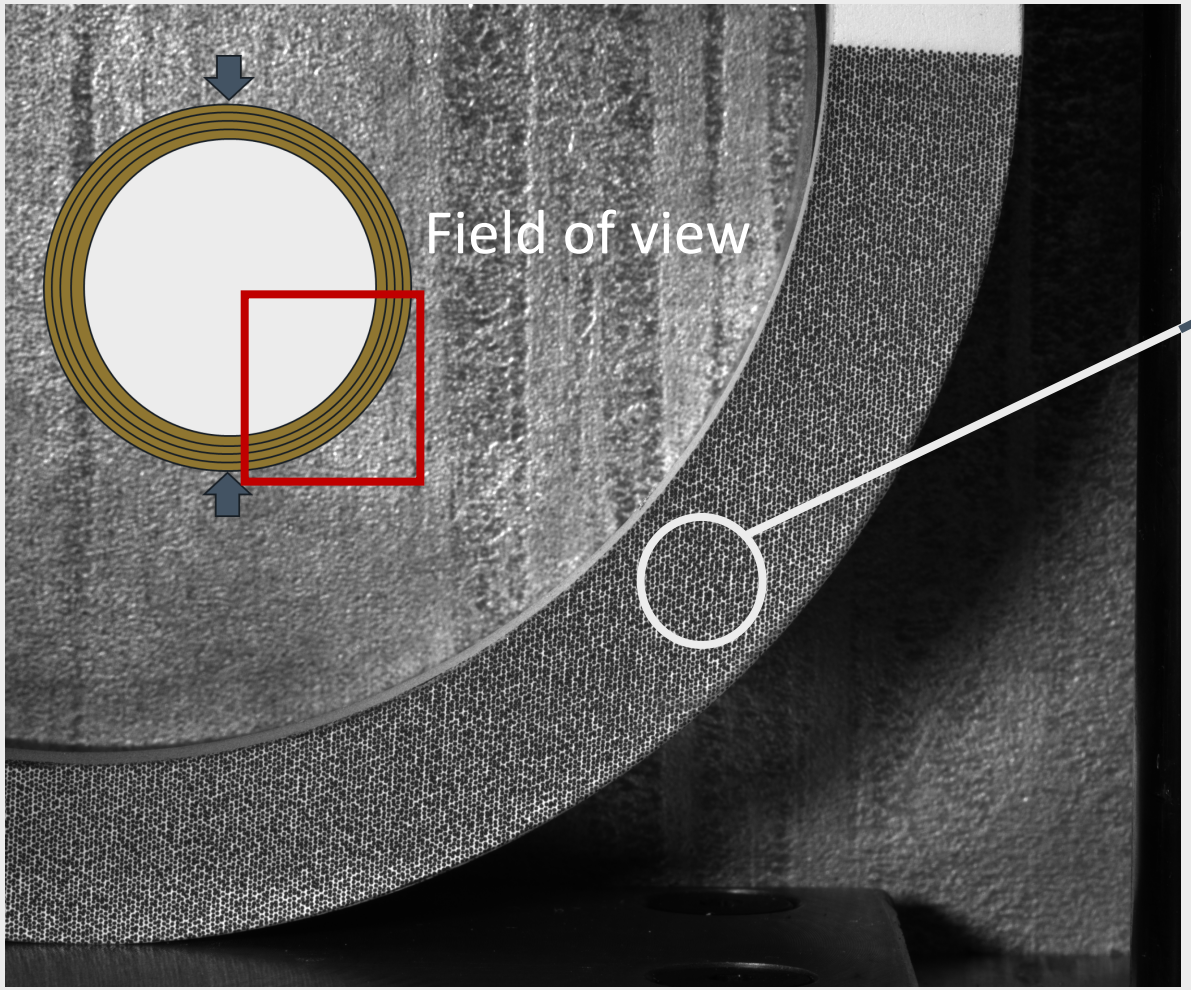

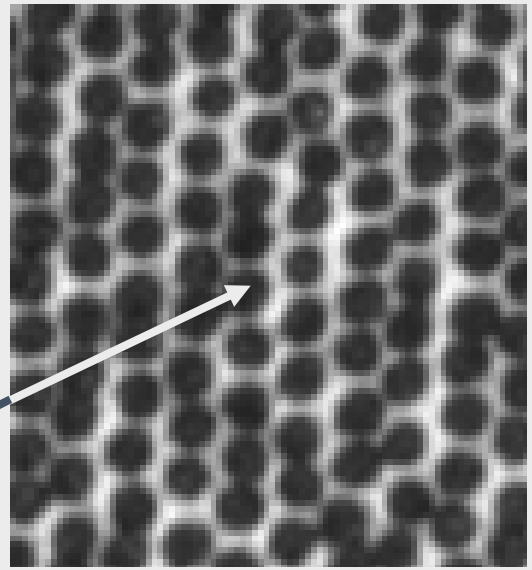

Laser engraved
250 µm dots

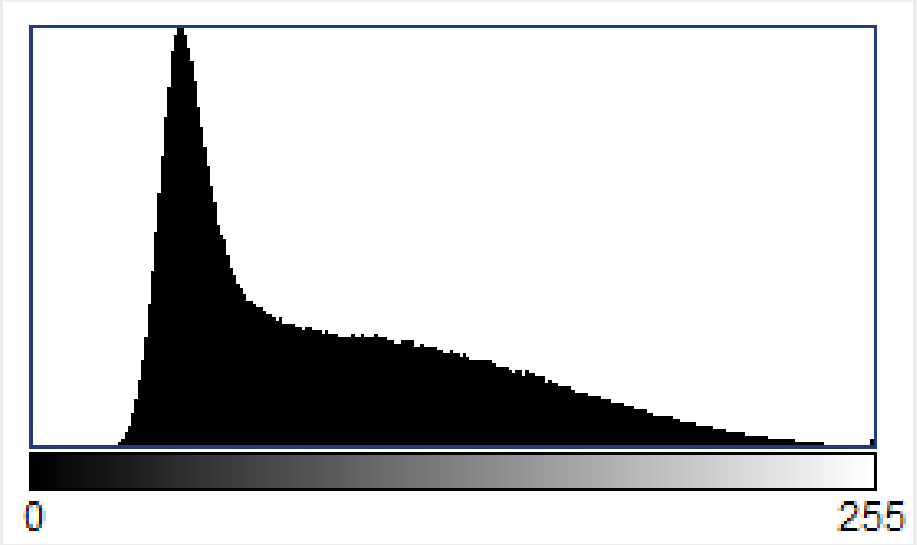

Histogram

Experimental protocol and DIC settings

- Calibration
- Stationary images: 100
  - Averaged reference images
- 5 load steps
  - 460, 892, 1322, 1760 and 2194 N
  - 100 averaged deformed images
  - All used for identification
- DIC setting
  - Subset: 21, step: 1
  - Strain window: 5 (Q4)
  - ZNSSD, affine shape functions, local bicubic splines

Digital Twin (DT): FEDEF Module

MatchID
Metrology beyond colors

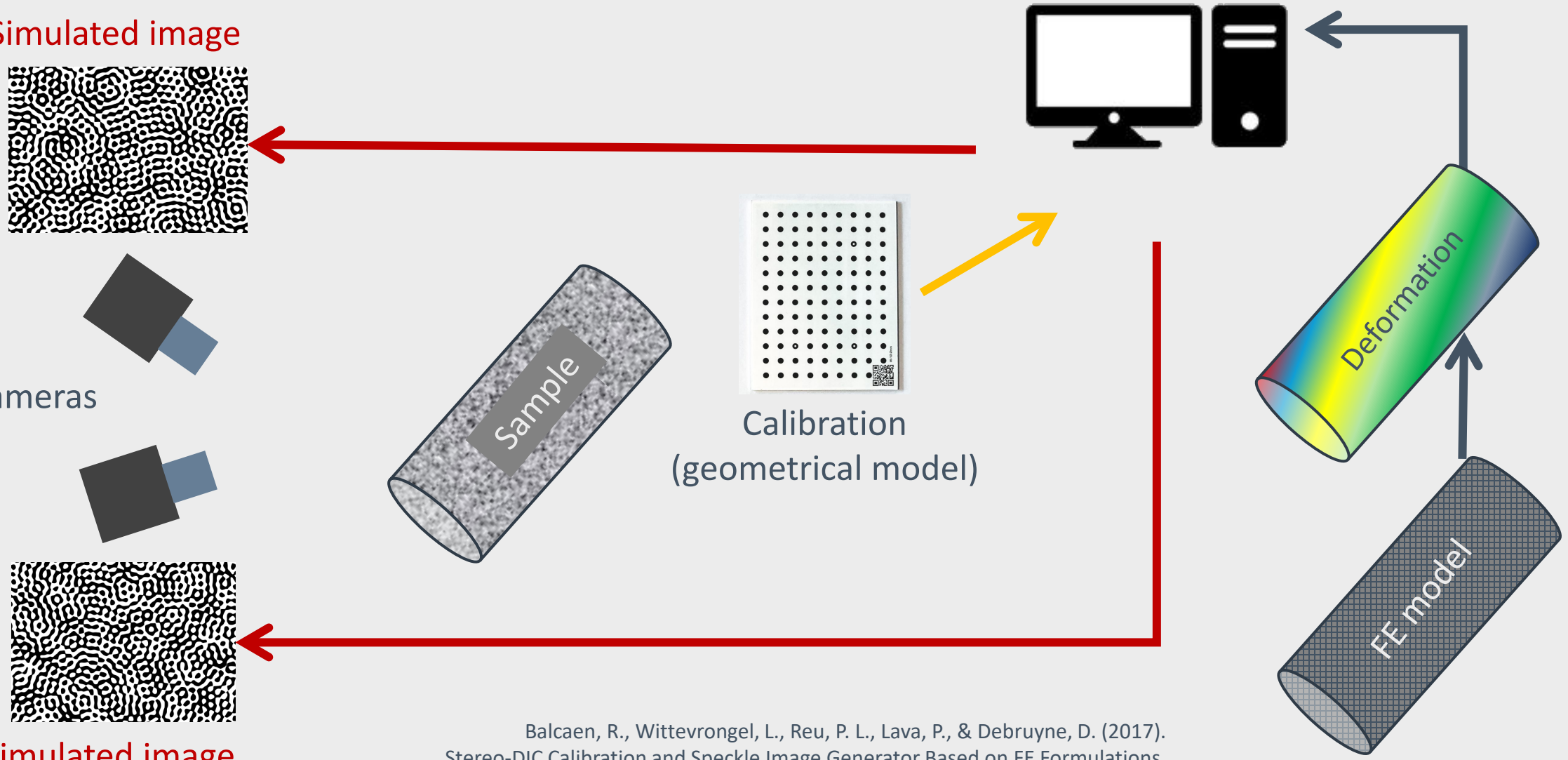

Balcaen, R., Wittevrongel, L., Reu, P. L., Lava, P., & Debruyne, D. (2017).
Stereo-DIC Calibration and Speckle Image Generator Based on FE Formulations.
Experimental Mechanics, 57(5), 703-718.

Last load step - $\varepsilon_{rr}(\mu\varepsilon)$

Experimental

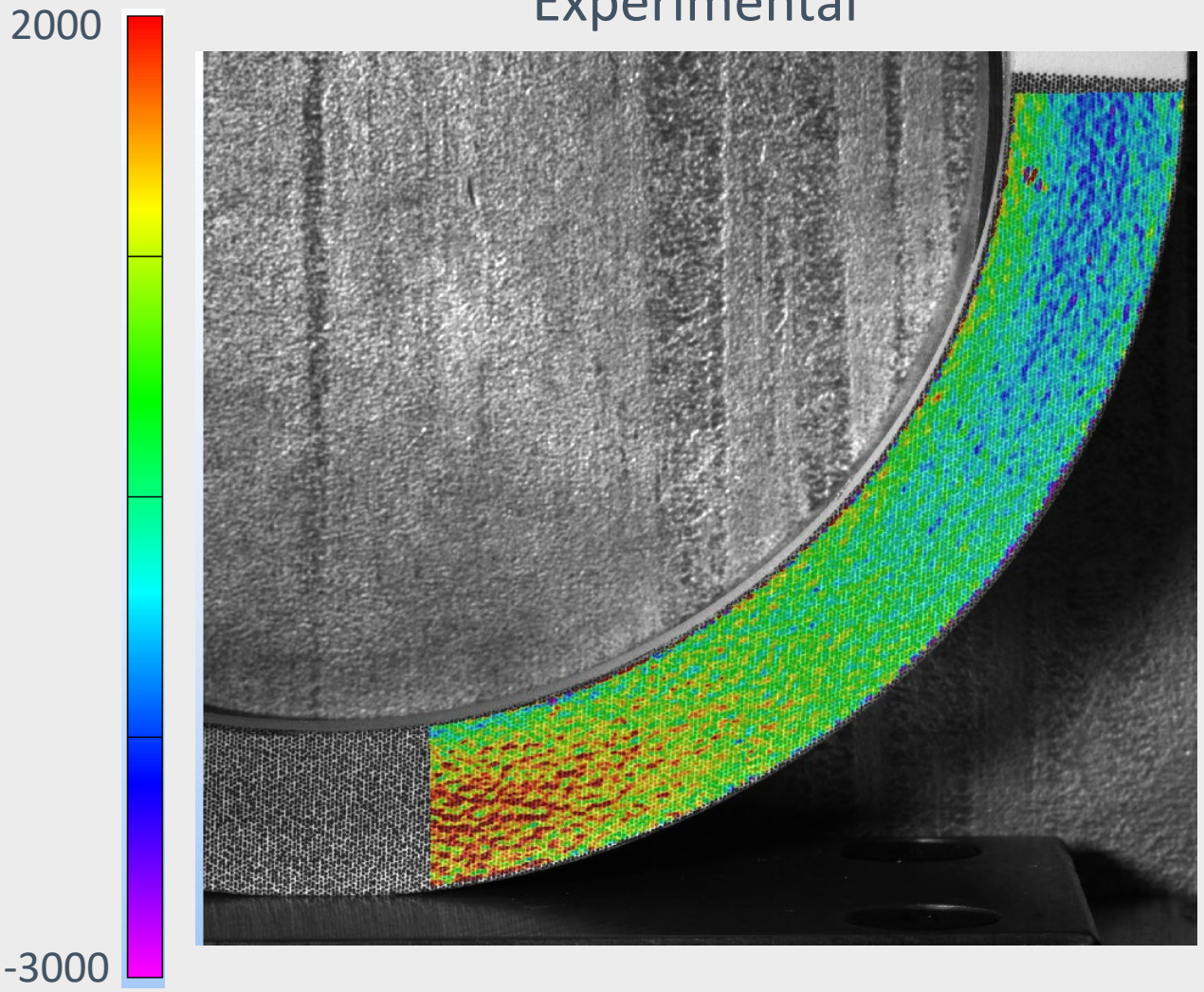

FE - DT

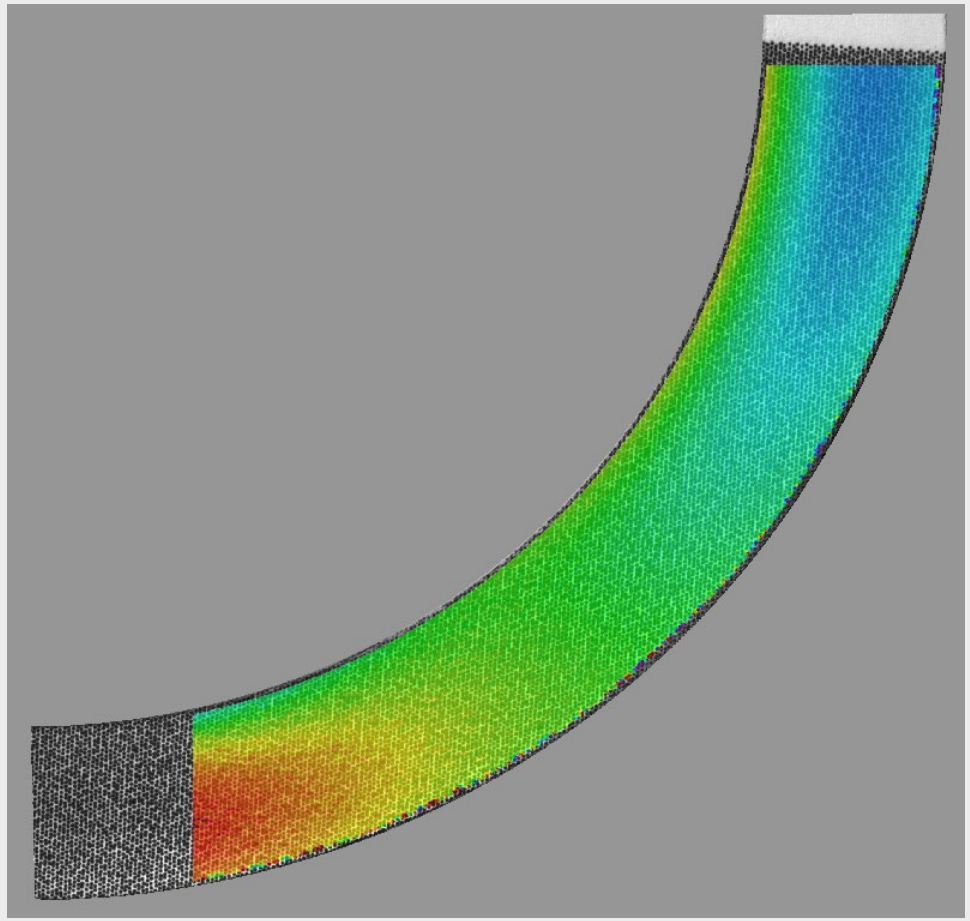

Last load step - $\varepsilon_{\theta\theta}(\mu\varepsilon)$

Experimental

FE - DT

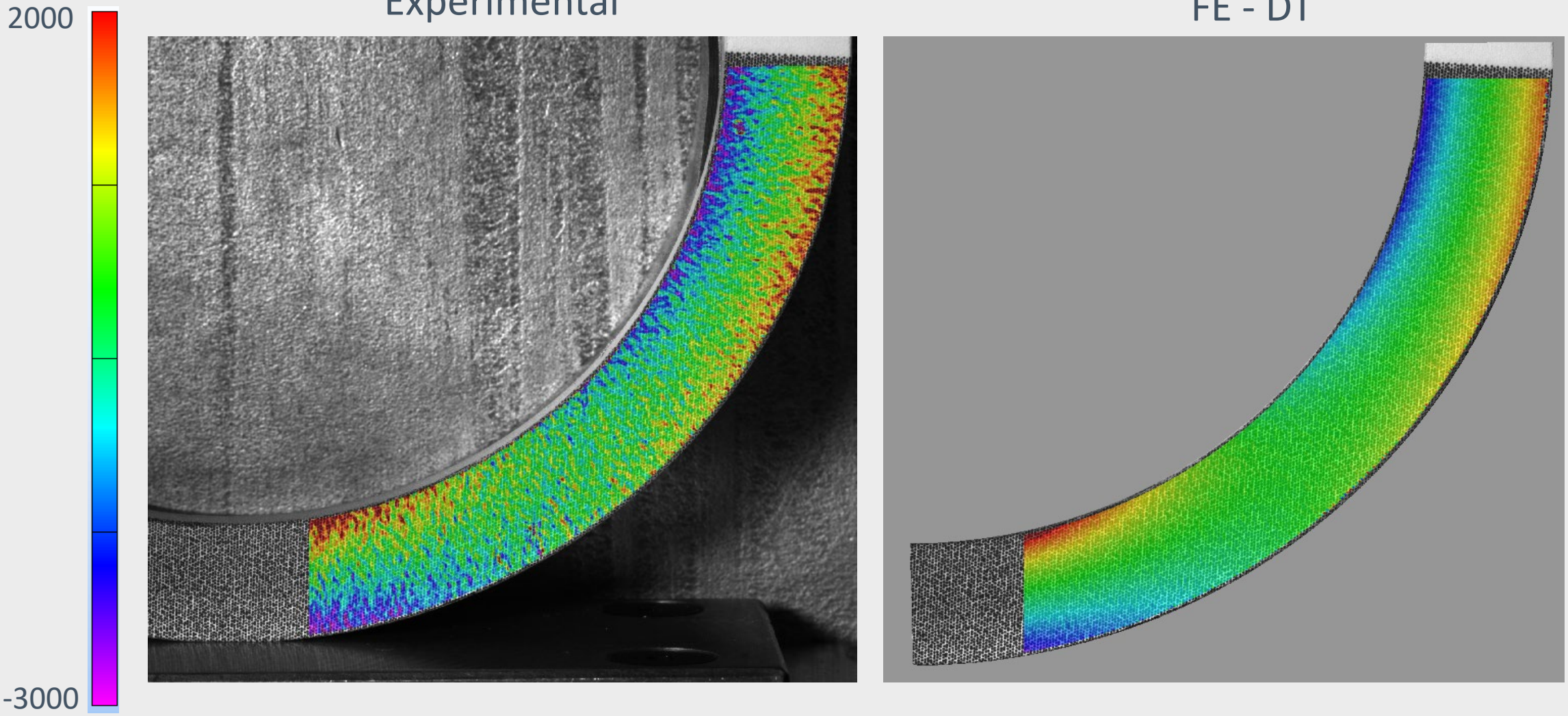

Last load step - $\varepsilon_{r\theta}(\mu\varepsilon)$



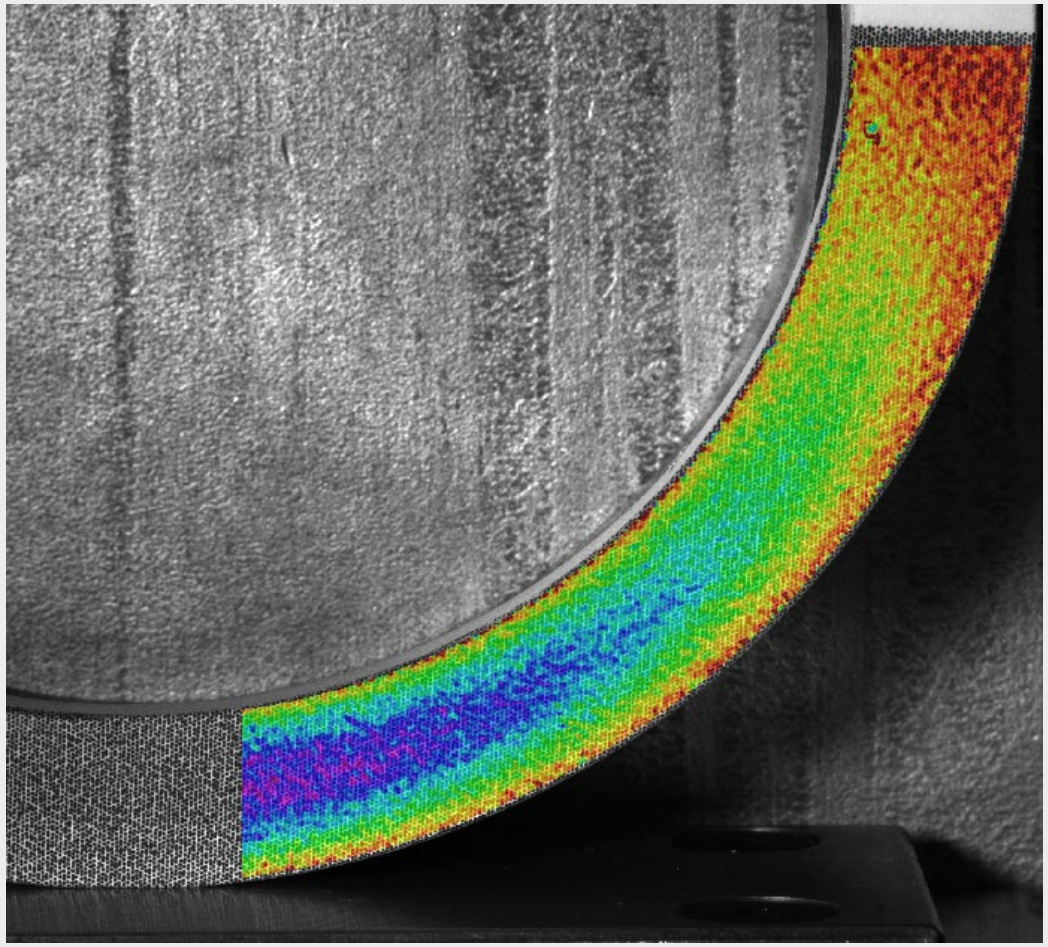

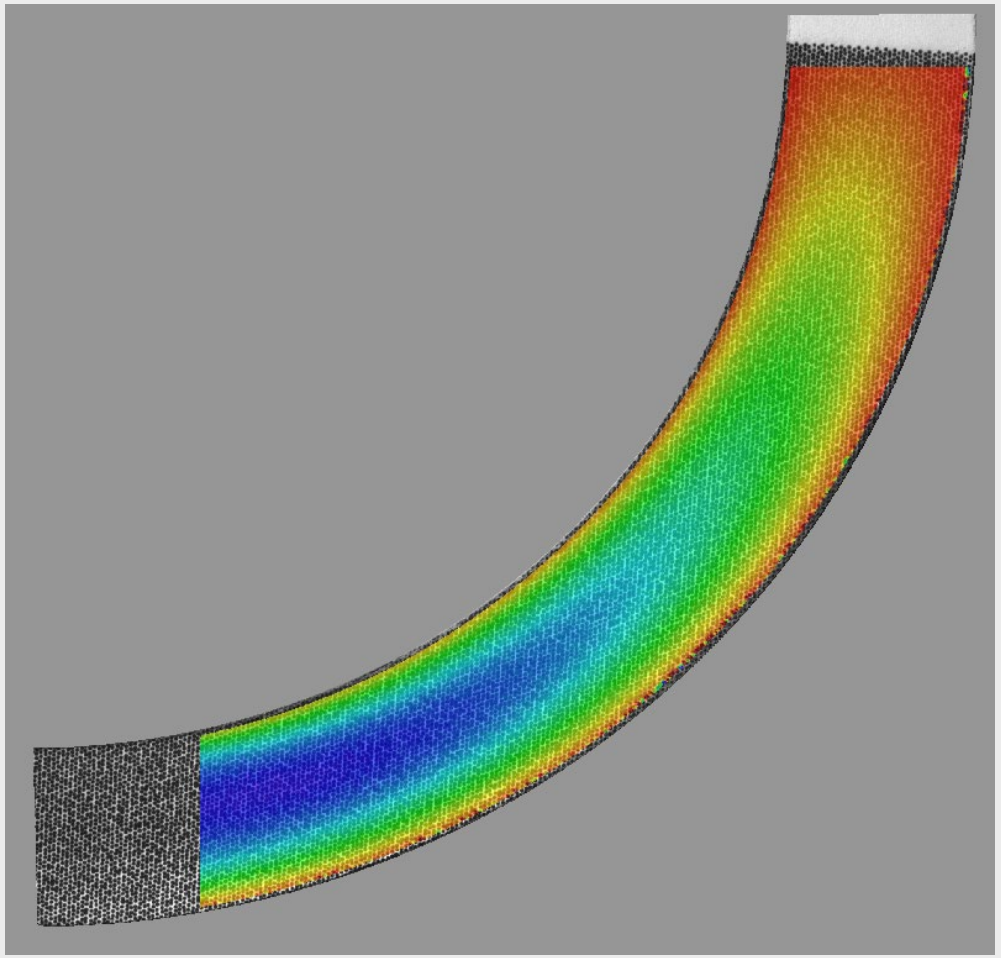

Sensitivity virtual fields

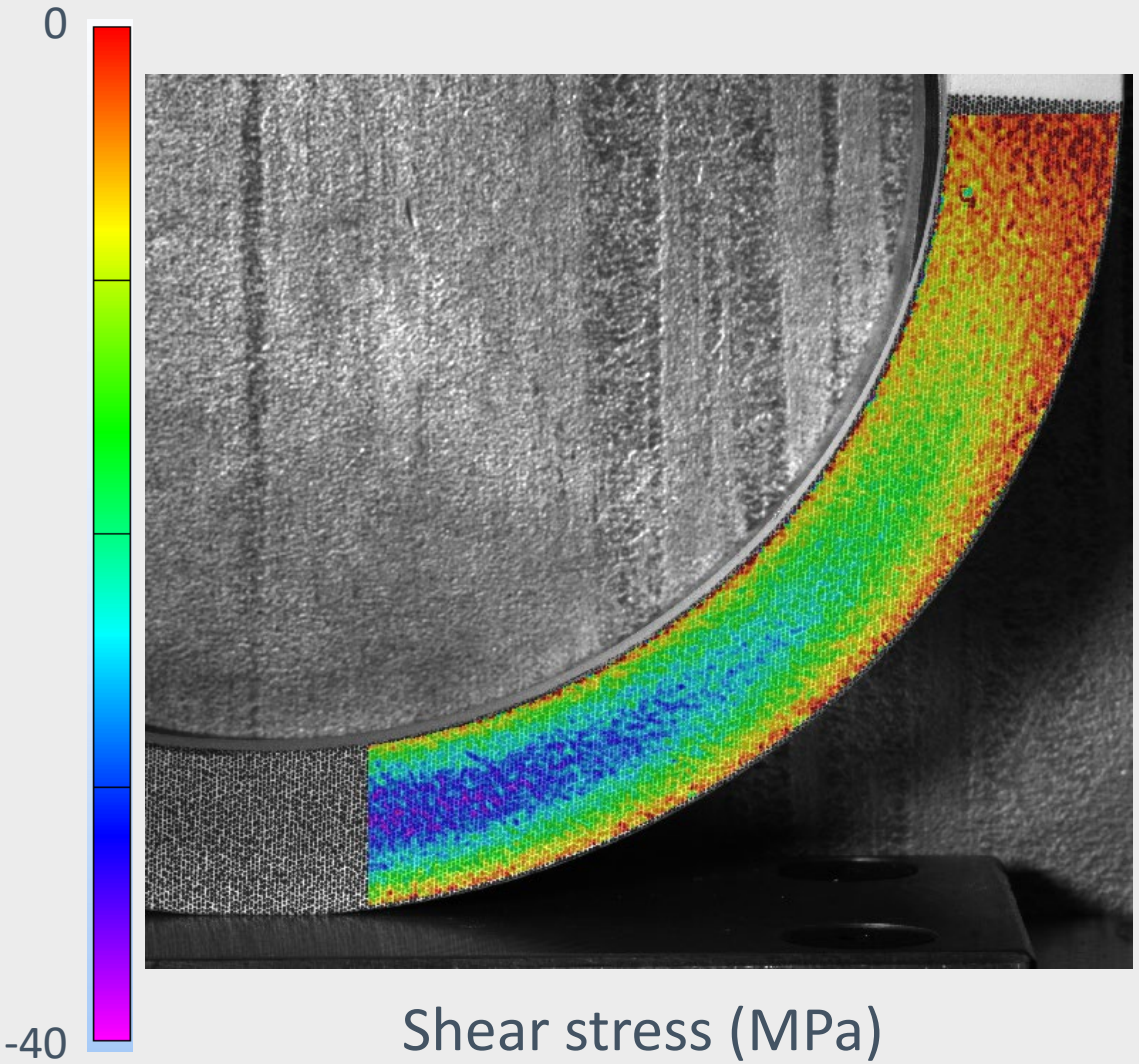

Shear stress (MPa)

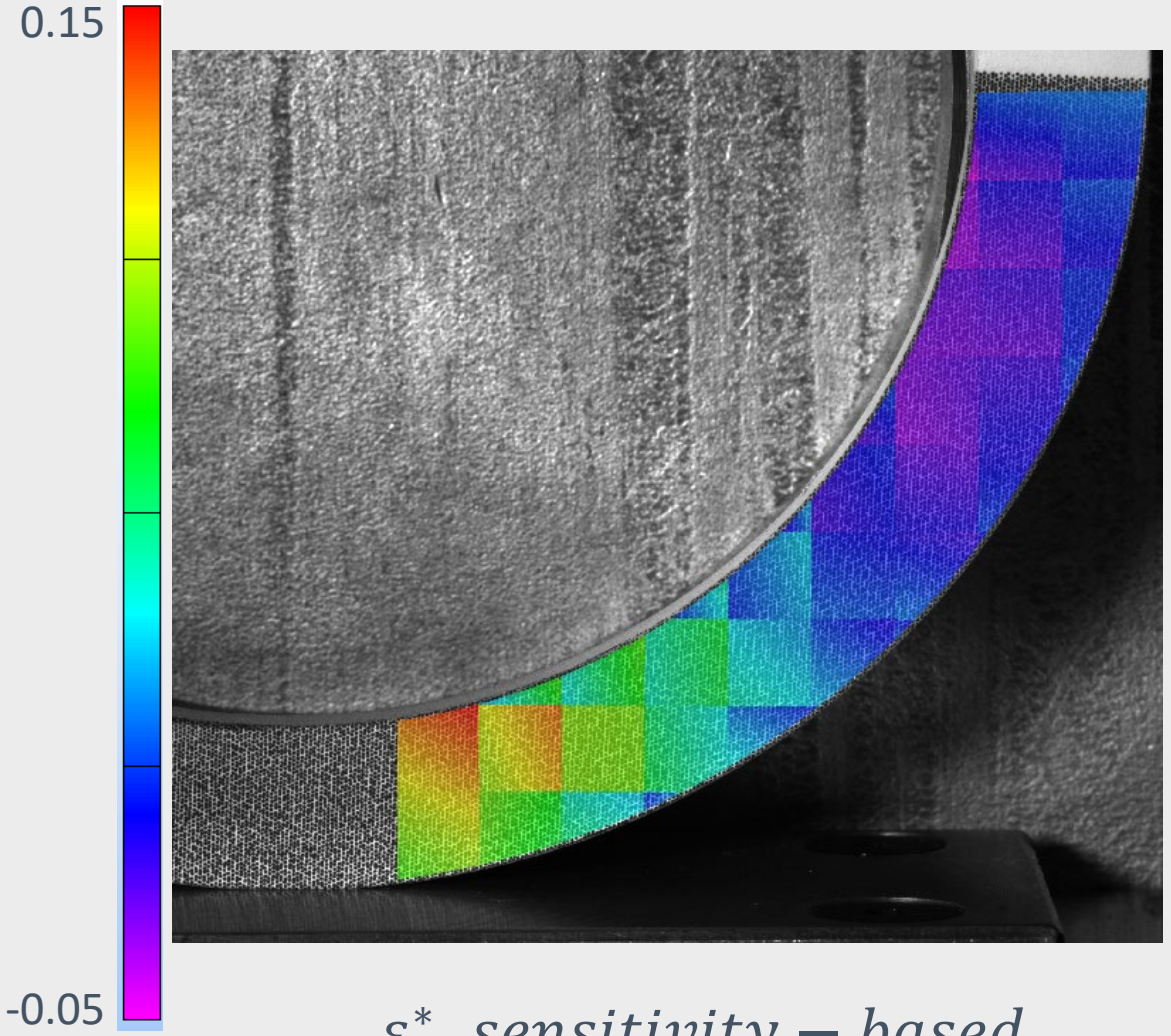

ε_{ss}^{*} *sensitivity – based*

Identification results

- VFM settings:

Strain window	Virtual mesh
5	9 x 9
10	9 x 9
10	6 x 6

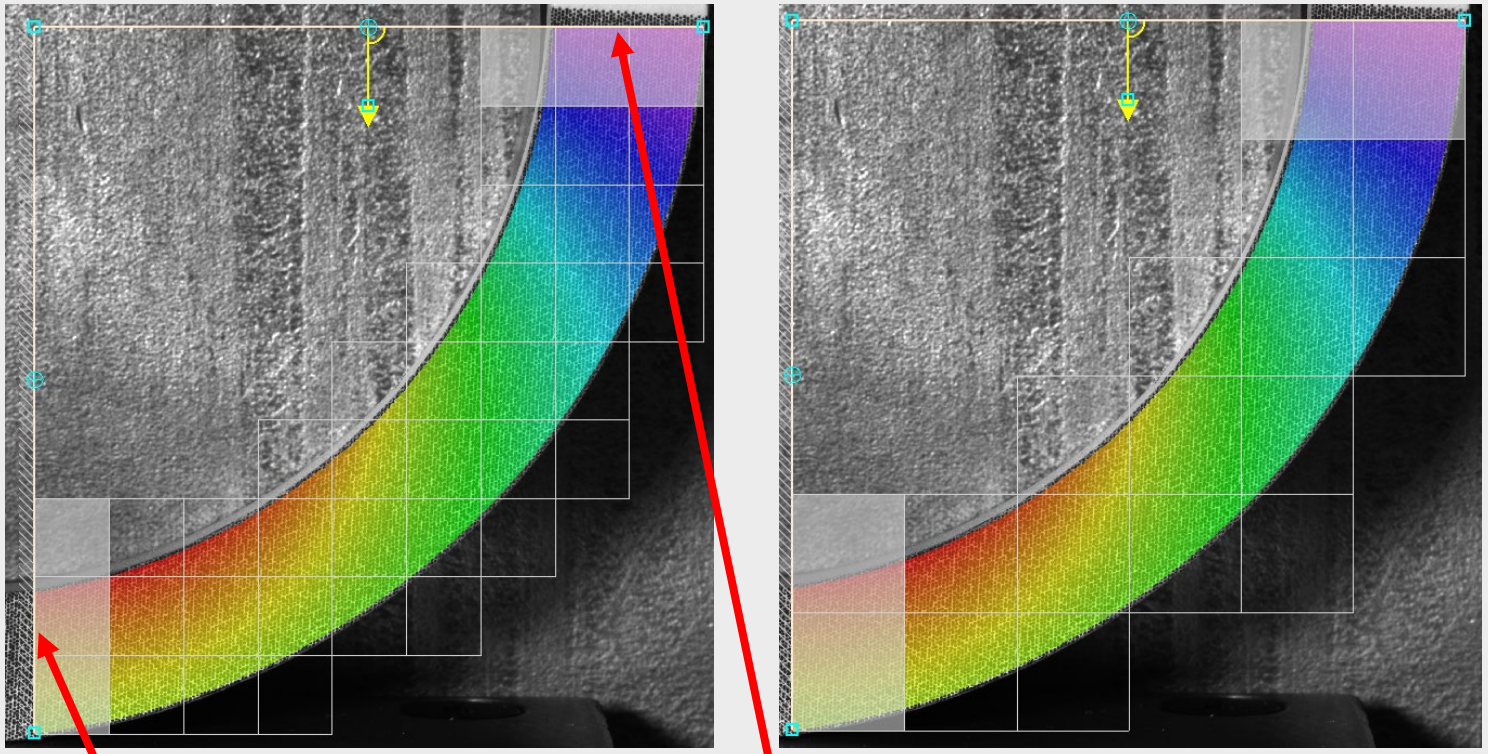

- Virtual boundary conditions

All virtual dofs fixed

Horizontal fixed
Vertical: constant

Results

- All load steps (5), all VFM settings (3), 15 results

	$E_{rr}\ (GPa)$	$E_{\theta\theta}\ (GPa)$	$\nu_{\theta r}\ (-)$	$G_{r\theta}\ (GPa)$
Mean	7.04	101	0.51	3.09
Coef. Var (%)	7.7	3.0	19	2.2

- Last load step (VFM sensitivity)

	$E_{rr}\ (GPa)$	$E_{\theta\theta}\ (GPa)$	$\nu_{\theta r}\ (-)$	$G_{r\theta}\ (GPa)$
Mean	7.82	106	0.54	3.06
Coef. Var (%)	0.2	1.3	8.4	0.9

Identification from Digital Twin

	$E_{rr}\ (GPa)$	$E_{\theta\theta}\ (GPa)$	$\nu_{\theta r}\ (-)$	$G_{r\theta}\ (GPa)$
Reference	7.82	106	0.54	3.06
Identified	8.35	157	0.26	3.61
Ref/Id.	0.93	0.67	2.07	0.85

Reason: missing edges*

Amplified by bending deformation

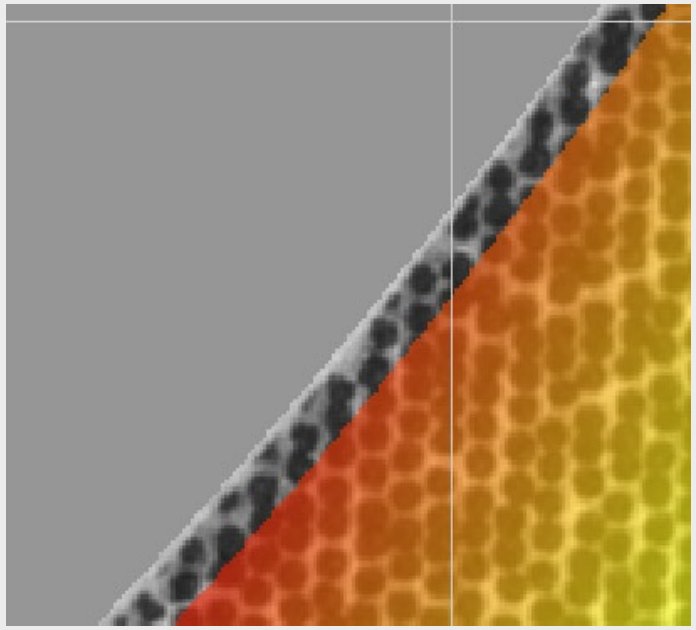

Underway: data padding approach

*Rossi, M., & Pierron, F. (2012). *Int. J. of Sol. and Struct., 49(3-4), 420-435.*

Corrected identified values

	$E_{rr}\ (GPa)$	$E_{\theta\theta}\ (GPa)$	$\nu_{\theta r}\ (-)$	$G_{r\theta}\ (GPa)$
Initial	7.82	106	0.54	3.06
Corrected	7.32	71.6	1.12	2.59

Possible shear nonlinearity

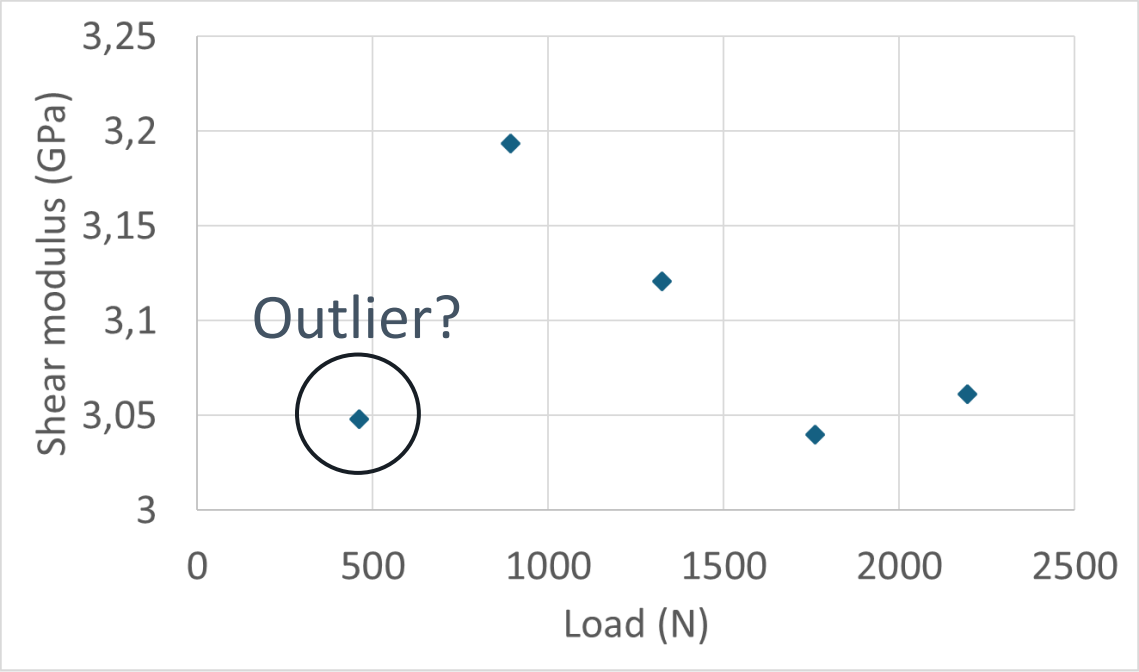

Conclusions

- Operational tool for MT2.0 on composites
- Outstanding feature: edge padding (underway)
- Digital Twin:
  - UQ
  - Correction of systematic errors
- Future work
  - Apply to other configurations
  - New standards

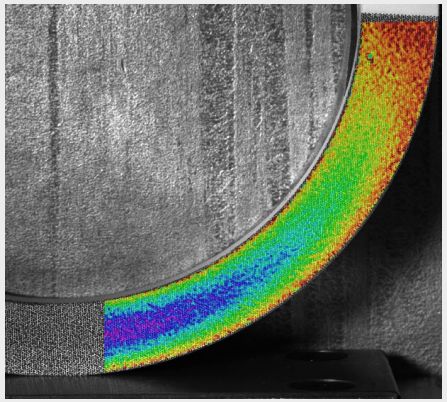

	$E_{rr}\ (GPa)$	$E_{\theta\theta}\ (GPa)$	$\nu_{\theta r}\ (-)$	$G_{r\theta}\ (GPa)$
Initial	7.82	106	0.54	3.06
Corrected	7.32	71.6	1.12	2.59

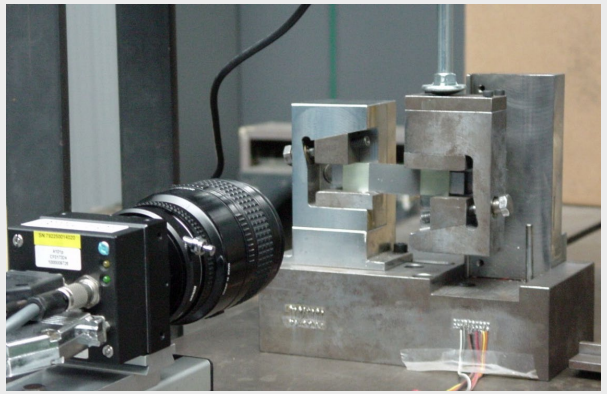

MatchID

Metrology beyond colors

Thank you for your attention

isabella.m.jacobsen@matchid.us

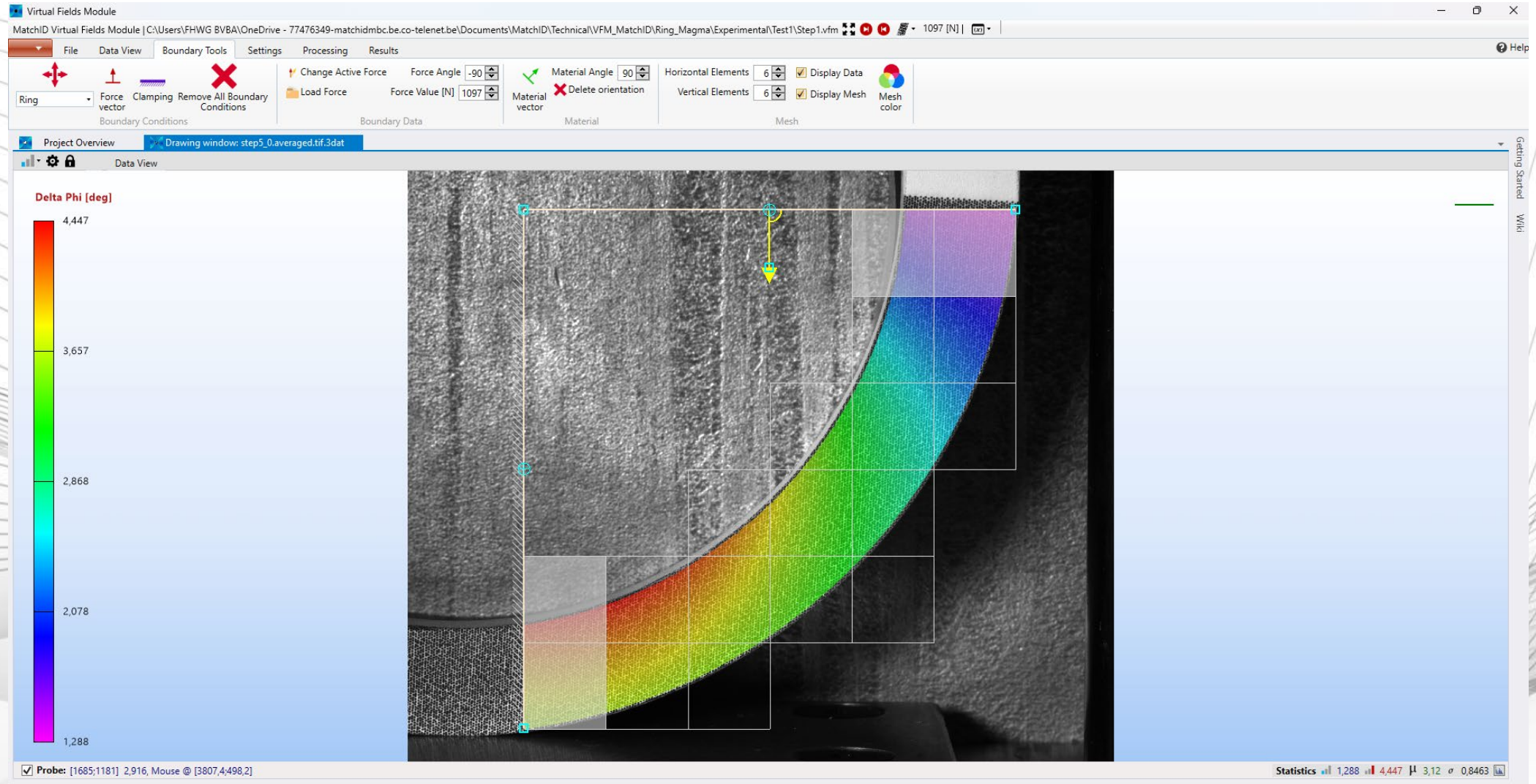

Development of Flame-retardant Medium Density Wood Fibreboards using Phosphorylated Casein and Polyamidoamine-epichlorohydrin Resin

Hanbin Lee, Nam Kyeun Kim and Debes Bhattacharyya

Centre for Advanced Materials Manufacturing and Design, The Department of Mechanical and Mechatronics Engineering, The University of Auckland, New Zealand

ICCM-24 Baltimore, Aug 4 – Aug 8, 2025

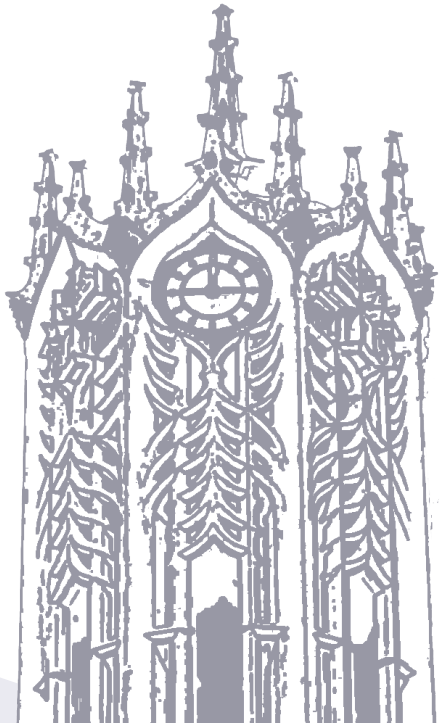

CENTRE FOR ADVANCED MATERIALS MANUFACTURING & DESIGN

UNIVERSITY OF AUCKLAND
Waipapa Taumata Rau
NEW ZEALAND

Background

Medium Density Fibreboard

- A type of engineering wood product
- Consisting of wood fibre and binder
- Good quality of surface

Application

- ❑ Furniture
- ❑ kitchen cabinets
- ❑ Mouldings
- ❑ door parts
- ❑ laminate flooring



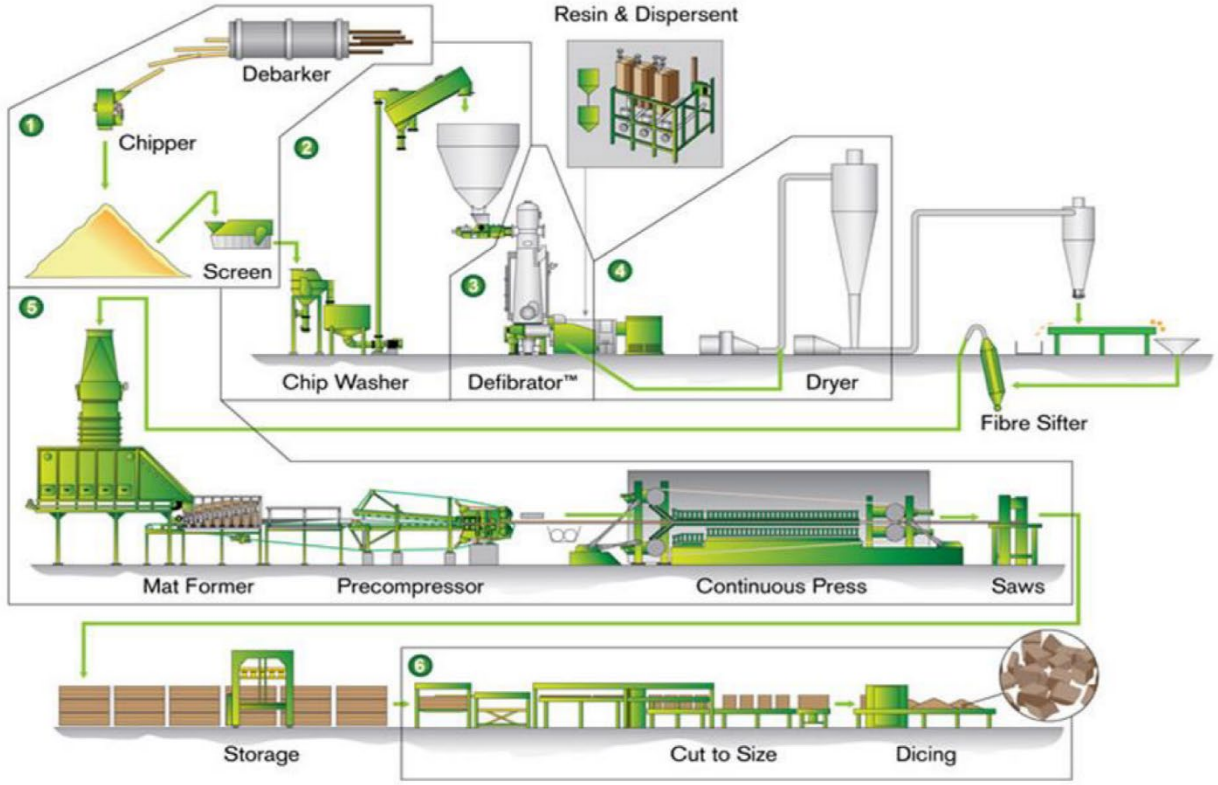

1. Getting wood chips from pulp, waste, residual wood and logging
2. Removing impurities from chips after screening
3. Refining wood chips using pressurised refiners (pressurised disk refining)
4. Blending wood fibres with binders and sometimes wax
5. Forming a mat and hot pressing
6. Cooling and cutting to size

Background

Fire Resistant Study

- (In 1963) Inorganic chemicals in solid pine wood, analysed by residual char weight measurement; Browne & Tang
- (In 1983) Polyurethan-based FR coating on plywood surfaces in the ASTM E119-20; White et al
- (In 2012) Nanoclay in UF-based MDF, analysed by TGA; Reza et al
- (In 2019) Combination of different types of chemicals in MUF-based MDF, analysed by cone calorimeter; George et al

Binder Toxicology Study

- (In 1992) Suspected formaldehyde emission from pressed-wood products; Oston & Fellin
- (In 1998) Regulated formaldehyde emission from building materials; Kavvouras et al
- (In 2004) Categorised formaldehyde as carcinogenic for humans; Gatlin et al
- (In 2013) MUF culminating the desirable bonding strength of MDF, but still higher emission of the formaldehyde; Zhang et al
- (In 2018) Combination of UF and MF complying with formaldehyde emission regulations (EC-32-17); Zhang et al

Challenges

Fire hazard

- (In 2007) The addition of 6 % inorganic salts, such as borax and diammonium phosphate, decreased the internal bond strength by ~33 % in the PF-based MDF samples; Ayrilmis et al
- (In 2009) The incorporation of 30 % mineral-based chemicals, such as sodium aluminate and aluminium trihydrate, dropped the internal bond strength of the UF-based MDF samples by ~26 %; Hashim et al

➢ Corrosive side effect
➢ Toxic fumes (during combustion)
➢ Mechanical properties drops

Toxic binder

- (In 2000) Adverse health effects (nausea, eye, and throat irritation) in humans at more than 0.1 mg/L airborne formaldehyde concentration ; Athanassiadou
- MDF products made in NZ based on a MUF binder have 0.3 mg/L formaldehyde emission that complies with JIA A 5905 standard (Max. 0.5 mg/L of formaldehyde emission)

➢ Residual formaldehyde in the binder
➢ Process of the binder manufacture
➢ Hydrolytic degradation of the cured binder, particularly under high temperature and humidity

Motivation and Concept

- **Combination binder system**

Polyamidoamine-epichlorohydrin (PAE)

- ✓ Relatively low toxicity
- ✓ Good bonding with natural materials

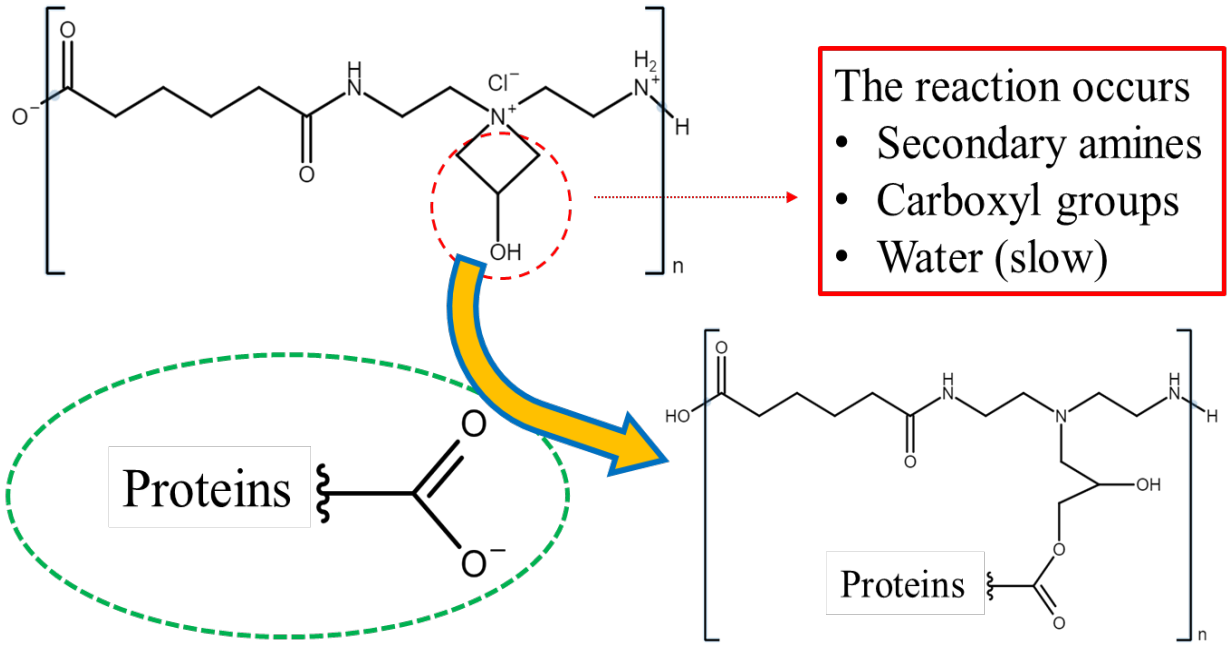

Casein

- ✓ Char forming ability due to a rich of acid sources and blowing agents (carboxyl/sialic groups & amine groups)
- ✓ The excellent flame-retardant performance of casein has been identified in different material systems (textile substrates and polymer composites); Alongi et al and Zhang et al

Material and Manufacturing Parameters

- Material composition of MDF panels

Sample	PAE (%)	Casein (%)	Moisture content (%)
4.4PAE8	4.4	-	8
4.4PAE8 30CP	4.4	30	8

- Manufacturing parameters

Resin content (%)	Moisture content (%)	Hot-pressing time (s)	Hot-pressing temperature (°C)	Target density (kg/m^3)
4.4	8	150	180	**750**

✓ Moisture content (MC) and the resin ratio were suggested from the supplier.

✓ Parameters are from the previous research regarding formaldehyde-free resin-based MDF manufacture.

✓ The resin system is a combination of modified soy flour and PAE resin.

✓ A density range of MDF is 650 – 800 kg/m^3

Manufacture of Casein-based MDF

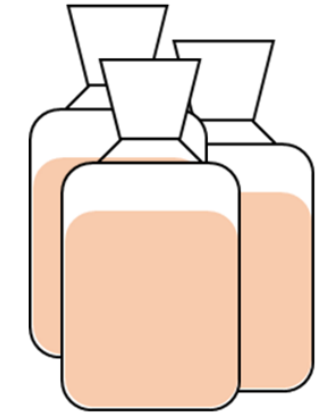

Wood fibres

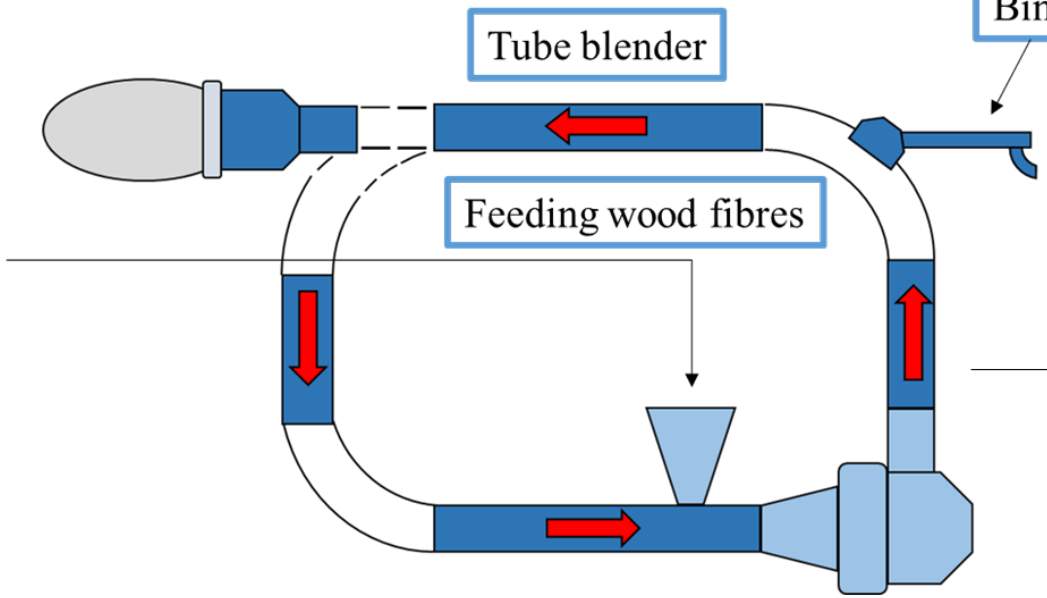

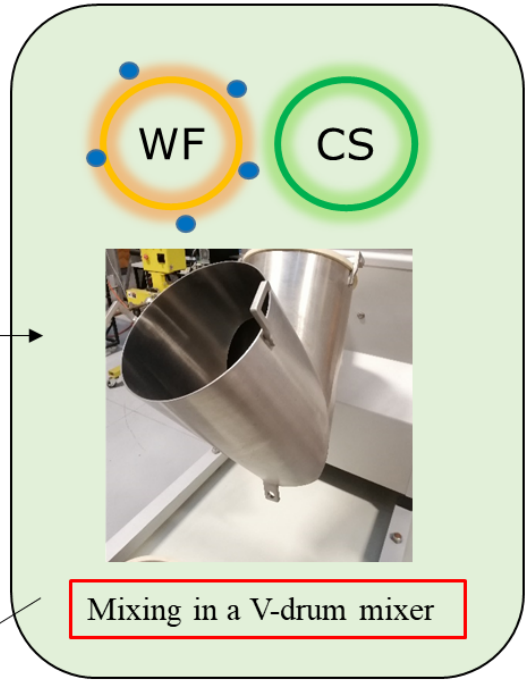

Mixing in a V-drum mixer

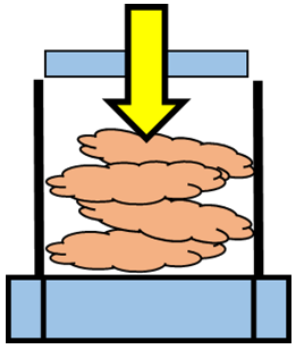

Pre-pressing and mat forming

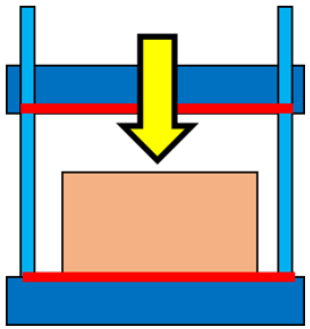

Hot pressing

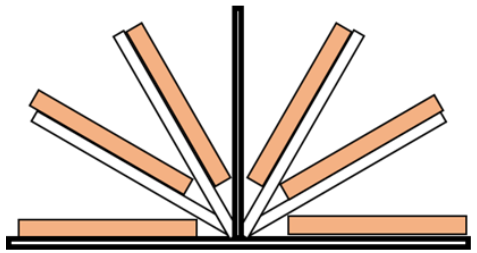

Cooling

- Wood fibres (WF) that have been sprayed with binders are mixed with casein particles in a mechanical mixer.

Heat Release Rate

- **Effect of casein on heat release rate of MDF**

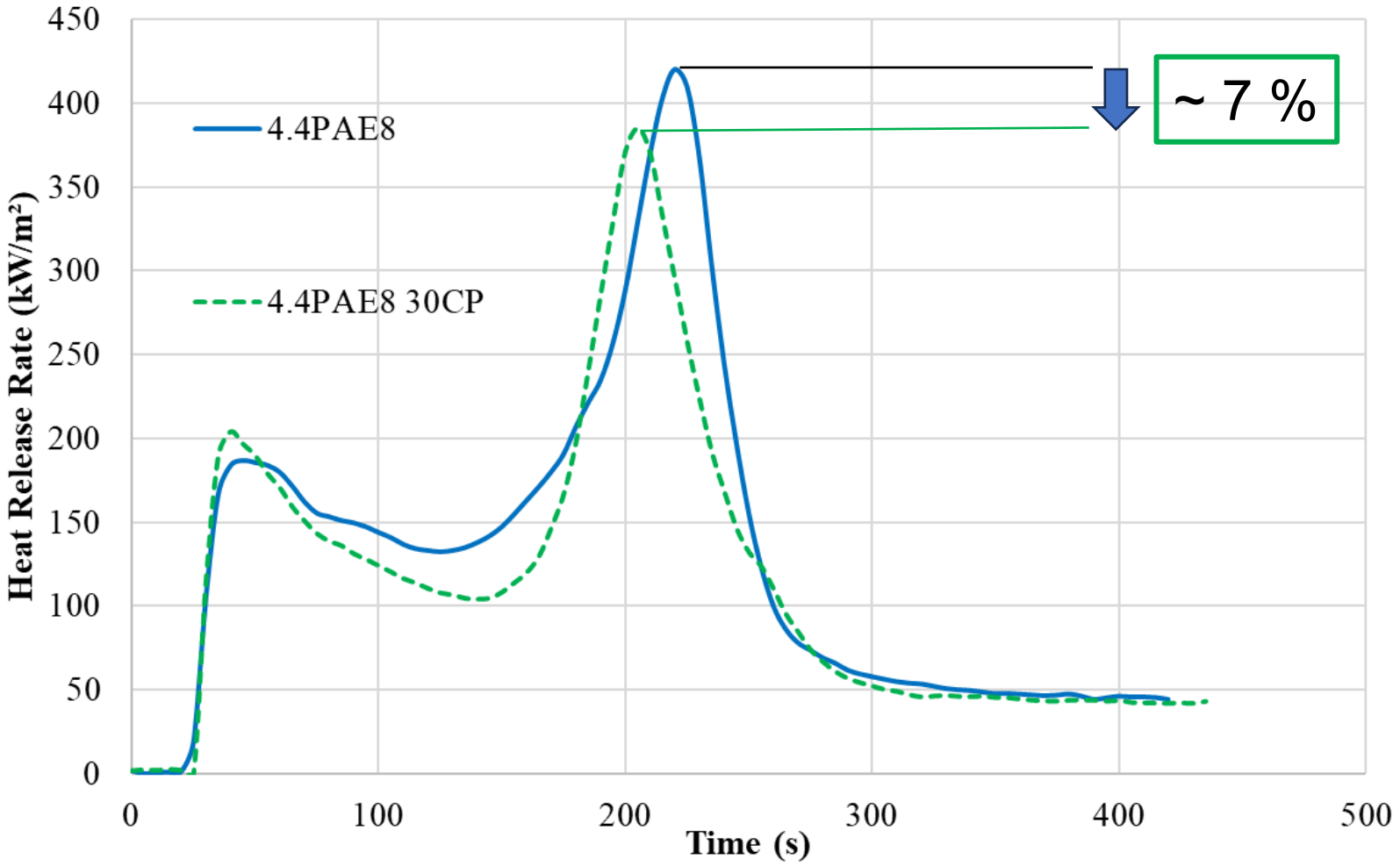

Heat release rate (HRR)

- ✓ The rate of fire growth
- ✓ The size of the fire
- ✓ An effective heat of combustion

The addition of 30 % casein particles reduces the peak heat release rate of the MDF sample by ~ 7 %.

Mechanical Properties

- **Mechanical properties of PAE-based MDF samples using casein particles**

➢ **Flexural strength**

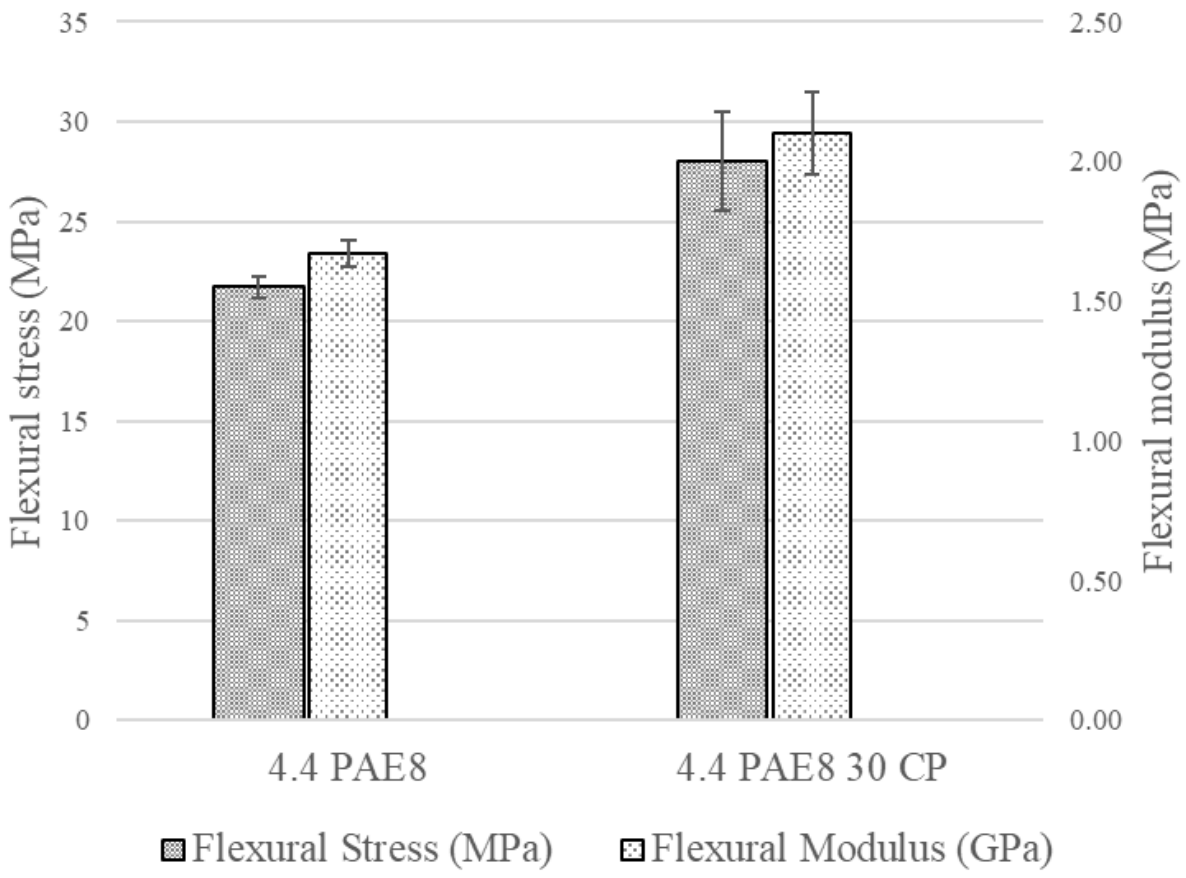

➢ **Internal bond (IB) strength**

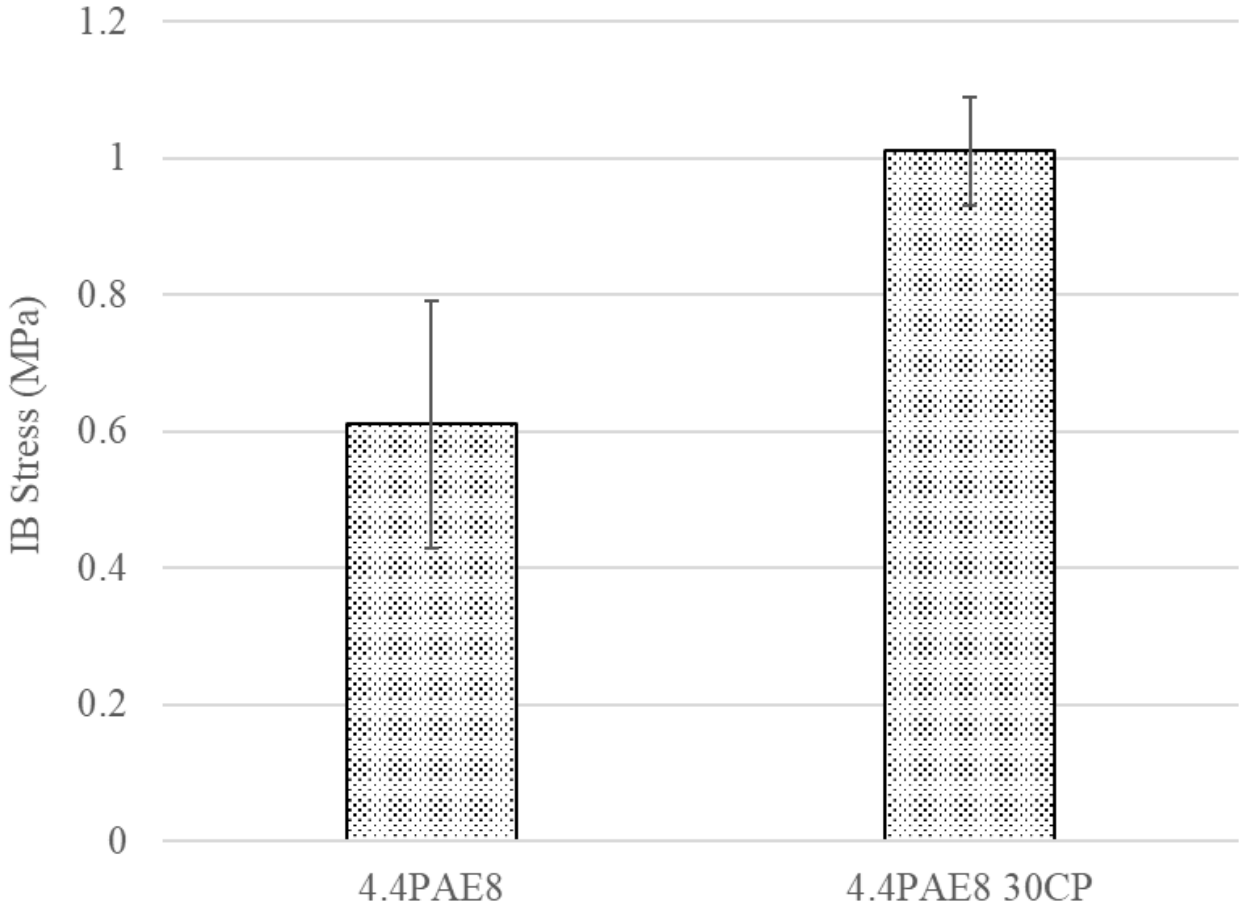

Phosphorylation of Casein

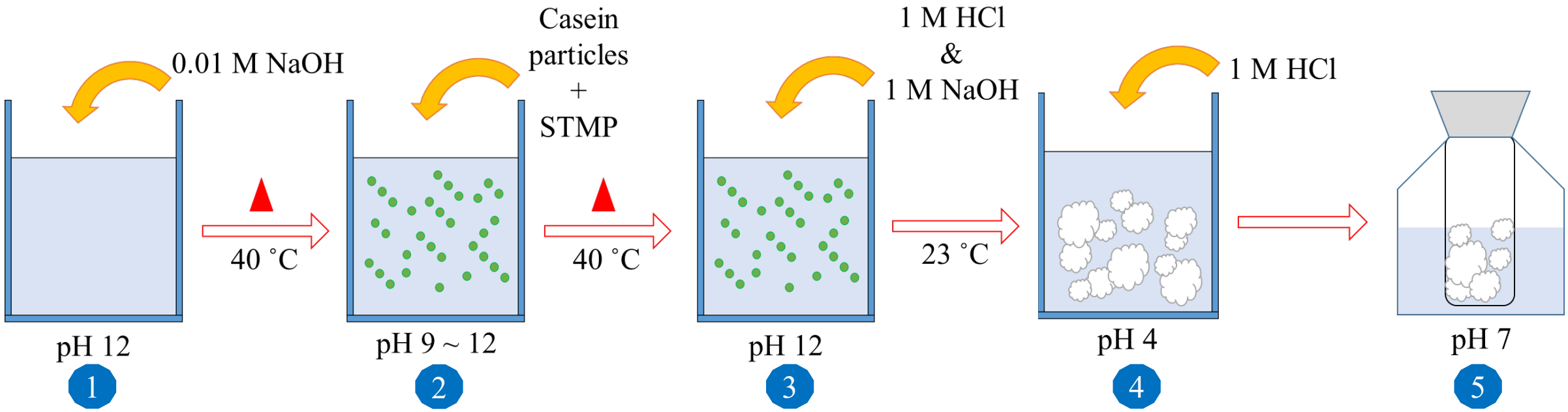

1. Preparing 0.01 M sodium hydroxide (NaOH) solution to make a pH 12 environment. Heating the NaOH solution at 40 ˚C.
2. Casein particles are added when the solution temperature reaches 40 ˚C. Sodium trimetaphosphate (STMP) is slowly added. (when STMP is added, the pH value decreases due to the reaction)
3. Dropping 1 M hydrogen chloride (HCl) or NaOH in the casein-STMP solution to remain the pH value at 12. Total reaction time is 1 hour.
4. Quenching the reaction by the removal of the heat. Decreasing the pH value at 4 by dropwise addition of 1 M HCl.
5. Collecting the treated casein curd by a coffee sieve and washing them with distilled water.

Fourier Transform Infrared Spectroscopy

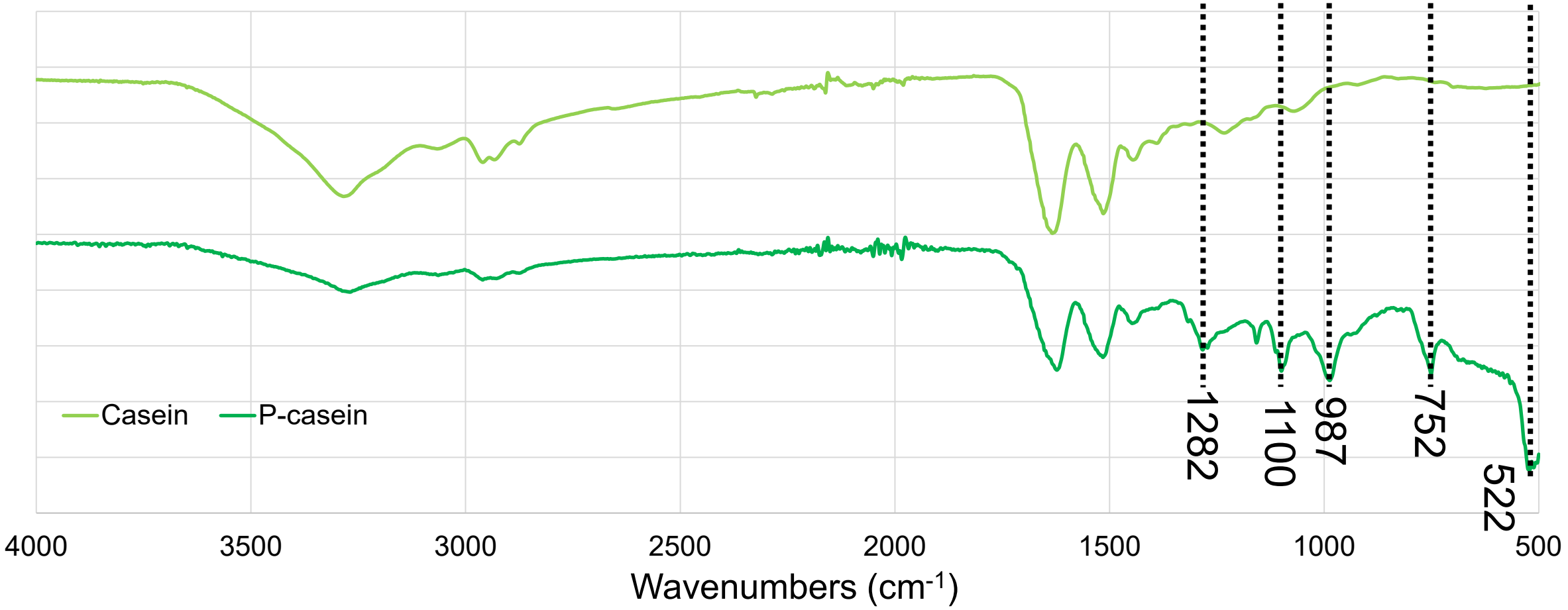

- 752 cm^{-1} is the most important peak to identify the bonding formation of hydroxide groups (casein) and phosphate groups (STMP) through phosphorylation.
- Other vibration bands; 522, 987, 1100, and 1282 cm^{-1} are attributed to O-P-O, P-OH, P-OH, and P=O stretching, respectively.

Energy dispersive X-ray (EDX)

- **Elemental composition of casein and phosphorylated casein**

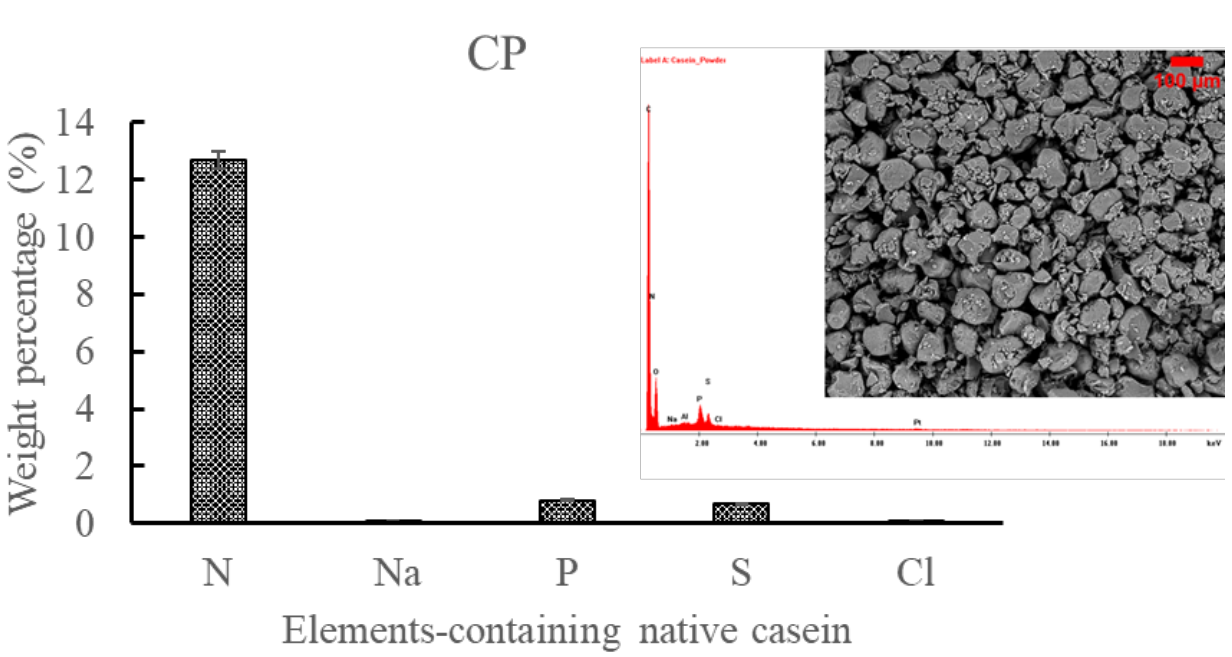

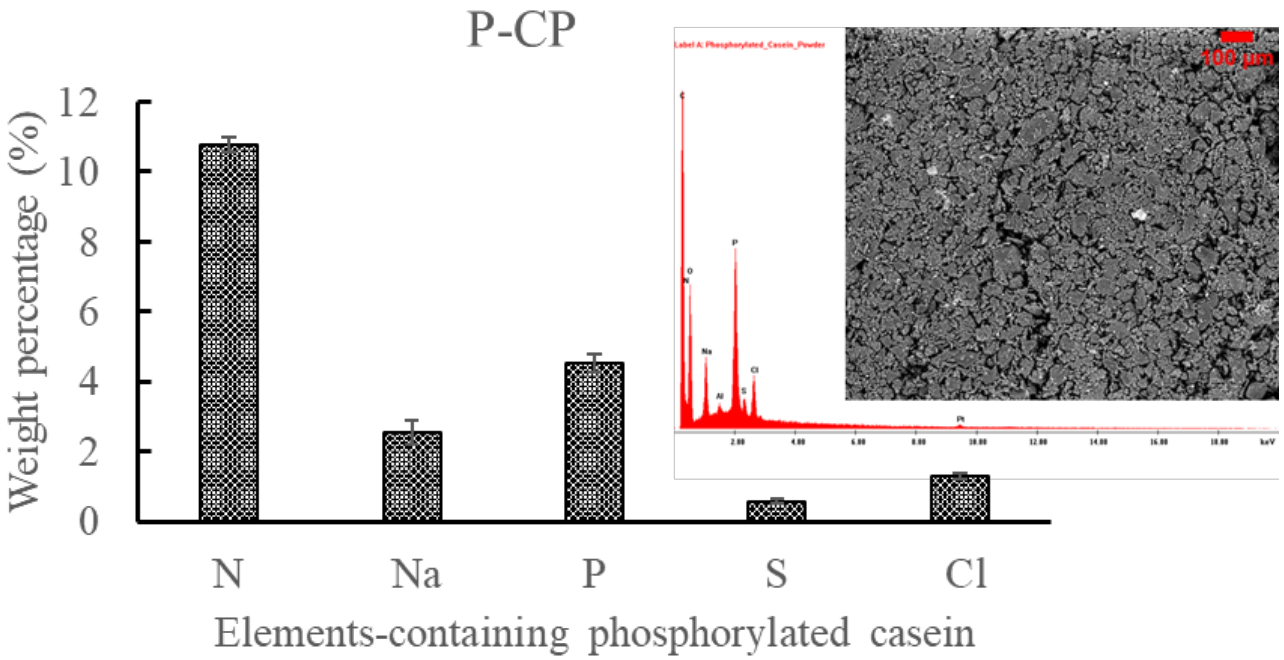

✓ Sodium (Na) and choline (Cl) contents in the structure of the phosphorylated casein increase by 2.3 % and 1.6 %, respectively.

Heat Release Rate

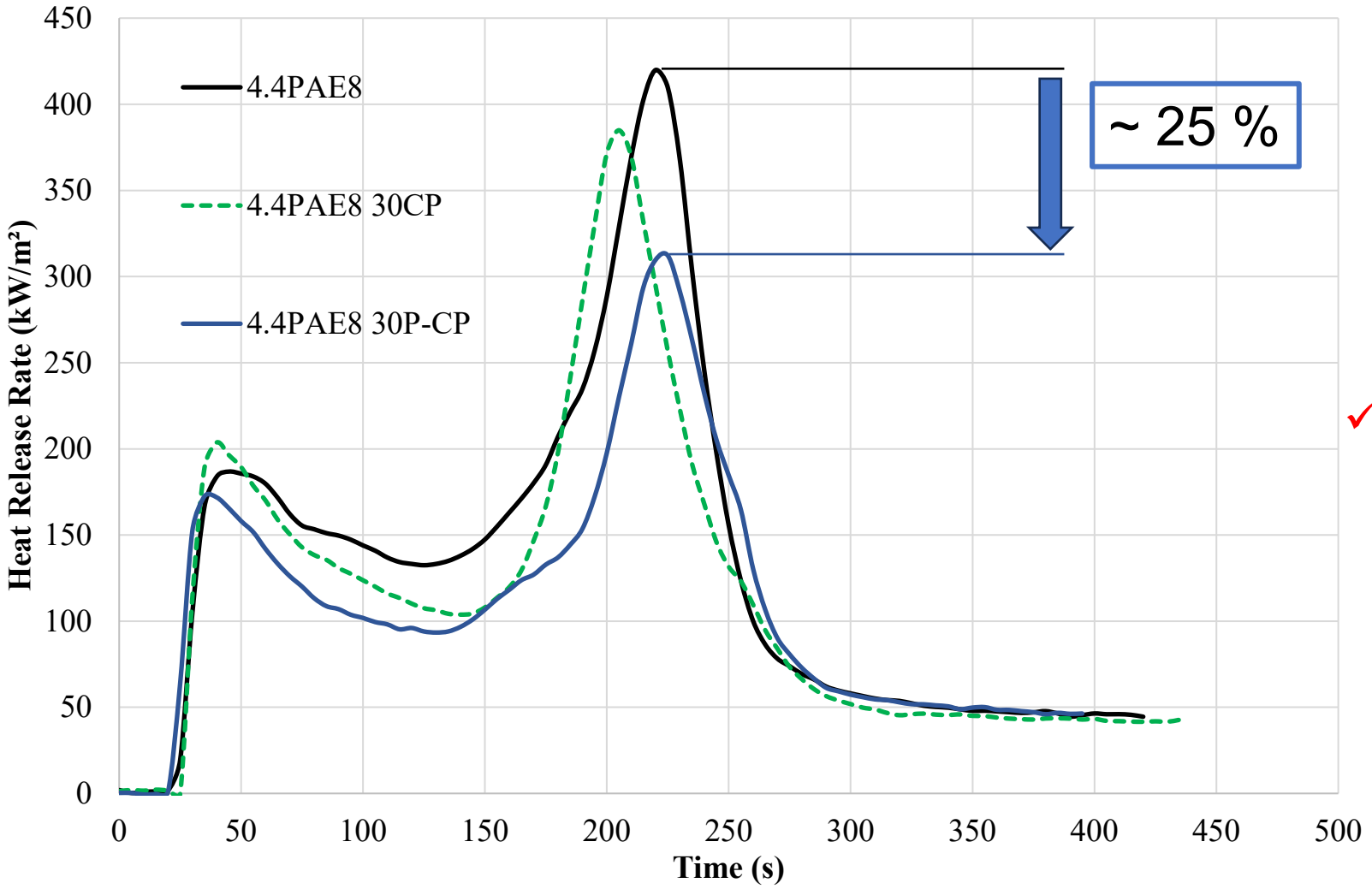

Heat release rate (HRR)

- ✓ The rate of fire growth
- ✓ The size of the fire
- ✓ An effective heat of combustion

✓ **The addition of 30 % phosphorylated casein particles most effectively reduces the peak heat release rate of the MDF sample by ~ 25 %.**

Mechanical Properties

- **Effects of 30 % P-CP addition on mechanical properties of 4.4PAE8 MDF**

➢ **Flexural strength**

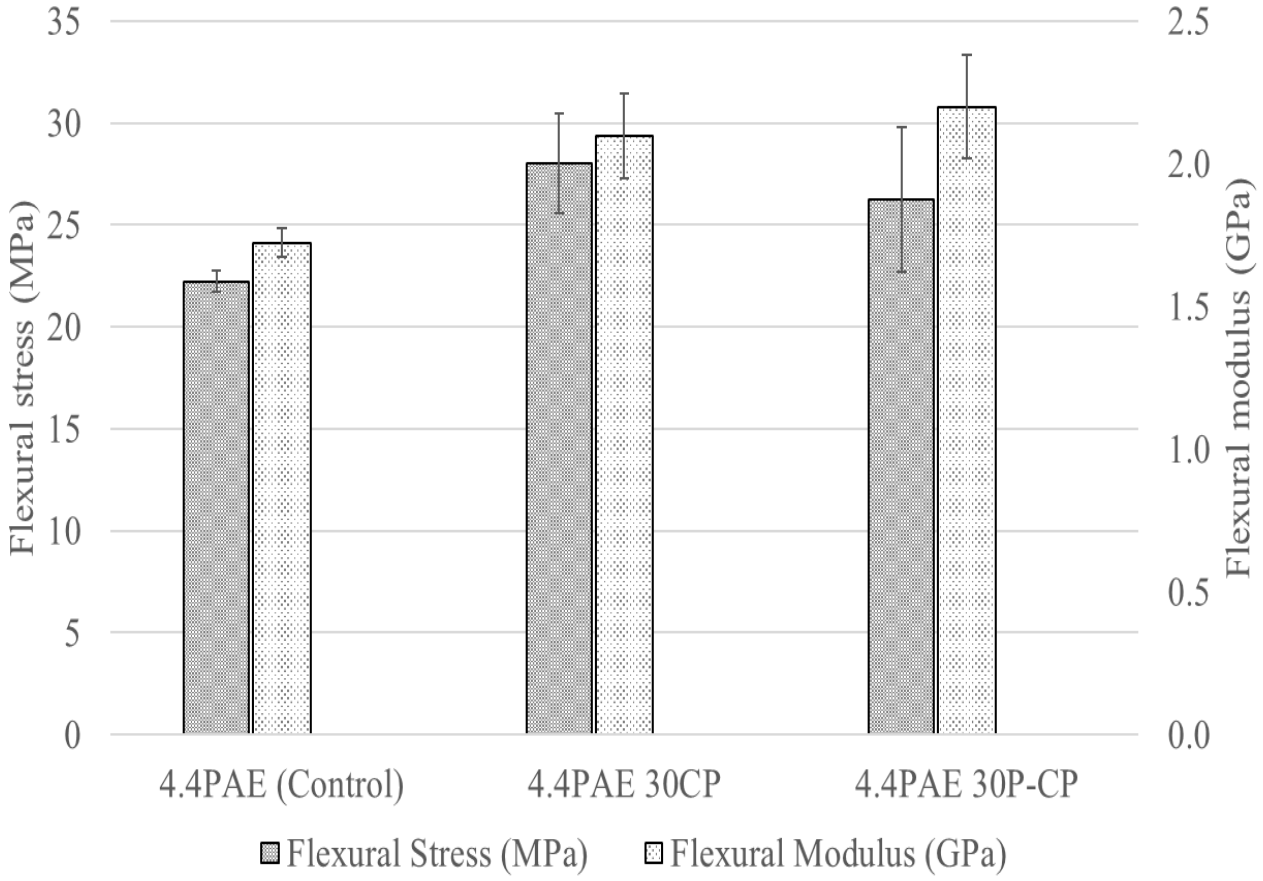

➢ **Internal bond (IB) strength**

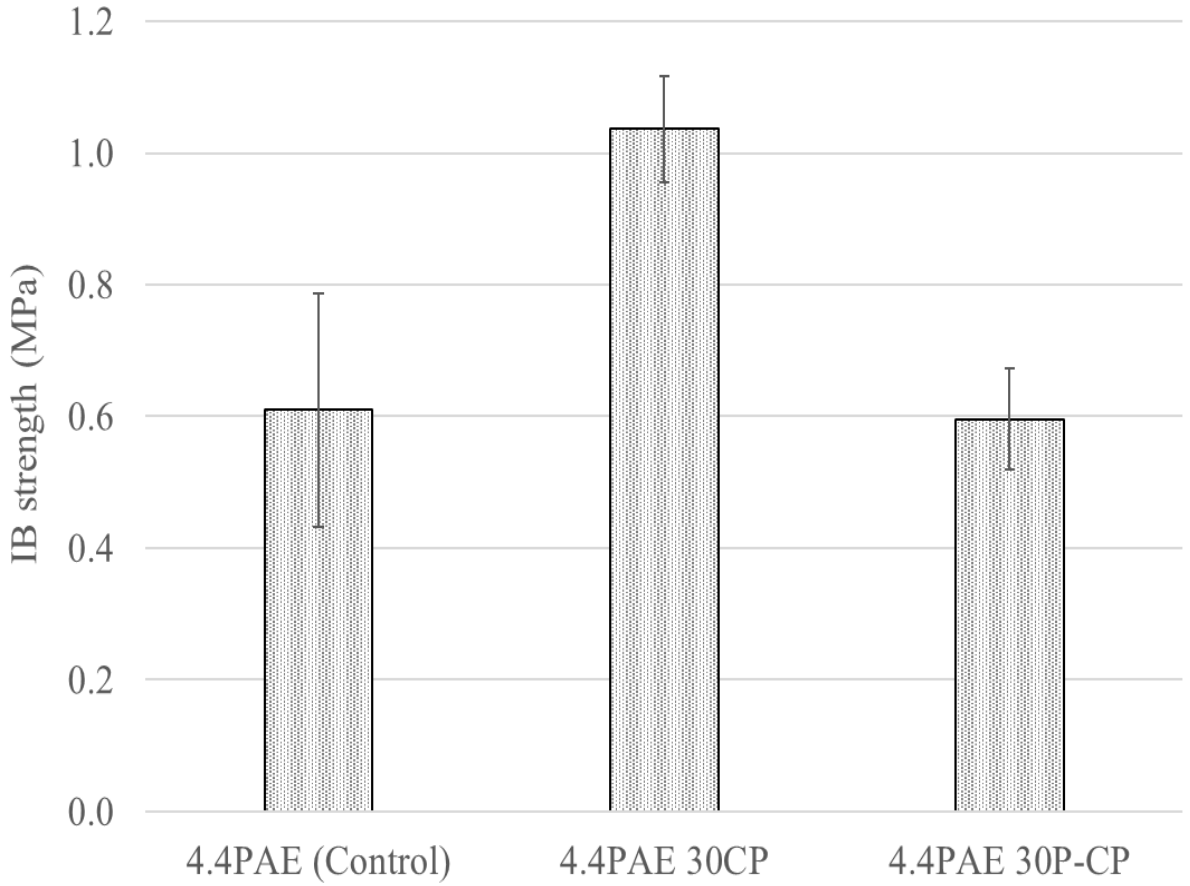

Hypothetical Reaction Disturbance

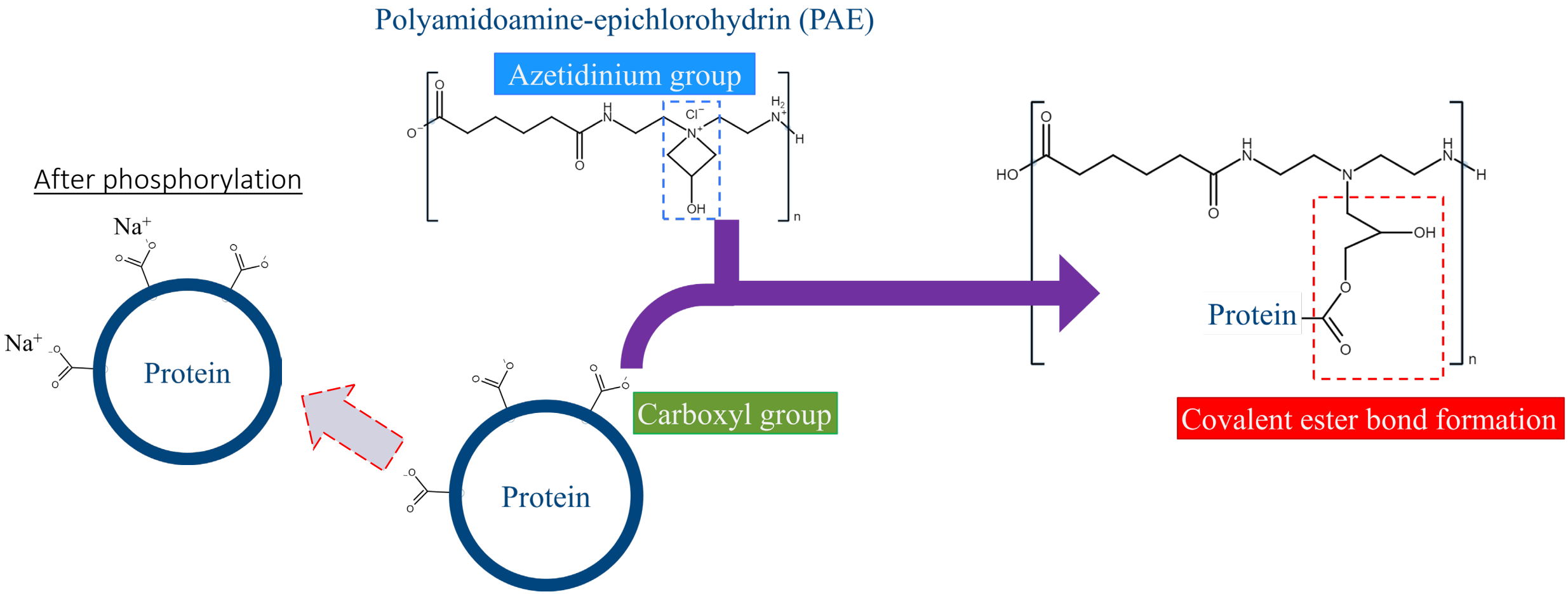

- ✓ It is assumed that sodium carboxylate (-COONa) like a sodium salt may not function as a carboxyl group capable of reacting with the azetidinium group of the PAE.

Conclusions

- Casein was successfully phosphorylated to improve its char forming capability.
- MDF panels with density of ~730 kg/m^3 were manufactured using casein powder and PAE resin as a formaldehyde-free binder.
- Phosphorylated casein reduced peak heat release rate (~ 25%) of MDF with more effective char formation in comparison with one of the panel with non-treated casein.
- The addition of phosphorylated casein to the MDF improved both flexural modulus (23 %) and stress (16 %), compared to the panel with non-treated casein.
- Phosphorylation of casein retained internal bond strength of MDF.

DEVELOPMENT AND SYNTHESIS OF NOVEL DOPO-MODIFIED EPOXY RESIN AND ITS GLASS AND SISAL-BASED 3D WOVEN FIBER-REINFORCED COMPOSITE

Shubham Agnihotri[1], Javed Sheikh[2], S.P Singh[3], B.K Behera[4]

[1]School of Interdisciplinary Research, Indian Institute of Technology, Delhi
Hauz Khas, New Delhi, India-110016
Email : srz218574@sire.iitd.ac.in

[2]Department of Textile and Fiber Engineering, Indian Institute of Technology, Delhi
Hauz Khas, New Delhi, India-110016
Email : jnsheikh@iitd.ac.in , web page : https://textile.iitd.ac.in

[3]Department of Mechanical Engineering, Indian Institute of Technology, Delhi
Hauz Khas, New Delhi, India-110016
Email: singhsp@mech.iitd.ac.in, web page: https://textile.iitd.ac.in

[4]Department of Textile and Fiber Engineering, Indian Institute of Technology, Delhi
Hauz Khas, New Delhi, India-110016
Email : behera@iitd.ac.in , web page : https://textile.iitd.ac.in

Keywords: flame retardant resin, 3D woven fiber reinforced composite, Glass fiber, Sisal fiber

ABSTRACT

The growing demand for advanced materials in the construction industry has led to an increased focus on developing flame-retardant and mechanically robust composites. Epoxy resins, known for their excellent adhesive and mechanical properties, have become popular for matrix materials in fiber-reinforced composites. However, conventional epoxy resins are inherently flammable, which limits their applicability in high-temperature or fire-prone environments. This study addresses this limitation by developing and synthesizing a novel flame-retardant epoxy resin with modified 9,10-dihydro-9-oxa-10-phosphaphenanthrene-10-oxide (DOPO). Modified DOPO epoxy resin was synthesized and utilized as a matrix for 3D woven glass and sisal fiber-reinforced composites to enhance their flame-retardant properties. The 3D woven structure of the composite was chosen to improve load-bearing capacity and impact resistance, addressing the limitations of conventional 2D woven or random fiber composites in structural applications. The development of 3D woven glass and sisal fiber reinforced composite was done by VARTM method. The developed resin was characterized by FTIR, ^{1}H NMR, and ^{31}P NMR. The composites were comprehensively characterized to assess their thermal stability and mechanical properties. Flame retardant properties of the composites were determined by limiting oxygen index (LOI), vertical burning tests, and cone calorimetry. Tensile and flexural strength tests are employed to evaluate the changes after modification. The highest LOI value achieved was 29.4. Cone calorimetry analysis demonstrated significant improvement in flame retardancy. The mechanical properties exhibited a decline in both tensile and flexural strength.

1. INTRODUCTION

Fiber-reinforced composites (FRCs) are widely utilized in the construction, automotive, and aerospace sectors owing to their superior mechanical strength, high strength-to-weight ratio, and design flexibility. Epoxy resins, frequently used as matrix components in these composites, provide exceptional mechanical and chemical resistance qualities [1–5]. Nonetheless, their intrinsic flammability considerably restricts their applicability in contexts where fire safety is paramount.

Inorganic (e.g., magnesium hydroxide, boric acid) and organic (e.g., phosphorus- and silicon-based compounds) flame-retardant additives have been integrated into epoxy resins to address this issue [6,7].

Glass fiber-reinforced composites (GFRC) are extensively utilized for their superior strength and rigidity, whilst natural fibers such as sisal provide ecological advantages, economic viability, and moderate mechanical properties [8,9]. Nonetheless, both glass and sisal fiber composites exhibit inadequate flame resistance, especially when integrated with combustible epoxy matrix. Recent advancements in flame-retardant resins and additives have enhanced fire performance; nonetheless, issues persist in attaining uniform dispersion and preserving mechanical integrity [10–14].

The majority of fiber-reinforced composites (FRCs) are constructed from two-dimensional woven, stitched, or braided fabrics, frequently demonstrating constrained interlaminar strength and damage tolerance. Conversely, 3D woven fabric structures provide superior mechanical qualities, particularly in the thickness dimension, through the integration of binder yarns [15,16]. Although the benefits of 3D woven composites are recognized, few research have investigated their incorporation with flame-retardant epoxy matrices.

This study fills the research gap by synthesizing novel DOPO-modified epoxy resin and employing it as a matrix for 3D woven glass and sisal fiber-reinforced composites. The main aim is to assess the flame-retardant and mechanical characteristics of the developed composites. Characterization encompasses Limiting Oxygen Index (LOI), vertical burning assessments (UL-94), cone calorimetry, and tensile and flexural strength evaluations to determine the efficacy of the DOPO alteration and the composite structure for high-performance, fire-resistant applications.

2. EXPERIMENTAL

2.1 Materials

9,10-Dihydro-9-oxa-10-phosphaphenanthrene-10-oxide (DOPO), terephthaldicarboxaldehyde (TDCA) was purchased by TCI India Pvt Ltd. E-Glass roving of 900 Tex was procured from Owens Corning (India) Private Limited. Sisal yarn of 1000 Tex was purchased from Dinesh Industries, Jaipur, India. Diglycidyl ether of bisphenol A(DGEBA) was obtained from Atul Industries Ltd., India.

2.2 Synthesis of resin

0.1 mole (13.41 gram) of terephthaldicarboxaldehyde (benzene-1,4-dicarbaldehyde) and 0.2 mole of DOPO (43.24 gram) were added in dry toluene of 250 mL in a three-necked flask under a nitrogen environment. The reaction mixture was refluxed for 5 h at 100°C. The reaction mixture was cooled to room temperature. It was filtered and washed with toluene. The obtained solid was dried at 70°C in an oven. The synthesized compound (modified DOPO) was confirmed by FTIR and NMR spectra.

FTIR (cm^{-1}): OH stretching (3240 cm^{-1}), C=H stretching (2860 cm^{-1}), C-H stretching (2820 cm^{-1}), C=C stretching (1590 cm^{-1}), C-H scissoring (1430 cm^{-1}), P=O stretching (1120 cm^{-1}), C-H rocking vibration (713 cm^{-1}).

^{1}H NMR (500 MHz, DMSO-d6, ppm): 5.10–5.45 (m, 2H), 7.62 (m, 1H), 7.78–7.90 (m,2H), 8.04 (m, 1H), 8.10–8.33 (m, 4H).

^{13}C NMR (500 MHz, DMSO-d6, ppm): 120.02, 124.00, 124.76, 124.94, 125.89, 127.02, 127.46, 131.17, 134.17, 136.68, 154.40

^{31}P NMR (500 MHz, DMSO-d6, ppm): 31.19.

DGEBA and modified DOPO were mixed in a molar ratio of 1:1 and heated up to 135°C. The reaction was carried out until a homogeneous solution was obtained for 45-55 min. Fig 1 depicts the synthesis scheme of the product. The reaction between DGEBA and modified DOPO is illustrated in Fig 1. The trap air was removed from the mixture under vacuum for 5 min. The resin was directly used for making composites.

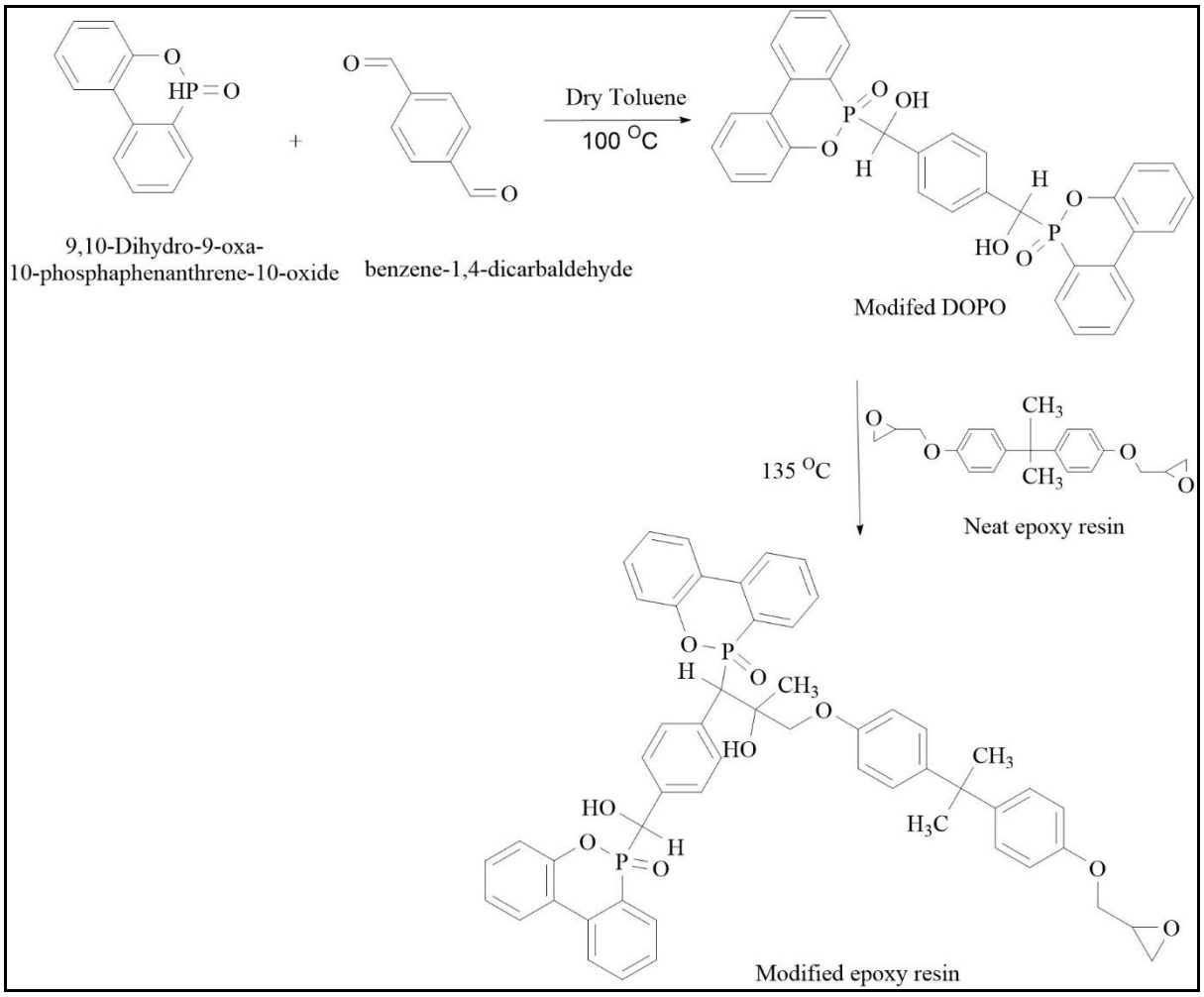

Figure 1: Synthesis of modified resin

2.3 Characterizations

FTIR spectra were obtained at wavenumber ranges of 400–4000 cm^{-1} using Nicolet iS50 FTIR spectrophotometer. All NMR spectra were performed on a Bruker 500 NMR spectrometer (500 MHz) using DMSO-d6 as solvent.

2.4 Development of fiber-reinforced modified epoxy resin-based composites

A four-layer 3D orthogonal fabric of glass and sisal fiber was developed in the customized rapier loom. Vacuum-assisted resin infusion (VARI) method was used to prepare composite materials [17]. The curing process was performed at ambient temperature for 8 h.

2.5 Measurement of flame-retardant properties of composites

The flammability of all the samples was determined using the limited oxygen index (LOI), according to ASTM D2863. Vertical flammability test was conducted according to the UL-94 standard. The cone calorimetry test was done according to the ASTM E1354.

2.6 Evaluation of mechanical properties of composites

According to ASTM D3039 and ASTM D7264, tensile strength and flexural rigidity were obtained.

3. RESULTS AND DISCUSSION

3.1 Characterization of intermediate and resins

Fig 2 indicates the FTIR spectra of modified DOPO. The FTIR spectra showed the bands of OH stretching (3240 cm^{-1}), C=H stretching (2860 cm^{-1}), C-H stretching (2820 cm^{-1}), C=C stretching (1590 cm^{-1}), C-H scissoring (1430 cm^{-1}), P=O stretching (1120 cm^{-1}), C-H rocking vibration (713 cm^{-1}).

This suggested the formation of modified DOPO.

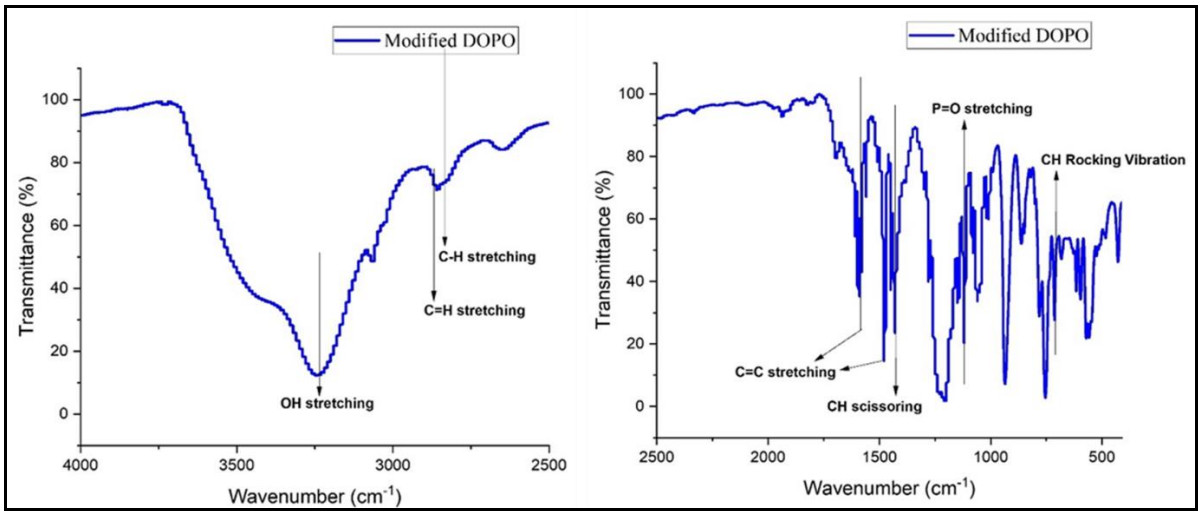

Figure 2: FTIR spectra of modified DOPO

^{1}H NMR spectra of modified DOPO are recorded in Fig 3. Types of A and B hydrogen showed multiplet in the 5.10-5.45 ppm region. Aromatic hydrogen showed various peaks: 7.62 (multiplet for one hydrogen), 7.78–7.90 (multiplet for two hydrogen), 8.04 (multiplet for one hydrogen), and 8.10–8.33 (multiplet for four hydrogen). Thus, it confirms the chemical structure.

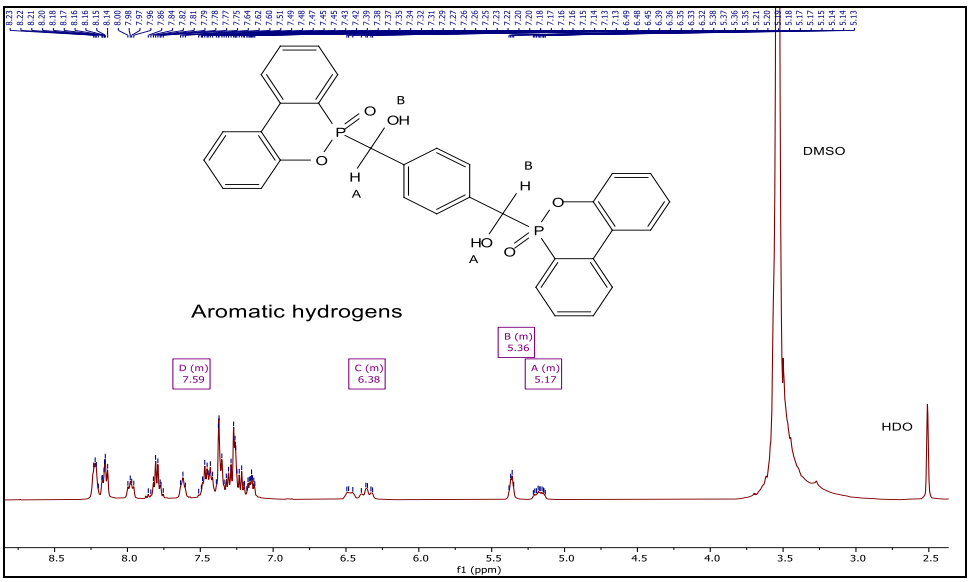

Figure 3: ^{1}H NMR spectra of modified DOPO

^{13}C NMR spectra of modified DOPO are recorded in Fig 4. Various carbon atom peaks were obtained at 120.02, 124.00, 124.76, 124.94, 125.89, 127.02, 127.46, 131.17, 134.17, 136.68, 154.40. As confirmed by ^{13}C NMR, the presence of various carbons suggested the chemical structure of modified DOPO.

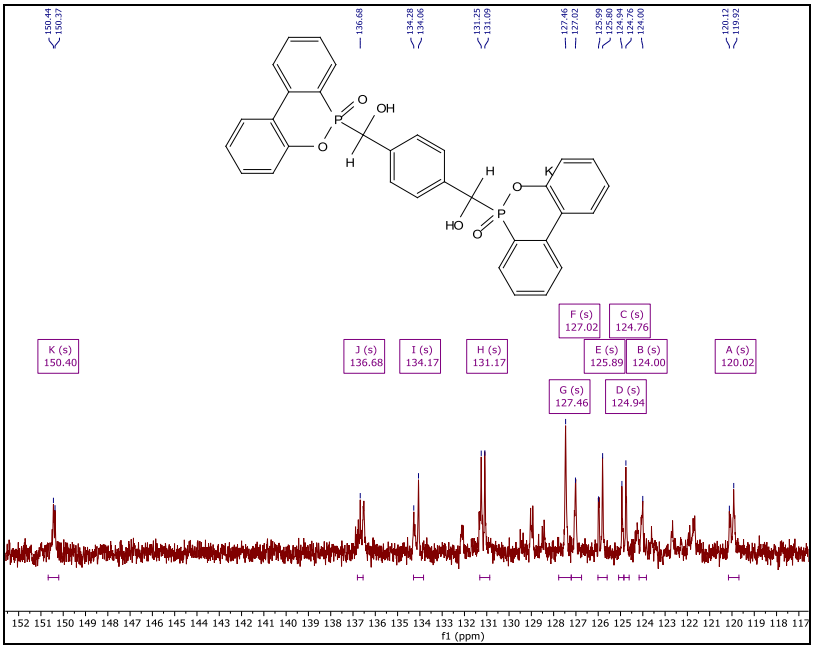

Figure 4: ^{13}C NMR spectra of modified DOPO

^{31}P NMR spectra of modified DOPO are depicted in Fig 5. One peak at 31.19 ppm was obtained due to one type of phosphorous atom attached to direct oxygen. Thus, FTIR and NMR spectra confirm the successful synthesis of modified DOPO.

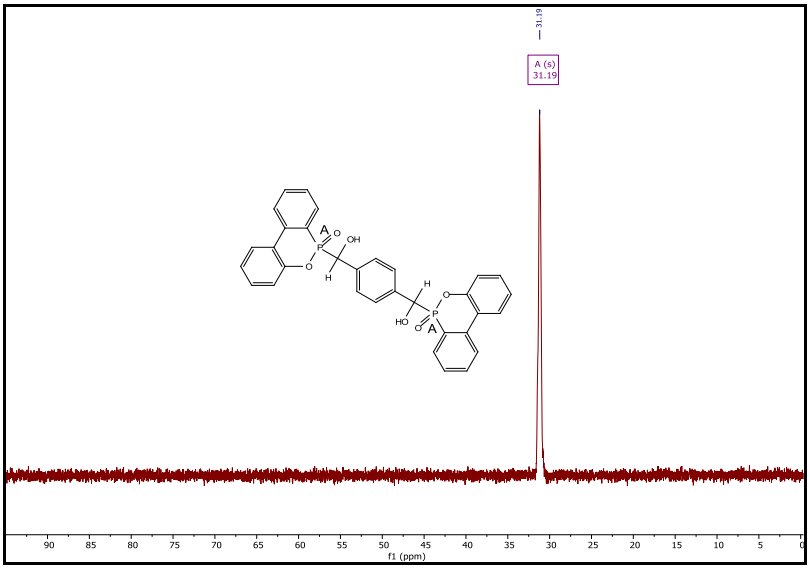

Figure 5: ^{13}C NMR spectra of modified DOPO

3.2 Flame retardant properties of composites

LOI (%) values of epoxy resin and modified epoxy resin-based glass and sisal fiber-reinforced composites are shown in Fig **6**. EP stands for neat epoxy resin; MEP indicates modified epoxy resin. The LOI (%) value was observed in the neat epoxy resin-based glass (EP-GC) and sisal fiber (EP-SC) composite, which was 22.5 and 22.8, respectively. After the modification in epoxy resin, the LOI (%) value of glass and sisal fiber composite became 29.4 and 28.6. The results show a significant improvement in the limiting oxygen index. This proves the efficiency of modified resin to protect composites from flames.

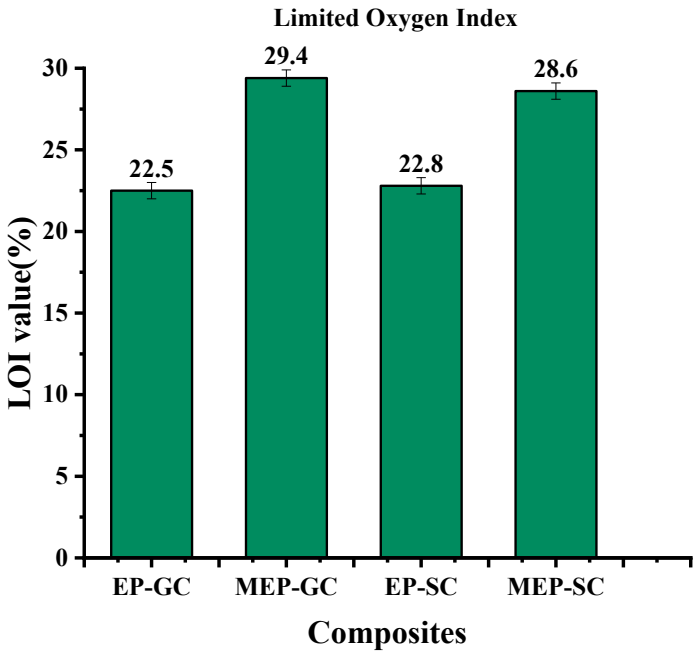

Figure 6: LOI value of neat and modified epoxy resin composite

The vertical burning test of composites is shown in Table 1. Results indicate that after the modification, the rating of composites has improved. The results demonstrate a significant improvement in the rating of vertical flammability, confirming the modified resin's effectiveness in enhancing the composites' flame resistance.

Table 1: UL 94 rating of composites

COMPOSITE SAMPLES	UL-94 TEST RATING	SIGNIFICANCE
EP-GC	NR	No rating
MEP-GC	V2	Burning stop in 30 seconds
EP-SC	NR	No rating
MEP-SC	V2	Burning stop in 30 seconds

3.3 Cone Calorimetry Test

Neat epoxy glass exhibits the highest peak heat release rate (pHRR) of 390.2 kW/m^2. After the modification, the pHRR value of the epoxy glass composite was 275.69 kW/m^2. The same patterns are

shown in the case of epoxy sisal and modified epoxy sisal composites (Fig 8), which exhibit 897.43 and 767.57 kW/m^{2,} respectively. Using the modified epoxy resin, a 29.3% reduction in the peak heat release rate was achieved with glass fiber, while a 14.47% reduction was observed with sisal fiber. These variations are attributed to the interaction between the resin and fibers and the distribution of the resin within the fiber matrix. Moreover, the modified resin exhibits an early release phenomenon (at a shorter time), which is attributed to the decomposition of flame-retardant moieties such as P=O, thereby protecting the composite from further burning.

Glass fiber is inherently flame-retardant; however, incorporating a neat flammable resin renders the composite flammable. The synthesized resin significantly enhances the flame-retardant properties of glass fiber-based composites, effectively making them inherently flame-retardant.

On the other hand, sisal is highly flammable. In this case, the developed resin protects the fiber and the entire composite, reducing its flammability. In conclusion, modifying the resin with phosphorus-containing groups imparts flame-retardant protection to the composites.

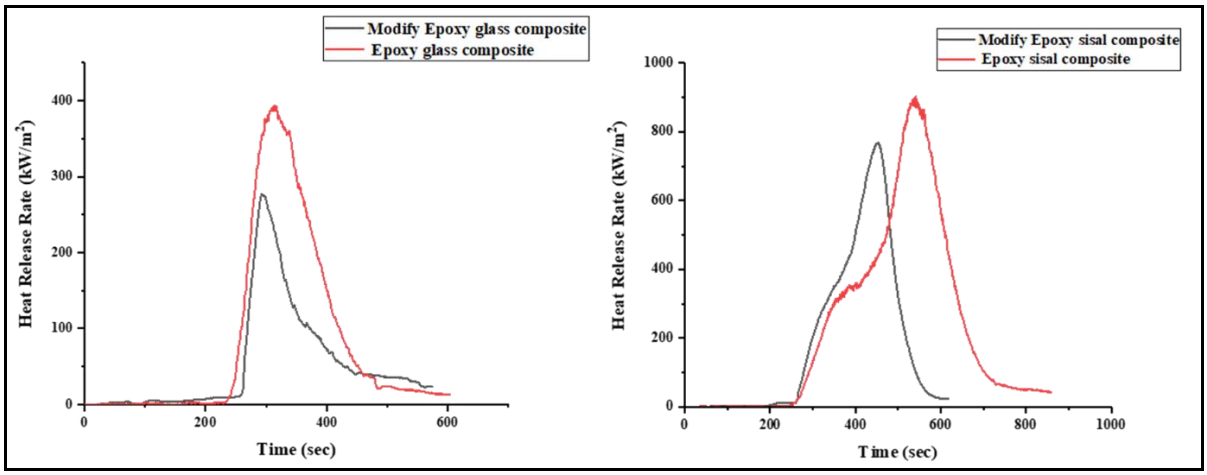

Figure 7: HRR value of neat and modified epoxy resin composite

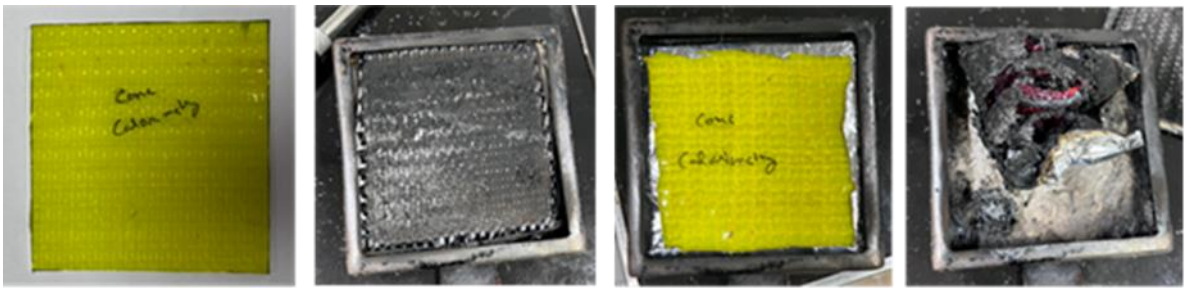

Figure 8: (Left) modified epoxy glass composite and (Right) modified epoxy sisal glass composite

3.6 Mechanical Properties of Composites

The tensile properties and flexural rigidity of neat and modified epoxy glass and sisal fiber-reinforced composites are presented in Figs 10 and 11. The curves in these figures show that the tensile and flexural properties of the modified composites are inferior to those of neat epoxy after incorporating modified DOPO into the epoxy resins. This decline in mechanical performance aligns with reported studies, which suggested that a high concentration of phosphorus-containing flame retardants often has a detrimental impact on the mechanical characteristics of the polymer matrix [18,19].

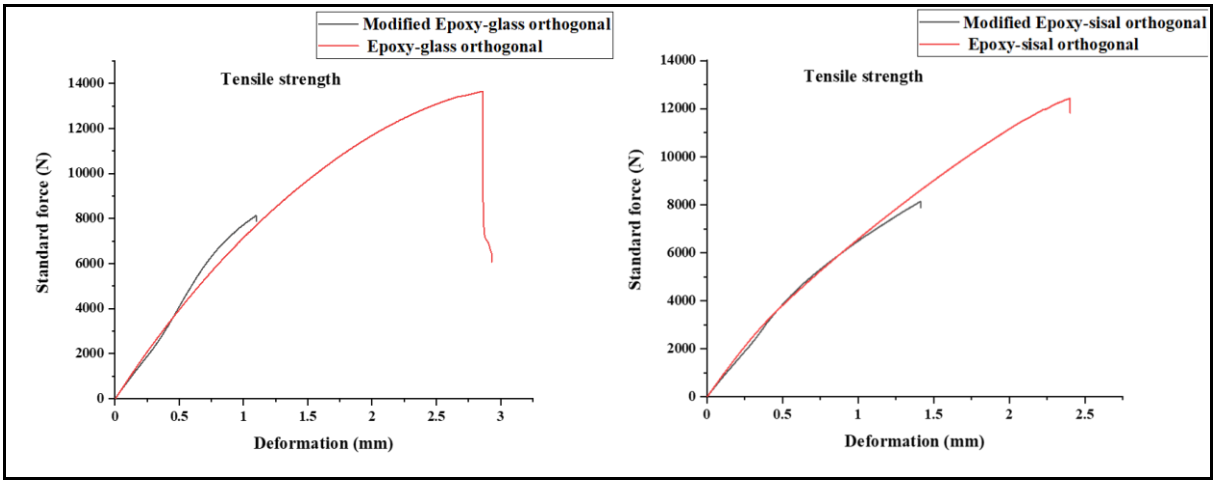

Figure 9: Tensile strength of composites

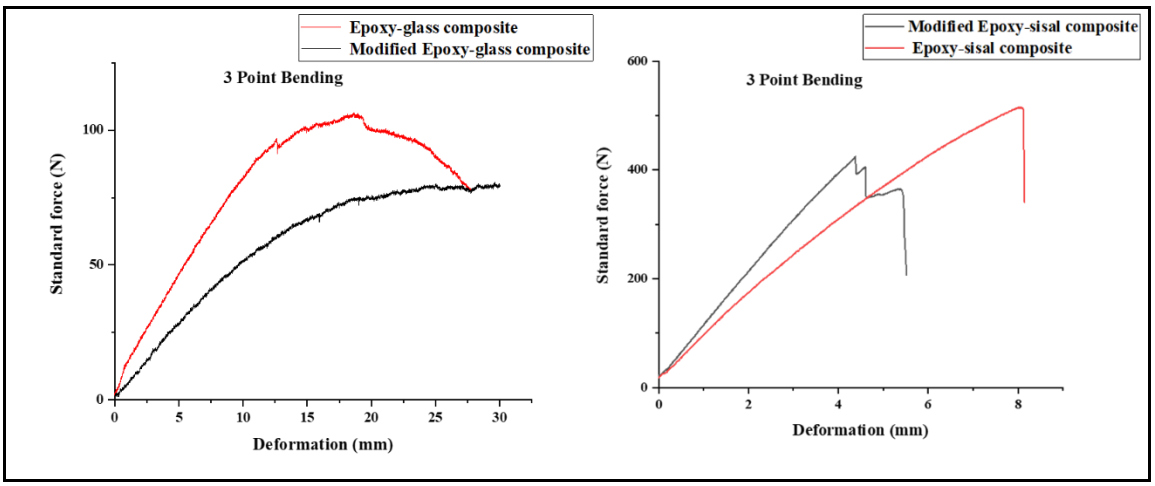

Figure 10: Flexural rigidity of composites

4. CONCLUSION

A novel DOPO-modified epoxy resin was successfully synthesized, and 1H NMR, 13C NMR, and 31P NMR confirmed its chemical structure. The high phosphorus content of the modified resin imparted excellent flame retardancy to epoxy resins. The LOI value of composites was increased from 21 to 29 and UL-94 test rating was improved from no rating to V-2 rating. The significant decrement of 30% s in case of glass and almost 15% in sisal shown in peak heat release rate. Using a 3D woven fiber architecture further contributed to improved structural performance, particularly in load-bearing and impact resistance. However, the integration of the flame-retardant additive resulted in a reduction in mechanical properties, including tensile and flexural strength. Overall, the study demonstrates a promising approach to enhancing fire safety in fiber-reinforced composites for construction and structural applications, highlighting the need to balance flame retardancy with mechanical performance. This work provides a novel route for developing efficient flame-retardant composites for high-performance materials for construction, automotive, and aerospace applications.

REFERENCES

[1] C. Li, J. Fei, T. Zhang, S. Zhao, L. Qi, Relationship between surface characteristics and properties of fiber-reinforced resin-based composites, Compos B Eng 249 (2023). https://doi.org/10.1016/j.compositesb.2022.110422.

[2] S.H. Aziz, M.P. Ansell, S.J. Clarke, S.R. Panteny, Modified polyester resins for natural fiber composites, Compos Sci Technol 65 (2005) 525–535. https://doi.org/10.1016/j.compscitech.2004.08.005.

[3] S. Agnihotri, J.N. Sheikh, S.P. Singh, B.K. Behera, Flame-retardant textile structural composites for construction application: a review, J Mater Sci (2024). https://doi.org/10.1007/s10853-023-09312-7.

[4] B.K. Kandola, L. Krishnan, J.R. Ebdon, P. Myler, Structure-property relationships in structural glass fiber reinforced composites from unsaturated polyester and inherently fire retardant phenolic resin matrix blends, Compos B Eng 182 (2020). https://doi.org/10.1016/j.compositesb.2019.107607.

[5] X. Zhao, L. Yang, F.H. Martin, X.Q. Zhang, R. Wang, D.Y. Wang, Influence of phenylphosphonate based flame retardant on epoxy/glass fiber reinforced composites (GRE): Flammability, mechanical and thermal stability properties, Compos B Eng 110 (2017) 511–519. https://doi.org/10.1016/j.compositesb.2016.10.090.

[6] L. Chen, Y.Z. Wang, A review on flame retardant technology in China. Part I: Development of flame retardants, Polym Adv Technol 21 (2010) 1–26. https://doi.org/10.1002/pat.1550.

[7] A. Kausar, I. Rafique, Z. Anwar, B. Muhammad, Recent Developments in Different Types of Flame Retardants and Effect on Fire Retardancy of Epoxy Composite, Http://Dx.Doi.Org/10.1080/03602559.2016.1163607 55 (2016) 1512–1535. https://doi.org/10.1080/03602559.2016.1163607.

[8] T.P. Sathishkumar, S. Satheeshkumar, J. Naveen, Glass fiber-reinforced polymer composites - A review, Journal of Reinforced Plastics and Composites 33 (2014) 1258–1275. https://doi.org/10.1177/0731684414530790.

[9] N. Agarwal, A. Singh, I.K. Varma, V. Choudhary, Effect of structure on mechanical properties of vinyl ester resins and their glass fiber-reinforced composites, J Appl Polym Sci 108 (2008) 1942–1948. https://doi.org/10.1002/app.27779.

[10] Z. Wang, W. Feng, J. Ban, Z. Yang, X. Fang, T. Ding, B. Liu, J. Zhao, Sisal-Fiber-Reinforced Polypropylene Flame-Retardant Composites: Preparation and Properties, Polymers 2023, Vol. 15, Page 893 15 (2023) 893. https://doi.org/10.3390/POLYM15040893.

[11] M. Vishnu Prabhakar, T. Rajasekaran, Machinability and flammability properties of sisal fiber reinforced polymer composites, in: IOP Conf Ser Mater Sci Eng, Institute of Physics Publishing, 2018. https://doi.org/10.1088/1757-899X/402/1/012035.

[12] N.R. Paluvai, S. Mohanty, S.K. Nayak, Studies on thermal degradation and flame retardant behavior of the sisal fiber reinforced unsaturated polyester toughened epoxy nanocomposites, J Appl Polym Sci 132 (2015) 42068. https://doi.org/10.1002/APP.42068.

[13] B.K. Kandola, A.R. Horrocks, P. Myler, D. Blair, Mechanical performance of heat/fire damaged novel flame retardant glass-reinforced epoxy composites, Compos Part A Appl Sci Manuf 34 (2003) 863–873. https://doi.org/10.1016/S1359-835X(03)00156-8.

[14] A. Hörold, B. Schartel, V. Trappe, M. Korzen, J. Bünker, Fire stability of glass-fiber sandwich panels: The influence of core materials and flame retardants, Compos Struct 160 (2017) 1310–1318. https://doi.org/10.1016/J.COMPSTRUCT.2016.11.027.

[15] B.N. Cox, On the tensile composites failure of 3D woven, (1996) 447–458.

[16] B.P. Dash, B.K. Behera, R. Mishra, J. Militky, Modeling of internal geometry of 3D woven fabrics by computation method, Http://Dx.Doi.Org/10.1080/00405000.2012.720850 104 (2013) 312–321. https://doi.org/10.1080/00405000.2012.720850.

[17] V.R. Tamakuwala, Manufacturing of fiber reinforced polymer by using VARTM process: A review, in: Mater Today Proc, Elsevier Ltd, 2021: pp. 987–993. https://doi.org/10.1016/j.matpr.2020.11.102.

[18] D. Liu, P. Ji, T. Zhang, J. Lv, Y. Cui, A bi-DOPO type of flame retardancy epoxy prepolymer: Synthesis, properties and flame-retardant mechanism, Polym Degrad Stab 190 (2021). https://doi.org/10.1016/j.polymdegradstab.2021.109629.

[19] Z. Chi, Z. Guo, Z. Xu, M. Zhang, M. Li, L. Shang, Y. Ao, A DOPO-based phosphorus-nitrogen flame retardant bio-based epoxy resin from diphenolic acid: Synthesis, flame-retardant behavior and mechanism, Polym Degrad Stab 176 (2020). https://doi.org/10.1016/j.polymdegradstab.2020.109151.

ENHANCING FIRE RESISTANCE OF CARBON FIBRE COMPOSITES USING FUNCTIONALIZED AMMONIUM POLYPHOSPHATE NANOPARTICLES

Wenmu Yang[1], Jiawei Wang[1], Wenkai Chang[1], Mohammad S. Islam[1], Zhao Sha[1], Cheng Wang[1], Jin Zhang[1], Guan Heng Yeoh[1], Cyrille Boyer[2], Chun Hui Wang[1]*
[1]School of Mechanical and Manufacturing Engineering, University of New South Wales, Sydney, NSW 2052, Australia
[2]Cluster for Advanced Macromolecular Design, School of Chemical Engineering, High Street, UNSW Sydney, Australia
Email: chun.h.wang@unsw.edu.au, web page: https://www.unsw.edu.au

Keywords: Ammonium polyphosphate, Flame retardancy, Mechanical properties, Finite elements

ABSTRACT

Epoxy-based carbon fibre reinforced composites (CFRPs) are widely used in aerospace, transportation, and construction due to their high strength-to-weight ratio. However, epoxy resins are flammable and can ignite and burn when exposed to fire, producing highly toxic smoke gases. The CFRPs' poor fire resistance is primarily due to the epoxy resin's inherent flammability. One common method to address this issue is to incorporate flame-retardant fillers into the matrix. However, existing flame-retardant particles typically range from tens to hundreds of microns, significantly decreasing the strength and fracture toughness of the composites.

To address this challenge, in this study, a novel strategy is proposed to functionalize ammonium polyphosphate (APP) with NH_3^+ groups from an amine-based hardener, yielding hardener-functionalized APP nanoparticles (HF-APP). These nanoparticles were further downsized from 14μm to 0.2μm by sonication and uniformly dispersed into the epoxy matrix of CFRPs. At a 30wt% loading, the modified composites exhibited a 50% reduction in peak heat release rate and an increase in the limiting oxygen index to 49. Additionally, substantial improvements were observed in flexural strength, short beam shear strength, and interlaminar fracture energy. Finite element analysis further revealed that HF-APP nanoparticles undergo filament-like separation at high stress levels, effectively mitigating interfacial stress concentration and preserving structural integrity. This multifunctional approach offers the significant potential for developing flame-retardant CFRPs capable of withstanding extreme environments while maintaining high mechanical and fracture properties, a feat previously unattainable with conventional methods.

1 INTRODUCTION

Epoxy resins and their composites are limited in their use in demanding fire protection environments due to the flammability of epoxy resins [1], their limiting oxygen index (LOI) is approximately 20%, rendering these materials extremely flammable even after the ignition source is removed [2]. This poses a serious threat to fire safety, especially in enclosed or high-risk environments such as rail tunnels and aircraft cabins. When exposed to fire, epoxy-based composites can undergo rapid thermal degradation, produce toxic smoke, and lose structural integrity, increasing the risk of structural failure, impeding evacuation and suppression measures. To mitigate these hazards, international flame-retardant standards have been established for materials used in railway vehicles and other public safety-critical areas, with emphasis on indicators such as ignition resistance, flame propagation, smoke release, and toxic gas emissions. However, meeting these standards while maintaining the high mechanical strength essential for structural performance remains a major engineering challenge.

To enhance the fire resistance of CFRPs, flame-retardant additives such as aluminium hydroxide, magnesium hydroxide, and APP are commonly incorporated into the matrix [3]. Organic additives,

including halogenated compounds and phosphorus-based molecules, are also widely used. While these approaches are effective in reducing flammability, high loadings (over 30wt%) are typically required hydroxide [4-6] which damage mechanical properties such as tensile and flexural strength. Moreover, the ununiform dispersion and weak interfacial bonding of large-sized additives (10 to 100 of microns) with the epoxy matrix can lead to stress concentrations and reduce fracture toughness [7]. Reactive strategies involving phosphorus, silicon, or halogen containing curing agents have been proposed to chemically integrate flame-retardant elements into the polymer network without significantly altering the resin's thermomechanical properties [6]. However, many of these approaches change the curing kinetics or final network structure of the epoxy, resulting in reduced stability or unpredictable performance.

In this study, we propose an innovative method to enhance the flame retardancy of epoxy and CFRP composites while maintaining or even improving their mechanical properties. APP particles were chemically functionalized via cationic ion exchange with NH_3^+ groups from an amine-based curing agent, yielding HF-APP particles [8]. This functionalization enabled the particles to participate in the curing reaction with eppxy, improving compatibility and interfacial adhesion with the epoxy matrix. The particles were further downsized via probe ultrasonication and filtration, resulting in submicron nanoparticles denoted as SHF-APP with improved dispersibility. Composites fabricated using these modified particles exhibited significantly enhanced flame-retardant performance, including a 50% reduction in peak heat release rate and a LOI value up to 49, while maintaining over 90% of the tensile strength of neat epoxy at 20wt% HF-APP loading. Mechanical tests further demonstrated improved flexural strength, short beam shear strength, and interlaminar fracture energy. Finite element analysis revealed that HF-APP particles can deform or split under stress, reducing their stress concentration effects and minimizing mechanical compromise. These results highlight the dual functionality of HF-APP in simultaneously curing and reinforcing the epoxy matrix, offering a potential solution for high-performance, fire-safe CFRP structures in transportation and construction industries.

2 GENERAL SPECIFICATIONS

2.1 Material and methods

The materials used in this study include bisphenol A-type epoxy resin (DGEBA), APP, and an amine-based hardener. APP was surface functionalized via mixing with the curing agent, enhancing its compatibility with the epoxy matrix. The functionalized APP was further downsized to nanoparticles and then incorporated into the epoxy resin at various loadings (10–30wt%) to prepare the modified systems. CFRP laminates were further fabricated using a hand lay-up process followed by vacuum-assisted resin transfer molding (VARTM). The flame-retardant performance of the composites was characterized by LOI, UL-94 vertical burning tests, and cone calorimetry, while mechanical properties were evaluated through tensile, flexural, and interlaminar shear strength tests. Scanning electron microscopy (SEM) was employed to analyze the morphology and dispersion of the modified particles within the matrix.

2.2 Results and discussion

2.2.1 Flame retardant tests results

The flame-retardant performance of epoxy matrix was significantly enhanced by incorporating HF-APP. In cone calorimetry, neat epoxy exhibited a peak heat release rate (PHRR) of 1841 kW/m² and a total heat release (THR) of 62.4 MJ/m². With 30wt% HF-APP, the PHRR drastically dropped to 37 kW/m², and the composite self-extinguished during testing, with THR approaching zero. In contrast, unmodified APP only reduced the PHRR to 856 kW/m² at the same loading. The total smoke release (TSR) was also significantly reduced by HF-APP, achieving a 95% decrease at 30wt% loading, compared to a 50% reduction by APP. The LOI increased from 20 (neat epoxy) to 44 for HF-APP/epoxy composites at 30wt%, highlighting their resistance to ignition.

For CFRP systems, the PHRR was reduced from 408 kW/m² (unmodified epoxy matrix) to 103 kW/m² with 30wt% HF-APP. LOI values rose from 36 to 49. Notably, only 10wt% HF-APP was sufficient to achieve the highest V-0 rating in UL-94 vertical burning tests, whereas 30wt% APP or 20wt% SHF-APP was required for the same level. The flame-retardant performance of SHF-APP composites was found to be intermediate between that of APP and HF-APP. While the further reduction in particle size led to a slight increase in PHRR, it also resulted in a decrease in THR, indicating a balance effect in performance matrix. Overall, SHF-APP exhibited flame-retardant behavior comparable to HF-APP, suggesting that the nanoscale particle size maintains thermal protection while offering potential advantages in mechanical reinforcement. These results highlight SHF-APP as an effective alternative that balances flame retardancy with enhanced structural performance.

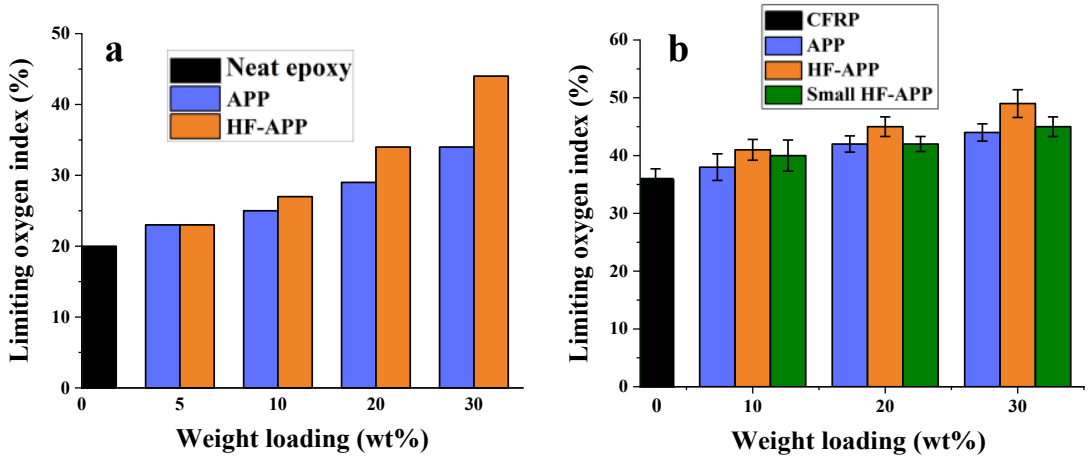

Fig. 1 LOI values of CFRPs with different weight loadings of APP, HF-APP, and SHF-APP in the epoxy matrix.

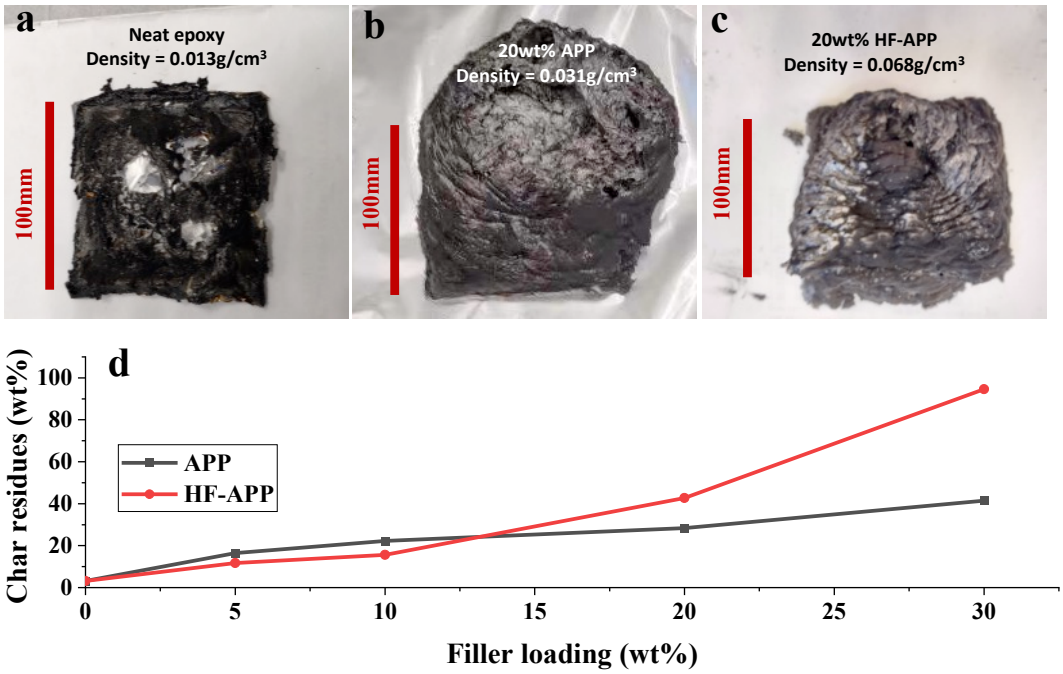

Fig. 2 Char residues: neat epoxy (a), 20 wt% APP/epoxy (b), 20 wt% HF-APP/epoxy (c) and weight percentage of residues (d) from cone calorimeter tests.

2.2.2 Mechanical tests results

The mechanical performance of CFRPs incorporating APP, HF-APP, and SHF-APP were systematically evaluated through tensile, short beam shear, and interlaminar fracture tests. The short beam shear strength was largely preserved even at high additive concentrations. Both APP and HF-APP modified composites maintained over 90% of the strength of the unmodified laminate at 30wt%. Notably, SHF-APP led to a 30% increase in short beam shear strength, attributed to more uniform matrix distribution, reduced interlaminar cracking, and improved fibre alignment. Interlaminar fracture energy (G_{IC}) was also investigated, showing that while APP and HF-APP caused moderate reductions at higher loadings, SHF-APP at 30wt% retained nearly the full fracture toughness of the baseline CFRP. These results indicate that HF-APP improves strength retention in epoxy matrices, and SHF-APP enhances interlaminar properties in CFRPs, offering a potential method to flame-retardant composites with minimal reduction in mechanical performance.

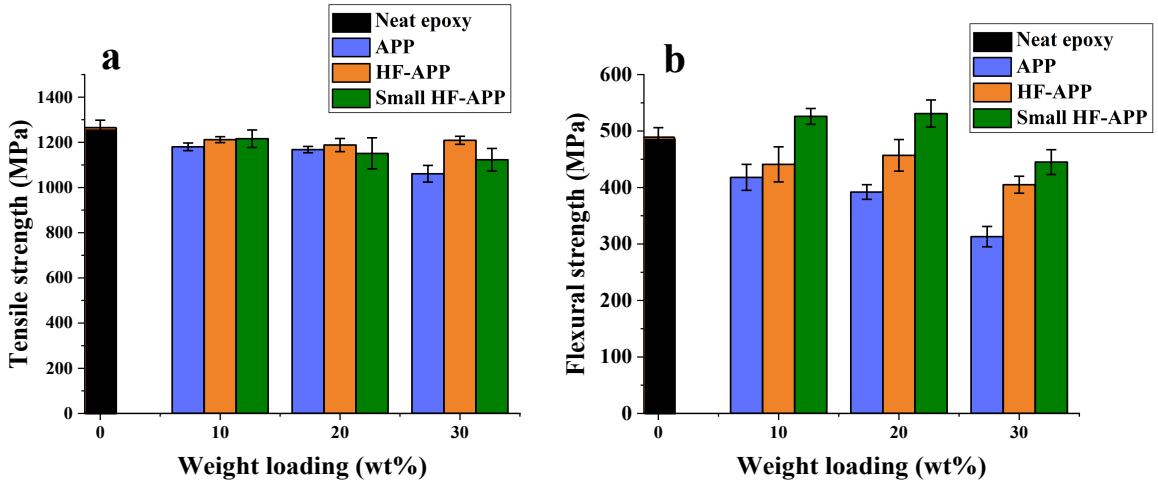

Fig. 3 Strengths of CFRPs with different weight loadings of APP, HF-APP, and SHF-APP particles: tensile strength (a) and flexural strength (b).

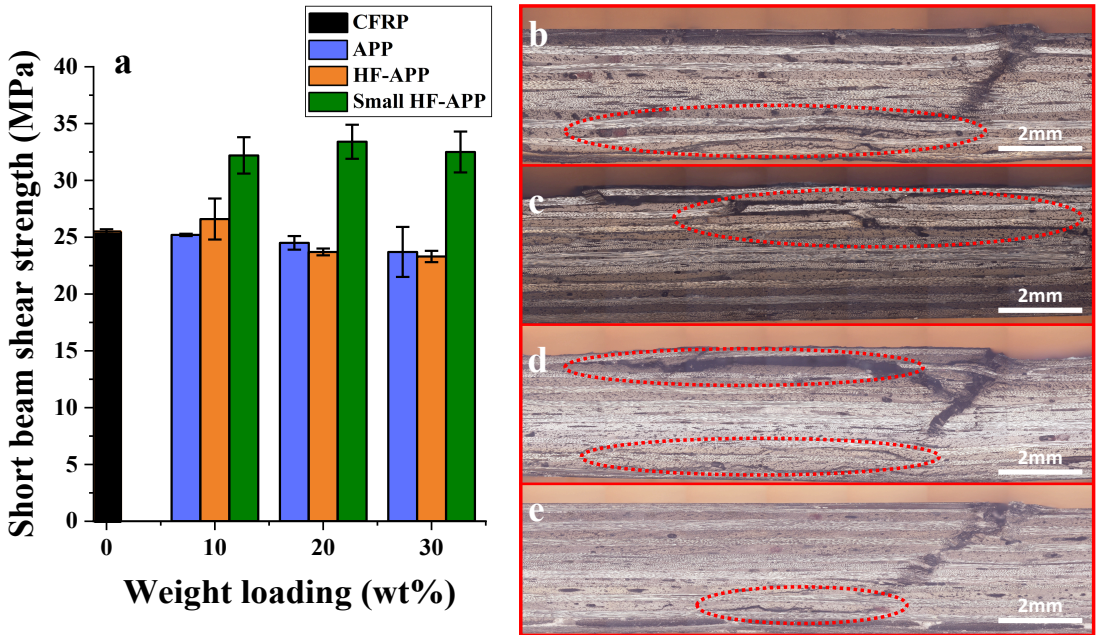

Fig. 4 Short beam shear strength (a) of CFRP with different weight concentrations of APP, HF-APP, and SHF-APP. Microscopic optical images of samples' cross sections of CFRP (b) and CFRP with 30wt% APP (c), HF-APP (d), and SHF-APP (d) after short beam shear test.

2.2.3 Comparison of the key results

A comparative analysis of mechanical strength retention and flame-retardant performance was conducted for epoxy matrix and CFRP systems incorporating unmodified APP, HF-APP, and SHF-APP, alongside other modification strategies such as ATNi [9], and DDM [10] functionalized APP. In the epoxy matrix system, tensile tests revealed that at 10wt% loading, HF-APP achieved the highest retention of mechanical strength, closely matching the performance of APP@ATNi, while also delivering the most obvious reduction in PHRR. HF-APP exhibited comparable enhancements in LOI, char residue, and total heat release (THR), demonstrating its balanced improvement in both structural and flame-retardant properties.

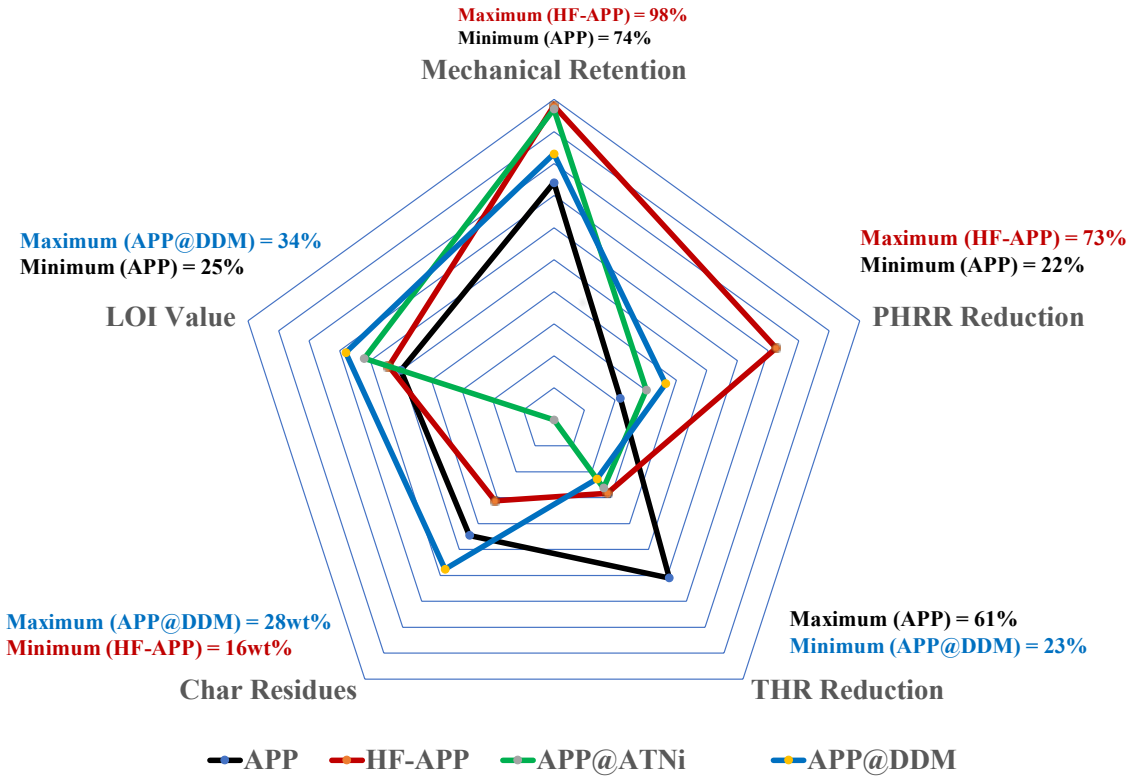

Fig. 5 Comparisons of the unmodified APP and HF-APP with APP@ ATNi and APP@DDM at 10wt% loading.

In contrast, SHF-APP demonstrated the best mechanical advantages. Specifically, the short beam shear strength and interlaminar fracture toughness were significantly improved by SHF-APP compared to both APP and HF-APP, while maintaining flame-retardant effectiveness equivalent to HF-APP. Furthermore, the cumulative percentage changes across seven key performance indicators highlighted SHF-APP as the most balanced and effective additive for CFRP applications. These results suggest that while HF-APP is optimal for preserving tensile performance in epoxy matrices, SHF-APP particles are more suitable for CFRP composites where interlaminar properties and fire safety must be simultaneously optimized.

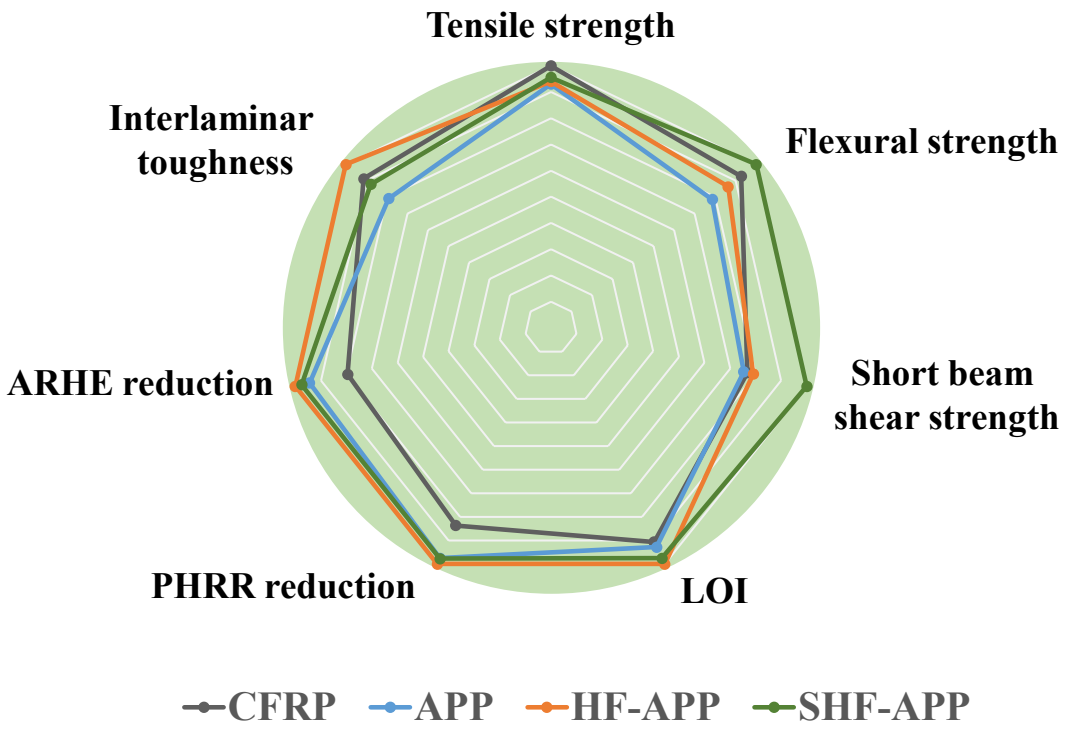

Fig. 6 Comparison of the mechanical and fire-retardant performance indicators of the four types of CFRPs.

3 CONCLUSION

In this study, a novel strategy was developed to enhance the flame-retardant performance and retain the mechanical integrity of epoxy resins and their CFRPs through the functionalization of APP using an amine-based curing agent. In the epoxy system, the resulting HF-APP exhibited strong interfacial compatibility with the matrix and a filamentous morphology that effectively mitigated stress concentrations. At 20wt% loading, HF-APP reduced the peak heat release rate and total heat release by 87% and 83%, respectively, while maintaining 92% of the tensile strength of the neat epoxy. By reducing the average particle size of HF-APP from 14μm to 0.12μm via probe ultrasonication, SHF-APP particles were obtained. These particles preserved the flame-retardant performance of HF-APP while further improving short beam shear strength and interlaminar fracture toughness due to enhanced matrix uniformity and fibre alignment. These improvements were attributed to improved dispersion, stress transfer, and the formation of dense char layers during combustion. The modified system met the highest fire safety classification (HL3) under EN 45545-2:2013, demonstrating its suitability for railway applications. The findings of this study provide new insights into the structure–property relationships of flame-retardant fillers in polymer composites, offering potential methods for developing multifunctional CFRPs that meet both fire safety standards and mechanical performance requirements for applications in transportation, infrastructure, and high-performance engineering.

REFERENCES

1. Petersen, M.R., et al., *Mechanical properties of fire-retardant glass fiber-reinforced polymer materials with alumina tri-hydrate filler.* Composites Part B-Engineering, 2015. **78**: p. 109-121.

2. Zhang, L.W., A.O. Sojobi, and K.M. Liew, *Sustainable CFRP-reinforced recycled concrete for cleaner eco-friendly construction.* Journal of Cleaner Production, 2019. **233**: p. 56-75.
3. Kim, H., et al., *Thermal barrier coating for carbon fiber-reinforced composite materials.* Composites Part B-Engineering, 2021. **225**: p. 109308.
4. Yang, W.M., et al., *Nanoparticles of polydopamine for improving mechanical and flame-retardant properties of an epoxy resin.* Composites Part B-Engineering, 2020. **186**: p. 107828.
5. Yang, W.M., et al., *Effects of waste coffee grounds on the mechanical properties, flame retardancy and toxic gas production of epoxy composites.* Materials & Design, 2022. **224**: p. 111347.
6. Mukhtar, M., D. Klosterman, and A.B. Morgan, *Preparation, Cure, Characterization, and Mechanical Properties of Reactive Flame-Retardant Cyanate Ester/Epoxy Resin Blends and their Carbon Fiber Reinforced Composites.* Composites Part B-Engineering, 2024. **282**: p. 111580.
7. Li, Y.T., et al., *Processing, thermal conductivity and flame retardant properties of silicone rubber filled with different geometries of thermally conductive fillers: A comparative study.* Composites Part B-Engineering, 2022. **238**: p. 109907.
8. Yang, W.M., et al., *A novel strategy for high flame retardancy and structural strength of epoxy composites by functionalizing ammonium polyphosphate (APP) using an amine-based hardener.* Composite Structures, 2024. **327**: p. 117710.
9. Sui, Y.L., et al., *Superior radical scavenging and catalytic carbonization capacities of bioderived assembly modified ammonium polyphosphate as a mono-component intumescent flame retardant for epoxy resin.* European Polymer Journal, 2021. **156**: p. 110601.
10. Wang, F., et al., *Fabrication of Diaminodiphenylmethane Modified Ammonium Polyphosphate to Remarkably Reduce the Fire Hazard of Epoxy Resins.* Polymers (Basel), 2021. **13**(19): p. 3221.

ICCM24
AUGUST 4-8, 2025
BALTIMORE CONVENTION CENTER
BALTIMORE, MARYLAND, USA

No Technical Paper Submission for:

Anil Netravali

EFFECT OF THERMAL MODIFICATION ON THE FIRE PERFORMANCE OF STRAND-BASED MASS TIMBER COMPOSITE PANELS

A. Chanda[1], R. Adhikari[2,3], M.K.B Bakri[4], M. Aro[5] and V. Yadama[6]

[1]Composite Materials and Engineering Center, Department of Civil and Environmental Engineering, Washington State University, Pullman, WA, 99164
Email: avishek.chanda@wsu.edu, Web page: https://cmec.wsu.edu/person/avishek-chanda/

[2]Product Engineering, Codes and Standards, Weyerhaeuser, Federal Way, WA, 98001
[3]Composite Materials and Engineering Center, Department of Civil and Environmental Engineering, Washington State University, Pullman, WA, 99164
Email: rajan.adhikari@wsu.edu, Web page: https://www.linkedin.com/in/rajan-adhikari-pe-010b3b197/

[4]Composite Materials and Engineering Center, Washington State University, Pullman, WA, 99164
Email: m.khusairybinbakri@wsu.edu, Web page: https://cmec.wsu.edu/person/muhammad-khusairy-bin-bakri/

[5]Wood Products, Natural Resources Research Institute, University of Minnesota, Duluth, MN
Email: maro@d.umn.edu, Web page: https://nrri.umn.edu/faculty-staff/matt-aro-ms

[6]Composite Materials and Engineering Center, Department of Civil and Environmental Engineering, Washington State University, Pullman, WA, 99164
Email: vyadama@wsu.edu, Web page: https://cmec.wsu.edu/person/vikram-yadama/

Keywords: Thermal modification; Cross laminated timber; Sustainable building construction materials; Wood strand composite; Fire reaction properties; Fire resistance properties

ABSTRACT

The demand for mass timber panels has risen sharply, driven by the growing need for sustainable construction materials. However, concerns regarding the durability and fire performance of wood-based composite materials have led to the development of various treatment processes. Among them, thermal modification is a widely adopted process in the industry to enhance the dimensional stability and durability of wood-based materials. At the same time, the emphasis on high-quality lumber for cross-laminated timber (CLT) panels has diminished the utilization of small-diameter timber (SDT) for CLT panels. Effective use of SDT is essential for maintaining forest health and mitigating forest fires. This study explores the use of SDT strands, both untreated and thermally modified, in the production of mass timber panels. Thermal treatment was conducted in an industrial autoclave to ensure uniform processing. The resulting composite panels exhibited excellent mechanical performance, notably enhanced shear strength due to the reduction of rolling shear effects. Fire testing revealed that thermal modification had no significant impact on either fire reaction or fire resistance properties of the mass timber panels produced using control and thermally modified wood strand composite material. While the flexural stiffness remained largely unchanged, the panels demonstrated slight reductions in flexural strength and significant improvements in shear and internal bond strength.

1 INTRODUCTION

Sustainable materials have seen an increase in interest for different applications in the built environment [1]. The use of cross-laminated timber (CLT), which can transfer forces in two directions, has been one such application in demand as a sustainable building construction material [2].

Traditionally, these CLT panels are made from high-quality lumber, the processing of which is economically viable to the sawmills [2]. The manufacturing cost of CLTs is higher than that of other wood-based panels due to the stringent quality control protocols for the lumber that is used in the panels. However, low-quality small-diameter logs are readily available in the US forests as a result of hazardous fuel-removal thinning operations to mitigate forest fires and ensure healthy forests [3-5]. There is commercial interest in producing value-added products using these small-diameter logs, and manufacturing mass timber panels using strand-based technology fits the bill as it does not require high-quality lumber for the production of wood strand composite materials [3, 6-8].

One of the primary challenges in using cross-laminated timber (CLT) for exterior applications is its high susceptibility to moisture uptake [9], which significantly limits its use in outdoor environments. To address this limitation, various strategies have been explore, most notably, chemical modification of the wood to enhance its dimensional stability and overall durability. However, chemical modifications, such as chromated copper arsenical and micronized copper azole, are known to be hazardous to the environment. Enhancing the usability of SDT necessitates procedures that improve its longevity, dimensional stability, and overall product performance while imparting minimal damage to the environment. This study proposes the method of thermal modification of strands to achieve more dimensionally stable and more durable mass timber panels [1]. Thermal modification has been studied extensively for lumber to enhance its dimensional stability and durability. Thermal modification (TM) provides a sustainable substitute for chemical alteration, using heat as the principal agent in either dry or wet conditions. In wet processes, water or steam is used, with the possibility of recycling waste for energy recovery or biofuel generation. Dry techniques use air or inert atmospheres for comparable advantages [10]. TM reduces wood's hydrophilicity by partially extracting hemicellulosic sugars [11], thus improving dimensional stability and decay resistance. Pressurized settings further expedite the breakdown of the complex hemicellulose structure, thus imparting decay resistance and decreasing moisture absorption while preserving or marginally increasing stiffness as the degree of crystallinity is increased [12]. Therefore, the current research employed a pressurized TM technique for the strands to augment hemicellulose breakdown, strengthen resistance to fungal decay, and alleviate moisture-related problems while preserving mechanical integrity.

Fire performance is a critical consideration for mass timber panels, especially in light of increasingly stringent global fire safety regulations for building materials. While wood offers several advantages as a structural material, its inherent combustibility poses challenges in applications requiring enhanced fire resistance [13]. One potential mitigation strategy involves the use of organic wood preservatives—traditionally applied to protect against biological degradation, which may also influence the material's combustion behavior [14]. Investigations examining the combustion characteristics of prevalent species such as Norway spruce (*Picea abies*) and Scots pine (*Pinus sylvestris*) have shown distinct species-specific variations in burn patterns, mass loss, and charring zone thickness [15]. Similar variations are found in heat-treated woods. The findings are affected by wood density, resin content, and preservative treatments [15]. Comprehensive studies on the influence of TM on the fire performance of full-scale structures are limited. Additionally, there is also a divided belief on the advantages or disadvantages of TM on the fire performance of mass timber panels [8, 9]. Thus, it is also critical to have a comprehensive understanding of the influence of TM on strand-based mass timber panels, in both fire reaction and fire resistance properties. Therefore, the objectives of this study are to evaluate the effects of thermal modification on the structural performance of the proposed strand-based wood composite mass timber panels and to investigate the influence of thermal modification on the fire reaction and fire resistance properties of the panels.

2 MATERIALS AND METHODS

2.1 Panel production

Wood strands were produced from lower-grade lumber sourced from small-diameter Engelmann spruce (*Picea engelmannii*) and lodgepole pine (*Pinus contorta*), referred to as ESLP. The materials were procured from Idaho Forest Group. The sourced timber (thickness between 25.4 to 50.8 mm) was cut into 150 mm long slats, soaked in water to increase the moisture content above the fiber saturation point to around 40-50%, and stranded using a CAE disc strander (Kadant, Inc.) at WSU's Composite

Materials and Engineering Center (CMEC). The generated wood strands were approximately 148 mm in length, 19 mm to 38 mm in width, and 0.381 mm to 0.508 mm in thickness. The produced stands were then conditioned at 21.1°C and 65% relative humidity (RH) to attain a moisture content of 12% before thermal modification. The TM was carried out in an industrial autoclave at Therma Wood Technologies (TWT), Ronan, Montana, USA. The modification was carried out in an inert condition, using nitrogen, at 165°C and 0.8 MPa pressure in a 12 m^3 autoclave for 7.5 h.

After thermal treatment, the strands were again conditioned at 21.1°C and 65% RH for about three weeks before making flat 6.35 mm thick, 1220 mm wide, and 2440 mm long veneers with a target density of 640 kg/m^3. Polymeric methyl diphenyl diisocyanate (pMDI) adhesive, supplied by Henkel, was applied at 5 wt.% and atomized onto the strands using a drum blender. The veneers were made with strands oriented primarily along the long direction in a hot press (Ironworks Press Machine). The veneers were then assembled into laminated strand veneer lumber (LSVL) with final dimensions of 38.1 mm in thickness, 610 mm in width, and 2440 mm in length. The sanded veneers were initially coated using a 10 wt% aqueous solution of primer (Loctite HB 3105) before applying the polyurethane (PUR) adhesive (HBX 602 PURBOND). PUR was applied at a coverage rate of 20 g/m^2, using the automated glue spreading technique of the USNR CLT Press 1.83 m by 3.66 m (USNR, Woodland, Washington, USA), available at WSU's CMEC. The same press from Ironworks was then used to make the LSVL panels, details of which are provided in [1]. The LSVL panels were then cross-laminated to develop the cross-laminated strand veneer lumber (CLSVL), using the same PUR adhesive with a 20 g/m^2 spread rate. Cold pressing was used for making both LSVL and CLSVL panels. The final CLSVL panels were made at a thickness of 114.3 mm, a length of 3000 mm, and a width of 1830 mm. The USNR CLT Press was utilized to make the CLSVL panels.

2.2 Mechanical performance

Flatwise third-point bending tests were performed according to ASTM D198-22a [18], where a span-to-depth ratio of 18 was maintained for the CLSVL (2286 mm by 305 mm by 114 mm) panels. A 222 kN load cell, attached to a hydraulic actuator, with string pots having stroke lengths of 250 mm, available at WSU's CMEC, was used for performing the flexural tests. The test setup is provided in Figure 1 (a). Flatwise center-point bending tests were again conducted to ascertain the shear characteristics of the mass timber panels, again as per ASTM D198-22a standard [18]. Here, the span-to-depth ratios for both the panel types were reduced to four, as per the standard, resulting in 203 mm long, 89 mm wide, and 38 mm thick LSVL panels and 584 mm long, 305 mm wide, and 114 mm thick CLSVL panels. The same 222 kN load cell and strain pots were used. The testing setup is illustrated in Figure 1 (b).

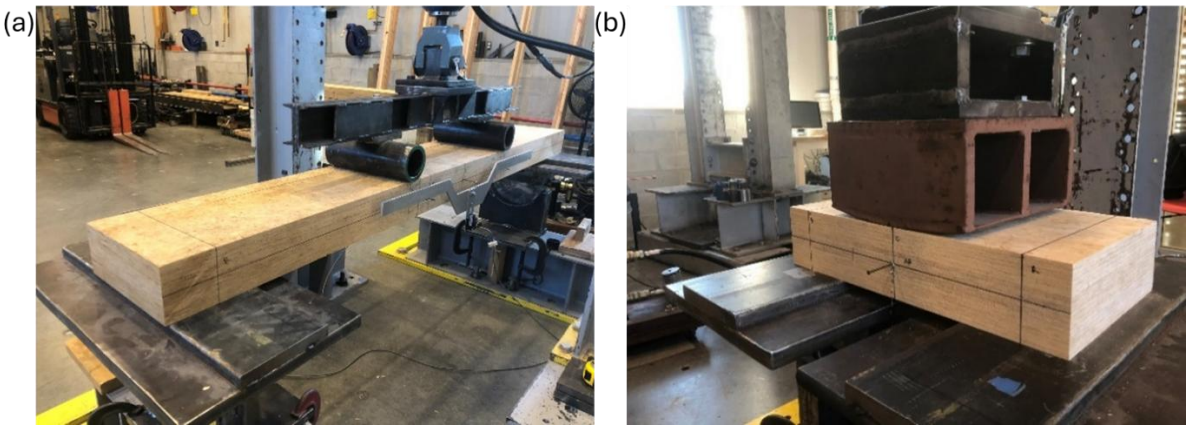

Figure 1: Illustration of the testing setups for (a) flexural test and (b) shear test as per ASTM D198-22a standard [18].

2.3 Fire performance

Bench-scale cone calorimeter tests were also conducted as per the ASTM E1354-23 [19]. The tests were carried out in the horizontal orientation at the University of Auckland (UoA), New Zealand, on the CLSVL panels prepared from both thermally treated strands and untreated (control) strands. The

limitation in sample holder thickness at UoA (50 mm) required the CLSVL samples to be cut in half to ensure the thickness of each specimen was less than 50 mm. The sample dimensions were maintained at 100 mm by 100 mm. The ASTM E119-24 [20] standard was followed to perform the fire resistance testing at two different scales on the CLSVL panels at Western Fire Center. A small-scale furnace test was eventually carried out with 1.19 m by 1.5 m by 0.11 m samples, which were not loaded and the fire rating was calculated based on either the time the wall resisted the heat transmission in a way that the unexposed side did not reach a temperature of 139°C or the time when the panel failed structurally due to buckling at the junctions under gravity load. Sixteen thermocouples were installed on each panel to monitor temperatures at every 38.1 mm increment through the panel thickness, extending up to 114.3 mm from the exposed surface to also monitor the temperature on the unexposed side. The full-scale furnace tests on horizontal walls were then carried out with 3.01 m by 3.5 m by 0.11 m samples, as per the ASTM E119-24 standard. The standard requires a minimum 9.3 m^2 surface area of exposure, which was met in the current study. The samples were loaded in compression with a uniformly distributed load of 355.86 kN, which resulted in 9.43 kN/m of loading as per the anticipated loading of 2-layered structures. The fire rating was again calculated based on either the time the wall with the compression loads resisted the heat transmission until the temperature on the unexposed side reached 139°C or the time when the wall panels failed under the gravity and applied loads. Twenty thermocouples were used in each panel, six equally distributed at 38.1 mm depths until the unexposed side was reached, with two at the junctions on the unexposed side created during the assembly of the LSVL panels.

3 RESULTS AND DISCUSSIONS

Mechanical testing revealed significant advantages of the strand-based mass timber panels, termed cross-laminated strand veneer lumber (CLSVL), over conventional CLT panels; particularly the elimination of rolling shear, a common failure mode that limits the load-carrying capacity of CLT in high-rise constructions. Additionally, CLSVL demonstrated comparable or superior mechanical performance in several aspects when compared to other mass timber panels made from the same species [21]. Figures 2 (a) and (b) illustrate the comparative effective bending and shear stiffnesses, respectively, of the mass timber panels. The elimination of rolling shear failure [6] resulted in a significant increase in the shear stiffness of the strand-based panels, resulting due to the distribution in grain orientation in the plane of the panel. Internal bond strengths of the composites, as per ASTM D1037-13 [22], also showed enhanced performance with values of 1.08 MPa (COV = 16 %) compared to only 0.3 MPa (COV = 46 %) for the panels made from control or not thermally modified strands.

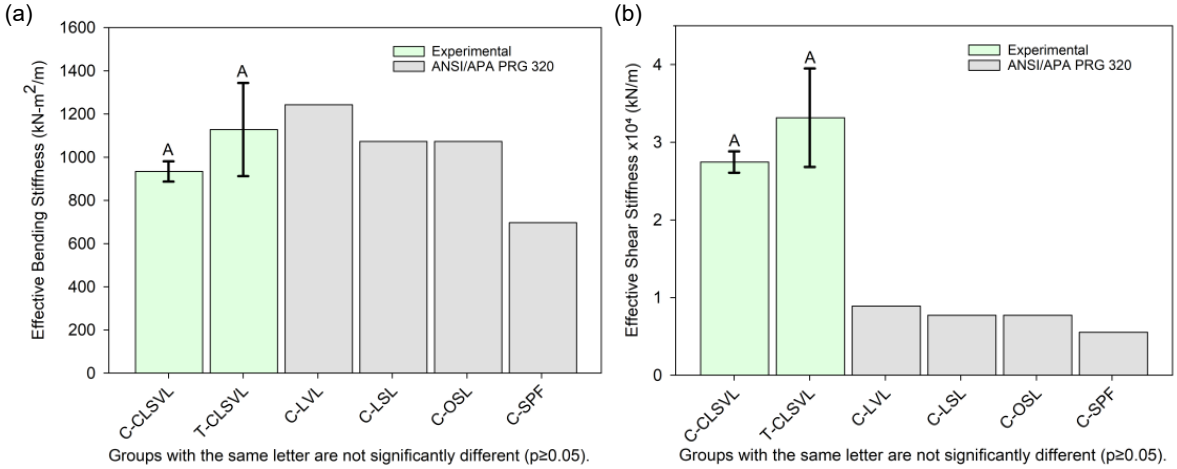

Note: C-LVL = CLT from Laminated Veneer Lumber, C-LSL = CL from Laminated Strand Lumber, C-OSL = CLT from Oriented Strand Lumber, C-SPF = CLT from SPF lumber

Figure 2: Comparative test results for (a) effective bending stiffness and (b) effective shear stiffness.

Fire reaction property analysis using a bench-scale cone calorimeter, as per ASTM E1354-23, showed similar trends in heat release rate (HRR) and mass loss for both CLSVL panels made from control (C-CLSVL) and thermally modified (T-CLSVL) strands, as illustrated in Figure 2. The peak

heat release rate (PHRR) shifted, with higher values for the T-CLSVL (351.7 ± 41.1 kW/m^2), compared to 310.1 ± 10.1 kW/m^2 for the control samples, Figure 3 (a). Although the time to PHRR was longer for the T-CLSVL panels (45 ± 5.4 sec) compared to 35 ± 6.2 sec for the control. The total heat evolved was also almost similar for both the panel types tested. The time to ignition was longer for the T-CLSVL panels by about 33% compared to the C-CLSVL panels, which can be attributed to the reduced amount of weak hemicellulose and volatiles from the surface. The time to flameout was almost similar with only 6% average variation. This indicates that although the time to ignition was later, the amount of fuel in the material reduced during the TM process, resulting in a similar time of flameout. Both samples showed good barriers against flame propagation, with an initial peak in HRR and then a steady, low HRR throughout the burning phase, as can be observed from Figure 3 (a). These are synchronous to fire-resistant specimens, showing a significant amount of char formation on the upper layers that can protect the subsequent layers, giving a good amount of time for evacuating the premises during fire. The mass loss rate was similar for both samples, as can be observed from Figure 3 (b). The char formed in the T-CLSVL samples was 3.3% of the initial mass, 40% higher than that of the control specimen. The T-CLSVL samples also took 33% longer to ignite and 22% longer to reach the PHRR, indicating better fire reaction properties compared to the control. However, the time to flameout was lower by 6%, which again can be attributed to the lower availability of fuel due to the loss in TM. The total heat evolved was almost similar, with the T-CLSVL having a slightly higher PHRR by about 11.8%. Overall, both the C-CLSVL and the T-CLSVL showed promising fire reaction properties.

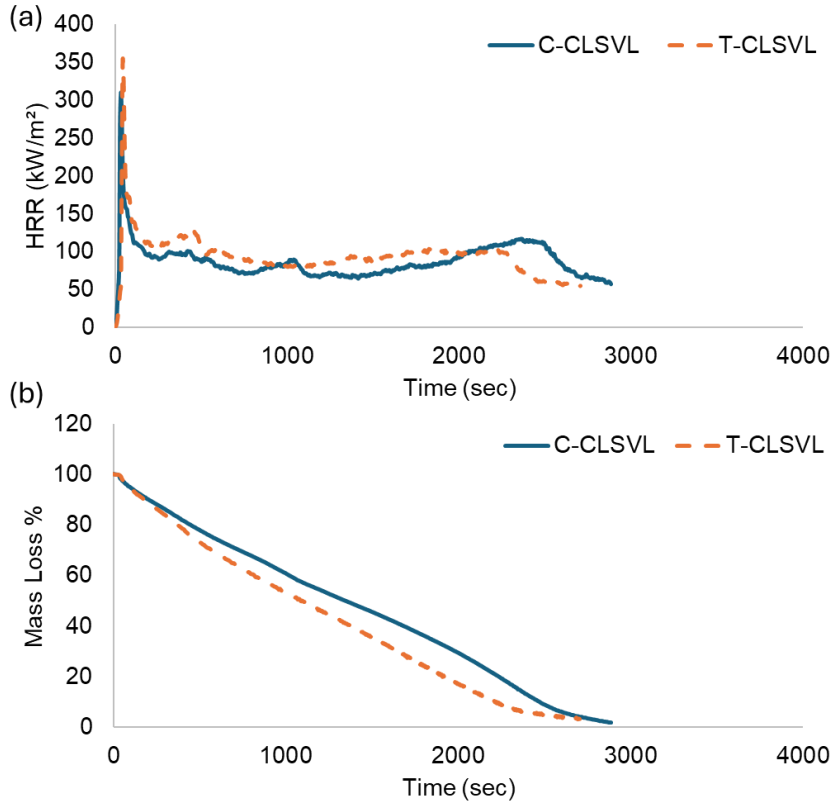

Figure 3: Representation of the (a) HRR and (b) mass loss percentage of the control and TM CLSVL panels when tested in the cone-calorimeter as per the ASTM E1354-23 standard

Small-scale fire resistance tests on C-CLSVL and T-CLSVL panels, based on ASTM E119-22 standard, were performed. Control and TM strands were used to fabricate 24 veneers that were 1.22 m by 1.83 m (4 ft by 6 ft) for the layup of the panels. The control veneers had an average density of 642.34 ± 40 kg/m^3 (40.1 ± 2.5 lb/ft^3), and the TM veneers had 644.58 ± 16.02 kg/m^3 (40.24 ± 1 lb/ft^3). The final wall assembly, after installation, was 1.19 m by 1.5 m by 0.11 m. These specimens were not loaded, therefore, the main criterion for judgment, as per ASTM E119-20, was that the transmission of heat through the wall will not have raised the temperature on its unexposed side more than 139°C (average) above its initial temperature, or if a temperature higher than 30% (181°C) of the specified limit occurs

at any one point (single-point) on the unexposed side of the assembly. Both specimens were able to meet the 1-hr wall rating requirement, with the control being able to maintain the testing criteria for 102 min (rounded off to the nearest integral minute). The treated had a successful test for 64 min (corrected time), after which, although the sample did not fail, the testing apparatus failed to maintain pressure. A comparison of the temperatures on the three levels of the panels (1.5 in or 38.1 mm layer, 3 in or 76.2 mm layer, and unexposed side) at 60 mins showed that the C-CLSVL samples had better fire resistance compared to the TM counterparts.

Finally, full-scale vertical fire resistance testing, as per ASTM E119-20, was carried out on the panels with a continuous compressive load on the top surface, as illustrated in Figure 4. The load-bearing calculations were carried out as per the expected loading on 2-layered structures, which came out to be 9.43 kN/m or 6957 lb/ft, giving a total load of 355.86 kN or 80,000 lbs. The utilization ratio of 0.163, as per interaction equations, was used to understand the loading requirements. The results further strengthened the previous conclusion from the small-scale test, that both wall structures successfully met the 1-hr load requirements. However, similar to small-scale testing, the C-CLSVL panel was able to withstand the load for 71 mins, compared to 64 mins by the T-CLSVL wall specimen. The control performed slightly better under fire resistance, which might be attributed to the reduction in strength due to the TM of the strands. It must also be noted that the panels failed due to buckling under compression loads at the joints in the outer layer, as illustrated in Figure 3. Thus, if the veneers were laminated directly without processing them into lumber, the buckling issue could be eliminated. This has the potential to enhance the fire rating of the panels and possibly impart better fire resistance properties of the T-CLSVL panels due to the enhanced stiffnesses.



Figure 3: Loaded full-scale wall test for (a) C-CLSVL and (b) T-CLSVL before and after fire test as per ASTM E119-20 vertical wall testing procedure.

4 CONCLUSIONS

Thermal modification had an overall positive impact on the mechanical properties of the panels, evidenced by a 260% increase in internal bond strength and a 21% improvement in both effective bending and shear stiffnesses, without a statistically significant change in flexural strength. In contrast, its effect on fire performance was largely neutral, with no significant differences in most fire reaction and resistance metrics; however, a slight decline in the overall fire rating was observed. To address this limitation and meet fire safety standards, the application of an external fire-resistant layer—such as gypsum board, which is commonly used in buildings worldwide—is proposed. Given the environmental concerns and non-renewable nature of gypsum, alternative solutions are being explored. Preliminary research is investigating the use of fire-resistant fabrics, which may enhance fire performance while reducing reliance on gypsum-based materials in residential construction. Additionally, the lab-scale requirement of sectioning the LSVL panels for sanding and priming, if eliminated, can potentially reduce the buckling issues at the joints and possibly increase the fire rating of the overall panels, where the enhanced stiffness due to thermal modification can potentially also help increase the fire resistance properties of the panels.

ACKNOWLEDGEMENTS

This study is based upon work supported by the National Science Foundation under Grant No. 1827434 and the USFS Wood Innovation Grant No. 20-DG-11062765-743. The authors would also like to acknowledge Therma Wood Technology (TWT), Montana, for helping with the thermal modification process, and the University of Auckland, New Zealand, for assisting with the cone calorimeter studies.

REFERENCES

[1] R. Adhikari, “CROSS-LAMINATED STRAND-VENEER COMPOSITE MASS TIMBER PANELS FOR BUILDING CONSTRUCTION”.
[2] R. Brandner, G. Flatscher, A. Ringhofer, G. Schickhofer, and A. Thiel, “Cross laminated timber (CLT): overview and development,” *Eur. J. Wood Wood Prod.*, vol. 74, no. 3, pp. 331–351, May 2016, doi: 10.1007/s00107-015-0999-5.
[3] S. W. Weight and V. Yadama, “Manufacture of laminated strand veneer (LSV) composite. Part 1: Optimization and characterization of thin strand veneers,” *Holzforschung*, vol. 62, no. 6, 2008, doi: 10.1515/HF.2008.126.
[4] R. Jerves, V. Yadama, M. Aro, and M. R. Pelaez-Samaniego, “Cross-laminated strand veneer lumber mass timber panels from thermally modified strands,” *Constr. Build. Mater.*, vol. 368, p. 130370, Mar. 2023, doi: 10.1016/j.conbuildmat.2023.130370.
[5] S. W. Weight and V. Yadama, “Manufacture of laminated strand veneer (LSV) composite. Part 2: Elastic and strength properties of laminate of thin strand veneers,” *Holzforschung*, vol. 62, no. 6, 2008, doi: 10.1515/HF.2008.127.
[6] R. Adhikari *et al.*, “Performance of Thermally Modified Wood Strands and Thin Veneers for Use in Durable Mass Timber Panels,” 2025. doi: 10.2139/ssrn.5228063.
[7] F. B. T. Imamura, Y. Chen, L. Deng, and Y. H. Chui, “Moisture and mould growth risk of cross-laminated timber basement walls: Laboratory and field investigation,” *Constr. Build. Mater.*, vol. 428, p. 136150, May 2024, doi: 10.1016/j.conbuildmat.2024.136150.
[8] M. R. Pelaez-Samaniego, V. Yadama, E. Lowell, and R. Espinoza-Herrera, “A review of wood thermal pretreatments to improve wood composite properties,” *Wood Sci. Technol.*, vol. 47, no. 6, pp. 1285–1319, Nov. 2013, doi: 10.1007/s00226-013-0574-3.
[9] W. E. Hillis, “High temperature and chemical effects on wood stability: Part 1: General considerations,” *Wood Sci. Technol.*, vol. 18, no. 4, pp. 281–293, 1984, doi: 10.1007/BF00353364.
[10] T. Ding, L. Gu, and X. Liu, “Influence of steam pressure on chemical changes of heat-treated Mongolian pine wood,” *BioResources*, vol. 6, no. 2, pp. 1880–1889, Apr. 2011, doi: 10.15376/biores.6.2.1880-1889.

[11] A. Chanda, N. K. Kim, W. Wijaya, and D. Bhattacharyya, “Fire reaction of sandwich panels with corrugated and honeycomb cores made from natural materials,” *J. Sandw. Struct. Mater.*, vol. 23, no. 8, 2021, doi: 10.1177/1099636221989234.
[12] É. Lublóy, D. T. Mészáros, L. G. Takács, Z. Cimer, and H. Norbert, “Examination of the fire performance of wood materials treated with different precautions,” *J. Therm. Anal. Calorim.*, vol. 148, no. 10, pp. 4129–4140, May 2023, doi: 10.1007/s10973-023-12050-2.
[13] C. A. S. Hill, *Wood Modification: Chemical, Thermal and Other Processes*, 1st ed. Wiley, 2006. doi: 10.1002/0470021748.
[14] P. Mitrenga, M. Vandlíčková, M. Konárik, and K. Košútová, “Impact of Heat Treatment of Spruce Wood on Its Fire-Technical Characteristics Based on Density and the Side Exposed to Fire,” *Appl. Sci.*, vol. 12, no. 13, p. 6452, Jun. 2022, doi: 10.3390/app12136452.
[15] J. Martinka, E. Hroncová, T. Chrebet, and K. Balog, “The influence of spruce wood heat treatment on its thermal stability and burning process,” *Eur. J. Wood Wood Prod.*, vol. 72, no. 4, pp. 477–486, Jul. 2014, doi: 10.1007/s00107-014-0805-9.
[16] D07 Committee, *ASTM D198-22a: Standard Test Methods of Static Tests of Lumber in Structural Sizes*. doi: 10.1520/D0198-22.
[17] ASTM International, “ASTM E1354-17 Standard Test Method for Heat and Visible Smoke Release Rates for Materials and Products Using an Oxygen Consumption Calorimeter,” *Annu. Book ASTM Stand.*, vol. 44, no. 42, 2017.
[18] E05 Committee, *ASTM E119-24: Test Methods for Fire Tests of Building Construction and Materials*. doi: 10.1520/E0119-20.
[19] APA, *Standard for performance-rated crosslaminated timber. ANSI/APA PRG, 320*. doi: https://www.apawood.org/ansi-apa-prg-320.
[20] ASTM, “ASTM D1037-13 Standard test methods for evaluating properties of wood-base fiber and particle,” 2013.

piep
innovation
in polymer
engineering

www.piep.pt



Burning behavior of thermoplastic glass fiber composites for a bumper beam application

ICCM24 – 24st International Conference on Composite Materials

August, 2025, Baltimore – USA

Joana Malheiro
Helena Rocha
Andreia Vilela
Paulo Antunes
Liliana Ferreira
Paula Peixoto

BeNeutral
PRR Plano de Recuperação e Resiliência
REPÚBLICA PORTUGUESA
Financiado pela União Europeia NextGenerationEU

Contents

Introduction

Testing

Production

Fire test

Conclusions

BeNeutral
PRR Plano de Recuperação e Resiliência
REPÚBLICA PORTUGUESA
Financiado pela União Europeia NextGenerationEU

Introduction

Research Framework

- Development under Be.Neutral project
- Reduction of CO_2 emission
- Mobility solutions
- Bumper beam solution with integrated sensors
- Lightweight
- Recyclability / Repairability

Introduction

Materials



$(0_2/\pm45_4/0_2)$

Reinforcements

Unidirectional glass-fiber (640 g/m^2)

Biaxial ±45° glass-fiber (400 g/m^2)

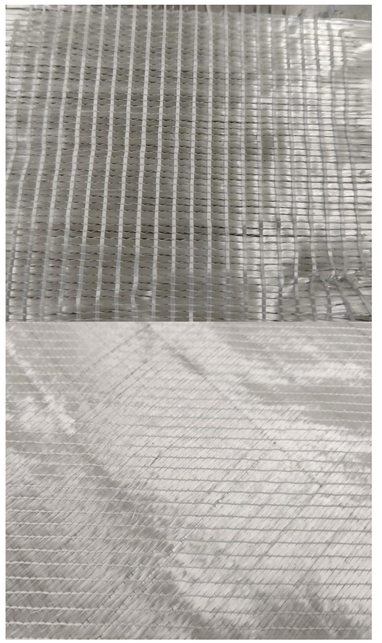

BeNeutral
PRR Plano de Recuperação e Resiliência
REPÚBLICA PORTUGUESA
Financiado pela União Europeia NextGenerationEU

Introduction

Materials



Acrylic Resin

ELIUM® 188 XO

Curing agent

PERGAN

PEROXAN BP-Pulver 50 W

Introduction

Materials

Fire retardants

ATH - Aluminum trihydroxide or alumina trihydrate ($Al(OH)_3$)

APP - Ammonium polyphosphate ($[NH_4PO_3]n(OH)_2$)



Introduction

Manufacturing Process

Vacuum Assisted Resin Infusion (VARI)

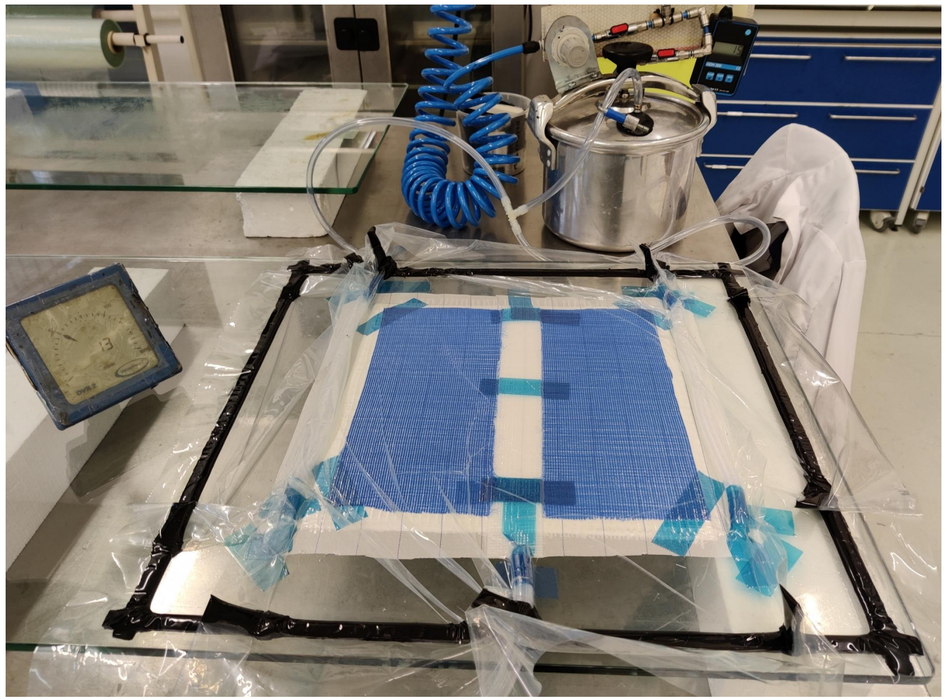

Testing

TGA test

Test method	ASTM E1131-20
Temperature program	**Stage 1** – heating: 30 - 450°C, rate 10°C/min, nitrogen atmosphere **Stage 2** – cooling: 450 - 300°C, rate 10°C/min, nitrogen atmosphere **Stage 3** – heating: 300 – 530°C, rate 10°C/min, oxidizing atmosphere

Testing

TGA test

Sample location

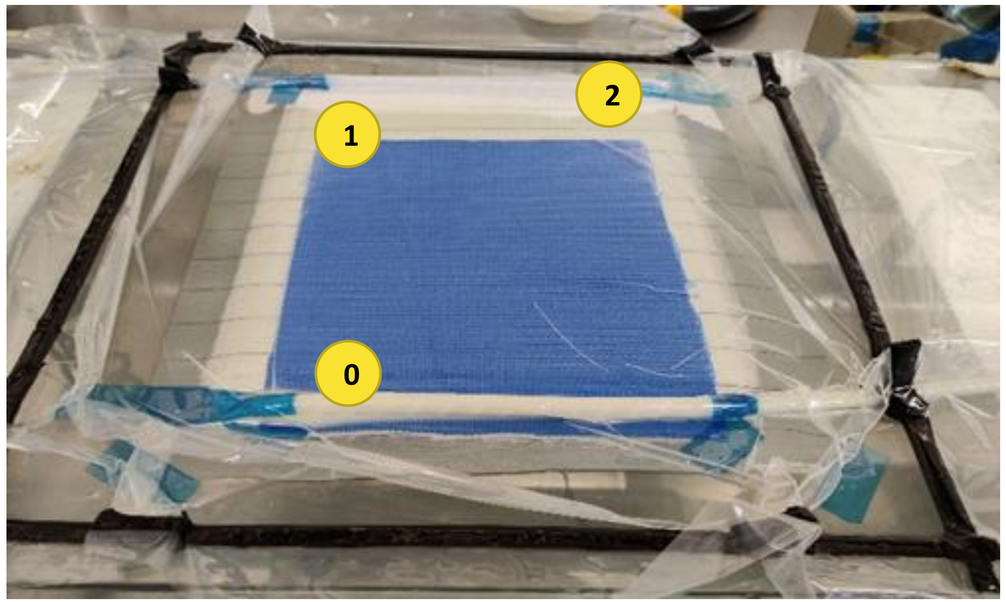

Chemical composition of samples (TGA analysis % - ASTM E1131-20)

Sample	Resin	ATH ($Al(OH)_3$))	Glass fiber
0	25,4	1,98	72,7
1	24,8	3,30	71,8
2	25,5	0,21	74,3

TGA results for samples with 30% of ATH in weight of resin (w/wR)

Testing

TGA test

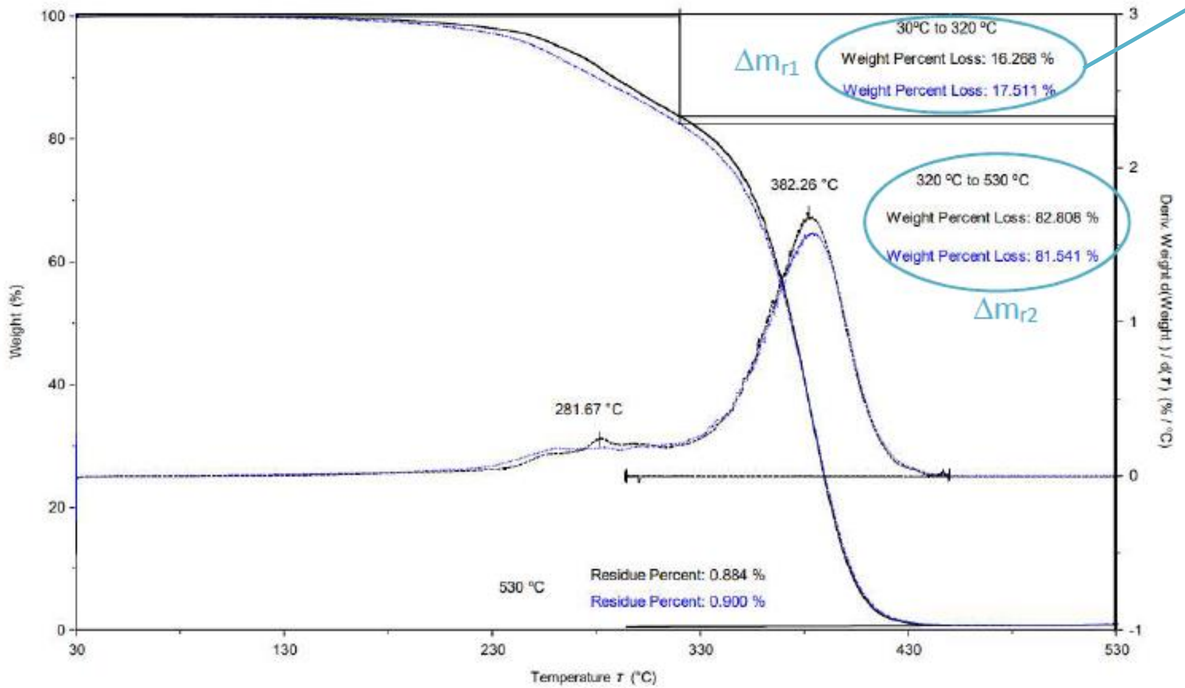

Weight loss and derivative related to temperature for PMMA Arkema Elium 188 XO

Weight loss for PMMA Arkema Elium 188 XO:

16,89%

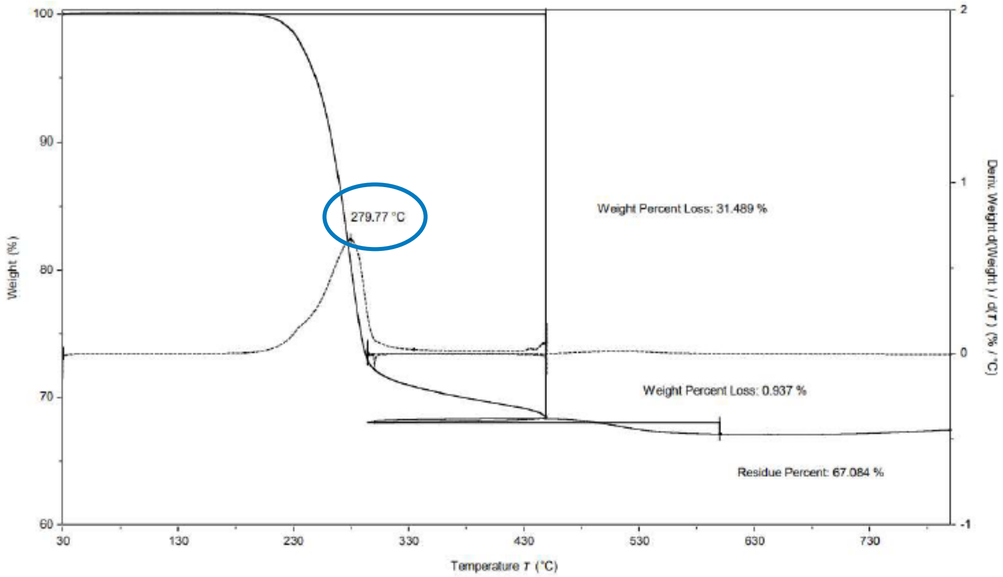

Weight loss and derivative related to temperature for ATH

ATH and PMMA weight losses occur in same temperature range

BeNeutral
PRR Plano de Recuperação e Resiliência
REPÚBLICA PORTUGUESA
Financiado pela União Europeia NextGenerationEU

Testing

TGA test

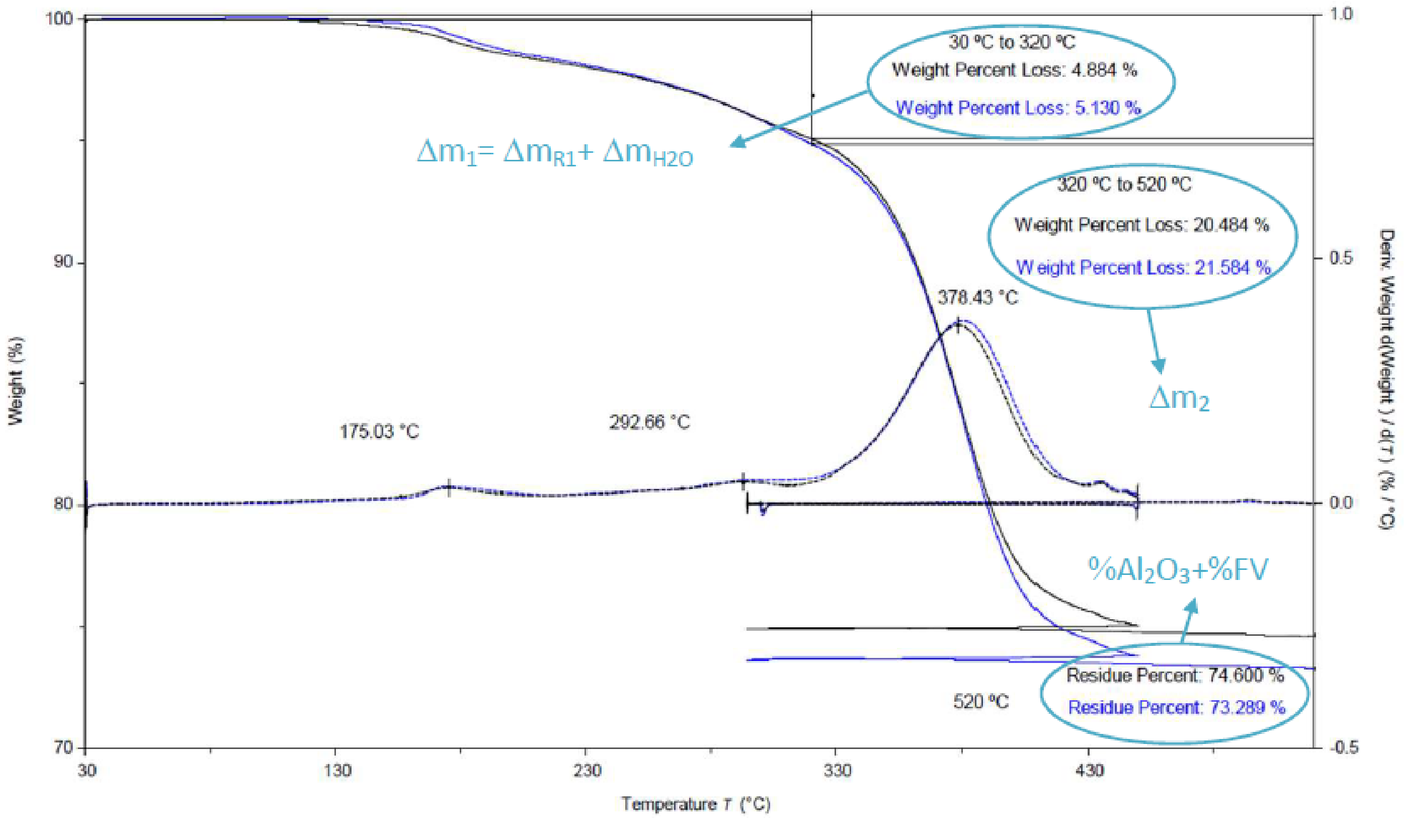

Weight loss and derivative related to temperature for sample **0**

Weight loss related with resin

$$\Delta m_{R1} = \Delta m_2 \times \Delta m_{r1} / \Delta m_{r2}$$

Weight loss from ATH decomposition

$$\Delta m_{H2O} = \Delta m_1 - \Delta m_{R1}$$

Stoichiometric relations

$$\%Al(OH)_3 = \Delta m_{H2O} \times 156/54$$

$$2\ Al(OH)_3\ (s) \rightarrow Al_2O_3\ (s) + 3\ H_2O\ (g)$$

(156) (102) (54)

BeNeutral
PRR Plano de Recuperação e Resiliência
REPÚBLICA PORTUGUESA
Financiado pela União Europeia NextGenerationEU

Production

VARI – Vacuum Assisted Resin Infusion

- Dispersion improvement FR particles (ATH and APP)

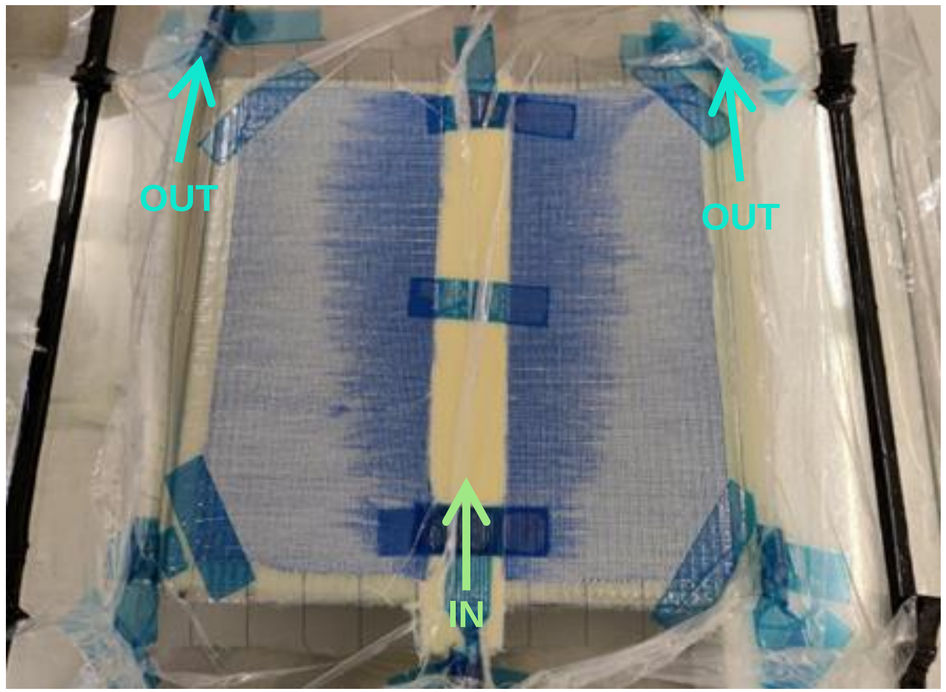

Fire test

Testing

- ISO 3795: 1989
- Conditioning (23±2)°C and (50±10)% for 24 hours
- Fire performance

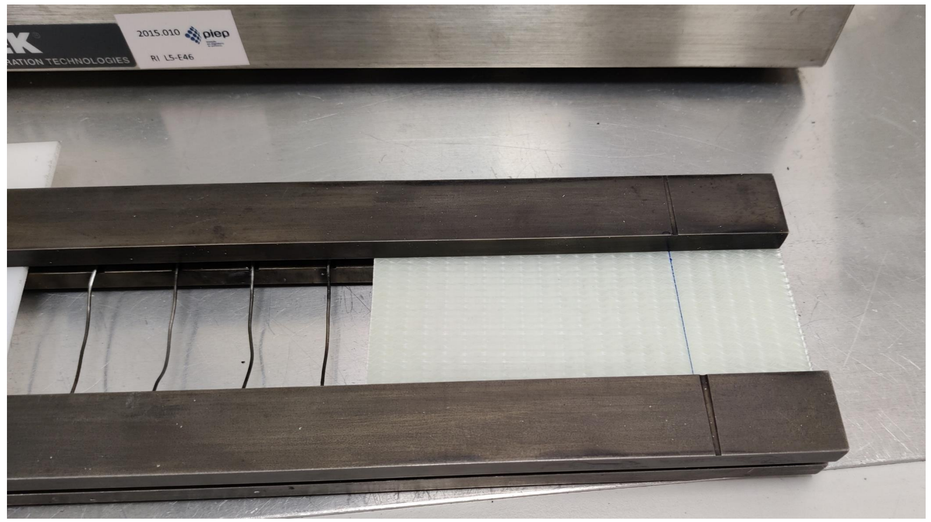

Fire test

Results

Samples	Thickness	Time to combustion (s)	Distance covered by flame (mm)	Combustion speed, B (mm/min)
0% ATH + 0% APP	3,32	0,0	0	0,0
	3,32	559,1	119	12,8
	3,25	598,1	114	11,4
	3,29	588,7	118	12,0
	3,27	570,3	112	11,8

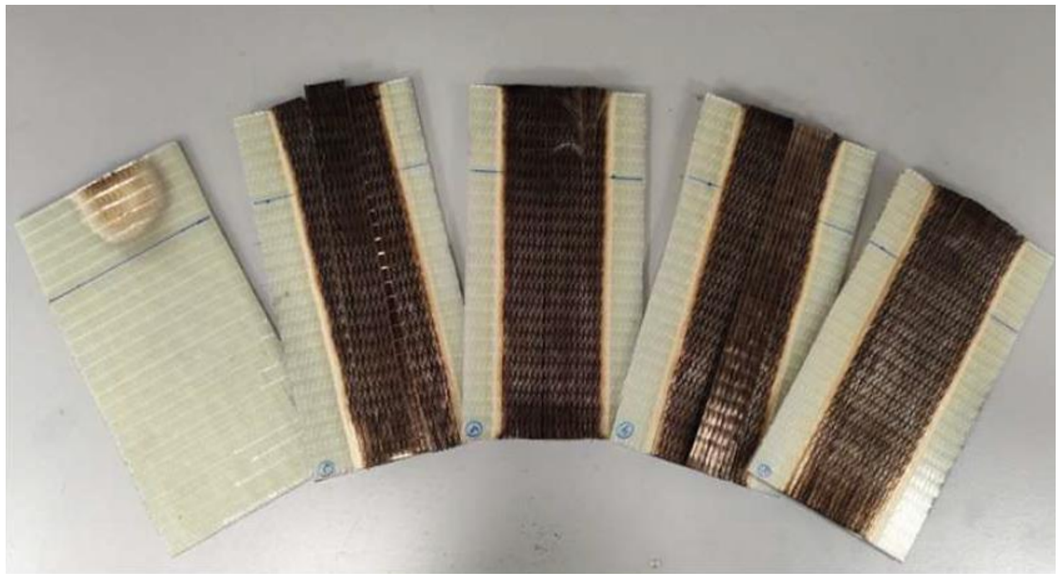

Fire test

Results

Samples	Thickness	Time to combustion (s)	Distance covered by flame (mm)	Combustion speed, B (mm/min)
15% ATH + 0% APP	3,23	364,7	60	9,9
	3,38	0,0	0	0,0
	3,38	0,0	0	0,0
	3,33	0,0	0	0,0
	3,29	401,7	55	8,2

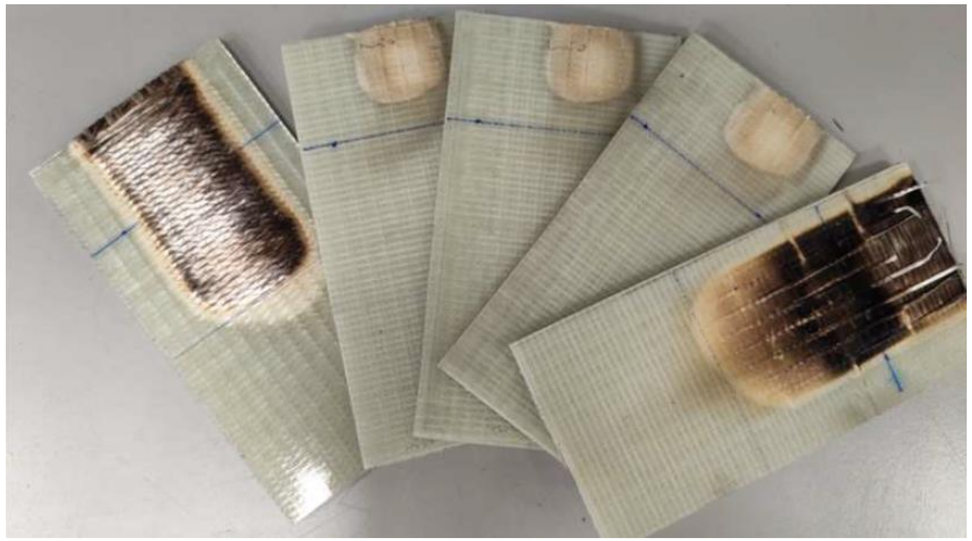

Fire test

Results

Samples	Thickness	Time to combustion (s)	Distance covered by flame (mm)	Combustion speed, B (mm/min)
30% ATH + 0% APP	3,36	0,0	0	0,0
	3,26	0,0	0	0,0
	3,27	0,0	0	0,0
	3,29	0,0	0	0,0
	3,28	0,0	0	0,0

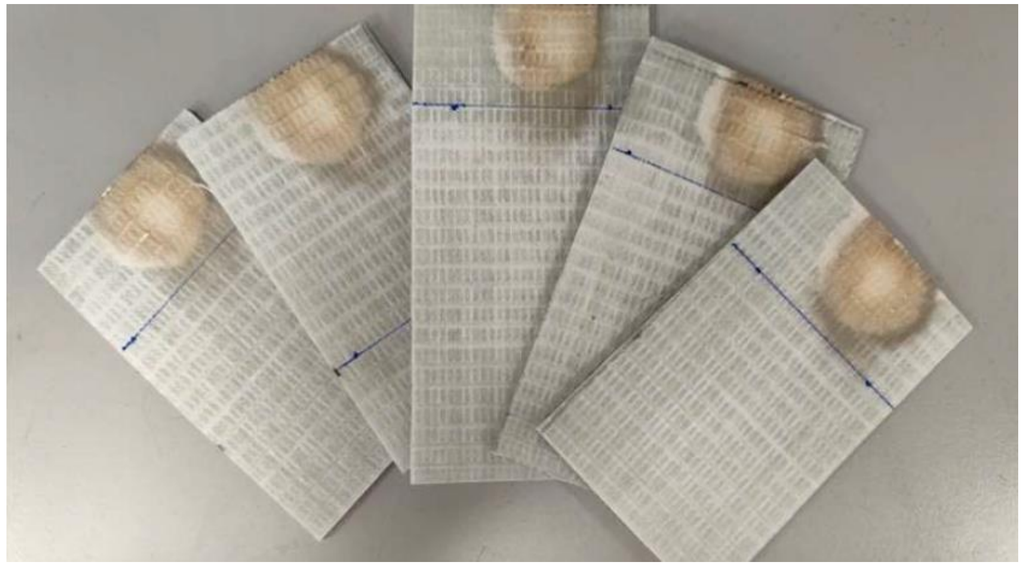

BeNeutral
PRR Plano de Recuperação e Resiliência
REPÚBLICA PORTUGUESA
Financiado pela União Europeia NextGenerationEU

Fire test

Results

Samples	Thickness	Time to combustion (s)	Distance covered by flame (mm)	Combustion speed, B (mm/min)
7,5% ATH + 7,5% APP	3,36	0,0	0	0,0
	3,33	0,0	0	0,0
	3,25	0,0	0	0,0
	3,29	0,0	0	0,0
	3,25	0,0	0	0,0



BeNeutral
PRR Plano de Recuperação e Resiliência
REPÚBLICA PORTUGUESA
Financiado pela União Europeia NextGenerationEU

Fire test

Results

Samples	Thickness	Time to combustion (s)	Distance covered by flame (mm)	Combustion speed, B (mm/min)
0% ATH + 15% APP	3,27	109,9	30	16,4
	3,17	0,0	0	0,0
	3,20	633,2	110	12,8
	3,26	652,5	110	12,8
	3,25	0,0	0	0,0

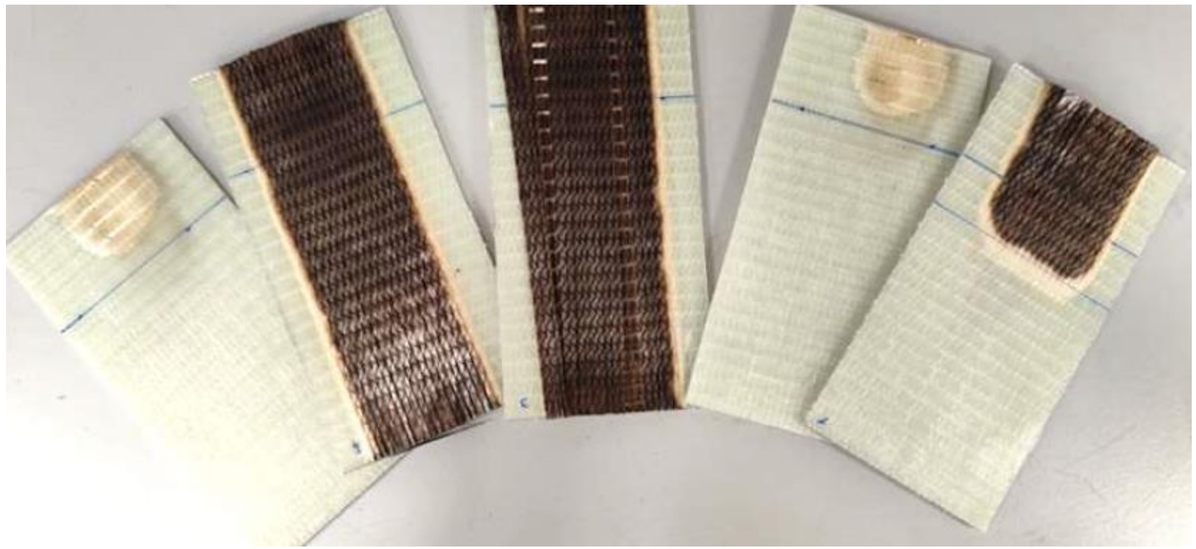

BeNeutral
PRR Plano de Recuperação e Resiliência
REPÚBLICA PORTUGUESA
Financiado pela União Europeia NextGenerationEU

Fire test

Results – double check

Samples	Thickness	Time to combustion (s)	Distance covered by flame (mm)	Combustion speed, B (mm/min)
7,5% ATH + 7,5% APP	3,13	0,0	0	0,0
	3,13	0,0	0	0,0
	3,22	0,0	0	0,0
	3,16	0,0	0	0,0
	3,10	0,0	0	0,0

From resin inlet side



BeNeutral
PRR Plano de Recuperação e Resiliência
REPÚBLICA PORTUGUESA
Financiado pela União Europeia NextGenerationEU

Fire test

Results – double check

Samples	Thickness	Time to combustion (s)	Distance covered by flame (mm)	Combustion speed, B (mm/min)
7,5% ATH + 7,5% APP	3,11	0,0	0	0,0
	3,12	0,0	0	0,0
	3,10	0,0	0	0,0

From resin outlet side



Conclusions

- VARI is difficult for particle distribution, producing some “filtration” and sedimentation (in flow media);
- ATH particles showed good fire retardant properties for 30%;
- Samples with 7,5% ATH + 7,5% APP show the best compromise between weight and fire behaviour;
- Laminate using 7,5% ATH + 7,5% APP is self extinguishable, no flame no fire.

BeNeutral
PRR Plano de Recuperação e Resiliência
REPÚBLICA PORTUGUESA
Financiado pela União Europeia NextGenerationEU



ACKNOWLEDGEMENTS

This article was developed within the scope of the Innovation Pact Mobility Agenda for Carbon Neutrality in Cities by the Consortium Be.Neutral – co-financed by NextGenerationEU, through the 'Business Innovation Agendas' investment from the Recovery and Resilience Plan (RRP).

(351) 253 510 050

geral@piep.pt

www.piep.pt

PIEP - Pólo de Inovação em Engenharia de Polímeros,
Universidade do Minho, Campus de Azurém, Edifício 15
4800-058 Guimarães, Portugal

Follow PIEP on social networks

BeNeutral

PRR Plano de Recuperação e Resiliência

REPÚBLICA PORTUGUESA

Financiado pela União Europeia NextGenerationEU

HYDROCHAR-BASED FLAME RETARDANTS FROM BREWERS' SPENT GRAIN FOR HIGH-PERFORMANCE COMPOSITES

A. Pantaleoni[1], I. Bavasso[1], M.P. Bracciale[1], P. Russo[2], J. Tirillò[1], G. Malucelli[3], E. Maccaferri[4], L. Giorgini[4], A. Marrocchi[5], F. Sarasini[1]

[1]Department of Chemical Engineering Materials Environment, University of Rome La Sapienza. UdR INSTM, Via Eudossiana 18, 00184 Rome, Italy
Email: alessia.pantaleoni@uniroma1.it, irene.bavasso@uniroma1.it, mariapaola.bracciale@uniroma1.it, jacopo.tirillo@uniroma1.it, fabrizio.sarasini@uniroma1.it, web page: http://www.uniroma1.it

[2]Institute for Polymers, Composites and Biomaterials, National Research Council, Via Campi Flegrei 34, 80078 Pozzuoli (Na) (Italy)
Email: pietro.russo@ipcb.cnr.it, web page: https://www.cnr.it/

[3]Department of Applied Science and Technology, Politecnico di Torino, Viale Teresa Michel 5, 15121 Alessandria, Italy
Email: giulio.malucelli@polito.it, web page: https://www.polito.it/

[4]Department of Industrial Chemistry "Toso Montanari", University of Bologna, Viale Risorgimento 4, 40136 Bologna, Italy
Email: emanuele.maccaferri3@unibo.it, loris.giorgini@unibo.it, web page: https://www.unibo.it/it

[5]Department of Chemistry, Biology and Biotechnology, University of Perugia, Via Elce di Sotto 8, 06123 Perugia (Italy)
Email: assunta.marrocchi@unipg.it, web page: https://www.unipg.it/

Keywords: Biocomposites, Hydrochar, Flame resistance, Mechanical properties, Phytic acid

ABSTRACT

In this study, a sustainable flame-retardant biocomposite was developed by incorporating hydrochar (HC) derived from Brewers' Spent Grain (BSG) into a polylactic acid (PLA) matrix. HC was produced via hydrothermal carbonization (HTC), yielding a porous, carbon-rich material characterized by a high content of oxygen-containing functional groups. The filler was further functionalized with phytic acid (PA) to introduce phosphorus-based flame-retardant functionalities (HC-P). The effectiveness of the modification was confirmed through FT-IR, while SEM-EDS, BET and elemental analysis were used to assess the structural and surface properties of HC. PLA composites containing 20 wt.% of HC and HC-P were prepared via melt blending and compression molding, and characterized by TGA, DSC, DMA, and flexural testing. HC incorporation led to earlier thermal degradation and reduced mechanical performance, attributed to poor interfacial adhesion and filler aggregation. However, PA functionalization improved thermal stability and partially restored mechanical properties by enhancing filler–matrix compatibility and dispersion. Cone calorimeter tests revealed that the HC-P composite exhibited improved flame-retardant performance, with reductions of 15% in peak heat release rate (pHRR), 13% in total smoke release (TSR), 12.5% in specific extinction area (SEA), and 12.9% in MARHE compared to the unmodified composite. These results highlight the dual role of phytic acid in promoting char formation and limiting flammable volatile release, demonstrating the potential of functionalized hydrochar as an effective bio-based flame retardant for PLA composites.

1 INTRODUCTION

The rapid expansion of manufacturing industries has increased the demand for materials with improved strength, lower density, reduced cost, and enhanced sustainability. Composite materials have

emerged as one of the materials that can meet this growing demand. Growing environmental awareness has highlighted the impact of plastic pollution and fossil fuel use, driving industries to adopt renewable raw materials and develop biobased polymers to reduce environmental impact [1]. Among biopolymers, polylactic acid (PLA) stands out as a promising material produced from renewable sources like corn starch and sugarcane [2]. Its biodegradability, biocompatibility, and suitable mechanical performance have made it a widely used alternative to traditional petroleum-based plastics in various fields, including packaging, textiles, biomedical applications, and composite materials. However, biopolymers like PLA are generally more expensive than petroleum-based plastics, limiting their broader adoption [3]. A common strategy to reduce costs while preserving environmental benefits involves creating biocomposites by partially replacing the polymer with low-cost, natural waste-derived fillers [4]. Moreover, PLA exhibits certain drawbacks that limit its use in more demanding applications, as low thermal stability, brittleness, and high flammability [5]. To address these limitations, recent research has focused on incorporating functional reinforcement to enhance performance and lower production costs.

Various additives and fillers—such as antioxidants, plasticizers, stiffeners, and flame retardants—are widely used to enhance specific polymer properties. However, some stiffening fillers fail to balance stiffness and toughness, and many conventional fillers raise environmental and health concerns due to their toxicity (e.g., phthalates, PBDEs [6]). As a result, there is increasing interest in greener alternatives that combine performance with safety. Carbon-based materials like carbon nanotubes, carbon black, biochar, and graphene [7,8] are particularly promising due to their high surface area, carbon content, and hydrophobicity. However, materials such as grapheneand nanotubes remain costly and complex to produce. Biochar (BC) is a sustainable carbon-based filler with high thermal stability, hardness, surface area, chemical stability, and electrical conductivity [9]. These properties make it a promising alternative to conventional fillers for improving the mechanical, electrical, and flame-resistant performance of PLA-, HDPE-, and PP-based composites. Among carbon-based materials, hydrochar (HC) is emerging as a sustainable and promising filler for polymer composites, although it remains less studied than biochar, carbon black, or carbon nanotubes. HC is produced via hydrothermal carbonization (HTC), a low-temperature (180–300 °C), water-based thermochemical process that converts wet biomass under autogenous pressure [10]. Unlike pyrolysis, HTC allows direct processing of high-moisture feedstocks, such as agricultural residues or food waste, eliminating energy-intensive drying and offering higher solid yields. These features support its economic viability and align with circular economy principles by converting organic waste into valuable carbon-based materials. When combined with biodegradable polymers like PLA, HC contributes to the development of sustainable, carbon-neutral or even carbon-negative composites. In this work, we propose hydrochar (HC) derived from Brewers' Spent Grain (BSG) via hydrothermal carbonization (HTC) as a sustainable carbon-based filler for PLA composites. BSG is the primary by-product of the brewing industry, accounting for around 85% of its total waste, with an estimated annual output of 25–40 million tonnes globally and 3.4 million tonnes within the EU [11]. This lignocellulosic residue is rich in organic matter but contains a high moisture content (70–90 wt.%), making it prone to microbial decomposition and the development of unpleasant odors. In warm climates, its shelf life may be limited to 7–10 days, posing challenges for storage and transportation [12]. As a result, BSG is often disposed of through unsustainable practices such as landfilling. HTC offers an effective valorization route by processing wet biomass without prior drying, making it particularly suitable for BSG and contributing to circular waste management strategies. To the best of the authors' knowledge, no study has investigated the use of hydrochar (HC) derived from Brewers' Spent Grain (BSG) as a filler in polymer composite materials. Only a few studies have explored HC obtained from other biomass sources for composite applications. Ye et al. conducted a comparative study on HC and biochar from wood chips as fillers in PBAT-based biodegradable composites. HC acted as a nucleating agent and influenced the hydrophobicity of the composites. Unlike biochar, which increased stiffness at the expense of toughness, HC provided an improved balance between stiffness and toughness, with optimal performance achieved at 10 wt.% HC treated at 300 °C [13]. Nizamuddin et al. developed PLA-based composites incorporating 5–20 wt.% HC from rice husk via melt processing. The addition of HC significantly increased the tensile modulus (from 2.63 to 4.24 GPa at 20 wt.%) due to mechanical interlocking and polymer infiltration into HC pores. However, tensile strength and elongation at break decreased, attributed to weak interfacial adhesion and particle agglomeration. HC also acted as a nucleating agent and enhanced the thermal stability of the composites [14]. Bejenari et al. investigated

HC from spruce bark waste in an aromatic bio-epoxy resin system, where HC acted as both a filler and a co-reactant in the crosslinking process. This dual role led to increased reaction enthalpy, a reduced curing temperature range, and significantly improved thermal stability and hardness, demonstrating HC's potential to produce stiffer and more sustainable materials [15]. Therefore, using HC as a filler in biopolymers offers a promising strategy for developing biocomposite materials by lowering costs, potentially enhancing the polymer's mechanical properties, and adding value to waste in accordance with circular economy principles. However, one of the main problems with biocomposite materials persists: their poor fire resistance. Biopolymers like PLA are inherently highly flammable [16]. Flame retardants (FRs) are essential for improving the fire safety of composite materials by preventing ignition and slowing combustion. While halogen-based FRs were widely adopted in the 1970s for their high efficiency at low loadings, their use has raised serious environmental and health concerns due to the release of toxic gases and persistent pollutants. As a result, increasing regulations and environmental awareness have driven the development of halogen-free, bio-based flame retardants as safer and more sustainable alternatives [17]. Among halogen-free alternatives, phosphorus-based flame retardants are gaining significant interest due to their structural versatility, variable phosphorus content, and oxidation states (0 to +5), which enable tailored flame-retardant mechanisms suited to different polymer matrices [18,19]. Incorporating flame retardants (FRs) directly into the polymer matrix is the most common method to enhance fire resistance of bio-based composites. However, this approach often results in compatibility issues between the FRs and PLA, negatively impacting the mechanical properties of the composites due to increased melt viscosity and potential phase separation [20,21]. An alternative strategy involves grafting or adsorbing the FR onto the filler, thus improving fire resistance without compromising composite integrity, especially in systems using hydrophilic FRs and hydrophobic polymer matrices, such as PLA [22]. In this paper, we aim to address key challenges associated with polymeric biocomposites, such as high cost and poor fire resistance, by developing a PLA-based biocomposite reinforced with hydrochar (HC) derived from beer production waste. To enhance fire resistance, we also propose the surface modification of the filler using phytic acid. Phytic acid (PA), with its high phosphorus content (~28%) and non-toxic, eco-friendly profile, is gaining attention as a sustainable flame retardant and alternative to halogenated compounds [23]. It acts in both the condensed and gas phases, promoting char formation and releasing phosphorus radicals that quench flame-propagating species, while generating inert gases that dilute combustible elements [24]. In composite materials, PA has been used to modify reinforcing phases to enhance flame resistance. Liu et al. treated ramie fibers with PA, increasing LOI and char yield but reducing mechanical strength, which was mitigated through hybridization with glass fibers [25]. Costes et al. improved PLA flame retardancy by melt blending lignin with PA, achieving a 44% reduction in peak heat release rate, UL-94 V-2 classification, improved thermal stability, and enhanced elongation at break [26]. In the literature, one study reports the use of carbon-based materials as fillers in combination with phytic acid: Zhong et al. prepared flame-retardant bamboo biochar (mBC) via hydrogen peroxide oxidation followed by modification with phytic acid and urea to add phosphorus and nitrogen groups. Incorporating 10 wt.% mBC into PLA improved flame retardancy, achieving UL-94 V-0 and raising the LOI from 20.7% to 28.3%. Cone calorimeter tests showed a decrease in ignition time (63 to 38 s at 20 wt.% mBC) and reduced heat release due to stable char formation. Despite some loss in mechanical strength from filler–matrix incompatibility, performance remained acceptable [27]. In this study, hydrochar was produced from Brewers' Spent Grain (BSG). Compared to biochar, hydrochar naturally possesses a surface rich in oxygen-containing functional groups and exhibits a highly porous structure. These features eliminate the need for oxidative pretreatment, thereby avoiding the associated safety risks. The use of hydrochar not only reduces energy consumption during filler production but also makes the modification process more sustainable. The produced hydrochar was characterized for its structure by Scanning Electron Microscopy (SEM) coupled with Energy Dispersive Spectroscopy (EDS), its chemical composition through elemental analysis, and its porosity by Brunauer–Emmett–Teller (BET) measurements. Following characterization, the hydrochar was modified by reaction with phytic acid. This modification was carried out in aqueous solution at room temperature, with pH adjustment facilitating the formation of ionic and hydrogen bonds. The modified filler (HC-P) was analyzed by Fourier Transform Infrared Spectroscopy (FT-IR) to confirm the effectiveness of the surface modification and subsequently

incorporated into polylactic acid (PLA) matrices at a loading of 20 wt.%. The resulting composites were evaluated for their mechanical, thermal, and flame retardant properties using cone calorimetry.

2 MATERIALS AND METHODS

2.1 MATERIALS

A PLA Luminy® LX175 (96% L-isomer), provided by TotalEnergies Corbion, was utilized as the polymer matrix. Brewers' Spent Grain (BSG) was provided by research center CERB (Italian Brewing Research Centre, Perugia, Italy). Phytic acid solution 50 % (w/w) in H_2O and sodium hydroxide (NaOH) were obtained from Merck KGaA (Darmstadt, Germany).

2.2 HYDROCHAR SYNTHESIS AND COMPOSITE MANUFACTURING

Brewers' Spent Grain (BSG), with a moisture content of 83.5%, was first homogenized by grinding and then mixed with distilled water to obtain a dry-to-water ratio of 1:2. The resulting mixture was placed in an autoclave hydrothermal reactor, where hydrochar (HC) was produced through hydrothermal carbonization (HTC). The reaction was conducted at 230 °C for 4 hours.

5g of hydrochar were reacted with 13.1 mL (14.4 mmol) of phytic acid. The pH was adjusted to 4.5 using sodium hydroxide (NaOH), and the mixture was stirred at room temperature for 24 hours. The modified hydrochar (HC-P) was then collected by filtration.

Fabrication of the PLA reinforced with untreated hydrochar (PLA-HC) and PLA reinforced with modified hydrochar (PLA_HC-P) composites was performed using Brabender-like equipment (Rheocord EC, Haake Inc.) and a lab hydraulic press (Collin model P400E) to process them into plates (100mm × 100mm × 4mm). Before compounding, the HC and HC-P as well as the PLA pellets were dried in a vacuum oven at 70 °C for 4 h. The micro compounder was used to mix HC and HC-P with PLA setting the rotation speed of 60 rpm at 180 °C for 5 min. The PLA composites were then compression molded at 180 °C using a pressure profile as follows: 2 min at 0 bar – 1 min at 5 bar – 1 min at 10 bar and 1 min at 20 bar. Finally, the cooling step down to room temperature was carried out while maintaining the material at the maximum pressure set (20 bar). The reinforcement content was kept at 20 wt.%.

2.3 CHARACTERIZATION TECHNIQUES

The effectiveness of hydrochar (HC) modification with phytic acid was evaluated using Fourier Transform Infrared Spectroscopy (FT-IR). Spectra were recorded with a Bruker VERTEX 70 spectrometer equipped with a diamond attenuated total reflectance (ATR) accessory. Measurements were performed in the mid-infrared range (400–4000 cm^{-1}) at a resolution of 4 cm^{-1}, averaging 128 scans per sample.

The surface morphology of the hydrochar (HC) was examined using Field Emission Scanning Electron Microscopy (FE-SEM) combined with Energy Dispersive X-ray Spectroscopy (EDS). Imaging was performed on a Tescan Mira3 system at an accelerating voltage of 10 kV. Prior to analysis, the samples were sputter-coated with a thin layer of gold to enhance conductivity.

Thermogravimetric analysis (TGA) was performed in accordance with ISO 11358, using a TG209 F1 Libra instrument (Netzsch). Samples were heated from room temperature to 800 °C at a constant rate of 10 °C/min under a nitrogen atmosphere.

Differential scanning calorimetry (DSC) was carried out in accordance with ISO 11357 using a DSC 300 Caliris (Netzsch), under a nitrogen flow of 40 mL/min. The thermal program consisted of a heating–cooling–heating cycle from 25 °C to 200 °C at a rate of 10 °C/min. Melting and crystallization temperatures, along with the degree of crystallinity (Xc, see Equation 1), were determined as the average values from three independent measurements:

$$\chi_c = \frac{(\Delta H_m - \Delta H_{cc})}{\Delta H_m^0 \, x \, \varphi} \, x \, 100 \qquad (1)$$

where ΔH_{cc} and ΔH_m represent the cold crystallization and melting enthalpies of the PLA composites, respectively; φ is the weight fraction of PLA in the composite; and ΔH_m^0 (93 J/g) is the enthalpy of fusion for 100% crystalline PLA [28].

Elemental composition was analyzed using a UNICUBE® elemental analyzer.

Surface area and porosity were measured by N_2 adsorption–desorption isotherms at −196 °C using a Micromeritics Triflex analyzer. Samples were outgassed at 300 °C for 4 hours before analysis. Isotherms (p/p_0 = 0.01–0.99) were analyzed with 3Flex software (v4.05), and the BET equation was applied to calculate the specific surface area.

The thermal conductivity of the composites was measured using a TCi C-Therm thermal conductivity analyzer (C-Therm Technologies Ltd., Fredericton, Canada).

Dynamic mechanical analysis (DMA) was used to evaluate the thermo-mechanical behavior of the materials in the solid state under oscillatory loading. The storage modulus (E′), loss modulus (E″), and damping factor ($\tan\delta = E''/E'$) were recorded as a function of temperature. Tests were performed in three-point bending mode using a DMA 242 E Artemis instrument (Netzsch), in accordance with ISO 6721. Specimens (60 × 10 × 4 mm³) were heated from 25 °C to 75 °C at a rate of 2 °C/min, with a constant oscillation frequency of 1 Hz.

Flexural tests were performed on 80 × 10 × 4 mm^3 specimens using a Zwick/Roell Z2.5 machine, following ISO 178 (span-to-thickness ratio 16:1, crosshead speed 5 mm/min).

Fire behavior was evaluated using an oxygen consumption-based cone calorimeter (CCT), specifically the FFT Cone Calorimeter model from Fire Testing Technology Limited. In accordance with ISO 5660 standards, tests were conducted with an incident heat flux of 35 kW/m². The specimens, placed horizontally under a cone-shaped heater, measured 100 × 100 mm² with a thickness of 4 mm. Each formulation was tested using three replicate samples.

3 RESULTS AND DISCUSSION

The raw material, Brewers' Spent Grains (BSG), and the resulting hydrochar (HC) produced via hydrothermal carbonization (HTC) were morphologically characterized by SEM analysis as shown in Figure 1. The BSG (Figure 1a) exhibits a compact and relatively smooth surface morphology, with aggregated structures and limited visible porosity. After HTC treatment, a substantial morphological transformation is observed (Figure 1b): the HC displays a more fragmented and porous structure, characterized by rougher surfaces and irregular agglomerates. This change is consistent with the partial carbonization and structural reorganization of the lignocellulosic matrix induced by the HTC process.

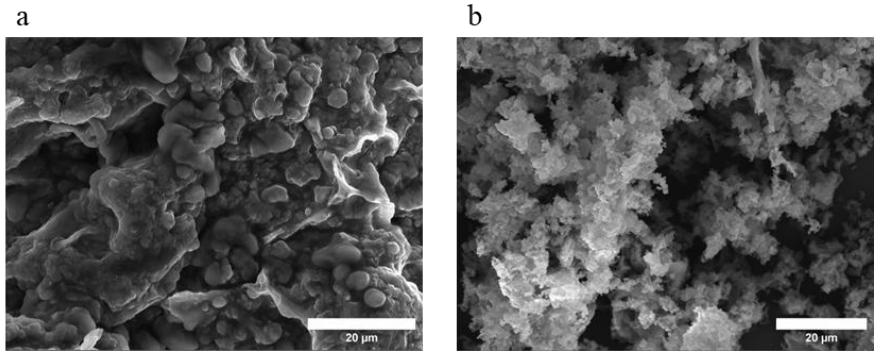

Figure 1: SEM analysis of (a) as-received Brewers' Spent Grains (BSG) and (b) hydrochar (HC)

Elemental analysis was performed on both dried BSG and the resulting hydrochar. The raw BSG exhibited a composition of 46.3% carbon, 4.71% hydrogen, 3.79% nitrogen, and 0.063% sulfur. After HTC treatment, the hydrochar showed a composition of 60.5% carbon, 6.9% hydrogen, 2.8% nitrogen, and 0.3% sulfur. The observed increase in carbon and hydrogen content, together with the relative decrease in nitrogen, reflects the fundamental chemical transformations induced by the HTC process. Specifically, HTC promotes the removal of nitrogen-containing compounds via volatilization or dissolution in the aqueous phase, resulting in a more carbon-enriched solid. This behavior is consistent with findings reported by Kruse et al., who attributed the decrease in nitrogen content to the degradation

of proteins into amino acids and subsequently into volatile species such as ammonia and amines. The preferential loss of nitrogen and retention of carbon-rich structures leads to a more aromatic and condensed hydrochar, particularly when protein-rich feedstocks like BSG are used [29]. The BET specific surface area of HC was measured at 6.63 m^2/g, while the pore volume derived from BJH analysis remains low, suggesting the presence of a predominantly mesoporous to macroporous network. These textural features are consistent with those typically observed in non-activated hydrochars produced under mild hydrothermal conditions [30,31]. The hydrochar was then functionalized with phytic acid units via a reaction carried out at room temperature using water as the solvent. This functionalization aimed to introduce phosphate groups onto the hydrochar surface, potentially enhancing its effectiveness as a flame retardant for biocomposites. The FT-IR spectra of HC show a broad band between 3100 and 3700 cm^{-1} attributed to O–H stretching vibrations in hydroxyl and carboxyl groups. Peaks at 2921 and 2855 cm^{-1} correspond to aliphatic C–H stretching and deformation vibrations [32]. The band at around 1060 cm^{-1} is associated with β-glycosidic bonds in cellulose and hemicellulose [33]. An absorption peak near 1515 cm^{-1} indicates aromatic ring stretching vibrations, suggesting the presence of aromatic structures [34]. The peak at approximately 1700 cm^{-1} corresponds to C=O groups, while bands in the range 1030–1160 cm^{-1} relate to cellulose components [33]. The FT-IR spectrum of HC-P showed new signals at 1059 cm^{-1} and 921 cm^{-1}. Phytic acid typically exhibits signals associated with the asymmetric and symmetric stretching vibrations of P–O–C groups at 1071 cm^{-1} and 996 cm^{-1}, respectively[35]. The shift in the newly observed signals may suggest interactions between phytic acid and functional groups on the hydrochar surface [36]. PLA-based composites were prepared by incorporating 20 wt.% of either HC or HC-P as reinforcing agents. The thermal degradation behavior of neat PLA and its composites with HC and HC-P was investigated by TGA, as reported in Table 1. The incorporation of HC into the PLA matrix leads to an earlier degradation, as evidenced by the decrease in T_5%, T_{10}%, and T_{max} values. This behavior can be attributed to two main mechanisms. The first is related to the presence of HC, a carbonaceous material with a porous structure and high surface area, which facilitates the formation of thermally conductive networks within the PLA matrix. Indeed, the thermal conductivity of PLA reinforced with HC increased by approximately 80% compared to neat PLA, enhancing heat transfer efficiency throughout the material. As a result, the composite heats up more uniformly and rapidly under thermal stress, leading to an earlier onset of thermal degradation [37]. The second possible mechanism involves chemical interactions between the biochar surface and the PLA matrix. Similar observations have been reported for PLA composites containing grapevine-derived biochar (GVC), where the filler was found to catalyze the scission of PLA macromolecular chains. This resulted in a reduced average molecular weight and a narrower molecular weight distribution. Such molecular-level degradation can also contribute to the earlier thermal decomposition observed in PLA/HC composites [38]. Interestingly, the composite containing phytic acid-modified hydrochar (PLA_HC-P) shows slightly delayed degradation compared to PLA_HC, with T_5% and T_{10}% values of 301.1 °C and 332.6 °C, respectively. Its T_{max} (368.1 °C) is also close to that of neat PLA (369.6 °C). While thermal conductivity remains similar to PLA_HC, this delayed degradation suggests a stabilizing effect of phytic acid. Such behavior may be attributed to phosphorus-containing groups from phytic acid, which are known to promote char formation and interfere with radical degradation pathways [39]. Moreover, the final residue increases significantly with the addition of HC (8.93%) and even more so in PLA_HC-P (10.3%), compared to neat PLA (1.5%). This trend reflects the presence of the carbon-rich filler and the additional contribution of phytic acid, which is known to promote carbonization reactions and enhance char yield during thermal decomposition [40].

	$T_{5\%}$ °C	$T_{10\%}$ °C	T_{max} °C	Residue wt.%
PLA	340.2	347.3	369.6	1.5
PLA_HC	297.3	319.2	359.0	8.9
PLA_HC-P	301.1	332.6	368.1	10.3

Table 1: TGA results of PLA, PLA_HC and PLA_HC-P

Composites materials were then characterized by DSC analysis (Table 2). The incorporation of 20 wt.% hydrochar (HC) into PLA resulted in a decrease in the glass transition temperature (T_g). This reduction may be attributed to a combination of factors. On one hand, the presence of polar functional groups on the HC surface can increase the free volume between PLA chains, enhancing chain mobility and thereby lowering T_g [41,42]. On the other hand, the possible presence of residual moisture and hydroxyl groups on HC may have contributed to partial degradation of PLA chains during melt mixing, leading to a lower molecular weight and, consequently, a reduced T_g [43]. However, an increase in the crystallinity was observed. This is likely due to the ability of HC particles to act as nucleating agents, promoting crystal growth and enhancing overall crystallinity [13]. This effect thus seems to coexist with an increase in the amorphous fraction, as indicated by the shift in T_g. This could be the result of heterogeneity in HC dispersion or partial PLA degradation, leading to localized changes in chain mobility and crystal structure. PLA reinforced with phytic acid-functionalized hydrochar (PLA_HC-P) showed a slight increase in T_g compared to PLA_HC. This may be attributed to improved interfacial interactions between HC and the PLA matrix, promoted by phytic acid, which can reduce the interfacial free volume and limit chain mobility [26]. Nonetheless, the T_g remained lower than that of neat PLA, and a reduction in crystallinity was observed in comparison to PLA_HC.
This behavior could be explained by multiple concurrent phenomena, including a potential and mild plasticizing effect of phytic acid on the PLA matrix, which can increase chain flexibility and thus reducing crystallinity [44,45].

Sample	T_g (°C)	T_{cc} (°C)	T_m (°C)	ΔH_{cc} (J g^{-1})	ΔH_m (J g^{-1})	χ_c (%)
PLA	59.6	117.6	147.9	11.4	15.9	4.9
PLA-HC	53.6	118.9	147.2	19.1	23.8	6.3
PLA_HC_P	54.8	115.9	146.7	22.5	24.8	3.1

Table 2: DSC results of PLA, PLA_HC and PLA_HC-P

Dynamic mechanical analysis (Table 3) provided further insights into the thermomechanical behavior of the composites. The storage modulus (E′) of PLA_HC was significantly lower than that of neat PLA, suggesting a plasticizing effect induced by the presence of hydrochar. This reduction in stiffness may be attributed to the limited interfacial adhesion between HC and the PLA matrix, and the tendency of HC particles to form aggregates, which can act as stress concentrators and disrupt efficient load transfer[46]. Consistent with DSC findings, the glass transition temperature (T_g) of PLA_HC was shifted to lower values, indicating increased chain mobility likely related to the presence of polar groups on HC and possible partial degradation of PLA during processing. Interestingly, the PLA_HC-P sample exhibited a moderate increase in storage modulus compared to PLA_HC and a less pronounced shift in T_g. This suggests that the phytic acid functionalization may improve compatibility and interfacial interaction between HC and the PLA matrix [26].

Sample	E' (MPa)			T_g (°C)
	at 40 °C	at 50 °C	at 60 °C	
PLA	3229	3130	398	63.8
PLA_HC	2487	527	22	58.2
PLA_HC-P	2687	2023	20	59.5

Table 3: DMA results of PLA, PLA_HC and PLA_HC-P

The flexural tests showed (Table 4) a decrease in flexural strength and elastic modulus for both PLA_HC and PLA_HC-P composites compared to neat PLA, with strain at maximum load remaining relatively unchanged. Although DSC analysis revealed an increase in crystallinity for PLA_HC, the mechanical weakening observed can be attributed to poor interfacial adhesion and the formation of HC aggregates, which act as stress concentrators and impair effective load transfer [13]. Conversely, PLA_HC-P exhibited reduced crystallinity relative to PLA_HC, which might lower stiffness. Nevertheless, interfacial interactions due to phytic acid functionalization help recover mechanical performance by minimizing aggregation and promoting better stress transfer. This balance results in PLA_HC-P having somewhat better flexural properties than PLA_HC, despite the decreased crystallinity.

	Strain %	**Flexural Strength MPa**	**Flexural modulus GPa**
PLA	3.9 ± 0.1	98.6 ± 1.7	3.5 ± 0.2
PLA_HC	3.2 ± 0.3	53.5 ± 3.0	2.5 ± 0.2
PAL-HC-P	3.9 ± 0.1	57.0 ± 4.3	2.5 ± 0.7

Table 4: Flexural results of PLA, PLA_HC and PLA_HC-P

The PLA composite reinforced with phytic-acid-modified hydrochar (PLA_HC-P) showed notable improvements in fire behavior compared to the unmodified system (PLA_HC). Specifically, cone calorimetry revealed a 15% reduction in peak heat release rate (pHRR), a 13% decrease in total smoke release (TSR), a 12.5% reduction in specific extinction area (SEA), and a 12.9% decrease in maximum average rate of heat emission (MARHE). These results indicate that the incorporation of phytic acid enhances the flame-retardant performance of the composite. The phosphorus-rich structure of phytic acid likely promotes the formation of a stable and protective char layer during combustion, which limits heat and mass transfer. Moreover, the modification alters the thermal degradation pathway, reducing the release of flammable volatiles and smoke. This suggests a synergistic flame-retardant effect, combining condensed-phase char promotion and gas-phase flame inhibition, resulting in improved fire safety of the PLA-based composite.

4 CONCLUSIONS

This work demonstrates the potential of hydrochar (HC) derived from Brewers' Spent Grain (BSG) as a sustainable filler for PLA-based biocomposites. The hydrothermal carbonization (HTC) process enabled the direct valorization of wet agro-industrial waste into a porous, carbon-rich material without the need for drying or activation. Structural, morphological, and chemical characterization of the HC—through SEM-EDS, FT-IR, BET, elemental analysis, and Boehm titration—confirmed the development of a heterogeneous, oxygen-functionalized surface suitable for further chemical modification. Surface functionalization with phytic acid (PA) introduced phosphorus-containing groups onto the HC, as confirmed by FT-IR analysis, with the aim of enhancing flame retardancy and improving compatibility with the PLA matrix. Thermal analysis indicated that HC alone tended to promote earlier degradation of PLA, while phytic acid modification delayed degradation and enhanced char formation, suggesting increased thermal stability. Calorimetric data showed changes in crystallinity behavior, with HC promoting nucleation and PA-modified HC slightly suppressing it, likely due to altered filler–matrix interactions.

Dynamic mechanical and flexural tests highlighted a reduction in stiffness and strength with HC, partially recovered when the filler was functionalized, confirming the positive effect of PA on dispersion and interfacial adhesion. Cone calorimeter tests showed that the addition of phytic-acid-modified hydrochar (PLA_HC-P) resulted in improvements in fire behavior, with reductions of 15% in pHRR, 13% in TSR, 12.5% in SEA, and 12.9% in MARHE compared to the unmodified composite. Overall, the combined use of hydrochar and phytic acid offers a promising strategy to produce bio-based composites with improved thermal stability, enhanced flame retardancy, and acceptable mechanical properties, while promoting circular economy principles through the upcycling of food industry residues.

ACKNOWLEDGEMENTS

Financed by the European Union - NextGenerationEU (National Sustainable Mobility Center CN00000023, Italian Ministry of University and Research Decree n. 1033 - 17/06/2022, Spoke 11 - Innovative Materials & Lightweighting). The opinions expressed are those of the authors only and should not be considered as representative of the European Union or the European Commission's official position. Neither the European Union nor the European Commission can be held responsible for them.

REFERENCES

[1] Walker T R and Fequet L 2023 Current trends of unsustainable plastic production and micro(nano)plastic pollution *TrAC - Trends in Analytical Chemistry* **160**

[2] McKeown P and Jones M D 2020 The Chemical Recycling of PLA: A Review *Sustainable Chemistry* **1** 1–22

[3] Wang L, Tong Z, Ingram L O, Cheng Q and Matthews S Green Composites of Poly (Lactic Acid) and Sugarcane Bagasse Residues from Bio-refinery Processes

[4] Morreale M, Liga A, Mistretta M C, Ascione L and La Mantia F P 2015 Mechanical, Thermomechanical and Reprocessing Behavior of Green Composites from Biodegradable Polymer and Wood Flour *Materials 2015, Vol. 8, Pages 7536-7548* **8** 7536–48

[5] Mary S K, Sara Thomas M, Rose Koshy R, Pillai P K, Pothan L A and Thomas S 2021 Adhesion in Biocomposites: A Critical Review **6** 531–58

[6] Hirai H, Takada H, Ogata Y, Yamashita R, Mizukawa K, Saha M, Kwan C, Moore C, Gray H, Laursen D, Zettler E R, Farrington J W, Reddy C M, Peacock E E and Ward M W 2011 Organic micropollutants in marine plastics debris from the open ocean and remote and urban beaches *Mar Pollut Bull* **62** 1683–92

[7] Bartoli M, Arrigo R, Malucelli G, Tagliaferro A and Duraccio D 2022 Recent Advances in Biochar Polymer Composites *Polymers (Basel)* **14**

[8] Guo R, Ren Z, Bi H, Xu M and Cai L 2019 Electrical and Thermal Conductivity of Polylactic Acid (PLA)-Based Biocomposites by Incorporation of Nano-Graphite Fabricated with Fused Deposition Modeling *Polymers 2019, Vol. 11, Page 549* **11** 549

[9] Ogunsona E O, Codou A, Misra · Manjusri and Mohanty A K 1234 Thermally Stable Pyrolytic Biocarbon as an Effective and Sustainable Reinforcing Filler for Polyamide Bio-composites Fabrication *J Polym Environ* **26** 3574–89

[10] Marrocchi A, Cerza E, Chandrasekaran S, Sgreccia E, Kaciulis S, Vaccaro L, Syahputra S, Vacandio F, Knauth P and Di Vona M L 2024 Hydrochar from Pine Needles as a Green Alternative for Catalytic Electrodes in Energy Applications *Molecules* **29** 3286

[11] Lynch K M, Steffen E J and Arendt E K 2016 Brewers' spent grain: a review with an emphasis on food and health *Journal of the Institute of Brewing* **122** 553–68

[12] Ikram S, Huang L Y, Zhang H, Wang J and Yin M 2017 Composition and Nutrient Value Proposition of Brewers Spent Grain *J Food Sci* **82** 2232–42

[13] Ye C, Yu F, Huang Y, Hua M, Zhang S and Feng J 2022 Hydrochar as an environment-friendly additive to improve the performance of biodegradable plastics *Science of the Total Environment* **832**
[14] Nizamuddin sabzoi, Jadhav A, saeed Qureshi sundus, Ahmed Baloch H, siddiqui M H, Mubarak N M, Griffin G, Madapusi srinivasan, tanksale A and Imran Ahamed M synthesis and characterization of polylactide/rice husk hydrochar composite
[15] Bejenari I, Dinu R, Montes S, Volf I and Mija A 2021 Hydrothermal Carbon as Reactive Fillers to Produce Sustainable Biocomposites with Aromatic Bio-Based Epoxy Resins *Polymers 2021, Vol. 13, Page 240* **13** 240
[16] Chow W S, Teoh E L and Karger-Kocsis J 2018 Flame retarded poly(lactic acid): A review *Express Polym Lett* **12** 396–417
[17] Shen J, Liang J, Lin X, Lin H, Yu J and Wang S 2022 The flame-retardant mechanisms and preparation of polymer composites and their potential application in construction engineering *Polymers (Basel)* **14**
[18] Przystas A, Jovic M, Salmeia K A, Rentsch D, Ferry L, Mispreuve H, Perler H and Gaan S 2018 Some Key Factors Influencing the Flame Retardancy of EDA-DOPO Containing Flexible Polyurethane Foams *Polymers 2018, Vol. 10, Page 1115* **10** 1115
[19] Velencoso M M, Battig A, Markwart J C, Schartel B and Wurm F R 2018 Molecular Firefighting—How Modern Phosphorus Chemistry Can Help Solve the Challenge of Flame Retardancy *Angewandte Chemie* **130** 10608–26
[20] Bar M, Alagirusamy R and Das A 2015 Flame retardant polymer composites *Fibers and Polymers* **16** 705–17
[21] Zhang Q, Wang W, Gu X, Li H, Liu X, Sun J and Zhang S 2019 Is there any way to simultaneously enhance both the flame retardancy and toughness of polylactic acid? *Polym Compos* **40** 932–41
[22] Zhang L, Li Z, Pan Y T, Yáñez A P, Hu S, Zhang X Q, Wang R and Wang D Y 2018 Polydopamine induced natural fiber surface functionalization: a way towards flame retardancy of flax/poly(lactic acid) biocomposites *Compos B Eng* **154** 56–63
[23] Sykam K, Försth M, Sas G, Restás Á and Das O 2021 Phytic acid: A bio-based flame retardant for cotton and wool fabrics *Ind Crops Prod* **164** 113349
[24] Yang Y, Wang X, Fei B, Li H, Gu X, Sun J and Zhang S 2021 Preparation of phytic acid-based green intumescent flame retardant and its application in PLA nonwovens *Polym Adv Technol* **32** 3039–49
[25] Liu S, Wang B, Wang C, Pei X, Li M and Fu G 2024 Study on flame retardant modified ramie reinforced composites and their mechanical properties *Journal of Reinforced Plastics and Composites* **43** 84–96
[26] Costes L, Laoutid F, Brohez S, Delvosalle C and Dubois P 2017 Phytic acid–lignin combination: A simple and efficient route for enhancing thermal and flame retardant properties of polylactide *Eur Polym J* **94** 270–85
[27] Zhong J, Wang E, Sun Y, Yin N, Tian S, Ying W, Li W and Zhang W 2023 Fabrication of Phytic Acid/Urea Co-Modified Bamboo Biochar and Its Application as Green Flame Retardant for Polylactic Acid Resins *Polymers 2023, Vol. 15, Page 360* **15** 360
[28] Turner J F, Riga A, O'Connor A, Zhang J and Collis J 2004 Characterization of drawn and undrawn poly-L-lactide films by differential scanning calorimetry *J Therm Anal Calorim* **75** 257–68
[29] Kruse A, Koch F, Stelzl K, Wü D and Zeller M 2016 Fate of Nitrogen during Hydrothermal Carbonization

[30] Kambo H S and Dutta A 2015 A comparative review of biochar and hydrochar in terms of production, physico-chemical properties and applications *Renewable and Sustainable Energy Reviews* **45** 359–78
[31] Marrocchi A, Cerza E, Chandrasekaran S, Sgreccia E, Kaciulis S, Vaccaro L, Syahputra S, Vacandio F, Knauth P and Di Vona M L 2024 Hydrochar from Pine Needles as a Green Alternative for Catalytic Electrodes in Energy Applications *Molecules* **29** 3286
[32] Guo S, Dong X, Liu K, Yu H and Zhu C 2015 Chemical, energetic, and structural characteristics of hydrothermal carbonization solid products for lawn grass *Bioresources* **10** 4613–25
[33] Liu Z, Quek A, Kent Hoekman S and Balasubramanian R 2013 Production of solid biochar fuel from waste biomass by hydrothermal carbonization *Fuel* **103** 943–9
[34] Nitsos C K, Matis K A and Triantafyllidis K S 2013 Optimization of hydrothermal pretreatment of lignocellulosic biomass in the bioethanol production process *ChemSusChem* **6** 110–22
[35] Hong R, Ting L and Huijie W 2017 Optimization of extraction condition for phytic acid from peanut meal by response surface methodology *Resource-Efficient Technologies* **3** 226–31
[36] De Carli L, Schnitzler E, Ionashiro M, Szpoganicz B and Rosso N D 2009 Equilibrium, thermoanalytical and spectroscopic studies to characterize phytic acid complexes with Mn(II) and Co(II) *J Braz Chem Soc* **20** 1515–22
[37] Feng X, Wang X, Cai W, Qiu S, Hu Y and Liew K M 2016 Studies on Synthesis of Electrochemically Exfoliated Functionalized Graphene and Polylactic Acid/Ferric Phytate Functionalized Graphene Nanocomposites as New Fire Hazard Suppression Materials *ACS Appl Mater Interfaces* **8** 25552–62
[38] Huang C C, Chang C W, Jahan K, Wu T M and Shih Y F 2023 Effects of the Grapevine Biochar on the Properties of PLA Composites *Materials 2023, Vol. 16, Page 816* **16** 816
[39] Yang X, Song X, Wang Y, Yu E, Wei Z and Erlei Yu C 2022 Synthesis of phytic acid-based compounds for improving the mechanical properties and fire performances of poly(lactic acid)
[40] Wu F, Xu J, Qiu X, Lin S, Zhang M, Ma M, Shi Y, He H, Chen S and Wang X 2021 Super-Low-Addition Biobased Flame Retardant Dedicated to Polylactic Acid through Ionic Reaction between Phytic Acid and Taurine *ACS Appl Polym Mater* **3** 4579–86
[41] Chen Z J, Tsou C H, Tsai M L, Guo J, De Guzman M R, Yang T, Gao C, Lei Y, Gan P W, Chen S, Tu L J, Qu C L, Wang R Y and Wu C S 2021 Barrier Properties and Hydrophobicity of Biodegradable Poly(lactic acid) Composites Reinforced with Recycled Chinese Spirits Distiller's Grains *Polymers 2021, Vol. 13, Page 2861* **13** 2861
[42] Zouari M, Devallance D B and Marrot L 2022 Effect of Biochar Addition on Mechanical Properties, Thermal Stability, and Water Resistance of Hemp-Polylactic Acid (PLA) Composites *Materials 2022, Vol. 15, Page 2271* **15** 2271
[43] Righetti M C, Cinelli P, Mallegni N, Massa C A, Bronco S, Stäbler A and Lazzeri A 2019 Thermal, Mechanical, and Rheological Properties of Biocomposites Made of Poly(lactic acid) and Potato Pulp Powder *International Journal of Molecular Sciences 2019, Vol. 20, Page 675* **20** 675
[44] Zhang M, Wang Y, Huang J, Wang D, Li T, Wang S and Dong W 2023 Phytic acid–based flame retardant and its application to poly(lactic acid) composites *New Journal of Chemistry* **47** 19494–503

[45] Guo Q, Cao J, Han Y, Tang Y, Zhang X and Lu C 2017 Biological phytic acid as a multifunctional curing agent for elastomers: towards skin-touchable and flame retardant electronic sensors *Green Chemistry* **19** 3418–27

[46] Mysiukiewicz O and Barczewski M 2019 Utilization of linseed cake as a postagricultural functional filler for poly(lactic acid) green composites *J Appl Polym Sci* **136** 47152

DESIGN AND PROTOTYPING OF COMPOSITE DEPLOYABLE BOOMS FOR SOLAR SAILS

Flavia Palmeri[1], Lorenzo Martinazzoli and Susanna Laurenzi

Department of Astronautical Electrical and Energy Engineering, Sapienza University of Rome, Via Salaria 851-881, Rome, 00138, Italy Email: susanna.laurenzi@uniroma1.it.

[1]Current address: California Institute of Technology, 1200 E. California Boulevard, MC 105-50, Pasadena, CA 91125-4600

Keywords: Ultrathin composites, Deployable structures, Buckling analysis, Solar sails, Finite elements

ABSTRACT

The solar sail is a promising propulsion concept that utilizes solar radiation pressure to navigate in space without propellant, enabling missions otherwise unattainable with traditional propulsion methods (e.g., electric or chemical propulsion). This paper presents the design of the structural subsystem of a 35x35 monolithic solar sail, with a specific focus on composite the deployable booms responsible for deploying and tensioning the sail membrane. Structural numerical analyses are conducted both on a full-scale model of a single boom and on the solar sail system. The former is intended to estimate the critical buckling load of the composite booms, the latter is used to determine the axial load acting on the boom tips due to membrane tension and to evaluate maximum sail displacements caused by solar radiation pressure. The axial load acting on the boom tip must remain below the critical buckling value, and the maximum displacement of the sail must not exceed 1% of the sail's side length. In this work, we designed composite deployable booms to meet these requirements and prototyped them at lab-scale.

1 INTRODUCTION

Solar sail propulsion systems have long been of great interest for space missions. Unlike chemical or electric propulsion, which require onboard propellants, solar sailing uses an external source of propulsion, harnessing the Sun's power through the momentum transfer of photons that impact and reflect off the membrane [1].

Spencer and co-authors provide a survey of the state-of-the-art of the solar sailing technology [2]. According to their work, the first advanced conceptual study dates to the late 1970s when the Jet Propulsion Laboratory designed a spacecraft that would make a rendezvous of Halley's Comet. Later, the DLR-ESA-INVENT carried out the first ground test of a fully deployable solar sail structure in 1999. During the test, four carbon fiber reinforced polymer (CFRP) booms were deployed with the four triangular segments of the sail [3]. In 2010, the interplanetary kite-craft accelerated by radiation of the Sun (IKAROS), sponsored by the JAXA, was launched and successfully deployed a 196 m2 solar sail on route to Venus [4]. Meanwhile, NASA developed the Nano Sail-D mission to demonstrate both the deployment of a sail from a three-unit CubeSat and the sail capability of accelerating spacecraft de-orbiting thanks to the increased atmospheric drag. The first Nano Sail-D unfortunately underwent a launch failure, whereas its flight spare satellite, NanoSail-D2, successfully deployed a 10m2-sail from a three-unit CubeSat. However, the results were not those expected since NanoSail-D2 remained in orbit for 240 days before re-entry even if it was supposed to deorbit from the initial 650 km altitude in 70-120 days [5]. Likewise, the LighSail programme, by the Planetary Society, involved solar sail technology using three-unit CubeSat. During this programme, LightSail-1 successfully deployed a 32 m2-solar sail [6] and, for the first time, LightSail-2 exploited the solar radiation pressure to perform an

apogee raising from a low Earth orbit (LEO) [8]. On April 23, 2024, the NAS's mission Advanced Composite Solar Sail System (ACS3) featuring a square-shaped solar sail with an approximate 0 m side was launched and successfully deployment of the composite boom solar sail in LEO in August 2024 [7].

For solar sail missions, the general trend is to use four deployable booms to unfurl and tension the sail. Deployable booms can be categorized according to the cross-section geometry, the most popular being: Storable Tubular Extendible Member (STEM), Collapsible Tubular Mast (CTM), and Triangular Rollable and Collapsible (TRAC). A STEM is generally made of a thin-walled composite shell with circular cross-section [8], a CTM is made of two thin flexible shells with a bi-convex shape bonded at their edges cite [9,10] a TRAC is composed by two curved C-shaped section joined along one[11,12], and a SHEARLESS boom is formed by coupling the edges of two cylindrical shells front-to-front by a tightly-fitted outer sheath [13,14]. In this work, we consider CTMs.

The design of deployable booms serving as fundamental structural component in the solar sail system is particularly delicate. These booms must apply enough tension to the membrane to avoid significant out-of-plane deflections, while also withstanding compression without buckling. While numerical analysis can come at hand, structural simulations of solar sail systems often struggle with convergence due to the nonlinearities introduced by the large, thin membranes and the slender, flexible booms [15]. In 2002, Murphy and co-authors proposed a pre-tensioning method to solve convergence issues [16]. The pre-tensioning step allows the membrane to get out-of-plane stiffness to run the subsequent dynamic analysis and get the system's first ten natural modes. Talegani et al. maintained the same strategy and, in addition to predict the vibration modes, performed a geometrically nonlinear static analysis to evaluate the full-scale deformations of the pre-tensioned solar sail systems [17]. Sleight and Muheim performed a parametric study on a 150 m sail with a variable pre-stress at the center of its triangular segments (from 0.1 to 5 psi) [18]. After pre-tensioning, the sail deflection shows an inflection point as the pre-stress level increases from 1 to 3 psi, while the boom deflections increase continuously, as well as its compression level. Sleight and Muheim used a fictitious thermal load to contract the cables connecting the booms and the sail corners. Different thermal field results in a variable pre-tensioning scenario. Other methods were proposed to simulate pre-tensioning such as the quasi-random application of small out-of-plane forces to get a feasible static sail [19]. In this work, we use the pre-tensioning method with a fictitious thermal field.

In previously presented works, system-level models of solar sail structures often lack detail in the representation of individual booms. These components are frequently simplified as one-dimensional beams, with the material typically assumed to be isotropic, whereas in reality, booms are thin-walled shells that may exhibit local instabilities and are often made of composite materials with inherently anisotropic properties. In this work, we aim to investigate the behavior of the boom more thoroughly, treating it as an integral part of the solar sail structure. To this end, we perform a structural analysis of both a single boom and the full solar sail system, modeling the boom in both cases as a two-dimensional shell with anisotropic properties. Two full-scale finite element method (FEM) models are developed. The first is a model of the boom, aimed at evaluating its critical buckling load. The second is a system-level FEM model of the solar sail, consisting of the sail membrane and the boom acting as a support structure. This model is intended to assess the maximum out-of-plane displacement of the sail under solar radiation pressure. The buckling analysis results from the first analysis are then compared with the compression forces acting on the boom to verify whether the boom is truly capable of providing the required tensioning.

2 FINITE ELEMENT MODELS

This section describes the numerical model of the boom used to evaluate its buckling load and the numerical model of the solar sail system developed to identify the compression induced on the booms due to sail's tensioning and the deflection of the tensioned membrane due to solar pressure. The ABAQUS software has been used, which has been compared and validated against other finite element software [17].

2.1 BOOM FINITE ELEMENT MODEL

To ensure efficient impulse transfer and manoeuvrability, the membrane must be placed under tension. As a result, the booms are primarily subjected to axial compression, necessitating a buckling analysis. This analysis provides estimates of the critical load that would cause structural collapse, enabling the application of appropriate pre-tensioning.

The boom is modelled by sketching its cross-section geometry, shown in Fig. 1, where r_1 = 39 mm is the radius of the central arc segment, r_2 = 18 mm is the radius of the edge arc segment, w = 6 mm is the width of the flange, called web, and the subtended angle $\alpha_1 = \alpha_2 = 90°$. The cross-section has then been extruded to a length of 24.75 m. This length was selected to be half of the diagonal of a 35 m square, as the CTMs are intended to support the 35-by-35 meter monolithic solar sail. The boom is modelled as two separate shells, bonded along the web region through tie constraints.

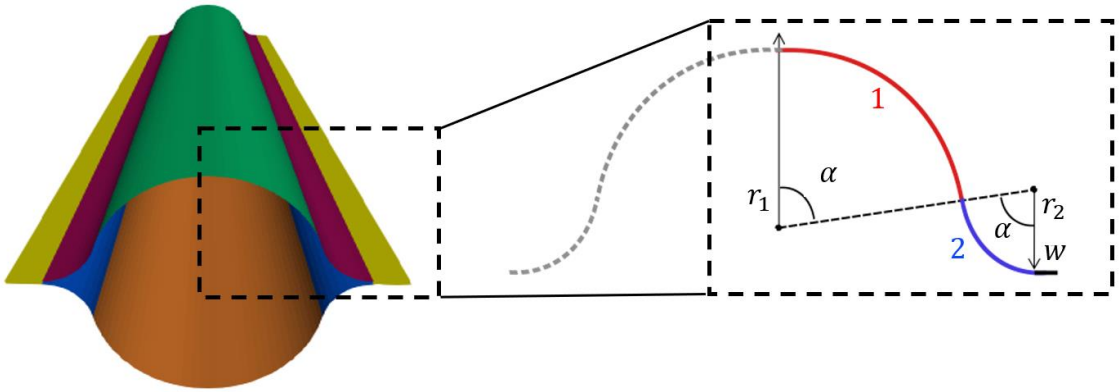

Figure 1. Geometric description on the composite boom.

The mesh consists of 60,500 shell-S4R elements for each shell. In this model, the edge points at the root cross-section are fully constrained in translation and rotation to simulate the interlocking with the bus. In contrast, the edge points at the tip cross-section are constrained in z-rotation only. Additionally, a unit load is applied at the CTM's tip.

The boom is made of a 2-ply composite laminate featuring an anti-symmetric lay-up with fiber orientations of ±45°, a total thickness of 0.16 mm, and a density of 1371 kg/m³. The reinforcement is composed of 6k Toray T300 carbon fiber spread tows, woven into a plain weave fabric. The matrix is the CYTECH CYCOM® 823 epoxy. The mechanical behavior of such material is represented using the ABD stiffness matrix, initially computed via classical laminate theory (CLT). The ABD entries were subsequently refined based on an experimental characterization campaign conducted on specimens made from the same material system. The ABD matrix is as follows, where sub-matrix A is in N/m, while sub-matrix D is in Nm:

$$ABD = \begin{bmatrix} 4.357e+06 & 3.903e+06 & 0 & 0 & 0 & 0 \\ 3.903e+06 & 4.357e+06 & 0 & 0 & 0 & 0 \\ 0 & 0 & 4.074e+06 & 0 & 0 & 0 \\ 0 & 0 & 0 & 9.296e-03 & 8.327e-03 & 6.362e-03 \\ 0 & 0 & 0 & 8.327e-03 & 9.296e-03 & 6.362e-03 \\ 0 & 0 & 0 & 6.362e-03 & 6.362e-03 & 8.692e-03 \end{bmatrix} \quad (1)$$

In this model, the edge points at the root cross-section are fully constrained in translation and rotation to simulate the interlocking with the bus. In contrast, the edge points at the tip cross-section are constrained in z-rotation only. Additionally, a load is applied at the CTM's tip.

The simulation consists of a preliminary linear buckling analysis, followed by a non-linear Riks analysis [14, 20]. In the linear analysis, a unit tip load is applied to the boom to determine its critical buckling load. This critical load is then used in the subsequent non-linear analysis, which is conducted on an imperfect geometry. Geometric imperfections are introduced by superimposing the first three buckling modes, obtained from the linear analysis, onto the undeformed boom geometry. The amplitudes of the mode shapes are scaled to 1%, 0.5%, and 0.25% of the laminate thickness for the first, second, and third modes, respectively. The non-linear analysis is performed using the arc-length method [21–23], with the load applied incrementally through adaptive step sizes.

2.2 SOLAR SAIL SYSTEM FINITE ELEMENT MODEL

The solar sail system is composed by four supporting booms, placed along the diagonals of a 35 m square solar sail. The sail is supported by four 20 cm cables, which simulate the connection between the booms and the sail. The inner ends of the cables are attached to the corners of the sail, while the outer ends are connected to the tips of the booms via MPCs. Interactions between the assembly parts are modelled through the *General contact giving a "Hard" Contact normal behavior which avoids penetration between their surfaces.

The sail is modeled as a membrane, whose section has a thickness of 2.5 μm [24]. The sail is discretized by M3D4R elements, which are 4 node quadrilateral membrane elements, with reduced integration and hourglass control.

Each cable is modelled as a wire with a circular cross-section of radius 1.58 mm. Cables are discretized by T3D2 elements which are 2-node linear 3-D truss.

The booms are modeled as shells. Its geometric description is given in subsection 2.1. The booms are discretized by S4R elements

The sail and the cables are made of Kapton and Kevlar respectively. Their density and mechanical properties are taken from literature, and they are given in Table 1 [17].

Properties		Kapton	Kevlar
E	[GPa]	2.48	62
ν	–	0.34	0.36
ρ	[Kg/m^3]	1425.2	1440.0

Table 1: Properties of Kapton and Kevlar [17]

The simulation consists of two steps. The first step is the sail tensioning, which involves providing the connection cables with a thermal field. This field is fictitious and acts on cables only, therefore the coefficient of thermal expansion (CTE) is given only for Kevlar, with CTE = $4.6\ 10^{-6} \circ C^{-1}$ [8]. A decrease in temperature causes the cables to contract, which results in tensioning the membrane. In this step, geometric non-linearity is considered. The second step involves applying solar pressure, where a pressure of 2.0334×10^{-5} Pa is applied to surface of the tensioned membrane facing the Sun.

The Interactions, loads and boundary conditions acting in the FEM model of the solar sail system are shown in Fig. 2.

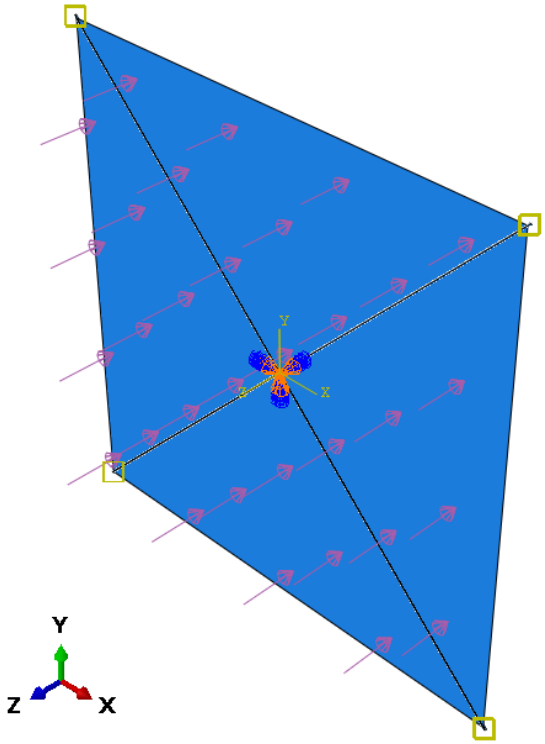

Figure 2. Interactions, loads and boundary conditions acting in the FEM model of the solar sail system.

A dynamic explicit procedure is used, with default values of automatic stabilization. The "improvedDTmethod" algorithm is used to improve the speed of the analysis, allowing to identify the critical time step and avoiding numerical singularities. To further control the analysis, a viscous pressure is introduced as damping effect, limiting the rise of the system kinetic energy and simulating a quasi-static analysis. The viscous pressure used is $3.6\ 10^{-6}$, considering a c_v of $2\ 10^{-2}$ accordingly to Mallikarachchi and Pellegrino's work [25].

3 RESULTS

This section presents both the results of the simulation at the individual component level and at the system-level. The results at the system-level are reported separately for the two consecutive analysis steps: the pre-tensioning and the solar pressure loading results are provided in Sec.3.2.1 and Sec.3.2.2, respectively.

3.1 BOOM FINITE ELEMENT MODEL RESULTS

Firstly, results of the mesh sensitivity analysis are reported in Fig. 3. The starting mesh was composed of about 30000 elements, with an approximate global size of 2 cm. It's shown that the critical buckling load converges at a value of about 1.71 N for a number of elements greater than 60500 for each boom, which is an optimal trade-off between computational time and results accuracy. Such a mesh determined a critical load of 1.7018 N, deviating from the convergence value by approximately 0.65%. The first three buckling modes are presented in Fig. 3.

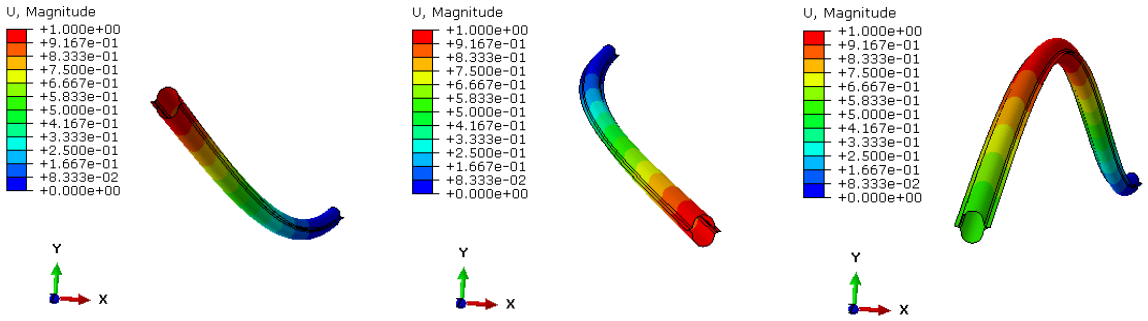

Figure 3. First three linear buckling modes; from the left: 1.7018 N, 1.7607 N, 15.318 N.

The Riks analysis yields the force at the tip vs. tip displacement curve, shown in Fig. 4. The maximum of the curve determines the buckling load of the first mode. The non-linear simulation shows that instabilities occurred at about 1.696 N, reaching 99.7% of the axial load computed in the linear analysis.

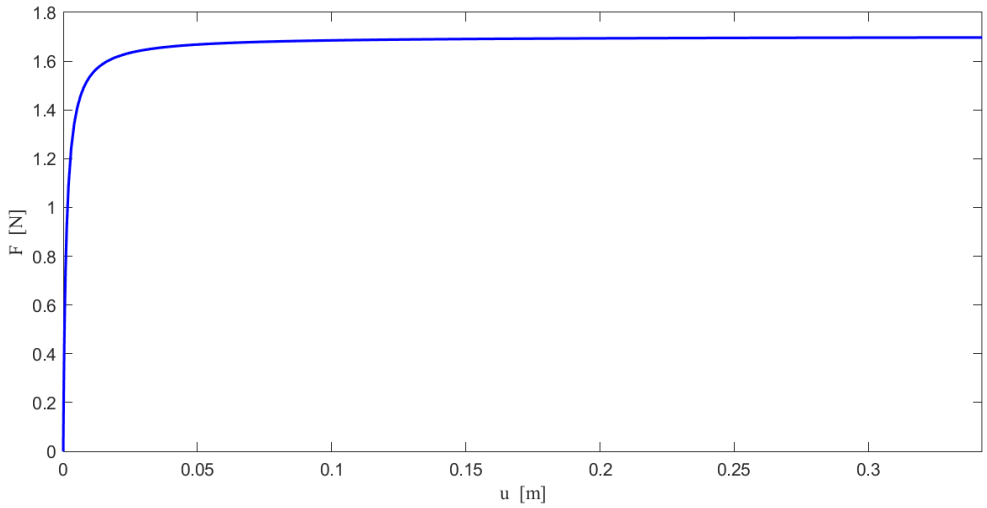

Figure 4. Axial load vs tip displacement curve by the nonlinear buckling analysis.

3.2 SOLAR SAIL SYSTEM FINITE ELEMENT MODEL RESULTS

In Sec.3.2.1 the minimum stress of the membrane due to the pre-tensioning is provided after a sensitivity analysis. Tensioning the sail will cause its stretching. So, the displacement fields are presented as well to evaluate how much and in which directions the membrane is stretched. Subsequently, in Sec.3.2.2 we present the displacements obtained from the solar radiation pressure application to the tensioned system. In plane and out-of-plane fields are evaluated for the membrane, showing very small deformation and therefore the capability of the proposed design to operate properly in the working.

3.2.1 Pre-tensioning results

In Fig. 5 shows the stress distribution over the sail after the pre-tensioning step is shown, where it was determined that a thermal load of -500°C is consistent with the loads observed on the sail surface. Indeed, a stress intensification is registered at the four corners of the sail, with a maximum value of about 2.2 MPa, while the remainder of the membrane is stretched with a stress of the order of Kpa, that

are compatible with the sail material properties, as established in [24]. At this point, the stress over the cables is 49 KPa, that induce a tensioning force on the boom tip of 0.38 N, preserving the integrity of the structure as the nonlinear critical load is about 1.696 N.

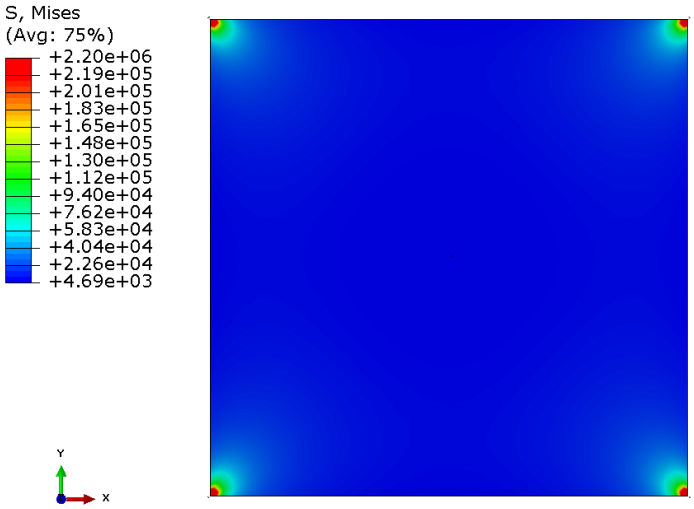

Figure 5. Mises stress distribution over the sail after pre-tensioning phase.

The in-plane displacement observed are less than 1 mm, denoting that the membrane is practically flat and stretched over all the surface, as shown in Fig. 6. Since the sail was defined with membrane-type elements, the out-of-plane displacements cannot be computed without an orthogonal load.

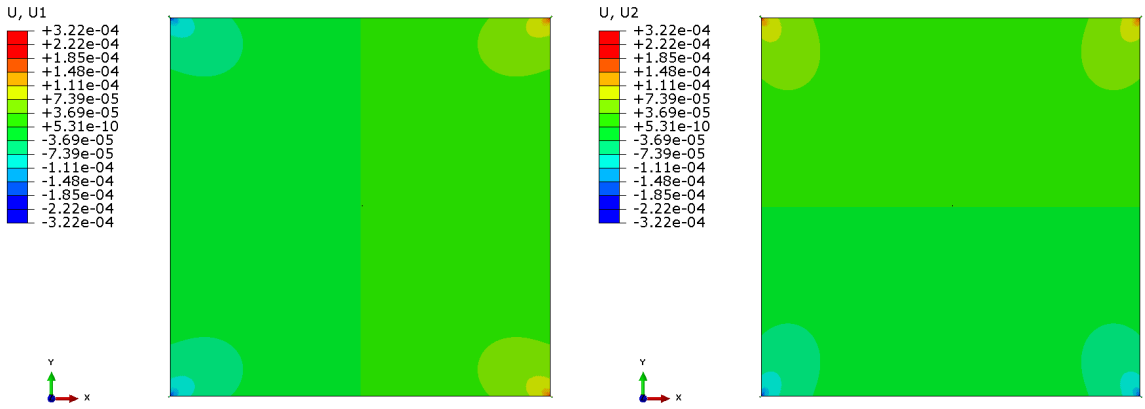

Figure 6. In-plane displacements of the sail after pre-tensioning phase: horizontal displacement on the left, vertical displacement on the right.

3.2.2 Solar pressure loading results

After the application of the solar radiation pressure, perpendicularly to the sail surface, the stress level changed slightly, preserving the same distribution of the previous step as reported in Fig. 7. The stress

value on the cables is slightly reduced compared to the simple tensioning phase; consequently, the boom structures will be able to sustain the overall load computed in the nonlinear analysis avoiding buckling occurrence.

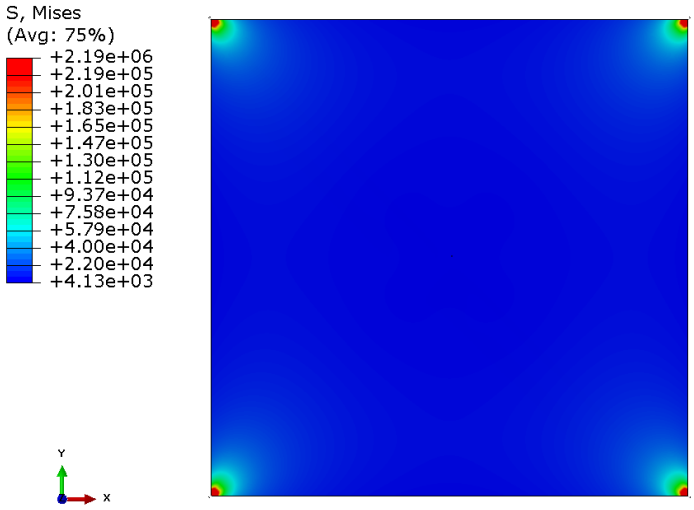

Figure 7. Mises stress distribution over the sail after solar pressure loading.

Similarly, the in-plane displacements are substantially unchanged, Fig. 8, while a negative out-of-plane displacement is observed, aligned to the solar radiation pressure. Due to the presence of the boom structure behind the solar sail, the contact region is identified and highlighted in the contour plot in Fig. 9.

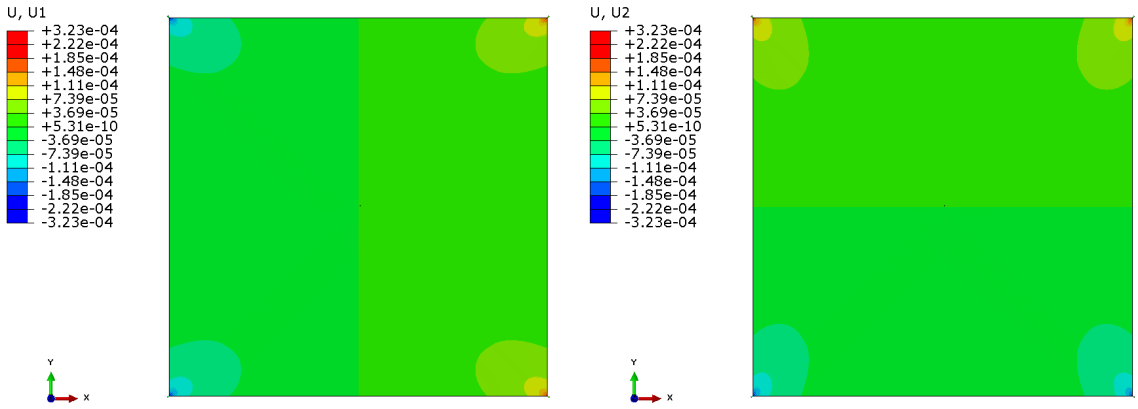

Figure 8. In-plane displacements of the sail after solar pressure loading: horizontal displacement on the left, vertical displacement on the right.

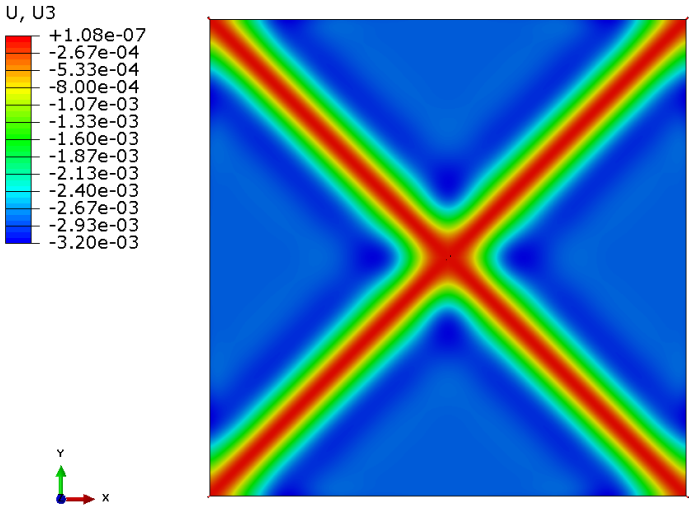

Figure 9. Out-of-plane displacement over the sail after the solar pressure loading.

4. LAB-SCALE BOOM PROTOTYPING

Lab-scale CTMs, each 70 cm in length and with a cross-section featuring all characteristic dimensions scaled at a 2:3 ratio compared to the reference design, were fabricated using a two-step, out-of-autoclave curing process. The two composite shells were cured separately and subsequently bonded together during a second curing cycle.
For each shell, the laminate lay-up and consumable layers were manually draped over a custom-designed mold, Fig. 10.

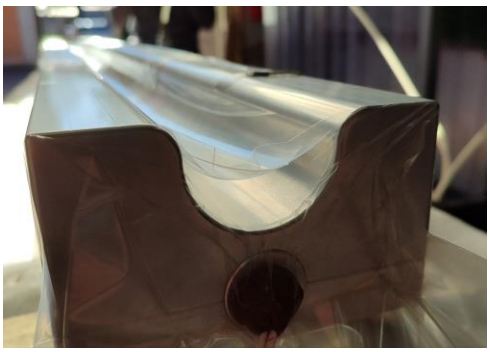

Figure 10. Customized mold for out-of-autoclave boom manufacturing.

The lay-up was then vacuum-bagged together with the mold, and the curing was performed using a feedback-controlled thermal system. This system consists of electric heating cartridges for heat input, a thermocouple for temperature monitoring, and a proportional-derivative temperature controller that regulates current flow to the cartridges. The heating cartridges are inserted into a through-hole running along the axis of the mold, while the thermocouple is placed directly on the mold surface to accurately track its temperature. The temperature controller is positioned for easy access and operation throughout the curing process. The components are shown in Fig. 11.

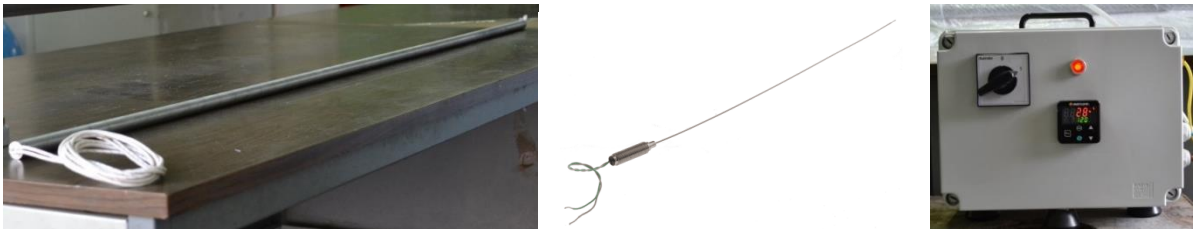

Figure 11. Feedback thermal control system.

The temperature cycle set at the temperature controller is the curing cycle as established per data sheet of CYCOM®823 RTM. (Cure temperature: 125°C, Cure time: 60 mins, Heat up rate: 2°C/min, Pressure: 0bar). At the end of the first cure, the shells were allowed to cool to room temperature and the demolding was performed. Then, a single ply of structural adhesive AF163 − 2K was used to bond together the two shells along their edges, with a cure cycle of 60 mins at 135°C.
In Fig. 12 the manufacturing steps are presented alongside and the prototype, which is characterised by a mean thickness of 0.16 mm.

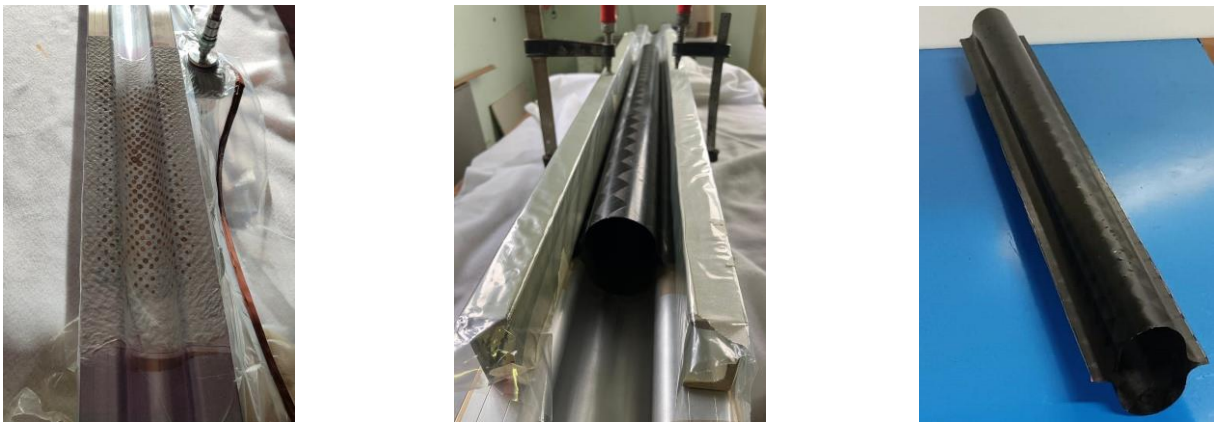

Figure 12. Subsequent steps of boom manufacturing: shell curing cycle with vacuum bag lay-up, adhesive curing cycle, finished boom prototype.

9 CONCLUSIONS

In this work, the design for the boom supporting a 35 by 35 monolithic solar is presented, investigating its structural performances. First of all, the boom critical load at buckling is evaluated. Then the structural behaviour of the solar sail at a system level is investigated. A pre-tensioning value is selected such that the sail achieves stiffness without compromising the boom stability, i.e., compression load acting on the boom tip smaller than its critical buckling value. Within the limits of the maximum stress the sail can sustain, a load on the cables of 0.38 N is reached and the integrity of the boom structures is preserved. Finally, the out-of-plane displacements of the tensioned sail after the application of the solar radiation pressure are evaluated showing negligible deflections. Indeed, the out-of-plane maximum displacements of the membrane is about 3 mm, and the membrane-sail can be considered satisfactorily flat, thus providing a proper solar thrust. Based on these promising results a lab-scale boom prototype has been developed using an out-of-autoclave manufacturing process. Particularly, a two-step technique is proposed, realizing the two half shells of the boom and bonding them with a structural adhesive. The final prototype presents a mean thickness of 0.16 mm and well-aligns with the nominal curvature provided by the mold.

ACKNOWLEDGEMENTS

This work is performed under the Agreement between the Italian Space Agency and DIAEE – Sapienza University of Rome n. 2019-28-HH.0 - CUP n. F84I19001070005 related to R&D activities on solar photonic propulsion.

REFERENCES

[1] G. Vulpetti, L. Johnson and G.L. Matloff, *A Novel Approach to Interplanetary Travel*, Praxis, 2008.

[2] D.A. Spencer, L. Johnson, and A.C. Long, Solar sailing technology challenges. *Aerospace Science and Technology*, ***93***, 2019, 105276. (doi: 10.1016/j.ast.2019.07.009)

[3] M. Leipold, M. Eiden, C.E. Garner, L. Herbeck, D. Kassing, T. Niederstadt, ... and W. Unckenbold, Solar sail technology development and demonstration, *Acta astronautica*, ***52(2-5)***, 2003, pp. 317-326. (doi: 10.1016/S0094-5765(02)00171-6)

[4] Y. Tsuda, O. Mori, R. Funase, H. Sawada, T. Yamamoto, T. Saiki, ... and J.I. Kawaguchi, Flight status of IKAROS deep space solar sail demonstrator. *Acta astronautica*, ***69*(9-10)**, 2011, pp. 833-840. (doi; 10.1016/j.actaastro.2011.06.005)

[5] L. Johnson, M. Whorton, A. Heaton, R. Pinson, G. Laue, and C. Adams. NanoSail-D: A solar sail demonstration mission, *Acta astronautica*, ***68*(5-6)**, 2011, pp. 571-575. (doi: 10.1016/j.actaastro.2010.02.008)

[6] D. A. Spencer, B. Betts, J.M. Bellardo, A. Diaz, B. Plante and J.R. Mansell. The LightSail 2 solar sailing technology demonstration. *Advances in Space Research*, ***67*(9)**, 2021, pp. 2878-2889. (doi: 10.1016/j.asr.2020.06.029)

[7] W.K. Wilkie, Overview of the nasa advanced composite solar sail system (acs3) technology demonstration project. *AIAA Scitech 2021 Forum*, January 11–15 and 19–21, 2021, virtual event.

[8] M. Aguirre-Martinez, D.H. Bowen, R. Davidson, R.J. Lee, and T. Thorpe. (1986, September). The development of a continuous manufacturing method for a deployable satellite mast in CFRP. In *British Plastics Congress*, September, 1986, University Park, PA, pp. 107-110.

[9] L. Herbeck, M. Leipold, C. Sickinger, M. Eiden, and W. Unckenbold. Development and test of deployable ultra-lightweight cfrp-booms for a solar sail. *European Conference on Spacecraft Structures, Materials and Mechanical Testing*, November 29 - December 1, 2000, ESTEC, Noordwijk, The Netherlands, ESASP-468, 2001, p.107

[10] B. Jeremy and M. Thomas, Performance validation of the triangular rollable and collapsible mast, *24th Annual AIAA/USU Conference on Small Satellites*, 2010

[11] T.W. Murphey, D. Turse, and L. Adams, TRAC boom structural mechanics, *4th AIAA spacecraft structures conference*, 2017.

[12] J.M. Fernandez, Advanced deployable shell-based composite booms for small satellite structural applications including solar sails, *International Symposium on Solar Sailing*, 2017.

[13] J.M. Fernandez, *Sheath-based rollable lenticular-shaped and low-stiction composite boom*, 2018, (No. Patent Number: US-Patent-9,863,148).

[14] D. Barbera and S. Laurenzi. Nonlinear buckling and folding analysis of a storable tubular ultrathin boom for nanosatellites. *Composite Structures*, ***132***, 2015, pp. 226-238. (doi: 10.1016/j.compstruct.2015.05.024)

[15] S. Gong and M. Macdonald. Review on solar sail technology. *Astrodynamics*, ***3***, 2019, pp. 93-125. (doi: 10.1007/s42064-022-0136-2)

[16] D. Murphy, T. Murphey, and P. Gierow. Scalable solar sail subsystem design considerations, *43rd AIAA/ASME/ASCE/AHS/ASC Structures, Structural Dynamics, and Materials Conference*, April 22-25, 2002, Denver, Colorado, p. 1703.

[17] B. Taleghani, D. Sleight, D. Muheim, K. Belvin, and J. Wang, Assessment of analysis approaches for solar sail structural response, *39th AIAA/ASME/SAE/ASEE Joint Propulsion Conference and Exhibit*, July 20-23, 2003, Huntsville, Alabama, p. 4796.

[18] D. Sleight, and D. Muheim, Parametric studies of square solar sails using finite element analysis, *45th AIAA/ASME/ASCE/AHS/ASC Structures, Structural Dynamics & Materials Conference*, April 19 – 22, 2004, Palm Springs, California, p. 1509.

[19] D. B. Holland, *Static and dynamic characteristics of end-loaded beams with specific application in square solar sails*, Duke University,

[20] C. Leclerc, and S. Pellegrino, Nonlinear elastic buckling of ultra-thin coilable booms, *International Journal of Solids and Structures*, ***203***, 2020, pp. 46-56, (doi: 10.1016/j.ijsolstr.2020.06.042)

[21] N. Vasios, Nonlinear Analysis of Structures, The Arc Length Method: Formulation, Implementation and Applications, PhD thesis. Harvard, 2015

[22] M. Fafard. and B. Massicotte. Geometrical interpretation of the arc-length method. *Computers & structures*, ***46*(4)**, 1993, pp. 603-615. (doi: 10.1016/0045-7949(93)90389-U)

[23] N.D. Gavin, G. Pretti, W.M. Coombs, J.C. Brigham, and C.E. Augarde, On the implementation of a material point-based arc-length method. *International Journal for Numerical Methods in Engineering*, ***125*(9)**, 2024, e7438. (doi: 10.1002/nme.7438)

[24] L. Boni, M. Bassetto, L. Niccolai, G. Mengali, A.A. Quarta, C. Circi, ... and E. Cavallini, Structural response of Helianthus solar sail during attitude maneuvers. *Aerospace Science and Technology*, ***133***, 2023, 108152. (doi: 10.1016/j.ast.2023.108152)

[25] H.M.Y.C. Mallikarachchi, and S. Pellegrino. Quasi-static folding and deployment of ultrathin composite tape-spring hinges. *Journal of Spacecraft and Rockets*, ***48*(1)**, 2011, pp. 187-198. (doi: 10.2514/1.47321)

Characterization and Mitigation of Droplet-Induced Impact Damage in Wind Blade Leading-edge Coatings

Po-Wen(Brian) Wang

PI: Nancy Sottos

University of Illinois Urbana-Champaign

24th ICCM Conference August 2025

Outline

1. Introduction & Background
2. Calibration & Setup Optimization
3. Material Evaluation for Stress Wave Dissipation
4. Summary and Future Work

Leading Edge Erosion Damage





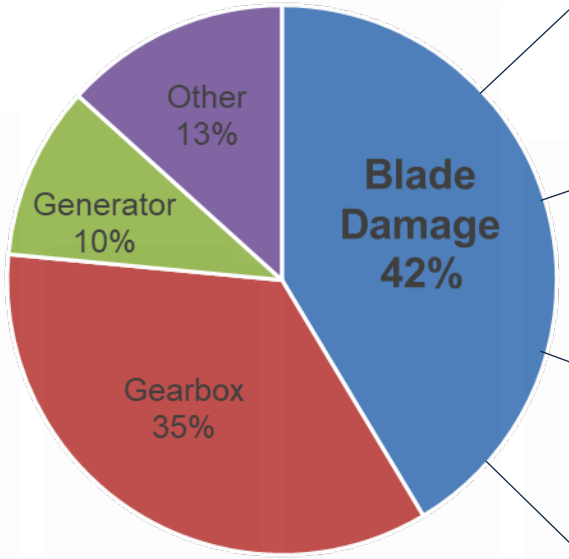

- 25% of the levelized cost
- Blade lifetime decline (7%↑)
- Annual energy production reduce (5%↑)
- Other blade damage

Elhadi Ibrahim, et al., Materials, 2020

Mishnaevsky, et al., Wind Energy, 2020

Shohag, et al., Wind Engineering, 2017

Mishnaevsky, Renewable Energy, 2019

Leading-Edge Erosion Mechanism

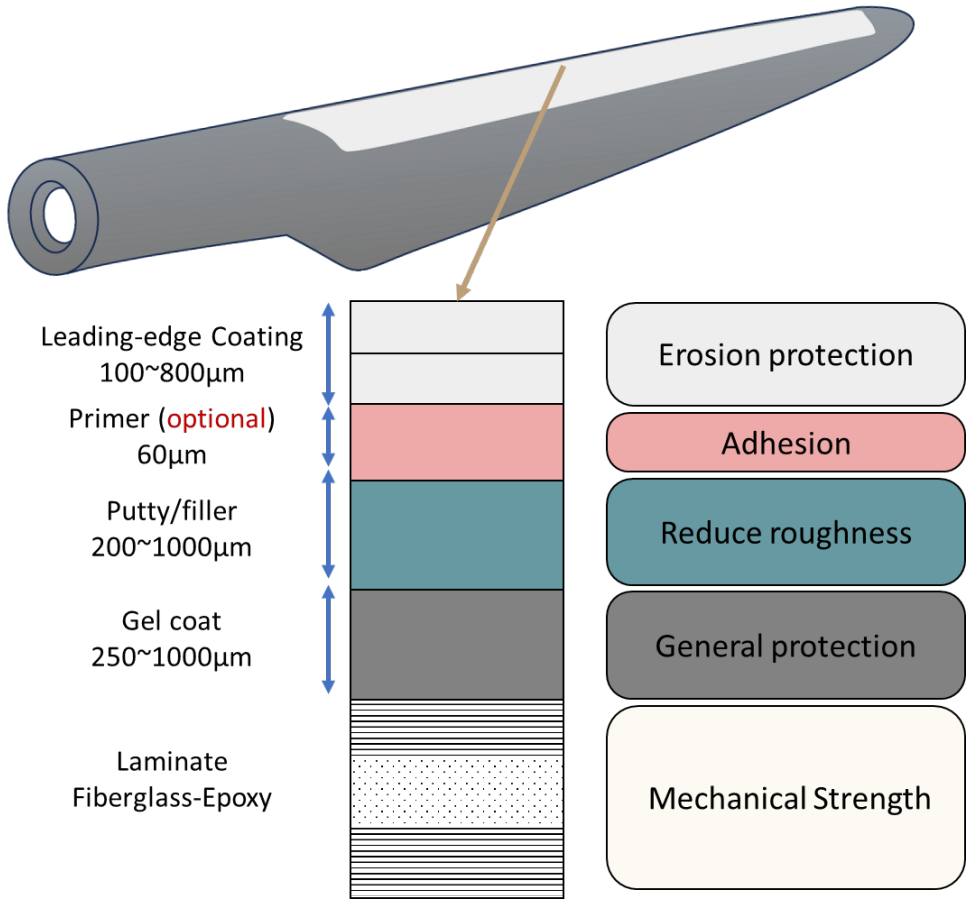

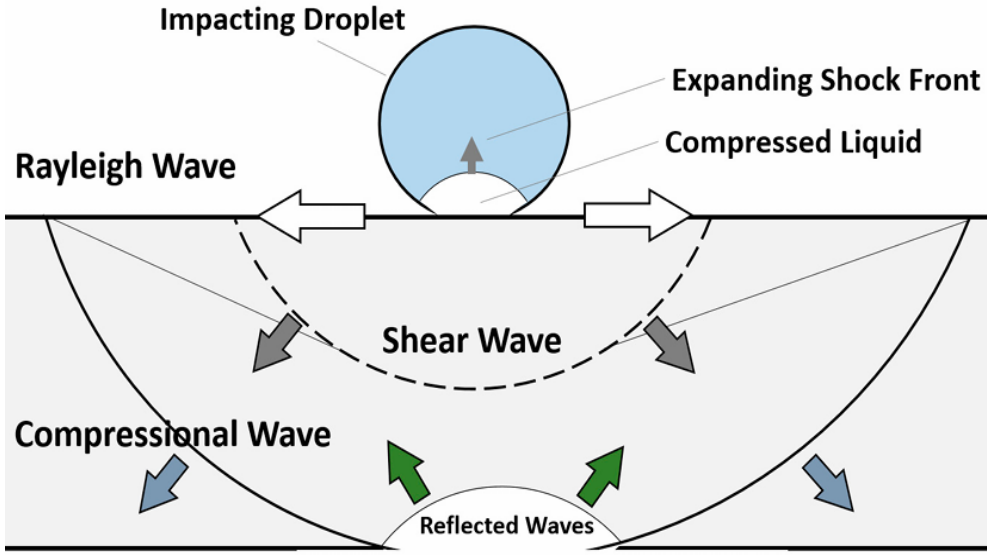

- Erosion is caused by the high-velocity impact of rain droplets near the blade tip
- The impact induces stress waves that lead to fatigue damage of the surface coating

Cortés, et al., *Materials* (2017) Mishnaevsky Jr, et al., *Wind Energy* (2020) Ahmed, et al., *Polymers* (2021) Elhadi Ibrahim, M., & Medraj, M. *Materials* (2019)

Simulate Droplet Impact Using Laser-induced Stress Waves

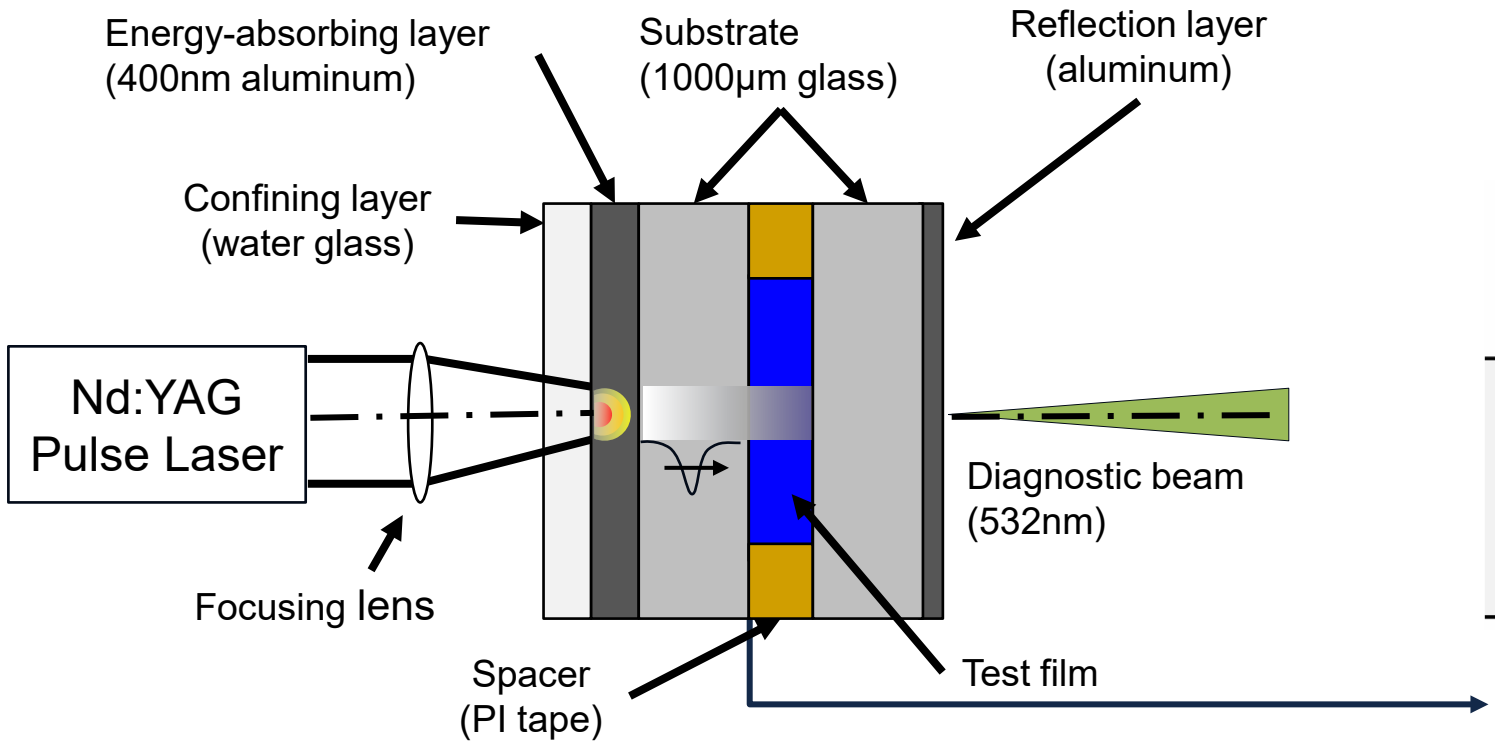

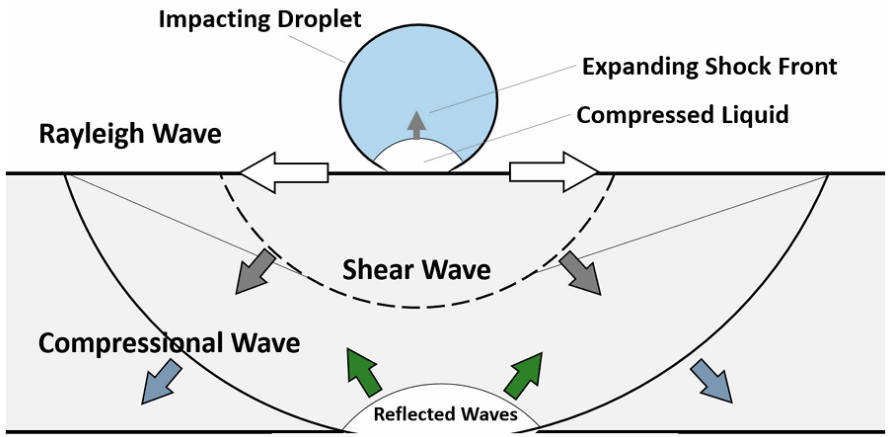

Elhadi Ibrahim, M., & Medraj, M. Materials, (2019)

Laser Induced Stress Waves Setup

Nd:YAG
Pulse Laser

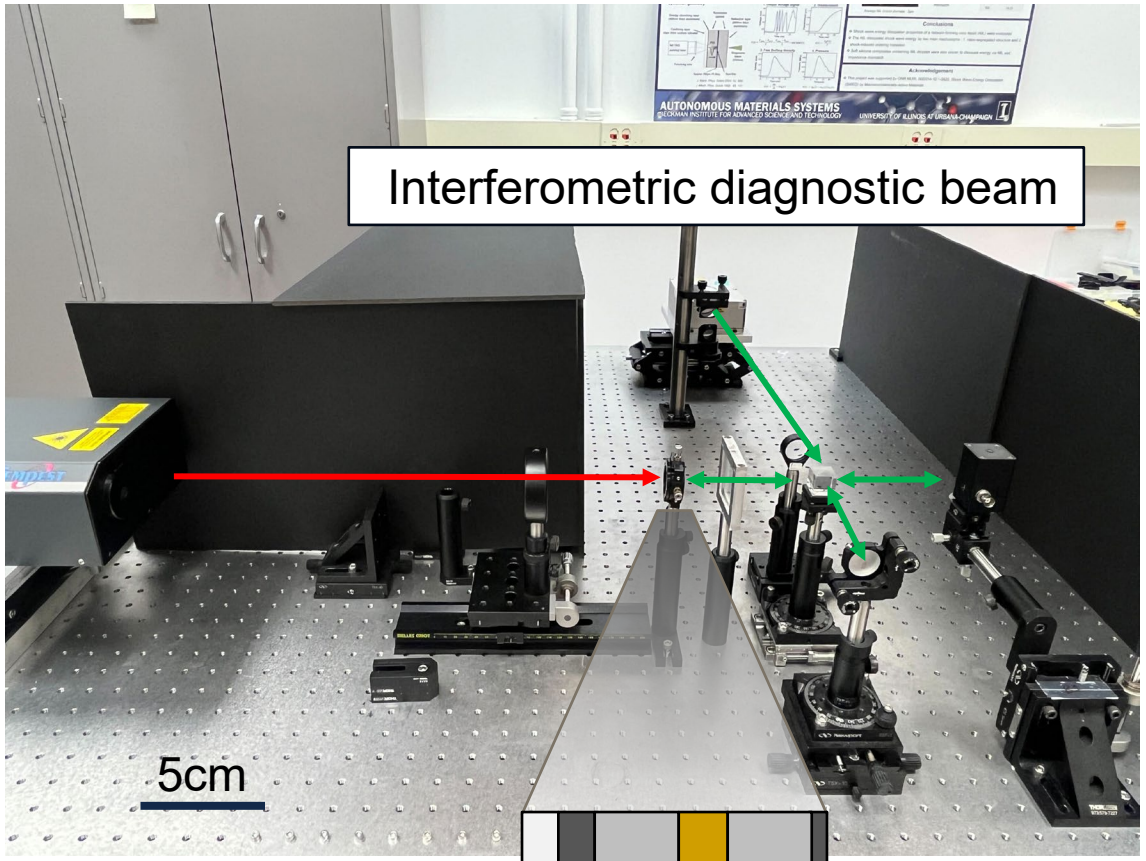

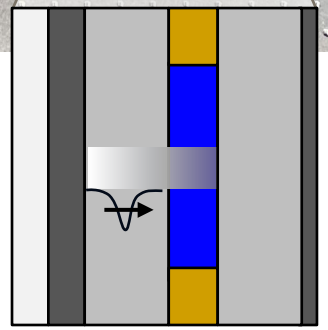

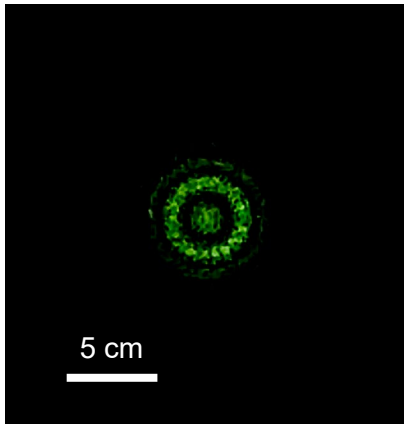

Change of fringes over time n(t)

↓

Displacement over time u(t)

↓

Substrate stress over time $\sigma_{sub}(t)$

Interferometric Data Analysis

Output Voltage Signal V(t)

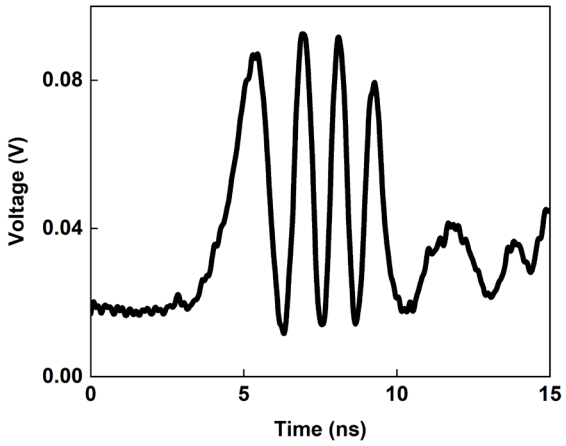

$$V(t) = \frac{V_{max} + V_{min}}{2} + \frac{V_{max} - V_{min}}{2}\sin(2\pi n(t))$$

Displacement u(t)

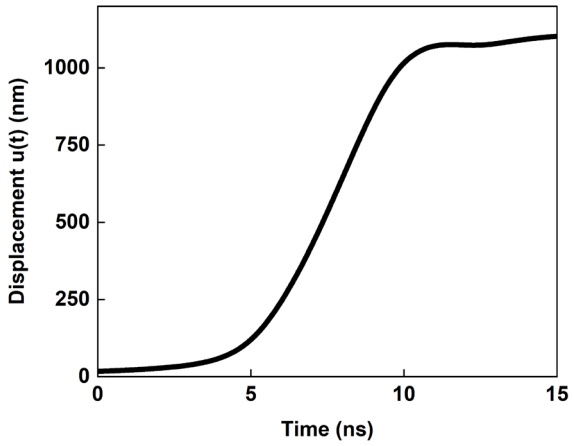

$$u(t) = \frac{\lambda_0 n(t)}{2}$$

Substrate Stress $\sigma_{sub}(t)$

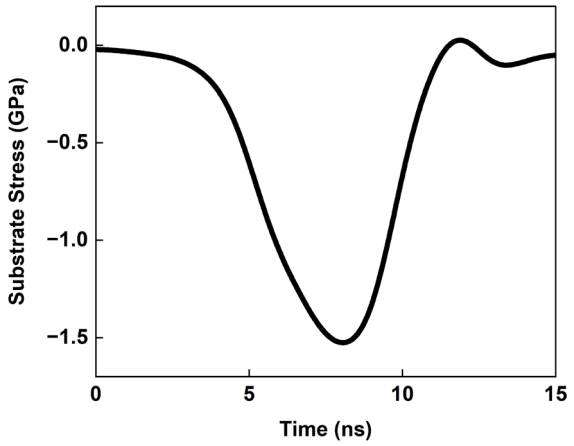

$$\sigma_{sub}(t) = -\frac{1}{2}(\rho C_d)_{sub}\frac{du}{dt}$$

Energy / Area J(t)

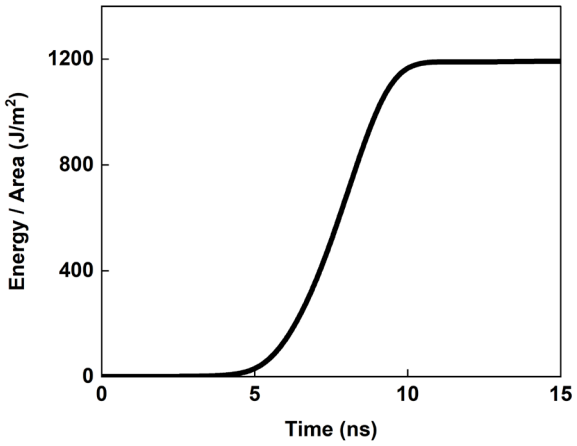

$$J(t) = \int_0^t \sigma_{sub}\,\frac{du}{dt}\,dt$$

Calibration & Setup Optimization

Effect of Confining Layer Thickness

Investigate the impact of the confining layer thickness on controlling the generation and measurement of stress waves.

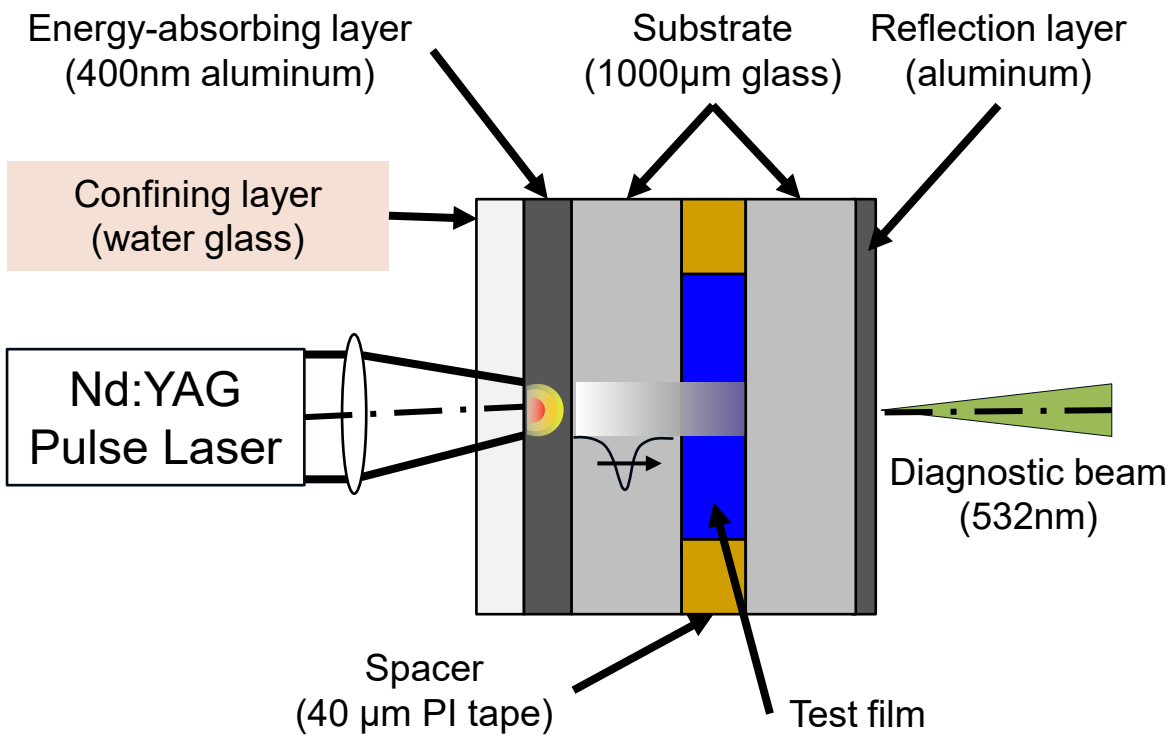

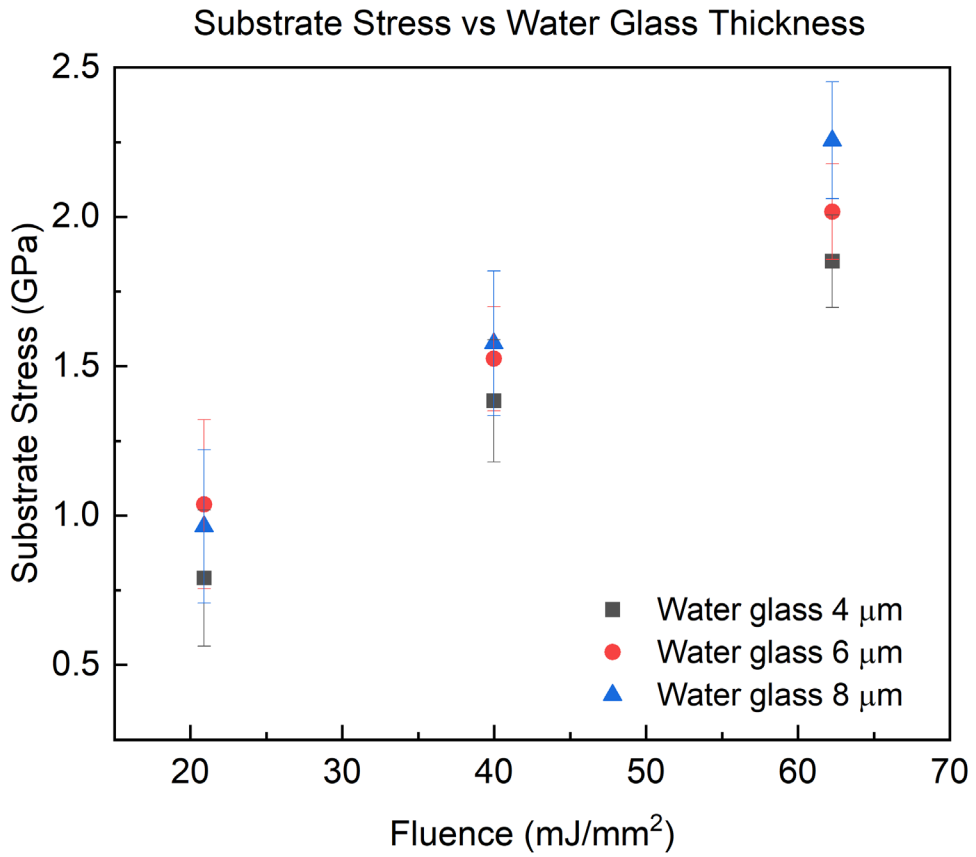

Material Evaluation for Stress Wave Dissipation

Polyurethane Coating Preparation

PU Coating Preparation :

Etch the glass substrate using 30% nitric acid → Apply a 40 µm Kapton spacer → Mix and degas the PU components → Drop-cast the PU resin onto the etched substrate → Place a second glass substrate on top to form the sandwich structure → Vitrify at room temperature for 24 hours → Cure in an oven at 50 °C for 24 hours

Components	Desmodur E 30700	1,4 butanediol	DABCO	$MgSO_4$
Mole ratio	1	1	0.05	0.05
Role	Isocyanate prepolymer	Chain extender	Catalyst	Desiccant

Polystyrene Coating Preparation

PS Coating Preparation :

Etch the glass substrate using 30% nitric acid → Prepare a 5 wt% solution of polystyrene in toluene → Sonicate the solution for 1 hour → Spin coat the solution at 5000 rpm (ramp: 15 s, dwell: 30 s) → Dry the coated sample in a toluene-saturated environment

Spin coating steps	Ramp	Dwell	RPM
Time (s)	15	30	5000

Polyurethane Coating Stress Wave Dissipation

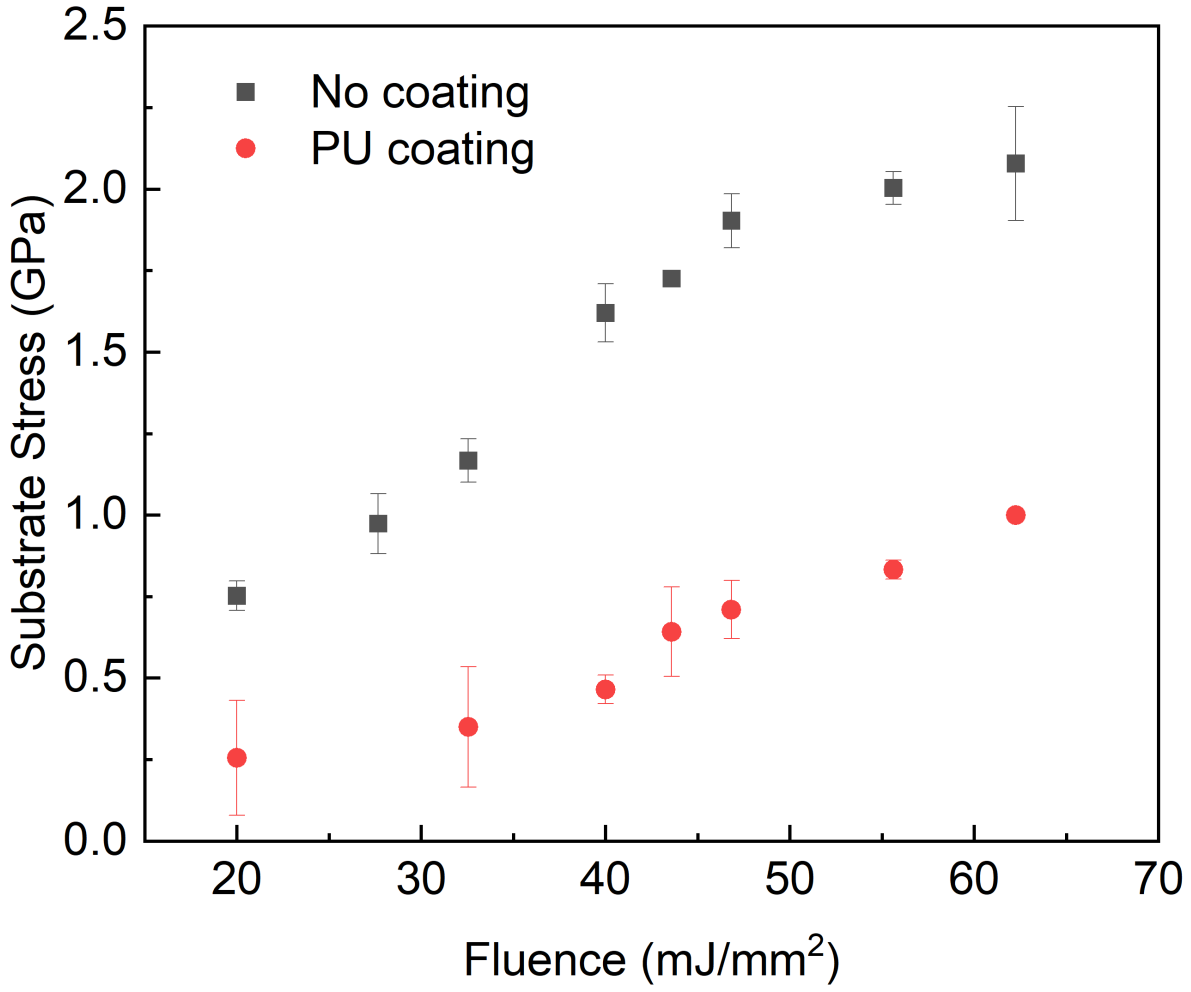

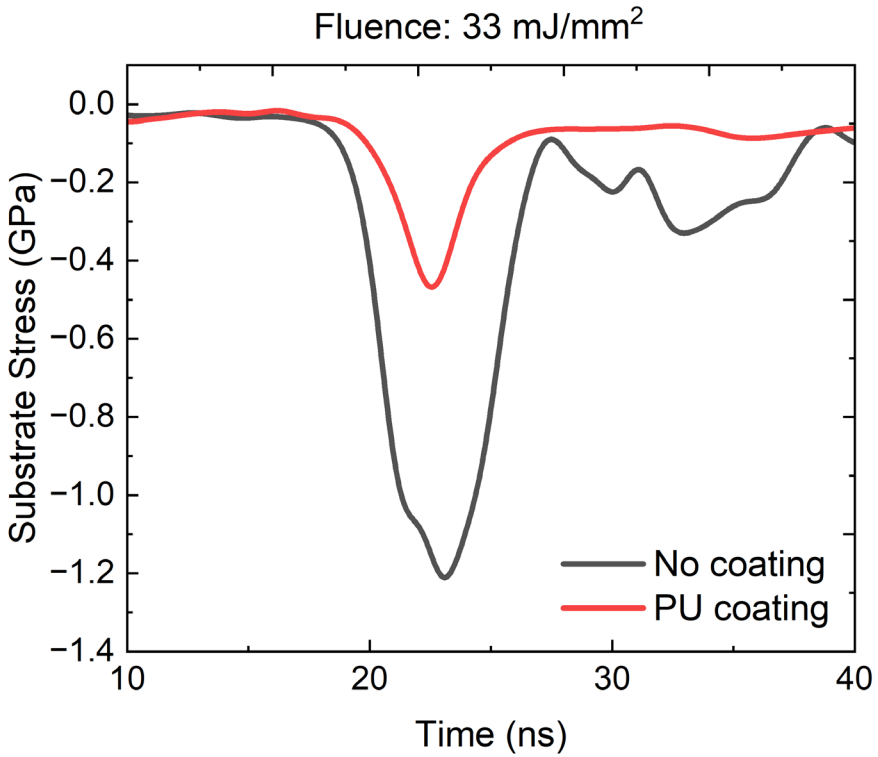

PU sample stacking	Sandwich
Water glass	8 µm
PU coating	40 µm
Reflection	200 nm

Polystyrene Coating Stress Wave Dissipation

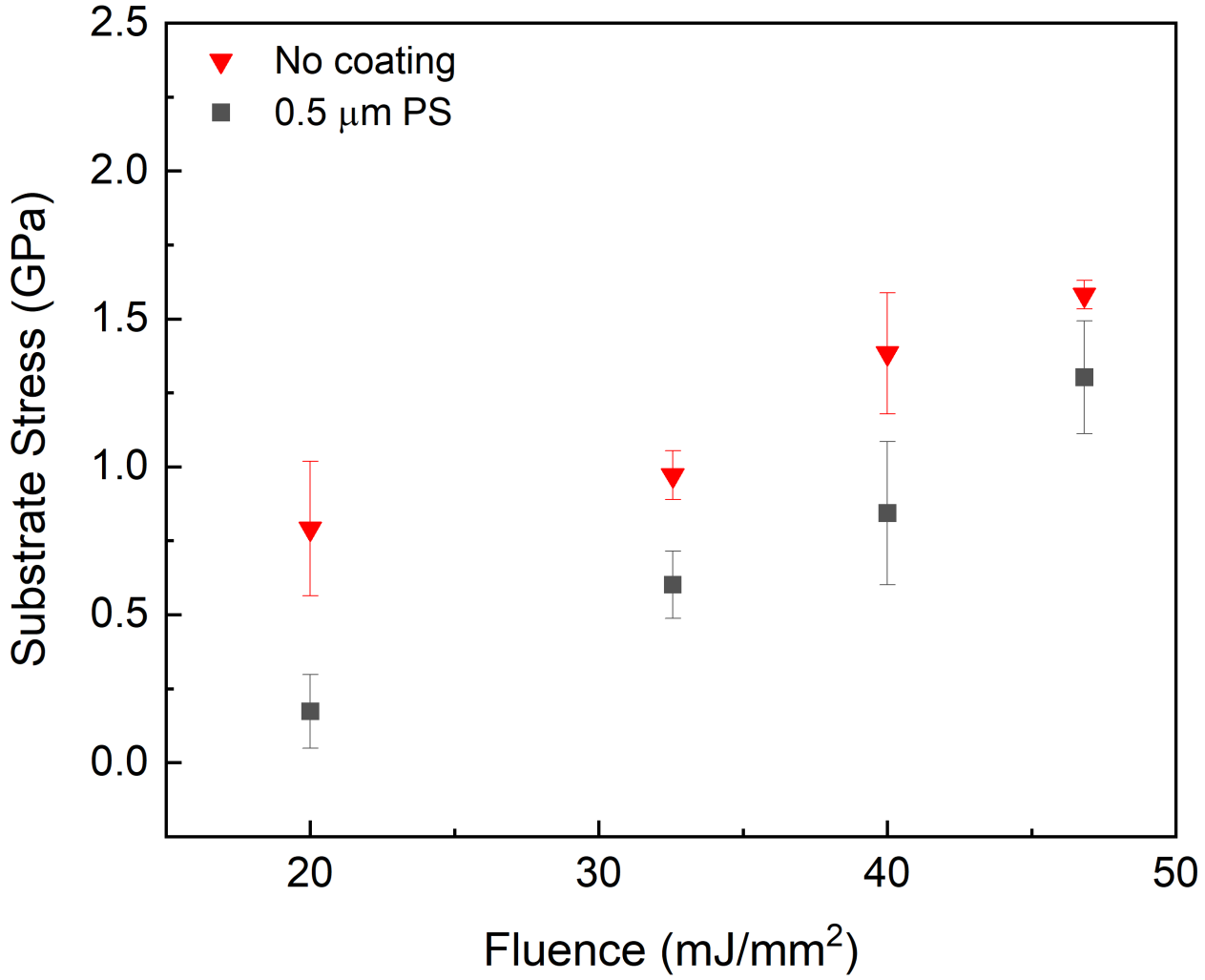

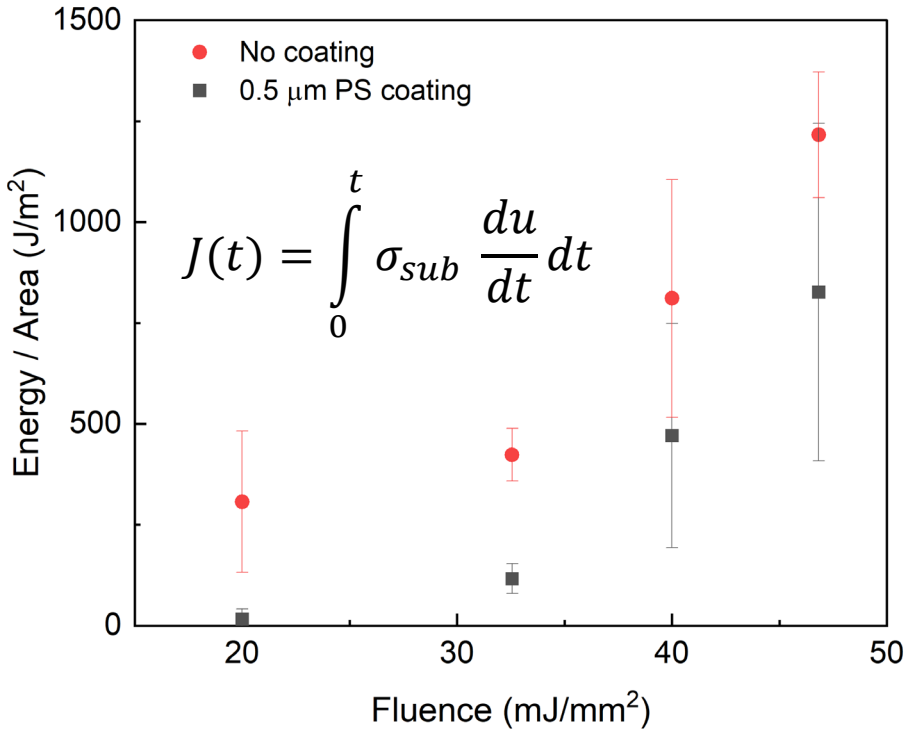

PS sample stacking	Sandwich
Water glass	4 μm
PS coating	0.5 μm
Reflection	200 nm

Preliminary Comparison of Stress Wave Energy Absorption by PU and PS Coatings

We evaluated the stress wave energy absorption by polyurethane (PU) and polystyrene (PS) coatings compared to an uncoated control

Total transmitted energy J(t) (J/m^2)

$$J(t) = \int_0^t \sigma_{sub} \frac{du}{dt} dt$$

Percent energy absorption (%)

$$= \frac{J_0 - J(t)}{J_0}$$

J_0: Transmitted energy of the substrate stress
J(t): Transmitted energy of the sample without coating

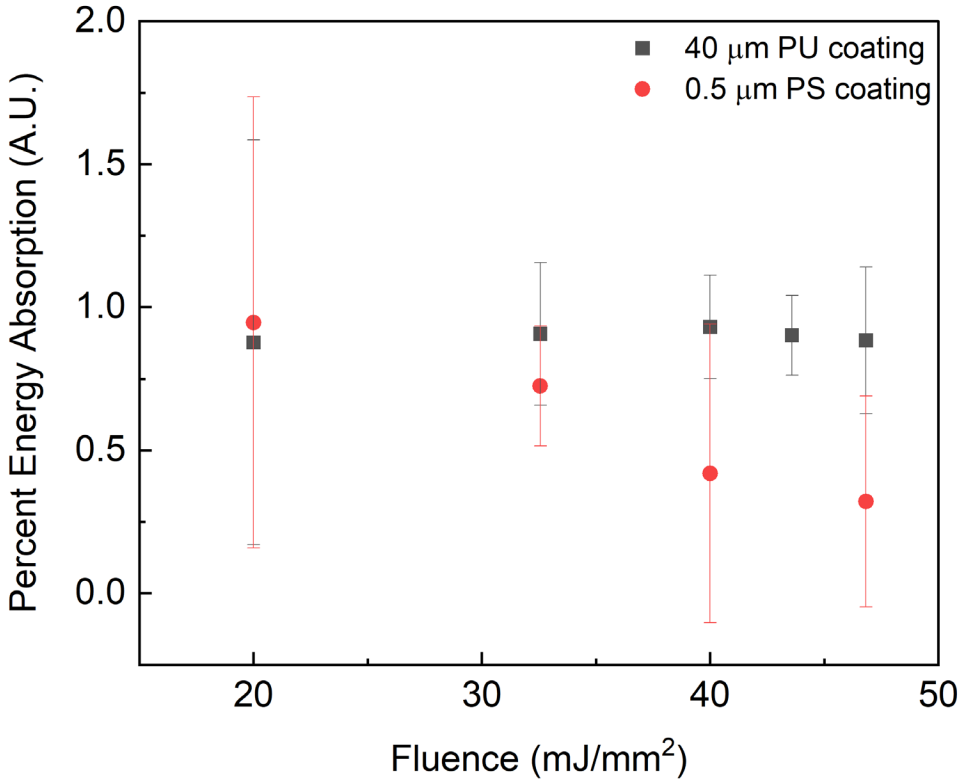

The effects of thickness on dissipation will be studied in future work.

Summary

- Developed a high-throughput, material-efficient laser-induced stress wave platform for evaluating erosion-mitigating coatings on coupon-scale samples.
- Demonstrated tunable stress wave generation by adjusting laser fluence and confinement layer thickness.
- Preliminary results show both polyurethane (PU) and polystyrene (PS) coatings reduce transmitted stress wave energy compared to uncoated samples.
- Future work will incorporate self-healing functionality and dynamic networks into coatings to achieve active mitigation of erosion damage.

Acknowledgments

Prof. Nancy Sottos

Dr. Eric Doskocil

Sottos Group

AMS Group

Materials Research Laboratory

Beckman Institute for Advanced Science and Technology





INSTITUT CLÉMENT ADER

Numerical and Experimental Analysis of Residual Deformations in Composite Plates : Integration of Part/Mold Interaction and Compensated Mold Design

24th International Conference on Composite Materials (ICCM24)

*Elias DELSOL, Wiyao AZOTI, Bruno CASTANIE, **Philippe OLIVIER** and Léon RATSIFANDRIHANA*

IMT Mines Albi École Mines-Télécom · INSA TOULOUSE · isae SUPAERO · Université de Toulouse · cnrs · Communauté d'universités et établissements de Toulouse

Introduction

- Composite materials play a key role in the aerospace industry
- Significant mass reduction
- Manufacturing processes are costly, partly due to process-induced deformations
- Prediction methods lack accuracy, especially for thin composite parts

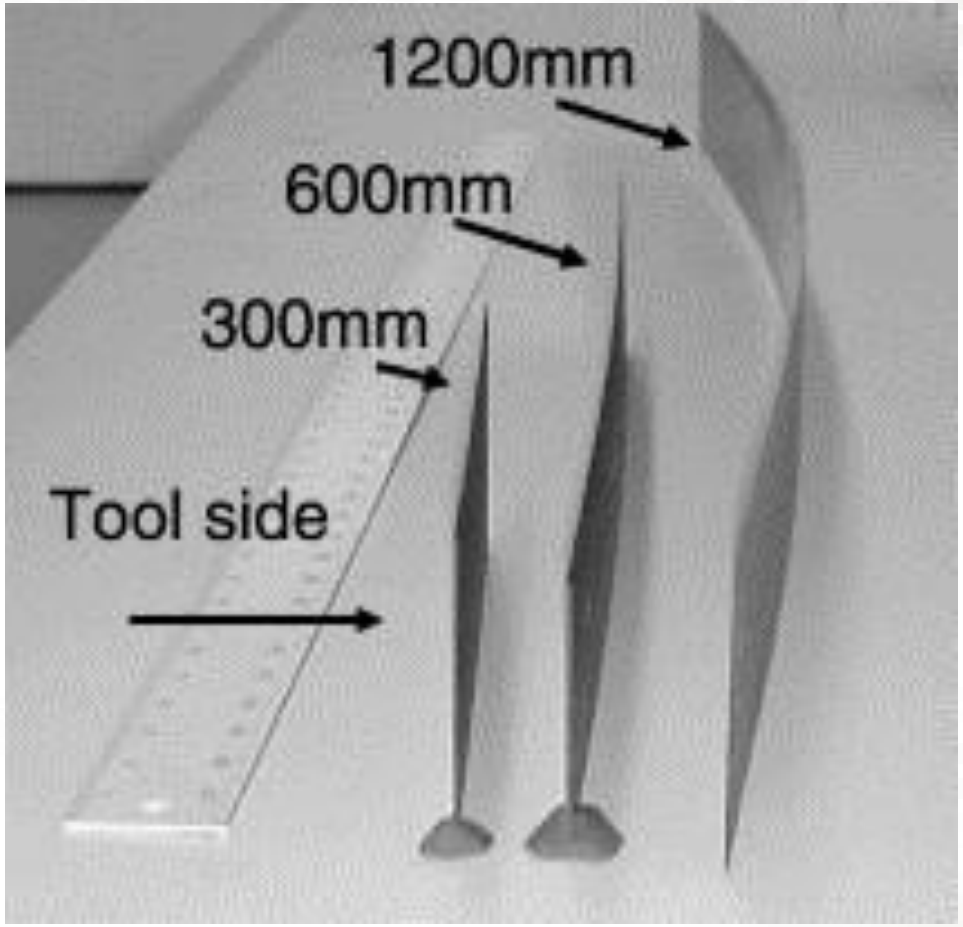

Thin plate warpage [Twigg 2004]

Need for a more accurate model for thin composite parts

Residual deformations of composite parts manufactured in autoclave

- "Composite parts never have the same dimensions as the tool on which they are processed " [Kappel 2018],
- Two types of deformation: spring-in and warpage [Moretti 2020],
- Need to design a compensated mold [Wucher 2014],
- Costly process: based on experimental iterations.

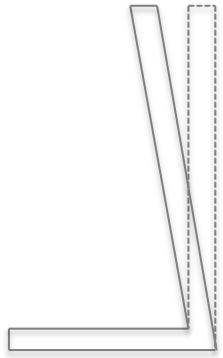

Spring-in



Warpage



Industrial and scientific challenges : prediction of residual deformations, and limiting experimental iterations

The main mechanisms generating residual deformations

- Thermal expansion mismatch [Wisnom 2006],
- Chemical shrinkage [Li 2004],
- Part/mold interaction [Twigg 2004] ,
- Thermal gradients [Bogetti 1992] ,
- Fiber volume fraction [Hubert 2001] .

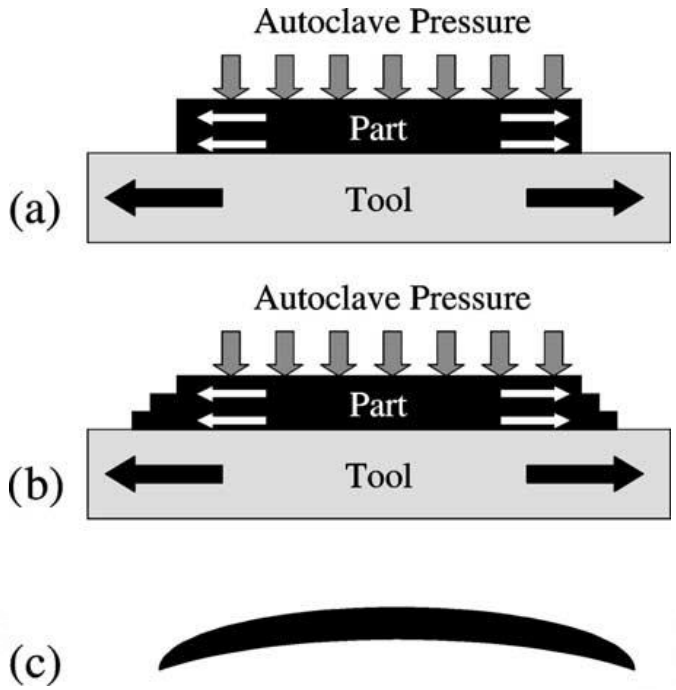

Part/Mold Interaction [Twigg 2004]

Numerous mechanisms with variable influence: multiphysical modeling is necessary

Table of contents

- Experimental analysis of thin plates process-induced deformations
- Numerical analysis of thin plates process-induced deformations
- Conclusions and perspectives

Laminated Plate Manufacturing

- Size 250 x 250 mm,
- Material AS4/8552,
- Layups : [0,90,90,0], [0,90,0,90], [-45,45,45,-45], [-45,45,-45,45],
- Aluminum mold,
- Application of the cycle indicated in the documentation.

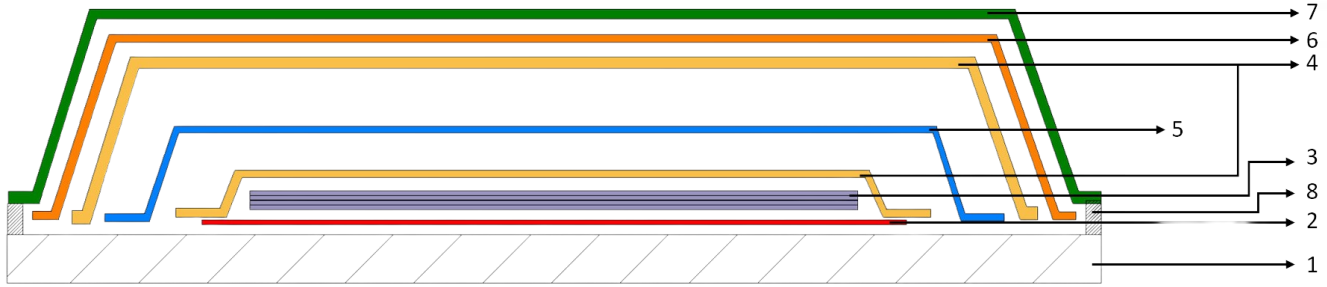

Reference	Designation
1	Aluminium mold
2	Peel ply
3	Composite part
4	Perforated release film
5	Bleeder ply
6	Breather ply
7	Vacuum bag
8	Sealant tap

Indirect measurement of the tool/part interaction effect

Displacement field measurement

- Dimensional control by stereo **DIC**: non-contact measurement,
- Low dispersion across repeated tests
- Large out-of-plane deflections observed, despite symmetric layup

Layup	Measured Flatness
[-45,45,-45,45]	25,6 mm
[0,90,0,90]	11,2 mm
[-45,45,45,-45]	7,8 mm
[0,90,90,0]	2,2 mm

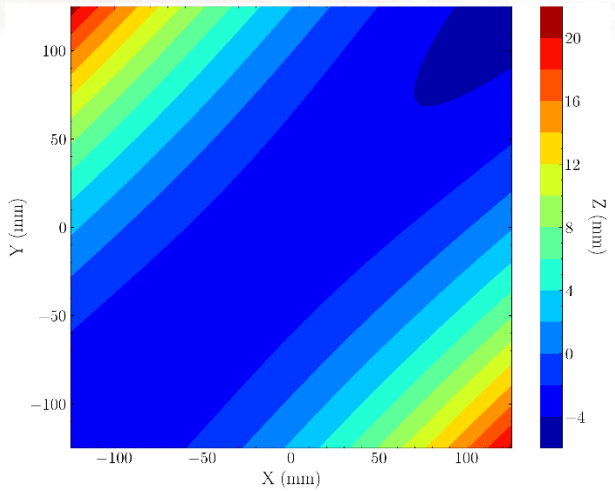

[-45,45,-45,45]

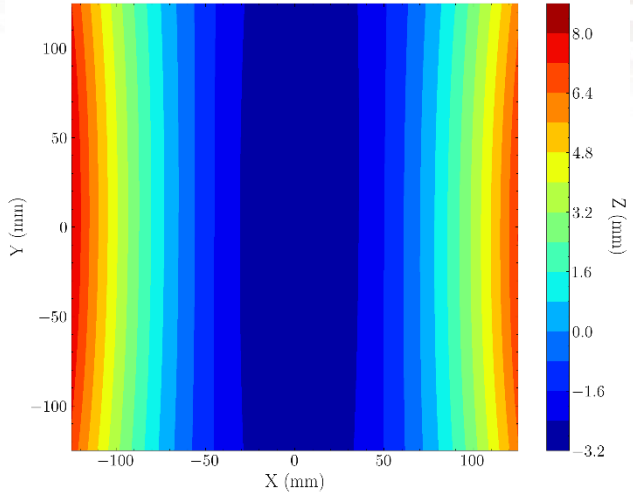

[0,90,0,90]

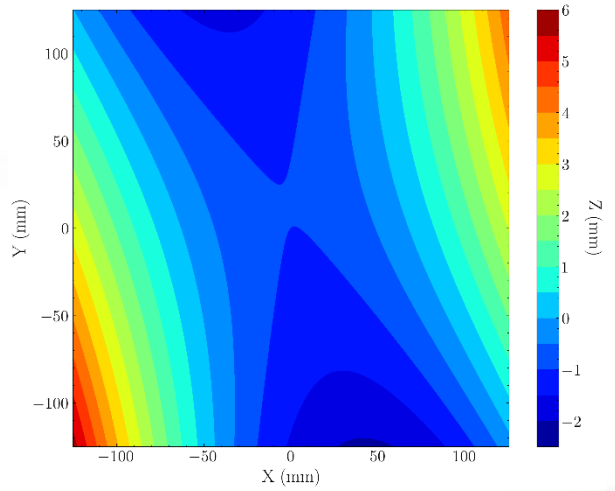

[-45,45,45,-45]

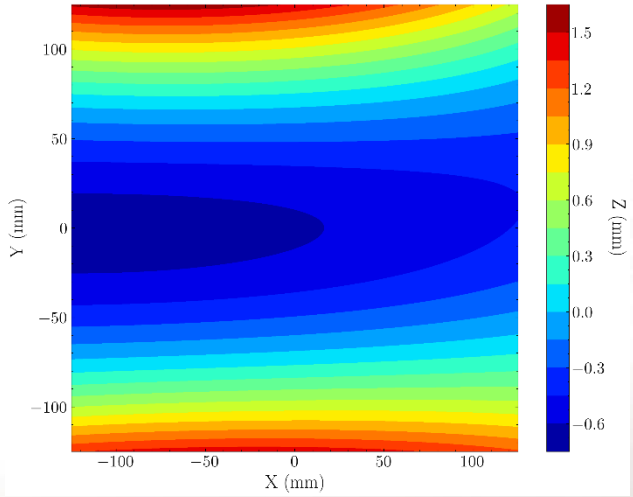

[0,90,90,0]

Significant influence of the tool–part interaction mechanism

Cure modelling

- Development of a UMAT user subroutine in Abaqus : use of the CHILE model
- Frictional contact between mold and part
- Application of pressure and thermal cycles
- After demolding : isostatic positioning

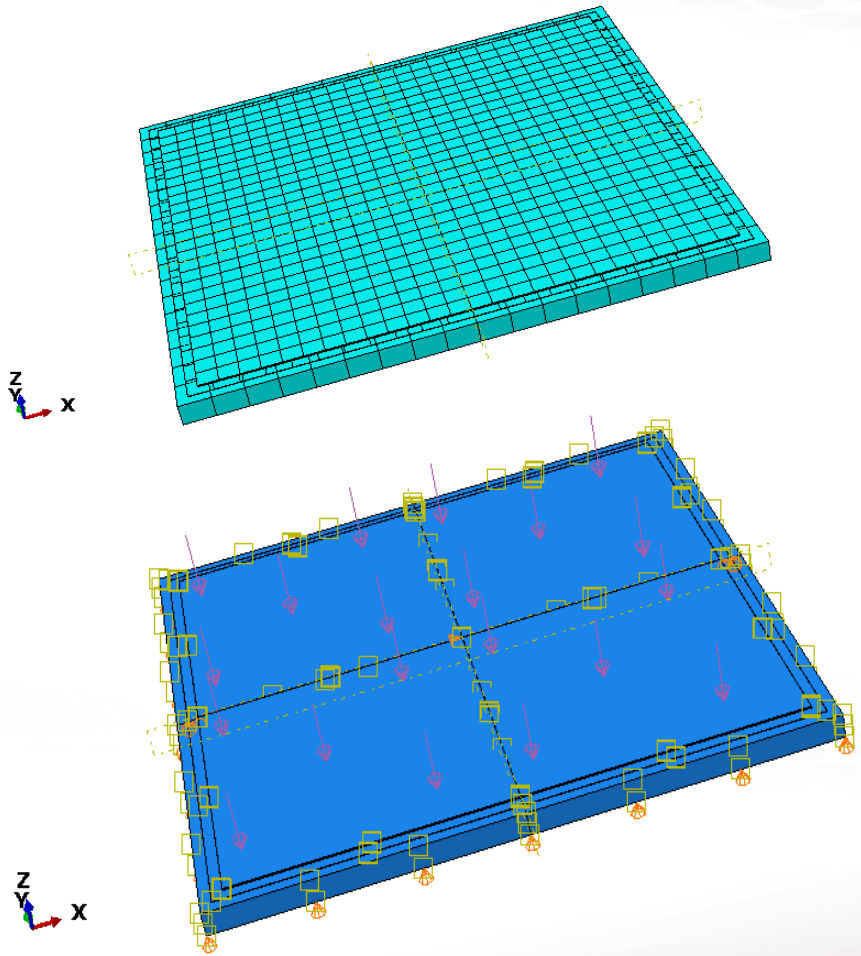

Boundary conditions for demolding affect the displacement field ➔ comparison with experimental results is impossible

Correction of the displacement field

- Need to correct the displacement fields,
- Minimizing the gap between the initial and final shapes,
- Find the translation and rotation matrices of the vector base,
- Then, apply the translation and rotation to the final shape

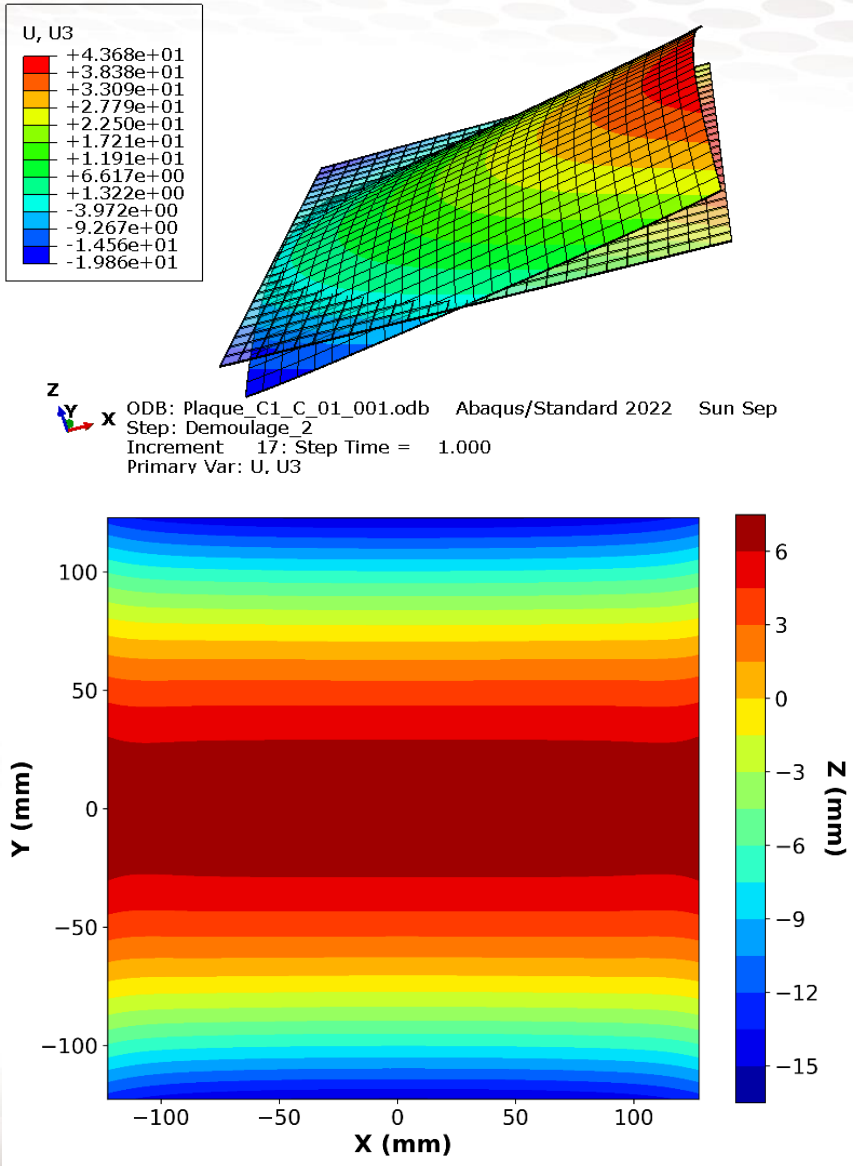

Full cure modelling

- Main assumption : part free of stress before gelation
- Friction interaction occurs during a small temperature variation before glassy state,
- Practically no stress storage due to the tool/part interaction

The assumption of a stress-free part before gelation is incorrect ?

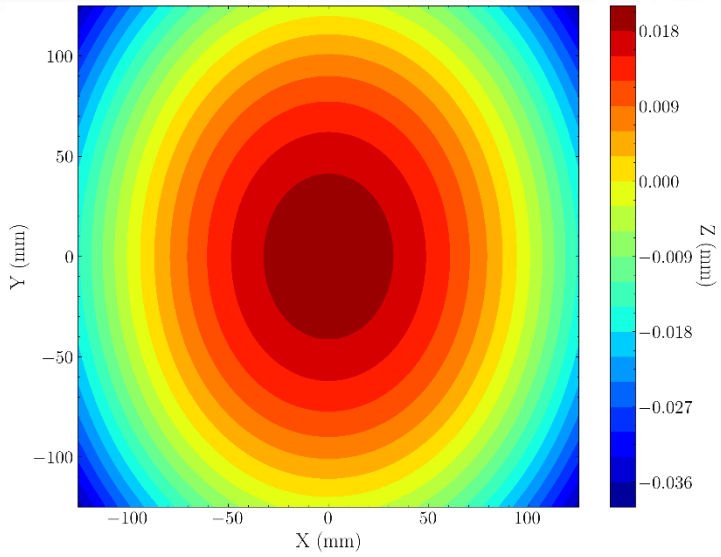

[0,90,90,0]

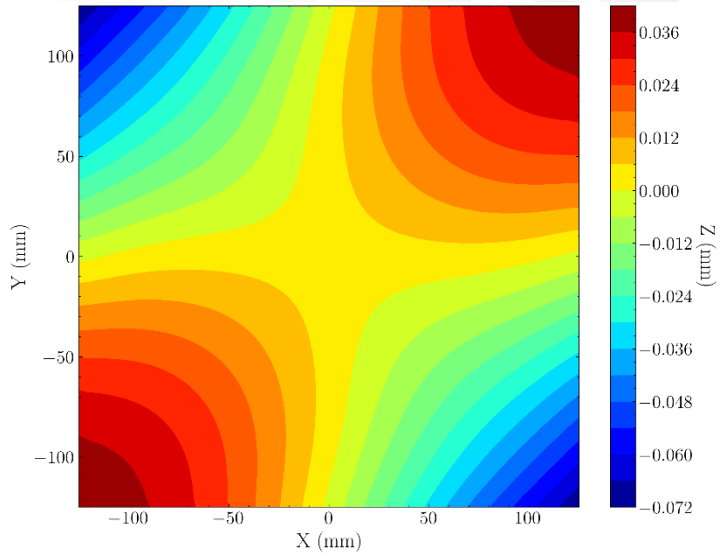

[-45,45,45,-45]

Layup	Measured Flatness	Predicted Flatness
[-45,45,-45,45]	25,6 mm	27,48 mm
[0,90,0,90],	11,2 mm	11,63 mm
[-45,45,45,-45]	7,8 mm	0,11 mm
[0,90,90,0]	2,2 mm	0,06 mm

Investigation of Tool–Part Mechanical Interaction Effects

- Some fibers remain in contact with the mold surface
- The assumption of a stress-free state before gelation is not valid
- A sliding friction condition occurs between the mold and the fiber bed
- Tensile stresses are locked-in in the fibers constrained by the mold

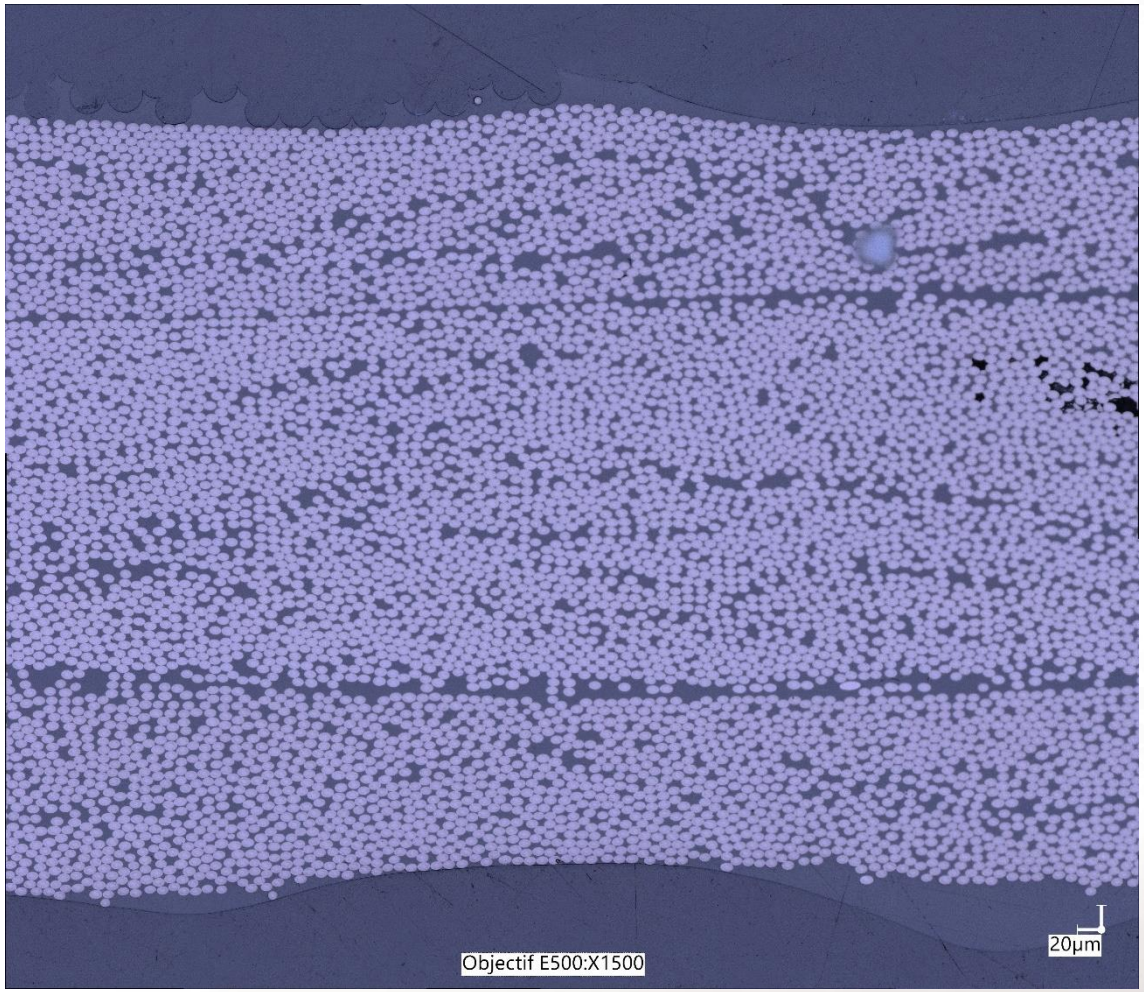

The assumption of a stress-free part before gelation is incorrect

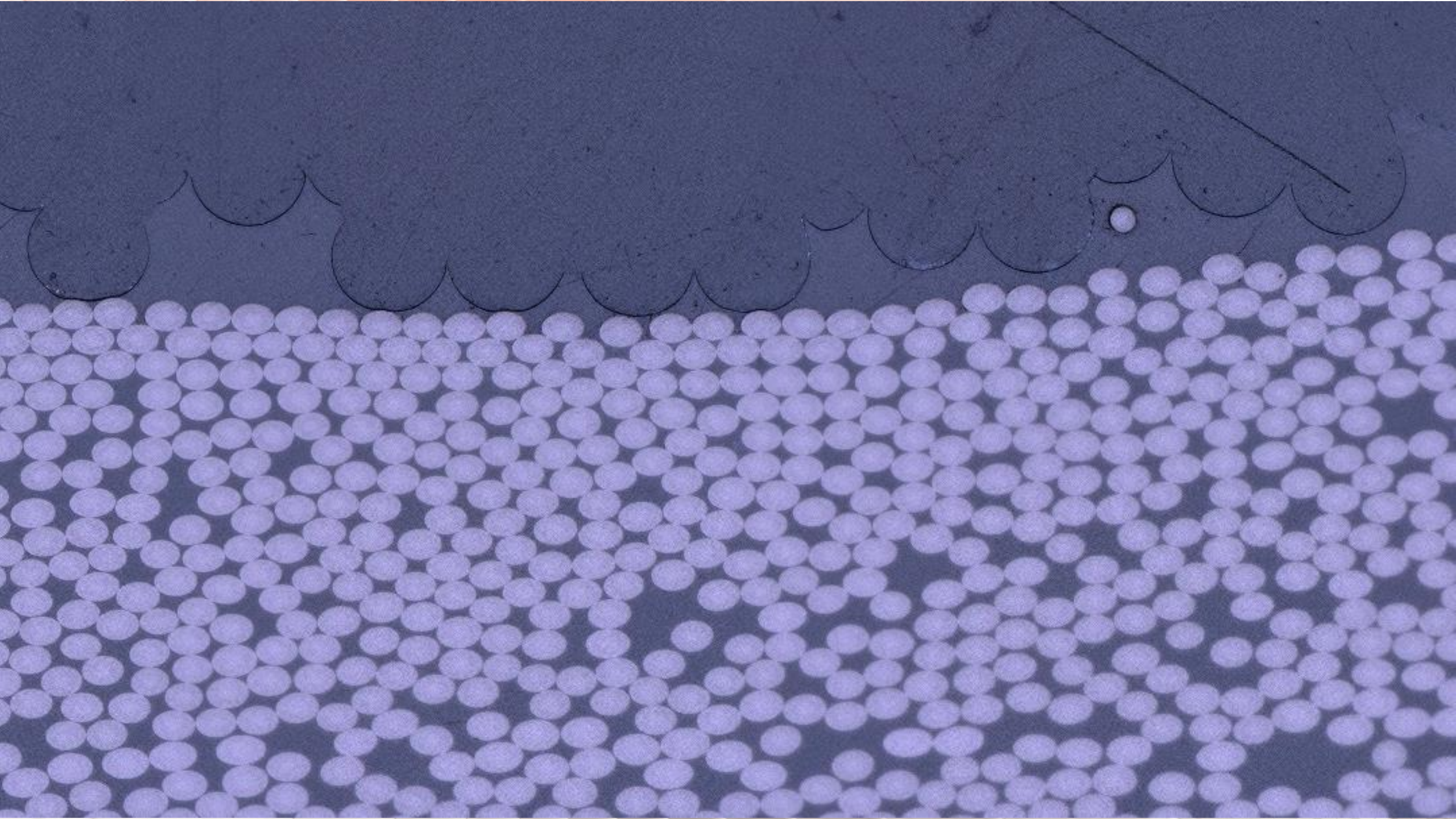

Full cure modelling with tool part interaction : viscous stage

- Simulation without considering the microscale,
- Two materials during the viscous phase
- Frictional contact between mold and part (with f=0.1)
- Displacement continuity assumption between composites plies

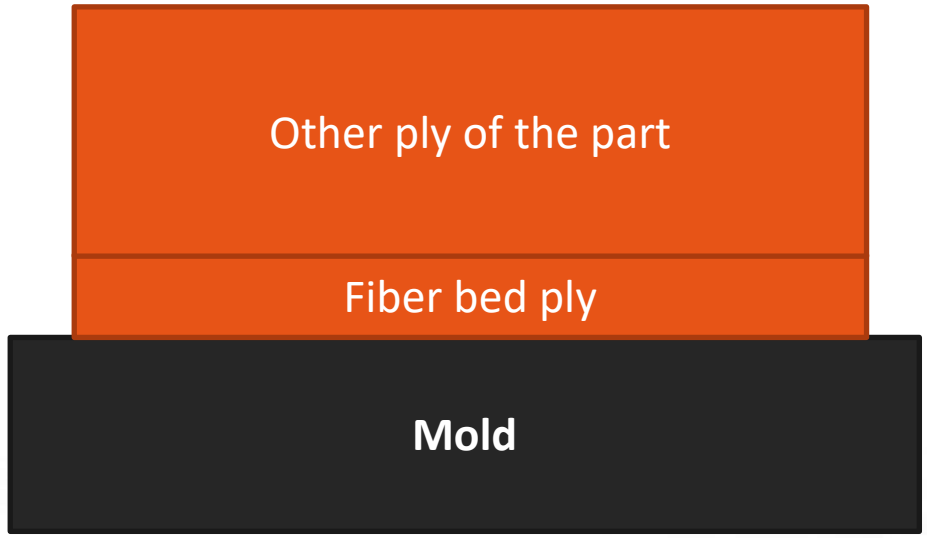

Modelization of the fiber bed stress by considering a ply of fiber in contact with the mold

Full cure modelling with tool part interaction : results

- Development of a UMAT user subroutine in Abaqus : use of the CHILE model
- Frictional contact between mold and part (with f=0.1),
- Considerable improvement of the prediction,

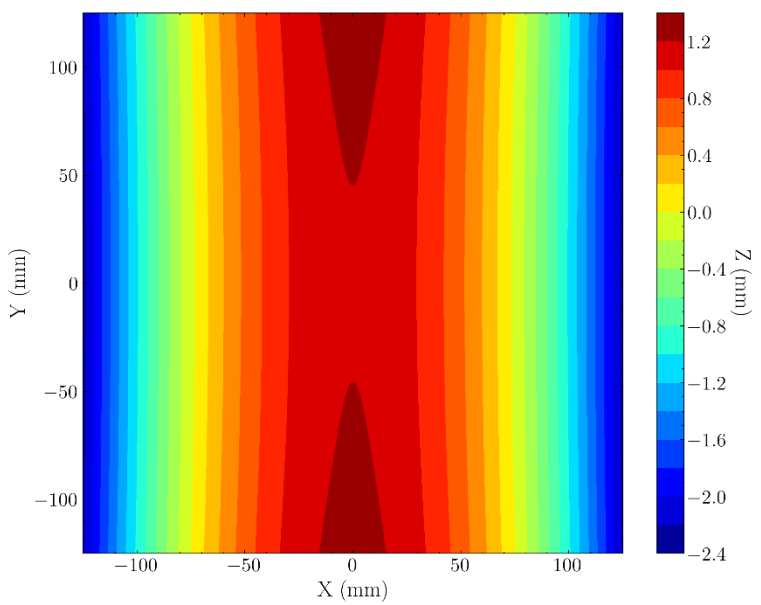

[0,90,90,0]

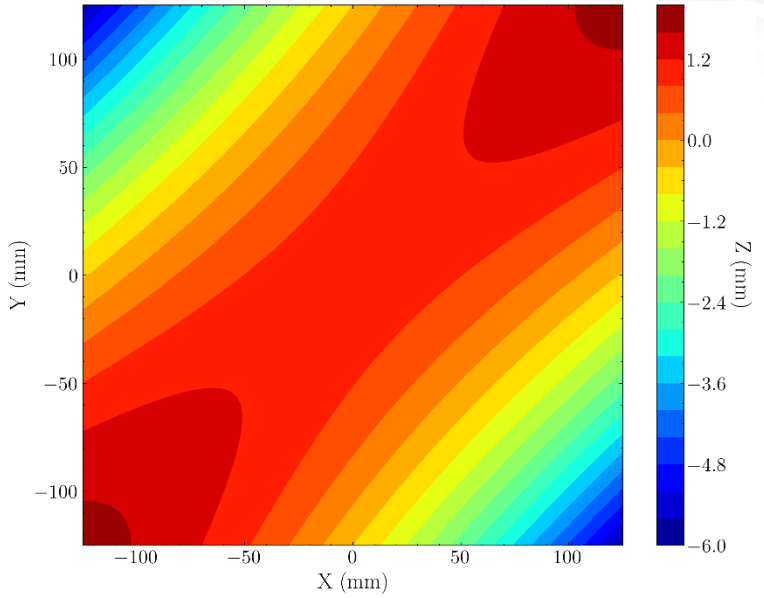

[-45,45,45,-45]

Layup	Measured Flatness	Predicted Flatness
AS45	25,6 mm	27,48 mm
AS90	11,2 mm	11,63 mm
S45	7,8 mm	6,60 mm
S90	2,2 mm	3,46 mm

Full cure modelling with tool part interaction : results

- Asymmetrical layup : out-of-plane residual displacements developed during the glassy stage,
- A friction interaction only during the rubbery stage can not describe the tool part interaction effect,
- Tool part interaction phenomenon takes place during the viscous stage,

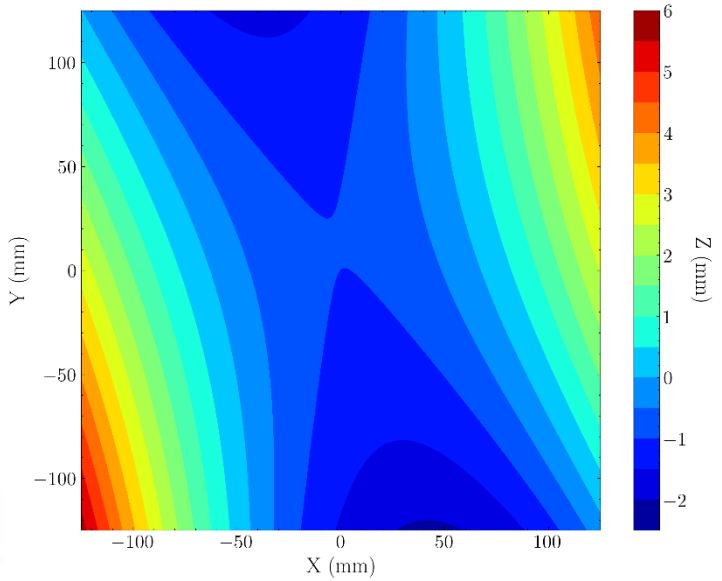

Measured shaped (part is returned)

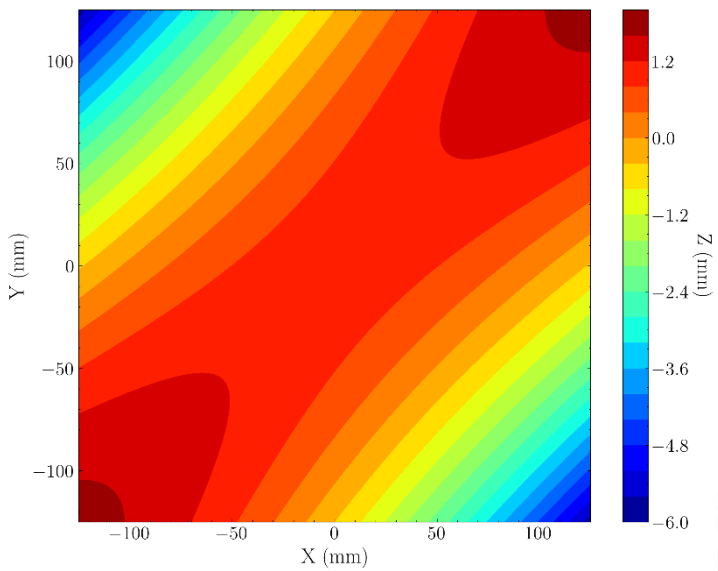

Predicted shaped

Further investigations are needed to improve model accuracy

Conclusions and Perspectives

Conclusions

- An experimental analysis of residual deformations was conducted
- The tool–part interaction was investigated
- A complete simulation method was developed
- A significant improvement in warpage prediction was achieved by accounting for tool–part interaction

Perspectives

- Improve the tool–part interaction modeling through micromechanical analysis
- Focus upon the role of peel-ply
- Apply the in-house digital compensating mold design method
- Validate the compensating mold design using the current part configurations

Sources

[Twigg 2004] Twigg, G., Poursartip, A., & Fernlund, G. (2004). Tool–part interaction in composites processing. Part I: experimental investigation and analytical model. *Composites Part A: Applied Science and Manufacturing*, *35*(1), 121-133.

[Kappel 2018] Kappel, E. (2018). Compensating process-induced distortions of composite structures: a short communication. *Composite Structures*, *192*, 67-71.

[Moretti 2020] Moretti, L., Castanié, B., Bernhart, G., & Olivier, P. (2020). Characterization and modelling of cure-dependent properties and strains during composites manufacturing. *Journal of composite materials*, *54*(22), 3109-3124.

[Wucher 2014] Wucher, B., Lani, F., Pardoen, T., Bailly, C., & Martiny, P. (2014). Tooling geometry optimization for compensation of cure-induced distortions of a curved carbon/epoxy C-spar. *Composites Part A: Applied Science and Manufacturing*, *56*, 27-35.

[Wisnom 2006] Wisnom, M. R., Gigliotti, M., Ersoy, N., Campbell, M., & Potter, K. D. (2006). Mechanisms generating residual stresses and distortion during manufacture of polymer–matrix composite structures. *Composites Part A: Applied Science and Manufacturing*, *37*(4), 522-529.

[Li 2004] Li, C., Potter, K., Wisnom, M. R., & Stringer, G. (2004). In-situ measurement of chemical shrinkage of MY750 epoxy resin by a novel gravimetric method. *Composites Science and Technology*, *64*(1), 55-64.

[Bogetti 1992] Bogetti, T. A., & Gillespie Jr, J. W. (1992). Process-induced stress and deformation in thick-section thermoset composite laminates. *Journal of composite materials*, *26*(5), 626-660.

[Hubert 2001] Hubert, P., & Poursartip, A. (2001). Aspects of the compaction of composite angle laminates: an experimental investigation. *Journal of Composite Materials*, *35*(1), 2-26.

INSTITUT CLÉMENT ADER

Numerical and Experimental Analysis of Residual Deformations in Composite Plates : Integration of Part/Mold Interaction and Compensated Mold Design

*Elias DELSOL, Wiyao AZOTI, Bruno CASTANIE, **Philippe OLIVIER** and Léon RATSIFANDRIHANA*

Thank you for your attention

IMT Mines Albi École Mines-Télécom · INSA TOULOUSE · isae SUPAERO · Université de Toulouse · cnrs · Communauté d'universités et établissements de Toulouse

We support the



bid for ICCM26 Toulouse 2029 organisation

IMT Mines Albi École Mines-Télécom · INSA Toulouse · isae SUPAERO · Université de Toulouse · cnrs · Communauté d'universités et établissements de Toulouse

ICCM24
AUGUST 4-8, 2025
BALTIMORE CONVENTION CENTER
BALTIMORE, MARYLAND, USA

No Technical Paper Submission for:

Andrejs Pupurs

DEVELOPMENT OF HIGH-PERFORMANCE BIPOLAR PLATES BY ELECTRODE INTEGRATION FOR VANADIUM REDOX FLOW BATTERIES

Amanpreet Kaur[1] and Jun Woo Lim[2]

[1]Graduate School of Flexible and Printable Electronics & LANL-JBNU Engineering Institute-Korea, Jeonbuk National University, 567 Baekje-daero, Deokjin-gu, Jeonju-si, Jeonbuk State, 54896, Republic of Korea
Email: amankhamano@gmail.com, web page: https://ascl.jbnu.ac.kr

[2]Graduate School of Flexible and Printable Electronics & LANL-CBNU Engineering Institute Korea & Department of Mechatronics Engineering & JBNU-KIST Industry-Academia Convergence Research, Jeonbuk National University, 567 Baekje-daero, Deokjin-gu, Jeonju-si, Jeonbuk State, 54896, Republic of Korea
Email: jul170@jbnu.ac.kr, web page: https://ascl.jbnu.ac.kr

Keywords: Vanadium redox flow battery, Integrated structure, Low interfacial contact resistance, High conductivity, Multi-cell structure.

ABSTRACT

The bipolar plate is a crucial element of the vanadium redox flow battery (VRFB) as it serves as both the electrical path for the electrolyte and the structural support for the cell within the VRFB stack. The graphite material has been used as the bipolar plate, mostly due to its excellent electrical conductivity. A significant limitation of the VRFB is the presence of several core components. Hence, the internal contact resistance (ICR) arises between the electrode and bipolar plate within the cell stack, and it is significantly greater than the bulk resistance of the corresponding specimens. This study focuses on creating an integrated assembly of the electrode and bipolar plate to address the limitations of the ICR. The integrated assembly was constructed using a single carbon felt specimen. The study resulted in the development of an electrode-integrated BP that exhibited a 28% decrease in overall resistance and a 175% improvement in mechanical properties. Gas permeability and acid aging tests confirmed that the electrode-integrated BP exhibited zero gas permeability and was therefore durable. In conclusion, a two-cell charge/discharge test confirmed that the energy efficiency of the integrated structure had increased by 6.3%. The proposed integrated structure is thus a potentially advantageous substitute for conventional BP and CF electrode assemblies.

1 INTRODUCTION

There is a growing interest in using renewable resources for power production due to environmental concerns about the usage of non-renewable resources like fossil fuels [1,2]. Solar and wind energy are highly accessible, cost-effective, and environmentally friendly sources of energy [3,4]. Nevertheless, the generation of power from these renewable energy sources is irregular, requiring the development of large electrical energy storage systems [5]. This issue has led to significant progress in the research and development of electrical energy storage devices, particularly in the past few decades. Vanadium redox flow batteries (VRFB) show great potential as energy storage systems due to their optimum combination of safety, durability, stability, and efficiency. A standard Vanadium Redox Flow Battery (VRFB) consists of several cells, two pumps, and two electrolyte tanks. The structure of each cell consists of two bipolar plates (BPs), two electrodes, and a membrane.

The membrane acts as a barrier between the two half-cells in the VRFB. The electrode facilitates the formation of reactive sites and electrical pathways for the electrolyte. It is often made of carbon and graphite felt. The VRFB stores energy in the two electrolytes containing different redox couples, V^{2+}/V^{3+} and VO^{2+}/VO_2^{+}, which generate a potential difference through an electrochemical redox reaction. This

results in a charge-discharge reaction. The BPs provide pathways for electrical current to flow between adjacent cells while also isolating each individual cell. Consequently, a BP must possess certain characteristics, including a high electrical conductivity, a low permeability of vanadium sulfuric acid electrolytes, and chemical stability. Although VRFB (Vanadium Redox Flow Battery) is being more commercialized, there is still a persistent requirement to investigate further methods of improving efficiency and lowering expenses. The power capacity of the VRFB is governed by the size of the stack area and the number of stacks, while the energy capacity is dictated by the quantity of electrolyte. In the case of a multiple-stack VRFB, improving cell resistance might lead to enhanced performance.

In VRFB, there is a contact between the Bipolar Plate (BP) and electrode in the VRFB. This interface gives rise to problems associated with interfacial resistance (ICR) as shown on Fig. 1. In order to address these ICR (Internal Cell Resistance) difficulties, it is necessary to apply a high compaction pressure to the VRFB (Vanadium Redox Flow Battery) stack. However, the VRFB experiences a low applied pressure due to structural constraints, resulting in a decrease in viscous dissipation. Therefore, the internal contact resistance (ICR) has a substantial impact on the cell efficiency of the vanadium redox flow battery (VRFB) and causes a reduction in efficiency. Lim et al. proposed an integrated structure of a carbon felt electrode (CFE) and BP for VRFB, which was created by local thermoplastic welding [6]. The structure of the CFE-BP assembly demonstrated a decrease in electrical resistance and an increased level of energy efficiency due to the reduction in contact resistance. However, the mechanical characteristics of the CFE can be compromised because to the reduction in porosity caused by the compaction pressure applied during the production process.

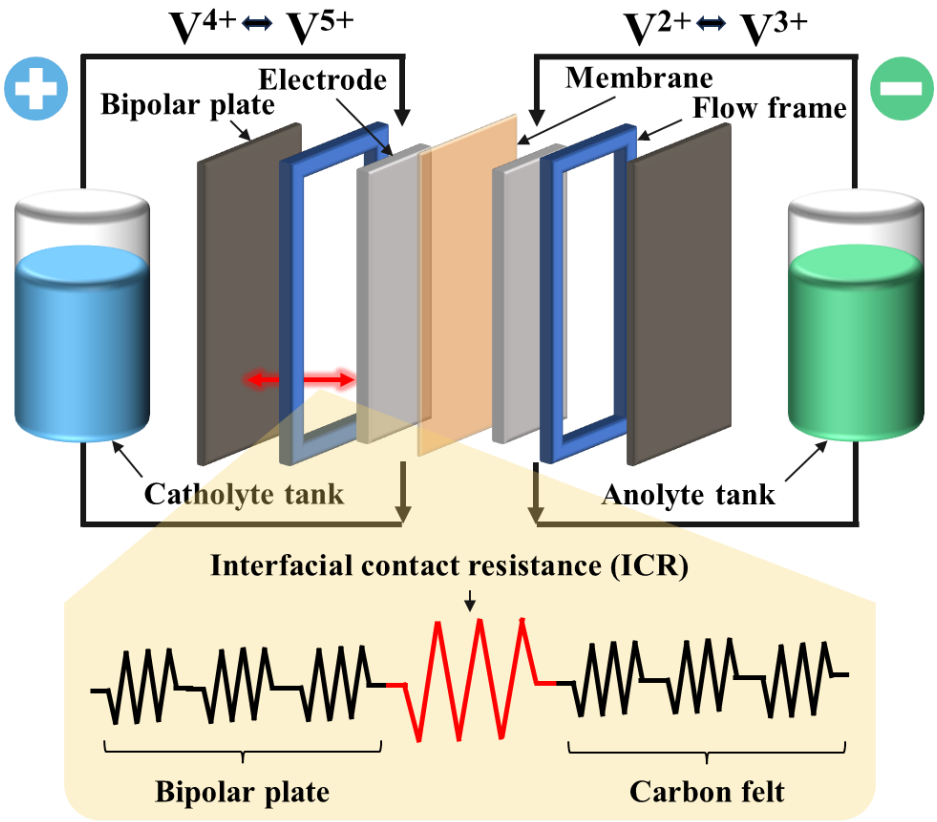

Figure 1: Schematic of vanadium redox flow battery (VRFB) and interfacial contact resistance.

We proposed a carbon felt electrode (CFE)-BP-Carbon felt electrode (CFE) (CFE-BP-CFE) composite structure that generates repetitive units of multi-cell arrays from a single CF in order to overcome these issues. By utilizing this approach, the degradation of mechanical properties caused by the compressive pressure of the CF electrode is prevented. The CFE-BP-CFE composite structure was

fabricated using one single CF in order to reduce contact resistance between the CFE and BP, as well as adjacent cells; this structure established an electrode-BP-electrode interconnection with the CF fibers. By partially impregnating the electrode section with a soluble resin, the CFE section, which measured 4 mm in thickness from both surfaces of a 10 mm single CF, was rendered impermeable. This impregnated CFE section was protected from the compaction pressure utilized during BP fabrication. Significant hydrophilicity was achieved by thermal treatment, enabling the electrode section to be filled with regular glucose and porosity to be eliminated under CF pressure. Following this fabrication, a two-cell test was conducted to evaluate the total resistance, gas permeability, and charge/discharge cycle of the battery.

2 EXPERIMENTAL SECTIONS

2.1 Fabrication of the integrated structure

The CFE-BP-CFE integrated structure was fabricated from the single CF. The properties of the CF are shown in Table 1. The assembly is prepared in the compression mold. The carbon felt electrode portion is filled with the regular glucose to secure it from the pressure of the compression mold. The bipolar plate portion is fabricated by the epoxy resin by partial impregnation in the vacuum oven and subsequently in compression mold. The detailed procedure of fabrication is shown in Fig. 2.

Thickness	Density	Tensile strength	Porosity
10 mm	0.08 g/cm^3	0.15 MPa	92-94%

Table 1. Properties of carbon felt.

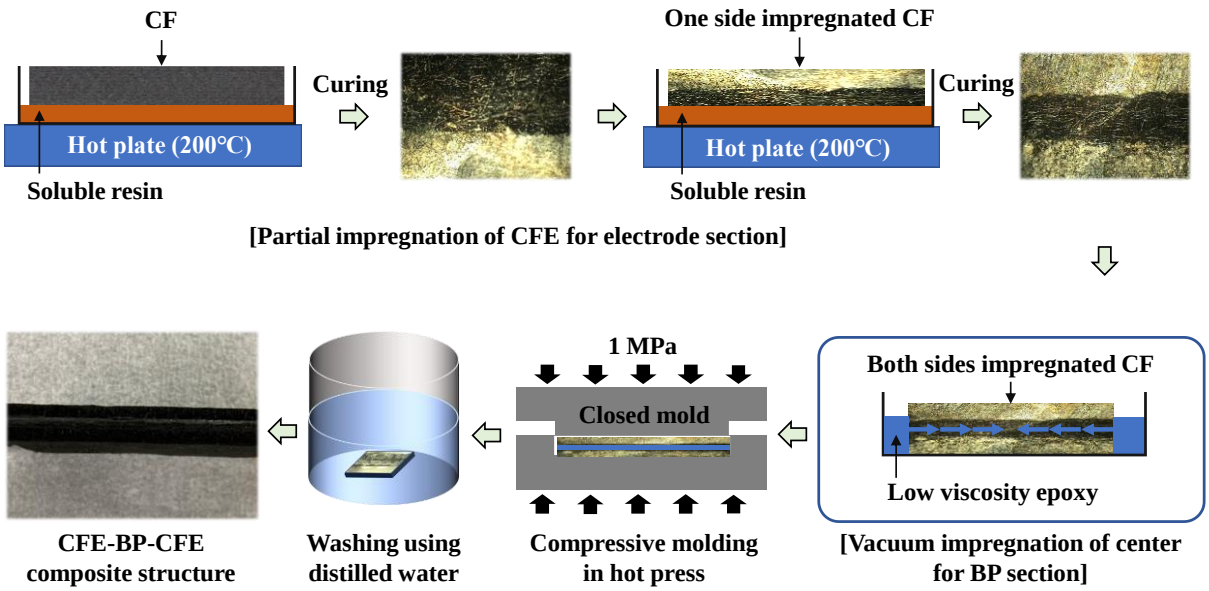

Figure 2: Experimental procedure of the carbon felt electrode-bipolar plate-carbon felt electrode (CFE-BP-CFE) composite structure.

2.2 Characterizations

The areal specific resistance has been calculated using the four-point probe method. The permeability of the CFE-BP-CFE composite structure was measured using gas sensors. Acid-aging test has been conducted to check the stability of the bipolar plate. Charge-discharge test was carried out to check the performance of the integrated assembly of the electrode and bipolar plater for VRFB. The setup pf charge discharge test using integrated structure is shown in Fig. 3.

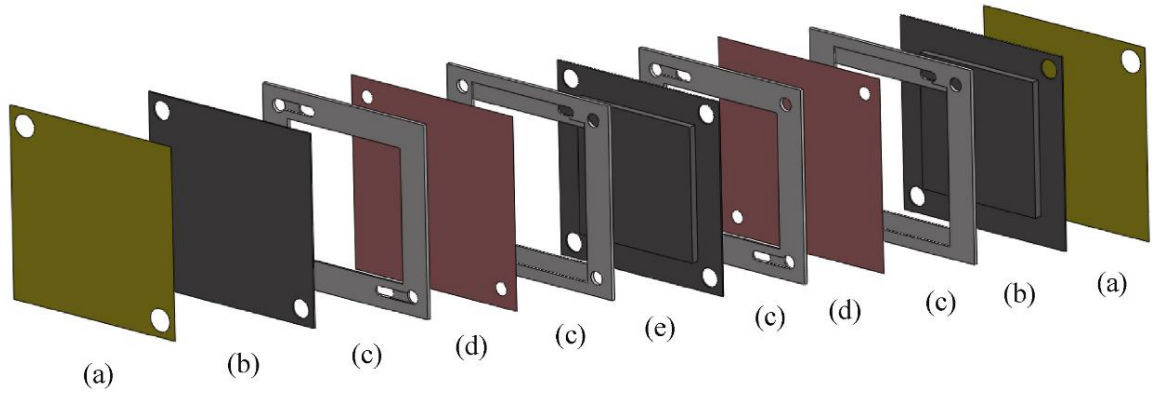

Figure 3: Schematic of core components of two-cell assembly: (a) Current collector; (b) Bipolar plate-carbon felt electrode (BP-CFE) composite structure; (c) Flow frame; (d) Membrane; (e) Carbon felt electrode-bipolar plate-carbon felt electrode (CFE-BP-CFE) composite structure.

3 RESULTS AND DISCSUSSION

An optical microscope image of the 4-mm-thick impregnated layer is presented in Fig. 4(a). The same procedure was applied to the opposite side of the CF. Fig. 4(b) displays the CF with glucose partially impregnated from both sides. Fig. 4(c) presents optical microscope images of the cross-section of the fabricated CFE–BP–CFE composite structure. The central region, corresponding to the bipolar plate (BP), shows uniform epoxy impregnation. Notably, Fig. 4(c) reveals the presence of interconnected carbon fibers bridging the BP and CFE layers. These fiber connections establish a continuous electrical pathway between adjacent cells, thereby improving the overall electrical conductivity of the integrated BP–CFE structure.

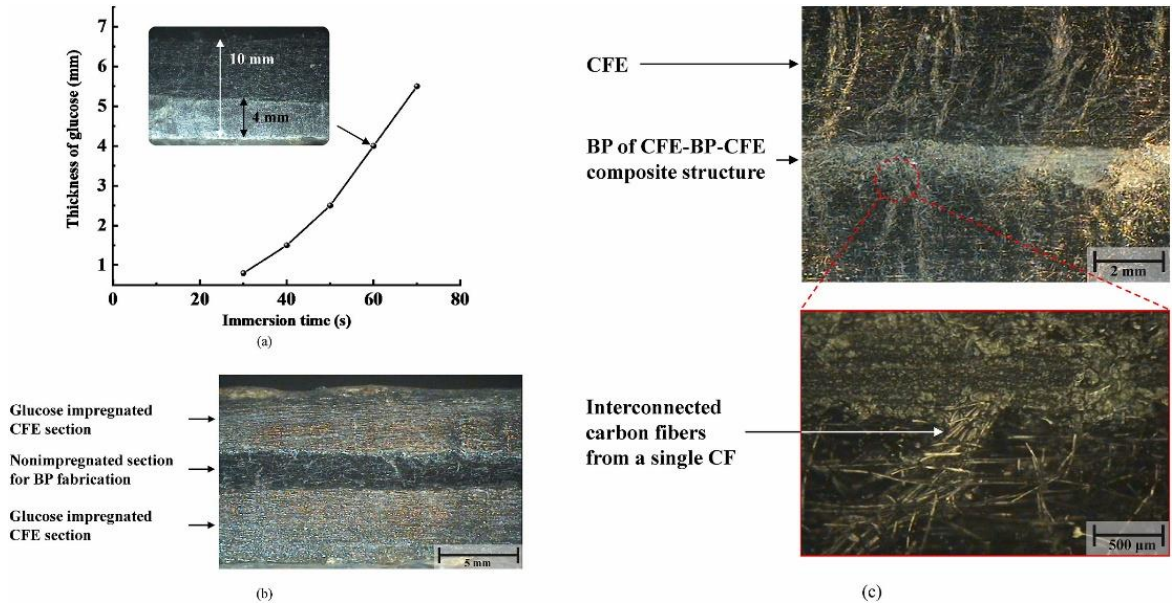

Figure 4: Optical microscope images: (a) Thickness of glucose in partially impregnated carbon felt (CF) as a function of immersion time; (b) Cross-section of carbon felt electrode (CFE) showing glucose impregnation from both sides; (c) Cross-section of the CFE–BP–CFE composite structure.

Figure 5 demonstrates the overall resistance of three structures: the conventional structure with commercial graphite composite BP, the CFE, and the designed CFE-BP-CFE composite structure. As expected, the total electrical resistance decreased in proportion to the increase in compaction pressure. The total resistance of the CFE-BP-CFE composite structure was measured to be about equivalent to

that of the CFE. However, the resistance of the CFE was found to be 28% lower than that of the conventional construction. The reason for this is that the CFE-BP-CFE composite structure consists of a single CFE, and both surfaces of the CFEs are consistently linked with carbon fibers through the central BP section.

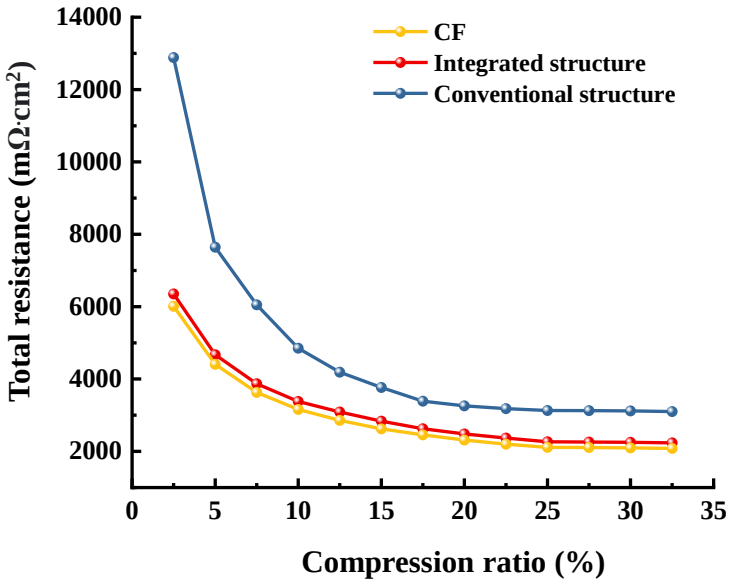

Figure 5: Total resistance of CF, Integrated structure and Conventional structure.

Figure 6 demonstrates the results of the charge/discharge test for both the integrated and conventional assemblies using a two-cell VRFB configuration. The galvanostatic charge/discharge test of the integrated structure demonstrated a reduced discharge voltage and a higher charge voltage. The energy and voltage efficiency of the CFE-BP-CFE composite structure two-cell assembly were enhanced by a significant 6.3%. The decrease in the Ohmic loss in the cell was attributed to the integration of BP and CFEs, resulting in a reduction in the total resistance of the cell. The performance of the CFE-BP-CFE composite structure was improved by the interconnected fibers of BP and CFEs, which created continuous electrical paths. However, the coulombic efficiency remained constant for both setups.

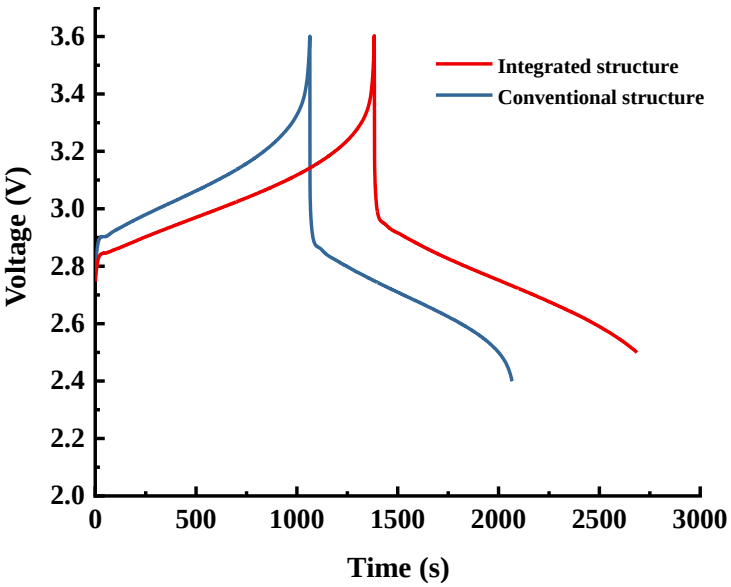

Figure 6: Charge discharge curve of Integrated structure and Conventional structure.

4 CONCLUSIONS

This paper presents the development of a composite structure consisting of a CFE-BP-CFE configuration, achieved through the utilization of a novel fabrication technique that effectively addresses the issue of ICR. The electrode and BP parts were linked together using carbon fibers, since the integrated structure was created from a single sheet of carbon fiber (CF). The proposed structure demonstrated a 28% reduction in resistance compared to the standard structure, which was roughly equivalent to the resistance of a single CFE. Additionally, the charge/discharge test conducted on the suggested construction with two cells showed a longer duration for both charging and discharging, as well as a 6.3% improvement in energy efficiency compared to the conventional structure. This improvement can be attributed to a decrease in Ohmic potential and a reduction in total resistance. The CFE-BP-CFE composite structure minimizes the quantity of core components in the VRFB stack while preserving the stack's efficiency through the use of lower compaction pressure. Hence, the created CFE-BP-CFE composite structure has the potential to serve as a substitute for traditional VRFB components, offering enhanced performance. Furthermore, the VRFB system can be successfully commercialized based on its economic and engineering viability.

ACKNOWLEDGEMENTS

This study was supported by the Guwon Scholarship Foundation (No. 2023-12-01). Their support is greatly appreciated.

REFERENCES

[1] Z.X. He, Y.Q. Jiang, W. Meng, J. Zhu, Y. Liu, L. Dai, L. Wang, Advanced $LiTi(PO_4)_3$@N-doped carbon anode for aqueous lithium ion batteries, Electrochimica Acta, 222, 2016, pp. 1491–1500 (doi: 10.1016/j.electacta.2016.11.127).

[2] A. Kaur, K. Il Jeong, S.S. Kim, J.W. Lim, Optimization of thermal treatment of carbon felt electrode based on the mechanical properties for high-efficiency vanadium redox flow batteries, Composite Structures, 290, 2022, 115546 (doi: 10.1016/j.compstruct.2022.115546).

[3] Z.L. Zhang, Y.P. Yuan, L.P. Ouyang, H.Q. Zhang, X.L. Cao, L.L. Sun, P.E. Phelan, Thermal properties of ternary carbonate/T-ZnOw for thermal energy storage in high-temperature concentrating solar power systems, Composites Part A: Applied Science and Manufacturing, 93, 2017, pp. 177–184 (doi: 10.1016/j.compositesa.2016.12.013).

[4] Y.Q. Jiang, Z.H. Liu, Y.R. Lv, A. Tang, L. Dai, L. Wang, Z.X. He, Perovskite enables high performance vanadium redox flow battery, Chemical Engineering Journal, 443, 2022, 136341 (doi: 10.1016/j.cej.2022.136341).

[5] X. Luo, J.H. Wang, M. Dooner, J. Clarke, Overview of current development in electrical energy storage technologies and the application potential in power system operation, Applied Energy, 137, 2015, pp. 511–536 (doi: 10.1016/j.apenergy.2014.09.081).

[6] J.W. Lim, D.G. Lee, Carbon fiber/polyethylene bipolar plate–carbon felt electrode assembly for vanadium redox flow batteries (VRFB), Composite Structures, 134, 2015, pp. 483–492 (doi: 10.1016/j.compstruct.2015.08.113).

Korea Aerospace University

The 24th International Conference on Composite Materials (ICCM24)

Sustainable Oxide/Oxide ceramic composites with atomic oxygen protection for VLEO satellite applications

*Chae-Hwan Lim[1], Dong-Jun Hong[1], Hannah Jang[1], Seung-Hyeon Kang[1], Sang-Hun Lee[2], Hyeon-Seok Ko[2], Won-Ho Choi[3] and Young-Woo Nam[1, 4†]

[1]Graduate School of Aerospace and Mechanical Engineering, Korea Aerospace University
[2]Materials Digitalization Center, Korea Institute of Ceramic Engineering & Technology
[3]Aerospace R&D Center, Korean Air
[4]Department of Smart Drone Engineering, Korea Aerospace University

August 07, 2025

MCML MULTIFUNCTIONAL COMPOSITES & MANUFACTURING LABORATORY

Table of Contents

I. Introduction

II. Materials preparation

III. Methods

IV. Results and discussion

V. Conclusions

I. Introduction

Background

❖ *Oxide-Oxide ceramic matrix composites (CMCs)*

By raw materials

- Non-oxide ceramics
  - Alumina Nitride
  - Silicon Nitride
  - Silicon Carbide
- Oxide ceramics
  - **Alumina oxide**
  - Zirconia oxide
  - Boron and Mullite oxide

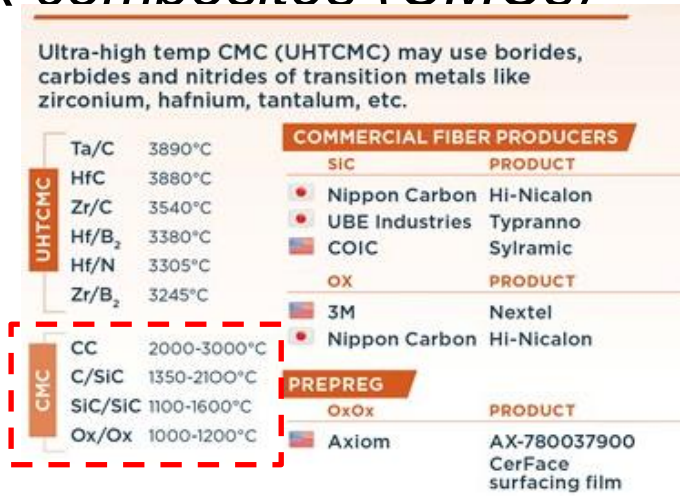

<CMC prepreg and developed products[1]>

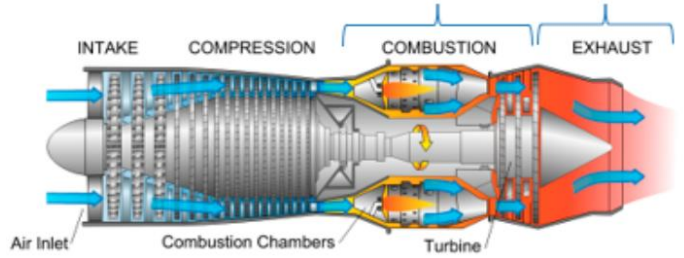

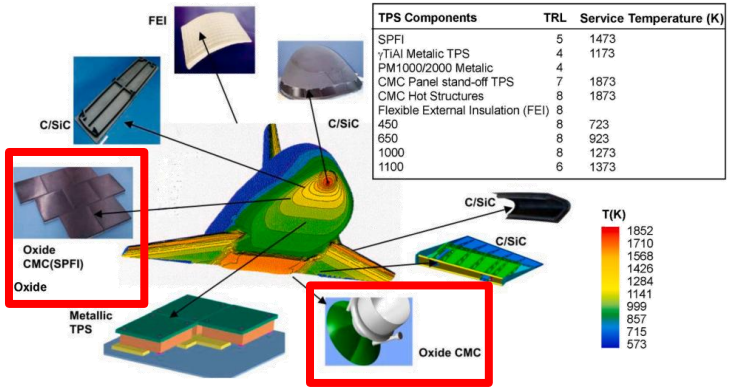

Ceramics

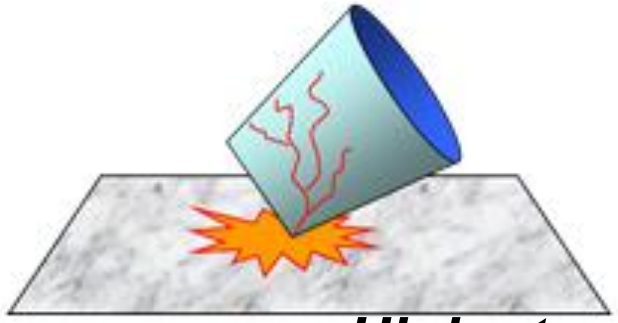

Ceramic matrix composites

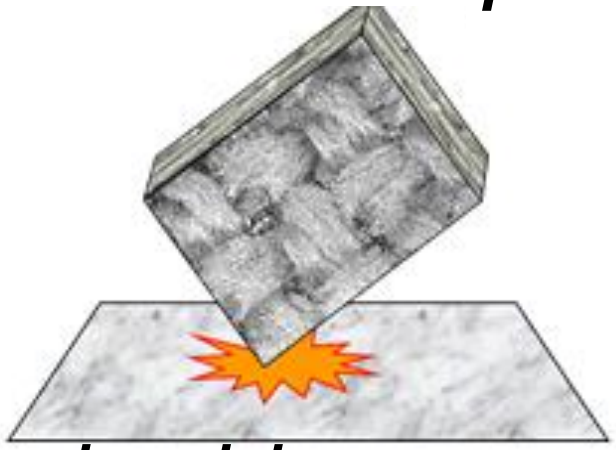

High strength and modulus

High-temperature stability in oxidation

Oxide-Oxide CMCs increased

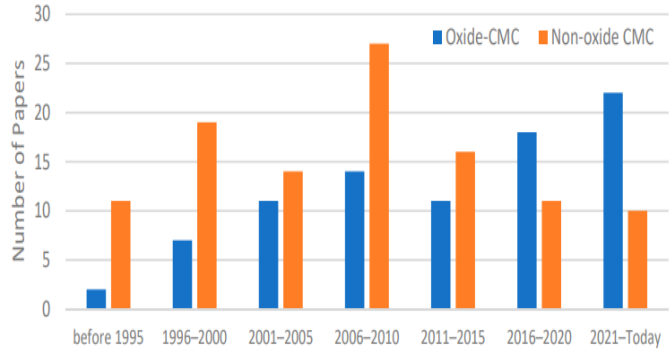

<Oxide vs Other composites materials research>

[1] NITE, "What is NITE Process?" [Online]. Available: https://nite.co.jp/what-is-nite-process-2/.

[2] Le, Vinh Tung, Ngoc San Ha, and Nam Seo Goo. "Advanced sandwich structures for thermal protection systems in hypersonic vehicles: A review." *Composites Part B: Engineering* 226 (2021): 109301.

Background

❖ *Very low earth orbit (VLEO) environment*

Benefit

- Reduced launch cost
- Reduced communication latency
- Self-cleaning orbit (large constellation)

Challenge

- Exposure to atomic oxygen (AO)
- Atmospheric drag
- Fuel consumption

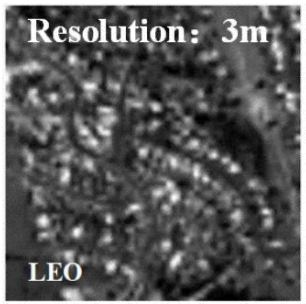



<Resolution comparison[4]>


< Self-cleaning orbit[5]>


< Large constellation[5]>

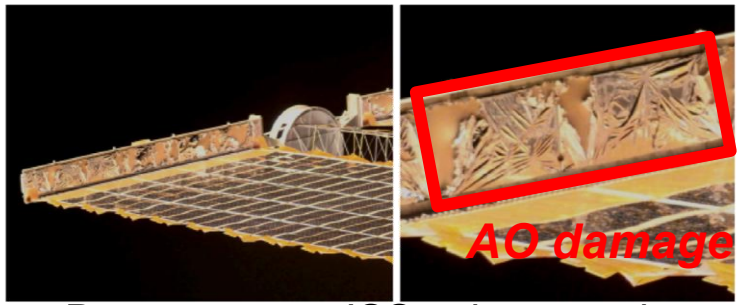

<Damage to an ISS solar array by AO exposure[6]>

LEO environment & VLEO environment[3]

Condition	LEO environment	VLEO environment
Altitude	450 ~ 2,000 km	160 ~ 450 km
AO flux	$\mathbf{10^{12} \sim 10^{13}}$ **atoms/**$\boldsymbol{cm^2 \cdot s}$	$\mathbf{10^{14} \sim 10^{15}}$ **atoms/**$\boldsymbol{cm^2 \cdot s}$
Atmospheric density	$\mathbf{10^{-12}}$ **kg/**$\boldsymbol{m^3}$	$\mathbf{10^{-9}}$ **kg/**$\boldsymbol{m^3}$
Vacuum	$10^{-6} \sim 10^{-10}$ Torr	$10^{-5} \sim 10^{-6}$Torr
Temperature	-150 ~ 150℃	-150 ~ 150℃
Heat cycle	90~110 min	90~110 min
UV radiation	100 ~ 400 nm	100 ~ 400 nm

[3] Han, Joo-Hyun, and Chun-Gon Kim. "Low earth orbit space environment simulation and its effects on graphite/epoxy composites." Composite structures 72.2 (2006): 218-226.
[4] Chen, Guoquan, et al. "VLEO Satellite Constellation Design for Regional Aviation and Marine Coverage." IEEE Transactions on Network Science and Engineering (2023).
[5] Llop, J. Virgili, et al. "Very low earth orbit mission concepts for earth observation: Benefits and challenges." Reinventing Space Conference. 2014.
[6] Kimoto, Yugo, et al. "MDM: a flight mission to observe materials degradation in-situ on satellite in super low Earth orbit." *Acta Astronautica* 179 (2021): 695-701.

Background

❖ *Discharge wall of the hall effect thruster*

Discharge wall must satisfy the requirements: high-temperature resistance, thermal shock resistance, high thermal conductivity low thermal expansion, and dielectric properties[8]

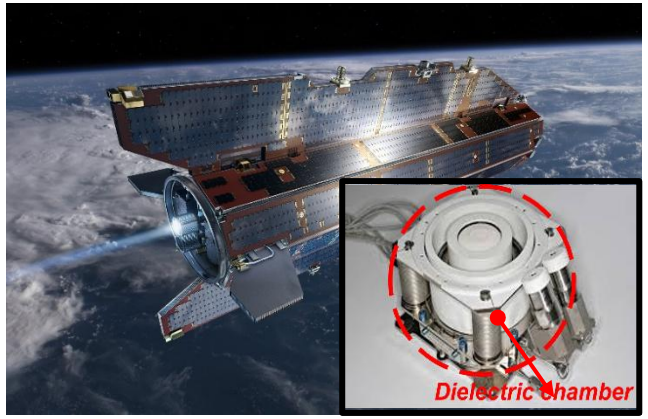

<GOCE satellite>

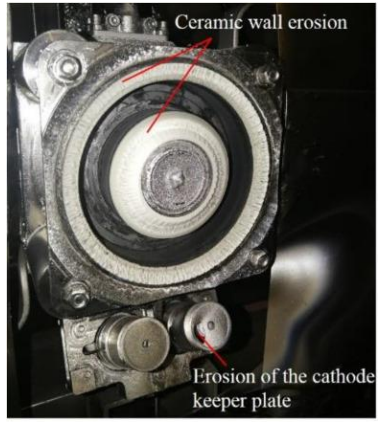

<Plasma thruster discharge walls[7]>

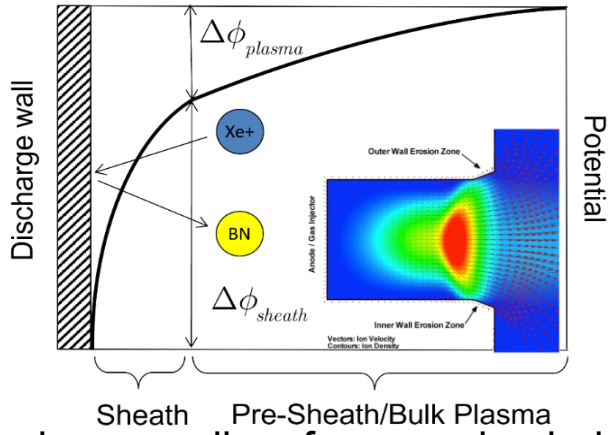

<Discharge wall surface erosion induced by Xe^+ ions in plasma thrusters[6]>

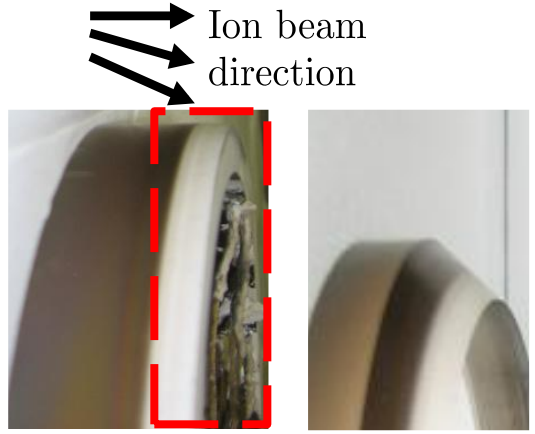

<Surface degradation of plasma thruster discharge walls[7]>

Discharge wall erosion rate[8]

$$\varepsilon = j_{i\perp} Y\left(E,\theta\right) \qquad \Delta\phi_{plasma} = \phi_d - \phi_{sheath\ edge}$$

$$E = E_{plasma} + E_{sheath} \qquad E_{sheath} = E_{sheath}\left(\Delta\phi_{sheath}\right)$$

$$E_{plasma} = E_{plasma}\left(\Delta\phi_{plasma}\right) \qquad \Delta\phi_{sheath} = \Delta\phi_{sheath}\left(T_e\right)$$

$$Y = \left(0.0099 + \alpha^2 6.04\times10^{-6} - \alpha^3 4.75\times10^{-8}\right)\sqrt{\varepsilon_i}\left(1-\sqrt{\frac{58.6}{\varepsilon_i}}\right)^{2.5}$$

Sigmund theory[8]

$$Y(E) \approx \alpha \frac{S_n(E)}{U_o}$$

$Y(E) = Sputtering\ yield$

$S_n(E) = Nuclear\ stopping\ power$

$\alpha = Correction\ factor$

$U_o = Surface\ binding\ energy$

[6] Mikellides, I. G., Katz, I., Hofer, R. R., and Goebel, D. M., "Design of a Laboratory Hall Thruster with Magnetically Shielded Channel Walls, Phase III: Comparison of Theory with Experiment," AIAA-2012-3789, July 2012
[7] Precision Ceramics. (n.d.). Boron nitride uses in Hall effect ion thrusters

Literature survey (1/5)

Korea Aerospace University

MCML MULTIFUNCTIONAL COMPOSITES & MANUFACTURING LABORATORY

❖ *Magnetically shielded hall thruster*

Magnetically shielded Hall thrusters reduce discharge wall erosion but may reduce anode efficiency and thrust by about 20% under the same operating conditions

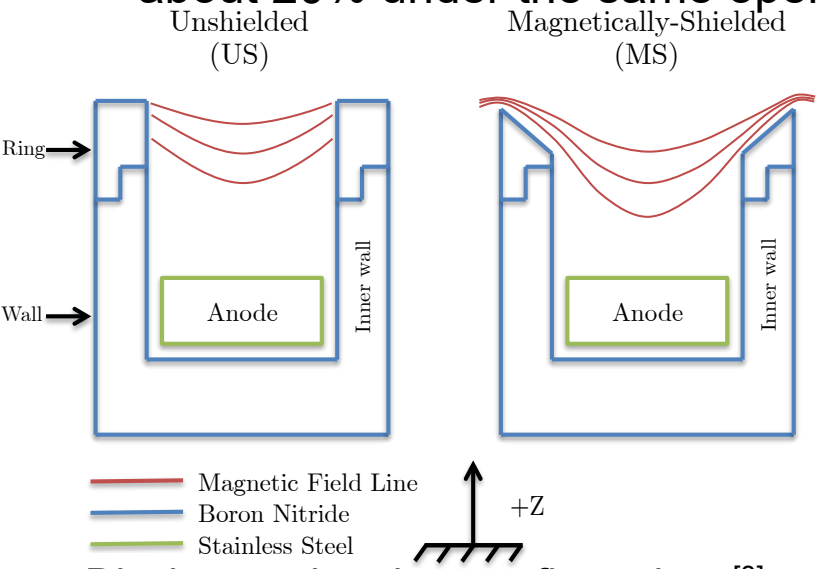

<Discharge chamber configurations[8]>

<Plasma temperature according to thruster type[6]>

Thruster Configuration	Temperature (c)
US (Inner)	500
US(Outer)	510
MS (Inner)	422
MS(Outer)	447

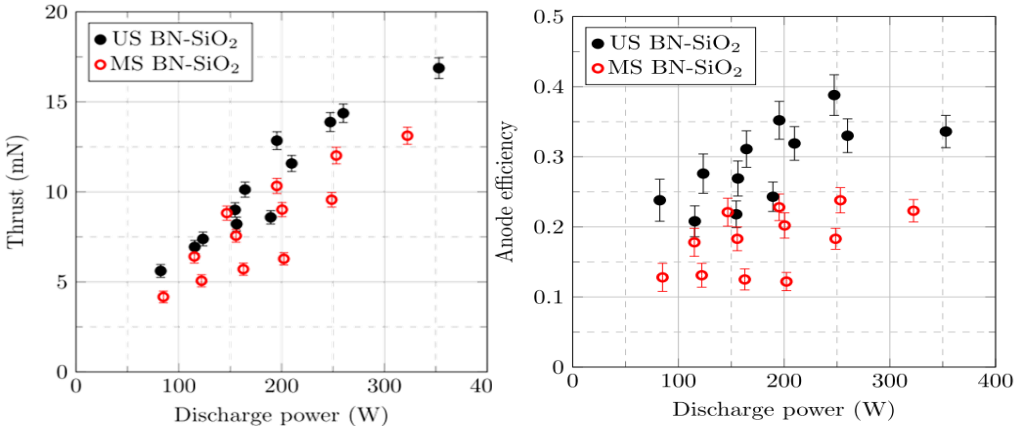

<Comparison between the thrust, anode efficiency of the US and MS thrusters with ceramic wall[8]>

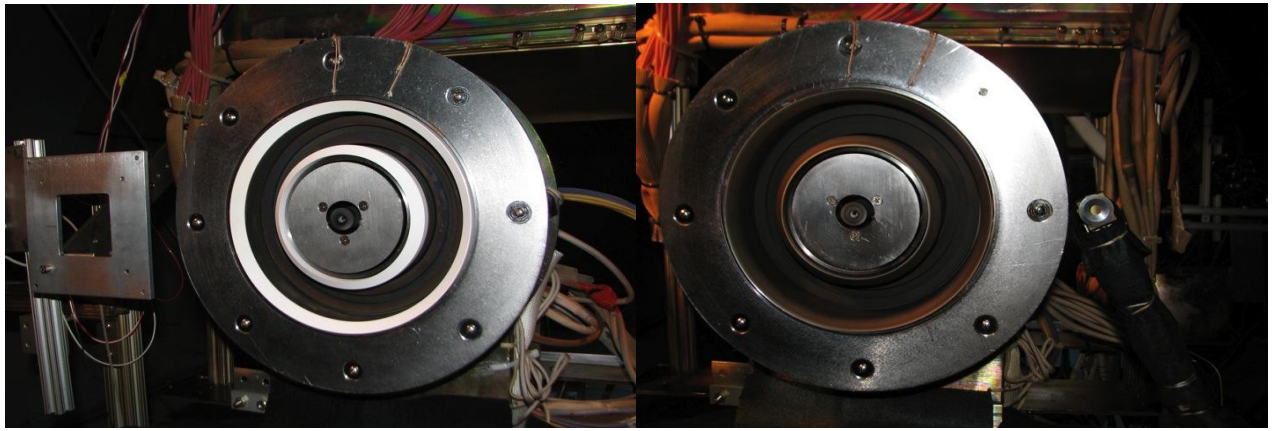

<Hall plasma discharge wall materials left: BN, right: graphite[8]>

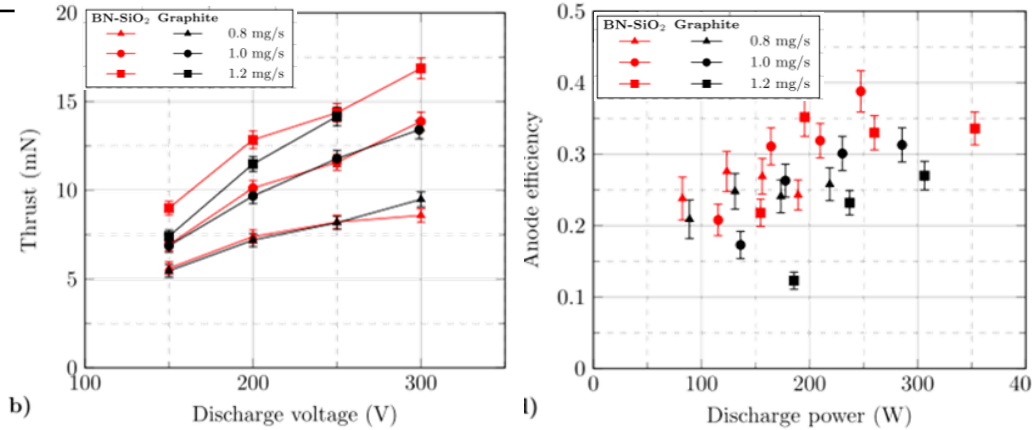

< BN-SiO2 and graphite left: thrust, right: anode efficiency[8]>

[8] Grimaud, Lou, and Stéphane Mazouffre. "Performance comparison between standard and magnetically shielded 200 W Hall thrusters with BN-SiO2 and graphite channel walls." *Vacuum* 155 (2018): 514-523.

Literature survey (2/5)

❖ *BN–CaO-Y_2O_3-Al_2O_3 of plasma resistance*

The sputtering damage of h-BN grains by Xe ions includes B–N bond breaking and layer delamination, while composite erosion involves joint damage with mullite and separation of h-BN grains from the surface

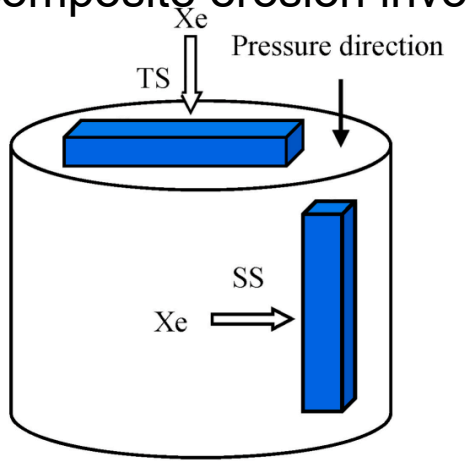

<Test direction of sample[10]>

Lattice distortion

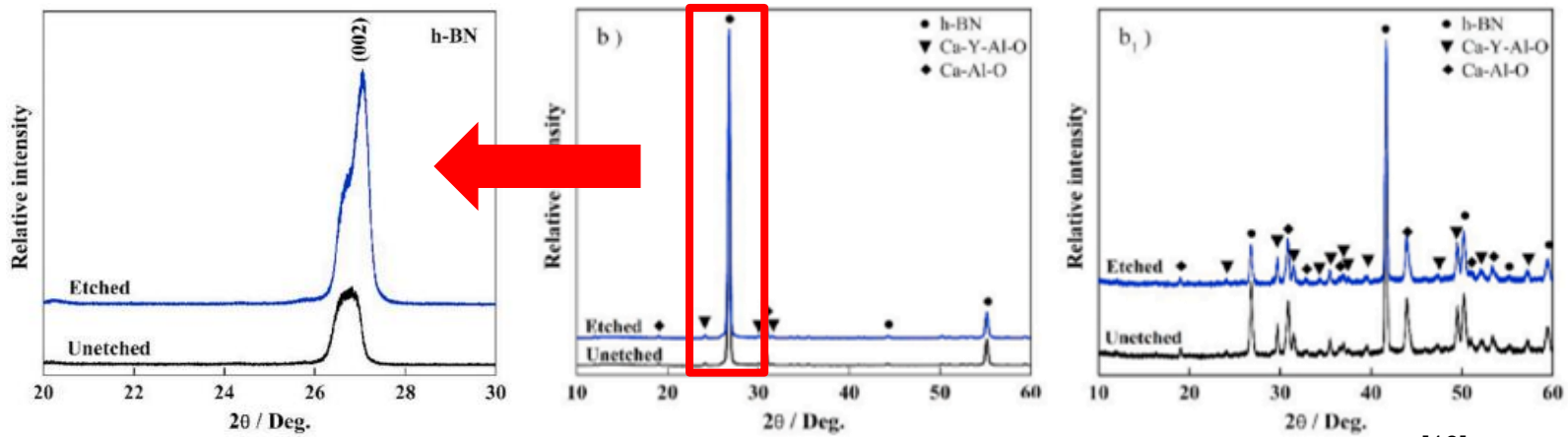

<Phase analysis results of sample surface before and after etching[10]>

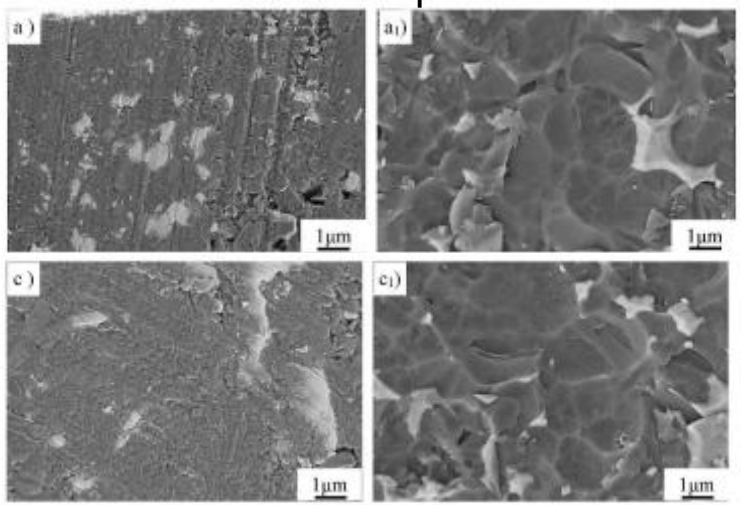

<Micro morphology of textured ceramics before and after etching[10]>

<Mass etching rate (M_m) and line etching rate (M_l) of textured ceramics[10]>

No	Mass etching rate	Line etching rate
1-TS	1.15	4.96
1-SS	1.19	5.14
2-TS	1.05	4.53
2-SS	1.09	4.71
4-TS	1.16	4.99
4-SS	1.15	4.93

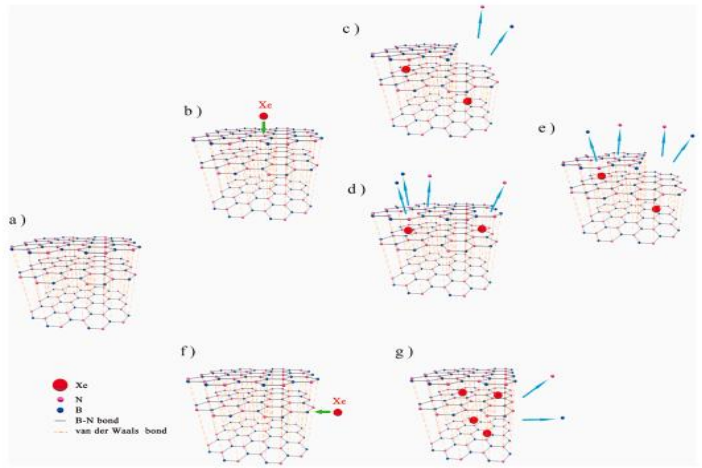

<Damage model of h-BN crystal by Xe ion etching[10]>

[10] Tian, Zhuo, et al. "Etching resistance and etching behavior of h-BN textured ceramics under Xe plasma condition." *Ceramics International* 48.7 (2022): 9099-9106.

Literature survey (3/5)

❖ *Y_2O_3-based ceramics etching by Xe plasma*

Y_2O_3-based composites exhibit enhanced plasma erosion resistance with increasing Al_2O_3 content, owing to improved densification and reduced grain detachment

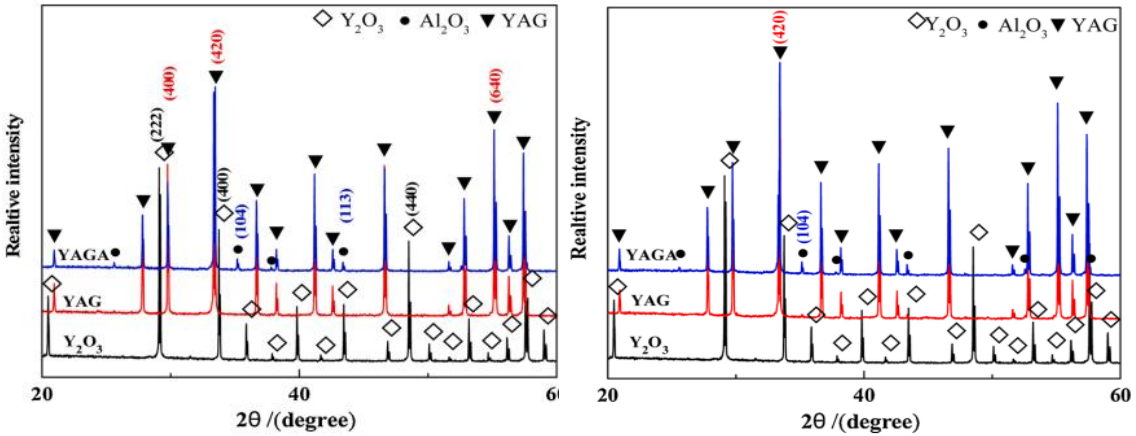

<Phase composition of the sintered material>

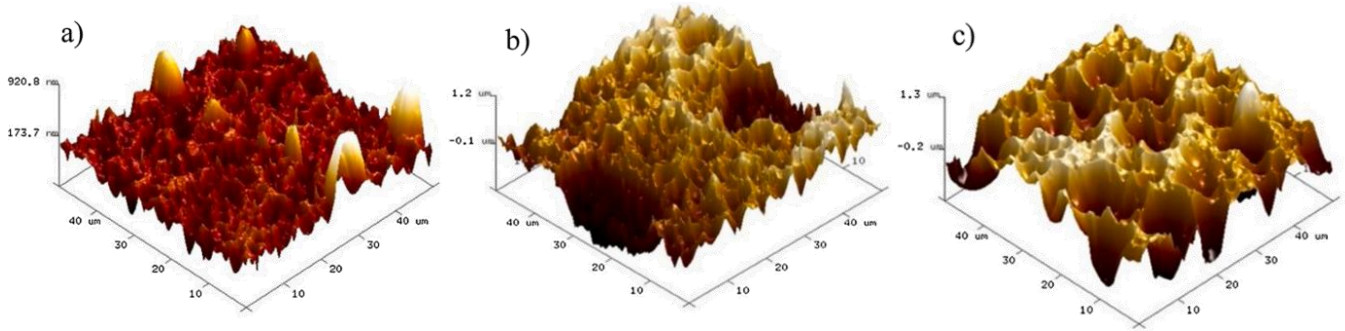

<Etching surface 3D images by AFM microscope[9]>

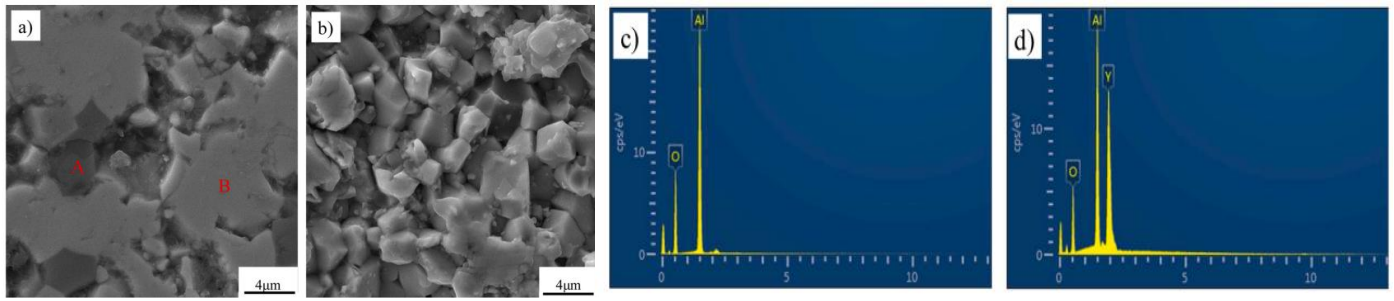

<Surface morphology before and after etching and energy spectrum analysis (YAGA). a) before b) after c) energy spectrum of A grains; d) energy spectrum of B grains[9]>

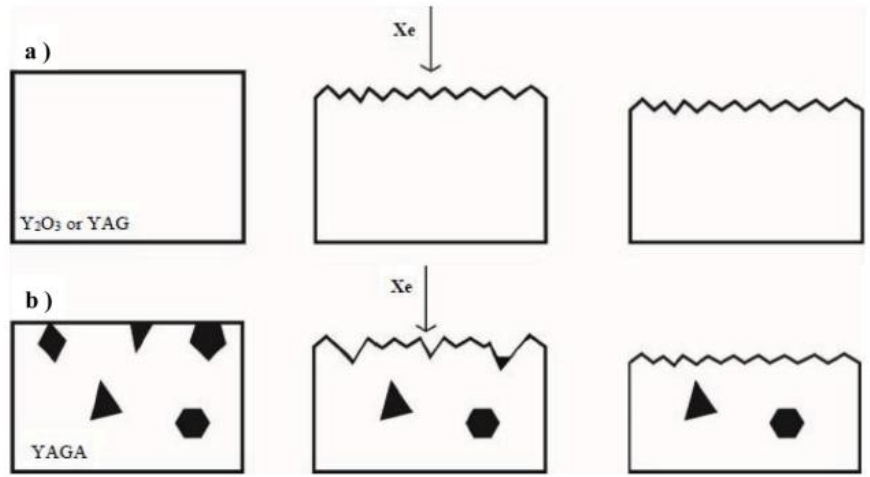

<Schematic of the mechanism of the plasma etching process for sintered ceramics

[9] Tan, Yicheng, et al. "Sputtering resistance and damage mechanism of Y2O3-based ceramics etching by Xe plasma." Materials Today Communications 26 (2021): 101775.

Literature survey (4/5)

Korea Aerospace University

MCML MULTIFUNCTIONAL COMPOSITES & MANUFACTURING LABORATORY

❖ *AO damage mechanism of ZrC-C/C composites*

The performance evolution of ZrC-C/C composite under AO exposure involves two stages including the improvement stage, substantial damage stage

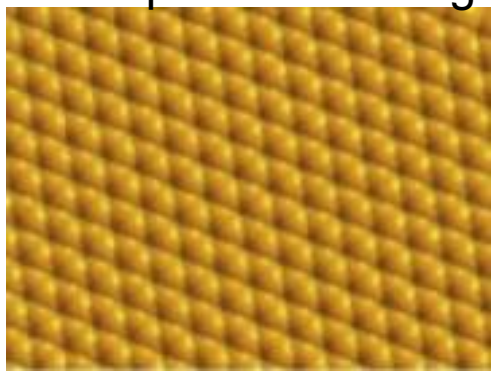

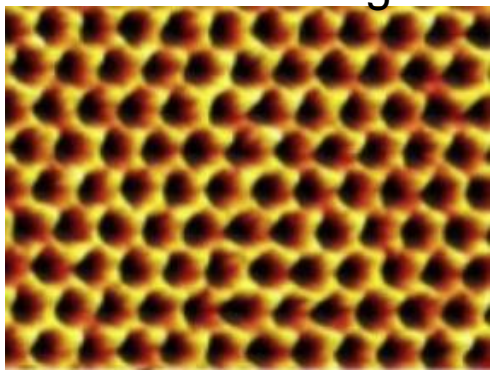

< Non–exposed, Exposed C/C composite[11]>

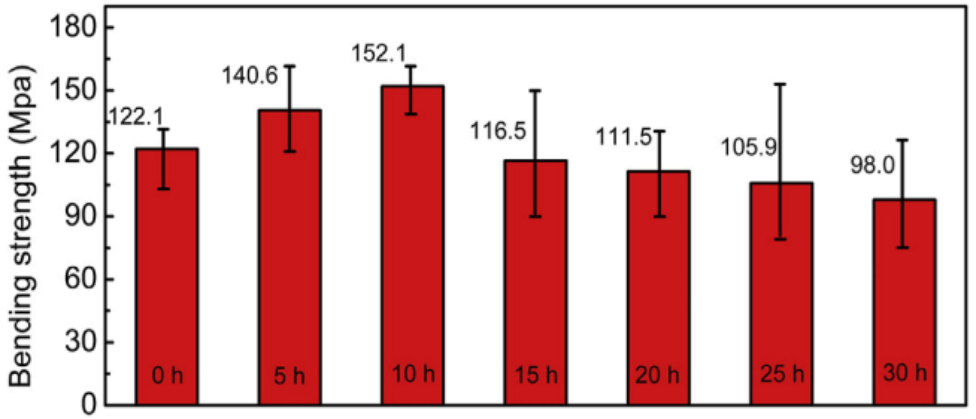

$$ZrC_{(s)} + 4AO_{(p)} \rightarrow ZrO_{2(s)} + CO_{(g)} + CO_{2(g)}$$

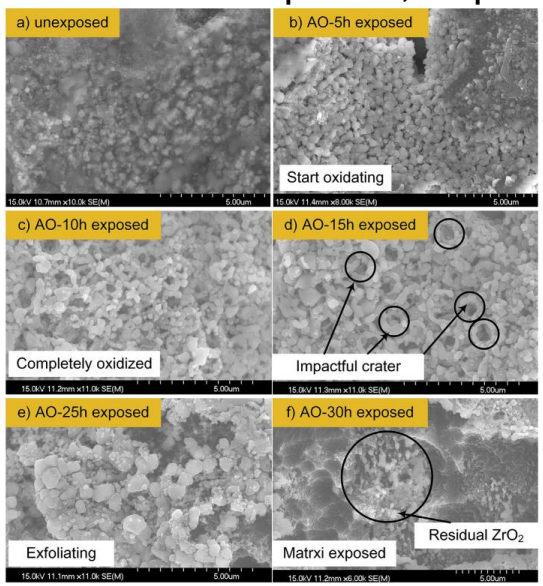

<Morphologies of the ZrC grain evolution of AO exposure [11]>

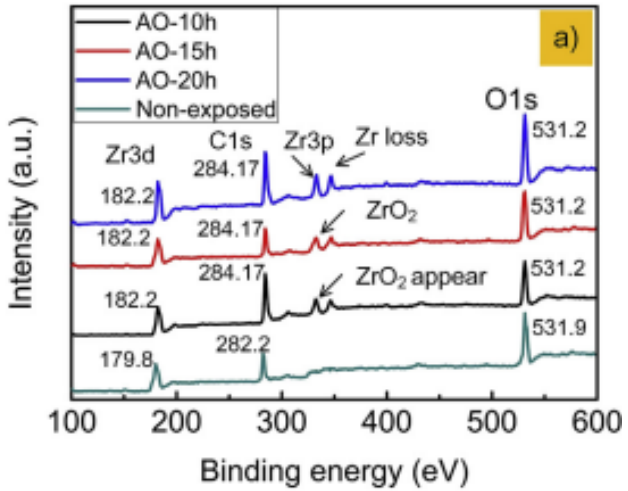

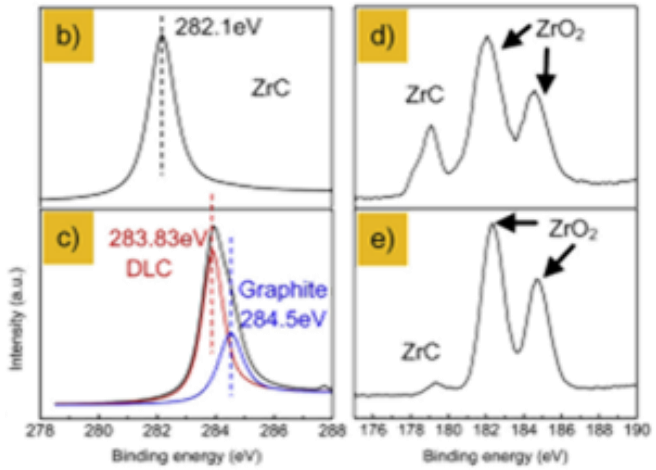

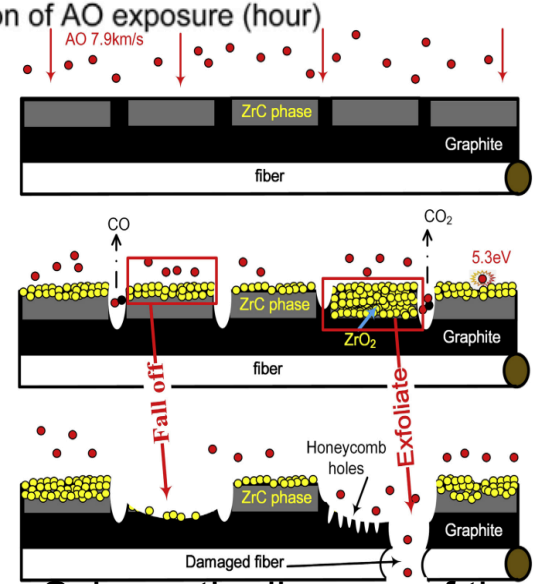

. <Schematic diagram of the AO damage process on ZrC–C/C [11]>

[10] Liu, Guanghai, et al. "Damage behavior of atomic oxygen on zirconium carbide coating modified carbon/carbon composite." *Ceramics International* 46.3 (2020): 3324-3331.

Literature survey (5/5)

❖ *AO erosion resistance on Al_2O_3/SiO_2 film coated PI*

Korea Aerospace University

MCML MULTIFUNCTIONAL COMPOSITES & MANUFACTURING LABORATORY

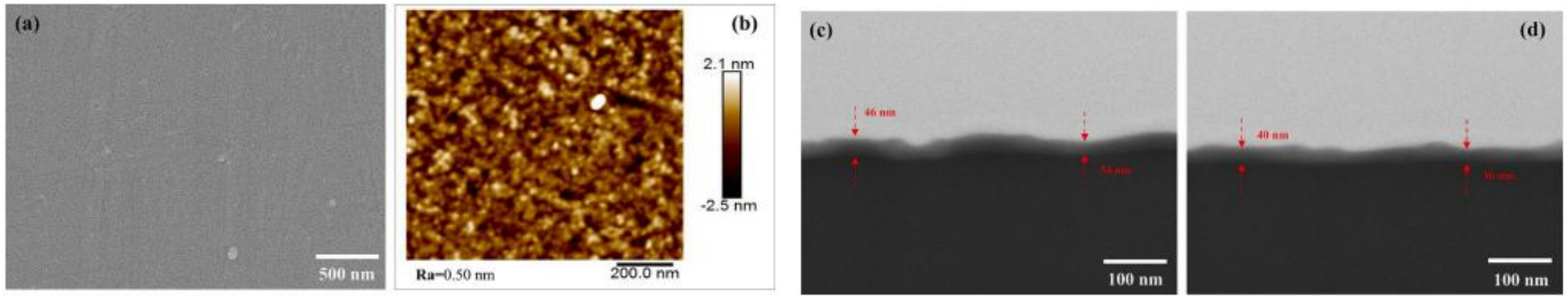

<(a) FESEM of Al_2O_3/SiO_2@PI (b) AFM of 30 nm Al_2O_3/SiO_2@PI (c) Cross-section of SiO_2@PI (d) Cross-section of Al_2O_3/SiO_2@PI>

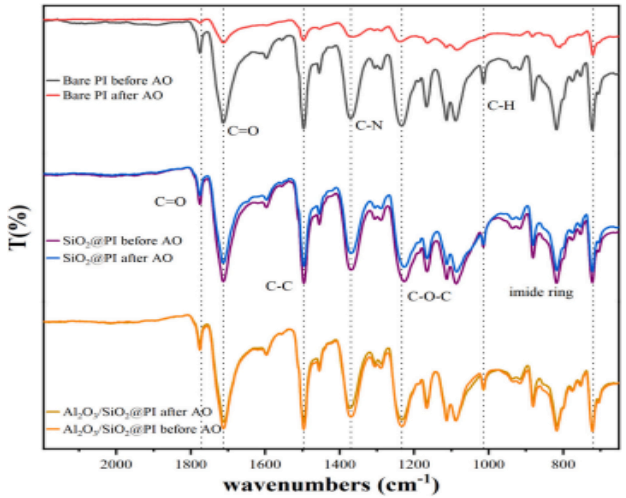

<FTIR spectra of PI, SiO_2@PI, and Al_2O_3/SiO_2@PI before and after AO>

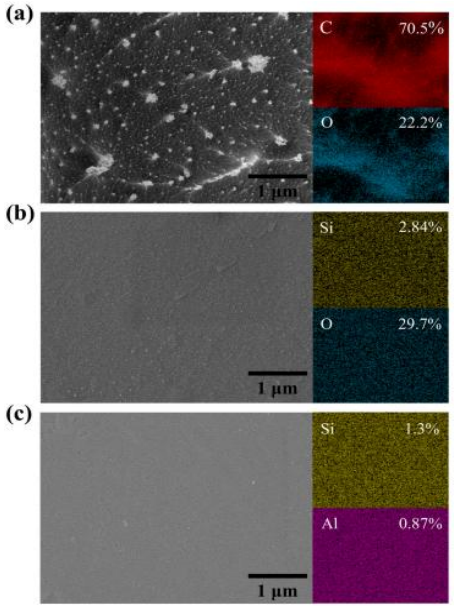

<FESEM images and EDS element mapping of PI after AO erosion

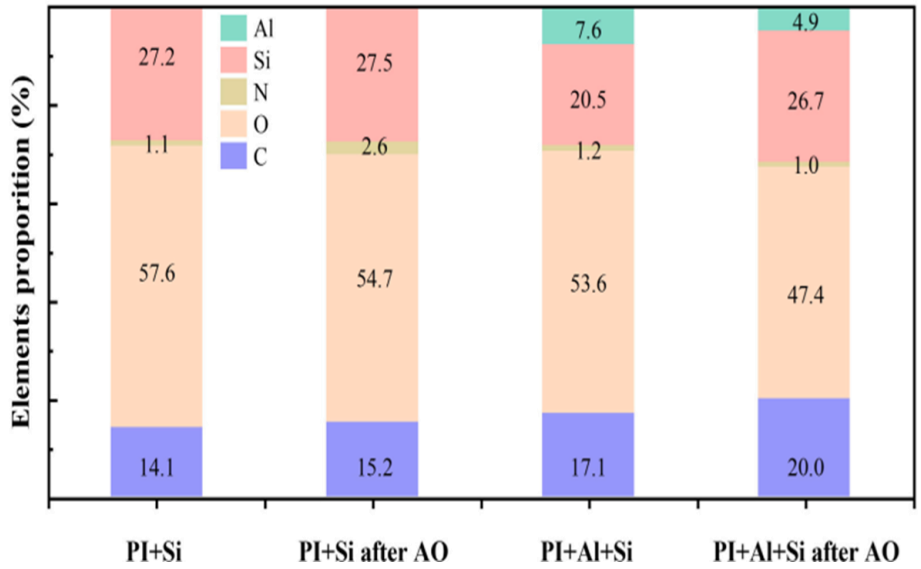

<XPS spectrum analysis of ALD@PI surface before and after AO irradiation: Surface elemental contents>

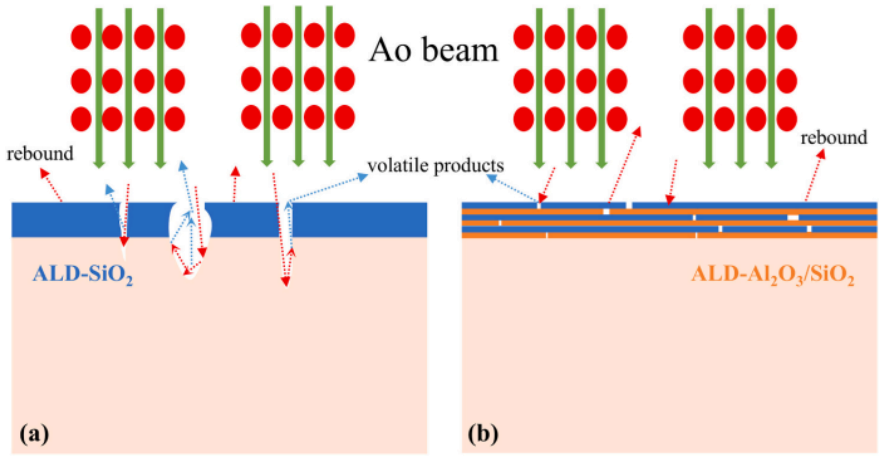

<Schematic of AO beam erosion path through ALD-SiO_2@PI and ALD-Al_2O_3/SiO_2@PI>

[10] Yan, Chi, et al. "Fabrication of high-performance ALD-Al2O3/SiO2 nanolaminate coating for atomic oxygen erosion resistance on polyimide." Surface and Coatings Technology 502 (2025): 131960.

Research highlights

VLEO satellite

Korea Aerospace University

MCML
MULTIFUNCTIONAL COMPOSITES & MANUFACTURING LABORATORY

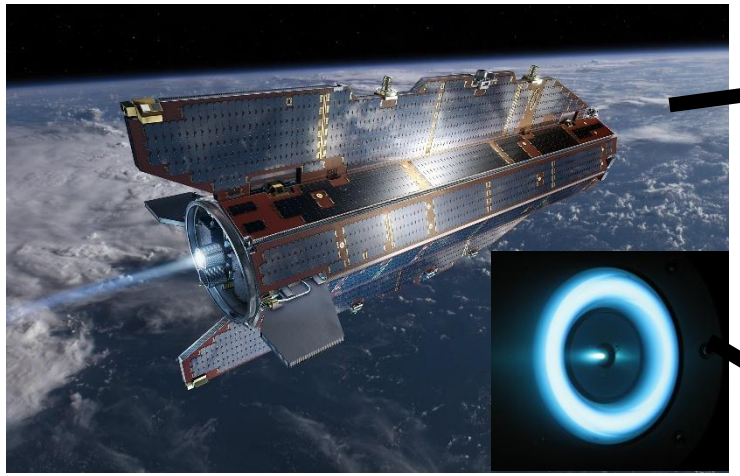

VLEO environment

Atomic oxygen
Thermal cycle
UV light
Vacuum

Ox/Ox CMCs

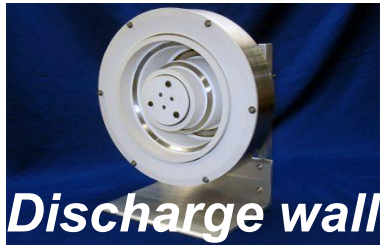



Plasma

"Develop a new concept of plasma thruster discharge wall using Ox/Ox CMCs"

Conventional Methods

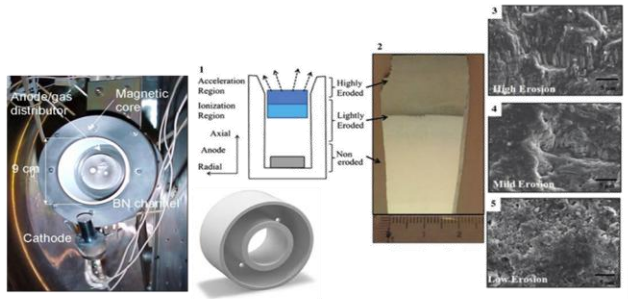

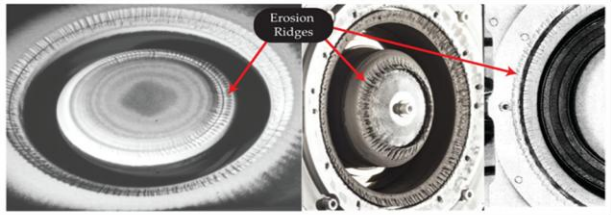

- Low costs
- Low temperatures
- Low pressures
- High mechanical properties
- Autoclave curing (Slurry methods)
- etc.

KAU KICET 한국세라믹기술원
Korea Aerospace University

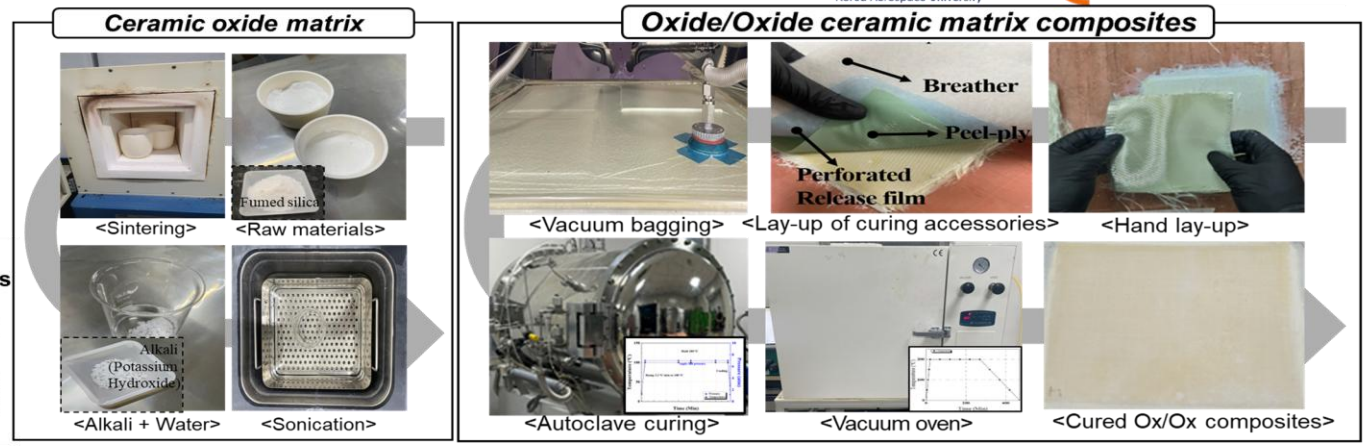

Proposed Methods of Oxide/Oxide Ceramic Matrix Composites

"New method of Ox/Ox CMCs for plasma thruster discharge wall"

II. Materials preparation

Materials preparation

Korea Aerospace University

MCML MULTIFUNCTIONAL COMPOSITES & MANUFACTURING LABORATORY

❖ *Ceramic oxide fiber*



<Ceramic roving>

- Metal oxide-based material (99%)
- Low secondary electron emission (SEE)
- Low coefficient of thermal expansion (CTE)
- High-temperature resistance
- High-plasma resistance

<Surface energy by type of composites[12~14]>

Sample	Surface free energy [mN/m]
Ox-Ox composites[14]	**50 ~ 70**
CFRP[13]	30
GFRP[12]	30

❖ *Ceramic oxide matrix*



<Ceramic powder>

<Alkali + Water>

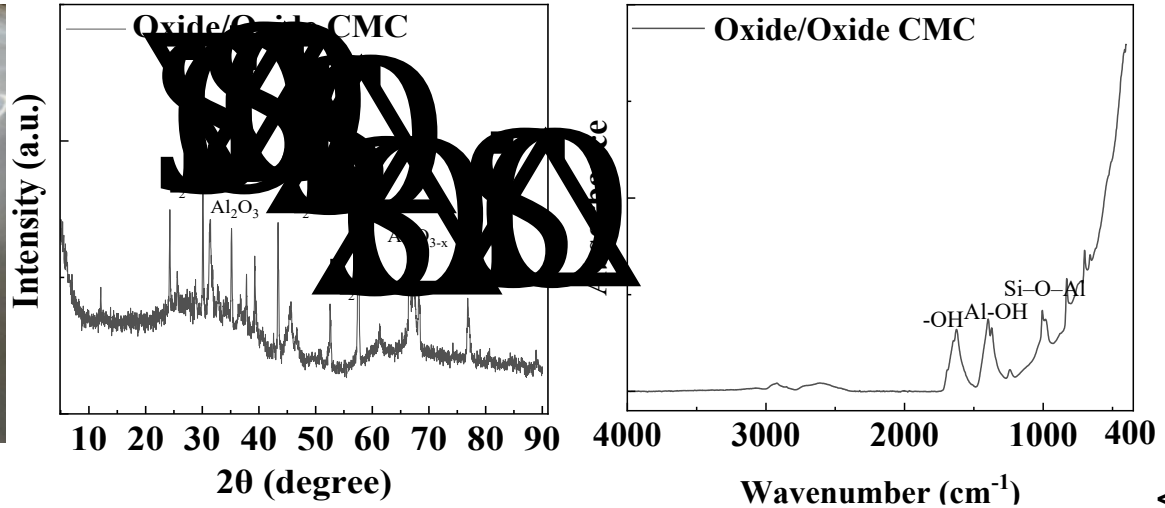

<XRD and FTIR results for Oxide/Oxide CMCs>

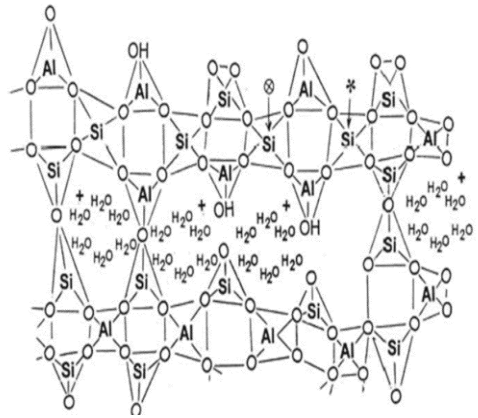

<Structural oxide ceramic network[14]>

[12] Jia, Dechang, et al. Geopolymer and geopolymer matrix composites. Singapore: Springer, 2020.
[13] Aliheidari, et al. "Retaining high fracture toughness in aged polymer Composite/adhesive joints through optimization of plasma surface treatment." Composites Part A: Applied Science and Manufacturing 176 (2024): 107835.
[14] Yang, Chengjuan, et al. "Functionalized CFRP surface with water-repellence, self-cleaning and anti-icing properties." Colloids and Surfaces A: Physicochemical and Engineering Aspects 586 (2020): 124278.

Materials preparation

❖ *Fabrication of Oxide/Oxide CMCs*

Ceramic oxide matrix

<Sintering>

<Raw materials>

<Alkali + Water>

<Sonication>

<Ceramic matrix>

Oxide/Oxide ceramic matrix composites

<Autoclave curing>

<Vacuum bagging>

<Lay-up of curing accessories>

<Hand lay-up>

<vacuum oven>

<Cured Ox/Ox composites>

<Cutting process>

<Specimens>

III. Methods

Method

❖ *VLEO space environment simulated facility*

- Chamber size (inside): 600×500×250 mm
- Atomic oxygen generator: DC supply & Ion beam gun
- Atomic oxygen flux: 1.35×10^{17} atoms/cm^2·s
- Ultraviolet (UV) lamp: 280 ~ 420 nm
- Thermal cycle: -80 ~ 150 ℃ / 90 min/cycle
- Max temperature 1,000 ℃
- Vacuum: 10^{-7} Torr

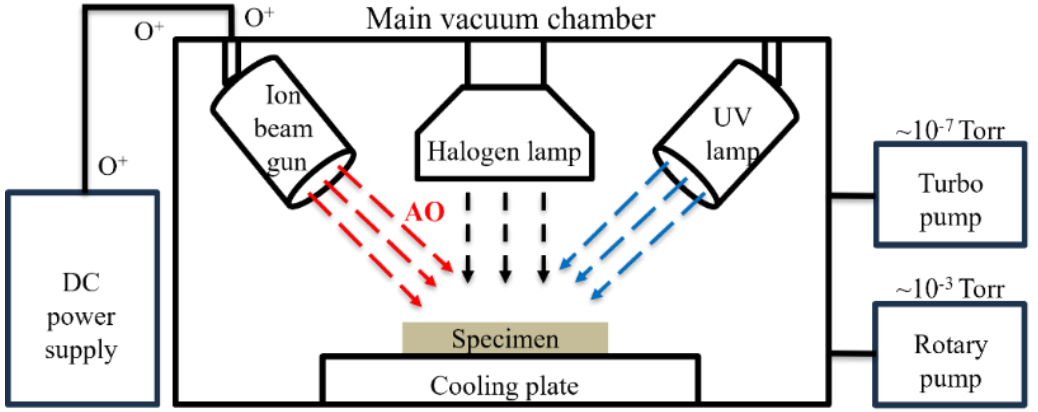

<Schematic of VLEO space chamber>

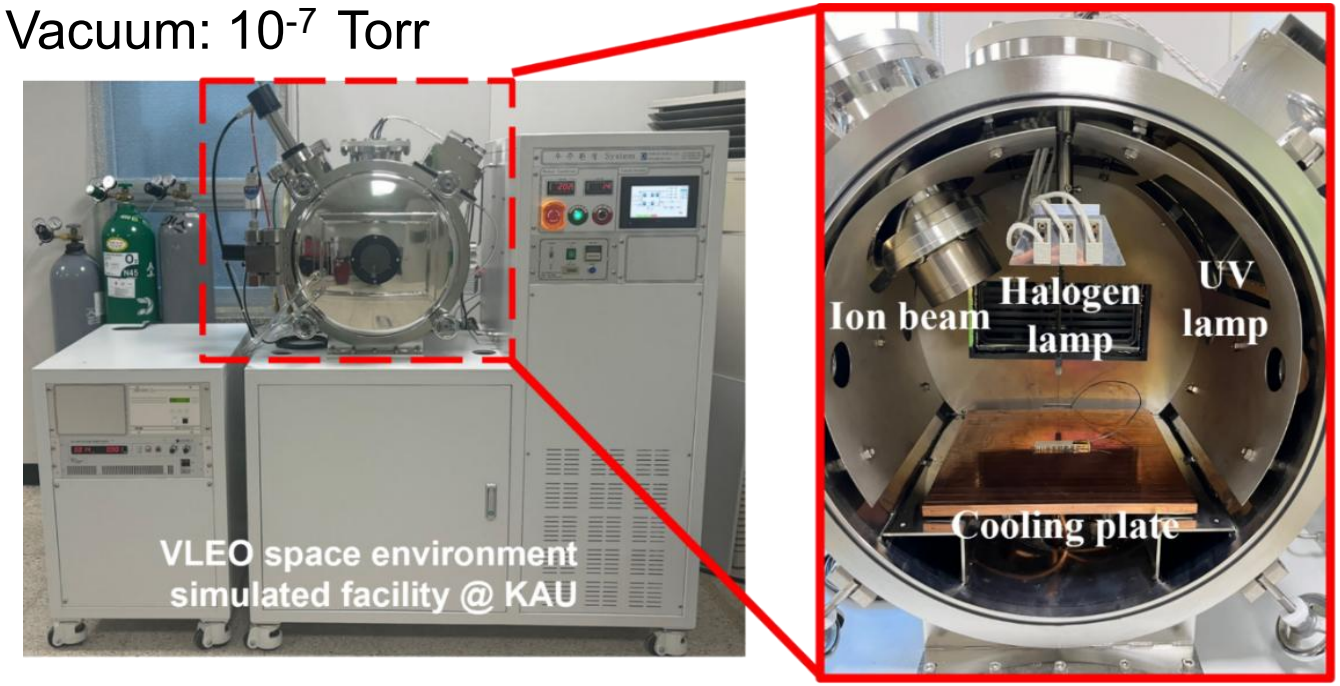

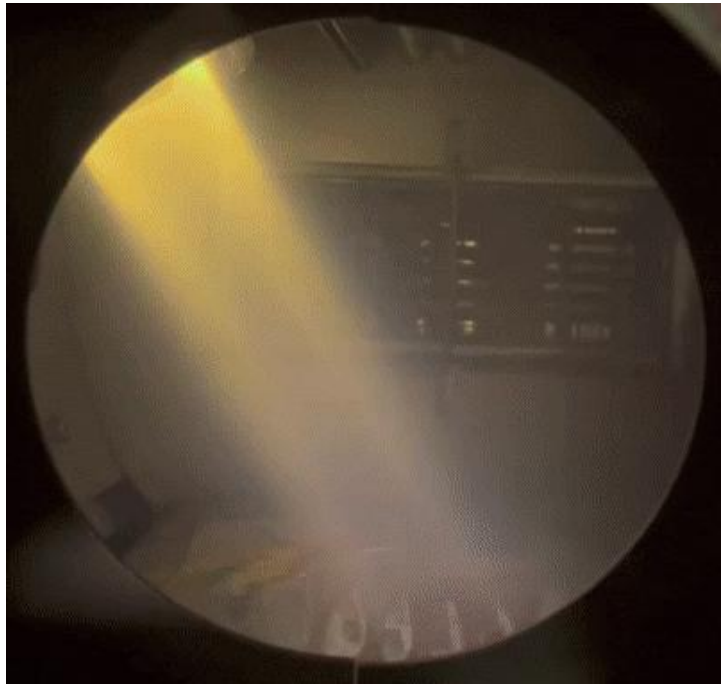

<VLEO space chamber @KAU MCML Lab>

Method

❖ *Plasma test conditions*

- Materials: Ox/Ox CMCs, h-BN, Al_2O_3
- Gas: Argon
- Gas flow rate: 10 SCCM
- Time: 4 Hours
- Angle: 0°[16]
- Beam energy: 1,000 eV

❖ *VLEO space environment test conditions*

- Materials: Ox/Ox CMCs
- Atomic oxygen: 1.35 ×10^{17} atoms /cm^2·s
- Thermal cycle: -80 ~ 150℃ / 90 min
- Vacuum: 1 × 10^{-6} Torr
- UV lamp: 280 ~ 420 nm
- Exposure time: 0, 7.5, 15, 24 Hours

Korea Aerospace University

MCML
MULTIFUNCTIONAL COMPOSITES & MANUFACTURING LABORATORY

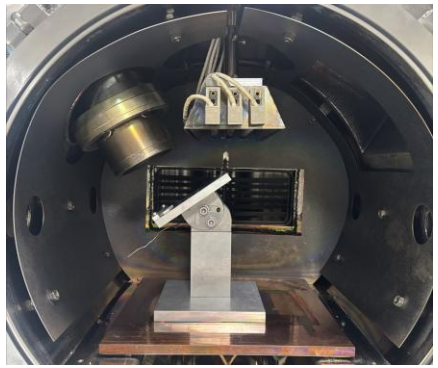

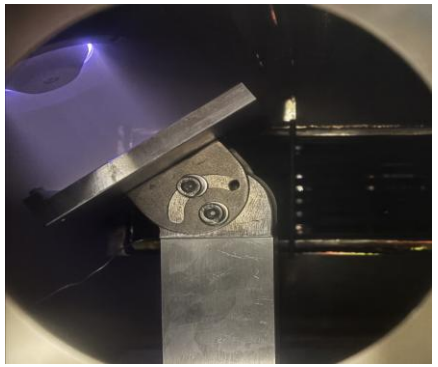

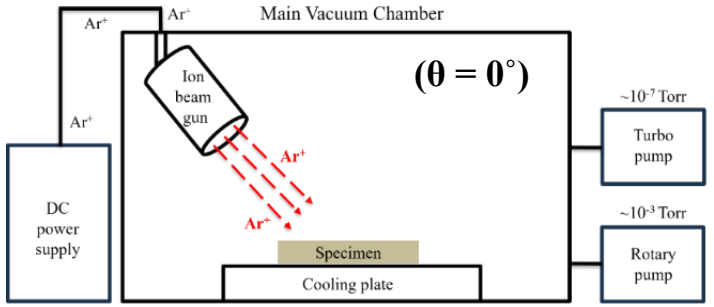

< Plasma erosion test>

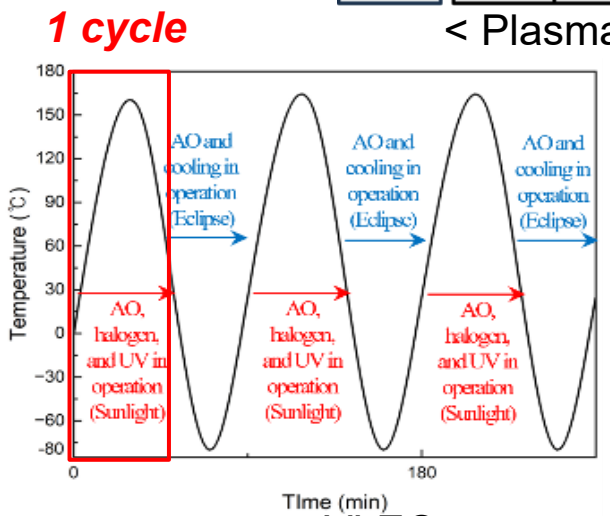

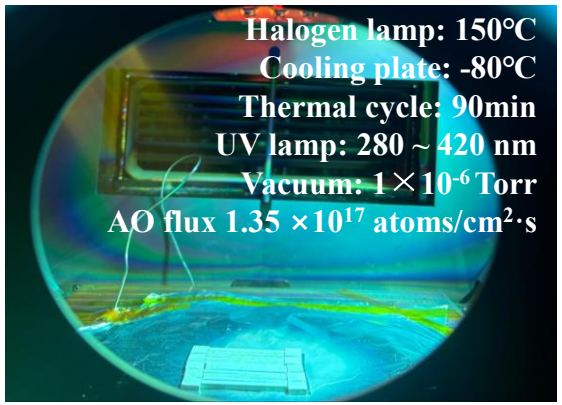

<VLEO space environment test >

[16] Tan, Yicheng, et al. "Sputtering resistance and damage mechanism of Y2O3-based ceramics etching by Xe plasma." *Materials Today Communications* 26 (2021): 101775.

IV. Results and discussion

Results and discussion

❖ *Results of the VLEO environment test*

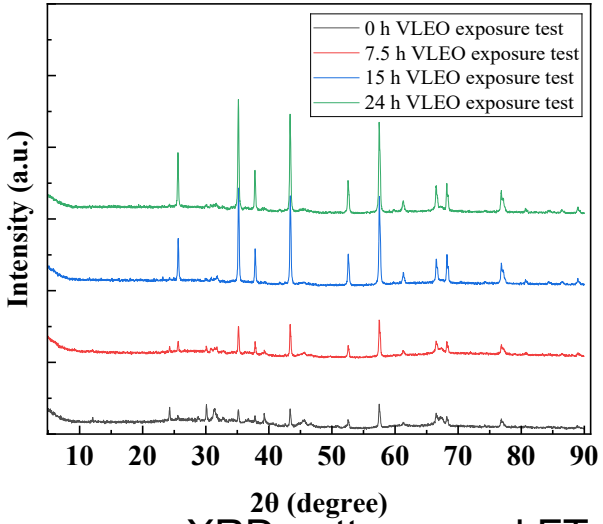

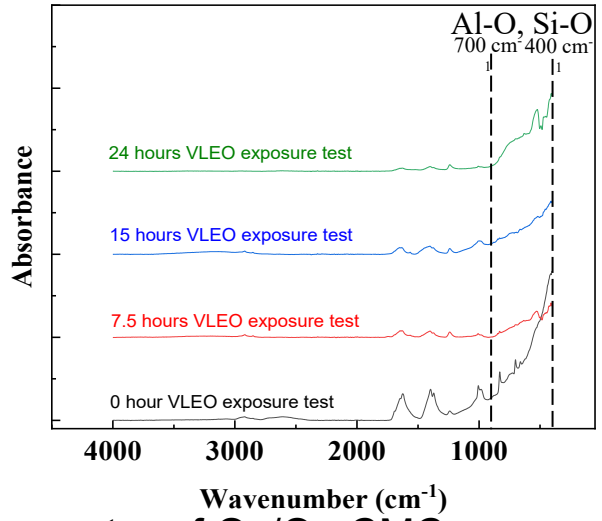

< XRD patterns and FT-IR spectra of Ox/Ox CMCs after VLEO environment exposure>

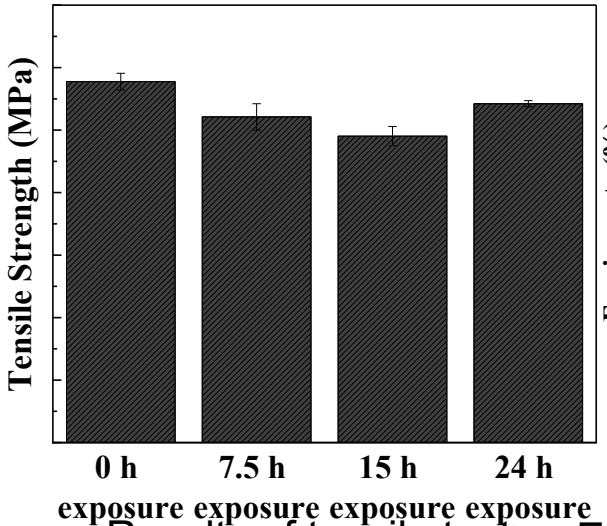

<Results of tensile test>

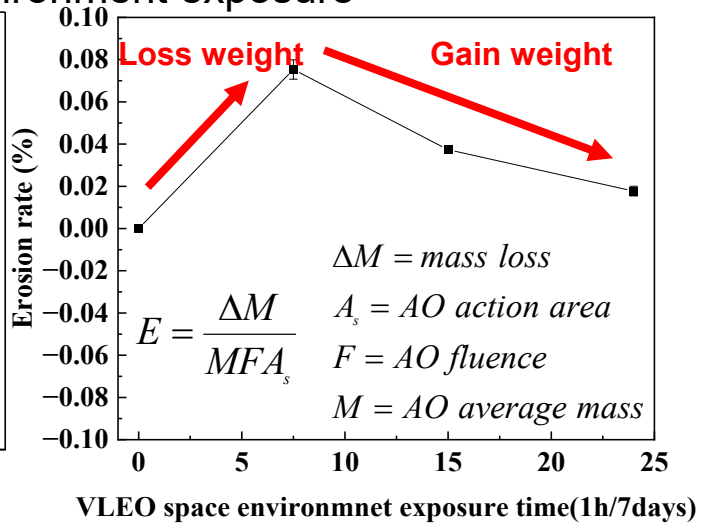

<Erosion rate of oxide/oxide composites>

<Erosion rate of atomic oxygen>

No.	Materials	Erosion rate
This study	**Ox-Ox composite**	**0.02**
Liu et al. [16]	SiC-Carbon/Carbon	-0.02
Luan et al. [17]	Carbon/SiC-HfC	0.22
Liu et al. [18]	TaC-Carbon/Carbon	0.23
Zhai et al. [19]	Carbon/CE	0.425
Choi et al. [20]	OG POSS/epoxy	1.0
Han et al. [21]	Graphite/Epoxy	1.5

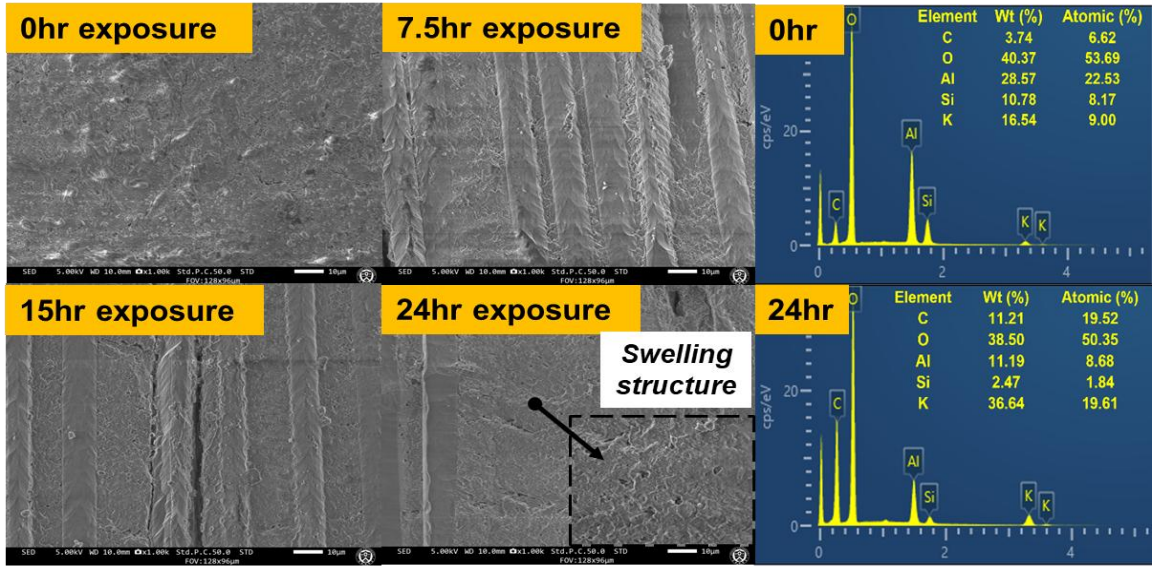

<SEM images after exposure to the VLEO environment>

[16] Liu, Guanghai, et al. "Damage behavior of atomic oxygen on zirconium carbide coating modified carbon/carbon composite." Ceramics International 46.3 (2020): 3324-3331
[17] Damage behavior of atomic oxygen on a hafnium carbide-modified C/ SiC composite
[18] Atomic oxygen damage behavior of TaC coating-modified C/C composite

Results and discussion

❖ *Results of the plasma etching test*

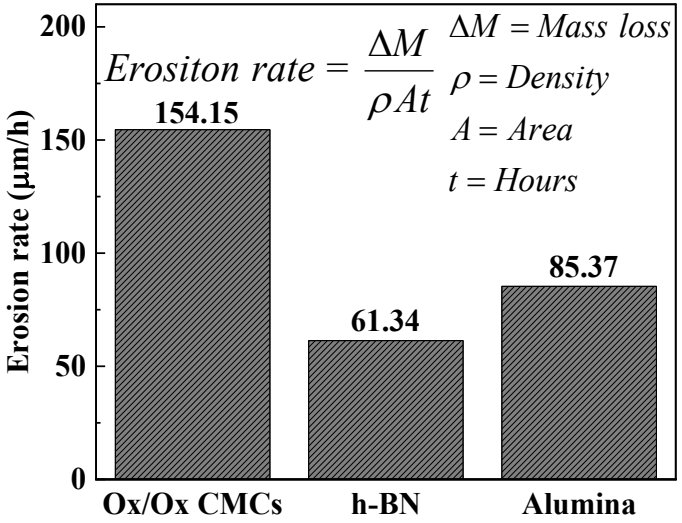

<Results of erosion rate for plasma>

<Results of density>

Sample	Density (g/m³)
This study	**2.85**
h-BN	1.9
Alumina	3.9

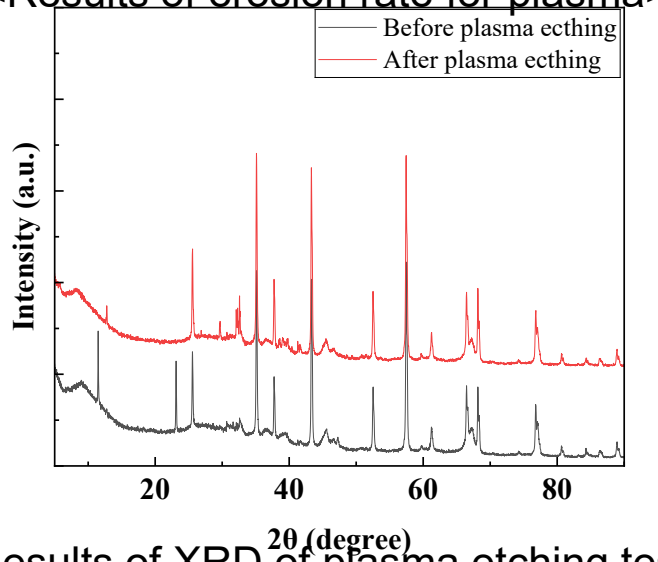

< Results of XRD of plasma etching test >

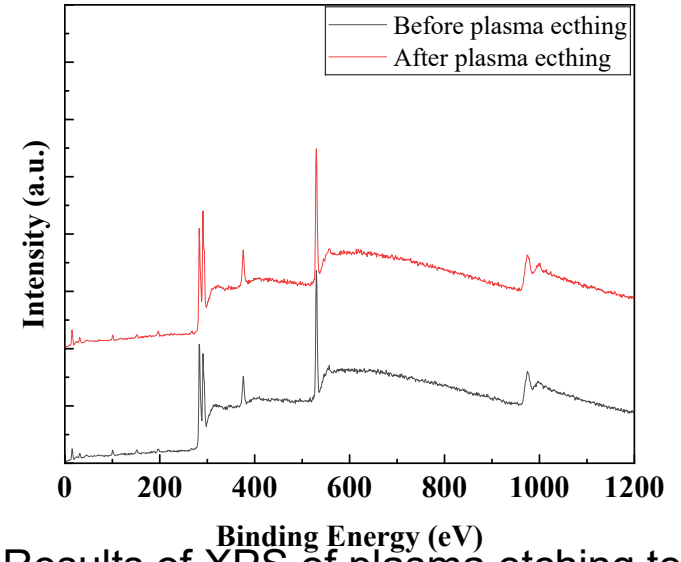

< Results of XPS of plasma etching test >

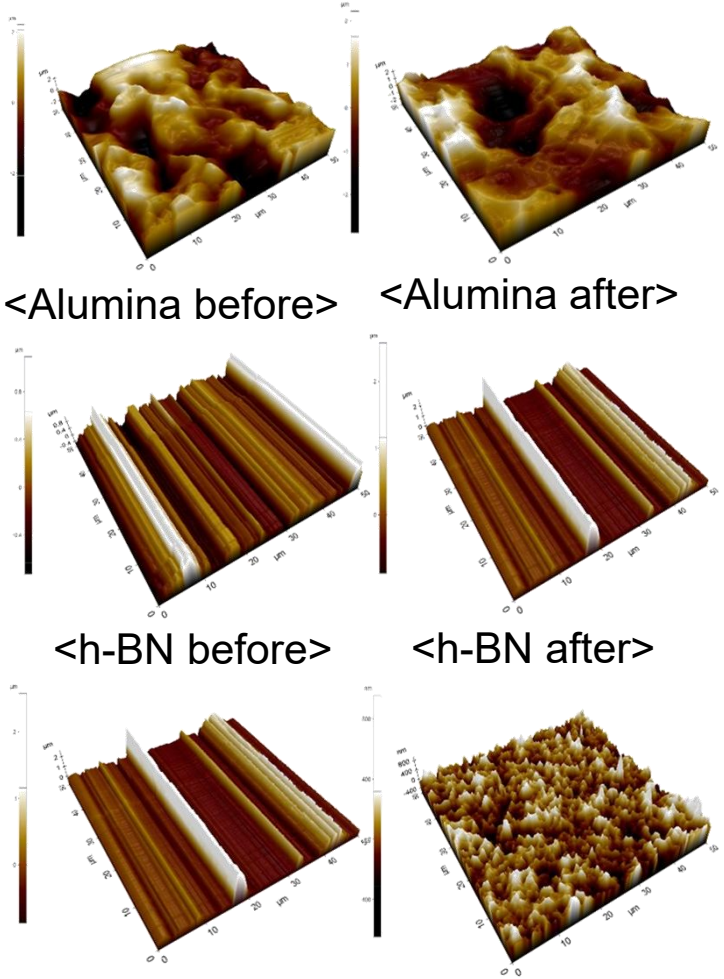

<Alumina before> <Alumina after>

<h-BN before> <h-BN after>

<Ox/Ox CMCs before> <Ox/Ox CMCs after>

< Analysis of the AFM>

[19] Synergistic effects of atomic oxygen and thermal cycling in low earth orbit on polymer-matrixed space materia
[20] Enhanced resistance to atomic oxygen of OG POSS/epoxy nanocomposites
[21] Low earth orbit space environment simulation and its effects on graphite/epoxy composites

V. Conclusions

Conclusions

Korea Aerospace University

MCML
MULTIFUNCTIONAL COMPOSITES & MANUFACTURING LABORATORY

- In this study, we conducted space environment assessments and thermal shock evaluations to develop a new concept discharge wall for a plasma thruster operating in VLEO.
- The evaluation of the VLEO environment showed no significant changes in chemical structure or tensile strength after prolonged exposure to atomic oxygen.
- Plasma erosion tests showed that the material had a higher erosion rate than Boron Nitride Grade HP, and no phase transformation was observed.
- **In future works,** the investigation will be expanded to evaluate structural integrity under plasma-exposed conditions.

Korea Aerospace University

Korea Aerospace University

MCML
MULTIFUNCTIONAL COMPOSITES & MANUFACTURING LABORATORY

Thank you for your attention

This work was partly supported by the National Research Foundation of Korea (NRF) grant funded by the Ministry of Science and ICT (RS-2024-00397400) and this work was supported by Korea Research institute for defense Technology planning and advancement (KRIT) Grant funded by Defense Acquisition Program Administration (DAPA)(KRIT-CT-22-028)

Presenter chaehwan@kau.kr

Professor ywnam@kau.ac.kr

Web page https://mcml.kau.ac.kr

KOREAN AIR

ACT

MCML
MULTIFUNCTIONAL COMPOSITES & MANUFACTURING LABORATORY

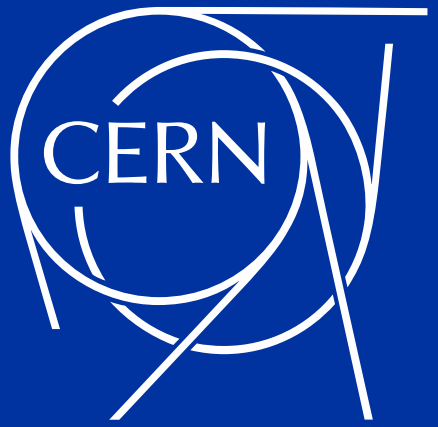

Electrical Insulation for Nb_3Sn Superconducting Cables

Roland Piccin, Vincent Schenk, Javier Osuna, Christian Scheuerlein, Francois-Olivier Pincot (CERN/TE/MSC/SMT)

07/08/2025, ICCM Conference Baltimore

Table of contents

1. Introduction to Superconductivity and Particle Accelerators
2. The Challenge of Electrical Insulation in Nb_3Sn Magnet
3. Insulation Materials and Processing
4. Electrical Performance
5. Conclusions and Perspectives

From Discovery of Superconductivity to Large-Scale Particle Accelerators



- **Superconductivity** is a property of certain materials that exhibit **zero electrical resistance** below a critical temperature (Tc). Enables current flow without power loss due to **absence of the Joule effect**.

- **Discovered in 1911** at Leiden University (Netherlands) by **Heike Kamerlingh Onnes**. He was awarded the 1913 Nobel Prize in Physics.



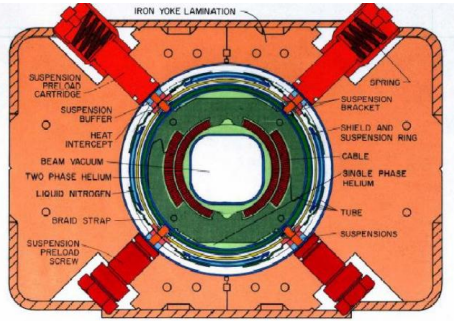

- In **the 80's** the **first large-scale applications** of superconductivity begun to appear: **Tevatron** particle accelerator built at Fermilab (USA). 774 x 4.3T dipoles 6-m long used to bend the particles in the ring.

- **In 2006** the **Large Hadron Collider (LHC)** was commissioned at CERN (Switzerland). The largest existing particle accelerator with a 27-km circumference.

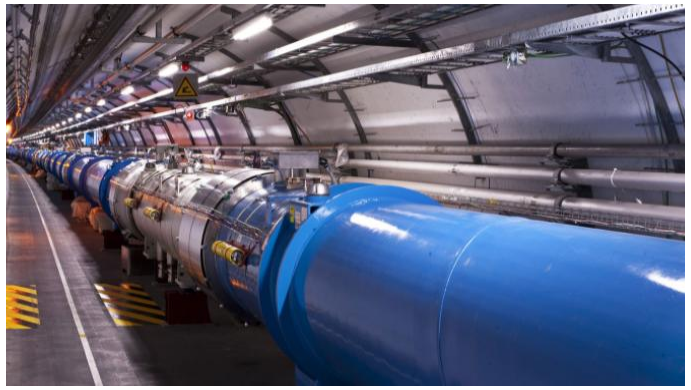

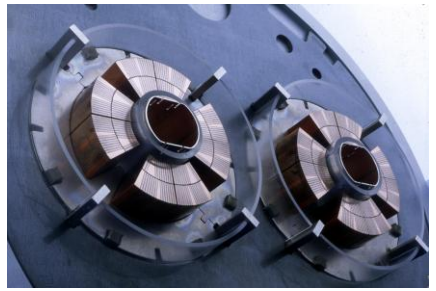

HL-LHC and Beyond... Future Circular Collider (FCC) at CERN

- The next step for CERN is the **High-Luminosity upgrade (HL-LHC)** aiming at increasing the collisions thus the view of rare phenomena, precision of the measurements and opening the way to new discoveries.
- **For the first time, Nb_3Sn magnet will be installed in an accelerator**. 30 powerful quadrupoles installed around ATLAS and CMS detectors
- **HL-LHC will start operation in 2030.**

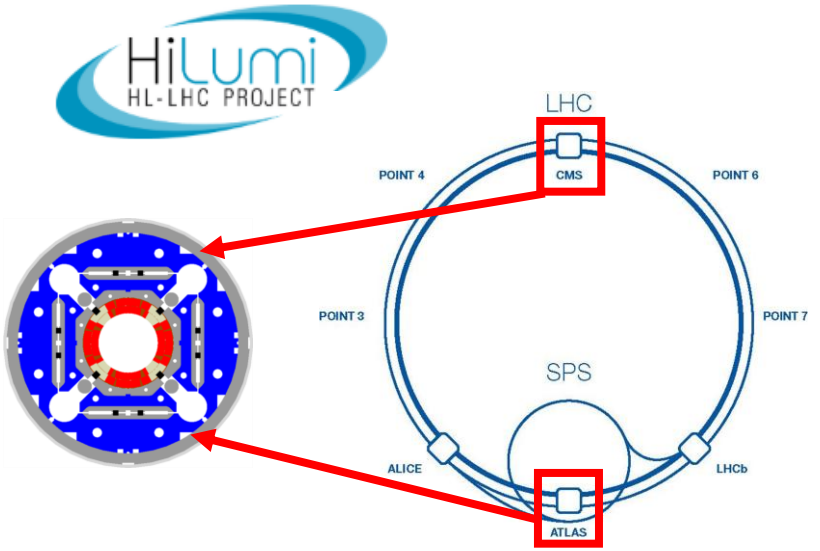

- Scienitfic community is discussing about a 90.7-km-Circumference **Future Circular Collider (FCC)** at CERN developed with a 2-stage approach: FCC-ee from the **mid-2040s** and FCC-hh from **the 2070s**.

- It calls for development of **Nb_3Sn accelerator dipole magnets with 14 T operational field** with focus on **sustainability**, **cost** and **large-scale production**. This is the scope of **High Field Magnet (HFM) program**

HFM
High Field Magnets

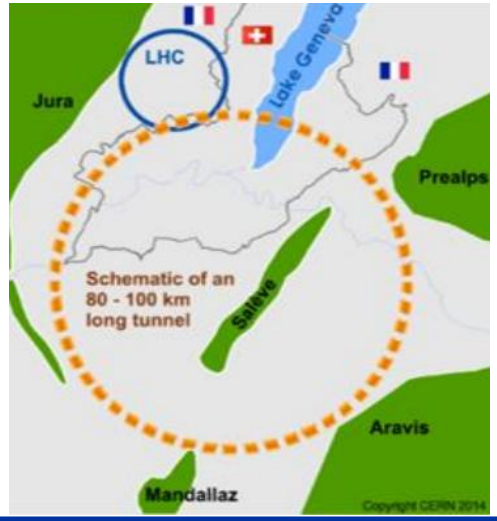

Nb_3Sn Coil Insulation Systems

- During construction and operation, superconducting magnets as well as their insulation systems are exposed to cryogenic temperature (1.9 K), high radiation levels (1 – 30 MGy) and mechanical loads, especially during assembly (~100 MPa).
- A robust electrical insulation is key to assure reliability and performance of the magnets.
- Within HFM program, an R&D work package is devoted to the development of **enhance electrical insulation systems** for Nb_3Sn coil.



Nb_3Sn Rutherford-type cable

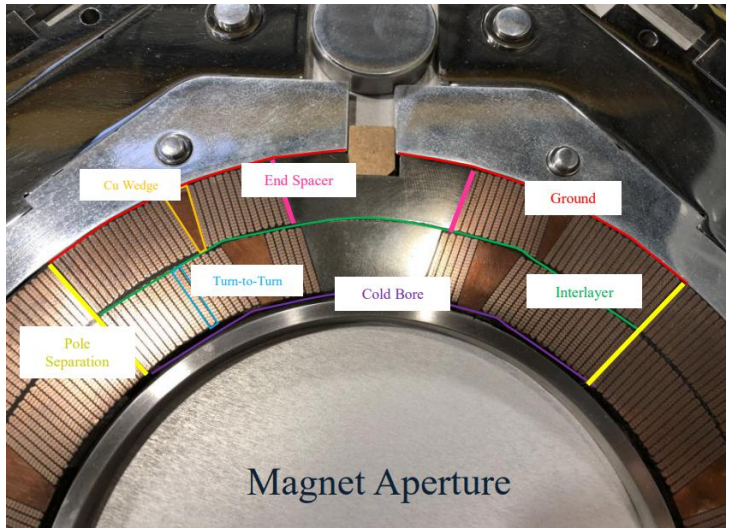

What is demanded to an insulation system for HFM?

- To have **high dielectric strength (voltage withstand ~ 2 kV)**
- To have **good mechanical properties** (at each stage of magnet manufacturing and operation, loads ~100 MPa)
- To have a **high radiation hardness (up to 30 MGy)**
- To be as thin as reasonably achievable (in consideration of all other requirements)
- To possibly have **good thermal properties** (high heat capacitance and conductivity)
- Others…

Manufacturing a Nb_3Sn coil (1/2)

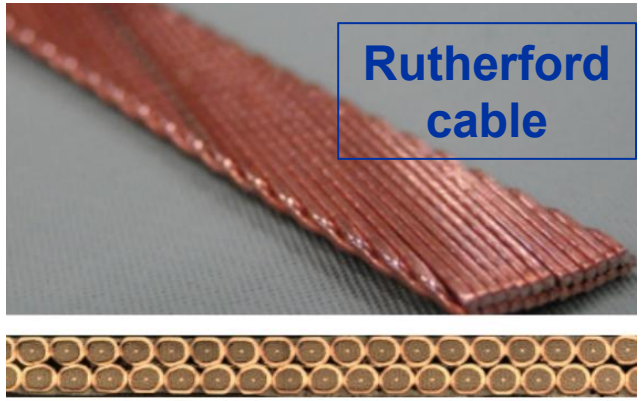



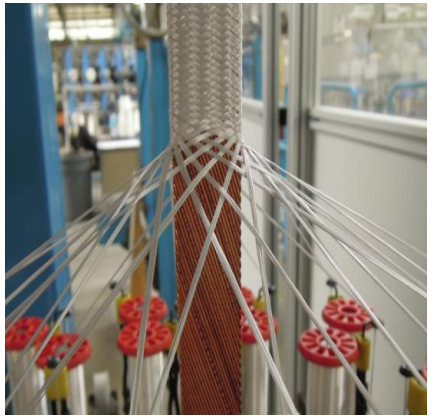

Courtesy of CGP (Omerin Group)

INSULATION

The insulation is constituted by a glass fibers braided onto the Nb_3Sn cable.

Topic #1



COIL WINDING

The cable is wound around a pole mounted on a steel mandrel. For long coils (> 8 m) the winding process is carried out by an automatic winding machine.

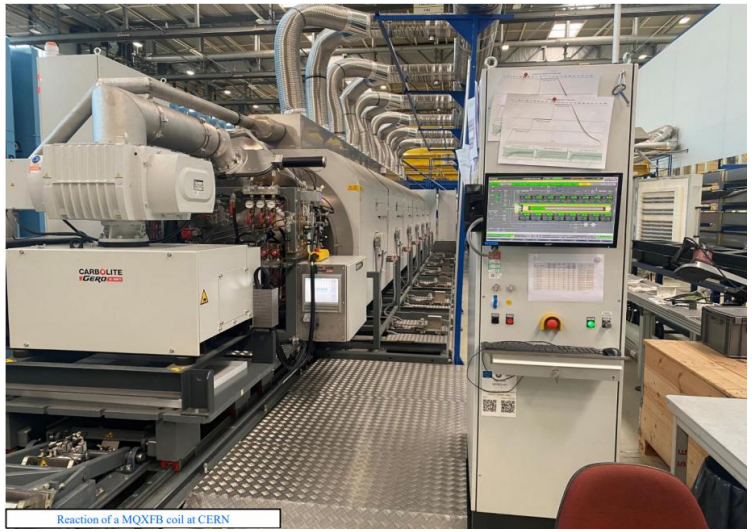

REACTION HEAT TREATMENT

The “reaction” process is required to create the intermetallic compound Nb_3Sn. Coil heated to about 650-700 °C in vacuum or inert gas (argon) atmosphere for roughly 50 hours.

Topic #2

Manufacturing a Nb3Sn coil (2/2)


MQXFB coil inside the impregnation tank CERN



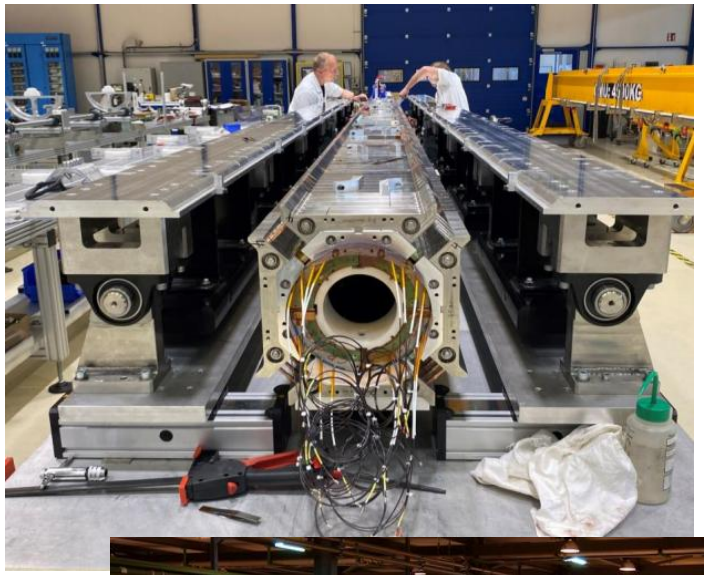



VACUUM IMPREGNATION

After reaction the Nb_3Sn becomes brittle. Carefull handling is required. The coil is vacuum impregnated with epoxy to create a monoholitc component and provide dielectric insulation.

Topic #3

The following steps include the assembly of the coils in a coil-pack, assembly of the yoke, welding, insertion in the cryostat, testing and installation…

Cable Insulation

Cable Insulation

- Fiber is **braided** directly around the Rutherford-type conductor
- Typically, **S2 glass** is chosen for the higher mechanical properties and thermal stability compared other glass fibers
- Conductor **insulation thickness 0.145 ± 0.05 mm**

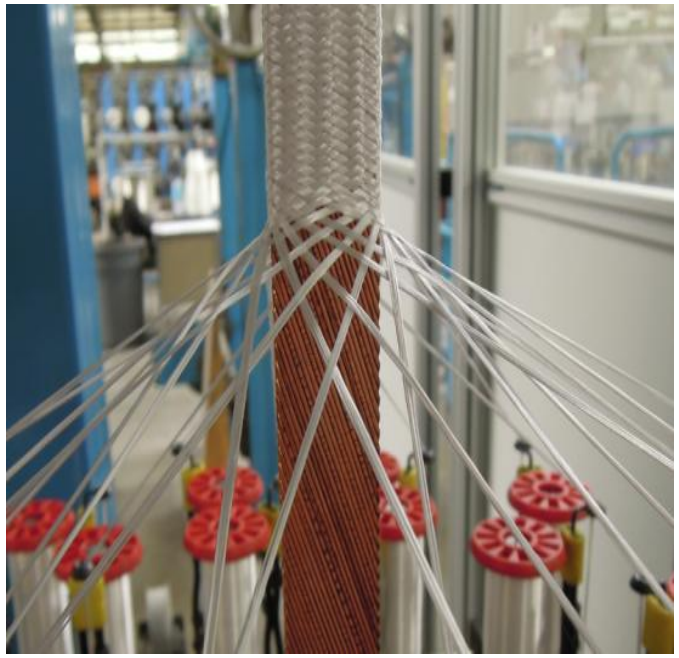

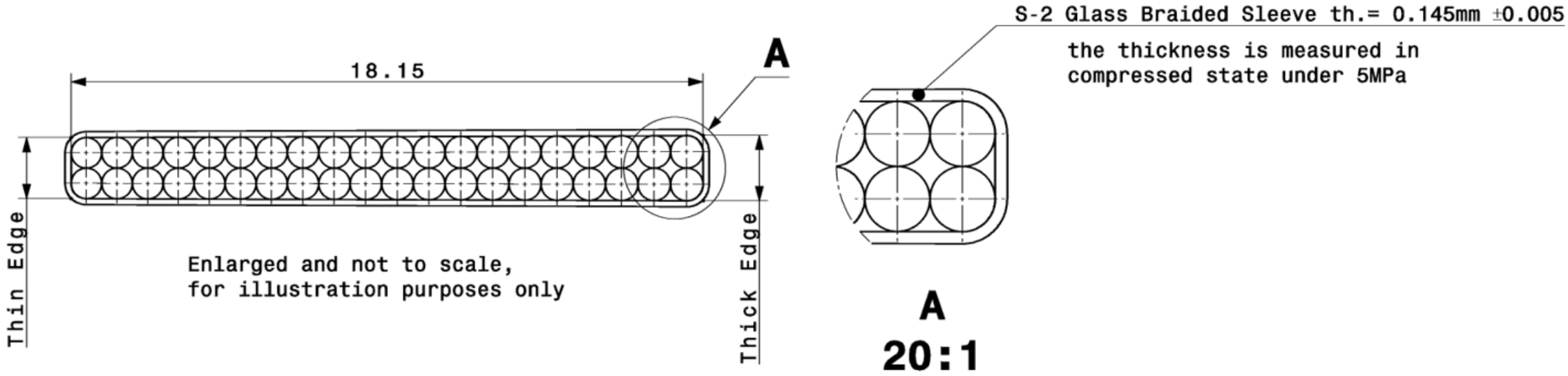

Control of Insulation thickness

- The **target insulation thickness** is achieved tuning the braiding pitch.
- **Control of insulation thickness** is extremely important because tight tolerances required during the magnet assembly.

$$p = LVDT_{insulated}(\sigma_t) - LVDT_{bare}(\sigma_t) = \boldsymbol{t_{insulation}} * 20$$

- **Quality control** of each insulated Unit Length (UL) is measured with "**10-stack**". Difference of consecutive measurements of a stack of 10 conductors with braided sleeve and without:

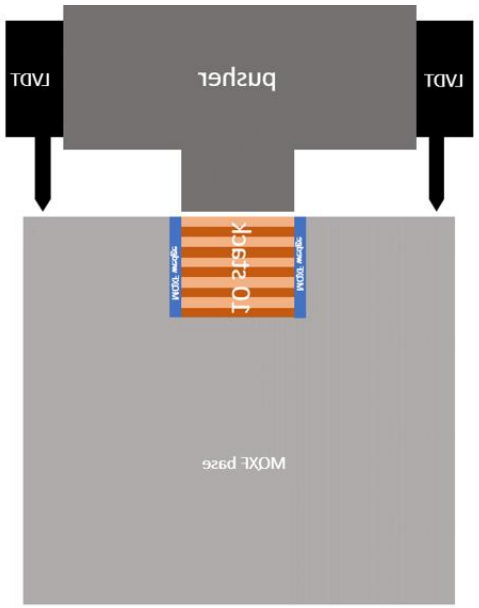

Insulation thickness set-up: "10-stack measurement"

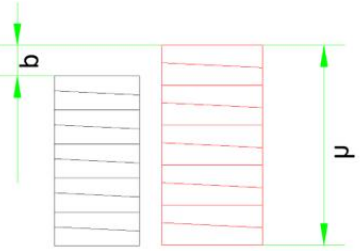

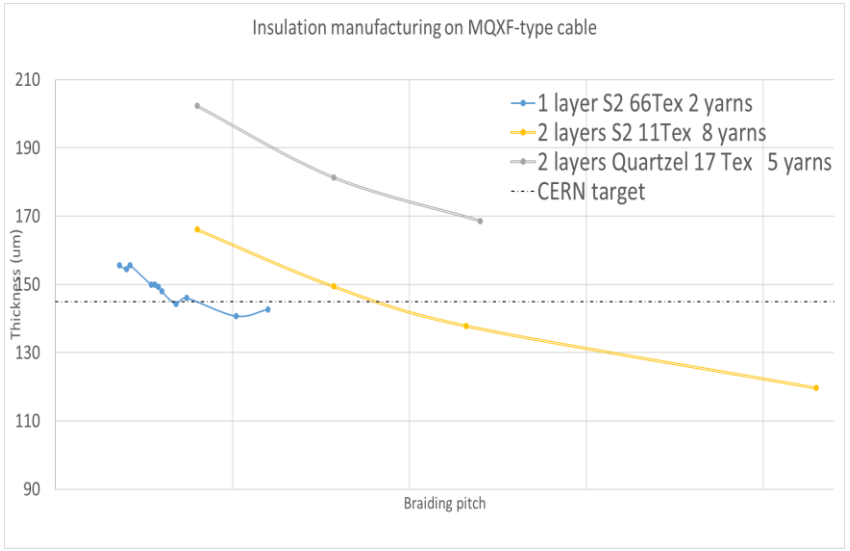

Insulation thickness for different braiding pitches

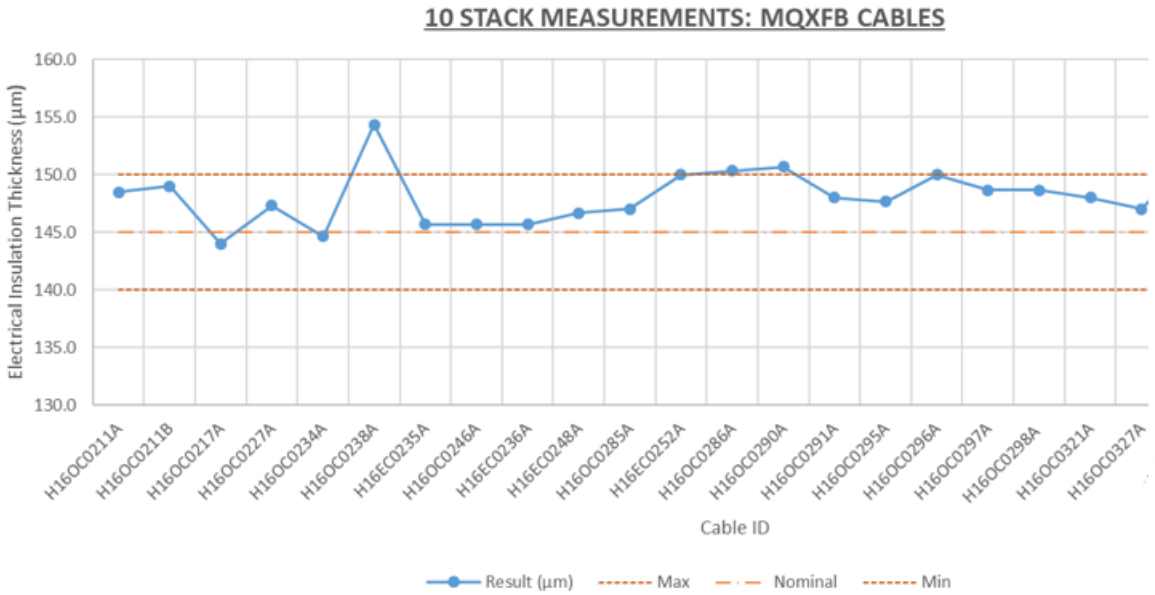

Insulation thickness for different UL (E. Fernandez Mora)

Braided Insulation Layout

- **Fibre volume fraction Vf** determine final properties of the insulation dielectric strength, mechanical strength, thermal conductivity and Coefficient of Thermal Expansion (CTE)

- Typical **target of fibre volume fraction is > 50%**

- Two types of braiding layout: **single** (filament Ø=9 µm) and **double sleeve** (filament Ø=5 µm). Both types display a **Vf ~ 60%**

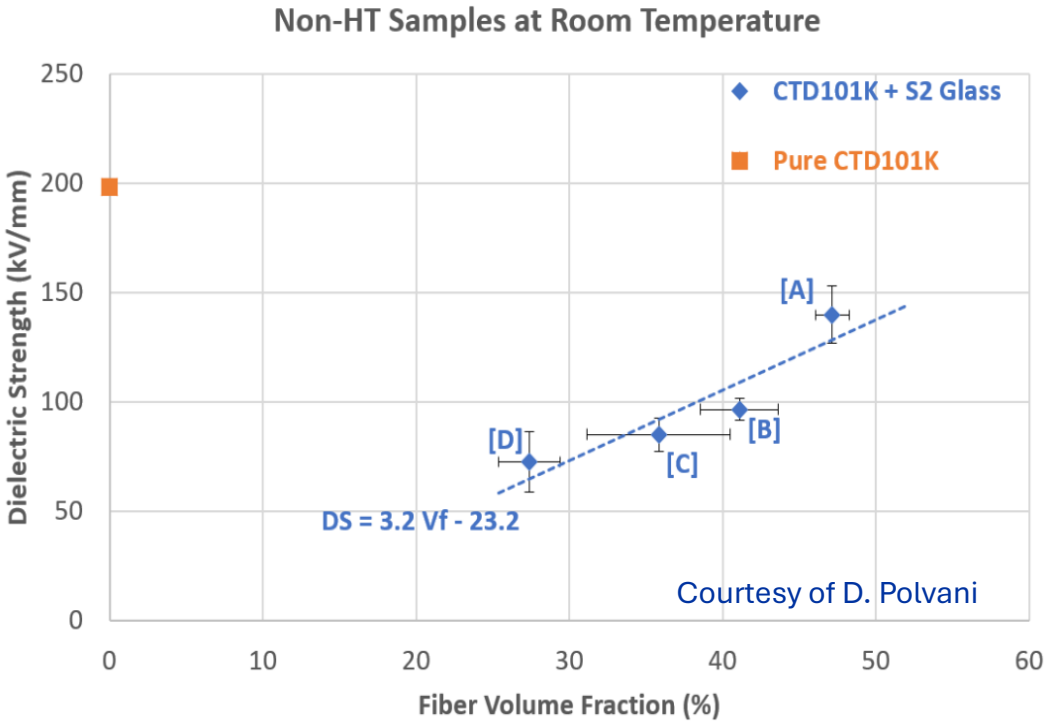

Braided Insulation Layout

Double sleeve has the advantage of having smaller epoxy volumes therefore less stored strain energy (accumulated during cooldown 300 K -> 4K). Epoxy cracks when stored strain energy is grater than work of fracture

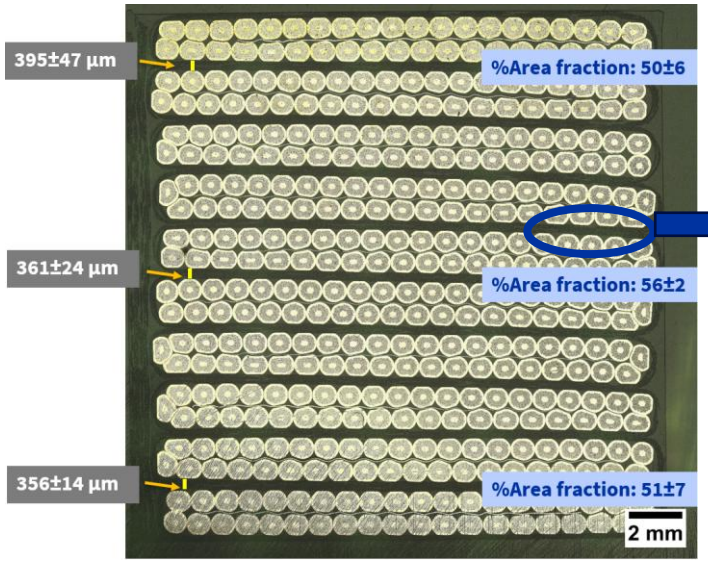

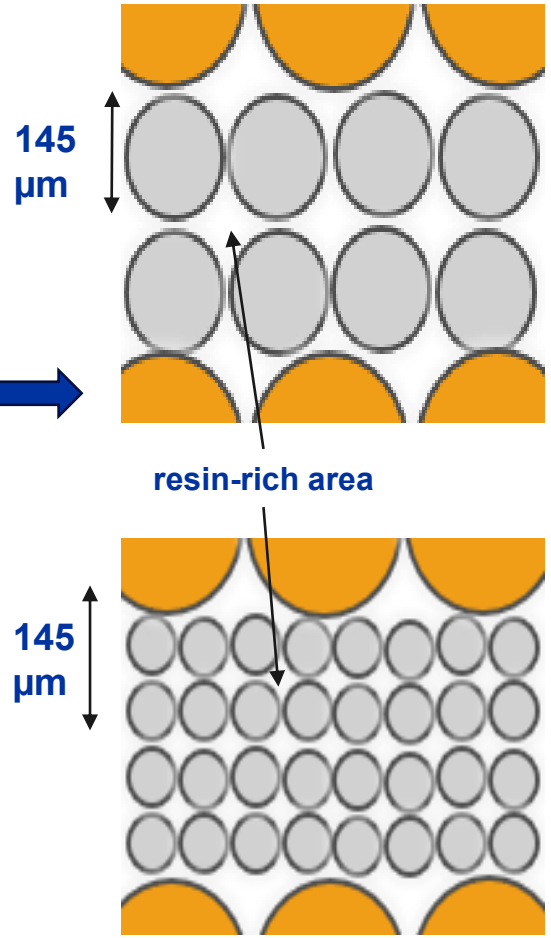

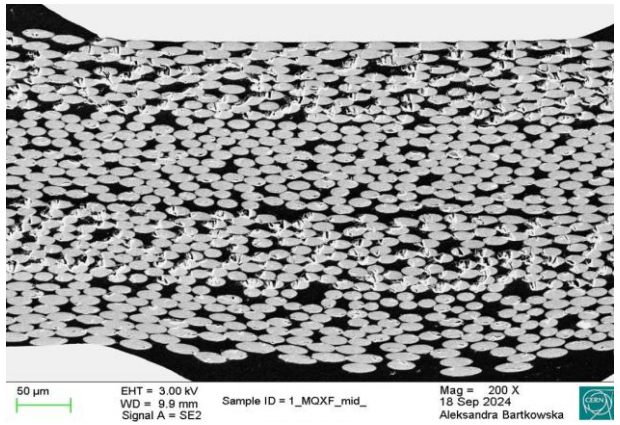

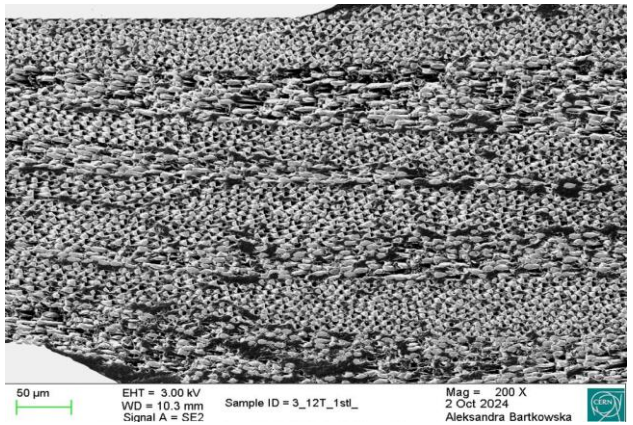

Fiber desizing

Nb_3Sn reaction treatment: Desizing effect

- The insulated coil is heated to about 650-700 ℃ in vacuum or inert gas (argon) atmosphere for roughly 50 hours. This is the reaction cycle of Nb_3Sn.
- The sizing undergoes a **pyrolysis** leaving **conductive products** on the fibers.
- Conductive products **impact the dielectric strength** of the insulation. The effect is less dramatic at cryogenic temperatures

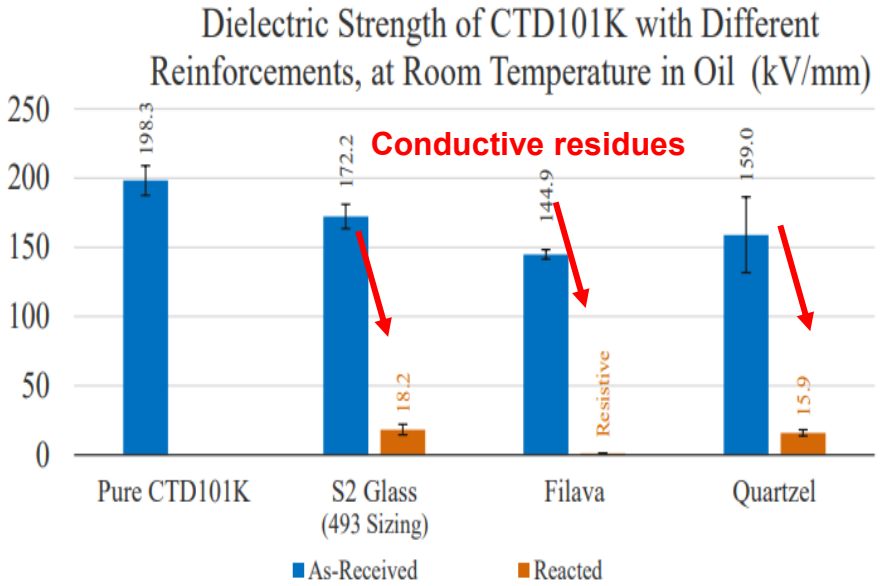

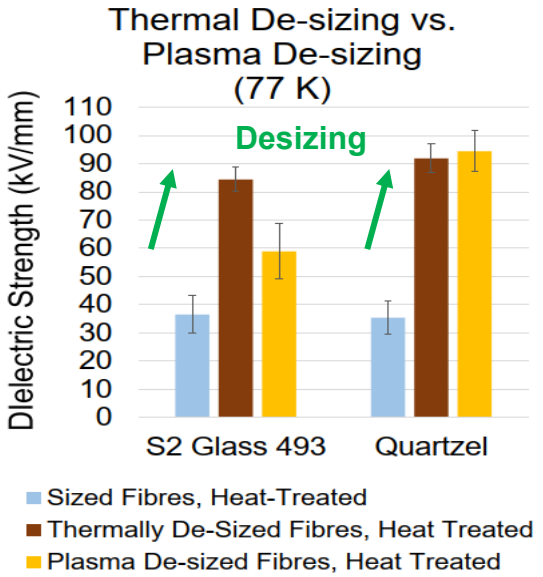

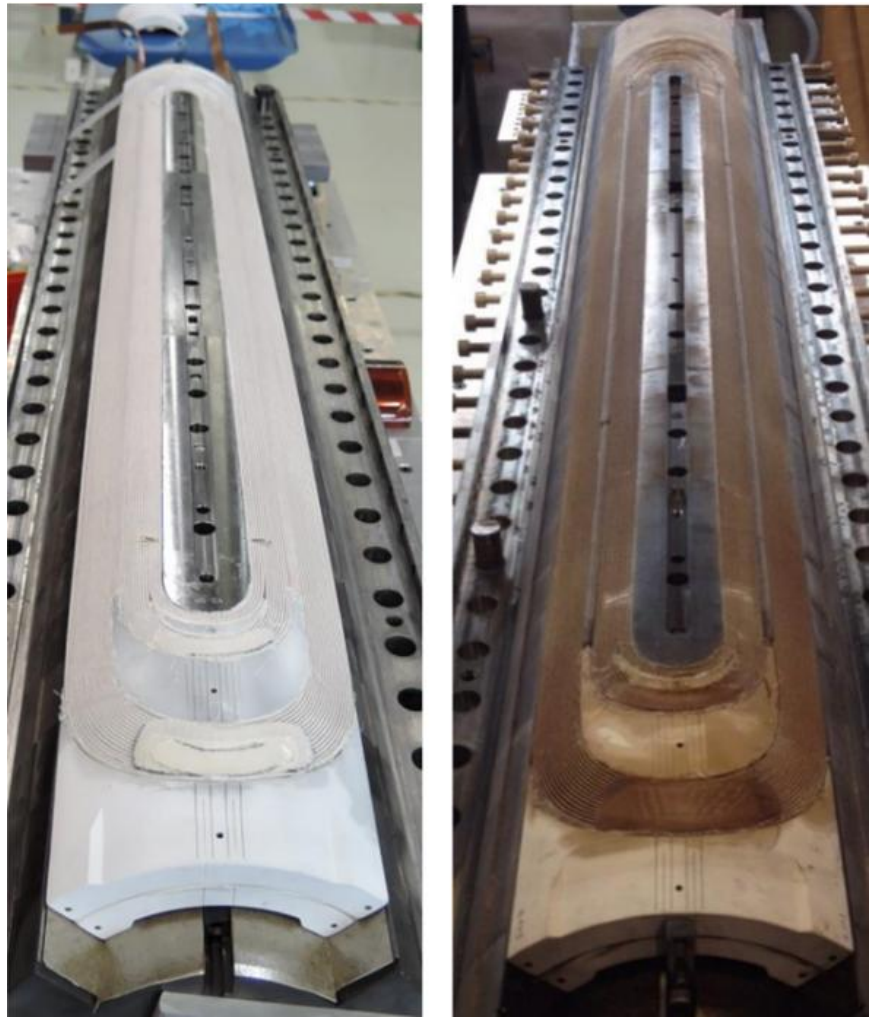

Superconducting coil before and after heat treatment

J. Osuna et al, *"Advanced Composite Insulation Systems in Nb3Sn Superconducting Magnets for Accelerators: Electrical Characterization of Laminates at Cryogenic Temperatures"*, accepted for ICEC/ICMC 2024

Thermal and Plasma Desizing

Desizing methods:

- **Thermal desizing** consists of injecting oxygen to burn off the sizing during the reaction treatment
- **Plasma desizing** consists of using a plasma torch to burn off the sizing before the cable is wound

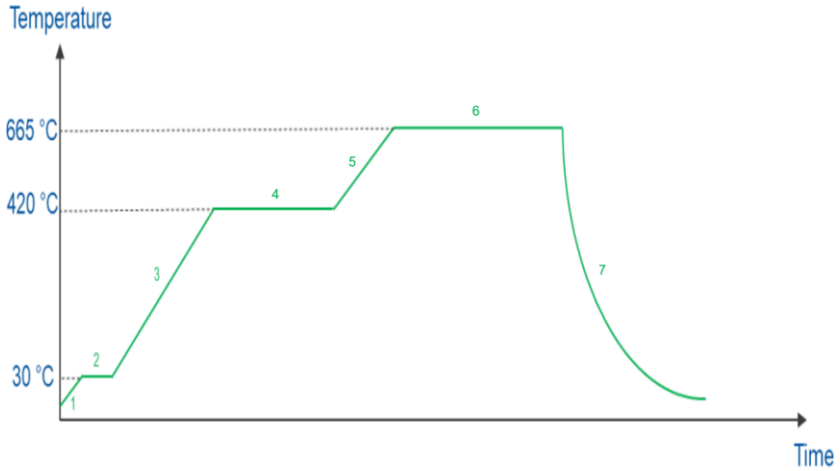

Typical Nb3Sn reaction cycle

Plasma →

Thermal →

1. Braiding
2. Winding
3. Reaction
4. Impregnation







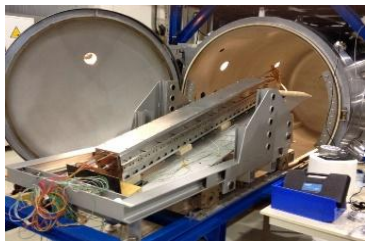

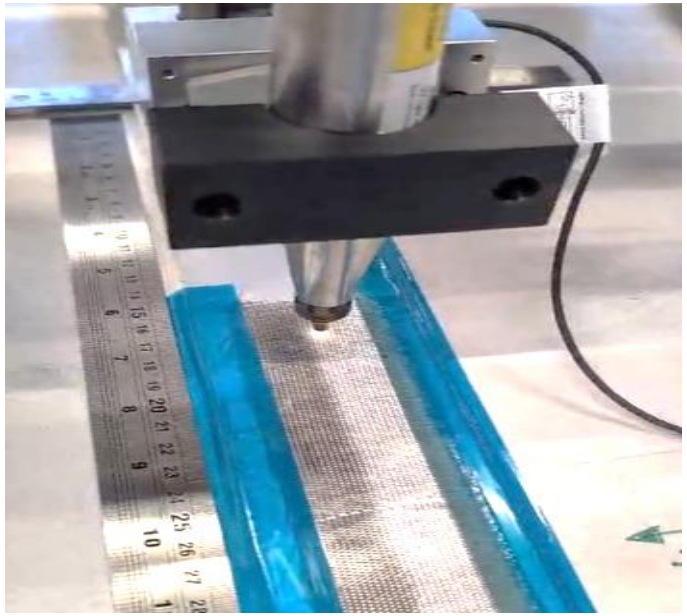

Plasma treatment on reacted glass fibres

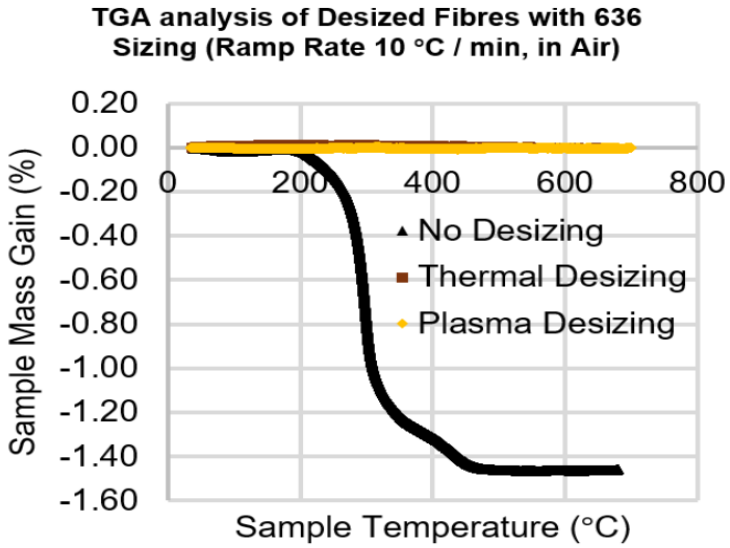

Epoxy systems

Impregnation systems

Current status on impregnation systems:

- In most cases, **epoxies** are used for impregnation
- Among them, two families of hardeners can be used: **amine and anhydride**
- Other chemicals can be added to tailor processing and end properties such as accelerator or flexibiliser

Desired properties for processing:

- **Low viscosity / long pot life** (coils are 8 to 15 m long)
- Low shrinkage during curing and low exothermic behaviour
- **Low curing temperature** to reduce thermal stresses

Desired end properties:

- **High dielectric strength**
- **Good mechanical properties**
- Thermal shock resistance
- **High radiation hardness (dose depends on where the magnet is installed in the accelerator – few MGy to 30 MGy)**
- Lowest possible CTE mismatch with coil constituents

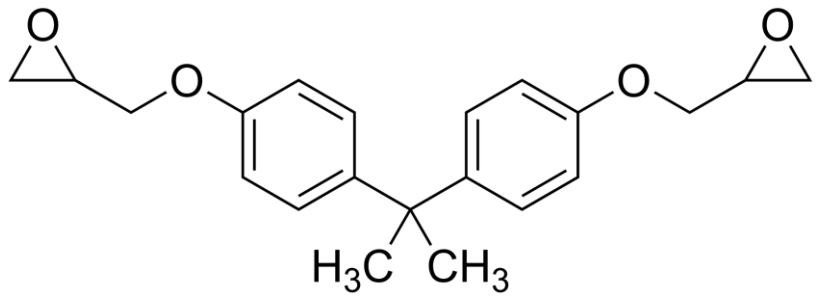

DGEBA epoxy resin

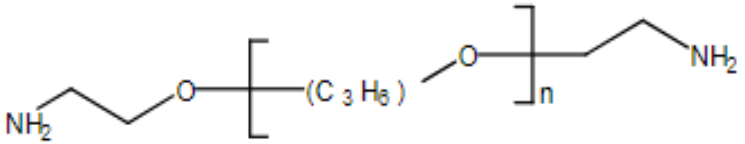

Amine hardener

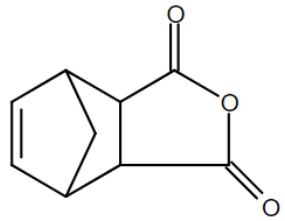

Anhydride hardener

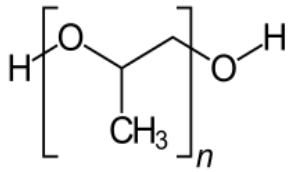

Flexibiliser

Fracture toughness of epoxies

Fracture toughness of different epoxies at room temperature and 77 K:

- Overall, the **fracture toughness of anhydride epoxies is lower than amine epoxies, especially at low temperatures**
- To toughen CTD101K epoxy, a flexibiliser DY040 was added (10 and 20 w%), leading to a toughness increased by 50 % at 77 K

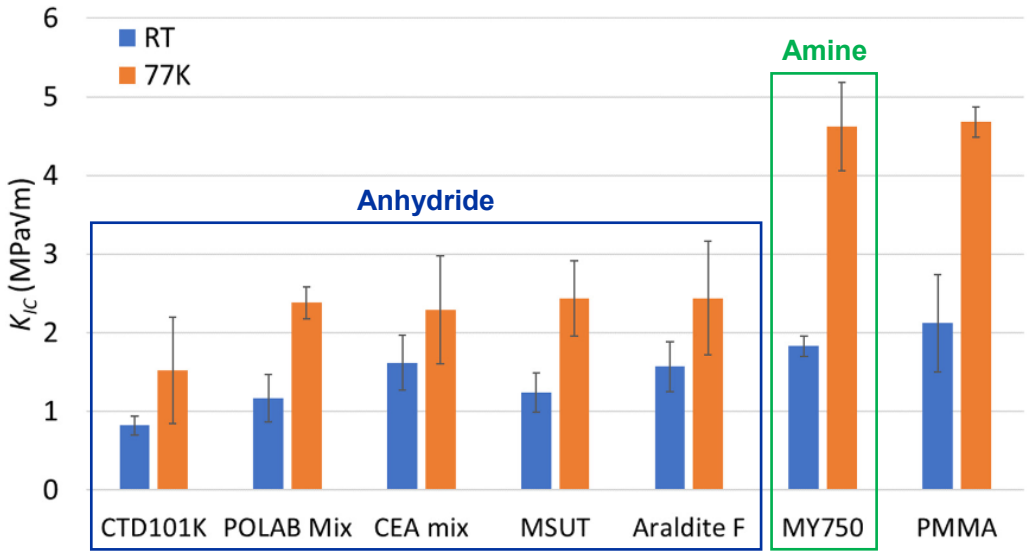

Fracture toughness of different polymers

Epoxy resin + flexibiliser

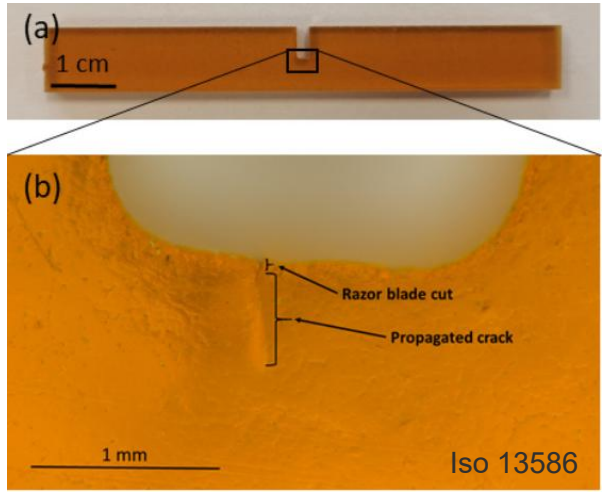

Fracture toughness test sample

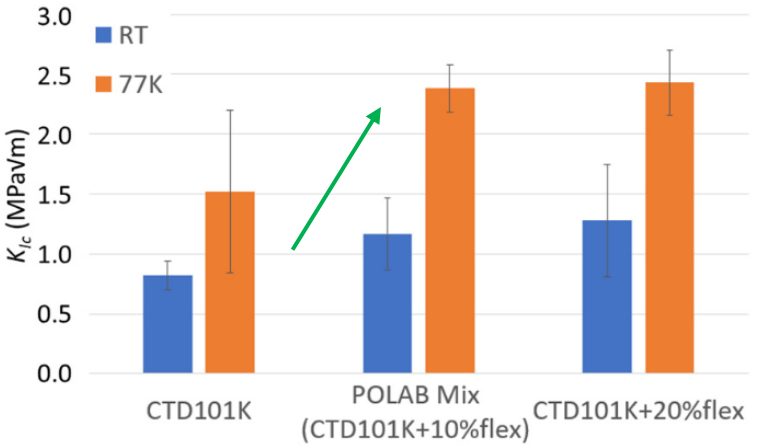

Fracture toughness of CTD101 flexibilised

A. Gaarud, et al, "*Fracture toughness, radiation hardness and processibility of polymers for superconducting magnets*" Polymers 2024, 16(9), 1287

Influence of the chemistry on the radiation hardness

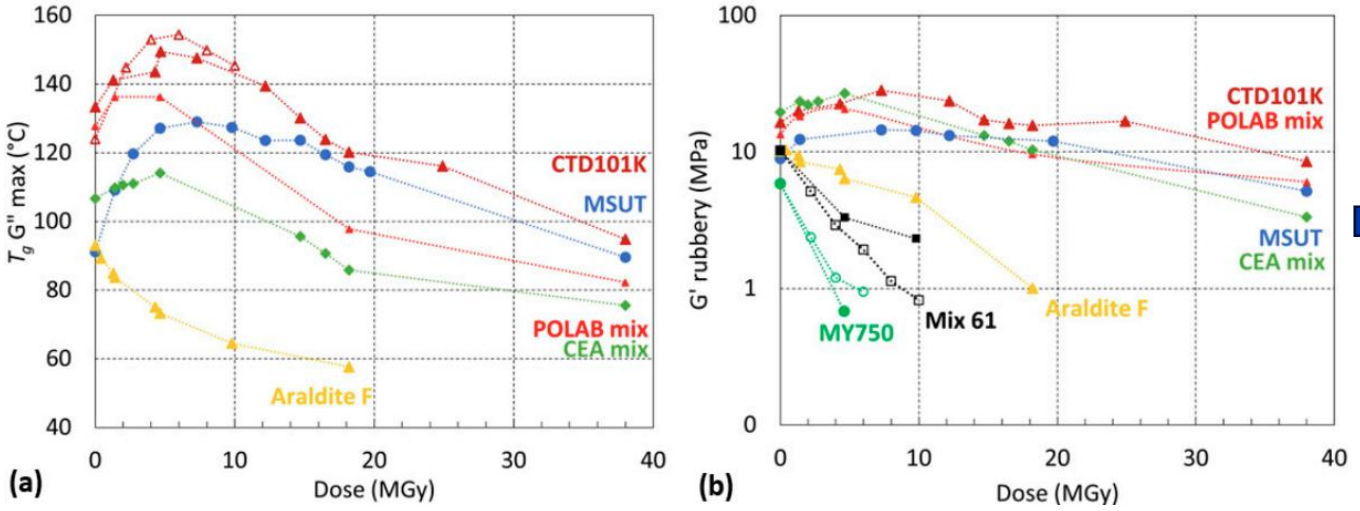

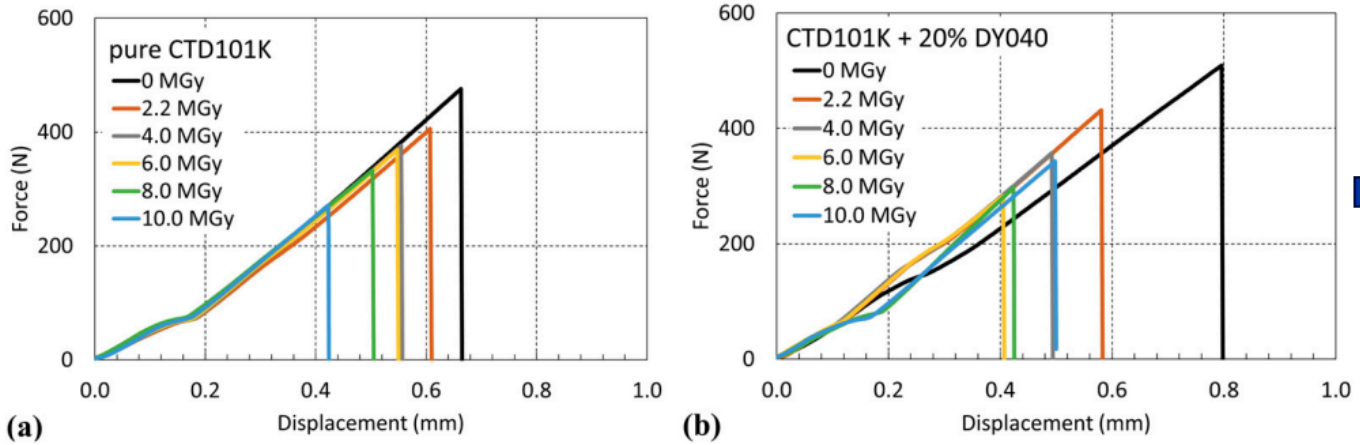

Dynamic Mechanical Analysis (DMA) study of irradiated epoxies:

- **The epoxies with anhydride hardeners are more resistant to radiation** e.g. CTD101K, MSUT (MY740) and CEA mix (CY 192-1) compared to epoxies using amine- based hardeners (Mix 61 and MY750)

CTD101K vs CTD101K + DY040 (POLAB mix):

- DMA (up to 38 MGy) and 3-point bending (up to 20 MGy) studies did not reveal significant change of radiation hardness between the two systems
- **DY040 can be used to increase fracture toughness without impacting the radiation hardness**

D.M. Parragh, et al, "*Irradiation induced aging of epoxy resins for impregnation of superconducting magnet coils*", IEEE Trans. Appl. Supercond., 34 (3), (2024), Art. no. 7800107
A. Gaarud, et al, "*Fracture toughness, radiation hardness and processibility of polymers for superconducting magnets*" Polymers 2024, 16(9), 1287

Influence of irradiation environment and temperature

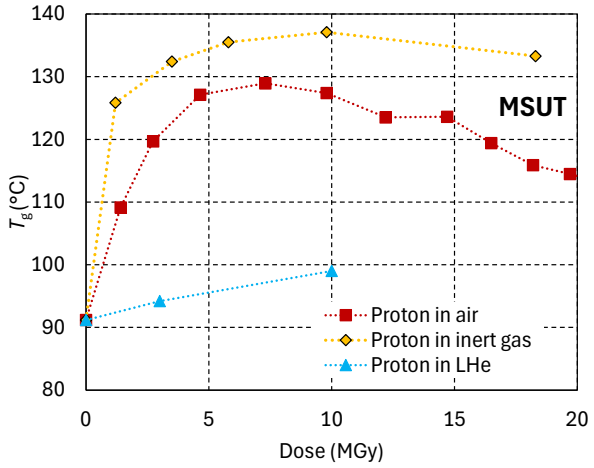

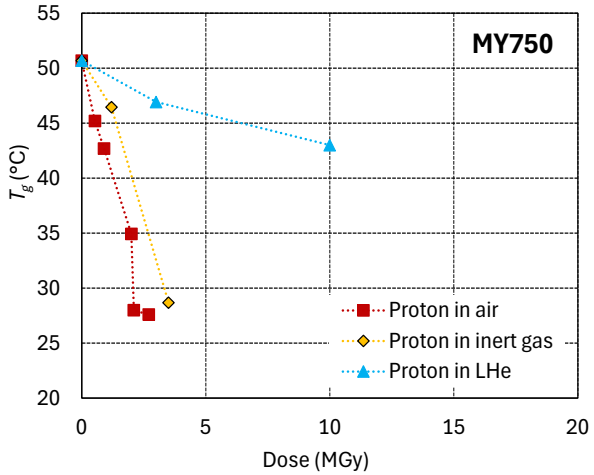

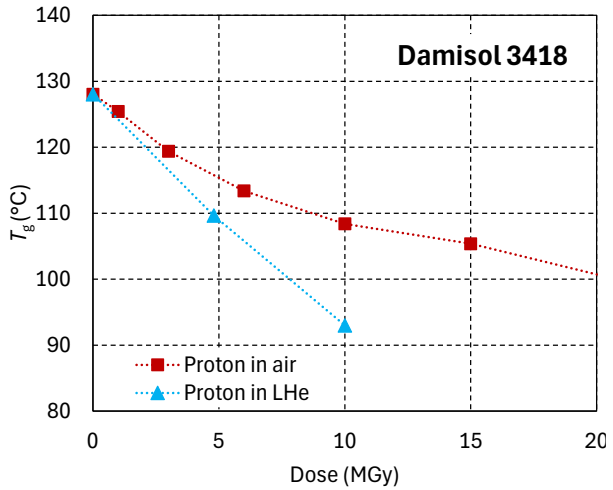

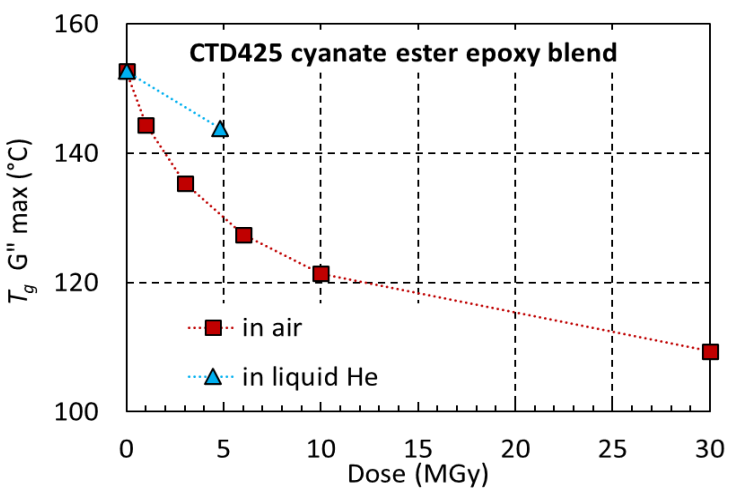

DMA study of irradiated epoxies in air, inert gas or liquid helium:

- Strong different efficiency for producing radiation damage, depending on the irradiation temperature
- More cross-linking and less chain scission in inert gas
- **Cross-linking is nearly completely suppressed in liquid helium**
- The temperature effect on chain-scission is materials dependent

To predict the dose limits of organic materials in superconducting magnets, **irradiations need to be performed at cold**

New set up for cold irradiation test campaign under construction at CERN

D.M. Parragh, et al, "*Irradiation induced aging of epoxy resins for impregnation of superconducting magnet coils*", IEEE Trans. Appl. Supercond., 34 (3), (2024), Art. no. 7800107
A. Gaarud, et al, "*Fracture toughness, radiation hardness and processibility of polymers for superconducting magnets*" Polymers 2024, 16(9), 1287

Electrical Performance

Insulation Quality and Electrical Performance

- For High Field Magnets expected **voltages to ground and between turns** range approximately around **1.5 kV** and **100 V** respectively.

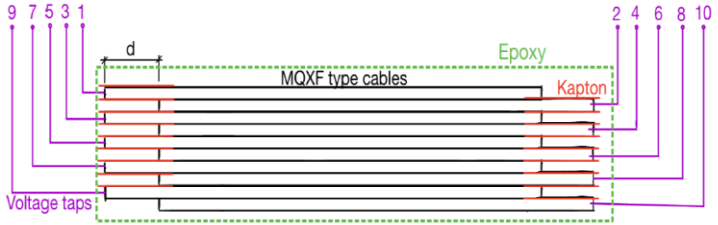

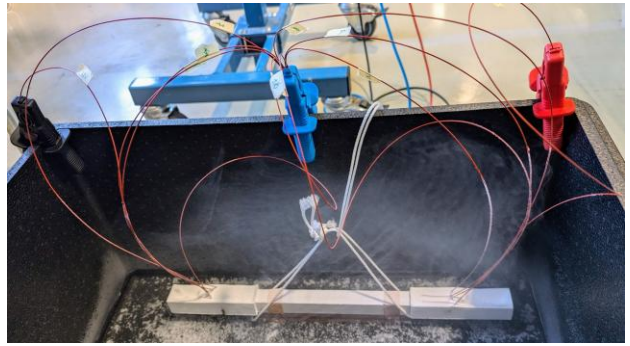

Representative samples of turn-to-turn insulation (HV 10-stacks)

- The **quality** of the insulation is assessed **by voltage withstand test** and **partial discharge (PD).**

- Turn-to-Turn insulation withstand >2.5 kVdc before and after controlled cold thermal cycles down to 77 K (LN_2)

- **Partial Discharges (PD)** are localized breakdowns. It can appear in voids, cracks, across the insulation surfaces and in air (corona).

- **PDs can reveal the presence of defects** in the insulation that may develop in failures if subjected to repeated thermal cycles or mechanical loads

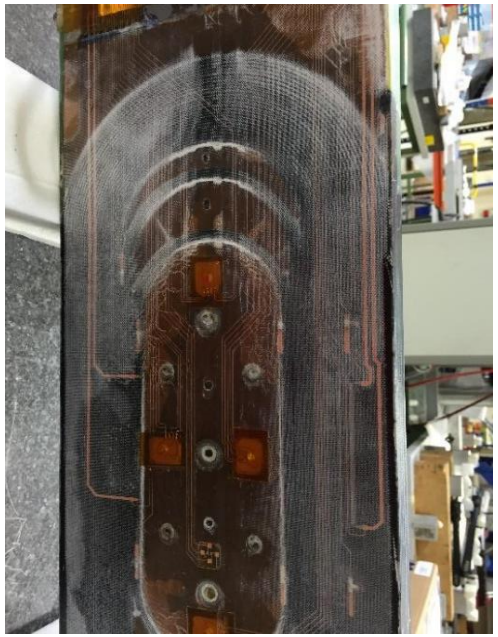

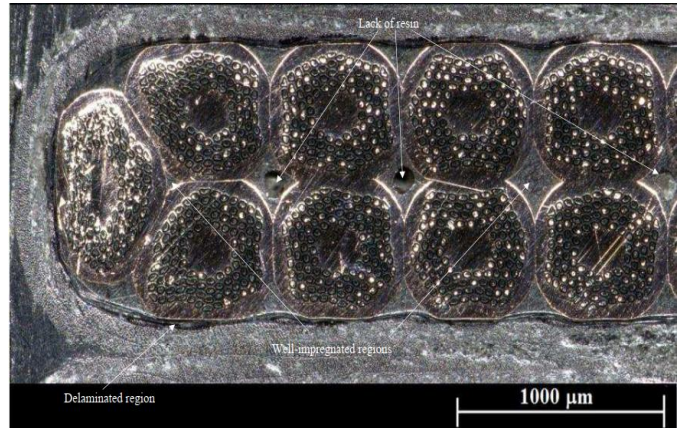

Example of carking on coil after exposure to liquid Helium (right); delamination and cavities on insulated cable. SMC coils (Courtesy of J.C. Perez)

Partial Discharges

- The size and shape of a defect can be estimated by **Paschen Law of gases**, the PD inception voltage (**PDIV**)* and the interpretation of the Phase-Resolved PD (**PRPD**) pattern.

- Defect free Turn-to-Turn insulation are **PD free up to ~ 8 kV**. It is possible to assume that **cavities**, if present, **<~ 6 µm**.

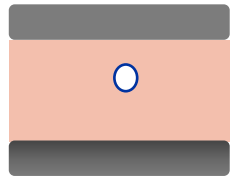

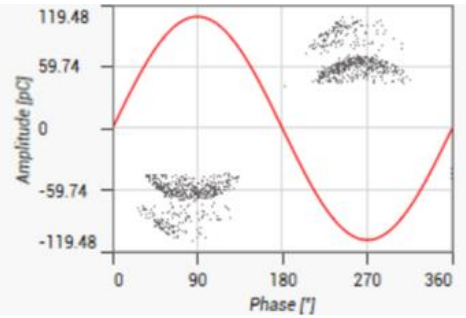

- **PDIV** occurs on some samples around **4 kV**. Possible **flat cavity or delamination** of approximately **10 µm** (or spherical voids ~25 µm).

- PD inception voltage of insulation that underwent **five thermal cycles in LN2** was on the range of **2.5 kV.** Possible flat cavity or delamination of approximately **15 µm** (or spherical voids ~30 µm).

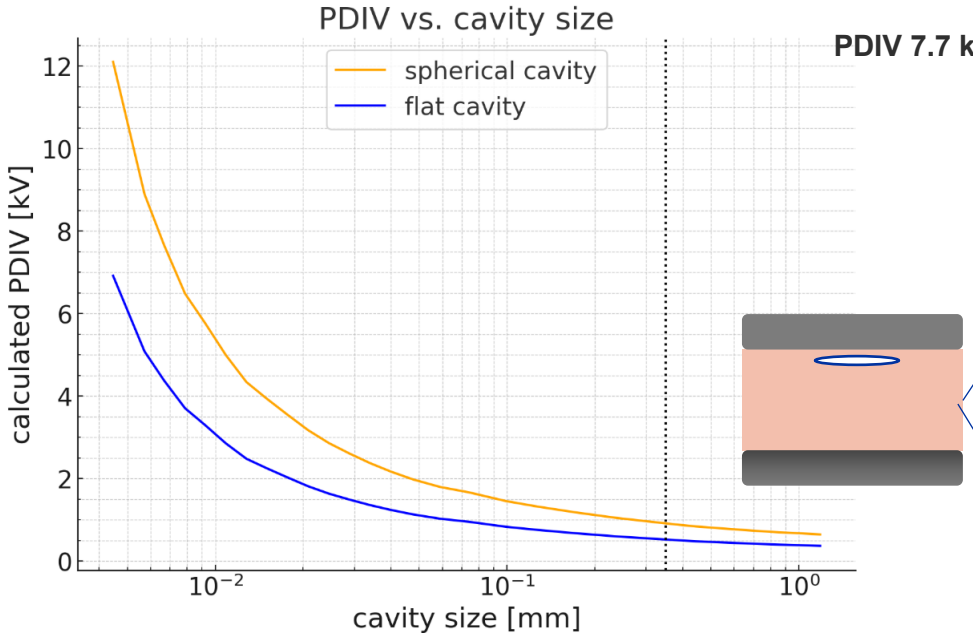

PDIV 7.7 kV; PRPD attributed to micro-voids

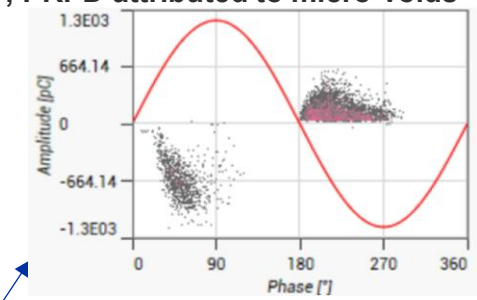

PDIV 4 kV; PRPD attributed to delamination

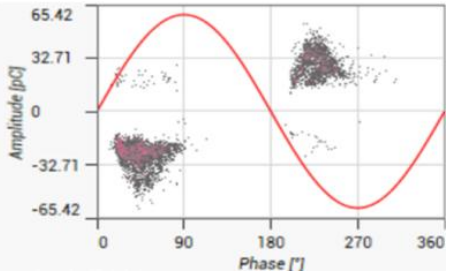

PDIV 2.5 kV; PRPD attributed to delamination

***voltages expressed in peak values**

PD data from D. Polvani - internal document (EDMS)

Conclusions and perspectives

- **Robust electrical insulation** is essential for the reliability of Nb_3Sn superconducting magnets for particle accelerators
- **Control of the braiding process** is necessary to meet tight magnet construction tolerances and insulation quality.
- **Desizing techniques** (thermal, plasma) are promising in improving dielectric performance, but scale-up and validation in coils are ongoing.
- An epoxy system tailored with flexibiliser can **enhance fracture toughness** at cryogenic temperature without compromising radiation hardness – critical for long-term performance.
- **Partial Discharge (PD)** testing is a valuable diagnostic tool to assess insulation quality and detect early signs of degradation due to thermal-mechanical induced stresses.

Thank you for your attention

Optimum boundaries for maximum load-carrying capacity for misaligned water-lubricated composite journal bearing based on elastohydrodynamic lubrication

Wonvin Kim, Su Hyun Lim, Wonki Kim, Donghyeon Cho, Kiyaranu Putra Pakartiwan, Muhammad Salman Sarfraz, Seong Su Kim*

Department of Mechanical Engineering, KAIST

2025.08.07

INDEX

01. Introduction

02. Numerical analysis

03. Result & Discussion

04. Conclusion

01. INTRODUCTION

Water-lubricated journal bearing

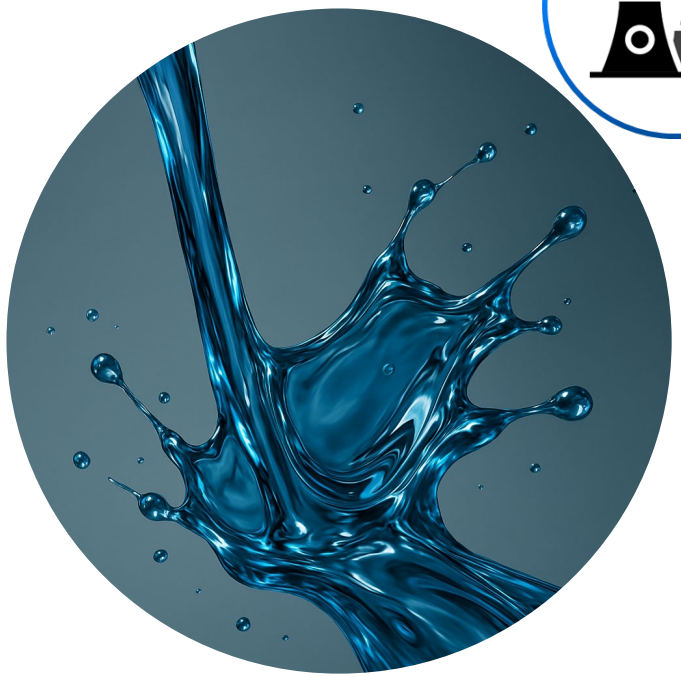

Water lubrication

- Eco-friendly
- Simplicity
- Low Viscosity
- Thermal stability

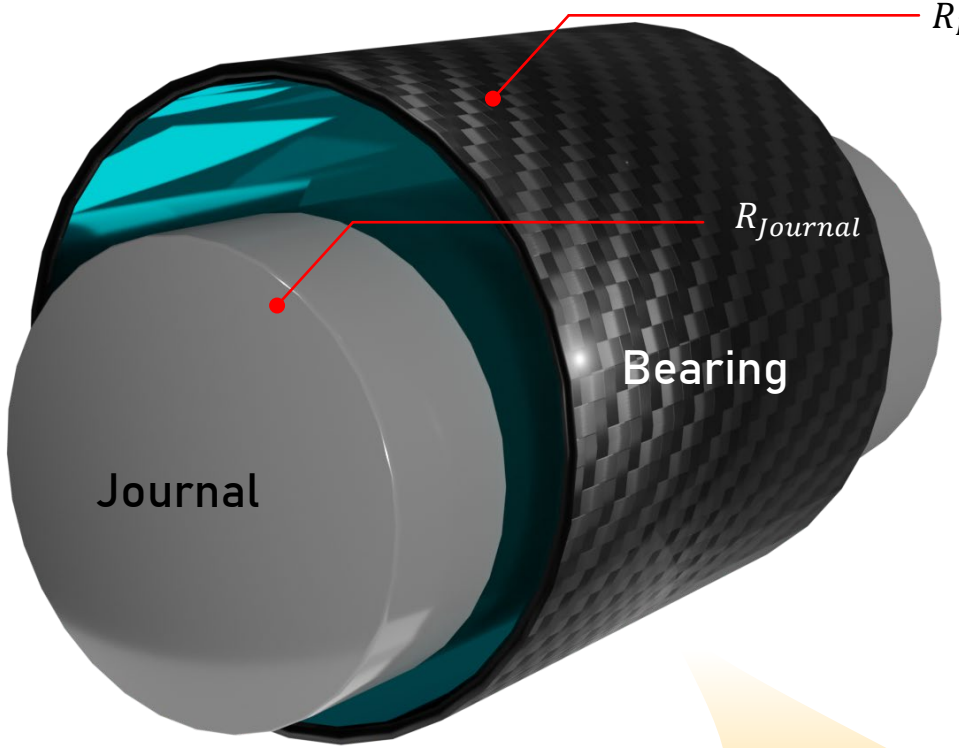

Design parameter:

$$Clearance, c = R_{Bearing} - R_{Journal}$$

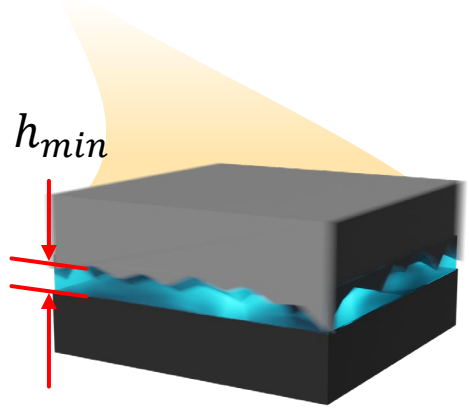

Composite bearing liner

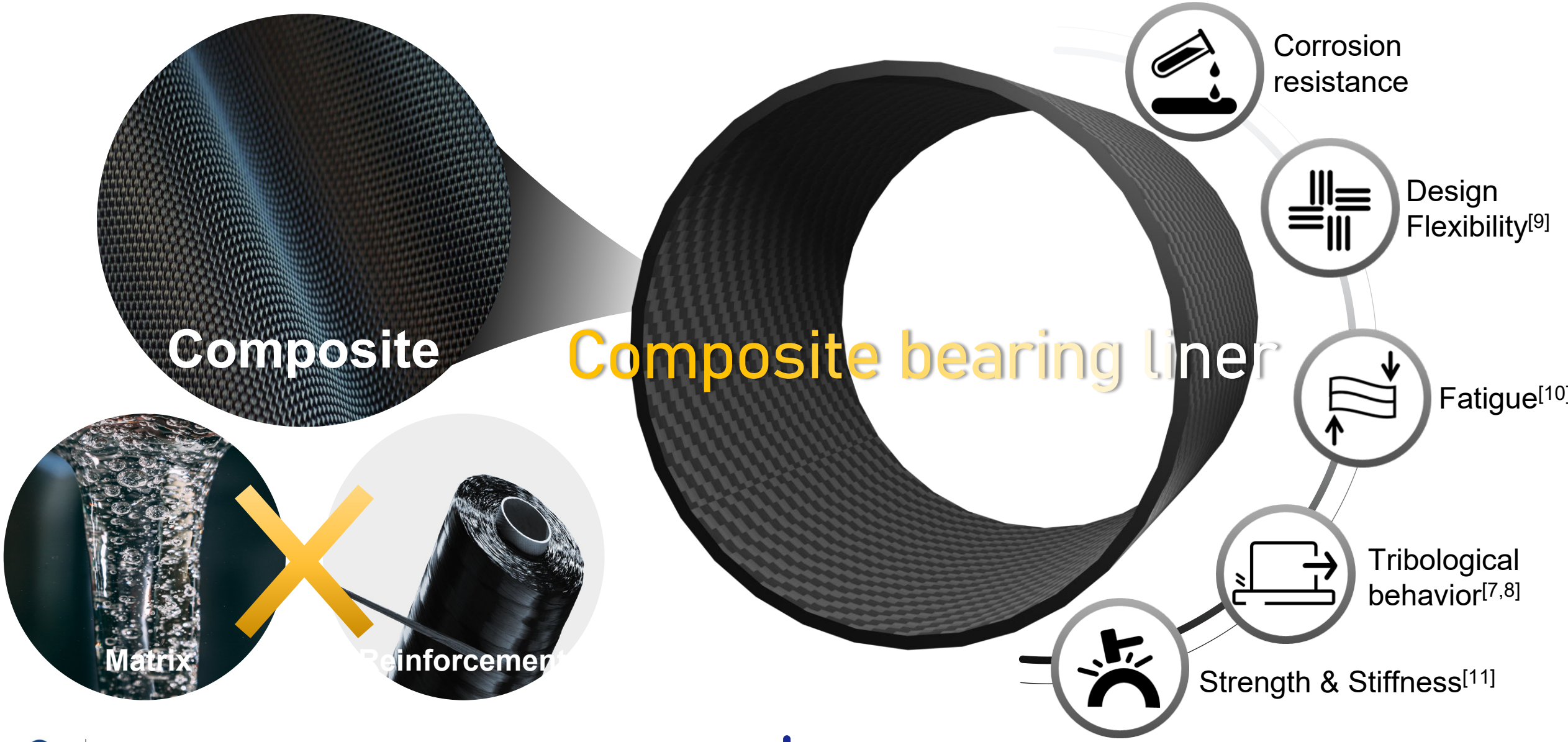

Bearing deformation & Misalignment

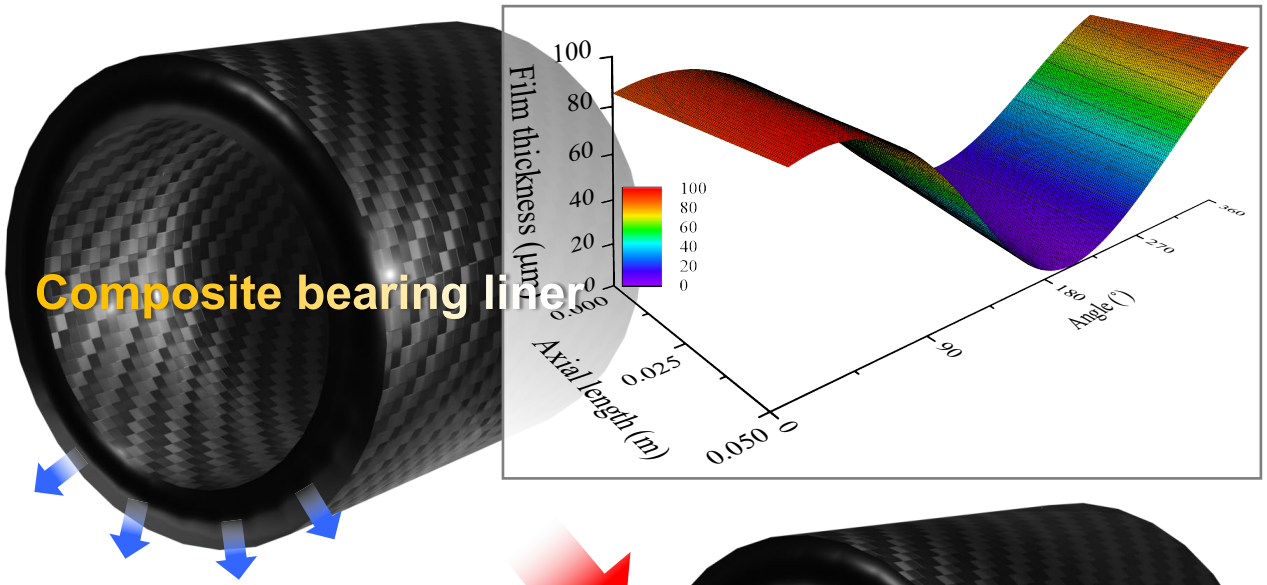

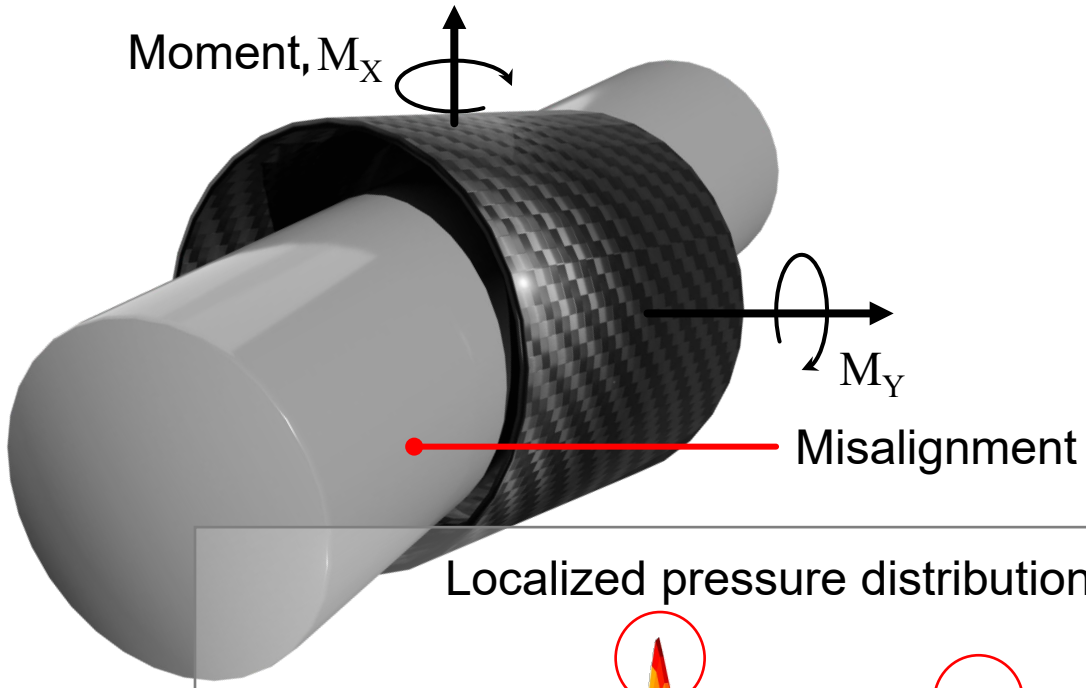

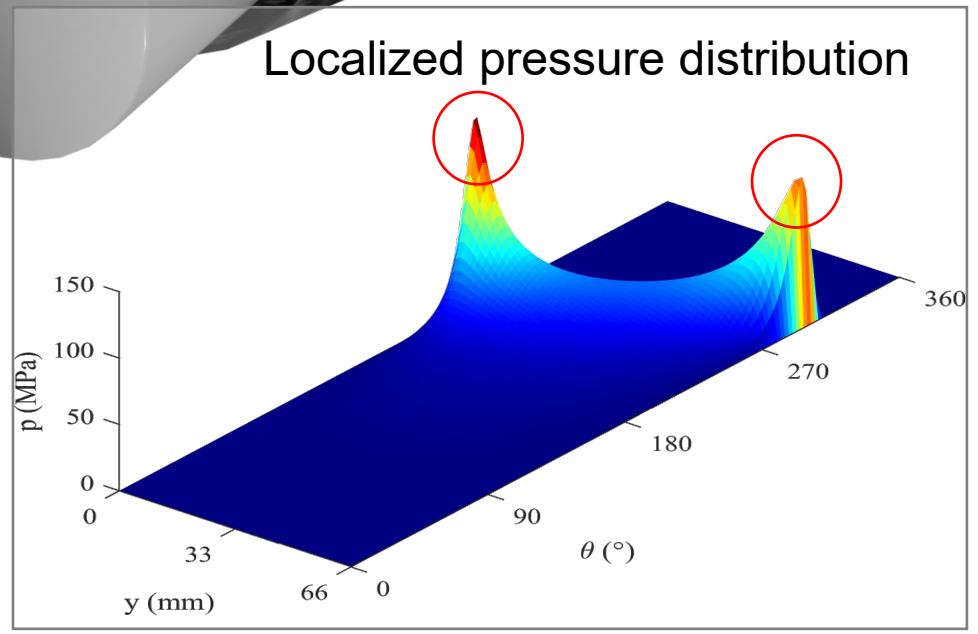

Journal bearing

Geometry

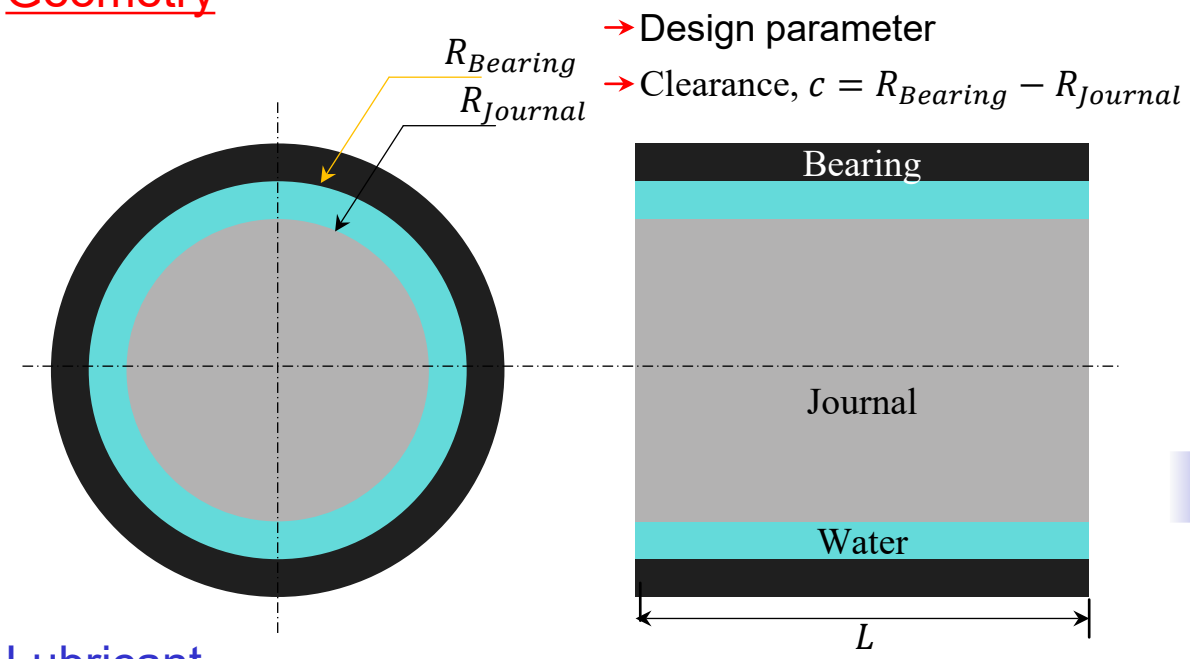

Lubricant

Viscosity, μ; Density, ρ

Operating condition

Angular velocity, ω; Load, W

Bearing materials

Elastic constants, C_{ij}

Main principle

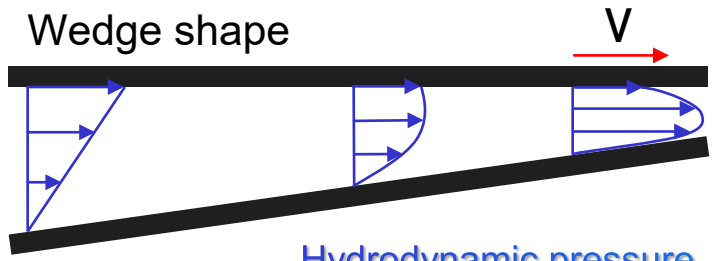

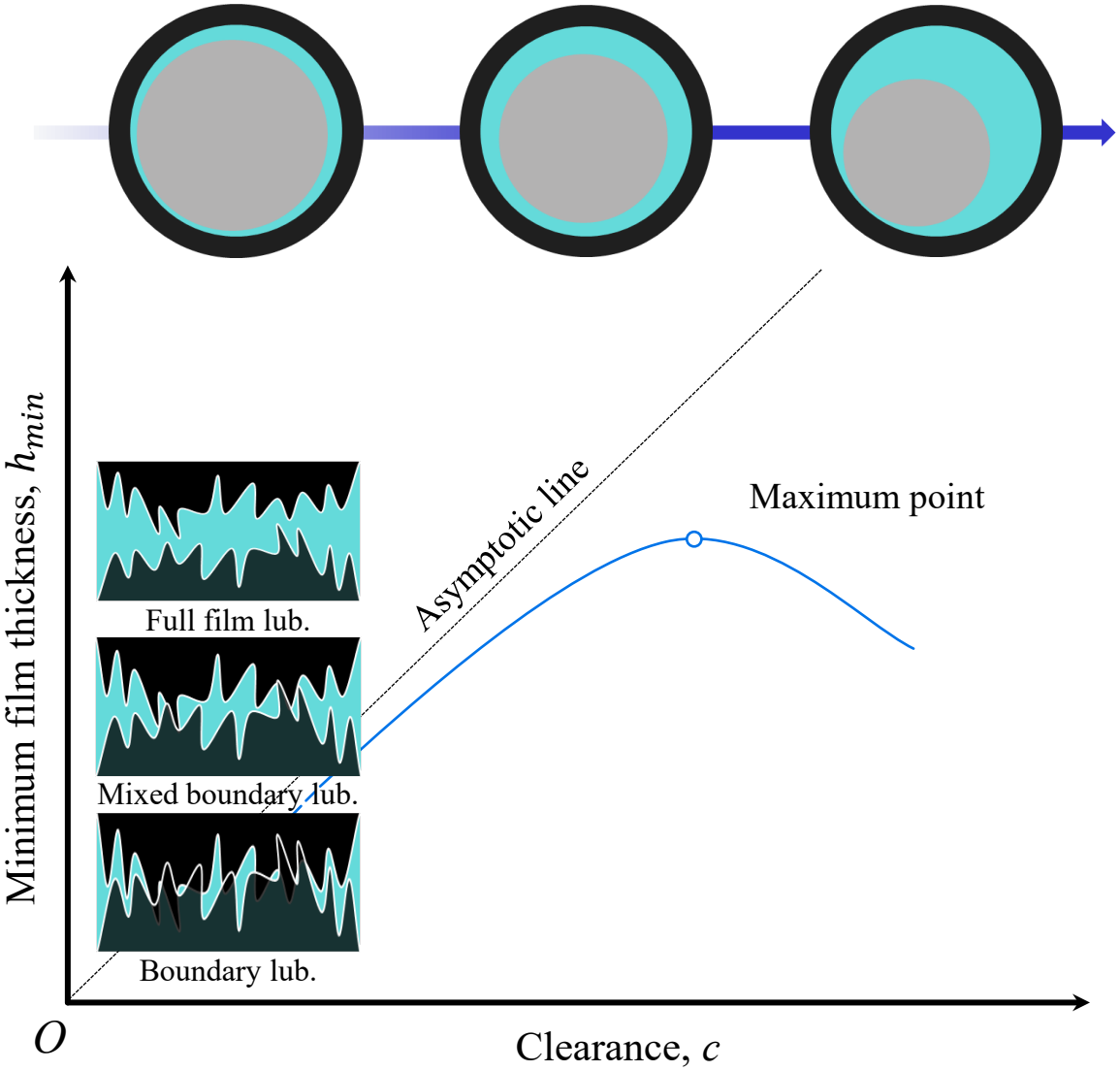

Journal bearing

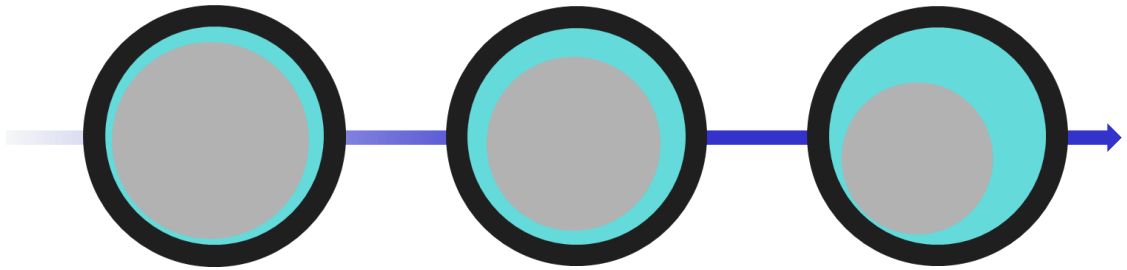

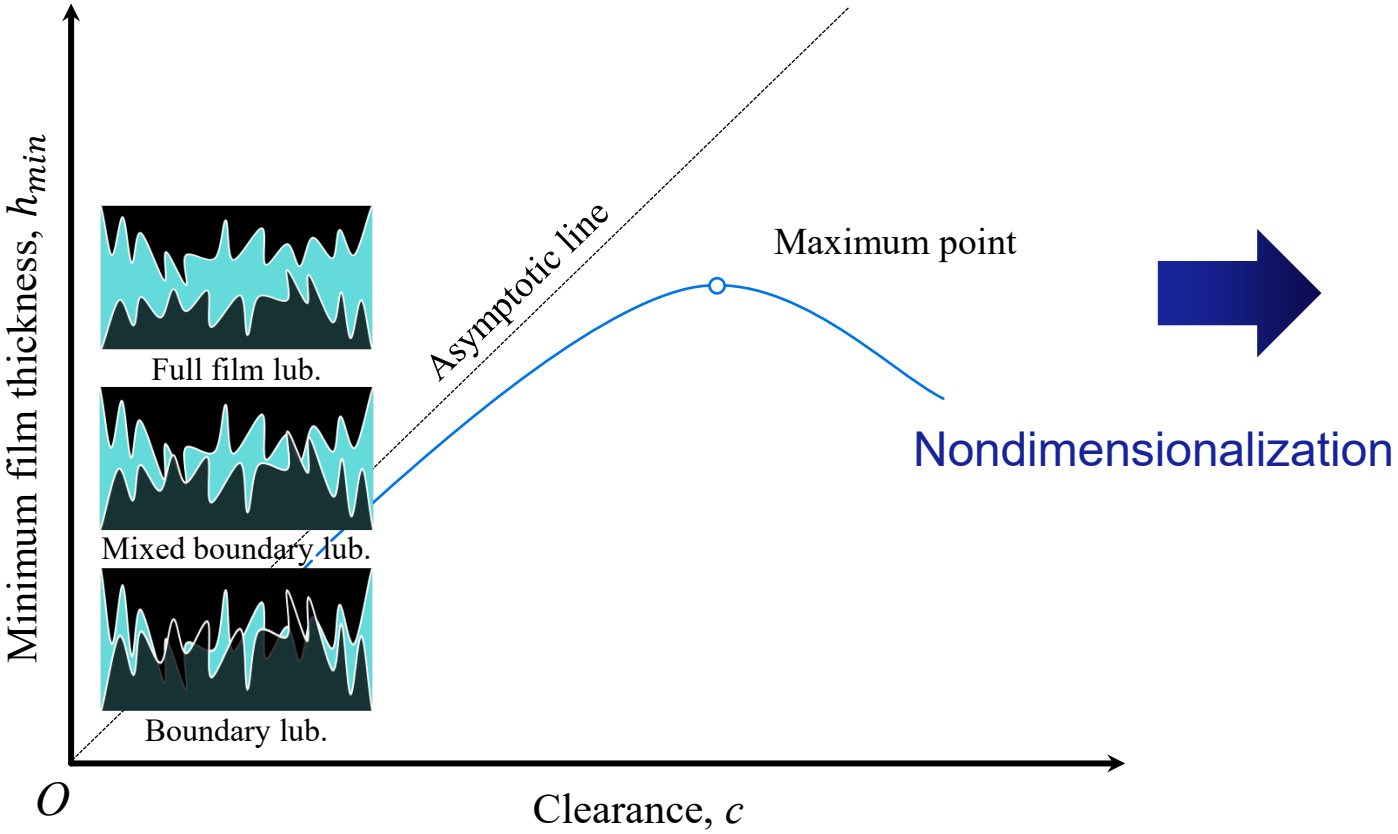

Nondimensionalization

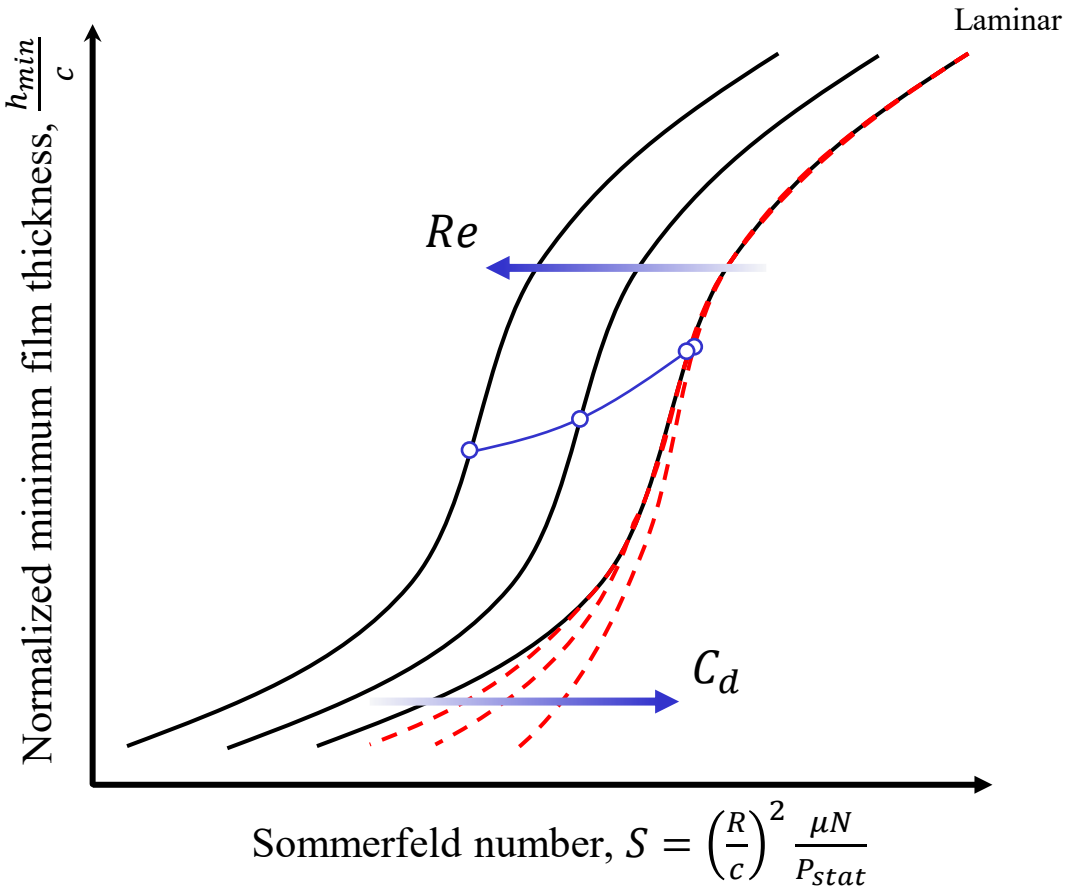

Previous work

Composite Bearing Deformation[13]

Restriction by housing
Long axial length

Hooke's law (Orthotropic material)

$$\begin{bmatrix} 0 \\ 0 \\ \varepsilon_3 \\ \varepsilon_4 \\ \varepsilon_5 \\ \varepsilon_6 \end{bmatrix} = \begin{bmatrix} S_{11} & S_{12} & S_{13} & 0 & 0 & 0 \\ S_{21} & S_{22} & S_{23} & 0 & 0 & 0 \\ S_{31} & S_{32} & S_{33} & 0 & 0 & 0 \\ 0 & 0 & 0 & S_{44} & 0 & 0 \\ 0 & 0 & 0 & 0 & S_{55} & 0 \\ 0 & 0 & 0 & 0 & 0 & S_{66} \end{bmatrix} \begin{bmatrix} \sigma_1 \\ \sigma_2 \\ -p \\ \sigma_4 \\ \sigma_5 \\ \sigma_6 \end{bmatrix}$$

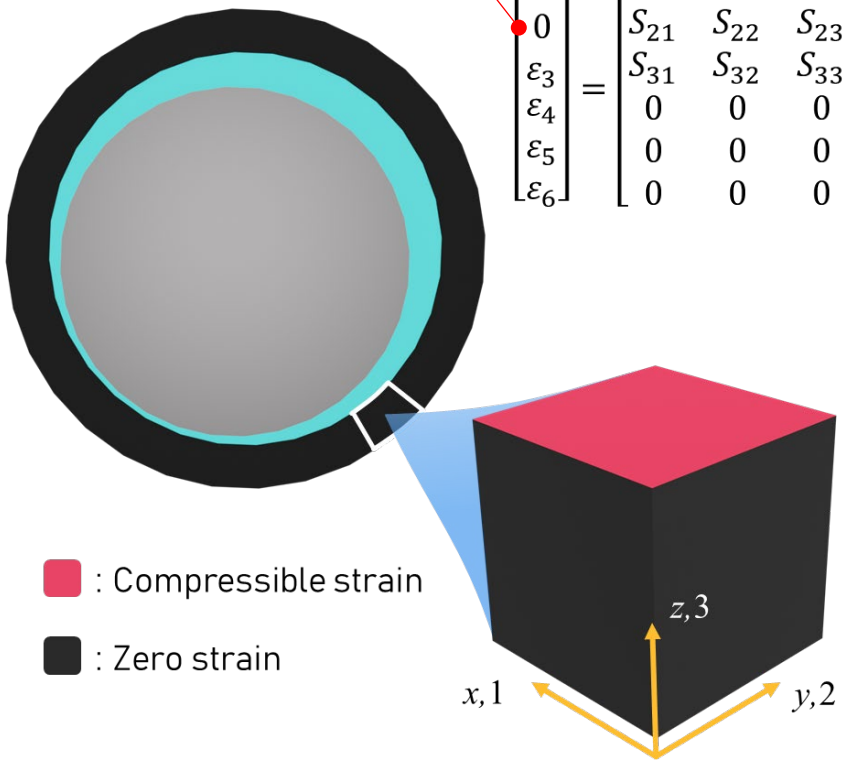

$$\delta = -pt_b \left(\frac{S_{31}(S_{13}S_{22} - S_{23}S_{12})}{S_{22}S_{11} - S_{12}S_{21}} + \frac{S_{32}(S_{13}S_{21} - S_{23}S_{11})}{S_{12}S_{21} - S_{22}S_{11}} - S_{33} \right)$$

Optimum boundaries for maximum load-carrying capacity [13]

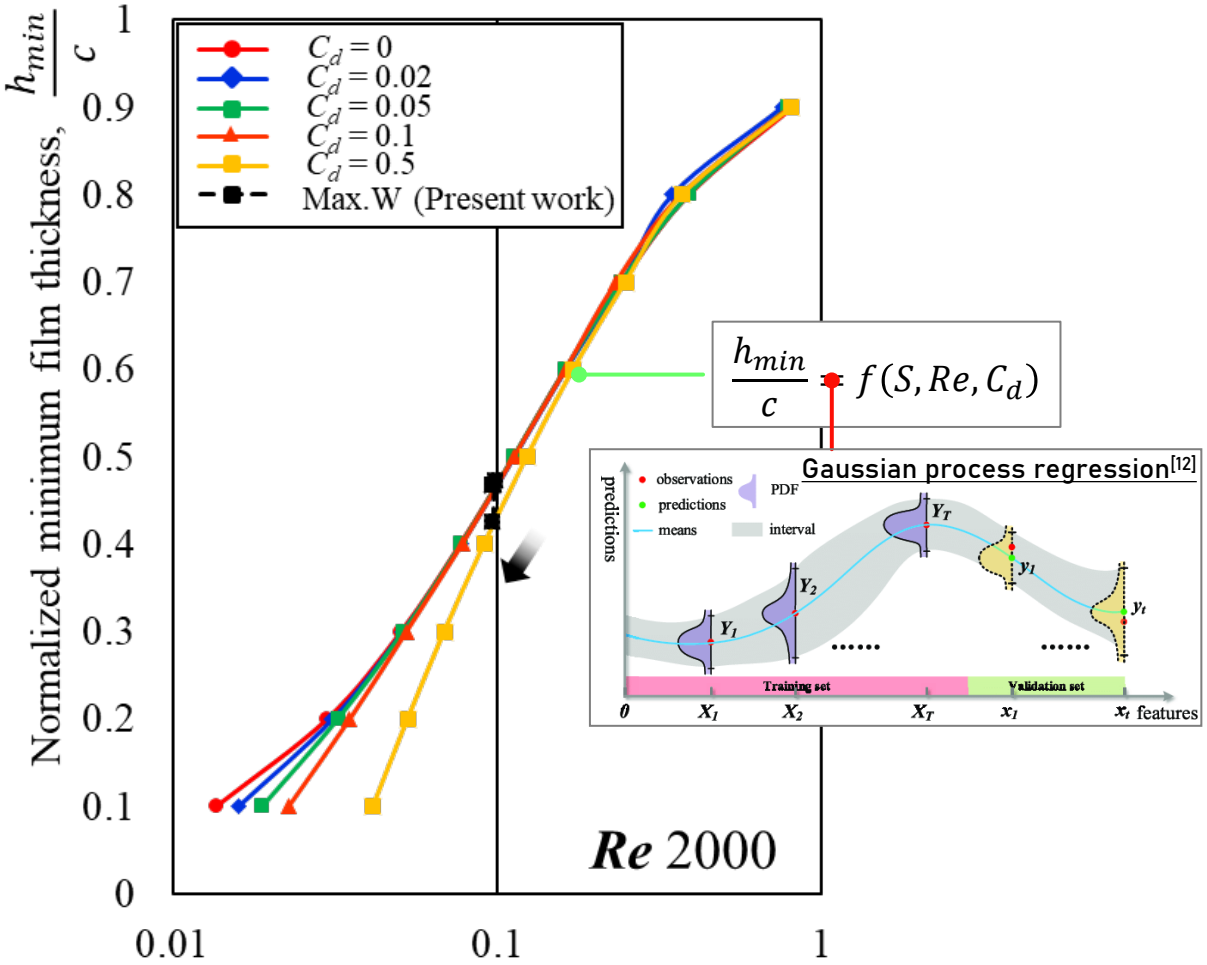

OBJECTIVE

- Provide the optimum boundary for maximum load-carrying capacity in misaligned water-lubricated composite journal bearings
- Analyze the behavior of optimum boundaries incorporating turbulence, bearing deformation, and misalignment

WORK FLOW



Numerical analysis

- Governing equation for steady-state analysis
- Analytical method for bearing deformation
- Boundary conditions
- Algorithm for EHL
- Optimum boundary for maximum load-carrying capacity



Result & Discussion

- Validation
- FEM-based bearing performance
- Effectiveness of analytical approach
- Recommended operating region
- Behavior of optimum boundaries



Conclusion

- Conclusion

02. NUMERICAL ANALYSIS

Governing equation

Misaligned water-lubricated composite journal bearing

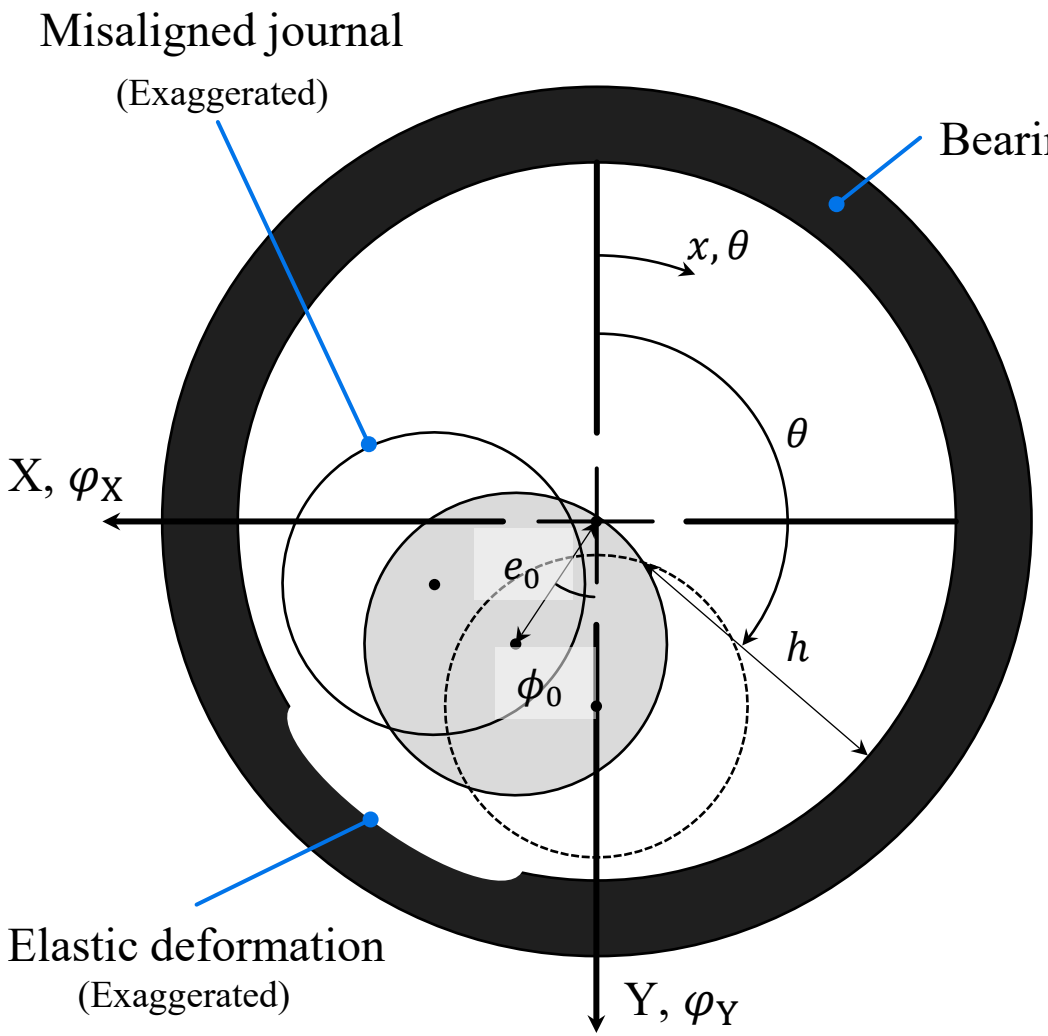

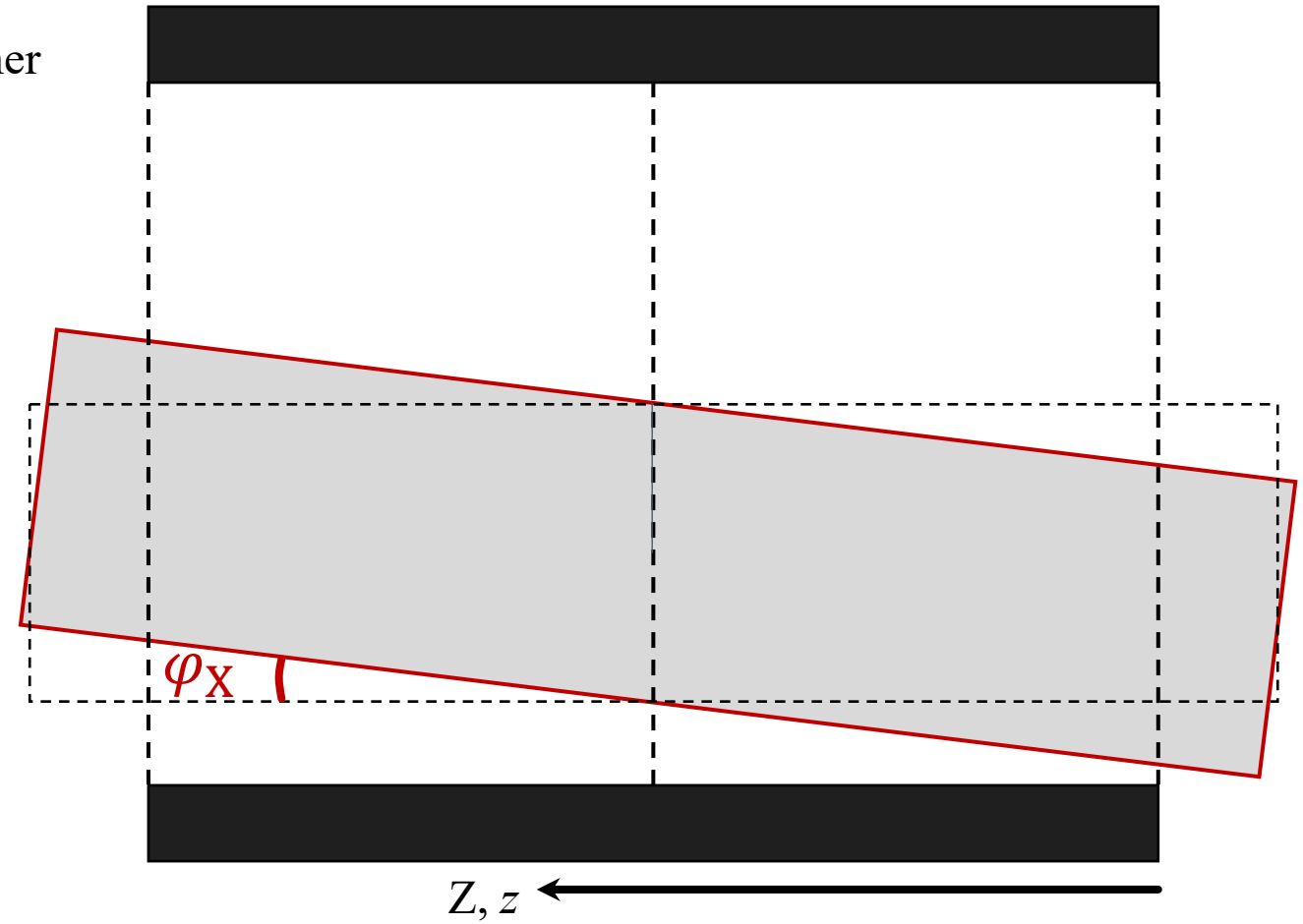

Governing equation

Fluid domain

Assumption:

- Isothermal condition
- Incompressible
- $c << R$

Reynolds equation

$$\frac{\partial}{\partial x}\left(\frac{h^3}{k_x \mu}\frac{\partial p}{\partial x}\right)+\frac{\partial}{\partial z}\left(\frac{h^3}{k_z \mu}\frac{\partial p}{\partial z}\right)=\frac{U}{2}\frac{\partial h}{\partial x}+\frac{\partial h}{\partial t}$$

where

Laminar $\begin{cases} k_x = 12 \\ k_z = 12 \end{cases}$ Turbulent $\begin{cases} k_x = 12 + 0.0136\boldsymbol{Re}^{0.9} \\ k_z = 12 + 0.0043\boldsymbol{Re}^{0.96} \end{cases}$

p: pressure
c: clearance
μ: viscosity

h: film thickness eqn.
U: Linear velocity

Table. Operating condition

Parameter	Symbol	Unit	Value
Bearing length	L	m	0.050
Journal radius	R	m	0.025
Radial clearance	c	μm	50
Angular velocity	N	rad/s	100π

Film thickness eqn. w/ misalignment

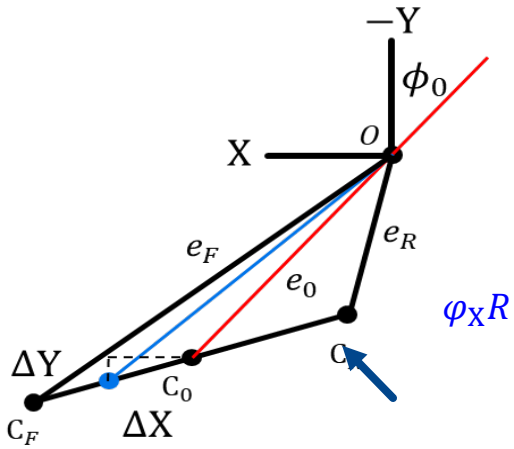

Projection of axis of journal

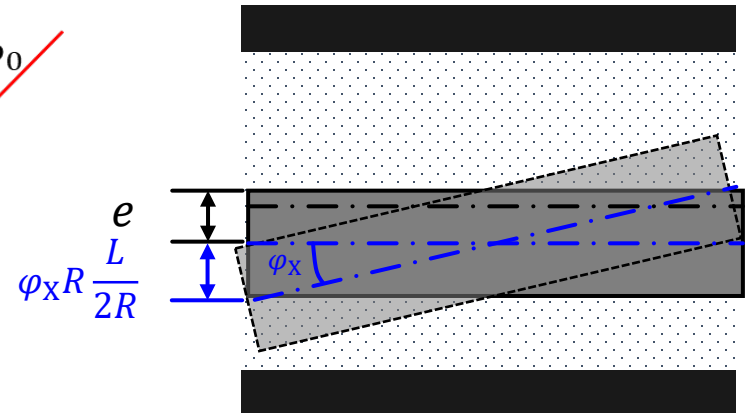

Tilting of the journal

Bearing deformation

$$\tilde{h}(\theta,z) = 1+\varepsilon_0 \cos(\theta-\phi_0)+\left(\frac{L}{R}\right)\left(\frac{R}{c}\right)\left(\left(\bar{z}-\frac{1}{2}\right)\cdot\varphi_Y\cdot\sin\theta-\left(\bar{z}-\frac{1}{2}\right)\cdot\varphi_X\cdot\cos\theta\right)+\delta$$

Misalignment effect

Load dir. only

Misalignment ratio, $\lambda_m = \frac{\varphi_X R}{c}$

Analytical method for bearing deformation

Elastic deformation of the bearing liner

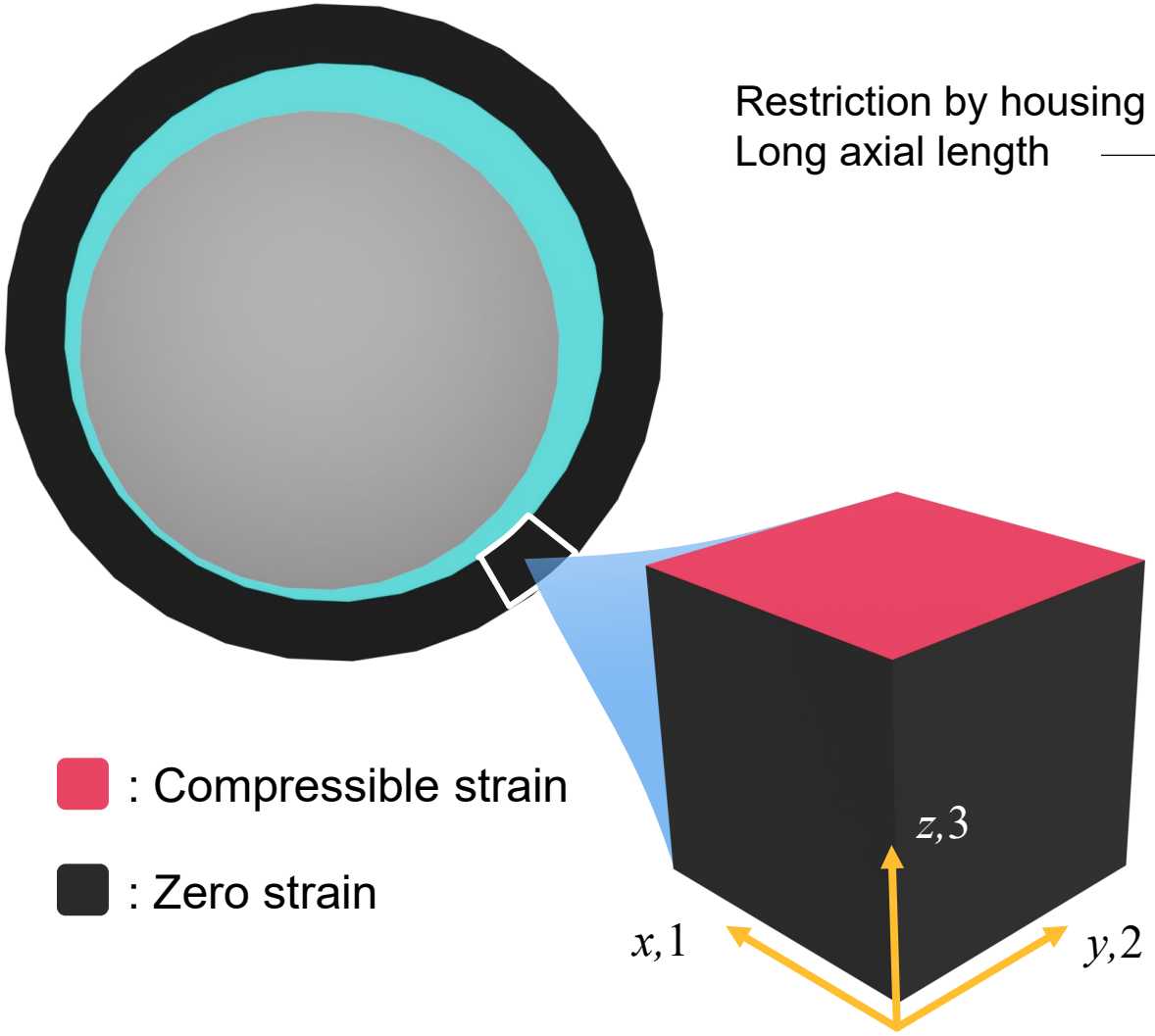

- Hooke's law (Orthotropic material)

Restriction by housing
Long axial length

$$\begin{bmatrix} 0 \\ 0 \\ \varepsilon_3 \\ \varepsilon_4 \\ \varepsilon_5 \\ \varepsilon_6 \end{bmatrix} = \begin{bmatrix} S_{11} & S_{12} & S_{13} & 0 & 0 & 0 \\ S_{21} & S_{22} & S_{23} & 0 & 0 & 0 \\ S_{31} & S_{32} & S_{33} & 0 & 0 & 0 \\ 0 & 0 & 0 & S_{44} & 0 & 0 \\ 0 & 0 & 0 & 0 & S_{55} & 0 \\ 0 & 0 & 0 & 0 & 0 & S_{66} \end{bmatrix} \begin{bmatrix} \sigma_1 \\ \sigma_2 \\ -p \\ \sigma_4 \\ \sigma_5 \\ \sigma_6 \end{bmatrix}$$

- Analytical relation of elastic deformation and pressure

$$\delta = -pt_b \left(\frac{S_{31}(S_{13}S_{22} - S_{23}S_{12})}{S_{22}S_{11} - S_{12}S_{21}} + \frac{S_{32}(S_{13}S_{21} - S_{23}S_{11})}{S_{12}S_{21} - S_{22}S_{11}} - S_{33} \right)$$

$$= -pt_b\lambda$$ ← Deformation parameter

- Deformation coefficient

$$C_d = \frac{t}{c}\left(\frac{R}{c}\right)^2 \mu N \left(\frac{S_{yx}(S_{xy}S_{zz} - S_{zy}S_{xz})}{S_{xz}S_{zx} - S_{zz}S_{xx}} + \frac{S_{yz}(S_{xy}S_{zx} - S_{zy}S_{xx})}{S_{xz}S_{zx} - S_{zz}S_{xx}} - S_{yy} \right)$$

$$= \frac{t}{c}\left(\frac{R}{c}\right)^2 \mu N\lambda$$

Governing equation

Structural domain

Constitutive equation of the bearing liner

$$\rho \ddot{u}_i = \frac{\partial \sigma_{ji}}{\partial x_j} + f_i \; in \; D$$

Weak formulation

$$\int \sigma_{ji} \frac{\partial \bar{u}_i}{\partial x_j} d\boldsymbol{\Omega} + \int \left(\hat{k}_{ij}(u_j - g_j) - t_i\right)\bar{u}_i d\boldsymbol{\Gamma} = \int f_i * \bar{u}_i \, d\boldsymbol{\Omega} \; in \; D$$

where

$u_i = u_x\hat{\imath} + u_y\hat{\jmath} + u_z\hat{k}$ — Displacement

$f_i = f_x\hat{\imath} + f_y\hat{\jmath} + f_z\hat{k}$ — Body force

$\sigma_{ij} = C_{ijkl}\varepsilon_{kl}$ — Stress-strain

Discretization

Volume element

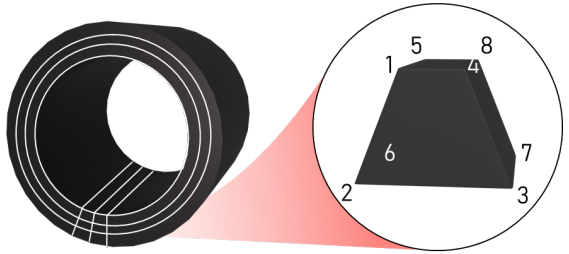

Surface element

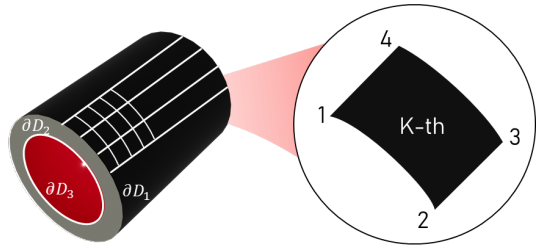

Global matrix eqns.

$$K_{pq}u_q = L_p$$

K_{pq}: *Global stiffness matrix*

L_p: *Global load vector*

u_q: *Displacement vector*

Table. Bearing materials

	t_b	E	E_{11}	E_{22}	E_{33}	ν	ν_{12}	ν_{13}	ν_{23}	G	G_{12}	G_{13}	G_{23}
Unit	(mm)			(GPa)								(GPa)	
Steel	1	200				0.3							
Glass fiber reinforced polymer (GFRP), PEEK	1		6.2	6.2	2.1		0.408	0.41	0.41		2.11	0.98	0.98
Low-density polyethylene (LDPE)	1	0.09				0.35				0.033			

Boundary conditions

Fluid domain

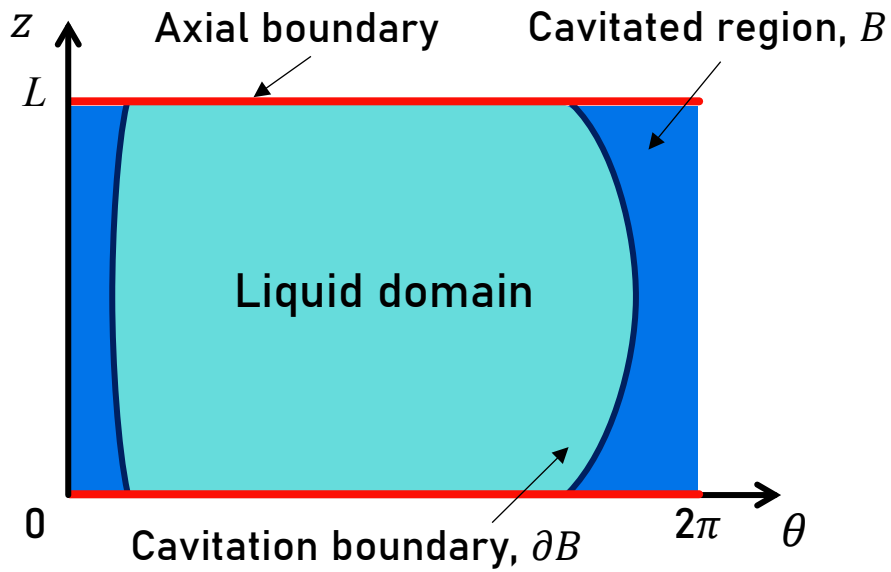

Reynolds boundary condition (Cavitation):

$$p = 0 \; on \; B \qquad p = \frac{\partial p}{\partial x} = 0 \; on \; \partial B$$

Axial B.C.

$$p_{z=0} = p_{z=L} = 0$$

Bearing liner

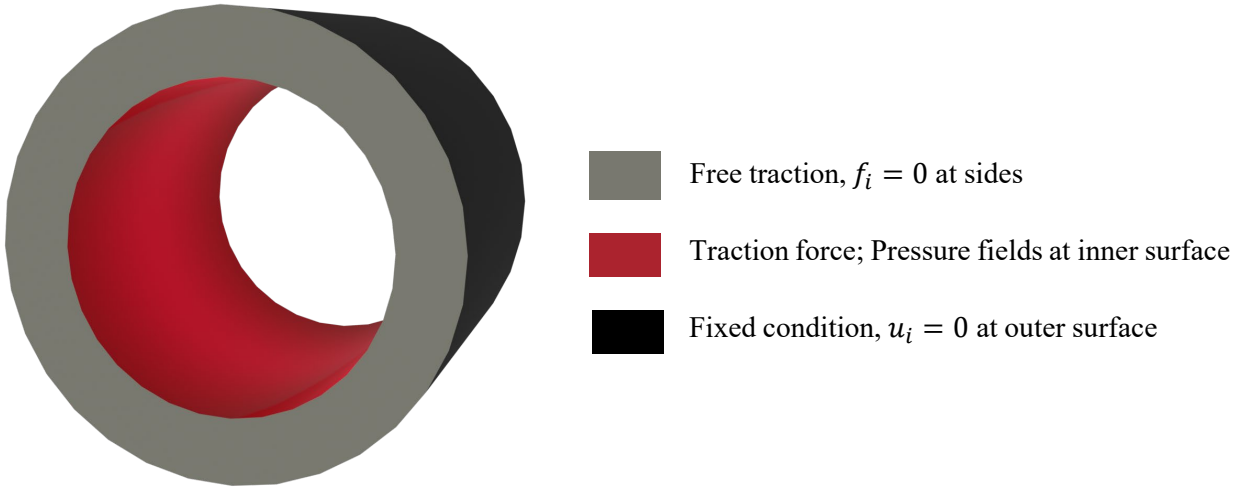

At Outer surface, $u_i = 0$

At Inner surface, $f_i = \sigma_{ji} n_j$ (Hydrodynamic pressure)

At Axial-end surface, $f_i = 0$

Algorithm for EHL

Algorithm

Options

I. Constitutive equation (FEM)
II. Analytical relation

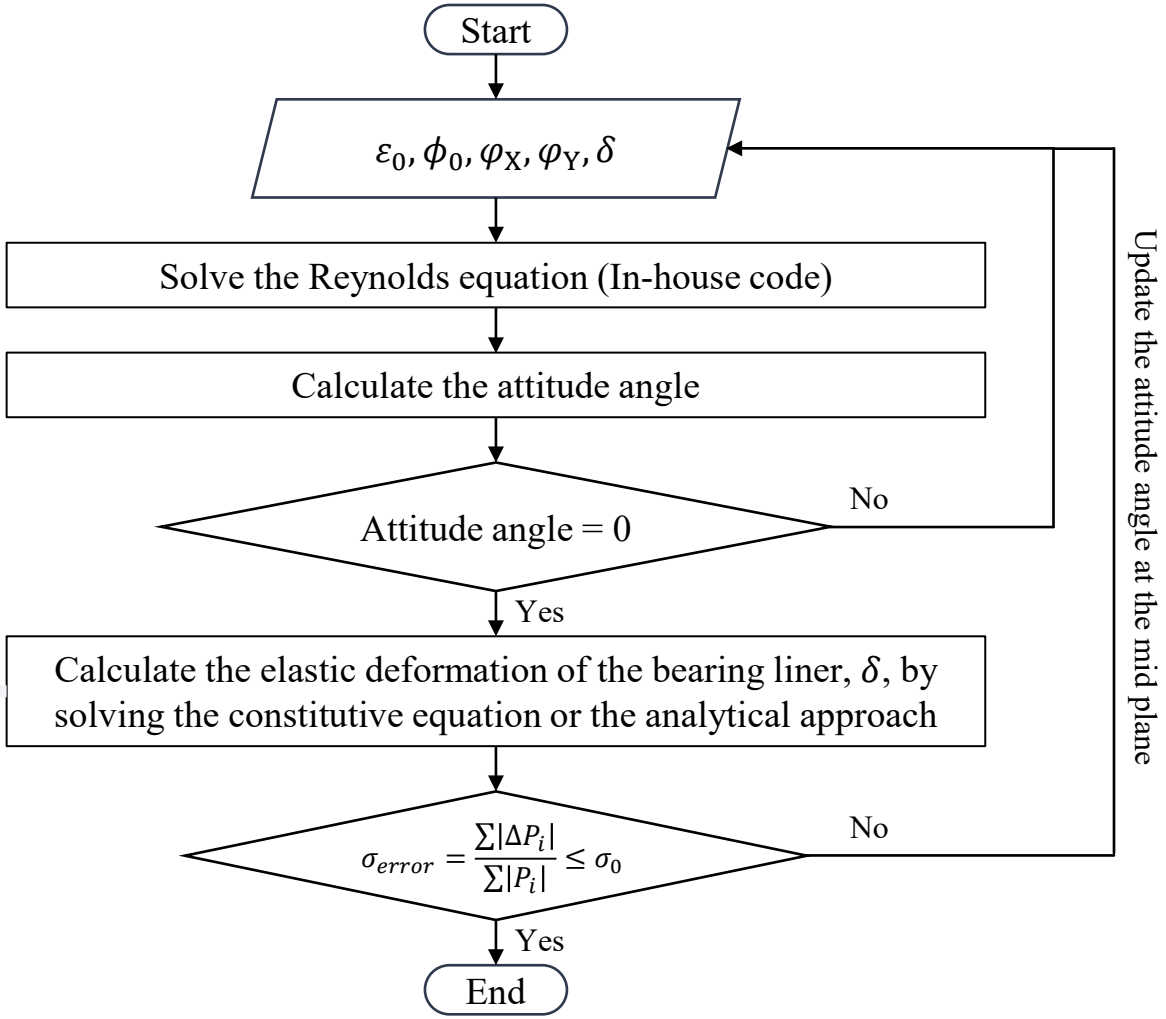

Optimum boundary

Bisection method-based algorithm

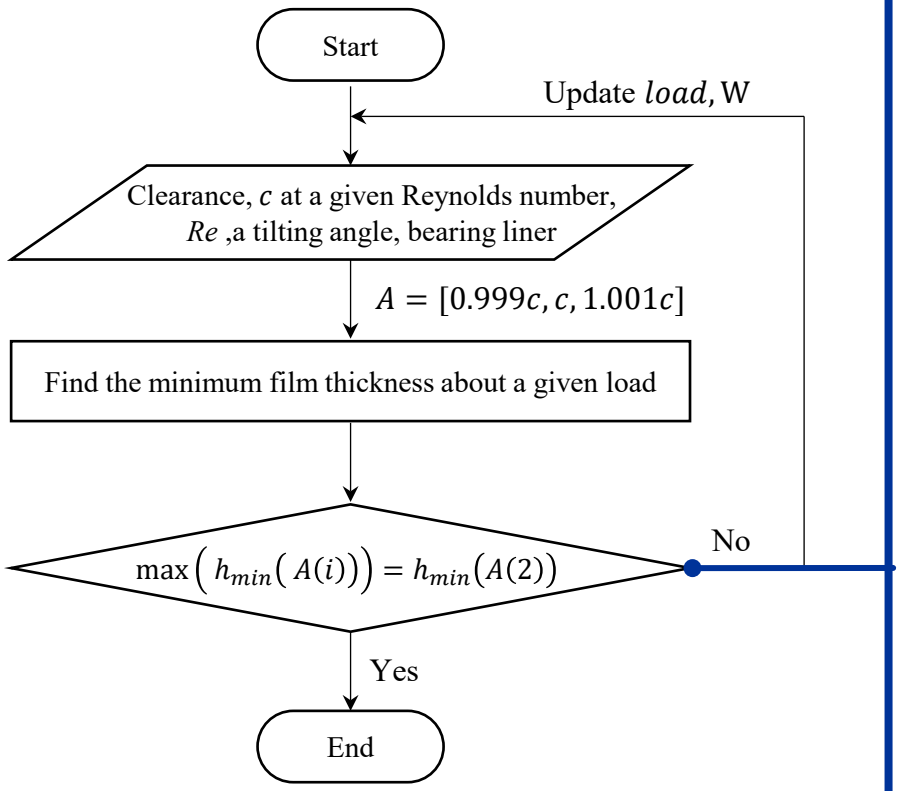

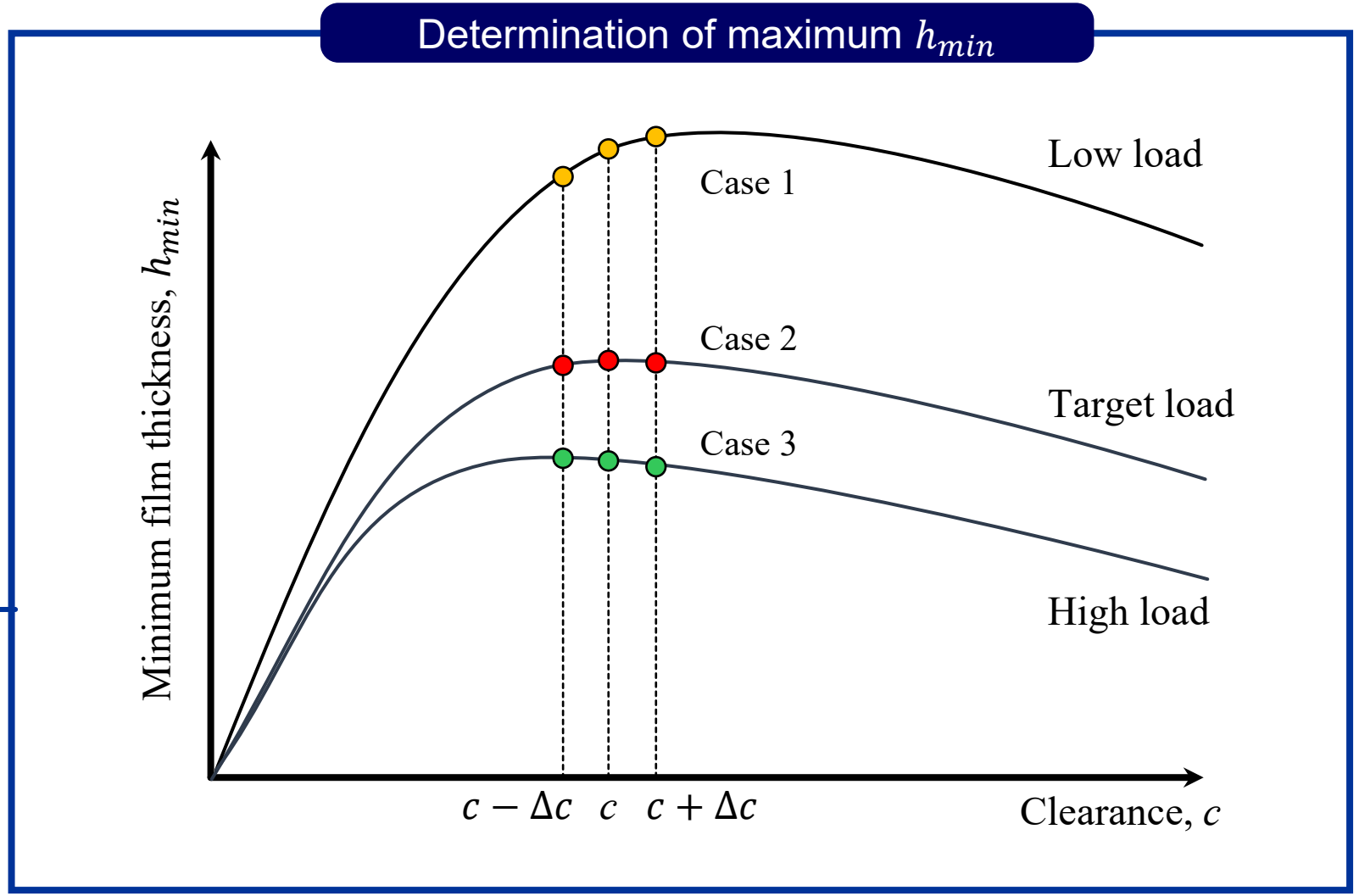

03. RESULT & DISCUSSION

Verification of the present work

Validation (Static performance)

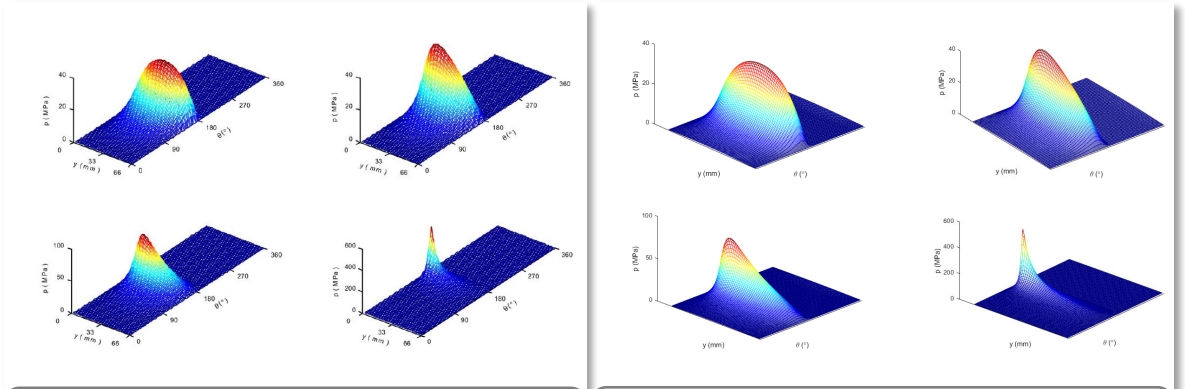

Sun et *al.* [14] | Present work

$\varphi_0 = \alpha = 0°$

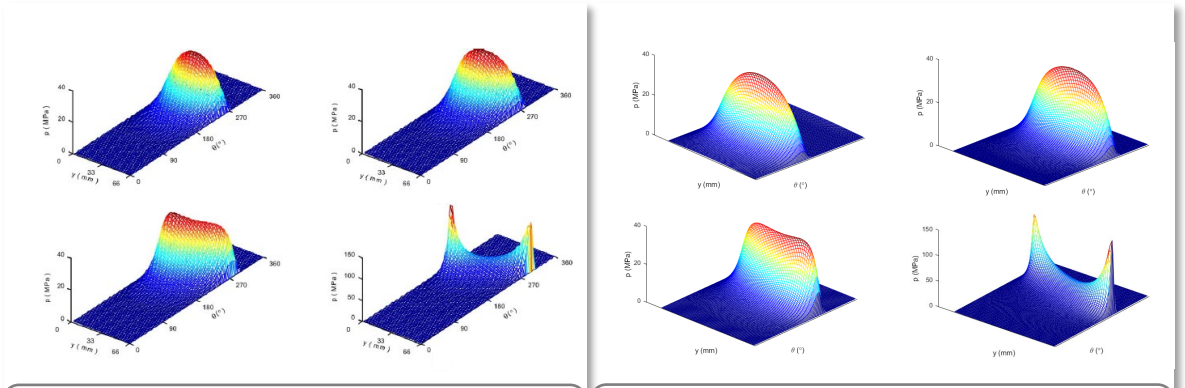

Sun et *al.* [14] | Present work

$\varphi_0 = \alpha = 90°$

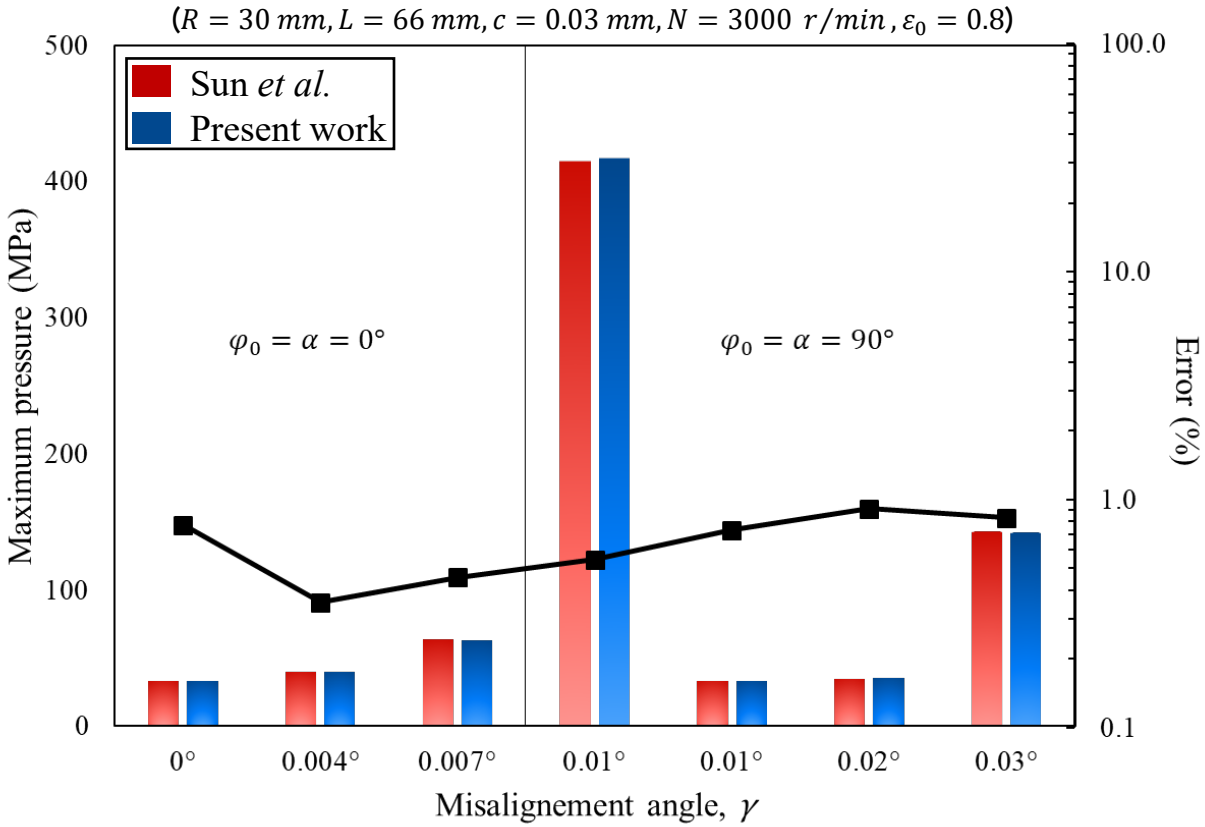

Cf. Film thickness eqn.

$$h(\theta, z) = c + e_0 \cos(\theta - \varphi_0) + \tan\gamma \cdot \left(z - \frac{L}{2}\right) \cos(\theta - \alpha - \varphi_0)$$

Bearing deformation & Misalignment

Pressure fields & Film thickness distribution ($\varepsilon_0 = 0.9, \lambda_m = 0.1$)

	Pressure	Film thickness distr.	Pressure	Film thickness distr.
Steel	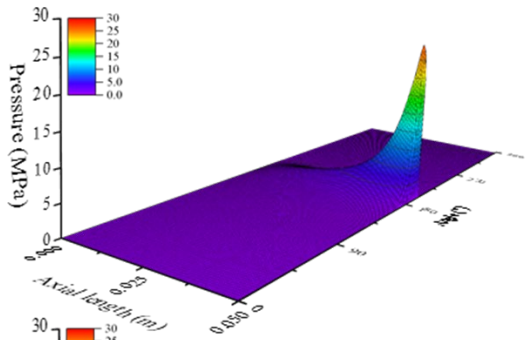	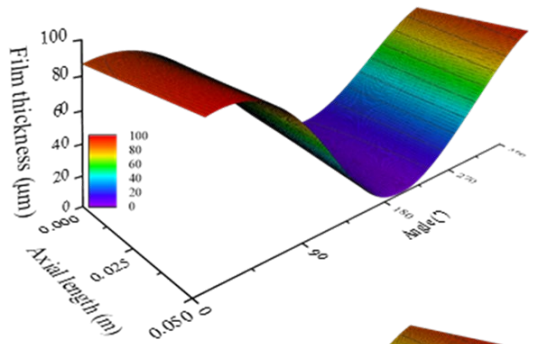	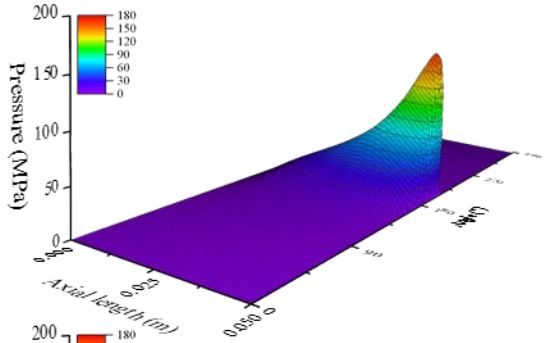	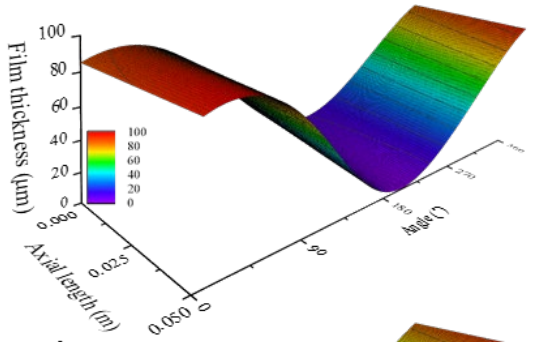
GFRP	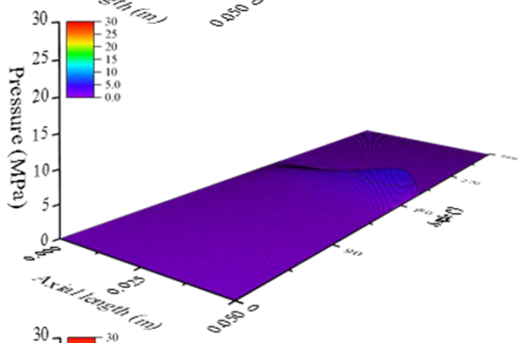	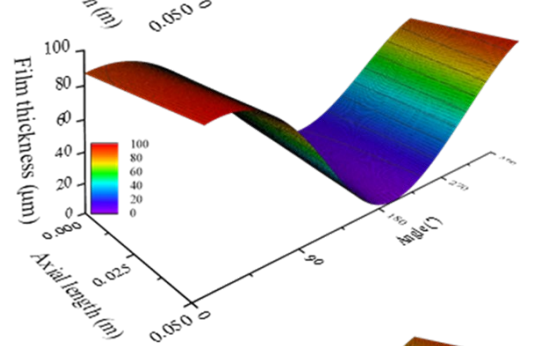	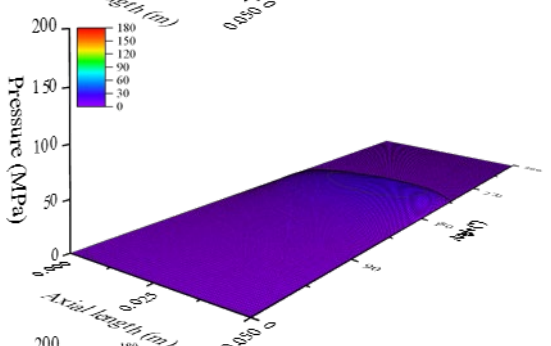	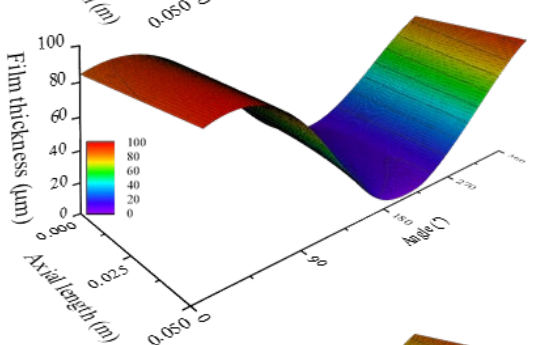
LDPE	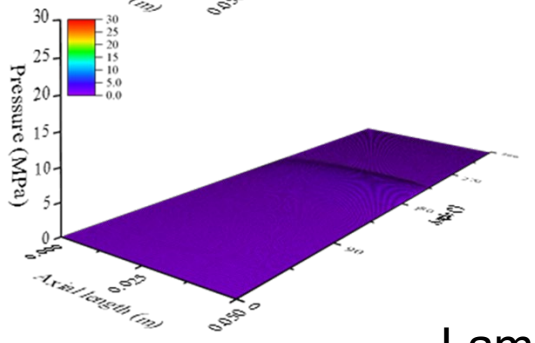	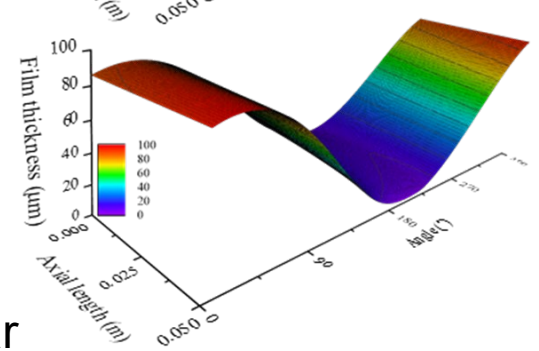	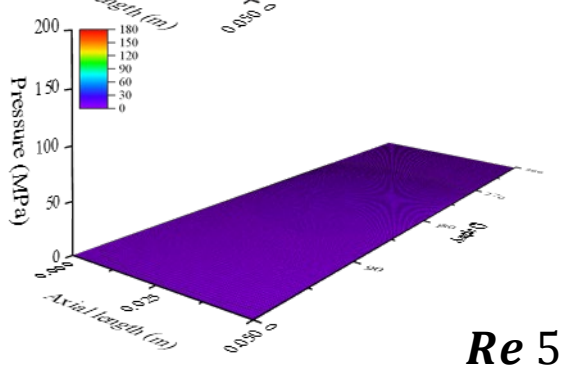	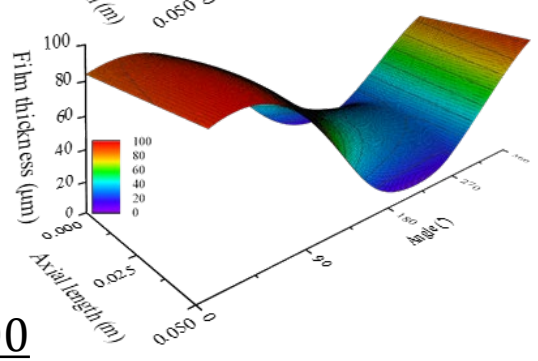

Laminar

Re 5000

Bearing deformation & Misalignment

Bearing performances

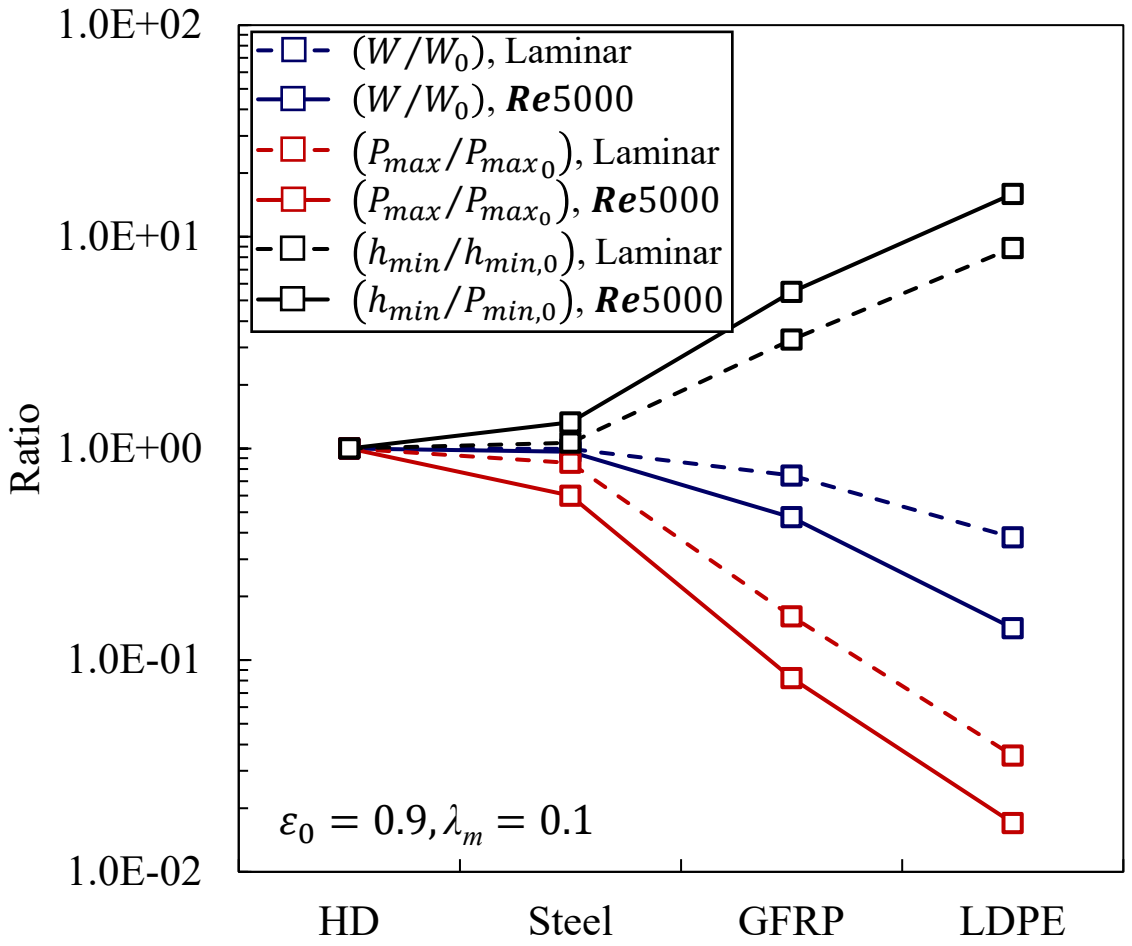

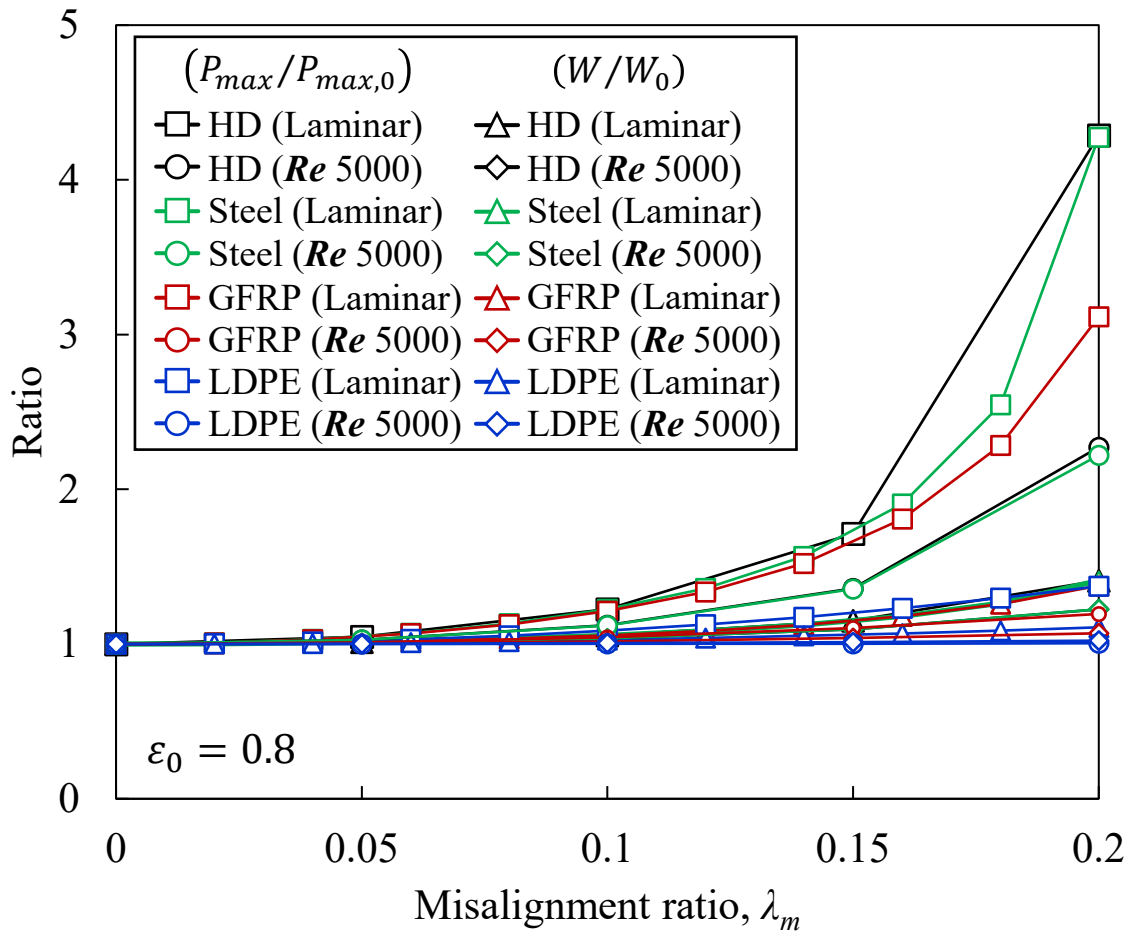

- Suppression of the wedge effect caused by bearing deformation

Validation of analytical method

FEM vs. Analytical method ($\varepsilon_0 = 0.9, \lambda_m = 0.1$)

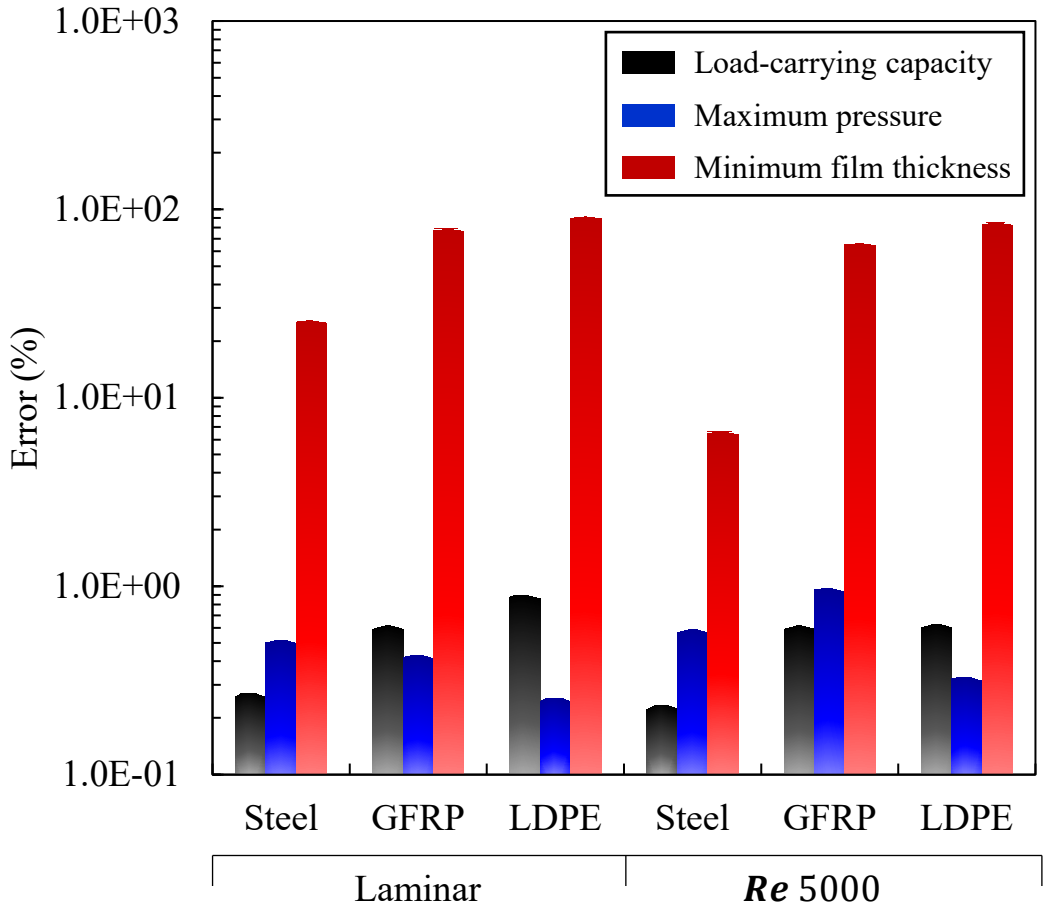

At maximum pressure;

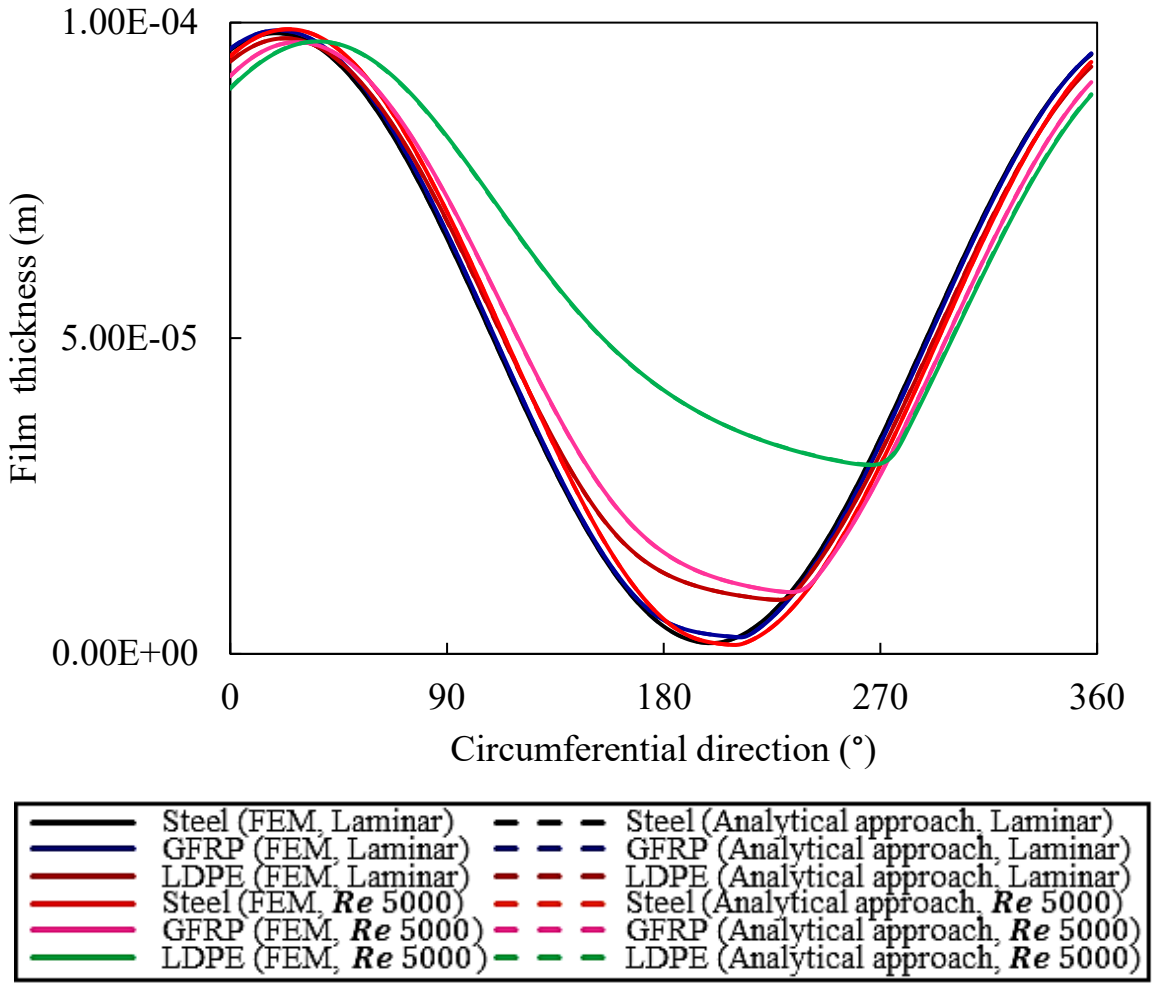

Validation of analytical method

FEM vs. Analytical method ($\varepsilon_0 = 0.9, \lambda_m = 0.1$)

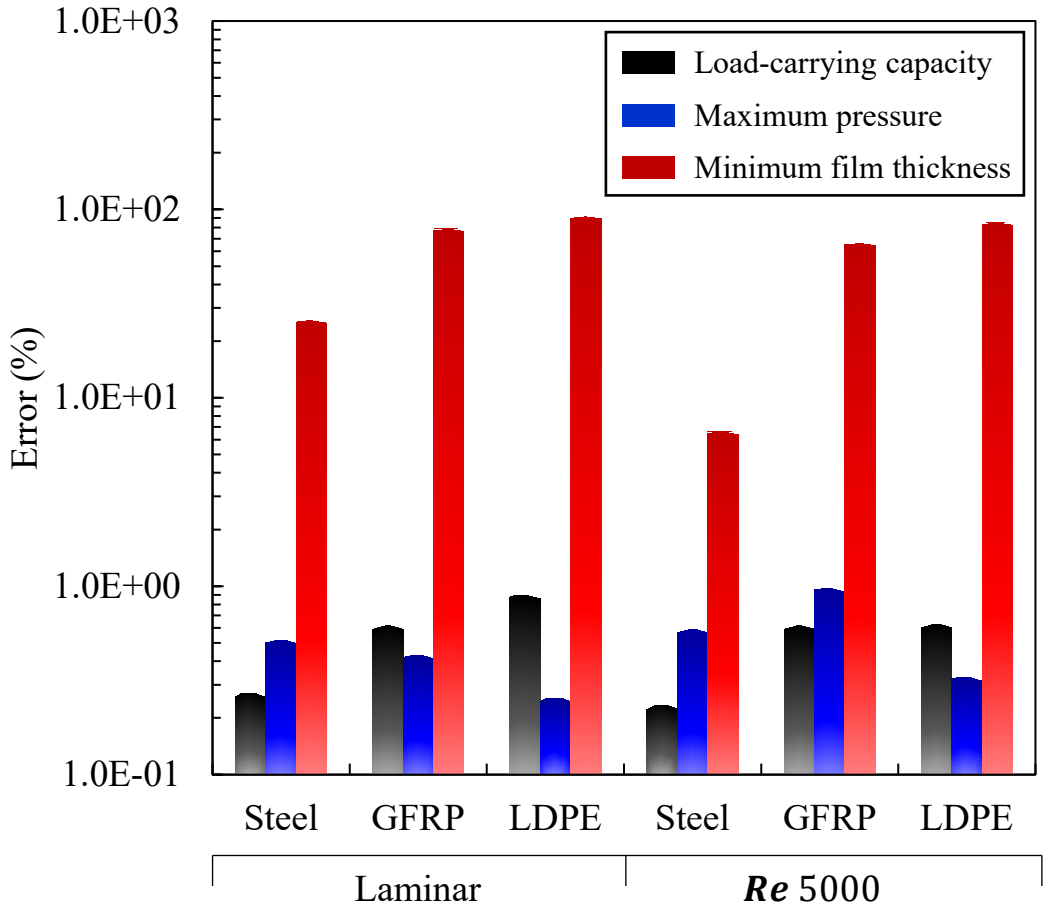

At maximum pressure;

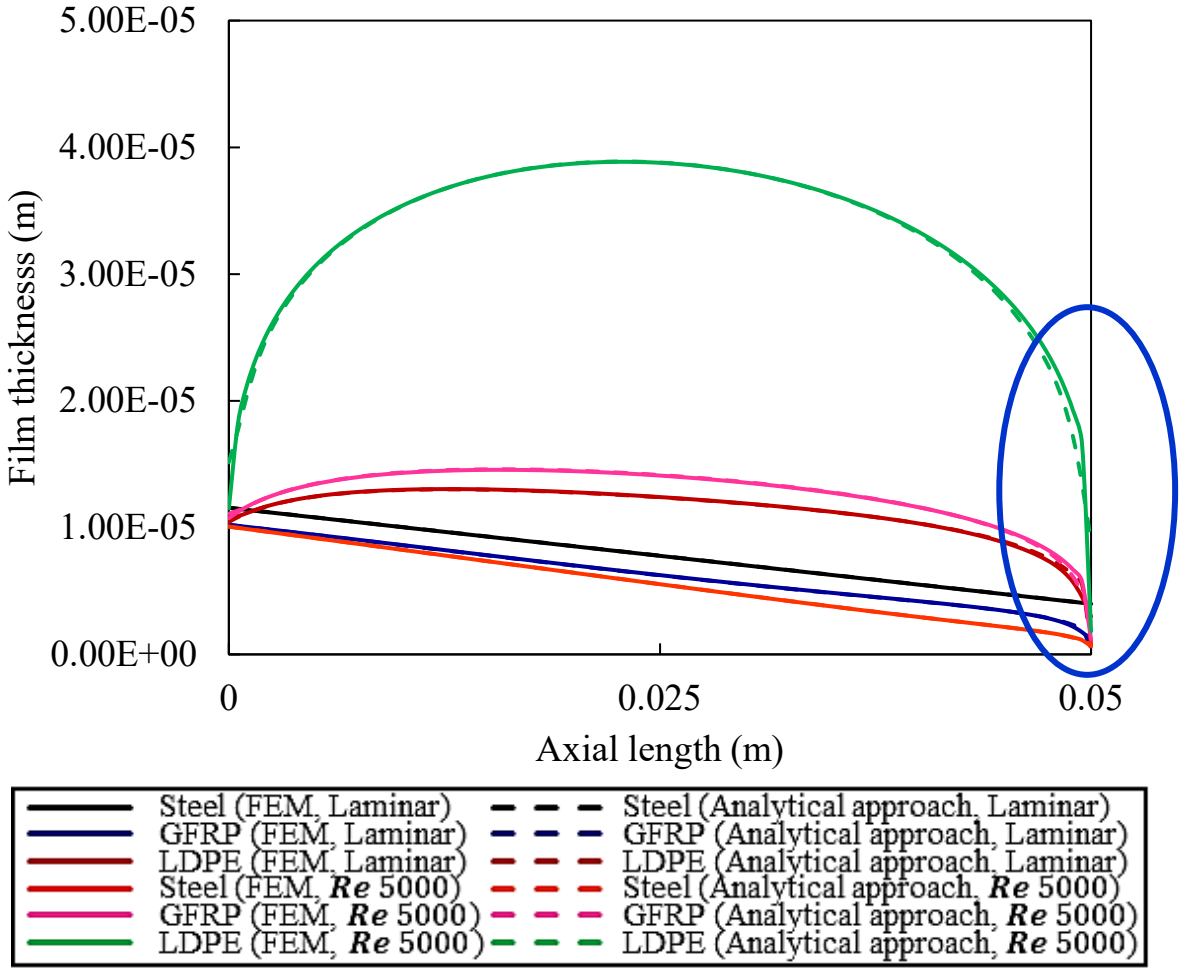

Validation of analytical method

FEM vs. Analytical method ($\varepsilon_0 = 0.9, \lambda_m = 0.1$)

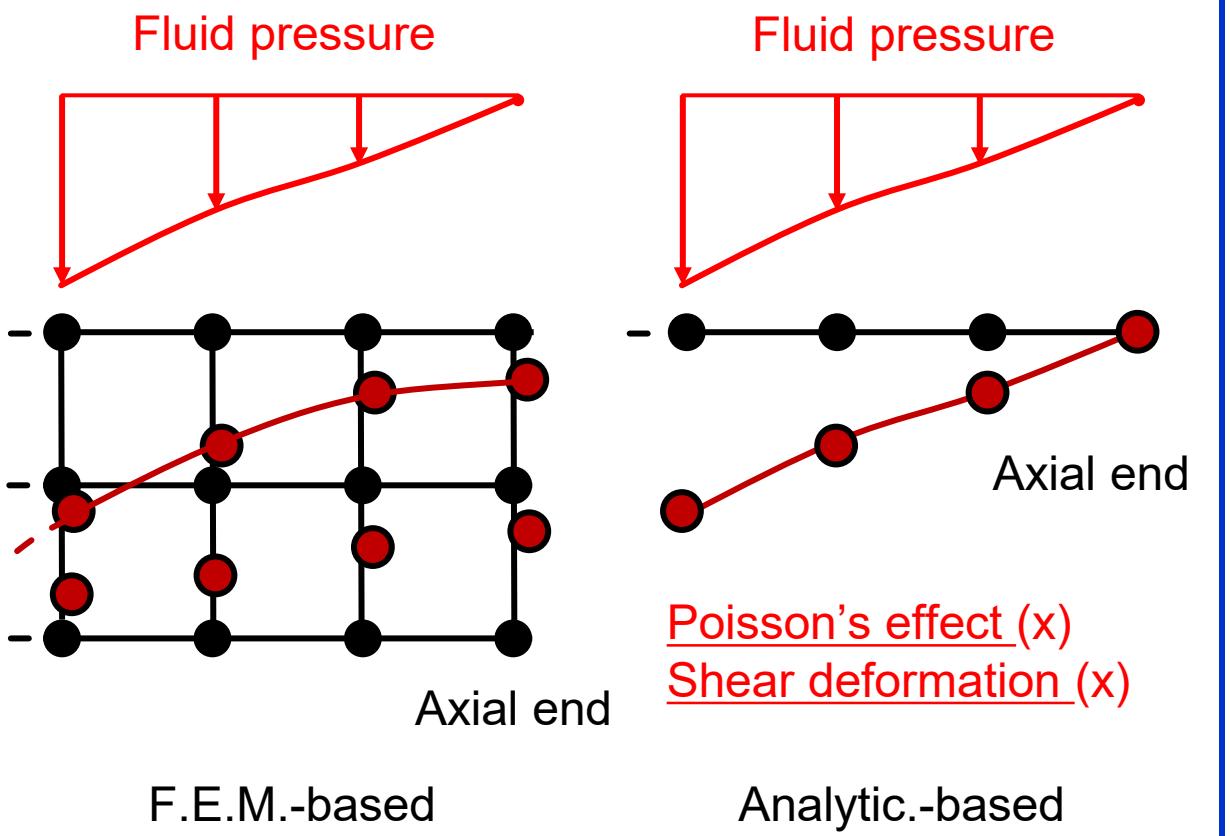

At maximum pressure;

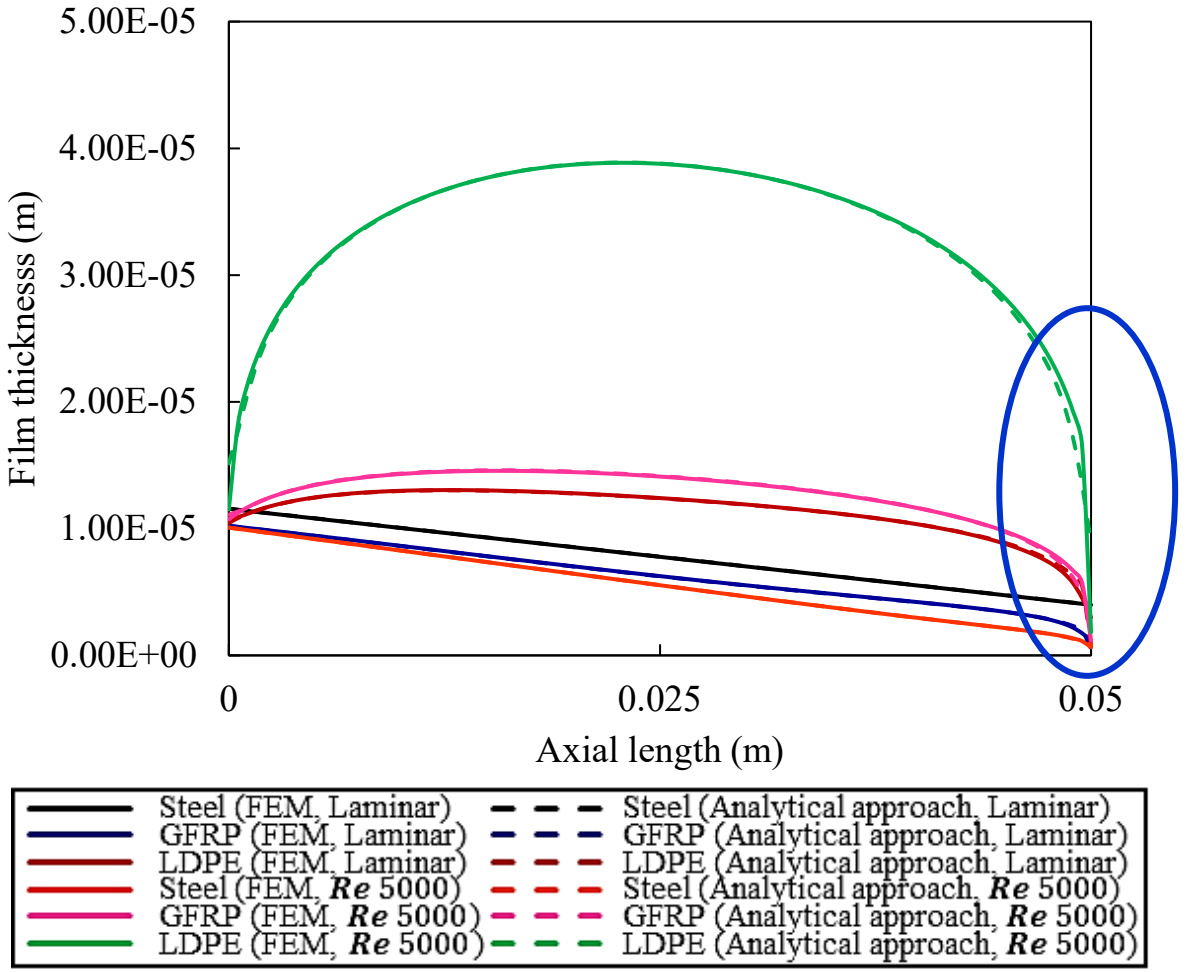

Optimum boundary

Turbulence & Misalignment

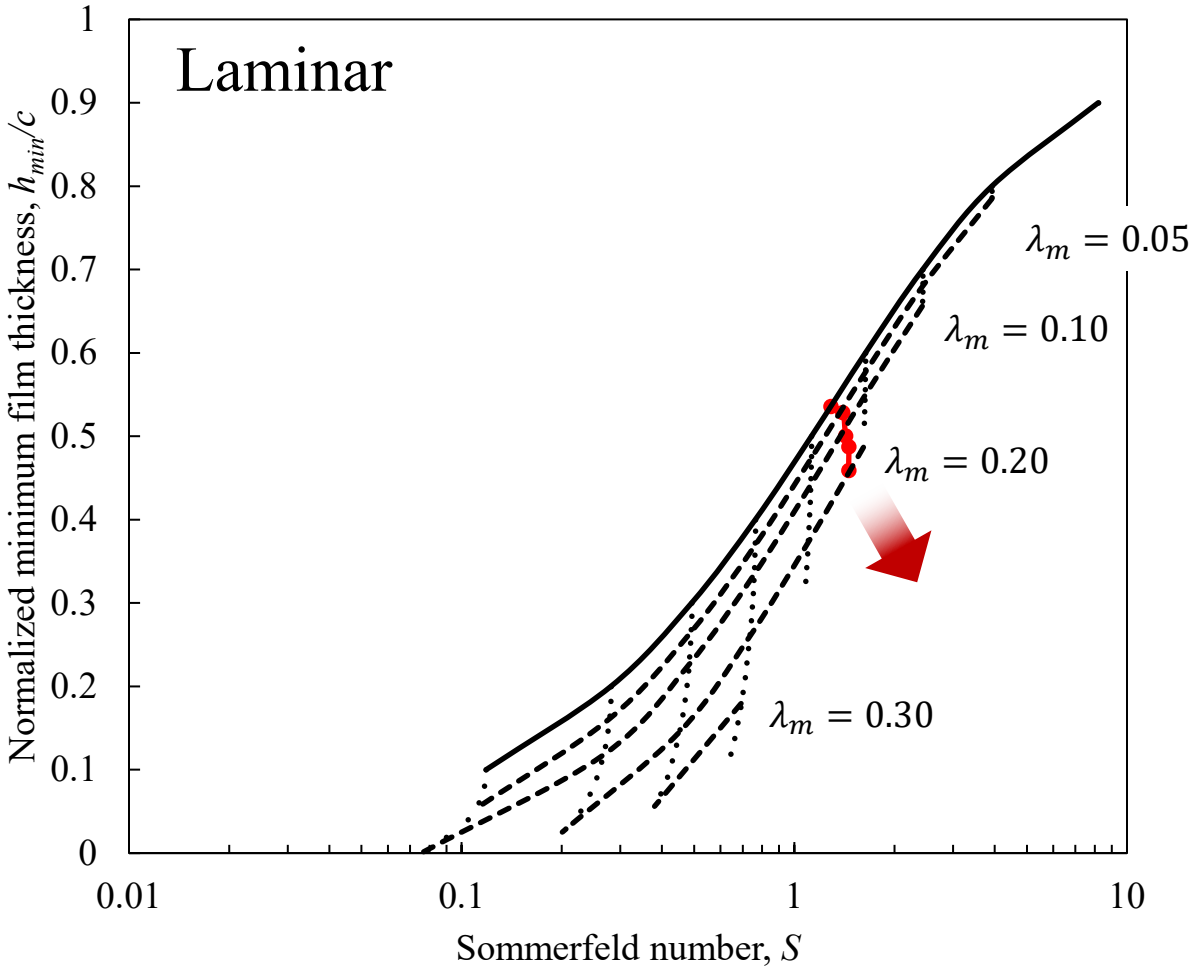

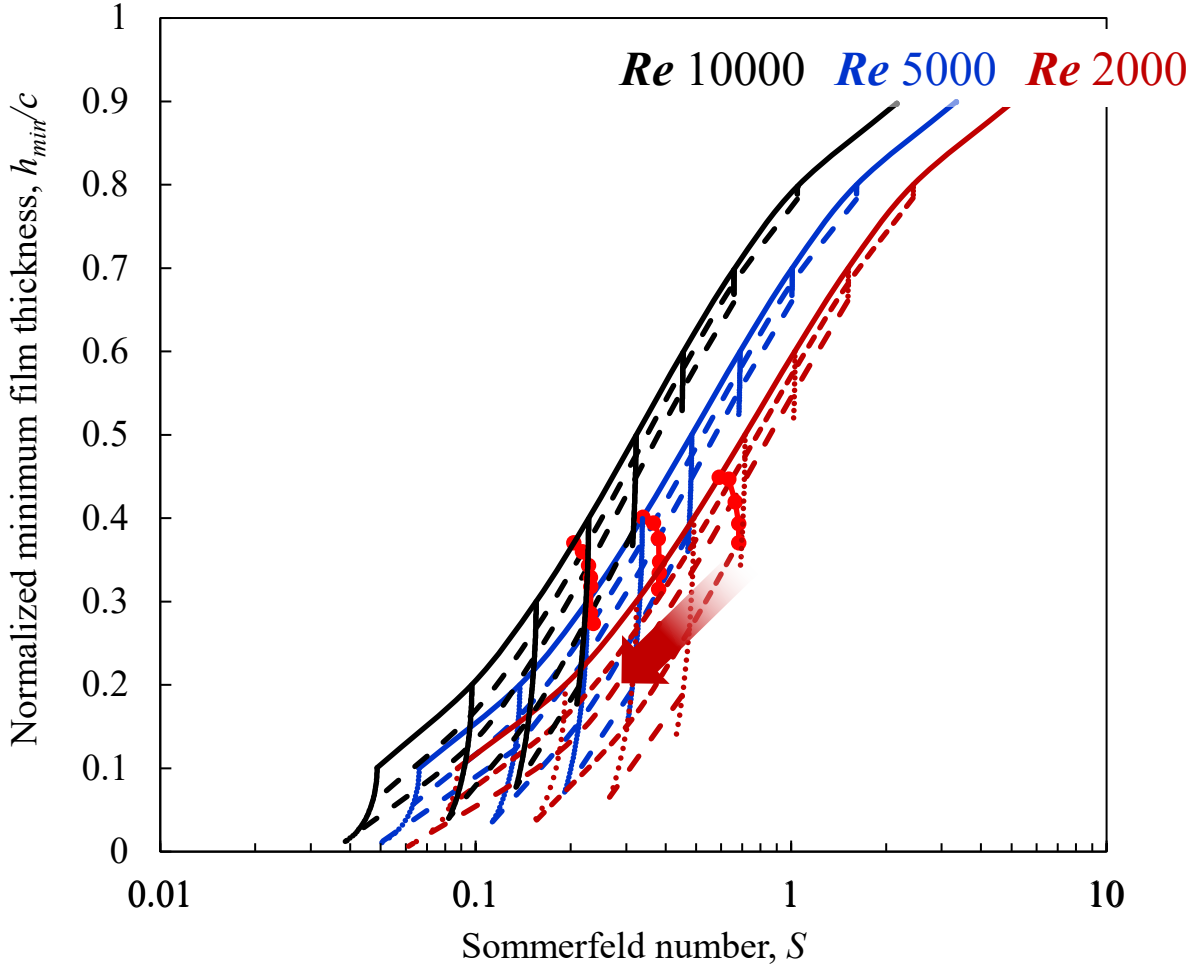

Optimum boundary for maximum load-carrying capacity Data points (FEM results) No misalignment

Behavior of optimum boundary

Turbulence effect

Cf. Given: Load, Velocity, Viscosity (μ)

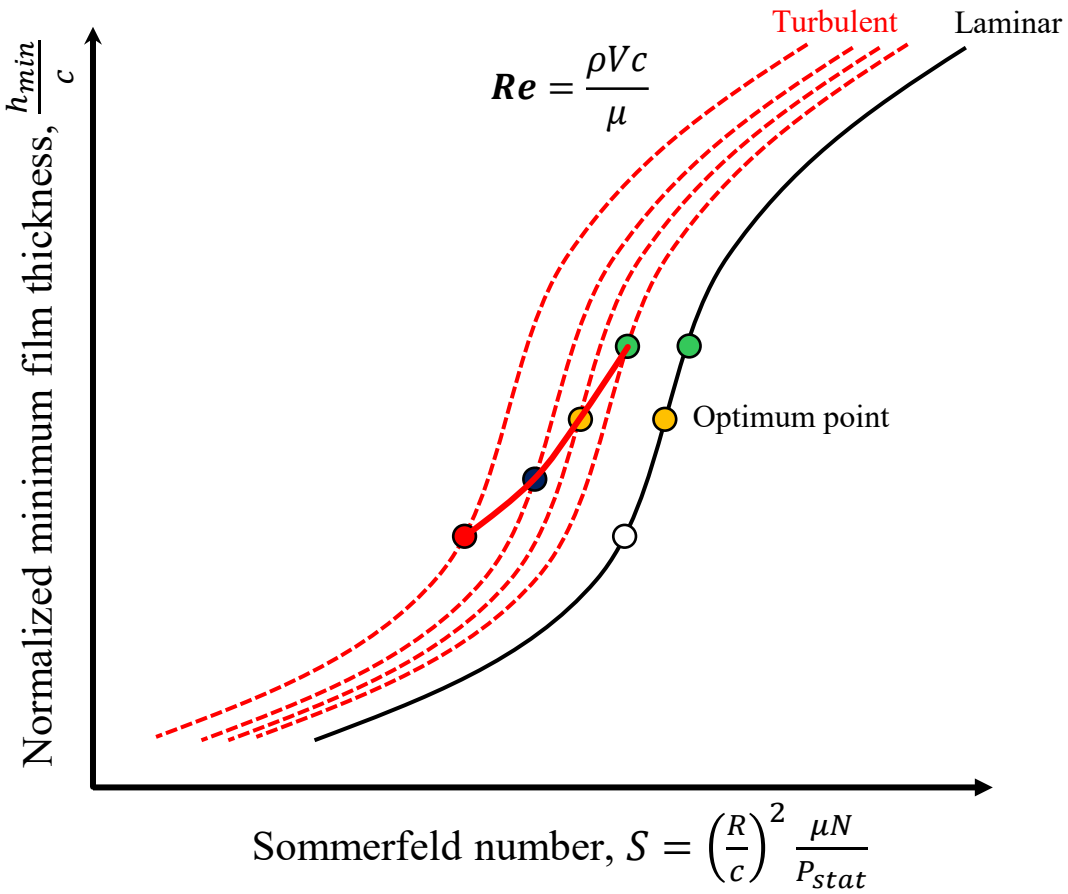

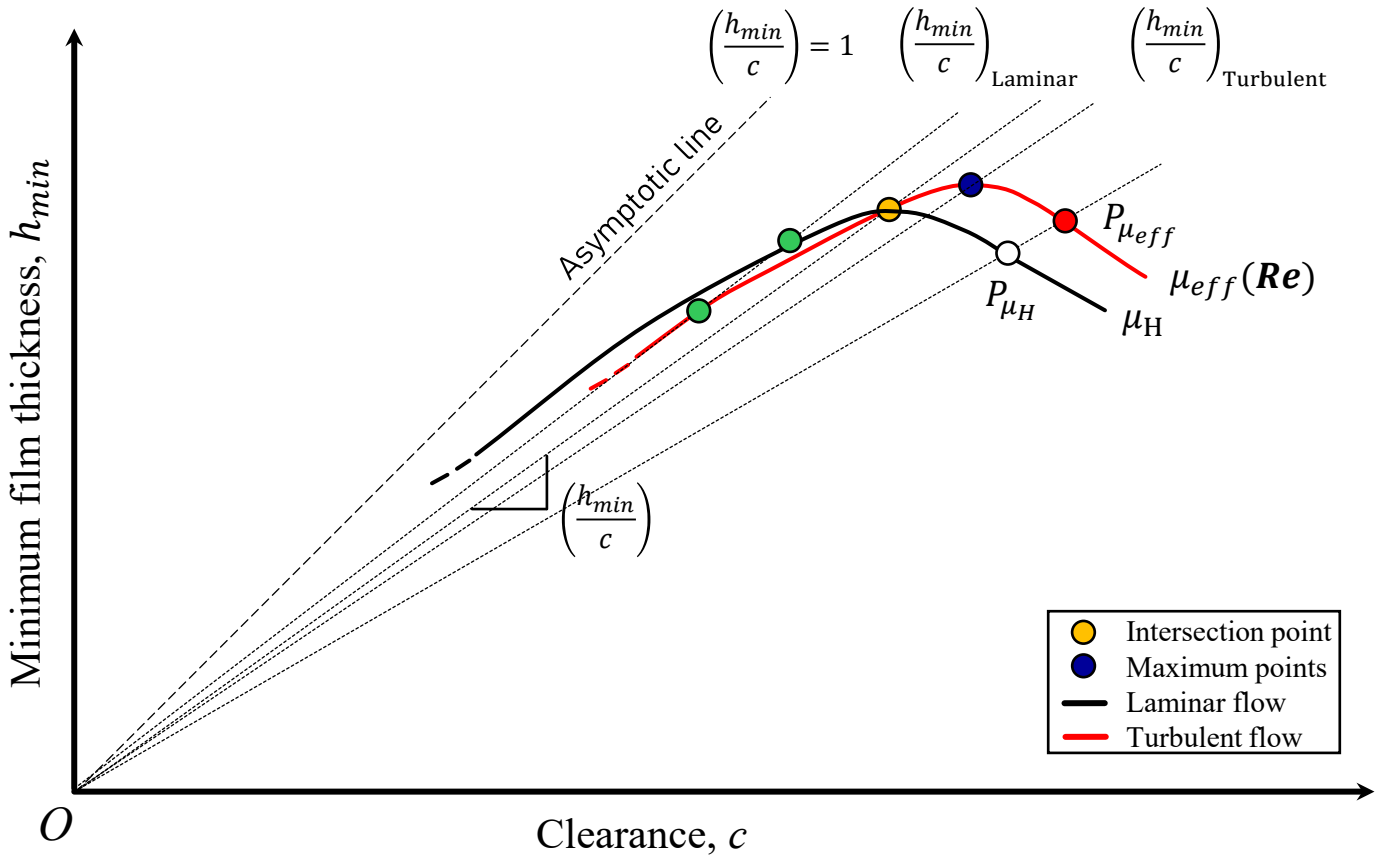

Optimum boundary

Bearing deformation & Misalignment

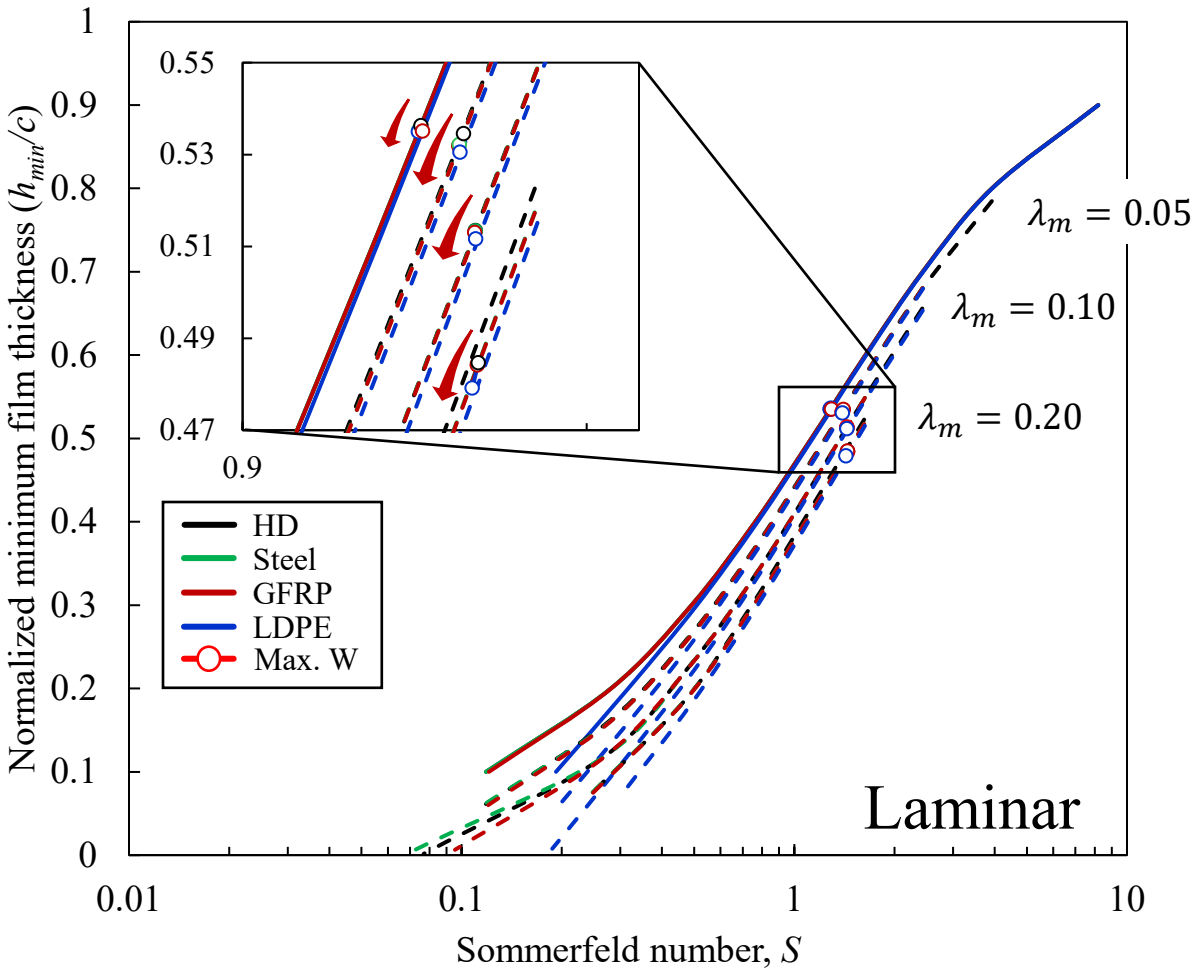

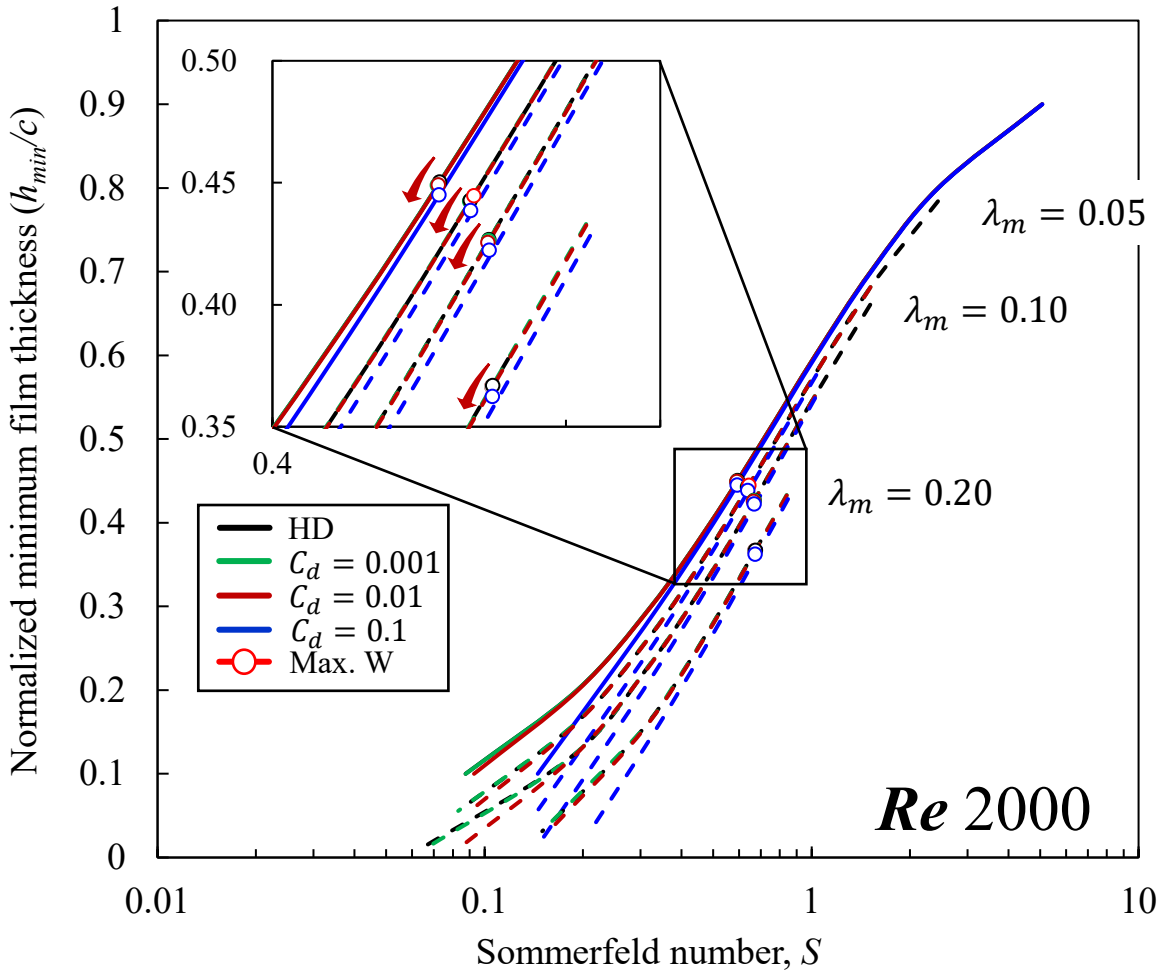

Optimum boundary

Bearing deformation effect

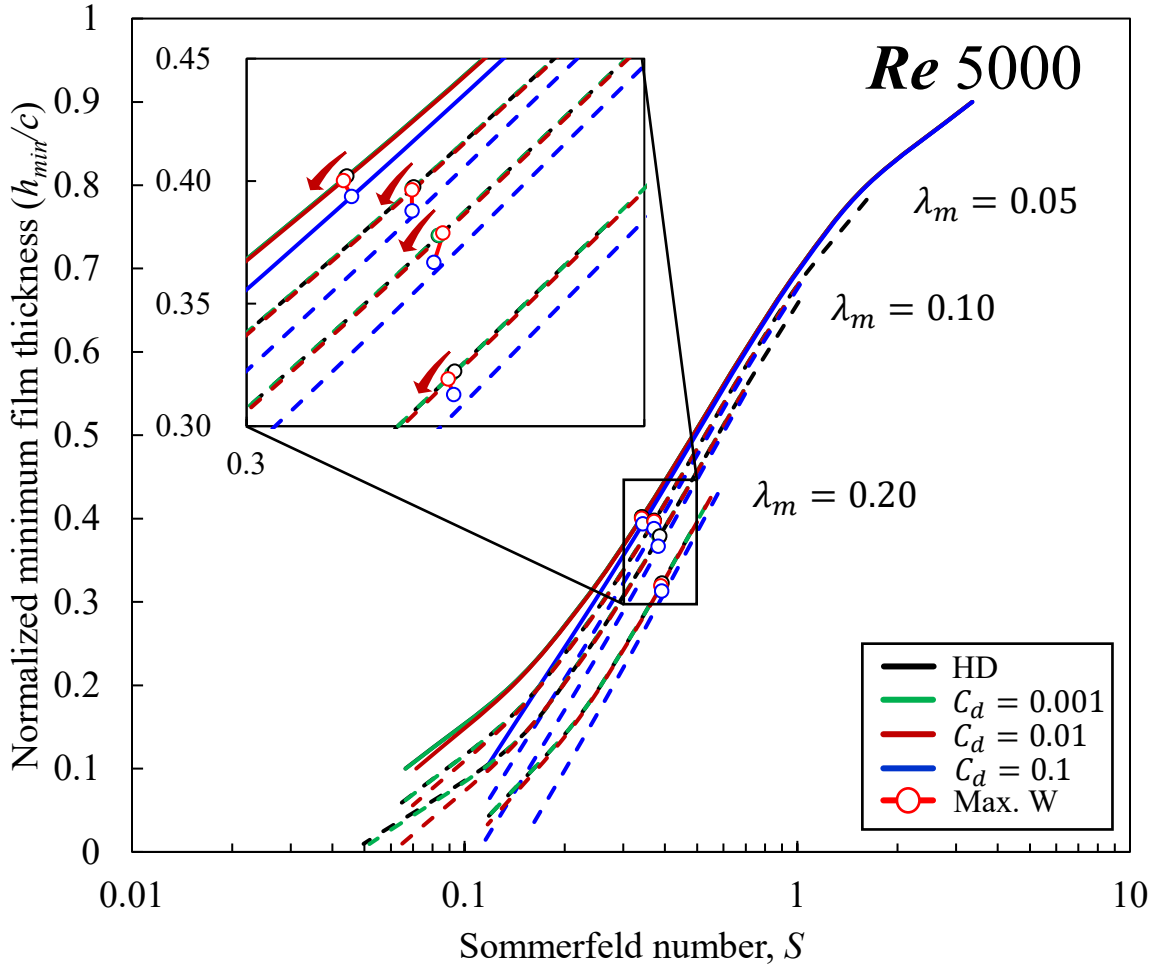

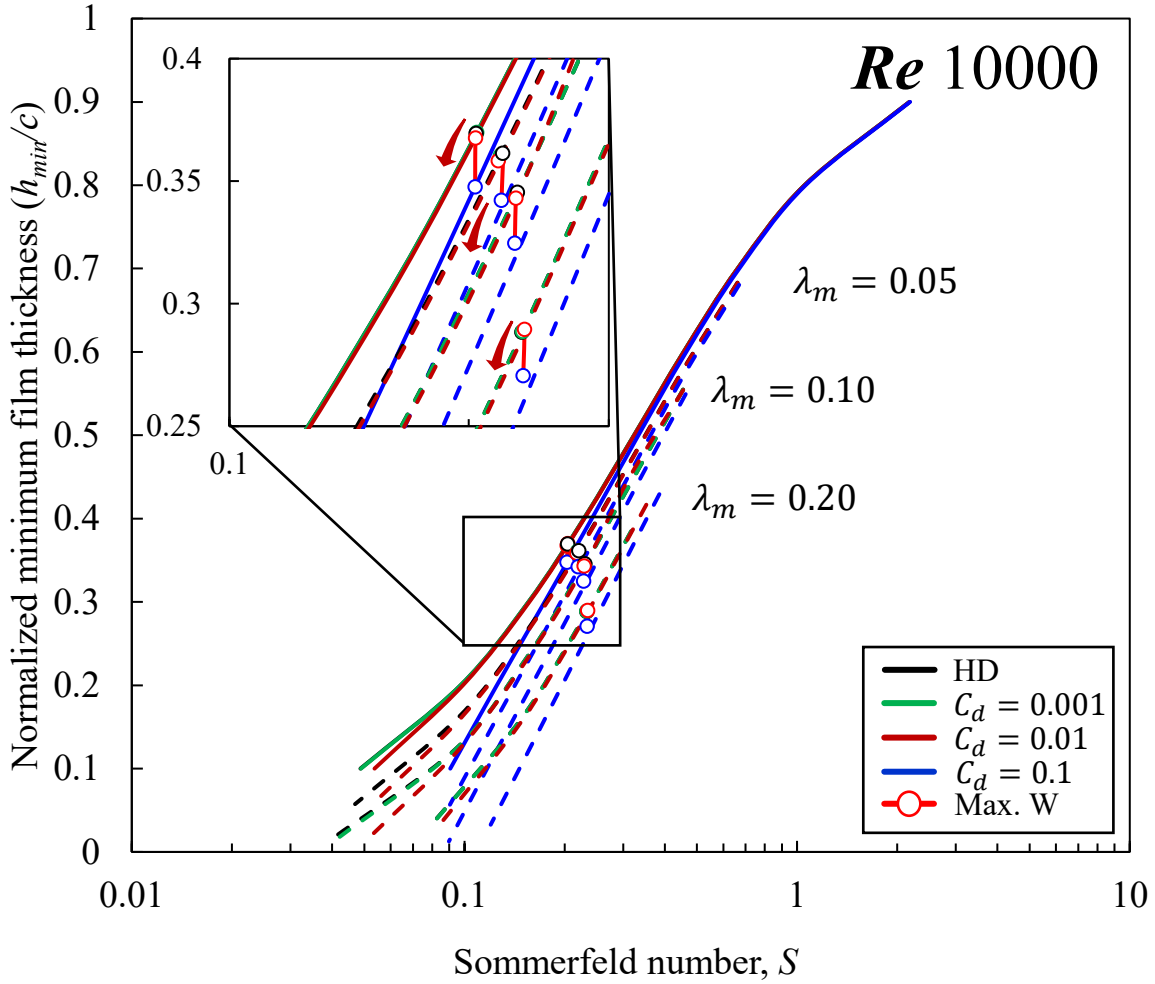

Behavior of optimum boundary

Bearing deformation & Misalignment

Separation point: A point where indicated effects become significant

Cf. Given: Load, Velocity, Viscosity (μ)

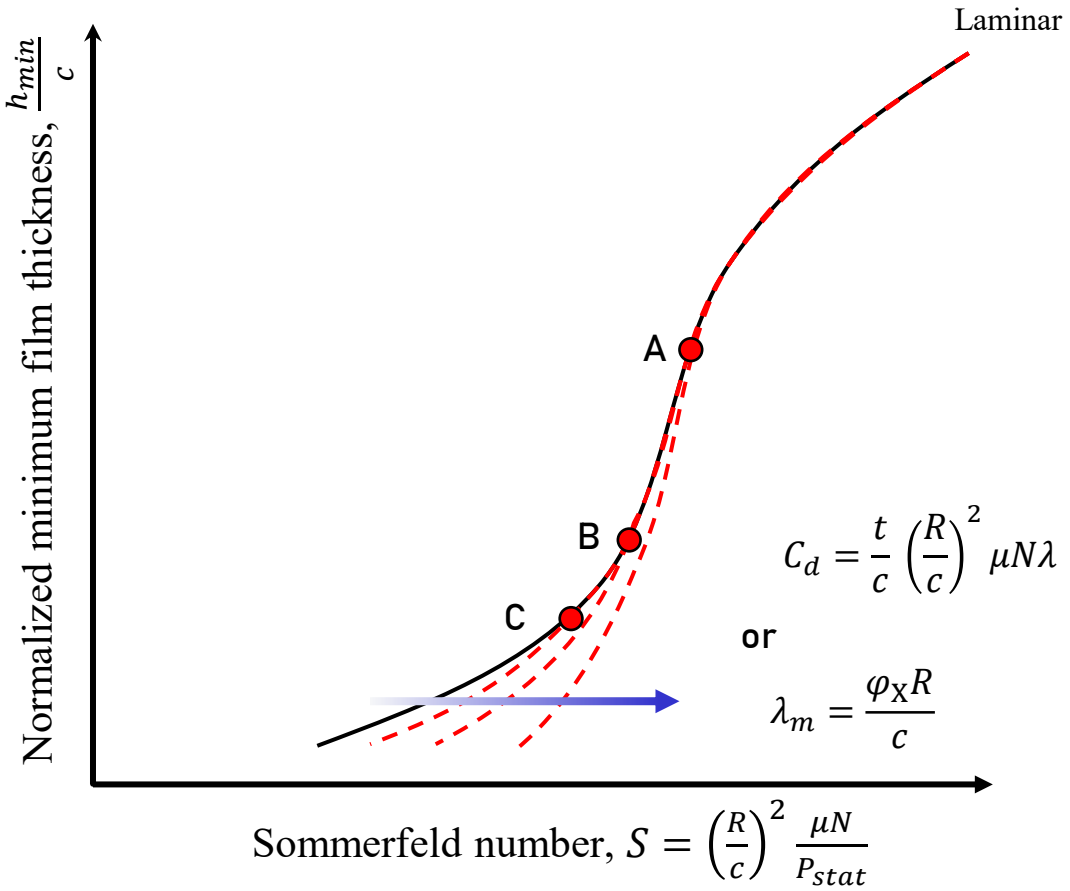

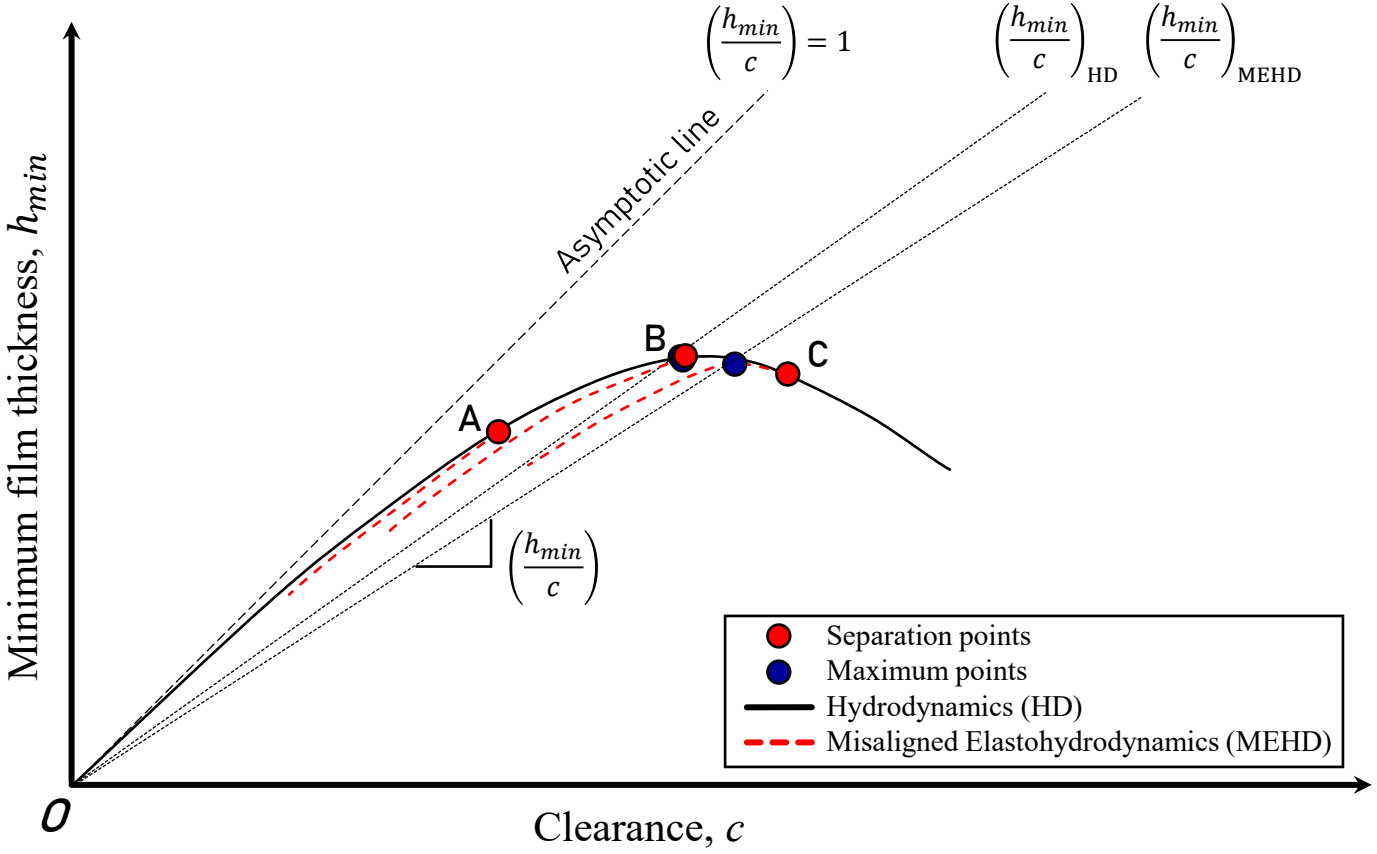

04. CONCLUSION

Conclusion

1. This study is the first to propose the **optimal boundary for achieving maximum load-carrying capacity, incorporating the effects of turbulence, bearing deformation, and misalignment**.

2. The inclusion of these factors **narrowed the recommended operating range**, highlighting the importance of considering them to ensure the high reliability of the system.

3. Furthermore, this research introduces **novel frameworks** to explain **the shift in optimal boundaries for maximum load-carrying capacity** caused by **turbulence, bearing deformation, and misalignment**.

References

[1] https://ourworldindata.org/ghg-emissions-by-sector

[2] https://www.climatechange.ie/un-shipping-climate-talks-captured-by-industry/

[3] https://www.imo.org/en/MediaCentre/HotTopics/Pages/Cutting-GHG-emissions.aspx

[4] https://splash247.com/japanese-make-breakthroughs-in-ammonia-ship-race/

[5] Xia, Chong, et al. "Simulation study on transient performance of a marine engine matched with high-pressure SCR system." International Journal of Engine Research 24.4 (2023): 1327-1345.

[6] https://www.tecnoveritas.net/media/newsletters/marine-industry/revamping-or-scrapping-decisions/

[7] Kim, Seong Su, and Dong Chang Park. "Characteristics of carbon fiber phenolic composite for journal bearing materials." Composite structures 66.1-4 (2004): 359-366.

[8] Lee, Hak Gu, and Seong Su Kim. "Effect of compacted wear debris on the tribological behavior of carbon/epoxy composites." Composite structures 74.2 (2006): 136-144.

[9] Htang, Aung, Masahiro Ohsawa, and Hiroshi Matsumoto. "Fatigue resistance of composite restorations: effect of filler content." Dental Materials 11.1 (1995): 7-13.

[10] Yang, Junbo, et al. "Optimal design of blended composite laminate structures using ply drop sequence." Composite Structures 135 (2016): 30-37.

[11] Kim, Wonvin, et al. "Research trends and future perspective in nonconventional machining of fiber-reinforced polymers: a review." Functional Composites and Structures 3.2 (2021): 022001.

[12] Zhang, Zhendong, et al. "Solar radiation intensity probabilistic forecasting based on K-means time series clustering and Gaussian process regression." Ieee Access 9 (2021): 89079-89092.

[13] Kim, Wonvin, et al. "Optimum boundaries for maximum load-carrying capacity in water-lubricated composite journal bearings incorporating turbulences and inertial effects based on elastohydrodynamic analysis." Journal of Computational Design and Engineering 9.6 (2022): 2506-2523.

THANK YOU FOR YOUR ATTENTION!



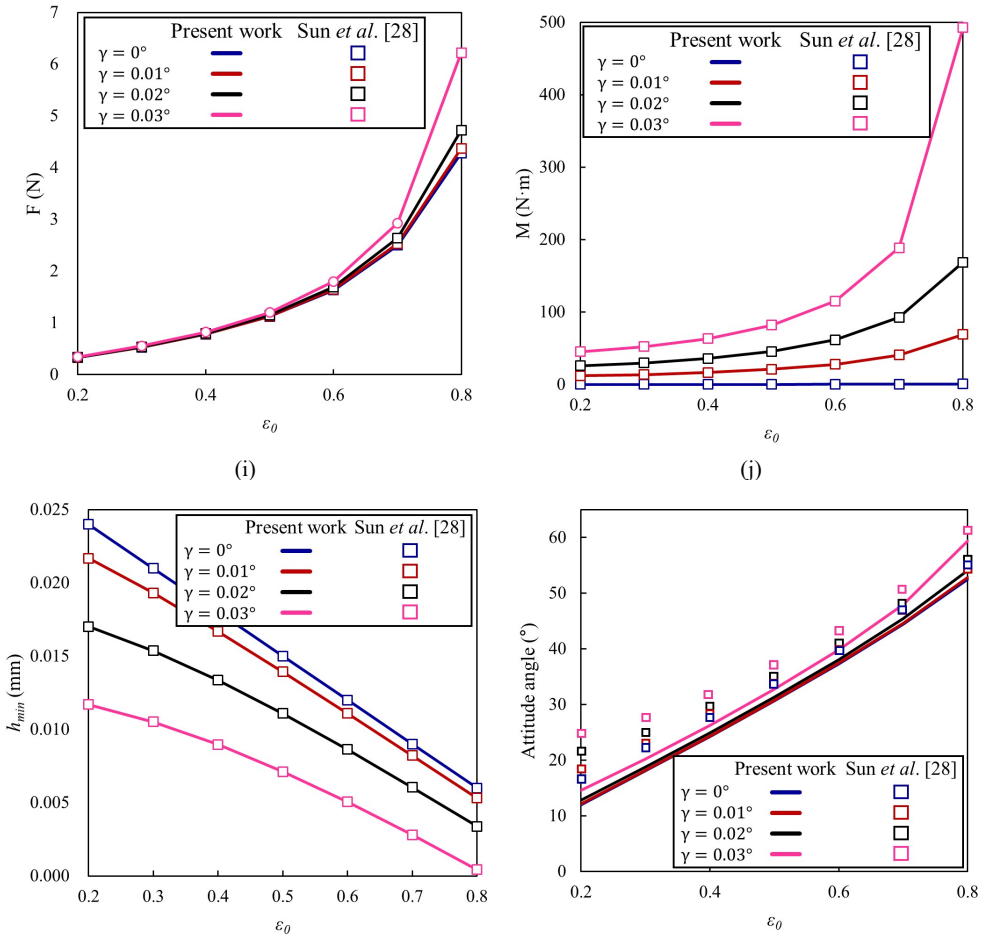

Figure 7. Validation of this work with the reference (R = 30 mm, L = 66 mm, c = 0.03 mm, n = 3000 r/min, $\varepsilon_0 = 0.8$) pressure fields at different angle γ of misalignment (a) $\gamma = 0°$, (b) $\gamma = 0.004°$, (c) $\gamma = 0.007°$, (d) $\gamma = 0.01°$ for $\psi_0 = \alpha = 0°$, (e) $\gamma = 0°$, (f) $\gamma = 0.01°$, (g) $\gamma = 0.02°$, (h) $\gamma = 0.03°$ for $\psi_0 = \alpha = 90°$, (i) load-carrying capacity, (j) moment, (k) minimum film thickness, and (l) attitude different angle γ of misalignment against eccentricity ratio

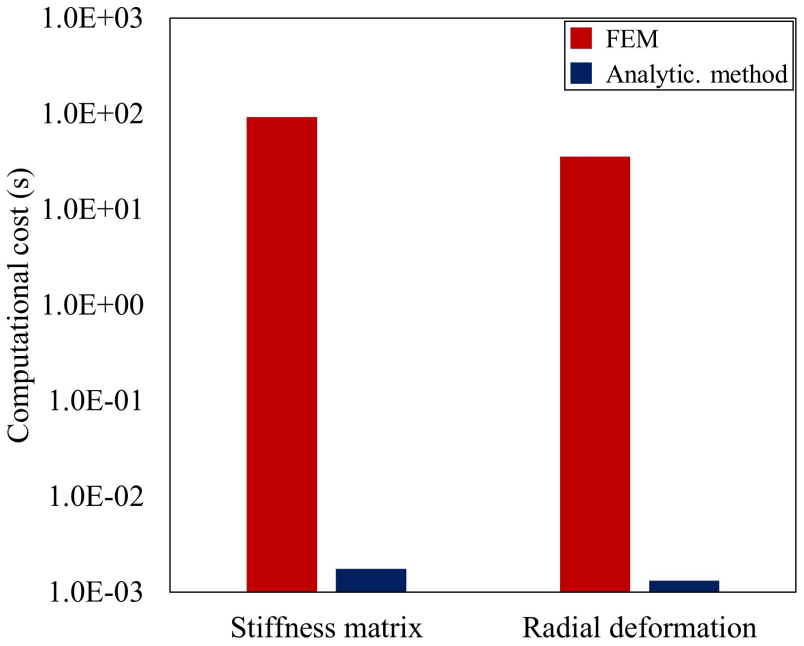

Figure 15. A comparison of computational costs in a single iteration

Pressure fields ($\varepsilon_0 = 0.8$)

Cf.

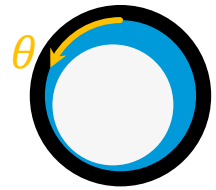

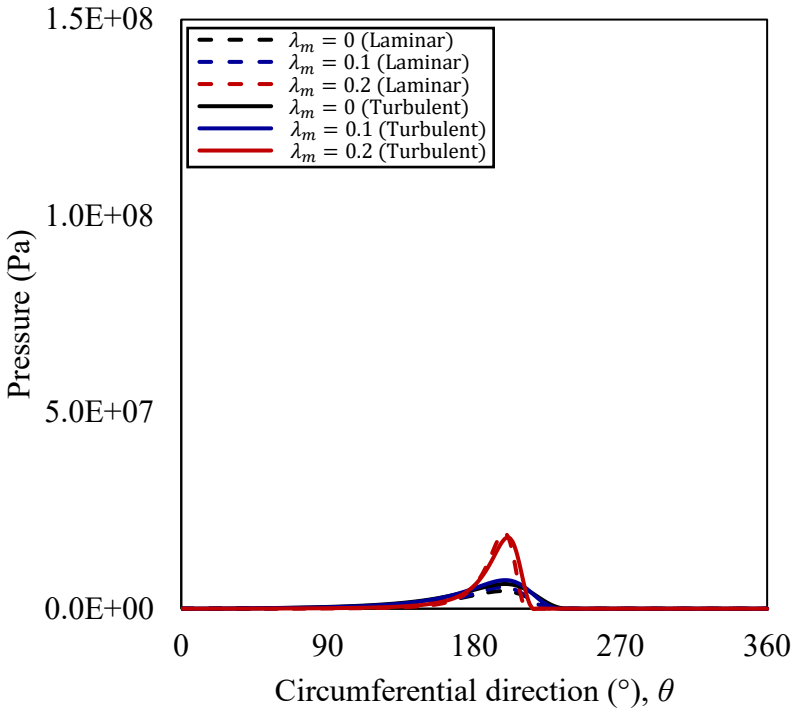

Re 2000

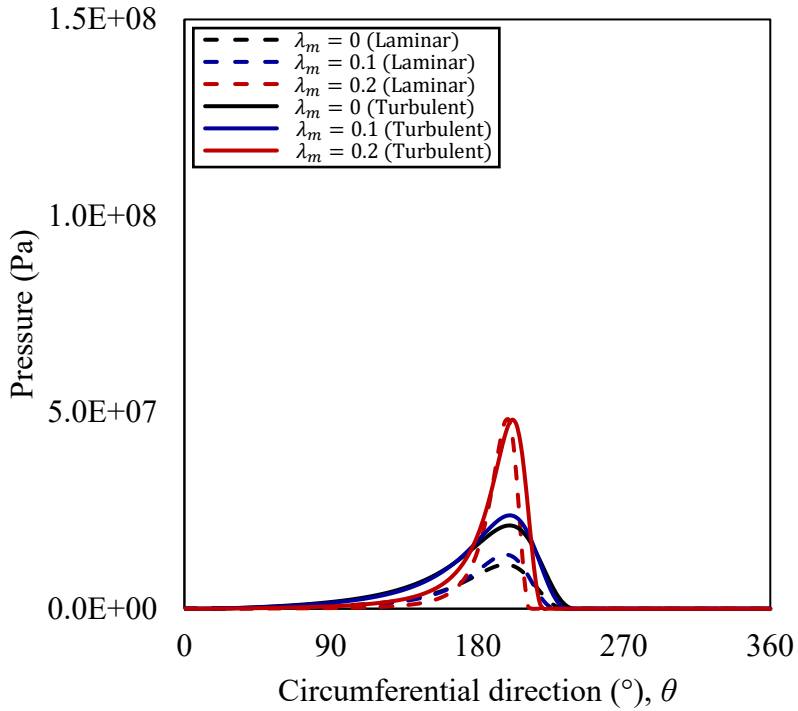

Re 5000

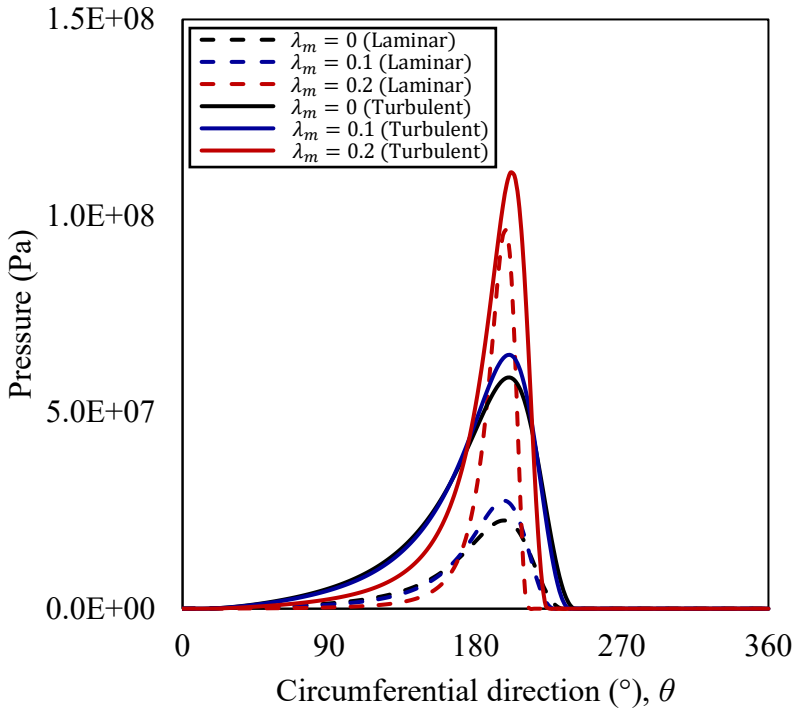

Re 10000

Bearing performances ($\varepsilon_0 = 0.8$)

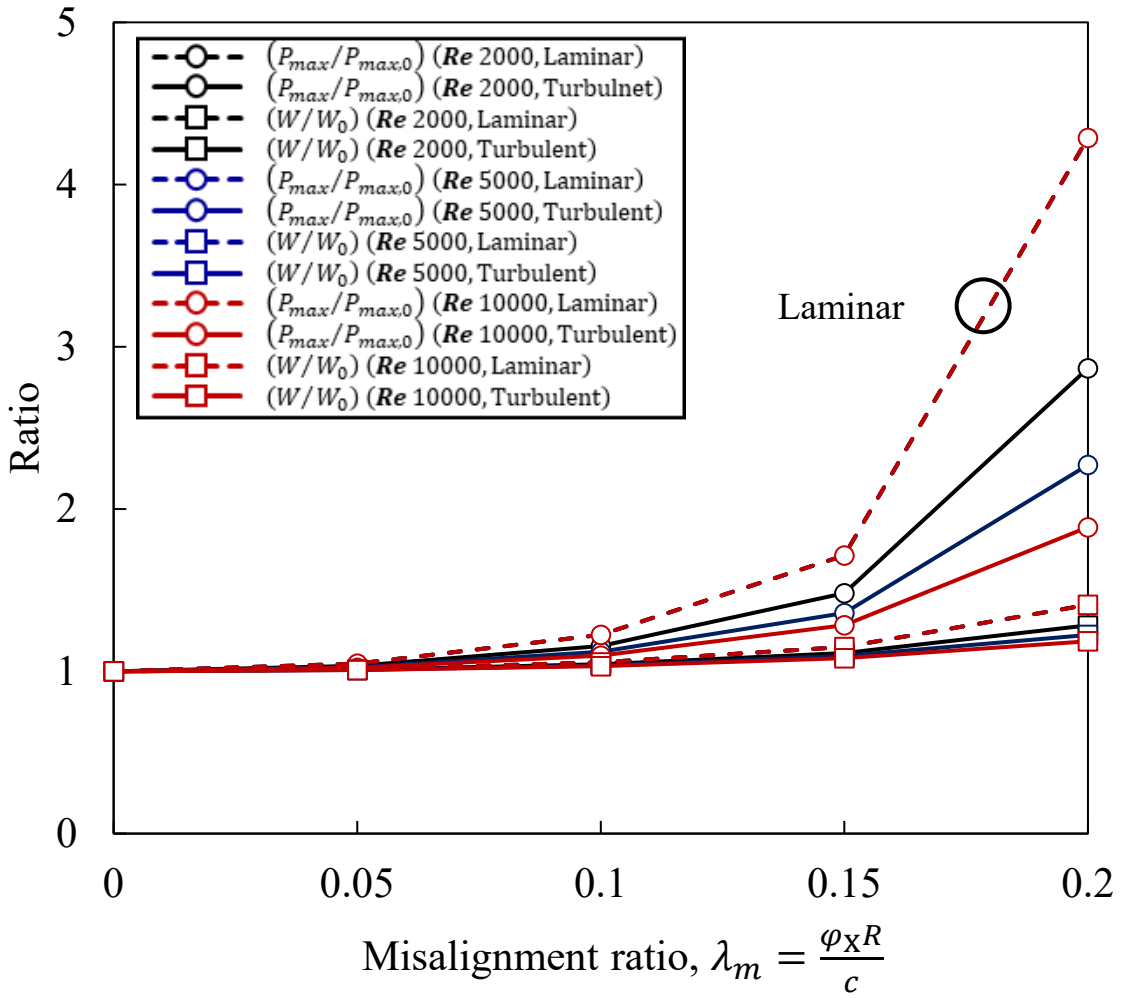

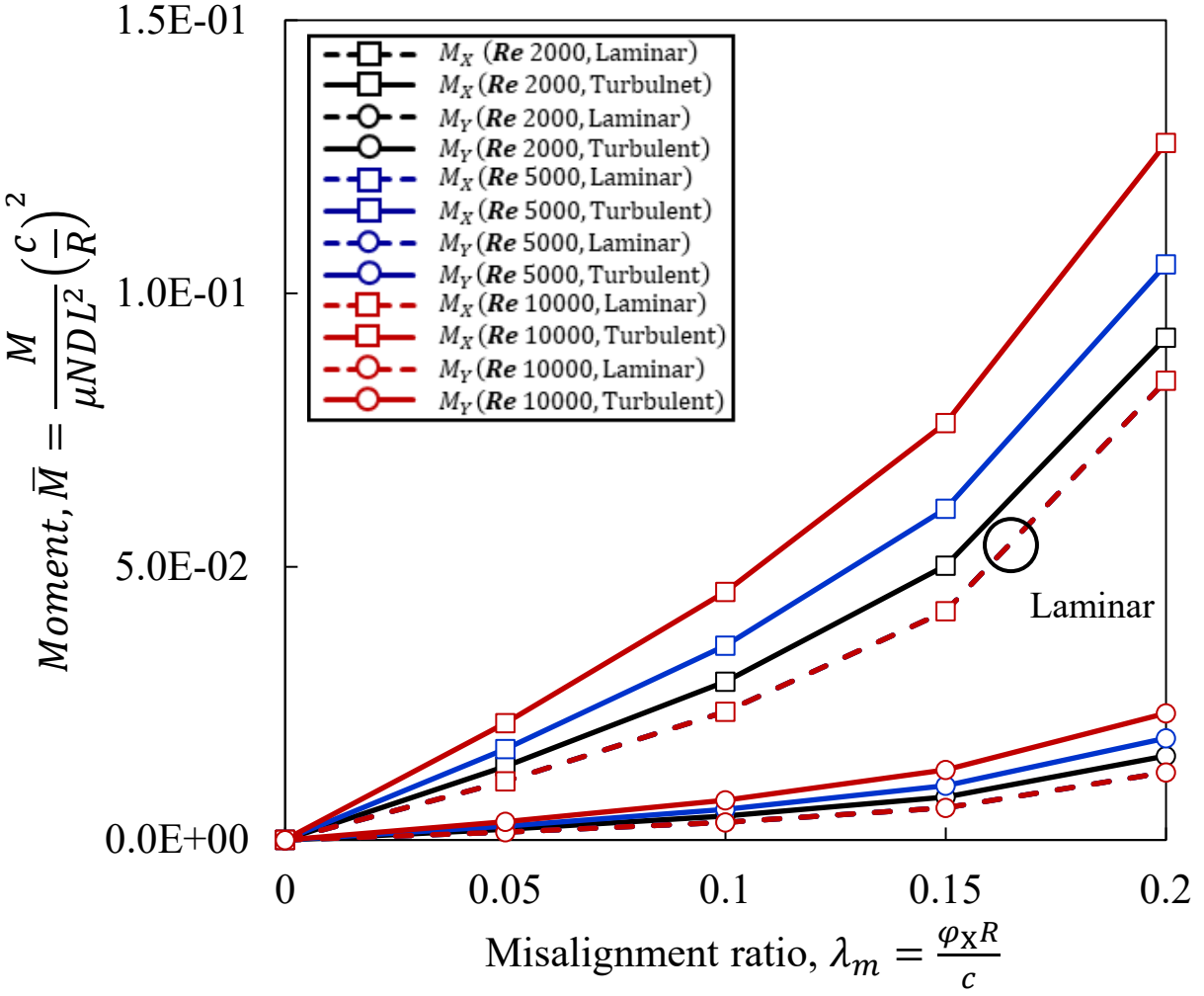

LIGHTWEIGHT COMPOSITE MATERIALS FOR RADIATION SHIELDING VIA ELECTROSPINNING FABRICATION

Maria Gabriella Santonicola[1], Gianluca Ciarleglio[1], Elisa Toto[1] and Susanna Laurenzi[2]

[1]Department of Chemical Engineering Materials Environment, Sapienza University of Rome
Via del Castro Laurenziano 7, 00161 Rome, Italy
Email: mariagabriella.santonicola@uniroma1.it, web page: https://www.uniroma1.it/it

[2] Department of Astronautical, Electrical and Energy Engineering, Sapienza University of Rome
Via Salaria 851-881, 00138 Rome, Italy
Email: susanna.laurenzi@uniroma1.it, web page: https://www.uniroma1.it/it

Keywords: Composite fibers, Electrospinning, Radiation shielding, Thermal properties, Electron microscopy

ABSTRACT

This work focuses on the design and fabrication of innovative polymer-based radiation shields by using the electrospinning technique. A strategic architecture of the fibers is developed to enhance the radiation shielding properties of the composite material, and to preserve flexibility and adaptability to different surfaces. The polymer-based fibers are synthesized using a non-toxic solvent mixture, following a sustainable and environmentally friendly approach that avoids the use of conventional toxic solvents. The polymer concentration and solution formulation were optimized to ensure electrospinnability. The influence of electrospinning parameters (voltage, flow rate, and collector distance) on fiber morphology was systematically investigated. To explore potential improvements in shielding performance, high-Z lead-free fillers (Bi_2O_3, Gd_2O_3, and WO_3) were considered in simulation studies and theoretically evaluated for their photon attenuation efficiency when embedded in the polymer matrix. Photon attenuation properties were analyzed using the XCOM database across a wide energy range (0.001–10 MeV), relevant to space environments, including solar X-rays, solar gamma rays, and cosmic gamma radiation. Several experimental techniques were used to analyze the properties of the electrospun mats. Fourier-transform infrared spectroscopy (FTIR) was used to investigate the chemical structure, while scanning electron microscopy (SEM) provided insights into the microfiber morphology. Differential scanning calorimetry (DSC) was carried out to evaluate the thermal properties of the electrospun fibers, also in consideration of the temperature fluctuations that are typically found during space exploration missions.

1 INTRODUCTION

As human space exploration advances toward longer and more complex missions, the development of advanced radiation shielding materials becomes increasingly critical to protect both astronauts and spacecraft electronics from the harmful effects of ionizing radiation [1]. This radiation arises primarily from solar particle events, solar-origin X-rays and γ-rays, and high-energy galactic cosmic rays, all of which pose cumulative biological and technological risks in low-Earth orbit and beyond [2]. Conventional shielding strategies have long relied on bulk metallic barriers, particularly lead, due to their high density and effective photon attenuation. However, such materials are inherently rigid, heavy, and environmentally hazardous, making them unsuitable for modern aerospace systems where weight constraints, flexibility, and sustainability are essential [3].

In response to these limitations, there is growing interest in the design of polymeric composite materials that combine lightweight polymer matrices with high-Z fillers capable of attenuating high-energy radiation [4]. This approach enables the fabrication of shielding materials that are not only mechanically adaptable but also engineered at the micro- or nanoscale to enhance radiation interaction cross-sections. Among advanced polymeric materials, polyimide (PI) stands out due to its exceptional

thermal and chemical stability, high mechanical strength, and inherent flexibility, making it a preferred material for aerospace applications [5-7].

Meanwhile, the pursuit of sustainable technologies has accelerated the replacement of toxic heavy metals with lead-free high-Z oxides, such as bismuth oxide (Bi_2O_3), gadolinium oxide (Gd_2O_3), and tungsten oxide (WO_3) [8, 9]. These materials offer high photon attenuation performance across broad energy ranges and have been increasingly explored for use in next-generation shielding composites [10]. To fabricate these advanced fibrous composite structures, electrospinning has emerged as a powerful and versatile fabrication method. This technique enables the production of uniform fiber mats with a high surface-area-to-volume ratio and allows for precise control over fiber morphology and architecture [11, 12]. Electrospinning is scalable from laboratory to industrial production, making it a promising route for large-scale production of lightweight shielding composites.

In the present work, polyimide fibers were successfully fabricated via electrospinning using non-toxic solvents and characterized using scanning electron microscopy (SEM), Fourier-transform infrared spectroscopy (FTIR), and differential scanning calorimetry (DSC). To explore their applicability in radiation shielding, a simulation-based study was conducted to evaluate the theoretical performance of these fibrous structures when integrated with lead-free high-Z oxide fillers. Photon attenuation properties were calculated using the XCOM photon cross-section database over a wide energy range (0.001 to 10 MeV), encompassing the primary spectral domains of space radiation. The findings support the viability of these polyimide-based composites as lightweight and sustainable alternatives to conventional metallic shielding for future space missions.

2 MATERIALS AND METHODS

2.1 Materials

The following chemicals were obtained from the indicated sources and used without further purification: 2,2-bis [4-(4-aminophenoxy)phenyl] hexafluoropropane (4-BDAF, Tokyo Chemical Industry, Tokyo, Japan); 2,2-bis(3,4-dicarboxyphenyl) hexafluoropropane dianhydride (6FDA, Alfa Aesar, Kandel, Germany); dimethyl isosorbide (DMI, Sigma-Aldrich, Milan, Italy); acetone (ACS reagent, ≥99.5%); acetic anhydride (Chem-Lab, Zedelgem, Belgium) and pyridine (Honeywell Riedel-de Haën, Charlotte, NC, USA). Ultrapure water (resistivity 18.2 MΩ cm) was obtained from a Direct-Q3 UV water purification system (Millipore, Molsheim, France).

2.2 Electrospinning

The polyimide (PI) used in this study was synthesized via a two-step process, as previously described in our earlier work [5]. After synthesis and purification, the resulting polyimide was obtained as a dry powder. The PI powder was dissolved in a solvent mixture of acetone and DMI at suitable ratio before the electrospinning process.

A custom-made experimental setup for electrospinning/electrospraying was employed to fabricate the polyimide fibers, providing precise control over process conditions and reproducibility [13-15]. A green electrospinning approach was employed by use of the non-toxic DMI/acetone solvent system. Process parameters (polymer concentration, solvent ratio, applied voltage, and flow rate) were optimized to yield uniform fibers. The optimized conditions, identified through preliminary screening, were applied throughout. Following electrospinning, the resulting fiber mats were subjected to thermal treatment at 150 °C for 2 hours to ensure complete removal of residual solvents and to promote further imidization of the polymer structure.

2.3 Characterization methods

The morphology of PI microfibers was examined via SEM (VEGA II LSH, Tescan, Czech Republic) after gold sputter-coating (Cressington 108, UK). Fiber diameter distribution was quantified using ImageJ (v1.51w) with the DiameterJ plugin (v1.018). Thermal behavior was assessed by DSC (Pyris DSC 8500, PerkinElmer, USA) under nitrogen flow (40 mL/min), using ~10 mg samples in sealed aluminum pans, scanned from 25 to 300 °C at 10 °C/min. FTIR analysis was performed with a Nicolet™

Summit spectrometer (Thermo Fisher Scientific, USA) equipped with a diamond ATR, recording spectra in the 4000–600 cm^{-1} range at 4 cm^{-1} resolution (64 scans, air background subtracted).

2.4 Radiation shielding simulations

Simulations of the composites radiation shielding properties were performed using the XCOM photon cross section database developed by NIST, incorporating total attenuation coefficients inclusive of coherent scattering [16]. The study focused on photon interactions within the 0.01–10 MeV energy range, encompassing the most relevant spectral domain for radiation exposure in low Earth orbit (LEO) and interplanetary space [17]. This range includes contributions from solar X-rays, gamma radiation from solar flares, and galactic cosmic photons, making it representative of operational space conditions [18]. Simulations were performed on pure polyimide ($C_{46}H_{12}F_6O$), high-Z oxides (PbO, Bi_2O_3, Gd_2O_3, and WO_3), and their corresponding composites with polyimide as the matrix. The selected fillers include lead oxide (PbO) as a conventional reference and three lead-free alternatives, bismuth oxide (Bi_2O_3), gadolinium oxide (Gd_2O_3), and tungsten oxide (WO_3), chosen for their high atomic numbers, chemical stability [19-21]. Two filler loadings (20 and 50 wt%) were selected as the most realistic concentrations, balancing processability, dispersion quality, and shielding effectiveness, under the assumption of uniform distribution within the polymer matrix. The total linear attenuation coefficient (μ) for each sample was calculated using the rule of mixtures, accounting for the weighted contributions of each component's mass attenuation coefficient (μ/ρ) and density. To assess the relative performance of the composites with respect to the neat polymer, a dimensionless attenuation ratio R was introduced, defined as:

$$R = \frac{(\mu/\rho)_{composite}}{(\mu/\rho)_{PI}} \quad (1)$$

where $(\mu/\rho)_{composite}$ is the mass attenuation coefficient of the filled system, and $(\mu/\rho)_{PI}$ is that of the pristine PI. This ratio, evaluated at a reference energy of 0.5 MeV, enables a direct and density-independent comparison of shielding efficiency across all compositions [22].

3 RESULTS AND DISCUSSION

3.1 Fabrication of PI microfibers by electrospinning

The electrospinning process was optimized by varying polymer concentration, solvent composition, voltage, and flow rate. Uniform fibers were obtained using a polyimide solution in a non-toxic binary DMI/acetone solvent system. The resulting mats were thermally treated at 150 °C for 2 h to remove residual solvents and promote further imidization. Figure 1a shows a representative SEM image of the thermally treated fibers, revealing smooth, bead-free, randomly oriented filaments. The corresponding diameter distribution (Fig. 1b), obtained using DiameterJ, resulted in a mean diameter of 1.16 ± 0.59 μm, with 36.9% porosity and an intersection density of 0.43 intersections/μm^2. This microstructure indicates a highly porous and interconnected architecture suitable for functional filler integration.

A qualitative assessment of flexibility is shown in Figure 1c. The mat was manually folded and released, demonstrating elastic recovery without visible damage or permanent deformation.

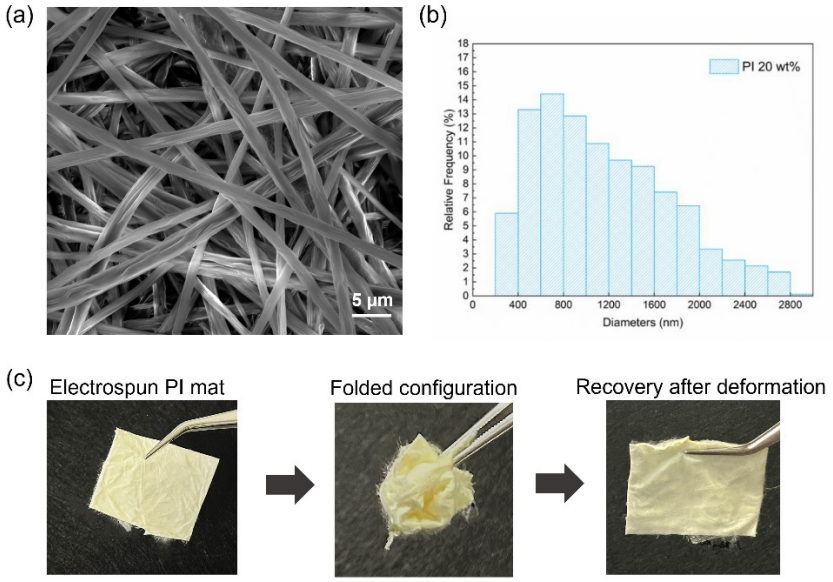

Figure 1: (a) SEM image of electrospun polyimide fibers after thermal treatment at 150 °C for 2 hours. (b) Fiber diameter distribution histogram. (c) Qualitative flexibility assessment: the mat is shown in its original state (left), after folding (middle), and following shape recovery (right).

3.2 Chemical and Thermal Properties of PI electrospun fibers

FTIR spectroscopy was employed to assess the chemical structure of electrospun polyimide fiber mats (20 wt%). Figure. 2a shows the chemical structure of aromatic PI with trifluoromethyl functional groups. The spectrum (Fig. 2b) exhibits well-defined imide-associated absorption bands, including the asymmetric and symmetric C=O stretching vibrations at 1784 and 1724 cm^{-1}, respectively. The C=C stretching of the aromatic moiety is evident at 1504 cm^{-1} and remains unaltered. The absorption at 1379 cm^{-1}, assigned to C–N stretching, and the band at 724 cm^{-1}, corresponding to C=O bending, further corroborate the presence of the imide group. The absence of characteristic bands associated with unreacted amine and carboxylic acid groups (3330, 1710, 1650, and 1550 cm^{-1}) indicates a high conversion degree of poly (amic acid) into polyimide [5]. Minor features in the 2921–2850 cm^{-1} region are attributed to C–H stretching vibrations from residual solvent species.

Differential scanning calorimetry (DSC) was employed to evaluate the thermal behavior of electrospun PI fiber mats. The thermogram of the untreated fibers showed two distinct exothermic peaks at 220 °C and 232 °C during the heating (Fig. 2c). In contrast, the thermogram of the thermally treated PI fibers (150 °C for 2 h) does not exhibit any thermal events within the investigated temperature range, confirming the absence of residual transitions or structural rearrangements. The absence of thermal events up to 300 °C confirms the thermal stability of the treated fibers, making them suitable for aerospace applications requiring resistance to prolonged thermal exposure.

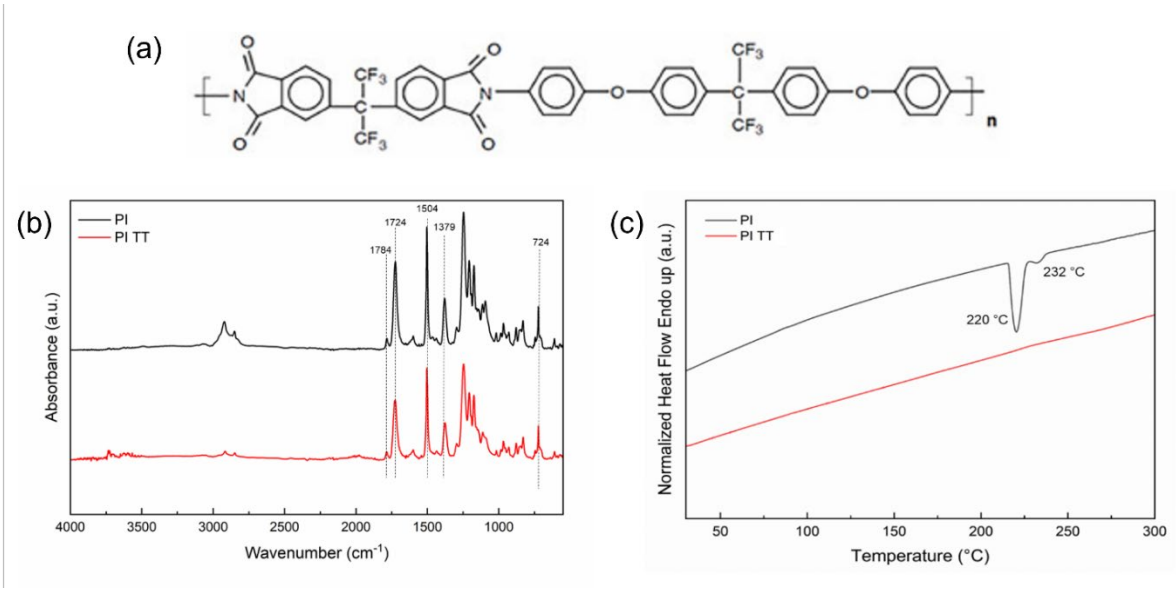

Figure 2: (a) Chemical structure of the in-house synthesized polyimide [5]. (b) FTIR spectra of electrospun PI fiber mats, untreated and thermally treated at 150 °C for 2 hours. Data are offset for clarity. (c) DSC thermograms of untreated and thermally treated PI fibers.

3.3 Simulations of radiation shielding capability

Figure 4 presents the simulated mass attenuation coefficients (μ/ρ) of the investigated fillers and polyimide-based composites across the 0.001–10 MeV photon energy range. As expected, PbO exhibited the highest attenuation due to its high atomic number. However, Bi_2O_3 demonstrated nearly equivalent performance, particularly within the 0.01–1 MeV range, which is highly relevant for shielding against solar and cosmic photon fluxes in low Earth orbit (LEO).

Upon incorporation into the PI matrix at 20 wt% and 50 wt% loading (Fig. 4c and 4e), all fillers led to an increase in attenuation relative to the pristine polymer. This effect becomes more pronounced at higher concentrations, with clear differences observed in the 0.1–1 MeV range (Figure. 4d and 4f), which corresponds to the energy window where Compton scattering dominates and shielding demands are most relevant to space radiation environments [23]. A comprehensive summary of the simulated mass attenuation coefficients (μ/ρ) at 0.5 MeV and the corresponding normalized attenuation ratios (R) relative to pristine PI is presented in Table 1. At 50 wt% filler loading, the Bi_2O_3-filled composite demonstrated superior attenuation performance compared to the PbO-based sample, with a marginally higher R value (1.416 vs 1.407).

Although composites incorporating WO_3 and Gd_2O_3 show comparatively lower R values, they still provide a significant improvement over unfilled polyimide. These results validate the role of high-Z oxide fillers in improving the photon-attenuation ability of polymer-based materials. In particular, Bi_2O_3 emerges as a very promising lead-free alternative that can offer attenuation performance equal to or marginally better than that of conventional lead-containing materials, while providing enhanced environmental sustainability and chemical stability features required for next-generation aerospace shielding materials.

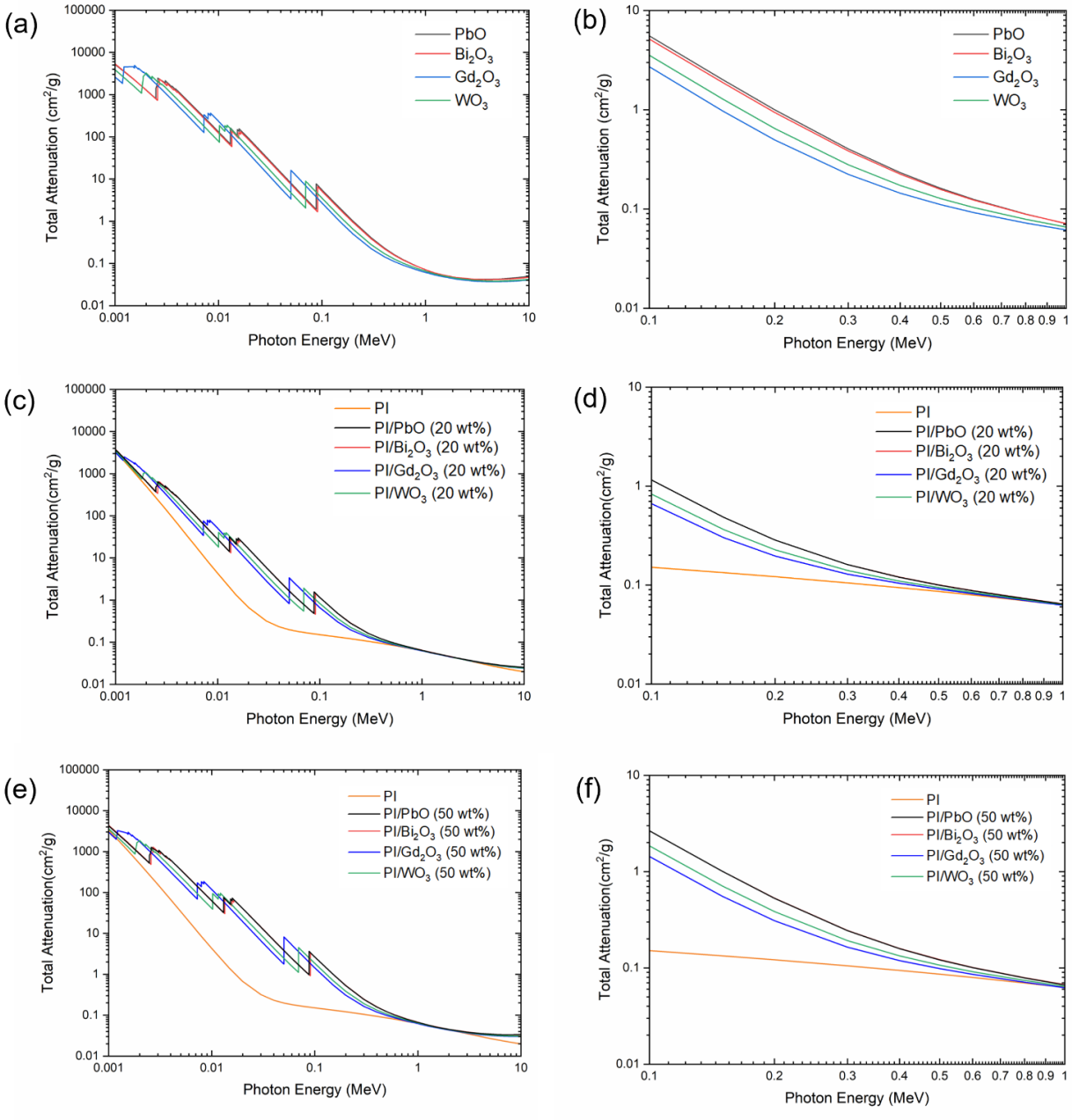

Figure 4: Simulated photon attenuation of polyimide (PI) composites using XCOM. Total attenuation coefficients (0.001–10 MeV) were computed via the NIST XCOM database, including coherent scattering. Plots of (a,b) PbO and lead-free oxides (Bi_2O_3, Gd_2O_3, WO_3), (c, d) PI composites with 20 wt% fillers, (e, f) PI composites with 50 wt% fillers. (b, d, f) Enlarged area of plots showing the 0.1–1 MeV range relevant to LEO radiation environments.

Table 1: Attenuation performance of neat polyimide (PI) materials and polyimide composites at 0.5 MeV. Total attenuation coefficients (μ/ρ) and the corresponding normalized attenuation ratios (R) relative to neat PI calculated at 0.5 MeV using XCOM.

Sample	Total Attenuation (cm^2/g) at 0.5 MeV	R at 0.5 MeV
PI	0.086	1.000
PbO	0.161	1.875
Bi_2O_3	0.158	1.831
Gd_2O_3	0.110	1.283
WO_3	0.127	1.480
PI/PbO (20 wt%)	0.100	1.163
PI/Bi_2O_3 (20 wt%)	0.100	1.166
PI/Gd_2O_3 (20 wt%)	0.091	1.057
PI/WO_3 (20 wt%)	0.094	1.096
PI/PbO (50 wt%)	0.121	1.407
PI/Bi_2O_3 (50 wt%)	0.122	1.416
PI/Gd_2O_3 (50 wt%)	0.098	1.142
PI/WO_3 (50 wt%)	0.107	1.240

4 CONCLUSIONS

Flexible polyimide-based fibrous mats were successfully fabricated via green electrospinning using a non-toxic solvent system and subsequently stabilized by heat treatment. The resulting materials exhibited uniform morphology, flexibility, and thermal stability up to 300 °C, confirming their suitability for use in space environment. A comprehensive characterization revealed smooth, bead-free fibers with a highly porous and interconnected microstructure. Radiation shielding simulations using XCOM demonstrated that PI composites loaded with lead-free high-Z oxides significantly enhance photon attenuation. Among the candidates, Bi_2O_3 showed performance comparable to or exceeding that of Pb, particularly in the 0.1–1 MeV range relevant to space radiation. These findings highlight the potential of PI/Bi_2O_3 composite mats as lightweight, flexible, and more sustainable alternatives to conventional shielding materials for future space missions.

ACKNOWLEDGEMENTS

This work was financially supported through the projects EFIBER-SHIELDS and FLEX-PI-MATER-SPACE funded by Sapienza University of Rome. G. C. was partially supported by a research fellowship financed by the Rome Technopole Project (ECS 0000024 Rome Technopole – CUP B83C22002820006, PNRR Mission 4 Component 2 Investment 1.5, funded by the European Union – NextGenerationEU).

REFERENCES

[1] J. C. Chancellor, G. B. I. Scott, and J. P. Sutton, Space Radiation: The Number One Risk to Astronaut Health beyond Low Earth Orbit, *Life,* vol. 4, no. 3, pp. 491-510, 2014, doi: https://doi.org/10.3390/life4030491.

[2] M.-H. Y. Kim, K. A. George, and F. A. Cucinotta, Space Environment (Natural and Induced), 2007.

[3] N. J. Abualroos, K. A. Yaacob, and R. Zainon, Radiation attenuation effectiveness of polymer-based radiation shielding materials for gamma radiation, *Radiat. Phys. Chem.,* vol. 212, p. 111070, 2023/11/01/ 2023, doi: https://doi.org/10.1016/j.radphyschem.2023.111070.

[4] S. Bagheri, H. Khalafi, M. R. Tohidifar, and S. Bagheri, Thermoplastic and thermoset polymer matrix composites reinforced with bismuth oxide as radiation shielding materials, *Compos. B Eng.,* vol. 278, p. 111443, 2024/06/01/ 2024, doi: https://doi.org/10.1016/j.compositesb.2024.111443.

[5] E. Toto, S. Laurenzi, R. C. Pellegrini, E. Cavallini, and M. G. Santonicola, Eco-friendly synthesis of high-performance polyimide materials using bio-based greener solvents: Towards sustainable technologies in space environment, *Mater. Today Sustain.,* vol. 25, p. 100657, 2024/03/01/ 2024, doi: https://doi.org/10.1016/j.mtsust.2023.100657.

[6] J. Chang, H. Niu, and D. Wu, 12 - High performance polyimide fibers, in *Structure and Properties of High-Performance Fibers*, G. Bhat Ed. Oxford: Woodhead Publishing, 2017, pp. 301-323.

[7] I. Gouzman, E. Grossman, R. Verker, N. Atar, A. Bolker, and N. Eliaz, Advances in Polyimide-Based Materials for Space Applications, *Adv. Mater.,* vol. 31, no. 18, p. 1807738, 2019, doi: https://doi.org/10.1002/adma.201807738.

[8] V. Singh *et al.*, Heavy Metal Contamination in the Aquatic Ecosystem: Toxicity and Its Remediation Using Eco-Friendly Approaches, *Toxics,* vol. 11, no. 2, p. 147, 2023, doi: https://doi.org/10.3390/toxics11020147.

[9] B. Hwang and J.-S. Lee, Lead-free, air-stable hybrid organic–inorganic perovskite resistive switching memory with ultrafast switching and multilevel data storage, *Nanoscale,* vol. 10, no. 18, pp. 8578-8584, 2018, doi: https://doi.org/10.1039/C8NR00863A.

[10] E. Toto, L. Lambertini, S. Laurenzi, and M. G. Santonicola, Recent Advances and Challenges in Polymer-Based Materials for Space Radiation Shielding, *Polymers,* vol. 16, no. 3, p. 382, 2024, doi: https://doi.org/10.3390/polym16030382.

[11] C. Giuliani *et al.*, Advanced Electrospun Composites Based on Polycaprolactone Fibers Loaded with Micronized Tungsten Powders for Radiation Shielding, *Polymers,* vol. 16, no. 18, p. 2590, 2024, doi: https://doi.org/10.3390/polym16182590.

[12] F. Fadil, N. D. N. Affandi, M. I. Misnon, N. N. Bonnia, A. M. Harun, and M. K. Alam, Review on Electrospun Nanofiber-Applied Products, *Polymers,* vol. 13, no. 13, p. 2087, 2021, doi: https://doi.org/10.3390/polym13132087.

[13] G. Ciarleglio, T. Russo, S. Vella, E. Toto, and M. G. Santonicola, Electrospray Fabrication of pH-Responsive Microspheres for the Delivery of Ozoile, *Macromol. Symp.,* vol. 413, no. 4, p. 2400031, 2024, doi: https://doi.org/10.1002/masy.202400031.

[14] G. Ciarleglio, M. Placido, E. Toto, and M. G. Santonicola, Dual-Responsive Alginate/PNIPAM Microspheres Fabricated by Microemulsion-Based Electrospray, *Polymers,* vol. 16, no. 19, p. 2765, 2024, doi: https://doi.org/10.3390/polym16192765.

[15] G. Ciarleglio, T. Russo, E. Toto, and M. G. Santonicola, Fabrication of Alginate/Ozoile Gel Microspheres by Electrospray Process, *Gels,* vol. 10, no. 1, p. 52, 2024, doi: https://doi.org/10.3390/gels10010052.

[16] M. J. Berger and J. H. Hubbell, XCOM: Photon cross sections on a personal computer, 1987.

[17] J. A. Jones, F. Karouia, L. Pinsky, and O. Cristea, Radiation and Radiation Disorders, in *Principles of Clinical Medicine for Space Flight*, M. R. Barratt, E. S. Baker, and S. L. Pool Eds. New York, NY: Springer, 2019, pp. 39-108.

[18] V. G. Kurt, B. Y. Yushkov, V. I. Galkin, K. Kudela, and L. K. Kashapova, CORONAS-F observation of gamma-ray emission from the solar flare on 2003 October 29, *New Astron.,* vol. 56, pp. 102-112, 2017/10/01/ 2017, doi: https://doi.org/10.1016/j.newast.2017.05.002.

[19] D.-E. Kwon, D.-H. Han, K.-H. Jung, S.-J. Lee, J.-O. Kim, and C.-H. Baek, Performance and feasibility evaluation for radiation shielding of metal oxides: Monte Carlo simulation, *J. Korean Phys. Soc.,* vol. 82, no. 8, pp. 813-817, 2023/04/01 2023, doi: https://doi.org/10.1007/s40042-023-00744-7.

[20] F. Bakri, P. L. Gareso, and D. Tahir, Advancing radiation shielding: A review the role of Bismuth in X-ray protection, *Radiat. Phys. Chem.,* vol. 217, p. 111510, 2024/04/01/ 2024, doi: https://doi.org/10.1016/j.radphyschem.2024.111510.

[21] A. Safari, P. Rafie, S. Taeb, M. Najafi, and S. M. J. Mortazavi, Development of Lead-Free Materials for Radiation Shielding in Medical Settings: A Review, *J. Biomed. Phys. Eng.,* vol. 14, no. 3, pp. 229-244, 2024, doi: https://doi.org/10.31661/jbpe.v0i0.2404-1742.

[22] W. M. Al-Saleh, M. Elsafi, H. M. Almutairi, I. M. Nabil, and M. A. El-Nahal, A comprehensive study of the shielding ability from ionizing radiation of different mortars using iron filings and bismuth oxide, *Sci. Rep.,* vol. 14, no. 1, p. 10014, 2024/05/01 2024, doi: https://doi.org/10.1038/s41598-024-60188-2.

[23] H. O. Tekin *et al.*, Enhanced radiation shielding via incorporating europium oxide in 316L stainless steel: Synthesis, physical, microstructural, shielding, and mechanical properties, *J. Mater. Res. Technol.,* vol. 34, pp. 184-194, 2025/01/01/ 2025, doi: https://doi.org/10.1016/j.jmrt.2024.12.054.

ICCM24
AUGUST 4-8, 2025
BALTIMORE CONVENTION CENTER
BALTIMORE, MARYLAND, USA

No Technical Paper Submission for:

Clement Hiel

FORMING WRINKLE-FREE CURVED C CHANNEL WITH UNIDIRECTIONAL FIBER REINFORCED COMPOSITES

Suk Young Chey[1], Sung-Hoon Ahn[1,2]

[1]Department of Mechanical Engineering, Seoul National University, South Korea
1, Gwanak-ro, Gwanak-gu, Seoul, Republic of Korea, 08826
Email: schey1@snu.ac.kr

[2]Institute of Advanced Machinery and Design, Seoul National University, South Korea
1, Gwanak-ro, Gwanak-gu, Seoul, Republic of Korea, 08826
Email: ahnsh@snu.ac.kr, web page: https://fab.snu.ac.kr/

Keywords: Unidirectional fiber, Laminate Wrinkling, Double Diaphragm Forming, Prepreg

ABSTRACT

Wrinkling is a critical challenge when forming complex, double-curved shapes using unidirectional fiber composites. These defects degrade mechanical properties and dimensional accuracy, limiting industrial applicability. While Double Diaphragm Forming (DDF) is used to suppress wrinkles using elastic diaphragms, it is less effective for thick laminates, particularly those with quasi-isotropic fiber orientations. High interply shear resistance in such laminates restricts internal deformation, causing wrinkling. Additionally, diaphragms between the tool and laminate reduce precision and complicate removal.

This study presents a novel forming technique that sequentially laminates thin layers directly on the mold surface to achieve the required thickness. It uses a long inflatable tube to press the laminate during forming, replacing the traditional diaphragm. The tube can be removed after forming, eliminating interply shear and enabling wrinkle-free forming on the tool surface. The material used is SKYFLEX USN150A (SK Chemical), a unidirectional carbon fiber prepreg with epoxy resin (4900 MPa strength, 240 GPa modulus, 1.82 g/cm³ density, 150 g/m² areal weight, 36% resin content, no scrim). Though not aerospace-grade, it is well-suited for process development.

The method was validated by forming a C-channel with eight plies (stacking sequence: (0/90/45/–45)s) using four two-ply forming cycles. The final part measured 1140 mm in length with a 1000 mm inner flange radius. Thickness was measured at 268 points using micrometers, yielding an average of 2.149 mm and a standard deviation of 0.081 mm. Minor variations were observed at edges and flanges, influenced by fiber orientation and curvature. Differences between 0°/90° and ±45° laminates suggest the need for preform shape adjustment. After forming, the part was vacuum-bag cured at 125°C under 200 kPa for 2 hours.

This technique offers a practical, wrinkle-free forming process for unidirectional composites with potential for industrial application.

1 INTRODUCTION

Curved C-channel structures are commonly used in aircraft fuselages as lightweight, high-stiffness frame components. These elements offer an efficient moment of inertia and enable easy access for joining processes such as riveting and bonding. When paired in a fuselage cross-section, they function similarly to I-beam webs, effectively sharing structural loads with the skin under pressure and bending. Their geometry also allows for relatively simple manufacturing processes. As aircraft structures evolve toward more efficient and lightweight designs, forming such curved components from fiber-reinforced composites has become increasingly desirable.

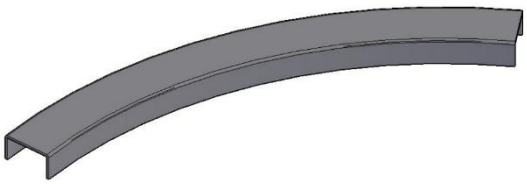

Figure 1: A curved C channel.

Among composite materials, unidirectional (UD) carbon fiber prepregs are widely used in the aerospace industry, where the strength-to-weight ratio plays a crucial role. During forming, longitudinal deformation along the fiber direction is limited due to the high directional stiffness of the fibers. As a result, plies with different fiber orientations require distinct deformation modes. This mismatch necessitates interply slippage—the relative movement between adjacent laminate layers—when shaping complex geometries using UD prepregs with quasi-isotropic layups, such as (0/90/45/–45)s, which contain multiple plies with different fiber orientations within a laminate [1, 2, 3]. Forming such stacks over double-curved molds introduces resistance to deformation and promotes buckling or wrinkling. Wrinkle defects are not only visually undesirable but also detrimental to structural performance, affecting dimensional accuracy and load-bearing capabilities. These issues have limited the widespread industrial adoption of composite forming, especially for aerospace-grade structures.

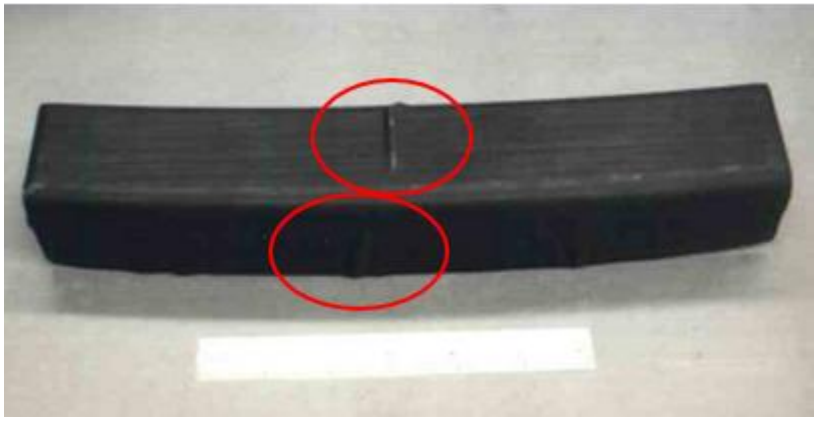

Figure 2: laminate wrinkle on a curved C channel part.

Double Diaphragm Forming (DDF) is one of the most established techniques used to address these challenges. In this method, the composite laminate is placed between two elastic diaphragms, and vacuum is applied to draw the laminate tightly against the forming tool. The elastic tension in the diaphragms applies pressure from both sides, helping to prevent out-of-plane buckling. While DDF is effective for thin laminates, it becomes less reliable with increased thickness or complex stacking sequences. For quasi-isotropic laminates, the combined effects of internal strain, limited ply compatibility, and interply shear resistance lead to persistent wrinkling.

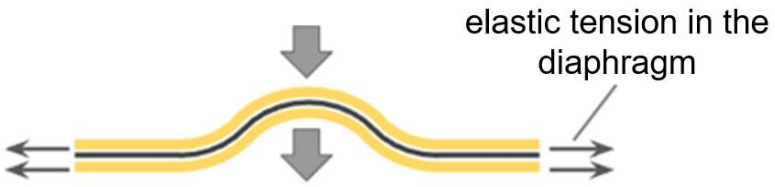

Figure 3: illustration of diaphragm pressure generated by the elastic tension.

Experimental results confirm this limitation. Curved C-channels formed with quasi-isotropic stacking using DDF consistently showed severe wrinkling along the flanges and curved surfaces, regardless of component size. This observation suggests that the fundamental mechanics of interply behavior and laminate deformation must be reconsidered. It also highlights the need for alternative forming strategies that reduce or eliminate interply slippage while maintaining compatibility with existing composite manufacturing workflows.



Figure 4: laminate wrinkling formed during double diaphragm forming process.

This research addresses the limitations of conventional forming methods by exploring a sequential forming technique for unidirectional prepregs. Instead of forming a thick laminate at once, thin layers are shaped individually and laminated progressively to build up the required thickness. By forming each ply or small stack directly on the mold surface, interply slippage is minimized or eliminated. This approach offers better conformity to complex shapes and prevents wrinkle formation, paving the way for more precise, defect-free composite components suitable for demanding applications.

2 A NEW FORMING METHOD FOR WRINKLE-FREE LAMINATES

Wrinkling in quasi-isotropic composite laminates remains a significant challenge in forming double-curvature geometries, especially when using unidirectional (UD) fiber prepregs. This issue arises primarily due to the limited interply slippage needed to accommodate the different in-plane deformation behaviors of plies with varying fiber orientations. In contrast, cross-ply laminates (e.g., 0°/90° or ±45°) can deform through a trellising mechanism, in which adjacent plies rotate locally relative to each other, reducing the need for slippage. However, quasi-isotropic layups—which combine multiple cross-ply orientations such as 0°/90° and ±45°—introduce conflicting deformation patterns among plies. In Figure 5, the trellising deformation of the blue laminate requires longitudinal slippage of the red ply (thick section). This mismatch increases interply resistance, elevates internal stresses, and often leads to out-of-plane buckling or wrinkle formation. Similar behavior has been observed in dry woven fabric composites as well [2, 4, 5, 6].

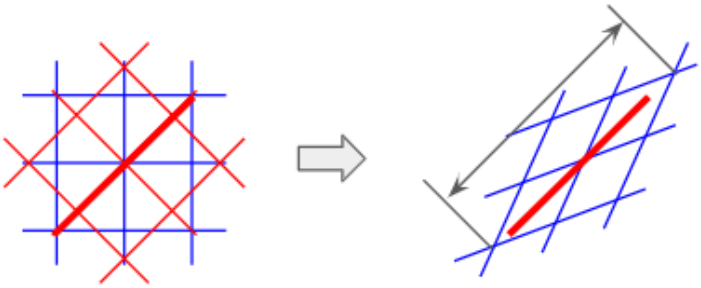

Figure 5: Illustration of the necessary interply slippage between plies with different fiber orientations during in-plane deformation. In quasi-isotropic laminates, misaligned fiber directions (e.g., ±45° vs.

0°/90°) require longitudinal slippage to accommodate trellising, leading to increased interply shear and potential wrinkling during forming.

To address this challenge, a new forming approach is proposed that eliminates the need for interply slippage by sequentially forming multiple thin laminates, one layer at a time, on top of previously shaped layers. In this method, each ply or sub-laminate is formed directly onto the tool surface or a pre-formed layer. By avoiding the bulk deformation of a thick laminate stack, the material can more easily conform to complex geometries without inducing significant interlaminar shear strains.

A critical requirement of this approach is to support the laminate from the both sides to suppress out-of-plane buckling during forming—while ensuring that no material remains trapped between the laminate and the tool. In conventional double diaphragm forming (DDF), the laminate is supported by diaphragms on both sides; however, one diaphragm remains between the tool and the laminate, as shown in Figure 6, and cannot be easily removed after forming.

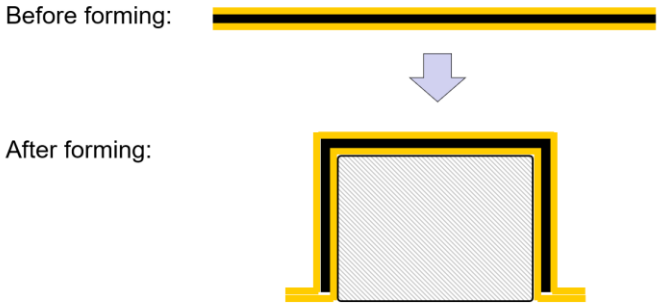

Figure 6: Schematic showing one of the diaphragms trapped between the composite laminate and the forming tool after forming with DDF.

To overcome this limitation, the proposed method employs inflatable tubes or long balloons placed adjacent to the tool surface to support the laminate during forming. As the forming completes, the balloons are fully deflated and removed, allowing the laminate to make direct contact with the tool surface.

The process begins by placing a thin composite prepreg on the diaphragm and the supporting table. A forming tool is then positioned on top of the laminate, as shown in Figure 7(a). Note that the color representing the diaphragm has been changed in Figure 7—from yellow in Figure 6 to a new color—to indicate the use of a natural rubber sheet. Figure 7(b) provides an angled view of the same setup, where inflatable tubes are placed adjacent to the forming tool. The composite laminate located beneath the inflatable tubes is visible in the magnified image. A top plate holds the tool in place throughout the forming process as the diaphragm inflates and exerts upward pressure against it. This top plate can be made from a transparent material, such as polycarbonate, to enable real-time observation of the forming progression.

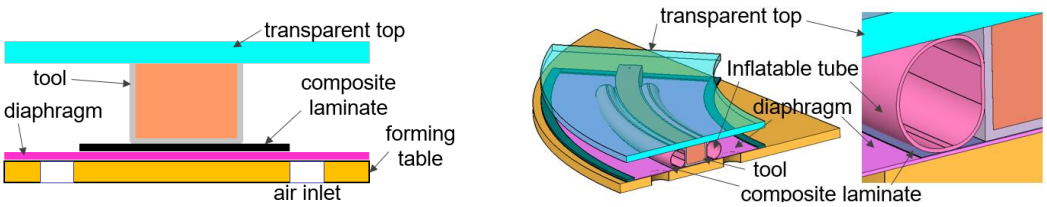

(a) cross sectional view (b) angled view with inflatable tubes

Figure 7: Schematic diagrams to illustrate the setup with tool on the laminate and diaphragm.

During forming, air pressure inflates the diaphragm, pressing the laminate toward the tool while the inflatable tube, positioned between the laminate and the tool, applies localized pressure to support the laminate. As forming progresses, air within the inflatable tube is gradually released to maintain appropriate contact pressure without obstructing the forming process. Figure 8 illustrates how the inflatable tubes deform while the diaphragm inflates. Once forming is complete, the inflatable tube is fully deflated and removed. The next ply is then placed and formed in the same manner. By repeating this process layer by layer, the total laminate thickness is gradually built up, reducing interply stress and effectively preventing wrinkle formation.

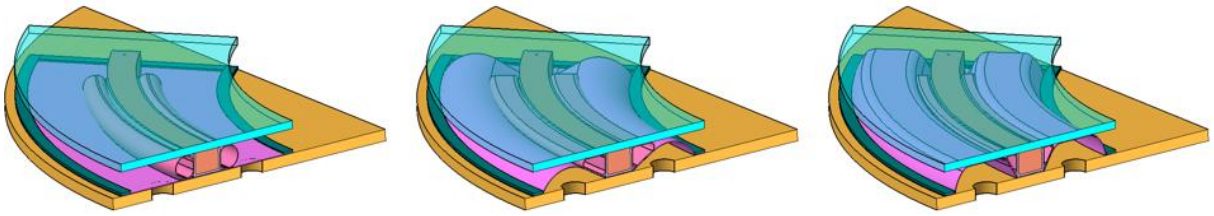

Figure 8: As the diaphragm inflates, the laminate deforms and the inflatable tubes are squeezed and exert supporting pressure on the laminate to prevent out of plane buckling.

This approach offers several advantages. First, it enables wrinkle-free forming of quasi-isotropic layups by sequentially forming thin laminates. Second, because the laminate is formed directly on the tool surface, in-place curing is possible without the need for repositioning. Third, the sequential nature of the process supports semi-automation, allowing integration of preform cutting, layer placement, and forming into a continuous workflow. Finally, desired stacking sequences such as $(0/90/\pm45)_s$ can be achieved by alternating between (0°/90°) and (±45°) layups during each cycle. This method offers a practical path forward for producing geometrically accurate, structurally sound composite parts with complex shapes. It opens new possibilities for forming high-performance UD laminates for aerospace and automotive applications, where shape fidelity and defect minimization are essential.

Figure 9 illustrates the progression of the forming process and indicates the point at which the inflated tube or balloon is removed—after Step 4—to allow the laminate to form directly on the tool surface. Step 6 demonstrates the repeatability of the process for building up laminate thickness.

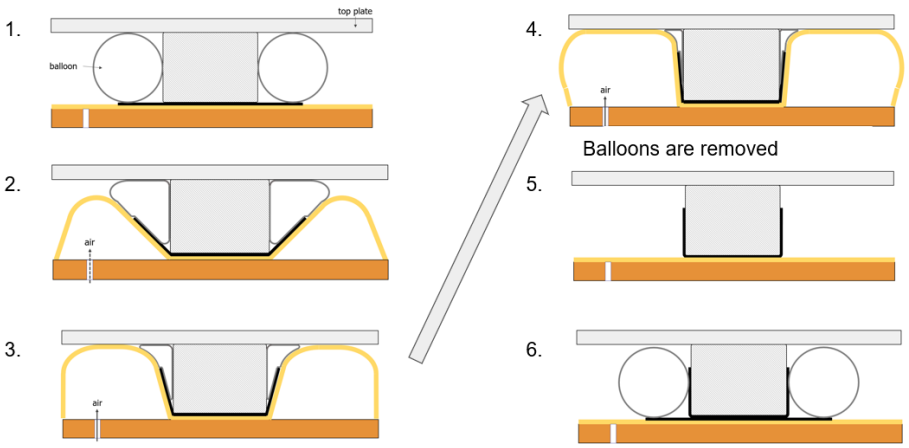

Figure 9: Step-by-step sequence of the proposed sequential forming process.

3 PRODUCED PARTS

Two composite parts with curved C-channel geometries were produced using the newly developed wrinkle-free forming method. The primary goal of the experiments was to evaluate the feasibility of sequentially forming cross-ply unidirectional (UD) laminates without introducing interply shear or laminate wrinkling. The first part, with dimensions of 30 cm in length and a channel height of 3 cm, was manufactured using a mold embedded with heating elements for in-situ curing. The laminate configuration consisted of eight plies arranged in a quasi-isotropic sequence: (0°/90°/+45°/−45°)s. This part was successfully cured, but localized defects such as bridging were observed, particularly in regions with high curvature. These defects indicated partial separation between the laminate and the tool surface during forming, prompting design refinements in the support structure.

The second part incorporated improvements including refined support mechanisms and better laminate placement, minimizing the chances of interlaminar bridging. A mixed-material mold—constructed from aluminum for structural rigidity and wood for thermal insulation—was used to facilitate even heat distribution. The same stacking sequence and dimensions were used, and inflatable bladders were employed beneath the diaphragm to maintain consistent pressure on the laminate from both tool and air-side surfaces. Notably, the second part demonstrated successful wrinkle-free forming, with no signs of buckling or delamination. Visual inspection and surface flatness assessments confirmed the structural integrity of the part.

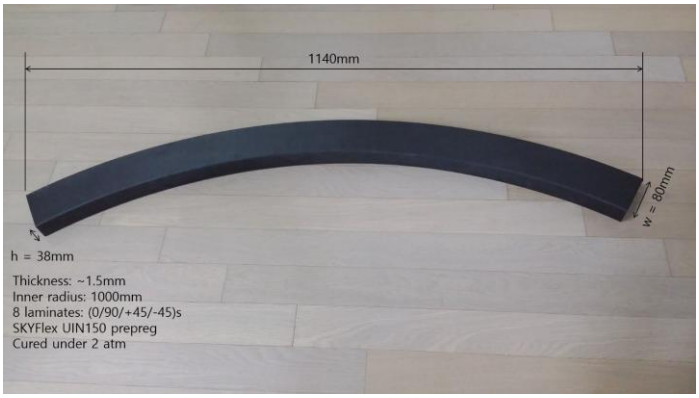

Figure 10: dimensions of the second curved C channel without wrinkles.

The successful fabrication of these components validates the proposed method's capability to form complex geometries in composite laminates without the introduction of defects typically encountered in double-diaphragm forming. Moreover, the modularity of this process allows for scaling to larger parts and different ply orientations, marking a significant advancement in out-of-autoclave composite

4 THICKNESS MEASUREMENT

Thickness uniformity across composite structures is essential for maintaining mechanical performance and ensuring predictable load-bearing behavior. To assess the effectiveness of the newly developed forming process, detailed thickness measurements were conducted on the second, wrinkle-free curved C-channel part. The specimen was marked with adhesive tapes at evenly spaced 5 cm intervals along the circumference to establish consistent measuring points. A micrometer equipped with extensions was used to measure the thickness of the top surface and both flanges, accounting for curved and constrained geometries.

The average thickness of the top surface was measured to be 2.17 mm, with a standard deviation of 0.05 mm. This indicates that the forming process provided excellent consistency in the laminate stacking and consolidation. The inner and outer flanges were measured separately to evaluate local variation. The average thicknesses were found to be 2.15 mm for the inner flange and 2.12 mm for the outer flange,

with no significant thickness gradient observed across the part height.

Further evaluation was conducted at high, middle, and low sections along the vertical height of the flange to analyze possible variations due to gravity or differential compaction pressures. The thickness values recorded were within ±0.1 mm of the average, demonstrating that the laminate layers remained well-aligned and that the support method effectively minimized thickness deviation. The measurement results confirm that interply slippage and wrinkling were successfully suppressed, allowing even consolidation of the laminate throughout the part.

These findings demonstrate the viability of the sequential cross-ply stacking and forming approach for producing geometrically complex, multi-ply composite parts with tight dimensional tolerances. The precise control over laminate thickness is particularly important for applications in aerospace structures, where uniform mechanical properties and dimensional accuracy are essential.

5 CONCLUSIONS

A novel forming method was developed to eliminate wrinkling in quasi-isotropic unidirectional composite laminates. By supporting the laminate from both sides using removable diaphragms and inflatable bladders, the process avoids interply slippage and enables direct forming on the tool surface. This method facilitates sequential cross-ply laminate stacking and in-situ curing, addressing key limitations of traditional double-diaphragm forming.

Two curved C-channel parts were produced, with the second part exhibiting wrinkle-free geometry and uniform thickness. Measurements showed an average thickness of 2.15 mm with minimal variation, confirming consistent consolidation throughout the part.

The proposed process is scalable and compatible with semi-automated manufacturing, making it a practical solution for industries requiring lightweight, high-integrity composite structures. It offers a reliable approach for forming complex geometries without defects, particularly in aerospace and advanced structural applications [2, 6].

ACKNOWLEDGEMENTS

This work builds upon the authors' earlier contributions, including U.S. Patent No. US11745408B2 and the publication titled "Forming Wrinkle-Free Curved C Channel with Unidirectional Fiber Reinforced Composites," published in the International Journal of Precision Engineering and Manufacturing-Green Technology [1, 7]. The present study expands and refines the forming process itself—now the focal point of this work—through revised explanations, enhanced illustrations, and additional discussion.

The authors gratefully acknowledge the mentorship of Professor Timothy Gutowski during the first author's earlier academic training, which provided foundational experiences that contributed to this research. This work was fully self-funded by the authors.

REFERENCES

[1] Chey, S.Y., Ahn, SH. Forming Wrinkle-Free Curved C Channel with Unidirectional Fiber Reinforced Composites. *Int. J. of Precis. Eng. and Manuf.-Green Tech.* (2025). https://doi.org/10.1007/s40684-025-00700-9

[2] Gutowski, T. G., Dillon, G., Chey, S., & Li, H. (1995). Laminate wrinkling scaling laws for ideal composites. *Composites Manufacturing, 6*(3–4), 123–134.

[3] P. Hallander, M. Akermo, C. Mattei, M. Petersson, T. Nyman, An experimental study of mechanisms behind wrinkle development during forming of composite laminates, *Composites Part A: Applied Science and Manufacturing*, Volume 50, 2013, Pages 54-64.

[4] F. Yu, S. Chen, L.T. Harper, N.A. Warrior, Investigation into the effects of inter-ply sliding during double diaphragm forming for multi-layered biaxial non-crimp fabrics, *Composites Part A: Applied Science and Manufacturing*, Volume 150, 2021, 106611.

[5] G.D. Lawrence, S. Chen, N.A. Warrior, L.T. Harper, The influence of inter-ply friction during double-diaphragm forming of biaxial NCFs, *Composites Part A: Applied Science and Manufacturing*, Volume 167, 2023, 107426.

[6] Li, Z.; Song, Q.; Liu, J.; Liu, W.; Chen, P.; Yue, G. Modeling of Preforming Process for Unidirectional Prepreg Composites Using Simplified Linear Friction Model and Fiber-Tracking Method. *Polymers* 2025, *17*, 1321. https://doi.org/10.3390/polym17101321.

[7] S. Y. Chey, *Material forming apparatus and material forming method*, U.S. Patent 11,745,408 B2, Sep. 5, 2023.

ICCM24 24TH INTERNATIONAL CONFERENCE ON COMPOSITE MATERIALS
AUG 4-8, 2025 • BALTIMORE CONVENTION CENTER • BALTIMORE, MARYLAND

DRAPING TOOL GENERATION FOR IMAGE-BASED SURROGATE DRAPING MODELS USING FREE FORM DEFORMATION AND TOPOGRAPHY MODIFICATION

Sophia Keller[1], Franz Maier[1], Anna Trauth[2], Markus G.R. Sause[2] and Roland M. Hinterhölzl[1]

[1]Department of Lightweight Design and Composite Materials, University of Applied Sciences Upper Austria
Stelzhamerstrasse 23, 4600 Wels, Austria
Email: sophia.keller@fh-wels.at, web page: http://www.fhooe.at

[2]Department of Material Resource Management, Augsburg University
Universitaetsstrasse 2, 86159 Augsburg, Germany
web page: https://www.uni-augsburg.de

Keywords: Draping simulation, Topography modification, Free form deformation, Parametric draping tool, Preforming

ABSTRACT

In the context of composite manufacturing process development, digital twins are often used to conduct parametric studies in order to determine the optimum process parameters without the need of extensive trial-and-error experiments. Process simulation using finite element (FE) method has become a well-established tool for performing such tasks. However, the major drawback of this method is the high computational cost (especially in the context of preforming when draping dry materials), which restricts calculations to a limited set of configurations that must be carefully selected by experts. Therefore, modern approaches increasingly focus on surrogate modeling using artificial intelligence. One possible surrogate model architecture is the image-based U-Net model that maps input images to resulting output images. When trained with sufficient data, this kind of model is able to predict results for different draping parameters quite accurately for draping tool geometries included in the training data (see [1]). When it comes to unknown tool geometries (that were not within the training data), however, predictions become unreliable. This paper describes the generation of a parametric tool that covers a range of different tool geometries in order to expand the prediction accuracy for unseen geometries. By training the surrogate model on draping tools with different similarities to a reference, it can interpolate within this similarity range, enabling accurate predictions for unknown draping tools that lie between known configurations. The parametric tooling uses a similarity measure to evaluate the degree of similarity between two tools of different similarities to a certain reference tool. The goal is to use these generated tools within a routine to automatically create training data and then train the surrogate using the simulation results for the varying tools. The developed parametric draping tool uses Free Form Deformation and the *Downhill Simplex method* to achieve shapes of different similarities.

1 INTRODUCTION

Over the last decades, artificial intelligence (AI)-based surrogate modeling became an increasingly popular strategy for approximating the complex behavior of various processes with faster yet still reliable alternatives. It is already applied across different disciplines such as biomedical applications [2], environmental science [3] or material science [4]. In the field of material forming and process simulation, there are also multiple applications in standard manufacturing such as metal forming [5, 6]. Most recent advances also show the use of surrogate models within the field of textile draping and composite manufacturing [7, 8]. Reported approaches range from rather low complexity (e.g., using linear regression models), to metamodeling [9] and neural networks of different complexities [10] up to highly complex full simulation models (e.g., using Position-Based Dynamics approaches) [8].

A quite common approach for the approximation of process parameters is the use of convolutional neural networks (CNNs) – especially in form of a U-Net architecture. U-Nets, originating from the field of biomedical image segmentation [2], are supervised learning models, usually trained on labeled images, where each data entry contains an input with an associated output image. A properly trained model allows for a readily available prediction, with only moderately complex architecture.

In a preliminary study, we established the applicability of a U-Net surrogate model to predict the draping behavior of a fabric onto a rib tool [1]. Findings confirmed the ideal suitability of the image-based surrogate to approximate the draping behavior and provide accurate predictions for the rib tool geometry it was trained on. However, the main disadvantage of those kind of models is their poor extrapolation capabilities, meaning that the model cannot provide accurate predictions for draping tools that were not included in the training data. This means, if we want to use the surrogate model for a new draping tool geometry, a whole new training data, including the new tool geometry, must be generated annihilating the time-savings by this approach. The objective of this study is therefore to create a parametric tool that enables the generalization of the U-Net surrogate model in order to enhance the prediction quality of unseen geometries.

2 METHODS

The idea of creating a parametric draping tool is based on the assumption that U-Net surrogate models are capable of interpolating between similar solutions (i.e., data augmentation, see [2]). The surrogate model used in [1] should therefore be expanded by training with tools of different similarities, enhancing generalizability and thus, the overall applicability of image-based surrogate models. To implement this approach, we developed a python script that is able to targetedly modify surfaces based on a reference surface in order to achieve tools with different degrees of similarity to the reference. The following subsections show a detailed description of the generalization concept, script architecture, working principle and algorithm specifics.

2.1 Overall Objective and Generalization Concept

In the aircraft industry, component and draping tool design play a crucial role in ensuring the component's structural integrity within the whole assembly. Oftentimes, tool geometries need to be slightly adapted in order to suit the varying application requirements. This results in various draping tools that differ in shape while still maintaining a certain degree of similarity. To ensure that the image-based surrogate model manages to deal with those kind of variations, they need to be reflected within the training data. In order to achieve that, we developed the following concept for the parametric tool creation:

First, a set of representative tool geometries (derived from real-world application components) must be defined. These serve as reference tools for creating variations with different degrees of similarity. The user provides their surface topology as *.stl* meshes. Examples of such geometries (e.g., based on typical aircraft components) are shown in Figure 1.

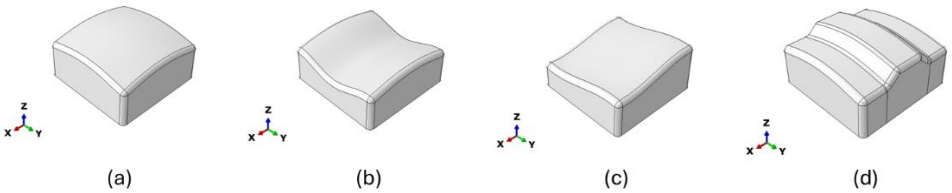

Figure 1: Examples of representative reference tools for aircraft components: (a) spheric calotte, (b) saddle-shaped, (c) double sine and (d) curved hat profile

Modifications of such tools are always limited to manufacturing constraints, such as maximum z-displacements. Therefore, additionally to the reference tools, the user needs to define the manufacturing constraints that limit maximum displacements and thus the distortion of the whole profile. These displacement constraints are based on user expertise, resulting in a maximum possible "dissimilarity" for the tool variations of a respective reference.

For proof of concept, we used a double sine (i.e., *Usecase 1*) and a parabolic geometry (i.e., *Usecase 2*) as tool references:

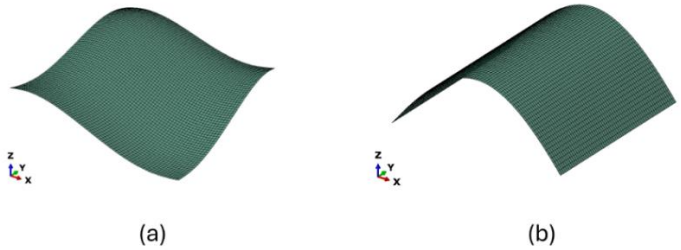

Figure 2: Reference meshes for (a) *Usecase 1* and (b) *Usecase 2*.

The developed routine should systematically generate variations with different similarities to those two geometries, while satisfying the predefined manufacturing constraints (which define the maximum dissimilarity for each shape). In a subsequent step the variations can be used for training the surrogate model, enabling a generalization of the model.

2.2 Script architecture

The developed python script includes the targeted surface modification, similarity assessment and export of created tools as *.stl* files. It can be divided into three main building blocks composing the algorithm:

a) Tool Deformation using Free Form Deformation (FFD)
b) Similarity Measure
c) Solver

Tool Deformation. The deformation of the tool is done via Free Form Deformation (FFD) using the python modules *splinepy* and *gustaf* [11]. This specific technique is used to deform geometrical objects by enclosing them with a hull based on 3D curves (e.g., B-splines or NURBS). By transforming the spline control points of the hull, the contained geometry can then be deformed [12] (see Figure 3). When selecting a reference tool (in our case an FE mesh, e.g., a double sine geometry), the number of spline points in each direction of a cartesian coordinate system can be specified. Distinct control points can then be selected to deform the tool.

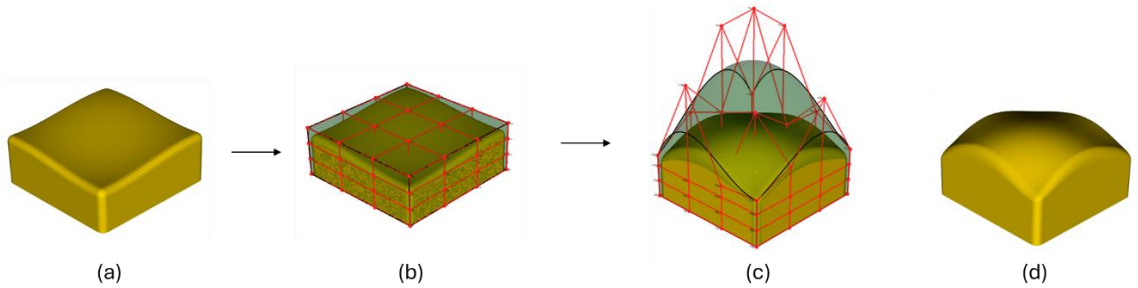

Figure 3: Schematic sketch of the working principle of FFD for a (a) double sine geometry as initial configuration, (b) enclosed in a spline hull and an exemplary deformed configuration (c) with and (d) without spline hull.

Similarity Measure. The similarity measure used to assess the degree of similarity between a reference mesh and the deformed mesh is the root mean square value (RMS) of the nodal distances d_i between the reference mesh and the deformed mesh (see equation (1)).

$$RMS = \sqrt{\frac{1}{n}\sum_{i} \boldsymbol{d}_i^2} \tag{1}$$

Different strategies for the similarity measure (such as the structural similarity index (SSIM) [13] or the comparison of histograms) were analyzed, however, the RMS measure provided the most suitable solution since the other approaches implied a loss of spatial correspondence (due to data summarization for histograms 2D conversion for SSIM).

Due to the manufacturing constraints explained above, the magnitude of the RMS value is limited to certain bounds. This constraint is implemented by calculating a maximum RMS value within predefined displacement bounds and normalizing the RMS value as shown in equation (2):

$$RMS_{norm} = \frac{RMS}{RMS_{max}} \tag{2}$$

This simultaneously ensures comparability between the RMS values of different configurations of the deformed mesh by normalizing the RMS value to a range of [0,1]. Spline control points can be displaced to achieve a certain similarity to the reference while considering the manufacturing constraints. The maximum possible RMS value is specific to the reference geometry as well as depending on the displacement bounds in z-direction. The RMS_{max} value is therefore determined in the following manner:

- *(1) Calculate Candidate z-values*. For each node in the reference mesh, the z-coordinate that lies furthest away from the point (within predefined bounds, either in positive or negative z-direction) is calculated.
- *(2) Enforce Neighbor Constraint*. The extreme values for the z-coordinates are adjusted so that a point does not exceed a fixed distance threshhold to its neighbors. This is done iteratively until convergence.
- *(3) Local Refinement*. The z-values with respected neighbor constraints are then again optimized to maximize the deviation (i.e., the RMS value).

Figure 4 shows a schematic visualization of the working principle in a 2D case:

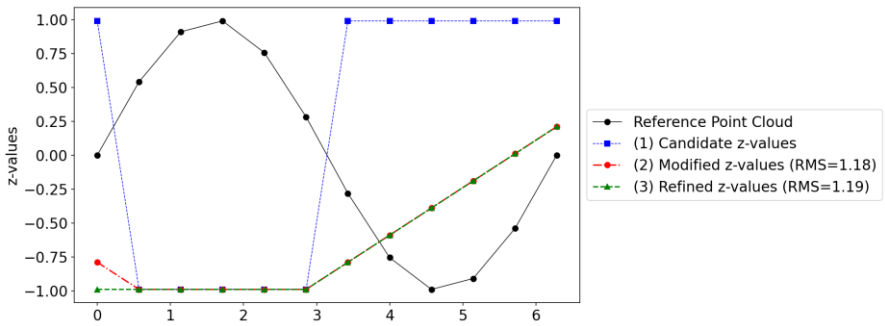

Figure 4: Schematic visualization of the working principle of the algorithm to determine RMS_{max} shown by the example of a 2D reference point cloud and the calculated (1) candidate values, (2) modified values based on the neighbor constraint and (3) refined values to maximize the RMS value.

Using this metric, different similarities to the reference within the design space can be determined by displacing the spline control points along the z-axis. Thereby, we can obtain shapes with different similarity to a reference, as demonstrated in Figure 5.

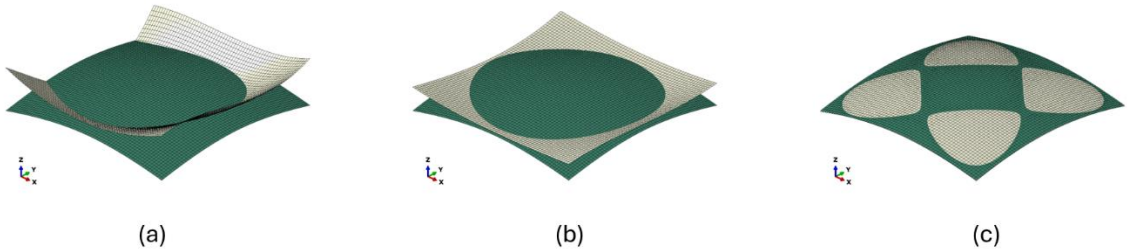

Figure 5: Possible solutions for (a) total dissimilarity (i.e., $RMS_{norm} = 0$), (b) medium similarity (i.e., $RMS_{norm} = 0.5$) and (c) total similarity ($RMS_{norm} = 1$) to the reference.

To automatically determine the spline displacement values necessary to achieve a possible configuration with target RMS value, we used the solver described in the following paragraph.

Solver. In order to determine a certain transformation array (i.e., array of z-displacements) for the spline control points to achieve a target similarity of the current deformed mesh to the reference mesh, an optimization algorithm was used. This algorithm enables a targeted topography modification to achieve a certain target value (T_v) for the similarity. Different optimization algorithms were analyzed on their suitability for the topography modification. For our purpose of optimizing the RMS value, we needed a derivative-free optimization algorithm, whereby the *Downhill Simplex Method (*also known as *Nelder-Mead method*) suited our application best since it allows for the optimization of non-linear functions with multiple parameters. In our case, the parameters to be optimized are the z-displacements of the spline control points and the objective function $f(\boldsymbol{x})$ to be minimized is the difference between the target value T_v and the normalized RMS value of the nodal distances $\boldsymbol{d}(\boldsymbol{x})$ between reference and deformed mesh (depending on the current z-displacement array $\boldsymbol{x}$ of the spline points):

$$f(\boldsymbol{x}) = T_v - RMS_{norm}\big(\boldsymbol{d}(\boldsymbol{x})\big), \tag{3}$$

The found geometry for a specific T_v is thereby one candidate solution that depends on the chosen starting point $\boldsymbol{x_0}$**.** Different starting points lead to different solutions which would all qualify for expanding the interpolation space of the surrogate model.

2.3 Topography Modification Procedure

Based on the three building blocks in section 2.1, the topography modification procedure is done using the *Downhill Simplex* algorithm combined with the FFD for the tool deformation and the similarity measure. Before delving into the working principle of the algorithm, we want to clarify the *terminology* to enhance understanding:

- A ***vertex*** (n-dimensional) in the context of the *Downhill Simplex Method* is one full candidate solution. It contains n entries which, in our case, reflects the number spline control points for which the z-displacement can be modified (e.g., $n = 16$).
- A ***simplex*** is a collection of $n + 1$ vertices (i.e., in our case, 17 arrays with dimension $n + 1$ each).
- The goal is to minimize the value of the ***objective function*** $f(\boldsymbol{x})$ where $\boldsymbol{x} \epsilon \mathbb{R}^n$ (in our case $\boldsymbol{x} \epsilon \mathbb{R}^{16}$). We want to reach a certain degree of similarity based on the similarity measure RMS_{norm}. Therefore, our objective is to reach a target value T_v by:

$$\min|f(\boldsymbol{x})| = \min|T_v - RMS_{norm}(\boldsymbol{x})| \tag{4}$$

To get a clear understanding of the topography modification via *Downhill Simplex Method*, the 6 individual steps (performed within a loop) are as follows [14]:

0) Initialization of Simplex Δ

The procedure starts by defining a **starting point** $\boldsymbol{x_0}$ and a **step size** s. The starting point x_0 is defined by our initial z-displacement of the spline points, which is an array of size n (i.e., number of modifiable spline points):

$$\boldsymbol{x_0} = [x_{01}, x_{02}, \dots, x_{0n}] \tag{5}$$

The initial simplex Δ then consists of $n + 1$ entries, whereby $\boldsymbol{x}_0$ initially serves as our first vertex within the simplex:

$$\Delta = \{\boldsymbol{x_0}, \boldsymbol{x_1}, \dots, \boldsymbol{x_n}\} \tag{6}$$

The residual 16 arrays are created by iteratively creating modified copies of $\boldsymbol{x}_0$ in the following manner:

$$\boldsymbol{x_i} = \boldsymbol{x_0} + s \cdot \boldsymbol{e}_i, \tag{7}$$

where s is the defined step size and $\boldsymbol{e_i} \in \mathbb{R}^n$ is the standard basis vector with 1 in the i-th position and 0 elsewhere.

The objective function f is then evaluated at each entry of the simplex Δ, to get a score for each vertex:

$$f_i = f(\boldsymbol{x_i}) \quad \text{for } i \in [0, n], \tag{8}$$

resulting in a set of pairs:

$$\{(x_i, f(x_i))\}_{i=0}^{n} \tag{9}$$

1) Order Vertices

In a second step, the set of pairs is sorted by score, from best to worst: $f(\boldsymbol{x_1}) \leq f(\boldsymbol{x_2}) \leq \cdots \leq f(\boldsymbol{x_{n+1}})$, with $\boldsymbol{x_1}$ being the vertex with the best score and $\boldsymbol{x_{n+1}}$ being the vertex with the worst score.

2) Compute Centroid of Simplex

The centroid $\boldsymbol{x_c}$ of the simplex is calculated without considering $\boldsymbol{x_{n+1}}$ (i.e., without the array with the worst score):

$$\boldsymbol{x_c} = \frac{1}{n}\sum_{i=1}^{n} \boldsymbol{x_i} \tag{10}$$

3) Reflection

The worst vertex $\boldsymbol{x_{n+1}}$ is then reflected using the centroid $\boldsymbol{x_c}$ by:

$$\boldsymbol{x_r} = \boldsymbol{x_c} + \alpha(\boldsymbol{x_c} - \boldsymbol{x_{n+1}}), \tag{11}$$

with α being the reflection coefficient. The reflected vertex $\boldsymbol{x_r}$ is then again evaluated using the objective function $f(\boldsymbol{x_r})$. If $\boldsymbol{x_r}$ achieves a better score than the second worst result $\boldsymbol{x_n}$, but not better than the best result $\boldsymbol{x_1}$, the worst result $\boldsymbol{x_{n+1}}$ is replaced by $\boldsymbol{x_r}$ and the iteration is terminated:

$$\boldsymbol{x_{n+1}} \leftarrow \boldsymbol{x_r} \qquad \text{if } f(\boldsymbol{x_1}) \leq f(\boldsymbol{x_r}) < f(\boldsymbol{x_{x+1}}) \tag{12}$$

Else the iterations move on to step 4a) or 4b), based on the score of the reflected vertex $\boldsymbol{x_r}$.

4a) If $f(\boldsymbol{x_r}) < f(\boldsymbol{x_1})$: Expansion

If the reflected array $\boldsymbol{x_r}$ achieves a better score than the best array $\boldsymbol{x_1}$, the expansion step is performed as follows:

$$\boldsymbol{x_e} = \boldsymbol{x_c} + \gamma(\boldsymbol{x_r} - \boldsymbol{x_c}), \tag{13}$$

with γ being the expansion coefficient. If the evaluation of $f(\boldsymbol{x_e})$ achieves a better score than $f(\boldsymbol{x_r})$, the expanded array $\boldsymbol{x_e}$ replaces the worst array $\boldsymbol{x_{n+1}}$:

$$\boldsymbol{x_{new}} = \begin{cases} \boldsymbol{x_e} & \text{if } f(\boldsymbol{x_e}) < f(\boldsymbol{x_r}) \\ \boldsymbol{x_r} & \text{otherwise} \end{cases} \tag{14}$$

$$\boldsymbol{x_n} \leftarrow \boldsymbol{x_{new}} \tag{15}$$

In either case, the current iteration is terminated, and the next iteration is started at step 1).

4b) If $f(\boldsymbol{x_r}) \geq f(\boldsymbol{x_n})$: Contraction

In case that the reflected array $\boldsymbol{x_r}$ performs worse than the second worst result $\boldsymbol{x_n}$, the contraction step is performed as follows:

- If $f(\boldsymbol{x_r}) < f(\boldsymbol{x_{n+1}})$: **Outside Contraction**

$$\boldsymbol{x_{co}} = \boldsymbol{x_c} + \gamma(\boldsymbol{x_r} - \boldsymbol{x_c}), \tag{16}$$

with γ being the contraction coefficient. If the contracted vertex $\boldsymbol{x_{co}}$ performs better than the reflected vertex $\boldsymbol{x_r}$, the worst vertex $\boldsymbol{x_{n+1}}$ is replaced by the contracted point $\boldsymbol{x_{co}}$ (i.e., $\boldsymbol{x_{n+1}} \leftarrow \boldsymbol{x_{co}}$), the iteration is terminated and the next iteration is started at step 1). Else, the iteration continues with step 5).

- If $f(\boldsymbol{x_r}) \geq f(\boldsymbol{x_{n+1}})$: **Inside Contraction**

$$\boldsymbol{x_{ci}} = \boldsymbol{x_c} - \gamma(\boldsymbol{x_{n+1}} - \boldsymbol{x_c}), \tag{17}$$

with γ being the contraction coefficient. If the contracted vertex $\boldsymbol{x_{ci}}$ performs better than the worst vertex $\boldsymbol{x_{n+1}}$, the worst vertex $\boldsymbol{x_{n+1}}$ is replaced by the contracted point $\boldsymbol{x_{ci}}$ (i.e., $\boldsymbol{x_{n+1}} \leftarrow \boldsymbol{x_{ci}}$) and the iteration is terminated (next iteration from step 1) on). Else, the iteration continues with step 5).

5) Reduction / Shrink (if expansion and contraction fail)

This step shrinks the simplex to narrow down to a local optimum, in case steps 3) and 4) fail. Thereby, all vertices of the simplex (except the best vertex $\boldsymbol{x_1}$) are replaced using:

$$\boldsymbol{x_{red}} = \boldsymbol{x_1} + \sigma(\boldsymbol{x_i} - \boldsymbol{x_1}), \tag{18}$$

with σ being the shrink coefficient. That way, all vertices are moved towards the best vertex and the next iteration starts at step 1).

In our case, for each step from 3) to 5), the current mesh is modified (using the current parameter set of the simplex), the nodal distances to the reference mesh, the corresponding RMS value is calculated, and the objective function is evaluated. Based on the respective score of the objective function, a decision is made to terminate the iteration or to continue with a subsequent step. This process is repeated until a certain termination criterion (also checked within each evaluation step) is reached.

2.2.1 Dynamic penalty

The z-displacement contraints are implicitly contained in the target value through RMS_{max}. However, this constraint also needs to be forwarded to the solver in order to ensure parameter exploration within the constraints. Therefore, we adapted the *Downhill Simplex* algorithm by including a dynamic penalization approach. This penalty is designed to constrain the z-displacements in compliance with manufacturing constraints and thereby prevent excessive deformations. The idea behind the dynamic penalty is to discourage displacements that deviate significantly from the residual displacements:

First, the bounds for the tolerable distance range are calculated using the interquartile range (IQR) and the lower (b_l) and upper (b_u) bound are defined as:

$$b_l = Q1 - i * IQR,\ b_u = Q3 + i * IQR, \tag{19}$$

with $Q1$ and $Q3$ being the lower and upper quartile and i being a multiplier that can be adapted according to the desired sensitivity to outliers. The entries of the spline point displacement array $\boldsymbol{x}$ are then filtered as 'below', 'above' or 'within' the bounds. For outliers below the lower bound, the individual penalty magnitude p_i is then calculated by:

$$p_i = (b_u - x_i)^2 \tag{20}$$

Similarly, the penalty for outliers above the upper bound is calculated as:

$$p_i = (x_i - b_l)^2 \tag{21}$$

We decided on a quadratic penalty function so that the solution performs exponentially worse with each point lying outside the IQR and with increasing distance. Before evaluating the individual score $f(\boldsymbol{x})$ of each step, the sum of all penalties $\sum p_i$ is added. This way, excessive distortions are considered rather unsuitable and the algorithm searches for alternative solutions.

2.3 Usecases for the Proof of Concept

For the proof of concept, we used the double sine and the parabolic geometry shown in Figure 2 as reference mesh and a plate geometry as initial mesh for the deformation. We conducted a parametric study with target values reaching from 0 (i.e., total dissimilarity) to 1 (i.e., identical meshes) in steps of 0.1 to evaluate the functionality of the developed routine. The hull for the FFD of our component consists of 4 x 4 x 2 spline control points, whereas only the top control points ($n = 16$) were enabled for the z-displacement (i.e., displacement in height direction).

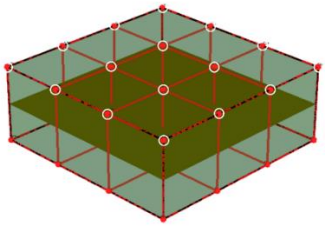

Figure 6: Spline hull for the deformation of the initial mesh for the usecases, with the modifiable control points marked in white.

This constraint was imposed to keep the calculation effort within a reasonable time. The parameters for the topography modification were chosen as follows:

- starting point $\boldsymbol{x_0} = [0,0,\dots,0] \in \mathbb{R}^{16}$
- step size $s = 0.1$
- the reflection, expansion, contraction and shrink coefficients were set to standard values [14]: $\alpha = 1, \gamma = 2, \rho = 0.5, \sigma = 0.5$

The convergence criterion is based on the number of consecutive iterations with improvements below $10e^{-6}$. The procedure is terminated as soon as 100 consecutive improvements below that threshold are reached.

3 RESULTS

The parametric studies were conducted on the two generic geometries: the double sine and the parabolic geometry. The following sections contain the results of the RMS_{max} determination as well as the parametric study.

3.1 RMS_{max} for the Usecases

Usecase 1. The automatically determined value for RMS_{max} resulted in 0.3. This value is reached when the points of the deformed mesh are furthest away from the reference, without leaving the space bounds and without violating the constraint for excessive distortion. A surface with those extreme values is shown in Figure 7:

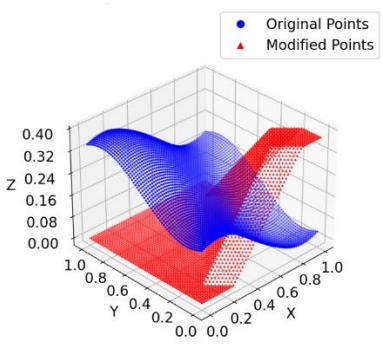

Figure 7: Configuration within the space bounds that leads to the highest RMS_{max} value for *Usecase 1* with reference mesh (blue) and modified mesh (red).

Usecase 2. As for *Usecase 1*, the maximum RMS value was automatically determined by calculating the deformed configuration which would lead to the largest distances between reference and deformed mesh. The RMS_{max} resulted in 0.3 (also similar to *Usecase 1*). The following figure shows the theoretical configuration that achieves the highest RMS value:

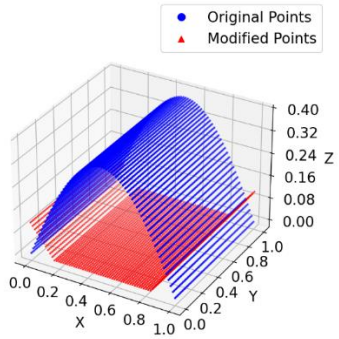

Figure 8: Configuration within the space bounds that leads to the highest RMS_{max} value for *Usecase 2* with reference mesh (blue) and modified mesh (red).

Even though these configurations are not possible to be reached using FFD (since the spline points always ensure a smooth surface without rough edges), they give an indication for the maximum possible RMS value that cannot be exceed by any of the tool modifications using FFD – thus it is suitable for normalization.

3.2 Results Parametric Study for the Usecases

Usecase 1. The surface modification was performed using a double sine geometry as a reference mesh and a planar geometry as deformable mesh. An exemplary mesh modification result for $T_v = 1$, including the hull and the modified spline points, is shown in Figure 9. The initial mesh (Figure 9a) is deformed by modifying the top row of spline control points in order to achieve a configuration similar to the reference mesh (Figure 9b).

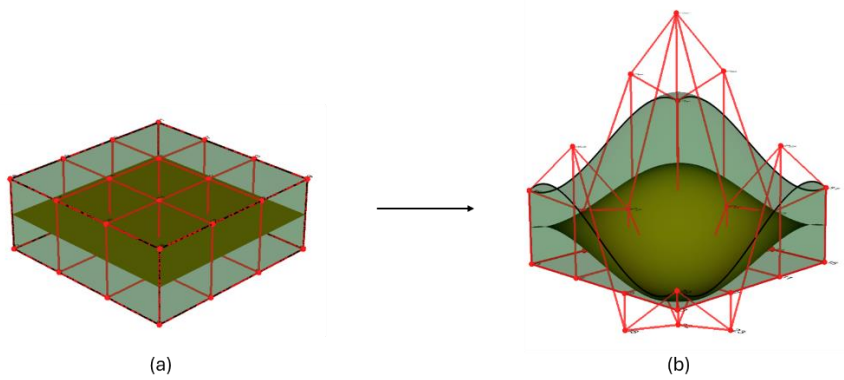

Figure 9: (a) Initial mesh and (b) deformed configuration for $T_v = 1$ with an achieved objective value of $f(\boldsymbol{x}) = 0.0019$

This procedure was done with target values from 0 to 1 in steps of 0.1. Figure 10 shows the resulting deformed meshes for the different target values (including the achieved score from the objective function) in superposition to the reference mesh.

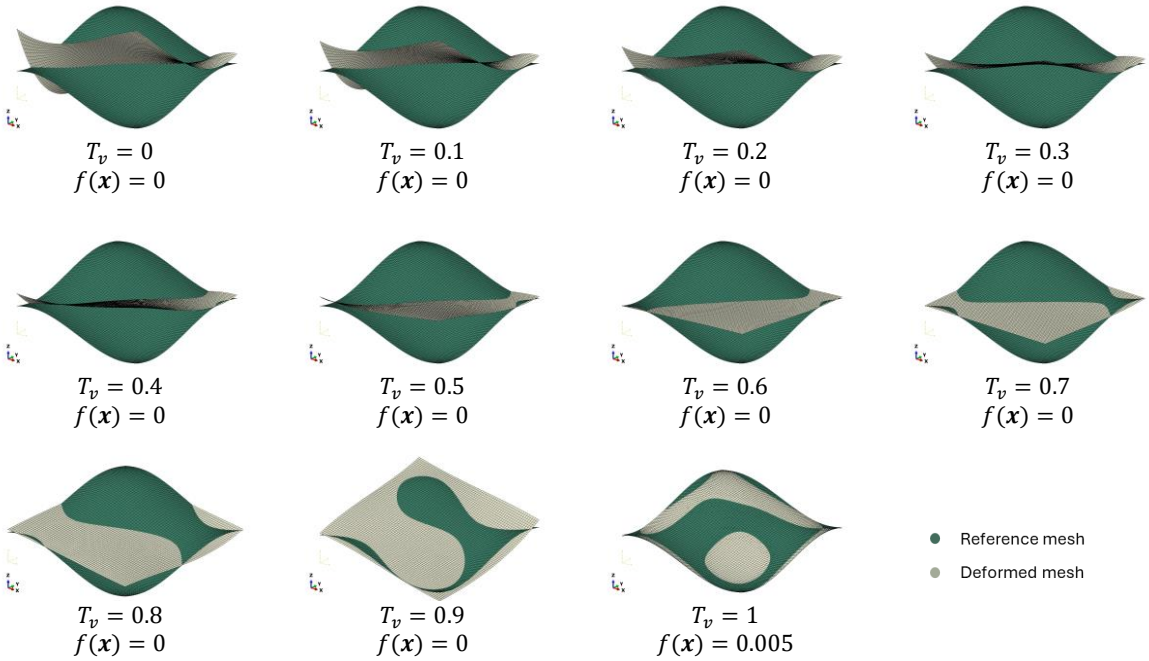

Figure 10: Resulting meshes depending on the target value, with the achieved objective value $f(\boldsymbol{x})$ indicating the difference to the respective desired target value for the double sine reference mesh.

For all target values except $T_v = 1$, the optimization algorithm found a solution matching the specified target RMS value. For a uniform starting point $\boldsymbol{x_0} = [0,0,\dots,0] \in \mathbb{R}^{16}$, the deformed meshes for $T_v = 0$ to $T_v = 0.5$ only show varying degrees of the same geometric shape. This indicates that the algorithm found the same local minimum for those target values, converging toward it to varying degrees. To mitigate this behavior, alternative starting points can be selected for those configurations to guide the algorithm toward a different local optimum. In case of $T_v = 1$, the RMS value only deviates by about 0.2 % from the target. Looking at the superposition of the reference and the deformed mesh in Figure 10, the meshes only deviate slightly. From a manufacturing perspective, these slight deviations from the desired tool shape will not affect the draping result drastically. The precision of the draping tool is therefore sufficient for the generation of tools with different degrees of similarity.

Usecase 2. Similar to *Usecase 1*, the surface modification was done using a parabolic geometry as reference mesh and a planar geometry as deformable mesh. Figure 11 shows an exemplary deformation result for $T_v = 1$ including the hull and the modified spline control points.

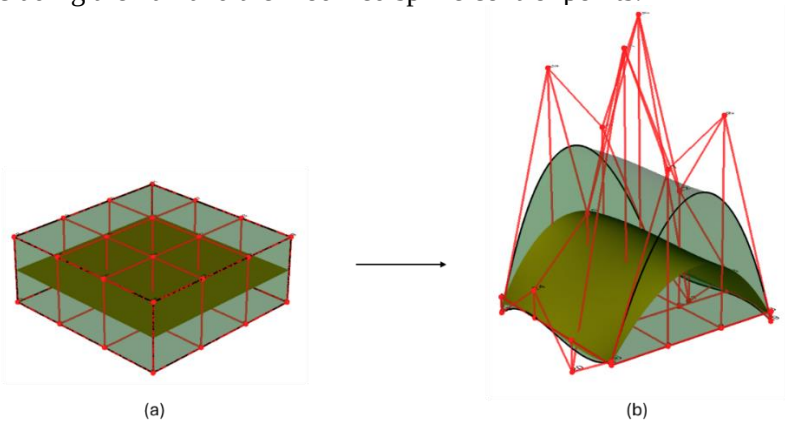

Figure 11: (a) Initial mesh and (b) deformed configuration for $T_v = 1$ with an achieved objective value of $f(\boldsymbol{x}) = 0.0018$.

Again, for each target value from 0 to 1 (in steps of 0.1), a deformed configuration was calculated. As for *Usecase 1*, the algorithm found solutions matching the specified target value, except for $T_v = 1$. Since for this usecase, the solver also tends to converge to the same local minimum (but to different extents) for target values below $T_v = 0.5$, only selected results are shown in Figure 12:

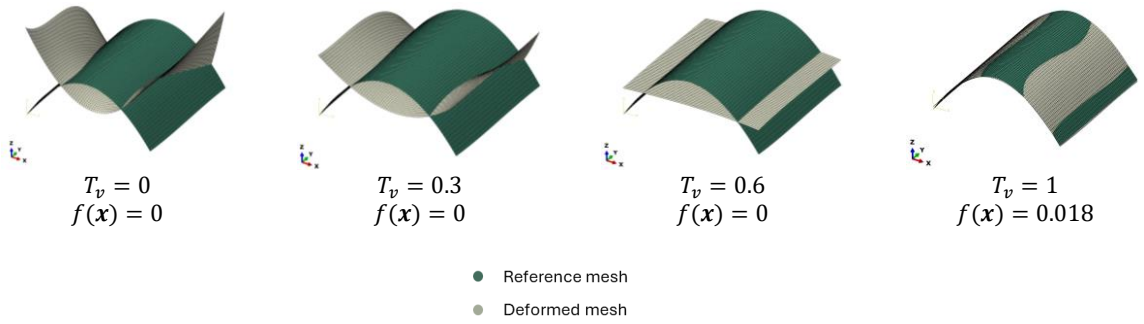

Figure 12: Resulting meshes depending on the target value, with the achieved objective value $f(\boldsymbol{x})$ indicating the difference to the respective desired target value for the parabolic reference mesh.

To demonstrate the dependency of the solution on the chosen starting point $\boldsymbol{x_0}$, Figure 13 shows different solutions calculated for $T_v = 0.5$ for different starting points $\boldsymbol{x_0}$.

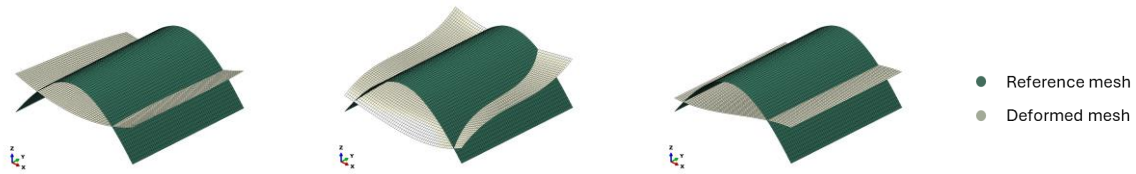

$$\boldsymbol{x_0} = \begin{bmatrix} 0, & 0, & 0, & 0, \\ 0, & 0, & 0, & 0, \\ 0, & 0, & 0, & 0, \\ 0, & 0, & 0, & 0] \end{bmatrix} \quad \boldsymbol{x_0} = \begin{bmatrix} -0.1, & 0.1, & -0.1, & 0.1, \\ -0.1, & 0.1, & -0.1, & 0.1, \\ -0.1, & 0.1, & -0.1, & 0.1, \\ -0.1, & 0.1, & -0.1, & 0.1] \end{bmatrix} \quad \boldsymbol{x_0} = \begin{bmatrix} -0.2, & -0.2, & 0.2, & 0.2, \\ -0.2, & -0.2, & 0.2, & 0.2, \\ -0.2, & -0.2, & 0.2, & 0.2, \\ -0.2, & -0.2, & 0.2, & 0.2] \end{bmatrix}$$

Figure 13: Resulting meshes for $T_v = 0.5$ depending on the starting point $\boldsymbol{x_0}$ (with the achieved objective value $f(\boldsymbol{x})$ for the parabolic reference mesh).

All resulting geometries match the desired T_v of 0.5. The starting point, however, influences the resulting shape. This emphasizes the need for further investigations concerning the selection of the starting point $\boldsymbol{x}_0$. Beside that, the interaction between the three building blocks of the routine works quite well since linking the three components (FFD, similarity measure and optimization algorithm) provides a plausible set of configurations for the different target values and shapes can be controlled using different starting points.

4 CONCLUSIONS

The developed routine provides a robust, repeatable way to generate draping tools of different similarities for generic shapes such as a double sine and a parabolic geometry. There is still potential for improvement concerning the tendency of solutions within a certain target to converge to the same solution but with varying degrees. A detailed study on the starting point $\boldsymbol{x_0}$ selection as well as a more in-depth analysis on the penalty function are planned for future studies to guide the optimization algorithm toward different local optimum solutions from the outset. Additional next steps are to include real component tools in the representative tool set. If this step works out well, the U-Net surrogate model explained in [1] should be trained with the different tools and the prediction quality should be evaluated.

ACKNOWLEDGEMENTS

We want to thank the Austrian Research Promotion Agency (FFG) and the Austrian Ministry for Climate Action, Environment, Energy, Mobility, Innovation and Technology for the financial support of the projects *Jarvis4Pre* (Grant No. 886871) in the scope of the "Take Off" funding program and *AutoDrape* (Grant No. 895980).

REFERENCES

[1] S. Keller, F. Maier, P. M. Blies and R. M. Hinterhoelzl. Creating Training Data for Surrogate Models using FE Draping Simulation. *Proceedings of the 23rd International Conference on Composite Materials (ICCM)*, Belfast, 2023.

[2] O. Ronneberger, P. Fischer, T. Brox. U-Net: Convolutional Networks for Biomedical Image Segmentation. *Computer Vision and Pattern Recognition*, pp. 234-241, 2015.

[3] M. L. Taccari, J. Nuttall, X. Chen, et al. Attention U-Net as a surrogate model for groundwater prediction. *Advances in Water Resources*, Volume 163, 2022.

[4] B.R. Swain, D. Cho, J. Park, et al. Complex-Phase Steel Microstructure Segmentation Using UNet; Analysis across Different Magnifications and Steel Types. *Materials*, MDPI, Volume 16, 2023.

[5] H. Zhou, Q. Xu and N. Li, A study on using image based machine learning methods to develop the surrogate models of stamp forming simulations, *Journal of Manufacturing Science and Engineering*, Vol. 144, Issue 2, 2020.

[6] J. Jakumeit, M. Herdy, M. Nitsche. Parameter optimization of the sheet metal forming process using an iterative parallel kriging algorithm. *Structural and Multidisciplinary Optimization 29*, pp. 498-507, 2005.

[7] C. Zimmerling, C. Poppe and L. Kärger, Estimating optimum process parameters in textile draping of variable part geometries - A reinforcement learning approach, Procedia manufacturing, *Proceedings of the 23rd International Conference on Material Forming, ESAFORM 2020*, Cottbus, Germany, Elsevier, 2019, pp. 426–431.

[8] P. M. Blies, S. Keller, U. Kuenzer et al. Towards the Automation of Woven Fabric Draping via Reinforcement Learning and Extended Position Based Dynamics. *Journal of Manufacturing Processes*, Volume 141, pp. 336-350, 2025.

[9] M. H. A. Bonte, A. H. V. D. Boogaard, J. Huétink, A metamodel based optimisation algorithm for metal forming processes, *International Journal of Forming Processes*, 2007.

[10] H. Jedda, A. Ghith and S. Faouzi, Prediction of fabric drape using the Neural Networks, *International Conference of Applied Research in Textile (CIRAT-2)*, Tunisia, 2006.

[11] J. Lee, *splinepy – Library for prototyping spline geometries of arbitrary dimensions and degrees, and IGA*, 2024, tataratat.github.io/splinepy [accessed: 19.05.2025]

[12] T.W. Sederberg, S.R. Parry, Free-form deformation of solid geometric models, *ACM SIGGRAPH Computer Graphics*, 20, 1986, pp. 151-160 (doi:10.1145/15886.15903).

[13] Z. Wang, H. R. Sheikh, Image Quality Assessment: From Error Visibility to Structural Similarity, *IEEE Transactions on Image Processing*, Vol. 13, No. 4, 2004.

[14] J. C. Lagarias, J. A. Reeds, M. H. Wright and P. E. Wright, Convergence Properties of the Nelder-Mead Simplex Method in Low Dimensions, *SIAM Journal on Optimization*, Vol. 9, No. 1, pp. 112-147, Society for Industrial and Applied Mathematics, 1998.

COMPACTION AND FLUID-STRUCTURE INTERACTION LEADING TO FIBER DISPLACEMENT IN RESIN INFUSION OF COMPOSITE MANUFACTURING

Debabrata Adhikari[1], Jesper John Lisegaard[1], Jesper Henri Hattel[1] and Sankhya Mohanty[1]

[1]Department of Civil and Mechanical Engineering, Technical University of Denmark
Produktionstorvet, Building 425, DK-2800, Kgs. Lyngby, Denmark
Email : debaa@dtu.dk,

Keywords: Preform, Resin flow, Permeability, Compaction, Fluid-structure-interaction

ABSTRACT

Accurately predicting flow behavior in dry fiber preforms is essential for many liquid molding processes, including resin transfer molding (RTM). One of the main challenges in RTM is obtaining precise permeability values to ensure complete saturation of the preform during infusion. Conventionally, permeability predictions are made using flow experiments on compacted dry fiber layers or by predictive flow simulation assuming an idealised preform. During RTM, the fabric undergoes initial compaction, subsequent relaxation at the arrival of the resin flow front, and eventually full saturation. To address the complex fluid-structure interactions, one approach would be to model the preform deformation during compaction and then study the change in fiber volume fraction during the steady state flow of resin. In this work, a mechanical model accounting for the frictional contact between the yarns was developed in order to predict the displacement during the initial compaction of the dry yarn assembly. The post-compaction deformed geometry is subsequently used within one-way coupled fluid-structure interaction simulations to predict the final fiber distribution within the modelled domain as well as the resultant steady state saturated permeability.

1 INTRODUCTION

Fiber-reinforced polymers (FRPs) are known for their high specific strength, excellent stiffness-to-weight ratio and durability, making them ideal for applications across civil infrastructure, aerospace, wind energy, marine, and automotive industries. Vacuum-assisted resin transfer molding (VARTM) is a widely adopted method for manufacturing large-scale composite structures, such as wind turbine blades. In VARTM, resin is infused into a dry fiber preform under near-vacuum conditions by maintaining a small pressure differential between the inlet and the outlet. This slow vacuum-driven infusion, followed by curing in external ovens, eliminates the need for expensive autoclaves. However, VARTM-produced components often exhibit local variations in fiber volume fraction, as the final saturation is influenced by the interplay between the resin's flow capacity (commonly defined by the preform's permeability) and the localized compaction pressure (leading to fiber deformation) [1,2]. The overall permeability of the VARTM mold system, which includes the core, the fiber preform, the distribution media and the peel ply, is affected by the geometric features occurring across multiple scales. At the macro scale (cm to m), elements such as the distribution media, the peel ply, the release film, and the flow channels in the core significantly influence the global resin flow. At the meso-macro scale (mm to cm), the type of weave or the non-woven structure, as well as the lay-up sequence within the laminate, govern how resin propagates through the layers. At the micro-meso scale (µm to mm), factors such as the intra-yarn and the inter-yarn spacing and the packing arrangement become more critical for local permeability. In essence, the macro-scale permeability dictates the resin distribution speed across the mold (helping to prevent large dry spots) while the meso- and the micro-scale permeabilities govern the uniformity of the resin infusion between fibers and the saturation levels (i.e. they impact the inter- and intra-tow micro-void formation).

During VARTM, the dry fiber preform undergoes a sequence of mechanical and fluid interactions beginning with compaction during vacuum bagging, followed by partial relaxation as the resin front

arrives, and concluding with full saturation. These stages introduce complex fluid-structure interactions due to both infusion and compaction effects. Typically, researchers have taken a two-step approach to predict permeability and flow behavior [3]. The first step addresses preform deformation, modeling the yarn's behavior using elastic or hypoelastic properties to capture its deformation during compaction [4] then studying the permeability based on change of fiber volume fraction [5]. Studies have considered fiber displacement due to shear deformation in angle-ply reinforcements [6] due to draping and yarn slippage of woven fiber layups [7], but a significant challenge remains in exporting the predicted deformed geometry to create a fluid domain for flow analysis.

In this study, a model to simulate the yarn deformation and the displacement during the initial compaction of a dry fiber assembly was developed using the mechanical solver within ANSYS Workbench. Realistic boundary conditions corresponding to the vacuum bagging step were applied alongside appropriate contact definitions to prevent yarn interpenetration and to accurately replicate the physical compaction behavior. Following the mechanical simulation, the deformed yarn geometry was transferred to the CFD software ANSYS FLUENT to evaluate the resulting flow behavior and assess the impact on permeability. Key parameters such as the change in global fiber volume fraction (V_f), the yarn slippage, and the potential overlap were analysed to compare the permeability between the undeformed and the compacted configurations of the fiber preform. The use of one-way fluid-structure interaction (FSI) coupling within the unified ANSYS Workbench environment enabled a more refined estimation of both the initial mechanical compaction and the corresponding local flow characteristics to propose more accurate, deformation-dependent permeability predictions.

2 STRUCTURAL MODEL - COMPACTION

The deformation of the fiber layup has been studied in the linear elastic regime (Equation 1) for UD glass fibers considering frictional contact between the yarns. Here, $\boldsymbol{\sigma}$ and $\boldsymbol{\varepsilon}$ are the stress and the strain tensor of the material respectively, while the material properties E of the UD fiber correspond to those of Epoxy E-Glass UD with orthotropic elastic properties (Table 1). A static structural analysis is performed in this study while implementing a displacement-based control for the compaction of yarn layups.

$$\boldsymbol{\sigma} = E\,\boldsymbol{\varepsilon} \tag{1}$$

Table 1: Material properties of Epoxy E-Glass UD (Orthotropic) fiber composite.

Epoxy E-Glass UD	**Values**	**Unit**
Density (ρ)	2000	kg/m^3
Young modulus X direction (E_x)	45000	*MPa*
Young modulus Y direction (E_y)	10000	*MPa*
Young modulus Z direction (E_z)	10000	*MPa*
Poisson's ratio XY (v_{xy})	0.3	
Poisson's ratio YZ (v_{yz})	0.4	
Poisson's ratio XZ (v_{xz})	0.3	
Shear modulus XY (G_{xy})	5000	*MPa*
Shear modulus YZ (G_{yz})	3846.2	*MPa*
Shear modulus XZ (G_{xz})	5000	*MPa*

Initially an idealised yarn layup consisting of three layers of unidirectional (UD) fibers is placed between two plates. For simplicity, the same frictional contact type has been assumed between the yarns and between the yarn and the mould plate [8], with a friction coefficient value of 0.2. A fixed support was applied to the bottom face of the bottom plate (label A in Figure 1), which fully restrained all translational and rotational degrees of freedom for the bottom plate. The top face of the top plate (label B in Figure 1) was subjected to a displacement of 3mm in the Y-direction. To avoid rigid body motion, the out-of-plane displacement of the yarn side faces across XY plane is set to zero with no translation

along X axis except the translation and compaction along Y-axis (label C in Figure 1). Additionally, on the side face of yarn YZ-plane, the out-of-plane displacement is also set to zero keeping Y-axis free to move (label D in Figure 1). To avoid excessive penetration between the yarns, the pinball radius is set to 0.05mm. The direct numerical scheme with sub-steps control has been considered, thus accounting for over 200 sub-steps allowing large deflection for the yarns. The final displacement of the top plate (0.21 mm) to the maximum allowable distance has been simulated with 3 intermediate displacement load states.

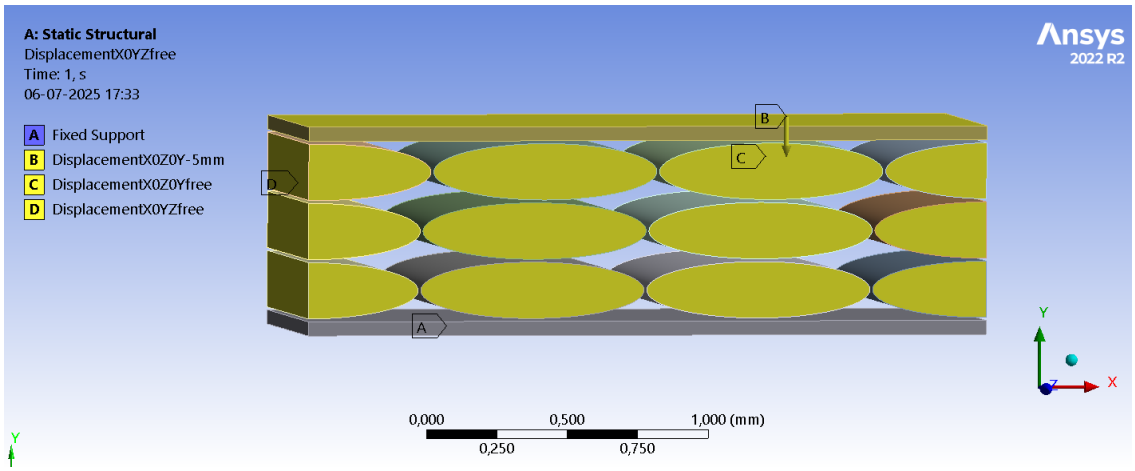

Figure 1:Load state and the boundary conditions for compaction of yarn layup.

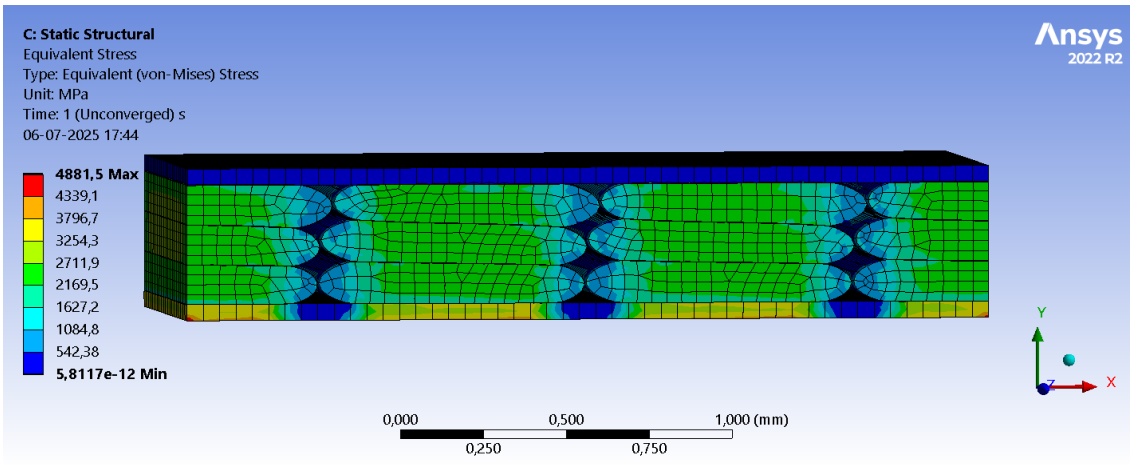

Figure 2: Equivalent stress observed on the layup and the compaction plate.

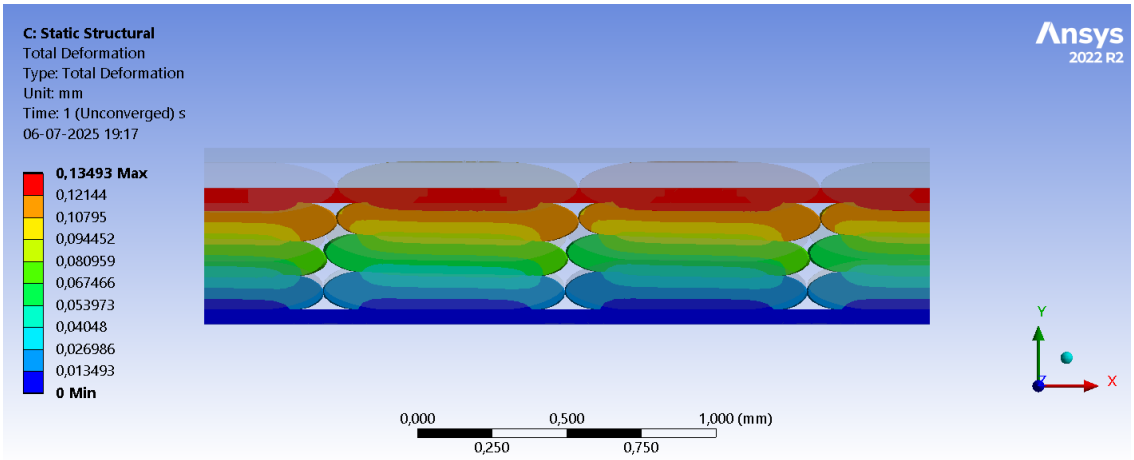

Figure 3: Deformed state of compacted yarn layup and yarns overlap

Figure 2 illustrates the equivalent stresses during the final displacement load state of the top plate. Stress concentrations are visibly evident around the interfaces between the yarn layup, indicating that each yarn experiences substantial mechanical loading as the top plate closes the gap. The symmetrical stress patterns highlight uniformity and periodicity within the internal structure. Figure 3 illustrates the total deformation field in the compacted yarn layups. The central zones, where the yarns are closely packed, exhibit higher deformation magnitudes, suggesting significant compaction induced displacement and mechanical interaction. Additionally, yarn slippage/overlap is also observed between yarn in a layer. These overlapping areas are critical in modeling realistic fiber architecture behavior, as they reflect the actual physical phenomena encountered during manufacturing processes. It is estimated that the global fiber volume fraction V_f increases from 46.54% to 62.55%, while the intra fiber V_f of each yarn is updated from 64% in undeformed configuration to 67.28% (in Table 2) in the deformed state.

Table 2: Change in local intra yarn and global preform fiber volume fraction.

Preform Configuration	**Local intra yarn v_f [%]**	**Global V_f [%]**
Undeformed	64	46.54
Deformed	67.28	62.55

3 FLUID MODEL – PERMEABILITY

The compacted yarn layup has been extracted for subsequent CFD simulations to estimate the permeability and predict the flow behaviours. The surface maps of the compacted yarn from the deformed stated are curated to create a suitable mesh for the flow simulation within ANSYS Fluent. It has been assumed that the intra yarn fiber volume fraction (v_f) is 64%. In the Gebert model [9], the micro-scale longitudinal (k_{ll}) and transverse ($k_\perp$) permeability characterization is based on the geometrical arrangement of individual fibers and utilize the fiber diameter and the volume fraction of the yarn. Equation 2, provide the analytical permeability for the hexagonal packing of the individual fiber arrangement in the unit cell of a yarn. Intra-yarn permeability ($k_{ll}, k_\perp$) has been predicted from the Gebert's model considering fibers are arranged in a hexagonal pattern.

$$k_{ll} = \frac{8r^2}{53}\frac{(1-v_f)^3}{v_f^2}$$
$$k_\perp = \frac{16}{9\pi\sqrt{6}}\frac{\left(\sqrt{\frac{v_{fmax\_hex}}{v_f}}-1\right)^{2.5} r^2}{v_f^2} \quad (2)$$

Here, v_{fmax_hex} refers to the maximum $v_f (= \frac{\pi}{2\sqrt{3}})$ achieved in the hexagonal packing when the circular fiber touches each other within a yarn. A resin with density (ρ) of 1212kg/m^3 and viscosity (μ) of 0.09 Pa.s has been used as the fluid medium, with the inlet and the outlet pressure being set at 100 Pa and 10 Pa respectively along the fiber direction of the yarn. A schematic of the flow simulation has been shown in Figure 4.

As depicted in Equation 3, Darcy's law has been used to describe the fluid flow behaviour in the porous media.

$$v = \frac{1}{\mu} \boldsymbol{K}.(\nabla P + \rho g) \tag{3}$$

where the volume averaged Darcy velocity v was correlated to the pressure gradient ∇P, the dynamic resin viscosity μ, as well as the resin density ρ, through the permeability tensor $\boldsymbol{K}$ and g the gravitational constant. Moreover, to ensure the resin flow between the porous yarn and the adjacent flow channels, the Brinkmann model has been used. The meso-scale permeability [10] is then estimated based on the calculated flowrate across the outlet surface and the applied pressure gradient between the inlet and the outlet.

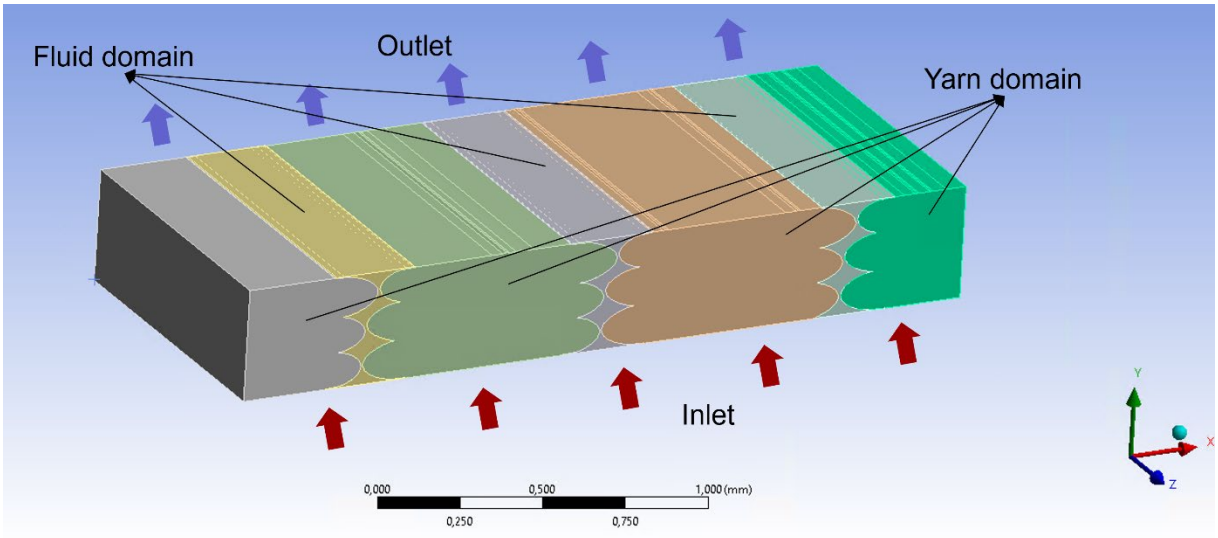

Figure 4: Flow configuration of the deformed preform considering porous yarn.

The pressure profiles presented in Figure 5 shows a smooth and continuous gradient from the inlet to the outlet, indicating that a steady-state resin flow has been established in both the undeformed and deformed configurations of the preform. This steady gradient suggests that the flow front has fully propagated through the domain and the pressure distribution has stabilized across the fiber assembly. However, a closer examination of the undeformed configuration reveals that the yarn boundaries near the outlet face exhibit localized pressure variations when compared to the surrounding matrix. This discrepancy may be attributed to the idealized geometry in the undeformed state, where uniform fiber packing and regular channel pathways may not accurately capture the true resin flow resistance encountered at the microstructural level. In contrast, the deformed configuration accounting for the compaction-induced yarn displacement and the change in both the local and the global fiber V_f shows more realistic flow resistance and pressure drop behavior.

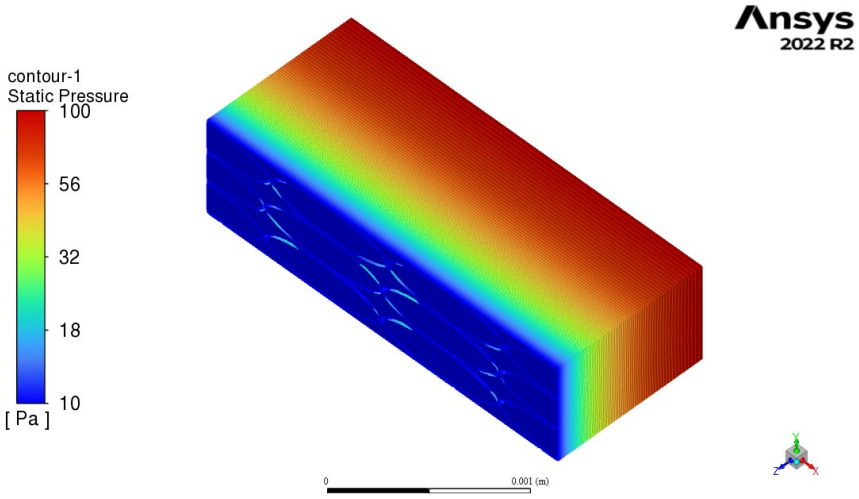

(a)

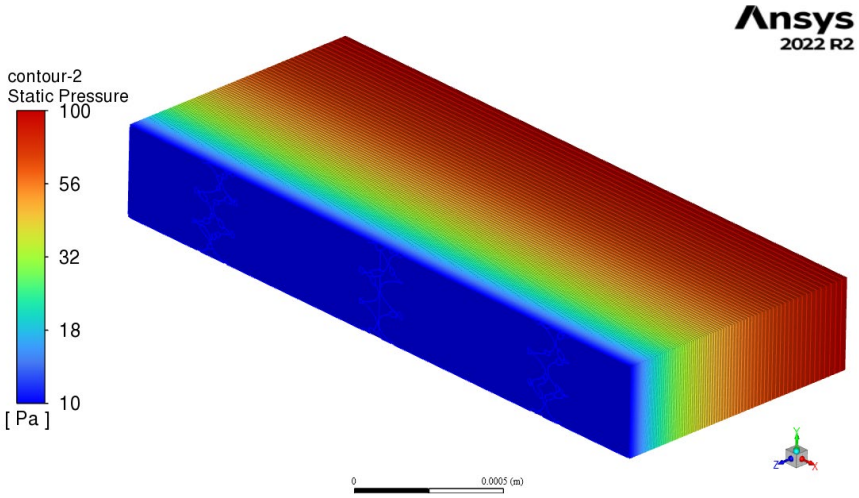

(b)

Figure 5: Infusion pressure profile in (a) undeformed and (b) deformed state of the preform.

In Figure 6, the velocity profiles during resin infusion through the fiber preform in both the undeformed and deformed states are presented. It is observed that, in the undeformed configuration, the velocity profile reveals significantly higher peak value up to approximately 0.01 m/s in the intra yarn spaces. Thus, the uniform geometry of the undeformed preform, containing relatively large open channels, allows for an easier resin passage. Correspondingly, as shown in Table 3, the undeformed preform exhibits a higher permeability. In contrast, the deformed configuration shows significantly lower flow velocity (around 5.7e-4 m/s) with flow localized along narrower paths. The deformation caused by the mechanical compaction and the yarn displacement altered the internal geometry of the preform, consequently increasing the flow resistance and reducing the overall permeability (by 2-orders of magnitudecompared to the undeformed state). From the contour line of velocity profile, it is also noted that level of yarn saturation in the intra yarn porous space is comparatively low in the deformed configuration than the undeformed state.

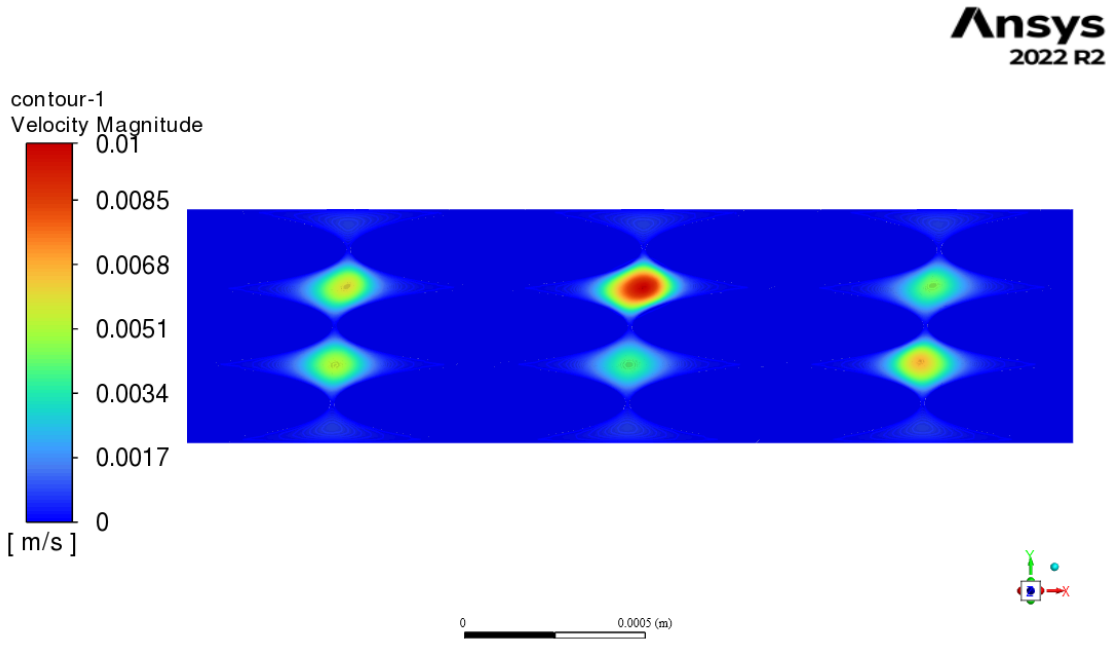

(a)

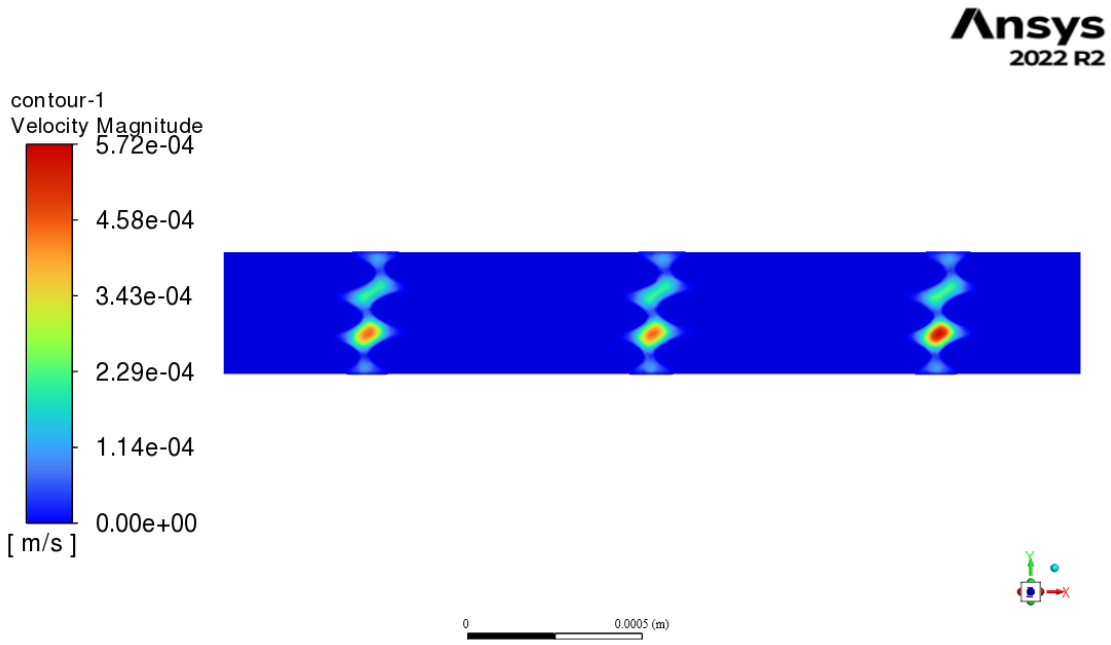

(b)

Figure 6: Velocity profile in (a) undeformed and (b) deformed state of the preform.

Table 3: Estimated permeability in undeformed and deformed state of preform.

Preform configuration	**Global V_f [%]**	**Permeability [m^2]**	**Mass flow rate [kg/s]**
Undeformed	46.54	1.8572e-10	6.4826459e-07
Deformed	62.55	5.4767e-12	1.3291301e-08

This clearly demonstrates that ignoring the preform deformation can lead to substantial overestimation of flow and permeability. Upon incorporating these deformations, the resulting flow pattern becomes more constrained and non-uniform, better reflecting real manufacturing conditions. These findings emphasize the critical role of coupled fluid-structure interaction modelling in accurately predicting the resin infusion behavior in composite manufacturing processes.

4 CONCLUSIONS

This study presents an integrated numerical approach to model compaction-induced deformation and its influence on resin flow in dry fiber preforms during VARTM. By employing a one-way fluid-structure interaction (FSI) framework within ANSYS Workbench, the yarn deformation under mechanical compaction was accurately captured, and the resulting deformed geometry was utilized to simulate the resin flow and predict the permeability. The analysis revealed that compaction significantly alters the internal geometry of the preform, increasing the global fiber volume fraction and reducing the available flow channels, which in turn leads to a substantial decrease in permeability by nearly two orders of magnitude compared to the undeformed configuration. The pressure and the velocity profiles demonstrate that idealized undeformed geometries overestimate the flow uniformity and the resin saturation. It is thus necessary to incorporate the deformation-dependent flow domains within VARTM simulations to enhance the permeability prediction accuracy (and improve the reliability of composite manufacturing process modelling).

ACKNOWLEDGEMENTS

The work of Debabrata Adhikari, Jesper Henri Hattel and Sankhya Mohanty has received funding from Horizon Europe, the European Union's Framework Programme for Research, and Innovation, under Grant Agreement No. 101058054 (TURBO). The work of Jesper John Lisegaard has been supported by the Energy Technology Development and Demonstration Programme: Automated Lay-up processes in blade Manufacturing (ALMA) project (Grant No. 640222-495998).

REFERENCES

[1] S. G. Advani, E. M. Sozer, Process modeling in composites manufacturing, *CRC press*, 2002.

[2] A. Endruweit, P. McGregor, A. Long, M. Johnson, Influence of the fabric architecture on the variations in experimentally determined in-plane permeability values, *Composites Science and Technology* 66 (11-12) (2006) 1778–1792.

[3] Loix, Fabrice, et al. "Woven fabric permeability: From textile deformation to fluid flow mesoscale simulations." *Composites science and Technology* 68.7-8 (2008): 1624-1630.

[4] Khan, M. Aurangzeb, et al. "Numerical and experimental analyses of woven composite reinforcement forming using a hypoelastic behaviour. Application to the double dome benchmark." *Journal of materials processing technology* 210.2 (2010): 378-388.

[5] Pierce, Robert S., Brian G. Falzon, and Mark C. Thompson. "A multi-physics process model for simulating the manufacture of resin-infused composite aerostructures." *Composites Science and Technology* 149 (2017): 269-279.

[6] Badel, Pierre, Emmanuelle Vidal-Sallé, and Philippe Boisse. "Computational determination of in-plane shear mechanical behaviour of textile composite reinforcements." *Computational materials science* 40.4 (2007): 439-448.

[7] Simon, J., et al. "A yarn-scale woven fabric model including significant slippage formulated within the Arbitrary Lagrangian Eulerian framework." *Computer Methods in Applied Mechanics and Engineering* 420 (2024): 116741

[8] Bai, Renzi, Bo Chen, Julien Colmars, and Philippe Boisse. "Physics-based evaluation of the drapability of textile composite reinforcements." *Composites Part B: Engineering* 242 (2022): 110089.

[9] B. R. Gebart, Permeability of unidirectional reinforcements for RTM, *Journal of composite materials* 26 (8) (1992) 1100–1133.581.

[10] D. Adhikari, J. J. Lisegaard, J. H. Hattel, S. Mohanty, An efficient approach for mesoscale virtual

permeability predictions using realistic fiber geometry extracted via micro-ray computed tomography, in: *21st European Conference on Composite Materials*, 2024, pp. 467–474.

ASSESSING THE INFLUENCE OF FLAX FIBERS HUMIDITY ON PROPERTIES AND MANUFACTURING AT CONTROLLED CAPILLARY NUMBER

Jean-Baptiste Jouenne[1], Antoine Levée[2] Bernard Miranda Campos[3] and Joël Bréard[1]
[1]ABTE, UR 4651 Université de Caen Normandie,
Bd Maréchal Juin, 14032 Caen, France
Email: jean-baptiste.jouenne@unicaen.fr

[2]DEPESTELE/Teillage Vandecandelaère, Research & Development, 14540 Bourguébus, France

[3]Laboratoire CRISMAT, Normandie Université, ENSICAEN, UNICAEN, CNRS,
14050 Caen, France

Keywords: Liquid Composite Molding, Natural Fiber, Moisture Effect , Controlled flow rate

ABSTRACT

This paper introduces a new method to perform liquid composite molding with a controlled resin flow rate, enabling the manufacture of plant fiber-reinforced composites with varying water contents. The manufacturing of plant fiber composites is still poorly controlled, as existing techniques are often adapted from synthetic fiber composites, despite the hydrophilic nature of natural fibers making such transpositions problematic. We propose that by monitoring fiber water content, it is possible to master the manufacturing process and optimize the structural integrity of the final part. To achieve this, we developed a novel infusion method that maintains a constant resin flow front velocity and allows processing at a target Capillary number (*Ca*). Our results show that drying natural fibers is not always necessary for successful infusion. This work demonstrates that composite parts can be manufactured while preserving fiber integrity, reducing energy consumption, and minimizing environmental impact.

1 INTRODUCTION

The manufacturing of plant fiber-reinforced composites has been a challenge since the beginning of the 21st century. It has been established that the plant fibers specificities, all the more so flax fibers, differ from those of synthetic ones. One of the major differences between these two types of materials lies in the hydrophilic nature of plant fibers. Many studies have shown that during the processing of such composites, controlling the amount of water contained by the fibers to improve understanding microstructural material state [1]. Moreover, manufacturing processes used for plant fiber-reinforced composites are mostly carried out through the direct transposition of methods and technologies used for the production of synthetic ones. This approach does not ensure preservation of the structural integrity of the flax fibers, nor does it optimize the properties of the composite material produced.
Liquid composite molding processes (LCM) such as resin infusion are commonly used in many industrial fields to fabricate composites [2]. In liquid resin infusion, the pressure difference between the polymer bucket and the mold outlet drives the polymer flow [3]. As the polymer flow front progresses into the fibrous preform, the pressure gradient decreases. Consequently, the velocity v of the polymer flow front also decreases with time. Using the capillary number (*Ca)* in injection process, where μ is the liquid viscosity and γ the liquid/gas surface tension, authors [4] have demonstrated the necessity to monitor polymer flow front velocity in order to minimize the void content in the final composite part.
In addition to these physical parameters, the water contained by plant fibers can have a significant impact during processing. Due to the hydrophilic nature of plant fibers, their moisture sorption mechanisms have been widely studied in a wide range of humid environments [5]. Authors have highlighted that “water sorption in fibers and their composites has been found to significantly affect their dimensional and structural properties”. Therefore, when compressing preforms, hygro-thermal

conditions must also be controlled and monitored, in order to take hygro-mechanical specificities of plant fibers into account. Other authors [6], [7] showed that water contained in plant fibers also influences the resin crosslinking.

Recently, a low-tech dedicated setup has been developed in the laboratory allowing to control the flow front velocity *v*. This study aims to introduce a unique research tool in the field of composite manufacturing by liquid infusion process allowing scientist the study of natural fibers processability at controlled *Ca*. Using fiber's moisture management, it is first proposed to measure the influence of humidity on properties and manufacturing of natural fiber reinforced composites. A second outlook for this work is to show that our new setup enables the manufacturing of optimized plant fiber-reinforced composite parts by piloting resin flow at the appropriate *Ca*.

This work is the starting point of a project that aims at bringing new insights on liquid composites manufacturing processes using low environmental impact technologies and to the formation of microstructural defects.

2 EXPERIMENTAL SECTION

2.1 Description of the research tool

The upper mold is a 20 mm thick transparent glass to prevent mold deformation and the lower part of the mold is an aluminum plate of 10 mm thick (figure 1a). Spacers of predefined thickness are placed on the side of mold to obtain final parts of the target thickness. In this study, spacers of 3 mm will be use to reach 30 % volumetric fiber fraction with 4 flax plies. Two grooves are cut in the lower part of the mold and seals are placed in them creating two cavities: the inner cavity in which the preform is placed, and the outer cavity in which a vacuum is done (figure 1b). This vacuum is referred to as *peripheral vacuum* reaches -980 mbar and is the first novelty of this method. Because vacuum is not directly applied on the preform stack as in most of LCM processes, the resin is allowed to freely go through the preform. In addition, the *peripheral vacuum* applies on the preform a constant pressure of around 0.1 MPa which is used for fiber compaction. The second novelty of this method is the use of a peristaltic pump to transfer resin from the reservoir to the preform. A peristaltic pump can transfer fluids without exposing them to contamination for example for sterile or corrosive fluids. It is mainly used for pharmaceutical, medical and agro application. The principle is that a flexible tubing is mounted inside a circular pump housing with rotating rollers. As the rollers turns, the tube is compressed then released continuously causing the fluid to circulate in one direction (figure 1a). With the combination of these two principles, fiber preform can be impregnated at controlled flow rate and constant flow front velocity. The pump is a Masterflex™ L/S™ capable of delivering a constant flow rate from 0.36 to 3400 mL/min, with a reverse flow option that is particularly useful for cleaning the hoses after manufacturing. Hoses are made from silicone with an outer diameter of 7 mm and an inner diameter of 5 mm. Before the preform impregnation, both parts of the mold are waxed and polished with a release agent to facilitate demolding. The preform is then positioned inside the mold, with a gutta seal placed around it to minimize edge effects during the impregnation. Then the peripheral vacuum is applied to compact the preform. After compaction, a 15 minutes relaxation phase is done to reach target thickness before starting impregnation. The resin will first full the space at the inlet of the cavity where there are no fibers (figure 2a). Once this space is full, the resin will go through the preform with a perfect straight line of flow front (figure 2b). Once filled, the resin progresses through the preform with a straight flow front (Figure 2b). When the resin reaches the end of the preform, the pump is stopped and the inlet tube is clamped to prevent leakage. The tube is then cut, and any remaining resin is returned to the reservoir using the pump's reverse function. The tube is cleaned with ethanol followed by water, allowing it to be reused. Demolding is done by releasing the peripheral vacuum. Disposable items include the section of hose embedded in cured resin, the gutta seal, and the resin container.

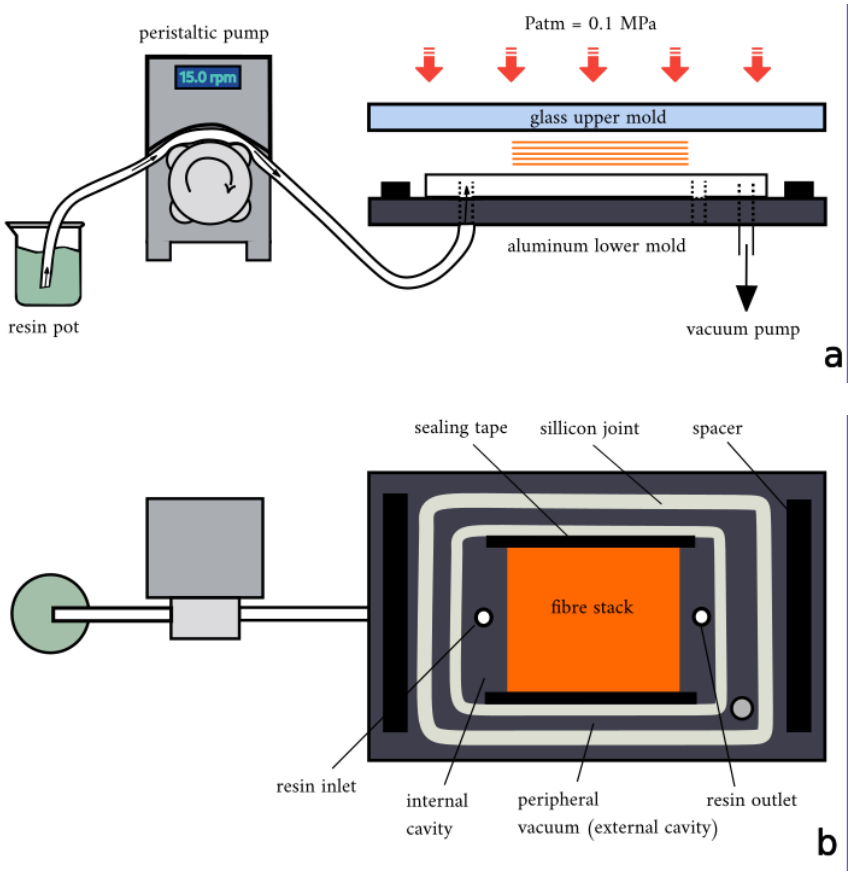

Figure 1: Schematic representation of the *THMClight* experimental setup

The fabrics used are 2 x 2 linen twills with a weight per unit area of 300 g/m^{2}meter supplied by *Depestel (Teillage Vandecandelaere, France)*. The polymer used is an epoxy-amine system consisting of *Greenpoxy SR8100* epoxy precursor and *SD8824* amine hardener, both supplied by *SICOMIN*. The experimental setup was designed to be low-tech, requiring only long-life equipment and very few consumables (hoses, mixing pot, sealant tape).

For conditioning, the linen fabrics were stored in a humidity-controlled enclosure at a constant temperature of 23°C. The storage time for the plies was based on a prior assessment of the time required to reach water saturation. Parameters and resulting water content are described in table 1.

Designation	**HR0%**	**HR50%**	**HR70%**	**HR90%**
Relative humidity	0	50	700	90
Temperature	103	23	23	23
Conditioning time (h)	24	24	24	24
Water content (wt%)	0 - 2	7,6	9,9	16,7
Density (kg/m^3)	1490	1470	1465	1420

Table 1: Preform conditioning

2.2 Measuring the flow front velocity

Since the main objective of the THMClight is to impregnate fibrous preforms at a controlled flow rate, it is essential to measure the flow front velocity. THMClight is, above all, a research tool designed to help scientists and industrial partners better understand impregnation mechanism. The upper mold is made of glass allowing user to observe the progression of the resin flow front. A camera is installed above the experimental set up to capture the entire impregnation phase (figure 2). After the recording, the flow front velocity of the resin is measured with FIJI (ImageJ). After setting the scale, a straight line was drawn between the edge of the preform at the onset of impregnation and the resin front. A value noted as *Xt*, corresponding to the position of the resin front over time, was then determined (figure 2).

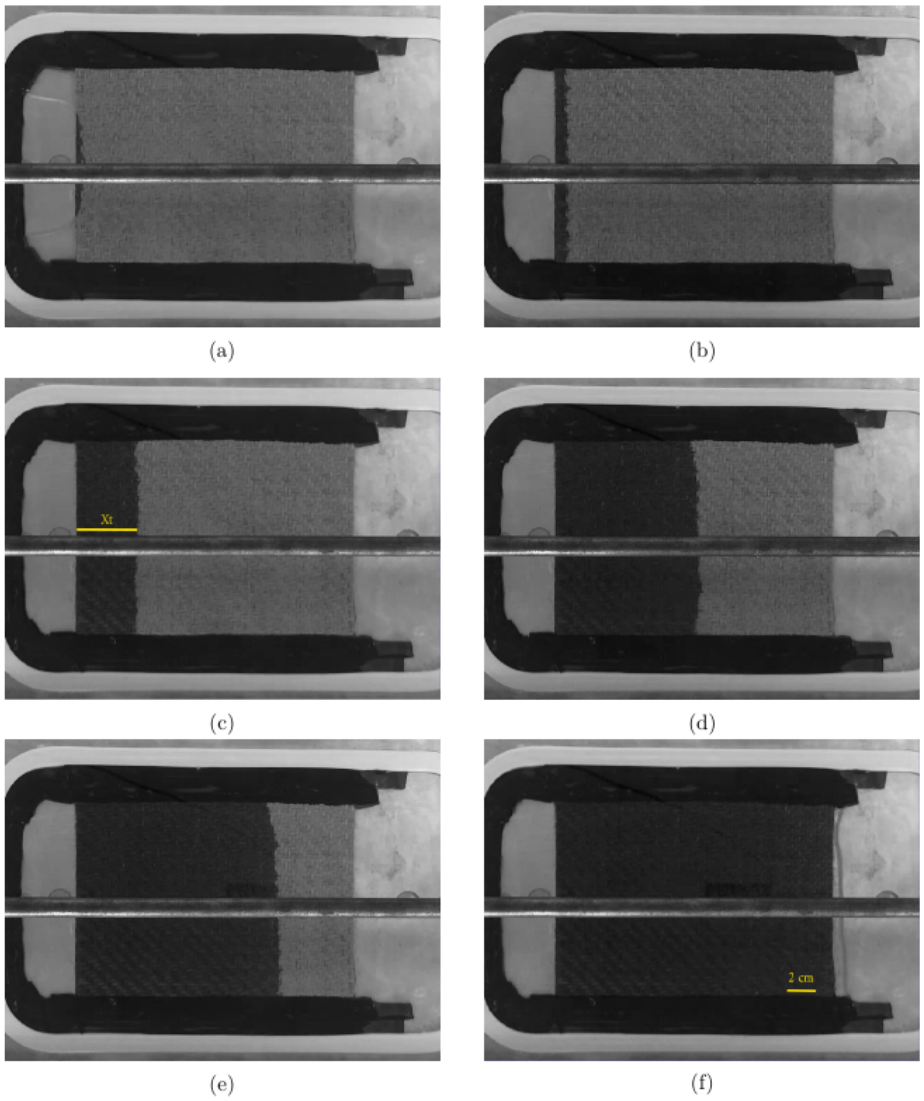

Figure 2: Resin flow front progression through a dry preform at constant rate

By plotting the graph $Xt = f(t)$, a series of data points was obtained, enabling the characterization of the resin front advancement profile. A linear regression of this dataset (constrained to pass through the origin) is performed to determine the velocity at which the resin front propagates through the preform.

3 RESULTS

3.1 Validation of the tool

The main objective of the T*HMClight* was to allow liquid composite manufacturing at constant resin flow front. Validation of the tool was conducted by manufacturing composite plates reinforced with dry flax fibers at a flow rate corresponding to optimal capillary number ($Ca_{opt} \cong 10^{-3}$) as proposed by other researchers [8], [9], [10], [11]. The pump speed was set to 15 rpm (22.5 mL/min) and manufacturing done in triplicate to demonstrate the robustness of the method. The evolution of the resin front position over time for each trial is shown in figure 3.

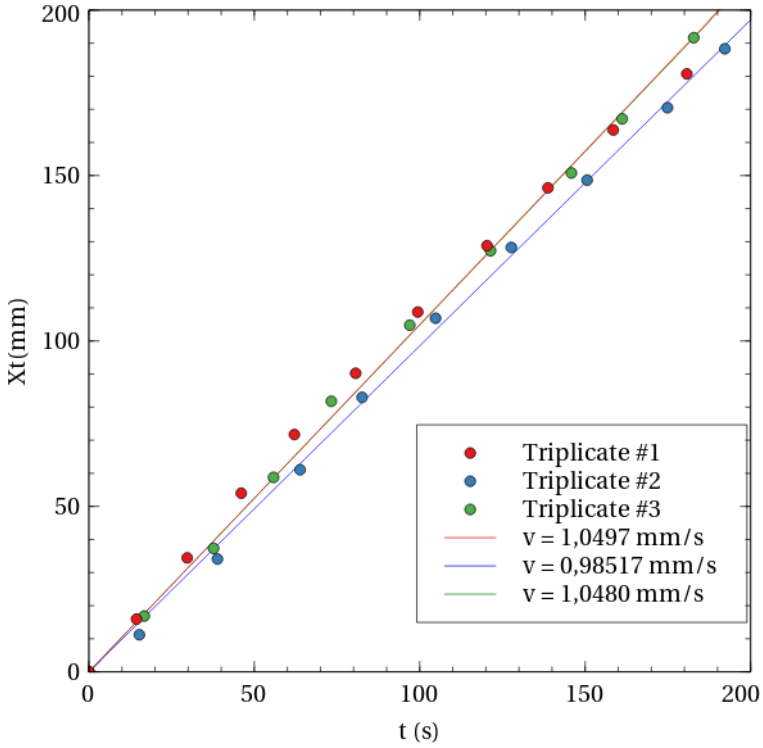

Figure 3: Resin flow front position (Xt) over time during manufacturing (Q = 22,5 mL/min)

Each point on the graph corresponds to the position of the resin front along the plate over time. A measurement was taken approximately every 2 cm along the plate. During controlled flow impregnation, the resin front formed a straight line with an angular deviation between 0 and 5°. Edge effects that can distort this front were occasionally observed and are attributed to poor distribution of the yarns along the parting line typically due to the absence of a yarn in the X-direction. Owing to the regularity of the resin front, the *Xt* values could be measured at the center of the plate during impregnation. The resulting plot is a linear function,which confirms that the resin front advances at a constant velocity. The average value of the flow front rate is $1{,}02 \pm 0{,}03$ mm/s which is in good agreement with other researchers that succeed to impregnate synthetic fibers at controlled flow rate [8], [11].

3.2 Influence of preform water content

Multiple composite plates were manufactured using different flow rates to target various *Ca*. Preform with various fiber water contents were also used to assess the influence of natural fiber humidity on the manufacturing. Table 2 summarizes the parameters set for the experiment and figure 4 shows the calculated *Ca* after based on the front velocity measurements for each plate.

Target *Ca*	Velocity *v* (m/s)	Flow rate *Q* (mL/min)
$1{,}0.10^{-3}$	$1{,}37.10^{-4}$	2,93
$7{,}68.10^{-3}$	$1{,}05.10^{-3}$	22,5
$2{,}0.10^{-2}$	$2{,}39.10^{-3}$	51
$2{,}75.10^{-2}$	$3{,}76.10^{-3}$	80

Table 2: Parameters for target *Ca* determination

The range of Capillary numbers studied allowed evaluation of the influence of flax fiber water content from low flow rate ($Q = 3$ mL/min, $Ca = 1.10^{-3}$) to high flow rate ($Q = 86$ mL/min $Ca = 2{,}75.10^{-2}$). At low flow rate of resin (close to Ca_{opt}) fiber water content had a little effect on the flow front velocity since the target *Ca* was reached for all humidity levels. However, at higher flow rates, significant variations in the calculated Capillary number were observed, reflecting changes in flow front velocity. Although, preforms containing 7 - 10 wt% water content show the closest values to target capillary number. This result strengthen the idea of a strict control of the fiber water content during manufacturing.

3.3 A deformed preform after manufacturing

During several manufacturing trials, deformation of the preform was observed after resin impregnation. For example, the figure 5 shows the deformation of a 16.2wt% water content preform manufactured at the same flow rate of resin used during the validation of the method. The deformation of the preform can be a consequence of a high fiber water content and a high flow rate of resin. In order to show this phenomenon we built a phase diagram with the flow rate of resin and the fiber water content. The diagram is shown figure 6 and evidences the effect of a high capillary number and fiber water content on the preform during manufacturing.

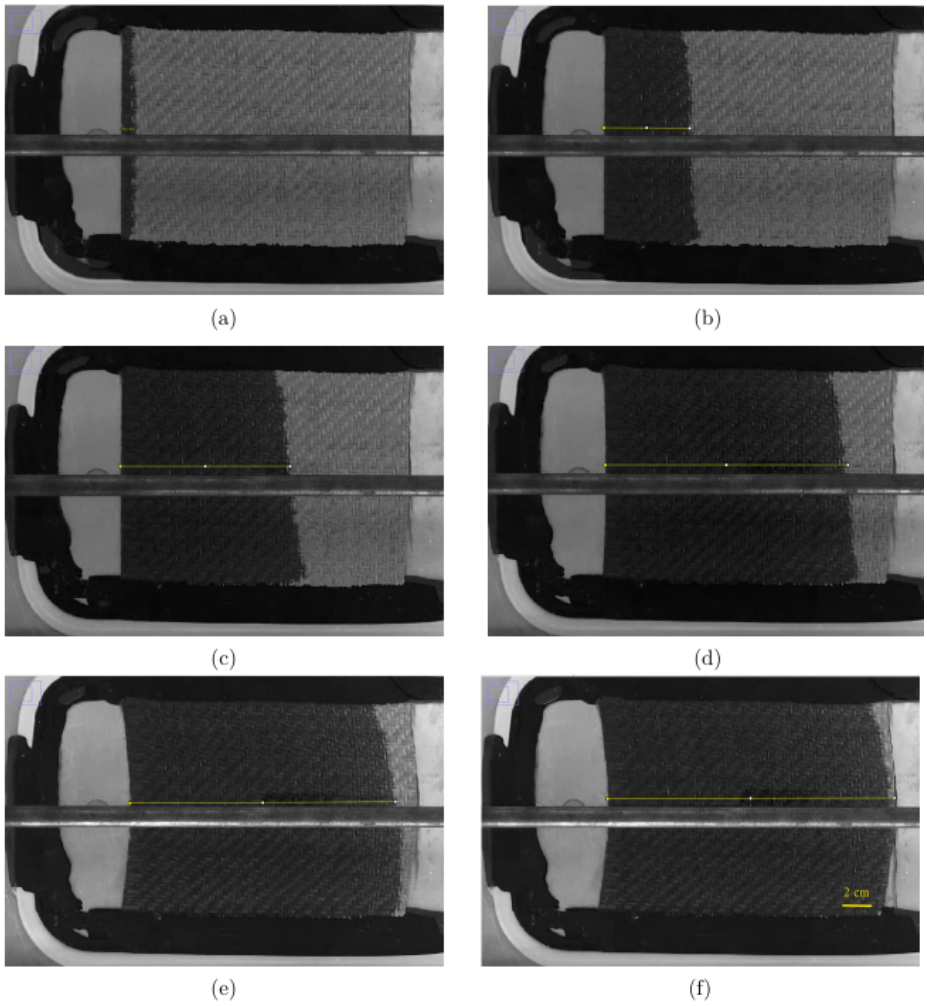

Figure 5: Resin flow front progression through a preform with 16,2wt% water content

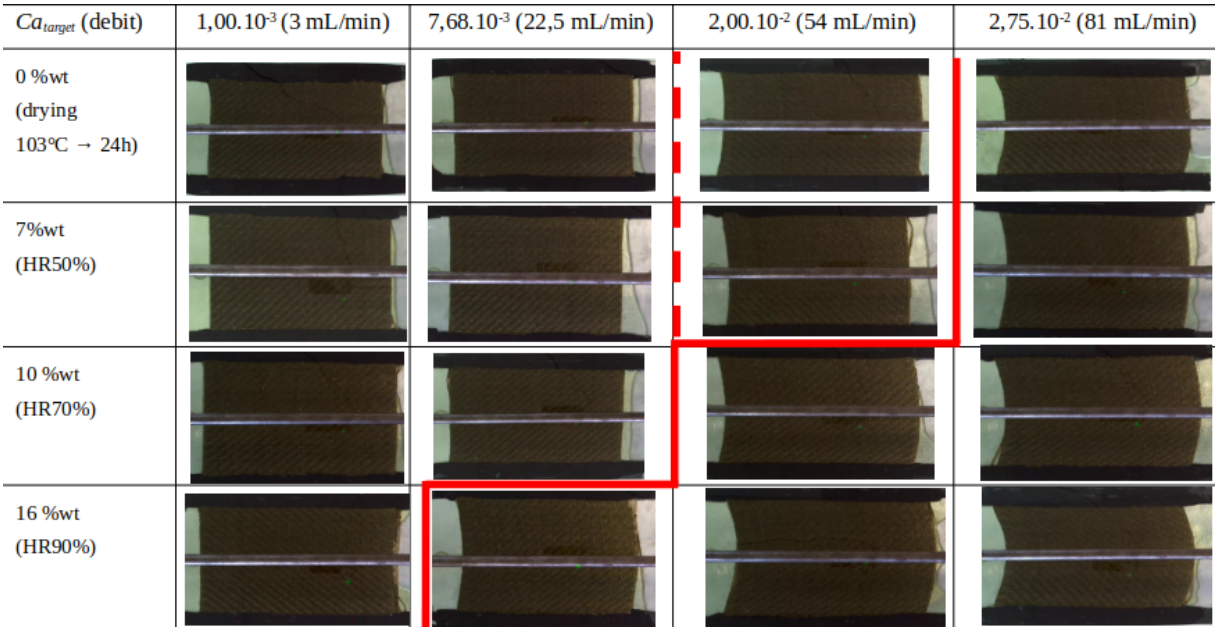

Figure 6: Processability window

During impregnation, the resin applies a pressure on the fibrous preform in the thickness direction. As the resin progresses through the preform, the applied pressure increase. If this pressure exceeds the compaction (holding) pressure applied to the preform stack, the preform may slip, leading to deformation of the final part (figure 7).

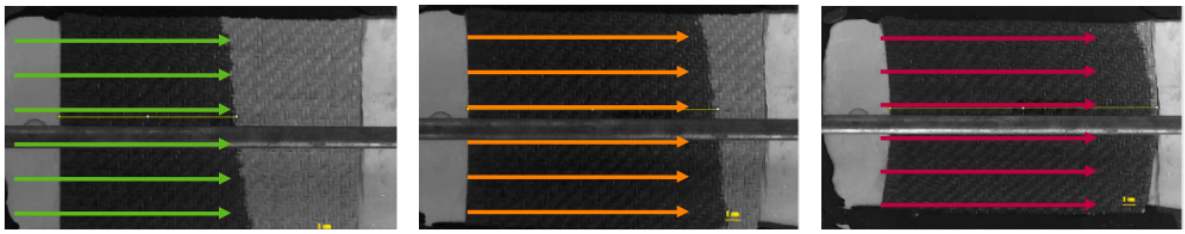

Figure 7: Illustration of the threshold pressure phenomenon observed during the controlled infusion process

The threshold pressure can be calculated by using Terzaghi's law [12]. The threshold pressure is then assimilated to the effective stress in this case σ_{eff}.

$$\sigma_{eff} = \sigma_{tot} - P_0 \quad (1)$$

with σ_{eff} the effective stress in MPa, σ_{tot} the total stress applied on the preform in MPa and P_0 the pressure applied by the resin in MPa. P_0 is calculated using the following equation based on Darcy's law:

$$P_0 = (Q/A)^2 (\mu/K)t \quad (2)$$

with Q the flow rate of resin in m^3/s, A the section of the preform corrected by the volumetric fiber fraction in m^2, μ the dynamic viscosity of the resin in Pa.s, K the permeability of the preform in m^2 and t is time in s.

In this study, permeability was taken as $K = 5.10^{-10}$ m^2 based on previous work [13], [14]. For the total stress, a constant initial force of $\sigma_{tot} = 0.1$ MPa is applied. The preform relaxes during compaction, therefore, the total stress needed to reach target thickness decreases due to this relaxation and tends to an asymptotic value. A recent work of our team on NCF flax preform showed that the relaxation phenomenon increases with the fiber water content. Since this study is on 2 x 2 flax twill preform we approximate the total stress value in function of the preform water content following the table below.

Average water content wt%	Relaxed σ tot (MPa)
0	0,08
7,6	0,07
9,9	0,06
16,7	0,05

Table 3: Values of the total stress σ_{tot} applied on the preform after relaxation for different preform water content

Effective stress has been calculated for varous combination of flow rate and fiber water content and results are plotted in figure 8. It gives rise to a surface plot representing the threshold pressure, described as effective stress. When the pressure applied by the resin on the preform exceeds the value of effective stress, slippage occurs. This chart allow the manufacturer to know which thermo-hygrometric conditionning should be applied to the preform to allow manufacturing at target flow rate (*Ca*) without causing slippage of the preform.

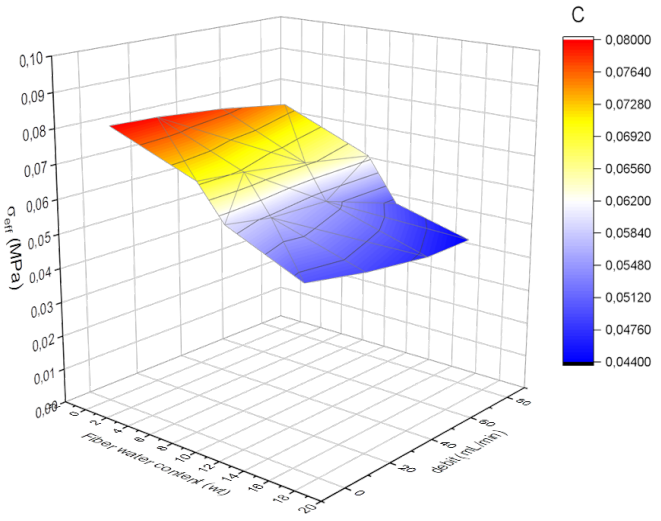

Figure 8: 3D representation of effective stress calculation
with flow rate and water content variations

3.3 Mechanical properties

The mechanical properties of composites made with the *THMClight* at various water contents were assessed using flexural trial test. The stress at break and the flexural modulus have been plotted in an Ashby diagram (figure 8).

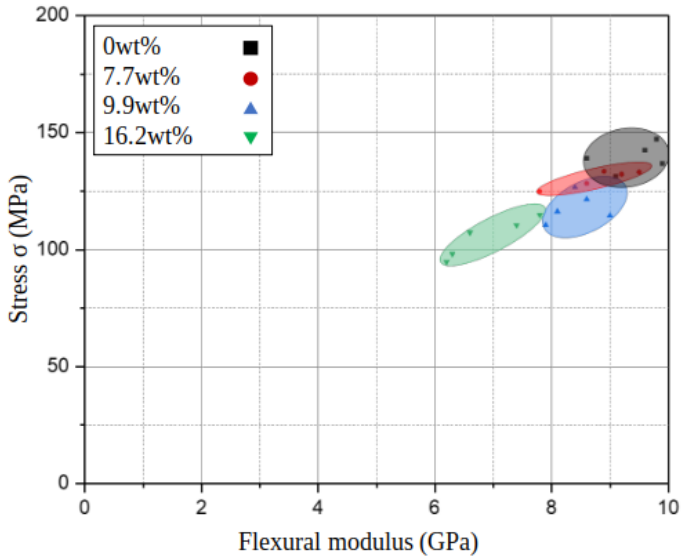

Figure 9: Effect of preform water content on mechanical
properties of flax / epoxy composites

A clear degradation in both flexural modulus and flexural stress is observed as the moisture content increases from 0% to 16wt%. Composites produced from dry preforms (0wt%) exhibit the highest

mechanical performance, with an average flexural modulus of approximately 9 GPa and a flexural stress near 180 MPa. In contrast, composites manufactured with highly humid preforms (16wt%) show significantly reduced properties, with a modulus of ~6 GPa and strength below 130 MPa. However, we would like to point out the fact that the gap in mechanical performances between dry preform composites and 7wt% water content composites are not so different and can. Considering this, a composites reinforced by a preform that contains 7wt% can be suitable for a particular application. This brings the idea of a more reasonable conception of composite parts. If the drying phase is not mandatory to satisfy mechanical requirements then it should be avoid for cost and energy savings.

4 CONCLUSIONS

In this work we successfully developed a new research tool and a potential industrial method for composite part production. The *THMClight* system enables the manufacturing of composite plate at controlled flow rate of resin with a low-tech experimental setup. By controlling the flow rate, it becomes possible to maintain a constant resin flow front, allowing manufacturing at a target Capillary number and thus minimizing void content. Using this LCM method, the influence of natural fiber water content on manufacturing has been studied. Results showed that at optimal *Ca*, humidity has a limited effect on capillary number but at higher *Ca* significant variations can be observed. Due to hydrophilic nature of flax fiber, preform with high water content slipped during manufacturing at several flow rates. This was attributed to a decrease in permeability with increasing moisture content, leading to a higher fiber volume fraction. Consequently, the pressure exerted by the resin exceeded the compaction pressure from the mold, resulting in fiber movement. Mechanical testing revealed that composites made from dry preforms did not exhibit significantly superior properties compared to those made from preforms containing 5–7 wt% water. This opens the door to reconsidering the necessity of drying preforms prior to manufacturing. If mechanical requirements can be met without a drying phase, the process can be made more energy- and cost-efficient. By mastering the effect of water content during process it is then possible to avoir drying phase of preform that is energy consumming and cost effective for industrials. This will also reduce carbon footprint of natural fiber reinforce composite manufacturing.

ACKNOWLEDGEMENTS

The authors would like to thank DEPESTELE/Teillage Vandecandelaère for their support and contribution to this work.

REFERENCES

[1] A. A. Bachchan, P. P. Das, and V. Chaudhary, “Effect of moisture absorption on the properties of natural fiber reinforced polymer composites: A review,” *Mater. Today Proc.*, vol. 49, pp. 3403–3408, 2022, doi: 10.1016/j.matpr.2021.02.812.

[2] S. Bickerton, Q. Govignon, and P. Kelly, “7 - Resin infusion/liquid composite moulding (LCM) of advanced fibre-reinforced polymer (FRP),” in *Advanced Fibre-Reinforced Polymer (FRP) Composites for Structural Applications*, J. Bai, Ed., in Woodhead Publishing Series in Civil and Structural Engineering. , Woodhead Publishing, 2013, pp. 155–186. doi: https://doi.org/10.1533/9780857098641.2.155.

[3] A. Hindersmann, “Confusion about infusion: An overview of infusion processes,” *Compos. Part Appl. Sci. Manuf.*, vol. 126, p. 105583, Nov. 2019, doi: 10.1016/j.compositesa.2019.105583.

[4] C. H. Park, A. Lebel, A. Saouab, J. Bréard, and W. I. Lee, “Modeling and simulation of voids and saturation in liquid composite molding processes,” *Compos. Part Appl. Sci. Manuf.*, vol. 42, no. 6, pp. 658–668, Jun. 2011, doi: 10.1016/j.compositesa.2011.02.005.

[5] A. Célino, S. Fréour, F. Jacquemin, and P. Casari, “The hygroscopic behavior of plant fibers: a review,” *Front. Chem.*, vol. 1, 2014, doi: 10.3389/fchem.2013.00043.

[6] M. Boutin, A. Rogeon, M. Aufray, R. Piquet, and A. Rouilly, “Influence of flax fibers on network formation of DGEBA/DETA matrix,” *Compos. Interfaces*, vol. 28, no. 1, Art. no. 1, 2021, doi: 10.1080/09276440.2020.1736454.
[7] J.-B. Jouenne, D. Barbier, V. Hounkpati, L. Cauret, and A. Vivet, “Influence of flax fibers on the curing kinetics of bio-based epoxy resin,” *J. Mater. Sci.*, Jul. 2024, doi: 10.1007/s10853-024-09891-z.
[8] S. Arnaud, “Contribution à la compréhension de la formation de défauts d’élaboration par RTM d’un composite stratifié Carbone/Epoxy – Influences sur le comportement hygrothermique et abattement des propriétés thermomécaniques,” Université de Caen, 2013.
[9] N. Patel, V. Rohatgi, and L. J. Lee, “Micro scale flow behavior and void formation mechanism during impregnation through a unidirectional stitched fiberglass mat,” *Polym. Eng. Sci.*, vol. 35, no. 10, pp. 837–851, May 1995, doi: 10.1002/pen.760351006.
[10] J. S. Leclerc and E. Ruiz, “Porosity reduction using optimized flow velocity in Resin Transfer Molding,” *Compos. Part Appl. Sci. Manuf.*, vol. 39, no. 12, pp. 1859–1868, Dec. 2008, doi: 10.1016/j.compositesa.2008.09.008.
[11] G. Cazaux, “Faisabilité des procédés LCM pour l’élaboration de composites renfort continu à matrice thermoplastique polyamide,” Université du Havre, 2016.
[12] K. Terzaghi, *Theoretical Soil Mechanics*, John Wiley&Sons, Inc. 1943.
[13] S. Comas-Cardona, P. Le Grognec, C. Binetruy, and P. Krawczak, “Unidirectional compression of fibre reinforcements. Part 1: A non-linear elastic-plastic behaviour,” *Compos. Sci. Technol.*, vol. 67, no. 3–4, pp. 507–514, Mar. 2007, doi: 10.1016/j.compscitech.2006.08.017.
[14] S. Comas-Cardona, C. Binetruy, and P. Krawczak, “Unidirectional compression of fibre reinforcements. Part 2: A continuous permeability tensor measurement,” *Compos. Sci. Technol.*, vol. 67, no. 3–4, pp. 638–645, Mar. 2007, doi: 10.1016/j.compscitech.2006.07.020.

EFFECT OF ANISOTROPY IN FIBRE BUNDLE SPACING ON MACROVOID FORMATION IN VISCOUS-FLUID IMPREGNATION TO WOVEN GLASS FIBRE

T. Ito[1,†], M. Inagawa[1], S. Yamashita[1,+] and I. Ueno[2]

[1] Division of Mechanical & Aerospace Engineering, School of Science & Technology, Tokyo University of Science 2641, Yamazaki, Noda, Chiba 278-8510, Japan
[†] Email: 7524502@ed.tus.ac.jp

[2] Department of Mechanical & Aerospace Engineering, Faculty of Science & Technology, Tokyo University of Science, 2641 Yamazaki, Noda, Chiba 278-8510, Japan
Email: ich@rs.tus.ac.jp

+ Original affiliation: Division of Mechanical Engineering (affiliation name was changed after the graduation)

Keywords: RTM, Fibres, Resins, Anisotropy

ABSTRACT

We conduct a series of experiments on impregnation of viscous fluid into woven fibre bundles placed between parallel plates to simulate resin impregnation near the substrates in VARTM method. This study particularly focuses on the impact of anisotropy in fibre bundle spacing on macrovoids formation. It is found that flow near the flow front changes by varying anisotropy in fibre bundle spacing. We reveal that aspect ratio of the space among fibre bundle dramatically affects macrovoid formation.

1 INTRODUCTION

Fibre-reinforced plastic (FRP) is a composite material manufactured by impregnating fluid, such as epoxy or phenolic resin, into fibre bundles. FRP exhibits high strength and stiffness, together with low weight and ease of processing. Due to its superior specific strength compared to metals, FRP has been widely used as a substitute for metallic materials in various applications, including aerospace components and automotive bodies. Among the forming techniques for FRP, one notable method is Liquid Composite Molding (LCM). One prominent example is the VARTM (Vacuum Assisted Resin Transfer Molding) method, which accelerates resin impregnation by using vacuum pump, has numerous advantages and ability to mold materials and manufacture in any type of shape with a wide range of spatial scales with low cost. However, it also has the disadvantage that entrapments of gas remained in the mold are prone to occur due to unintended insufficient impregnation during the resin flow. Entrapped gas, or void, can cause stress concentration and significantly decrease the trustworthiness of manufactured composites. To maintain quality of composite materials, it is essential to elucidate the conditions for void formation and suppression. Two types of voids have been defined: microvoids which form within fibre bundles, and macrovoids which form between fibre bundles [1]. This study focuses on the latter, as it has more significant impact on tensile and compressive strength of materials [2]. Extensive research has been conducted on the behavior of fluid impregnation within fibre bundles in the VARTM process. Total volume of residual voids varies with some factors such as the capillary number (Ca), a dimensionless number representing the characteristic velocity of fluid, and wettability [3,4].

$$\mathrm{Ca} = \frac{\mu U}{\sigma}, \tag{1}$$

where μ, σ, and U, represent the viscosity, the surface tension, and the impregnation velocity of the test fluid, respectively. When Ca is small—that is, when capillary forces dominate—the test fluid preferentially flows between the fibre tows and gradually fills the interior of each tow. In this regime,

macrovoids are prone to form between fibre bundles. Conversely, when Ca is large, the formation of macrovoids is suppressed; however, micro-voids tend to form within the fibre bundles with higher probability. Although the optimal capillary number (Ca) depends on multiple factors, including the structure of fibre bundles and is therefore difficult to determine uniquely, a value of $Ca \approx 10^{-3}$ is regarded as effective threshold for suppressing void formation across various conditions [5,6]. Furthermore, it has been experimentally demonstrated that increasing the contact angle at the solid-liquid interface—i.e., reducing wettability—suppresses deformation of the flow front, thus reducing macrovoid formation even under low Ca conditions [7,8]. It has also revealed that wettability has a significant influence on flow patterns within porous media, particularly on void geometry and residual void content through X-ray 3D scanning of fluid displacement in carbon fibre preforms [8]. This study targets on woven fibre bundles placed between parallel plates to simulate resin impregnation near the substrates in the VARTM method, and particularly focuses on the impact of anisotropy in fibre bundle spacing on the viscous fluid impregnation dynamics.

2 EXPERIMENTS

The experimental apparatus used in this study is schematically illustrated in Fig. 1. To prepare a mold, we settle the single-layer woven glass fibre mat between acrylic flat plates on both sides, which are fixed by jigs made of SUS. To prevent gas-liquid leakage into or out of the mold, an O-ring is installed between each acrylic plate and the jig. The inlet of the mold is connected to a reservoir of test liquid, and the outlet is connected to a vacuum pump (DA-60D, ULVAC, Inc., Japan) to create a pressure difference within the mold, each via rubber tubes. The pressure difference within the mold is adjusted using two regulators (IRV 10-C08L, SMC, Corp., Japan) connected between the outlet of the mold and the vacuum pump, and measured with a pressure meter (MT300-D01, Yokogawa Test & Measurement Corporation, Japan). 350-cSt silicone oil (KF-96-350 CS, Shin-Etsu Chemical Co., Ltd., Japan) is employed as test liquid, and fluorescent particles are mixed in the liquid as tracers for visualization. Light emitting diode (LED) (AITEC SYSTEM, Co., LTD., Japan) is placed to visualize the flow front of the impregnating liquid with white light. Additionally, a continuous laser light of 532 nm in wavelength is irradiated at the imaging area through a half-mirror to excite the fluorescent particles to visualize particle behavior in the liquid. The images of the impregnation process are recorded by using charge-coupled device (CCD) camera (C9300 − 221, Hamamatsu Photonics, K.K., Japan) of 640 x 480 pixel at 20 fps from the underside of the mold with 60 mm lens (Micro-Nikkor 60mm f/2.8D, Nikon, Inc., Japan). To prevent the CCD camera from receiving the laser light, a short-pass filter is placed between the CCD camera and the half mirror. Before conducting each experiment, the sealed container containing the test liquid is subjected to ultrasonic vibration for one hour to obtain a uniformly dispersed mixture of particles. Also, the test liquid is degassed under -90 kPa for at least three hours to remove residual air within the liquid. Figure 2 shows the woven glass fibre mats (Featherfield, K.K., Japan) with different anisotropies in fibre bundle spacing used in this study. Fibre bundles aligned in the main flow direction are referred to as warp, while those oriented in the spanwise direction are referred to as weft. The aspect ratios of the gaps, where neither warp nor weft fibre bundles are present, are varied as (a) 1:1, (b) 1:3, and (c) 3:1. The fibre mat used in each experiment consisted of fibres with a diameter of 17 μm.

The density per area is (a) 550 g/m², and (b) and (c) 462 g/m². The test liquid is silicone oil as aforementioned, whose kinematic viscosity, density, and surface tension are 350 mm^2/s, 967.4 g/m^3, 21.1 mN/m respectively. All experiments are conducted under constant conditions at a room temperature of 22 °C.

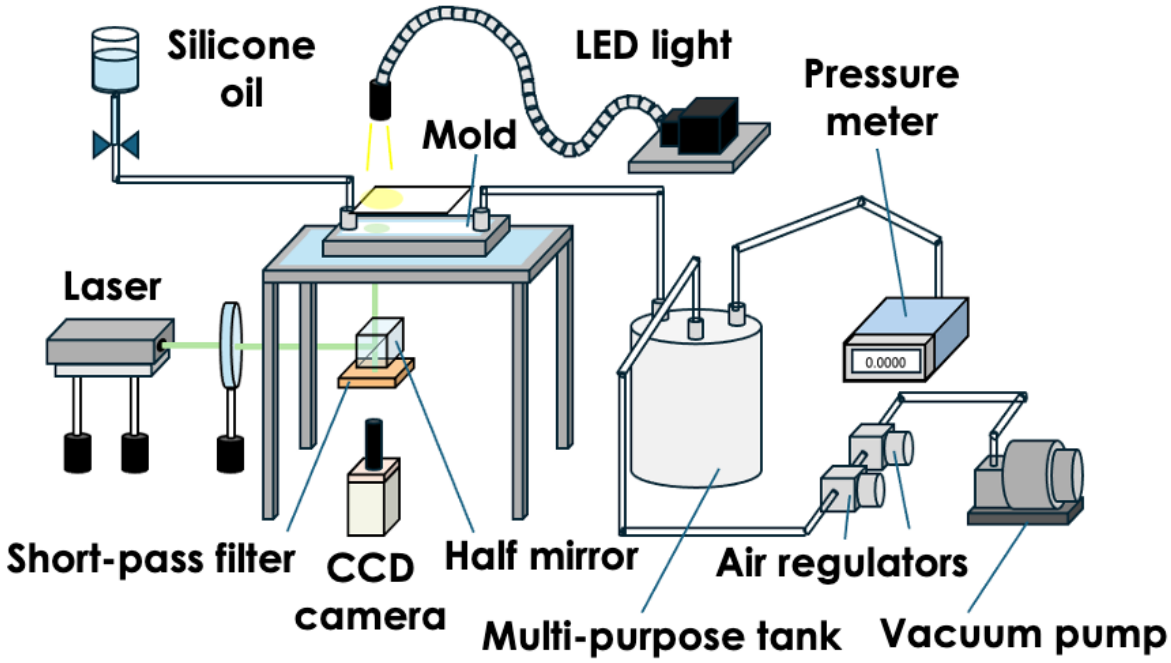

Figure 1: Experimental apparatus for visualizing impregnation process into woven glass fibre mats in mold.

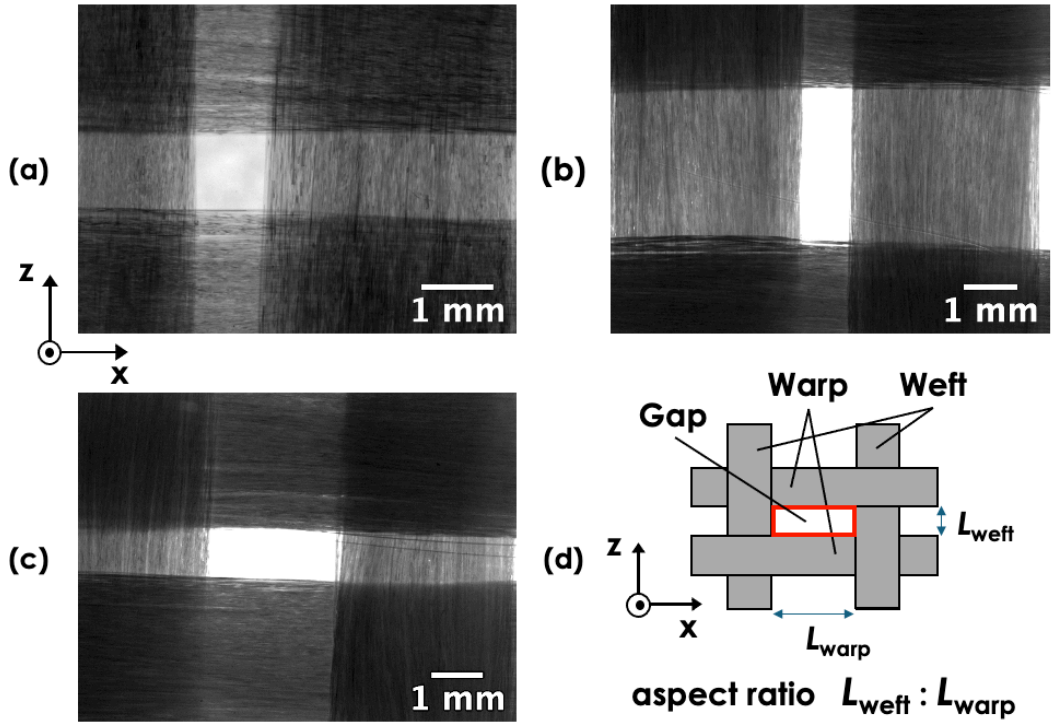

Figure 2: Three types of woven glass fibre mats with anisotropy in fibre bundle spacing. Aspect ratio of each gaps, $L_{weft} : L_{warp}$, is (a) 1:1 (b) 1:3 (c) 3:1.

3 RESULTS&DISCUSSION

Figure 3 shows a representative example of impregnation behavior. The left three columns represent experimental results, and the rightmost column shows results of numerical simulation [9]. The experimental results include instantaneous fields near the flow front at two representative time points ($t - t_0 = 0$ [s],10 [s]) and pathline images obtained by integrating instantaneous fields over these time intervals. Under all conditions, the warp fibre bundles in the upper left and lower right crimp are positioned in the foreground (from the viewing side), and the same applies to the weft fibre bundles in the upper right and lower left crimp. This study replicates the flow front behavior in the snap-off process, as previously observed by simulation [7] and by experiments [7,10]. Snap-off refers to a phenomenon in which advancing flow front moves around the gap, resulting in spontaneous filling of the weft fibre at the downstream side of the gap and disconnection of the non-wetting phase [11]. The flow behavior near the flow front is visualized by tracking fluorescent particles. Under each condition, at the upstream side of the gap, the liquid near the flow front moves around the gap, resulting in a flow velocity component in the z-axis direction at both the upper and lower sides. As impregnation progresses, the liquid flows along the warp fibre bundles in the lower-right crimp (as indicated as (iii)), resulting in dominant flow velocity component in the x-axis direction. In contrast, in the upper-right crimp (i), the liquid permeates along the weft fibre at the downstream side of the gap (ii), resulting in a flow velocity component in the z-axis direction. This phenomenon is particularly noticeable in Panel (c). These results are well reproduced by the present numerical simulation (rightmost column in Fig. 3) for each gap geometry. The liquid motion along the weft fibres in the downstream side of the gap (ii) enhances the curvature of the flow front near the boundary between the gap and weft fibre bundle (as shown at the right edge of the gap), thereby increasing the Laplace pressure. As a result, it suppresses macrovoid formation by inducing detachment of the interface at the warp fibre edge in the gap. This tendency is particularly pronounced under the condition of a 3:1 aspect ratio gap (Panel (c)), supporting the results by Matsuzaki et al. [12], which showed that macrovoid formation is less likely in fibre mats with lower $L_{\mathrm{weft}} / L_{\mathrm{waft}}$. It is important to note that the weft and warp fibre bundles have different thicknesses in their study.

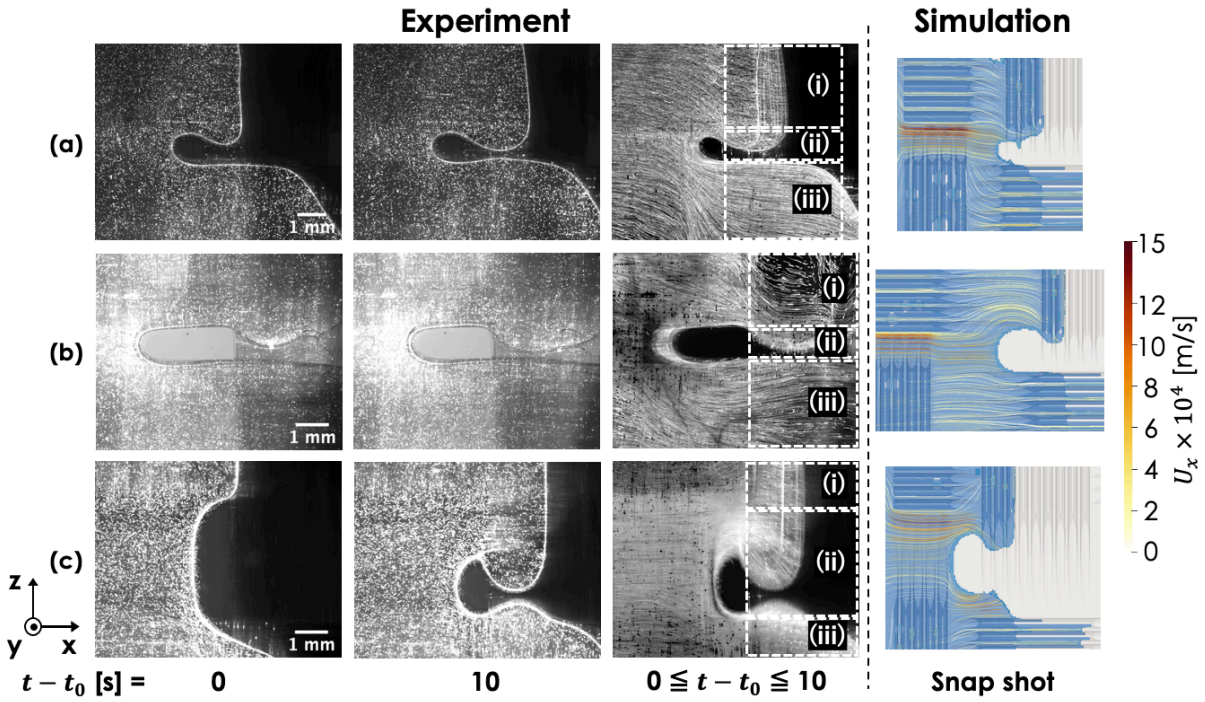

Figure 3: Representative examples of impregnation behavior under each gap aspect ratio: (a) 1:1, (b) 1:3, and (c) 3:1. The left three columns represent experimental results, while the rightmost column shows numerical results.

Figure 4 shows an instantaneous field of the observation region captured by the CCD camera. A dashed line in the figure indicates the evaluation line defined for evaluating the representative impregnation velocity of the liquid. The left panel shows the raw image data, while the right panel displays the velocity field obtained via PIV analysis, overlaid on the raw image. PIV data are processed using filter based on the discrete cosine transform (DCT) [13]. The impregnation velocity of the test liquid is evaluated using the velocity data obtained from the PIV. We define the representative impregnation velocity $\overline{U_{x,20s}}$ as the time-averaged x-direction velocity along the inspection line over 20-second interval, selected after the flow front has sufficiently advanced and the flow has stabilized. The same evaluation method is applied under all aspect ratio conditions.

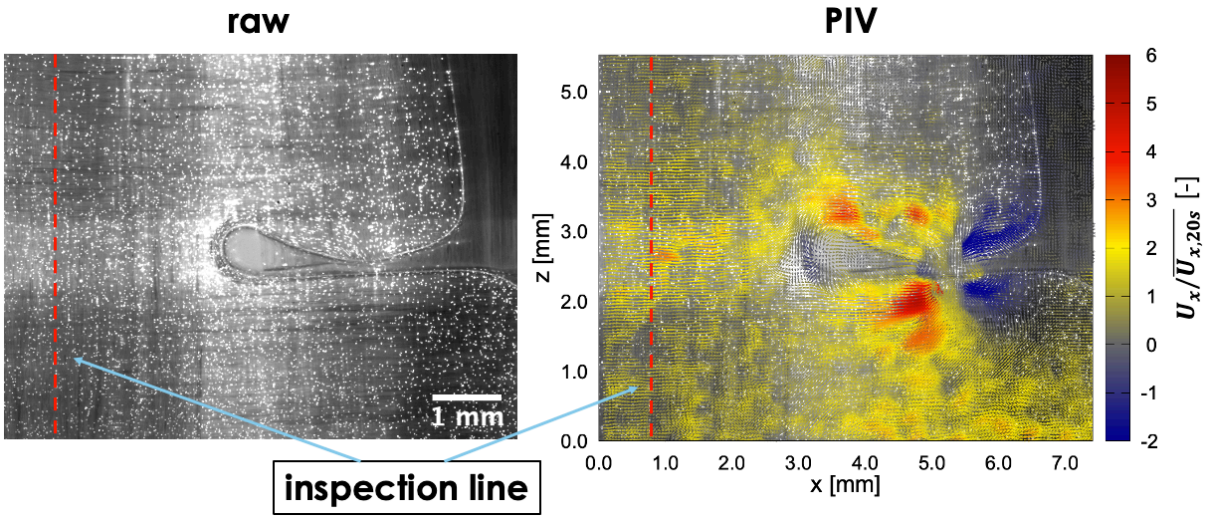

Figure 4: Instantaneous field of observation region with dashed evaluation line used for evaluating $\overline{U_{x,20s}}$ The left panel shows the raw image data, while the right panel displays the velocity field obtained from the PIV, visualized using the filter based on DCT.

Figure 5 shows instantaneous field immediately after snap-off for each aspect ratio condition. The left two columns represent experimental results, and the rightmost column shows results by the numerical simulation [9]. The first column of experimental results illustrates the raw instantaneous field overlaid with a schematic of the local fibre orientation and highlighted gas-liquid interfaces. The closed interfaces entrapped in the gap region are marked in green, while the leading flow front is highlighted in pink. The second column of experimental results displays a magnified view of the velocity vector field obtained by the PIV (with DCT filter) focusing on the snap-off region, with the gas-liquid interfaces emphasized in the same color scheme. The color distribution in the vector field is determined by the x-direction velocity normalized by the representative impregnation velocity $\overline{U_{x,20s}}$ defined above. The same image processing and analysis procedure is applied to all aspect ratio conditions (a)1:1, (b)1:3, and (c)3:1. Regarding the velocity field, particularly in conditions (a) and (c), large velocity vectors are observed along the gas-liquid interfaces. Along the interface highlighted in green, positive velocities appear both above and below a negative velocity region located near the snap-off region. In contrast, along the interface highlighted in pink, the velocity near the snap-off region is positive, while negative velocities are observed above and below it. This velocity distribution is attributed to the rapid deformation of the gas-liquid interface caused by snap-off, which draws in the surrounding liquid and leads to the expansion of the constriction between gas-liquid interfaces in the x-direction. Although a similar tendency is observed under the condition of a 1:3 aspect ratio gap (Panel (b)), no prominent velocity distribution appears in any region. The tendency for the constricted region to exhibit an opposite velocity to that of upper and lower regions is also well reproduced by the present numerical simulations for each gap shape. In the presentation, we also incorporate experimentally obtained shear fields into

our discussion, alongside the results of numerical results.

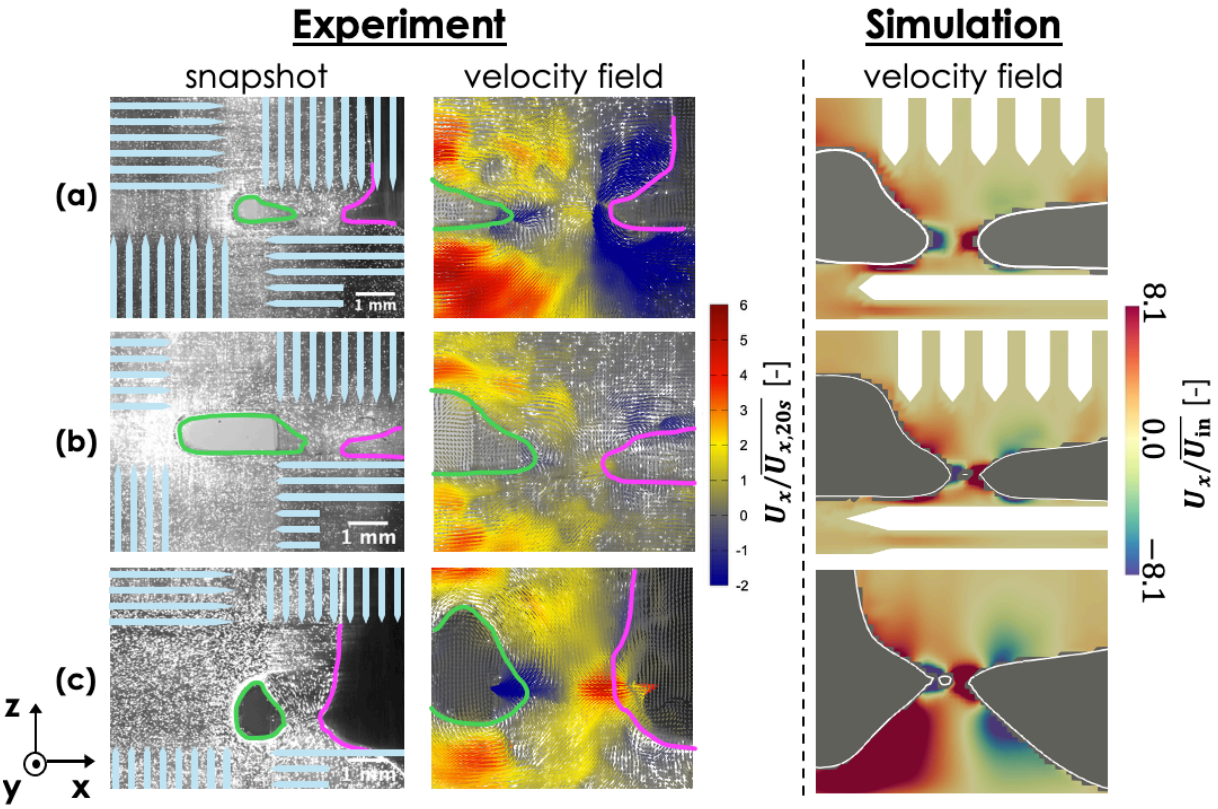

Figure 5: Velocity fields immediately after snap-off for each aspect ratio: (a) 1:1, (b) 1:3, and (c) 3:1. The left two columns show the experimental results, and the rightmost column shows the numerical simulation results. The left column presents raw image data, while the center column displays a magnified view of velocity field obtained via the PIV. In both experimental columns, a schematic of the local fibre orientation and highlighted gas-liquid interfaces are overlaid.

3 CONCLUDING REMARKS

This study investigates the impregnation behavior of a viscous fluid into woven fibre bundles placed between parallel plates, with particular focus on the impact of the anisotropy in fibre bundle spacing influences the impregnation behavior. We prepared three kinds of fibre mats with different gap aspect ratio: 1:1, 1:3, and 3:1. We mixed fluorescent tracer particles into test liquid to examine impregnation behavior. For each aspect ratio condition, comparisons between experimentally obtained pathline and velocity fields predicted by numerical simulations showed good agreement in overall trends. The results demonstrated that the magnitude of spanwise velocity along weft fibres in the downstream of the gap has a significant impact on macrovoid formation in this system.

ACKNOWLEDGEMENTS

This research was partially supported by the Grant-in-Aid for scientific Research (B) (Grant No.: 24K00824) from the Japan Society for the Promotion of Science (JSPS). One of the authors, MI, acknowledges the Advanced Centre for Computational Materials Science (ACCMS), Kyoto University, for providing their supercomputer resources (JFY2024 & 2025) for the part of the present simulations.

REFERENCES

[1] J. M. Lawrence, P. Frey, A. A. Obaid, S. Yarlagadda and S. G. Advani, Simulation and validation of resin flow during manufacturing of composite panels containing embedded impermeable inserts with the VARTM process, *Polymer composites,* **28,** 2007, pp. 442-450 (doi: 10.1002/pc.20293).

[2] J. Varna, R. Joffe, L.A. Berglund, T.S. Lundström, Effect of voids on failure mechanisms in RTM laminates, *Composites Science and technology,* **53**, 1995, pp. 241-249 (doi: 10.1016/0266-3538(95)00024-0).

[3] N. Patel and L. J. Lee, Effects of fibre mat architecture on void formation and removal in liquid composite molding, *Polymer Composites,* **16**, 1995, pp. 386-399 (doi: 10.1002/pc.750160507).

[4] C. Zhao, B. Yang, S. Wang, C. Ma, S. Wang and F. Bi, Three-dimensional numerical simulation of meso-scale-void formation during the mold-filling process of LCM, *Applied Composite Materials,* **26,** 2019, pp. 1121-1137 (doi: 10.1007/s10443-019-09770-w).

[5] N. Patel and L. J. Lee, Modeling of void formation and removal in liquid composite molding. Part II: Model development and implementation, *Polymer Composites,* **17**, 1996, pp.104-114 (doi: 10.1002/pc.10595).

[6] C. DeValve and R. Pitchumani, Simulation of void formation in liquid composite molding processes, *Composites Part A: Applied Science and Manufacturing,* **51**, 2013, pp.22-32 (doi: 10.1016/j.compositesa.2013.03.016).

[7] K. Yoshihara, Y. Kamei, A. Mizuno, H. Ohgaki, T. Hori and I. Ueno, Effect of wettability on viscous liquid impregnation in single-layer woven-fibre bundles driven by pressure difference, *Composites Part A: Applied Science and Manufacturing,* **138**, 2020, 106049 (doi: 10.1016/j.compositesa.2020.106049).

[8] H. Teixidó, B. Caglar, and V. Michaud, Effect of wettability and textile architecture on fluid displacement and pore formation during infiltration of carbon fibrous preforms, *Composites Part A: Applied Science and Manufacturing,* **174**, 2023, 107733 (doi:10.1016/j.compositesa.2023.107733).

[9] M. Inagawa, T. Ito, S. Yamashita and I. Ueno, Numerical analysis of macrovoid formation process in a single-layered woven fibre bundle confined between parallel plates, *24th International Conference on Composite Materials* (*ICCM24*) (Aug. 2025, Baltimore, MD, USA) (to be presented).

[10] N. Kuentzer, P. Simacek, S. G. Advani and S. Walsh, Permeability characterization of dual scale fibrous porous media, *Composites Part A: Applied Science and Manufacturing,* **37**, 2006, pp.2057-2068 (doi: 10.1016/j.compositesa.2005.12.005).

[11] K. Singh, T. Bultreys, A. Q. Raeini, M. Shams and M. J. Blunt, New type of pore-snap-off and displacement correlations in imbibition, *Journal of Colloid and Interface Science,* **609**, 2022, pp.384-392 (doi: 10.1016/j.jcis.2021.11.109).

[12] R. Matsuzaki, D. Seto, M. Naito, A. Todoroki and Y. Mizutani, Analytical prediction of void formation in geometrically anisotropic woven fabrics during resin transfer molding, *Composites Science and Technology,* **107**, 2015, pp.154-161 (doi: 10.1016/j.compscitech.2014.12.013).

[13] D. Garcia, Robust smoothing of gridded data in one and higher dimensions with missing values, *Computational statistics & data analysis,* **54**, 2010, pp.1167-1178 (doi: 10.1016/j.csda.2009.09.020).

ICCM24
AUGUST 4-8, 2025
BALTIMORE CONVENTION CENTER
BALTIMORE, MARYLAND, USA

No Technical Paper Submission for:

Arjen Koorevaar

inegi driving science & innovation

CONVERTING KNOWLEDGE INTO VALUE FOR OVER 35 YEARS

Since 1986

Real-Time Predictive Monitoring and Adaptive Control in Vacuum Infusion: Development of a Physics-Based Digital Twin

João Machado
Nuno Correia

U.PORTO

ICCM24
24TH INTERNATIONAL CONFERENCE ON COMPOSITE MATERIALS

© INEGI all rights reserved

1.

Introduction

- Vacuum infusion
- Control/feedback methodologies
- Digital Twins

Since 1986

© INEGI all rights reserved

Vacuum infusion

Manufacturing steps

1. Lay-up

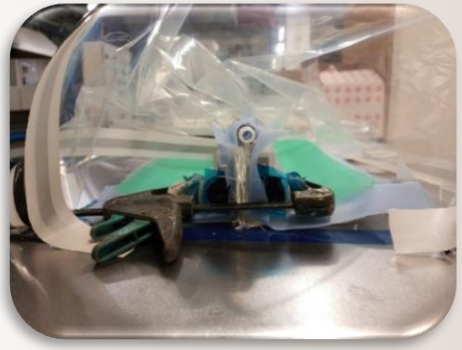

2. Infusion



3. Demoulding



© INEGI all rights reserved

Vacuum infusion

Problems

Dry spots





Voids



Incomplete curing

Distortions

...

© INEGI all rights reserved

Control/feedback methodologies

Digital twins

Real-time manufacturing data



Digital twin

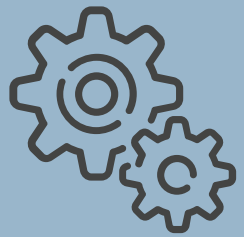

Manufacturing parameter adjustment



© INEGI all rights reserved

Digital Twins

Numerical *vs.* Data-driven

Numerical methods

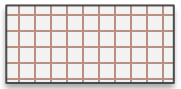

Input data
- Mesh
- Process data (permeability, BCs, ...)

Computational time
- Depends on numerical scheme and mesh refinement

Output
- Physically accurate output
- Resolution can be adjusted by mesh refinement

Machine learning



Input data
- Large dataset
- Process data (permeability, BCs, ...)

Computational time
- Faster than generic CFD solvers

Output
- Reliability depends on amount of training data, model size, part geometry, etc...

© INEGI all rights reserved

Digital Twins

Remote computing

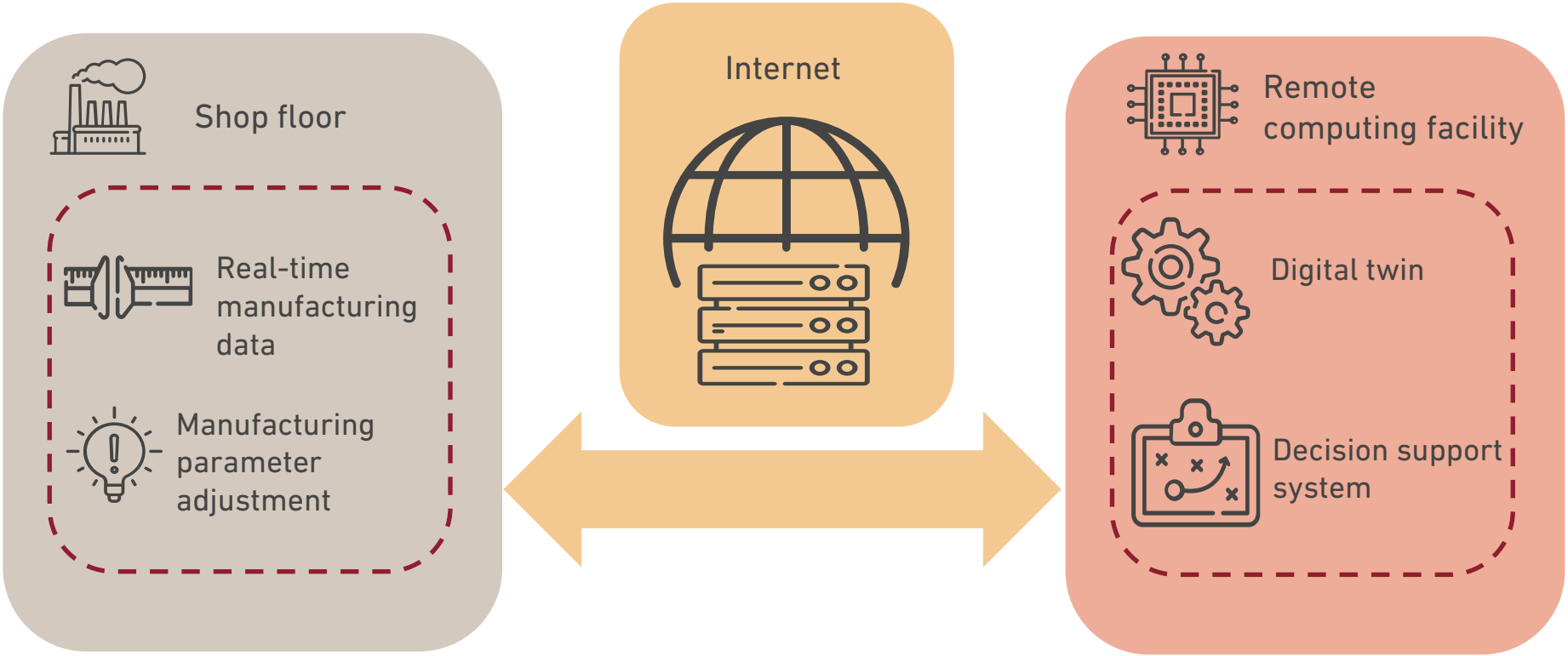

© INEGI all rights reserved

2.

Framework

- Overview
- Network interface
- Domain mapping
- Simulation
- Permeability calibration

Since 1986

© INEGI all rights reserved

Overview

Overview

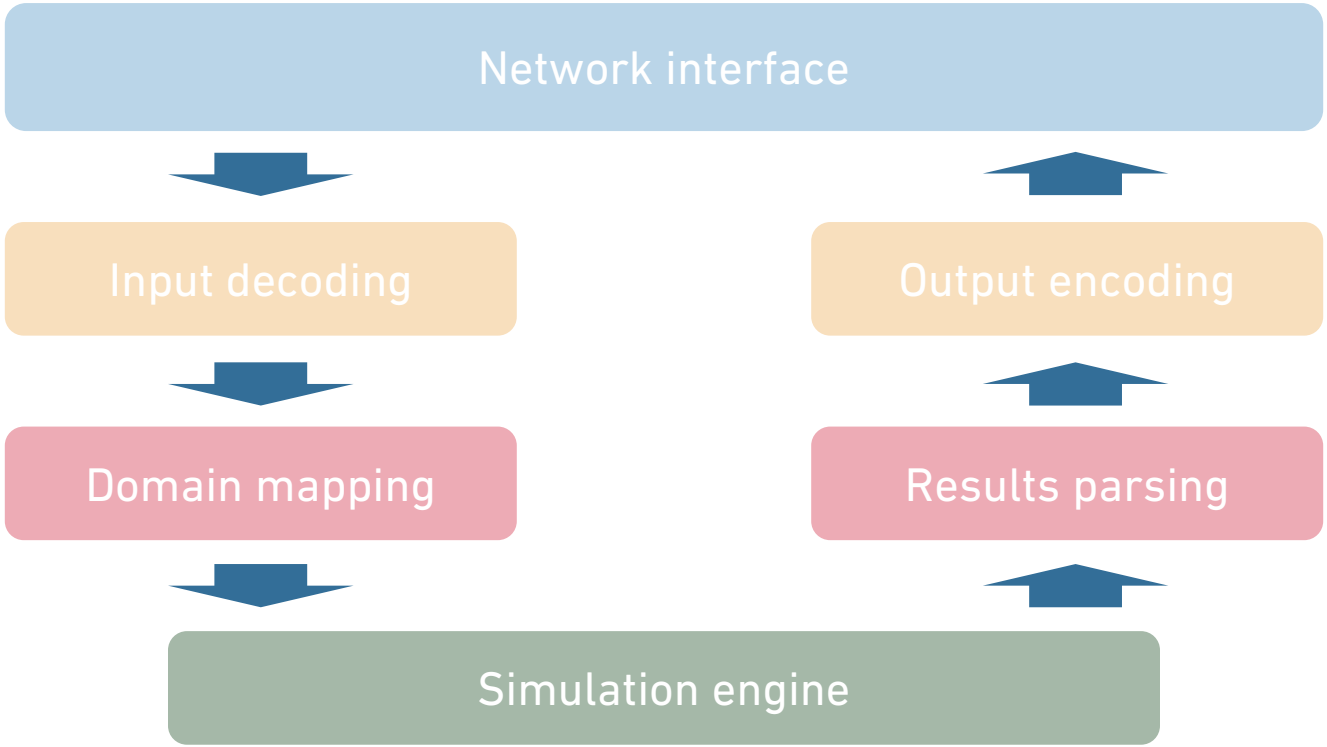

© INEGI all rights reserved

Network interface

Overview

- ✓ MQTT protocol communication
- ✓ Automatic sensor recognition (following specified JSON structure)
- ✓ Domain is updated when new data is available
- ✓ Simulations are only performed when requested (resource efficient)
- ✓ Timestamp in data packets allow for time synchronization & performance checks

© INEGI all rights reserved

Domain mapping

Overview

Saturated area extraction

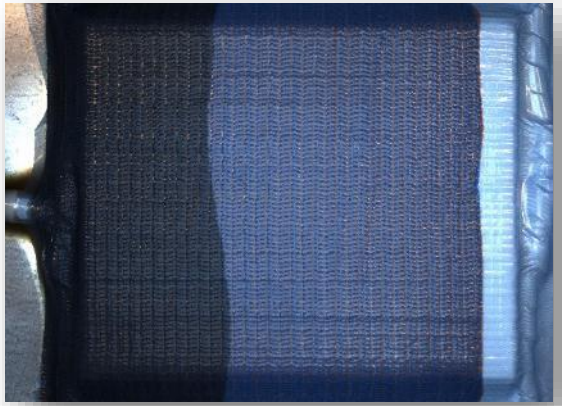

Coordinates

$$\begin{pmatrix} x1, y1 \\ x2, y2 \\ \dots \end{pmatrix}$$

Correlation with mesh control volumes coordinates

$$\begin{pmatrix} CV1 \\ CV2 \\ \dots \end{pmatrix}$$

Superposition to FEM model mesh

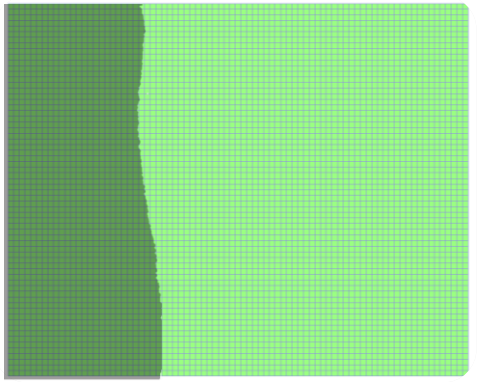

© INEGI all rights reserved

Simulation

Overview

Creation of DUMP file

Control volume fill factor setting

BC coordinates & value setting

Field data (permeability, fibre volume fraction setting)

Creation of LBASIC script

LIMS simulation (command line)

Result parsing from DUMP file

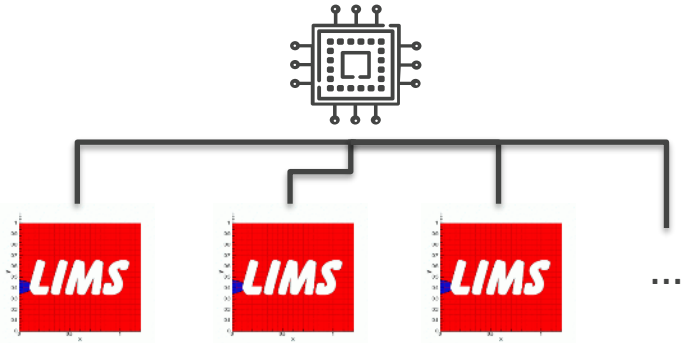

Parallelization is key

© INEGI all rights reserved

3.

Validation

- Experiments
- Results

Since 1986

© INEGI all rights reserved

Experiments

Experimental setup

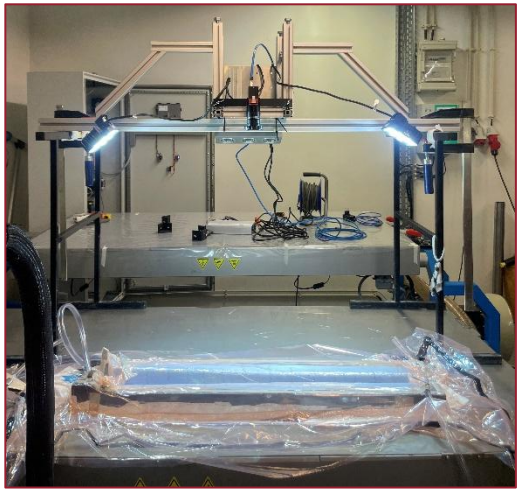



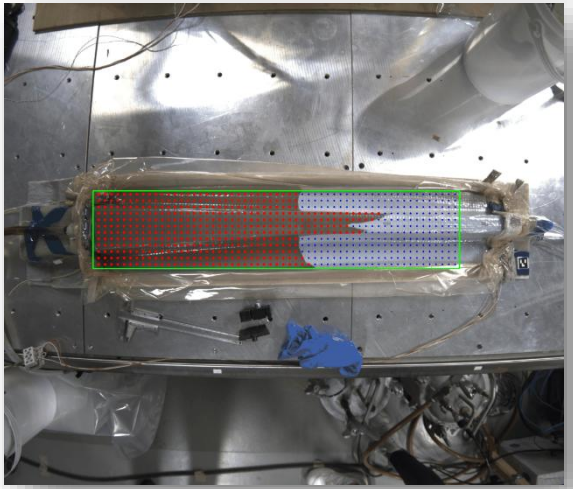

© INEGI all rights reserved

Results

Real-time simulations

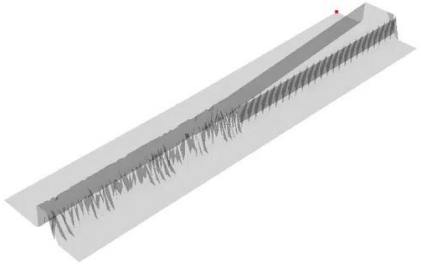

Real-time prediction based on flowfront mapping

Part (FEM mesh)

Flowfront mapping

Simulation prediction (dt=10s)

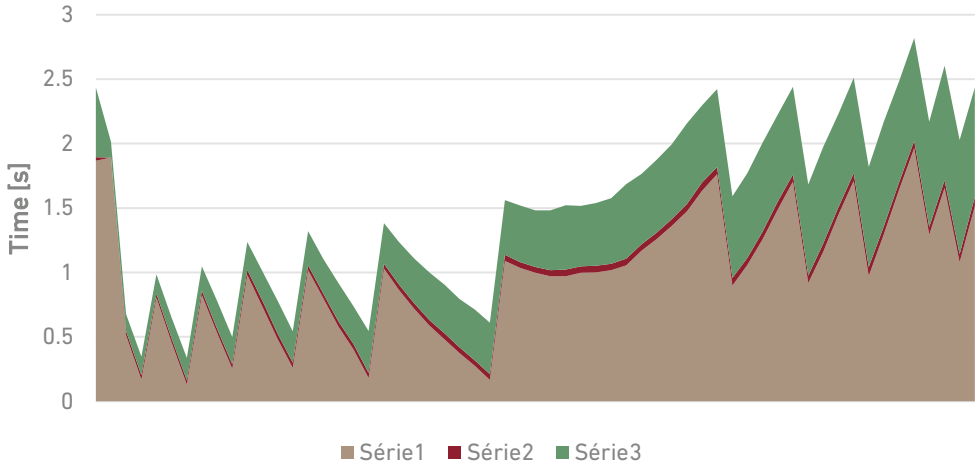

© INEGI all rights reserved

Results

Permeability calibration

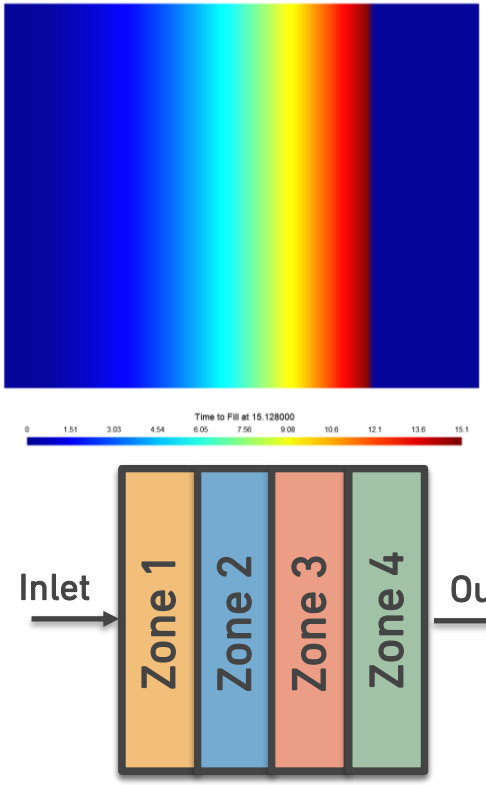

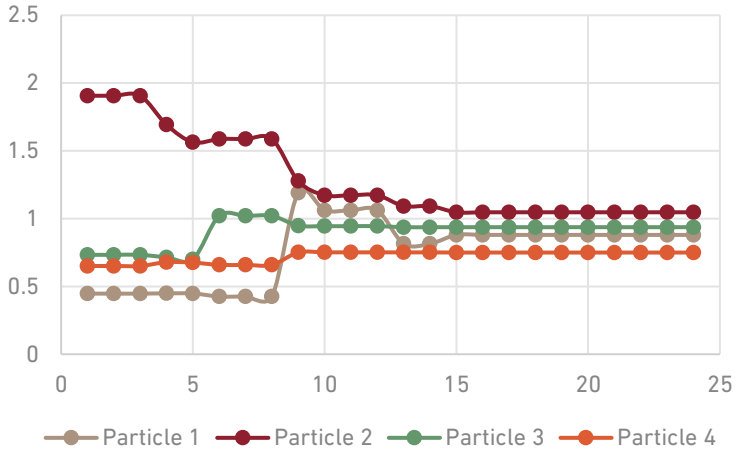

- Mesh size: 5346 elements (shell)
- Calibration runtime: 37.05s
- Total number of simulations: 96

Workstation: Intel® Core™ i7-8700K CPU @ 3.70GHz / 16GB RAM

© INEGI all rights reserved

4.

Conclusions & Future Work

- Conclusions
- Future Work
- Acknowledgements

Since 1986

© INEGI all rights reserved

Conclusions

The proposed digital twin can achieve low computational times, which allow:

- A timely prediction of future results
- The calibration of intrinsic material properties, leading to a self-adjusting behaviour

Remote computing capability eliminates the need for extensive computational hardware on the shop floor

© INEGI all rights reserved

Future work

- Enhance property calibration methods
- Validate system through increasingly complex manufacturing scenarios
- Add additional phenomena to the digital twin (curing, distortion, etc)

© INEGI all rights reserved

Acknowledgements

FLASH-COMP (Flawless and sustainable production of composite parts through a human centred digital approach) - European Union's Horizon Europe research innovation programme under grant agreement No.101058458.

© INEGI all rights reserved

inegi driving science & innovation

CONVERTING KNOWLEDGE INTO VALUE FOR OVER 35 YEARS

Since 1986

João Machado

jmmachado@inegi.up.pt

INSTITUTE OF SCIENCE AND INNOVATION IN MECHANICAL AND INDUSTRIAL ENGINEERING

www.inegi.pt

ICCM24

24TH INTERNATIONAL CONFERENCE ON COMPOSITE MATERIALS

U.PORTO

© INEGI all rights reserved

FLEXIBLE AND EFFICIENT MANUFACTURING OF TAILORED CABIN INTERIOR PANELS FOR URBAN AIR MOBILITY APPLICATIONS

Johannes Baur, Johannes Bauer, Gerd Falk, Benjamin Grisin, Furkan Özcan, Olivier Benetreau, Stefan Carosella and Peter Middendorf

Institute of Aircraft Design - IFB, University of Stuttgart
Allmandring 5b, 70569 Stuttgart, Germany
Email: baur@ifb.uni-stuttgart.de, web page: https://www.ifb.uni-stuttgart.de/

Keywords: Automated Fibre Placement, Tailored Fibre Placement, Adaptive tooling, Lightweight design, Composite panels

ABSTRACT

Urban Air Mobility (UAM) faces demanding challenges on weight reduction, efficiency, and sustainability in electric vertical take-off and landing (eVTOL) aircrafts. This research presents and compares three ultra-lightweight composite panel manufacturing concepts, tailored for interior applications, using adaptive moulds and fibre placement technologies. The first concept is a selectively reinforced panel using Tailored Fibre Placement (TFP) with functional integration, achieving surface weights as low as 1.640 g/m². The second is a selectively reinforced sandwich panel, topology optimized and realized using TFP with towpregs, reducing weight further to 650 g/m². The third concept employs robotic near-net-shape Automated Fibre Placement (AFP) of bindered or prepreg tapes directly onto adaptive moulds. Although highly automated and capable of 3D deposition, this approach is currently limited to straight fibre paths and less suited for function integration. Comparative results show trade-offs between flexibility, automation, material efficiency, and design complexity. The integration of adaptive tooling and modular placement strategies opens new pathways for rapid, cost-effective, and sustainable production of composite panels. While this work focuses on aircraft cabin interiors, the presented methods demonstrate broader applicability for next-generation lightweight structures across the UAM sector and beyond.

1 INTRODUCTION

Recent technological developments in the field of electrical vertical take-off and landing (eVTOL) have contributed to further interest and innovations in the field of urban air mobility (UAM) [1]. Nevertheless, a number of challenges concerning the power-to-weight ratio and electrical efficiency must be overcome before eVTOLs can be realised. The overall weight reduction is an important factor as it results in lowered energy consumption or allows for batteries with higher capacities [2]. In addition, studies have shown that the utilisation phase is responsible for up to 99 % of emissions in aviation, and sustainability highly depends on the use of lightweight components [3].

This is where ultra-lightweight approaches become very attractive. The efficiency of composite materials can be improved by optimizing their orientation, taking full advantage of their anisotropic properties. Topology optimization aims to generate load optimized structures, often enabled by additive manufacturing approaches. Thanks to the high degree of design freedom, the material can be optimally distributed, resulting in an increased performance [4]. The use of composites for these structures offers the potential for further optimization of the performance and the lightweight character. The production of composite structures with oriented fibres is crucial for their realization. Automated Fibre Placement (AFP) [5] technologies offer great freedom for the manufacturing of these structures. The Dry Fibre Placement (DFP) is used in a process named Crosslayer [6]. It uses spread dry carbon fibre tows (FixedTows or tapes) that are fixed by the application of an auxiliary binder system [7]. They are placed linearly by activating the binder system, mostly by heating, and enabling adhesion to the tooling surface [8]. That way, load-optimized preform layups are automatically produced near-net-shape [6–9]. Another preform manufacturing approach is the Tailored Fibre Placement (TFP). This process uses embroidery

technology to place continuous fibres according to the load paths in a 2D plane [10]. Different fibres like carbon fibres (CF), glass fibres (GF), and natural fibres (NF) can be used. The dry fibres are stitched on an embroidery base material using a zig-zag stitch pattern. Thanks to the variable orientation of fibres, the resulting preforms can be highly optimized in terms of load-bearing ability and material efficiency. For the selective reinforcements, anisotropic topology optimization can be applied depending on the supporting material layup [11].

Especially cabin interior panels, which are non-structural, are predestined for implementing ultra-lightweight construction approaches. Nowadays, interior panels for commercial aircraft are made of sandwich panels, manufactured as a combination of honeycomb core and glass fibre reinforced plastic (GFRP) face sheets in closed press tools [12]. With standard surface weights higher than 2.000 g/m^2 [13], they have great potential for material savings in the final part and for reducing production waste by developing more efficient processes. As the established production process for sandwich panels is complex, expensive, time-consuming, and hardly automated [12,14], production costs can be significantly reduced by the automated, modular, and versatile manufacturing strategies presented in this research. To unfold the full potential of quickly customizable preforming processes, an adaptive mould is investigated. The surface of this mould can be manipulated to different shapes automatically, which can reduce investment costs, storage costs, and production times [15]. The flexibility gained by the combination of adaptive tooling and fibre placement processes can help reduce the gap between design and production, and enable the fabrication of complex geometries. Though showcasing the manufacturing abilities using the example of cabin interior panels, this paper aims to provide an insight on the versatile application possibilities enabled by variable axial fibre placement technologies in general, not only for UAM applications.

2 METHODS AND MATERIALS

This research aims to introduce and compare three manufacturing methods for tailoring UAM interior panels to achieve significant weight savings at the expense of rigidity. All methods include the use of adaptive moulds and are based on the AFP technologies which are presented next.

2.1 Adaptive tooling

Most samples were produced on the adaptive mould “Mini” from Adapa A/S (Aalborg, Denmark), which is shown in Figure 1.



Figure 1: Adaptive mould Adapa "Mini"

The flexible membrane allows for the generation of double-curved continuous surfaces that can be transformed within minutes. It is controlled by 64 pistons in an 8 × 8 configuration. This results in an active area of 600 mm × 600 mm, and a maximum area of 850 mm × 850 mm. As a constraint, the minimum radius is 400 mm. It must be noted, that the “Mini” is the research mould from Adapa A/S, larger moulds are available in different sizes and can provide areas of up to 9.000 mm × 9.000 mm.

2.2 Tailored Fibre Placement

In this work, a TFP machine TCWM-102 from Tajima Industries Ltd. (Kasugai, Japan), as shown in Figure 2, is used. This twin-head machine has two continuous feeding devices installed and offers a maximum working area of 1.550 mm × 950 mm.



Figure 2: TFP embroidery machine Tajima TCWM-102

2.3 Dry Fibre Placement

The dry fiber tapes are produced from CF with a spreading machine from M&A Dieterle GmbH (Ottenbach, Germany) and can be processed with a Crosslayer placement head of the same company. Basically, the Crosslayer end effector actively feeds bindered or pre-impregnated tape material, activates the adhesive with an IR-lamp and presses it to the tool surface [6]. This is usually done on the Crosslayer portal machine with a working area of 2.000 mm × 1.000 mm. Both machines are presented in Figure 3.

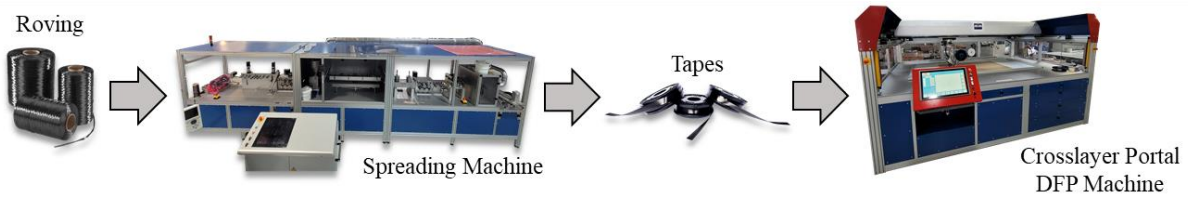

Figure 3: Spreading machine for tape production and Crosslayer portal machine for DFP

2.4 Universal Robot UR20

Figure 4 a) displays the collaborative robot (cobot) Universal Robots UR20 from Teradyne Robotics GmbH (Munich, Germany) with a maximum payload of 20 kg. One major advantage of the cobot is, that it does not need any safety housing, so its application possibilities are very flexible. For robotic AFP, a modified Crosslayer tape placement end effector, shown in Figure 4 b), is mounted. This tool can be used to directly apply tapes to 2D- or 3D-shaped surfaces.

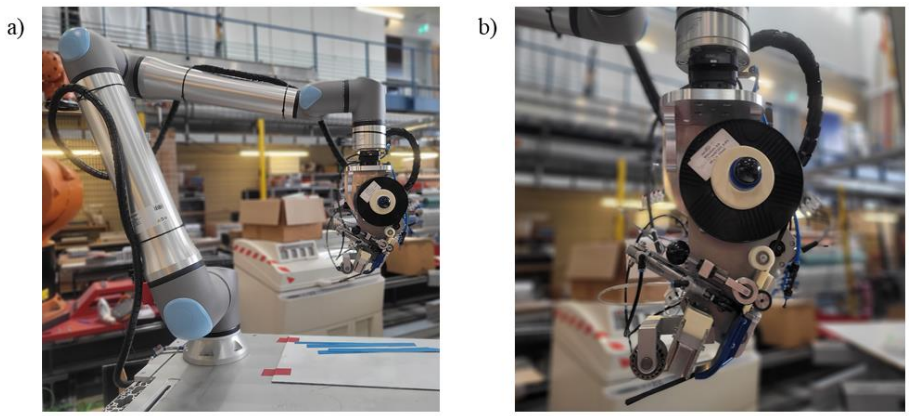

Figure 4: Robotic DFP: a) Cobot UR20; b) Crosslayer placement head

2.5 Materials

During the manufacturing experiments, CF rovings of different filament counts are used. A 12K CF roving Tenax™-E HTS40 F13 12K from Teijin Carbon Europe GmbH (Wuppertal, Germany) is used for towpreg production. For dry TFP processing, a 50K roving Sigrafil® C T50 from SGL Carbon SE

(Wiesbaden, Germany) is used. The 30K roving Pyrofil™ TRH50 30K from Mitsubishi Chemical Corporation (Tokyo, Japan) is used for the production of tapes for the DFP process.

The GF base material for embroidery is E-glass woven fabric HexForce 02116 1260 TF970 from Hexcel Corporation (Stamford, Connecticut, USA). It was purchased from Wela Handelsgesellschaft mbH (Geesthacht, Germany). It weighs 105 g/mm^2. As an alternative, NF base material flax fibre twill 2/2 fabric ampliTex™ 5040 from Bcomp Ltd. (Fribourg, Switzerland) with 300 g/m^2 is chosen.

As a core material, pressure stable polyester nonwoven Soric® XF 6 with a thickness of 6 mm is chosen. In addition to its core function, it can also serve as an infusion medium. The dry weight of Soric® XF 6 is 345 g/m^2, the infiltrated weight is 3.600 g/m^2. It is produced by Lantor B.V. (Veenendaal, Netherlands) and was purchased from Gaugler & Lutz GmbH & Co. KG (Aalen-Ebnat, Germany).

Two resin systems are used throughout the experiments. Both possess low viscosity and long pot life. For the towpreg production, EPIKOTE™ Resin MGS RIMR 135 is used in combination with EPIKURE™ Curing Agent MGS RIMH 137 from Hexion B.V. (Rotterdam, Netherlands). All other Infusions are done with Epoxy Resin L and Hardener GL2 from R&G Faserverbundwerkstoffe GmbH (Waldenbuch, Germany). Especially for optical applications, the high transparency of this resin is beneficial.

3 DESIGN AND MANUFACTURING CONCEPTS

This chapter presents and compares three distinct manufacturing concepts, each implemented in the form of ultra-lightweight panel prototypes, which are described in Chapter 4. All approaches are developed to be compatible with adaptive mould systems, supporting both, dry fibre placement followed by resin infusion, or prepreg-based processing routes. The concepts differ in their design philosophies, functional integration capabilities, and fibre placement strategies, yet all target significant weight reduction and high shape adaptability – key features for next-generation aerospace interior components, especially within Urban Air Mobility (UAM) applications.

3.1 Selectively Reinforced Panel

The first concept is a tailored ceiling panel with integrated functionality, following a design-driven and bionically inspired approach. Drawing inspiration from nature, in this case leaves, the panel design emphasizes load path efficiency and multifunctionality. The central design feature is the selective reinforcement of fibre paths, strategically placed to mimic natural vein structures for optimized mechanical performance. A distinguishing element of this panel is the integration of connection functions. By including loops at the distal ends of the fibre arms, simple mechanical attachment without additional hardware is enabled.

Furthermore, the base material is variable, supporting the use of different materials for focus on aesthetics, lightweight design or sustainability. The TFP reinforced base is stacked together with optional added layers onto the tool surface. The whole panel is then infiltrated using vacuum assisted resin infusion (VARI) or vacuum assisted process (VAP®). This concept is illustrated in Figure 5.

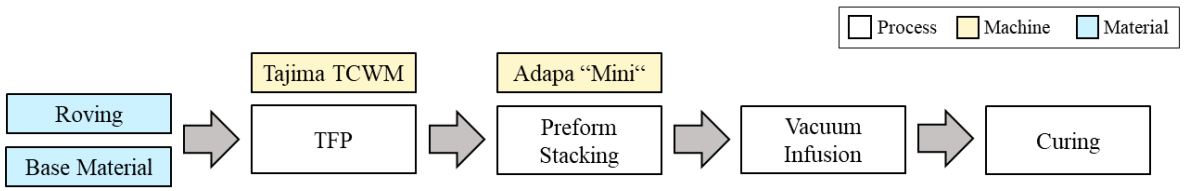

Figure 5: Process diagram of the manufacturing process for the selectively reinforced panel

3.2 Selectively Reinforced Sandwich Panel

The second concept adopts a methodical, performance-optimized approach focused on maximizing mechanical stiffness through sandwich panel construction. This concept relies on the well-established mechanical principle that panel height contributes significantly to bending stiffness, which is enhanced by employing a low-density core material and stiff top and bottom skins. Selective reinforcement is

applied only where structurally necessary, thereby reducing the overall fibre volume and optimizing material usage. The design process, illustrated in Figure 6, is driven by topology optimization, which informs the creation of a modified reinforcement grid, termed the “Opti-Grid”, that serves as the basis for TFP paths.

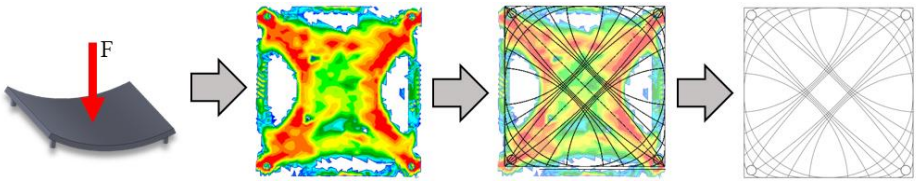

Figure 6: Design process of the "Opti-Grid", starting from solid reference model, going through topology optimization and resulting in an optimized fibre path

For the panel fabrication using TFP technology, it is necessary to use material with compatibility to the embroidery process. The core material must be stitchable, flexible, and capable of maintaining its height under needle load and under surface load. Experiments demonstrated high potential for the lightweight Soric® XF polyester core material. To avoid filling this porous core material with resin, an alternative to vacuum infusion is needed. At this point, pre-impregnated rovings, so-called towpregs, were chosen to be placed with TFP. Towpreg-based TFP offers a resin-contained process with minimal resin waste, making it well-suited for low-mass applications. A known downside of this approach is the contamination of embroidery equipment with pre-impregnated material, requiring periodic cleaning.

The embroidery-based process deposits fibres directly onto two substrates: One layer is placed directly onto the Soric® XF core material, the other is stitched onto a base layer of the glass fibre woven fabric. These preforms are subsequently stacked and shaped on the adaptive mould, followed by vacuum bagging and curing. Figure 7 illustrates the concept of this process, which eliminates the vacuum infusion step.

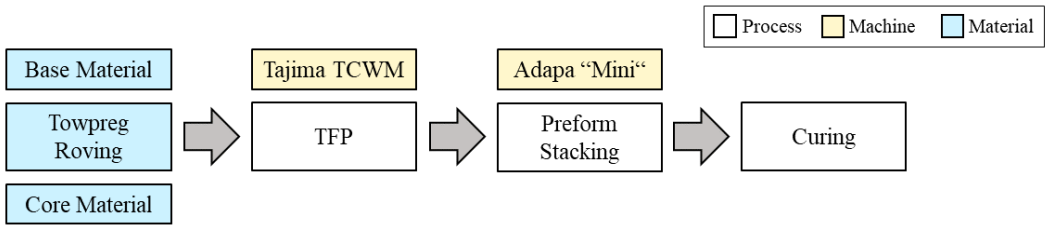

Figure 7: Process diagram of the manufacturing process for the selectively reinforced sandwich panel

3.3 Near-Net-Shape Robotic AFP Panel

The third manufacturing concept employs automated, robotic near-net-shape fibre placement of fibre tapes. This approach leverages an industrial robotic setup wherein spread fibre tapes are applied directly to the adaptive mould surface in their final geometry, avoiding intermediate draping or reshaping steps. The consistent-width bindered dry fibre tapes are prepared from carbon fibre rovings with the M&A Dieterle spreading unit. These are used either dry or pre-infiltrated within a Crosslayer placement head, that is guided precisely over the adaptive mould surface by an UR20 robotic arm. The placement head consists of a tape supply for a film spool and uses an infrared (IR) heating unit to activate the binder or resin on the tapes. Subsequently, a roller system presses the tape with defined force, controlled by the UR20 onto the tool surface. This approach is limited to linear fibre paths due to the nature of the spread tape material and the placement head, but enables highly repeatable and efficient processing. The direct 3D deposition onto the adaptive mould aims to eliminate common defects like wrinkles or bridging, often found in manually draped laminates. Using this process, either monolithic or sandwich design can be realised. For sandwich panels, a core is placed on the bottom reinforcement layer and then covered with the top reinforcement layer. Figure 8 gives an overview on the robotic AFP process with dry bindered tapes and with prepreg tapes.

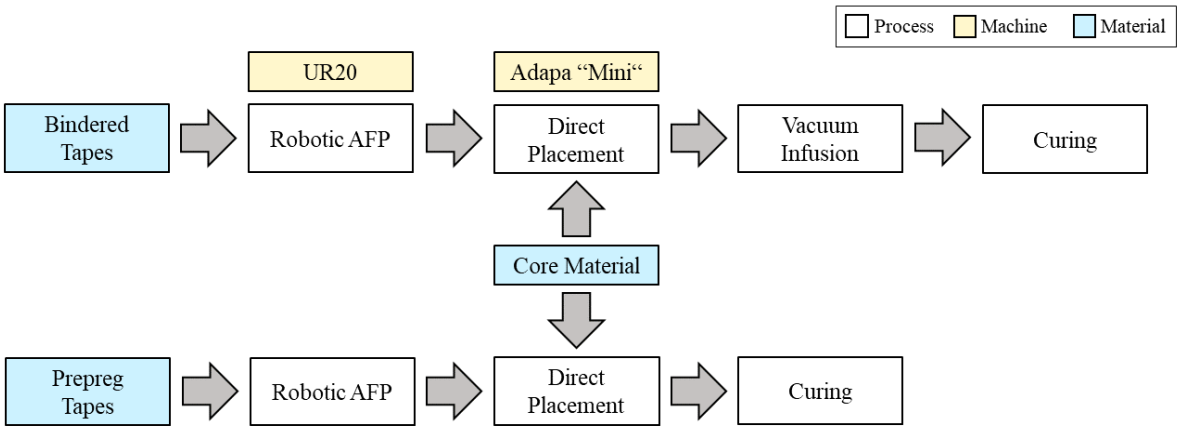

Figure 8: Process diagram of the manufacturing process for the robotic AFP panel with bindered tapes or with prepreg tapes

4 RESULTS

The selectively reinforced panel and the selectively reinforced sandwich panel are evaluated on the basis of the production of panel prototypes. For the robotic AFP, the concept is assessed based on calculations. All three processes differ in their intended application, in their weight, and in their stiffness.

4.1 Selectively Reinforced Panel

The prototype for this manufacturing concept is a cabin interior ceiling panel with a length of 2.400 mm. For this prototype, the moulding area of the lab-scale Adapa "Mini" was too small. Therefore, a standard tooling made from Polyurethane (PU) was used. The TFP process and the resulting panel are presented in Figure 9.

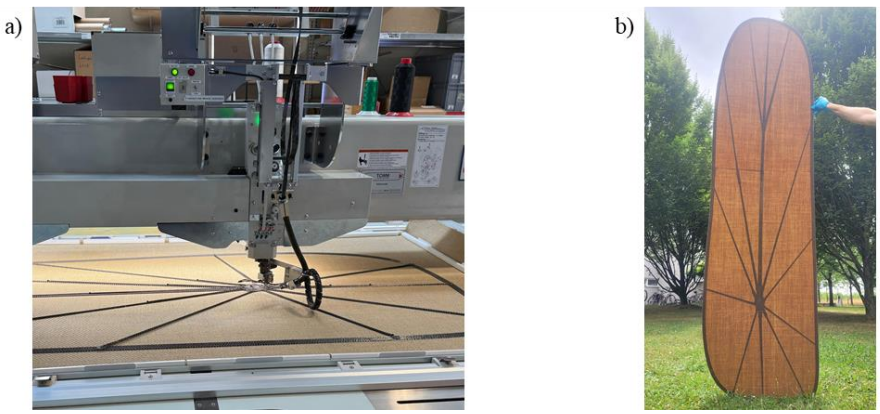

Figure 9: Manufacturing of cabin interior ceiling panel prototype: a) TFP on NF base with CF; b) front side of final NF panel prototype

The NF reinforced panel structure includes two layers of ampliTex™ 5040 woven flax fabric and weighs 2.700 g, which converts to 1.640 g/m^2. Connector functions were successfully integrated in this structure while creating an aesthetic bionically inspired panel. This concept showcases the potential of design-centric fibre placement to integrate functionality without compromising lightweight objectives.

4.2 Selectively Reinforced Sandwich Panel

This panel, sized 700 mm × 700 mm, was produced on the Adapa mould with a radius of 400 mm. Towpreg TFP was done with 12K CF roving, preimpregnated with epoxy resin system RIMR 135/ RIMH 137, on the GF base material and on the Soric® XF core. The needle and the fibre guide unit of the TFP machine had to be cleaned thoroughly after these works.

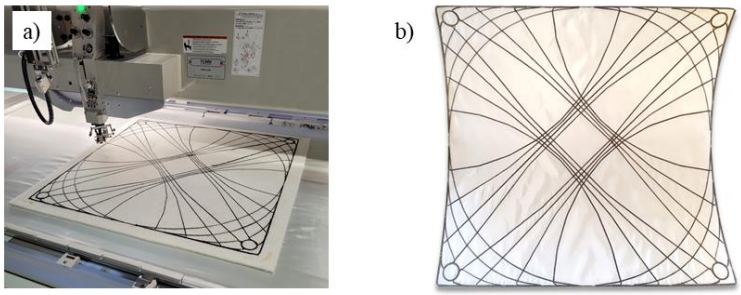

Figure 10: Manufacturing of selectively reinforced sandwich panel: a) TFP on core material with towpreg; b) panel prototype

The resulting prototype demonstrates excellent mass reduction at 320 g, which is equivalent to a surface weight of 650 g/m². This approach highlights how methodically placed fibres in a lightweight sandwich architecture can yield high mechanical efficiency with minimum material usage.

4.3 Near-Net-Shape Robotic AFP Panel (Concept)

The feasibility is proven for this third manufacturing approach. The DFP end effector was successfully implemented and tested in combination with UR20. First layups have been realized on the Adapa “Mini”, one of them shown in Figure 11.

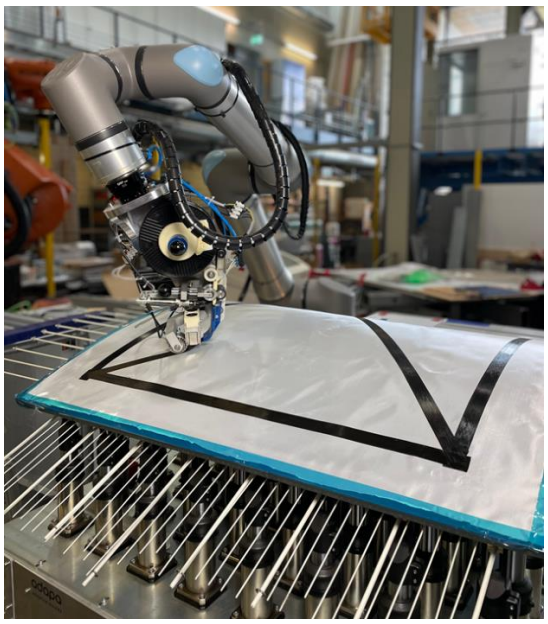

Figure 11: DFP with UR20 on adaptive mould Adapa "Mini"

As no prototype panel was manufactured to date, the concept is evaluated on the basis of weight calculations for a 700 mm × 700 mm sized panel. For the DFP panel with subsequent vacuum infusion setup, the core material is fully filled with epoxy resin. Therefore, this material is the most robust, but also by far the heaviest. The final weight can be calculated with the following formula:

$$m_{panel} = m_{core} \times (w_{panel} \times l_{panel}) + m_{tape,\ infiltrated} \times l_{fibre\ path} \times n_{tape\ layers} \quad (1)$$

The surface weight of the infiltrated core material is $m_{core} = m_{core,\ infiltrated} = 3.600$ g/m², the panel width is $w_{panel} = 0{,}7$ m, and the panel length is $l_{panel} = 0{,}7$ m. The weight of an infiltrated 30K tape is $m_{tape,\ infiltrated} = 3$ g/m and the totalled length of the fibre path for top and bottom layer is $l_{fibre\ path} = 18$ m. For $n_{tape\ layers} = 1$, this results in a potential panel weight $m_{panel,\ DFP} = 1.818$ g, or 3.710 g/m². Therefore, the robotic DFP processing route is not very promising. This is why future research aims to include the

AFP of prepreg tapes. The goal is to combine non-infiltrated Soric® XF with 30K CF prepreg tape. For a 700 mm × 700 mm sized sandwich panel, the part weight is also calculated using equation (1). The same values as above are used here, only varying the weight of the core $m_{core} = m_{core,\,dry} = 345$ g/m^2. This results in a potential panel weight $m_{panel} = 223$ g, which is equivalent to 455 g/m^2. Compared to the TFP sandwich panel, weight is mainly saved thanks to the renunciation of GF base material.

Although the near-net-shape robotic AFP obtains the highest automation potential, it is limited by a less flexible fibre architecture due to the restriction to straight-line paths. Therefore, this concept does not currently support function integration, like loops for the mounting of connectors. Nevertheless, this technique provides a high-throughput, robust solution for producing contoured interior panels with excellent material distribution and very low manual labour input.

4.4 Comparison

Each of the three approaches demonstrates a viable path toward highly efficient, lightweight, and application-specific composite panel manufacturing. The three approaches are compared in Table 1.

Feature/Concept	**Selectively Reinforced Panel**	**Selectively Reinforced Sandwich Panel**	**Near-Net-Shape Robotic AFP Panel Concept**
Fibre Placement Process	TFP	TFP	Robotic AFP
Fibre Material	Roving	Towpreg	Bindered Tape / Prepreg Tape
Fibre Placement Geometry	Variable Axial Design	Variable Axial Design	Straight Lines
Near-Net-Shape	2D	2D	3D
Compatible with Adaptive Moulds	Yes	Yes	Yes
Design Philosophy	Aesthetic & Functional	Stiffness Optimization	Process Efficiency
Functional Integration	Connectors	Connectors	Not Integrated
Process Automation	Medium	Medium	High
Areal Weight (g/m²)	1.640	650	3.600* (infusion) 455* (prepreg) *calculated values

Table 1: Comparison of flexible manufacturing concepts

The selective panel emphasizes design and function, the sandwich panel highlights mechanical performance via structural optimization, and the robotic AFP concept provides industrial scalability with streamlined automation. The choice between them ultimately depends on the specific application context, performance priorities, and available production infrastructure.

5 CONCLUSIONS

This process study presented and compared three advanced manufacturing strategies for ultra-lightweight composite cabin interior panels, all leveraging variable axial fibre placement technologies in combination with adaptive tooling. The findings highlight the immense potential of tailored fibre architectures to significantly reduce component weight while enabling either structural optimization or functional integration.

The selectively reinforced panel demonstrated that variable axial fibre placement using TFP allows integration of secondary functionalities such as mechanical connectors without compromising aesthetics

or sustainability. The proposed multifunctional concept is particularly efficient in scenarios where design, functionality and material diversity are of the utmost importance.

The selectively reinforced sandwich panel emphasized performance-driven design, utilizing topology optimization to guide fibre placement for maximum stiffness-to-weight ratios. Through the use of stitchable cores and towpregs, this method eliminated vacuum infusion, achieving the lowest prototype areal weight (650 g/m²) while simplifying processing.

The robotic AFP concept, although still under development, highlighted the benefits of high automation and near-net-shape capability. While limited by its restriction to straight fibre paths, the use of dry or prepreg tapes in combination with adaptive moulding shows promise for future high-throughput manufacturing, especially with further refinement of resin handling and tool-path generation.

Overall, the study reveals that each concept offers unique advantages depending on the application focus – be it function, performance, or scalability. Adaptive moulds played a key enabling role in reducing tooling complexity, cost, and development time, demonstrating their compatibility with all presented processes.

Future research will explore mechanical characterization, long-term durability, and the integration of sensors or active components. Ultimately, these approaches support the growing need for sustainable, lightweight, and functionally integrated solutions not only in UAM but across all mobility sectors.

ACKNOWLEDGEMENTS

This work is supported by the Federal Ministry for Economic Affairs and Energy as part of the LuFo VI-2 research project “KONKAV” (FKZ: 20K2105F).

Supported by:



on the basis of a decision
by the German Bundestag

REFERENCES

[1] A.P. Cohen, S.A. Shaheen and E.M. Farrar, Urban Air Mobility: History, Ecosystem, Market Potential, and Challenges, *IEEE Trans. Intell. Transport. Syst.* **22** (2021), 6074–6087.

[2] H. Pak, L. Asmer, P. Kokus, B.I. Schuchardt, A. End, F. Meller, K. Schweiger, C. Torens, C. Barzantny, D. Becker, J.M. Ernst, F. Jäger, T. Laudien, N. Naeem, A. Papenfuß, J. Pertz, P.S. Prakasha, P. Ratei, F. Reimer, P. Sieb, C. Zhu, R. Abdellaoui, R.-G. Becker, O. Bertram, A. Devta, T. Gerz, R. Jaksche, A. König, H. Lenz, I.C. Metz, F. Naser, L. Schalk, S. Schier-Morgenthal, M. Stolz, M. Swaid, A. Volkert and K. Wendt, Can Urban Air Mobility become reality? Opportunities and challenges of UAM as innovative mode of transport and DLR contribution to ongoing research, *CEAS Aeronaut J* (2024).

[3] D. Krause, L. Schwan, S. Wehrend and K. Zumach, Steigerung der Nachhaltigkeit im Luftverkehr: Potenziale rund um die Flugzeugkabine, in: *DGLR-Mitgliedermagazin "Luft- und Raumfahrt"*, pp. 28–31.

[4] L. Peng, S. Xiuli, D. Shaojing and F. Yufan, Topology optimization methods and its applications

in aerospace: a review, *Struct Multidisc Optim* **68** (2025).
[5] S. Carosella, S. Hügle, F. Helber and P. Middendorf, A short review on recent advances in automated fiber placement and filament winding technologies, *Composites Part B: Engineering* **287** (2024), 111843.
[6] B. Grisin, S. Carosella and P. Middendorf, Dry Fibre Placement: The Influence of Process Parameters on Mechanical Laminate Properties and Infusion Behaviour, *Polymers* **13** (2021).
[7] F. Helber, B. Schrick, S. Carosella and P. Middendorf, Production with Customizable UD Materials for Hybrid, in: *SAMPE Europe Conference 2017*.
[8] F. Helber, S. Carosella and P. Middendorf, Quantitative Assessment of Reactive and Non-Reactive Binder Systems on First Ply Adhesion for Dry Fiber Placement Processes, *KEM* **926** (2022), 1317–1326.
[9] G.S. Dutta, M. Feyrer, G. Ziegmann, J. Bauer, S. Carosella, P. Middendorf, G. Oehl and J. Guhathakurta, Zero-waste prepreg production through the combination of automated fiber Placement and Online-Prepreg Technology. Tagungsband 6. Symposium Materialtechnik: 20. bis 21. Februar 2025 (2025).
[10] C. Cherif, ed., *Textile Werkstoffe für den Leichtbau: Techniken - Verfahren - Materialien - Eigenschaften*, Springer, Berlin, Heidelberg, 2011.
[11] J. Schwingel and P. Middendorf, Topological design using multivariate laminate stackings for tailored fiber placement, *Journal of Composite Materials* **56** (2022), 2047–2061.
[12] H. Eschen, F. Kalscheuer and T. Schüppstuhl, Optimized process chain for flexible and automated aircraft interior production, *Procedia Manufacturing* **51** (2020), 535–542.
[13] SHOWA AIRCRAFT INDUSTRY CO., LTD., *Datasheet AeroRigid 2623: Composites Panel for Aircraft Interiors*, Tokyo, 2017.
[14] E.A. Franco-Urquiza, P.I. Alcántara Llanas, V. Rentería-Rodríguez, R.S. Saleme, R. Ramírez Aguilar, C. Zarate Pérez, M. Torres-Arellano and S. Piedra, Innovation in Aircraft Cabin Interior Panels. Part II: Technical Assessment on Replacing Glass Fiber with Thermoplastic Polymers and Panels Fabricated Using Vacuum Forming Process, *Polymers* **13** (2021), 3258.
[15] C. Raun and P.H. Kirkegaard, Adaptive Mould - A Cost-Effective Mould System Linking Design and Manufacturing of Double-Curved Panels, in: *Proceedings of the IASS-SLTE 2014 Symposium*, 2014.

Hollow Ball Core (HBC) Technology for Novel Sandwich Structured Composites

Won Gyo Seo, Gavin Stoker, Henry Shaw,

Advisor: Prof. Dae Han Sung

24th International Conference on Composite Materials August 4-9, 2025 in Baltimore, MD

ICCM24
24TH INTERNATIONAL CONFERENCE ON COMPOSITE MATERIALS

STATE U | UtahState University

FICAM Functional Intelligent Composites & Advanced Manufacturing

00 Outline

- Introduction and motivation
- Hollow Ball Core(HBC) Manufacturing Ap proach for Panel Tests
- Characterization of HBC Panels
- Key Advantages and Applications
- Future Works & Acknowledgements

01 Introduction and Research Motivation

Sandwich cores

Homogeneous Support of the skins

Open/closed c ells, no cells

Foam cores

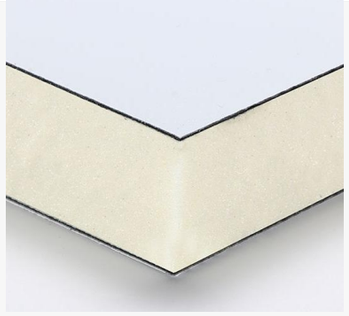

Structured (non-homogeneous) support of the skins

Punctual structure

Open

pin cores

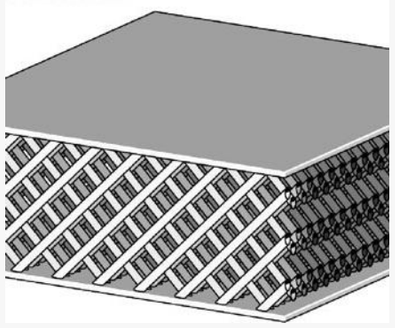

Regional structure

Open to both side

Cup shape cores



Unidirectional structure

Open to one side

corrugated cores

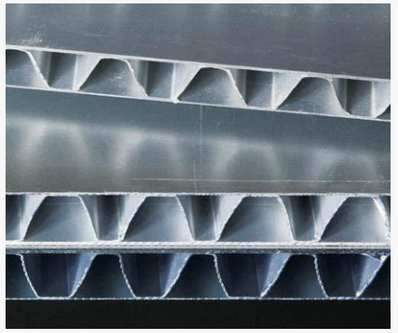

Bi-directional Structure

Open in thickness d irection

Honeycomb cores

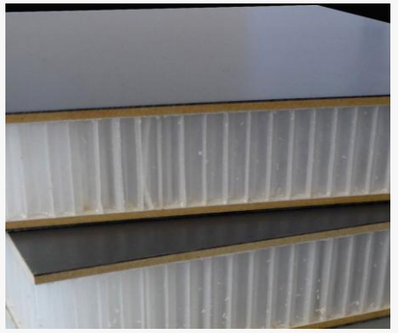

01 Introduction and Research Motivation

Corrugated Core

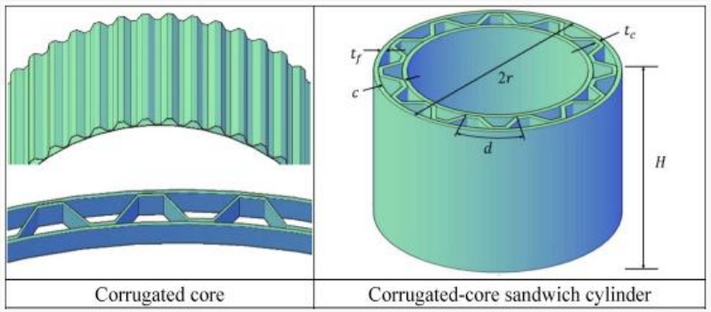

Truss Core

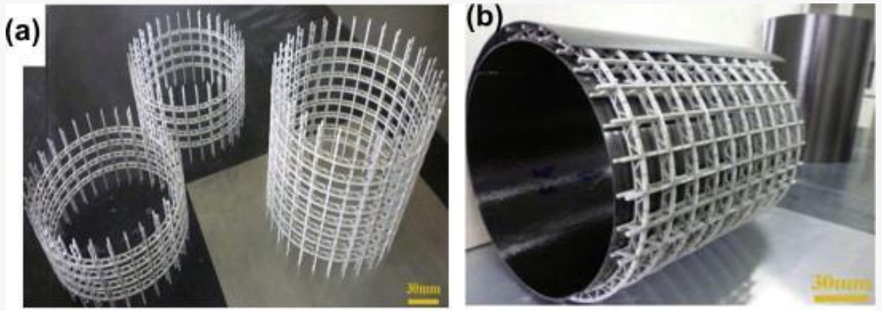

3D Printed Core

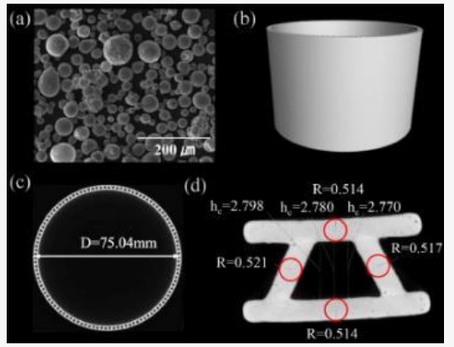

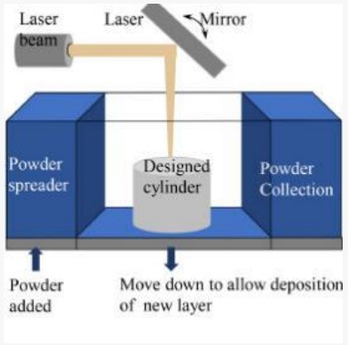

- **Limitation: Sandwich for Complex Structures**
  - **Complex curvatures**
  - **Cylinders and enclosed molds**

01 Introduction and Research Motivation

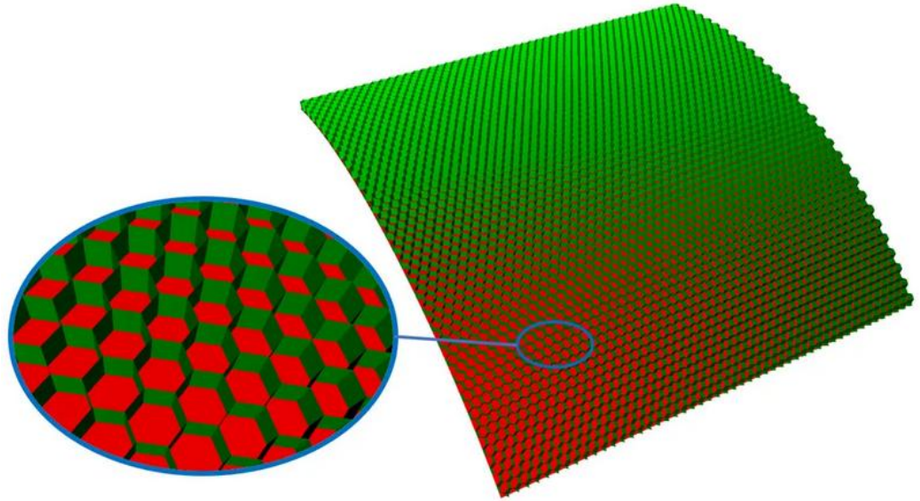

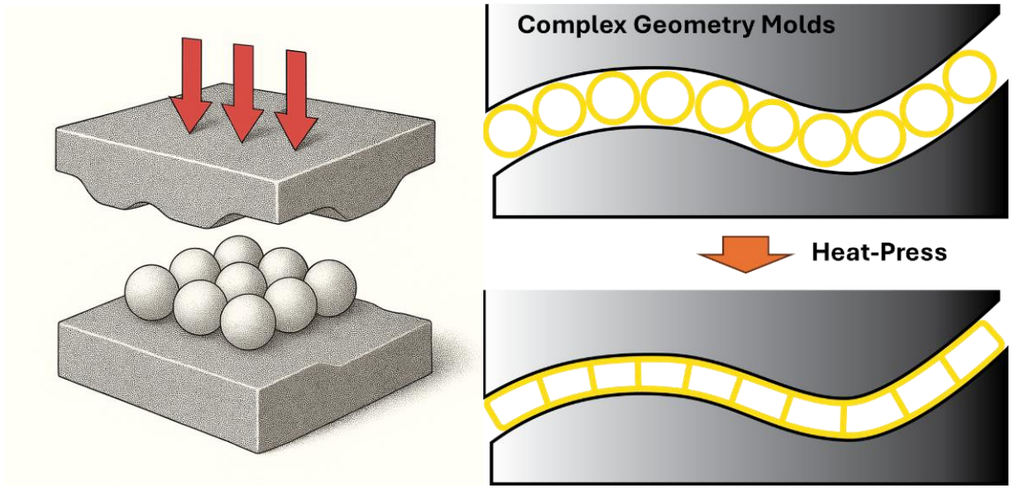

01 Introduction and Research Motivation

- **Key Advantages**
  - HBC can accommodate the complex geometry sandwich structures only through ball packing optimization
  - 100% recyclable materials (thermoplastics) are used
- **Potential Applications**
  - Replacing closed mold processes (e.g., UAM parts)
  - Enclosed molds

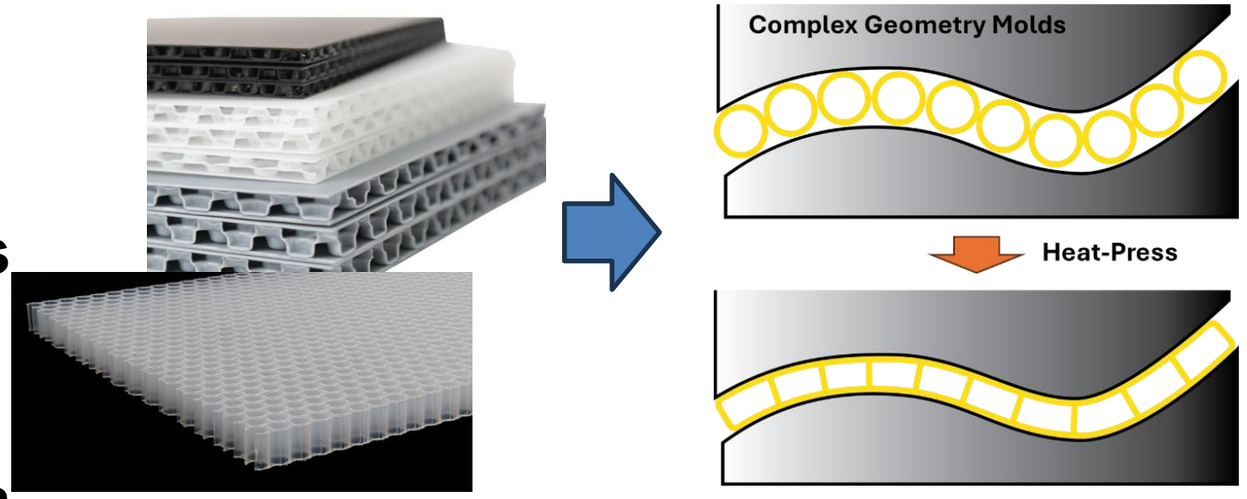

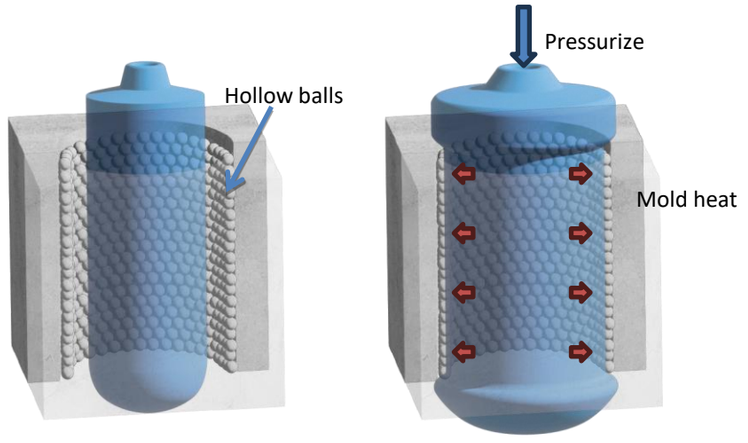

Ball placement in mold

Mold heat / bladder inflation

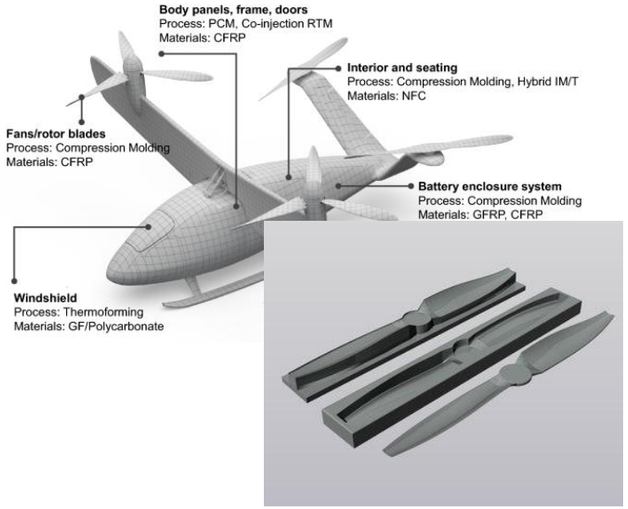

02 Hollow Ball Core material properties

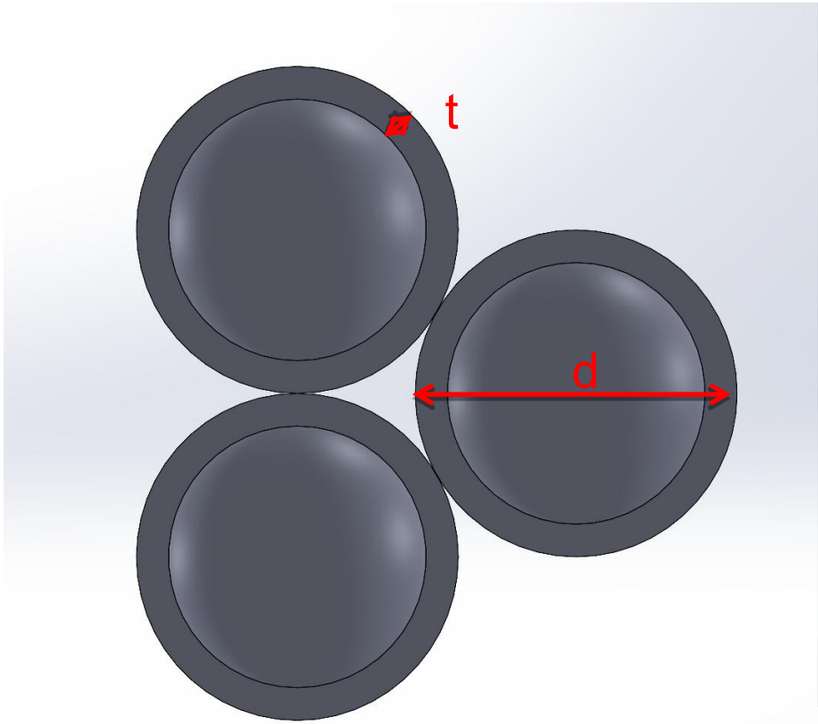

Cutaway view of HBC unit cell



Thermoplastic ball

02 Hollow Ball Core material properties



Thermoplastic ball

02 DSC – crystallization kinetics for heating/cooling rate control

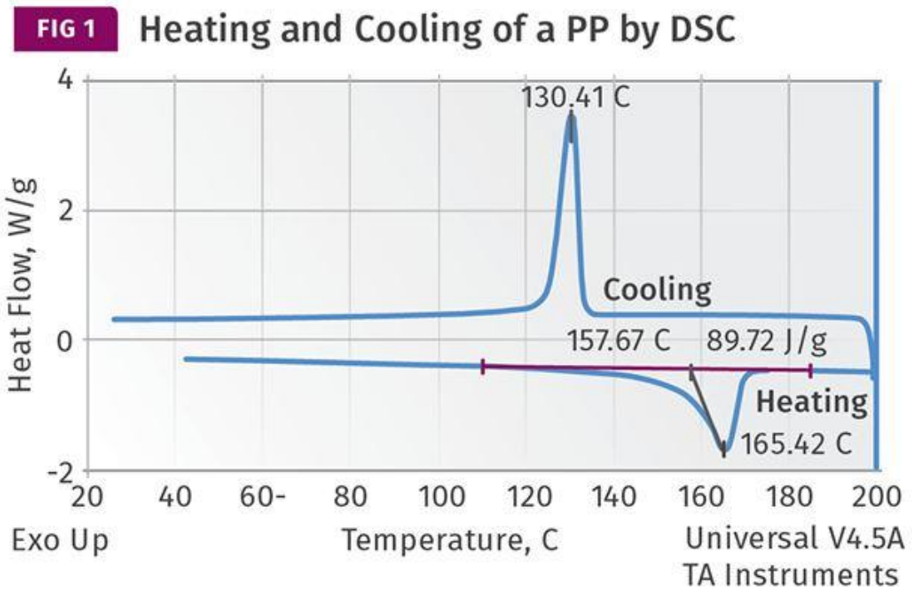

02 Dynamic Mechanical Analysis

- DSC & DMA results validation
- Identify Interdiffusion temperature
- Onset point,
  - rapid drop of storage modulus E’
- 166°C = 330°F
  - Initial process temperature

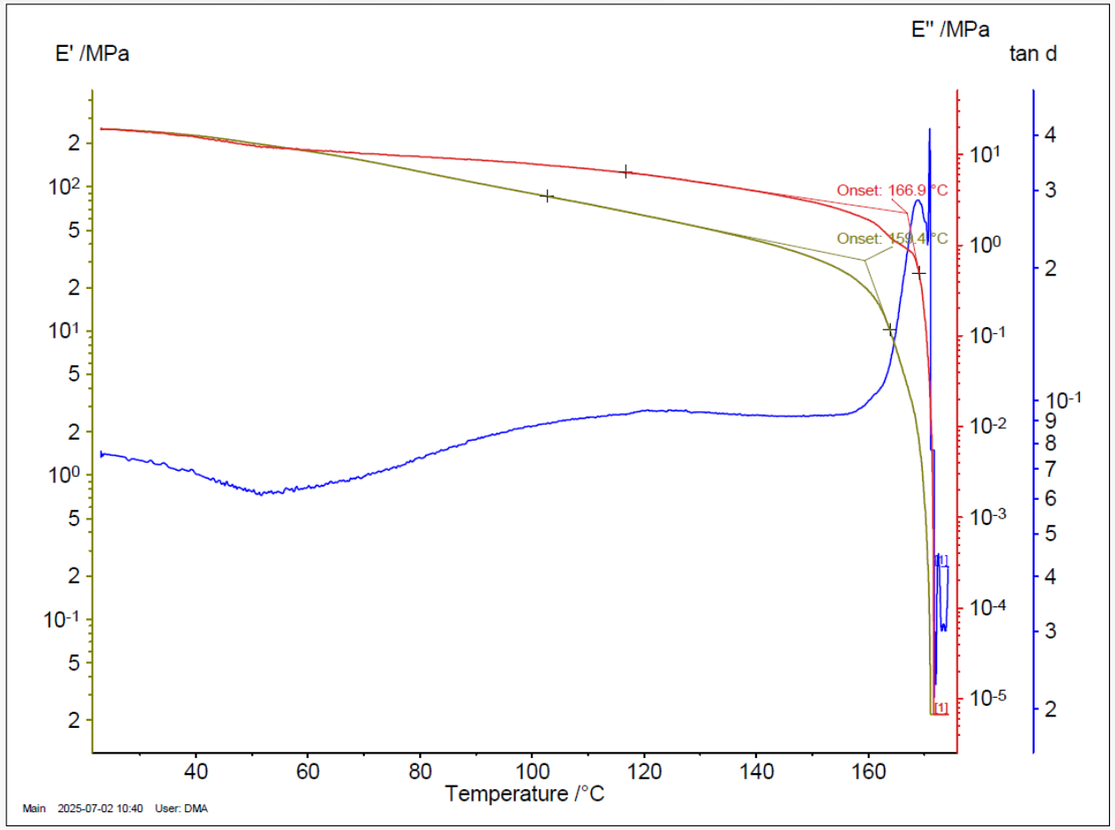

- Glass transition temperature, but below melting temperature

03 Hollow Ball Core(HBC) Manufacturing Process

- **Experimental Procedure and Processing Flow**
  - **Material property**
  - **Heating**
  - **Pressing and bonding**
  - **Cooling**
  - **Bonding check**
  - **Structure testing**

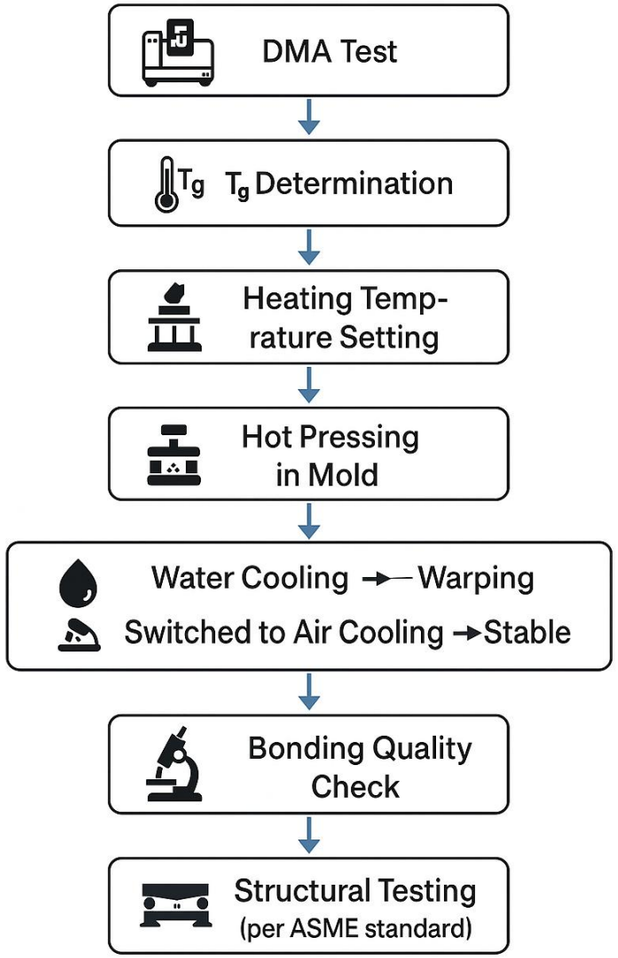

03 HBC Manufacturing Process





Single cell without mold

Dimensional Change during Process

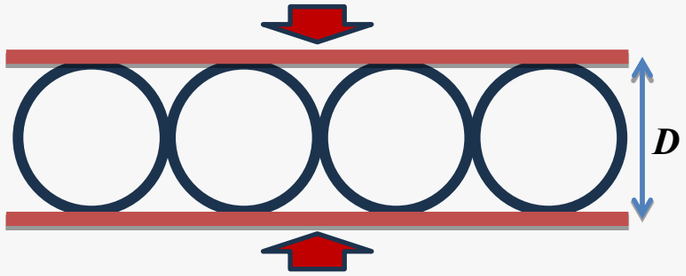

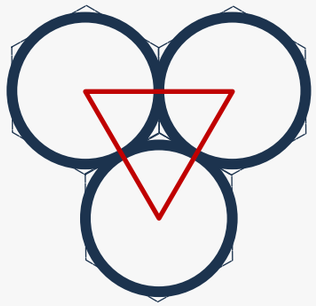



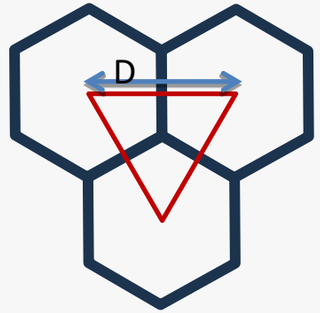

$$\frac{1}{2}\times\frac{4}{3}\pi\left(\frac{D}{2}\right)^3=\left(\frac{D}{2}\times\frac{\sqrt{3}}{2}D\right)\times H$$

$$H=\frac{\pi}{3\sqrt{3}}D$$

$$H=0.605D$$

The reduced height after compaction is approximately 60% of ball diameter

03 HBC Manufacturing Process

- **Thermoplastic (Polypropylene – PP) hollow spheres are heat-pressed**
- **Dwell time 10 min at 340 °F**



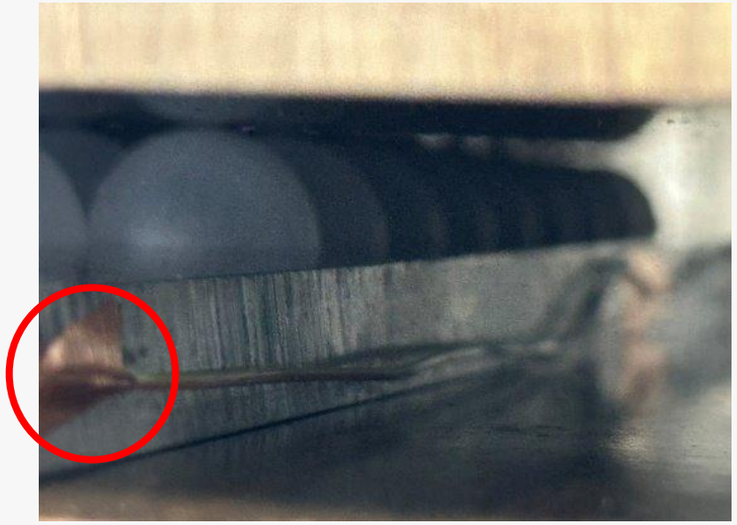

Temperature probe location k-type

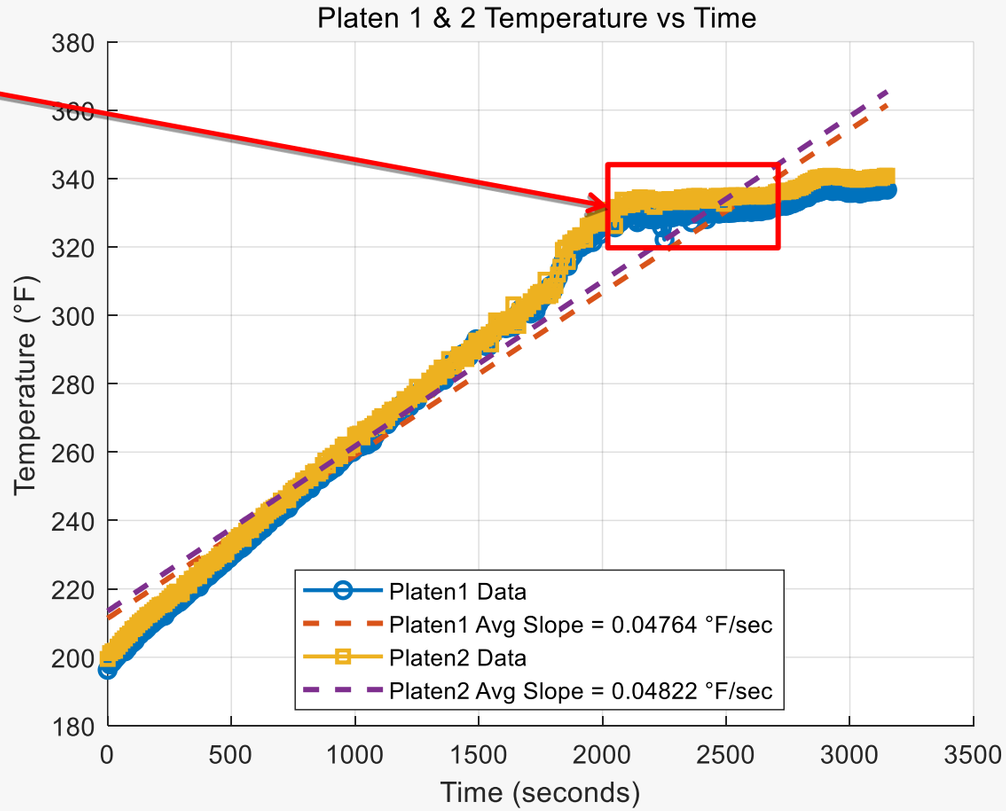

03 Hollow Ball Core(HBC) Manufacturing Process

- **Thermoplastic (Polypropylene – PP) hollow spheres are heat-pressed**
- **Cell bonding temperature 350 °F**
- **Ramping up temperature**
- **Press is already completed at this point**



Cell fail to weld with l
ower temperature

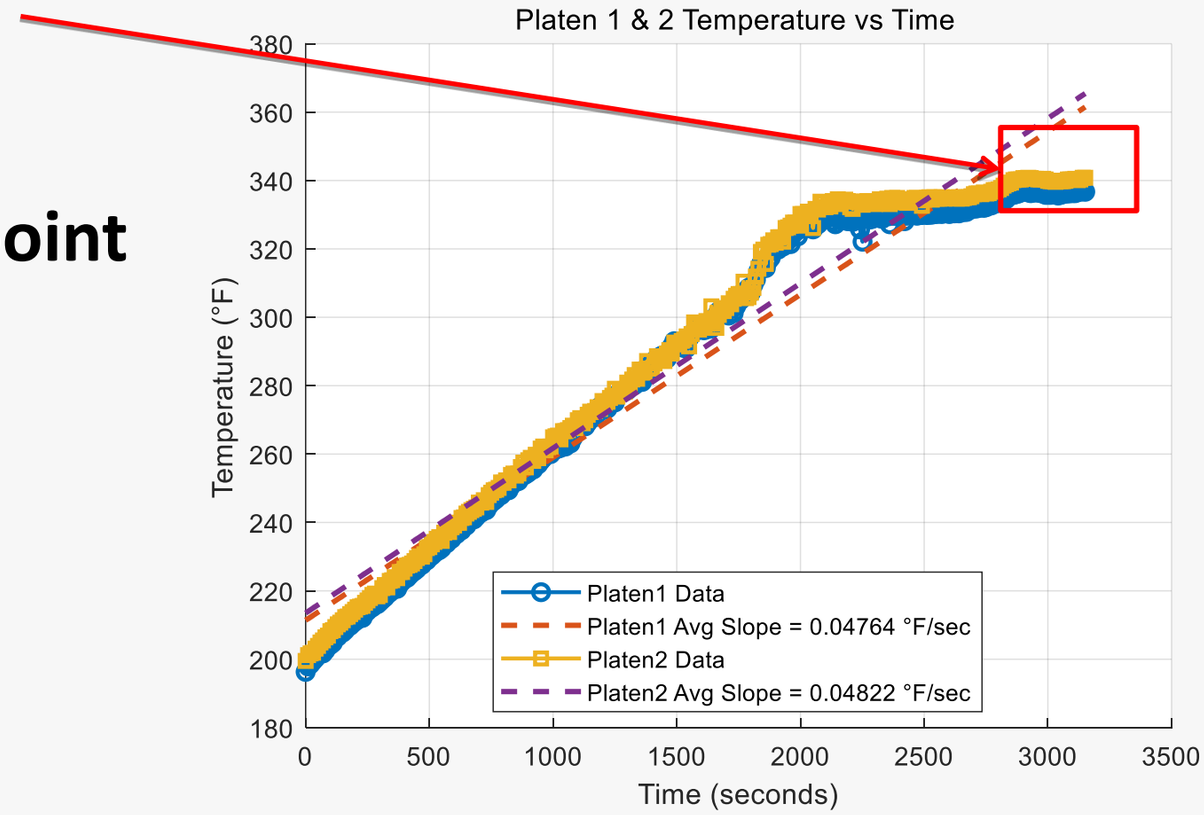

03 Hollow Ball Core(HBC) Manufacturing Process

- Thermoplastic (Polypropylene – PP) hollow spheres are cooled
- Crystallization temperature 266°F
- Cooling methods
  - Water cooled
  - Air cooled
- Press is already completed at this point



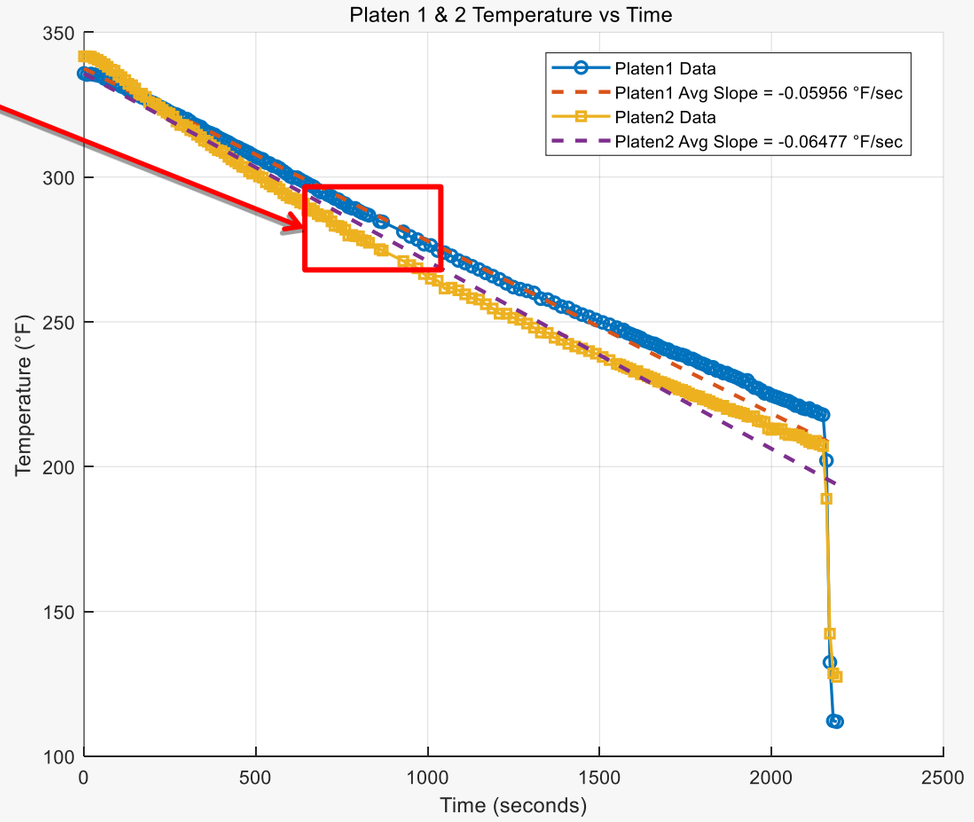

04 HBC Manufacturing Process

Cooling rate and smooth surface process



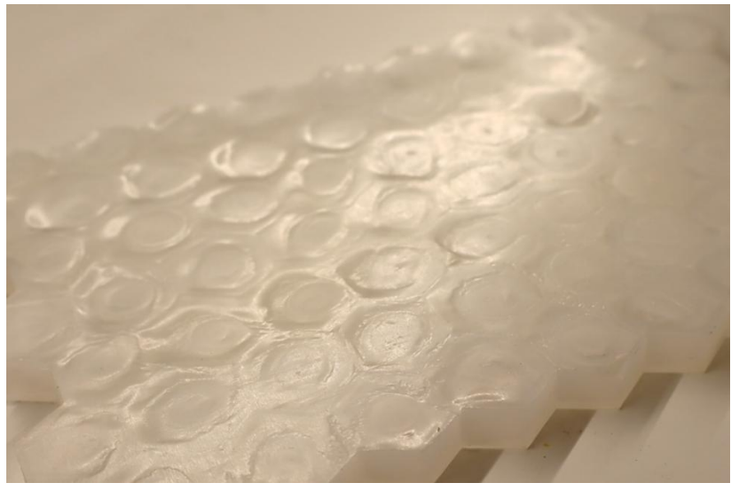

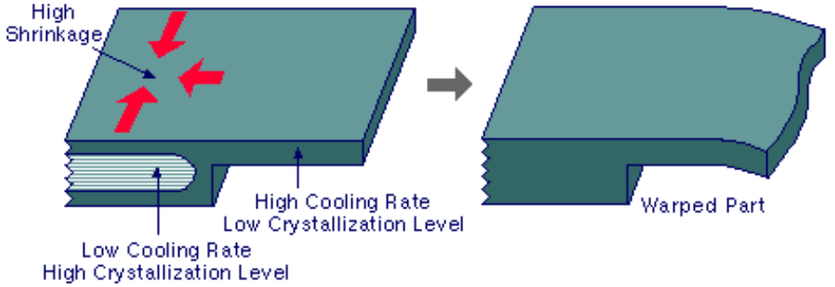

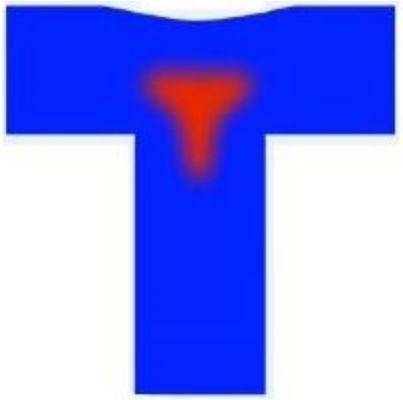

https://blogs.solidworks.com/tech/2018/09/your-part-is-shrinking.html

04 Characterization of HBC Panel

- **Flexural Test – water vs air cooled**
  - **Equivalent weight**

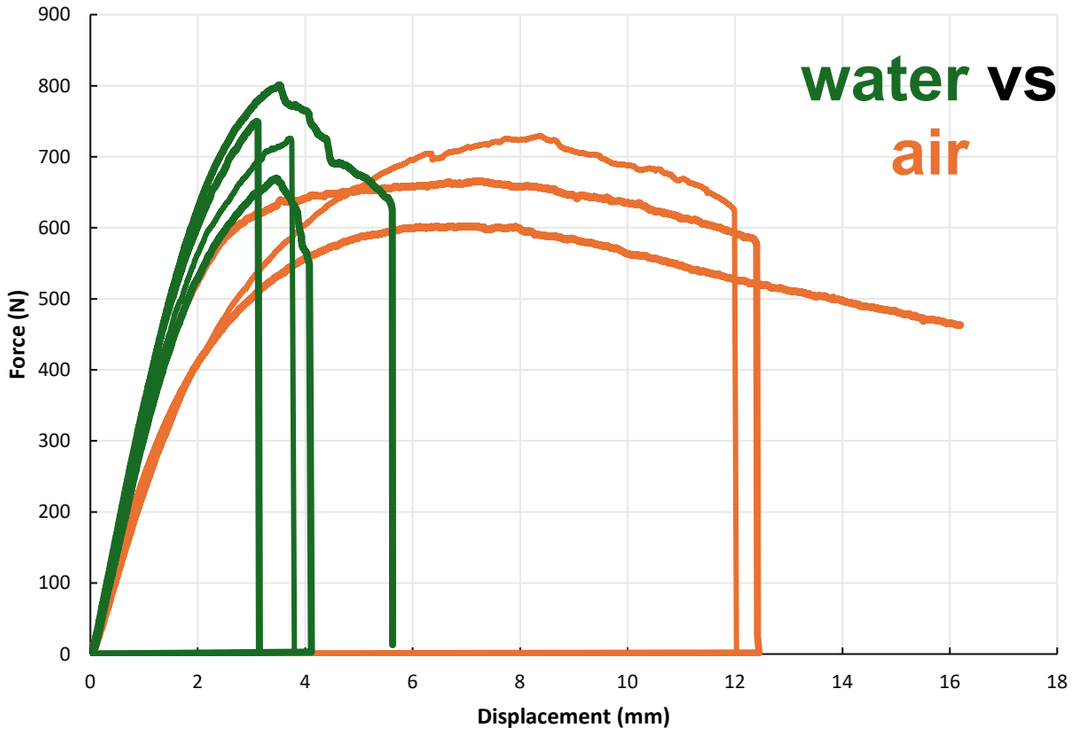





- **Air cooled panel showed ductility**
  - **Strong bond, uniform quality**
  - **Force distributed well thru the joints**

04 Characterization of HBC Panel

- **Flexural Test – HBC vs Solid**
  - **Equivalent weight**

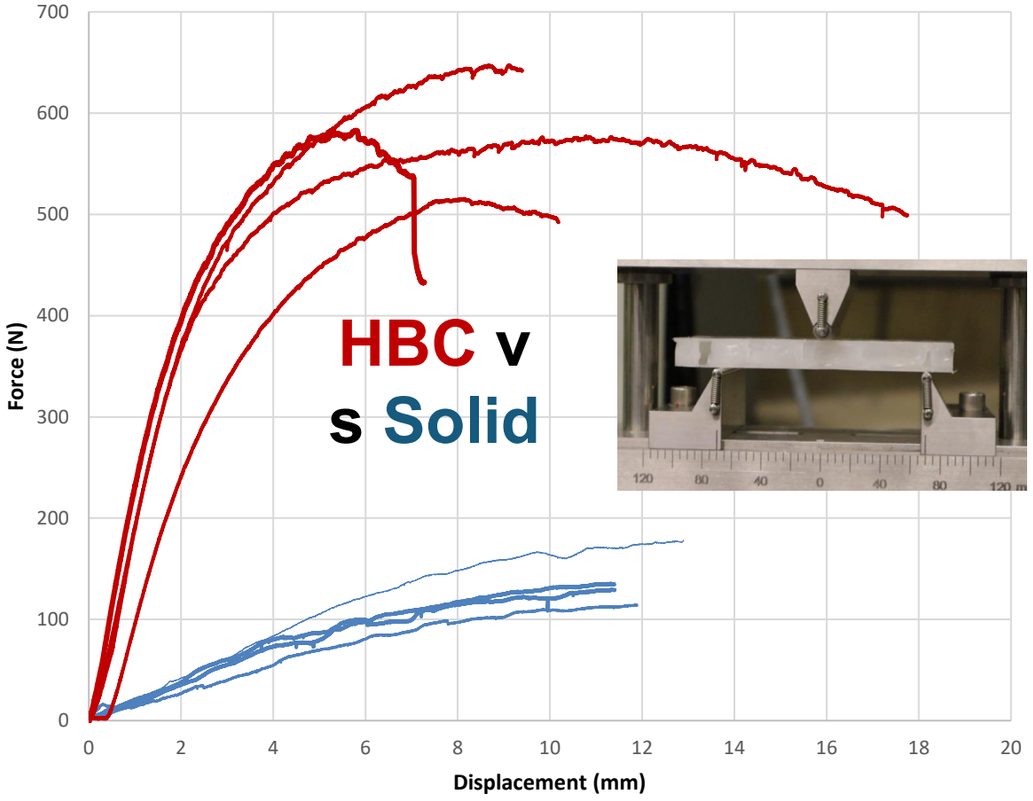

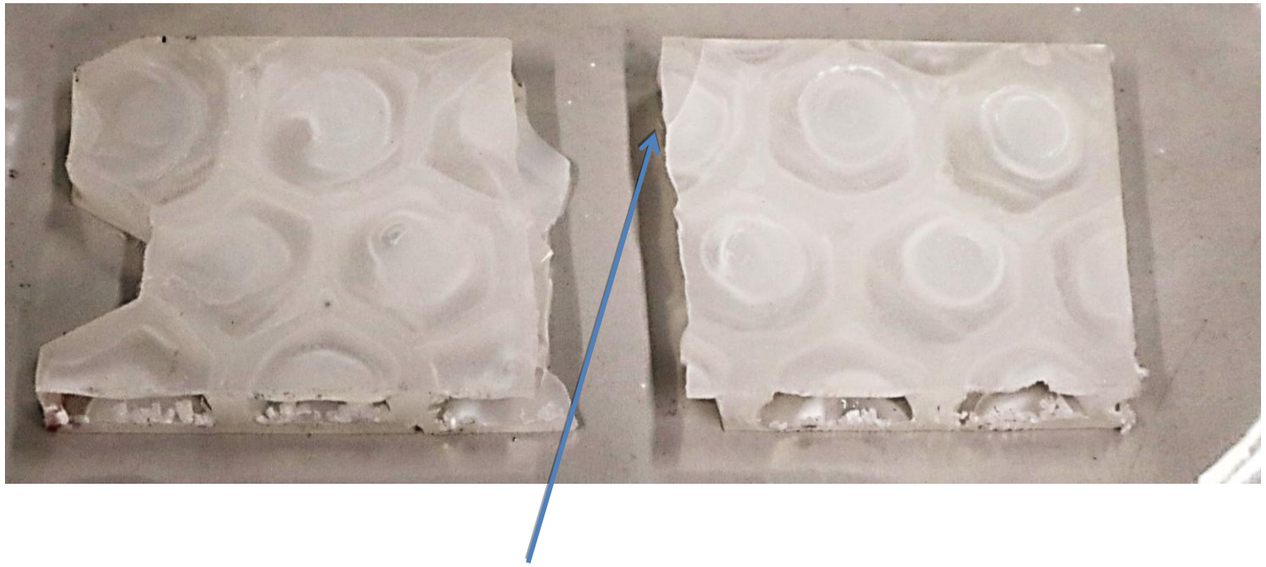

- **Fracture does not occur at the b all interfaces**
  - **Strong bond, uniform quality**

04 Characterization of HBC Panel

- **Thermoplastic (Polypropylene – PP) hollow spheres**

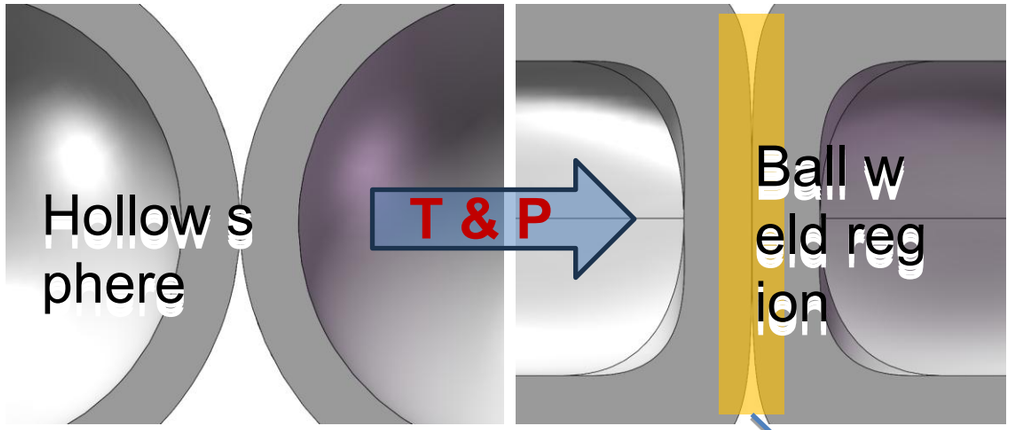

Light Reflections f
rom photography

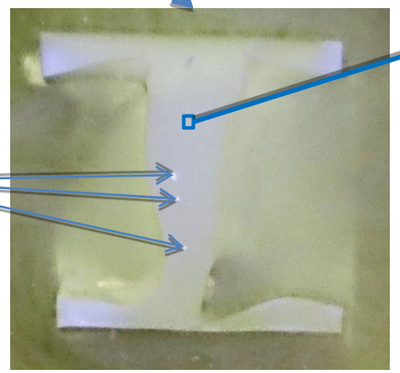

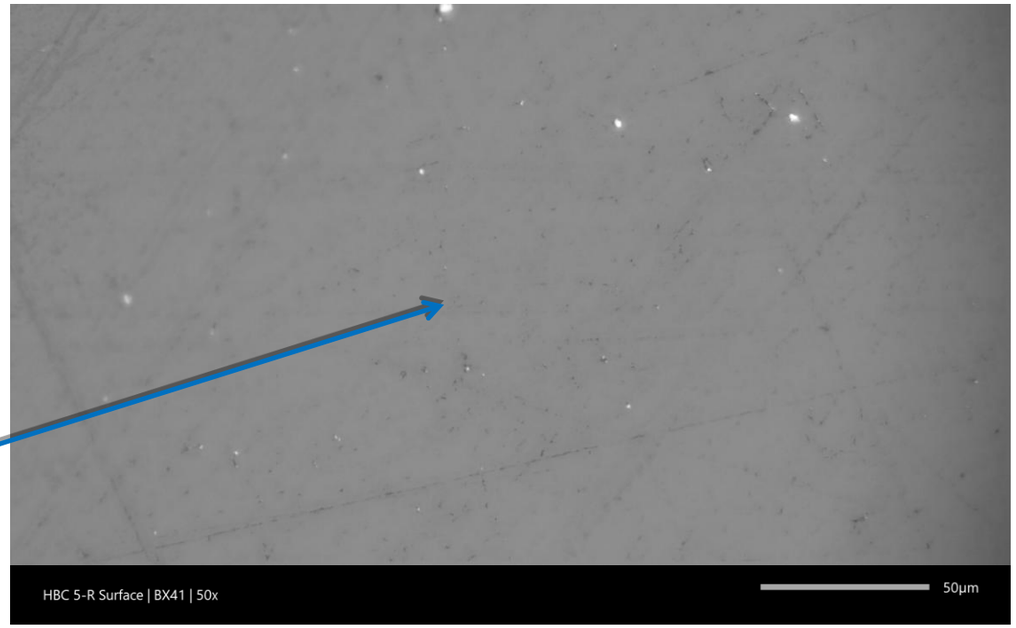

- Thermally joined line is invisible
- Homogeneously welded

05 Conclusive Remarks

- Pressing was feasible near the thermoplastic's Tg
- Cell fusion occurred at higher Tg in DSC vs. DMA
- Slow cooling enhanced crystallization and bonding
- Flat mold fabrication was simple and effective
- Potential shown for use with complex molds

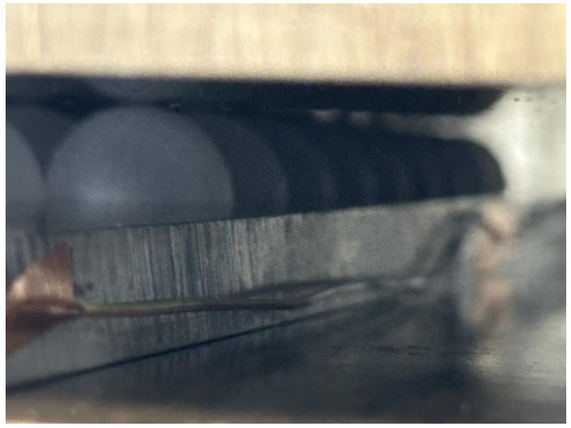



05 Future Work

- **Further characterization**
  - **HBC manufacture effect on tensile strength**
  - **HBC impact strength**
  - **Crystallization kinetics of ball polymers**
- **Process optimization**
  - **Thermo-mechanical property modeling via ANSYS**
  - **Improved temperature and pressure monitoring and control**

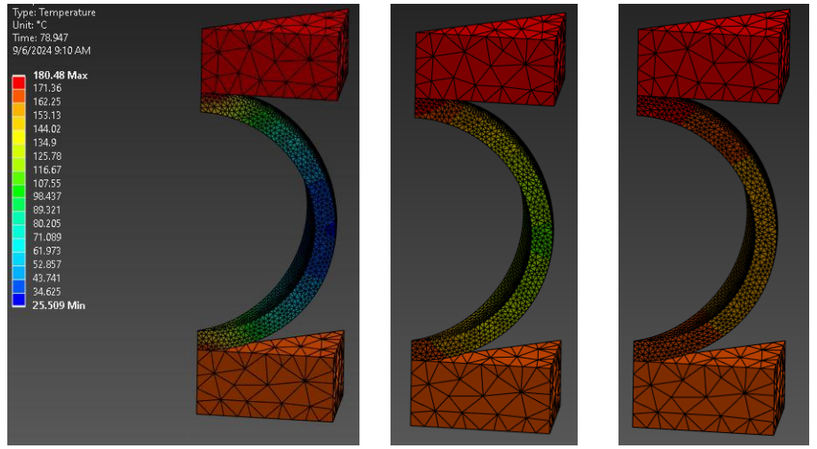

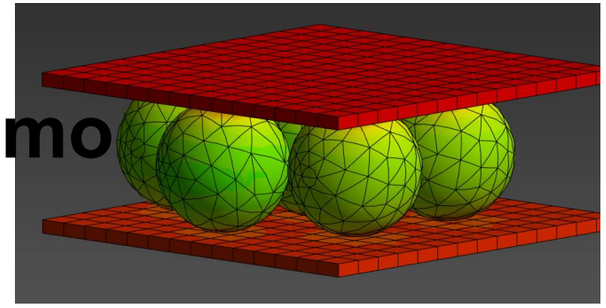



05 Acknowledgements

- **FICAM Lab**
  - **Gavin Stoker, Henry Shaw, Prof. Dae Han Sung**
- **CDMAM Lab**
  - **Dr. Greg Anderson**
- **USU Machinist, Terry Zollinger**
- **Utah State University**
- **ICCM 24**



Q&A

FICAM

Supplementary

02 Hollow Ball Core(HBC) Manufacturing Process

- **Thermoplastic (Polypropylene – PP) hollow spheres are heat-pressed**

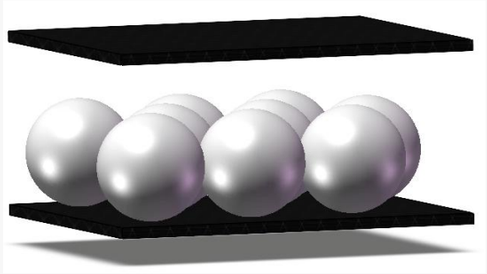

Blow-molded hollow spheres

Heat Press

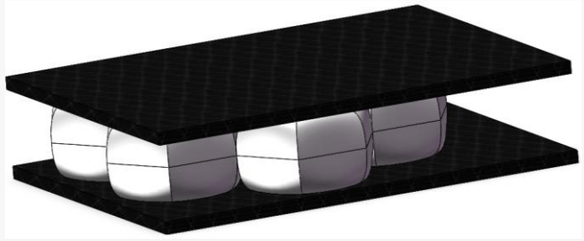





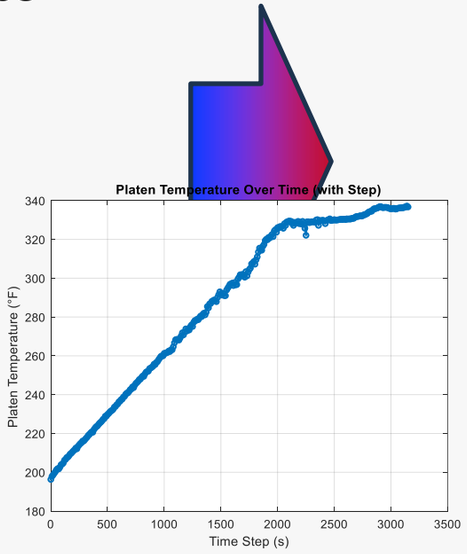

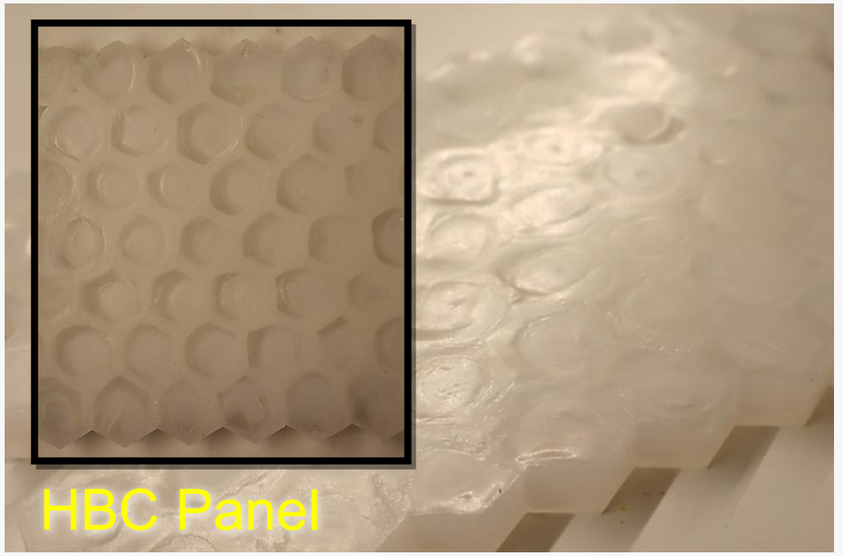

02 HBC Manufacturing Process

- **Height reduction after packing**

$$\frac{1}{2}\times\frac{4}{3}\pi\left(\frac{D}{2}\right)^3=\left(\frac{D}{2}\times\frac{\sqrt{3}}{2}D\right)\times H$$

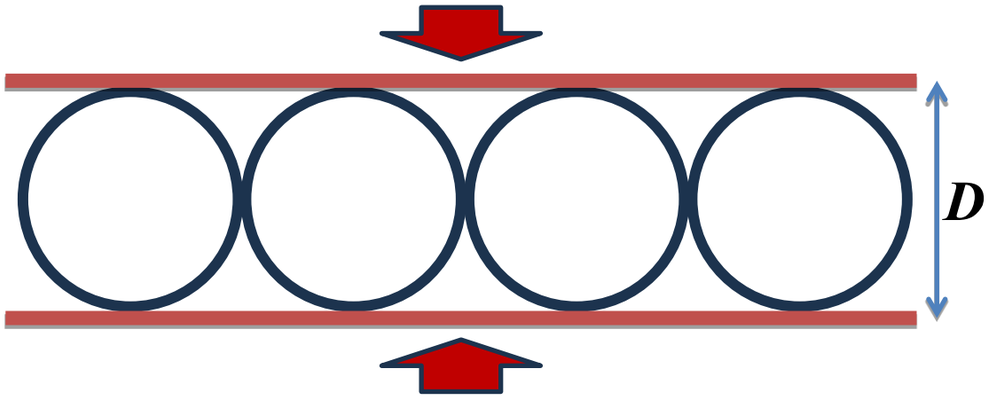

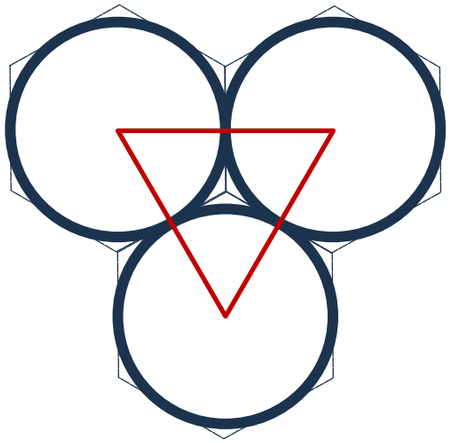



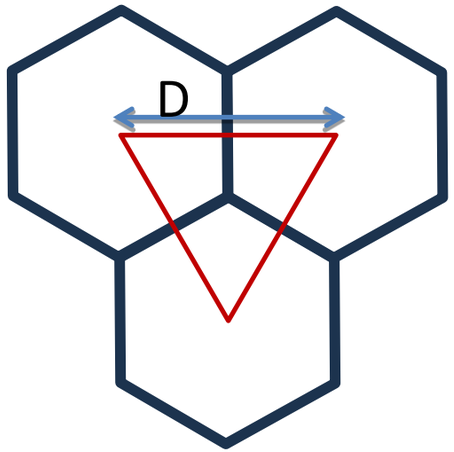

$$H=\frac{\pi}{3\sqrt{3}}D$$
$$H=0.605D$$

The reduced height af ter compaction is app roximately 60% of bal l diameter

03 Characterization of HBC Panel



Solid Panel
Same mass of material
Same area

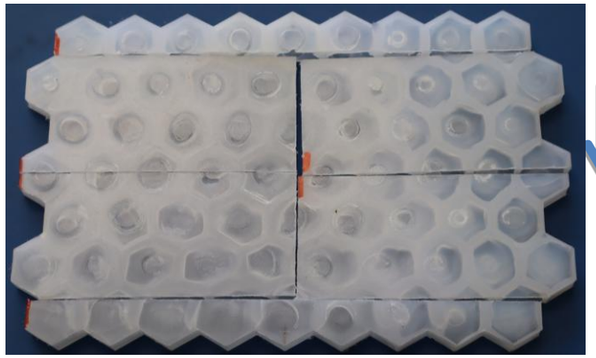

Cut to same sample shape
Allows for comparative testing

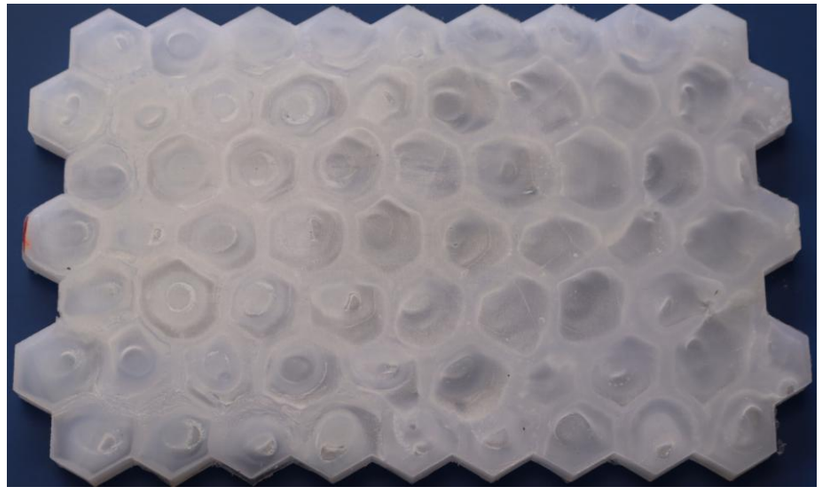

Sample Panel
HBC geometry

ICCM24

24TH INTERNATIONAL CONFERENCE ON COMPOSITE MATERIALS

caelestis

aimen TECHNOLOGY CENTRE

Hyperconnected simulation ecosystem supporting probabilistic design and predictive manufacturing of next generation aircraft structures – **CAELESTIS Project**

Baltimore, August 4-8, 2025

Dr. Cristian Builes Cárdenas, Mario Román Rodríguez, Ivette Coto Moretti, Sabela Sánchez, Andrés Fernández

Dr. Elena Rodriguez Senín (*presenter*)

Funded by the European Union

Funded by the European Union. Views and opinions expressed are however those of the author(s) only and do not necessarily reflect those of the European Union or [EUROPEAN CLIMATE, INFRASTRUCTURE AND ENVIRONMENT EXECUTIVE AGENCY (CINEA)]. Neither the European Union nor the granting authority can be held responsible for them.

CONTENT

- ✓ INTRODUCTION TO CAELESTIS PROJECT
- ✓ OBJECTIVES
- ✓ MATERIALS AND METHODOLOGY
- ✓ EXPERIMENTAL RESULTS
- ✓ CONCLUSIONS

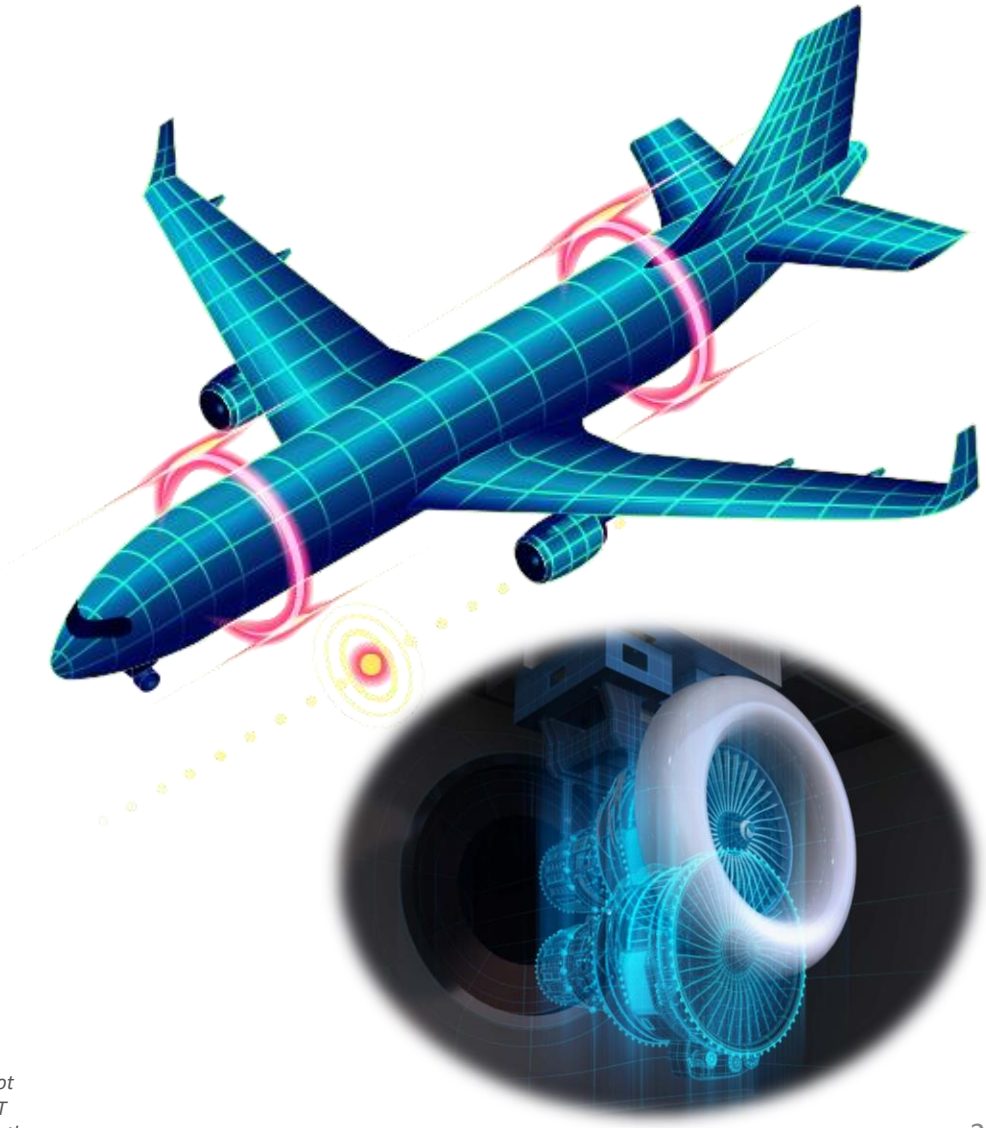

Funded by the European Union

Funded by the European Union. Views and opinions expressed are however those of the author(s) only and do not necessarily reflect those of the European Union or [EUROPEAN CLIMATE, INFRASTRUCTURE AND ENVIRONMENT EXECUTIVE AGENCY (CINEA)]. Neither the European Union nor the granting authority can be held responsible for them.

Introduction to CAELESTIS project

Funded by the European Union

Funded by the European Union. Views and opinions expressed are however those of the author(s) only and do not necessarily reflect those of the European Union or [EUROPEAN CLIMATE, INFRASTRUCTURE AND ENVIRONMENT EXECUTIVE AGENCY (CINEA)]. Neither the European Union nor the granting authority can be held responsible for them.

Driver….

Adopting a new breed of aircraft is essential for reaching climate neutrality by 2050

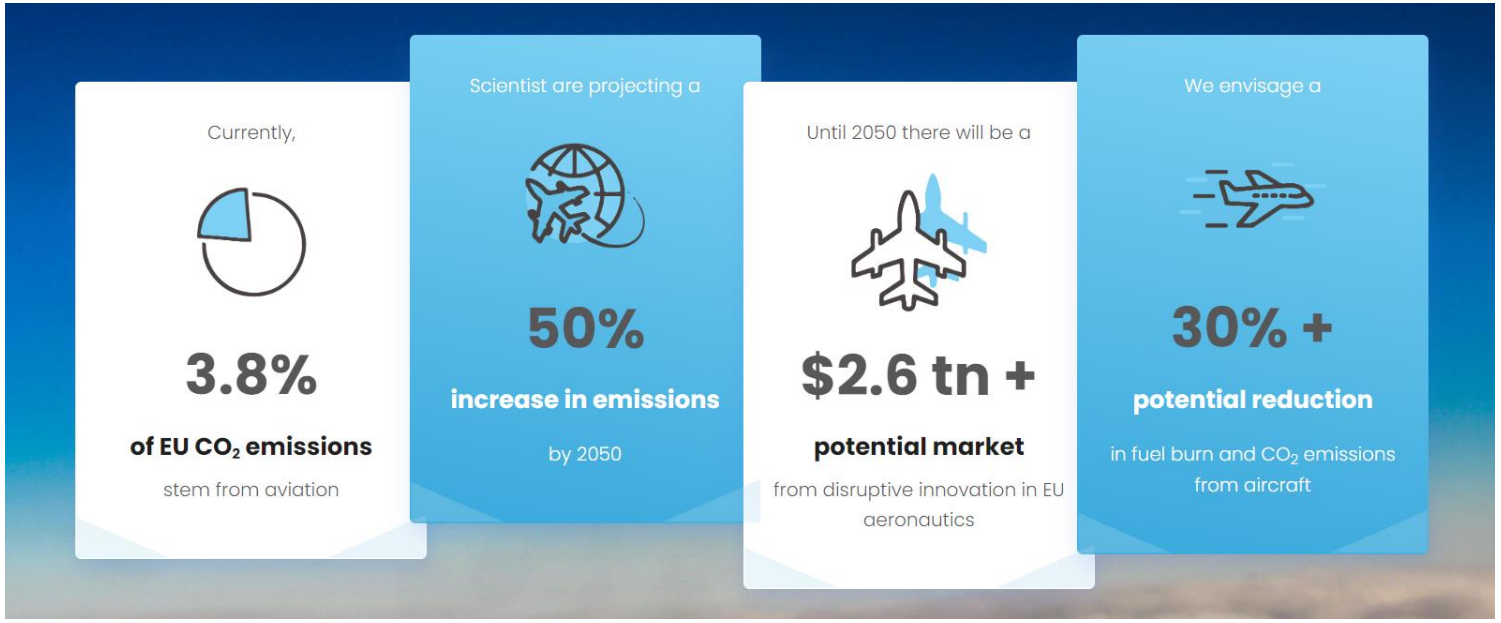

According to the aeronautics community, **virtual engineering** has a big potential to be the **key enabling technology** in achieving these objectives and making **zero carbon aviation** a reality.

Funded by the European Union

Funded by the European Union. Views and opinions expressed are however those of the author(s) only and do not necessarily reflect those of the European Union or [EUROPEAN CLIMATE, INFRASTRUCTURE AND ENVIRONMENT EXECUTIVE AGENCY (CINEA)]. Neither the European Union nor the granting authority can be held responsible for them.

Scope and Consortium

The chief aim is to develop a robust and secure **digital ecosystem**, utilizing s**imulation-driven design** to innovate a **new manufacturing methodology** able to transform the European aircraft industry – and reduce emissions.



11 partners
8 countries
Coordinated by: aimen TECHNOLOGY CENTRE

START **May 2022**

FINISH **October 2025**

Consortium

We are a multi-sector **Innovation and Technology Centre**, that develops **R&D&i activities** and provides **technological services** in the fields of:

Digitization of Processes		Advanced Manufacturing		Inspection and Testing	Sustainability
Sensor Solutions & Process Control	Simulation and Digital Twin	Laser Technologies	Joining Technologies	Inspection and Structural Integrity	Environmental and Biobased Technologies
Robotics and Mechatronics	Artificial intelligence	Advanced Composites	Additive Manufacturing	Materials Analysis and Testing	Sustainability Analysis

AIMEN is in O Porriño

*(15km to **Vigo**)* **Galicia**, **Spain**.

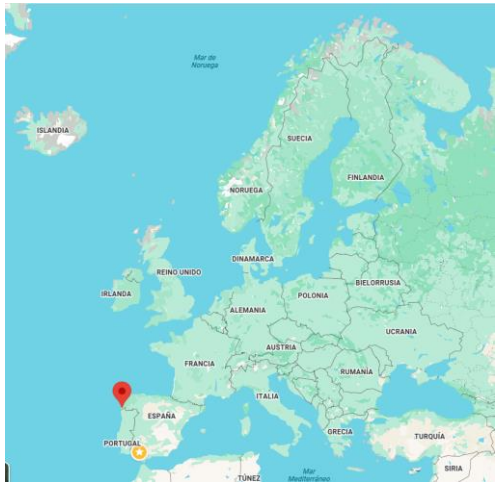

Funded by the European Union

Funded by the European Union. Views and opinions expressed are however those of the author(s) only and do not necessarily reflect those of the European Union or [EUROPEAN CLIMATE, INFRASTRUCTURE AND ENVIRONMENT EXECUTIVE AGENCY (CINEA)]. Neither the European Union nor the granting authority can be held responsible for them.

COMPTech

Advanced Composites Technologies

aimen TECHNOLOGY CENTRE

Advanced Composites Manufacturing

Additive Manufacturing

Smart Materials

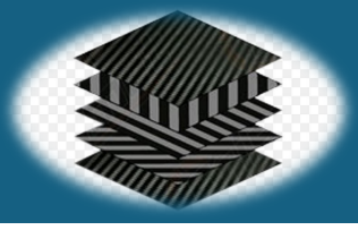





40 Researchers
12 PhD

Projects:
17 Nationals
18 European

Monitoring – Control

Automated / Robotized

Digitalization
(Process and Product)

Sustainable Materials and Manufacturing

Analysis and Testing



Concept

CAELESTIS develops an **end-to-end Interoperable Simulation Ecosystem** (ISE) that will perform **multidirectional dataflow** across the aircraft value chain **linking product design and distributed engineering teams´ CAD-CAE tools**, to accelerate the design and engineering optimization of disruptive aircraft and engine configurations.

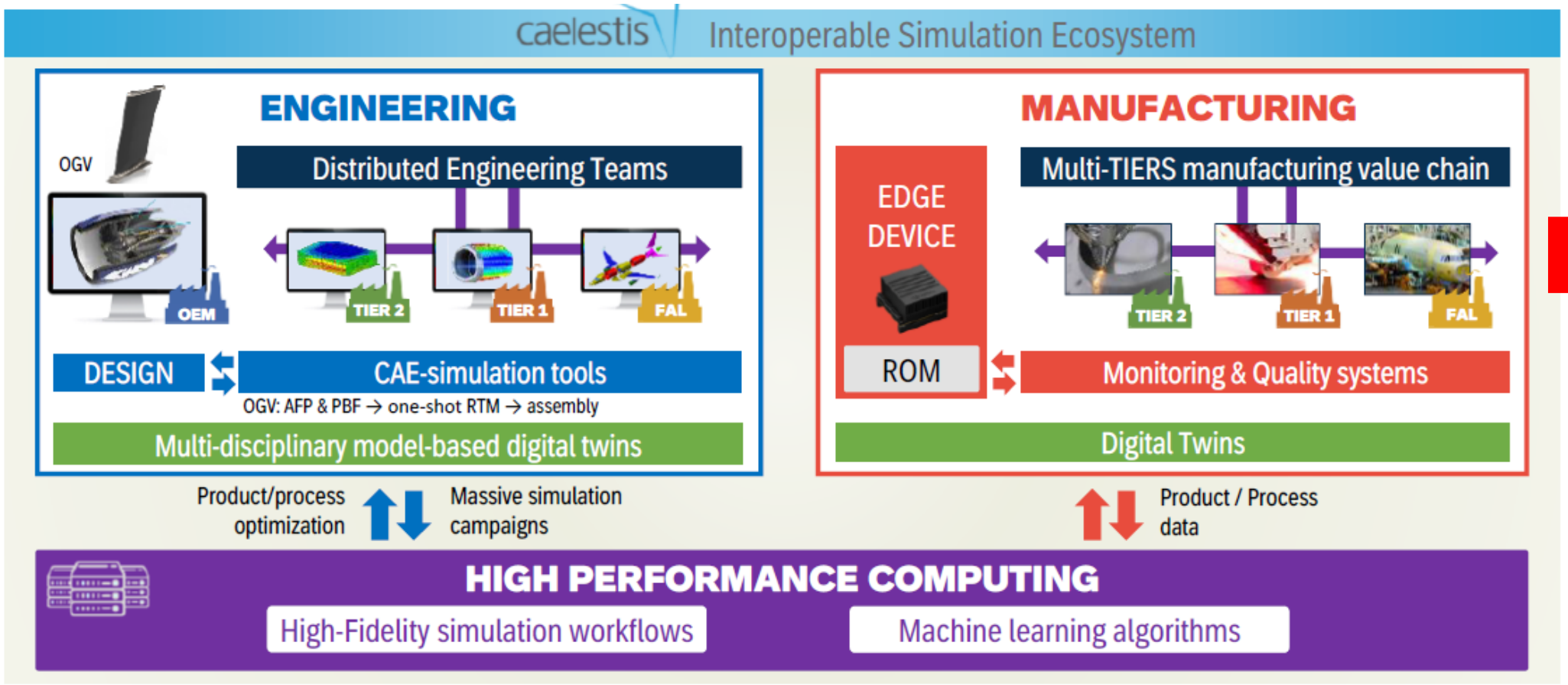

Automation and Digitalization of Composites Manufacturing (AFP, RTM)

OBJECTIVES

Funded by the European Union

Funded by the European Union. Views and opinions expressed are however those of the author(s) only and do not necessarily reflect those of the European Union or [EUROPEAN CLIMATE, INFRASTRUCTURE AND ENVIRONMENT EXECUTIVE AGENCY (CINEA)]. Neither the European Union nor the granting authority can be held responsible for them.

This work is focused on the AFP process parametrization and the digitalization of the dry preform using on-line monitoring systems (*digital twin*)

Objectives*:*

- To understand the effect of the **AFP process parameters** on the dry fiber preform quality (***tape adhesion***) and, at the end, on the composite mechanical performance.
- To analyze the influence of AFP parameters on **resin permeability** behavior, and, at the end, on the RTM processing performance.
- To **digitalize the dry-fiber preform** manufacturing based on **on-line quality control systems *(SmartHub tool)***.

To give input from experimental data to process modelling / digital twin – data workflow
To contribute to the CAELESTIS ISE *(interoperable simulation ecosystem)*

Funded by the European Union

Funded by the European Union. Views and opinions expressed are however those of the author(s) only and do not necessarily reflect those of the European Union or [EUROPEAN CLIMATE, INFRASTRUCTURE AND ENVIRONMENT EXECUTIVE AGENCY (CINEA)]. Neither the European Union nor the granting authority can be held responsible for them.

Materials and methodology

Funded by the European Union

Funded by the European Union. Views and opinions expressed are however those of the author(s) only and do not necessarily reflect those of the European Union or [EUROPEAN CLIMATE, INFRASTRUCTURE AND ENVIRONMENT EXECUTIVE AGENCY (CINEA)]. Neither the European Union nor the granting authority can be held responsible for them.

Materials and Methodology

Carbon dry fiber preform by AFP (Automated Fiber Placement) and RTM (Resin Transfer Molding)

aimen TECHNOLOGY CENTRE

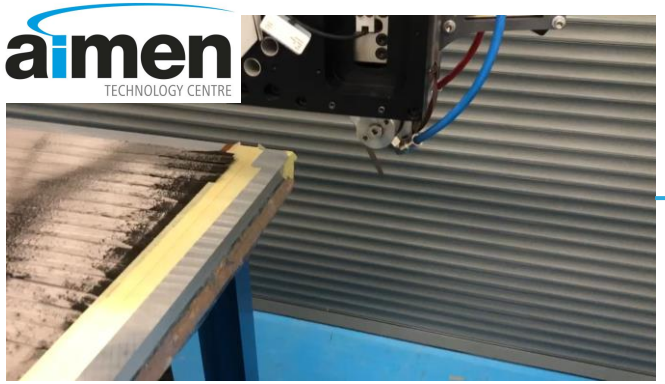

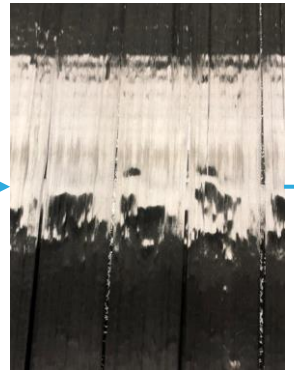

Fiber preform

Titanium inserts by AM (PBF)

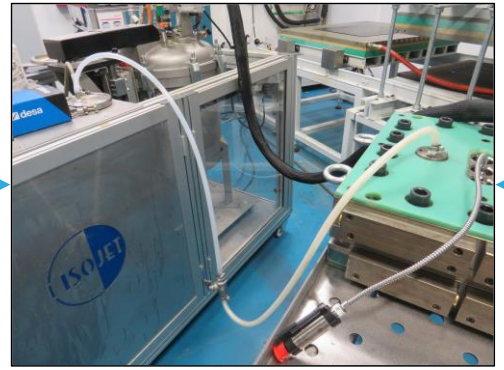

Ti-composite Resin Injection

Outlet Guide Vane (OGV)

GKN AEROSPACE

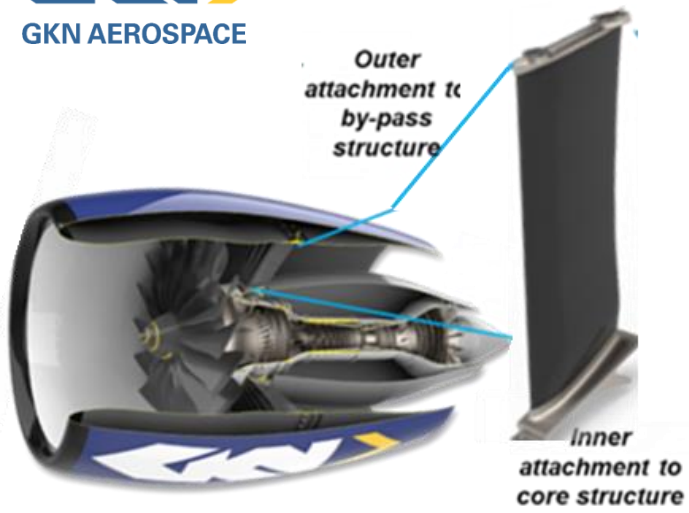

Ti + composite OGV *(one-shot RTM)*

Funded by the European Union

Funded by the European Union. Views and opinions expressed are however those of the author(s) only and do not necessarily reflect those of the European Union or [EUROPEAN CLIMATE, INFRASTRUCTURE AND ENVIRONMENT EXECUTIVE AGENCY (CINEA)]. Neither the European Union nor the granting authority can be held responsible for them.

Materials and Methodology

Defects on dry fiber preform during AFP

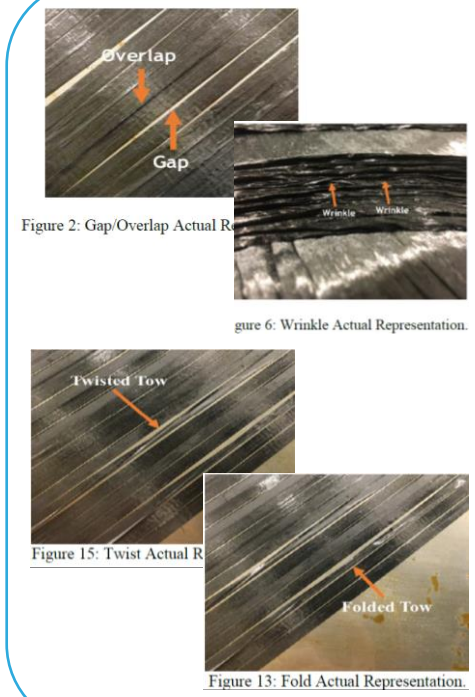

Harik, R., Saidy, C., Williams, S. J., Gurdal, Z., & Grimsley, B. (2018).

Quality control on-line monitoring systems:

- ✓ Thermal camera - temperature measurements
- ✓ Profilometry - fiber layup topography map

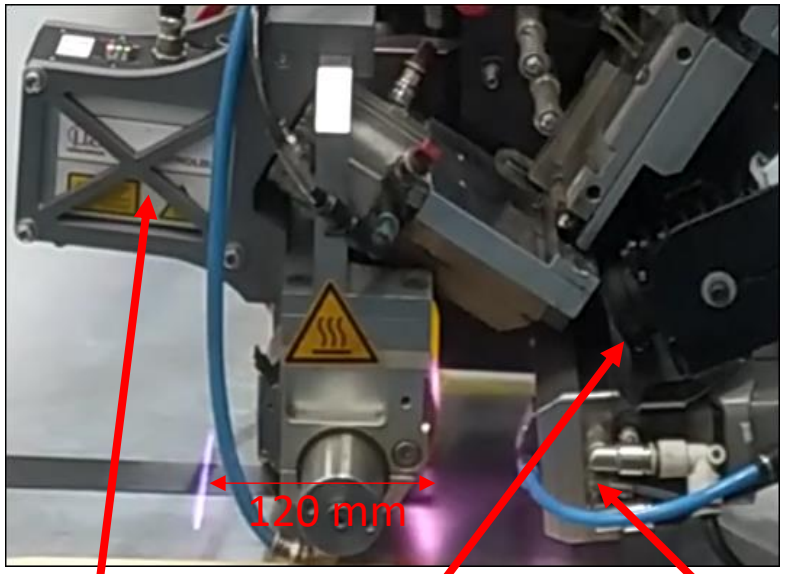

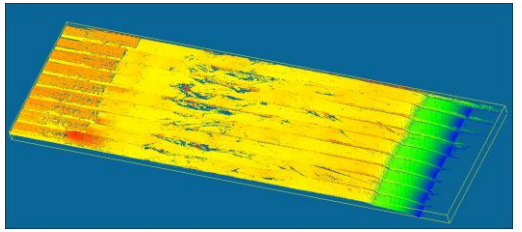

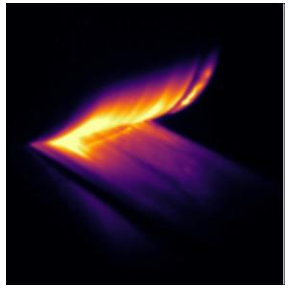

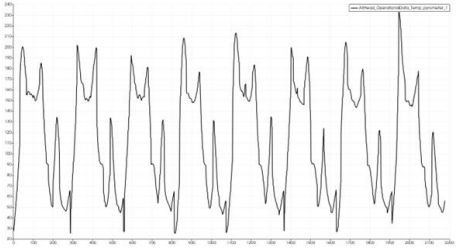

Profilometer ***Thermal Camera*** ***VCSELs (High power laser)***

Funded by the European Union

Funded by the European Union. Views and opinions expressed are however those of the author(s) only and do not necessarily reflect those of the European Union or [EUROPEAN CLIMATE, INFRASTRUCTURE AND ENVIRONMENT EXECUTIVE AGENCY (CINEA)]. Neither the European Union nor the granting authority can be held responsible for them.

Materials and Methodology

AFP (Automated Fibre Placement)

TeXtreme

Ref 5172: 194 UD IMS65 VO /25:194 SPREAD TOW
Toho Tenax E IMS65 E23 24K 830tex
Binder: Spunfab® PA1206 6 g/m2

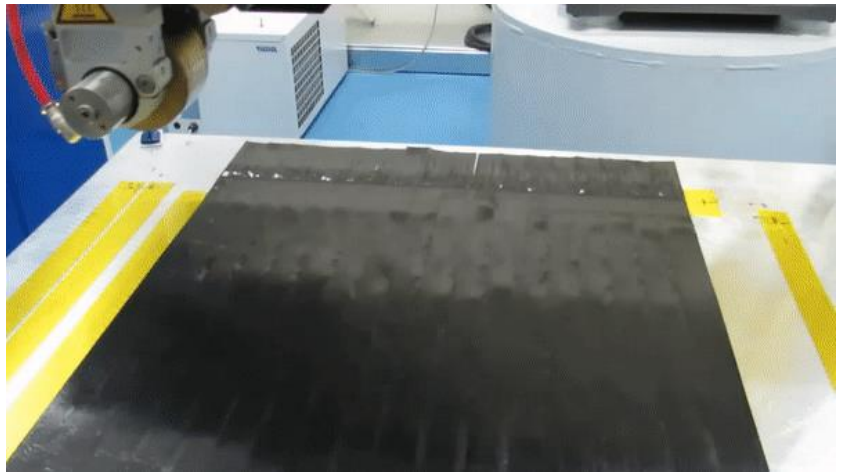

aimen TECHNOLOGY CENTRE

AFP deposition of UD tape

RTM (Resin Transfer Molding)

HEXCEL

HexFlow RTM6 Epoxy resin

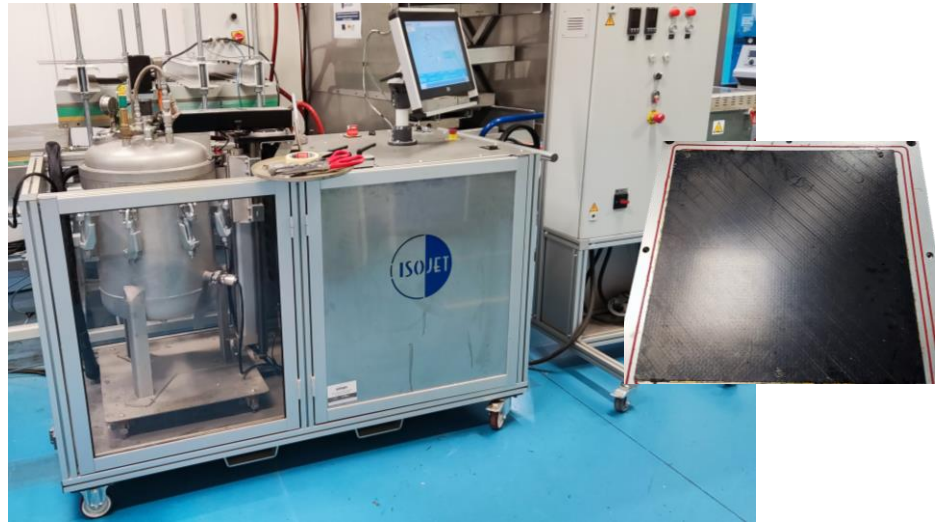

aimen TECHNOLOGY CENTRE

RTM machine

Funded by the European Union

Funded by the European Union. Views and opinions expressed are however those of the author(s) only and do not necessarily reflect those of the European Union or [EUROPEAN CLIMATE, INFRASTRUCTURE AND ENVIRONMENT EXECUTIVE AGENCY (CINEA)]. Neither the European Union nor the granting authority can be held responsible for them.

AFP head and laser heating system (*VCSEL*)



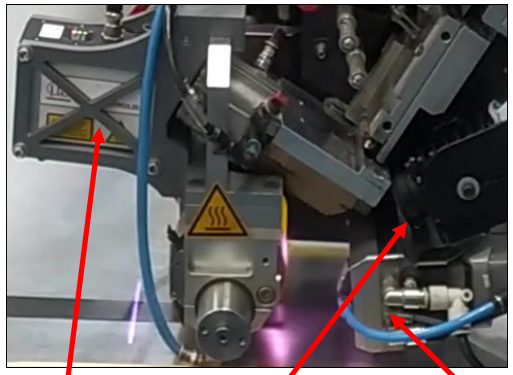

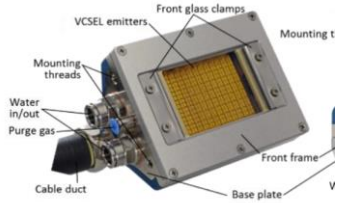

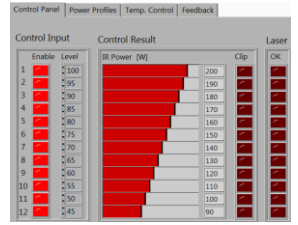

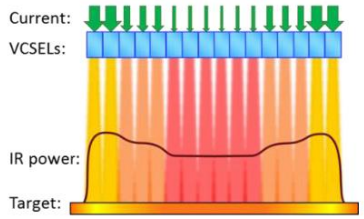

Heating: IR VCSEL system (2,4 kW):

- ✓ 12 independent heating zones *(adjustable power)*
- ✓ 5 zones were selected to concentrate heating on CF tape *(1 inch width)*

  Total power: 1000W
- ✓ Process monitoring (*thermal camera*)

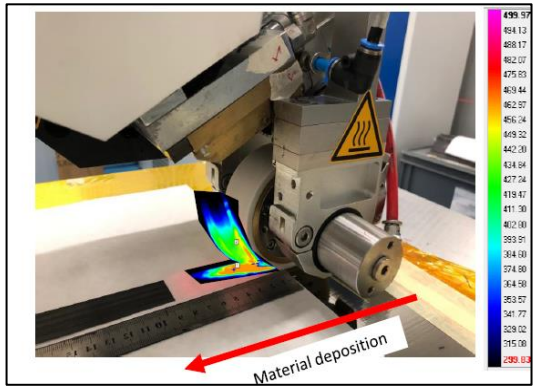

Funded by the European Union

Funded by the European Union. Views and opinions expressed are however those of the author(s) only and do not necessarily reflect those of the European Union or [EUROPEAN CLIMATE, INFRASTRUCTURE AND ENVIRONMENT EXECUTIVE AGENCY (CINEA)]. Neither the European Union nor the granting authority can be held responsible for them.

Main parameters that affect the AFP process:

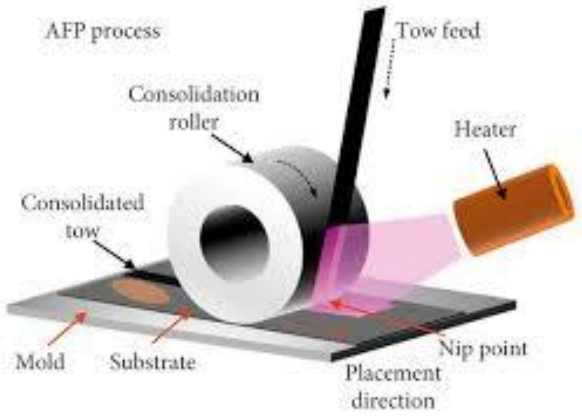

Factor	Measurement unit	Variable type
Head/roll pressure	N	Quantitative
Deposition velocity	mm/s	Quantitative
Heating source power	W	Quantitative
Fiber areal weight	g/m^2	Quantitative
Tape thickness	mm	Quantitative
Binder type	-	Qualitative
Head/roll material	-	Qualitative
Lay-up sequence	-	Qualitative
Font position, inclination	mm, °	Quantitative
Stagger	mm	Quantitative

Funded by the European Union

Funded by the European Union. Views and opinions expressed are however those of the author(s) only and do not necessarily reflect those of the European Union or [EUROPEAN CLIMATE, INFRASTRUCTURE AND ENVIRONMENT EXECUTIVE AGENCY (CINEA)]. Neither the European Union nor the granting authority can be held responsible for them.

Study: Effect of AFP selected variables on dry fiber preform properties:

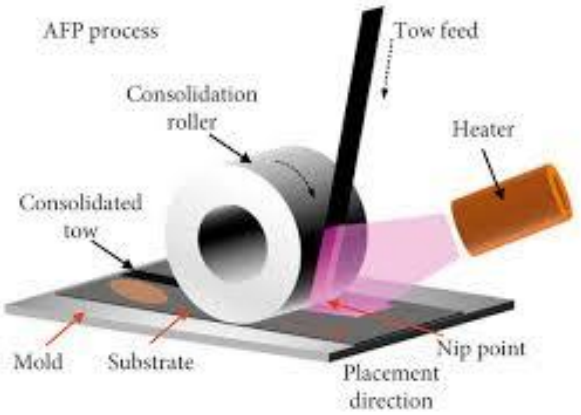

Factor	Effect	Unit	Type	Evaluation
Head/roll pressure	Tape thickness	mm	Quantitative	Direct measurement
	Preform compaction	m^2	Quantitative	Permeability test
Deposition velocity	Manufacturing time	s	Quantitative	Direct measurement
	Tape temperature	°C	Quantitative	Pyrometers and thermal camera
Heating input	Tape temperature	°C	Quantitative	Power consumption

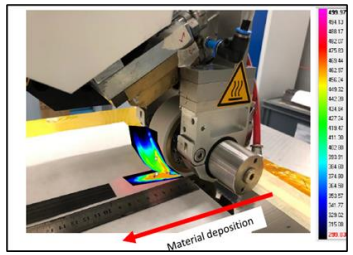

Tape-by-tape consolidation (adhesion) – dry fiber preform compaction

Funded by the European Union

Funded by the European Union. Views and opinions expressed are however those of the author(s) only and do not necessarily reflect those of the European Union or [EUROPEAN CLIMATE, INFRASTRUCTURE AND ENVIRONMENT EXECUTIVE AGENCY (CINEA)]. Neither the European Union nor the granting authority can be held responsible for them.

Dry Carbon Fiber AFP process parameters – SoA and AIMEN expertise

Heat Source	Dry Fiber	Heat power (W)	Temperature at nit point (ºC)	Compaction force (N)	Deposition speed (mm/s)		[Ref]
					1ª	Other	
Laser 3 kW	Carbon fiber + epoxi/ thermoplastic binder	-	200	446	-	400	[6]
Laser	Carbon fiber 24K (weight in área: 194 g/m^2) + thermoplastic binder	800	200 (800 m/s)	200	400	800	[5]
			320 (400 m/s)				
Laser 3 kW	Carbon fiber + binder	200	200	446	-	400	[4]
		357	300				
Hot Gas Torch	-	-	176	311	25,4	100	[3]
Laser	PRISM TX1100	-	160	160	-	200	[7]
Laser 6 kW	Carbon fiber	-	-	446	-	100,200,400,800	[8]
Laser	Carbon fiber 24K UD (weight in área: 194 g/m^2) + thermoplastic binder	800	250	200	-	100	[9]
IR halogen lamp	Carbon fiber	360	110	-	-	850	[10]
Laser	Carbon fiber (HFW160PA)	-	160	160	-	200	[11]
Laser	Carbon fiber 24K Ud (weight in area;:194 g/m^2) + thermoplastic binder	800	250	200	-	1000	[12]

Determination of process window

The DOE parameter levels (V, Pres, Pow) have been adjusted based on the AIMEN AFP equipment, our expertise and the experimental previous works.

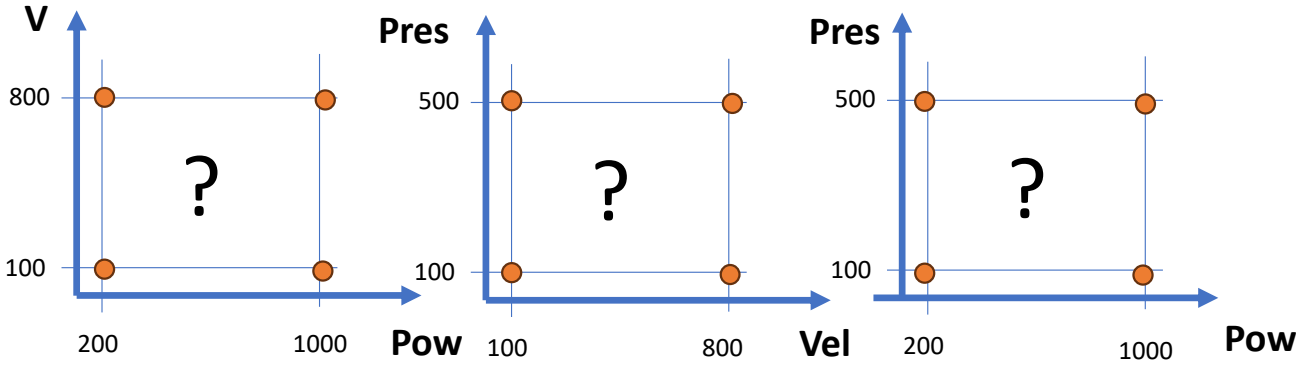

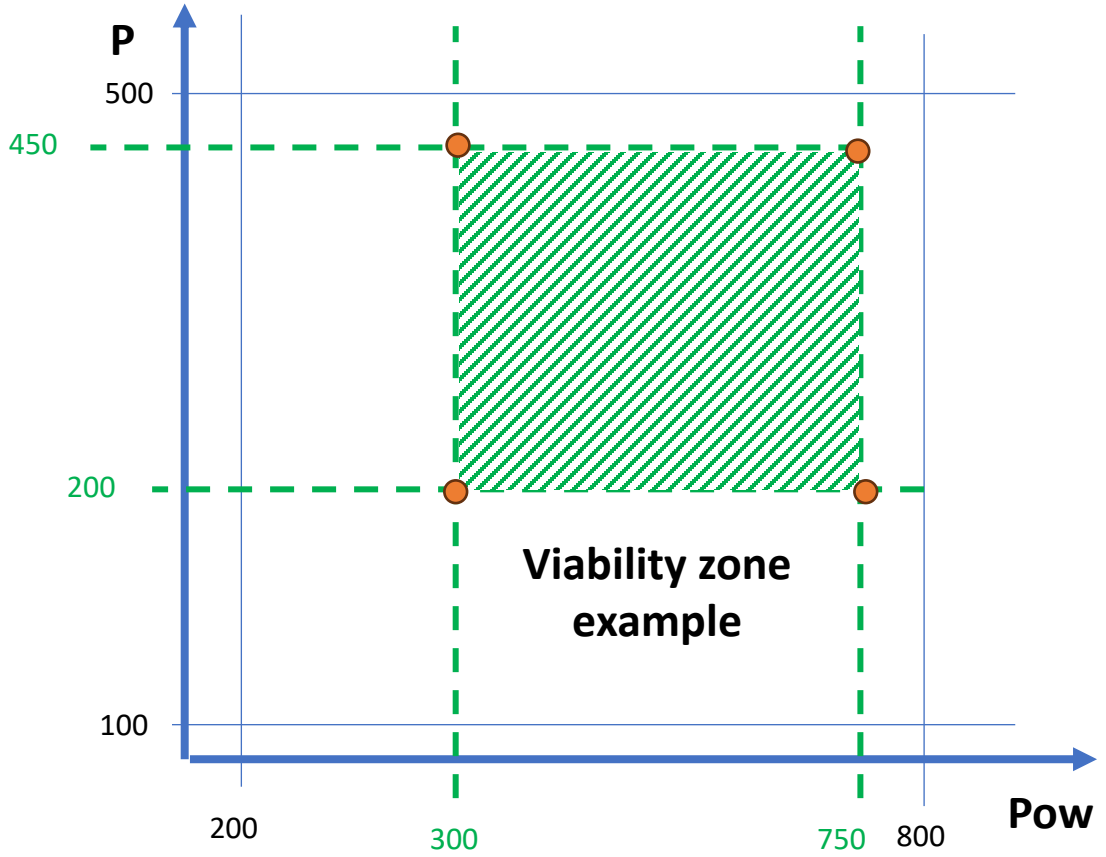

Funded by the European Union

Funded by the European Union. Views and opinions expressed are however those of the author(s) only and do not necessarily reflect those of the European Union or [EUROPEAN CLIMATE, INFRASTRUCTURE AND ENVIRONMENT EXECUTIVE AGENCY (CINEA)]. Neither the European Union nor the granting authority can be held responsible for them.

Selection of parameters levels to perform AFP DOE

Factor	Measurement unit	Min	Max	Variable type
Head/roll pressure	N	250	500	Quantitative
Deposition velocity	mm/s	100	400	Quantitative
Heating source power (5 zones)	W	100 (10%)	400 (40%)	Quantitative

- Pressure < 250 N results in pulling/dragging effect of the dry CF (no adhesion)
- Velocities > 400 mm/s surpasses the AFP head reliability with dry CF (velocity not uniform for the short sample length)
- Power > 400 W makes the fibers and binder burn.

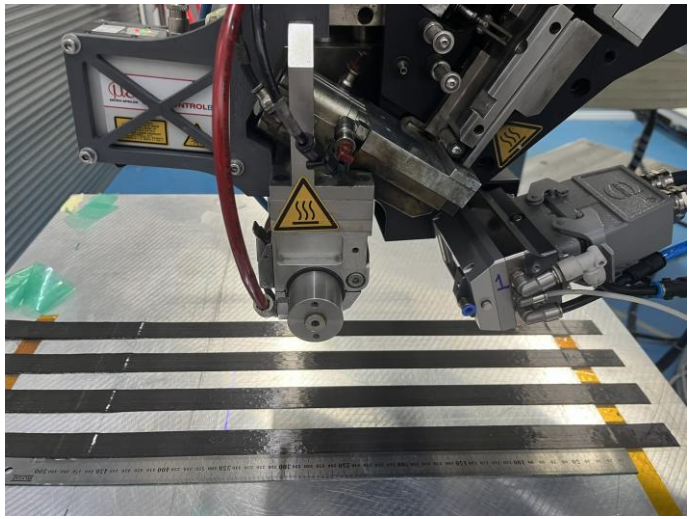

Funded by the European Union

Funded by the European Union. Views and opinions expressed are however those of the author(s) only and do not necessarily reflect those of the European Union or [EUROPEAN CLIMATE, INFRASTRUCTURE AND ENVIRONMENT EXECUTIVE AGENCY (CINEA)]. Neither the European Union nor the granting authority can be held responsible for them.

Evaluation of adhesion between dry CF layers

Peeling test

- Quantitative evaluation of adhesion between layers using an adapted set-up for peeling test [1-2]:
  - ✓ Able to measure the adhesion between layers *(there are not standards for dry fiber)*
  - ✓ No large quantities of material are required for this analysis (*usually requires to manufacture a complete laminate to be injected and later analyzed)*
- The samples have been made using 4 CF layers.
- Peeling length: 135 ± 5 mm.
- Peeling test was performed by holding 1 or 2 layers (no difference found)

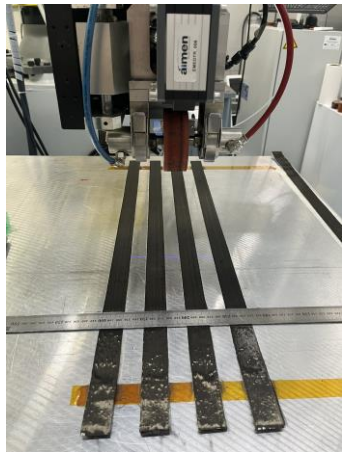

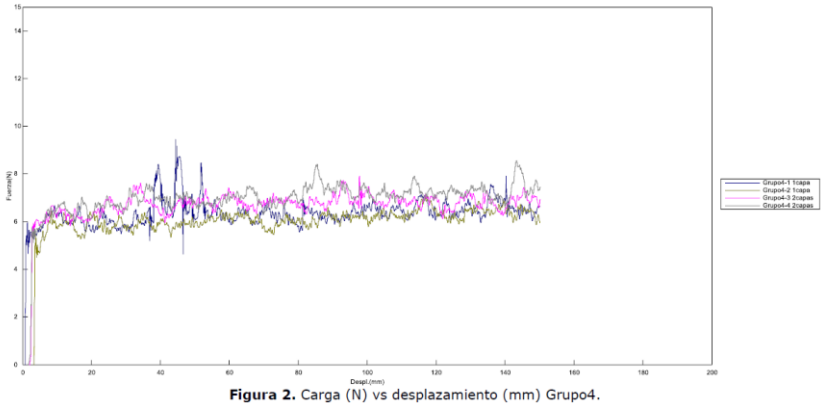

Figura 2. Carga (N) vs desplazamiento (mm) Grupo4.



Funded by the European Union

Funded by the European Union. Views and opinions expressed are however those of the author(s) only and do not necessarily reflect those of the European Union or [EUROPEAN CLIMATE, INFRASTRUCTURE AND ENVIRONMENT EXECUTIVE AGENCY (CINEA)]. Neither the European Union nor the granting authority can be held responsible for them.

Permeability tests

Darcy´s Law can provide the **preforms' permeability** (in-plane) along the linear flow direction (k):

- x_{ff} is the flow front position at the injection time t_{ff}
- Φ is the porosity of the preform
- μ is the viscosity of the injected fluid that is used for the tests *(calibrated oil)*
- ΔP is the pressure difference between the inlet and the outlet locations (constant)

$$K = -\frac{x_{ff}^2 \cdot \Phi \cdot \mu}{2 \cdot \Delta P \cdot t_{ff}}$$

Preforms 2mm thickness, 11 layers, layup 0°)

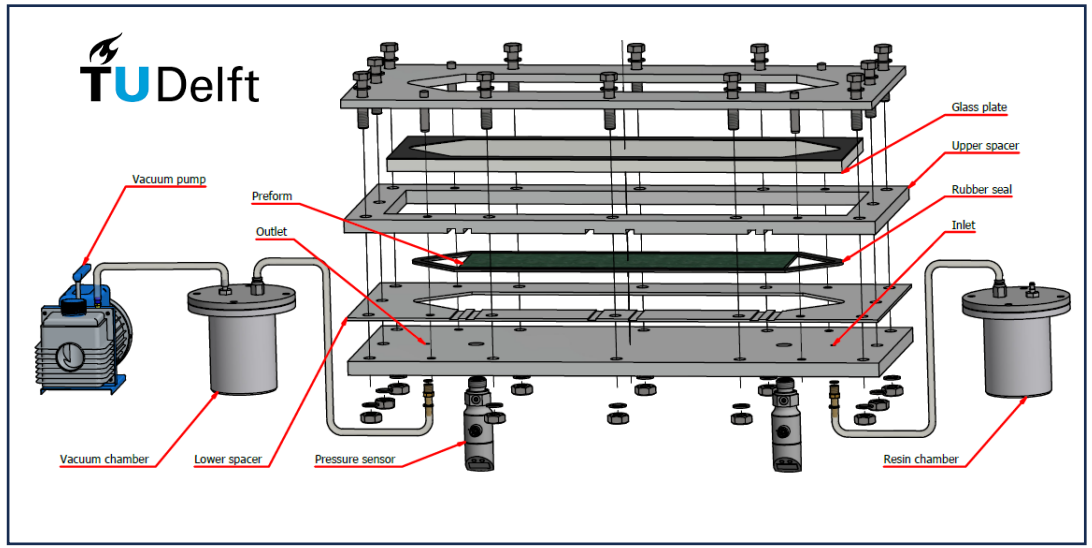

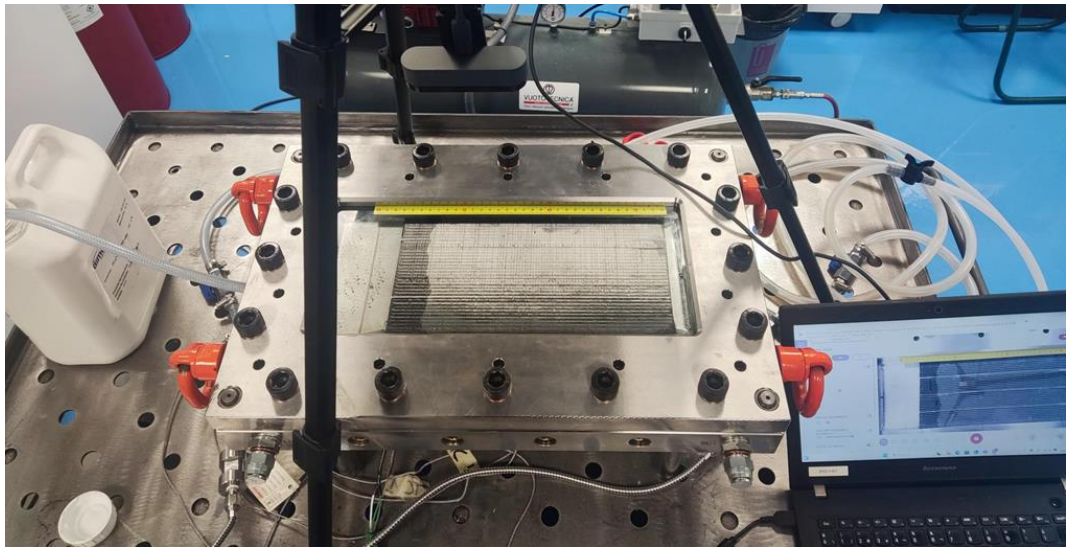

Funded by the European Union

Funded by the European Union. Views and opinions expressed are however those of the author(s) only and do not necessarily reflect those of the European Union or [EUROPEAN CLIMATE, INFRASTRUCTURE AND ENVIRONMENT EXECUTIVE AGENCY (CINEA)]. Neither the European Union nor the granting authority can be held responsible for them.

Experimental Results - AFP parametrization

Funded by the European Union

Funded by the European Union. Views and opinions expressed are however those of the author(s) only and do not necessarily reflect those of the European Union or [EUROPEAN CLIMATE, INFRASTRUCTURE AND ENVIRONMENT EXECUTIVE AGENCY (CINEA)]. Neither the European Union nor the granting authority can be held responsible for them.

Tape adhesion – peeling strength

Samples	Speed (mm/s)	Power (W)	Pressure (N)	Peeling strength (N/m)	ST. Dev.
1	100	100	250	No adhesion	
2	400	100	250	No adhesion	
3	100	400	250	77,6 ±13,5	13,5
4	400	400	250	29,7 ±12,1	12,1
5	100	100	500	No adhesion	
6	100	100	500	No adhesion	
7	100	400	500	123,0 ±14,7	14,7
8	400	400	500	71,2 ±8,1	8,1
15	250	250	375	44,1 ±2,2	2,2

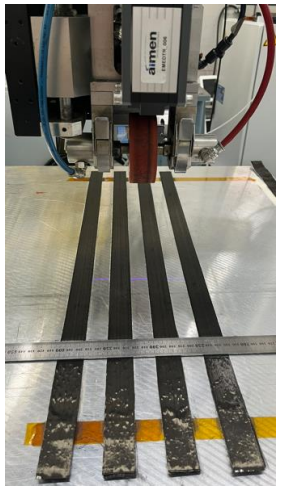





Funded by the European Union

Funded by the European Union. Views and opinions expressed are however those of the author(s) only and do not necessarily reflect those of the European Union or [EUROPEAN CLIMATE, INFRASTRUCTURE AND ENVIRONMENT EXECUTIVE AGENCY (CINEA)]. Neither the European Union nor the granting authority can be held responsible for them.

Tape adhesion – peeling strength

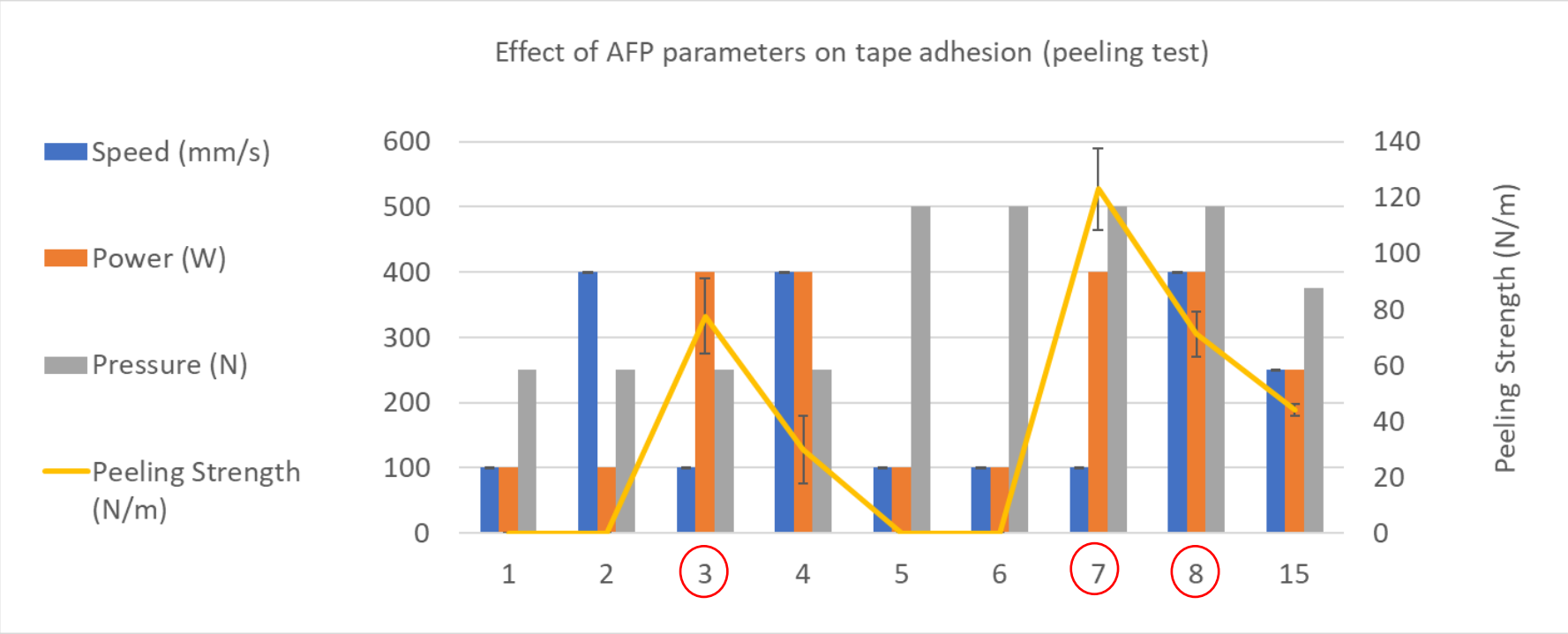

The higher peel strength values occur:

- ✓ At higher power
- ✓ At lower speed

Both parameters have influence on the temperature input on the tape.

It seems that pressure is the lowest influent parameter.

Funded by the European Union

Funded by the European Union. Views and opinions expressed are however those of the author(s) only and do not necessarily reflect those of the European Union or [EUROPEAN CLIMATE, INFRASTRUCTURE AND ENVIRONMENT EXECUTIVE AGENCY (CINEA)]. Neither the European Union nor the granting authority can be held responsible for them.

Tape adhesion – peeling strength

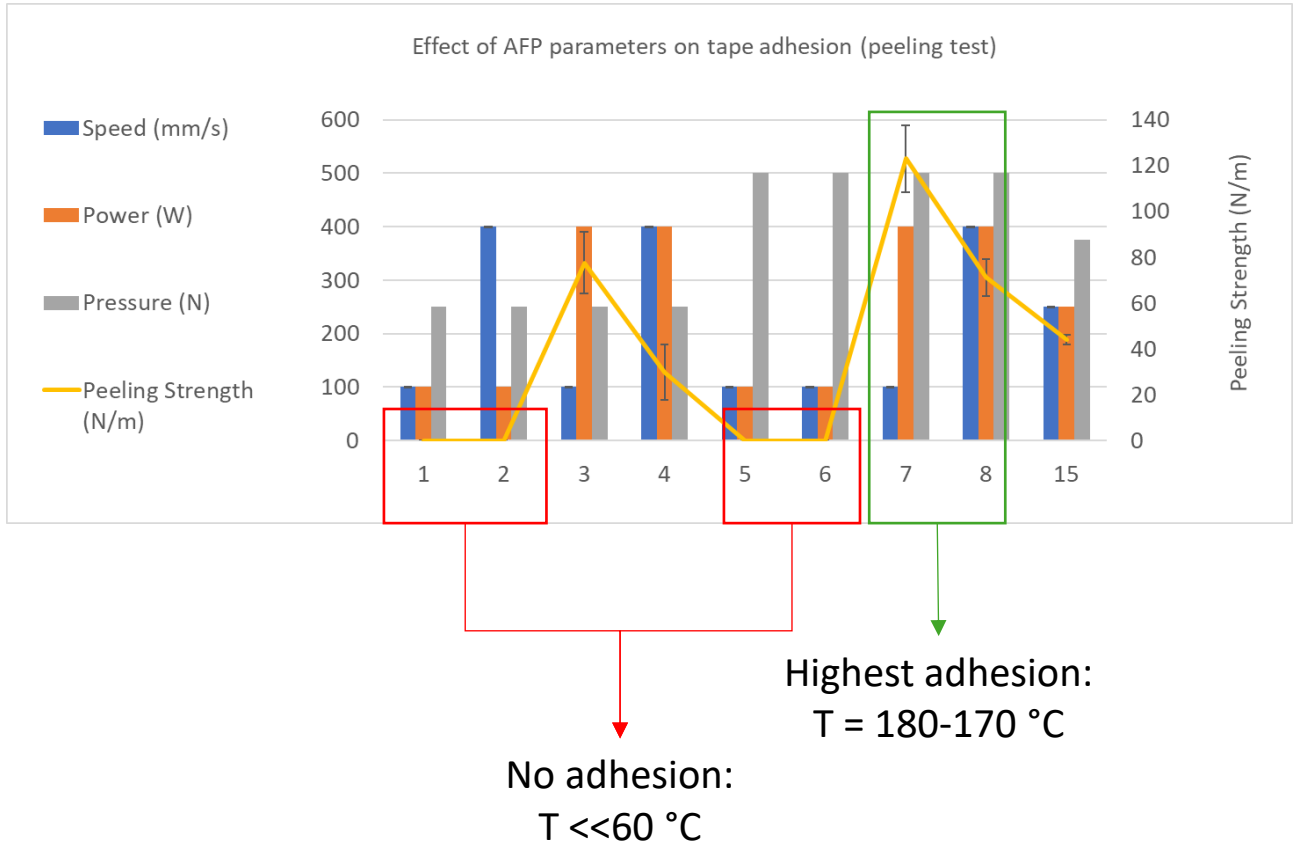

No adhesion:
T <<60 °C

Highest adhesion:
T = 180-170 °C

Thermal camera data on real time

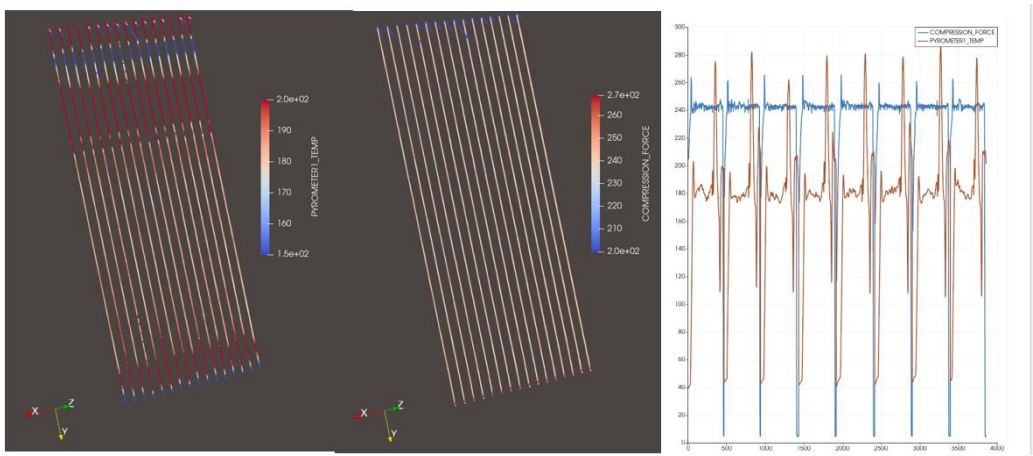

TeXtreme

Binder: Spunfab® PA1206 6 g/m2
Tm: 160-170 °C

Funded by the European Union

Funded by the European Union. Views and opinions expressed are however those of the author(s) only and do not necessarily reflect those of the European Union or [EUROPEAN CLIMATE, INFRASTRUCTURE AND ENVIRONMENT EXECUTIVE AGENCY (CINEA)]. Neither the European Union nor the granting authority can be held responsible for them.

Permeability tests

	Permeability (m^2) x(10^{-12})				
Sample	k_{Z1} (zone 1)	k_{Z2} (zone 2)	k_{Z3} (zone 3)	Mean	Peeling Strength (N/m)
# 3	7,0354	8,1455	9,1325	8,1045	77,6
# 4	10,204	9,8208	26,6957	10,5661	29,7
# 7	4,2073	9,6302	-	6,9188	123,0

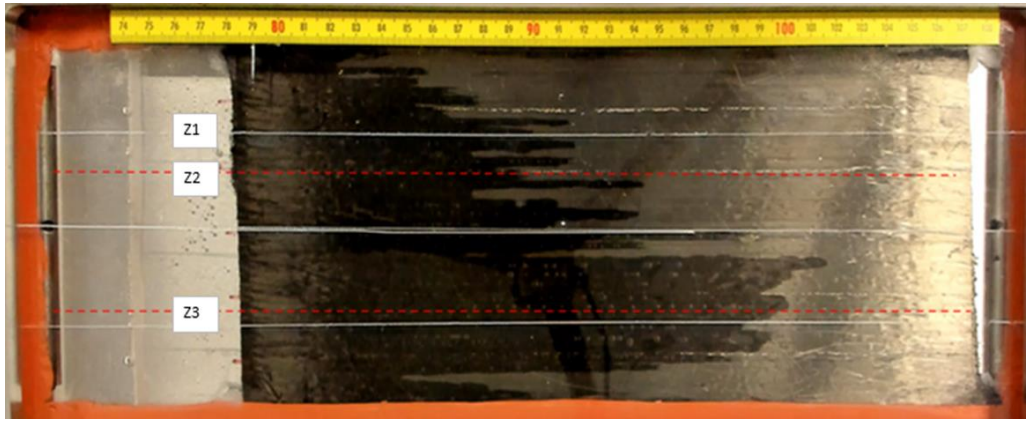

- Race-tracking (*fast resin channels*) have been observed in all the samples due to the gaps between tapes.
- The permeability has been estimated discarding the fast tracks.

Reference permeability values using similar material/process were not found. Some UD-CF studies showed values between 6-20 x10^{-12} m^2.

Funded by the European Union

Funded by the European Union. Views and opinions expressed are however those of the author(s) only and do not necessarily reflect those of the European Union or [EUROPEAN CLIMATE, INFRASTRUCTURE AND ENVIRONMENT EXECUTIVE AGENCY (CINEA)]. Neither the European Union nor the granting authority can be held responsible for them.

Permeability results

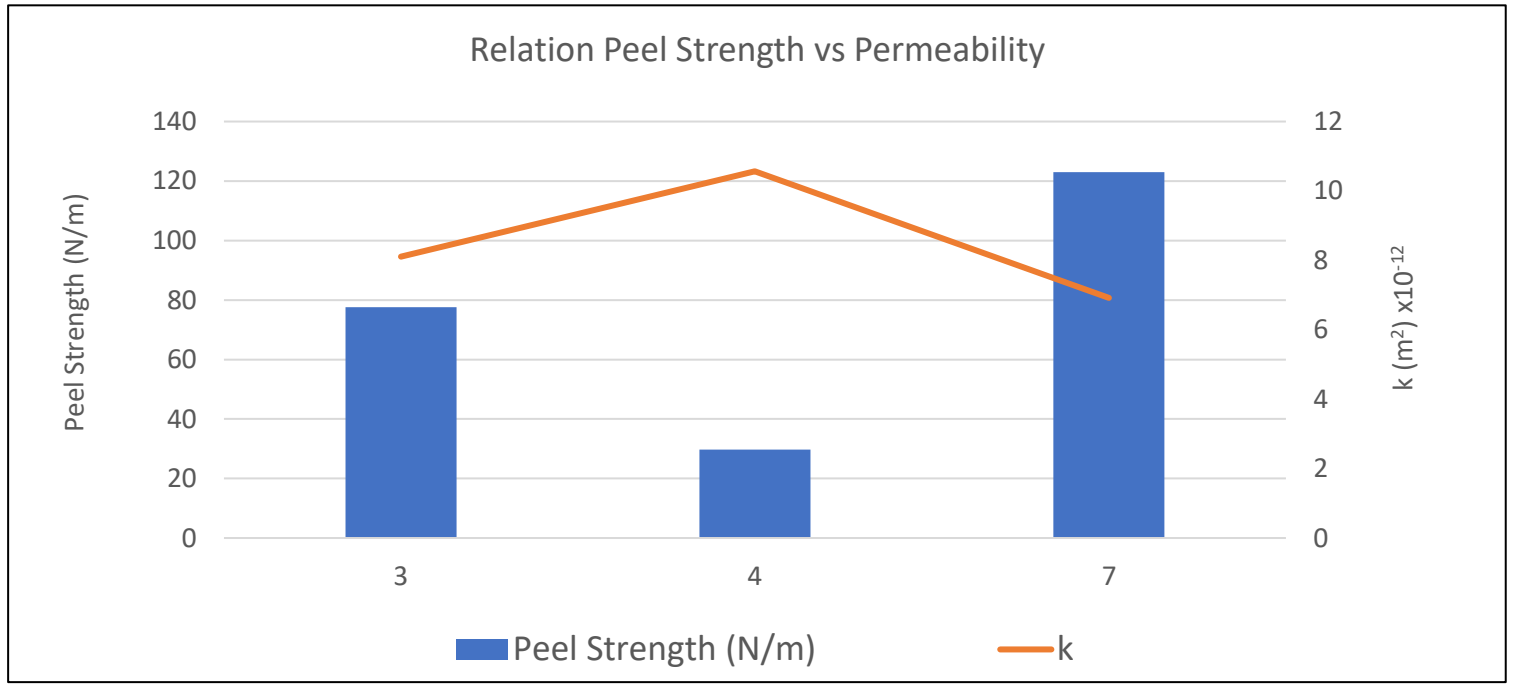

- ✓ Higher peel strength (higher compaction) results in lower permeability.
- ✓ Less dry fiber preform compaction results in a better permeability.

Low dry fiber preform compaction means better permeability but… how this can affect during RTM in the %resin?



Funded by the European Union

Funded by the European Union. Views and opinions expressed are however those of the author(s) only and do not necessarily reflect those of the European Union or [EUROPEAN CLIMATE, INFRASTRUCTURE AND ENVIRONMENT EXECUTIVE AGENCY (CINEA)]. Neither the European Union nor the granting authority can be held responsible for them.

Experimental Results - AFP on-line quality control

Funded by the European Union

Funded by the European Union. Views and opinions expressed are however those of the author(s) only and do not necessarily reflect those of the European Union or [EUROPEAN CLIMATE, INFRASTRUCTURE AND ENVIRONMENT EXECUTIVE AGENCY (CINEA)]. Neither the European Union nor the granting authority can be held responsible for them.

AFP on-line quality control

A profilometer was installed in the AFP head to scan every ply of the preform.

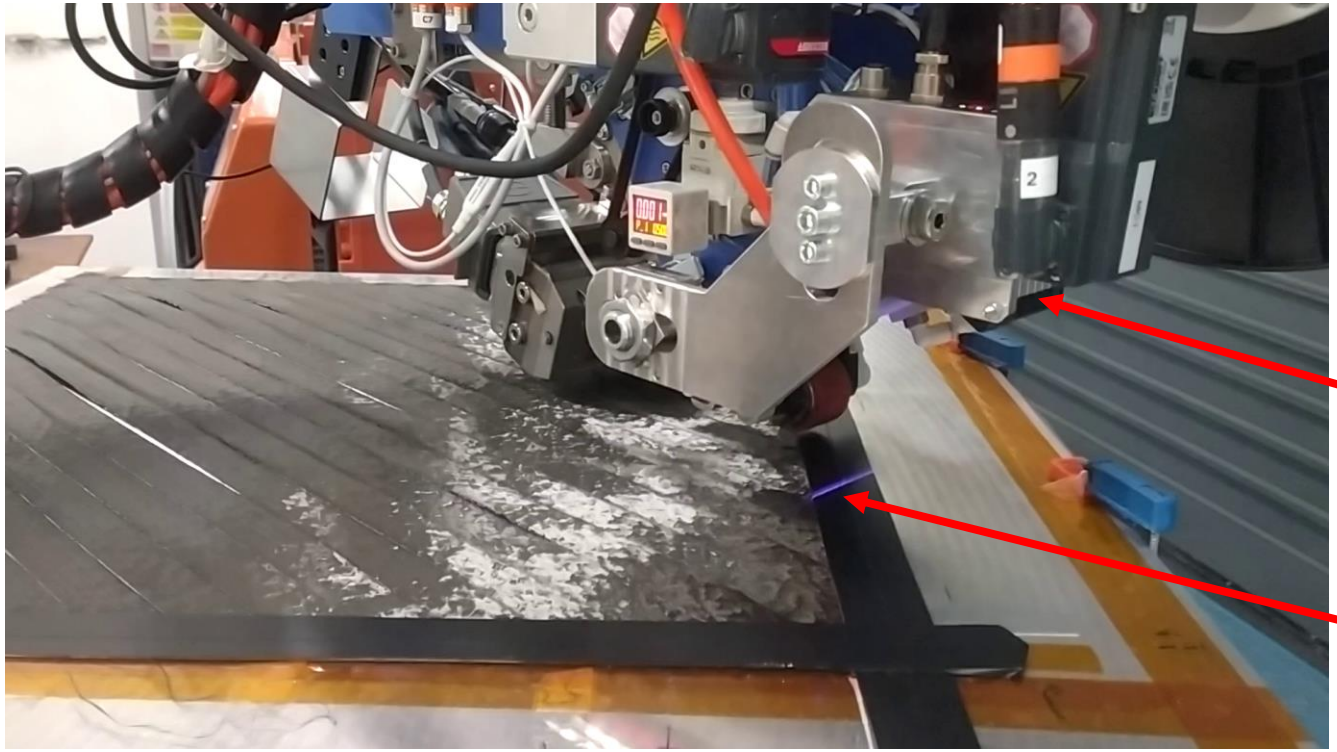

Funded by the European Union

Funded by the European Union. Views and opinions expressed are however those of the author(s) only and do not necessarily reflect those of the European Union or [EUROPEAN CLIMATE, INFRASTRUCTURE AND ENVIRONMENT EXECUTIVE AGENCY (CINEA)]. Neither the European Union nor the granting authority can be held responsible for them.

AFP on-line quality control

Profilometer scanning process is carried out tow by tow to generate a 3D point cloud of each ply

(*see video*)

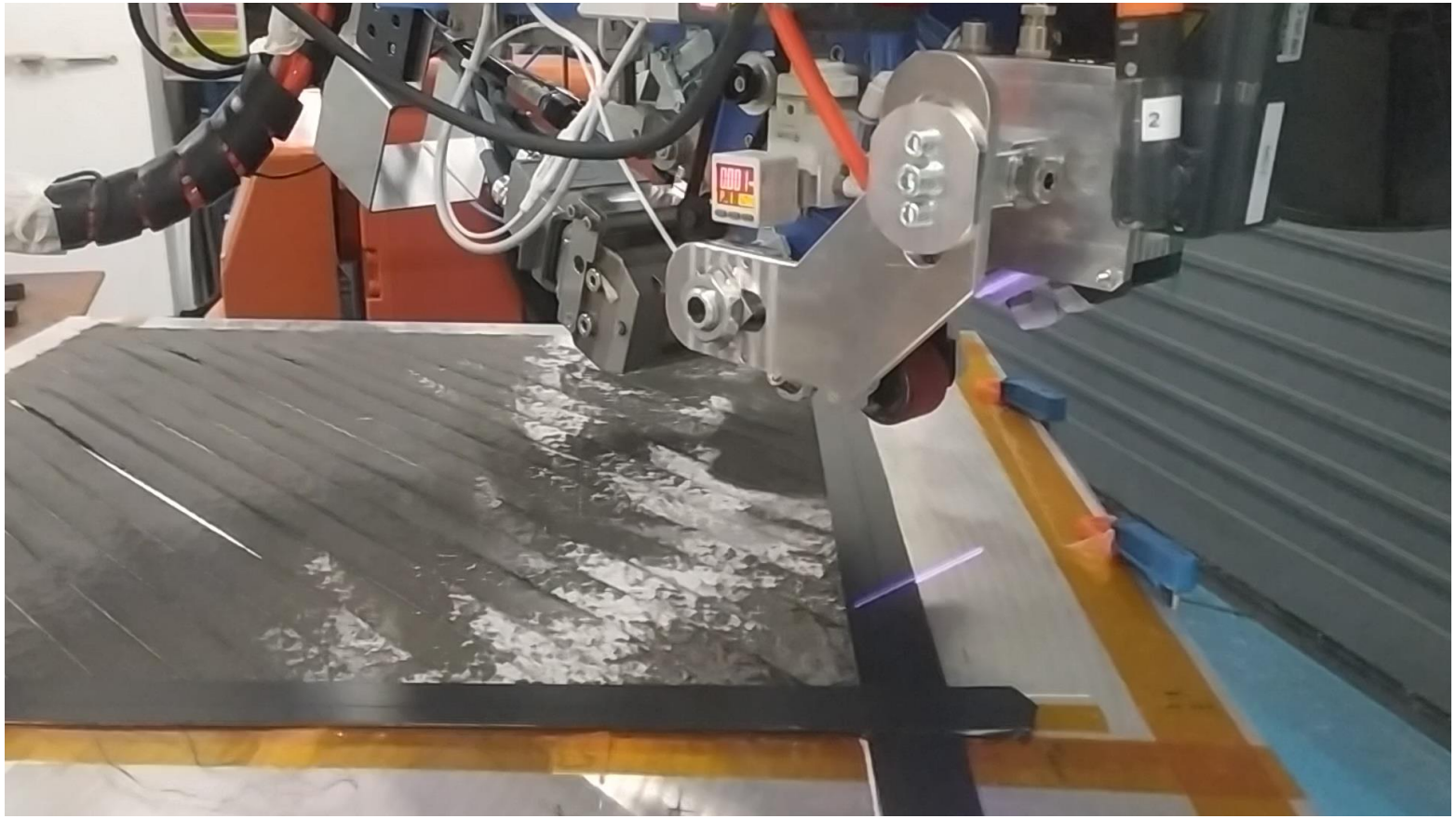

Funded by the European Union

Funded by the European Union. Views and opinions expressed are however those of the author(s) only and do not necessarily reflect those of the European Union or [EUROPEAN CLIMATE, INFRASTRUCTURE AND ENVIRONMENT EXECUTIVE AGENCY (CINEA)]. Neither the European Union nor the granting authority can be held responsible for them.

AFP on-line quality control

Each scanned tow individually by the profilometer is located next to the next one to be displayed as a whole ply.

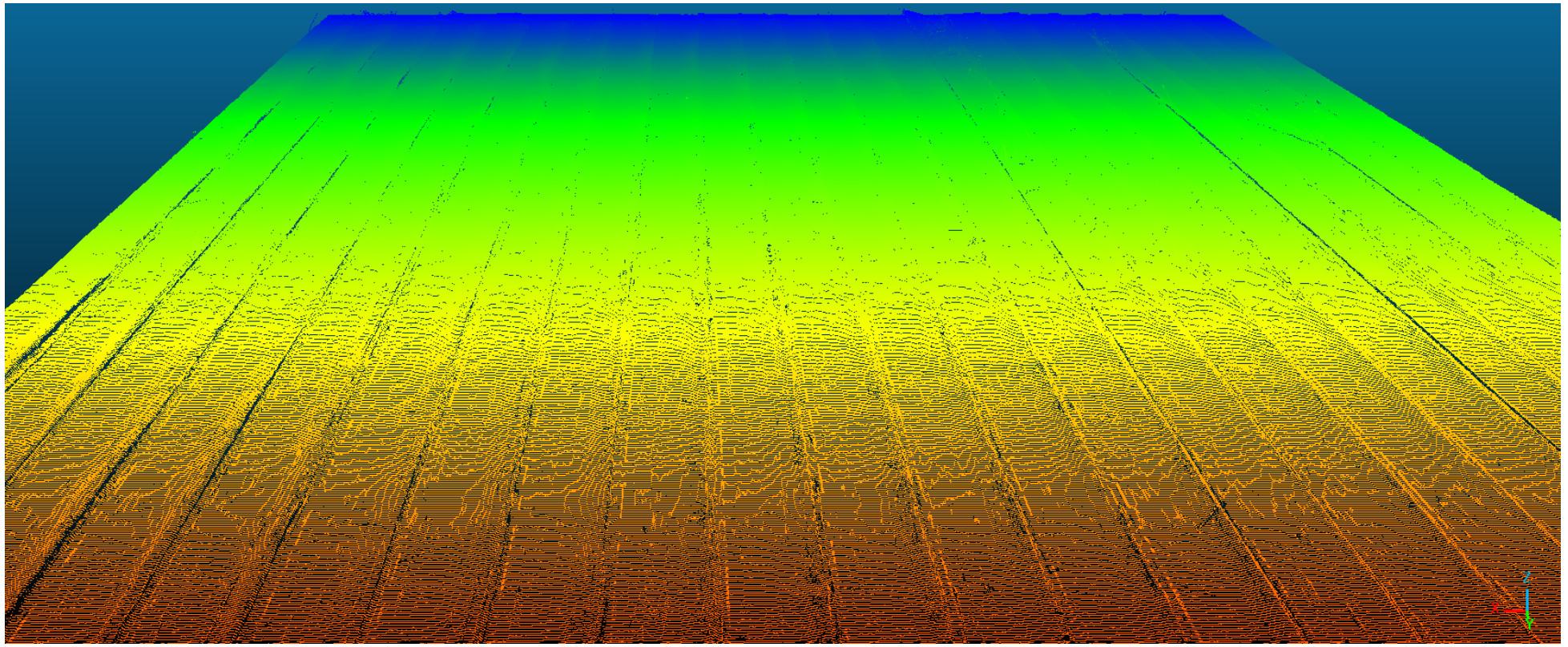

Funded by the European Union

Funded by the European Union. Views and opinions expressed are however those of the author(s) only and do not necessarily reflect those of the European Union or [EUROPEAN CLIMATE, INFRASTRUCTURE AND ENVIRONMENT EXECUTIVE AGENCY (CINEA)]. Neither the European Union nor the granting authority can be held responsible for them.

AFP on-line quality control

- Tow with a 5 mm **gap** defect in both sides.

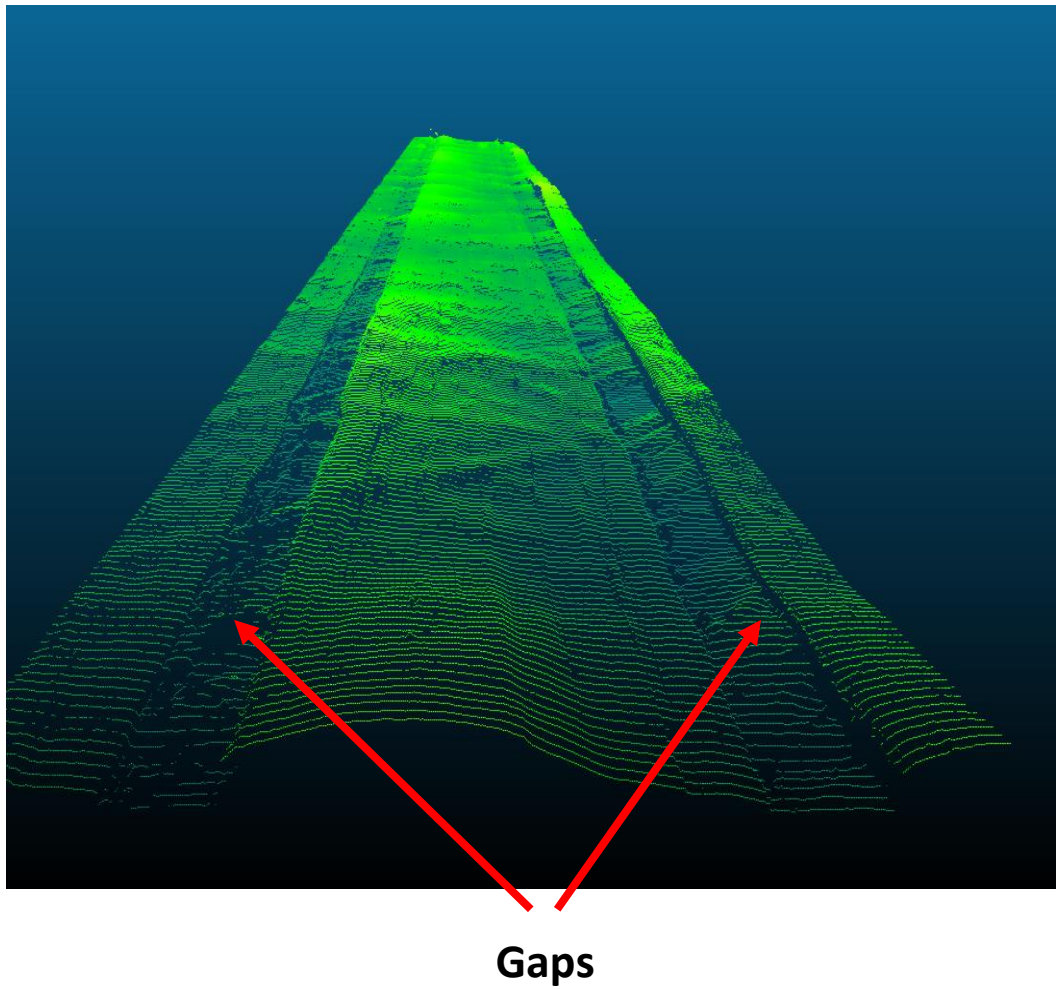

- Tow with a 5mm **overlap** defect in both sides.

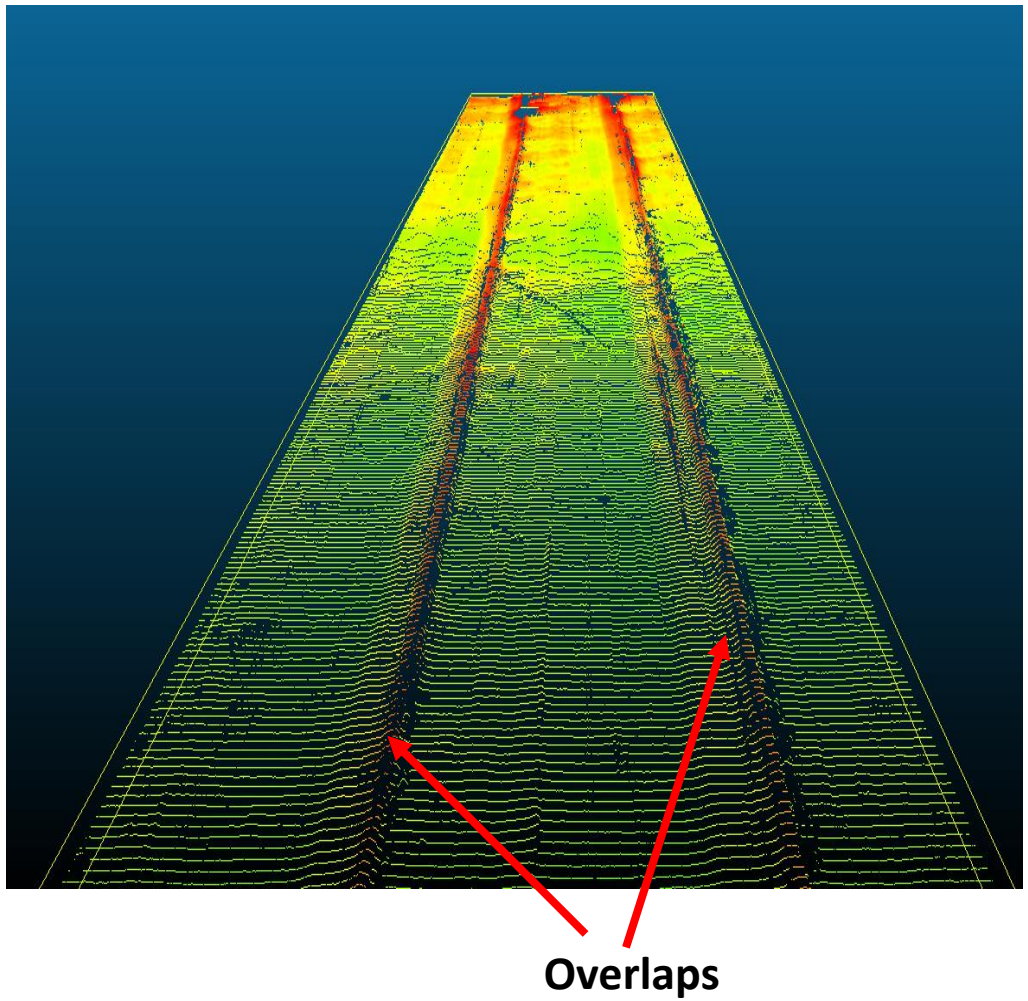

AFP on-line quality control

Complete ply with artificial 5 mm **overlap** defects.

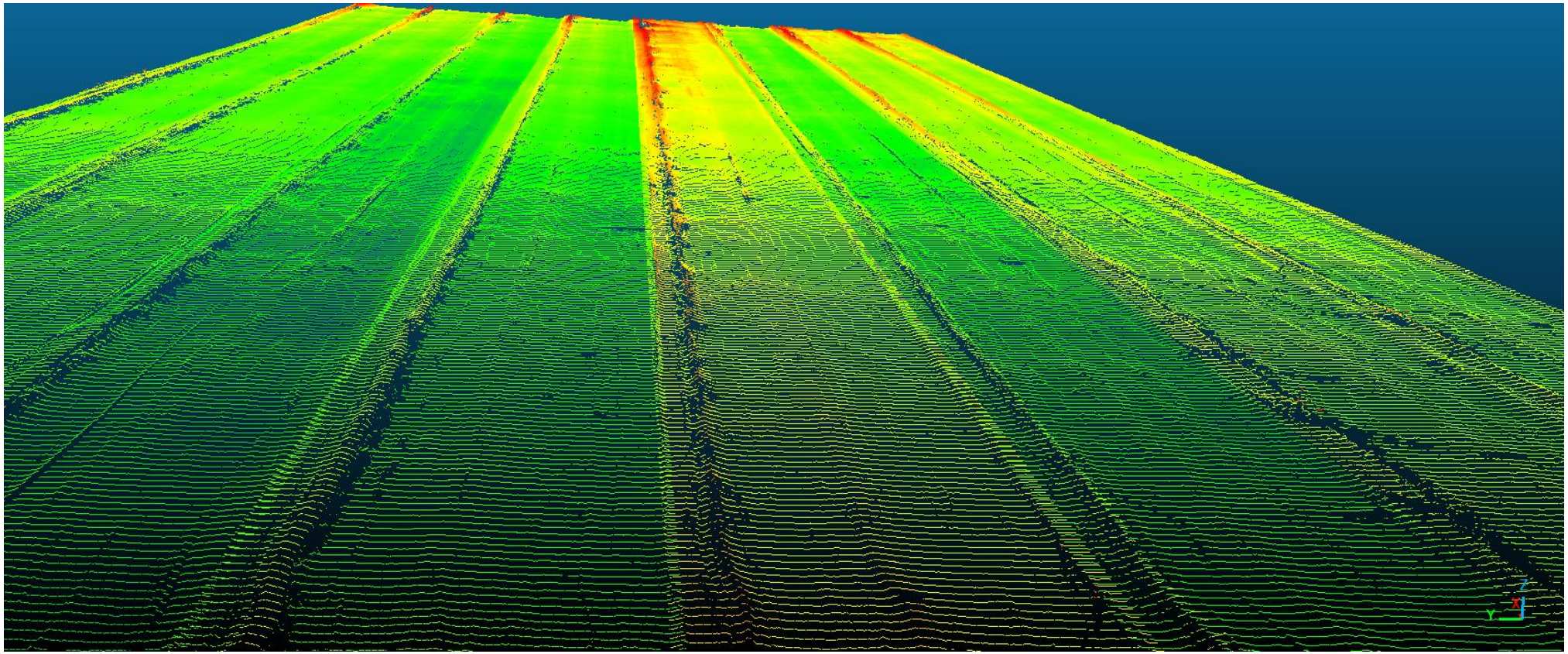

Funded by the European Union

Funded by the European Union. Views and opinions expressed are however those of the author(s) only and do not necessarily reflect those of the European Union or [EUROPEAN CLIMATE, INFRASTRUCTURE AND ENVIRONMENT EXECUTIVE AGENCY (CINEA)]. Neither the European Union nor the granting authority can be held responsible for them.

AFP on-line quality control

To match AFP-fry fiber defects with any possible RTM defect, it is necessary to reference the 3D point cloud scan of each ply with the robot manufacturing trajectories.

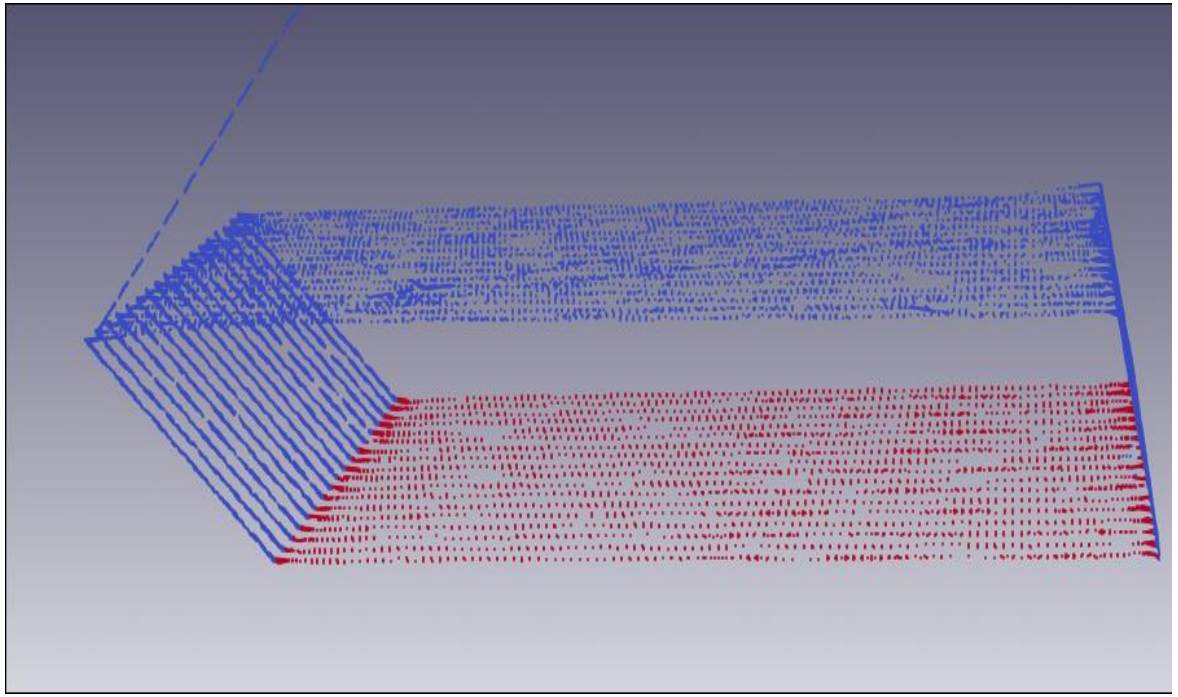

Robot manufacturing trajectories for one ply

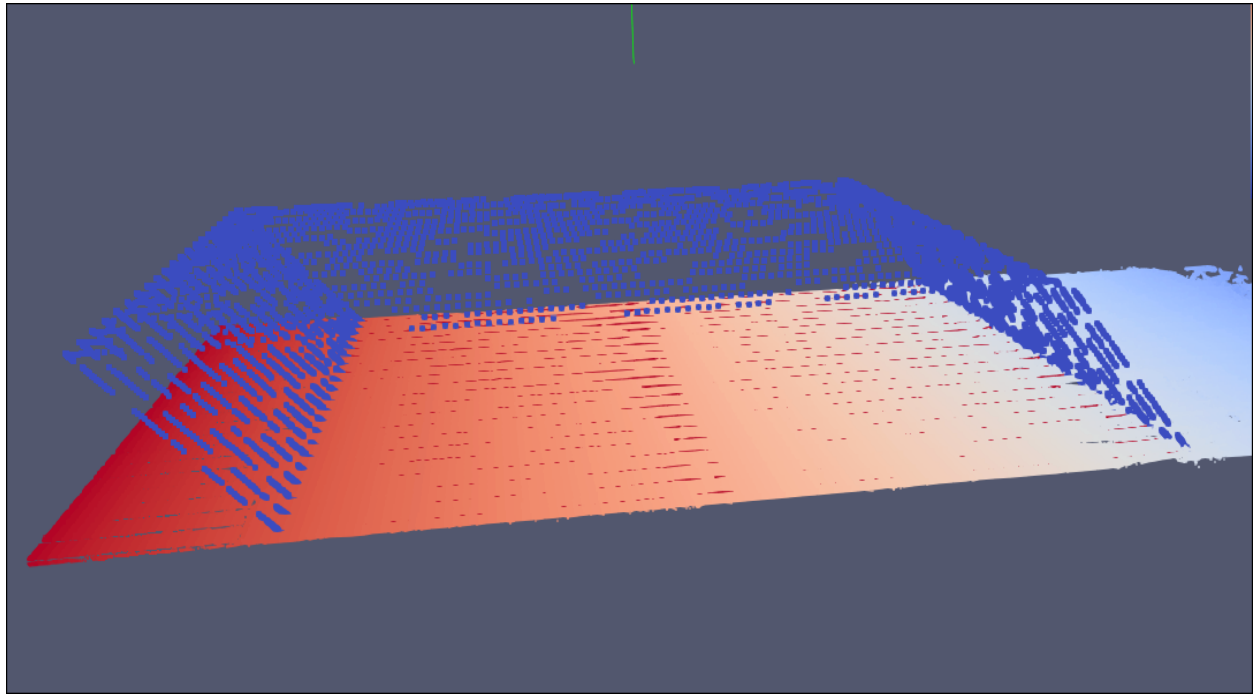

3D point cloud scan of one ply overlapped with robot trajectories

Funded by the European Union

Funded by the European Union. Views and opinions expressed are however those of the author(s) only and do not necessarily reflect those of the European Union or [EUROPEAN CLIMATE, INFRASTRUCTURE AND ENVIRONMENT EXECUTIVE AGENCY (CINEA)]. Neither the European Union nor the granting authority can be held responsible for them.

Thermal camera that provides thermal images for off-axis temperature measurement

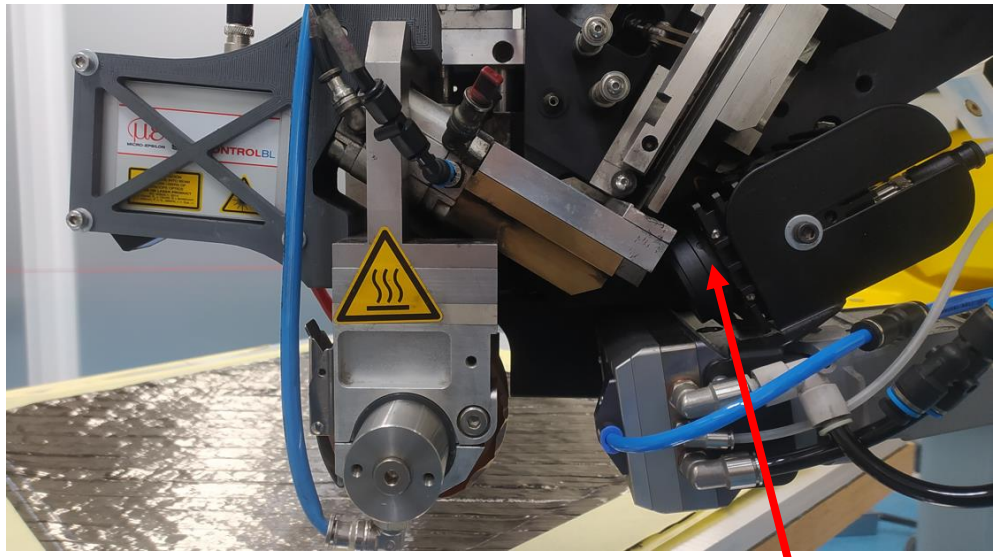

Thermal Camera
FLIR A70

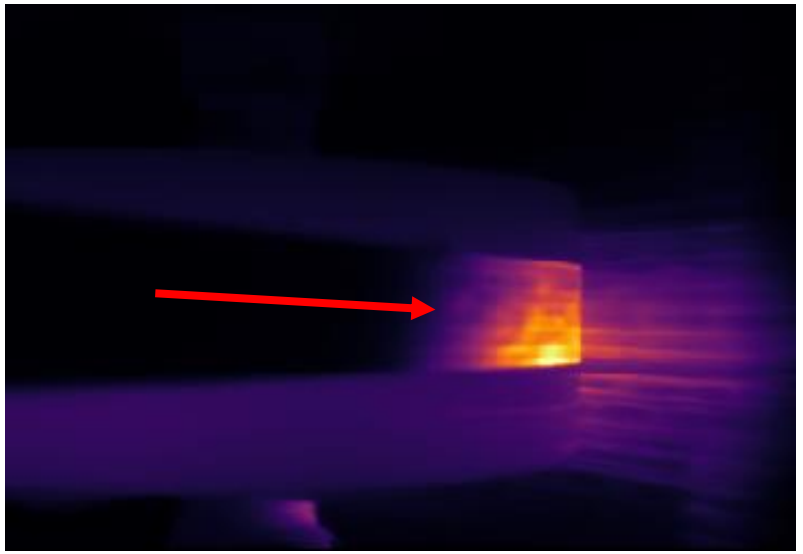

Thermal image of the AFP process

Funded by the European Union

Funded by the European Union. Views and opinions expressed are however those of the author(s) only and do not necessarily reflect those of the European Union or [EUROPEAN CLIMATE, INFRASTRUCTURE AND ENVIRONMENT EXECUTIVE AGENCY (CINEA)]. Neither the European Union nor the granting authority can be held responsible for them.

AFP on-line quality control

Thermal data analysis of the AFP process:

- Plot 1 shows the profile temperature of one tow while laser is ON (*area within the red circle is the relevant)*
- Plot 2 shows the profile temperature of several consecutive tows.
- Plot 3 represents the average temperature of the relevant area of all tows for each layer of the whole preform.

1

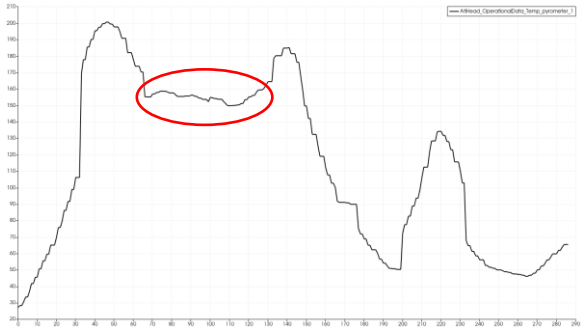

2

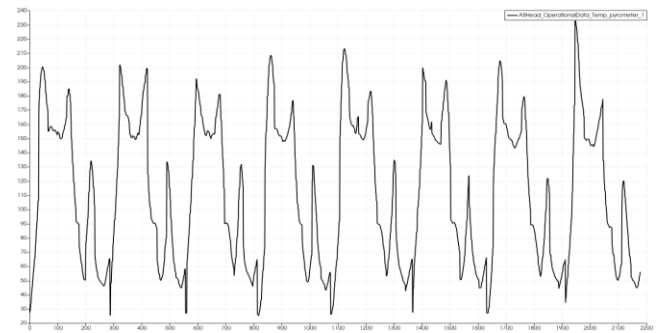

3

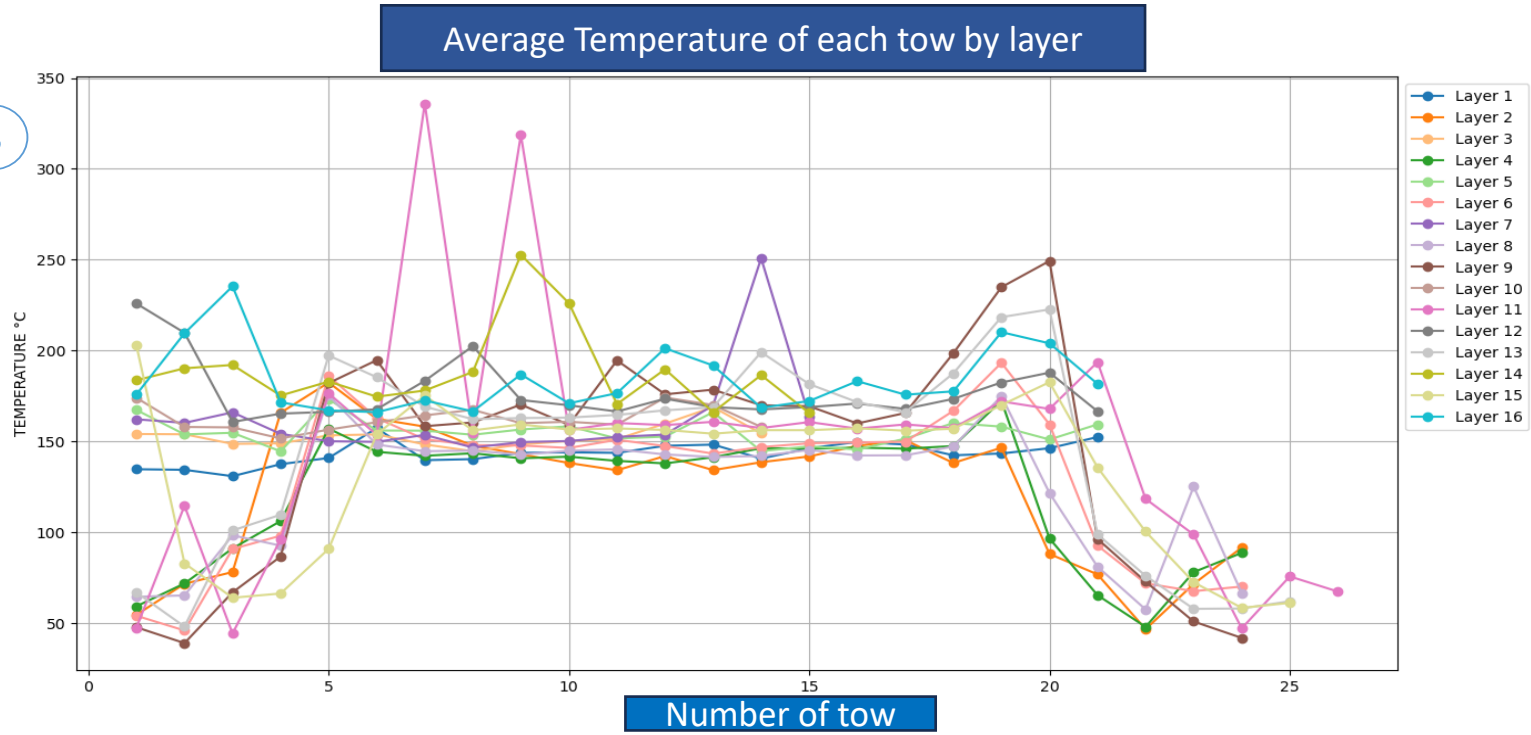

Funded by the European Union

Funded by the European Union. Views and opinions expressed are however those of the author(s) only and do not necessarily reflect those of the European Union or [EUROPEAN CLIMATE, INFRASTRUCTURE AND ENVIRONMENT EXECUTIVE AGENCY (CINEA)]. Neither the European Union nor the granting authority can be held responsible for them.

AFP on-line quality control

Complete information for AFP on-line quality control:

Overlapping Profilometer + Thermal camera + Robot position

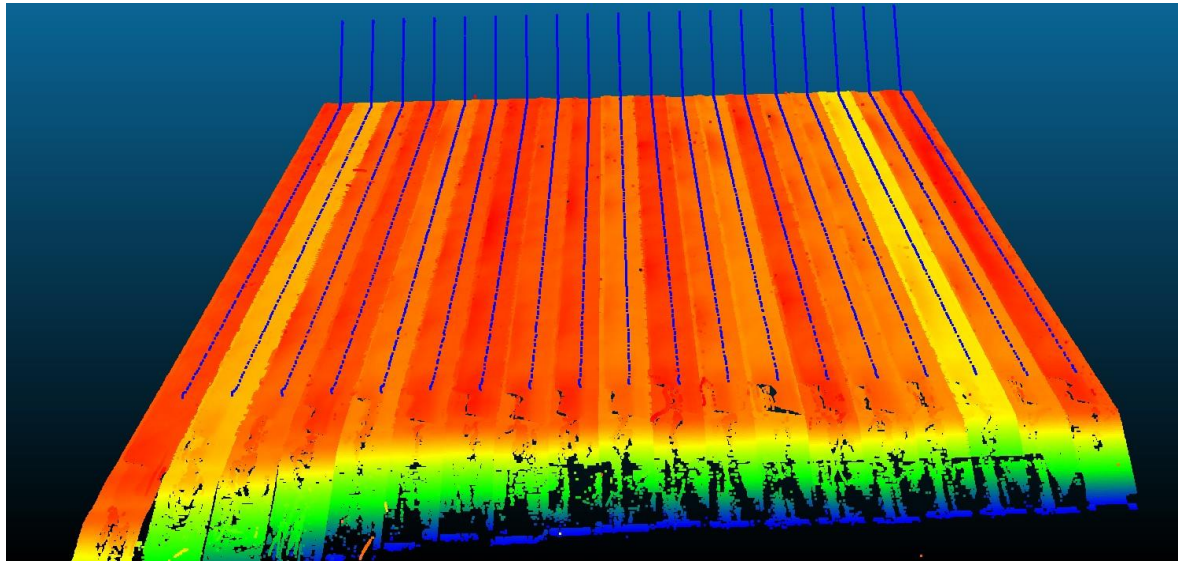

Funded by the European Union

Funded by the European Union. Views and opinions expressed are however those of the author(s) only and do not necessarily reflect those of the European Union or [EUROPEAN CLIMATE, INFRASTRUCTURE AND ENVIRONMENT EXECUTIVE AGENCY (CINEA)]. Neither the European Union nor the granting authority can be held responsible for them.

AFP on-line quality control

“SmartHub” TOOL: Complete collection of information of AFP manufacturing (VIDEO)

Funded by the European Union

Funded by the European Union. Views and opinions expressed are however those of the author(s) only and do not necessarily reflect those of the European Union or [EUROPEAN CLIMATE, INFRASTRUCTURE AND ENVIRONMENT EXECUTIVE AGENCY (CINEA)]. Neither the European Union nor the granting authority can be held responsible for them.

Experimental Results - Demonstrator manufacturing

Funded by the European Union

Funded by the European Union. Views and opinions expressed are however those of the author(s) only and do not necessarily reflect those of the European Union or [EUROPEAN CLIMATE, INFRASTRUCTURE AND ENVIRONMENT EXECUTIVE AGENCY (CINEA)]. Neither the European Union nor the granting authority can be held responsible for them.

DEMONSTRATOR

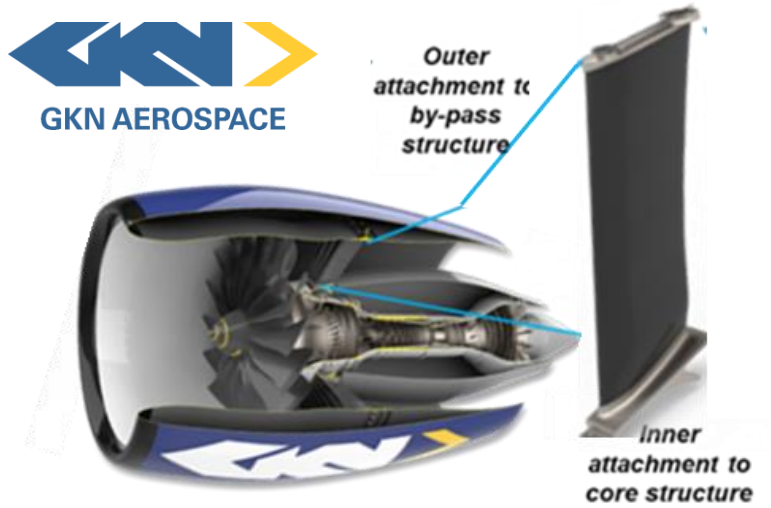

Ti + composite OGV
(one-shot RTM)

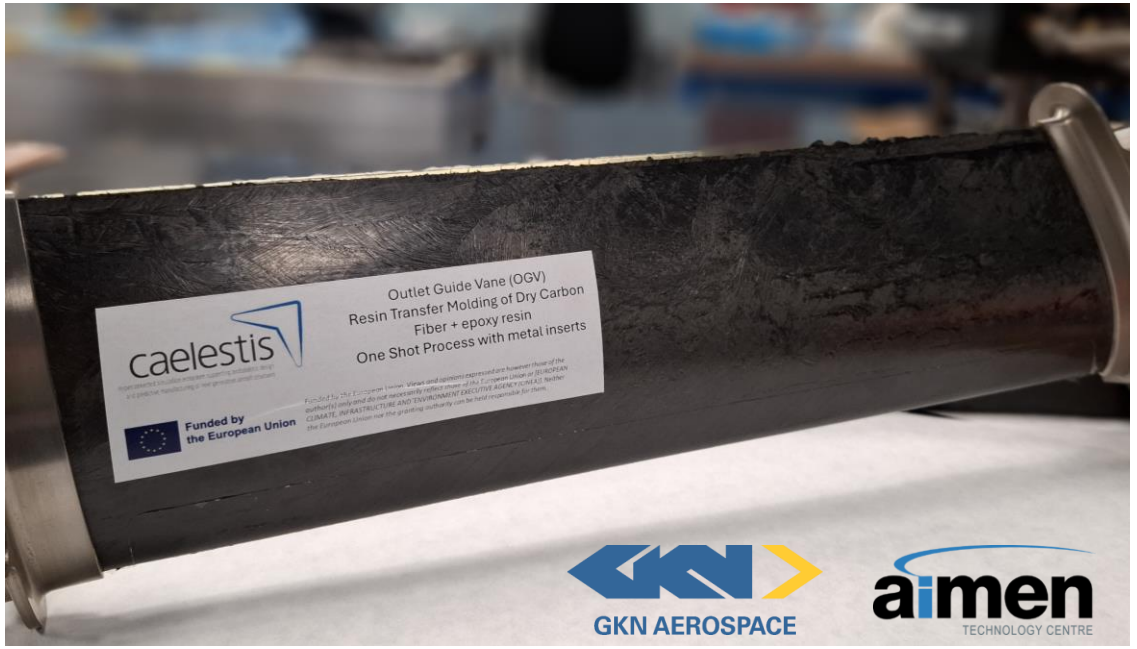

Funded by the European Union

Funded by the European Union. Views and opinions expressed are however those of the author(s) only and do not necessarily reflect those of the European Union or [EUROPEAN CLIMATE, INFRASTRUCTURE AND ENVIRONMENT EXECUTIVE AGENCY (CINEA)]. Neither the European Union nor the granting authority can be held responsible for them.

CONCLUSIONS AND FUTURE WORK

Funded by the European Union

Funded by the European Union. Views and opinions expressed are however those of the author(s) only and do not necessarily reflect those of the European Union or [EUROPEAN CLIMATE, INFRASTRUCTURE AND ENVIRONMENT EXECUTIVE AGENCY (CINEA)]. Neither the European Union nor the granting authority can be held responsible for them.

Conclusions and future work

- ✓ The AFP parameter that has more influence in the compaction (peel strength) of the dry fiber is the heating input (resulted from laser power and velocity).
- ✓ The optimum AFP process T > T_m *(binder activation)* T < $T_{degradation}$
- ✓ The higher permeabilities occur at the lower compaction of the dry preform.
- ✓ The "SmartHub" tool allow us the on-line quality control and manufacturing data analysis

On-going next steps:

- ✓ To study the effect of the dry fiber preform quality on the RTM process and on the mechanical properties of the final laminates.
- ✓ To give input to the CAELESTIS simulation workflow

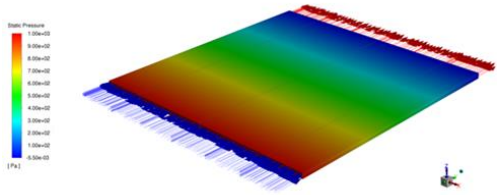

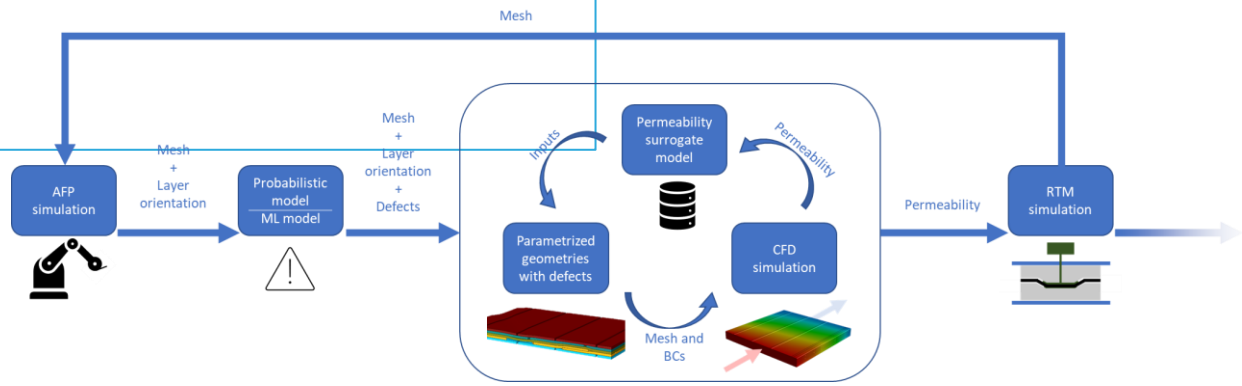

Funded by the European Union

Funded by the European Union. Views and opinions expressed are however those of the author(s) only and do not necessarily reflect those of the European Union or [EUROPEAN CLIMATE, INFRASTRUCTURE AND ENVIRONMENT EXECUTIVE AGENCY (CINEA)]. Neither the European Union nor the granting authority can be held responsible for them.

Quality control - online monitoring technologies (RTM)



Sensorized RTM mold

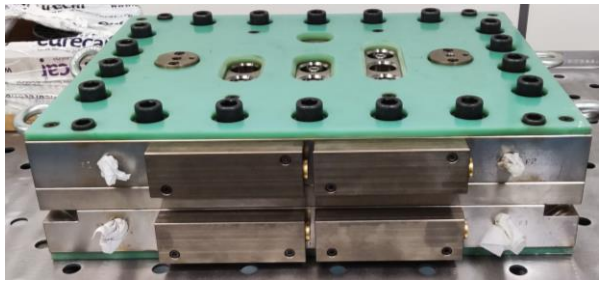

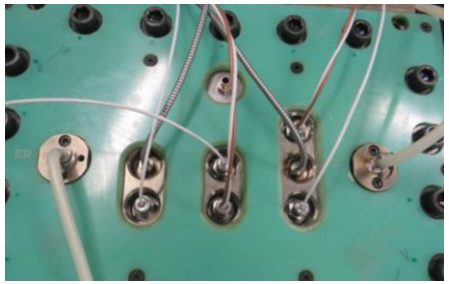

Resin flow front

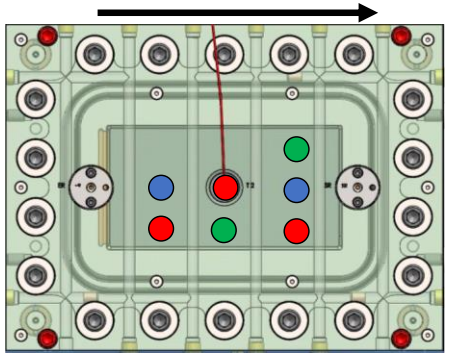

- Pressure sensor
- Cure degree sensor
- Resin Arrival + T sensor

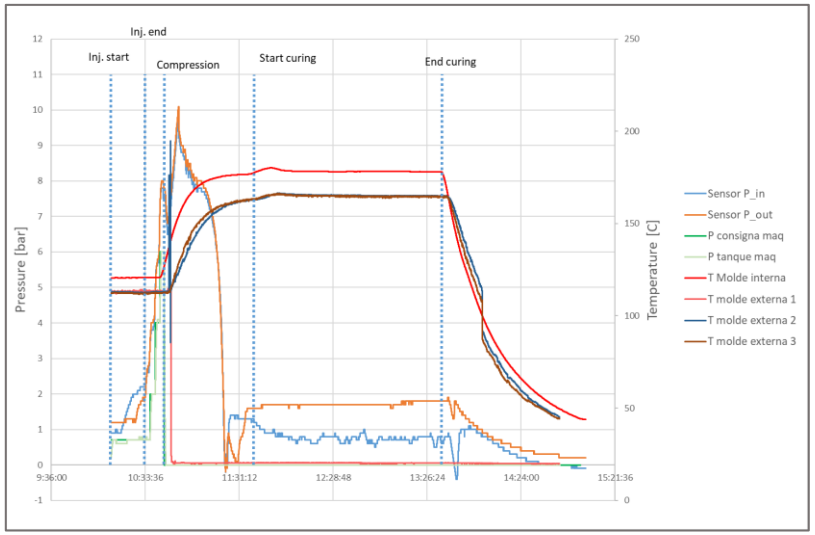

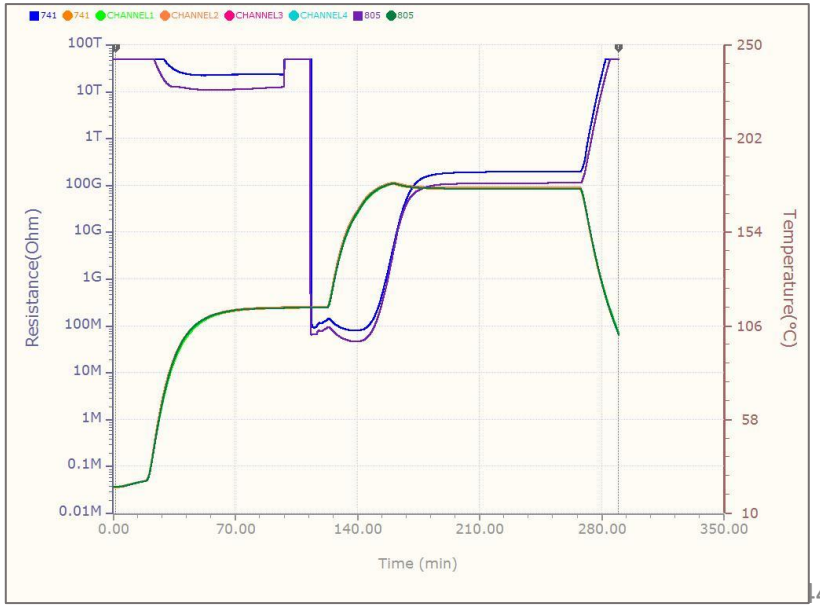

Funded by the European Union

Funded by the European Union. Views and opinions expressed are however those of the author(s) only and do not necessarily reflect those of the European Union or [EUROPEAN CLIMATE, INFRASTRUCTURE AND ENVIRONMENT EXECUTIVE AGENCY (CINEA)]. Neither the European Union nor the granting authority can be held responsible for them.

Thanks for your attention!

Dr. Elena Rodríguez Senín| Head of Advanced Composites Technologies
erodriguez@aimen.es | +34 986 344 000 Ext. 2133 - +34 637 149 677

caelestis

Hyperconnected simulation ecosystem supporting probabilistic design and predictive manufacturing of next generation aircraft structures

Funded by the European Union

Funded by the European Union. Views and opinions expressed are however those of the author(s) only and do not necessarily reflect those of the European Union or [EUROPEAN CLIMATE, INFRASTRUCTURE AND ENVIRONMENT EXECUTIVE AGENCY (CINEA)]. Neither the European Union nor the granting authority can be held responsible for them.

TIME-DEPENDENCY PHENOMENA IN BIAXIALLY ORIENTED POLYPROPYLENE and SELF REINFORCED POLYPROPYLENE LAMINATES

Anna Kandinskaia, Arianna Tavano, Pauline Koslowski, Laurens van Audenaerde, Nathan Vanden Bulcke, Ignaas Verpoest, Yentl Swolfs

AGENTSCHAP INNOVEREN & ONDERNEMEN

Samsonite

KU LEUVEN MATERIALS ENGINEERING

Composite Materials Group

ORIENTED POLYMERS

Uniaxial orientation

- ⊕ High properties along **ONE** direction
- ⊖ **Large** property **GAPS** between the stretched and not stretched directions

SRPP tapes

Biaxial orientation

- ⊕ Good properties along **TWO** directions
- ⊕ **Limited** property **GAPS** between the two directions

BOPP films

ORIENTED POLYMERS

BOPP films

SRPP fabrics

Excellent interfaces

ORIENTED POLYMERS

BOPP films

SRPP fabrics

Excellent interfaces

Recyclability

ORIENTED POLYMERS

BOPP films

SRPP fabrics

Excellent interfaces

Recyclability

High toughness

ORIENTED POLYMERS

BOPP films

SRPP fabrics

Excellent interfaces

Recyclability

High toughness

Low cost

ORIENTED POLYMERS

BOPP films

SRPP fabrics

Excellent interfaces

Recyclability

High toughness

Low cost

Formability

ORIENTED POLYMERS

BOPP films

SRPP fabrics

Excellent interfaces

Recyclability

High toughness

Low cost

Formability

Different textural look

ORIENTED POLYMERS

BOPP films

ORIENTED POLYMERS

BOPP films



ORIENTED POLYMERS

BOPP films

SRPP fabrics



ORIENTED POLYMERS

BOPP films



SRPP fabrics



TIME-DEPENDENCY ANALYSIS



TIME ?



TIME





TIME ?



TIME

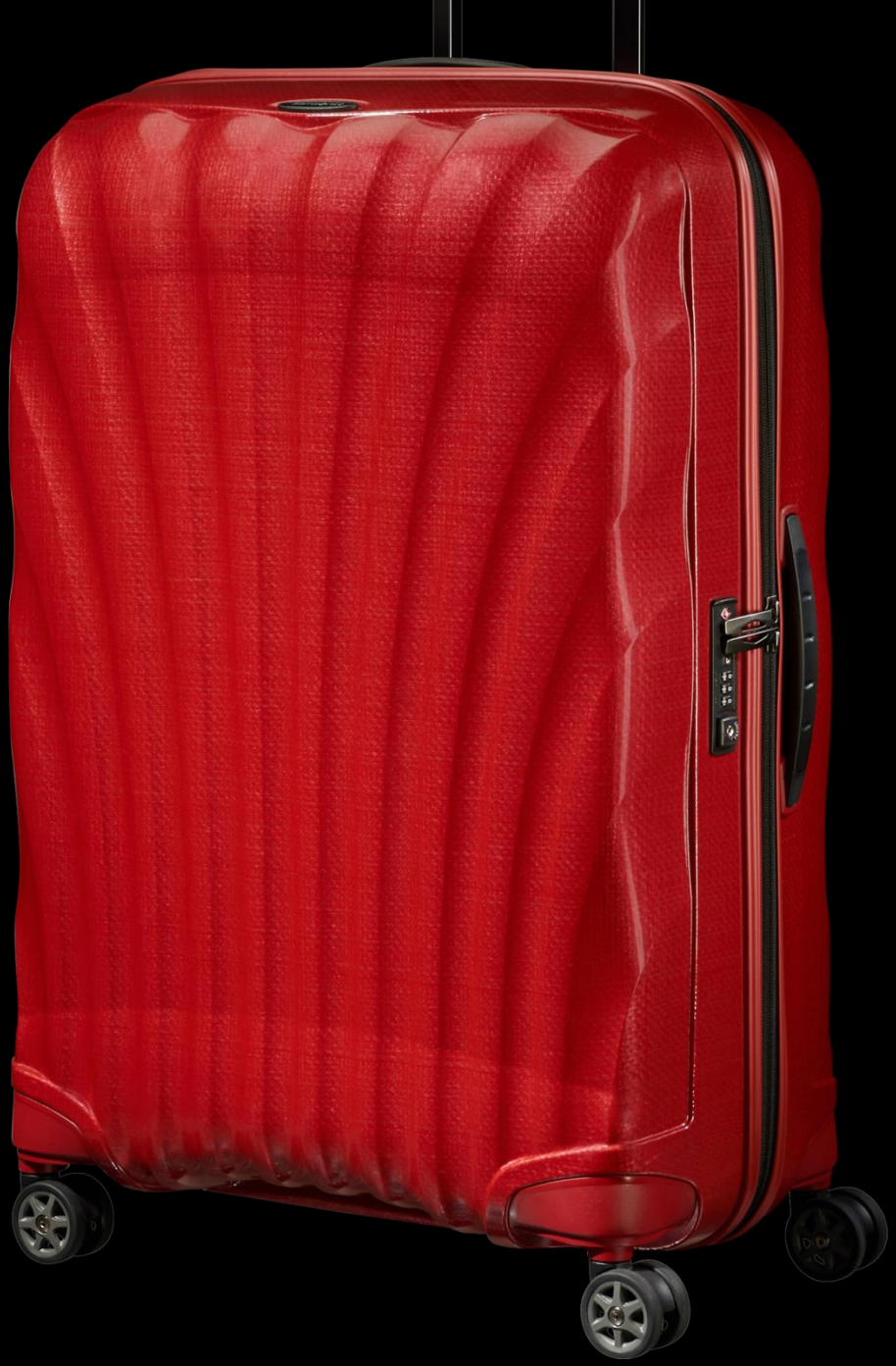

EXPERIMENTAL PART

MANUFACTURING

BOPP film laminate

MANUFACTURING

BOPP film laminate



MANUFACTURING

BOPP film laminate

SRPP woven laminate



MANUFACTURING

BOPP film laminate



SRPP woven laminate



MANUFACTURING

BOPP film laminate

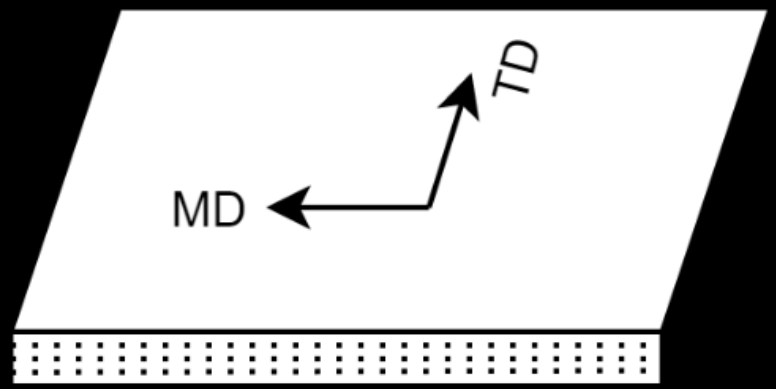

SRPP woven laminate

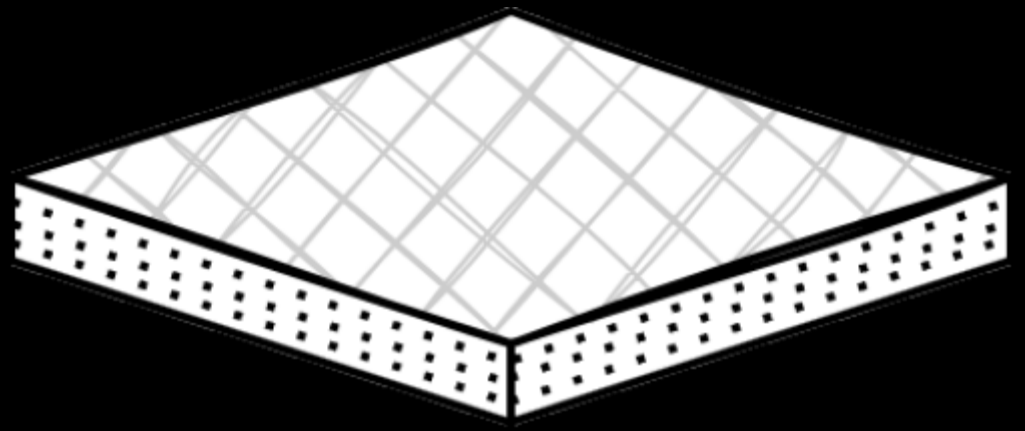

MANUFACTURING

BOPP film laminate

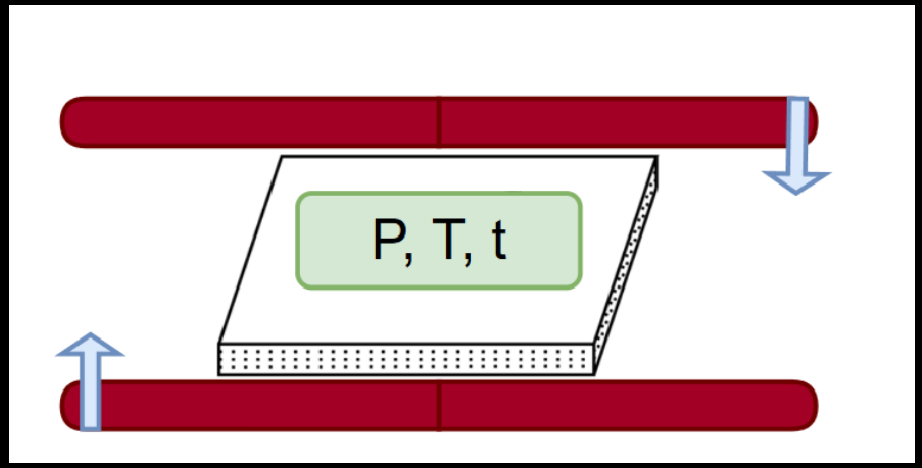

SRPP woven laminate

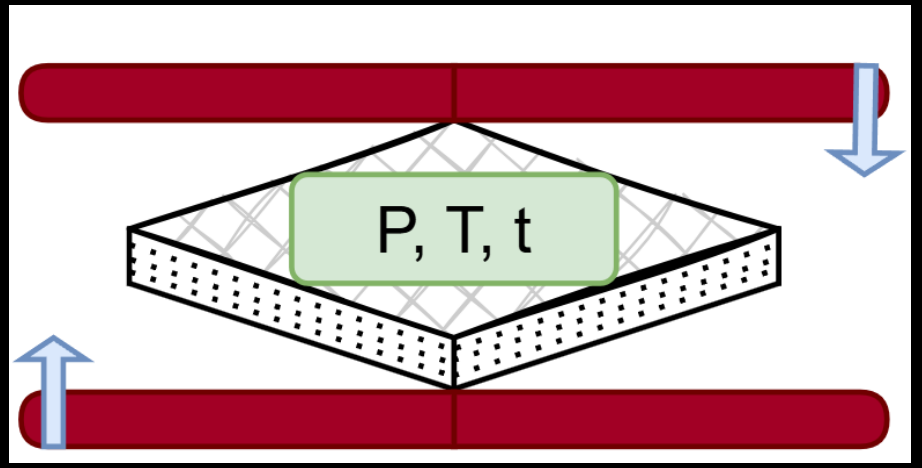

TESTING

BOPP film laminate

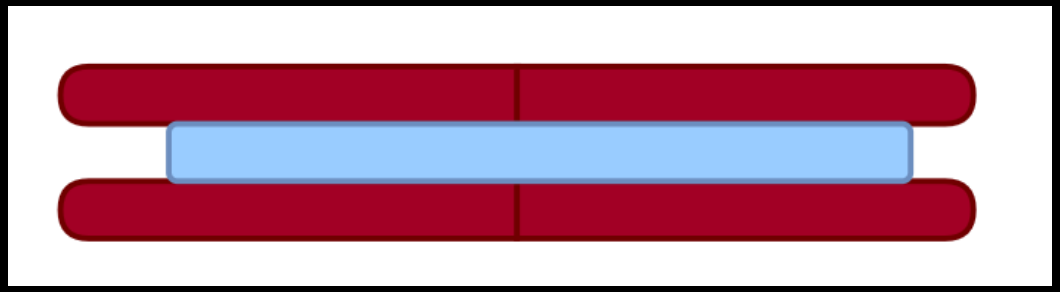

SRPP woven laminate

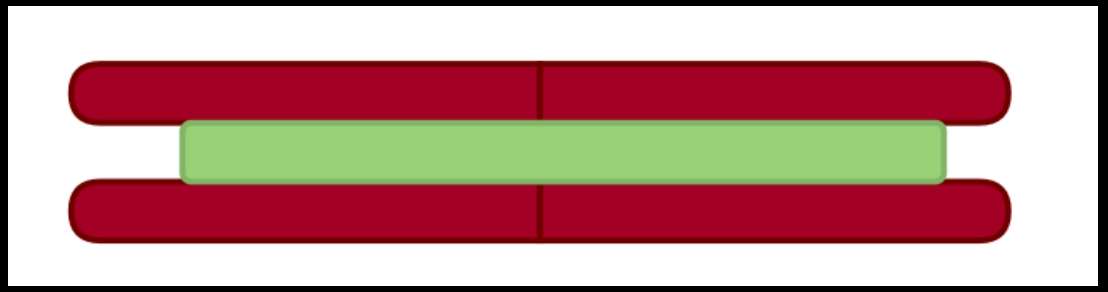

TESTING

BOPP film laminate

SRPP woven laminate

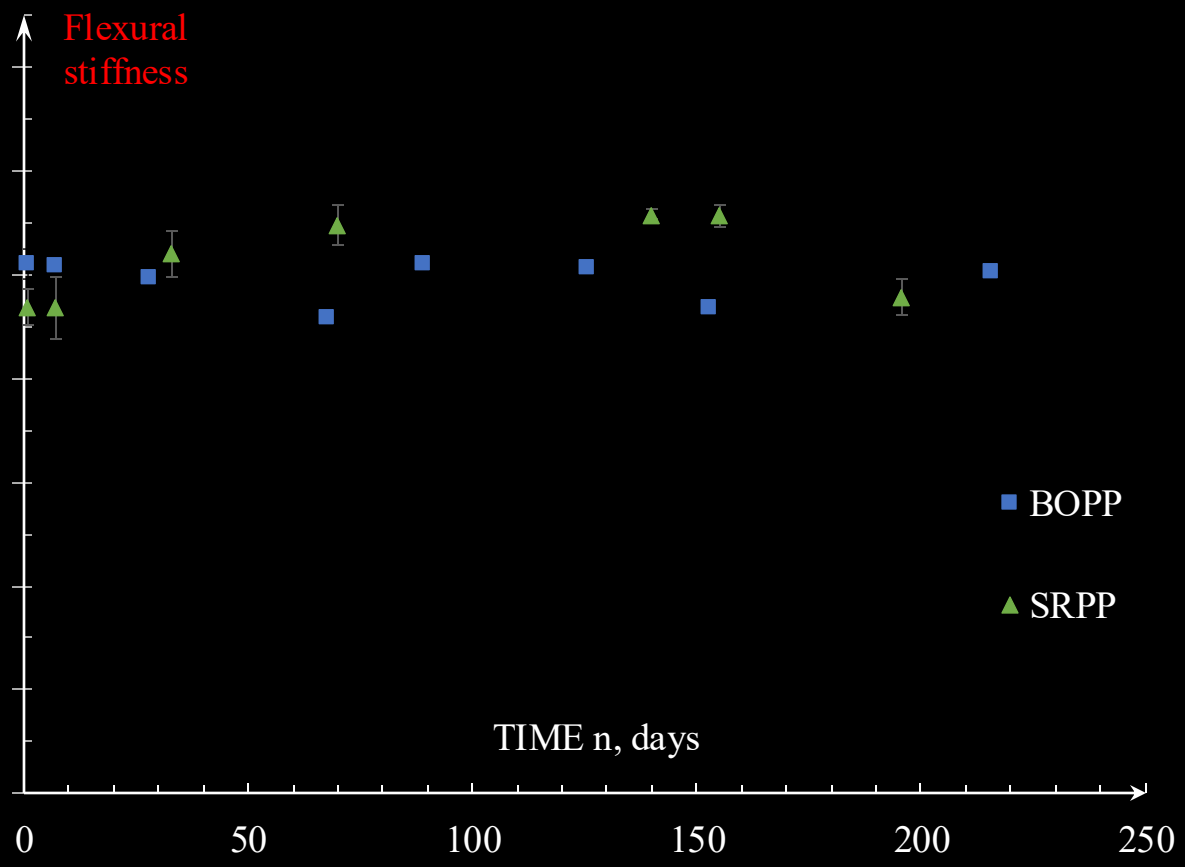

TESTING

BOPP film laminate

SRPP woven laminate

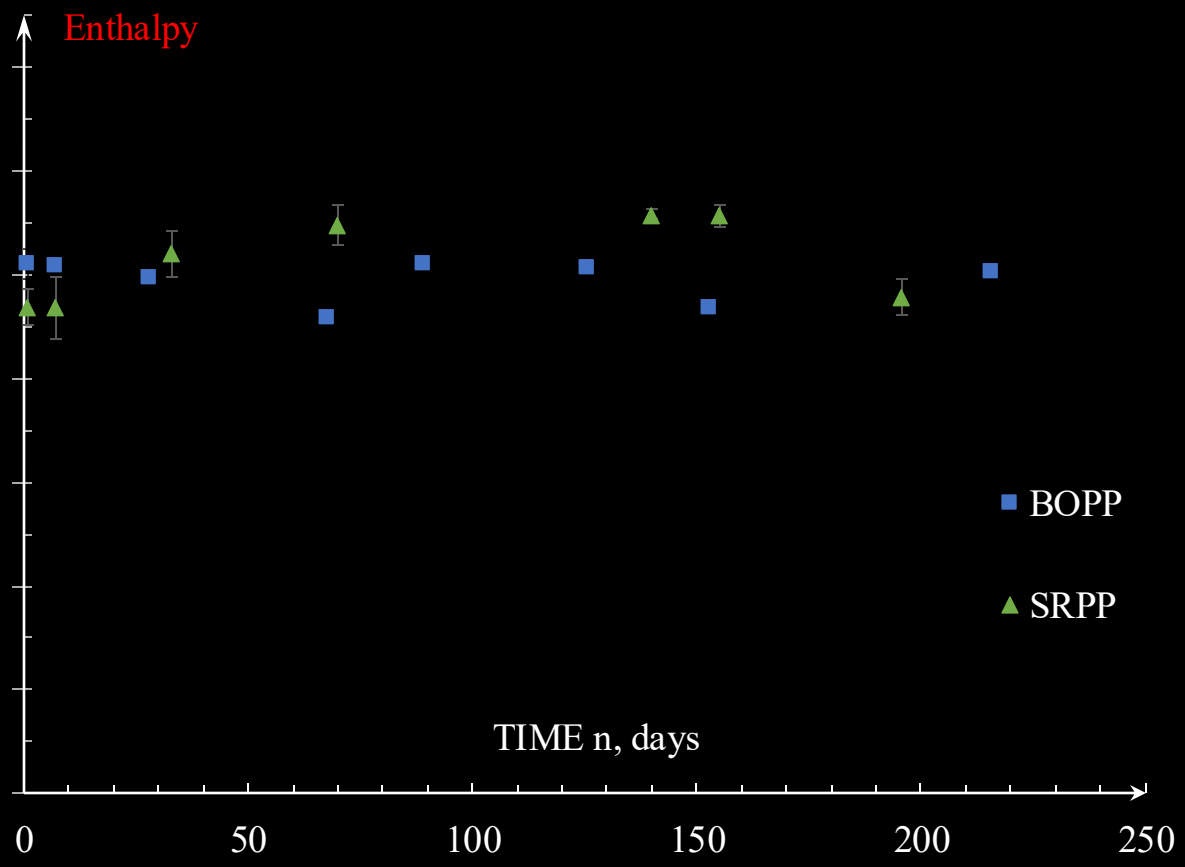

Three-point bending test results

BOPP





Three-point bending test results

BOPP





Three-point bending test results

BOPP

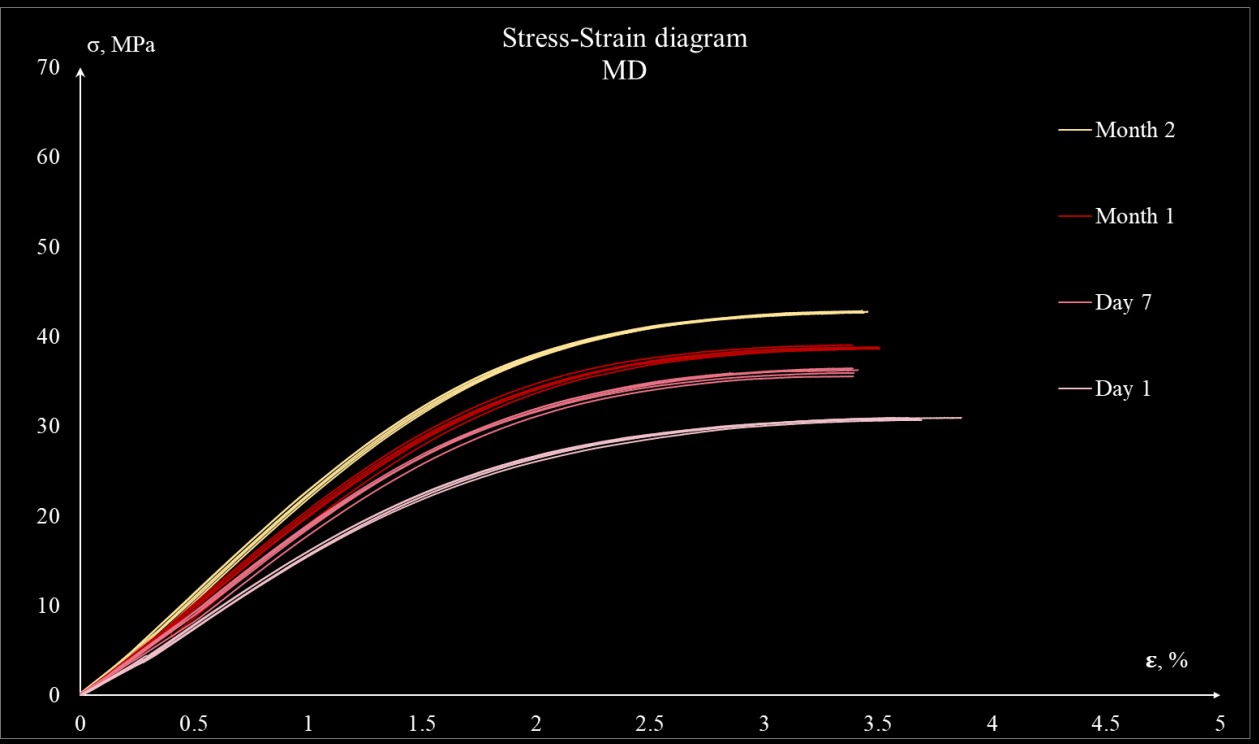

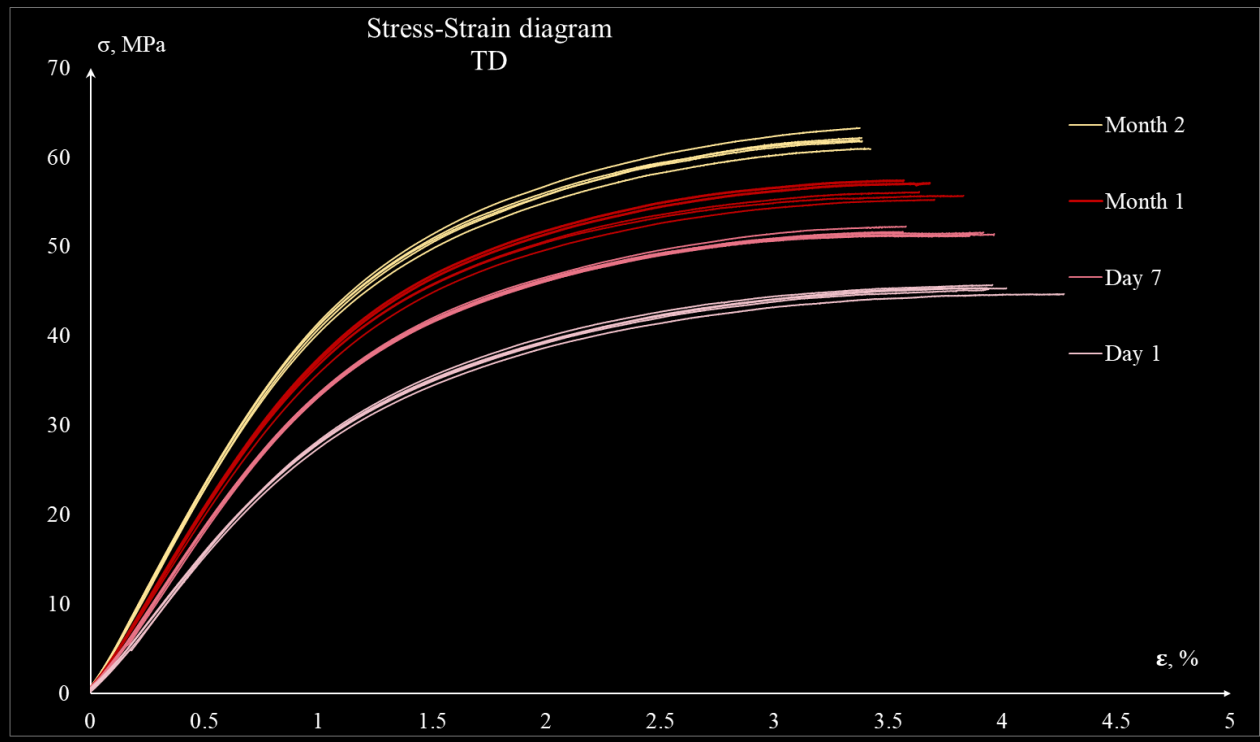

Three-point bending test results

BOPP

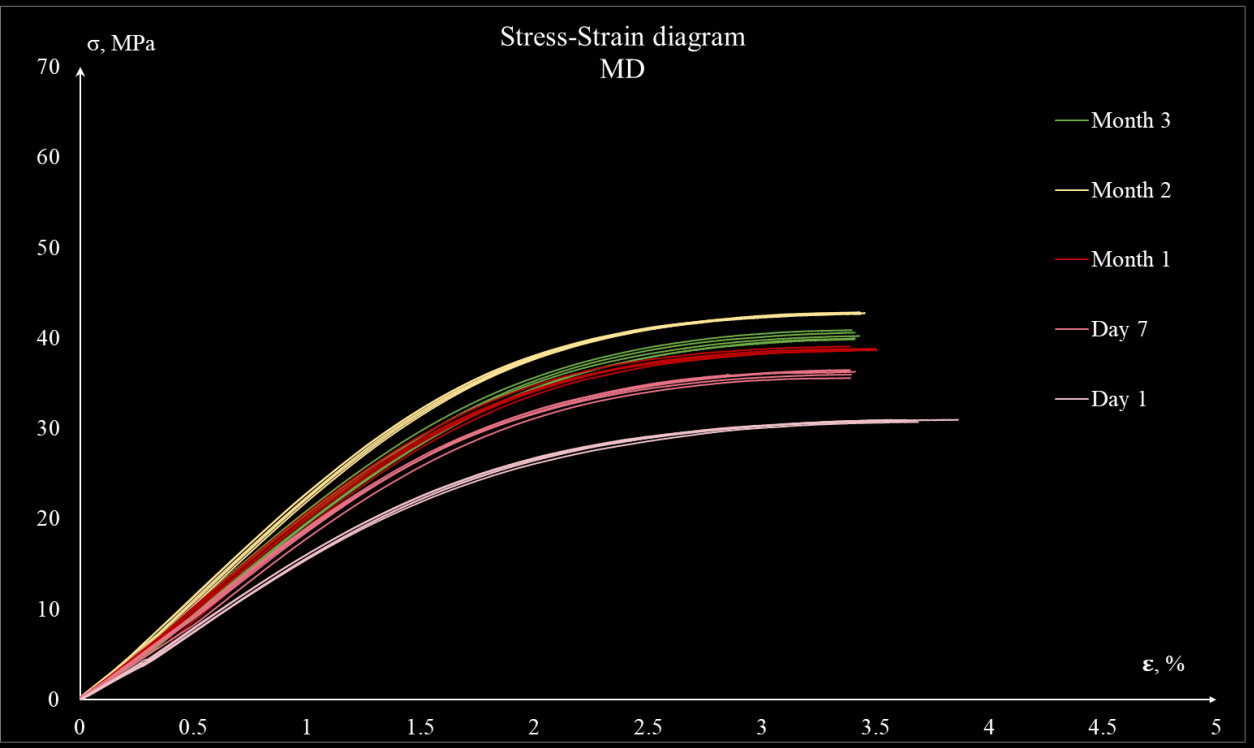

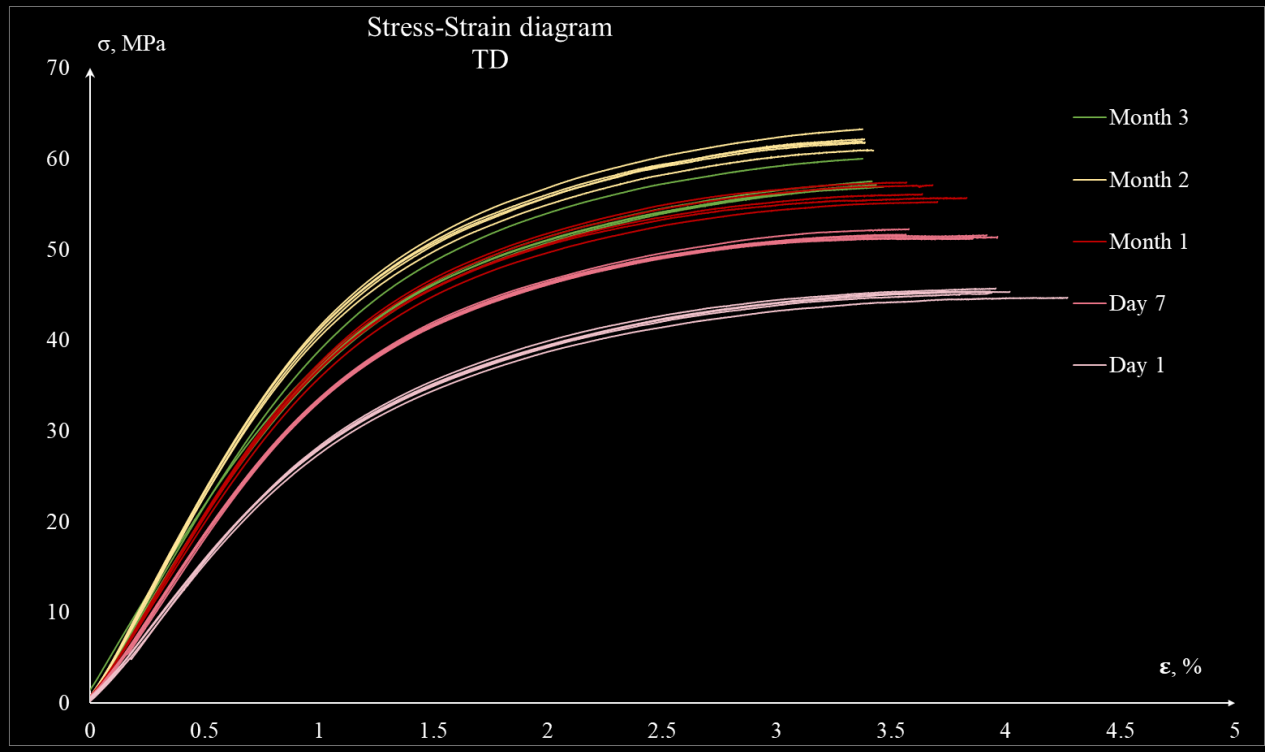

Three-point bending test results

BOPP

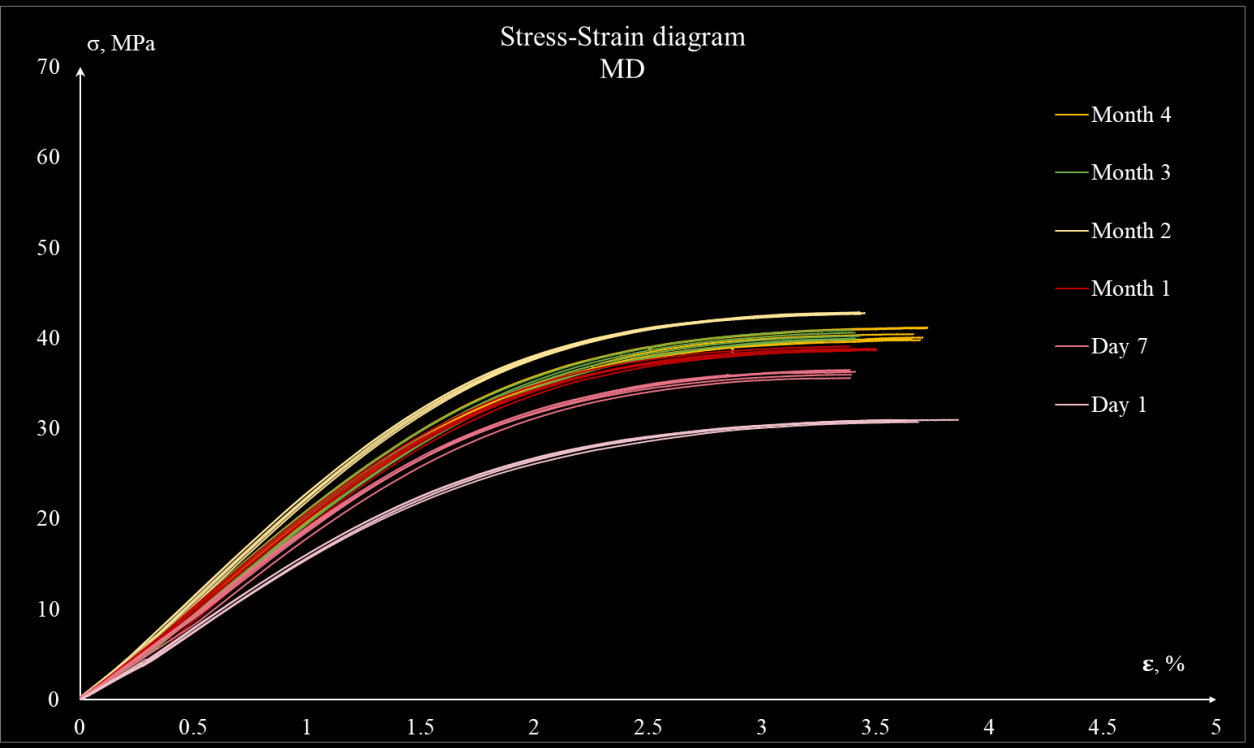

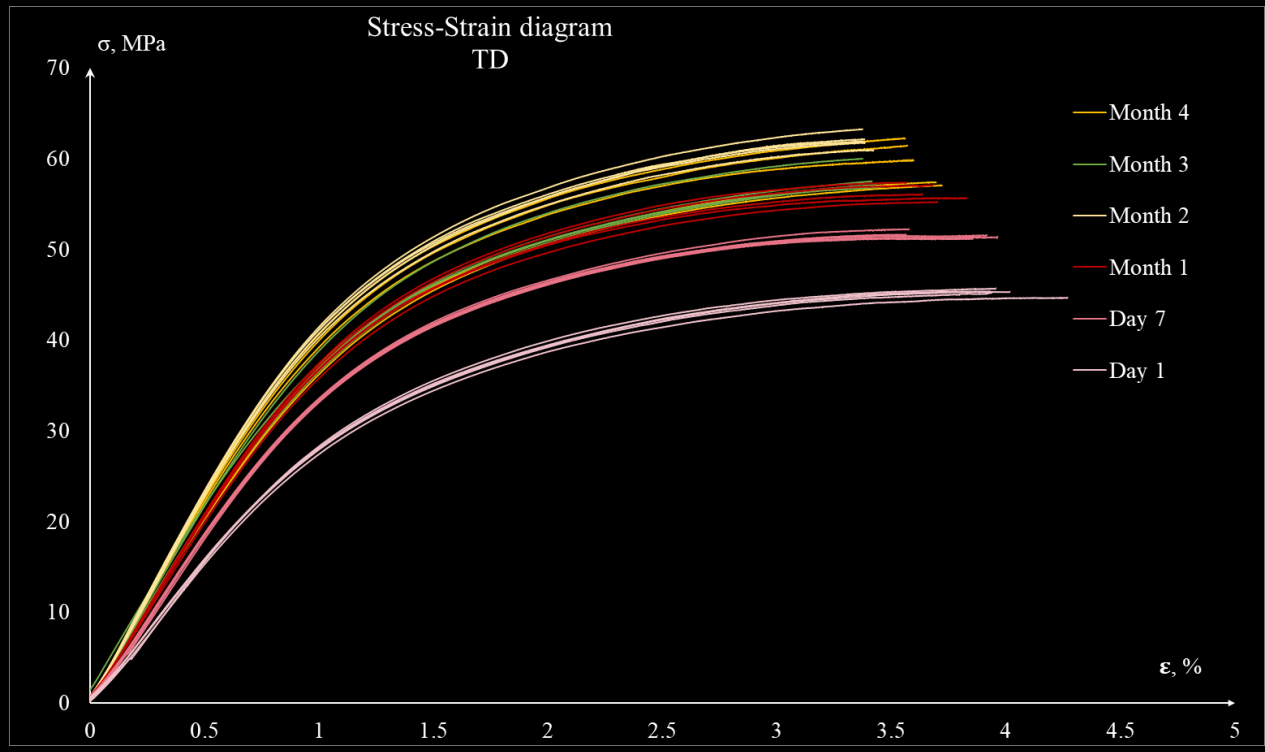

Three-point bending test results

BOPP

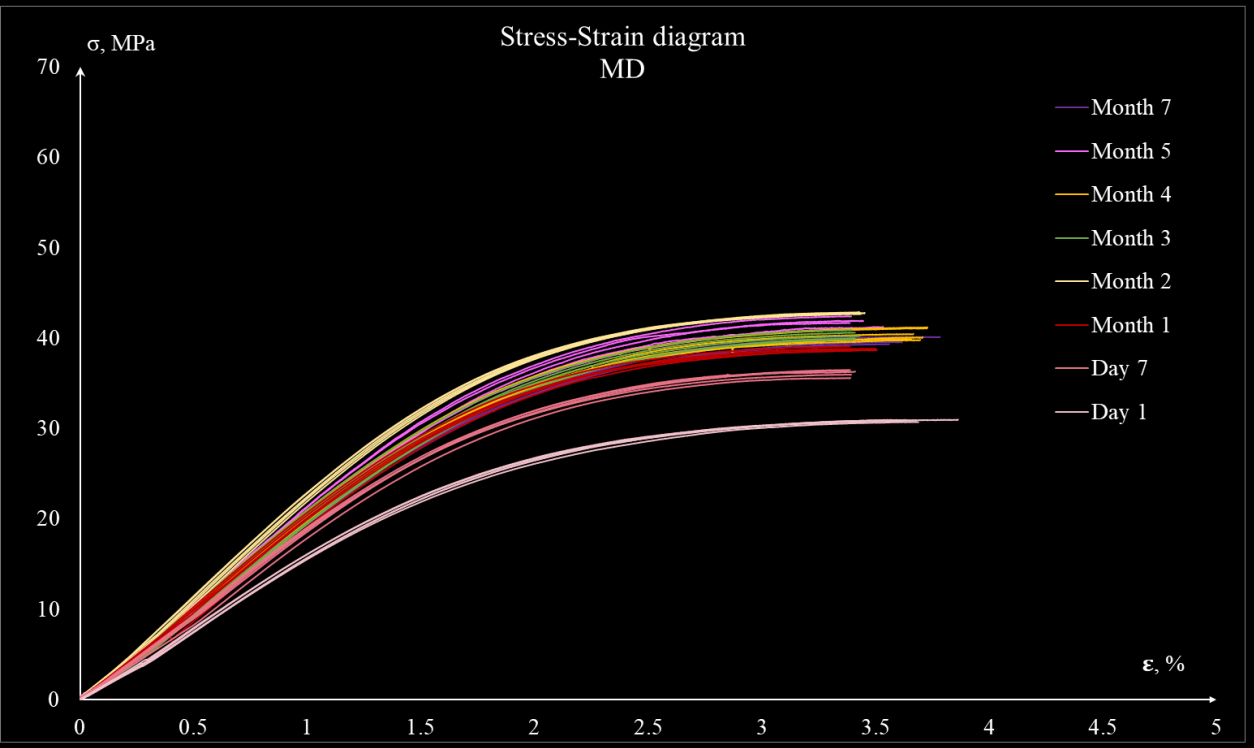



Three-point bending test results

SRPP

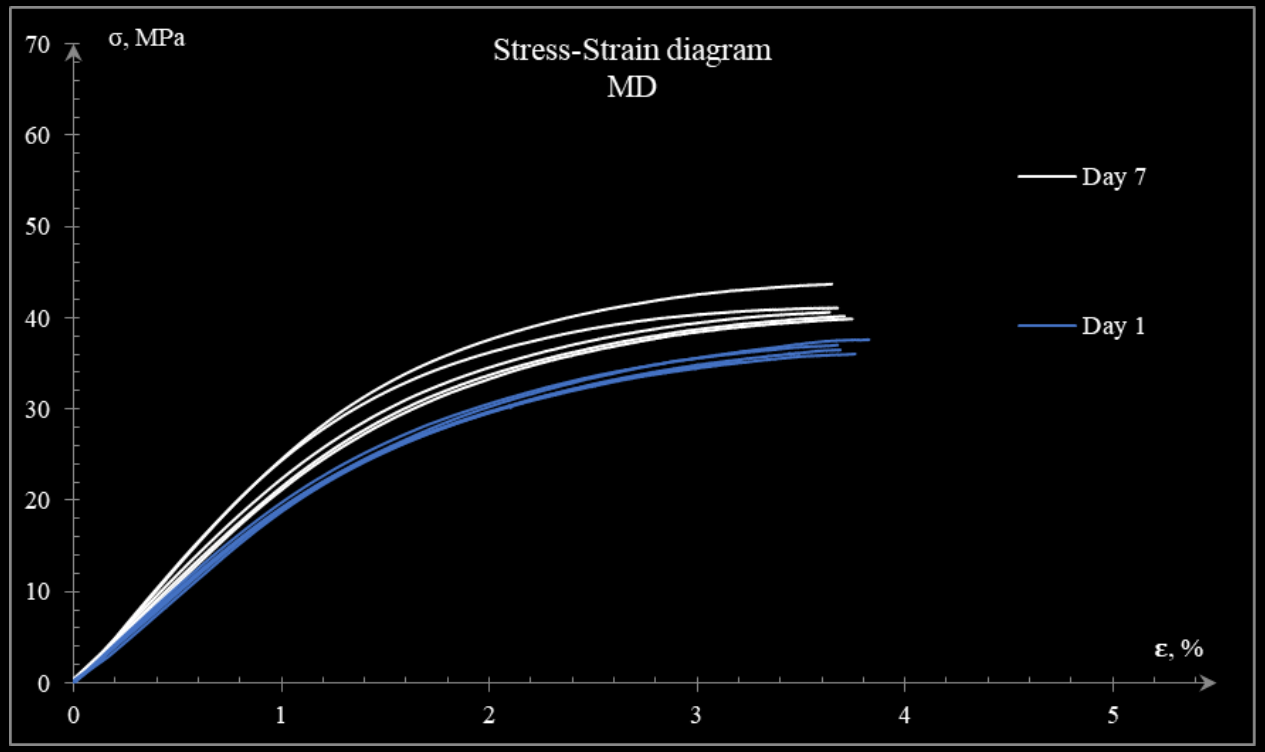

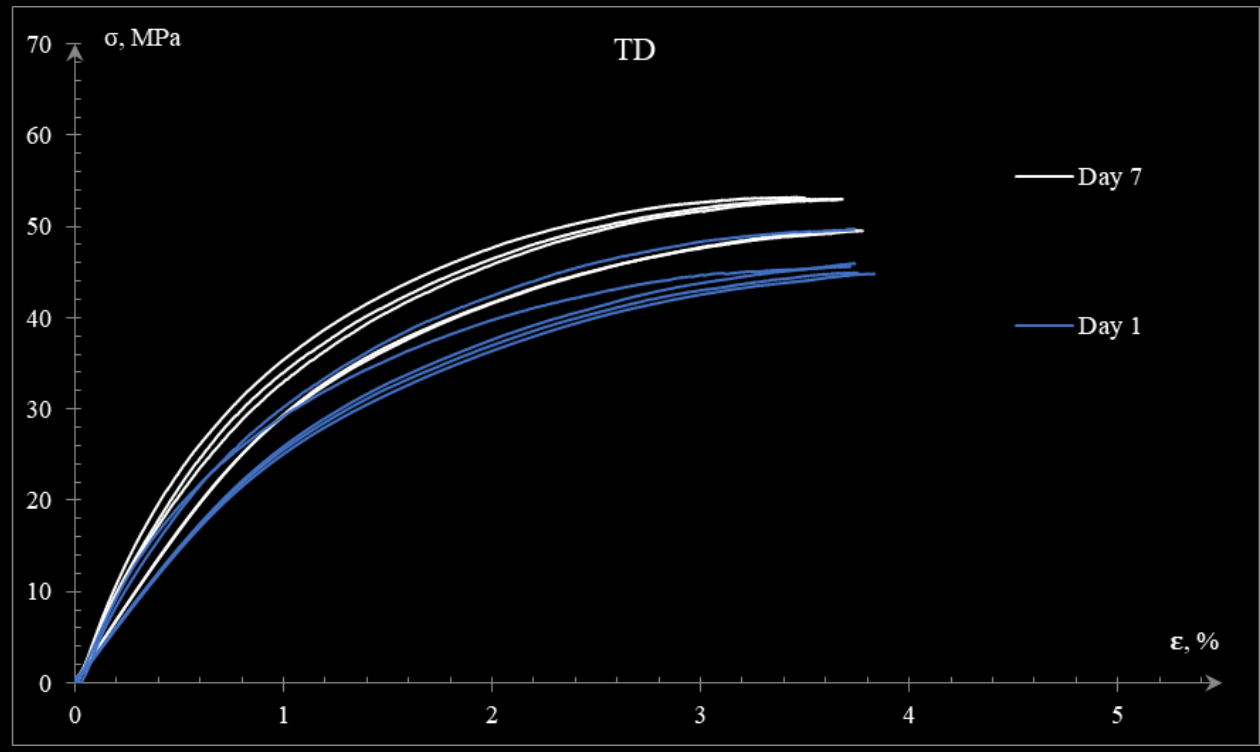

Three-point bending test results

SRPP

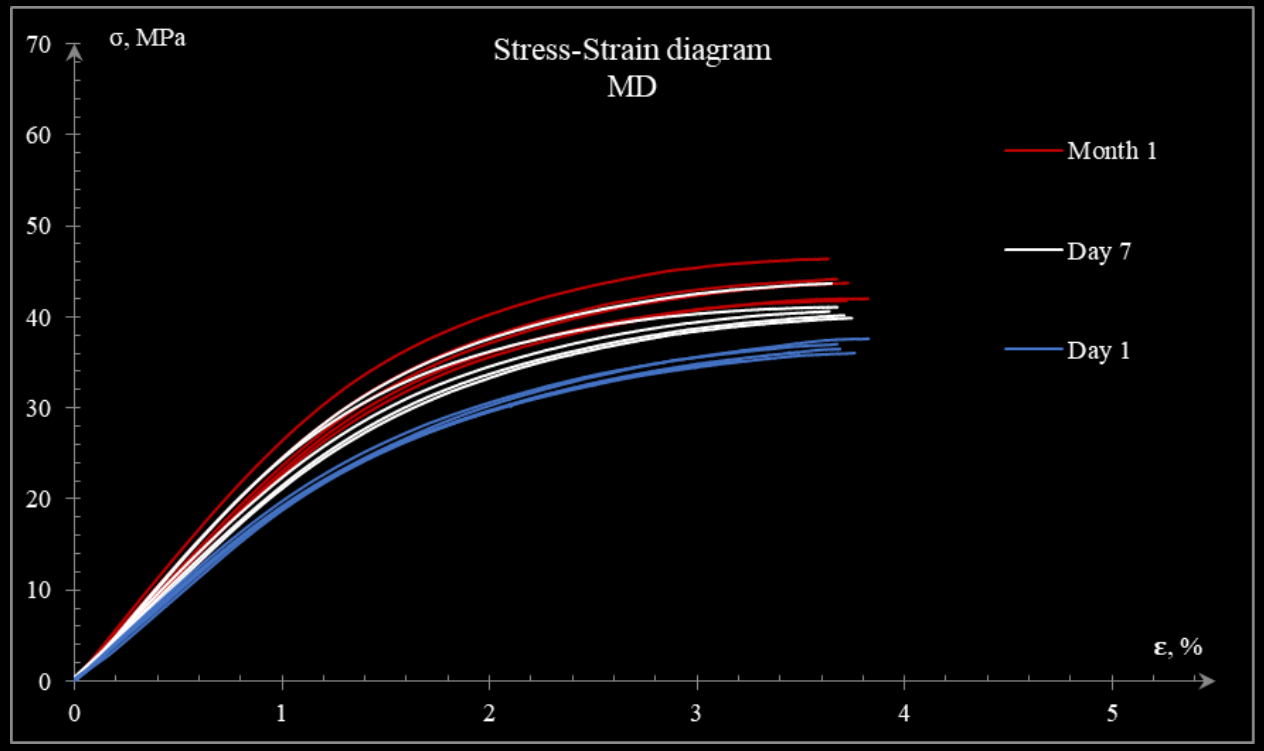

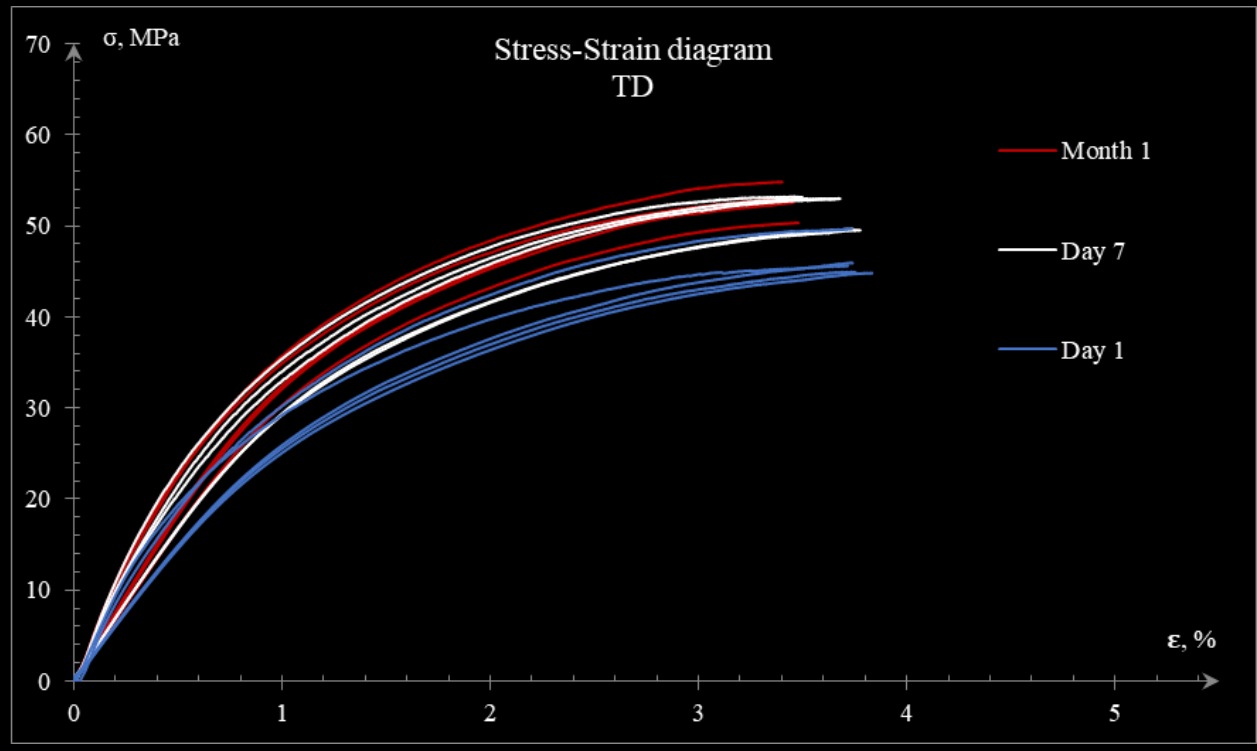

Three-point bending test results

SRPP

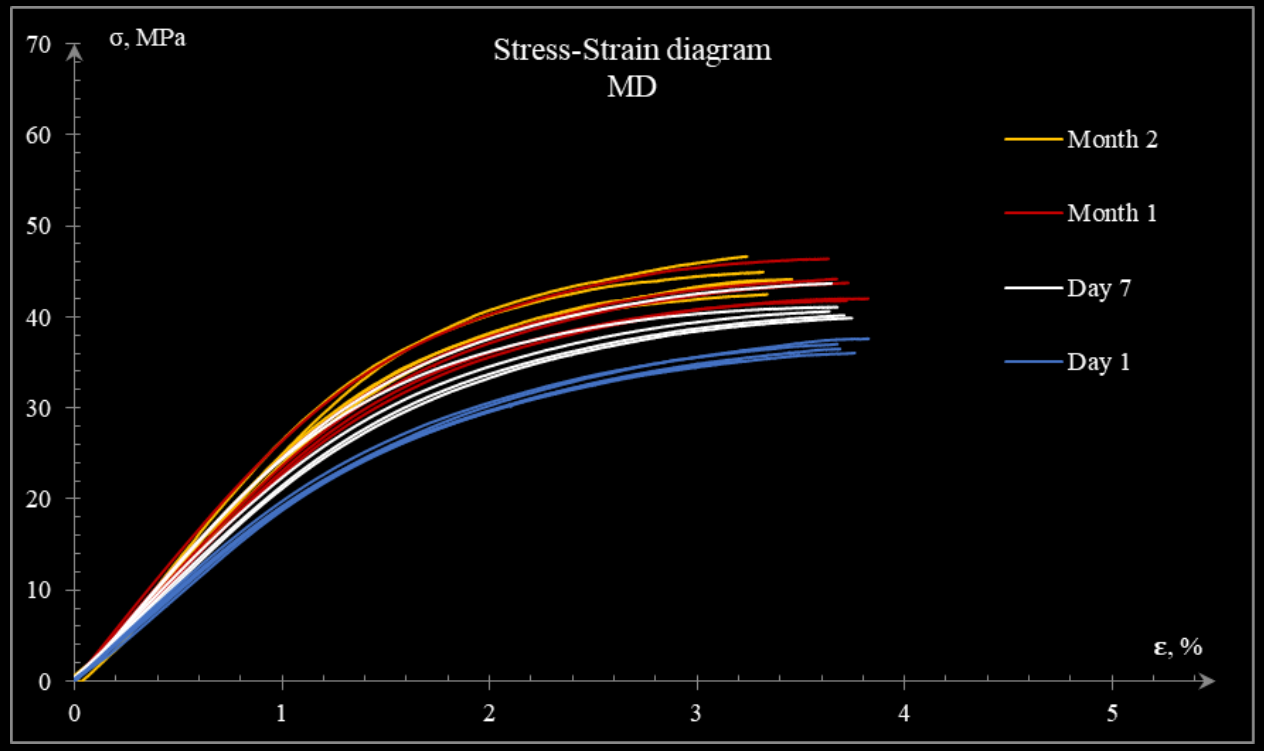

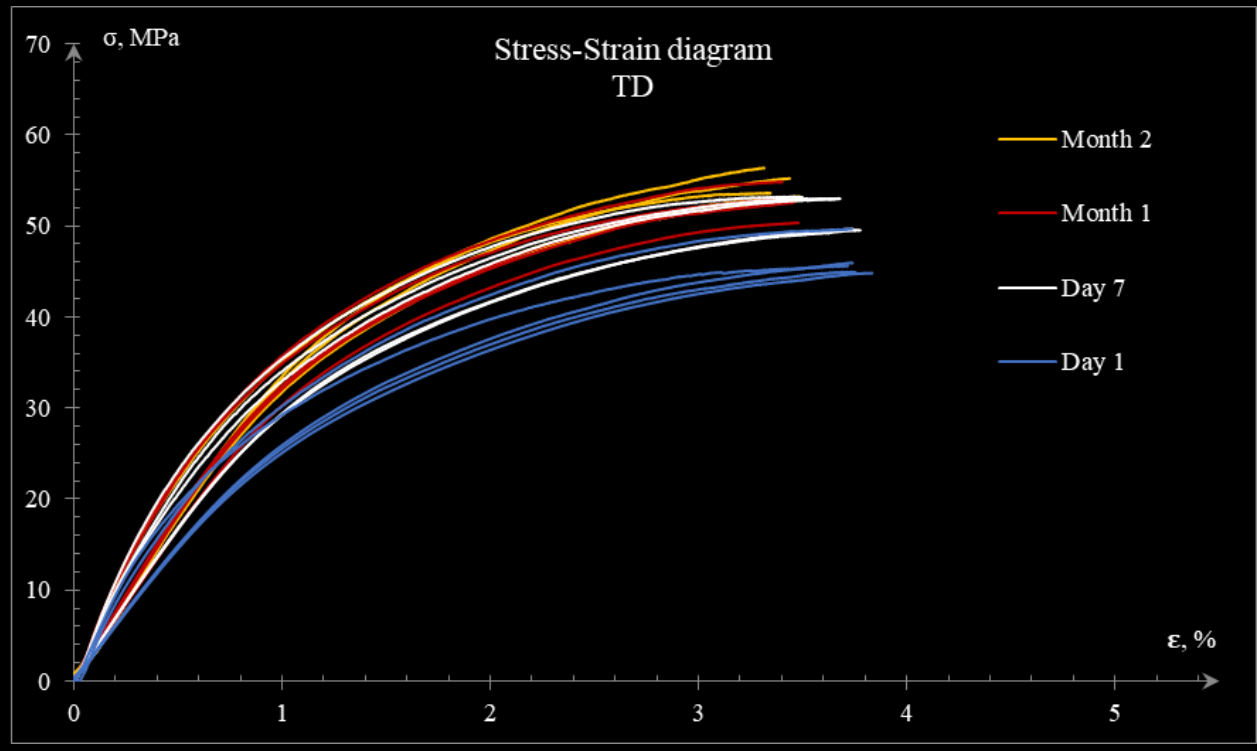

Three-point bending test results

SRPP

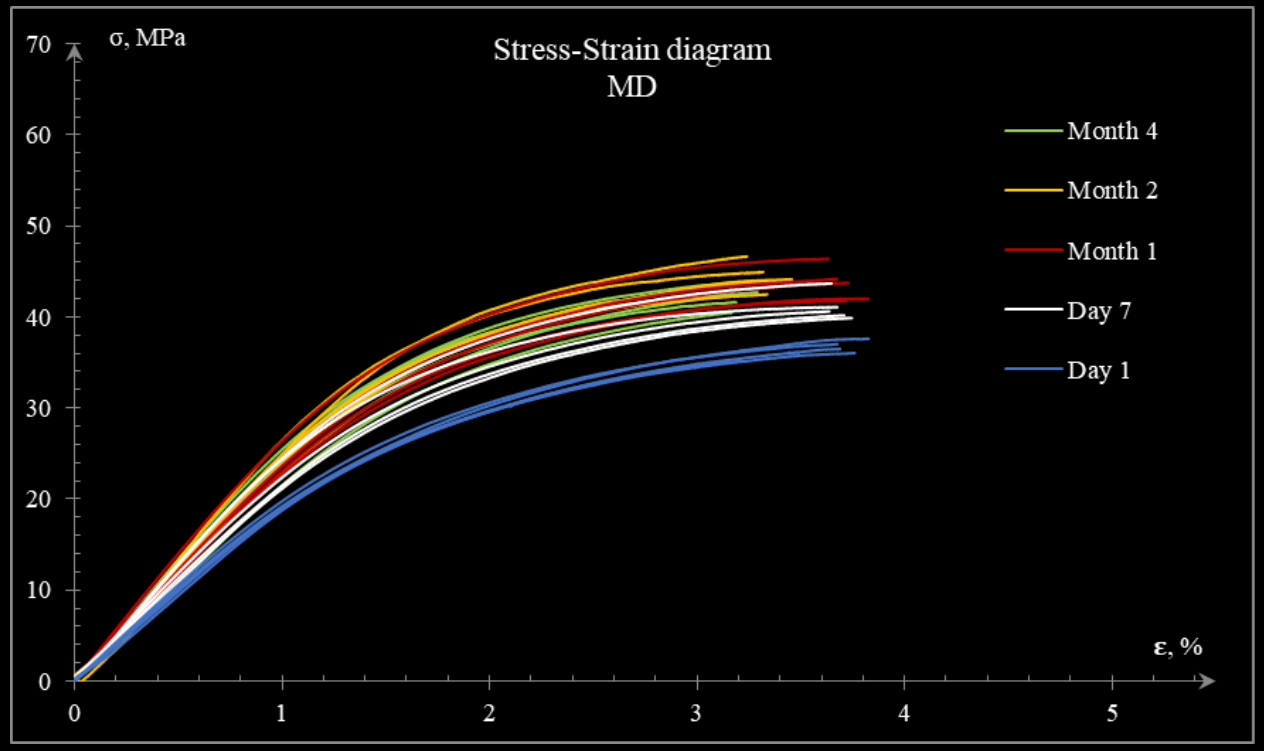

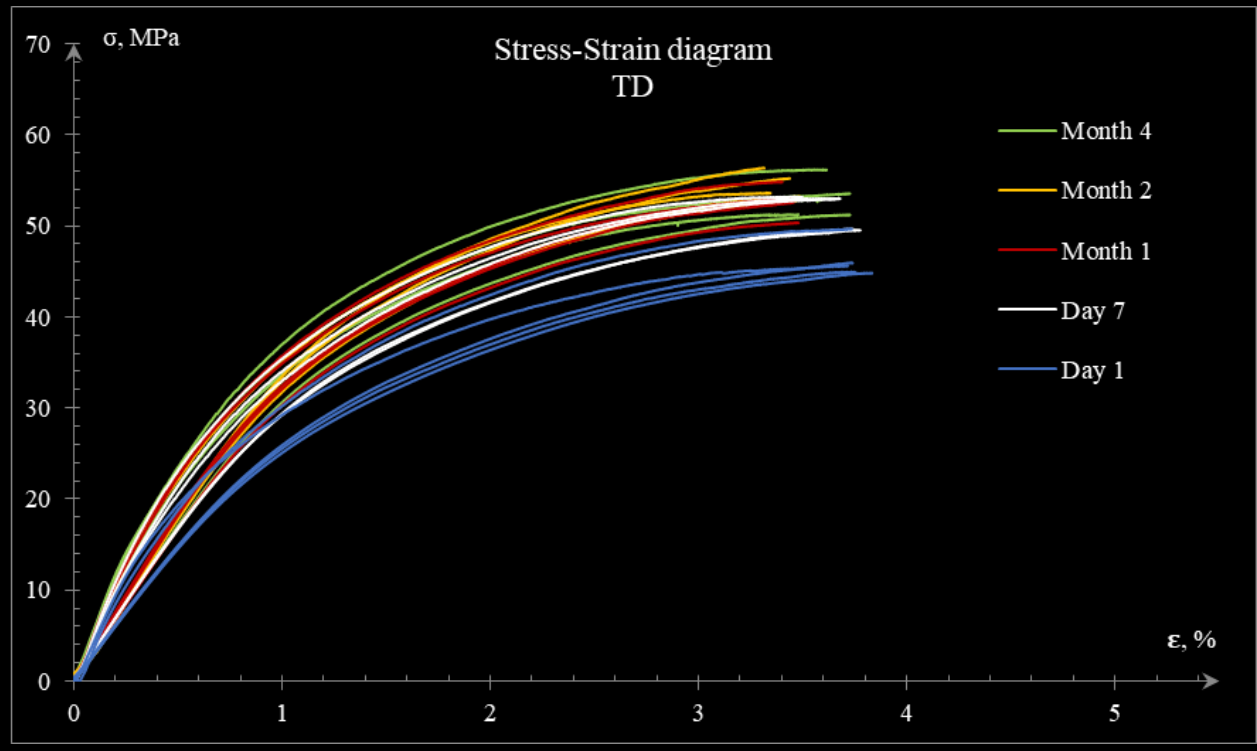

Three-point bending test results

SRPP

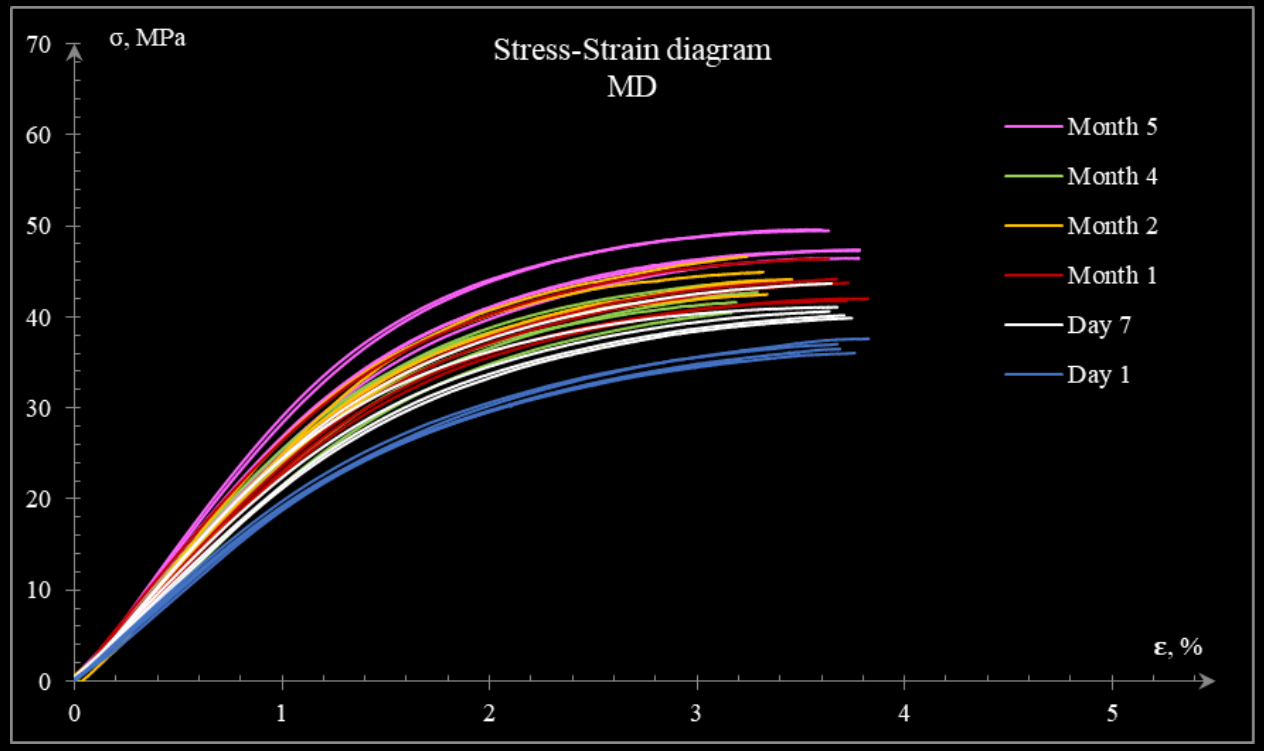

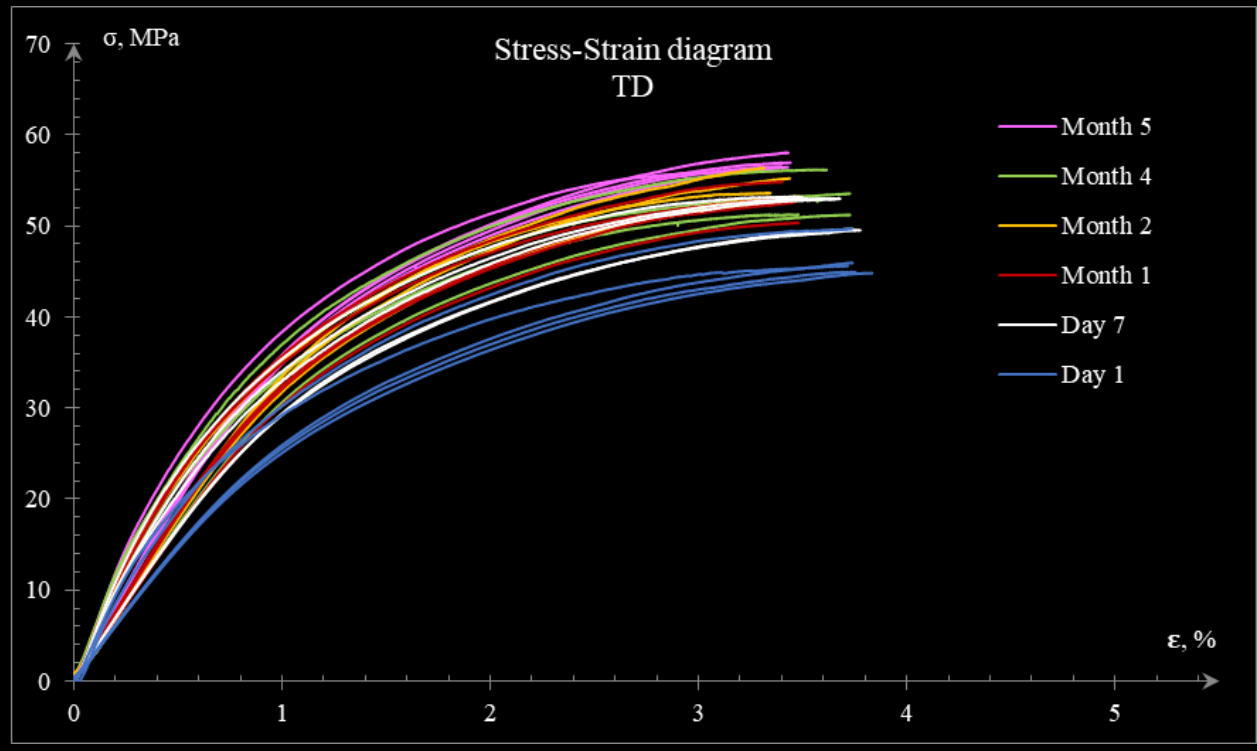

Three-point bending test results

SRPP

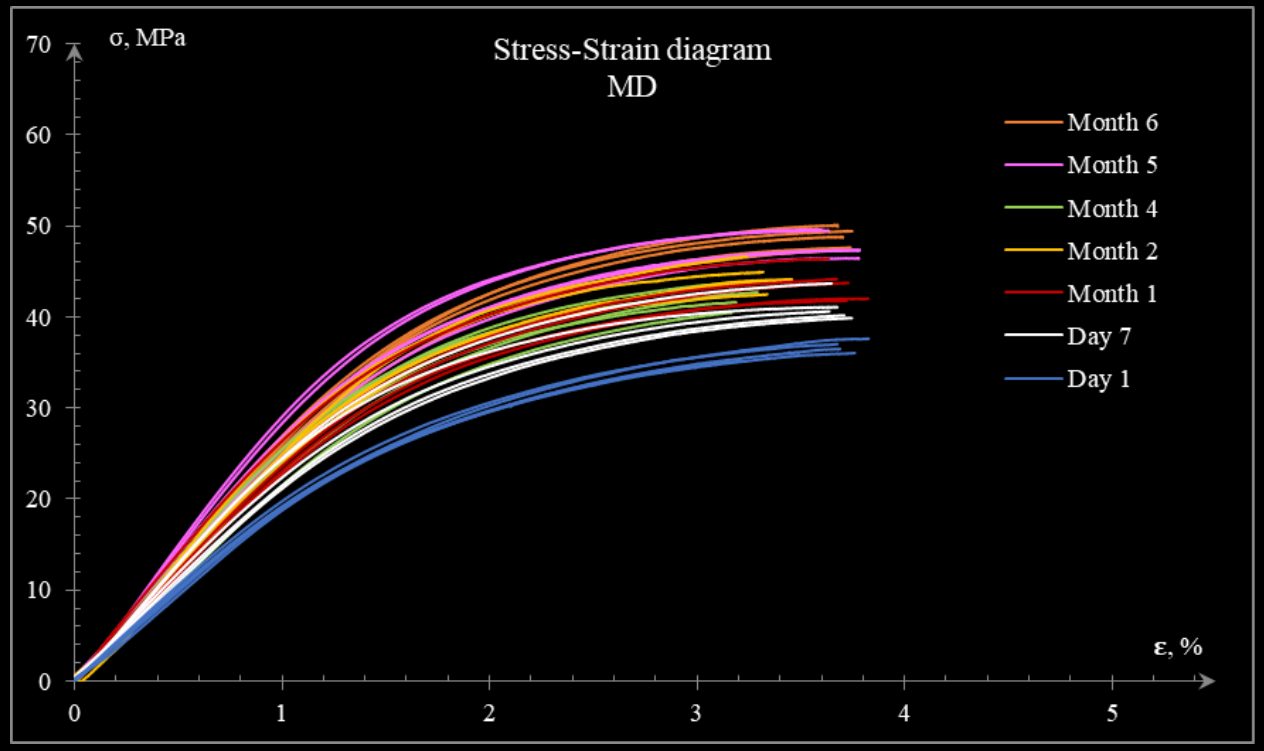

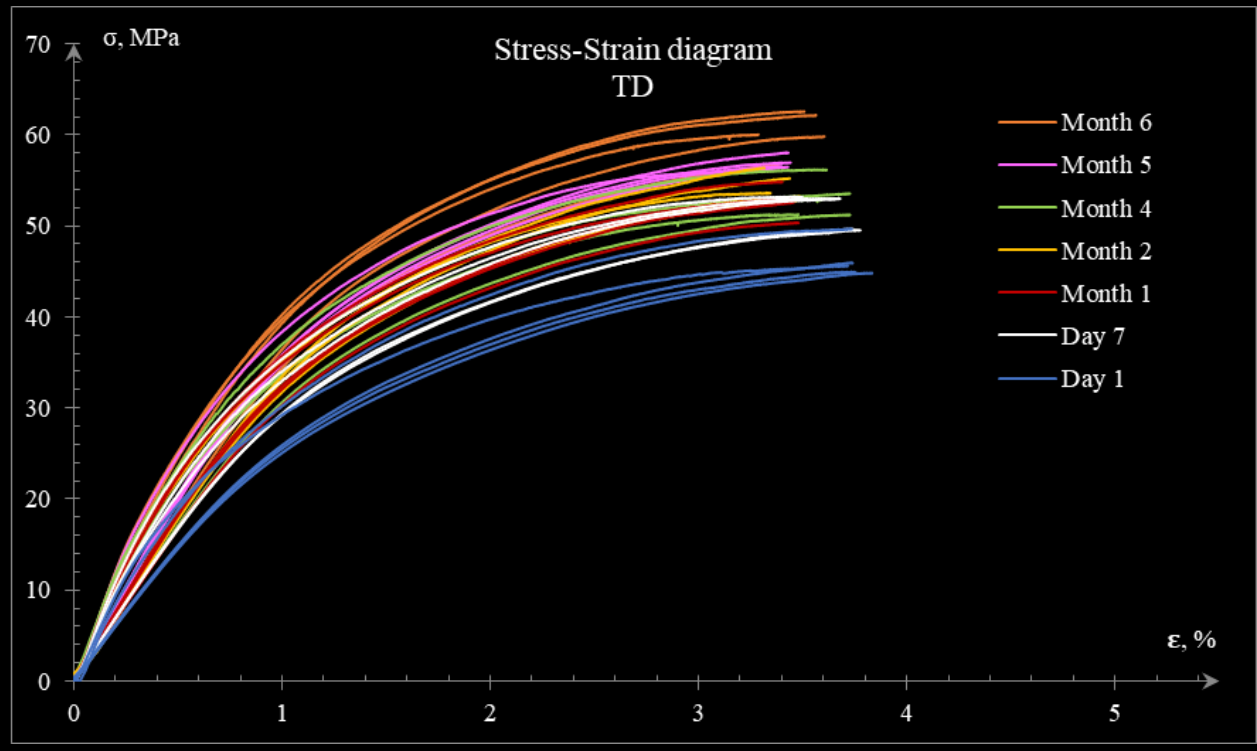

Three-point bending test results

SRPP

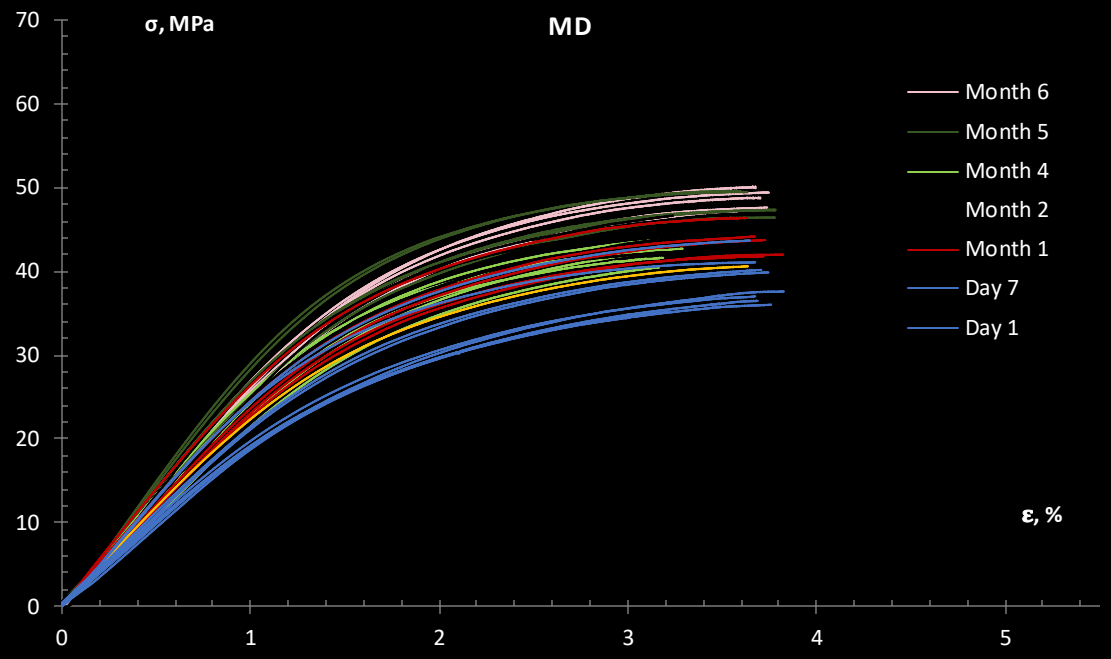

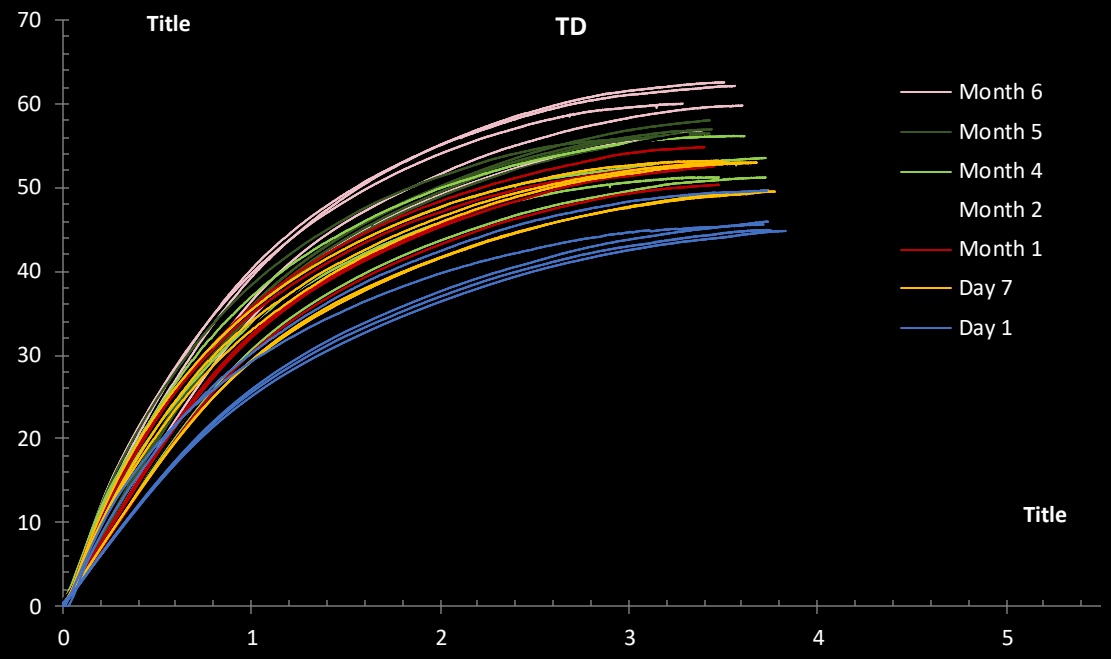

Three-point bending test results

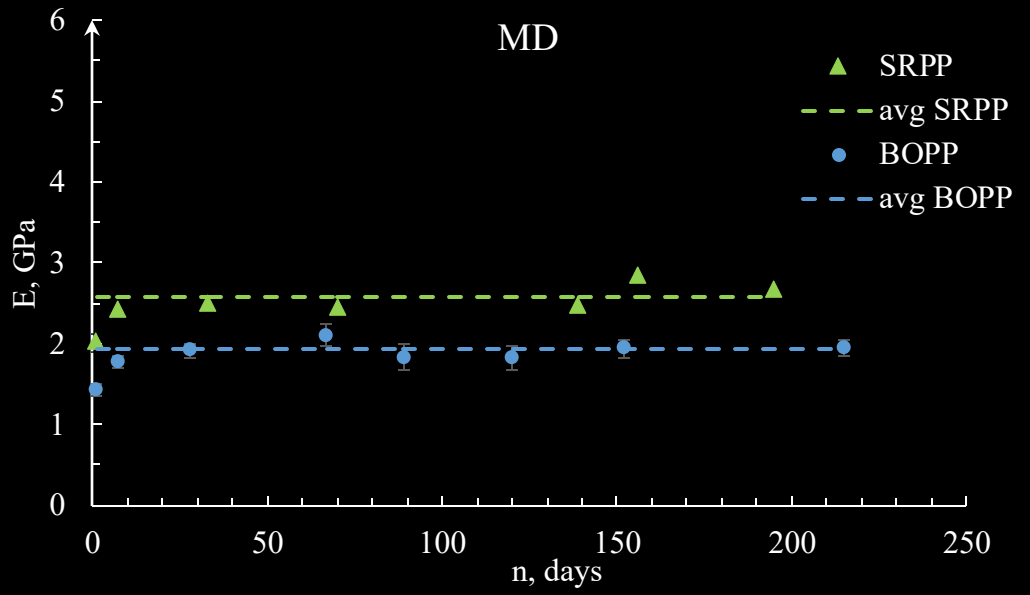

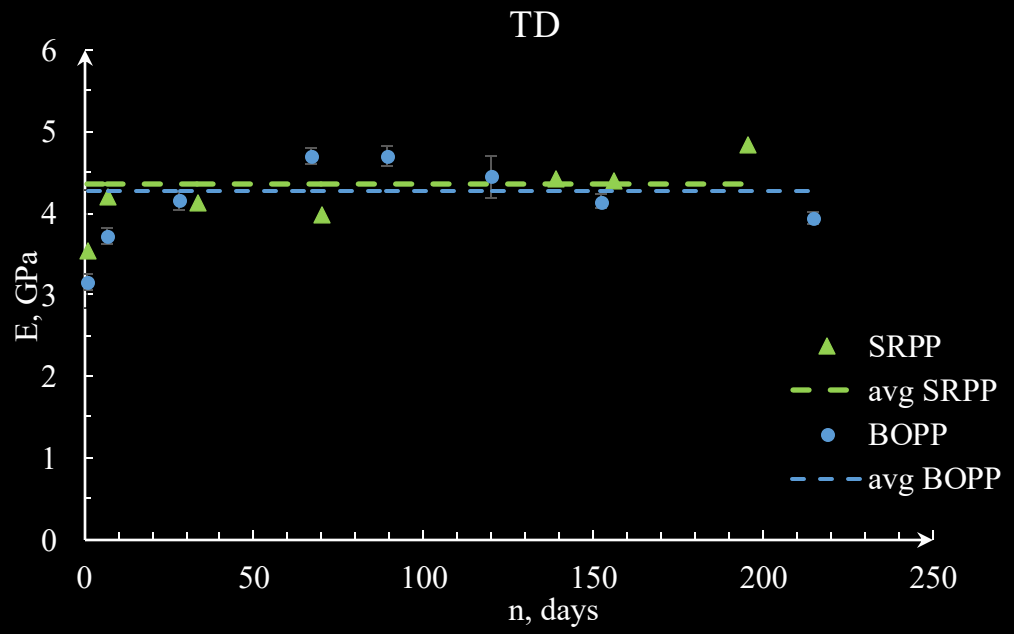

Gaps between timeslots statistically analyzed

BOPP

MD: 34% in 1 months

TD: 32% in 1 months

Stabilization after 1 month

MD = Machine Direction; TD = Transverse Direction

Three-point bending test results

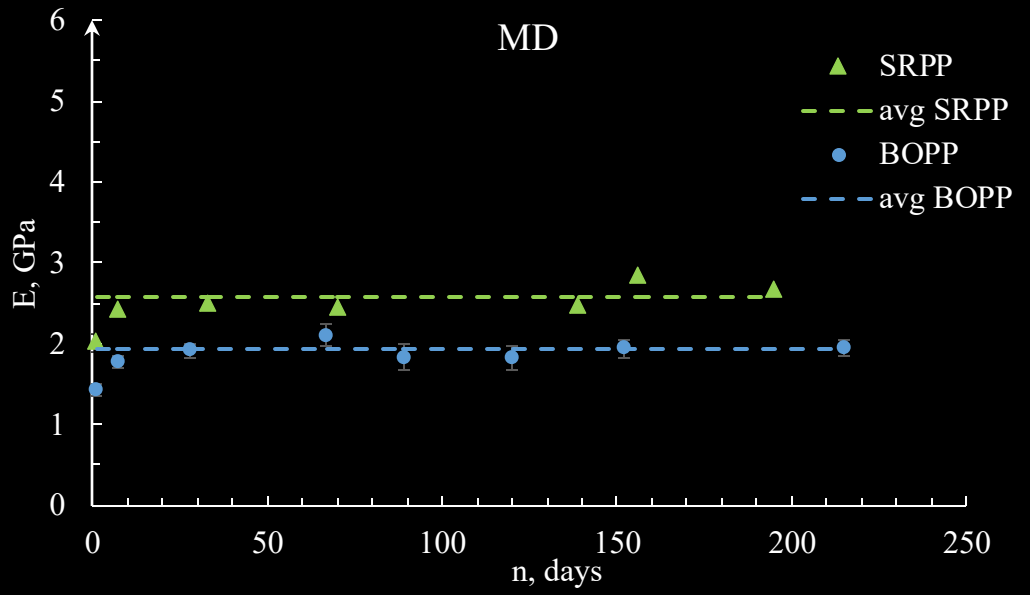

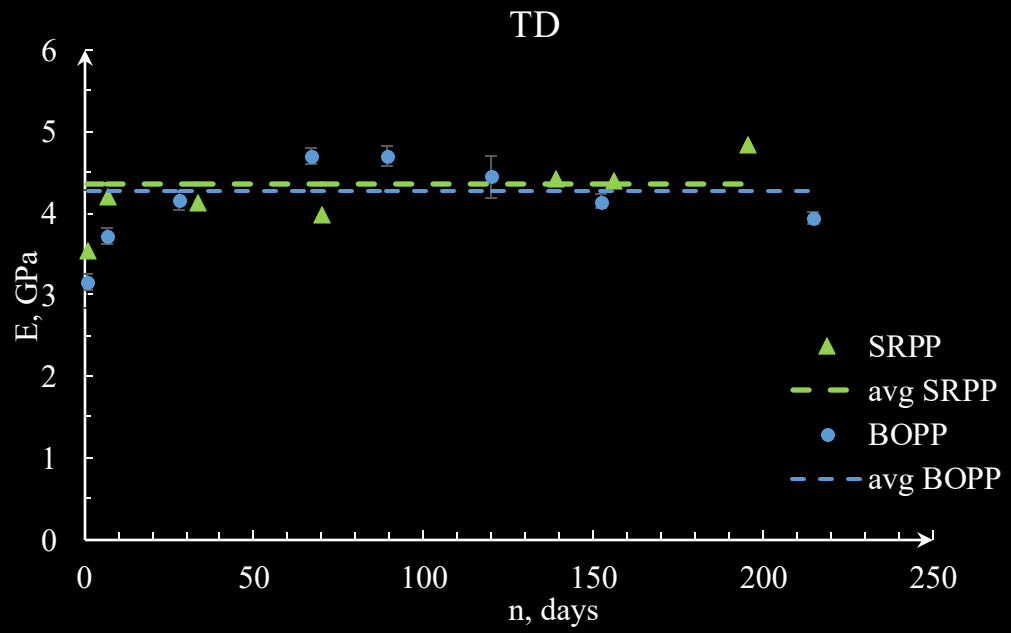

Gaps between timeslots statistically analyzed

BOPP

- MD: 34% in 1 months
- TD: 32% in 1 months
- Stabilization after 1 month

SRPP

- MD: +24% in 1 month
- TD: +16% in 1 month
- Stabilization after 1 month

MD = Machine Direction; TD = Transverse Direction

DSC analysis

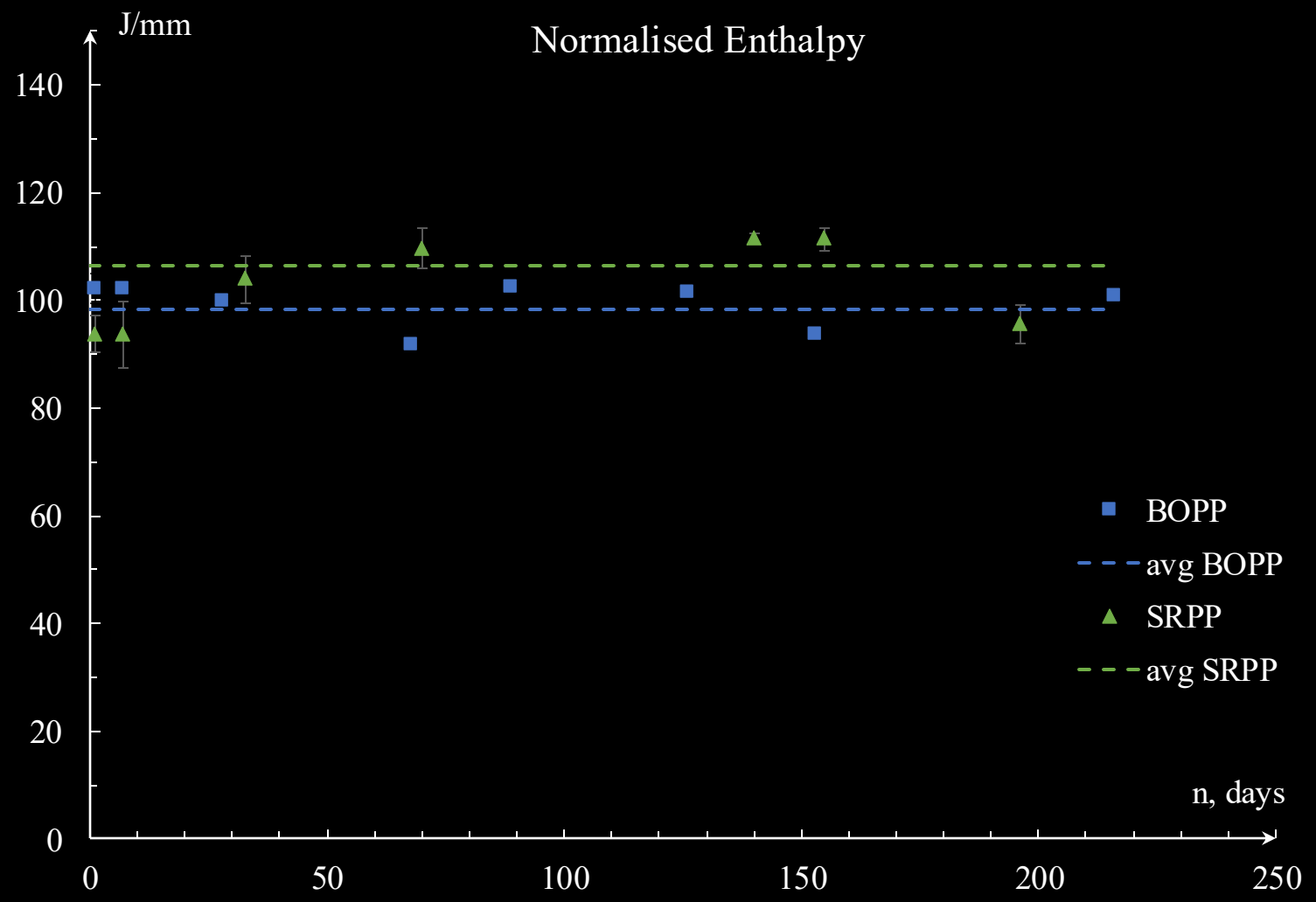

BOPP Variation < 10%

SRPP Variation < 20%

CONCLUSIONS

BOPP

Flexural properties are **TIME-DEPENDENT**

Crystallinity degree is **NOT AFFECTED** by time

Ideal testing time:
AT LEAST AFTER ONE MONTH

SRPP

Flexural properties are **TIME-DEPENDENT**

Crystallinity degree is MORE **AFFECTED** by time

Ideal testing time:
AT LEAST AFTER ONE MONTH

Future work

BOPP

SRPP

Study on the internal stresses and its contribution

TIME-DEPENDENCY PHENOMENA IN BIAXIALLY ORIENTED POLYPROPYLENE and SELF REINFORCED POLYPROPYLENE LAMINATES

Anna Kandinskaia, Arianna Tavano, Pauline Koslowski, Laurens van Audenaerde, Nathan Vanden Bulcke, Ignaas Verpoest, Yentl Swolfs

AGENTSCHAP INNOVEREN & ONDERNEMEN

Samsonite

KU LEUVEN MATERIALS ENGINEERING

Composite Materials Group

ICCM24
24TH INTERNATIONAL CONFERENCE ON COMPOSITE MATERIALS

UNIVERSITÄT BAYREUTH

POLYMER ENGINEERING

ICCM 24 Baltimore, Maryland | 4.-8. August 2025

Understanding Towpreg Manufacturing – Combining Advanced Resin Formulation and Improved Processing Techniques for the Next Generation of Pressure Vessels

Marius Luik, Prof. Dr.-Ing. H. Ruckdäschel | 7.08.2025

Department of Polymer Engineering | Prof. Dr.-Ing. H. Ruckdäschel | polymer-engineering.de

Digitalization for Sustainability

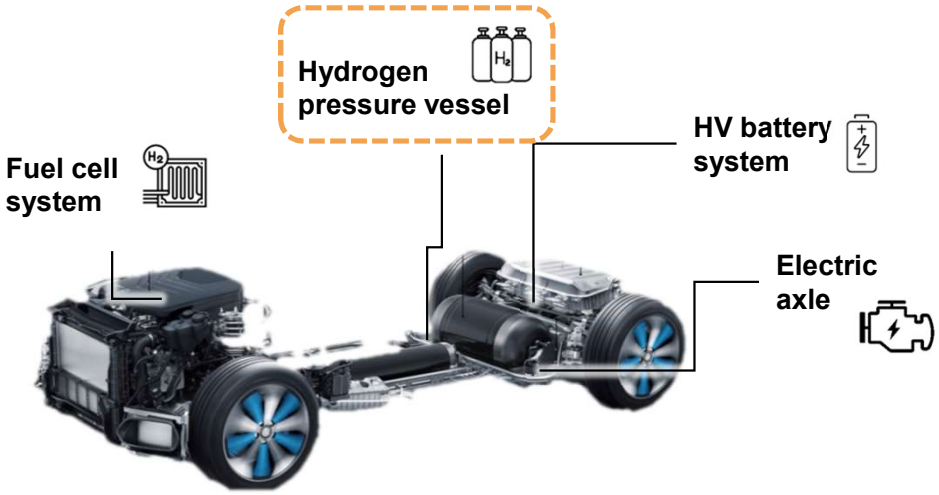

- **Lack of digital predictability** of EV components necessitates validation
- Hardware- and resource-intensive in **conflict with sustainability objectives**

DigiTain

Federal Ministry for Economic Affairs and Energy

Project duration: 1.1.2023-31.12.2025
Total project volume ~ 38 mio Euro
28 Project partners

ARENA2036 · AVL · BMW GROUP · Constellium · DAIMLER TRUCK · DYNA MORE · EDAG · FORWARD ENGINEERING · Fraunhofer EMI · Fraunhofer IWM · GREENING · HEXAGON · INATECH · iPoint · JWS · KIRCHHOFF AUTOMOTIVE · Leibniz-Institut für Verbundwerkstoffe · Mercedes-Benz · SGS · TÜV SAAR · UNIVERSITÄT BAYREUTH · TECHNISCHE UNIVERSITÄT DRESDEN · TECHNISCHE UNIVERSITÄT DARMSTADT · Universität der Bundeswehr München · Universität Stuttgart · VDA · XPLM · ZF · SW

Image: GLC F-Cell, 2018 ©Mercedes-Benz Group

Next generation of hydrogen pressure vessel

Type I Solid metal shell

Type II Metal shell with composite overwrap

Type III Metal liner with composite overwrap

Type IV Thermoplast liner with composite overwrap

HDPE/PA – thermoplastic liner acts as hydrogen barrier

Type V **Linerless** composite shell



Simpler/cheaper manufacturing process



10-20% lighter than type IV vessels



Improved exploitation of **vessel space**

Development of optimized composite for permeation reduction

Manufacturing methods

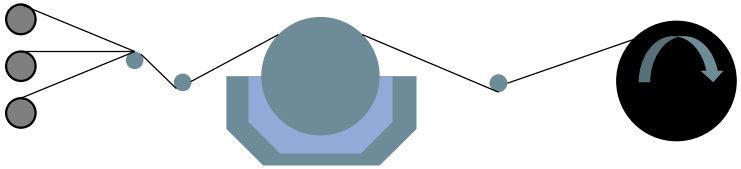

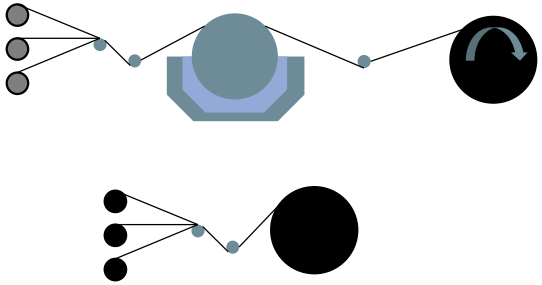

Wet-winding (state of the art)

- **Low viscosity**
- Winding speed up to **60 m/min**
- Variation in FVC



Towpreg winding

- **High viscosity.**
- Winding speed up to **240 m/min**
- Pre-impregnated products allow precise FVC control



Towpreg winding improves process precision significantly

https://www.addcomposites.com/post/filament-winding; download: 06.01.2025

Next generation of hydrogen pressure vessel

Permeability of different polymers at varying temperature:

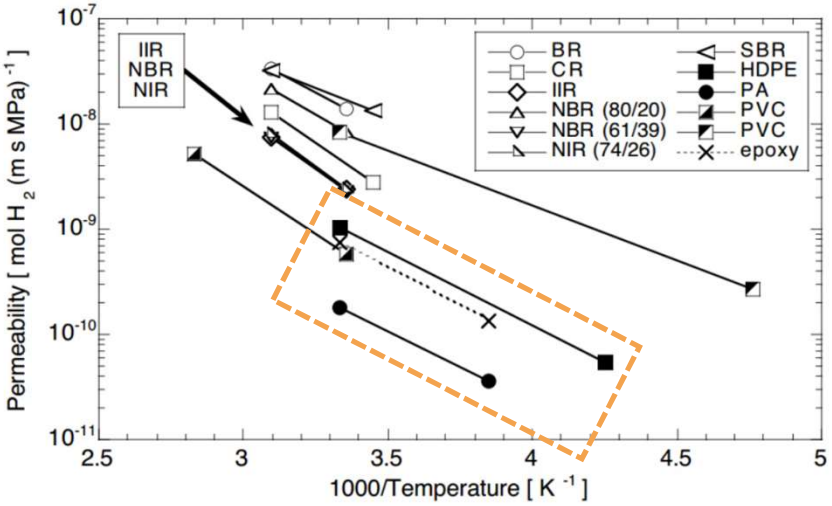

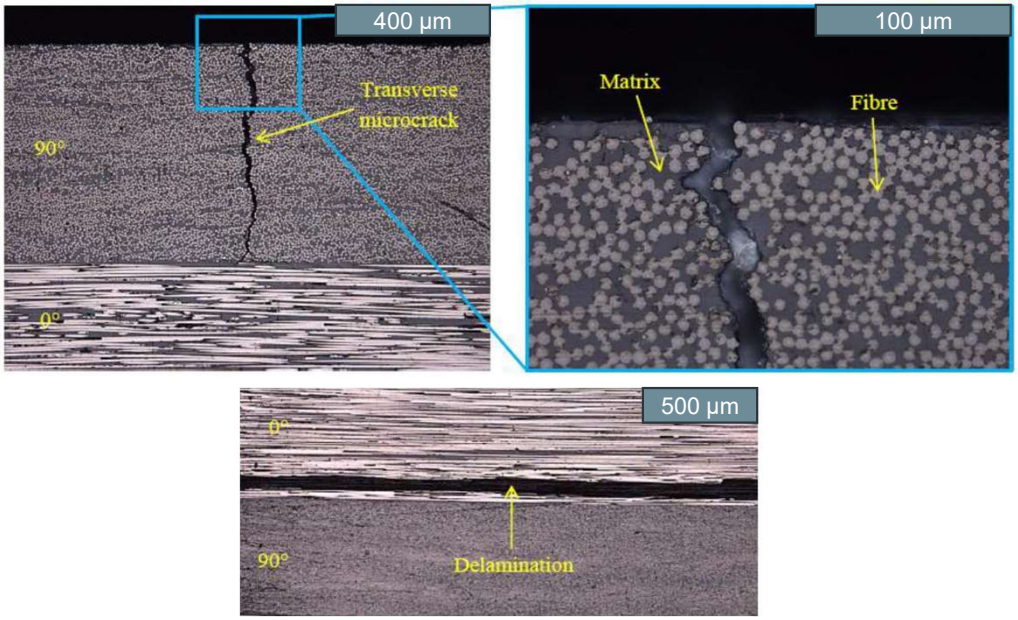

Crack formation in composite leads to permeation pathways – crack initiation and reduction necessary

Polymers for Hydrogen Infrastructure and Vehicle Fuel Systems, Barth **2013**;
Damage and permeability in linerless composite cryogenic tanks, David M. Grogan **2015**

Manufacturing and material challenges

Type V

Challenges:

Cracks in composite due to mechanical/thermal stress might **lead to leakage**

Optimisation of manufacturing to **avoid defects**

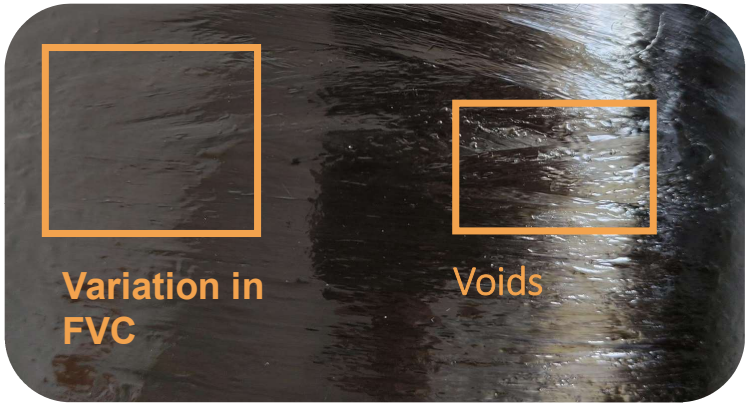

wet-wound structure

- How can we improve the composite material to minimize crack formation/propagation?
- How can we improve the manufacturing process to reduce irregularities and defects?

OVERVIEW



Development of Type V resin systems for pressure vessels



Optimizing process control for Towpreg manufacturing



Mechanical testing of filament wound composites

OVERVIEW



Development of Type V resin systems for pressure vessels

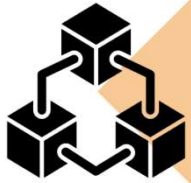

Optimizing process control for Towpreg manufacturing



Mechanical testing of filament wound composites

Tensile properties of resin systems

2 Formulations:

- Latent hardener + Curing agent
- Similar viscosity profile

Olin EPOXY

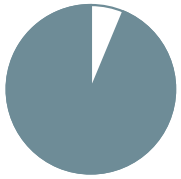

Digitow-1:
$DGEBA_{(low\ visc.)}$:$DGEBA_{(high\ visc.)}$
T_G: 140 °C



Digitow-2:
50:50 $DGEBA_{(low\ visc.)}$:Novolak
T_G: 160 °C

Toughening agent:

- Polysiloxane block copolymer (**BCP**)

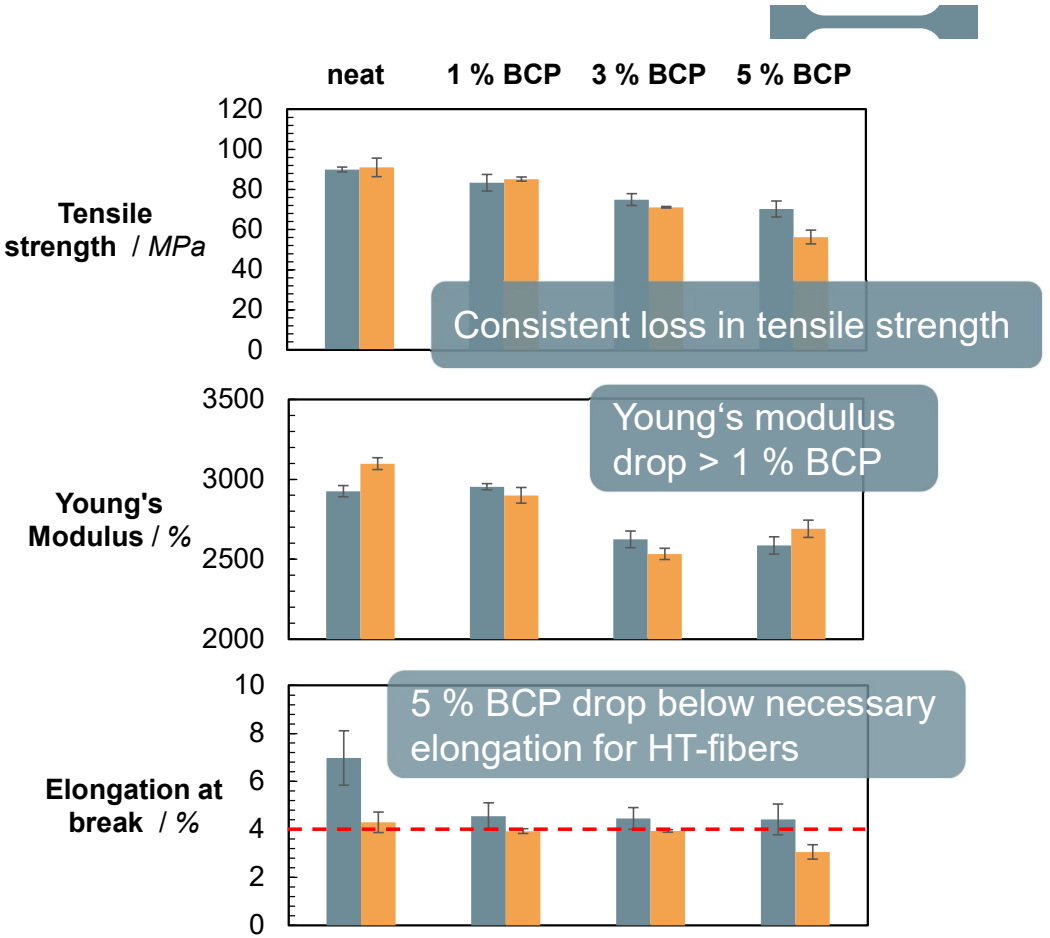

T_G: DSC 10 K/min, N2, point of inflection; Tensile properties: ISO-527/2, cast moulded

Resin fracture mechanics

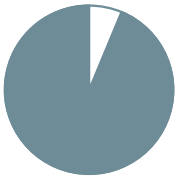

Digitow-1 – medium T_G
T_G: 140 °C



Digitow-2 – high T_G
T_G: 160 °C

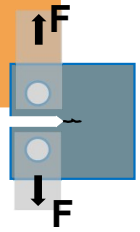

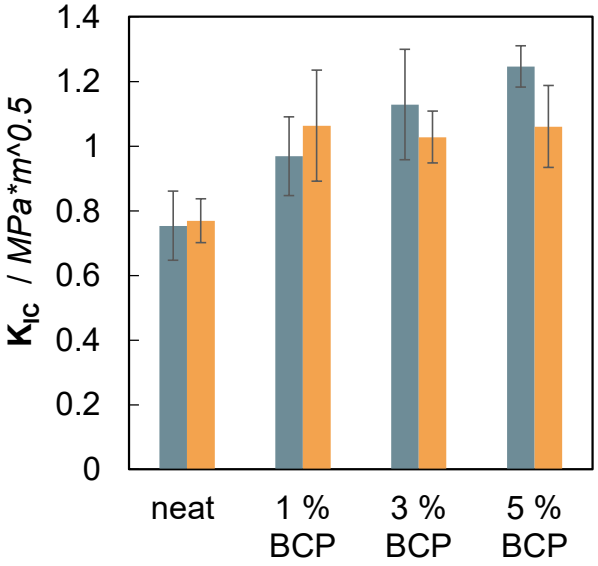

- Comparable K_{IC}
- Plateau for Digitow-2

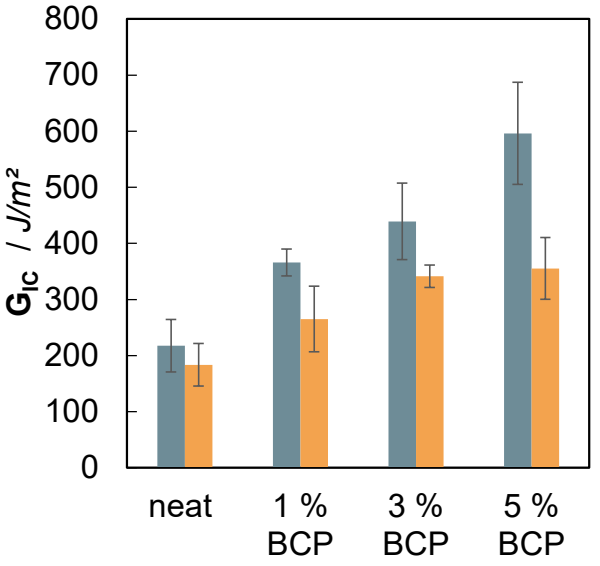

G_{IC} – benefits from higher BCP concentrations

- More ductile resin allows significantly higher toughening – dispite minor **E** differences
- 3 % BCP sweet spot between mechanical + fracture mechanical properties

Fatigue crack propagation

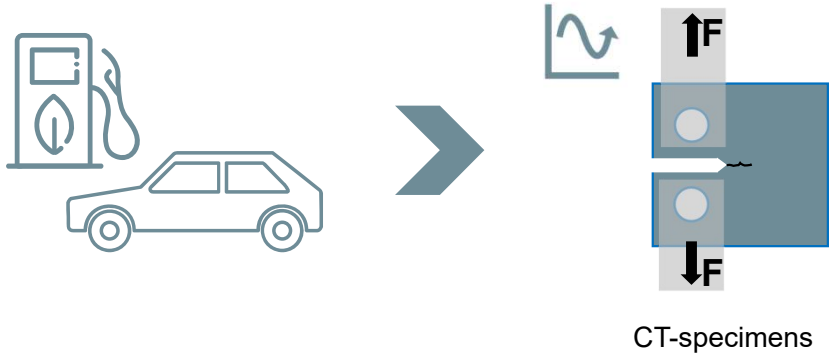

CT-specimens

Crack propagation

- ASTM E647-2
- Curves from single specimen
- Following crack propagation through mechanical signal

Potential synergistic effects

combining BCP + SiO_2-NP ?

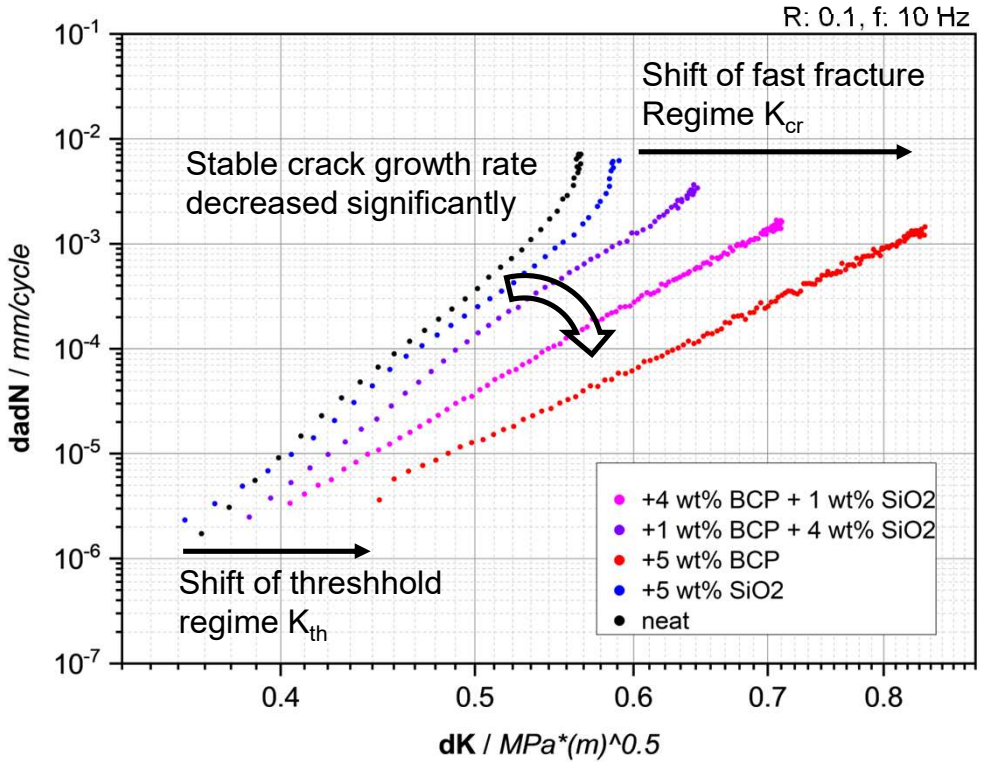

BCP decreases crack growth significantly up to 5 wt%

Overview



Development of Type V resin systems for pressure vessels



Optimizing process control for Towpreg manufacturing



Mechanical testing of filament wound composites

Modifications of the winder unit – SC filament winder (ETC)

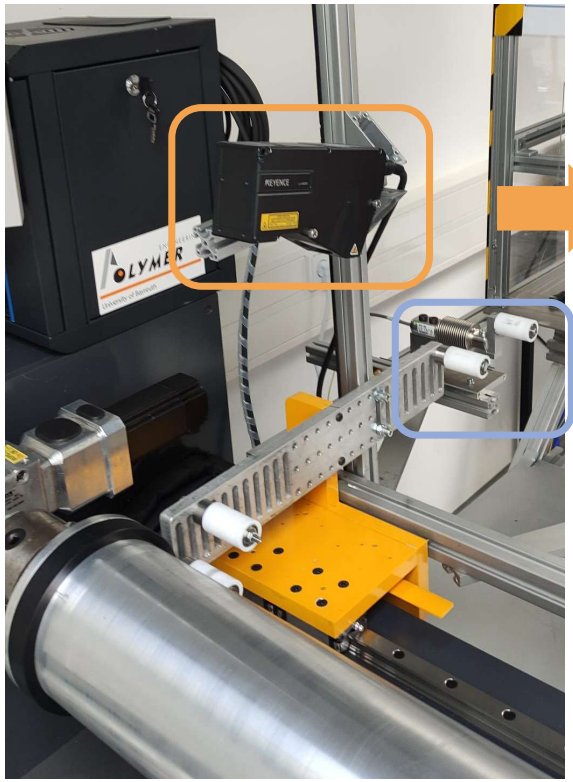

Width measurement

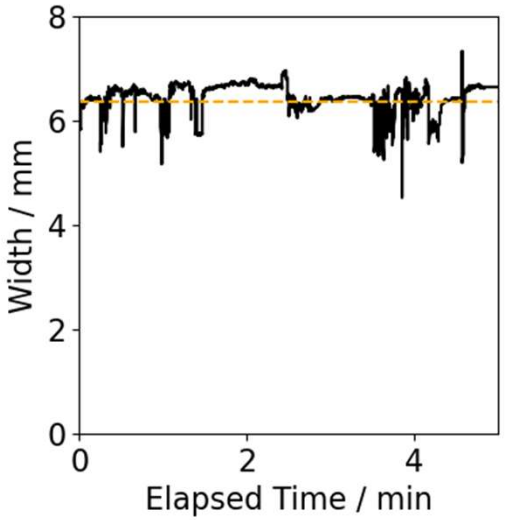

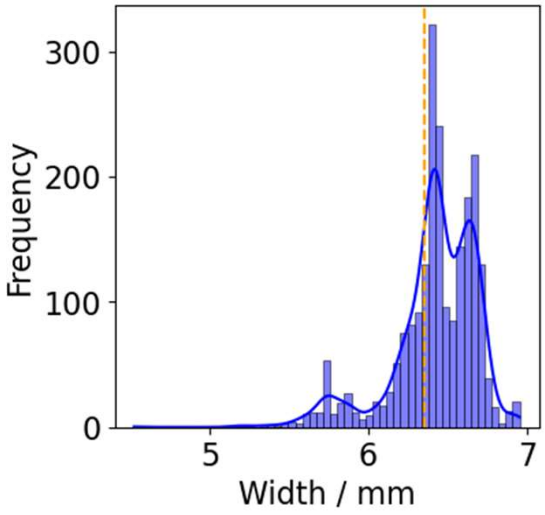

Fiber tension measurement

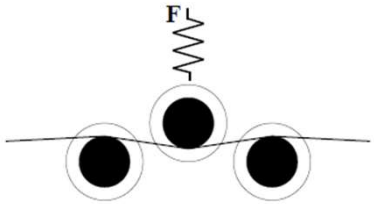

Fiber tension up to
100 N / Roving measurable

Consistent unwinding process – consistent impregnation process

Modifications of the winder unit

Impregnation

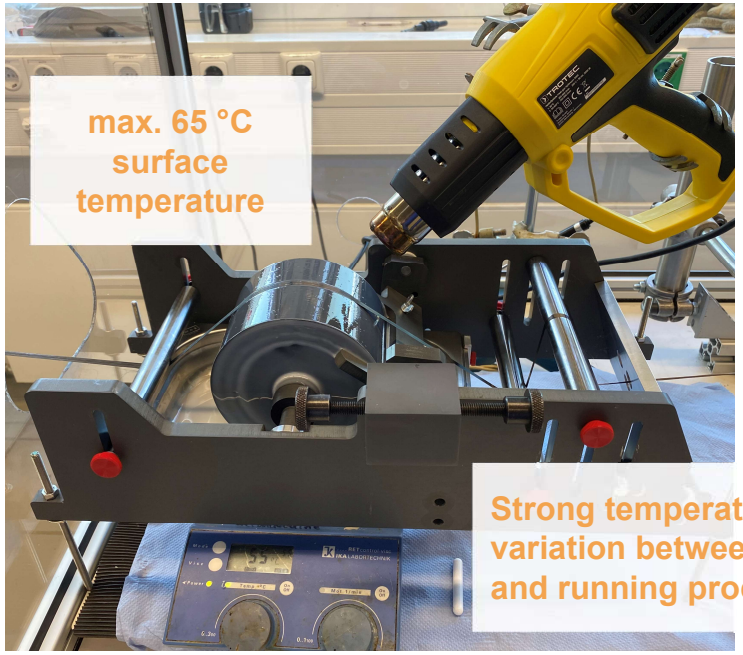

Low heat transfer



Constant surface temperature of up to 95 °C

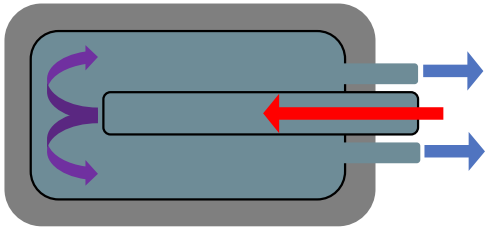

More stable and precise parameter tuning possible

How to manufacture Towpregs?

Winding tension

- Low roving tension < 1350 cN
- Tension too high:

Rovings “merge”

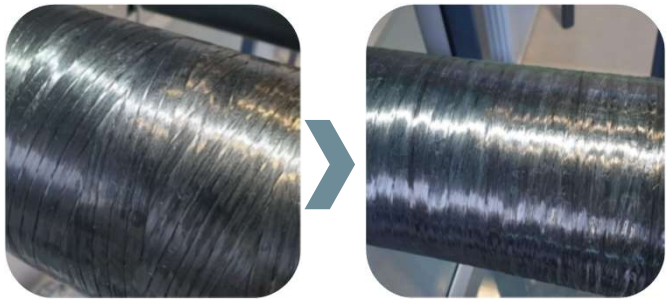

After winding | 2 h @ RT

Impregnation temperature

- Low enough to allow consistent impregnaton
- High enough to avoid de-wetting

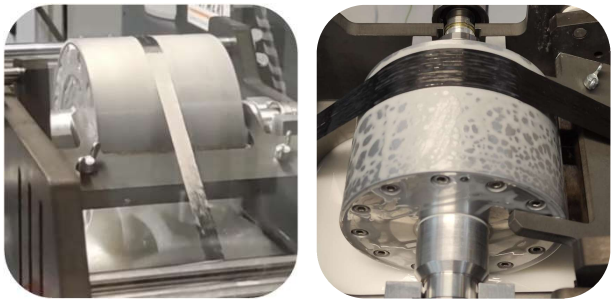

70 °C | 85 °C

Winding pattern

- Low winding angles < 70 ° show increase in fiber rupture due to uptake of underlaying filaments

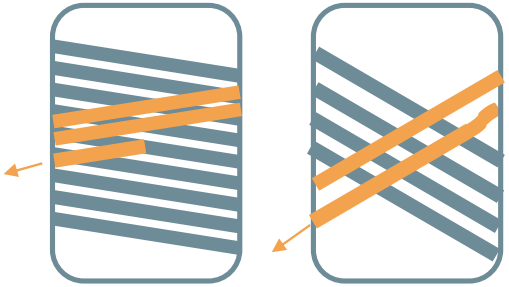

Sweet spots in fiber tension and impregnation temperature to be found!

Overview



Development of Type V resin systems for pressure vessels

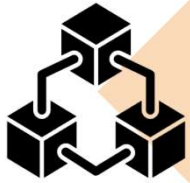

Optimizing process control for Towpreg manufacturing



Mechanical testing of filament wound composites

Mechanical testing of composite specimens

NOL-split disk (tensile) testing

Naval Ordnance Laboratory,
White Oak Maryland





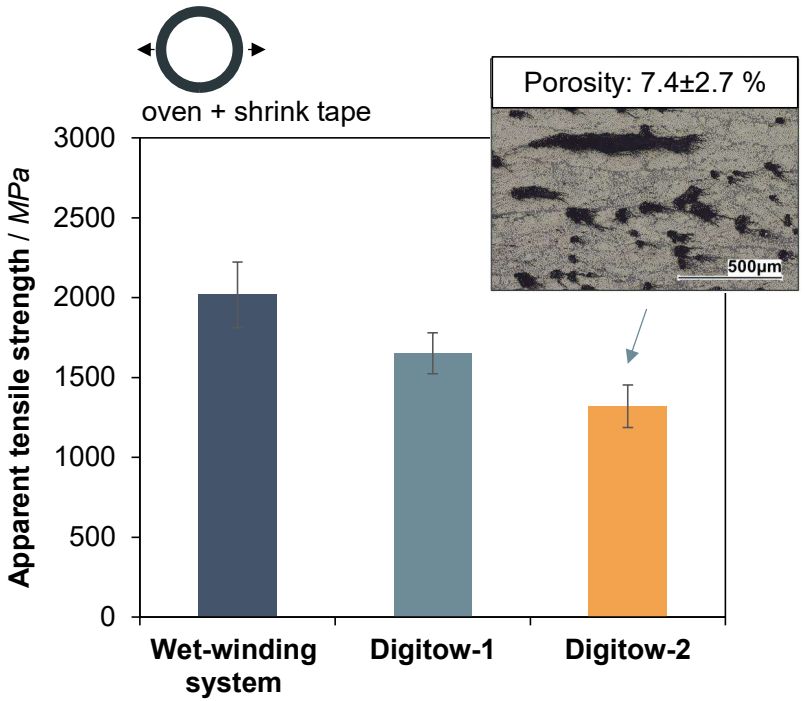

Optimization of winding parameters necessary

ISO-527/5 – 0°

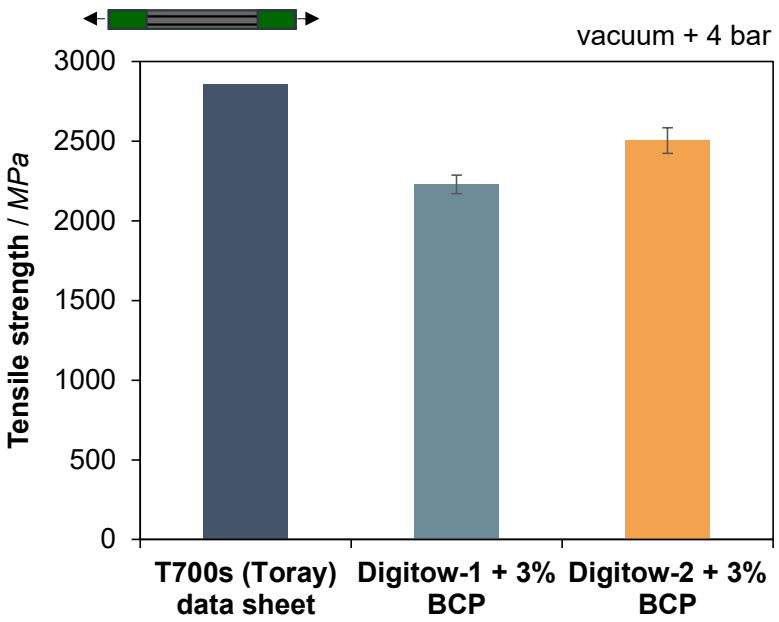

Digitow-2 reaches expected 0°-strength

 Szpoganicz 2025; Reference resin: Araldite® LY 556/Aradur® 917-1/Accelerator 960-1; FVC: Toray T700s: 60 % DT-1: 61 % DT-2: 67 %

Summary

- Successful toughening of Towpreg resin systems ✓
- Impregnation process successfully monitored ✓
- Mechanical testing of filament wound structures successful ✓

Outlook

? Transfer of fracture toughness to composite level

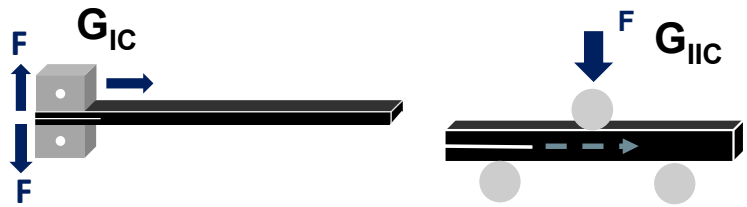

? Can the optimization of processing parameters improve the mechanical performance

Questions?



Contact:

Marius Luik, M.Sc.
Composites Group

University of Bayreuth
Department of Polymer Engineering
Universitätsstr. 30
95447 Bayreuth
Phone: +49 (921) 55 - 7564
Mail: marius.luik@uni-bayreuth.de

Chair: *Prof. Dr.-Ing. Holger Ruckdäschel*
http://www.polymer-engineering.de

Project:

Digitain - FKZ: 19S22006Q

Special thanks to:

Federal ministry for economic affairs and energy

For the financial support

Olin Corporation for the supply of resin

Funded by the European Union
NextGenerationEU

Supported by:
Federal Ministry for Economic Affairs and Energy
on the basis of a decision by the German Bundestag

ICCM24
AUGUST 4-8, 2025
BALTIMORE CONVENTION CENTER
BALTIMORE, MARYLAND, USA

No Technical Paper Submission for:

Sagar Patil

EXFOLIATION AND DISPERSION OF MXENE IN EPOXY RESIN USING DISPERSING AGENTS AND THREE-ROLL MILLING

Kristina Zukiene, Daiva Milasiene, Vladimir Spacek, and Daiva Zeleniakiene

MXene. Structure and Properties

- MXenes, a rapidly emerging class of 2D transition metal carbides, nitrides, and carbonitrides, possess a unique layered structure.
- Their outstanding electrical conductivity, large surface area and controllable surface chemistry make them ideal for the production of advanced composites.

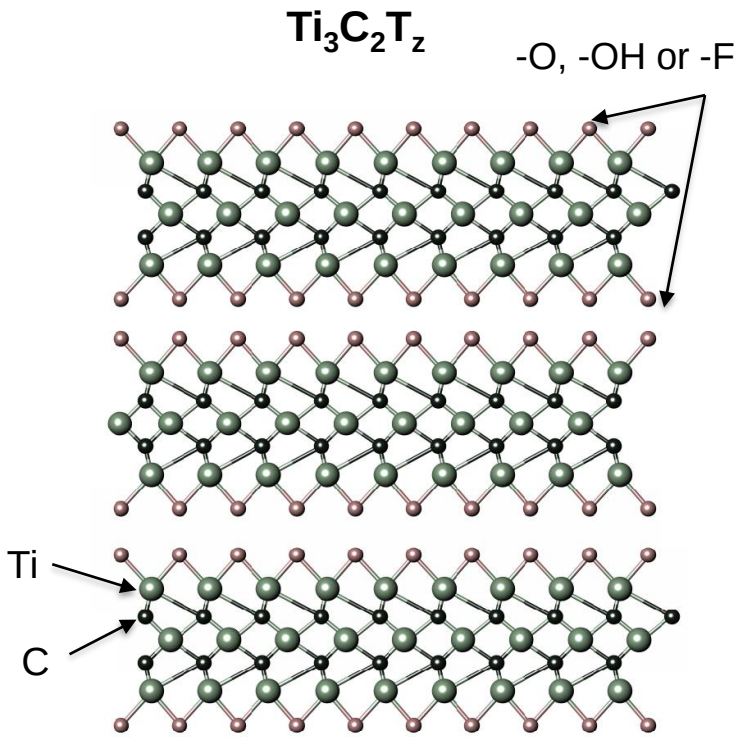

Overcoming Dispersion Challenges in Epoxy

Polarity Mismatch

Polar functional groups hinder dispersion of MXene in polymer matrices, leading to agglomeration and limiting broader application.

Dispersion-driven performance

Insufficient dispersion limits performance in advanced composites (e.g., EMI shielding, electrical conductivity).

Need for effective methods to achieve homogeneous dispersion.

Aim

- To identify the most effective dispersant for achieving homogeneous dispersion of $Ti_3C_2T_x$ MXene powder in an epoxy resin matrix, and to evaluate the performance of three-roll milling techniques in facilitating uniform MXene distribution.

$Ti_3C_2T_x$

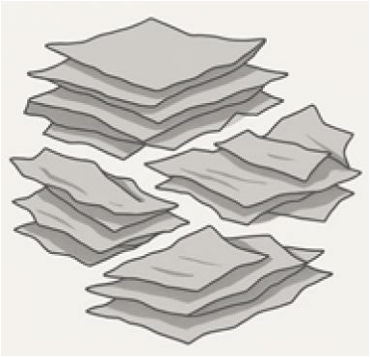

Dispersant

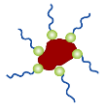

Three-Roll Milling



Strategies for Enhanced Dispersion

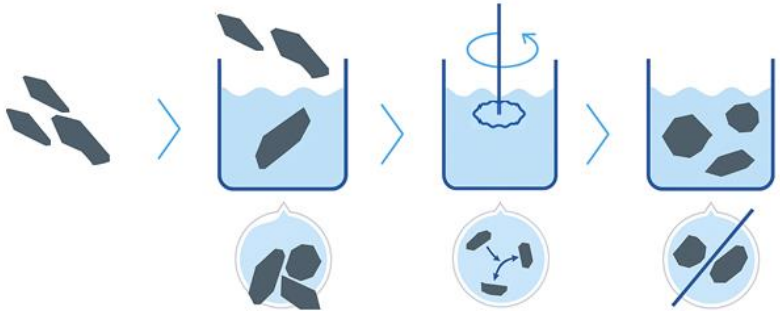

Dispersing Agents

Surfactants and copolymers reduce surface tension and provide steric or electrostatic repulsion, preventing MXene aggregation.



Three-Roll Milling

Applying high shear forces effectively exfoliates and disperses 2D nanoparticles within the polymer matrix.

Materials

- **MXene $Ti_3C_2T_x$** (Laizhou Kai Kai Ceramic Materials Co., Ltd, Shandong Province, China)
- **CHS-EPOXY® 520 Bisphenol-A-based epoxy resin** (Spolchemie Company, Czech Republic)
- **Curing agent - Jeffamine D230:Jeffamine D2000 4:1** (Huntsman Corporation, The Woodlands, TX, USA)
- **Dispersants - DISPERBYK-180 and BYK-9076** (BYK-Chemie GmbH, Wesel, Germany)

Introducing Steric Dispersing Agents

- **DISPERBYK-180** is a hydroxy-functional carboxylic acid ester with particles-affinic groups.
- **DISPERBYK-180** deflocculates particles by means of steric stabilization. As a result of the small particle sizes can be achieved.

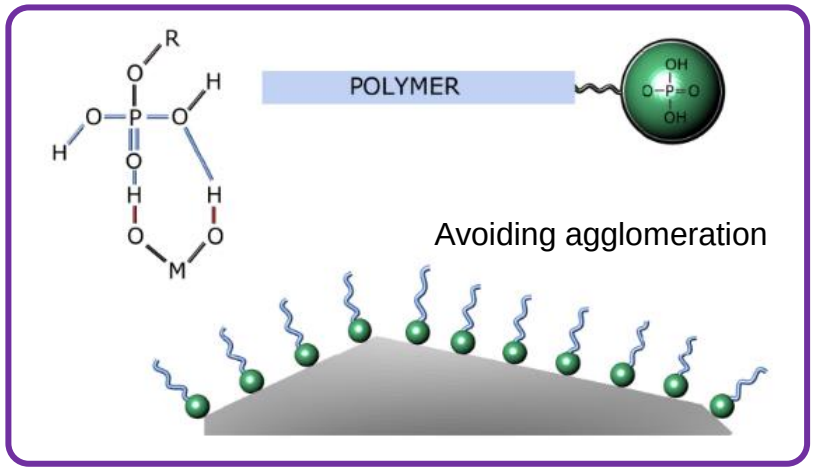

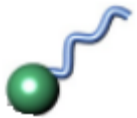

Acidic particle-affinic group

Solvent/resin-affinic part

Introducing Steric Dispersing Agents

- **BYK-9076** is an alkylammonium salt of a high molecular weight copolymer containing amine groups and carboxylic functionalities.
- **BYK-9076** separate particles by means of **steric stabilization**. It also generates a uniform electrical charge in the particles (**electrostatic stabilization**). The resulting repulsion effect and the steric stabilization prevent any aggregation.

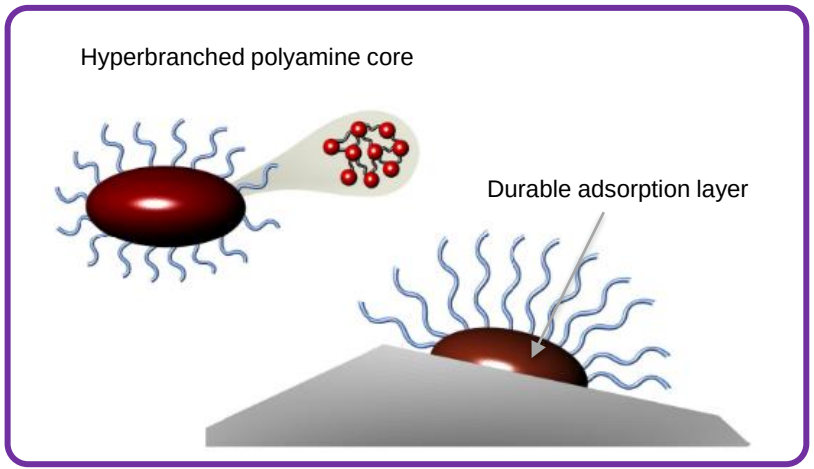

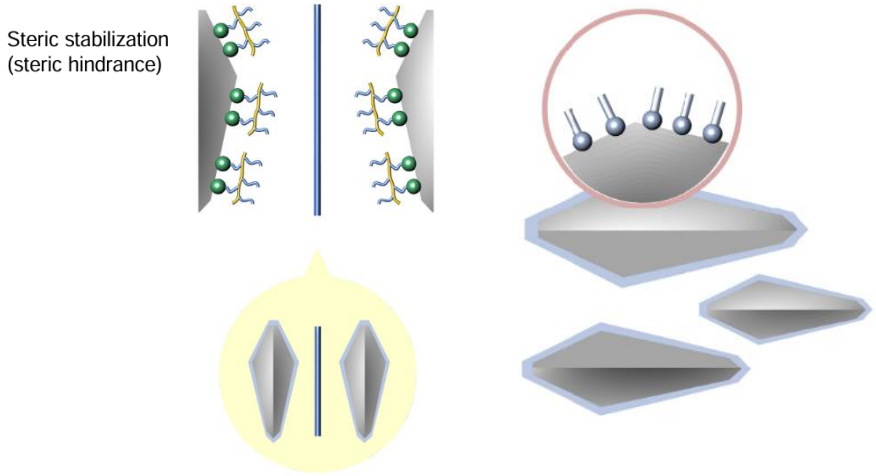

Preparation of MXene/Epoxy Films

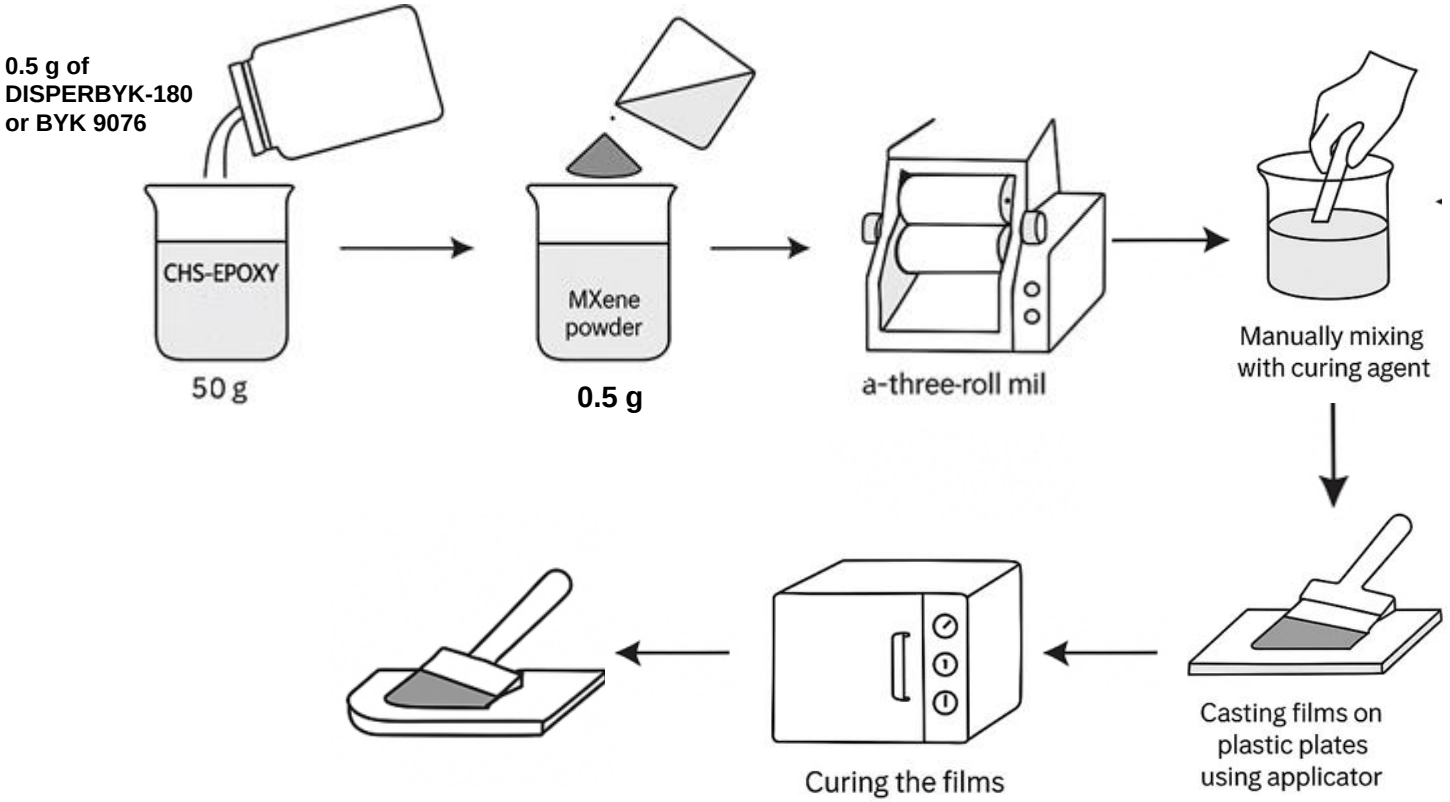

MXene Distribution in Epoxy Matrix

Without Dispersant

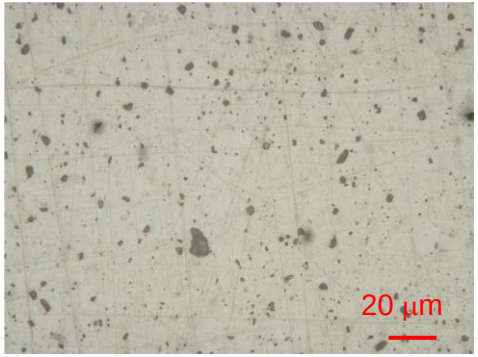

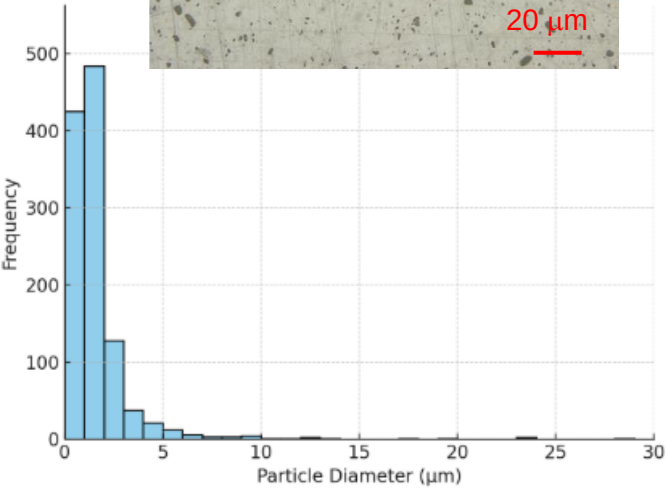

With BYK-9076

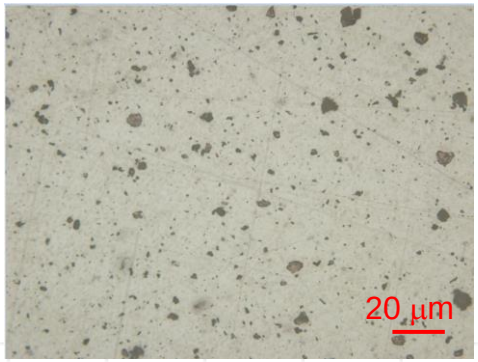

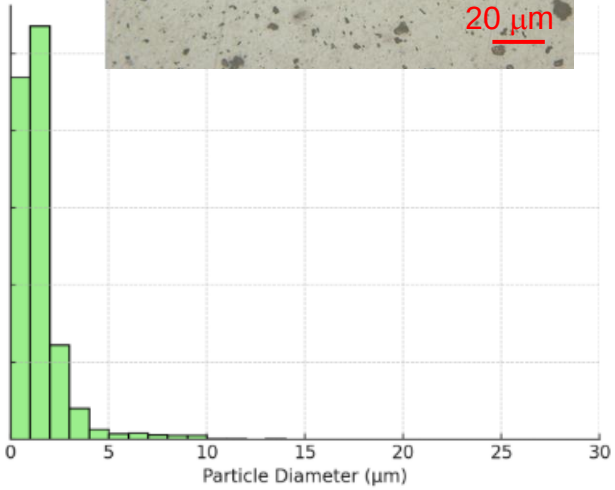

With DISPERBYK-180

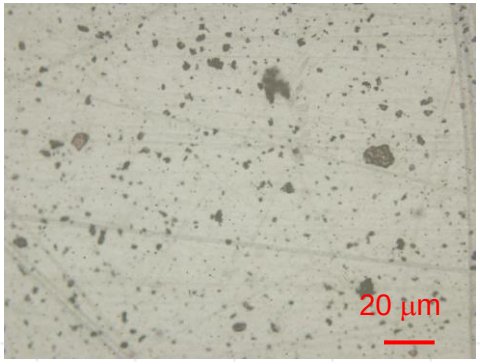

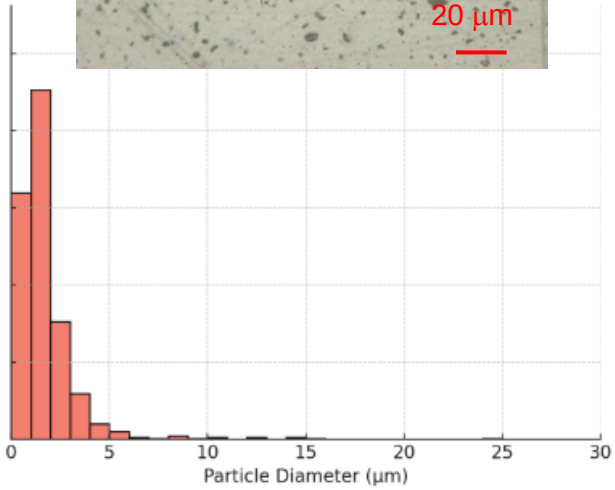

MXene Distribution in Epoxy Matrix

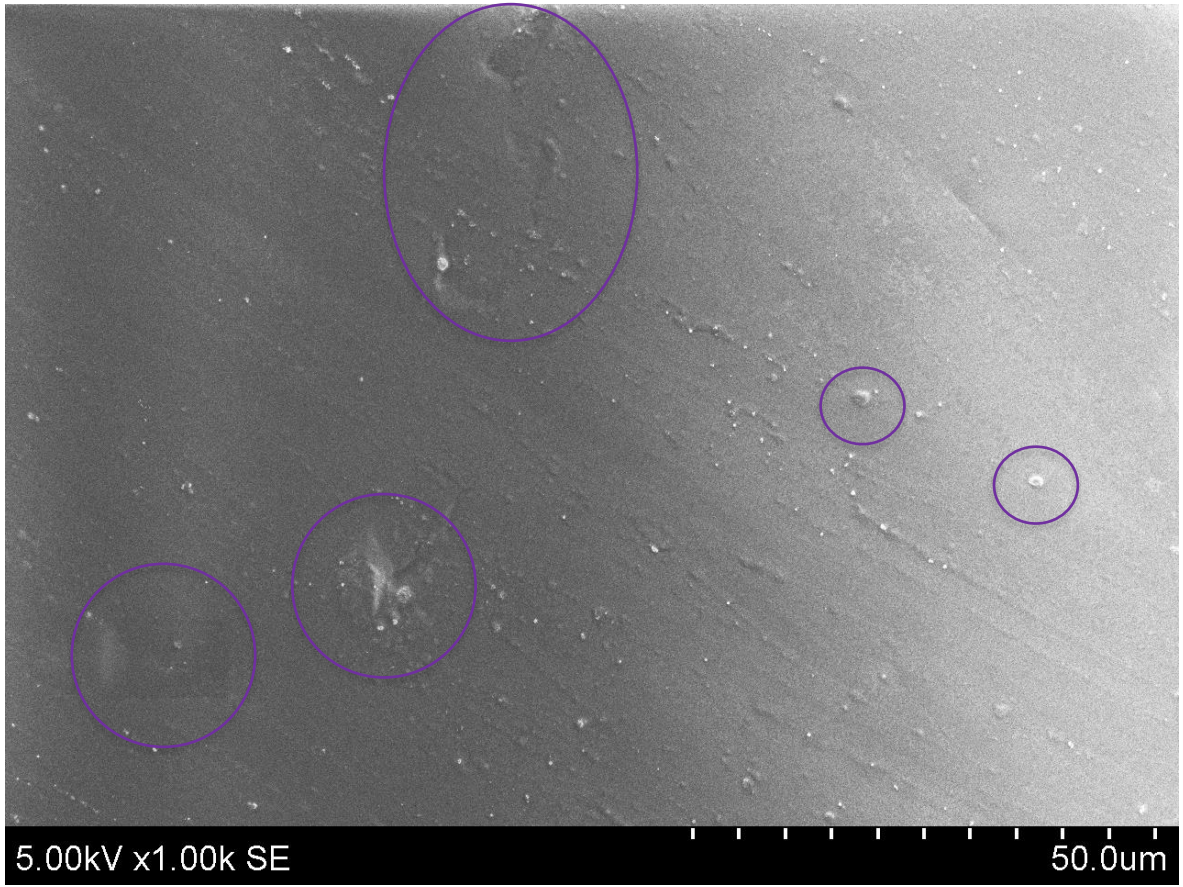

The Structural Properties of MXene/Epoxy Composites

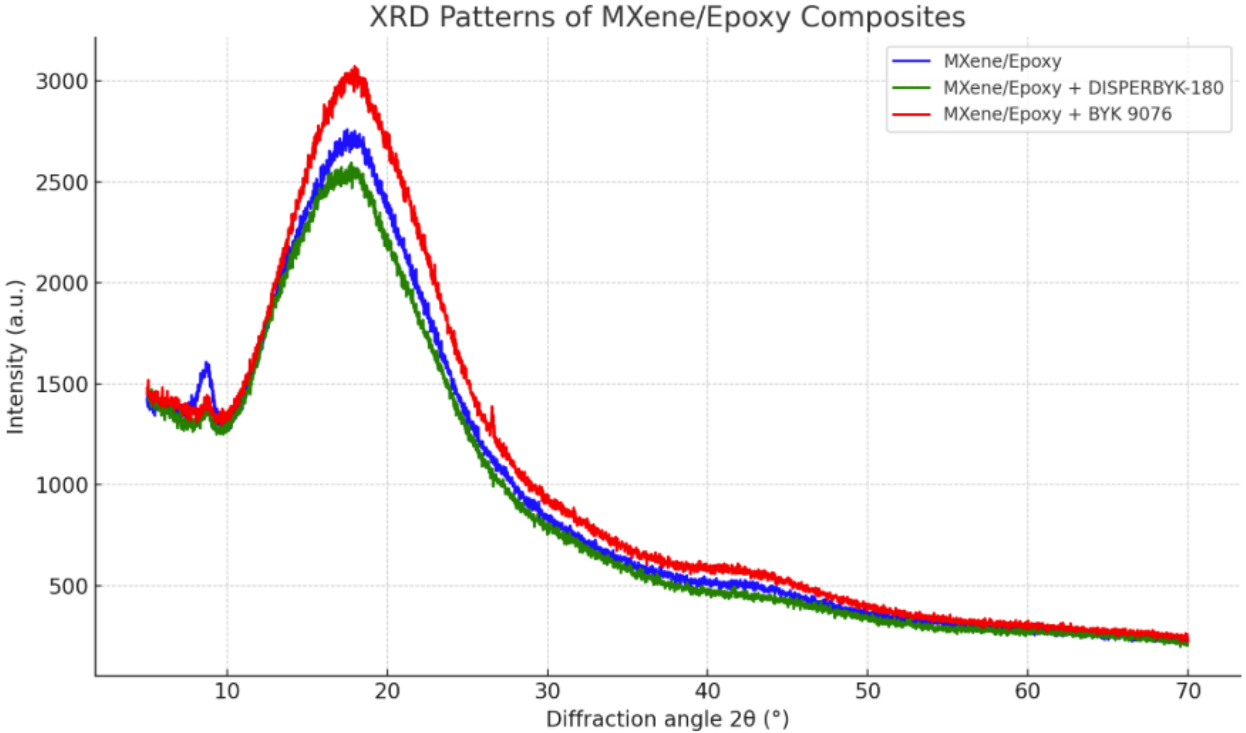

The reduced intensity and broadening of the (002) peak at 8° in XRD patterns indicate improved exfoliation of MXene layers.

Impact on Mechanical Properties

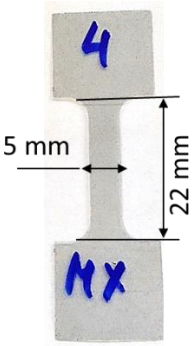

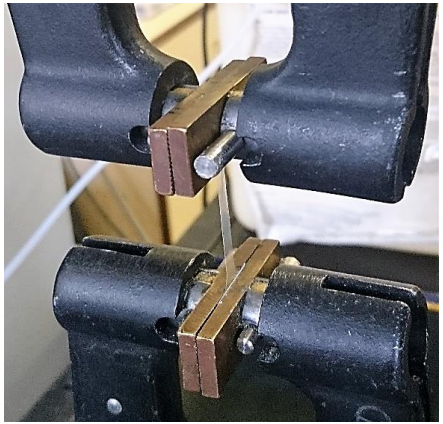

Tensile Testing Parameters

- **Equipment**: Testing Machine (Admel Lhomargy, France)
- **Load Cell**: 100 N
- **Crosshead Speed**: 1 mm/min
- **Gauge Length**: 22 mm.

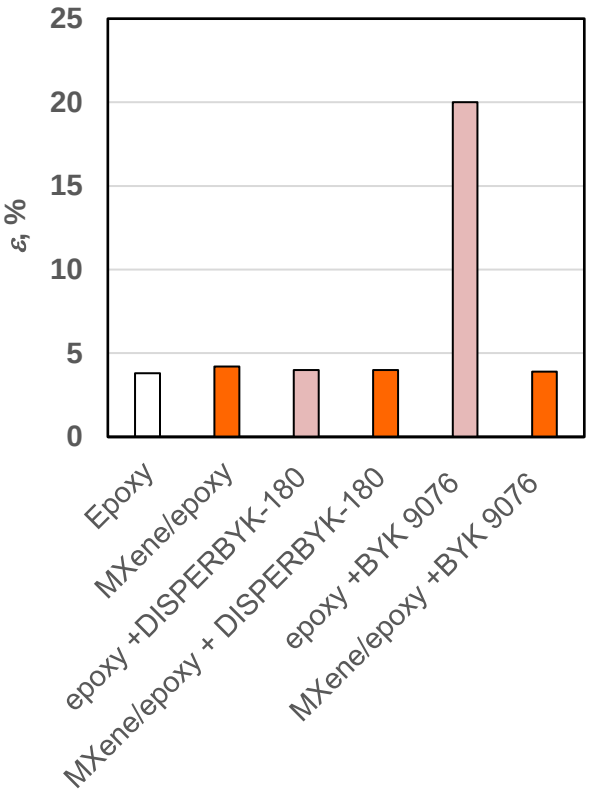

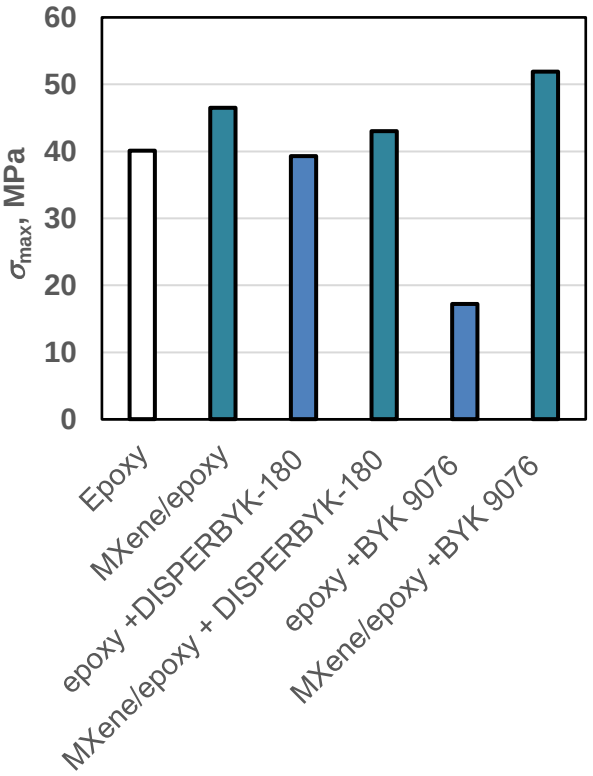

Conclusions

- Effective exfoliation and homogeneous dispersion of MXene in epoxy resin were achieved through a synergistic approach combining dispersing agents with high-shear three-roll milling.
- The use of dispersants and high-shear three-roll milling ensured a uniform distribution of exfoliated MXene throughout the epoxy matrix, minimising agglomeration.
- BYK-9076 acts as an effective dispersant and compatibiliser for MXenes in an epoxy matrix. It can also be used to functionalise the MXene surface, enhancing compatibility with the polymer matrix and improving the mechanical properties of the nanocomposite.

Thank you for your attention

Funded by the European Union

This research is funded by the European Union Horizon Europe Programme under Grant Agreement No. 101182521. Views and opinions expressed are however those of the author(s) only and do not necessarily reflect those of the European Union or European Research Executive Agency. Neither the European Union nor the granting authority can be held responsible for them.

ICCM24
AUGUST 4-8, 2025
BALTIMORE CONVENTION CENTER
BALTIMORE, MARYLAND, USA

No Technical Paper Submission for:

Quentin Marechal

Molecular Dynamics-derived Mode I Traction Laws for Crystalline UHMWPE Fibrils

Iveena Mukherjee, **Nuwan Dewapriya**, John W. Gillespie Jr. and Joseph M. Deitzel



UNIVERSITY OF DELAWARE
CENTER FOR COMPOSITE MATERIALS
Celebrating 50 Years

Overall Problem Statement - UHMWPE

Goal: Understand how **consolidation process variables** (temp., pres., and time) can be used to **control composite microstructure** (*reduce voids, minimize filament damage*) in order to **improve composite performance** (*reduce weight, maximize energy absorption*).

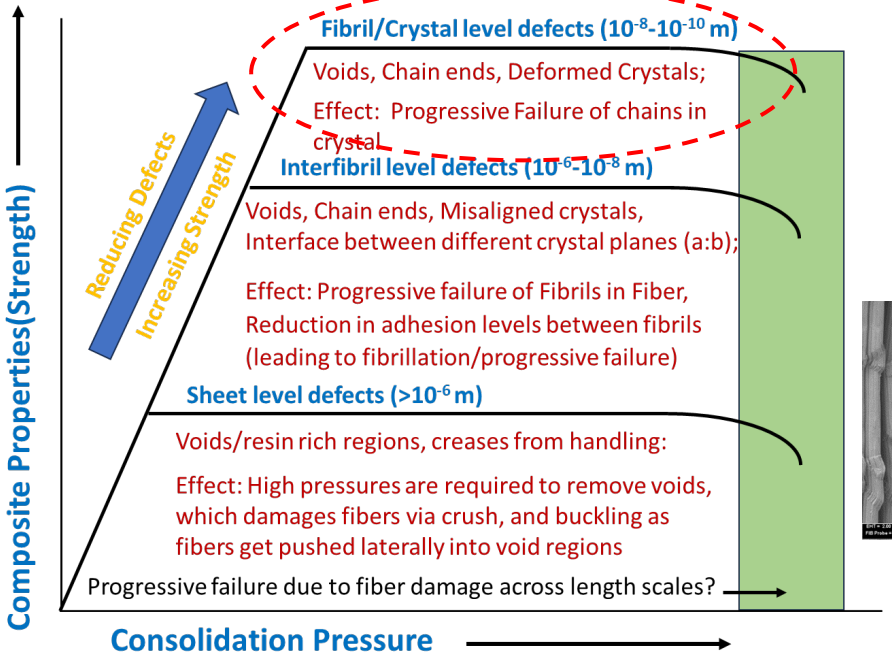

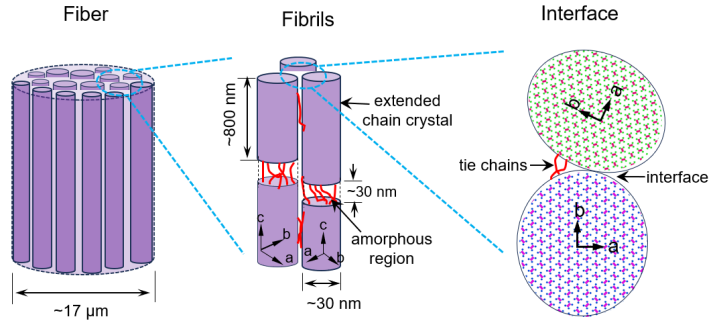

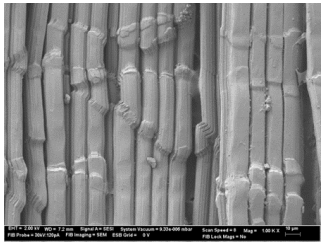

Hypothesis: *Void content reduction will increase tensile strength until a plateau strength is achieved*

- Plateau strength is governed by the remaining critical defects at lower length scales
- Process optimization provides a route to control critical defects and increase plateau strength
- Excessive consolidation pressure may damage fibers at all length scales and reduce strength

Technical Approach

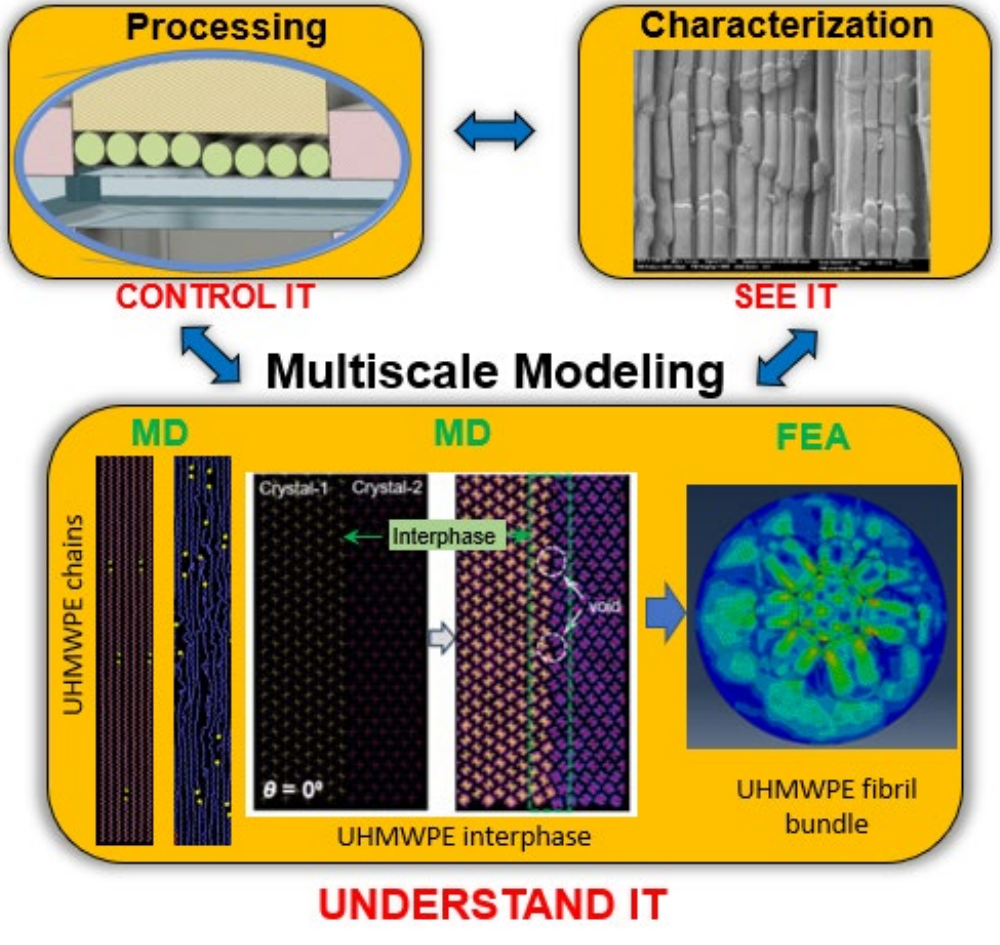

Research Method: Molecular Dynamics (MD)

- MD simulations are widely used to study the structures and properties of materials at the nanoscale.
- MD solves Newton's equation of motion ($F=ma$), and it is much faster than QM and DFT simulations.
- Atomic interactions are described by interatomic potential fields.
- Selection of the proper potential is very important for accurate predictions of properties.
- We use AIREBO-M (developed for hydrocarbons) to model polyethylene.
- Used LAMMPS, OVITO.

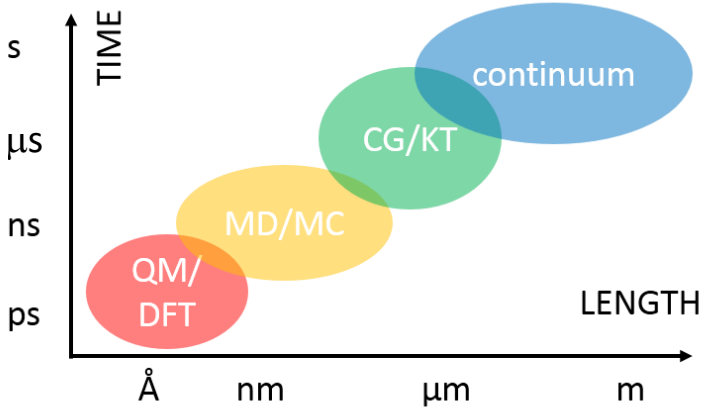

http://chemwiki.ucdavis.edu

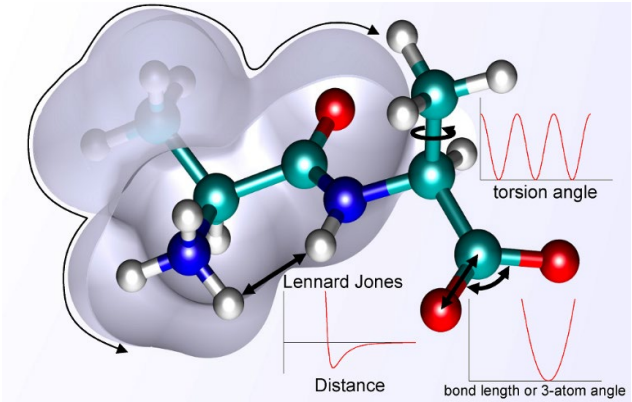

https://wikipedia.org/

Multiscale Modeling: MD Informed FEA

MD

Chain ends

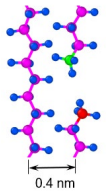

Misaligned interfaces

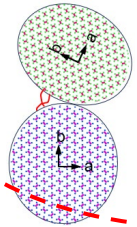

Voids at interfaces

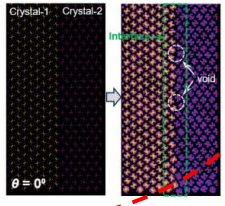

Collapsed voids & wavy chains

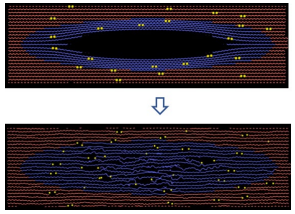

Amorphous regions

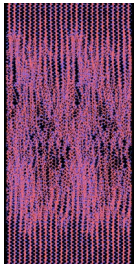

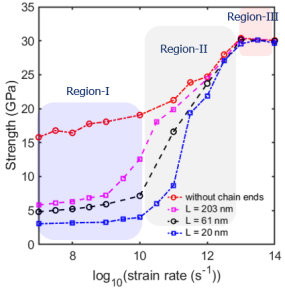

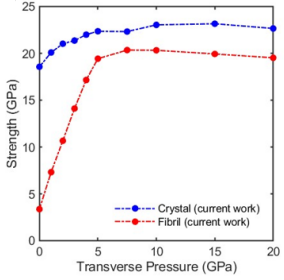

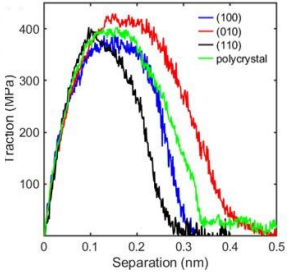

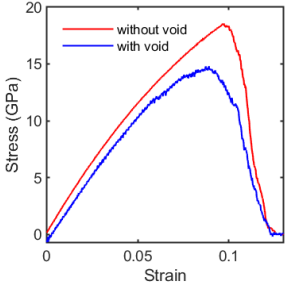

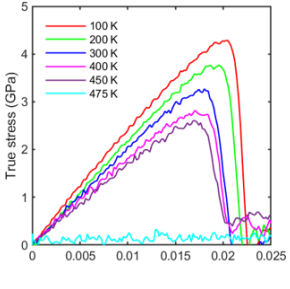

FE

Collapse of voids between oriented fibrils

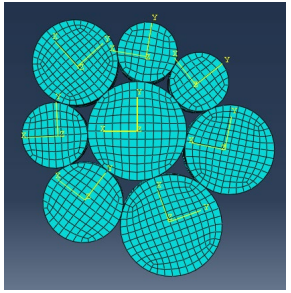

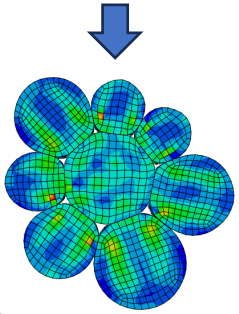

- MD simulations predict the 3D stress-strain response and cohesive traction laws for crystalline/amorphous PE.
- These predictions consider various factors, such as defects, strain rate, molecular weight, transverse pressure from impact, and temperature on progressive failure.
- The MD results serve as input for bridging length scales in FE.

Mode-I Traction Laws of UHMWPE Crystals

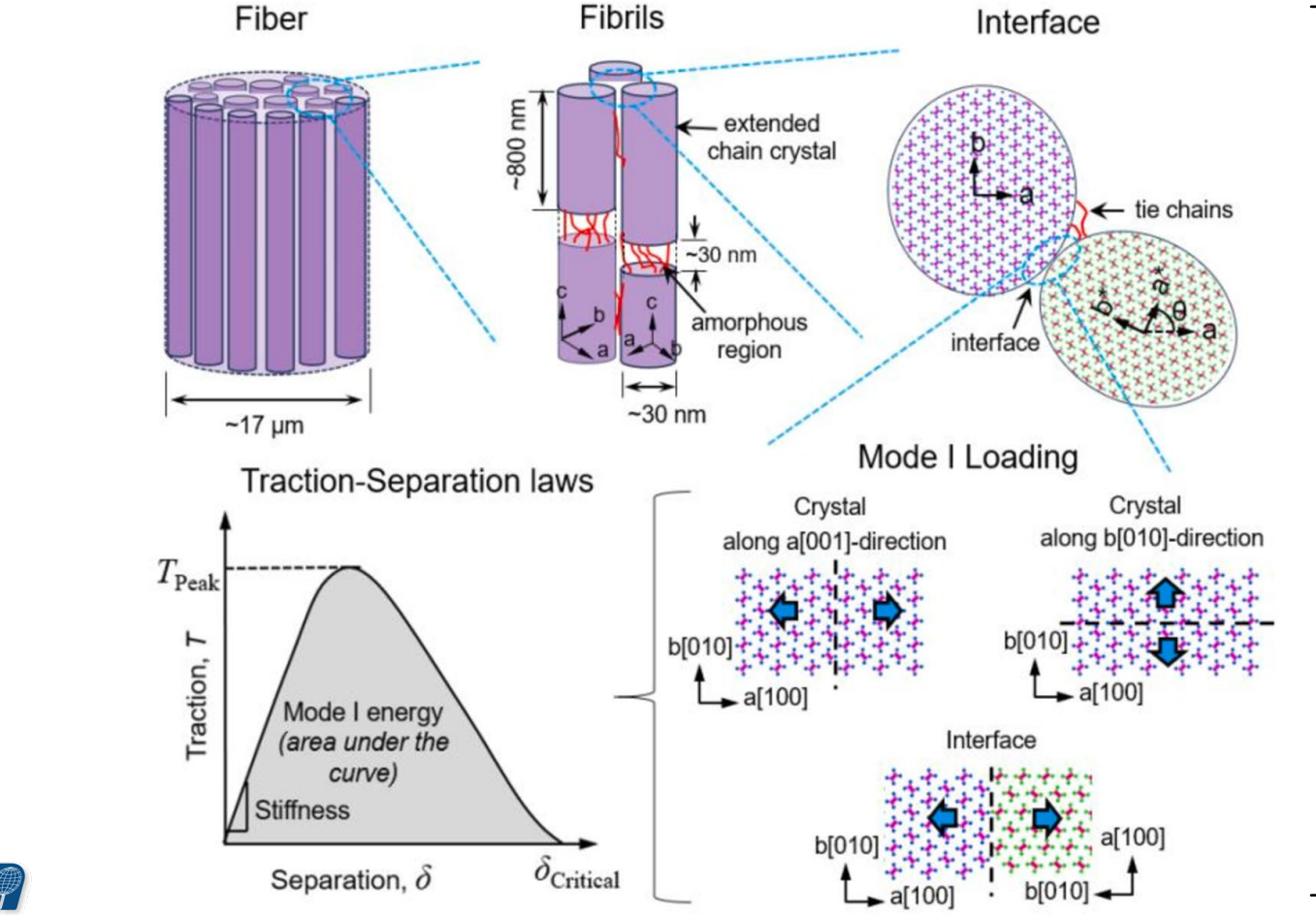

FEA

Collapse of voids between oriented fibrils

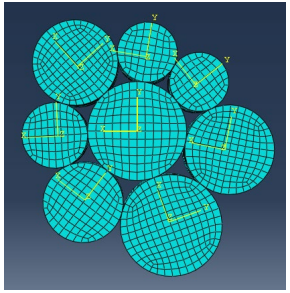

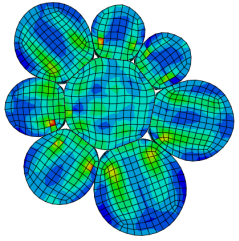

PE Unit Cell & Crystal Planes

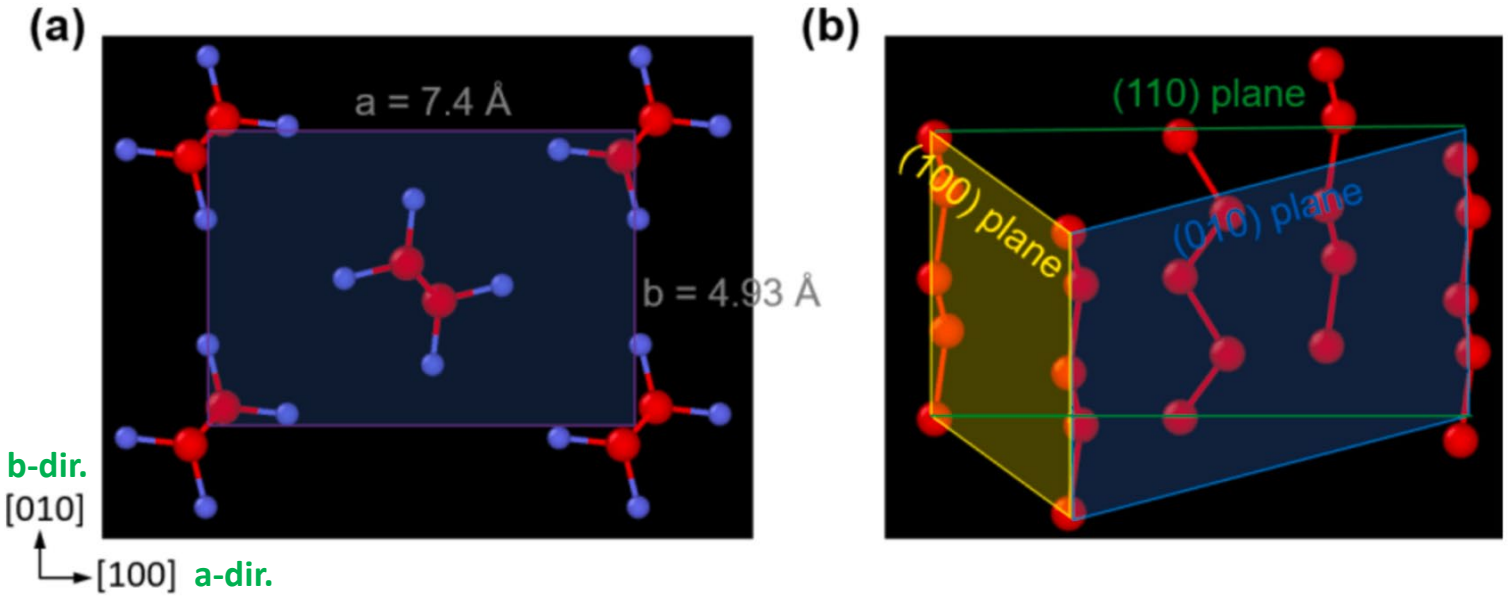

Mukherjee *et al*. Compute. Mater. Sci. 247 (2025)

Selection of Interphase Thickness

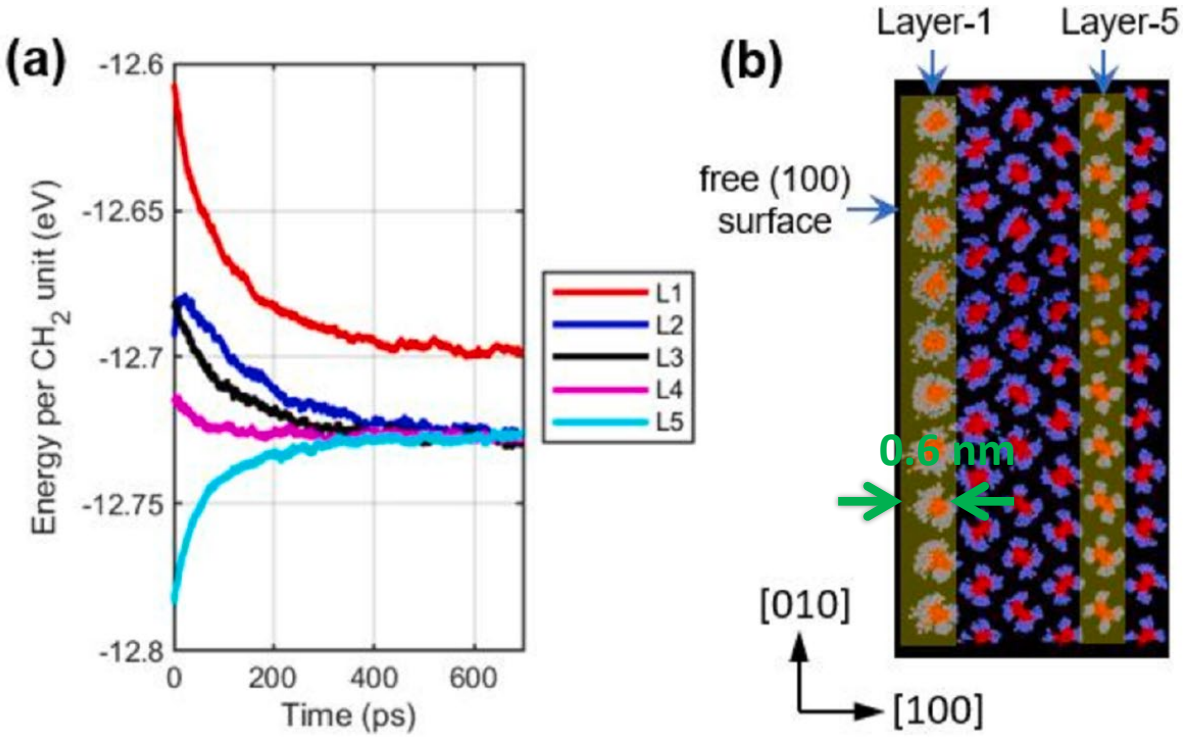

Mukherjee *et al*. Compute. Mater. Sci. 247 (2025)

Mode-I Traction-Separation Response

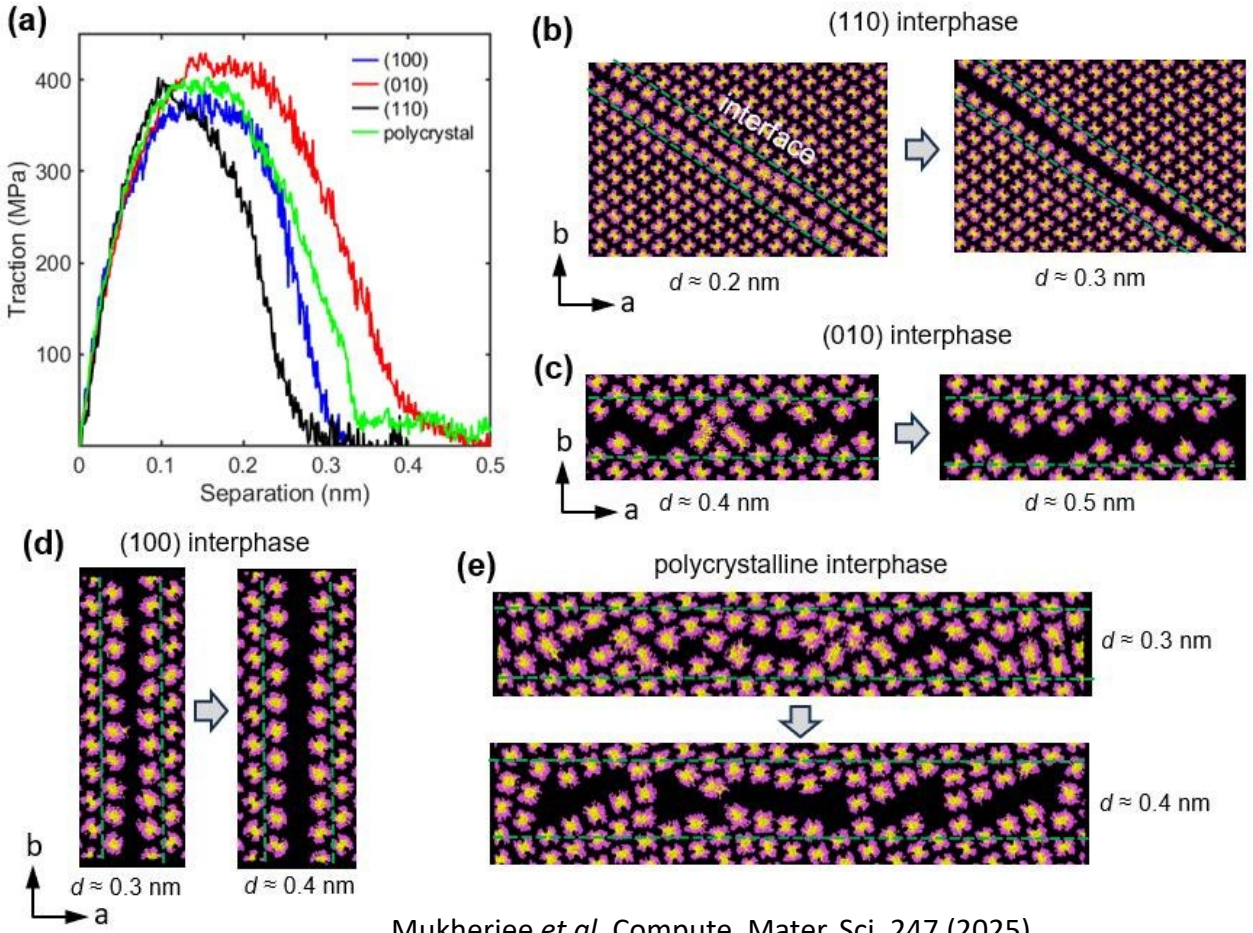

Mukherjee *et al*. Compute. Mater. Sci. 247 (2025)

Misaligned a-b Interfaces

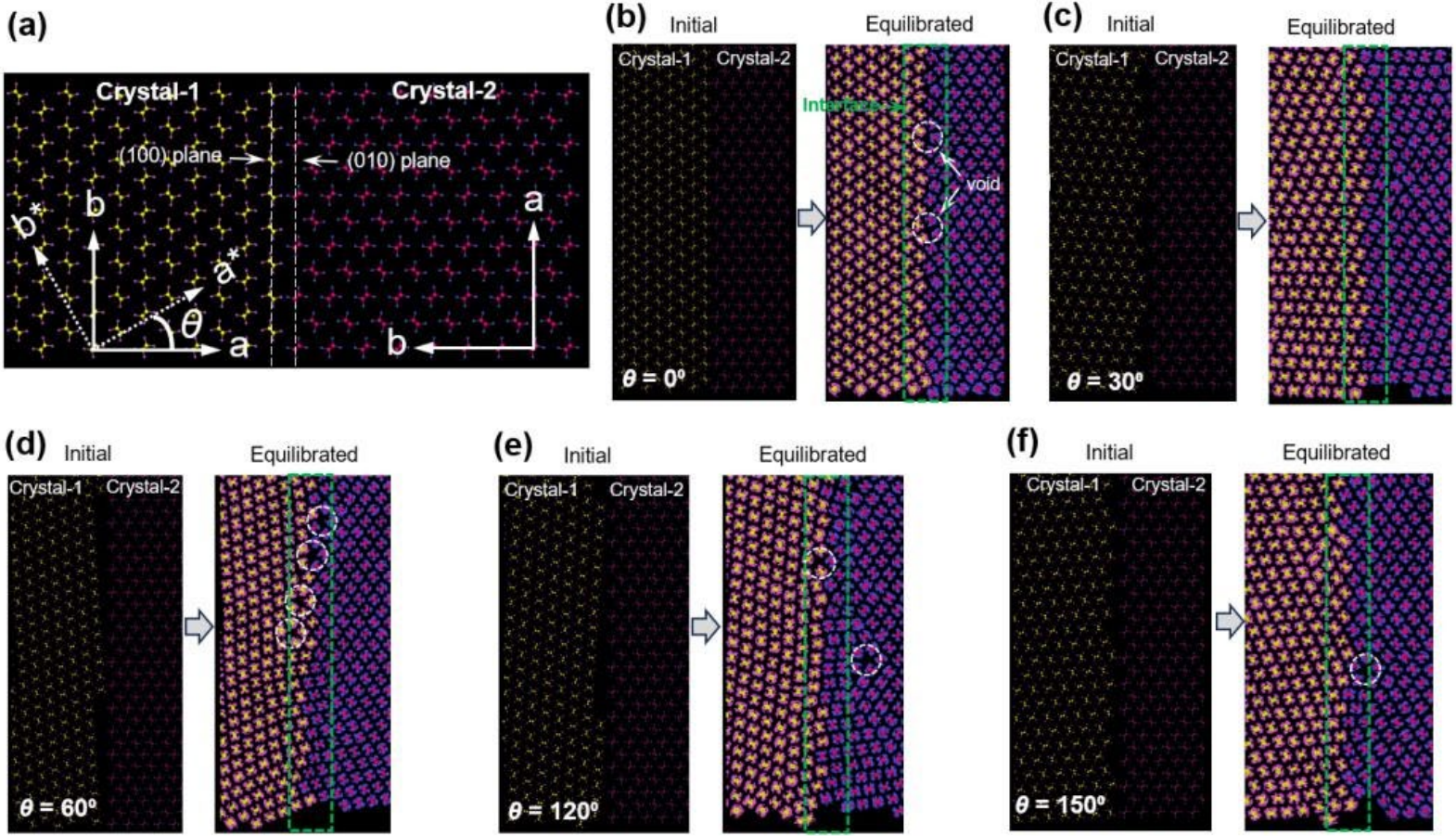

Mukherjee *et al*. Compute. Mater. Sci. 247 (2025)

Mode-I Response of Misaligned a-b Interfaces

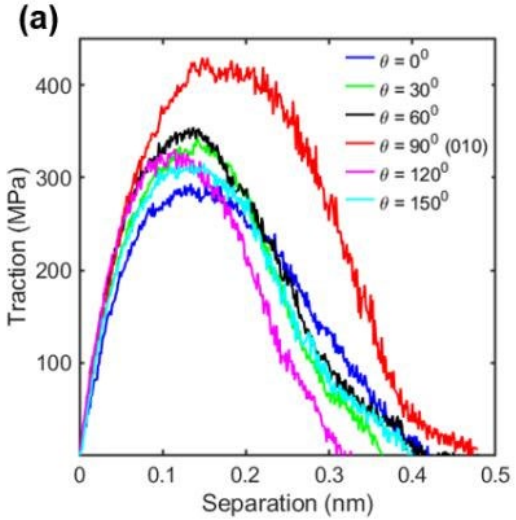

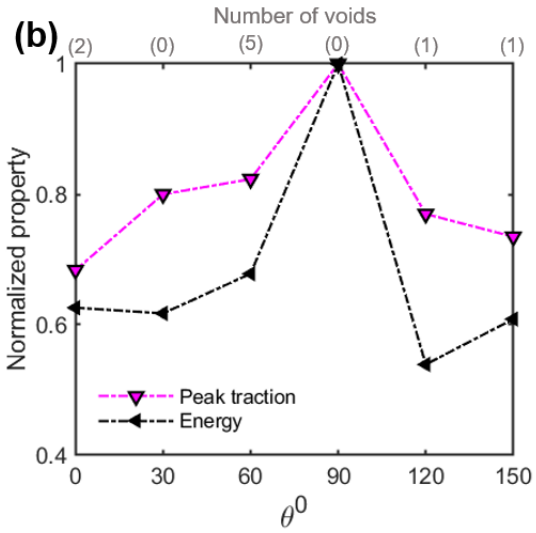

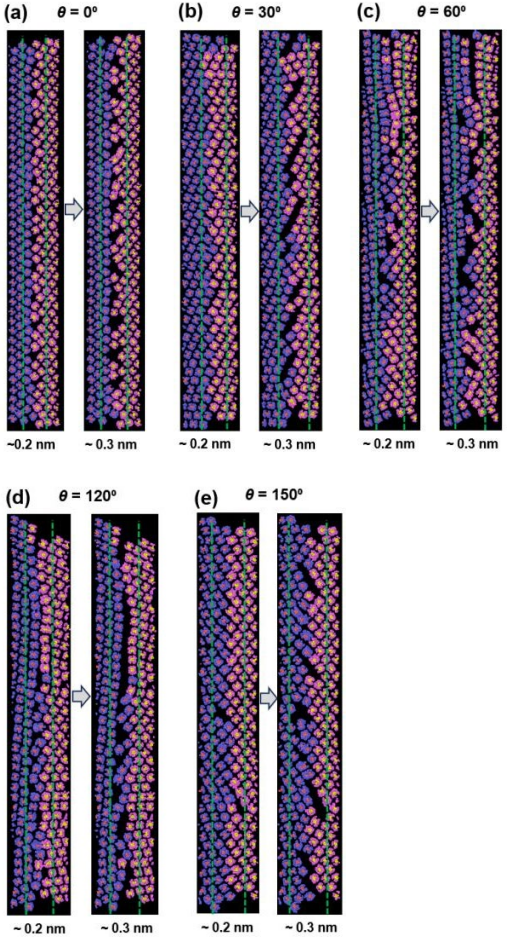

- Critical separation is between ~0.3 to 0.4 nm.
- The interfacial properties remain unaffected by voids (the relatively small size of the voids).
- The relatively weak van der Waals forces allow the chains to easily readjust themselves to minimize any emerging stress concentration.

Mukherjee *et al*. Compute. Mater. Sci. 247 (2025)

Parameter Fitting for a Cohesive Zone Model

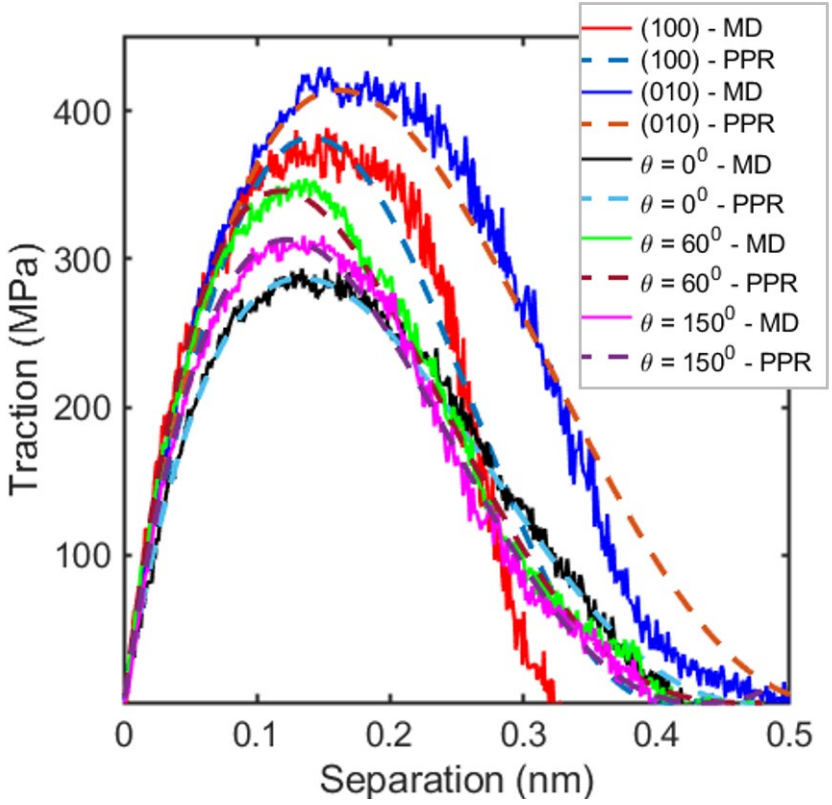

Mukherjee *et al*. Compute. Mater. Sci. 247 (2025)

Park–Paulino–Roesler (PPR) cohesive zone model

Park *et al*. J. Mech. Phys. Solids 57 (2009)

$$\Psi(\Delta_n) = \Gamma_n \left(1 - \frac{\Delta_n}{\delta_n}\right)^{\alpha} \left(\frac{m}{\alpha} + \frac{\Delta_n}{\delta_n}\right)^{m} + \Phi_n$$

where, Γ_n is the Mode I energy constant; Δ_n is the normal separation distance; δ_n is the critical separation distance; α is the shape parameter and m is the non-dimensional exponent.

$$T_n(\Delta_n) = \frac{\Gamma_n}{\delta_n}\left[m\left(1 - \frac{\Delta_n}{\delta_n}\right)^{\alpha}\left(\frac{m}{\alpha} + \frac{\Delta_n}{\delta_n}\right)^{m-1} - \alpha\left(1 - \frac{\Delta_n}{\delta_n}\right)^{\alpha-1}\left(\frac{m}{\alpha} + \frac{\Delta_n}{\delta_n}\right)^{m}\right]$$

Acknowledgements

The research was sponsored by the **Army Research Laboratory** and was accomplished under Cooperative Agreement Number W911NF-23-2-0022. The views and conclusions contained in this presentation are those of the authors and should not be interpreted as representing the official policies, either expressed or implied, of the Army Research Office or the U.S. Government. The U.S. Government is authorized to reproduce and distribute reprints for Government purposes, notwithstanding any copyright notation herein.

Thank you for your attention!

Effect of Consolidation Pressure on Void Reduction and Effective Properties in a Stochastic UHMWPE Fibril Array

Dr. Abdalsalam Fadeel, Dr. Joseph M. Deitzel, Prof. Jack Gillespie

Date: August 4-8, 2025

UNIVERSITY OF DELAWARE
CENTER FOR COMPOSITE MATERIALS
Celebrating 50 Years

OVERVIEW

Goal: Understand how consolidation process variables Temperature(T), Pressure(P) and time (t) control composite microstructure (*Reduce voids*, *Increase fiber volume fraction*, *Minimize filament damage*) to improve composite performance (*Reduce weight*, *Maintain Performance*, *Reduce dynamic deflection*, *Maximize energy absorption*).

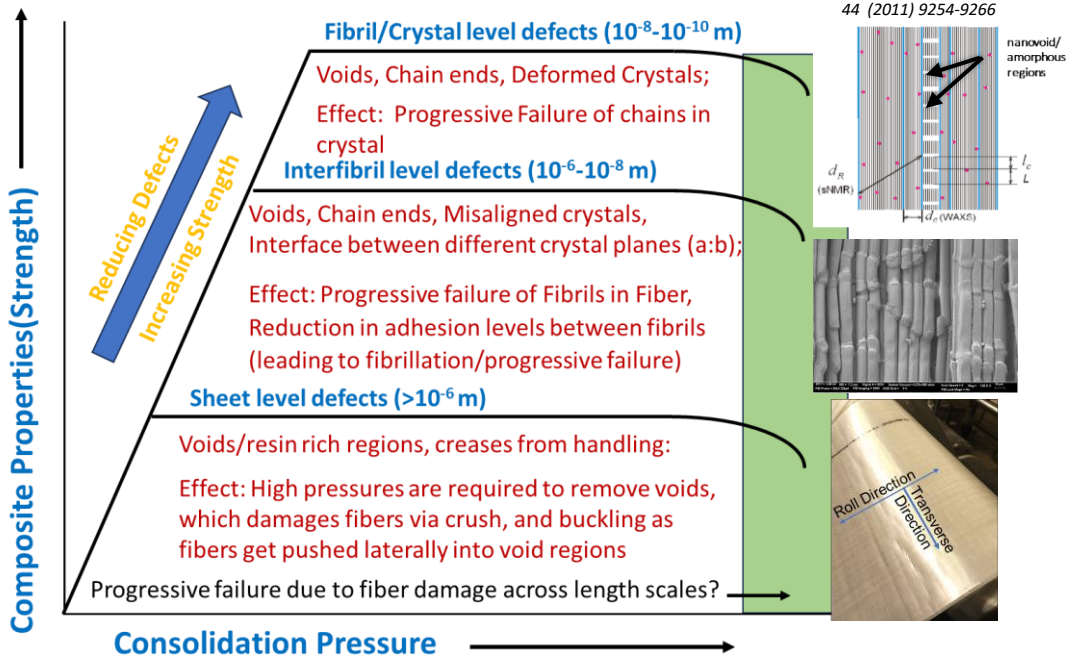

Litvinov et al., Maromolecules 44 (2011) 9254-9266

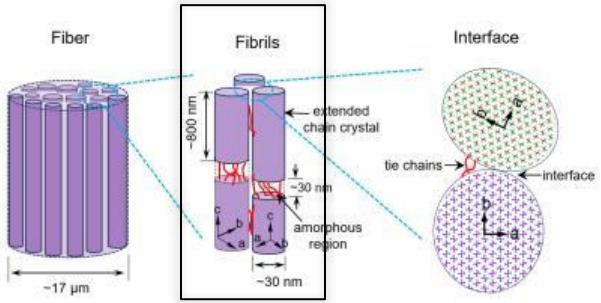

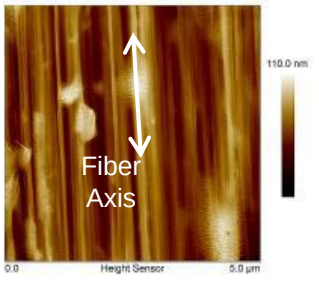

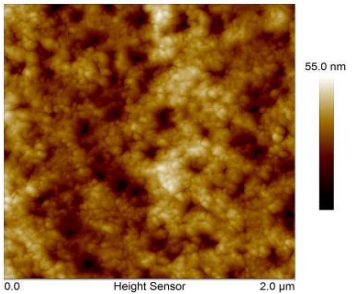

AFM images of the microtomed surface of the UHMWPE fiber

PROBLEM STATEMENT AND MODELING OBJECTIVE

- What is the effect of consolidation pressure on the stochastic fibril level microstructure within a fiber at processing temperature?
  - Fibril deformation, shape, and fibril-fibril contact areas.
  - Inter-fibril void content.
- What is the effect of microstructure on the effect properties of the fiber at room temperature?

Single fiber 12-15 microns
contains 200,000+ fibrils.

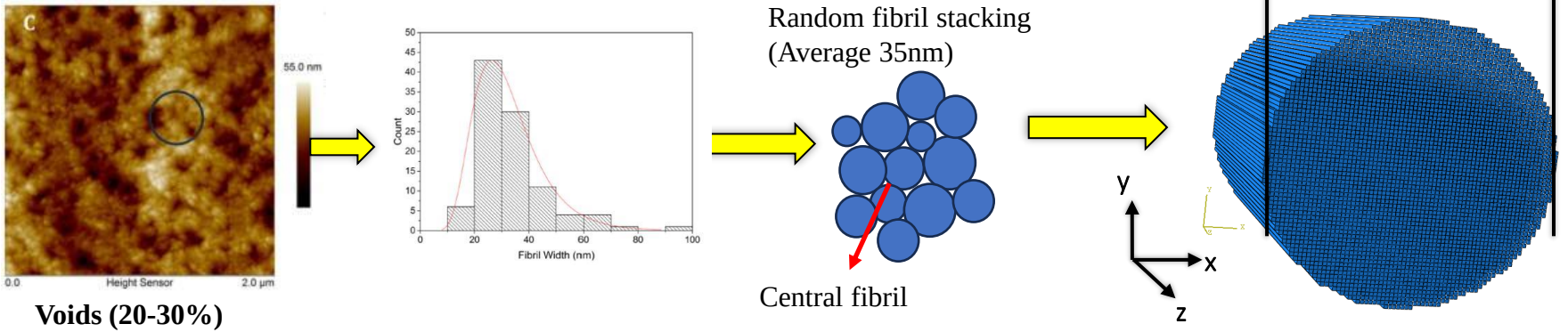

Voids (20-30%)

- Based on AFM imaging, the microstructure of polyethylene (PE) fibers consists of aligned fibrils and interstitial voids. Under hydrostatic pressure, this structure undergoes reformation, directly influencing fiber performance.
- The following objectives are pursued:
  - **Develop** a methodology to correlate consolidation pressure with microstructural evolution.
  - **Predict** inelastic deformation, contact area growth, and progressive void reduction.
  - **Determine** effective isotropic mechanical properties using finite element analysis (FEA).

APPROACH

- **Develop a methodology to apply hydrostatic pressure on a fibril array**
  - Constant diameter
  - Stochastic diameter distribution

- **Use a methodology to predict microstructure evolution.**
- **Define RVE for constant fibril diameter and statistical fibril diameter distribution**
  - Fibril diameter distribution
  - Equivalent interstitial void content

- **Develop methodology to calculate effective properties of the fibril array as a function of hydrostatic pressure/void content**

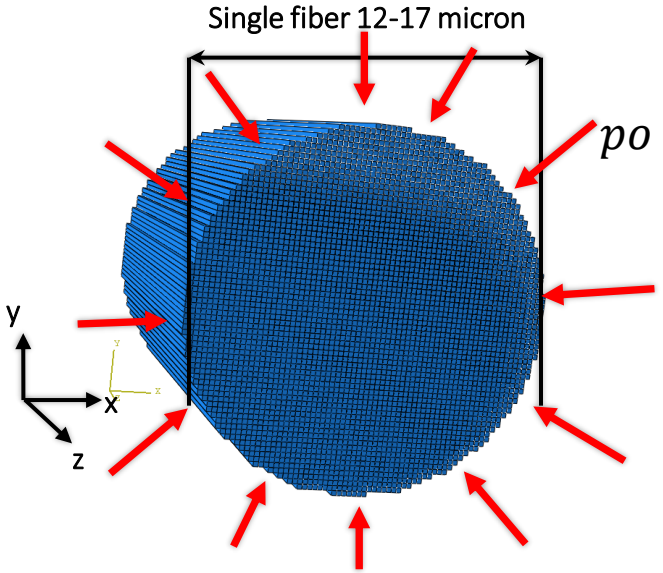

MODELING STRATEGY FOR FIBRIL ARRAYS

- **Step 1: Uniform Fibrils Model**
  - Used to demonstrate methodology and validate simulation approach
  - Enables use of RVE to save computational time
- **Step 2: Statistical Geometry Generation**
  - Generated fibril array geometries from statistical fibril diameter data.
  - Used the Monte Carlo method to reduce the array size while preserving representative fibril diameter distribution and interstitial void content.
- **Step 3: Realistic Simulation of Fibril Microstructure Subjected to Hydrostatic Pressure During Consolidation at 125C**
  - Optimal configuration applied to validated model
  - Leads to realistic and accurate predictions with reduced complexity

MATERIAL INPUT PROPERTIES USED IN MODELS

- The data are based on molecular dynamics (MD) simulations of UHMWPE at sheet process conditions:
- 125 °C over a wide range of consolidation pressure

- According to N. Dewapriya et al. (2023, 2024), the most recent mechanical properties were obtained from MD simulations conducted at a strain rate of 10^9/s at 125 °C.

- The yield stresses $\sigma_{ay}, \sigma_{by}, and\ \tau_{aby}$ correspond to the a-direction, b-direction, and a–b shear plane, respectively.

- These values were used to define the anisotropic yield behavior.

- This table summarizes the elastic properties used in the plane strain FEA model.

E_a, GPa	E_b, GPa	E_c, GPa	G_{ab}, GPa	G_{bc}, GPa	G_{ca}, GPa
3.346	4.3	263.53	2.78	1.30	1.77
ν_{ab}	ν_{bc}	ν_{ac}	σ_{ay},GPa	σ_{by},GPa	τ_{aby},GPa
0.48	0.006	0.007	0.34	0.093	0.213

STEP 1: UNIFORM FIBRILS MODEL

Key Steps in Modeling Hydrostatic Pressure on Fibril Arrays

1. Hexagonal Packing and Void Content Estimation

- Select the optimal fibril ring geometry and number of rings to replicate initial void content.
- Perform convergence study to ensure accuracy and model stability (see next slide).

2. Pressure Application Strategy

- Establish a method for uniform hydrostatic pressure application across the external surface of outermost fibril in the array.
- Surround fibrils with an incompressible matrix material to transmit uniform hydrostatic pressure (details in Slide 9).
- All fibril surfaces are frictionless

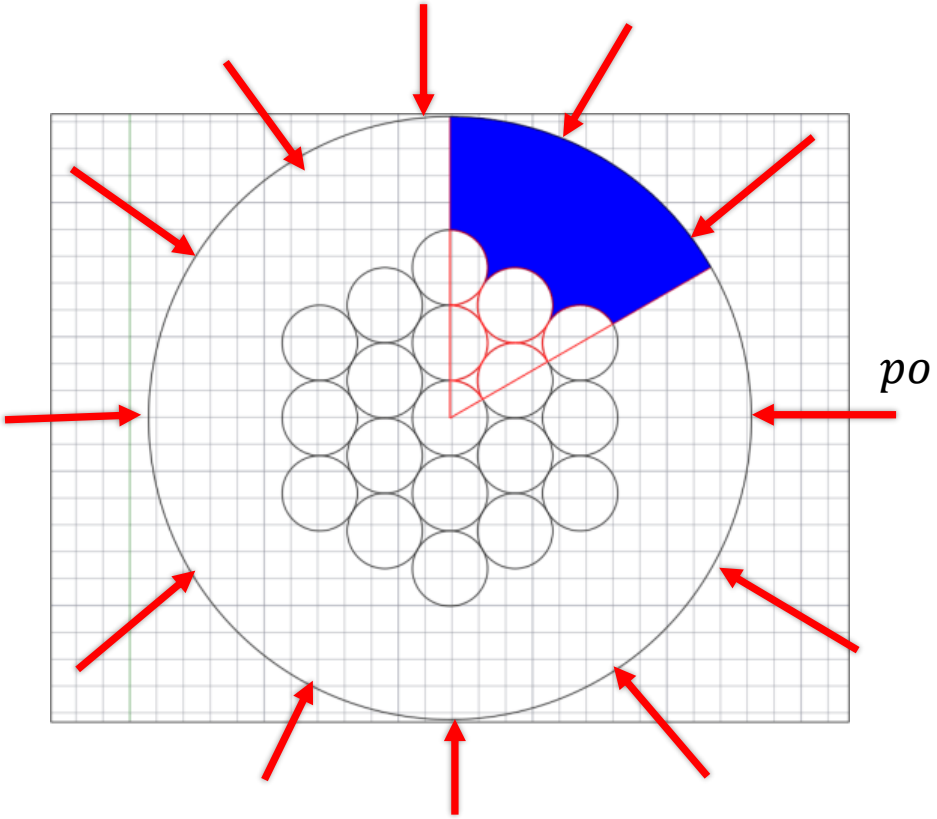

To reduce computational cost and improve simulation efficiency, the RVE was modeled using one-eighth of the circular fibril array as shown above.

STEP 1: UNIFORM FIBRILS MODEL

Key Steps in Modeling Hydrostatic Pressure on Fibril Arrays

1- Hexagonal Packing and Void Content Estimation



Table 1. Comparison of void fraction values obtained analytically from Equation (1) and measured using AutoCAD, as a function of the number of fibrils derived from Equation (2).

Number of rings (n)	Void Fraction (Theoretical)	Void Fraction (CAD)	Number of of fibrils (N)
1	0.042142104	0.042	7
2	0.06088869	0.0608	19
3	0.069691669	0.069	37
4	0.074742231	0.0747	61
5	0.078007966	0.078	91

- Equations (1) and (2), derived from uniform circular geometry, show excellent agreement with AutoCAD results for n=1 to 4, validating their accuracy for larger ring counts.

$$Voids\ Fraction = \frac{n^2\left(\sqrt{3}-\frac{\pi}{2}\right)}{n^2.\left(\sqrt{3}-\frac{\pi}{2}\right)+\pi\left(\frac{1}{6}+\frac{n(n+1)}{2}\right)} \quad \text{....(1) , } n \text{ is the number of rings}$$

$$N(n) = 1 + 3n(n+1) \quad \text{..... (2), } N \text{ is the number of fibrils}$$

- However, due to computational limitations associated with ABAQUS simulations, and considering that our goal is to approximate the methodology rather than achieve full convergence, selecting two rings is deemed appropriate for the current model.

STEP 1: UNIFORM FIBRILS MODEL

Key Steps in Modeling Hydrostatic Pressure on Fibril Arrays

Constitutive Model for Incompressible Material

- The blue region is modeled using a Mooney–Rivlin hyperelastic material:

Strain Energy Function:

$$U = C_{10}(\bar{I}_1 - 3) + C_{01}(\bar{I}_2 - 3) + (1/D_1)(J^{el} - 1)^2 \quad \ldots..(1)$$

Material Constants:

$$\mu_0 = 2(C_{10} + C_{01}), \qquad K_0 = 2/D_1$$

μ_0 Shear modulus

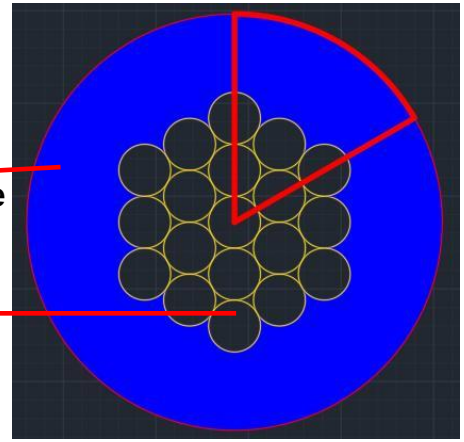

Schematic of the micromechanical model.

- The shear modulus was reduced to ensure the matrix can carry the applied pressure without stress relaxation (see Equation 2) based on Ogden, R.W. (1997) and Bonet, J., & Wood, R.D. (2008).

Incompressible Material Cauchy Stress Tensor:

$\sigma = -p\,I + \mu\,B$ ……. (2), $B=FF^T$ is the left Cauchy-Green deformation tensor. μ is the shear modulus

- Thus, the lowest value of the shear modulus will ensure the material accurately carries the hydrostatic pressure.

STEP 1: UNIFORM FIBRILS MODEL

UNIVERSITY OF DELAWARE
CENTER FOR COMPOSITE MATERIALS
Celebrating 50 Years

Element Type for Incompressible Region: ABAQUS

- 3D hybrid elements were used in the finite element model.
- The element type selected is C3D8H, which is appropriate for modeling incompressible materials.
- These elements are ideal for capturing the behavior under uniform hydrostatic pressure.
- The mesh ensures accurate stress transmission through the incompressible matrix to the fibril structure.

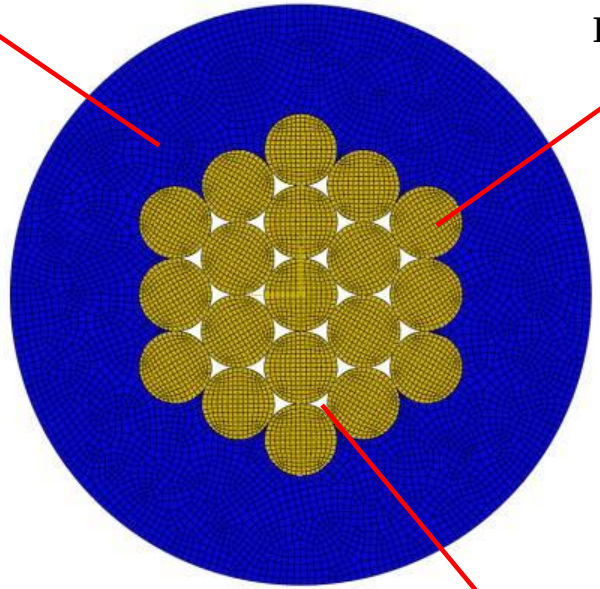

Element Type for Fibril Region

- Fibrils were modeled using 3D brick elements (C3D8) with full integration.
- A nonlinear mesh convergence study was conducted to balance accuracy and computational cost.
- Although modeled in 3D, plane strain boundary conditions were applied on surfaces normal to the cross-section.

The void region

STEP 1: UNIFORM FIBRILS MODEL

Volume Change and Equivalent Property Estimation

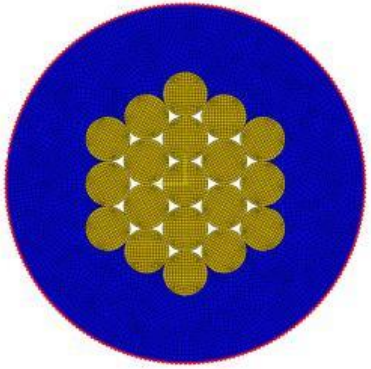

For 2D plane strain conditions, the following equations are used to calculate the equivalent mechanical properties:

$$K = -V\frac{dP}{dV} \ldots\ldots\ldots (1) \quad K = \frac{E}{2(1+\nu)(1-2\nu)} \ldots\ldots\ldots (2)$$

$$\varepsilon_r = \frac{-P}{E}(1+\nu)(1-2\nu) \ldots\ldots\ldots (3)$$

Based on the extracted data for volume change and strain variation with applied pressure, the following equivalent mechanical properties can be computed:

- **Equivalent Elastic Modulus (E)**
- **Bulk Modulus (K)**
- **Stress–Strain Relationship**

These values are determined by solving the constitutive relations shown in the equations above.

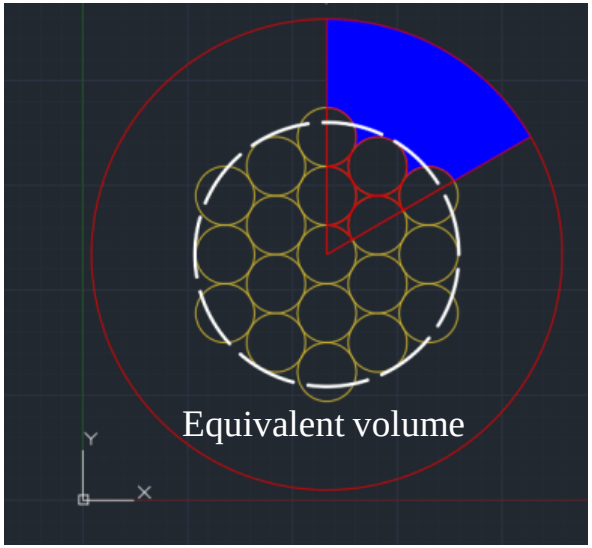

- Equivalent volume representations were computed for both fibrils and voids based on their volumes.
- All final results and visualizations were based on these equivalent circle approximations.

STEP 1: UNIFORM FIBRILS MODEL

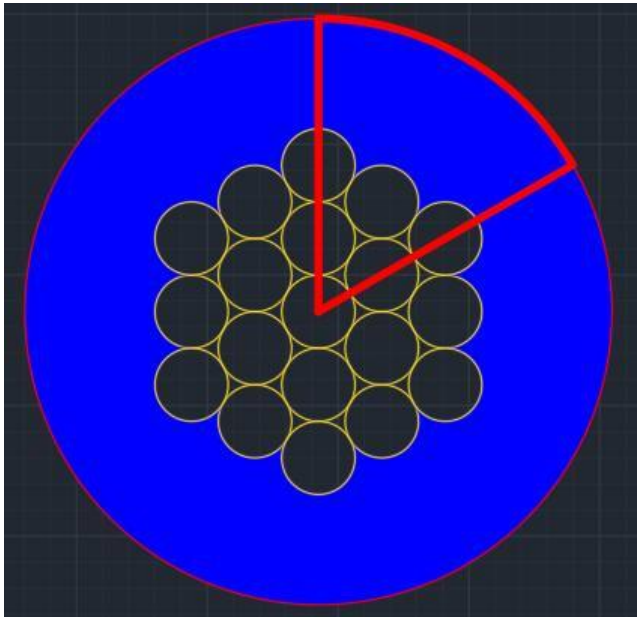

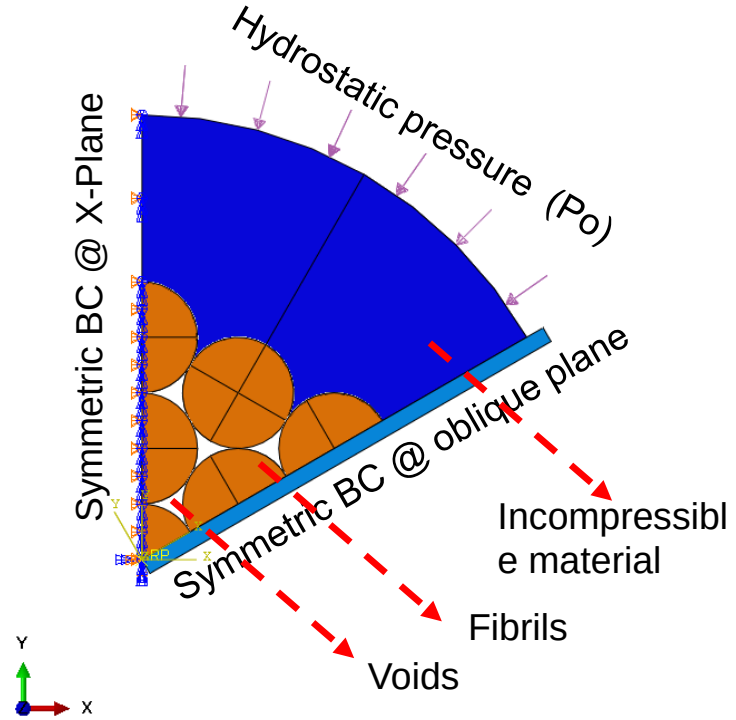

- The repeated geometric pattern was constructed using AutoCAD and employed for representative volume element (RVE) micromechanical modeling. Periodic boundary conditions (PBCs) were applied to simulate the infinite material response. Additionally, symmetry boundary conditions were imposed along the X-plane and an oblique plane inclined at 30 degrees to the horizontal, as illustrated.

STEP 1: UNIFORM FIBRILS MODEL

UNIVERSITY OF DELAWARE
CENTER FOR COMPOSITE MATERIALS
Celebrating 50 Years

Initial Results: Incompressible Material Response Under Hydrostatic Loading

S11=Radial stresses=Applied pressure

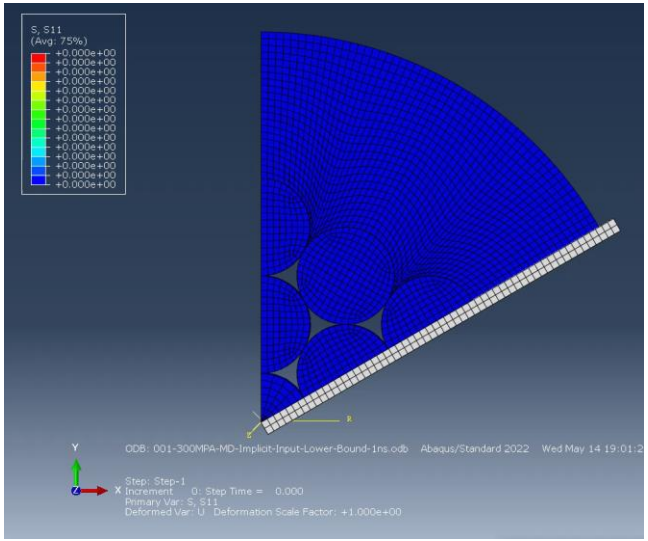

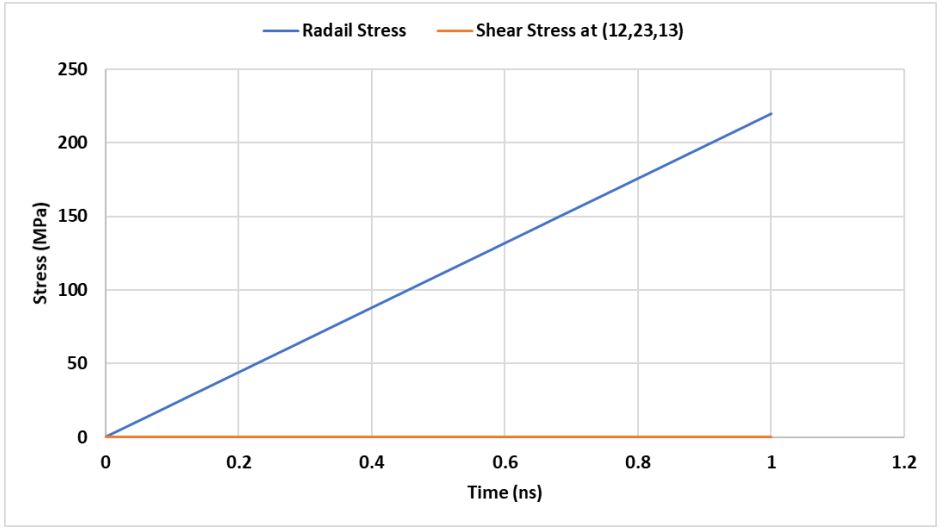

- The **radial stresses** in the incompressible material are **uniform** and match the applied hydrostatic pressure.
- **Shear stresses remain negligible**, confirming the incompressible material behavior.
- These results validate the pressure transfer mechanism and satisfy **Equation (2)** (Ogden, R.W. (1997) and Bonet, J., & Wood, R.D. (2008)) $\sigma = -p\,I + \mu\,B$ ……. (2)

STEP 1: UNIFORM FIBRILS MODEL

Void Reduction and Deformation Stages at 125C

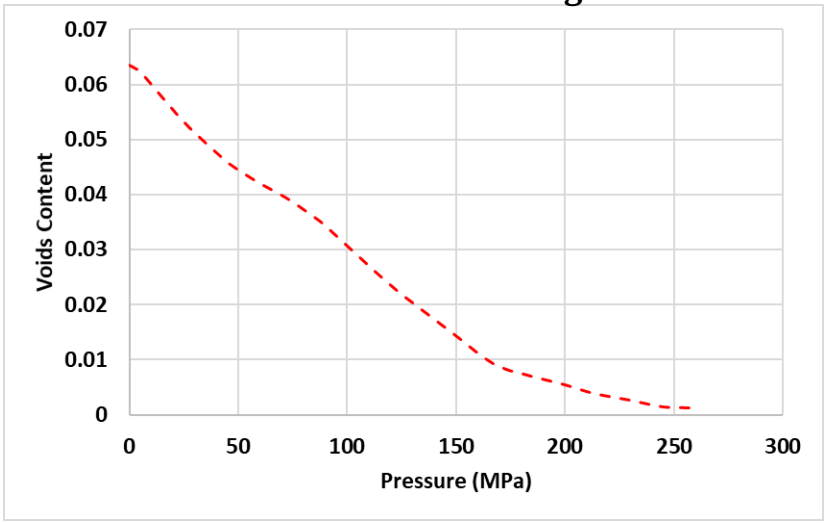

- In the MD configuration, complete void elimination occurs at an applied pressure of approximately **250 MPa (1% void content is achieved at 160 MPa)**.
- The void reduction process can be categorized into **three distinct stages**:
  - **Elastic deformation (0 to 50 MPa)**
  - **Elastic-plastic softening (50 to 150 MPa)**
  - **Bulk modulus stiffening (150 to 250 MPa)**
- The initial void fraction for the uniform fiber array with two rings is **6.31%**.
- The structure undergoes **inelastic deformation** until a fully void-free configuration is achieved at 250 MPa.

STEP 1: UNIFORM FIBRILS MODEL

Plane Strain Bulk Modulus vs. Void Content at 125C

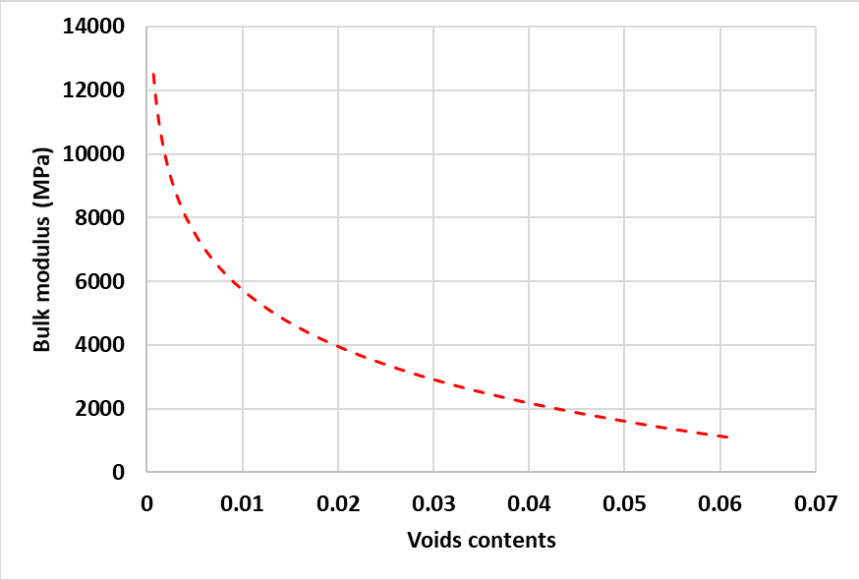

The bulk modulus was calculated from the volume-pressure plot, considering the equivalent volume changes of the fibrils and voids.

$$K = -V\frac{dP}{dV} \quad \ldots\ldots\ldots (1)$$

At an initial void content of 6.3%, the bulk modulus is at its minimum value of 1101.8 MPa. As pressure increases, voids collapse and stiffness rises. When the void fraction approaches zero, the bulk modulus rapidly increases and converges toward the fully dense value of 55,750 MPa, as predicted by Equation (2). This trend is clearly shown in the plot, where the bulk modulus increases sharply as porosity diminishes.

$$K = \frac{E}{2(1+\nu)(1-2\nu)} \quad \ldots\ldots\ldots (2)$$

STEP 1: UNIFORM FIBRILS MODEL

Effective Stress-Strain of the model under hydrostatic pressure

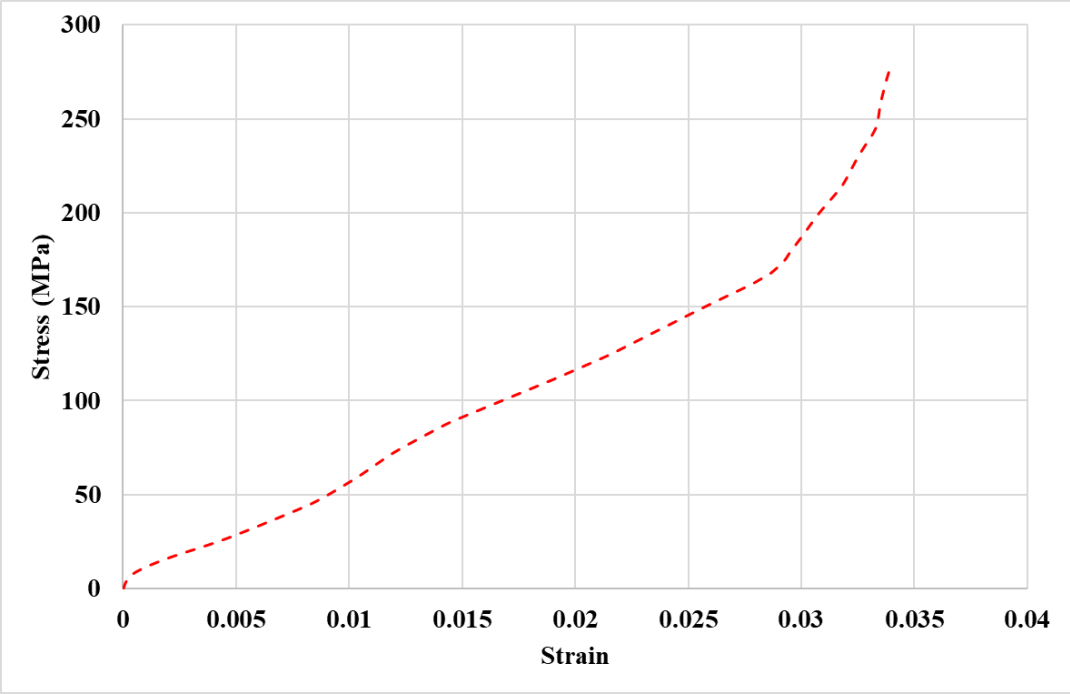

The effective elastic strain response exhibits a typical three-stage behavior: an initial elastic regime, a plateau region, and a final densification phase. Densification occurs at a lower strain due to the influence of the bulk modulus.

STEP 1: UNIFORM FIBRILS MODEL

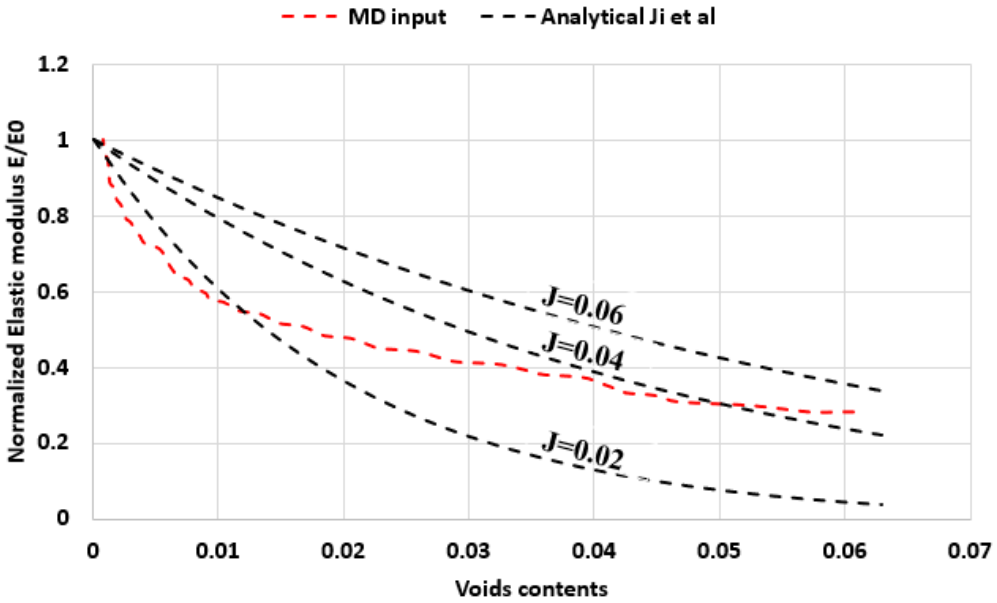

The normalized elastic modulus was compared to the analytical inverse correlation proposed by Ji et al. (2006) for the effect of porosity on mechanical properties:

$E/E0 = (1 - P)^{\frac{1}{J}}$, where P is the void content and J is the fractal parameter. A value of J=0.04 provided the best correlation with the data.

•The elastic modulus at **zero porosity** tends to match the modulus of the **constituent material** used in the simulation or experiment.

STEP 2: STATISTICAL GEOMETRY GENERATION

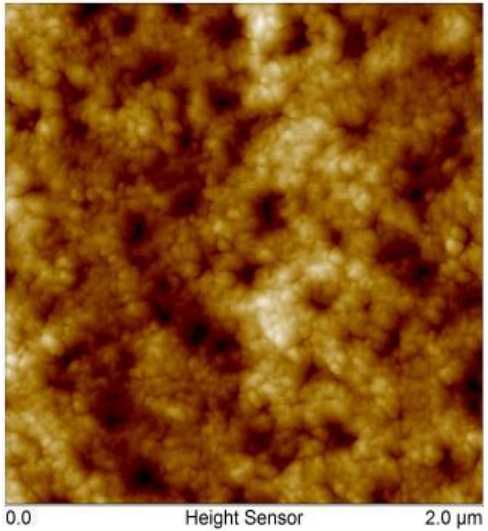

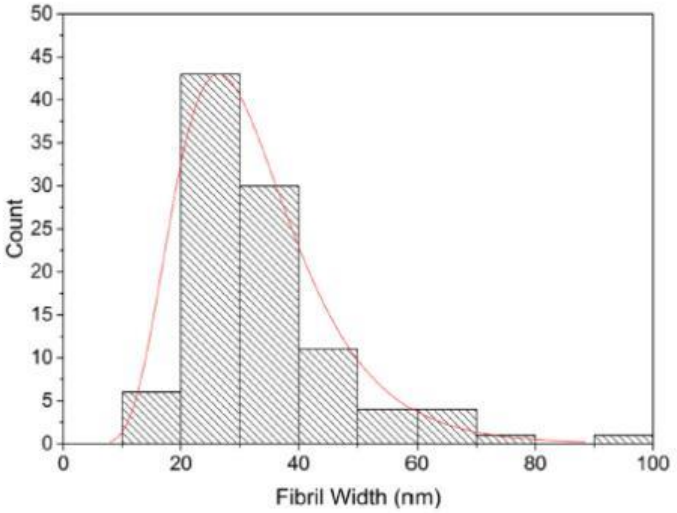

Morphology of UHMWPE Fiber (McDaniel et al., 2015)

- AFM imaging reveals aligned fibrils with interstitial voids in PE fibers.
- Surface fibrils show width variations following a log-normal distribution.
- Direct measurements validate the statistical trend across the fiber surface.
- This distribution serves as a baseline for structural modeling.

STEP 2: STATISTICAL GEOMETRY GENERATION

UNIVERSITY OF DELAWARE
CENTER FOR COMPOSITE MATERIALS
Celebrating 50 Years

- **Efficient Modeling Through Monte Carlo and CAD**

1.Statistic representative

CAD/VBA Modeling Output

Statistical Parameters of Void Content

Reduce the number of fibrils

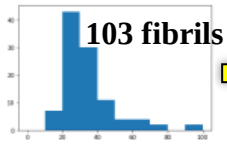

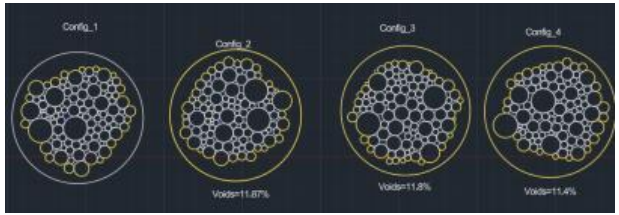

10 configurations

Mean (μ)	Standard deviation (σ)
10.4%	2.76%

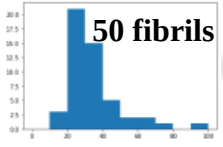

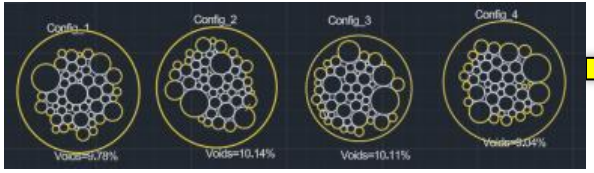

10 configurations

Mean (μ)	Standard deviation (σ)
9.30%	3.17%

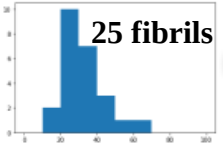

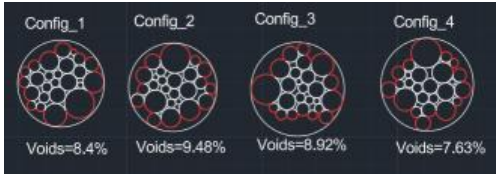

10 configurations

Mean (μ)	Standard deviation (σ)
8.01%	2.84%

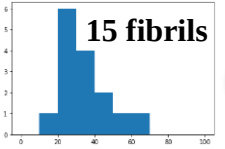

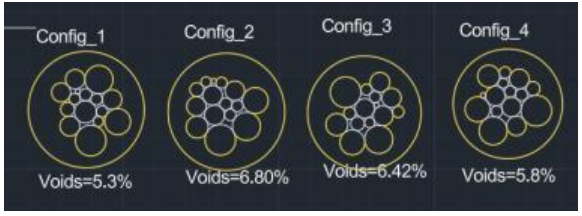

10 configurations

Mean (μ)	Standard deviation (σ)
6.24%	4.0%

- We applied Monte Carlo sampling to statistical fibril data and used CAD to generate ten configurations for each case.
- The 25-fibril model balanced accuracy and efficiency, reducing simulation time by over 86% compared to the full model.

STEP 3: REALISTIC SIMULATION

•One representative geometry out of ten configurations was selected for detailed FE simulation.

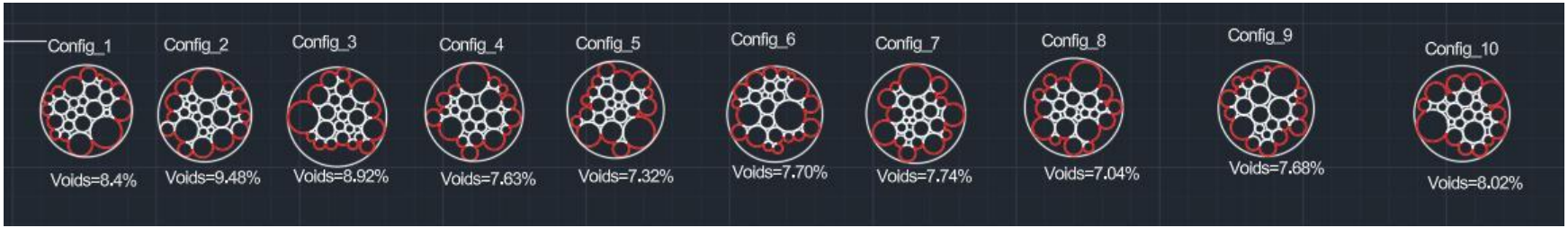

- Based on CAD-generated distributions, multiple fibril array configurations were created.
- Among these, one configuration was selected for finite element modeling in ABAQUS.
- Configuration 2, characterized by the largest initial void content, was chosen to represent the most critical case for assessing consolidation and mechanical response

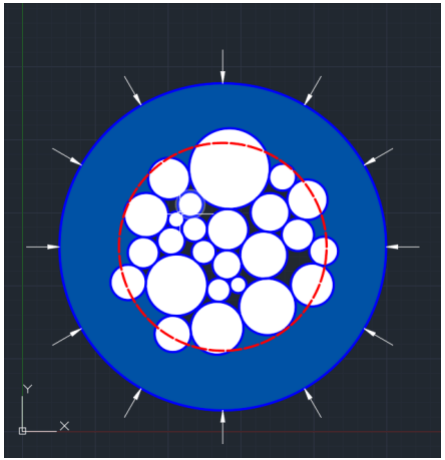

- Schematic of the model for 25-fibril arrays with initial voids of 9.48%.
- The red-dash line is the equivalent radius for the fibrils and voids with equivalent volume.

STEP 3: REALISTIC SIMULATION

•**The results: Contour plots.**

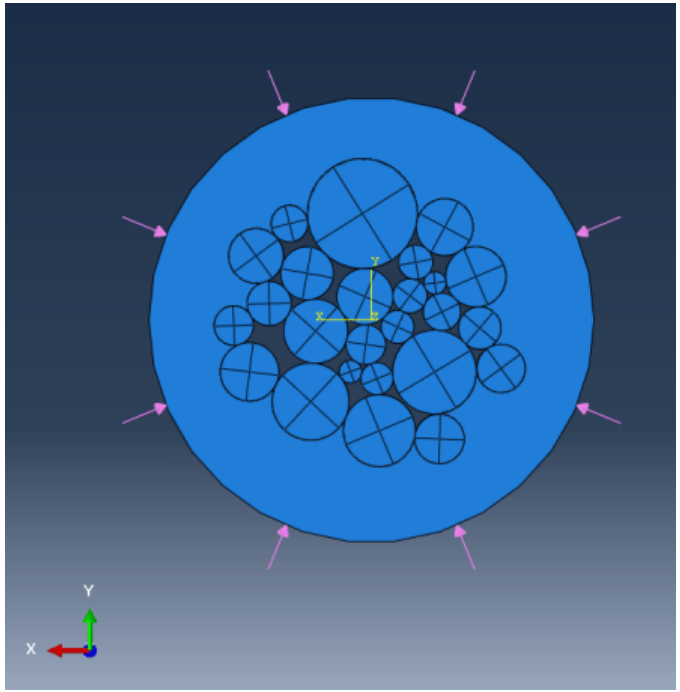

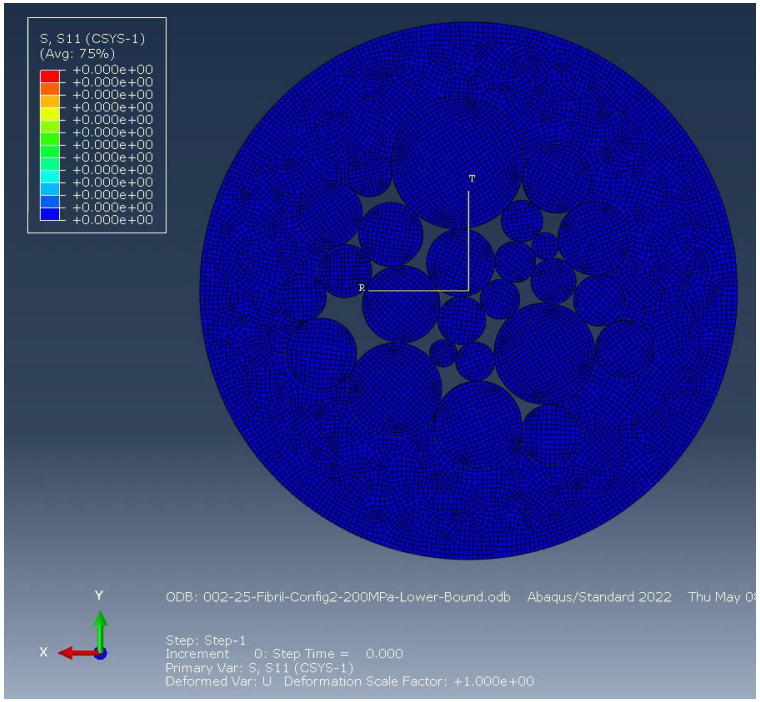

•The same modeling approach used for the uniform fibril array was applied to the stochastic configuration. However, in this case, hydrostatic pressure was applied uniformly along the entire circumference of the fibril array to accurately simulate realistic compaction behavior. Voids gradually decrease with increasing pressure. Complete void-free occurs at 166 MPa.

STEP 3: REALISTIC SIMULATION

- **Void's content reduction with increasing hydrostatic pressure at 125C**

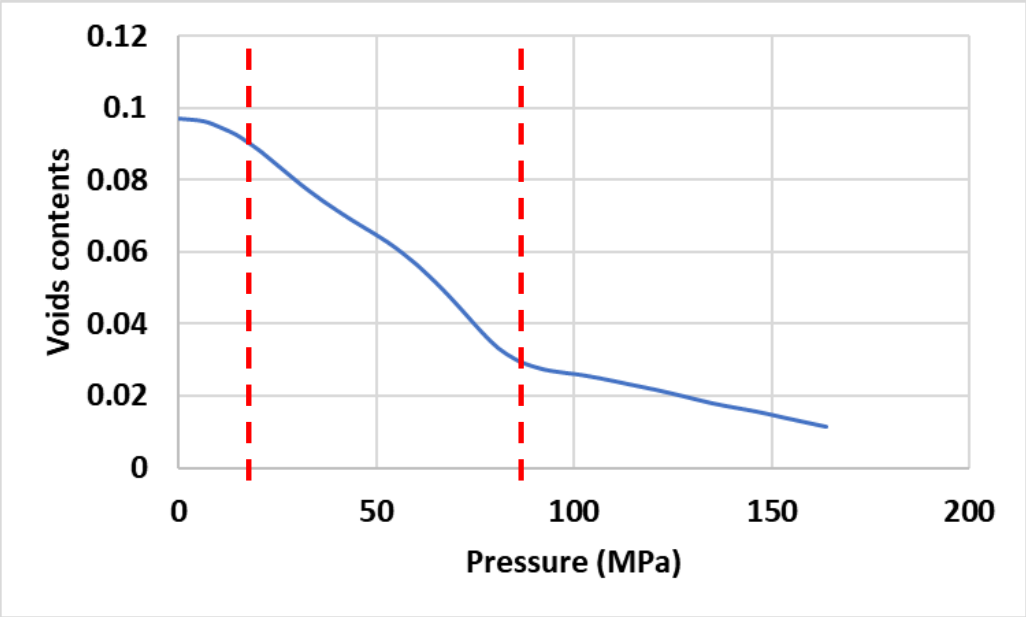

- Initial void content is 9.48% (0.0948) is much closer to the measured porosity
- Three stages of the plots (Elastic deformation, Elastic-plastic softening, Bulk modulus stiffening) exist.
- Hydrostatic pressure of 160 MPa reduced Void Content to 1% for the Stochastic fibril array (9.48% to 1%). In comparison, 160MPa reduced Void Content from 6.3% to 1%).
- Predicted evolution of microstructure for Stochastic fibril array is more realistic (fibril shape, contact and relative orientation of PE crystals) for FEA simulations considering fibrillation failure modes

EQUIVALENT BULK MODULUS WITH VOID CONTENTS

UNIVERSITY OF DELAWARE
CENTER FOR COMPOSITE MATERIALS
Celebrating 50 Years

➢ **The results :Bulk Modulus Evolution During Void Elimination , Based on MD at 125C Input**

- For the plane strain condition, the effective bulk modulus K is calculated from the volumetric strain vs. pressure plot using the relation: $K = -\frac{\Delta P}{\Delta V/V}$ ……. (1)
- Analytically, the bulk modulus of the fully dense constituent material (from MD input properties) is determined from Equation (2): $K = \frac{E}{2(1+\nu)(1-2\nu)}$ … … … (2)
- Substituting the MD-derived values yields: K=56.1 GPa
- As void content vanishes, the effective bulk modulus approaches that of the solid, confirming pressure-induced densification and stiffness recovery.

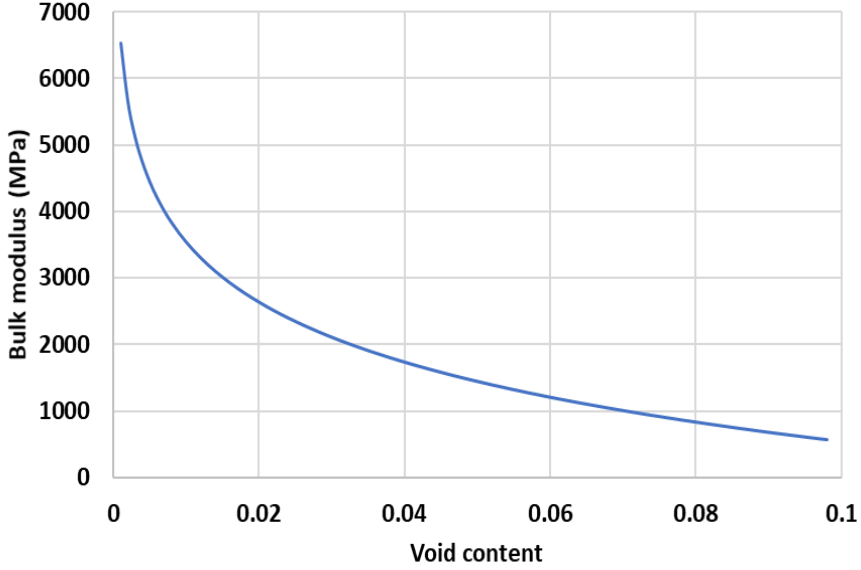

STEP 3: REALISTIC SIMULATION

- **The results: The equivalent stress-strain, Based on MD at 125C Input**

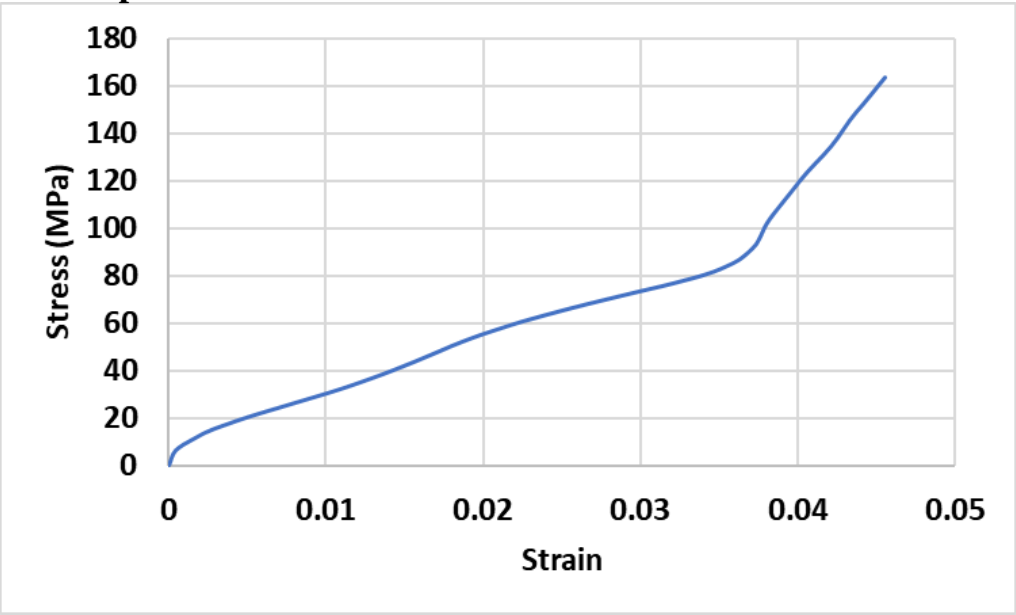

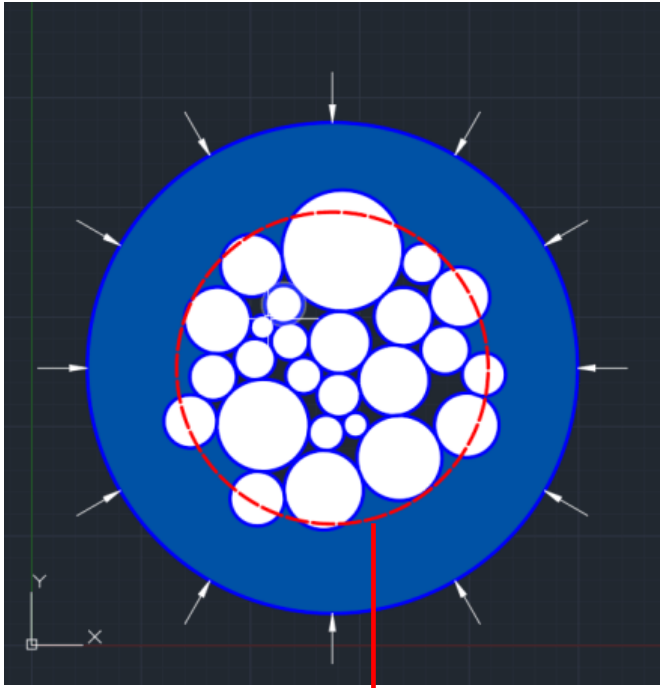

Equivalent volume

- Effective stress–strain computed at the red-dotted effective circle, it can be seen that the stages are Elastic deformation, Elastic-plastic softening, Bulk modulus stiffening.

EQUIVALENT ELASTIC MODULUS WITH VOIDS (125C⁰)

The results: Effective elastic modulus, Based on MD at 125C Input

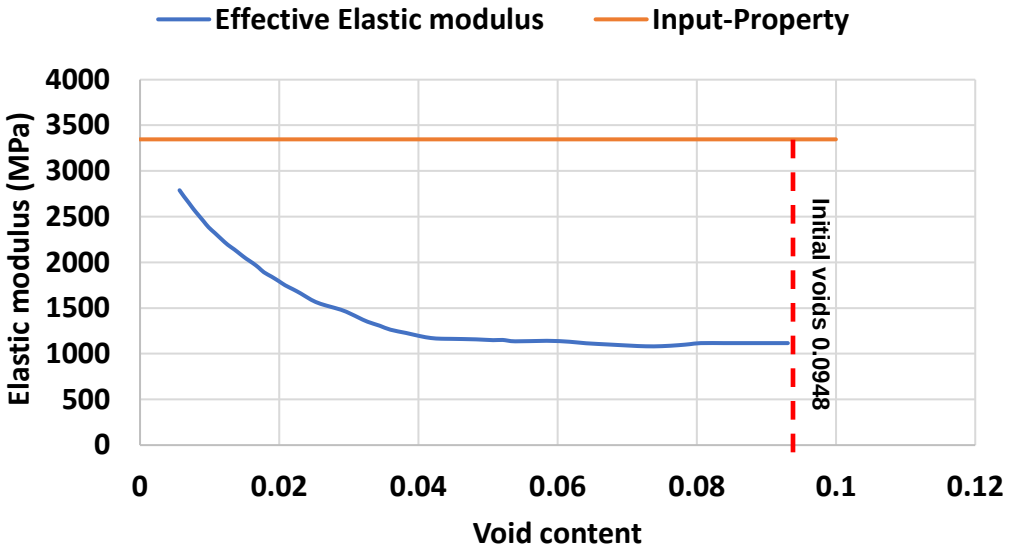

- At an initial void content of 9.48%, the elastic modulus was 1115.9 MPa. As voids diminished, stiffness increased steadily, reaching 3345 MPa at zero porosity. The void-free modulus closely matches the solid input property, confirming the correlation.

CONCLUSIONS AND FUTURE WORK

- A novel micromechanical model was developed to simulate the effect of consolidation pressure on polyethylene (PE) fibril arrays with interstitial voids.
- The model incorporates fibril distribution and void content inspired by AFM imaging.
- A Mooney–Rivlin hyperelastic model successfully represented the incompressible polymer, transmitting uniform hydrostatic pressure.
- Parametric studies confirmed the model's ability to capture inelastic fibril deformation, void collapse, and contact area growth.
- The evolved microstructure provides a realistic basis for multiscale modeling of fibril interaction and compaction behavior.
- The methodology enables prediction of effective mechanical properties as functions of microstructural change.
- Plane strain bulk modulus, Young’s modulus, and stress–strain response show nonlinear increases with pressure.
- As voids are eliminated, the effective properties approach those of fully dense fibrils.

Future Work:

- Use the predicted microstructure to evaluate effective mechanical properties at room temperature (RT).
- Apply the predicted contact areas between fibrils to model defibrillation behavior under axial and transverse loading conditions.

ACKNOWLEDGEMENT

- Presented research was funded under the cooperative agreement award number W911NF-23-2-0022.
- To the CCM-UD family and staff.
- Team Members:
  - Professor Jack Gillespie
  - Dr. Joseph Deitzel
  - Dr. John Tierney
  - Dr. Nuwan Dewapriya and Molla Ali
- ARL TPOC:
  - Dr. Travis Bogetti
  - Dr. Mike Yeager

ICCM24
AUGUST 4-8, 2025
BALTIMORE CONVENTION CENTER
BALTIMORE, MARYLAND, USA

No Technical Paper Submission for:

Muhammad Yasir Khalid

ICCM24
AUGUST 4-8, 2025
BALTIMORE CONVENTION CENTER
BALTIMORE, MARYLAND, USA

No Technical Paper Submission for:

Tae Kyeom Kim

ICCM24
AUGUST 4-8, 2025
BALTIMORE CONVENTION CENTER
BALTIMORE, MARYLAND, USA

No Technical Paper Submission for:

Muzafar Hussain

ICCM24
AUGUST 4-8, 2025
BALTIMORE CONVENTION CENTER
BALTIMORE, MARYLAND, USA

No Technical Paper Submission for:

Erdem Yildiz

SUSTAINABLE PHASE CHANGING FIBER-REINFORCED COMPOSITES

Aidan D. Holihan[1], Philip R. Barnett[1,2]

[1]Tickle College of Engineering, The University of Tennessee, Knoxville, TN, USA
Email: aholihan@vols.utk.edu

[2]The University of Tennessee-Oak Ridge Innovation Institute, The University of Tennessee, Knoxville, TN, USA
Email: pbarnet3@utk.edu, web page: https://volweb2.utk.edu/~pbarnet3/

Keywords: *Carbon fiber; Discontinuous reinforcement; Porosity; Thermomechanical; Recycling*

ABSTRACT

Sustainable composites made of a thermoplastic polyphenylene sulfide matrix reinforced with recycled carbon fibers were produced and infiltrated with a bio-based phase change material to enhance their temperature resistance. By varying molding pressure, the void content of the composites was controlled, thereby allowing for variable phase change material content. Flexural testing revealed that the inclusion of phase change material enhances the flexural modulus of the composites. Similarly, the thermal conductivity of the composites was found to improve with the addition of phase change material, which filled the pore spaces within the composite that prevented effective heat transfer. While typically viewed as a detriment, we showed that targeted porosity infiltrated with a phase change material can enhance the functionality of composites with minimum flexural stiffness loss.

1 INTRODUCTION

Carbon fiber reinforced polymers are the material of choice for high performance structures subjected to moderate thermal loads. For more intense thermal loading, microvascular composites offer sustained high temperature performance that is otherwise limited by the polymeric matrix[1]. However, structures do not always undergo sustained thermomechanical loading, instead often experiencing brief temperature excursions during operation in applications such as batteries and motors in electric vehicles and aircraft during acceleration or take-off/landing. As such, the active cooling of composites may not always be the most appropriate design choice due to the additional complexity and weight associated with the hardware required to actively pump the coolant through vasculature. Phase change materials (PCMs) offer a passive alternative to active cooling.

Few authors have studied the use of PCMs as a means of thermal regulation in composite materials. Casado et al.[2] filled cavities in an injection molded rail flanged plate with PCM to extend fatigue life by more than 400% through reduced temperature rise of the polyamide matrix. Yoo et al. [3,4] incorporated PCM microcapsules into a glass fiber/epoxy laminate to enhance thermal energy storage. They found that the PCM led to a decrease in thermal conductivity, an increase in thermal storage capacity, an increase in dimensional stability, and a significant decrease in the mechanical properties of the composites. The thermal stability of the composites was unaffected by the inclusion of PCM. Fredi et al. [5] mixed paraffin microcapsules into carbon fiber/PMMA composites and found that the activation energy of PCM composite glass transition was not significantly impacted by the PCM with a melting point of 43 °C. Their dynamic mechanical analysis (DMA) results indicated that the embedded PCM caused a brief pause in the gradual storage modulus decrease during heating.

In this study, we investigated the manufacturing of recycled carbon fiber composites containing embedded phase change materials. Unlike the prior work, which focused primarily on microcapsules mixed into the resin, we show that low-cost sustainable composites containing PCM can be produced using a scalable vacuum infiltration process. We showed that recycled carbon fiber nonwoven preforms can be used to manufacture composites with highly connected porosity when processed by compression molding following the author's prior work[6]. Recycled carbon fibers offer a significant reduction in carbon emissions, while maintaining near virgin fiber mechanical properties. The PPS matrix offers high toughness, solvent resistance, and is commonly found in under-the-hood automotive applications. We

produced samples with varying molding pressures and resin content to induce varying void content, which was characterized by density measurements and optical microscopy. We filled the connected pore space with a biobased PCM having a heat storage capacity near 200 Jg^{-1} using a vacuum infiltration process. We then characterized flexural performance and transverse thermal conductivity. This work sets the foundation for creating multifunctional composites for thermal energy storage using sustainable reinforcement and PCMs.

2 MATERIALS AND METHODS

2.1 Carbon Fiber

Recycled carbon fiber preforms, provided by Gen2 Carbon (formerly ELG Carbon Fibre), containing fibers recovered via a pyrolysis process and then upcycled into a nominally 200 gm^{-2} nonwoven fabric produced using carding and cross-lapping processes, were used in this work. Prior testing revealed that the fibers exhibit standard modulus properties[7]. Fiber length was greater than 25 mm, for which mechanical properties significantly exceeding typical short fiber composites have been realized. The use of recycled carbon fibers makes this reinforcement choice both low cost and sustainable. Reducing manufacturing waste and re-using fibers from end-of-life parts aids in the development of a circular economy for composite materials.

2.2 Polyphenylene Sulfide

Polyphenylene sulfide (PPS) is a semicrystalline aromatic thermoplastic offering high toughness, solvent resistance, and performance comparable to many common structural epoxies. The high melt temperature of the polymer, in combination with the high levels of crystallinity that enables its use well beyond its glass transition temperature, makes PPS a strong candidate for applications in which thermal resilience is required. PPS films of 0.127 mm thickness (Solvay, Ryton QC160P) were purchased from CS Hyde for use as the matrix in the composites manufactured in this study. In addition to the beneficial thermal, mechanical, and chemical properties of PPS, the recyclability of thermoplastic matrix composites is of key importance to the development of a circular economy for composites materials. PPS can be melt processed to form new composites from end-of-life components and manufacturing waste[8], unlike traditional thermosets that are typically pyrolyzed or chemically digested for fiber recovery and subsequent integration into new parts.

2.3 Phase Change Materials

A commercially-available PCM was purchased (Entropy Solutions, PureTemp). The material, referred to as 48X, was a white wax as a solid and a clear, low viscosity liquid as a melt. According to the manufacturer, the 48X PCM shows a melting point of 48 °C, a thermal conductivity of 0.25 $W\ m^{-1}\ K^{-1}$, and a heat storage capacity of 230 $J\ g^{-1}$. PCMs are emerging as an option to improve the thermal efficiency of buildings through thermal energy storage[9]. Their integration into low-cost composite materials would enable new architectural designs with enhanced sustainability.

2.4 Composite Manufacturing

Composites were manufactured through a compression molding process. Relative to traditional composite manufacturing techniques such as autoclave and oven curing of thermosets, compression molding is a rapid and low energy process capable of meeting high volume demand. First, organosheets, or single plies of carbon fiber reinforced thermoplastic, were produced by compressing a single nonwoven layer between two PPS films at 300 °C and 1 MPa pressure for 5 minutes, followed by cooling under pressure to 60 °C. The organosheets were then cut into 150 mm × 150 mm plies and placed in a closed mold of the same dimensions to form plaques for testing. Due to anisotropy in the preforms[6], special care was taken to track the laminate orientation. Processing times and temperatures were the same for organosheets and composite plaques, while the pressure used to manufacture plaques was varied from 0.5 to 4 MPa to achieve differing levels of porosity.

Samples were cut from the plaques for flexural, thermal conductivity, and dynamic mechanical analysis testing using a wet diamond saw and subsequently milled to the final dimensions. Once at the

final dimensions, the density of the composites was evaluated using an analytical balance and measurements of the length, width, and thickness. Some of the samples were evaluated as-cut, while others were infiltrated with the PCM before testing. Initial density measurements using a helium pycnometer revealed that the porosity within the uninfiltrated samples was highly connected. PCM infiltration was achieved by placing the samples in a beaker of PCM melt inside a vacuum oven for 10 minutes at greater than 26" Hg.

2.5 Micrographic Analysis

Specimens extracted from the plaques were polished for optical microscopy. Images were acquired at 200X resolution (0.96 μm/pixel) over a 12.7 mm wide section of the composites using a Keyence VHX-7100 automated stage microscope. The fiber volume fraction was determined by segmenting the images in ImageJ and using a pixel-counting script developed in MATLAB. This method has been shown to yield good agreement with measurements using Archimede's Principle[7]. Multiple cross sections were evaluated to capture local variability.

2.6 Flexural Testing

Flexural testing was performed on samples according to the ASTM D790 standard on specimens of 50.8 mm × 12.7 mm at a span-to-depth ratio of 16 at a strain rate of 1% per minute. Five samples containing PCM and five neat samples were tested per molding condition. Additionally, neat PCM samples were tested.

2.7 Thermal Conductivity

Transverse (through-thickness) thermal conductivity was measured using the double-sided transient plane source method (TPS 2500S, Hot Disk). Three measurements were taken per sample at each molding pressure on neat samples. The neat samples were then infiltrated with PCM and re-tested to ensure that local microstructural variability did not significantly influence the measurement.

3 RESULTS AND DISCUSSION

3.1 Multiscale Characteristics

The composites were evaluated at both the bulk and microstructure scales to elucidate the effects of varying pressure during molding. The density of the composites was found to increase as a function of the applied molding pressure, as shown in Figure 1. Previous work by the author[10] has shown that increasing the molding pressure leads to greater fiber compaction and enhanced consolidation. Too little pressure leads to porosity due to resin starvation. Interestingly, the density measured by helium pycnometry was largely consistent, ranging from 1.482 to 1.507 g/cc. The void-free density was estimated to be 1.494 g/cc based on the densities of the constituent components. This indicates that the pores within the composite were highly connected.

The void content before and after infiltration with the PCM is also shown in Figure 1. A major reduction in void content was apparent when comparing the measured density for PCM infiltrated composites with the theoretical density of a composite in which all the voids were filled with PCM. For samples molded at pressures of 2 and 4 MPa, the initial porosity was so low that the PCM had no significant effect on further decreasing porosity. This indicates that there is a limit to the pore connectivity in the composites.

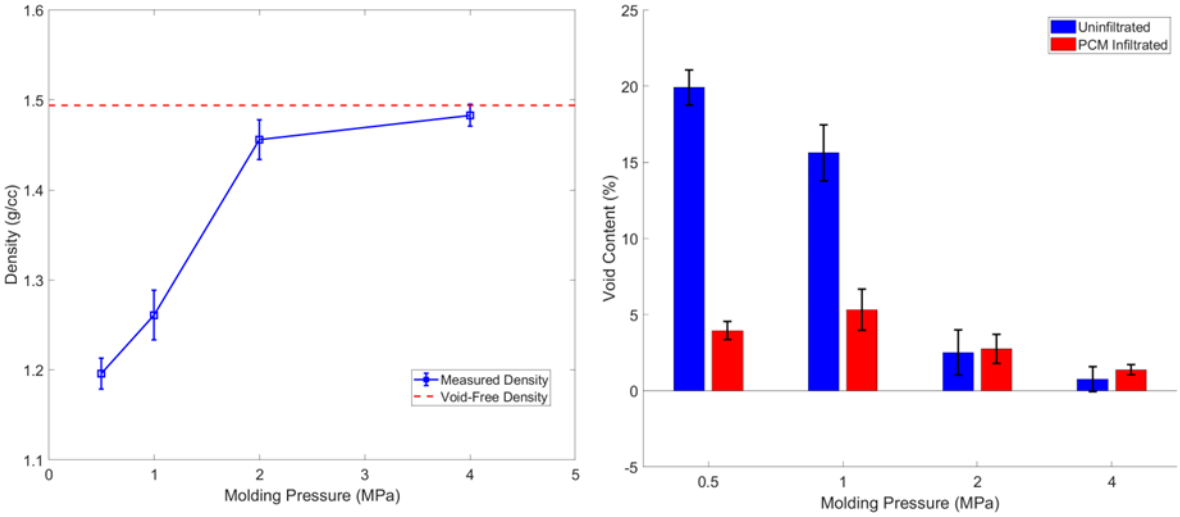

Figure 1: Additional molding pressure significantly increases composite density (left) and most of the voids are filled with PCM (right).

Example optical micrographs acquired for the samples are shown in Figure 2 and the resulting fiber volume fraction analysis is found in Table 1. For low molding pressure, significant interlaminar voids are present, indicating that resin migrated either from the center of the preforms and toward the interfaces or from the interfaces and to the center during consolidation. The high loft of recycled carbon fiber nonwovens makes this behavior likely to occur, although additional study is required to understand the mechanism. As the pressure increased to 1 MPa, the voids became more dispersed and spherical in shape, indicating entrapped gas as opposed to resin migration. At and above 2 MPa, the voids were nearly gone, with a consistent distribution of fibers. Likewise, the fiber volume fraction was a function of the total applied pressure, in addition to the matrix film thickness. The maximum was achieved at or beyond 2 MPa molding pressure, representing complete infiltration of the matrix film. The fiber content saturates at this level as there is no way of removing excess resin in the closed mold used in this study. For discontinuous fiber composites, this represents a significant improvement over incumbent materials such as long fiber thermoplastics and injection molding compounds.

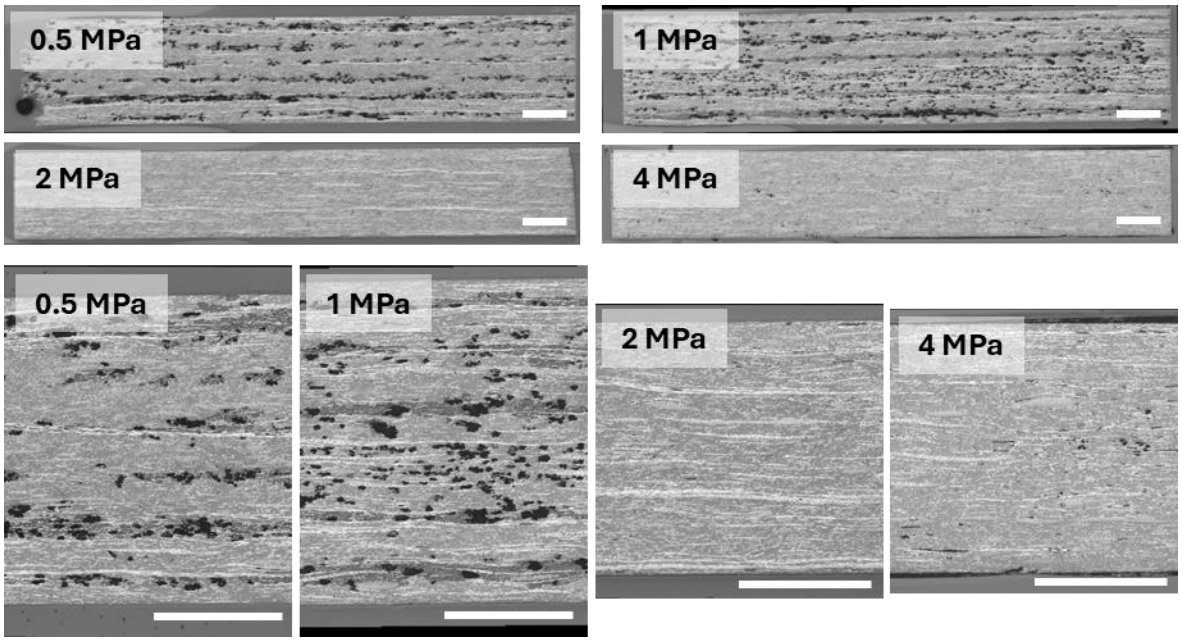

Figure 2: Representative micrographs of compression molded composites before infiltration.

Molding Pressure	Fiber Volume Fraction (%)
0.5 MPa	27.73 ± 1.64
1 MPa	26.89 ± 1.77
2 MPa	35.25 ± 2.23
4 MPa	33.65 ± 1.51

Table 1: Fiber volume fraction measured from optical micrographs

3.2 Flexural Testing

Flexural testing of the neat PCM revealed extremely low mechanical properties. The flexural strength was 1.17 MPa ± 0.019 MPa and the flexural modulus was 0.41 GPa ± 0.09 GPa. A simple Rule of Mixtures approximation for the properties of the infiltrated composites is as follows:

$$P_{infiltrated} = P_{composite}(1 - V_{PCM}) + P_{PCM}V_{PCM} \quad (1)$$

where P refers to the property (strength or modulus) of interest for the composite or PCM phase and V refers to the volume fraction of each phase. Due to the small volume of PCM and its low mechanical properties compared to the composite, the PCM is not expected to contribute significantly to the mechanical properties of the infiltrated composites.

Surprisingly, flexural testing of the composites revealed a significant increase in modulus in the samples containing PCM, as shown in Figure 3. This modulus increase cannot be simply explained by the Rule of Mixtures but instead is likely the result of more complex micromechanical mechanisms that require further exploration. It is theorized that the filled voids may provide an elastic support for fibers subjected to bending within the composite. Due to the small fiber diameter, bending of fibers near voids is expected to be significant. By filling the void with PCM, the neighboring fibers can be supported against bending. Future work will be required to evaluate this proposed mechanism of stiffness retention.

The flexural strength of the composites was not significantly improved by the addition of PCM, indicating that the reduction in void space did little to change the failure of the composites. This behavior is expected from the Rule of Mixtures, as the strength of the neat PCM was very low relative to the composite strength. It is worth noting the error bars in Figure 3. The variability in properties is more significant for the composites manufactured at lower molding pressures. Much of this variability may be attributed to the microstructural inhomogeneity in discontinuous fiber composites, in which regions of fiber misorientation or variable fiber volume fraction may lead to premature localized failure that is amplified by inhomogeneous void distribution. Hence, the lower the void content, the less variable the strength. The variability in this work could be better understood with further testing that is beyond the scope of this manuscript. Despite this limitation, the trends are clear: the flexural strength of composites infiltrated with PCM is largely unaffected, while their flexural modulus generally improves.

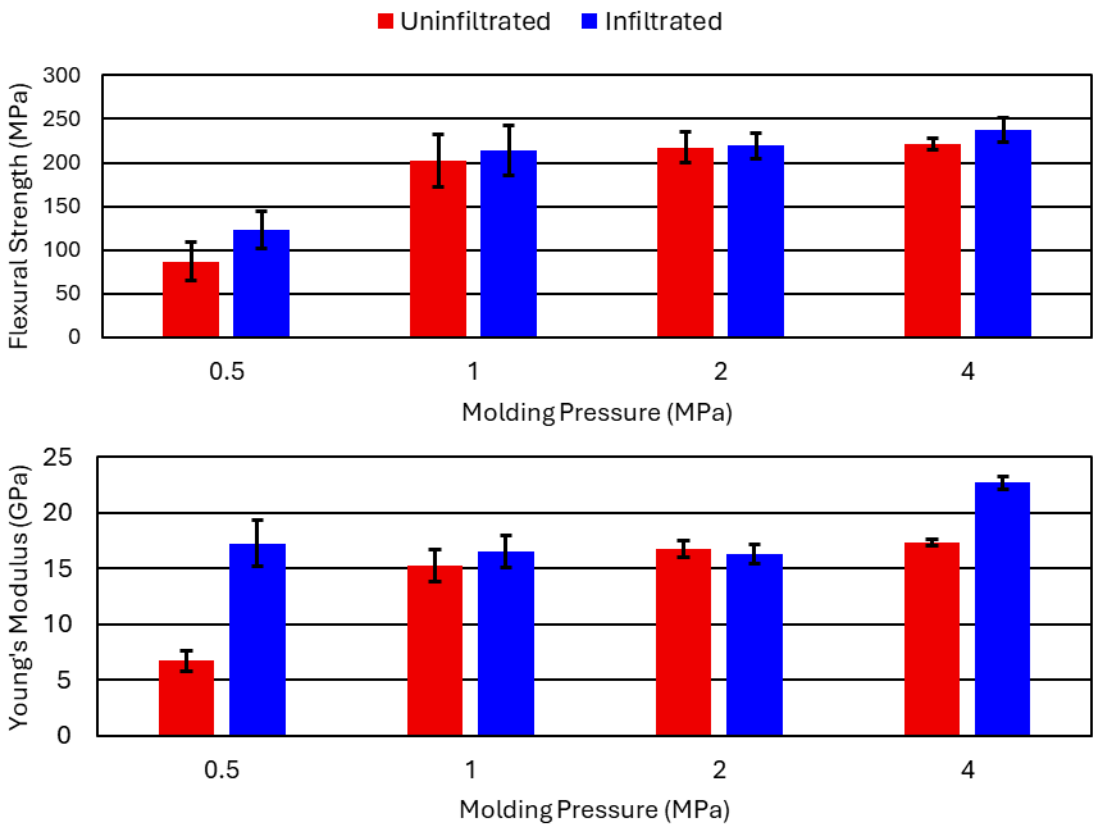

Figure 3: Flexural strength (top) and modulus (bottom) of neat and PCM-containing composites manufactured at different molding pressures.

3.3 Thermal Conductivity

The measured transverse thermal conductivity of the composites is shown in Figure 4. The thermal conductivity of the neat PPS was reported as 0.30 W m^{-1} K^{-1} by the manufacturer. The transverse thermal conductivity of composites is matrix-dominated due to the matrix regions separating fibers. Furthermore, the transverse thermal conductivity of carbon fibers is typically much lower than the axial thermal conductivity. Due to these properties, in combination with the high void content of the composites manufactured at low molding pressures, the thermal conductivity of composites molded below 2 MPa was lower than even the neat polymer. However, the addition of PCM to fill the porosity led to a significant increase in the transverse thermal conductivity of the composites despite its low thermal conductivity. For all molding pressures tested, the infiltrated composites reached approximately their full thermal conductivity with the addition of PCM.

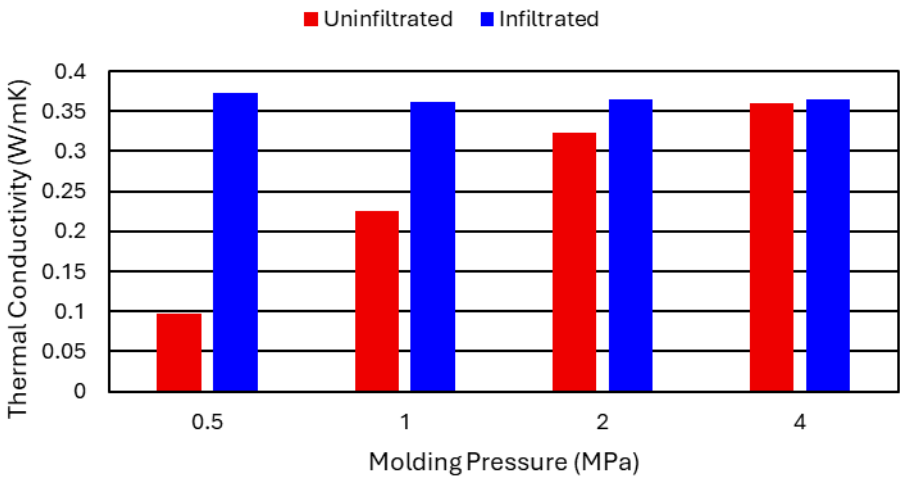

Figure 4: Thermal conductivity of neat and PCM-containing composites manufactured at different molding pressures.

9 CONCLUSIONS

In this work, we developed low-cost, sustainable composites containing embedded phase change materials. The use of low-cost recycled carbon fiber reinforcement, an easily recyclable thermoplastic matrix, and rapid compression molding processing makes such materials attractive to high volume markets in which cycle and time and cost are key factors driving decision making. We showed that porosity in these composites can be controlled by varying the applied pressure during molding. After molding, parts can be vacuum infiltrated with a PCM melt in a scalable process. The embedded PCM offers several benefits, including synergistically enhanced flexural modulus and improved thermal conductivity. The PCM is also anticipated to enable brief excursions beyond typical use temperatures or sensing through thermal energy storage. This work shifts the paradigm of void content in composites from a detriment to a beneficial feature. Beyond the ability to withstand brief thermal excursions, this material system also adds passive thermal energy storage capabilities. The addition of PCM into sustainable composites may aid in an acceleration of the shift to composite materials in the transportation and construction industries by integrating additional thermal regulation capabilities without the need for active coolant pumping.

Future work will seek to evaluate the pore morphology of these composites, understand the impact of the embedded PCM on the activation energy of transition processes in the composites, and exploring the viscoelastic and fatigue properties of these materials. The use of recycled carbon fibers paired with a thermoplastic matrix and bio-based PCM makes this material a strong candidate for low carbon footprint multifunctional composites.

ACKNOWLEDGEMENTS

We acknowledge Dayakar Penumadu for providing access to the Hot Disk system for thermal conductivity measurements and microscopy facilities. We thank David Harper and Joshua Crabtree for helpful discussions in the formulation of this concept. We are grateful to Andy Baker for providing us with machining expertise for sample preparation.

REFERENCES

[1] Coppola AM, Warpinski LG, Murray SP, Sottos NR, White SR. Survival of actively cooled microvascular polymer matrix composites under sustained thermomechanical loading. *Composites Part A: Applied Science and Manufacturing*, **82**, 2016, pp. 170–9. (https://doi.org/10.1016/j.compositesa.2015.12.010).

[2] Casado JA, Gutiérrez-Solana F, Carrascal I, Diego S, Polanco JA, Hernández D. Fatigue behavior enhancement of short fiber glass reinforced polyamide by adding phase change

materials. *Composites Part B: Engineering*, **93**, 2016, pp. 115–22. (https://doi.org/10.1016/j.compositesb.2016.02.059).

[3] Yoo S, Kandare E, Shanks R, Al-Maadeed MA, Afaghi Khatibi A. Thermophysical properties of multifunctional glass fibre reinforced polymer composites incorporating phase change materials. *Thermochimica Acta*, **642**, 2016, pp. 25–31. (https://doi.org/10.1016/j.tca.2016.09.003).

[4] Yoo S, Kandare E, Mahendrarajah G, Al-Maadeed MA, Khatibi AA. Mechanical and thermal characterisation of multifunctional composites incorporating phase change materials. *Journal of Composite Materials*, **51**, 2017, pp. 2631–42. (https://doi.org/10.1177/0021998316673894).

[5] Fredi G, Dorigato A, Pegoretti A. Dynamic-mechanical response of carbon fiber laminates with a reactive thermoplastic resin containing phase change microcapsules. *Mechanics of Time-Dependent Materials*, **24**, 2020, pp. 395–418. (https://doi.org/10.1007/s11043-019-09427-y).

[6] Barnett PR, Gilbert CL, Penumadu D. Repurposed/recycled discontinuous carbon fiber organosheet development and composite properties. *Composites Part C: Open Access*, **4**, 2021. (https://doi.org/10.1016/j.jcomc.2020.100092).

[7] Barnett PR, Young SA, Chawla V, Foster DM, Penumadu D. Thermo-mechanical Characterization of Discontinuous Recycled/Repurposed Carbon Fiber Reinforced Thermoplastic Organosheet Composites. *Journal of Composite Materials*, 2021. (https://doi.org/10.1177/00219983211015721).

[8] Barnett PR, Hmeidat NS, Zheng B, Penumadu D. Toward a circular economy: zero-waste manufacturing of carbon fiber-reinforced thermoplastic composites. *Npj Materials Sustainability*, **2**, 2024, pp. 1–12. (https://doi.org/10.1038/s44296-024-00006-y).

[9] Faraj K, Khaled M, Faraj J, Hachem F, Castelain C. Phase change material thermal energy storage systems for cooling applications in buildings: A review. *Renewable and Sustainable Energy Reviews*, **119**, 2020, pp. 109579. (https://doi.org/10.1016/j.rser.2019.109579).

[10] Barnett PR, Cook ZA, Hulett BM, Varma NH, Penumadu D. Influence of processing parameters on permeability and infiltration of compression molded discontinuous carbon fiber organosheet composites. *Composites Part A: Applied Science and Manufacturing*, **152**, 2022, pp. 106682. (https://doi.org/10.1016/j.compositesa.2021.106682).

ICCM24 24TH INTERNATIONAL CONFERENCE ON COMPOSITE MATERIALS
AUG 4-8, 2025 • BALTIMORE CONVENTION CENTER • BALTIMORE, MARYLAND

MEASURING THE MECHANICAL AND ELECTRICAL PERFORMANCE OF CONFORMAL LOAD-BEARING ANTENNA STRUCTURES UNDER MECHANICAL LOADING

Mitch Dunn[1], Thien Bui[1], Samuel Munro[1], Michael Adams[1], Alice Greenan[1], Clement Beteille[1] and Martin Veidt[1]

[1]School of Mechanical & Mining Engineering, The University of Queensland
Brisbane, Australia
Email: m.dunn1@uq.edu.au

Keywords: Smart materials; Hybrid; Laminates; Electrical properties; Mechanical properties.

ABSTRACT

Conformal Load-Bearing Antenna Structures (CLAS) are multifunctional composite materials that integrate structural and radio communication capabilities, offering significant potential for aerospace applications. While these structures are named for their load-bearing capabilities, experimental studies validating their electromechanical performance under mechanical loading remains limited. This paper presents proof-of-concept experimental methodologies for characterising the electrical behaviour of embedded patch antennas within composite laminates subjected to tensile and flexural loads.

To minimize interference from test fixtures, custom setups using low-dielectric polymer components were developed, enabling antennas to radiate primarily into free space. Microstrip-fed rectangular patch antennas were fabricated using glass/epoxy laminates with laser-cut copper foil. Electrical performance was assessed during loading, including return loss, resonant frequency and radiation pattern.

Results show that mechanical strain induces predictable shifts in resonant frequency consistent with theoretical models. Flexural testing confirmed that fixture design and proximity to dielectric and conductive material surfaces influence antenna performance. Realised gain measurements under bending reveal the impact of laminate deformation on antenna radiation pattern.

These findings demonstrate the feasibility of simultaneous mechanical and radio frequency (RF) testing methodologies for assessing CLAS performance and for supporting design workflows that combine simulation and experimental verification. This work contributes to advancing multifunctional composite technologies through rigorous electromechanical characterisation, aiding future integration of conformal load-bearing antenna structures into high-performance aerospace systems.

1 INTRODUCTION

Conformal load-bearing antenna structures (CLAS) are a class of multifunctional composite structures capable of functioning as antennas for radio communication in addition to their role as load-bearing structural components. Multidisciplinary technology development driven by the CLAS concept over the past few decades has led to many configurations, but patch antennas (and arrays) made by layering thin copper foil into laminated structures are commonly featured and many designs rely on this fundamental building block. Understanding how these elements perform under load is essential to understanding the coupled mechanical-electrical behaviour of these structures, and critical to designing high performing aerospace vehicles.

Literature studies on CLAS have primarily focused on novel methods to manufacture different configurations of antennas and less focus has been paid to electromechanical performance. Some studies have looked at the performance of antennas after a loading or damage event [1], though most are limited to simulation studies [2]. The use of simulations is a natural choice for designers, as commercially available software is necessary to design patch antennas given the interaction between electromagnetic

radiation and surrounding structural material. This study presents methods for collecting experimental antenna performance data of these structures under load to confirm the findings of simulation studies.

The performance of an antenna against its design parameters can be measured in many ways: realised gain, radiation pattern, resonant frequency, bandwidth, impedance, polarisation and more. These measures can range from single values such as centre/resonant frequency, to multi-dimensional functions such as realised gain which is a function of two polar coordinates and frequency.

An additional consideration is that many antenna measurements are in fact measurements of a larger electrical network. Commonly this includes coaxial cables used to carry electrical signals, and connections between elements. In the case of antennas embedded into composite laminates, there is generally a standard radio frequency (RF) connector (such as Type N or SMA [3, 4]) attached to the composite and soldered to the active element or feed network. Electrical measurements of a CLAS are therefore measurements of the antenna, feed network including solder joints, RF connectors and cables.

The breadth of measurable characteristics, complexity of measured data, and the requirement for a whole-of-system approach means that experimental testing requires some thought and care, whether one is seeking to compare different antennas, compare the performance of a loaded CLAS to an unloaded CLAS, or perform quality assurance on as-manufactured CLAS. One final complication is that conductive or dielectric materials near an antenna influence its radiation pattern. Experimentally characterising antenna performance on aircraft such as UAVs is complicated by the influence of nearby aircraft body [5, 6] for example. Measured experimental results for combined mechanical and RF testing are therefore a function of any apparatus used for fixturing and applying load.

This paper describes some proof-of-concept experimental measurements of antenna characteristics that largely focus on the following research questions:

1. Can we modify standard mechanical tests to reduce the influence of test fixtures on measured antenna characteristics?
2. Can we collect antenna performance data of load-bearing antenna structures under load to compare with simulation studies?

The remainder of this paper is structured as follows:

- Section 2 outlines the theoretical basis for predicting frequency shifts in microstrip-fed patch antennas under mechanical load.
- Section 3 details the design and fabrication of experimental specimens.
- Section 4 describes the testing methodologies developed to minimise fixture interference during tensile and flexural loading.
- Section 5 presents and analyses the electromechanical performance results.
- Section 6 concludes with key findings and recommendations for future research.

2 MICROSTRIP-FED RECTANGULAR PATCH ANTENNA

Figure 1 shows the typical design of a microstrip-fed rectangular patch antenna on a dielectric substrate with a ground plane. The following geometric parameters of the rectangular patch antenna determine the characteristics of the antenna:

- Length (L): determines frequency of fundamental mode
- Width (W): chosen to maximise radiation efficiency
- Substrate height (h): determined by application
- Relative permittivity (ε_r): material property
- Microstrip width (W_0): chosen to match impedance of source; function of h and ε_r
- Recess length (y_0): chosen to match impedance of patch

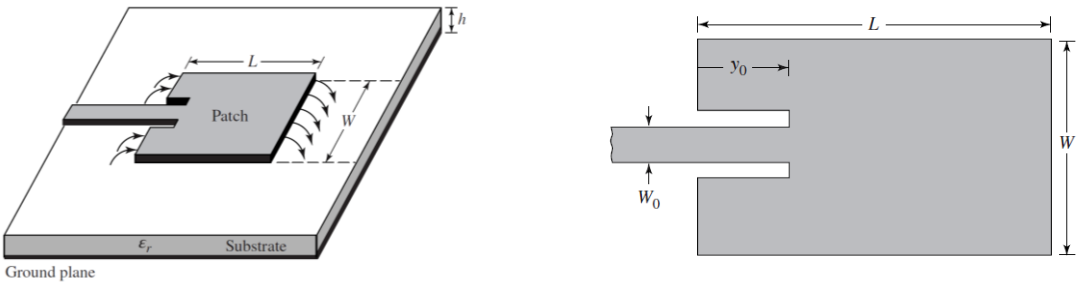

Figure 1: Typical design of a microstrip-fed rectangular patch antenna [7]

Modelling the antenna as a resonant cavity between patch and ground plane [7], the frequency of the fundamental mode, f_{010}, is ultimately a function of patch length, patch width and substrate height (Equation 1); however the influence of patch length is greater than patch width or substrate height.

$$f_{010} = \frac{c}{2L_{eff}\sqrt{\epsilon_{r,eff}}} \quad (1) \qquad \epsilon_{r,eff} = f(W,h) \quad (2) \qquad L_{eff} = f(L,W,h) \quad (3)$$

Mechanical strain of a conformal load-bearing antenna structure can change the characteristic frequency of the antenna. Since the fundamental mode of a rectangular patch antenna depends strongly on patch length, strain along the length direction of a rectangular patch changes the resonant frequency of the antenna; a positive change of length will decrease the frequency. While many conformal load-bearing antennas are not designed using rectangular patches, any planar antenna undergoing strain will change characteristics in a similar fashion. The rectangular patch is a simple, easy to analyse design for studying general trends and answering our research questions.

3 EXPERIMENTAL SPECIMENS

Figure 2 shows the specimen design used in this work for investigating the effect of tensile loading along the length direction (L) of a microstrip-fed rectangular patch antenna. The Tensile Specimen consists of a fibre-reinforced composite laminate having a laser-cut copper foil patch antenna and microstrip feed on the top side and a copper foil ground plane on the bottom side. These specimens are manufactured using two layers of 8-harness satin weave glass/epoxy prepreg, and the copper foil elements are laid up into the laminate prior to vacuum bag cure in an oven.

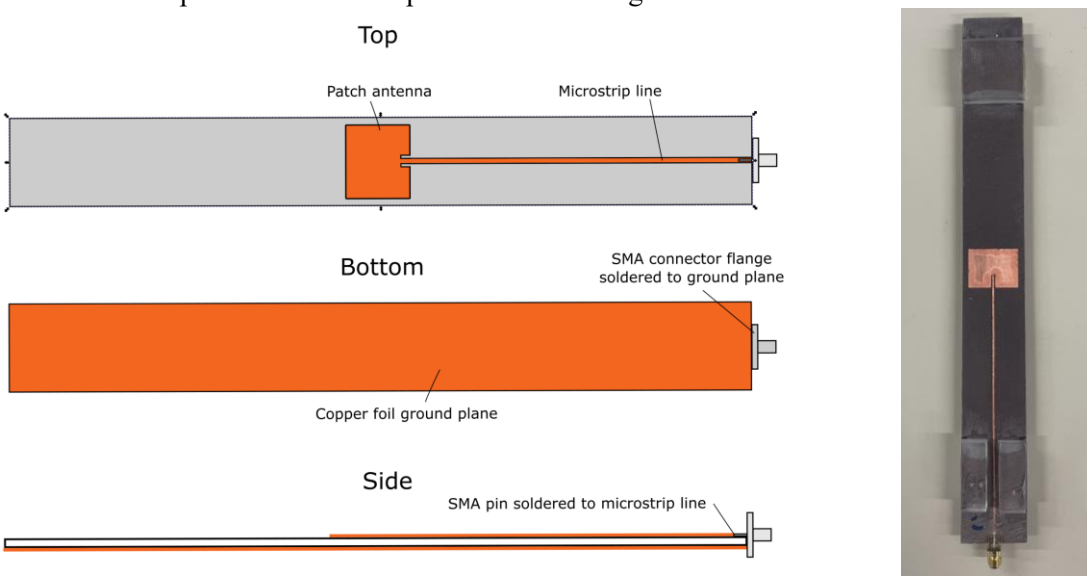

(a) (b)

Figure 2: Specimen design used to investigate the effect of tensile loading

The microstrip line is terminated by an SMA connector; the pin is soldered to the microstrip, and the ground flange is soldered to the ground plane. Perspex tabs are bonded onto both sides of the specimen at each end. The tabs serve two purposes: to ensure that standard mechanical testing machine grips do not contact the microstrip and to ensure an air gap above the microstrip. If a dielectric material were to sit on the surface of the specimen, over the microstrip, this would change the characteristic impedance of the microstrip and affect antenna performance.

A similar design of specimen is used for flexural testing (Flexural Specimen A in Table 1), however no tabs are bonded to these samples. Flexural Specimen B is an alternative flexural testing specimen design where the total height of the laminate is kept fixed, but the active antenna element is embedded one ply beneath the surface. Since flexural strain is dependent on distance from the neutral axis, the antenna elements in Flexural Specimens A and B experience different levels of strain for the same radius of curvature. The microstrip and patch dimensions are adjusted to take into account the effect of the superstrate ply on effective permittivity and microstrip impedance.

Table 1: Specimen parameters for tensile and flexural testing experiments

Specimen Parameter		Tensile Specimen	Flexural Specimen A	Flexural Specimen B
Patch length, L	[mm]	18.9	30.8	30.3
Patch width, W	[mm]	23.9	39.1	38.3
Substrate height*, h	[mm]	0.55	1.10	0.825
Superstrate height, h^+	[mm]	–	–	0.275
Material	–		E-Glass/epoxy	
Substrate relative permittivity, ε_r	–	4.3	4.3	4.3
Microstrip width, W_0	[mm]	0.96	1.90	1.39
Recess length, y_0	[mm]	6.2	10.1	9.9
Specimen length	[mm]	250	210	210
Specimen width	[mm]	30	65	65

*Due to manufacturing variability, the cured substrate height is observed to vary by up to 5% from these nominal values.

Figure 3 shows layup schematics for the two flexural specimens, and for a case where paint is applied as a cosmetic coating to Flexural Specimen A. These schematics are not to scale and are intended to illustrate that the antennas are fabricated by manufacturing a larger composite laminate panel containing multiple antennas, which are later waterjet cut from the panel. While Figure 3 shows two patch antennas per panel, this process scales to higher numbers of antenna per panel.

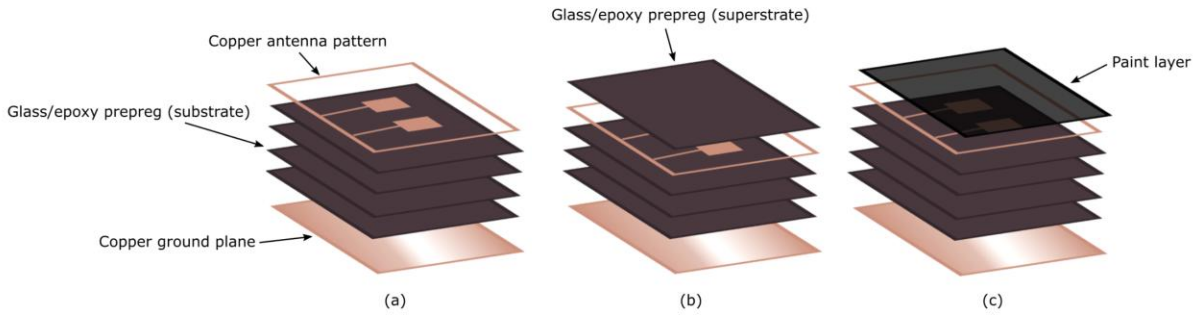

Figure 3: Layup schematics for (a) Flexural Specimen A, (b) Flexural Specimen B, (c) Flexural Specimen A with paint

The final experimental specimen type produced for this study is a sandwich-structured composite panel; its design form is very similar to the Tensile Specimen and Flexural Specimen A, with the inclusion of a polymethacrylimide (PMI) foam core and an additional face sheet/skin, as shown in Figure

4. Two configurations for this specimen exist; Configuration 1 is designed to undergo flexural strain of the opposite sign to Configuration 2, i.e. tensile vs compression strain.

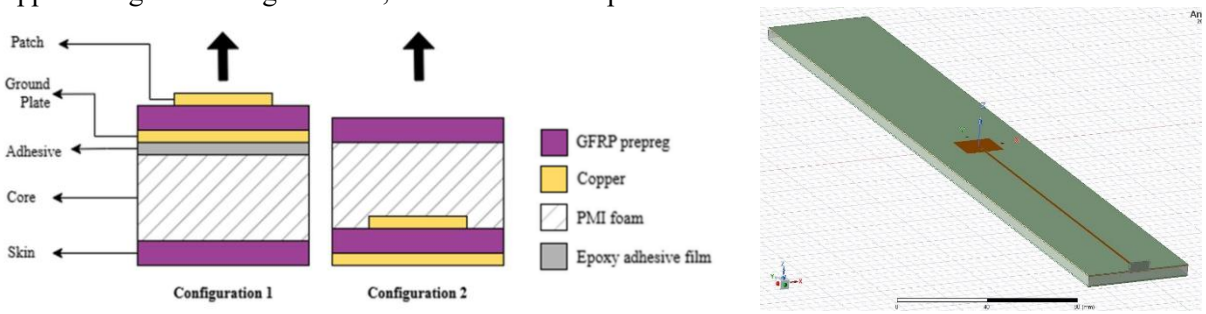

(a) (b)

Figure 4: (a) Layup configurations for the Sandwich Panel test coupons, (b) Ansys HFSS model of Configuration 1

Table 2: Specimen parameters for sandwich panel antennas for flexural testing

Specimen Parameter		Sandwich Panel
Patch length, L	[mm]	10.1
Patch width, W	[mm]	13
Substrate height, h	[mm]	0.275
Substrate material	–	E-Glass/Epoxy
Core material	–	PMI foam (3mm)
Substrate relative permittivity, ε_r	–	4.3
Microstrip width, W_0	[mm]	0.54
Recess length, y_0	[mm]	3.4
Specimen length	[mm]	350
Specimen width	[mm]	50

4 EXPERIMENTAL METHODOLOGIES

Figure 5 shows the experimental test setup for tensile testing; a tensile testing machine is used to load specimens in tension while a Vector Network Analyser (VNA) is used to measure return loss, S_{11} (Equation 4). The specimens are loaded to 2% nominal strain, which is calculated by crosshead displacement. Periodically during the tests, at increments of 0.25% nominal strain, each sample is analysed using the VNA and S_{11} measured. A video extensometer is also used to measure the average strain over the length of the patch. From each S_{11} curve, the resonant frequency (minimum in return loss) value is recorded so that a change in frequency can be observed as a function of applied strain.

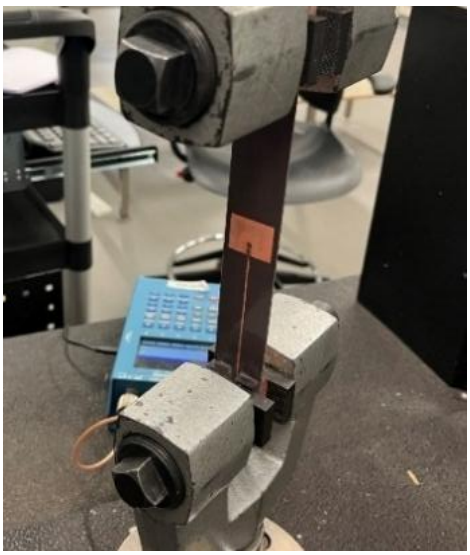

Figure 5: Experimental test setup for tensile testing

$$S_{11}(dB) = 10\log\left(\frac{Reflected\ Power}{Incident\ Power}\right) \qquad (4)$$

For flexural testing, multiple experimental setup concepts have been developed and trialled. Traditional four-point bending test fixtures for universal test machines are made of steel, including the loading pins. The close proximity of the loading pins to the microstrip, and the proximity of both the four-point bending fixture and the universal test machine to the antenna during testing make conventional flexural testing undesirable for composite laminates with embedded antenna elements. The main goals of the developed experimental setup concepts were to:

1. Replace all text fixture structure with polymer fixtures to reduce influence on antenna.
2. Replace loading pins with polymer pins to reduce influence on microstrip and antenna.
3. Reduce the amount of radiated power that could be reflected back to the antenna, either by:
    a. Absorbing the radiation, or
    b. Allowing the antenna to radiate into as much free space as possible.

Figure 6 shows the first of these concepts, a small anechoic box designed to fit to a universal test machine. The chamber is lined with RF absorbing foam, rated to the frequencies of interest of the antennas under test. Four-point bending fixtures have been designed and 3D printed from PLA, and polycarbonate loading pins are used. Figure 6(b) shows Flexural Specimens sitting in the test chamber (without the top loading fixture or top of box present). An access hole allows routing of a coaxial cable for VNA testing of the antenna while under load. Conventional four-point bending testing can be performed on these samples with a slow rate of crosshead displacement and continuous recording of the VNA to yield resonant frequency and bandwidth of the antenna at different strain levels.

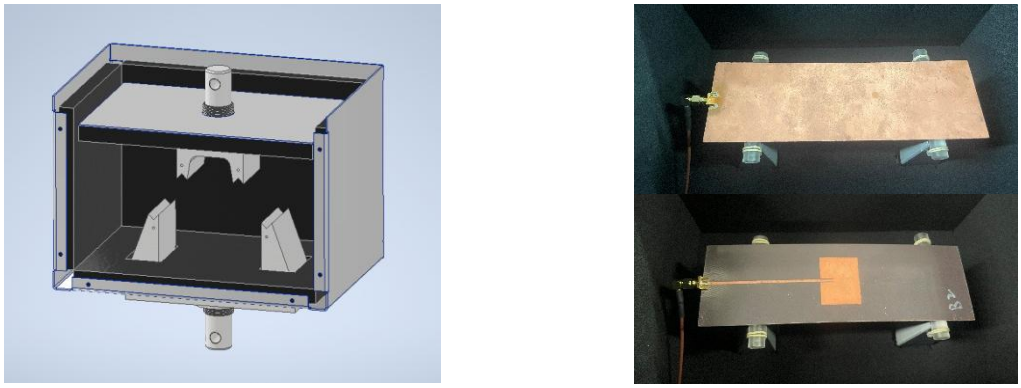

(a) (b)

Figure 6: Anechoic box concept for flexural testing of multifunctional composite laminates

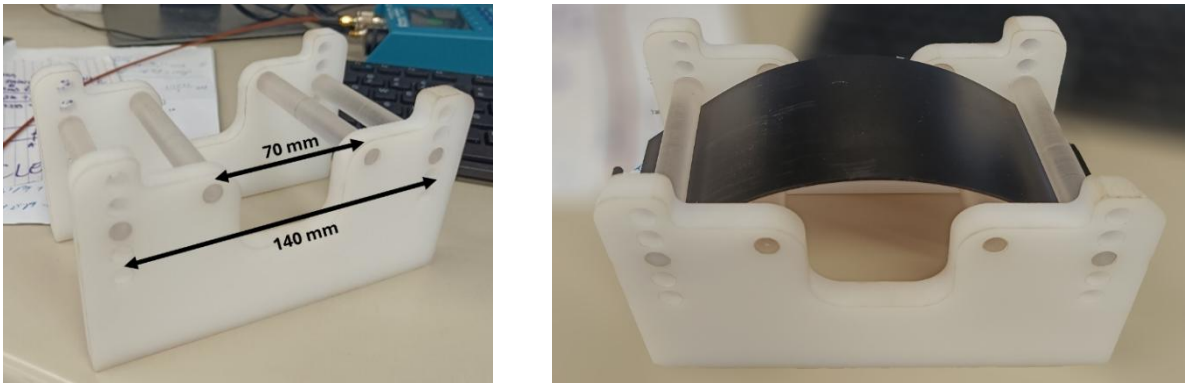

(a) (b)

Figure 7: Test fixture for placing multifunctional composite laminates under flexural strain without external loading.

Figure 7 shows a text fixture that is designed to place multifunctional composite laminates under flexural strain without the use of an external loading device such as a universal test machine. The motivation for this concept is to allow for radiation pattern testing of the antenna while it is under flexural strain. For example, this test fixture can be used in a conventional antenna pattern measurement setup in an anechoic chamber that simulates free space. The test fixture outer pins can move, so that five discrete levels of flexural strain or curvature can be applied to the test specimen. Figure 7(b) shows a painted Flexural Specimen A installed into the test fixture and deformed into the "20mm" position, which is equivalent to 20 mm of crosshead displacement if the anechoic box loading fixture were used in a universal test machine.

A set of experiments was performed to compare four-point bending using the developed anechoic box concept (Figure 6) to four-point bending using the static testing fixture designed to eliminate the need for external loading (Figure 7). Using the universal testing machine and anechoic box fixture, five Flexural Specimen A type samples were loaded such that the patch antenna is put into tensile strain; the patch elongates and theory predicts a drop in resonant frequency. VNA measurements were taken at 0, 5, 10, 15 and 20 mm of crosshead displacement. Similarly, three Flexural Specimen A type samples were placed in the static testing fixture at curvatures equivalent to 0, 10 and 20 mm of crosshead displacement. Changes in resonant frequency were calculated for each specimen and the results of this analysis are shown in Section 5.

Finally, a concept has been developed for performing four-point bending in a universal testing machine, utilising low-dielectric polymer supports, where the antenna is allowed to radiate mostly into free space (see Figure 8(a)). The antenna faces straight down into over a metre of free space, under which RF absorbing foam rests on the testing machine structure. Figure 8(b) shows a little more detail including VNA connected to the test specimen during loading. As for the previous concepts, this setup allows for the measurement of S_{11} of the antennas to investigate how resonant frequency shifts with flexural deformation. Specimens are loaded to 30 mm of crosshead displacement, with return loss measurements taken at 5 mm increments of crosshead displacement.

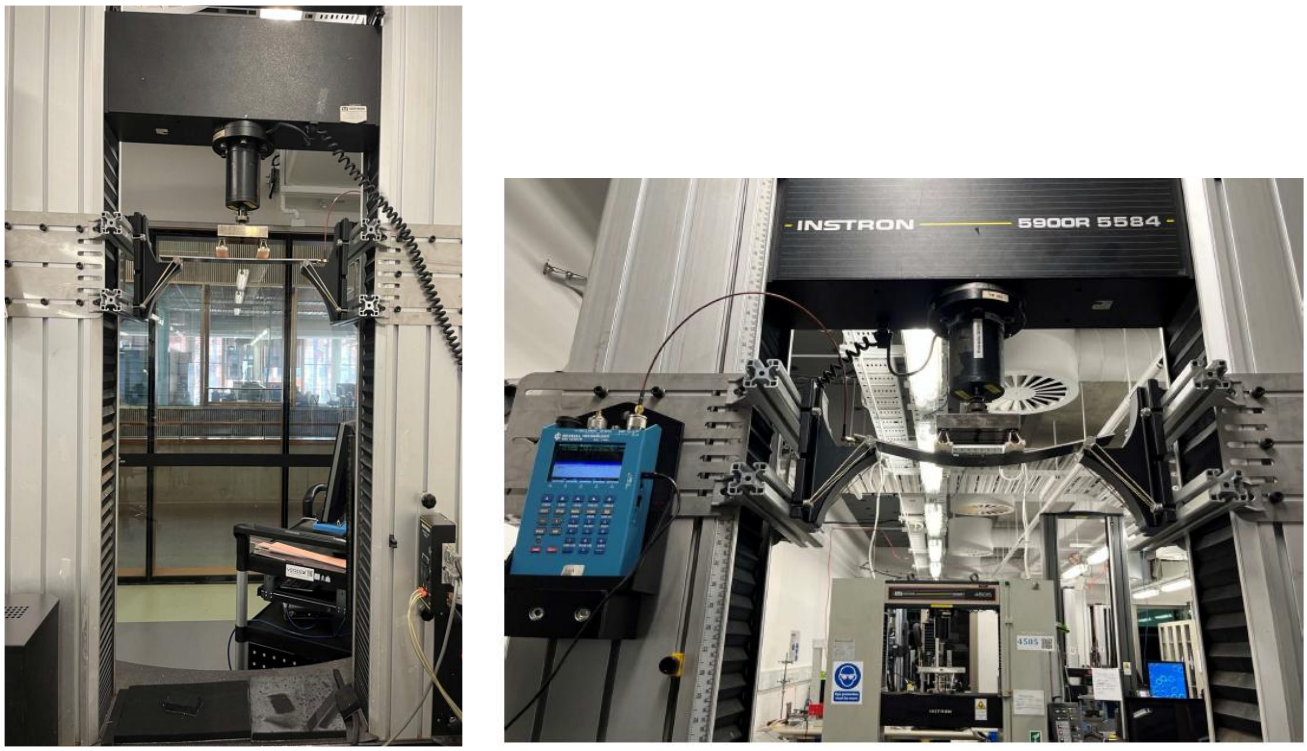

(a) (b)

Figure 8: Experimental setup for four-point bending of a Sandwich Panel

5 EXPERIMENTAL RESULTS

Six Tensile Specimens were manufactured for this work and loaded in tension using the methodology described in Section 4. Figure 9 shows an example of S_{11} curves obtained for a single specimen, at nine levels of crosshead displacement. Figure 10 shows the main result of this testing: the change in frequency for all six specimens is shown (marker average, error bars min and max) along with the change in frequency predicted by basic theory model presented in Section 2. Note in Figure 10, the x-axis is the average strain across the patch measured using video extensometer, ϵ_{patch}, whereas the strain values listed in in Figure 9 are nominal strains calculated from crosshead displacement.

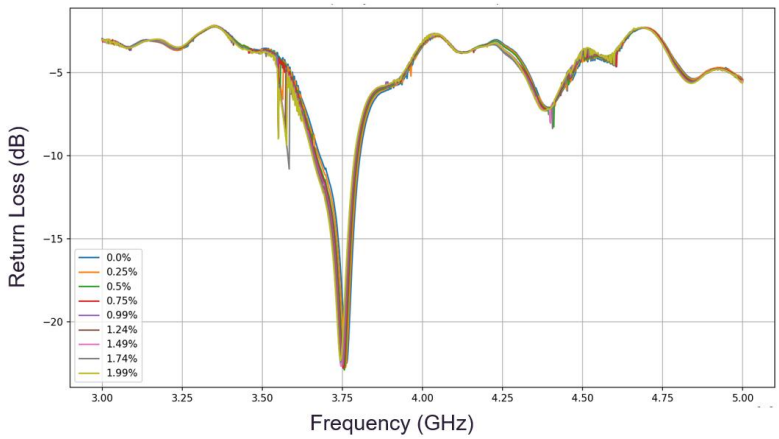

Figure 9: Example of return loss vs frequency data for tensile specimen.

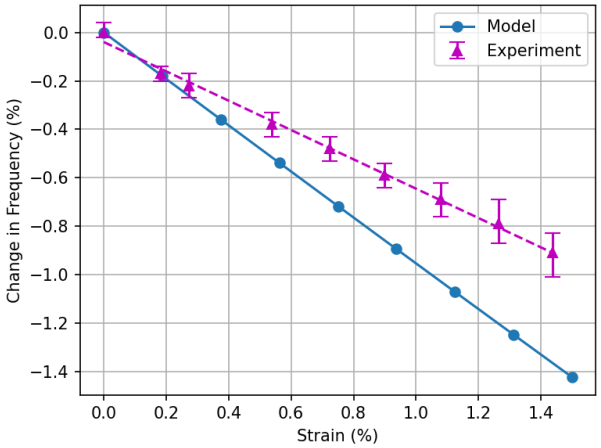

Figure 10: Measured vs. theoretical resonant frequency shift in tensile specimens as a function of strain of patch (measured with video extensometer).

The experimental data for tensile testing agrees somewhat with the predictions of basic theory, which are obtained using Equation 1 with L_{eff} calculated from $L(1 + \epsilon_{patch})$. The relatively narrow spread of results and good linearity of the experimental trend are promising results for this testing concept. The discrepancy between model and experiment of approximately 25-40% is similar to that reported in literature for strain-sensing patch antennas [e.g. 9,10]. We noted during our testing, out-of-plane deformation of the specimens were observed due to the unsymmetrical layup of the composite; copper is much stiffer than the glass/epoxy substrate and one side of the specimen has a ground plane occupying the entire face. This out-of-plane deformation is not captured by the basic model and could easily explain the results; this deformation also makes numerical simulation of the coupled mechanical-electrical problem challenging using commercial software such as Ansys HFSS.

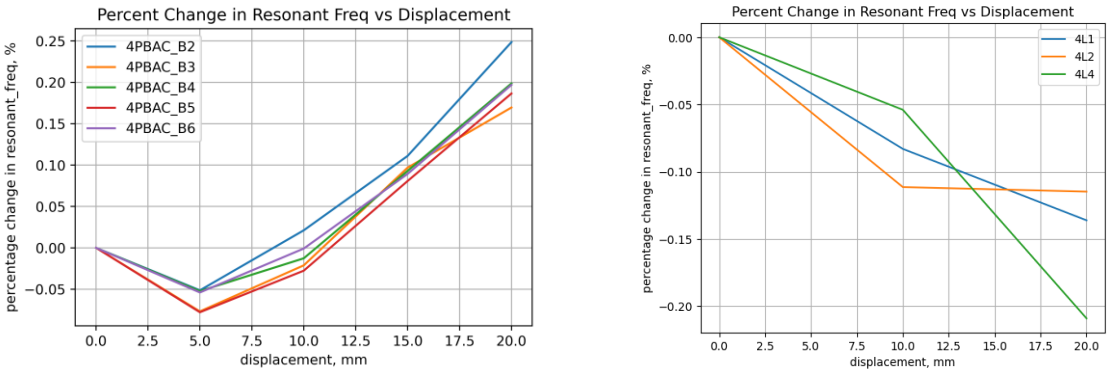

(a) (b)

Figure 11: Change in resonant frequency vs crosshead displacement for (a) anechoic box concept, and (b) static test fixture.

Figure 11 shows the main results comparing the anechoic box test setup to the static test fixture. Figure 11(a) shows an initial decrease in resonant frequency for all samples as predicted, but then a steady increase in resonant frequency for all samples as flexural strain increases. On further observation and analysis, the authors have concluded that the frequency increase is likely due to the antenna element moving closer to the bottom of the loading fixture and internal surface of the box as it strains, due to curvature of the part. The stand-off distance between the antenna and absorbing foam not remaining constant during testing is not desirable for fair comparison of experimental data points. Ultimately, the findings of these experiments have led to the abandonment of the anechoic box concept by the authors.

Figure 11(b) shows a general downward trend of resonant frequency for the static test fixture experiments, which is in good agreement with predictions. There is a large spread in the data, which may be attributed to the difficulty of precise and repeatable positioning of the specimen within the current fixture design. This concept does not have an issue with the antenna moving closer to a surface during testing, as the antenna is radiating into free space above the test fixture.

The final four-point bending testing concept was trialled using Sandwich Panel specimens described in Section 3. Figure 12(a) shows a specimen of Configuration 1 in the text fixture; the side of the specimen with an antenna is under tension, and the length of the patch should increase, leading to a decrease in resonant frequency. Specimens of Configuration 2 on the other hand, with an antenna on the back face sheet, and are placed under compression in this setup, and this should lead to an increase in the resonant frequency. The results in Figure 12(b) confirm these trends, with the two configurations seeing a frequency trend of approximately equal magnitude but opposite sign. These results represent a successful proof-of-concept of using low-dielectric polymer material for a conventional four-point bending experimental apparatus while ensuring the antenna is radiating into mostly free space.

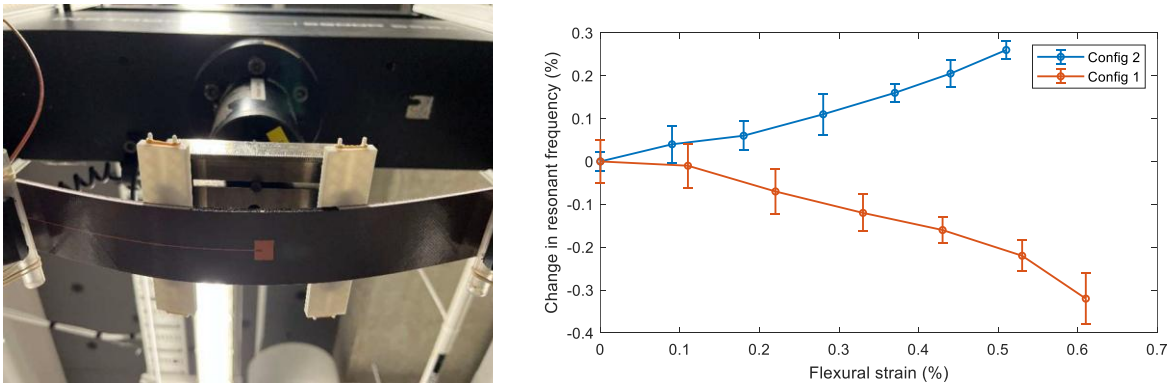

(a) (b)

Figure 12: (a) Sandwich Panel specimen (Configuration 1) bending under load, (b) change in frequency vs. flexural strain for Sandwich Panel specimens (Configurations 1 and 2).

Based on the success of the static test fixture in simple tests for resonant frequency, some preliminary experiments were performed to measure the radiation pattern of specimens under different levels of curvature. Near-field measurements were acquired in an *MVG Starlab* system and processed to approximate far-field gain. Figure 13 shows Flexural Specimen A (painted) in the static test fixture, secured to the central plinth of the *Starlab* system. Realised gain was calculated relative to a standard gain antenna, for frequencies between 2.0 and 3.0 GHz, in 101 steps of 10 MHz, for a 3D field in steps of 3 degrees for azimuth and 3 degrees for elevation. This was repeated for each specimen in the undeformed (0 mm) and deformed (20 mm equivalent crosshead displacement) cases.

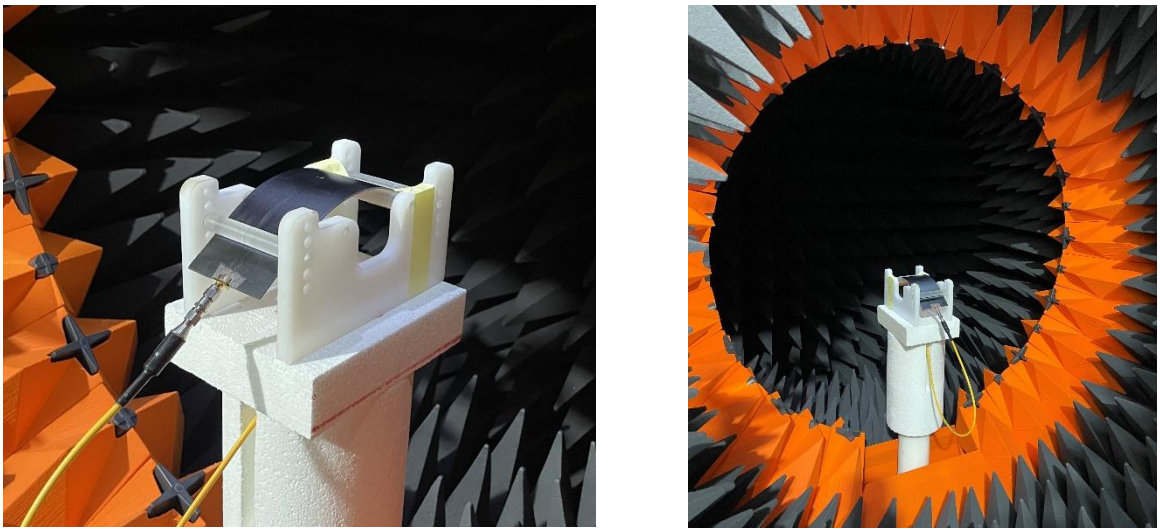

(a) (b)

Figure 13: Flexural Specimen A (painted) in the static test fixture, secured to the central plinth of the MVG Starlab system.

Figure 14 shows the maximum realised gain at each frequency between 2.0 and 3.0 GHz for Flexural Specimens A and B, each in the undeformed and deformed state. This shows peak realised gain occurs at 2.41 GHz in all tests.

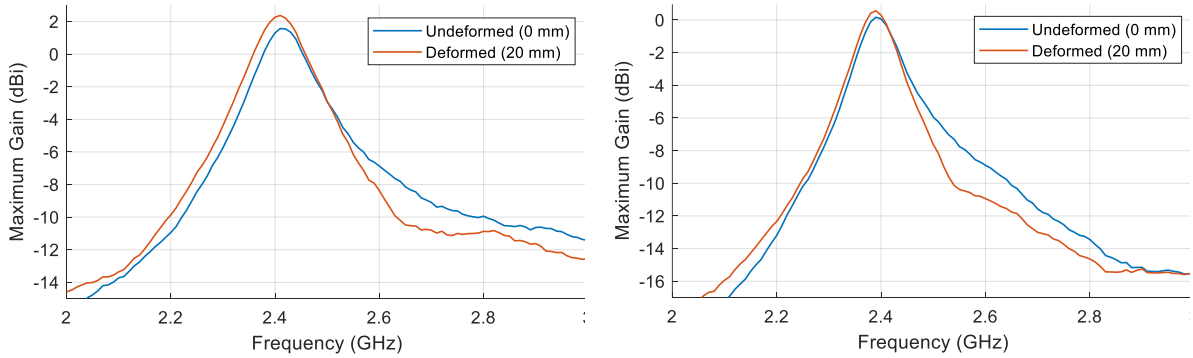

Figure 14: Maximum realised gain vs. Frequency for (a) Flexural Specimen A, painted and (b) Flexural Specimen B.

The antenna radiation patterns at 2.41 GHz are shown in Figure 15 (E-plane) and Figure 16 (H-plane). The E-plane results show that the main lobe of both undeformed specimens has a flat top, separated into two peaks. Flexural deformation of the structures produces a protrusion of this lobe directly away from the patch. The H-plane intersects with this protrusion, and the H-plane results show a consistent increase in gain under deformation.

The effect of laminate curvature on radiation pattern appears identical in form and magnitude between specimen types. This is despite the patch antenna undergoing a different strain magnitude; the patch in Flexural Specimen B is closer to the neutral axis of bending and therefore will experience a lower degree of in-plane strain due to bending. It can therefore be concluded that the change in radiation pattern is attributed to the deformation, i.e. the change of shape, and not a strain effect. Similar results have been shown for wearable antennas, where there is change of shape but no substrate strain [e.g. 11].

These results represent a successful proof-of-concept of using a static test fixture made from low-dielectric polymer material for the measurement of radiation patterns of conformal load-bearing antenna structures under flexural loads.

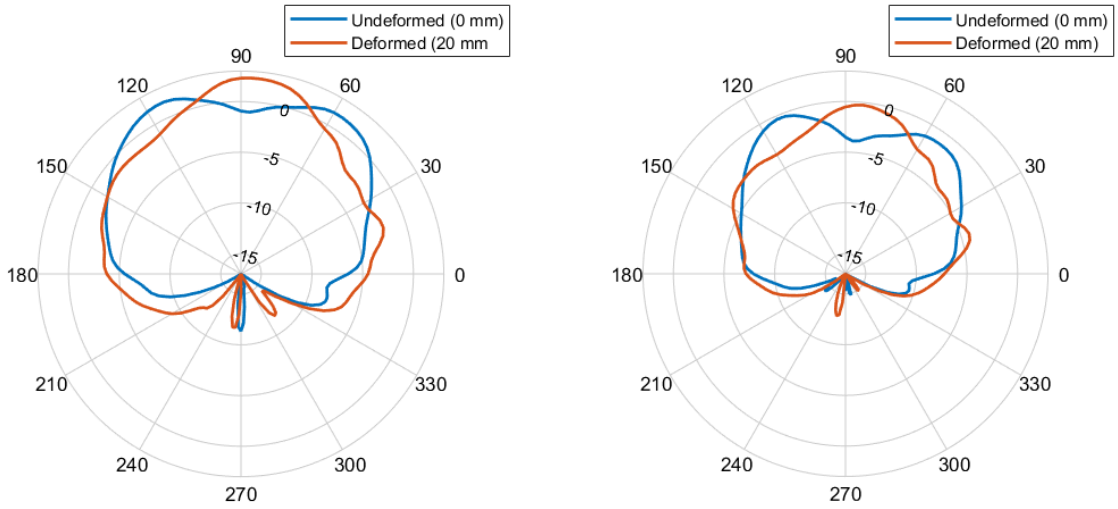

Figure 15: E-plane radiation patterns at 2.41 GHz for (a) Flexural Specimen A, and (b) Flexural Specimen B

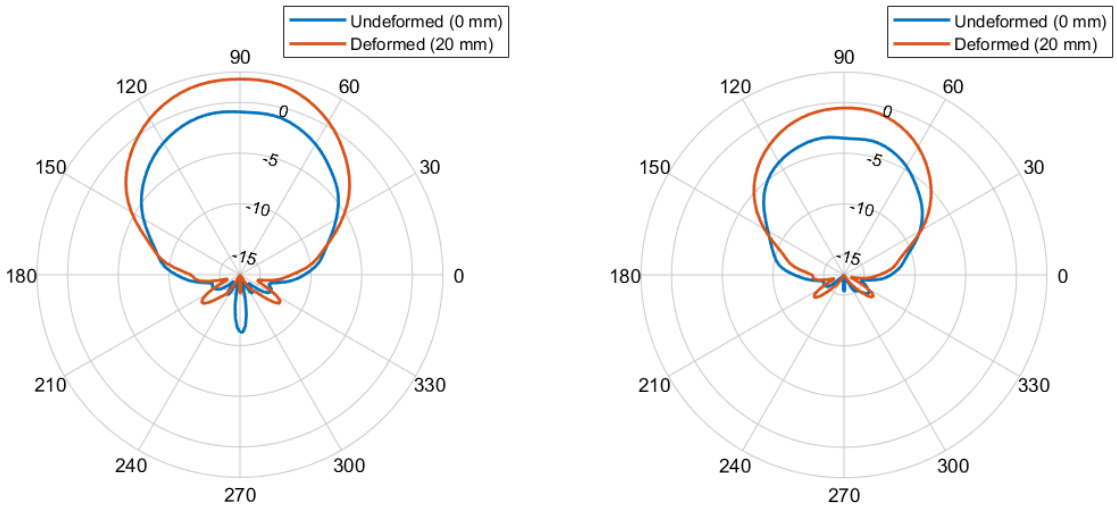

Figure 16: H-plane radiation patterns at 2.41 GHz for (a) Flexural Specimen A, and (b) Flexural Specimen B

6 CONCLUSIONS

This paper describes successful proof-of-concept experimental work to reduce the influence of test fixtures on measured electrical characteristics of conformal load-bearing antenna structures. The developed experimental setup concepts focus on using low-dielectric polymer materials for test fixtures and redesigning experiments such that antennas propagate mostly into free space.

Methods for performing conventional tensile and flexural testing of multifunctional composite laminates have been demonstrated that allow for simultaneous performance characterisation of embedded antennas. The observed trends in data collected during these proof-of-concept experiments tend to agree with predictions made using basic theory of rectangular patch antennas. A methodology that allows conformal load-bearing antenna structures to be fixed under flexural strain while radiation pattern measurements are made has been successfully demonstrated.

This work is an important step towards developing design workflows that include verifying the results of coupled mechanical-electrical numerical simulations with experimental data. For complicated structures, experimental testing is not a feasible pathway toward designing conformal load-bearing antenna structures that perform as expected in real-world applications, and numerical simulations must fill this gap. Experimental work of the type described in this paper can be used to verify and validate simple simulation cases to increase confidence in the results of the design workflow.

ACKNOWLEDGEMENTS

This paper includes work that was supported by the Australian Government Department of Education through Australia's Economic Accelerator Program. This paper includes work that was supported by DMTC Limited (Australia). The authors have prepared this paper in accordance with the intellectual property rights granted by a DMTC Project Agreement.

The authors gratefully acknowledge Kelvin Nicholson from the Defence Science and Technology Group (DSTG) for their contributions to this research and access to radiation pattern measurement facilities through DMTC Project 3.196.

REFERENCES

[1] Y. Lu, J. Healey, and P. Callus, "Experimental investigation of electromechanical performance of CLAS under tensile and fatigue loading," Composite Structures, vol. 320, p. 117845, 2025. doi: 10.1016/j.compstruct.2025.117845.

[2] J. Healey, Y. Lu, and P. Callus, "Mechanical loading effects on conformal load-bearing antenna structures: Simulation of tensile, biaxial, and twisting configurations," Defence Science and Technology Group, Australia, 2022. doi: 10.1016/j.compstruct.2022.115123.

[3] K. J. Nicholson, T. C. Baum, J. E. Patniotis, and K. Ghorbani, "Discrete Holographic Antenna Embedded in a Structural Composite Laminate," IEEE Antennas and Wireless Propagation Letters, vol. 19, no. 2, pp. 358–362, Feb. 2020. doi: 10.1109/LAWP.2019.2962902.

[4] T. C. Baum, R. W. Ziolkowski, K. Ghorbani, and K. J. Nicholson, "Embroidered active microwave composite preimpregnated electronics - pregtronics," IEEE Transactions on Microwave Theory and Techniques, vol. 64, no. 10, pp. 3175–3186, Oct. 2016.

[5] N. C. Matson, J. Camp and D. Rajan, "Effect of Antenna Orientation and UAV Position on UAV Communications in 3D Space," 2022 IEEE Latin-American Conference on Communications (LATINCOM), Rio de Janeiro, Brazil, 2022, pp. 1-6, doi: 10.1109/LATINCOM56090.2022.10000517.

[6] M. Badi, J. Wensowitch, D. Rajan and J. Camp, "Experimentally Analyzing Diverse Antenna Placements and Orientations for UAV Communications," IEEE Transactions on Vehicular Technology, vol. 69, no. 12, pp. 14989-15004, Dec. 2020, doi: 10.1109/TVT.2020.3031872.

[7] C. A. Balanis, Antenna Theory: Analysis and Design, 4th ed. Wiley, 2016.

[8] B. Mekimah, A. Messai, and A. Belhedri, "Analysis of the effect of dielectric losses on the bandwidth of microstrip patch antenna in stacked geometry and modelling," SN Applied Sciences, vol. 2, Article 767, 2020. doi: 10.1007/s42452-020-2292-4.

[9] J. Wang, Y. Hao, and C. Parini, "Strain measurement using microstrip patch antennas," IEEE Transactions on Antennas and Propagation, vol. 64, no. 6, pp. 2508–2513, Jun. 2016. doi: 10.1109/TAP.2016.2547381

[10] D. Tata, S. K. Sharma, and L. Shafai, "Patch antennas for strain sensing applications," IEEE Transactions on Antennas and Propagation, vol. 57, no. 3, pp. 610–617, Mar. 2009. doi: 10.1109/TAP.2009.2014574

[11] I. Adam, M. R. Kamarudin, A. H. Rambe, N. Haris, H. A. Rahim, W. Z. A. W. Muhamad, A. M. Ismail, M. Jusoh, M. N. M. Yasin, “Investigation on Wearable Antenna under Different Bending Conditions for Wireless Body Area Network (WBAN) Applications,” International Journal of Antennas and Propagation, 2021, 5563528, 9 pages, 2021. https://doi.org/10.1155/2021/5563528

EVALUATING THE IMPACT OF CARBON-BASED NANOMATERIALS ON THE THERMO-MECHANICAL PROPERTIES OF HIGH-PERFORMANCE POLYMER FIBRES

Stergios Goutianos[1] and Ton Peijs[2]

[1]Departmentof Manufacturing and Civil Engineering, Norwegian University of Science and Technology, Gjøvik, Norway
Email: stergios.goutianos@ntnu.no, web page: http://www.ntnu.no

[2]University of Warwick, WMG, Materials Engineering Centre, CV4 7AL, Coventry, UK
Email: t.peijs@warwick.ac.uk, web page: https://warwick.ac.uk

Keywords: Carbon nanotubes, Carbon nanoplatelets, Nanocomposites, Polymer fibres, Mechanical strength, Thermal conductivity

ABSTRACT

The paper examines the reinforcing effect of carbon-based nanomaterials on high-performance polymer fibres. Based on various experimental studies, which show that even with relatively high contents of carbon-based nanomaterials - despite their exceptionally high mechanical properties - only modest increases in strength are achieved, the present study investigates whether this suggests that the initially promised enhancements cannot be fully realized. The paper then extends the analysis to explore the potential for improving thermal conductivity by adding carbon-based nanomaterials. The primary focus is on reinforcing high-performance polymer fibres. Both analytical and numerical modelling are employed. The results demonstrate that, for realistic carbon nanotube (CNT) contents and aspect ratios, the extraordinary strength of CNTs cannot be fully exploited in high-performance polymer fibres. However, the addition of carbon nanoplatelets (CNPs) can significantly enhance the thermal conductivity of these fibres.

1 INTRODUCTION

Since their discovery, carbon-based nanomaterials and in particular carbon nanotubes (CNTs) [1], have been extensively studied as a reinforcement to develop composites with superior mechanical, thermal and electrical properties due to their exceptional properties [2]. However, despite their strength (~100 GPa) which is an order of magnitude greater than the strongest carbon fibre (~7 GPa), the initial expectations have not been realised [3]. Weak interfacial adhesion to the polymer matrix, agglomeration, and random orientation are some of the limiting factors [3]. A key parameter to better utilize the intrinsic properties of CNTs is to orient them along the loading axis for example by applying an electric field [4]. An alternative method is to align the CNTs during polymer processing, for example by fibre spinning [5]. In this way, polymer fibres reinforced with CNTs can be produced, with the promise of achieving superior properties [5,6]. However, while some improvement in mechanical properties is observed, none of these reinforced fibres exhibit mechanical performance comparable to that of commercial high-performance fibres.

Carbon-based nanomaterials can also be used to enhance other properties, such as the thermal conductivity of polymers or polymer fibres, due to their exceptional thermal conductivity. For example, graphene nanoplatelets (GNPs) have a thermal conductivity ranging from 1000 to 5300 $W \cdot m^{-1} \cdot K^{-1}$ [7]. Siginifcant imrpovements in thermal conductivity have been reported for a range ogf polymers. For example with 10 wt % GNPs in polyvinyl alcohol matrix, an increase in thermal conductivity of about 1800% has been reported [8].

Based on the above, it appears that carbon-based nanomaterials have a strong positive effect on enhancing the thermal properties of polymers, whereas their effect on improving mechanical properties is generally insignificant. Even in cases where a significant increase in the strength of polymer fibres is

reported, there remains the question of whether this improvement is an indirect effect resulting from a modification of the polymer matrix by the nanofiller [9].

The paper, therefore, focuses on polymer fibres and aims to address whether carbon-based nanomaterials can, even in theory, effectively reinforce such fibres in terms of strength. In parallel, it seeks to determine the maximum limits of thermal conductivity that can be achieved. CNTs will be used to address the first part of the question, and GNPs the second. Analytical and numerical models will be employed, assuming that the carbon-based nanomaterials are perfectly aligned and homogeneously dispersed within the polymer fibre.

2 MODEL DESCRIPTION

In this section, the models used in the present paper are briefly presented.

2.1 Analytical modelling of mechanical behaviour

A large number of analytical micromechanical models exist for analysing the mechanical response of aligned single-fibre composites. In the present work, the model developed by Sørensen [10], originally developed to study debonding initiation and growth from a fibre break for an infinitely long fibre, is employed (see Fig. 1). This model accounts for interface debonding, sliding due to friction, and residual stresses. Previous work has shown that modelling a single fibre (CNT) yields results similar to those obtained for multiple aligned CNTs embedded in a polymer fibre [9].

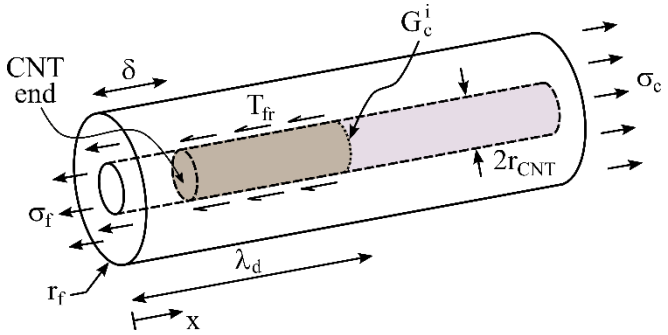

Figure 1: A single aligned CNT in a polymer fibre.

In Fig. 1, σ_c is the applied stress in the CNT reinforced polymer fibre. When σ_c reaches a critical value, σ_c^i, interface debonding initiates from the CNT end (at $x = 0$ in Fig.1). The debonding initiation stress is given by [10]:

$$\frac{\sigma_c^i}{E_c} = \frac{(1 - V_{CNT})E_f}{E_c}\Delta\epsilon^T + 2\sqrt{\frac{(1 - V_{CNT})E_f}{E_c}\left(\frac{G_c^i}{E_{CNT}\, r_{CNT}}\right)} \tag{1}$$

where E_c is the Young's modulus of the CNT-reinforced polymer fibre and E_f the Young's modulus of the polymer fibre itself. r_{CNT} is the radius of the CNT and V_{CNT} the CNT volume fraction. $\Delta\epsilon^T$ is the misfit strain. G_c^i is the mode II (shear) fracture energy and influences σ_c^i. Assuming a linear softening traction separation cohesive law, the maximum interface peak traction is:

$$\hat{T} = 0.5\, G_c^i\, \delta \tag{2}$$

where δ is the critical tangential interface separation. The frictional stress, T_{fr}, results in an increase of the applied stress, σ_c, as the debond length, λ_d, increases [10]:

$$\frac{\sigma_c}{E_c} = \frac{\sigma_c^i}{E_c} + 2\left(\frac{T_{fr}}{E_{CNT}}\right)\left(\frac{\lambda_d}{r_{CNT}}\right) \tag{3}$$

where E_{CNT} is the Young's modulus of the CNT. The debond length is given by [10]:

$$\frac{\lambda_d}{r_{CNT}} = \frac{E_{CNT}}{2\,T_{fr}}\left(\frac{\sigma_c}{E_c} - \frac{(1-V_{CNT})E_f}{E_c}\Delta\epsilon^T\right) - \frac{E_{CNT}}{T_{fr}}\sqrt{\frac{(1-V_{CNT})E_f}{E_c}\left(\frac{G_c^i}{E_{CNT}r_{CNT}}\right)} \tag{4}$$

2.2 Finite element modelling of thermal behaviour

As mentioned in the previous Section, the thermal conductivity enhancement of the polymer fibres is examined using graphene nanoplatelets (GNPs) with in-plane dimensions λ_x and λ_y, and out-of-plane thickness λ_z. The GNPs are assumed to be perfectly aligned along the y-axis, forming a regular staggered 3D array within the polymer fibre, as shown in Fig. 2. The Representative Volume Element (RVE), highlighted in Fig. 2, is used to evaluate the effective conductivity of the GNP-reinforced polymer fibres.

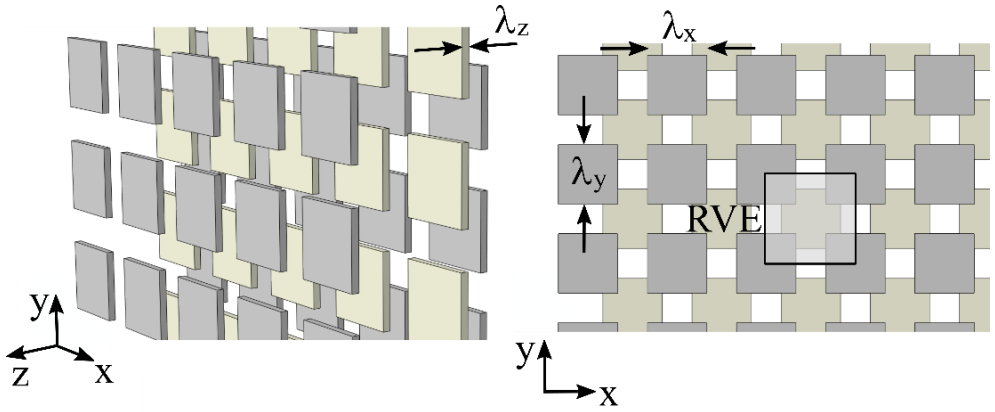

Figure 2: Representative Volume Element (RVE) of a polymer fibre containing CNPs.

The RVE shown in Fig. 2 is analysed using the commercial finite element software Abaqus. It should be noted that, within the RVE, the outer GNPs have a thickness of $\lambda_z/2$. Periodic boundary conditions are applied using the Micromechanics Plugin for Abaqus. The effective thermal conductivity is calculated in all three principal directions.

3 RESULTS: MECHANICAL PERFORMANCE OF CNT-REINFORCED FIBRES

Fig. 3 shows the debonding initiation stress, σ_c^i, as function of the polymer fibre's Young's modulus, and the interface peak traction for 10% CNT volume fraction. Assuming zero interfacial frictional stresses are zero, σ_c^i corresponds to the strength, σ_f^u of the CNT-reinforced polymer fibres. These strength values can then be directly compared with the superimposed strengths of various commercial high-performance polymer fibres. The CNT Young's modulus was assumed to be 1 TPa.

If we consider the Spectra 900 fibre with σ_f^u equal to 2.1 GPa, then an interface peak traction greater than 110 MPa is required to increase the strength from 2.1 to 3 GPa (a 30% increase). However, this interface peak traction exceeds the shear strength of the fibre itself. Similar results are observed also for the Zylon HM fibre. To achieve a strength increase of approximately 30%, the interface peak traction must exceed 125 MPa. It may be added that for a CNT volume fraction of 1%, achieving a fibre strength of 3 GPa for Spectra 900 would require an interface peak traction of 200 MPa (results not shown). However, for the Zylon HM fibre, a slightly lower interface peak traction (75 MPa) is required to achieve a strength increase of about 30%. This value is still relatively high compared to the shear strength of high-performance polymer fibres.

The results above assume, as previously mentioned, the absence of frictional stresses, and therefore can be considered a lower-bound estimate of the strength of CNT-reinforced polymer fibres. Next, in Fig. 4 the effect frictional stresses is considered (Eqs. 3 and 4). It can be seen that the applied stress increases linearly with the debond length after debonding has initiated. It is assumed that the debond length increases in a stable manner; therefore, the applied stress at which the CNT is fully debonded provides an estimate of the strength of the CNT-reinforced polymer fibre.

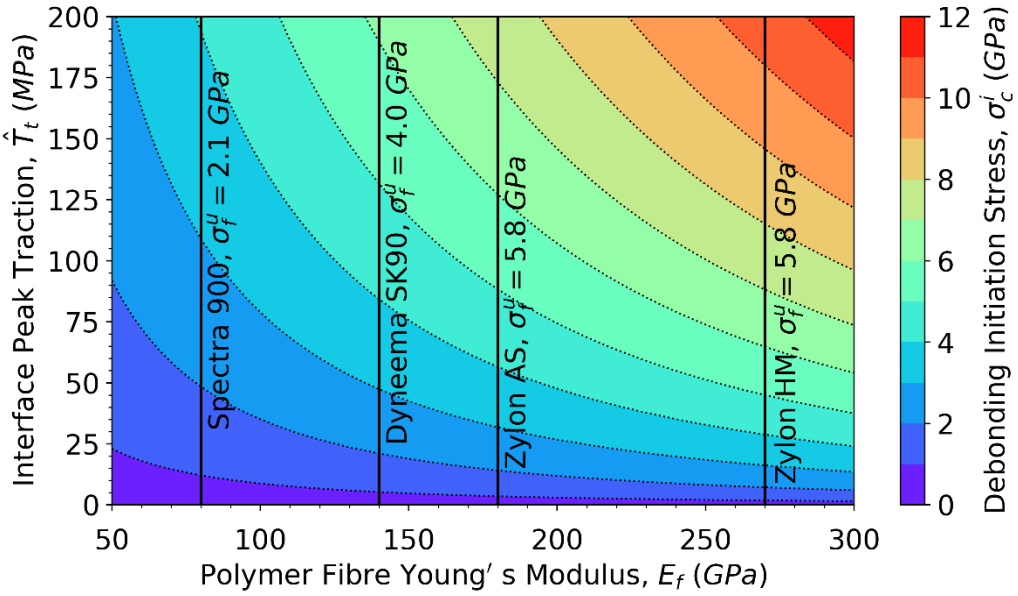

Figure 3: Debonding initiation stress, σ_c^i, as a function of the polymer fibre Young's modulus, E_f, and the interface peak traction, $\hat{T}$. V_{CNT}=10%, δ=5 nm, T_{fr}=0.

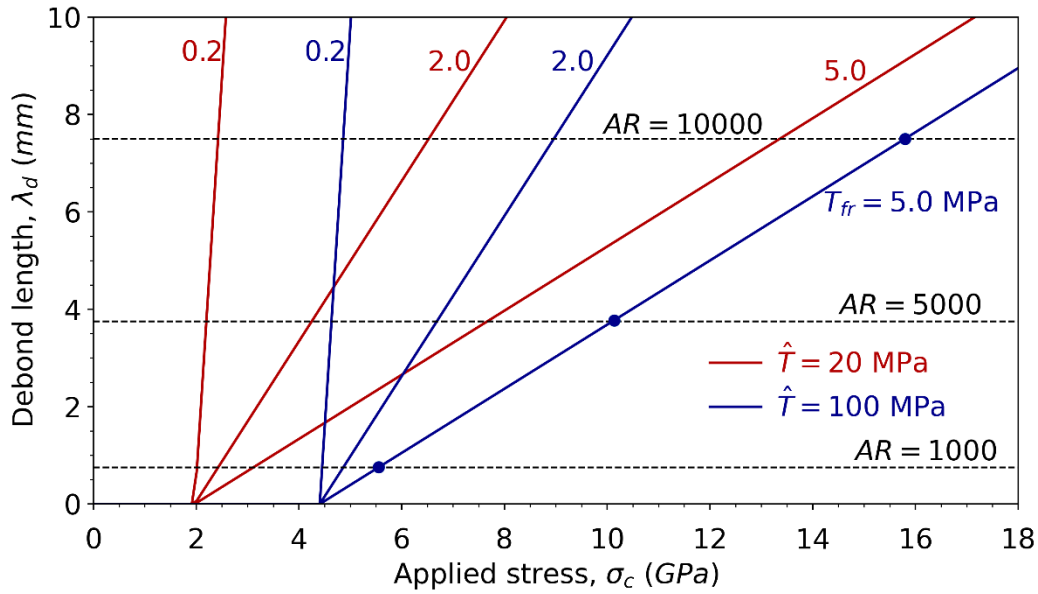

Figure 4: Debond length, λ_d, as a function of the applied stress, σ_c, for different interface frictional stresses, T_{fr}. V_{CNT}=10%, δ=5 nm. The dashed lines show when the CNT becomes fully debonded for the corresponding aspect ratio.

In Fig. 4, the debond length is plotted against the applied stress for two different interface peak tractions (20 and 100 MPa). As expected, a higher peak traction delays the onset of debonding. Afterwards, the debond length increases linearly with applied stress. Fig. 4 also presents results for three different values of interfacial frictional stress: 0.2, 2, and 5 MPa. If we consider the case of $\hat{T}$ =100 MPa and an interface frictional stress equal to 5 MPa, the strength of the CNT-reinforced fibre is approximately 5.5 GPa - an increase of about 20% compared to the stress at debonding initiation. This result corresponds to CNTs with an aspect ratio (AR) of 1000. If the aspect ratio is 5000, the strength of the CNT-reinforced fibre increases to approximately 10.1 GPa, representing an increase of about 55%. Finally, for an aspect ratio of 10000, the strength reaches 15.8 GPa - an increase of more than 70% compared to the debonding initiation stress. It should be noted that these significant increases in strength

require a high interfacial frictional stress. As shown in Fig. 4, if the frictional stress is 0.2 MPa, then the fibre strength for a CNT aspect ratio of 10000 is approximately 4.9 GPa, corresponding to an increase of only about 8% compared to the debonding initiation stress.

4 RESULTS: THERMAL PERFORMANCE OF CNP-REINFORCED FIBRES

In this section, the results for thermal conductivity of the polymer fibre reinforced with GNPs (Graphene Nanoplatelets) are presented. In Fig. 5, the principal thermal conductivity of the GNP-reinforced polymer fibres is plotted as a function of the GNPs' in-plane conductivity and the axial conductivity of the polymer fibres. Typical values for some commercial high-performance fibres (also used in the previous section on mechanical response) are 5–10 W/m·K for Dyneema fibres [11] and approximately 13 W/m·K for Zylon fibres [12]. It is worth mentioning that the thermal conductivity of isotropic (bulk, unaligned) polyethylene is around 0.3 to 0.5 W/m·K [13]. The GNP volume fraction is set to 1%. The in-plane thermal conductivity of the GNPs varies from 0 to 5000 W/m·K, with 5000 W/m·K likely representing the upper limit [14]. For practical applications, values on the order of 1700 to 2000 W/m·K are more realistic [15].

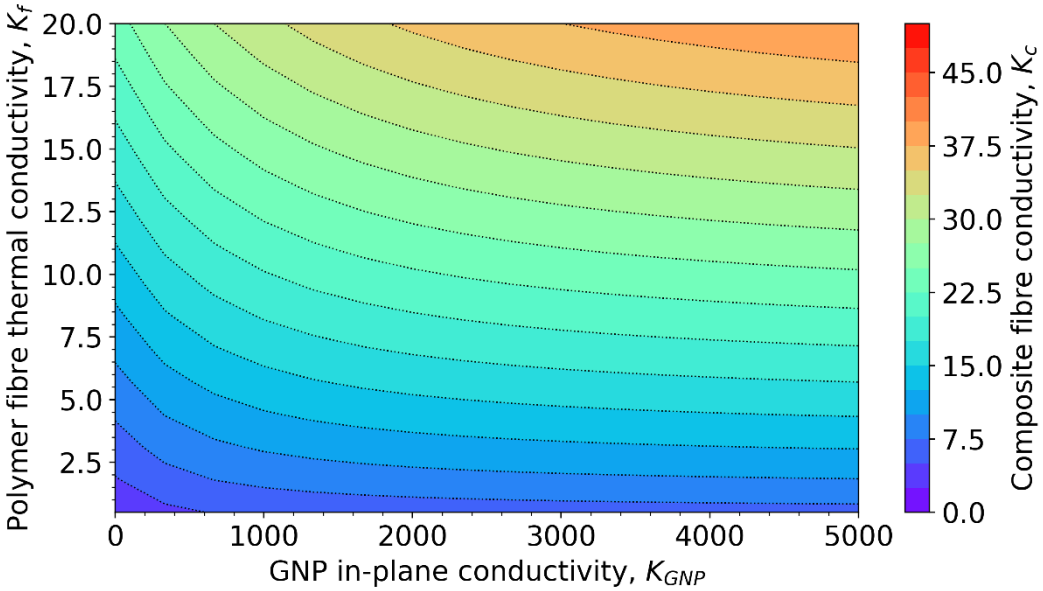

Figure 5: Principal thermal conductivity of the GNP-reinforced polymer fibre, K_c, as a function of the GNP in-plane thermal conductivity, K_{GNP} and the axial polymer fibre thermal conductivity, K_f. $V_{GNP} = 1\%$ and the aspect ratio $AR = \lambda_y/\lambda_z$=500 with $\lambda_x = \lambda_y$. The thermal conductivity is given in W/m·K.

If we consider Dyneema or Spectra polymer fibres with a thermal conductivity of 9.6 W/m·K and add 1% by volume of GNPs, the thermal conductivity of the composite fibre reaches 18 W/m·K when the conductivity of the GNP is 1750 W/m·K. If the conductivity of the GNP is 5000 W/m·K, then the conductivity of the composite fibre becomes 22.1 W/m·K. In the first case, the conductivity of the Dyneema or Spectra polymer fibres increases by approximately 1.9 times, while in the second case it increases by nearly 2.3 times. A similar trend is observed for Zylon fibres, assuming an intrinsic thermal conductivity of 13.5 W/m·K. When the in-plane thermal conductivity of the GNPs is 1750 W/m·K, the effective conductivity of the reinforced fibre increases to 22.65 W/m·K - approximately a 1.7-fold enhancement. For a GNP in-plane conductivity of 5000 W/m·K, the fibre conductivity reaches 27.61 W/m·K, representing nearly a twofold increase.

It is also interesting to consider the effect of adding GNPs to bulk isotropic polyethylene with a thermal conductivity of 0.5 W/m·K. Adding 1% by volume of GNPs with a thermal conductivity of 1750 W/m·K results in composite fibres with a conductivity of 4.6 W/m·K (more than a 9-fold increase). Adding GNPs with a thermal conductivity of 5000 W/m·K produces composite fibres with a thermal

conductivity of 6.2 W/m·K (approximately a 12-fold increase). Therefore, GNPs have a more pronounced impact when the base polymer fibre has a lower thermal conductivity..

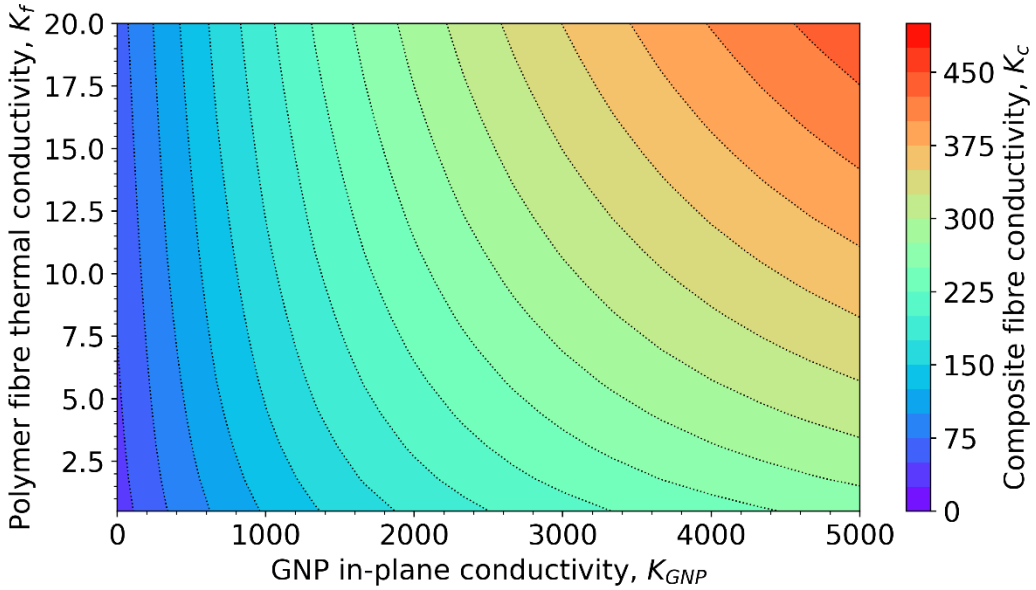

Figure 6: Principal thermal conductivity of the GNP-reinforced polymer fibre, K_c, as a function of the GNP in-plane thermal conductivity, K_{GNP} and the axial polymer fibre thermal conductivity, K_f. $V_{GNP} = 10\%$ and the aspect ratio $AR = \lambda_y/\lambda_z$=500 with $\lambda_x = \lambda_y$. The thermal conductivity is given in W/m·K.

Fig. 6 is similar to the previous figure, but with V_{GNP} increased to 10%. It can be seen that for Dyneema or Spectra fibres with a thermal conductivity of 9.6 W/m·K, the resulting composite fibre has a thermal conductivity of 135 W/m·K (14 times higher) when the GNPs have a thermal conductivity of 1750 W/m·K. For a Zylon fibre and assuming that K_{GNP} is 1750 W/m·K, the composite fibres have a thermal conductivity of 144 W/m·K (10 times higher). The trends are similar to those described for the case where V_{GNP} equals 1%, but the thermal conductivities obtained for the reinforced fibres are now much higher. In all cases, the enhancement of thermal conductivity is greater when the starting polymer fibre has a lower thermal conductivity.

It should be noted that higher thermal conductivities can be obtained, for example, by increasing the aspect ratio whilst maintaining the same GNP volume fraction. In the present work, we have chosen to use the simplest staggered 3D distribution of GNPs and have fixed the aspect ratio, whilst also using $\lambda_x = \lambda_y$.

5 CONCLUSIONS

In the present work, the effect of reinforcing high-performance polymer fibres with carbon-based nanomaterials was investigated using simulations, with the aim of determining whether carbon-based nanomaterials can enhance the mechanical and thermal properties of the fibres.

It was shown that several conditions must be met simultaneously, such as exceptional aspect ratio of CNTs, substantial frictional stresses, and significant volume content of CNTs, in order to achieve an increase of several times (3-4 times) in the polymer fibre strength.

On the other hand, it was shown that adding only small amounts (1% by volume) of GNPs increases the thermal conductivity of polymer fibres by a factor of 2. Increasing the content of GNPs to 10% results in an increase by a factor of 15 for Dyneema fibres, using a typical thermal conductivity of 1750 W/m·K for the GNPs.

Therefore, it can be argued that carbon-based nanomaterials are promising materials for enhancing the thermal properties of polymer fibres, but not the mechanical properties.

REFERENCES

[1] S. Iijima, Helical Microtubules of Graphitic Carbon, *Nature*, **354**, 1991, pp. 56-58.
[2] E.T. Thostenson, Z. Ren and T.-W. Chou, Advances in the science and technology of carbon nanotubes and their composites: A review, *Composites Science and Technology*, **61**, 2001, pp. 1899-1912.
[3] I.A. Kinloch, J. Suhr, J. Lou, R.J. Young and P.M. Ajayan, Composites with carbon nanotubes and graphene: An outlook, *Science*, **362**, 2018, pp. 547-553.
[4] C.A. Martin, J.K.W. Sandler, A.H. Windle, M.-K. Schwarz, W. Bauhofer, K. Schulte and M.S. P. Shaffer, Electric field-induced aligned multi-wall carbon nanotube networks in epoxy composites, *Polymer*, **46**, 2005, pp. 877-886.
[5] P. Ciselli, Z. Wang and T. Peijs, Reinforcing potential of carbon nanotubes in oriented polymer fibres, *Materials Technology*, **22**, 2007, pp. 10-21.
[6] A. Mikhalchan and J.J. Vilatela, A perspective on high-performance CNT fibres for structural composites, *Carbon*, **150**, 2019, pp. 191-215.
[7] W.H. Danial and Z.A. Majid, Recent advances on the enhanced thermal conductivity of graphene nanoplatelets composites: A short review, *Carbon Letters*, **32**, 2022, pp. 1411-1424.
[8] Y. Liu, K. Wu, F. Luo, M. Lu, F. Xiao, X. Du, S. Zhang, L. Liang and M. Lu, Significantly enhanced thermal conductivity in polyvinyl alcohol composites enabled by dopamine modified graphene nanoplatelets, *Composites Part A: Applied Science and Manufacturing*, **117**, 2019, pp. 134-143.
[9] S. Goutianos and T. Peijs, On the low reinforcing efficiency of carbon nanotubes in high-performance polymer fibres, *Nanocomposites*, **7**, 2021, pp. 53-69.
[10] B.F. Sørensen, Micromechanical model of the single fiber fragmentation test, *Mechanics of Materials*, **104**, 2017, pp. 38-48.
[11] S. Shen, A. Henry, J. Tong, R. Zheng and G. Chen, Polyethylene nanofibres with very high thermal conductivities, Nature Nanotechnology, **5**, 2010, pp. 251-255.
[12] T. Yamamoto and T. Itoh, Thermal conductivity of high-strength polymer fibers measured by the laser flash method, *Journal of Applied Polymer Science*, vol. **76**, 2000, pp. 927-931.
[13] C.L. Choy, Thermal conductivity of polymers, *Polymer*, **18**, 1977, pp. 984-1004.
[14] A.A. Balandin, S. Ghosh, W. Bao, I. Calizo, D. Teweldebrhan, F. Miao and C.N. Lau, Superior Thermal Conductivity of Single-Layer Graphene, *Nano Letters*, **8**, 2008, pp. 902-907.
[15] K.M.F. Shahil and A.A. Balandin, Thermal properties of graphene and multilayer graphene: Applications in thermal interface materials, *Solid State Communications*,n**152**, 2012, pp. 1331-1340.

ICCM24
AUGUST 4-8, 2025
BALTIMORE CONVENTION CENTER
BALTIMORE, MARYLAND, USA

No Technical Paper Submission for:

Amit Chaudhari



Processing and Characterization of 3D Vascular Carbon-Carbon Composites

Henry Holman, Mark Olima and Dr. Michael Keller

Department of Mechanical Engineering, The University of Tulsa, Tulsa OK, USA.

THE UNIVERSITY of TULSA

SOLAR ENERGY TECHNOLOGIES OFFICE
U.S. Department Of Energy

ADVANCED COMPOSITE MATERIALS LAB

U.S. DEPARTMENT OF ENERGY | Office of Science

C_f/C_m composites can be used in Concentrated Solar Power (CSP) receivers for power generation



Ivanpah Solar Power Facility in the Mojave Desert, CA [1]

Inconel 718 ⟶ Carbon-Carbon Composite

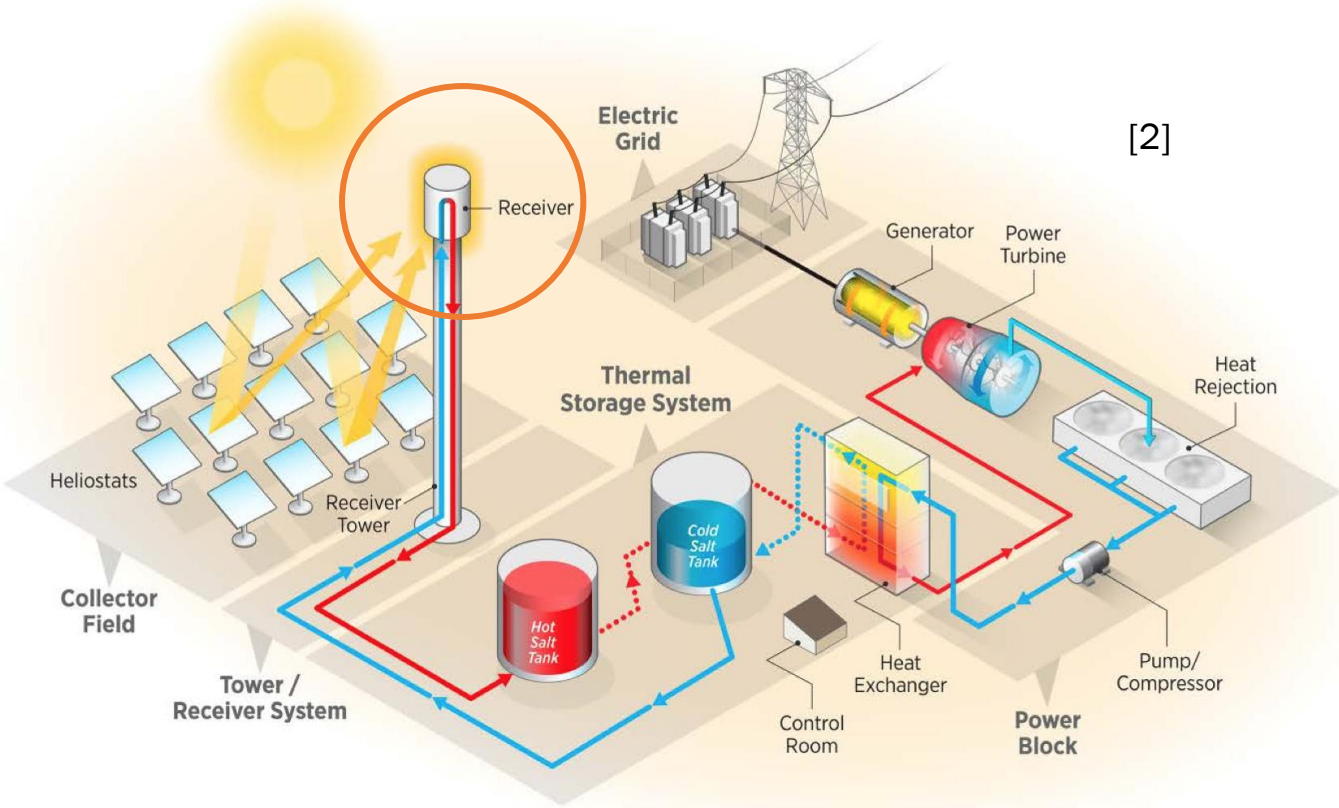

[2]

Illustration of molten-salt power tower with a thermal storage system[2]

[1] Getty Images
[2] Concentrating Solar Power Gen3 Demonstration Roadmap. https://www.nrel.gov/docs/fy17osti/67464.pdf

C_f/C_m Composites have a better specific strength and Coefficient of Thermal Expansion (CTE)

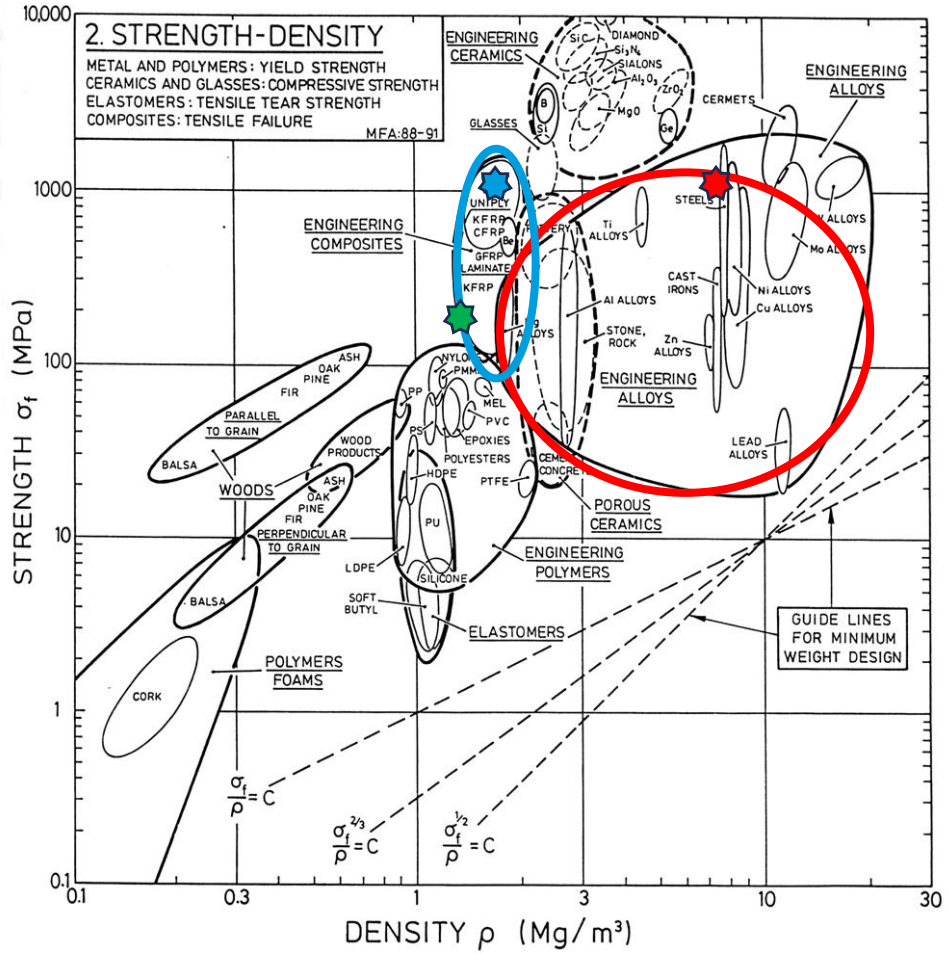

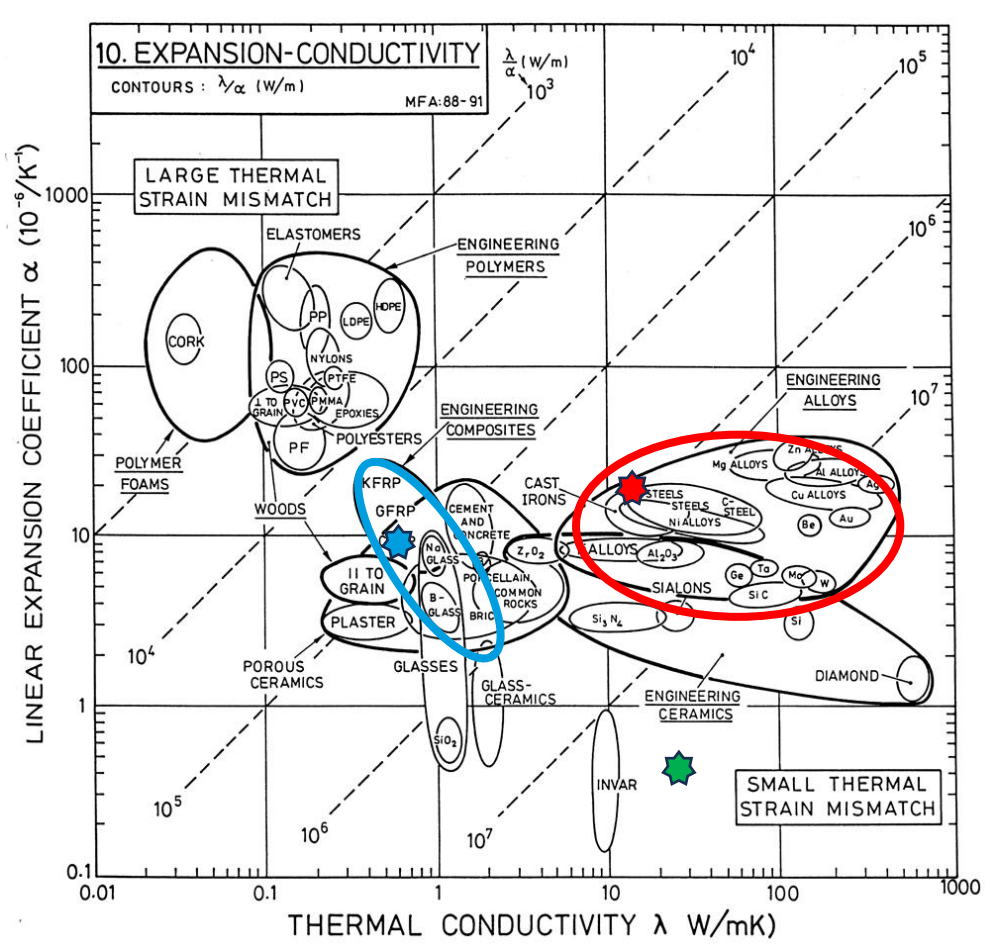

- Metals
- Inconel 718
- Engineering Composites
- Carbon Fiber Reinforced Plastics
- C_f/C_m Composite

ADVANCED COMPOSITE MATERIALS LAB

[3] Michael F. Ashby, Material Selection in Mechanical Design

[4] Cordeiro Jr, J. C., Zuzelski, M., Olima, M. H., Crunkleton, D. W., Otanicar, T., Ramsurn, H., & Keller, M. W. (2024). Vascular Carbon/Carbon composites for concentrated solar power. Composites Part A: Applied Science and Manufacturing, 108069

[5] Shi, S., Wang, Y., Jiang, T., Wu, X., Tang, B., Gao, Y., Zhong, N., Sun, K., Zhao, Y., Li, W., & Yu, J. (2022). Carbon Fiber/Phenolic Composites with High Thermal Conductivity Reinforced by a Three-Dimensional Carbon Fiber Felt Network Structure. ACS omega, 7(33), 29433–29442. https://doi.org/10.1021/acsomega.2c03848

Microvascular carbon-carbon composite with a straight channel

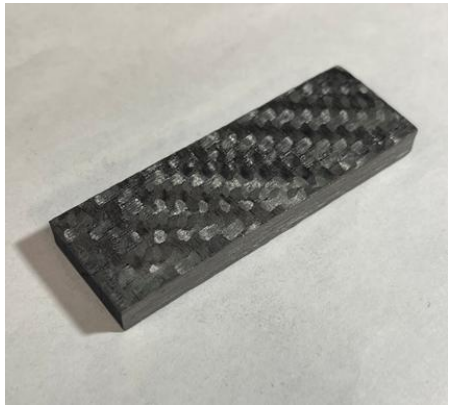

Micro-channel

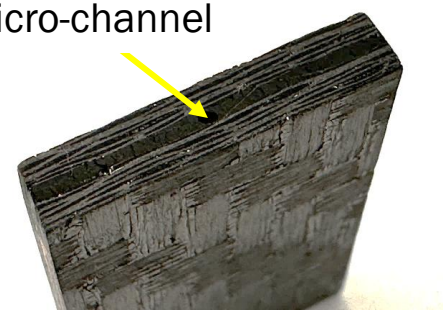

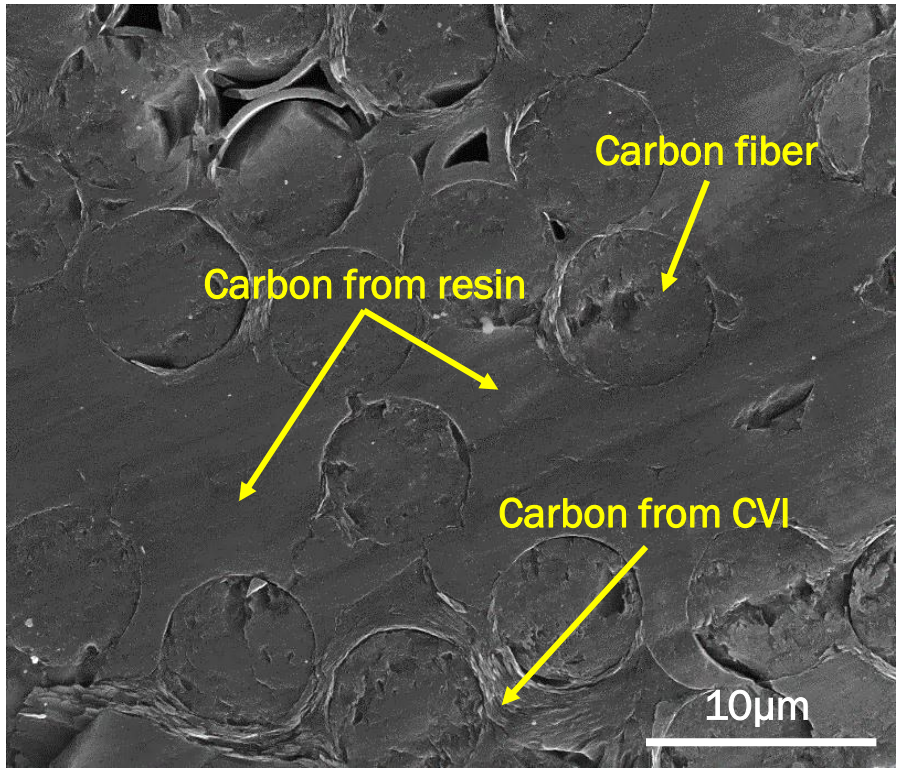

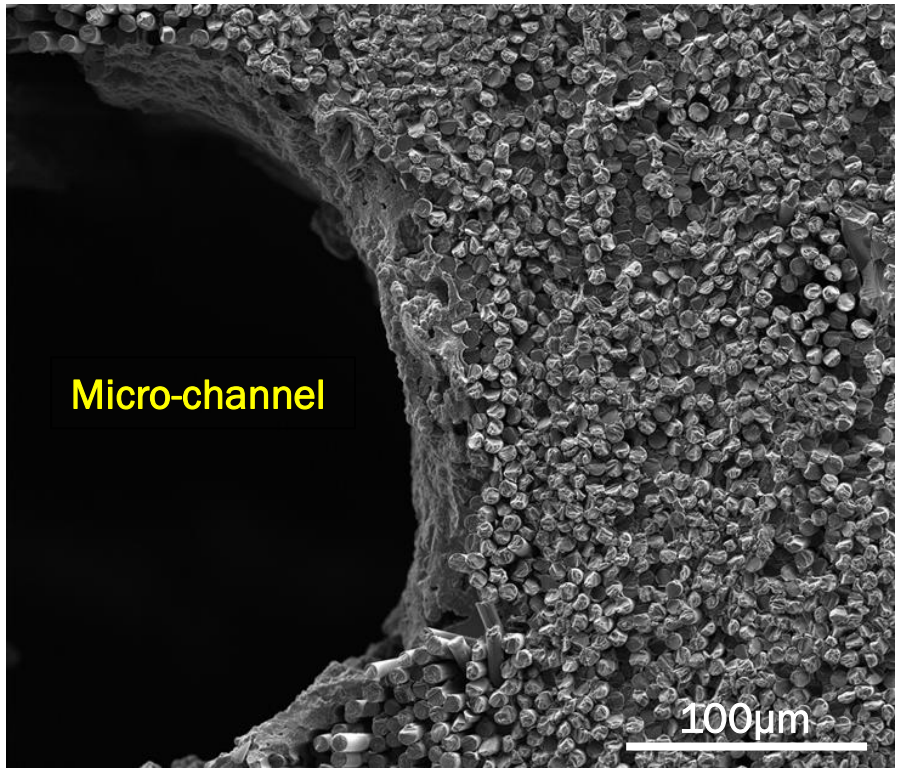

[4] Cordeiro Jr, J. C., Zuzelski, M., Olima, M. H., Crunkleton, D. W., Otanicar, T., Ramsurn, H., & Keller, M. W. (2024). Vascular Carbon/Carbon composites for concentrated solar power. Composites Part A: Applied Science and Manufacturing, 108069

CFD simulations in search for an optimal 2D channel geometry using ANSYS Fluent

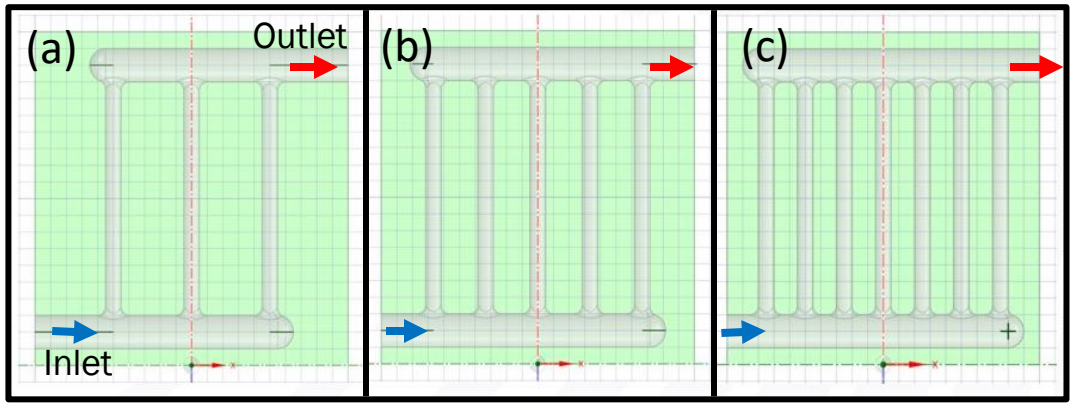

Channel geometries with (a) 3 paths (b) 5 paths and (c) 7 paths

Input parameters	Metric
CTE (m^{-1})	$4x10^{-6}$, $5.75x10^{-6}$
Thermal Conductivity (W/mK)	3, 4.5, 6, 7.5, 9, 10.5, 12
Solar Flux (W/m^2)	750,000
Pressure Drop (psi)	5
Inlet Temperature (K)	473, 573, 673, 873, 973, 1073
Pipe Roughness (m)	$3.2x10^{-6}$
Absorptivity	.94
Emissivity	.88

ADVANCED COMPOSITE MATERIALS LAB

[6] Keller, M. W., Otanicar, T. P., Crunkleton, D. W., Cordeiro, J. C., Ramsurn, H., & Davis, R. E. (2023). Carbonized Microvascular Composites for Gas Receivers.

THE UNIVERSITY of TULSA

CFD results: surface temperature and efficiency contours of different heat transfer fluids

Material	Density (kg/m^3)	Cp (J/kg*K)	Viscosity (kg/m*s)	Thermal Conductivity (W/m*K)
sCO_2	49.31	1247	4.31E-05	0.09402
Na	801.7	1257.52	2.04E-04	62.5
KCl-$MgCl_2$	1557.044	1010.2062	3.4627E-03	0.442

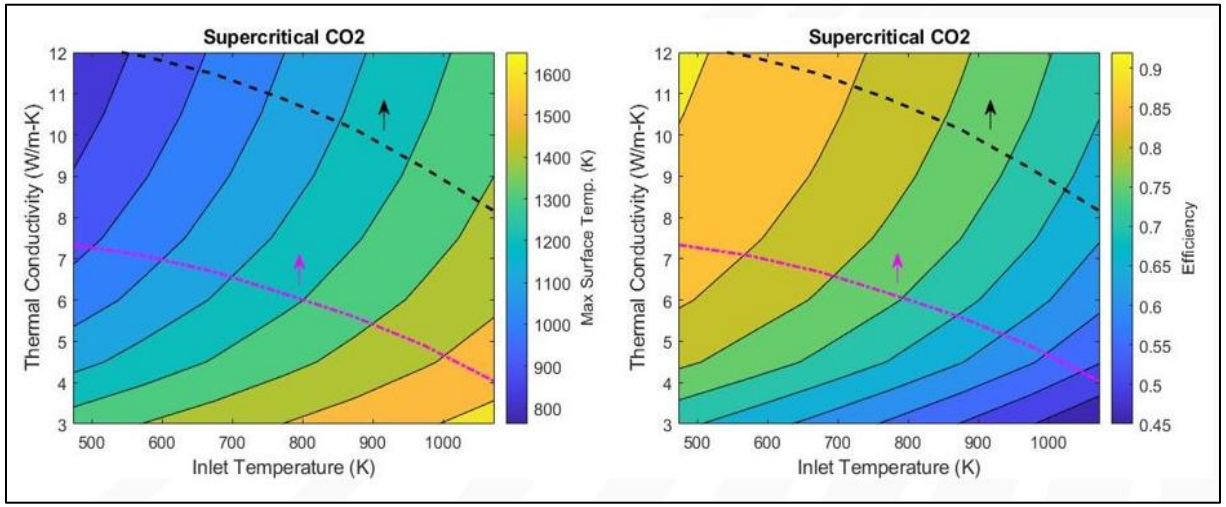

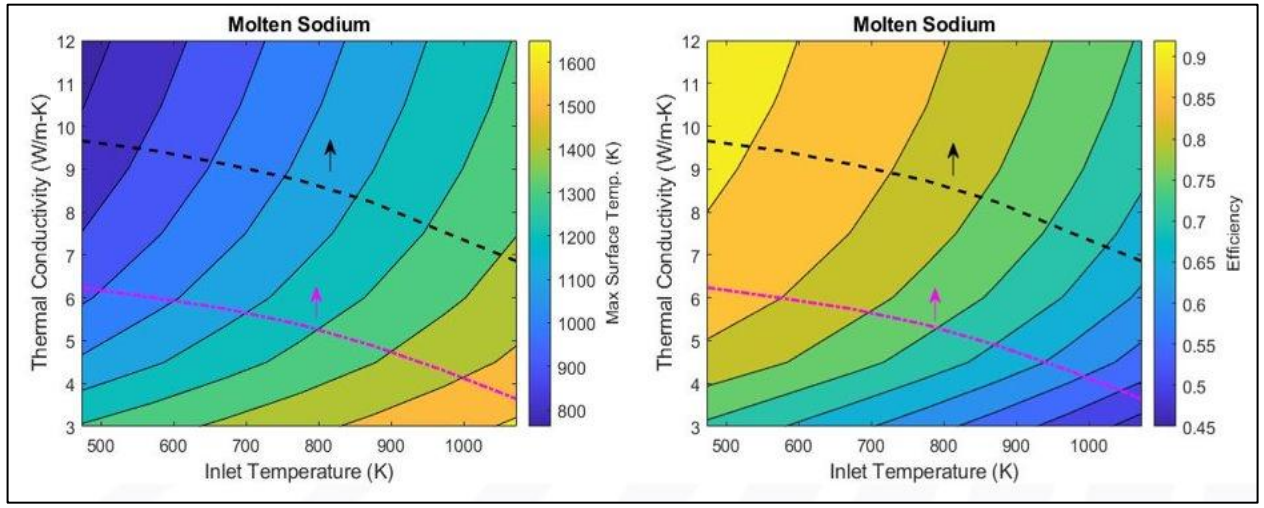

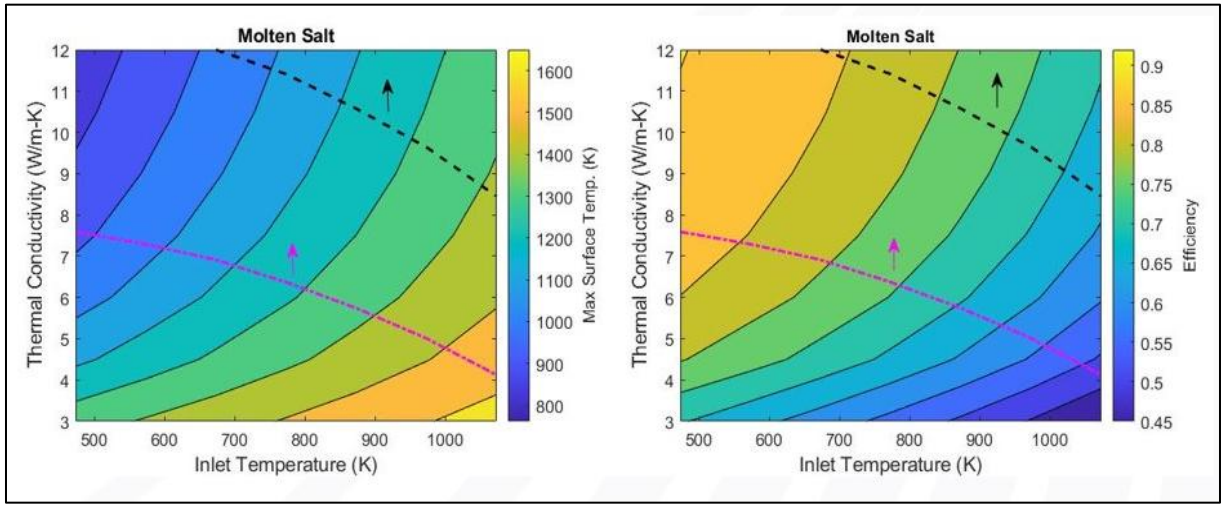

[6] Keller, M. W., Otanicar, T. P., Crunkleton, D. W., Cordeiro, J. C., Ramsurn, H., & Davis, R. E. (2023). Carbonized Microvascular Composites for Gas Receivers.

Multiple paths provide for a lower max surface temperature and higher efficiency

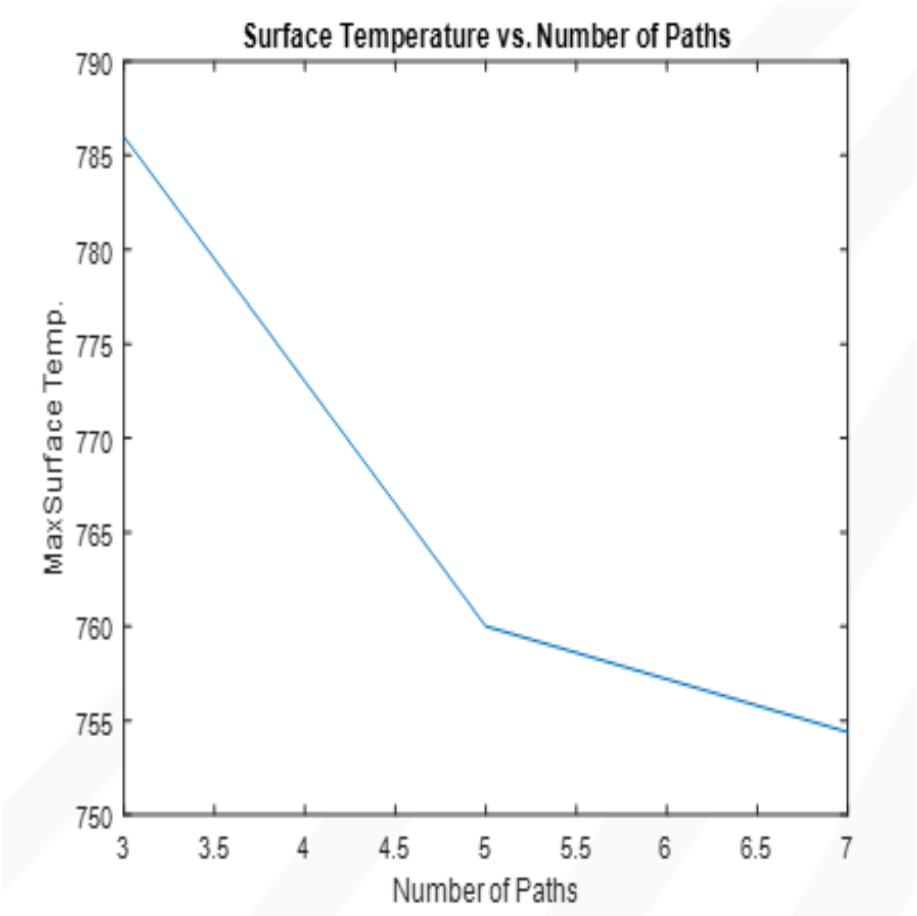

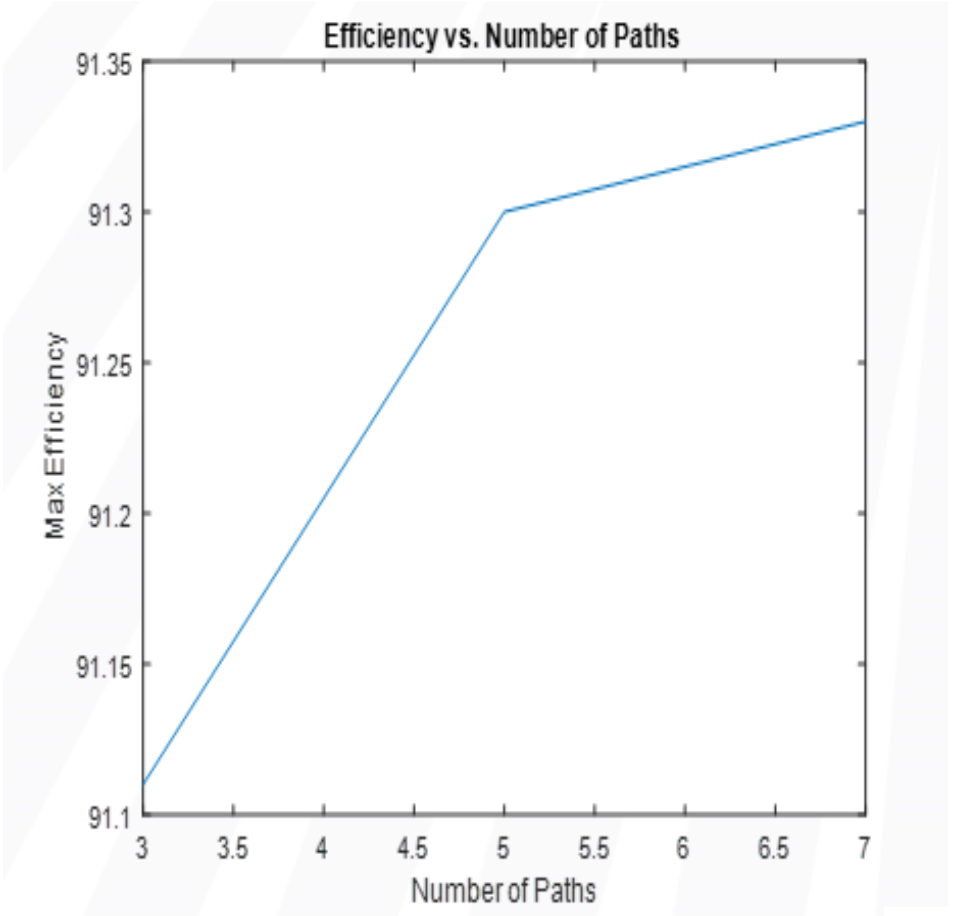

[6] Keller, M. W., Otanicar, T. P., Crunkleton, D. W., Cordeiro, J. C., Ramsurn, H., & Davis, R. E. (2023). Carbonized Microvascular Composites for Gas Receivers.

Successful fabrication of a polymer matrix composite (PMC) with 3D channels

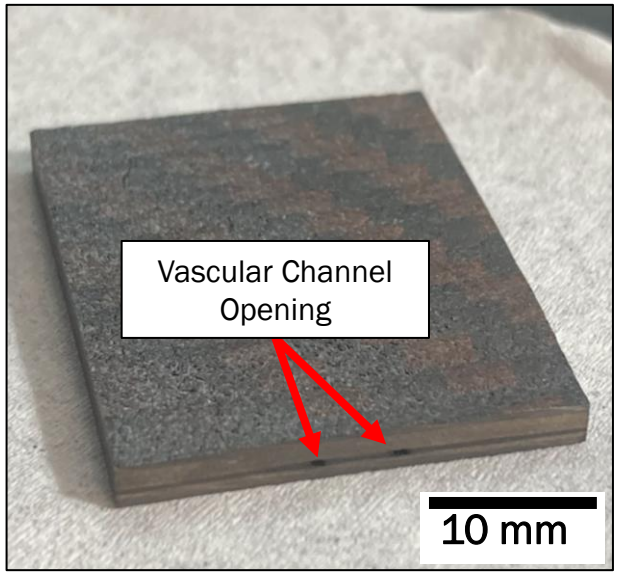



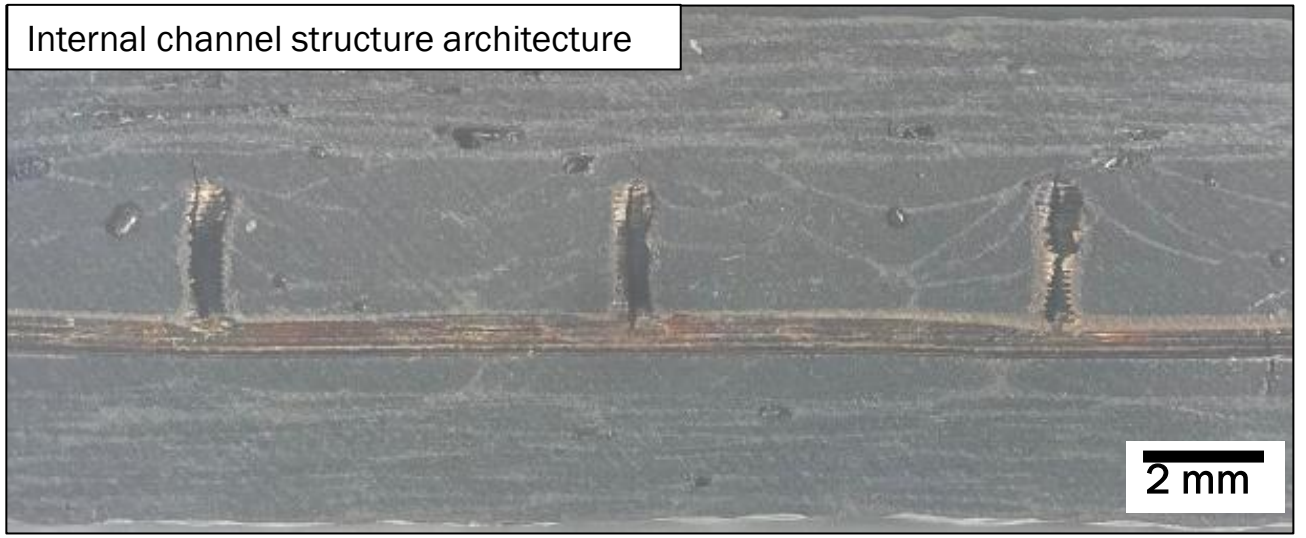

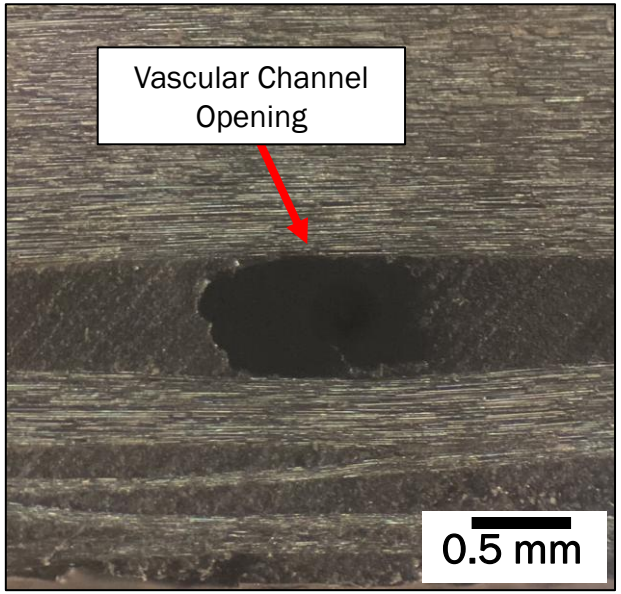

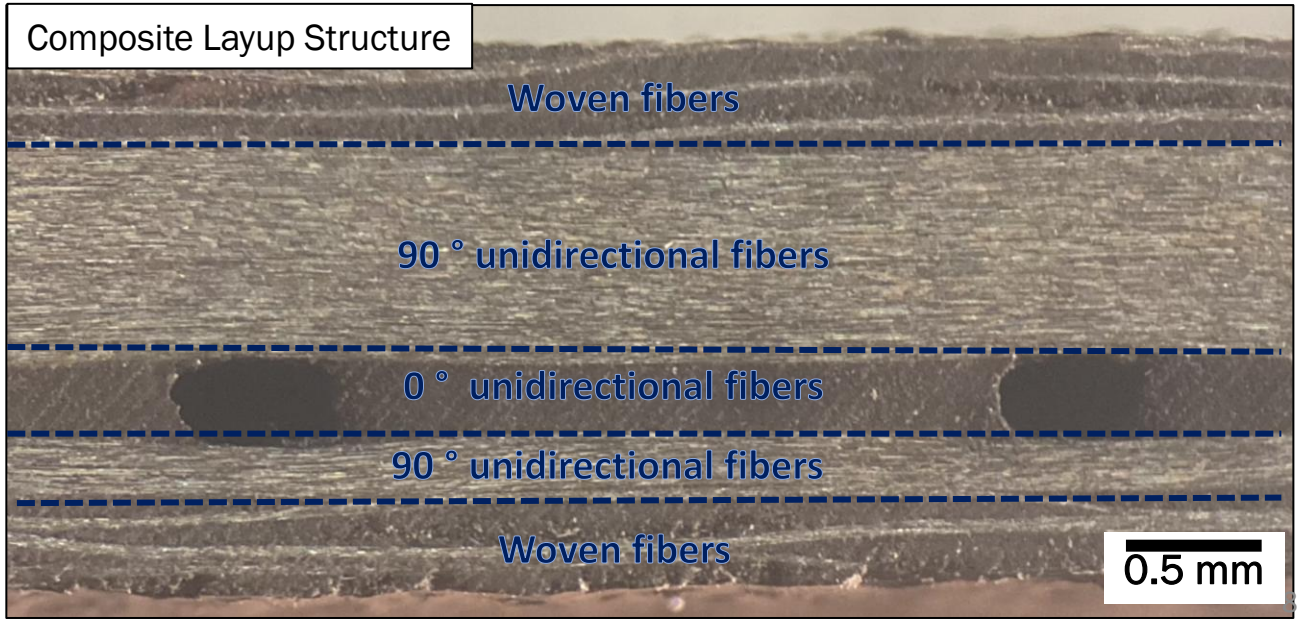

3DHX samples had better flexural properties than 2DHX samples

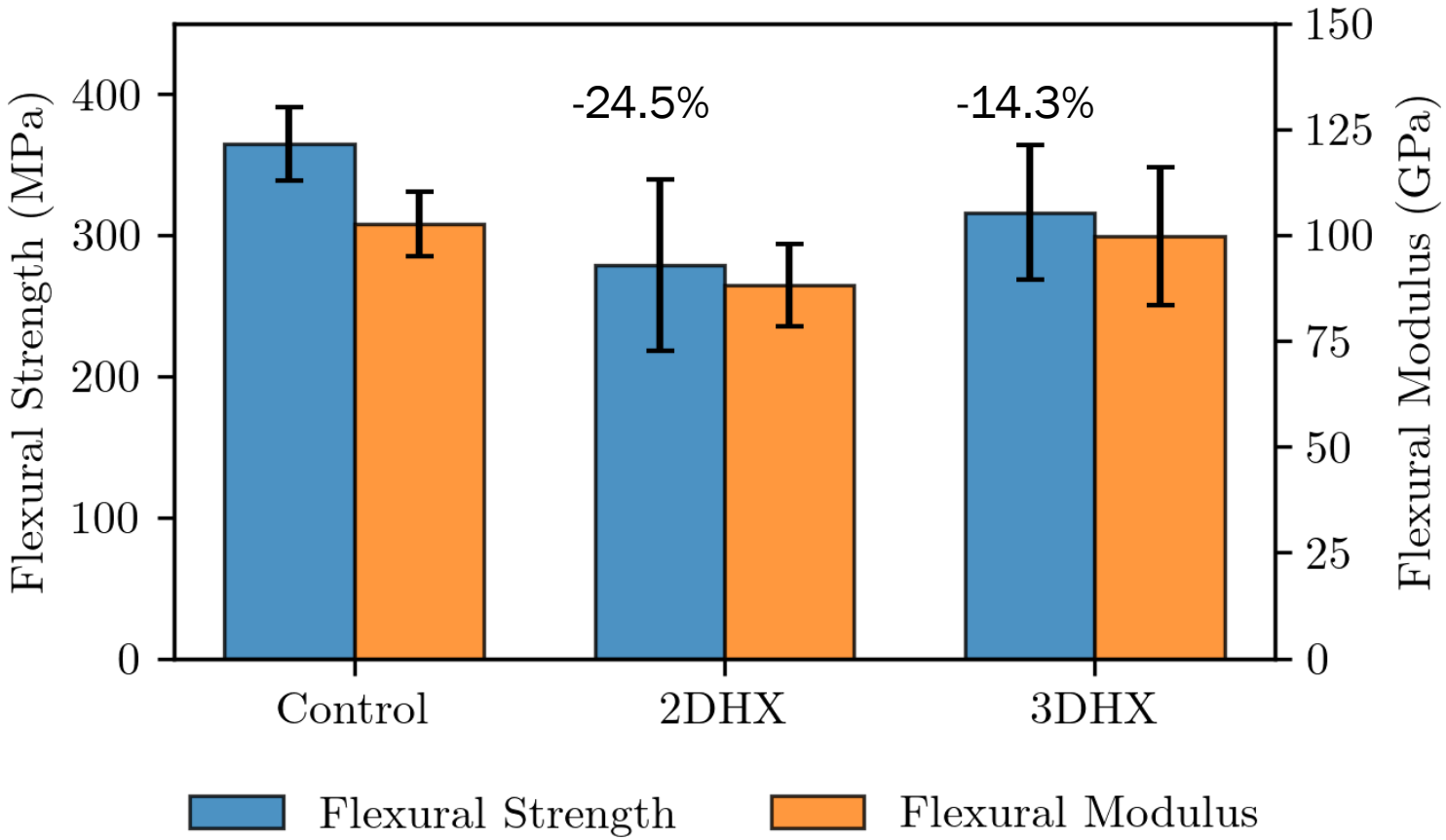

Sample	P-value
Control vs 2DHX	0.0369
Control vs 3DHX	0.0847

Carbon-carbon composite fabrication is specialized

1. Prepreg

- Pitch carbon fiber
- Curing of phenolic resin
  - Up to 140 °C
  - 80 psi & vacuum
- Depolymerize at 260°C for 12 hours in vacuum

Autoclave curing

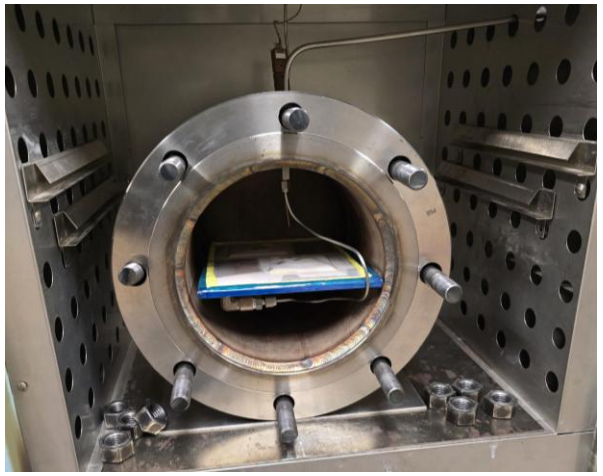

2. Carbonization

- Convert resin into carbon
  - Nitrogen atmosphere
  - 1000 °C
  - 1 hour
- Followed by intermediate graphitization at 2200°C for 1 hour

Quartz tube furnace



3. Densification

- Chemical Vapor Infiltration (CVI)
  - Methane
  - 1000 °C
  - Four 20 hours cycles

CVI in a quartz tube furnace



4. Graphitization

- Convert carbon matrix into graphite
  - Argon atmosphere
  - 2200 °C
  - 3 hours

Graphitization furnace



[4] Cordeiro Jr, J. C., Zuzelski, M., Olima, M. H., Crunkleton, D. W., Otanicar, T., Ramsurn, H., & Keller, M. W. (2024). Vascular Carbon/Carbon composites for concentrated solar power. Composites Part A: Applied Science and Manufacturing, 108069

Carbon-carbon composite with 3D channel network

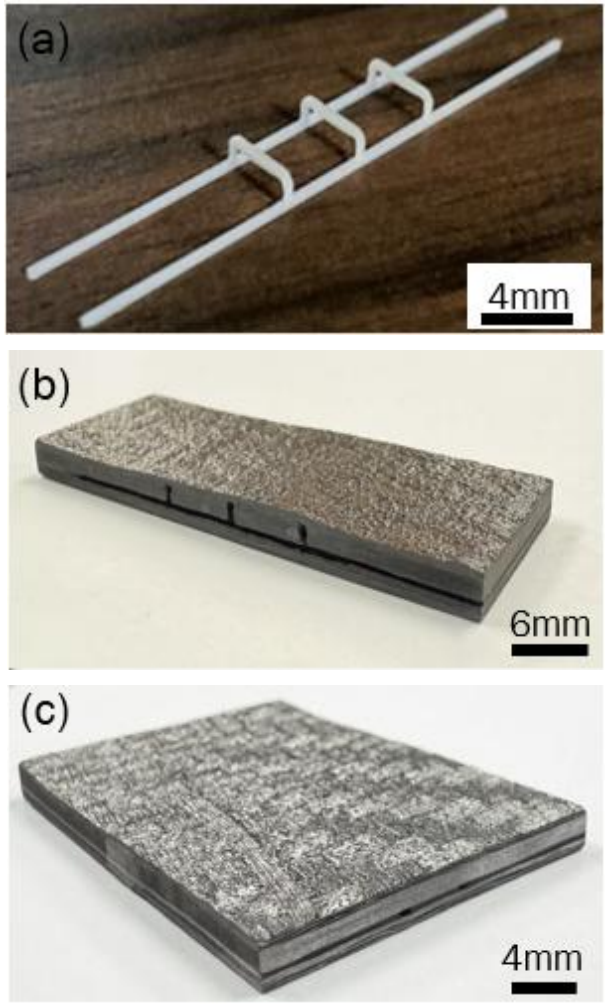

- 3D sacrificial catalyzed PLA template
- Cross-section of green part showing clear channels
- Graphitized 3D heat exchanger carbon-carbon composite

micro-CT images of the sample show clear channels and bridges

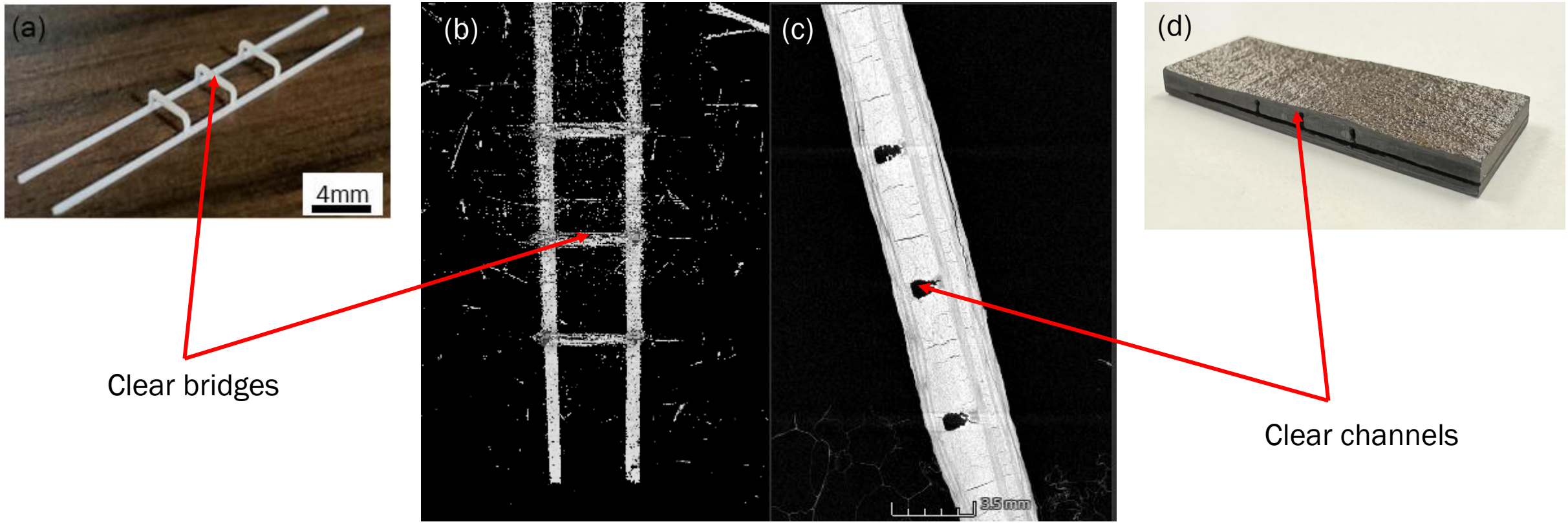

Carbon/Phenolic Composite (pre carbonization)

Experimental setup to determine the pressure limit of the channels in the composite

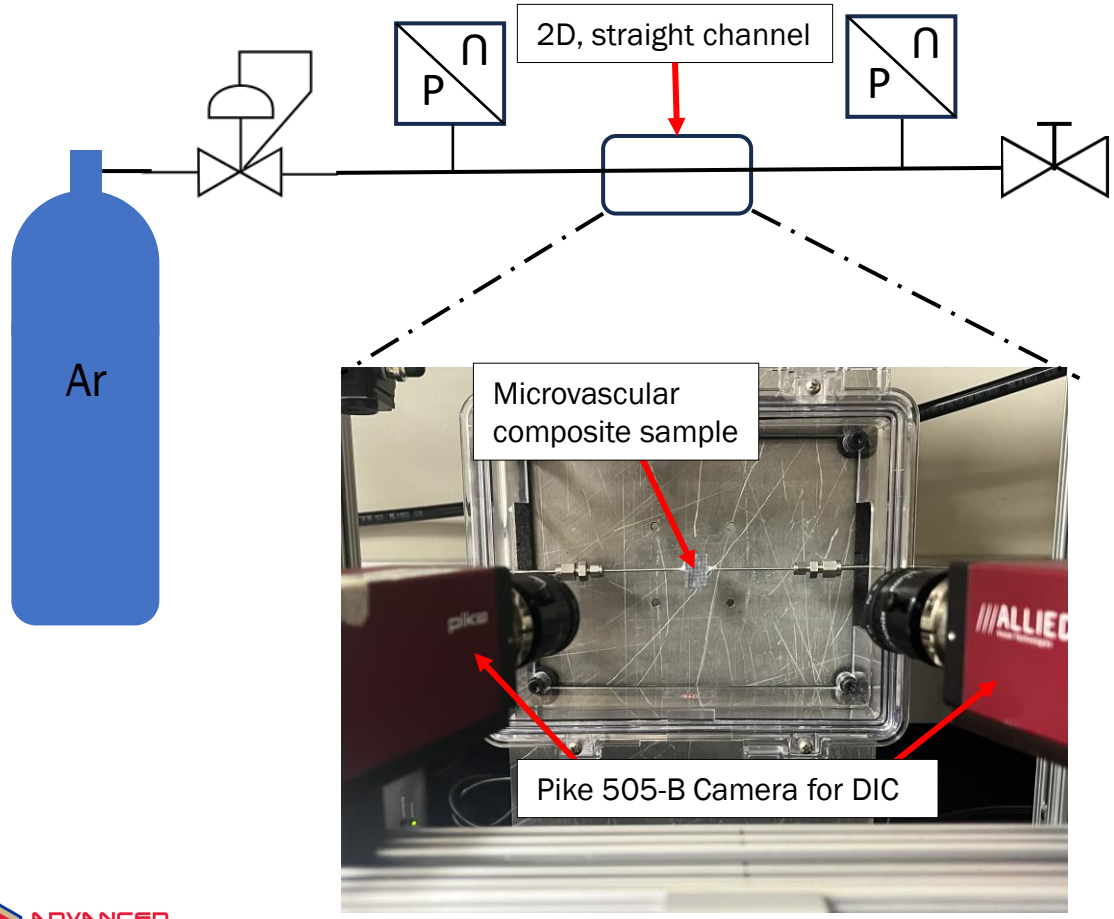

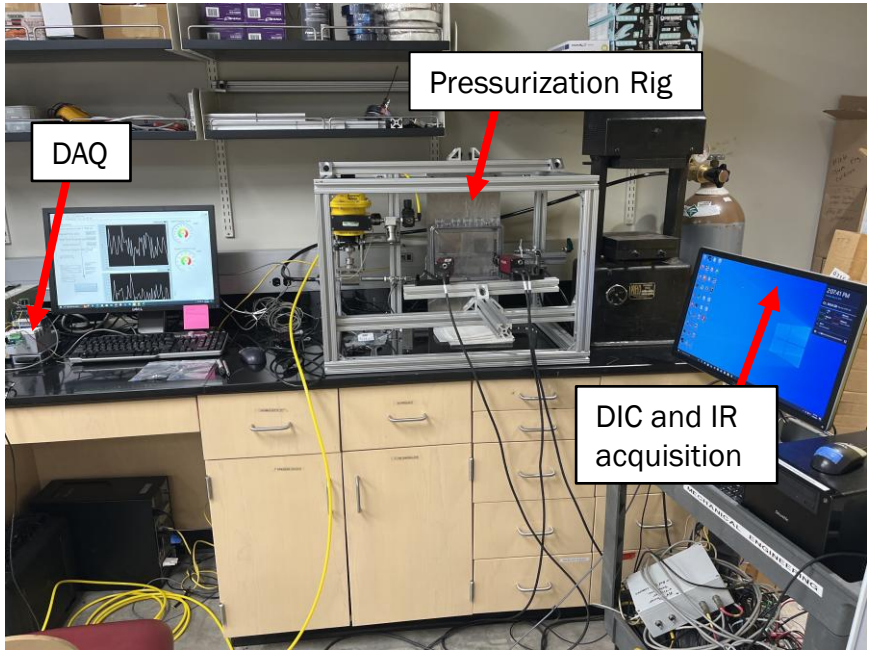

- Argon gas
- FLOWSERVE® Kammer Electropnumatic actuator with air-to-open action

The pressurization rig can achieve 1100psi with no leaks

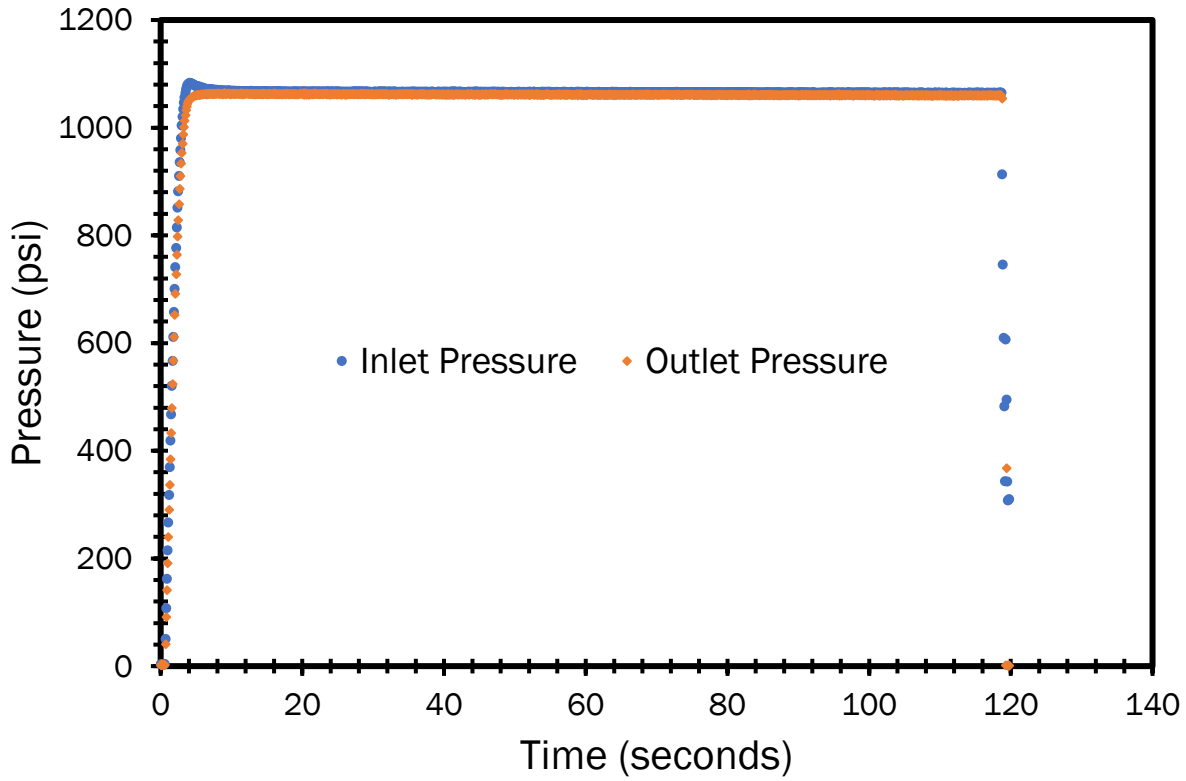

Heat transfer capacity of S-CO_2

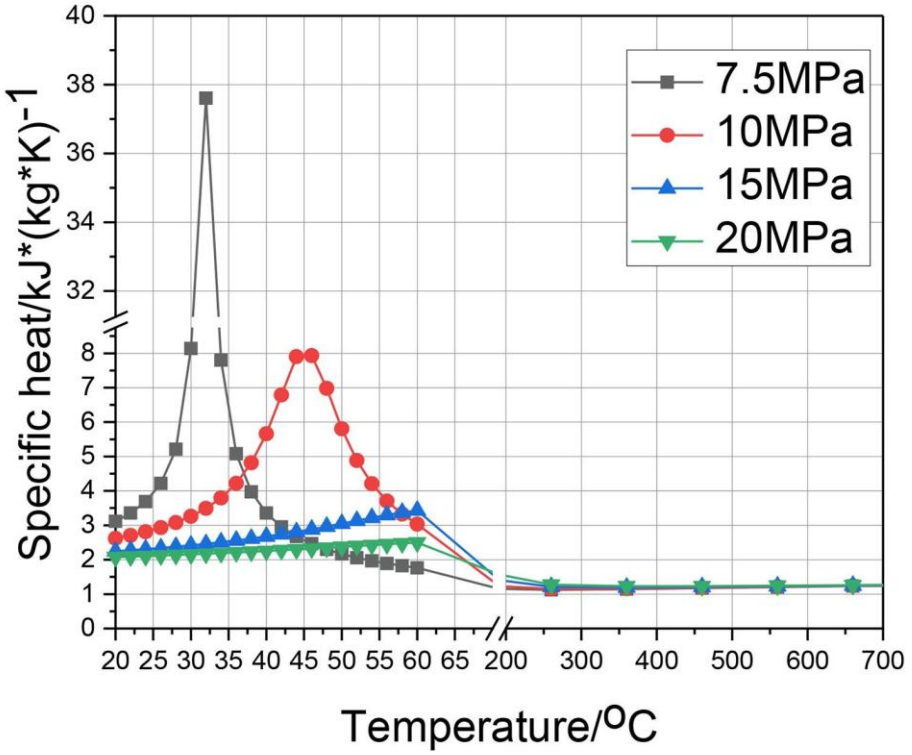

Wu et. al. *A review of research and development of supercritical carbon dioxide Brayton cycle technology in nuclear engineering applications*. 2020

ADVANCED COMPOSITE MATERIALS LAB

Fluid was injected into the channels using a syringe pump and composite sample monitored using an IR camera setup

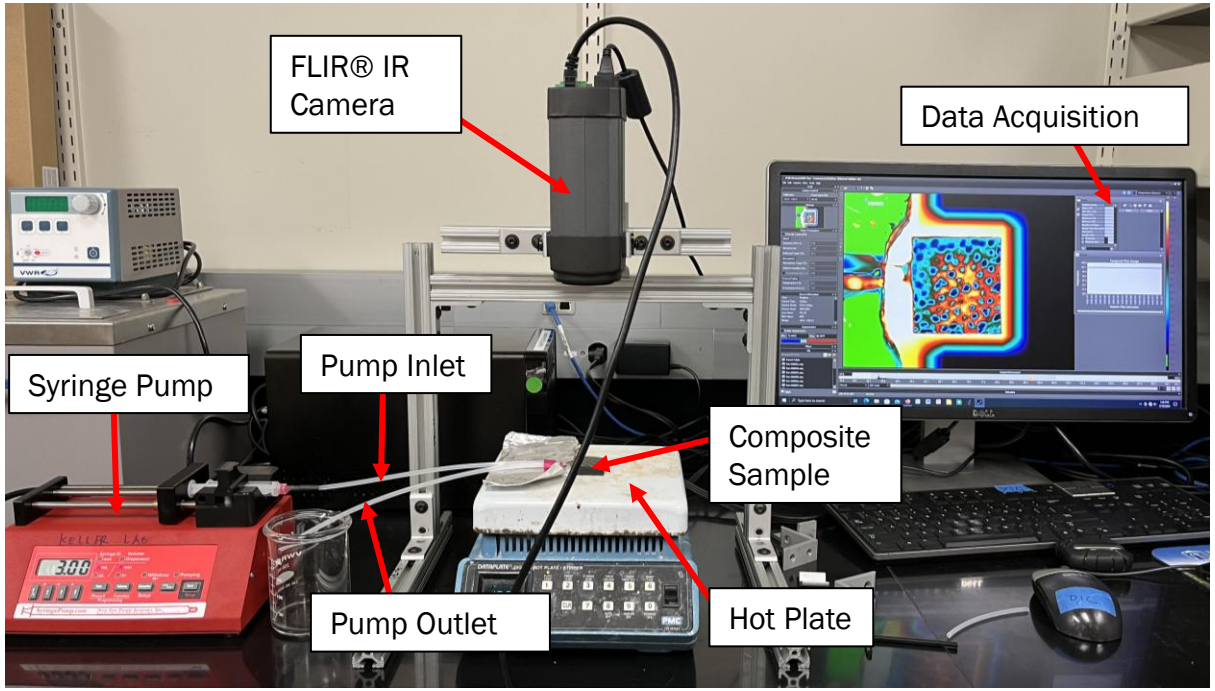

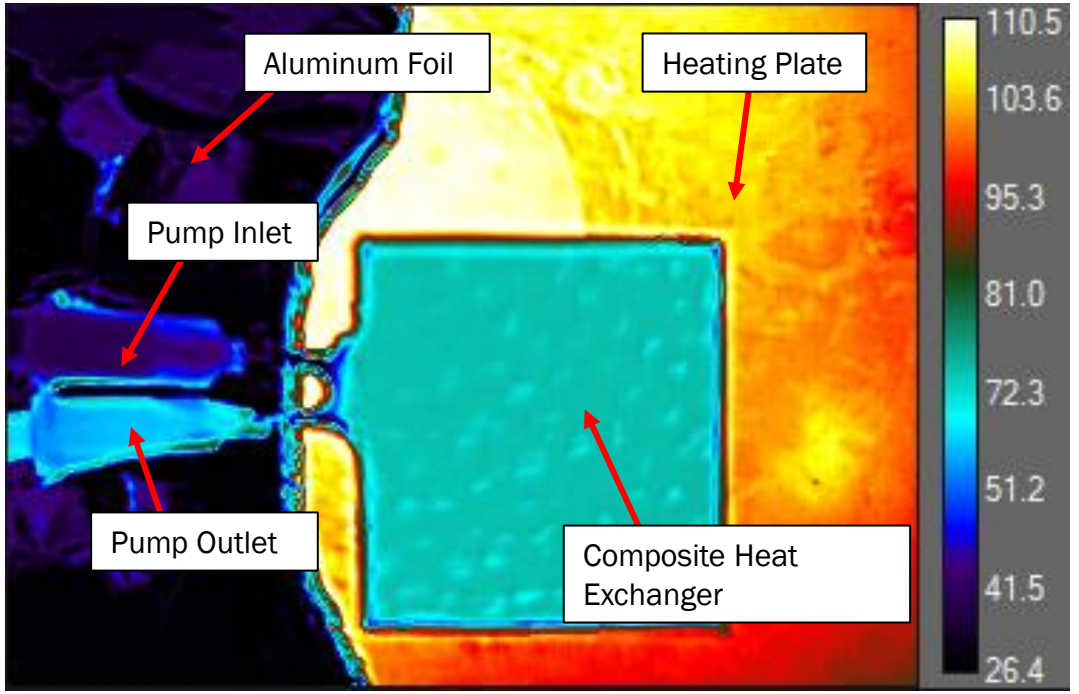

- Working fluid is water at 2, 4, 6, and 10* mL/min
- Heating plate set a constant 100°C

Higher fluid flowrates improved the effectiveness of the 3D channels as a heat exchanger

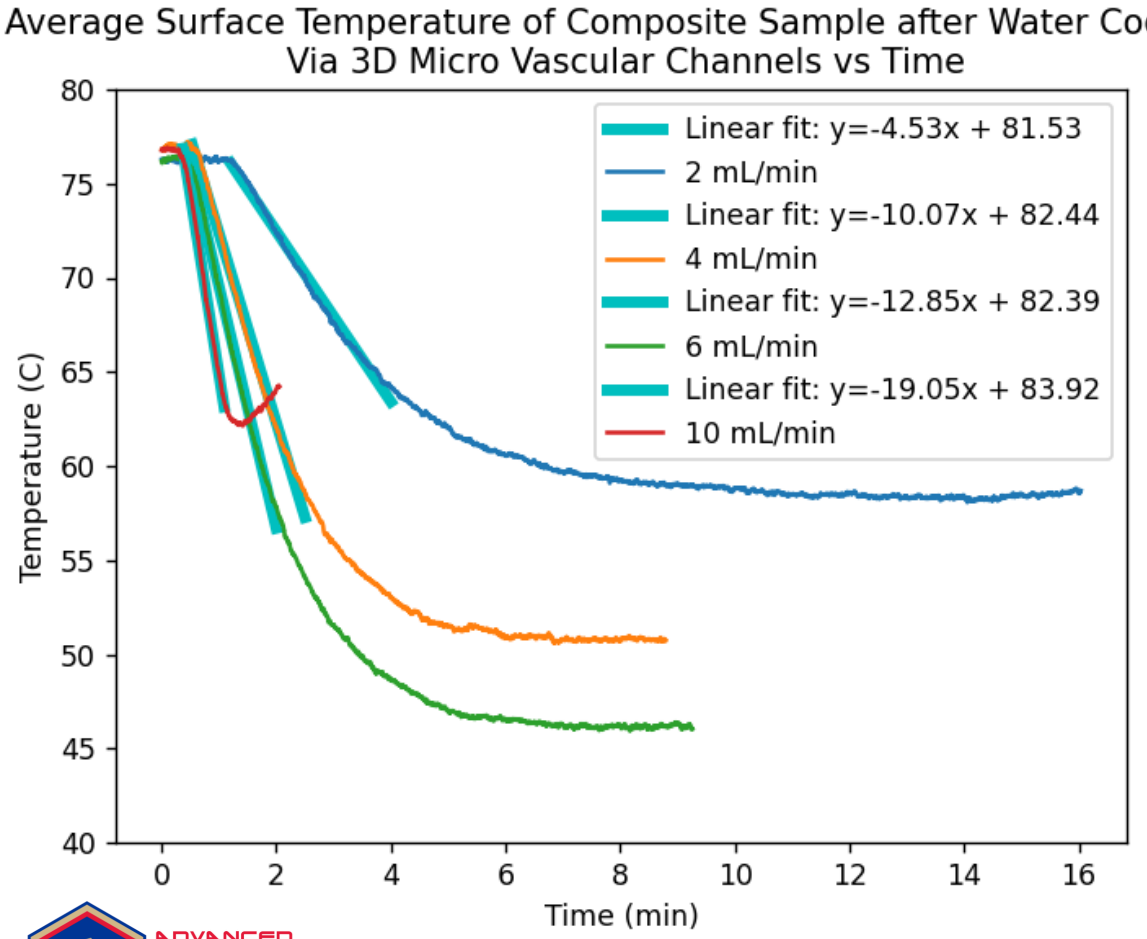

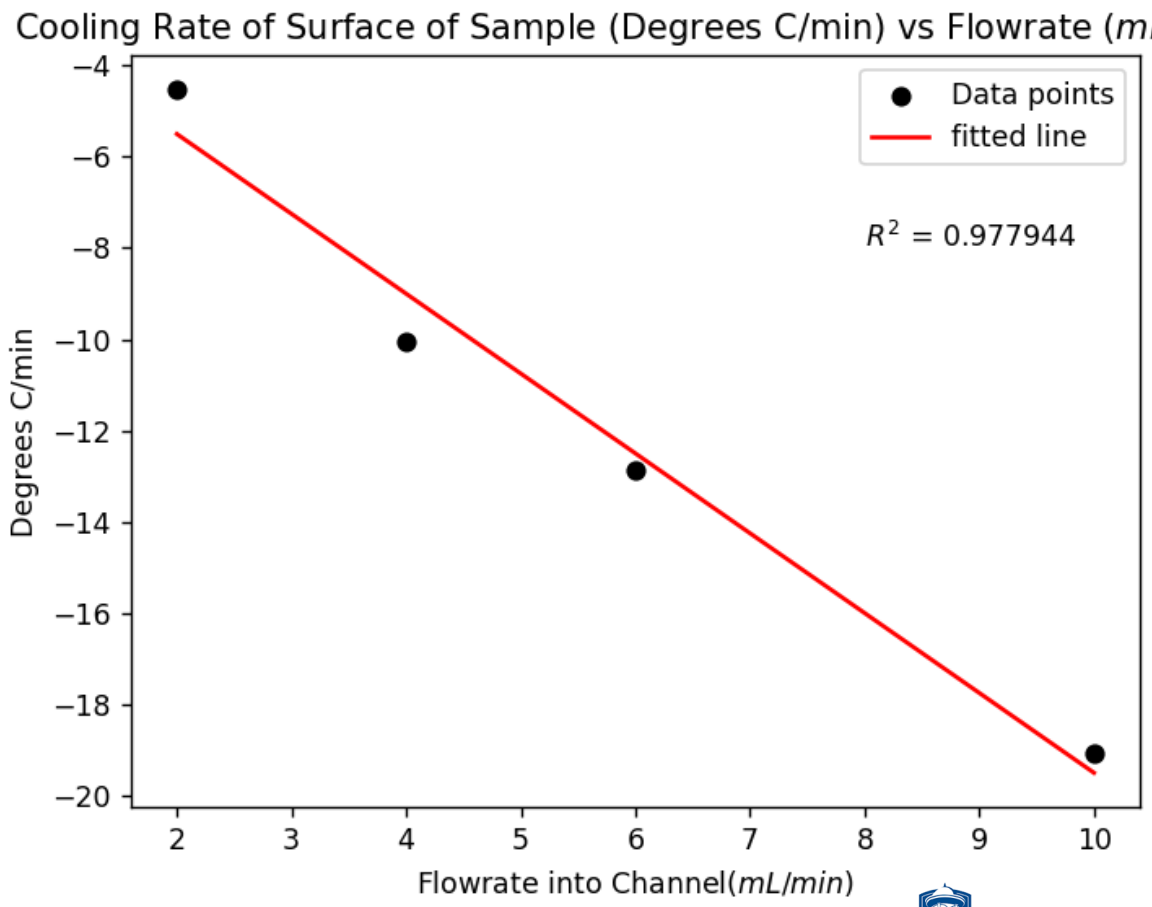

ADVANCED COMPOSITE MATERIALS LAB

THE UNIVERSITY of TULSA

Manufactured vascular carbon-carbon composite sustained 800 PSI without failure

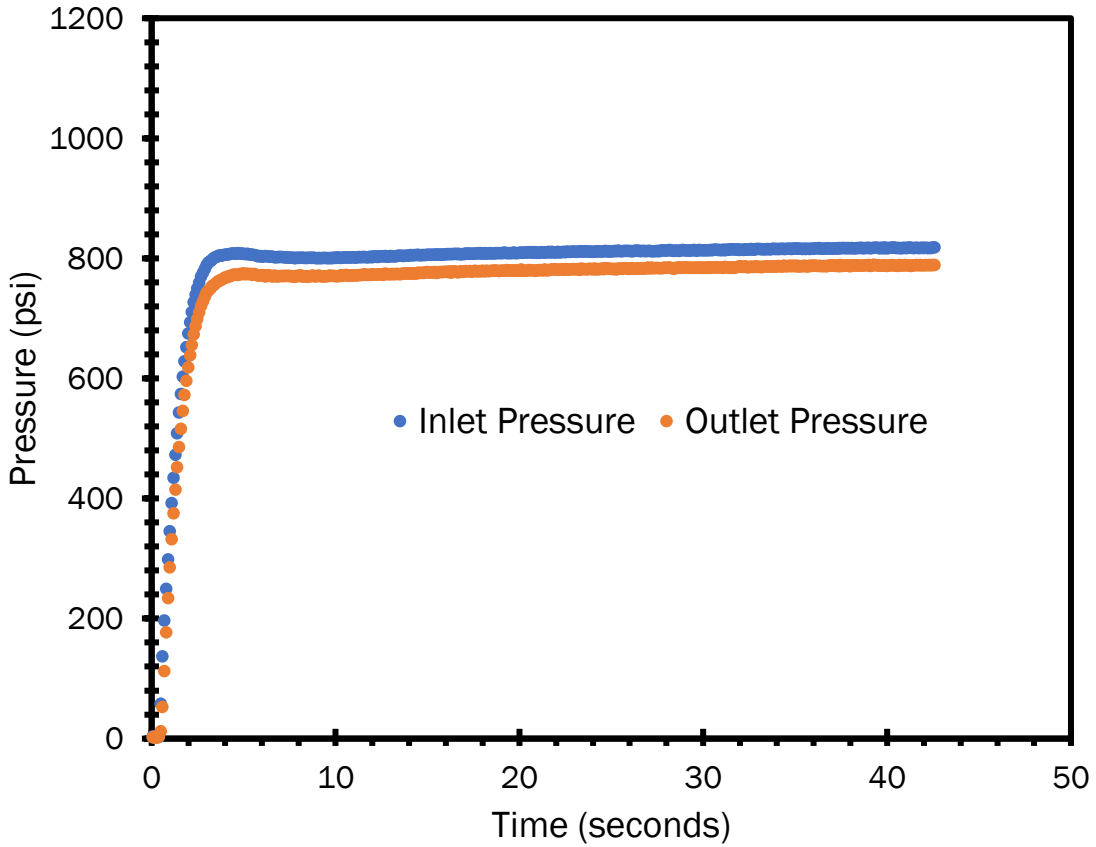

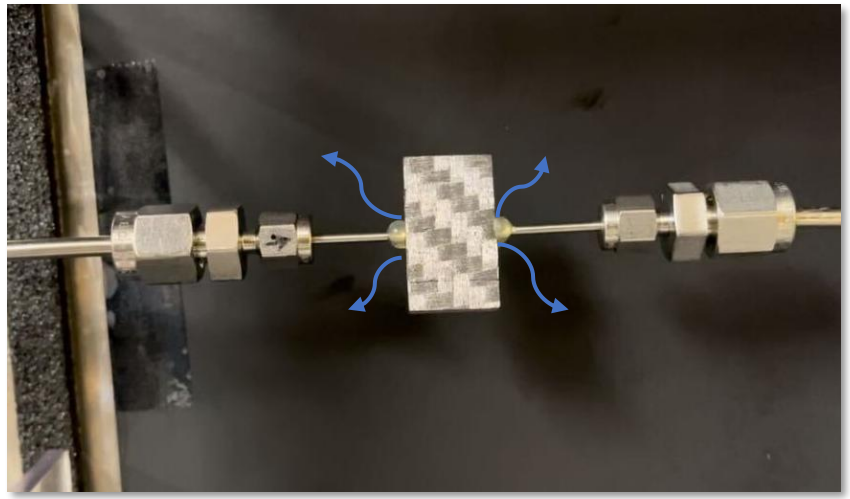

Leak at the tube and channel interface

ADVANCED COMPOSITE MATERIALS LAB

THE UNIVERSITY of TULSA

Summary

- Ability to manufacture Carbon-Carbon Composite heat exchanger
- Demonstrate effectiveness of a 3D cooling network up to 19°C/min
- Channel structure can handle up to xxx psi

Future work

- Use different mediums like Helium or sCO_2
- Optimize channel architecture for better thermal and mechanical performance using FEA



Instron.com

Acknowledgments

Research Group Professor

- Dr. Michael Keller

Research Group Colleague

- Mark Olima

Questions?

Heat-pipe-cooled leading edge. Molybdenum-Rhenium embedded in C_f/C_m

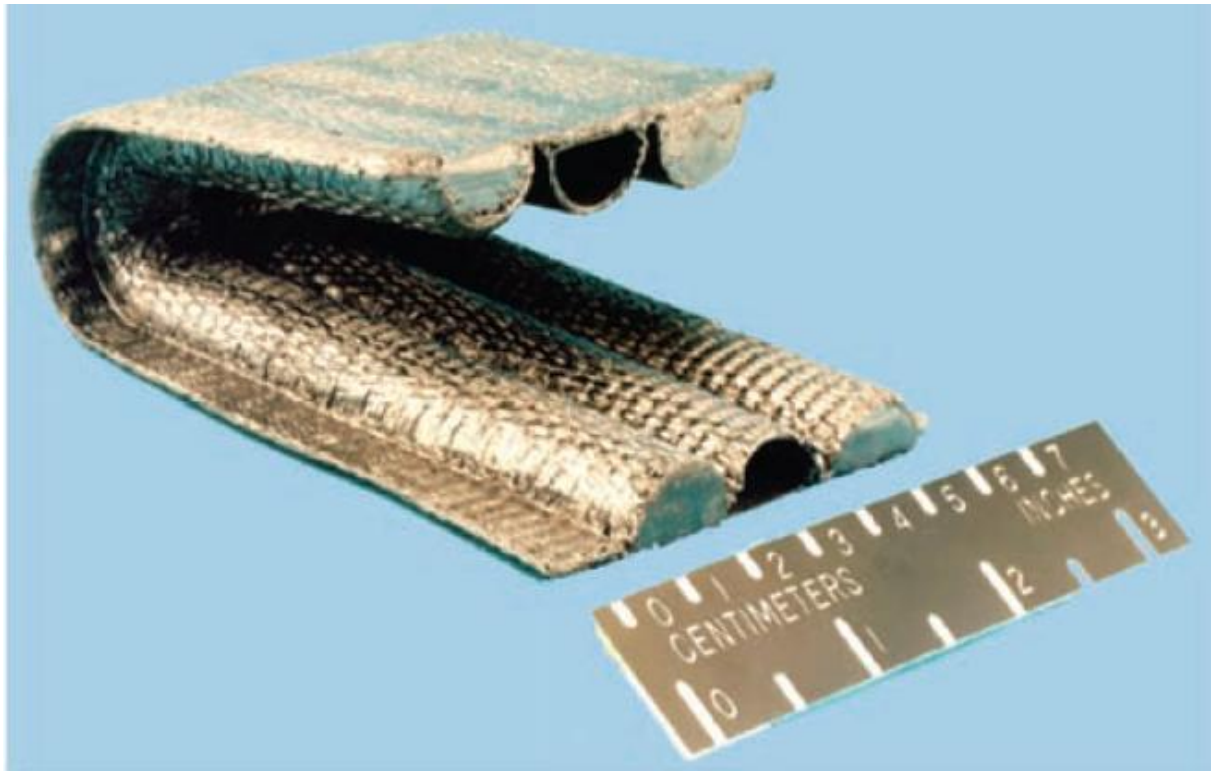

Glass, David. "Ceramic matrix composite (CMC) thermal protection systems (TPS) and hot structures for hypersonic vehicles." *15th AIAA international space planes and hypersonic systems and technologies conference*. 2008.

EFFECTS OF COOLING RATE ON THE MECHANICAL AND THERMAL PROPERTIES OF SELF-REINFORCED POLYETHYLENE COMPOSITES

Yelin Ni[1*], Yao Qiao[1*], Raveen John[1], Ethan Nickerson[1], Khaled Shahwan[1], Kevin Simmons[1*]

[1]Energy and Environment Directorate, Pacific Northwest National Laboratory, Richland, Washington, USA

Emails of corresponding authors:
Yelin Ni (yelin.ni@pnnl.gov)
Yao Qiao (yao.qiao@pnnl.gov)
Kevin Simmons (kl.simmons@pnnl.gov)

Keywords: Thermoplastic composite, Self-reinforced composite, Polyethylene, Cooling rate, Tensile properties, Thermal properties

ABSTRACT

Self-reinforced polyethylene (PE) composites offer advantages of interfacial compatibility, enhanced mechanical performance, and full recyclability potential due to their homopolymer composition. This study investigates the effect of cooling rate during composite fabrication on the mechanical and thermal properties of self-reinforced PE composites consisting of ultrahigh molecular weight polyethylene (UHMWPE) fabric and high-density polyethylene (HDPE) matrix. Composite sheets with 50 wt.% fabric content were manufactured using powder impregnation and hot compaction techniques, with cooling rates varied from 0.76 to 424.92 °C/min through controlled air cooling, cold metal block transfer, and ice immersion methods. The uniaxial quasi-static tensile testing revealed bilinear stress-strain behavior, presumably attributed to yarn de-crimping followed by the elastic behavior of the composite, with modulus values ranging from 2.2 to 3.8 GPa in the initial region and higher values (8.1 to 11.3 GPa) in the elastic region. Mechanical properties showed minimal dependence on cooling rate. Thermal analysis revealed that the melting temperature (T_m) of HDPE decreased from ~130 °C to ~126.5 °C with increasing cooling rate, following a linear correlation with logarithmic cooling rate. The total degree of crystallinity of the PE composites (i.e., the sum of crystallinity of HDPE matrix and UHMWPE fabric) decreased from ~85% to ~75% with increasing cooling rate, approaching the theoretical mixing rule value of 72.4%. These findings suggest that self-reinforced PE composites exhibit relative insensitivity to cooling rate variations in the range of 0.76 to 424.92 °C/min, which may be attributed to low interfacial strength between PE matrix and PE fabric compared to conventional fiber-reinforced composites.

1 INTRODUCTION

Self-reinforced thermoplastic composites are materials in which both the matrix and the reinforcing phase consist of the same polymer, with the benefits of interfacial compatibility, enhanced mechanical performance, and the potential for full recyclability and re-processing [1–3]. The self-reinforced polyethylene (PE) composites are also known for its lightweight, low energy cost during manufacturing, waterproof and high durability. These composites are typically manufactured by consolidating highly oriented PE fibers or films into a bulk matrix, utilizing the high crystallinity and molecular alignment of the reinforcement to achieve significantly higher tensile strength and stiffness than the isotropic PE [2,4]. During composite manufacturing, the control of thermal history is critical to maintain fiber orientation and ensuring optimal interfacial bonding between the fiber and the matrix [3,5]. It has been reported that polyether ether ketone (PEEK) matrix as a semi-crystalline thermoplastic polymer exhibited a transition from brittle to ductile performance as the cooling rate became faster [6,7]. Whether such a transition could be observed for other semi-crystalline polymer composites such as the self-reinforced PE composites is unknown. In this work, we present the

preliminary studies on the mechanical and thermal properties of self-reinforced PE composites affected by the cooling rates during manufacturing.

2 EXPERIMENTAL

2.1 Powder Impregnation

PE composite sheets were fabricated from ultrahigh molecular weight polyethylene (UHMWPE) fabric (Avient Corporation) and high-density polyethylene (HDPE) powder (Microthene FA70000, LyondellBasell), with 50 wt.% of fabrics, by powder impregnation and compression molding techniques. The UHMWPE fabrics and HDPE powders were used as received.

Two 6" × 4" (152.4 mm × 101.6 mm) pieces were cut from the plain weave UHMWPE fabric, with the cutting direction aligned parallel to the warp and weft fiber directions. The HDPE powder was poured into a 250-micron sieve and sprayed onto the mold by manually vibrating the sieve above the mold. Figure 1(a) shows the top layer of HDPE powder distributed on a piece of UHMWPE fabric. A total of three layers of powder and two layers of fabric were alternately laid up in a mold, as shown in Figure 1(b).

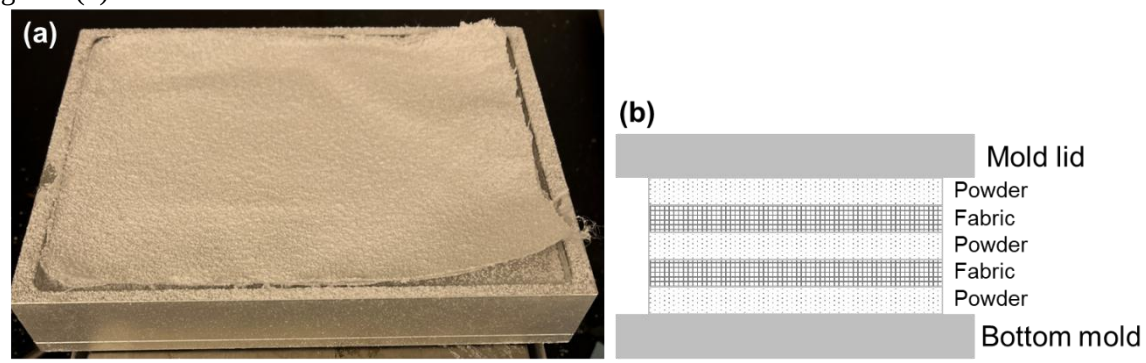

Figure 1. (a) The HDPE powder deposits on the top of, in between, and at the bottom of two UHMWPE fabrics in a mold. (b) Layup of UHMWPE fabric and HDPE powder layers in the mold.

2.2 Compression Molding with Different Cooling Rates

The mold was transferred to a hot press (Carver) pre-heated to 140 °C, and held at 1100 lbs (approximately 45.8 psi or 0.3 MPa) for 15 min on the compression molder before cooling down in place. The processing parameters were optimized in a previous study [8]. A typical temperature profile during compression molding is shown in Figure 2, where the temperature inside the mold were in between 135 °C and 140 °C for more than 10 min. The temperature range was chosen to completely melt the HDPE powder but keep the fabric intact. The compression molder was equipped with an air-cooling accessory. By adjusting the cooling air pressure, cooling rates ranging from 0.76 °C/min to 3.61 °C/min were obtained.

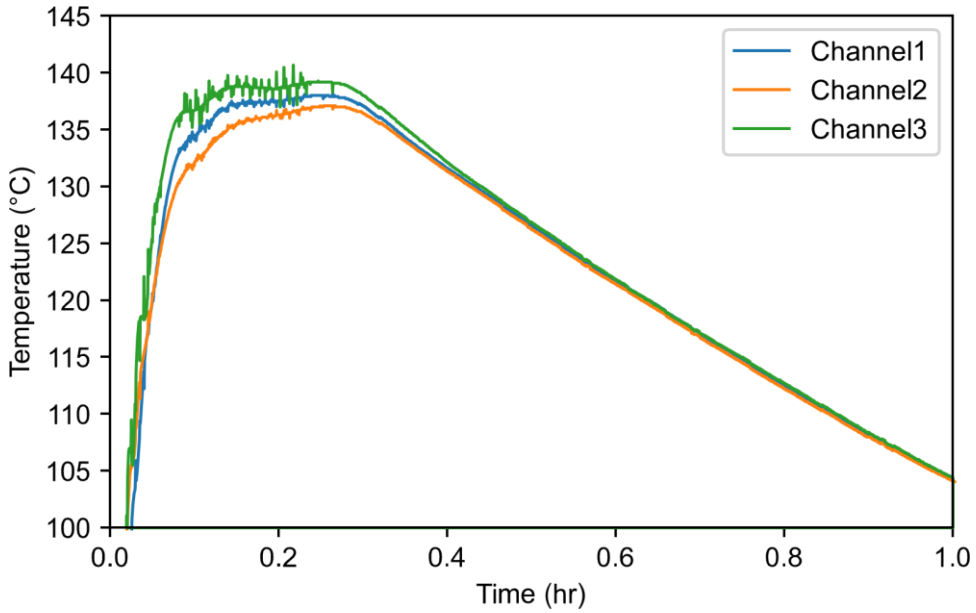

Figure 2. Temperature readings of three thermocouples placed at three different locations inside the mold, in between the composite and mold lid.

Higher cooling rates (above 50 °C/min) were achieved by transferring the mold onto cold metal blocks (Figure 3a) and into an ice bucket (Figure 3b). A second batch using the ice-immersion method was performed to achieve an even higher cooling rate up to 424.92 °C/min. The cooling rates were calculated from the initial cooling periods (e.g., above 100 °C), as listed in Table 1.

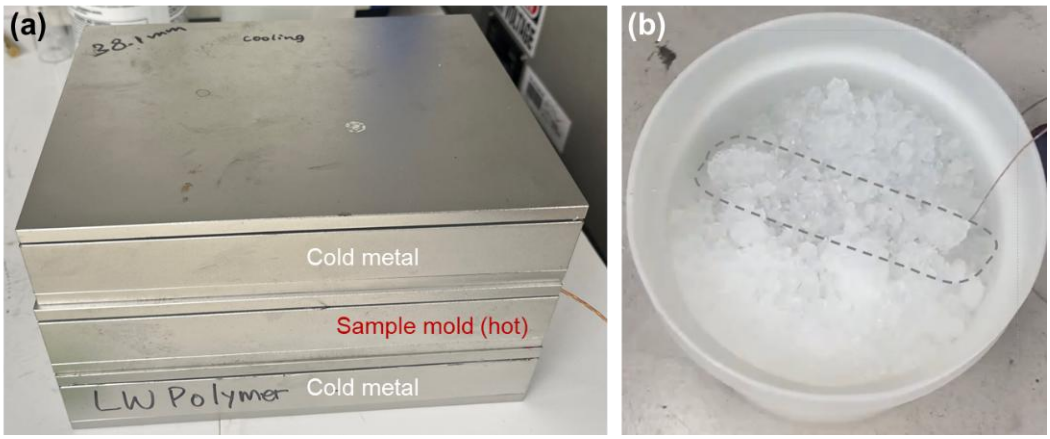

Figure 3. (a) Cooling down the mold with composite sample in between two empty metal molds initially at 25 °C. (b) A mold immersed in a bucket of ice. The grey dashed line indicates the location of the mold.

Table 1. Cooling rate at the initial cooling period using different cooling methods.

Cooling Method	Cooling Rate (°C/min)
Adjusting cooling air pressures on the compression molder	0.76
	0.80
	1.18
	3.61
Cold metal blocks	62.48
Ice immersion	167.27
	424.92

2.3 Tensile Testing

From each composite sheet, five rectangular specimens of 0.5” × 5” (12.7 mm × 127 mm) were cut along the principal fiber orientations (0°/90°). Uniaxial quasi-static tensile tests were performed at room temperature on an Instron 5582 test frame at a controlled displacement rate of 2 mm/min. The crosshead movement direction was aligned with the yarn axis. A gauge section of 2.6” (66 mm) long and full width was pre-speckled and monitored by the digital image correlation (DIC, Correlated Solutions) cameras for strain calculation.

2.4 Thermal Analysis

Melting and crystallization behaviors of as-purchased UHMWPE fabric, HDPE powder, and the composite specimens were characterized on the Differential Scanning Calorimetry (DSC, TA Instruments Q2000) in cyclic temperature ramps between 0 and 200 °C. The heating and cooling rates were 10 °C/min. The tests were performed under N_2 gas flow of 50 mL/min.

The melting point (T_m) was determined as the temperature corresponding to peak maxima of the melting peaks in the first heating cycle. The enthalpy (ΔH) was calculated as the trapezoidal area under the heat capacity curve, as shown in Figure 4. The baseline for peak area calculation was chosen to be the line connecting the 60 °C and 180 °C points. These two points were chosen as they were located on the flat portion of the heat capacity curve at each side of the peak. Degree of crystallinity (χ) was calculated as a ratio of heat of fusion (ΔH_f) measured on the endothermic peaks (during heat cycles) to the heat of fusion of 100% crystalized PE (ΔH_f^0 = 293 J/g [9]).

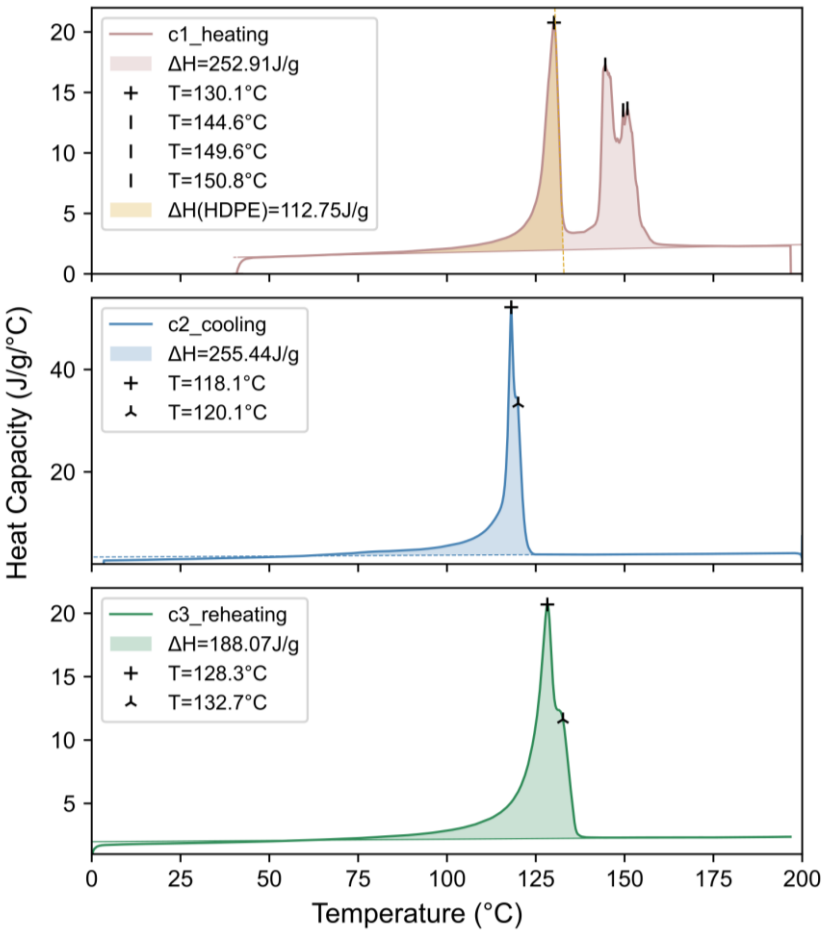

Figure 4. Heat capacity in three cycles of DSC test for a self-reinforced PE composite: c1 – initial heating from 40 to 200 °C, c2 – cooling cycle from 200 to 0 °C, c3 – re-heating from 0 to 200 °C. The shaded area represents enthalpy (ΔH). The dashed line represents the baseline for area calculation.

2.5 Microscopic Imaging

The cross-section of square samples of 0.5" × 0.5" (12.7 mm × 12.7 mm) cut from composite sheets were imaged on an Olympus DSX1000 microscope. Prior to imaging, the cross-section was first grinded using sandpapers of 180 grit, 600 grit and 1200 grit, and then polished with two pads each soaked with 3 μm and 0.5 μm polishing solution. In between the grinding and polishing steps, the surface was cleaned with soap and water, rinsed with ethanol and dried using compressed air.

3 RESULTS

3.1 Tensile Properties

Tensile properties along the longitudinal direction were obtained by uniaxial tension test. The actual strain rate as calculated from DIC strain was approximately 3×10^{-4}/s. Representative stress-strain curves are shown in Figure 5 for composites obtained at different cooling rates.

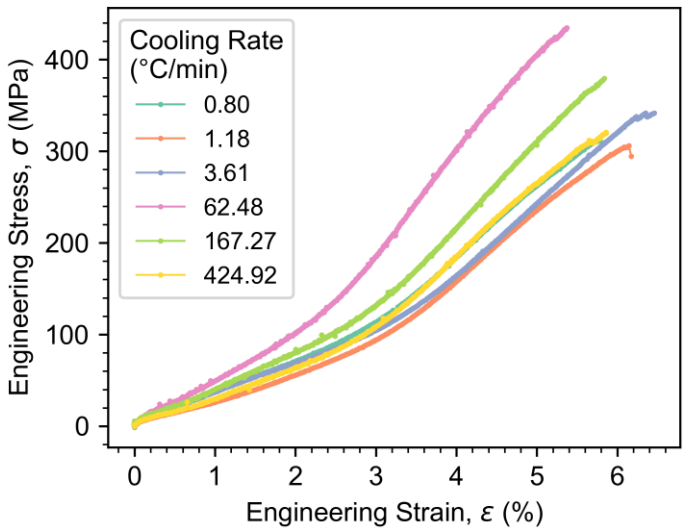

Figure 5. Engineering stress vs. engineering strain for PE composites under uniaxial tension. The strain was obtained by DIC. One curve out of five replicates was plotted for composites made at the same cooling rate.

All curves in Figure 5 showed a bilinear behavior, with the slope becoming steeper at around 2 – 3% strain. Opposite to the typical stress-strain behavior of polymers, the transition at around 2 – 3% strain was not a yield point but the onset of a hardening region. For a single yarn detached from woven fabric, a small toe region within 1% strain was associated with fiber de-crimping, i.e., straightening and realigning of the yarn, where the stress almost did not increase and the modulus was near-zero [10,11]. It was assumed that the initial linear region (below 2 – 3 % strain and 100 MPa) observed for PE composites in Figure 5 was a result of de-crimping of yarns in the specimen. The modulus of the initial linear region ranged from 2.2 to 3.8 GPa, much higher than the modulus of pure HDPE (0.8 GPa), suggesting that a portion of yarns had contributed to the stiffness of the composite while other yarns were not fully straightened. The second linear region (beyond 3% strain) corresponds to the elastic behavior of the composites. The modulus of the composite was calculated from the second linear region.

The modulus, tensile strength and ultimate elongation were plotted as a function of cooling rate as shown in Figure 6. The mechanical properties did not show a significant dependence on the cooling rate. The largest differences were observed when the cooling rate increased from 3.61 °C/min to 62.48 °C/min, where the average strength and modulus increased by 57.74 MPa (16%) and 3.15 GPa (39%) respectively. The strength and modulus slightly decreased with cooling rates above 62.48 °C/min. Several factors may explain why mechanical properties remain unaffected by cooling rate: (1) the crystal morphology and crystal size of self-reinforced PE composites were not affected by cooling

rates in the investigated range, though effects might become apparent at lower cooling rates; (2) the interfacial strength between PE matrix and PE fabric (0.5 – 2 MPa) was low, compared to carbon fiber(CF)/epoxy matrix (60 – 100 MPa) or CF/PEEK (30 – 50 MPa).

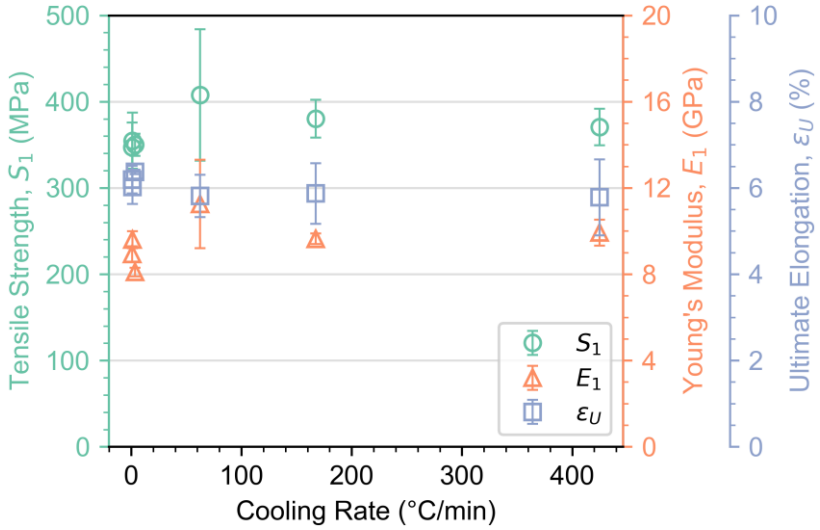

Figure 6. Tensile strength and modulus of the UHMWPE/HDPE composites as a function of cooling rate.

3.2 Microscopic Morphology

Figure 7(a) showed the micrographs of the as-received fabric, confirming a plain weave architecture. Warp yarns can be clearly observed from the cross-sectional images of the PE composites, as exemplified in Figure 7(b). The presence of crimped yarns supports the hypothesis that yarn de-crimpling was associated with the low-stiffness initial linear region on the stress-strain curve.

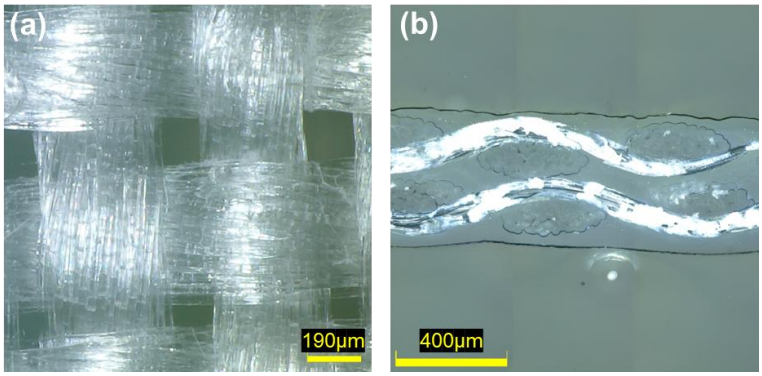

Figure 7. Microscopic images of (a) UHMWPE woven fabric as received, (b) cross-section of the self-reinforced PE composite cooled down at 167.27 °C/min.

3.3 Thermal Properties

It is well-established that thermal properties of semi-crystalline polymers are affected by cooling rates [12,13]. From the DSC signals as exemplified in Figure 4, the HDPE matrix and UHMWPE fabric in the PE composite showed separate endothermic peaks in the initial heating cycle, but these peaks collapsed into one peak with a shoulder in the re-heating cycle, since the effects of processing histories specifically the cooling rates on thermal properties of composites were erased by annealing the samples at 200 °C, i.e., the PE crystals had melted and re-crystalized. Therefore, thermal properties, including the T_m of HDPE and χ of the composites, were determined from the first heating cycle.

The heat capacity signals in the first heating cycle were plotted in Figure 8 for one representative sample of the three replicates of the PE composites made at the same cooling rate. Two melting peaks were visible: the melting of HDPE located between 126 °C to 130 °C, and the melting of UHMWPE located above 140 °C. The UHMWPE peak was a convolution of multiple split peaks, which is a signature for highly-oriented UHMWPE fibers with draw ratios typically above 50. The split peaks correspond to transitions of different crystal phases, such as transition from orthorhombic into hexagonal crystals [14].

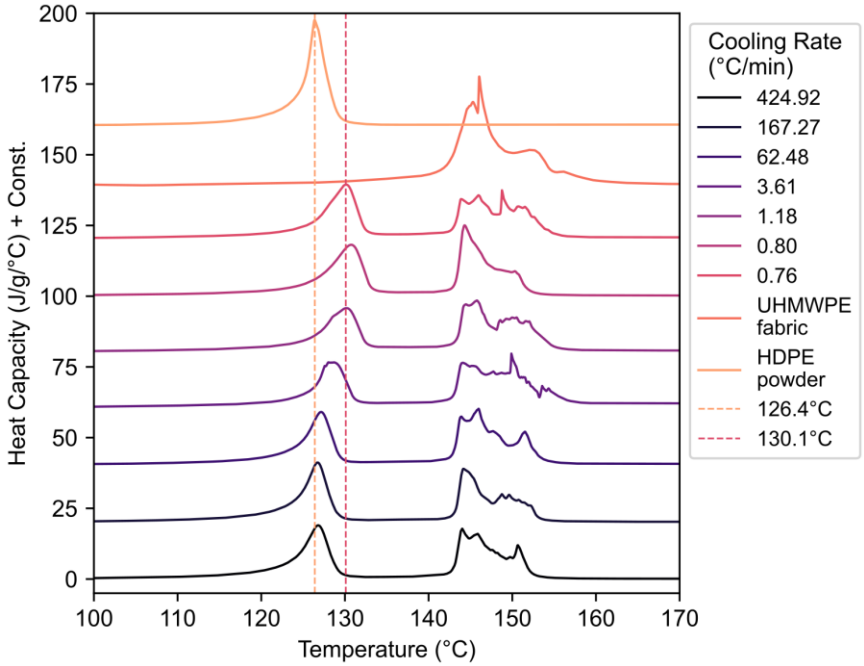

Figure 8. Heat capacity during the initial heating ramp of PE composites manufactured with difference cooling rates, and the as-received HDPE powder and UHMWPE fabric samples. One out of three replicates were plotted. The curves were vertically shifted for clarity.

As shown in Figure 8, the melting peaks of UHMWPE in the composite were not affected by cooling rate, which was expected considering that the manufacturing temperature of the composites (140 °C) was below the melt temperature of highly oriented UHMWPE crystals. However, T_m of HDPE shifted from ~130 °C to ~126.5 °C as the cooling rate increased, approaching the T_m of as-received HDPE powder. The qualitative trend was within expectation as higher cooling rates promoted formation of imperfect crystals with a lower T_m. The decrease in the T_m of HDPE was most significant when the cooling rate was slow (below 62.48 °C/min). Phenomenologically, T_m of HDPE showed a linear correlation with the log of cooling rate, as shown in Figure 9.

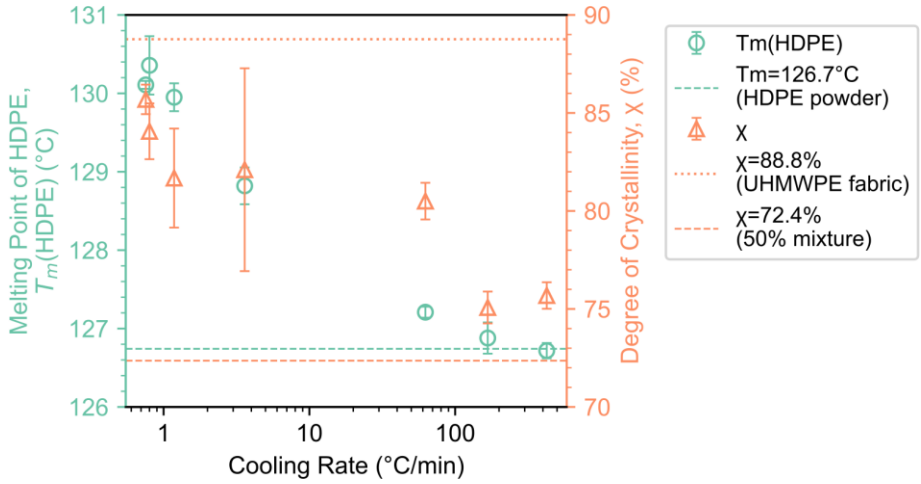

Figure 9. T_m of HDPE and the total degree of crystallinity (χ) of the UHMWPE and HDPE portions in the self-reinforced PE composites, as a function of cooling rate. The green dashed line represents the T_m of as-received HDPE powder. The orange dashed line represents the theoretical χ of composites based on the mixing rule. The dotted orange line represents the χ of as-received UHMWPE fabric.

Crystallinity of the composite (χ) was calculated based on the area under the heat capacity curve, as demonstrated in Figure 4. The χ decreased with cooling rate from ~85% to ~75%, as shown in Figure 9, approaching the average crystallinity based on the mixing rule (72.4%) for a composite consisting of 50 wt.% fabric and 50 wt.% matrix. The χ decreased most rapidly in two regions: (1) when cooling rates were below 1.2 °C/min, and (2) from 62.48 to 167.27 °C/min. In both regions the modulus of the composite showed a slight decrease, as shown in Figure 6.

4 SUMMARIES

In summary, self-reinforced PE composites were manufactured from UHMWPE fabric and HDPE matrix by powder impregnation and compression molding. The cooling rates were varied from 0.76 °C/min to 424.92 °C/min. The mechanical and thermal properties of UHMWPE/HDPE composites were not significantly affected by cooling rates. The melt temperature of HDPE matrix decreased with cooling rates and linearly correlated with the logarithmic cooling rates. The total degree of crystallinity of the composites decreased with cooling rates especially in the ranges of 0.76 – 1.18 °C/min and 62.48 – 167.27 °C/min, where the modulus also decreased slightly.

ACKNOWLEDGEMENTS

This work is supported by U.S. Department of Energy, Office of Energy Efficiency and Renewable Energy, Vehicle Technologies Office (EERE-VTO-DE-LC-000L078). This work was performed at the Pacific Northwest National Laboratory (PNNL). PNNL is operated by Battelle for U.S. Department of Energy under contract DE-AC05-76RL01830.

REFERENCES

[1] Y. Qiao, L.D. Fring, M.R. Pallaka, K.L. Simmons, A review of the fabrication methods and mechanical behavior of continuous thermoplastic polymer fiber–thermoplastic polymer matrix composites, Polymer Composites 44 (2023) 694–733. https://doi.org/10.1002/pc.27139.

[2] J. Colwell, P. Halley, R. Varley, P. Heidarian, T. McNally, T. Peijs, L. Vandi, Self-reinforced biodegradable thermoplastic composites, Adv Compos Hybrid Mater 7 (2024) 128. https://doi.org/10.1007/s42114-024-00939-x.

[3] C. Gao, L. Yu, H. Liu, L. Chen, Development of self-reinforced polymer composites, Progress in Polymer Science 37 (2012) 767–780. https://doi.org/10.1016/j.progpolymsci.2011.09.005.

[4] Á. Kmetty, T. Bárány, J. Karger-Kocsis, Self-reinforced polymeric materials: A review, Progress in Polymer Science 35 (2010) 1288–1310. https://doi.org/10.1016/j.progpolymsci.2010.07.002.
[5] F. Vannucchi de Camargo, E. da Silva Fernandes, C.S. ten Caten, A.K. Alves, C.P. Bergmann, G. Minak, In-Plane Shear Strength of Single-Lap Co-Cured Joints of Self-Reinforced Polyethylene Composites, Materials 14 (2021) 1517. https://doi.org/10.3390/ma14061517.
[6] S.-L. Gao, J.-K. Kim, Cooling rate influences in carbon fibre/PEEK composites. Part 1. Crystallinity and interface adhesion, Composites Part A: Applied Science and Manufacturing 31 (2000) 517–530. https://doi.org/10.1016/S1359-835X(00)00009-9.
[7] S.-L. Gao, J.-K. Kim, Cooling rate influences in carbon fibre/PEEK composites. Part II: interlaminar fracture toughness, Composites Part A: Applied Science and Manufacturing 32 (2001) 763–774. https://doi.org/10.1016/S1359-835X(00)00188-3.
[8] Y. Qiao, S. Ko, J.L. Ramos, E.K. Nickerson, A.C. Denny, G.M. Schuler, N.L. Brown, A. Guzman, C.E. Moriel, M.R. Pallaka, Y. Ni, K.W. Shahwan, K.L. Simmons, Effects of processing temperature, pressure, and fiber volume fraction on mechanical and morphological behaviors of fully-recyclable uni-directional thermoplastic polymer-fiber-reinforced polymers, Composites Part C: Open Access 14 (2024) 100497. https://doi.org/10.1016/j.jcomc.2024.100497.
[9] B. Wunderlich, C.M. Cormier, Heat of fusion of polyethylene, Journal of Polymer Science Part A-2: Polymer Physics 5 (1967) 987–988. https://doi.org/10.1002/pol.1967.160050514.
[10] H. Wang, P.J. Hazell, K. Shankar, E.V. Morozov, Z. Jovanoski, A.D. Brown, Z. Li, J.P. Escobedo-Diaz, Tensile properties of ultra-high-molecular-weight polyethylene single yarns at different strain rates, Journal of Composite Materials 54 (2020) 1453–1466. https://doi.org/10.1177/0021998319883416.
[11] M. Li, P. Wang, F. Boussu, D. Soulat, Effect of Fabric Architecture on Tensile Behaviour of the High-Molecular-Weight Polyethylene 3-Dimensional Interlock Composite Reinforcements, Polymers 12 (2020) 1045. https://doi.org/10.3390/polym12051045.
[12] M. Zinet, Z. Refaa, M. Boutaous, S. Xin, P. Bourgin, Thermophysical Characterization and Crystallization Kinetics of Semi-Crystalline Polymers, Journal of Modern Physics 4 (2013) 28–37. https://doi.org/10.4236/jmp.2013.47A2005.
[13] M. van Drongelen, P.C. Roozemond, G.W.M. Peters, Non-isothermal Crystallization of Semi-Crystalline Polymers: The Influence of Cooling Rate and Pressure, in: F. Auriemma, G.C. Alfonso, C. de Rosa (Eds.), Polymer Crystallization II: From Chain Microstructure to Processing, Springer International Publishing, Cham, 2017: pp. 207–242. https://doi.org/10.1007/12_2015_344.
[14] J.-T. Yeh, S.-C. Lin, C.-W. Tu, K.-H. Hsie, F.-C. Chang, Investigation of the drawing mechanism of UHMWPE fibers, J Mater Sci 43 (2008) 4892–4900. https://doi.org/10.1007/s10853-008-2711-1.

MOLECULAR MODELING OF A BISMALEIMIDE RESIN

TREVOR WAVRUNEK
MICHIGAN TECHNOLOGICAL UNIVERSITY
ADVISOR: DR. GREGORY ODEGARD

CMMR Lab™

MOTIVATION: NEXT GENERATION COMPOSITES

- Polymer-CF composites are dominant materials for high specific strength & stiffness applications
- Significant potential improvement in specific properties with polymer nanocomposites
- Multiscale simulation can significantly cut down on material design costs (ICME)



Rocket Lab Electron (2023)

The Institute for Ultra-Strong Composites by Computational Design *NASA* (2017).

ROLE OF MOLECULAR SIMULATION

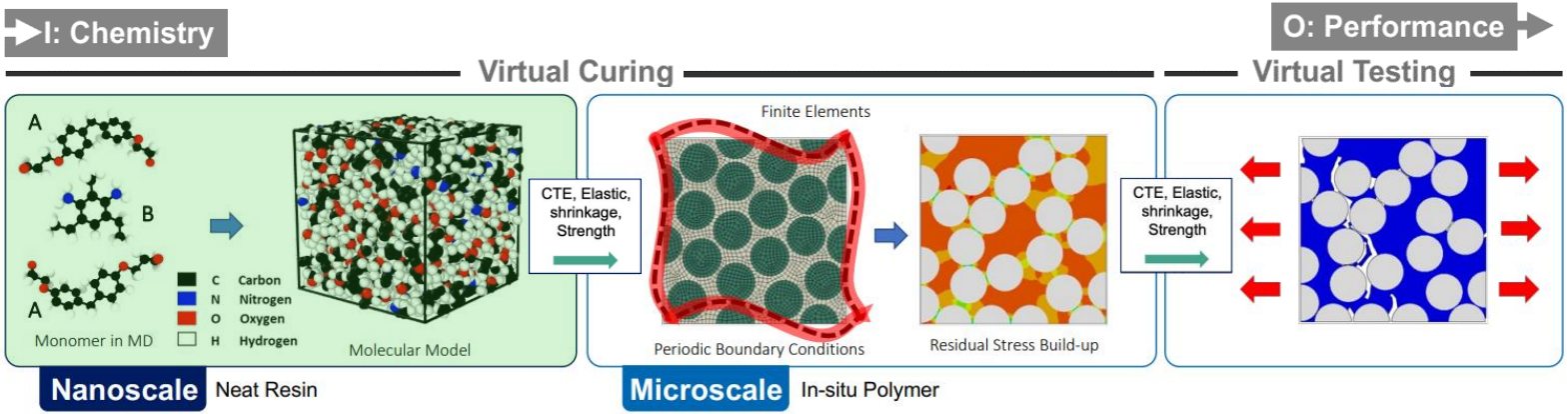

- MD directly informs residual stress buildup and cracking from chemical and thermal factors
- Experimental methods to obtain mid-cure properties are difficult or nonexistent

Shah, S. P., et. al, *Mech Adv Mater Struc* **30**, 486–497 (2021).

MOLECULAR DYNAMICS

- **Premise:**

  Atoms' dynamic behavior can be modeled using classical physics.

- Numerical, iterative solution of a dynamical physics problem using classical equations of motion:

$$m_i \ddot{\boldsymbol{r}}_i = \boldsymbol{f}_i = -\frac{\partial}{\partial \boldsymbol{r}_i} E_{pot}$$

$$E_{pot} = E_{bond} + E_{angle} + E_{torsion} + E_{nonbond}$$

- Energies are calculated with the help of (usually) empirical forcefields

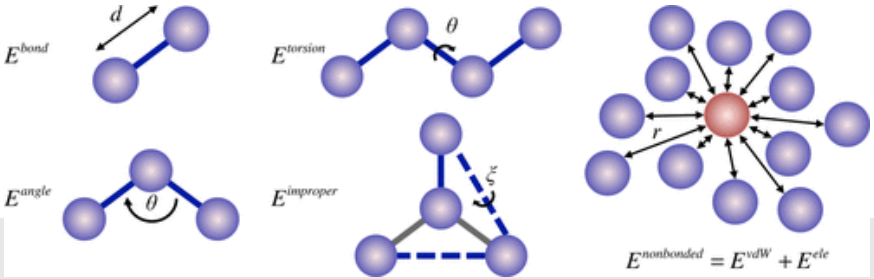

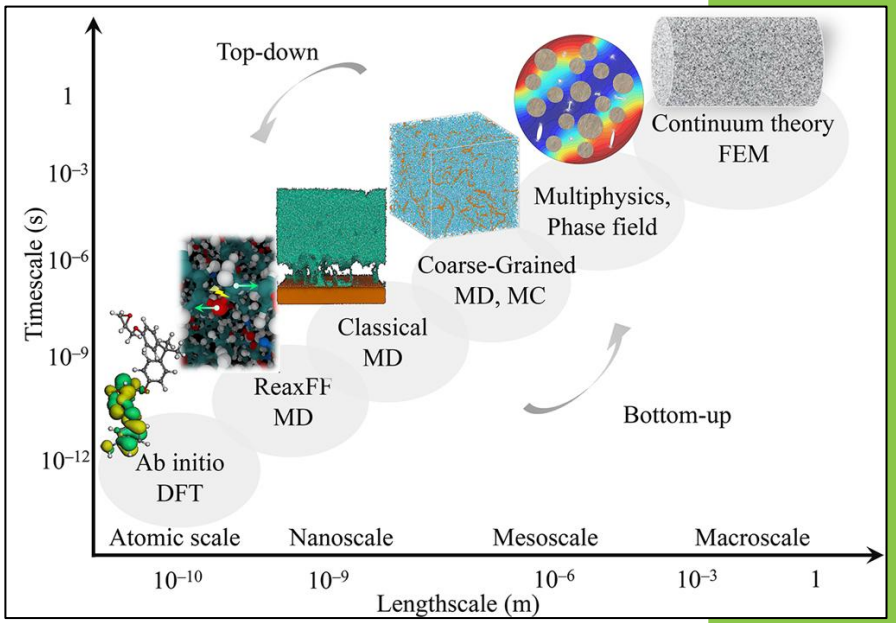

Lin, K. & Wang, Z. *Commun Mater* **4**, 1–16 (2023).
Riniker, S. *J. Chem. Inf. Model* ***15*** *565-578 (2018).*

PROJECT GOAL

Predict the thermomechanical property evolution and polymer structure of a 3-component HP Bismaleimide resin as a function of degree of cure for use in a multi-scale model.

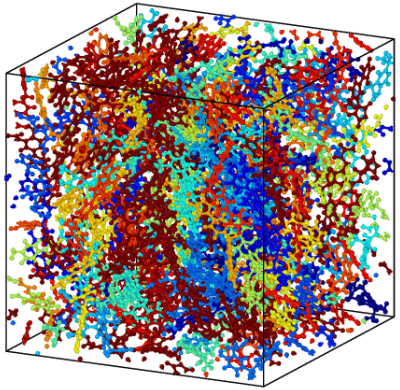

Virtual Polymerization

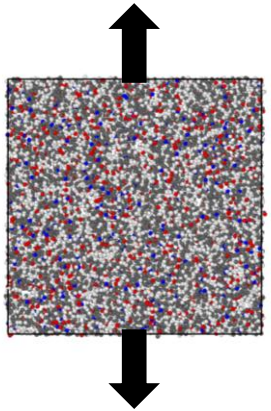

Simulated Tests

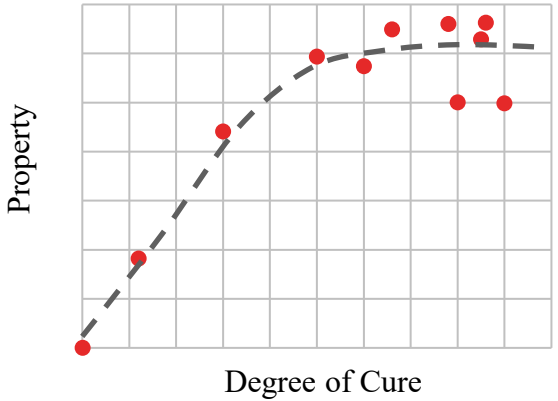

Process Insights

BISMALEIMIDE RESIN

- High-performance variant based on a classic 2-component system
  - Easily processable
  - Good adhesion to fibers
  - Great thermal properties
- Utilizes 2-stage cure:
  1. “Initial Cure”
  2. “Post Cure”

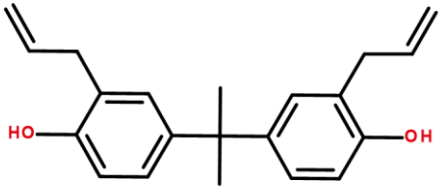

o,o’-diallylbisphenol A
(DABPA)

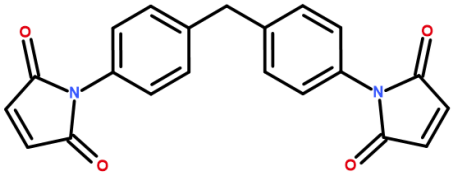

4,4’-Bismaleimidodiphenylmethane
(BMPM)

THEORIZED BMI CHEMISTRY

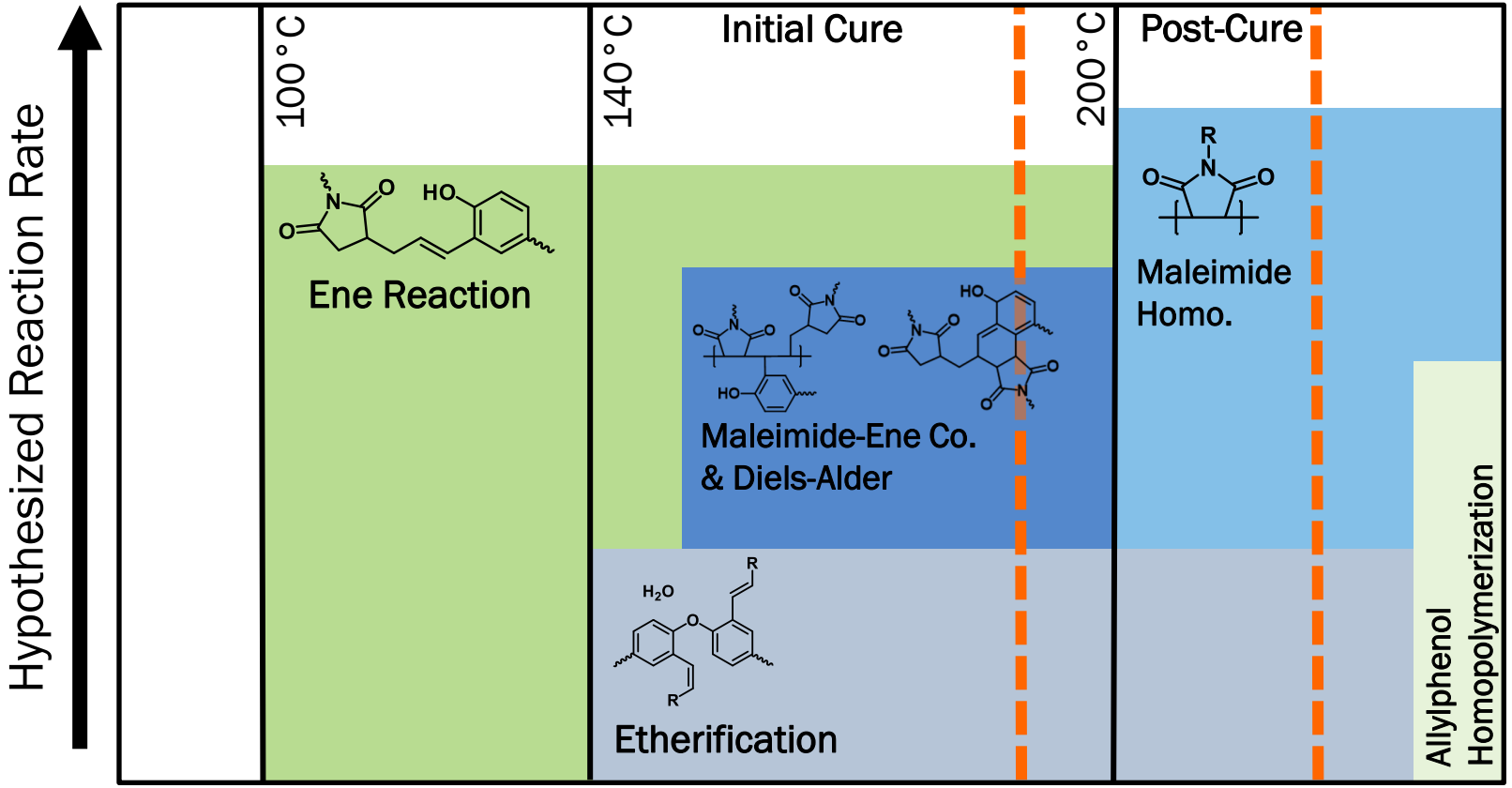

Morgan, R. J. et al. *Polymer* **38**, 639–646 (1997).
Evsyukov, S. E. & Pohlmann, T. *Current Trends in Polymer Science* **20**, (2020).
Phelan, J. C. & Sung, C. S. P. *Macromolecules* **30**, 6837–6844 (1997).
Rozenberg, B. A., et al. *Polym. for Adv. Technologies* **13**, 837–844 (2002).
Mijović, J. & Andjelić, S. *Macromolecules* **29**, 239–246 (1996).

MOLECULAR DYNAMICS WORKFLOW

Build un-crosslinked system of monomers (LUNAR), densify to liquid (1.2g/cc) in LAMMPS

Crosslink using combination of proposed reactions (REACTER)

Cool and relax system to 300K & 1.0 atm

Deform and measure energy, pressure, & geometry changes

Use these to estimate thermomechanical properties *(G, E, K, v, σ, T_g, & CTE)*

Simulation Construction

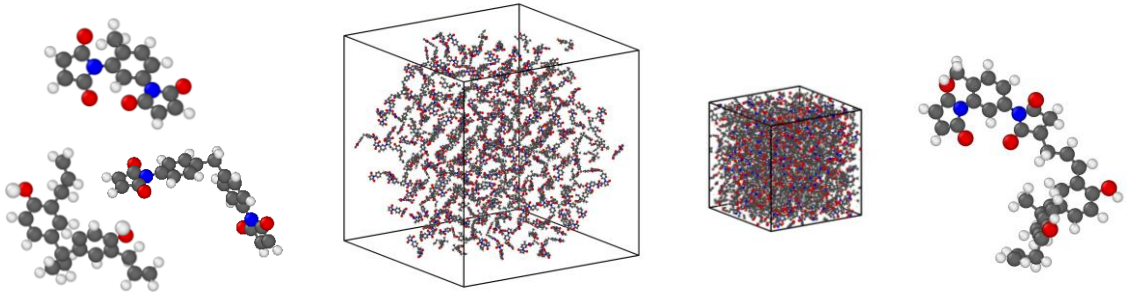

Property Prediction

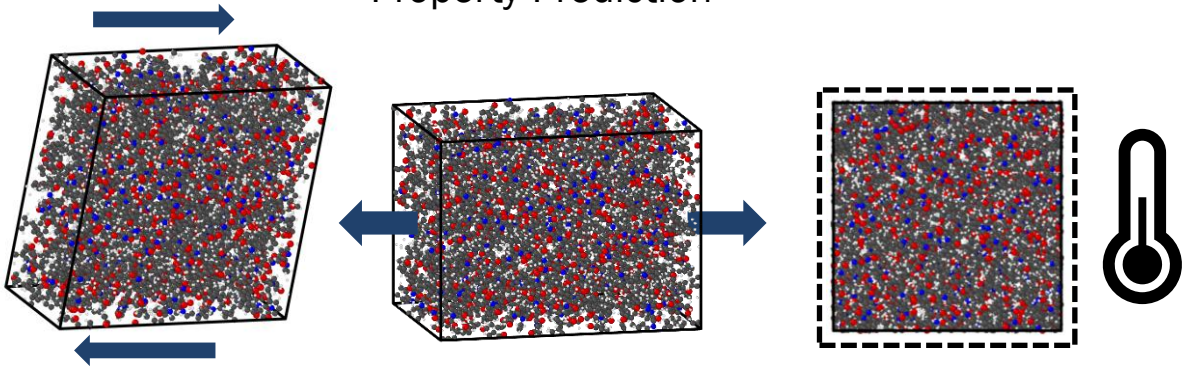

Gissinger, J. R., et al., *Polymer* (2017) 128 : p. 211-217.
Kemppainen, J et al., *J. Chem. Inf. Model.* (2024) 64 : p5108–5126.

SIMULATION PARAMETERS

- x5 replicates, 15k atoms
- 2-stage polymerization with ramps
  - NVT, ρ=1.2 g/cc during production
  - Temperature +100K from resin datasheet
- Mechanical testing at 1e8 s^{-1}
  - RFR analysis, no PCFF-2xe
- Annealing simulation
  - 50 K/ns heating rate
  - Hyperbola fit + bilinear regression used

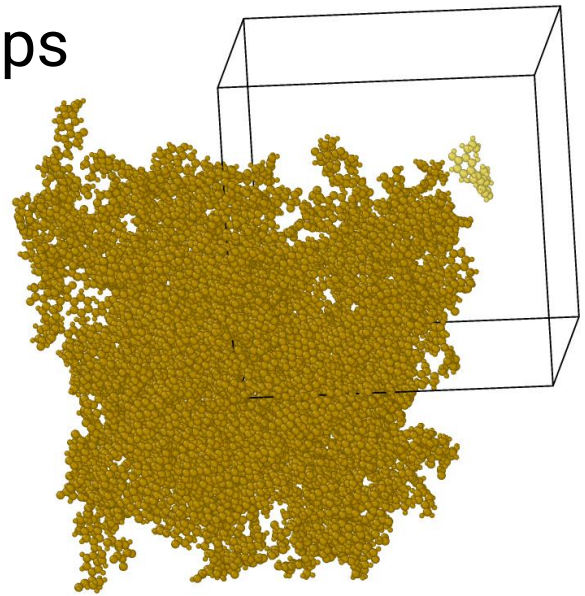

KINETIC AND GEOMETRIC PARAMETERS

- Arrhenius Equation

$$p(reaction) = Ae^{-\frac{E_a}{R(T+T')}}$$

- Pre-exponential taken as order of magnitude
- Non-constrained pre-exponential (A) and E_a tuned to match experimental data

Reaction	A $(mol\text{-}s)^{-1}$	E_a (kcal/mol)	Source
Ene	1e6	16.9	[1]
Radical from Maleimide	**parametric**	21.9	[1]
Radical from Ene	**parametric**	18.0	-
Etherification	**parametric**	10	-

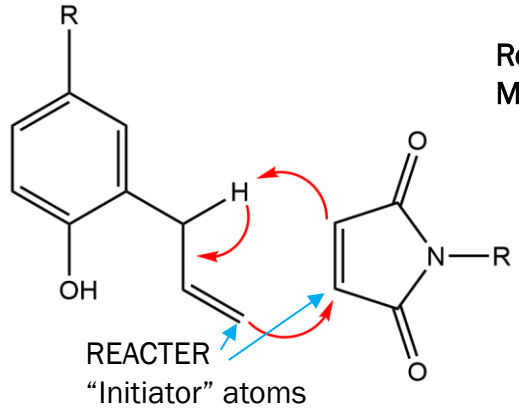

Reaction Mechanism

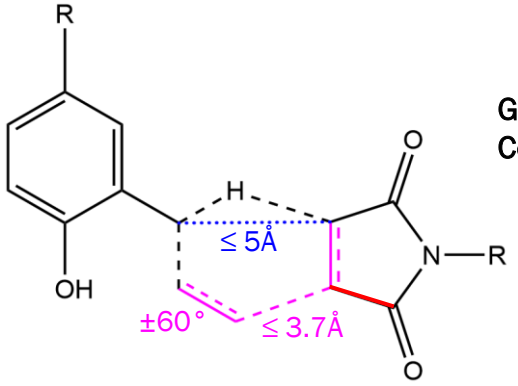

Geometric Constraints

[1] Rozenberg, B. *et al. Polymers for Advanced Technologies* **13**, 837–844 (2002).

EFFECT OF PRE-EXPONENTIAL (A)

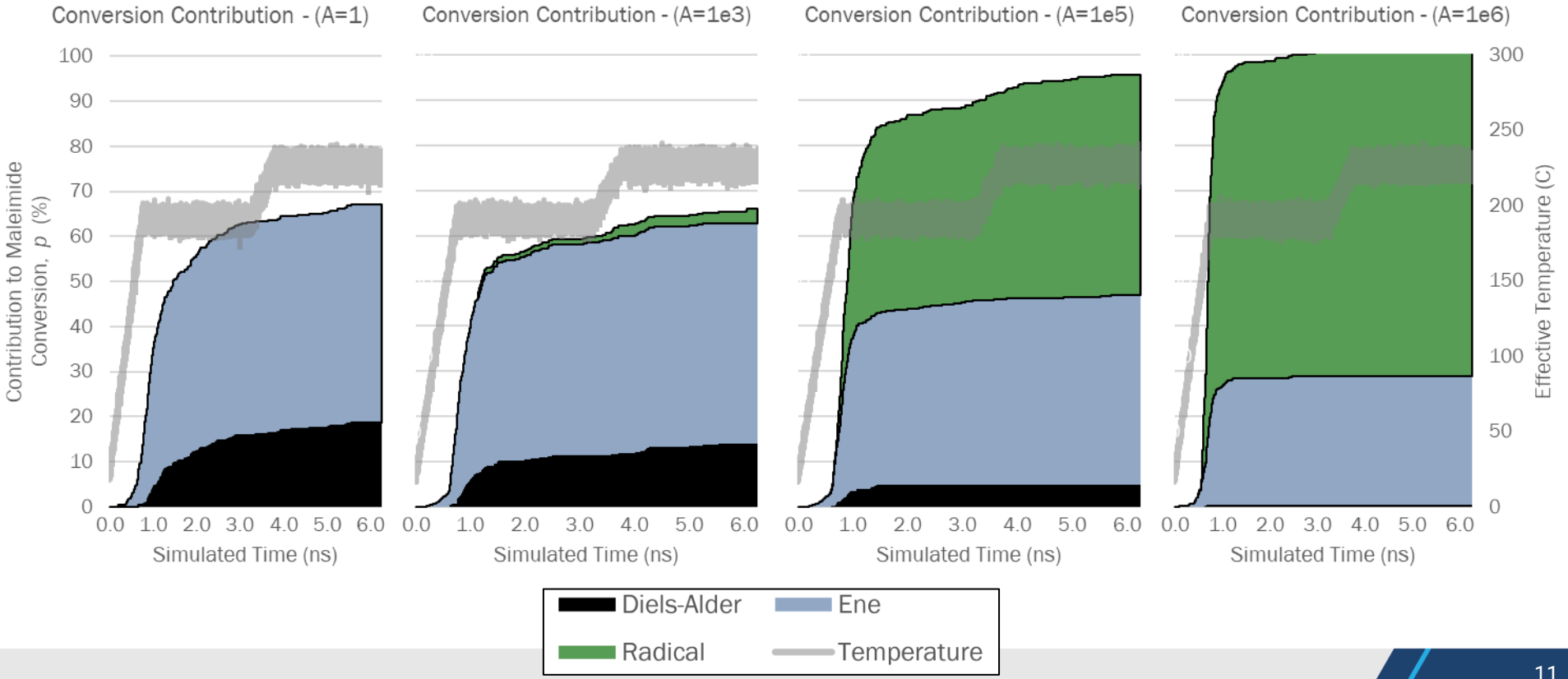

GEL POINT DETERMINATION

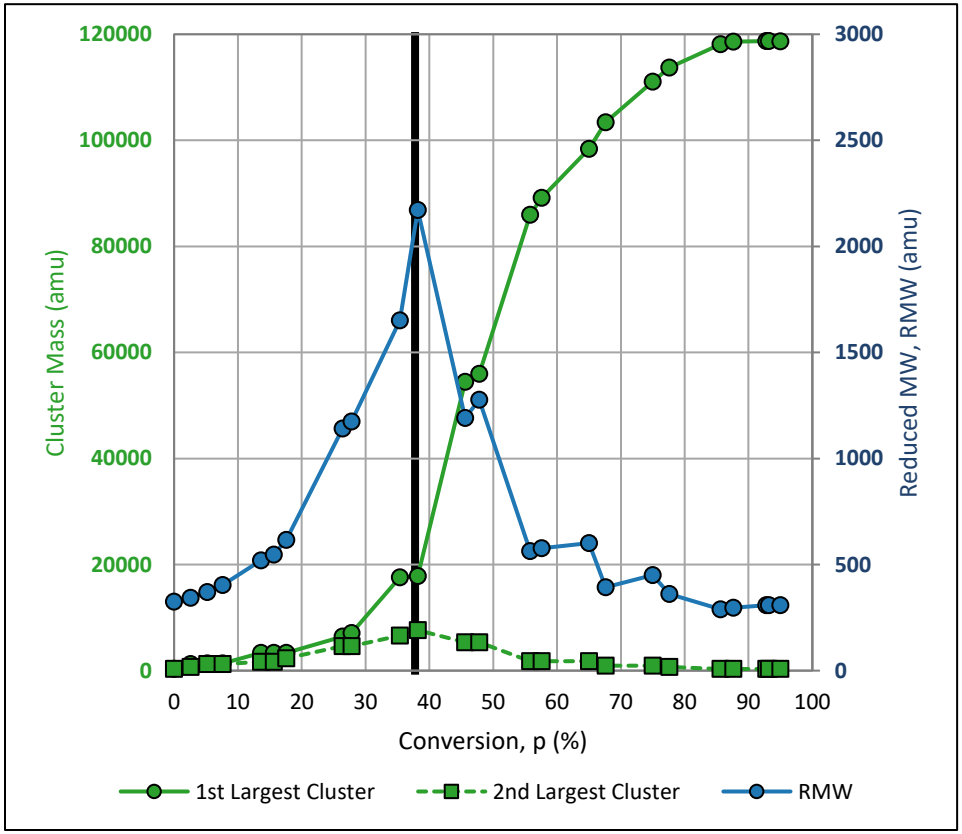

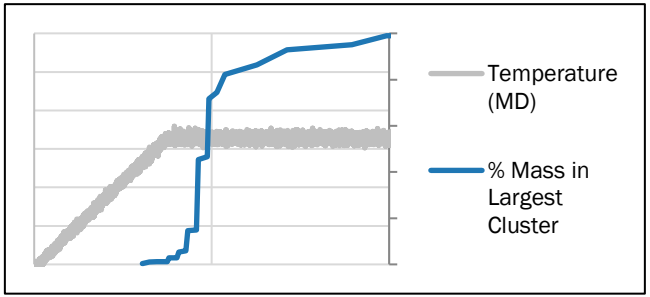

Replicate	Gel Point
1	38.2
2	38.6
3	43
4	37.6
5	38.2
Average	39.1 ± 2.2

SHRINKAGE AT PROCESS TEMPERATURE

- Shrinkage within range of expected values
  - Pure BMPM: **0.7%**
  - Matrimid 5292: **5.2%**
  - This study: **1.81%**
- Room Temp. density is close to spec.
  - MD: **1.259 g/cc**
  - Spec: **1.250 g/cc**

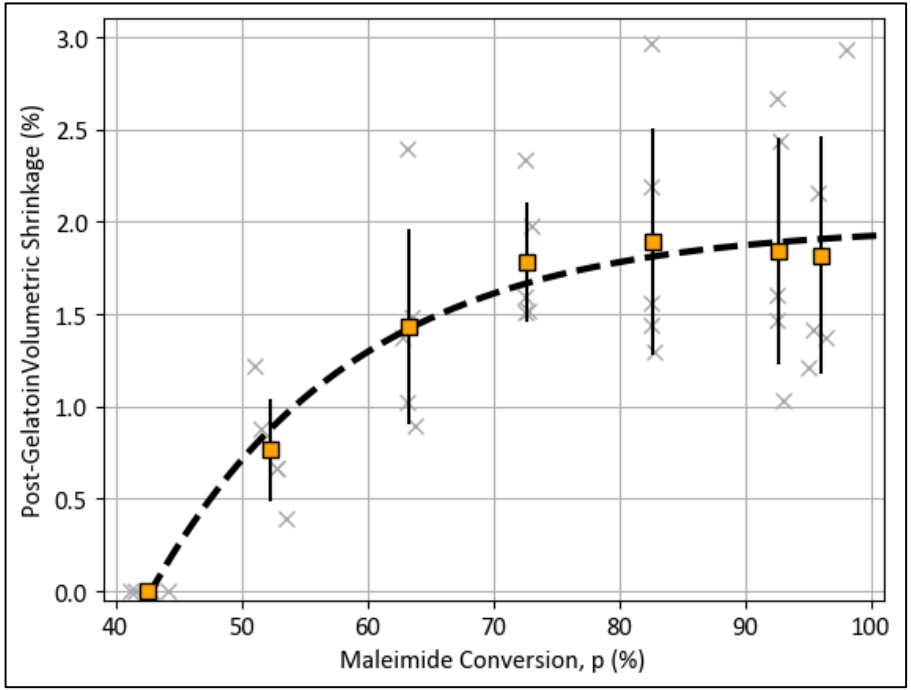

Leung, C. Lee, C, Technical Report “Development of High Temperature Low Cure Shrinkage Adhesives” (1999).

MECHANICAL PROPERTY PREDICTION

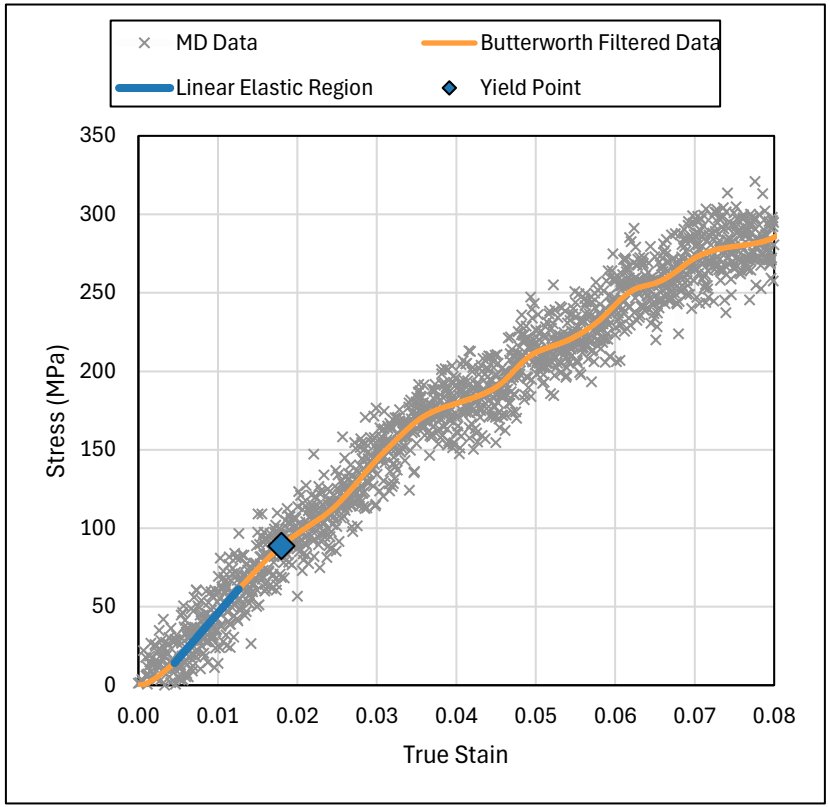

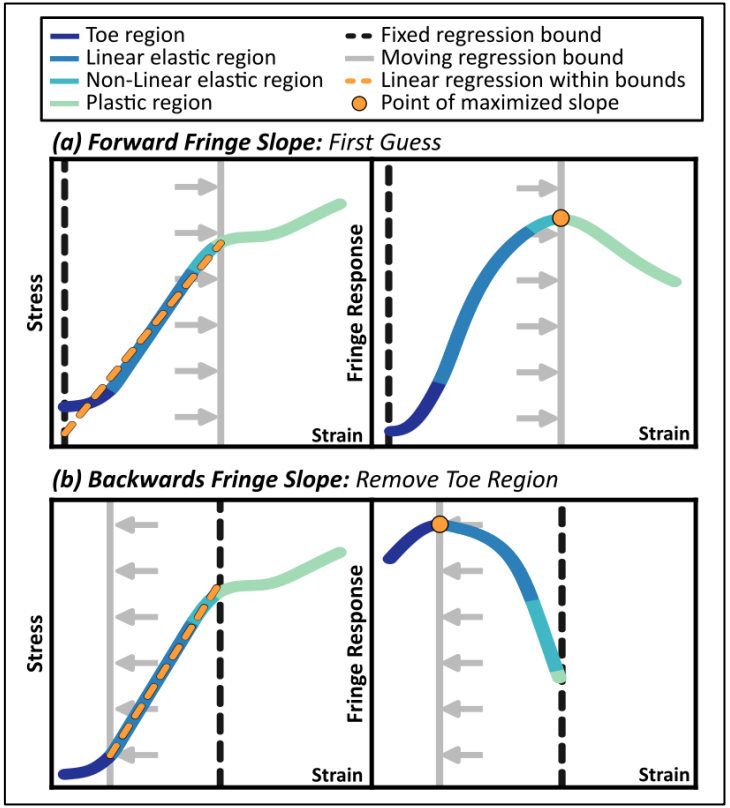

MECHANICAL RESULTS

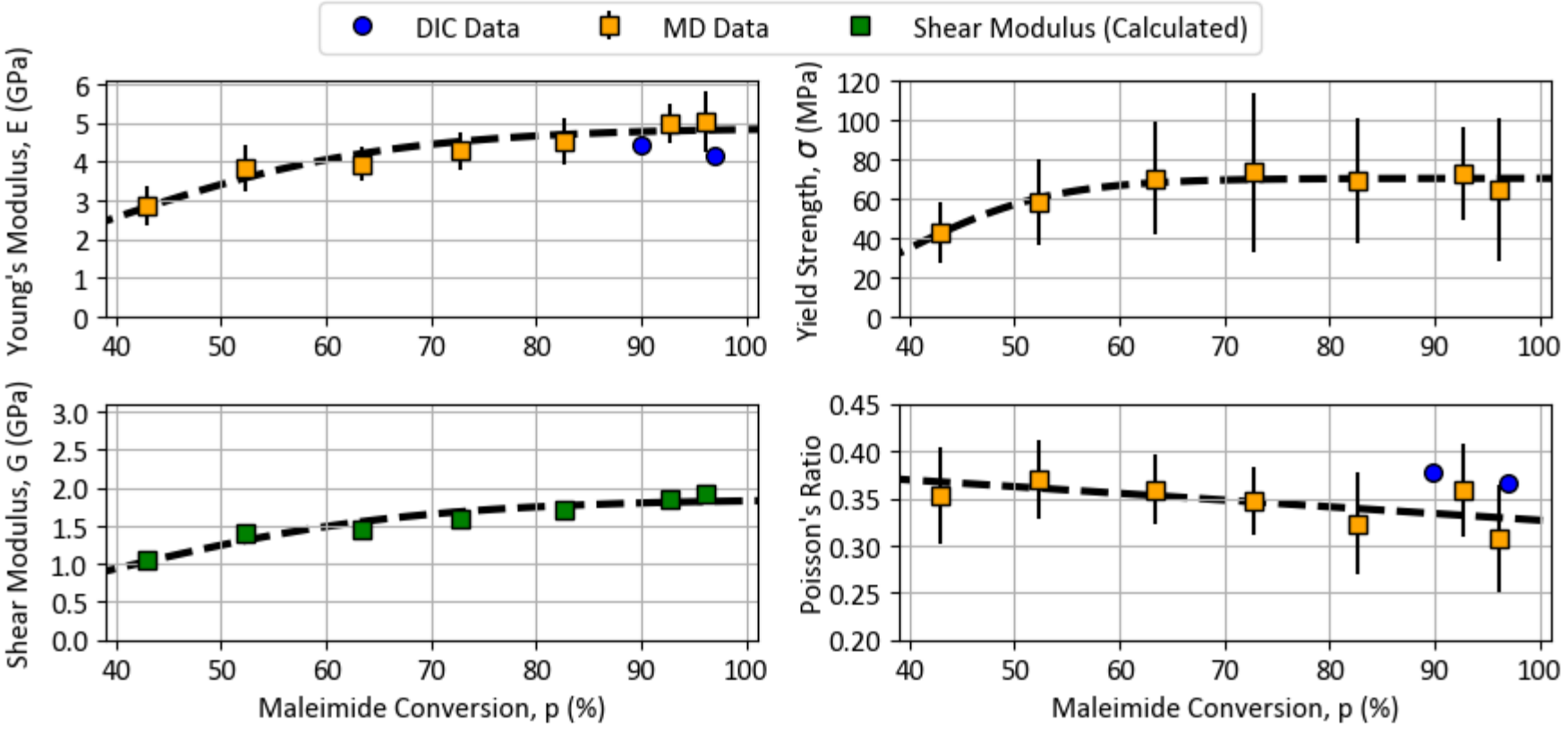

THERMAL RESULTS

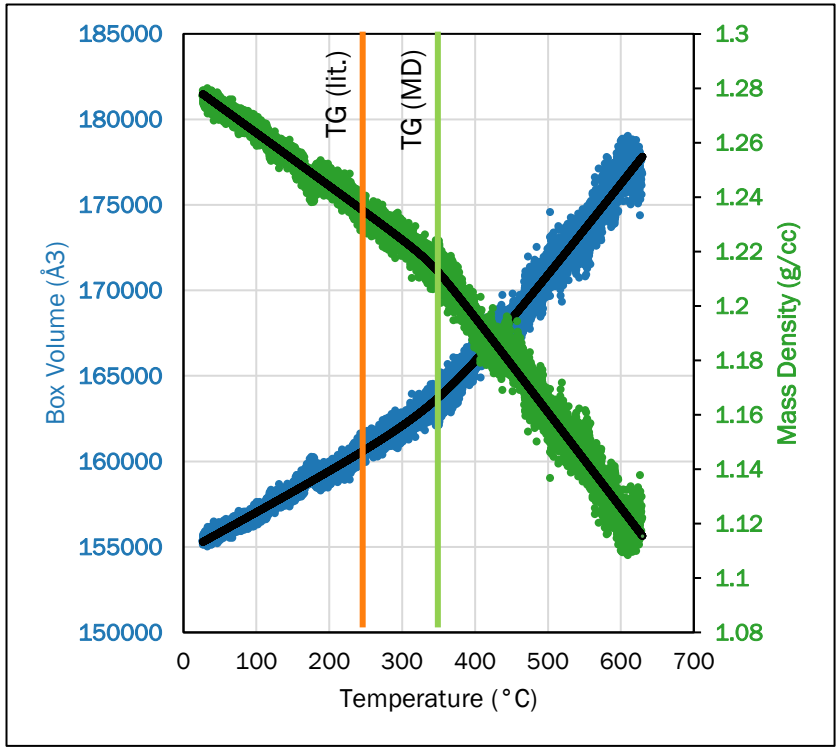

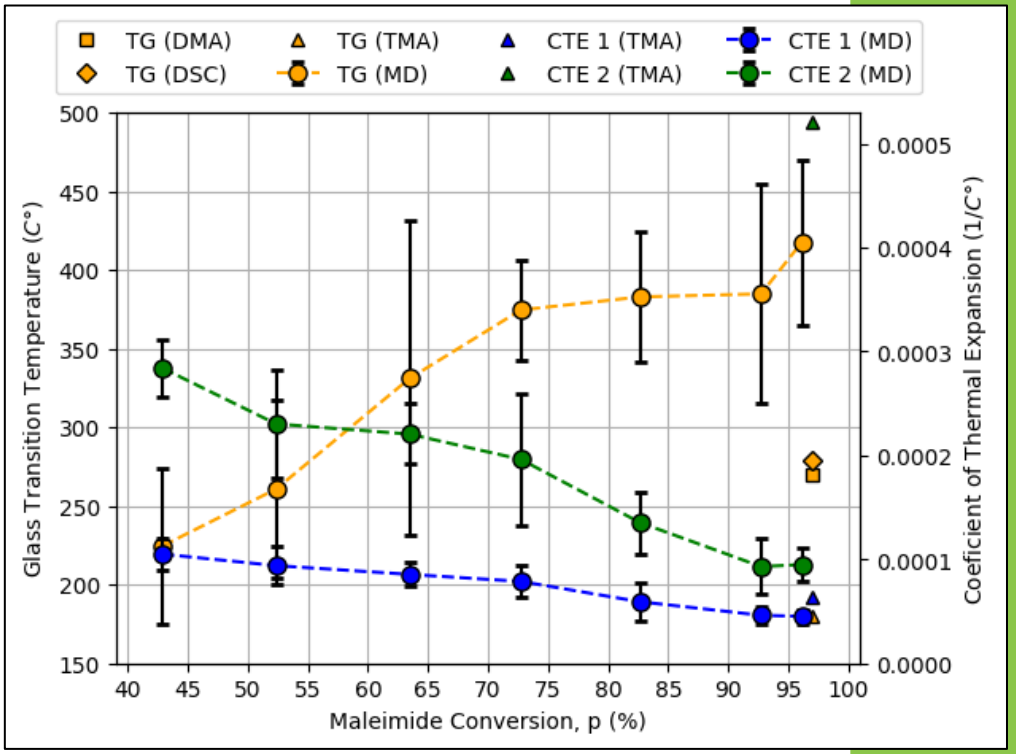

SUMMARY

- Implementation of competing reaction kinetics was incorporated into a process model for an engineering BMI thermoset
- Cure kinetics, as well as physical and mechanical properties are compliant, although T_G is overpredicted
- Higher fidelity ICME could inform improved resin cure processes and manufacturing design of thermoset matrix composites

ACKNOWLEDGEMENTS

Thanks to:

Dr. Greg Odegard

The Computational Mechanics and Materials Research (CMMR) Lab

Dr. Jake Gissinger, Dr. Mia Siochi, Dr. Kris Wise

Dr. Britannia Vondrasek, Cecil Evers, Kaylee Thaggard

The Institute for Ultra-Strong Composites by Computational Design (USCOMP)

Superior HPC at MTU



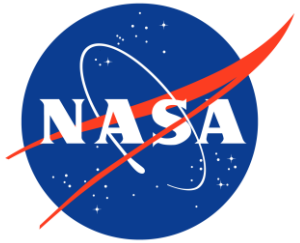

Michigan Tech



CMMR Lab™



US COMP

CMMR Lab™
COMPUTATIONAL MECHANICS
& MATERIALS RESEARCH

Thermomechanical Properties Of Polybenzoxazine Resin in a Molecular Dynamics Model as a Function of Degree of Cure and Temperature

7-Aug-2025

Tristan Muzzy[1]

Dr. Gregory M. Odegard[1]

[1]Mechanical and Aerospace and Engineering, Michigan Technological University

Outline

- Motivation
- Background
- Objectives
- Methodologies
- Results
- Conclusions
- Acknowledgements

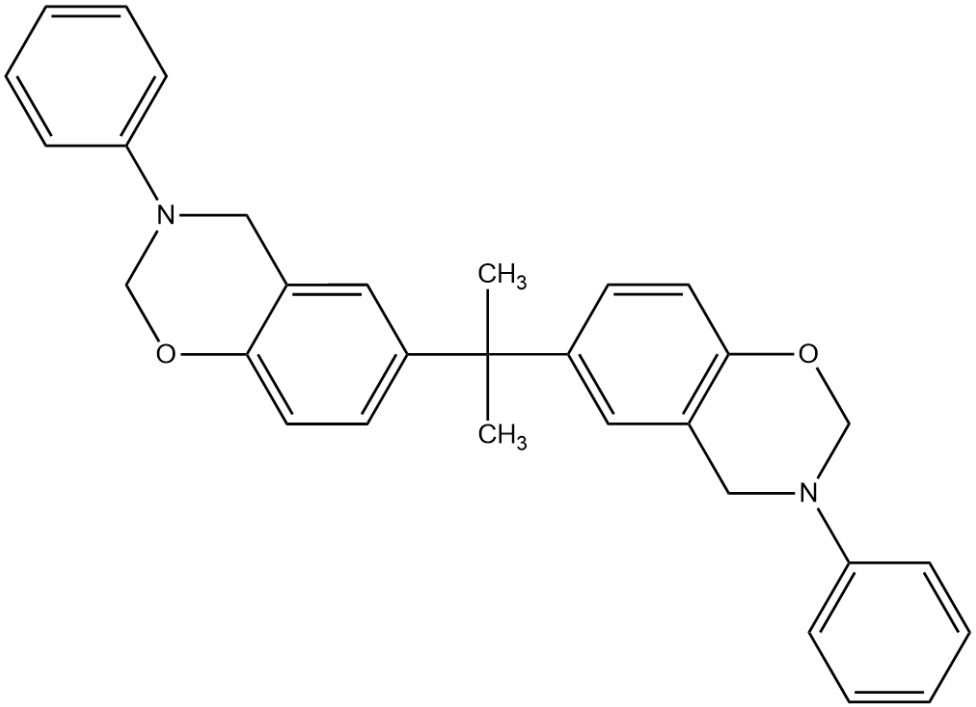

What We Need

- **Advanced composites to reach space exploration milestones**
  - Extreme temperatures
  - Thermal protection
  - Lightweight materials
- **Manufacturing challenges**
  - Samples to useable parts
  - Process Modeling
  - Changing material properties

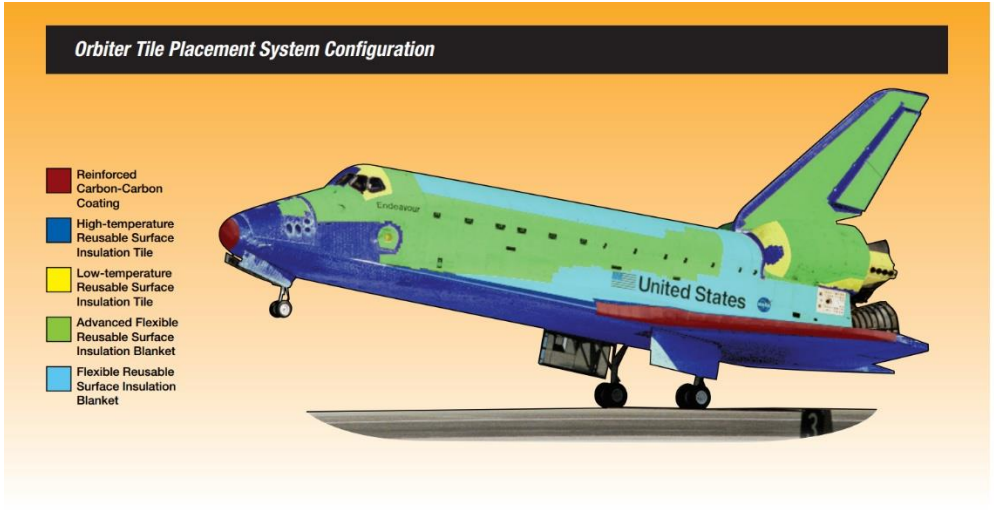

From https://interestingengineering.com/transportation/what-keeps-spaceships-from-burning-up-during-reentry

Other Materials Have desirable properties

- Curing → Shrinkage
- Pyrolysis → Porosity
- This can create voids and initialize cracks
- Minimizing formation during processing can improve overall material properties
- Other materials have cure expansion

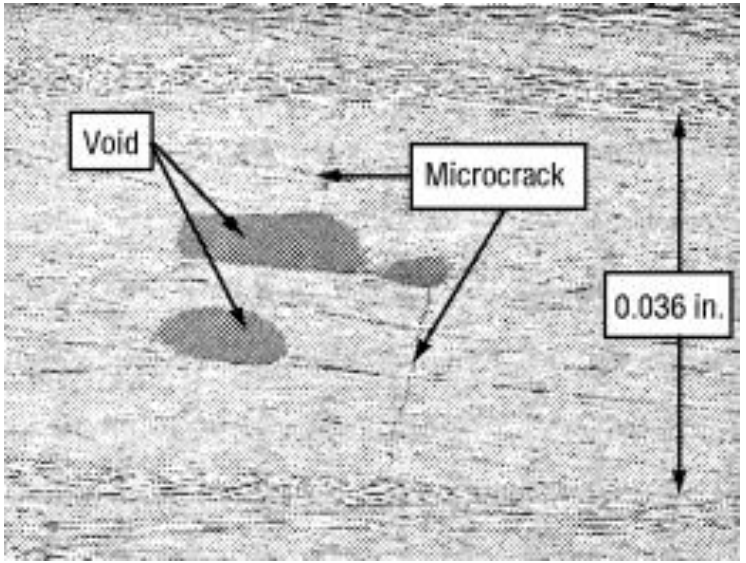

Credit: NASA-Evaluation of Microcracking in Two Carbon-Fiber/Epoxy-Matrix Composite Cryogenic Tanks

[3]Savage, *Carbon-Carbon Composites* (1993)

Objectives

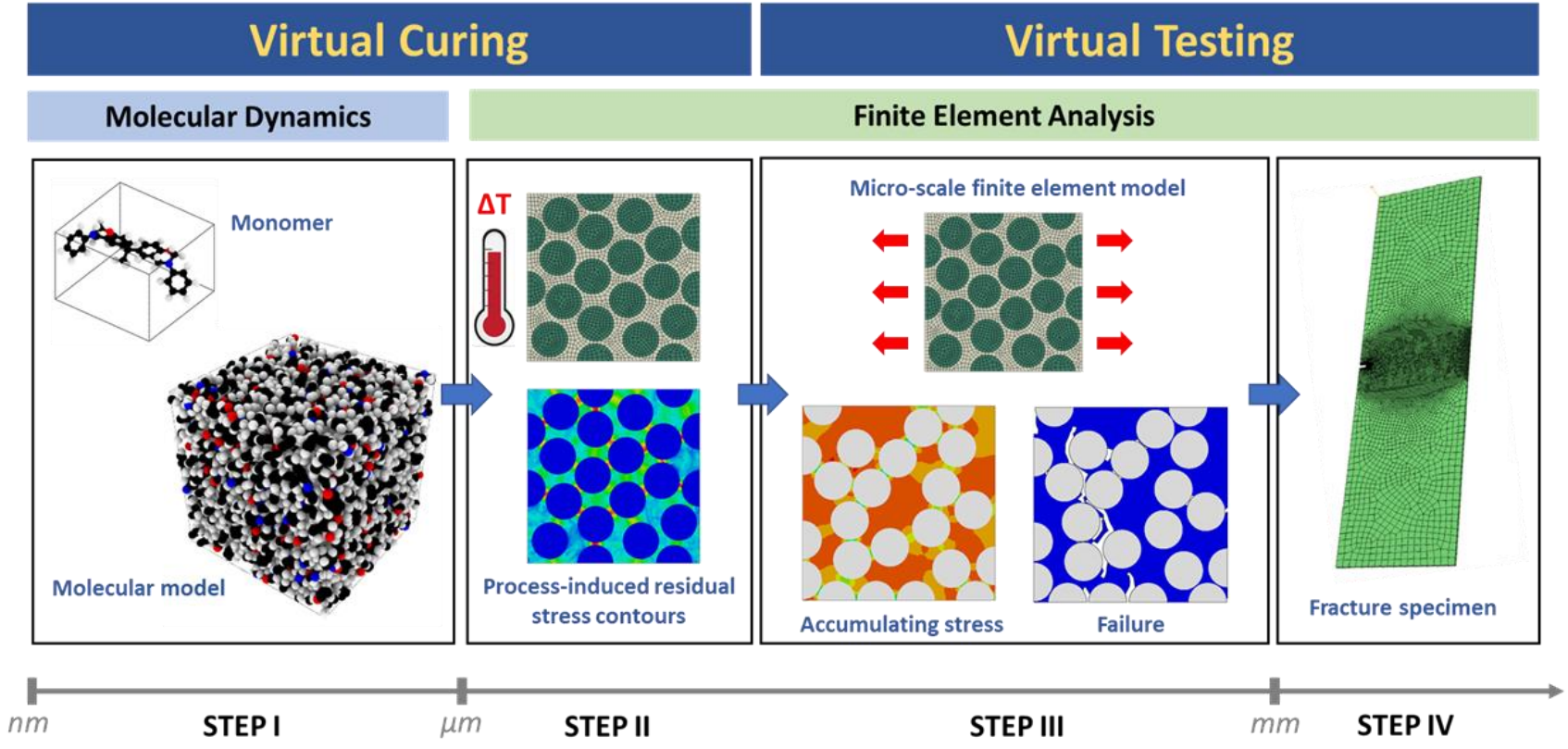
Virtual Curing
Virtual Testing
Molecular Dynamics
Finite Element Analysis
Monomer
Molecular model
ΔT
Process-induced residual stress contours
Micro-scale finite element model
Accumulating stress
Failure
Fracture specimen
nm
STEP I
μm
STEP II
STEP III
mm
STEP IV

What We Can Do With Molecular Dynamics

- **Perfect Microscope**
- **DSC data**
- **Tracers and diffusion**
- **XRD**
- **Mechanical Testing**
- **Thermal properties**
- **Chemical reactions**
- **Spectroscopy**

…At the same time!

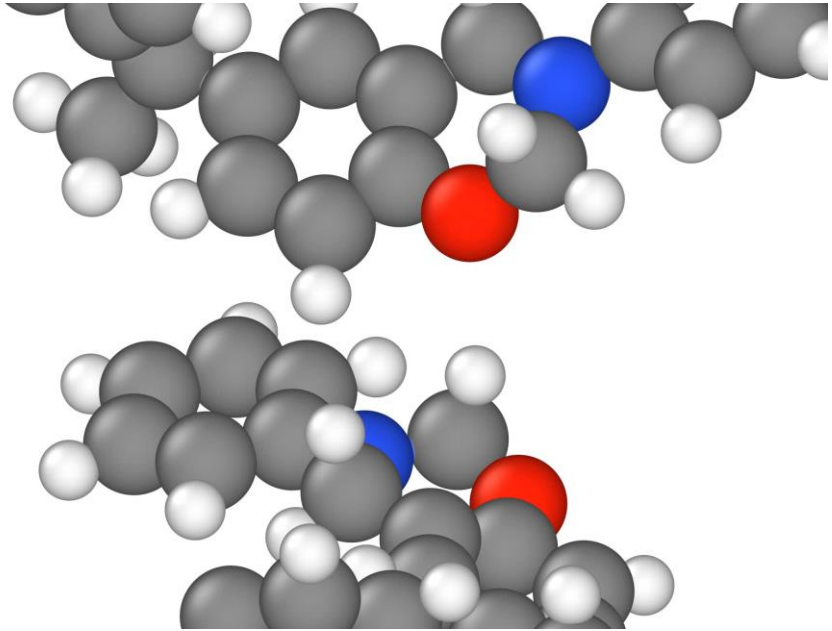

LAMMPS stands for **L**arge-scale **A**tomic/**M**olecular **M**assively **P**arallel **S**imulator.

Polybenzoxazine (PBZ) Introduction

- **bisphenol-A aniline benzoxazine (BA-a) monomer**
  - Same reaction twice on both sides
  - Other PBZ precursors are also in use
- **Thermoset resin**
  - Ring opening homopolymerization, partially understood
  - “Ionically activated” / “thermally accelerated polymerization”
  - Evidence for autocatalyzation from polarized groups
- **Desirable properties**
  - **Little to no cure shrinkage, but why and how?**
  - Good mechanical properties
  - High glass transition temperature (Tg)
  - No byproducts

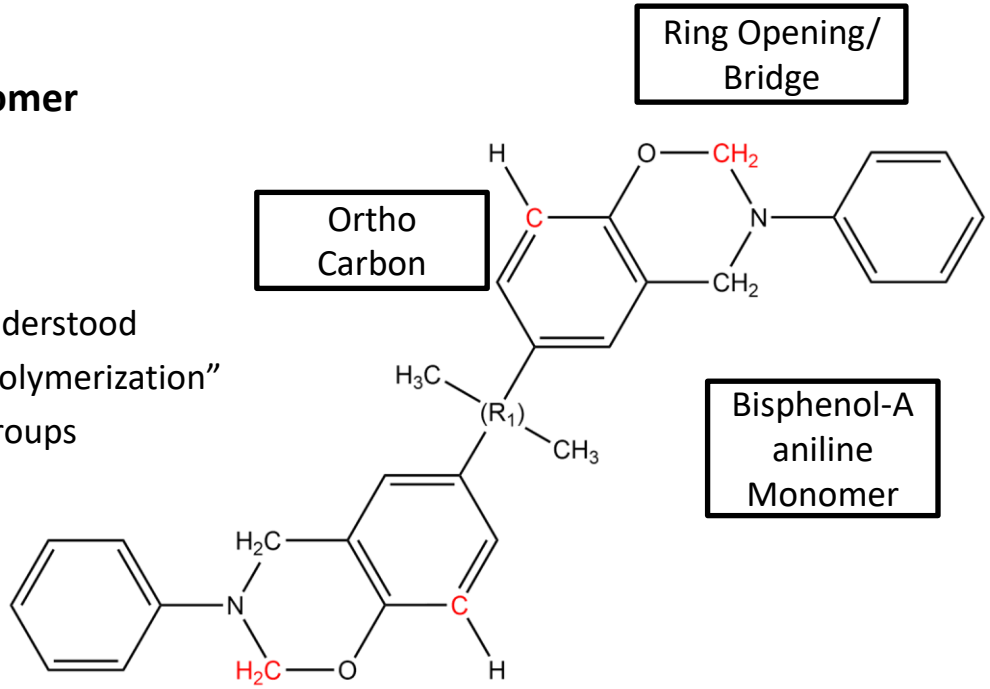

Gaikwad[2] et al., ACS Applied Polymer Materials 2021 3 (12), 6407-6415 DOI: 10.1021/acsapm.1c01164
Ishida et al., *Handbook of benzoxazine resins*: Elsevier, 2011, pp. 3-81.

Reaction Steps

Bisphenol-A aniline PBZ

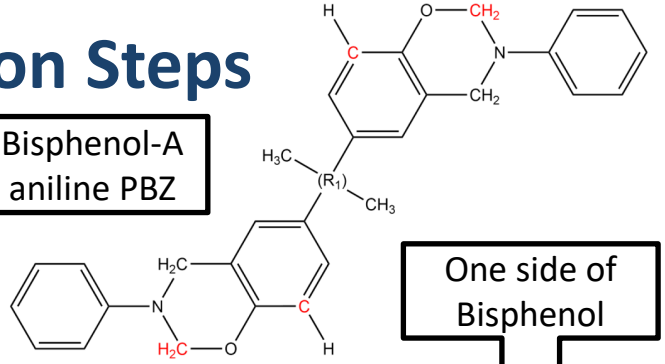

One side of Bisphenol

May Receive Bridge (Used Ring)

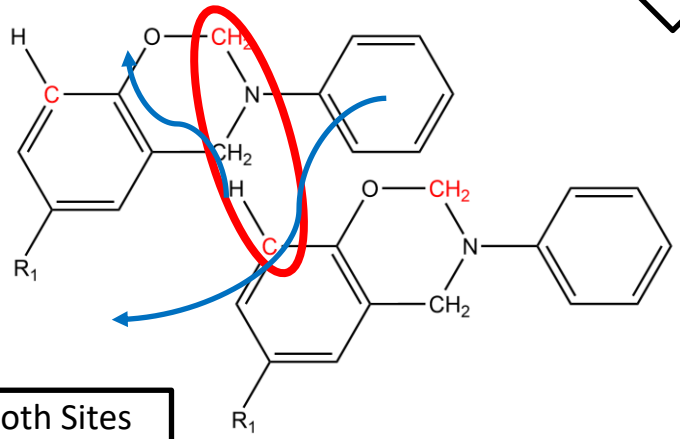

Both Sites Unused

Post Reaction

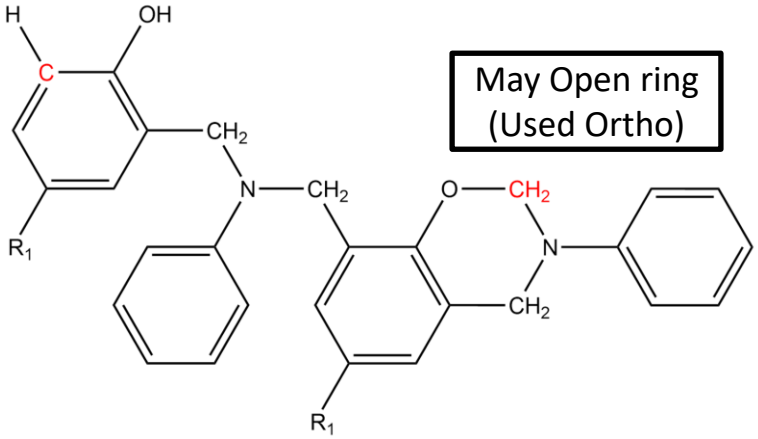

May Open ring (Used Ortho)

PBZ Density evolution

$$Volume\ shrinkage = \left(\frac{\rho_{cured}}{\rho_{uncured}} - 1\right) * 100\%$$

PBZ

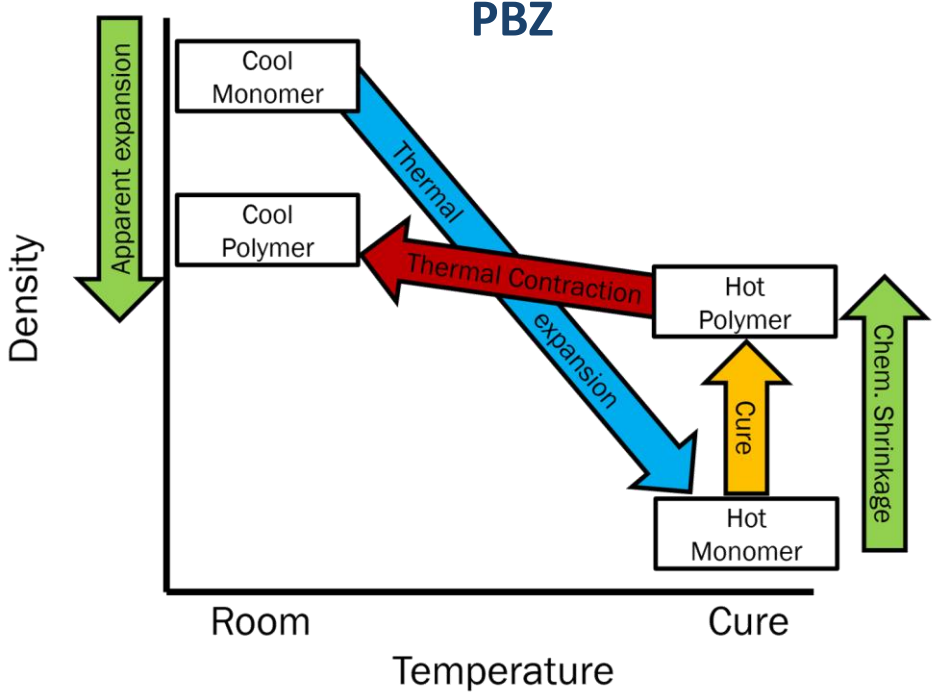

Other Materials

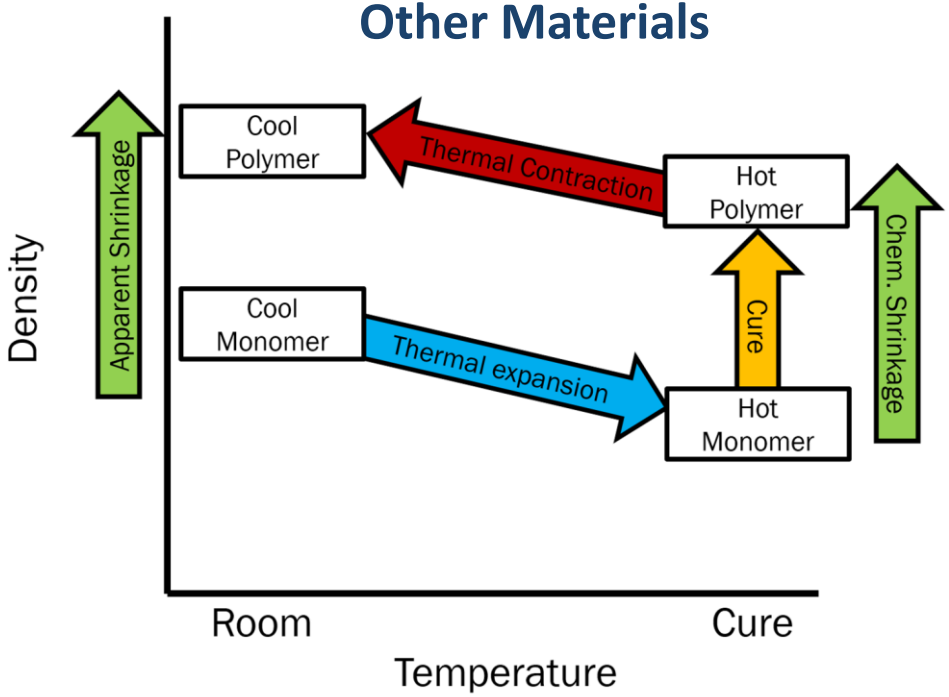

Ishida[3] et al., "A study on the volumetric expansion of benzoxazine-based phenolic resin," *Macromolecules,* vol. 30, no. 4, pp. 1099-1106, 1997

Modeling

- **Start with randomized monomer gas at 0.25 g/cc**
  - Monomer from Chemdraw
  - Randomized Replication in Python script 250 molecules: 16250 atoms
  - PCFF-IFF applied in LUNAR[4] (with modified H-σ)
- **Repeat to make five 250 monomer replicates**
- **Densify to liquid density and Relax**
- **Cure using Reaction templates[5]**
- **Post cure Annealing**
- **Measure Properties**
- **Heat from 200K – 800K**

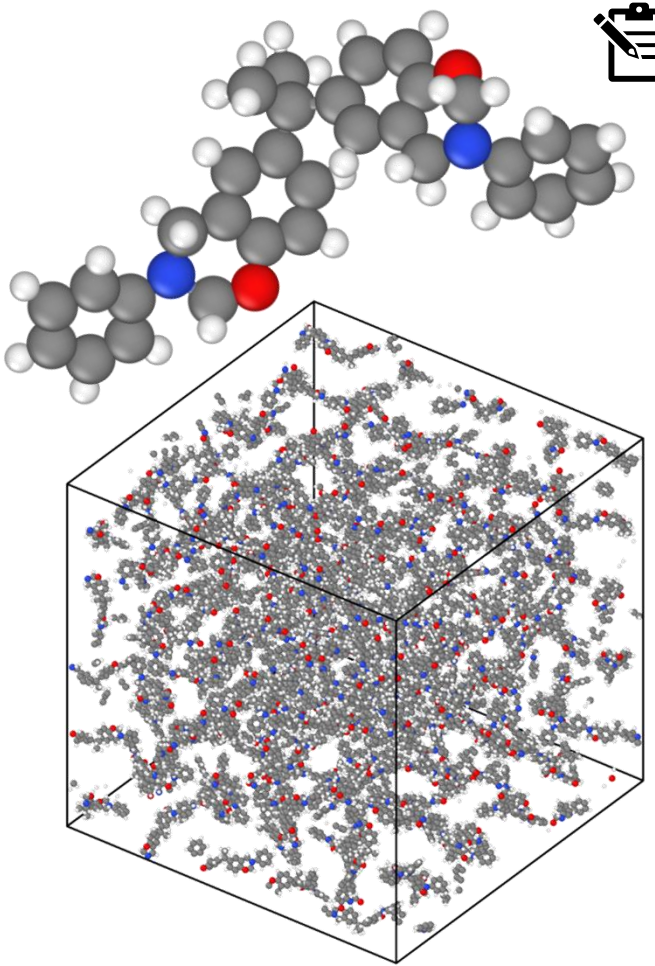

Kemppainen[4] et al., "LUNAR: Automated Input Generation and Analysis for Reactive LAMMPS Simulations," 2024, doi: 10.26434/chemrxiv-2024-9tqz2.

Gissinger[5] et al., "REACTER: A heuristic method for reactive molecular dynamics," *Macromolecules,* vol. 53, no. 22, pp.

Cured Models

- **Uncured Density Validation**
  - This study experimental 295K: 1.183 ± 0.024 g/cc
  - Simulated 300K: 1.184 ± 0.002 g/cc
- **Post Cure Density Comparison**
  - Experimental density [2] is the closest density at 1.182 g/cc, other literature values are higher.
  - Full Cure models at 1.173g/cc with best method
- **Closest method is the blue line**
  - Cluster evolution data every 1%
  - Density evolution every 5%
  - Tensile and CTE evolution every 10%

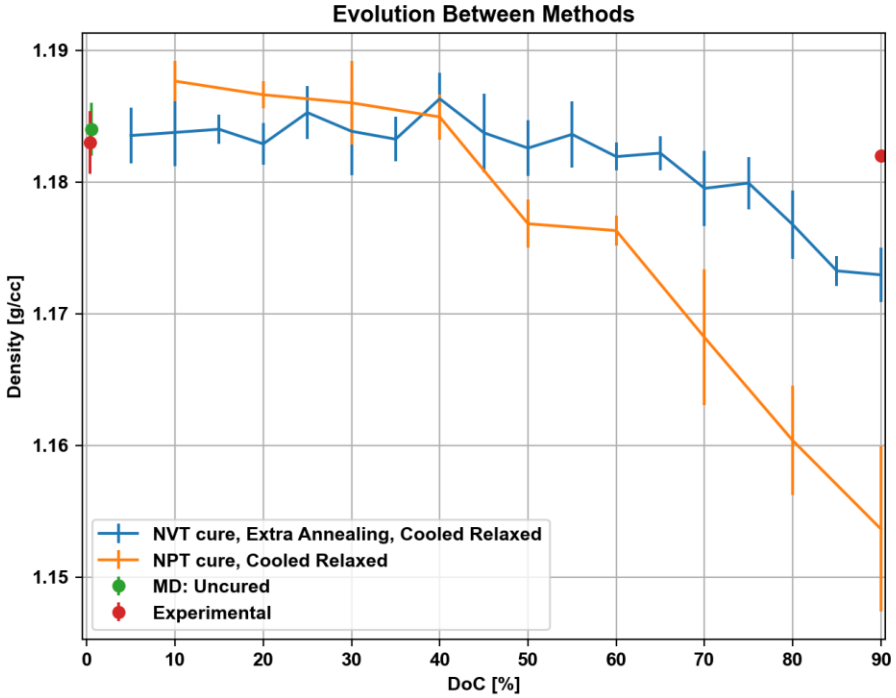

What is Free Volume

$$V_{System} = V_{Free} + V_{Atom}$$

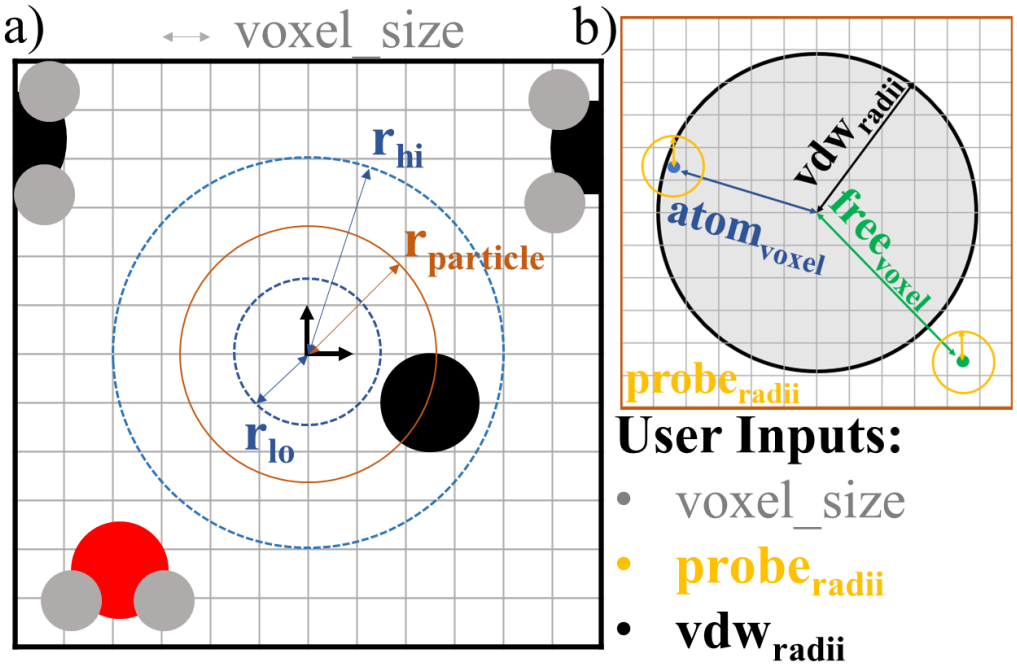

User Inputs:

- voxel_size
- $probe_{radii}$
- vdw_{radii}

DETDA Monomer

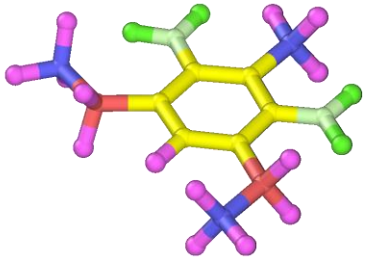

Gsêê ŵộĺụṇê ắŋắĺỳṣîṣ sêṣụĺʧṣ
Dêŋṣîʧỳ
Şîṇụĺắʧîộŋ çêĺĺ ŵộĺụṇê
Aʧộṇ ŵộĺụṇê
Gsêê ŵộĺụṇê
Rêsçêŋʧ Gsêê ŵộĺụṇê

Atom Volume

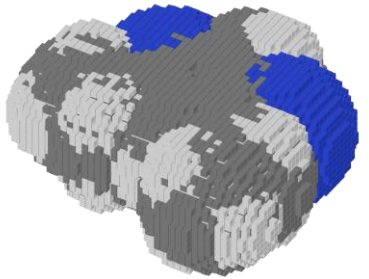

PBZ Thermal and Cure Density Evolution

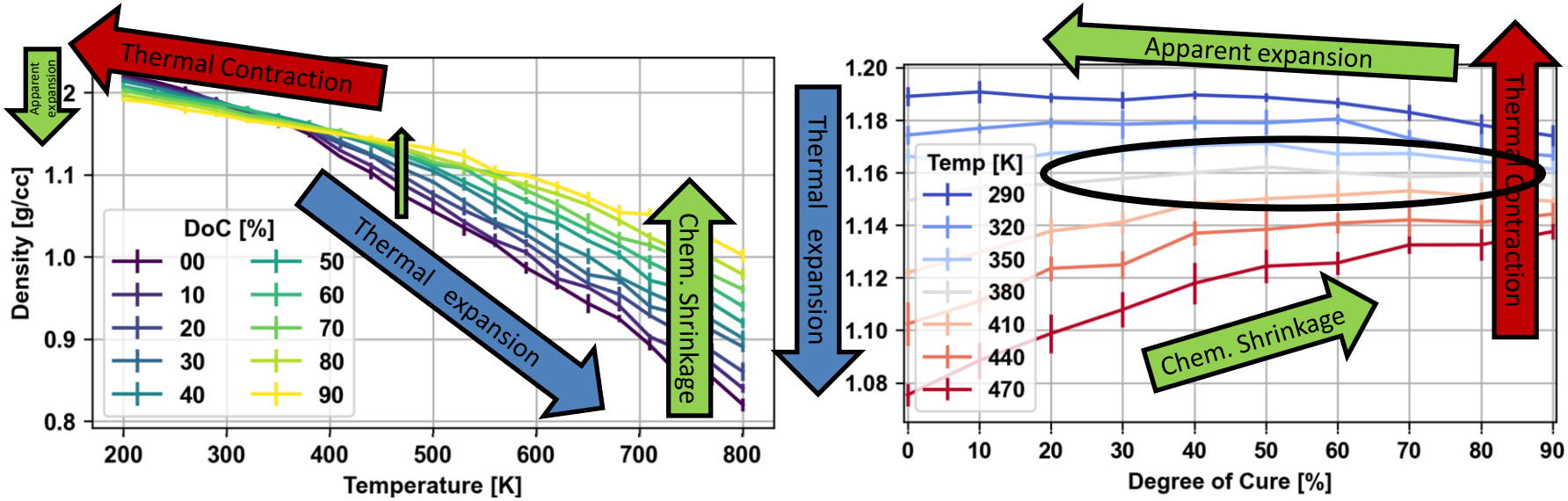

PBZ Thermal and Cure Atom Volume Evolution

$$V_{System} = V_{Free} + V_{Atom}$$

- - (dashed) System Volume
___ (solid) Atom Volume

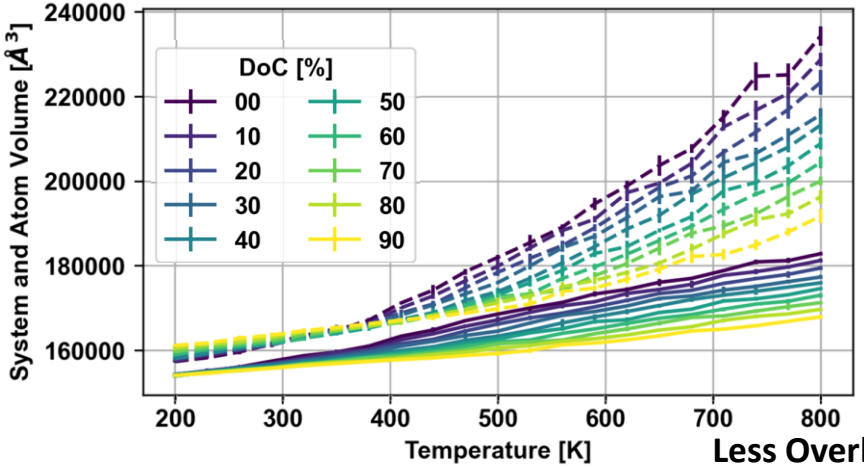

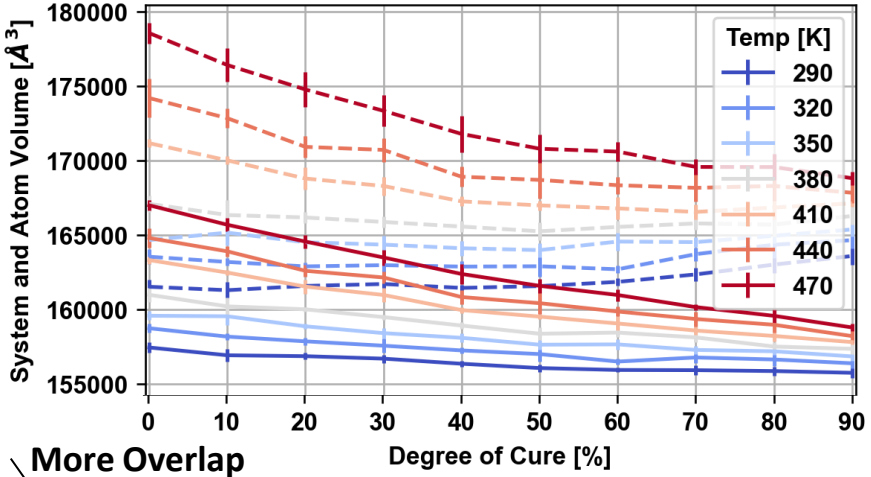

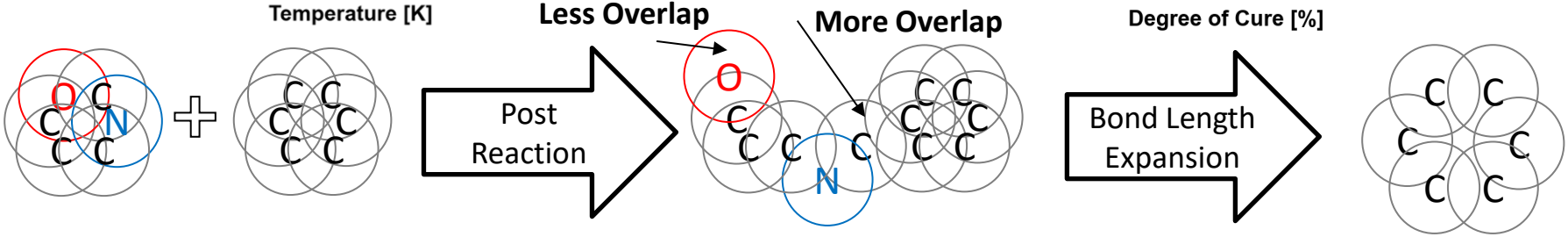

PBZ Thermal and Cure Free Volume Evolution

$$V_{System} = V_{Free} + V_{Atom}$$

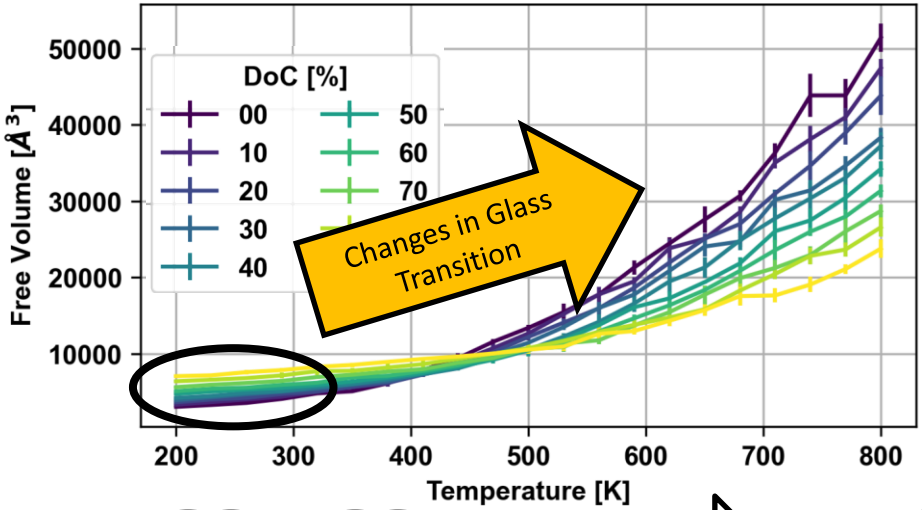

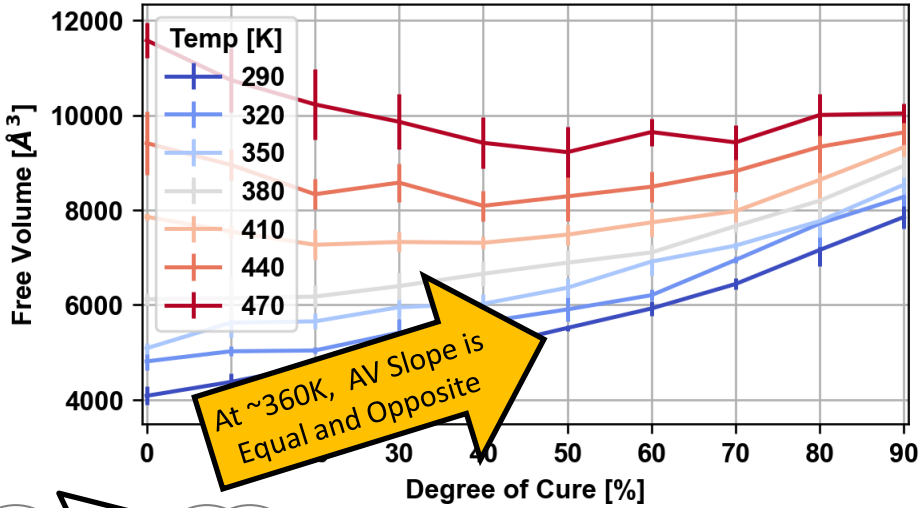

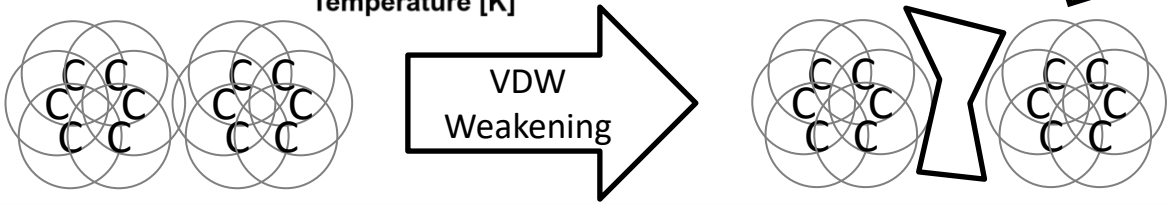

Summary

- **Cure shrinkage analysis using Free volume is Insightful**
  - More analysis possible using bond length and dihedral angle distributions
- **Residual Stress can be modulated with Temp and Cure rate**

- **More material Properties**
  - Tensile data in progress
  - Tg and CTE from same data
- **Future projects**
  - Improve Tg fitting
  - Study H-sigma effects
  - Modify PBZ FF parameters
  - PBZ variants

Acknowledgements

- Dr. Greg Odegard (MTU)
- CMMR Lab (MTU)
- SUPERIOR HPC (MTU)
- Cecil Evers (FSU)
- C3MD
- USCOMP





Thank you! Questions?

Regression Fringe Response Modulus Method

- **Tensile simulations using class2-xe Force Field***
- **Automated processing* of Stress-Strain data (QR code)**
  1. Low pass filter of MD data
  2. Algorithm to determine linear elastic region
  3. Algorithm to find yield point
  4. Process full array of 3 directions-5 replicates-many DoC-many Temps
  5. Determine outliers

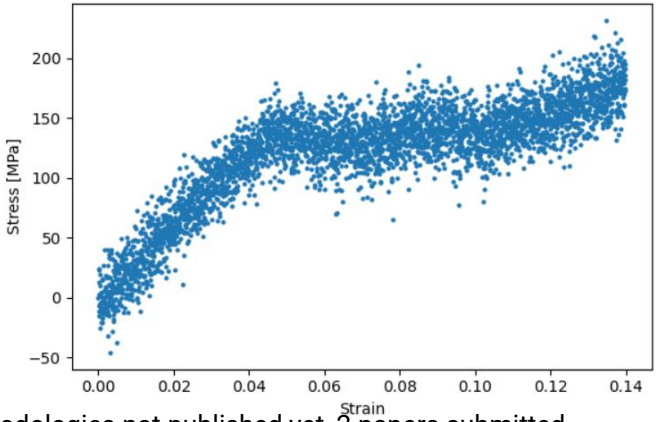

LUNAR RFR

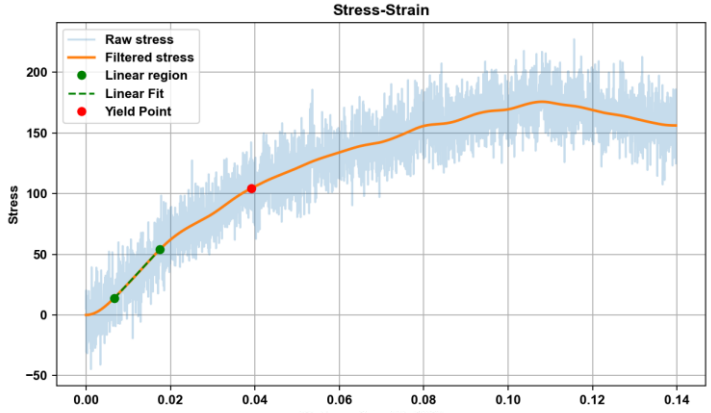

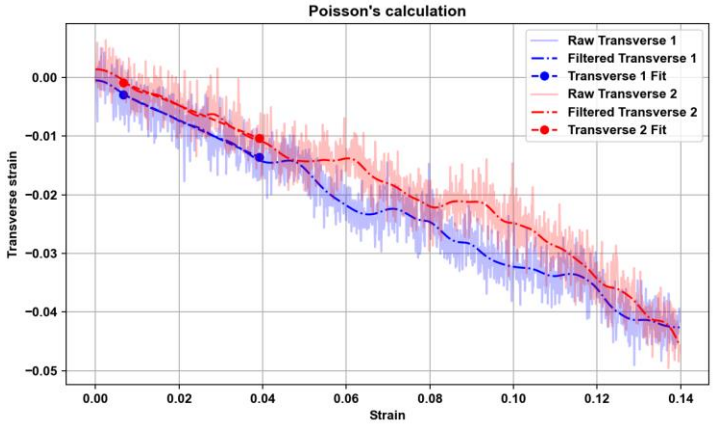

*Methodologies not published yet, 2 papers submitted

Mechanical Property Evolution

- **Independent variables**
  - 0%-90% cure
  - 300k – 475K
  - 3 directions, 5 replicates (mean and std of these)
- **Dependent variables**
  - Filter Cutoff Frequency
  - Linear region / Young's Modulus
  - Yield Stress / Yield Strain
  - Poisson's ratio in transverse directions
- **No outliers removed Currently**
  - Negative Poisson's
  - large Y intercept
- **Experimental: Modulus, 5.49 ± 0.33 GPa; Yield, 49.2 ± 2.02 MPa [2]**

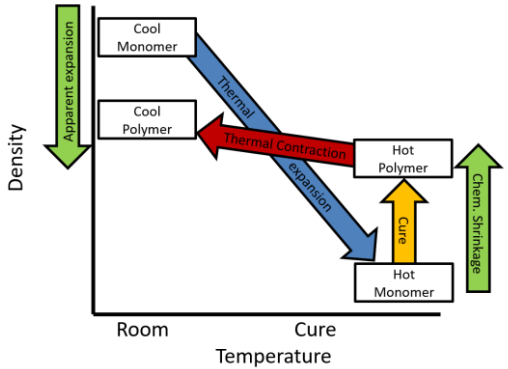

Modulus Data [MPa]

Cure:Temp	300K	325K	350K	375K	400K	425K	450K	475K
0%	1824.8	1112.8	1106.4	975.4	998.2	755.3	866.2	805.7
10%	2054.1	nan	nan	nan	nan	nan	nan	1019.6
20%	2058.1	nan	nan	nan	nan	nan	nan	1626.0
30%	2532.9	nan	nan	nan	nan	nan	nan	1355.7
40%	2751.7	nan	nan	nan	nan	nan	nan	1790.2
50%	2819.9	nan	nan	nan	nan	nan	nan	2038.2
60%	3221.2	nan	nan	nan	nan	nan	nan	2290.4
70%	3193.3	nan	nan	nan	nan	nan	nan	2542.2
80%	3689.8	nan	nan	nan	nan	nan	nan	2909.6
90%	4074.2	3551.2	3743.8	3607.9	3902.8	3276.9	3196.2	3040.1

Mechanical Property Evolution

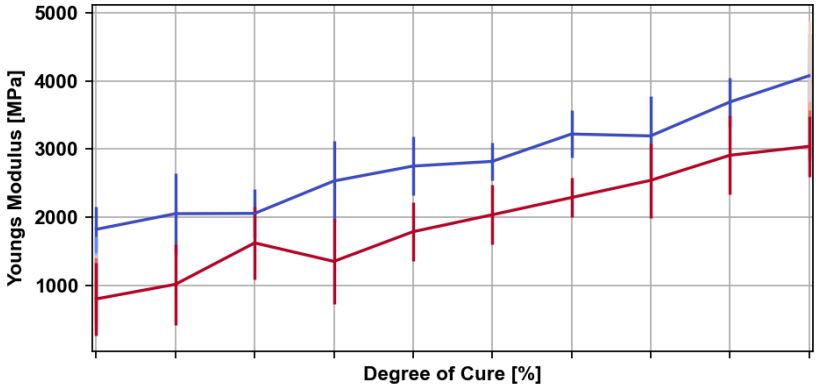

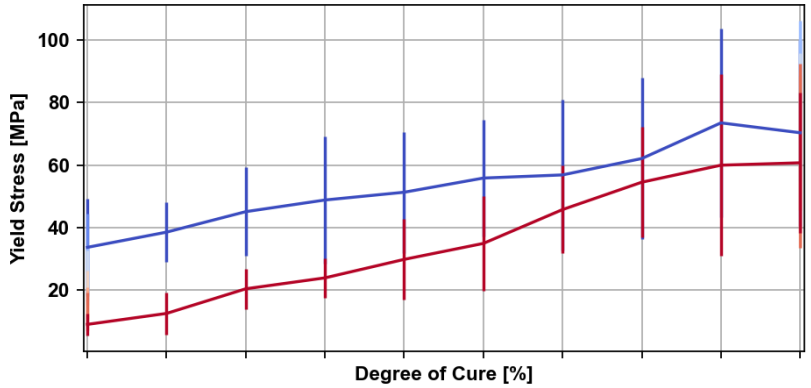

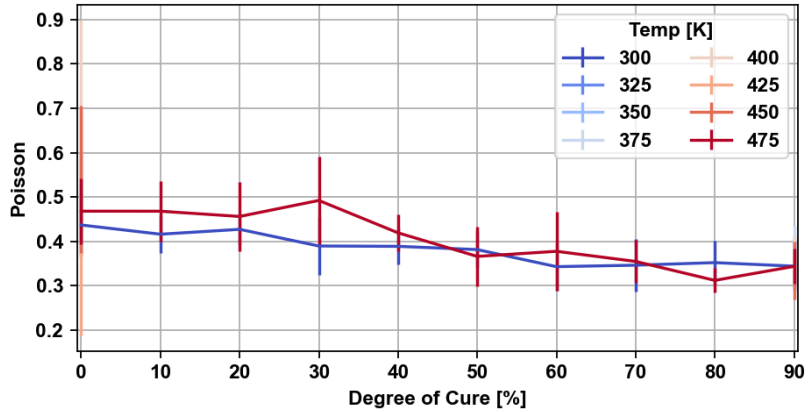

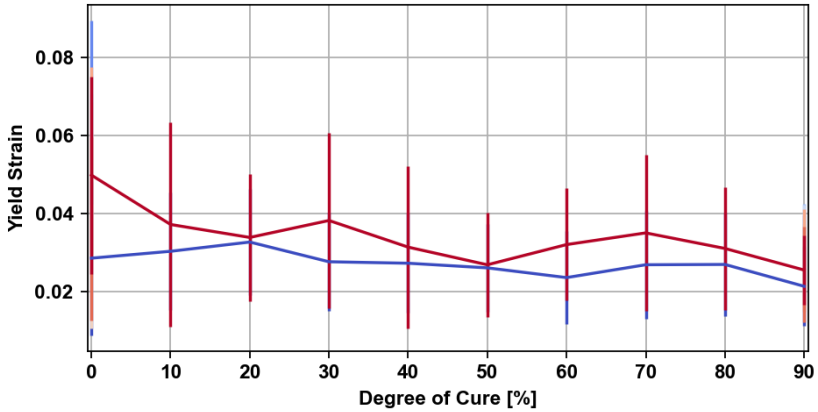

Mechanical property evolution

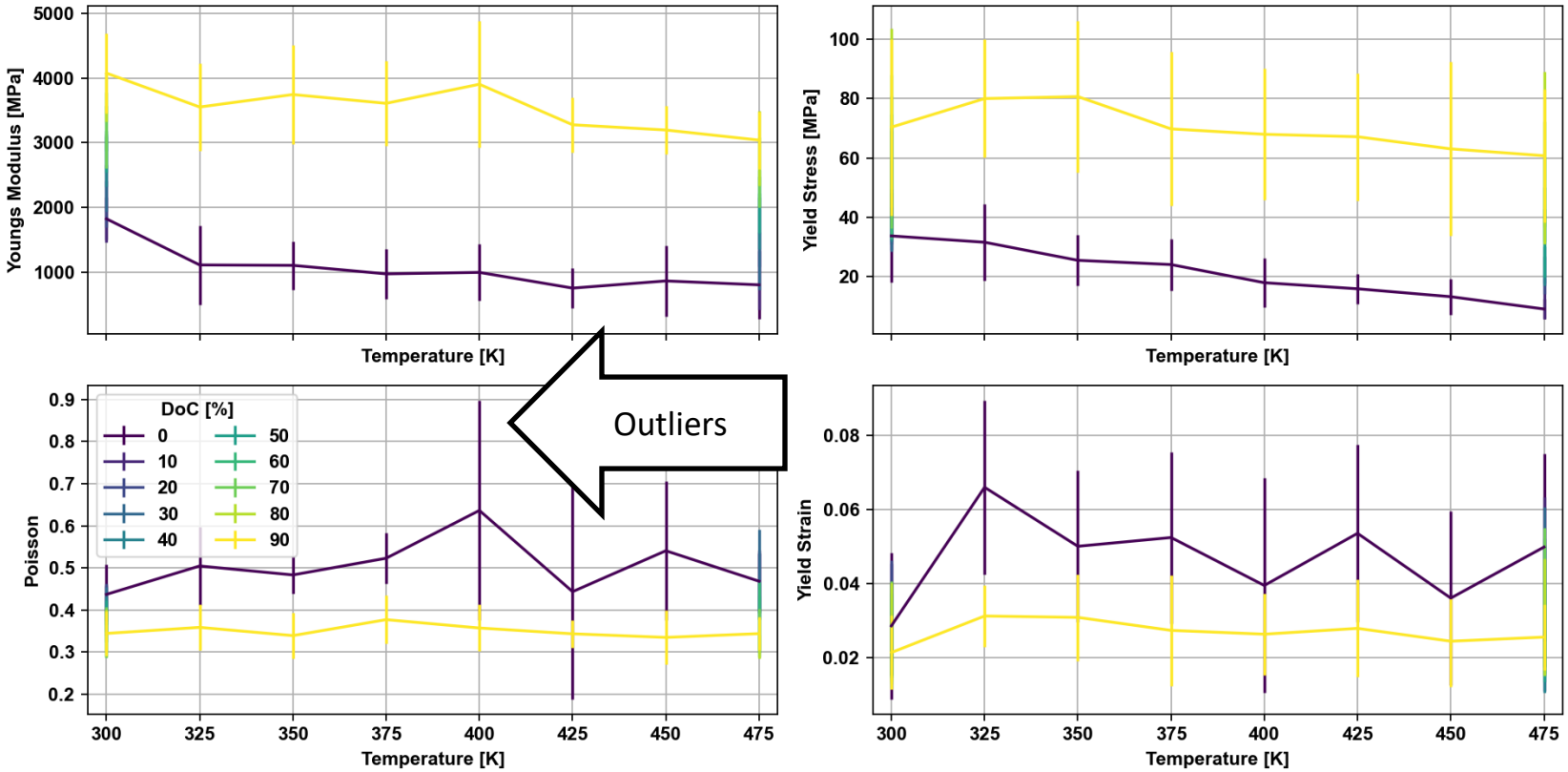

PBZ Glass Transition Evolution

- **Fit volume with hyperbola model**
  - Fit depends on range used
  - Top from 200K to 800K
  - Bottom uses -13C to 287C
- **Will further explore fitting methods**

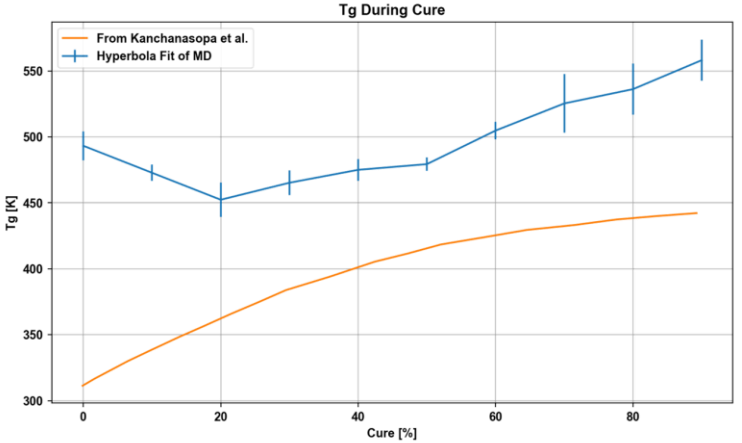

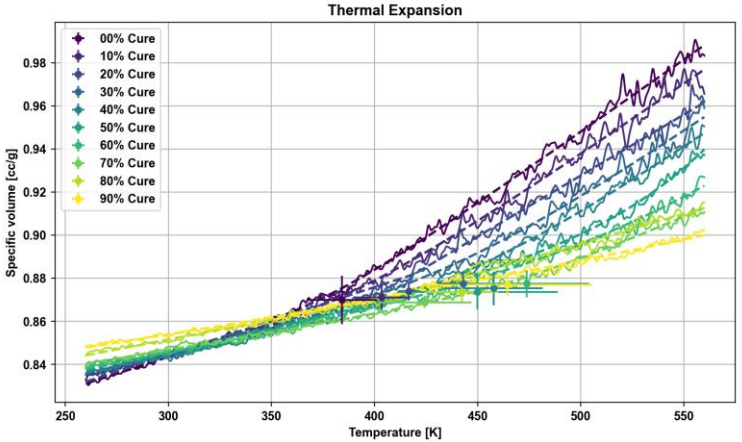

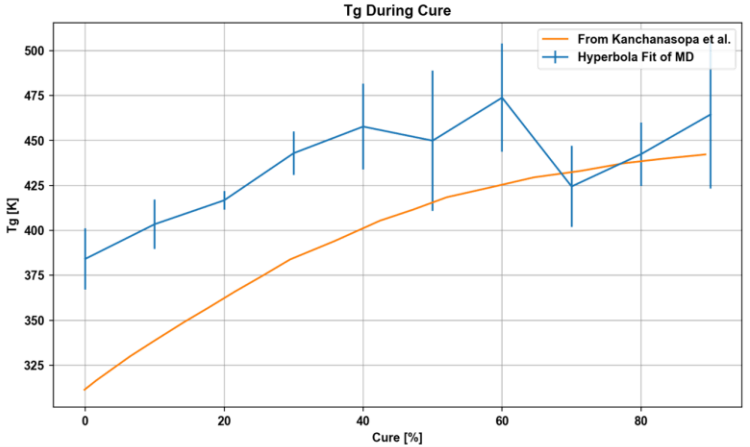

PBZ Thermal and Cure Evolution

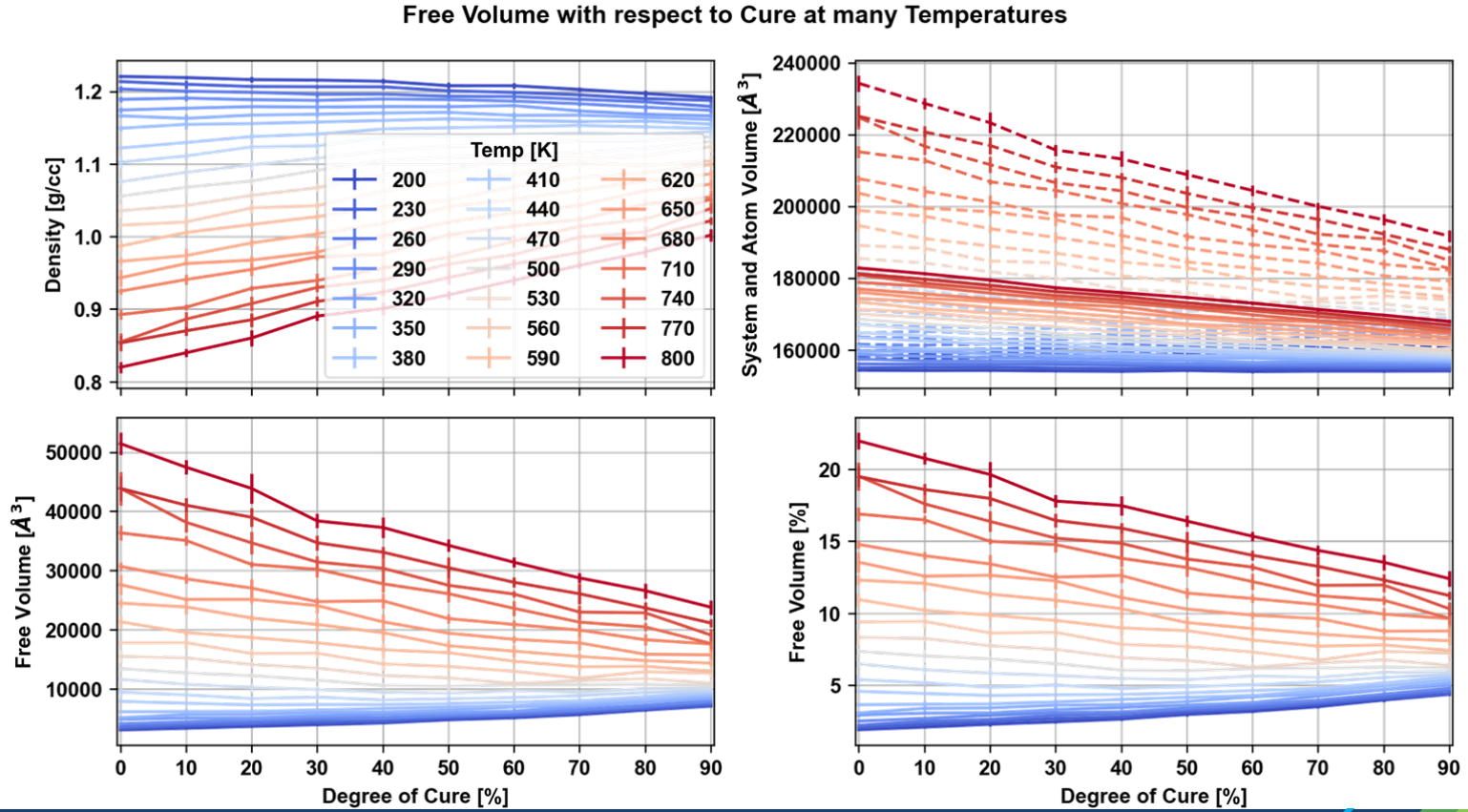

PBZ Thermal Expansion Simulations

- **Start with annealed models**
  - Every 10% cure
  - Five 16250 atom systems
- **Cool to 200K**
- **Relax for 1 ns**
- **Heat at 75K/ns**
  - Data files every 30K
  - Average density
  - Average energies
- **Fit volume with hyperbola model[6]**

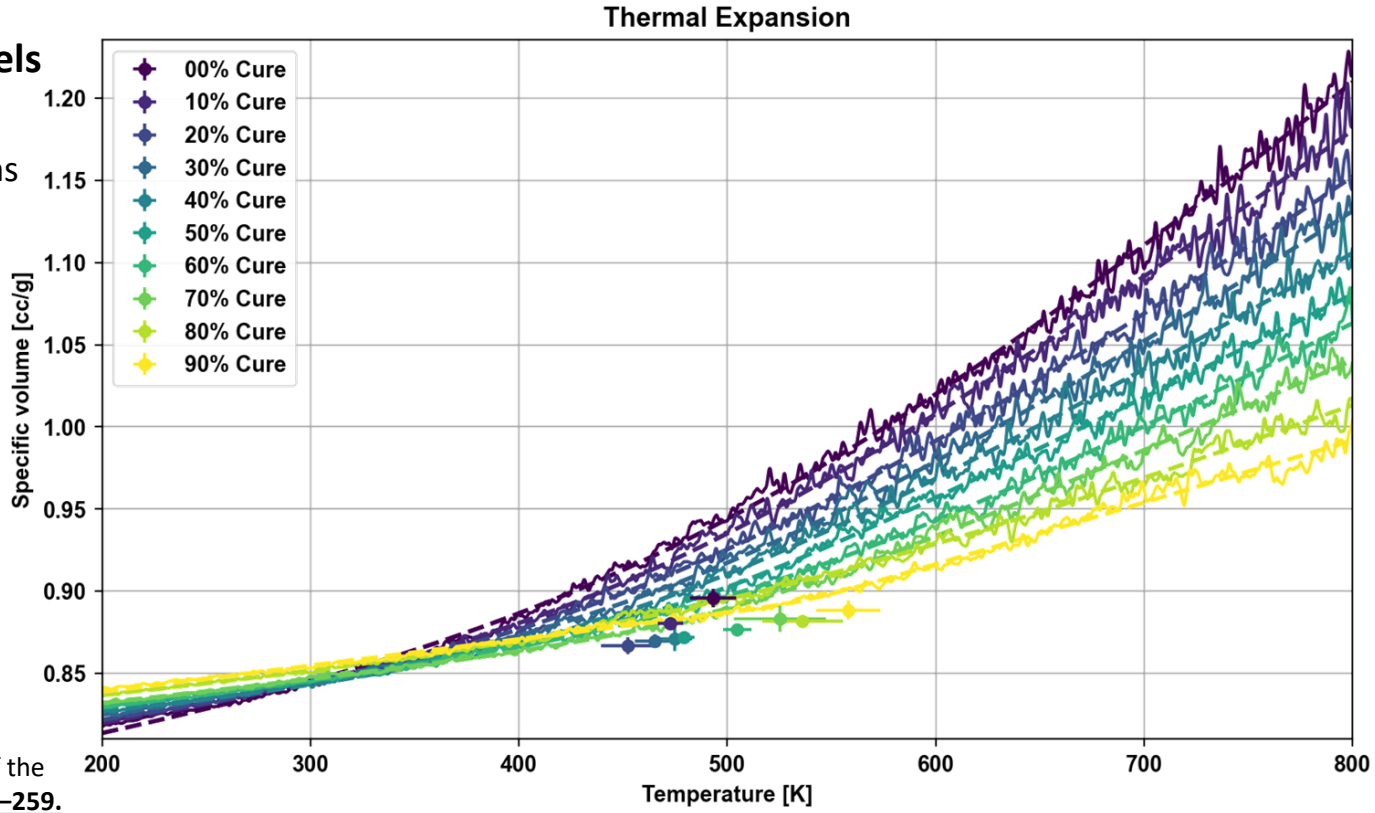

Patrone[6], P. N., et al. (2016). "Uncertainty quantification in molecular dynamics studies of the glass transition temperature." Polymer **87: 246–259.**

PBZ CTE Evolution

- **Fit volume with hyperbola model**
  - Fit depends on range used
  - Top from 200K to 800K
  - Bottom uses -13C to 287C
- **Will further explore fitting methods**
- **Find experimental sourse**

Reading Free Volume or Mechanical Property Plots

- **Points are average and standard dev. between runs**
- **x-axis for independent variable**
  - Temperature
  - Time
  - Degree of Cure
- **Color for 2nd independent variable**
  - Degree of Cure
  - Temperature
  - Processing Method
- **y-axis data from post process**
  - Density, Atom volume Free volume
  - Elastic modulus, yield, Poisson

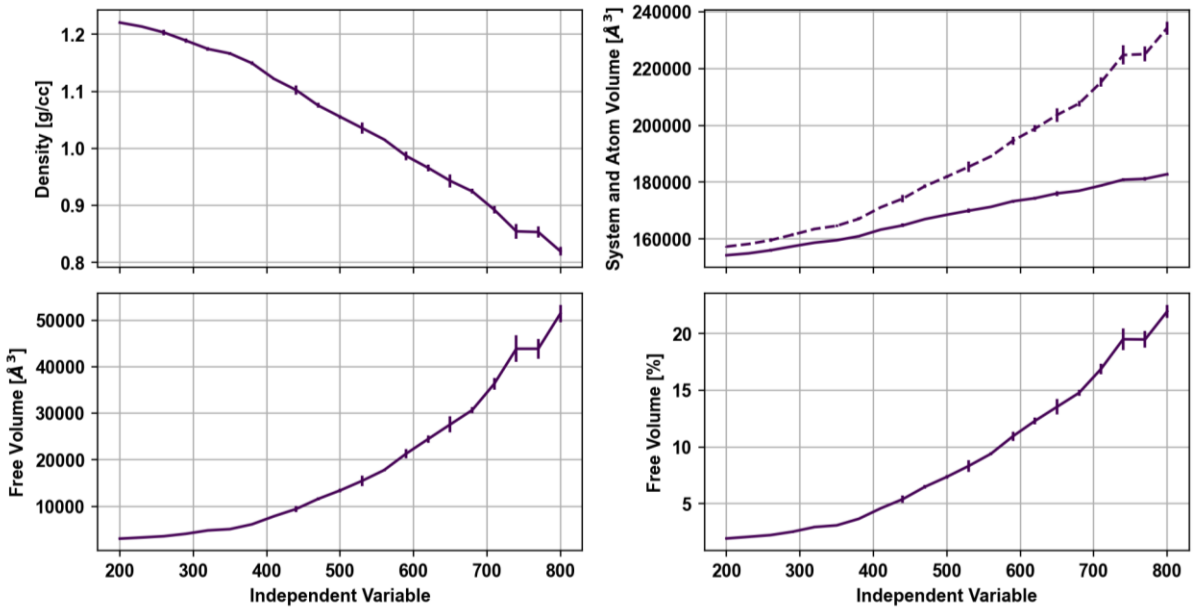

PBZ Thermal and Cure Free Volume Evolution

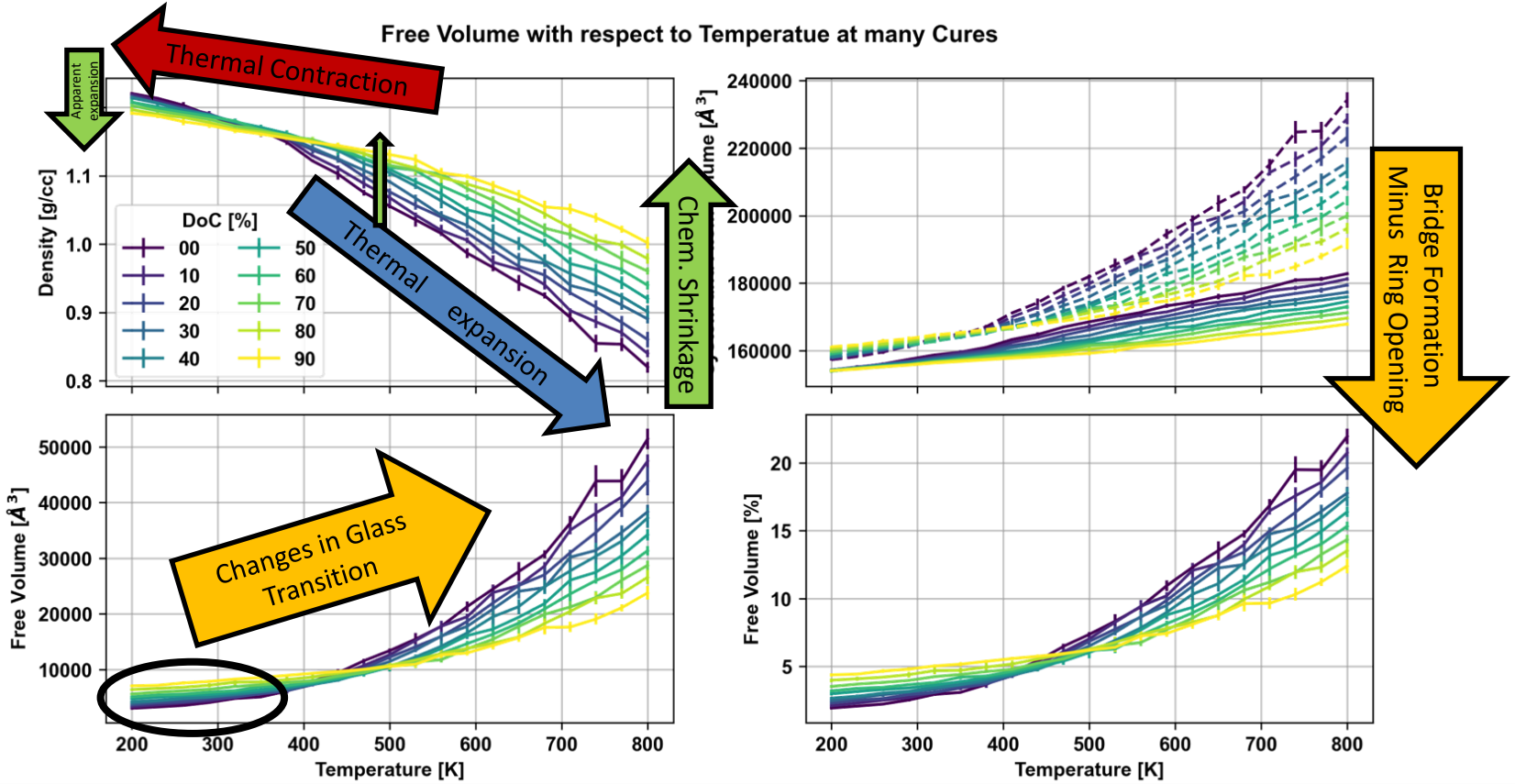

PBZ Thermal and Cure Evolution

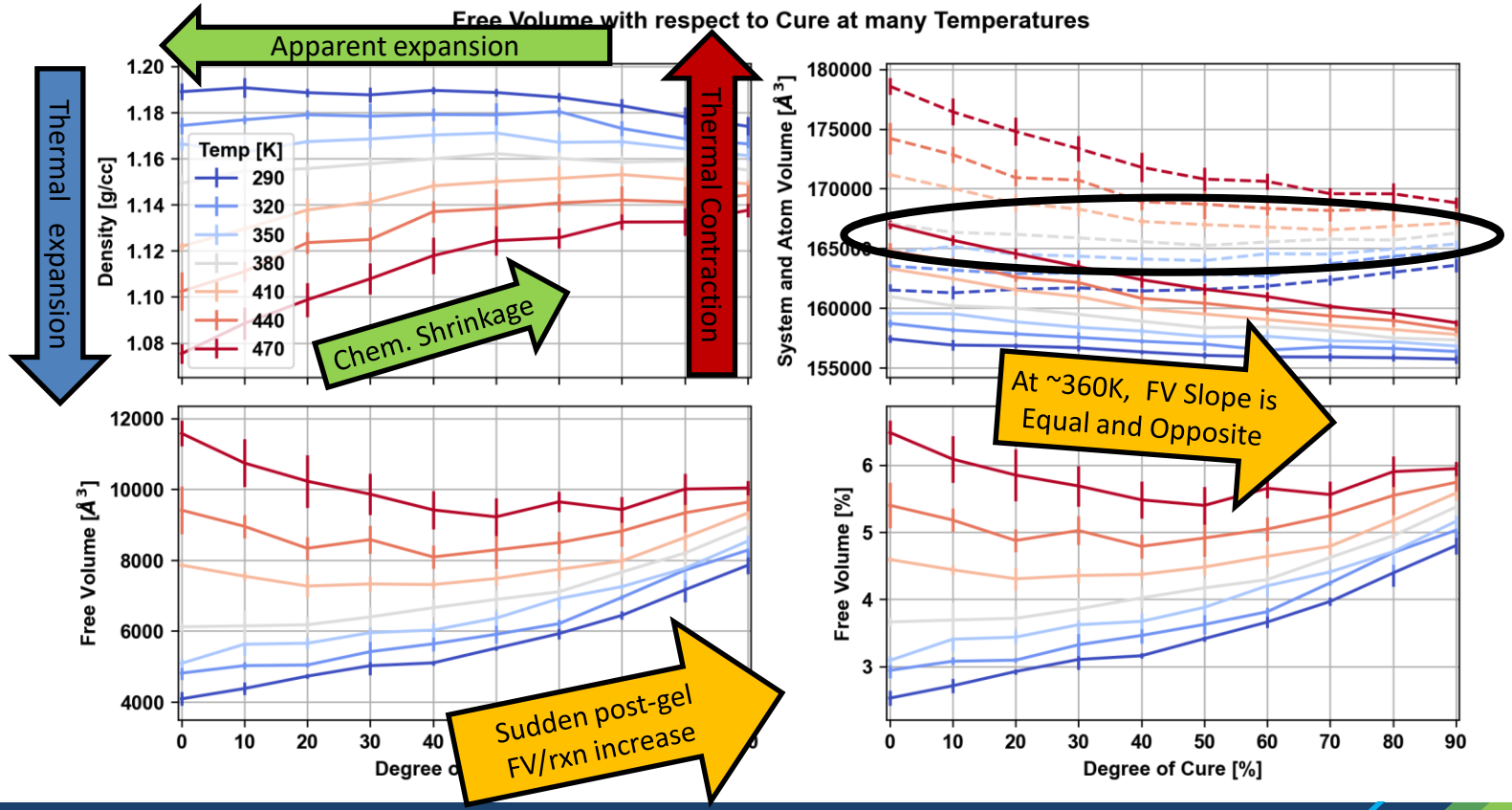

EPON-862 Free Volume

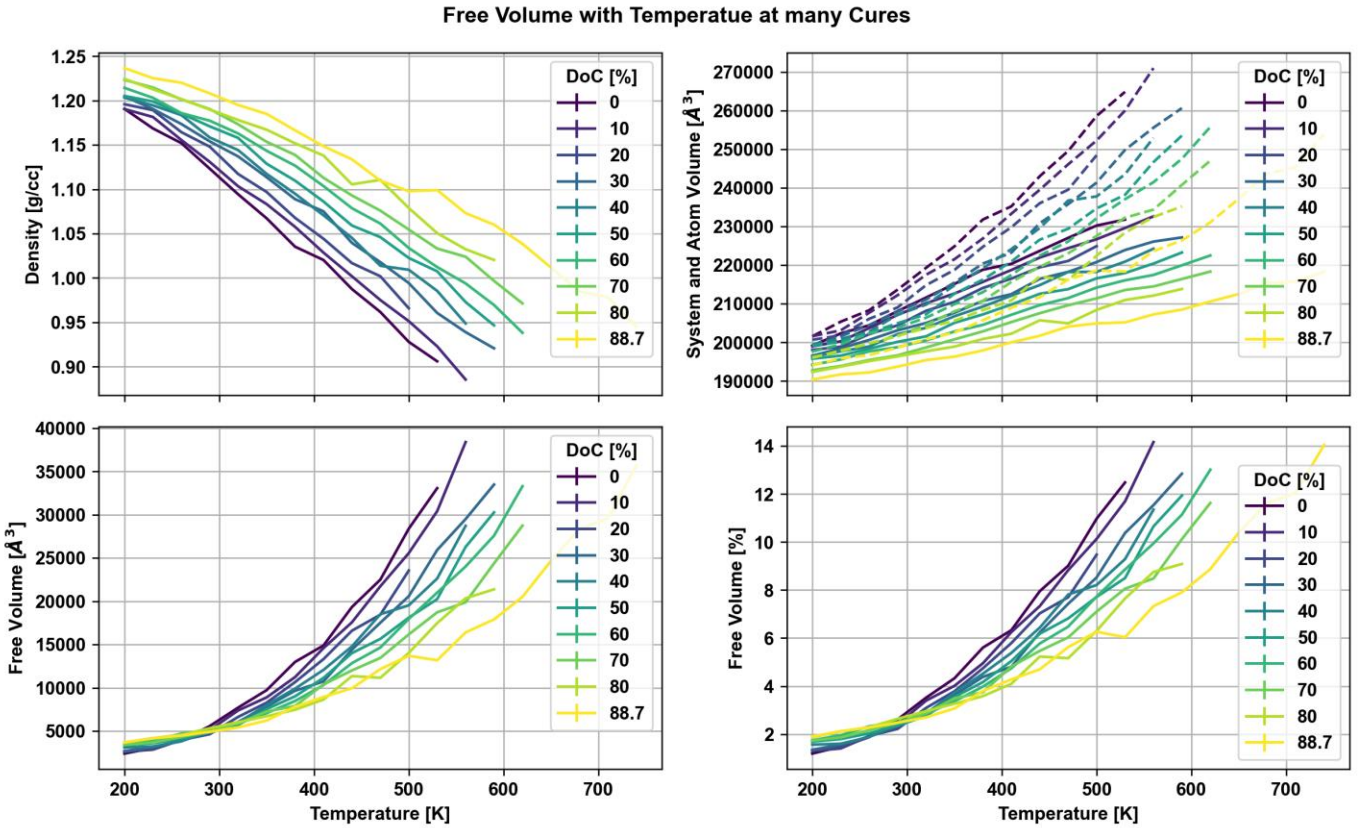

Free Volume Evolution With and Without anneal

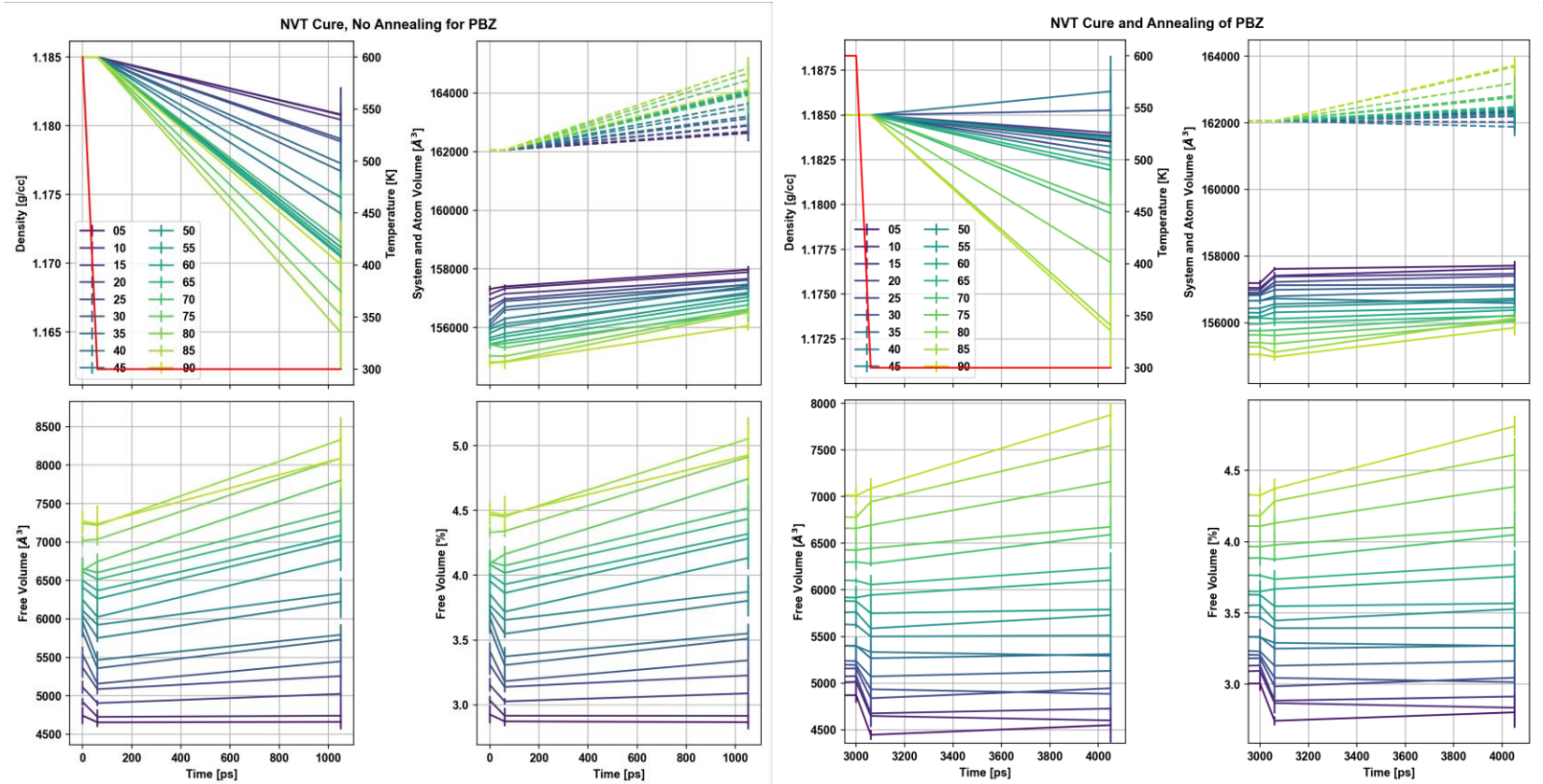

Gel Point Determination

- **Inflection point of largest cluster**
  - standard method for CMMR
- **Uses every 1% cure averaged between 5 replicates**
  - Standard deviation in mass at same DoC shown
- **Now fittable with constructed function**
  - Future work to finalize function choice, it may possibly become a sperate paper.
  - "Double Gaussian Turn" is shown and works well
- **PBZ is consistently just over 50%**
  - 53.2% for constant volume final run
  - 52.7% for constant pressure final run
  - ~51% in early testing
  - ~40% with reaction rate error

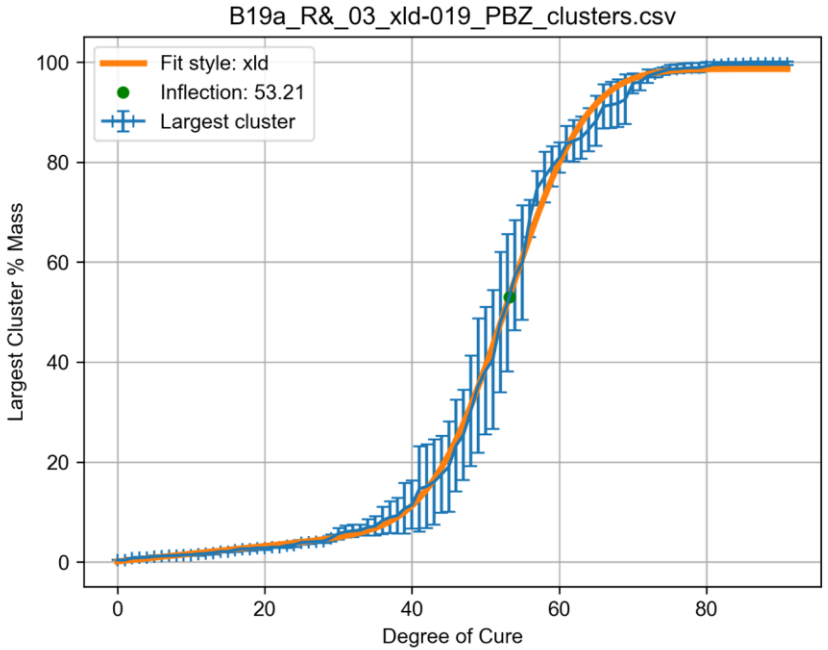

Final cure method data

- **Cure NPT @475k: get density @475k, 50k/ns cool, 2ns NPT @300k get density**
- **Cure NVT @ 600k 1.185 g/cc: Hold 3ns NVT, NVT cool at 5k/ps, 1ns NPT @300k get density**

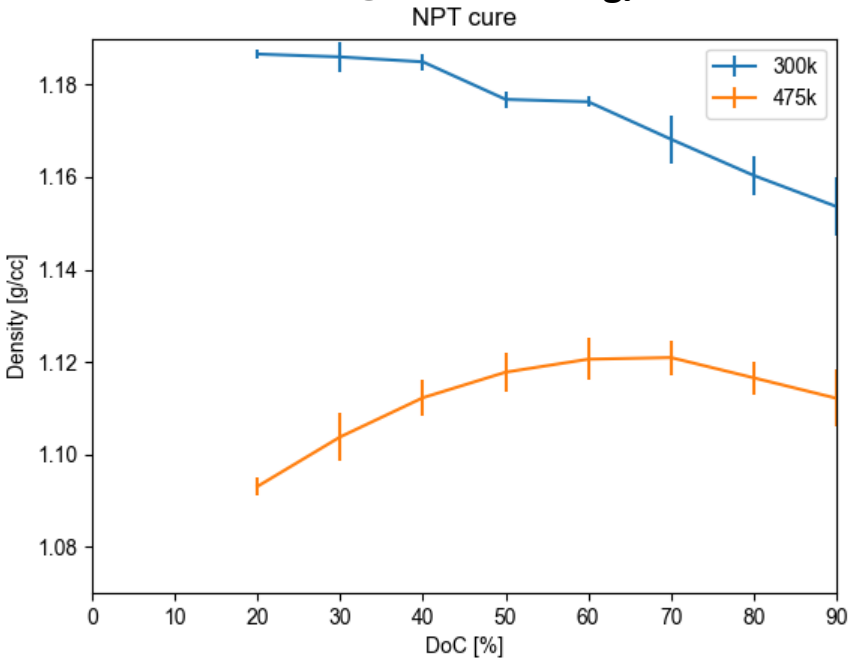

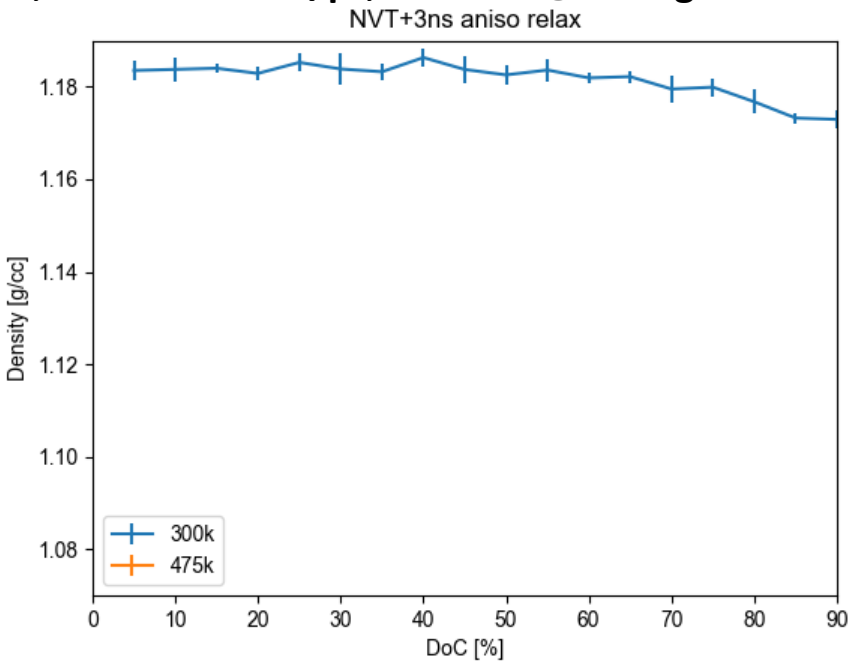

Final cure method data + Thermal cycle

- **Cure NPT @475k: get density @475k, 50k/ns cool, 2ns NPT @300k get density**
- **annealed NVT (last slide) + 2ns NPT @475k, 50k/ns cool, 2ns NPT @300k get density**

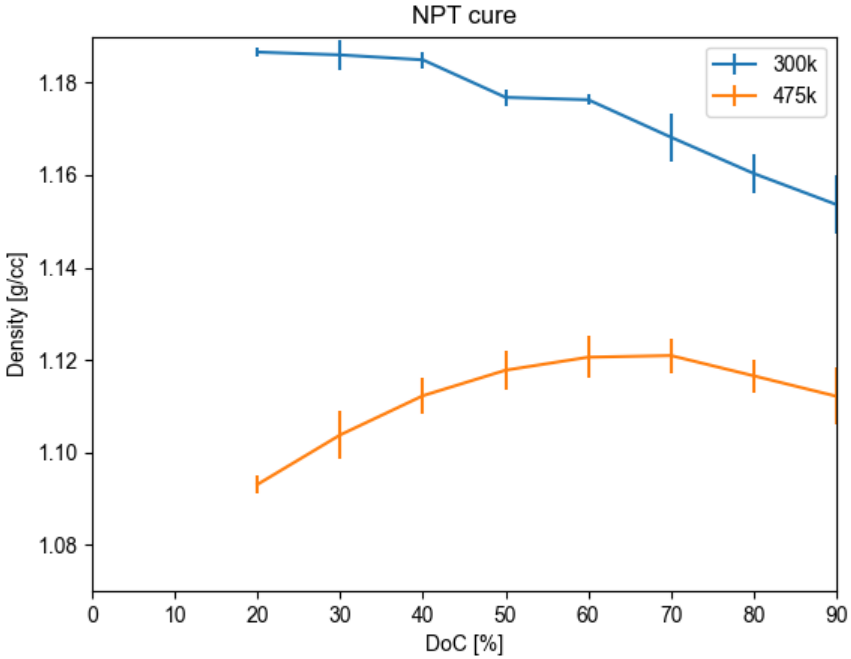

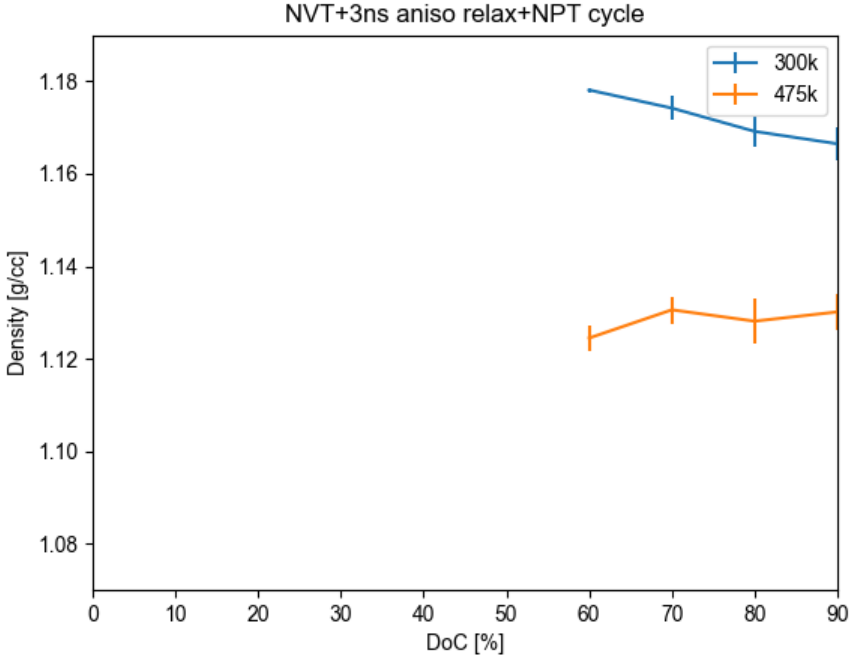

PBZ Cure cycle

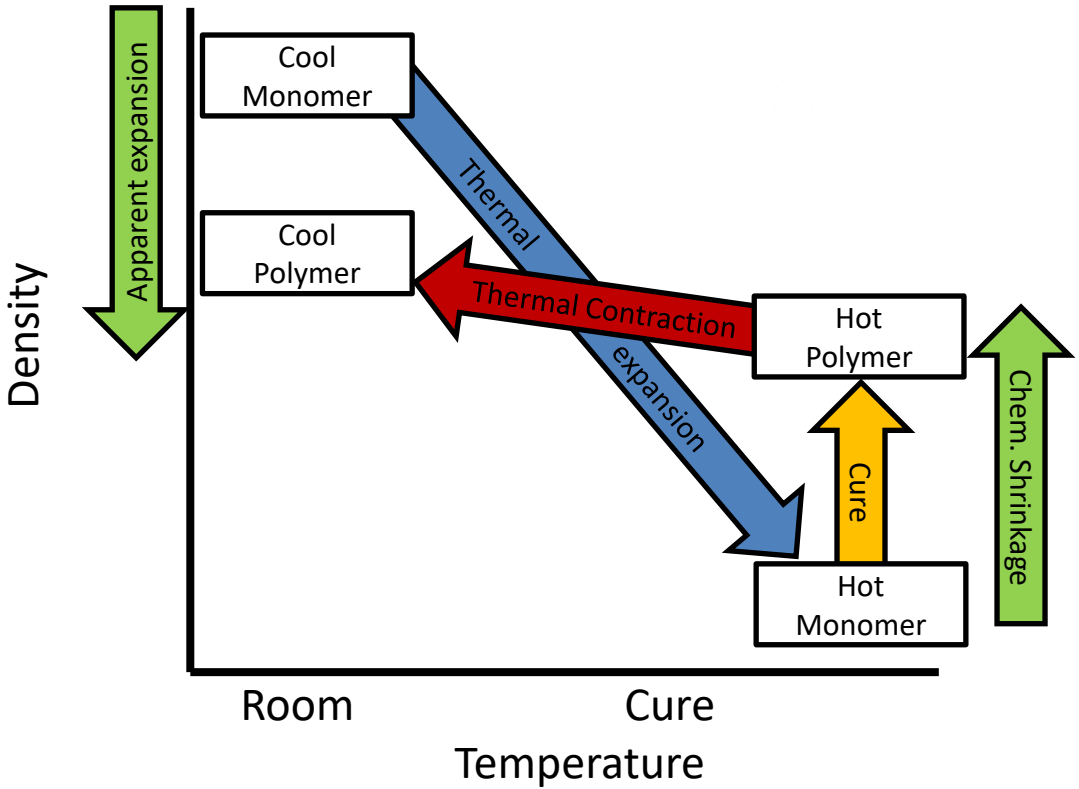

Normal Cure cycle

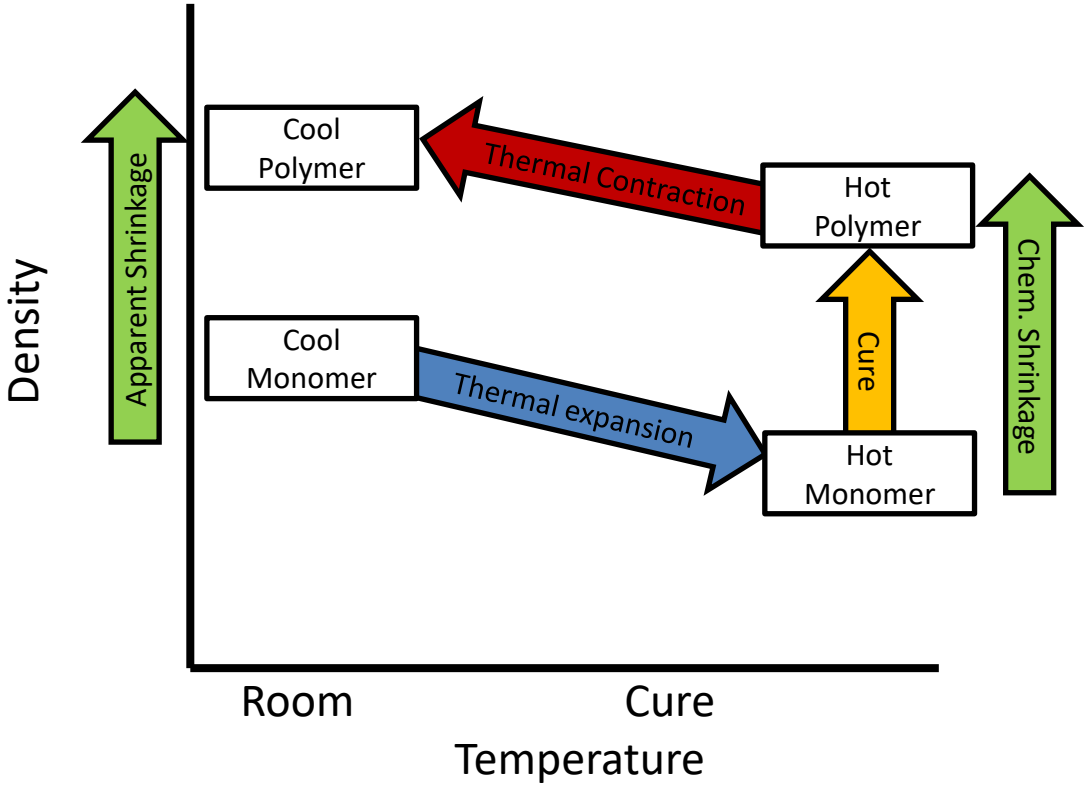

ICCM24 24TH INTERNATIONAL CONFERENCE ON COMPOSITE MATERIALS
AUG 4-8, 2025 • BALTIMORE CONVENTION CENTER • BALTIMORE, MARYLAND

TENSILE CYCLIC BEHAVIOR OF OPEN-HOLE CFRP LAMINATES WITH ULTRA-THIN PLIES

Carlos Sandino[1], Roberto Prieto-García[2], Serafín Sánchez-Carmona[3] and Elena Correa[4]

[1]Group of Elasticity and Strength of Materials
Department of Continuum Mechanics and Structural Analysis, Universidad de Sevilla
Camino de los Descubrimientos s/n, 41092 Sevilla, Spain
Email: csandino@us.es, web page: https://prisma.us.es/investigador/5831

[2]Group of Elasticity and Strength of Materials
Department of Continuum Mechanics and Structural Analysis, Universidad de Sevilla
Camino de los Descubrimientos s/n, 41092 Sevilla, Spain
Email: robprigar@alum.us.es

[3]Group of Elasticity and Strength of Materials
Department of Continuum Mechanics and Structural Analysis, Universidad de Sevilla
Camino de los Descubrimientos s/n, 41092 Sevilla, Spain
Email: sscarmona@us.es, web page: https://prisma.us.es/investigador/7003

[4]Group of Elasticity and Strength of Materials
Department of Continuum Mechanics and Structural Analysis, Universidad de Sevilla
Camino de los Descubrimientos s/n, 41092 Sevilla, Spain
Email: ecorrea@us.es, web page: https://prisma.us.es/investigador/931

Keywords: Carbon fibre, Fatigue, Stress concentrations, Non-destructive testing, Delamination, Thin films.

ABSTRACT

The phenomenon of *scale effect* in composite materials is defined by reduced damage onset associated with a decrease in ply thickness. This effect has garnered renewed interest with the advent of low-grammage prepregs, prompting an upsurge in research into the use of ultra-thin plies in composite laminate manufacturing. In this regard, previous studies have primarily concentrated on the effects of the use of ultra-thin plies in the case of cross-ply laminates subjected to cyclic tensile loads.

Given this context, the present experimental study explores the integration of ultra-thin plies in multidirectional CFRP composite laminates, specifically in open-hole configurations, to assess damage evolution under tension-tension fatigue. The analysis compares quasi-isotropic laminates consisting of conventional thickness plies with their equivalent versions incorporating 90º ultra-thin plies, maintaining the same stacking sequences. Additionally, two distinct stacking sequences are investigated. The primary objective is to assess the impact of 90º ultra-thin plies and their distribution through the laminate thickness on damage evolution, aiming to identify potential improvements in laminate performance.

Following quasi-static tensile characterisation, the open-hole specimens are subjected to tension-tension fatigue testing with a stress ratio of R=0.1, where the maximum stress represents a fraction of the ultimate tensile strength. Damage onset and progression during cyclic loading are monitored using ultrasonic inspection. The results demonstrate that laminates with ultra-thin plies exhibit slower damage evolution and reduced sensitivity to the presence of the open hole at equivalent load levels. Moreover, the findings underscore the critical role of stacking sequence reorganization, particularly in mitigating free-edge damage mechanisms.

These observations suggest that multidirectional laminates featuring ultra-thin plies deliver superior performance under tensile fatigue loading. The results support their potential for enhanced structural durability, reinforcing the viability of implementing ultra-thin ply technology at an industrial scale.

1 INTRODUCTION

Recent interest in understanding the so-called *scale effect* [1] has driven growing research on the use of ultra-thin plies in the fabrication of composite laminates. Several studies have examined how these plies influence the performance of cross-ply laminates subjected to cyclic tensile loading [2]. Findings consistently show that the damage mechanisms in 90° plies vary significantly depending on whether the plies are of conventional or ultra-thin thickness, with the latter delaying damage initiation and leading to a less severe onset of degradation.

Following the approach of these previous studies, the present study explores whether incorporating ultra-thin plies can enhance the mechanical response of quasi-isotropic laminates. In particular, it focuses on open-hole carbon fibre/epoxy laminates [3], comparing configurations made entirely with conventional plies to those where only the 90° plies are replaced by ultra-thin plies.

In this regard, previous investigations into open-hole quasi-isotropic specimens have primarily examined how ply thickness influences mechanical performance under quasi-static [4–7] and cyclic tensile loading [8–9]. For instance, in [9], tension–tension fatigue tests compared laminates made with thin, intermediate, and thick plies—where all plies were uniformly scaled in thickness—focusing on stiffness degradation and internal damage evolution via X-ray radiography.

In contrast, the present work adopts a different strategy. Two laminate configurations with identical stacking sequences were designed: one composed entirely of conventional plies, and another where only the 90° plies were substituted with ultra-thin plies. Both configurations were tested using two distinct stacking sequences, ensuring identical proportions of 0°, ±45°, and 90° orientations. Following specimen fabrication, cyclic tensile tests were performed on open-hole samples to assess how 90° ply thickness and placement influence damage initiation and growth, especially around the hole. To track damage progression, non-destructive ultrasonic inspections were carried out at predefined cycle intervals, enabling a direct comparison of the four laminate designs and potential performance gains.

The paper is organised into four main parts. Section 2 outlines the manufacturing process of the open-hole specimens. Section 3 details the experimental methodology, including the procedures and results for static and cyclic tensile testing as well as damage assessment. Finally, Section 4 presents the key conclusions and discusses potential directions for future research.

2 MANUFACTURING PROCESS

The open-hole tensile specimens used in this experimental programme were designed in accordance with the specifications provided in [10]. The central hole, located at the midpoint of both the specimen's length and width, was drilled and reamed following the recommendations of the standard to minimise any risk of damage in its vicinity. Since the presence of the hole generates an adequate stress concentration to induce failure, no additional tabs were employed.

Two stacking sequences were selected: $[+45/-45/0/90]_{2s}$, as recommended by the standard [10], and $[+45/90/-45/0]_{2s}$. For each stacking sequence, two laminate configurations were fabricated. The first consisted entirely of plies with conventional thickness (150 g/m²), while the second replaced the 90° plies with ultra-thin plies (50 g/m²), keeping all remaining plies at the conventional 150 g/m² grammage. This approach enabled a direct comparison between the two configurations without increasing the total ply count or manufacturing time.

The laminates were produced using TP 402/T700SC carbon fibre/epoxy prepreg supplied by North Thin Ply Technology and were cured using a standard autoclave process. The resulting four specimen types, along with their geometric parameters—length (L), width (w), thickness (t), and hole diameter (Ø=w/6)—are summarised in Table 1.

Specimens	*L* (mm)	*w* (mm)	*ø* (mm)	*t* (mm)	Stacking sequence	90º ply grammage (g/m^2)	0° and ±45° ply grammage (g/m^2)
OH.A	200	36	6	2.7	$[+45/-45/0/90]_{2s}$	150	150
OH.B				2.2		50	
OH.C				2.6	$[+45/90/-45/0]_{2s}$	150	
OH.D				2.1		50	

Table 1: Dimensions of the specimens.

3 EXPERIMENTAL PROGRAMME

3.1 Quasi-static tests

Quasi-static tensile tests were carried out to determine the tensile strength (σ_U) of the laminates. This value represents a key parameter for defining the load levels used later in cyclic testing. The strength values were computed based on the ultimate load and the gross cross-sectional area. For each of the four laminate configurations, five specimens were tested. Testing was performed using an Instron 4483 universal testing machine equipped with a 150 kN load cell.

The results, summarised in Table 2, include the mean σ_U for all specimen types, accompanied by their standard deviation and coefficient of variation. Overall, laminates incorporating ultra-thin 90° plies (OH.B and OH.D) exhibited higher tensile strength compared to those made exclusively with conventional plies. Additionally, the stacking sequence $[+45/90/–45/0]_{2s}$ produced slightly higher strength values than the $[+45/–45/0/90]_{2s}$ sequence.

Specimens	Stacking sequence	σ_U (MPa)	SD (MPa)	CV (%)
OH.A	$[+45/-45/0/90]_{2s}$	387.94	7.48	1.93
OH.B		446.74	6.10	1.36
OH.C	$[+45/90/-45/0]_{2s}$	415.29	24.52	5.90
OH.D		465.36	40.69	8.74

Table 2: Tensile strength (σ_U) for all specimen types.

3.1 Cyclic tests

The tensile fatigue performance of open-hole composite specimens was assessed through tension–tension (T–T) fatigue testing, conducted at a stress ratio of R=0.1. For each specimen configuration, the tensile strength (σ_U) was first determined to establish a baseline reference. The maximum applied stress for fatigue testing corresponded to 80% of the respective tensile strength for each configuration.

Four specimens from each configuration were tested under these conditions. All experiments were performed using an Instron 8801 universal dynamic testing machine equipped with a 100 kN load cell, operating at a loading frequency of 3 Hz.

Fatigue tests were periodically interrupted at predefined intervals—specifically, after 2,500; 5,000; 10,000; 20,000; 50,000; 75,000; 100,000; 150,000; and 200,000 load cycles—to evaluate the evolution of damage. At each interruption, ultrasonic inspection was employed to monitor damage initiation and propagation, facilitating comparative assessment of the different specimen configurations. The progression of damage is depicted for representative specimens in Figures 1 and 2, with OH.A and OH.B shown in Figure 1, and OH.C and OH.D in Figure 2.

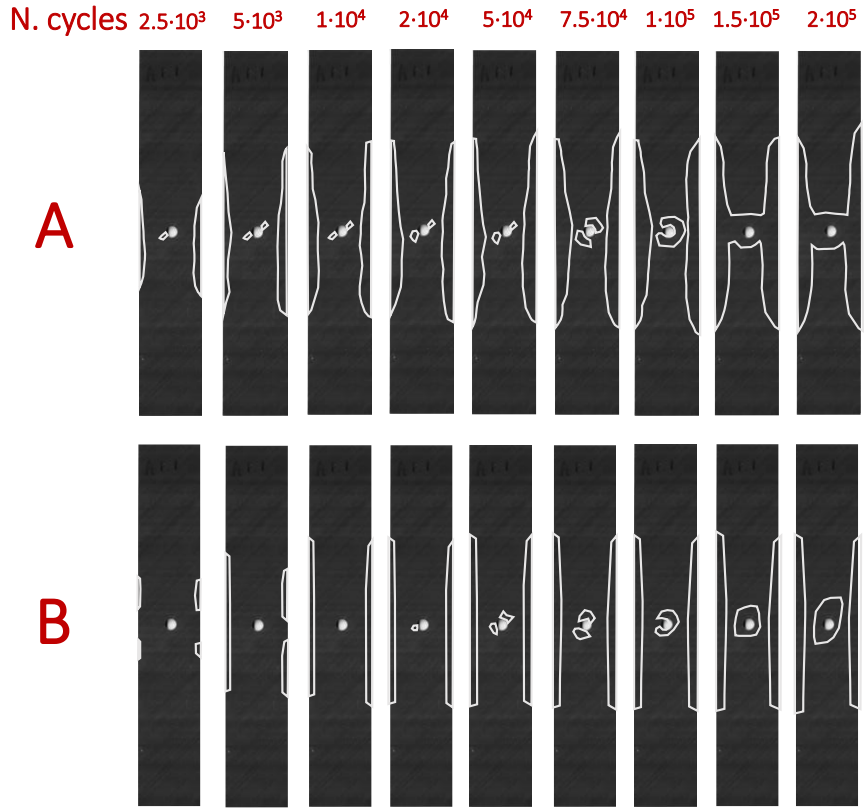

Figure 1: Evolution of the extent of damage for laminates OH.A and OH.B.

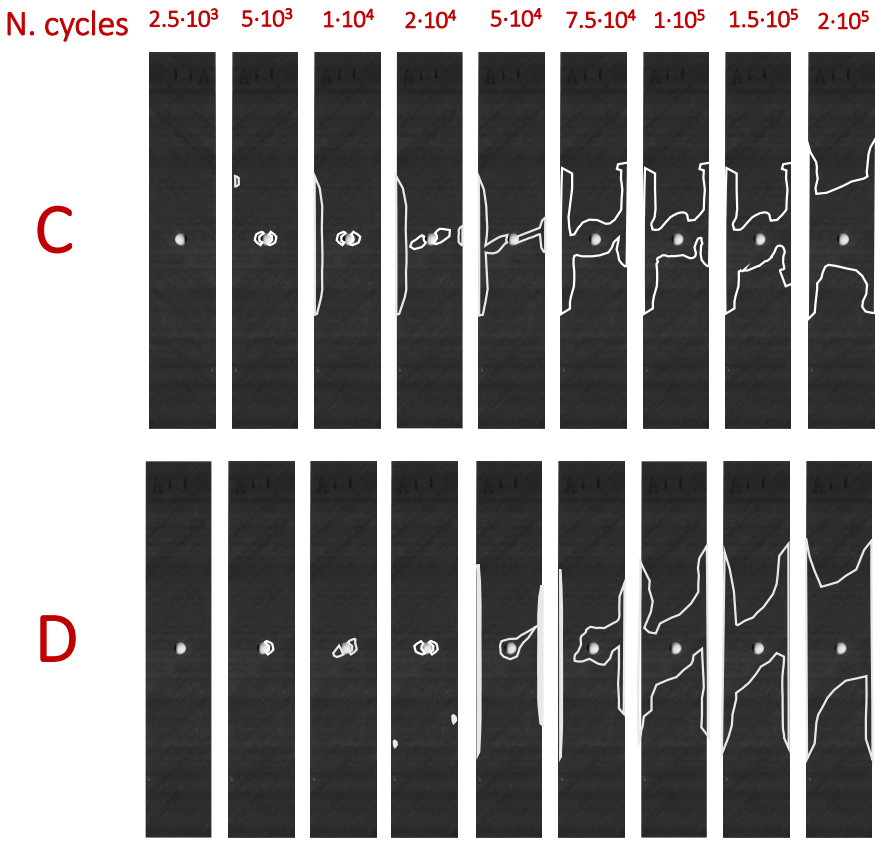

Figure 2: Evolution of the extent of damage for laminates OH.C and OH.D.

Comparative analysis of OH.A and OH.B specimens highlights the beneficial role of incorporating ultra-thin 90° plies within the $[+45/–45/0/90]_{2s}$ laminate. In OH.B specimens, free-edge damage was observed to initiate at a higher number of cycles relative to OH.A. Moreover, damage surrounding the open hole tended to manifest only after the free-edge damage had extended along the specimen free-edges, excluding the clamped regions. Consequently, the delayed onset of free-edge damage in OH.B specimens correspondingly postpones the initiation of hole-adjacent damage, effectively retarding the overall damage progression mechanism.

In the comparison shown in Figure 2 for specimens with the $[+45/90/-45/0]_{2s}$ stacking sequence (OH.C and OH.D), a delay in the initiation of free-edge damage is again observed due to the inclusion of ultra-thin 90° plies. However, this delay does not influence the overall progression of damage. Beyond approximately 100,000 load cycles, the extent of free-edge damage becomes nearly identical in both specimen types. Furthermore, unlike the behaviour noted for the $[+45/90/-45/0]_{2s}$ laminate, the delayed free-edge damage does not coincide with a postponed onset of damage around the hole. Consequently, the free-edge and open-hole damage mechanisms appear to evolve independently.

4 CONCLUSIONS

The experimental results indicate that substituting conventional 90° plies with ultra-thin plies in quasi-isotropic open-hole laminates enhances tensile fatigue performance for the $[+45/–45/0/90]_{2s}$ configuration. The use of ultra-thin plies delays the progression of the damage mechanisms, highlighting their potential as a design feature for improving fatigue life. These findings underscore the suitability of ultra-thin 90° plies for quasi-isotropic laminates subjected to cyclic tensile loading and support their potential adoption in industrial applications.

In contrast, this benefit is not evident for the $[+45/90/-45/0]_{2s}$ configuration. Although the initiation of free-edge and open-hole damage is postponed by incorporating ultra-thin 90° plies, the overall damage levels in both laminate types converge after extended cycling.

Future work will focus on refining the understanding of damage evolution in quasi-isotropic open-hole laminates through advanced inspection methods capable of resolving through-thickness damage localization. Such approaches will help clarify the contribution of ultra-thin plies to damage progression. Additionally, numerical modelling will be employed to optimise laminate design strategies incorporating ultra-thin plies.

ACKNOWLEDGEMENTS

This work was supported by:

- Consejería de Economía y Conocimiento Junta de Andalucía. Project P18-FR-3360 corresponding to the I+D+ I Programa Operativo FEDER 2014-2020 and Junta de Andalucía and European Social Fund.
- Spanish Ministry of Universities: 'Margarita Salas' grants for the training of young doctors. Funded by the Spanish Recovery, Transformation and Resilience Plan and Next Generation EU.
- Spanish Ministry of Science and Innovation. Project PID2021-126279OB-I00 corresponding to the State Plan 2021-2023: Knowledge Generation Projects.

REFERENCES

[1] F. París, M. L. Velasco, and E. Correa. The scale effect in composites: An explanation physically based on the different mechanisms of damage involved in failure. *Compos Struct*, 257, 113089, 2021.

[2] S. Sánchez-Carmona, E. Correa, A. Barroso, and F. París P. Experimental observations of fatigue damage in cross-ply laminates using carbon/epoxy ultra-thin plies. *Compos Struct*, 306, 116564, 2023.

[3] O.J. Nixon-Pearson, S.R. Hallett, P.J. Withers and J. Rouse Damage development in open-hole composite specimens in fatigue. Part 1: Experimental investigation. *Compos Struct,* 106:882–889, 2013.
[4] R. Aoki, R. Higuchi, T. Yokozeki, K. Aoki, Kazuyuki, S. Uchiyama and T. Ogasawara. Effects of ply thickness and 0°-layer ratio on failure mechanism of open-hole and filled-hole tensile tests of thin-ply composite laminates. *Compos Struct*, 280, 114926, 2021.
[5] G. Czél, T. Rev, M. Jalalvand, M. Fotouhi, M.L. Longana, O.J. Nixon-Pearson, and M.R. Wisnom. Pseudo-ductility and reduced notch sensitivity in multi-directional all-carbon/epoxy thin-ply hybrid composites. *Compos. - A: Appl. Sci. Manuf,* 104:151–164, 2018.
[6] B.G. Green, M.R. Wisnom, and S. Hallett. An experimental investigation into the tensile strength scaling of notched composites. *Compos. - A: Appl. Sci. Manuf,* 38(3):867-878, 2007.
[7] S.R. Hallett, B.G. Green, W.G. Jiang and M.R. Wisnom, An experimental and numerical investigation into the damage mechanisms in notched composites. *Compos. - A: Appl. Sci. Manuf,* 40(5):613-624, 2009.
[8] S. Sihn, R.Y. Kim, K. Kawabe and S. W. Tsai. Experimental studies of thin-ply laminated composites. *Compos Sci Technol*, 67(6): 996-1008, 2007.
[9] R. Aoki, R. Higuchi and T. Yokozeki. Progressive damage and residual strength of open-hole thin-ply CFRP laminates under tensile fatigue loading. *Compos Struct,* 314:116973, 2023.
[10] ASTM International. ASTM D5766 / D5766M-11 - Standard Test Method for Open Hole Tensile Strength of Polymer Matrix Composite Laminates. West Conshohocken, PA. ASTM International; 2018.

ICCM24 24TH INTERNATIONAL CONFERENCE ON COMPOSITE MATERIALS
AUG 4-8, 2025 • BALTIMORE CONVENTION CENTER • BALTIMORE, MARYLAND

EFFECT OF WEAVE ARCHITECTURE AND STUFFER TO BINDER RATIO ON MECHANICAL PERFORMANCE OF 3D-WOVEN COMPOSITE CORE-BASED SANDWICH PANELS

Prabhjot Singh[1], Javed Sheikh[2] and B. K. Behera[3]

[1]Department of Textile and Fibre Engineering, Indian Institute of Technology Delhi,
Hauz Khas, New Delhi, India – 110016
Email: prbjotsingh.k@gmail.com

[2] Department of Textile and Fibre Engineering, Indian Institute of Technology Delhi,
Hauz Khas, New Delhi, India – 110016
Email: jnsheikh@iitd.ac.in, web page: https://textile.iitd.ac.in

[3] Department of Textile and Fibre Engineering, Indian Institute of Technology Delhi,
Hauz Khas, New Delhi, India – 110016
Email: behera@iitd.ac.in, web page: https://textile.iitd.ac.in

Keywords: 3D woven composite; sandwich panels; flexural performance; impact properties; damage analysis.

ABSTRACT

Metal-faced sandwich panels with solid composite cores are increasingly used in structural applications due to their high strength-to-weight ratio, excellent fatigue resistance, stiffness, and superior impact tolerance. These characteristics make them ideal for demanding environments in aerospace, automotive, and defence sectors. However, conventional sandwich structures are often limited by core materials that lack sufficient delamination resistance and fail to distribute loads efficiently under extreme conditions. This study investigates the mechanical enhancement of fibre metal laminate (FML) sandwich panels by incorporating 3D-woven fabric-reinforced composite cores. Three weave architectures—3D orthogonal, 3D angle-interlock, and 3D warp-interlock—were explored across three stuffer-to-binder yarn ratios: 1:2, 1:1, and 2:1. Flexural testing revealed that the 3D angle-interlock cores exhibited the highest load-bearing capacity due to their inclined binder yarns that engage more effectively under bending stress. In contrast, 3D orthogonal cores demonstrated superior flexural stiffness, attributed to the near-vertical alignment of binder yarns enhancing through-thickness shear resistance. Panels with higher stuffer-to-binder ratios (2:1) consistently achieved greater peak loads and deflections, indicating enhanced energy absorption due to the increased volume of in-plane stuffer yarns. Notably, the 1:2 stuffer-to-binder ratio with an orthogonal weave offered a balanced improvement in both metrics. These findings offer valuable insights for designing high-performance sandwich composites for critical applications in the aerospace and defence sectors.

1 INTRODUCTION

Metal-faced sandwich panels with solid composite cores are advanced lightweight structural materials that combine the durability and strength of metal facesheets with the tailored properties of a solid composite core [1,2]. Typically, the facesheets are made from metals such as aluminum or stainless

steel, which provide excellent flexural stiffness, damage tolerance and surface hardness. The core, on the other hand, is a homogeneous composite material—often a polymer matrix composite—that offers excellent fatigue resistance, shear strength, and energy absorption. These characteristics make these composites ideal for demanding structural applications in aerospace, automotive, and defence sectors.

A lot of literature has already been published showing excellent fatigue resistance [3–5] and impact damage tolerance [6–8] of metal-faced sandwich panels with 2D and UD cores. They exhibit exceptional fatigue resistance, as the fibre layers act to arrest and slow the growth of cracks that initiate in the metal layers, significantly extending the material's lifespan under cyclic loading. FMLs are also highly damage-tolerant, maintaining much of their structural integrity even after sustaining impact or localized damage [9]. However, the flexural performance of conventional sandwich structures can be limited by the properties of the core material, which may struggle to effectively mitigate delamination and distribute loads under extreme conditions [10–12]. Numerous studies have investigated the flexural performance of metal-faced solid core sandwich structures, particularly those with unidirectional (UD) and 2D FRP cores. Lawcock et al. [13] reported that the flexural behaviour of CARALL laminates is highly influenced by the bonding strength at the metal–composite interface, which affects interlaminar shear but not tensile strength. To enhance flexural performance, several researchers have focused on improving interfacial adhesion in FML sandwich composites [14–16]. However, in designs prioritizing flexural modulus, increasing layer thickness has been shown to reduce flexural modulus linearly, with minimal impact on flexural strength [17].

Recent advancements in 3D-woven composites have demonstrated their potential to enhance the mechanical performance of FMLs over traditional two-dimensional (2D) woven and unidirectional (UD) composites, particularly in demanding engineering applications. One of the primary benefits is their superior resistance to delamination, a common failure mode in 2D and UD composites where layers separate under flexural or impact loading. This is achieved by incorporating fibers in the through-thickness (z) direction, which greatly enhances the structural integrity and reduces the risk of layer separation. Offering improved resistance to delamination, higher energy absorption, and more efficient load transfer [18,19]

The 3D-woven preforms can also be further modified to tailor the mechanical performance of the metal-faced sandwich composite panels by varying the weave architecture and stuffer-to-binder ratio of the woven preforms. As these two parameters are critical while determining the mechanical performance of the 3D-woven composites. Varying these parameters can further help analyse the change in the impact and flexural performance of the 3D-woven core-based metal-faced sandwich composite panels.

2 MATERIAL AND METHODS

2.1 Materials

The sandwich panels used in this study incorporate three different types of 3D-woven solid composite core preforms: 3D orthogonal, 3D angle interlock, and 3D-warp interlock. All 3D core preforms are 4-layer to maintain consistency. A total of 9 core fabric preforms were fabricated, varying weave architecture and three different stuffer to binder ratios (1:2, 1:1, 2:1). The facesheets used are made of aluminium (Al-6063) with a thickness of 0.5mm. All samples were designed with identical dimensions: a core height of 2 mm and facesheet thickness of 0.5 mm. PLEXUS MA311 adhesive was used to bond the aluminium facesheets and core. The construction parameters of the core preforms are listed in Table 1. All core fabrics were fabricated using 600 tex E-glass rovings on a customized 3D rigid rapier weaving loom. A pictorial representation of the 3D orthogonal, 3D angle interlock, and 3D-warp interlock preforms is shown in Figure 1. All composite cores were consolidated using the Vacuum-Assisted Resin Transfer Moulding (VARTM) process, employing Epoxy LY556 resin and Aradur HY951 hardener.

Table 1: Construction parameters of 3D Solid Structures for core

Weave	3D orthogonal	3D angle interlock	3D warp interlock
Stuffer linear density (tex)	600	600	600
Binder linear density (Denier)	300	300	300
Filler linear density (Denier)	600	600	600
Number of stuffer layers	4	4	4
Number of filler layers	5	5	5
Stuffer + binder ends per inch	1:2 - 22 1:1 - 30 2:1 - 36	1:2 - 22 1:1 - 30 2:1 - 36	1:2 - 22 1:1 - 30 2:1 - 36
Filler ends per inch	10	10	10

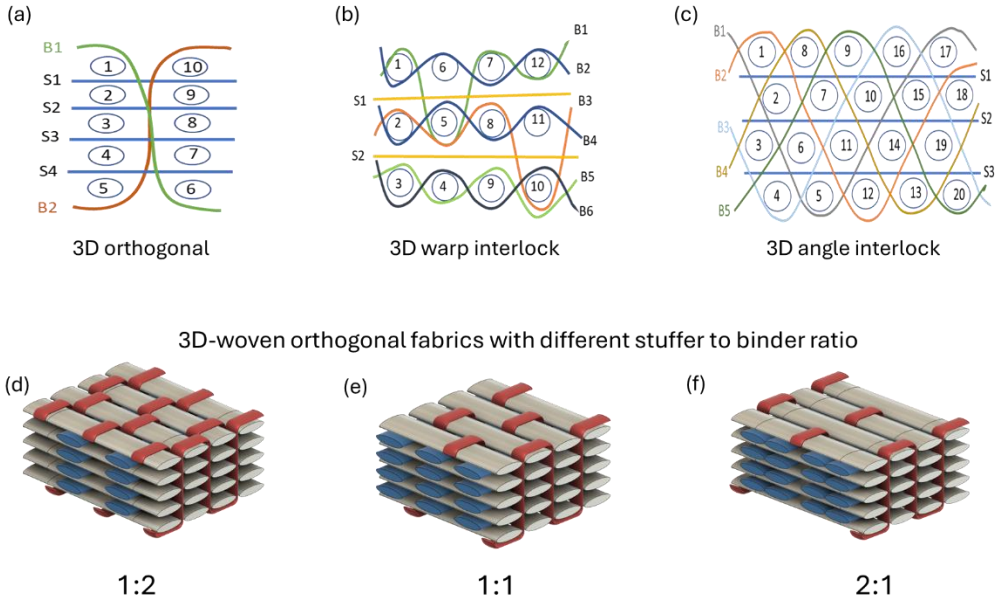

Figure 1: (a-c) Weave design of different structures; (d-f) 3D-woven orthogonal fabrics with different stuffer-to-binder ratios

2.2 Preparation of sandwich panels

The sandwich structures were assembled using a hand layup method (illustrated in Fig. 2). Prior to bonding, the aluminium surfaces were sandblasted and cleaned with ethanol to improve adhesive bonding by removing surface contaminants. A uniform pressure was applied during bonding by placing a metallic plate of known weight over the sandwich assembly to expel entrapped air and ensure even adhesive distribution. To maintain a consistent adhesive layer, jigs were used to control the bond-line thickness, particularly at the corners. After the bonding process, the sandwich panels were allowed to cure at room temperature as per the adhesive manufacturer's recommendation. Following curing, the bonded sandwich panels were cut into standard test specimens using a precision band saw cutting machine. All specimens were inspected for uniformity in geometry and absence of visible defects before further testing.

2.3 Three-point bending

The three-point bending (TPB) tests on sandwich panels are conducted according to the ASTM D7264 standard. A characteristic label was used for each specimen to facilitate the analysis. The TPB tests were carried out on sandwich beams with different core types and aluminium and composite sheets of equivalent thickness. The span-to-width ratio was kept at 16:1, and the width of the sandwich panels was kept at 20mm. The Zwick Roell Z250 UTM machine was used for the tests with a crosshead speed of 2 mm/min for all TPB tests.

The flexural strength and flexural stiffness of the sandwich composite panels were calculated using equations 1 and 2,

$$\sigma_f = \frac{3P.L}{2bd^2} \tag{1}$$

Where σ_f is the flexural strength (MPa), P is the maximum load prior to failure (N), L is the span length (mm), b and d are the sandwich width (mm) and thickness (mm), respectively.

$$D = \frac{l^2.a.\Delta P}{16 f_1} \tag{2}$$

Where, D is the flexural stiffness (N.mm^2), l is the span length (mm), a is overhanging arm length (mm), $\Delta P/f1$= slope of linear load-deformation curve (N/mm).

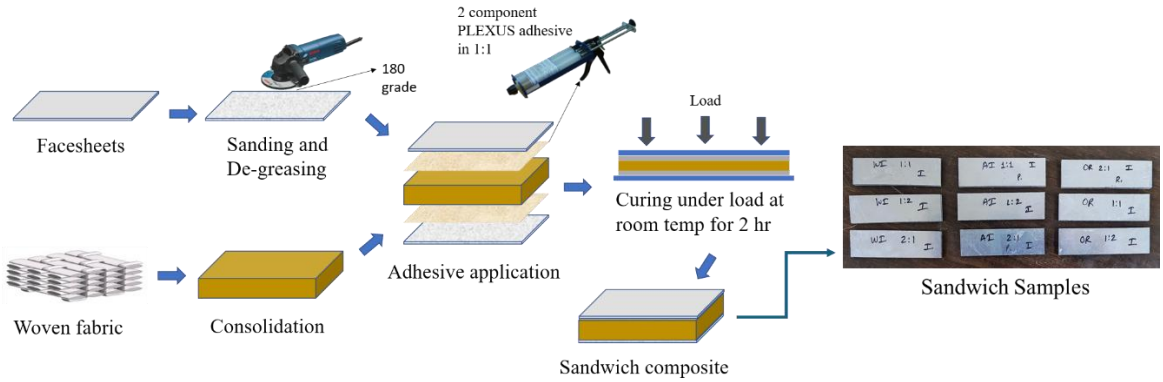

Figure 2: Sandwich preparation by Hand-layup process and final prepared 3D woven composite core sandwich panels

3 RESULTS AND DISCUSSION

3.1 Flexural Performance of Sandwich Composites

Figure 3 (a) and (b) illustrate the flexural strength and flexural stiffness, respectively, of aluminium-faced sandwich composites reinforced with 3D orthogonal, 3D angle-interlock, and 3D warp-interlock FRP cores. Each core configuration was studied at three different stuffer-to-binder yarn ratios: 1:2, 1:1, and 2:1.

From Fig. 3(a), it is evident that the 3D angle-interlock core sandwich panels consistently exhibited the highest flexural strength across all three stuffer-to-binder ratios. This was followed by the 3D orthogonal and then the 3D warp-interlock structures. The superior performance of the angle-interlock

architecture can be attributed to the orientation of its binder yarns, which are inclined rather than aligned purely in the thickness (Z) direction. This inclined arrangement enhances load transfer along the loading axis, thereby improving the panel's capacity to resist bending loads. Notably, the flexural strength increases with higher stuffer-to-binder ratios (from 1:2 to 2:1) in all three architectures, likely due to the increased volume of load-bearing stuffer yarns enhancing in-plane strength.

In contrast, the trend in flexural stiffness, as shown in Fig. 3(b), presents a different behaviour. The 3D orthogonal core sandwich panels demonstrated the highest flexural stiffness, especially prominent at the 1:2 stuffer-to-binder ratio. The orthogonal architecture benefits from binder yarns aligned nearly in the Z-direction, which enhances through-thickness stiffness and improves resistance to deformation under bending. The near-orthogonal arrangement of the binder, stuffer, and filler yarns contributes to a more integrated and rigid structure, improving shear stress transfer across the laminate. This results in a more uniform stress distribution during bending.

Interestingly, the flexural stiffness of the angle-interlock and orthogonal cores are nearly comparable at the 1:1 and 2:1 ratio, indicating that at equal or higher stuffer to binder ratios, angled binders can achieve stiffness close to that of orthogonal binders as the collective binder effect reduces per unit area. However, for the 1:2 ratio, the 3D orthogonal cores outperform the other two, while the warp-interlock configuration consistently shows the lowest flexural strength and stiffness in both graphs. This can be linked to the limited number of through-thickness binders in the warp-interlock design, which reduces the panel's resistance to both bending and shear deformation.

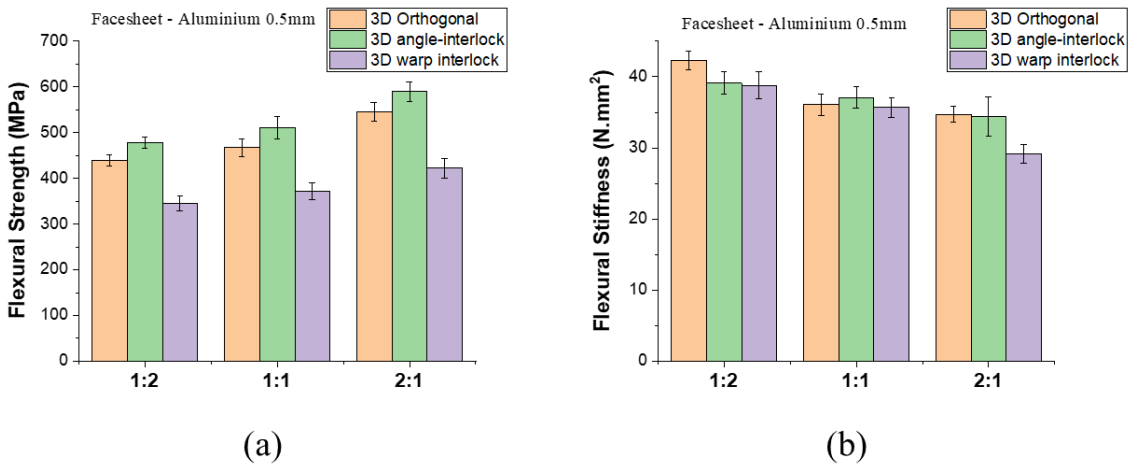

Figure 3: (a) Flexural strength; (b) flexural stiffness of sandwich panels with different core weave architecture and stuffer-to-binder ratio.

Figure 4 presents the load–displacement responses of sandwich panels with 3D orthogonal (OR), 3D angle-interlock (AI), and 3D warp-interlock (WI) composite cores under three different stuffer-to-binder ratios (1:2, 1:1, and 2:1). Specifically, Figure 2(a) compares the load–displacement curves of the three core architectures at a fixed 1:2 ratio, while Figures 4(b), 4(c), and 4(d) illustrate the effect of stuffer-to-binder ratio on the flexural behaviour of OR, AI, and WI cores, respectively.

From Figure 4(a), it is evident that the angle-interlock (AI) core exhibited the highest peak load, followed by the orthogonal (OR) and warp-interlock (WI) cores. The superior flexural load capacity of the AI core can be attributed to its angled binder yarns, which are better aligned with the direction of applied bending loads, allowing for enhanced load transfer and energy absorption. In contrast, the WI core, which contains fewer effective through-thickness reinforcements, shows the lowest peak load and early softening in the curve, indicating a reduced ability to resist delamination and through-thickness shear.

Figures 4(b–d) further reveal that increasing the stuffer-to-binder ratio consistently enhances the flexural load capacity across all core types. This trend is most evident in the AI and OR cores, where the 2:1 ratio configurations reach the highest peak loads. The improvement in performance at higher stuffer-to-binder ratios is due to the greater number of in-plane stuffer yarns per unit area, which directly contribute to carrying bending stresses. These yarns offer enhanced resistance to tensile and compressive forces developed on the tension and compression sides of the core during flexure.

Interestingly, the difference between the 1:2 and 1:1 configurations is minimal in terms of peak load, suggesting that the in-plane reinforcement (stuffers) is similar in both cases. However, a closer look at the slope of the initial linear region reveals that flexural stiffness is higher in the 1:2 ratio panels, especially for the OR cores (Fig. 2b). This increased stiffness can be attributed to the greater number of binder yarns in the through-thickness (Z) direction, which improve shear resistance and contribute to structural rigidity. On the other hand, the 2:1 configuration, despite showing the highest load-bearing capacity, exhibits slightly lower stiffness, particularly in WI cores (Fig. 4d), likely due to the reduced binder content, which weakens through-thickness integrity.

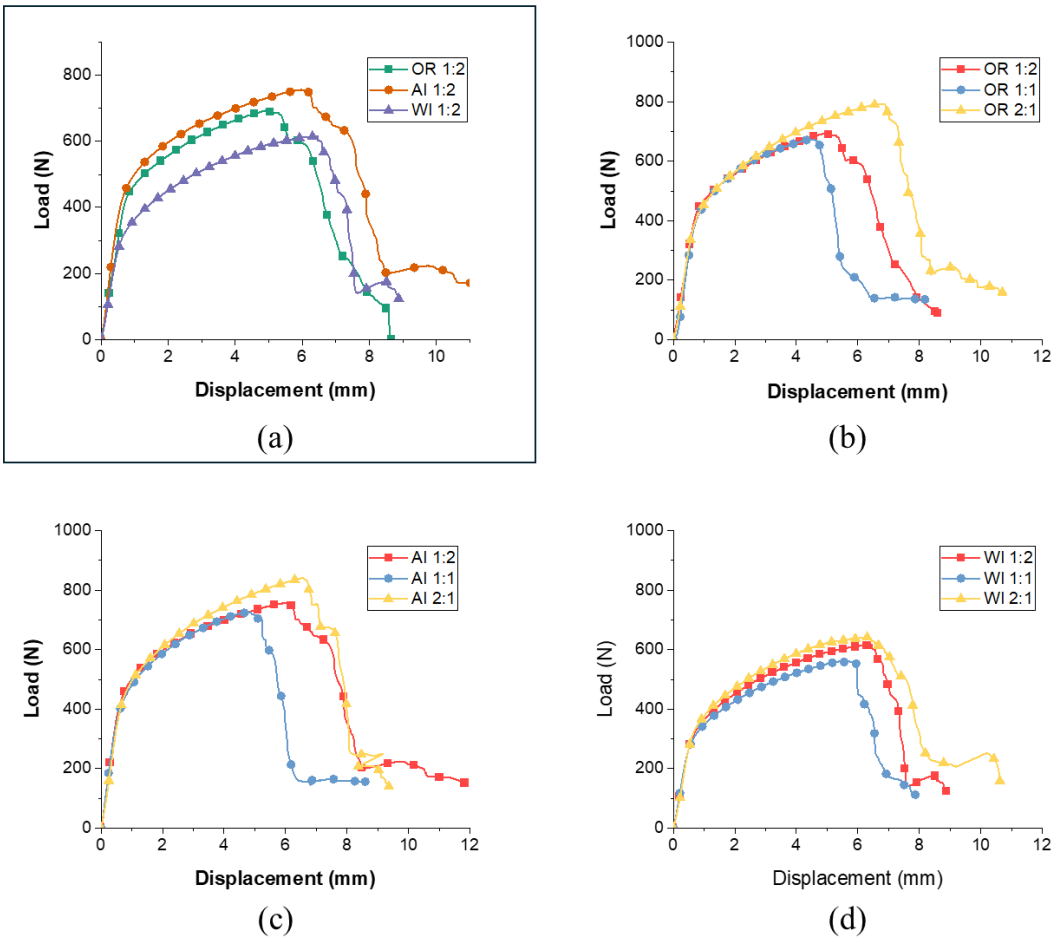

Figure 4: Load–displacement curves of sandwich panels with 3D OR, AI, and WI cores. (a) Comparison at 1:2 ratio; (b–d) effect of stuffer-to-binder ratios on OR, AI, and WI cores, respectively.

Figure 5 shows the post-flexural failure images of the sandwich panels reinforced with 3D angle-interlock, 3D orthogonal, and 3D warp-interlock composite cores, each tested at three different stuffer-to-binder ratios (1:2, 1:1, and 2:1). A consistent observation across all samples is the absence of

debonding or delamination between the core and the aluminum facesheets, indicating effective adhesive bonding and good interfacial integrity.

The dominant failure mode observed is a combination of core shear/yield, followed by bottom facesheet yielding under tension. During bending, the compressive stresses on the top face are absorbed without fracture, while the core initially undergoes localized deformation. As the loading progresses, the tension side of the panel (bottom facesheet) yields, ultimately leading to final failure. Samples with higher stuffer-to-binder ratios (2:1) exhibit larger deformation before failure, as evident from their more pronounced bending in Figure 5. This is because a higher ratio indicates greater in-plane stuffer yarn content, which enhances the core's ability to resist bending loads, delays the onset of failure, and allows more energy absorption. In contrast, the 1:2 specimens exhibit relatively smaller deformation, correlating with earlier onset of failure and reduced energy absorption due to fewer stuffer yarns available to share the in-plane tensile and compressive stresses.

These visual observations are in agreement with the flexural load-displacement curves presented earlier (Figure 4), where panels with a 2:1 ratio showed the highest load-bearing capacity and deflection before failure. While the external damage is visible, the internal core damage mechanisms, such as microcracking, yarn pull-out, or delamination within the core layers, remain areas of ongoing investigation and will be further studied using micro-computed tomography (μCT) analysis for comprehensive damage assessment.

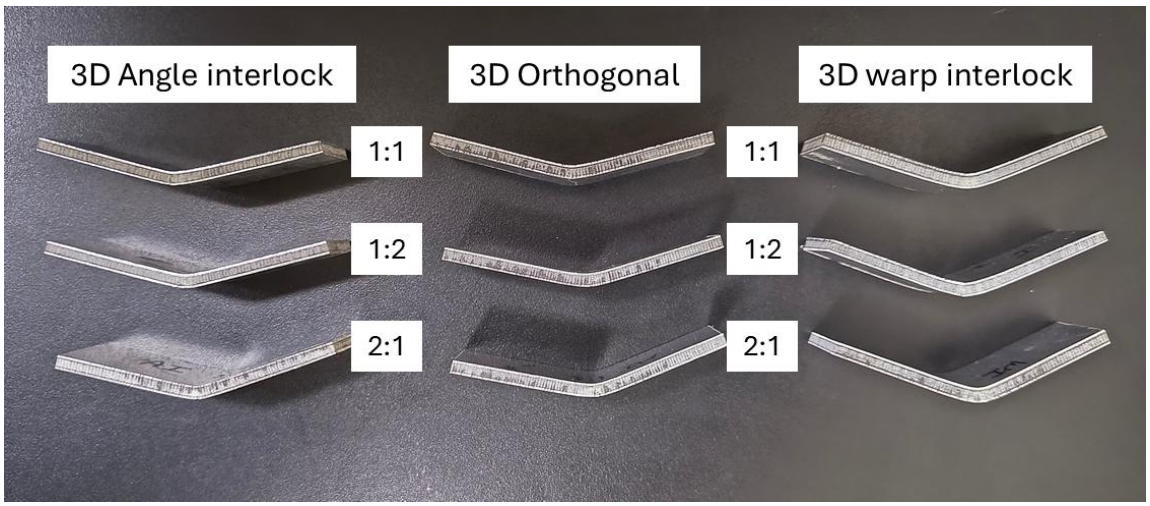

Figure 5: Fractured sandwich samples of different weave architecture (3D orthogonal, angle interlock, and warp interlock) and stuffer-to-binder ratio (1:2, 1:1, 2:1)

9 CONCLUSIONS

This study investigated the flexural behaviour of aluminium-faced sandwich composite panels reinforced with three different 3D woven core architectures—orthogonal, angle-interlock, and warp-interlock—at varying stuffer-to-binder ratios (1:2, 1:1, and 2:1). The results demonstrated that both core architecture and stuffer-to-binder ratio significantly influence the flexural strength, stiffness, and failure mechanisms of the sandwich panels.

Among the three architectures, the 3D angle-interlock core exhibited the highest flexural strength, attributed to its inclined binder yarns that effectively engage under bending loads. The 3D orthogonal core showed superior flexural stiffness, especially at lower stuffer-to-binder ratios, due to its vertically aligned Z-binders, which enhance through-thickness shear resistance. The 3D warp-interlock cores consistently exhibited lower mechanical performance, likely due to fewer effective through-thickness reinforcements.

An increase in the stuffer-to-binder ratio led to improved flexural load capacity across all core types, confirming that higher stuffer content enhances in-plane load distribution. However, this came at the expense of slightly reduced stiffness due to a corresponding decrease in binder yarns. Post-fracture analysis revealed that all panels failed through a combination of core shear/yielding and bottom facesheet tension failure, without any evidence of core–face debonding, indicating robust interfacial adhesion. The deformation profiles and fracture characteristics observed in flexural testing were consistent with the load-displacement behaviour, validating the role of textile architecture and yarn orientation in tailoring sandwich panel performance

REFERENCES

[1] P. Singh, J. Sheikh, B.K. Behera, Metal-faced sandwich composite panels: A review, Thin-Walled Struct. 195 (2024) 111376. https://doi.org/10.1016/j.tws.2023.111376.

[2] J. Fan, W. Cantwell, Z. Guan, The low-velocity impact response of fiber-metal laminates, J. Reinf. Plast. Compos. 30 (2011) 26–35. https://doi.org/10.1177/0731684410386133.

[3] J.J. Homan, Fatigue initiation in fibre metal laminates, Int. J. Fatigue 28 (2006) 366–374. https://doi.org/10.1016/j.ijfatigue.2005.07.030.

[4] R. Alderiesten, Fatigue in fibre metal laminates: The interplay between fatigue in metals and fatigue in composites, Fatigue Fract. Eng. Mater. Struct. 42 (2019) 2414–2421. https://doi.org/10.1111/ffe.12995.

[5] N.L. Feng, S. DharMalingam, K.A. Zakaria, M.Z. Selamat, Investigation on the fatigue life characteristic of kenaf/glass woven-ply reinforced metal sandwich materials, J. Sandw. Struct. Mater. 21 (2019) 2440–2455. https://doi.org/10.1177/1099636217729910.

[6] Z. Wang, J. Mao, K. Yuan, K. Wei, S. Yao, Investigation on impact damage and residual in-plane compression strength of FML laminates, Int. J. Impact Eng. 189 (2024) 104956. https://doi.org/10.1016/j.ijimpeng.2024.104956.

[7] A. Serubibi, P.J. Hazell, J.P. Escobedo, H. Wang, E. Oromiehie, G.B. Prusty, A.W. Phillips, N.A. St John, Fibre-metal laminate structures: High-velocity impact, penetration, and blast loading – A review, Compos. Part Appl. Sci. Manuf. 173 (2023) 107674. https://doi.org/10.1016/j.compositesa.2023.107674.

[8] A. Vlot, Impact properties of Fibre Metal Laminates, Compos. Eng. 3 (1993) 911–927. https://doi.org/10.1016/0961-9526(93)90001-Z.

[9] G. Caprino, G. Spataro, S. Del Luongo, Low-velocity impact behaviour of fibreglass–aluminium laminates, Compos. Part Appl. Sci. Manuf. 35 (2004) 605–616. https://doi.org/10.1016/j.compositesa.2003.11.003.

[10] S. Khalili, S.M.R. Khalili, R.E. Farsani, P. Mahajan, Flexural properties of sandwich composite panels with glass laminate aluminum reinforced epoxy facesheets strengthened by SMA wires, Polym. Test. 89 (2020) 106641. https://doi.org/10.1016/j.polymertesting.2020.106641.

[11] X. Wu, Y. Pan, G. Wu, Z. Huang, R. Tian, S. Sun, Flexural Behaviour of CFRP/MG Hybrid Laminates with Different Layers Thickness, Adv. Compos. Lett. 26 (2017) 096369351702600505. https://doi.org/10.1177/096369351702600505.

[12] M.R. Abdullah, W.J. Cantwell, The impact resistance of polypropylene-based fibre–metal laminates, Compos. Sci. Technol. 66 (2006) 1682–1693. https://doi.org/10.1016/j.compscitech.2005.11.008.

[13] G. Lawcock, L. Ye, Y.-W. Mai, C.-T. Sun, The effect of adhesive bonding between aluminum and composite prepreg on the mechanical properties of carbon-fiber-reinforced metal laminates, Compos. Sci. Technol. 57 (1997) 35–45. https://doi.org/10.1016/S0266-3538(96)00107-8.

[14] F. Mottaghian, F. Taheri, On the flexural response of nanoparticle-reinforced adhesively bonded joints mating 3D-Fiber Metal Laminates – A coupled numerical and experimental investigation, Int. J. Adhes. Adhes. 120 (2023) 103278. https://doi.org/10.1016/j.ijadhadh.2022.103278.

[15] S.M.R. Khalili, V. Daghigh, R. Eslami Farsani, Mechanical behavior of basalt fiber-reinforced and basalt fiber metal laminate composites under tensile and bending loads, J. Reinf. Plast. Compos. 30 (2011) 647–659. https://doi.org/10.1177/0731684411398535.

[16] R. Keshavarz, H. Aghamohammadi, R. Eslami-Farsani, The effect of graphene nanoplatelets on the flexural properties of fiber metal laminates under marine environmental conditions, Int. J. Adhes. Adhes. 103 (2020) 102709. https://doi.org/10.1016/j.ijadhadh.2020.102709.
[17] X. Wu, Y. Pan, G. Wu, Z. Huang, R. Tian, S. Sun, Flexural Behaviour of CFRP/MG Hybrid Laminates with Different Layers Thickness, Adv. Compos. Lett. 26 (2017) 096369351702600505. https://doi.org/10.1177/096369351702600505.
[18] P. Singh, J. Sheikh, B.K. Behera, Flexural Behaviour of 3D-Woven Fabric-Reinforced Epoxy Composite Core-Based Metal-Faced Sandwich Panels, in: B.K. Behera, M. Takatera, R.K. Mishra (Eds.), Adv. Multifunct. Compos. Mater., Springer Nature, Singapore, 2025: pp. 25–34. https://doi.org/10.1007/978-981-97-6968-1_3.
[19] B.K. Behera, B.P. Dash, Mechanical behavior of 3D woven composites, Mater. Des. 67 (2015) 261–271. https://doi.org/10.1016/j.matdes.2014.11.020.

ADVANCED THERMOPLASTIC HONEYCOMB CORES: EFFICIENCY GAINS THROUGH COEXTRUDED FOAMED CELL WALLS IN SANDWICH STRUCTURES

Gregor Jesse[1], Friedrich Zerling[2], Robert Zarnekow[2], Jochen Pflug[2], Robert Böhm[1]

[1]Faculty of Engineering, Leipzig University of Applied Sciences (HTWK Leipzig)
P.O. Box 30 11 66, Karl-Liebknecht-Straße 134, 04277 Leipzig, Germany
Email: gregor.jesse@htwk-leipzig.de, robert.boehm@htwk-leipzig.de,
web page: https://www.htwk-leipzig.de/

[2]Research and Development, ThermHex Waben GmbH
Merseburger Straße 235, 06130 Halle (Saale), Germany
Email: friedrich.zerling@thermhex.com, web page: https://thermhex.com/en

Keywords: Honeycomb, Thermoplastics, Sandwich, Foams, Buckling, Mechanical properties, FEA

ABSTRACT

As part of the research project “ExSaZell – Efficiency and Performance Enhancement of Thermoplastic Honeycomb Cores through Innovative, Extrusion-Based, Foamed Cellular Wall Systems with Sandwich Structure”, an advanced three-layer cellular wall concept was developed in collaboration of ThermHex, Kunststoff-Zentrum Leipzig (KUZ), and HTWK Leipzig. This approach utilizes the co-extrusion of polypropylene into a multi-layer flat film, followed by continuous thermoforming into honeycomb cores. The resulting cell walls consist of two dense outer layers and a foamed, lower-density inner layer. This structured wall design enables significant improvements in mechanical performance, particularly under compressive loads, while maintaining a constant core density. The integration of a foamed middle layer reduces the overall material mass and increases the effective wall thickness, thereby enhancing buckling resistance, a critical parameter for honeycomb core performance under compressive and shear stresses. Initial industrial trials demonstrated an increase of 21.8% in flatwise compressive strength compared to a conventional monolithic thermoplastic core of equivalent density. The internal structuring was achieved via the targeted addition of a chemical blowing agent and nucleating agent into the base polymer of the inner layer. The concept development and industrial trials conducted by ThermHex were supported by nonlinear finite element analyses (FEA) from HTWK Leipzig and morphological as well as mechanical testing by KUZ Leipzig. The results underline the potential of this sandwich cell wall concept to replace traditional honeycomb core materials in lightweight applications, offering both economic and ecologic advantages through improved resource efficiency, recyclability, and production cost reductions.

INTRODUCTION

The global demand for transport services, whether by air, land, or water, continues to grow [1]. The automotive industry is currently one of the fastest-growing sectors, and this growth is accompanied by an increasing demand for lightweight components [2]. In 2018 alone, 95 million light vehicles were sold worldwide, and this number is expected to rise to 110 million units per year by 2025 [1], [3]. This sustained expansion in the transport sector, however, leads to significant energy consumption and increasing emissions of greenhouse gases, particularly carbon dioxide (CO_2) [1], [2], [4].

To address these challenges and enhance fuel efficiency, vehicle lightweighting is a crucial strategy [5]. Studies indicate that reducing vehicle mass by 10% not only lowers raw material consumption but also cuts car fuel consumption by between 6% to 8% [4]. Every 100 kg removed from a motor vehicle reduces CO_2 emissions by 9 grams per kilometer [2]. For Battery Electric Vehicles (BEVs), the specific consumption saving achievable through 100 kg mass reduction, known as the Energy Reduction Value (ERV), ranges from 0.47 to 1.17 kWh/(100 km × 100 kg), with larger vehicles and more dynamic driving cycles exhibiting higher ERV values [6]. Lightweighting also offers advantages beyond raw material and fuel efficiency [2], such as improved energy efficiency, reduced noise, vibration, and harshness (NVH) [1], and enhanced energy absorption capabilities [3], [5]. Furthermore, lighter materials like aluminum absorb impact better than steel in accidents. Vehicle weight is identified as the most significant factor influencing fuel consumption, accounting for approximately 70% to 75% of total fuel use [2], [4]. For instance, a 30% mass reduction on the body-in-white (BIW) structure of a typical compact car (e.g. Volkswagen Golf) over a lifetime road performance of 150,000 km can lead to fuel savings of around 398 liters (equivalent to ~998 kg CO_2 savings). This implies a saving of approximately 0.3 L/100 km for each car [5]. Overall, studies suggest that a total vehicle weight reduction of up to 12.6% can be achieved, which translates to a CO_2 emission reduction of 25.2 grams per kilometer [4].

In this context, sandwich structures have emerged as a prevalent method for replacing traditional, heavier materials. A typical sandwich structure comprises two solid, force-absorbing face sheets and a lightweight core material that keeps these face sheets separated. This design allows for achieving high mass-specific bending stiffness, strength, and optimal fatigue resistance, while simultaneously reducing the overall weight and cost of the component [7]. Sandwich panels can also be formed into complex shapes, enabling significant component consolidation and simplifying manufacturing processes [3], [5]. Their applications span from floors for heavy-duty trailers and air cargo containers [7], [8] to components for electric vehicles, including vehicle floors and exterior panels [1], [8], [9].

The core of a sandwich structure plays a critical role in the overall mechanical performance of the component, as it spaces the face sheets apart and primarily withstands shear and compressive forces [1]. Honeycomb cores are particularly interesting due to their excellent strength-to-weight ratio and good sound and thermal insulation properties [1], [10]. Various materials are used for honeycomb cores, including paper honeycomb, polypropylene (PP) honeycomb, aluminum honeycomb, and phenolic Nomex aramid fiber honeycomb [1], [9], [10]. It is important to note, however, that most "conventional" sandwich cores (such as traditional honeycomb, wood, or foam) generally contribute only marginally to the overall bending stiffness of the structure, serving primarily as low-density spacers [10].

Despite their shared classification as "honeycomb cores", significant differences exist in the properties and application areas of various materials. Nomex aramid fiber honeycomb, for instance, is extremely lightweight, non-metallic, and offers a unique profile of properties including a high strength-to-weight ratio, toughness, corrosion, fatigue, and impact resistance, as well as fire resistance and good dielectric and thermal insulation characteristics [10]. These superior properties make Nomex suitable for high-performance applications, such as airplane secondary components, but carry an extremely high carbon footprint and can only be calcinated at the end of lifecycle[10]. In contrast, thermoplastic honeycomb cores are characterized by efficient production techniques, their good flexibility and ease of formability, making them more cost-effective and adaptable for automotive applications like electric car floors [9]. Paper honeycomb, known for its low-cost raw material, compressibility during conversion, and low transportation cost, finds wide application in flat commodity products and packaging applications [1].

The selection of the appropriate honeycomb core material thus heavily depends on the specific application, performance requirements, and economic considerations. While the advantages of high-performance honeycombs like Nomex are undeniable in specialized fields, a key challenge for the automotive industry lies in developing cost-effective yet high-performing honeycomb solutions that meet the demands of mass production and optimally define and utilize the specific role of the honeycomb core in the overall bending stiffness of the sandwich structure.

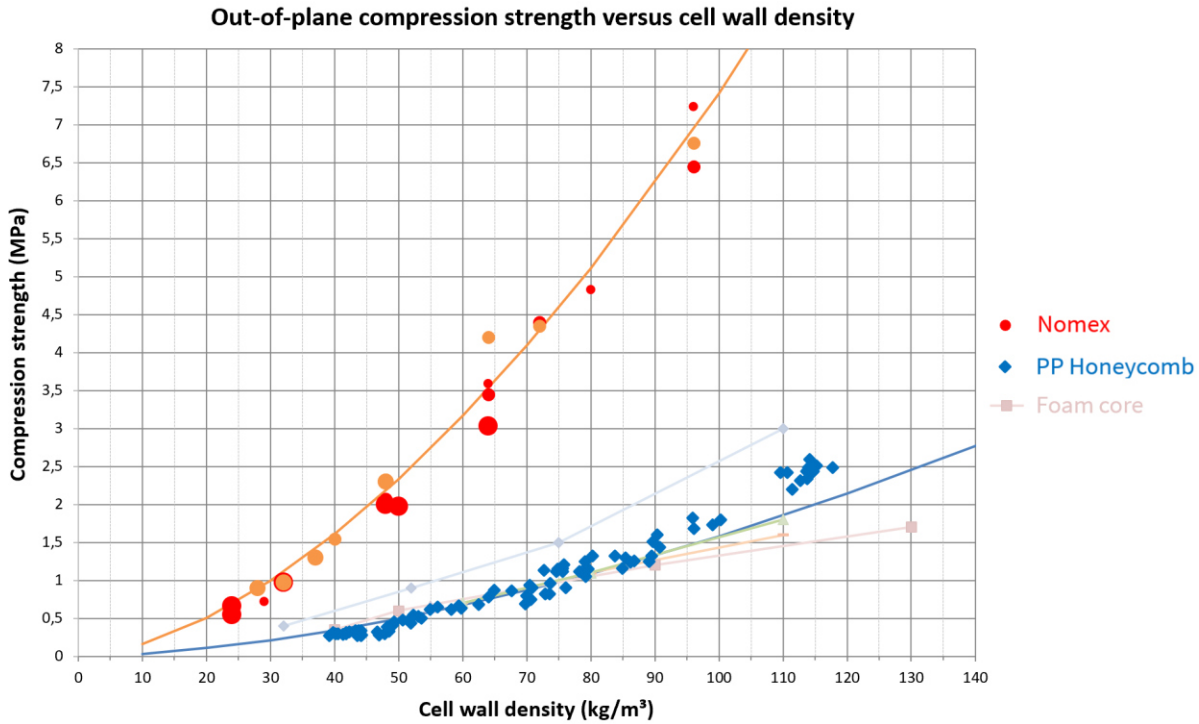

Figure 1: Honeycomb and foam cores in density dependent compression strength [11]

Conventional methods for producing sandwich components are hardly suitable for mass production due to their time and cost. To overcome this, the "ThermHex" honeycomb production process was developed and patented by EconCore N.V., which enables continuous in-line production of thermoplastic honeycomb cores [12]. This technology is applied in industrial scale by EconCore's daughter company ThermHex Waben GmbH in Germany.

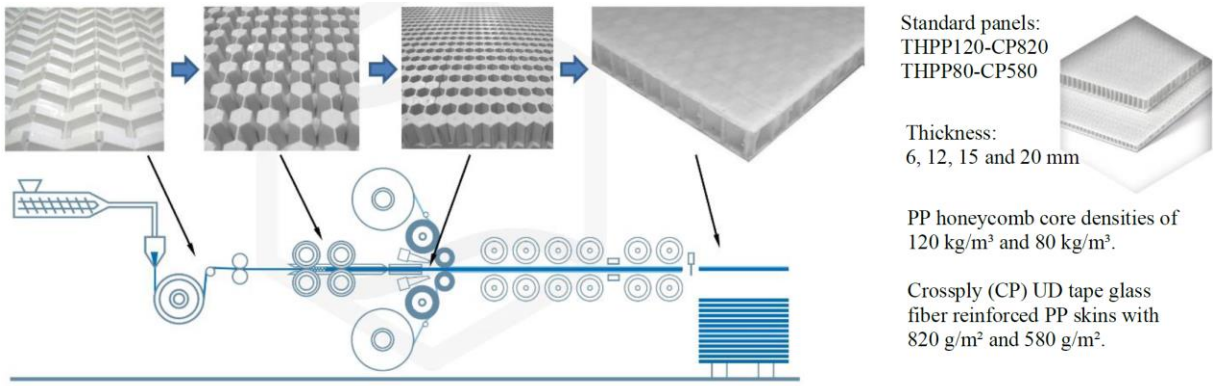

Figure 2: Continuous production of thermoplastic honeycomb sandwich panels [12].

Unlike stepwise batch methods, all production steps take place on a single line, starting with the extrusion of a flat film, followed by rotational vacuum forming, folding, laminating, and cutting [12], [13].

This inline efficiency allows for the production of over more than a million square meters of honeycomb cores per year at speeds of up to 10 meters per minute and cost advantages of more than 20% vs. traditional PP cores [12]. The inline-lamination of face sheets from thermoplastic tape laminates during honeycomb core production also enables the manufacturing of sandwich panels for large-scale series production with short cycle times. ThermHex honeycomb cores find wide application, for example in truck bodies and automotive interiors [12].

RESEARCH OBJECTIVE AND INVESTIGATED VARIANTS

A significant innovation in cell wall structure is being pursued in the research project "ExSaZell - Efficiency and performance enhancement of thermoplastic honeycomb cores through innovative, extrusion-based, foamed cellular wall systems with sandwich structure", a collaboration of Thermhex, Kunststoff-Zentrum Leipzig and HTWK Leipzig. The main interest of this research lies in further sub-structuring the cell wall via co-extrusion. A recurring problem in sandwich structures is the stability failure (buckling) of the cell walls oriented perpendicular to the face sheets under compressive and shear loads. An increase in buckling stiffness at constant weight and identical honeycomb core material is only possible through further structuring of the cell walls themselves.

The project's core innovation involves designing the honeycomb cell walls themselves in a sandwich construction consisting of a layered A-B-A cross sectional substructure. Here, the individual cell walls consist of a core layer (B) with lower density and outer face layers (A) with higher stiffness. PP serves as the material basis, where the individual layers, although chemically homogeneous, can vary through compounding or additivation to achieve specific properties. This allows for the use of high-strength PP homopolymers (PPH) or reinforced PP in the outer layers and lighter PP copolymers (PPC) in the inner layer. The subsequent crucial step for further density reduction and property enhancement is foaming the mid-layer (B) of the cell wall. This is expected to enable a weight-specific increase in the mechanical properties of the honeycomb core by up to 25%.

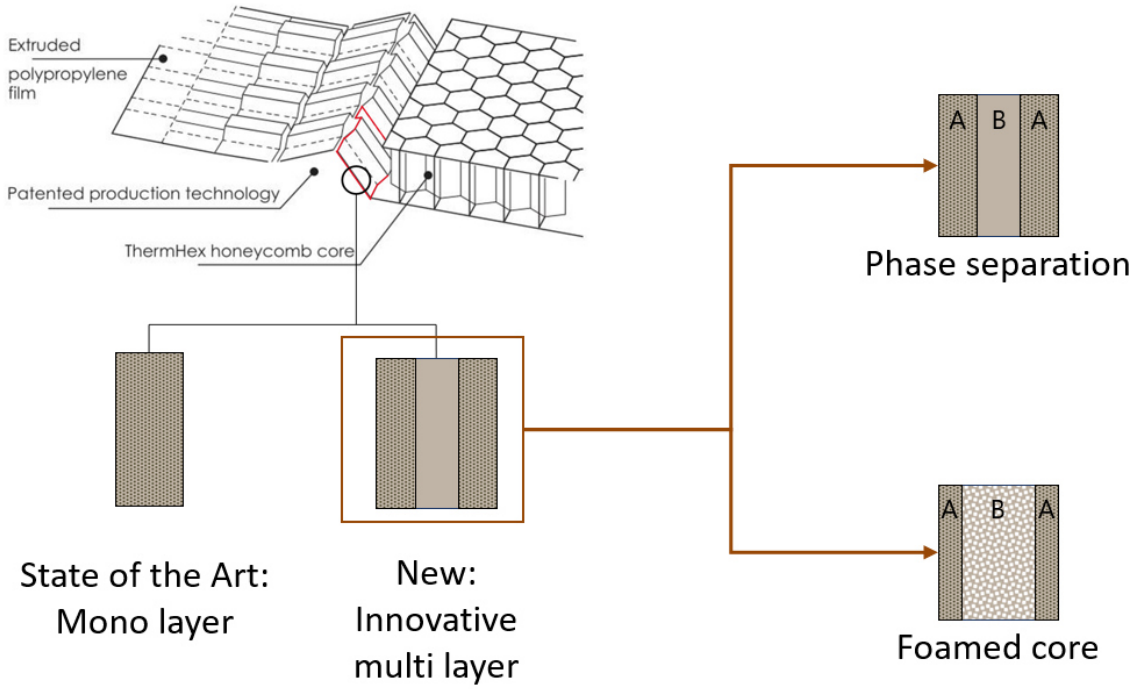

Figure 3: Multi-layer cell wall approach

The project primarily investigates three variants of cell wall structuring:

1. **Mono layer (reference):** This represents the current state of the art, where the cell walls consist of a homogenized polypropylene compound. This variant is characterized by good mechanical properties and efficient production.
2. **Phase separation:** The goal is a complete demixing of the components, enabling higher weight-specific properties through the use of stiffer/stronger materials in the outer layers and tougher materials in the core layer. This allows for gradients in stiffness and density.
3. **Foamed mid-layer:** In this variant, the density of the core layer (B) is reduced by foaming. This enables a greater cell wall thickness at constant weight and thus leads to increased buckling stiffness and better specific properties of the honeycomb core.

NUMERICAL MODELING

For the Finite Element Analysis (FEA) of honeycomb structures, the unit cell approach was employed in Ansys, leveraging the inherent regular and periodic pattern of hexagonal cell cores. This method significantly simplifies the model by considering only a single hexagonal unit cell, including its adjacent cell walls. The modeling was performed using “SOLSH190” Solid Structural Shell elements, allowing for a parametrically designed model with flexible adjustment of cell wall height, the distance between cell walls, the cell angle, and the thickness ratio of L-walls to W-walls. To enable a comprehensive material investigation, each cell wall was divided into two outer elements enclosing one middle element. This subdivision allowed for the free selection of mechanical properties for the outer and inner layers, as well as the mass fraction between two different materials.

This simulation approach enabled a detailed investigation of various material configurations. As for the reference variant, a monolayer honeycomb core was established where both outer and inner material layers were assigned identical mechanical properties, representing the homogeneous material mixture of the current production's PPH and PPC. The second variant was designed as a phase-separated honeycomb core, specifically assigning PPH properties to the outer layers and PPC properties to the inner layers of the cell walls. This distinction facilitates the analysis of the mechanical response of a heterogeneous material distribution. Furthermore, the model accounted for the foaming of PPC by treating it as a homogenized material with an effective 22.5% reduction of its original mechanical properties, reflecting the impact of the foaming process. It's important to note that the mechanical properties of both PPH and PPC materials were determined through tensile testing of the corresponding virgin materials, which was carried out by KUZ Leipzig. For the numerical model, a “Bilinear Isotropic Hardening” (BISO) material model was utilized, incorporating a tangential modulus of 17.2 MPa (see Table 1).

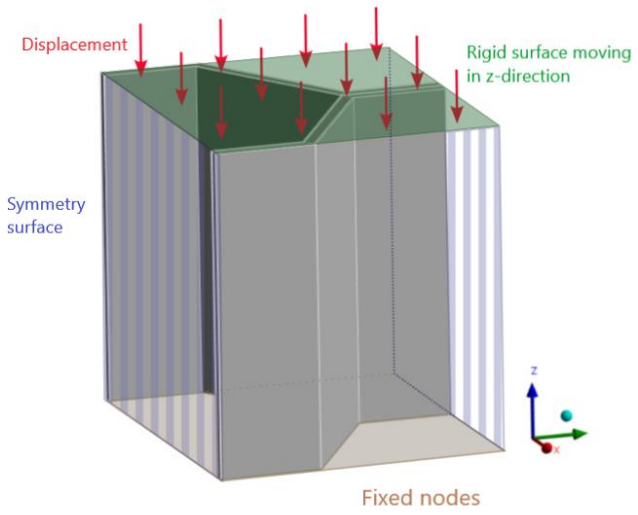

Figure 4: Unit-Cell with boundary conditions

To optimize computational efficiency for the nonlinear buckling analysis, the inherent X and Y axis symmetry of the honeycomb core allowed for the simulation of a quarter-section of the structure (see Figure 4). Specific boundary conditions were applied to represent the core's behavior under compressive loading: The bottom nodes were fixed to prevent any free translations or rotations, ensuring a stable base. Conversely, the nodes on the opposing (top) side were designated as "one-dimensional displacement nodes," constraining their movements in the X and Y directions, along with rotations about each axis, thereby permitting translation only along the Z-axis. Frictional contact was implemented between the cell walls to prevent unrealistic sliding or interpenetration during deformation. The nonlinear buckling analysis was then conducted by applying a displacement of 10^{-3} mm in the negative Z-direction to these top nodes.

Engineering constant		Polypropylene Homopolymer (PPH)	Polypropylene Copolymer (PPC)	Polypropylene Copolymer (foamed)
ρ	[g/cm³]	1.03	0.9	0.6975
E	[MPa]	1750	1440	1116
ν_{12}	–	0.3	0.3	0.3
K	[MPa]	1408	1200	930
G	[MPa]	650	554	430
σ	[MPa]	36	27	21
E_t	[MPa]	17.2	17.2	17.2

Table 1: Mechanical properties of PPC and PPH (virgin material)

MANUFACTURING AND MORPHOLOGICAL CHARACTERIZATION

ThermHex, leveraging its established production capabilities, can realize all three variants investigated in this research project. For the reference variant, the manufacturing process is straightforward. A single extruder is sufficient to melt the PP granulate. This molten material is then extruded through a dedicated die to form a PP foil, which is subsequently folded into the honeycomb core structure on the production line. The production of the phase-separated variant requires a more advanced setup. A second "co-extruder" is integrated into the process, allowing for the separate melting of two distinct material mixtures: one for the outer layer (Layer A) and another for the inner layer (Layer B). A specialized extrusion die, featuring a three-layered feedblock, then co-extrudes these materials simultaneously to create the desired three-layered foil. Finally, the foamed variant is achieved by incorporating a chemical foaming agent into the polypropylene granulate used for the inner layer. The foaming agent type and concentration were selected after an empirical benchmarking study of various combinations of different blowing and nucleating agents as well as their respective concentrations in a pre-investigation by ThermHex and KUZ. The blowing agent decomposes within the extruder, releasing gas. While this gas remains dissolved under pressure inside the extruder, upon exiting the die, a sudden pressure drop causes it to expand rapidly under the formation of gas bubbles, creating the desired cellular structure that is then fixed as the extrudate cools. To validate the desired geometrical and morphological aspects of the produced honeycomb core variants, X-Ray Computed Tomography (CT) scans were performed. CT scanning was chosen due to its ability to non-destructively visualize internal structures and confirm the distinct three-layer configuration of the honeycomb core, allowing clear differentiation of the layers through the material. This method also offered significant advantages in specimen preparation and contrast resolution compared to alternative techniques like optical microscopy, streamlining the validation process.

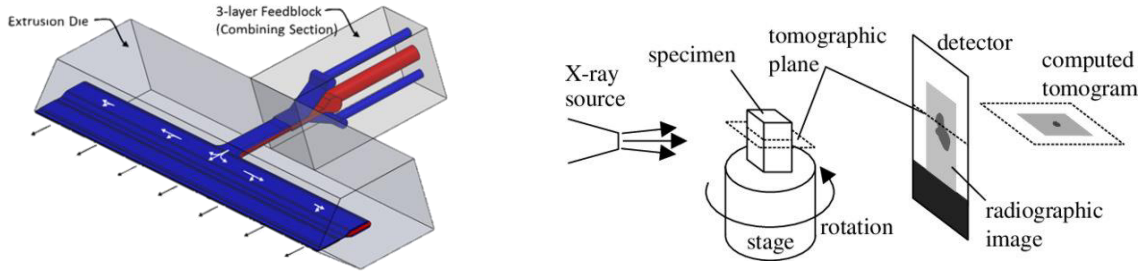

Figure 5: Schematic representation of coextrusion die system (left) and computed tomography for morphology assessment of produced specimens

EXPERIMENTAL MECHANICAL TESTING

Mechanical properties of each variant were evaluated using 100x100 mm² specimens tested under ASTM C365 conditions. This standard test method, officially titled "Standard Test Method for Flatwise Compressive Properties of Sandwich Cores," defines the procedure for measuring the flatwise compressive strength and modulus of core materials used in sandwich structures. Essentially, it assesses the load a core can withstand when compressed perpendicular to its surface (flatwise), thereby simulating the stresses sandwich cores experience in real-world applications.

RESULTS

The desired geometrical and morphological aspects of the produced honeycomb core variants were validated using Computed Tomography (CT) scans. Figure 6 displays scans of the reference configuration (1, top), phase-separated (2, middle), and foamed variants (3, bottom). The reference variant scan shows a consistent wall thickness of 0.23 mm. A tapering effect, caused by the vacuum thermoforming process, appears after the bending area and is visible in all variants. As expected, the reference core's material remains homogeneous. In the phase-separated and foamed variants, the distinct three-layer structure is clearly visible in the respective CT scans 2 and 3. This is due to the density difference between PPH (higher) and PPC (lower). The phase-separated variant's outer layers are 0.022 mm thick (≈ 20% of total thickness), while the foamed variant's outer layers are 0.016 mm thick (≈22% of total thickness). The cellular structure in the foamed variant is distinct. The extrusion process causes significant pore elongation, resulting in a more needle-shaped form rather than an ellipsoid. The average pore size is 90 x 20 x 250 µm³ (x, y, z). These CT images confirm that all three designed variants can be successfully manufactured in a production-like setting, validating their desired morphological characteristics.

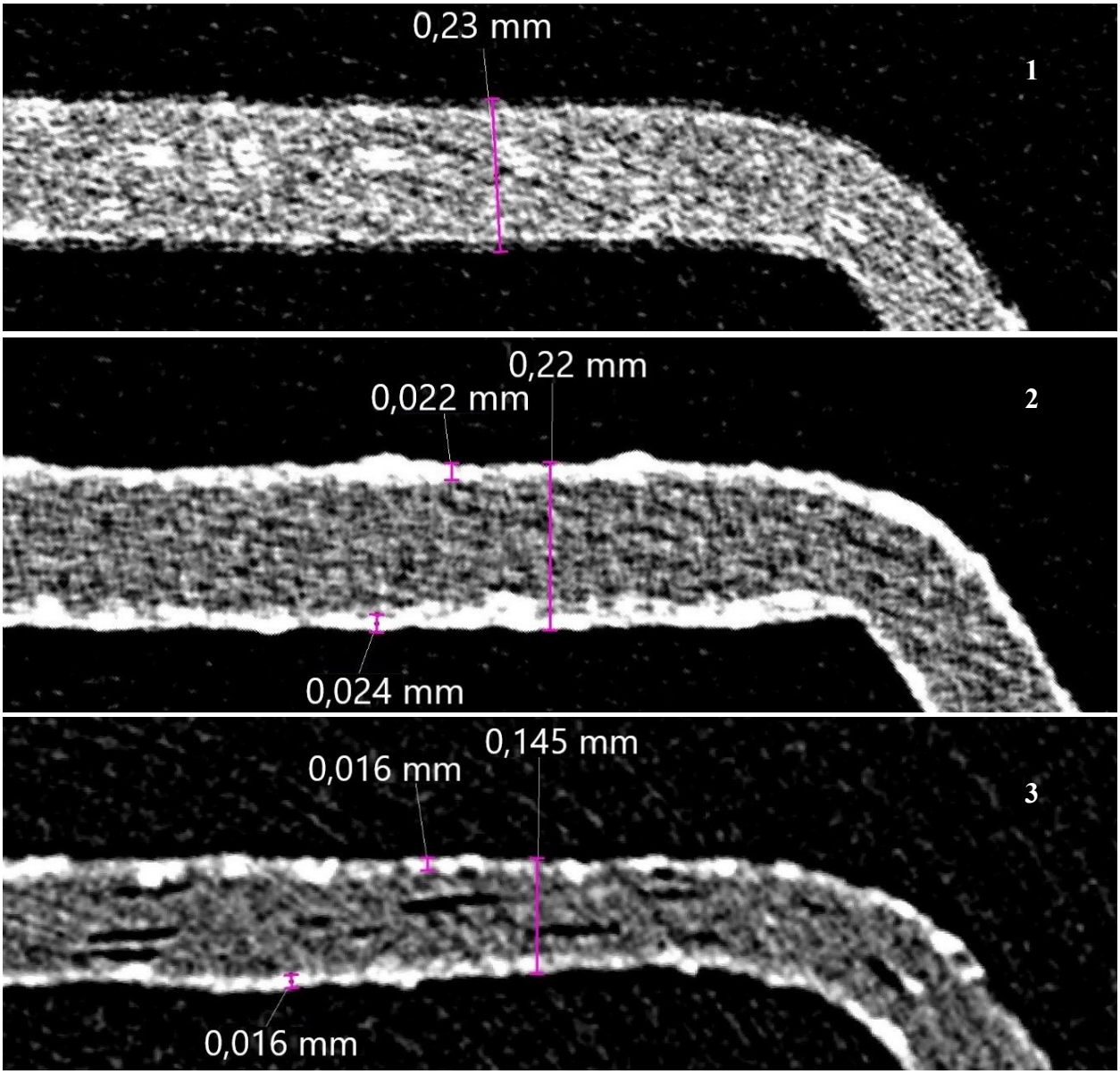

Figure 6: CT scan of developed specimens' cross section

The nonlinear buckling analysis under compressive loading yielded effective normal stresses and normal strains for each element until failure, which are presented in the form of stress-strain curves (see Figure 7). Initially, all configurations exhibit a linear elastic response, characterized by a proportional increase in effective normal stress with increasing strain. Upon reaching a critical stress level, local or global buckling phenomena initiate within the structure, marked by the attainment of a maximum point on the curve. Beyond this peak, the structural stability is compromised, and nonlinear effects become dominant. The post-peak behavior is governed by a combination of progressive buckling-induced instabilities and, depending on the material response, plastic deformation within the cell walls. This results in a reduction of the effective normal stress with further strain. The reference variant, with its homogeneous material composition, exhibited a maximum stress of 1.5 MPa. In contrast, the various three-layer core configurations (with outer layer thicknesses of 10%, 33%, 50%, and 90% and equal core density of 80 kg/m³) demonstrated significantly improved performance, achieving peak stresses ranging from 2.2 to 2.3 MPa. The highest peak stress was observed in the third variant, which incorporated a foamed middle layer, reaching a significant improvement up to 2.4 MPa.

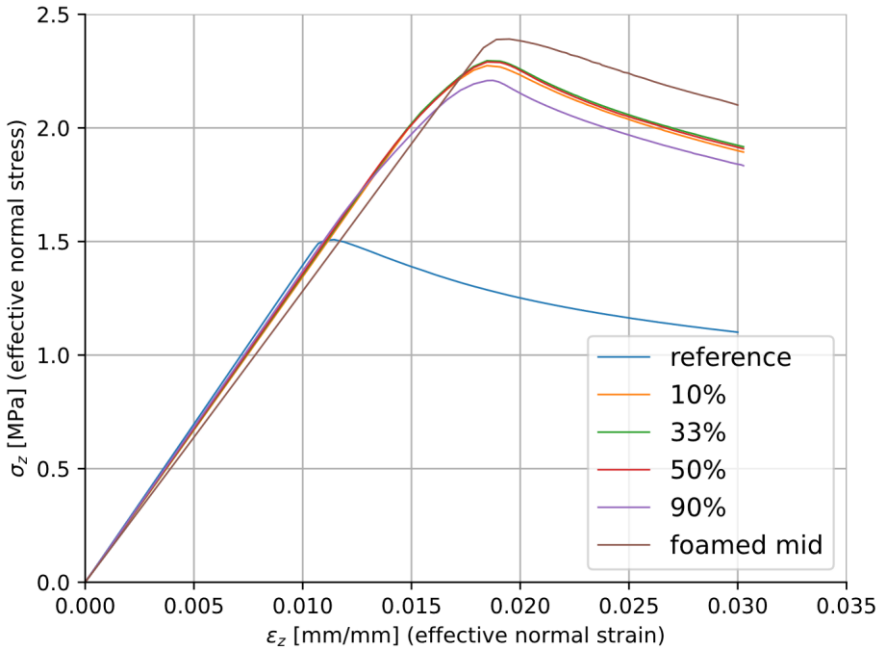

Figure 7: Stress-strain curves under compressive loading in FEA with varying layer thickness ratio (2xA/B)

Figure 8 displays an exemplary comparison of compression strength (in MPa) versus cell wall density (in kg/m³). These results from experimental mechanical testing validate the significant improvements achieved by the new honeycomb core designs. The phase-separated design, featuring high-density outer layers and a low-density core, showed a 12% improvement in compression strength, increasing from 1.19 MPa for the reference non-foamed honeycomb core to 1.33 MPa. Further enhancing performance, the introduction of a foamed middle layer in the third variant led to a 22% increase in compression strength, achieving 1.45 MPa. Notably, the density of all tested specimens remained consistent within usual process variation, ranging from approximately 81 to 83 kg/m³. This confirms that the new designs maintain weight efficiency while substantially improving mechanical properties.

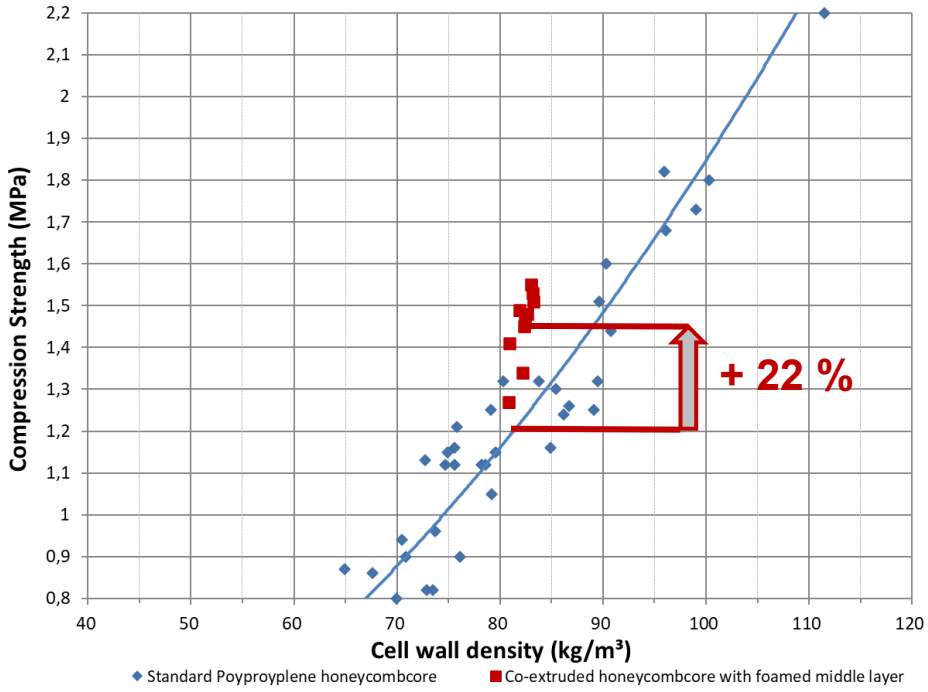

Figure 8: ThermHex honeycomb compression strength versus cell wall density

A comparison between the experimentally tested and numerically simulated compression strengths reveals an overestimation by the simulation. For the reference non-foamed honeycomb core, the average tested compression strength was 1.19 MPa, while the simulation yielded a higher value of 1.5 MPa, indicating an overestimation of 26%. Similarly, for the phase-separated variant, the tested compression strength was 1.33 MPa, compared to a simulated value of 2.0 MPa, representing an overestimation of 50%. The foamed variant also showed this trend, with a tested strength of 1.45 MPa and a simulated strength of 2.4 MPa, resulting in an overestimation of 65% (see Table 2).

		Reference	Phase separation	Foamed mid-layer
ρ	[kg/m³]	82.57	81.01	82.90
$R_{m,real}$	[N/mm²]	1.19	1.33	1.45
$R_{m,sim}$	[N/mm²]	1.5	2.0	2.4
Δ	[%]	26	50	65

Table 2: Comparison of experimental and simulated compression strengths

DISCUSSION

The observed discrepancies between simulated and experimentally determined compression strengths highlight several areas for consideration and potential refinement in the numerical model. Firstly, a primary source of potential overestimation lies in the material property input for the simulation. The mechanical properties of the PPH and PPC utilized in the model were derived from standardized tension tests on virgin material specimens. This approach inherently does not fully account for the effects of the extrusion and elongation processes that the material undergoes during the manufacturing of the thin honeycomb foils. These processes are known to induce molecular orientation and potentially alter the mechanical properties in a way not captured by bulk virgin material testing, likely leading to a reduction in actual performance compared to theoretical values. More accurate testing methods specifically designed for thin-section foils, or an alternative approach to determine the in-situ material properties of the extruded and elongated film, would be highly desirable for improving simulation accuracy. Secondly, the geometrical idealization of the honeycomb core in the simulation presents another potential source of deviation. The numerical model assumes perfectly straight cell walls, uniform cell distances, and precise angles. In reality, the manufacturing process invariably introduces imperfections and defects within the cell walls. These real-world flaws can act as stress concentrators or local weak points, promoting premature buckling and thus contributing to the lower experimental compression strengths compared to the idealized simulated performance. Future simulation efforts could benefit from incorporating representative manufacturing imperfections into the geometric model. This modification together with boundary conditions that not only allow for idealized z-direction displacement of the nodes, but also more realistic secondary in-plane-displacements can reduce the delta observed between testing and FEA. Other potential influences can include the imperfect test environment leading to uneven loading in flatwise compression tests if the load plates are not perfectly parallel. Despite these quantitative discrepancies, the parametric nature of the simulation model enables effective qualitative differentiation between variations in material properties and the relative proportions of outer and inner layers. This functionality provides a robust framework for informing design strategies, supporting the optimization of material selection and structural configurations during early-stage development and prototyping, even in the absence of precise numerical agreement with experimental results. The increasing delta of simulation vs. experiment for more challenging to produce configurations also hint at further improvement potential with more fine tuned manufacturing processes thereof.

The present investigation demonstrates that thermoplastic honeycomb cores can be significantly enhanced through sandwich-style cell wall structures, improving both mechanical performance and weight efficiency. Phase-separated and foamed middle-layer designs exhibit substantial gains in compression strength – 12% and 22% increases, respectively – without significant density variation.

This approach offers a notable advancement in enhancing structural performance without additional weight, critical for industries where material mass is a key design constraint. A salient advantage of this development is its recyclability. Exclusive utilization of thermoplastic materials without fiber reinforcement ensures uncompromised recyclability. This directly aligns with sustainability objectives by facilitating straightforward end-of-life recycling processes. First samples following a closed-loop approach by using post-consumer regranulate in the inner layer have already been manufactured in another coextrusion project by ThermHex. Consequently, these innovations position the novel honeycomb core configurations as highly promising for high-performance, lightweight applications, particularly within the automotive industry. Their synergistic combination of enhanced mechanical strength, consistent low density, and excellent recyclability presents significant potential for reducing vehicle mass, improving fuel efficiency, and contributing to more sustainable manufacturing.

CONCLUSION

This investigation successfully demonstrates that advanced thermoplastic honeycomb cores can be significantly enhanced through innovative sandwich cell wall structures, leading to improved mechanical performance and weight efficiency. The research explored three key variants: a monolayer reference, a phase-separated design, and a foamed mid-layer configuration. Significant performance gains were achieved with the new designs. The phase-separated variant showed a 12% increase in compression strength (from 1.19 MPa to 1.33 MPa), while the foamed mid-layer design delivered an even more remarkable 22% increase (reaching 1.45 MPa) compared to the reference. Crucially, these improvements were accomplished while maintaining a consistently low density across all tested samples (approx. 81-83 kg/m³), confirming their weight efficiency. Numerical simulations further supported these findings, predicting peak stresses up to 2.4 MPa for the idealized foamed variant. The feasibility of continuous production for all three variants was validated using the established production process at company ThermHex, Germany. Computed Tomography (CT) scans confirmed the successful creation of the desired morphological properties in a production-like environment. A major sustainability advantage of these materials lies in their uncompromised recyclability, stemming from the exclusive use of thermoplastics without fiber reinforcement. This characteristic aligns with sustainability goals by enabling straightforward end-of-life recycling, making these novel honeycomb cores highly promising for lightweight applications, particularly in the automotive industry, to reduce vehicle mass and improve fuel efficiency or allow for compensation of heavier electronics integration.

However, challenges in production and reproducibility were identified. A notable discrepancy was observed between simulated and experimental compression strengths, with simulations overestimating results by 26% to 65%. This overestimation is primarily attributed to using virgin material properties in simulations, which do not fully account for the effects of extrusion and elongation processes on thin foils, as well as idealized geometrical models and boundary conditions not reflecting real-world manufacturing and test setup imperfections. Despite these quantitative differences, the parametric simulation model remains valuable for qualitative differentiation and early-stage design optimization. Future work will focus on further developing hierarchical or hybrid designs to continuously optimize the properties of these advanced honeycomb core structures.

For future industrial implementation, further research and development efforts are essential to optimize the reproducibility and consistency of the manufacturing process. As with the scaling of any novel material system, achieving stringent process control and minimizing variabilities in material distribution and cellular morphology will be critical for ensuring robust and predictable performance across larger production batches and enabling widespread adoption of these advanced honeycomb core designs.

REFERENCES

[1] Dymriton, "Application of Honeycomb Sandwich Composite Materials in Automotive Exterior Parts - Dymriton Composites." Accessed: Jun. 13, 2025. [Online]. Available: https://www.dymriton.com/application-of-honeycomb-sandwich-composite-materials-in-automotive-exterior-parts-tissu-fibre-de-carbone/, https://www.dymriton.com/application-of-honeycomb-sandwich-composite-materials-in-automotive-exterior-parts-tissu-fibre-de-carbone/

[2] G. P. Chirinda and S. Matope, "The Lighter the Better: Weight Reduction in the Automotive Industry and its Impact on Fuel Consumption and Climate Change," Dec. 2020.

[3] T. R. Neu, K. Heim, W. Seeliger, P. H. Kamm, and F. García-Moreno, "Aluminum Foam Sandwiches: A Lighter Future for Car Bodies," *JOM*, vol. 76, no. 5, pp. 2619–2630, May 2024, doi: 10.1007/s11837-024-06460-2.

[4] G. Refiadi, I. S. Aisyah, and J. P. Siregar, "Trends in Lightweight Automotive Materials for Improving Fuel Efficiency and Reducing Carbon Emissions," *Automot. Exp.*, vol. 2, no. 3, pp. 78–90, Oct. 2019, doi: 10.31603/ae.v2i3.2984.

[5] J. Njuguna, *Lightweight composite structures in transport: design, manufacturing, analysis and performance*. in Woodhead Publishing series in composites science and engineering. Oxford: Woodhead Publishing, 2016.

[6] F. Del Pero, L. Berzi, A. Antonacci, and M. Delogu, "Automotive Lightweight Design: Simulation Modeling of Mass-Related Consumption for Electric Vehicles," *Machines*, vol. 8, no. 3, p. 51, Sep. 2020, doi: 10.3390/machines8030051.

[7] A. Kausar, I. Ahmad, S. A. Rakha, M. H. Eisa, and A. Diallo, "State-Of-The-Art of Sandwich Composite Structures: Manufacturing—to—High Performance Applications," *J. Compos. Sci.*, vol. 7, no. 3, p. 102, Mar. 2023, doi: 10.3390/jcs7030102.

[8] J. Galos, M. Sutcliffe, D. Cebon, and Golam Newaz, "Lightweighting road freight semi-trailers through the application of composites in trailer decking," 2015, doi: 10.13140/RG.2.1.1115.3042.

[9] I. C. Sukmaji, W. R. Wijang, S. Andri, K. Bambang, and T. Teguh, "Application of sandwich honeycomb carbon/glass fiber-honeycomb composite in the floor component of electric car," presented at the International Conference on Engineering, Science and Nanotechnology 2016 (ICESNANO 2016), Solo, Indonesia, 2017, p. 030056. doi: 10.1063/1.4968309.

[10] J. Pruez, S. Shoukry, G. Williams, and M. Shoukry, "Lightweight Composite Materials for Heavy Duty Vehicles," None, 1116021, Aug. 2013. doi: 10.2172/1116021.

[11] F. Zerling and R. Zarnekow, "Increasing the efficiency and performance of thermoplastic honeycomb cores through co-extruded foam core sandwich cell walls," presented at the 8th International Conference on Cellular Material (CellMAT 2024), Magdeburg, Germany, Nov. 2024.

[12] J. Pflug, F. Zerling, R. Schlimper, and T. Gläßer, "Continuous Production of Thermoplastic Honeycomb Sandwich Panels for Thermoformed and Functionalized Automotive Parts," presented at the 13th International Conference on Sandwich Structures (ICSS-13), Knoxville - USA, Oct. 2022.

[13] J. Pflug, B. Vangrimde, I. Verpoest, and P. Bratfisch, "Honeycomb Core Materials: New Concepts for Continuous Production," *Sampe J.*, vol. 39, Sep. 2003.

ICCM24 24TH INTERNATIONAL CONFERENCE ON COMPOSITE MATERIALS
AUG 4-8, 2025 • BALTIMORE CONVENTION CENTER • BALTIMORE, MARYLAND

IMPACT AND DAMAGE RESISTANCE OF SANDWICH BEAMS MADE FROM SUSTAINABLE MATERIALS AT LOW TEMPERATURES

Gabriel Sánchez Escudero, Enrique Barbero and Sonia Sánchez Sáez

Department of Continuum Mechanics and Structural Analysis, Universidad Carlos III de Madrid, Av. Universidad 30, 28911 Leganés, Madrid, España
Email: gabsanch@pa.uc3m.es, web page: https://www.uc3m.es

Keywords: Sustainable sandwich composites, Flax/epoxy composites, Recycled PET core, Low-velocity impact, Low-temperature

ABSTRACT

This study investigates the response to low-velocity impact of sustainable and conventional sandwich beams tested at two temperatures: room temperature and -40°C. The sustainable sandwich beams are made by two flax/epoxy skins with a recycled PET foam core, while the conventional beams use glass/epoxy skins and a PVC foam core. Both types of sandwich beams were impacted with energies ranging from 2.5 J to 20 J using a drop-weight tower, and their responses were evaluated in terms of absorbed energy, peak force, energy absorption ratio, and effective flexural modulus. The results indicate that the conventional structure exhibits superior impact performance and lower temperature sensitivity. However, the flax/PET sandwich beam achieved peak loads comparable to the conventional sandwich, with minimal variation due to temperature, and demonstrated efficient energy absorption at low impact energies under cold conditions.

1 INTRODUCTION

Sandwich structures are widely employed in the aerospace, automotive, marine, and rail sectors due to their excellent stiffness-to-weight ratio, high energy absorption capacity, and superior performance under flexural loads. These structures are made of two stiff composite skins and a lightweight core. They offer additional benefits such as thermal and acoustic insulation. Conventional sandwich cores are often made from synthetic materials and include polymeric foams, honeycombs, or corrugated sheets [1].

During operation, sandwich panels may be subjected to accidental low-velocity impacts, such as tool drops during maintenance or debris strikes in high-speed trains. Depending on the impact energy level, these impacts can result in barely visible damage or catastrophic failure. One of the main drawbacks of these structures is their limited impact resistance [1], especially in cases where internal damage may not be externally detectable. Prior studies have extensively characterized the impact behaviour of traditional sandwich structures combining synthetic cores and composite skins [2], though most focus on ambient conditions.

However, in real-world applications such as cryogenic storage, Arctic operations, or aerospace thermal cycling, these structures may be exposed to low temperatures. At these temperatures, core and matrix brittleness typically increases, and mismatched thermal expansion coefficients between skin and core can introduce residual stresses [1], significantly modifying impact response.

Due to growing environmental concerns and the increasing demand for sustainable materials, research has intensified into the development of bio-based sandwich structures. Natural fibres such as flax have emerged as a promising alternative to glass fibres thanks to their relatively high specific strength, low density, and renewable origin [3], [4]. However, there are certain limitations to their use, including high moisture uptake, reduced thermal stability, and a strong dependency of mechanical properties on processing conditions or seasonal variations [5].

Recycled polymeric foams, particularly thermoplastic-based materials, have attracted increasing attention as sustainable core alternatives. Thermoset polymers such as polyurethane or Polymethacrylimide are difficult to recycle, whereas thermoplastics like polyethylene terephthalate (PET) are widely available and industrially recycled. PET foams offer favourable mechanical properties, including high specific strength and stiffness, along with low thermal conductivity [6]. These features, combined with the large volume of post-consumer PET waste, make them an attractive ecological solution for sandwich core applications.

Despite the growing interest in sustainable alternatives, the impact behaviour of these eco-sandwich configurations, particularly at sub-zero temperatures, remains insufficiently explored [1], [7]. Moreover, findings obtained for specific core–skin combinations and geometries cannot be generalized, as their response is highly dependent on structural configuration, stacking sequence, and test conditions.

This study investigates the low-velocity impact behaviour of sandwich beams made from flax/epoxy skins combined with recycled PET foam cores. The performance is compared against a conventional configuration comprising glass/epoxy skins and a PVC foam core. Tests were conducted at both room temperature and −40°C to assess the influence of temperature on structural performance. The analysis focuses on critical mechanical response parameters such as peak impact force, absorbed energy, effective flexural stiffness, and failure mechanisms observed via high-speed imaging. The findings aim to enhance the understanding of sustainable sandwich composites and support their future implementation in structural applications subjected to impact loading.

2 MATERIALS AND METHODS

2.1 Materials

A sustainable sandwich structure was analysed and compared to a conventional reference configuration. Both were manufactured with identical stacking sequences and resin systems, but differed in fibre type and core material. The sustainable sandwich was made by two composite skins of a symmetric laminate with four plies of a flax/epoxy woven fabric with a fibre content of 49%, supplied by Simcas Composites (EPC 300-F200T-5043-52-1000). The lay-up sequence used was [0/90]s. The core was made from a recycled PET foam (ArmaPET GR200, 200 kg/m³), provided by Composites Quimiber.

The reference sandwich used the same stacking sequence and resin system, but incorporated a glass fibre woven fabric (EPC300-G200T-40-1270) in place of flax. The core of the reference configuration was a PVC foam (Divinycell HP200, 200 kg/m³), supplied by DIAB.

Rectangular beam specimens with dimensions of 270 mm in length and 50 mm in width were extracted from the manufactured sandwich panels. All specimens featured a core thickness of 10 mm and skin

thicknesses of 1.2 mm. The fabrication process was carried out at the Composite Materials Laboratory of the Instituto Nacional de Técnica Aeroespacial (INTA), in strict adherence to the manufacturing guidelines specified in the technical datasheets of the materials.

2.2 Low velocity impact test

Low-velocity impact tests were performed using a drop-weight impact tower (CEAST Fractovis 6875). The striker had a semicylindrical head of 20 mm in diameter and a total mass of 3.995 kg. A piezoelectric load cell mounted on the striker allowed for the continuous recording of the impact force. The impact velocity was measured using a photoelectric sensor, which also activated a rebound prevention system to ensure single-impact events. The tests were conducted according to ASTM D7136, covering impact energies of 2.5, 5, 7.5, 10, 12.5, 15, 17.5, and 20 J. All configurations were tested at room temperature and at -40°C. At least five specimens were tested per configuration.

From the force-time signal recorded during each impact, the displacement of the striker tip was computed via double integration, using the initial impact velocity as a starting point. Assuming continuous contact between the striker and the specimen, this displacement was taken as representative of the vertical deflection at the mid-span of the beam. The energy transferred to the specimen was calculated as the area under the resulting force–displacement curve. Energy-time plots were constructed accordingly. In tests where no catastrophic failure occurred, the final energy value on the curve was interpreted as the absorbed energy during damage progression. In contrast, for specimens that failed during impact, the maximum value reached was considered as the absorbed energy up to failure, as the curve does not drop afterward (Sánchez et al., 2005).

2.3 Digital image correlation method (DIC)

Each test was recorded using a PHOTRON FASTCAM SA-Z high-speed camera, positioned perpendicular to the front face of the specimen and operating at 30,000 frames per second. The footage was processed using a 2D Digital Image Correlation (DIC) technique, which enabled the visualization and analysis of the strain fields developed during the impact event. The speckle pattern was designed such that each spot covered approximately 3–5 pixels to ensure high correlation accuracy.

In this study, the DIC method was employed as a verification tool to assess the validity of the Euler–Bernoulli beam theory under low-velocity impact conditions. **Figure 1** presents as an example the strain distribution obtained from a flax/PET sandwich specimen impacted at 12.5 J under room temperature conditions.

Figure 1 (a) show the vertical strain component ε_{yy}. The mean strain along the beam length remains close to zero, showing that the transverse deformation is negligible. However, a localized compressive region is clearly observed beneath the impactor (C_0), corresponding to core indentation and local crushing phenomena. In contrast, at a remote location away from the impact zone (P_0), the strain remains negligible, further supporting the assumption of negligible vertical strain in the global response.

Figure 1 (b) represents the longitudinal strain field ε_{xx}. Two virtual extensometers were defined: E_0 on the upper skin and E_1 on the lower skin. The results indicate that the top face experiences compressive strains, while the bottom face undergoes tensile strains, consistent with pure bending behaviour. These

observations confirm that the global deformation of the sandwich beam under the studied impact conditions adheres to the assumptions of Euler–Bernoulli beam theory.

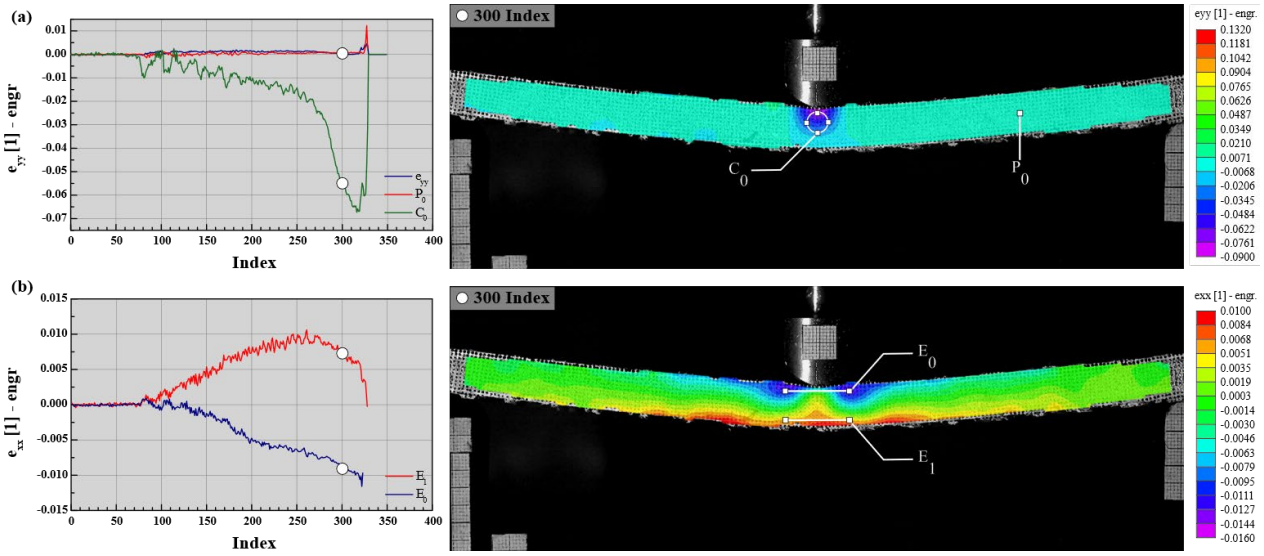

Figure 1. (a) Transverse strain distribution and (b) longitudinal strain distribution in the Flax/PET sandwich beam under low-velocity impact at −40 °C.

Based on these results, the effective Young's modulus of the system was subsequently estimated using the beam bending equation for a 3-point bending configuration:

$$E_{eff} = \frac{L^3}{4bh^3}\left(\frac{F}{\delta}\right) \quad (1)$$

where L is the span length, b the beam width, h the total thickness, F the applied load, and δ the mid-span deflection.

3 RESULTS AND DISCUSSION

This section examines the main results obtained from the low-velocity impact tests conducted on the sustainable (Flax/PET) and conventional (Glass/PVC) sandwich beams. The variables analysed include absorbed energy, energy absorption ratio, peak impact force, and equivalent flexural modulus, under two temperature conditions: room temperature (20°C) and sub-zero temperature (−40°C). Additionally, high-speed recordings were used to correlate the failure evolution with the load evolution.

3.1 Energy absorption and energy ratio

Figures 2-3 show the evolution of the absorbed energy and the energy ratio, respectively, as a function of the impact energy for both sandwich configurations at room temperature and -40°C. In all cases, the absorbed energy increases linearly with impact energy up to a threshold, beyond which the curve either plateaus or, in specific configurations, begins to decrease slightly. This behaviour marks a transition from sub-critical damage mechanisms, such as matrix cracking and fibre debonding [8], to more severe failure modes, including core shear, indentation, or partial perforation.

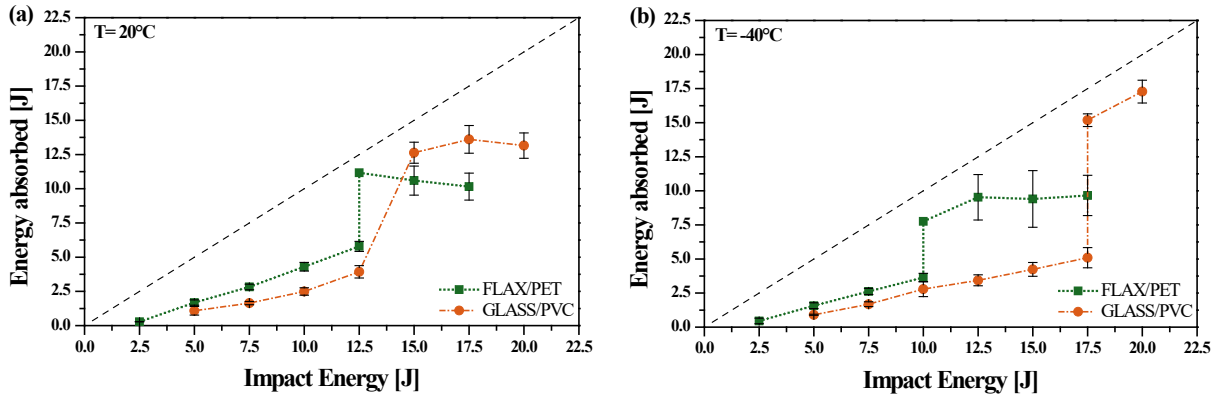

Figure 2. Absorbed energy as a function of impact energy for both sandwich configurations: (a) room temperature and (b) −40°C.

For the Flax/PET sandwich, the absorbed energy increases significantly with impact energy, but shows a sharp rise at 12.5 J under ambient conditions and 10 J at -40°C, indicating a shift in the dominant failure mode. This behaviour is also reflected in the energy ratio, as shown in **Figure 3**. The Flax/PET system reaches values near unity at the transition energy, indicating that nearly all the impact energy is dissipated through irreversible damage. Beyond this point, the ratio tends to decrease, as the structure is no longer capable of absorbing additional energy, suggesting that the beams are close to complete collapse.

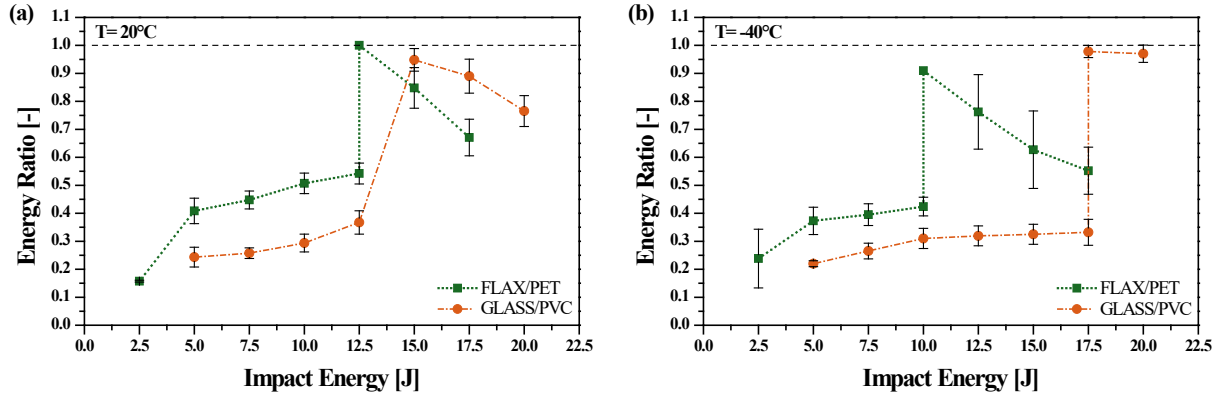

Figure 3. Energy absorption ratio as a function of impact energy for both sandwich configurations: (a) room temperature and (b) −40°C.

Meanwhile, the Glass/PVC configuration displays a more gradual increase in both absorbed energy and energy ratio. No clear transition is observed at room temperature, although the data suggests that the threshold energy lies between 12.5 J and 15 J. Additionally, the influence of temperature on this configuration appears to be limited, as the overall trends between 20°C and -40°C remain relatively similar. This implies that the onset of extensive damage occurs at slightly higher energies compared to the PET configuration, albeit with less efficient energy dissipation.

At higher impact energies (15 J at 20°C and 17.5 J at −40°C), the energy ratio of the Glass/PVC system surpasses that of the Flax/PET sandwich. However, this apparent advantage does not reflect superior energy

absorption performance, but rather the fact that the PVC structure is still resisting and has not yet reached complete failure. By comparison, the PET system has already undergone its full damage progression and begins to lose efficiency as the dominant failure modes saturate. Overall, these results demonstrate that the Flax/PET sandwich exhibits superior energy absorption performance, particularly under moderate impact energies and cold environments, although it is related to a higher level of damage.

3.2 Peak load and failure response

Figure 6 shows the variation of the peak impact force as a function of impact energy. In all cases, the peak load increases with energy until a threshold value is reached, beyond which the growth rate diminishes. This trend reflects the onset of damage mechanisms and the associated reduction in structural stiffness.

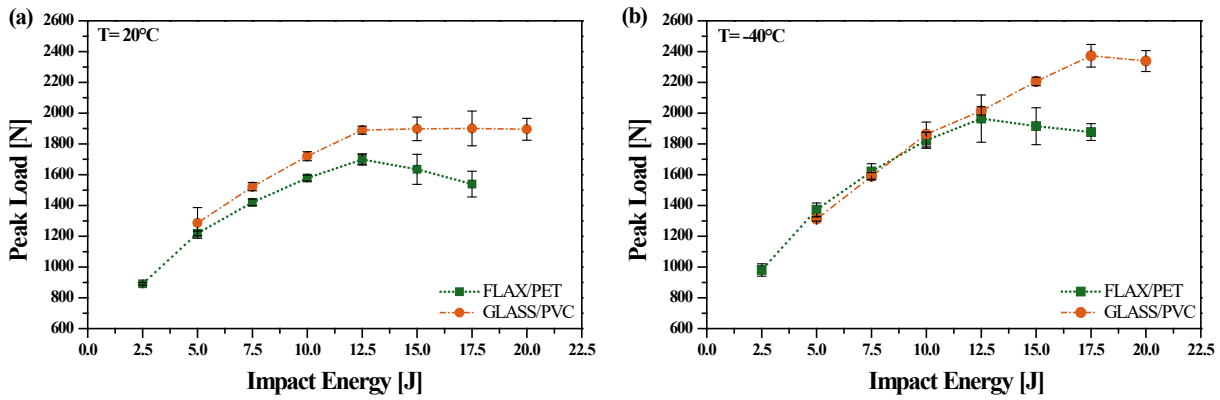

Figure 6. Peak impact force as a function of impact energy for both sandwich configurations: (a) room temperature and (b) −40°C.

In the Flax/PET sandwich, the peak load exhibits a similar trend at both temperatures, with nearly identical values across the entire energy range. This indicates that the mechanical properties of the PET foam, namely stiffness and strength, are minimally affected by the temperature reduction.

As shown in **Figure 7**, multiple diagonal cracks initiate just after the point of maximum load, coinciding with a sudden drop in the measured force. This damage sequence is captured in frames A to F, and involves the formation of diagonal shear cracks at approximately 45° within the PET foam core (frame C), followed by their propagation through the core thickness (frame D), and subsequent core-skin debonding beneath the impactor (frames E and F). This damage sequence compromises the structural integrity of the beam and prevents elastic recovery, thereby resulting in full energy absorption without rebound.

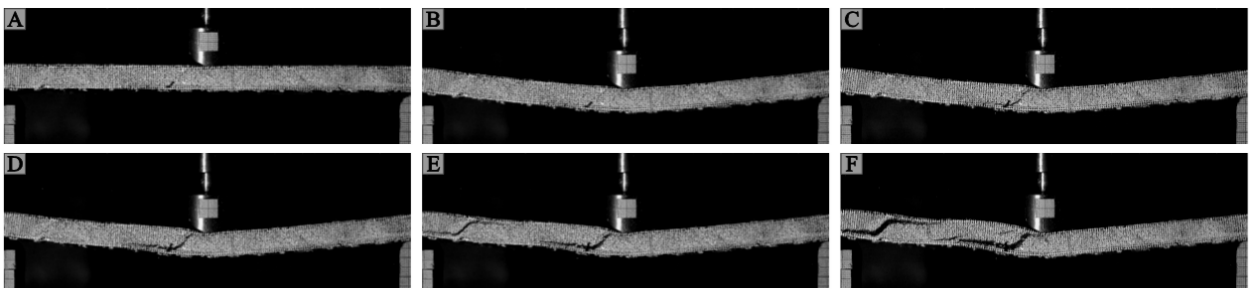

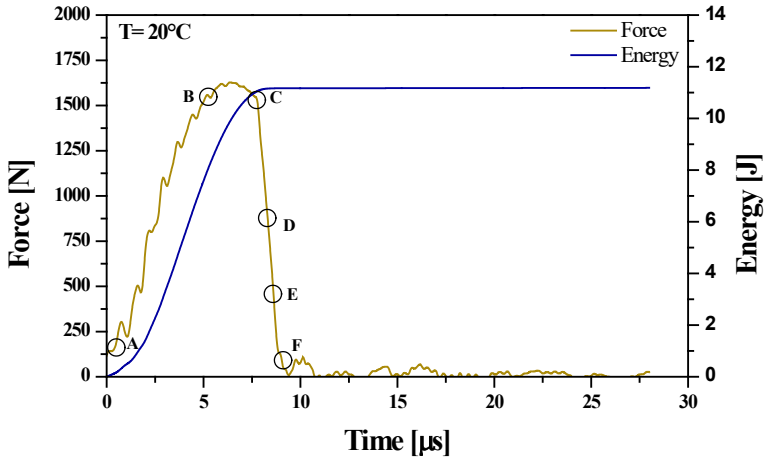

Figure 7. Force–time and energy–time curves for PET-core sandwich at 12.5 J and 20°C.

In contrast, the response of the Glass/PVC sandwich differs significantly beyond the threshold energy. As observed in **Figure 6**, temperature has little influence below the threshold, where peak force remains stable. This limited thermal sensitivity aligns with observations by Castellanos et al. [1], who studied PVC-core sandwiches with carbon/vinylester skins under -50°C impacts. However, while those authors reported a decrease in peak force at low temperature, our results show an increase at -40°C once the threshold energy is exceeded. This discrepancy may stem from the lower temperature sensitivity of the glass/epoxy skins used in this work, which are less brittle compared to the carbon/vinylester laminates employed by Castellanos et al. [1]. Additionally, differences in specimen geometry and impact configuration, such as the use of rectangular panels and hemispherical impactors, could further contribute to the different behaviour observed.

At the threshold energy, barely any damage is observed in the PVC core. As shown in **Figure 8**, damage is confined to compressive failure of the upper skin, with no significant visible damage in the core region. This damage pattern begins with localized core crushing (frame C), followed by top skin failure (frame D). The absence of rebound confirms that the residual energy remains trapped within the damaged structure, likely due to plastic collapse and progressive fracture in the core. The force–time curve of the Glass/PVC beam does not exhibit a sharp drop to zero, unlike the Flax/PET sandwich, which is consistent with a more localized and gradual failure mode.

These results indicate that the Glass/PVC sandwich beam sustains higher peak loads and exhibits delayed damage initiation compared to the Flax/PET sandwich.

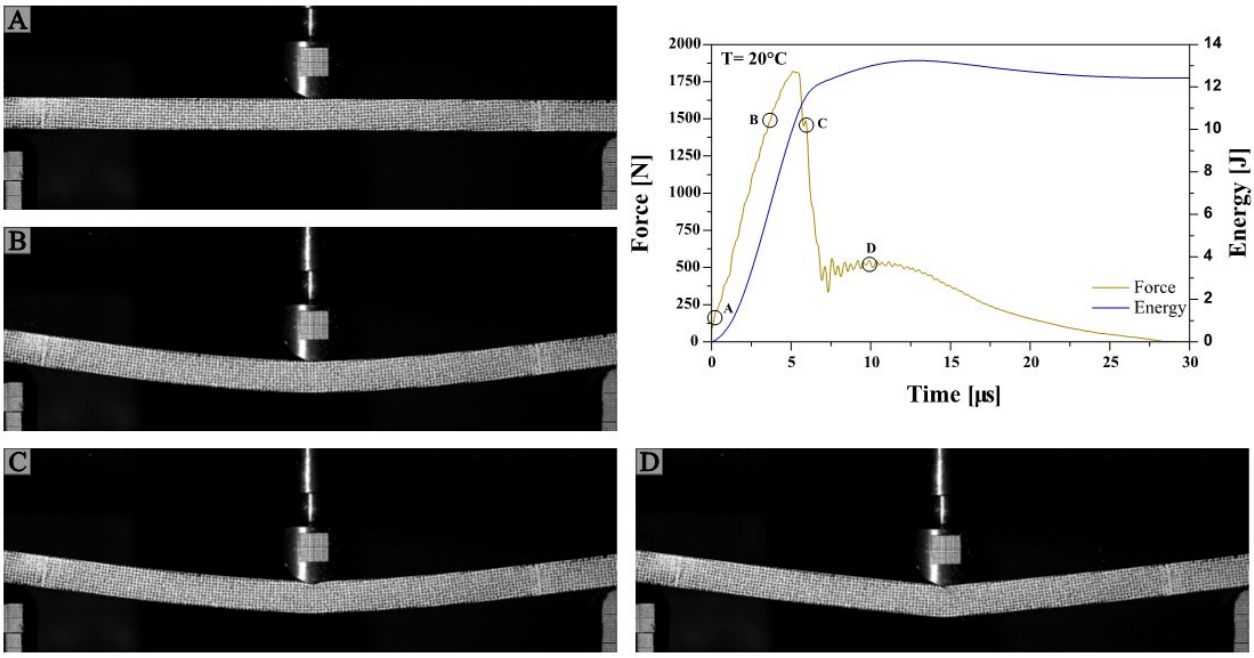

Figure 8. Force–time and energy–time curves for PVC-core sandwich at 17.5 J and 20°C.

3.3 Effective flexural modulus

Figure 9 shows the evolution of the effective flexural modulus as a function of impact energy, estimated from the linear portion of the force–displacement curve under the assumption of Euler–Bernoulli beam behaviour. The effective modulus remains nearly constant across the studied energy range, indicating that both sandwich systems are relatively insensitive to the associated strain rate. A difference of approximately 10% is observed between the Flax/PET and Glass/PVC configurations.

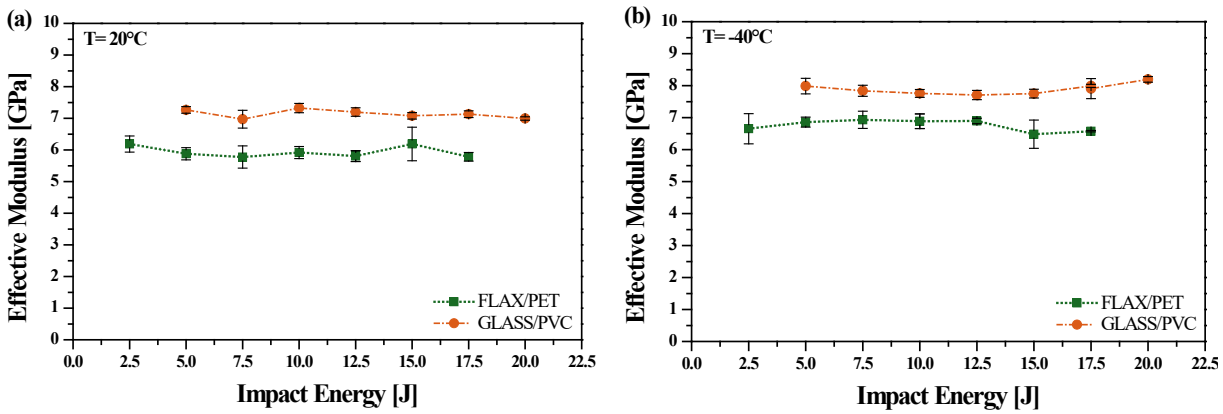

Figure 9. Effective flexural modulus as a function of impact energy: (a) room temperature and (b) −40°C.

Both materials exhibit a slight increase in stiffness at −40 °C compared to room temperature, with gains of approximately 20% for Flax/PET and 15% for Glass/PVC. This suggests a temperature-induced stiffening effect. Interestingly, this trend contrasts with the energy absorption behaviour, where both systems displayed

increased brittleness. These results indicate that, despite a reduction in damage tolerance at low temperatures, the initial elastic response of both configurations improves moderately.

4 CONCLUSIONS

This study analysed the low-velocity impact response of two sandwich beam configurations tested at two temperatures. In the energy range and thermal conditions considered, sandwich beams manufactured with natural and sustainable materials exhibited inferior performance compared to conventional sandwich structures composed of glass/epoxy skins and PVC foam cores. This outcome is consistent with the superior mechanical properties of the constituent materials in the reference system. In particular, the Glass/PVC sandwich showed a higher threshold energy, and its impact response remained largely unaffected by temperature variations.

Additionally, the conventional sandwich exhibited a progressive and localized failure mode, whereas the Flax/PET configuration showed a more abrupt and catastrophic failure when subjected to impact energies at or above its threshold. However, in terms of peak impact force, the Flax/PET system demonstrated performance comparable to the reference sandwich, with limited temperature sensitivity. These results suggest that, while sustainable sandwich structures can match the load-bearing capacity of conventional designs, their damage tolerance and energy thresholds are more susceptible to environmental conditions. Therefore, further improvements in core toughness and interfacial strength are required to enhance their impact resistance and make them more competitive in demanding applications.

ACKNOWLEDGEMENTS

This publication is part of the R&D project PID2021-127174OB-I00, funded by the Spanish State Research Agency (AEI) and the European Regional Development Fund (FEDER/UE).

REFERENCES

[1] A. G. Castellanos and P. Prabhakar, “Elucidating the mechanisms of damage in foam core sandwich composites under impact loading and low temperatures,” *Journal of Sandwich Structures & Materials*, vol. 24, no. 1, pp. 337–359, Jan. 2022, doi: 10.1177/1099636221993848.

[2] S. Chahardoli, T. N. Tran, S. M. Hossaeini Marashi, F. Masoumi, and S. Tatyana Yu, “Experimental investigation of the crushing characteristics in sandwich panels in the application of light vehicles using three-point bending tests,” *Eng Fail Anal*, vol. 129, p. 105725, Nov. 2021, doi: 10.1016/j.engfailanal.2021.105725.

[3] M. Pervaiz and M. M. Sain, “Carbon storage potential in natural fiber composites,” *Resour Conserv Recycl*, vol. 39, no. 4, pp. 325–340, Nov. 2003, doi: 10.1016/S0921-3449(02)00173-8.

[4] L. Yan, N. Chouw, and K. Jayaraman, “Flax fibre and its composites – A review,” *Compos B Eng*, vol. 56, pp. 296–317, Jan. 2014, doi: 10.1016/J.COMPOSITESB.2013.08.014.

[5] M. Ramesh, “Flax (Linum usitatissimum L.) fibre reinforced polymer composite materials: A review on preparation, properties and prospects,” *Prog Mater Sci*, vol. 102, pp. 109–166, May 2019, doi: 10.1016/J.PMATSCI.2018.12.004.

[6] P. Mazzuca, “Flexural behaviour of GFRP sandwich panels with eco-friendly PET foam core for the rehabilitation of building floors,” *Structures*, vol. 60, p. 105815, Feb. 2024, doi: 10.1016/J.ISTRUC.2023.105815.

[7] F. Sarasini *et al.*, “Impact behavior of sandwich structures made of flax/epoxy face sheets and agglomerated cork,” *Journal of Natural Fibers*, vol. 17, no. 2, pp. 168–188, Feb. 2020, doi: 10.1080/15440478.2018.1477084;REQUESTEDJOURNAL:JOURNAL:WJNF20;SUBPAGE:STRING:ACCESS.

[8] S. Samlal and R. Santhanakrishnan, “Low-Velocity Impact Behavior of Foam Core Sandwich Panels with Inter-Ply and Intra-Ply Carbon/Kevlar/Epoxy Hybrid Face Sheets,” *Polymers (Basel)*, vol. 14, no. 5, p. 1060, Mar. 2022, doi: 10.3390/POLYM14051060.

DESIGN AND OPTIMIZATION OF FUNCTIONALLY GRADED HONEYCOMB STRUCTURES FOR OUT-OF-PLANE STIFFNESS AND ENERGY ABSORPTION

Ali Nabizadeh[1,2] and Kaan Yildiz[2,3]

[1]Department of Aeronautical Engineering, Istanbul Technical University
Istanbul, 34469, Türkiye

[2]Aerospace Research Center, Istanbul Technical University
Istanbul, 34469, Türkiye

[3]Aviation Institute, Istanbul Technical University
Istanbul, 34469, Türkiye

Keywords: Graded materials, Honeycomb, Out-of-plane properties

ABSTRACT

Honeycomb structures, inspired by nature, are widely valued for their remarkable strength-to-weight ratios, making them indispensable in aerospace, automotive, and other engineering applications. This study explores the mechanical performance of functionally graded honeycomb structures with various thickness gradation configurations. Seven designs, including uniform and staged thickness variations, were analyzed through finite element method (FEM) simulations and validated with experimental testing to assess their behavior under compressive loading. The results demonstrate that incorporating thickness gradation significantly enhances mechanical properties compared to uniform designs. Staged configurations improved compressive strength, energy absorption, and crushing force efficiency, with the number and placement of thickness variations playing a critical role. While increasing the number of gradation stages refined stability and crushing force efficiency, it also resulted in trade-offs, such as reduced load-bearing capacity and energy absorption. Designs with strategically placed thin regions outperformed others in terms of energy dissipation and stability, highlighting their suitability for applications requiring controlled deformation and impact resistance. This study provides valuable insights into the design and optimization of functionally graded honeycomb structures, offering a pathway for developing lightweight, high-performance materials tailored to specific engineering needs.

1 INTRODUCTION

Honeycomb structures, inspired by the natural design of beehives, have long been recognized for their outstanding combination of low density and high stiffness [1], making them ideal for a range of applications across industries such as aerospace [2], automotive [3], architecture [4], and biomedicine [5]. The unique cellular configuration of honeycombs offers exceptional strength and energy absorption [6-9], particularly in sandwich composite designs, which are widely used in critical structures where weight reduction and impact resistance are paramount [10, 11]. Under out-of-plane loads, honeycombs exhibit high stiffness due to axial extension or compression of their cell walls, which provide structural support [12]. However, the in-plane stiffness of honeycomb structures remains relatively low, primarily due to the bending stresses arising from the distinct geometry of the cells [13].

Recent advancements in honeycomb design have sought to optimize their mechanical properties, particularly to enhance the in-plane behavior of these materials. This has led to efforts to adjust the geometry of honeycomb cells, including the angles of hexagonal cells, to create tailored materials suited for specific applications. One notable development in this field involves the integration of auxetic materials—materials that exhibit a negative Poisson's ratio—into traditional honeycomb structures [14, 15]. These auxetic designs, such as hybrid honeycombs with split vertical struts, have been shown to significantly improve compressive strength, energy absorption, and the overall deformation patterns of honeycombs, which are crucial for controlled collapse and maintaining structural integrity in dynamic load conditions [16].

Alongside these geometric optimizations, the concept of functionally graded materials (FGMs) has emerged as a promising approach to enhance honeycomb performance. FGMs allow for a gradual variation in material properties across the structure, resulting in improved strength, durability, and environmental resistance [17]. This gradual change in properties, unlike traditional composites that feature abrupt transitions, enables the design of more efficient structures with tailored mechanical characteristics, such as modulus, density, and thermal conductivity [18-20]. Initially developed for aerospace applications requiring efficient thermal barriers, FGMs have since expanded into sectors such as biomedical, chemical, nuclear, and energy engineering, where high- performance materials are critical [21].

Building on these advancements, recent research has explored functionally graded honeycomb structures, which incorporate varying geometries of unit cells across their panels to achieve tailored mechanical properties. By adjusting the geometries, honeycomb structures can exhibit enhanced stiffness-to-weight ratios, which is particularly beneficial for lightweight mechanical and aerospace applications. The introduction of FGMs into these gradient honeycombs has demonstrated improvements in overall stiffness, shear modulus, and bending performance, further enhancing the suitability of these structures for applications that demand precise mechanical performance and optimized strength-to-weight ratios [22- 24].

In this study, we focus on the design and manufacturing of functionally graded honeycomb structures with linear thickness variations in the out-of-plane direction in each stage. Specifically, seven configurations are considered:

1. Uniform average thickness
2. A single-stage thick-thin variation
3. A double-stage thick-thin-thick variation
4. A double-stage thin-thick-thin variation
5. A triple-stage thin-thick-thin-thick variation
6. A quadruple-stage thin-thick-thin-thick-thin variation
7. A quadruple-stage thick-thin-thick-thin-thick variation

To validate these designs, finite element method (FEM) simulations were performed to predict mechanical performance under out-of-plane compressive loading. Experimental tests using a universal testing machine (UTM) were carried out to validate these simulations and characterize key mechanical properties, including stiffness, densification displacement, mean crushing force, and energy absorption capacity. This study aims to deepen the understanding of functionally graded honeycombs and their potential applications in high-performance scenarios, such as in aerospace, automotive, and packaging industries, where tailored mechanical responses are essential for optimized structural performance.

2 MATERIALS AND METHODS

2.1 Materials

Esun PLA+ filaments which are known for their combination of low melting point and high strength were used in this study for printing functionally graded honeycomb structures. The dog-bone shaped tensile test specimens, 165 mm in length and 19 mm in width, were produced using Bambu Lab P1S 3D printer. The tensile properties of the filaments were obtained by tensile tests using a UTM equipped with a 50 kN load cell according to ASTM D638 standard. The stress strain data of the filaments under tensile loading are depicted in Figure 1.

All samples were printed with 100% infill value as it ensures uniform mechanical properties across the material. This helps the object retain its shape and structural integrity especially under prolonged applied loads. The recommended nozzle temperature for Esun PLA+ filament is reported to be between 210-230 °C, therefore, 220 °C was selected for 3D printing. The installed nozzle has 0.4 mm extrusion diameter for finer resolution of samples. Bed temperature of 50 °C provided adequate adhesion and minimized warping effects for the samples. Additionally, the printing speed of 100 mm/min was found to be sufficient for desirable quality of the samples.

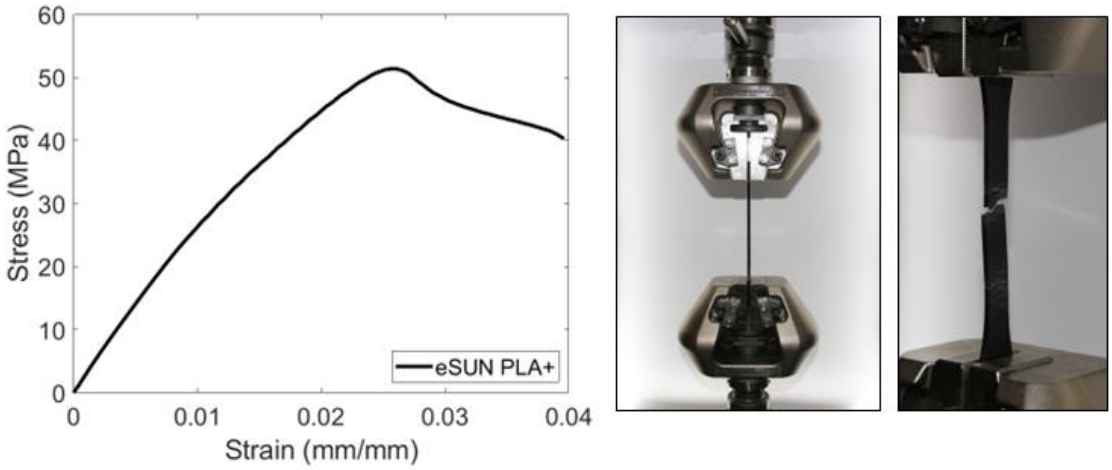

Figure 1: Esun PLA+ material experimental tensile stress-strain curve and testing apparatus.

2.2 Design and Fabrication of Graded Honeycomb Structures

The unit cell used in this study is shown in Figure 2 where parameters L, H, t_1, t_2, t_{avg}, and θ represent the side length, unit cell height, thickness of the thin section, thickness of the thick section, average thickness where $t_{avg} = (t_1 + t_2)/2$, and interior angle of the unit cell, respectively. The geometrical dimensions of the honeycomb unit cells are as follows: the side length L is 15 mm, the unit cell height H is 30 mm, the thickness t_1 is 0.5 mm, t_2 is 1.5 mm, t_{avg} is 1 mm, and the interior angle θ is 30°. For this study, the average thickness of 1 mm was maintained across all samples to ensure equal mass, regardless of variations in the design pattern. This approach eliminates the need to use mass-normalized, specific values for comparison. A double-stage unit cell is shown in Figure 2, clarifying the average thickness concept for tapered configurations.

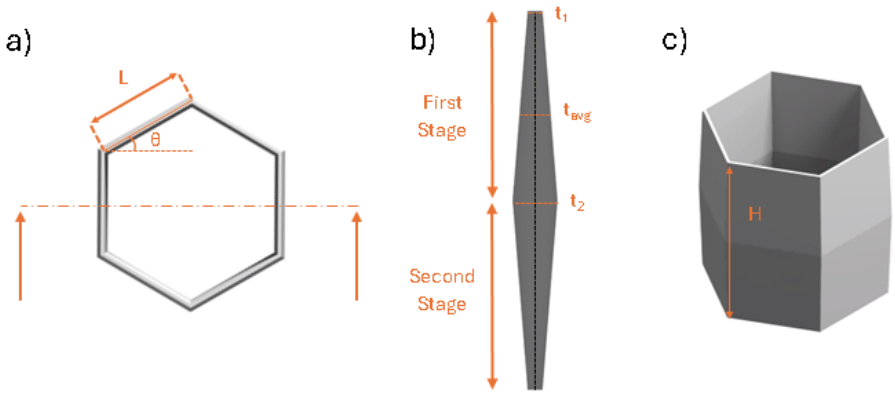

Figure 2: An illustration of a double-stage unit cell: a) Top view, b) side view of a single cell wall, and c) isometric view of the unit cell.

Model designs of honeycomb unit cells were developed using CATIA V5 software. The models were generated with a symmetric design approach, where the unit cells are arranged radially around a central origin point, leading to an axisymmetric design. This circular distribution facilitates compression testing by allowing the samples to be directly tested without the need for additional plates. Moreover, this design minimizes the area occupied by the samples, allowing them to fit efficiently within the standard circular plates of the UTM machine.

A systematic approach was adopted for naming different honeycomb configurations based on their thickness variations. The naming convention uses a combination of letters and numbers to represent the configuration type, ensuring clarity and brevity. The prefix H was used for all structures, indicating the honeycomb geometry. Depending on the variations in the thickness, U stands for uniform thickness whereas SS, DS, TS, and QS refer to linear thickness variations in a single stage, a double stage, a triple stage, and a quadruple stage in an alternating thinning and thickening sense. Then, numeric characters were used in between to describe the thickness values at the top face of honeycombs getting in contact with the load applying platen in mm.

This design scheme leads to only one configuration in honeycombs with an odd number of stages since having a thin or thick cell wall at the top face generates the same configuration, upside down. However, for an even number of stages, two different configurations arise and the top face thickness becomes important. For example, H-0.5SS stands for a single stage honeycomb where the thickness linearly varies between 0.5 and 1.5 mm from top to bottom. On the other hand, H-1.5QS denotes a sample with four stages where in each sample the thickness varies between 0.5 and 1.5 mm with the thickness at the top face is 1.5 mm. To maintain consistency, the codes and their corresponding configurations have been documented in Table 1. Furthermore, computer aided designs (CAD) of the corresponding configurations are depicted in Figure 3.

Configuration Description	**Honeycomb**
Uniform thickness of 1 mm	H-1U
Single stage variation (0.5 mm to 1.5 mm)	H-0.5SS
Double stage with 1.5 mm thickness at the top face	H-1.5DS
Double stage with 0.5 mm thickness at the top face	H-0.5DS
Triple stage with 0.5 mm thickness at the top face	H-0.5TS
Quadruple stage with 1.5 mm thickness at the top face	H-1.5QS
Quadruple stage with 0.5 mm thickness at the top face	H-0.5QS

Table 1: Configuration descriptions and their corresponding codes.

2.3 Energy Absorption Characteristics

The energy absorption characteristics of cellular structures are primarily described using six key indices: densification displacement (x_d), mean crushing force (F_m), peak force (F_{max}), crushing force efficiency (e_f), and energy absorption (EA). Among these, the most prominent parameters are x_d and F_m. The expressions of these parameters are obtained based on the energy absorption efficiency approach as noted by Li et al. [25] and detailed below.

The energy absorption efficiency $\eta(x)$ is defined as:

$$\eta(x) = \frac{1}{F(x)H}\int_{x_y}^{x} F(\bar{x})d\bar{x} \tag{1}$$

where $F(x)$ represents the compressive force, H is the specimen height, and x_y denotes the displacement value at the end of the linear region. The densification displacement corresponds to the displacement at which $\eta(x)$ achieves its maximum value, determined by:

$$\left.\frac{d\eta(x)}{dx}\right|_{x=x_d} = 0 \tag{2}$$

The peak force is the maximum compressive force observed until densification begins. The mean crushing force, a critical parameter reflecting the energy absorption capability of the structure in the plateau phase, is then calculated as follows:

$$F_m = \frac{\int_{x_y}^{x_d} F(\bar{x})d\bar{x}}{x_d - x_y} \tag{3}$$

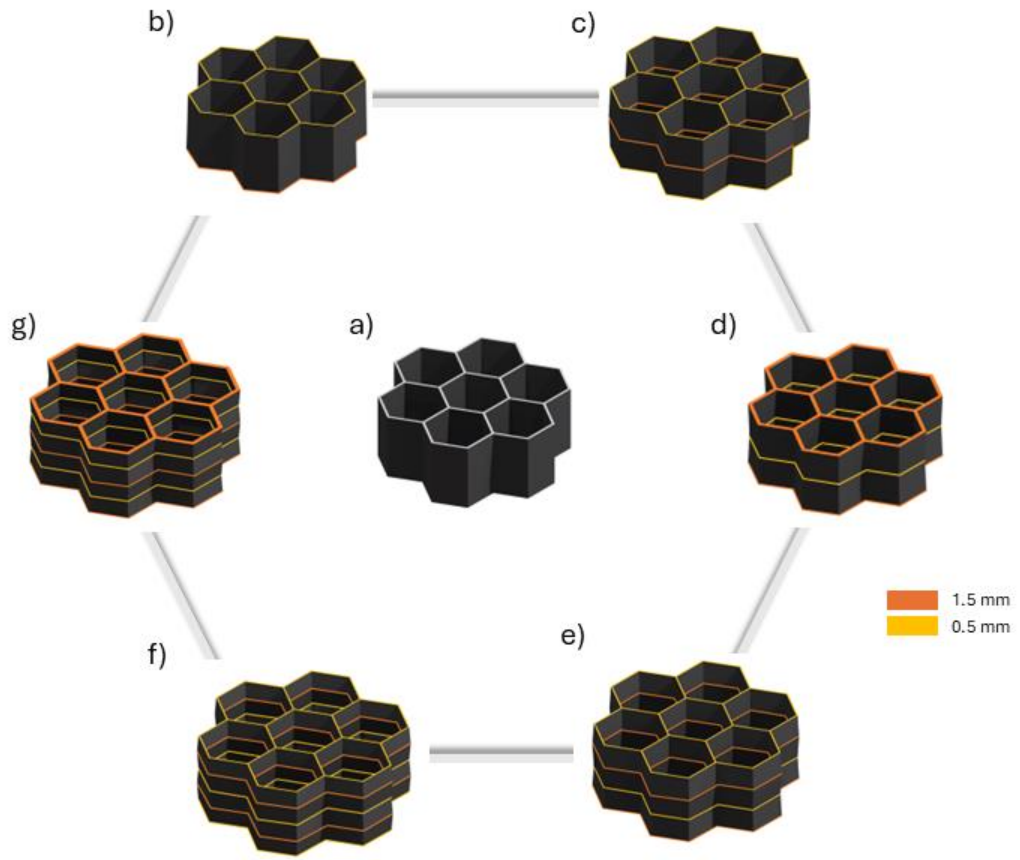

Figure 3: Computer aided drawing designs of functionally graded honeycomb lattice structures: a) H-1U, b) H-0.5SS, c) H-0.5DS, d) H-1.5DS, e) H-0.5TS, f) H-0.5QS, and g) H-1.5QS.

Energy absorption represents the total energy absorbed by the cellular structure during compression and is determined as the area under the force-displacement curve:

$$EA = \int_0^{x_d} F(\bar{x})d\bar{x} \tag{4}$$

Furthermore, the crushing force efficiency is the ratio of the mean crushing force to the peak force:

$$e_f = \frac{F_m}{F_{max}} \tag{5}$$

Finally, stiffness is a material or structure's fundamental resistance to elastic deformation when a force is applied. It is quantitatively measured as the ratio of force to displacement $\boldsymbol{k = F/\delta}$, typically in N/m. In our study, it specifically refers to the initial out-of-plane compressive stiffness of honeycomb structures, where a balance of stiffness and controlled deformation is key for effective energy absorption in impact applications.

2.4 Finite Element Analysis

ABAQUS commercial software was employed to analyze the mechanical behavior of honeycomb structures under compression loading and validate experimental findings. To perform the simulations, a dynamic-explicit solver with smooth loading was selected, which is suitable for quasi-static loading conditions. A total time step of 0.05 s was considered to expedite the simulations while retaining quasi-static conditions. To confirm the validity of the quasi-static analysis conducted using the dynamic-explicit solver, the kinetic energy values must be negligible compared to the internal energy values [26]. This verification is illustrated in Figure 4 which confirms the accuracy of the simulation model.

A general contact approach was used to model interactions between the structural components, with a friction coefficient of 0.2. The lower surface was fixed while the upper surface underwent axial displacement loading to replicate the boundary conditions of the experimental tests. The structure was meshed using C3D8R elements, and a mesh size of 0.3 mm was used.

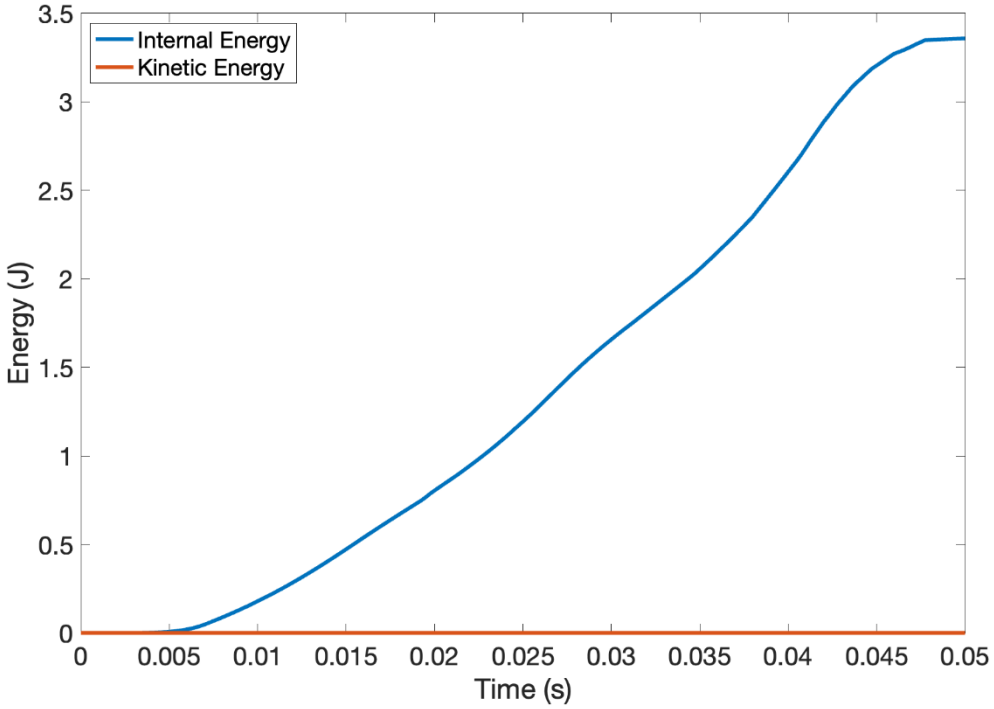

Figure 4: Internal and kinetic energies for H-1U under out-of-plane FEM compression test.

2.5 Experimental Characterization

Compression testing of physical samples were carried out by Shimadzu AGS-X UTM with a 50 kN load cell. Samples were subjected to compression tests with a persistent displacement rate of 3 mm/min until 80% strain is achieved for each model. At least three samples were tested according to ASTM C365 guidelines, and the obtained force-displacement data were utilized to calculate mechanical properties including peak force, densification displacement, energy absorption, mean crushing force, and crushing force efficiency.

3 RESULTS AND DISCUSSION

As an illustrative case, the experimental results obtained from three different samples and the finite element analysis results of H-1U samples are shown in Figure 5 where EXP stands for the experimental data. Based on the results presented in Figure 5, the printing quality among three different samples is quite similar, evinced from the force-displacement behavior of the samples showing almost identical results until around 6 mm, beyond which the impurities start altering the behavior. Furthermore, the FEM and experimental results are in close agreement, indicating the accuracy of the FEM simulations.

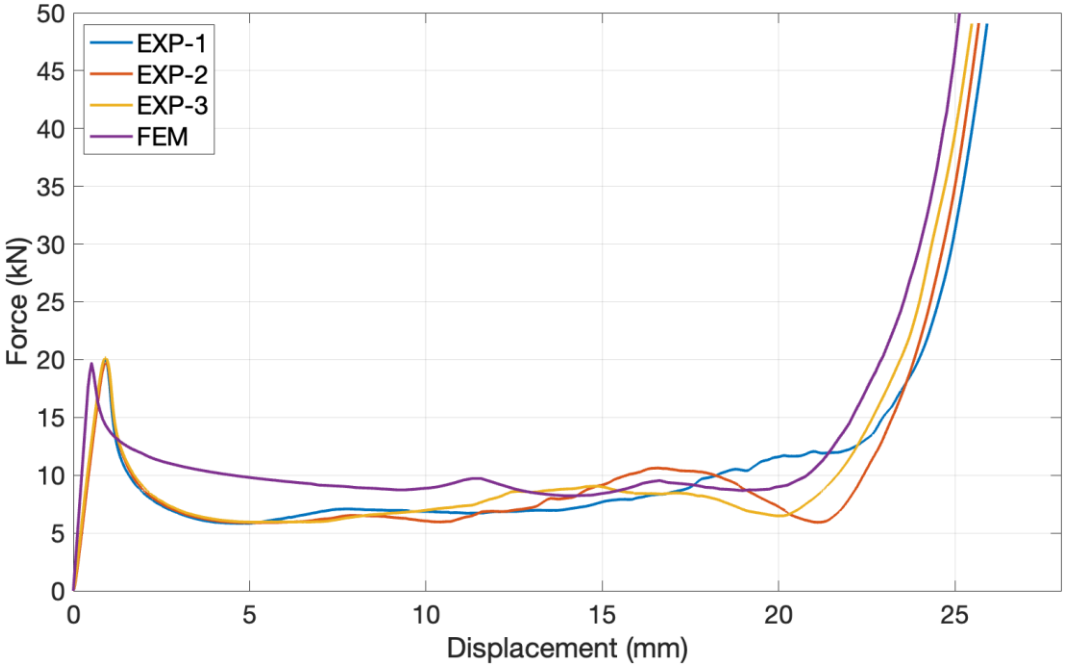

Figure 5: Experimental and numerical (FEM) out-of-plane force-displacement curves for H-1U.

A MATLAB code which utilizes the force displacement curves as inputs was developed to calculate the important performance metrics pertinent to mechanical characteristics of honeycomb structures in the out-of-plane direction such as densification displacement, peak force, mean crushing force, crushing force efficiency, and energy absorption. The force-displacement curves for FEM and experimental tests are shown in Figures 6 and 7, respectively. The performance metrics obtained via the developed MATLAB code are tabulated in Table 2. The tabulated results provide a comprehensive overview of the mechanical performance of seven distinct honeycomb configurations; each designed with variations in out-of-plane thickness. By analyzing key metrics such as stiffness, densification displacement, mean crushing force, and energy absorption, one can discern clear trends and identify optimal designs for specific applications.

Regarding initial deformation behavior, the uniform H-1U configuration stands out with the longest linear region (0.94±0.01 mm), indicating its superior ability to withstand elastic deformation before permanent yielding. In contrast, designs like H-0.5SS, H-0.5DS, and H-0.5TS, characterized by thinner top sections or a single-stage linear variation, exhibit significantly lower linear regions, suggesting they begin to deform plastically much earlier. This trade-off implies that while H-1U is more resilient to initial deformation, the graded designs might be more suitable for applications where controlled, early initiated plastic deformation is a desired mechanism for protection systems.

When considering the structure's capacity for energy absorption through deformation, the densification displacement becomes crucial. Here, H-0.5TS configuration excels, demonstrating the highest densification displacement (23.99 ± 0.31 mm). This indicates that the triple-stage design with a thin top face can effectively absorb energy over a larger deformation range before fully compacting. Similarly, H-0.5QS and H-0.5SS also show high densification displacements, positioning these graded structures as superior choices for impact protection and scenarios requiring prolonged energy dissipation. Conversely, H-1.5DS, which features a thick top face, exhibits the lowest densification displacement, suggesting a more rapid compaction and thus a smaller effective energy absorption range.

In terms of load-carrying capacity and energy absorption efficiency, the peak force, mean crushing force, and crushing force efficiency metrics offer valuable insights. H-0.5TS consistently leads in both peak force (22.72 ± 2.98 kN) and mean crushing force (11.90 ± 0.28 kN), highlighting its robust load-bearing capacity and effective energy absorption during the crushing phase. While H-0.5TS shows strong performance, H-0.5DS distinguishes itself with the highest crushing force efficiency (66.87 ± 5.03%). This high efficiency suggests a very stable and consistent crushing behavior after the initial peak load, which is highly beneficial for predictable energy dissipation in crashworthiness applications.

In contrast, the uniform H-1U and the thicker top-faced H-1.5DS and H-1.5QS configurations generally exhibit lower crushing force efficiencies, indicating a more abrupt force drop after the peak load.

The ultimate measure of a structure's impact resistance is its total energy absorption capacity. The results overwhelmingly favor the graded designs, with H-0.5TS absorbing a remarkable 281.98 ± 10.64 J of energy, significantly outperforming all other configurations. H-0.5QS and H-0.5SS also demonstrate excellent energy absorption capabilities, reinforcing the benefits of functional grading for impact protection. The H-1.5DS, with its thicker top face, shows the lowest energy absorption, underscoring that certain grading strategies are more effective for maximizing energy dissipation.

Finally, regarding stiffness, which reflects the structure's resistance to initial elastic deformation, H-1.5DS exhibits the highest value (25.60 ± 1.33 N/m). The uniform H-1U also demonstrates good stiffness. While the graded designs like H-0.5TS and H-0.5QS show comparable stiffness values, those with thinner top faces (H-0.5SS and H-0.5DS) tend to be slightly less stiff. This suggests that for applications demanding maximum initial rigidity, configurations with uniform thickness or thicker starting layers might be marginally preferable, though the differences in stiffness among most graded samples are not as dramatic as the differences in energy absorption.

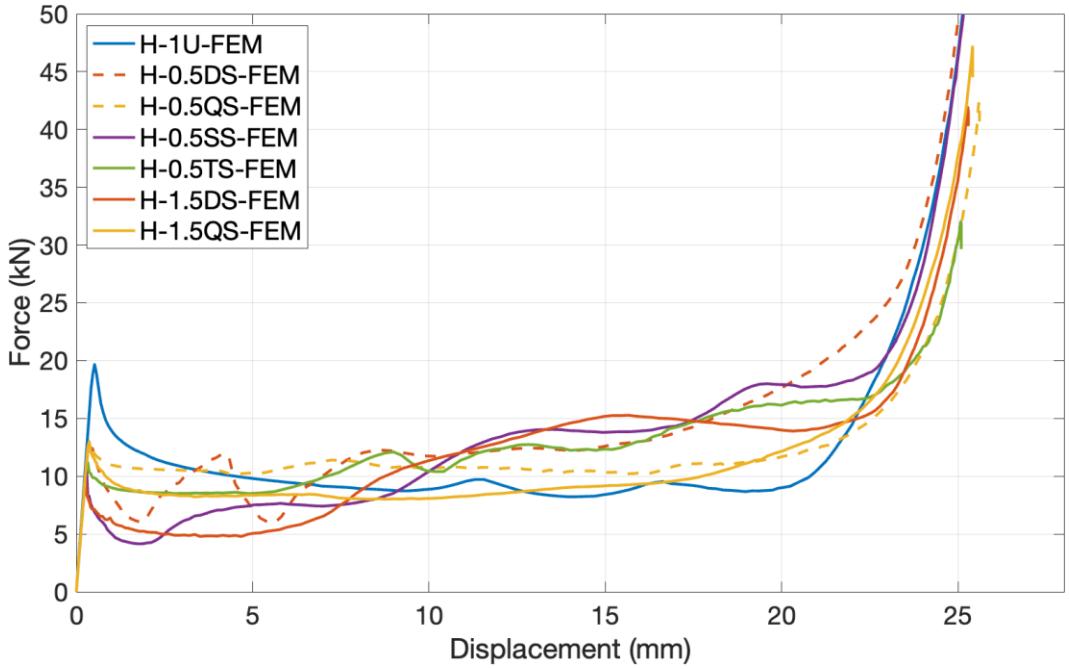

Figure 6: Force-displacement curves of honeycomb samples from FEM analyses.

Sample	x_y (mm)	x_d (mm)	F_{max} (kN)	F_m (kN)	e_f (%)	EA (J)	K (kN/mm)
H-1U	0.94 ± 0.01	21.01 ± 0.88	19.79 ± 0.23	7.80 ± 0.23	39.41 ± 1.39	167.02 ± 10.98	24.38 ± 0.26
H-0.5SS	0.47 ± 0.02	22.13 ± 0.44	17.62 ± 2.00	9.88 ± 0.39	56.42 ± 4.48	216.14 ± 12.97	20.20 ± 1.67
H-0.5DS	0.54 ± 0.03	20.99 ± 0.43	14.15 ± 1.18	9.42 ± 0.11	66.87 ± 5.03	195.72 ± 4.41	21.93 ± 0.77
H-1.5DS	0.76 ± 0.02	17.81 ± 0.29	15.82 ± 0.80	7.30 ± 0.39	46.27 ± 4.42	130.81 ± 7.97	25.60 ± 1.33
H-0.5TS	0.58 ± 0.00	23.99 ± 0.31	22.72 ± 2.98	11.90 ± 0.28	52.74 ± 5.67	281.98 ± 10.64	23.09 ± 1.73
H-0.5QS	0.70 ± 0.02	23.16 ± 0.38	17.36 ± 2.95	10.41 ± 0.20	60.96 ± 8.58	238.78 ± 8.53	23.05 ± 1.02
H-1.5QS	0.70 ± 0.04	21.97 ± 0.20	19.29 ± 2.36	8.94 ± 0.46	46.54 ± 3.33	194.78 ± 11.96	23.45 ± 2.22

Table 2: Mechanical properties of the honeycomb samples.

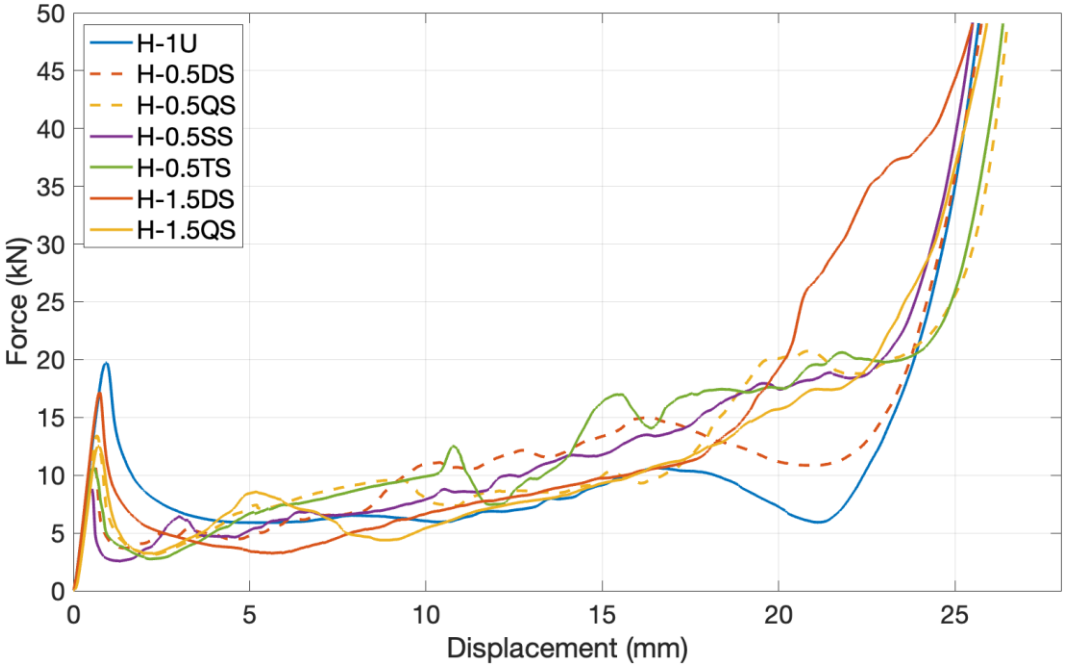

Figure 7: Experimental force-displacement curves of honeycomb samples.

4 CONCLUSIONS

This study thoroughly investigated the compressive behavior of various honeycomb structures, comparing uniform (H-1U) and functionally graded designs. The experimental and FEM simulation results showed very good agreement, validating the simulation approach adopted. Through a user-friendly MATLAB script, key performance metrics including compressive force, mean crushing force, crushing force efficiency, energy absorption, densification displacement, and stiffness were evaluated.

The results demonstrate that functionally graded honeycomb structures offer significant advantages over uniform designs, particularly in energy absorption capacity and crushing force efficiency. The triple-stage configuration (H-0.5TS), characterized by a thin top face, consistently emerged as the superior design for applications demanding high impact resistance and effective energy dissipation, absorbing a remarkable 281.98 ± 10.64 J of energy. While uniform designs like H-1U showed longer elastic region (resilience to initial elastic deformation) and H-1.5DS exhibited the highest stiffness, the overall gains in energy absorption and controlled crushing behavior observed in graded structures like H-0.5QS and H-0.5SS were substantial.

In conclusion, although certain graded designs may demonstrate earlier permanent deformation or exhibit slightly reduced initial stiffness, their enhanced capacity for energy dissipation—achieved through controlled deformation and prolonged energy absorption—renders them highly advantageous. These results underscore the potential of functionally graded structures to enable tailored mechanical responses, offering significant promise for high-performance applications in impact-critical sectors such as aerospace and automotive engineering.

5 ACKNOWLEDGEMENTS

The authors gratefully acknowledge the partial financial support received from Istanbul Technical University Scientific Research Projects Coordination Unit (Project ID: PMA-2025-46714). The authors would like to extend their sincere gratitude to the members of Istanbul Technical University Aerospace Research Center.

REFERENCES

[1] J. Zhang, G. Lu, Z. You, Large deformation and energy absorption of additively manufactured auxetic materials and structures: A review, Composites Part B: Engineering 201 (2020) 108340. doi:https://doi.org/10.1016/j.compositesb.2020.108340.

[2] Q. Z. F. X. Meng, J. L. Yang, Improvement of crashworthiness behaviour for simplified structural models of aircraft fuselage, International Journal of Crashworthiness 14 (2009) 83–97. doi:10.1080/13588260802517360.

[3] Z. Wang, Y. Zhou, X. Wang, X. Zhang, Multi-objective optimization design of a multi-layer honeycomb sand- wich structure under blast loading, Proceedings of the Institution of Mechanical Engineers, Part D: Journal of Automobile Engineering 231 (2017) 1449–1458. doi:10.1177/0954407016672606.

[4] C. M. Geng, The Feasibility of Honeycomb Structure to Enhance Daylighting and Energy Performance for High-Rise Buildings, Ph.D. thesis, 2022.

[5] S. Wang, Z. Shi, L. Liu, Z. Huang, Z. Li, J. Liu, Y. Hao, Honeycomb structure is promising for the repair of human bone defects, Materials Design 207 (2021) 109832. doi:https://doi.org/10.1016/j.matdes.2021.109832.

[6] D. Ruan, G. Lu, B. Wang, T. Yu, In-plane dynamic crushing of honeycombs—a finite element study, Interna- tional Journal of Impact Engineering 28 (2003) 161–182. doi:https://doi.org/10.1016/S0734-743X(02)00056-8.

[7] M. Yamashita, M. Gotoh, Impact behavior of honeycomb structures with various cell specifica- tions—numerical simulation and experiment, International Journal of Impact Engineering 32 (2005) 618–630. doi:https://doi.org/10.1016/j.ijimpeng.2004.09.001, fifth International Symposium on Impact Engineering.

[8] L. Aktay, A. F. Johnson, B.-H. Kro¨plin, Numerical modelling of honeycomb core crush behaviour, Engineering Fracture Mechanics 75 (2008) 2616–2630. doi:https://doi.org/10.1016/j.engfracmech.2007.03.008, fracture of Composite Materials.

[9] Y. Tao, M. Chen, H. Chen, Y. Pei, D. Fang, Strain rate effect on the out-of-plane dynamic compres- sive behavior of metallic honeycombs: Experiment and theory, Composite Structures 132 (2015) 644–651. doi:https://doi.org/10.1016/j.compstruct.2015.06.015.

[10] Experimental and numerical characterization of honeycomb sandwich composite panels, Simulation Modelling Practice and Theory 17 (2009) 1533–1547. doi:https://doi.org/10.1016/j.simpat.2009.05.008.

[11] M. He, W. Hu, A study on composite honeycomb sandwich panel structure, Materials Design 29 (2008) 709–713. doi:https://doi.org/10.1016/j.matdes.2007.03.003.

[12] C. Qiu, Z. Guan, X. Guo, Z. Li, Buckling of honeycomb structures under out-of-plane loads, Journal of Sandwich Structures & Materials 22 (2020) 797–821. doi:10.1177/1099636218774383.

[13] A.-J. Wang, D. L. McDowell, In-plane stiffness and yield strength of periodic metal honeycombs, Journal of Engineering Materials and Technology 126 (2004) 137–156. doi:10.1115/1.1646165.

[14] M. Xu, D. Liu, P. Wang, Z. Zhang, H. Jia, H. Lei, D. Fang, In-plane compression behavior of hybrid honeycomb metastructures: Theoretical and experimental studies, Aerospace Science and Technology 106 (2020) 106081. doi:https://doi.org/10.1016/j.ast.2020.106081.

[15] A. Ingrole, A. Hao, R. Liang, Design and modeling of auxetic and hybrid honeycomb structures for in-plane property enhancement, Materials Design 117 (2017) 72–83. doi:https://doi.org/10.1016/j.matdes.2016.12.067.

[16] M. Safikhani Nasim, A. Yaghootian, R. Mosalmani, Energy absorption of the additively manufactured novel re-entrant auxetic structure in comparison with honeycomb structure: experimental and numerical analysis, Journal of the Brazilian Society of Mechanical Sciences and Engineering 45 (2023) 275. doi:10.1007/s40430- 023-04178-x.

[17] M. Naebe, K. Shirvanimoghaddam, Functionally graded materials: A review of fabrication and properties, Applied Materials Today 5 (2016) 223–245. doi:https://doi.org/10.1016/j.apmt.2016.10.001.

[18] R. Duraibabu, R. Prithvirajan, M. Sugavaneswaran, G. Arumaikkannu, Compression behavior of function- ally graded cellular materials fabricated with fdm, Materials Today: Proceedings 24 (2020) 1035–1041. doi:https://doi.org/10.1016/j.matpr.2020.04.417, international Conference on Advances in Materials and Manu- facturing Applications, IConAMMA 2018, 16th -18th August, 2018, India.

[19] B. Garrido Silva, F. Alves, M. Sardinha, et al., Functionally graded cellular cores of sandwich panels fabricated by additive manufacturing, Proceedings of the Institution of Mechanical Engineers, Part L: Journal of Materials: Design and Applications 236 (2022) 1814–1828. doi:10.1177/14644207221084611.

[20] S. Huo, B. Du, Y. Zhao, H. Liu, Y. Shi, X. Chen, Thermal design of functionally graded cellular structures with multiple microstructure configurations through topology optimization, Composite Structures 313 (2023) 116922. doi:https://doi.org/10.1016/j.compstruct.2023.116922.

[21] B. Saleh, J. Jiang, R. Fathi, T. Al-hababi, Q. Xu, L. Wang, D. Song, A. Ma, 30 years of functionally graded materials: An overview of manufacturing methods, applications and future challenges, Composites Part B: Engineering 201 (2020) 108376. doi:https://doi.org/10.1016/j.compositesb.2020.108376.

[22] D. Qi, Q. Lu, C. He, Y. Li, W. Wu, D. Xiao, Impact energy absorption of functionally graded chiral honeycomb structures, Extreme Mechanics Letters 32 (2019) 100568. doi:https://doi.org/10.1016/j.eml.2019.100568.

[23] J.-h. Zhang, B.-j. Dong, B. He, Y. Sun, Free vibrations and impact resistance of a functionally graded honeycomb sandwich plate, Shock and Vibration 2021 (2021) 8043368. doi:https://doi.org/10.1155/2021/8043368.

[24] T. Fan, Dynamic crushing behavior of functionally graded honeycomb structures with random defects, International Journal of Materials Research 107 (2016) 783–789. URL: https://doi.org/10.3139/146.111403. doi:doi:10.3139/146.111403.

[25] X. Z. Qixun Li, F. Fan, Quasi-static compressive behaviour of 3d-printed origami-inspired cellular structure: experimental, numerical and theoretical studies, Virtual and Physical Prototyping 17 (2022) 69–91. doi:10.1080/17452759.2021.1987051.

[26] Ehsan Etemadi, Mohammad Bashtani, Hong Hu, Novel auxetic metamaterials inspired from geometry patterns of an Iranian Mosque with improved energy absorption capability, Materials Today Communications, Volume 41, 2024, 110470, ISSN 2352-4928, https://doi.org/10.1016/j.mtcomm.2024.110470.

ICCM24
AUGUST 4-8, 2025
BALTIMORE CONVENTION CENTER
BALTIMORE, MARYLAND, USA

No Technical Paper Submission for:

Istvan Nemes-Karoly

STOCHASTIC MODELLING OF THE SPATIALLY DISTRIBUTED VISCOELASTICITY OF SHORT FIBER-REINFORCED COMPOSITES USING RANDOM FIELDS

Eduard Klatt[1], Natalie Rauter[1]

[1]Chair of Solid Mechanics, Helmut-Schmidt-University / University of the Federal Armed Forces
Holstenhofweg 85, 22043 Hamburg, Germany
Email: klatte@hsu-hh.de, web page: https://www.hsu-hh.de/mechanik/
Email: natalie.rauter@hsu-hh.de, web page: https://www.hsu-hh.de/mechanik/

Keywords: Short fiber-reinforced composite, Viscoelasticity, Random fields, Multiscale, Tensile creep test

ABSTRACT

Short fiber-reinforced composites, such as Polybutylene Terephthalate with a fiber mass fraction of 30%, exhibit enhanced mechanical properties due to embedded reinforcing short fibers. However, the reinforcing fibers and hence the microstructural randomness cause pronounced spatially distributed viscoelastic behavior, resulting from microstructural randomness. This study presents a combined experimental and numerical investigation to model and analyze the local distribution of viscoelastic parameters in short fiber-reinforced composites, both at the microscale and component level. In the experimental context, the viscoelastic behavior of the material is characterized using tensile testing at the component level and nanoindentation at the microscale. These analyses reveal significant variability in the creep properties of fiber-reinforced specimens compared to those of unreinforced Polybutylene terephthalate. The numerical multiscale simulation is based on random fields, where the viscoelastic behavior is described through a generalized Maxwell model by using a Prony series representation. With this, a connection between the microscale and component level is established. Therefore, at the microscale, artificial microstructures are generated based on statistical descriptors of fiber geometry and orientation. The material properties of the homogenized material are obtained through numerical simulations that respect Hill's condition. In order to account for the stochastic nature resulting from the microstructure at the component level, spatially varying material parameters are represented via second-order Gaussian random fields, discretized using the Karhunen-Loève expansion. With the presented multiscale approach, the spatial randomness of the viscoelastic behavior is successfully incorporated into numerical simulations. The findings of the numerical simulation exhibited a robust alignment with the experimental data, thus providing additional support for its practical relevance.

1 INTRODUCTION

Short Fiber-Reinforced Composites (SFRCs) are formed by combining two or more constituent materials during an injection molding process [2]. In this specific case, thermoplastic Polybutylene terephthalate (PBT) is generally used as the matrix, while short fibers are utilized to provide mechanical reinforcement, resulting in increased stiffness and strength. However, polymer-based composites, such as PBT GF30 (with 30% fiber mass fraction), exhibit time-dependent deformation under sustained mechanical loads, a phenomenon generally referred to as viscoelasticity. This behavior is primarily attributed to the viscoelastic nature of the polymer matrix [5]. Since PBT GF30 can be processed by injection molding, its applications are found in the automotive, aerospace, and electronics industries. For these applications, a precise characterization of viscoelastic behavior is essential for reliable performance prediction [9].

The generalized Maxwell model is a widely used approach to describe the viscoelastic response of SFRCs [13]. This model conceptualizes the behavior of the material using a network of springs and dashpots, respectively representing elastic and viscous effects [13]. Due to its standardized structure, the Maxwell model is implemented in most commercial Finite Element Method (FEM) software packages [1]. The numerical implementation is typically based on the representation of the Prony series [13].

Although the addition of short fibers enhances the mechanical properties of SFRCs, it also introduces a notable drawback, such as the spatial heterogeneity of mechanical properties at the component level [10]. This heterogeneity is derived from the microstructure of the material itself [4, 11], which is primarily influenced by the manufacturing process, such as mold injection [2]. During mold injection, variations in flow velocity and the resulting shear forces in the cross-section of the melt flow cause non-uniform microstructural characteristics [2]. Consequently, this results in spatially distributed mechanical properties at the microscale and component levels.

The probabilistic nature of the microstructure is characterized by probability density functions of fiber length, fiber diameter, and fiber orientation [4, 12]. Due to the considerable disparity in the length scales, where the fiber length is much smaller than the overall dimensions of the component, a multiscale approach is essential to accurately capture the mechanical behavior of the SFRCs at the component level [10].

One potential framework for modeling the spatial distribution of mechanical parameters is to utilize random fields, thereby allowing for the representation of the behavior of inhomogeneous materials at the component level [14]. The numerical discretization of these random fields is based on the Karhunen-Loève expansion [7]. In this work, a two-dimensional cross-section of a standardized tensile test specimen, conforming to DIN EN ISO 527-2 type 1A, is used within a numerical framework to model at the component level and in an experimental context. First, the entries of the anisotropic elasticity tensor are determined using an artificial microstructure, which is described in detail in [10, 12]. The artificial microstructure is generated based on the probabilistic characteristics of fiber length, fiber orientation, and fiber diameter. The numerical simulation at the microscale is conducted using linear elastic modeling for both the fibers and the matrix material. Finally, the component-level numerical results obtained using a second-order Gaussian random field are compared with the experimental tensile creep data.

2 THEORETICAL FRAMEWORK

Viscoelasticity effects are defined as a time-dependent deformation process that occurs under constant load and temperature conditions, involving both elastic and viscous contributions. This phenomenon is of particular significance in polymer-based materials, which exhibit viscoelastic behavior, combining time-independent elasticity with time-dependent viscous flow. Due to the heterogeneity of the material, these time-dependent mechanical properties are spatially distributed. To effectively capture and analyze this phenomenon, a probabilistic approach is necessary.

2.1 Viscoelasticity

Creep is a component of viscoelasticity, defined as the time-dependent deformation of a material under constant load and temperature. This phenomenon is commonly observed in polymer-based materials, which exhibit a combination of elastic and viscous behavior [13]. This behavior is often referred to as viscoelastic behavior. Creep deformation is generally understood to occur in three stages: primary, secondary, and tertiary creep, as demonstrated in Figure 1, which presents a schematic representation of the strain ε, as a function of time t.

As illustrated in Figure 1 the primary creep stage is characterized by a deceleration in the strain rate. It occurs immediately after stress application, with the initial strain $\varepsilon(0)$ representing the elastic response. A constant strain rate marks the secondary creep stage and is crucial to evaluating long-term material behavior. This is usually the longest stage. In the tertiary creep stage, the strain accelerates rapidly, ultimately leading to material failure.

The total strain $\varepsilon_{\text{total}}(t)$ over time of the specimen under constant loads, as schematically presented in Figure 1, can be expressed additively as

$$\varepsilon(t) = \varepsilon_{\text{total}}(t) = \varepsilon_{\text{linear elastic}} + \varepsilon_{\text{creep}}(t). \tag{1}$$

Here, $\varepsilon_{\text{linear elastic}}$ represents the immediate strain response upon the application of stress, following Hooke's law for linear elasticity. This component remains constant over time and does not contribute to the time-dependent deformation behavior of the material. However, the creep deformation $\varepsilon_{\text{creep}}(\text{t})$ accounts for the viscoelastic deformation that evolves under sustained loading, including all three stages.

In this study, the focus is on the primary and secondary stages because capturing the tertiary stage is time-consuming and experimentally challenging.

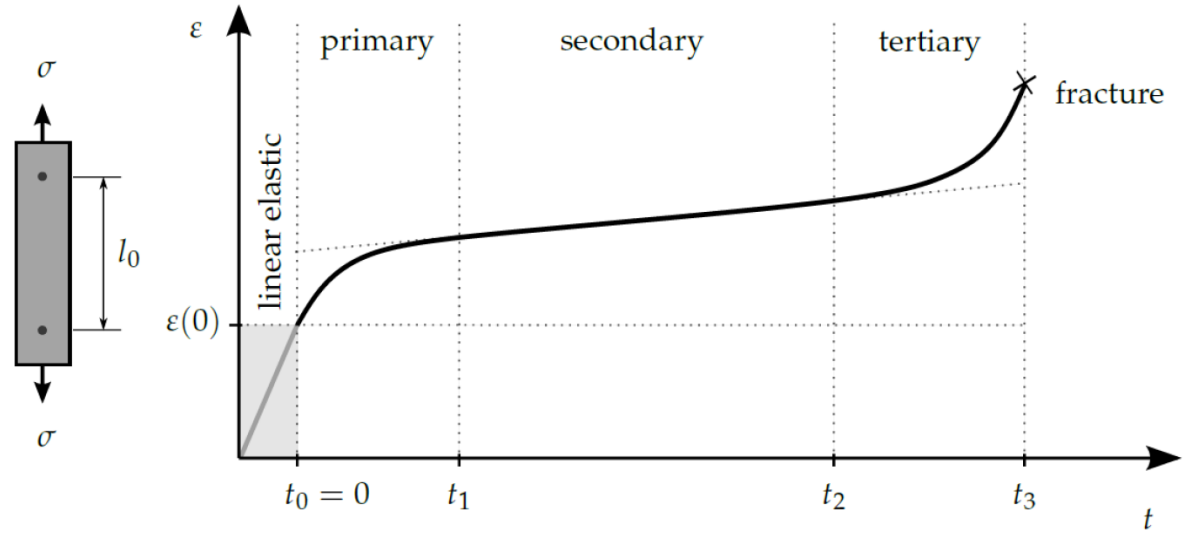

Figure 1: Schematic representation of the typical behavior of creep strain ε, which is divided into three distinct stages, while constant load σ and temperature T are applied to a sample.

The mathematical models are derived using rheological elements that describe the stress-strain relations for the viscoelastic behavior [13]. These elements are depicted in Figure 2, where the spring element represents Hooke's law with stiffness K_{eq}. According to Newton's law, a dashpot is defined as a purely viscous material characterized by its dynamic viscosity, denoted by η. When the spring and dashpot are connected in series, it is referred to as the Maxwell element. Furthermore, by employing a parallelization approach with the N_i-th Maxwell elements and the equilibrium spring K_{eq}, the concept of the generalized Maxwell model is introduced.

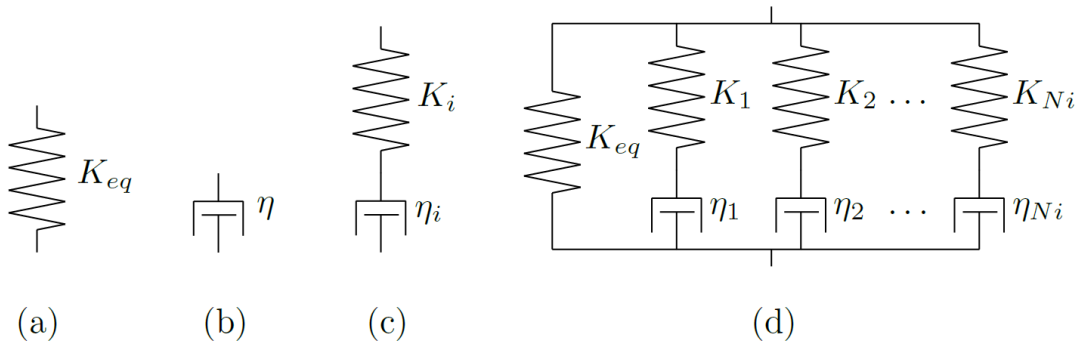

Figure 2: Representation of rheological elements to describe viscoelasticity: a) a spring with the stiffness K_{eq} following Hooke's law, b) a dashpot representing purely viscous behavior, c) a Maxwell element consisting of a spring and dashpot in series, and d) a generalized Maxwell model.

For the generalized Maxwell model with $K_{Ni} = 1$, as detailed in [13], the stress-strain relationship for viscoelastic materials is formulated as a differential equation

$$\frac{\mathrm{d}\sigma(t)}{\mathrm{d}t} + \frac{K_1}{\eta_1}\sigma(t) = \left(K_{eq} + K_1\right)\frac{\mathrm{d}\varepsilon(t)}{\mathrm{d}t} + \frac{K_{eq}K_1}{\eta_1}\varepsilon(t). \tag{2}$$

This differential equation models the viscoelastic response of complex materials, encompassing stress relaxation and creep behavior [13].

A commonly used approach to characterize the time-dependent viscoelastic response is the Prony

series, which can be derived by applying the Laplace transform to the differential formulation of the generalized Maxwell model [13], as demonstrated in Equation 2. The Prony series effectively describes the time-dependent deformation behavior of materials, expressed as [13]

$$K(t) = K_{eq} + \sum_{i=1}^{N_i} K_i \, e^{-t/\tau_i}. \tag{3}$$

The relaxation function $K(t)$ characterizes the time-dependent decrease in material stiffness due to viscoelastic effects. Each exponential term corresponds to a Maxwell element with a distinct relaxation time τ_i, which captures different rates of stiffness relaxation [13]. In practical applications, the parameters of the Prony series K_{eq}, K_i, and τ_i are determined by fitting the Prony series to experimental data. The fitting process typically involves applying optimization techniques to minimize the discrepancy between the model's predictions and observations [5, 8]. The result of this process is a viscoelastic model that is tailored to the material under investigation.

2.2 Karhunen-Loève expansion

2.2.1 Second-order Gaussian random field

Quantities that are derived from random experiments and governed by the rules of probability theory are known as random variables, denoted as $Z(\omega)$. In a mechanical context, specific material properties, such as Young's modulus, are not constant but instead vary due to natural heterogeneity uncertainty. A well-known approach to representing this distribution is the Gaussian distribution, which is characterized by its first two statistical moments and thereby defines the normal distribution [14]. The statistical moments are the expected value, μ, and the standard deviation, σ.

By extending the random variable $Z(\omega)$ to the spatial coordinates x, over the defined domain, one speaks of a random field [14]

$$Z(x) = Z(\omega, \boldsymbol{x}). \tag{4}$$

A Gaussian random field is fully characterized by the mean value $\mu(\mathbf{x})$, the standard deviation $\sigma(\mathbf{x})$, and the dimensionless correlation coefficient $\rho(x_1, x_2)$ [6, 14]. The correlation coefficient is a measure of the relationship between two points, $\mathbf{x_1}$ and $\mathbf{x_2}$, of a random field. When combined with the covariance, it can be expressed as

$$\rho_{12} = \rho_{Z_1,Z_2} = \frac{Cov[Z_1, Z_2]}{\sigma_1 \sigma_2}. \tag{5}$$

One speaks of the auto-correlation when Z_1 and Z_2 are from the same random field $Z(\mathbf{x})$. Otherwise, it involves cross-covariance and cross-correlation.

It is assumed that the random fields are homogeneous. This indicates that the mean value and the standard deviation are independent of spatial coordinates and thus remain constant over a realization [14]. Additionally, the correlation is translation-independent and is therefore described by relative coordinates $\boldsymbol{\xi}$.

2.2.2 Karhunen-Loève expansion of Gaussian random field

The Karhunen-Loève (KL) expansion provides a comprehensive framework for representing second-order Gaussian stochastic random field, functioning as a probabilistic analog to the classical Fourier transform [7]. This expansion is expressed as follows

$$X(\omega, \boldsymbol{x}) = \sum_{n=0}^{\infty} \sqrt{\lambda_n}\ \phi_n(\boldsymbol{x})\, Z_n(\omega), \tag{6}$$

where $Z_n(\omega)$ is an uncorrelated random variable, and λ_n and $\phi_n(\mathbf{x})$ are eigenpairs of a Fredholm integral of second-order. This Fredholm integral of second-order is written as

$$\int_D Cov[Z_1, Z_2]\ \phi_n(\boldsymbol{x_1})\, \mathrm{d}\boldsymbol{x_1} = \lambda_n\, \phi_n(\boldsymbol{x_2}). \tag{7}$$

Moreover, the correlation must be established before generating a random field. However, a closed solution is feasible only for a limited number of correlation functions and domain shapes. Consequently, numerical methods are necessary. Furthermore, the random field is divided into deterministic and stochastic components, which are represented as

$$\begin{aligned} Z(\omega, \boldsymbol{x}) &= \mu(\boldsymbol{x}) + \alpha(\omega, \boldsymbol{x}) \\ &= \mu + X(\omega, \boldsymbol{x}). \end{aligned} \tag{8}$$

Here, the mean of the random field $\mu(\mathbf{x})$ represents the deterministic part of it, while $\alpha(\omega, \mathbf{x})$ represents the stochastic part with an expected value of zero.

For the numerical generation of random fields, the optimal linear estimation expansion method is employed, as introduced in [6]. First, the covariance matrix, denoted by $\mathbf{C}$, is calculated for the predefined and discretized two-dimensional shape using the triangular function. The two-dimensional model of the tensile test specimen is schematically illustrated in Figure 3. This step is expressed as

$$\boldsymbol{C}(\boldsymbol{x_1}, \boldsymbol{x_2}) = \rho(\xi_1, \xi_2), \tag{9}$$

where $\mathbf{C}$ is a N $\times$ N symmetric positive semi-definite matrix.

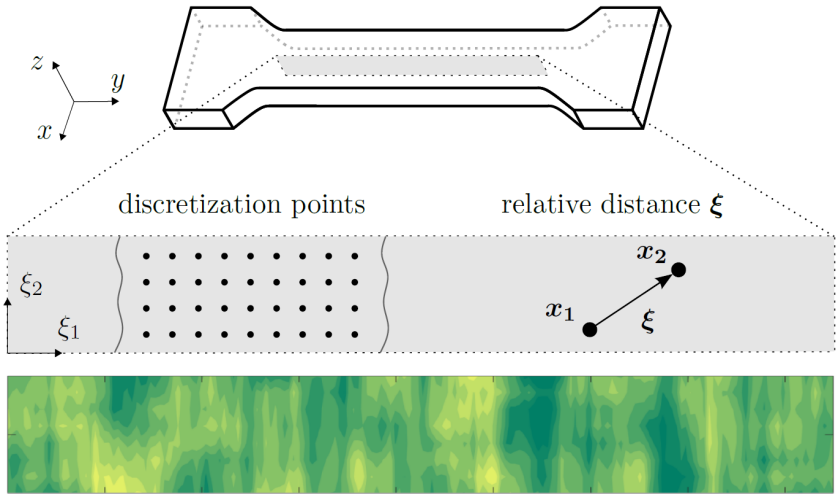

Figure 3: Standard tensile test specimen featuring a two-dimensional model representation, illustrating the discretization points and the relative distance $\boldsymbol{\xi}$ between the points $\mathbf{x_1}$ and $\mathbf{x_2}$ are shown schematically. Furthermore, a numerically generated second-order Gaussian random field for this two-dimensional model is exemplified.

This leads to the eigenvalue problem

$$\boldsymbol{C}(\boldsymbol{x_1}, \boldsymbol{x_2})\, \phi_n = \lambda_n\, \boldsymbol{\phi_n}, \tag{10}$$

where the eigenpair (λ_n and $\phi_n(\mathbf{x})$) are determined. Furthermore, the eigenpair is used for the M-th truncated random fields $\hat{Z}$.

$$\hat{Z}(\omega, \boldsymbol{x}) = \mu + \sum_{n=1}^{M} \sqrt{\lambda_n}\, \phi_n(\boldsymbol{x}) Z_n(\omega). \tag{11}$$

This approximation is referred to as the truncated Karhunen–Loève expansion. An exemplary representation of a second-order Gaussian random field is provided in Figure 3.

2.3 Multiscale modeling framework

A Representative Volume Element (RVE) is crucial for modeling heterogeneous materials, such as SFRCs. The RVE must be sufficiently large to capture the statistical features of the heterogeneity while remaining small enough to function as a material point at the component level and independent of the RVE size, as demonstrated schematically in Figure 4 a). In contrast, smaller domains that do not fully satisfy these criteria are referred to as Statistical Volume Elements (SVEs). The purpose of SVEs is to investigate the variability of effective properties resulting from microstructural randomness.

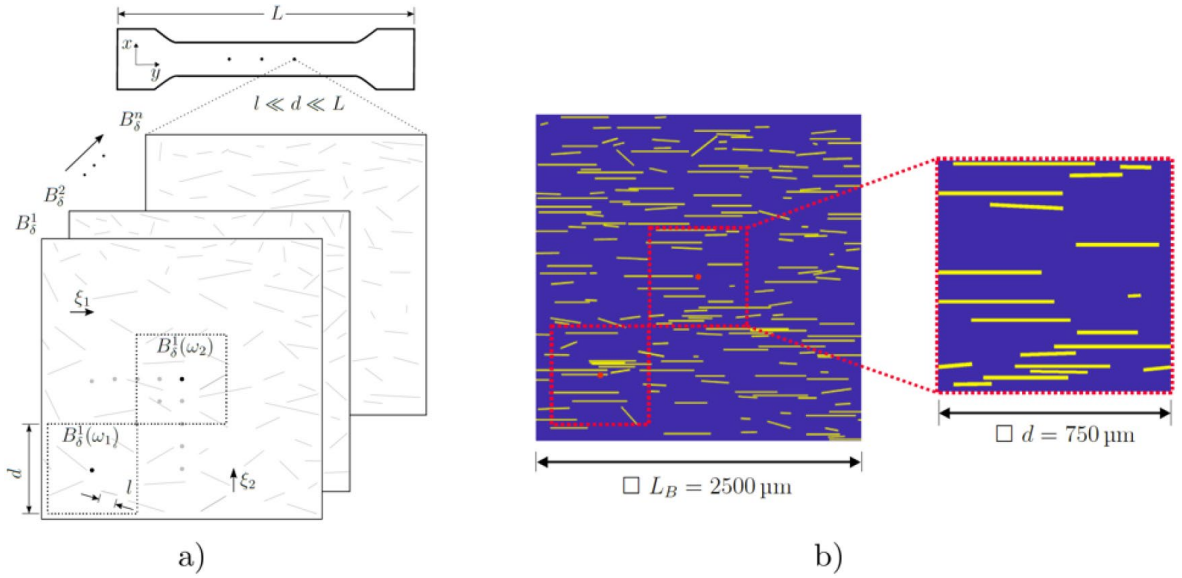

Figure 4: Representation of the definition of the scale $l \ll d \ll L$ based on a tensile test specimen: a) various unique microstructures at different positions at the component level, and b) numerically modeled artificial microstructure.

Using the numerically modeled artificial microstructure, as depicted in Figure 4 b), the material properties are determined by Hill's condition [3]

$$\langle \boldsymbol{\sigma} : \boldsymbol{\varepsilon} \rangle = \langle \boldsymbol{\sigma} \rangle : \langle \boldsymbol{\varepsilon} \rangle. \tag{12}$$

The generation of this artificial microstructure, considering the probabilistic characteristics of fiber length, fiber diameter, and fiber orientation, as detailed in [10-12]. The properties of the materials used for the linear elastic model are summarized in Table 1.

	Fiber	PBT (Matrix)
Young's modulus	83.9 GPa	2.67 GPa
Poisson's ratio	0.22	0.41
Density	2500 kg m^{-3}	1300 kg m^{-3}

Table 1: Fiber and PBT (matrix) material properties for modeling the artificial microstructure.

The effective material properties can be calculated by applying three independent load cases for each type of boundary condition, namely Dirichlet and Neumann types, to the numerical artificial microstructure. By averaging $\langle\cdot\rangle$ the properties calculated in the domain, the homogenized material properties are written as

$$\langle \boldsymbol{\sigma} \rangle = \mathbf{C}^{\text{eff}} : \langle \boldsymbol{\varepsilon} \rangle \tag{13}$$

and

$$\langle \boldsymbol{\varepsilon} \rangle = \mathbf{S}^{\text{eff}} : \langle \boldsymbol{\sigma} \rangle \tag{14}$$

where $\mathbf{C}^{\text{eff}}$ and $\mathbf{S}^{\text{eff}}$ represent the effective stiffness and the compliance tensor, respectively. In the case of time-dependent behavior, the relation exemplarily for stiffness behavior is written as

$$\langle \boldsymbol{\sigma}(\boldsymbol{t}) \rangle = \mathbf{C}^{\text{eff}}(\boldsymbol{t}) : \boldsymbol{\varepsilon_0} \tag{15}$$

Here, only the matrix material is modeled as viscoelastic using a Prony series with a single branch, as shown in Figure 2, with $K_{Ni} = 1$. These Prony parameters, which were obtained through experimental means and are specific to unreinforced PBT, are listed in Table 2. This is achieved by fitting the experimental data with the Levenberg-Marquardt algorithm. The identified Prony parameters for PBT are applied exclusively to the matrix phase of the artificial microstructures, with the corresponding results shown in Figure 10 a) for five different microstructures. The five microstructures considered are subdomains (d) extracted from the larger volume (LB) shown in Figure 4 b).

	Prony parameters for matrix		
Brunch	K_{eq} [GPa]	K_1 [MPa]	τ_1 [s]
1	2.5	119.54	108.92

Table 2: Prony parameter obtained through fitting the experimental data of the unreinforced material PBT.

3 EXPERIMENTAL INVESTIGATION

This section presents the motivation for employing the probability modeling approach to model spatially distributed mechanical properties. The experimental findings are presented at the microscale and component level of PBT and PBT GF30. This is achieved through a tensile creep test at the component level and nanoindentation at the microscale.

3.1 Materials used in composite

In this comprehensive experimental investigation, a standardized tensile test specimen is utilized, which is directly molded with reinforced fibers (PBT GF30) and without fibers (PBT). The matrix material is a thermoplastic Polybutylene Terephthalate, representing the primary component, which is marketed under the trade name ULTRADUR B 4520 by BASF. The reinforcing component of the composite is E-Glass, designated as FGCS 3540 and provided by STW. The manufacturing of all specimens was carried out using an injection molding process at Kunststoff-Zentrum Leipzig GmbH.

3.2 Experimental setup and specimen preparation

3.2.1 Investigation at the microscale

For the experimental investigation at the microscale, a ZHN nanoindenter from ZwickRoell, equipped with a Berkovich indenter, was used. To do this, a small specimen is removed from the tensile test sample, as illustrated in Figure 5. The extracted specimen was prepared by grinding and polishing, as detailed in [4]. The nanoindentation tests are performed with a force of 1750 mN and a hold phase of 300 s. The creep value Cr represents the viscoelastic property and is expressed as

$$\text{Creep} = Cr = h_2 - h_1, \tag{16}$$

where h_2 and h_1 are the maximum depth of the indentation test and the beginning of the holding phase, respectively, as shown in Figure 6.

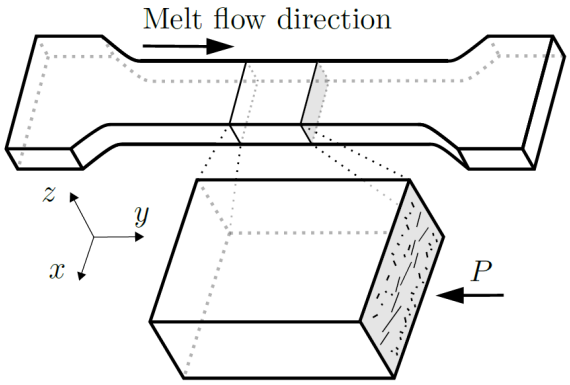

Figure 5: A small sample is extracted from the tensile test specimen. The gray marked surface is of interest for the indentation test.

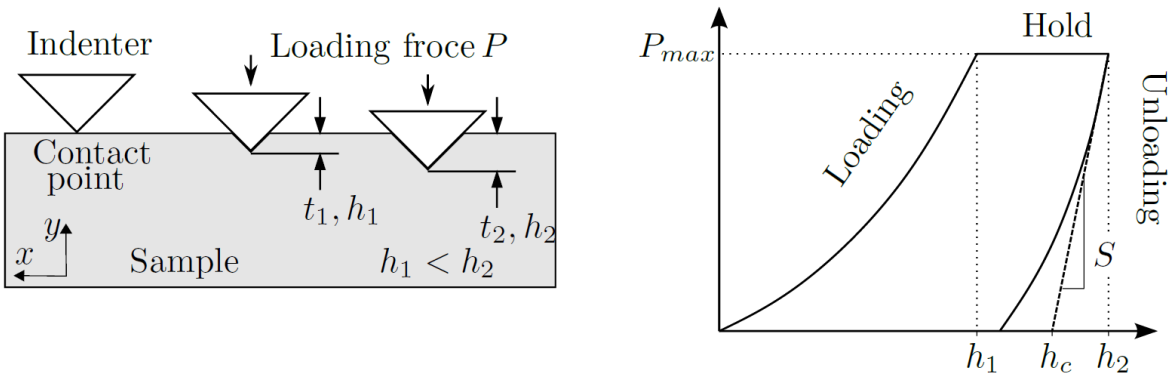

Figure 6: Schematic representation of the nanoindentation curve derived from the indentation test. This includes an example of the nanoindentation test procedure, illustrating the search for the contact point, the beginning of the hold phase at h_1, and the end of the hold phase at h_2.

3.2.2 Investigation at the Component level

For the experimental investigation at the component level, the specimen is divided into $L = 15$ areas, each with an initial length of 5 mm, as depicted in Figure 7. Creep behavior in these areas is measured using the ARAMIS 3D digital image correlation system. Consequently, the assessment of creep behavior is conducted within these designated areas, allowing for the determination of its local distribution across the specimen. A detailed description of this experimental setup and conditions can be found in [5].

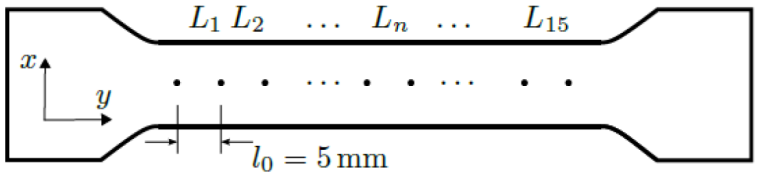

Figure 7: Tensile test specimens were divided into 15 areas with an initial length of 5 mm to measure local viscoelasticity properties.

3.3 Experimental results and validation

3.3.1 Experimental results at the microscale

To evaluate the variations in microscale viscoelastic behavior, nanoindentation measurements were conducted across the specimen's cross-section, as shown in Figure 5 and 6. The distribution of creep values is displayed in Figure 8. For PBT, the unreinforced matrix exhibits a fairly uniform response. In contrast, PBT GF30 exhibits significant variability in microscale viscoelastic behavior, indicating microstructural heterogeneity resulting from the embedded short fibers.

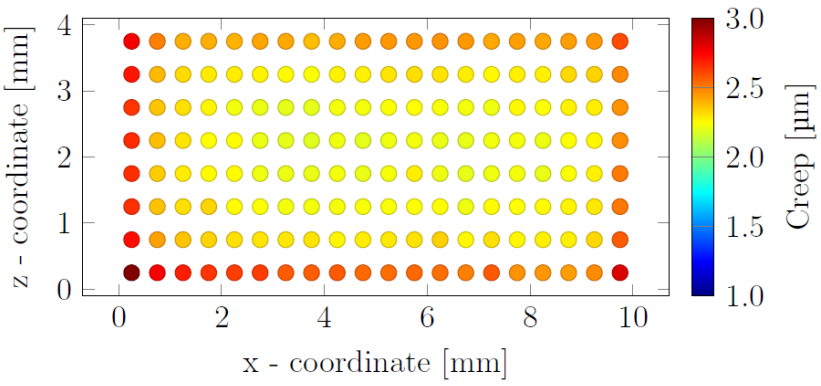

(a) PBT

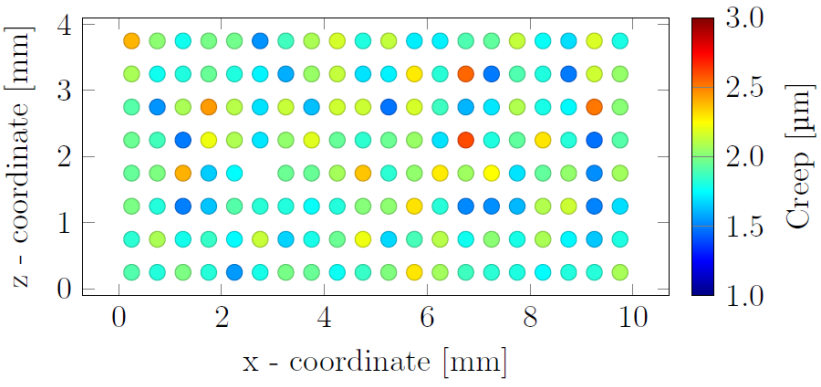

(b) PBT GF30

Figure 8: Creep value Cr of 160 measurement points over the cross-section, a) represents the unreinforced material PBT, and b) the short fiber-reinforced material PBT GF30.

3.3.2 Experimental results and validation at the component level

This microscale trend is also observed at the component level, as demonstrated in Figure 9, which illustrates the distribution of the viscoelastic parameter K_i. In that figure, the local distribution of K_i, as introduced in Equation 3, is presented. This distribution is derived from the Prony series after five

minutes of creep testing for both PBT and PBT GF30 using the Levenberg-Marquardt method. The unreinforced PBT specimen shows a relatively uniform distribution of K_i values. Conversely, the PBT GF30 specimen exhibits a substantial increase in scatter, indicative of considerable spatial variability resulting from the limited fiber reinforcement.

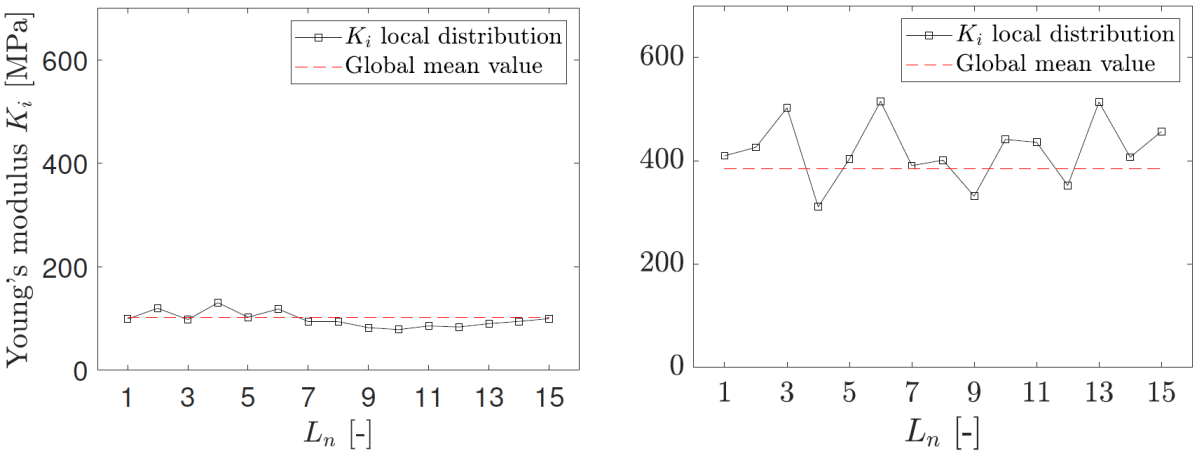

Figure 9: The local distribution at the component level for one specimen, as introduced in Figure 3, shows the Prony parameter K_i obtained by fitting Equation 3 using the Levenberg-Marquardt algorithm. The global mean value is obtained experimentally over a length of 75 mm and represents 20 specimens.

Finally, Figure 10 b) presents a comparison between the experimental creep data and the numerically predicted results obtained using the Karhunen-Loève based stochastic modeling approach. The close agreement observed demonstrates the model's ability to accurately capture the spatially varying viscoelastic behavior of the fiber-reinforced composite. The 15 areas introduced in Figure 7 at the component level are illustrated here, aligning with both the experimental and numerical data.

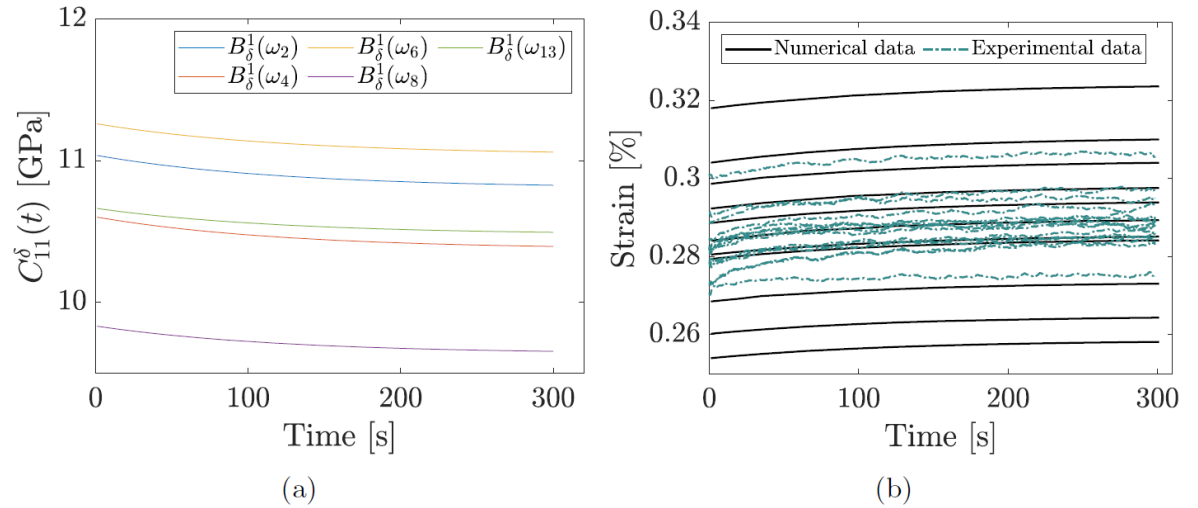

Figure 10: Numerical results include a) numerical results of $C_{11}(t)$ of the time-dependent at five different artificial microstructures, and b) a comparison between experimental creep data and numerical results modeled using the Karhunen-Loève approach, all 15 areas are shown.

4 CONCLUSION

The experimental investigations on both the component level and microscale demonstrate that the presence and distribution of short fibers significantly influence the spatial distribution of viscoelastic properties. The obtained results clearly indicate the need for a probabilistic modeling approach to accurately capture the behavior of the distributed mechanical properties. In this context, the Karhunen-Loève expansion is a suitable method that offers a compact and efficient representation of second-order Gaussian random fields. The numerical results derived from this approach demonstrate strong agreement with the experimental data, providing further validation of its applicability.

REFERENCES

[1] DASSAULT Systèmes, Abaqus 6.14 Analysis User's Guide, Providence, RI, USA, 2014.

[2] C.-T. Huang, X.-W. Chen, W.-W. Fu, Investigation on the fiber orientation distributions and their influence on the mechanical property of the co-injection molding products, Polymers 12 (2020) https://doi.org/10.3390/polym12010024

[3] R. Hill, The elastic behaviour of a crystalline aggregate, Proceedings of the Physical Society. Section A 65 (1952) https://doi.org/10.1088/0370-1298/65/5/307

[4] E. Klatt, I.M. Widera, N. Rauter, A procedure for determination of the microstructural probabilistic characteristics from micrographs and their impact on subsequent results, PAMM 22 (2023) https://doi.org/10.1002/pamm.202200277

[5] E. Klatt, B. Zimmering, B. Niggemann, N. Rauter, A comparative characterization of the creep behavior of short-fiber reinforced composites based on the prony series and fractional derivative-based creep models, Preprints (2025) https://doi.org/10.20944/preprints202506.1262.v1

[6] C. Li, A.D. Kiureghian, Optimal discretization of random fields, Journal of Engineering Mechanics 119 (1993)

[7] C. Maccone, Deep Space Flight and Communications: Exploiting the Sun as a Gravitational Lens, Springer Praxis Books. Springer, (2009). https://books.google.de/books?id=nGBhKDE1SFEC

[8] E. Marino, M. Flaschel, S. Kumar, L. D. Lorenzis, Automated identification of linear viscoelasticity constitutive laws with EUCLID, Mechanics of Materials 181 (2023). https://doi.org/10.1016/j.mechmat.2023.104643

[9] T.A. Oswald, G. Menges, Materials Science of Polymers for Engineers, Carl Hanser Verlag GmbH Co KG, (2012). https://doi.org/10.1007/978-1-56990-524-1

[10] N. Rauter, A computational modeling approach based on random fields for short fiber-reinforced composites with experimental verification by nanoindentation and tensile tests, Computational Mechanics 67 (2021) https://doi.org/10.1007/s00466-020-01958-3

[11] N. Rauter, R. Lammering, Experimental characterization of short fiber-reinforced composites on the mesoscale by indentation tests, Applied Composite Materials 28 (2021) https://doi.org/10.1007/s10443-021-09937-4

[12] N. Rauter, R. Lammering, Correlation structure in the elasticity tensor for short fiber-reinforced composites, Probabilistic Engineering Mechanics 62 (2020) https://doi.org/10.1016/j.probengmech.2020.103100

[13] N.W. Tschöegl, The Phenomenological Theory of Linear Viscoelastic Behavior: an Introduction, Springer, (1989). https://doi.org/10.1007/978-3-642-73602-5

[14] E. Vanmarcke, Random Fields: Analysis and Synthesis, G - Reference, Information and Interdisciplinary Subjects Series. World Scientific, (2010). https://books.google.de/books?id=0MCxDV1bonAC

ICCM24
AUGUST 4-8, 2025
BALTIMORE CONVENTION CENTER
BALTIMORE, MARYLAND, USA

No Technical Paper Submission for:

Lichang Lu

DETECTION OF DELAMINATION IN CFRP LAMINATES BY INTEGRATED FIBER-OPTIC STRAIN DISTRIBUTION SENSORS

Tatsuro Kosaka [1] and Serina Nakajima[2]

[1]Department of Systems Engineering, Kochi University of Technology
185 Miyanokuchi, Kami, Kochi 7828502, Japan
Email: kosaka.tatsuro@kochi-techac.jp, web page: http://www.kochi-tech.ac.jp

[2]Shinmeiwa Industries Inc
1-1 Shinmeiwa-cho, Takarazuka, Hyogo 665-0052, Japan
web page: https://www.shinmaywa.co.jp/

Keywords: NDT, Rayleigh scattering, Detection of delamination, CFRP laminates, Distributed strain sensing

ABSTRACT

Carbon fiber reinforced plastic (CFRP) offers excellent properties such as low weight and high strength, but internal delamination caused by impact or fatigue is difficult to detect. To address this, we explored the use of Rayleigh scattering-based optical fiber sensors that measure surface strain distributions via Rayleigh scattering to detect delamination in real time. A CFRP laminate was prepared with artificial delamination of 35 mm or 55 mm in length at two depths: the 10th layer (1.0 mm from the surface) and the 50th layer (3.5 mm deep). Three-point bending tests were conducted, and strain distributions were measured using a distributed fiber-optic sensor. Finite element analysis (FEM) was also performed to verify the experimental results. The strain profiles from both the test and simulation showed good agreement. At the delamination tip, the strain curve exhibited a valley for shallow delamination and a peak for deeper ones. FEM results revealed that the shape and magnitude of the surface strain anomaly are sensitive to delamination depth, especially when the delamination is near the sensing surface. When the sensor was on the tensile side, characteristic strain valleys and peaks were observed around the delamination tip, varying with depth. On the compressive side, the effect was less pronounced unless the delamination was close to the surface. These findings suggest that depth estimation is possible by placing sensors on both sides of the laminate.

1 INTRODUCTION

CFRP laminated plates, known for their light weight, high strength, and high rigidity, are widely used in aircraft and other applications due to their ability to be integrally molded with stringers. However, interlaminar delamination caused by impact or fatigue is difficult to detect visually. Therefore, non-destructive testing (NDT) methods are essential for ensuring safety during regular inspections.

Conventional NDT techniques such as ultrasonic testing, X-ray inspection, and infrared thermography have been introduced and play an important role in aircraft maintenance. However, these methods require halting operations and are limited in scanning range, resulting in prolonged inspection times and increased operational costs. To reduce downtime and improve reliability, real-time structural health monitoring (SHM) is gaining attention [1].

Real-time SHM involves embedding sensor systems directly into the structure and monitoring during operation. If wide-area measurements can be achieved using a minimal number of sensors and a compact measurement system, SHM of large-scale structures—such as aircraft—could become feasible even in-flight.

Various sensor systems have been studied, including micro piezoelectric elements and electrical resistance-based sensors. Among these, distributed optical fiber sensors are particularly well-suited for detecting delamination between stringers and skins, as they can monitor strain over long distances using a single fiber. However, the commonly used Optical Time Domain Reflectometry (OTDR)

technique, while cost-effective, has limited spatial resolution (on the order of sub-meters) and is inadequate for detecting delamination at the centimeter scale required for aircraft structures.

Therefore, we focus on a Rayleigh scattering-based distributed optical fiber sensor using Optical Frequency Domain Reflectometry (OFDR), which offers spatial resolution on the order of millimeters. By measuring strain and temperature distributions, it becomes possible to detect damage more precisely [2]. Our previous work demonstrated that delamination tips could be identified at the millimeter level by analyzing surface strain distributions measured at 1 mm intervals. In particular, Mode I and Mode II delamination tips were detected by observing peaks in the strain profiles. However, the influence of delamination depth and specimen thickness on this detection method has not been fully explored.

In this study, we conducted three-point bending tests and finite element analysis (FEA) to investigate how the depth and thickness of delamination affect surface strain distributions, aiming to clarify the detection limits and improve reliability in practical SHM applications.

2 EXPERIMENTAL METHOD

3.1 Rayleigh scattering distribution sensor

A Rayleigh scattering-based distributed sensor measures the backscattered light along the length of an optical fiber and detects local strain changes using the cross-correlation method on the spatial frequency distribution of the scattered signal. Rayleigh scattering originates from refractive index mismatches at the core-cladding interface and reflects geometrical changes in the fiber. Unlike Brillouin scattering, Rayleigh scattering does not involve a frequency shift proportional to strain. However, OFDR (Optical Frequency Domain Reflectometry) provides extremely high spatial resolution, allowing hundreds of data points per millimeter. The resulting frequency spectrum shifts toward lower frequencies when the fiber is stretched. By performing cross-correlation with a reference spectrum, the amount of frequency shift can be quantified and converted to strain. In this study, the spatial interval over which the spectrum is analyzed is defined as the gauge length, which can be adjusted post-measurement.

Strain distributions were measured using a Rayleigh scattering-type distributed optical fiber sensor (ODiSI A-50, LUNA Technologies). The system supports measurement ranges from 1 to 50 meters, with a minimum spatial resolution (pitch) of 1 mm, a strain measurement range of ±10,000 με, resolution of 1 με, and a sampling rate of up to 5 Hz, allowing simultaneous acquisition of strain and temperature distributions.

3.2 Experimental method

In this study, unidirectional CFRP specimens were fabricated using 60 plies of CFRP prepreg (TR350C100S, Mitsubishi Chemical) through hot press molding. To introduce delamination, a 0.1 mm thick Teflon sheet was placed between the 50th and 51st plies. Specimens with delamination lengths of 35 mm, 45 mm, and 55 mm were prepared by varying the length of the Teflon insert.

A three-point bending static test was conducted with a support span of 100 mm and a displacement rate of 0.5 mm/min (Figure 2). A fiber optic sensor was bonded to the bottom surface using instant adhesive (Figure 3). Additionally, the specimens were tested in both upright and inverted orientations, positioning the delamination at either 10 or 50 plies from the measurement surface. The load was paused at a predetermined value, and strain distributions were recorded during the test. Strain analysis was performed with a 1 mm measurement pitch and a 10 mm gauge length.

3.3 Analysis method

Finite element analysis was conducted using Abaqus with a two-dimensional model of the three-point bending test. The material properties were longitudinal Young's modulus E_L=137GPa, transverse modulus E_T=9.76GPa, shear modulus, G_{LT}=5.17GPa, Poisson's ratio ν_{LT}=0.32. While the experiments focused on delamination at two depths (10 and 50 plies), the simulation covered a broader range of delamination depths. To evaluate the influence of plate thickness, simulations were also performed using a 9 mm thick model—twice the experimental specimen thickness.

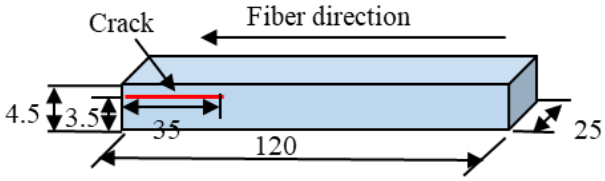

Figure 1: CFRP specimen with artificial delamination

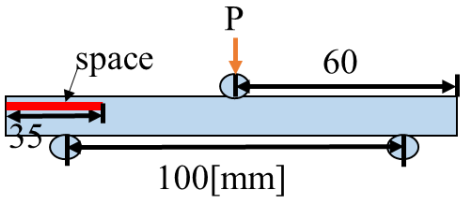

Figure 2:3-point bending test

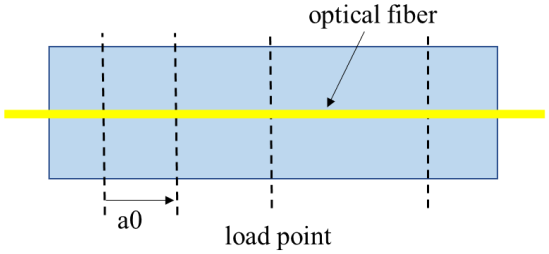

Figure 3: Location of optical fiber sensor

3 EXPERIMENTAL RESULTS AND DISCUSSION

3.1 Detection of position of delamination tip

Figures (a)–(c) show the strain distributions obtained from the optical fiber sensor, along with the corresponding finite element analysis (FEA) results under the same load, for specimens with delamination lengths of 35 mm, 45 mm, and 55 mm, respectively. The horizontal axis represents the distance from the specimen edge, and the numbers 10 and 50 indicate the delamination depths from the sensor surface, expressed as ply numbers.

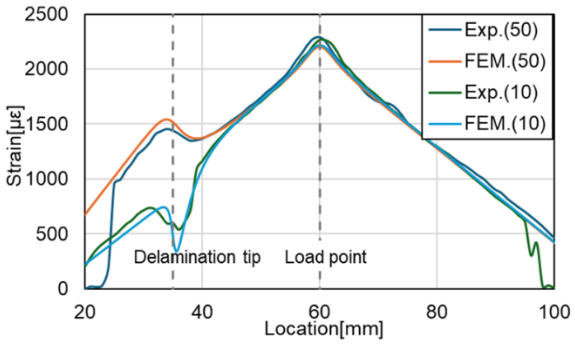

(a) 35mm delamination

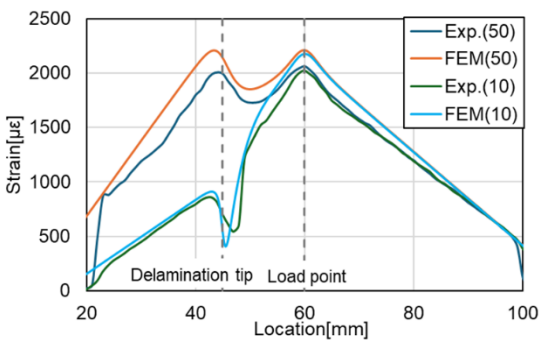

(b) 45mm delamination

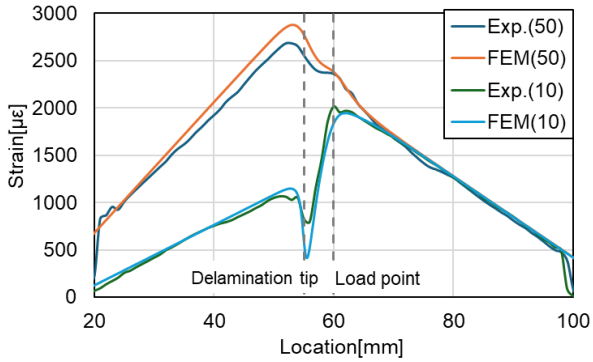

(c) 55mm delamination

Figure 4: Measured and FEM-calculated strain distribution at 3-point bending tests.

As shown, the experimental and FEA results show good agreement across all delamination lengths, confirming that the Rayleigh scattering-based distributed sensor provides highly accurate and spatially resolved strain measurements.

In all cases, a consistent relationship was observed between the surface strain distribution and the delamination front: a peak appeared 1 mm to the left of the delamination tip, and a sharp valley was observed 1 mm to the right when the delamination was close to the sensor surface. Notably, at a delamination length of 55 mm, the maximum global strain was located near the delamination tip rather than at the loading point

3.2 Effect of depth-wise position of delamination

The measurement surfaces were set as the upper and lower surfaces, and FEM analysis was performed by changing the delamination position. Figure 5 shows the strain distribution when the measurement surface was set as the lower surface, for delamination lengths of 35 mm and 55 mm. Figure 6 shows the strain distribution when the measurement surface was set as the upper surface, for delamination lengths of 35 mm and 55 mm. In both figures, the delamination depth is expressed as a percentage of the thickness from the lower surface.

From Figure 5, it was found that the delamination depth reaches a maximum value 1 mm to the left of the delamination tip at all positions. As the depth increases toward the 50% thickness position of the specimen (depth 2.25 mm), the maximum value increases, but from 50% depth to 66.7% depth, the maximum value remains almost unchanged. Additionally, this trend was found to be independent of the delamination length.

Figure 6 shows the compression side, where strain is negative. However, when the delamination depth is close to the sensor (61.1−77.8%), a sharp valley appears compared to the tensile side shown in

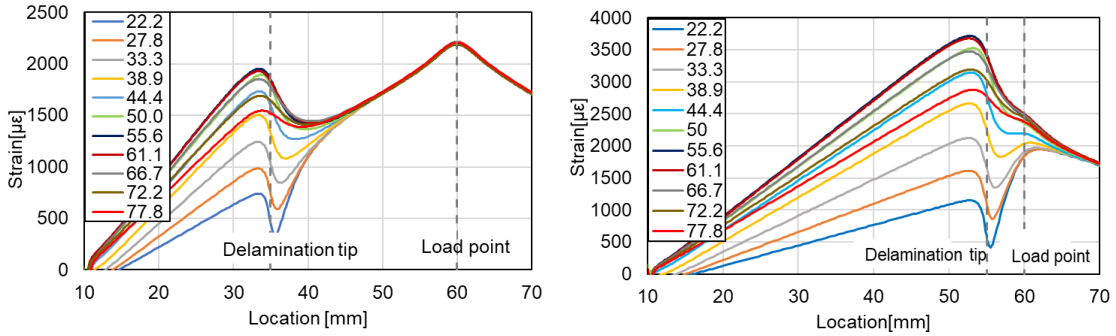

(a) Delamination length of 35mm (b) Delamination length of 55mm

Figure 5: Surface strain distribution on the tensile side at 3-point bending tests with delamination exists at various depth..

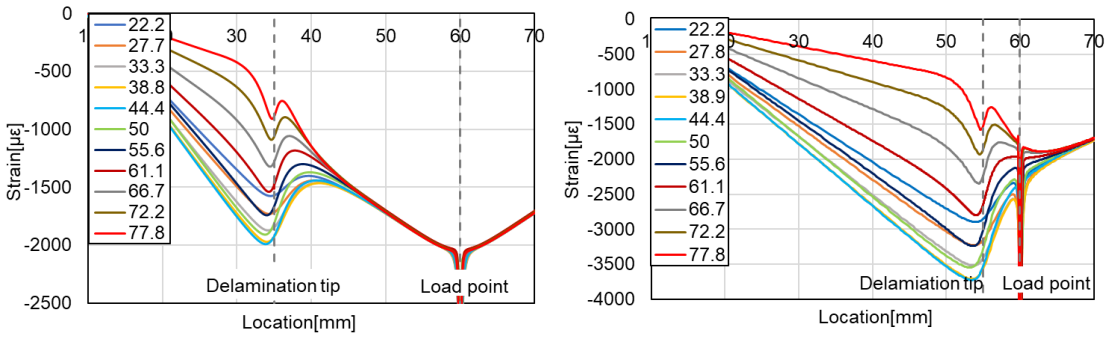

(a) Delamination length of 35mm (b) Delamination length of 55mm

Figure 6: Surface strain distribution on the compressive side at 3-point bending tests with delamination exists at various depth.

Figure 5, indicating that the strain perturbation at the delamination tip differs between the tensile and compression sides. This is because the tensile side layer is subjected to concentrated loads due to the fulcrum, whereas the compressive side receives loads through the peel surface. When measuring the compressive side, similar to the tensile side, the depth of the peel from the sensor surface increases as the delamination depth progresses toward the center, causing the valley depth of the strain peak to increase, but decreases as the peel moves away from the center.

Based on the above results, it was found that determining the delamination depth is difficult using only the peak height measurement of one side, except when the delamination depth is near the sensor surface. Therefore, it is considered necessary to place sensors on both the upper and lower surfaces to achieve accurate delamination depth determination. Rayleigh scattering-type distribution sensors can measure a very long range with a single sensor, so it is believed that simultaneous measurement of both upper and lower surfaces through appropriate sensor placement enables the identification of depth positions.

3.3 Relationship between strain perturbation peak and depth-wise position

It has been clarified that the peak height of strain is influenced by the depth position. Therefore, to quantitatively clarify this relationship, the strain distribution on the surface of a laminated plate without delamination was used as a reference, and the strain distribution in the presence of delamination was subtracted to obtain the perturbation distribution caused by delamination. The normalized distribution of the perturbation relative to the load point strain is shown in Figure 7. Additionally, to investigate the influence of plate thickness, FEM analysis was also performed for a plate thickness of 9 mm.

From the figure, it can be seen that in both thicknesses, when the delamination is inserted at a depth of 33.3% from the measurement surface, a clear valley is observed. On the other hand, as the delamination moves away from the measurement surface, only peaks appear. It was found that up to a

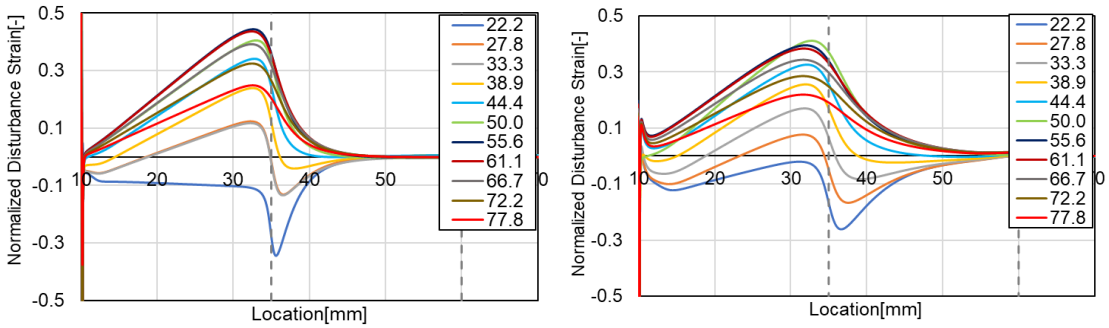

(a) 4.5mm thickness (b) 9mm thickness

Figure 7: Perturbation of strain by delamination at 3-point bending tests.

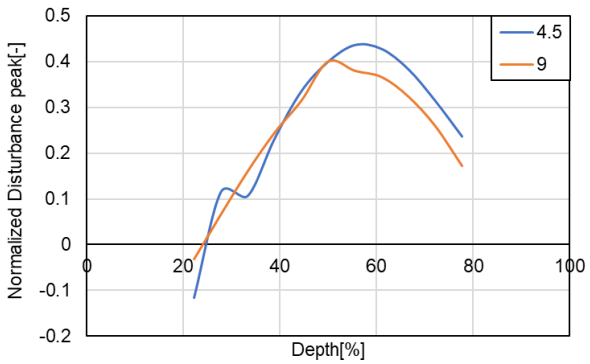

Figure 8: Relationship between normalized perturbation peak caused by delamination at 3-point bending tests for specimens of 4.5- and 9-mm thicknesses.

depth of 50%, the size of the peaks increases monotonically with the depth of the delamination. This trend is similar regardless of thickness, indicating that the size of the peaks is a useful feature for estimating depth. On the other hand, it was also found that as the thickness increases, the peak shapes of the peaks and valleys become less pronounced. Therefore, it was found that although plate thickness affects the distribution of strain perturbations caused by delamination, it is likely possible to detect the depth from the perturbation peak within the range from the measurement surface to the central thickness.

Figure 8 shows the relationship between the height of the disturbance peak and the delamination depth position normalized by plate thickness for plate thicknesses of 4.5 mm and 9 mm, respectively. From the figure, it can be seen that in the case of a thickness of 9 mm, the depth increases monotonically up to 50%, and the peak value decreases monotonically beyond 50%. However, in the case of 4.5 mm, it can be seen that the depth decreases once at 33.3%. This is likely due to stress concentration at the support point influencing the perturbation distribution.

In summary, regardless of plate thickness, it was found that the depth of delamination can be estimated from the height of the perturbation peak. Additionally, when the delamination depth is close to the sensor surface, the height of the perturbation valley is a better indicator.

4 CONCLUSIONS

In this study, we investigated the effects of delamination depth and plate thickness on the detection of interlaminar delamination in CFRP using a Rayleigh scattering-type distribution sensor. Experimental and FEM analysis results showed good agreement, demonstrating that the spatial resolution and accuracy of the sensor are sufficient for detecting the leading edge position of interlaminar delamination. Furthermore, the analysis results indicated that the position of the delamination depth is strongly correlated with the normalized strain peak. This correlation showed a similar trend even when the plate thickness varied. However, since the peak height is maximum near the center of the specimen, it is necessary to determine whether the delamination depth is close to the sensor surface. However, when the delamination depth is near the sensor surface, a characteristic valley is observed, making identification easy.

Therefore, by using this sensor on both the upper and lower surfaces, it was found that it is possible to simultaneously determine the position and depth of the interlaminar delamination tip.

REFERENCES

[1] N. Takeda, S. Takeda, Y. Nagao, A. Franceschetti and X. Liu, Detection of internal damage in CFRP using embedded optical fiber sensors, *Composites Part A*, **42**(6), 2011, pp. 669–676 (doi: 10.1016/j.compositesa.2011.02.006).

[2] M. Froggatt and J. Moore, High-spatial-resolution distributed strain measurement in optical fiber with Rayleigh scatter, *Applied Optics*, **37**(10), 1998, pp. 1735–1740.

ICCM24
AUGUST 4-8, 2025
BALTIMORE CONVENTION CENTER
BALTIMORE, MARYLAND, USA

No Technical Paper Submission for:

Yushen Wang

No Technical Paper Submission for:

Societal and Industrial Impact Workshop

STRUCTURAL INTEGRITY ASSESSMENT OF REPURPOSED EOL WIND TURBINE BLADE COMPOSITE COMPONENTS USING ACOUSTIC EMISSION TESTING AND I*B*-VALUE ANALYSIS UNDER VARIOUS LOADING AND TEMPERATURE CONDITIONS

P. Johst[1,2], M. Shin[3], S. Lee[3,4], E. Kim[3,4], R. Böhm[1], W. Na[3,5*]

[1]Faculty of Engineering, Leipzig University of Applied Sciences (HTWK Leipzig)
Karl-Liebknecht-Straße 132, 04277 Leipzig, Germany
Email: philipp.johst@htwk-leipzig.de, robert.boehm@htwk-leipzig.de, web page: https://fing.htwk-leipzig.de/fakultaet/professuren/prof-robert-boehm

[2]Faculty of Mechanical Science and Engineering, Dresden University of Technology (TU Dresden)
Holbeinstraße 3, 01307 Dresden, Germany
Email: philipp.johst@mailbox.tu-dresden.de, web page: https://tu-dresden.de/

[3]Composite Materials Applications Research Center, Korea Institute of Science and Technology
92 Chudong-ro, Bongdong-eup, Wanju-gun, Jeonbuk 55324, Republic of Korea
Email: t24088@kist.re.kr, leesungbi@kist.re.kr, t20468@kist.re.kr, namossi@kist.re.kr, web page: https://jb.kist.re.kr:7443/eng/main/main.do

[4]Department of Materials Science and Engineering and Research Institute of Advanced Materials
Seoul National University, 1 Gwanak-ro, Gwanak-gu, Seoul, 08826 Republic of Korea
Email: leesungbi@kist.re.kr, t20468@kist.re.kr, web page: https://en.snu.ac.kr/

[5]Department of JBNU-KIST Industry-Academia Convergence Research, Jeonbuk National University
567 Baekje-daero, Deokjin-gu, Jeonju-si, Jeollabuk-do, 54896 Republic of Korea
Email: namossi@kist.re.kr (W. Na, **Corresponding Author*), web page: https://jbnu.ac.kr/web/index.do

Keywords: Wind turbine blade, Polymer-matrix composites, Spar cap components, Non-destructive testing, Acoustic emission

ABSTRACT

Wind energy is an essential renewable energy source; however, the disposal of end-of-life (EoL) wind turbine blades (WTBs) presents significant challenges. Repurposing EoL WTB components, such as spar caps, for use in the construction sector is a sustainable alternative; however, pre-existing damage can affect their mechanical performance. This study investigates an acoustic emission (AE)-based approach that incorporates improved *b*-value (I*b*-value) analysis to assess the structural integrity of EoL WTB spar cap specimens. Tensile and bending tests are performed at 23 °C and 67 °C to evaluate damage propagation for potential construction applications. AE data analysis confirmed the method's effectiveness in detecting early degradation. Furthermore, the influence of temperature on the mechanical properties of the composite material is investigated. The findings indicate that I*b*-value analysis is a viable non-destructive testing method for assessing structural repurposed EoL WTB components under various loading conditions. The extension of this approach to other EoL WTB components has the potential to enhance circular economy strategies in the wind energy and construction sectors.

1 INTRODUCTION

Wind power is a crucial renewable energy source, with a substantial volume of end-of-life (EoL) wind turbine blade (WTB) material anticipated globally by 2050 [1], with Germany contributing a major share [2]. However, the management of EoL WTBs poses significant challenges due to the

environmental impact of disposal [3]. The utilization of composites as the primary material in WTBs is predominantly attributable to their high specific mechanical properties [4]. However, their thermoset-based polymer matrix makes recycling difficult [5]. Under circular economy principles [6], the repurpose strategy offers a promising alternative [7-9], especially for structural components of EoL WTBs [10]. By repurposing EoL WTB composite components in a second life application with a new function, this strategy seeks to extend the service life of the composite materials while preserving their structural integrity. Unidirectional (UD) reinforced spar cap beams, which are characterized by their excellent mechanical properties, are assumed to be suitable for repurposing in large quantities in various industrial sectors, including the construction industry. However, the possibility of pre-existing damage resulting from the manufacturing process or the first life cycle cannot be discounted, as this may lead to mechanical degradation [11]. Understanding these effects and defining their reliability is essential for the structural repurpose of EoL WTB components in second-life applications.

Previous research has presented a method for assessing the structural integrity of composite components using acoustic emission (AE) testing combined with I*b*-value analysis [12, 13]. AE is a well-established, non-destructive testing (NDT) technology with high resolution. The *b*-value analysis, which monitors the cumulative amplitude distribution, demonstrated sufficient feasibility with modification. The improved *b*-value (I*b*-value) was combined to assess the structural integrity of EoL WTB spar cap specimens [14]. The method has been studied and concluded to be effective in identifying early damage propagation under tensile loading at room temperature (RT).

However, the robustness of this technique for other loading conditions and at elevated temperatures (ET) remains to be validated. This study explores the feasibility of I*b*-value analysis for tensile and bending loading at ET conditions, considering repurpose in the construction sector. The ET of 67 °C is determined in accordance with a German guideline (*BUEV recommendations*) that holds validity in the construction sector. To this end, tensile and bending tests are carried out at RT (23 °C) and ET (67 °C). The AE data collected during these tests are used to perform a comparative behavior analysis of the tensile and bending specimens at RT and ET. The present study focuses on the *b*-/I*b*-value analysis to evaluate the reliability of this method in different loading scenarios.

2 MATERIALS AND METHODS

2.1 Materials and EoL WTB specimen preparation

An EoL WTB (E40 wind turbine; Enercon, Germany) with a service life of approximately 20 years is used as the base material in this study. The WTB extends along a longitudinal direction (LD) measuring 19.3 m, while the transverse direction (TD) is perpendicular to the LD, with a maximum width of 1.92 m (Figure 1a). The spar cap component (Figure 1a, Section A-A), consists of glass fiber-reinforced polymer (GFRP) composites. The extraction of UD GFRP spar cap samples is conducted in alignment with the sectioning approach described by Joustra *et al.* [10].

Initially, TD cuts are performed using a wire saw to separate the EoL WTB segments (Figure 1a, dashed lines). Subsequent to this, LD cuts are performed to extract the shear web and sandwich elements from the spar cap beams (Figure 1b). The spar cap beams are then cut (Figure 1c) into square-shaped components measuring 200 mm in length (Figure 1d) and are further processed into tensile and bending specimens. Consequently, one side of each spar cap component is flattened with a CNC router, following the process of wheel cutting to obtain samples with a thickness of 4 mm. Any sharp edges are smoothed with sandpaper. For tensile testing, 1.6 mm thick GFRP tabs are bonded to 50 mm of both ends of each tensile sample using an epoxy film adhesive (UCS-I-95; UCS, China), resulting in a gauge length of 100 mm. The final tensile specimens have overall dimensions of 200 x 20 x 4 mm (Figure 1e). The specimens for the bending tests are produced from the tensile specimens through the use of a waterjet machine and measure 80 x 20 x 4 mm (Figure 1f). The glass fiber volume fraction of the UD specimens is estimated to be approximately 43.9% (density glass fiber: 2.48 g/cm^3, density matrix: 1.19 g/cm^3). As the tests are planned at ET, the glass transition temperature of the matrix material is determined to be 100 °C using differential scanning calorimetry (DSC) in accordance with ISO 11357.

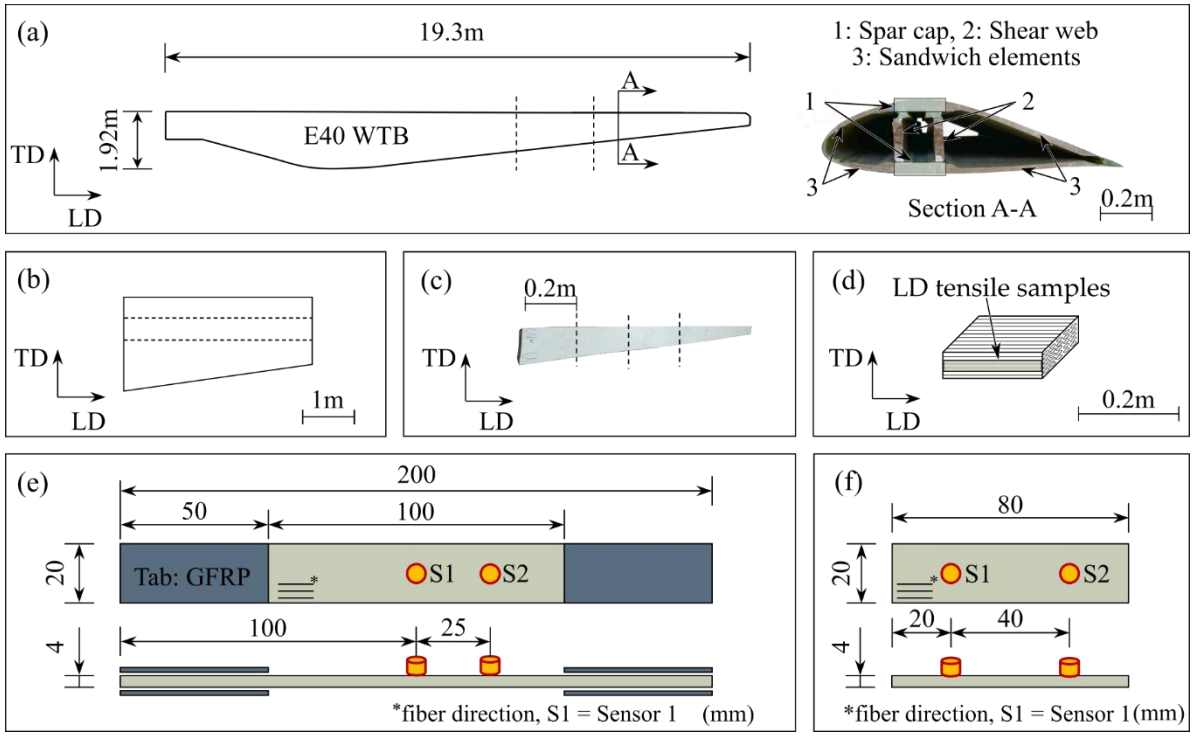

Figure 1: Preparation process of EoL spar cap specimens: (a) EoL WTB; (b) EoL WTB segment; (c) Spar cap beam; (d) Square-shaped spar cap component; (e) Dimensions of tensile specimens and sensor locations; (f) Dimensions of bending specimens and sensor locations.

2.2 Material characterization at different temperatures

The mechanical properties of the prepared EoL specimens are evaluated through tensile and bending tests performed at two different temperatures: room temperature (RT, 23 °C) and elevated temperature (ET, 67 °C). Tensile tests are conducted following the standards outlined in ASTM D3039 and are carried out on a universal testing machine equipped with a temperature chamber (Instron 5985; Instron, USA) at a crosshead speed of 0.5 mm/min (Figure 2a). The selection of this strain rate is driven by the objective of minimizing the strong overlap of AE signals, especially after 50 % of the specimen life when signal density increases significantly. In order to reduce measurement noise, neither an extensometer nor a strain gauge is used. A minimum of seven tensile specimens are tested at each temperature condition. In addition, bending tests are conducted at RT and ET, following ASTM D790, and are performed on a universal testing machine equipped with a temperature chamber (Instron 5985; Instron, USA) at a crosshead speed of 0.9 mm/min (Figure 2b). The span length is 33.6 mm. A minimum of six bending specimens are tested at each temperature condition. AE monitoring is performed simultaneously during the material characterization tests.

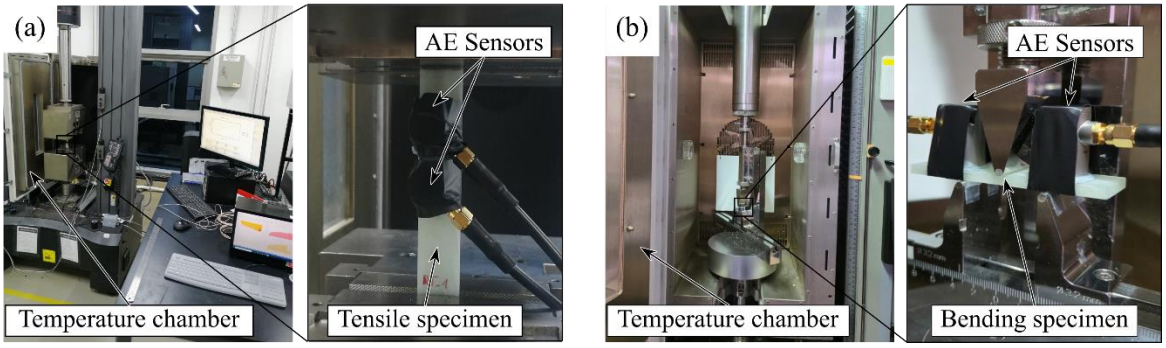

Figure 2: (a) Tensile test equipment; (b) Bending test equipment.

2.3 Acoustic emission testing

Wide-range piezoelectric AE sensors (IDK-AES-H150; IDK Co., Ltd., Republic of Korea) with a frequency range of 100-900 kHz were used for AE monitoring. During both tensile and bending tests, two AE sensors are attached to each specimen and secured with silicone grease (HIVAC-G; Shin-Etsu, Japan) and vinyl tape (Figure 2a and Figure 2b). The locations of the sensors (S1 and S2) are labeled "S" in Figure 1e and Figure 1f. The sensor placement remained constant throughout all experiments for both testing temperatures.

Before the experiments, the sensitivity of both AE sensors is verified. The AE signals are amplified using preamplifiers (IDK-AMP-S001-40/60; IDK Co. Ltd., Republic of Korea) with a gain of 40 dB_{AE}. During the testing phase, AE signals exceeding the 40 dB_{AE} threshold are detected with a digitizer (IDK-DAQ8; IDK Co. Ltd., Republic of Korea) at a sampling rate of 5 MSPS per channel. The AE signals are recorded under the conditions listed in Table 1. The time parameters are set as follows: peak definition time (PDT) at 200 µs, hit definition time (HDT) at 400 µs, and hit lockout time (HLT) at 4000 µs. Additionally, the amplitude, energy, and frequency characteristics of the AE signals are calculated and recorded, with the centroid frequency serving as the primary frequency characteristic for GFRP. AE signal analysis is based on key features including raw amplitude, hit frequency (hits per second), and AE frequency (peak frequency). Data processing is carried out using MATLAB software (version R2024a, MathWorks, USA).

	Threshold	Pre-amplifier	Sampling conditions		
			Sampling rate	Pre-trigger	Length[1]
Value	40	40	5	100	1000
Unit	dB_{AE}	dB_{AE}	MSPS	μs	µs

[1]Length: Recording time for each acoustic emission (AE) signal after the AE signal exceeds a certain threshold.

Table 1: Acoustic emission testing conditions.

As shown in previous studies, the dominant failure modes in UD reinforced specimens include matrix cracking, interfacial failure, and fiber breakage/fracture [15]. In FRPs, AE signals typically fall within the 100 kHz to 600 kHz range when a band-pass filter is applied, with specific frequency ranges corresponding to distinct fracture modes. High frequencies (400 - 600 kHz) are indicative for fiber breakage/fracture, low frequencies (100 – 220 kHz) correspond to matrix cracking, and intermediate frequencies (220 – 400 kHz) are associated with interfacial failure mechanisms. Multiple specimens are tested under each temperature condition (tensile and bending), resulting in minimal variation in AE parameters and characteristics. This reproducibility enabled the selection of a representative dataset for further analysis.

2.4 *b*-/I*b*-value analysis

For *b*-/I*b*-value analysis, the amplitude of AE signals is recorded, and the cumulative distribution function (CDF) is plotted according to Equation (1):

$$N(A) = \int_{A}^{\infty} n(A')dA' \tag{1}$$

here, A denotes a specific amplitude, while A' is an auxiliary amplitude variable used for integration, n(A') is the number of AE hits corresponding to each particular amplitude, and N(A) represents the cumulative number of hits with amplitudes equal to or greater than A. Although A' is mathematically equivalent to A, the distinction is introduced for notational clarity. In AE analysis, the amplitude A [dB_{AE}] is defined by Equation (2), using a reference voltage 1 µV as V0.

$$A = 20 * log_{10}\frac{V_1}{V_0} \tag{2}$$

The concept of *b*-value was introduced by Gutenberg through the Gutenberg-Richter equation, which is defined as the negative slope of the CDF, as shown in Equation (3). Originally developed for seismological analysis, this method has also been applied to materials such as concrete [16].

$$log_{10} * N(A) = a - bA \tag{3}$$

where a is an empirical constant, and b is the *b*-value, representing the slope of the linear relationship, typically determined by the least-square method. The *b*-value remains positive as long as the CDF shows a declining trend. In the early damage phase, dominated by microcracking, many low-amplitude and few high-amplitude AE signals are recorded, resulting in a high *b*-value (green line, Figure 3a). As macrocracks develop, the number of high-amplitude AE signals increases, shifting the CDF and reducing the *b*-value (orange line, Figure 3a) [17]. This decline near failure indicates that the *b*-value effectively reflects structural health. In composite materials, where multiple cracks propagate independently, tracking major crack regions using the mean value (μ) and standard deviation (σ) of AE amplitudes is more practical. This localized form of analysis, known as the I*b*-value, was introduced by Shiotani [18] and further studied by Jung and Na [12]. The I*b*-value is described in Equation (4):

$$log_{10} * N(A) = a - IbA \ldots (\mu - \alpha_1\sigma < A < \mu + \alpha_2\sigma) \tag{4}$$

α_1 and α_2 are constants defining the lower $(\mu - \alpha_1\sigma)$ and upper $(\mu + \alpha_2\sigma)$ amplitude limits (Figure 3b). The amplitude range is $(\alpha_1 + \alpha_2)\sigma$, typically with an $\alpha_1 : \alpha_2$ ratio of 1:1 or 1:2; in this study, both were set to 1. The parametric values are calculated after every 500 AE hits for the tensile specimens and after every 100 AE hits for the bending specimens (i.e., 1st to 100/500th, 1st to 200/1000th, ..., up to 400/2000th). The slopes of *b*-/I*b*-values are determined using the least-squares method. High values indicate a dominance of microscopic fractures, while low values suggest increasing macroscopic fracture activity (i.e., large amplitude signals).

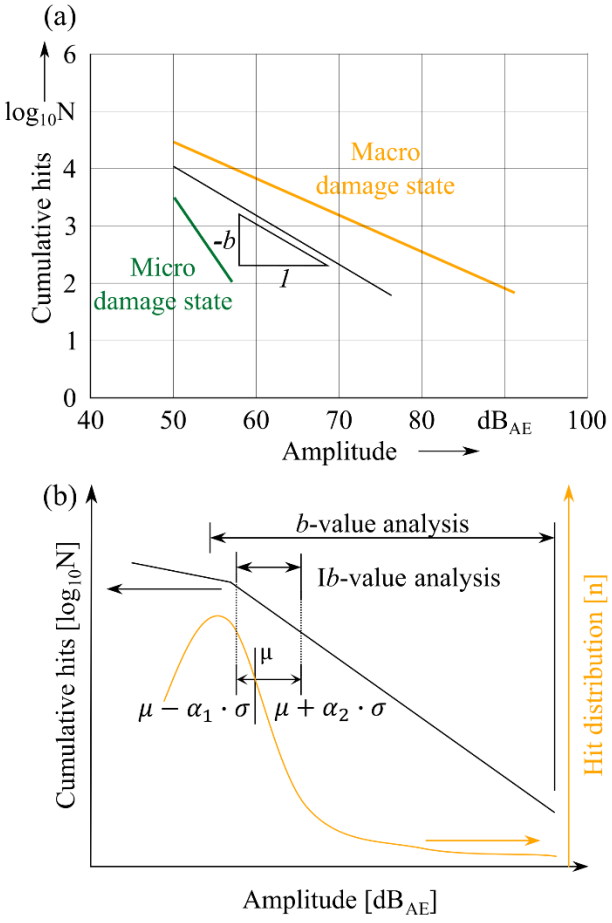

Figure 3: (a) Interpretations and (b) Definition of *b*-/I*b*-value analysis [14].

3 RESULTS

3.1 Analysis of the failure behavior of the EoL spar cap composites at RT and ET

Tensile loading: The RT tensile specimens show an average ultimate tensile strength (UTS) of 683 MPa, while the ET specimens exhibit a slightly lower average UTS of 598 MPa. The UTS represents 100 % of the tensile specimen lifetime and marks the point of total failure. At both test temperatures, the tensile specimens exhibit linear elastic stress-strain behavior until they reach total failure. The influence of different temperature settings on material behavior under tensile loading is explored in the frequency domain. Figures 4a and 4b present the acoustic emission (AE) frequency analysis results for the RT and ET specimens, respectively.

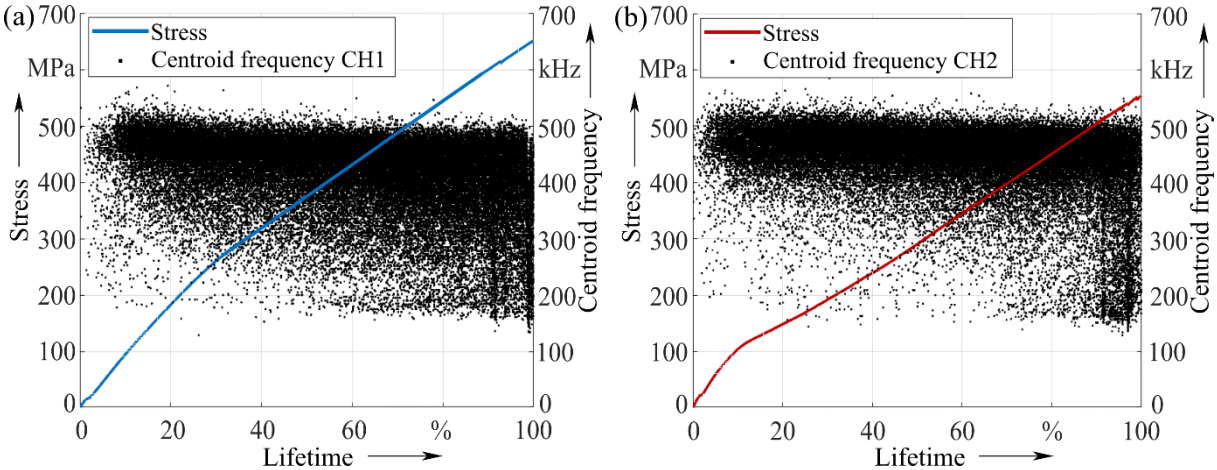

Figure 4: Centroid frequency range as the total hits for (a) RT and (b) ET tensile specimens.

The overall frequency range is broad; however, distinct preferred centroid frequency ranges are identified. For both RT and ET specimens, high frequencies (400 – 600 kHz) associated with fiber breakage are dominant. As the specimen's approach total failure, a significant number of intermediate (220 – 400 kHz) and low frequency (100 – 220 kHz) hits are detected. In particular, the RT specimens exhibited a significantly higher number of mid-frequency hits (corresponding to interfacial failure) compared to the ET specimens from 20% lifetime onward. This trend is also illustrated in Figure 5.

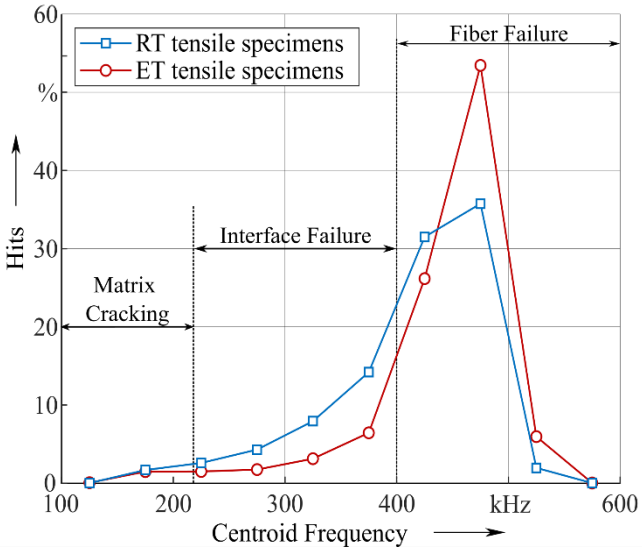

Figure 5: AE distribution showing the centroid frequency at RT and ET (each AE hit fraction was normalized to the total number of AE hits).

In the context of ET, the polymer matrix undergoes partial softening, resulting in a reduction of its load-carrying capacity and the appearance of slight ductility. These two effects have opposing implications for interfacial adhesion: softening tends to weaken the interface, while increased ductility may enhance it. However, the overall impact appears to be dominated by the negative influence of matrix softening. Considering the significant mismatch in mechanical properties between the fibers and the matrix, as well as the intrinsic brittleness of the fibers, the potential benefits of increased ductility appear to be negligible in tensile specimens loaded in LD.

Bending loading: The RT bending specimens exhibit an average ultimate flexural strength (UFS) of 1,174 MPa, while the ET specimens show a reduced average UFS of 890 MPa. UFS is defined as the maximum bending load a specimen can sustain before complete structural failure. Although the EoL bending specimens display a moderate reduction in bending strength under ET conditions, their mechanical performance remains comparatively high. Analogous trends are observed in the tensile specimens tested at ET. These findings underscore the viability of repurposing EoL spar cap components in structural second life applications, including those exposed to ET, such as in the construction sector.

Figures 6a and 6b present representative stress–strain curves and trend lines under bending load, along with corresponding AE hits in the frequency domain. Up to approximately 60% of the specimen's lifetime, both curves exhibit a similar slope ($b_{RT1} = b_{ET1}$), indicating comparable stiffness during the initial loading phase. Beyond this point, a reduction in slope is observed ($b_{RT2} < b_{RT1}$; $b_{ET2} < b_{ET1}$), particularly in the ET specimens. The secondary linear slope (b_{ET2}) is lower than that of the RT specimens (b_{RT2}), which may contribute to the lower UFS under ET conditions.

The AE data also reflect this transition. During the initial 60% of the lifetime, the AE signals predominantly lie within a narrow frequency range of 400–600 kHz for RT and ET bending specimens, a range associated with fiber breakage. After this point, the frequency distribution becomes significantly broader. In addition to high-frequency events, intermediate- and low-frequency AE hits (100–400 kHz) are increasingly apparent, suggesting the onset of additional damage mechanisms such as matrix cracking or interfacial debonding.

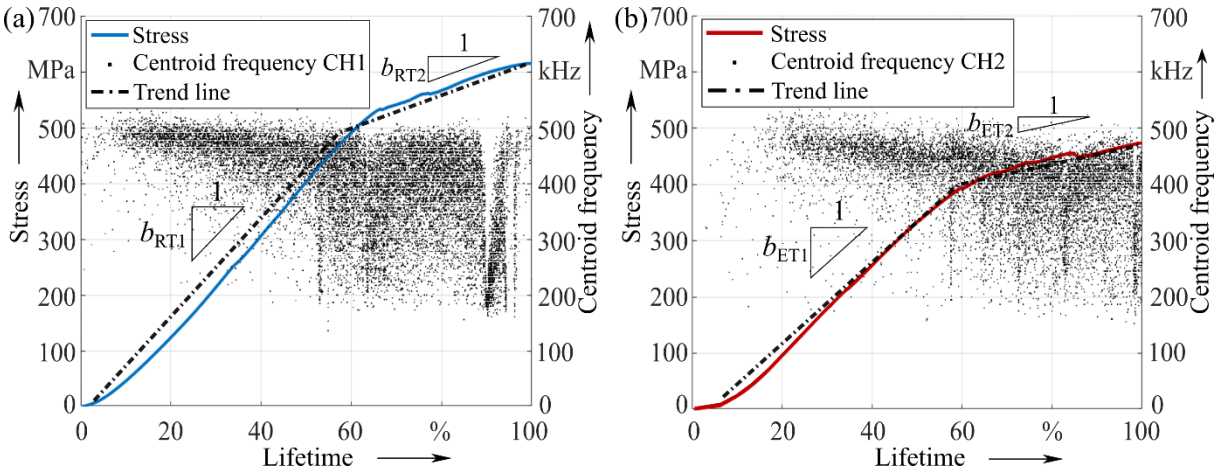

Figure 6: Centroid frequency range as total hits for (a) RT bending and (b) ET bending specimens.

Fundamentally, since tensile failure dominates in this material system, the AE distribution of centroid frequencies observed under bending closely resembles that observed in tensile failure. The centroid frequency ranges remain generally similar for the bending specimens tested at both temperatures. Notably, the ET specimens exhibit a slightly higher number of high-frequency AE hits compared to those tested at RT. This trend is illustrated in Figure 7.

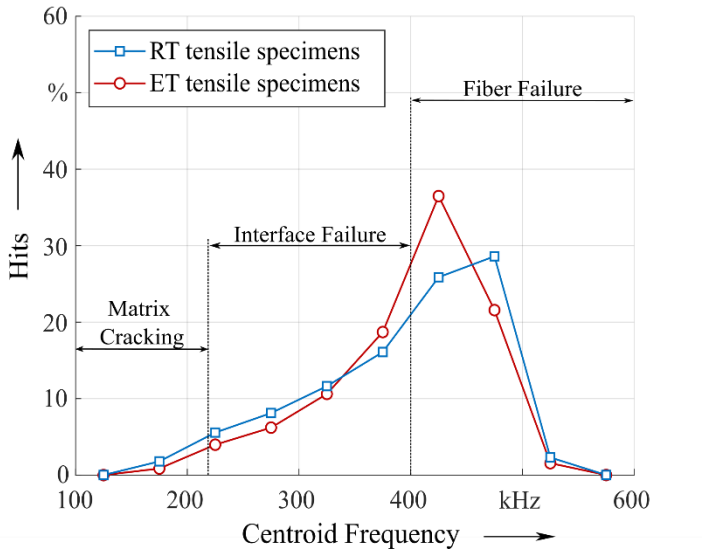

Figure 7: AE distribution for both bending temperatures (each AE hit fraction was normalized to the total number of AE hits).

3.2 *b*-/I*b*-value analysis of tensile and bending tests at different temperatures

The *b*-/I*b*-value analysis uses data from the first 30% of the specimen's lifetime to ensure sufficient AE activity and to allow the specimen to undergo complex microdamage behavior in the early stages. This period typically exhibits numerous microcracks and rising *b*-values, which do not reliable indicate structural integrity. To improve data quality, the first 50 AE hits—primarily considered noise—are excluded from the analysis.

As shown in Figure 8, the *b*-value does not exhibit a consistent trend over the lifetime of the tensile and bending specimens tested at RT and ET. Depending on the loading condition, the *b*-value either increases or decreases, indicating variability rather than a clear progression. This inconsistency suggests a potential overemphasis of micro-cracks activity in the results. Consequently, the *b*-value is not considered valid as a reliable indicator in terms of SHM purposes.

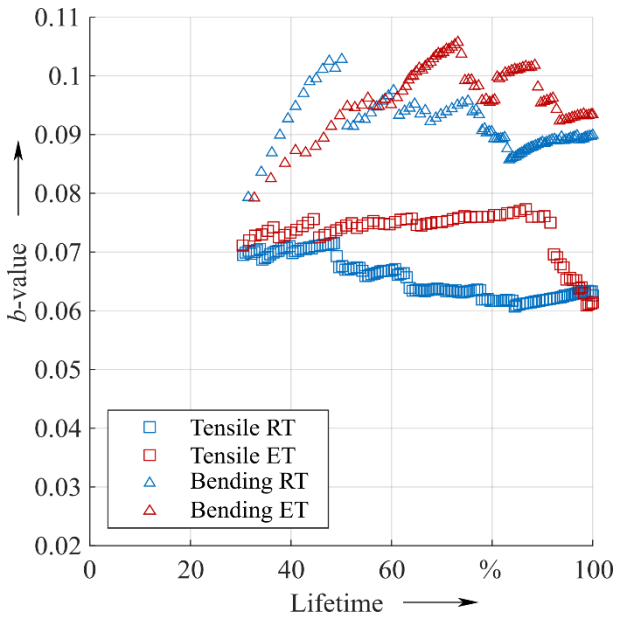

Figure 8: Lifetime dependence of *b*-values during tensile and bending tests at RT and ET.

The I*b*-value analysis presented in Figure 9 shows a decreasing trend for both tensile and bending specimens, indicating greater reliability as a damage assessment criterion. It demonstrates potential for representing the structural health of EoL composite materials.

The final I*b*-value for the tensile tests (Figure 9a) ranges from 0.05 to 0.055 at RT, and increases slightly to approximately 0.06 under ET conditions. This increase may result from temperature-induced changes in the matrix properties or a weakened fiber-matrix interface.

In bending tests (Figure 9b), the final I*b*-value ranges from 0.055 to 0.06 at RT and increases slightly to approximately 0.065 under ET conditions. At both temperatures, the I*b*-value exhibits a two-phase trend: a typical decreasing phase followed by a slower decreasing phase beginning at approximately 60% of the specimen's lifetime. This transition corresponds to the change in slope observed in the stress-strain response, indicating a shift from major crack propagation to the final failure phase, which is characterized by the formation of numerous microcracks. Sudden jumps in the I*b*-value are likely caused by the abrupt formation of individual microcracks.

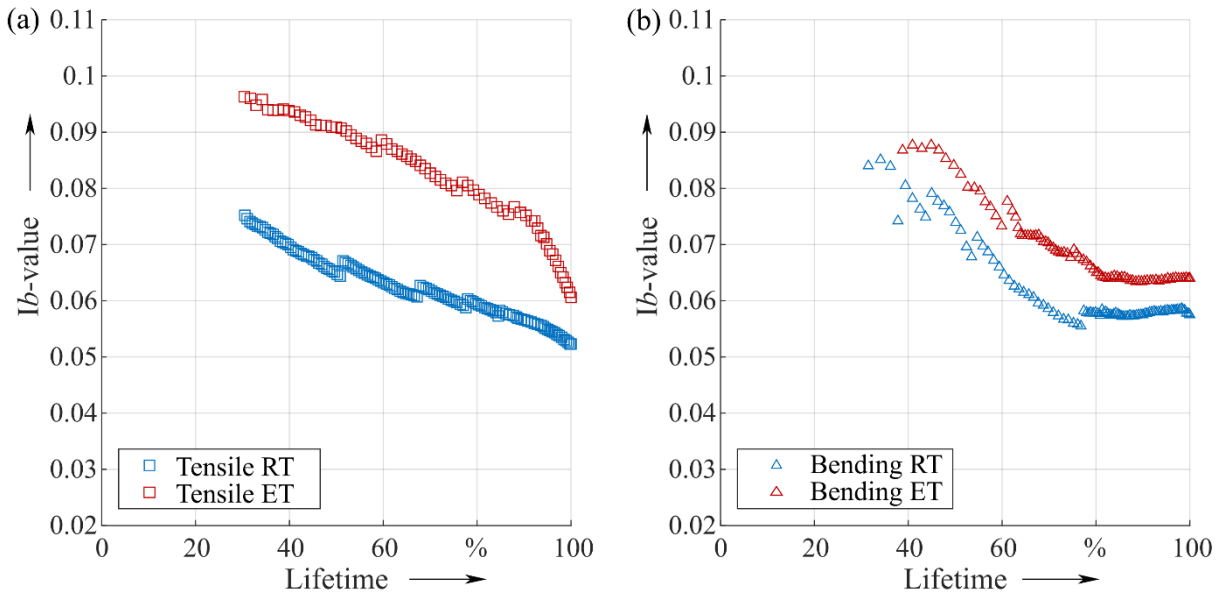

Figure 9: Lifetime dependence of I*b*-values during (a) tensile tests at RT and ET and (b) bending tests at RT and ET.

3.3 Comparison I*b*-value analysis for tensile and bending specimens

The I*b*-value is found to be sensitive to varying loading conditions. Therefore, its interpretation as an indicator of structural condition should be adapted to the specific loading scenario. The corresponding Ib-values, categorized by load scenario, are summarized in Table 2.

I*b*-value tensile RT	I*b*-value tensile ET	I*b*-value bending RT	I*b*-value bending ET	Structural condition
I*b* > 0.1	I*b* > 0.1	I*b* > 0.1	I*b* > 0.1	No/slight damage
0.1 > I*b* > 0.07	0.1 > I*b* > 0.08	0.1 > I*b* > 0.07	0.1 > I*b* > 0.075	Moderate damage
0.07 > I*b* > 0.06	0.08 > I*b* > 0.07	0.07 > I*b* > 0.06	0.075 > I*b* > 0.065	Severe damage
0.06 > I*b*	0.07 > I*b*	0.06 > I*b*	0.065 > I*b*	Near to fracture

Table 2: Structural health assessment criteria based on I*b*-values for repurposed EoL composites under different loading conditions.

Based on these criteria, the following assumptions can be made:

- If the structural condition is classified as moderately damaged, repair of the monitored structure is recommended.
- If the Ib-value indicates severe damage, structural replacement should be considered as a viable option.
- If the structure approaches fracture, safety concerns arise, and immediate intervention may be necessary.
- If loading conditions are considered in the interpretation of the Ib-value, the feasibility of Ib-value analysis for SHM of repurposed GFRP beams is further supported.

4 DISCUSSIONS

The results demonstrate that the I*b*-value exhibits a consistent decreasing trend, independent of the applied loading condition. This observation supports the reliability and repeatability of I*b*-value analysis across both tensile and bending load scenarios. Since second life applications of composite components may involve varying dominant loading scenarios, this dependency must be carefully considered when employing the I*b*-value as a structural health indicator. Notably, final failure in all cases occurred at an I*b*-value of approximately 0.06, suggesting that this value may serve as a threshold indicator of critical damage. Under ET conditions, the final I*b*-values tended to be slightly higher than those observed at RT. This behavior likely reflects the combined influence of increased microcrack generation and thermal softening of the matrix. Given the comparable internal structural conditions of the specimens, it is reasonable to attribute the dominant effect to the latter, indicating that matrix weakening under ET contributes more significantly to the observed increase in I*b*-value.

This study advances the current understanding of the I*b*-value approach by examining its response not only to different loading modes but also to variations in temperature. The ability of the I*b*-value to capture damage evolution under these divers' conditions highlights its potential as a robust diagnostic tool for SHM.

However, this study also has certain limitations. Notably, the behavior of the I*b*-value under cyclic bending loading, especially beyond the onset of phase 2 (where damage localization becomes dominant), remains unexplored. Future research should address this aspect and explore the scalability of the approach, for example, by applying it to larger structural elements such as 1000 mm long spar cap beams. Additionally, validating the technique across different composite components from EoL WTBs would support a broader assessment of its applicability for SHM in sustainable energy infrastructure.

5 CONCLUSIONS

This study presents an AE-based structural integrity assessment of EoL WTB components subjected to varying loading and temperature conditions. Key AE features, namely peak amplitude, cumulative hits, and centroid frequency, are evaluated in accordance with established failure analysis methodologies. Compared to RT specimens, ET specimens exhibit slightly reduced UTS and UFS, reflecting temperature-dependent material degradation.

In the *b*-/I*b*-value analysis, a representative segment extraction method based on mean values is introduced. The results show that the *b*-value does not exhibit a consistent trend over the specimen lifetime, limiting its reliability. In contrast, the I*b*-value demonstrates a more robust and reproducible response, establishing it as a more reliable indicator of structural degradation.

Regardless of the specific form a monitoring criterion may take, the findings highlight the need for standardized methods to track the evolution of dominant crack regions during progressive failure. As the repurposing of composite materials gains increasing relevance, SHM approaches tailored to previously serviced materials under different loading conditions are essential. In particular, ensuring the structural integrity of components during the early stages of their second application is critical. The extended I*b*-value approach proposed in this study provides a promising foundation for SHM of repurposed composites and shows potential for practical implementation in industrial sectors such as wind energy and construction.

ACKNOWLEDGEMENTS AND FUNDING

This work was supported by a travel grant from the Graduate Academy of the TU Dresden. The study has been performed within the HORIZON-CL4-2021-RESILIENCE-01 project "European recycling and circularity in large composite components (EuReComp)", call "A Digitized, Resource-Efficient and Resilient Industry 2021", HORIZON Research and Innovation Actions, Contract Number 101058089. Views and opinions expressed are however those of the author(s) only and do not necessarily reflect those of the European Union or HADEA. Neither the European Union nor HADEA can be held responsible for them.

This work was supported from KIST institutional program. This work was supported by the Commercialization Promotion Agency for R&D Outcomes (COMPA) grant funded by the Korean Government (Ministry of Science and ICT) (RS-2023-00304729). EZ Composites (Gimje, Republic of Korea) manufactured the EoL specimens for tensile and bending tests.

REFERENCES

[1] P. Liu and C. Y. Barlow, Wind turbine blade waste in 2050, *Waste management (New York, N.Y.)*, **62**, *2017*, pp. 229–240 (doi: 10.1016/j.wasman.2017.02.007).

[2] P. Johst, M. Bühl, C. Enderle, R. Kupfer, N. Modler and R. Böhm, Forecasting wind turbine blade waste with material composition and geographical distribution: Methodology and application to Germany, *Resources, Conservation and Recycling*, **211**, *2024* (doi: 10.1016/j.resconrec.2024.107876).

[3] J. Beauson, A. Laurent, D. P. Rudolph and J. Pagh Jensen, The complex end-of-life of wind turbine blades: A review of the European context, *Renewable and Sustainable Energy Reviews*, **155**, *2022* (doi: 10.1016/j.rser.2021.111847).

[4] L. Mishnaevsky, K. Branner, H. N. Petersen, J. Beauson, M. McGugan and B. F. Sørensen, Materials for Wind Turbine Blades: An Overview, *Materials*, **10**, *2017* (doi: 10.3390/ma10111285).

[5] Y. Yang, R. Boom, B. Irion, D.-J. van Heerden, P. Kuiper and H. de Wit, Recycling of composite materials, *Chemical Engineering and Processing: Process Intensification*, **51**, *2012*, pp. 53–68 (doi: 10.1016/j.cep.2011.09.007).

[6] J. Potting, M. Hekkert, E. Worrell, and A. and Hanemaaijer, Circular Economy: Measuring innovation in the product chain, Accessed: Jan. 25, 2023. [Online]. Available: https://www.pbl.nl/sites/default/files/downloads/pbl-2016-circular-economy-measuring-innovation-in-product-chains-2544.pdf

[7] K. Ruane *et al.*, Construction and Cost Analysis of BladeBridges Made from Decommissioned FRP Wind Turbine Blades, *Sustainability*, **15**, *2023* (doi: 10.3390/su15043366).

[8] P. Johst *et al.*, Identification and Environmental Assessments for Different Scenarios of Repurposed Decommissioned Wind Turbine Blades, *Mater Circ Econ*, **5**, *2023* (doi: 10.1007/s42824-023-00085-7).

[9] P. Johst *et al.*, Concept and Life Cycle Assessment of a Tiny House Made from Root Section Structures of a Decommissioned Large-Scale Wind Turbine Blade as a Repurposed Application, *Mater Circ Econ*, **6**, *2024* (doi: 10.1007/s42824-023-00093-7).

[10] J. Joustra, B. Flipsen and R. Balkenende, Structural reuse of wind turbine blades through segmentation, *Composites Part C: Open Access*, **5**, *2021* (doi: 10.1016/j.jcomc.2021.100137).

[11] M. Kucher, P. Johst, M. Lizaranzu, F. Lahuerta and R. Böhm, A Micromechanical Modeling Approach for the Estimation of the Weathering-Induced Degradation of Wind Turbine Blades, *Mater Circ Econ*, **5**, *2023* (doi: 10.1007/s42824-023-00088-4).

[12] D. Jung and W. Na, Acoustic Emission Testing and Ib-Value Analysis of Ultraviolet Light-Irradiated Fiber Composites, *Applied Sciences*, **11**, *2021* (doi: 10.3390/app11146550).

[13] D. Jung, W.-R. Yu and W. Na, Use of acoustic emission b(Ib)-values to quantify damage in composites, *Composites Communications*, **22**, *2020* (doi: 10.1016/j.coco.2020.100499).

[14] P. Johst, S. Lee, E. Kim, S. Bae, R. Böhm and W. Na, Structural integrity assessment of repurposed wind turbine blade composite components with acoustic emission testing and Ib-value analysis, *Composites Part B: Engineering*, **301**, *2025* (doi: 10.1016/j.compositesb.2025.112490).

[15] H. Suzuki, T. Kinjo, Y. Hayashi, M. Takemoto and K. Ono, Wavelet transform of acoustic emission signals, *Journal of acoustic emission*, *1996*, pp. 69–84.

[16] B. Gutenberg, The energy of earthquakes, *QJGS*, **112**, *1956*, pp. 1–14 (doi: 10.1144/GSL.JGS.1956.112.01-04.02).

[17] T. Schumacher, C. C. Higgins and S. C. Lovejoy, Estimating Operating Load Conditions on Reinforced Concrete Highway Bridges with b-value Analysis from Acoustic Emission Monitoring, *Structural Health Monitoring*, **10**, *2011*, pp. 17–32 (doi: 10.1177/1475921710365424).

[18] T. Shiotani, X. Luo, H. Haya and M. Ohtsu, Damage quantification for concrete structures by improved b-value analysis of AE *Proceedings of the International Conference on Fracture*, *Italy, October 1, 2005*.

VALIDATION OF POSSIBLE APPLICATIONS OF FLAKE LAMINATES FOR RECYCLING OF PA6-CF PRODUCTION SCRAP

Johanna Beckmann[1], André Bachmann[2], Philipp Brandes[3], Thorsten Marten[4], Thomas Tröster[5], Elmar Moritzer[6]

[1]Chair for Automotive Lightweight Design, University of Paderborn
Warburger Straße 100, 33098 Paderborn, Germany
Email: johanna.beckmann@uni-paderborn.de, web page: https://mb.uni-paderborn.de/leichtbau

[2]Chair for Automotive Lightweight Design, University of Paderborn
Warburger Straße 100, 33098 Paderborn, Germany
Email: bachmann_andre@outlook.de, web page: https://mb.uni-paderborn.de/leichtbau

[3]Chair of Plastics Technology and Plastics Processing, University of Paderborn
Warburger Straße 100, 33098 Paderborn, Germany
Email: philipp.brandes@ktp.uni-paderborn.de, web page: https://ktp.uni-paderborn.de/

[4]Chair for Automotive Lightweight Design, University of Paderborn
Warburger Straße 100, 33098 Paderborn, Germany
Email: thorsten.marten@uni-paderborn.de, web page: https://mb.uni-paderborn.de/leichtbau

[5]Chair for Automotive Lightweight Design, University of Paderborn
Warburger Straße 100, 33098 Paderborn, Germany
Email: thomas.troester@uni-paderborn.de, web page: https://mb.uni-paderborn.de/leichtbau

[6]Chair of Plastics Technology and Plastics Processing, University of Paderborn
Warburger Straße 100, 33098 Paderborn, Germany
Email: elmar.moritzer@ktp.uni-paderborn.de, web page: https://ktp.uni-paderborn.de/

Keywords: Carbon fibre, Recycling, Mechanical properties, Forming

ABSTRACT

To facilitate the future application of mechanically shredded production scrap of polyamide 6-carbon fiber (PA6-CF), a comprehensive assessment of its potential use cases is essential. As a first step, the influence of selected process parameters on the processing behavior and quality of the resulting laminates was systematically investigated. Based on 3-point bending and tensile tests possible applications of flake laminates with structural or visual requirements are looked at and compared to sheet molding laminates out of chopped carbon fiber tape reinforced thermoplastics (SM-CTT). The results indicate that the mechanical properties of the recycled PA6-CF flake laminates are comparable to those of SM-CTT materials, suggesting analogous fields of application. Despite minor surface defects, a largely smooth surface finish was attainable. From an ecological standpoint, a significant advantage of this recycling approach is the direct reutilization of production scrap without the need for fiber-matrix separating or the addition of external materials.

1 INTRODUCTION

Lightweight construction is a key technology for enhancing resource and energy efficiency across various industries, particularly in the transportation sector. In automotive engineering, reducing mass-dependent driving resistances contributes significantly to the reduction of energy consumption and greenhouse gas emissions. [1] Fiber-reinforced polymer composites (FRPs; if carbon-fiber-reinforced: CFRPs), in particular thermoplastic-based variants (tFRPs), offer high potential for lightweight design due to their excellent specific mechanical properties. Compared to thermoset systems, tFRPs enable shorter processing times, lower material costs and improved end-of-life recyclability. [2, 3]

Especially organosheets, a semi-finished tFRP, offer significant weight-saving potential. Organosheets are typically manufacturers in flat sheet form through consolidation processes and later shaped into complex parts using thermoforming or pressforming techniques. Despite careful planning, the production with organosheets often generates considerable scrap, particularly in high-volume processes. [4, 5]

This paper investigates a strategy for the reutilization of production scrap from thermoplastic composite manufacturing. The aim is to evaluate the material and structural performance of reprocessed crap material and to assess its suitability for reintegration into functional components. By establishing methods for the reuse of tFRP production waste, the overall sustainability and material efficiency of composite-based lightweight systems can be significantly improved.

Traditional recycling approaches for composite waste include mechanical processing, thermal recycling or the separation of individual components through solvolysis. After the mechanical recycling of thermoplastics, shredded waste can be reused via processes such as injection molding or extrusion. However, the original fiber length is significantly reduced, leading to a decrease in the mechanical properties of the recycled material. [6, 7]

An innovative and promising recycling alternative takes advantage of the thermoplastic matrix and its re-meltability and re-moldability – fibers and matrix are not separated. Because the production waste can vary greatly in size, the approach starts by segmenting tFRP scrap into cm-sized more manageable pieces, called flakes. In the next step the flakes can be consolidated into a semi-finished product by evenly distributing, heating them above melting point and compressing them. The semi-finished product can be manufactured like organosheets by thermoforming or pressforming techniques. This method facilitates the creation of a new type of laminate that combines material and energy efficiency, making it suitable for applications with moderate mechanical property requirements. [7] This not only undermines the ecological and economic benefits of lightweight construction but also presents a largely untapped secondary resource.

2 PROCEDURE/METHOD

The semi-finished laminate, a consolidated panel, could be used in two different use cases of thermoforming: applications with structural requirements and visible parts. A simple isothermal manufacturing process is looked at to reduce process complexity. To ensure a stable thermoforming process the process conditions for the semi-finished product must be evaluated. Based on differential scanning calorimetry (DSC) and Design of Experiments, the main process parameters for the isothermal manufacturing process including pre-heating temperature, pre-heating duration, press force, cavity temperature and press time are varied. This is to analyze the effect of the parameters on the mechanical properties. Three-point-bending tests are carried out to analyze the mechanical properties. A low bending stress and flexural modulus should indicate insufficient consolidation. Consolidation was also assessed visually and qualitatively based on surface continuity and absence of visible delamination. An additional qualitative assessment was performed using tap test, in which the acoustic response of the sheet was evaluated. A high-pitched, metallic sound is indicative of proper consolidation, while a dull sound may suggest internal defects or insufficient consolidation. Goal is a flake laminate which is fully consolidated and could reach structural or visual requirements.

After finding the best process parameters, the mechanical properties of the process are analyzed and compared to traditional materials like SM-CTT. In the second application for visible parts the focus is on fiber cohesion and surface defects, evaluating whether the panel could meet visual requirements.

3 EXPERIMENTAL INVESTIAGTIONS

3.1 Materials

The experimental procedure involves using PA6-CF tape with a fiber mass content of 60 wt.% from Envalior GmbH (Germany) as the virgin material, which is consolidated, and chopped into flakes measuring 6 mm to 14 mm in equivalent diameter. According to the tape manufacturer, the tape properties are the following:

Properties	Unit	Typical Data	Test Method
Density	(kg/m³)	1450	ISO 1183
Fiber content (V/V)	(%)	49	ISO 11667
Tensile modulus – 0°	(GPa)	135	ISO 527-4
Stress at break – 0°	(MPa)	1700	ISO 527-4
Strain at break – 0°	(%)	1.4	ISO 527-4
Melting temperature	(°C)	220	ISO 11357-1

Table 1: Properties of the PA6-CF tape according to the datasheet.

Figure 1 shows the PA6-CF tape after consolidating and chopping in the form of flakes. This material has a three-dimensional, voluminous, loose structure.



Figure 1: Chopped flakes.

3.2 Manufacturing

The isothermal process includes two main manufacturing steps:

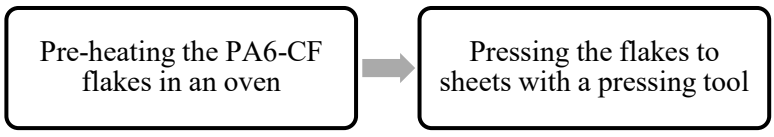

The series of pictures in Figure 2 illustrates the manufacturing process.



1. Evenly distributed flakes on a metal sheet



2. Heating in the oven

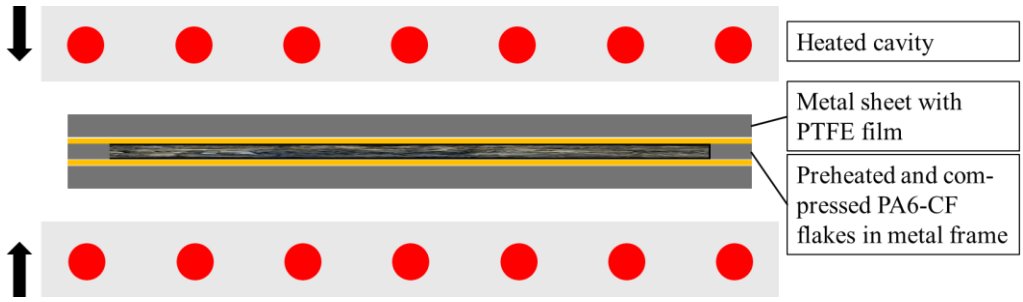

3. Pressing tool with preheated flake material



4. Consolidated flake laminate

Figure 2: Manufacturing process of flake laminates by isothermal process.

For pre-heating, the tFRP-flakes are evenly distributed between two metal sheets. To contain the flakes and prevent material leakage during pressing, a 2 mm thick metal frame is inserted between the sheets. This also leads to equal sheet thicknesses. To enhance demoldability one side of each sheet is lined with polytetrafluorethylene (PTFE)-film. The stack is heated in a convection oven of the company Nabertherm GmbH (Germany), type TR 240. In order to identify suitable process conditions for pre-heating, the relevant parameters were systematically varied as follows:

- Pre-heating temperatures: 225 °C, 250 °C, 275 °C
- Pre-heating duration: 10 min, 12.5 min, 15 min, 17.5 min, 20 min

The weight of the covering metal sheet compresses the CFRP flakes, resulting in a pre-compacted structure. After completing the pre-heating cycle, the stack is manually transferred to the pressing tool with a planar mold cavity. The size of the cavity measures 350 mm x 300 mm. Both halves of the mold are equipped with electrically heated cartridges for temperature control. Consolidation is carried out using a servo-motorized screw press (Synchropress GmbH (Germany), type: 1M-300) under the following process parameters:

- Forming pressure: 20 bar, 40 bar, 80 bar
- Cavity temperature: 80 °C, 100 °C, 120 °C
- Holding time: 30 s, 60 s, 120 s

The forming pressure p is set using the known area of the cavity A and the set pressing force F (cf. Equation 1).

$$\boldsymbol{p = F/A} \tag{1}$$

After passing the holding time the press returns to the starting position and the stack can be ejected manually.

3.3 Sample preparation and test methods

Mechanical properties are evaluated through three-point bending and tensile tests, following DIN EN ISO 14125 and DIN EN ISO 527-4 standards, respectively. Both geometries can be cut out of the produced flake-laminate sheets by waterjet cutting. For tensile tests the specimen measures 250 mm x 25 mm. Three-point bending samples measure 100 mm x 15 mm. Since PA6 tends to absorb water, the specimens were dried at 80 °C for 5 hours in a climate chamber and afterwards conditioned at 23 °C and 50 % relative humidity for 8 hours. Tests are performed on a servo-electric (type: Criterion C45.105) universal testing machine from MTS Systems Corporation (USA) with a testing speed of 2 mm/min. To assess potential anisotropy, specimens are extracted in both the 0° and 90° directions.

4 RESULTS

4.1 Influence of process parameters on degree of consolidation and mechanical properties

The pre-heating temperature has a significant impact on the degree of consolidation and resulting mechanical properties of the PA6-CF flake laminates. At a pre-heating temperature of 225 °C, approximately 5 °C above the peak melting point determined via DSC, insufficient consolidation was observed. The produced laminates were fragmented and unsuitable for mechanical testing. Increasing the pre-heating temperature to 250 °C improved consolidation significantly, as indicated by a smoother surface appearance and enhanced structural integrity. Further increasing the temperature to 275 °C yielded to no noticeable differences in surface quality and mechanical properties compared to 250 °C, as confirmed by three-point bending tests (bending stress: (102.52 ± 19.23) MPa vs. (116.34 ± 22.11) MPa; flexural modulus: (10812.64 ± 1401.88) MPa vs. (10614.54 ± 990.77) MPa).

In a subsequent experimental series, the influence of pre-heating duration was investigated. A pre-heating duration of 10 minutes resulted in poor consolidation with extensive surface defects and fragmentation. Extending the duration to 12.5, 15 and 17.5 minutes led to notable improvements (bending stress: (103.64 ± 13,87) MPa, (102.52 ± 19,23) MPa, (165.95 ± 16.18) MPa; flexural modulus (8820.65 ± 1245.19) MPa, (10812.64 ± 1401.88) MPa, (12556.67 ± 1930.39) MPa), indicating more complete consolidation. The characteristic metallic sound during tap testing further supported this observation. However, further extending the duration to 20 minutes, caused a decline in mechanical performance (bending stress: (120.79 ± 25.14) MPa; flexural modulus: (11138.02 ± 4250.62) MPa). Since thermal degradation at this temperature and time frame is unlikely, the decrease in properties is attributed to extended transfer durations between oven and press, which may have led to a significant drop in laminate temperature before pressing.

The press force also influenced the consolidation outcome. At 250 °C pre-heating temperature, a forming pressure of 20 bar was insufficient to ensure complete consolidation, resulting in visibly defective surfaces. Pressures of ≥ 40 bar were required to obtain nearly defect-free laminate surfaces at this temperature. No significant mechanical differences were observed between samples pressed at 40 bar and 80 bar (bending stress: (102.52 ± 19.23) MPa vs. (97.19 ± 11.26) MPa; flexural modulus: (10812.64 ± 1401.88) MPa vs. (9733.37 ± 647.42) MPa). At elevated pre-heating temperatures, a pressure of 20 bar was found to be adequate.

The pressing tool enables a slow, controlled cooling of the laminate, which promotes crystallization and improves mechanical performance. However, variation in temperature did not lead to significant differences in three-point bending properties between 80 °C and 100 °C temperature (bending stress: (114.41 ± 24.34) MPa vs. (102.52 ± 19.23) MPa; flexural modulus: (9415.86 ± 1899.78) MPa vs. (10812.64 ± 1401.88) MPa). At 120 °C both values declined by approximately 50 %, indicating suboptimal cooling conditions.

A holding time of 60 seconds in the press yielded the best mechanical performance (bending stress: (102.52 ± 19.23) MPa; flexural modulus: (10812.64 ± 1401.88) MPa). A shorter duration of 30 seconds led to lower values (bending stress: (82.68 ± 13.37) MPa; flexural modulus: (7454.42 ± 1242.22) MPa), while an extended time of 120 seconds show no further benefit (bending stress: (80.66 ± 21.64) MPa; flexural modulus: (8133.93 ± 1166.30) MPa).

The results underline the importance of carefully controlled pre-heating temperature and duration and indicate them as the two main controlling process parameters of the whole process. Heat loss during manual transfer between oven and press – characteristic of this isothermal process – can result in suboptimal consolidation and surface defects, as the material temperature may fall below the ideal processing range. To counteract this the pre-heating temperature must be set above peak melting point indicated by DSC.

Based on these results, the following process parameters should at least be achieved to ensure sufficient consolidation and mechanical performance for the investigated material:

- Pre-heating temperature: > 250 °C
- Pre-heating duration: > 17.5 minutes
- Forming pressure: > 25 bar
- Cavity temperature: 100 °C
- Press holding time: 60 s

Initial trials were conducted using reduced amount of flake material compared to the amount used in the subsequent production of full-sized laminate sheets. To evaluate the internal heat-up behavior of larger flake stacks, a thermocouple was embedded centrally during pre-heating. At an oven setpoint of 250 °C, the core of the stack required more than 65 minutes to reach the target temperature of 250 °C. This suggests that prior specimens processed with lower flake mass may not have fully reached processing temperature, potentially explaining earlier inconsistencies. By increasing the oven temperature to 275 °C this duration was reduced to 23.5 minutes, while at 290 °C the target temperature was achieved after 17.5 minutes.

These findings demonstrate the relatively slow heat transfer into the flake material. To ensure that the flakes remain above melting temperature during transfer to the mold and subsequent consolidation, the oven temperature and pre-heating duration must be adjusted.

Based on the results of these thermal evaluations, the process parameters in Table 2 were selected to produce flake laminates for three-point bending and tensile tests. The forming pressure was maintained at 25 bar, the cavity temperature was set to 100 °C, and a consistent holding time of 60 s was applied in all cases.

Sample	**Pre-heating temperature** (°C)	**Pre-heating duration** (min)
275°C_24min	275	24
275°C_29min	275	29
290°C_19min	290	19
300°C_19min	300	19

Table 2: Pre-heating temperatures and durations for the manufacturing process of different samples.

4.1 Mechanical properties in comparison to similar laminates

The processed sheets have a shiny and nearly defect-free surface and a metallic sound which indicates sufficient consolidation. They would be suitable for visual applications. The investigation of mechanical properties will show if the sheets can also be used in structural parts with mechanical requirements.

The mechanical characterization of the PA6-CF flake laminates was conducted via three-point bending and tensile testing. A comparison of specimens oriented in 0° and 90° direction revealed no statistically significant anisotropy, suggesting that the laminates exhibit quasi-isotropic behavior. As a result, test data are presented independent of extraction direction.

Figure 3 illustrates the average bending stress and flexural modulus values obtained for various processing parameters (cf. Table 2).

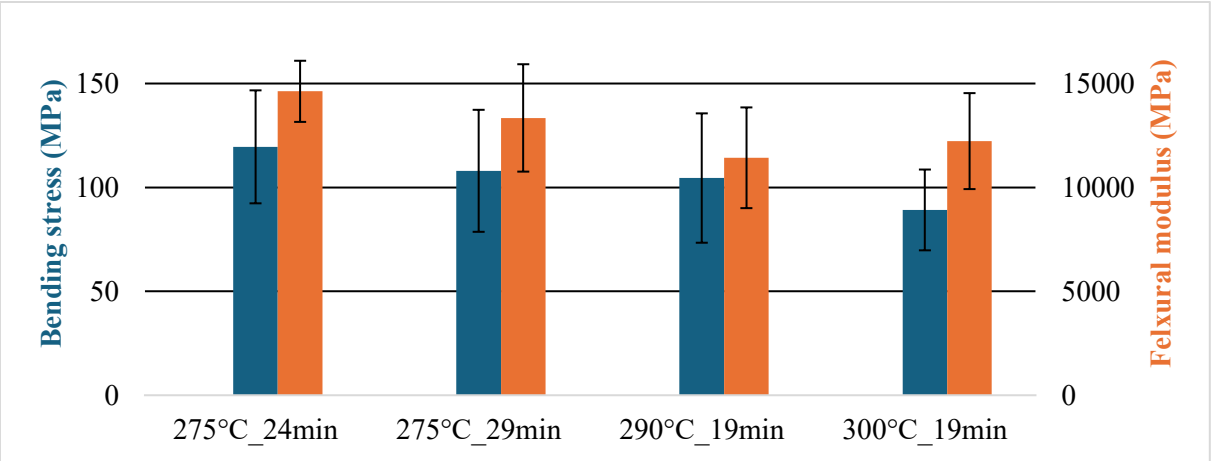

Figure 3: Average bending stress and flexural modulus of consolidated PA6-CF flake laminates.

The flexural modulus ranges from 11426.07 MPa (290°C_19min) to 14623.23 MPa (275°C_24min) with standard deviations between 1470.71 MPa and 2584.05 MPa. Notably, samples processed at an oven temperature of 275 °C with varying pre-heating durations yielded nearly identical flexural moduli within the margin of experimental uncertainty. Laminates processed at 290 °C and 300 °C with shorter pre-heating durations (19 minutes) achieve comparable modulus values. The relatively high standard deviation is attributed to process-related fluctuations, particularly variable transfer times between oven and press. Because of this instability and a slow heat transfer into the flake material the small changes in temperature or pre-heating duration have little to no significant impact on the flexural moduli.

Bending stress values vary between 89.17 MPa (300°C_19min) and 119.52 MPa (275°C_24min) with standard deviations from 19.44 MPa to 31.13 MPa. Across all variants, the bending stress results remain at a comparable level, reinforcing the hypothesis that inconsistent transfer times may have led to temporary temperature drops below the optimal consolidation window.

For reference, the flexural modulus of pure PA6, as specified in the material data sheet [8] of the material used in [9], is 1961 MPa which is approximately one-sixth of the values obtained for the flake laminates. In contrast, a PA6-CF with a similar fiber volume fraction exhibits a flexural modulus of 98112.4 MPa [10]. In comparison the flake laminates reach approximately 14,9 % of the flexural modulus of virgin continuous fiber composite, making them suitable for applications with moderate mechanical requirements.

Table 3 summarizes the tensile test results for PA6-CF flake laminates and compares them with reference materials, including pure PA6, SM-CTT with similar fiber volume content and the virgin continuous PA6-CF tape. The tensile modulus could only be determined for the 275°C_29min test series, as the slopes of the linear elastic regions in the other specimens exhibited significant variability, preventing a consistent evaluation.

Material	Tensile modulus (MPa)	Stress at break (MPa)	Strain at break (%)	Tensile Strength (MPa)
PA6-CF flake laminates				
275°C_24min	-	14.80 ± 9.32	0.01 ± 0.003	16.96 ± 9.45
275°C_29min	42.84 ± 3.64	23.09 ± 10.32	1.56 ± 1.1	31.46 ± 6.94
290°C_19min	-	27.47 ± 7.46	0.01 ± 0.002	27.75 ± 7.2
300°C_19min	-	22.97 ± 11.91	0.01 ± 0.003	26.84 ± 9.26
References				
Pure PA6 [11]	52000	-	28.70	28.70
SM-CTT (3t) (V/V=52.4 %) [9]	33.2 ± 2.9	-	0.9 ± 0.1	259.6 ± 39.1
PA6-CF tape (0°) [12]	135000	1700	1.4	1910

Table 3: Average mechanical properties for PA6-CF samples with different pre-heating temperature and duration and references from literature.

The highest mechanical performance among the flake laminates was achieved with a pre-heating regime of 275 °C for 29 minutes. The observed scatter in mechanical data is likely a result of uncontrolled variations in transfer time.
The tensile modulus of the flake laminates exceeded that of the SM-CTT reference, indicating their suitability as a replacement in applications where stiffness is a primary design criterion. However, the tensile strength and strain-at-break values fell significantly short of those achieved by continuous fiber-reinforced PA6-CF tape due to the inherently random fiber orientation in the flake structure. This structural limitation reduces the ability of the fiber phase to effectively carry axial load, which is reflected in the lower mechanical performance metrics.
The 275°C_29min reach roughly half of the values as SM-CTT and PA6-CF tape at strain at break when considering the high standard deviation. The tensile strength of the flake laminates was comparable to neat PA6 and reached approximately one-tenth of the SM-CTT reference. Despite this, the performance enhancement relative to the matrix alone demonstrates the reinforcing effect of the flakes and underscores the viability of this material for cost-sensitive, less demanding applications.
The mechanical properties show that some values are higher than pure PA6 and similar to SM-CTT. The PA6-CF tape has, as could be expected, better mechanical properties. Concluding that PA6-CF flake laminates are recommendable for visual applications or applications with medium to low standards on mechanical properties.

5 CONCLUSIONS

This study demonstrates the feasibility of manufacturing PA6-CF flake laminates via an isothermal compression molding process using recycled material. The mechanical characterization revealed that, despite their randomly oriented microstructure, the laminates exhibit quasi-isotropic behavior and provide significantly enhanced stiffness compared to pure PA6. Although they fall short of the mechanical performance achieved by continuous or chopped fiber-reinforced tapes (e.g., SM-CTT or virgin PA6-CF), their performance is sufficient for structural applications with low to moderate mechanical demands, as well as for purely visual or semi-structural components as an intermediate layer or filling material.
The findings suggest that flake laminates offer a sustainable alternative to more resource-intensive fiber composites, particularly in contexts where full structural load-bearing capacity is not critical.

Overall, the study highlights the potential of mechanically recycled FRP composites in lightweight design and resource-efficient component production, supporting circular economy principles within tFRP processing.

ACKNOWLEDGEMENTS

Many thanks go to Johannes Terhechte of W8SVR for providing the virgin material and Winand Kok and Hans Luinge of Spiral RTC for shredding. Further thanks go to all former and current colleagues as well as students at the Chair for Automotive Lightweight Design and Chair of Plastics Technology and Plastics Processing who supported this study.

REFERENCES

[1] A. Candela, G. Sandrini, M. Gadola, D. Chindamo, and P. Magri, "Lightweighting in the automotive industry as a measure for energy efficiency: Review of the main materials and methods," (in eng), *Heliyon*, vol. 10, no. 8, e29728, 2024, doi: 10.1016/j.heliyon.2024.e29728.

[2] AVK, Industrievereinigung Verstärkte Kunststoffe, *Handbuch Faserverbundkunststoffe/Composites: Grundlagen, Verarbeitung, Anwendungen,* 4th ed. Wiesbaden: Springer Vieweg, 2013.

[3] R. Stewart, "Thermoplastic composites — recyclable and fast to process," *Reinforced Plastics*, vol. 55, no. 3, pp. 22–28, 2011, doi: 10.1016/S0034-3617(11)70073-X.

[4] J. P. Snudden, C. Ward, and K. Potter, "Reusing automotive composites production waste," *Reinforced Plastics*, vol. 58, no. 6, pp. 20–27, 2014, doi: 10.1016/S0034-3617(14)70246-2.

[5] P. K. Mallick, "Thermoplastics and thermoplastic–matrix composites for lightweight automotive structures," in *Materials, Design and Manufacturing for Lightweight Vehicles*: Elsevier, 2010, pp. 174–207.

[6] C. Capela, S. E. Oliveira, J. Pestana, and J. Ferreira, "Effect of fiber length on the mechanical properties of high dosage carbon reinforced," *Procedia Structural Integrity*, vol. 5, pp. 539–546, 2017, doi: 10.1016/j.prostr.2017.07.159.

[7] S. M. Aldosari *et al.,* "Mechanical Recycling of Carbon Fiber-Reinforced Polymer in a Circular Economy," (in eng), *Polymers*, vol. 16, no. 10, 2024, doi: 10.3390/polym16101363.

[8] M-Base Engineering + Software GmbH, *Material Data Center | Datasheet KOPA® KN177N.* [Online]. Available: https://www.materialdatacenter.com/ms/en/Kopa/Kolon/KOPA%C2%AE+KN177N/43c4cab9/1395 (accessed: Jul. 8 2025).

[9] Y. Wan, H. Suganuma, and J. Takahashi, "Effects of fabrication processes and tape thickness on tensile properties of chopped carbon fiber tape reinforced thermoplastics," *Composites Communications*, vol. 22, p. 100434, 2020, doi: 10.1016/j.coco.2020.100434.

[10] ORIBI Composites, *Carbon Fiber/PA6: (CF/PA6).* [Online]. Available: https://oribicomposites.com/oribicomposites/wp-content/uploads/sites/9/MKT-1006-Carbon-Fiber-PA6-Data-Sheet.pdf (accessed: Jul. 8 2025).

[11] H. J. An, J. S. Kim, K.-Y. Kim, D. Y. Lim, and D. H. Kim, "Mechanical and thermal properties of long carbon fiber-reinforced polyamide 6 composites," *Fibers Polym*, vol. 15, no. 11, pp. 2355–2359, 2014, doi: 10.1007/s12221-014-2355-5.

[12] Celanese Materials Database, *CELSTRAN® CFR-TP PA6 CF60-03: CELESTRAN® CFR-TP*.

RECYCLING OF END-OF-LIFE WIND TURBINE BLADES INTO POLYMER COMPOSITES: EFFECT OF REPROCESSING ON SECONDARY COMPOSITES

Shashank Tumkur Karnick[1], Dr. Nataliya Lushnikova[1], Prof. dr. ir. H. J. H (Jos) Brouwers[1] and Prof. dr. Florent Gauvin[1]

[1]Department of Built Environment, Eindhoven University of Technology
P.O. Box 513, Groen Loper 3, 5612AE Eindhoven, Netherlands
Email: s.tumkur.karnick@tue.nl Web page: https://www.tue.nl/en/

Keywords: Recycling, Secondary polymer composites, Wind turbine blade waste, Polypropylene, Reprocessing

ABSTRACT

The increase in composite waste from decommissioned wind turbine blades must be managed through recycling to alleviate environmental issues. To provide a competitive alternative to traditional virgin composites, this study investigates the potential use of waste wind turbine blades (WWTB) as a sustainable reinforcement material in secondary polypropylene (PP) composites. WWTB and a coupling agent (maleic anhydride-grafted polypropylene, or MAPP) were combined to create PP composites through extrusion and injection moulding. To assess their recyclability and performance retention, these composites underwent three reprocessing cycles, which included the addition of manufacturing waste produced during extrusion. The samples were characterized using Fourier transform infrared (FTIR) spectroscopy, Differential scanning calorimetry (DSC), tensile test, three-point bending test, and melt flow index (MFI). Due to the compatibilization, the composites exhibited an increase in mechanical properties compared to both uncompatibilized composites and pure PP. The reprocessed composites in the second and third cycles further exhibited improved mechanical performance, attributed to lower melt temperature and screw speed during injection moulding. FTIR analysis revealed that the functional groups remained unaffected across reprocessing cycles. Upon MAPP addition, DSC revealed higher melting points and crystallinity of composites, and reprocessing had little effect on the degree of crystallinity. Furthermore, following repeated reprocessing, the MFI values increased, suggesting a reduction in the molecular weights of the composites.

1 INTRODUCTION

Global Wind Energy Council (GWEC) has increased its growth estimate for 2024–2030 (1210GW) by 10% [1]. The onshore installed capacity is expected to reach over 5000 GW by 2050, with offshore contributing 1000 GW [2]. As the wind energy industry grows, 330,000 t/year of composite materials manufactured from wind turbine blades will be deposited or burned globally until 2028, and 418,000 t/year between 2028 and 2040 [3]. Circularity of materials has received more attention from industry and scholars in recent years, especially in the wind energy sector, which generates enormous amounts of outdated turbine components, such as blades [4].

Steel, copper wire, hardware, and outfitting make up 85% of wind turbine components. The remaining 15% consists mostly of waste glass or carbon fibre composites from wind turbines, which are environmentally hazardous due to their 60% reinforcing fibre and 40% resin content. The cross-linked polymer chains of thermoset resins, such as polyester and epoxy, further complicate recycling. Recycling such composite wastes is quite challenging since these blades have been designed to endure extreme mechanical and environmental stresses for many years [2], [5], [6]. Recent years have seen several studies on the recycling of waste fiber-reinforced epoxy resins (WFREs) by pyrolysis [7] and chemical treatment [3], emphasizing the breakdown of epoxy resins to recover high-value carbon fibers. However, thorough research is still needed to recover glass fibers using these two techniques.

On the other hand, mechanical recycling, which involves grinding the composite to generate a mixture of single fibres, resin chunks, and fibre matting embedded in resin, is one of the simplest methods for handling decommissioned blades out of all the recycling systems now in use [8]. Due to its lower energy consumption of 0.1–4.8 MJ/kg and lower process cost compared to the value of recycled material, mechanical recycling is the most sought-after recycling method among industries [9].

In 2024, Pu et al. developed polypropylene composites via injection moulding by using wind turbine blade waste as a filler up to 50 wt% along with other compatibilizers. These composites exhibited a significant increase of 37.3% of tensile strength, 147.3% of tensile modulus, and 165.5% of flexural strength [10]. Similarly, Mamanpush et al. used such wind turbine blade waste as a feedstock alongside high-density polyethylene (HDPE) to extrude profiled composites. Such secondary composites showed improved mechanical and physical properties and further proving the potential capability of using waste wind turbine blades in secondary polymer composites [11].

However, the price of virgin glass fibre, which is approximately €2/kg [12] should be considered while recycling glass fibers from wind turbine blades. The lower energy demand for recycling (10–20 times lower) compared to the embodied energy of manufacturing for virgin glass (13–32 MJ/kg) [13] is equally imperative. To tackle such competitiveness in the raw materials, many investigations have been done in the past related to the reprocessing capability of glass fibre reinforced polypropylene composites. Colucci et al. investigated how recycling affected the performance behaviour of virgin glass fibre/polypropylene composites using injection moulding. However, the samples were only mechanically recycled once, and the mechanical characteristics were found to be lower than those of non-recycled polypropylene [14]. Chen et al. investigated the impact of three (3) injection moulding machine processing cycles on the characteristics of long glass fibre and PP. Their results demonstrated that the thermo-mechanical, rheological, and thermal characteristics of the composite are not significantly affected by mechanical recycling [15]. A similar investigation of reprocessing was done by Touati et al. on isotactic polypropylene (PP)/Cloisite 15A (OMMT) (5 wt.%) nanocomposites in the presence of maleic anhydride grafted polypropylene used as a compatibilizer [16]. Achukwu et al. confirmed that glass fibre reinforced polypropylene composites can be reprocessed for a maximum of 3 cycles without significant deterioration of mechanical properties or chemical structure [17].

Up until now, research on the reprocessing of glass fibre-reinforced polypropylene (GF-PP) composites has mostly focused on systems that use virgin glass fibres; similarly, manufacturing waste produced during the reprocessing process has received less attention. Therefore, to make the secondary composites more competitive against virgin composites, the current study examines the effects of 3 reprocessing cycles on secondary polypropylene composites reinforced with waste from shredded wind turbine blades, a non-virgin, post-industrial source of glass fibre. And to better replicate actual recycling situations, this work not only uses the recycled reinforcement but also ingeniously combines manufacturing waste generated during extrusion with the shredded secondary composites. For fair comparison, these composites were compared with pure PP.

2 MATERIALS AND METHODOLOGY

2.1 Materials

For the fabrication of the novel secondary polymer composites, a primary raw material, specifically mechanically recycled waste wind turbine blade (WWTB), was obtained from PreZero Gestion De Residuos SA (Spain), exhibiting a particle size of below 20 mm. It was further sieved, and the size fraction above 500 µm was considered for extrusion. The matrix utilized in this work is a thermoplastic polymer, specifically polypropylene (SABIC PP 520P), acquired from Resinex (Netherlands). At 2.16 kg of load and 230°C, the melt flow rate of PP is 10.5 g/10min. A coupling agent, maleic anhydride-graft-polypropylene (MAPP), was purchased from Sigma Aldrich (Netherlands).

2.2 Composite preparation and reprocessing

Different formulations (*Table 1*) of PP and WWTB were used to produce new secondary composites using two major processing methods: twin-screw extrusion and injection moulding. At first, the primary and secondary feeders of twin screw extruder (HAAKE Rheomex OS twin screw, ThermoFischer) were supplied with PP + MAPP and WWTB, respectively at 110 rpm rotation speed at processing temperatures of 180 °C for zone 1 and zone 2, 190 °C for zone 3 up to zone 8 and 200 °C for zone 9 and zone 10. Thoroughly compounded granules or pellets were extruded for three different cycles. Then, the dried pellets were used to produce tensile (75 mm × 5 mm × 2 mm) and bending specimens (80 mm × 10 mm × 4 mm) using a BOY XS injection moulding. The following parameters were used for injection moulding: melt temperature (200 °C), mould temperature (210 °C), injection speed (110 mm/s), injection time (15 s), cooling time (15 s), and cycle time (120 s).

In the first cycle, virgin PP was compounded with WWTB to produce secondary composites without a coupling agent. Similarly, for composites with a coupling agent, MAPP was compounded with virgin PP and WWTB (*Figure 2*). Later, a similar procedure was used for an additional two cycles, where the shredded composites, along with the corresponding pellets from the same cycle, which can be considered as manufacturing waste, were compounded to produce new composites. For instance, to produce a second cycle composite, tested samples from the first cycle were shredded and mixed with the pellets of corresponding composition from the first cycle, which are then extruded and injection moulded into second cycle composites, as shown in *Figure 1*.

From here on, the following nomenclature has been adopted for each composition: XA/YB/ZC, where X corresponds to the concentration of polypropylene by weight, Y to the recycled material from WWTB by weight, and Z to the coupling agent by weight. Similarly, A, B, and C correspond to the short names of the material. For instance, 73PP/25RM/2CA is a formulation with 73 wt.% of polypropylene, 25 wt.% of recycled material from WWTB, and 2 wt.% of coupling agent.

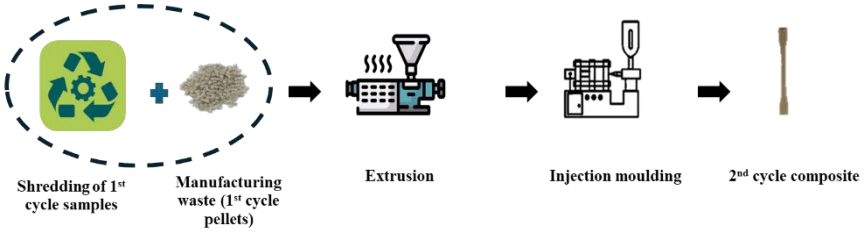

Figure 1: Illustration of the reprocessing method for each cycle

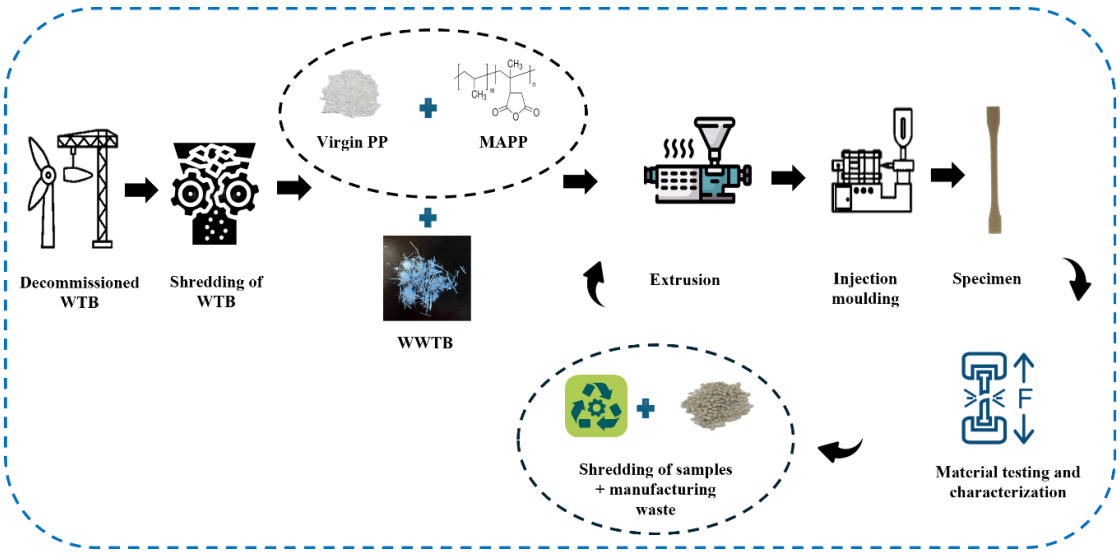

Figure 2: Schematic representation of the reprocessing of secondary composites

Table 1: Formulation of secondary polymer composites

Sample	Polypropylene (wt.%)	Recycled material (wt.%)	Coupling agent (wt.%)
100PP	100	0	0
75PP/25RM	75	25	0
50PP/50RM	50	50	0
73PP/25RM/2CA	73	25	2
48PP/50RM/2CA	48	50	2
70PP/25RM/5CA	70	25	5
45PP/50RM/5CA	45	50	5

2.3 Characterization

Chemical (structural) analysis

Fourier transform infrared spectroscopy (FTIR): This technique was employed to characterise the functional groups present in the secondary composites after multiple reprocessing cycles. Using the Frontier Spectrometer from Perkin Elmer, Fourier transform infrared spectroscopy was conducted in the range of 400 cm^{-1} to 4000 cm-1 with 20 scans per measurement.

Thermal analysis

Differential scanning calorimetry (DSC): The degree of crystallinity (X_c), melting and crystallization behaviours of all the extruded samples were determined using DSC – Q2000 (TA Instruments Co., Ltd., USA). The analysis was carried out in a temperature range between -90 °C and 220 °C under a nitrogen atmosphere with a flow rate of 50 mL/min and employing 5 °C/min for both heating and cooling cycles. All the samples were subjected to two heating and one cooling cycle. The following equation was used in the calculation of X_c:

$$Xc = \frac{\Delta H_m}{\Delta H_m^*} \times 100 \qquad (1)$$

Where ΔH_m denotes the melting enthalpy of the PP in the composition and ΔH_m^* enthalpy of melting of fully crystalline PP, taken as 209 J/kg [18].

Mechanical testing

Tensile and three-point bending test: To determine the tensile and flexural properties of the injection moulded composites, both tensile and three-point bending tests were conducted according to ISO 527 – 2 and ISO 178, respectively, using a Zwick Roell ZW010 equipped with a 2.5 kN load cell. The standard test parameters of 5 mm/min and 10 mm/min cross-head speed were used for the tensile test and bending test, respectively. However, tensile testing of third-cycle PP was conducted at a cross-head speed of 50mm/min. The flexural tests were carried out up to 10% deformation. The results were determined based on the average of five samples for each composition.

Rheology

Melt flow rate (MFR): Measurement of the MFI for all the extruded samples was performed according to ISO 1133-1 (Method A) with Cflow Extrusion Plastometer (Zwick Roell 4100). A standard method by using an applied weight of 2.16 kg at 230 °C was used. Melt flow rate (MFR) was calculated according to equation (2):

$$MFR = \frac{600m}{t} \qquad (2)$$

Where m denotes the average mass, in grams, of the cut-offs, and t denotes the cut-off time interval, in seconds

3 RESULTS AND DISCUSSION

Chemical (structural) analysis

The possible chemical structure changes within the composites for different reprocessing cycles were examined by FT-IR spectra *(Figure 3*). In all the reprocessing cycles of PP, the medium CH_2 bending vibration was observed at 1457 cm^{-1}, whereas the C–H stretch bond is represented by the absorption band at 2950 cm^{-1}. Also, CH_3 bending vibrations were obtained approximately at 1375 cm^{-1} [17]. Touati et al. also reported a weak intensity carbonyl band that represents MAPP compatibilizer at 1720 $cm^{-1,}$ and the FT-IR spectra of pure PP did not show this carbonyl band [16]. The stretching vibration of the Si-O bonds inside SiO_2 is responsible for the peak at 1100 cm^{-1} [10]. Similar results were observed by several researchers, which indicate that no significant structural change, such as oxidative degradation, has occurred even after multiple reprocessing cycles of reinforced PP composites [16], [17], [19].

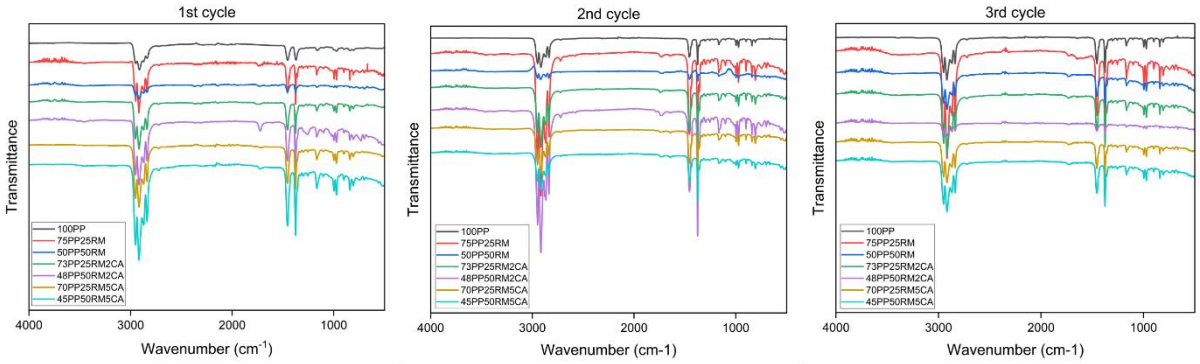

Figure 3: FTIR spectra of all the composites at different reprocessing cycles

Thermal analysis

The DSC thermograms, as shown in *Figure 4* represent the melting and cooling curves of all the extruded samples for different reprocessing cycles. The melting point of pure PP in the first cycle was 162.91 °C. However, with the addition of WWTB, the melting point of the composites 75PP25RM and 50PP50RM increased to 165 °C. Meanwhile, after the compatibilization, the melting points of the composites were reduced. A similar behaviour was observed by Hassan et al [18].

The ΔH_m is an essential parameter since its value is directly correlated with the polymer's total crystallinity content [20]. Similar to Hassan et al. report, ΔH_m of both uncompatibilized and compatibilized composites reduced compared to pure PP, which is attributed to the reduction of the degree of crystallinity of the PP matrix with the incorporation of fibres. The incorporation of glass fibres disrupts the linear crystallizable arrangement of the PP chains, resulting in a reduced degree of crystallinity and an increased proportion of flexible amorphous material[18]. On the other hand, the integration of MAPP into the composites has enhanced the level of crystallinity, which indicates that the coupling agent's presence has enhanced the matrix nucleation [21], [22]. In addition, Pu et al. reported that the composites with a lower amount of WWTB augment the crystallinity due to the nucleation-inducing effect of WWTB, which can be seen from *Figure 5*. However, the increased viscosity at larger WWTB contents prevented PP chains from arranging regularly, which resulted in a noticeable reduction in crystallinity [10].

The melting and crystallization points of compatibilized and uncompatibilized composites had an insignificant decrease after three cycles, except PP, where melting and crystallization points increased as the number of reprocessing cycles increased. The crystallinity index of all the composites, including PP, exhibited a negligible reduction after the second cycle extrusion, however, the X_c of PP after the second cycle was not considered here due to an inappropriate value. In the third cycle, X_c of PP had a slight reduction compared to the first cycle. Meanwhile, X_c of all the other composites either had a slight improvement or similar values even after three reprocessing cycles.

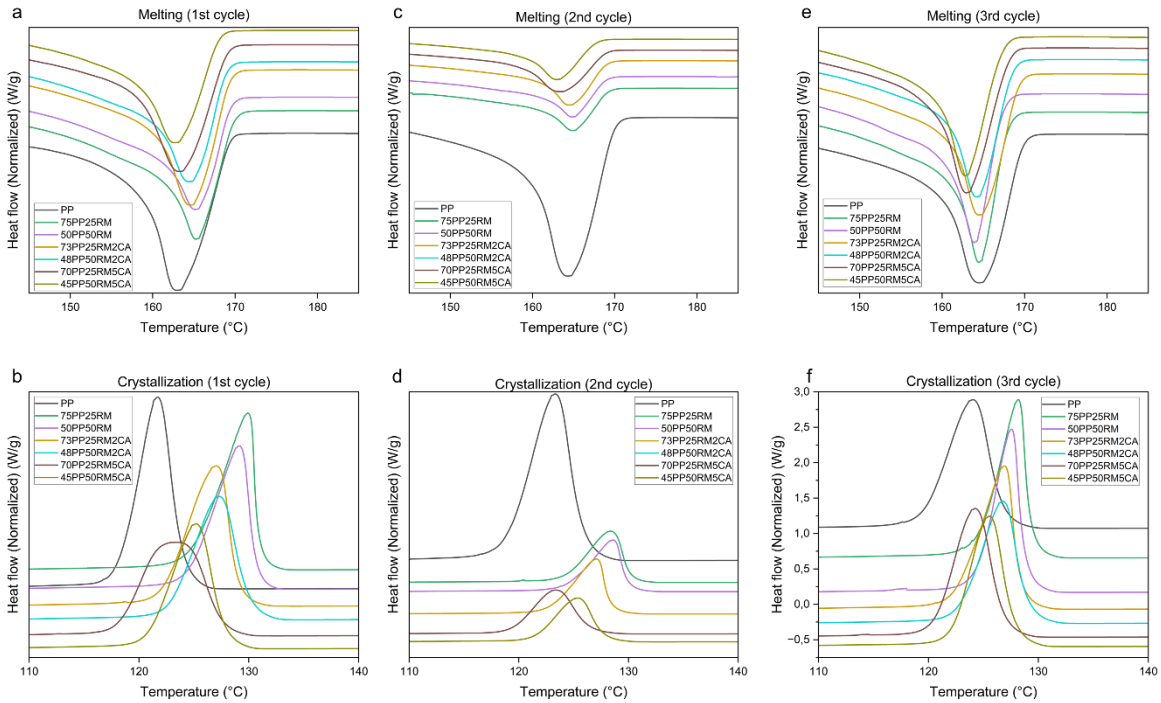

Figure 4: DSC thermograms of all the composites at different reprocessing cycles: (a, c, e) melting; (b, d, f) crystallization

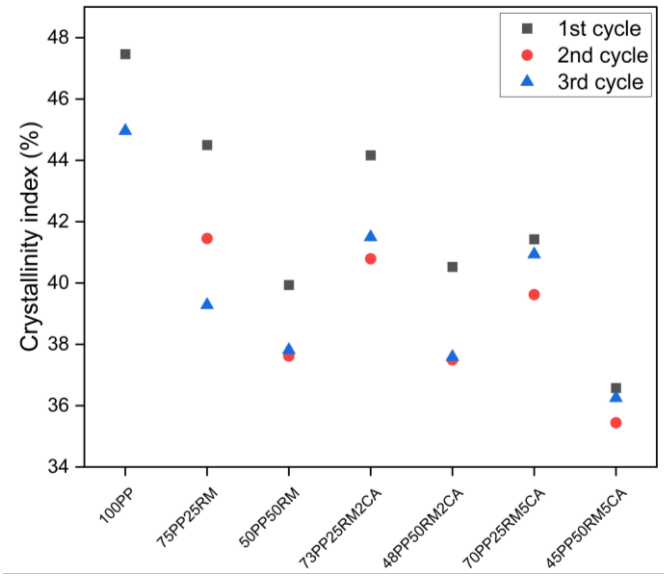

Figure 5: Crystallinity index of all the composites at different reprocessing cycles

Mechanical testing

Tensile properties

The tensile properties of the first cycle secondary composites, such as 75PP25RM, which are WWTB reinforced PP composites, had a similar tensile strength to pure PP, with a higher stiffness. However, further reductions in tensile strength were observed with increased recycled material content. The 50PP50RM composites exhibited a lower tensile strength due to poor interfacial strength between the matrix and recycled fibre from WWTB, which consists of epoxy residue on its surface. For this reason, it can be assumed that the stress applied cannot be transferred from the matrix to the fibres [23]. However, the problem of poor adhesion was addressed with the addition of a coupling agent, which led to a slight improvement of 9% in those composites after the addition of 2 wt% (48PP50RM2CA) and 5 wt% (70PP25RM5CA) coupling agent compared to pure PP. Moreover, the higher weight percentage of CA showed an improvement in the stiffness of the composite while maintaining a good tensile strength, as shown in *Figure 6*.

In the second and third cycles, the tensile properties of all the composites, including pure PP, have been increased compared to their counterparts from the first cycle. According to Huang et al. this improvement in the tensile could be attributed to several processing factors of injection moulding such as lower screw speed and lower melt temperature. Less damage to the PP molecular chains results in higher molecular densities and which in turn increases the tensile strength of reprocessed composites. Similarly, at lower melt temperature, the arrangement of molecular chains will not disorganize, resulting in higher tensile strength [24].

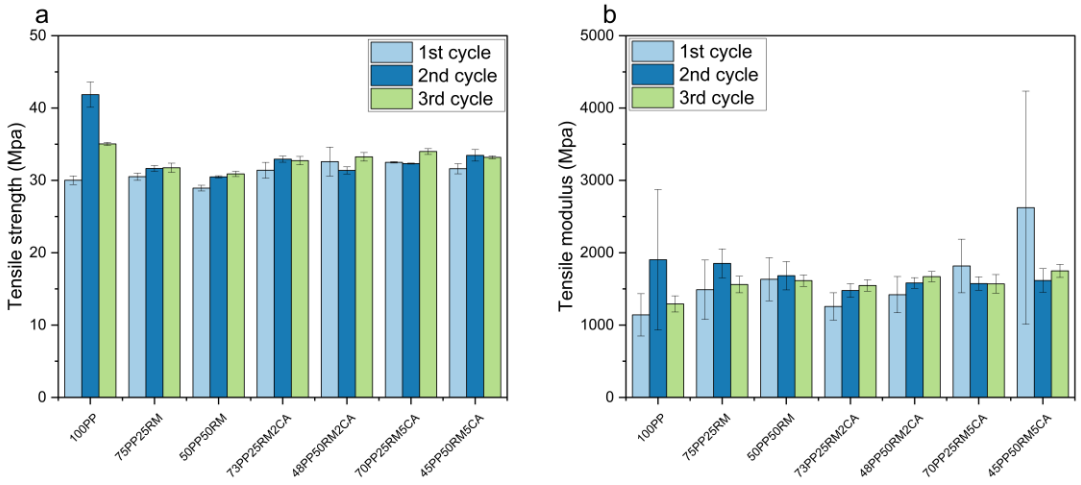

Figure 6: Tensile strength (a) and Tensile modulus (b) of different composites at three reprocessing cycles

Flexural properties

Unlike tensile properties, there were some significant improvements in the flexural properties of the secondary composites, even without a CA, over pure PP, as shown in *Figure 7*. In the first cycle, the flexural strengths showed an increase in all the composites, with 50PP50RM and 45PP50RM5CA exhibiting the highest changes of 18% and 21%, respectively. However, the samples without a CA had high stiffness, as indicated by their higher flexural modulus compared to all the other samples with a coupling agent, which shows the positive effect of using a CA on the secondary composites. The second cycle composites, however, exhibited an improvement in their flexural properties. All the second-cycle composites showed an increase in flexural strength compared to their counterparts from the first cycle. The flexural modulus of all the composites with a CA, except 45PP50RM5CA, was increased, making them stiffer than the composites without a CA, which had a lower flexural modulus compared to the first

cycle. Despite having a reduction in the flexural strength in the third cycle, these composites performed better than their counterparts from the first cycle. Similar observations were made in terms of flexural modulus. Again, these improvements can be attributed to the processing parameters of injection moulding.

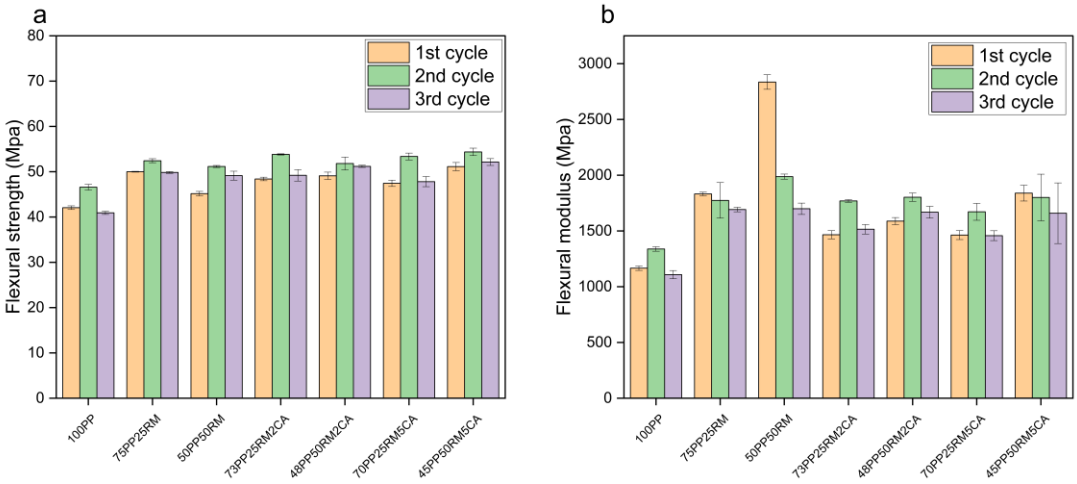

Figure 7: Flexural strength (a) and Flexural modulus (b) of different composites at three reprocessing cycles

Rheology

Melt flow index (MFI)

The MFI of composites was determined to study the effects of reprocessing on viscosity and molecular weight. *Figure 8* shows the MFI of pure PP and different composites with and without CA for three reprocessing cycles. For pure PP, MFI progressively increased with every reprocessing cycle, beginning from 10.5 g/10min up to 13.2 g/10min in the third cycle, resulting in a 25% increase. A similar trend was observed with all the other composites, suggesting a decrease in the molecular weight of polypropylene during the three reprocessing cycles.

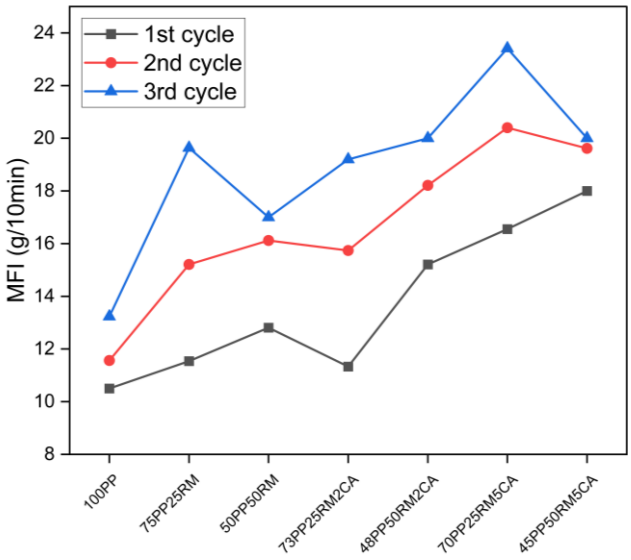

Figure 8: MFI properties of different secondary composites subjected to three reprocessing cycles

In addition, an increasing trend of MFI was observed with the higher dosage of CA in the composites. The highest increase of MFI of 41% was observed for the 70PP25RM2CA composite when it was reprocessed for the third time. The Ara´ujo et al. confirm that an increase in the MFI results in a drop in the melt viscosity and, as a result, a negative change in the molecular weight of the plastic and also noticed that reduction in intermolecular interaction and entanglements results in a decrease in polymer viscosity, which in turn causes a decrease in molecular weight and polymer chain length [25]. Spicker et al. also showed that their PP subjected to ten reprocessing cycles had improved MFI, decreased average molecular weight and viscosity, all of which corresponded to the occurrence of β-scission reactions [26].

4 CONCLUSIONS

In order to make the secondary polymer composites more competitive against virgin composites, reinforcement from WWTB was used to prepare PP composites via injection moulding and thereafter subjected to 3 reprocessing cycles along with manufacturing waste derived during extrusion. The resulting polymer composites were examined in terms of their mechanical, thermal, rheological, and structural properties. Therefore, it may be concluded that:

- The addition of coupling agent (MAPP) to the secondary composites showed a positive effect of 9% improvement in tensile strength of 48PP50RM2CA and 70PP25RM5CA. Similarly, a 21% improvement was seen in the flexural strength of 45PP50RM5CA. Higher amounts of WWTB and MAPP had a positive impact on the mechanical properties. In 2nd and 3rd cycle composites, tensile and flexural properties were further improved, which can be attributed to the lower screw speed and melt temperature of injection moulding;
- FT-IR spectra showed that functional groups present in the composites were unaffected even after 3 reprocessing cycles, which proves that the degradation is thermo-mechanical, not thermo-oxidative;
- Melting points of uncompatibilized composites were increased to 165 °C. The integration of MAPP into the composites has enhanced the degree of crystallinity, which indicates that the coupling agent's presence has enhanced the matrix nucleation. In all the composites, including pure PP, a slight reduction or similar degree of crystallinity was observed even after 3 reprocessing cycles;
- The MFI of all the composites was increased after 3 reprocessing cycles, suggesting a decreased viscosity and lower molecular weight, all of which happened due to the β-scission reactions.

The findings of this study demonstrate the potential of waste wind turbine blades (WWTB) as a viable reinforcement material in secondary polypropylene composites. The ability of these composites to undergo reprocessing with performance trends comparable to those reinforced with virgin glass fibres highlights their promise as a competitive and sustainable alternative to conventional virgin composites. Furthermore, a detailed comparative study has to be done between these secondary composites and virgin PP-GF composites.

ACKNOWLEDGEMENTS

This work was supported by the European Union's Horizon Europe Research and Innovation Programme under grant agreement no. 101096437 (Blades2build). Funded by the European Union. Views and opinions expressed are, however, those of the author(s) only and do not necessarily reflect those of the European Union or the European Climate, Infrastructure and Environment Executive Agency (CINEA). The author would also like to thank Guido Smets and Bas Koolen from Fontys University of Applied Sciences, Netherlands, for their continuous support with polymer processing.

REFERENCES

[1] "GWEC's Global Wind Report 2024." Accessed: Jun. 07, 2025. [Online]. Available: https://www.gwec.net/reports/globalwindreport/2024

[2] R. Fonte and G. Xydis, "Wind turbine blade recycling: An evaluation of the European market potential for recycled composite materials," *J Environ Manage*, vol. 287, Jun. 2021, doi: 10.1016/j.jenvman.2021.112269.

[3] C. Mattsson, A. André, M. Juntikka, T. Tr nkle, and R. Sott, "Chemical recycling of End-of-Life wind turbine blades by solvolysis/HTL," in *IOP Conference Series: Materials Science and Engineering*, IOP Publishing Ltd, Oct. 2020. doi: 10.1088/1757-899X/942/1/012013.

[4] Ž. Kavaliauskas *et al.*, "Recycling of Wind Turbine Blades into Microfiber Using Plasma Technology," *Materials*, vol. 16, no. 8, Apr. 2023, doi: 10.3390/ma16083089.

[5] M. J. Leon, "Recycling of wind turbine blades: Recent developments," Feb. 01, 2023, *Elsevier B.V.* doi: 10.1016/j.cogsc.2022.100746.

[6] H. K. Jani, S. Singh Kachhwaha, G. Nagababu, and A. Das, "A brief review on recycling and reuse of wind turbine blade materials," *Mater Today Proc*, vol. 62, no. P13, pp. 7124–7130, Jan. 2022, doi: 10.1016/j.matpr.2022.02.049.

[7] D. Åkesson, Z. Foltynowicz, J. Christéen, and M. Skrifvars, "Microwave pyrolysis as a method of recycling glass fibre from used blades of wind turbines," *Journal of Reinforced Plastics and Composites*, vol. 31, no. 17, pp. 1136–1142, Sep. 2012, doi: 10.1177/0731684412453512.

[8] A. Moslehi, A. Ajji, M. C. Heuzey, A. Rahimizadeh, and L. Lessard, "Polylactic acid/recycled wind turbine glass fiber composites with enhanced mechanical properties and toughness," *J Appl Polym Sci*, vol. 139, no. 15, Apr. 2022, doi: 10.1002/app.51934.

[9] R. M. Gonçalves, A. Martinho, and J. P. Oliveira, "Recycling of Reinforced Glass Fibers Waste: Current Status," Feb. 01, 2022, *MDPI*. doi: 10.3390/ma15041596.

[10] Z. Pu, S. Yang, and Q. Wang, "Recycling of waste wind turbine blades for high-performance polypropylene composites," *J Appl Polym Sci*, vol. 141, no. 23, Jun. 2024, doi: 10.1002/app.55474.

[11] S. H. Mamanpush, H. Li, K. Englund, and A. Tavousi Tabatabaei, "Extruded Fiber-Reinforced Composites Manufactured from Recycled Wind Turbine Blade Material," *Waste Biomass Valorization*, vol. 11, no. 7, pp. 3853–3862, Jul. 2020, doi: 10.1007/s12649-019-00659-0.

[12] "EMPHASIZING project investigates glass fiber upcycling | CompositesWorld." Accessed: Jun. 07, 2025. [Online]. Available: https://www.compositesworld.com/news/emphasing-project-investigates-glass-fiber-upcycling

[13] G. Leeke, G. Oliveux, and S. Pickering, "Composite Recycling: Where are we now?," Berkhamsted, 2016.

[14] G. Colucci, H. Simon, D. Roncato, B. Martorana, and C. Badini, "Effect of recycling on polypropylene composites reinforced with glass fibres," *Journal of Thermoplastic Composite Materials*, vol. 30, no. 5, pp. 707–723, May 2017, doi: 10.1177/0892705715610407.

[15] T. Chen, C. D. Mansfield, L. Ju, and D. G. Baird, "The influence of mechanical recycling on the properties of thermotropic liquid crystalline polymer and long glass fiber reinforced polypropylene," *Compos B Eng*, vol. 200, p. 108316, Nov. 2020, doi: 10.1016/J.COMPOSITESB.2020.108316.

[16] N. Touati, M. Kaci, S. Bruzaud, and Y. Grohens, "The effects of reprocessing cycles on the structure and properties of isotactic polypropylene/Cloisite 15A nanocomposites," *Polym Degrad Stab*, vol. 96, no. 6, pp. 1064–1073, 2011, doi: 10.1016/j.polymdegradstab.2011.03.015.

[17] E. O. Achukwu *et al.*, "Recycling effects on the bending, rheological, and structural properties of glass fiber-reinforced isotactic polypropylene composites," *Journal of Reinforced Plastics and Composites*, vol. 43, no. 9–10, pp. 532–546, May 2024, doi: 10.1177/07316844231167552.

[18] A. Hassan, N. A. Rahman, and R. Yahya, "Extrusion and injection-molding of glass fiber/MAPP/polypropylene: Effect of coupling agent on DSC, DMA, and mechanical properties," *Journal of Reinforced Plastics and Composites*, vol. 30, no. 14, pp. 1223–1232, Jul. 2011, doi: 10.1177/0731684411417916.

[19] E. Esmizadeh, C. Tzoganakis, and T. H. Mekonnen, "Degradation Behavior of Polypropylene during Reprocessing and Its Biocomposites: Thermal and Oxidative Degradation Kinetics," *Polymers 2020, Vol. 12, Page 1627*, vol. 12, no. 8, p. 1627, Jul. 2020, doi: 10.3390/POLYM12081627.

[20] W. J. Sichina, "Prediction of end-use characteristics of polyethylene materials using differential scanning calorimetry," *USA: Application Briff DSC-11*, 1994.

[21] M. Modesti, A. Lorenzetti, D. Bon, and S. Besco, "Thermal behaviour of compatibilised polypropylene nanocomposite: Effect of processing conditions," *Polym Degrad Stab*, vol. 91, no. 4, pp. 672–680, Apr. 2006, doi: 10.1016/J.POLYMDEGRADSTAB.2005.05.018.

[22] S. L. Gao and E. Mäder, "Characterisation of interphase nanoscale property variations in glass fibre reinforced polypropylene and epoxy resin composites," *Compos Part A Appl Sci Manuf*, vol. 33, no. 4, pp. 559–576, Apr. 2002, doi: 10.1016/S1359-835X(01)00134-8.

[23] K. Oksman, A. P. Mathew, R. Långström, B. Nyström, and K. Joseph, "The influence of fibre microstructure on fibre breakage and mechanical properties of natural fibre reinforced polypropylene," *Compos Sci Technol*, vol. 69, no. 11–12, pp. 1847–1853, Sep. 2009, doi: 10.1016/J.COMPSCITECH.2009.03.020.

[24] P. W. Huang and H. S. Peng, "Number of Times Recycled and Its Effect on the Recyclability, Fluidity and Tensile Properties of Polypropylene Injection Molded Parts," *Sustainability 2021, Vol. 13, Page 11085*, vol. 13, no. 19, p. 11085, Oct. 2021, doi: 10.3390/SU131911085.

[25] E. A. F. Araújo, L. L. Y. Visconte, A. L. N. da Silva, L. Sirelli, and É. B. A. V. Pacheco, "Effect of clay amount and reprocessing cycles on thermal, morphological, and mechanical properties of polypropylene/organovermiculite nanocomposites," *Polym Eng Sci*, vol. 59, no. 10, pp. 2110–2120, Oct. 2019, doi: 10.1002/PEN.25213.

[26] C. Spicker, N. Rudolph, I. Kühnert, and C. Aumnate, "The use of rheological behavior to monitor the processing and service life properties of recycled polypropylene," *Food Packag Shelf Life*, vol. 19, pp. 174–183, Mar. 2019, doi: 10.1016/j.fpsl.2019.01.002.

TIN-CATALYZED EPOXY VITRIMER MATRIX: AN APPROACH TO WASTE REDUCTION IN EPOXY COMPOSITES

E. Waechter[1], M. Gresil[1*]

[1]Department of Materials Science and Engineering, Monash University,
Clayton, VIC 3800, Australia;
Email: matthieu.gresil@monash.edu

Keywords: Epoxy vitrimer, organotin catalyst, composite, recycling, reprocessing, vitrimerization

ABSTRACT

The growing demand for epoxy fibre-reinforced composites raises significant environmental concerns due to the large amounts of waste produced. This study investigates the use of vitrimers - polymers that combine the durability of thermosets with the reprocessability of thermoplastics- to reduce such waste. Our approach involves substituting traditional, irreversible epoxy matrices with inherently reversible epoxy vitrimer systems.

We present a novel vitrimer system synthesized from a conventional epoxy monomer, a carboxylic acid curing agent, and an organotin catalyst. The material is synthetized via a simple one-pot process using easily accessible raw materials, to enhance its suitability for industrial adoption. The catalyst's thermal properties contribute to the generation of a robust network that resists degradation during reprocessing. In addition, vitrimerization is used to convert a cured, traditional epoxy material into a vitrimer, highlighting the potential for waste valorization. Finally, an efficient chemical recycling method is presented for epoxy vitrimer composites, showcasing the potential for material recovery in composite applications.

1. INTRODUCTION

Epoxy fibre-reinforced composites are widely used in industries such as aerospace, automotive, and construction. However, they generate a lot of waste, largely due to the use of epoxies as matrix materials. The underlying issue lies in their chemistry: traditional epoxy resins, which belong to the thermosetting class of polymers, form irreversible, covalently crosslinked networks **[1]**. While this structure provides them excellent thermomechanical properties -at a reasonable cost and with great versatility-, it also makes them extremely difficult to recycle or repair, and impossible reshape. As the market for these composites continues to grow, a surge in waste is expected, amplifying environmental concerns and underscoring the urgent need for innovative solutions **[2]**.

Vitrimers, a new class of dynamic polymers discovered in 2011 **[3, 4]**, have emerged as a promising solution for designing materials that generate less waste. Above a critical topology freezing temperature (Tv), their networks can rearrange without losing covalent connectivity thanks to accelerated associative bond exchange reactions, allowing them to flow and fully relax stresses **[5, 6]**. When used as matrices, vitrimers enable the development of recyclable, repairable, weldable, and reshapable composites **[7-14]**. However, their heavy reliance on expensive or commercially unavailable raw materials has so far hindered their adoption by industry **[15-31]**.

In this work, we demonstrate the potential of epoxy vitrimers to address both future and existing epoxy composite waste. First, we present a recyclable epoxy matrix that maintains its thermal and dynamic properties after recycling, offering a viable strategy to reduce future waste generation. We also present a simple chemical recycling method that enables the recovery of fibres with clean surfaces within two hours. Furthermore, we show that fully cured, irreversible epoxy thermosets can be converted into reprocessable vitrimers through a vitrimerization process **[32]**, providing a promising route for valorising existing epoxy waste.

2. MATERIALS AND METHODS

2.1 Materials

Matrix. The formulation was based on D.E.R. 332 diglycidyl ether of bisphenol A (DGEBA, eew 177.0 g/mol, Sigma-Aldrich) as diepoxy monomer and sebacic acid (SA, meq 101.2 g/mol relative to the epoxy group, Sigma-Aldrich) as curing agent. Monobutyltin oxide (Sn, meq 208.8 g/mol, Tokyo Chemical Industry) was employed as catalyst. Chemical structures are presented in **Table 1**.

Reinforcement. 3K twill weave carbon fibre fabric (200gsm, Enhanced Composites) was used to reinforce the matrix.

Role	Chemical compound	Chemical structure
Monomer	Diglycidyl ether of bisphenol A (DGEBA)	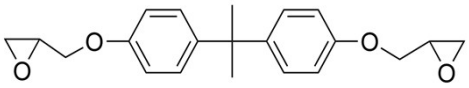
Curing agent	Sebacic acid (SA)	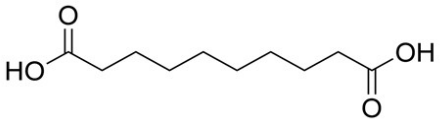
Catalyst	Monobutyltin oxide (Sn)	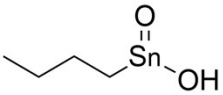

Table 1: Chemical structures of the raw materials used

2.2 Sample preparation and recycling

Preparation and recycling of epoxy samples. Overall, four matrix materials were developed and compared (see **Figure 1**). First, two initial epoxy systems were synthetized: a vitrimer (v), as well as a conventional thermoset (TS) prepared without any catalyst. Both systems were then reprocessed to produce a recycled vitrimer (Rv) and a vitrimerized thermoset (vTS). The formulations were prepared using a 1:1 ratio of epoxy to carboxylic acid functional groups, with the catalyst added at 5 % molar equivalent (meq.) relative to the epoxy.

The two initial epoxy systems (v and TS) were prepared by mixing SA powder with DGEBA using an overhead stirrer at 60 °C and 250 rpm for 24 hours. For the vitrimer system (v), the catalyst (Sn) was then added to the mixture, followed by an additional 30 minutes of stirring. After mixing, the formulations were degassed at 90 °C for 4 hours. The curing process was completed by heating the samples for 8 hours at 145 °C, followed by 8 hours at 160 °C. The recycled vitrimer (Rv) was prepared by cryo-grinding the original vitrimer (v) into a powder, followed by compression molding at 200 °C for 1 hour, under approximately 5 MPa of pressure. In case of the vitrimerized vitrimer (vTS), the conventional thermoset (TS) was cryo-ground together with the catalyst, added at 5 % meq. relative to the epoxy group, and then processed using the same compression molding conditions.

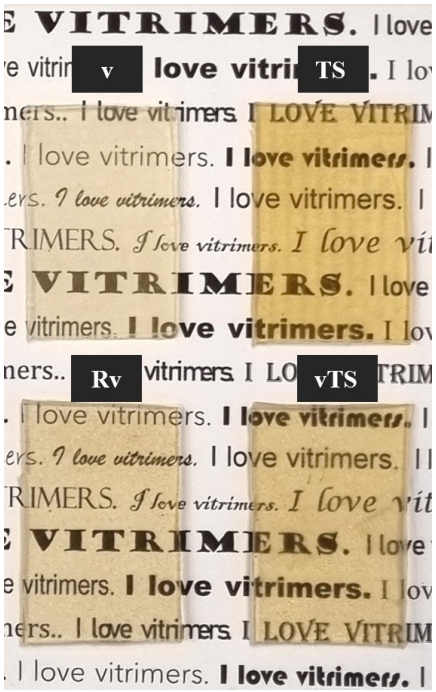

Figure 1: Preparation of two original (v, TS) and two recycled epoxy systems (Rv, vTS).

Preparation and recycling of fibre-reinforced epoxy samples. A vitrimer composite sample (CFRv) was manufactured using carbon fibres and the original vitrimer (v) resin developed in the first part of the study. Eight plies were placed in a steel mold and stacked in a 0/90° ply orientation. As each layer was positioned, the degassed resin was gradually poured between the plies to ensure proper impregnation. Once the lay-up was complete, the composite was compression-molded overnight at 145 °C under a pressure of approximately 5 MPa.

To evaluate the recyclability of the fibre-reinforced composite material, a solvolysis procedure was conducted. A composite sample measuring approximately 15 mm × 15 mm × 3 mm was immersed in about 35 mL of diethylene glycol and heated at 180 °C for 2 hours. For comparison purposes, fibres were recovered after both 10 minutes and 2 hours of immersion using tweezers, then washed with acetone and fully dried for 1 day at 160 °C before characterization.

2.3 Sample characterization

Dynamic mechanical analysis (DMA) was carried out using a TA Instruments DMA 850 and a film tensile clamp geometry. A sinusoidal stress with a frequency of 1 Hz and an amplitude of 10 µm was applied while the temperature was increased from –20 °C to 150 °C at a constant rate of 1 °C/min, following a 20-minute soak period.

Thermogravimetric analysis (TGA) was conducted using a NETZSCH TG 209F1 Libra analyzer to evaluate the thermal stability of the materials. Samples were heated from 35 °C to 800 °C at a constant rate of 10 °C/min under a nitrogen atmosphere.

Stress relaxation behavior was studied using a TA Instruments Discovery HR30 rotational rheometer fitted with a torsion clamp. Measurements were taken at multiple temperatures above the glass transition temperature (Tg), with each temperature held for 4 hours. A constant strain of 1 % was applied at each step, and the temperature was increased in 10 °C increments from 150 °C to 200 °C.

Scanning Electron Microscopy (SEM) was used to visually evaluate the quality of the recycled fibres. The analysis was performed using a FEI Nova NanoSEM 450 FEGSEM equipped with an ETD detector. Samples were prepared by applying a 10 nm carbon coating prior to imaging.

3. RESULTS AND DISCUSSION

3.1 Impact of matrix reprocessing on its thermal properties

The impact of matrix reprocessing on the thermal properties of the materials was evaluated using DMA, with a focus on the glass transition temperature (Tg) and rubbery storage modulus (see **Figure 2**).

First, a comparison between the original vitrimer (v) and thermoset (TS) reveals that the vitrimer has a higher Tg and rubbery plateau (measured at T = Tg + 30 °C). This is likely caused by an increase in crosslink density, resulting from the addition of the tin catalyst to the network, expected to accelerate curing and promote branching reactions in this diepoxy-diacid vitrimer systems **[33]**. This is consistent with the rise in storage modulus at high temperatures, implying that the material continues to undergo reactions that increase its crosslink density. Moreover, comparing the peak heights of tan delta for v and TS reveals that TS exhibits a higher peak, indicating greater molecular mobility within its network **[34, 35]**. This is expected for non-catalyzed diacid-diepoxy systems, where polyaddition reactions between epoxy and carboxylic acid groups likely dominate **[36, 37]**, resulting in the formation of long, linear hydroxyester chains **[33, 38]**.

It is interesting to note that the recycled vitrimer (Rv) shows a 6 % reduction in Tg and a 20 % lower rubbery storage modulus values compared to v, along with a slightly higher tan delta peak height. This suggests a material with greater flexibility, which is unexpected for a recycled material.

When comparing the original (TS) and vitrimerized (vTS) thermosets, an increase in Tg and rubbery plateau, as well as a decrease in tan delta peak height, is observed for vTS. The introduction of rigid domains into the network could be responsible for this effect, correlating with the visible shoulder at low temperatures indicative of microstructural variation **[39]**. Such heterogeneity could originate from inadequate integration of the catalyst into the network, leading to the formation of non-dynamic thermoset regions, further characterized by shorter chains than those of TS due to potential chain scission occurring during reprocessing. Still, despite these noticeable differences, the Tg and storage modulus values indicate that the vitrimerization process doesn't compromise such thermomechanical properties.

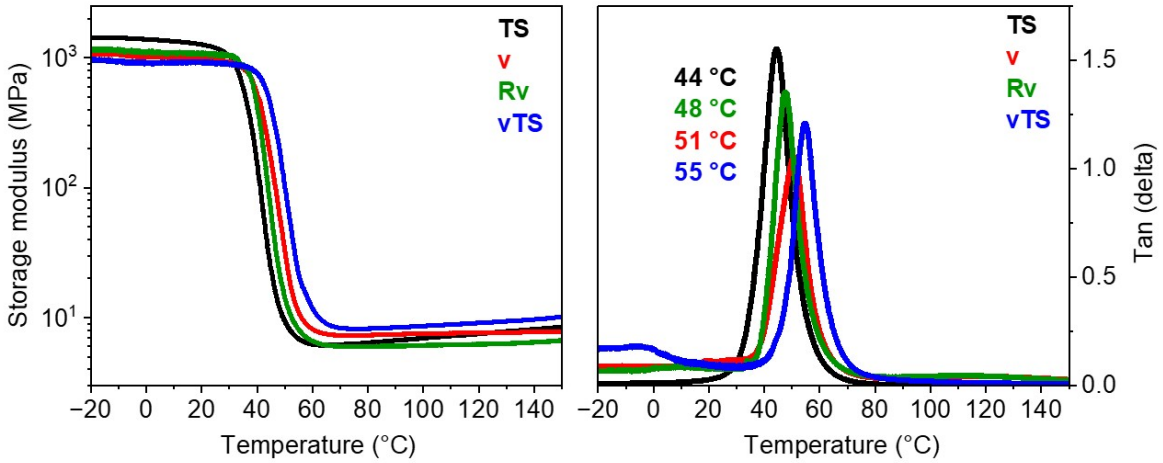

Figure 2: DMA of conventional thermoset (TS), original vitrimer (v), recycled vitrimer (Rv), and vitrimerized thermoset (vTS). Temperature-dependent evolution of the storage modulus and tan delta.

TGA results (see **Figure 3**) further support the preserved thermal stability of the vitrimer system after reprocessing: the original (v) and recycled (Rv) vitrimers exhibit nearly identical thermal degradation profiles. Specifically, their initial degradation temperatures (T_{onset}), defined as the temperatures at which 5 % weight loss occurs, are 328 °C and 331 °C, respectively. Their peak degradation temperatures (T_{max}), corresponding to the maximum rate of weight loss determined from the derivative thermogravimetric (DTG) curves, are 414 °C and 415 °C. And their residual weight at 800 °C falls within the range of 15 - 17 %. While the vitrimerized thermoset (vTS) exhibits very

similar behaviour, a slight distinction is observable, with its T_{onset}, T_{max}, and residual weight reaching 345 °C, 423 °C, and 17 %, respectively. This subtle increase in thermal stability might be attributed to a higher proportion of irreversible -hence more stable- bonds in the network compared to the non-vitrimerized vitrimers.

In contrast, the conventional thermoset (TS) exhibits a notably higher initial degradation temperature (approximately 60 °C above that of the vitrimer systems) highlighting the commonly observed trade-off between thermal stability and reversibility. A lower onset of degradation in vitrimers is indeed expected, given their ability to flow at elevated temperatures.

Overall, the similarity in thermal degradation profiles among v, Rv, and vTS indicates that neither the recycling process nor vitrimerization significantly affected the thermal resistance of the matrix. In particular, the nearly identical behavior of v and Rv confirms that the material remained largely unaffected by the recycling process, which aligns with the DMA results and underscores the excellent thermal robustness of the vitrimer system. In addition, the comparable thermal stability of Rv and vTS reinforces the potential of vitrimerization as an effective approach for thermoset recycling, enabling material recovery without loss of thermal performance.

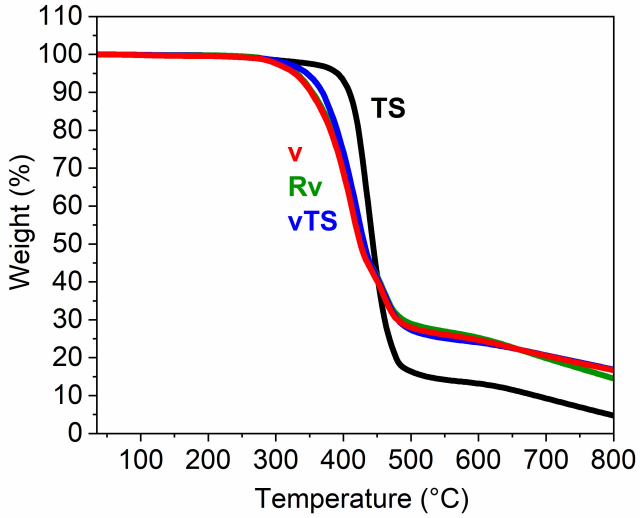

Figure 3: TGA curves for conventional thermoset (TS), original vitrimer (v), recycled vitrimer (Rv), and vitrimerized thermoset (vTS).

3.2 Impact of matrix reprocessing on its dynamic properties

Stress relaxation experiments were conducted to assess the dynamic behavior of the vitrimer systems and evaluate the effect of reprocessing on their flow properties. In such tests, a constant strain is applied, and the decrease in stress over time is monitored. At 200 °C, the original (v) and recycled (Rv) vitrimers exhibit full stress relaxation, while the vitrimerized thermoset (vTS) shows slightly reduced relaxation due to the presence of non-exchangeable covalent crosslinks. In contrast, the conventional thermoset (TS) shows negligible relaxation, as expected given the absence of dynamic bond exchanges (see **Figure 4**).

The characteristic stress relaxation times were determined using the Maxwell model of stress relaxation **[5]**. The results show that the recycled vitrimer (Rv) relaxes at a rate nearly identical to that of the original vitrimer. For instance, at 200 °C, both systems exhibit a relaxation time of 10 minutes. This highlights that the recycling process preserved the dynamic behavior of the vitrimer network. Interestingly, the vitrimerized thermoset (vTS) displays notably slower stress relaxation kinetics. At 200 °C, the relaxation time of vTS is 23 minutes -more than twice that of v and Rv. Stress relaxation in vitrimers is primarily governed by the rate of dynamic exchanges **[5, 34, 40]**, namely, in this case, transesterification reactions between hydroxyl and ester groups **[41, 42]**. Therefore, the slower stress relaxation observed in vTS indicates that the dynamic exchanges occur at a reduced rate. A greater proportion of irreversible bonds may account for this, by increasing the network's rigidity and the

average distance between dynamic moieties. Such a phenomenon could result from insufficient or uneven catalyst incorporation, a common challenge in vitrimerization **[32, 43]**.

In summary, the results confirm that an irreversible thermoset can be transformed into an inherently recyclable material through vitrimerization. In the case of Rv, the findings highlight that the recycling process has minimal impact on the dynamic properties of the vitrimer. However, the slower stress relaxation observed in vTS implies that the vitrimerization process impacted the material's dynamic properties, possibly due to suboptimal incorporation of the catalyst into the network. To improve this, reducing the particle size of the thermoset powder or increasing the compression molding time could be considered **[43]**.

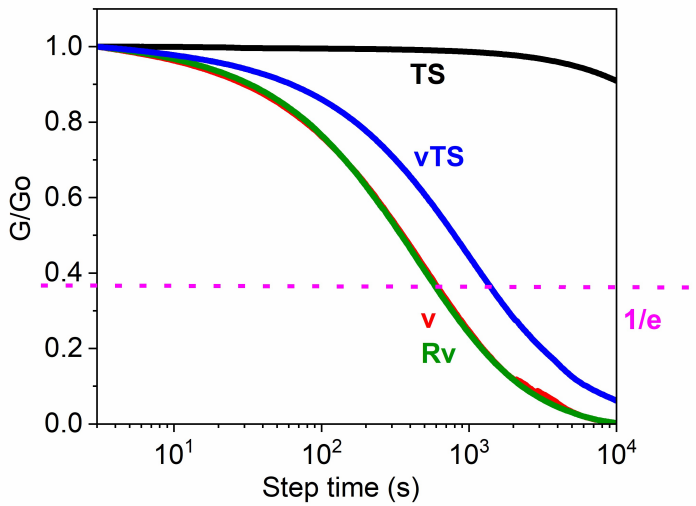

Figure 4: Stress relaxation behaviour at 200 °C for conventional thermoset (TS), original vitrimer (v), recycled vitrimer (Rv), and vitrimerized thermoset (vTS).

3.3 Impact of composite recycling on fibre quality

The chemical recycling process (see **Figure 5**) enabled to separate the fibres from the vitrimer matrix (v) after only 10 minutes of immersion in diethylene glycol (diEG). The solvent's active role in dynamic transesterification exchanges allows the vitrimer matrix to depolymerize, thereby enabling the separation of fibres from the matrix **[4, 44]**. Both the temperature of the process and the amount of solvent used significantly influence the rate of depolymerization.

It is worth noting that the dissolved matrix could be recovered and reused to produce a new chemically recycled vitrimer matrix. However, in practice, complete removal of the solvent remains a challenge. The recovered material typically retains residual solvent, resulting in a plasticized matrix with considerably higher flexibility than the original due to a higher amount of hydroxyl groups. While this may restrict its suitability for some applications, it could also offer opportunities in others where enhanced flexibility is desirable.

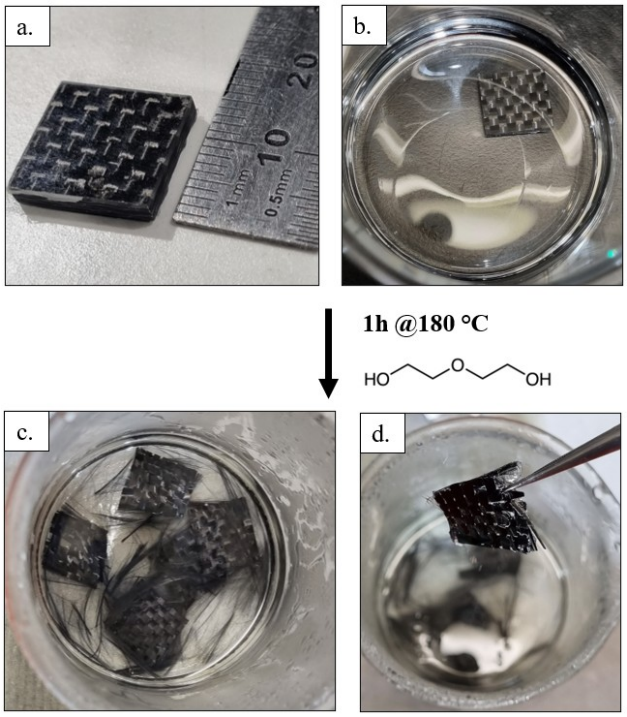

Figure 5: Pictures of composite chemical recycling: a) Preparation of CFRv sample, consisting of the original vitrimer (v) reinforced with carbon fibres. b) Sample immersion in diethylene glycol (diEG) at 180 °C. c) Fibres easily separated from the depolymerized matrix after 1 hour of immersion. d) Fibre recovery for characterization.

The surface quality of the recovered fibres was evaluated using SEM after immersion in diEG for two different immersion durations: 10 minutes and 2 hours (see **Figure 6**). SEM images reveal that, after 10 minutes, matrix residues are still clearly visible on fibre surface, whereas after 2 hours, these residues have substantially disappeared, indicating a more complete matrix depolymerization. To further assess fibre cleanliness and confirm the preservation of fibre quality, TGA will be conducted on the recovered fibres.

Overall, these results illustrate the strong potential of vitrimer-based matrices to facilitate composite recycling and enable the recovery of high-value materials.

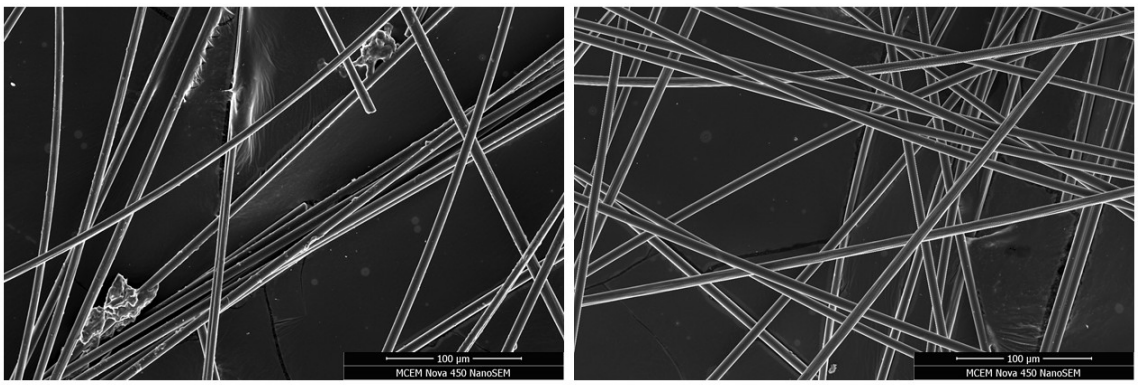

After 10 min chemical recycling **After 2 h chemical recycling**

Figure 6: SEM images of recycled fibres after 10 minutes (left) and 2 hours (right) of recycling, showing a visual comparison of their quality.

4. CONCLUSIONS

The vitrimer system developed in this work was synthesized using a conventional epoxy monomer, the biobased and affordable sebacic acid as curing agent, and an organotin catalyst. The resulting material exhibited a glass transition temperature of 51 °C and a characteristic stress relaxation time of 10 minutes at 200 °C. The synthesis process, combined with the material's thermal robustness and the accessibility of its raw materials, supports its industrial relevance. First, it was shown that this vitrimer system can be recycled without compromising its thermal and dynamic performance. After recycling, the material largely retained its Tg, rubbery plateau, thermal stability, and stress relaxation behavior, highlighting its excellent reprocessability. Additionally, a chemical recycling method was implemented to recover fibres from vitrimer-based composites. After two hours of immersion in diethylene glycol at 180 °C, SEM images revealed clean fibre surfaces. To tackle existing composite waste, the vitrimerization of fully cured conventional epoxy thermosets was also explored. The process successfully converted a thermoset into a reprocessable material, able to flow and significantly relax stresses at high temperature. A slight increase in Tg, rubbery plateau, and thermal stability was noticed compared to the original vitrimer, possibly due to the introduction of irreversible bonds into the network. While no loss of thermomechanical properties was observed, the results reveal a notably slower stress relaxation response -at least twice as slow as the original vitrimer-, which could be attributed to a higher proportion of irreversible bonds in the network, in line with our DMA and TGA results. This phenomenon could be explained by an inadequate integration of the catalyst into the network.

Overall, this study demonstrates the potential of epoxy vitrimers as a more sustainable alternative to conventional epoxy matrices for reducing composite waste. By substituting traditional, irreversible epoxy systems with dynamic, reprocessable vitrimer networks, this approach addresses both future and existing composite waste streams. Ultimately, this research aims to support a more environmentally responsible composite industry.

ACKNOWLEDGEMENTS

This work was supported by the Australian Research Council Discovery Project (DP240102221).
The authors acknowledge the use of ChatGPT for rephrasing purposes.

REFERENCES

1. Chabert, E., *Matériaux composites à matrices vitrimère et polymère supramoléculaire*. 2015.
2. Khurshid, M.F., et al., *Recent developments in the processing of waste carbon fibre for thermoplastic composites – A review.* Journal of Composite Materials, 2020. 54(14): p. 1925-1944.
3. Montarnal, D., et al., *Silica-like malleable materials from permanent organic networks.* Science, 2011. 334(6058): p. 965-8.
4. Yang, Y., et al., *Functional epoxy vitrimers and composites.* Progress in Materials Science, 2021. 120: p. 100710.
5. Capelot, M., et al., *Catalytic Control of the Vitrimer Glass Transition.* ACS Macro Letters, 2012. 1(7): p. 789-792.
6. Alabiso, W. and S. Schlögl *The Impact of Vitrimers on the Industry of the Future: Chemistry, Properties and Sustainable Forward-Looking Applications*. Polymers, 2020. 12, DOI: 10.3390/polym12081660.
7. Chabert, E., et al., *Multiple welding of long fiber epoxy vitrimer composites.* Soft Matter, 2016. 12(21): p. 4838-4845.
8. Weidmann, S., et al., *Investigations on thermoforming of carbon fiber reinforced epoxy vitrimer composites.* Composites. Part A, Applied science and manufacturing, 2022. 154: p. 106791.
9. Post, W., et al., *Healing of a glass fibre reinforced composite with a disulphide containing organic-inorganic epoxy matrix.* Composites science and technology, 2017. 152: p. 85-93.

10. Wu, Y., Y. Wei, and Y. Ji, *Carbon material/vitrimer composites: Towards sustainable, functional, and high-performance crosslinked polymeric materials.* Giant, 2023. 13: p. 100136.
11. Kissounko, D.A., P. Taynton, and C. Kaffer, *New material: vitrimers promise to impact composites.* Reinforced plastics (London), 2018. 62(3): p. 162-166.
12. Si, H., et al., *Rapidly reprocessable, degradable epoxy vitrimer and recyclable carbon fiber reinforced thermoset composites relied on high contents of exchangeable aromatic disulfide crosslinks.* Composites. Part B, Engineering, 2020. 199: p. 108278.
13. Poutrel, Q.-A., et al., *Thermolatent Heterogeneous Epoxy–Acid Formulation for the Manufacture of Preimpregnated Sheets and Composites with Vitrimer Properties.* ACS applied polymer materials, 2023.
14. Taynton, P., et al., *Repairable Woven Carbon Fiber Composites with Full Recyclability Enabled by Malleable Polyimine Networks.* Adv. Mater, 2016. 28(15): p. 2904-2909.
15. Denissen, W., et al., *Vinylogous Urea Vitrimers and Their Application in Fiber Reinforced Composites.* Macromolecules, 2018. 51(5): p. 2054-2064.
16. Yuan, Y., et al., *Multiply fully recyclable carbon fibre reinforced heat-resistant covalent thermosetting advanced composites.* Nature Communications, 2017. 8(1): p. 14657.
17. Wang, S., et al., *Facile: In situ preparation of high-performance epoxy vitrimer from renewable resources and its application in nondestructive recyclable carbon fiber composite.* Green chemistry : an international journal and green chemistry resource : GC, 2019. 21(6): p. 1484-1497.
18. Memon, H., et al., *An imine-containing epoxy vitrimer with versatile recyclability and its application in fully recyclable carbon fiber reinforced composites.* Composites science and technology, 2020. 199: p. 108314.
19. Liu, T., et al., *Carbon Fiber Reinforced Epoxy Vitrimer: Robust Mechanical Performance and Facile Hydrothermal Decomposition in Pure Water.* Macromol Rapid Commun, 2021. 42(3): p. e2000458-n/a.
20. Wang, H., et al., *A Triple Crosslinking Design toward Epoxy Vitrimers and Carbon Fiber Composites of High Performance and Multi-shape Memory.* Chinese journal of polymer science, 2021. 39(6): p. 736-744.
21. Wang, S., et al., *Fully recyclable and reprocessable polystyrene-based vitrimers with improved thermal stability and mechanical properties through nitrogen-coordinating cyclic boronic ester bonds.* Applied surface science, 2021. 570: p. 151157.
22. Wang, S., et al., *Facile preparation of recyclable cyclic polyolefin/polystyrene vitrimers with low dielectric loss based on semi-interpenetrating polymer networks for high-frequency copper-clad laminates.* Polymer (Guilford), 2021. 233: p. 124214.
23. Xu, Y., et al., *Reprocessable, Self-Adhesive, and Recyclable Carbon Fiber-Reinforced Composites Using a Catalyst-Free Self-Healing Bio-Based Vitrimer Matrix.* ACS Sustainable Chem. Eng, 2021. 9(48): p. 16281-16290.
24. An, X., et al., *Epoxy resin with exchangeable diselenide crosslinks to obtain reprocessable, repairable and recyclable fiber-reinforced thermoset composites.* Reactive & functional polymers, 2022. 172: p. 105189.
25. Kamble, M., et al., *Reversing fatigue in carbon-fiber reinforced vitrimer composites.* Carbon (New York), 2022. 187: p. 108-114.
26. Qiao, Z., et al., *High-Performance and Degradable Polybenzoxazine/VU Vitrimer and Its Application for Carbon Fiber Recycling.* ACS Sustainable Chem. Eng, 2022. 10(28): p. 9113-9122.
27. Wang, Y., et al., *Recyclable Carbon Fiber Reinforced Vanillin-Based Polyimine Vitrimers: Degradation and Mechanical Properties Study.* Macromolecular Materials and Engineering, 2022. 307(7): p. 2100893.
28. Xu, Y., et al., *Hyperbranched polyester catalyzed self-healing bio-based vitrimer for closed-loop recyclable carbon fiber-reinforced polymers.* Composites science and technology, 2022. **228**: p. 109676.

29. Yang, W., et al., *Design of inherent fire retarding and degradable bio-based epoxy vitrimer with excellent self-healing and mechanical reprocessability.* Composites science and technology, 2022. **230**: p. 109776.
30. Zhou, Z., et al., *Unraveling a path for multi-cycle recycling of tailored fiber-reinforced vitrimer composites.* Cell reports physical science, 2022. **3**(9): p. 101036.
31. Nabipour, H., et al., *A bio-based intrinsically flame-retardant epoxy vitrimer from furan derivatives and its application in recyclable carbon fiber composites.* Polymer degradation and stability, 2023. **207**: p. 110206.
32. Yue, L., et al., *Vitrimerization: A Novel Concept to Reprocess and Recycle Thermoset Waste via Dynamic Chemistry.* Glob. Challenges, 2019. **3**(7): p. 1800076.
33. Tangthana-umrung, K., Q.A. Poutrel, and M. Gresil, *Epoxy Homopolymerization as a Tool to Tune the Thermo-Mechanical Properties and Fracture Toughness of Vitrimers.* Macromolecules, 2021. **54**(18): p. 8393-8406.
34. Han, J., et al., *A Catalyst-Free Epoxy Vitrimer System Based on Multifunctional Hyperbranched Polymer.* Macromolecules, 2018. **51**(17): p. 6789.
35. Huang, Z., et al., *Surface engineering of nanosilica for vitrimer composites.* Composites science and technology, 2018. **154**: p. 18-27.
36. Menager, C., et al., *Polymerization kinetic pathways of epoxidized linseed oil with aliphatic bio-based dicarboxylic acids.* Journal of polymer science (2020), 2020. **58**(12): p. 1717-1727.
37. Schwaiger, M. and K. Resch-Fauster, *Mechanical flexible epoxy resins with 100% bio-based carbon content based on epoxidized vegetable oils.* Journal of applied polymer science, 2022. **139**(48): p. n/a.
38. Poutrel, Q.-A., et al., *Dicarboxylic acid-epoxy vitrimers: influence of the off-stoichiometric acid content on cure reactions and thermo-mechanical properties.* Polymer Chemistry, 2020. **11**(33): p. 5327-5338.
39. Altuna, F., C. Hoppe, and R.J.J. Williams, *Shape memory epoxy vitrimers based on DGEBA crosslinked with dicarboxylic acids and their blends with citric acid.* RSC Adv., 2016. **6**.
40. Altuna, F.I., C.E. Hoppe, and R.J.J. Williams, *Shape memory epoxy vitrimers based on DGEBA crosslinked with dicarboxylic acids and their blends with citric acid.* RSC Advances, 2016. **6**(91): p. 88647-88655.
41. Van Zee, N.J. and R. Nicolaÿ, *Vitrimers: Permanently crosslinked polymers with dynamic network topology.* Progress in Polymer Science, 2020. **104**: p. 101233.
42. Schenk, V., et al., *Vitrimer composites: current status and future challenges.* Materials Advances, 2022. **3**(22): p. 8012-8029.
43. Yue, L., et al., *Recycling Epoxy by Vitrimerization: Influence of an Initial Thermoset Chemical Structure.* ACS Sustainable Chem. Eng, 2020. **8**(33): p. 12706-12712.
44. Shi, Q., et al., *Solvent Assisted Pressure-Free Surface Welding and Reprocessing of Malleable Epoxy Polymers.* Macromolecules, 2016. **49**(15): p. 5527-5537.

POLITECNICO MILANO 1863

CENTRO NAZIONALE PER LA MOBILITÀ SOSTENIBILE

Sustainable alternatives to thermoset polymers for aerospace composites: a comparison using LCA

Andrea Bologna, Antonio Mattia Grande

Department of Aerospace Science and Technology (DAER), Politecnico di Milano

ICCM24, Baltimore, August 7 2025

Outline

- Introduction
- What is LCA?
- Scope definition
- Case study
- LCA modelling
- LCA results
- Conclusions

Introduction: European policies framework

- Aviation makes up for 13.9% of transport emissions and it's responsible for 4% of total EU GHG emissions [1]
- Emissions produced by general aviation could triple by 2050 according to ICAO [2]
- ICAO drew a resolution to decarbonise aerospace industry with sustainable market-based measures [2]
- EASA drew the European Aviation Environmental Report, one of the chapters is dedicated to technology and design [3]



Introduction: AAM market expectations

Total equivalent CO_2 emissions of a traditional aircraft life cycle:

- >99% from the use phase
- <1% from production and EoL [4]



$m \approx 10^{4/5}$ kg



$m \approx 10^{3}$ kg

What about UAM?
Market value forecast of 74 billion USD in the US for civil EVTOLs in 2035 [5]

Shorter lifecycle

Higher environmental impact from production and EoL: ranging from 20% to 75% according to different scenarios [6], [7]

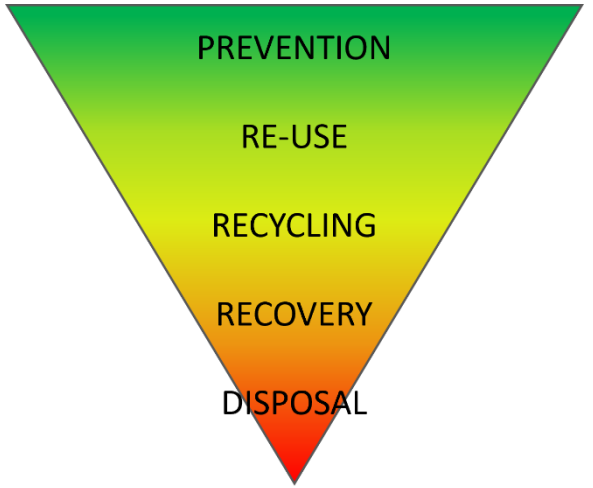

What is LCA?

LCA phases:

1) Goal and scope definition
2) LCI (Life Cycle Inventory)
3) LCIA (Life Cycle Impact Assessment)
4) Interpretation of the results

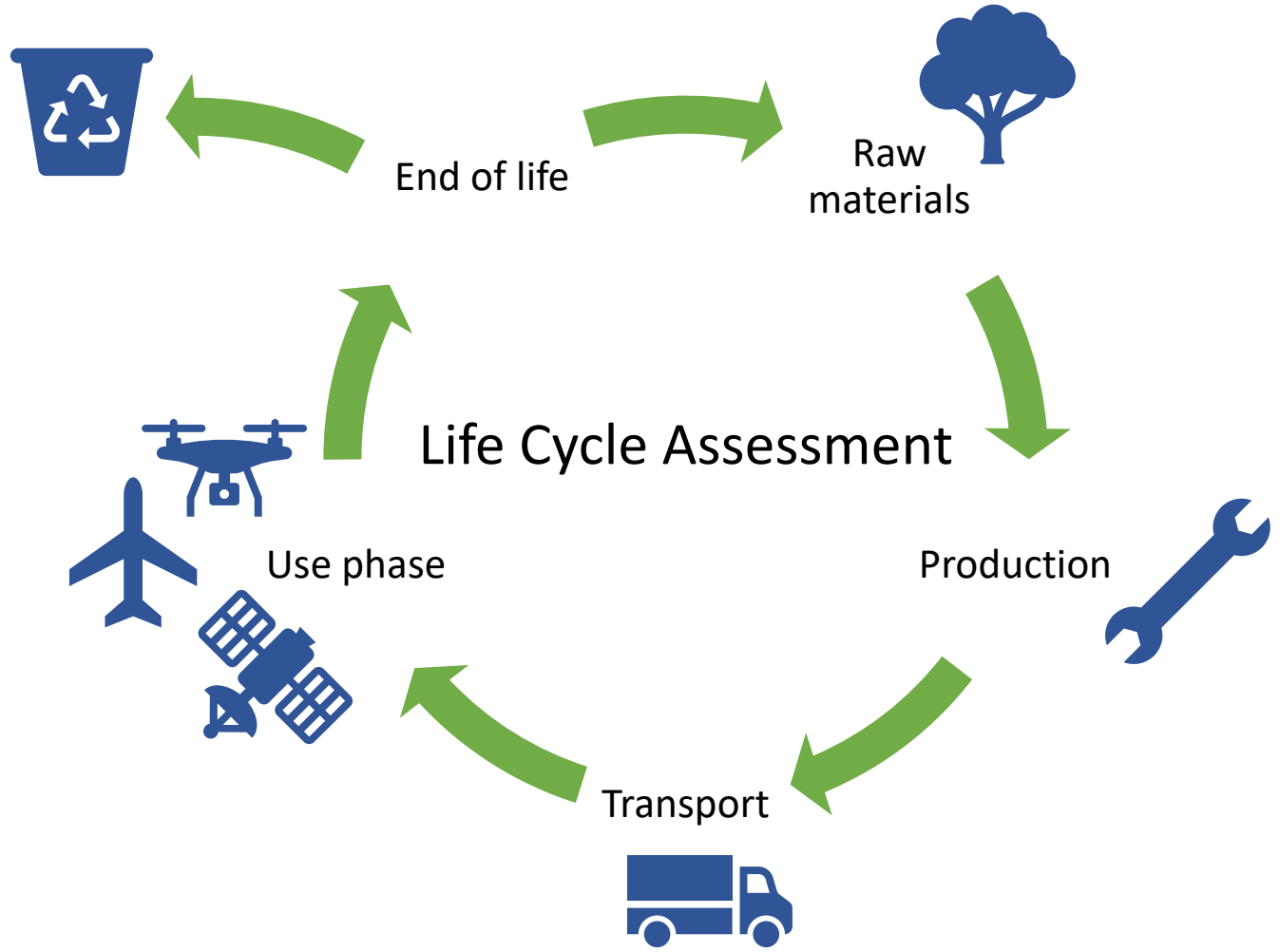

Scope definition

Scope definition:

Carry out a **preliminary comparison between different polymeric matrices**, analysing the Global Warming Potential associated to the production and EoL phases of an EVTOL.

Polymeric matrix	**Characteristics**
Thermoset resin	Epoxy resin is considered the standard solution in aerospace industry.
High-performance thermoplastics	Like the ketone family (PEEK, PEKK, etc.), high mechanical performance and chemical stability, offers the possibility to be reshaped.
Covalent adaptable networks	Similar to thermoset resins, but through a certain stimulus they can be reshaped. Still at research stage.

Case study

Functional unit: EVTOL structure, mass = **1465.5 kg**

Assumptions:

- The same fibers are used for all the matrices
- The use phase is neglected since the performance of the aircraft is expected to be similar in all cases
- The small difference in terms of performance is difficult to quantify



credits: NASA

Mass fraction for each material [7]

	Aluminium	Steel	Titanium	Carbon fiber	Glass fiber	Polymeric Matrix
Mass fraction	0.173	0.093	0.066	0.294	0.119	0.256

LCA modelling

Thermoset resin:
- Autoclave curing
- Mechanical recycling: industry adopted best option

Thermoplastic matrix:
- Production by thermoforming
- EoI mix of recycling and reshaping

Vitrimer:
- Production like thermoset
- EoL like thermoplastic

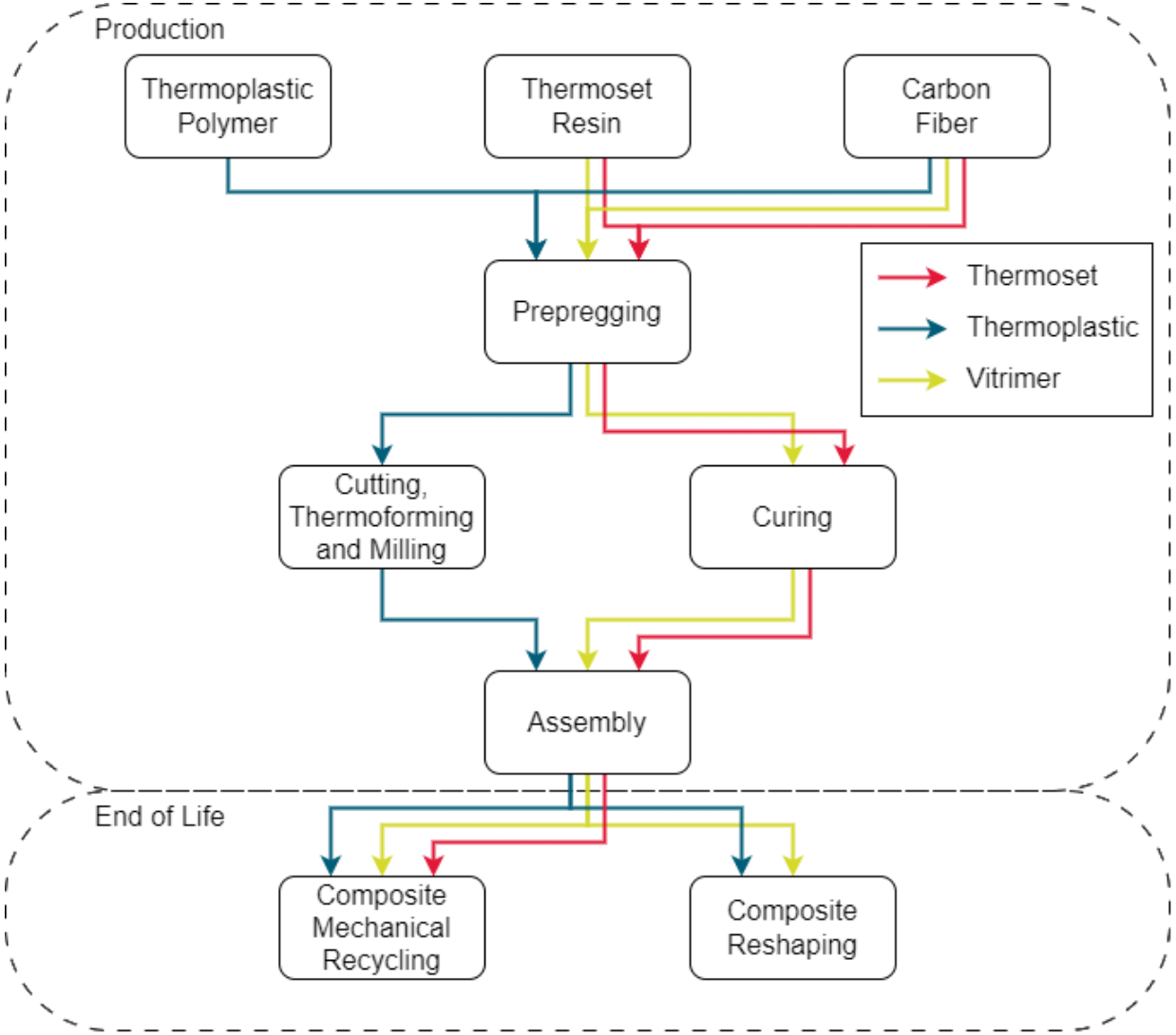

LCA results: GWP 1/2

- Results obtained using the ReCiPe 2016 method
- The lowest CO_2 emissions can be achieved with vitrimers
- The percentage of reused material strongly impact the GWP
- Thermoset resin results as the worst option in all the considered scenarios

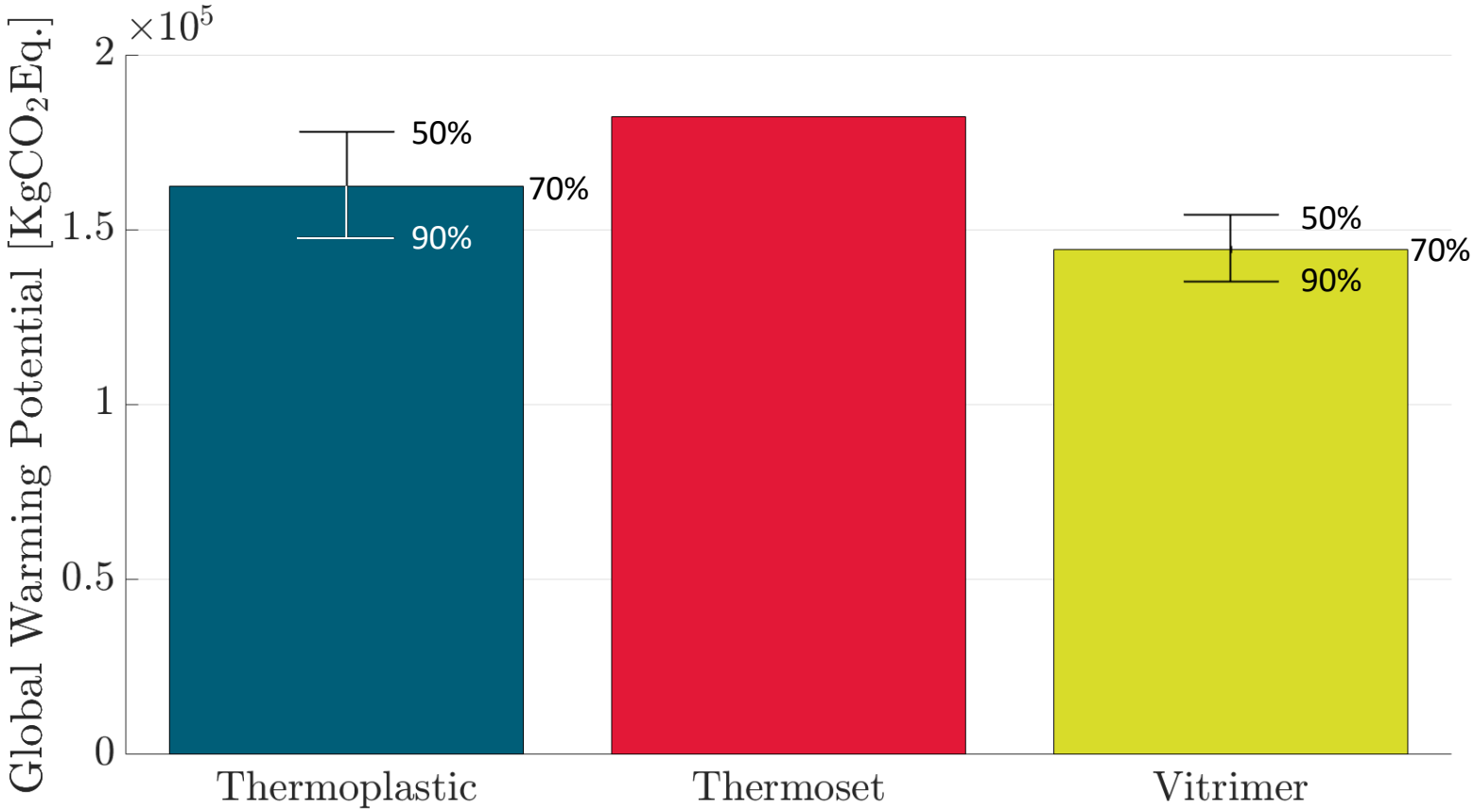

	Thermoplastic	Vitrimer
Avoided emissions	10.9%	20.8%

LCA results: GWP 2/2

- PEEK production produces more emissions with respect to thermoset resins
- Most of the GWP comes from energy production

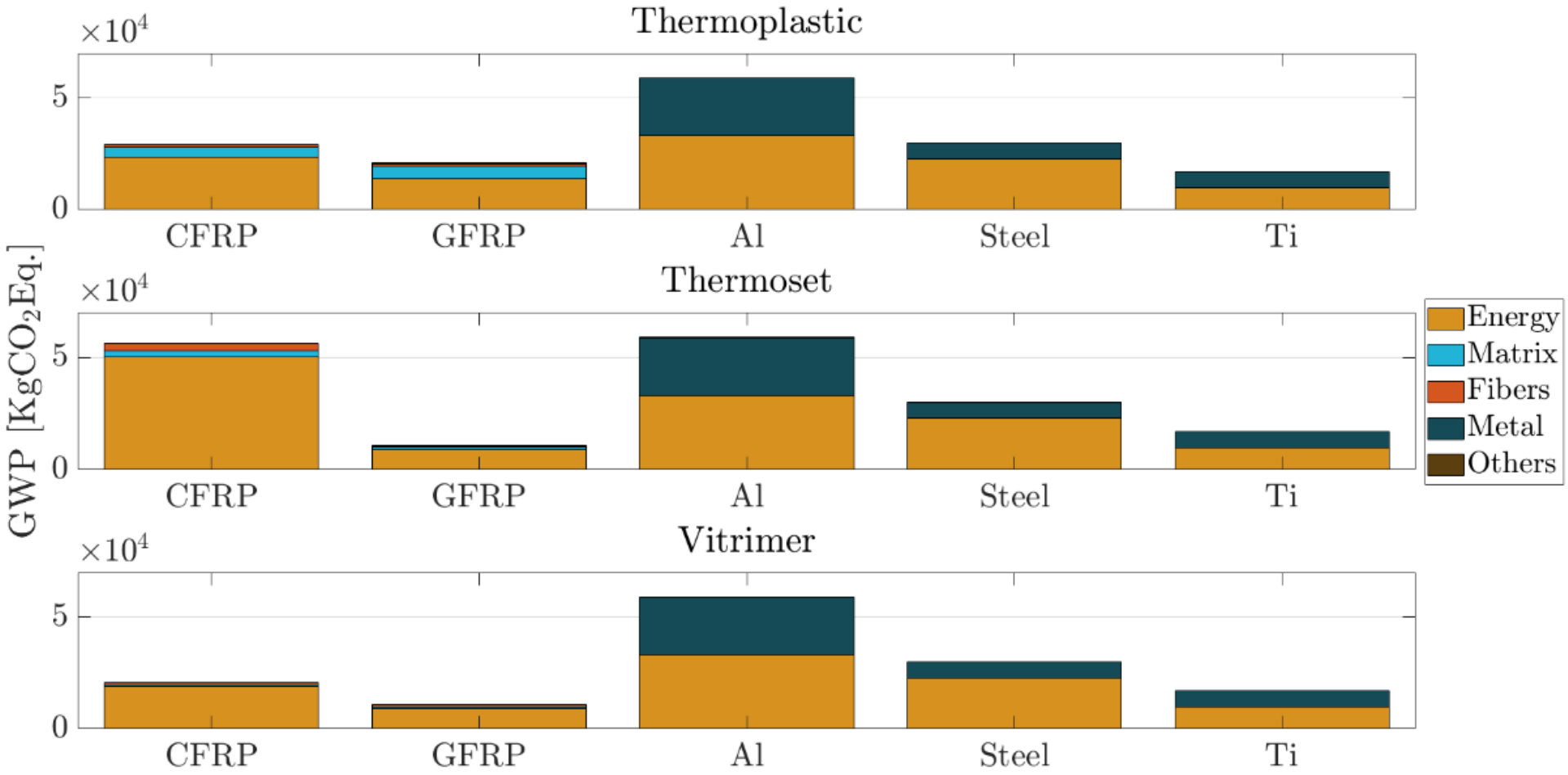

LCA results: CED

Looking at Cumulative Energy Demand (CED) it is clear that composites material request the highest energy for they production, which can be strongly mitigated by reuse strategies

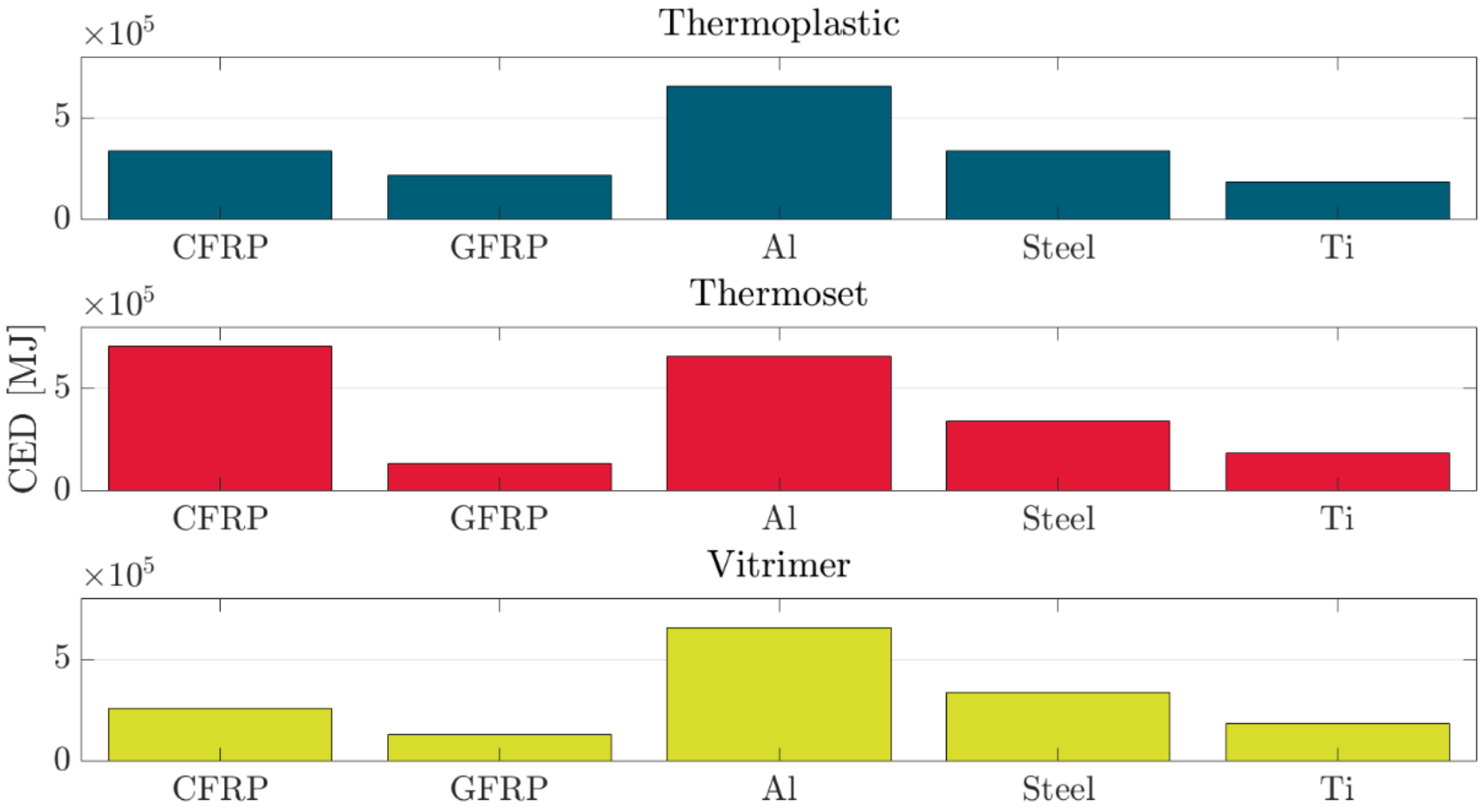

LCA results: sensitivity analysis

The breakeven point which justifies the adoption of PEEK is obtained when almost 50% of the material is reused.

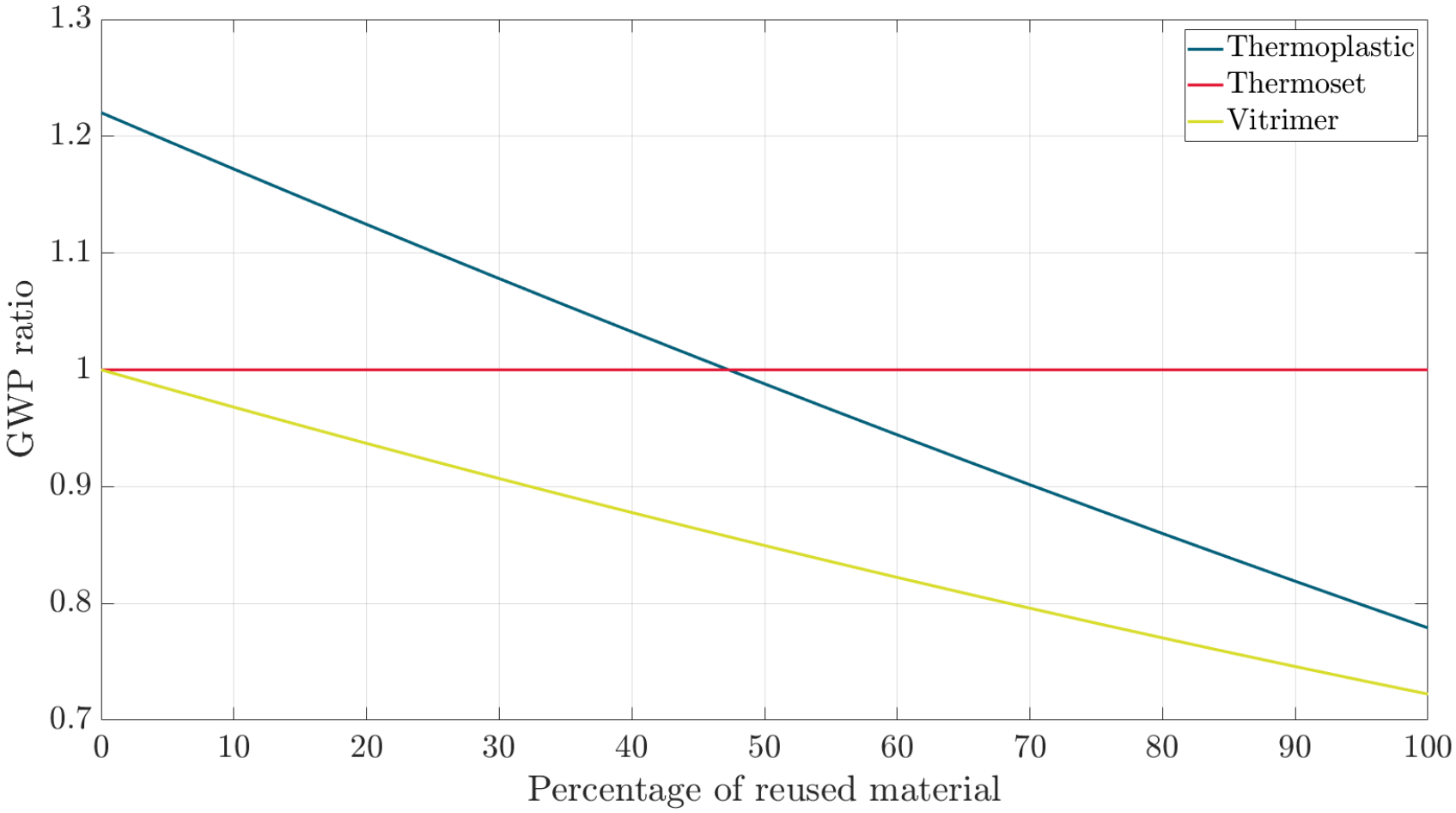

Conclusions

- Decarbonization is of paramount importance in the aerospace industry
- Looking at new trends, production and EoL will be more relevant
- Reshaping composite materials could give a relevant contribution

Future developments

- The LCA database should be widened with better quality data
- How many times the reshaping can be carried out with limited degradation of the material
- How environmental effects will impact the reshaping possibility and the performance

References

[1] https://climate.ec.europa.eu/eu-action/transport/reducing-emissions-aviation_en

[2] https://www.icao.int/environmental-protection/Pages/default.aspx

[3] https://www.easa.europa.eu/en/light/topics/european-aviation-environmental-report-2022

[4] I. Jakovljević, R. Mijailović, and P. Mirosavljević, “Carbon dioxide emission during the life cycle of turbofan aircraft,” Energy, vol. 148, pp. 866–875, Apr. 2018, doi: 10.1016/j.energy.2018.02.022.

[5] A. P. Cohen, S. A. Shaheen, and E. M. Farrar, “Urban Air Mobility: History, Ecosystem, Market Potential, and Challenges,” IEEE Transactions on Intelligent Transportation Systems, vol. 22, no. 9, pp. 6074–6087, Sep. 2021, doi: 10.1109/TITS.2021.3082767.

[6] R. Arvidsson, A. Nordelöf, and S. Brynolf, “Life cycle assessment of a two-seater all-electric aircraft,” International Journal of Life Cycle Assessment, vol. 29, no. 2, pp. 240–254, Feb. 2024, doi: 10.1007/s11367-023-02244-z.

[7] N. André and M. Hajek, “Robust environmental life cycle assessment of electric vtol concepts for urban air mobility,” in AIAA Aviation 2019 Forum, American Institute of Aeronautics and Astronautics Inc, AIAA, 2019, pp. 1–14. doi: 10.2514/6.2019-3473.

Q&A

Andrea Bologna
PhD student at the Department of Aerospace Science and Technology (DAER), Politecnico di Milano
andrea.bologna@polimi.it

Antonio Mattia Grande
Associate professor at the Department of Aerospace Science and Technology (DAER), Politecnico di Milano
antoniomattia.grande@polimi.it

Thank you for the attention!

SCAN ME!

DIPARTIMENTO DI SCIENZE E TECNOLOGIE AEROSPAZIALI
www.aero.polimi.it

Acknowledgments

This study was carried out within the MOST – Sustainable Mobility National Research Center and received funding from the European Union Next-Generation EU (PIANO NAZIONALE DI RIPRESA E RESILIENZA (PNRR) – MISSIONE 4 COMPONENTE 2, INVESTIMENTO 1.4 – D.D. 1033 17/06/2022, CN00000023). This manuscript reflects only the authors' views and opinions, neither the European Union nor the European Commission can be considered responsible for them.

Supplementary: LCA processes

Processes with energy cost

Process	Output Mass [kg]	Waste [kg]	ρ [kWh/kg]	P [kW]	t [h]	E [kWh]
CFRP TS						
Prepregging	1083,79		11,10			12030,10
Lay up	867,03	216,76				
Curing	693,63	173,41		6936,27	8,00	55490,17
GFRP TS						
Prepregging	437,85		11,10			4860,16
Lay up	350,28	87,57				
Curing	280,23	70,06		2802,25	8,00	22418,03
CFRP TP						
Prepregging	1205,89		11,10			13385,36
Panel prod.	964,71	241,18	6,10			5884,74
Processing	693,63	271,08				84000,44
GFRP TP						
Prepregging	487,18		11,10			5407,69
Panel prod.	389,74	97,44	6,10			2377,43
Processing	280,23	109,52				33936,18
Aluminium						
Machining	251,59	4780,26		120,00	1673,09	200771,08
Steel						
Machining	135,21	2568,99		120,00	1156,04	138725,21
Titanium						
Machining	95,84	191,69				58733,75

Supplementary: Carbon fibers inventory

Output	**Quantity**
Carbon fibers	1 Kg
Input	
Polyacrylonitrile fibres (PAN), from acrylonitrile and methacrylate, prod. mix, PAN w/o additives EU-27 S	1 Kg
Electricity, high voltage {DE}| market for | Cut-off, S	459 MJ/kg
Transport, freight, lorry 16e32 metric ton, euro3 {RER}| market for transport, freight, lorry 16e32 metric ton, EURO3 | Cut-off, S	2224 kgkm

A. D. La Rosa, S. Greco, C. Tosto, and G. Cicala, “LCA and LCC of a chemical recycling process of waste CF-thermoset composites for the production of novel CF-thermoplastic composites. Open loop and closed loop scenarios,” J Clean Prod, vol. 304, Jul. 2021, doi: 10.1016/j.jclepro.2021.127158.

Supplementary: Mechanical recycling of CFRP

Process	Item	Amount	Unit
Input	Composite	1	kg
	Electricity, medium voltage {IT}| electricity voltage transformation from high to medium voltage | APOS, S	0.27	MJ
Output	rCF	0.24	kg
	Fine powder	0.19	kg
	Coarse fraction	0.57	kg

M. Wu, J. Sadhukhan, R. Murphy, U. Bharadwaj, and X. Cui, “A novel life cycle assessment and life cycle costing framework for carbon fibre-reinforced composite materials in the aviation industry,” International Journal of Life Cycle Assessment, vol. 28, no. 5, pp. 566–589, May 2023, doi: 10.1007/s11367-023-02164-y.

Supplementary: LCI thermosplastic EVTOL

Process	Database	Unit	Quantity
Aluminium (waste treatment) {GLO}| recycling of aluminium | Cut-off, S	Ecoinvent 3	kg	4780,27
Aluminium, primary, ingot {IAI Area, EU27 & EFTA}| market for aluminium, primary, ingot | Cut-off, S	Ecoinvent 3	kg	5031,86
Electricity, high voltage {Europe without Switzerland}| market group for electricity, high voltage | Cut-off, S	Ecoinvent 3	MJ	343772,6
Electricity, medium voltage {RER}| market group for electricity, medium voltage | Cut-off, S	Ecoinvent 3	MJ	1955599
Glass fibre {RER}| glass fibre production | Cut-off, S	Ecoinvent 3	kg	302,58
Polyacrylonitrile fibres (PAN), from acrylonitrile and methacrylate, prod. mix, PAN w/o additives EU-27 S	ELCD	kg	748,96
PEEK (Polyetheretherketone)	IDEMAT2025	kg	641,53
Steel and iron (waste treatment) {GLO}| recycling of steel and iron | Cut-off, S	Ecoinvent 3	kg	2760,68
Steel, chromium steel 18/8 {GLO}| market for steel, chromium steel 18/8 | Cut-off, S	Ecoinvent 3	kg	2704,2
Titanium {GLO}| market for titanium | Cut-off, S	Ecoinvent 3	kg	287,53
Transport, freight, lorry 16-32 metric ton, EURO6 {RER}| market for transport, freight, lorry 16-32 metric ton, EURO6 | Cut-off, S	Ecoinvent 3	tkm	2090,929
Waste plastic, mixture {RER}| market group for waste plastic, mixture | Cut-off, S	Ecoinvent 3	kg	719,22

Supplementary: LCI thermoset EVTOL

Process	Database	Unit	Quantity
Aluminium (waste treatment) {GLO}| recycling of aluminium | Cut-off, S	Ecoinvent 3	kg	4780,27
Aluminium, primary, ingot {IAI Area, EU27 & EFTA}| market for aluminium, primary, ingot | Cut-off, S	Ecoinvent 3	kg	5031,86
Electricity, high voltage {Europe without Switzerland}| market group for electricity, high voltage | Cut-off, S	Ecoinvent 3	MJ	308962,1
Electricity, medium voltage {RER}| market group for electricity, medium voltage | Cut-off, S	Ecoinvent 3	MJ	1774903
Epoxy resin, liquid {RER}| market for epoxy resin, liquid | Cut-off, S	Ecoinvent 3	kg	576,58
Glass fibre {RER}| glass fibre production | Cut-off, S	Ecoinvent 3	kg	271,94
Polyacrylonitrile fibres (PAN), from acrylonitrile and methacrylate, prod. mix, PAN w/o additives EU-27 S	ELCD	kg	673,12
Steel and iron (waste treatment) {GLO}| recycling of steel and iron | Cut-off, S	Ecoinvent 3	kg	2760,68
Steel, chromium steel 18/8 {GLO}| market for steel, chromium steel 18/8 | Cut-off, S	Ecoinvent 3	kg	2704,2
Titanium {GLO}| market for titanium | Cut-off, S	Ecoinvent 3	kg	287,53
Transport, freight, lorry 16-32 metric ton, EURO6 {RER}| market for transport, freight, lorry 16-32 metric ton, EURO6 | Cut-off, S	Ecoinvent 3	tkm	2041,698
Waste asphalt {RoW}| market for waste asphalt | Cut-off, S	Ecoinvent 3	kg	390,17
Waste plastic, mixture {RER}| market group for waste plastic, mixture | Cut-off, S	Ecoinvent 3	kg	157,62

ICCM24
24TH INTERNATIONAL CONFERENCE ON COMPOSITE MATERIALS

MICHIGAN ENGINEERING
UNIVERSITY OF MICHIGAN

Mapping the Global Flow of Fiber-Reinforced Polymer Composites and Supply Chain Energy Requirements

Presenter: Zhuoer Li

Authors: Zhuoer Li, Dr. Daniel Cooper*

University of Michigan

*drcooper@umich.edu

Motivation to Decarbonize FRPC Production

Fiber-reinforced polymer composites (FRPCs) are becoming increasingly used across transport, electronics, wind energy and other sectors



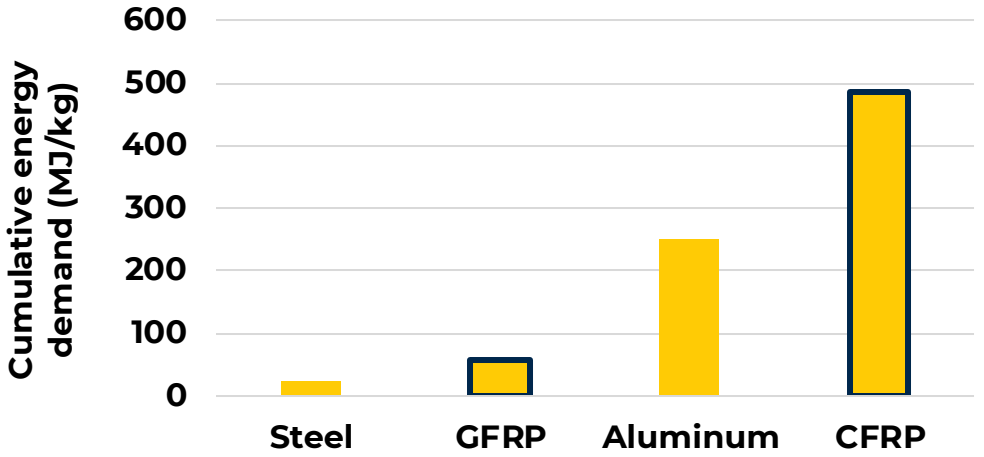

Fig. 1. Cumulative energy demand of materials

However, their production comes with environmental problems such as:

- High energy and emission intensities
- Low recycling rate at end-of-life (~2%)
- High process scrap rate (*e.g., prepreg cutting waste ~ 30-40%*) with most scrap landfilled

Aim: understanding decarbonization priorities within the global FRPC supply chain

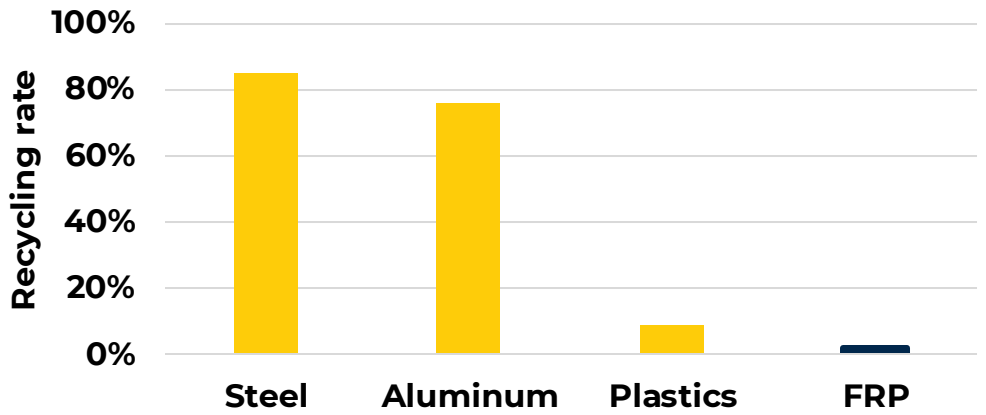

Fig. 2. Global recycling rate of materials

Life Cycle Analysis for Process-level Impacts

MICHIGAN ENGINEERING
UNIVERSITY OF MICHIGAN

Life cycle analysis (LCA)

- Most common method
- Focus on process-level impacts
- Examples findings for LCAs on FRPC:
  - A CFRP automotive part need ~ 4 times the **primary energy** of a steel one (Das, 2011; Ghosh et al., 2021)
  - High **resource depletion, water consumption** (Wegmann et al., 2022; Walker and Thies, 2022)
  - Bio-based composites need double the **land use** of C/GFRP and steel (Walker and Thies, 2022)

Limitations of LCA

Lacking material quantity considerations (intensity vs. demand), limiting guidance for research and investment prioritization

Table 1. An example of quantity & impact

	Glass fiber	**Carbon fiber**
Global production	~6,000 kt	~1,00 kt
Primary energy intensity	~22 MJ/kg	~350 MJ/kg

Material Flow Analysis - Environmental Impacts With Material Quantity Considerations

MICHIGAN ENGINEERING
UNIVERSITY OF MICHIGAN

Material flow analysis (MFA)

- Characterizes how a given material is transformed through a supply chain
- Enables the impact assessment across a supply chain on an equal footing

Existing MFA on FRPC

- J. Rybicka et al. (2015) mapped 4 different processes to capture FRPC mfg. scrap flows
- Shuaib et al., (2015) mapped the UK CFRP and GFRP supply chains
- Hamid et al. (2025) mapped global composites waste from wind turbine blades

Current Gap

There is only process-level, sectorial and regional, low-resolution supply-chain-level MFA on FRPC

To identify decarbonization priorities, we conducted an MFA on the global FPRC supply chain

This research: Material flow analysis (MFA) + Energy Analysis to Reveal FRPC Decarbonization Priorities

MICHIGAN ENGINEERING
UNIVERSITY OF MICHIGAN

Key contributions: using MFA to quantify the material efficiency and energy demand in global fiber reinforced polymer composite supply chain

1. Model the **mass** flows and their uncertainties in the global FRP composite supply chain with Bayesian inference

2. Quantify the **primary energy** attributable to FRP materials, processes and end-use sectors

3. Identify the **decarbonization opportunities** in the global FRPC production system

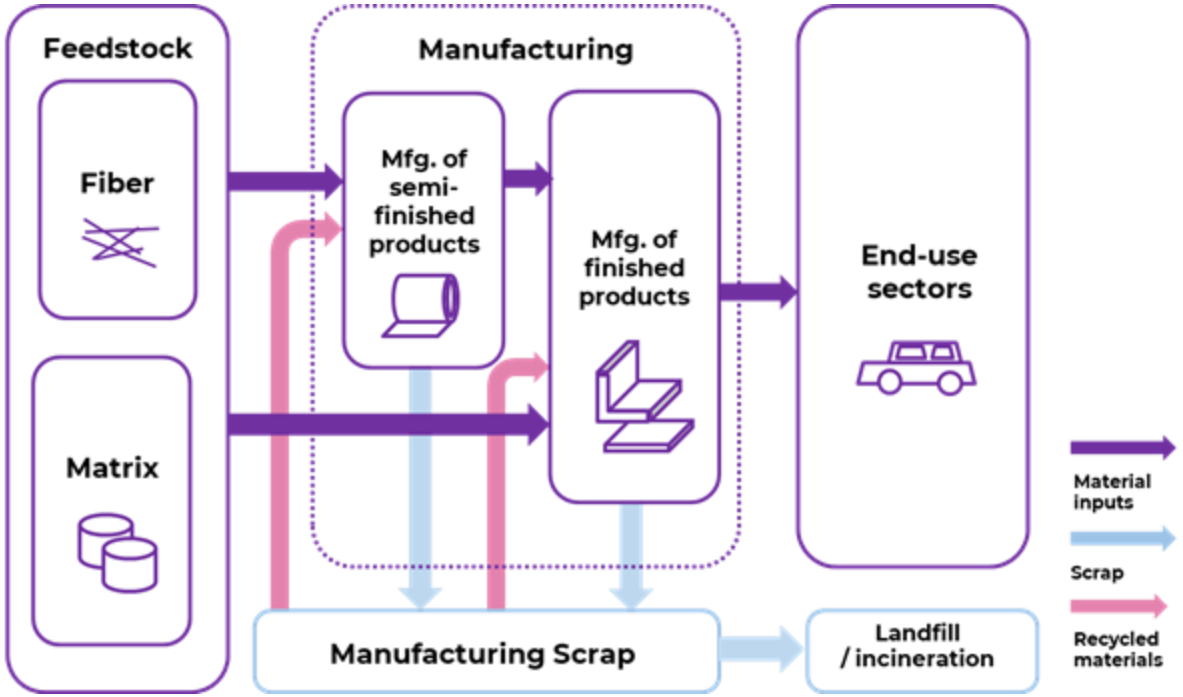

Fig. 3. Scope of this material flow analysis.

Methodology

MICHIGAN ENGINEERING
UNIVERSITY OF MICHIGAN

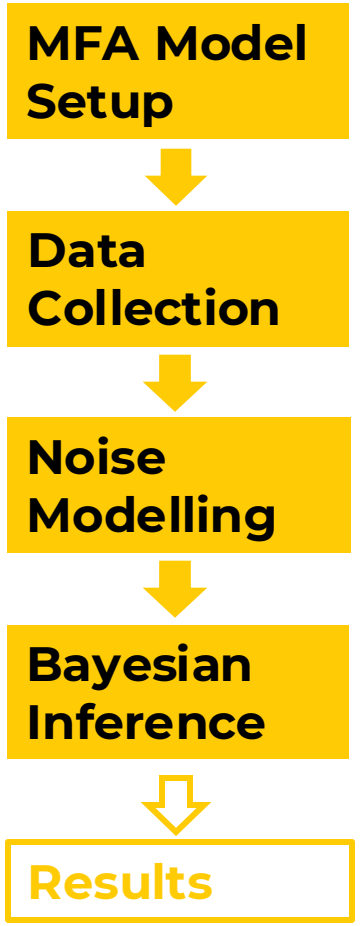

Material Flow Analysis - Model Structure

MICHIGAN ENGINEERING
UNIVERSITY OF MICHIGAN

- MFA Model Setup
- Data Collection
- Noise Modelling
- Bayesian Inference
- Results

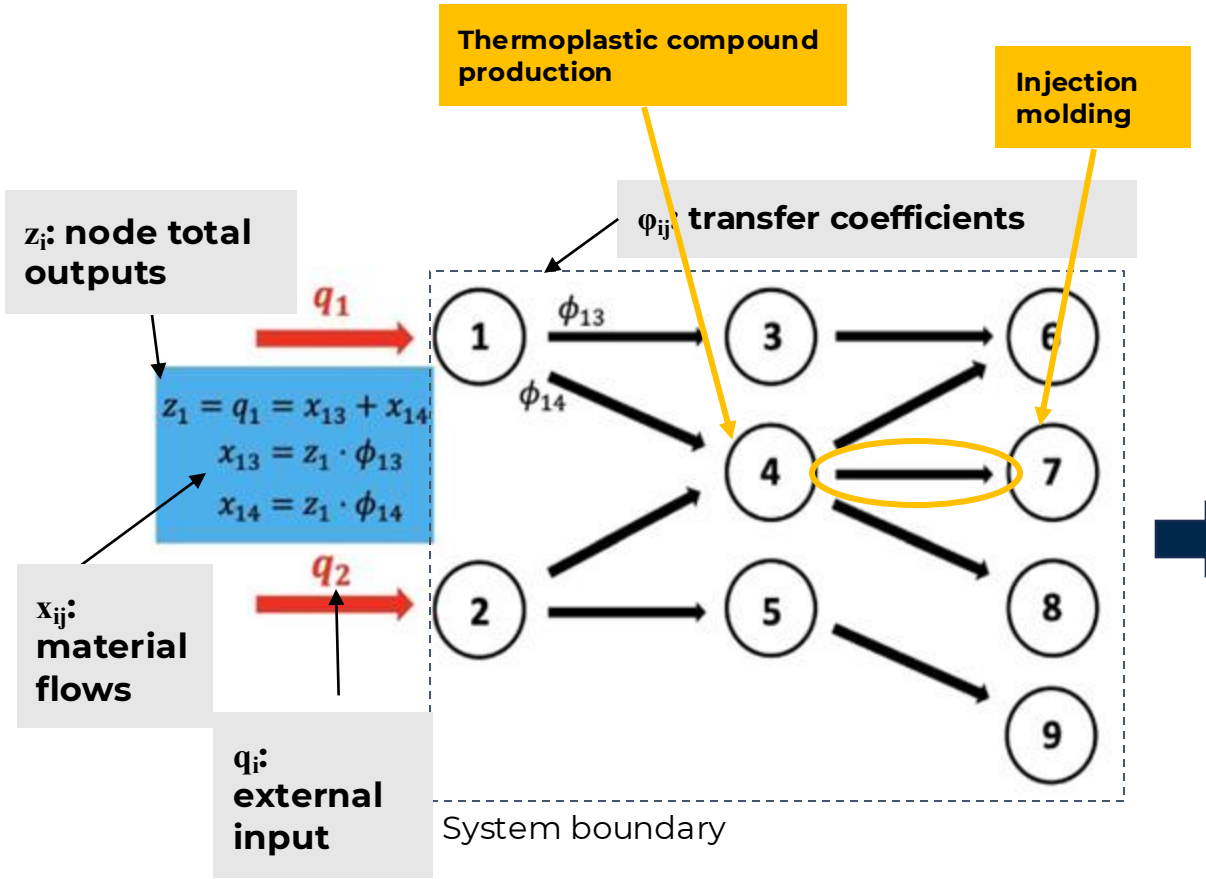

Fig. 4. An example MFA network (Dong et al., 2023)

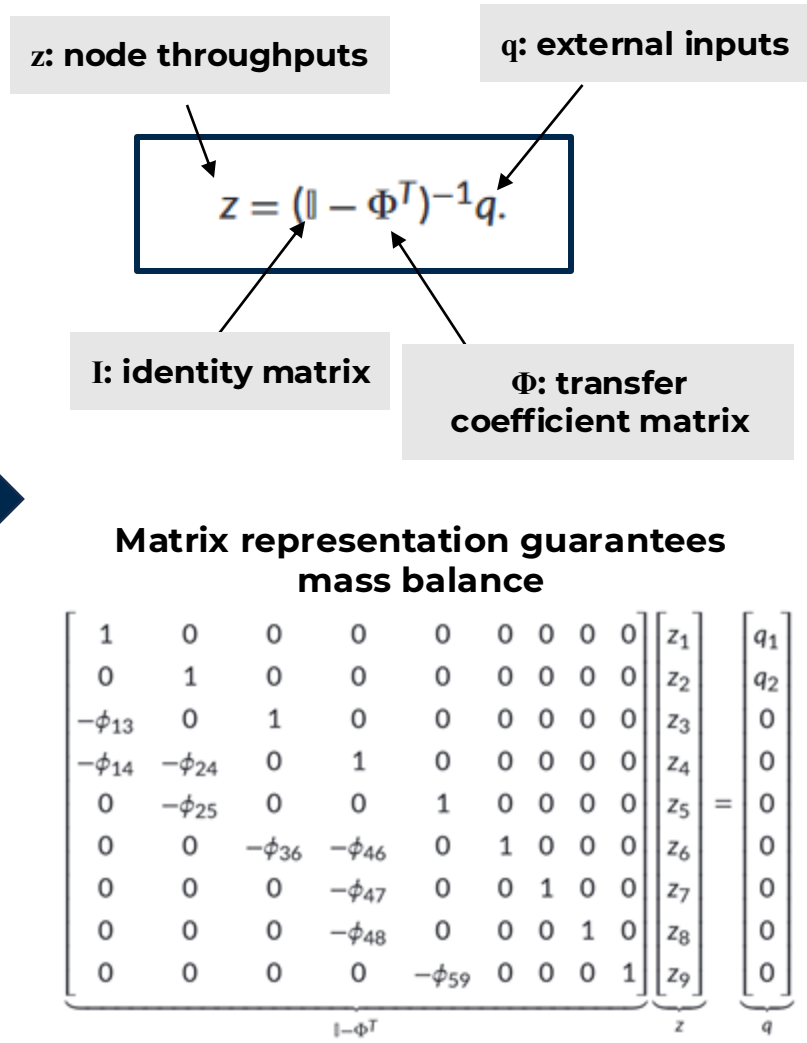

Material Flow Analysis - Data Collection

MICHIGAN ENGINEERING
UNIVERSITY OF MICHIGAN

MFA Model Setup

Data Collection

Noise Modelling

Bayesian Inference

Results

Data collection

- Material production and demand - market reports (e.g., JEC), research articles, OEM websites
- Primary energy intensities - Ecoinvent 3 database, LCA studies, industry reports (e.g., JCMA)

Data Format	Examples
Mass Flow Data	
Flow values (in kt)	The amount of aramid paper used in aramid honeycomb production is 3.4 kt globally.
Transfer coefficients (0 – 100%) (e.g., Scrap & recycling rates)	The process yield for GFRP prepreg production is 93%.
Technical coefficients (0 – 100%) (e.g., Fiber/matrix mass ratios)	The typical fiber fraction of open molded parts are 50 wt.% (40 vol.%). 32% of the composite products in marine application were manufactured via spray-up in 2022.
Percentage share of any process in a sum of processes (0 – 100%)	The volume of composite products in construction accounts for 26% of the total composite market in 2022 (JEC, 2023).
Node throughputs (in kt)	The volume of global composites market in construction applications was 3.3 mt in 2022 (JEC, 2023).
Sum of nodes (in kt)	The total volume of thermoset composites in the market is 7.8 Mt in 2022 (JEC, 2023).
Energy Intensity Data	
Primary energy intensities (in MJ/kg)	The primary energy intensity of glass fiber direct roving is 28 MJ/kg.

MFA Data Noise Modelling Using Pedigree Matrix

MICHIGAN ENGINEERING
UNIVERSITY OF MICHIGAN

MFA Model Setup
↓
Data Collection
↓
Noise Modelling
↓
Bayesian Inference
↓
Results

Why modelling data noise?

- Data are not 100% reliable or correct
- Enable transparent decision-making

Pedigree Matrix Approach

- For a given data, **assign data quality scores** (1-4, smaller numbers mean higher quality) for **5 data quality metrices** (reliability, completeness, temporal correlation, geographical correlation, other correlation)

- Calculate: **coefficient of variation (CV)** for normal distribution or **uncertainty parameter (U)** for lognormal distribution using:

For each quality metric: $CV_i = a * e^{b*(score_i - 1)}; U_i = 1 + \frac{CV_i}{100}$

Total noise for data: $CV_{total} = \sqrt{\sum CV_i^2}; U_{total} = \exp(\sqrt{\sum \ln(U_i)^2})$

$a_{not\ sensitive} = 0.375;\ a_{medium\ sensitive} = 0.75;\ a_{highly\ sensitive} = 1.5; b = 1.105$

Laner et al. "A novel approach to characterize data uncertainty in material flow analysis and its application to plastics flows in Austria." 2016

Uncertainty Quantification via Bayesian Inference

MICHIGAN ENGINEERING
UNIVERSITY OF MICHIGAN

MFA Model Setup

Data Collection

Noise Modelling

Bayesian Inference

Results

Data inconsistencies and uncertainties

- Discrepancies across data sources
- Various forms
- Data scarcity

Bayesian inference (BI)

BI uses **probability distributions** to represent data record with uncertainties and enables **updating of model parameter (material flow) uncertainties** as more data is collected (Lupton and Allwood, 2018)

Likelihood
Data records (with noise)

Priors
Initial knowledge (weakly informed)

$$P(\theta|D) = \frac{P(D|\theta)P(\theta)}{P(D)}$$

Posterior
Updated knowledge

Marginal likelihood
Normalizing factor

Bayes' Theorem

θ: model parameters
D: data records

Results – Global Flow of FRP Composites in 2024 (in Million tons)

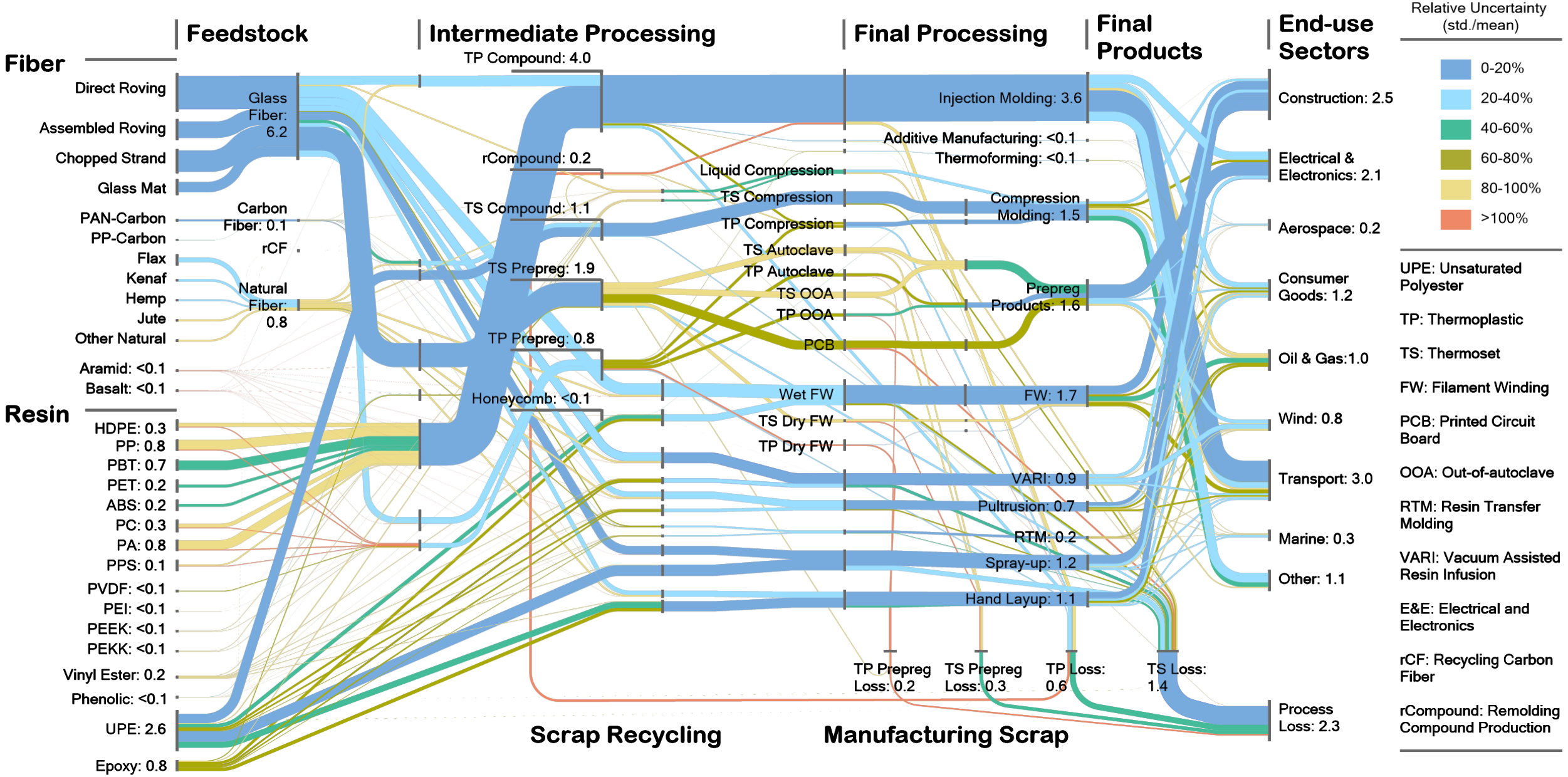

UPE: Unsaturated Polyester

TP: Thermoplastic

TS: Thermoset

FW: Filament Winding

PCB: Printed Circuit Board

OOA: Out-of-autoclave

RTM: Resin Transfer Molding

VARI: Vacuum Assisted Resin Infusion

E&E: Electrical and Electronics

rCF: Recycling Carbon Fiber

rCompound: Remolding Compound Production

Key information: material throughputs (thickness of flows), data uncertainty (color of flows), scrap flows

Material Efficiency of the Global FRPC Supply Chain

Scrap primarily come from

- **Thermoset processes** (>50%)
- **High-throughput processes** (injection molding, TP compound production, compound production)
- **Manual processes or semi-manual processes** (spray-up, hand layup, vacuum assisted resin infusion VARI etc.)

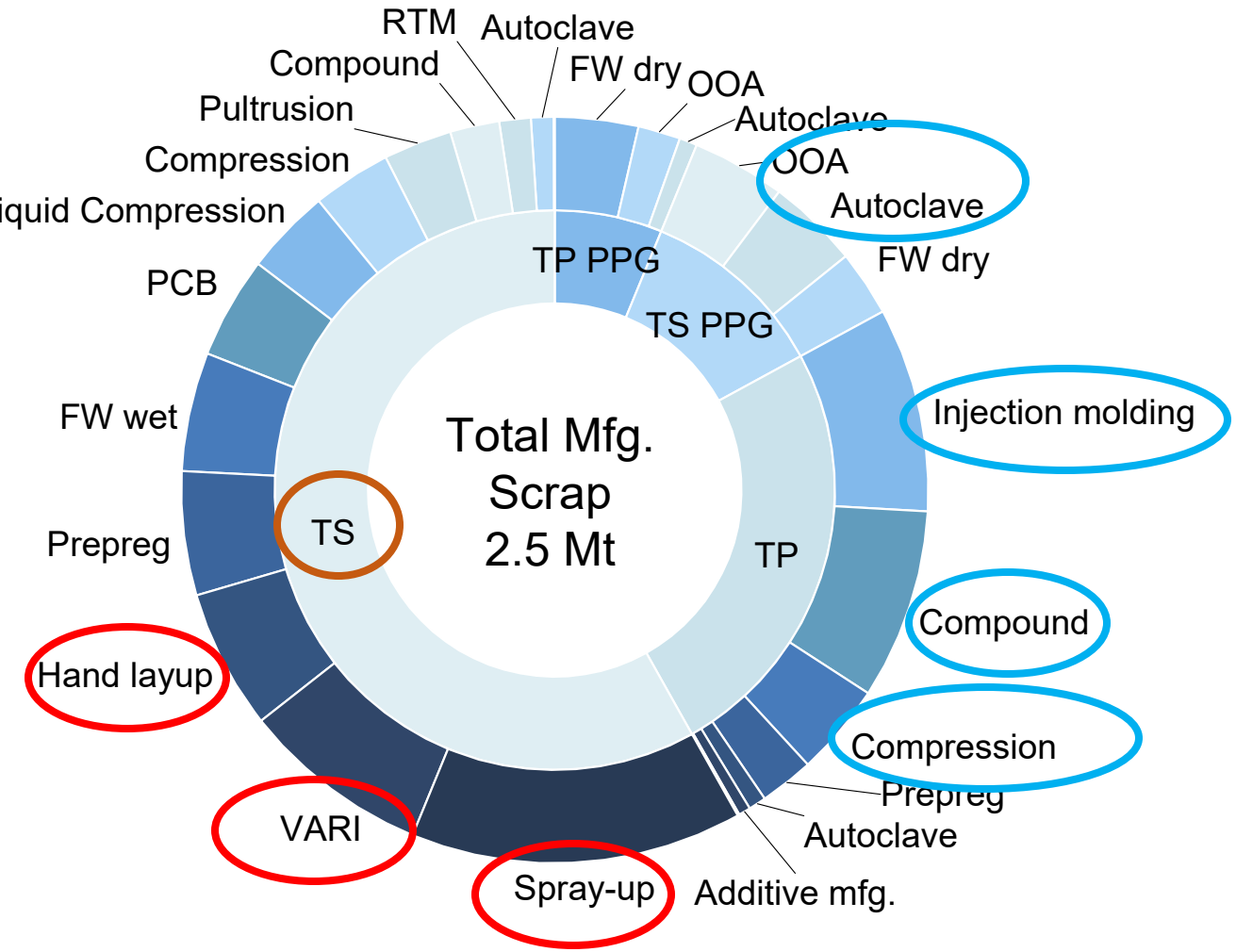

Fig. 5. Manufacturing scrap profile
(TS: thermoset; TP: thermoplastic; PPG: prepreg)

Primary Energy Demands of FRPC Materials and Processes

Energy Hotspots

- **Resin**, especially **unsaturated polyester (UPE)**
- **Autoclave curing**
- **Glass and natural fibers** (vs. carbon)

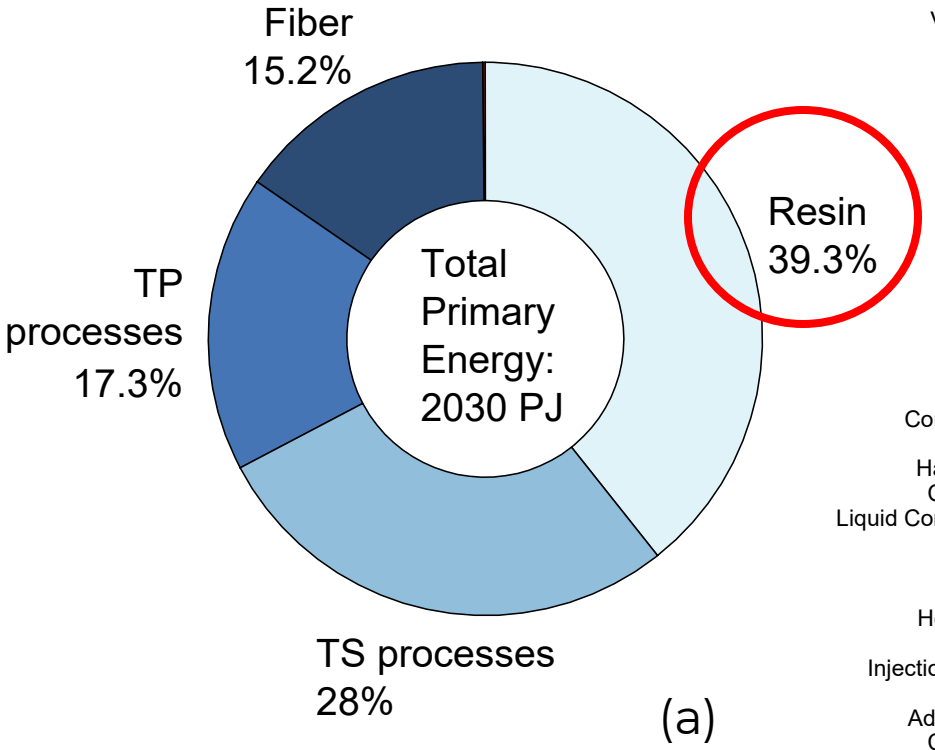

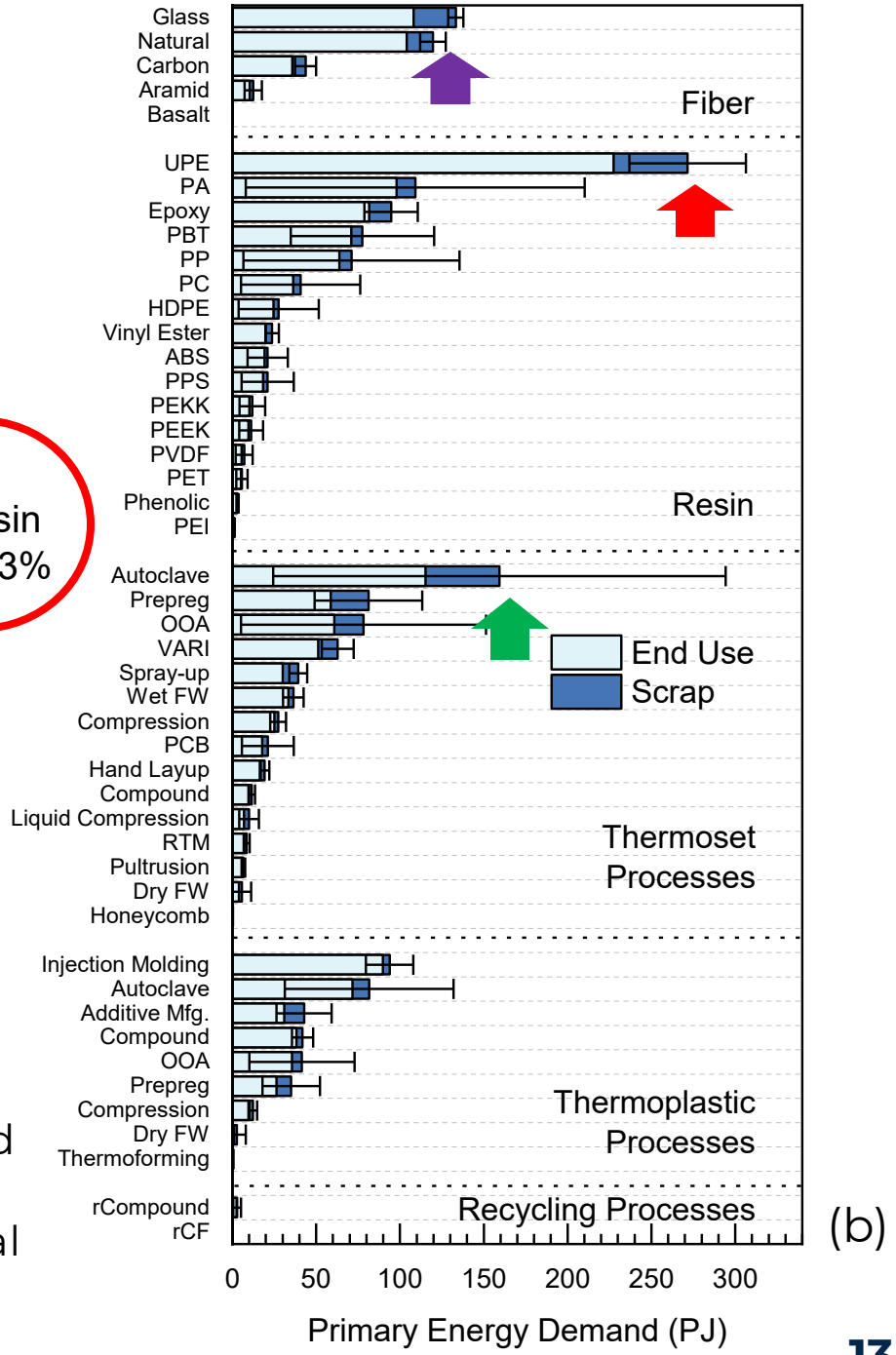

Fig. 6. (a) Total primary energy demand and
(b) primary energy demand by material and processes.

Attributing Primary Energy to Processes/Sectors

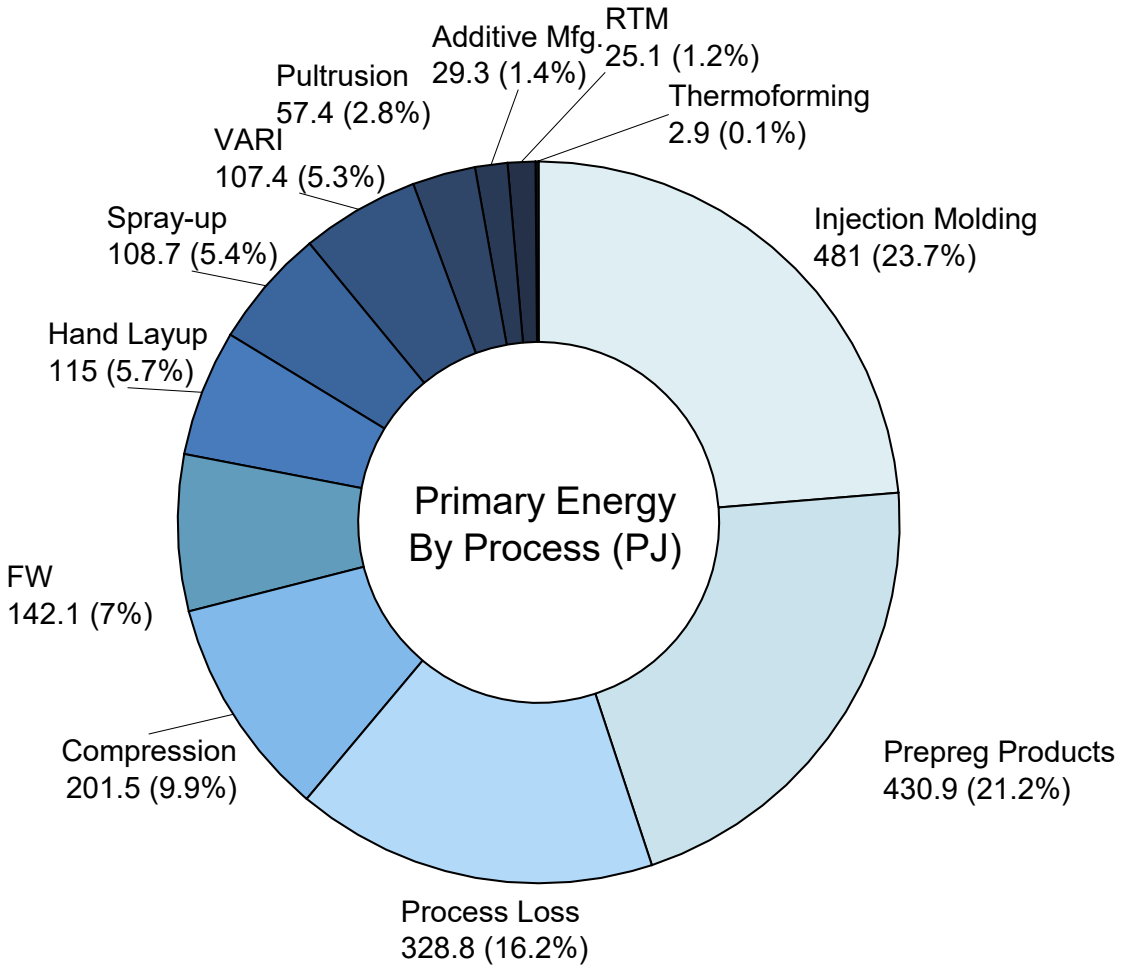

Fig. 7. Primary energy attributable to mfg. processes

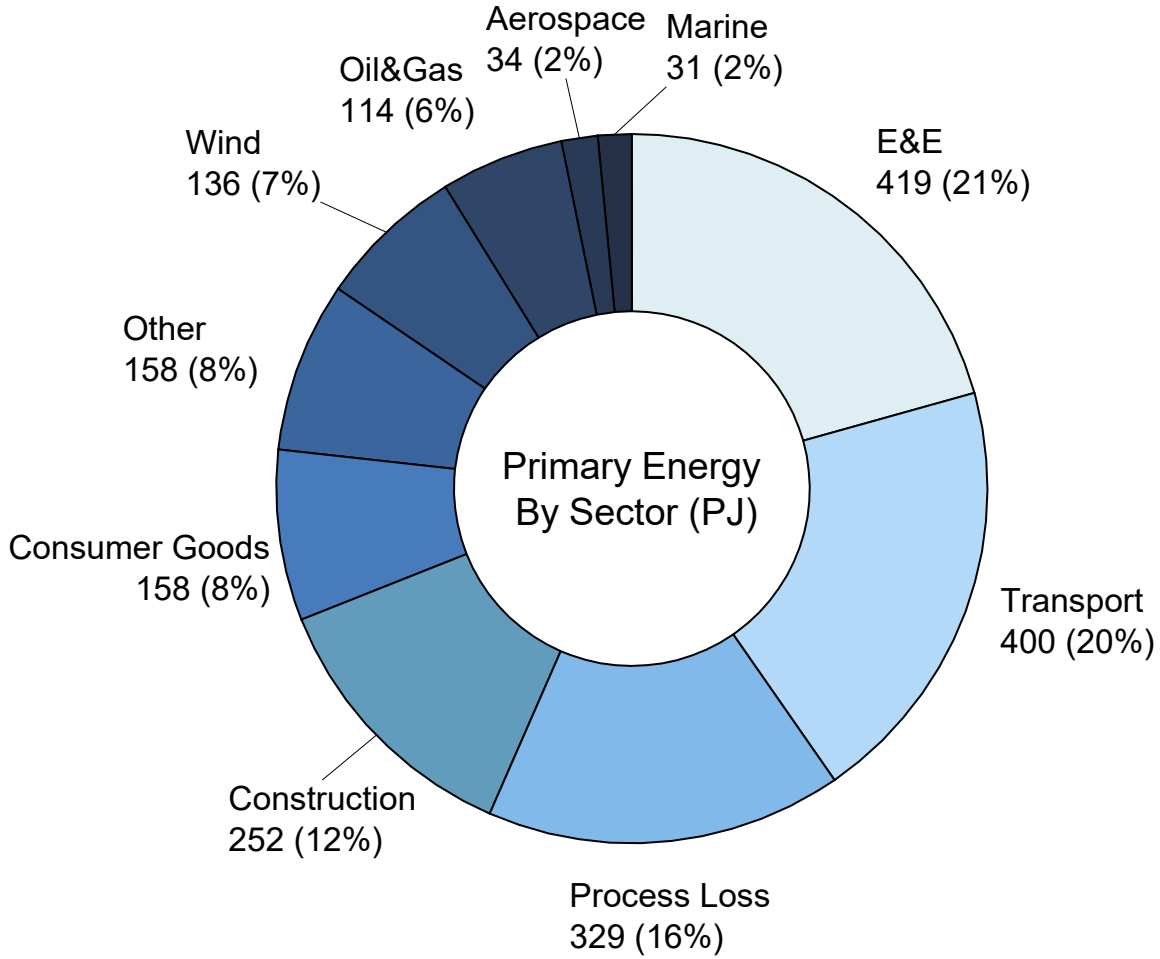

Fig. 8. Primary energy attributable to end-use sectors

Conclusions

MICHIGAN ENGINEERING
UNIVERSITY OF MICHIGAN

This study provides a new perspective on the material efficiency and energy demand distributions within the global FRPC supply chain.

Key take-aways

- **Low-value materials** and **high-throughput processes** have **large material and energy footprints** and **should be prioritized for decarbonization efforts.**
- **Resin production** accounts for **most primary energy requirement**. Substitution with bio-based options can potentially have a great impact on supply chain decarbonization.
- **Manufacturing scrap generation is significant** and scrap recycling remains minimal. **Yield improvement should focus on high-throughput processes manual processes.**

Thank You

Contact Information

Zhuoer Li
PhD Candidate
Mechanical Engineering
University of Michigan
lze@umich.edu

Dr. Daniel Cooper
Associate Professor
Mechanical Engineering
University of Michigan
drcooper@umich.edu

References

ATESCAN-YUKSEK, Y., MILLS, A., AYRE, D., KOZIOL, K. & SALONITIS, K. 2024. Comparative life cycle assessment of aluminium and CFRP composites: the case of aerospace manufacturing. *The International Journal of Advanced Manufacturing Technology,* 131**,** 4345-4357.

BeyondPlastics, 2022. “The Real Truth About the U.S. Plastics Recycling Rate.”

Das, S., Warren, J., West, D., and Schexnayder, S. M., 2016, "Global carbon fiber composites supply chain competitiveness analysis," Oak Ridge National Lab.(ORNL), Oak Ridge, TN (United States); The University of Tennessee, TN.

DONG, J., LIAO, J., HUAN, X. & COOPER, D. 2023. Expert elicitation and data noise learning for material flow analysis using Bayesian inference. *Journal of Industrial Ecology*.

GARG, N. & SHRIVASTAVA, S. Environmental and economic comparison of FRP reinforcements and steel reinforcements in concrete beams based on design strength parameter. Proceedings of the UKIERI Concrete Congress, Jalandhar, India, 2019. 5-8.

Gutowski, T. G., S. Sahni, J. M. Allwood, M. F. Ashby, and E. Worrell. 2013. The energy required to produce materials: Constraints on energy-intensity improvements, parameters of demand. Philosophical Transactions of the Royal Society A 371(1986):20120003. DOI: 10.1098/rsta.2012.0003.

Hamid, Saher, Christopher Niezrecki, and Annika Eberle. "Contextualizing Wind Turbine Blade Waste: Comparison to Other Global Waste Streams." *SAMPE Journal* 61.3 (2025).

Leontief, W. W., 1936, "Quantitative input and output relations in the economic systems of the United States," The review of economic statistics, pp. 105-125.

LIDDELL, H., DOLLINGER, C., FISHER, A., BRUESKE, S. & CRESKO, J. 2017. Bandwidth study on energy use and potential energy saving opportunities in US Carbon Fiber Reinforced Polymer Manufacturing. *Report number: DOE/EE-1662*.

LIDDELL, H., DOLLINGER, C., FISHER, A., BRUESKE, S., CARPENTER, A. & CRESKO, J. 2017. Bandwidth Study on Energy Use and Potential Energy Saving Opportunities in US Glass Fiber Reinforced Polymer Manufacturing.

LUPTON, R. C. & ALLWOOD, J. M. 2018. Incremental material flow analysis with Bayesian inference. *Journal of Industrial Ecology,* 22**,** 1352-1364.

RYBICKA, J., TIWARI, A., DEL CAMPO, P. A. & HOWARTH, J. 2015. Capturing composites manufacturing waste flows through process mapping. *Journal of cleaner production,* 91**,** 251-261.

SHUAIB, N. A., MATIVENGA, P. T., KAZIE, J. & JOB, S. 2015. Resource efficiency and composite waste in UK supply chain. *Procedia CIRP,* 29**,** 662-667.

The International Aluminium Institute (IAI), 2021. “Aluminium Recycling.”

U.S. Geological Survey, 2021. “IRON AND STEEL SCRAP.”

WEGMANN, S., RYTKA, C., DIAZ-RODENAS, M., WERLEN, V., SCHNEEBERGER, C., ERMANNI, P., CAGLAR, B., GOMEZ, C. & MICHAUD, V. 2022. A life cycle analysis of novel lightweight composite processes: Reducing the environmental footprint of automotive structures. *Journal of Cleaner Production,* 330**,** 129808.

Multiple Iteration of Recycling of Carbon Fiber Composites Enable by TuFF Technology

August 7, 2025

Joseph M. Deitzel, Ph.D.

University of Delaware Center for Composite Materials



UD-CCM At a Glance-50 Years

- Founded in 1974, CCM is an internationally recognized interdisciplinary center of excellence for composites education and research
  - Started in Mechanical Engineering
  - College-wide interdisciplinary center in 1978 timeframe (ME, CHE, MSE program)

- Three-Part Mission
  - Conduct basic and applied research
  - Educate scientists and engineers
  - Transition technology to industry

- More than 3000 alumni working in Industry, Government Labs or Academia

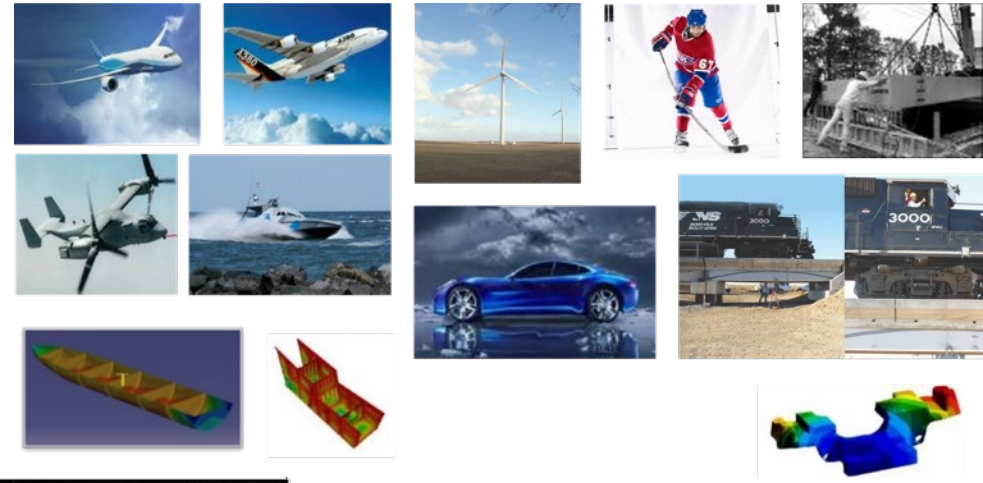





Circular Economy of Composites Enable By the TuFF Process

DOE/EERE/ Advanced Manufacturing Office (AMO) DE-EE000303

Goal: Demonstrate for commercial Carbon/Epoxy and Carbon-Elium composites can undergo ***multiple*** recycling iterations and maintain near full property translation.

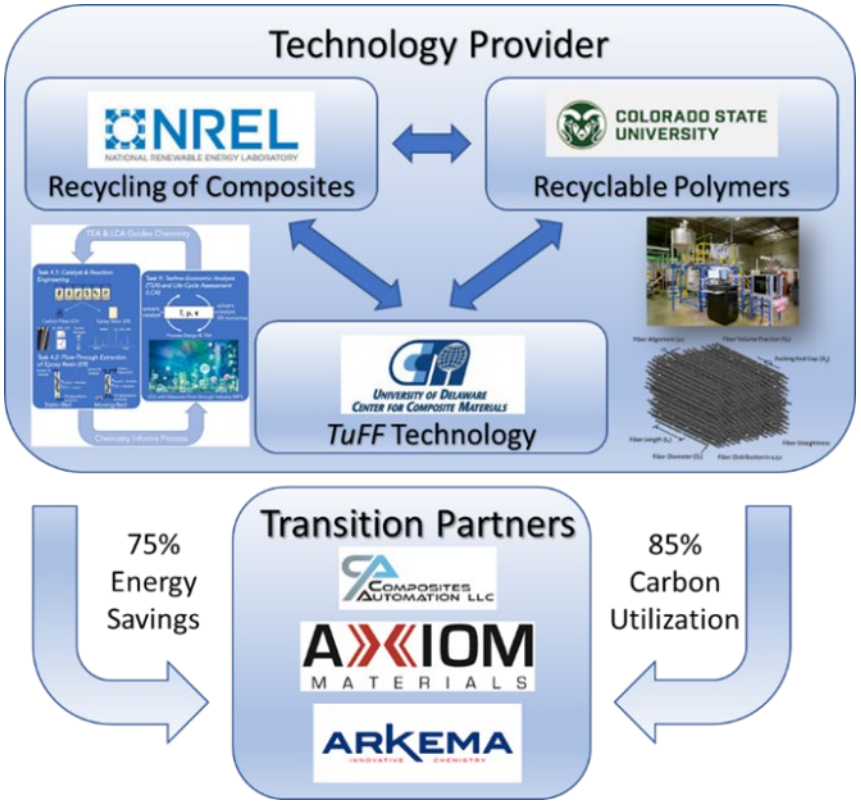

- ***Separate the CFC polymer and fiber content with catalyst and fiber recovery (NREL lead)***
- ***Demonstrate a new class of recyclable by-design polymers (CSU lead)***
- ***Process the recycled carbon fiber content into high-performance CFCs (UD-CCM lead)***

- ***Transition partners***
  - ***Axiom Materials: Pre-Preg manufacture***
  - ***Composites Automation: Composite fabrication***
  - ***Arkema: Resin production***
- ***Monthly technical meetings are held with DoE and Partners to share information and address challenges***

Composite Recycling Motivation:
Energy Savings, Supply Chain Stability, Environmental Stewardship

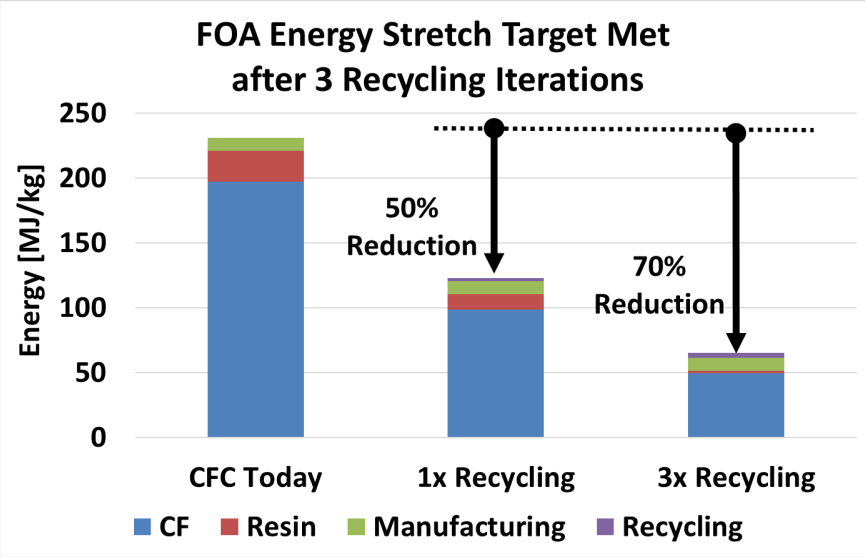

Data source: Suzuki, T; Takahashi, J;; The Ninth Japan International SAMPE Symposium; 2005

Zhang et al Composites Part B: Engineering Volume 250, 1 February 2023, 110463

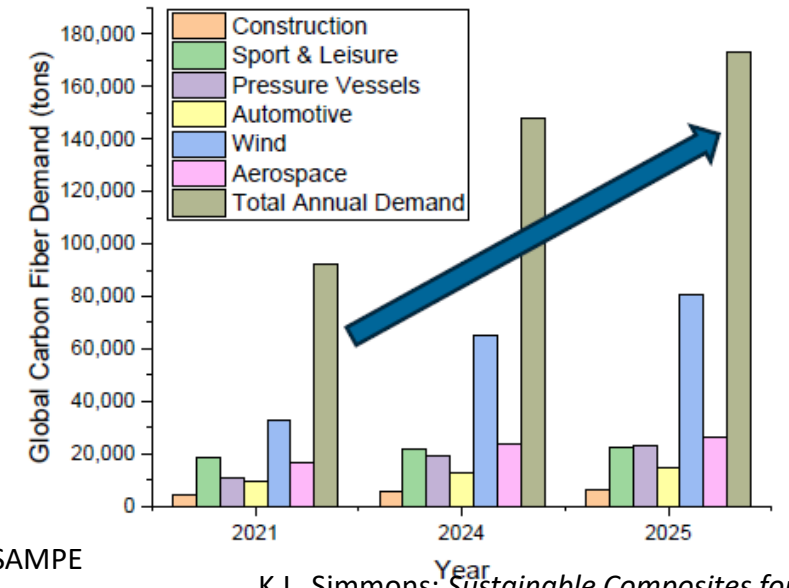

Data from https://www.igtpan.com/Ingles/mercado-carbono.asp

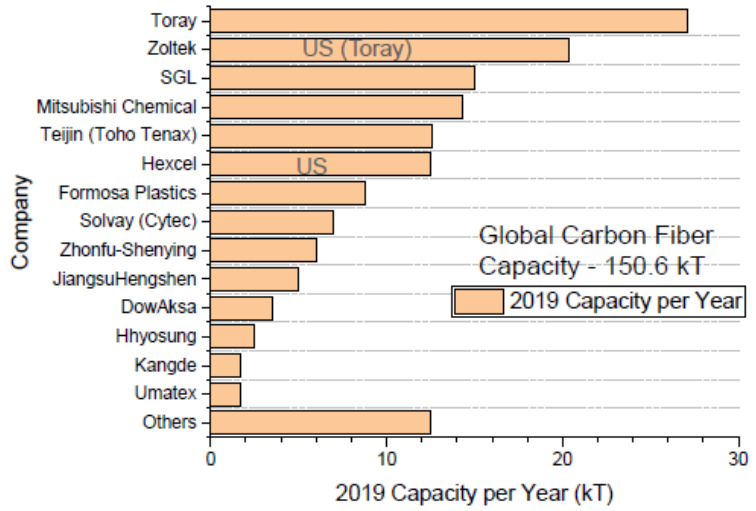

K.L. Simmons; *Sustainable Composites for Hydrogen Delivery and Storage*, SAMPE 2024

- CFC recycling approach can allow multiple iterations with fiber recovery, 50% energy saving after first recycling and ~70% after 3 recycling steps
- Majority of Industry predictions indicate Carbon fiber demand to exceed current world capacity
  - Growth in demand (10-13%) expected to exceed supply in the next decade(Drivers Wind, Pressure Vessels, etc)
  - ***Recycled/Waste CF sources can potentially expand domestic sources of carbon fibers for non-aerospace applications***

Challenges of Recycled CFC

- Recycling processes such as ***pyrolysis, thermolysis or solvolysis*** exist and have shown to recover *rCF* without significant fiber degradation
- Typically, size reduction (conversion to short fiber) is an inherent process step during fiber recovery
- Current state-of-the-art *rCF* are used as filler in injection molding and other low-performance processes
  - Low fiber volume fraction parts
  - Aspect ratio low ➔ reducing properties
  - Inherent ***value*** of CF lost
  - Down-cycled parts vs. true recycling
- Potential solutions
  - Maintaining original format: Recycling of fabric and tow
  - Aligned Discontinuous Fiber (HiPerDif, TuFF)

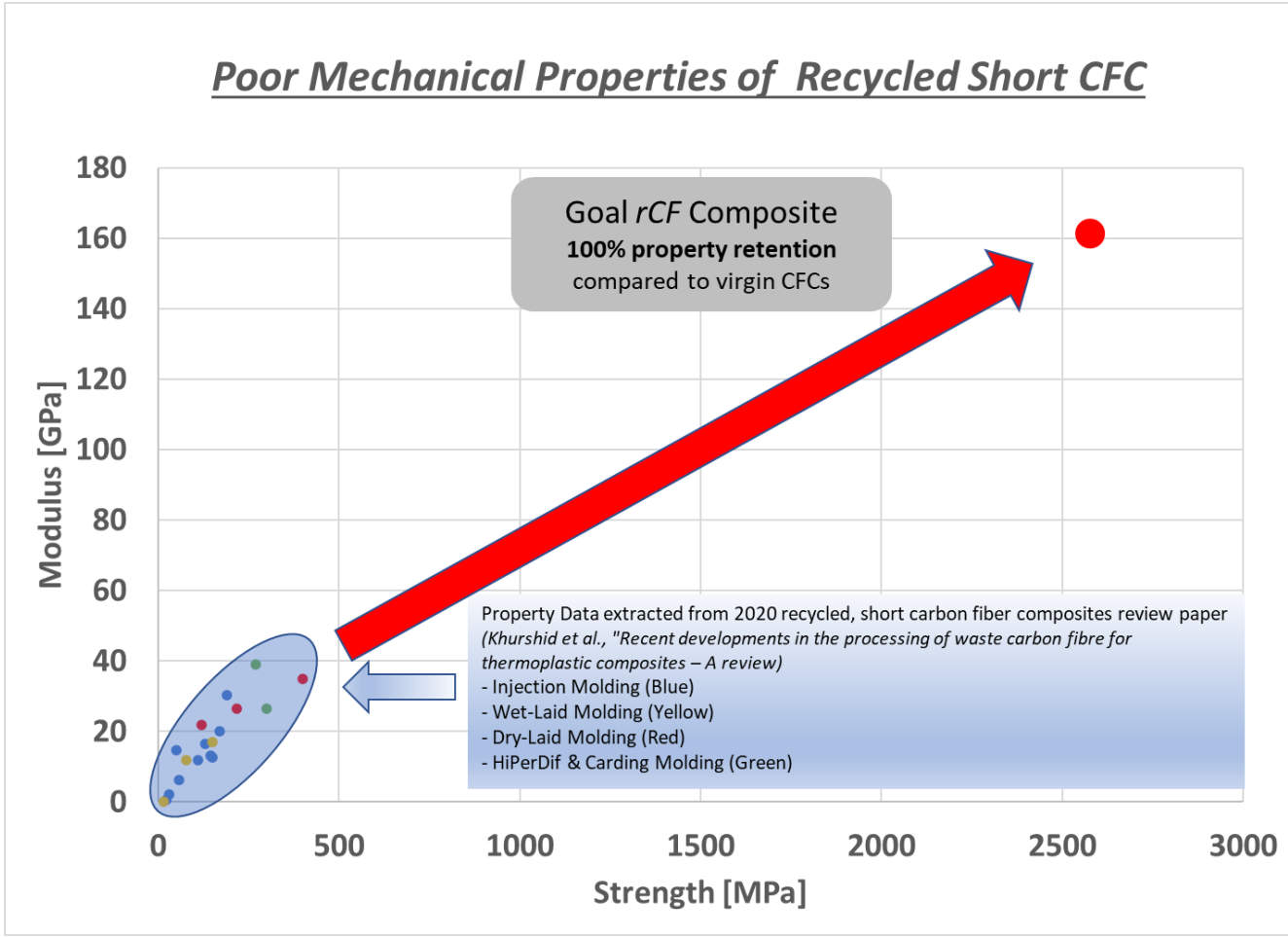

2017-Tailorable Universal Feedstock and Forming (TuFF)

TuFF is a <u>feedstock</u> comprised of a <u>highly-aligned</u> short fiber microstructure in tape, sheet and blank formats

- Millimeter long short fiber with filament level alignment control: > 95% ($\pm$ 5 $^{\circ}$)
- High fiber volume fraction >57%
- Properties equivalent to continuous fiber composites >370ksi (2.55GPa) strength and >23msi (159GPa) stiffness
- In-plane stretch allows metal-like forming at high throughputs
- Thin ply formats for improved damage tolerance and minimum gage designs (30gsm to standard areal weight)
- <u>Enables recycling of carbon fiber composites</u>

Two US Patents (10,669,659 B2 & 11,047,078) "ALIGNED DISCONTINUOUS FIBER PREFORMS, COMPOSITES AND SYSTEMS AND PROCESSES OF MANUFACTURE"

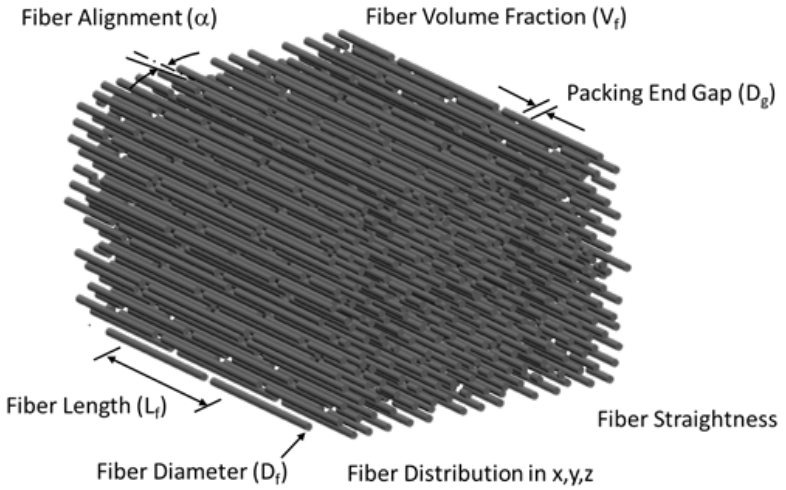

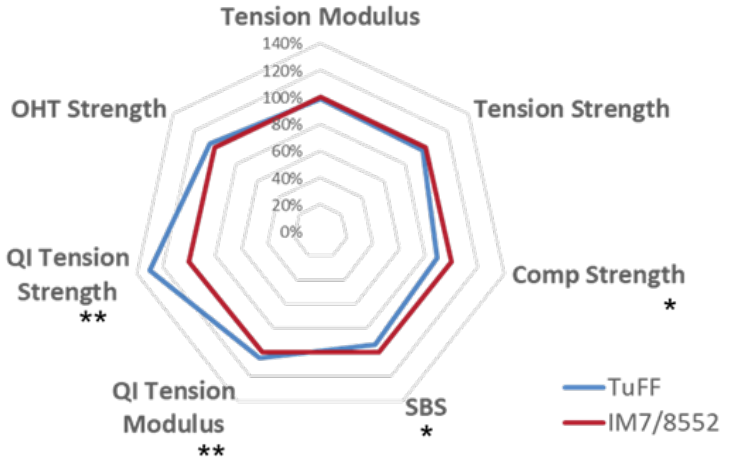

*** Compression Strength and SBS are resin dominated (PEI vs 8552 Epoxy)**
****QI comparison is thin-ply (60 gsm FAW) to thick-ply (192 gsm FAW)**
OHT Strength is from TuFF1, Rest are TuFF2; Normalized values

TuFF Enables Closed-Loop Recycling of Carbon Fiber Composites

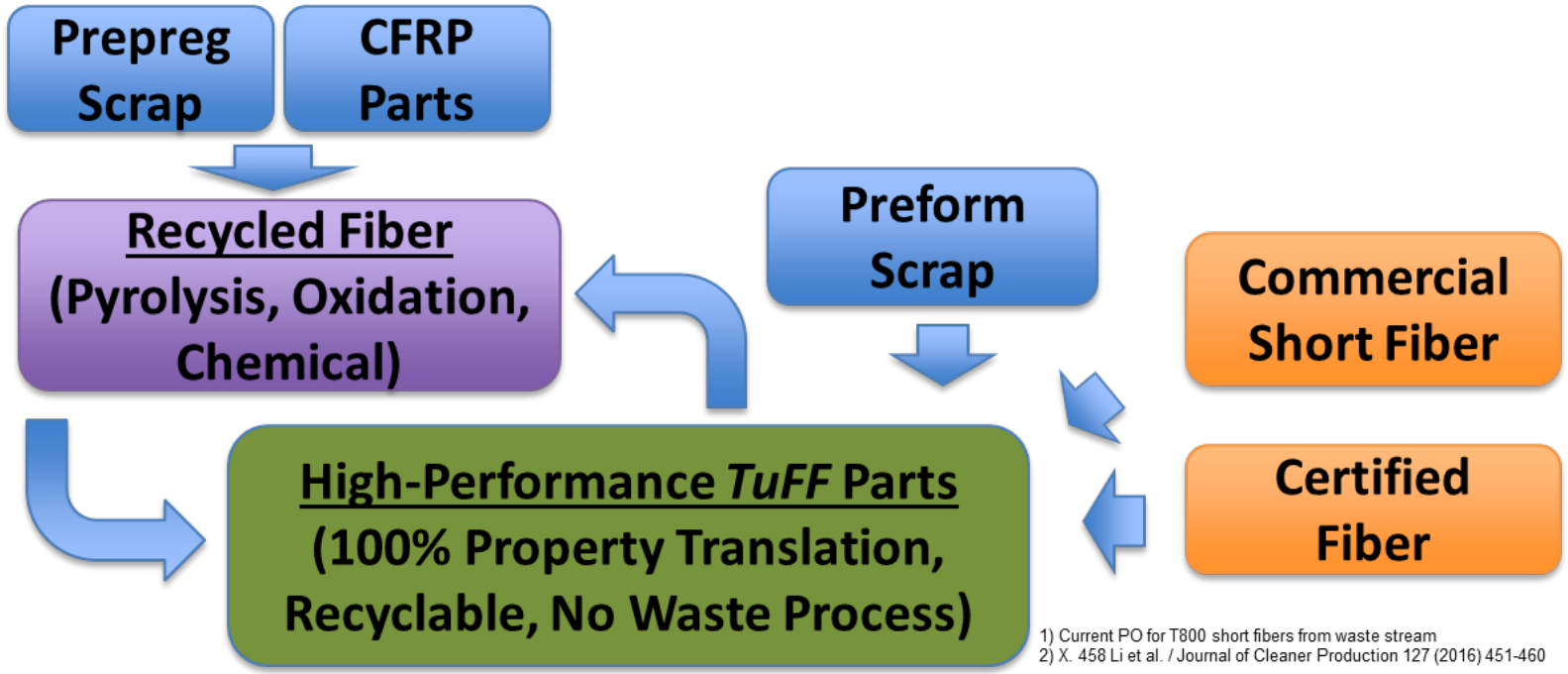

1) Current PO for T800 short fibers from waste stream
2) X. 458 Li et al. / Journal of Cleaner Production 127 (2016) 451-460

- Waste/Recycled fibers reduce material cost and environmental burden
  - Waste fiber price[1] ~$5/lb for intermediate modulus CF
  - Recycled fiber cost[2] estimated at ~$1.5/lb
- Commercial recycling processes exist and create discontinuous fiber material

➔ ***TuFF* process is key to convert recycled/waste fibers into high-performance parts**

➔ **Key challenges include fiber strength retention, fiber-resin adhesion, fiber length distribution, dispersion and alignment quality**

Recycled TuFF Process

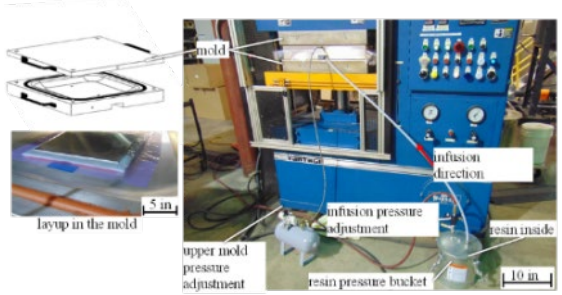

VARTM/High Pressure Bladder Mold



Compaction testing, Alignment Quality

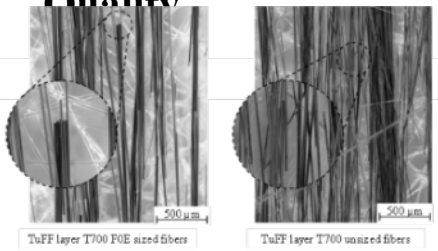

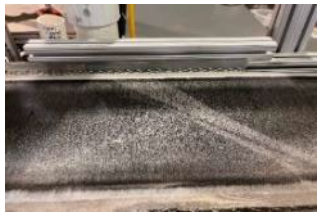

(Re-) Alignment of T700S Fibers within TuFF-Process

Composite production

Composite testing

Preform (re-) production

Recycling

Panel QC(C-scan, Microstructure

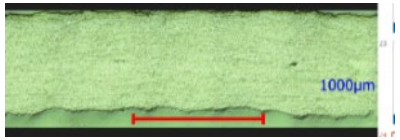

Mechanical Properties

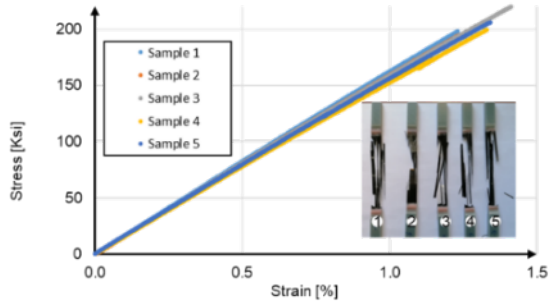

Fiber Surface preparation, Dispersion Evaluation

Pyrolysis
Thermolysis
Solvolysis



Challenges for Incoming Recycled Feedstock: Residue!

Waste Fiber T800
Dry fiber(minor residue)

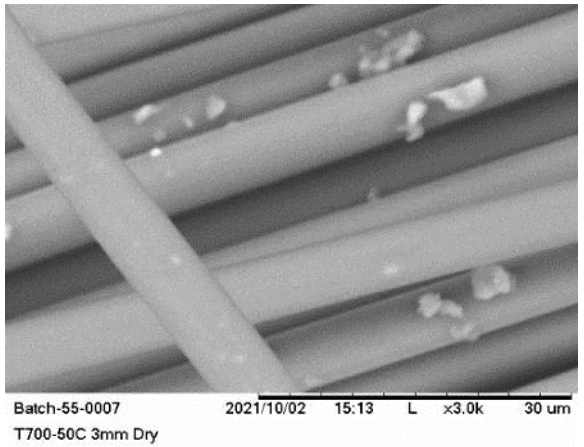

Recycled T700/Elium
Thermolysis(~2% residue)

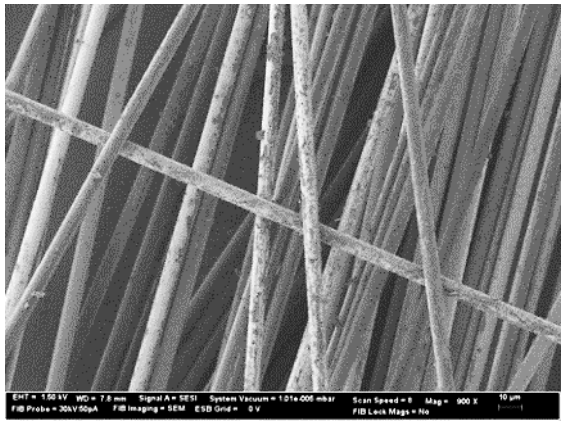

Recycled T800 Epoxy Prepreg
Solvolysis(5-10% Residue)

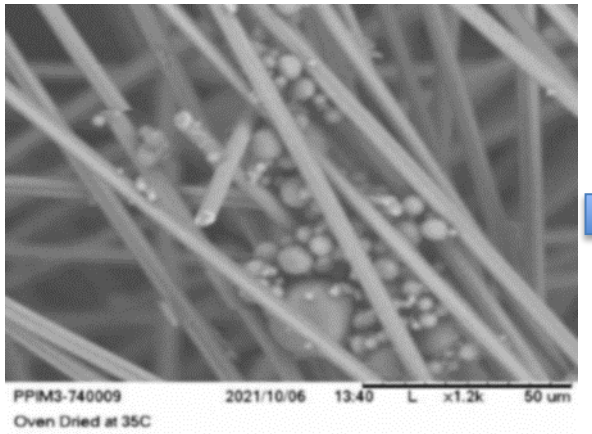

TuFF sheet made with
recycled T800



- Challenges of recycling prepreg and end-of-life parts for use in TuFF.
  - Residual material from recycling process can inhibit dispersion and resin adhesion
  - Broad distribution of fiber lengths
- Need for more efficient recycling approach and/or post recycling cleaning step
  - Elevated temperature oxidation- can harm fiber properties
  - Surfactants to aid in dispersion-requires chemicals that might adversely effect resin adhesion
  - Low temperature(50°-70°C) oxidative(ozone) cleaning-Potentially viable, but less efficient

Cleaning: Elevated Temperature Oxidation

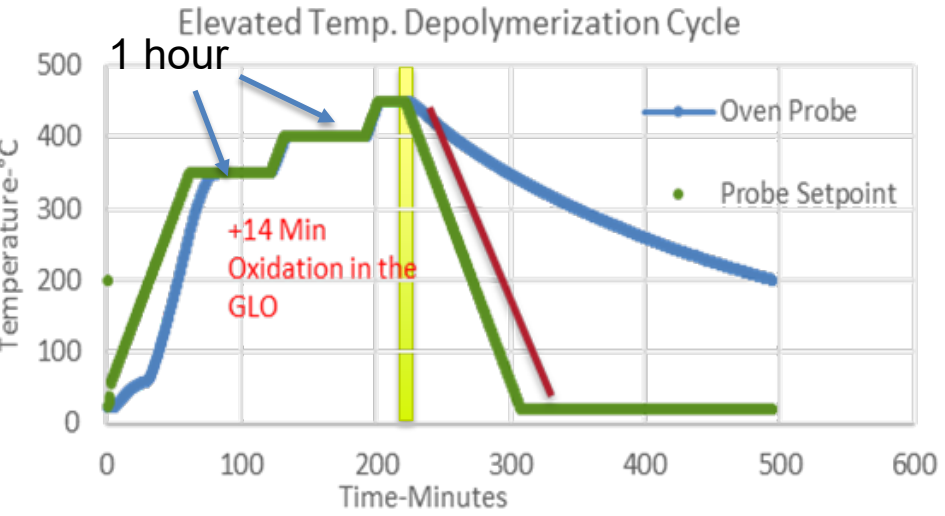

Recycling leaves ~2% residue
(Low MW Oils and Char)

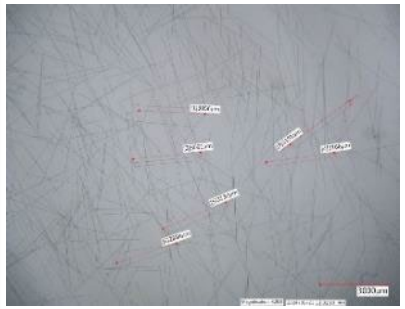

Recycled T700
dispersed in water

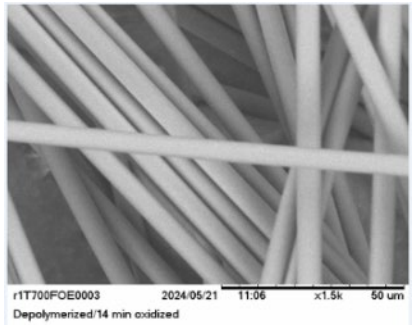

Recycled T700 SEM
Micrograph

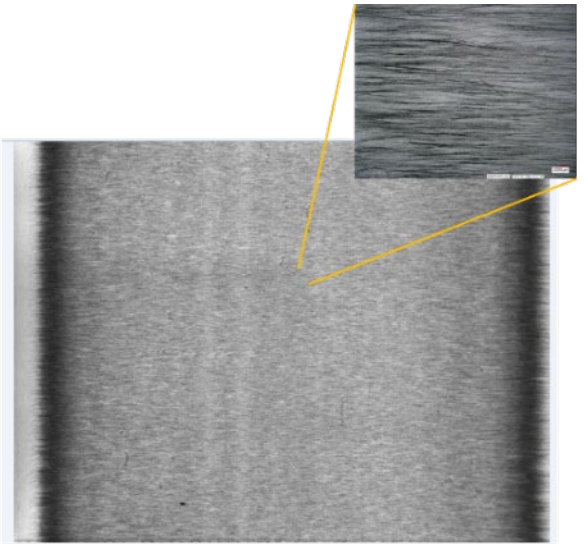

Elium/T700 FoE Recycle Iteration 1



Elium composites



Recycled T700 Fiber

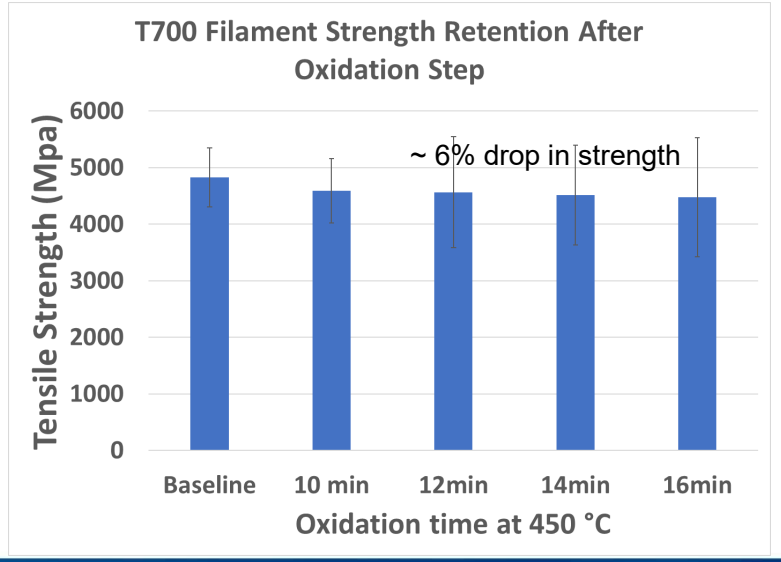

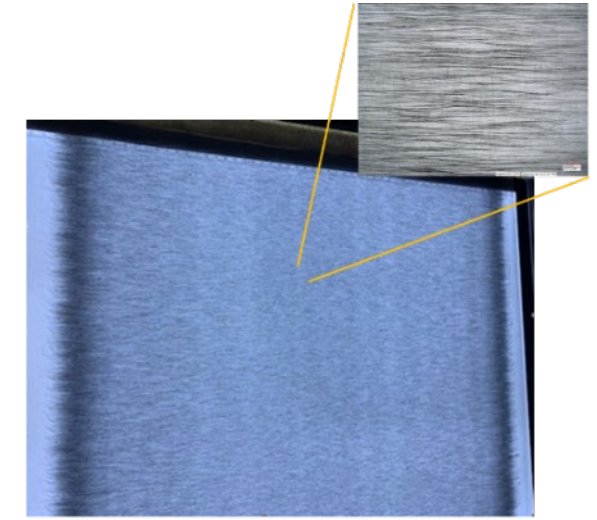

Elium/T700 FoE Recycle Iteration 2

Adhesion Promotion for Recycle Fibers

Fiber Pullout Steps

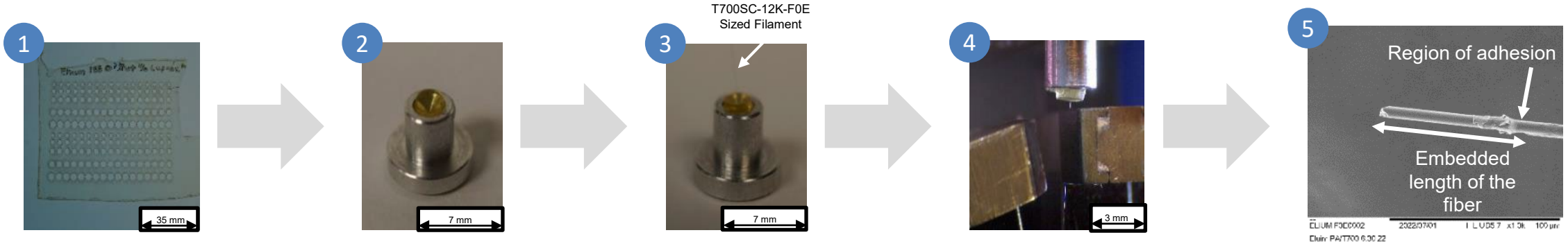

Laser Cut Cast Elium Film

Laser Cut Sample on Aluminum Crucible

Sample with Fiber ready for Pullout testing

Sample Loaded in Pullout Test Fixture

Measure Diameter and Embedded Length in the SEM

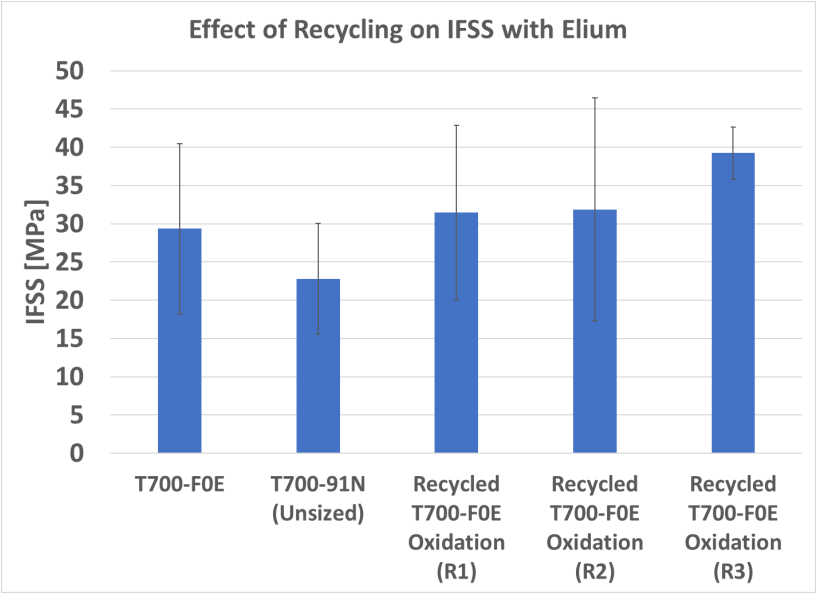

- Measured IFSS for Recycled fibers is comparable to Virgin fiber
- Mixed Mode(resin yielding) failure is observed in all cases
- IFSS for Elium resin system is (~30 MPa) is much lower than what is typical for Epoxy-CF systems(~78 MPa))

Evaluating Failure Mode

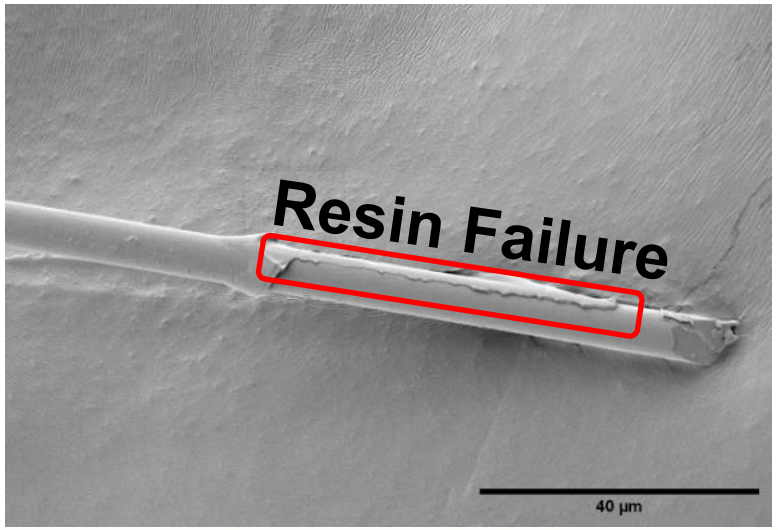

High Pressure Bladder Molding

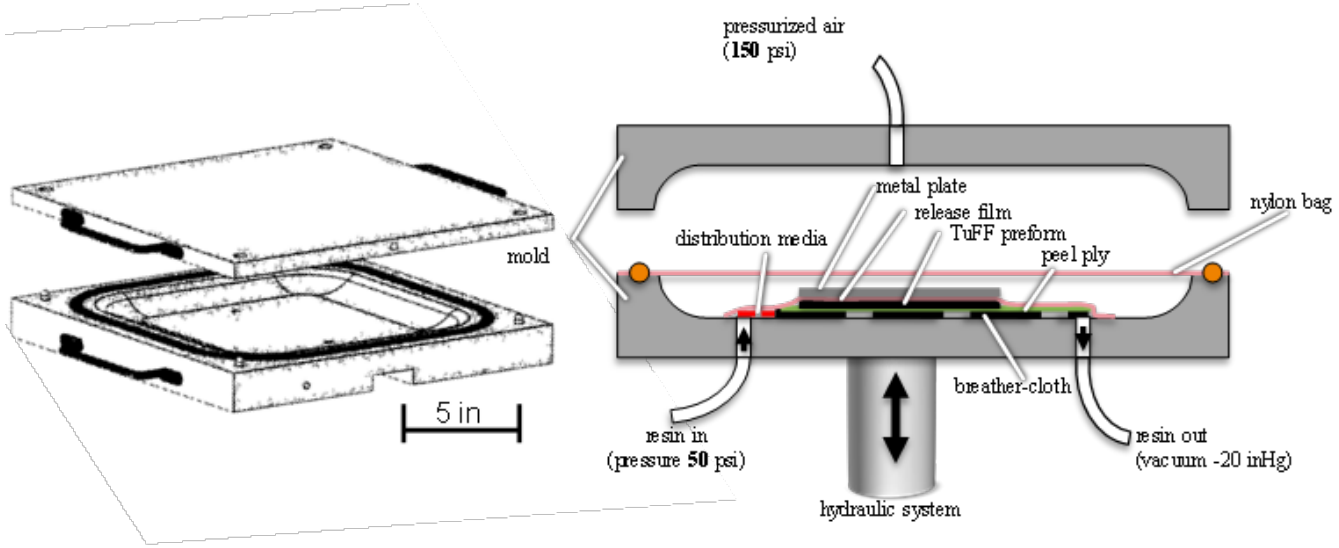

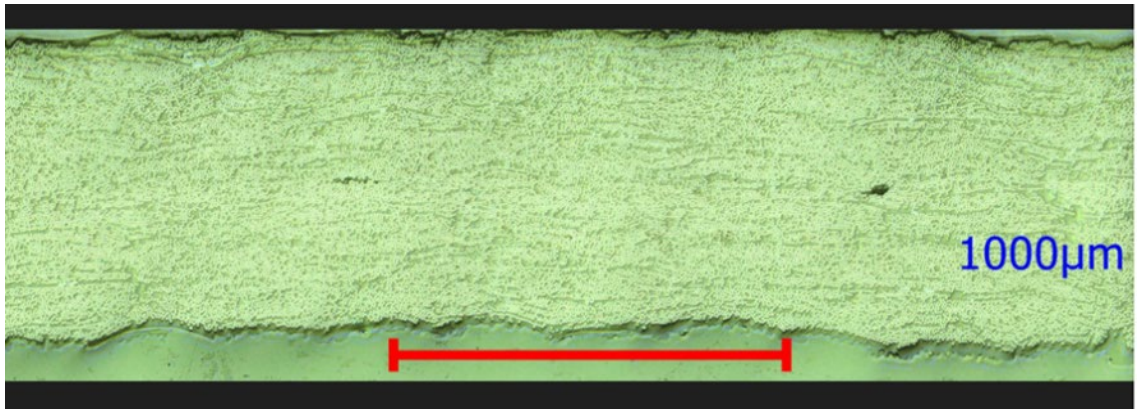

- Infusion parameters: 50 psi resin pressure, 200 psi bladder pressure for a total 150 psi consolidation pressure
- Polymerization:4 hours at 25 °C, 2 hours 80 °C under pressure

- Elium/T700 FOE Composite cross section
  - Arkema recommended Sizing
  - 1 mm thick panel with ~55% FvF

Strength, Modulus, SFTT and Fiber Length Measurements

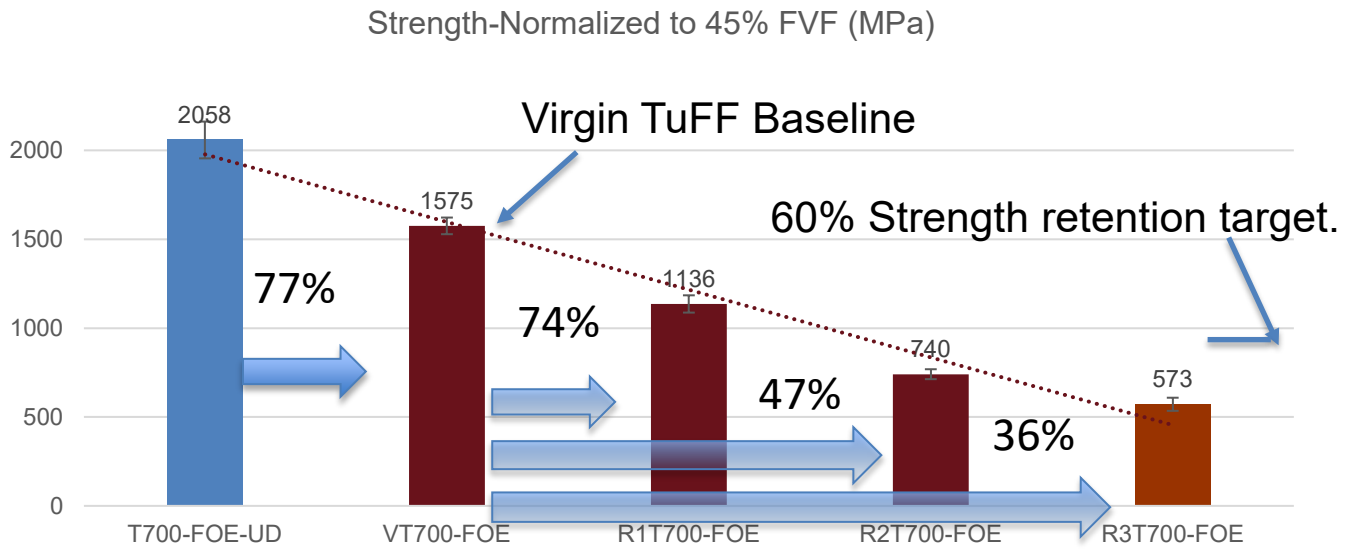

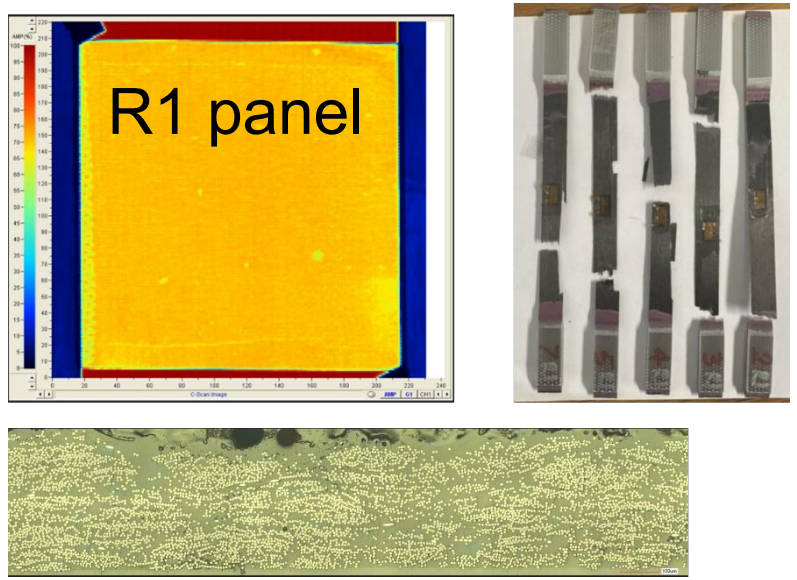

- We see 100 % retention of Stiffness across 3 recycling iterations
- Strength reduces with recycling iteration

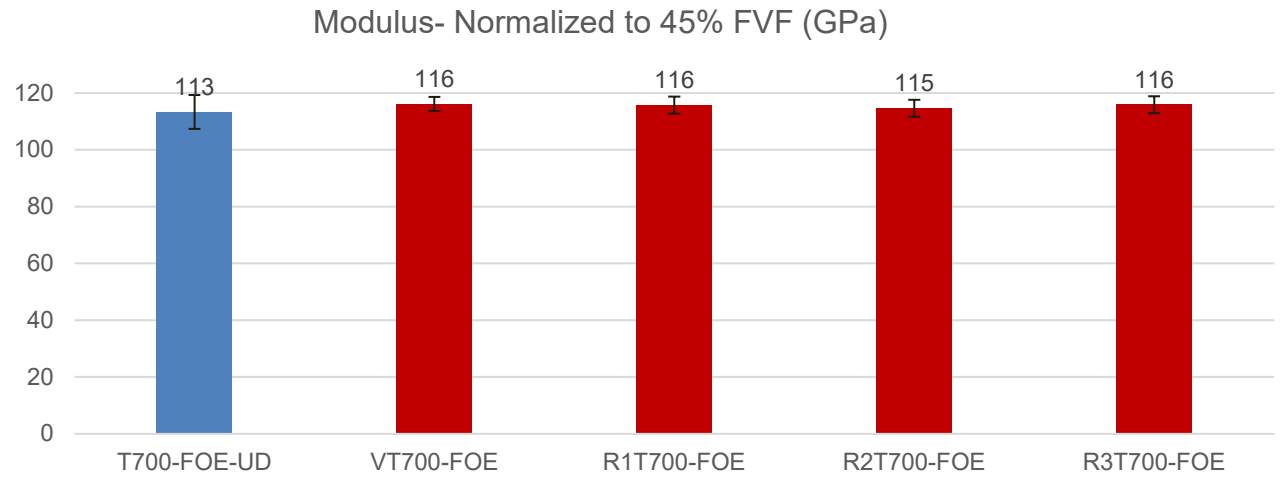

Strength, Modulus, SFTT and Fiber Length Measurements

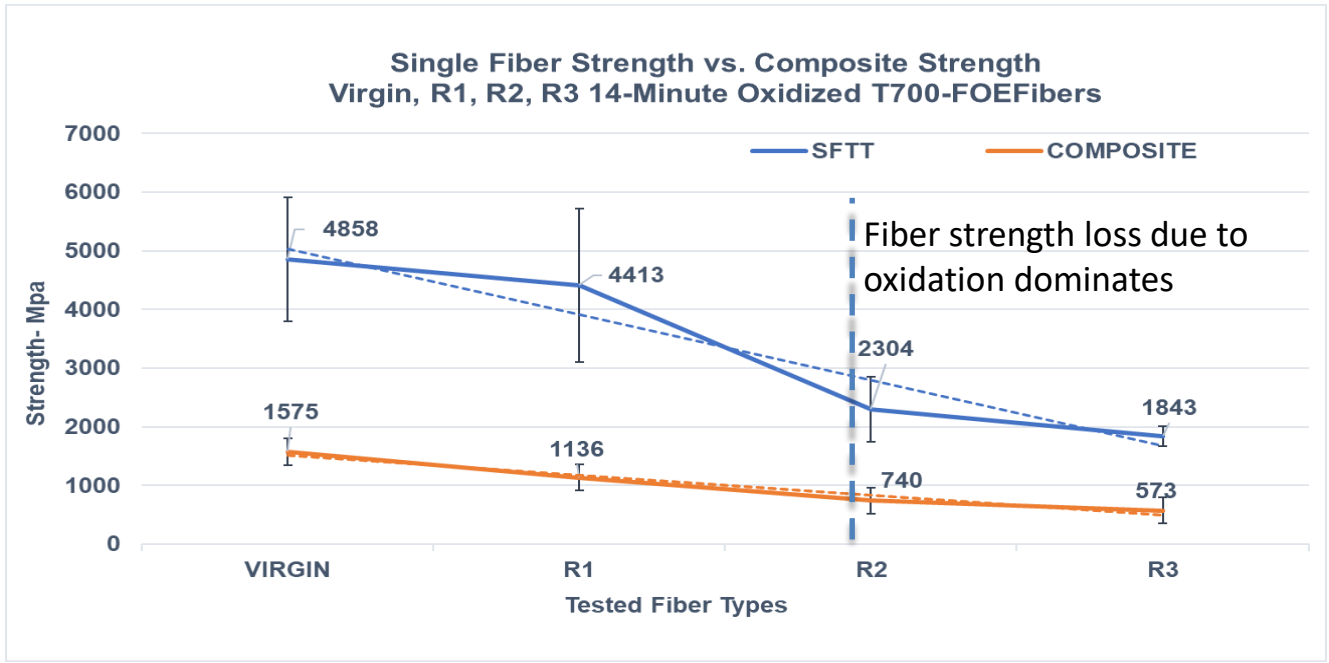

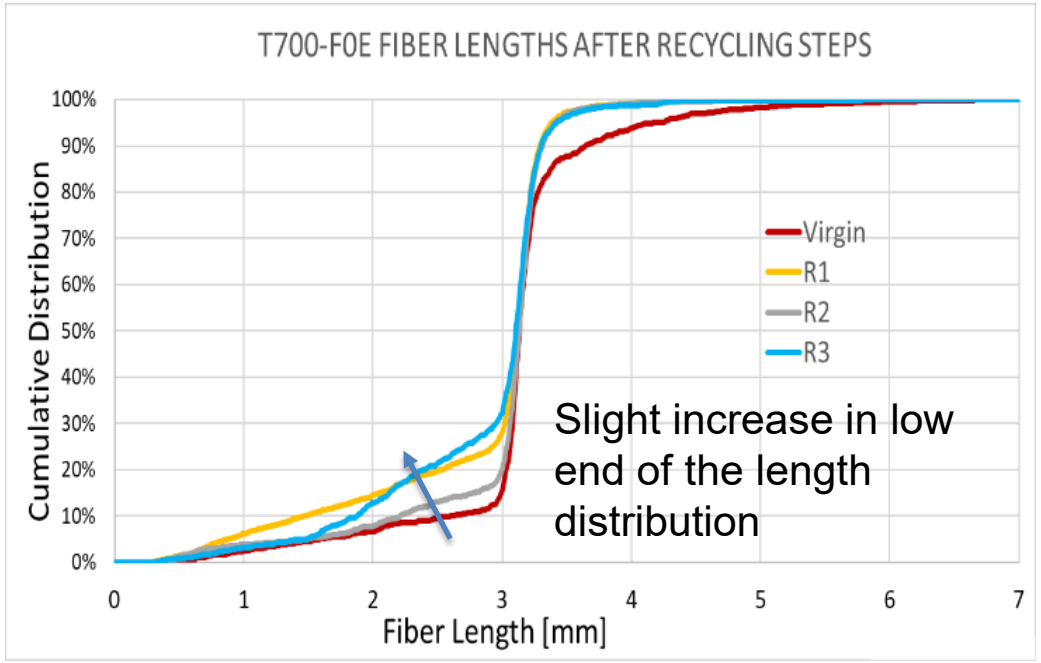

- Potential reasons for Strength reduction include:
  - Cumulative effect of multiple oxidative cleaning steps
  - Increase in low end of the fiber length distribution
    - Shorter fibers could lead to more end clusters

Multi-Iteration Elium/T700 Recycling Summary

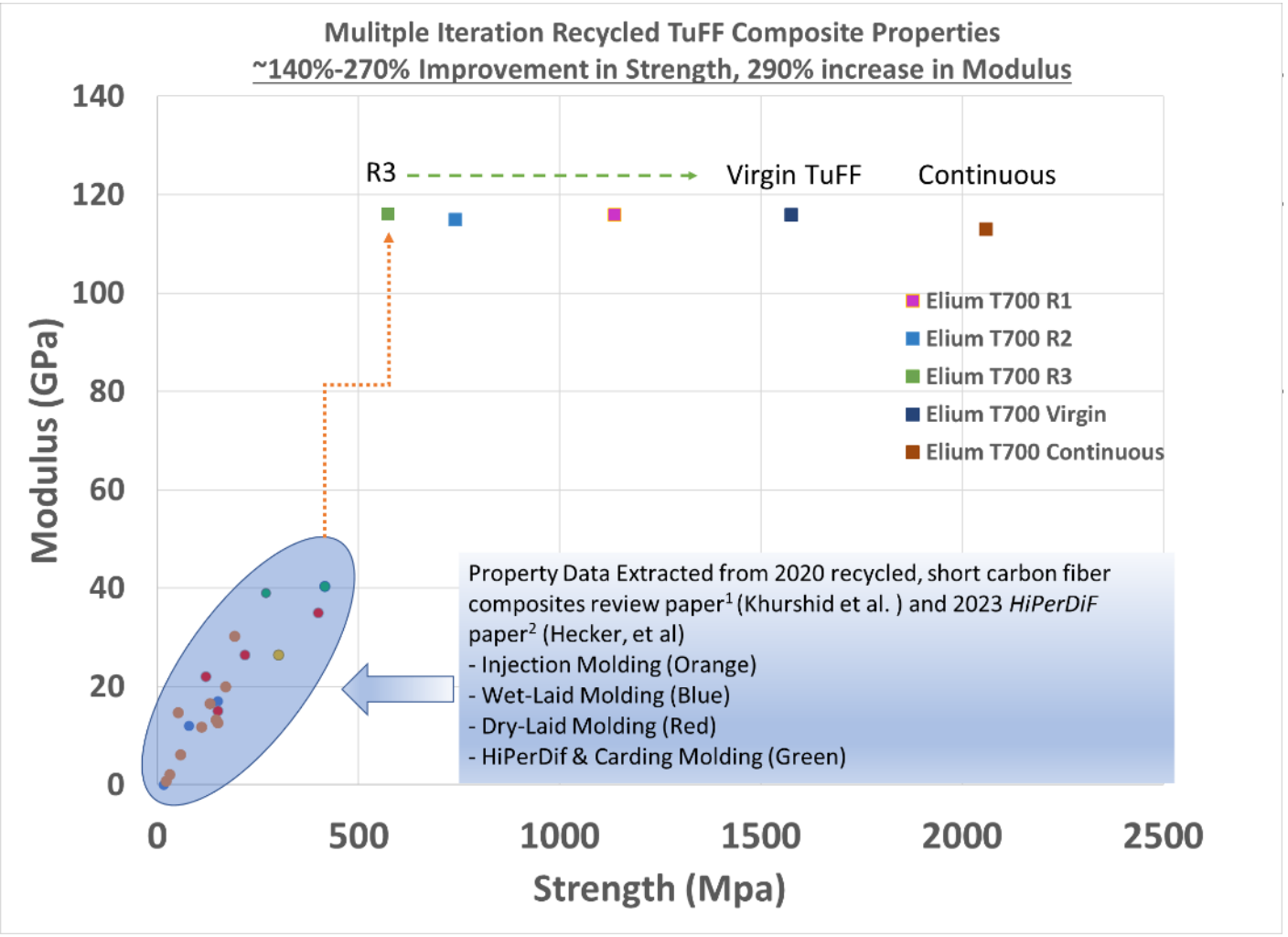

100% Translation of Modulus, independent of # of recycling iterations

Third iteration of recycled fibers show ~140% improvement in strength over majority of reported recycled short fiber composites

Key factors in reduction of composite strength include:

- Loss of filament strength due to multiple oxidative cleaning steps
- Small scale clusters of fiber end groups
- Broadening of fiber length distribution
- Fiber/Resin Adhesion

1. Muhammad Furqan Khurshid , Martin Hengstermann, Chokri Cherif, Journal of Composite Materials 54(14)
2. Hecker, Marcelle D., et al. ,Composites Part A: Applied Science and Manufacturing, 173 (2023): 107651.

Forming Elium-infused Virgin and R3 T700 blanks via Bead Mold Setup

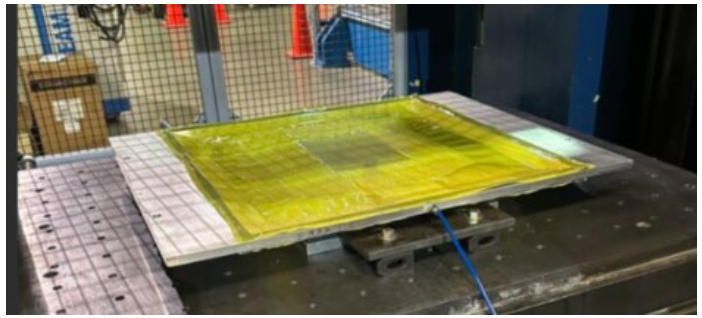



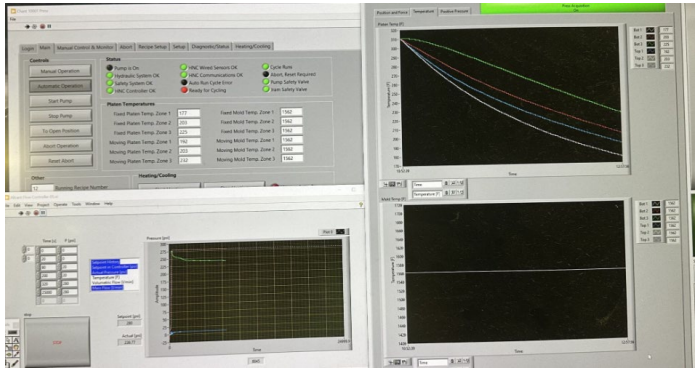

- Forming experiments with virgin and recycled TuFF blanks were successful
- The virgin blank had previous surface defects coming from the VARTM processing (After a pressure drop, leftover entrapped air formed a strip)
- Bead Mold Process conditions are as follows:
  - Heat press up to 155 ˚C
  - Prepare the blank in the mold, bag, and vacuum
  - Close the press and wait 20 minutes to get to the required resin viscosity
  - Increase pressure up to 280 psi and dwell 5 minutes
  - Start the cool-down process, remove the part





Commercial Prepregging of TuFF

(Axiom, Composite Automation and UD-CCM)



Axiom Commercial Prepreg line



CA-TuFF material being run



Final TuFF/Epoxy prepreg

- 120 gsm T700-50C TuFF dry preform with 2 64 gsm Axiom 2201 UD resin films
  - One film layer is used the carrier(100 ft roll fabricated at CA and transported to Axiom for prepreg processing)
  - No significant modification to the prepreg line was necessary

Summary & Opportunities for *rCF*

- Aligned discontinuous fiber formats have potential to re-capture original carbon fiber performance for rCF
  - *TuFF* formats have demonstrated 100% modulus and 74% strength to date for rCF compared to Virgin TuFF composites
- rCF quality must approach virgin carbon fiber quality
  - Surface cleanliness, eliminate polymer residue
    - Recycle-by-Design Resins!
  - Minimize or eliminate fiber flocks(cm) and fiber end aggregations(Microns to MM)
  - Approaches to reduce incoming breadth of fiber distribution
    - Too small – may affect strength translation
    - Too long – may affect formability
  - Sizing of rCF – may be needed
- Allows other unique part manufacturing processes enabled by the in-plane extensibility of *TuFF*

Acknowledgements: The Circular Economy Team!

DOE/EERE/ Advanced Manufacturing Office (AMO) DE-EE000303

- **UD-CCM**
  - Joseph Deitzel
  - Tekin Ozdemir
  - Munetaka Kubota
  - Udey Balaga
  - Markus Schwaiger
- **Composites Automation**
  - Mark Davis
  - Dirk Heider
  - Roger Crane
- **Axiom Materials**
  - Johnny Lincoln
  - Antonios Tontisakis
- **NREL**
  - Rebecca DiPucchio
  - William Michener
  - Ciaran Lahive
  - Kevin Sullivan
  - Katie Stevenson
  - Gregg Beckham
- **NREL cont**
  - Stephen Dempsey
  - Abhay Athaley
- **CSU**
  - Eswara Rao Chakkapu
  - Eugene Chen
- **Arkema**
  - Paul Boothe
  - Evan Martz
  - Mark Aubart

REPROCESSABLE HIGH PEROFRMANCE EPOXY IMINE VITRIMER COMPOSITES

Sharine Noelle O. Bendulo[1], Houlei Gan[2], Juan Zhang[3], Russell J. Varley[2*]

[1]Institute for Frontier Materials, Deakin University
75 Pigdons Rd, Waurn Ponds, Victoria, Australia
Email: s219444715@deakin.edu.au,

[2]School of Engineering, RMIT University
124 La Trobe St., Melbourne, Victoria, Australia
Email: houlei.gan@rmit.edu.au, russell.varley2@rmit.edu.au

[3]Institute for Polymer Composites, Jiangsu University of Technology
1801 Zhongwu St., Changzhou 213001, Jiangsu, China
Email: jane.zhang@jsut.edu.cn

Keywords: covalent adaptive networks, epoxy imine networks, repair

ABSTRACT

Vitrimers retain the structural integrity of thermosets while exhibiting flow-like properties under certain conditions, enabled by heat-activated dynamic bond exchange reactions. In this study, the effects of off-stoichiometric ratios in tailoring the properties and reprocessability of imine-epoxy vitrimers, focusing on a para-substituted imine-epoxy vitrimer is studied and compared to a standard thermoset based upon diglycidyl ether of bisphenol A. Furthermore, this work enabled an exploration of transimination—secondary bond exchange reaction where imine groups interact with unreacted amines—alongside imine metathesis. Stoichiometric balance starting from epoxy excess to amine excess were systematically varied to explore the impact upon static thermal and mechanical properties, as well as dynamic behaviour including the temperature of vitrimisation (T_v), adhesion, malleability and remouldability. These findings highlight how off-stoichiometric designs can optimize repairability and durability in highly aromatic epoxy vitrimers through dynamic imine chemistry, advancing the development of sustainable, reprocessable composites.

1 INTRODUCTION

Vitrimers are covalently crosslinked polymer networks modified with dynamic or reversible bonds capable of undergoing bond exchange reactions. These reactions enable topological rearrangements within the network without compromising the overall crosslink density.[1] The exchange can be triggered by external stimuli such as changes in temperature, pH, light, or the presence of chemical additives.[2-4] Examples of dynamic bonds commonly used in vitrimers include ester bonds, boronic esters, imines, and disulfide linkages.[5] As a result of the dynamic behavior, vitrimers can exhibit thermoplastic-like flow under specific conditions, a property not inherent in conventional thermosets, offering advantages in terms of recyclability, remouldability, and repair after curing.[6, 7]

Imines are particularly attractive due to their thermally activated bond exchange reactions and catalyst-free reprocessing. They undergo two types of bond exchange reactions, i.e., imine metathesis, which involves exchange between imine groups, and transimination, which occurs through reaction with free amine groups.[8] Since amine-based hardeners are commonly used in epoxy networks, varying the amine-to-epoxide stoichiometry can influence the amount of unreacted amine groups present in the cured network. These residual amines may participate in transimination reactions with imine bonds, not only during reprocessing but potentially during the curing process itself. This raises the question of how stoichiometry influences not only the curing process but also the post-cure properties and reprocessability of imine-based vitrimers. While off-stoichiometric formulations are

typically avoided in traditional thermosets due to their negative impact on thermal and mechanical properties, vitrimers may tolerate or even benefit from such formulations. Investigating this could provide valuable insights into how vitrimers differ from conventional thermosets, especially in terms of thermal and mechanical properties, reprocessability, and hydrolytic stability.

The role of stoichiometry in crosslinked polymers, particularly epoxy amine networks has been studied for many years and the relationships are well understood.[9-12] For the best combination of mechanical, thermal and physical properties, a stoichiometric, or small epoxide group excess is typically used because it will produce a homogenous network and provide the best opportunity for complete cure and a minimum of remaining reactive groups. Recent examples of systematic studies on epoxy networks and epoxy vitrimers include Senanayake et al. (2024) that reported on the impact of stoichiometry on the properties of epoxy/acid thermosets.[13] Jing and Xie (2022) investigated the effect of stoichiometry on the properties and reprocessability of epoxy/acid vitrimers facilitated by Zn^{2+}-catalyzed transesterification which was the first type of vitrimer reported. They varied the epoxy-fatty acid ratio and obtained glass transition temperatures between 20°C and 30°C and tensile strength between 2 to 4 MPa that decrease with increasing epoxy/acid ratio due to decreasing crosslink density.[14] Sheng and Guo (2023) did a similar study, varying the epoxy/acid ratio and found that the epoxy content increased glass transition temperature due to higher proportion of the rigid aromatic epoxide backbone from 40°C to 63°C and increased tensile strength increased from 26 to 43 MPa. In terms of repairability using a scratch test, increasing epoxy content enhanced repairability highlighting the importance of stoichiometry. [15]

In this work, an imine epoxy resin synthesized in house has been cured with diethyl toluene diamine (DETDA) using a range of stoichiometries from epoxy to amine excess and characterized for their static and dynamic properties. Various thermal, thermomechanical, and mechanical techniques were used to compare and contrast the dynamic network compared with a traditional epoxy amine network. Key dynamic properties such as material flow, topology freezing temperature, activation energy of dynamic behaviour, stress relaxation time, and adhesion strength were determined enabling dynamic behaviour to be better understood.

2 EXPERIMENTAL

2.1 Materials

Vanillin, 4-Aminophenol, benzyltriethylammonium chloride, (±)-epichlorohydrin, and 0.1N nitric acid in glacial acetic acid were purchased from Sigma-Aldrich (Missouri, USA). Isopropanol, ethanol, dichloromethane, and methanol were purchased from Chem-supply. Diethyltoluenediamine, DETDA 100, was purchased from Huntsman Corporation (Everberg, Belgium).

2.2 Sample Preparation

The para-substituted epoxy imine, pVAPI, was synthesized by mixing vanillin (0.02 mol) and 4-aminophenol (0.02 mol) in 30% aqueous ethanol at 50°C for two hours according to the following reaction sequence in Figure 1.

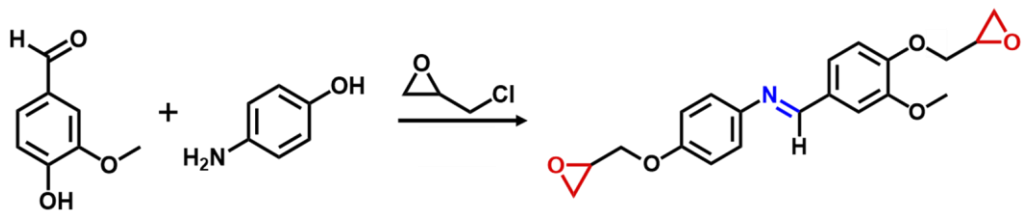

Figure 1: Synthesis of *p*VAPI epoxide from vanillin and *p*-aminophenol.

The precipitate was filtered, washed with deionized water, and dried overnight in an oven at 60°C. Epoxidation of pVAPI was carried out by mixing pVAPI (0.02 mol), epichlorohydrin (0.10 mol) and

benzyltriethylammonium chloride catalyst (2 mol %). The mixture was refluxed at 90°C for 2 hours. A water isopropanol solution of sodium hydroxide (0.10 mol) then added and mixing continued for 2 hrs at 60°C. After filtering, the product was concentrated in vacuo at 100°C then washed several times with deionized water. Finally, pVAPI epoxide was dried over anhydrous magnesium sulfate, and then isolated in vacuo. The yield for pVAPI epoxy was 98%.

The resin systems were prepared by mixing pVAPI epoxide and DETDA together using epoxide to active hydrogen ratios of 1:0.5, 1:0.7, 1:0.9: 1:1.2 and 1:1.5. The formulations were degassed and mixed together at 120°C for 10 minutes then poured into pre-heated silicone moulds and cured in a convection oven at 120°C for 2 hours, 150°C for 2 hours and 177°C for 5 hours. DGEBA-DETDA formulations were prepared in a similar manner.

2.3 Characterization

Dynamic thermomechanical analysis was conducted with TA Q800 DMA. Samples with dimensions of 12×50×2.5 mm^3 were prepared and placed in a dual cantilever fixture. A force amplitude of 15 µm with frequency of 1 Hz was applied from 30°C to 250°C at a rate of 3°C/min. The glass transition temperature, T_g, was determined from peak of the tan δ, and the crosslink density (υ_e) was calculated from the rubbery modulus, E_r, at $T_r = Tg + 50°C$, and with R which is the real gas constant, using the equation,

$$\upsilon_e = E_r/(3RT_r) \quad (1)$$

Thermal stability and degradation studies were done with Netzsch TG 209 F1 Libra. Samples of about 5 mg were prepared in Al_2O_3 pans. The temperature was ramped from 30 to 800°C at 10°C/min under nitrogen. Samples were characterized based upon the temperature at 5% mass loss, $T_{5\%}$, the temperature at the maximum rate of degradation, T_{max}, and the char yield at 800°C.

Thermomechanical analysis was conducted with the Netzsch Hyperion TMA. Polymer samples were cut into 5 mm disks with a drill press and placed in between ceramic plates. A force of 0.05 N was applied to ensure good contact between the samples. The temperature was increased from 30°C to 270°C at 3°C/min. The coefficients of thermal expansion for the glassy and rubbery regions were calculated from the slope before and after the glass transition temperature.

Flexural testing were conducted using an Instron 68TM-50 Universal Testing Machine. Flexural tests was based on ASTM D790 wherein resin bars with dimensions 12×60×2.5 mm^3 were prepared using a span-to-thickness ratio of 16:1, a crosshead displacement speed of 1.3 mm/min, and a 50 kN load cell. The modulus was measured from the slope of the stress−strain curve up to a flexural strain of 0.2%, and the flexural strength was measured from the maximum failure load.

To investigate test repeated adhesion, cured vitrimers placed on composite substrates were overlapped to an extent of 25 mm x 25 mm clamped together with a force of around 8 kN, and heated at 200°C for 3 hours in an oven. Adhesion was assessed according to a simple lap shear test using an Instron 5967 Universal Testing Machine

5 DISCUSSION

The cured resins are shown in Figure 2 illustrating the effect of stoichiometry on the colour of the cured resins. Clearly, imine networks become increasingly darker with higher levels of amine, reflecting the increasing vulnerability towards oxidation. In comparison the DGEBA DETDA networks are much less darker.

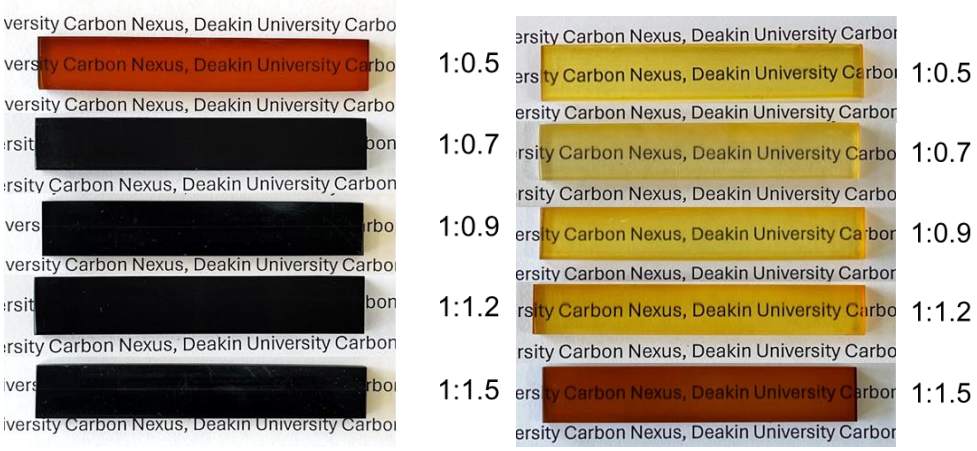

Figure 2: Images of the *p*VAPI-DETDA (left) and DGEBA-DETDA (right) networks after cure.

To evaluate the effect of stoichiometry on the thermomechanical properties of the vitrimer and non-vitrimer networks, dynamic mechanical analysis was performed. The DMTA spectra are shown in Figure 3 and the results are summarized in Table 1. Increasing amine content results in higher storage modulus and lower glass transition temperature which is also reflected in the lower crosslinking densities determined. All vitrimers have glass transition temperatures above 130°C, due to the rigid nature of the imine backbone. Unreacted amine groups led to a decrease in crosslinking density which is commonly observed in network polymers. The DMTA for the DGEBA DETDA networks had a higher storage modulus as well as lower glass transition temperature and crosslinking density.[10, 16] The tan delta peaks for all networks are symmetrical single peaks indicating homogeneous and fully cured networks formed even in the presence of excess epoxide and amine.

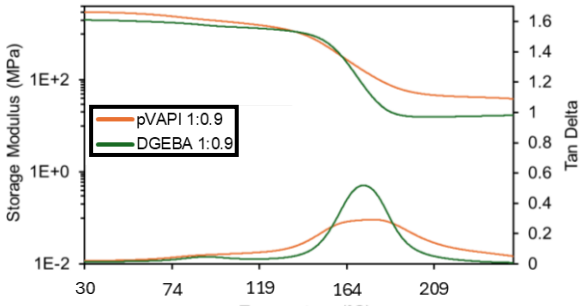

Figure 3: DMTA traces of the VAPI and DGEBA networks for 1:0.9 stoichiometry.

Thermomechanical analysis was performed to evaluate the effect of stoichiometry on the thermal expansion and dimensional stability. Figure 4 compares the raw thermogram from the DGEBA and pVAPI networks which show different behaviour. The DGEBA network appears quite standard with an inflection point corresponding to T_g, while the pVAPI imine does not appear to display an inflection point at T_g, again likely due to its rigid nature. The effect of stoichiometry on the CTE is shown in Table 1 where it can be seen that there is a gradual decrease in CTE with increasing amine content. In general the CTE of the DGEBA non vitrimer networks are lower than the vitrimer networks, suggesting it is more tightly constrained in the network.[10]

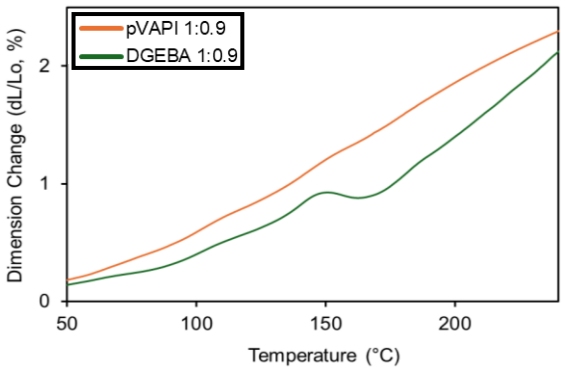

Figure 4: TMA traces of the VAPI and DGEBA networks for 1:0.9 stoichiometry.

The TGA thermograms show a typical mass loss transition in Figure 5. The important point to note is that the imine networks have a lower onset of degradation temperature and a high char yield compared to the DGEBA DETDA networks. As can be seen from the results, the effect of stoichiometry only has a modest impact upon degradation temperatures and char yields.[17]

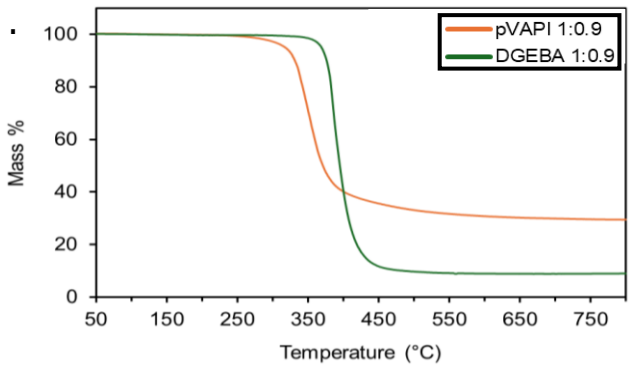

Figure 5: TGA thermograms showing mass loss from decomposition of the cured pVAPI 1:0.9 and DGEBA 1:0.9 networks.

Table 1: Summary of the thermal and thermomechanical properties of *p*VAPI-DETDA and DGEBA-DETDA networks.

Network	DMA				TGA			TMA
	T_g[a] (°C)	T_g[b] (°C)	$E'_{30°C}$ (GPa)	υ_e[c] (10^3 mol/m^3)	$T_{5\%}$ (°C)	T_{max} (°C)	Char yield (%)	α_g (10^{-6} K^{-1})
*p*VAPI-DETDA 1:0.5	192	166	2.9	3.3	313	347	33	71
*p*VAPI-DETDA 1:0.7	179	150	3.4	5.2	312	351	29	72
*p*VAPI-DETDA 1:0.9	178	142	3.0	3.6	317	350	30	72
*p*VAPI-DETDA 1:1.2	147	126	3.2	2.2	316	348	27	69
*p*VAPI-DETDA 1:1.5	123	104	3.3	1.3	309	354	26	67
DGEBA-DETDA 1:0.5	73	61	3.0	0.04	295	388	9	80
DGEBA-DETDA 1:0.7	121	99	3.0	0.4	347	386	10	57
DGEBA-DETDA 1:0.9	173	153	2.0	1.3	369	386	9	59
DGEBA-DETDA 1:1.2	180	163	2.2	2.1	366	386	9	58
DGEBA-DETDA 1:1.5	146	134	2.3	1.0	363	388	8	49

[a]Determined by the peak of tan δ. [b]Determined from the extrapolated onset of E'. [c]υ_e is the crosslink density per unit volume from the DMA curves at T_g + 40°C.

The mechanical properties of the pVAPI and DGEBA networks are shown in Table 2 which highlight the effect of stoichiometry for both networks, the vitrimer and non-vitrimer. An example of the stress strain curve for the 1:0.9 stoichiometry in Figure 6 in particular highlights their brittle failure, particularly for pVAPI. For the pVAPI network, increasing amine content increases the modulus and strength but does not significantly affect the strain at break. These trends are opposite to that of the benchmark thermoset which exhibits decreasing modulus and strength as well as increasing strain at break with increasing amine content. During curing, bond exchange reactions may be activated by the high temperature needed for curing which relaxes internal stress and decreases defects in the network leading to better mechanical properties. Increasing the ratio increases the number of amines that can participate in transimination reactions resulting in higher flexural modulus and strength. However, the strain at break remains the same with increasing amine content. This could be due to the similar chemical composition of the vitrimers.[14]

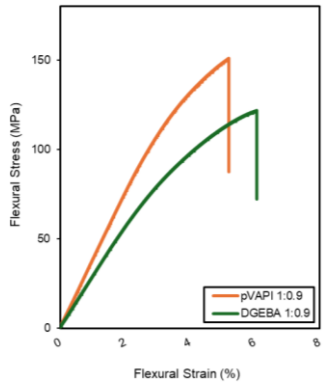

Figure 6: Flexural stress-strain curves for the pVAPI and DGEBA 1:0.9 networks.

Table 2: Summary of the mechanical properties of *p*VAPI-DETDA and DGEBA-DETDA networks.

Network	Flexural Strength (MPa)	Flexural Modulus (GPa)	Flexural Strain at Break (mm/mm)
*p*VAPI-DETDA 1:0.5	126	3.4	0.05
*p*VAPI-DETDA 1:0.7	150	3.9	0.05
*p*VAPI-DETDA 1:0.9	150	3.7	0.06
*p*VAPI-DETDA 1:1.2	155	3.9	0.06
*p*VAPI-DETDA 1:1.5	163	4.1	0.05
DGEBA-DETDA 1:0.5	30	3.3	0.01
DGEBA-DETDA 1:0.7	121	3.5	0.04
DGEBA-DETDA 1:0.9	122	2.9	0.08
DGEBA-DETDA 1:1.2	108	2.5	0.09
DGEBA-DETDA 1:1.5	95	2.7	0.11

Reversible or debondable adhesion of the vitrimers as a function of stoichiometry was investigated using lap shear. The load recovery is shown in Figure 7, where it can be seen that with increasing amine content, the load force increases. Clearly polymer chain diffusion and entanglement is therefore able to occur despite the fact that the polymer networks are fully cured. This highlights the molecular mobility of the imine functional group under heat and pressure. It is proposed that the dynamic covalent behaviour promotes transimination and imine metathesis between the surfaces enabling adhesion as the functional groups diffusion across the surfaces. Elevated temperatures increase the rate of these reversible exchange reactions that lead to topology rearrangements allowing faster chain diffusion. This experiment demonstrates the reprocessability of the VAPI vitrimer network while no diffusion for the DGEBA network was observed at all, despite efforts to do so. Figure 7 also shows the failure surfaces after re-processing highlight cohesive failure for stoichiometric and amine access networks.

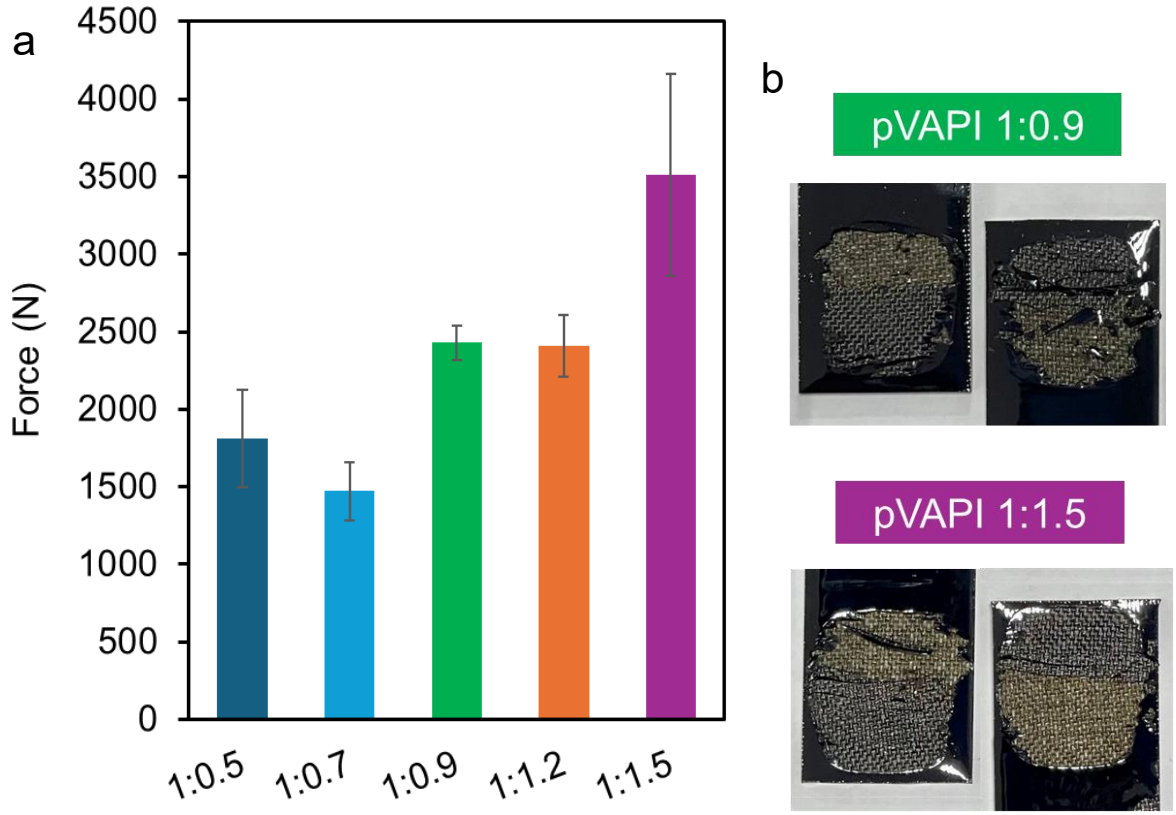

Figure 7: (a) Lap shear applied force of pVAPI-DETDA networks after welding the cured resins at 200°C for 3 hours. (b) Lap shear failure images of pVAPI-DETDA 1:0.9 and 1:1.5.

9 CONCLUSIONS

This study explored the impact of epoxide-amine stoichiometry on the properties and reprocessability of a highly aromatic imine-based epoxy vitrimer. This research provides insight into the bond exchange mechanism as a function of amine content and its application to the development of a reversible or debondable adhesive. The vitrimer properties were highly tunable achieving Tg's ranging from 120-210°C and flexural strength ranging from 120 to 160 MPa. This study is part of a broader study into the efficacy of imines as functional groups for high performance yet dynamic networks, and these results present excellent results that suggest that excellent mechanical and thermal properties, along with very good dynamic behaviour can go together in some high-performance networks.

REFERENCES

[1] H. Sharma, B. Krishnakumar, T. J. Dickens, G. J. Yun, A. Kumar, and S. Rana, A bibliometric survey of research trends in vitrimer, *Heliyon,* **9**, 2023, p. e17350, (doi: 10.1016/j.heliyon.2023.e17350).

[2] W. Denissen, J. M. Winne, and F. E. Du Prez, Vitrimers: permanent organic networks with glass-like fluidity, *Chem Sci,* vol. 7, no. 1, pp. 30-38, Jan 1 2016, doi: 10.1039/c5sc02223a.

[3] V. Schenk, K. Labastie, M. Destarac, P. Olivier, and M. Guerre, Vitrimer composites: current status and future challenges, *Materials Advances,* **3**, 2022, pp. 8012-8029, (doi: 10.1039/d2ma00654e).

[4] M. Kathan, C. Jurissek, P. Kovaříček, and S. Hecht, Imine-based dynamic polymer networks as photoprogrammable amine sensing devices, *Journal of Polymer Science Part A: Polymer Chemistry,* **57**, 2019, pp. 2378-2382, (doi: 10.1002/pola.29518).

[5] H. Memon, Y. Wei, L. Zhang, Q. Jiang, and W. Liu, An imine-containing epoxy vitrimer with versatile recyclability and its application in fully recyclable carbon fiber reinforced

composites, *Composites Science and Technology,* **199**, 2020 (doi: 10.1016/j.compscitech.2020.108314).

[6] H. Memon, Y. Wei, and C. Zhu, Recyclable and reformable epoxy resins based on dynamic covalent bonds – Present, past, and future, *Polymer Testing,* **105**, 2022 (doi: 10.1016/j.polymertesting.2021.107420).

[7] H. Memon *et al.*, Vanillin-Based Epoxy Vitrimer with High Performance and Closed-Loop Recyclability, *Macromolecules,* **53**, 2020, pp. 621-630, (doi: 10.1021/acs.macromol.9b02006).

[8] Y. Jin, Q. Wang, P. Taynton, and W. Zhang, Dynamic covalent chemistry approaches toward macrocycles, molecular cages, and polymers, *Acc Chem Res,* **47**, , pp. 1575-86(doi: 10.1021/ar500037v).

[9] G. R. Palmese and R. L. McCullough, Effect of epoxy–amine stoichiometry on cured resin material properties, *Journal of Applied Polymer Science,* **46**, 2003, pp. 1863-1873 (doi: 10.1002/app.1992.070461018).

[10] A. S. Sridhar, Effect of stoichiometry on crosslinked epoxy resin characteristics: structural heterogeneities, topological defects, properties, free volume and segmental mobility, *Soft Matter,* **18**, 2022, pp. 2354-2372 (doi: 10.1039/d1sm01825f).

[11] K. Yu, P. Taynton, W. Zhang, M. L. Dunn, and H. J. Qi, Influence of stoichiometry on the glass transition and bond exchange reactions in epoxy thermoset polymers, *RSC Adv.,* **4**, 2014, pp. 48682-48690 (doi: 10.1039/c4ra06543c).

[12] C. Bannister *et al.*, The influence of ambient cure chemistry and stoichiometry on epoxy coating surfaces, *RSC Adv,* **12**, 2022, pp. 28746-28754 (doi: 10.1039/d2ra05067f).

[13] R. B. Senanayake, H. Gan, J. Zhang, D. Liu, and R. J. Varley, Impact of Stoichiometry on the Network Structure, Properties, and Processing Relationships of an Epoxy Tannic Acid Resin System, *ACS Applied Polymer Materials,* **6**, 2024, pp. 2107-2117 (doi: 10.1021/acsapm.3c02212).

[14] F. Jing, R. Zhao, C. Li, Z. Xi, Q. Wang, and H. Xie, Influence of the Epoxy/Acid Stoichiometry on the Cure Behavior and Mechanical Properties of Epoxy Vitrimers, *Molecules,* **27**, 2022 (doi: 10.3390/molecules27196335).

[15] J. Sheng *et al.*, Using epoxy/acid stoichiometry to rationally tune the thermomechanical and reprocessing properties of epoxy vitrimers, *Journal of Applied Polymer Science,* **140**, 2023 (doi: 10.1002/app.54699).

[16] T. Liu *et al.*, Nitrogen-Free Tetrafunctional Epoxy and Its DDS-Cured High-Performance Matrix for Aerospace Applications, *Industrial & Engineering Chemistry Research,* **56**, 2017, pp. 7708-7719 (doi: 10.1021/acs.iecr.7b00096).

[17] A. Ruiz de Luzuriaga, G. Solera, I. Azcarate-Ascasua, V. Boucher, H.-J. Grande, and A. Rekondo, Chemical control of the aromatic disulfide exchange kinetics for tailor-made epoxy vitrimers, *Polymer,* **239**, 2022 (doi: 10.1016/j.polymer.2021.124457).

REJUVENATING OUT-OF-DATE PRE-PREGS WITH IMINE-EPOXY VITRIMERS

Sharine Noelle O. Bendulo[1], Houlei Gan[2], Juan Zhang[3], Russell J. Varley[2]

[1]Institute for Frontier Materials, Deakin University
75 Pigdons Rd, Waurn Ponds, Victoria, Australia
Email: s219444715@deakin.edu.au, sobendulo@gmail.com Web page: https://www.deakin.edu.au

[2]School of Engineering, RMIT University
124 La Trobe St., Melbourne, Victoria, Australia

[3]Institute for Polymer Composites, Jiangsu University of Technology
1801 Zhongwu St., Changzhou 213001, Jiangsu, China

Keywords: Composite welding, Out-of-date prepregs, Vitrimer, Epoxy, Imine

ABSTRACT

Composites have a strength-to-weight ratio, approximately nine times that of steel, making them desirable for demanding applications such as in wind turbine blades, aircraft and automotives. However, their commercial viability is constrained by logistical challenges, including the necessity for refrigerated transport and storage, as well as their inability to be molded or welded post-curing. Carbon fiber pre-pregs require refrigeration and must be maintained in a frozen state until use, complicating logistics and increasing waste due to spoilage during power outages. This study investigates the potential of vitrimers as a solution to rejuvenate out-of-date or improperly cured pre-pregs. Vitrimers are crosslinked polymer networks modified with dynamic bonds that undergo bond exchange reactions at elevated temperatures. This results in material flow which enables thermoforming and bonding even after curing which is not possible for existing thermosets. In this work, carbon fiber pre-pregs based on diglycidyl ether of bisphenol A, DGEBA, are cured to varying degrees of cure, and cured with an already fully cured imine-containing epoxy vitrimer, *p*VAPI-DETDA. The mechanical and thermal properties of the resulting laminates were characterized through three-point bending tests, dynamic mechanical analysis (DMA), thermogravimetric analysis (TGA), differential scanning calorimetry (DSC), and microscopy. The laminates demonstrated high glass transition temperatures of up to 177°C, degradation temperatures reaching 387°C, flexural strengths up to 1.31 GPa, and flexural moduli up to 105 GPa. These findings suggest that vitrimers can significantly mitigate waste and energy consumption while addressing the logistical limitations associated with thermoset carbon fiber pre-pregs. Moreover, this approach could enable the transport of composites similar to sheet metals, eliminating the need for refrigeration and enhancing their commercial potential.

1 INTRODUCTION

Fiber-reinforced polymer composites (FRPs) are advanced hybrid materials composed of a reinforcement—commonly fibers such as carbon, glass, or natural fibers—and a matrix, which can be a thermoset or thermoplastic polymer, ceramic, or metal.[1] Among these, carbon fiber-reinforced polymer (CFRP) composites are particularly attractive due to their high strength-to-weight ratio, excellent thermal stability, and mechanical robustness. These attributes make them ideal for aircraft structures, vehicle components, and wind turbine blades.[1-4]

CFRPs can be manufactured using various techniques, including hand lay-up, vacuum infusion, compression molding, and prepreg processing. Prepregs—fibers pre-impregnated with a polymer resin—are widely used, especially in the aerospace industry.[5-8] These prepregs are typically stored and transported in a frozen state to inhibit premature curing. Upon reaching the end user, they are

maintained under cold storage conditions until they are layed up in molds and consolidated under heat and pressure into the desired composite structure. For instance, aerospace manufacturers such as Boeing receive large rolls of prepregs that are kept frozen until final forming, requiring energy-intensive logistics. However, challenges arise when there are disruptions such as power outages or transportation delays.[9] In such cases, premature curing reactions between the epoxide and amine components may initiate, resulting in increased stiffness or boardiness of the prepreg. Boardy prepregs indicate partial cure, which reduces the availability of reactive functional groups essential for good interfacial bonding during composite formation. In severe cases where the prepregs are nearly or fully cured, they become non-adherent and unsuitable for further processing, leading to disposal and material wastage. This issue is rooted in the inherent intractability of thermosets, whose permanent crosslinked networks cannot be reshaped or remolded once cured.

To address this problem, the use of vitrimers is proposed—a class of crosslinked polymers that incorporate dynamic covalent bonds, enabling network rearrangement under specific conditions. Unlike conventional thermosets, vitrimers can exhibit thermoplastic-like flow behavior at elevated temperatures due to dynamic bond exchange reactions that facilitate topological reconfiguration. This property allows vitrimers to interdiffuse and entangle across interfaces, forming strong bonds even with thermosets. Furthermore, when vitrimers possess complementary functional groups, they can form covalent linkages with unreacted groups on partially cured prepreg surfaces, enabling chemical rejuvenation. Remarkably, vitrimers can achieve such interactions even when fully cured, offering post-curing reprocessability and welding capability.[10-13]

In this study, we exploited the weldability and reprocessability of an epoxy vitrimer based on dynamic imine bonds to rejuvenate out-of-date thermoset prepregs and maintain usability despite their boardy nature. Specifically, the initial cure state, i.e., the availability of residual functional groups affects vitrimer-assisted recovery. Thermoset prepregs of varying cure levels were interleaved with fully cured vitrimer single plies derived from *p*VAPI-DETDA, a vitrimer from an imine-epoxide synthesized from vanillin and 4-aminophenol, and the amine hardener diethyltolunediamine (DETDA), and hot-pressed into laminates. The resulting materials were characterized using differential scanning calorimetry (DSC), dynamic mechanical analysis (DMA), thermogravimetric analysis (TGA), and flexural testing to evaluate thermal and mechanical performance. Our results confirm that the vitrimer can effectively rejuvenate prepregs with sufficient unreacted functional groups by enabling covalent bonding. In cases where functional group availability is limited, vitrimer chain diffusion and physical entanglement still result in moderate property recovery. This study demonstrates that imine-epoxy vitrimers can extend the usability of out-of-date or improperly cured prepregs, offering a sustainable route to reduce composite material waste and retain performance.

2 METHODOLOGY

2.1 Sample Preparation

The vanillin-based imine-containing epoxide monomer was synthesized according to the method reported by Zhao, et al. (2018).[13] The resulting imine-epoxide, *p*VAPI epoxide, was then mixed with diethyltoluenediamine (DETDA) in a 1:1.5 ratio and dissolved in dichloromethane. Unidirectional carbon fibers were then impregnated with the mixture, the solvent was removed, vacuum bagged, and then cured in an oven at 120°C for 2 hours, 150°C for 2 hours and 177°C for 5 hours under vacuum. Thermoset prepregs were prepared from diglycidyl ether of bisphenol A (DGEBA) and DETDA in a 1:0.9 ratio. Unidirectional carbon fibers were impregnated with the mixture, vacuum bagged, and processed accordingly. Partially cured and fully prepregs were cured in an oven at 80°C and 150°C for 6 hours, respectively. As benchmark for out-of-date prepregs, a fresh uncured prepreg was prepared. This was done to simulate different stages of cure of improperly cured or out-of-date prepregs.

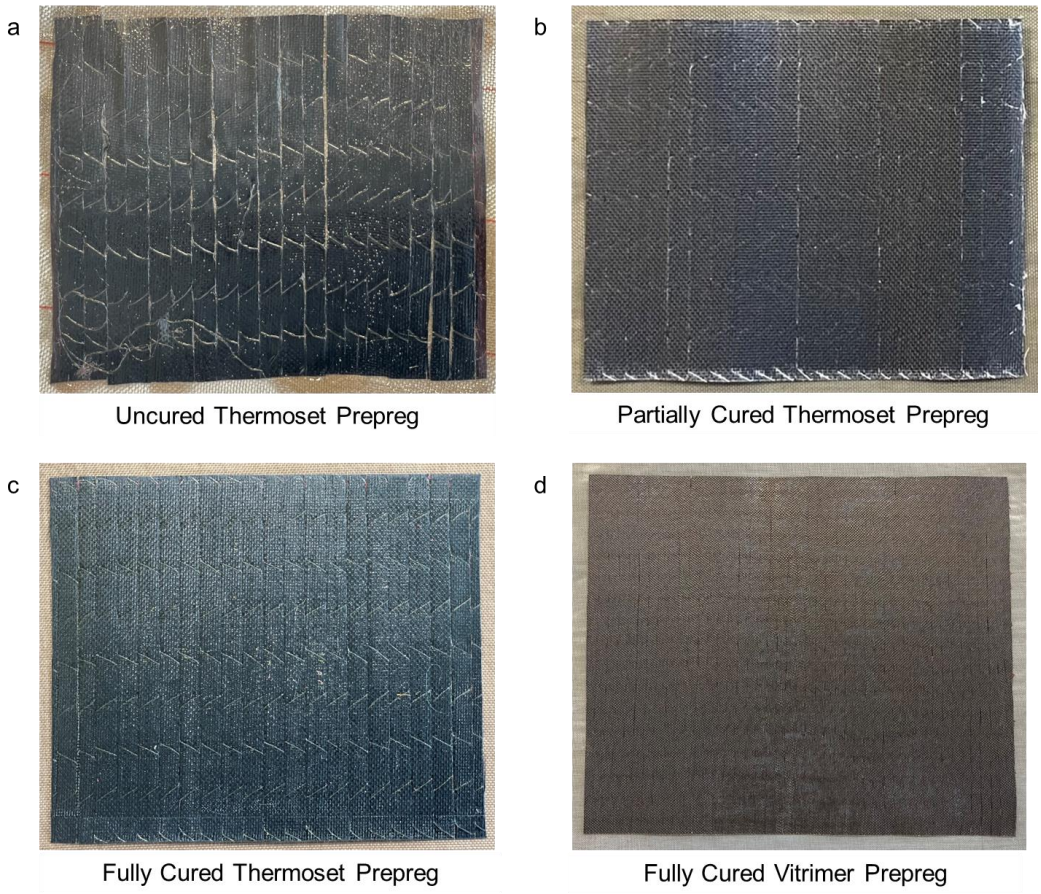

Figure 1: Images of (a) uncured, (b) partially cured and (c) fully cured DGEBA-DETDA carbon fibre prepregs and (d) fully cured *p*VAPI-DETDA carbon fibre prepreg.

Laminates designated as Unc VTCF, Par VTCF, and Ful VTCF, were then prepared from 8 alternating layers of uncured, partially cured and fully cured DGEBA-DETDA pre-pregs, respectively, with fully cured *p*VAPI-DETDA vitrimer single plies. The consolidation was done in a hot press at 200°C for 3 hours as shown in Figure 2. The pressure was kept constant at 2 tons.

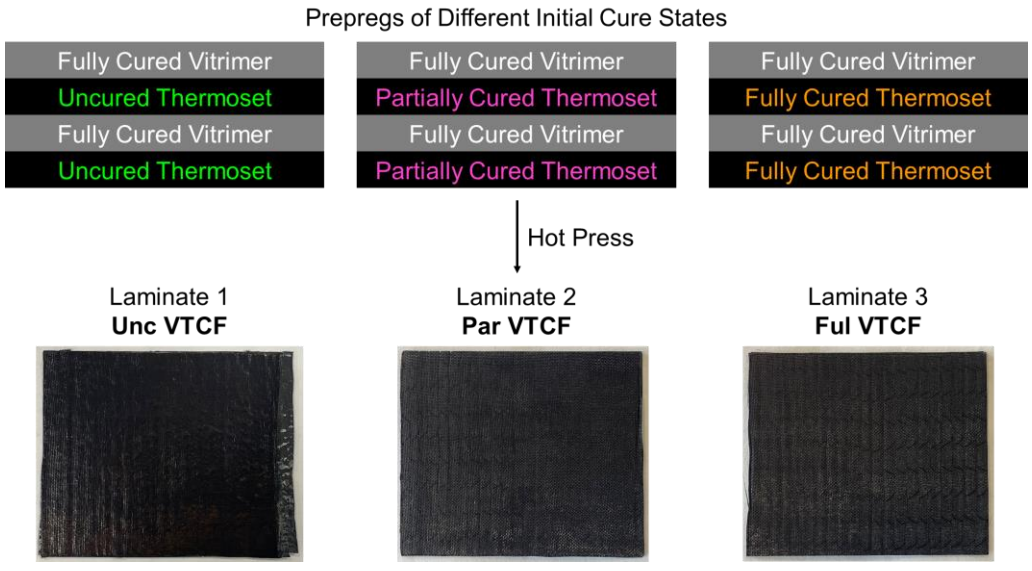

Figure 2: Schematic illustration of composite fabrication from alternating layers of the fully cured vitrimer single plies and thermoset prepregs of different initial cure states.

2.2 Thermal Analysis

Dynamic thermal analyses were done with Netzsch DSC 214 Polyma. Samples were prepared in concavus aluminum pans with lids pierced. The temperature was ramped from 30 to 320°C at a rate of 10°C/min under nitrogen. The data was processed with Proteus Analysis version 7.1.0 (2017, Netzsch-Geratebau GmbH, Germany).

Thermal stability and degradation studies were done with Netzsch TG 209 F1 Libra. Samples were prepared in Al_2O_3 pans. The temperature was ramped from 30 to 800°C at a rate of 10°C/min under nitrogen or air. The data was processed with Proteus Analysis version 8.0.2 (2020).

Dynamic thermomechanical analysis was conducted with TA Q800 DMA. Samples with dimensions of 12×32×3 mm^3 were prepared and placed in a single cantilever fixture. A force amplitude of 15 µm with frequency of 1 Hz was applied from 30°C to 300°C at a rate of 3°C/min. The data was processed with Universal Analysis version 4.5A.

2.3 Mechanical Testing

Flexural testing was conducted with Instron 68TM-50 Universal Testing Machine. Flexural tests were based on ASTM D790 wherein samples with dimensions 12×65×3 mm^3 were prepared and placed on support beams with a span of 48 mm. At least 10N was applied at a rate of 1.3 mm/min until fracture. The data was processed with BlueHill version 4.38.

3 RESULTS AND DISCUSSION

3.1 Preparation of Single Plies of Various Initial Cure States

Differential scanning calorimetry (DSC) was employed to assess the initial cure states of the uncured, partially cured, and fully cured thermoset prepregs, as well as the fully cured vitrimer single ply used in laminate fabrication. The DSC thermograms of the uncured and partially cured prepregs exhibited exothermic peaks beginning around 130°C, indicating that the curing reactions were incomplete. Notably, the uncured prepreg displayed a significantly larger exothermic peak area compared to the partially cured sample, reflecting a lower extent of initial cure of the former. The absence of a glass transition in the partially cured prepreg further confirms that it had not reached full cure. In contrast, both the fully cured thermoset prepreg and vitrimer single ply exhibited clear glass transition temperatures, consistent with complete network formation. These findings verify that the prepreg samples represent distinct cure states, validating their selection for studying the influence of initial cure on performance of the resulting laminates and the efficiency of vitrimers in rejuvenating out-of-date or improperly cured thermoset prepregs.

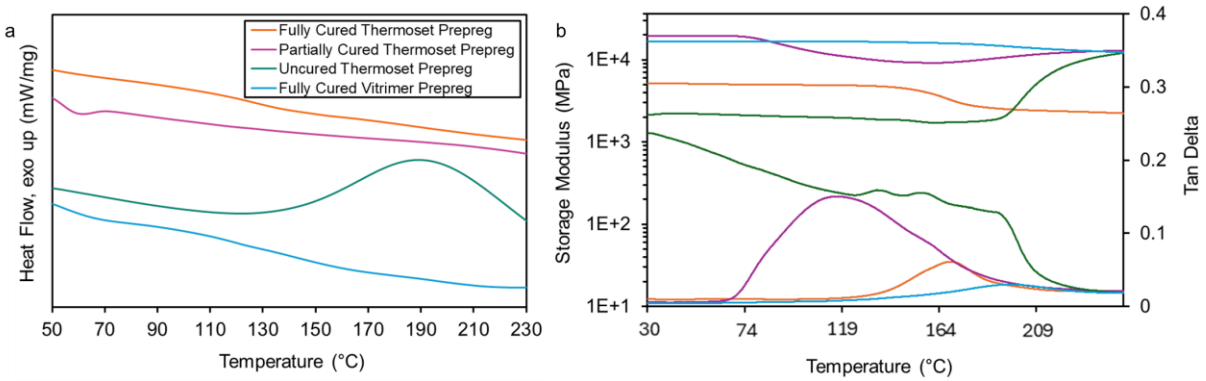

Figure 3: (a) DSC and (b) DMA thermograms of vitrimer and thermoset prepregs showing different stages of initial cure.

To further evaluate the curing states of the thermoset prepregs and the vitrimer single ply, dynamic mechanical analysis was performed, as illustrated in Figure 3. The tan δ and storage modulus curves for the uncured prepreg, Unc VTCF, are characteristic of an uncured network, displaying small tan δ peaks at around 131°C and 149°C. These peaks are followed by an increase in storage modulus, indicative of ongoing curing reactions during the thermal sweep. The partially cured prepreg, Par VTCF, exhibited a broad tan δ curve extending from approximately 60°C to 200°C, suggesting continued curing throughout the analysis along with glass transition. This is further supported by an increase in the storage modulus following the broad peak, similar to the uncured sample, further confirming in situ network formation during the analysis. In contrast, the fully cured prepreg, Ful VTCF, and the vitrimer single ply, *p*VAPI-DETDA, both displayed symmetrical, single tan δ peaks, signifying that their polymer networks were homogeneous and fully cured. Their storage modulus curves reveal a distinct glass transition followed by a rubbery plateau, further confirming their fully cured state. The measured glass transition temperatures, Tg, were 165°C for Ful VTCF and 192°C for *p*VAPI-DETDA. Notably, the ambient storage modulus and Tg of the vitrimer single ply exceeded that of Ful VTCF, suggesting that the selected vitrimer formulation does not compromise—and may even enhance—the thermal and mechanical performance of the resulting composite. This finding supports the suitability of the vitrimer for high-performance composite applications. Additionally, the broader and less intense tan δ peak observed for *p*VAPI-DETDA, compared to Ful VTCF, implies the presence of additional molecular motions at elevated temperatures. This broadening can be attributed to dynamic bond exchange reactions inherent to vitrimers, in addition to conventional segmental motion of the polymer chains. Overall, the DMA results clearly demonstrate the distinct stages of cure in the prepregs under investigation, confirming that the starting materials possess varying degrees of cure, which is essential for this work.

3.2 Fiber-Resin Content of Laminates

To determine the resin content of composites fabricated from alternating layers of the fully cured imine-epoxy vitrimer, *p*VAPI-DETDA, and DGEBA-DETDA prepregs in uncured, partially cured, or fully cured states, thermogravimetric analysis was employed. The analysis was initially performed under oxidative conditions to ensure complete degradation of the resin matrix. At 600°C, the carrier gas was switched from air to nitrogen to inhibit oxidation of the carbon fiber. The mass of the carbon fiber was estimated from the residual mass. All laminates exhibited char yields of approximately 70%, indicating a consistent composition with around 30% resin and 70% fiber content.

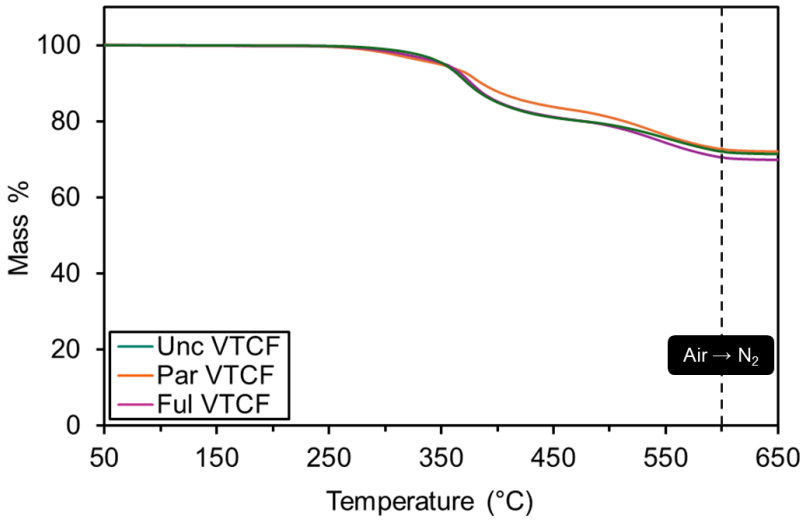

Figure 4: TGA thermograms of laminates from alternating layers of the fully cured vitrimer single plies and thermoset prepregs of different initial cure states under air atmosphere followed by nitrogen atmosphere.

3.3 Thermal Properties of Laminates

To assess how the initial cure state of thermoset prepregs influences the thermal properties of the resulting laminates, differential scanning calorimetry (DSC) was performed. All laminates exhibited DSC thermograms with no significant residual exothermic peaks, confirming complete curing across samples. The measured glass transition temperatures (Tg) were all comparable, around 140°C, indicating that the initial degree of cure of the prepregs had minimal impact on the final thermal properties of the composites. Interestingly, the laminate fabricated from the partially cured prepreg showed the highest Tg among the samples. This result may be attributed to the identical chemical composition of all laminates. Although variations in the initial cure states would typically lead to differences in crosslinking density after final curing, these differences were not reflected in the Tg values. This suggests that the fully cured vitrimer matrix may have facilitated effective network integration and crosslinking, contributing to the recovery or uniformity of thermal properties regardless of the prepreg's initial cure state.

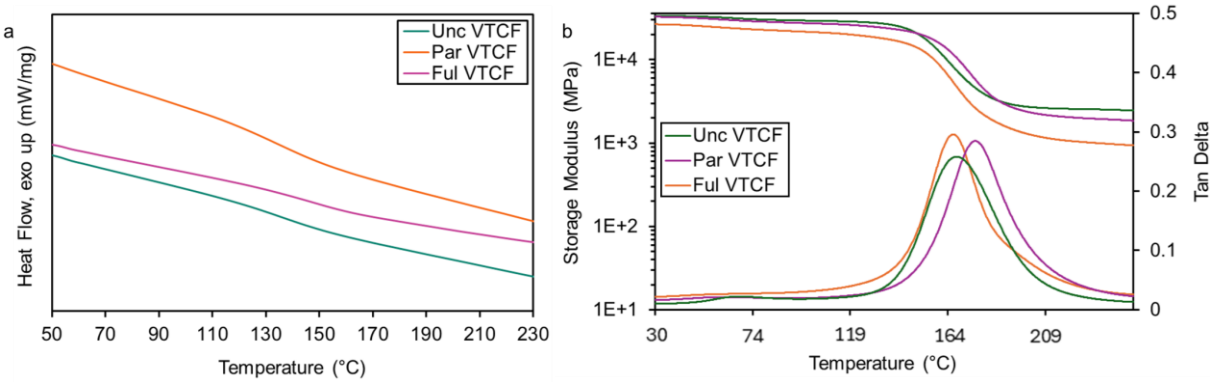

Figure 5: (a) DSC and (b) DMA thermograms of laminates from alternating layers of the fully cured vitrimer single plies and thermoset prepregs of different initial cure states.

To evaluate and compare the mechanical performance and viscoelastic behavior of laminates fabricated from prepregs with varying degrees of cure and vitrimer single plies, dynamic mechanical analysis was performed, as presented in Figure 5. All laminates exhibited symmetrical single peaks in their tan δ curves, indicating homogenous polymer networks and complete curing. The measured glass transition temperatures, Tg, were 169°C for the laminate from uncured prepregs, 177°C for that from partially cured prepregs, and 167°C for that from fully cured prepregs. These Tg values are relatively close, in alignment with differential scanning calorimetry results, and suggest effective integration of the vitrimer into all prepreg states, contributing to enhanced crosslinking. Furthermore, the Tg values lie between those of the neat DGEBA–DETDA and *p*VAPI–DETDA vitrimer single plies, reinforcing successful vitrimer integration.

Notably, the Tg of the laminate from partially cured prepregs was the highest among the three, implying that vitrimers can significantly improve the performance and usability of out-of-date prepregs with residual reactivity. Conversely, the lowest Tg was observed in the laminate from fully cured prepregs, which is consistent with their reduced number of available functional groups for vitrimer bonding, thereby limiting network rejuvenation. These observations highlight the influence of the initial cure state of the prepreg on the ability of the vitrimer to bond and rejuvenate the out-of-date prepreg. This trend is consistent with the storage modulus results. The storage moduli of laminates from uncured and partially cured prepregs were comparable, while the laminate from fully cured prepregs exhibited a lower modulus. Similarly, crosslink density followed the same pattern with the highest crosslink density observed was in the laminate from uncured prepregs, followed by that from partially cured prepregs, and with the lowest in the fully cured group. The comparable storage modulus and crosslinking density between the uncured and partially cured systems indicate that the presence of available reactive groups is critical for vitrimer integration. Moreover, this shows that a vitrimer single

ply is effective in restoring the mechanical properties and thermal properties of out-of-date prepregs without significant performance loss.

The effect of the prepreg cure state on the thermal stability and degradation behavior of resulting laminates was assessed with thermogravimetric analysis (TGA) under both non-oxidative and oxidative conditions, as illustrated in Figure 6. All laminates, prepared by alternating layers of fully cured imine-epoxy vitrimer single plies and DGEBA-DETDA prepregs in uncured, partially cured, or fully cured states, exhibit unimodal degradation within the range of 350–450°C. This degradation is primarily attributed to the thermolytic cleavage of C–N and C–O bonds. The onset degradation temperatures were measured to be 351°C, 353°C, and 359°C for laminates containing uncured, partially cured, and fully cured prepregs, respectively. A similar trend is observed in the maximum degradation temperatures, i.e., 375°C, 378°C, and 387°C for laminates from uncured, partially cured, and fully cured prepregs, respectively. The narrow range of these values suggests that the initial cure state of the prepregs has only a minor influence on the thermal stability and degradation behavior of the resulting composites. These properties are predominantly dictated by the chemical composition and molecular structure. Since all composites were fabricated from the same epoxy and hardener systems in fixed ratios, the observed thermal behaviors are consistent. Nonetheless, the observed differences align with the curing state, where a higher initial degree of cure correlates with slightly elevated onset and peak degradation temperatures. Laminates incorporating fully cured prepregs demonstrated the highest thermal stability, followed by those with partially cured and uncured prepregs. These elevated degradation temperatures which are significantly above typical service conditions indicate excellent thermal stability, affirming the suitability of these materials for high-performance structural applications. Notably, the degradation temperatures of the composites are substantially higher than those of the pure vitrimers, suggesting that interlayering with conventional high-performance thermosets can enhance the thermal stability of vitrimer-based systems. In terms of char yield, all laminates show values around 70%, indicating a resin content of approximately 30%. This consistency confirms that comparisons reflect the effect of cure state rather than differences in resin loading. In conclusion, the cure state of the out-of-date prepregs has only a minor impact on the thermal degradation behavior of the composites under non-oxidative environments. Even in laminates composed of fully cured prepregs and vitrimer single plies, degradation temperatures remain around 380 °C, reinforcing their potential for high-performance applications.

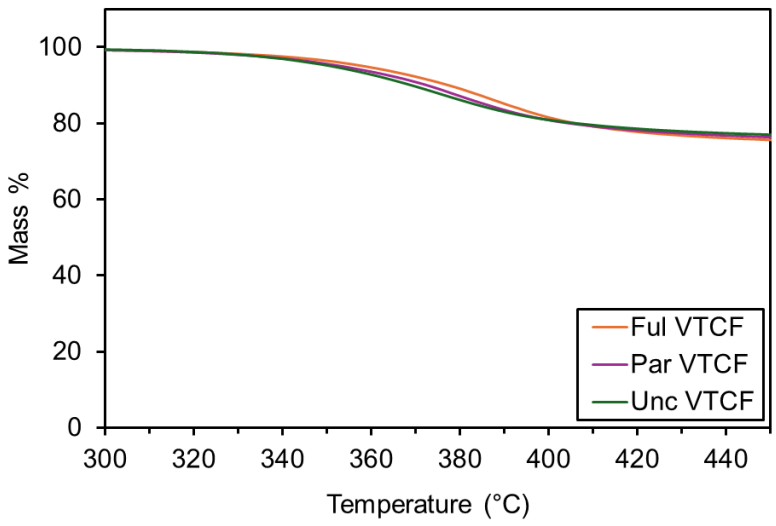

Figure 6: TGA thermograms of laminates from alternating layers of the fully cured vitrimer single plies and thermoset prepregs of different initial cure states under nitrogen atmosphere.

Under oxidative conditions as shown in Figure 4, the thermograms of the laminates composed of alternating layers of fully cured imine-epoxy vitrimer single plies and uncured prepregs display an initial unimodal degradation between 350–450°C, primarily resulting from the thermolytic cleavage of

C–N and C–O bonds just like under non-oxidative conditions. In contrast, laminates incorporating partially or fully cured prepregs exhibit bimodal degradation within the 300–450°C range. This bimodal behavior suggests that oxidative conditions amplify the influence of voids and interfacial adhesion differences introduced during laminate fabrication. The presence of partially or fully cured prepregs likely leads to poorer adhesion, increased void formation, or both. The onset degradation temperatures are 353°C, 354°C, and 349°C for laminates containing uncured, partially cured, and fully cured prepregs, respectively. Maximum degradation temperatures are 370°C, 375°C, and 385°C for laminates containing uncured, partially cured, and fully cured prepregs, respectively. While the overall trends are consistent with those observed under non-oxidative conditions, the laminate derived from fully cured prepregs displays the lowest onset degradation temperature. This indicates that, under oxidative conditions, the influence of defects such as poor interfacial adhesion and voids is more pronounced. Nevertheless, the difference in onset degradation temperatures compared to laminates prepared from uncured and partially cured prepregs remains relatively minor. A secondary degradation peak appears around 550°C in all samples, corresponding to the oxidative decomposition of residues formed by the epoxy networks which is not observed under non-oxidative conditions. To estimate resin content, the carrier gas was switched from air to nitrogen at 600°C to prevent oxidation of the carbon fiber. All laminates exhibited char yields near 70%, indicating a consistent resin content of approximately 30% and confirming that thermal behavior differences arise from prepreg cure state rather than formulation differences. In summary, the cure state of aged prepregs has only a minor effect on the thermal degradation behavior and stability of the laminates under both oxidative and inert conditions. Even laminates composed of fully cured prepregs and vitrimer plies degrade at high temperatures, 370–385°C, reinforcing their potential for high-performance structural applications.

3.4 Mechanical Properties of Laminates

The mechanical performance of composites fabricated from alternating layers of imine-epoxy vitrimer single plies and DGEBA-DETDA prepregs that were initially uncured, partially cured, or fully cured were evaluated via three-point bending tests, as illustrated in Figure 7. All laminates exhibited brittle failure, as indicated by the abrupt fracture observed in the stress–strain curves.

The flexural moduli for laminates fabricated from uncured, partially cured, and fully cured prepregs were 105 GPa, 105 GPa, and 98 GPa, respectively. These values are similar in value, suggesting that the modulus is predominantly dictated by the carbon fiber reinforcement, given its significantly higher stiffness relative to the matrix materials. Both the vitrimer and thermoset matrices are inherently stiff materials, which also contributes to the consistently high modulus values. The identical moduli of the laminates from uncured and partially cured prepregs, and their slightly higher values compared to those from fully cured prepregs, indicate that the vitrimer is highly effective in restoring or maintaining mechanical performance across varying cure states. When functional groups are available, as in the uncured and partially cured states, the vitrimer can form covalent bonds across the interface through transimination with unreacted amine groups, preserving interfacial integrity and mechanical performance. The slightly lower modulus observed in the laminate from fully cured prepregs suggests some reduction in adhesion efficiency due to limited availability of functional groups; however, the value remains high, implying that good bonding was still achieved through interfacial chain diffusion and entanglement by the vitrimer. Interlaminar adhesion plays a critical role in the mechanical performance of fiber-reinforced composites. Strong bonding between adjacent plies enables efficient stress transfer and uniform load distribution during bending. In contrast, poor interfacial adhesion can result in stress concentration at ply interfaces, leading to delamination, premature cracking, and failure under flexural loads. Insufficient bonding compromises load transfer, causing reductions in both flexural strength and stiffness.

The flexural strengths of the laminates from uncured, partially cured, and fully cured prepregs were 1.3 GPa, 1.1 GPa, and 0.7 GPa, respectively. These results confirm that the vitrimer was able to bond effectively across all prepreg conditions, including the fully cured state. The comparable strengths between laminates from uncured and partially cured prepregs suggest that the vitrimer successfully

underwent transimination reactions with unreacted amine groups at the interface, promoting strong interfacial bonding. The reduced strength observed in the laminate from fully cured prepregs likely arises from limited chemical reactivity due to the scarcity of available functional groups. In this case, vitrimer adhesion may rely more heavily on physical chain diffusion and entanglement as well as secondary interactions across the interface. Despite this limitation, a strength of 0.7 GPa was achieved, indicating that the vitrimer can still form mechanically robust interfaces with fully cured thermosets. Moreover, the presence of voids can further compromise mechanical performance by serving as stress concentrators, reducing the effective load-bearing volume of the composite. Voids typically arise during fabrication due to limited resin flow, particularly when bonding to fully cured prepregs. These defects reduce flexural strength and stiffness and contribute to early crack initiation and propagation during loading. Hence, the effects of differences in initial cure states of the prepregs resulting in differences in adhesion efficiency and void formation likelihood are more pronounced in the measured values of the flexural strength compared to the flexural modulus.

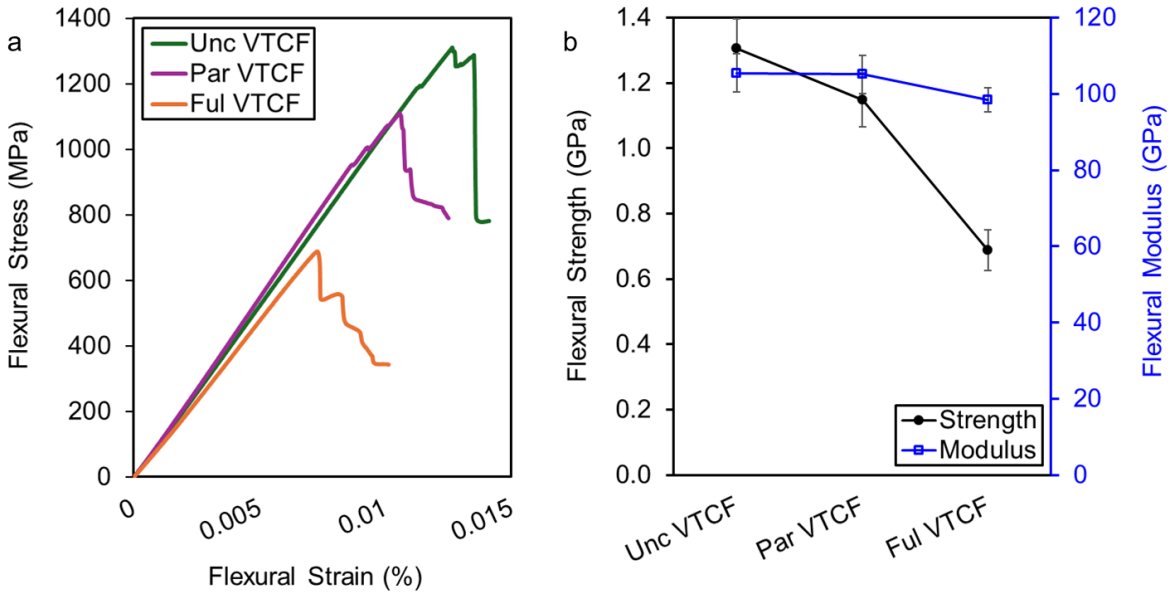

Figure 7: (a) Representative flexural stress-strain curves, (b) flexural strength and modulus of laminates from alternating layers of the fully cured vitrimer single plies and thermoset prepregs of different initial cure states.

Importantly, the mechanical performance of the laminate fabricated from partially cured prepregs is nearly equivalent to that from fresh uncured prepregs. This finding underscores the capacity of vitrimers to rejuvenate prepregs that have undergone partial cure and become boardy. It highlights the potential of imine-based vitrimers in restoring and reprocessing out-of-date prepregs for high-performance structural applications. Additionally, the initial cure state of the prepreg critically influences the bonding efficacy of the vitrimer and the extent of void formation, both of which significantly impact the resulting mechanical properties. For high-performance carbon fiber composites, optimizing interlaminar adhesion and minimizing void content are essential to maximizing flexural strength, stiffness, and toughness. Weak bonding or high void density can severely degrade performance, underscoring the importance of interfacial engineering when integrating vitrimer systems with thermoset prepregs.

3.5 Microscopy of Laminates

To evaluate the effect of initial cure states on the consolidation of the layers, optical images were obtained. Microscopy shows good consolidation in all samples. However, voids are present. The number of voids also increased as the initial cure state was more towards full curing. This could also

be the reason for the lower mechanical properties observed. But adhesion between the vitrimer and thermoset prepregs can be seen from optical images even if the prepreg was initially fully cured. This indicates that vitrimers can adhere to thermosets at different initial stages of cure. They are able to diffuse and entangle across the interface aside from covalent interactions with unreacted groups at the surface.

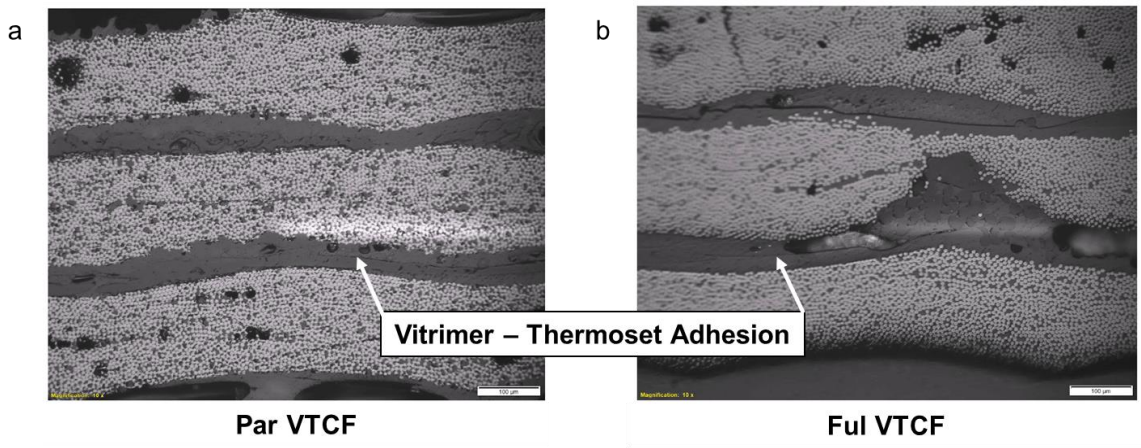

Figure 8: Optical images of cross-sections of the carbon fibre composites fabricated from alternating layers of the fully cured vitrimer single plies and (a) partially cured or (b) fully cured thermoset prepregs.

4 CONCLUSIONS

In this study, we leveraged the inherent weldability of fully cured imine-epoxy vitrimers and assessed their effectiveness in rejuvenating improperly cured or out-of-date thermoset prepregs. Traditional thermoset prepregs require refrigerated storage and transport, making logistics complex and increasing material waste due to spoilage during power outages. To simulate these conditions, thermoset prepregs from diglycidyl ether of bisphenol A, a commercially available resin, were pre-cured at varying temperatures to represent different degrees of initial cure, then interleaved them with fully cured vitrimer carbon fiber single plies. The resulting composites were evaluated for their thermal and mechanical properties. The results demonstrate that the initial cure state of the thermoset prepregs plays a critical role in dictating the resulting laminate properties. Laminates made with partially cured prepregs, i.e., cured at 80°C, exhibited thermal and mechanical properties comparable to those made with freshly prepared prepregs. This indicates that the presence of residual reactive groups such as unreacted amines allows for transimination reactions at the interface, forming covalent bonds between the vitrimer and thermoset, and near-complete property recovery. In contrast, prepregs cured at 150°C, which are fully crosslinked and lack functional groups capable of undergoing transimination, resulted in laminates with reduced mechanical properties. In this case, bonding was limited to physical mechanisms such as interfacial chain diffusion and entanglement. Nevertheless, microscopy confirmed ply adhesion, and thermal properties remained comparable with those of laminates made from fresh or partially cured prepregs, indicating partial recovery and successful consolidation. These findings highlight the critical role of interfacial chemistry specifically the availability of dynamic covalent bonding sites in determining the efficiency of vitrimer-assisted rejuvenation. Fully cured vitrimers can still adhere to fully cured thermoset prepregs and provide property recovery to a notable extent, even in the absence of covalent bonding. This capability presents a promising strategy to extend the usability of out-of-date prepregs, reduce material waste, and alleviate the challenges associated with refrigerated transport in composites manufacturing.

ACKNOWLEDGEMENTS

We would like to acknowledge the support of the Australian Research Council (DP220100130 and IH210100023) and Australian Composites Manufacturing Cooperative Research Centre (ACM CRC) (CRCXXIIIA000003) for partial funding of this research.

REFERENCES

[1] R. Phiri, S.M. Rangappa, S. Siengchin, O.P. Oladijo and T. Ozbakkaloglu, Advances in lightweight composite structures and manufacturing technologies: A comprehensive review, *Heliyon*, **10**, 2024, e39661 (doi: 10.1016/j.heliyon.2024.e39661)

[2] J. Zhang, G. Lin, U. Vaidya and H. Wang, Past, present and future prospective of global carbon fibre composite developments and applications, *Composites Part B: Engineering*, **250**, 2023, 110463 (doi: 10.1016/j.compositesb.2022.110463).

[3] J. Meegan, Some of the challenges faced by the Composites Industry in its bid to become more sustainable, *RSC Sustainability*, **1**, 2023, pp. 1737-1742 (doi: 10.1039/D3SU00200D).

[4] G. Nilakantan and S. Nutt, Reuse and upcycling of thermoset prepreg scrap: Case study with out-of-clave carbon fiber/epoxy prepre, *Journal of Composite Materials*, **52**, 2018, pp. 341-360 (doi: 10.1177/0021998317707253).

[5] D.J. Kwon, J.Y. Choi, P.S. Shin, K.L. DeVries and J.M. Park, Improvement in mechanical properties of recycled GF prepreg with CNT reinforced composites using a spray coating method, *Advanced Composite Materials*, **25**, 2016, pp. 515–524 (doi: 10.1080/09243046.2016.1145876).

[6] I. Bianchi, A. Forcellese, M. Marconi, M. Simoncini, A. Vita and V. Castorani, Environmental impact assessment of zero waste approach for carbon fiber prepreg scraps, *Sustainable Materials and Technologies*, **29**, 2021, e00308 (doi: 10.1016/j.susmat.2021.e00308).

[7] A.B., Irez and H. Yakar, Transformation of waste carbon fiber prepreg into sustainable composites: Application in the automotive industry components, *Polymer Composites*, **45**, 2024, pp. 9471-9486 (doi: 10.1002/pc.28421).

[8] E., Morici and N.T. Dintcheva, Recycling of Thermoset Materials and Thermoset-Based Composites: Challenge and Opportunity, *Polymers,* **14**, 2022, 4153 (doi: 10.3390/polym14194153).

[9] D. Budelmann, D. Gibhardt and B. Fiedler, A review on aging effects of thermoset prepregs, *Composites Part B: Engineering*, **303**, 2025, 112611 (doi:10.1016/j.compositesb.2025.112611).

[10] J. Masten-Davies, L.Q.T. Tran, J. Zhang and R.J. Varley, Investigating the welding and healing of epoxy anhydride vitrimer carbon fibre composites, *Composites Part A: Applied Science and Manufacturing*, **196**, 2025, 108956 (doi: 10.1016/j.compositesa.2025.108956).

[11] D. Montarnal, M. Capelot, F. Tournilhac and L. Leibler, Silica-like malleable materials from permanent organic networks, *Science*, **334**, 2011, pp. 965-968 (doi: 10.1126/science.1212648).

[12] M. Capelot, M. M. Unterlass, F. Tournilhac and L. Leibler, Catalytic Control of the Vitrimer Glass Transition, *ACS Macro Letters*, **1**, 2012, pp. 789-792 (doi: 10.1021/mz300239f).

[13] S. Zhao and M. M. Abu-Omar, Recyclable and Malleable Epoxy Thermoset Bearing Aromatic Imine Bonds, *Macromolecules*, **51**, 2018, pp. 9816-9824 (doi: 10.1021/acs.macromol.8b01976).

ICCM24
24TH INTERNATIONAL CONFERENCE ON COMPOSITE MATERIALS
AUG 4-8, 2025 • BALTIMORE CONVENTION CENTER • BALTIMORE, MARYLAND

Cure Kinetics of a Transesterification-type Vitrimer derived from a Commercial Epoxy-Anhydride Thermoset

Joshua Ilse, Pascal Hubert

7th August 2025



McGill
Structures & Composite Materials Laboratory

CREPEC
Research Center for High Performance Polymer and Composite Systems

Surveying Circularity in the Composites Industry

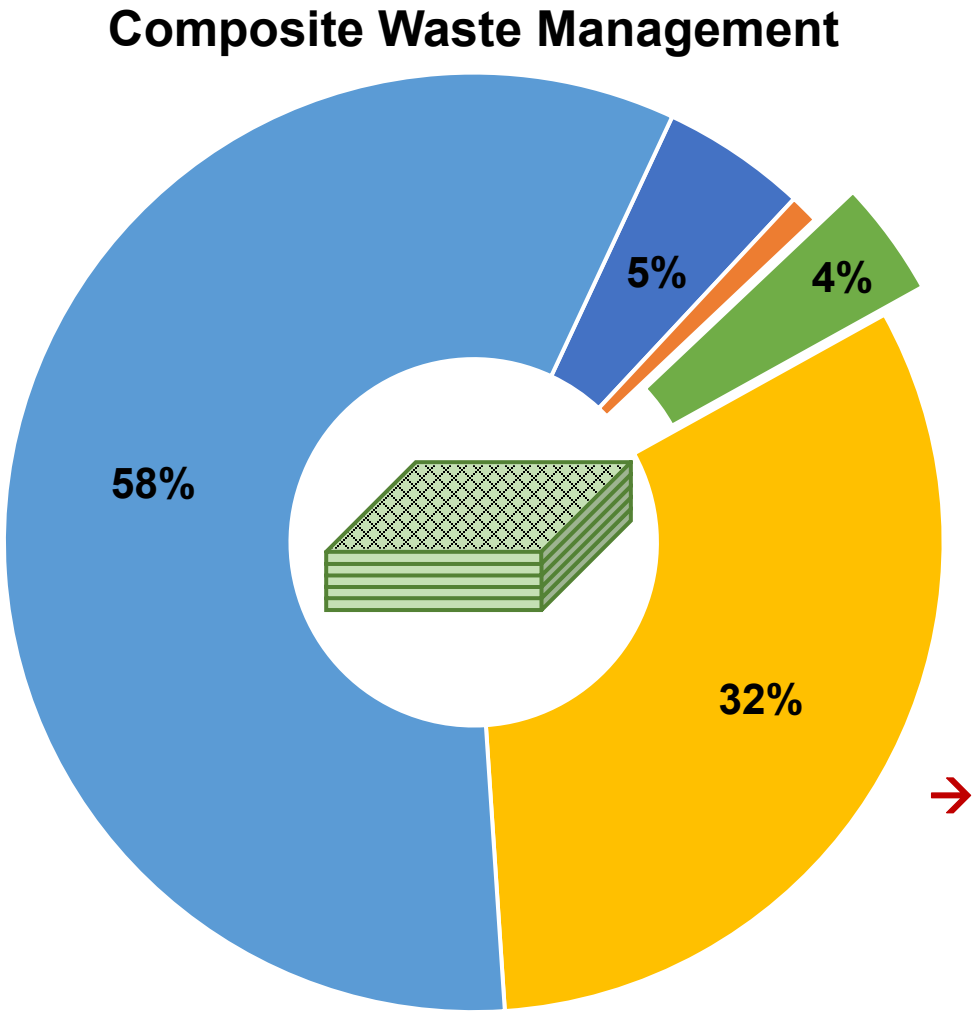

→ *Only **4%** of composites are recycled*

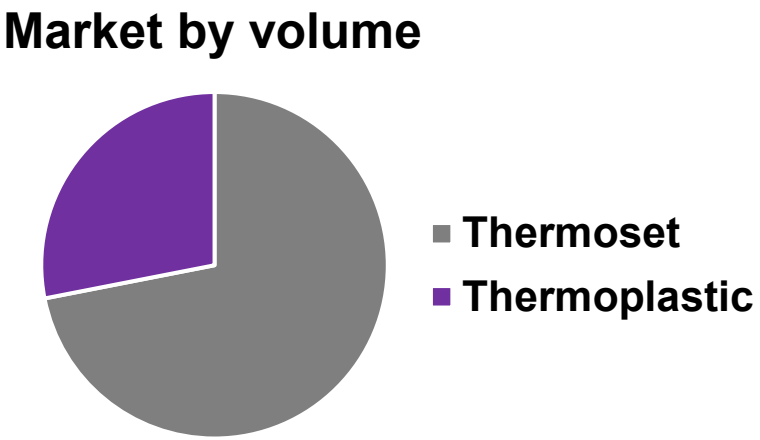

→ *How can we make future composites more recyclable?*

McGill
Structures & Composite Materials Laboratory

Data Source: *JEC Observer*

Surveying Circularity in the Composites Industry

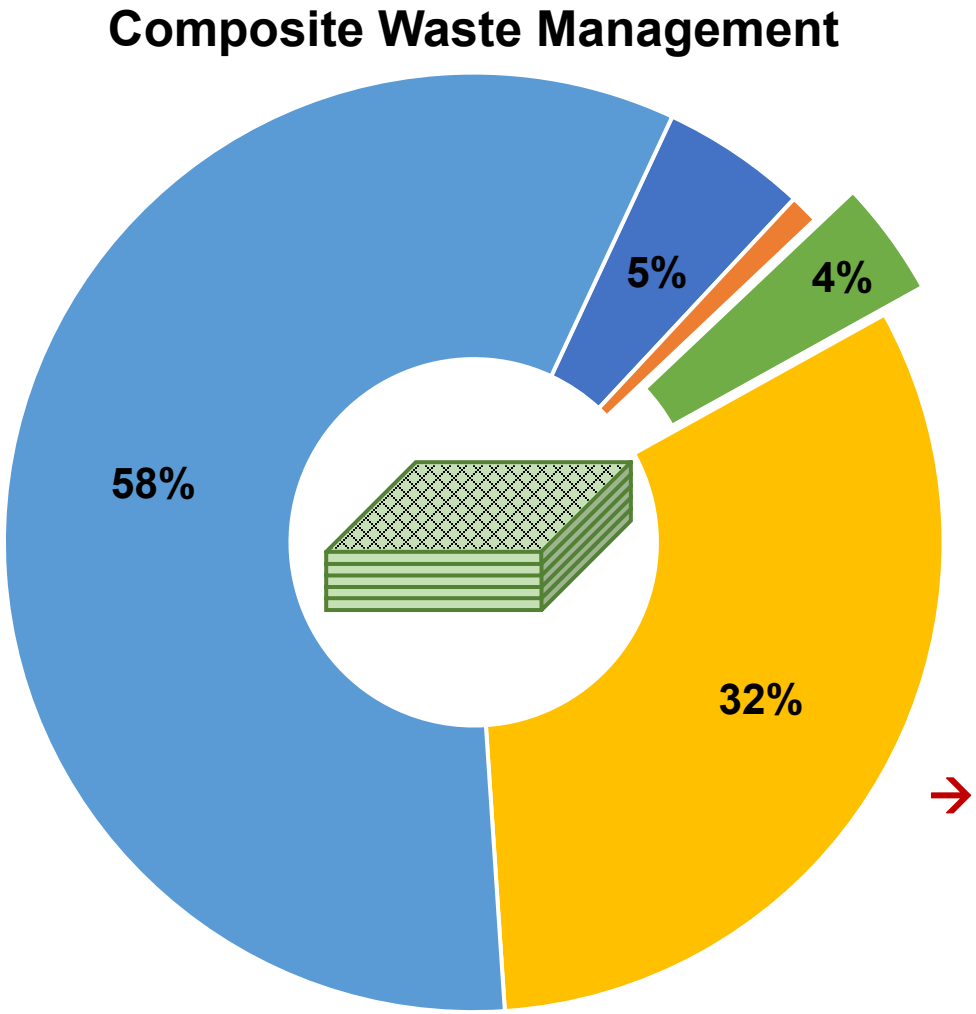

→ *Only **4%** of composites are recycled*

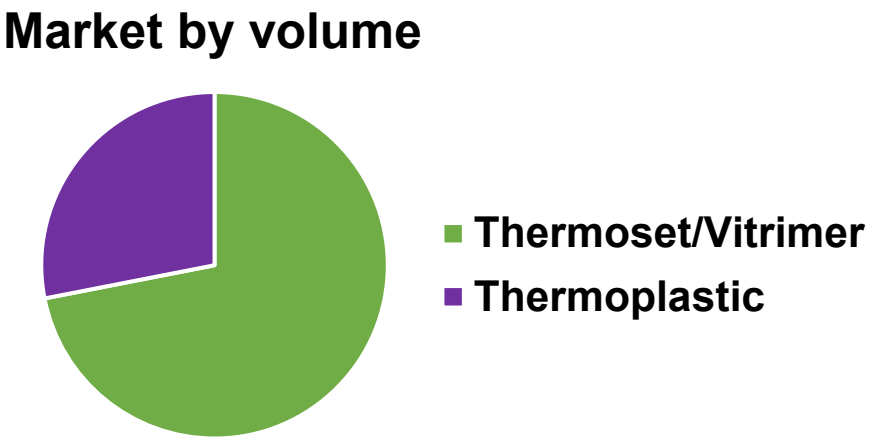

→ *How can we make future composites more recyclable?*

Vitrimers

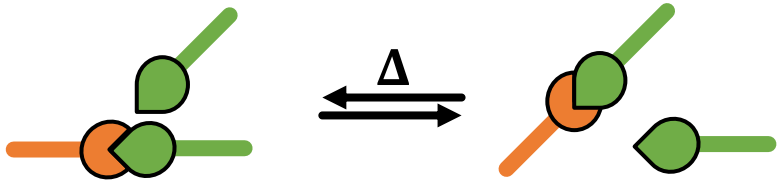

Data Source: *JEC Observer*

Methodology – Leverage Pre-Existing Materials & Processes

Table 1: Mix ratio (by weight).

	Resin (R)	Hardener (H)	Accelerator (A)	Vitrimer Catalyst (VC)
Thermoset	100	90	3	-
Vitrimer	100	45	3	14

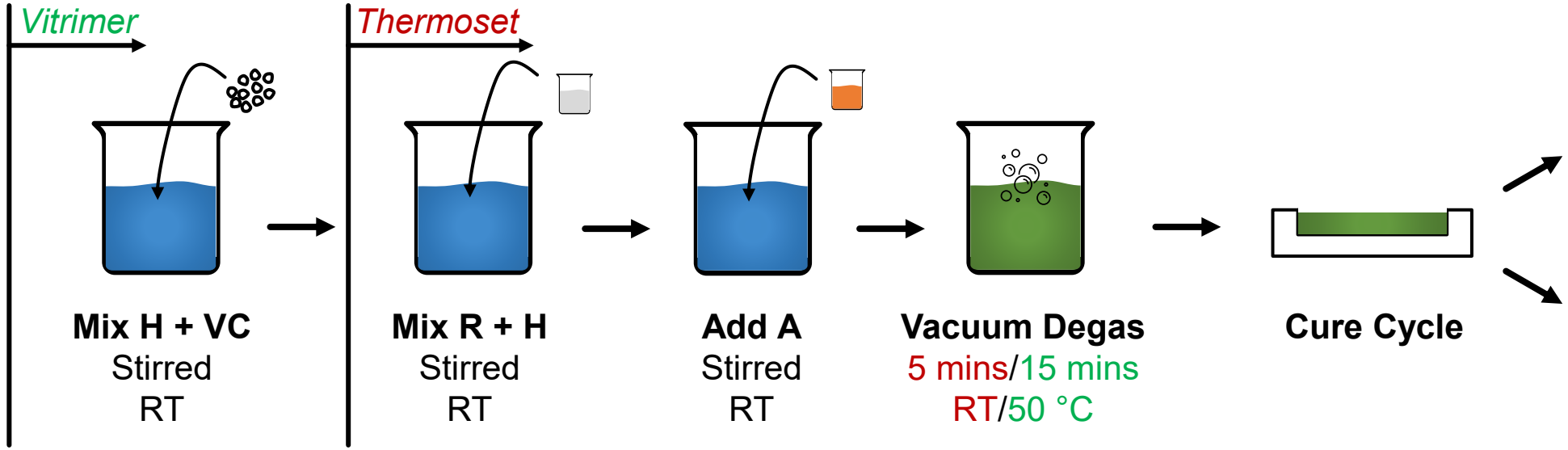



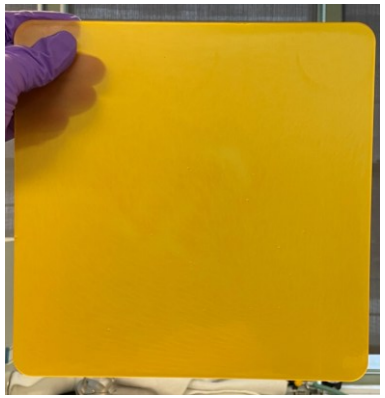

“Vitrimerization” of Commercial Thermoset

Objectives

Prior work: *is there vitrimer behaviour?*

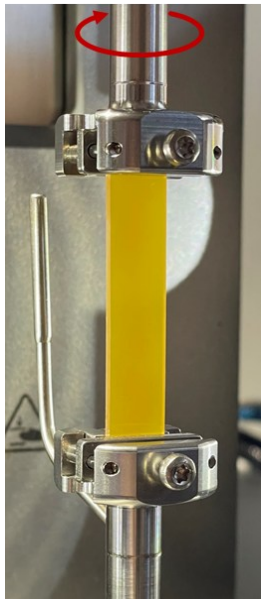



Cure Cycle
4 h @ 80 °C
+ 4 h @ 140 °C

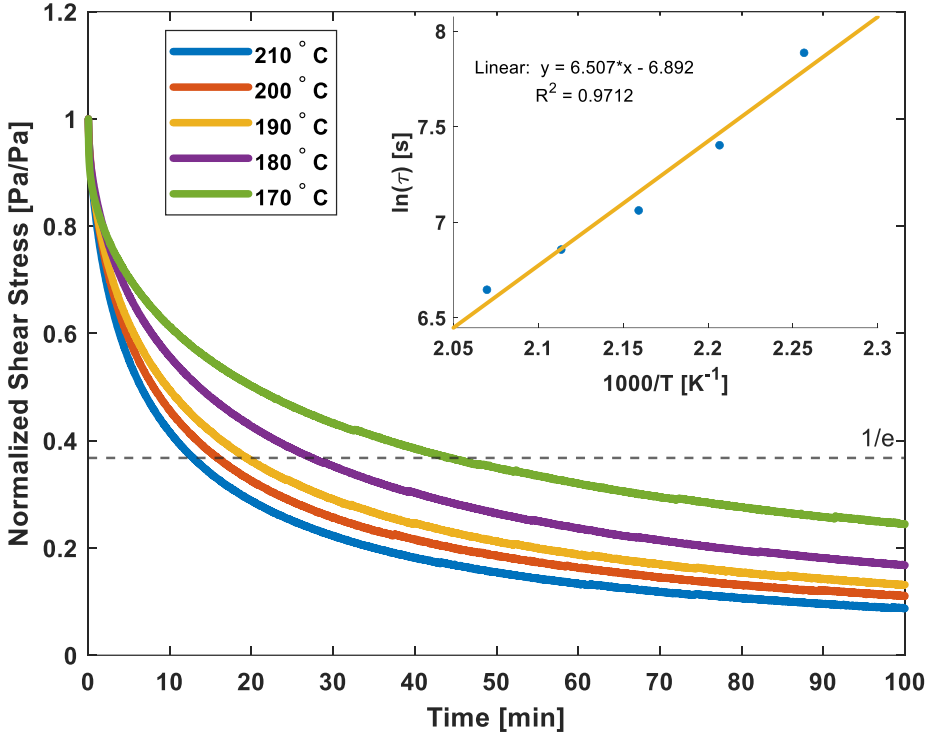

$$\tau(T) = \tau_0 \exp\left(\frac{E_a}{RT}\right)$$

Characteristic Relaxation Time

J.Ilse, P.Hubert. CANCOM2024.

This work: *how does cure behaviour change?*

- Differential Scanning Calorimetry (DSC)
  - Uncured resin (Thermoset/Vitrimer)
  - Isothermals: 80, 90, 100, 110, 120 °C
- Phenomenological model-fitting approach to cure kinetics:

$$\frac{d\alpha}{dt} = k(T)_i f(\alpha)_i$$

Reaction Rate | *Rate Constant* | *Reaction Model*

Results – Thermoset

Heat Flow vs. Time

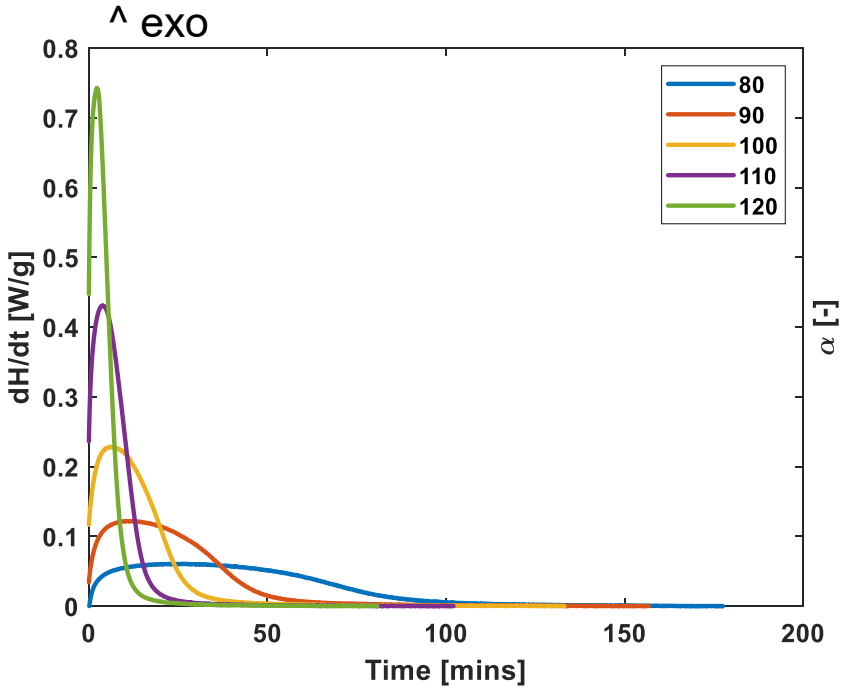

Conversion vs. Time

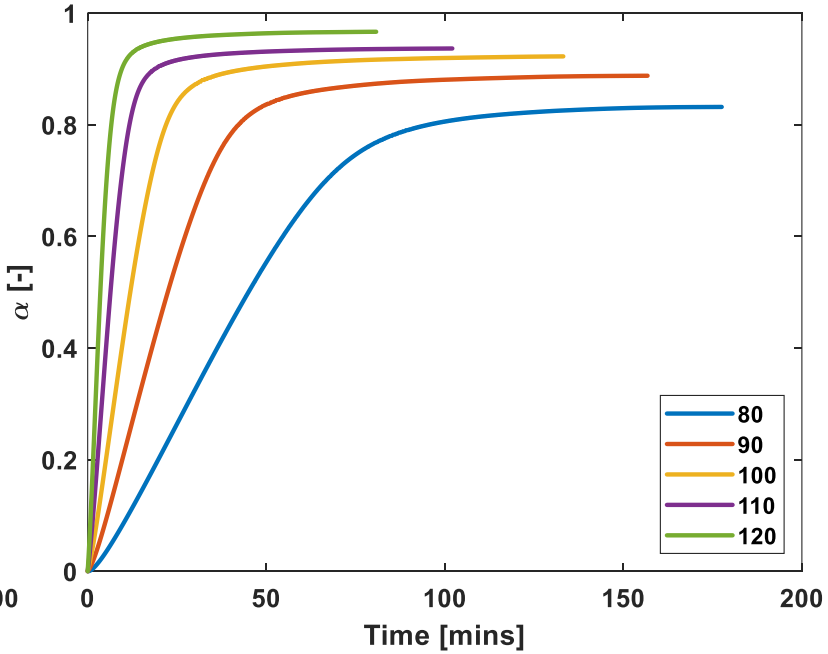

Reaction Rate vs. Conversion

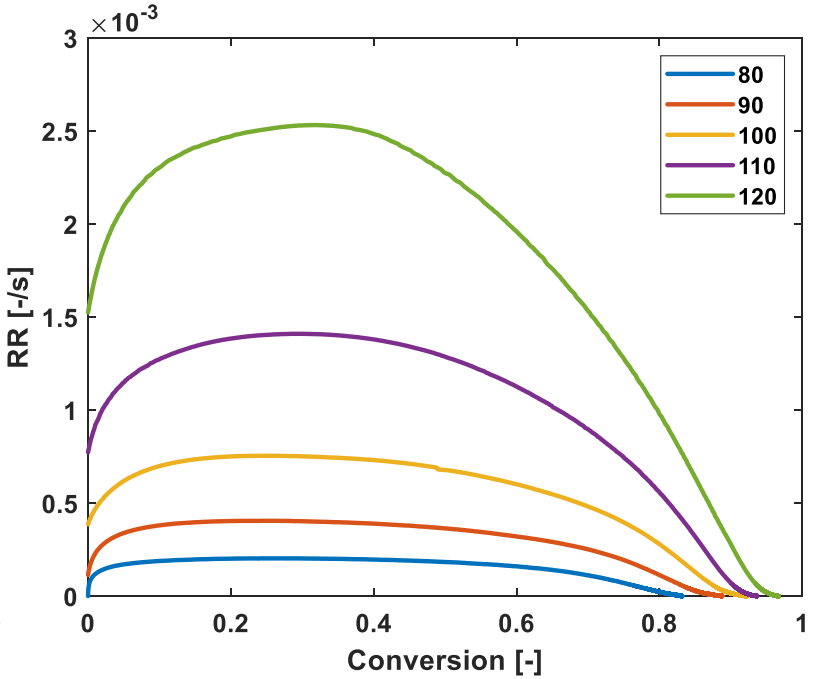

$$[1]\quad \Delta H_{tot} = \Delta H_{rxn} + \Delta H_{res}$$

ΔH_{tot}: *Total Heat of Reaction*
ΔH_{rxn}: *Heat of Reaction*
ΔH_{res}: *Residual Heat of Reaction*

$$[2]\quad \alpha(t) = \frac{\int_0^t \frac{dH}{dt}}{\Delta H_{tot}} = \frac{\Delta H_t}{\Delta H_{tot}}$$

H_t: *Heat of Reaction at time t*

$$[3]\quad \frac{d\alpha}{dt} = \frac{dH/dt}{\Delta H_{Tot}}$$

Results – Thermoset

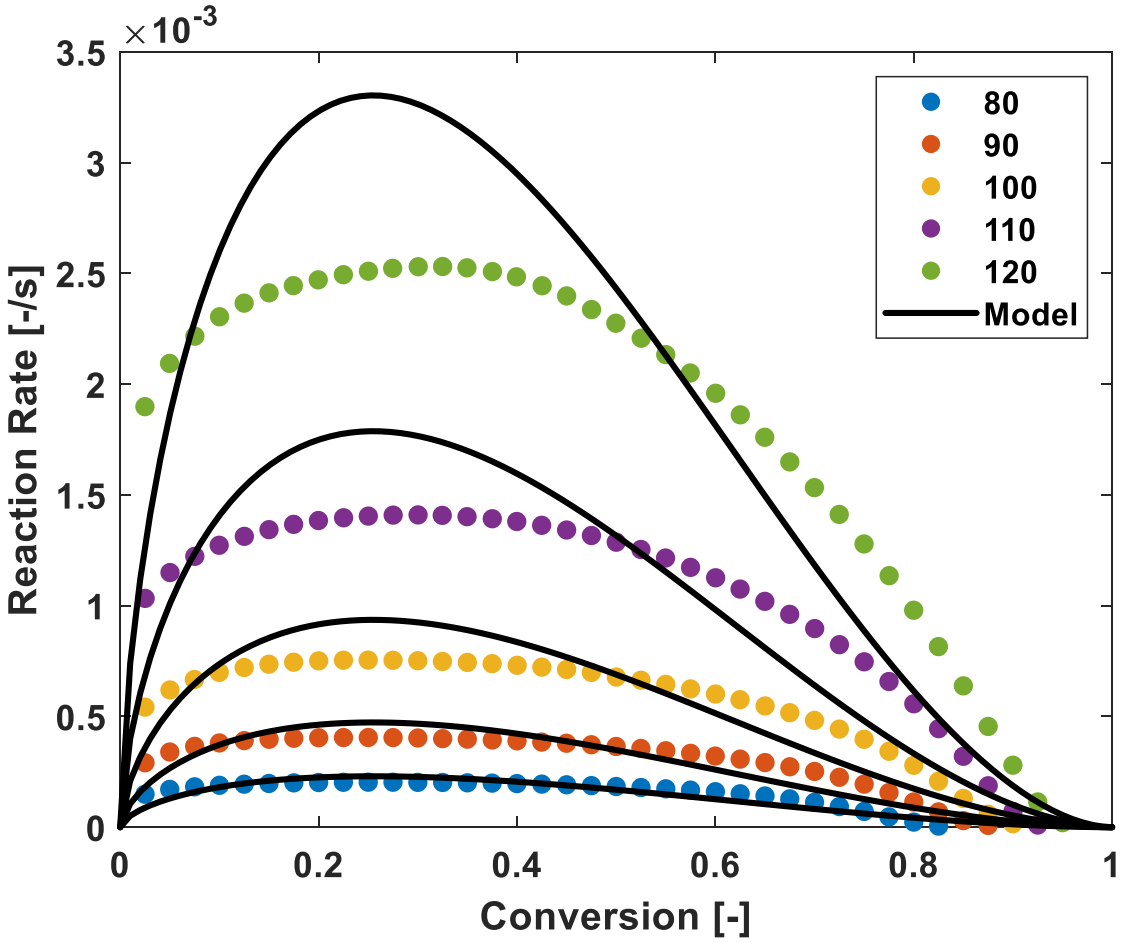

$$\frac{d\alpha}{dt} = k(T)f(\alpha)$$

Reaction Rate | *Rate Constant* | *Reaction Model*

→ Single-step reaction

Autocatalytic:

$$f(\alpha) = \alpha^m(1-\alpha)^n$$

Arrhenius:

$$k(T) = Aexp\left(-\frac{E_a}{RT}\right)$$

$$\frac{d\alpha}{dt} = Aexp\left(-\frac{E_a}{RT}\right)\alpha^m(1-\alpha)^n$$

→ 4 unknowns: A, E_a, m, n

$$lnA = 19.20\ [1/s]$$
$$E_a = 76.91\ [kJ/mol]$$
$$m = 0.6236\ [-]$$
$$n = 1.8208\ [-]$$

Results – Thermoset

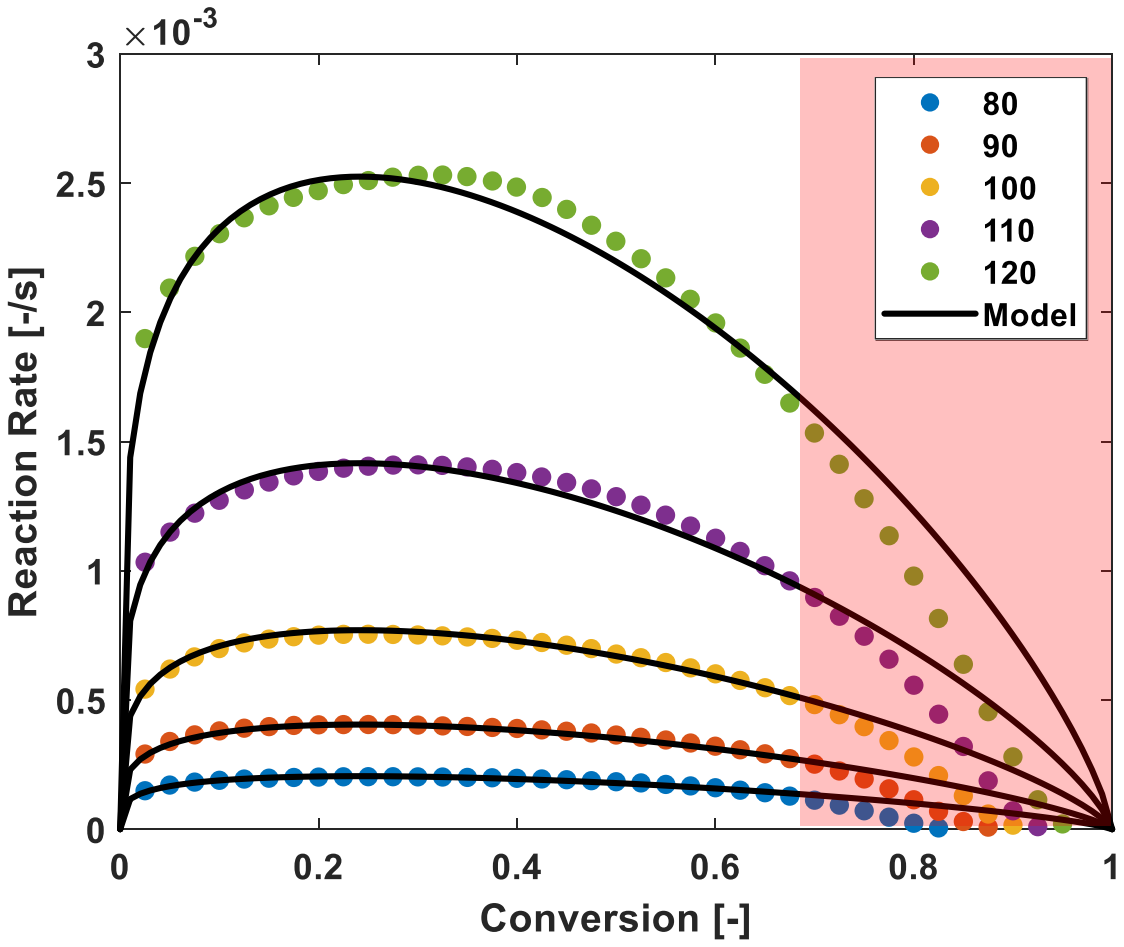

$$\frac{d\alpha}{dt} = k(T)f(\alpha)$$

Reaction Rate | *Rate Constant* | *Reaction Model*

→ Single-step reaction, 0 – 0.7 conversion

Autocatalytic:

$$f(\alpha) = \alpha^m(1-\alpha)^n$$

Arrhenius:

$$k(T) = Aexp\left(-\frac{E_a}{RT}\right)$$

$$\frac{d\alpha}{dt} = Aexp\left(-\frac{E_a}{RT}\right)\alpha^m(1-\alpha)^n$$

→ 4 unknowns: A, E_a, m, n

$$lnA = 16.73\ [1/s]$$
$$E_a = 72.43\ [kJ/mol]$$
$$m = 0.2406\ [-]$$
$$n = 0.7551\ [-]$$

Results – Vitrimer

Heat Flow vs. Time

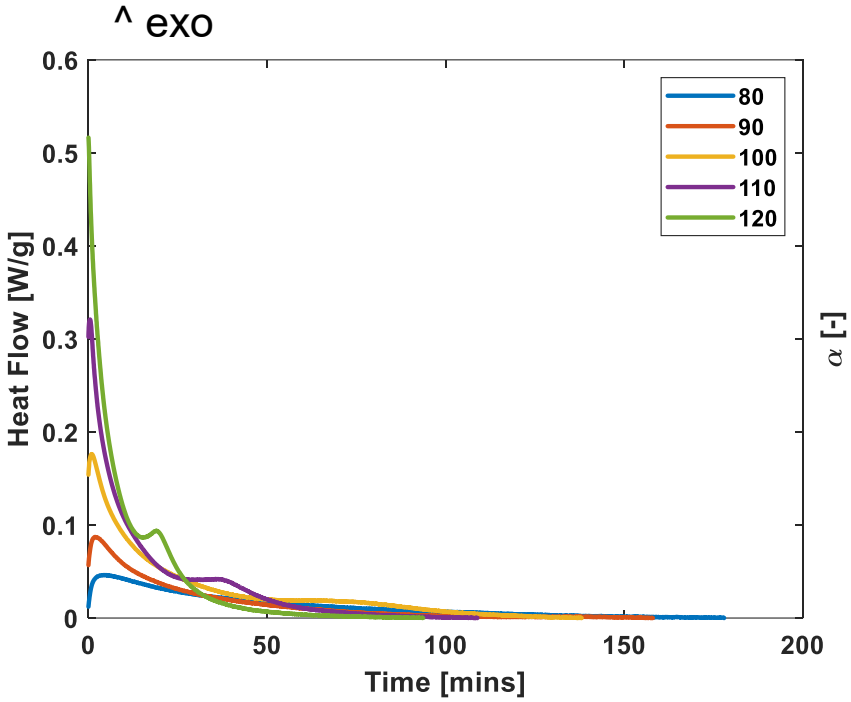

Conversion vs. Time

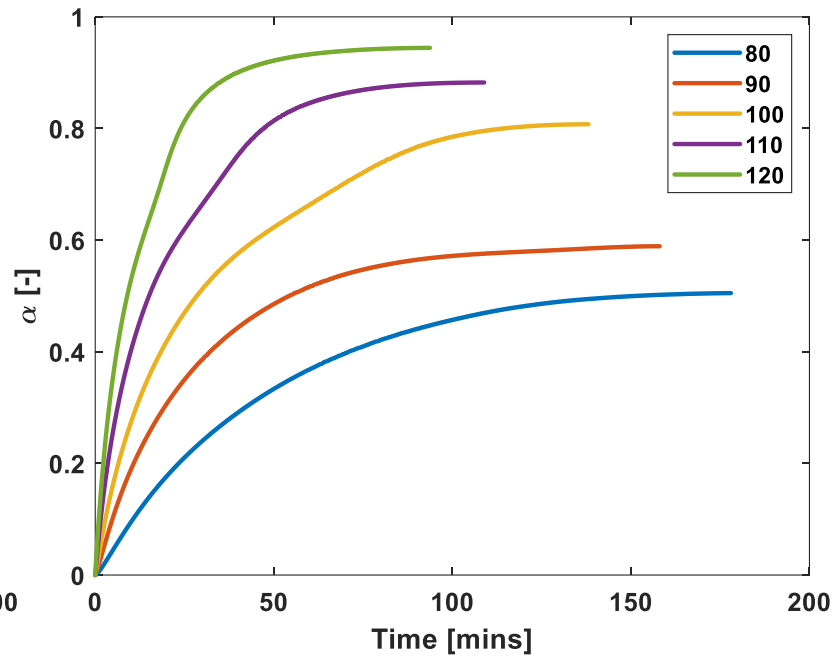

Reaction Rate vs. Conversion

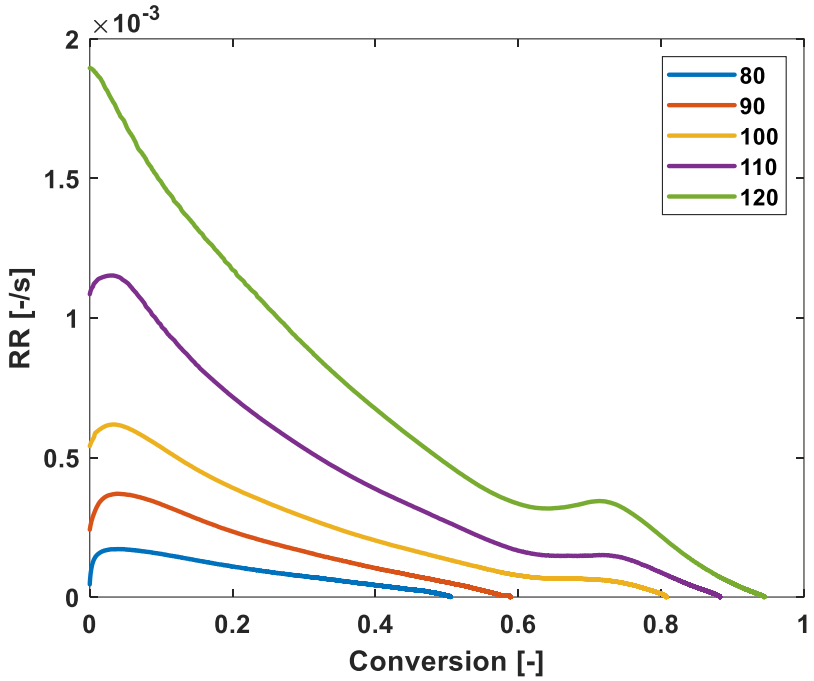

$$[1]\quad \Delta H_{tot} = \Delta H_{rxn} + \Delta H_{res}$$

ΔH_{tot}: *Total Heat of Reaction*
ΔH_{rxn}: *Heat of Reaction*
ΔH_{res}: *Residual Heat of Reaction*

$$[2]\quad \alpha(t) = \frac{\int_0^t \frac{dH}{dt}}{\Delta H_{tot}} = \frac{\Delta H_t}{\Delta H_{tot}}$$

H_t: *Heat of Reaction at time t*

$$[3]\quad \frac{d\alpha}{dt} = \frac{dH/dt}{\Delta H_{Tot}}$$

Results – Vitrimer

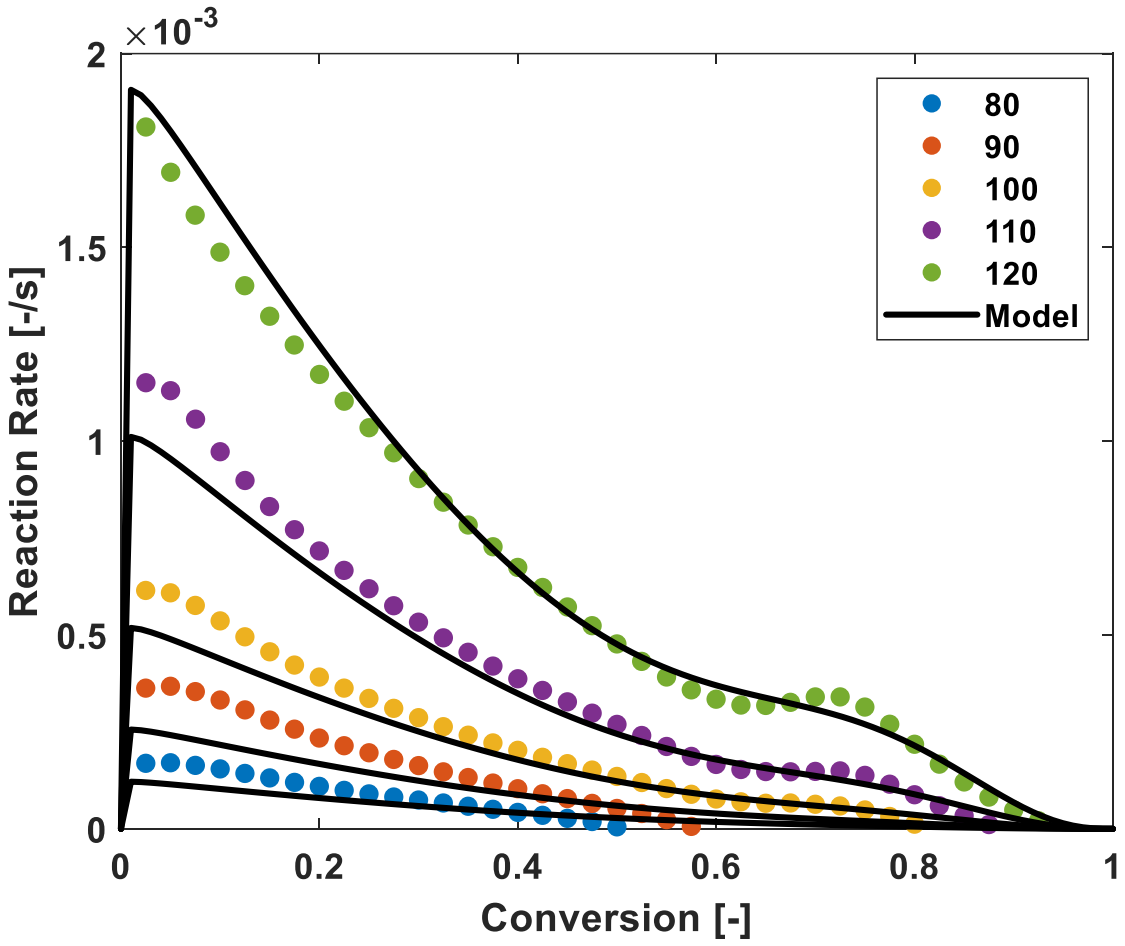

$$\frac{d\alpha}{dt} = k(T)_i f(\alpha)_i \qquad ; i = 2$$

Reaction Rate *Rate Constant* *Reaction Model*

Autocatalytic:

$$f(\alpha)_{1,2} = \alpha^m (1-\alpha)^n$$

Arrhenius:

$$k(T) = A exp\left(-\frac{E_a}{RT}\right)$$

$$\frac{d\alpha}{dt} = A_1 exp\left(-\frac{E_{a2}}{RT}\right) \alpha^{m_1}(1-\alpha)^{n_1} + A_2 exp\left(-\frac{E_{a2}}{RT}\right) \alpha^{m_2}(1-\alpha)^{n_2}$$

→ 8 unknowns: $A_1, E_{a1}, m_1, n_1, A_2, E_{a2}, m_2, n_2$

$lnA_1 = 18.17\ [1/s]$ $\quad lnA_2 = 34.92\ [1/s]$

$E_{a1} = 79.42\ [kJ/mol]$ $\quad E_{a2} = 121.5\ [kJ/mol]$

$m_1 = 0.02399\ [-]$ $\quad m_2 = 8.157\ [-]$

$n_1 = 2.33\ [-]$ $\quad n_2 = 2.883\ [-]$

Summary – Thermoset vs. Vitrimer 3D Model-Fit

Thermoset

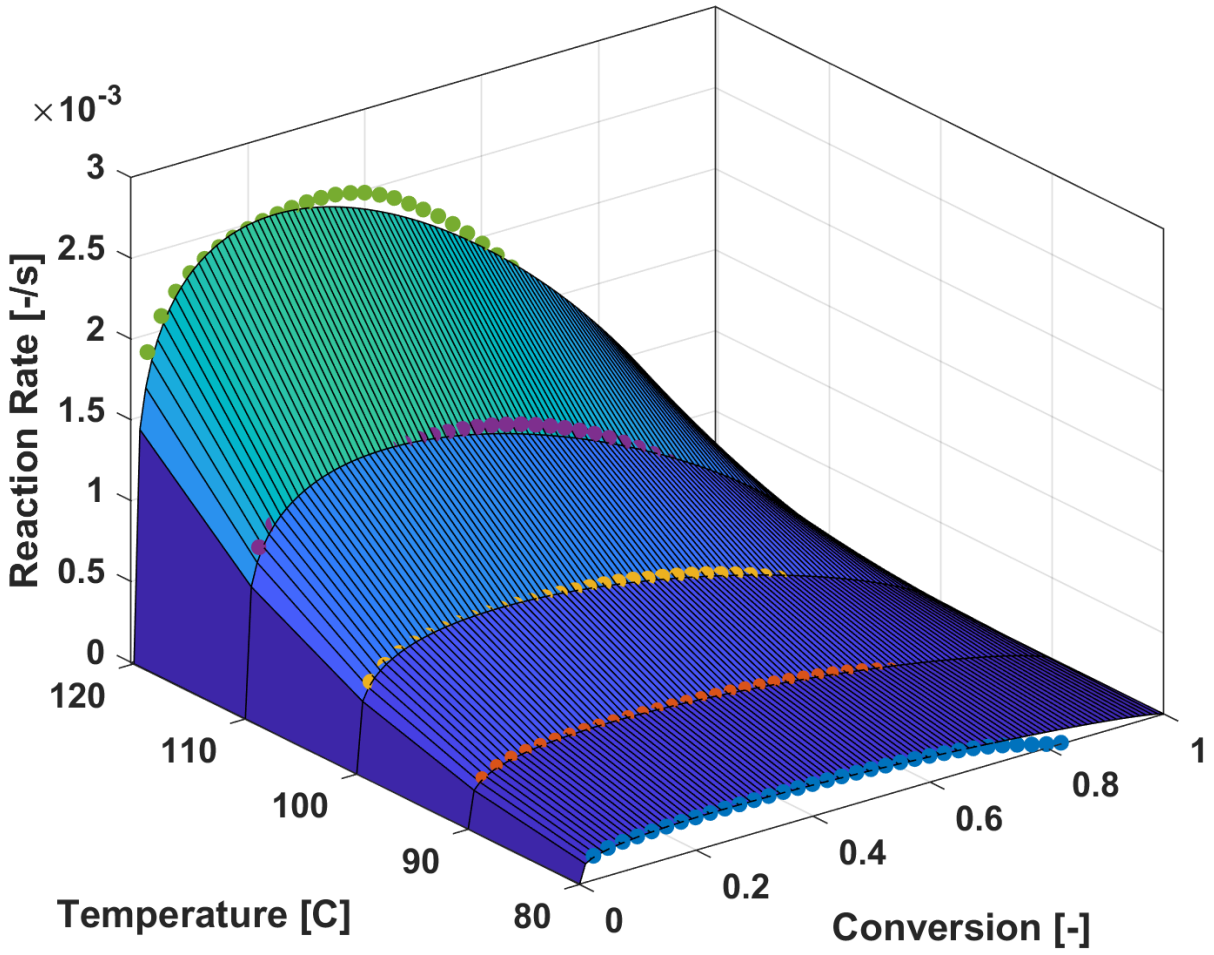

Vitrimer

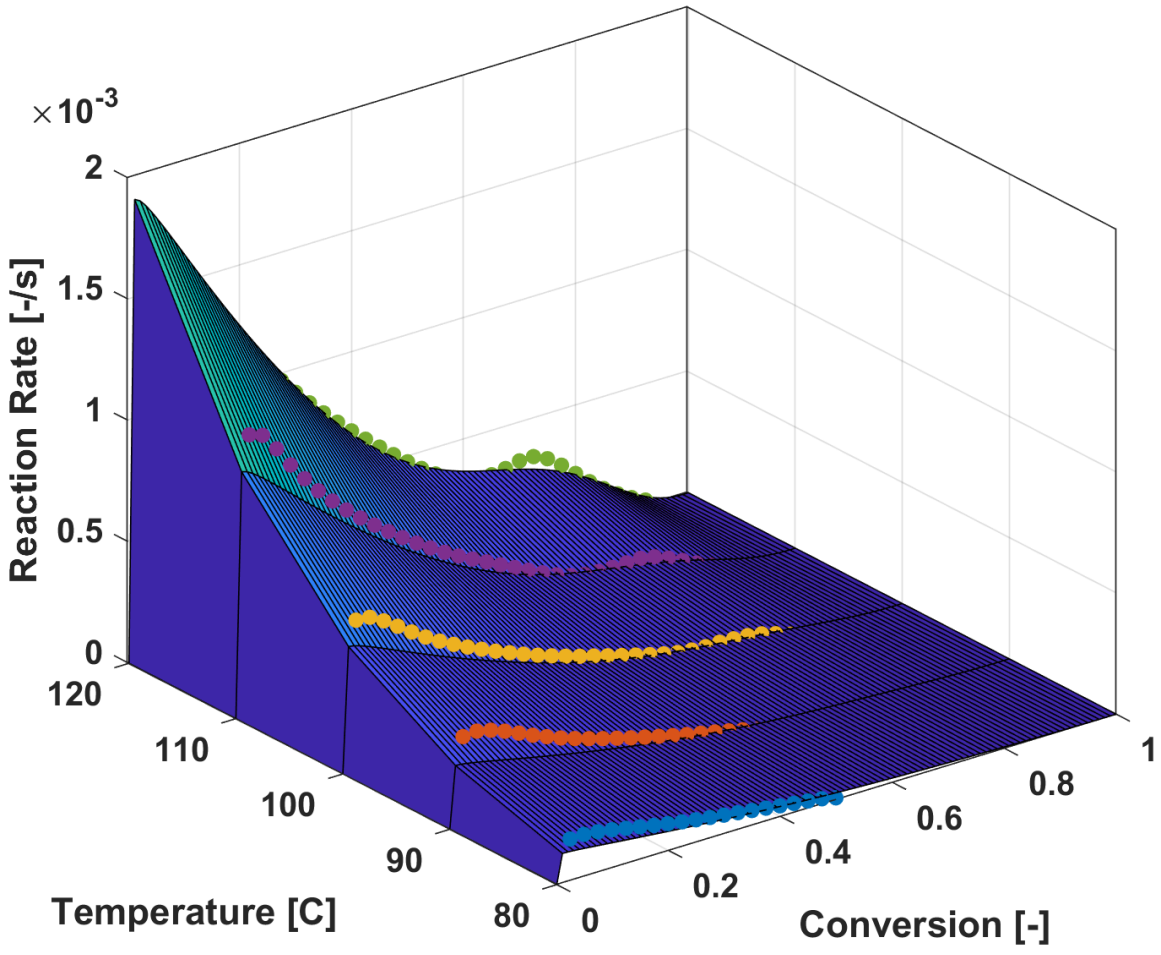

Acknowledgements

- Ms. Lucie Riffard (Lab Assistance)
- Huntsman (Materials)
- Vadasz (Fellowship)

CREPEC
Research Center for High Performance Polymer and Composite Systems

HUNTSMAN
Enriching lives through innovation

VADASZ SCHOLARS



Thank you

Questions?

Contact:

joshua.ilse@mail.mcgill.ca



ICCM24

24TH INTERNATIONAL CONFERENCE ON COMPOSITE MATERIALS

AUG 4-8, 2025 • BALTIMORE CONVENTION CENTER • BALTIMORE, MARYLAND

McGill

Structures & Composite Materials Laboratory

CREPEC

Research Center for High Performance Polymer and Composite Systems

ICCM24
AUGUST 4-8, 2025
BALTIMORE CONVENTION CENTER
BALTIMORE, MARYLAND, USA

No Technical Paper Submission for:

Simon Bickerton

ICCM24
AUGUST 4-8, 2025
BALTIMORE CONVENTION CENTER
BALTIMORE, MARYLAND, USA

No Technical Paper Submission for:

Stephen Tsai

LAMINATE HYBRIDIZATION USING HIGH MODULUS CARBON THIN PLIES FOR ENHANCED COMPRESSIVE PERFORMANCE

Joe Rifai

Wu, X., Pickard, L.R., Giuliano, A., & Wisnom, M.R.

Bristol Composites Institute, University of Bristol

Joe.Rifai@bristol.ac.uk

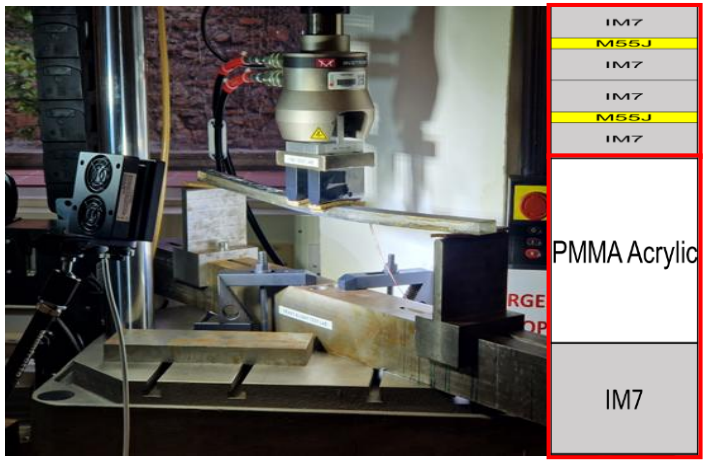

Next Generation Fibre-Reinforced Composites

IMPERIAL

The Composites Centre
for research, modelling, testing and training in advanced composites

University of BRISTOL
Bristol Composites Institute

UK Research and Innovation

Engineering and Physical Sciences Research Council

PRESENTATION OUTLINE

- Introduction
- Test methodology and hybrid laminate configurations.
- Experimental results of M55J in a carbon/carbon hybrid laminate.
- Fragmentation images of M55J fibres in an interrupted test.
- Experimental results of M55J in a glass/carbon hybrid laminate.
- Is the hybrid laminate failure affected as the thickness of M55J increases?
- Conclusion

IMPERIAL

Next COMP

University of BRISTOL
Bristol Composites Institute

NEXTCOMP

Aim: Develop a new generation of hierarchical composite materials to improve the compressive performance of fibre-reinforced composites.

Challenge: The longitudinal compressive strength of fibre-reinforced composites can be as low as half of their longitudinal tensile strength.

A collaboration between the University of Bristol and Imperial College London to address the challenges of longitudinal compression of composites.

Hierarchical problem

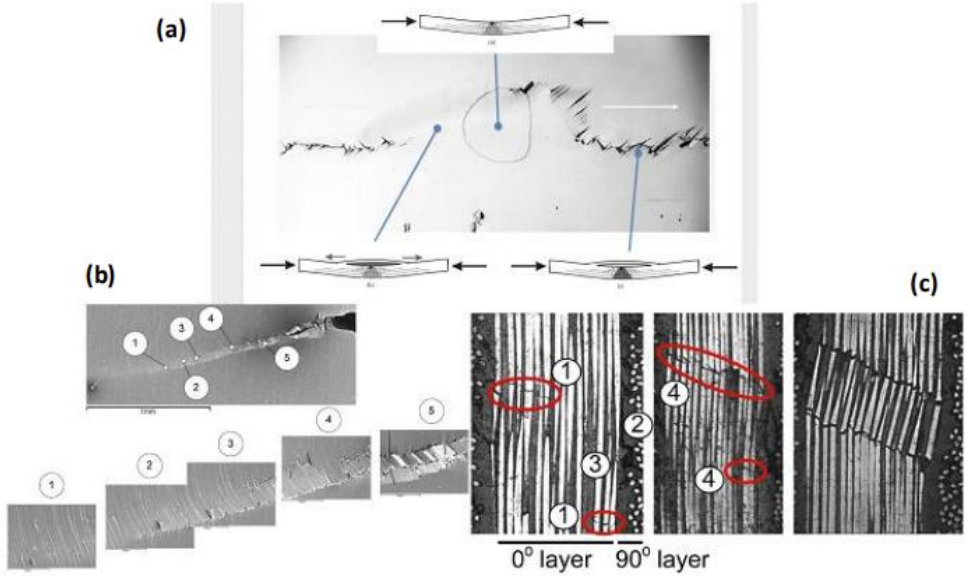

Modified from sources including; ST Pinho et al., On longitudinal compressive failure of carbon-fibre-reinforced polymer: from unidirectional to woven, and from virgin to recycled, *Philosophical Transitions of the Royal Society A*, Vol. 370, Issue 1965, 2012, 1871-1895; R Gutkin et al., On the transition from shear-driven fibre compressive failure to fibre kinking in notched CFRP laminates under longitudinal compression, *Composites Science and Technology*, Vol. 70, Issue 8, 2010, 1223-1231.

IMPERIAL

University of BRISTOL
Bristol Composites Institute

BACKGROUND

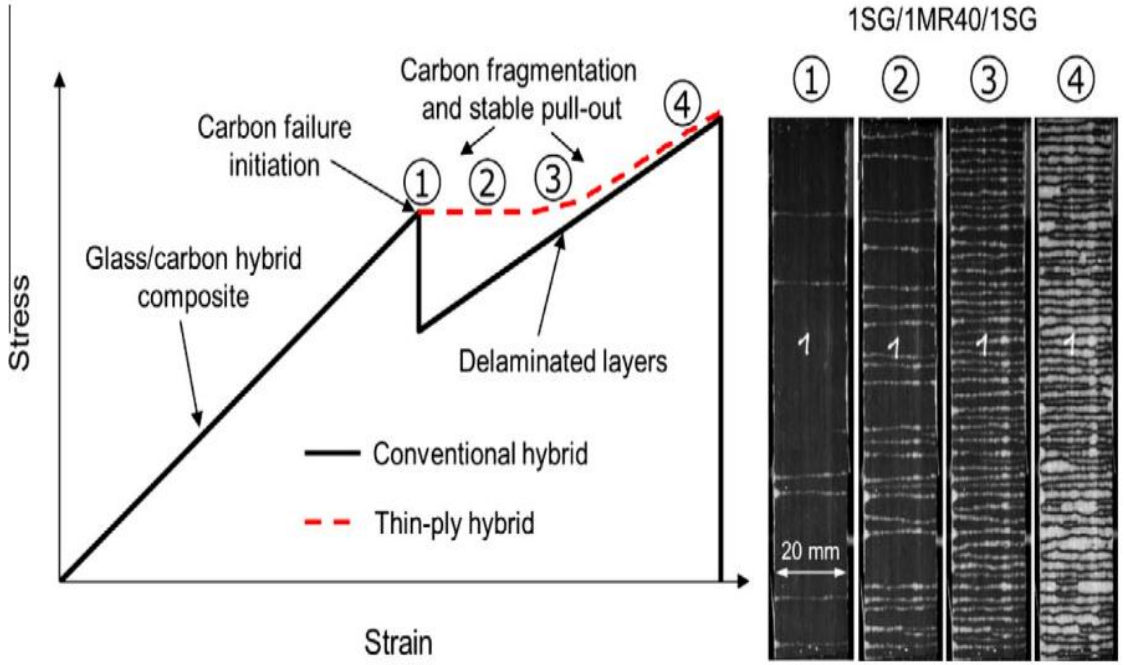

Tensile stress–strain response of conventional and thin-ply interlayer hybrid composites and typical appearance of thin-ply hybrid specimens at successive damage phases (dark areas show bonded, light areas show damaged glass/carbon interface through the translucent outer glass layer) [1].

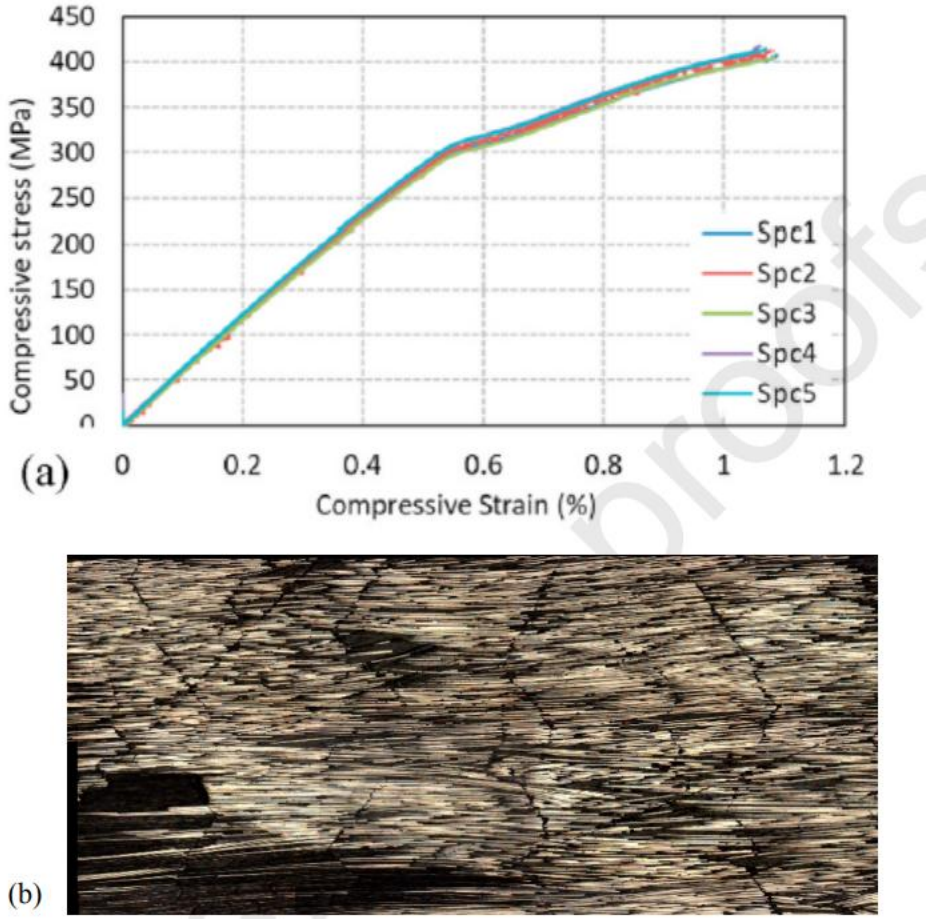

Compressive behaviour of $[\pm 27_7/0]S$ MR60/M55J carbon layup, a) Pseudo-ductile stress-strain response and b) compressive ply fragmentation in the central 0° plies [2].

HYBRID LAMINATES

Material	Ply thickness (mm)	E_{11} (GPa)	Compressive Strain	
IM7/epoxy	0.125	150	1.36%	[3]
M55J/epoxy	0.030	240	0.31%	[4]

- Observe if fragmentation of M55J occurs in a carbon/carbon hybrid laminate.
- Is the laminate failure affected as M55J thickness increases?

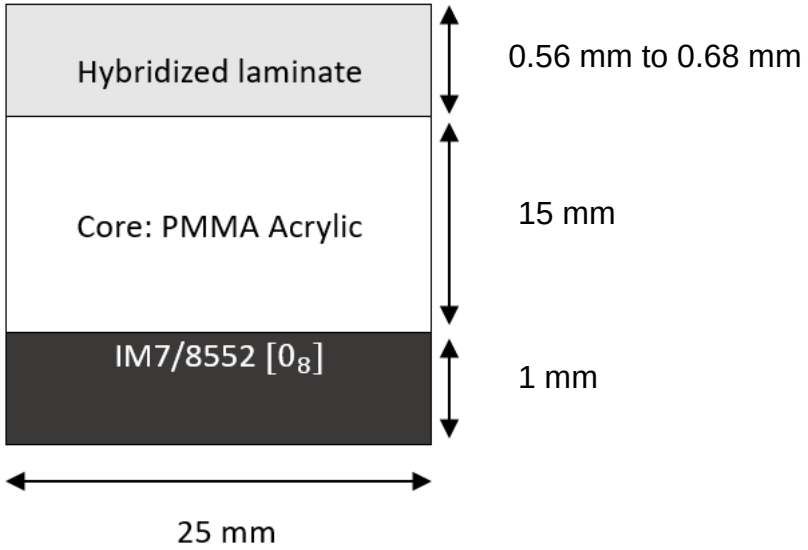

Cross-section view of the sandwich structure

Configuration 1 $E_{11} = 160\ GPa$ $t = 0.56\ mm$
IM7
M55J
IM7
IM7
M55J
IM7

Configuration 2 $E_{11} = 168\ GPa$ $t = 0.62\ mm$
IM7
M55J
M55J
IM7
IM7
M55J
M55J
IM7

Configuration 3 $E_{11} = 175\ GPa$ $t = 0.68\ mm$
IM7
M55J
M55J
M55J
IM7
IM7
M55J
M55J
M55J
IM7

IMPERIAL

Next COMP

University of BRISTOL
Bristol Composites Institute

TEST SET UP



- Instron 8872 Universal testing machine.
- Four-point bend test fixture.
- High speed camera recording at 50,000 fps.
- System 8000 data logger.
- AE sensors to detect fragmentation audially.

Note:
Support span of 550 mm.
Loading nose span of 60 mm (gauge section).
2 strain gauges attached on top and bottom skin.
2 AE sensors positioned in gauge section.

SINGLE PLY OF M55J

IM7
M55J
IM7
IM7
M55J
IM7

The maximum compressive strain of the hybrid laminate is 0.41% to 0.71%.

Intraply (fragmentation) failure of M55J followed by delamination failure of M55J and IM7 leading to catastrophic failure.

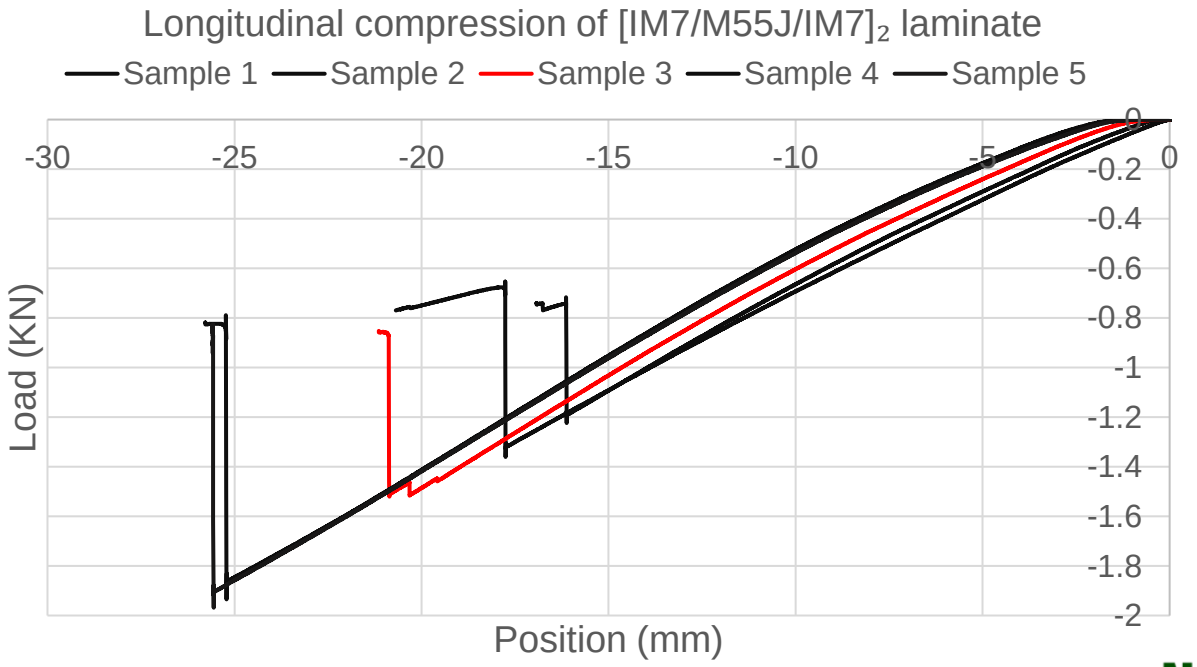

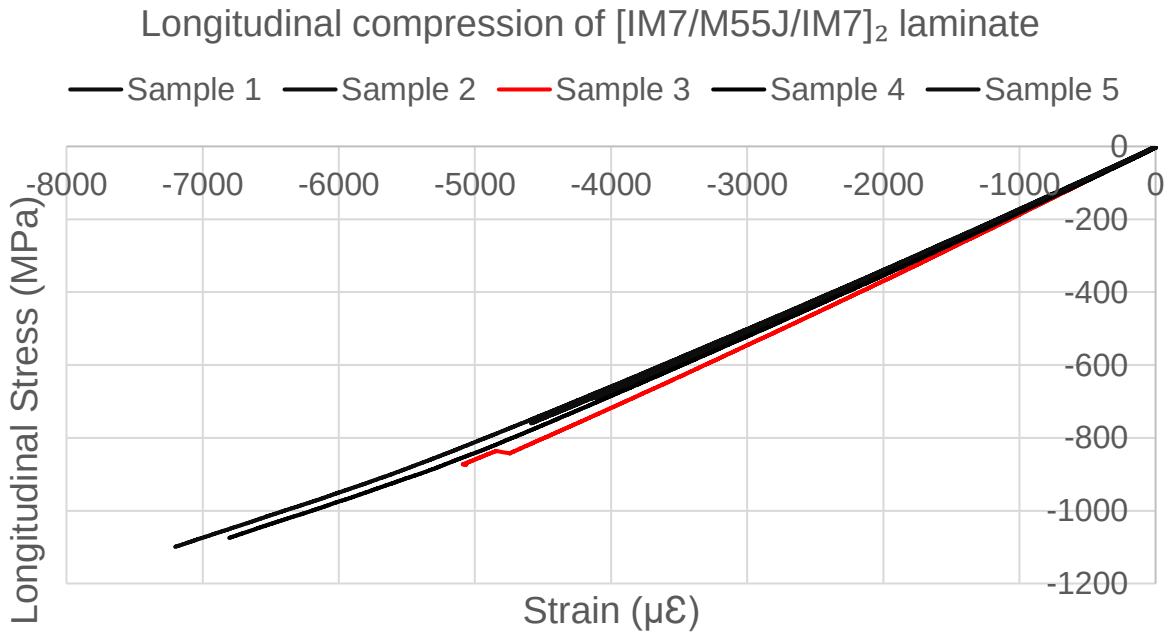

IMPERIAL

University of BRISTOL
Bristol Composites Institute

Pseudo-ductile response of Single ply of M55J in Carbon/Carbon Hybrid Laminates

High speed recording of sample 5 failure at 0.72% compressive strain.

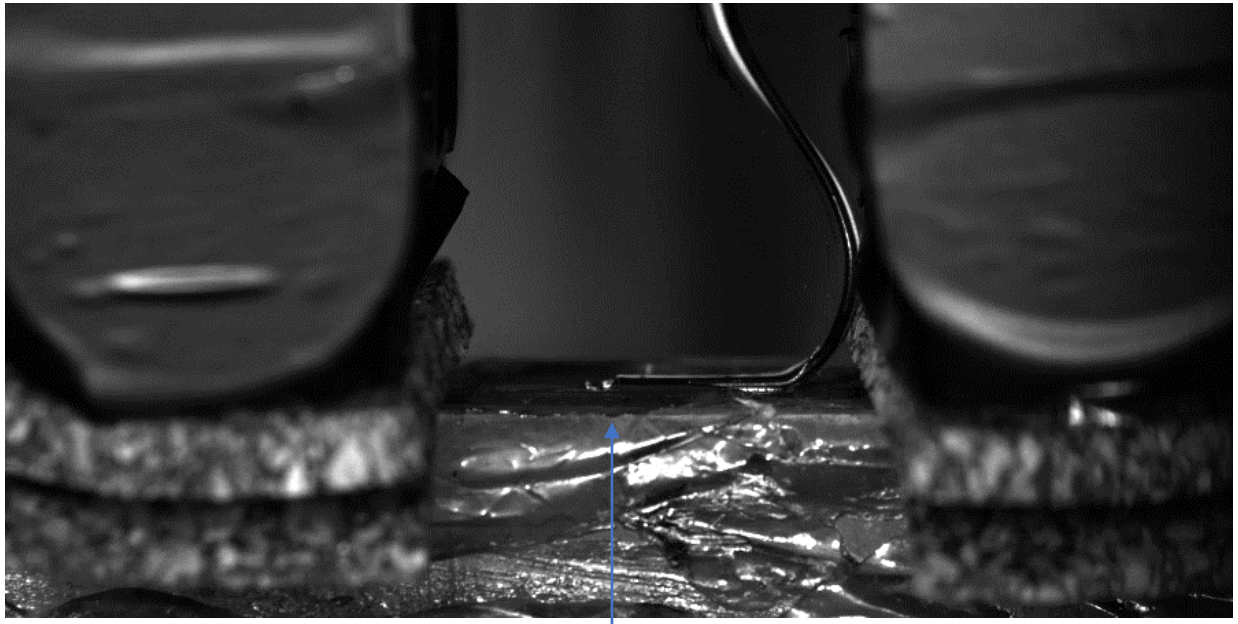

Observe this area

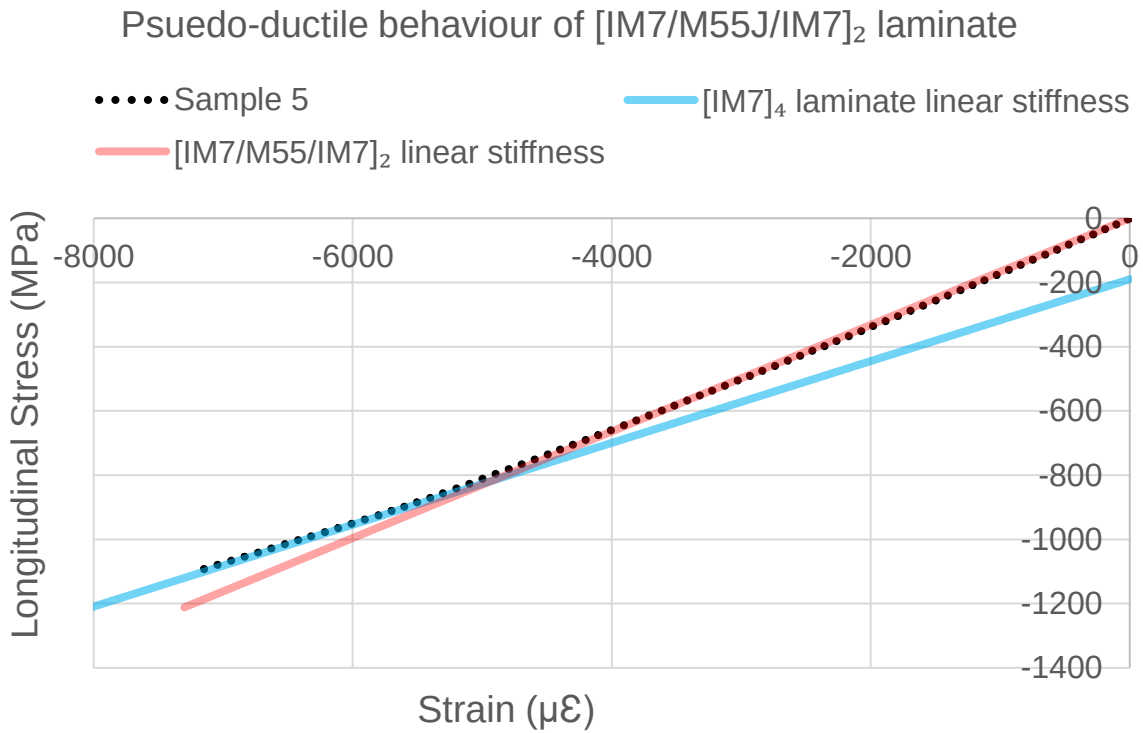

IMPERIAL

Next COMP

University of BRISTOL
Bristol Composites Institute

DOUBLE PLY OF M55J

IM7
M55J
M55J
IM7
IM7
M55J
M55J
IM7

The maximum compressive strain of the hybrid laminate is 0.44% to 0.51%.

Intraply (fragmentation) failure of M55J followed by instant delamination failure of M55J and IM7 leading to catastrophic failure.

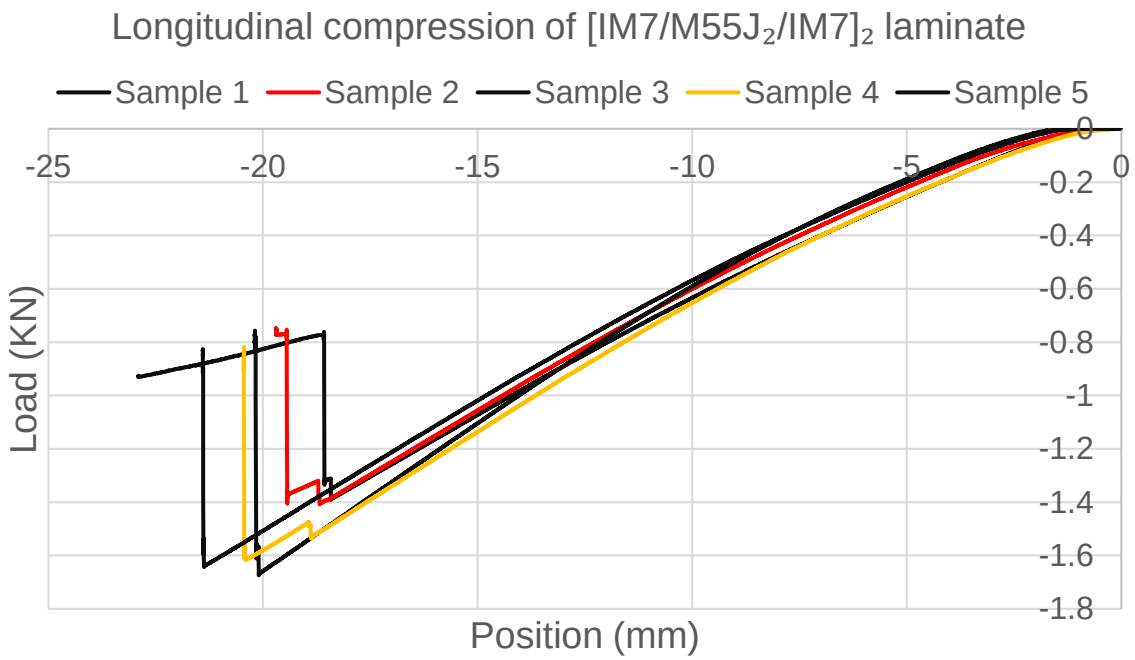

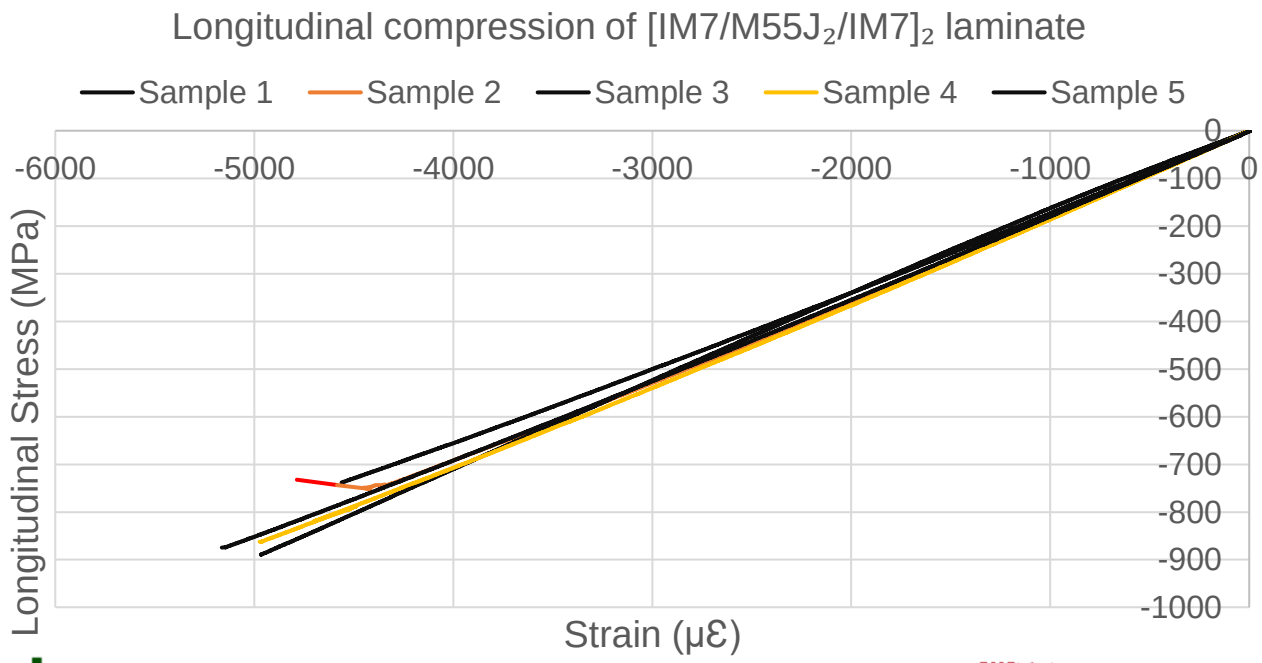

IMPERIAL

Next COMP

University of BRISTOL
Bristol Composites Institute

TRIPLE PLY OF M55J

The maximum compressive strain of the hybrid laminate is 0.36% to 0.47%.

Sample 5 was interrupted at 0.43% compressive strain after a load drop at 0.42% compressive strain.



IM7
M55J
M55J
M55J
IM7
IM7
M55J
M55J
M55J
IM7

High speed recording of sample 4 failure at 0.47% compressive strain.

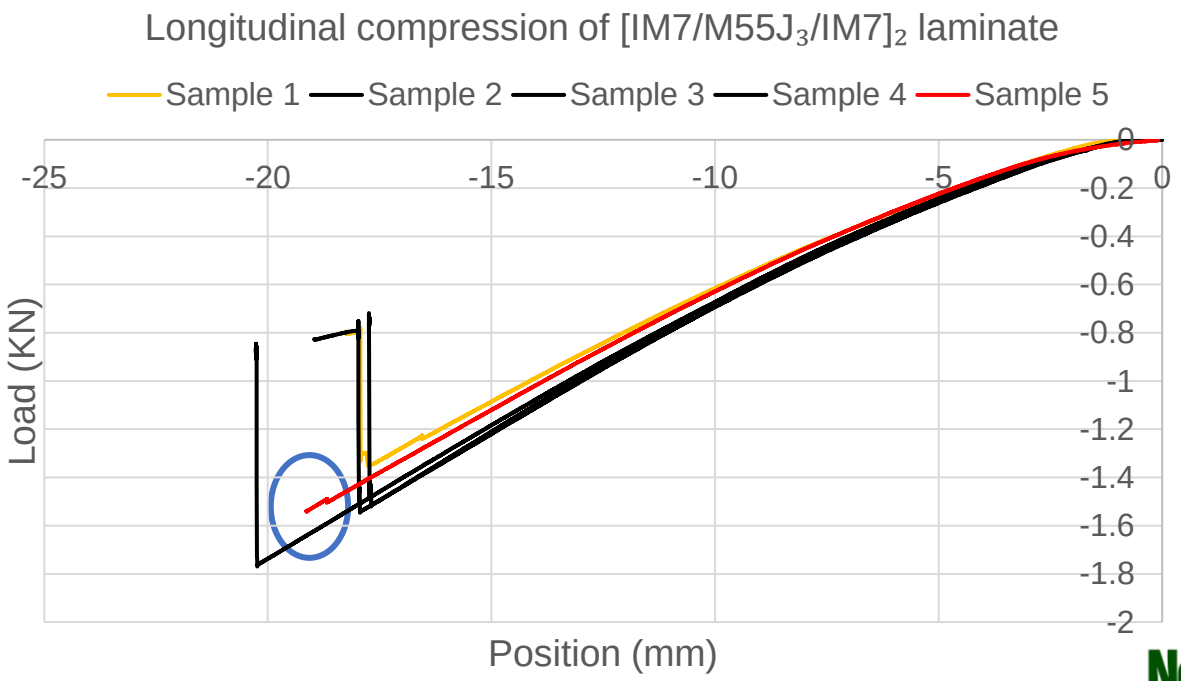

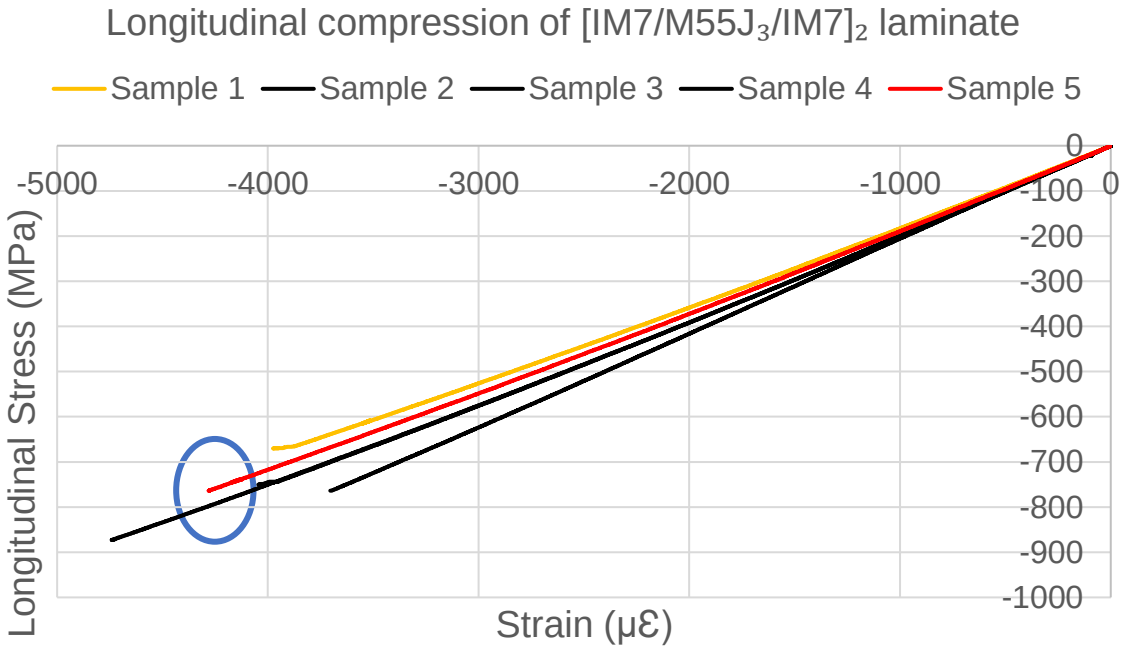

IMPERIAL

Next COMP

University of BRISTOL
Bristol Composites Institute

Triple ply of M55J

The sample was cut and polished to observe the fibre fragmentation of M55J.



Sample 5

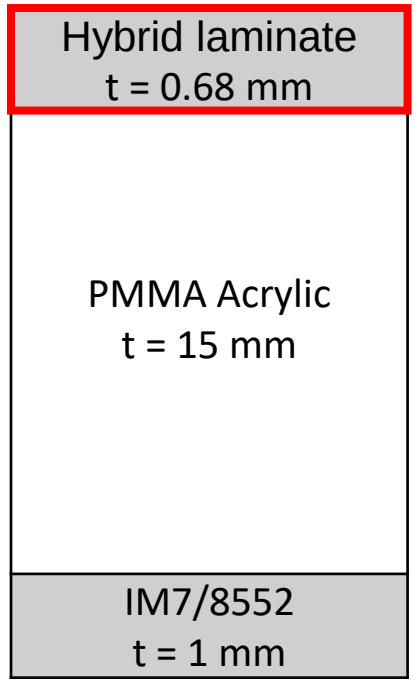

Sample 5 cross-section

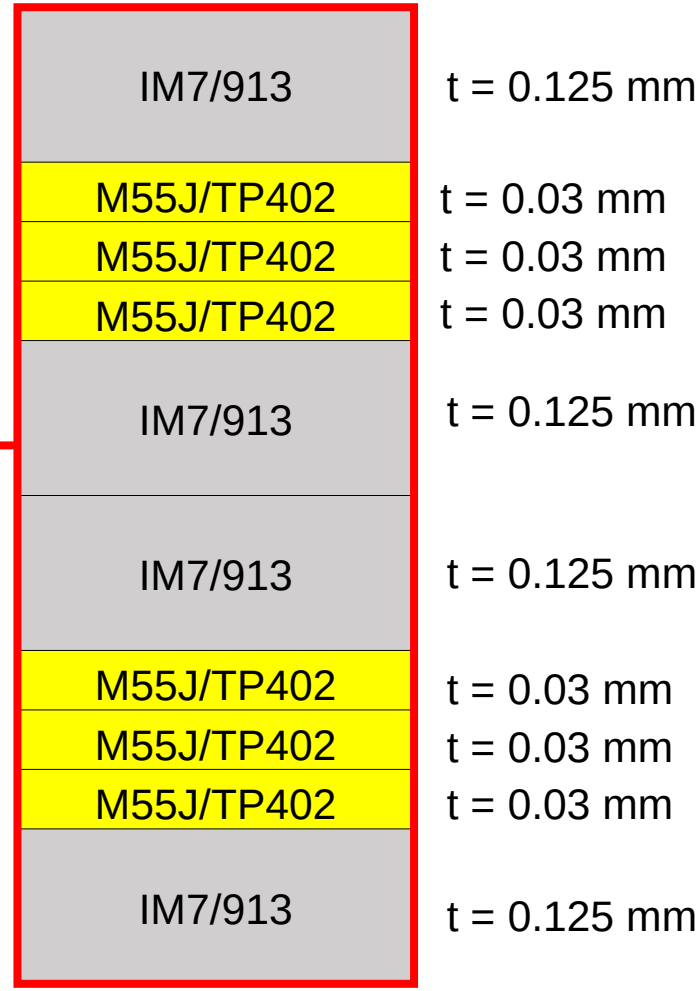

Sample 5 hybrid laminate cross-section

IMPERIAL

Next COMP

University of BRISTOL
Bristol Composites Institute

TRIPLE PLY OF M55J

Sample 5 hybrid laminate cross-section

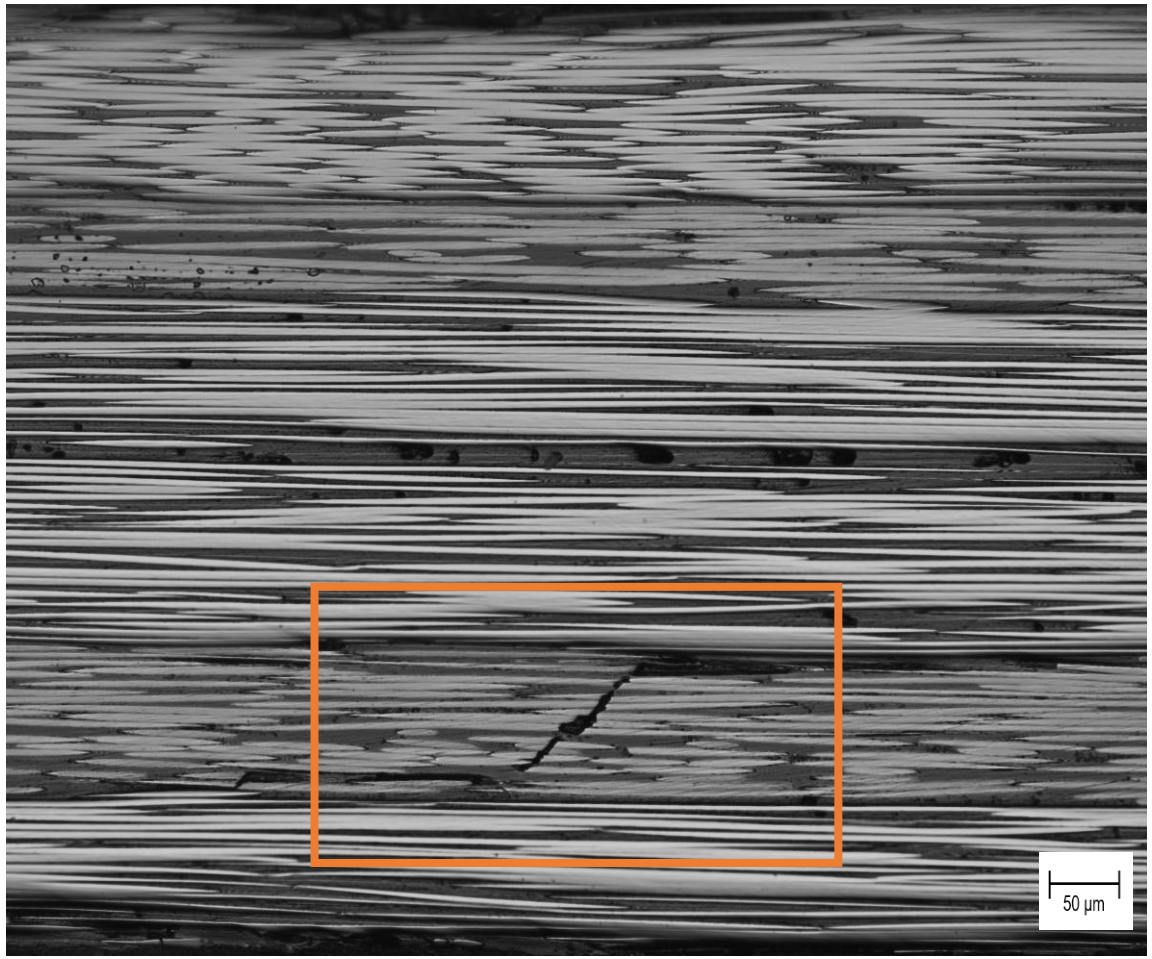

IM7/913	t = 0.125 mm
M55J/TP402	t = 0.03 mm
M55J/TP402	t = 0.03 mm
M55J/TP402	t = 0.03 mm
IM7/913	t = 0.125 mm
IM7/913	t = 0.125 mm
M55J/TP402	t = 0.03 mm
M55J/TP402	t = 0.03 mm
M55J/TP402	t = 0.03 mm
IM7/913	t = 0.125 mm

IMPERIAL

Next COMP

University of BRISTOL
Bristol Composites Institute

TRIPLE PLY OF M55J

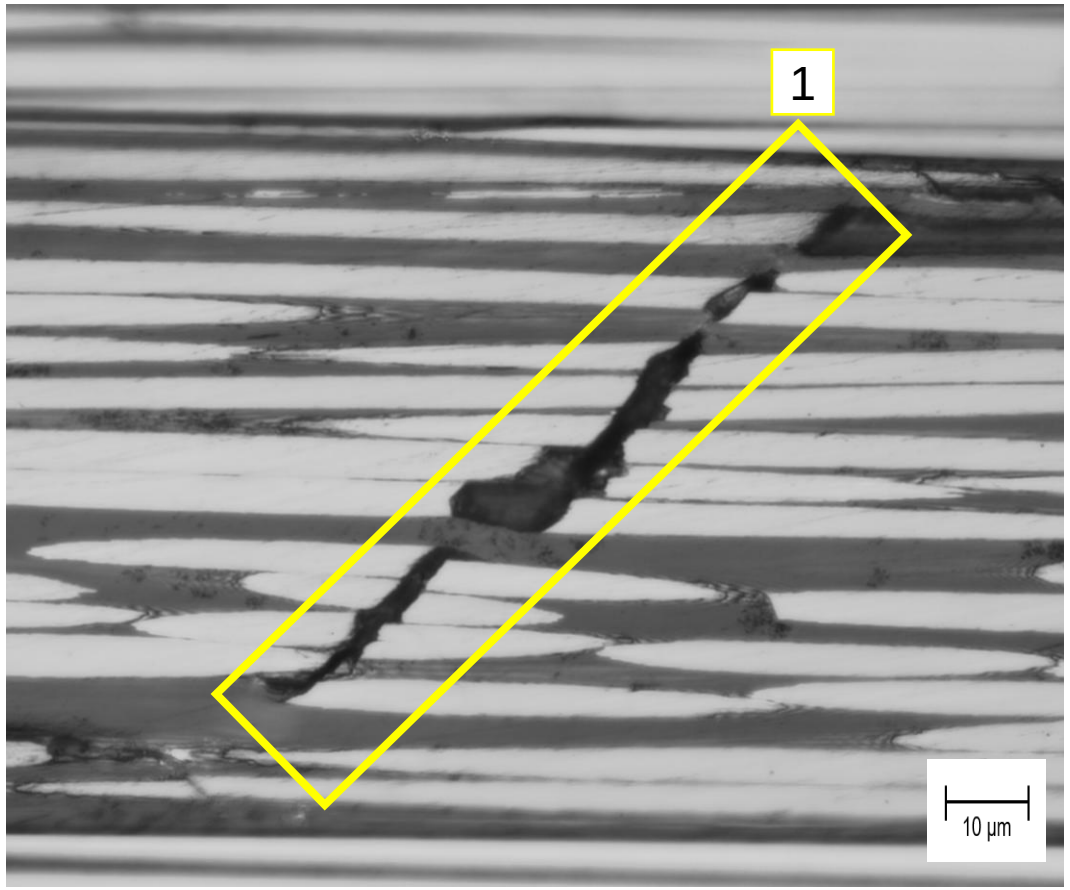

Fragmentation is observed on a fibre level and ply level

1. Compressive failure of M55J plies showing stable initial fragmentation.

IMPERIAL

Next COMP

University of BRISTOL
Bristol Composites Institute

TRIPLE PLY OF M55J

IM7
M55J
M55J
M55J
IM7
IM7
M55J
M55J
M55J
IM7

M55J baseline compressive strain of 0.31% and a knee point strain of 0.49% [4, 5].

Hybridization can support delayed compressive fragmentation of M55J.

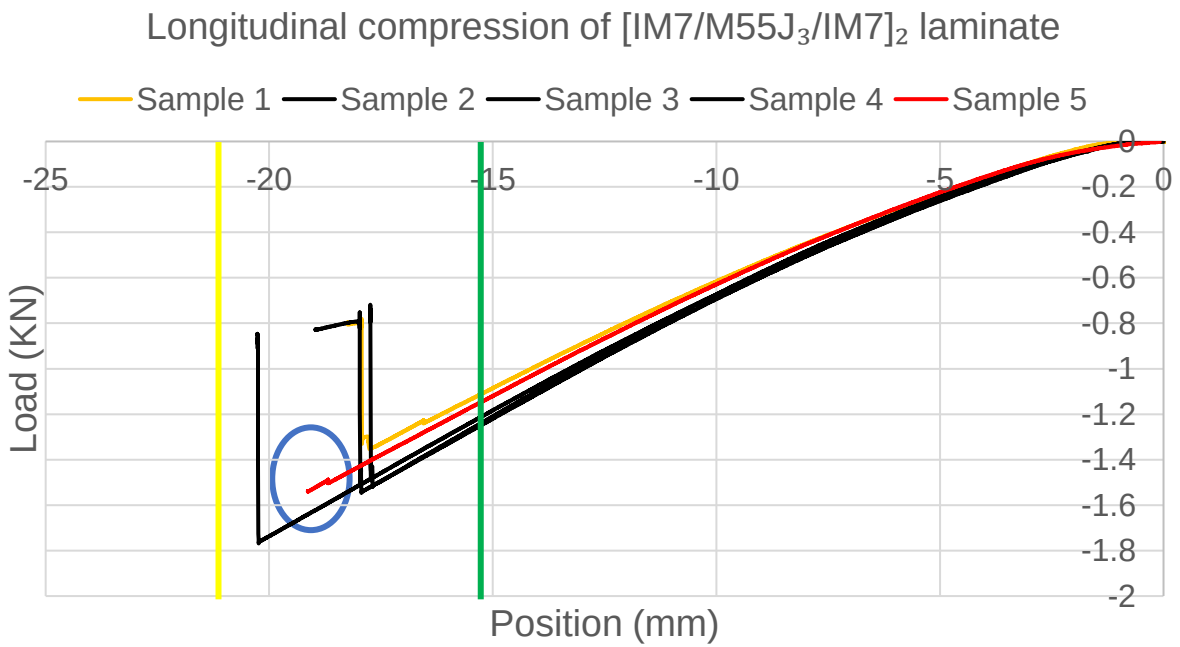

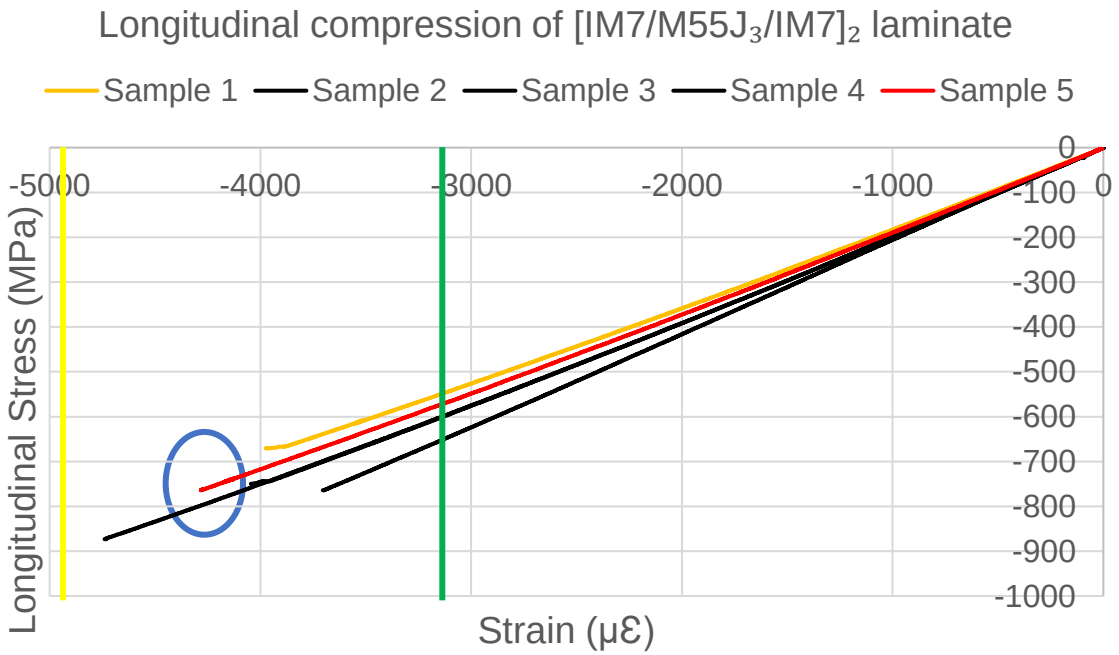

M55J Knee point strain

M55J Baseline compressive strain

Experimental Results of M55J in Glass/Carbon Hybrid Laminates

HYBRID LAMINATES

Material	Ply thickness (mm)	E_{11} (GPa)	Compressive Strain	
S-glass/epoxy	0.125	45.7	2.33%	[5]
M55J/epoxy	0.030	240	0.31%	[4]

- Visually/audibly observe the fragmentation of M55J in a glass/carbon hybrid laminate.
- Is the laminate failure affected as M55J thickness increases?

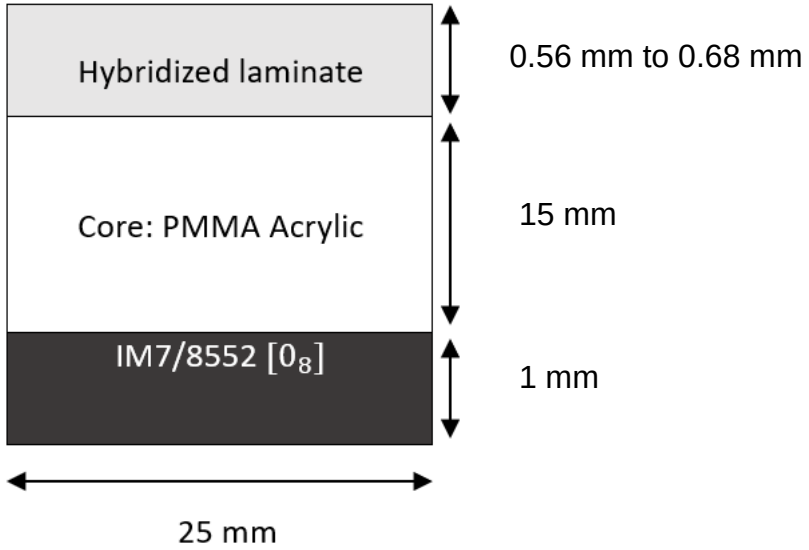

Cross-section view of the sandwich structure

Configuration 1 $E_{11} = 67.3\ GPa$ $t = 0.56\ mm$	Configuration 2 $E_{11} = 84.6\ GPa$ $t = 0.62\ mm$	Configuration 3 $E_{11} = 98.7\ GPa$ $t = 0.68\ mm$
S-glass	S-glass	S-glass
M55J	M55J	M55J
S-glass	M55J	M55J
S-glass	S-glass	M55J
M55J	S-glass	S-glass
S-glass	M55J	S-glass
	M55J	M55J
	S-glass	M55J
		M55J
		S-glass

IMPERIAL

Next COMP

University of BRISTOL
Bristol Composites Institute

SINGLE PLY OF M55J

S-glass
M55J
S-glass
S-glass
M55J
S-glass

The maximum compressive strain of the hybrid laminate is 1.22% to 1.5%.

Pseudo-ductile compressive failure showing a knee point indicating fragmentation of M55J fibres occurs as load is transferred to the surrounding S-glass fibres followed by catastrophic failure.

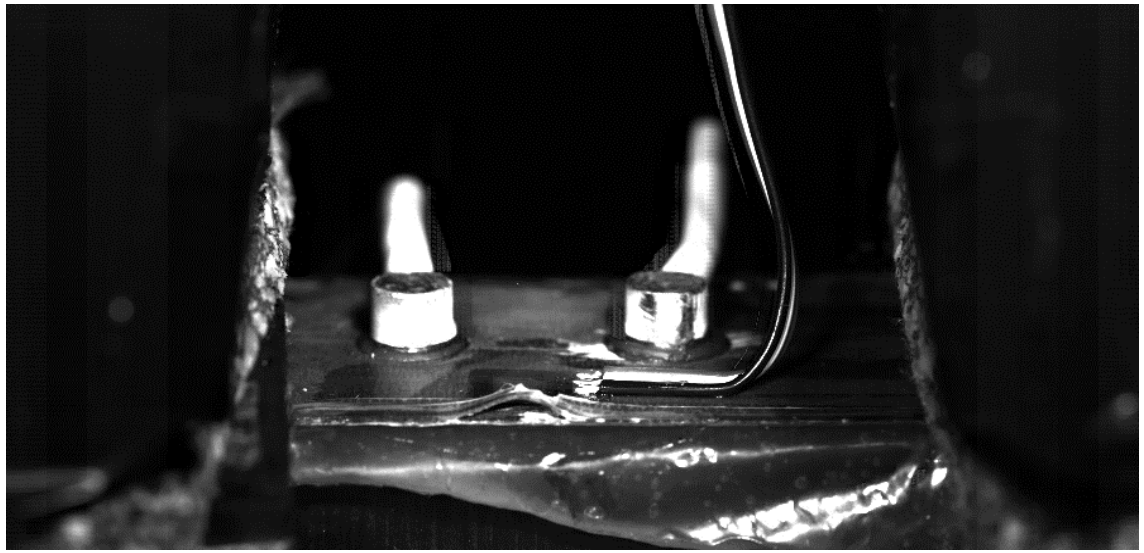

Sample 6 at a failure compressive strain of 1.29%.

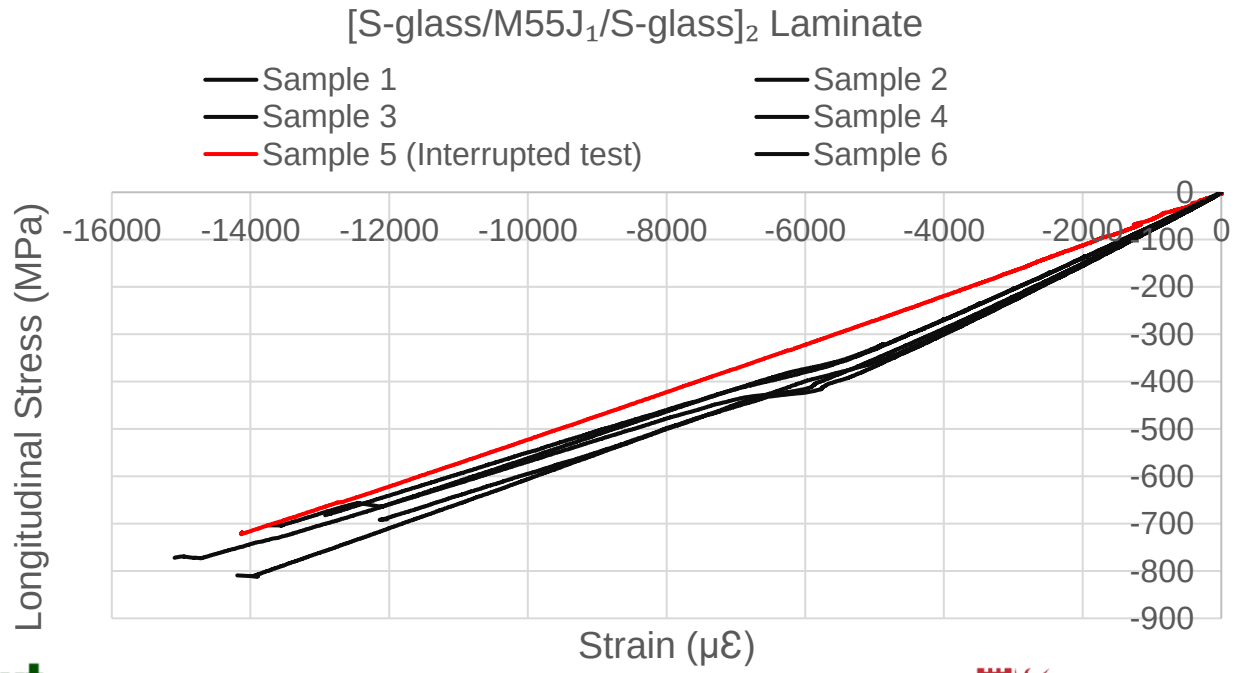

IMPERIAL

Next COMP

University of BRISTOL
Bristol Composites Institute

SINGLE PLY OF M55J REPEATED TEST

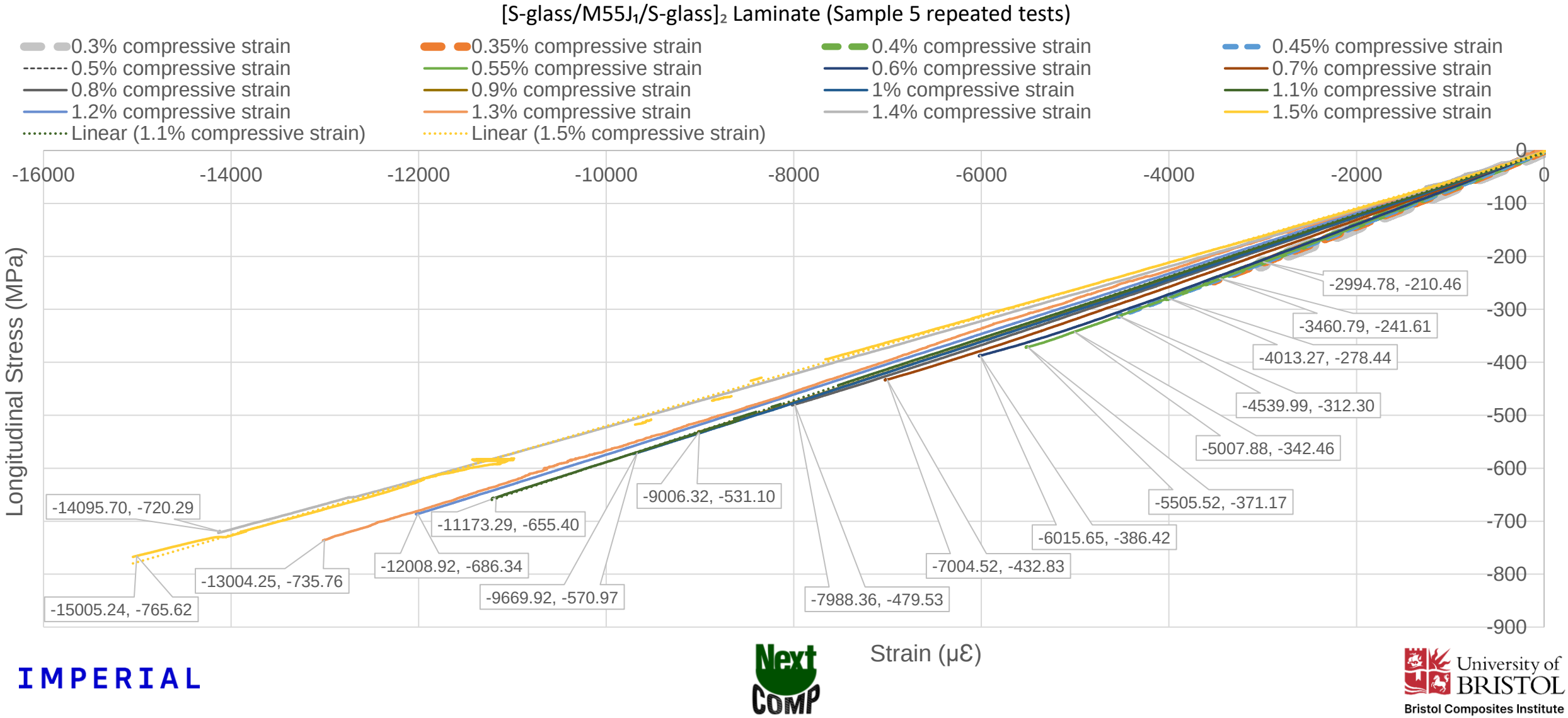

IMPERIAL

Next COMP

University of BRISTOL
Bristol Composites Institute

Double ply of M55J

S-glass
M55J
M55J
S-glass
S-glass
M55J
M55J
S-glass

The maximum compressive strain of the hybrid laminate is 0.7% to 0.92%.

Intraply (fragmentation) failure of M55J showing visible fibre breaks followed by delamination failure of M55J and load transfer to the surrounding S-glass fibres followed by catastrophic failure.

Psuedo-ductile compressive failure showing a knee point at 0.49% compressive strain.



Sample 4 failed at 0.86% compressive strain with M55J fibre fragments visible on laminate top plane.

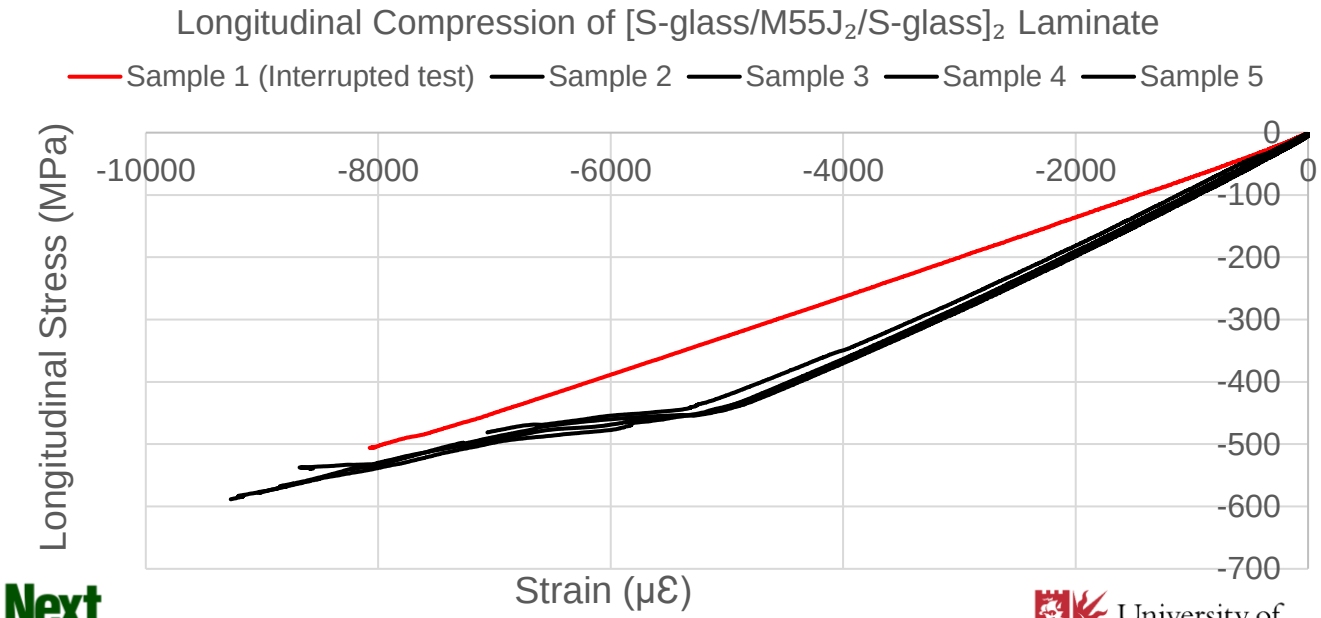

IMPERIAL

Next COMP

University of BRISTOL
Bristol Composites Institute

Double ply of M55J Repeated Test

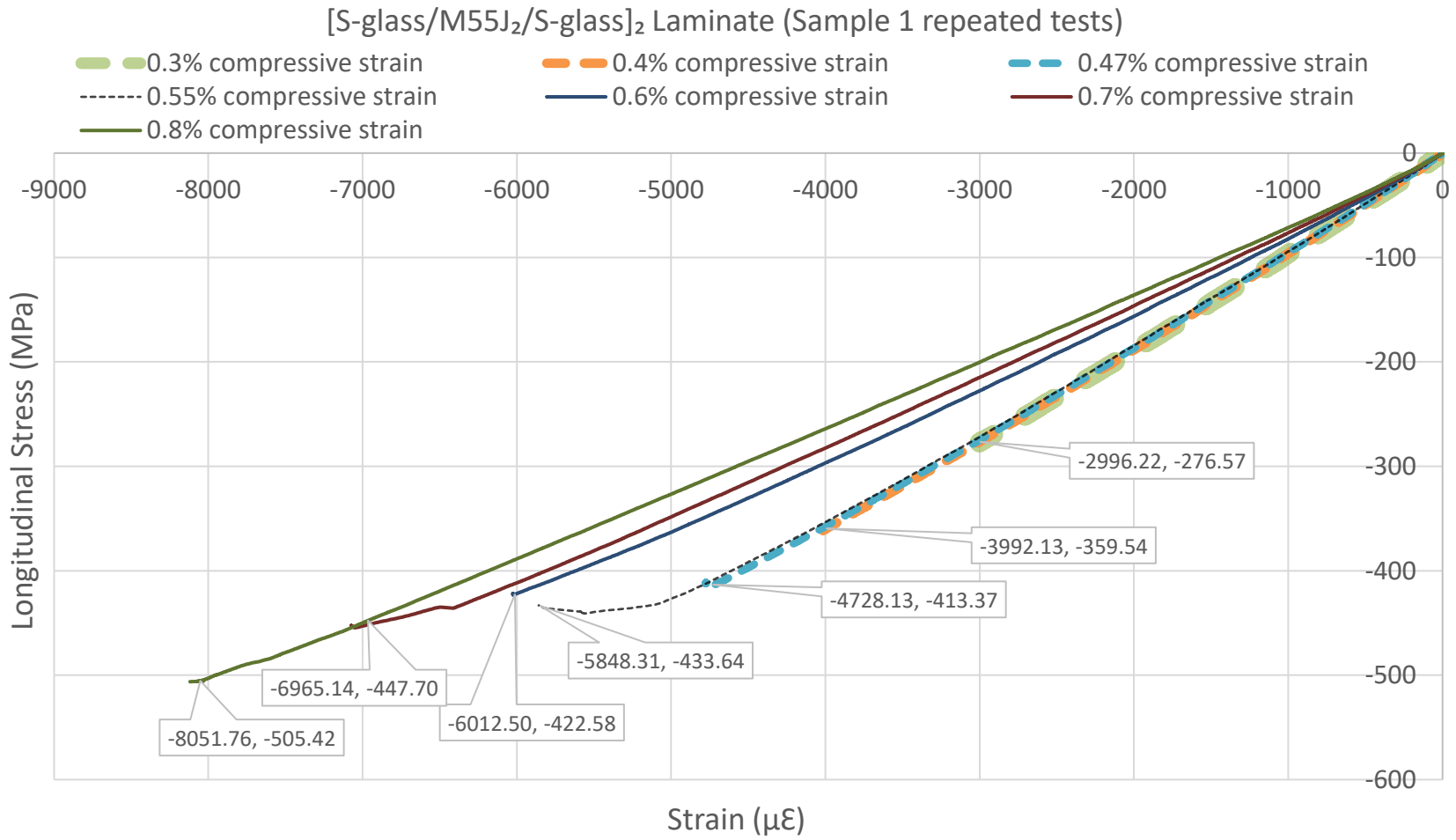

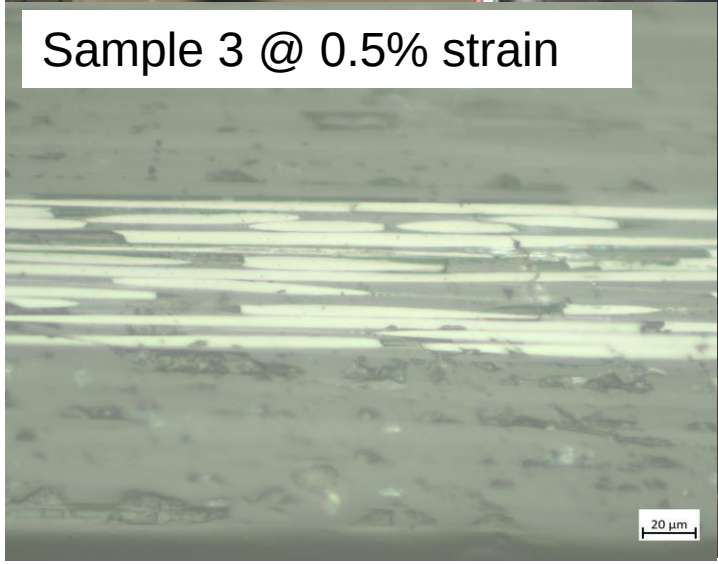

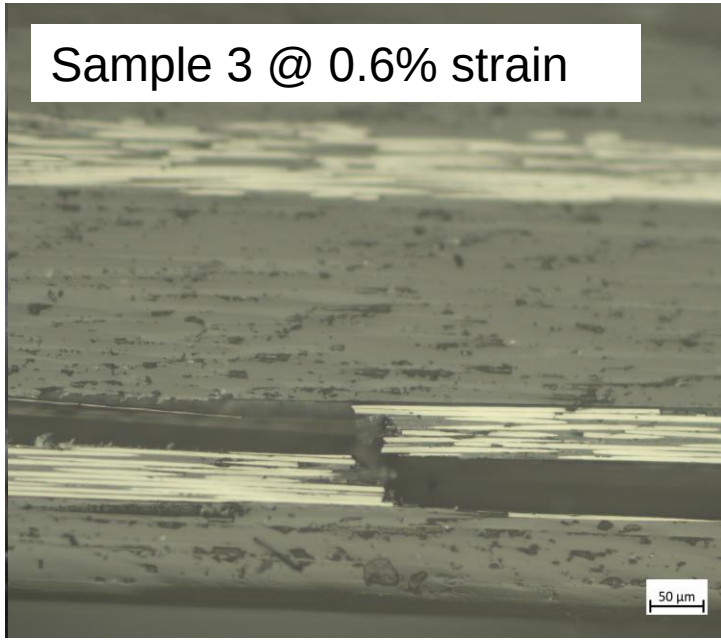

IMPERIAL

Next COMP

University of BRISTOL
Bristol Composites Institute

Triple ply of M55J

The maximum compressive strain of the hybrid laminate is 0.39% to 0.46%.

Intraply (fragmentation) failure of M55J leading to instant delamination and catastrophic failure.

S-glass
M55J
M55J
M55J
S-glass
S-glass
M55J
M55J
M55J
S-glass



Sample 4 failed at 0.46% compressive strain.

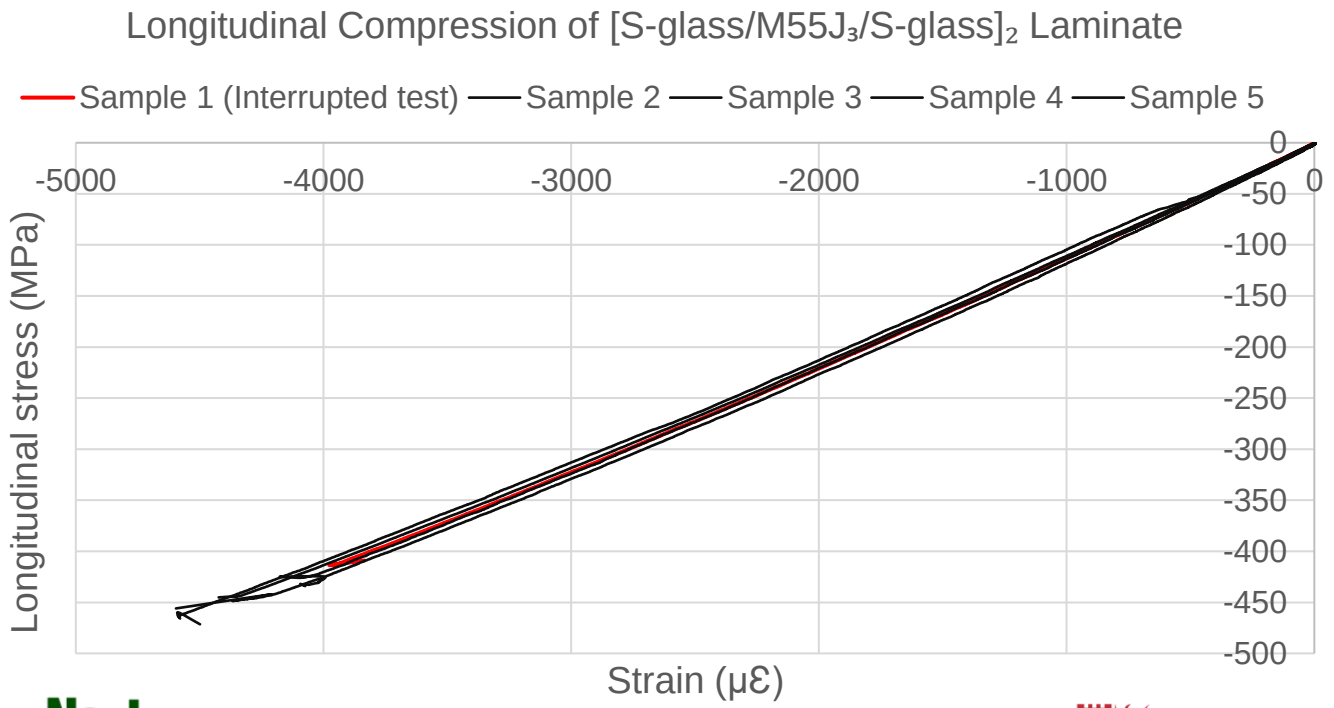

IMPERIAL

Next COMP

University of BRISTOL
Bristol Composites Institute

Triple ply of M55J Repeated Test

Sample 1 failed at 0.40% compressive strain.



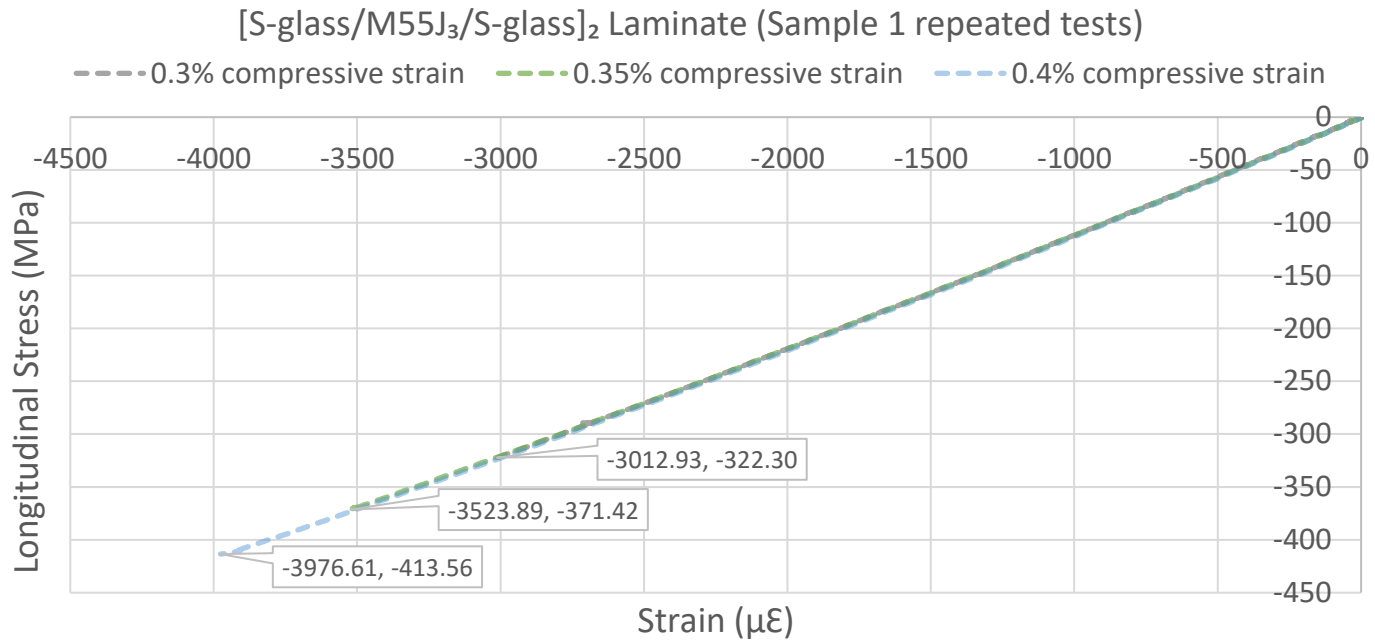

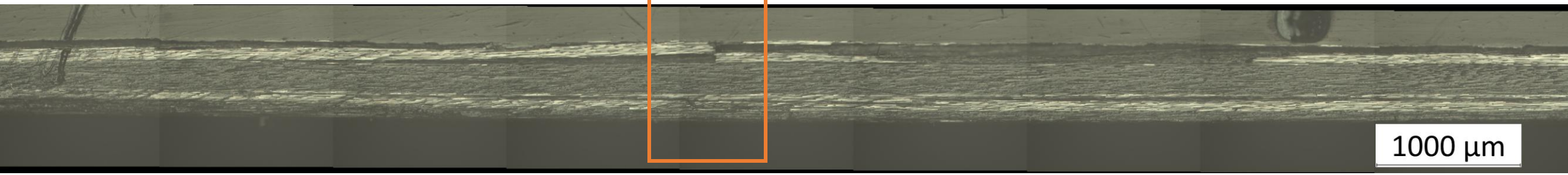

IMPERIAL

Next COMP

University of BRISTOL
Bristol Composites Institute

Maximum Compressive Strain of Hybrid Laminates

Average	CV (%)
4130	8.54
4320	6.27
4888	3.87
8360	9.49
5558	21.90
13667	7.21

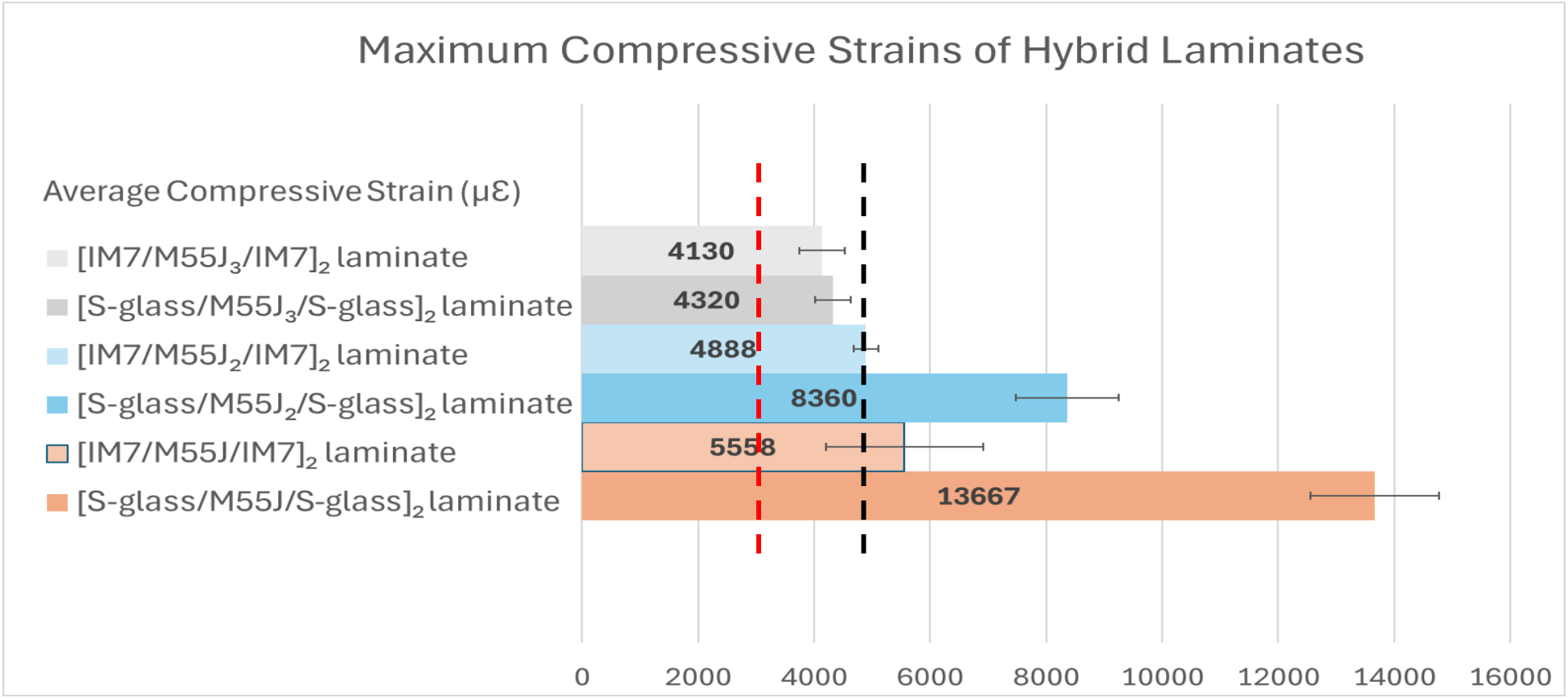

– – – Baseline strain [4]

– – – Knee point strain [5]

IMPERIAL

Next COMP

University of BRISTOL
Bristol Composites Institute

CONCLUSION

High modulus fibres can be used to increase the initial stiffness of fibre reinforced composite laminates.

Hybridization of M55J fibres demonstrates an increase in the compressive performance.

The failure mechanism shows compressive fragmentation of M55J fibres that eventually lead to delamination followed by catastrophic failure of the hybrid laminate.

The compressive strain of M55J shows a knee point at 0.49% against the literature's baseline value of 0.31% indicating an increase in the compressive performance.

Increasing M55J thickness reduces the maximum compressive strains of the hybrid laminate.

Carbon/carbon hybrid laminates show higher failure stresses and lower failure strains than glass/carbon hybrids.

IMPERIAL

Next COMP

University of BRISTOL
Bristol Composites Institute

REFERENCES

1. Czél, G., Jalalvand, M., Wisnom, M.R., & Czigany, T. Design and characterisation of high performance, pseudo-ductile all-carbon/epoxy unidirectional hybrid composites. Composites Part B: Engineering, 2017, Vol. 111, Pages 348–356. https://doi.org/10.1016/j.compositesb.2016.11.049

2. Wu, X., & Wisnom, M.R. Compressive failure strain of unidirectional carbon fibre composites from bending tests. Composite structures, 2023, Vol. 304. https://doi.org/10.1016/j.compstruct.2022.116467

3. Wu, X., Fuller, J.D., & Wisnom, M.R. Role of fibre fragmentation on pseudo-ductility of thin-ply +/- 27(7)/0 (s) carbon fibre laminates with high modulus 0 degrees plies under compressive and flexural loading. Composites Science Technology, 2020, Vol. 199. https://doi.org/10.1016/j.compscitech.2020.108377

4. Montagnier, O., & Hochard, C. Compression Characterization of High Modulus Carbon Fibers. Journal of Composite Materials, 2005, Vol. 39, Issue 1, Pages 35-49. https://doi:10.1177/0021998305046433

5. Suwarta, P., Wisnom, M.R., Fotouhi, M., Wu, X., & Czél, G. Pseudo-ductile compressive behaviour of unidirectional thin-ply carbon /glass fibre-epoxy hybrid composites. Composites Part A: Applied Science and Manufacturing. 2025, Vol. 195. https://doi.org/10.1016/j.compositesa.2025.108877

IMPERIAL

Next COMP

University of BRISTOL
Bristol Composites Institute



Next Generation
Fibre-Reinforced Composites

https://nextcomp.ac.uk

I would like to acknowledge funding which supported this work from the UK Research and Innovation - EPSRC Programme Grant; Next Generation Fibre-Reinforced Composites: A Full Scale Redesign for Compression (EP/T011653/1)

A collaboration between Imperial College London and University of Bristol

IMPERIAL

University of BRISTOL

Bristol Composites Institute

LOCALIZED HYBRIDIZATION USING BORON FIBERS: A ROUTE TO IMPROVE OPEN HOLE COMPRESSIVE PERFORMANCE

Gursahib. S. Bhatia[1], Hwei Linn Khoo[2], Torquato Garulli[3], Soraia Pimenta[4], Paul Robinson[5], Emile S. Greenhalgh[6] and Silvestre. T. Pinho[7]

[1]Department of Aeronautics, Imperial College London,
South Kensington, London SW7 2AZ, UK
Email: g.bhatia@imperial.ac.uk, web page: https://profiles.imperial.ac.uk/g.bhatia/about

[2]Department of Aeronautics, [2]Department of Mechanical Engineering,
Imperial College London, South Kensington, London SW7 2AZ, UK
Email: hwei.khoo18@imperial.ac.uk,

[3]AMADE, Polytechnic School, University of Girona,
C/Universitat de Girona 4, 17003 Girona, Spain,
Email: torquato.garulli@udg.edu, web page: https://profiles.imperial.ac.uk/t.garulli

[4]Department of Mechanical Engineering, Imperial College London,
South Kensington, London SW7 2AZ, UK
Email: soraia.pimenta@imperial.ac.uk, web page: https://profiles.imperial.ac.uk/soraia.pimenta

[5]Department of Aeronautics, Imperial College London,
South Kensington, London SW7 2AZ, UK
Email: p.robinson@imperial.ac.uk, web page: https://profiles.imperial.ac.uk/p.robinson

[6]Department of Aeronautics, Imperial College London,
South Kensington, London SW7 2AZ, UK
Email: e.greenhalgh@imperial.ac.uk, web page: https://profiles.imperial.ac.uk/e.greenhalgh

[7]Department of Aeronautics, Imperial College London,
South Kensington, London SW7 2AZ, UK
Email: silvestre.pinho@imperial.ac.uk, web page: https://profiles.imperial.ac.uk/silvestre.pinho

Keywords: Hybrid, Boron fibre, Compression, Microstructural design, Finite elements

ABSTRACT

In this study we propose a novel localized hybridization concept to enhance longitudinal compressive performance of composites containing open holes. The concept involves hybridization in the form of selective placement of individual boron fibres locally near the vicinity of a hole within 0° plies of a quasi-isotropic laminate made from a carbon-epoxy prepreg. The manufacturing of these novel hybrid laminates is realized using an in-house developed fibre placement fixture to precisely place the boron fibres at the required locations. The mechanical performance of the manufactured concept is benchmarked against a non-hybrid baseline laminate under quasi-static compressive loading following the ASTMD6484 standard. The proposed hybridisation strategy results in a significant (≈35%) increase in compressive strength over the corresponding baseline laminate. The improvement in compressive performance can be attributed to changes in failure mechanisms due to the presence of the boron fibres within the hybrid laminates, as revealed by post-test failure analysis (using X-ray scans and scanning electron microscopy) and finite element simulations. Our research demonstrates the success of this first of its kind locally hybrid design aimed at improving open hole compressive performance.

1 INTRODUCTION

Composite structures often include features like holes to serve various operational purposes, including cable or pipeline routing, fastener installations, and other functional requirements. However, these holes typically lead to localized stress concentrations [1]. Under compressive loading, these stress concentrations may result in microbuckling and unstable kink band growth near the hole edge, leading to catastrophic failure [2,3]. Hence, to improve the overall load-bearing capacity of such structures, it becomes crucial to devise a strategy to delay or suppress the progression of damage arising in the form of kink band growth from the hole.

In a previous study, by using commercial boron-carbon hybrid prepregs, Garulli et al. [4] observed that, for an edge-notched laminate under compression, both in-plane and out-of-plane kinking in carbon fibres can be arrested by the presence of boron fibres [4]. When the propagating kink band reaches a boron fibre, damage is interrupted and deflected by formation of a longitudinal split at the boron-epoxy interface. This work aims to utilize this deflection mechanism by developing an open hole-focused design wherein a patch of boron fibres is placed in accordance with the localized stress distribution around the hole.

The process involves hybridization of 0° plies of a quasi-isotropic carbon epoxy laminate by placing individual boron fibres aligned at 0° direction selectively at regular intervals in the transverse direction from the hole edge as shown in Fig. 1. To realize this, an in-house manufacturing procedure has been developed. The performance of hybrid laminates is benchmarked against a non-hybrid baseline laminate configuration under open hole compression as per ASTM D6484 test standard [5]. This study provides a practical localized approach for designers to enhance compressive strength near structural features like open holes, without affecting the overall global structural performance.

2 CONCEPT DESIGN, MATERIALS AND MANUFACTURING

2.1 Concept Design

In this work, we aim at improving the open hole compressive performance of a quasi-isotropic laminate ($[45_{10}/-45_{10}/0_{10}/90_{10}]_{3S}$) by embedding boron fibres within the block of 0_{10} plies resulting in a hybrid laminate ($[45_{10}/-45_{10}/0_{\text{Hybrid}}/90_{10}]_{3S}$) Each 0_{Hybrid} ply-block comprises of boron fibres embedded in the centre of 10 ultrathin carbon epoxy plies. However, the length of the boron fibres is relatively short compared to the overall length of the carbon fibres in 0° plies. Fig. 1 presents a schematic representation of 0° plies of a baseline and hybrid laminate samples tested in this work. The presence of the boron fibres is restricted to a local region in the vicinity of the hole resulting in a localized hybrid ply configuration. Fig. 1(c) presents a close-up view of the region near the hole for a hybrid sample showing distribution of the boron fibres. The variation in length of boron fibres follows the profile of variation of longitudinal stress with respect to the transverse distance from the edge of the hole.

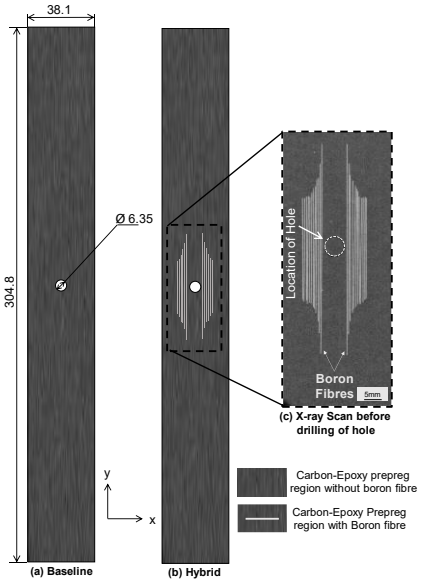

Figure 1: Schematic representation a 0° ply in the open hole specimens used in this study (a) baseline (non-hybrid) specimen (b) hybrid specimen (c) X-ray scan obtained during manufacturing stage, showing distribution of boron fibres within one hybrid 0° ply (note-figure (a) and (b) not to scale, all dimensions are in mm).

2.2 Materials

The required laminates were manufactured using a 15 gsm MR70/TP402 prepreg. The properties of this material have been reported by Garulli et al. [6]. For hybridization, 4-mil boron fibres supplied by Speciality Materials have been used. Boron fibres exhibit a unique combination of high compressive strength, high modulus and a large diameter [7]. The key material properties of boron fibres are presented in Table 1.

Property	Units	4-mil boron fibre
Diameter	µm	102
Density	g/cc	2.61
Thermal Expansion	PPM/°C	4.5
Tensile Strength	MPa	4000
Tensile Modulus	GPa	428
Compression Strength	MPa	>6000
Hardness	Knoop	3200

Table 1: Properties of the boron fibre used in this work [7].

2.3 Manufacturing

The manufacturing of the hybrid laminates was performed by a procedure developed in-house specifically for this study. As can be seen in Fig.1 (c), the hybrid plies contain individual boron fibres of different lengths placed at specific locations in the vicinity of the hole. This requirement led to the development of an in-house fibre placement fixture as shown in Fig. 2 (a). The overview of the whole process is presented in the form of a schematic diagram in Fig. 2 (b). The first step involves placing one ply of MR70/TP402 prepreg over the bottom plate of the fixture. The next step (Step-2 in schematic) involves placing the boron fibres one by one at required locations on the bottom prepreg. The guide plate provides a straight edge to align boron fibres parallel to the 0° direction (y-direction in Fig. 2(a)). The pitch between the boron fibres is controlled by moving the bottom plate with respect to the guide plate in x-direction. The bottom plate of the fixture is mounted over a linear x-stage which allows relative motion between the guide plate and the bottom plate in the x-direction as shown in Fig. 2(a). Once all

the required fibres are placed on the bottom prepreg, the guide plate along with the z-stage is removed from the fixture and another prepreg ply laid up on top of the previously arranged boron fibres and bottom prepreg, as shown in Step-3 in the schematic. Thereafter, the stack containing the two prepreg layers sandwiching the array of boron fibres between them, is brought onto a vacuum table and is subjected to vacuum for 30 minutes (Step-4). A caul plate is used during this step as shown in Step-4. Thereafter, the whole process (except Step-2) is repeated until four more top and bottom prepreg plies are added to the hybrid ply block.

In the end, one hybrid ply block comprises of a total of ten MR70/TP402 plies containing one array of boron fibres embedded in the middle. This one hybrid ply-block is represented as 0_{Hybrid} in the overall stacking sequence of $[45_{10}/-45_{10}/0_{\text{Hybrid}}/90_{10}]_{3S}$. In a similar way a total of six such hybrid 0° ply blocks are prepared and a final layup of $[45_{10}/-45_{10}/0_{\text{Hybrid}}/90_{10}]_{3S}$ is stacked. The curing of the layups is performed as per the curing parameters specified by manufacturer's datasheet [8]. The baseline laminates with stacking sequence $[45_{10}/-45_{10}/0_{10}/90_{10}]_{3S}$ were manufactured using similar manufacturing conditions except the process for the baseline laminates does not require the steps mentioned in Fig. 2 (b) due to the absence of boron fibres. The test specimens were machined out of the cured panels and the holes were drilled and reamed carefully to final dimensions as per ASTM D6484 [5]. The nominal dimensions of the specimens are shown in the schematic in Fig. 1 (a).

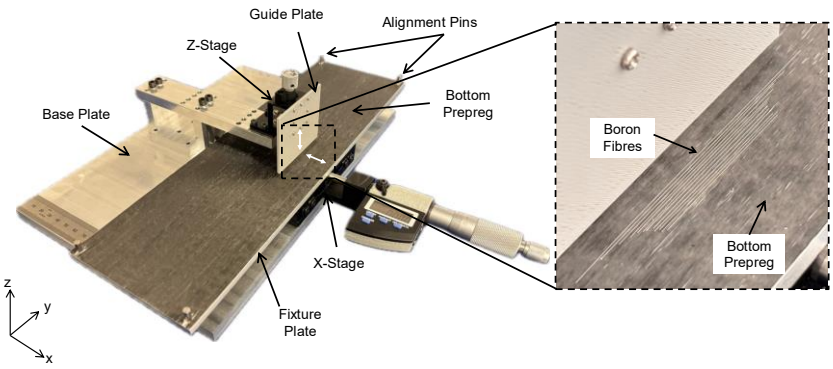

(a)

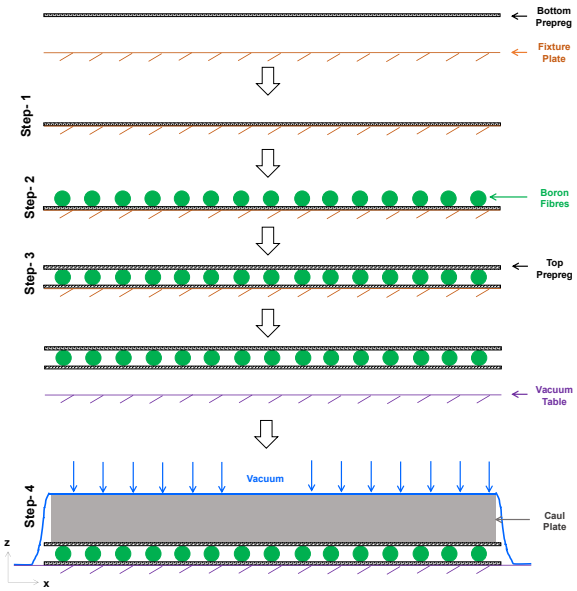

(b)

Figure 2: (a) Image of the fibre placement fixture used
(b) Schematic representation of the steps involved in preparing a hybrid ply;

3 TESTING AND MODELLING

3.1 Testing Methodology

The proposed hybrid concept was assessed against the baseline configuration by testing samples containing open holes subjected to compressive loading following the procedure described in ASTM D6484 [5]. A total of five samples for each configuration were tested. The load was introduced at a constant crosshead displacement rate of 1 mm/min. The test was stopped once a significant drop in load was observed. During the test, digital image correlation was employed to study development of strains in the vicinity of the hole. Fig. 3 shows an image of the test setup showing the main components. After the test, the samples were carefully removed from the test fixture. For the purpose of visual examination, digital photographs of tested specimens were obtained using a flatbed scanner. Thereafter, representative samples from both the baseline and hybrid configuration were further examined using two-dimensional X-ray scans. The specimens were then carefully dissected along the fracture path to examine the fracture surface using a scanning electron microscope (SEM).

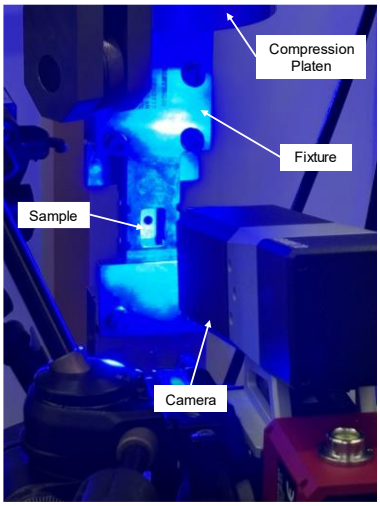

Figure 3: Experimental setup used for open hole compression testing using ASTM D6484.

3.2 Finite Element (FE) Modelling

A mesoscale modelling approach was used to understand the local stiffening effects due to the presence of additional reinforcement in the form of boron fibres around the hole. Two specimen models were generated: baseline and hybridised. Both specimen models follow the experimental specimen's dimensions as shown in Figs. 1 (a) and 4. The baseline specimen model consisted entirely of a carbon fibre reinforced polymer (CFRP) with uniform material properties. In the hybridised specimen model, the position, size, and shape of the hybrid regions ($CFRP_H$) were defined according to the boron fibre placement used in the experiments (Section 2.1). Both CFRP and $CFRP_H$ regions were modelled as homogeneous and linear-elastic within the specimen models for computational efficiency. The numerical simulation was conducted using Abaqus 2024 [9]; a uniform compression displacement (maximum displacement = 3 mm) was applied at the transverse edge of the specimen models. Implicit static analysis was used. Throughout the numerical simulation of each specimen model, the local strain ε_y^{local} was measured by a 7 mm virtual extensometer at the edge of the hole as shown in Fig. 4. The data obtained from this virtual extensometer was compared with the data obtained from a comparable 7 mm virtual extensometer used in processing DIC data, to obtain experimental strain data.

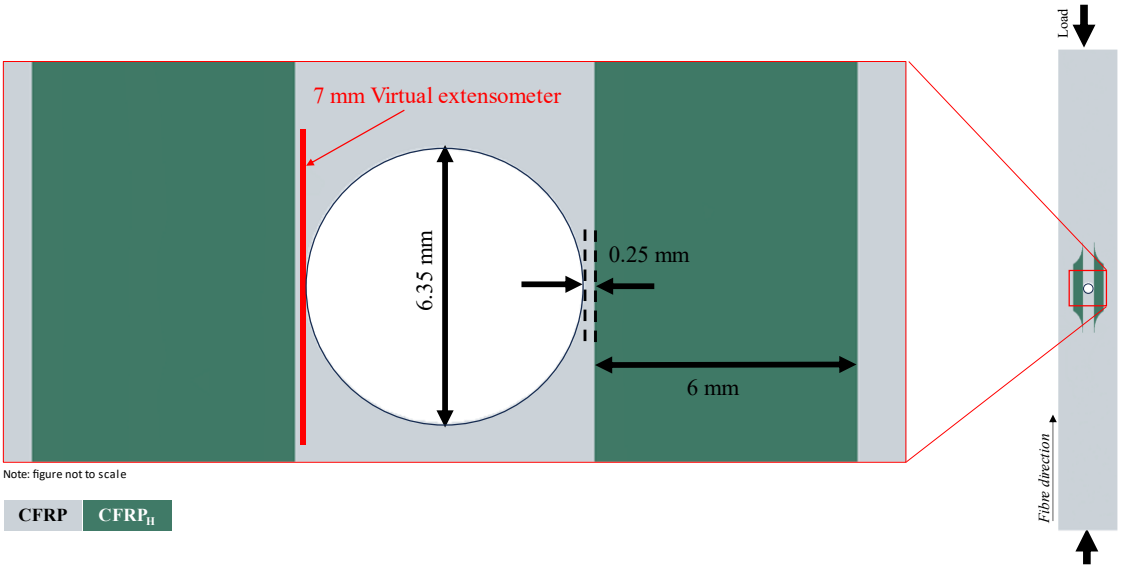

Figure 4: FE model geometry (0° ply) for the hybridised specimen]

4 RESULTS

The experimental gross compressive stress-crosshead displacement plots for a representative hybrid and a baseline sample are shown in Fig. 5 (a). It can be observed that both laminate configurations follow a similar loading trace with a catastrophic drop in load towards the end of the test. However, the stress and displacement at which this drop occurs is significantly different. Fig. 5 (b) shows a bar graph of average gross compressive strength of five samples under each configuration (Baseline and Hybrid). It is observed that the hybrid samples exhibit close to 35% higher compressive strength compared to the baseline samples. To understand the influence on localized stiffness around hole due to presence of boron fibres, the local strain from DIC and the FE model are plotted against the gross compressive stress for the same representative baseline and hybrid samples in Fig. 6 (a). These results from both the model and experiments indicate an increase in local stiffness in the vicinity of the hole. Fig 6 (b) shows a corresponding change in local compressive modulus for both laminates. Further, a bar graph showing difference in stress concentration at the edge of the hole within 0° plies of both baseline and hybrid configurations is shown in Fig. 6(c).

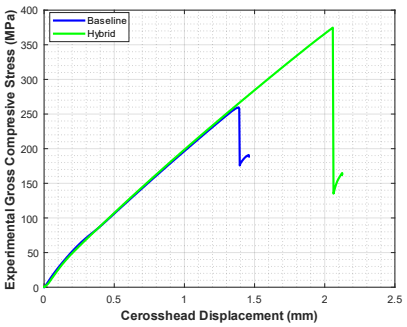

(a)

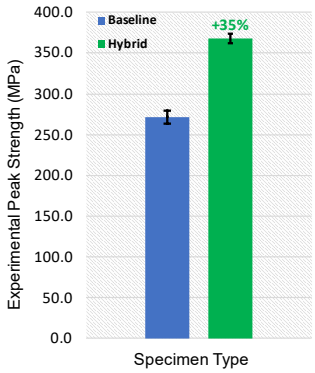

(b)

Figure 5: (a) Trace of experimental compressive stress with respect to crosshead displacement for a representative hybrid and baseline sample (b) Bar graph showing the average gross strength observed experimentally in each laminate configuration. Note- The error bars in Fig. (b) indicate a ± 1 standard deviation interval.

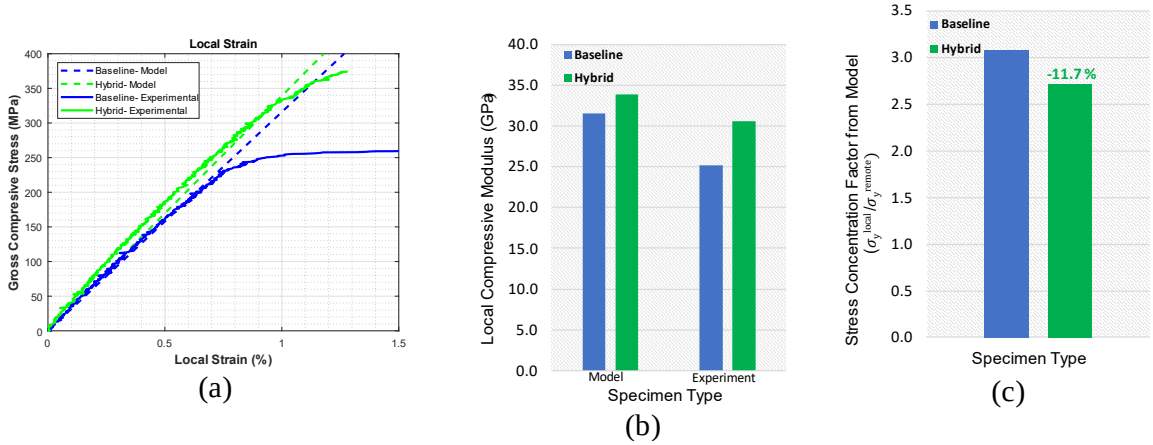

Figure 6: (a) Trace of gross compressive stress with respect to local strain for baseline and hybrid configurations using a virtual extensometer near the edge of the hole obtained from the mesoscale FE model and experiments (b) Bar graph showing the localized compressive modulus observed both experimentally and with the mesoscale FE model in each laminate (c) Bar graph showing the stress concentration factor at the edge of the hole observed with the mesoscale FE model in each laminate

The post-test X-ray scans are shown in Fig.7. These scans reveal a difference in the extent of the spread of damage between baseline and hybrid configurations. It can be noted that the damage in the longitudinal direction is more widespread in case of hybrid samples, suggesting a difference in the internal failure mechanisms. Fig. 8 shows the SEM micrographs obtained after dissecting the samples along the fracture path growing transverse to the loading.

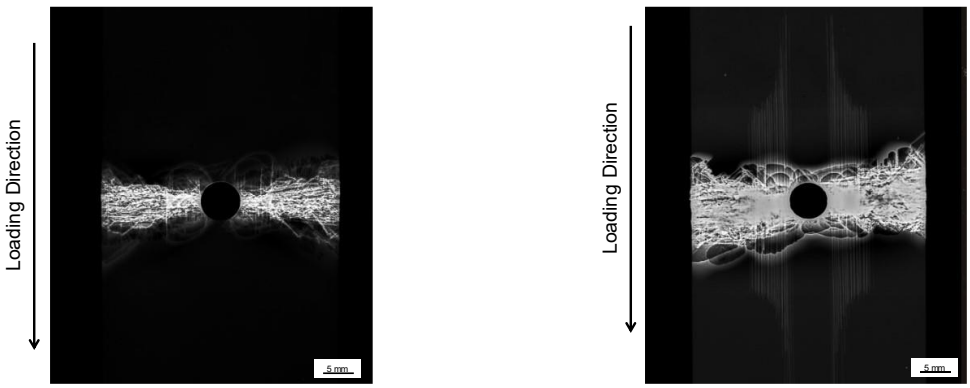

Fig. 7. Post OHC X-ray scan of (a) Baseline (b) Hybrid samples

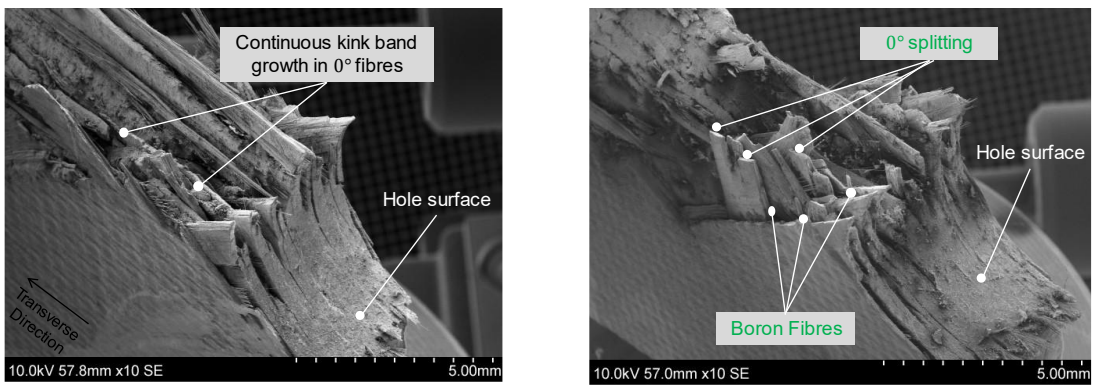

Figure 8: Post OHC SEM micrograph of (a) Baseline (b) Hybrid samples

5 DISCUSSIONS

The results presented in Section 4 show that the proposed local hybridization design about an open hole in quasi-isotropic CFRP laminates was successful in significantly improving the compressive performance. The increase in compressive strength of the hybrid laminate when compared to the baseline one was close to 35%. This improvement can be attributed partially to the reduction in the stress concentration at the hole edge (Fig. 6(c)) and partly to the formation of longitudinal splits within the 0° ply in the case of the hybrid laminates (Fig. 8 (b)). These longitudinal splits interrupt the unstable progression of kink bands in the transverse direction. This phenomenon is similar to the one reported by Garulli et al. [4] where they studied the damage mechanisms in boron-carbon hybrid laminates under compressive loading for edge-notched specimens. In fact, the presence of the longitudinal splits in the hybrid laminates leads to the formation of isolated strips of carbon fibres. This isolation of strips of carbon fibres results in a delay of the unstable kink band growth in a 0° ply, thus increasing the overall load and displacement (Fig. 5 (a)) at which catastrophic failure occurs. The presence of boron fibres (Fig. 6(b)) influences the local stiffness as observed by stress-local strain plots obtain from DIC and the FE model. On the other hand, the baseline samples exhibited evidence of continuous kink band growth (Fig. 8(a)), resulting in catastrophic failure at a lower load.

6 CONCLUSIONS

This research demonstrates the potential to increase the compressive strength of CFRP laminates structural features using a first-of-its-kind tailored strategy exploiting boron fibres to stop kink band propagation. Ultra-thin CFRP prepreg plies were reinforced locally using boron fibres. This has been achieved developing an in-situ manufacturing process for individual boron-fibre placement locally within the plies. The performance of hybrid boron-carbon laminates was assessed against baseline laminates under open-hole compression. The hybrid laminates exhibited an improvement of by 35% open hole compressive strength compared to baseline non-hybrid quasi-isotropic laminates.

In conclusion, this study underscores the efficacy of a localized hybridization approach in improving the compressive performance with insignificant influence on stiffness and weight of the laminates, thus offering a practical localized solution for designers to improve compressive strength near structural details such as open hole features without affecting the overall structure at a global level.

ACKNOWLEDGEMENTS

The authors acknowledge the funding for this research provided by UK Engineering and Physical Sciences Research Council (EPSRC) programme Grant EP/T011653/1, Next Generation Fibre-Reinforced Composites: a Full Scale Redesign for Compression in collaboration with University of Bristol.

For the purpose of open access, the authors have applied a Creative Commons Attribution (CC BY) license to any author accepted manuscript version arising.

The authors would thank Speciality Materials for providing the Boron fibres for this study. The authors would also like to thank the staff of the Composite Suite, PACT Lab and Aeronautics Workshop at Department of Aeronautics, Imperial College London for their assistance in manufacturing and testing of the samples for this study.

REFERENCES

[1] C. Soutis, N.A. Fleck, Static Compression Failure of Carbon Fibre T800/924C Composite Plate with a Single Hole, J Compos Mater 24 (1990) 536–558. https://doi.org/10.1177/002199839002400505.

[2] H. Suemasu, H. Takahashi, T. Ishikawa, On failure mechanisms of composite laminates with an open hole subjected to compressive load, Compos Sci Technol 66 (2006) 634–641. https://doi.org/10.1016/j.compscitech.2005.07.042.

[3] H. Suemasu, Y. Naito, K. Gozu, Y. Aoki, Damage initiation and growth in composite laminates during open hole compression tests, Advanced Composite Materials 21 (2012) 209–220. https://doi.org/10.1080/09243046.2012.723330.
[4] T. Garulli, T.J. Katafiasz, E.S. Greenhalgh, S.T. Pinho, Damage deflection and subsequent damage diffusion in carbon–boron fibre hybrid composites under longitudinal compression, Compos B Eng 291 (2025) 112025. https://doi.org/10.1016/j.compositesb.2024.112025.
[5] ASTMD6484/D6484M-23, Test Method for Open-Hole Compressive Strength of Polymer Matrix Composite Laminates, (2023). https://doi.org/10.1520/D6484_D6484M-23.
[6] T. Garulli, T.J. Katafiasz, E.S. Greenhalgh, S.T. Pinho, A novel bio-inspired microstructure for improved compressive performance of multidirectional CFRP laminates, Compos B Eng 264 (2023). https://doi.org/10.1016/j.compositesb.2023.110867.
[7] Boron Fiber Properties — Specialty Materials, (2025). https://www.specmaterials.com/boron-fiber-test-page.
[8] NTPT ThinPreg™ 402 data sheet Version 1.6, (2017). https://ntpt.tech/wp-content/uploads/2024/02/NTPT-DS-ThinPreg-402-May2017-v3.pdf.
[9] Abaqus/CAE | SIMULIA - Dassault Systèmes, (2024). https://www.3ds.com/products/simulia/abaqus/cae.

RESIDUAL STRAIN DEVELOPMENT IN CARBON FIBER REINFORCED METAL HYBRID LAMINATS: AN EXPERIMENTAL INVESTIGATION USING FBG STRAIN SENSORS

Maximilian Pollak, Michael Paulitsch and Roland M. Hinterhölzl

Research Group of Lightweight Design and Composite Materials, University of Applied Sciences

Contents

UNIVERSITY OF APPLIED SCIENCES UPPER AUSTRIA
OBERÖSTERREICH

- **Introduction**
- **Measurement System**
- **Experiments**
- **Results**
- **Outlook**

Motivation

Transformation of Mobility – “Imp4Zero”

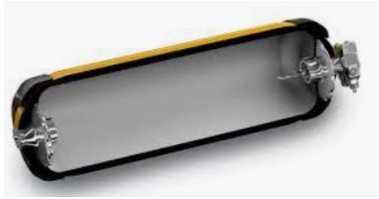

Non-destructive characterization of materials and components in 3D

Arc detection



[2]

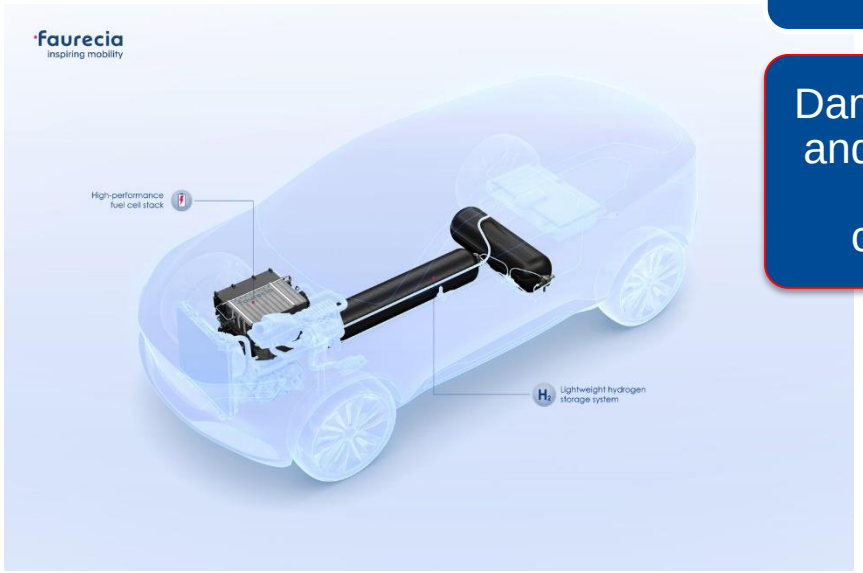

[1]

Damage detection and prevention in lightweight components

High-voltage testing



Motivation

Damage Detection

- **Improve safety of battery box and H2 pressure vessels**
- **Increasing service life**
- **Enhance Quality control**



[3]



[4]

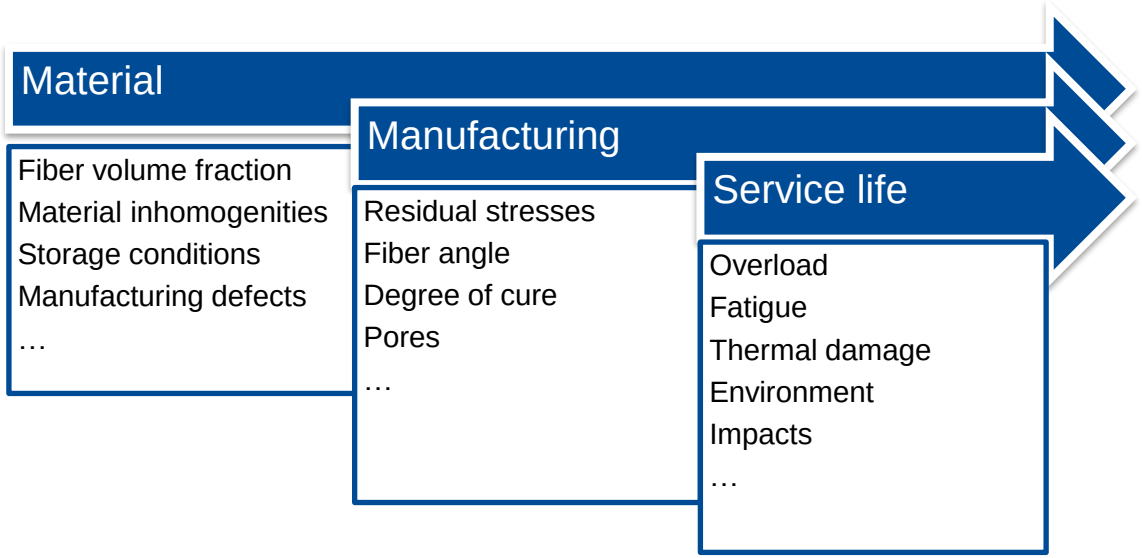

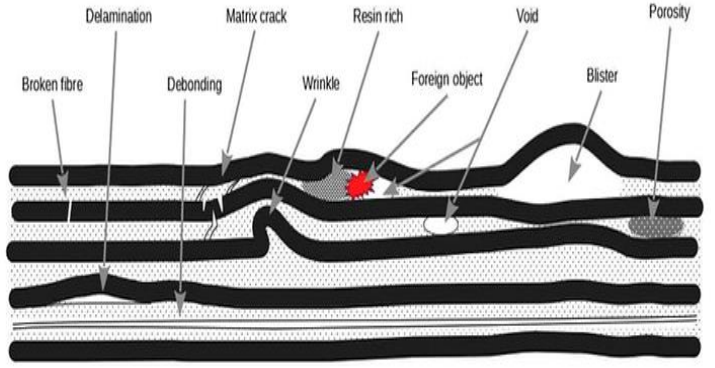

[5]

Goals

- **Development of a measuring system for condition monitoring of structural composite components**
- **Condition monitoring:**
  - during manufacturing
  - of structural tests in the context of component development
  - online during operation
- **Investigation of the influence of sensor integration on mechanical performance**

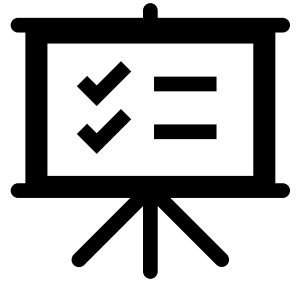

Methods - Building Blocks

UNIVERSITY OF APPLIED SCIENCES UPPER AUSTRIA
OBERÖSTERREICH

Produktzyklus

Process-induced effects, defects

Damage, service life

Raw material

Material and structural behaviour

DAQ-System

Digital Twin

Simulation

Damage, process/structural simulation, simulation chain,

Condition monitoring, FBG sensor, DAQ system, AE

Virtual Object

Data analysis

Model validation, feedback method

Sensor Calibration

Damage detection, damage index, prediction

Methods - Building Blocks

UNIVERSITY OF APPLIED SCIENCES UPPER AUSTRIA
OBERÖSTERREICH

Produktzyklus

Raw material

Process-induced effects, defects

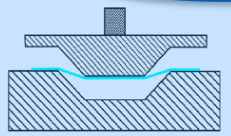

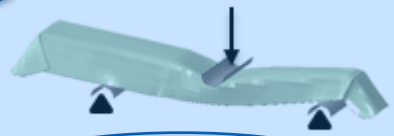

Material and structural behaviour

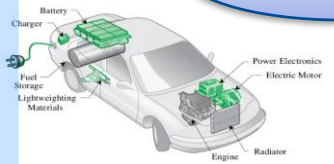

Damage, service life

DAQ-System

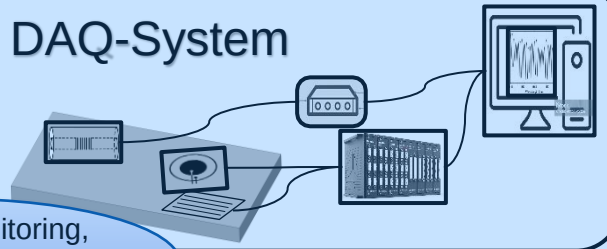

Condition monitoring, FBG sensor, DAQ system, AE

Digital Twin



Virtual Object

Simulation

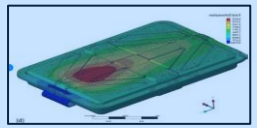

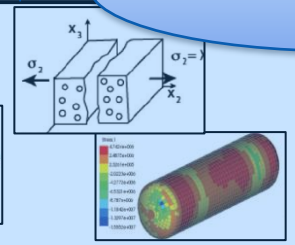

Damage, process/structural simulation, simulation chain,

Data analysis

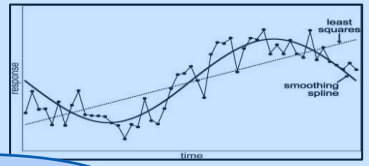

Sensor Calibration



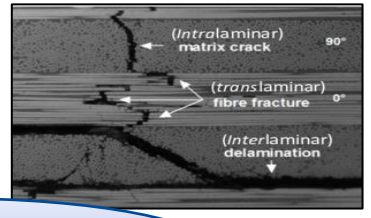

Damage detection, damage index, prediction

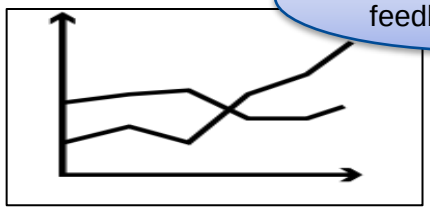

Model validation, feedback method

FBG Introduction

- **grating in the core of an optical fiber**
- **Small size ⌀150 µm, high sensitivity**
- **Acts as a wavelength-selective filter/mirror**
- **Sensitive to strain and temperature**
- **Wavelength shift:**

$$\Delta\lambda_B = (1 - p_e)\Delta\varepsilon + (\alpha + \zeta)\Delta T$$

p_e … photo − elastic constant

α … coefficient of thermal expansion

ζ … thermo − optic coefficient

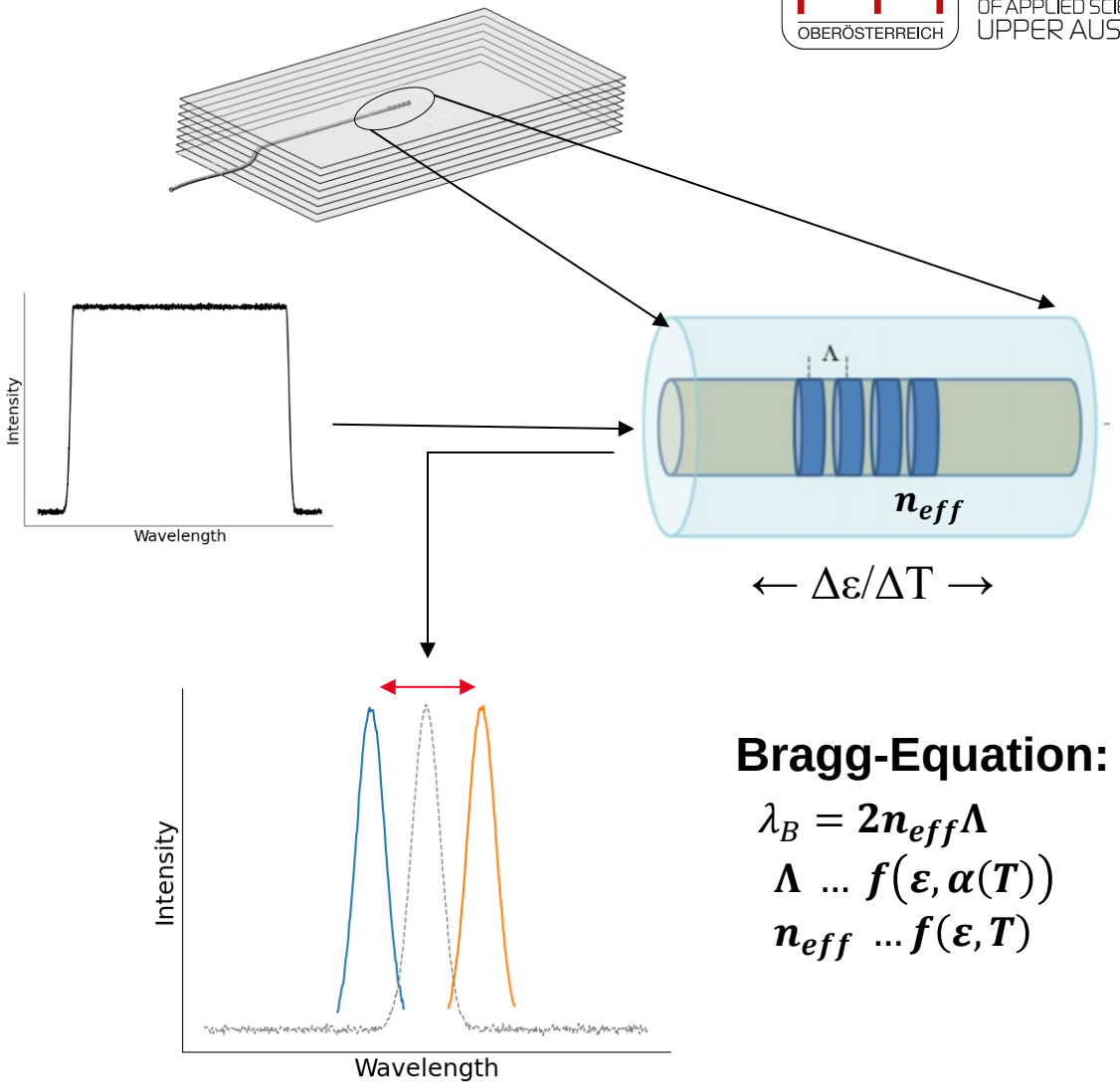

Bragg-Equation:

$\lambda_B = 2n_{eff}\Lambda$

Λ … $f(\varepsilon, \alpha(T))$

n_{eff} … $f(\varepsilon, T)$

Calibration Method

- **In-situ calibration with embedded FBG and thermo-couple in tensile test rig with temperature camber**
- **Strain calibration in range of 1500με**
- **Temperature in range -40°C – +180°C**
- **Temperature dependent CTE from TMA**

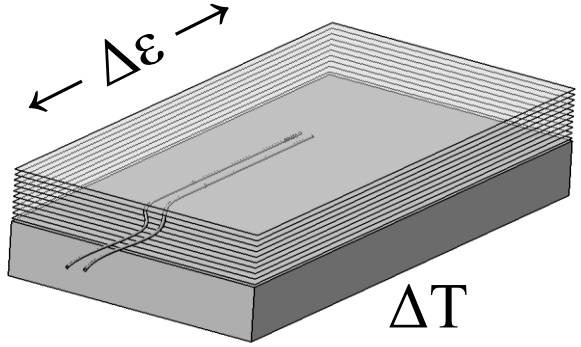

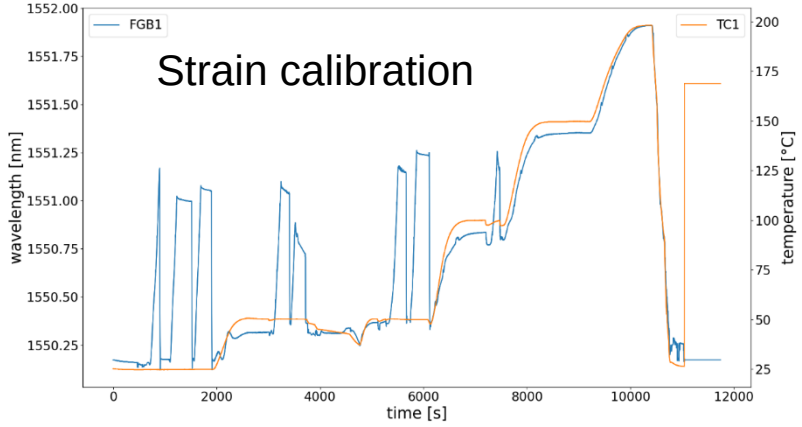

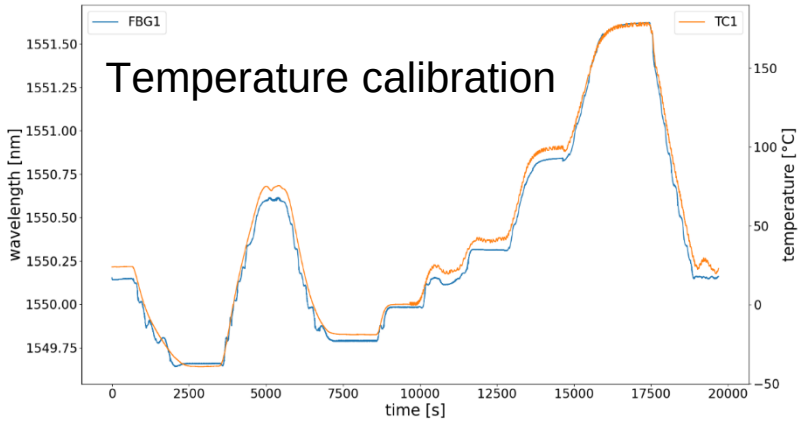

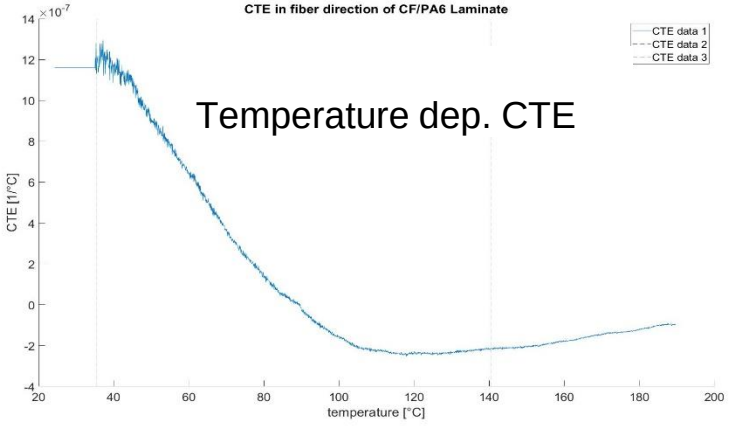

Calibration Models

- **Emperical calibration model with least square**
- **Total sensitivity:** $(\lambda - \lambda_0)_{\boldsymbol{total}} = (\lambda - \lambda_0)_{\varepsilon} + (\lambda - \lambda_0)_{\boldsymbol{\alpha}} + (\lambda - \lambda_0)_{\boldsymbol{T}}$
- **Strain sensitivity:** $(\lambda - \lambda_0)_{\varepsilon} = K_{\varepsilon} \Delta\varepsilon$
- **CTE sensitivity :** $(\lambda - \lambda_0)_{\alpha} = \alpha(T) \cdot \Delta T \cdot K_{\varepsilon}$
- **Temperature sensitivity :** $(\lambda - \lambda_0)_{T} = p_0 + p_1 \Delta T + p_2 \Delta T^2 + p_{\boldsymbol{3}} \Delta T^{\boldsymbol{3}} - \alpha(T) \cdot \Delta T \cdot K_{\varepsilon}$

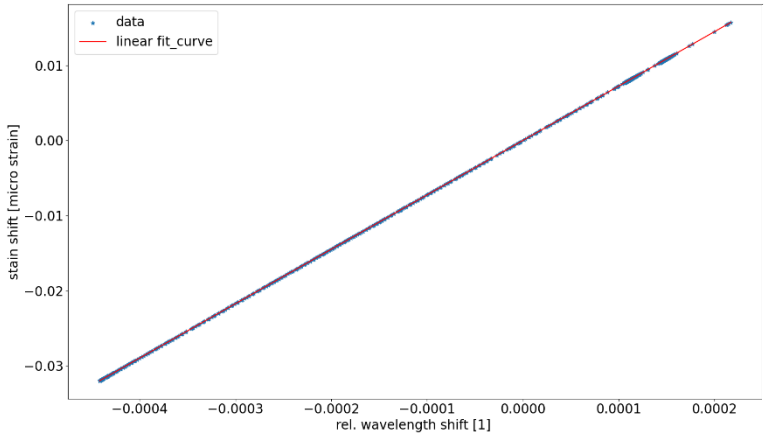

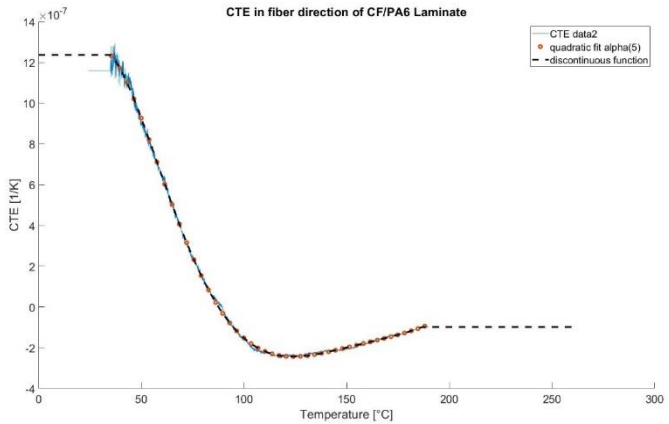

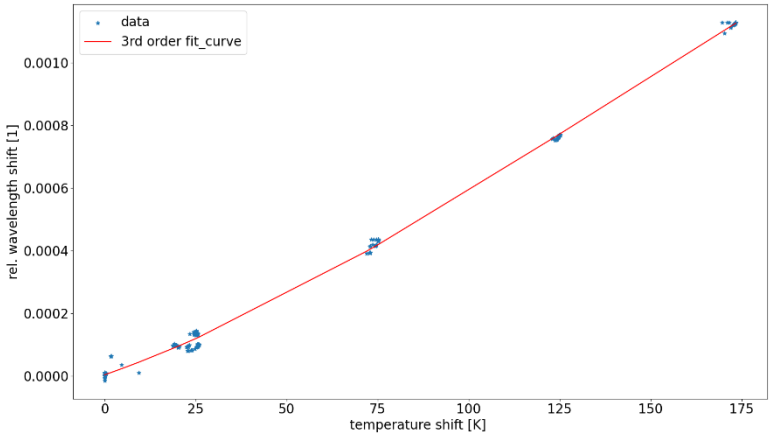

Materials



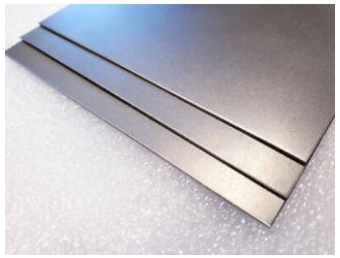

UNIVERSITY OF APPLIED SCIENCES UPPER AUSTRIA
OBERÖSTERREICH

TP-CFRP material:

- 0.2mm CF/PA6 Tape (SGL SIGRAPREG®TP C U157-0/NF-T340/46%)

Metal plates:

- 2mm stainless steel 1.4301
- 2mm aluminium plate EN AW-1050A

Adhesion promoter:

- Vestamelt Hylink (Evonik)

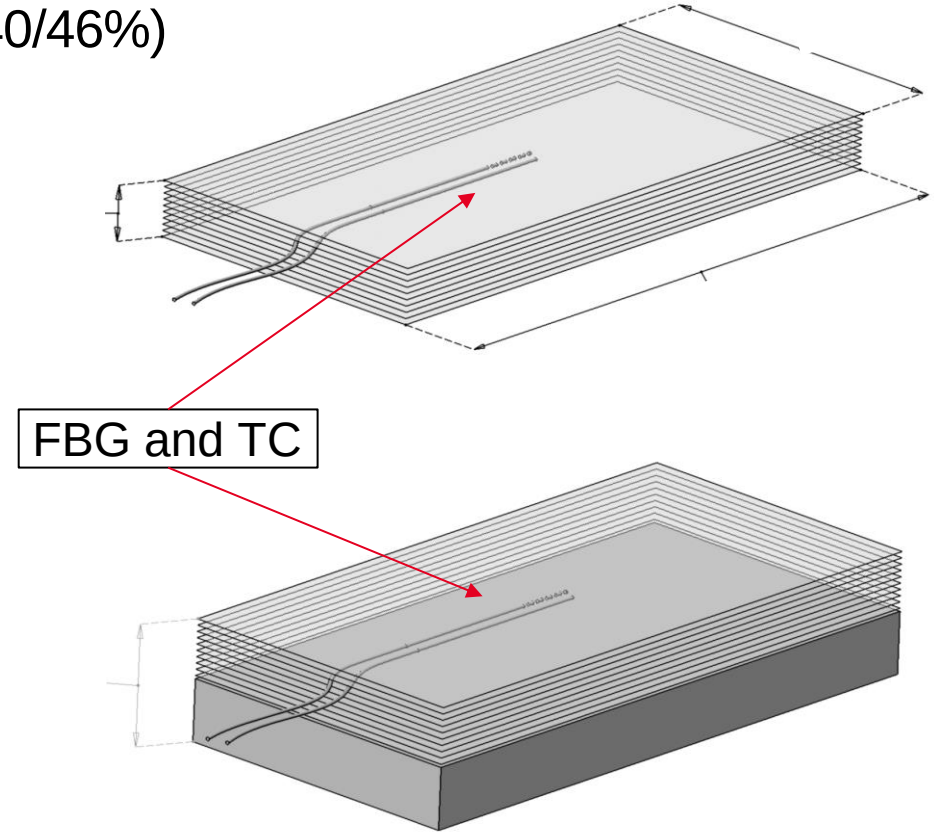

	Name	Layup	Sensor layer	Monitoring	Geometry
CFRP	symmetric-cross	$[0_2/90_2/0]_{2s}$	5/6	process	200x100x4mm
CFRP	unsymmetric cross	$[0_{12}/90_8]$	5/6	process	
Hybrid	CF/PA6-AL	$[0_{10}/AL_{2mm}]$	7/8	process, thermal cycling	
Hybrid	CF/PA6-ST	$[0_{10}/ST_{2mm}]$	7/8	process, thermal cycling	
Hybrid	cross-CF/PA6-AL	$[0_290_2/0_2/90_2/0_2/AL]$	7/8	process	
Hybrid	cross-CF/PA6-ST	$[0_290_2/0_2/90_2/0_2/ST]$	7/8	process	

Process Monitoring

- **Hot press mold with sensor feed-through**
- **FBG + TC embedded in stack**
- **230°C and 100kN**
- **CFRP and Hybrids investigated**

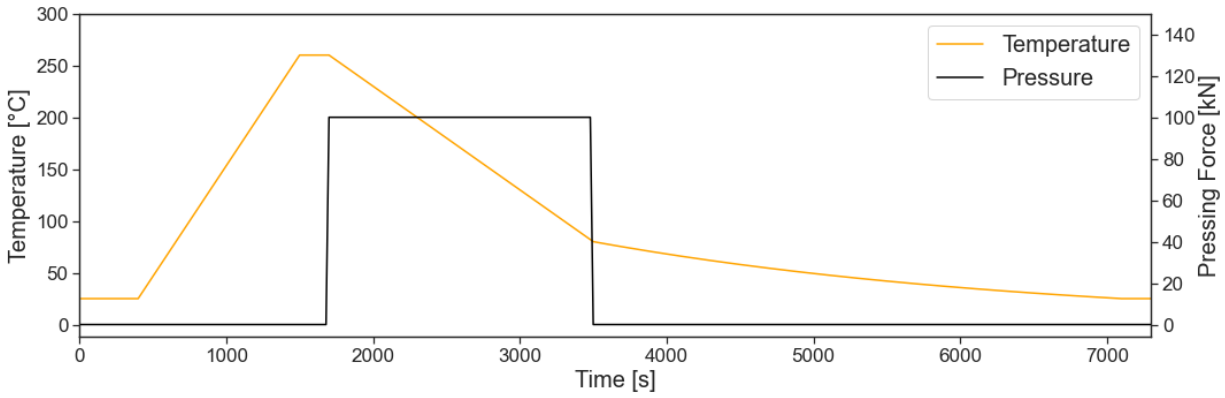



Thermal Cycling Test



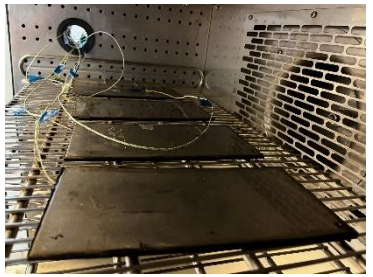

- **Climate chamber with sensor feed-through**
- **Aviation and Automotive cycle**
- **CF/PA6-ST and CF/PA6-AL specimens**

Cycle	Automotive	Aviation
Temperatures	-40°C, 40°C, 80°C, 40°C	-40°C, 80°C
Hold time	10h	1,5h
Cycles	4.5	50
Total time	180h (7day 12h)	150h (6day 6h)
Material	CF/PA6-ST	CF/PA6-AL
specimens	4 200x100x4mm	4 Stk. 200x100x4mm
Heating rate	Cooling: -4°C/min +8°C/min	

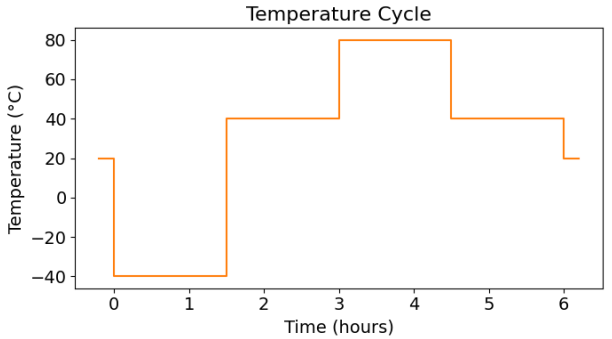

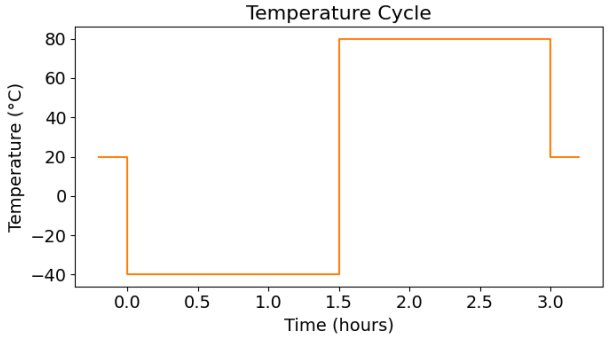

Results - Process Monitoring

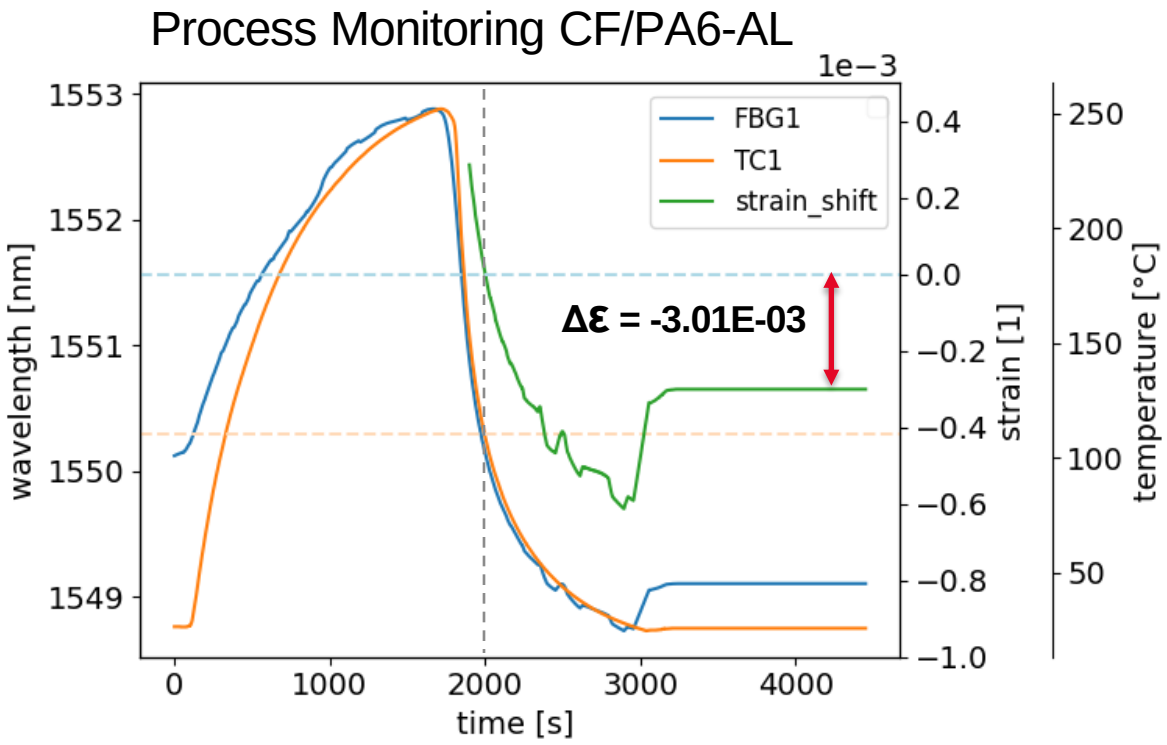

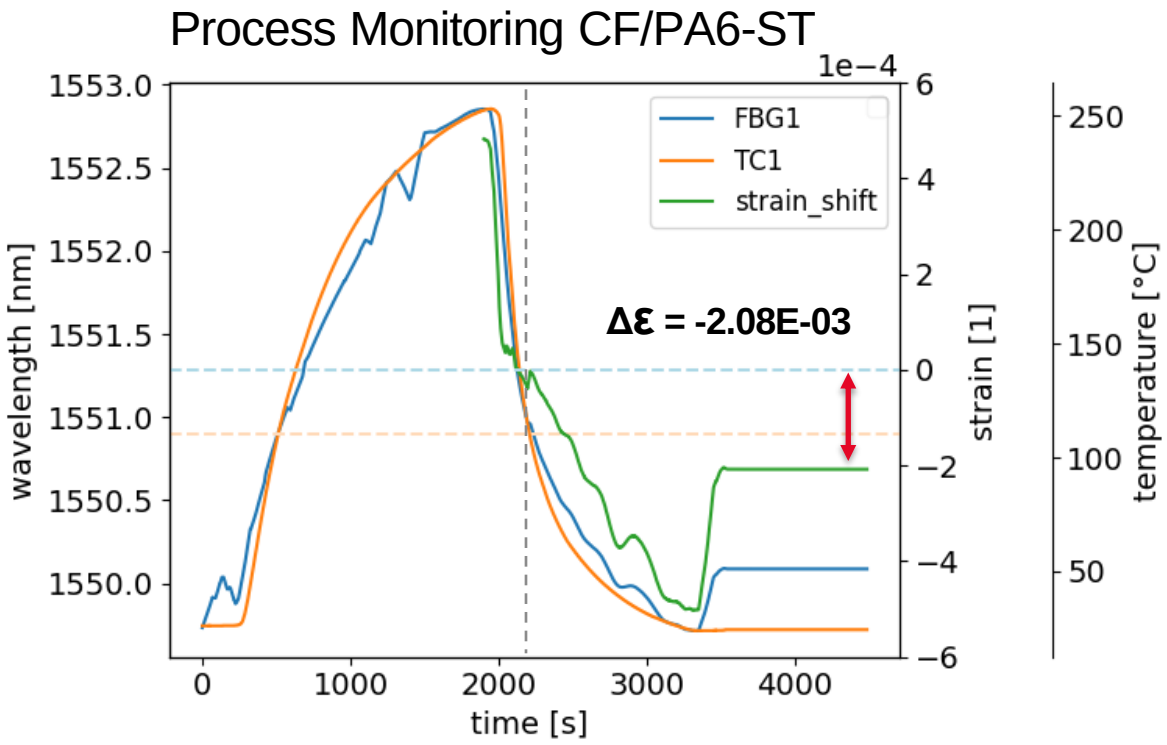

Results – Process Monitoring

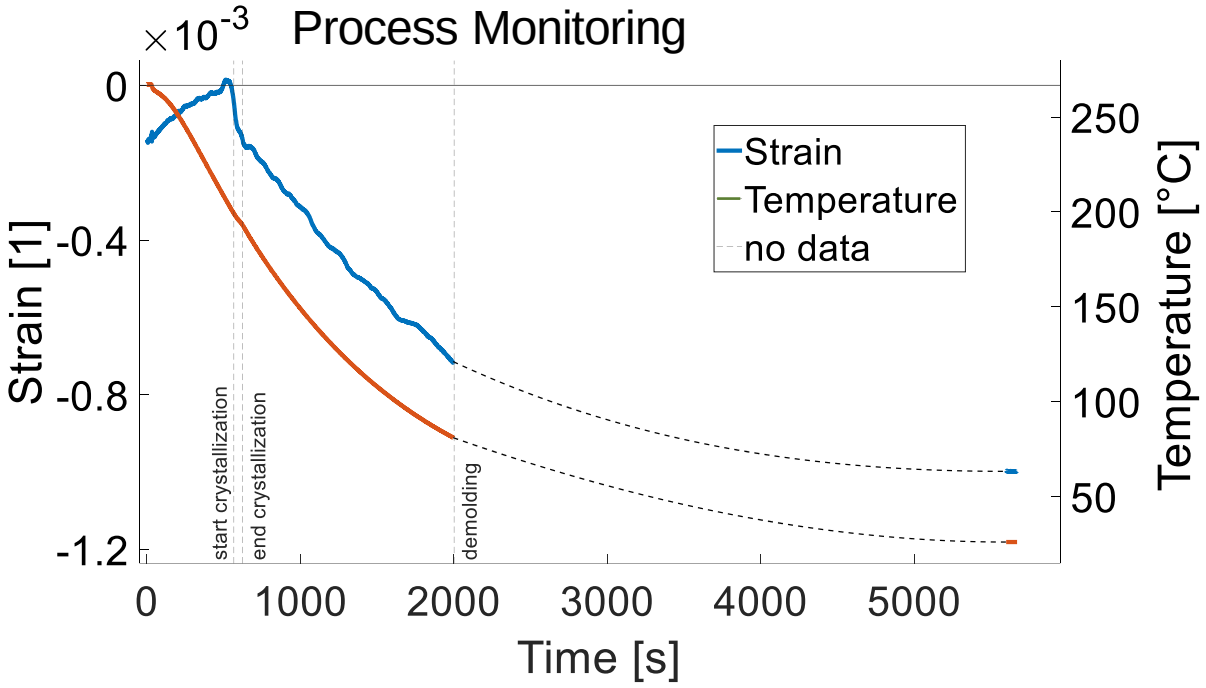

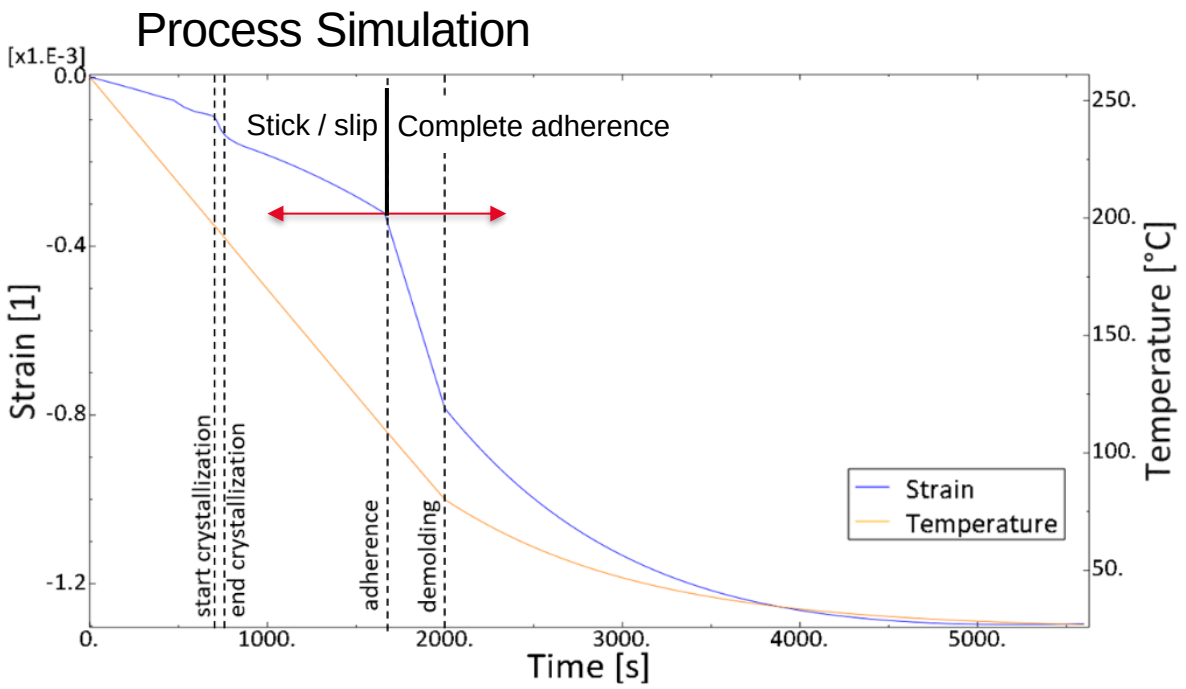

Results – Process Monitoring

Comparison measured strain vs. simulated strain

	Material Combination	Measurement Strain [10^{-3}]	Simulation Strain [10^{-3}]
CFRP	$[0_2/90_2/0_2/90_2/0_2]s$	-0.56	-0.55
		-0.49	-0.55
	$[0_{12}/90_8]$*	-0.59	-0.37
CFRP-metal hybrid	$[Al/0_{10}]$	-0.68	-0.95
		-0.67	-0.95
	$[Al/0_2/90_2/0_2/90_2/0_2]$	-1.22	-1.30
		-1.17	-1.30
	$[Steel/0_{10}]$	-0.47	-0.85
		-0.47	-0.85
	$[Steel/0_2/90_2/0_2/90_2/0_2]$	-1.00	-1.30
		-1.27	-1.30

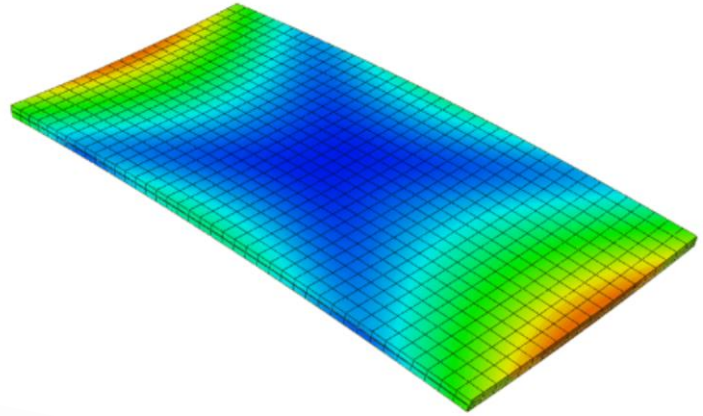

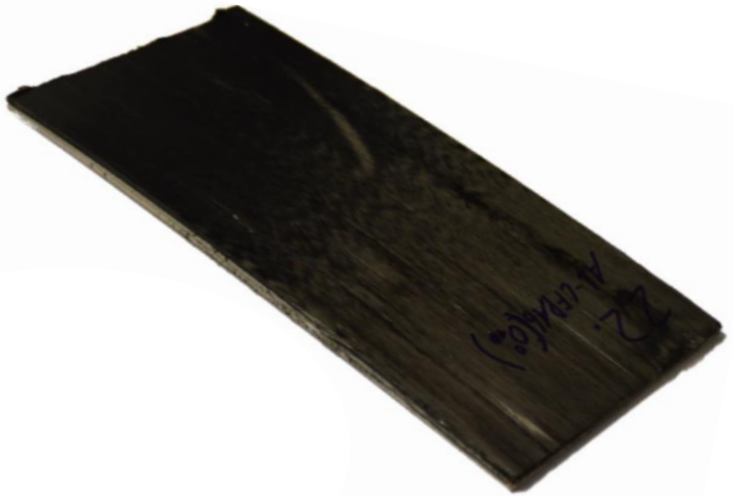

Results - Thermal Cycling

- **Investigated specimens**
  - **CF/PA6-ST (automotive)**
  - **CF/PA6-AL (aviation)**
- **No major relaxation observed**

Automotive cycle

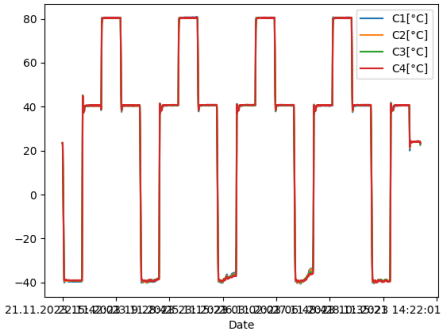

Aviation cycle

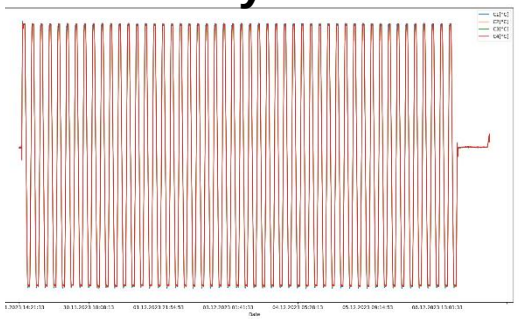

Automotive cycle

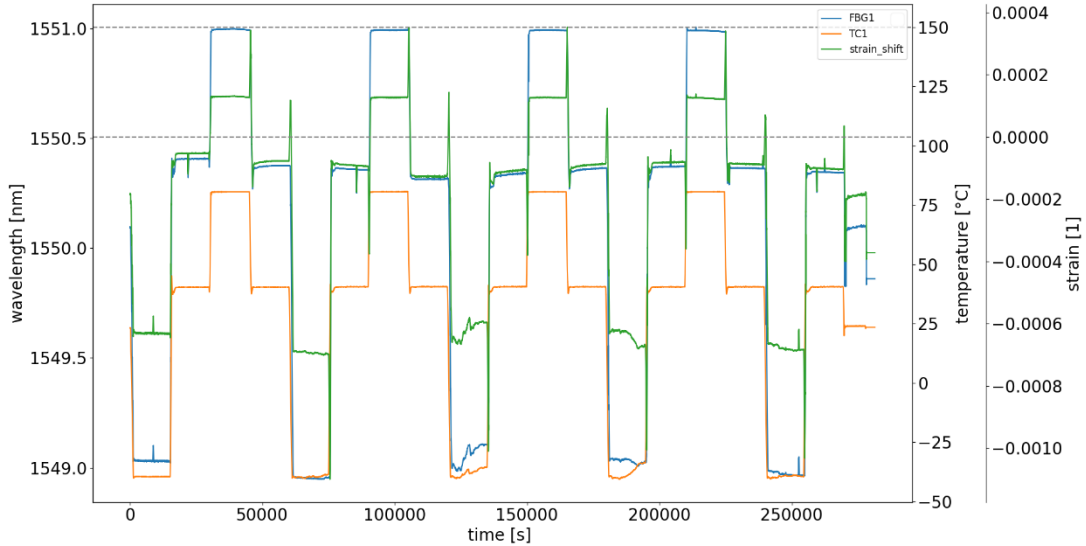

Results - Laser Scan

- **3D Laser scan of curved specimens**
- **Least-squares cylinder fitting**
- **Mean strain release 30-50με**
- **No release after cycling**

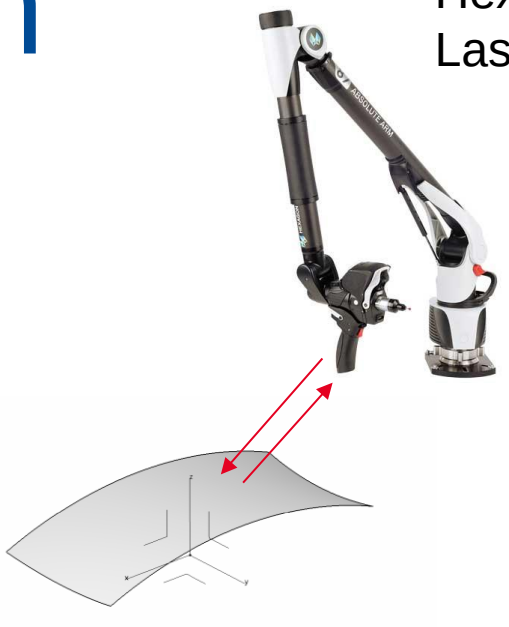

Hexagon
Laserscanner

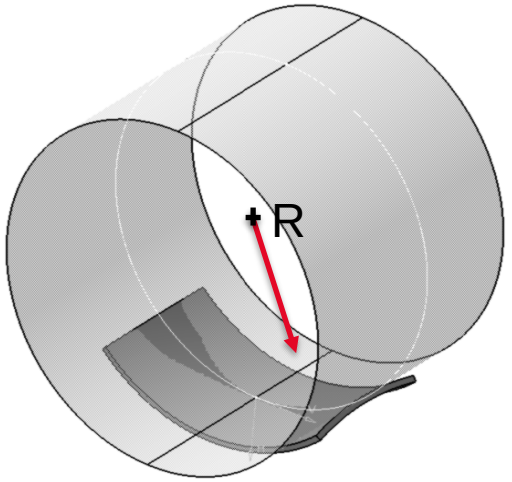

Curvature measurements

State	Curvatures		Strains at FBG layer	
	ST-CF/PA6	AL-CF/PA6	ST-CF/PA6	AL-CF/PA6
After manufacturing	2.63E-3	5.05E-3	-2.15E-3	-3.23E-3
Bevor thermal cycling	3.22E-3	6.01E-3	-1.64E-3	-2.94E-3
After thermal cycling	3.34E-3	6.21E-3	-1.64E-3	-2.91E-3

Methods - Building Blocks

UNIVERSITY OF APPLIED SCIENCES UPPER AUSTRIA
OBERÖSTERREICH

Produktzyklus

Process-induced effects, defects

Damage, service life

Raw material

Material and structural behaviour

DAQ-System

Digital Twin

Simulation

Damage, process/structural simulation, simulation chain,

Condition monitoring, FBG sensor, DAQ system, AE

Virtual Object

Data analysis

Sensor Calibration

Damage detection, damage index, prediction

Model validation, feedback method

Simulation-Chain “As-built“

- **Draping + Cure + Structural with mapped field variables**
- **Simulation „As-built“**
- **Mapping with user subroutines on intergration points**

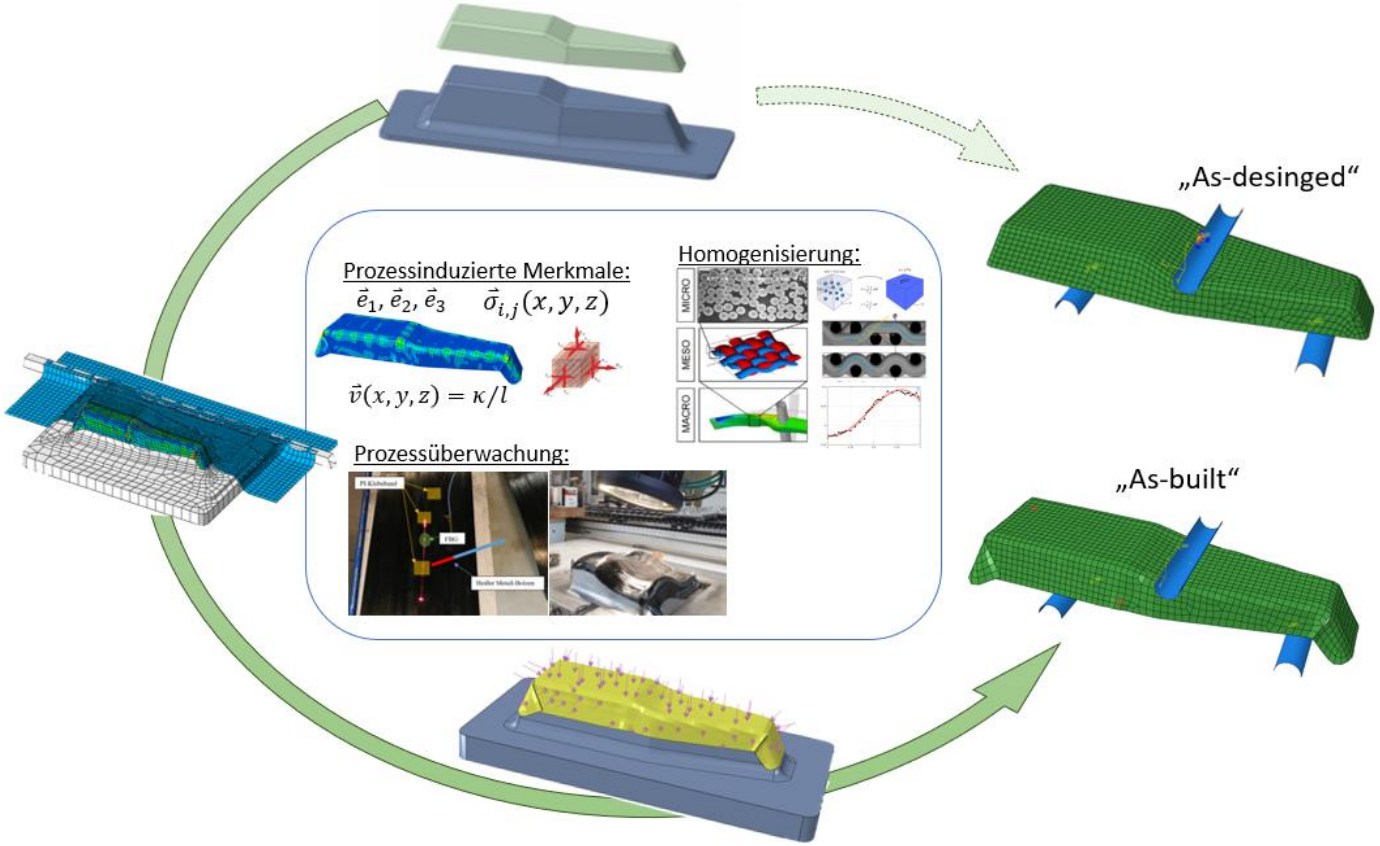

Results - “As-built“ Simulation

- **Matrix Tension in Region 1 caused by stress concentration at wrinkle**
- **Mesh size has major influence on concentration**

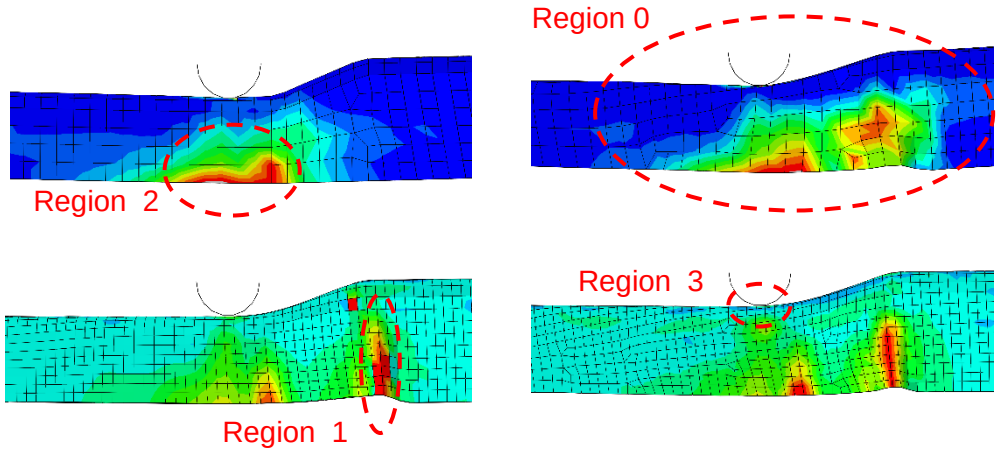

Hashin fiber tension initialisezion

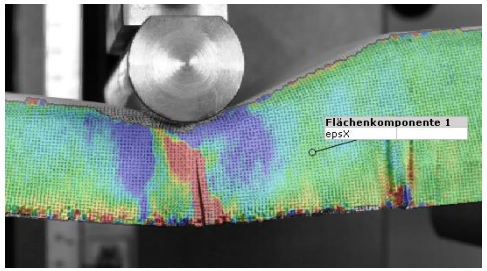

crack propagation beneth loading pin

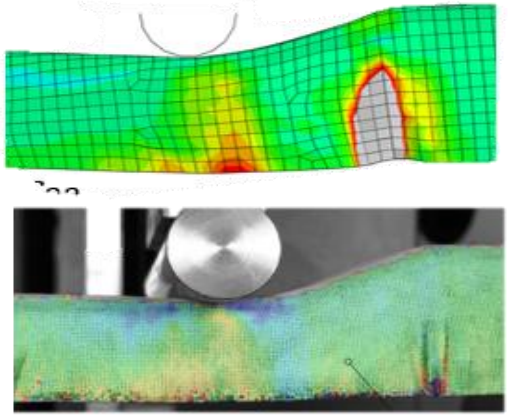

stress concentration observed in simulation and DIC

Results - “As-built“ Simulation

- **Comparison of reaction force of simulation and bending test**
- **Overestimated reaction force despite process induced effects**
- **Damage initialization of "As-built" agrees with test data**

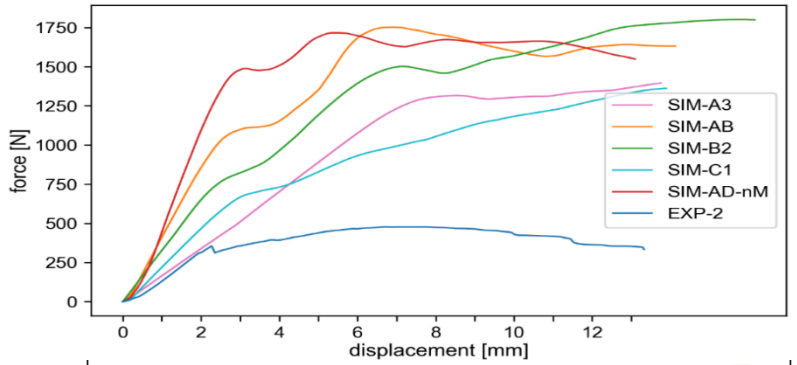

reaction force of loading pin

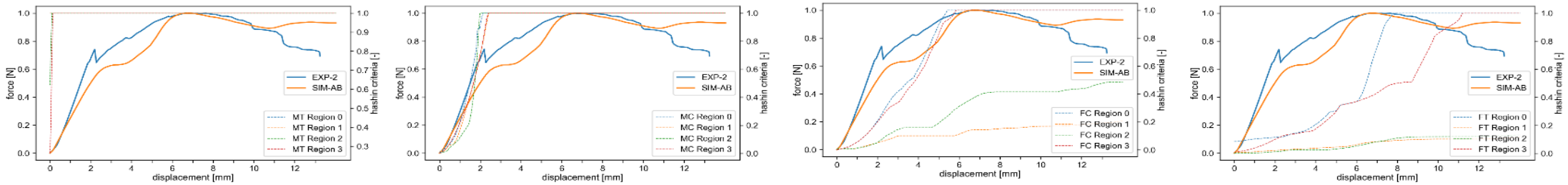

reaction force and Hashin criterion of simulation and bending test

Outlook

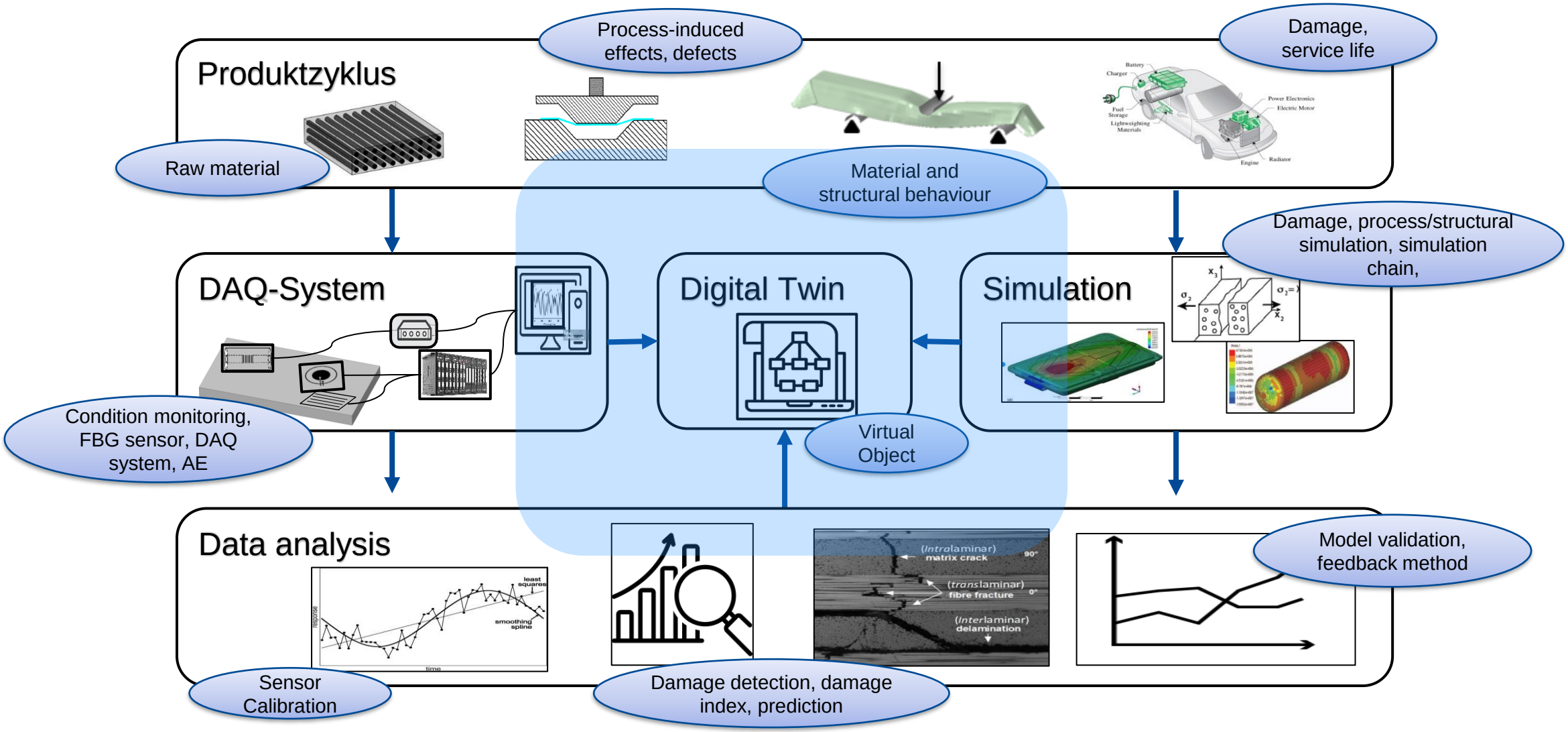
Produktzyklus
Process-induced effects, defects
Damage, service life
Raw material
Material and structural behaviour
DAQ-System
Digital Twin
Simulation
Damage, process/structural simulation, simulation chain,
Condition monitoring, FBG sensor, DAQ system, AE
Virtual Object
Data analysis
least squares
smoothing spline
(Intralaminar) matrix crack
(translaminar) fibre fracture
(Interlaminar) delamination
Model validation, feedback method
Sensor Calibration
Damage detection, damage index, prediction

Acknowledgement

This work was supported by the Upper Austrian Government through the project:

“IMP4Zero-E: Innovative Monitoring- und Prüfverfahren für den Zero-Emission-Antriebsstrang“

and under its FTI Structural-Funding Program:

“Erforschung von Methoden für die Mobilität der Zukunft” (Project No. Wi-2018-466449/18-WieM)“

and by the Austrian Research Promotion Agency (FFG) through the “ProSim“ project (No. 866878).



Contact

Maximilian Pollak

maximilian.pollak@fh-wels.at

Thank you for your attention!

CHARACTERISATION OF BINDER POWDERS IN GLASS FIBRE FABRICS USING LASER MICROSCOPY AND DEEP LEARNING SEGMENTATION METHODS

Jesper Lisegaard[1], Jesper Hattel[1] and Sankhya Mohanty[1]

[1]Department of Civil and Mechanical Engineering, Technical University of Denmark
Produktionstorvet, Building 425, DK-2800 Kgs. Lyngby, Denmark
Email: jejli@dtu.dk, web page: http://www.dtu.dk

Keywords: Binder Powders, Preforming, Machine Learning, Laser Microscopy, Image Analysis

ABSTRACT

Binder-stabilised preforms offer significant advantages in structural composite manufacturing, enhancing handling, repeatability, and overall process efficiency. However, the heterogeneous structure of the fabric, influenced by fibre orientations, binder powder distribution, and stitching patterns, presents challenges for process control and performance prediction. A detailed characterisation of these microstructural features is essential for optimising manufacturing parameters and ensuring consistent material properties. Laser microscopy combined with image analysis provides a powerful tool for quantifying these structural variations. Classical segmentation techniques, however, struggle to accurately delineate key features due to low contrast and complex material interfaces. In this work, we employ a deep learning-based segmentation approach using a U-Net model to overcome these challenges. The model enables robust segmentation of microscopy images, allowing for the extraction of critical microstructural properties, such as binder coverage, particle size distribution, and anisotropy, providing a quantitative basis for further analysis. The findings highlight the potential of deep learning in advancing automated image analysis for composite materials, paving the way for more data-driven approaches in material characterisation and process optimisation.

1 INTRODUCTION

Binder-powdered glass fibre fabrics show potential in composite manufacturing to create stable preforms that enable efficient, large-scale production e.g. for the wind turbine industry. Applying a polymer binder powder to the glass fibre fabrics gives the consolidated preforms mechanical stability upon activation (i.e. heat treatment under glass transition temperature), allowing them to be manipulated and transported. This stabilisation is essential for vacuum-assisted resin transfer moulding (VARTM) and similar processes, where consistent fibre distribution within preforms helps improve the flow of resin and, consequently, the overall quality of the final composite material.[1–5] Moreover, the use of binder powdered fabrics has the potential to parallelise the production stage, where the glass fibre fabrics are placed in the mould, ultimately reducing the lead time and cost associated with large-scale composite manufacturing.[6–8]

Despite the potential for widespread industrial application of binder powdered glass fibre fabrics (BP-GFF), current knowledge on the microstructural influence of binder powders is limited, particularly concerning how they interact with the fibres. The complex morphology of the binder powders and their heterogeneous distribution within the fibre preform poses multiple challenges for modelling the process. Existing methods often rely on simplified assumptions that do not capture the intricacies of the binder distribution and do not accurately represent the fibre-matrix interface.[9] This gap in robust modelling methodologies limits the predictability and optimisation of the manufacturing process, making it difficult to standardise quality control measures. As a result, there is a pressing need for more advanced characterisation techniques to facilitate accurate preform structure modelling and enhance binder powder composites' reliability.

Laser scanning confocal microscopy offers a promising approach by providing high-resolution imaging of BP-GFFs, enabling detailed analysis of the binder's distribution and morphology.[10]

These high-resolution images can be segmented through advanced image processing techniques to characterise the binder topology. Traditional segmentation methods, such as intensity threshold and feature-based segmentation, perform poorly for segmenting the laser microscopy images as the segmentation classes do not have separation in the intensity values nor the basic features. More recent advancements in machine learning, particularly convolutional neural networks (CNNs), allow for improved accuracy in segmenting complex, irregular structures. Badran et al. (2020) employed a deep neural network to segment 3D tomography images of SiC–SiC composites (i.e where fibre and matrix were made of same material), thereby facilitating automated analysis of fibre distribution and matrix cracking.[11] Hong et al. (2021) developed a deep learning model to segment short fibres in glass fibre reinforced concrete using X-ray micro-computed tomography images.[12] Guo et al. (2023) demonstrated the use of a U-Net for precise fibre segmentation in time-resolved computed tomography (CT) scans.[13] Vorobev et al. (2023) applied deep learning models to segment structural defects in polymer composite CT images, improving the detection of defects.[14] Dong et al. (2024) applied a U-Net model for segmenting 2D optical images to characterise the microstructure of fibre-hybrid polymer composites.[15]

In this study, we train and deploy a deep CNN based on U-Net to improve the segmentation of binders and glass fibres in laser scanning microscopy images of BF-GFFs.

2 DATA

The considered fabrics are Unidirectional Non-Crimp glass fibre Fabrics (UD NCF) and Biaxial (Biax) glass fibre fabrics, to which a semi-transparent polymer binder powder has been applied on the top surface of the fabrics. Both fabrics were acquired with the binder powder already applied.

The laser microscopy images are obtained using an Olympus LEXT laser microscope[16] using a 10X zoom objective and stitching multiple scans to cover more surface area than a single scan can. An example of a 4x4 stitched microscopy image of a UD NCF BP-GFF is shown below in fig. 1.

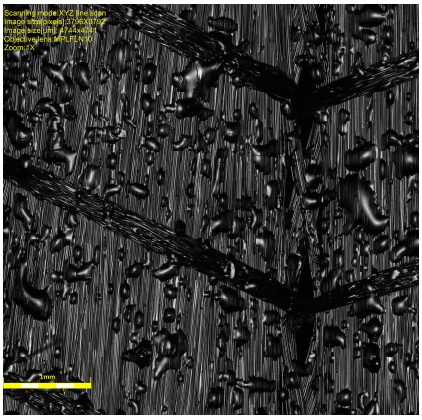

Figure 1: Laser scanning microscopy image of a UD NCF glass fibre fabric with polymer binder powder applied.

3 METHODS

3.1 Classical image segmentation methods

As seen on the microscopy image, the segmentation of binder powder and glass fibres is not a trivial task. The inherent features making the task difficult are, among others: 1) No significant contrast between binder powder and glass fibres. 2) Binder powders are semi-transparent, and the glass fibre structures come through. 3) The low contrast stitching makes the binder powder difficult to detect. Furthermore, manual segmentation is not a viable solution either, as even for quite small surface areas as the one shown in Fig. 1, there will be hundreds of particles present, making manual annotation of every one of them impractical.

These image features make it a difficult task to obtain good segmentations through classical imaging techniques. Intensity threshold and watershed methods will yield poor results, as there is no clear separation between classes in the intensity spectrum. More advanced methods, like the implementation [17] of the Structure Tensor method, which has previously been used to characterise fibre directions [18], can usually segment fibre images due to the directional information in the images. However, as the binder powder is semi-transparent, the directional information of the underlying glass fibres is also found in areas containing binder particles. Furthermore, the areas with stitching are also without any directional information and will therefore falsely be classified as binders. Therefore, these methods are inadequate for the segmentation task at hand.

3.2 Deep Learning segmentation

The dataset for training the deep learning segmentation model is established by cropping the original dataset into 512x512-pixel patches. Given the 8 original high-resolution images, this yields a total of 278 image patches. Of those, 90% (250 patches) will be used for training, and 10% (28 patches) will be used as the validation set during training. To guide the training, the images are partially annotated, separating areas that are binder powder and areas that are not binder powder. These masks have been encoded into three classes: {0, 1, 2} = {Unknown, Not Binder Powder, Binder powder}. Similarly to the original images, the masks are cropped into 278 patches, such that each training image patch has a corresponding mask patch holding some ground truth information.

The architecture used for the deep learning segmentation task is a U-Net, originally proposed by Ronneberger et al. (2015) [19]. In comparison with other architectures, U-Nets have proved excellent performance in image segmentation as the visual information is restored through the encoder-decoder architecture. 2) U-Nets do, in general, perform well on smaller datasets. The chosen architecture is further of the type utilising the deep CNN ResNet34 [20] as the backbone, where the ResNet34 is pre-trained on the ImageNet dataset [21]. The loss function used in the training of the U-Net is weighted categorical cross-entropy loss [22], where the classes {0, 1, 2} are assigned weight {0.0, 1.0, 1.0}, meaning no weight on the areas having no label and equal weight on the labelled areas. The network is trained using an ADAM optimiser for 200 epochs, showing a convergence of the training and validation losses in Fig. 2.

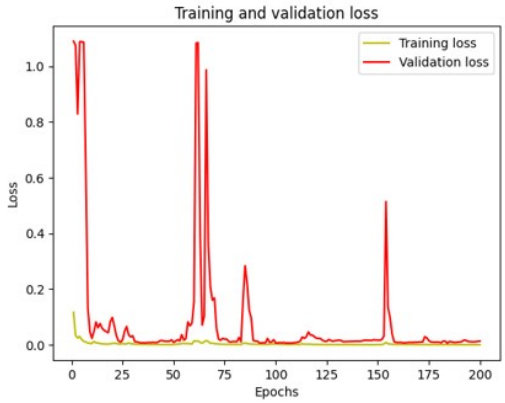

Figure 2: Training and validation loss curves for the U-Net segmentation model over 200 epochs.

4 RESULTS

The segmentation for a microscopy image produced by the U-Net segmentation model is shown in Fig. 3. The model has not seen this microscopy image during training, and therefore, it can be used to validate the model's performance.

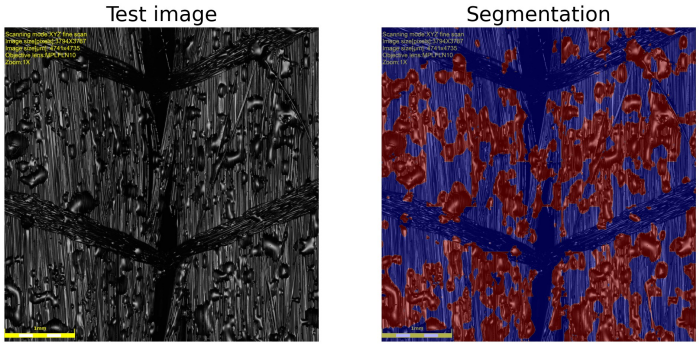

Figure 3: Microscopy image of a UD NCF BP-GFF (left) and corresponding U-Net segmentation output (right). Red pixels indicate binder powder; blue pixels indicate non-binder regions. This image was not part of the training set and is used for model validation.

Conferring Fig. 3, it can be difficult to assess whether the segmentation is a proper pixel-wise division of the microscopy image into the classes: binder powder and not binder powder. But certain metrics can aid in the assessment of the quality of the segmentation. The Intersection-over-Union (IoU) and Dice scores, both commonly used in the realm of image segmentation, are used in this study.

$$IoU = \frac{|A \cap B|}{|A \cup B|}, \quad Dice = \frac{2|A \cap B|}{|A| + |B|} \tag{1}$$

where A and B are the segmentation and annotation, respectively.

To properly compare the performance of each of the segmentation methods, IoU and Dice scores are computed for each of the methods against the annotation mask. The scores are only computed with regard to the annotated area corresponding to known classes. Furthermore, the confusion matrix is computed to evaluate the classification. The image used for validation is an image of UD NCF glass fibre fabrics that was acquired on the Olympus LEXT [16] from another sample, on another day, and that has not been part of either the training or the validation dataset. The image is the one shown in Fig. 3. This is to verify the robustness of the method, as it has to work on data that has not been seen by the model, while acquired under similar conditions to the training data.

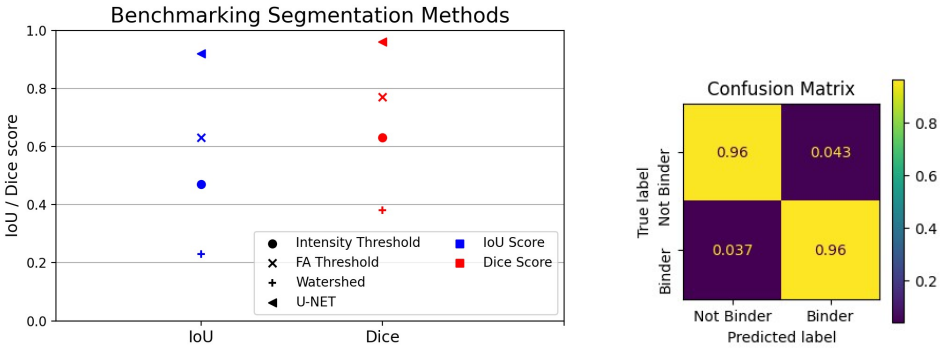

Figure 4: (Left) Intersection-over-Union (IoU) and Dice scores comparing classical and deep learning segmentation methods. (Right) Normalised confusion matrix for the U-Net model, showing 96% classification accuracy and balanced performance across classes.

As discussed, the scores in Fig. 4 demonstrate the fundamental limitations of classical methods in segmenting the microscopy images. The watershed approach fails to produce a meaningful segmentation, while intensity thresholding performs slightly better but remains insufficient for obtaining reliable segmentation results. This outcome is expected, as the image intensity spectrum lacks clear class separation. The structure tensor method using a fractional anisotropy measure

achieves a further improvement over the previous methods. However, its segmentation quality remains inadequate for meaningful post-processing. The U-Net segmentation model improves the scores significantly, as is seen in Fig. 4 (Left), where both IoU and Dice scores indicate a near-perfect match to the annotations. To further quantify the performance of the U-Net segmentation model, the normalised confusion matrix, Fig. 4 (Right), provides insights into how the classification performs and where it classifies incorrectly. Here it can be seen that the model correctly predicts 96\% of the pixels in each class, with a very low and equal rate of misclassification. This shows that there is no clear bias in the segmentation model. In total, this indicates that the segmentation model is successful and that the segmentation can be used for further processing.

The U-Net segmentation results provide a foundation for further analysis of material properties in the microscopy images. By leveraging the U-Net segmentation model, key characteristics such as binder coverage, particle size distribution, and particle aspect ratios can be quantified. These derived properties offer valuable insights into the material's composition and morphology, enabling a more detailed assessment. The U-Net segmentation model indicates that the binder coverage is approximately 50% in the microscopy image in Fig. 1, whereas the binder coverage is only approximately 34% in a similar microscopy image of a Biax glass fibre fabric. This indicates that the assumption of homogeneous binder powder distribution is inadequate.

Another derived result using the U-Net segmentation model is the particle size distribution. Using the ensemble of microscopy images acquired the particle size distribution is calculated. The resulting binder powder particle size distribution for assumed circular particles is shown in Fig. 5.

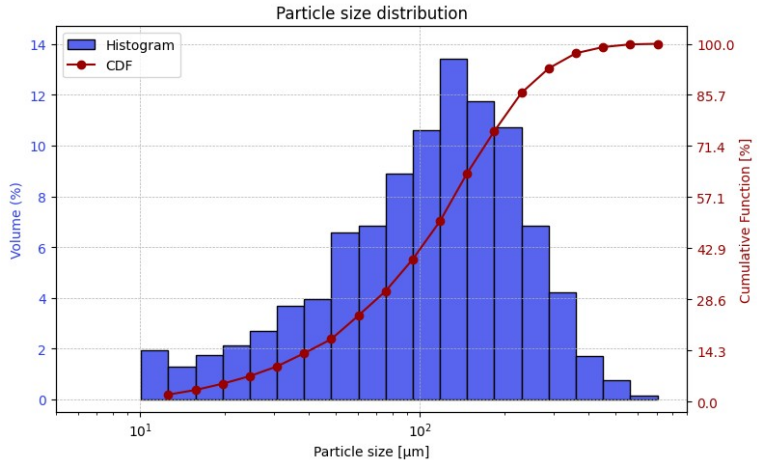

Figure 5: Distribution of binder powder particle sizes extracted from segmented microscopy images using the U-Net model. Particle sizes are estimated assuming circular geometry.

Furthermore, the binder powder particle aspect ratios, defined as the ratio of the longest axis to the shortest axis of the segmented particles, are of interest. First, to check whether the assumption of circular particles used for the particle sizes was violated, but secondly, because the binder powder morphology is of interest and poorly studied. Figure 6 summarises the binder powder particle aspect ratios of the particles in the microscopy images segmented using the U-net segmentation model.

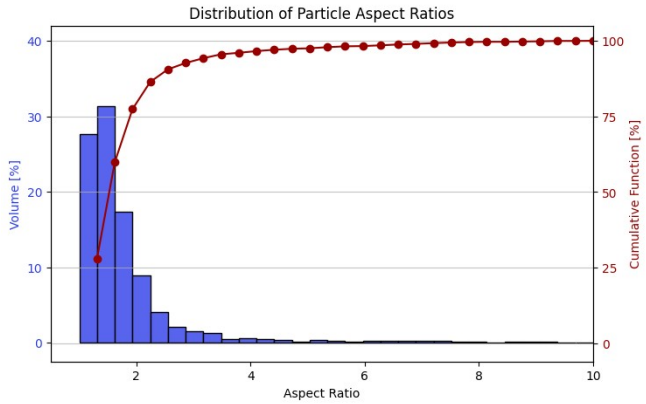

Figure 6: Distribution of aspect ratios (longest/shortest axis) of U-Net segmented binder particles, indicating general circularity.

The particle aspect ratios are as seen on Fig. 6, indicating that the particles are mostly approximately circular in shape, even though a smaller portion has slight ellipsoidal tendencies. It does, however, confirm that in general, it is not unreasonable to assume circular particles. These findings align well with microscopy image observations, e.g. see Fig. 1.

To give a more comprehensive understanding of the distribution of the binder powder on the glass fibre fabrics, one can investigate the binder coverage on smaller scales than the full microscopy images. This is because the region of influence for the particles is a lot smaller than the areas scanned, which makes it of interest to investigate whether there are areas with better or worse local coverage of the binder powder. The region of influence can be a moving window of a certain size, necessarily bigger than any individual powder particle. Using this moving window approach, a heatmap of local binder powder coverage percentages is constructed. Such a heatmap is overlaid on the example image (i.e. Fig. 1) in Fig. 7 below, where the moving window size is shown.

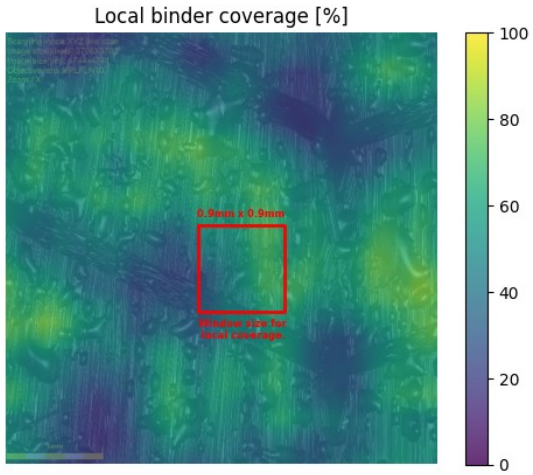

Figure 7: Heatmap of local binder powder coverage overlaid on the microscopy image from Fig. 1. The coverage is computed using a moving window approach to highlight spatial heterogeneity.

As seen in Fig. 7, the binder powder particles do not have a uniform coverage of the glass fibre fabric. Especially areas with stitching are lacking binder powder particles, resulting in near-zero coverage. Still, the deficient binder powder coverage is not limited to the stitching, as other areas are affected as well. Similarly, there are areas containing a lot of binder powders, which as a result yield the inhomogeneous distribution as indicated on the heatmap in Fig. 7.

To further quantify the local binder coverage of the considered fabrics, all of the microscopy images are considered to form a full distribution of local binder powder coverage percentages. That distribution is visualised in Fig. 8 below.

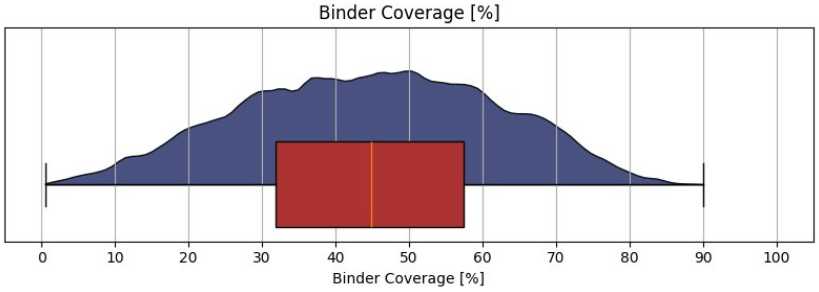

Figure 8: Distribution and boxplot of local binder powder coverage across all microscopy images.

The local binder powder particle coverage has a mean (and median) of approximately 47% but a standard deviation of approximately 17%-pts. The percentiles imply that 50% of the considered areas have a binder powder coverage between 32% and 57%, and that 95% of the considered areas have a binder powder coverage between 12% and 75%. This shows a wide range of local binder powder coverage, underlining the heterogeneous nature of the considered binder-powdered glass fibre fabrics.

5 CONCLUSIONS

Our findings using a U-Net deep CNN on partially annotated images suggest significantly improved segmentation of the microscopy images, resulting in accurate characterisation of the binder morphology and distribution. By comparing traditional and deep learning-based segmentation techniques, insights can be gained into the accuracy and reliability of each approach, paving the way for standardised, robust practices to characterise the binder powders applied to glass fibre fabrics. It has been shown how the distribution of local binder powder coverages has a large spread and can attain values from barely any binder powder to almost only binder powder. These insights contribute to a deeper understanding of the heterogeneity of the considered binder powder fabrics and the implications for composite processing and performance. The robust segmentation model developed highlights the potential for advanced automated image analysis tools for composite materials, which can pave the way for more data-driven approaches for material characterisation and better-informed processing.

ACKNOWLEDGEMENTS

The work of Jesper Lisegaard, Jesper Hattel and Sankhya Mohanty has received funding by the Energy Technology Development and Demonstration Programme: Automated Lay-up processes in blade Manufacturing (ALMA) project (Grant No. 640222-495998).

REFERENCES

[1] Helber F, Carosella S, Middendorf P. Effects of reactive and non-reactive tackifying agents on mechanical neat resin and composite performance for preforming processes and Liquid Resin Infusion (LRI) techniques. Adv Manuf Polym Compos Sci 2023;9:2205796. https://doi.org/10.1080/20550340.2023.2205796.

[2] Pierce RS. Challenges in permeability characterisation for modelling the manufacture of wind turbine blades. IOP Conf Ser Mater Sci Eng 2023;1293:012009. https://doi.org/10.1088/1757-899X/1293/1/012009.

[3] Tanoglu M, Robert S, Heider D, McKnight SH, Brachos V, Gillespie JW. Effects of thermoplastic preforming binder on the properties of S2-glass fabric reinforced epoxy composites. Int J Adhes Adhes 2001;21:187–95. https://doi.org/10.1016/S0143-7496(00)00050-6.

[4] Dickert M. Einfluss von Binder auf die Herstellung von Faserkunststoffverbunden. MyCoRe Community, 2015. https://doi.org/10.21268/20151210-093829.
[5] Neunkirchen S, Bender M, Schledjewski R. Effect of Binder Activation on in-Plane Capillary Flow in Multilayer Stacks of Carbon Fiber Fabrics. Appl Compos Mater 2024;31:709–19. https://doi.org/10.1007/s10443-023-10198-6.
[6] Ohlendorf J-H, Richrath M, Franke J, Brink M, Thoben K-D. Towards automation of wind energy rotor blade production: a review of challenges and application examples. Adv Manuf Polym Compos Sci 2020;6:173–90. https://doi.org/10.1080/20550340.2020.1838224.
[7] Schmidt S, Mahrholz T, Kühn A, Wierach P. Powder binders used for the manufacturing of wind turbine rotor blades. Part 2. Investigation of binder effects on the mechanical performance of glass fiber reinforced polymers. J Compos Mater 2019;53:2261–70. https://doi.org/10.1177/0021998318824784.
[8] Tanoğlu M, Tuğrul Seyhan A. Investigating the effects of a polyester preforming binder on the mechanical and ballistic performance of E-glass fiber reinforced polyester composites. Int J Adhes Adhes 2003;23:1–8. https://doi.org/10.1016/S0143-7496(02)00061-1.
[9] Broberg PH, Lindgaard E, Krogh C, Thompson AJ, Belnoue JP-H, Hallett SR, et al. That's how the preform crumples: Wrinkle creation during forming of thick binder-stabilised stacks of non-crimp fabrics. Compos Part B Eng 2024;273:111269. https://doi.org/10.1016/j.compositesb.2024.111269.
[10] Hovis D b., Heuer A h. The use of laser scanning confocal microscopy (LSCM) in materials science. J Microsc 2010;240:173–80. https://doi.org/10.1111/j.1365-2818.2010.03399.x.
[11] Badran A, Marshall D, Legault Z, Makovetsky R, Provencher B, Piché N, et al. Automated segmentation of computed tomography images of fiber-reinforced composites by deep learning. J Mater Sci 2020;55:16273–89. https://doi.org/10.1007/s10853-020-05148-7.
[12] Hong L, Zhang P, Liu D, Gao P, Zhan B, Yu Q, et al. Effective segmentation of short fibers in glass fiber reinforced concrete's X-ray images using deep learning technology. Mater Des 2021;210:110024. https://doi.org/10.1016/j.matdes.2021.110024.
[13] Guo R, Stubbe J, Zhang Y, Schlepütz CM, Gomez CR, Mehdikhani M, et al. Deep-learning image enhancement and fibre segmentation from time-resolved computed tomography of fibre-reinforced composites. Compos Sci Technol 2023;244:110278. https://doi.org/10.1016/j.compscitech.2023.110278.
[14] Vorobev R, Vasilev I, Kremnev I. Segmentation of structural defects in polymer composite computed tomography images with deep learning models. Tomogr Mater Struct 2023;3:100014. https://doi.org/10.1016/j.tmater.2023.100014.
[15] Dong J, Kandemir A, Hamerton I. Microstructural characterisation of fibre-hybrid polymer composites using U-Net on optical images. Compos Part Appl Sci Manuf 2025;190:108569. https://doi.org/10.1016/j.compositesa.2024.108569.
[16] - . Olympus Lext - Infinite Laser Microcope. - 2025. https://doi.org/10.57735/6163.
[17] Jeppesen N, Dahl VA. structure-tensor v0.1.2 2021. https://doi.org/10.5281/zenodo.4573913.
[18] Jeppesen N, Dahl VA, Christensen AN, Dahl AB, Mikkelsen LP. Characterization of the fiber orientations in non-crimp glass fiber reinforced composites using structure tensor. IOP Conf Ser Mater Sci Eng 2020;942:012037. https://doi.org/10.1088/1757-899X/942/1/012037.
[19] Ronneberger O, Fischer P, Brox T. U-Net: Convolutional Networks for Biomedical Image Segmentation 2015. https://doi.org/10.48550/arXiv.1505.04597.
[20] He K, Zhang X, Ren S, Sun J. Deep Residual Learning for Image Recognition. 2016 IEEE Conf. Comput. Vis. Pattern Recognit. CVPR, 2016, p. 770–8. https://doi.org/10.1109/CVPR.2016.90.
[21] Deng J, Dong W, Socher R, Li L-J, Li K, Fei-Fei L. ImageNet: A large-scale hierarchical image database. 2009 IEEE Conf. Comput. Vis. Pattern Recognit., 2009, p. 248–55. https://doi.org/10.1109/CVPR.2009.5206848.
[22] Ho Y, Wookey S. The Real-World-Weight Cross-Entropy Loss Function: Modeling the Costs of Mislabeling. IEEE Access 2020;8:4806–13. https://doi.org/10.1109/ACCESS.2019.2962617.

ICCM24
AUGUST 4-8, 2025
BALTIMORE CONVENTION CENTER
BALTIMORE, MARYLAND, USA

No Technical Paper Submission for:

Mahdi Tayybati

MODELING AND PREDICTION OF RESIDUAL STRENGTH OF POLYMER COMPOSITES EXPOSED TO HEAT

Jianhua Huang, Jack Gully and Matt Newsome

Materials Group, Luna Labs USA, LLC
3154 State Street, Blacksburg, VA 24060, USA
Email: jianhua.huang@lunalabs.us, web page: https://lunalabs.us

Keywords: Polymer Composites, Heat Damage, Kinetic Model, Residual Strength, Modeling

ABSTRACT

Composites are increasingly utilized in structural applications for military and commercial aircraft due to their high specific strength and stiffness. Despite these advantages over metal components, there is a significant risk if these structures are exposed to fires or high-temperature exhaust gas impingement. After an elevated temperature exposure, the composite properties may be significantly compromised even if minimal visible damage is apparent. Consequently, it is desired to have a rapid heat damage assessment and failure prediction tool based on operational and inspection data. This paper presents our efforts on developing models and simulation tools to predict residual strength of carbon/epoxy composites exposed to heat. A thermal decomposition kinetic model was developed based on the thermogravimetric data for the 5320-1 composite material. The residual short beam shear (SBS) strength of the composite was measured and related to the mass loss of the samples subjected to isothermal heating. Based on these results, a residual strength model was developed to predict the residual SBS strength of composite exposed to heat. The model has been validated and used to simulate degradation of carbon/epoxy composites subjected to isothermal heating. In addition, it was shown that the kinetic model derived for 5320-1 composites may be used with the residual strength data of other carbon/epoxy composites to develop a residual strength model for those composites.

1 INTRODUCTION

Aircraft polymer composite components are often exposed to extreme temperatures due to thermal events including exhaust impingement, engine fires, fuel fires, equipment overheating, brake fires, and lightning strikes. During thermal exposure, a chemical change in the matrix can occur and results in a reduction of composite mechanical properties. These chemical changes are difficult to detect with traditional Nondestructive Inspection (NDI) techniques (hardness, ultrasonic, visual inspection). This is classified as incipient heat damage. While some experimental methods such as Fourier Transform Infrared Spectroscopy (FTIR) technique may be used to inspect and disposition incipient heat damage on composite structures [1], development of a multi-physics model is desired to predict the structural response for a given temporal and spatial evolution of thermal environment.

To predict the post-fire mechanical response of single skin, flat composite laminates, Gibson et al. [2] proposed a model to predict the residual strength of polymer composites assuming the material has 100% and 0% strength left for the charred and uncharred portions of the material, respectively. Mouritz et al. [3, 4] proposed a simple two-layer model, one for the thermally affected region to have reduced or zero mechanical properties and a completely undamaged region with original mechanical properties. These models do not consider the property degradation in the resin decomposition region and cannot predict the residual strength of composites with incipient heat damage.

The goal of the present work is to develop a tool to predict residual strength of carbon/epoxy composites after a known time and temperature event. The time at temperature is such that the strength degradation is detectable whereas the physical damage (delamination) has not occurred yet. This is the region of highest interest for predictive capability and the focus of our efforts in this project. The mechanical property evaluation is focused on matrix sensitive short beam shear (SBS) strength test.

NAVAIR Public Release SPR# 2025-0430. Distribution Statement A - Approved for public release; Distribution is unlimited.

2 EXPERIMENTAL

2.1 Materials

Cycom 5320-1 prepreg (T650-35 3K plain weave fabric with resin content of 36%) manufactured by Solvay was used for making composites with single vacuum bag process. According to the manufacturer, Cycom 5320-1 is a toughened epoxy resin prepreg system designed for vacuum-bag-only (VBO) or out of autoclave (OOA) manufacturing of primary structural parts. The 5320-1 composites are also supported by an extensive set of multi batch mechanical and physical property databases [5].

2.2 Methods

Laminate and Test Coupon Preparation. Composite panels were fabricated using 16 pies of prepreg with single vacuum bag process cured in a convection oven with curing cycle recommended by the prepreg manufacturer. The cured panel has thickness of 0.122 inches. The panels were machined to generate test coupons with nominal dimension of 0.75”×0.25”×0.125” for thermal aging, mass loss and SBS tests. The coupons were dried at 80°C for 48 hours in a convection oven before used in the following treatments. The mass of dried samples was measured and used to calculate the mass loss of the composite after thermal aging.

Thermal Aging. Thermal aging of composite samples (SBS test coupons) was performed in a convection oven (Heratherm OMH60). A mineral wool insulation sheet was mounted in front of oven chamber to minimize the temperature drop when the oven door was opened. A small opening (3" × 1") was cut out on the sheet to allow the samples passing through the sheet. Two types of heating — isothermal heating and constant rate heating — were performed for thermal aging. To conduct the constant rate heating, heat oven to 50°C first, place composite samples (6 SBS test coupons as a set) in the oven and close the door. The oven was heated to target temperatures at the set heating rate. The samples were taken out of the oven when the target temperature was reached. The mass of aged samples was measured when the samples were cooled down.

Mass Loss Measurement. After heat exposure, the mass of the coupons was measured with balance with precision of 0.0001g. The mass loss of the samples is equal to the difference between the mass of the samples before and after heat exposure.

Short Beam Shear (SBS) Test. Short beam shear test for the aged samples was performed at room temperature on ADMET Expert 2611 Tester based on ASTM D2344 standard. The displacement rate was 0.05 inches/minute. Five specimens were evaluated to get average strength for each set of samples.

3 RESULTS AND DISCUSSION

3.1 Mass Loss and Kinetic Model of Composites

Mass Loss of the Composites. Mass loss (%) of 5320-1composites (SBS coupons) subjected to isothermal heating and constant rate heating is shown in Figure 1(a) and (b), respectively. The mass loss (%) is defined as $(m_0\text{-}m)/m_0 \times 100\%$, where m_0 and m are original mass and instantaneous mass at t, respectively. In general, mass loss depends on the aging time and temperature for isothermal heating. The higher temperature or longer time, the greater the mass loss values. For constant rate heating, the lower the heating rate, the greater the mass loss values. It is thus believed that mass loss can be a good indicator for severity of incipient heat damage of the composites.

Kinetic Model. According to the literature, the model or a mathematical description of the mass loss data is usually sought in terms of a `kinetic triplet' (i.e., Arrhenius parameters A and E, and the reaction model, $F(\alpha)$, also called the conversion function) which is related to the experimental data as follows [6]

NAVAIR Public Release SPR# 2025-0430. Distribution Statement A - Approved
for public release; Distribution is unlimited.

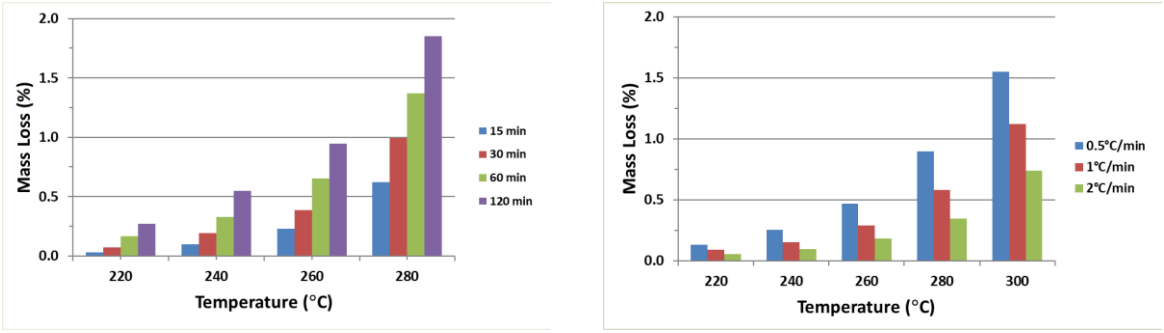

(a) (b)

Figure 1: Mass loss (%) of 5320-1 composites subjected to (a) isothermal and (b) constant rate heating.

$$\frac{d\alpha}{dt} = Aexp\left(-\frac{E}{RT}\right)F(\alpha) \tag{1}$$

where R is gas constant, T is temperature (K), α is the extent of conversion defined as

$$\alpha = (m_i - m)/(m_i - m_f) \tag{2}$$

where m_i, m and m_f are the initial, instantaneous and final mass of the material, respectively. For mass loss data obtained at a constant heating rate dT/dt=β, dα/dt in Eq.(1) can be replaced with β dα/dT:

$$\frac{d\alpha}{dT} = \frac{A}{\beta}exp\left(-\frac{E}{RT}\right)F(\alpha) \tag{3}$$

or

$$Ln\left(\beta\frac{d\alpha}{dT}\right) = -\frac{E}{RT} + Ln(A) + Ln(F(\alpha)) \tag{4}$$

For a fixed degree of progress α, the plots of Ln(βdα/dT) versus 1/T show parallel lines with a slope equal to –E/R, which leads to a method known as Friedman method for determining the activation energy E in the literature [7]. To get the α data, one needs not only initial and instantaneous mass of the material, but also the final mass of the material. If the final mass is not available or applicable, a fraction of mass loss α* as defined in

$$\alpha^* = (m_i - m)/m_i \tag{5}$$

may be used. Let

$$\lambda = m_i/(m_i - m_f) \tag{6}$$

we have

$$\alpha^* = \alpha/\lambda \tag{7}$$

With α being replaced with λα*, Eq.(1) can be rewritten as

$$\frac{d\alpha^*}{dt} = A^*exp\left(-\frac{E}{RT}\right)f(\alpha^*) \tag{8}$$

where A^* (=A/λ) and f(α*) represent the pre-exponential parameter and reaction model corresponding to α*. From this equation it follows that

$$Ln\left(\beta\frac{d\alpha^*}{dT}\right) = -\frac{E}{RT} + Ln(A^*) + Ln(f(\alpha^*)) \tag{9}$$

Comparing Eq.(9) and Eq.(4), it is apparent that the activation energy E can also be determined from dα*/dT. Figure 2 shows Ln α* as a function of temperature for 5320-1 composites subjected to constant

rate heating. As seen in the figure, d Ln α*/dT is a constant at a fixed heating rate, it is thus more convenient to use d Ln α*/dT instead of dα*/dT for the calculation. Rewrite Eq.(9) as

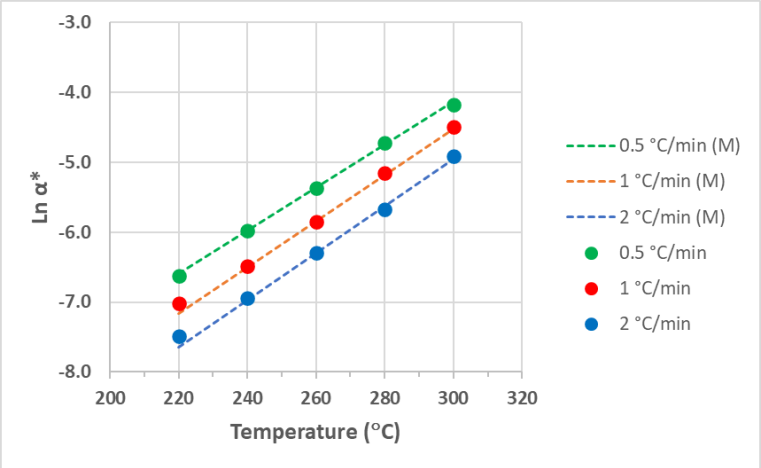

Figure 2: Ln α* as a function of temperature for 5320-1 composites subjected to constant rate heating. Closed circles represent measured data, dotted lines represent model predicted values.

$$Ln\left(\beta\frac{dLn(\alpha^*)}{dT}\right) = -\frac{E}{RT} + Ln(A^*) + Ln\big(f(\alpha^*)\big) - Ln(\alpha^*) \tag{10}$$

then the activation energy E can be determined from plots of Ln (β dLnα*/dT) versus $1/T$ at fixed α* levels. The result can be represented by

$$E = aLn\,\alpha^* + b = 19.22Ln\,\alpha^* + 230.92\ (kJ/mol) \tag{11}$$

From Eqs.(10)-(11) and the mass loss data, $f(\alpha^*) = \alpha^{*n}$ (where n is a constant) and A^* can be determined, Eq.(8) thus becomes

$$\frac{d\alpha^*}{dt} = A^* exp\left(-\frac{E}{RT}\right)\alpha^{*n} \tag{12}$$

Integration of Eq.(12) gives the α* of the composites subjected to isothermal heating

$$\alpha^* = \left[A^* kExp\left(-\frac{b}{RT}\right)(t - t_0) + (\alpha^*{}_0)^k\right]^{1/k} \tag{13}$$

where α^*_0 is α* at t_0 and $k = a/(RT)$-n+1, a and b are defined in Eq.(11). Given t_0 (=15 min) and α^*_0, the mass loss of composite at any time $t > t_0$ and T can be predicted using this equation. For composites subjected to constant rate heating, the mass loss becomes

$$\alpha^* = \alpha_0^* exp\left[\frac{A^*}{\beta} exp\left(-\frac{E_0}{RT_0}\right)(\alpha_0^*)^{n-1}(T - T_0)\right] \tag{14}$$

where α^*_0 is α* at T_0 and E_0 is the activation energy at $\alpha^* = \alpha^*_0$. The mass loss predicted using Eq.(14) and T_0 = 260°C is presented in Figure 2. As seen in the figure, the calculated values are in very good agreement with measured data for all heating rates and temperatures. The mass loss values calculated from Eq.(13) (data are not presented here) also agree with the measured data for the samples subjected to isothermal heating.

3.2 SBS Strength of Composites

Short beam shear strength of 5320-1 composites subjected to isothermal heating is given in Figure 3. Figure 4 shows the plots of SBS reduction versus mass loss for 5320-1 composites subjected to isothermal heating. Apparently, the relationship between SBS reduction and mass loss for a fixed aging

NAVAIR Public Release SPR# 2025-0430. Distribution Statement A - Approved
for public release; Distribution is unlimited.

time (15, 30, 60 and 120 minutes) can be represented by a linear equation. This means that, given exposure/aging time, the SBS strength reduction is proportional to the mass loss of the material.

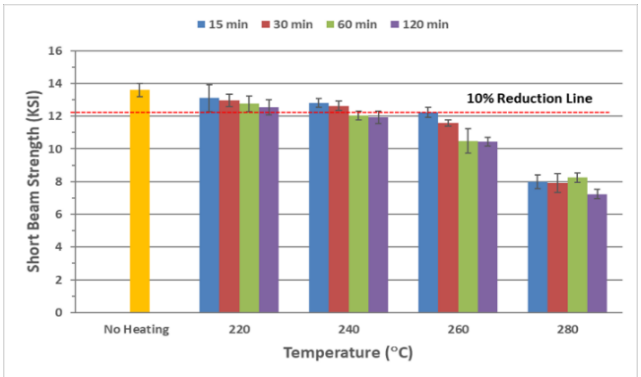

Figure 3: Short beam shear strength of 5320-1 composites subjected to isothermal heating.

The slope of lines was plotted against exposure time in Figure 5. The data can be fitted by a power law equation $y = 205.24x^{-0.452}$. Combining the results obtained from Figs.(4) and (5), we have:

$$\frac{\Delta F}{F_0} = ct^d \frac{\Delta M}{M_0} = 205.24t^{-0.452}\alpha^* \tag{15}$$

where $\Delta F = F_0 - F$, $\Delta M = M_0 - M$, M_0 and F_0 are the original mass and SBS strength of the material (no heat exposure), M and F represent the mass and SBS strength of the composite exposed to heat for t minutes.

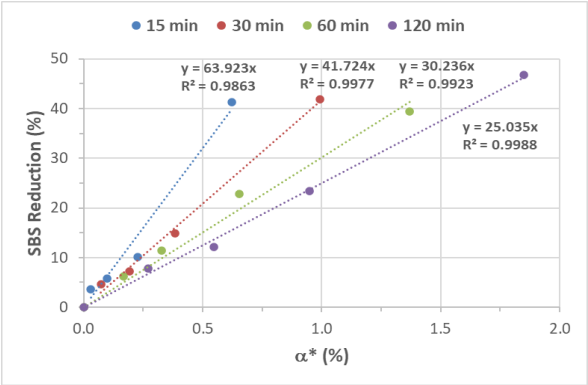

Figure 4: Plots of SBS strength reduction versus mass loss of 5320-1 composites subjected to isothermal heating with aging times indicated.

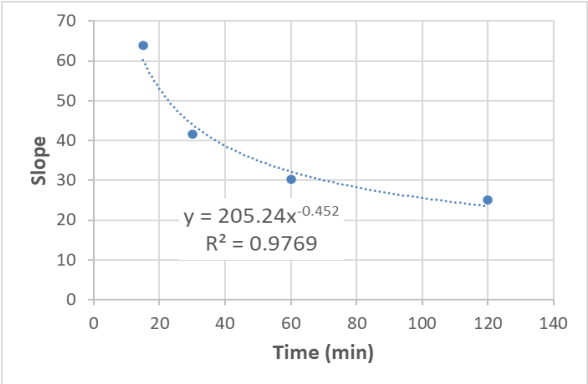

Figure 5: The plot of slope of lines in Figure 4 versus aging time.

NAVAIR Public Release SPR# 2025-0430. Distribution Statement A - Approved for public release; Distribution is unlimited.

3.3 Residual Strength Models for 5320-1 Composites

Based on the above equations, models have been developed to predict the residual SBS strength of the composites subjected to isothermal heating. From

$$F = F_0\left(1 - \frac{\Delta F}{F_0}\right) \tag{16}$$

it follows that

$$F = F_0\left\{1 - ct^d\left[A^*kExp\left(-\frac{b}{RT}\right)(t - t_0) + (\alpha^*{}_0)^k\right]^{1/k}\right\} \tag{17}$$

To verify/validate the residual strength models, the residual strength of 5320-1 composites subjected to isothermal heating were calculated from Eq.(17). The results together with the testing data are presented in Figure 6. As seen in the figure, the measured and predicted residual strengths are in very good agreement for all aging temperatures and times or heating rates. In fact, the predicted values are within the error bars of measured data in most cases. In other words, the difference between predicted and measured strength values are generally within the experimental errors. The result confirmed that the residual strength model works well for the composites.

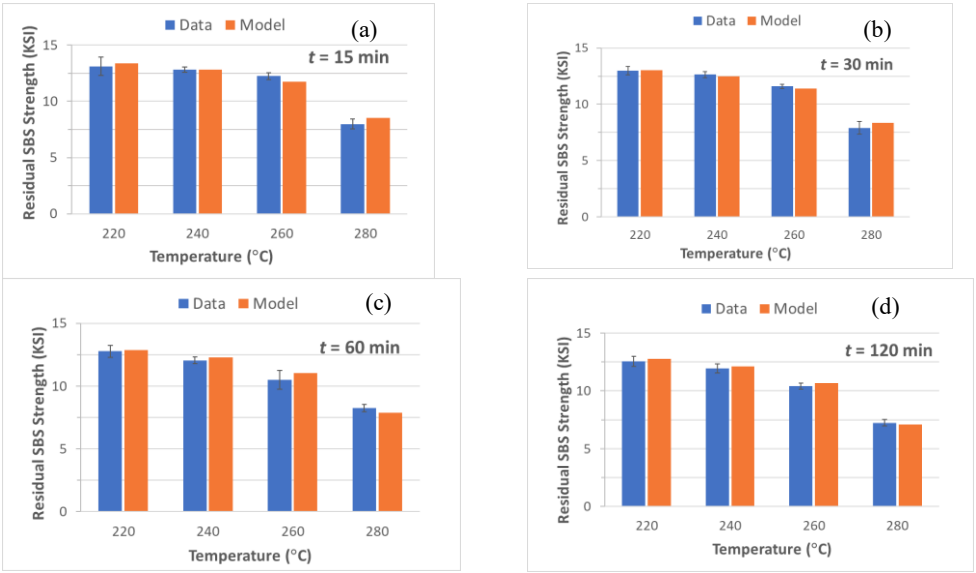

Figure 6: Comparison of model predicted and measured short beam strength for 5320-1 composites subjected to isothermal heating at 220~280°C for (a) 15, (b) 30, (c) 60 and (d) 120 minutes.

3.4 Residual Strength Prediction for Other Composites

A novel residual strength model has been developed and demonstrated successfully for short beam strength of CYCOM 5320-1 composite system. As lots of experimental work is needed to establish the residual strength models, a model or method is desired for prediction of residual strength of general carbon/epoxy composites (not limited to 5320-1) with no or minimal amount of experimental work required.

It was noticed that there were residual strength data sets (such as SBS, flexural and/or compressive strength data) for various carbon/epoxy composites exposed to heat with exposure conditions reported in the literature (see [8] for example). We have tried to "predict" the residual strength of the materials using our model (for 5320-1 composites) and then compare the result with the testing data to see how our model works for those materials. While good agreement between "predicted" and tested data was seen in some cases, poor results were observed in most cases. This means our model may not be

applicable to other materials in general. However, if our model is adapted to the new material and property first, it is possible to predict residual strength of the material without need for additional experiments. Below we will explain this further with some examples.

Figure 7(a) and (b) present the SBS strength reduction of dry and wet IM6/3501-6 carbon fiber/epoxy composites (data obtained from Ref [8]) versus mass loss of CYCOM 5320-1 exposed to heat with condition given in Ref [8], respectively. As seen in the figure, for either dry or wet samples, the SBS strength reduction of IM6/3501-6 and mass loss of dry 5320-1 composite can be represented by a linear equation as shown in the following equation:

$$\frac{\Delta F}{F_0} = c_x \alpha^*_S \tag{18}$$

where $\Delta F = F_0 - F$, F_0 and F are the original and instantaneous SBS strength of IM6/3501-6, α^*_S represents the mass loss of dry 5320-1 composite exposed to heat (obtained from Eq.(13)), c_x is the slope of the line which equals to 25.743 and 35.912 for the dry and wet IM6/3501-6 samples, respectively. Eq.(19) gives the residual SBS strength model (adapted model) for IM6/3501-6 subjected to isothermal heating

$$F = F_0(1 - c_x \alpha^*_S) = F_0 \left\{ 1 - c_x \left[A^* k Exp\left(-\frac{b}{RT}\right)(t - t_0) + (\alpha^*_0)^k \right]^{1/k} \right\} \tag{19}$$

where the expression for α^*_S was from Eq.(13). The measured and model predicted SBS strength of dry and wet IM6/3501-6 composites are shown in Figure 7(c) and (d), respectively. As seen in the figures, the model predicted and measured SBS strengths are in excellent agreement.

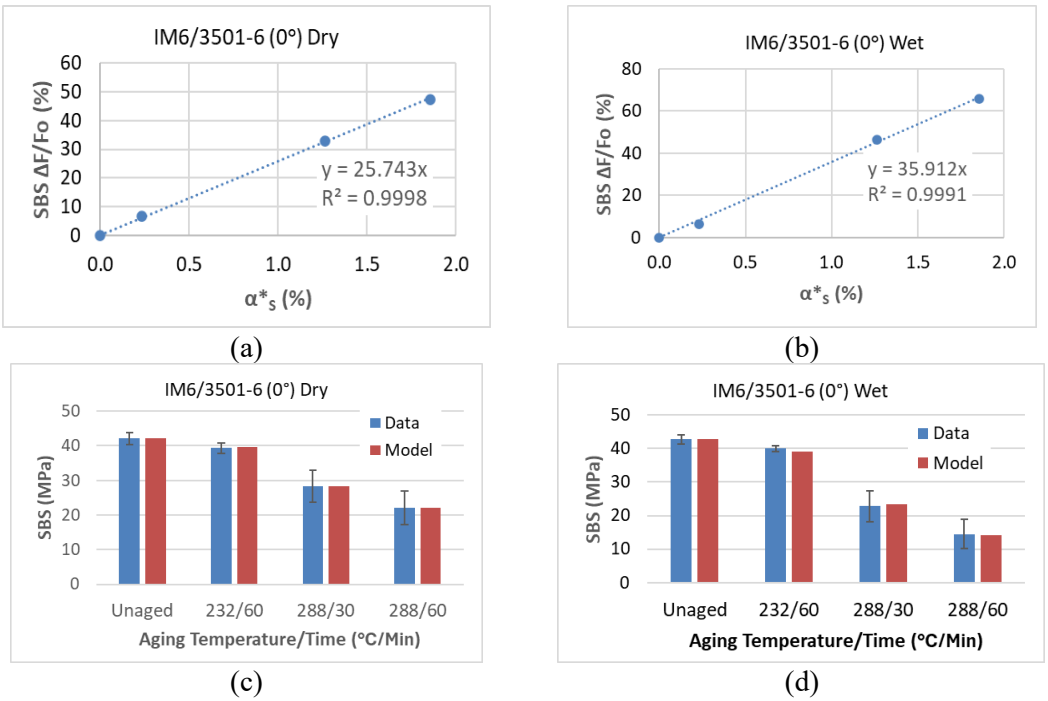

Figure 7: SBS strength reduction of dry (a) and wet (b) IM6/3501-6 carbon/epoxy composites versus mass loss of CYCOM 5320-1 exposed to heat. Comparison of measured and model predicted SBS strength of dry (c) and wet (d) IM6/3501-6 composites exposed to heat.

Similar results were obtained for residual flexural strength of IM6/3501-6 composites (Figure 8) with testing data obtained from Ref [8] as well. As seen in the figure, the flexural strength reduction of IM6/3501-6 and mass loss of dry 5320-1 composite can be represented by a linear equation, with slope being 32.819 and 31.315 for the dry and wet samples, respectively. A residual flexural strength model

can be derived for dry or wet IM6/3501-6 composites. As shown in Figure 8(c) and (d), the model predicted flexural strengths are in very good agreement with the testing data.

In summary, the adapted model can be derived by a) plotting strength reduction ($\Delta F/ F_0$) against mass loss (α^*_s) of 5320-1, b) finding relation $\Delta F/ F_0 = f(\alpha^*_s)$ (= $c_x\alpha^*_s$ in above examples) and, c) getting residual strength $F = F_0\,[1\text{-}f(\alpha^*_s)]$.

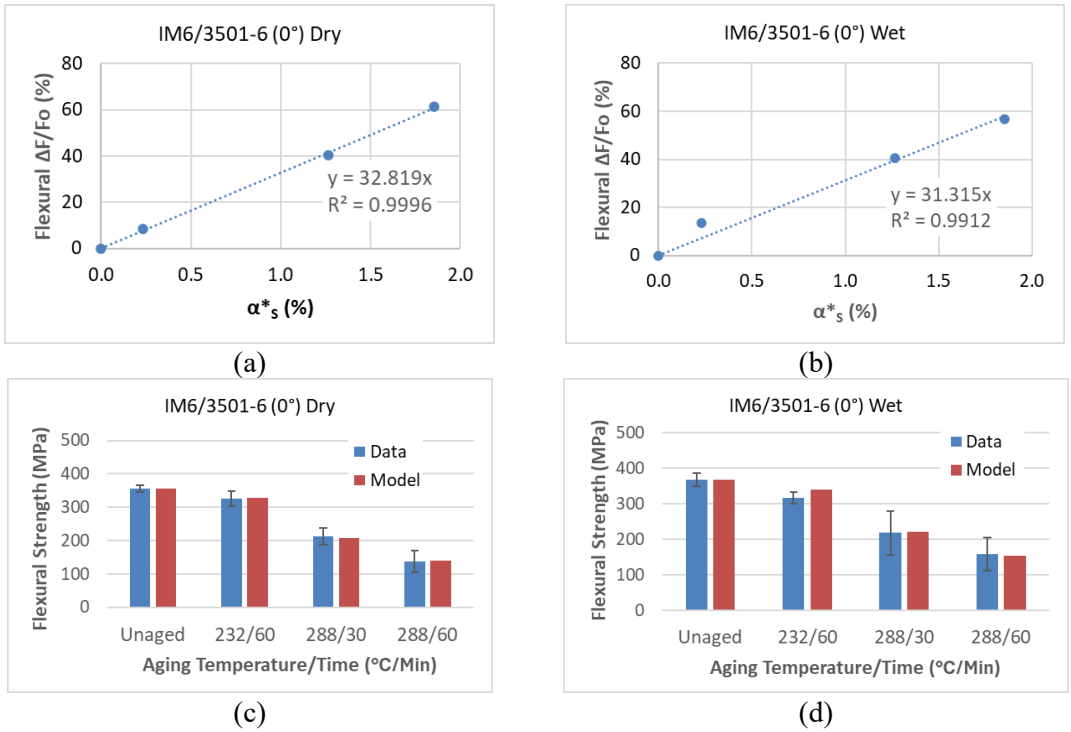

Figure 8: Flexural strength reduction of dry (a) and wet (b) IM6/3501-6 carbon/epoxy composites versus mass loss of CYCOM 5320-1 exposed to heat. Comparison of measured and model predicted flexural strength of dry (c) and wet (d) IM6/3501-6 composites exposed to heat.

4 CONCLUSIONS

Efforts have been made to model and simulate the incipient heat damage of carbon/epoxy composites exposed to excessive heat. A decomposition kinetic model has been developed based on the non-isothermal thermogravimetric data for the composite coupons for short beam shear (SBS) test. The result shows that the decomposition reaction can be represented by a power law model, and the reaction model may be determined without presuming the form of the model beforehand. The kinetic model has been verified using both non-isothermal and isothermal thermogravimetric data. The model predicted mass loss values are in excellent agreement with the experimental data. A quantitative relationship was established between mass loss and short beam shear (SBS) strength reduction of the composites subjected to isothermal heating. Based on the relationship and the kinetic model, a residual strength model has been developed to predict the residual strength of composites. The residual SBS strength of composites exposed to heat was measured and compared with the model predicted data. The result showed that the model predicted and measured strengths are in excellent agreement. In addition, the kinetic model derived for 5320-1 composites may be used with the residual strength data of other carbon/epoxy composites to establish a residual strength model for those composites.

ACKNOWLEDGEMENTS

This material is based upon work supported by the Naval Air Warfare Center under Contract No N68335-22-C-0228. Any opinions, findings and conclusions or recommendations expressed in this material are those of the author(s) and do not necessarily reflect the views of NAVAIR. The authors

would like to thank Diane Hoyns, Curtis Sharkey, Gabriel Murray (NAVAIR TPOCs) for guidance and support.

REFERENCES

[1] Massey, J.: "FTIR for Thermal Damage Inspection on Composite Aircraft" (2022), https://jteg.ncms.org/wp-content/uploads/2022/09/03-FTIR-for-Composite-Thermal-Damage - 2022-pdf.pdf.

[2] Gibson, A. G. et al.: "The Integrity of Polymer Composites During and After a Fire", Journal of Composite Materials, 38(15), 1283-1307 (2004).

[3] Mouritz, A.P., Mathys, Z.: "Post-fire mechanical properties of glass reinforced polyester composites" Composites Science and Technology, 61, 475–90 (2001).

[4] Mouritz, A.P., Mathys, Z., Gardiner, C.P.: "Thermomechanical modeling the fire properties of fiber-polymer composites", Composites, Part B, 35, 467-474 (2004).

[5] https://www.wichita.edu/industry_and_defense/NIAR/Research/cytec-5320-1/T650-3k-PW-2.pdf.

[6] Brown, M. E. et al.: "Computational aspects of kinetic analysis Part A: The ICTAC Kinetics project-data, methods and results", Thermochimica Acta 355(1-2), 125-143 (2000).

[7] Chairat, A. et al.: "Thermal degradation kinetics of a commercial epoxy resin - Comparative analysis of parameter estimation methods", J. Appl. Polym. Sci. 132, 42201 (2015), DOI: 10.1002/APP.42201.

[8] Janke, C J, et al. "Composite heat damage assessment" United States: N. p., 1993. Web https://www.osti.gov/servlets/purl/245551.

NAVAIR Public Release SPR# 2025-0430. Distribution Statement A - Approved for public release; Distribution is unlimited.

ICCM24
AUGUST 4-8, 2025
BALTIMORE CONVENTION CENTER
BALTIMORE, MARYLAND, USA

No Technical Paper Submission for:

Debes Bhattacharyya

EXPERIMENTAL EVALUATION OF INTERLAMINAR SHEAR STRENGTH OF CARBON NANOMATERIAL Z-THREADED CARBON FIBER-REINFORCED POLYMER LAMINATES AFTER EXPOSURE TO EXTREME ELEVATED TEMPERATURES

Ryan A. Warren[1], Obaidul Hasan[2] and Kuang-Ting Hsiao[3]

[1]Systems Engineering Program, University of South Alabama
150 Student Services Drive, Shelby Hall 4106. Mobile, Alabama
Email: raw1522@jagmail.southalabama.edu

[2]William B. Burnsed, Jr. Department of Mechanical Engineering, Aerospace, and Biomedical Engineering, University of South Alabama
150 Student Services Drive, Shelby Hall 3128. Mobile, Alabama
Email: oh2321@jagmail.southalabama.edu

[3]William B. Burnsed, Jr. Department of Mechanical Engineering, Aerospace, and Biomedical Engineering, University of South Alabama
150 Student Services Drive, Shelby Hall 3128. Mobile, Alabama
Email: kthsiao@southalabama.edu

Keywords: Carbon Nanofiber, Z-Threaded Carbon Fiber Reinforced Polymer, ILSS

ABSTRACT

Previous studies have shown that carbon nanofiber (CNF) z-threaded carbon fiber-reinforced polymer (ZT-CFRP) laminates exhibit improved mechanical performance in comparison to traditional carbon fiber-reinforced polymer (CFRP) laminates when exposed to extreme elevated temperatures. Z-threaded reinforcement is a technique for strengthening the through-thickness of a laminate by introducing perpendicularly aligned carbon nanomaterial to be threading into the continuous fiber array. Improved performance has already been observed in properties such as interlaminar shear strength (ILSS) without extreme heat exposure, but there has also been evidence that z-thread inclusion may mitigate strength loss due to thermal degradation of the matrix. This study examined how ILSS was diminished in both CFRP and ZT-CFRP samples with matrix degradation caused by extreme temperature exposure. Test samples were heated to 350 ˚C for 10 minutes and then allowed to return to room temperature. SBS testing in accordance with ASTM D2344 was conducted on both untreated and heat-treated samples for comparison. All samples were at room temperature during testing. It was found that ZT-CFRP samples (with 0.5wt% CNF concentration the matrix) exhibited higher ILSS with and without heat treatment over the traditional CFRP samples with and without heat treatment by +33.96% and +25.12%, respectively. ZT-CFRP ILSS was found to decrease by 10.584 MPa (-14.56%) after the extreme heat treatment, while CFRP ILSS decreased by only 4.627 MPa (-8.53%). Microscopic image analysis was also performed to provide insight into how the CNF z-threads may have provided a mechanism for retaining ILSS performance even with matrix thermal degradation.

1 INTRODUCTION

The high strength-to-weight ratios of carbon fiber reinforced polymers (CFRP) have caused it to become an increasingly used and researched material for structural designs. One of the disadvantages of CFRP is that they are anisotropic, with higher mechanical performance being restricted to loadings acting in the direction of the embedded reinforcing fibers. Even with the use of different stacking orientation techniques that can introduce more planar isotropy tendencies, there is still no reinforcing mechanism along the through-thickness of the composite. All reinforcement is confined to the plane of the fiber arrays. The novel Z-threaded nanomaterial reinforcement technique is a proven method for

increasing the through-thickness capabilities of CFRP. Within Z-threaded CFRP (ZT-CFRP), carbon nanomaterial is aligned and threaded perpendicularly through the reinforcing fiber array. A depiction of the concept of ZT-CFRP is provided in Figure 1 with carbon nanofibers (CNF) acting as the nanomaterial reinforcement.

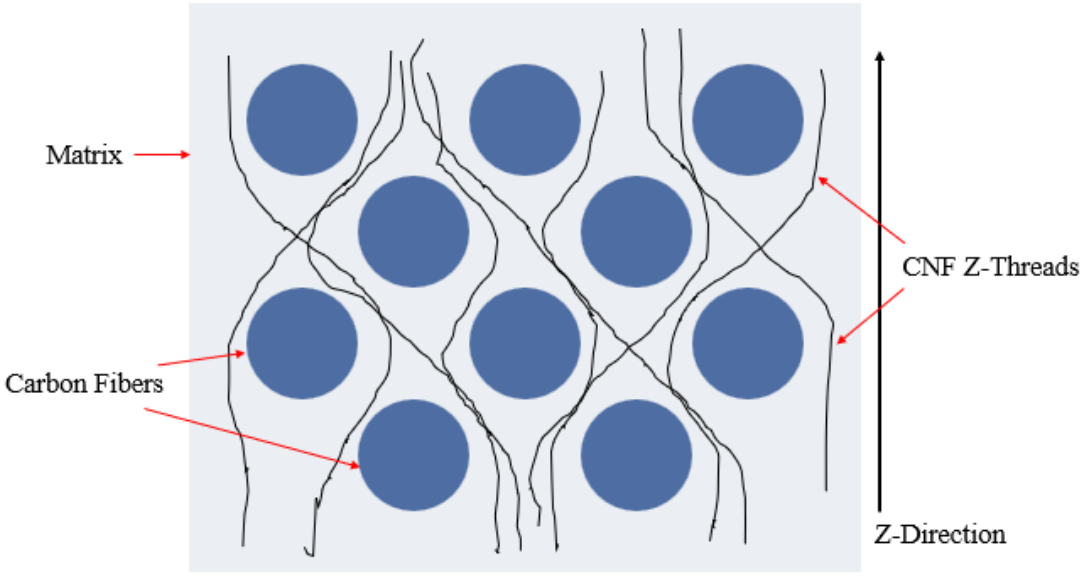

Figure 1: Illustration of ZT-CFRP showing how the nanomaterial reinforcement is threaded perpendicularly through fiber array.

Previous studies have already shown that ZT-CFRP exhibits improved through-thickness dependent material properties in comparison to traditional CFRP composites. This includes strengthened mechanical properties such as Mode-I delamination toughness [1] and longitudinal compressive strength [2], along with improved electrical [3, 4] and thermal conductivities [5]. Interlaminar shear strength (ILSS) is a mechanical property that saw significant increase in performance in comparison to traditional CFRP. With the inclusion of 1 wt% CNF z-threads, a 17% improvement in ILSS was observed. Traditional CFRP samples exhibited an average ILSS of 64.89 MPa while ZT-CFRP samples exhibited an average of 75.92 MPa [6].

Improved flammability characteristics have also been observed in ZT-CFRP using UL-94 testing, a standard for assessing the fire hazard of plastic materials. It was shown that ZT-CFRP took on average only 34.95 seconds to self-extinguish, while CFRP samples took on average 86.8 seconds. Self-extinguishing time for ZT-CFRP took only 40% of the time it took for CFRP samples. ZT-CFRP also showed a reduced chance of flame propagation in comparison to CFRP. None of the ZT-CFRP samples burned all the way to the clamp holding the specimen during testing, whereas 60% of the CFRP samples did [7].

A previous study on ILSS failure performance during extreme heat exposure provided evidence of improved strength capabilities and retention in extreme temperature environments of ZT-CFRP in comparison to CFRP. In this study an apparatus was designed and used to replicate the loading of a short beam shear (SBS) test within a muffle furnace chamber. Both CFRP and ZT-CFRP samples were placed inside the apparatus within the chamber and a static loading was exerted onto them. The temperature of the furnace was allowed to increase based on a consistent heating schedule until failure was observed within the testing samples. It was observed that the average failure temperature range for ZT-CFRP was between 384.0 ˚C to 398.4 ˚C, whereas CFRP samples failed on average at temperatures ranging from 349.6 ˚C to 368.2 ˚C. This was an approximate 30 ˚C increase in temperature handling capabilities exhibited by ZT-CFRP over CFRP [8].

Based on the temperature failure ranges observed from the previously mentioned study, there is evidence that ZT-CFRP may be better equipped at retaining strength during thermal degradation caused by extreme temperature exposure in comparison to traditional CFRP. This study examined the

retention of ILSS between CFRP and ZT-CFRP when exposed to extreme elevated temperatures that can cause thermal degradation within the matrix. This was accomplished by heat treating specimens at 350 ˚C within a muffle furnace for 10 minutes. The treated specimens were then removed and underwent SBS testing to experimentally determine their ILSS. Specimens subjected to no heat treatment were also tested to show how much strength was lost due to heat exposure and potential matrix degradation. Specimens for both cases were prepared and tested based on the specifications provided in ASTM D2344 [9]. Microscopic image analysis was also performed to determine how the z-threaded CNF microstructure may have contributed to the failure observed. The process of manufacturing and testing the specimens, testing data, and microscope images of the specimens are provided within this document.

1.1 Review of the Effect of Extreme Temperature Exposure on CFRP Behavior

Quintiere et al. [10] reported that the typical temperature range for the degradation of common aerospace CFRP composites is between 300 ˚C to 500 ˚C. The reduction in material properties observed at these elevated temperatures is not only due to the weakening molecular bonds but is also a result of the internal pressure caused by resin vaporization and the reinforcing fibers that hinder its escape. Bazli et al. [11] reported a similar degradation temperature range while also observing that composites loaded in either shear or compression failed at much earlier temperatures in comparison to those loaded in tension or flexure. Ningyun and Evans [12] performed short beam shear tests on fiber reinforced thermoplastic composites between 20 ˚C and 300 ˚C. Failure at low temperatures was found to be largely due to interlaminar shear and delamination. Large-scale inelastic deformation was observed within the test specimens at higher temperatures. These studies provide evidence that matrix sensitive material properties are more sensitive to extreme temperatures.

Nema et al. [13] found that both flexural strength and ILSS decreased linearly as temperature was increased to 200˚C. Significant decreases in flexural modulus were also observed at around 200 ˚C which was above the glass transition temperatures of the resin systems being used. Hegde et al. [14] also observed that composite strength and stiffness consistently fell as temperature began to approach the glass transition temperature. With steel and CFRP double strap joints, Nguyen et al. [15] saw load carrying capabilities diminish by 30% when exposed to temperatures around the glass transition temperature.

2 EXPERIMENTATION

2.1 Materials

All testing specimens utilized unidirectional HexTow AS7 carbon fiber from Hexcel with a density and areal weight of 1.79 g/cm^3 and 190 g/m^2, respectively, for reinforcement. The tow size was 12 K. CNFs used for z-thread nanomaterial reinforcement were PR-24-XT-PS grade from Pyrograph/ Applied Sciences Incorporated. This grade of nanofibers was reported to have an average diameter of 100 nm and lengths ranging between 50 μm to 200 μm. The base resin system utilized for all specimens consisted of a mixture of Epon-862, a diglycidyl ether of bisphenol F, and Epikure-W, a non-MDA aromatic amine curing agent containing diethylmethylbenzenediamine, both purchased from Miller-Stephenson Chemical Company. The surfactants Disperbyk-191 and Disperbyk-192, both purchased from BYK USA, were used in cases with CNF reinforcement to better disperse the nanomaterial within the resin mixture.

2.2 Prepreg Production

Two different cases of composite panels were manufactured for this study: control containing no nanomaterial reinforcement and ZT-CFRP. All prepreg used for the panels was manufactured through a proprietary production process developed by the Hsiao research group at the University of South Alabama that is illustrated within a pending patent application US20240149541A1 [16]. Both control and ZT-CFRP utilized a base blend of Epon-862 and Epikure-W mixed at a stochiometric ratio of

100:26.5, respectively. For the ZT-CFRP prepreg, CNF was added at 0.5 wt% of the overall resin matrix mixture. Both Disperbyk-191 and Disperbyk-192 were added at a ratio of 1:1:1 with CNF for better dispersion within the mixture. The resin mixture used for control prepreg manufacturing only contained Epon-862 and Epikure-W.

Both the control and ZT-CFRP resin mixture underwent five minutes of manual stirring once the components were measured out and combined as appropriate. For the ZT-CFRP mixture that contained nanomaterial reinforcement and surfactants, one hour of high shear mixing at 900 rpm using a Stir-Pack Laboratory Mixer was performed. The rotational direction of the mixer was alternated after 30 minutes. The high shear mixed reinforced resin then underwent two hours of sonication using a QSONICA Q700 sonicator. This step was taken to further disperse and reduce agglomerations of CNF within the resin mixture. A sample of the resin mixture was taken after this step to determine the quality of CNF dispersion underneath a Nikon Eclipse LV 150 microscope. Figure 2 provides an image of the final CNF dispersion quality within the resin mixture prior to moving to the next step of prepreg production.

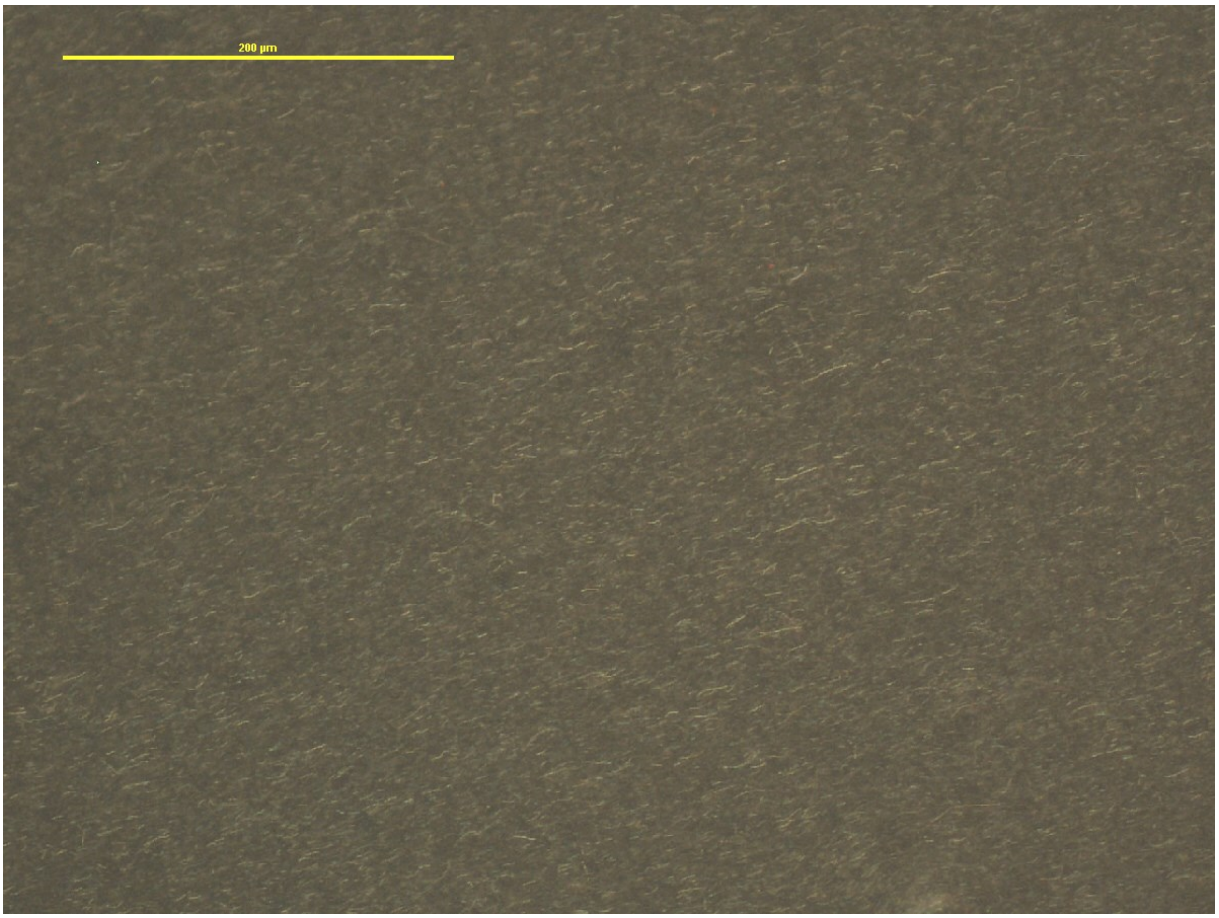

Figure 2: A microscope image showing dispersion quality of the CNF within the resin blend prior to prepreg manufacturing.

The appropriate amount of Epikure-W curing agent was added and manually stirred for 5 minutes into the dispersed CNF mixture to begin the B-staging process. The blend was then placed for approximately 1 hour inside a vacuum oven at 110 ˚C and -0.09 MPa. The vacuum applied to the resin during this process allowed for the removal of any trapped air within the mixture while also allowing it to partially cure. The control resin mixture also underwent the same B-staging process once Epikure-W was added.

The partially cured resin mixtures were then used in the proprietary ZT-CFRP prepreg production line to create hot melt resin films. An additional alignment process was performed to orientate the CNF reinforcement within the ZT-CFRP film. Alignment is accomplished through reinforced film

exposure to an electrical field for 150 seconds. The hot melt films created for both cases were then used to impregnate dry AS7 fiber fabric arrays. The alignment quality of the created ZT-CFRP prepreg was checked underneath a microscope. An example image of aligned prepreg is provided in Figure 3. Figure 4 provides a diagram detailing the process of making prepreg from start to finish.

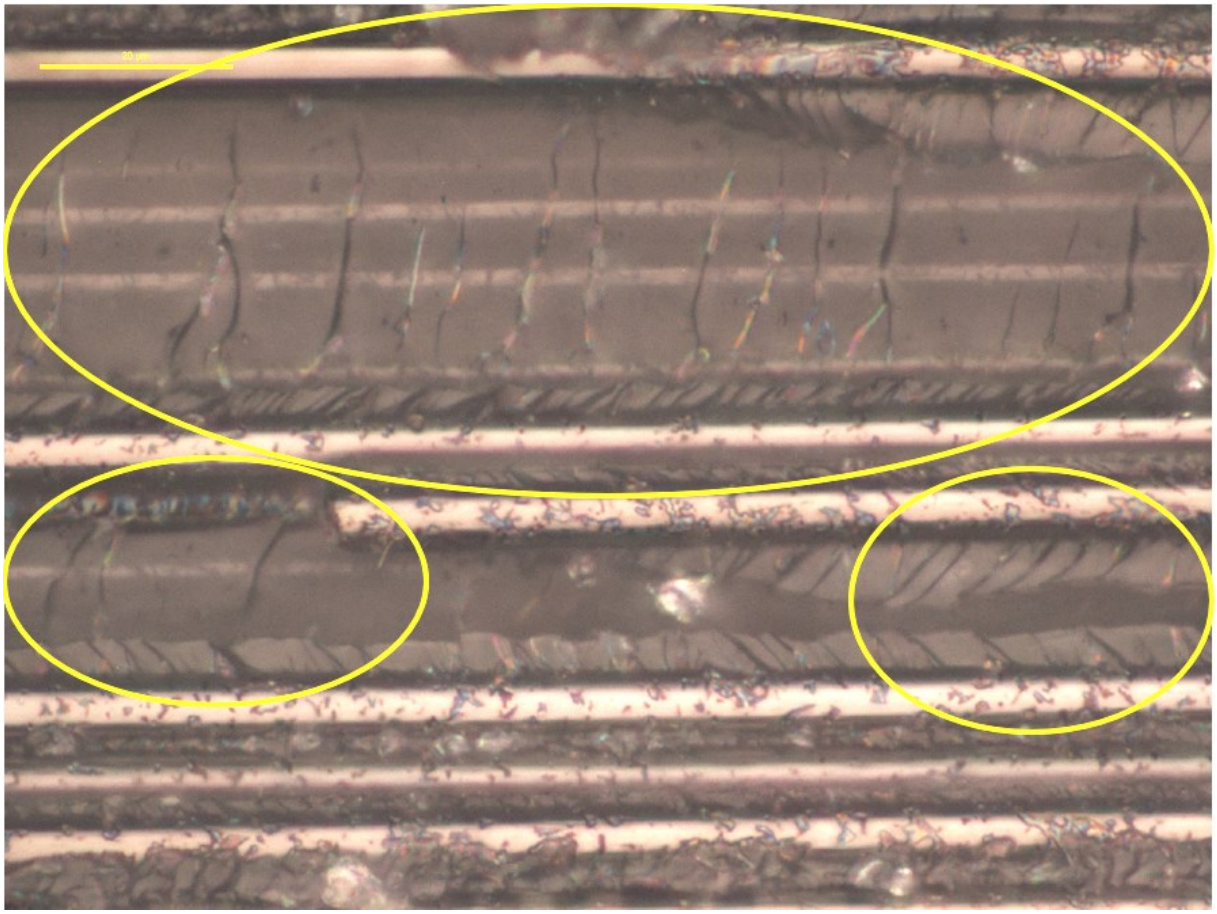

Figure 3: A microscope image of CNF alignment between carbon fibers (lines that are running horizontally) taken from a cured sample of prepreg

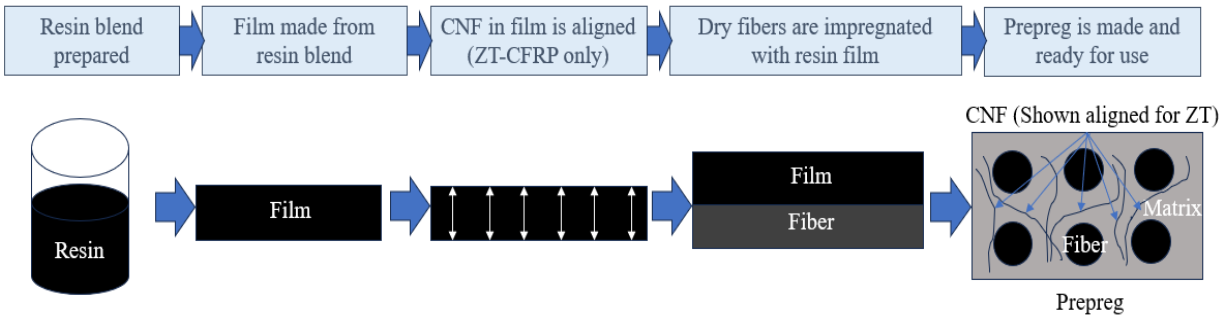

Figure 4: The prepreg making process is detailed in the diagram from preparing the resin blend to making prepreg.

2.3 Composite Panel and Test Specimen Production

The prepreg for both cases was cut into 127 mm x 127 mm sheets. Prepreg stacks of 16 plies were prepared by hand for both test cases. The prepreg was laid unidirectionally for both cases. The stacks were then cured using the out-of-autoclave vacuum bag-only (OOA-VBO) process detailed in Figure 5. In this process, an individual stack of prepreg is placed onto a release agent coated metal plate and is then covered by a vacuum bag after the peel ply, breather fabric, and other components are laid sequentially as shown in Figure 5. A vacuum pressure of -0.09 MPa was applied to the OOA-VBO assembly. A hot press was utilized to provide the necessary curing temperatures. The hot press was only used to simulate an oven and did not exert any force onto the OOA-VBO assembly. The temperatures and pressures utilized during the curing cycle for both composite panels are provided in Table 1.

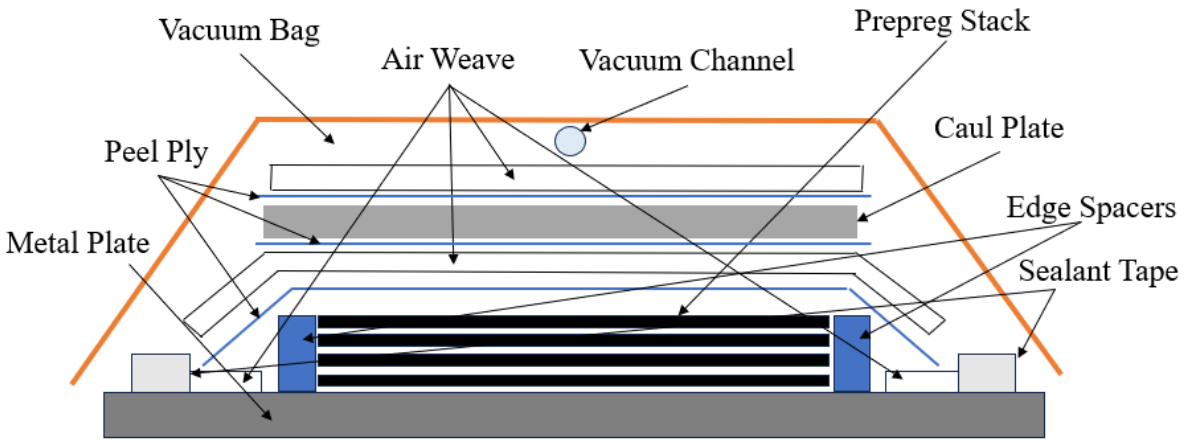

Figure 5: The OOA-VBO assembly and components are detailed in the diagram.

Composite Laminate Curing Cycle		
Time	**Temperature**	**Vacuum Applied**
60 minutes	22 ˚C (Room Temperature)	Yes
120 minutes	120 ˚C	Yes
360 minutes	180 ˚C	No

Table 1: The curing cycle that was utilized for manufacturing both the control and ZT-CFRP composites used in this study.

Once fully cured, the 127 mm x 127 mm laminate panels were cut to produce samples that fulfilled the criteria specified by the ASTM D2344 standard for SBS testing of fiber reinforced composites. The standard recommends the ratio between specimen thickness, width, and length should be 1:2:6, respectively [9]. With 16 plies, the nominal thickness of the two composite panels made for this study was 2.5 mm. Based off the recommendation by ASTM D2344, the dimensions of the test specimens were approximately 2.5 mm x 5 mm x 15 mm. The 15 mm length was parallel with the direction of the fibers. The ASTM D2344 standard requires that at least five specimens for each case are tested.

2.4 Specimen Heat Treating

An FB1400 model muffle furnace made by Barnstead Thermolyne Corporation was used for heat treating the test samples at 350 ˚C. The chamber was first preheated to 370 ˚C. The test specimens were put on a ceramic tray to be inserted within the chamber of the furnace. Once the chamber temperature stabilized, the ceramic tray with the specimens was placed inside the furnace. After two minutes of the ceramic tray being placed inside the chamber and the furnace door closing, the temperature setting of the oven was reduced to 350 ˚C. This heating procedure allowed the temperature of the specimens to rapidly increase to and hold at the desired exposure temperature of 350 ˚C. After 10 minutes within the furnace chamber, the ceramic tray and specimens were removed and allowed to cool to room temperature. Only five specimens at a time were heated within the furnace.

2.5 SBS Testing

The short beam shear tests done for this study were done using a Tinius Olsen 10ST universal testing machine. The loading nose and supports of the testing apparatus were both in compliance with ASTM D2344 with diameters of 6 mm and 3mm, respectively. The ASTM D2344 requires that the ratio between span length, or the distance between supporting pins, be four times the thickness of the testing specimen [9]. Since the testing specimens used in this study had a nominal thickness of 2.5mm, the span length was set to 10 mm. The crosshead movement rate of the loading nose was also in compliance and set at a rate of 1.0 mm/min. Data on the position of the loading crosshead and force during testing was output. Figure 6 provides a picture of the testing setup used for this study.

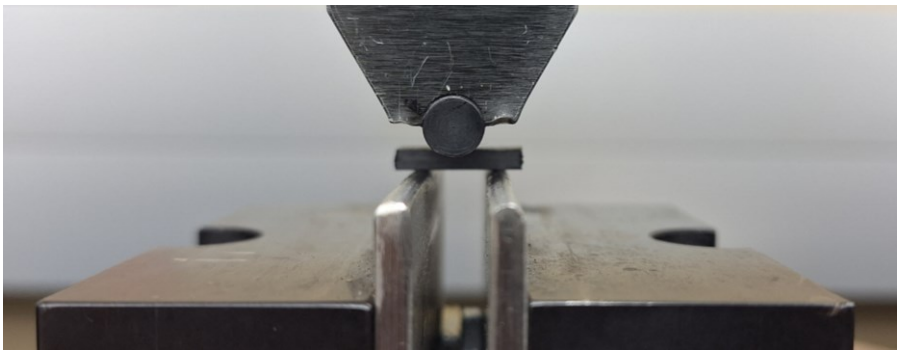

Figure 6: Photo of the SBS setup that was used for this study with a sample loaded.

3 RESULTS

3.1 Testing Data

The force testing output data was used to find the interlaminar shear stress acting on the specimens during SBS testing using the following formula from ASTM D2344:

$$F^{sbs} = 0.75\, x\, \frac{P}{b\, x\, h} \tag{1}$$

Where F^{sbs} is the interlaminar shear stress, P is the force due to the loading, b is the testing specimen width, and h is the testing specimen thickness [9]. The calculated stress values and crosshead displacement data from testing are plotted in Figure 7 for all four cases of specimens tested: control at room temperature, control after being heat treated at 350 ˚C, ZT-CFRP at room temperature, and ZT-CFRP after being heat treated at 350 ˚C

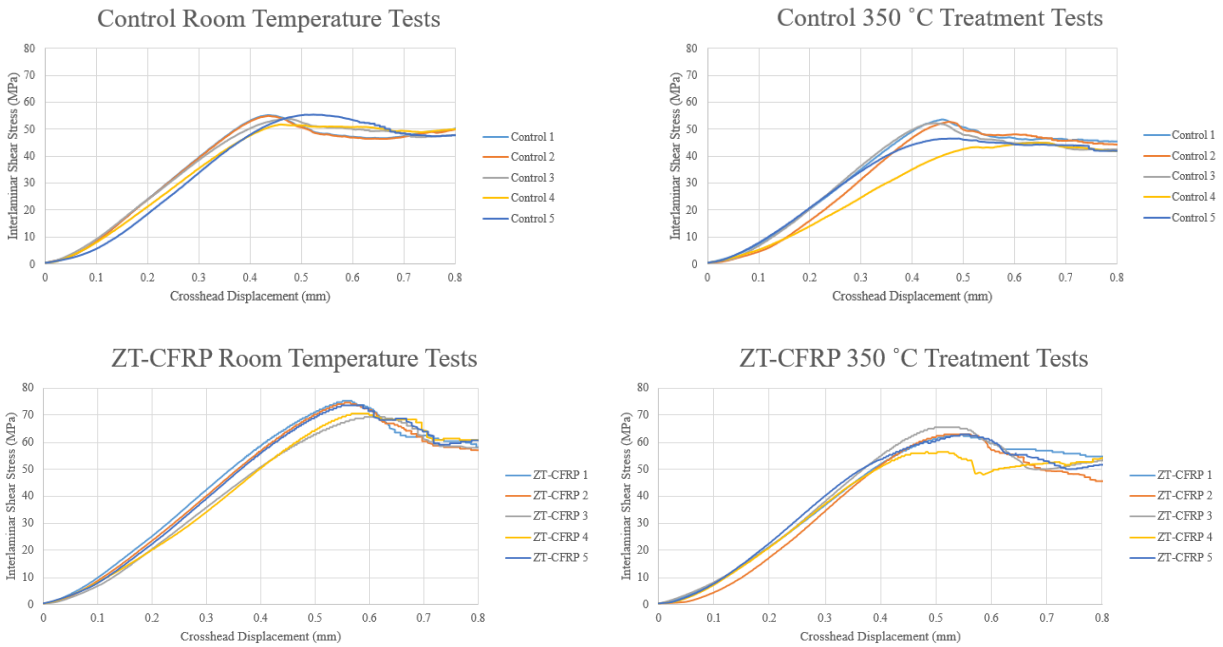

Figure 7: Crosshead displacement and interlaminar shear stress curves taken for the tested specimens.

The ILSS for each test sample is recorded in Table 2. The average ILSS for room temperature and 350 ˚C treated control CFRP samples was 54.253 MPa and 49.626 MPa, respectively. Based on the average control ILSS values, this was a 4.627 MPa (-8.53%) decline in strength after exposure to 350 ˚C for 10 minutes. A 10.584 MPa (-14.56%) decline in ILSS was observed between the average for room temperature and 350 ˚C treated ZT-CFRP samples, which was 72.676 MPa and 62.092 MPa, respectively. At room temperature, the average ILSS for ZT-CFRP was 18.423 MPa higher than that of control. Heat treated ZT-CFRP also had a higher average ILSS than heat treated control, with an observed 12.466 MPa difference between the two. It is interesting to note that the treated ZT-CFRP still had a higher ILSS (62.092 MPa) than that of the control CFRP without exposure of heat treatment (54.253 MPa).

ILSS (MPa)							
Room Temperature				**350 ˚C Treatment**			
Control 1	55.254	**ZT-CFRP 1**	75.308	**Control 1**	53.591	**ZT-CFRP 1**	62.759
Control 2	54.925	**ZT-CFRP 2**	74.606	**Control 2**	52.779	**ZT-CFRP 2**	62.882
Control 3	53.876	**ZT-CFRP 3**	69.317	**Control 3**	52.251	**ZT-CFRP 3**	65.525
Control 4	51.776	**ZT-CFRP 4**	70.564	**Control 4**	42.948	**ZT-CFRP 4**	56.413
Control 5	55.432	**ZT-CFRP 5**	73.584	**Control 5**	46.560	**ZT-CFRP 5**	62.880
AVERAGE	**54.253**	**AVERAGE**	**72.676**	**AVERAGE**	**49.626**	**AVERAGE**	**62.092**
Improvement	**-**		**+33.96%**		**-**		**+25.12%**
ST DEV	**1.350**	**ST DEV**	**2.333**	**ST DEV**	**4.161**	**ST DEV**	**3.024**

Table 2: ILSS values recorded for all tested specimens.

3.2 Microscope Image Analysis

Tested specimens were viewed underneath a Nikon Eclipse LV 150 microscope to provide a visualization of what mechanisms may have contributed to the interlaminar failure and strength discrepancies between the four test cases observed. Figure 8 provides images taken along the end of two specimens: one control and one ZT-CFRP that received no heat treatment. As can be seen, a much smaller interlaminar crack formed within the ZT-CFRP sample in comparison to the control sample.

This was likely due to the reinforcing CNF z-threads that helped to resist the formation and propagation of a larger scale crack.

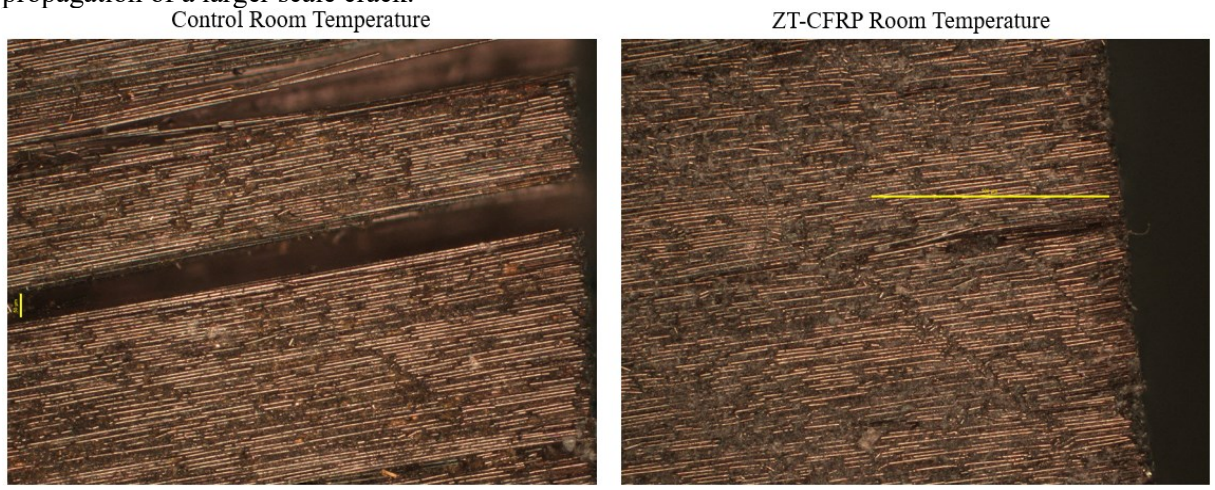

Figure 8: Images taken along interlaminar crack formed on the end of room temperature tested Control Sample 3*(left)* and ZT-CFRP Sample 5 *(right)*.

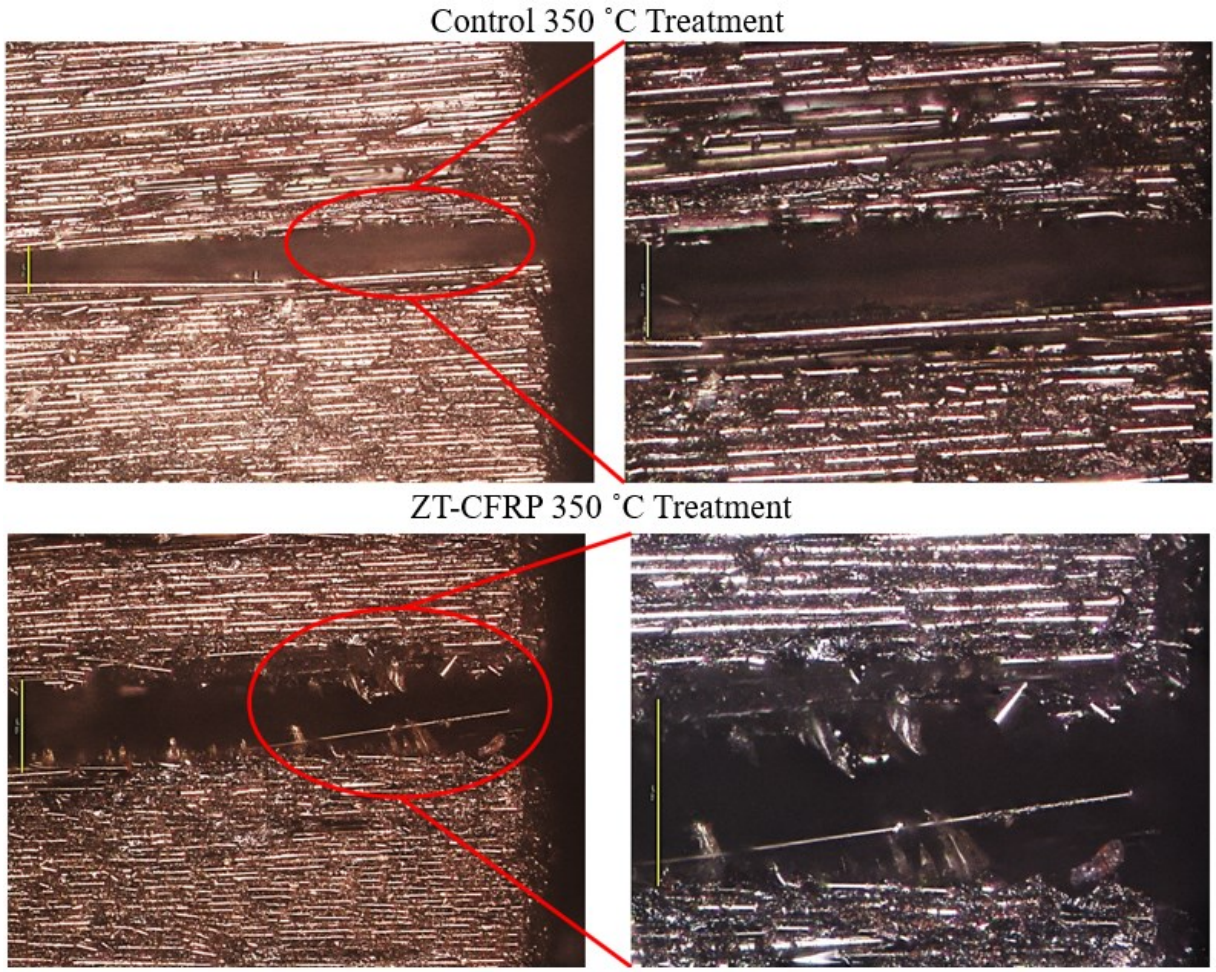

Figure 9: Images taken along interlaminar crack formed on the end of 350 ˚C treated tested Control Sample 1*(top)* and ZT-CFRP Sample 1 *(bottom)*.

Figure 9 shows images taken from two 350 ˚C pretreated samples: one control and one ZT-CFRP. As can be seen within the images taken along the interlaminar crack formation, the ZT-CFRP sample had a much more jagged edge in comparison to the control sample. Exposed CNF z-threads can also

be seen along the length of the crack formation. There also appears to be more misaligned carbon fibers near the interlaminar crack with the ZT-CFRP sample. The jagged edge, exposed z-threads, and greater fiber misalignment of the ZT-CFRP samples may help to support the argument made in the preceding paragraph that the CNF z-threads act as anchoring mechanism that resists delamination and interlaminar failure. The control samples only have the strength of the epoxy bond between layers to prevent delamination.

4 CONCLUSION

This study examined how the inclusion of CNF z-threads contributed to the retention of ILSS within CFRP composites after they have been exposed to extreme elevated temperatures. It was found that ZT-CFRP exhibited improved ILSS over traditional CFRP both with and without extreme temperature exposure. ZT-CFRP exhibited an average ILSS of 72.676 MPa without heat exposure and 62.092 MPa with a 350 ˚C heat treatment. The traditional CFRP samples exhibited an average ILSS of 54.253 MPa without heat exposure and 49.626 MPa with a 350 ˚C heat treatment. From the obtained ILSS data and microscope images taken of tested samples, there is evidence to suggest that the CNF z-threads provided a reinforcing mechanism that resisted interlaminar failure and crack propagation of the composite. This could be seen well in the extreme heat-treated samples where there was a diminished matrix due to thermal degradation. The CNF z-threads were apparent along the edges of the formed cracks and were likely significant contributors for ZT-CFRP heat treated samples still having higher ILSS than traditional CFRP samples that received no extreme heat exposure.

It was expected that the traditional CFRP samples would have a more diminished ILSS after heat exposure than was observed. This may have been a result of the CFRP samples being more resin dry in comparison to the ZT-CFRP samples despite having similar dimensions and being composed of the same amount of prepreg plies. There may have already been areas of diminished matrix in the CFRP samples in comparison to the ZT-CFRP samples that would not have been as affected by thermal degradation caused by the elevated temperatures.

The claims made in this publication can be further supported through additional testing in the future. Unaligned CNF reinforced CFRP would help to show that it is the z-threads and not just nanomaterial reinforcement that improves the ILSS capabilities. However, this has already been shown in samples with no extreme heat exposure [6]. Testing different exposure temperatures and/or times would also provide more insight into the effect of thermal degradation of the matrix on CFRP and ZT-CFRP interlaminar strength capabilities. Different CNF weight fractions could also better show the significance of z-threads for strength retention with smaller weight fractions likely not being able to retain ILSS as well as higher weight fractions.

ACKNOWLEDGEMENTS

The authors acknowledged the financial support by the National Science Foundation (Award numbers: 2044513 and 2419207) and NASA Alabama Space Grant Consortium Fellowship award (NASA Training Grant 80NSSC20M0044).

REFERENCES

[1] K.-T. Hsiao, et al., Effect of Carbon Nanofiber Z-Threads on Mode-I Delamination Toughness of Carbin Fiber Reinforced Plastic Laminates, *Composites Part A Applied Science and Manufacturing*, **91**(7), 2016 (doi :10.1016/j.compositesa.2016.10.022).

[2] S. Kirmse, et al., Effects of Carbon Nanofiber Z-Threads on the Longitudinal Compressive Strength of Unidirectional CFRP Laminates, *SAMPE 2019 (Society for the Advancement of Material and Process Engineering)*, *Charlotte, NC, 2019*.

[3] A. Scruggs, K. Henderson, and K.-T. Hsiao, Characterization of Electrical Conductivity of a Carbon Fiber Reinforced Plastic Laminate Reinforced With Z-Aligned Carbon Nanofibers, *CAMX 2016 (The Composites and Advanced Materials Expo), Anaheim, CA, 2016.*

[4] B. Ranabhat and K.-T. Hsiao, Improve the Through-Thickness Electrical Conductivity of CFRP Laminate Using Flow- Aligned Carbon Nanofiber Z-Threads, *SAMPE 2018 (Society for the Advancement of Material and Process Engineering), Long Beach, CA, 2018.*

[5] A. M. Scruggs, S. Kirmse, and K.-T. Hsiao, Enhancement of Through-Thickness Thermal Transport in Unidirectional Carbon Fiber Reinforced Plastic Laminates due to the Synergetic Role of Carbon Nanofiber Z-Threads*, Journal of Nanomaterials*, 2019: pp. 1-13 (doi : 10.1155/2019/8928917).

[6] S. Kirmse, B. Ranabhat, and K.-T. Hsiao, Experimental and analytical investigation on the interlaminar shear strength of carbon fiber composites reinforced with carbon nanofiber z-threads, *Materials Today Communications*, **25,** 2020 (doi : 10.1016/j.mtcomm.2020.101512).

[7] K.-T. Hsiao, et al., Flammability Characterization of Carbon Nanofibers and Nanotubes Z-Threaded CFRP Laminates, *CAMX- The Composites and Advanced Materials Expo, Anaheim, CA 2022.*

[8] R. Warren, et al., Experimental Study of ILSS Failure Performance of Carbon Nanofibers Z-Threaded CFRP During Extreme Heat Exposure, *SAMPE 2025 (Society for the Advancement of Material and Process Engineering)*, *Indianapolis, IN, 2025*.

[9] ASTM, *ASTM D2344: Standard Test Method for Short-Beam Strength of Polymer Matrix Composite Materials and Their Laminates*. 2022.

[10] J.G. Quintiere, R.N. Walters, and S. Crowley, *Flammability Properties of Aircraft Carbon-Fiber Structural Composite*, U.S.D.o. Transportation Editor, Federal Aviation Administration, 2007.

[11] M. Bazli and M. Abolfazli, Mechanical Properties of Fibre Reinforced Polymers under Elevated Temperatures: An Overview*, Polymers*, **12**(11), 2020, pp. 2600 (doi :10.3390/polym12112600).

[12] W. Ningyun and J.T. Evans, Collapse of continuous fibre composite beams at elevated temperatures, *Composites*, **26**(5), 1995, pp. 56-61 (doi :10.1016/0010-4361(94)P3630-J).

[13] A. Nema, et al., Effect of temperature on flexural and interlaminar shear strength properties of carbon-epoxy composites: Experiment and modeling*, Polymer Composites,* **45**(10), 2024, pp. 9139-9155 (doi :10.1002/pc.28399).

[14] S. Hegde, B.S. Shenoy, and K.N. Chethan, Review on carbon fiber reinforced polymer (CFRP) and their mechanical performance*, Materials Today: Proceedings*, **19**, 2019, pp. 658-662. (doi :10.1016/j.matpr.2019.07.749).

[15] T.-C. Nguyen, et al., Time-dependent behaviour of steel/CFRP double strap joints subjected to combined thermal and mechanical loading*, Composite Structures*, **94**(5), 2012 p. 1826-1833. (doi :10.1016/j.compstruct.2012.01.007)

[16] K.-T. Hsiao and S. Kirmse, *Novel Liquid Matrix Impregnation Method and Apparatus for Composite Prepreg Production*. 2022: United States.

ICCM24
AUGUST 4-8, 2025
BALTIMORE CONVENTION CENTER
BALTIMORE, MARYLAND, USA

No Technical Paper Submission for:

Jianhua Huang

ICCM24
AUGUST 4-8, 2025
BALTIMORE CONVENTION CENTER
BALTIMORE, MARYLAND, USA

No Technical Paper Submission for:

Debes Bhattacharyya

EXPERIMENTAL EVALUATION OF INTERLAMINAR SHEAR STRENGTH OF CARBON NANOMATERIAL Z-THREADED CARBON FIBER-REINFORCED POLYMER LAMINATES AFTER EXPOSURE TO EXTREME ELEVATED TEMPERATURES

Ryan A. Warren[1], Obaidul Hasan[2] and Kuang-Ting Hsiao[3]

[1]Systems Engineering Program, University of South Alabama
150 Student Services Drive, Shelby Hall 4106. Mobile, Alabama
Email: raw1522@jagmail.southalabama.edu

[2]William B. Burnsed, Jr. Department of Mechanical Engineering, Aerospace, and Biomedical Engineering, University of South Alabama
150 Student Services Drive, Shelby Hall 3128. Mobile, Alabama
Email: oh2321@jagmail.southalabama.edu

[3]William B. Burnsed, Jr. Department of Mechanical Engineering, Aerospace, and Biomedical Engineering, University of South Alabama
150 Student Services Drive, Shelby Hall 3128. Mobile, Alabama
Email: kthsiao@southalabama.edu

Keywords: Carbon Nanofiber, Z-Threaded Carbon Fiber Reinforced Polymer, ILSS

ABSTRACT

Previous studies have shown that carbon nanofiber (CNF) z-threaded carbon fiber-reinforced polymer (ZT-CFRP) laminates exhibit improved mechanical performance in comparison to traditional carbon fiber-reinforced polymer (CFRP) laminates when exposed to extreme elevated temperatures. Z-threaded reinforcement is a technique for strengthening the through-thickness of a laminate by introducing perpendicularly aligned carbon nanomaterial to be threading into the continuous fiber array. Improved performance has already been observed in properties such as interlaminar shear strength (ILSS) without extreme heat exposure, but there has also been evidence that z-thread inclusion may mitigate strength loss due to thermal degradation of the matrix. This study examined how ILSS was diminished in both CFRP and ZT-CFRP samples with matrix degradation caused by extreme temperature exposure. Test samples were heated to 350 ˚C for 10 minutes and then allowed to return to room temperature. SBS testing in accordance with ASTM D2344 was conducted on both untreated and heat-treated samples for comparison. All samples were at room temperature during testing. It was found that ZT-CFRP samples (with 0.5wt% CNF concentration the matrix) exhibited higher ILSS with and without heat treatment over the traditional CFRP samples with and without heat treatment by +33.96% and +25.12%, respectively. ZT-CFRP ILSS was found to decrease by 10.584 MPa (-14.56%) after the extreme heat treatment, while CFRP ILSS decreased by only 4.627 MPa (-8.53%). Microscopic image analysis was also performed to provide insight into how the CNF z-threads may have provided a mechanism for retaining ILSS performance even with matrix thermal degradation.

1 INTRODUCTION

The high strength-to-weight ratios of carbon fiber reinforced polymers (CFRP) have caused it to become an increasingly used and researched material for structural designs. One of the disadvantages of CFRP is that they are anisotropic, with higher mechanical performance being restricted to loadings acting in the direction of the embedded reinforcing fibers. Even with the use of different stacking orientation techniques that can introduce more planar isotropy tendencies, there is still no reinforcing mechanism along the through-thickness of the composite. All reinforcement is confined to the plane of the fiber arrays. The novel Z-threaded nanomaterial reinforcement technique is a proven method for

increasing the through-thickness capabilities of CFRP. Within Z-threaded CFRP (ZT-CFRP), carbon nanomaterial is aligned and threaded perpendicularly through the reinforcing fiber array. A depiction of the concept of ZT-CFRP is provided in Figure 1 with carbon nanofibers (CNF) acting as the nanomaterial reinforcement.

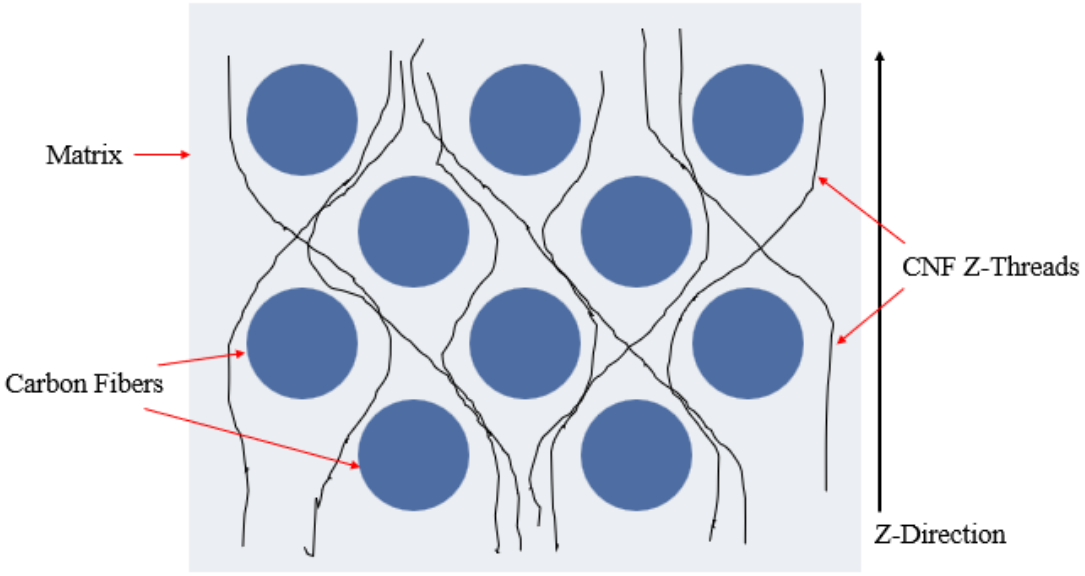

Figure 1: Illustration of ZT-CFRP showing how the nanomaterial reinforcement is threaded perpendicularly through fiber array.

Previous studies have already shown that ZT-CFRP exhibits improved through-thickness dependent material properties in comparison to traditional CFRP composites. This includes strengthened mechanical properties such as Mode-I delamination toughness [1] and longitudinal compressive strength [2], along with improved electrical [3, 4] and thermal conductivities [5]. Interlaminar shear strength (ILSS) is a mechanical property that saw significant increase in performance in comparison to traditional CFRP. With the inclusion of 1 wt% CNF z-threads, a 17% improvement in ILSS was observed. Traditional CFRP samples exhibited an average ILSS of 64.89 MPa while ZT-CFRP samples exhibited an average of 75.92 MPa [6].

Improved flammability characteristics have also been observed in ZT-CFRP using UL-94 testing, a standard for assessing the fire hazard of plastic materials. It was shown that ZT-CFRP took on average only 34.95 seconds to self-extinguish, while CFRP samples took on average 86.8 seconds. Self-extinguishing time for ZT-CFRP took only 40% of the time it took for CFRP samples. ZT-CFRP also showed a reduced chance of flame propagation in comparison to CFRP. None of the ZT-CFRP samples burned all the way to the clamp holding the specimen during testing, whereas 60% of the CFRP samples did [7].

A previous study on ILSS failure performance during extreme heat exposure provided evidence of improved strength capabilities and retention in extreme temperature environments of ZT-CFRP in comparison to CFRP. In this study an apparatus was designed and used to replicate the loading of a short beam shear (SBS) test within a muffle furnace chamber. Both CFRP and ZT-CFRP samples were placed inside the apparatus within the chamber and a static loading was exerted onto them. The temperature of the furnace was allowed to increase based on a consistent heating schedule until failure was observed within the testing samples. It was observed that the average failure temperature range for ZT-CFRP was between 384.0 ˚C to 398.4 ˚C, whereas CFRP samples failed on average at temperatures ranging from 349.6 ˚C to 368.2 ˚C. This was an approximate 30 ˚C increase in temperature handling capabilities exhibited by ZT-CFRP over CFRP [8].

Based on the temperature failure ranges observed from the previously mentioned study, there is evidence that ZT-CFRP may be better equipped at retaining strength during thermal degradation caused by extreme temperature exposure in comparison to traditional CFRP. This study examined the

retention of ILSS between CFRP and ZT-CFRP when exposed to extreme elevated temperatures that can cause thermal degradation within the matrix. This was accomplished by heat treating specimens at 350 ˚C within a muffle furnace for 10 minutes. The treated specimens were then removed and underwent SBS testing to experimentally determine their ILSS. Specimens subjected to no heat treatment were also tested to show how much strength was lost due to heat exposure and potential matrix degradation. Specimens for both cases were prepared and tested based on the specifications provided in ASTM D2344 [9]. Microscopic image analysis was also performed to determine how the z-threaded CNF microstructure may have contributed to the failure observed. The process of manufacturing and testing the specimens, testing data, and microscope images of the specimens are provided within this document.

1.1 Review of the Effect of Extreme Temperature Exposure on CFRP Behavior

Quintiere et al. [10] reported that the typical temperature range for the degradation of common aerospace CFRP composites is between 300 ˚C to 500 ˚C. The reduction in material properties observed at these elevated temperatures is not only due to the weakening molecular bonds but is also a result of the internal pressure caused by resin vaporization and the reinforcing fibers that hinder its escape. Bazli et al. [11] reported a similar degradation temperature range while also observing that composites loaded in either shear or compression failed at much earlier temperatures in comparison to those loaded in tension or flexure. Ningyun and Evans [12] performed short beam shear tests on fiber reinforced thermoplastic composites between 20 ˚C and 300 ˚C. Failure at low temperatures was found to be largely due to interlaminar shear and delamination. Large-scale inelastic deformation was observed within the test specimens at higher temperatures. These studies provide evidence that matrix sensitive material properties are more sensitive to extreme temperatures.

Nema et al. [13] found that both flexural strength and ILSS decreased linearly as temperature was increased to 200˚C. Significant decreases in flexural modulus were also observed at around 200 ˚C which was above the glass transition temperatures of the resin systems being used. Hegde et al. [14] also observed that composite strength and stiffness consistently fell as temperature began to approach the glass transition temperature. With steel and CFRP double strap joints, Nguyen et al. [15] saw load carrying capabilities diminish by 30% when exposed to temperatures around the glass transition temperature.

2 EXPERIMENTATION

2.1 Materials

All testing specimens utilized unidirectional HexTow AS7 carbon fiber from Hexcel with a density and areal weight of 1.79 g/cm^3 and 190 g/m^2, respectively, for reinforcement. The tow size was 12 K. CNFs used for z-thread nanomaterial reinforcement were PR-24-XT-PS grade from Pyrograph/ Applied Sciences Incorporated. This grade of nanofibers was reported to have an average diameter of 100 nm and lengths ranging between 50 μm to 200 μm. The base resin system utilized for all specimens consisted of a mixture of Epon-862, a diglycidyl ether of bisphenol F, and Epikure-W, a non-MDA aromatic amine curing agent containing diethylmethylbenzenediamine, both purchased from Miller-Stephenson Chemical Company. The surfactants Disperbyk-191 and Disperbyk-192, both purchased from BYK USA, were used in cases with CNF reinforcement to better disperse the nanomaterial within the resin mixture.

2.2 Prepreg Production

Two different cases of composite panels were manufactured for this study: control containing no nanomaterial reinforcement and ZT-CFRP. All prepreg used for the panels was manufactured through a proprietary production process developed by the Hsiao research group at the University of South Alabama that is illustrated within a pending patent application US20240149541A1 [16]. Both control and ZT-CFRP utilized a base blend of Epon-862 and Epikure-W mixed at a stochiometric ratio of

100:26.5, respectively. For the ZT-CFRP prepreg, CNF was added at 0.5 wt% of the overall resin matrix mixture. Both Disperbyk-191 and Disperbyk-192 were added at a ratio of 1:1:1 with CNF for better dispersion within the mixture. The resin mixture used for control prepreg manufacturing only contained Epon-862 and Epikure-W.

Both the control and ZT-CFRP resin mixture underwent five minutes of manual stirring once the components were measured out and combined as appropriate. For the ZT-CFRP mixture that contained nanomaterial reinforcement and surfactants, one hour of high shear mixing at 900 rpm using a Stir-Pack Laboratory Mixer was performed. The rotational direction of the mixer was alternated after 30 minutes. The high shear mixed reinforced resin then underwent two hours of sonication using a QSONICA Q700 sonicator. This step was taken to further disperse and reduce agglomerations of CNF within the resin mixture. A sample of the resin mixture was taken after this step to determine the quality of CNF dispersion underneath a Nikon Eclipse LV 150 microscope. Figure 2 provides an image of the final CNF dispersion quality within the resin mixture prior to moving to the next step of prepreg production.

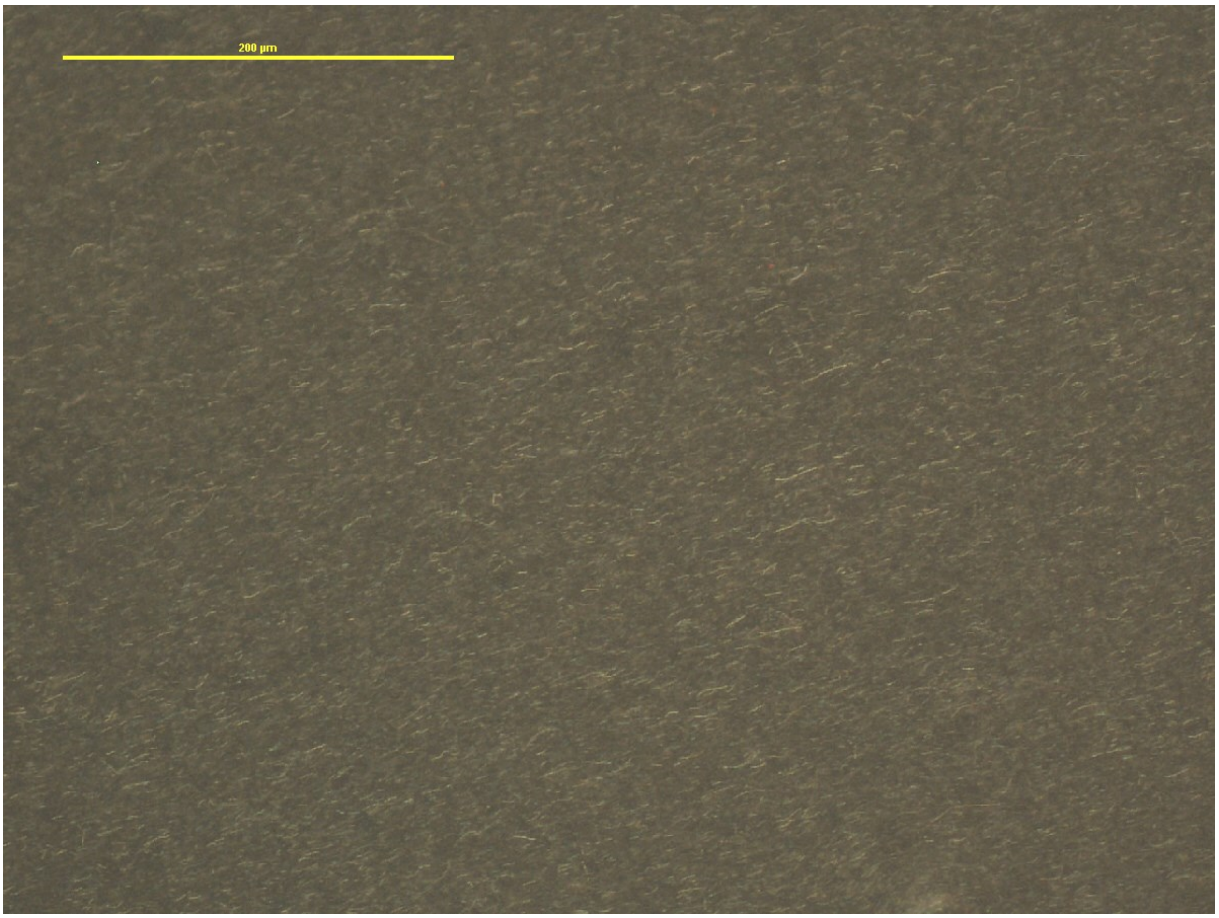

Figure 2: A microscope image showing dispersion quality of the CNF within the resin blend prior to prepreg manufacturing.

The appropriate amount of Epikure-W curing agent was added and manually stirred for 5 minutes into the dispersed CNF mixture to begin the B-staging process. The blend was then placed for approximately 1 hour inside a vacuum oven at 110 ˚C and -0.09 MPa. The vacuum applied to the resin during this process allowed for the removal of any trapped air within the mixture while also allowing it to partially cure. The control resin mixture also underwent the same B-staging process once Epikure-W was added.

The partially cured resin mixtures were then used in the proprietary ZT-CFRP prepreg production line to create hot melt resin films. An additional alignment process was performed to orientate the CNF reinforcement within the ZT-CFRP film. Alignment is accomplished through reinforced film

exposure to an electrical field for 150 seconds. The hot melt films created for both cases were then used to impregnate dry AS7 fiber fabric arrays. The alignment quality of the created ZT-CFRP prepreg was checked underneath a microscope. An example image of aligned prepreg is provided in Figure 3. Figure 4 provides a diagram detailing the process of making prepreg from start to finish.

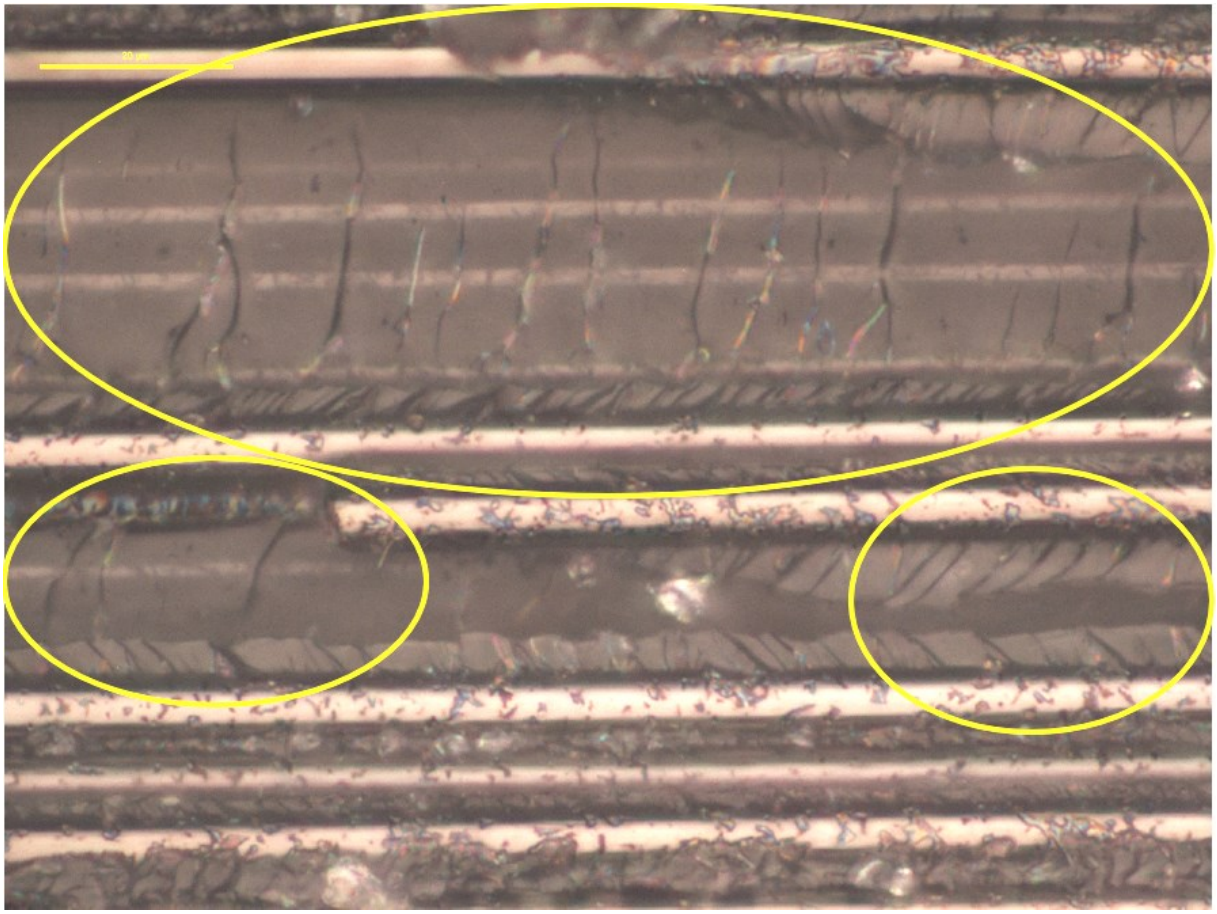

Figure 3: A microscope image of CNF alignment between carbon fibers (lines that are running horizontally) taken from a cured sample of prepreg

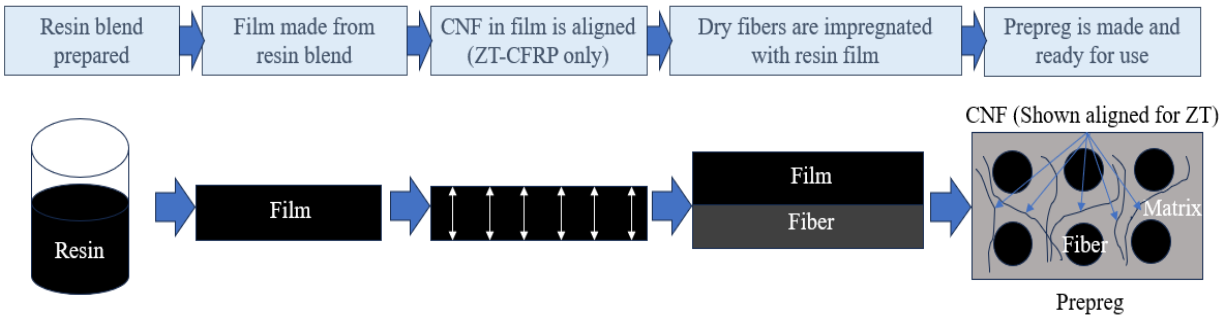

Figure 4: The prepreg making process is detailed in the diagram from preparing the resin blend to making prepreg.

2.3 Composite Panel and Test Specimen Production

The prepreg for both cases was cut into 127 mm x 127 mm sheets. Prepreg stacks of 16 plies were prepared by hand for both test cases. The prepreg was laid unidirectionally for both cases. The stacks were then cured using the out-of-autoclave vacuum bag-only (OOA-VBO) process detailed in Figure 5. In this process, an individual stack of prepreg is placed onto a release agent coated metal plate and is then covered by a vacuum bag after the peel ply, breather fabric, and other components are laid sequentially as shown in Figure 5. A vacuum pressure of -0.09 MPa was applied to the OOA-VBO assembly. A hot press was utilized to provide the necessary curing temperatures. The hot press was only used to simulate an oven and did not exert any force onto the OOA-VBO assembly. The temperatures and pressures utilized during the curing cycle for both composite panels are provided in Table 1.

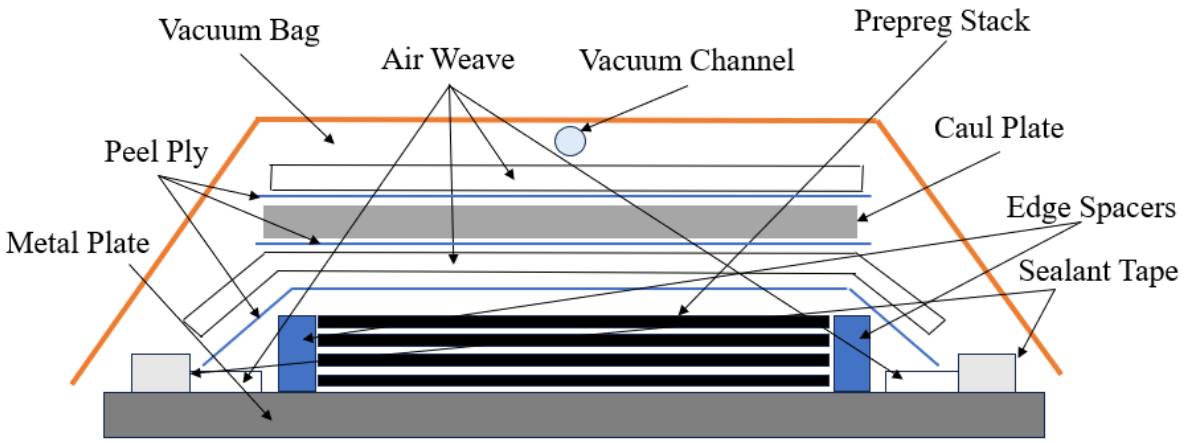

Figure 5: The OOA-VBO assembly and components are detailed in the diagram.

Composite Laminate Curing Cycle		
Time	**Temperature**	**Vacuum Applied**
60 minutes	22 ˚C (Room Temperature)	Yes
120 minutes	120 ˚C	Yes
360 minutes	180 ˚C	No

Table 1: The curing cycle that was utilized for manufacturing both the control and ZT-CFRP composites used in this study.

Once fully cured, the 127 mm x 127 mm laminate panels were cut to produce samples that fulfilled the criteria specified by the ASTM D2344 standard for SBS testing of fiber reinforced composites. The standard recommends the ratio between specimen thickness, width, and length should be 1:2:6, respectively [9]. With 16 plies, the nominal thickness of the two composite panels made for this study was 2.5 mm. Based off the recommendation by ASTM D2344, the dimensions of the test specimens were approximately 2.5 mm x 5 mm x 15 mm. The 15 mm length was parallel with the direction of the fibers. The ASTM D2344 standard requires that at least five specimens for each case are tested.

2.4 Specimen Heat Treating

An FB1400 model muffle furnace made by Barnstead Thermolyne Corporation was used for heat treating the test samples at 350 ˚C. The chamber was first preheated to 370 ˚C. The test specimens were put on a ceramic tray to be inserted within the chamber of the furnace. Once the chamber temperature stabilized, the ceramic tray with the specimens was placed inside the furnace. After two minutes of the ceramic tray being placed inside the chamber and the furnace door closing, the temperature setting of the oven was reduced to 350 ˚C. This heating procedure allowed the temperature of the specimens to rapidly increase to and hold at the desired exposure temperature of 350 ˚C. After 10 minutes within the furnace chamber, the ceramic tray and specimens were removed and allowed to cool to room temperature. Only five specimens at a time were heated within the furnace.

2.5 SBS Testing

The short beam shear tests done for this study were done using a Tinius Olsen 10ST universal testing machine. The loading nose and supports of the testing apparatus were both in compliance with ASTM D2344 with diameters of 6 mm and 3mm, respectively. The ASTM D2344 requires that the ratio between span length, or the distance between supporting pins, be four times the thickness of the testing specimen [9]. Since the testing specimens used in this study had a nominal thickness of 2.5mm, the span length was set to 10 mm. The crosshead movement rate of the loading nose was also in compliance and set at a rate of 1.0 mm/min. Data on the position of the loading crosshead and force during testing was output. Figure 6 provides a picture of the testing setup used for this study.

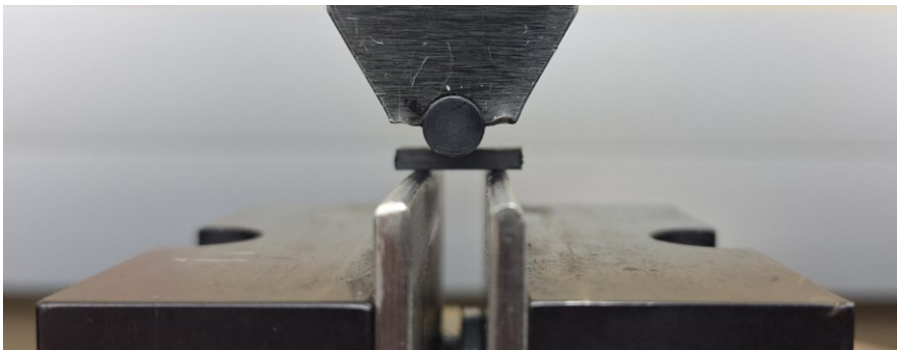

Figure 6: Photo of the SBS setup that was used for this study with a sample loaded.

3 RESULTS

3.1 Testing Data

The force testing output data was used to find the interlaminar shear stress acting on the specimens during SBS testing using the following formula from ASTM D2344:

$$F^{sbs} = 0.75\, x\, \frac{P}{b\, x\, h} \tag{1}$$

Where F^{sbs} is the interlaminar shear stress, P is the force due to the loading, b is the testing specimen width, and h is the testing specimen thickness [9]. The calculated stress values and crosshead displacement data from testing are plotted in Figure 7 for all four cases of specimens tested: control at room temperature, control after being heat treated at 350 ˚C, ZT-CFRP at room temperature, and ZT-CFRP after being heat treated at 350 ˚C

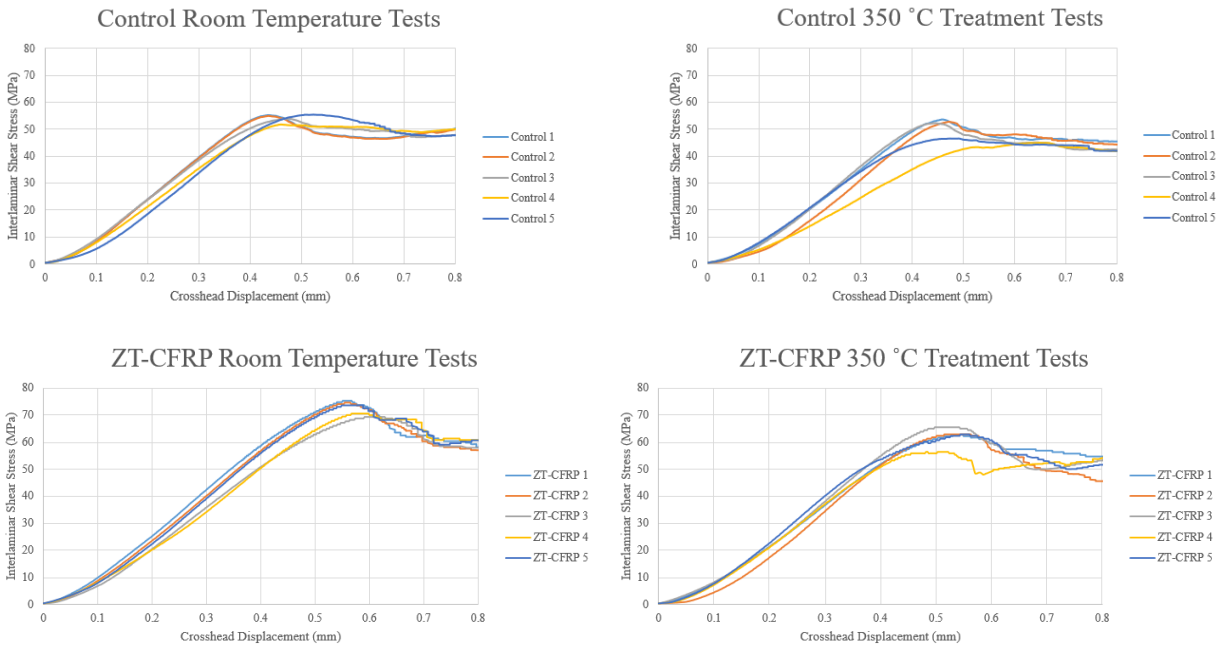

Figure 7: Crosshead displacement and interlaminar shear stress curves taken for the tested specimens.

The ILSS for each test sample is recorded in Table 2. The average ILSS for room temperature and 350 ˚C treated control CFRP samples was 54.253 MPa and 49.626 MPa, respectively. Based on the average control ILSS values, this was a 4.627 MPa (-8.53%) decline in strength after exposure to 350 ˚C for 10 minutes. A 10.584 MPa (-14.56%) decline in ILSS was observed between the average for room temperature and 350 ˚C treated ZT-CFRP samples, which was 72.676 MPa and 62.092 MPa, respectively. At room temperature, the average ILSS for ZT-CFRP was 18.423 MPa higher than that of control. Heat treated ZT-CFRP also had a higher average ILSS than heat treated control, with an observed 12.466 MPa difference between the two. It is interesting to note that the treated ZT-CFRP still had a higher ILSS (62.092 MPa) than that of the control CFRP without exposure of heat treatment (54.253 MPa).

ILSS (MPa)							
Room Temperature				**350 ˚C Treatment**			
Control 1	55.254	**ZT-CFRP 1**	75.308	**Control 1**	53.591	**ZT-CFRP 1**	62.759
Control 2	54.925	**ZT-CFRP 2**	74.606	**Control 2**	52.779	**ZT-CFRP 2**	62.882
Control 3	53.876	**ZT-CFRP 3**	69.317	**Control 3**	52.251	**ZT-CFRP 3**	65.525
Control 4	51.776	**ZT-CFRP 4**	70.564	**Control 4**	42.948	**ZT-CFRP 4**	56.413
Control 5	55.432	**ZT-CFRP 5**	73.584	**Control 5**	46.560	**ZT-CFRP 5**	62.880
AVERAGE	**54.253**	**AVERAGE**	**72.676**	**AVERAGE**	**49.626**	**AVERAGE**	**62.092**
Improvement	**-**		**+33.96%**		**-**		**+25.12%**
ST DEV	**1.350**	**ST DEV**	**2.333**	**ST DEV**	**4.161**	**ST DEV**	**3.024**

Table 2: ILSS values recorded for all tested specimens.

3.2 Microscope Image Analysis

Tested specimens were viewed underneath a Nikon Eclipse LV 150 microscope to provide a visualization of what mechanisms may have contributed to the interlaminar failure and strength discrepancies between the four test cases observed. Figure 8 provides images taken along the end of two specimens: one control and one ZT-CFRP that received no heat treatment. As can be seen, a much smaller interlaminar crack formed within the ZT-CFRP sample in comparison to the control sample.

This was likely due to the reinforcing CNF z-threads that helped to resist the formation and propagation of a larger scale crack.

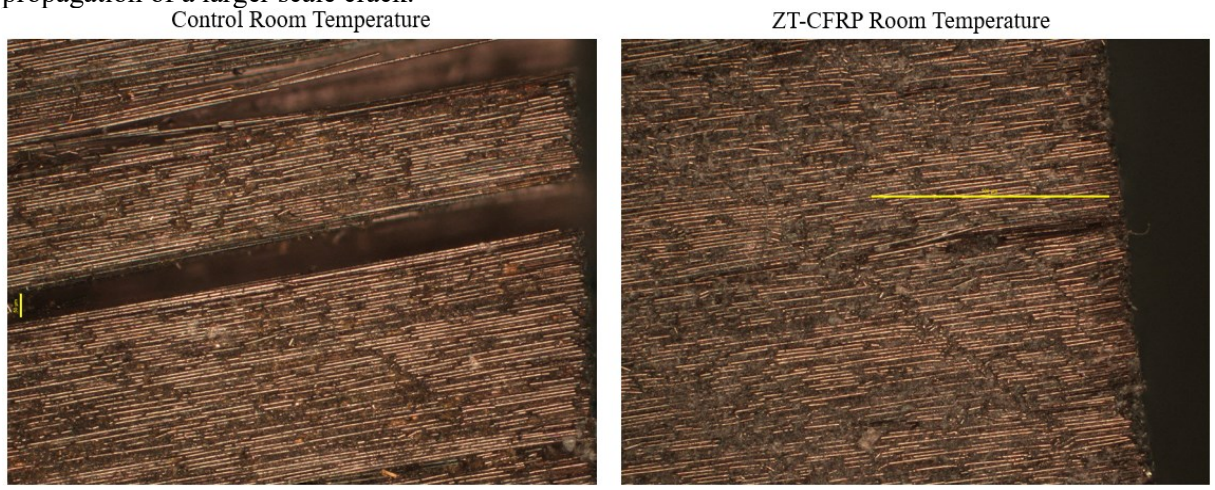

Figure 8: Images taken along interlaminar crack formed on the end of room temperature tested Control Sample 3*(left)* and ZT-CFRP Sample 5 *(right)*.

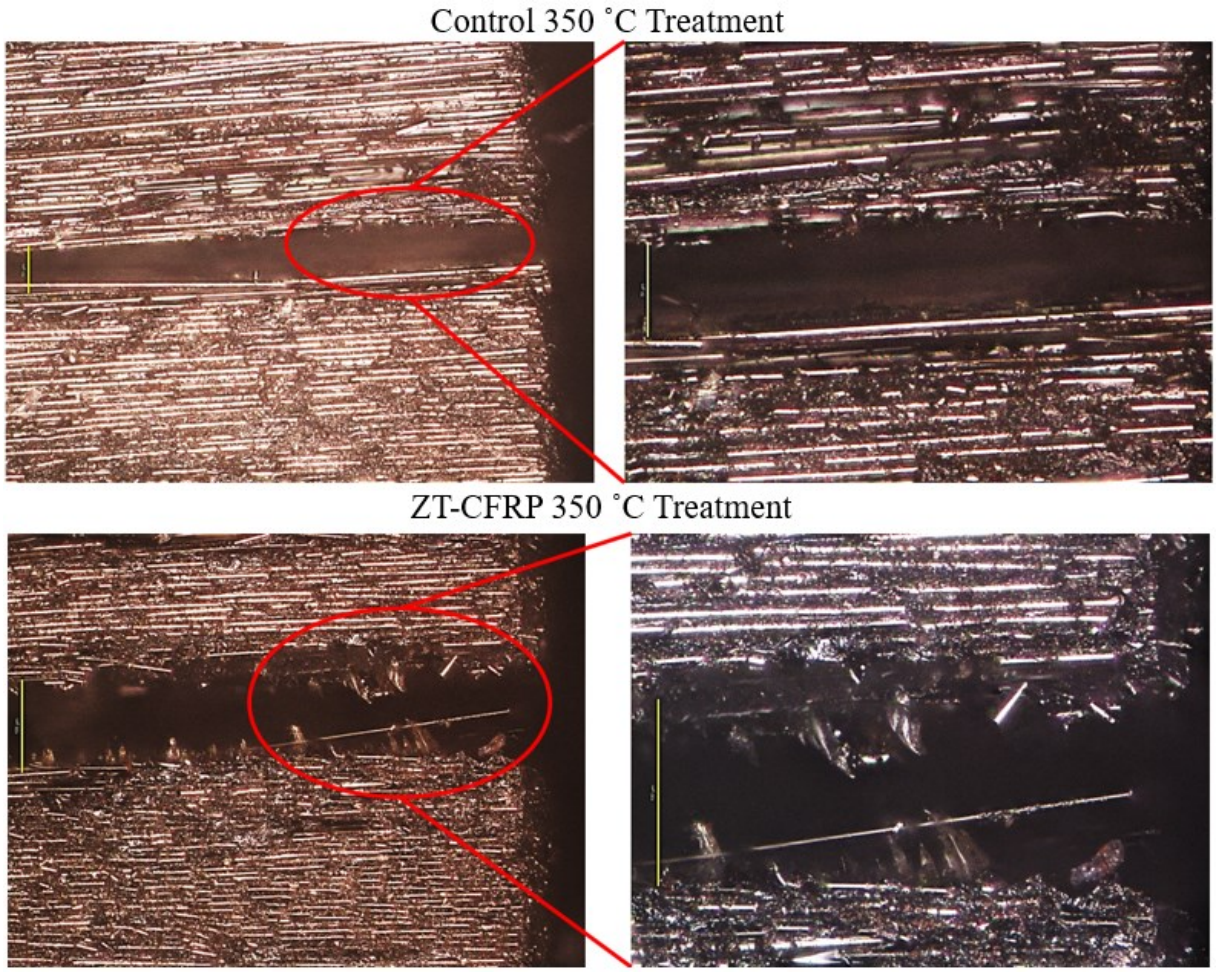

Figure 9: Images taken along interlaminar crack formed on the end of 350 ˚C treated tested Control Sample 1*(top)* and ZT-CFRP Sample 1 *(bottom)*.

Figure 9 shows images taken from two 350 ˚C pretreated samples: one control and one ZT-CFRP. As can be seen within the images taken along the interlaminar crack formation, the ZT-CFRP sample had a much more jagged edge in comparison to the control sample. Exposed CNF z-threads can also

be seen along the length of the crack formation. There also appears to be more misaligned carbon fibers near the interlaminar crack with the ZT-CFRP sample. The jagged edge, exposed z-threads, and greater fiber misalignment of the ZT-CFRP samples may help to support the argument made in the preceding paragraph that the CNF z-threads act as anchoring mechanism that resists delamination and interlaminar failure. The control samples only have the strength of the epoxy bond between layers to prevent delamination.

4 CONCLUSION

This study examined how the inclusion of CNF z-threads contributed to the retention of ILSS within CFRP composites after they have been exposed to extreme elevated temperatures. It was found that ZT-CFRP exhibited improved ILSS over traditional CFRP both with and without extreme temperature exposure. ZT-CFRP exhibited an average ILSS of 72.676 MPa without heat exposure and 62.092 MPa with a 350 ˚C heat treatment. The traditional CFRP samples exhibited an average ILSS of 54.253 MPa without heat exposure and 49.626 MPa with a 350 ˚C heat treatment. From the obtained ILSS data and microscope images taken of tested samples, there is evidence to suggest that the CNF z-threads provided a reinforcing mechanism that resisted interlaminar failure and crack propagation of the composite. This could be seen well in the extreme heat-treated samples where there was a diminished matrix due to thermal degradation. The CNF z-threads were apparent along the edges of the formed cracks and were likely significant contributors for ZT-CFRP heat treated samples still having higher ILSS than traditional CFRP samples that received no extreme heat exposure.

It was expected that the traditional CFRP samples would have a more diminished ILSS after heat exposure than was observed. This may have been a result of the CFRP samples being more resin dry in comparison to the ZT-CFRP samples despite having similar dimensions and being composed of the same amount of prepreg plies. There may have already been areas of diminished matrix in the CFRP samples in comparison to the ZT-CFRP samples that would not have been as affected by thermal degradation caused by the elevated temperatures.

The claims made in this publication can be further supported through additional testing in the future. Unaligned CNF reinforced CFRP would help to show that it is the z-threads and not just nanomaterial reinforcement that improves the ILSS capabilities. However, this has already been shown in samples with no extreme heat exposure [6]. Testing different exposure temperatures and/or times would also provide more insight into the effect of thermal degradation of the matrix on CFRP and ZT-CFRP interlaminar strength capabilities. Different CNF weight fractions could also better show the significance of z-threads for strength retention with smaller weight fractions likely not being able to retain ILSS as well as higher weight fractions.

ACKNOWLEDGEMENTS

The authors acknowledged the financial support by the National Science Foundation (Award numbers: 2044513 and 2419207) and NASA Alabama Space Grant Consortium Fellowship award (NASA Training Grant 80NSSC20M0044).

REFERENCES

[1] K.-T. Hsiao, et al., Effect of Carbon Nanofiber Z-Threads on Mode-I Delamination Toughness of Carbin Fiber Reinforced Plastic Laminates, *Composites Part A Applied Science and Manufacturing*, **91**(7), 2016 (doi :10.1016/j.compositesa.2016.10.022).

[2] S. Kirmse, et al., Effects of Carbon Nanofiber Z-Threads on the Longitudinal Compressive Strength of Unidirectional CFRP Laminates, *SAMPE 2019 (Society for the Advancement of Material and Process Engineering)*, *Charlotte, NC, 2019*.

[3] A. Scruggs, K. Henderson, and K.-T. Hsiao, Characterization of Electrical Conductivity of a Carbon Fiber Reinforced Plastic Laminate Reinforced With Z-Aligned Carbon Nanofibers, *CAMX 2016 (The Composites and Advanced Materials Expo), Anaheim, CA, 2016.*

[4] B. Ranabhat and K.-T. Hsiao, Improve the Through-Thickness Electrical Conductivity of CFRP Laminate Using Flow- Aligned Carbon Nanofiber Z-Threads, *SAMPE 2018 (Society for the Advancement of Material and Process Engineering), Long Beach, CA, 2018.*

[5] A. M. Scruggs, S. Kirmse, and K.-T. Hsiao, Enhancement of Through-Thickness Thermal Transport in Unidirectional Carbon Fiber Reinforced Plastic Laminates due to the Synergetic Role of Carbon Nanofiber Z-Threads*, Journal of Nanomaterials*, 2019: pp. 1-13 (doi : 10.1155/2019/8928917).

[6] S. Kirmse, B. Ranabhat, and K.-T. Hsiao, Experimental and analytical investigation on the interlaminar shear strength of carbon fiber composites reinforced with carbon nanofiber z-threads, *Materials Today Communications*, **25,** 2020 (doi : 10.1016/j.mtcomm.2020.101512).

[7] K.-T. Hsiao, et al., Flammability Characterization of Carbon Nanofibers and Nanotubes Z-Threaded CFRP Laminates, *CAMX- The Composites and Advanced Materials Expo, Anaheim, CA 2022.*

[8] R. Warren, et al., Experimental Study of ILSS Failure Performance of Carbon Nanofibers Z-Threaded CFRP During Extreme Heat Exposure, *SAMPE 2025 (Society for the Advancement of Material and Process Engineering)*, *Indianapolis, IN, 2025*.

[9] ASTM, *ASTM D2344: Standard Test Method for Short-Beam Strength of Polymer Matrix Composite Materials and Their Laminates*. 2022.

[10] J.G. Quintiere, R.N. Walters, and S. Crowley, *Flammability Properties of Aircraft Carbon-Fiber Structural Composite*, U.S.D.o. Transportation Editor, Federal Aviation Administration, 2007.

[11] M. Bazli and M. Abolfazli, Mechanical Properties of Fibre Reinforced Polymers under Elevated Temperatures: An Overview*, Polymers*, **12**(11), 2020, pp. 2600 (doi :10.3390/polym12112600).

[12] W. Ningyun and J.T. Evans, Collapse of continuous fibre composite beams at elevated temperatures, *Composites*, **26**(5), 1995, pp. 56-61 (doi :10.1016/0010-4361(94)P3630-J).

[13] A. Nema, et al., Effect of temperature on flexural and interlaminar shear strength properties of carbon-epoxy composites: Experiment and modeling*, Polymer Composites,* **45**(10), 2024, pp. 9139-9155 (doi :10.1002/pc.28399).

[14] S. Hegde, B.S. Shenoy, and K.N. Chethan, Review on carbon fiber reinforced polymer (CFRP) and their mechanical performance*, Materials Today: Proceedings*, **19**, 2019, pp. 658-662. (doi :10.1016/j.matpr.2019.07.749).

[15] T.-C. Nguyen, et al., Time-dependent behaviour of steel/CFRP double strap joints subjected to combined thermal and mechanical loading*, Composite Structures*, **94**(5), 2012 p. 1826-1833. (doi :10.1016/j.compstruct.2012.01.007)

[16] K.-T. Hsiao and S. Kirmse, *Novel Liquid Matrix Impregnation Method and Apparatus for Composite Prepreg Production*. 2022: United States.

University of BRISTOL

ncc innovating for industry

Bristol Composites Institute

Differential Eddy Current Sensing Probe and its Implementation in Automated Composite Manufacturing Applications

08/08/2025

Ege Arabul, Meirbek Mussatayev, Vincent K. Maes, James Kratz, Per Saunders, Robert Hughes



bristol.ac.uk/composites

InVIsion Carbon: Project Background

- What is Inductive sensing?
  - Eddy current testing (ECT)
  - Non-contact, non-destructive
  - Small electromagnets excite current flow within material; detect changes in the magnetic field produced by the material
- What can it do?
  - Fibre orientation, stacking sequence, local fibre volume fraction, consolidation, missing tows, sub-surface waviness.
- What is the current state of the technology?
  - Limited versatility in commercially available ECT systems
  - Limitless possible CFRP components with fixed sensor properties

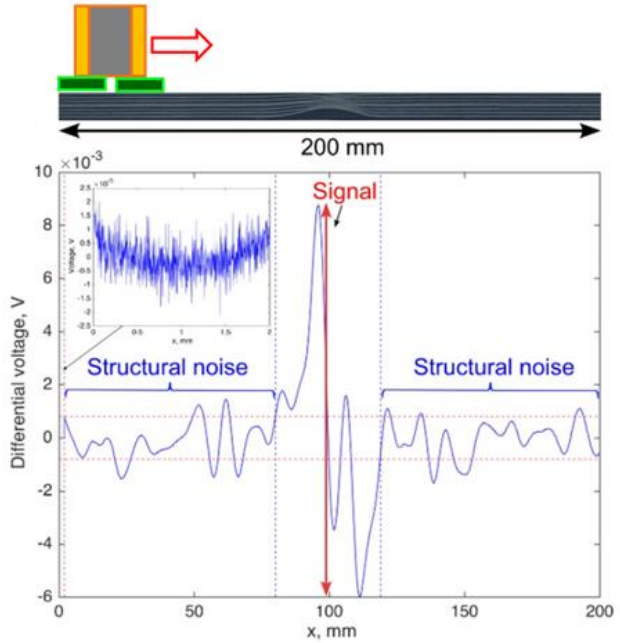

Position history of Eddy current scans over a defect

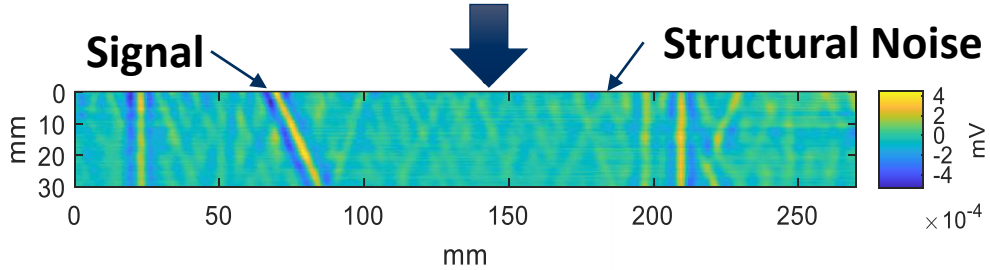

Eddy current scan image formed by combining multiple scans

InVIsion Carbon: Project Overview

- Challenge
  - In-line ECT monitoring in realistic CFRP manufacturing environments
  - Quantify and minimise noise and measurement uncertainties
  - Characterise sensitivity to material properties or features of interest

- Project Aim
  - Demonstrate and evaluate ECT on two automated manufacturing applications: **Automated Tape Laying** and **Filament Winding**

- Benefit
  - Non-contact, allowing for in-process inspection
  - High speed, applicable to industrial scale manufacturing
  - Quality monitoring, enabling early detection of manufacturing flaws
  - Improved manufacturing rates, due to reduction in inspection times



Integration of the Eddy-current probe in the ATL application



Integration of the Eddy-current probe in the FW application

Eddy Current Sensing Probe

The Eddy current sensing probe consists of three main components, including;

1. Driver coil to generate magnetic field
2. Pick-up coil to detect changes in the magnetic field, positioned in axial and transverse orientations.
3. Amplifier boards to on-board process the signal

Signal generated by the probe are transmitted to an USB oscilloscope (Handyscope) and interfaced via a LABVIEW PC program over USB

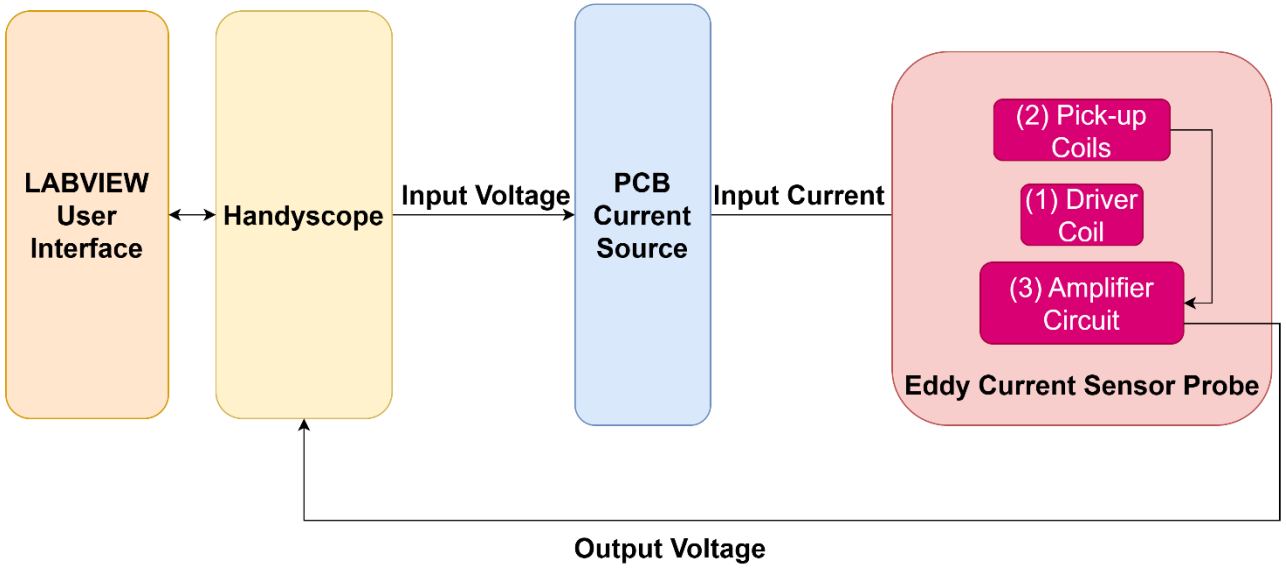

Electrical integration of the Eddy current sensing probe

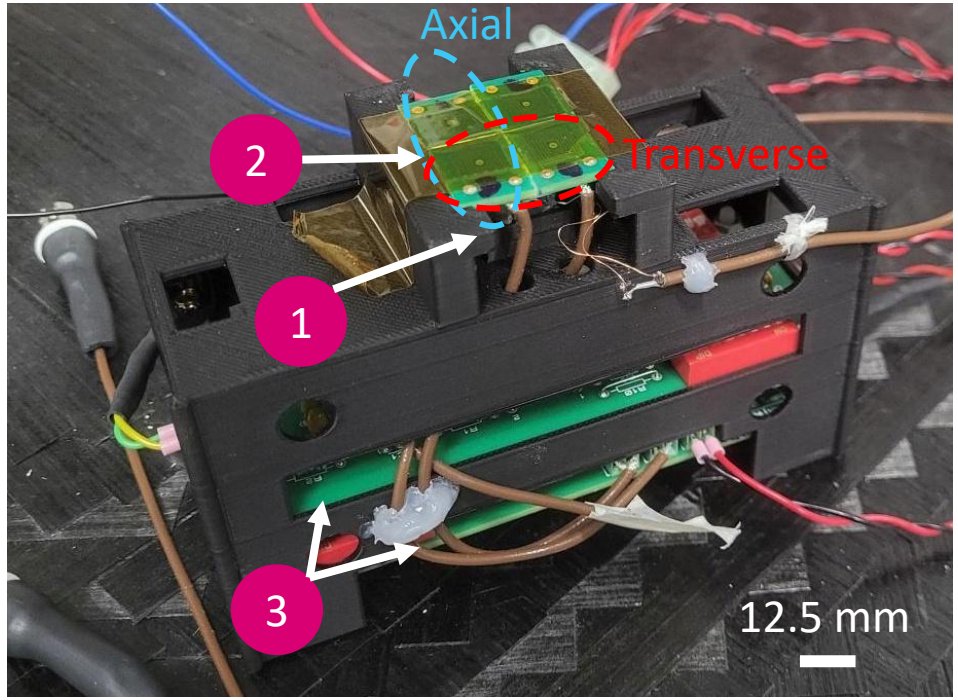

The Eddy current sensing probe with its key components highlighted

EC in Automated Tape Laying

Within the ATL application, the eddy current sensor was optimised and integrated into the ATL machine, and was proven to detect features including: Apparent defects (Delamination) and Subsurface defects
However, due to material availability and the project timelines, the data collection effort was shifted to the FW application.

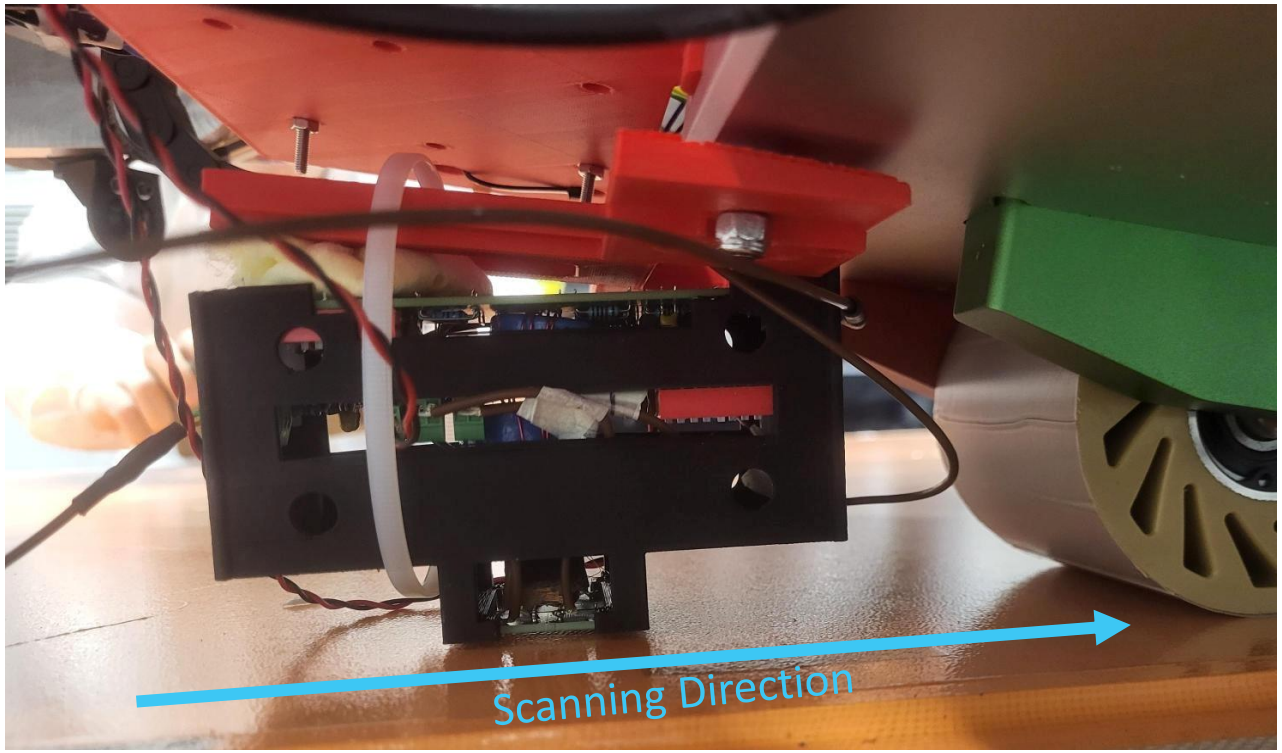

EC Sensor integrated into the ATL Machine

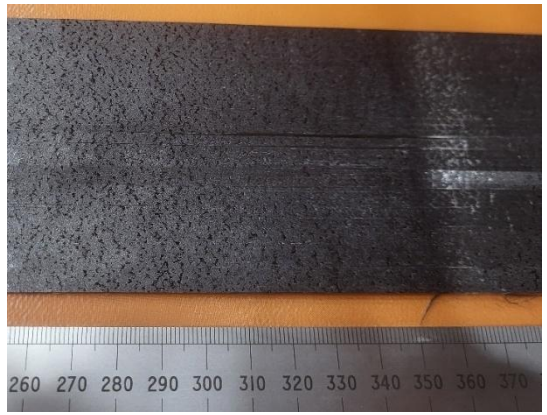

Delamination defect

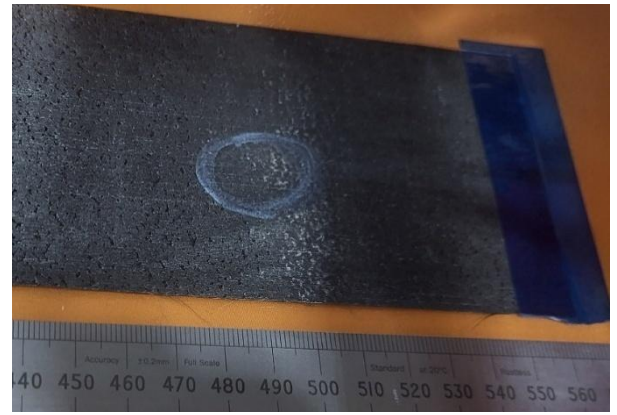

Subsurface defects

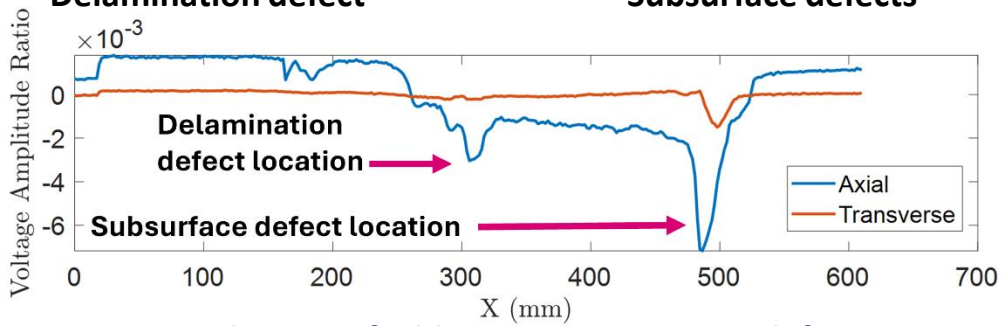

Position history of Eddy current scans over defects in ATL

Filament Winding Sensing Bench

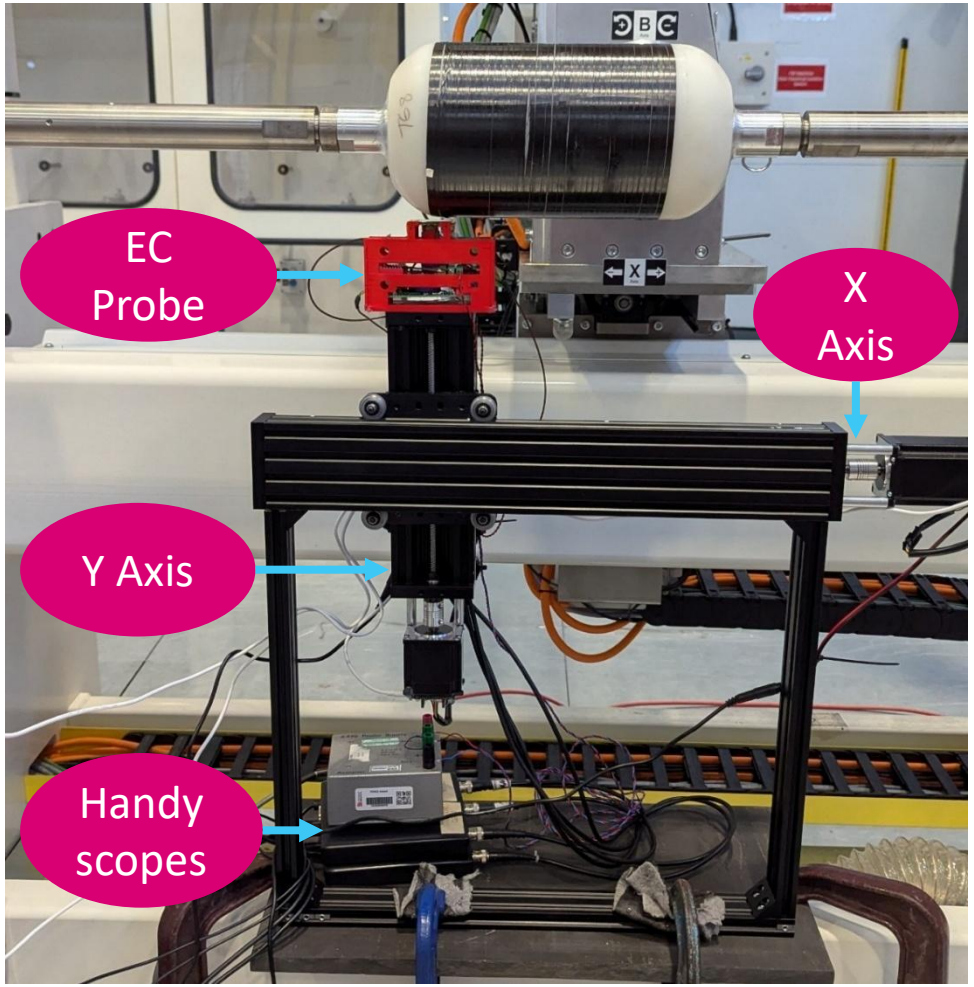

The FW Sensing Bench positioned within the cell

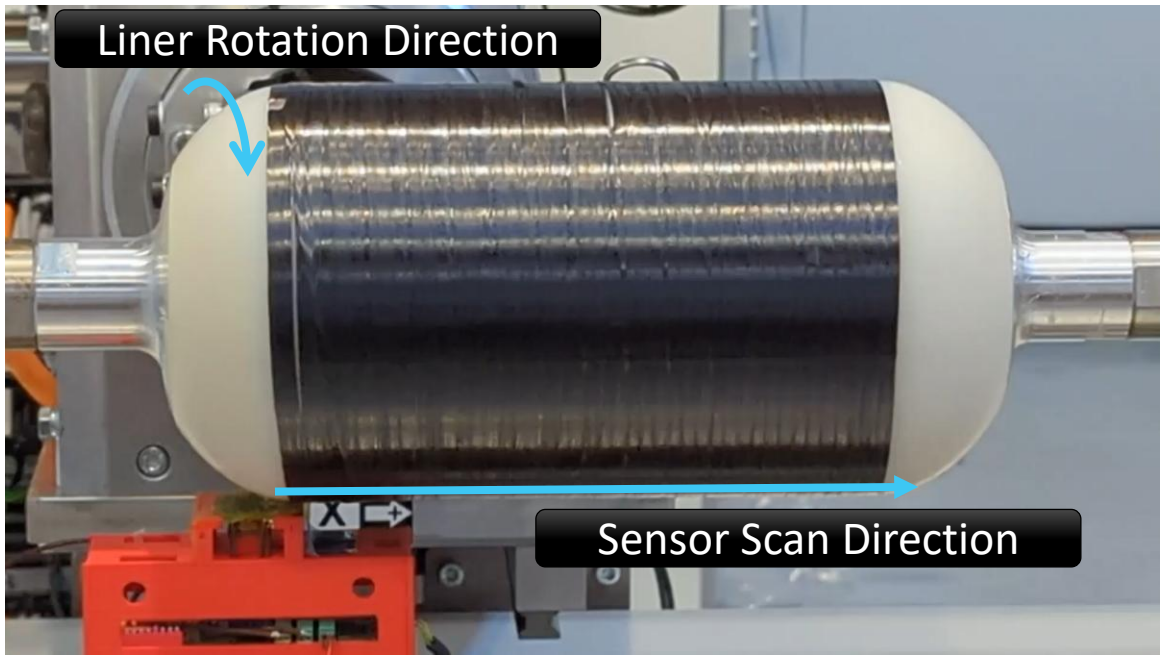

The operating principles of the FW Sensing Bench

A sensing bench was developed, featuring;

1. X axis for continuous movement across the liner
2. Y axis to automatically adjust the lift-off from the material surface

During scanning, the liner was continuously rotated as the probe scanned. This allowed for the complete characterisation of the liner.

Initial Defect Testing

To test the effectiveness of the sensor, samples with apparent defects were generated, featuring;

1. In-plane waviness defects generated by hex keys, which were used to create wrinkles of 0.5 to 4 mm. These wrinkles were pushed perpendicular to the fibre direction after the hex keys were removed, and covered by a secondary layer of tow-preg to create subsurface defects.
2. A pristine defect-free sample for comparison.

The samples were scanned with the sensing probe stationary and rotating the liner at a constant speed.



Generating in-plane waviness of varying sizes within the tow-preg samples

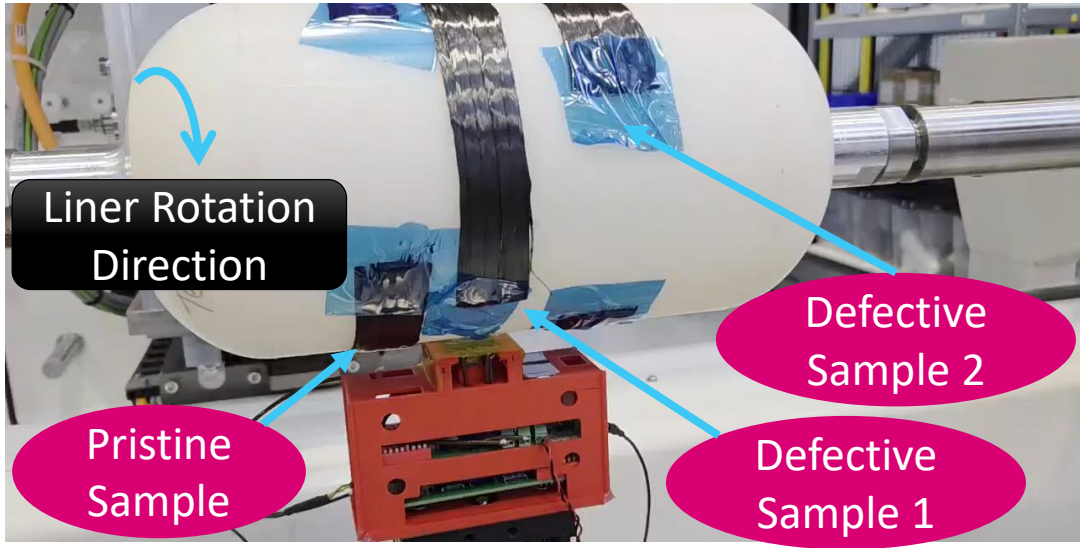

Scanning the pristine and the defective samples with the FW sensing bench stationary

Initial Defect Testing –Results

Initial calibration results showed that;

1. The data collected are repeatable across multiple runs.
2. High quality defect data can be collected up to 40 deg/s (6.67 RPM), corresponding to a linear speed of 52 mm/s.
3. The sensor response improved at operating frequencies closer to 3 MHz.
4. When the sensor is actuated as the liner rotates, the complete geometry can be scanned (continued in the next slide).

Repeatability Testing

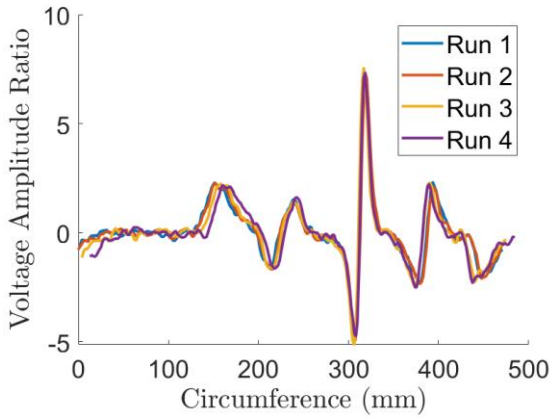

Varying Speed

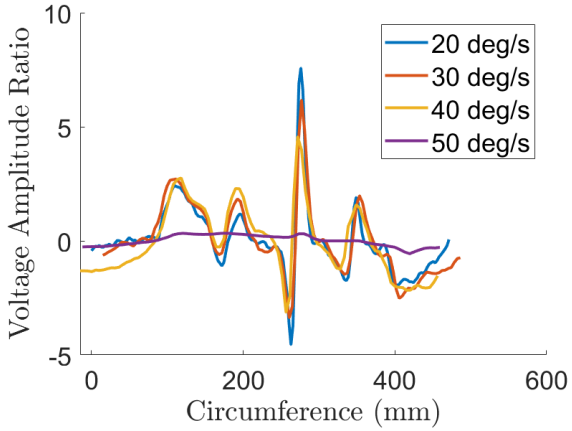

Varying Frequency

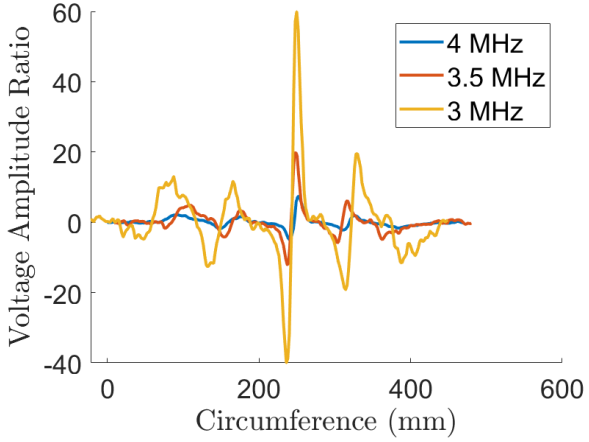

Scanning while Moving

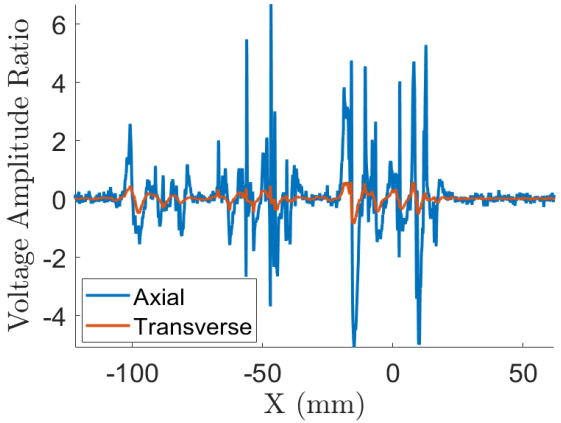

Initial Defect Testing –Scan While Move

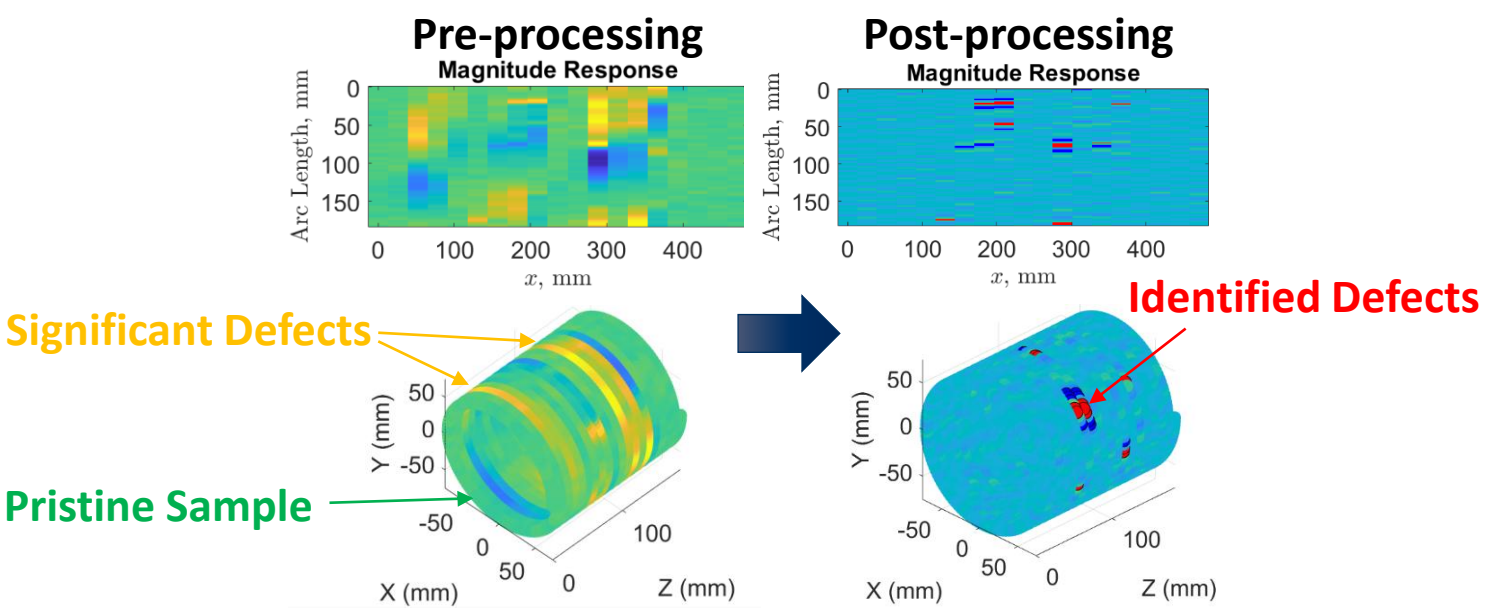

Axial Response

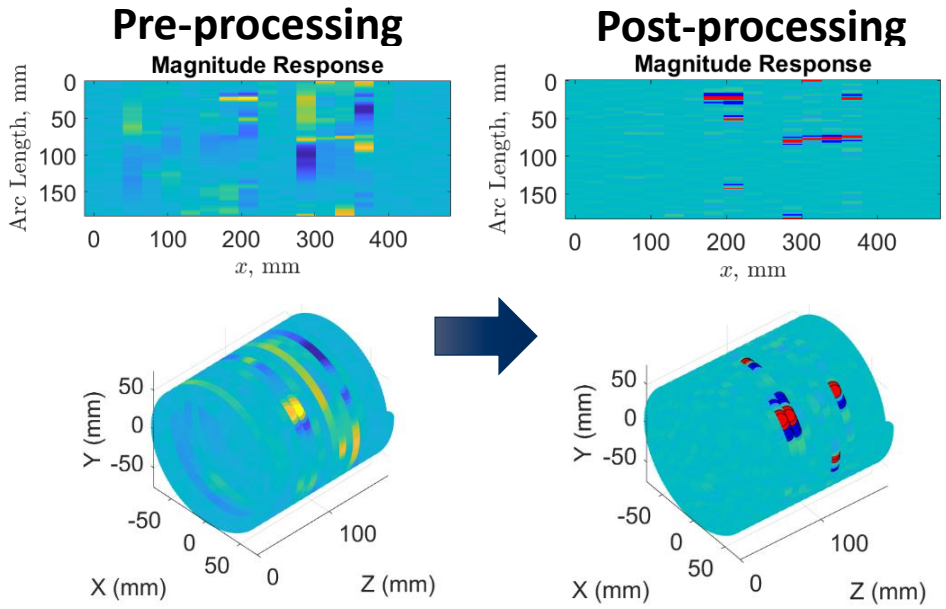

Transverse Response

By actuating the sensor while rotating the liner, defects and tow structure within the geometry were identified, where;

1. It was observed that the axial sensor responded more to the major changes in the tow structure (such as gaps in-between the tows) whereas the transverse sensor responded to the in-plane waviness more.
2. Post-processing allowed for subtracting the underlying tow structure and identifying locations of defects.

Multiple Hoop Layers Deposition

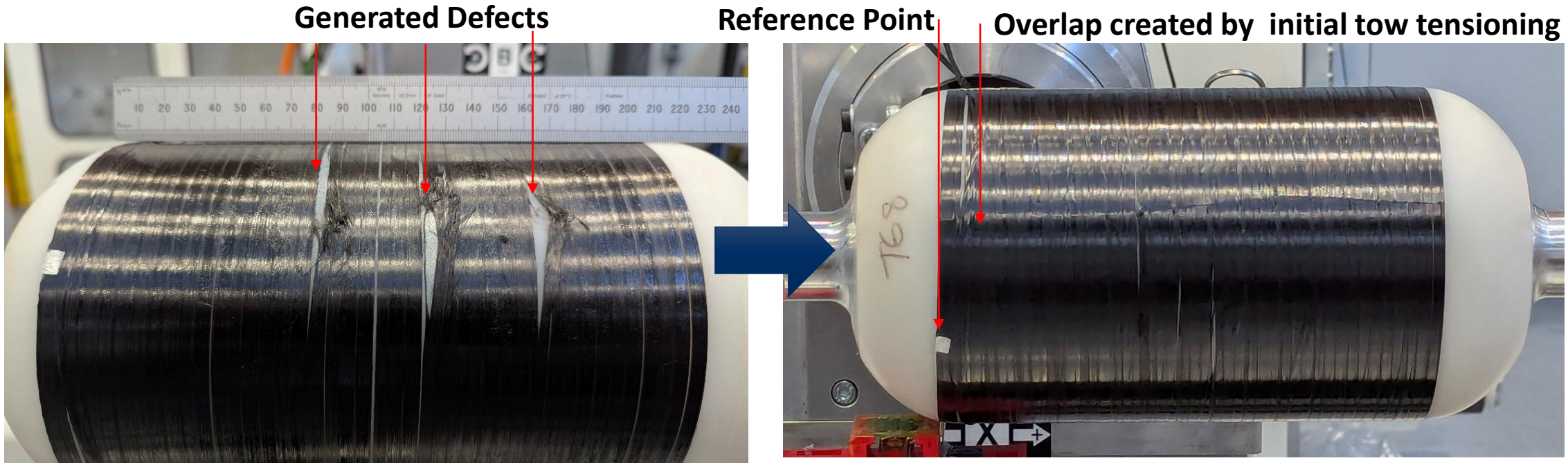

Defects generated in the first hoop layer

Covering the defects with multiple hoop layers

Following the initial calibration, multiple hoop layers were deposited to assess the effectiveness of the sensor, where;

1. An initial hoop layer was wound around the liner and several defects were embedded, along with a reference point.
2. This initial layer with defects was covered with multiple layers (six with the first layer) to assess the effectiveness of the sensor in detecting underlying defects.

The geometry was scanned at each layer for incremental quantification, along with optimising the lift-off from the surface.

Multiple Hoop Layers

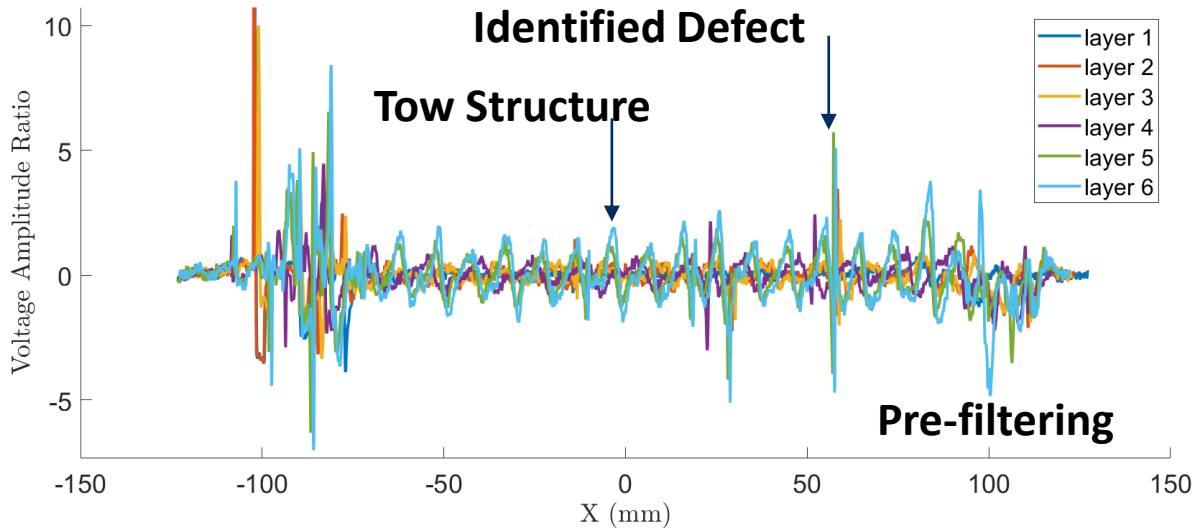

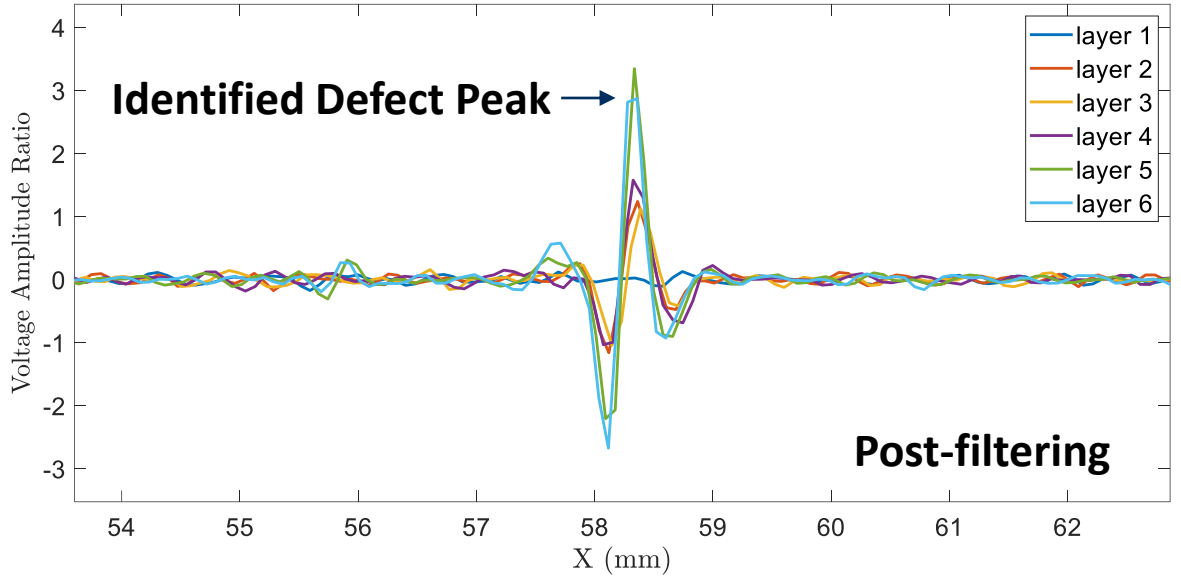

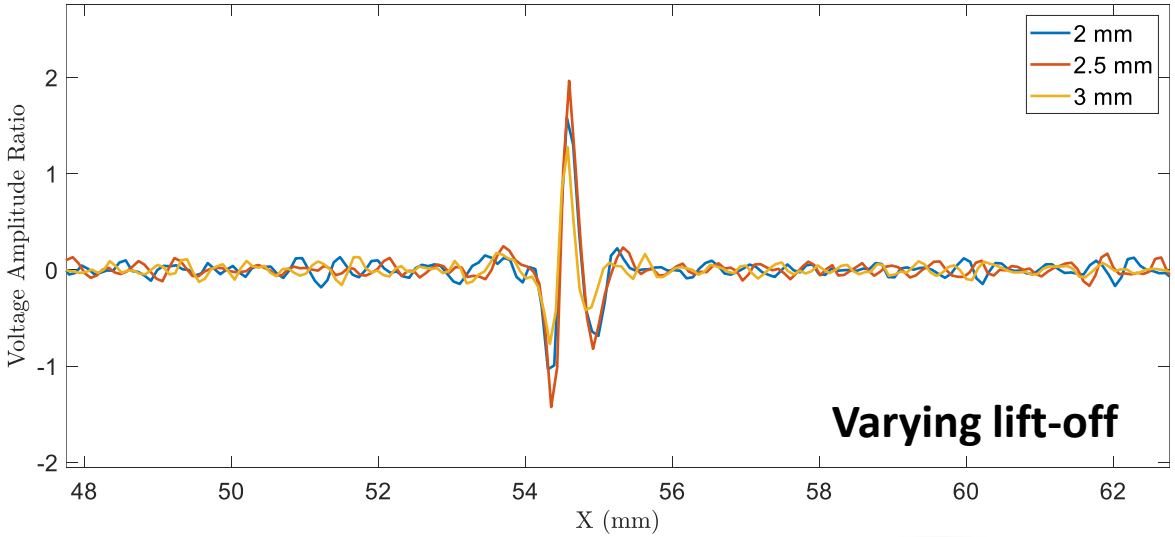

Scans of the multi-layer hoop geometry showed that;

1. Defects and tow structure visible after multilayer depositions.
2. EC response increased after multiple layers were deposited (possibly due to better contact between layers).
3. An optimum lift-off of 2.5 mm from the surface should be aimed for ideal response.

Multiple Hoop Layers Deposition

Applying post-processing to the sixth layer scan and analysing the complete geometry also showed that;

1. The axial sensor was able to identify all three defects, the reference point, and the initial tow tensioning defect even after five consecutive layers were deposited.
2. The transverse response can identify only some of the features, which could be due to the nature of the defects generated (in-plane waviness).
3. Tow structure can be subtracted by applying the post-processing to highlight only the defects.

This demonstrated the sensors capability in detecting sub-surface defects, as well as providing information regarding the nature of the defects detected.

Axial Response

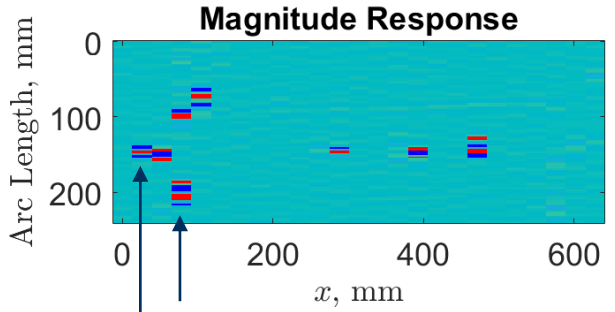

Transverse Response

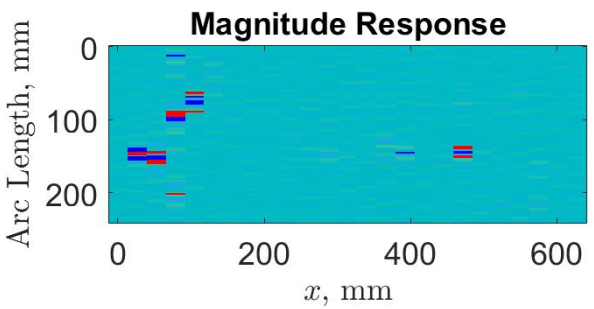

Tow Tensioning Defect

Reference Point

Identified Defects

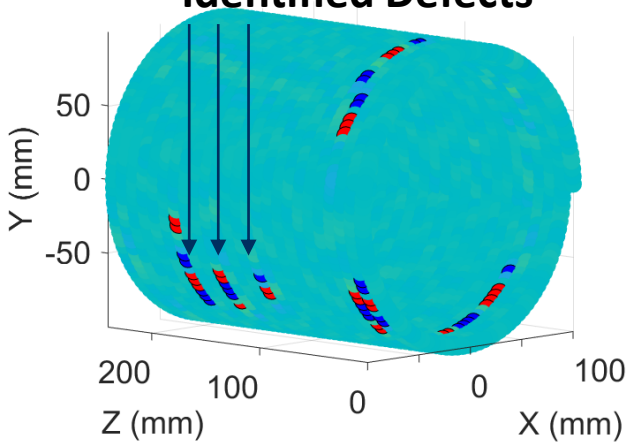

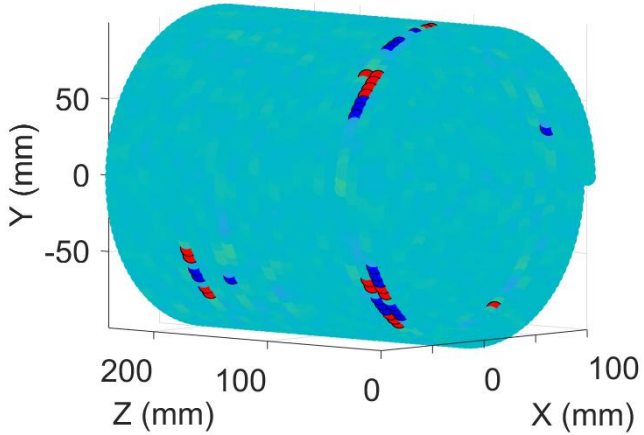

Depositing 22 Degree Layers

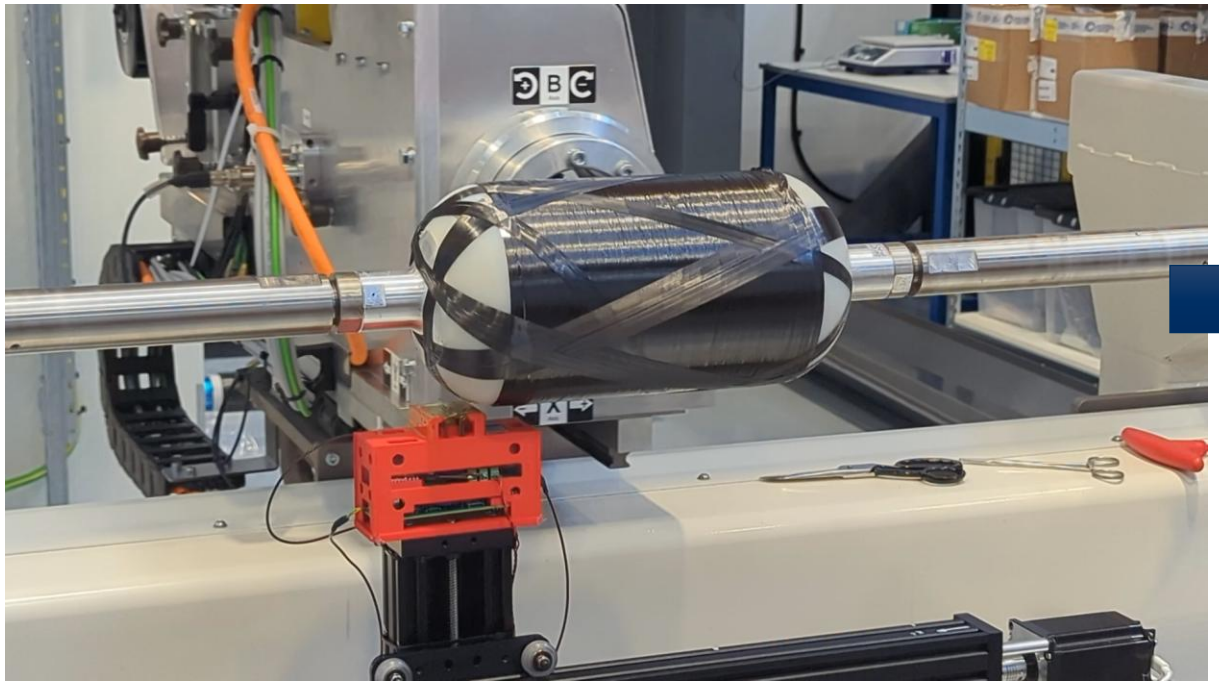

Winding the 22-degree layer on the geometry

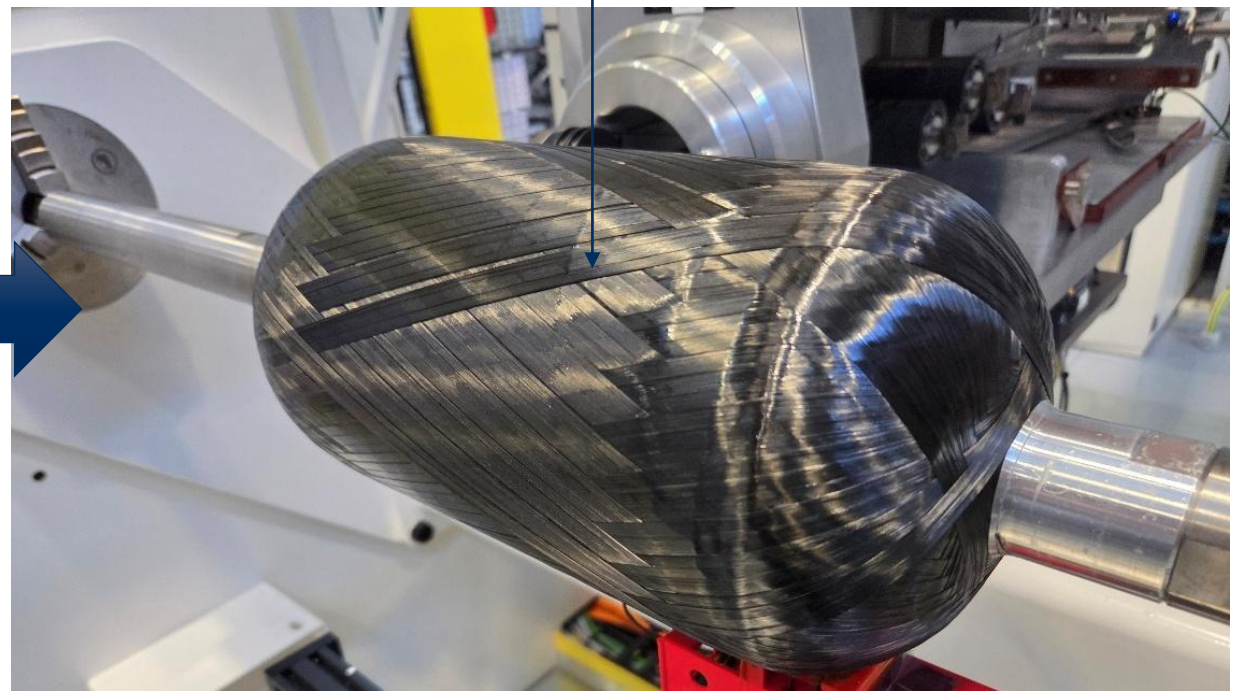

22-degree layer after deposition

Following the hoop-layer investigation, a 22-degree layer was deposited on top of the hoop layers, where;

1. The material was wound onto the liner after the technician adjusted the machine, resulting in a down-time. This could be a window to EC scans in a live implementation.
2. The wound geometry was scanned using the previous methodology.

Depositing 22 Degree Layers

Post-processing the scans after the deposition demonstrated that;

1. Several features were highlighted as defects, which could correspond to gaps, overlaps, end points of the deposition, as well as defects in the underlying layers.
2. The EC data can be used calculate deviations in the tow angles by tracing the detected features.

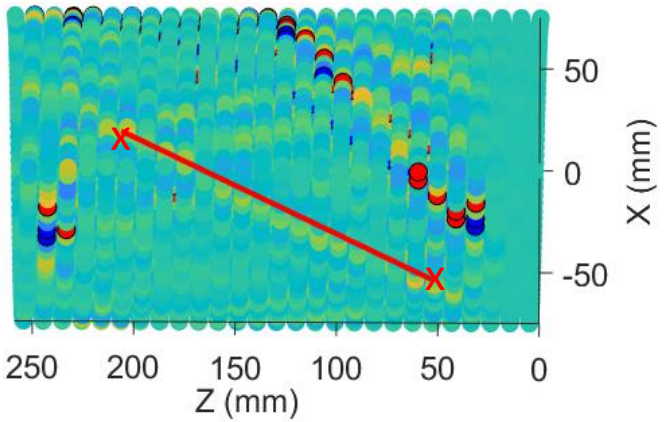

$$\tan^{-1}\frac{(0-55)}{(50-200)} = 0.34\,rad = \sim 20\,deg$$

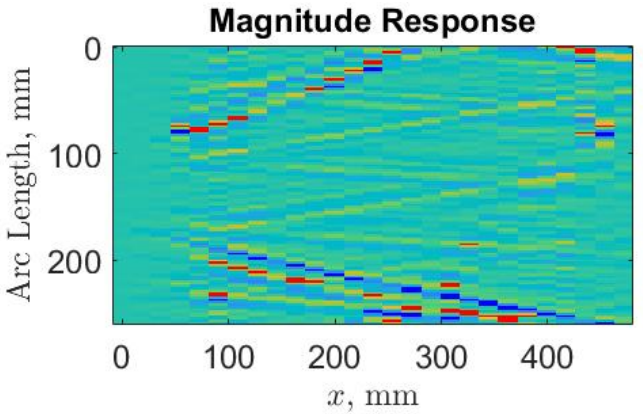

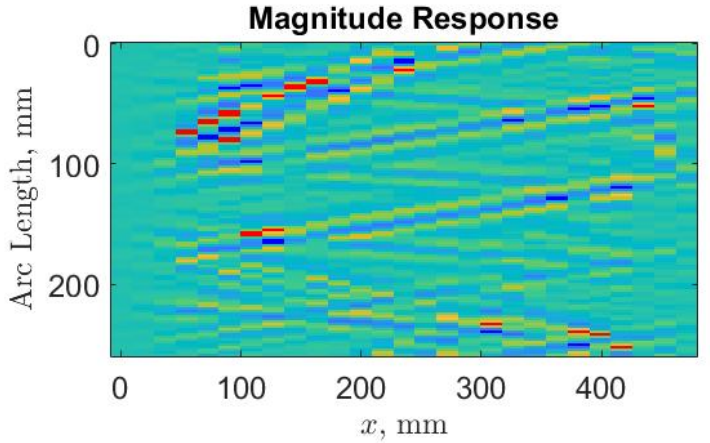

Axial Response

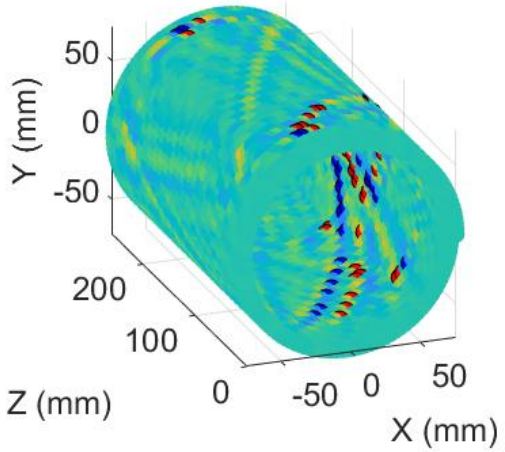

Transverse Response

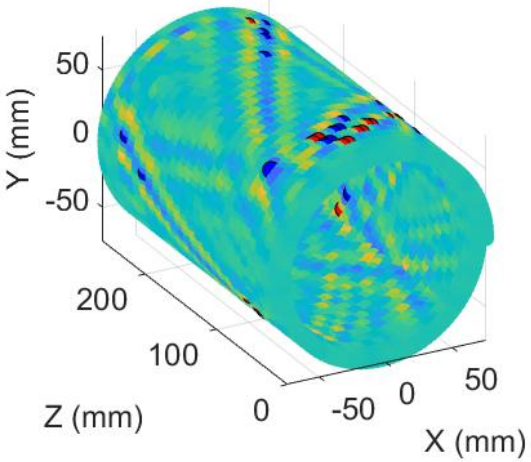

Depositing 22 Degree Layers

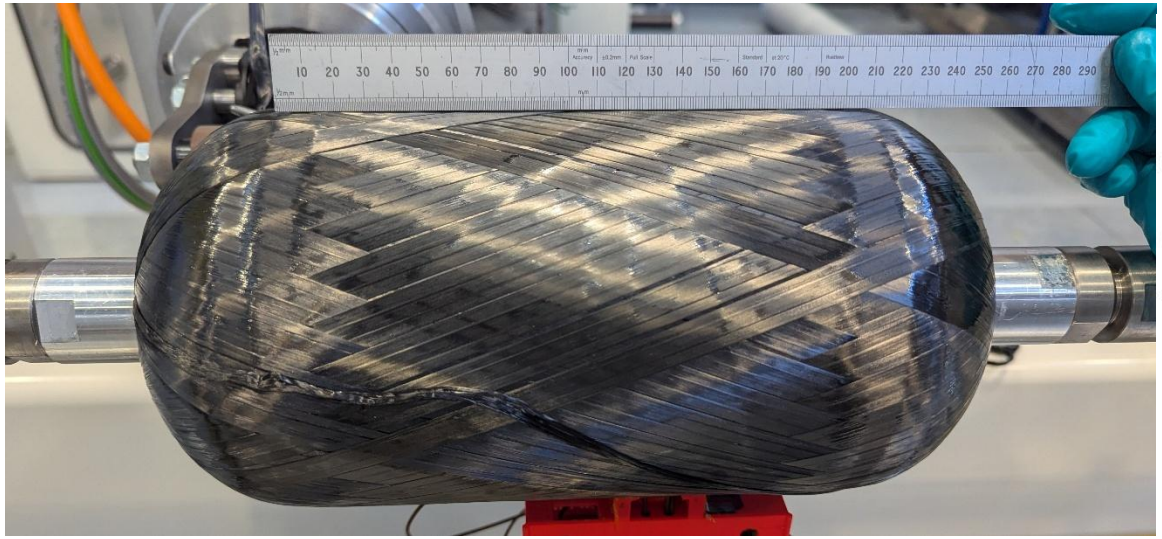

Defect embedded in the 22-degree layer

Following this quantification, a defect was embedded in the 22-degree layer and scanned, where;

1. The embedded defect was detected both by the axial and transverse sensors.
2. The underlying tow structure was still visible within the scans.

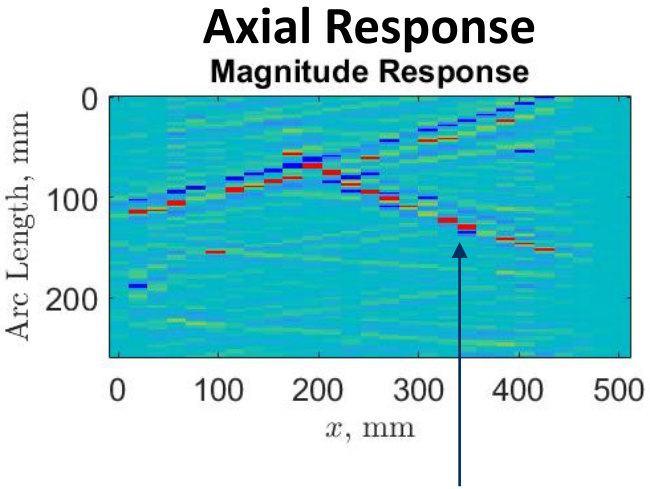

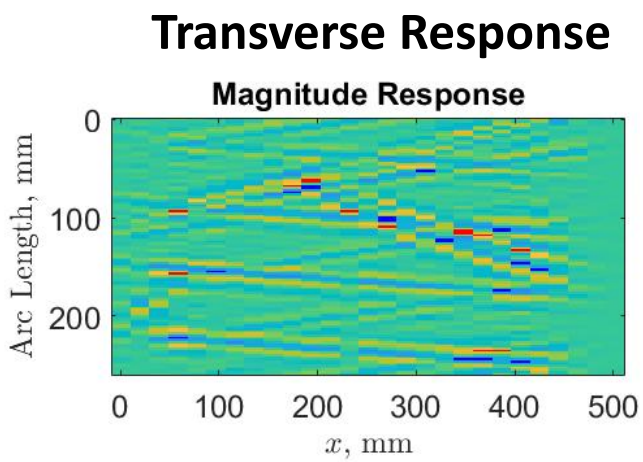

Embedded Defect

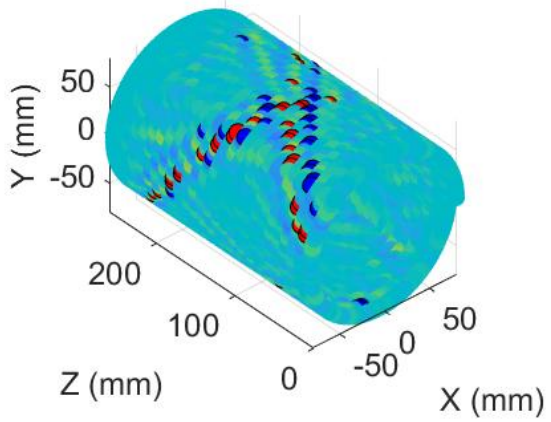

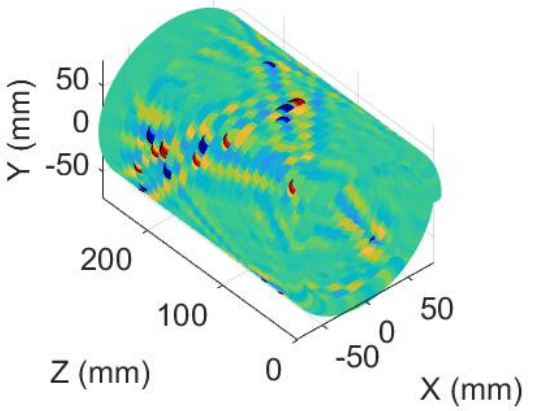

Defect Covered with Hoop Layer

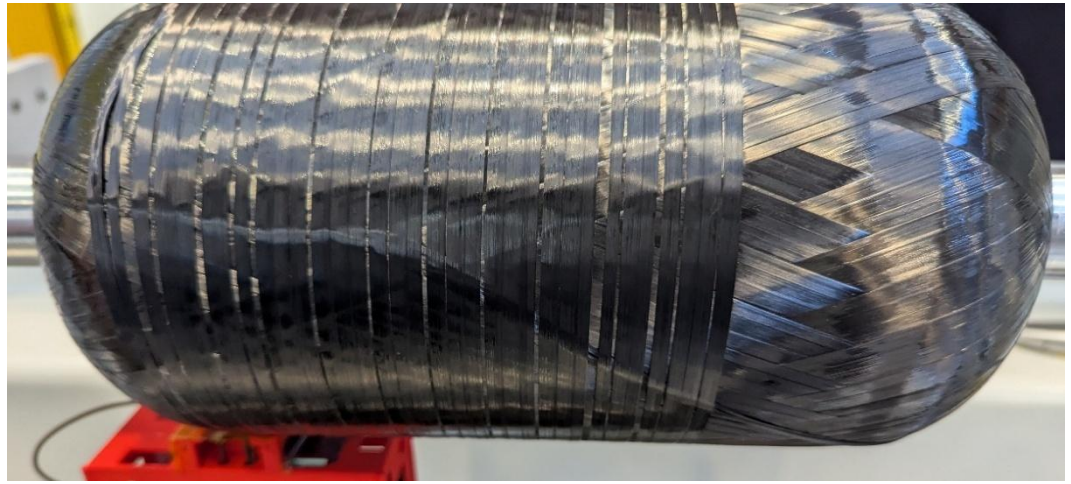

Hoop layer deposited on top of the 22-degree layer with the defect

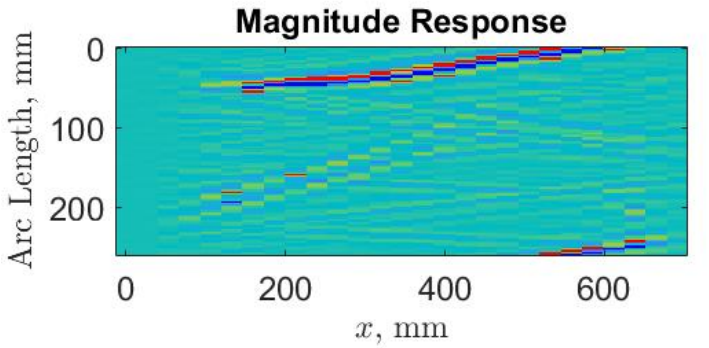

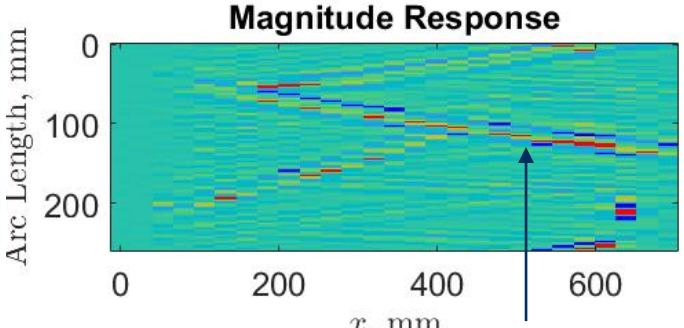

Embedded Defect

Axial Response

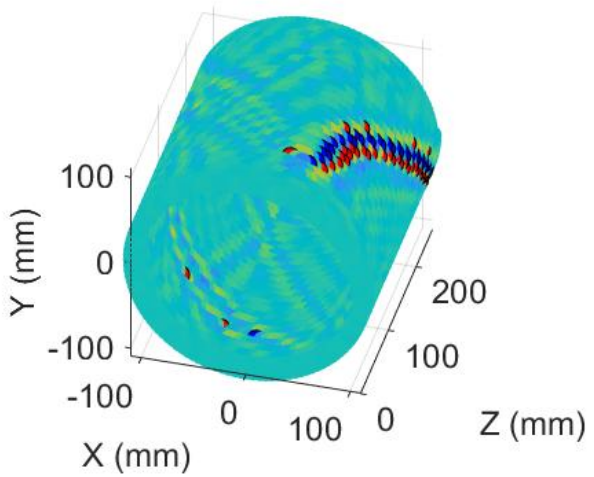

Transverse Response

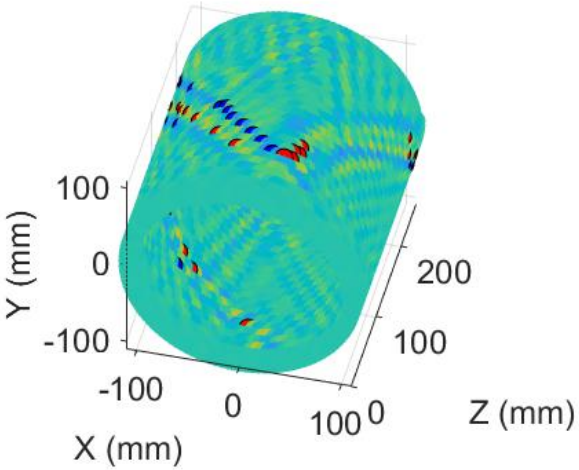

The 22-degree layer with the defect was then covered with another hoop layer and scanned. The results showed;

1. The embedded defect was still detected by the transverse sensor, whereas the axial sensor highlighted a different feature in the 22-degree layer.
2. The 22-degree layer was still visible within the scans.

Depositing 70 Degree

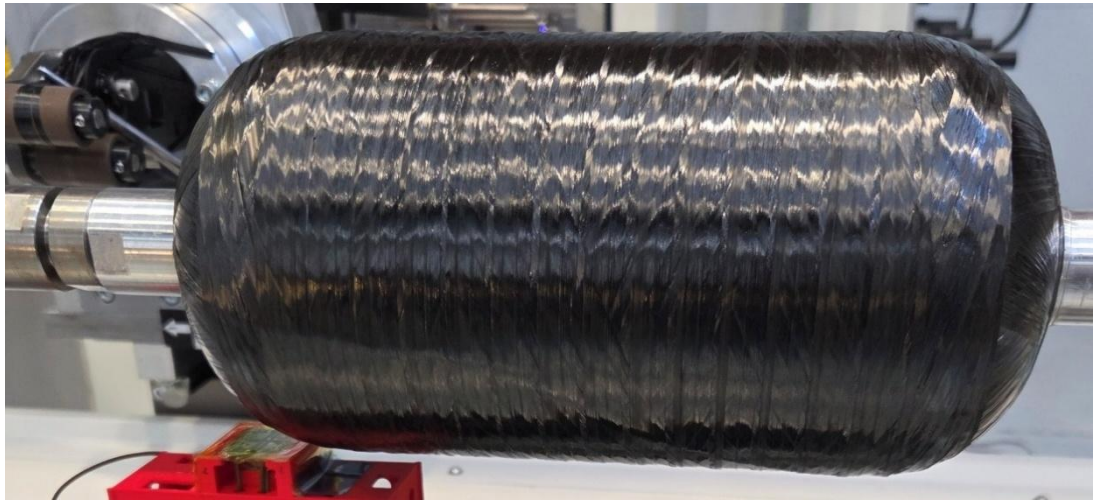

Hoop layer deposited on top of the 70-degree layer

The final two layers involved depositing a 70-degree layer, followed by another hoop layer. Final scans showed;

1. Due to the shallower angle of the 70-degree layers, the calculating the fibre orientation is more difficult. This could be improved by conducting measurements at a higher resolution.
2. The defect in the 22-degree layer was still visible within the scans.

Axial Response

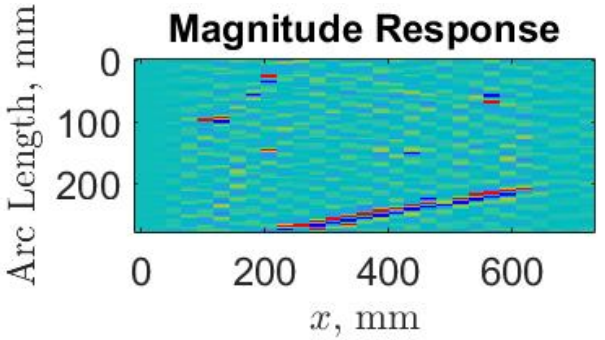

Transverse Response

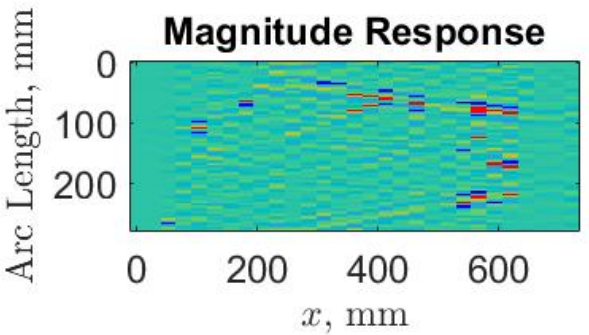

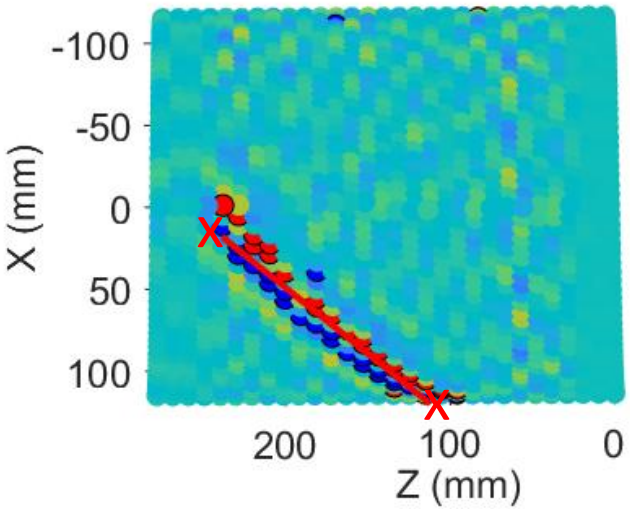

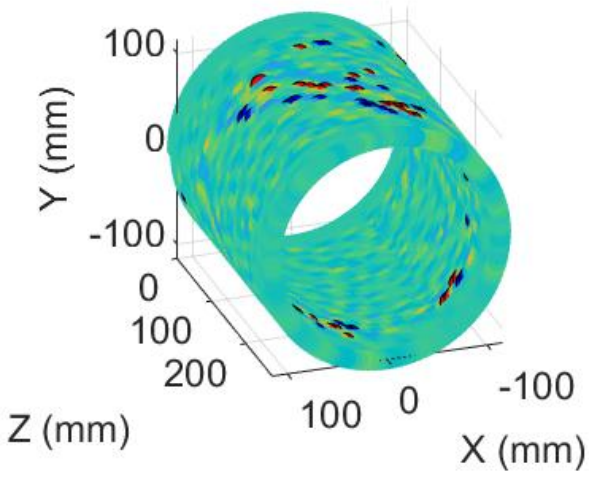

Conclusions & Future Work

Key Lessons Learned

- The manufactured geometries during ATL and filament winding processes can be in-line characterised using EC sensors.
- Automated defect detection allows for identifying features of interest.
- The performance of EC Sensor improves as more material is deposited, especially with different fibre orientations (even when the defects are buried deeper in the material.)
- Optimum parameters were selected, improvements to make for future measurements were identified (Liftoff, frequency, sampling rate…).

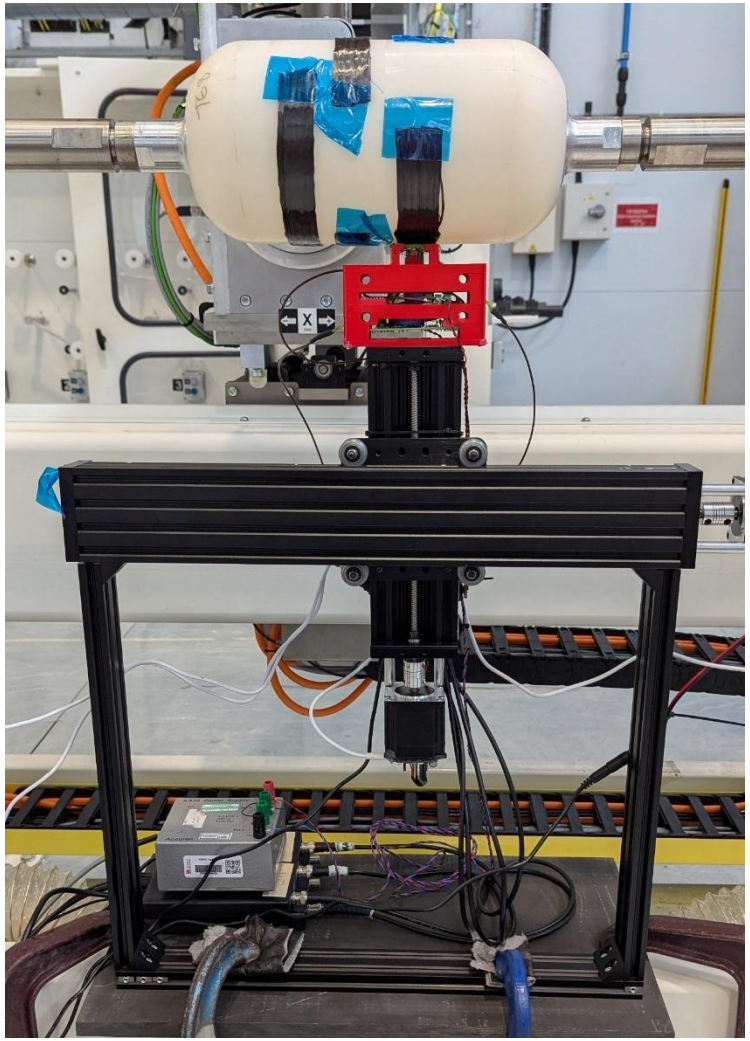

Conclusions & Future Work

Continuing the trials/ Finalising the TPT Project

- Comparison with XCT Data
- Developing capabilities to characterise the tank at the domes for validating models and CAM programming **(Request from FW team)**.
- In-process characterisation of a functional part e.g. hydrogen tank and/or varying process tension to create realistic defects.
- Development of the final EC probe resistant to environmental noise.
- Documenting the process within a journal article.

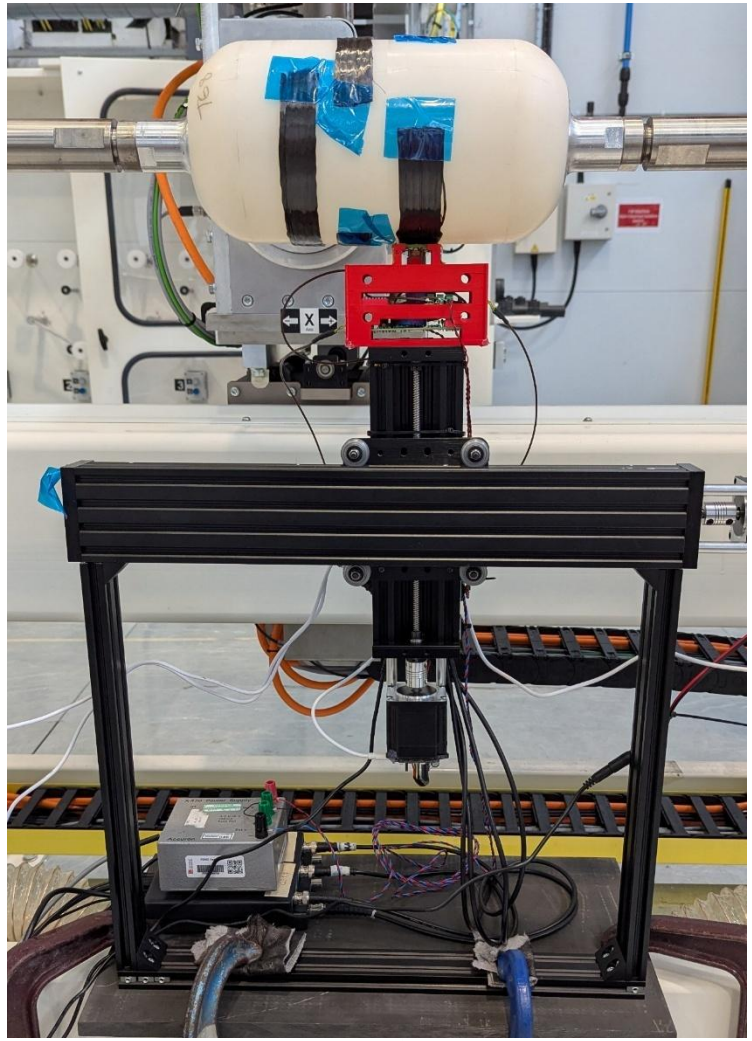



Bristol Composites Institute



ncc innovating for industry

bristol.ac.uk/composites

Filament Winding: Software

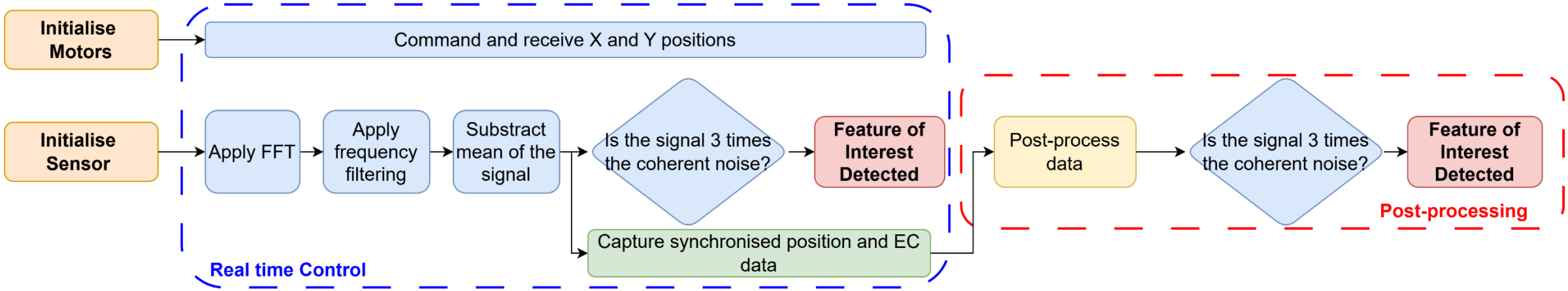

The control software for the FW sensing bench

The control software (operating at 100 Hz) features two defect detection systems based on MIL-HDBK-1823A* , where;

1. The in-line defect detection applies frequency filtering to detect defects during the process.
2. The off-line defect detection post-processes the data to highlight defects (<10 seconds upon collecting data).

*** Nondestructive evaluation system reliability assessment, Department of Defence Military Handbook (1999), 1823, MIL-HDBK-1**

PASS FREQUENCY AS A MEANS FOR INCREASED LATP PRODUCTIVITY

Emma Tobin[1], Hong Ma[2], Ronan M. O'Higgins[1] and Paul M. Weaver[1]

[1] Bernal Institute, School of Engineering, University of Limerick
Limerick, V94 T9PX, Ireland
Email: emma.tobin@ul.ie

[2]Department of Wind Energy, Technical University of Denmark
P.O. Box 49, Frederiksborgvej 399, DK-4000 Roskilde, Denmark

Keywords: Carbon fibre, Thermoplastic resin, Mechanical testing, Automated lay-up, Consolidation

ABSTRACT

Automated manufacturing of thermoplastic composites has gained increasing interest due to its potential for low-cost, high-rate production of composite structures. The matrix-dominated mechanical properties of a laminate manufactured by laser-assisted automated tape placement of thermoplastic composites are highly influenced by the selected processing parameters. Within this work, experimental analysis was conducted to investigate the effect of processing parameters and pass frequency on the laminate microstructure and short beam strength. In conjunction with mechanical characterisation, the process uses a thermo-mechanical model to simulate the thermal history of the manufacturing process. Two cylindrical mandrels with different diameters were used to vary the pass frequency whilst keeping the remaining process parameters constant. Findings show that increasing the pass frequency gradually increases the substrate temperature, reduces the specimen void content, and increases the short beam strength.

1 INTRODUCTION

Due to the long shelf life, high fracture toughness, and perceived recyclability, thermoplastic composites have gained interest in the aerospace industry. With composite materials making up more than 50% of structural weight of modern commercial aircraft, there is a growing need to manufacture thermoplastic composites more efficiently than by autoclave processing [1, 2]. As such, out-of-autoclave manufacturing, such as laser-assisted automated tape placement (LATP), may result in the production of low-cost thermoplastic composites with the potential for high-rate production. Additional benefits of in-situ consolidation of thermoplastic tape by LATP include lower energy consumption compared to autoclaving and reduced material waste [3]. However, as both the nip-point temperature and time under compaction are functions of time, manufacturing at high placement rates often results in a laminate with high porosity and lower levels of interlaminar bonding [4]. Therefore, processes need to be developed to ensure high levels of interlaminar bonding without compromising the production rate of composite laminates.

Several studies have compared the effect of placement rate on the short beam strength (SBS) of LATP laminates [5, 6]. Kirchhoff *et al.* [6] found that increasing the placement rate by 6 m/min at a constant processing temperature reduced the SBS of the laminate by 27% due to an increase in the void content. However, processing temperature can only be increased up to a certain level, noting that exceeding this critical temperature results in matrix degradation and reductions in SBS [7, 8].

Post-processing of LATP laminates in an autoclave has been demonstrated to reduce void content and increase SBS, resulting in laminates with properties comparable to those of autoclaved laminates [9]. However, the requirement for post-processing of LATP manufactured laminates may negate some of the cost and environmental benefits associated with in-situ consolidation. Alternative methods to post-processing, such as repass treatment or the use of a heated tool, have been studied as a means for improving laminate quality. However, repass treatment extends the required manufacturing time,

reducing the overall production rate [10], while the use of a heated tool may not prove beneficial for thick laminates [1] and involves greater energy costs. Therefore, alternative modifications to the manufacturing process may be necessary to increase laminate production without compromising quality.

Within this work, the time-temperature relationship during LATP manufacturing is studied, as well as the influence of substrate temperature on laminate microstructure and subsequent SBS. Specifically, while previous studies [11-13] have indicated that maintaining the substrate temperature of a laminate during manufacturing reduces the void content and increases the SBS, there is limited research on methods for maintaining substrate temperature without the use of an additional heat source.

3 MATERIAL AND METHODOLOGY

3.1 Material and Manufacturing Methods

Manufacturing trials were conducted using an AFPT GmbH produced laser-assisted automated tape placement system located within the University of Limerick. The LATP system consisted of a 3kW laser heat source attached to a Kuka robotic arm (Kuka, KR 240 L210-2). A thermal camera monitors the temperature of the incoming tape, substrate, and nip point, adjusting the laser power to maintain the programmed target temperature in a closed-loop system.

Unidirectional, 12 mm wide, carbon fibre/PEEK tape was used to manufacture a total of 14 wound specimens, with a layup of $[0°]_{30}$, using the processing parameters defined in Table 1. Specimens were manufactured with a constant pneumatic piston pressure of 2.5 Bar. Two cylindrical mandrels with two diameters were used: a large mandrel (diameter 250 mm) and a small mandrel (diameter 70 mm), to study the influence of pass frequency on the laminate microstructure and mechanical properties. Within the scope of this work, specimens are identified by the mandrel size (L or S, where Group L and S represent the specimens manufactured by large and small mandrels, respectively), the placement rate, and the processing temperature, as shown in Table 1. The pass frequency is defined as the inverse of the time required for one complete rotation of the mandrel, with different mandrel diameters resulting in different pass frequencies at the same placement rate, as shown in Table 2. Applying this naming convention, a specimen produced on the larger diameter mandrel at a placement rate of 9 m/min with a nominal nip point temperature of 450 °C is designated L-9-450.

Water jet cutting was used to extract specimens from the hoop laminate, ensuring a length of 40 mm for all specimens, as depicted in Fig. 1(a).

Parameters	Placement Rate (m/min)		
Temperature (°C)	3	9	15
400	3-400	9-400	15-400
450	3-450	9-450	15-450
500	3-500	9-500	15-500

Table 1: Processing parameters used during manufacturing. ID protocol consists of S or L (small or large, respectively) followed by process parameters.

Placement Rate (m/min)	Group S (Hz)	Group L (Hz)
3	0.228	0.058
9	0.680	0.173
15	1.136	0.287

Table 2: Pass frequency for two mandrel diameters and three placement rates used during manufacturing.

3.3 Characterisation and Analysis

Specimen void content was analysed using digital microscopy. The interlaminar bond line thickness was measured via point-to-point measurements at three locations within the overall specimen cross-section. Using the mandrel surface as a datum (0%) and the outer surface as the maximum value (100%), the bond line measurements were taken at 25%, 50%, and 75% of the specimen thickness.

As the degree of crystallinity can influence matrix-dominated mechanical properties, such as the short beam strength, digital scanning calorimetry (DSC) was conducted using a Netzsch 214 Polyma. The degree of crystallinity was tested for both the lower and upper surfaces of the specimen. Samples of 5-10 mg were taken from the specimens. A heating rate of 10 °C/min was used up to a maximum temperature of 400 °C. The degree of crystallinity is calculated from:

$$X_c = \frac{\Delta H_m - \Delta H_c}{\Delta H_{100} \times w_m} \times 100 \tag{1}$$

where ΔH_m is the melt enthalpy (J/g), ΔH_c is the cold crystallisation enthalpy (J/g), w_m is the mass fraction of the matrix (0.34), and ΔH_{100} is the full crystallisation enthalpy of PEEK (130 J/g) [14].

Mechanical testing of the short beam strength (SBS) was conducted in accordance with ASTM D2344 [15] for a curved specimen as depicted in Fig. 1(b). Specimens were loaded with a constant displacement rate of 1 mm/min using a Tinius Olsen H25K-S with a 5 kN load cell. The maximum load was recorded for each specimen, with SBS calculated using:

$$SBS = 0.75 \frac{P}{t \times w} \tag{2}$$

where P is the maximum load (N), t is the sample thickness (mm), and w is the sample width (mm).

A 2D thermo-mechanical model was developed to simulate the incoming tape and substrate on both mandrel diameters, providing the through-thickness temperature distribution during manufacturing. This model aids the discussion and understanding of the mechanisms at play during manufacturing. The model is based on, and validated by, previous work completed by Ma *et al.* [16]. Due to computational power limitations, only the initial four plies placed are modelled in this work. Further details of the computational model can be found in Tobin *et al.* [17].

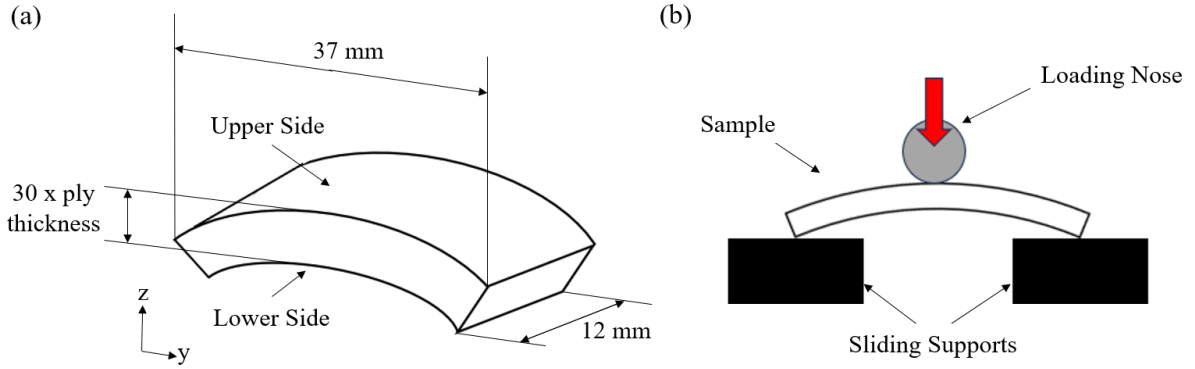

Figure 1: (a) SBS specimen geometry and (b) SBS loading set-up

4 RESULTS AND DISCUSSION

4.1 Computational Temperature Evolution

Thermo-mechanical modelling of the manufacturing process helps develop an understanding of the observed failure mechanisms. An initial comparison of the small and large mandrel models indicates that the simulated peak temperature on the incoming tape shows good agreement with the experimental processing temperature, indicating the acceptable accuracy of the model predictions.

When comparing the temperature evolution as shown in Fig. 2(a) and Fig. 3(a), it is apparent that higher substrate temperatures are reached in the small rather than the large mandrel. When placing ply two at a placement rate of 3 m/min and a processing temperature of 400 °C, ply 1 of S-3-400 reached a

maximum temperature of 400 °C, compared to 330 °C for L-3-400. However, it is worth noting that the substrate of L-3-400 remains below the melt temperature of PEEK during manufacturing, inhibiting interlaminar bonding. As the target temperature increases, computational thermal analysis indicates that the substrate reaches higher temperatures (Fig. 2(b) and Fig. 3(b)), with the large mandrel specimens being more sensitive to an increase in process temperature. The temperature sensitivity observed in the large mandrel specimens likely results from the difference in laser reflection patterns for the two mandrel diameters, which can be considered a limitation associated with the use of different mandrel diameters [17]. Analysing the temperature of the substrate for each layer suggests that the substrate temperature gradually increases with each rotation of the small mandrel, but not with the large mandrel. This observation becomes more apparent when comparing S-9-500 (Fig. 2(c)) and L-9-500 (Fig. 3(c)). For S-9-500, the first ply reaches a minimum temperature of 210 °C after the third layer is placed, however, L-9-500 cools to room temperature between each laser pass. When comparing L-9-500 to L-3-500, it is noted that the substrate temperature is lower for L-9-500 due to reduced time during the heating phase. While there is no thermo-mechanical model for placement rates of 15 m/min, it can be surmised that the observed trends when increasing the placement rate from 3 m/min to 9 m/min remain for higher placement rates. When considering the thermal history shown in Fig. 2 and Fig. 3, the influence of processing parameters can be inferred: increasing the processing temperature increases the substrate temperature, and increasing the placement rate can reduce the maximum temperature reached in the substrate while also reducing the cooling time. Additionally, comparing the thermal history displayed in both Figs. 2 and 3, it is noted that increasing the laser pass frequency can introduce gradual heating in the substrate, which can increase the degree of interlaminar bonding when manufacturing at high placement rates.

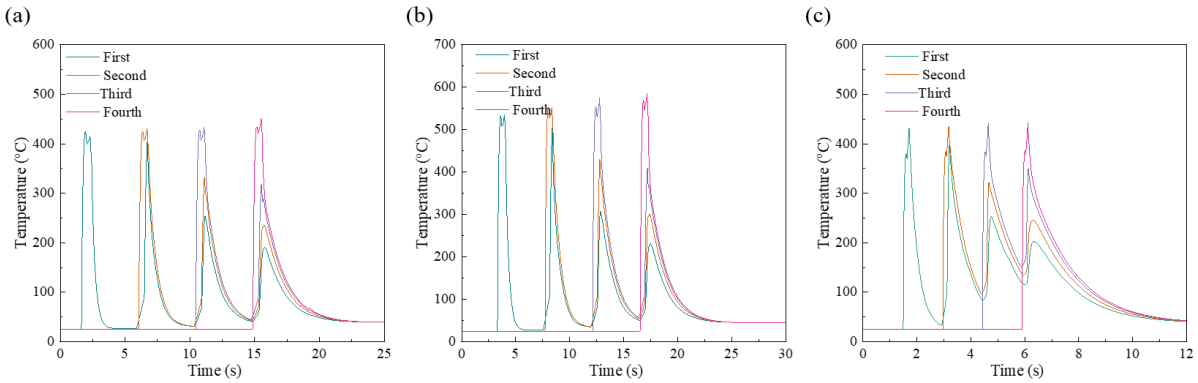

Figure 2: Thermal history of (a) S-3-400, (b) S-3-500 and (c) S-9-500. Different colours correspond to the ply placed (first ply to fourth ply).

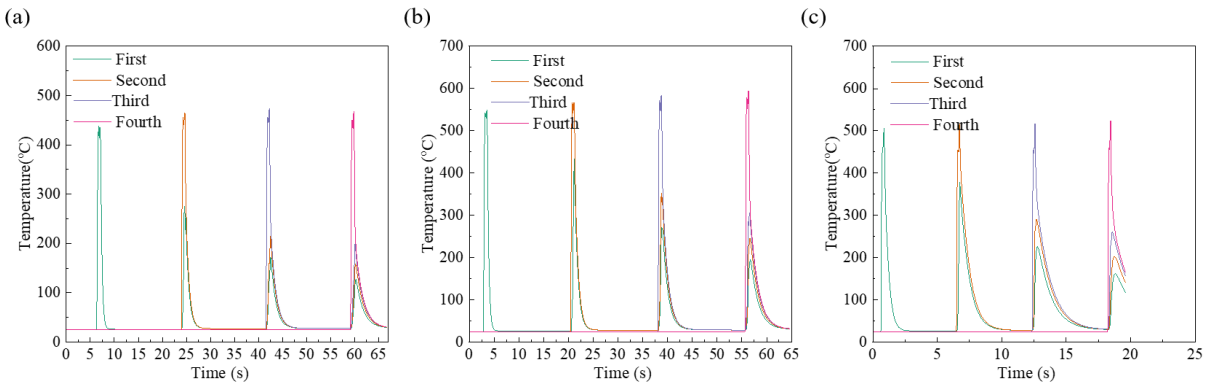

Figure 3: Thermal history of (a) L-3-400, (b) L-3-500 and (c) L-9-500. Each colour corresponds to the thermal history of the ply placed (first ply to fourth ply).

4.2 Microstructure Variation

Initial, qualitative comparison between laminate microstructures indicates that mandrel diameter and processing parameters affect the void content, location, and interlaminar bond line thickness. Specimen S-9-450 had the lowest overall void content (0.2%), whereas the highest void content was for L-3-400 (2.25%). When comparing the void content within both specimen groups at equivalent processing parameters, the void content in the small mandrel specimens was found to be lower than that in the large mandrel specimens (Fig. 4(a)). This difference was most apparent when manufacturing at 500 °C and 15 m/min, where the void content difference was 1.75% (Fig. 4(a)).

When considering the influence of processing parameters on void content, at low placement rates (3 m/min), increasing the processing temperature reduced the overall void content of the laminate. When considering the thermal history of the specimens, increasing the processing temperature resulted in a higher substrate temperature, which facilitates higher levels of interlaminar bonding due to increased matrix flow across the interlaminar bond line. By increasing the placement rate at a constant processing temperature, the void content increases, with the most prominent increase in void content observed when manufacturing on the large mandrel at 15 m/min. As previously mentioned, the level of interlaminar bonding is a function of the processing time, with an increase in placement rate reducing the laminate time under temperature or consolidation force. Fig. 3(c) shows that an increase in placement rate for the large mandrel reduces the maximum temperature reached by the substrate, which can serve to explain the void content observed in L-15-500. However, due to the gradual substrate heating with high pass frequency (Fig. 2(c)), S-15-500 has a lower void content than L-15-500 despite the maximum substrate temperature being relatively low.

In addition to void content variation, the predominant type of void observed, interlaminar or intralaminar, varied with processing parameters and mandrel diameter. Within the small mandrel specimens, intralaminar voids were the dominant void type for all processing parameters. However, specimens manufactured on the large mandrel exhibited both types of voids. At low placement rates (3 m/min), intralaminar voids were more prominent within specimens manufactured on the large mandrel, with few interlaminar voids observed. At higher placement rates, interlaminar voids became prominent. The void type occurs as a function of the tape temperature. According to thermal simulations, the substrate of L-9-500 remains below the melt temperature of PEEK, which can inhibit intimate contact formation, causing interlaminar voids to occur. While simulations were not conducted for a 15 m/min placement rate due to the associated computational costs, it can be assumed that this temperature difference would be exacerbated. Intralaminar voids can occur due to tape deconsolidation, as heating the tape can introduce void growth and migration, and rapid cooling reduces matrix flow [18]. Increasing the tape temperature to ensure the matrix is above the melt temperature allows intralaminar voids to be fully compacted during consolidation [19]. Additionally, increasing the pass frequency above 1 Hz at a constant placement rate can maintain a temperature above the glass transition temperature, which facilitates void compaction.

While there was little evidence of interlaminar voids within the small mandrel specimens, there were observed differences in the interlaminar bond line between the two mandrel size groups. An interlaminar resin-rich bond line is readily observed in all specimens; it was noted that increasing the processing temperature at a constant placement rate reduces the bond line thickness. For example, L-3-400, L-3-450, and L-3-500 had a resin-rich bond line thickness of 12.44, 8.74, and 7.92 μm, respectively. However, the bond line thicknesses for the small mandrel specimens are significantly lower than those for the equivalent large mandrel specimens, with S-3-400, S-3-450, and S-3-500 having bond line thicknesses of 9.73, 7,93, and 6.60 μm, respectively. Increasing the placement rate resulted in an increase in the bond line thickness at a constant processing temperature for both mandrel diameters. Despite an increase in the resin-rich bond line thickness with increasing placement rate, the observed trend of small mandrel specimens having a thinner resin-rich region was consistent. Additional observed differences between the mandrel size groups reflect the ply structure, with small mandrel specimens displaying significant out-of-plane ply waviness at high placement rates.

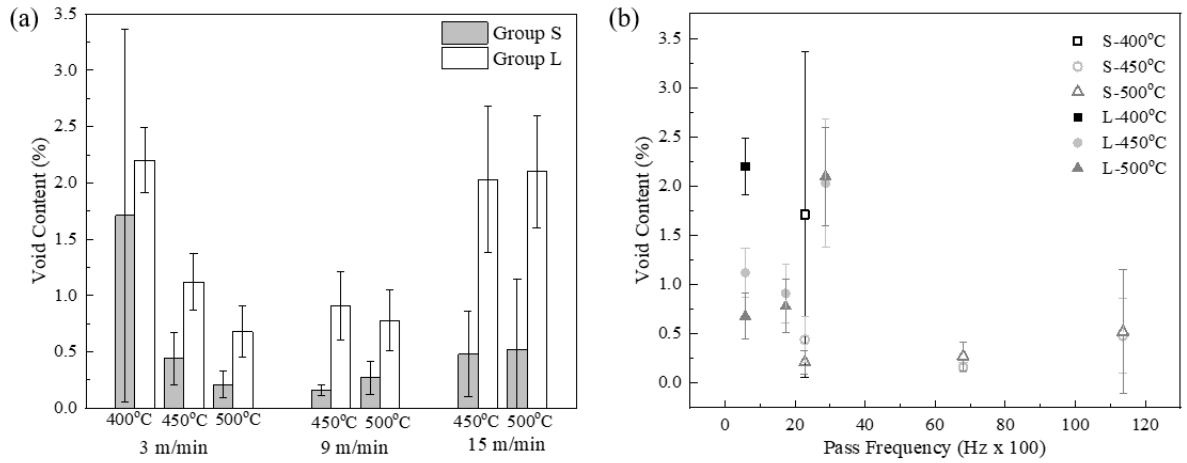

Figure 4: (a) Void content for processing parameters and (b) Void content variation with pass frequency

The degree of crystallinity can influence the mechanical properties of the matrix and, therefore, affect the SBS. When comparing the degree of crystallinity between the upper and lower surfaces, it is observed that the lower surface has a lower degree of crystallinity than the upper surface. Additionally, the upper surface's microstructure was found to be insensitive to changes in process parameters. When considering the degree of crystallinity at the lower surface, it is noted that at 3 m/min, increasing the processing temperature results in a five percent increase in the degree of crystallinity for both mandrel types. However, the average degree of crystallinity ranges between 20% and 25% (Fig. 5(a)), with the mandrel size and pass frequency having little effect on the average degree of crystallinity (Fig. 5(b)). When comparing the two mandrel sizes with equivalent processing parameters, it is observed that there was a 2-5% difference in degree of crystallinity, falling within the error margin of this analysis, despite the difference in pass frequency.

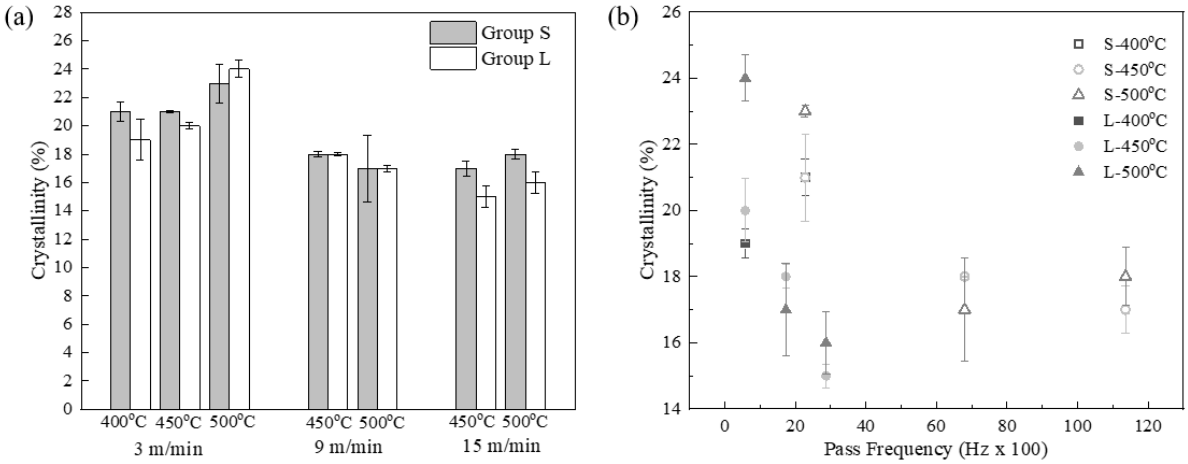

Figure 5: (a) Average crystallinity for specimens and (b) Crystallinity variation with pass frequency

4.3 SBS and Failure

The influence of processing parameters on SBS values is displayed in Fig. 6(a), with the effect of pass frequency shown in Fig. 6(b). A maximum SBS of 58 MPa is achieved with S-9-450. However, this value is still significantly lower than the expected SBS from an autoclave specimen (112 MPa [1]). From Fig. 6(a), it is noted that the specimens manufactured on the small mandrel have a higher SBS than the equivalent large mandrel specimens. Initial assumptions for this apparent difference are based on geometric differences; however, according to finite element simulations (Details on simulation available in Tobin *et al.* [17]), geometrical differences in specimens in this study have a negligible effect

on the SBS value. Additionally, the difference between SBS values for small and large mandrels is not consistent across the process parameters. This observation, combined with the knowledge that the degree of crystallinity can be considered equivalent for the two mandrel types, indicates that the pass frequency affects the SBS.

Comparing the influence of processing parameters on the SBS of both mandrel diameters indicates that the large mandrel specimens are more sensitive to variations in temperature and placement rate (Fig. 6(a)). Comparing L-3-500 to L-9-500, the increase in placement rate results in a reduction in substrate temperature in the large mandrel specimen, correlating with a 6% decrease in SBS. With an increased placement rate, there was a reduction in exposure time to laser flux, thereby reducing the maximum temperatures reached in the substrate. At a placement rate of 9 m/min and temperature of 500 °C, the first ply of L-9-500 reached a temperature of roughly 350 °C, with no subsequent ply reaching the melt temperature. Although above the matrix melt temperature (343 °C), as shown in Fig. 3(c), a rapid drop in temperature occurs due to the cooling effect of the consolidation roller. It can be assumed that a similar thermal history trend exists when further increasing the placement rate to 15 m/min. As a result, void growth, void migration, and fibre decompaction can occur during the heating phase, but the rapid temperature drop during consolidation prevents matrix flow [18]. The high void content in the large mandrel specimens, as a result of low processing temperature, can serve to explain the further reduction in SBS at 15 m/min, as there is a documented correlation between void content and SBS.

The range of SBS observed for large mandrel specimens is 23-47 MPa, compared to a variation of 48-58 MPa for the small mandrel specimens. The consistency of SBS results for the small mandrel specimens indicates that higher pass frequency can be beneficial for SBS. As there is a correlation between void content and SBS [20], specimens with low overall void content have higher SBS values. As observed with void content measurements, the large mandrel specimens were more sensitive to the temperature increase than the smaller mandrel specimens due to the difference in substrate temperatures. It was determined that increasing the processing temperature resulted in a reduction in void content and interlaminar bond line thickness for both mandrel diameters when processing at a speed of 3 m/min. The simulated thermal history for both mandrels indicates that increasing the processing temperature results in an increase in the substrate temperature. The increase in substrate temperature reduces matrix viscosity, which facilitates void compaction during manufacturing. This reduction in void content and matrix bond line width increases the SBS for the specimen, as voids act as stress concentrations and therefore serve as crack initiators.

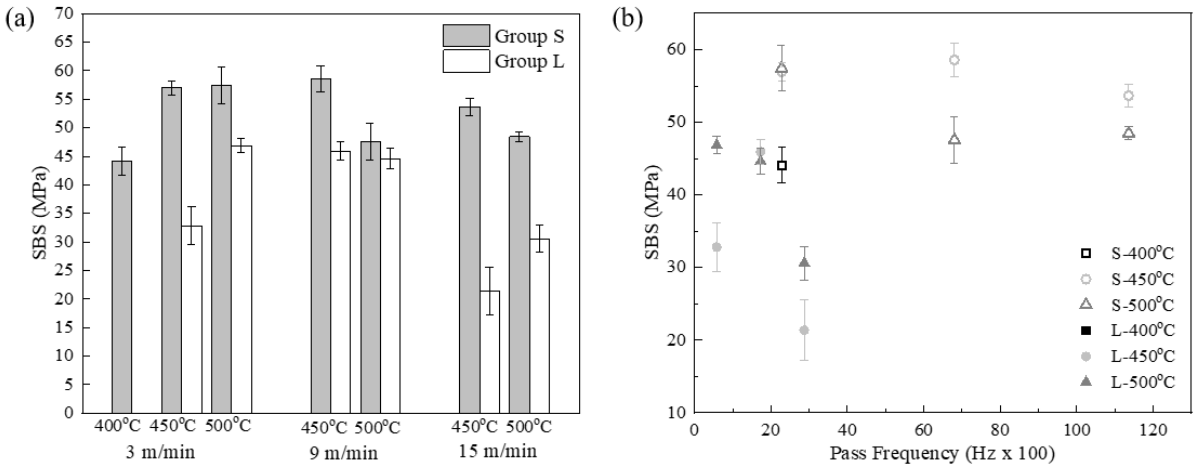

Figure 6: (a) Average SBS for processing parameters and (b) SBS variation with pass frequency

To understand the failure mechanism of SBS specimens, microscopical analysis was conducted to compare the failure locations and fracture surfaces. Fig. 7(a-b) displays the failure crack for the specimen with the lowest (L-3-400) and the highest SBS values (S-9-450). From Fig. 7(a), it is noted that failure occurs along the interlaminar bond line, with little to no crack deflection observed. This failure likely

occurs due to relatively poor interlaminar bonding as a result of a substrate temperature that was too low, as indicated in Fig. 3(a). When analysing the fracture surfaces of L-3-400, which had clear interlaminar failure, no sign of matrix deformation is observed (Fig. 7(c)), further indicating poor interlaminar bonding. Contrary to the interlaminar failure observed for L-3-400, failure S-9-450 occurred within the ply with significant crack deflection (Fig. 7 (b)). When analysing the failure surface of S-9-450 in Fig. 7(d), there are signs of matrix deformation correlating with the higher SBS value. Additionally, S-9-450 has significant matrix remaining on the fibre surfaces, indicating high levels of fibre-matrix adhesion, probably due to increased processing temperature, which improves the fibre-matrix bonding.

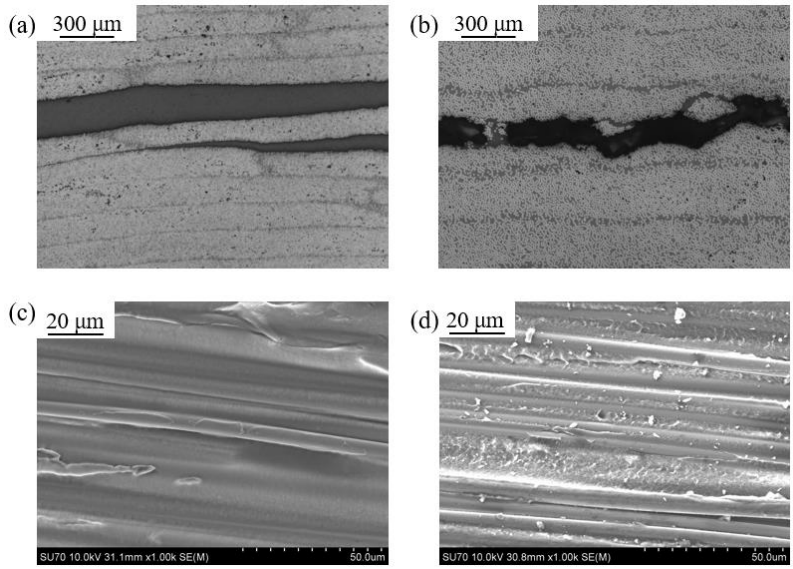

Figure 7: Fractured mid-plane of (a) L-3-400 and (b) S-9-450, and fracture surface of (c) L-3-400 and (d) S-9-450

4.4 The effect of pass frequency on SBS

While the effect of processing parameters on the SBS has been documented within Section 4.3, the influence of pass frequency on the microstructure and subsequent SBS variations has yet to be discussed. While there may be a difference in residual stress formation within the specimens due to the different mandrel diameters, Ma *et al.* [16] showed that variations in residual stress do not correlate with changes in the SBS. Changes, therefore, occur as a result of differences in the specimen's microstructure. As the consolidation force was held constant during manufacturing, the difference in microstructure between the two mandrel geometries can be explained by comparing their thermal histories.

In order to ensure intralaminar void compaction, the matrix should be held above the melt temperature [19]. However, once the matrix is above the glass transition temperature, it is possible to compress interlaminar and intralaminar voids [21]. From Fig. 2(c) and Fig. 3(c), it is noted that the substrate temperature of S-9-500 gradually increases, whereas for L-9-500 it does not. The increases in substrate temperature occur due to an increase in pass frequency from 0.173 Hz to 0.680 Hz. At elevated pass frequencies, the LATP head completes a full rotation of the mandrel before the previous ply fully cools, with the next ply being placed onto a warm substrate. The increase in substrate temperature at high pass frequencies is similar to the higher substrate temperature introduced while manufacturing on a heated tool, which has been shown to reduce void content and increase SBS [22]. Although the thermal history of manufacturing at 15 m/min was not simulated, the trends observed for S-9-500 and L-9-500 are likely to occur at a higher placement rate. Specifically, the substrate temperature of the specimens manufactured on the small mandrel at 15 m/min will not have fully cooled at a pass frequency of 1.136 Hz. This effect is due to the higher pass frequency, which results in lower void content in S-15-450 and S-15-500 compared to both L-15-450 and L-15-500. Despite the substrate temperature being lower at

high placement rates (Fig. 2 and Fig. 3), the substrate remains above the glass transition temperature for longer, which facilitates void compaction and interlaminar bonding.

The thermal history variation between the two mandrels highlights that increasing the pass frequency can aid in maintaining the substrate temperature, thereby reducing void content, and subsequently increasing the SBS. However, from Fig. 5(b) and Fig. 6(b), it is noted that the relationship between pass frequency and SBS is non-monotonic, with a maximum SBS being achieved (S-9-450) and subsequently decreasing. However, it is also worth noting that the maximum SBS value also varies with mandrel geometry, as the laser flux varies with diameter. Using the relationship between void content and pass frequency as a metric for optimisation, with the lowest void content being considered optimum, it was noted that this optimum was achieved at 9 m/min and 450 °C (0.680 Hz), and with the void content increasing with increases in pass frequency. However, when manufacturing large structures, this level of pass frequency is likely unattainable when manufacturing with a single LATP head. Therefore, future developments of the LATP systems, such that they are similar to the thermoplastic pipe manufacturing industry, where multiple heads work in unison, may facilitate the required high pass frequency [23]. Based on the thermal histories displayed in Fig. 2 and Fig. 3, the maximum substrate temperature is highly dependent on the placement rate. In order to further increase the pass frequency, it is necessary to increase the processing temperature further. However, when comparing the maximum temperatures achieved when processing at a pass frequency of 0.173 Hz and 0.680 Hz, it is noted that with the same nip-point temperature, the higher pass frequency results in a substrate temperature approximately 100 °C higher. This temperature difference indicates that although there is a requirement for increasing the target nip-point temperature with higher placement rates, increasing the pass frequency results in a lower temperature being needed, reducing the potential for matrix degradation.

6 CONCLUSIONS

LATP manufacturing was used to produce specimens on various diameter mandrels, allowing for the study of the effect of pass frequency on the specimen microstructure and subsequent variations in SBS. A thermo-mechanical finite element model was utilised to determine the thermal history of the laminates, providing a deeper understanding of the influence of processing on microstructural changes. Characterisation tests were conducted to analyse the influence of the microstructural changes due to pass frequency on the interlaminar bond strength through SBS testing.

Results show that increasing the placement rate increases the overall laminate void content due to insufficient matrix temperatures being reached. While the temperature is above the matrix glass transition temperature, at high placement rates (15 m/min), the substrate does not reach the melt temperature. This scenario facilitates tape deconsolidation while also inhibiting matrix flow, thereby increasing the void content. Due to an increase in void content, the maximum SBS obtained is 32 MPa (0.287 Hz). However, increasing the pass frequency to 1.136 Hz (57 MPa) at the same placement rate and temperature causes the substrate to gradually heat, increasing the window of time for consolidation to occur. Due to this gradual substrate heating, the void content reduced and SBS increased for equivalent process parameters, but at a higher pass frequency.

However, there are limitations associated with this study. While the use of two mandrel diameters introduced methods for varying the pass frequency, it became apparent that the laser flux was different for the two mandrel diameters. As a result, the maximum temperatures reached during ply placement differed for the same processing parameters. However, despite the temperature differences observed during initial placement, the thermal history trends with increasing pass frequency are expected to be representative. From the results and discussion presented in this work, it is apparent that a pass frequency of 0.680 Hz at 450 °C provided the highest SBS. However, for large-diameter structures, this pass frequency is likely unattainable with a single LATP head. Therefore, this study aims to highlight potential future developments in LATP manufacturing optimisation, aiming to achieve high-rate manufacturing without compromising interlaminar bond strength.

ACKNOWLEDGEMENTS

The authors would like to thank Science Foundation Ireland (SFI) for funding Spatially and Temporally VARIable COMPosite Structures (VARICOMP) Grant No. (15/RP/2773) under its Research Professor

programme. The authors would also like to thank David Jones for assisting in the manufacturing process using LATP.

REFERENCES

[1] Comer A. J., Ray D., Obande W. O., Jones D., Lyons J., Rosca I., et al. Mechanical characterisation of carbon fibre–PEEK manufactured by laser-assisted automated-tape-placement and autoclave. *Composites Part A: Applied Science and Manufacturing*.(2015);69:10-20; 10.1016/j.compositesa.2014.10.003.

[2] Clancy G., Peeters D., Oliveri V., Jones D., O'Higgins R. M., Weaver P. M. A study of the influence of processing parameters on steering of carbon Fibre/PEEK tapes using laser-assisted tape placement. *Composites Part B: Engineering*.(2019);163:243-51; 10.1016/j.compositesb.2018.11.033.

[3] Suzuki T. Prediction of energy intensity of carbon fiber reinforced plastics for mass-produced passenger cars2005.

[4] Stokes-Griffin C. M., Compston P. The effect of processing temperature and placement rate on the short beam strength of carbon fibre–PEEK manufactured using a laser tape placement process. *Composites Part A: Applied Science and Manufacturing*.(2015);78:274-83; 10.1016/j.compositesa.2015.08.008.

[5] Tobin E., Kumar Bandaru A., O'Higgins R. M., Weaver P. M. The influence of temperature and placement rate on wound laminated carbon fibre/PEEK hoop specimens manufactured by in-situ consolidated LATP. *Composite Structures*.(2024);341:118243; https://doi.org/10.1016/j.compstruct.2024.118243.

[6] Kirchhoff J. G., Heathman N. T., Yap T., Koirala P., Hudson T. B., Tehrani M. Interlaminar bonding in thermoplastic composites: A comparative analysis of laser AFP and post-processing. *Composites Part B: Engineering*.(2025);294:112156; https://doi.org/10.1016/j.compositesb.2025.112156.

[7] Oromiehie E., Gain A. K., Prusty B. G. Processing parameter optimisation for automated fibre placement (AFP) manufactured thermoplastic composites. *Composite Structures*.(2021);272:114223; 10.1016/j.compstruct.2021.114223.

[8] Oromiehie E., Garbe U., Gangadhara Prusty B. Porosity analysis of carbon fibre-reinforced polymer laminates manufactured using automated fibre placement. *Journal of Composite Materials*.(2020);54(9):1217-31; 10.1177/0021998319875491.

[9] Qureshi Z., Swait T., Scaife R., El-Dessouky H. M. In situ consolidation of thermoplastic prepreg tape using automated tape placement technology: Potential and possibilities. *Composites Part B: Engineering*.(2014);66:255-67; 10.1016/j.compositesb.2014.05.025.

[10] Shadmehri F., Hoa S., Fortin-Simpson J., Ghayoor H. Effect of in situ treatment on the quality of flat thermoplastic composite plates made by automated fiber placement (AFP). *Advanced Manufacturing: Polymer & Composites Science*.(2018);4(2):41-7;

[11] Wang X., Chen C., Hu S., Chen Z., Jiang W., Shen G., et al. In-situ infrared annealing for laser-assisted automated fiber placement to enhance interlaminar properties without sacrificing laydown efficiency. *Composites Part A: Applied Science and Manufacturing*.(2024);183:108214; https://doi.org/10.1016/j.compositesa.2024.108214.

[12] Shadmehri F., Hoa S. V., Fortin-Simpson J., Ghayoor H. Effect of in situ treatment on the quality of flat thermoplastic composite plates made by automated fiber placement (AFP). *Advanced Manufacturing: Polymer & Composites Science*.(2018);4(2):41-7; 10.1080/20550340.2018.1444535.

[13] Raps L., Chadwick A. R., Schiel I., Schmidt I. CF/LM-PAEK: Characterisation and sensitivity to critical process parameters for automated fibre placement. *Composite Structures*.(2022);284:115087; https://doi.org/10.1016/j.compstruct.2021.115087.

[14] Chang I. Y., Hsiao B. S. Thermal properties of high performance thermoplastic composites based on poly(ether ketone ketone) (PEKK). International SAMPE Symposium and Exhibition (Proceedings). pt 2 ed1991. p. 1587-601

[15] Materials A. C. D.-o. C. Standard test method for short-beam strength of polymer matrix composite materials and their laminates. 100 Barr Harbour Drive PO box C-700 West Conshohocken, Pennsylvania 19428-2959, United States: ASTM International; 2006
[16] Ma H., Bandaru A. K., Weaver P. M. The effect of laser assisted tape placement processing conditions on microstructural evolution, residual stress and interlaminar shear strength of carbon fibre/PEEK laminates. *Composites Part B: Engineering*.(2024);274:111293; https://doi.org/10.1016/j.compositesb.2024.111293.
[17] Tobin E., Ma H., O'Higgins R. M., Weaver P. M. Effect of automated tape placement pass frequency on matrix-dominated mechanical properties and microstructure of wound CF/PEEK. *Composites Part A: Applied Science and Manufacturing*.(2025);194:108901; https://doi.org/10.1016/j.compositesa.2025.108901.
[18] Çelik O., Bussink T., Peeters D., Teuwen J., Dransfeld C. The effect of Laser-Induced deconsolidation on the compaction behavior of thermoplastic composite tapes. *Composites Part A: Applied Science and Manufacturing*.(2021);151:106670; 10.1016/j.compositesa.2021.106670.
[19] Çelik O. Consolidation during laser assisted fiber placement: Heating, compaction and cooling phases. Delft, NL: Delft University of Technology; 2021.
[20] Jeong H. Effects of Voids on the Mechanical Strength and Ultrasonic Attenuation of Laminated Composites. *Journal of Composite Materials*.(1997);31(3):276-92; 10.1177/002199839703100303.
[21] Stokes-Griffin C. M., Compston P. Investigation of sub-melt temperature bonding of carbon-fibre/PEEK in an automated laser tape placement process. *Composites Part A: Applied Science and Manufacturing*.(2016);84:17-25; https://doi.org/10.1016/j.compositesa.2015.12.019.
[22] Chadwick A. R., Kotzur K., Nowotny S. Moderation of thermoplastic composite crystallinity and mechanical properties through in situ manufacturing and post-manufacturing tempering: Part 1 – Mechanical characterisation. *Composites Part A: Applied Science and Manufacturing*.(2021);143:106286; https://doi.org/10.1016/j.compositesa.2021.106286.
[23] Ridgway Machines Ltd., *RTP & TCP Taping Machines* (2024) https://www.ridgwayeng.com/rtp-machines/ (Last Accsessed: September 2024)

ICCM24

24TH INTERNATIONAL CONFERENCE ON COMPOSITE MATERIALS



aimen TECHNOLOGY CENTRE

Innovation & Technology

Sequential resistance welding of a thermoplastic composite leading edge demonstrator: From laboratory testing to full-scale welding

M. Russello, E. Chemello, R. González Gil, A. Martínez Domínguez, E. Rodríguez Senín

HERWINGT

CLEAN AVIATION

Co-funded by the European Union

Massimiliano Russello
Team Leader of Composite Welding Technologies

02-08-25

Ultrasonic Welding

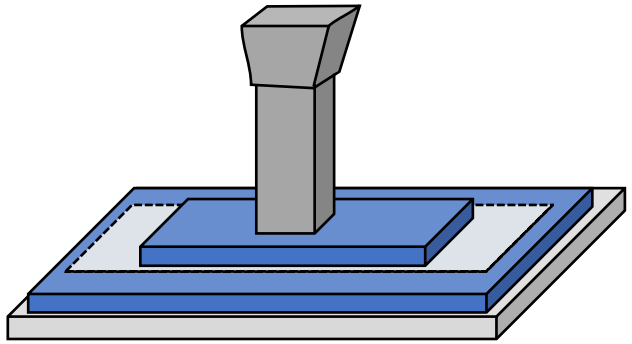

Resistance Welding

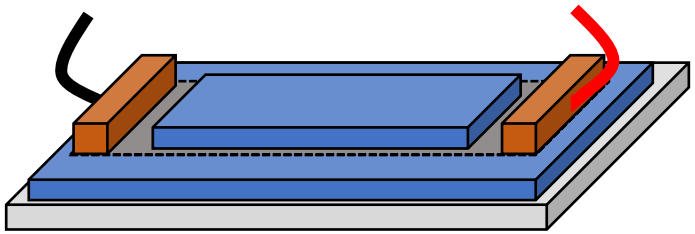

Induction Welding

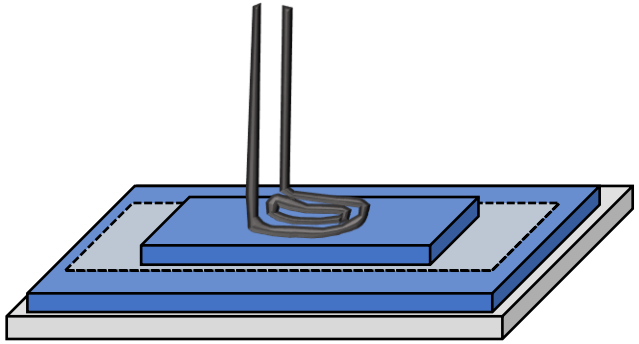

Conduction Welding

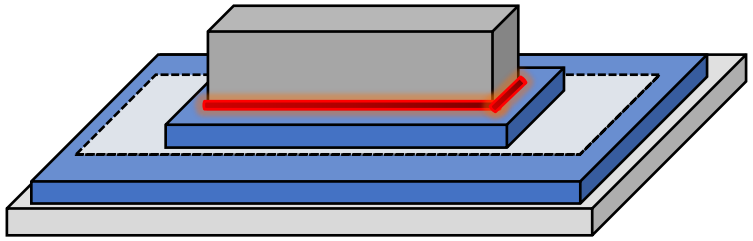

AIMEN technology centre

Process Understanding

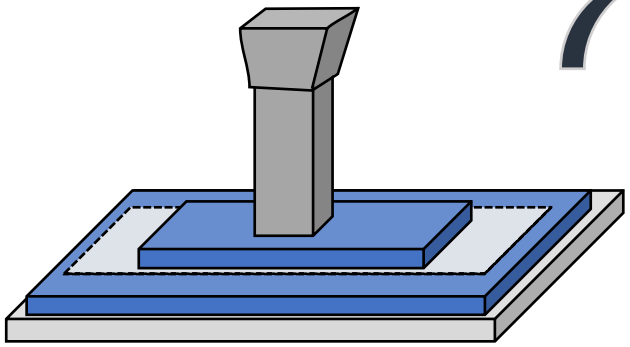

Equipment manufacturing

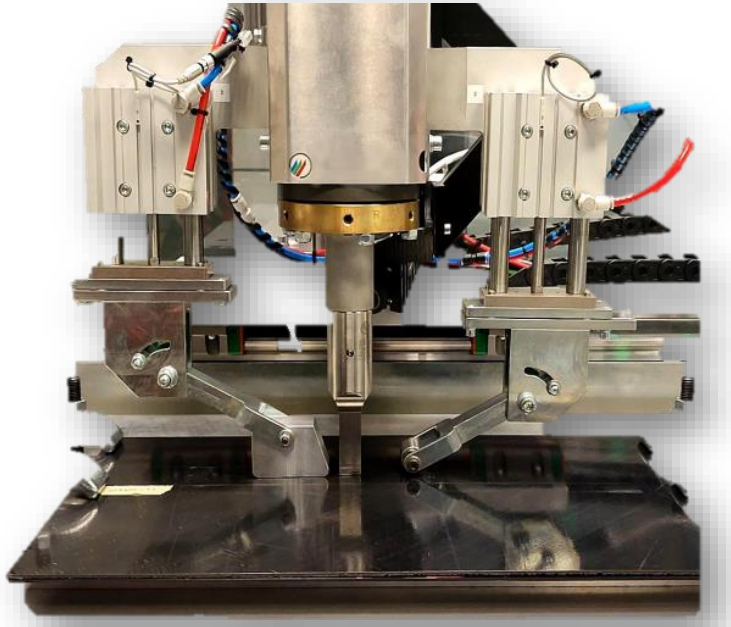

Automation and Monitoring





INTRODUCTION - WELDER

Resistance Welding
The frame couplings

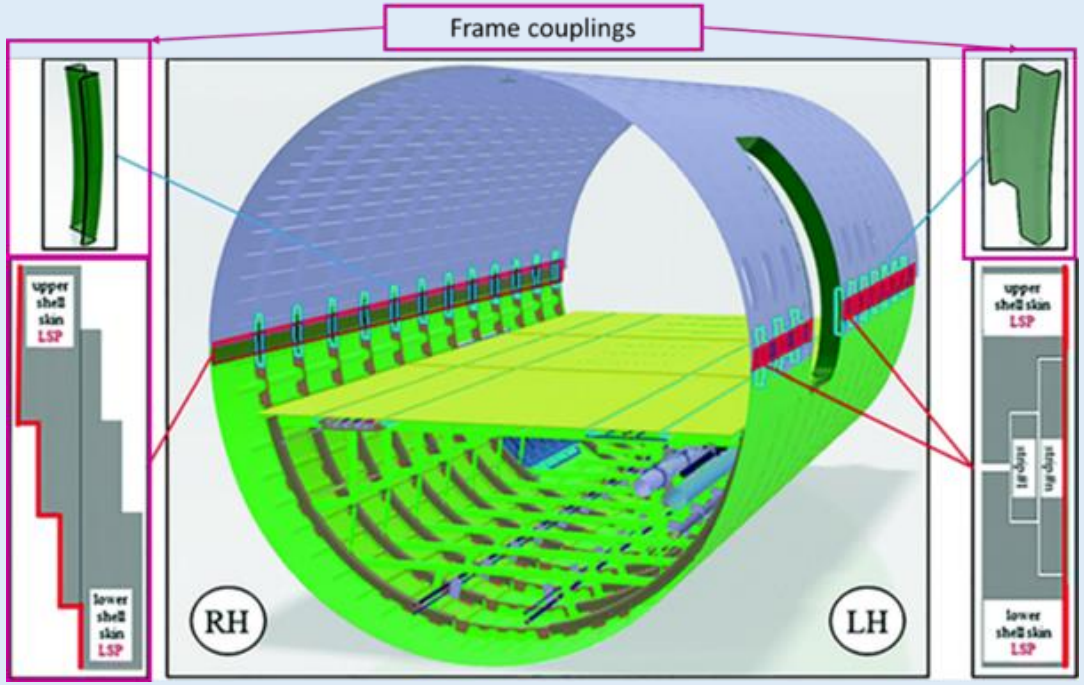



Scale-up challenge:

- Multiple in-series welds
- Automatic process
- Uniform performance



This Project has received funding from Clean Sky 2 Joint Undertacking (JU) under grant agreement Nº101007814

INTRODUCTION - HERWINGT

Sequential Resistance Welding Thermoplastic Leading Edge

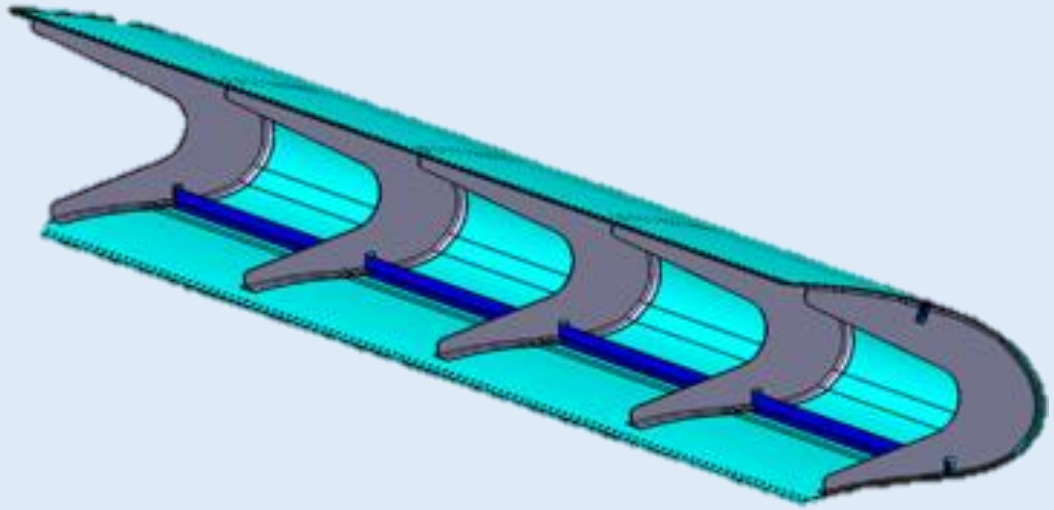

Scale-up challenge:

- 2.5 m structure
- Variable thickness
- Uniform performance
- Controllable temperatures
- High key performance

BASE MATERIAL :
High Temperature Thermoplastic Composites

INTRODUCTION

Current aeronautic needs:

- Innovative materials: Thermoplastics among these
- Flexible and adaptable manufacturing systems
- Shorter manufacturing cycles
- Environmental friendliness
- Energy efficiency
- Higher productivity

THERMOPLASTIC WELDING

- ✓ ROBUST
- ✓ RELIABLE
- ✓ EFFICIENT
- ✓ COMPATIBLE
- ✓ SAFE

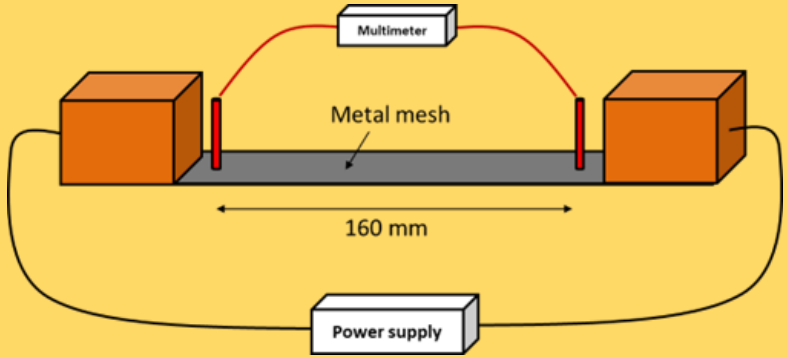

Parameters and variables:

- Pressure
- Power/Current
- Time
- Cooling
- Part layup and size
- Conductivity
- Thickness

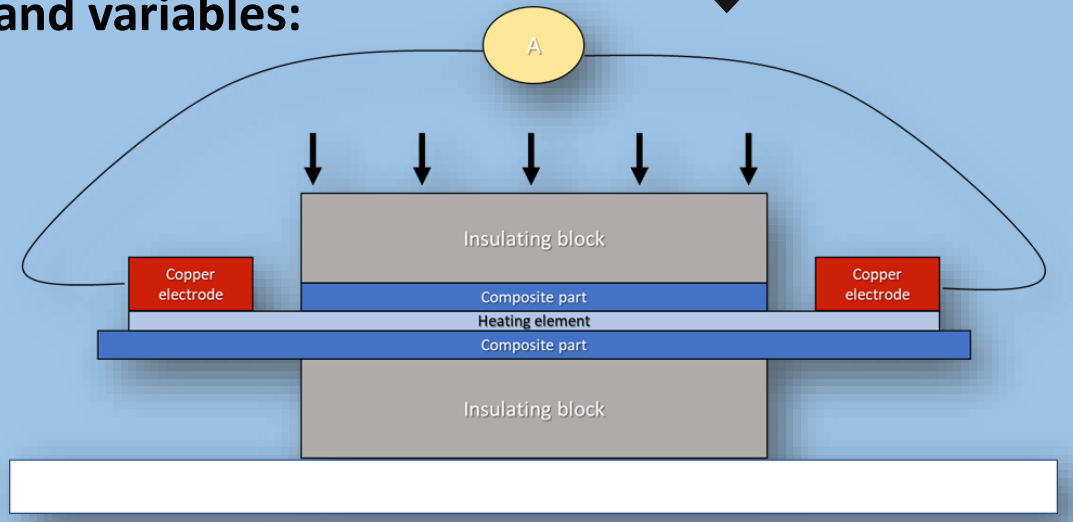

THE SCALING-UP CHALLENGE

Scale-up challenge

Welding: Setups and Parameters investigation

Monitoring:

Process investigation involving technological and process parameters, in-use monitoring

Analysis, Testing and data interpretation: Performance, robustness, processability.

Progressive Scale-up

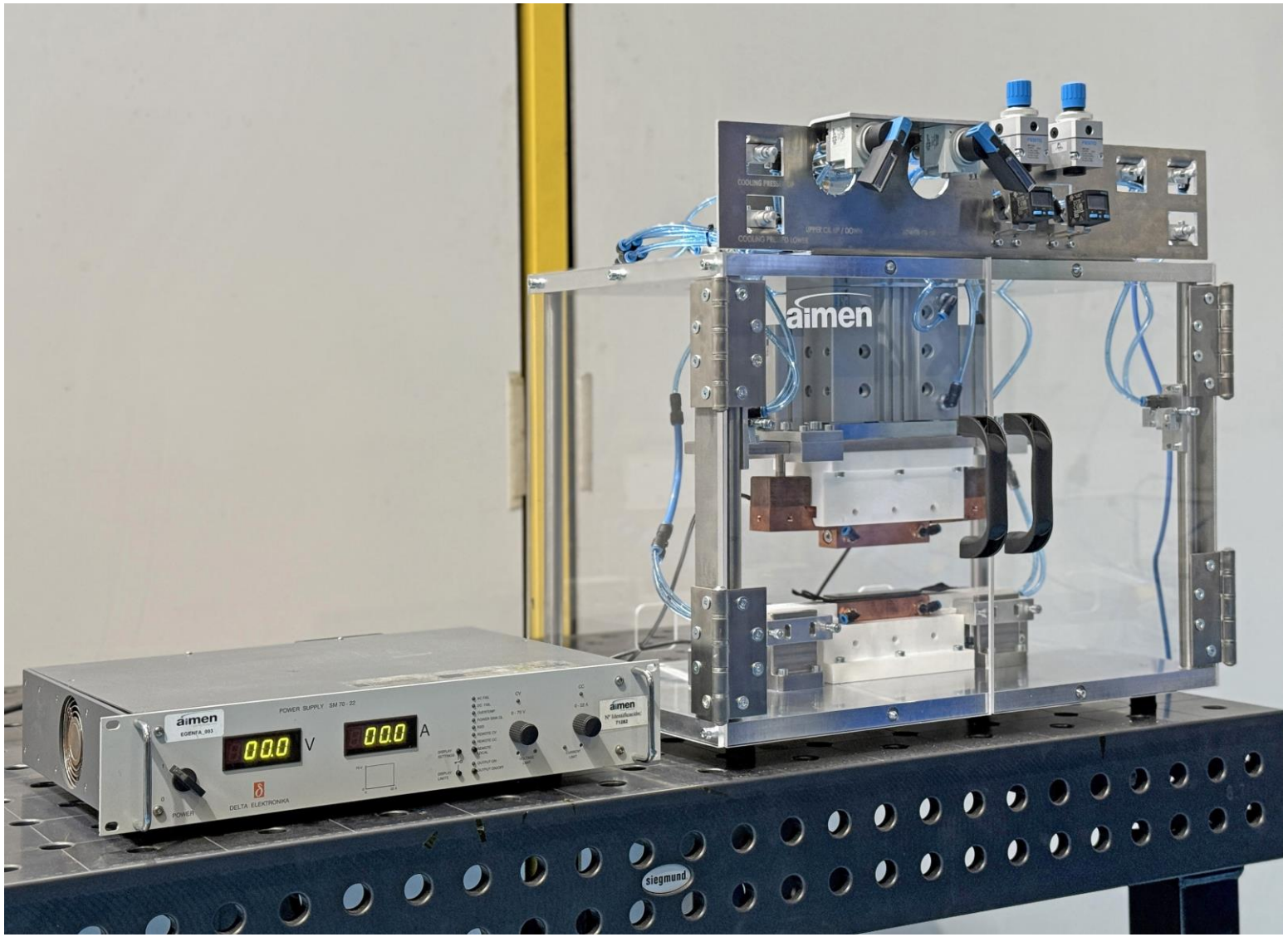

The Heating Element

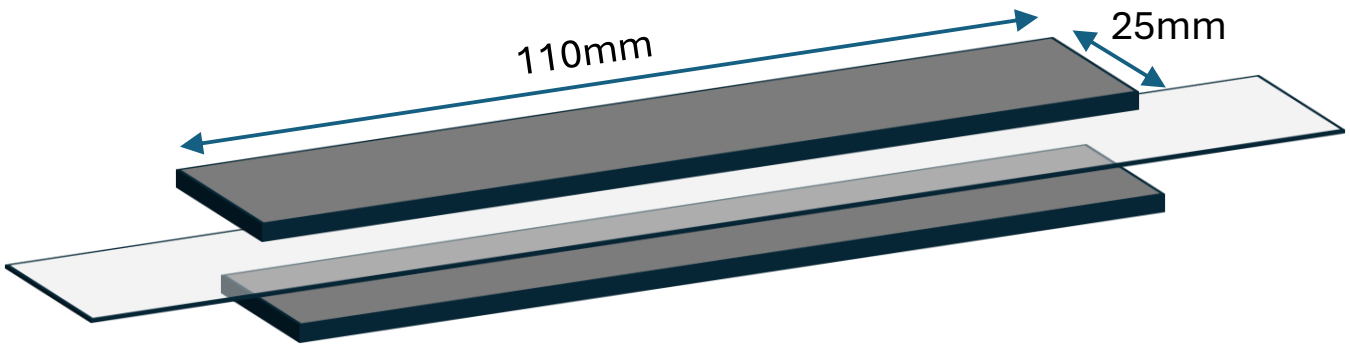

Metal Heating Element

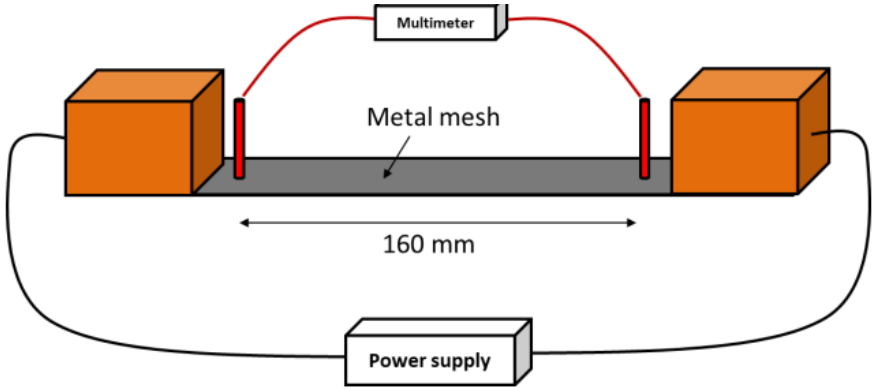

Carbon Based Heating Element

$$\rho_s(m\Omega) = \frac{R(\Omega) \cdot w(mm)}{l\,(mm)} \cdot 1000$$

The Heating Element – Electrical Properties

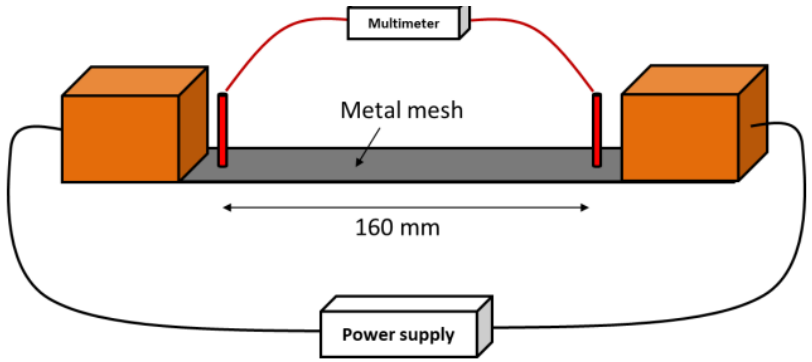



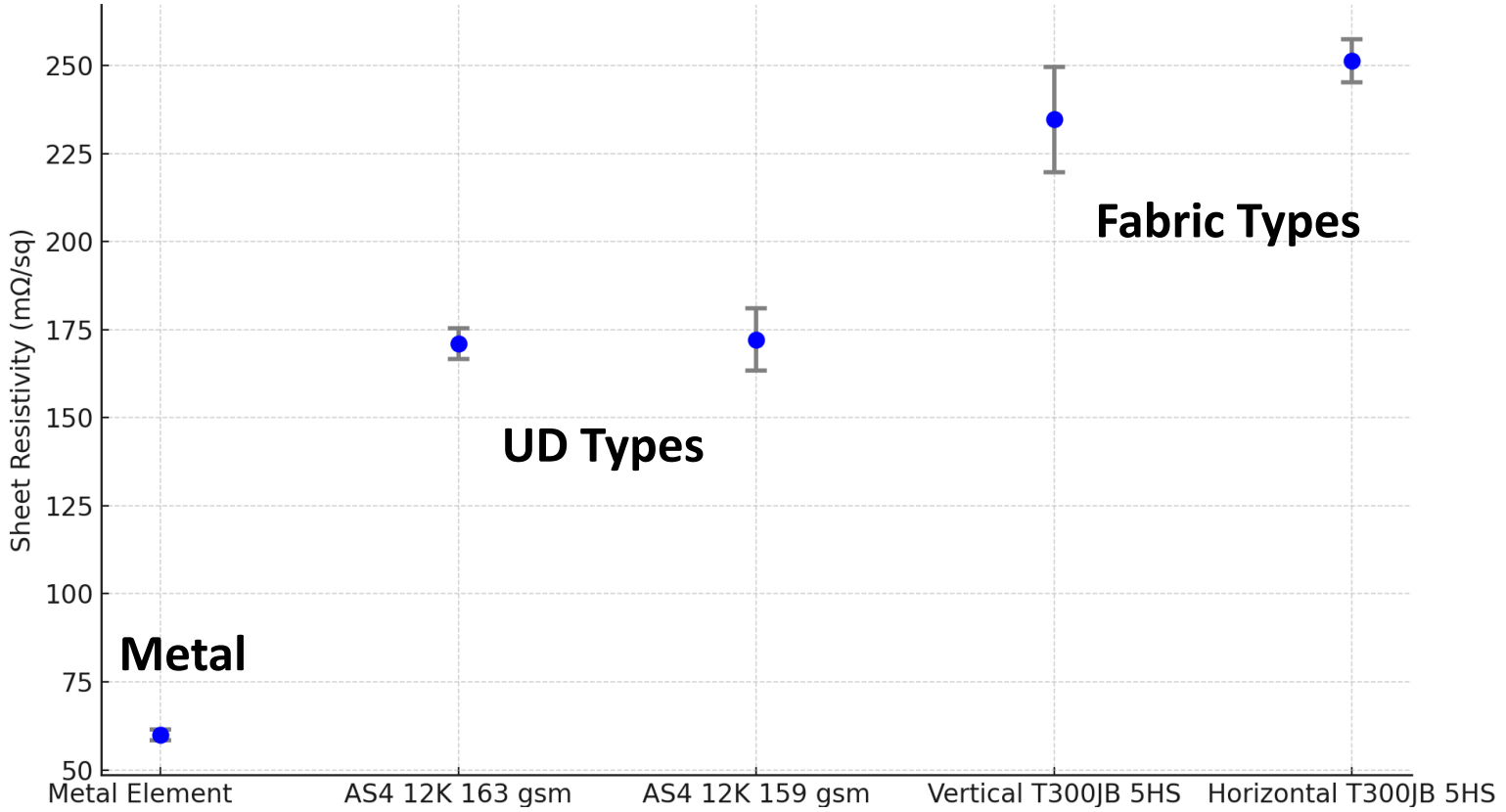

The effect of the Heating element Width

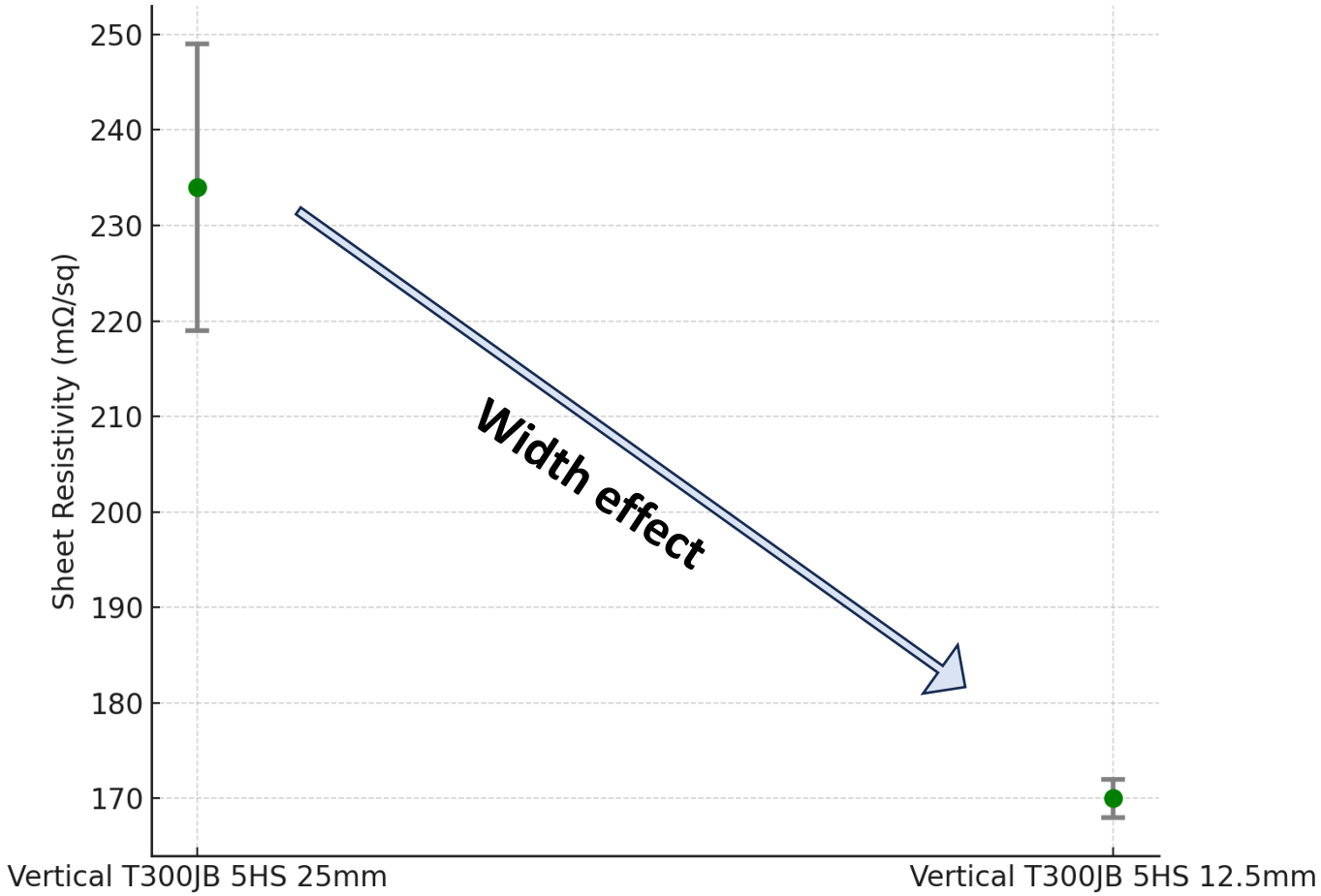

Monitoring of the Heating Element

MONITORING ADVANTAGES

- ✓ Correlate the technological parameters to the physical changes









Thermal Characterization

UD Type

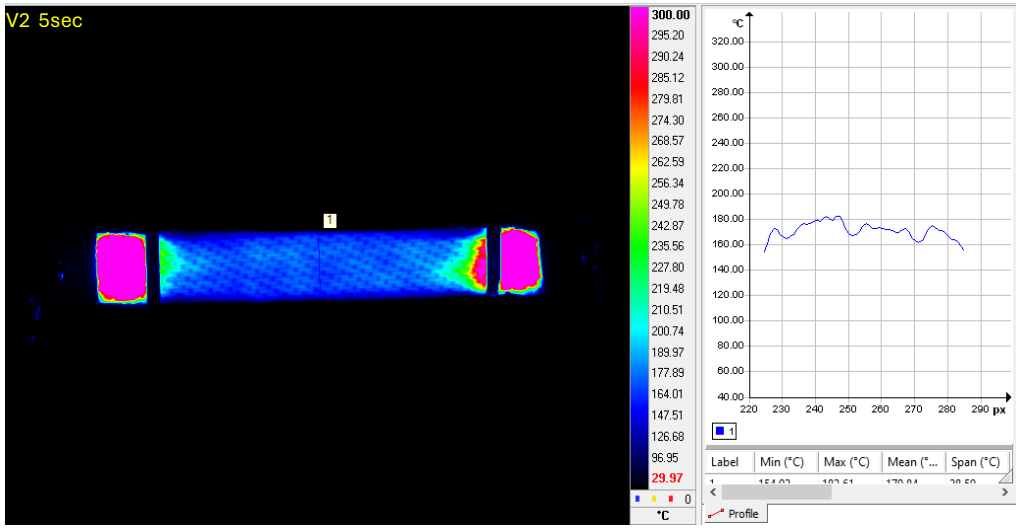

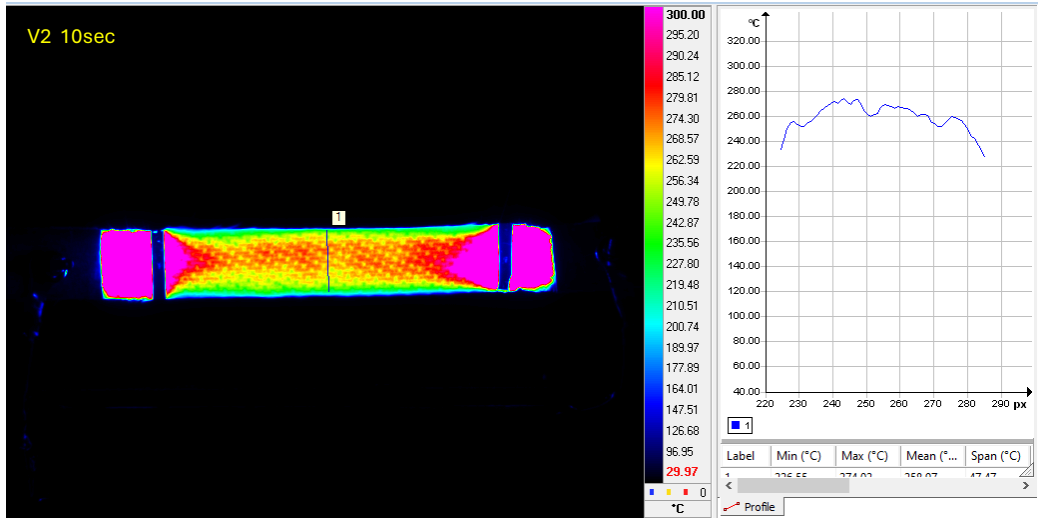

Fabric Type

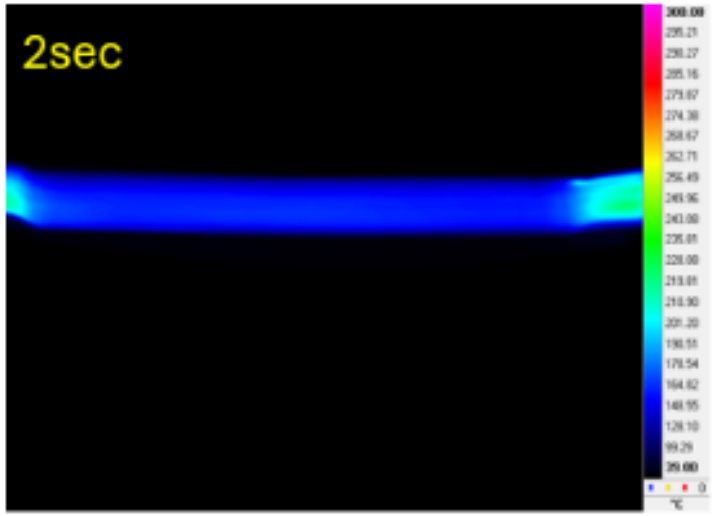

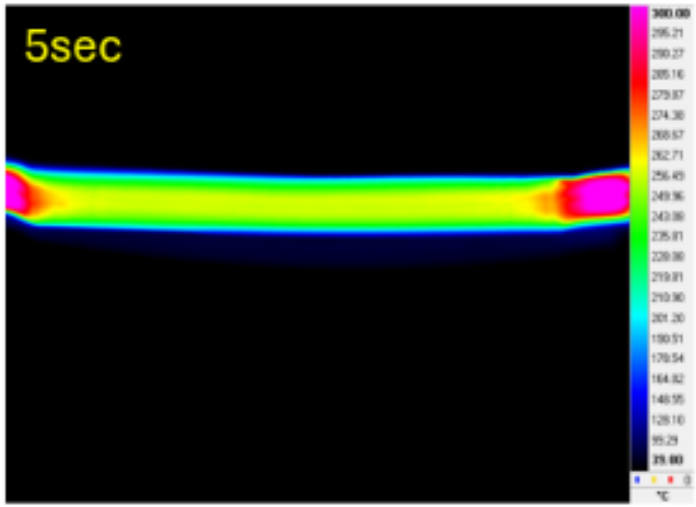

Scalability Issues

Electrical Signal → **Tuned Thermal Output**

Issues

- Heating element Reliability and Consistency (Electrical and Thermal Properties)
- Component to be welded (Material, Length, Thickness)
- Control and Monitoring

Possible Solutions

- Definition of acceptable processing windows
- Development of a Calibration processes
- Development of a Control and Monitoring System

Scalability Issues

Thermal Output

- Constant Electrical Input >> Time-Variable Thermal Output

- Variable Electrical Input >> Tuned Thermal Output
  - Batch Calibration >> Affected by Variability and Setup Variations
  - Individual Calibration >> No affected by Variability but affected by setup variation
  - Individual Calibration on Specific Setup >> No affected by Variability nor by Setup Variations
  - Real-Time control by Feedback > No affected by Variability nor by Setup Variations (Complex)

Batch Calibration



Individual Calibration



Individual Calibration on Setup

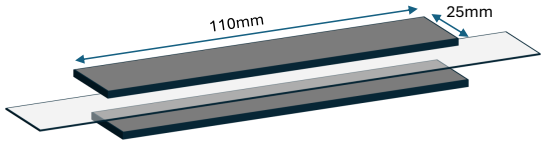

Real-Time Monitoring and Control



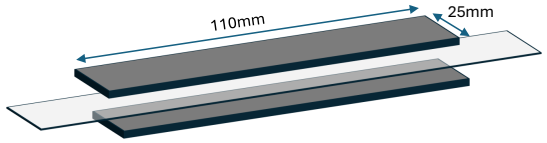

Real-Time Monitoring and Control

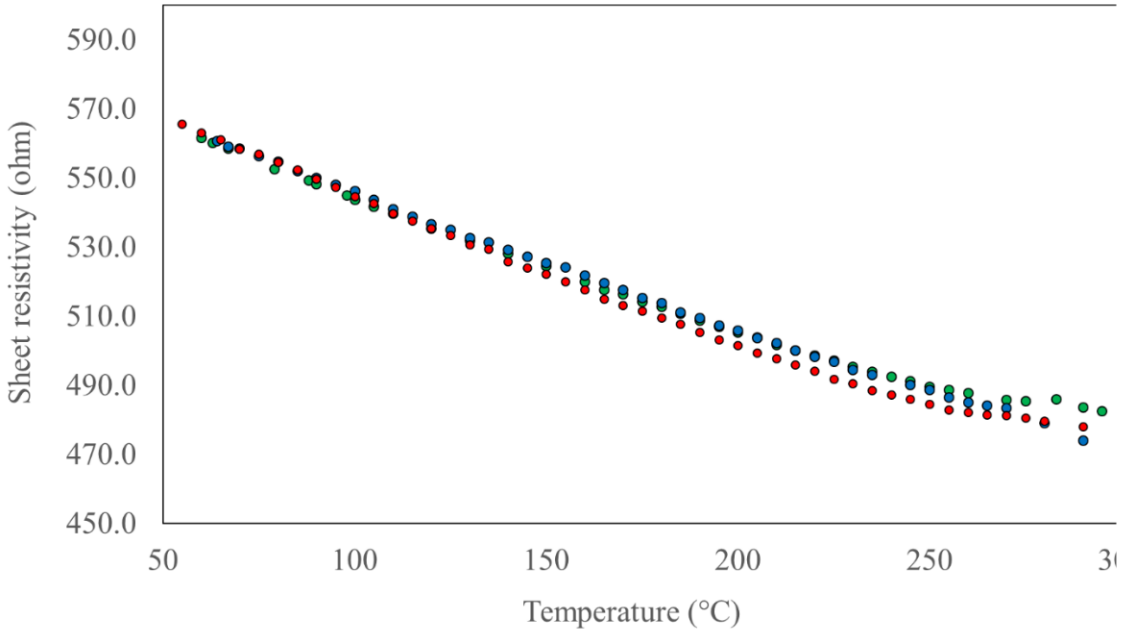

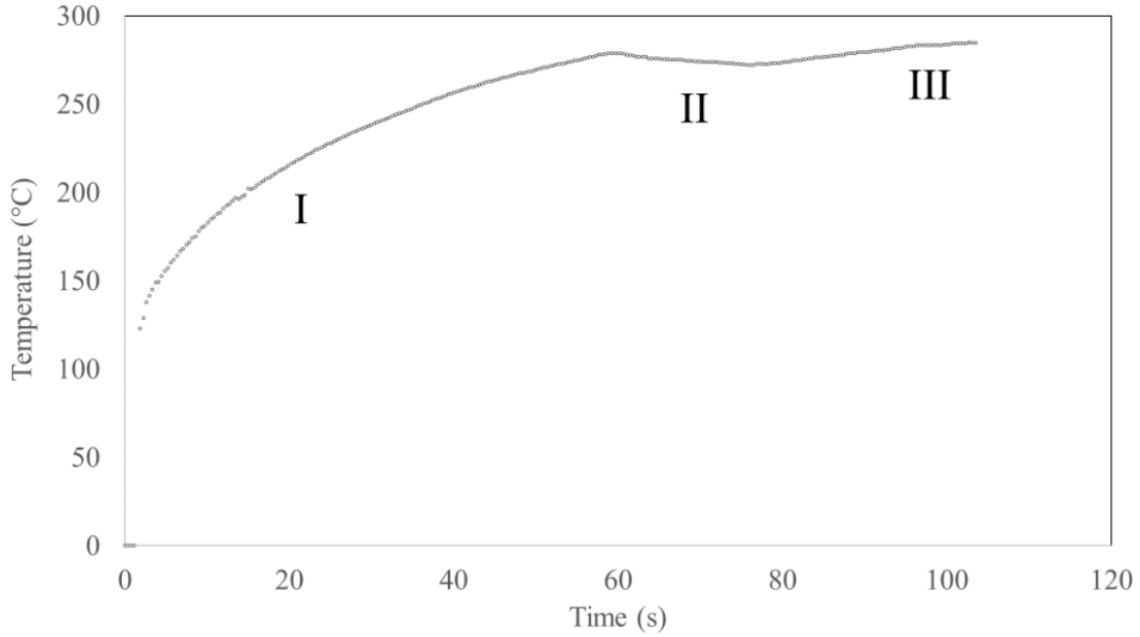

$$T = T_0 + \frac{\rho - \rho_0}{\omega}$$

LABORATORY SCALE TESTING

Laboratory scale….

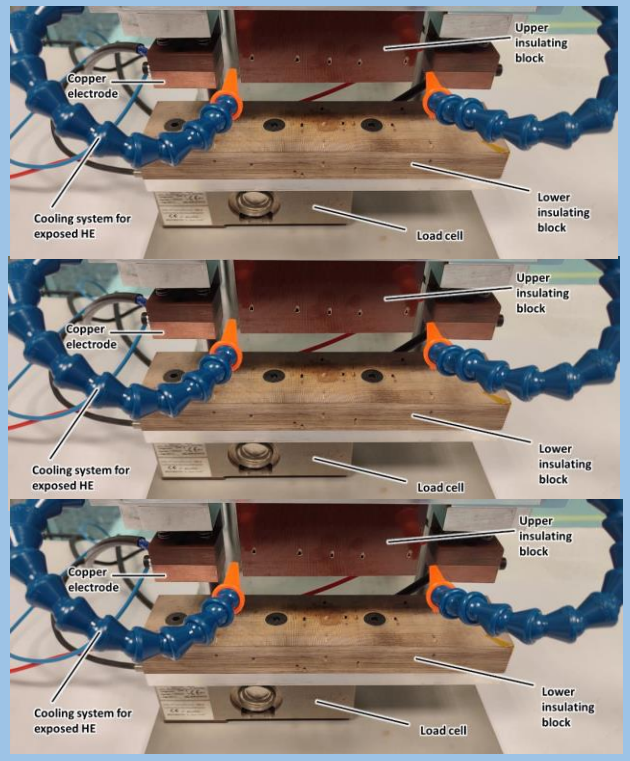



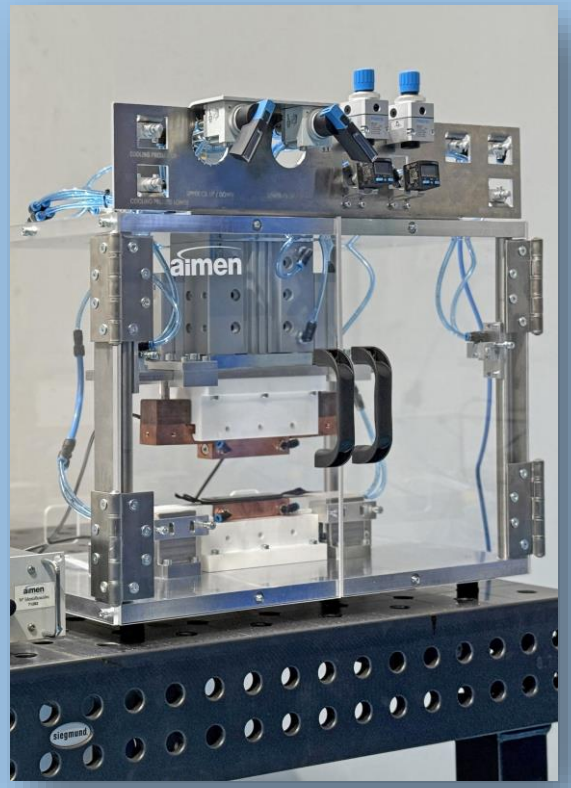

This Project has received funding from Clean Sky 2 Joint Undertacking (JU) under grant agreement Nº101007814

SCALE UP PROCESS

Demonstrator scale….

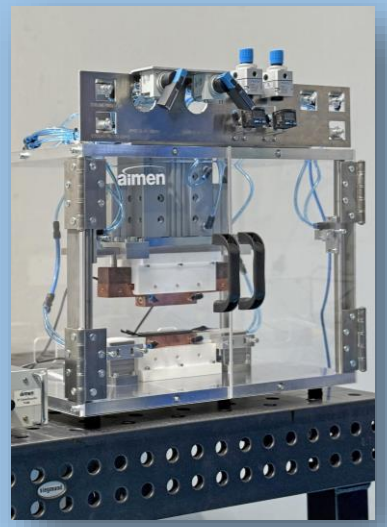

Energy director installation

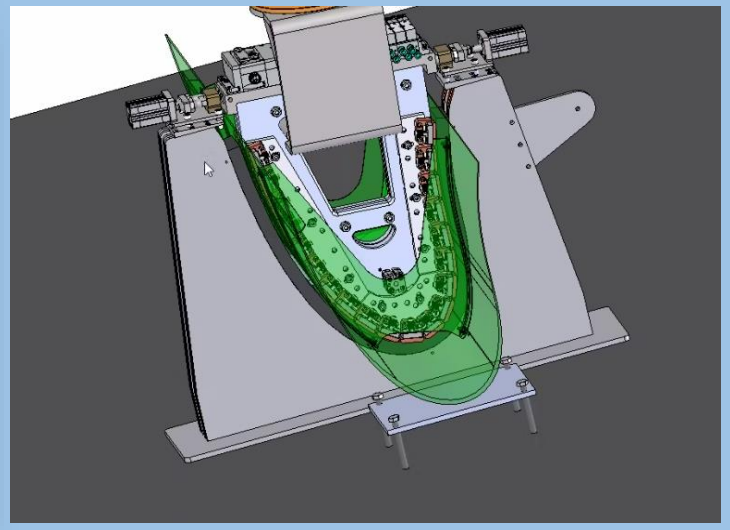

Tooling and Head design

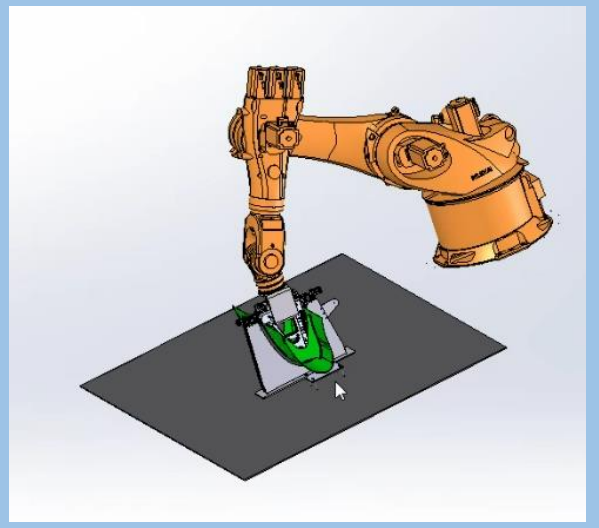

Automation and control systems

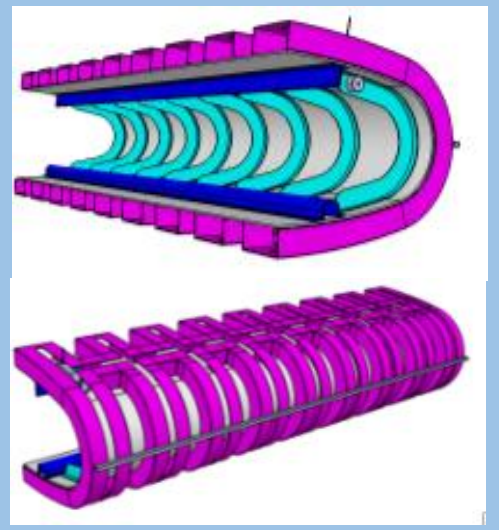

Final Welding Process

This Project has received funding from Clean Sky 2 Joint Undertacking (JU) under grant agreement Nº101007814

SCALE UP PROCESS

Other Success Stories

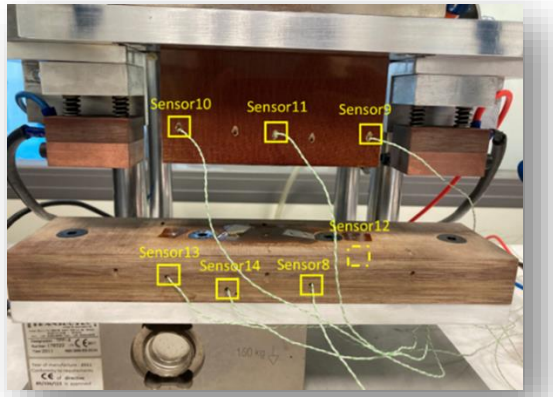

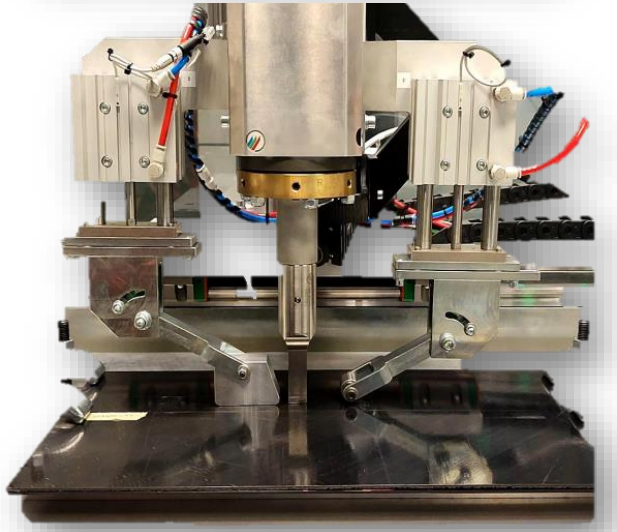





This Project has received funding from Clean Sky 2 Joint Undertacking (JU) under grant agreement Nº101007814

CONCLUSION

REMARKS

- Future applications of current manufacturing, assembly, and welding technologies are being developed in the direction of rapid, reliable and efficient processes.
- In the aviation industry, as well as other industries, research and analysis on the scalability of manufacturing methods can have a significant impact on future applications.



This Project has received funding from Clean Sky 2 Joint Undertacking (JU) under grant agreement №101007814

aimen
TECHNOLOGY CENTRE

Headquarters
Laser Applications Centre
Polígono Industrial de Cataboi
SUR-PPI-2 (Sector 2) Parcela 3
E36418 O PORRIÑO
Pontevedra - Spain
Phone: +34 986 344 000

Torneiros Facilities
Armando Priegue Building
Relva 27 A – Torneiros
E36410 O PORRIÑO
Pontevedra – Spain
Phone: +34 986 344 000

A Coruña Office
Polígono Industrial de Pocomaco
Parcela D-22 Oficina 20
E15190 A Coruña - Spain
Phone.: +34 637 127 253

Madrid Office
C/ Rodríguez San Pedro, 2
Planta 6, Oficina 609 Edificio Inter
E28015 Madrid - Spain
Phone: +34 687 448 915

North Office
Parque Tecnológico de Zamudio
Edificio 103, Planta 2
E48170 ZAMUDIO - Vizcaya
Phone: +34 662 489 181

aimen@aimen.es
www.aimen.es



THANK YOU FOR YOUR ATTENTION

Ultrasonic welding of metal and fibre reinforced thermoplastics – bond formation and joint strength

Moritz Liesegang

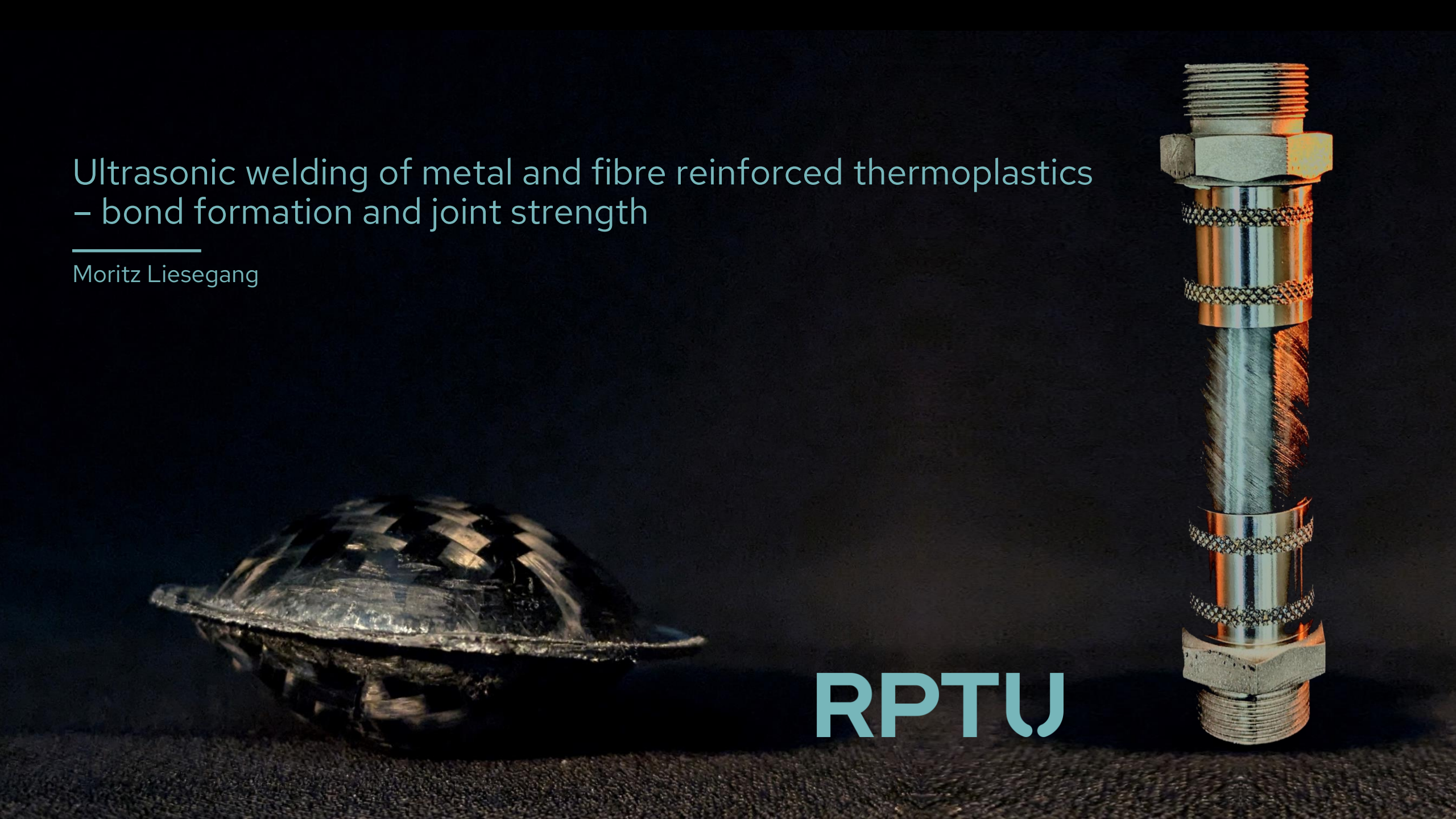

Ultrasonic welding of multi-material joints – Motivation

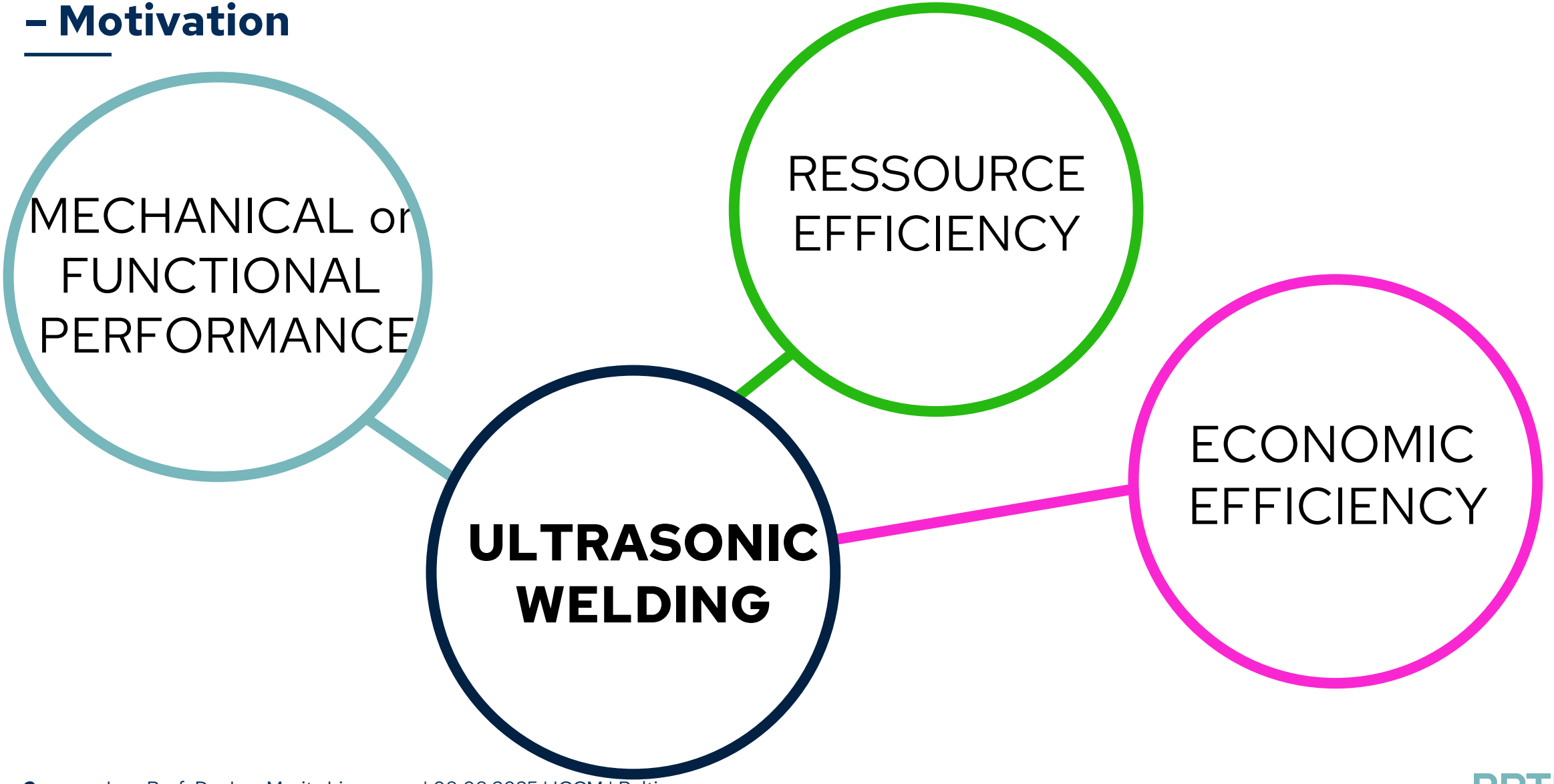

RPTU

Basics of ultrasonic welding – Types of ultrasonic welding

polymer ultrasonic welding

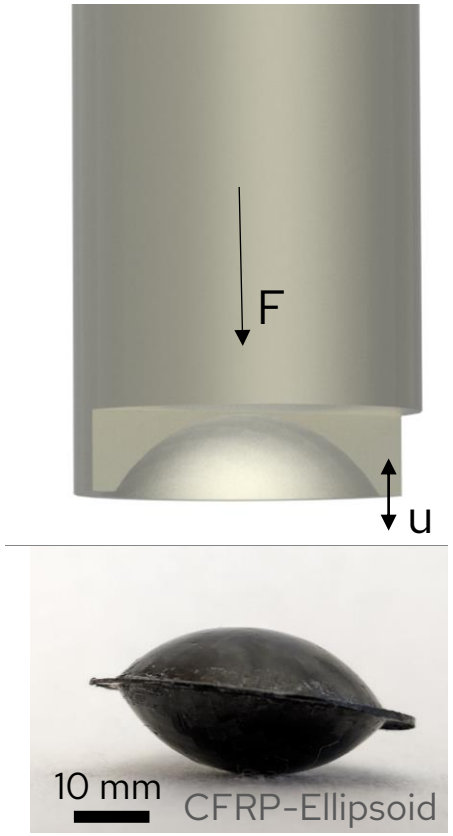

metal ultrasonic welding

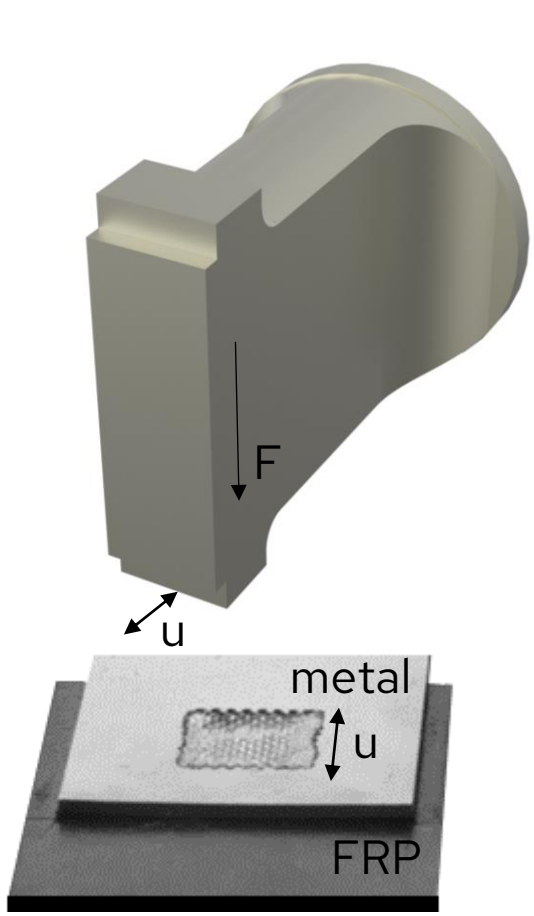

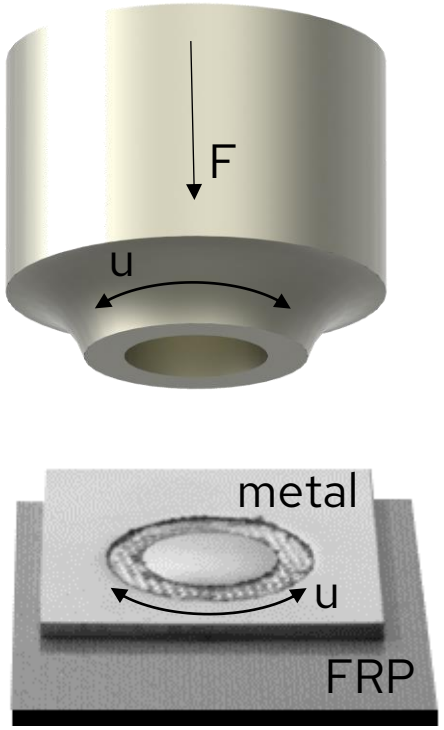

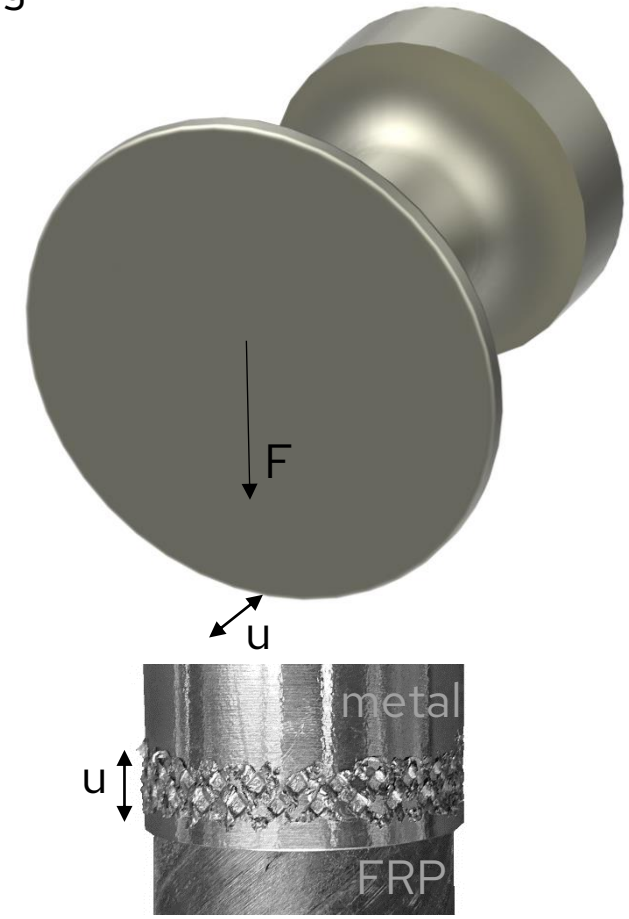

RPTU

Basics of ultrasonic welding – Oscillation system

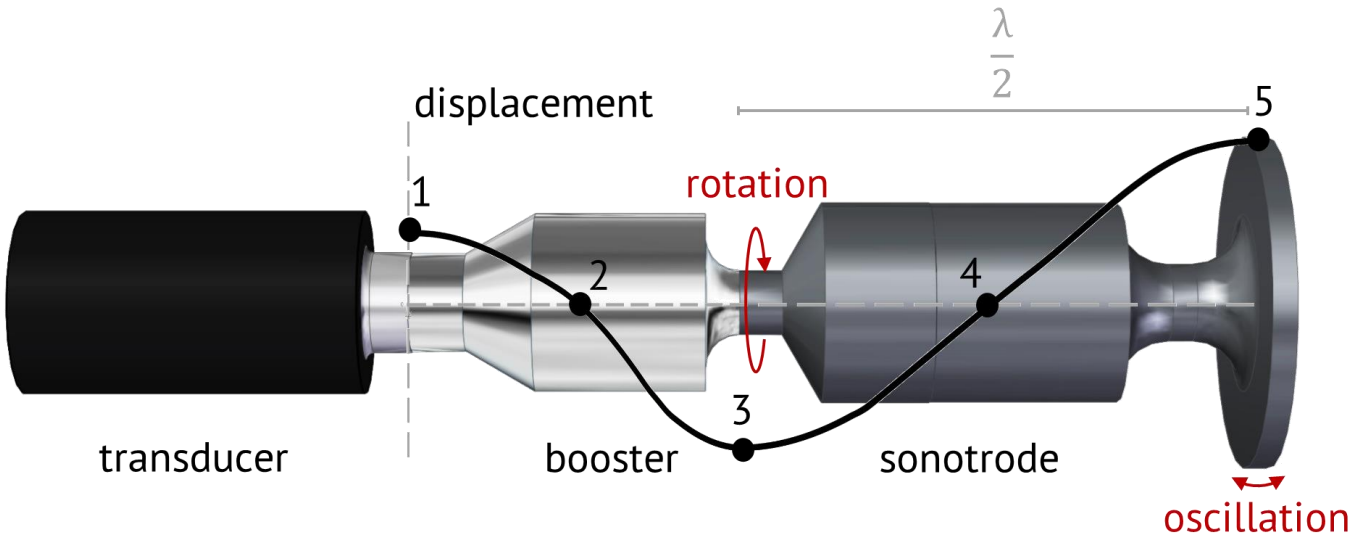

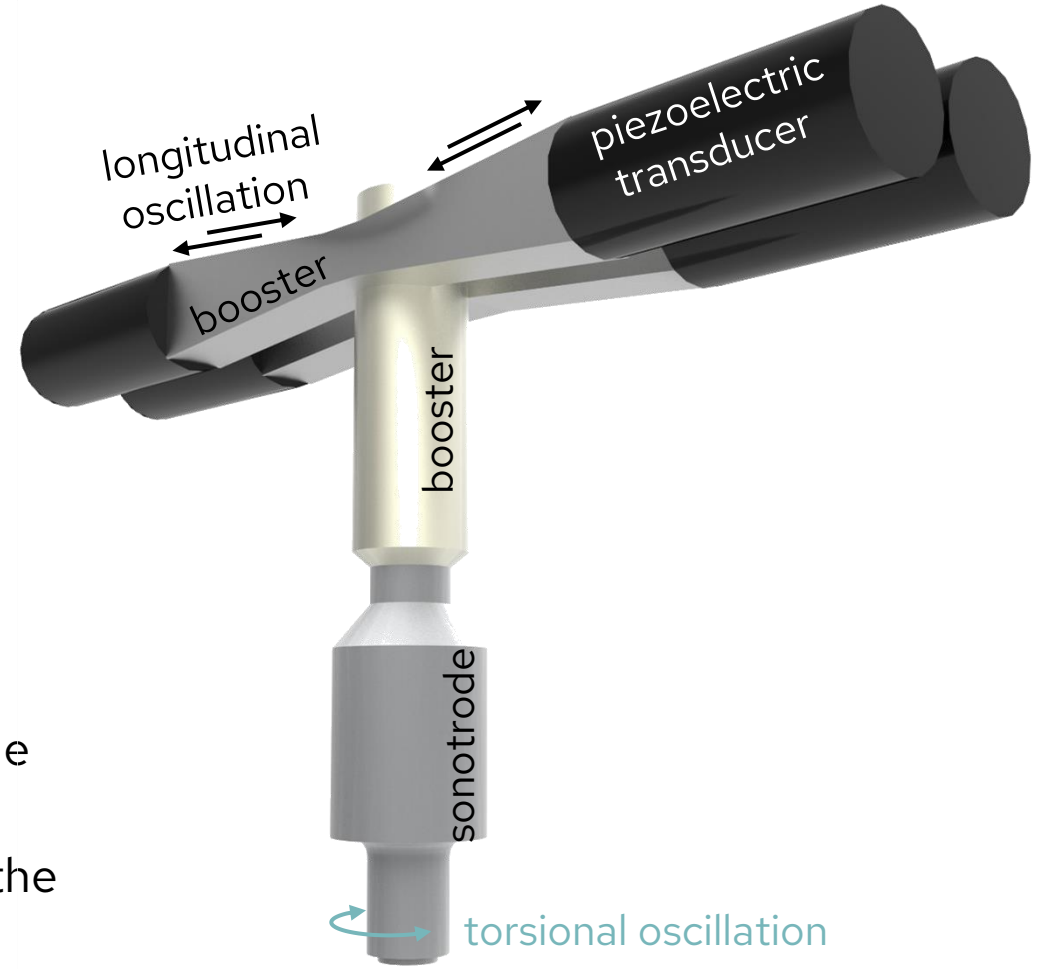

- Initiate an oscillation by inverse piezo electric effect close to the natural frequency of the system
- Acoustic translation of the boosters and the sonotrode affect the resulting amplitude at the sonotrode tip

Basics of ultrasonic welding – Industrial applications of ultrasonic welding

packaging materials

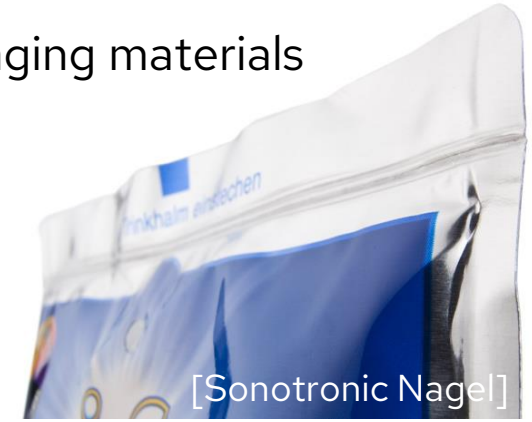

thermoplastic bodies

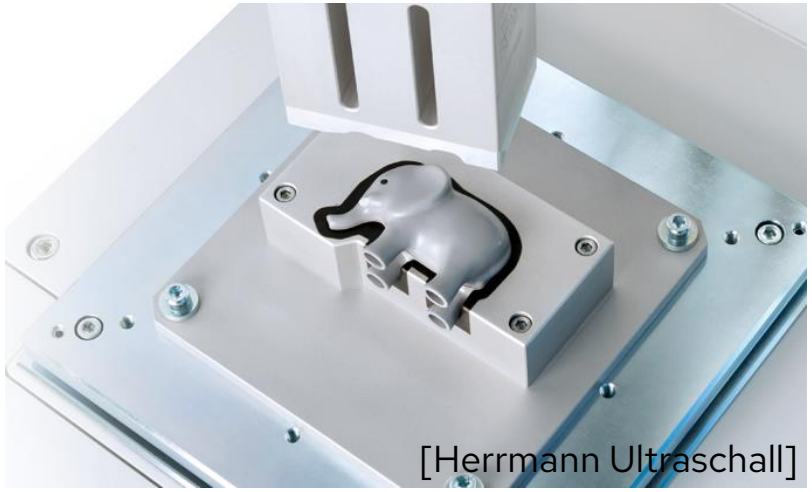

metallic foils



[Schunk Sonosystems]

electric conductors

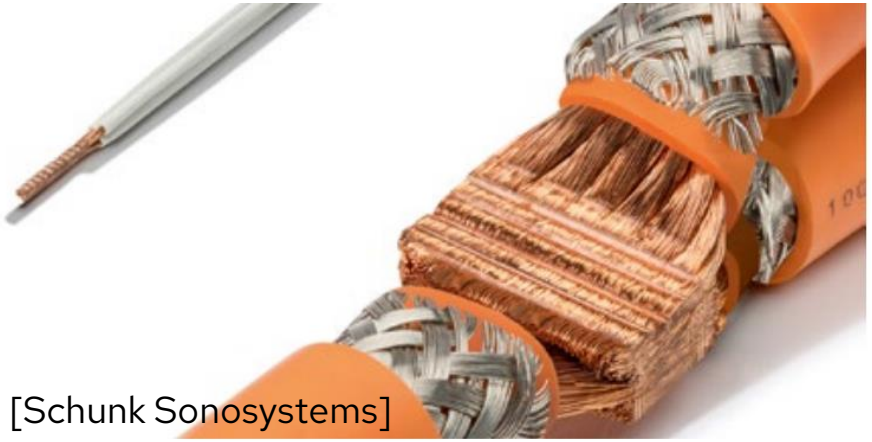

solar collectors

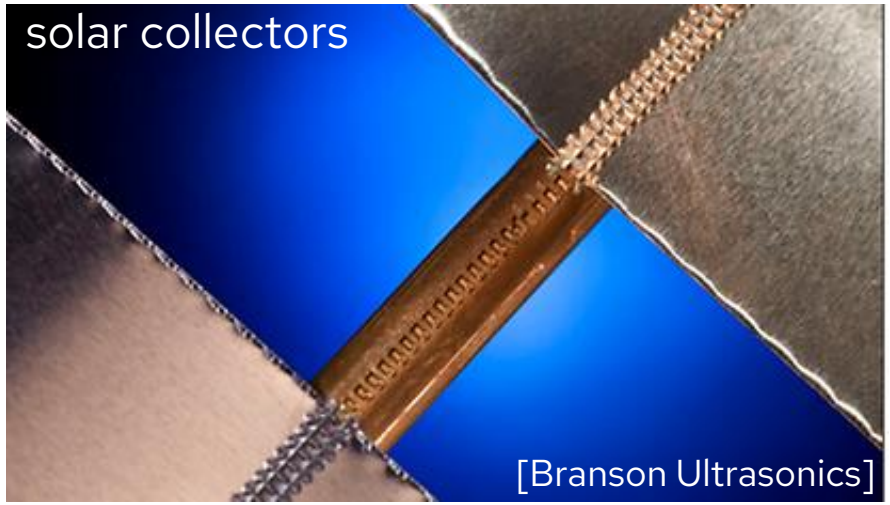

RPTU

Basics of ultrasonic POLYMER welding – Joint and interface formation

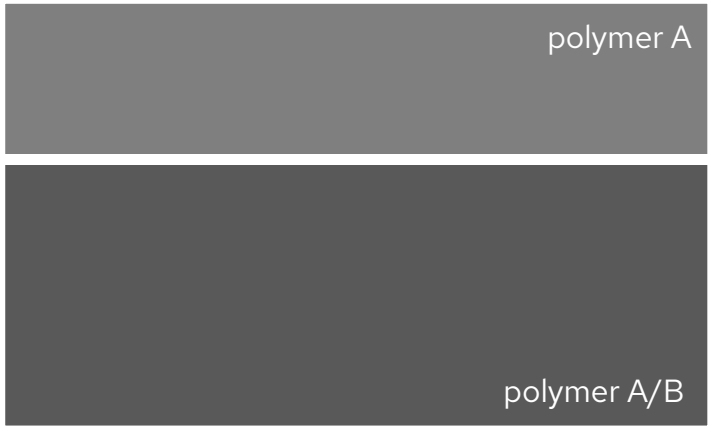

- single material or blend by melting and diffusion

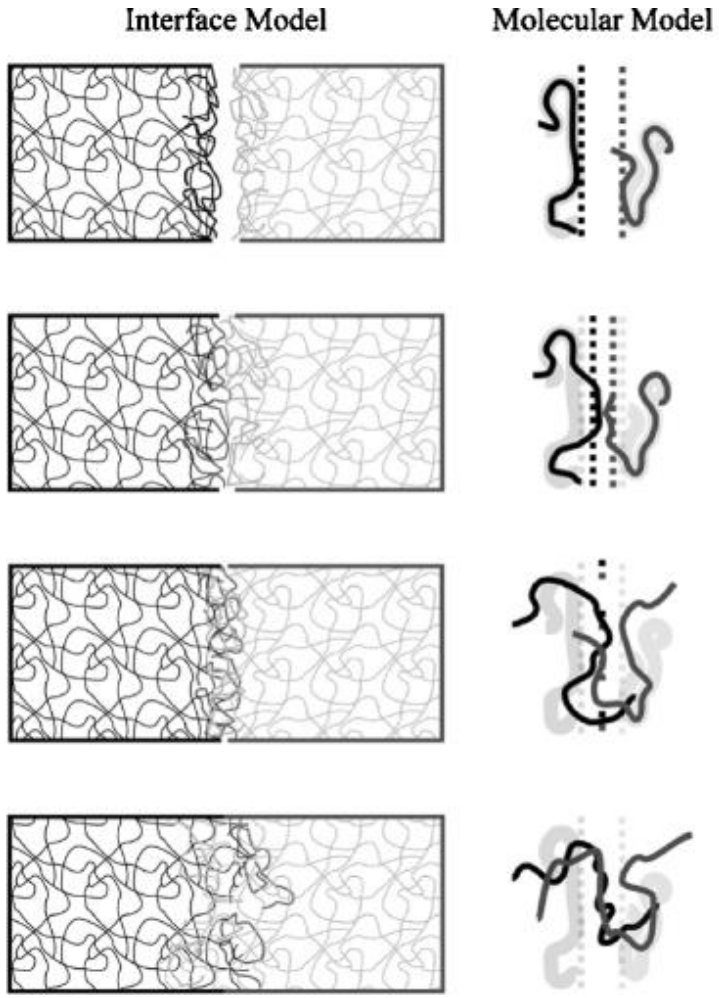

Zhang, H., Lamnawar, K. & Maazouz, A. Rheological modeling of the diffusion process and the interphase of symmetrical bilayers based on PVDF and PMMA with varying molecular weights. *Rheol Acta* **51**, 691–711 (2012). https://doi.org/10.1007/s00397-012-0629-7

Basics of ultrasonic METAL welding – Joint and interface formation

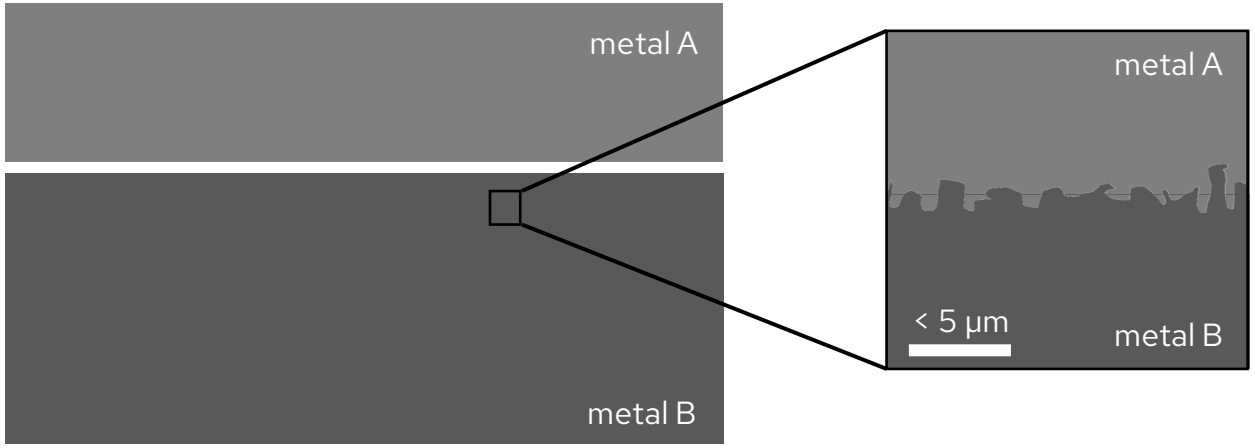

1. Shearing off topographie peaks
2. Breaking up oxide layers
3. Pure metal/metal contact
4. Interlocking by plastic deformation

- metallugical multi-metal joints by plastic deformation and diffusion

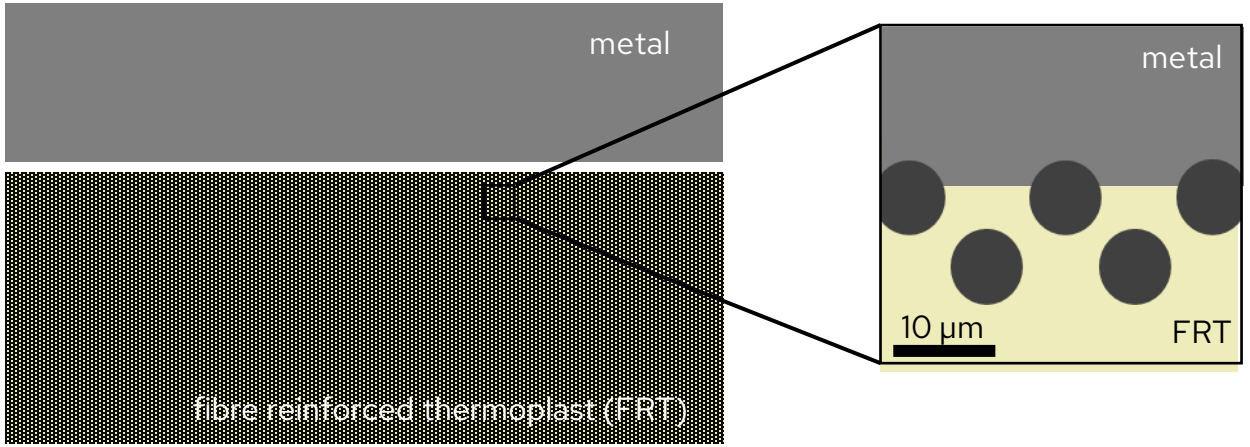

1. Fusing of thermoplastic matrix
2. Approximation of metal and fibres
3. Interlocking of metal and fibres

- adhesive bonding
- mechanical interlocking by plastic deformation
- and ?

RPTU

Multi-material Ti6Al4V/CF-PEEK-joints – Orbital ultrasonic welding

AIRBUS Parker CTC we are composites an AIRBUS company

HUTCHINSON PFW Aerospace GmbH HYDAC

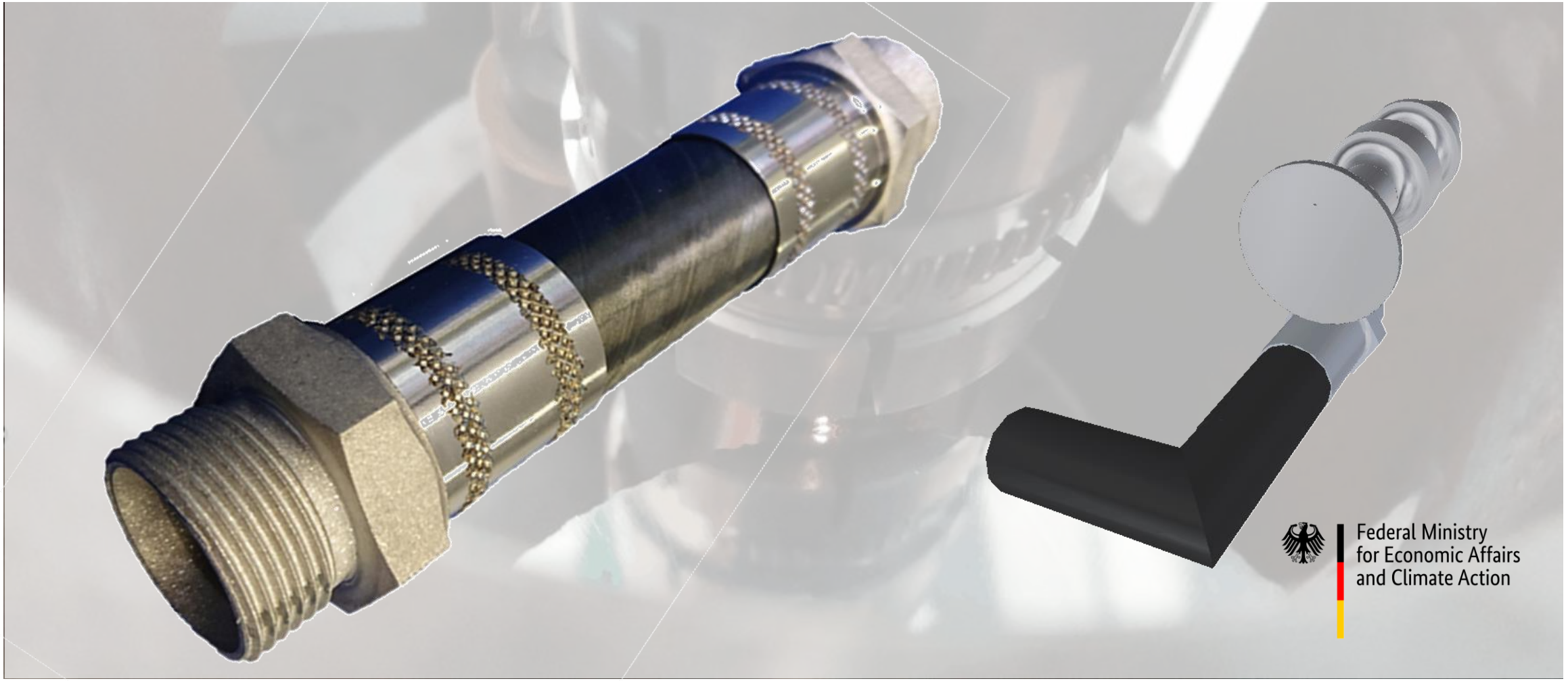

Multi-material Ti6Al4V/CF-PEEK-joints – Interface formation and strength

- No fibre-metal-contact
- Insufficient amount of welding energy to form high strength joint

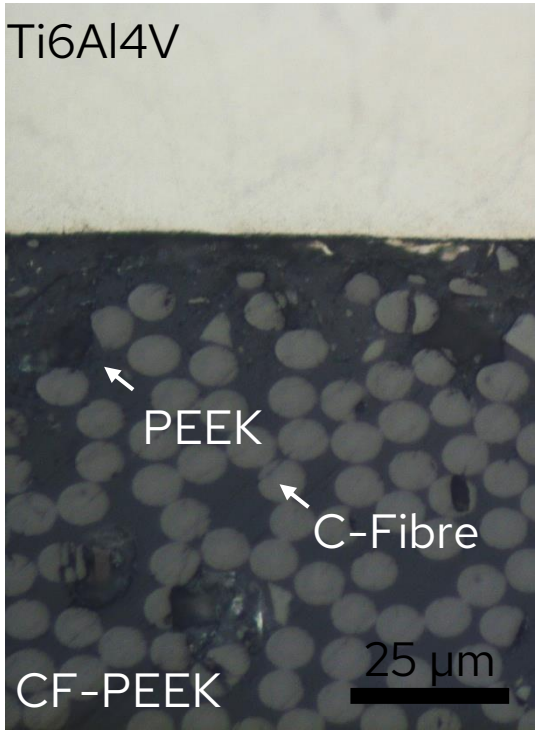

- Fibre-metal-contact
- No cavities

➡ Suitable process parameters

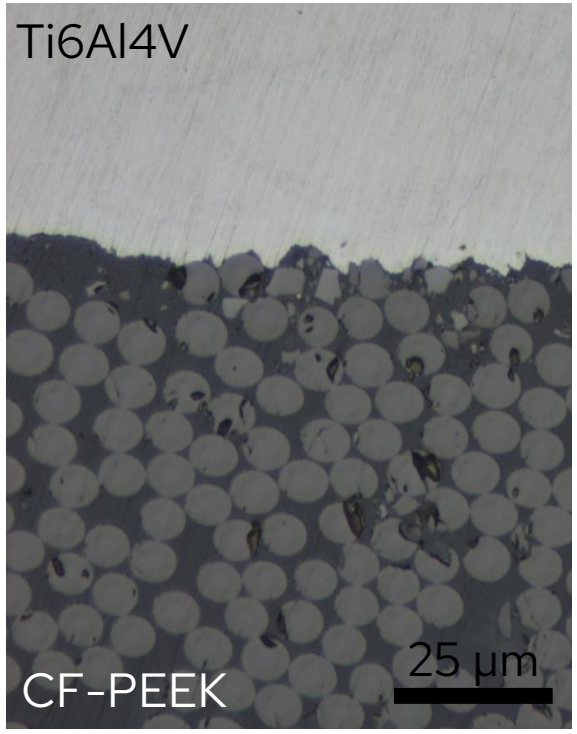

- Large cavities
- PEEK decomposition

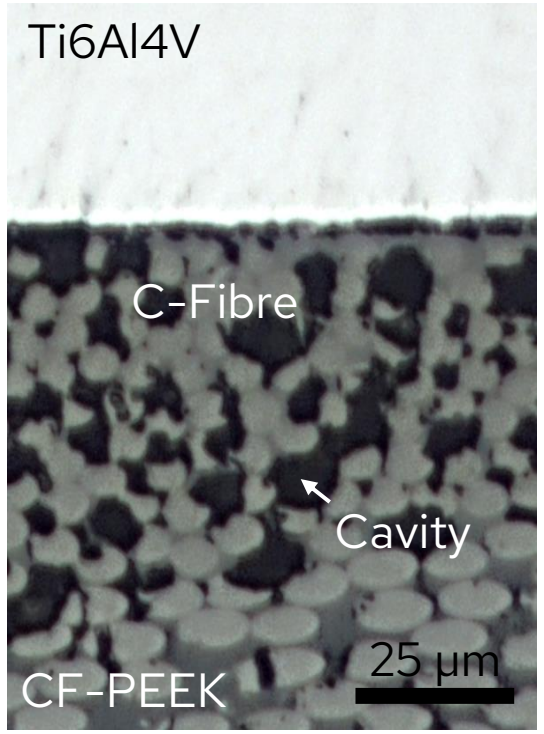



AIRBUS

Parker

CTC we are composites an AIRBUS company

HUTCHINSON PFW Aerospace GmbH

HYDAC

Federal Ministry for Economic Affairs and Climate Action

https://doi.org/10.3390/jmmp5020030 https://doi.org/10.26204/KLUEDO/6290

RPTU

FE modelling of Multi-material-joints – Overview

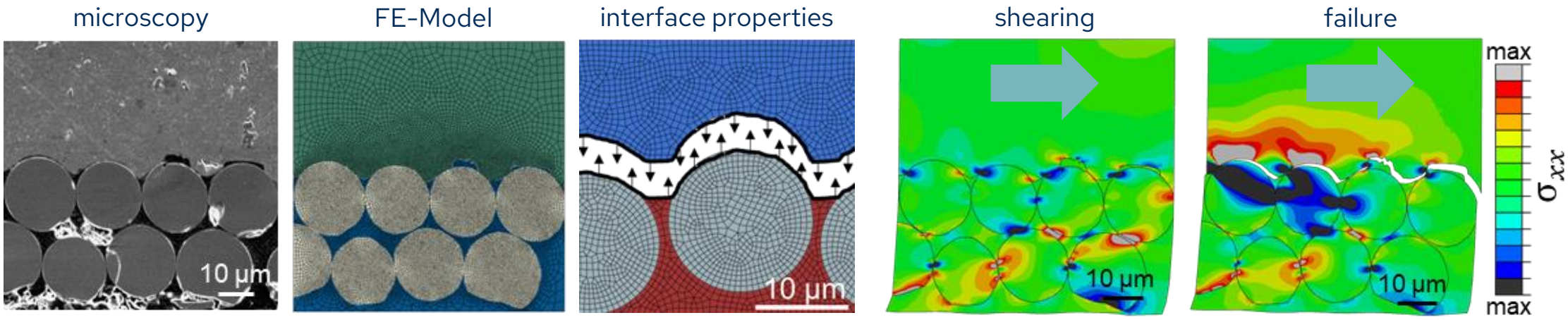

- **Interface characterisation and categorisation**
- **FE-Simulations of real 2D structures**
- **FE-Simulations of 3D models**

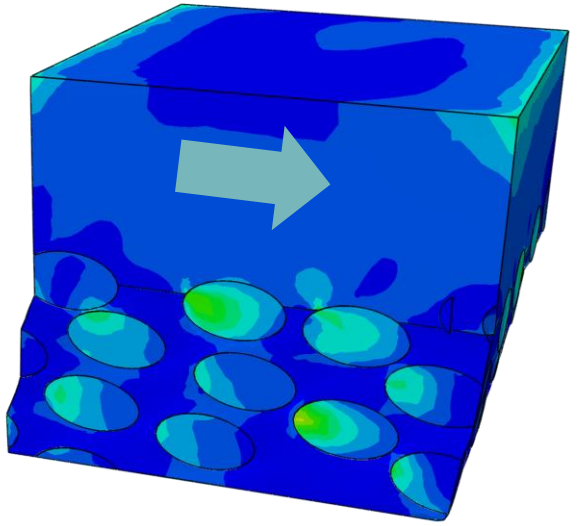


Sophie Arweiler

Arweiler-Böllert, S., Liesegang, M., Beck, T. *et al.* Relation Between Interface Geometry and Tensile Shear Strength of Ultrasonically Welded Joints. *J. of Materi Eng and Perform* **32**, 10469–10485 (2023). https://doi.org/10.1007/s11665-023-08325-2

RPTU

FE modelling of Multi-material-joints – Categorisation of interface structures

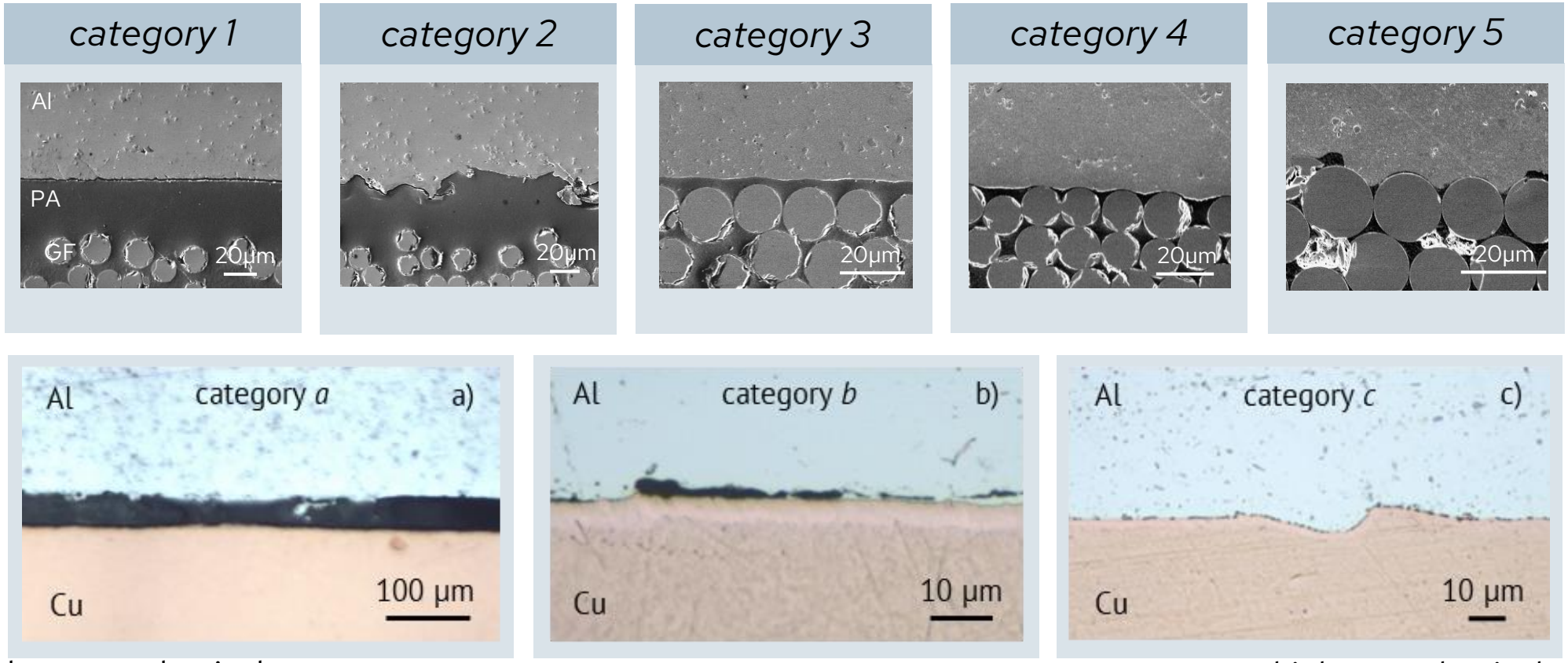

lower mechanical strength

higher mechanical strength

RPTU

FE modelling of Multi-material-joints – External Loading and Boundary Conditions

Calculation of the displacement in the microsection using the results from the tensile shear tests

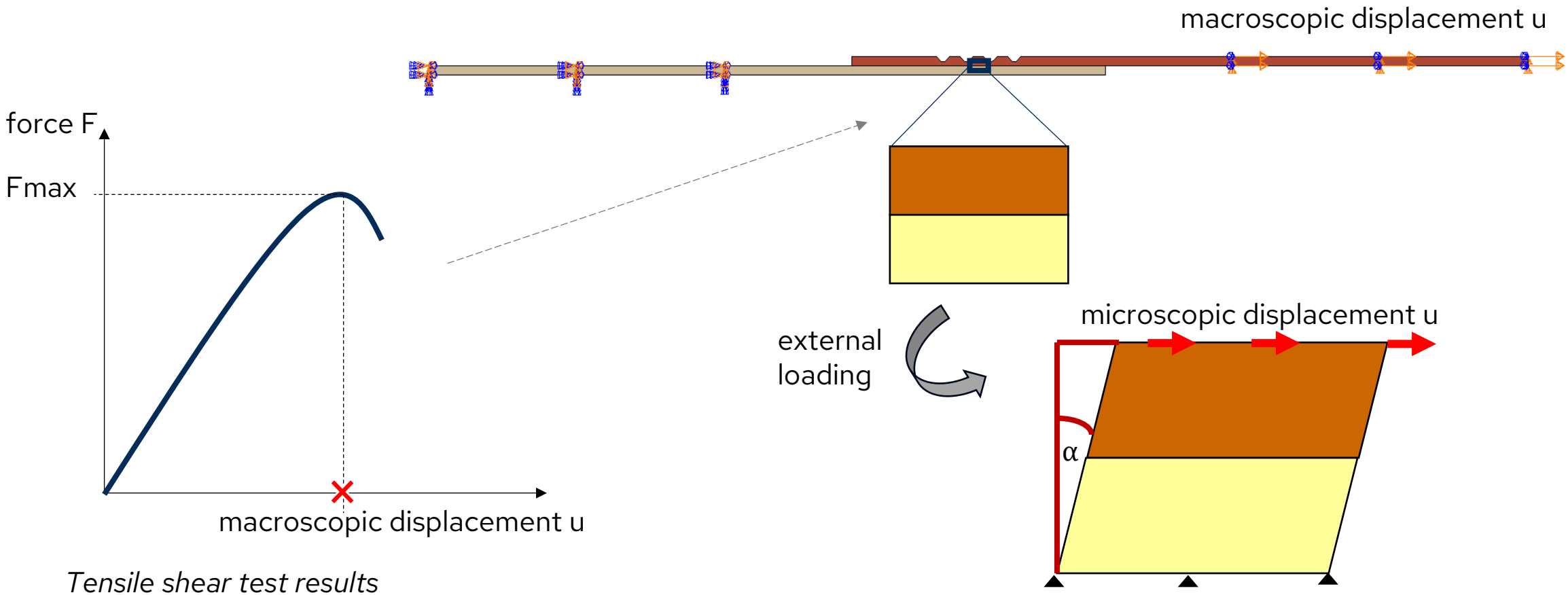

Tensile shear test results

RPTU

FE modelling of Multi-material-joints – Contact Model and Contact Conditions

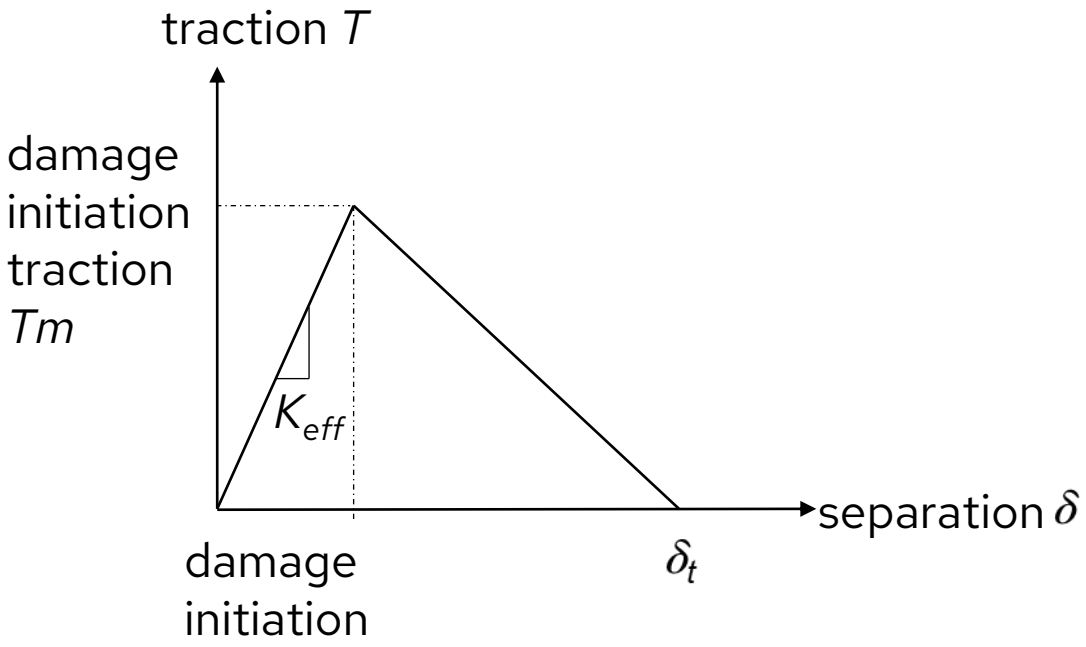

bilinear traction-separation law

- K_{eff} – contact stiffness
- Tm – maximum traction; start of contact damage
- δ_t – total separation between 2 nodes

Variation of the contact conditions by varying Tm:

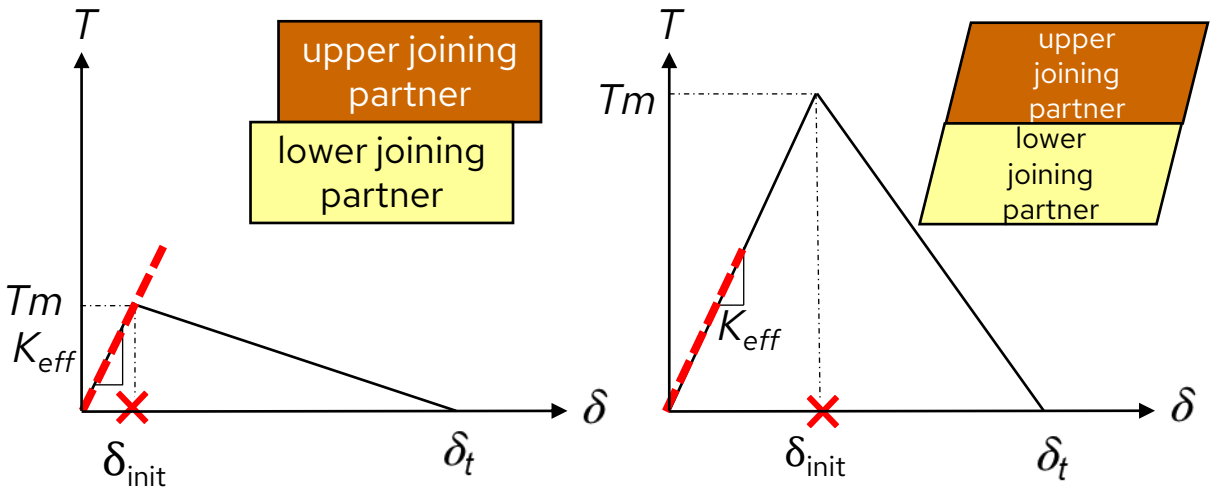

RPTU

FE modelling of Multi-material-joints – Correlation between joint strength and interface geometry

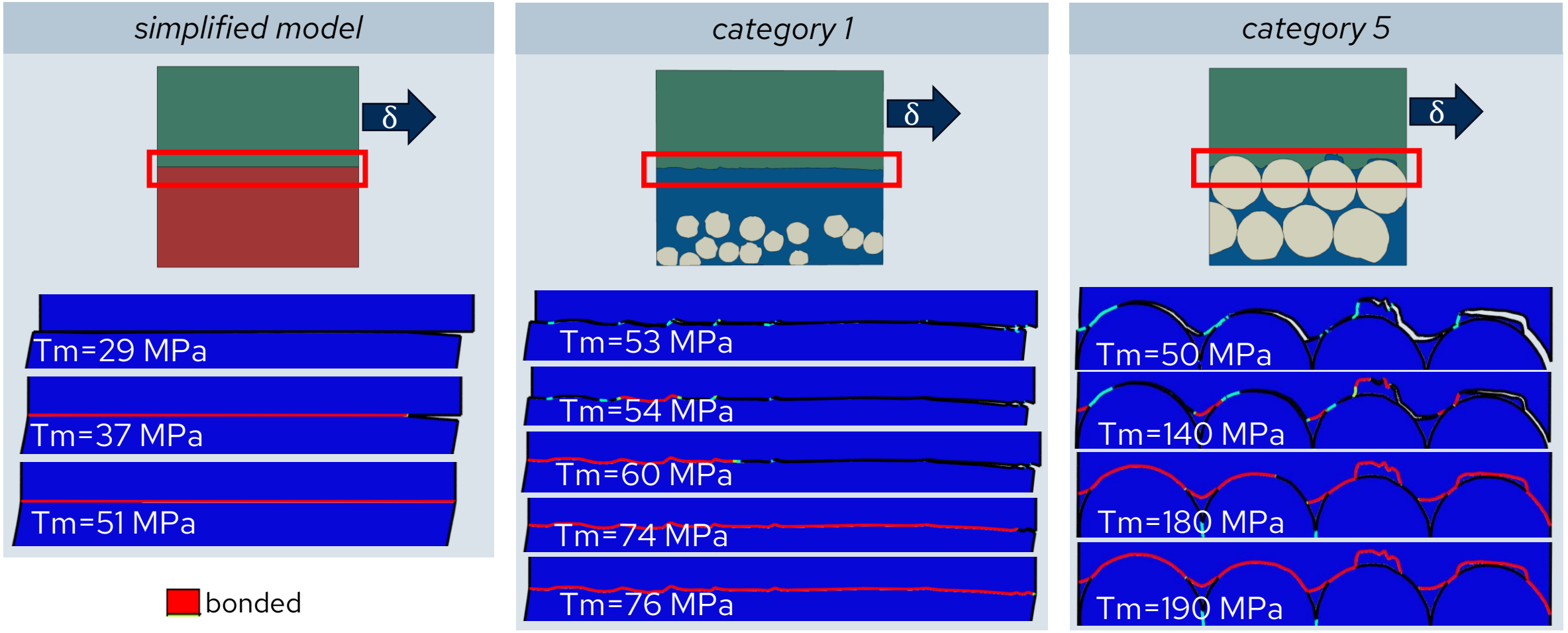

RPTU

FE modelling of Multi-material-joints – Outlook

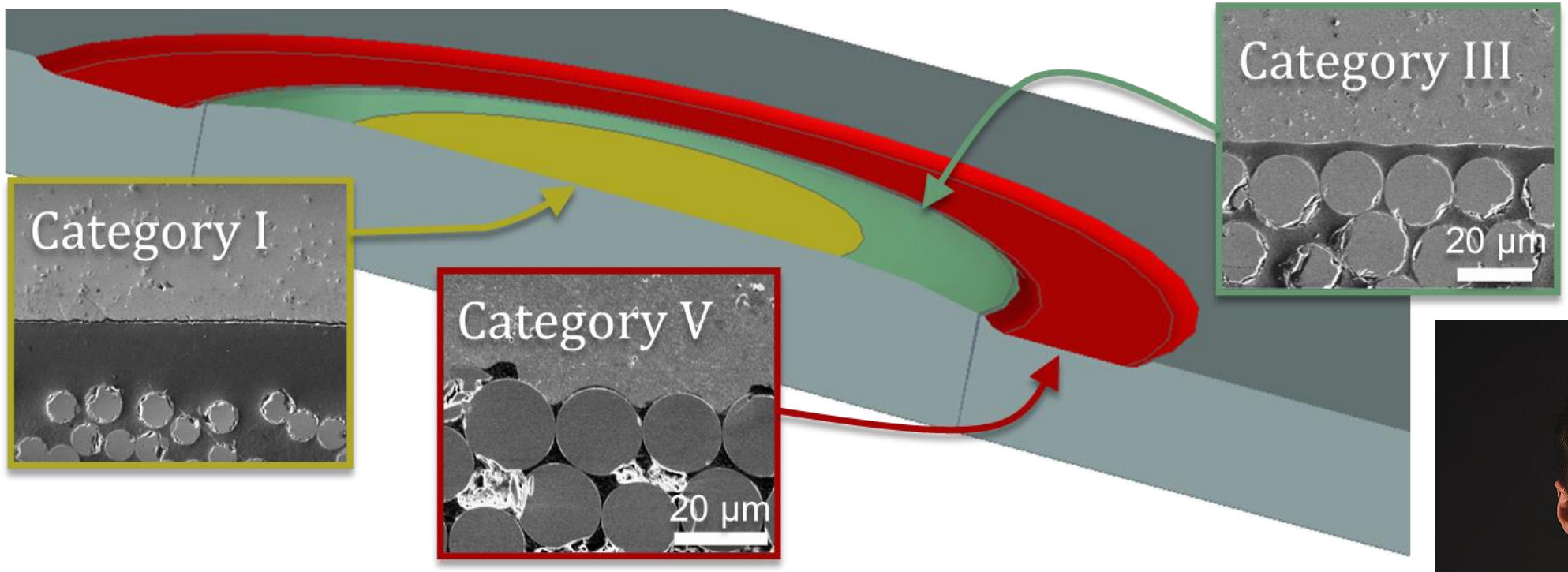

- **in-situ µ-CT-scans during loading**
- **FE-Simulations of real 3D structures**

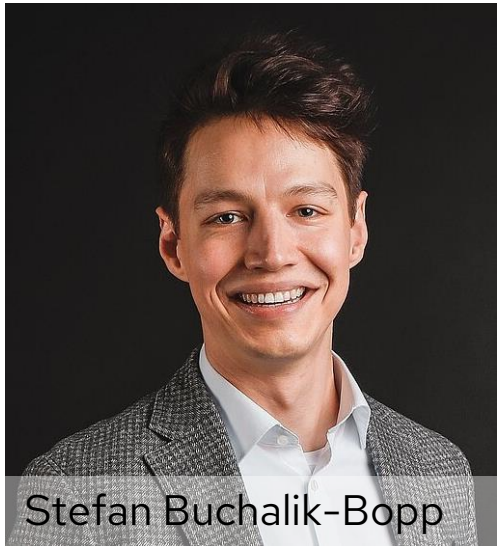

DFG Deutsche Forschungsgemeinschaft

Thank you!

Jun.-Prof. Dr.-Ing **Moritz Liesegang**

Power Ultrasonics

Institute of Materials Science and Engineering (WKK)

RPTU Kaiserslautern-Landau, Germany

m.liesegang@mv.rptu.de

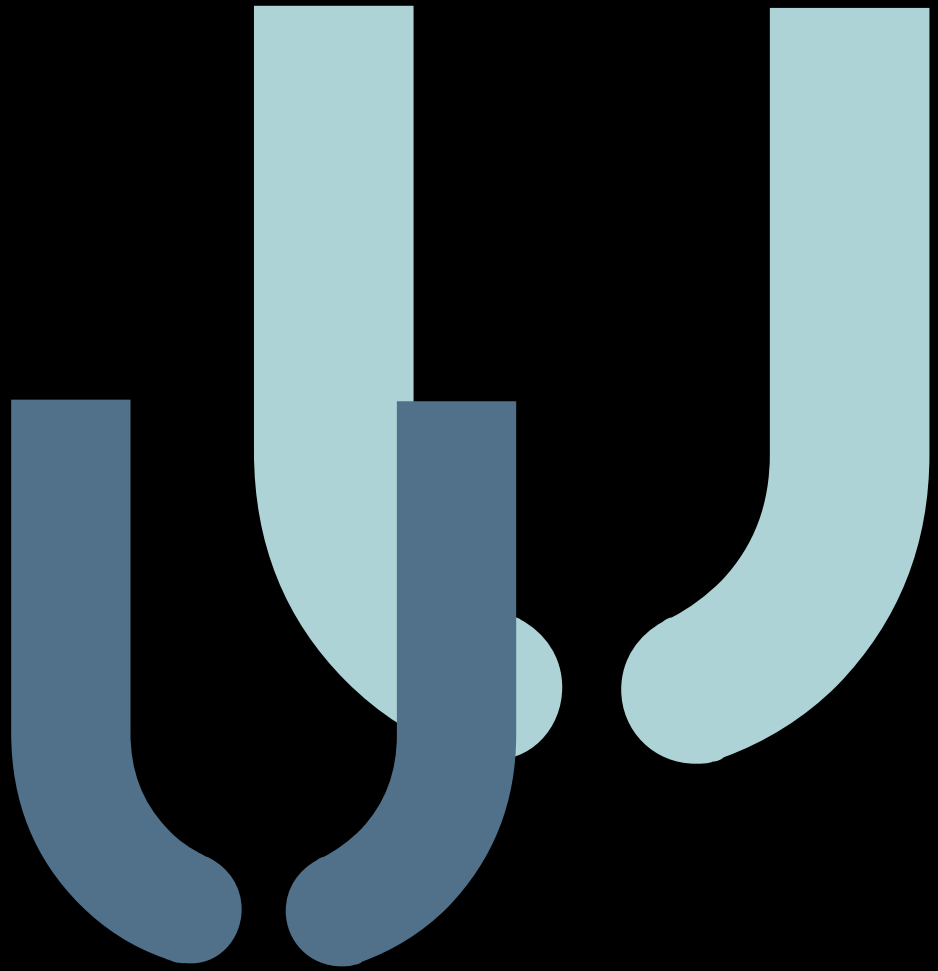

RPTU

ICCM24
AUGUST 4-8, 2025
BALTIMORE CONVENTION CENTER
BALTIMORE, MARYLAND, USA

No Technical Paper Submission for:

Casey Barrett

ICCM24
AUGUST 4-8, 2025
BALTIMORE CONVENTION CENTER
BALTIMORE, MARYLAND, USA

No Technical Paper Submission for:

Koki Tsuda

Multiscale modeling for bottom-up prediction of failure parameters of unidirectional carbon fiber reinforced composite lamina: from atoms to lamina-scale

Yoshiaki Kawagoe, Tadashi Watanabe, Yamato Hoshikawa, Kazuki Ryuzono, Keiichi Shirasu, and Tomonaga Okabe

The University of Tokyo, Tohoku University, Japan

Introduction: CFRP


*1


*2

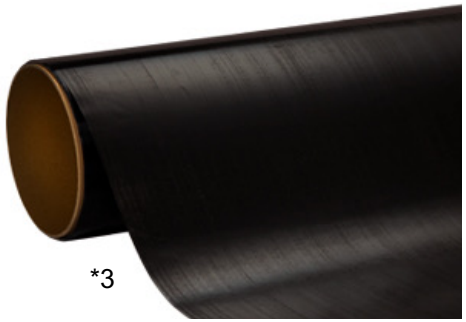
*3


*4

Carbon fiber + Resin **Composite** **Structure**


*2

Compared to metallic materials:

- ✓ Superior specific strength and stiffness
- ✓ Significant weight reduction benefits

→ **Increasing adoption in the aerospace field**

*1 https://www.torayca.com/lineup/product/pro_001.html
*3 https://www.torayca.com/lineup/product/pro_003.html

*2 https://stock.adobe.com/jp/
*4 https://commons.wikimedia.org/wiki/File:787fuselage.jpg

Introduction: Selection of matrix



*2

Conventional matrix resin: epoxy resin

エポキシ主剤

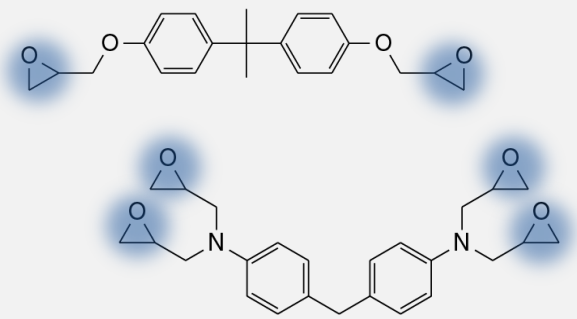

硬化剤

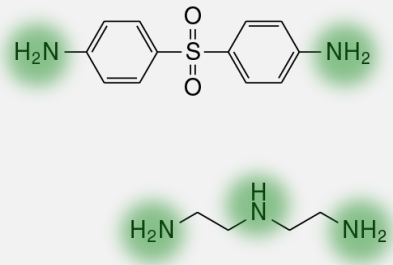

Epoxy / curing agent reaction → 3D crosslinking

Functionality tailored by resin/curing agent selection

Environmental resistance / Flame retardancy / Moldability…

Matrix selection: A key design factor for CFRP

*2 https://stock.adobe.com/jp/

Introduction: Hierarchical structure of CFRP

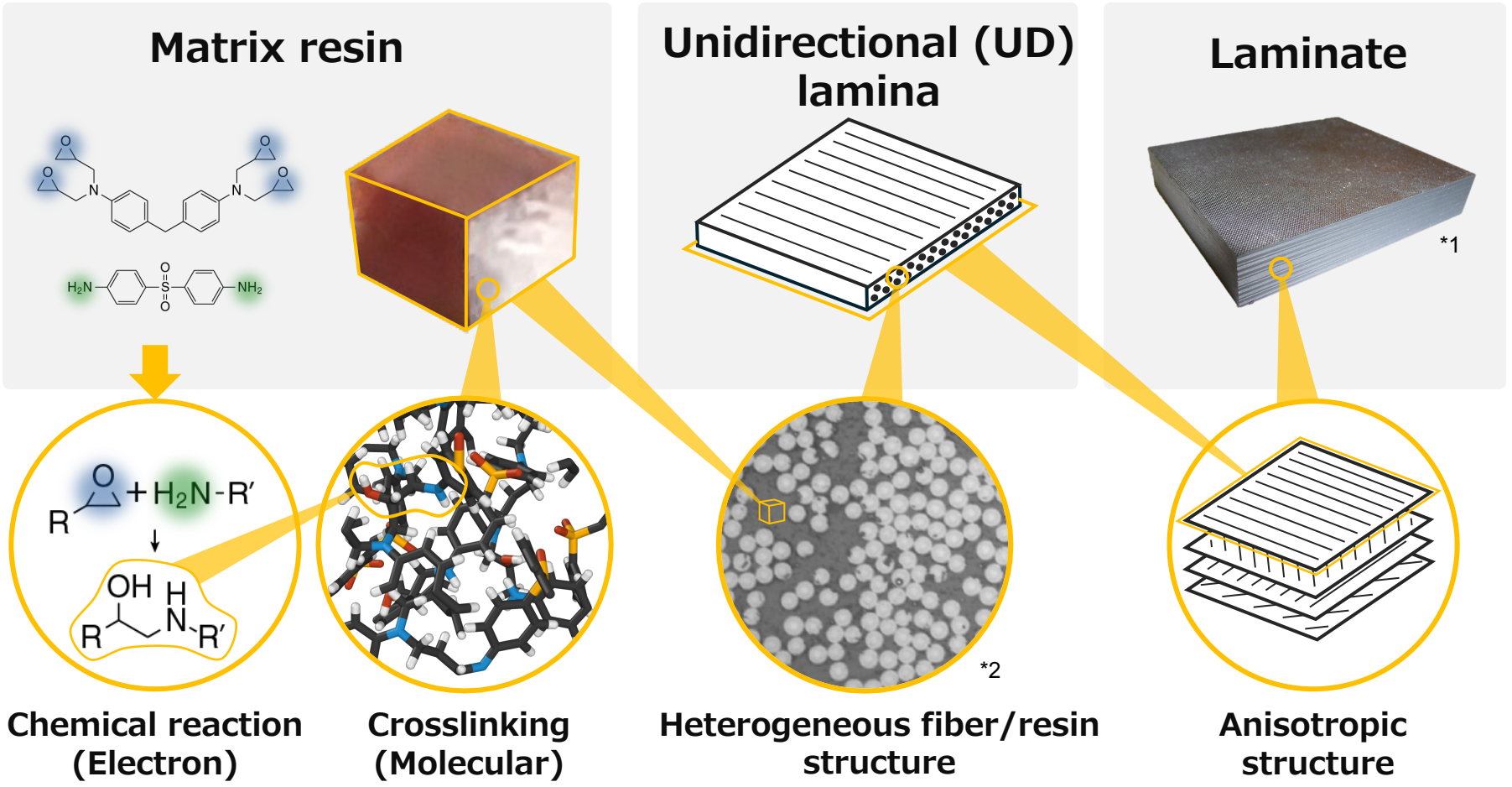

Interactions across scales result in complex and coupled failure mechanisms

*1 https://commons.wikimedia.org/wiki/File:Composite_laminate_specimen.JPG, Simon.white.1000

*2 M. Herráez et al., *Composites Part A*, 2020, 129, 105691

Introduction: Hierarchical structure of CFRP

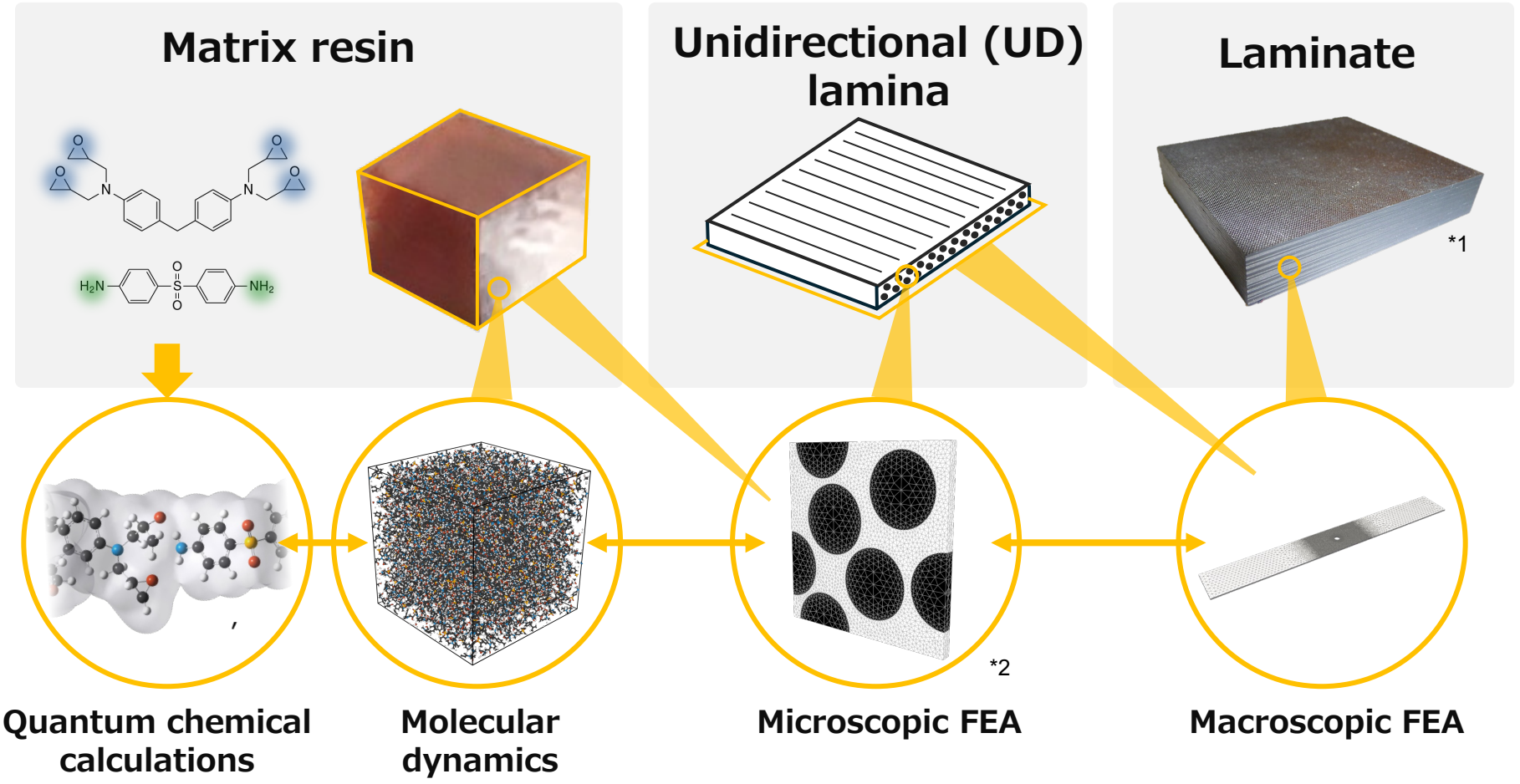

Objective:

CFRP strength parameters are estimated in a bottom-up manner through multiscale modeling, combining models specialized for each scale

Introduction: Hierarchical structure of CFRP

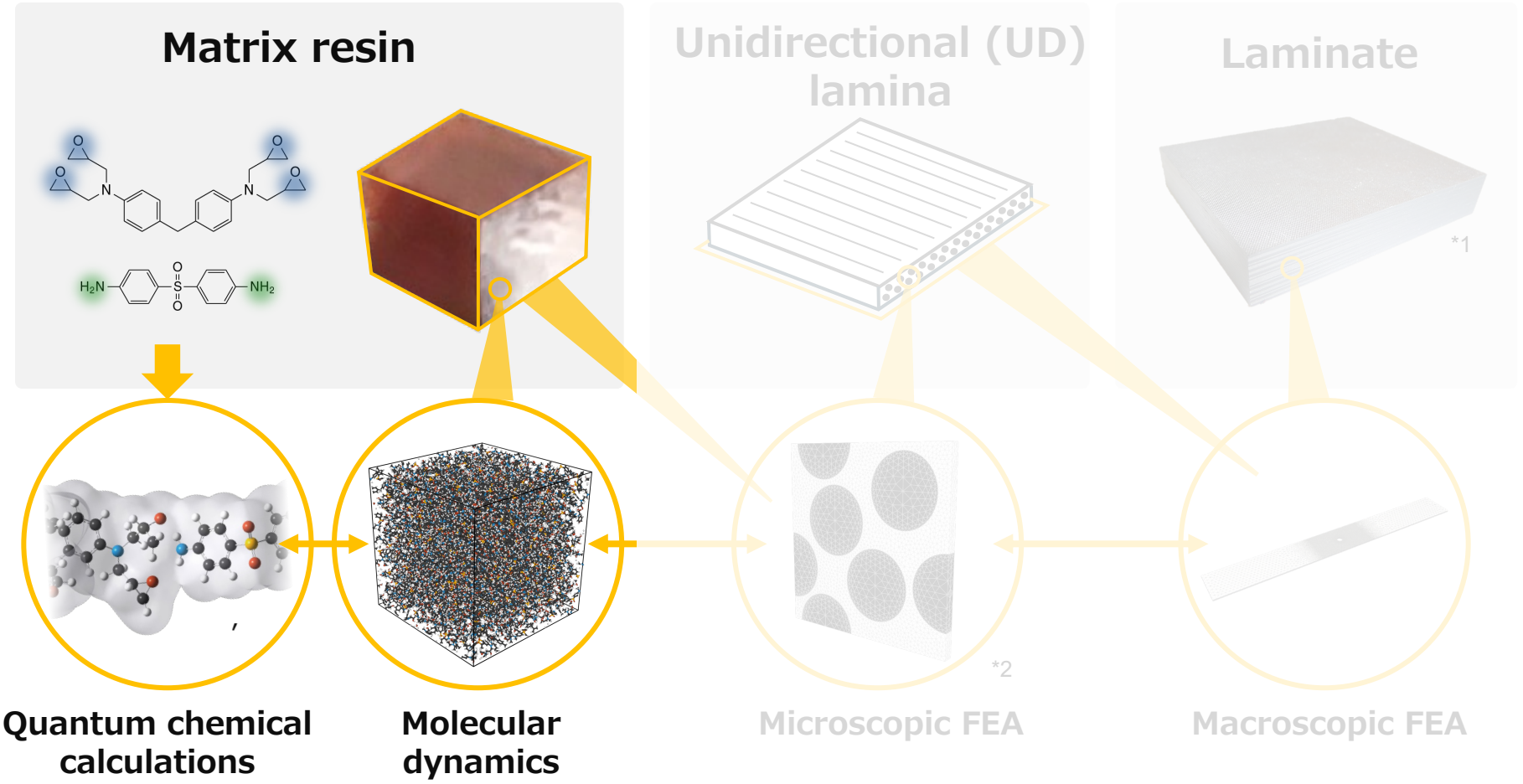

Objective:

CFRP strength parameters are estimated in a bottom-up manner through multiscale modeling, combining models specialized for each scale

Target base resin / curing agent

Base resin

Curing agent

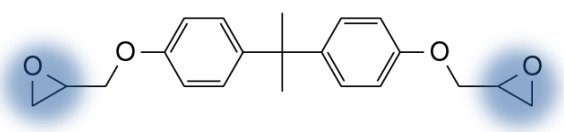

DGEBA

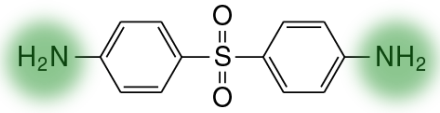

4,4′-DDS

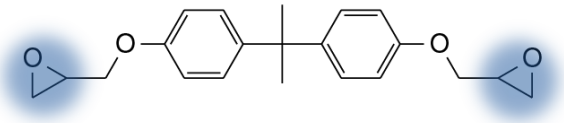

DGEBA

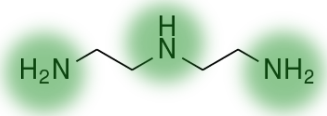

DETA

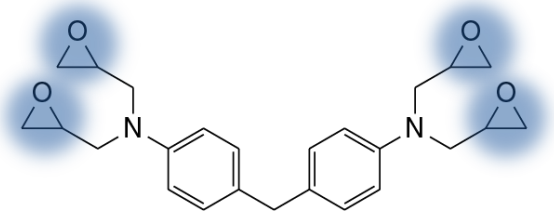

TGDDM

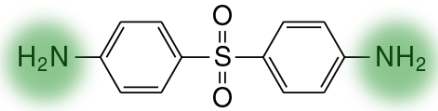

4,4′-DDS

Three typical epoxy systems for aerospace applications are selected as case studies

Quantum chemical calculations

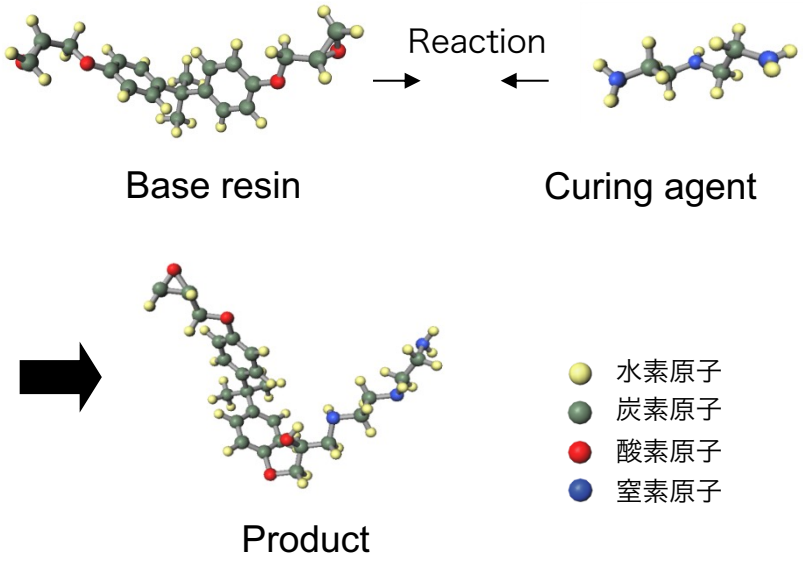

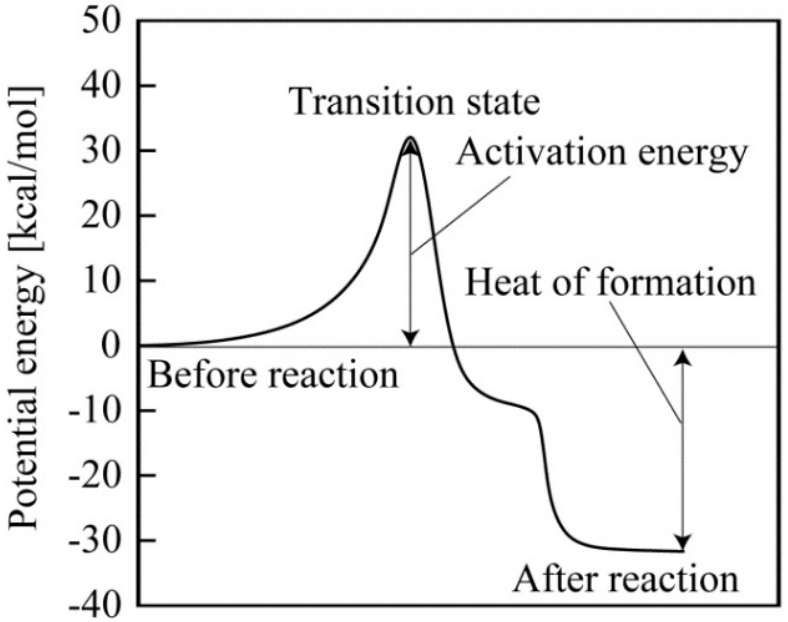

Energy profile of the crosslinking reaction

Reaction characteristics are specific to each material combination

→ Reaction pathways elucidated using the quantum chemical tool GRRM

Table 1
Activation energies, E_a, and heat of formation, H_f, obtained in GRRM.

Reaction type	E_a [kcal/mol]	H_f [kcal/mol]
DGEBA/4,4′-DDS		
Epoxy/primary amine	50.01	25.04
Epoxy/secondary amine	41.10	20.33
DGEBA/DETA		
Epoxy/primary amine	46.56	26.60
Epoxy/secondary amine (corner)	43.23	23.46
Epoxy/secondary amine (center)	46.68	22.15
TGDDM/4,4′-DDS		
Epoxy/primary amine	42.18	25.65
Epoxy/secondary amine (corner)	41.80	22.01

Y. Kawagoe, et al. Mechanics of Materials 170 (2022) 104332

Molecular dynamics (MD): Curing simulation

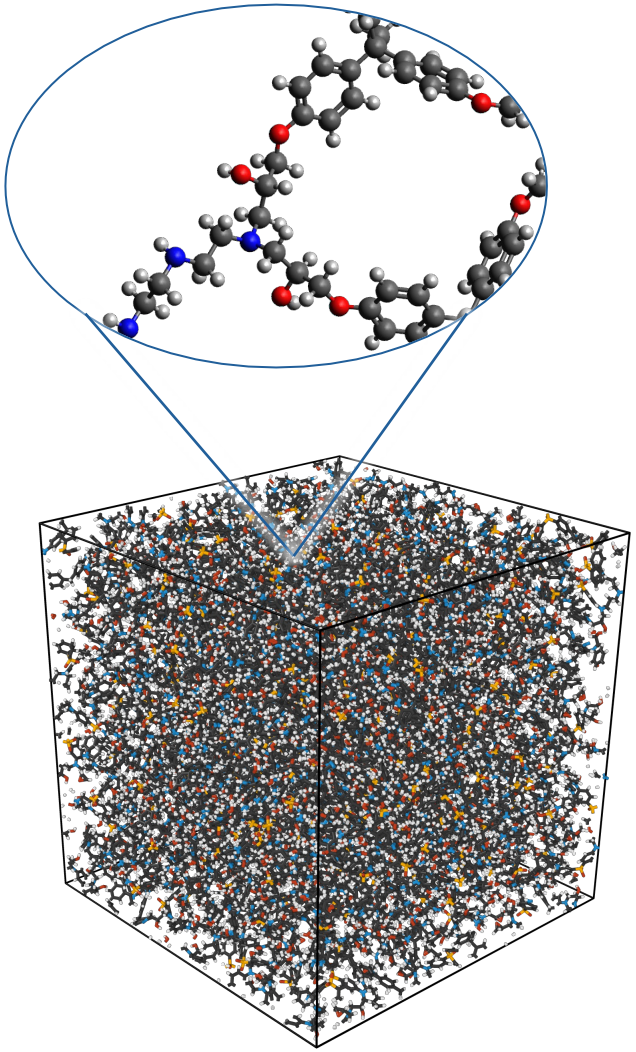

Arrhenius-type reaction model

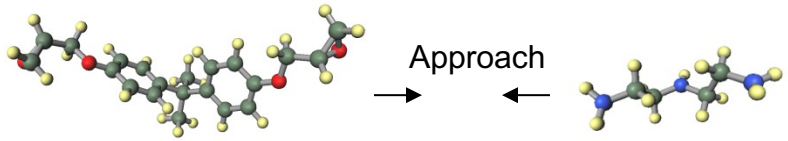

Base resin (DGEBA)

Curing agent (DETA)

Reaction probability

$$p = A \exp\left(-\frac{E_a}{RT}\right)$$

Heat of formation

$$E_{\mathrm{Kin,after}} = E_{\mathrm{Kin,before}} + H_f$$

Curing simulated via MD with explicit molecular structures

→ Resin model constructed

T. Okabe, et al. Polymer 54 (2013) 4660e4668

MD : Numerical mechanical testing

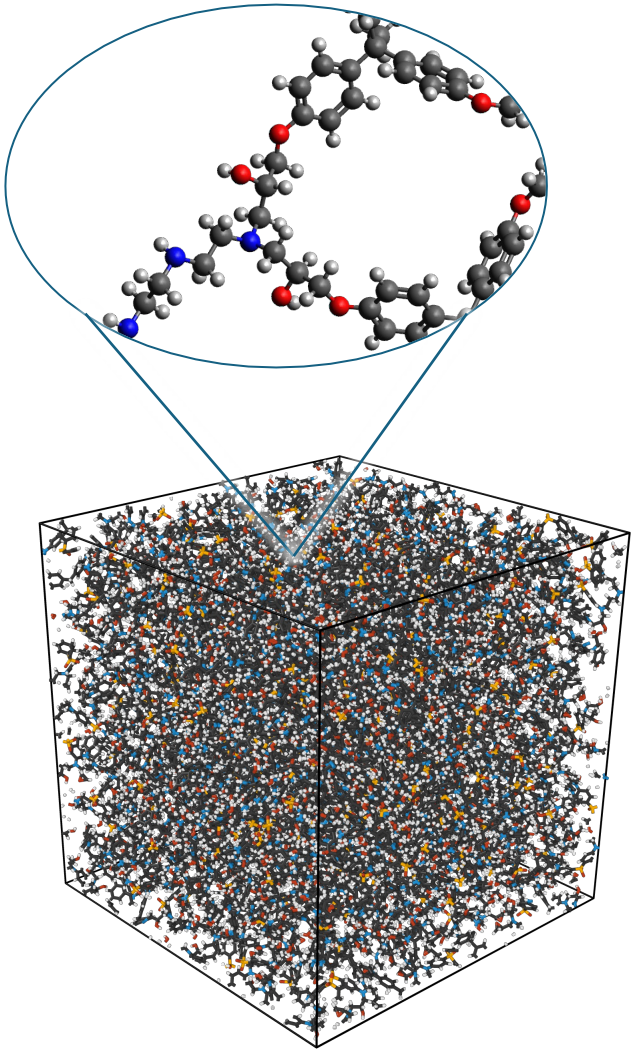

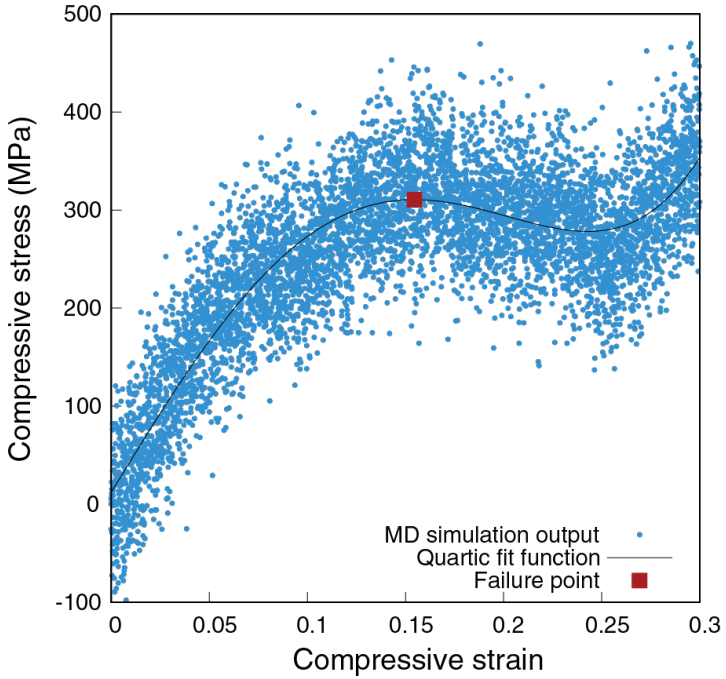

Mechanical behavior of the resin model evaluated numerically

→ Obtained properties: **strength**, stiffness, **nonlinear response**, and CTE

Y. Kawagoe, et al. Mechanics of Materials 170 (2022) 104332
T. Watanabe, et al. International Journal of Solids and Structures 283 (2023) 112489

MD : Resin strength estimation

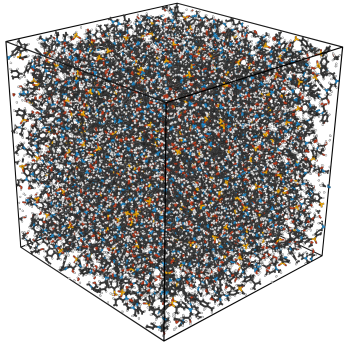

Limitations of mechanical testing via MD

Simulation times (~ns) → Extremely high strain rates

→ **Strength tends to be significantly overestimated**

Strain-rate adjustment using Argon's theory of molecular chain buckling (Sundararaghavan and Kumar, *Int. J. Plasticity*, 2013)

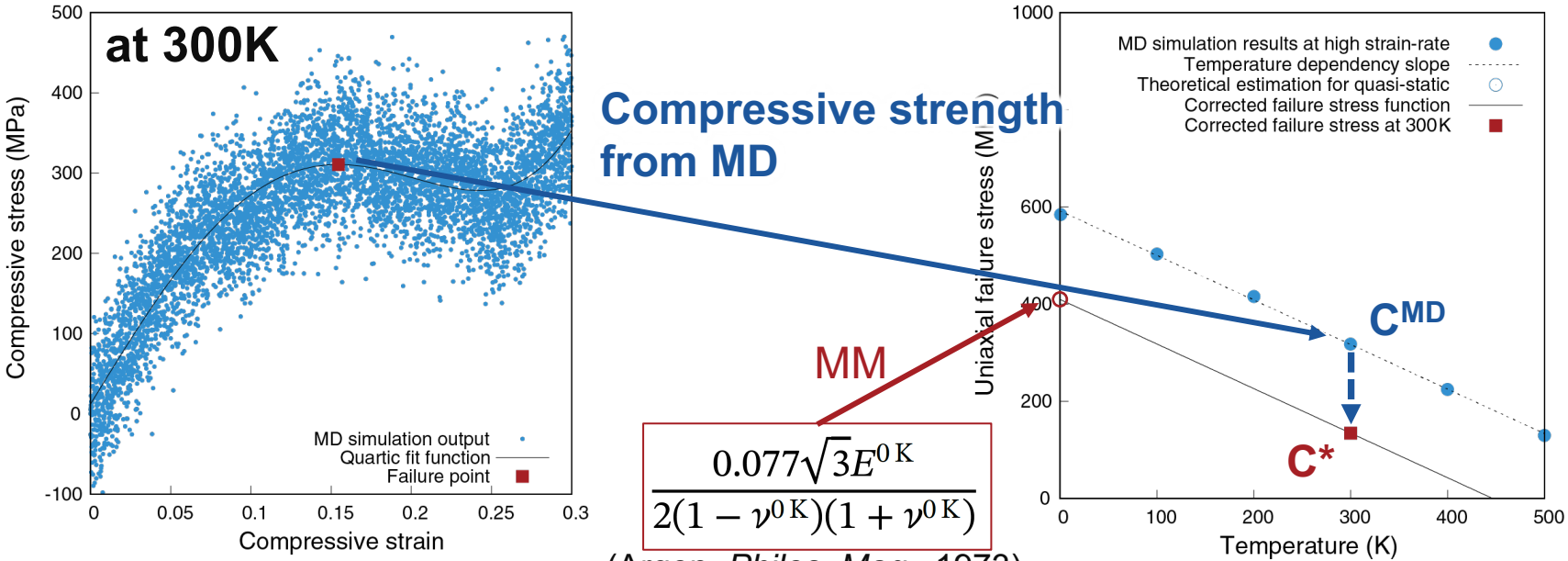

MD : Resin strength estimation

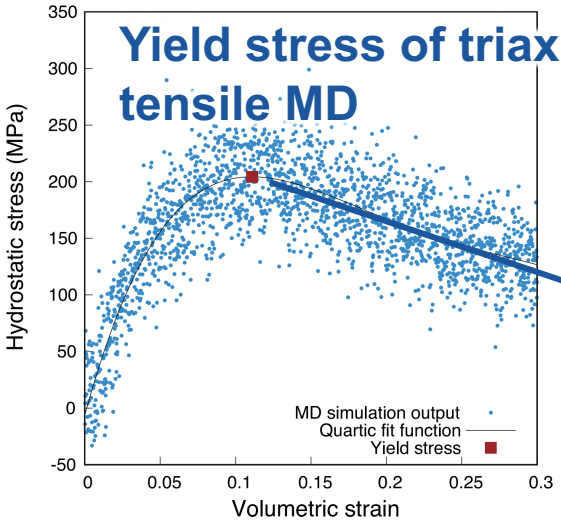

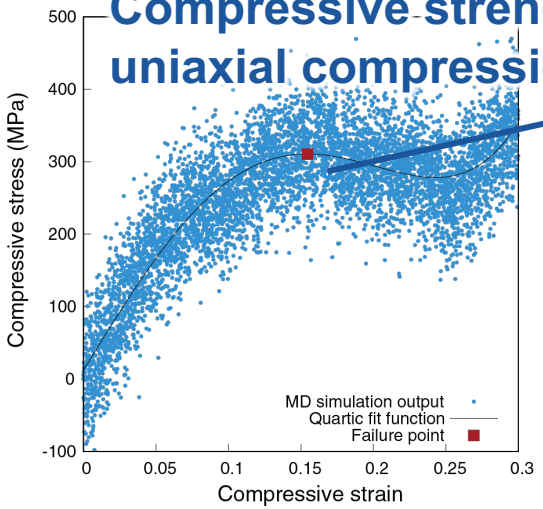

Christensen's failure criteria:

$$3\left(1-\frac{T}{C}\right)\frac{\sigma_{\mathrm{m}}}{C}+\left(\frac{\bar{\sigma}}{C}\right)^{2}\leq\frac{T}{C}$$

(Christensen, *J. Appl. Mech.*, 2019)

Lload is applied hydrostatically
→ von Mises stress is zero

$$\frac{T}{C}=\frac{3\sigma_{\mathrm{m}}^{\mathrm{f}}}{C+3\sigma_{\mathrm{m}}^{\mathrm{f}}}$$

※ T/C is strain-rate independent

As a result, the following strengths are obtained:

- ✓ **Strain-rate corrected compressive strength: C***
- ✓ **Brittle–ductile index: T/C**
- ✓ **Corrected tensile strength: T* = (T/C)·C***

MD : Resin nonlinear response

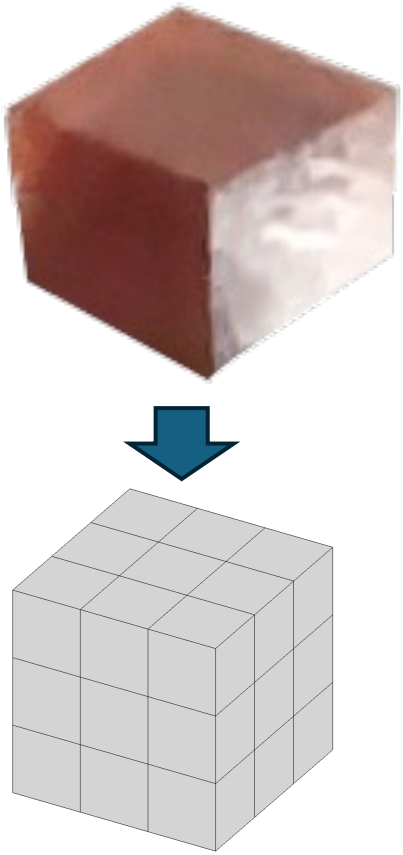

Elasto-viscoplastic constitutive law

(Kobayashi, *Transaction of JSME Series A*, 2004)

$$\dot{\boldsymbol{\sigma}} = \boldsymbol{C}_{\mathrm{m}} : \dot{\boldsymbol{\epsilon}} - \frac{3\mu\dot{\bar{\epsilon}}^{\mathrm{p}}}{\bar{\sigma}}\boldsymbol{\sigma}'$$

$$\dot{\bar{\epsilon}}^{\mathrm{p}} = \dot{\epsilon}_{\mathrm{r}}\left(\frac{\bar{\sigma} + \beta\sigma_{\mathrm{m}}}{g\left(\bar{\epsilon}^{\mathrm{p}}\right)}\right)^{\frac{1}{k}} \qquad g\left(\bar{\epsilon}^{\mathrm{p}}\right) = g_1\left(\bar{\epsilon}^{\mathrm{p}}\right)^{g_2} + g_3$$

E_{m} , ν_{m} : Elastic parameter

g_1 , g_2 , g_3 : Plastic parameter

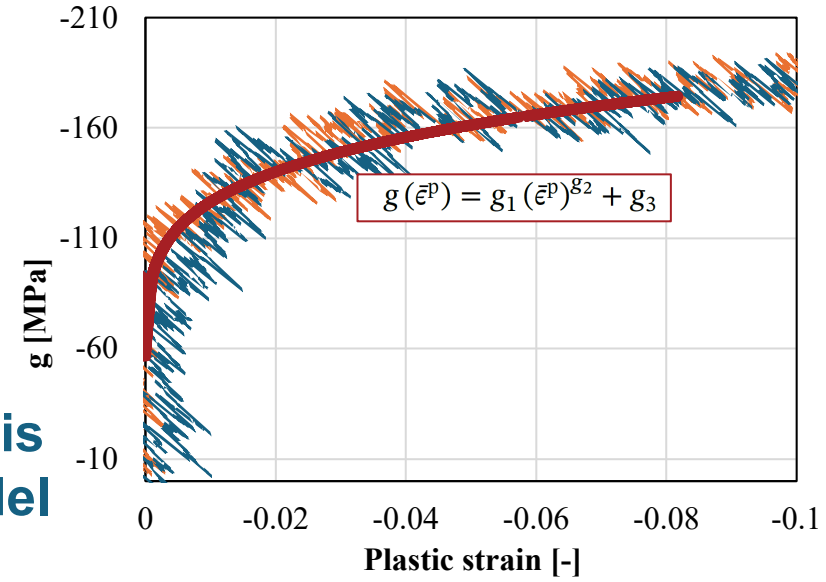

Plastic response obtained from MD is approximated by a constitutive model

Introduction: Hierarchical structure of CFRP

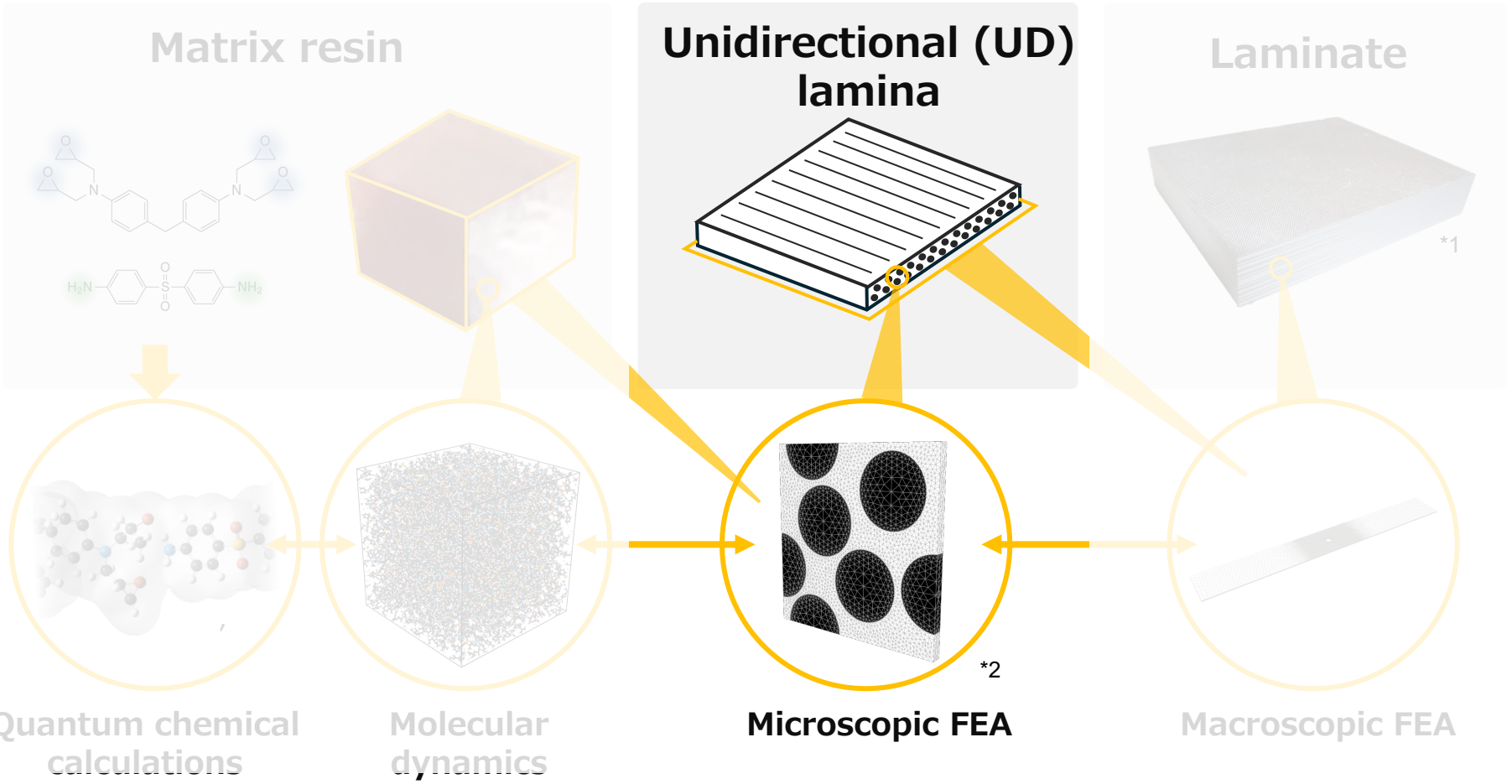

Objective:

CFRP strength parameters are estimated in a bottom-up manner through multiscale modeling, combining models specialized for each scale

Microscopic FEA for UD lamina

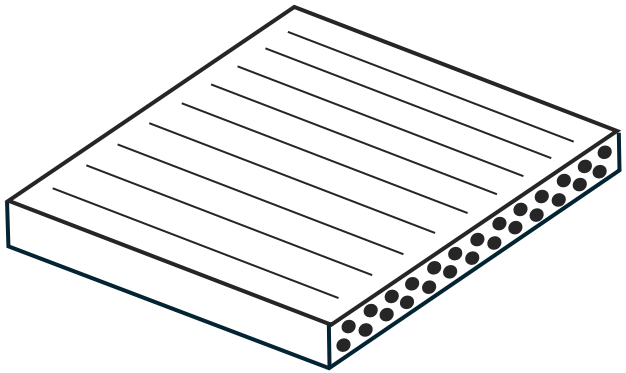

Mechanical properties of UD lamina

- ✓ Transversely isotropic elasticity
- ✓ Plastic model considering hydrostatic pressure dependence
  (Yokozeki et al., *Compos. Sci. Technol.*, 2007)
- ✓ Failure criterion for transversely isotropic materials (Christensen, *J. Appl. Mech.*, 2013)

RVE analysis

(Okabe et al., *Int. J. Solids Struct.*, 2011)

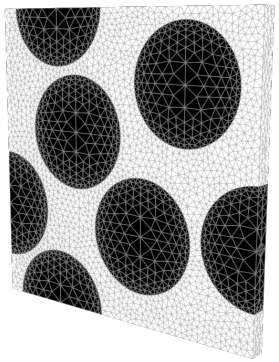

Fiber kink theory

(Budiansky and Fleck, *J. Mech. Phys. Solids*, 1993)

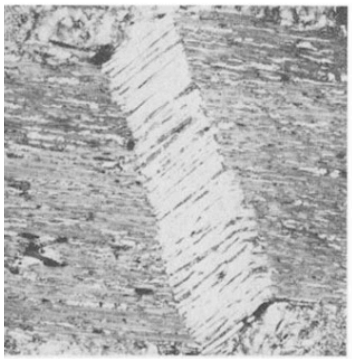

*1

Spring element model

(Okabe et al., *Compos. Sci. Technol.*, 2005)

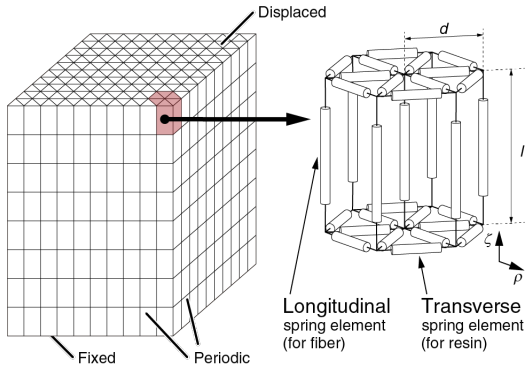

Other mechanical properties

Fiber-direction strength

Compressive **Tensile**

*1 B. Budiansky, *Comput. Struct.*, 1983, 16(1), 3–12

Microscopic FEA for UD lamina

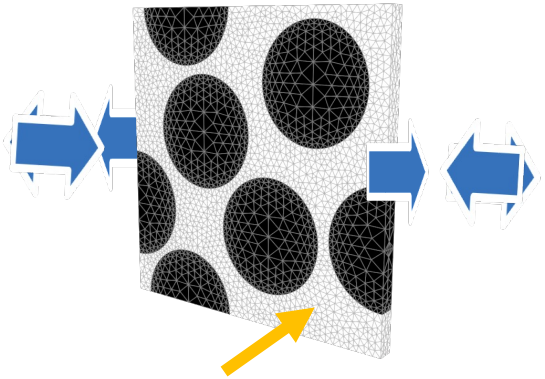

Resin properties from MD

E_m , ν_m C

g_1 , g_2 , g_3 T/C

Homogenization techniques

(Suquet, 1987. *Lecture Notes in Physics*, 1987)

$$E_{LL}\ ,\ E_{TT}\ ,\ G_{LT}$$
$$\nu_{LT}\ ,\ \nu_{TT}$$

Elastoplastic parameter identification using off-axis loading simulations

$\rightarrow$ $a_{66},\ A_1,\ n_1,\ A_2,\ n_2,\ \bar{\sigma}^{t}_{eff}$

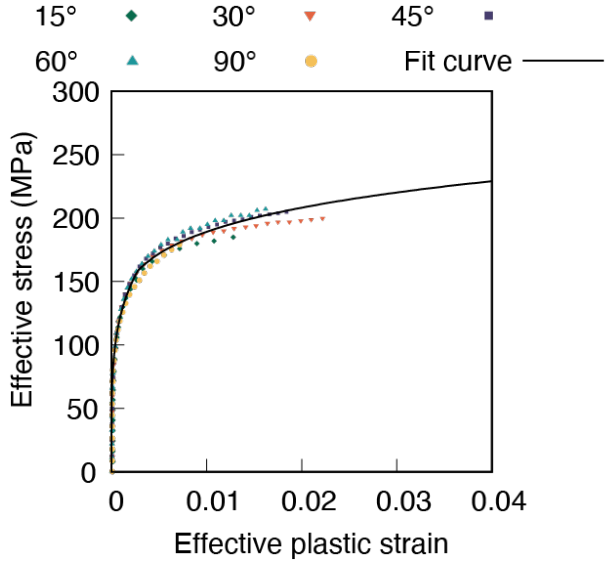

$$\bar{\sigma}_{eff} = \sqrt{\frac{3}{2}\left[(\sigma_{22}-\sigma_{33})^2 + 2a_{44}\sigma_{23}^2 + 2a_{66}\left(\sigma_{12}^2+\sigma_{13}^2\right)\right] + a_1^2\sigma_{11}^2} + a_1(\sigma_{11}+\sigma_{22}+\sigma_{33}),$$

$$d\epsilon_{ij}^{p} = \frac{\partial\bar{\sigma}_{eff}}{\partial\sigma_{ij}} d\bar{\epsilon}_{eff}^{p},$$

$$\bar{\epsilon}_{eff}^{p} = \begin{cases} A_1(\bar{\sigma}_{eff})^{n_1} & \text{if } \bar{\sigma}_{eff} \le \bar{\sigma}^{t}_{eff}, \\ A_2(\bar{\sigma}_{eff})^{n_2} & \text{if } \bar{\sigma}_{eff} \ge \bar{\sigma}^{t}_{eff}, \end{cases}$$

Microscopic FEA for UD lamina

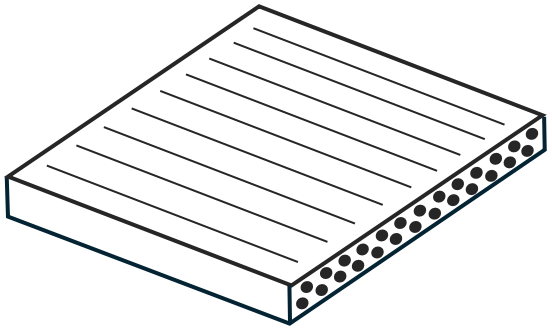

Christensen's failure criterion for transversely isotropic materials

(Christensen, *J. Appl. Mech.*, 2013)

$$\left(\frac{1}{T_{TT}}-\frac{1}{C_{TT}}\right)(\sigma_{22}+\sigma_{33})+\frac{1}{T_{TT}C_{TT}}(\sigma_{22}+\sigma_{33})^2 +\frac{1}{S_{TT}^2}(\sigma_{23}^2-\sigma_{22}\sigma_{33})+\frac{1}{S_{LT}^2}(\sigma_{12}^2+\sigma_{31}^2) \leq 1$$

$$\left(\frac{1}{T_{LL}}-\frac{1}{C_{LL}}\right)\sigma_{11}+\frac{1}{T_{LL}C_{LL}}\sigma_{11}^2 \leq 1$$

$$S_{TT}^2=\left(\frac{1+\frac{T_{TT}}{C_{TT}}}{3+5\frac{T_{TT}}{C_{TT}}}\right)T_{TT}C_{TT}$$

Simulating resin failure in composite materials

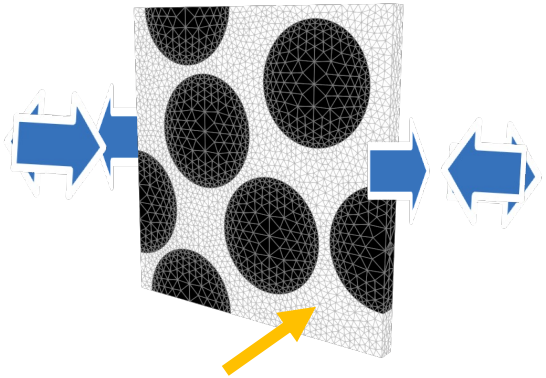

$T_{TT},\ C_{TT},\ S_{LT},\ C_{LL},\ T_{LL}$

Resin properties from MD

E_m , ν_m C

g_1 , g_2 , g_3 T/C

Fibre direction compressive strength

Budiansky's fiber kink theory

(Budiansky and Fleck, *J. Mech. Phys. Solids*, 1993)

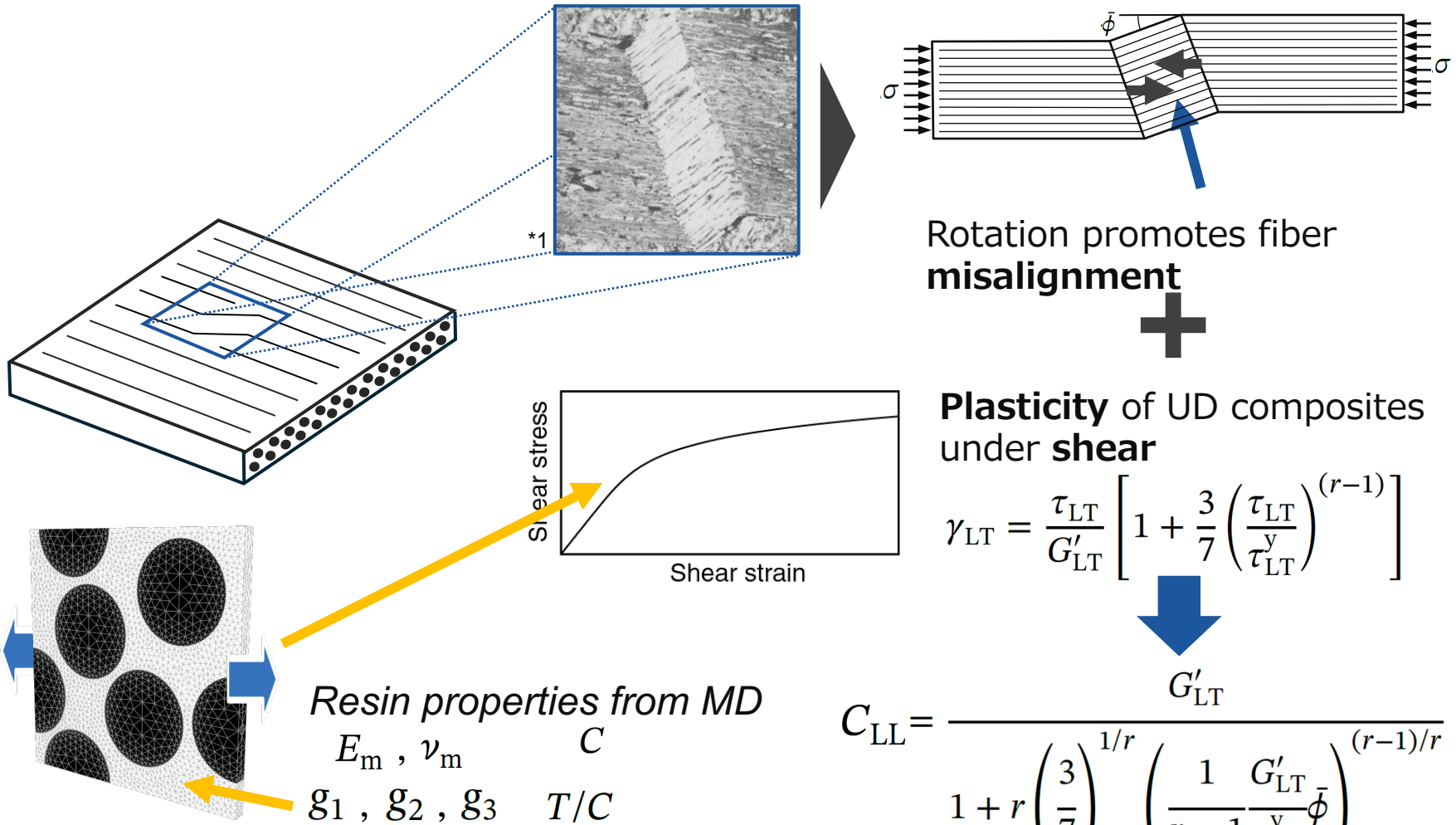

Rotation promotes fiber **misalignment**

+

Plasticity of UD composites under **shear**

$$\gamma_{LT} = \frac{\tau_{LT}}{G'_{LT}}\left[1 + \frac{3}{7}\left(\frac{\tau_{LT}}{\tau^{y}_{LT}}\right)^{(r-1)}\right]$$

Resin properties from MD

E_m , ν_m C

g_1 , g_2 , g_3 T/C

$$C_{LL} = \frac{G'_{LT}}{1 + r\left(\frac{3}{7}\right)^{1/r}\left(\frac{1}{r-1}\frac{G'_{LT}}{\tau^{y}_{LT}}\bar{\phi}\right)^{(r-1)/r}}$$

T. Watanabe, et al. International Journal of Solids and Structures 283 (2023) 112489

Fiber direction tensile strength

Spring element model

(Okabe et al., *Compos. Sci. Technol.*, 2005)

Mathematical model for failure prediction considering:

- ✓ Probabilistic fracture of individual fibers
- ✓ Shear stress transfer to broken fibers

Shear yield stress of resin:

$$\tau^{\mathrm{f}} = \sqrt{\frac{TC}{3}}$$

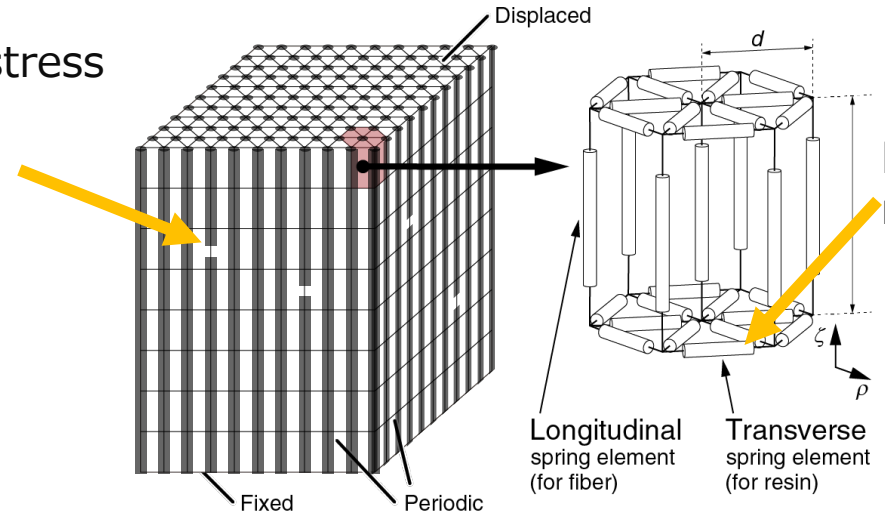

Resin shear modulus:

$$G_{\mathrm{m}} = \frac{E_{\mathrm{m}}}{2(1+\nu_{\mathrm{m}})}$$

$$T_{\mathrm{LL}}$$

Estimated material properties

Epoxy resin material properties from MD

	C		T/C	
	MD	Experiment	MD	Experiment
DGEBA/4,4′-DDS	180 MPa	142 MPa	0.670	0.714
DGEBA/DETA	134 MPa	101 MPa	0.657	0.700
TGDDM/4,4′-DDS	247 MPa	207 MPa	0.603	0.544

UD lamina material properties

	Young's modulus		Poisson's ratio		Shear modulus
	E_{LL}	E_{TT}	ν_{LT}	ν_{TT}	G_{LT}
DGEBA/4,4′-DDS	162 GPa	6.12 GPa	0.230	0.397	3.20 GPa
DGEBA/DETA	162 GPa	4.92 GPa	0.231	0.389	2.43 GPa
TGDDM/4,4′-DDS	162 GPa	6.15 GPa	0.226	0.387	3.26 GPa

※ T800S carbon fiber is assumed

Estimated material properties

Plastic behavior of each composite material

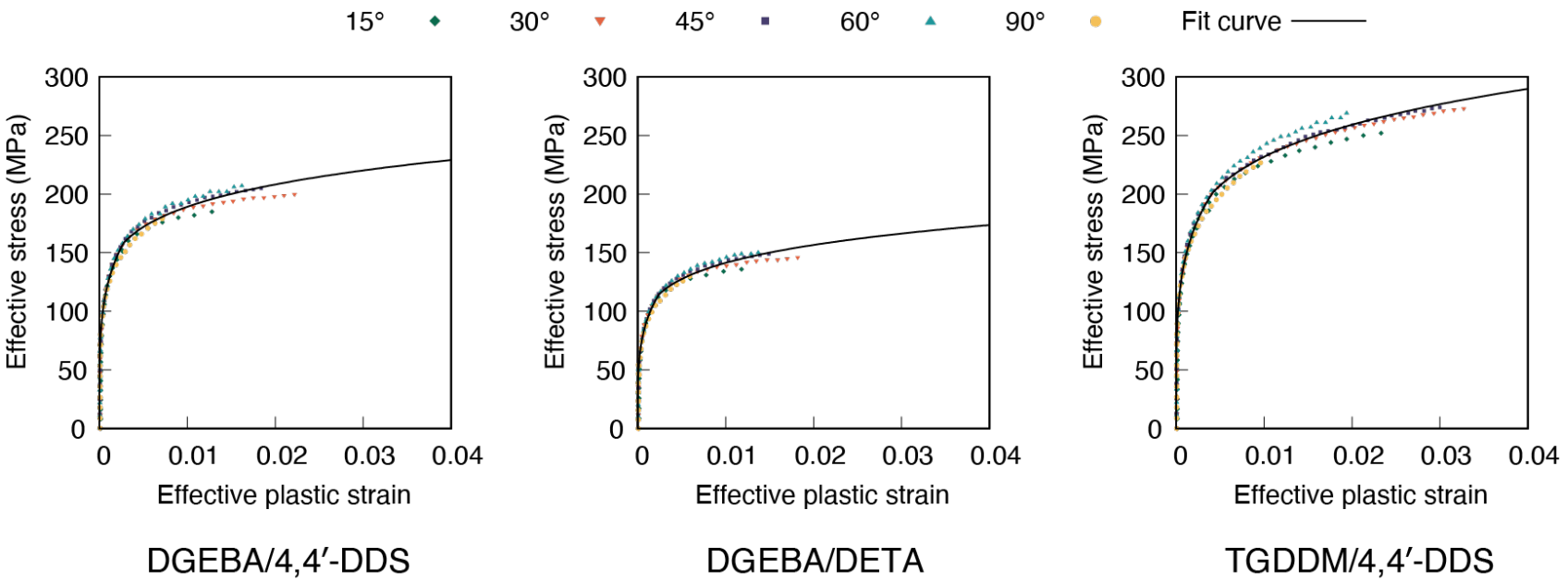

DGEBA/4,4′-DDS | DGEBA/DETA | TGDDM/4,4′-DDS

	a_{66}	A_1	n_1	A_2	n_2	$\bar{\sigma}^{t}_{eff}$
DGEBA/4,4′-DDS	2.59	1.28×10^{-12}	4.24	3.10×10^{-19}	7.25	159 MPa
DGEBA/DETA	2.56	2.13×10^{-11}	3.91	3.16×10^{-17}	6.74	115 MPa
TGDDM/4,4′-DDS	2.64	7.39×10^{-13}	4.23	2.09×10^{-17}	6.21	201 MPa

Estimated material properties

Five strengths of each composite material

	T_{TT}	C_{TT}	S_{LT}	C_{LL}	T_{LL}
DGEBA/4,4′-DDS	69 MPa	150 MPa	63 MPa	1157 MPa	2888 MPa
DGEBA/DETA	49 MPa	109 MPa	47 MPa	863 MPa	2894 MPa
TGDDM/4,4′-DDS	74 MPa	187 MPa	81 MPa	1254 MPa	2846 MPa

Experimental strengths of similar materials

	T_{TT} *1	C_{TT} *1	S_{LT} *2	C_{LL} *3	T_{LL} *1
T800S/3900-2B	67 MPa	193 MPa	119 MPa	1242 MPa	3100 MPa

*1 Morimoto et al., *JAXA advanced composites database*, 2018
*2 Raju and Acosta, *Crashworthiness of composite fuselage structures*, 2010
*3 Yokozeki et al., *Composites Part A*, 2006

Summary and Applications

- ✓ In this study, **five composite strength** parameters were estimated in a bottom-up manner by integrating **quantum chemical calculations,** molecular dynamics (**MD**), finite element analysis (**FEA**), and **theoretical models.**
- ✓ The seamless linkage of these methods enables both bottom-up and top-down analyses, clarifying the correlation between microscopic **molecular structure** and **macroscopic strength**.
- ✓ The five obtained strength parameters can be applied to **laminate-scale analyses**, such as open hole tension (OHT) and compression (OHC) simulations.

E_{LL}, E_{TT}, G_{LT} a_{66}, A_1, n_1
ν_{LT}, ν_{TT} $\bar{\sigma}^{t}_{eff}, A_2, n_2$
T_{TT}, C_{TT}, S_{LT}
C_{LL} T_{LL}

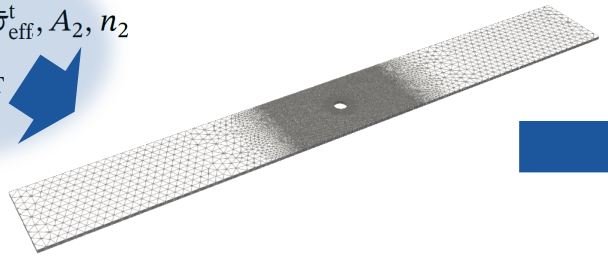

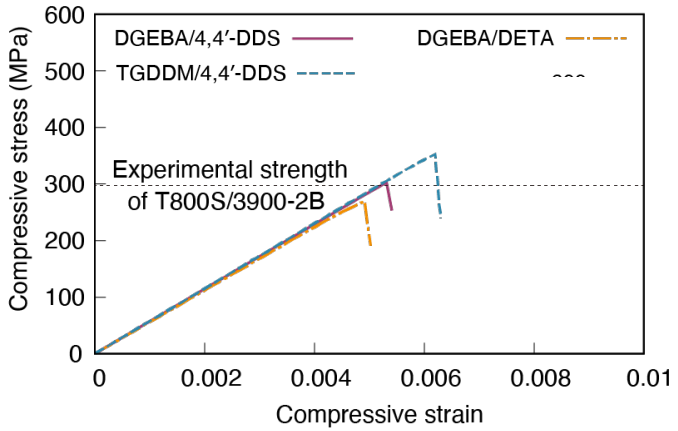

Open hole compression

A Novel Multi-Scale Digital Image Correlation Approach for Monitoring Stable Skin-Stringer Delamination Growth in Post-buckled Composite Panels

Andrés M. Pereira, Christos Kassapoglou, Sergio R. Turteltaub

Faculty of Aerospace Engineering,

Delft University of Technology,

The Netherlands



24th International Conference on Composite Materials (ICCM24)

TU Delft

From Fuselage to Single-Stringer Specimen

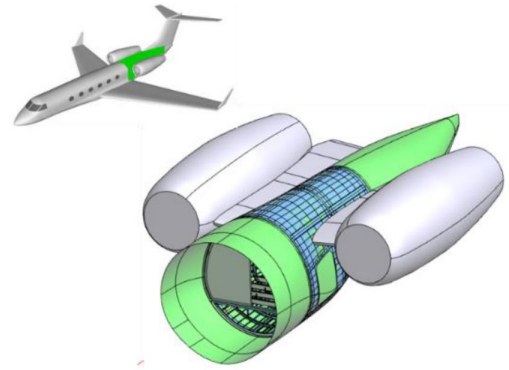

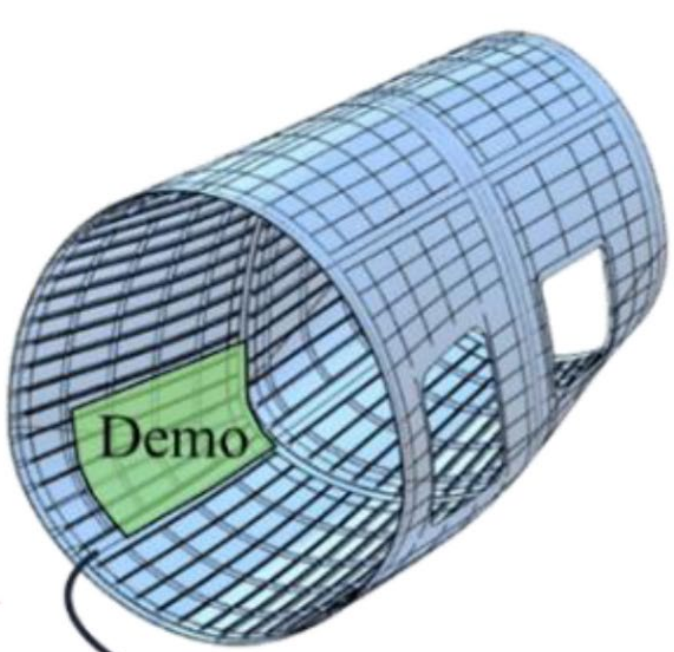

Rear Fuselage Section

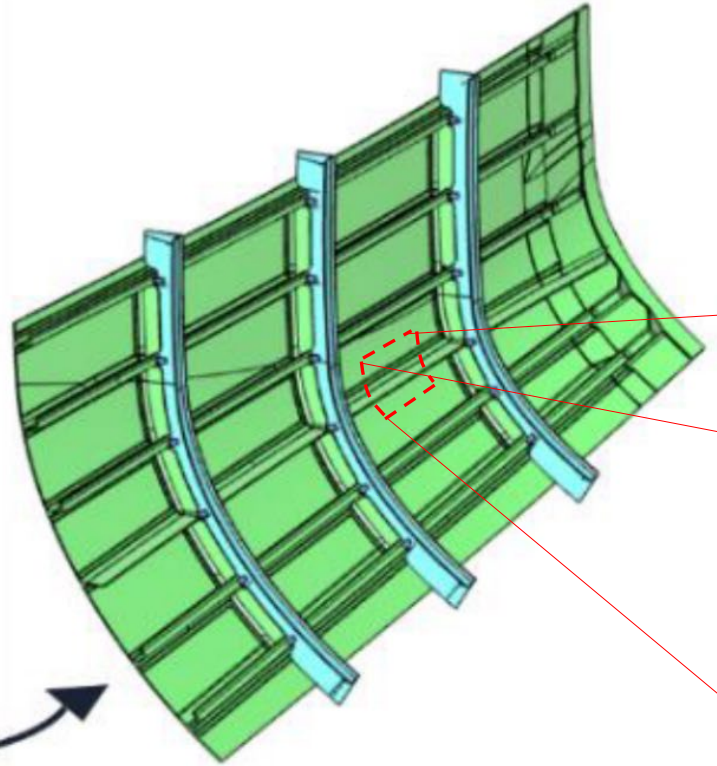

Fuselage Panel

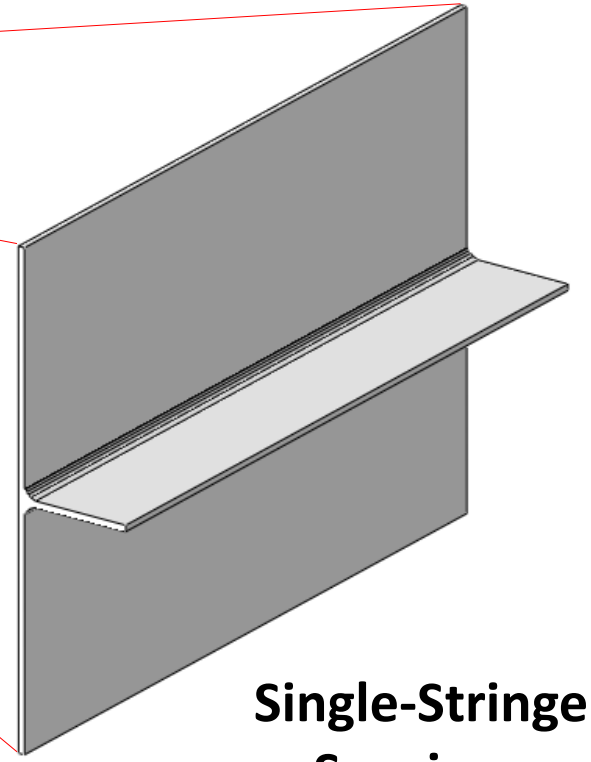

Single-Stringer Specimen

J.W. van Ingen, J.E.A. Waleson, A. Offringa, and M. Chapman. “Double Curved Thermoplastic Orthogrid Rear Fuselage Shell,” SAMPE Europe Conference, France, 2019.

Butt-joint Single-Stringer Specimen

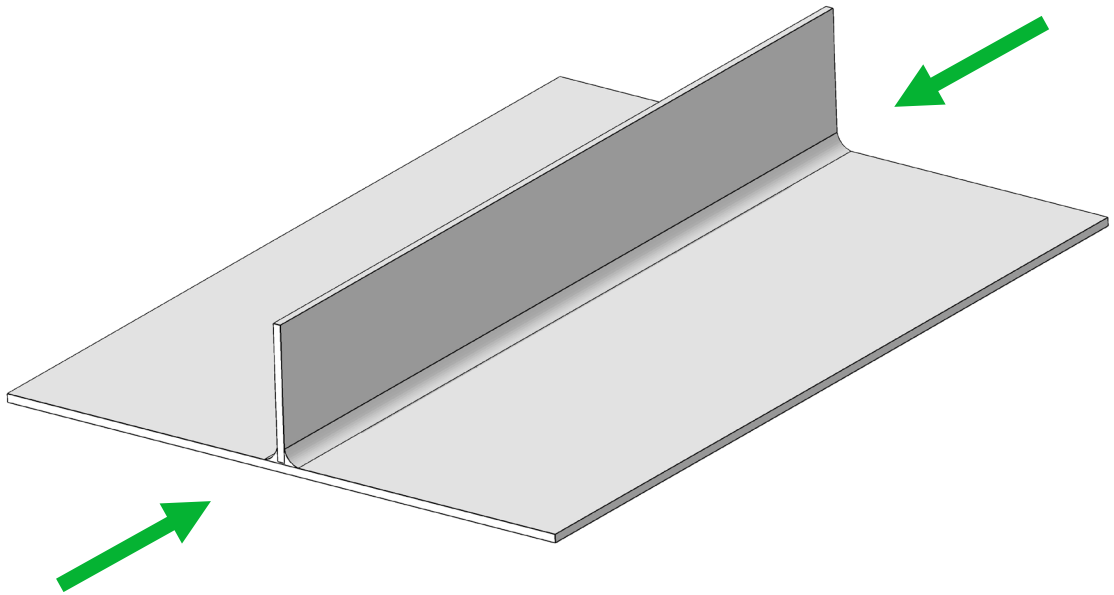

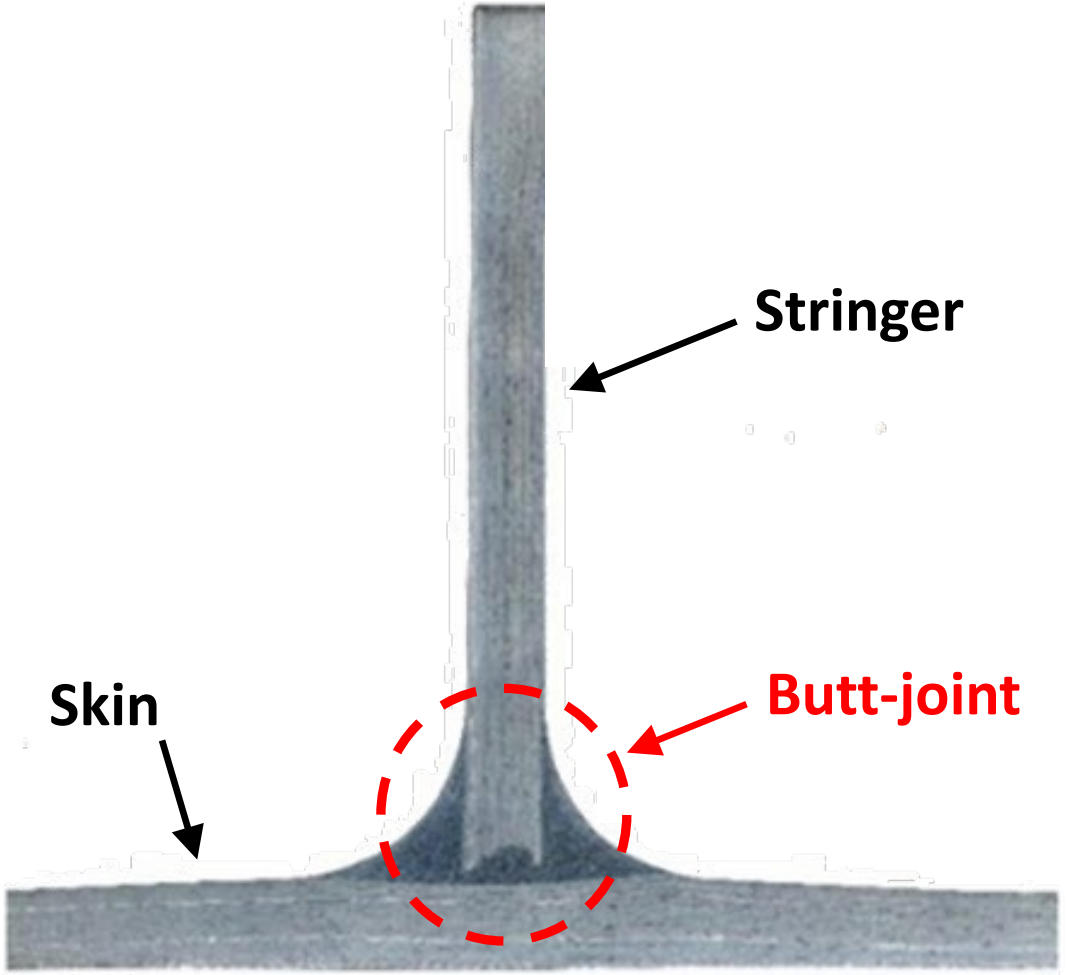

Tracking Delamination Growth in Post-Buckling

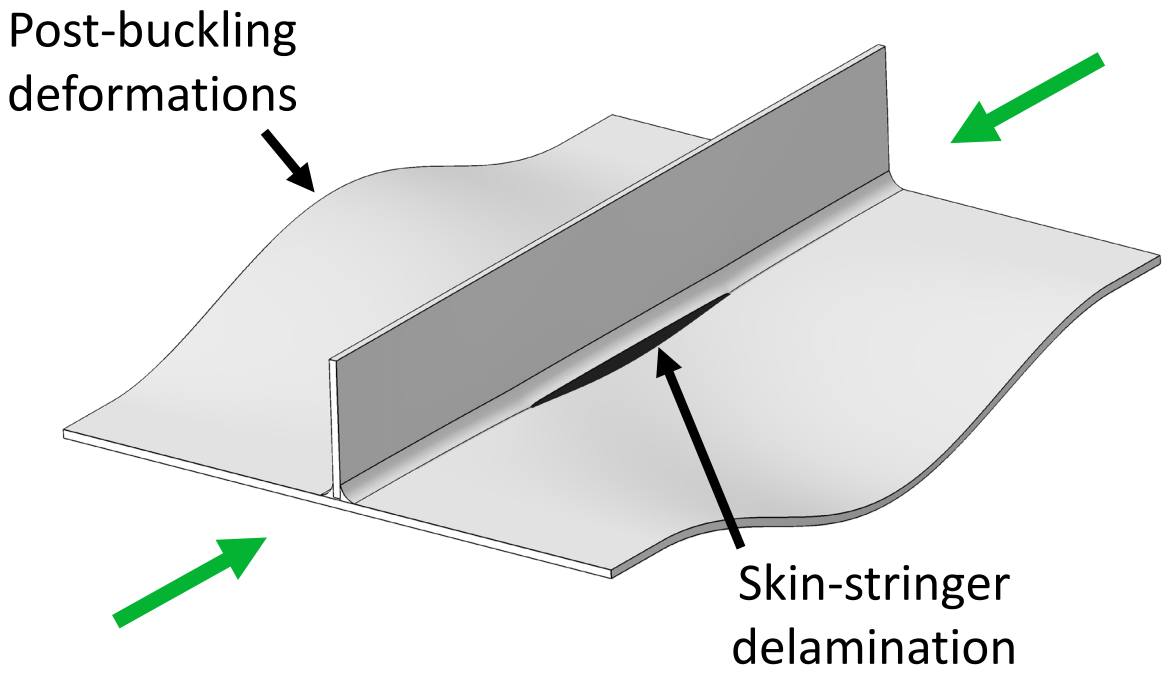

Current Challenge

Experimental methods cannot continuously capture skin-stringer delamination growth in detail during post-buckling.

Why It Matters

Lack of detailed data limits calibration and validation of advanced numerical damage models.

Research Objective

Experimental tracking of skin-stringer delamination growth in post-buckled composite panels.

Opportunity

High-fidelity experimental data can improve prediction accuracy, supporting certification of composite airframe post-buckling designs.

Outline

- ✓ **Design of Experiment**
- ✓ **Monitoring Methodology**
- ✓ **Results**
- ✓ **Conclusions & Future Work**

Design of Experiment: Specimen

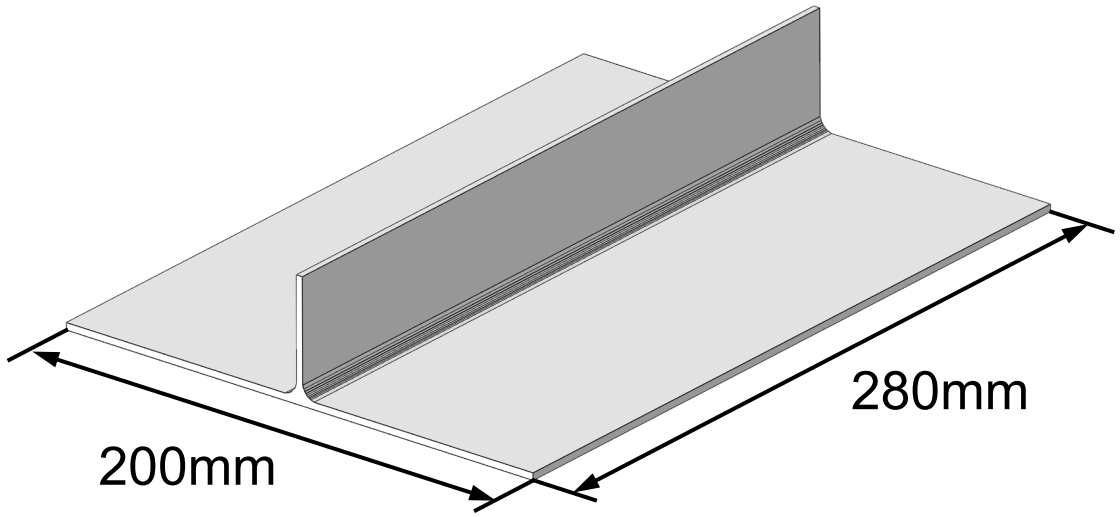

Component	Material
Skin	UD AS4D/PEKK
Web	UD AS4D/PEKK
Filler	SCRP CF/PEKK

DoE Objective:

Dimensions, layups and boundary conditions were optimized using FEA to maximize stable skin-stringer delamination growth.

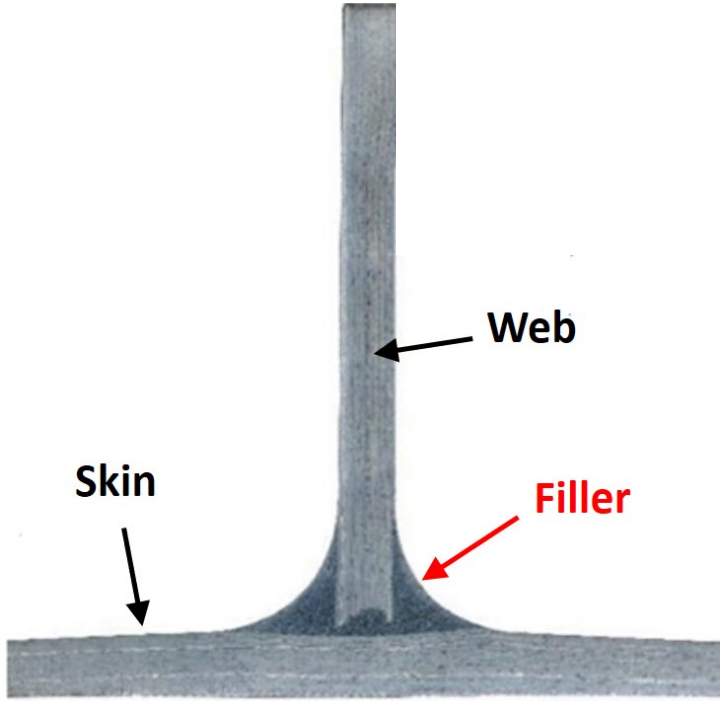

Design of Experiment: FEM Setup

Element Types	Color
SC8R	
C3D8I	
C3D6	

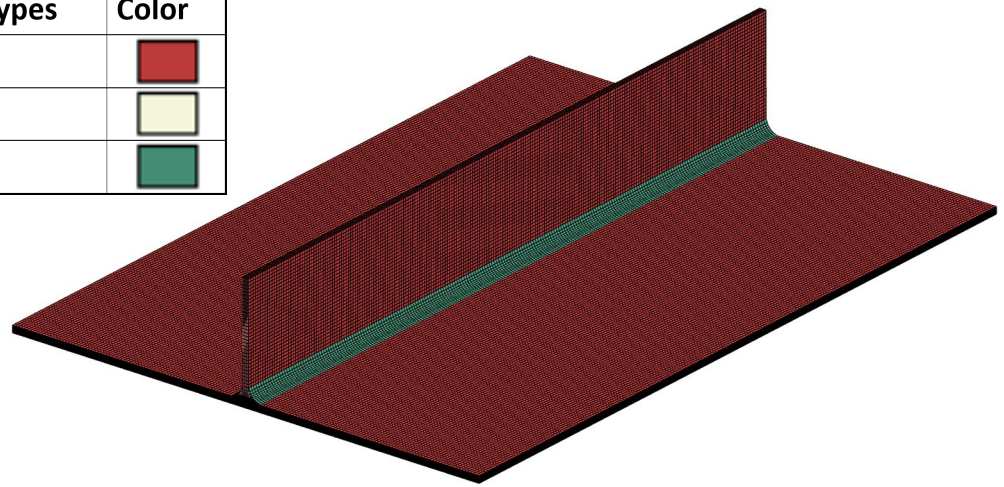

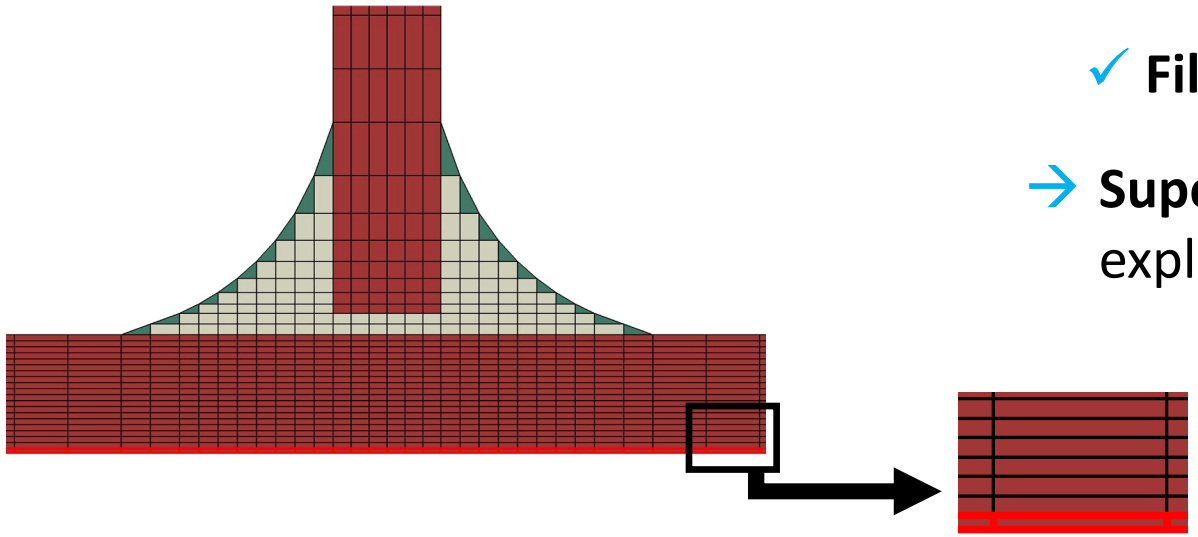

FE Software: Abaqus 2023

Model Details:

- **Mesh seed size**: 1.25mm
- **Local mesh refinement** at the stringer
- **Total elements**: 869,568
  - ✓ **Laminated components**: SC8R elements
  - ✓ **Filler**: C3D8I and C3D6 elements
- **Superficial resin layer** on OML side explicitly modeled (SC8R elements)

Design of Experiment: Boundary Conditions

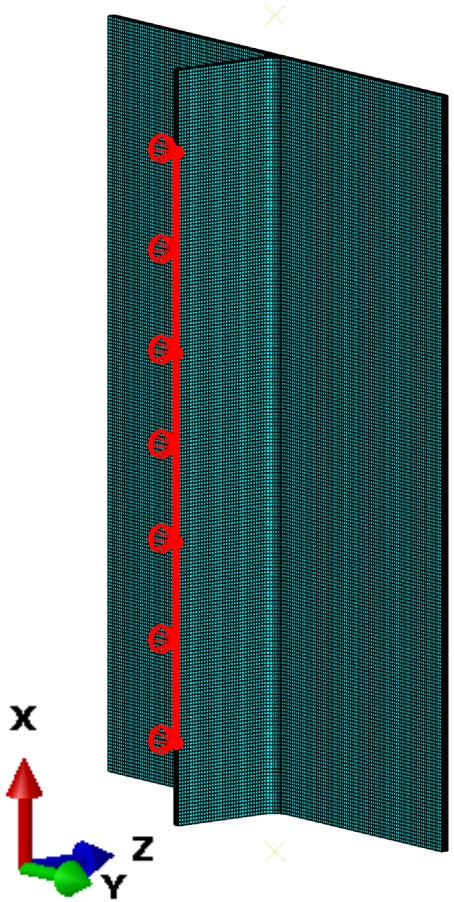

Simply-supported web
(U2 = 0)

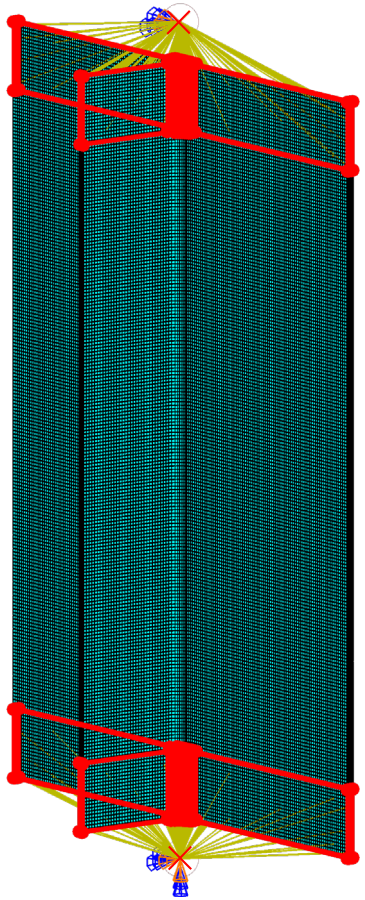

Clamped ends



Aluminum blocks
as end tabs

Fixture enforcing a simply-supported web.

Design of Experiment: Loading

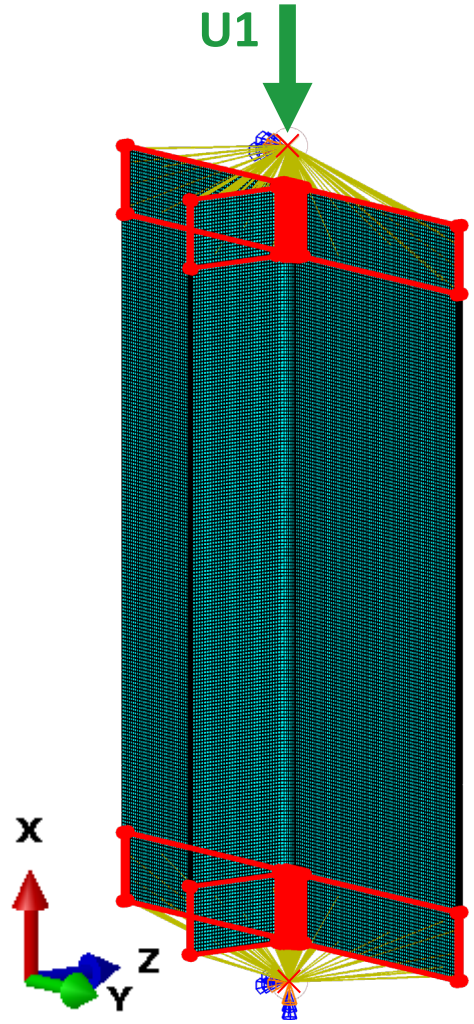

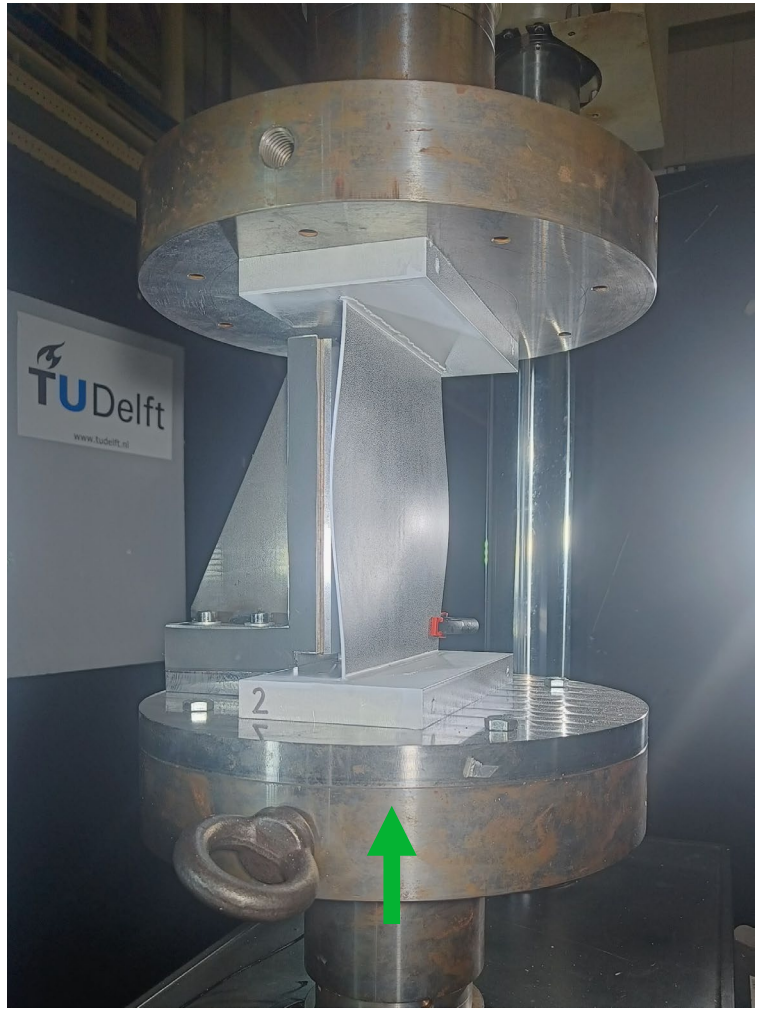

Quasi-static application

Displacement control @ 0.04 mm/min

Design of Experiment: Damage Growth Using VCCT

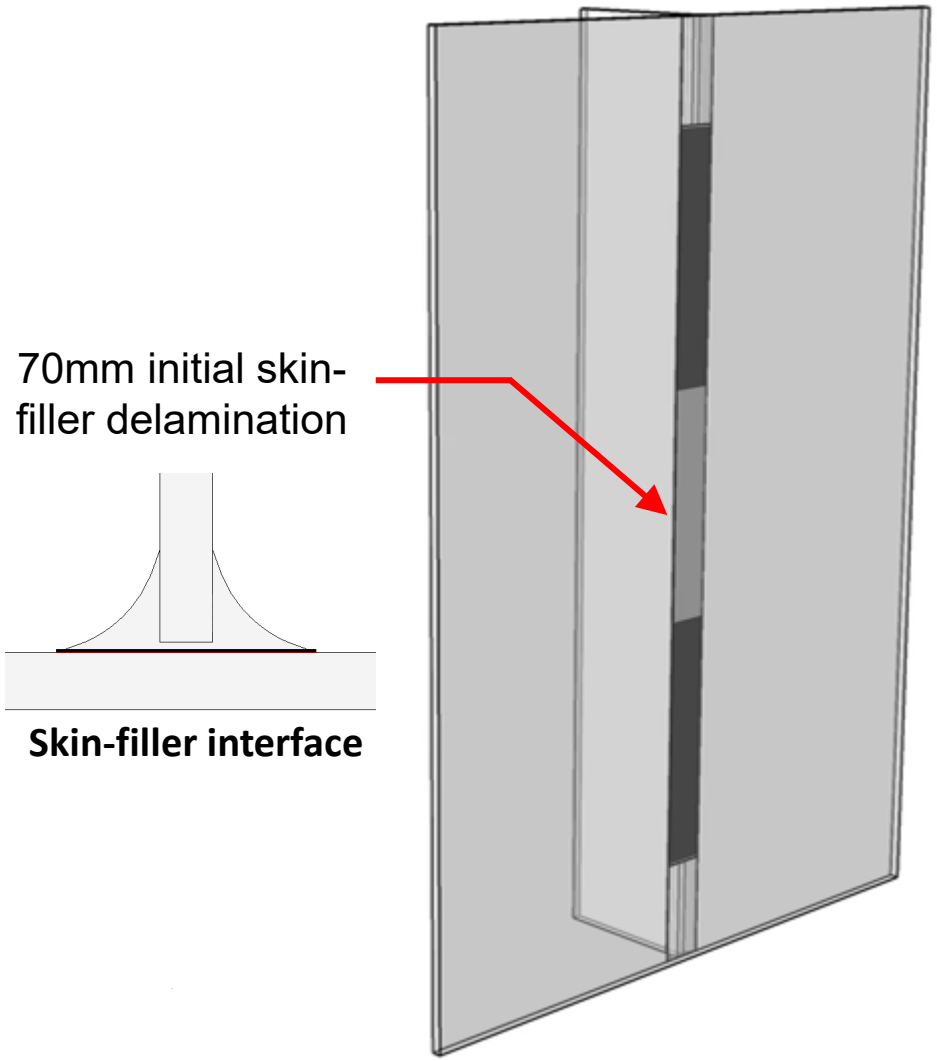

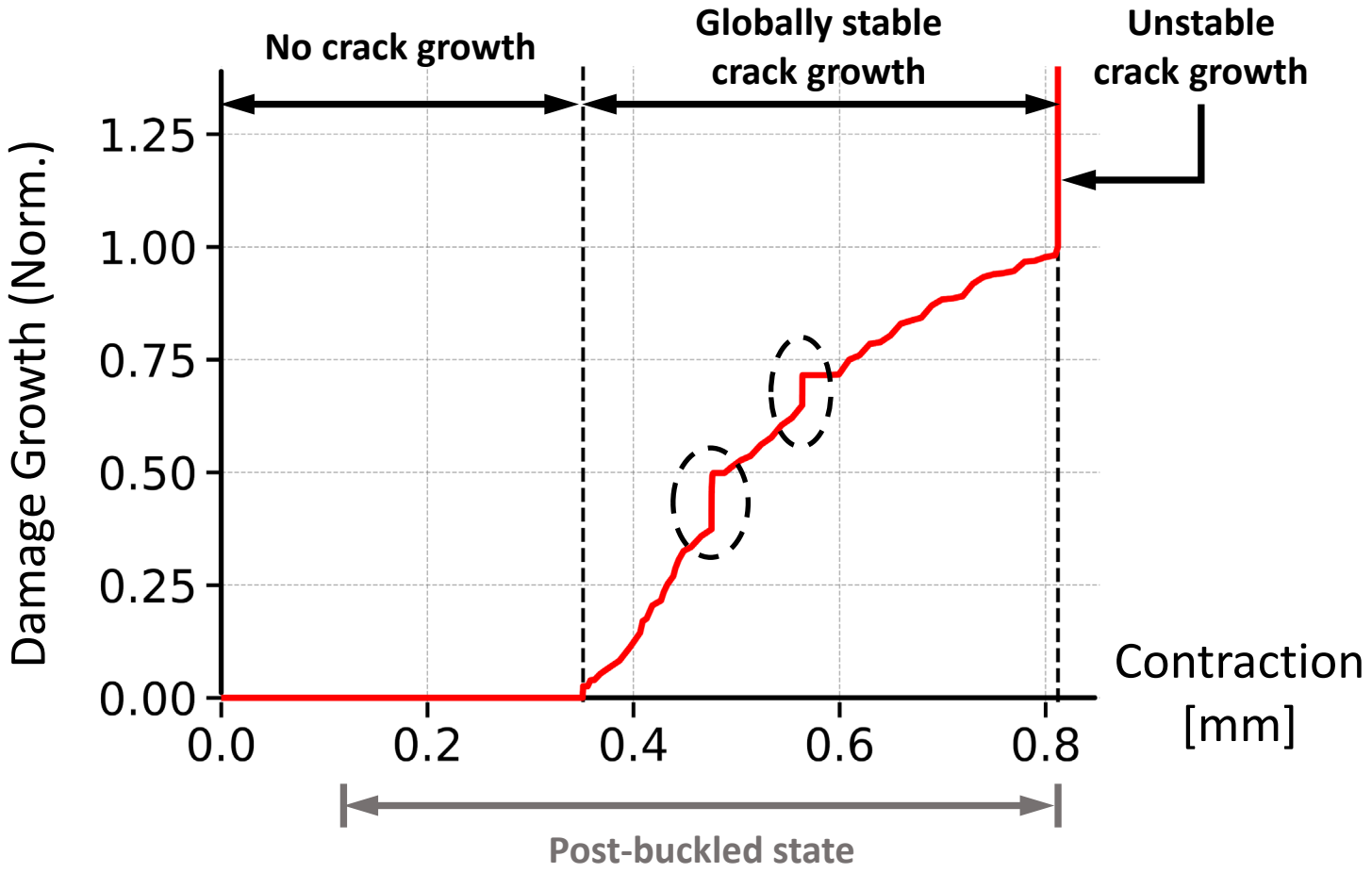

Design of Experiment: Damage Growth Using VCCT

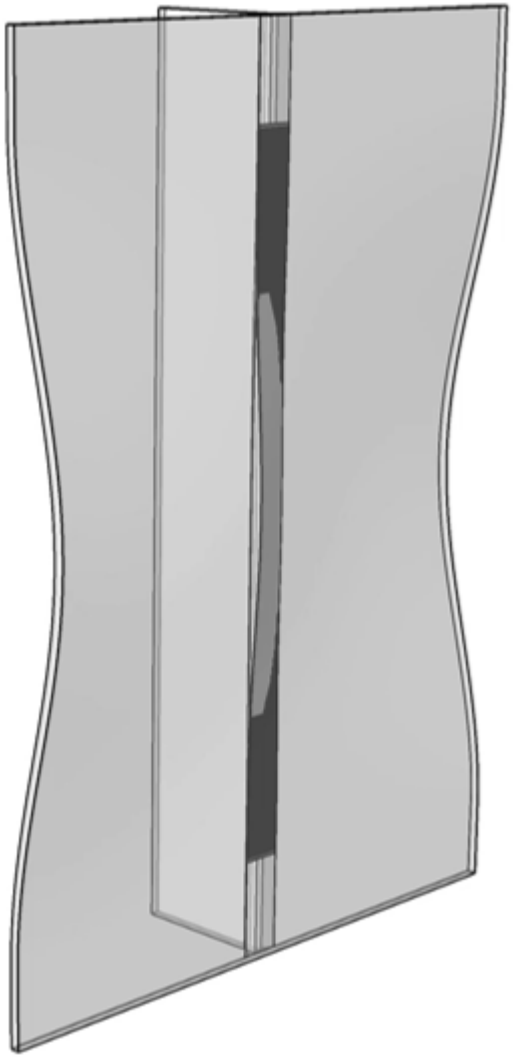

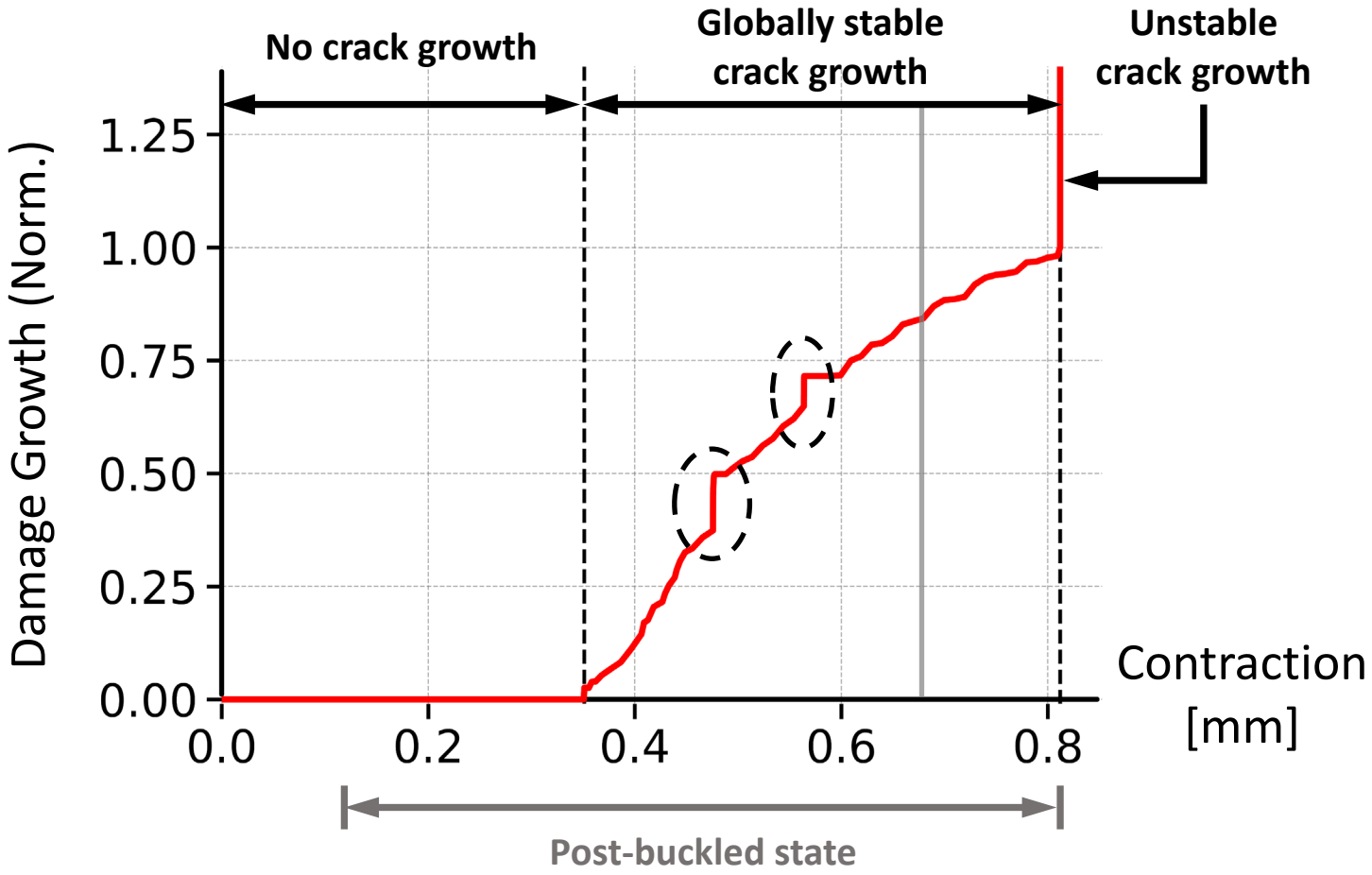

Strain Concentrations at Delamination Fronts

Indicator 1: Minimum in-plane principal strain on the Outer Mold Line (OML) surface

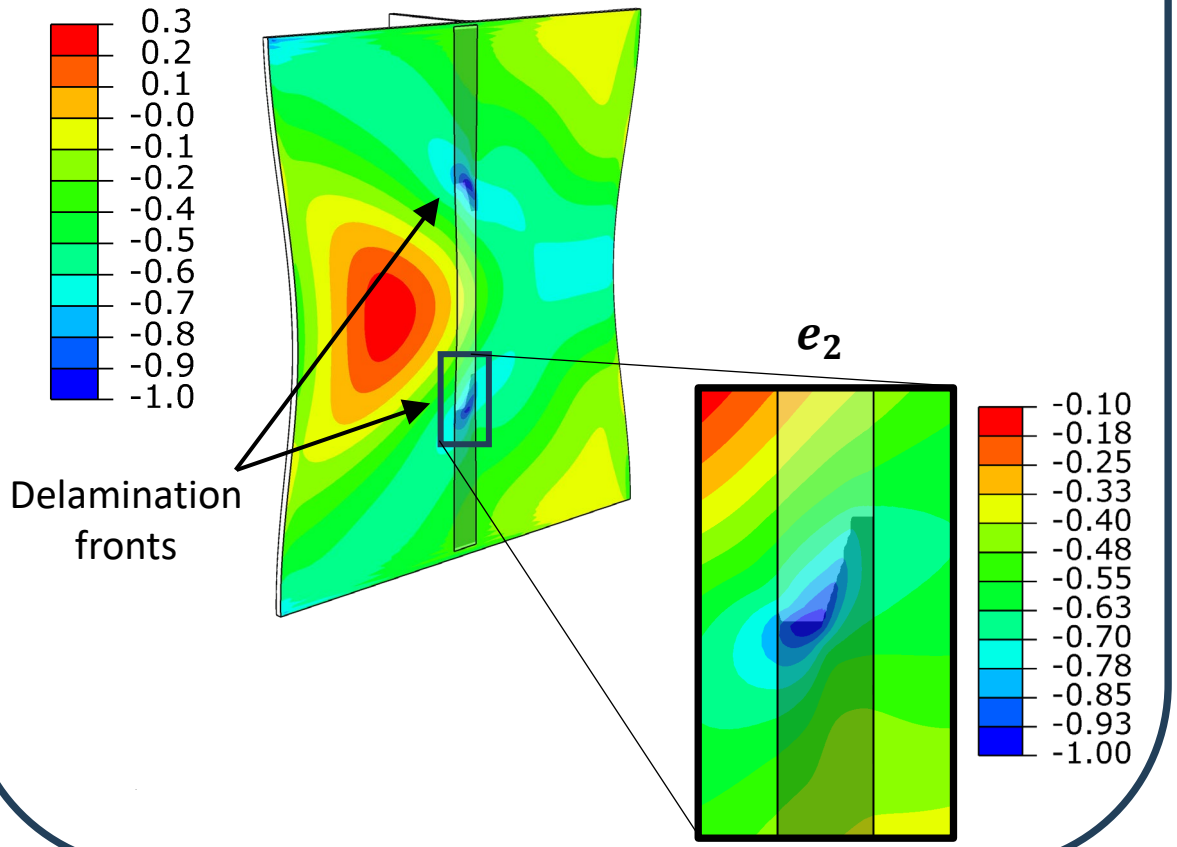

Indicator 2: Shear strain on the OML surface relative to a system aligned with the stringer

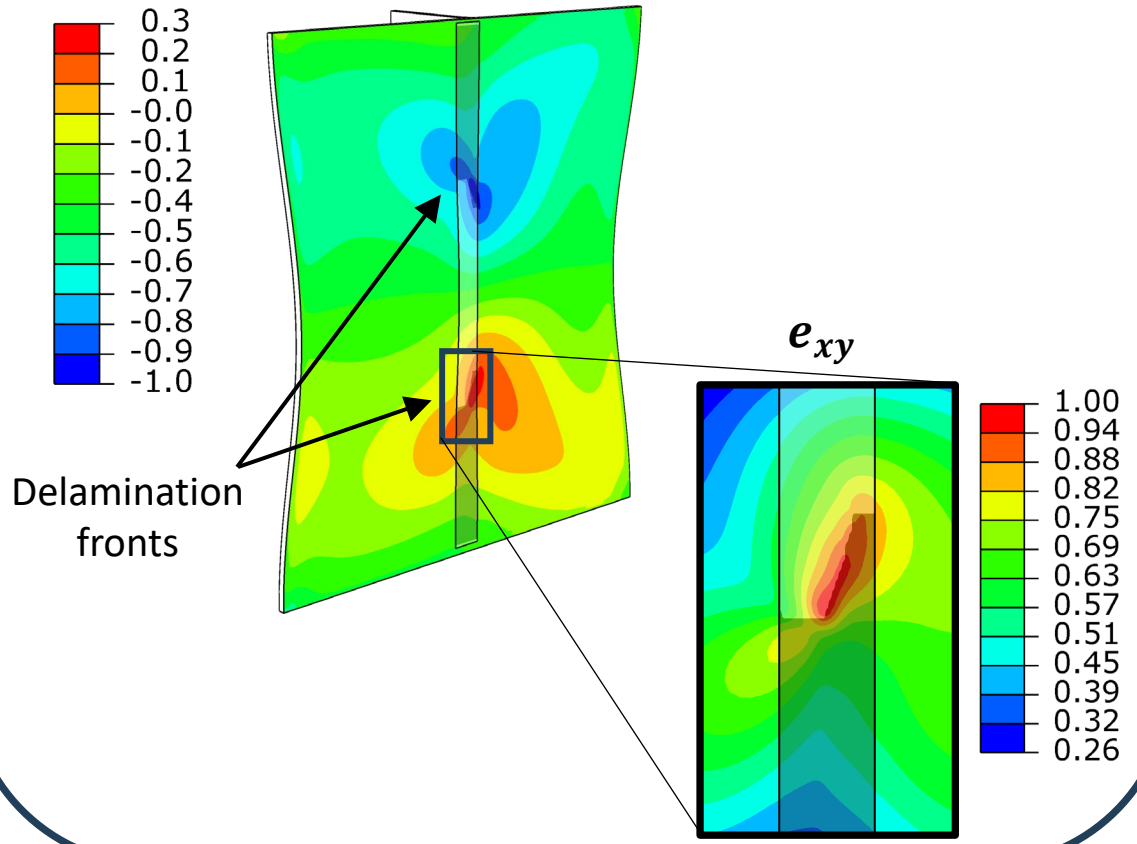

Strain Concentrations at Delamination Fronts

Indicator 1: Minimum in-plane principal strain on the Outer Mold Line (OML) surface

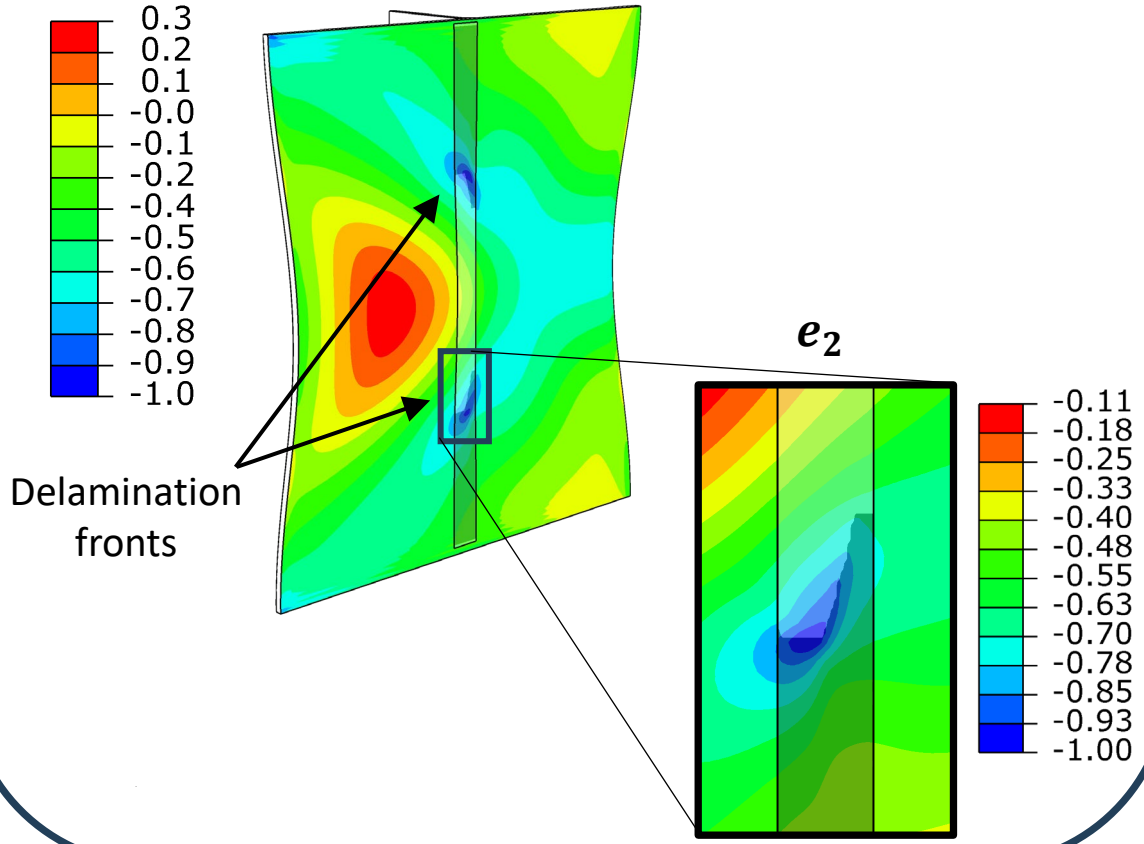

Indicator 2: Shear strain on the OML surface relative to a system aligned with the stringer

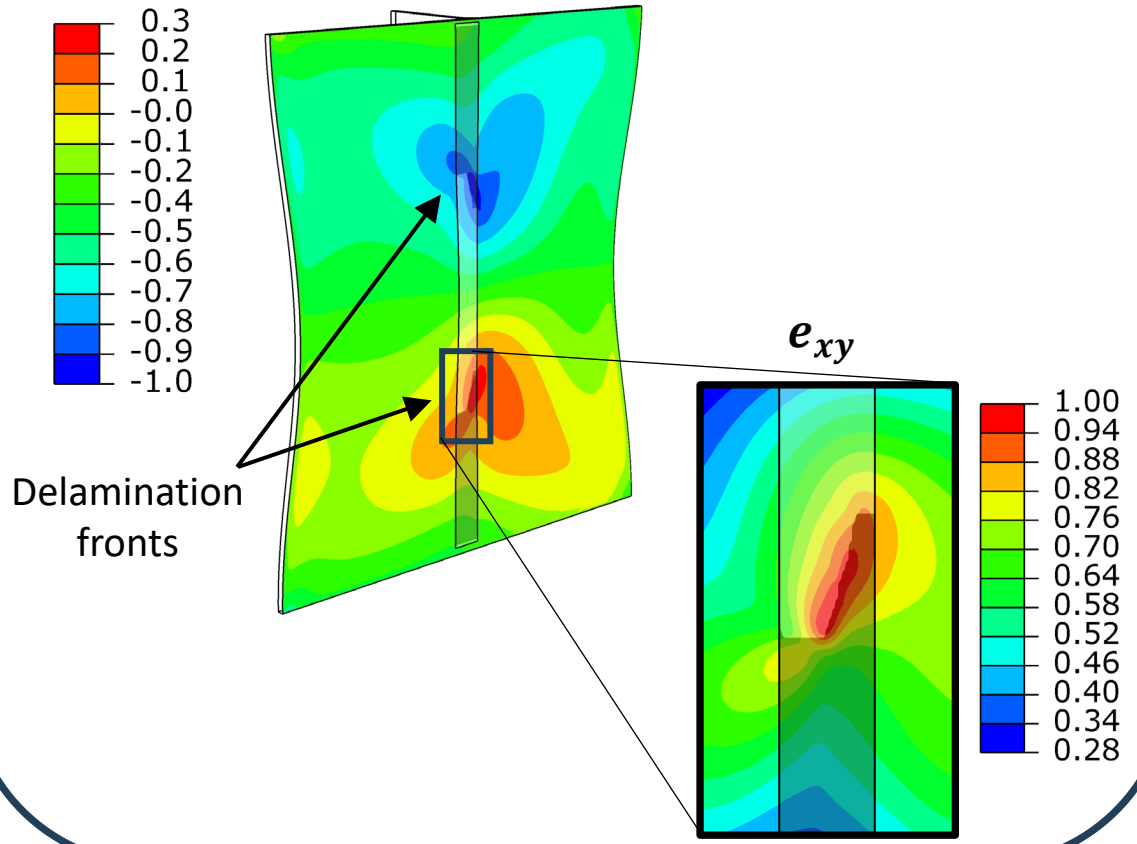

Monitoring Methodology: DIC-based Crack Front Estimation

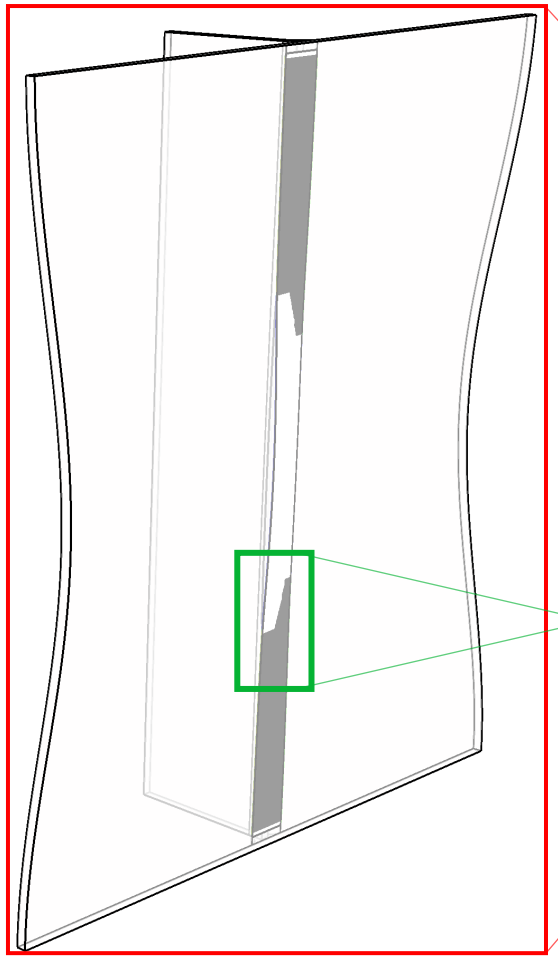

Global DIC

Local DIC

Global DIC: Capture out-of-plane post-buckling deformations.

W

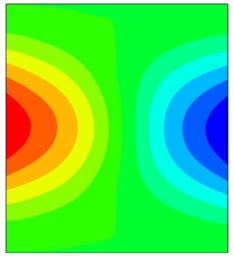

Local DIC: Capture strain concentrations at lower skin-stringer delamination front.

e_2 e_{xy}

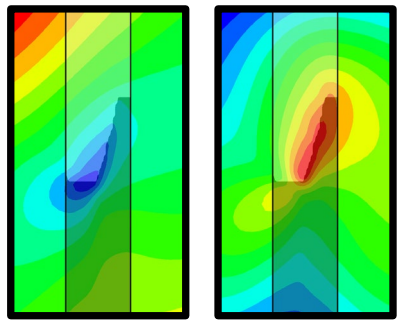

Validation: C-scans of the damage are acquired at different load levels and compared to DIC-based crack front estimates.

Global/Local DIC: Multi-Scale Pattern Design

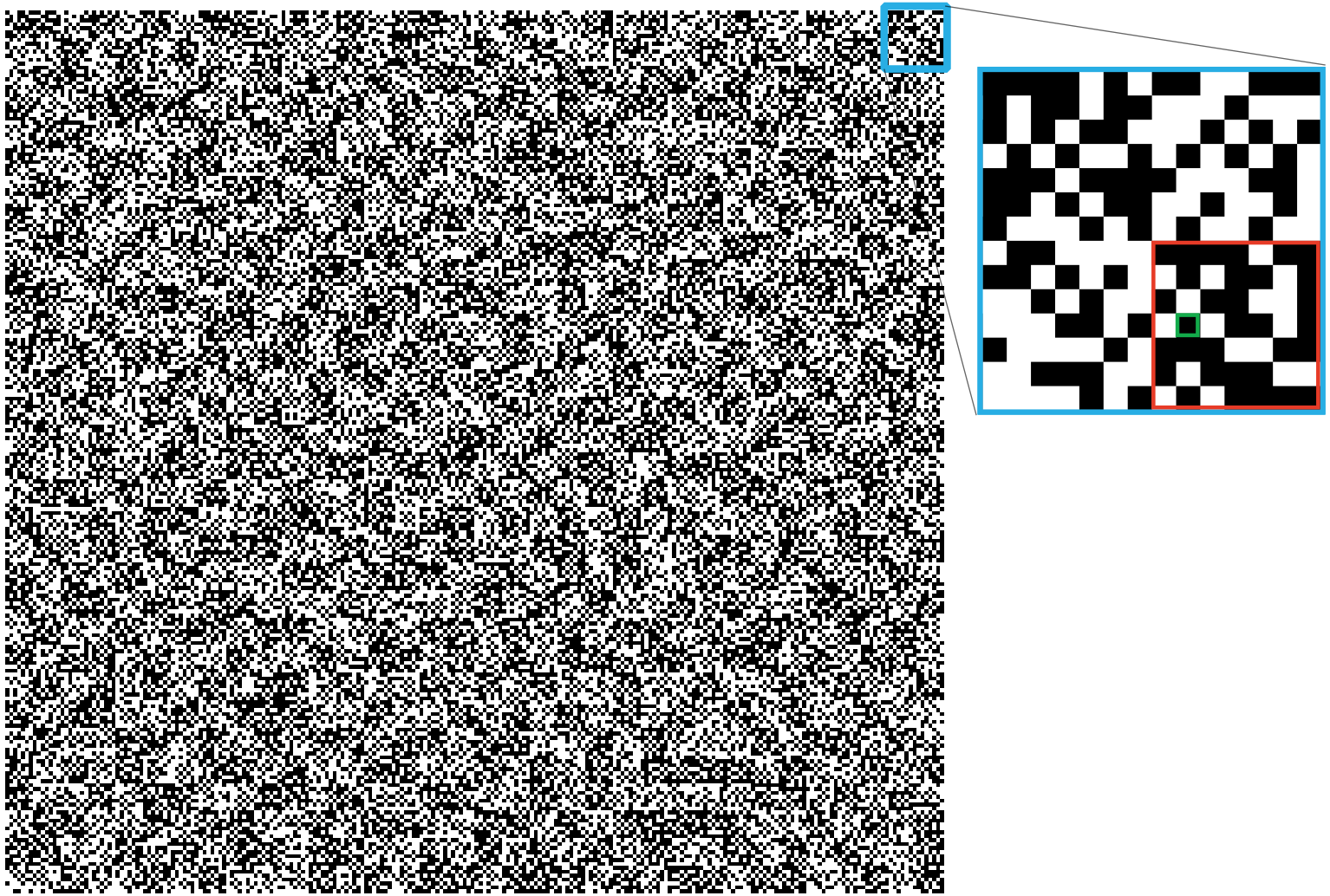

Target feature size: ~ 5px

Global DIC
- Resolution: 2048 × 2448 px
- Field of View: 256 x 305 mm

Global feature

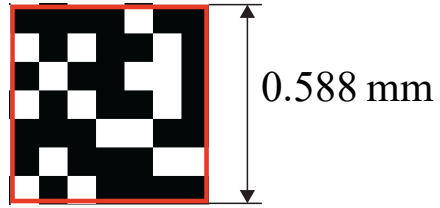

Local DIC
- Resolution: 2160 × 4096 px
- Field of View: 34 × 65 mm

Local feature

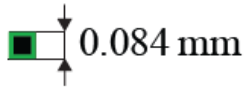

G. F. Bomarito, J. D. Hochhalter, and T. J. Ruggles, “Development of optimal multiscale patterns for digital image correlation via local grayscale variation,” *Experimental Mechanics*, vol. 58, no. 7, pp. 1169–1180, Sep. 2018.

Global/Local DIC: Experimental Setup

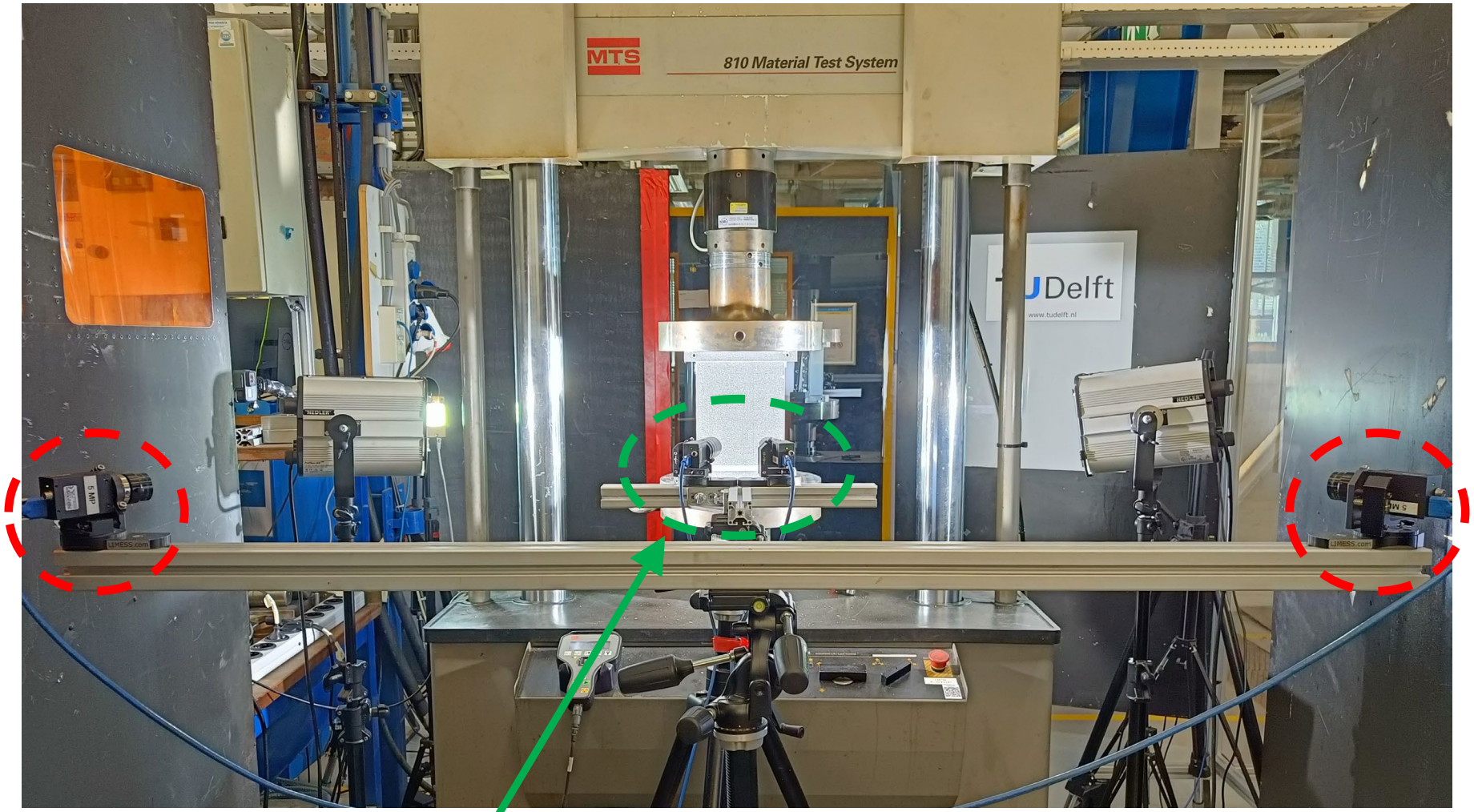

Global/Local DIC: Fields of View

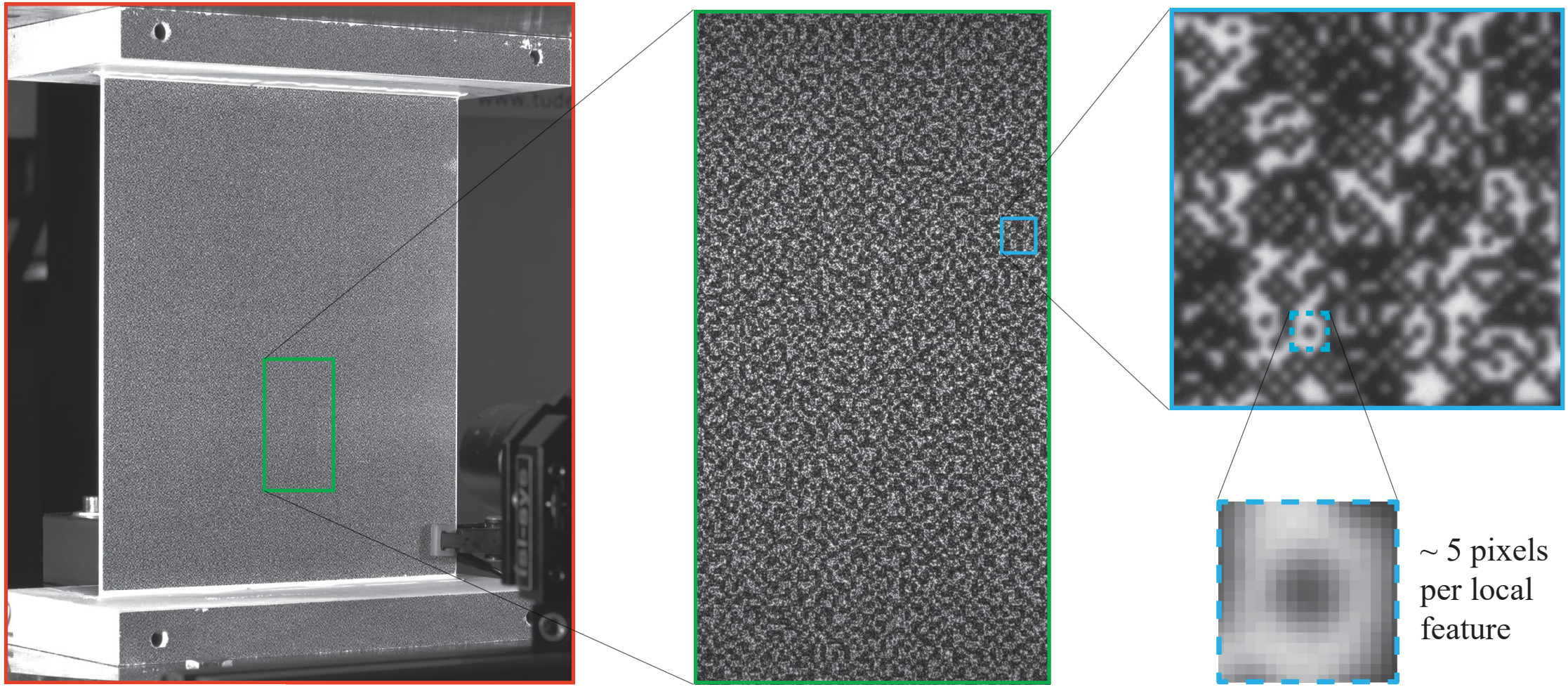

C-Scan Data: Reference for Validating Crack Front Monitoring

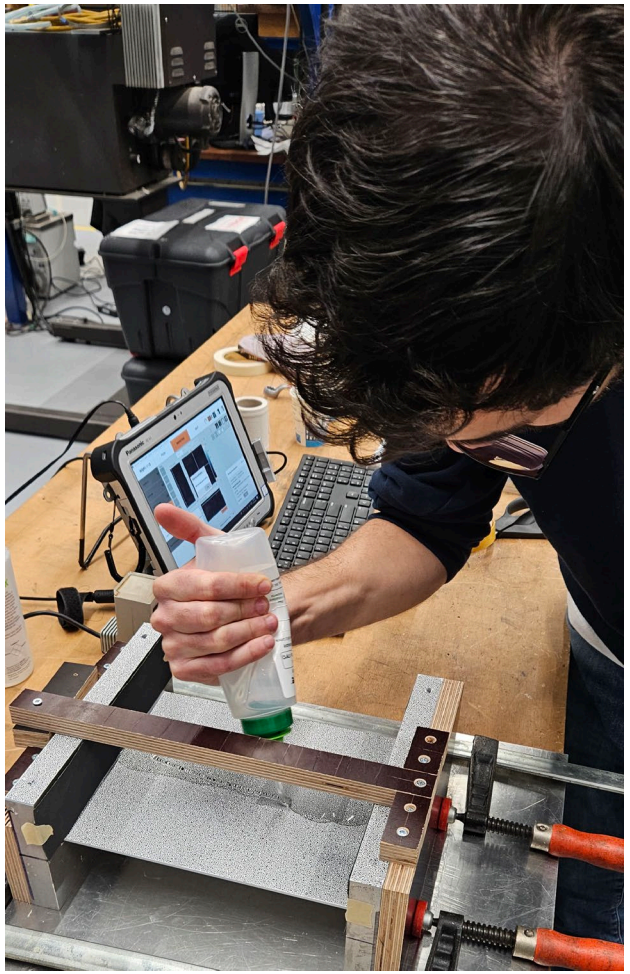

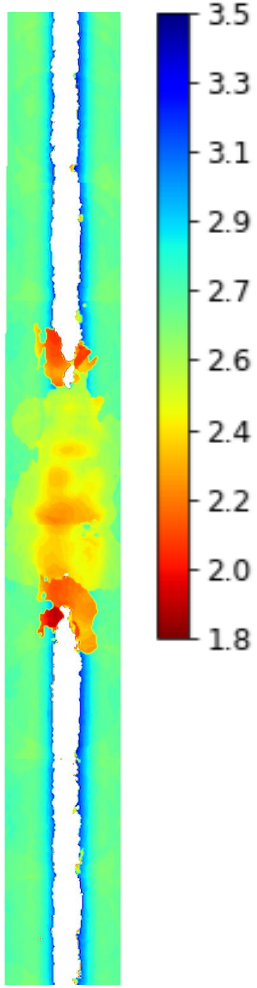

Detailed information on damage morphology (area, location, and depth) is obtained at different instances during the stable crack growth process.

↓

High-fidelity reference measurements for validating DIC-based crack front monitoring.



Dolphicam 2

C-Scan Data: Damage Evolution with Increasing Load

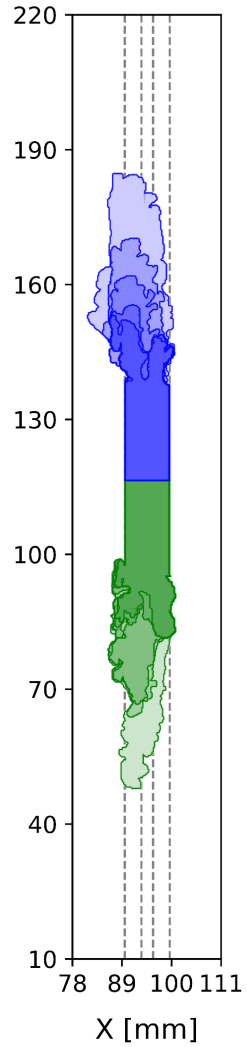

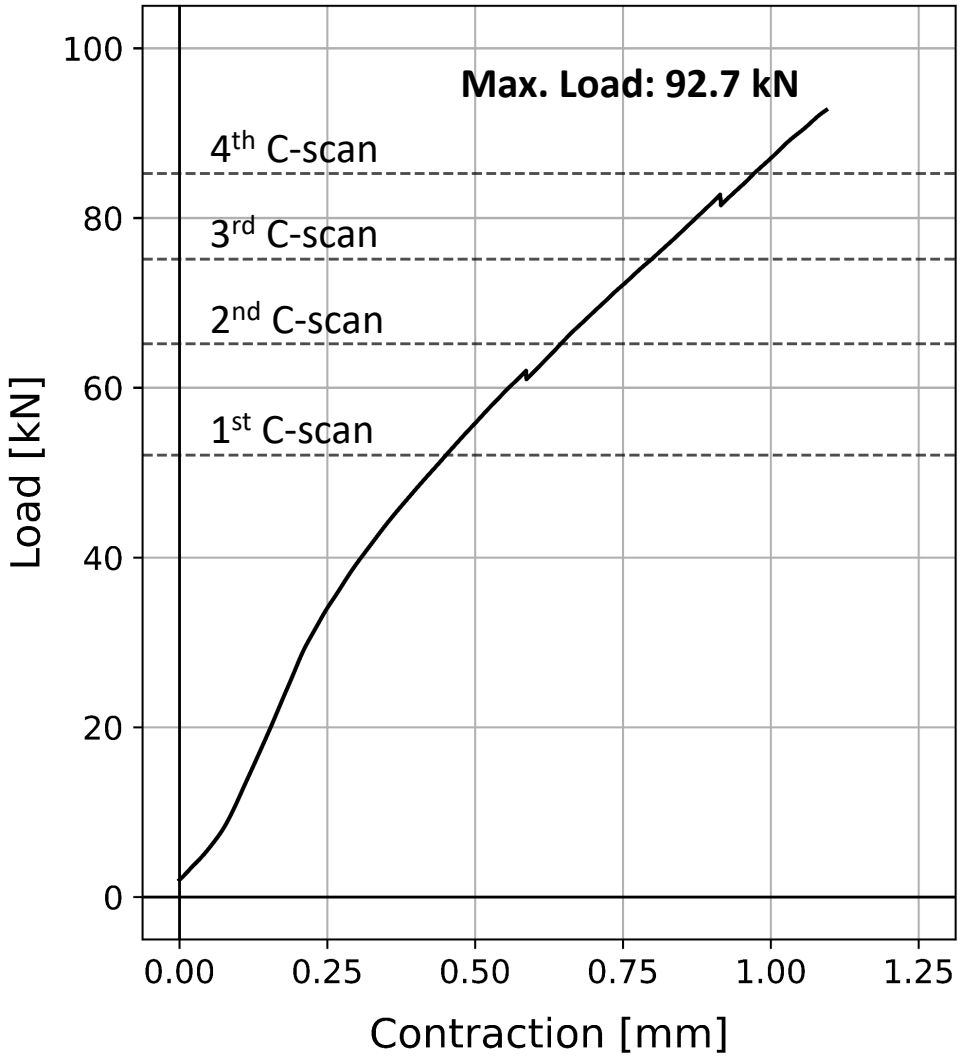

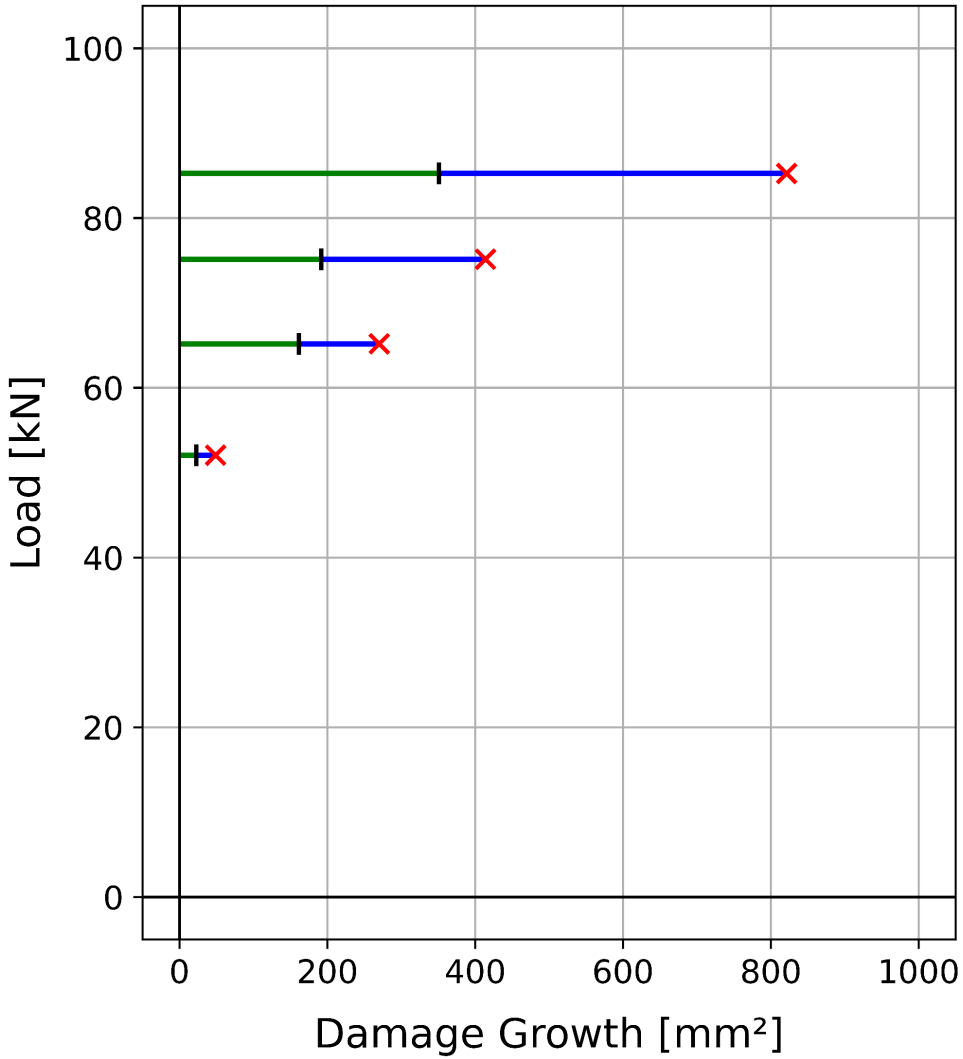

Validation of the DIC-based Crack Front Monitoring Method

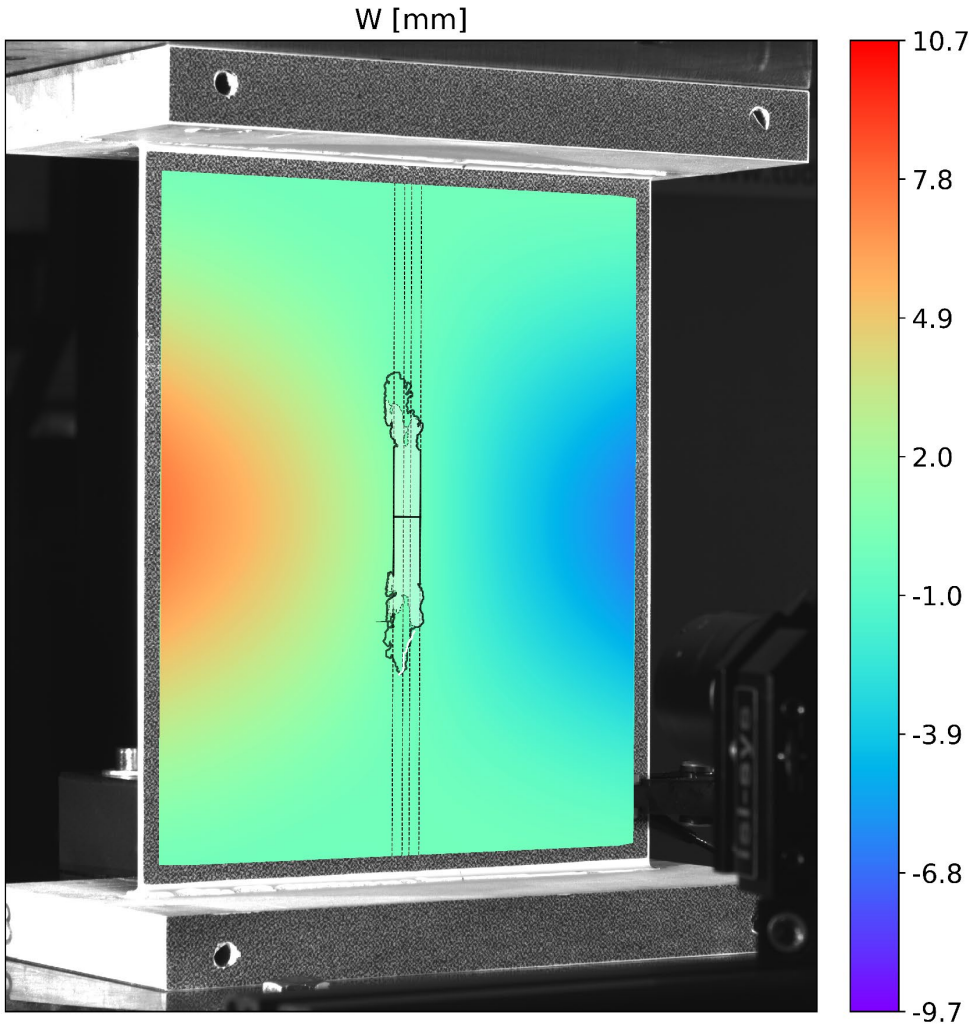

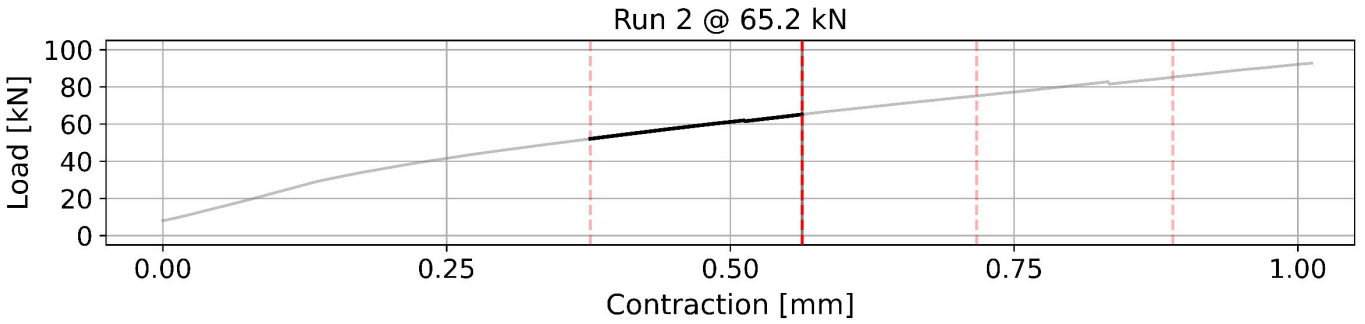

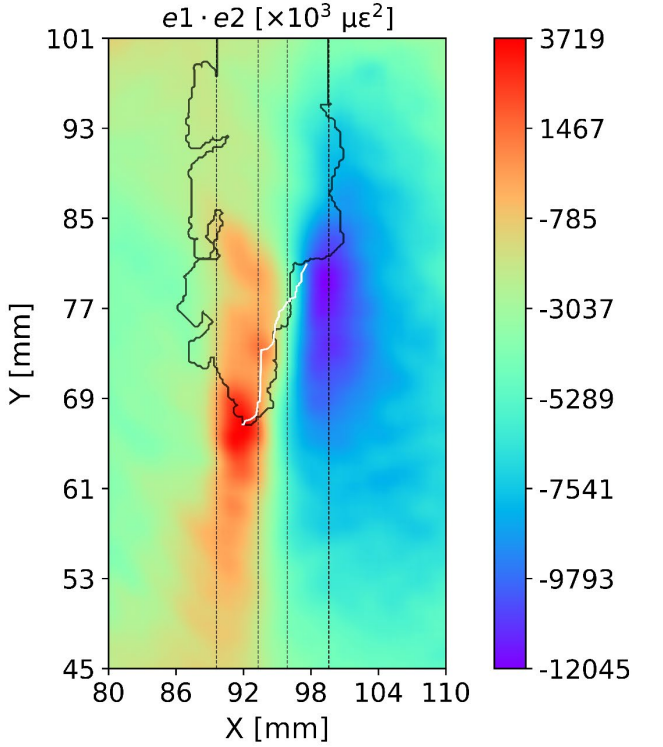

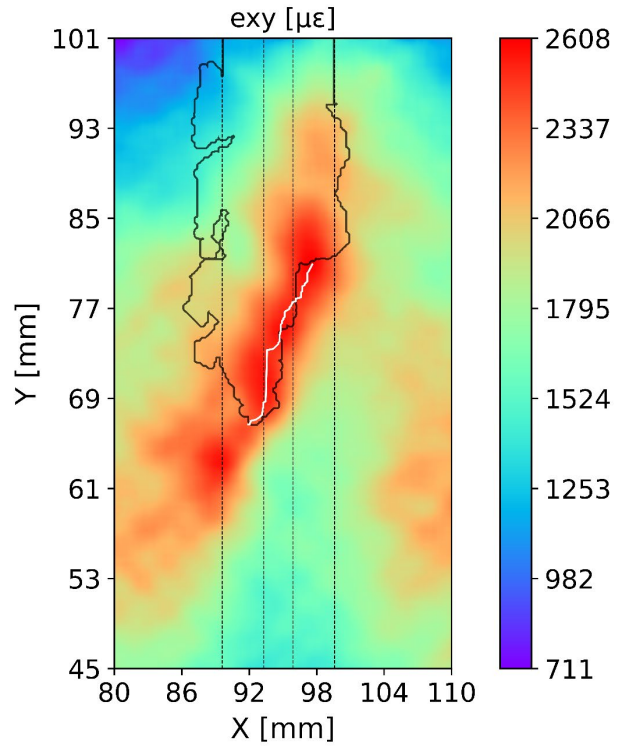

Validation of the DIC-based Crack Front Monitoring Method

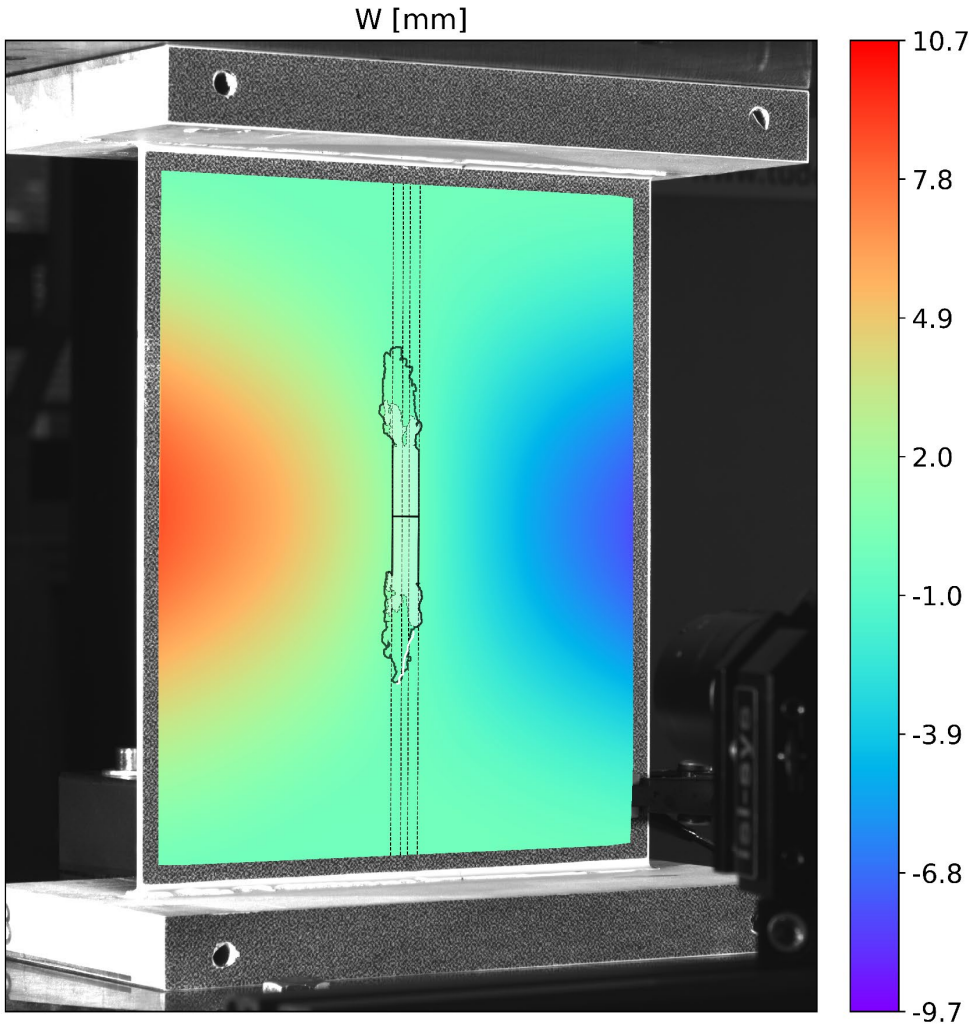

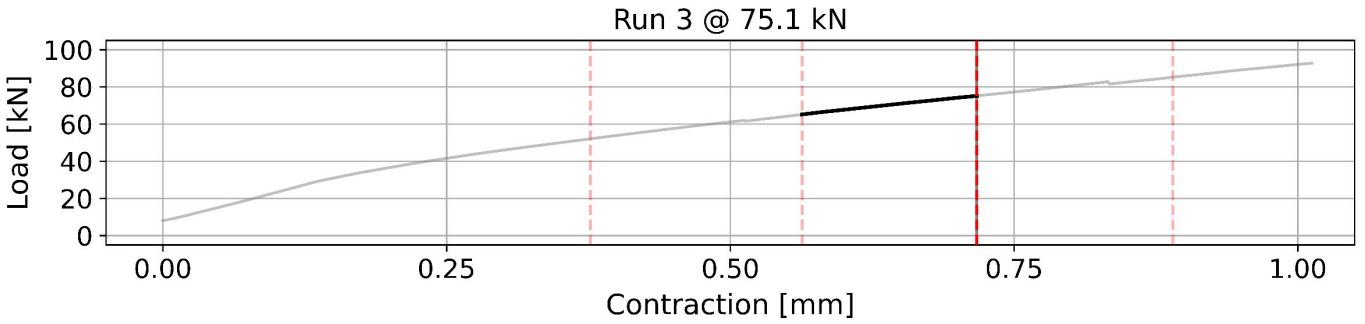

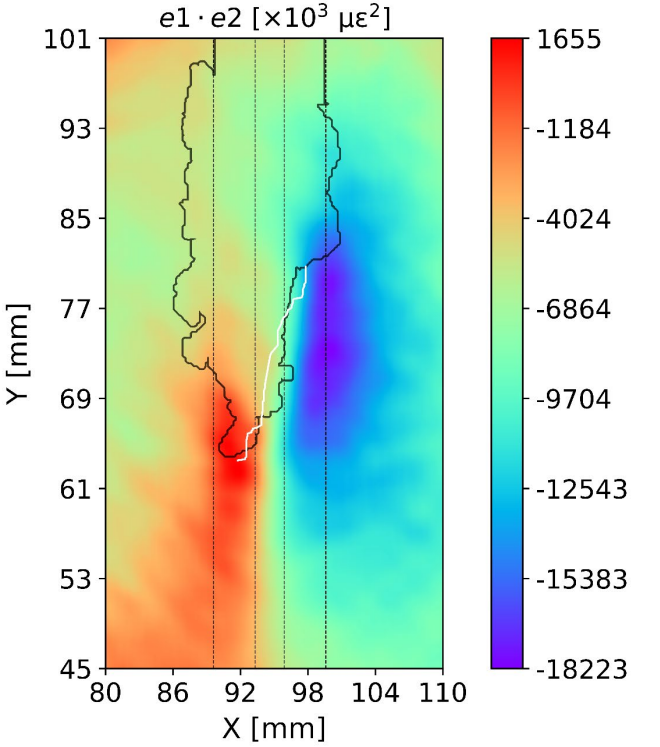

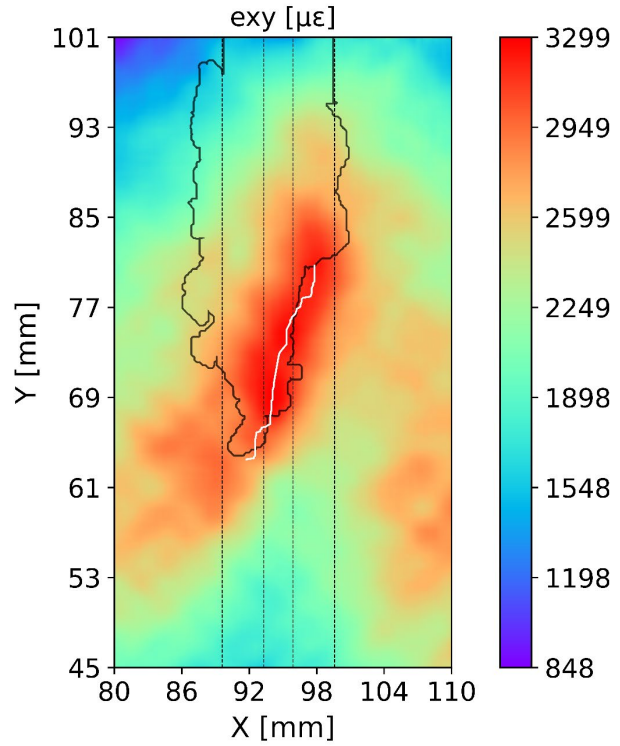

Validation of the DIC-based Crack Front Monitoring Method

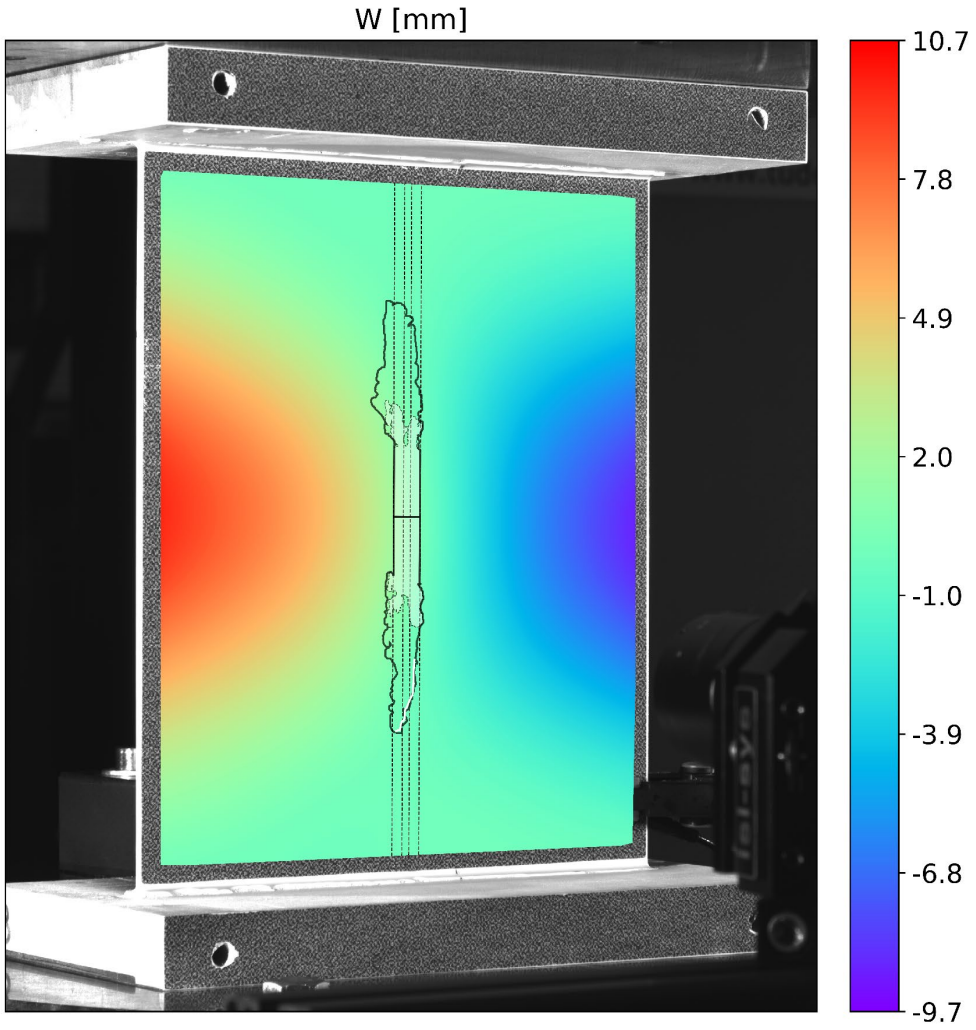

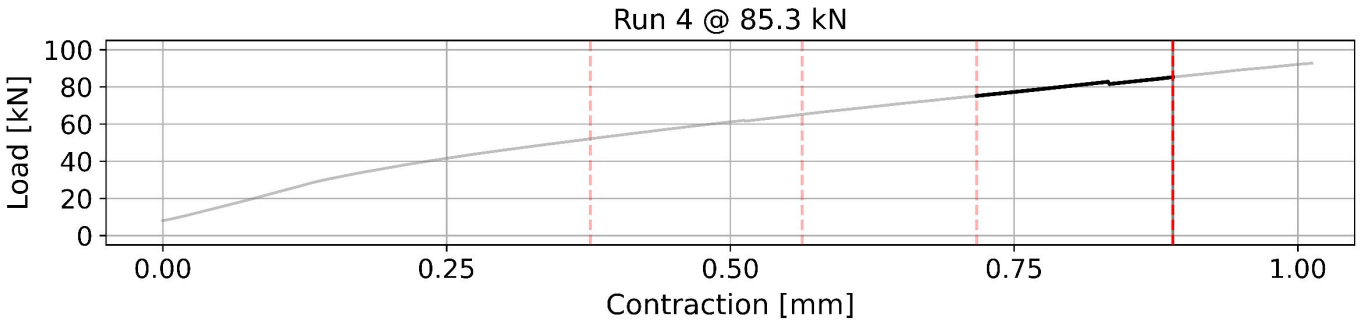

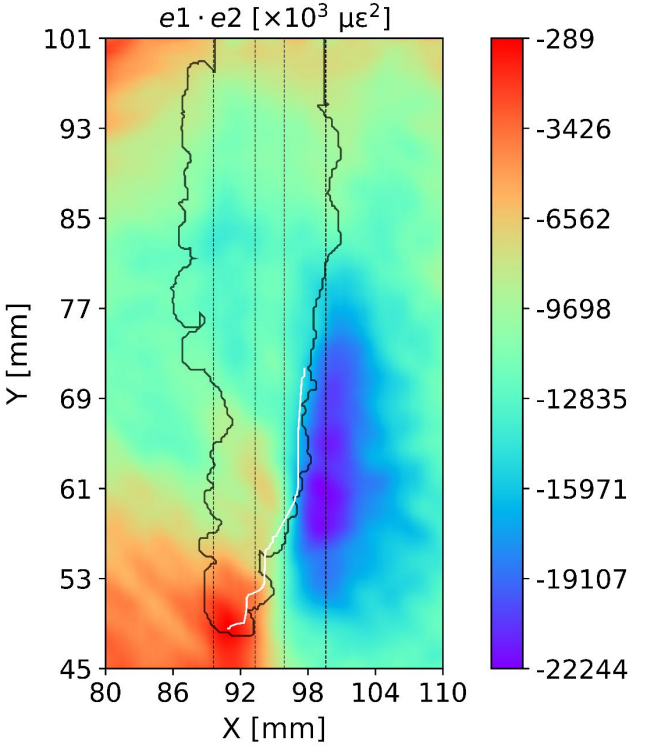

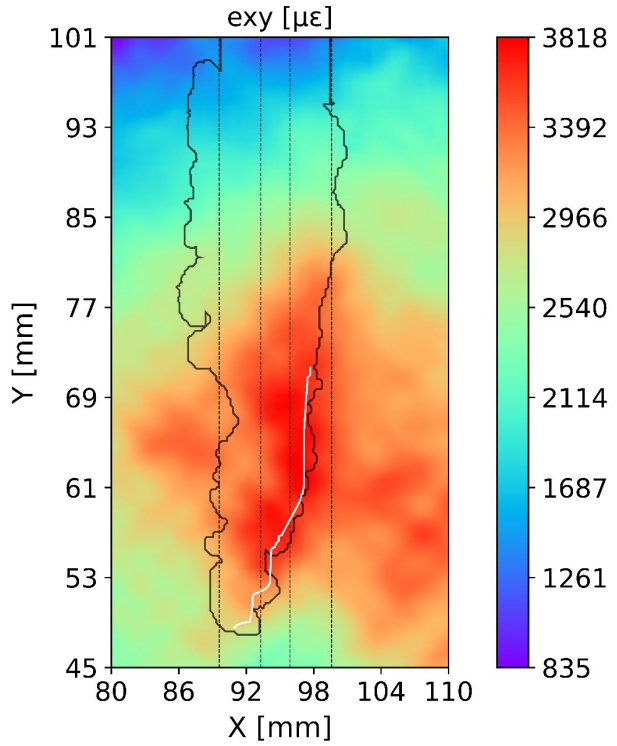

Enhanced Damage Quantification via Crack Front Monitoring

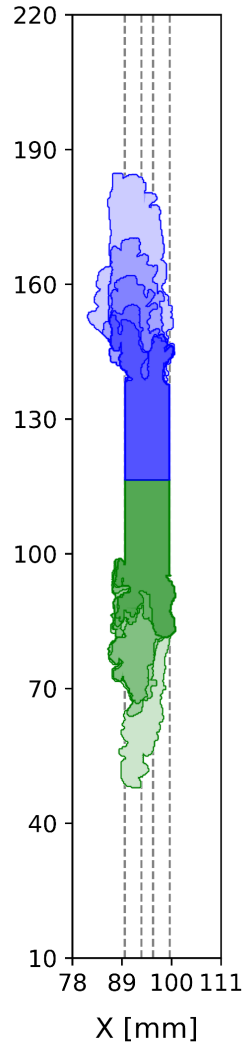

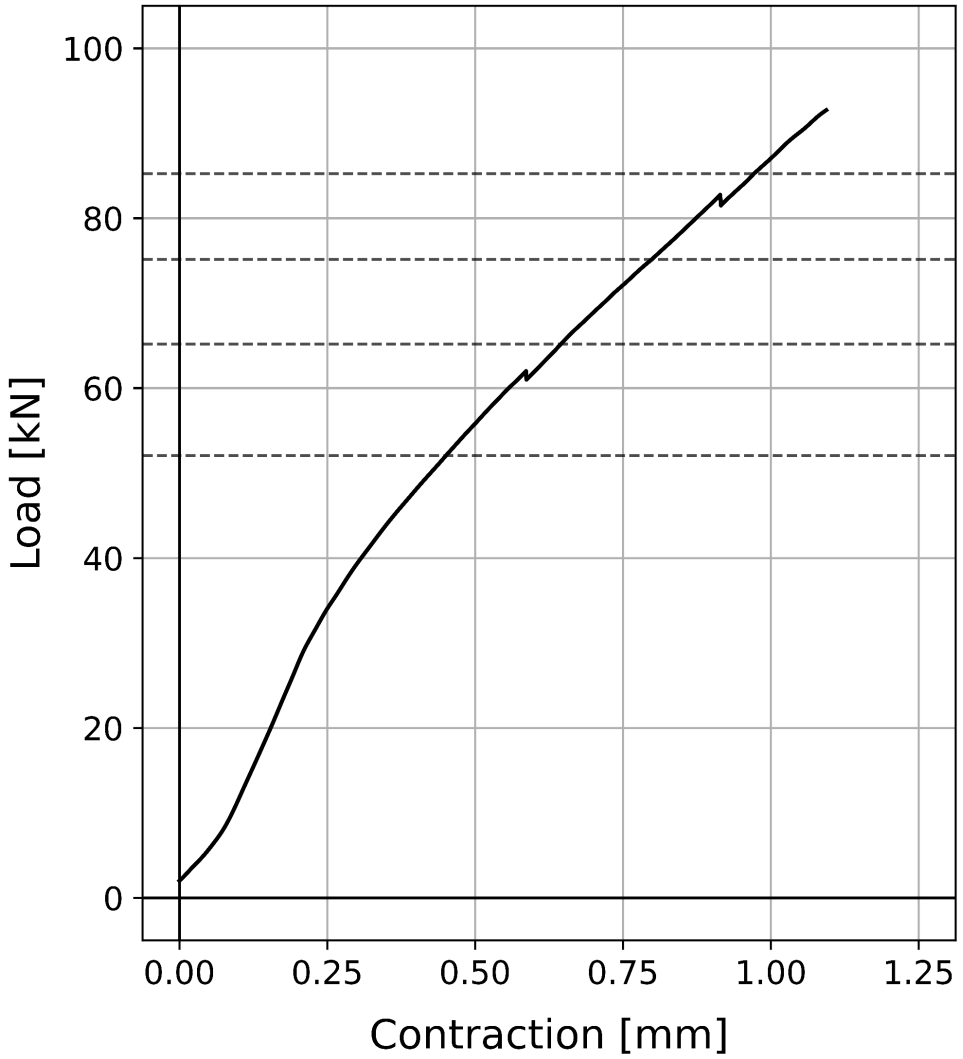

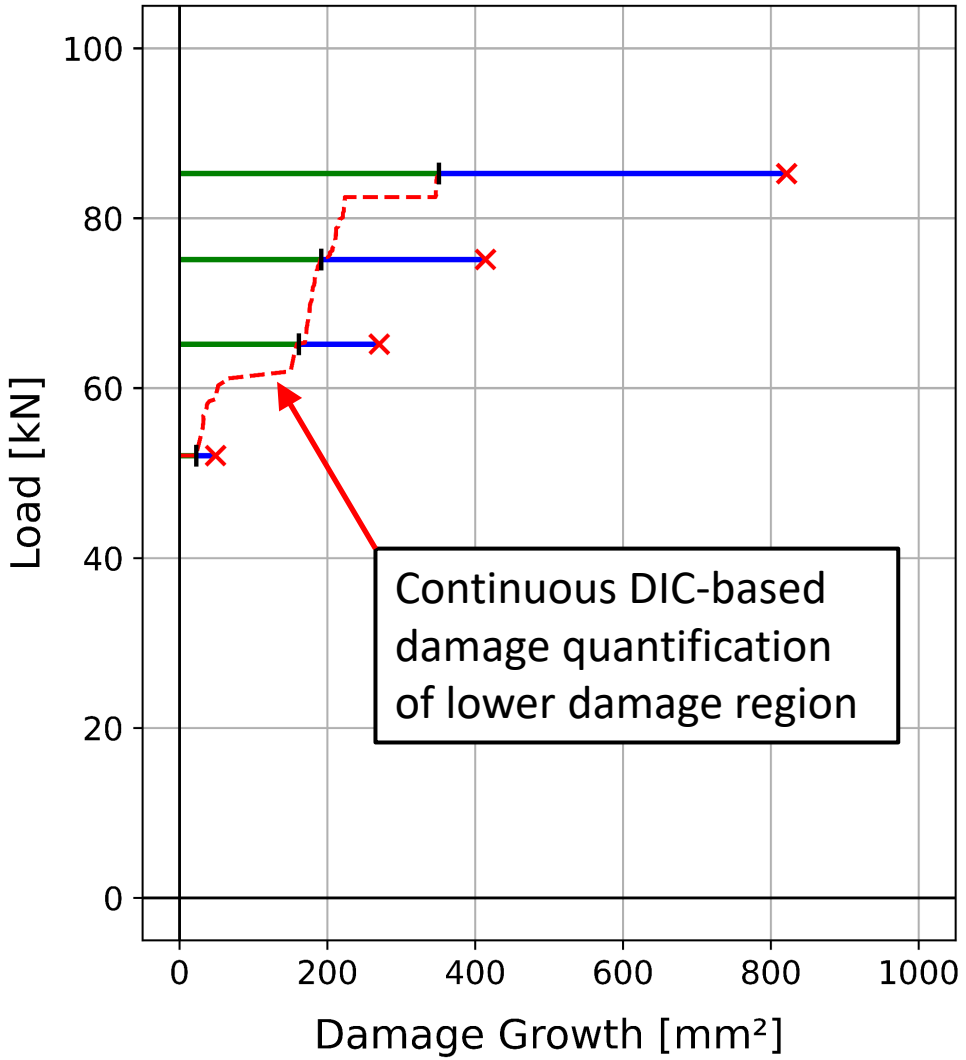

Conclusions & Future Work

- ✓ **Developed** and **validated** a novel DIC-based method for monitoring skin-stringer delamination growth in post-buckled composite panels.
- ✓ Enabled **continuous crack front tracking** during testing, advancing damage quantification beyond current standard approaches.
- ✓ The resulting data will **support validation of a high-fidelity numerical model**.
- ✓ The method will next be applied to a post-buckled **5-stringer panel**, representative of an actual airframe structure, to further demonstrate its capabilities.

A Novel Multi-Scale Digital Image Correlation Approach for Monitoring Stable Skin-Stringer Delamination Growth in Post-buckled Composite Panels

Andrés M. Pereira, Christos Kassapoglou, Sergio R. Turteltaub

Faculty of Aerospace Engineering,

Delft University of Technology,

The Netherlands



24th International Conference on Composite Materials (ICCM24)

TU Delft

ICCM24
AUGUST 4-8, 2025
BALTIMORE CONVENTION CENTER
BALTIMORE, MARYLAND, USA

No Technical Paper Submission for:

Mustafa Okumus

EXPERIMENTAL STUDY ON THE FATIGUE PERFORMANCE OF CFRP BEAMS WITH STRUCTURED SURFACE LOAD INTRODUCTION UNDER CYCLIC LOADING

Torben Deutschmann[1], Floyd Bischop[2], Marc Gadinger[3], Sandro Wartzack[4] and Dieter Krause[5]

[1]Institute of Product Development and Mechanical Engineering Design (PKT), Hamburg University of Technology (TUHH)
Denickestr. 17, 21073 Hamburg, Germany
Email: torben.deutschmann@tuhh.de, web page: https://tuhh.de/pkt

[2]Institute of Product Development and Mechanical Engineering Design (PKT), Hamburg University of Technology (TUHH)
Denickestr. 17, 21073 Hamburg, Germany
Email: floyd.bischop@tuhh.de, web page: https://tuhh.de/pkt

[3] Engineering Design, Friedrich-Alexander University of Erlangen-Nuremberg,
Martensstr. 9, 91058 Erlangen, Germany
Email: gadinger@mfk.fau.de, web page: https://www.mfk.tf.fau.de

[4] Engineering Design, Friedrich-Alexander University of Erlangen-Nuremberg,
Martensstr. 9, 91058 Erlangen, Germany
Email: wartzack@mfk.fau.de , web page: https://www.mfk.tf.fau.de

[5]Institute of Product Development and Mechanical Engineering Design (PKT), Hamburg University of Technology (TUHH)
Denickestr. 17, 21073 Hamburg, Germany
Email: krause@tuhh.de, web page: https://tuhh.de/pkt

Keywords: CFRP, Fatigue testing, 3-point bending, Load introduction, Cyclic loading

ABSTRACT

CFRP is widely used in lightweight structures subjected to cyclic loading. However, the fatigue performance at the structural level, particularly with mechanical joints, remains insufficiently understood. This study investigates the fatigue behavior of quasi-isotropic CFRP square tubes under cyclic 3-point bending, with a focus on a load introduction concept using bolted connections with structured surface plates. The specimens are tested under fully reversed loading at 1 Hz. Quasi-static baseline tests reveale linear behavior up to failure and high reproducibility between specimens. Cyclic tests show a clear increase in fatigue life with decreasing load amplitude. Hysteresis analysis reveals asymmetric behavior and narrowing around the zero-crossing prior to failure, especially in high-cycle specimens. The specimen with the highest cycle count exhibited a distinct fiber fracture on the tensile side, suggesting a change in failure mode compared to quasi-static loading. The results highlight the relevance of the hysteresis loop shape as a potential indicator for fatigue damage and structural monitoring. The findings underscore that fatigue failure may occur in locations different from those under static loading, suggesting that conventional design approaches based on static safety factors may be insufficient for the design of CFRP structures.

1 INTRODUCTION

Carbon fiber reinforced polymers (CFRP) are increasingly used in lightweight structural applications due to their excellent strength-to-weight ratio, corrosion resistance, and stiffness. They are well established in high-performance industries such as aerospace, automotive, and wind energy [1]. With rising production volumes and falling costs, CFRP has also become economically viable for

simpler structural components, such as square tube profiles, where mechanical performance and cost-efficiency must be balanced [2]. These components are gaining relevance in applications that demand robustness under repeated mechanical loading.

Cyclic loads are common in many operational environments. Despite the damage-tolerant nature of CFRP laminates under fatigue loading, the long-term performance of composite structures remains difficult to predict – especially at the structural level [3]. Most studies are limited to small-scale coupon specimens or highly application-specific configurations, leaving a research gap between elementary material tests and full-scale system evaluations [4].

A critical factor for structural CFRP components is a reliable load introduction. Bolted connections are widely used due to their mechanical reliability and ease of disassembly. However, they locally interrupt the fiber alignment and induce matrix cracking or delamination, making the joint region particularly vulnerable to fatigue degradation. Previous research has shown that structured surfaces at the interface can improve the load transfer capabilities of bolted joints by enhancing both mechanical interlocking and friction [5]. Understanding the fatigue behavior of such connections under realistic loading is essential for ensuring structural reliability and safe design margins. Moreover, being able to detect or predict fatigue-induced degradation is highly relevant for the development of structural health monitoring systems. In particular, hysteresis loop evolution under cyclic loading offers a promising approach for characterizing internal damage states [6], [7].

This study aims to address the outlined gap by investigating the fatigue performance of quasi-isotropic CFRP square tube beams under cyclic 3-point bending. A special focus is placed on the role of bolted load introduction with structured surfaces. The work builds upon earlier investigations of small-scale joint behavior and evaluates the structural-level fatigue response, with attention to both global mechanical performance and fatigue-induced changes in hysteresis characteristics.

2 RESEARCH PROBLEM AND OBJECTIVE

Fatigue in CFRP laminates is generally considered damage-tolerant, with gradual degradation rather than sudden failure. However, the load introduction zone remains a critical weak point, where local stress concentrations can initiate damage and accelerate failure processes [8]. Current research on cyclically loaded CFRP connections is fragmented and often based on simplified coupon tests, which limits its applicability to structurally relevant components [4].

Bolted connections are widely used for load introduction in CFRP due to their mechanical robustness, disassembly capability, and suitability for high force transfer. The load is transmitted through bearing stress, directly from the bolt into the laminate. However, the required drilling of holes leads to fiber interruption, causing matrix cracking and delamination in the surrounding region, which compromises structural integrity [9]. The fatigue strength of such connections can be improved through interference fits [8] and clamping pressure, although these effects depend strongly on geometry and assembly parameters [9]. Failure mechanisms in bolted CFRP joints can be categorized into four main types, each influenced by geometry and boundary conditions [10]. Bearing failure is considered the most desirable mode. It occurs as a localized compression failure near the bolt, typically characterized by resin crushing and fiber buckling. This failure is less brittle and more damage-tolerant, and is favored when a high plate width-to-hole diameter ratio is maintained [11]. In contrast, net-tension failure is a brittle mode resulting from high tensile stresses across the remaining ligament between the hole and the edge. It typically occurs when large bolts are used in narrow components, leading to sudden transverse cracking and rapid failure. Shear-out failure is another brittle mechanism, characterized by shear fracture along the bolt axis, often occurring when the end distance is too small. It frequently appears as a secondary failure following bearing damage, particularly in in-plane loading scenarios [12]. Lastly, cleavage failure combines features of net-tension and shear-out. It initiates at the end of the plate, especially when both edge and end distances are insufficient and the longitudinal fiber content is high, leading to crack propagation along an inclined path. Ensuring proper geometric ratios helps to avoid this mode [13]. To mitigate these failure mechanisms, it is essential to maintain precise hole manufacturing and sufficient edge distances [14]. Additional measures, such as embedded metal foils or localized reinforcement layers, can improve bearing strength and reduce sensitivity to geometric constraints [15]. Despite these measures, fatigue failure in bolted CFRP

connections remains difficult to predict, as it is highly dependent on load spectra, joint design, and laminate configuration [16].

Previous research has primarily focused on idealized test coupons. To address the lack of structural-level data, the present study investigates the fatigue performance of quasi-isotropic CFRP square tubes under cyclic 3-point bending. The aim of this study is to provide experimental data on the fatigue behavior of CFRP components at the structural level and to evaluate the effectiveness of a load introduction concept based on bolted connections with structured surfaces. By applying cyclic bending loads to full-scale square tube specimens, this work seeks to identify dominant failure mechanisms and assess the stability of the connection under fatigue.

3 SPECIMEN DESIGN AND TESTING APPROACH

The fatigue behavior of CFRP structures is investigated using a 3-point bending test setup. The test specimens consist of CFRP square tubes with dimensions of 75 × 75 × 750 mm and a wall thickness of 3 mm. The geometric dimensions of the specimens are shown in Figure 1, including mean values across all beams and their maximum deviations. Dimensions up to 75 mm were measured using a micrometer, while larger values were obtained with a caliper. The corner radius was determined via optical microscopy. Notable deviations are observed in the wall thickness and corner radius, whereas all other dimensions exhibited high dimensional accuracy. For the milled bolt holes, the measured radius deviation is at the limit of the measurement accuracy.

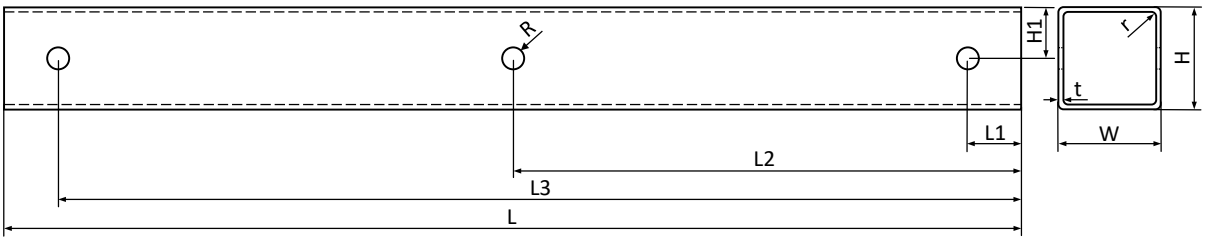

	W	H	L	$L1$	$L2$	$L3$	$H1$	R	r	t	$m\,(g)$
Ø (mm)	75.00 ± 0.002	75.00 ± 0.002	750.00 ± 0.1	40.00 ± 0.002	375.00 ± 0.1	710.00 ± 0.1	37.50 ± 0.002	8.00 ± 0.001	3.50 ± 1.011	3.15 ± 0.062	972.67 ± 6.30

Figure 1: Dimensions of the test specimens.

The laminate was manufactured using a prepreg process in an aluminum negative mold and featured a 12 layer quasi-isotropic layup, following the stacking sequence $[0°, 60°, -60°, 0°, -60°, 60°]_S$. To introduce the load, a bolted connection with structured surface plates is developed (see Figure 2). The bearing plates with structured contact surfaces are mounted on threaded pieces, which are pressed against the CFRP square profile by a locknut. These threaded elements are then fitted onto bolts through which the load is applied. This design enables both form-fit and clamping effects, aiming to enhance load transfer by increasing contact friction and minimizing stress concentrations. The structured surfaces featured pyramidal elements with a tooth height of 0.3 mm. The tooth geometry was selected based on literature [17] to ensure high friction and allowable surface pressure. The holes in the CFRP profile are manufactured with high dimensional accuracy to ensure a precise fit between bolt and laminate, as literature shows that even small clearance gaps can lead to a significant reduction in load transfer capacity [14].

To prevent overheating during high-cycle testing, compressed air is introduced through the hollow interior of the CFRP beam to provide active cooling. On the opposite side of the profile, an FFP2 filter is installed. This serves a dual purpose: first, to collect fine dust particles that might be expelled by the cooling airflow; and second, to create flow resistance, thereby improving air distribution through the beam and enhancing the overall cooling efficiency.

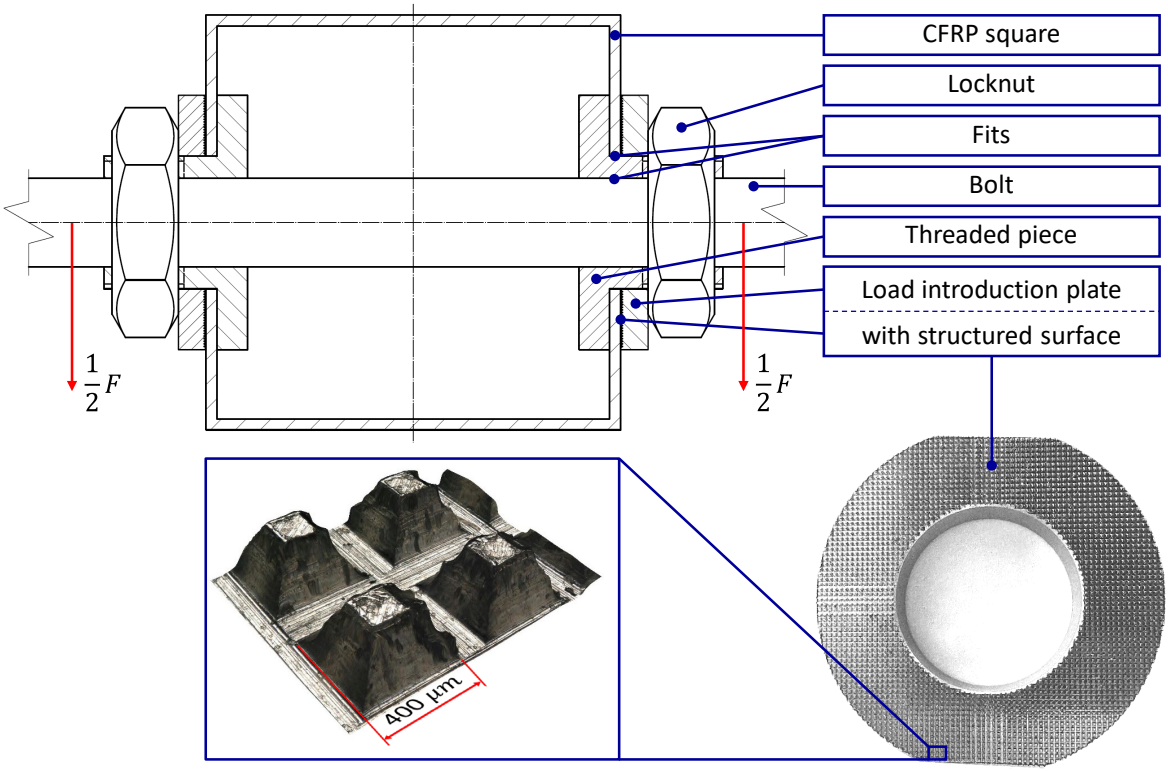

Figure 2: Load introduction design with structured surface and three-dimensional enlargement of the pyramid-shaped surface structure.

The experiments were carried out on a servo-hydraulic testing system with a maximum actuator force of 125 kN. The two outer supports are equipped with roller-bearing guides to compensate for axial displacement caused by beam deflection. Load is measured via a 125 kN load cell, and displacement is recorded both by the integrated actuator position sensor and an external laser displacement sensor, which is aligned with the midplane of the test setup. In addition, the temperature at the top flange of the CFRP profile is monitored using a Type K thermocouple.

At the beginning of the test series, two quasi-static destruction tests were performed to determine the maximum load capacity of the CFRP beams. This value serves as the basis for selecting the amplitude for the subsequent fatigue tests. The following cyclic tests were conducted under fully reversed loading at a frequency of 1 Hz. The first fatigue test was carried out at 85% of the previously determined maximum load, while the load amplitude was gradually reduced in the subsequent tests to assess the fatigue performance at lower stress levels.

4 RESULTS AND DISCUSSION

The structured surface embedding using the pyramidal profile was successfully implemented. No loosening of the locknuts was observed during cyclic testing, indicating stable mechanical fixation throughout the test duration. The cooling system proved effective, with a maximum temperature increase of only 1 °C at the measurement point. In contrast, a reference test without internal cooling, conducted at 1 Hz and a cyclic load of 45 kN, resulted in a temperature rise of approximately 23 °C after 30 minutes.

4.1 Quasi-static testing

The quasi-static tests reveal a linear force–displacement behavior up to the point of failure, indicating elastic material response across the tested load range. Maximum load capacity is observed at approximately 53 kN. Figure 3 shows the force–displacement diagram obtained from the quasi-static bending tests. Failure occurs suddenly, suggesting a brittle failure mechanism under bending load. A very good agreement is observed in the linear-elastic range of the force–displacement response.

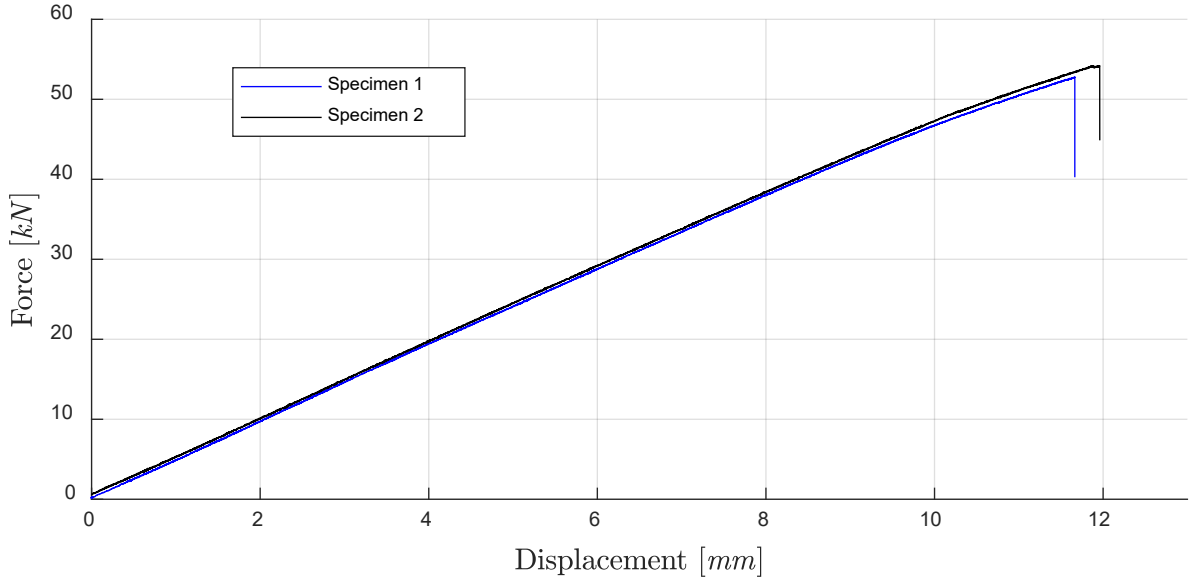

Figure 3: Force-displacement diagram of quasi-static tests.

Figure 4 presents the failure patterns of the two quasi-static specimens. The beams exhibit local buckling at the lower flange, combined with matrix detachment and interlaminar delamination, consistent with typical compression-induced failure mechanisms in fiber-reinforced polymer structures under bending. These failures are driven by local instability in matrix-dominated regions, which are especially sensitive to interlaminar shear stresses and separation. Notably, Specimen 1 failed at an off-center position, rather than directly at midspan where the highest bending moment occurs, and thus the failure, would be expected. A possible explanation for this behavior is that the load introduction locally reinforces the beam, especially the vertical webs of the square tube, thereby stabilizing the midsection and shifting the critical failure zone outward.

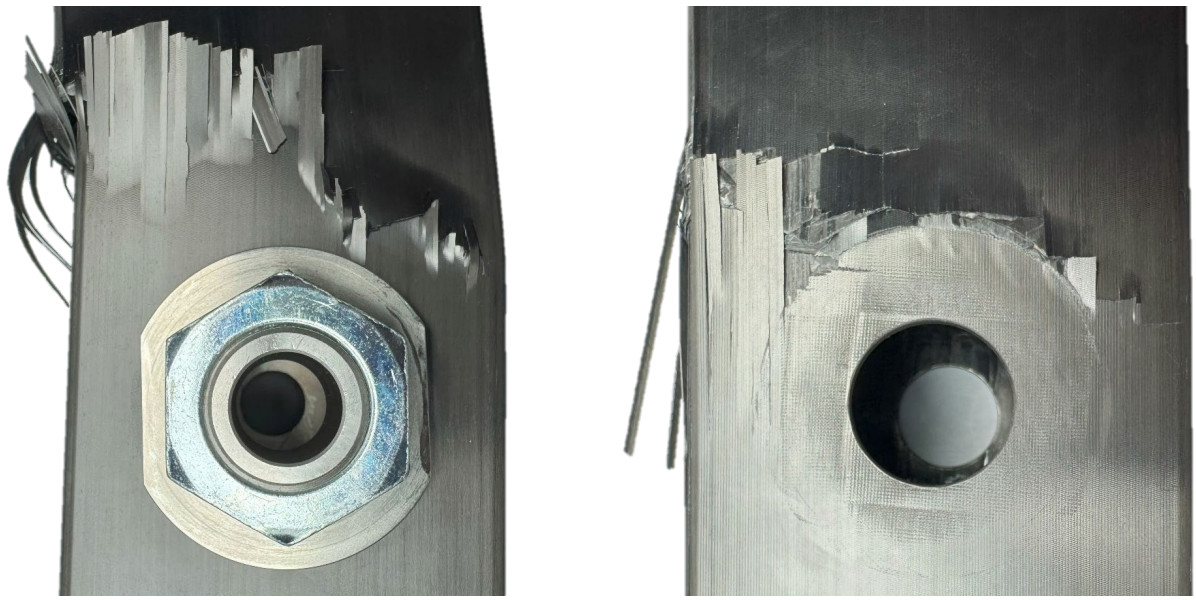

Figure 4: Failure of Specimen 1 with load introduction (left) and Specimen 2 without load introduction (right).

Specimen 2 exhibited a central failure fracture, as shown in Figure 4 (right). The fracture path runs around the load introduction region. As with Specimen 1, this suggests a stabilizing effect of the load introduction unit, likely due to the local reinforcement.

4.2 Cyclic testing

To evaluate the fatigue performance of the CFRP beams under cyclic loading conditions, a series of 3-point bending tests was carried out at decreasing load amplitudes. Table 1 summarizes the applied maximum force and the corresponding number of cycles to failure for each specimen. As expected, the number of cycles to failure increases with decreasing load level, indicating a typical fatigue response. While specimens tested at higher loads failed within a few thousand cycles, Specimen 7, sustained nearly 150,000 cycles before failure. The comparatively low cycle count of Specimen 5 suggests a potential outlier.

Test Specimen	Force [kN]	Number of Cylces to Failure
Specimen 3	45	2077
Specimen 4	43	10312
Specimen 5	40	2681
Specimen 6	38	12977
Specimen 7	35	149480

Table 1: Overview of tests.

Figure 5 compares the hysteresis behavior of Specimen 7 at cycle 100 and cycle 149,479, the cycle before final failure. A reduction in hysteresis area is observed at the later stage, indicating decreased energy dissipation, which is characteristic of advanced material degradation [18]. The loading and unloading paths converge near the zero-crossing, suggesting a nearly elastic response with no measurable plasticity or damping, a sign of structural exhaustion. While the overall stiffness appears unchanged, internal damage accumulation is likely near critical. A slight asymmetry and narrowing of the curve further points to localized effects such as delamination, matrix cracking, or fiber-matrix debonding. This observation is consistent with findings, where individual fiber bundles delaminated at the sides or corners of the beam, away from the eventual failure location, prior to global failure. This indicates that localized damage initiation can occur independently of the final fracture zone and further supports the interpretation of progressive internal degradation despite externally stable load-displacement behavior.

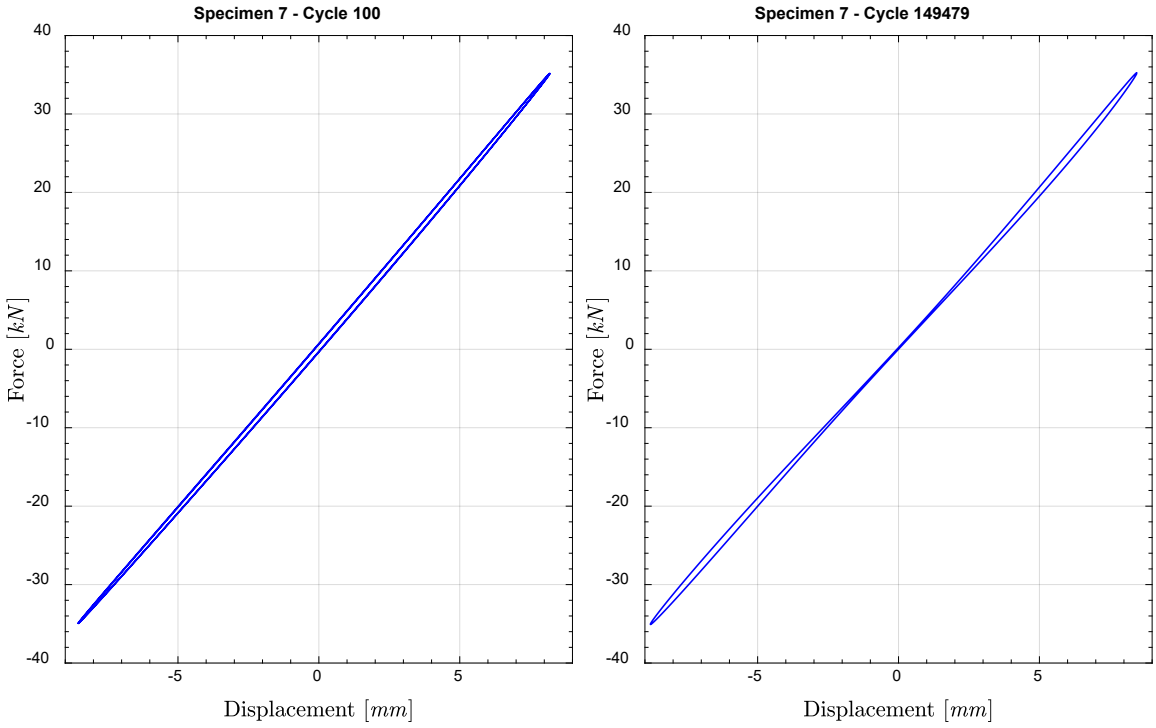

Figure 5: Hysteresis behavior of Specimen 7 at cycle 100 and 149479.

These features collectively indicate that the material has exhausted its damage tolerance and that failure is imminent. This progression highlights how the collapse of the hysteresis loop at the neutral axis could be precursor of final failure in fatigue-loaded composites. Such behavior could be relevant for structural health monitoring, as it highlights the need to detect early-stage internal damage. Localized delamination or fiber–matrix debonding could serve as early indicators of fatigue degradation. This aspect will be investigated in future tests. To enable a more detailed analysis of local damage progression, strain gauges will be applied at critical locations on the beam surface. This will allow for a broader and more spatially resolved dataset.

The convergence of the loading and unloading paths near the zero-crossing in Specimen 7 developed progressively over the final 40,000 cycles. A similar trend is observable in Specimens 4 and 6, where the hysteresis loops also narrow around the neutral axis as failure approaches. Furthermore, all specimens exhibit increasing asymmetry in their hysteresis behavior toward the end of their fatigue life, though with varying degrees of intensity.

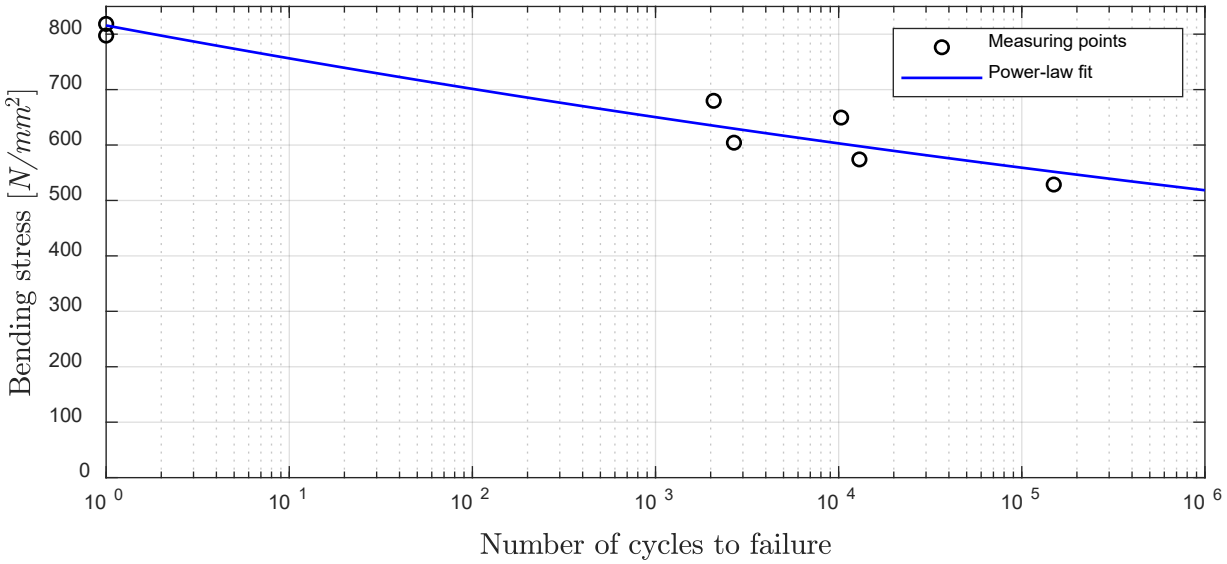

Figure 6: S-N curve with power-law fit trendline.

Figure 6 displays the bending stress versus the number of cycles to failure for all tested specimens. The results from the quasi-static tests are included as reference points with a cycle count of 1. To illustrate the overall trend in fatigue behavior, a power-law fit is applied to the data. This trendline provides a first approximation of the fatigue life curve, highlighting the expected decrease in maximum stress with increasing cycle number.

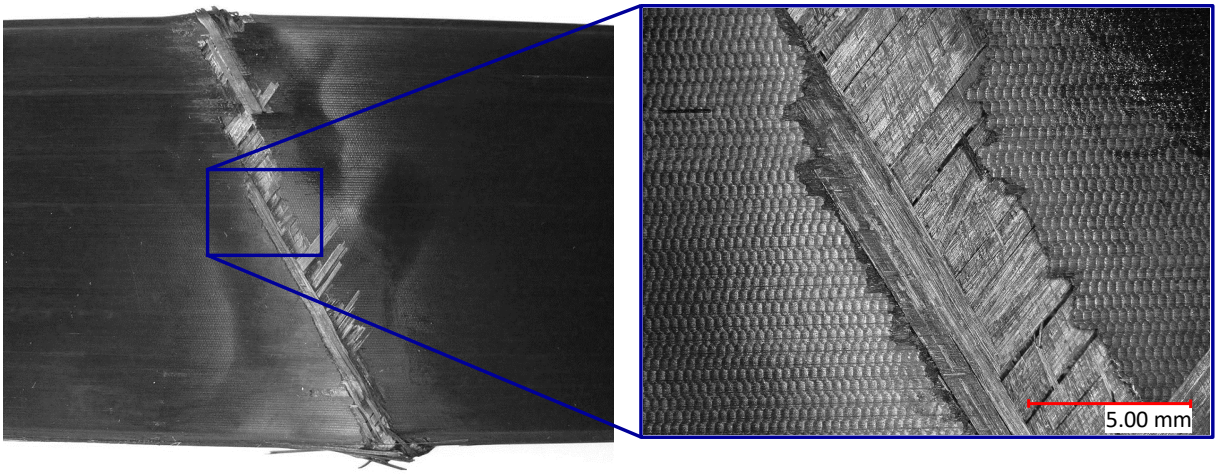

Figure 7: Failure of Specimen 7 with magnified view.

At low cycle counts, the observed failure modes are similar to those in the quasi-static tests, characterized by local buckling and delamination at the lower flange. However, at cycle numbers exceeding 10^4, delamination occurs on both sides of the specimen, which is consistent with the alternating loading applied during fatigue testing.

An exception appears in Specimen 7, where a distinct failure mode emerges. Instead of buckling on the compression side, as typically seen, the failure occurred on the tension side of the profile, where a fiber fracture accrued. This result is shown in Figure 7. Such a shift in failure location under fatigue loading is particularly relevant for design practice, as it challenges the assumption that fatigue failure occurs at the same critical location as static failure. In many current design approaches, fatigue is accounted for by applying a global safety factor to the static strength. This strategy may be insufficient when fatigue failure initiates in different regions of the structure. Since only a single specimen was tested in this high-cycle regime, further tests are planned to statistically validate this observation and assess its reproducibility.

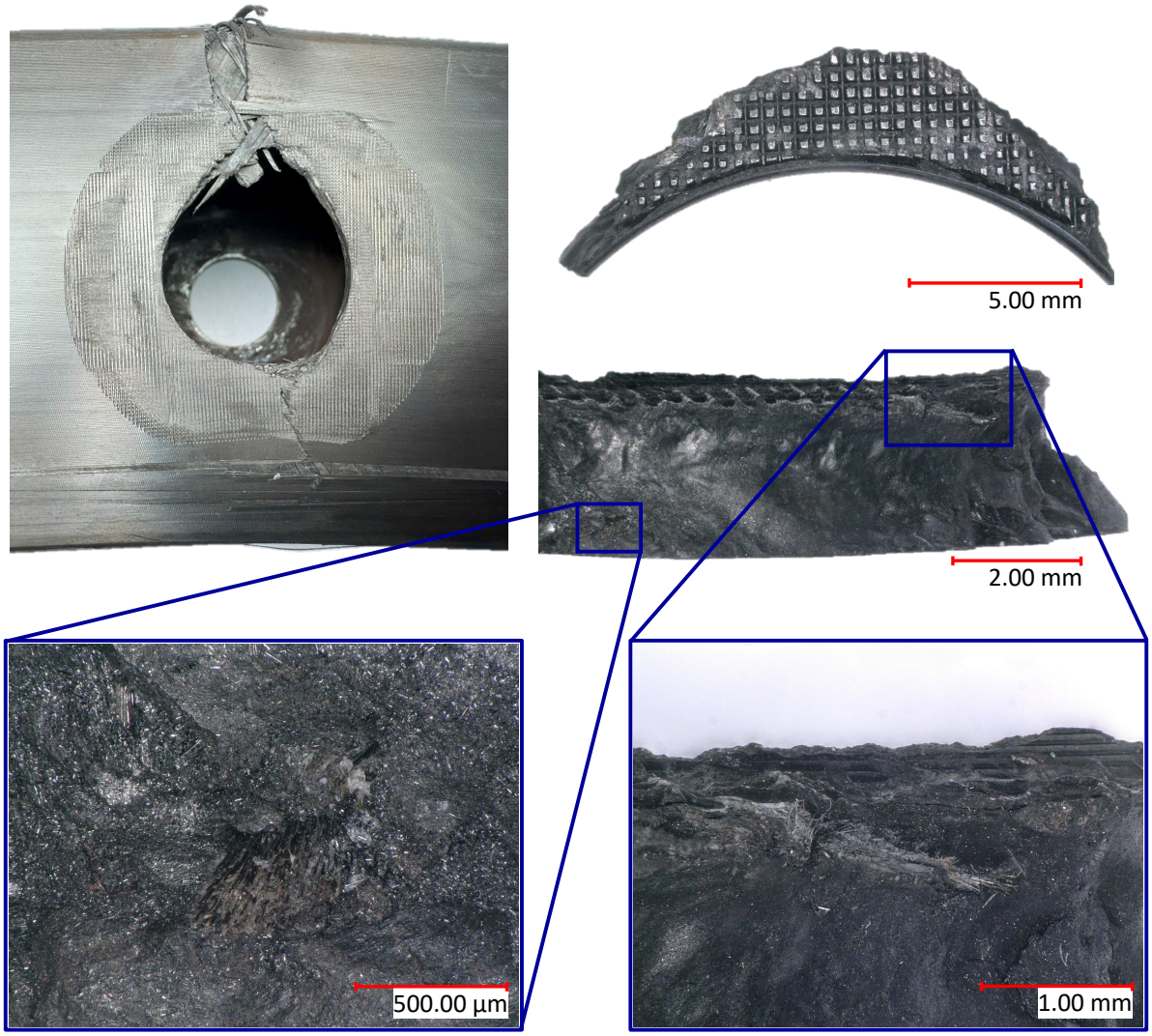

Figure 8: Top view of the damage on Specimen 7 (top left) and the detached fragment (top right). The fracture surface is shown in the middle right image, with magnified views of the fracture edge and exposed fiber bundles (bottom).

None of the tested specimens exhibited catastrophic failure at the load introduction area. However, in two cyclically tested specimens, seizure (galling) occurred between the bolt and the threaded insert. In both cases, localized damage to the CFRP in the load introduction zone is observed (see Figure 8).

The material appears brittle, and during disassembly, a portion of the laminate fractured and detached, shown on the right top in Figure 8. Below that, the fracture surface of the detached laminate fragment is shown. The surface exhibits a dark, discolored appearance, which visually resembles thermal damage or burning. Only two small areas with visible fibers can be identified, which are shown in magnified view in the lower part of the figure.

A possible explanation is that localized frictional heating during galling led to temperatures exceeding the glass transition temperature of the CFRP matrix, resulting in material degradation. Although this was not the primary failure mode of the beams, the finding emphasizes the critical importance of the load introduction zone in the fatigue design of CFRP structures. Even if structural failure occurs elsewhere, thermo-mechanical interactions at the interface may compromise long-term performance and must be accounted for in design and monitoring strategies.

5 CONCLUSION

This study contributes to the understanding of the fatigue performance of CFRP structures at the component level. CFRP square beams were tested under both quasi-static and cyclic 3-point bending, with the load introduced via structured bolted plates that ensured both form-fit and force-fit conditions. The quasi-static tests showed good repeatability across specimens, with linear behavior up to failure, followed by sudden collapse. The load introduction concept demonstrated a stabilizing effect on the beam structure.

Under cyclic loading up to 45 kN, the expected increase in the number of cycles to failure with decreasing load amplitude was observed. Notably, several specimens exhibited distinct hysteresis behavior prior to failure, including asymmetry and a progressive narrowing near the zero-crossing in high-cycle regimes. The specimen with the highest cycle count failed through a fiber break on the tensile side, suggesting a different failure mechanism compared to the quasi-static case.

These observations highlight the potential of hysteresis behavior as an indicator of internal damage, making it a promising approach for future structural health monitoring applications. Upcoming test series will focus on high-cycle regimes and will incorporate strain gauge measurements to further investigate the link between hysteresis characteristics and damage evolution. From a design perspective, the findings emphasize that fatigue failure may occur at locations different from those predicted by static analysis. Therefore, applying conventional safety factors to static designs may be insufficient for fatigue-critical CFRP structures. A more nuanced approach to fatigue assessment is needed – especially when mechanical connections are involved.

ACKNOWLEDGEMENTS

This research was funded by the Deutsche Forschungsgemeinschaft (DFG, German Research Foundation) – 508331526 with the title „ZoE – Erforschung der Übertragbarkeit des Zeitfestigkeitsverhaltens bei Faser-Kunststoff-Verbunden von Couponproben auf optimierte Halbzeuge zur Entwicklung einer konstruktionstechnischen Auslegungsrichtlinie“.

REFERENCES

[1] A. K. Hamzat, M. S. Murad, I. A. Adediran, E. Asmatulu, und R. Asmatulu, „Fiber-reinforced composites for aerospace, energy, and marine applications: an insight into failure mechanisms under chemical, thermal, oxidative, and mechanical load conditions“, *Adv Compos Hybrid Mater*, Bd. 8, Nr. 1, Feb. 2025, doi: 10.1007/s42114-024-01192-y.

[2] H. Guo, M. Zhou, P. Li, M. Lv, und Y. Zhang, „Prospects of carbon fiber composites applications in hydraulic supports“, *Front. Mater.*, Bd. 9, Aug. 2022, doi: 10.3389/fmats.2022.997258.

[3] R. Guo, C. Li, Y. Niu, und G. Xian, „The fatigue performances of carbon fiber reinforced polymer composites – A review“, *Journal of Materials Research and Technology*, Bd. 21, S. 4773–4789, Nov. 2022, doi: 10.1016/j.jmrt.2022.11.053.

[4] P. Alam, D. Mamalis, C. Robert, C. Floreani, und C. M. Ó Brádaigh, The fatigue of carbon fibre reinforced plastics - A review, *Composites Part B: Engineering*, Bd. 166, S. 555–579, Juni 2019, doi: 10.1016/j.compositesb.2019.02.016.

[5] T. Deutschmann, M. Gadinger, S. Wartzack, und D. Krause, Design of the Load Introduction of Continuous Fibre-Reinforced Components for Cyclic Loading, in *DS 133: Proceedings of the 35th Symposium Design for X (DFX2024)*, The Design Society, 2024, S. 115–124. doi: 10.35199/dfx2024.12.

[6] N. Rozo Lopez, J. Chen, und C. Hopmann, A micromechanical model for loading and unloading behavior of fiber reinforced plastics under cyclic loading, *Polymer Composites*, Bd. 41, Nr. 9, S. 3892–3902, Sep. 2020, doi: 10.1002/pc.25684.

[7] P. Xing und H. Yu, Tension-tension fatigue behavior and its modelling for life estimation of rivet-bonding CFRP/CFRP single lap joints, *Composite Structures*, Bd. 275, S. 114367, Nov. 2021, doi: 10.1016/j.compstruct.2021.114367.

[8] J. Wang, C. Zhu, Y. Yang, Y. Zhang, und Y. Bi, Effect of riveting displacement on the mechanical behavior of CFRP bolted joints with elliptical-head non-lug self-locking rivet nut, *Int J Adv Manuf Technol*, Bd. 125, Nr. 5–6, S. 2161–2182, März 2023, doi: 10.1007/s00170-023-10823-5.

[9] J. Godzimirski, M. Rośkowicz, M. Jasztal, und I. Barca, Static and Fatigue Strength and Failure Mechanisms of Riveted Lap Joints of CFRP Composites, *Materials*, Bd. 16, Nr. 5, S. 1768, Feb. 2023, doi: 10.3390/ma16051768.

[10] J. Qureshi, A Review of Fibre Reinforced Polymer Structures, *Fibers*, Bd. 10, Nr. 3, S. 27, März 2022, doi: 10.3390/fib10030027.

[11] N. S. Matharu und J. T. Mottram, Plain and threaded bearing strengths for the design of bolted connections with pultruded FRP material, *Engineering Structures*, Bd. 152, S. 878–887, Dez. 2017, doi: 10.1016/j.engstruct.2017.10.003.

[12] A. M. Girão Coelho und J. T. Mottram, Numerical Evaluation of Pin-Bearing Strength for the Design of Bolted Connections of Pultruded FRP Material, *J. Compos. Constr.*, Bd. 21, Nr. 5, S. 04017027, Okt. 2017, doi: 10.1061/(ASCE)CC.1943-5614.0000809.

[13] A. M. Girão Coelho und J. T. Mottram, A review of the behaviour and analysis of bolted connections and joints in pultruded fibre reinforced polymers, *Materials & Design*, Bd. 74, S. 86–107, Juni 2015, doi: 10.1016/j.matdes.2015.02.011.

[14] G. Kelly und S. Hallström, Bearing strength of carbon fibre/epoxy laminates: effects of bolt-hole clearance, *Composites Part B: Engineering*, Bd. 35, Nr. 4, S. 331–343, Jan. 2004, doi: 10.1016/j.compositesb.2003.11.001.

[15] A. Kötter, B., Bearing strength high performance fibre metal thin-ply laminates, Bd. Proceedings of the 20th European Conference on Composite Materials-Composites Meet Sustainability (Vol 1-6), Dez. 2022, doi: 10.5075/EPFL-298799_978-2-9701614-0-0.

[16] F. Liu, M. Xie, Y. Ji, und M. Zhou, Progressive fatigue damage analysis of composite bolted joint using equivalent stress model, *Science Progress*, Bd. 103, Nr. 1, S. 0036850419874234, Jan. 2020, doi: 10.1177/0036850419874234.

[17] A. Elter, *Hochbelastbare, reibkraftschlüssige Krafteinleitungen für Faser-Kunststoff-Verbunde auf Basis strukturierter Oberflächen: Grundlagen, Untersuchungen, Anwendungen und Auslegungsempfehlungen*. in Schriftenreihe Konstruktiver Leichtbau mit Faser-Kunststoff-Verbunden. Aachen: Shaker Verlag, 2015.

[18] R. De Finis und D. Palumbo, Estimation of the Dissipative Heat Sources Related to the Total Energy Input of a CFRP Composite by Using the Second Amplitude Harmonic of the Thermal Signal, *Materials*, Bd. 13, Nr. 12, S. 2820, Juni 2020, doi: 10.3390/ma13122820.

Friedrich-Alexander-Universität
Faculty of Engineering

Engineering Design
Prof. Dr.-Ing. Sandro Wartzack

Impact of Stacking Sequence on Tensile and Fatigue Performance of Quasi-isotropic Carbon/Epoxy Laminates

Marc Gadinger, Torben Deutschmann, Dieter Krause, Sandro Wartzack

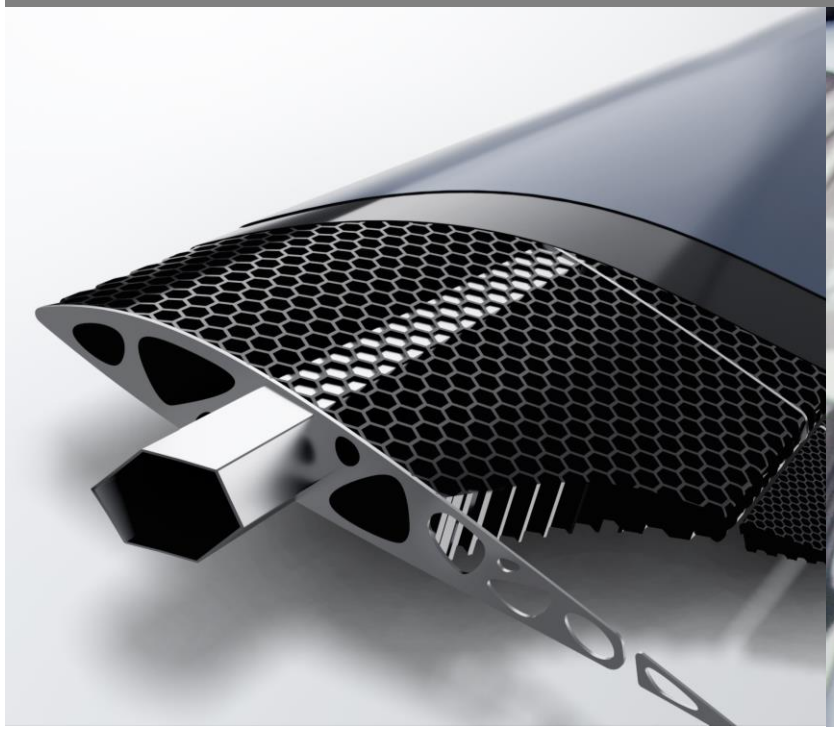

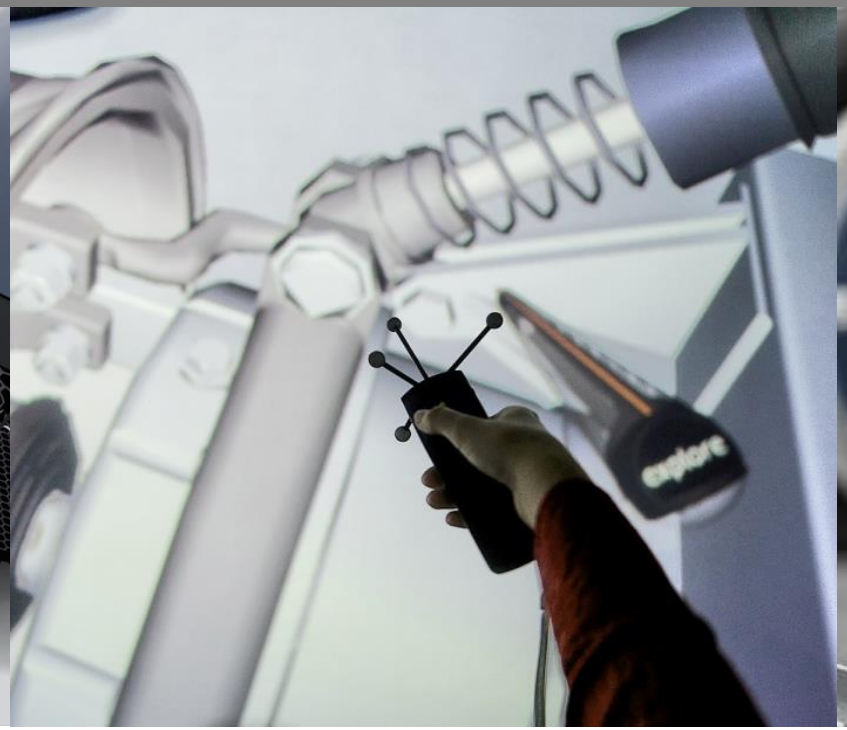

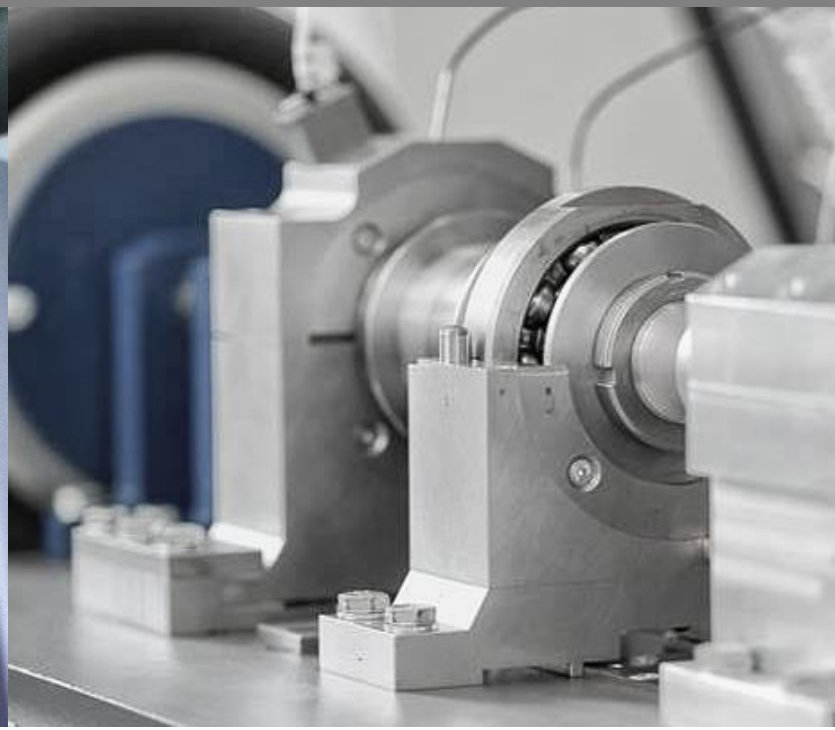

Outline



- Interlaminar stresses
- Research problem and research goal
- Methods and procedures
- Results and discussion

Interlaminar stresses

Problems with classical laminate theory

Classical laminate theory

- Only stresses within the plane $\sigma_x, \sigma_y, \tau_{xy}$
- Neglecting the spatial stress components σ_z, τ_{xz}, τ_{zy}
- Prediction of physically impossible stress states, e.g. along the free edges

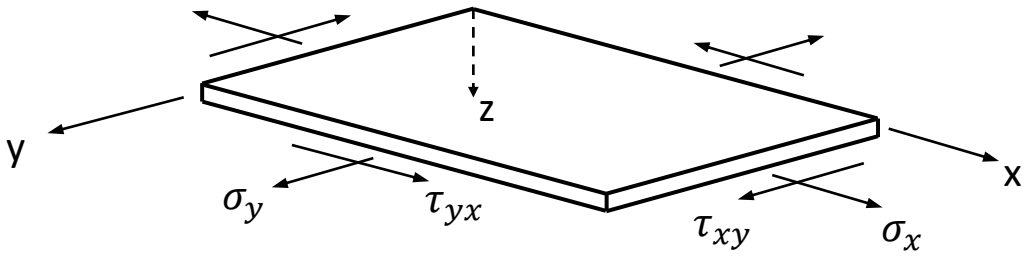

Interlaminar stresses

- Between the layers, as well as along free edges, borders and surfaces of the laminate
- Triggering various failure mechanisms in many composite materials

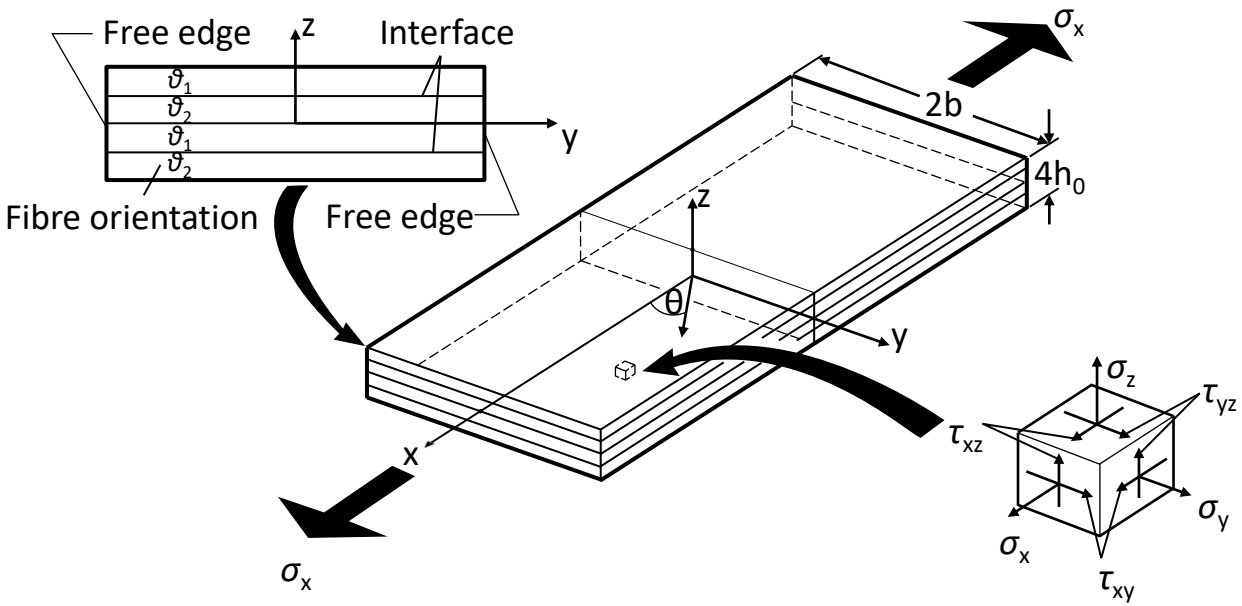

Jones, R.M. Mechanics of Composite Materials. 2nd Ed. Taylor & Francis. 1999.

Interlaminar stresses

Ausgeglichener Winkelverbund

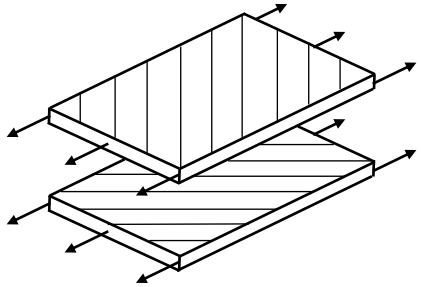

Layers under tension

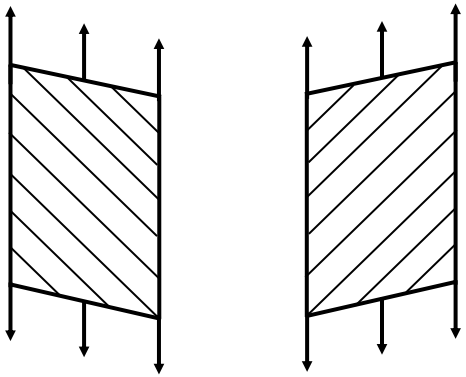

Layers under tension and shear (no shear deformation)

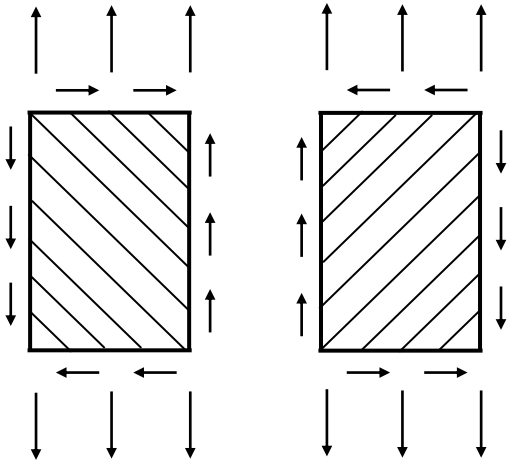

Stress distribution at free edge

- Complex curves with high stress peaks
- Can be influenced by changing the stacking sequence

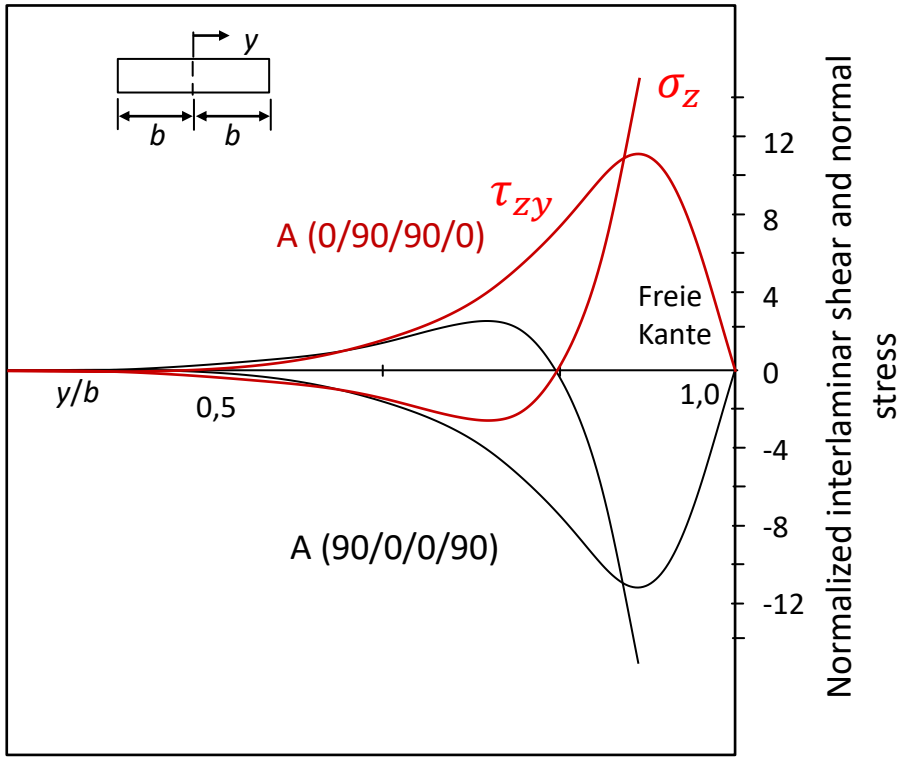

Jones, R.M. Mechanics of Composite Materials. 2nd Ed. Taylor & Francis. 1999.

Research problem and research goal

- Problem statement
  - Free-edge delamination can dominate strength & fatigue life in quasi-isotropic carbon/epoxy laminates

- Research goal
  - Compare two quasi-isotropic lay-ups with opposite edge stress signatures
    1. [90°, 45°, 0°, –45°]s → outer 90° plies → compressive edge σ_z
    2. [45°, –45°, 0°, 90°]s → outer ±45° plies → tensile edge σ_z
  - Assess effects on:
    - Ultimate tensile strength
    - Stiffness degradation & damage evolution under fatigue
    - Cycles-to-failure at constant max load

Methods and procedures

Materials & Specimens

- Material system: unidirectional carbon/epoxy prepreg
- Lay-ups tested:
  - Quasi-isotropic, 8 plies (symmetrical)
  - Thickness per ply = 0.2 mm
- Specimen geometry & preparation
  - Rectangular coupons per ASTM D3039-76 (tension) / D3479-96 (fatigue)
  - Tabs bonded to prevent grip damage

Test Setup & Environment

- Test machine: ZwickRoell servo-hydraulic, 25 kN load cell
- Lab conditions: 21 ± 1 °C, 50 ± 4 % RH
- Instrumentation
  - Force & grip-to-grip displacement logged continuously
  - IR thermometer maintained surface temp stability
- Test regimes
  - Quasi-static tension: monotonic pull to failure
  - Fatigue: sinusoidal, R = 0.1, f = 4 Hz, Pmax = 25 kN

Results and discussion

Quasi-Static Tension

Metric	[90°, 45°, 0°, –45°]s	[45°, –45°, 0°, 90°]s	Δ
UTS (MPa)	582.4 ± 2.8	520.9 ± 15.5	**+11 %**
Tensile Modulus (GPa)	40.93	40.80	~equal
Failure Strain (%)	1.88	1.98	~equal

Damage observations

- 90°-outer lay-up: no delamination; matrix cracking ruled failure
- ±45°-outer lay-up: early edge delamination between 90° plies

Results and discussion

Fatigue Behavior

Stiffness-degradation trends

- ±45°-outer: sharp early drop due to edge delamination
- 90°-outer: gradual decline; matrix cracks dominate

Cycles-to-failure

- Both lay-ups ≈ 18 k cycles (no significant difference) at 25 kN max load
- Highlight distinct initial slopes; annotate similar end-of-life points

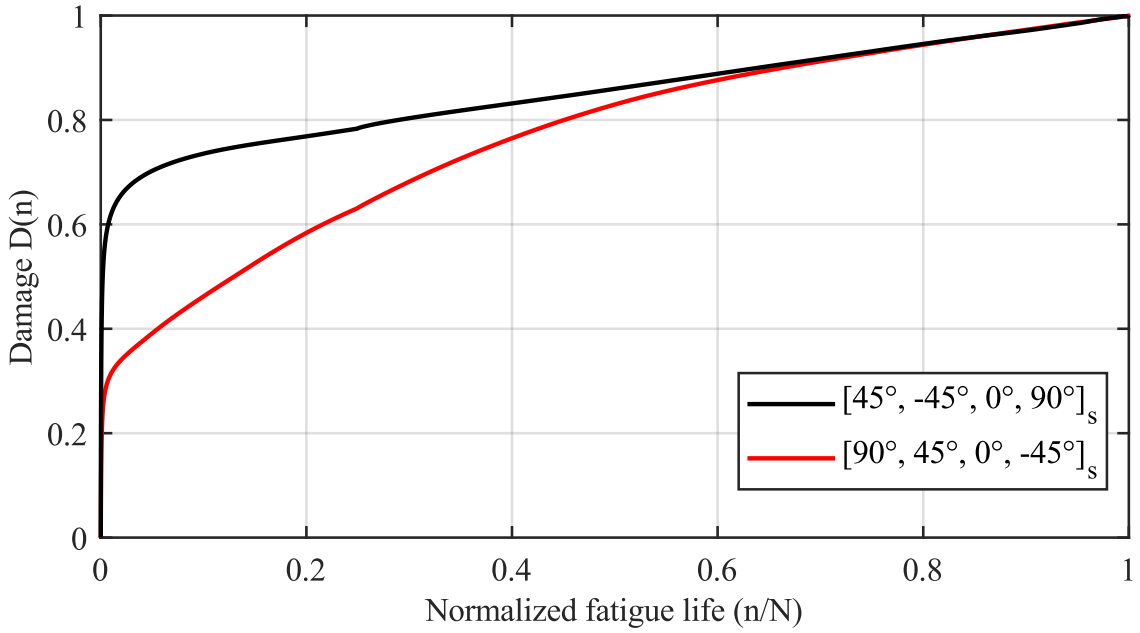

Results and discussion

Edge stress state governs initiation mechanism

- Compressive σ_z (90°-outer) delays delamination → boosts UTS
- Tensile σ_z (±45°-outer) accelerates edge delamination → lowers UTS

Why fatigue life converged

- Once delamination achieved steady growth, both stacks relied on matrix crack propagation & fiber rupture → similar life

Design takeaway

- For static strength-critical parts, place 90° outermost in quasi-isotropic laminates
- For fatigue-critical parts at moderate R-ratios, edge stress tailoring alone may not extend life; need multi-scale damage mitigation

Next steps

- Vary stress ratio & amplitude
- Extend to thicker laminates / different ply drop

Thank you for your attention!

Marc Gadinger, M. Sc.

Research Associate

gadinger@mfk.fau.de

FASTBLADE: A FATIGUE TESTING FACILITY FOR FULL-SCALE BLADES

Sergio Lopez Dubon[1], Fergus Cuthill[2], Marek Munko[3], Miguel A. Valdivia-Camacho[4], Conchúr M. Ó Brádaigh[5], and Edward D. McCarthy[6]

[1]School of Engineering, University of Edinburgh
Sanderson Building, Robert Stevenson Road, The King's Buildings, Edinburgh, EH9 3FB, U.K.
Email: Sergio.LDubon@ed.ac.uk , web page: https://www.fastblade.eng.ed.ac.uk/

[2]School of Engineering, University of Edinburgh
Sanderson Building, Robert Stevenson Road, The King's Buildings, Edinburgh, EH9 3FB, U.K.
Email: Fergus.Cuthill@ed.ac.uk , web page: https://www.fastblade.eng.ed.ac.uk/

[3]School of Engineering, University of Edinburgh
Sanderson Building, Robert Stevenson Road, The King's Buildings, Edinburgh, EH9 3FB, U.K.
Email: s1728055@sms.ed.ac.uk , web page: https://www.fastblade.eng.ed.ac.uk/

[4]School of Engineering, University of Edinburgh
Sanderson Building, Robert Stevenson Road, The King's Buildings, Edinburgh, EH9 3FB, U.K.
Email: MA.Valdivia@ed.ac.uk , web page: https://www.fastblade.eng.ed.ac.uk/

[5]School of Engineering, University of Sheffield
The University of Sheffield, Western Bank, Sheffield, S10 2TN, U.K.
Email: c.obradaigh@sheffield.ac.uk , web page: https://www.sheffield.ac.uk/engineering

[6]School of Engineering, University of Edinburgh
Sanderson Building, Robert Stevenson Road, The King's Buildings, Edinburgh, EH9 3FB, U.K.
Email: Ed.McCarthy@ed.ac.uk , web page: https://www.fastblade.eng.ed.ac.uk/

Keywords: Fatigue; Testing; Composites; Failure

ABSTRACT

Fatigue in composite tidal turbine blades presents a critical challenge for the long-term viability of tidal energy systems. These blades are subjected to millions of high-load cycles in harsh marine environments, and predicting their fatigue performance numerically is difficult due to complex material behaviour, loading conditions, and modelling assumptions. Offshore mechanical testing has emerged as a practical solution, enabling equivalent oceanic loads to be applied within accelerated timeframes in a controlled environment, thereby allowing for reliable structural assessments.

FastBlade, a unique facility developed by the University of Edinburgh, addresses longstanding issues in fatigue testing through a regenerative digital displacement hydraulic pump/motor system. This innovative approach enables precise, programmable cyclic loading of full-scale blades, resulting in up to 75% reduction in energy consumption compared to conventional hydraulic systems. FastBlade's platform is particularly suited for stiff composite structures that cannot be tested at resonance due to thermal limitations.

This paper, as part of the MaxBlade project, synthesises a review of research conducted at FastBlade, focusing on fatigue tests of a tidal blade using both single and multi-actuator configurations. Target hydrodynamic loads were derived from site-specific velocity data and simulated using Reynolds-Averaged Navier–Stokes (RANS) methods. During testing, the blade endured the equivalent of 20 years of tidal loading without catastrophic failure. However, variations in tip

displacements and strain responses across different actuator configurations highlighted the importance of refined load introduction methods and monitoring strategies.

Analysis of the test data informs improvements in control algorithms, actuator coordination, sensor placement, and calibration techniques. These enhancements enhance the reliability and repeatability of fatigue tests, contributing to the development of more robust and efficient blade designs. FastBlade's approach demonstrates the future of sustainable structural testing and offers broader applications across marine, wind, aerospace, and civil sectors.

1 INTRODUCTION

The increasing urgency to transition from fossil fuels to renewable energy has led to a surge of interest in marine energy systems, particularly tidal stream turbines. Tidal energy offers a unique advantage: it is a predictable and consistent source of power that complements intermittent sources, such as solar and wind [1]. As global energy systems evolve, the tidal energy sector is poised to play a critical role, especially in coastal regions with strong and reliable tidal currents [2].

The tidal energy industry traces its roots to early installations such as the La Rance tidal barrage in France (1967) [3]. Since then, advances in technology—particularly horizontal axis tidal turbines (HATs)—have enabled more practical, scalable, and less environmentally intrusive solutions [4]. The potential for tidal stream energy to contribute up to 100 GW to the EU grid by 2050 underscores its strategic importance [5]. However, realising this potential requires addressing key engineering challenges, most notably the structural reliability and fatigue life of turbine blades operating in a dense, high-load marine environment [6-7].

Tidal turbine blades must withstand millions of load cycles in harsh underwater conditions characterised by strong currents, turbulence, and biofouling. The risk of structural failure is significant, with consequences that extend beyond repair costs to include downtime and safety issues [8]. Unfortunately, much of the data informing blade design remains proprietary, and in situ testing, though valuable, is limited by uncontrolled environmental variables. Hydrodynamic model testing in flumes or tanks, such as at the FloWave facility in Edinburgh [9-10], provides controlled insight at a more minor scale, but cannot replicate the full complexity of real-world, full-scale blade behaviour [11-12].

To address these limitations, full-scale fatigue testing has emerged as an essential tool. Among recent advancements, the FastBlade facility in Scotland represents a significant leap forward [13]. Utilising a regenerative digital displacement hydraulic actuation system, FastBlade enables precise and energy-efficient cyclic loading of full-scale blades [14-15]. In 2022, FastBlade conducted high-load tests simulating over 21 years of tidal cycles, both with single- and triple-actuator setups, and continued testing until blade failure occurred, thereby setting a new benchmark in composite blade validation [13, 16, 17].

FastBlade's design directly addresses the inefficiencies of conventional servo-hydraulic rigs, particularly for stiff composite blades that cannot be excited at resonance without thermal damage. The facility's integration of simulation technologies, digital twins, and advanced monitoring further exemplifies a new paradigm in structural validation [18].

This paper synthesises research from across FastBlade's development and testing campaigns. Specifically, we investigate the structural performance and fatigue behaviour of a full-scale composite tidal turbine blade under both static and fatigue loading. We compare blade responses under single-and multiple-actuator configurations, examining how load frequency and control strategies affect displacement and strain. The study aims to inform future improvements in blade testing, design validation, and certification practices, supporting the development of more efficient and reliable tidal energy systems.

2 OVERVIEWS OF THE FASTBLADE FACILITY

FastBlade, located in Rosyth, Scotland, is the world's first test facility to implement regenerative digital displacement hydraulics designed explicitly for the large-scale fatigue testing of long, stiff composite structures, such as tidal turbine blades measuring between 2 and 14 meters. The facility enables both accelerated fatigue and static loading, providing high-fidelity data on structural performance under simulated real-world marine conditions. It can resist a moment of up to 11.96 MNm and a shear load of 2.13 MN in static tests, as well as a moment of 4.70 MNm and a shear load of 0.94 MN during accelerated fatigue tests.

At the heart of FastBlade is a 70-tonne reaction frame (see Figure 1), engineered to withstand substantial loads during both static and dynamic fatigue tests. The structural setup includes a reaction plane, support wall, T-Slot bed plates, and a custom adapter plate, all anchored on bridge bearings recessed into a 2.5-meter-deep floor pit, ensuring stability and repeatability during high-load testing scenarios.

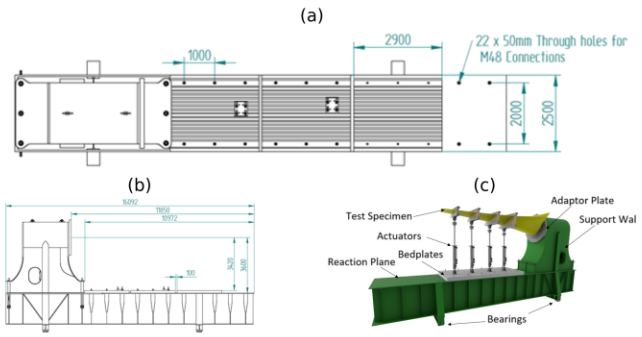

Figure 1: General arrangement and dimensions of the reaction frame at FastBlade. (a) Top view, (b) Lateral view, and (c) General view [13].

The facility's hydraulic actuation system is powered by four Digital Displacement™ reversible pumps developed by Danfoss. These pumps deliver a reversible hydraulic flow rate of 880 litres per minute, enabling precise actuator control and the simulation of complex ocean interaction loads. Additionally, the regenerative nature of the hydraulic system allows energy recovery, making FastBlade up to 75% more energy-efficient than conventional hydraulic testing systems of a similar scale. FastBlade is a cutting-edge platform designed not only to validate the structural integrity of tidal blades but also to support the advancement of sustainable marine energy technologies through efficient, data-rich, and environmentally conscious testing methodologies

3 ENERGY EFFICIENCY AND HYDRAULIC INNOVATION

FastBlade's hydraulic innovation lies in its use of Digital Displacement Pump (DDPMs) [19], which form the backbone of its regenerative hydraulic actuation system (see Figure 2). Unlike traditional servo-valve hydraulic setups, which lose significant energy as heat during load cycling, DDPMs offer a smarter, energy-efficient alternative. These digitally controlled units dynamically regulate flow and pressure by precisely timing valve openings in sync with the rotating shaft, eliminating the need for energy-wasting throttling.

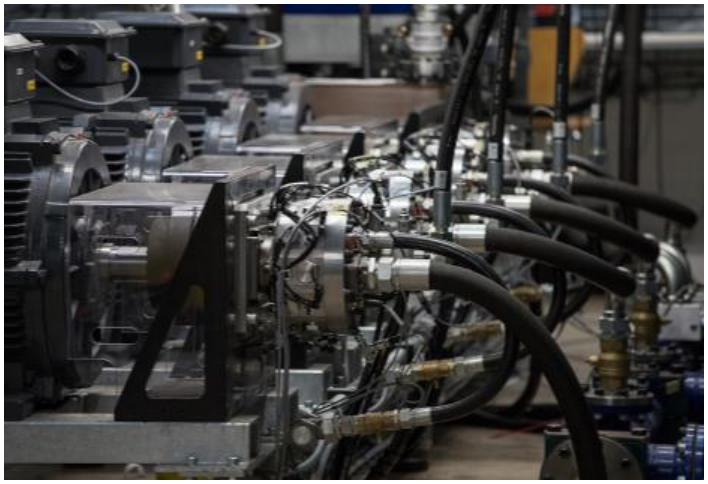

Figure 2: Digital Displacement Pumps and Motors at FastBlade.

A key advantage of this system is its ability to recover and reuse energy. During cyclic loading, the mechanical energy that would typically be dissipated is instead captured from the rotating inertia of the hydraulic drive and fed back into the system. This bidirectional flow capability means the actuators can alternate between applying loads and harvesting energy, depending on the structural response of the test specimen, as shown in Figure 3 for a test in which the power from the grid was cut and the system ran solely on the accumulated inertia.

This innovation results in energy savings of up to 75%, making FastBlade significantly more efficient than conventional fatigue testing systems. Such efficiency is particularly valuable when testing large, thick composite structures, such as tidal turbine blades, where resonant testing is impractical due to high damping properties and the risk of thermal buildup [20]. In addition to reducing power consumption, the regenerative system also enables more prolonged and more intensive test campaigns without compromising sustainability. The precise control afforded by DDPMs allows engineers to replicate complex, real-world marine load conditions, including quasi-steady flows and asymmetric stresses, while minimising environmental impact.

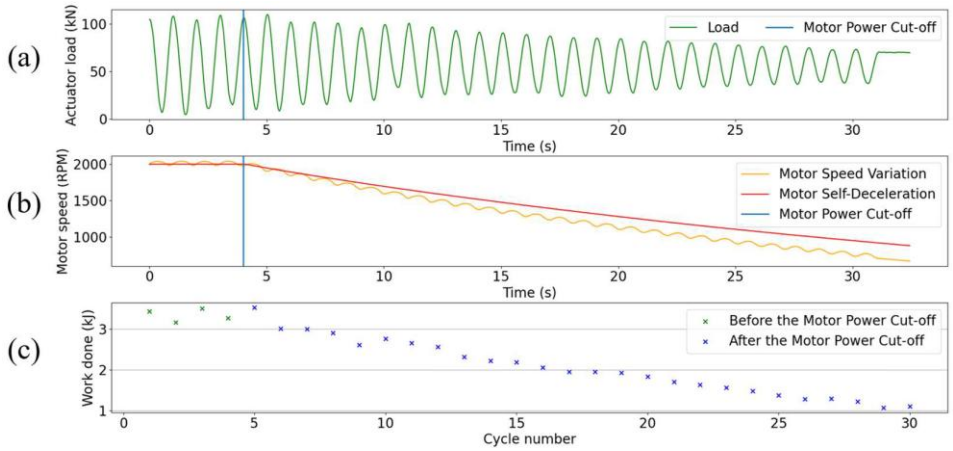

Figure 3: In the regeneration test, power to the VLT (Variable Load Terminal) is cut at 5 seconds. (a) The loading cycle continues even without power, with the amplitude gradually decreasing. After 25 cycles, the transferred energy drops to about one-third of its original level. (b) The motor slows down once power is cut. If loading is also stopped, the system slows down smoothly (as shown by the red trace). If loading continues, the motor decelerates slightly faster. This slight difference shows the high energy recovery (round-trip efficiency) of the system. (c) The energy transferred between the flywheel and the load also decreases over time, though not in a classic exponential (logarithmic) pattern. For the first 3 seconds after the power cut, the energy remains relatively steady, as the flywheel supplies the required power. [19].

5 FATIGUE TESTING

FastBlade enables accelerated life-cycle testing of full-scale composite tidal blades using static and fatigue test protocols aligned with IEC TS 62600-3 [21]. Tests are run at non-resonant frequencies to prevent internal heating, particularly for thick-sectioned tidal blades made of carbon or glass-fibre composites. Advanced sensing technologies such as strain gauges, DIC, and embedded instrumentation capture strain localisation, damage progression, and global stiffness. Actuators apply loads in both single-point and multi-point configurations to replicate the hydrodynamic moments observed in real-world deployments.

The 5.25 m long tidal turbine blade, tested, with a cross-section based on the NACA 63-4XX aerofoil series, was initially designed by Tidal Generation Limited and manufactured by Aviation Enterprises Limited for the DeepGen project. It came from a decommissioned 500 kW tidal stream turbine that operated at EMEC's Fall of Warness site for approximately two years. Some original design documents were unavailable, and Airborne has since acquired the design rights. Structurally, the blade features an 8 mm-thick glass-fibre skin, 3 mm GFRP ribs, and a spar cap made of 75% unidirectional carbon fibre epoxy prepreg. ±45° carbon fibre epoxy shear webs provide additional torsional strength. A rear GFRP spar, positioned 100 mm from the trailing edge, helps reduce peel stresses and improve fatigue performance.

To obtain the testing loads, high-fidelity simulations are a central component of FastBlade's methodology [22]. Actuator line modelling and RANS-based CFD simulations derive realistic load distributions from site-specific data. This includes modelling flow shear during ebb and flood tides and translating it into spatially and temporally varying blade loads (see Figure 4). These simulations guide the placement of actuators and force profiles. Furthermore, synthetic resonance, a method that mimics structural response through non-resonant actuation, bridges the gap between real-world conditions and laboratory constraints. This simulation-informed testing reduces the risk of over-conservatism and allows designers to optimise blade mass, stiffness, and geometry.

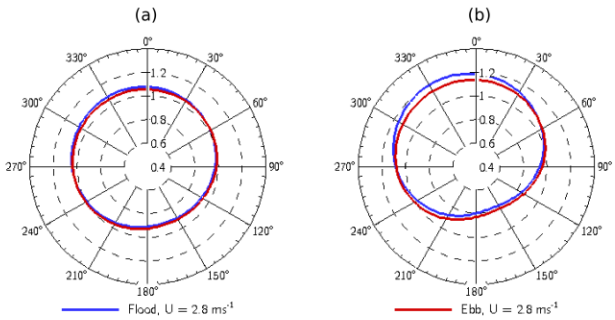

Figure 4: Hydrodynamic Simulation Results. The azimuthal variation of the normalized blade root bending moments in (a) the flapwise and (b) edgewise directions is depicted for both flood (blue) and ebb (red) tides. The rotor operates at a hub-height flow speed of U=2.8 m/s. [13]

The blade was tested under different setups (see Figure 5), following [21], the natural frequency was taken at the beginning and the end of the entire test program in setup (see Figure 5(a)), later on, the blade was tested with a single actuator which is a conventional test setup (see Figure 5(b)), a three actuator setup (see Figure 5(c)) to compare the benefits and challenges of more contact points as shown in [8] and finally a three actuator setup for extreme loads (see Figure 5(d)). The root bending moments for setups 5b and 5c were 1000 kNm for the static test and 650 kNm for the fatigue test. Nevertheless, after approximately 120000 cycles, the loads were changed to test different clamping system materials (see [24]) and evaluate the blade's response to higher load fatigue cycles. For setup 6d, the root bending moments during the static tests were up to 1400, 1600, 1800, and 3060 kNm. For fatigue with configuration 6d, first, a series of cycles at 1330 kN.m (almost twice the mean water velocity load) is applied to scale up to 1750 kN.m (nearly 2.7 times the mean water velocity load).

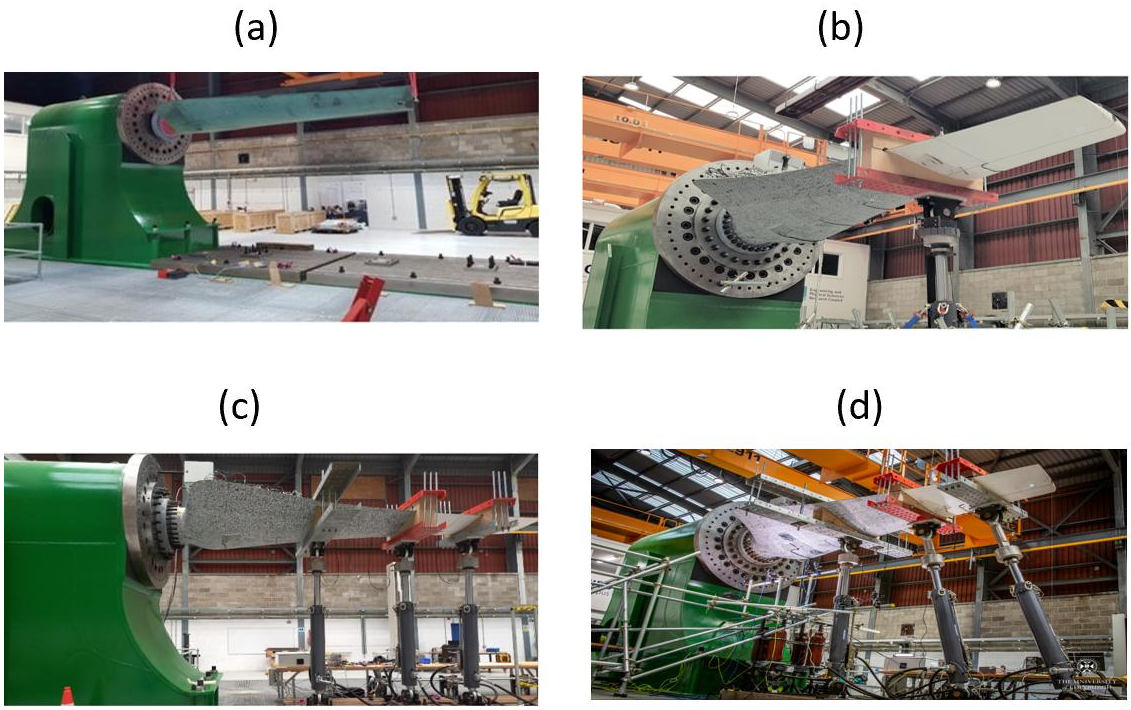

Figure 5: Testing setups. (a) No actuators for natural frequency, (b) Single actuator, (c) three actuators for design loads, (d) three actuators for extreme loads.

Testing credibility is reinforced through statistical validation techniques. FastBlade integrates real-time Process Capability Indices (PCIs) to monitor how closely the applied loads match prescribed values [15]. Load traces from historic and real-time data are compared to identify anomalies and deviations. These metrics ensure traceability, allowing engineers to diagnose actuator drift or calibration errors. Combined with redundant sensors, specialised anomaly detection algorithms[23] and automated control systems, this statistical approach guarantees repeatable and certifiable test outcomes, aligning with emerging marine energy certification frameworks. As a result of these controls, the results of displacement and root bending moments for the different fatigue tests are presented in Figure 6.

FastBlade has significantly advanced the understanding of tidal turbine blade mechanics under operational conditions. The research outputs inform the development of the next generation of certification standards, reduce design conservatism, and enable predictive maintenance strategies. FastBlade's principles, energy-efficient actuation, integrated simulation, and digital intelligence are extendable to aerospace wings, bridge components, offshore platforms, and wind turbine blades. As such, the facility serves as a model for structural testing in high-capital, high-reliability industries. Using all these valuable lessons, FastBlade approaches the new MaxBlade project.

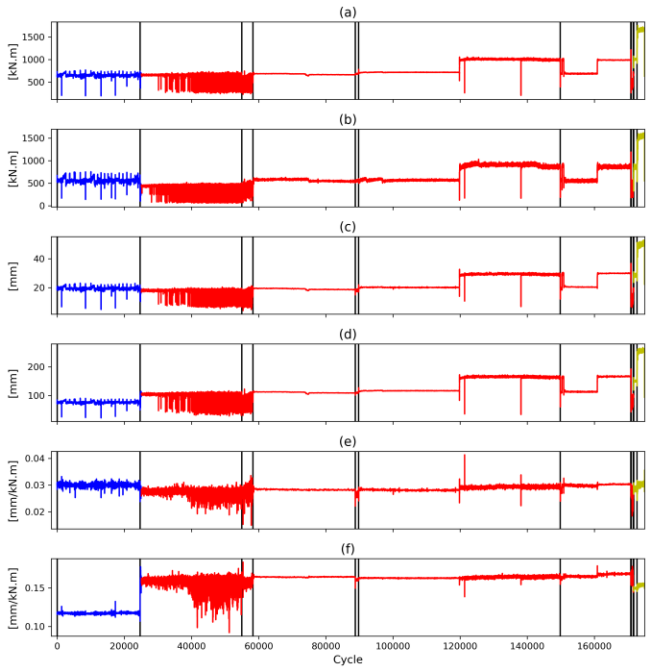

Figure 6: . Results from the different fatigue tests. The vertical black lines indicate a static test. The colour blue indicates the single actuator test, the colour red indicates the use of 3 actuators, and the colour yellow indicates the use of 3 actuators for high loads: (a) Root Bending Moment at the crest of each cycle, (b) Twice the amplitude of the Root Bending Moment at each cycle (c) Displacement at the blade's centre during the crest of each cycle, (d) Displacement at the blade's tip during the crest of each cycle, (e) Relation between displacement at the blade's centre and the root bending moment during the crest of each cycle, and (f) Relation between displacement at the blade's tip and the root bending moment during the crest of each cycle.

9 CONCLUSIONS

FastBlade represents a significant advancement in structural testing for tidal energy systems. By combining regenerative hydraulic actuation, simulation-informed load design, and advanced monitoring systems, it enables efficient and realistic fatigue testing of full-scale composite blades. The facility's use of digital displacement pump/motors (DDPMs) reduces energy consumption by up to 75%, making long-duration, high-load testing both feasible and cost-effective, particularly for stiff, high-damping structures where resonant testing is impractical.

Through a combination of static and fatigue tests, FastBlade has demonstrated the ability to simulate decades of tidal loading in a matter of weeks. Configurable actuator setups and precise control systems allow replication of realistic hydrodynamic moments, while embedded instrumentation provides valuable data on strain, displacement, and damage progression.

Simulation plays a key role in test planning, with hydrodynamic loads derived from RANS-based models and actuator line methods that capture the complex effects of tidal direction and flow shear. These simulations ensure that laboratory loads reflect real-world operational conditions. Quality assurance is further enhanced through statistical control tools such as Process Capability Indices, which support consistent and traceable testing.

The integration of digital twin technology adds a forward-looking dimension to FastBlade's approach. These models, ranging from data-driven to physics-informed, enable predictive insights, inform control strategies, and offer potential pathways for real-time condition monitoring of deployed blades.

Overall, FastBlade provides a practical and forward-compatible platform for validating the structural integrity of tidal turbine blades. Its contributions extend beyond marine energy, offering applicable methodologies for other sectors requiring high-fidelity fatigue testing. As the industry continues to evolve, facilities like FastBlade will play a crucial role in supporting safer, more efficient, and cost-effective renewable energy solutions.

ACKNOWLEDGEMENTS

All the authors: the MaxBlade project funded via the Horizon Europe MaxBlade project (Grant No. 101096891), co-funded by United Kingdom Research and Innovation (UKRI) and the European Commission.

All the authors: the Supergen ORE Hub for funding received through the Flexible Fund Award FF2020-1063

M. Munko: Babcock International and The Data Lab for research funding.

M.A. Valdivia-Camacho: Wind & Marine Energy Systems & Structures (WAMESS) CDT under the Engineering and Physical Sciences Research Council grant agreement EP/S023801/1.

REFERENCES

[1] Walker, S., & Thies, P. R. (2021). A review of component and system reliability in tidal turbine deployments. Renewable and Sustainable Energy Reviews, 145, 111084. https://doi.org/10.1016/j.rser.2021.111084

[2] Thanthirige, T. R. M., Goggins, J., & Flanagan, M. (2023). A state-of-the-art review of structural testing of tidal turbine blades. *Energies, 16*(10), 4061. https://doi.org/10.3390/en16104061

[3] Blunden, L. S., & Bahaj, A. S. (2007). Tidal energy resource assessment for tidal stream generators. Proceedings of the Institution of Mechanical Engineers, Part A: Journal of Power and Energy, 221(2), 137–146. https://doi.org/10.1243/09576509JPE248

[4] Igwemezie, V., Mehmanparast, A., & Kolios, A. (2019). Current trend in offshore wind energy sector and material requirements for fatigue resistance improvement in large wind turbine support structures–A review. *Renewable and Sustainable Energy Reviews, 101*, 181–196. https://doi.org/10.1016/j.rser.2018.11.002

[5] Gonabadi, H., Oila, A., Yadav, A., & Bull, S. (2022). Fatigue life prediction of composite tidal turbine blades. *Ocean Engineering, 258*, 111647. https://doi.org/10.1016/j.oceaneng.2022.111647

[6] D. M. Grogan, S. B. Leen, C. R. Kennedy, C. M. Brádaigh, Design of composite tidal turbine blades, Renewable Energy 57 (2013) 151–162. doi:10.1016/J.RENENE.2013.01.021

[7] C. R. Kennedy, S. B. Leen, C. M. Brádaigh, A preliminary design methodology for fatigue life prediction of polymer composites for tidal turbine blades, http://dx.doi.org/10.1177/1464420712443330 226 (2012) 203–218. doi:10.1177/1464420712443330

[8] Dubon, S. L., Cuthill, F., Vogel, C., & Ó Brádaigh, C. M. (2024). A full-scale composite tidal blade fatigue test using single and multiple actuators. Composites Part A: Applied Science and Manufacturing, 184, 107460. https://doi.org/10.1016/j.compositesa.2024.107460

[9] Moideen, R., Venugopal, V., Chaplin, J., & Borthwick, A. G. L. (2025). VIV-induced strain on a lazy wave dynamic marine power cable in a steady current. Ocean Engineering, 328, Article 121081. https://doi.org/10.1016/j.oceaneng.2025.121081

[10] Lam, R., Lopez Dubon, S., Sellar, B., Vogel, C. R., Davey, T., & Steynor, J. (2023). Temporal and spatial characterisation of tidal blade load variation for structural fatigue testing. Renewable Energy, 208, 665-678. https://doi.org/10.1016/j.renene.2023.03.117

[11] Gao, Z., Bingham, H. B., Ingram, D., & Kolios, A. (2018). Committee V.4: Offshore renewable energy. In C. G. Soares (Ed.), Progress in the Analysis and Design of Marine Structures (pp. 193–217). IOS Press. https://doi.org/10.3233/978-1-61499-864-8-193

[12] Borthwick, A. G. L. (2016). Marine renewable energy seascape. Engineering, 2(1), 69–78. https://doi.org/10.1016/J.ENG.2016.01.007

[13] Lopez Dubon, S., Vogel, C., Cava, D. G., Cuthill, F., & McCarthy, E. (2023). FASTBLADE: A TECHNOLOGICAL FACILITY FOR FULL-SCALE TIDAL FATIGUE TESTING. In SAMPE 2023 Conference and Exhibition (International SAMPE Technical Conference; Vol. 2023-April). Soc. for the Advancement of Material and Process Engineering. https://doi.org/10.33599/nasampe/s.23.0062

[14] Munko, M., Lopez Dubon, S., Cuthill, F., Rampen, W., & Ó Brádaigh, C. M. (2024). Monitoring Energy Recovery in a Full-Scale Fatigue Test. In Proceedings of the 20th International Conference on Condition Monitoring and Asset Management British Institute of Non-Destructive Testing. Advance online publication. https://doi.org/10.1784/cm2024.6a3

[15] Munko, M., Connolly, K. N., Cuthill, F., Valdivia Camacho, M. A., McCarthy, E., & Lopez Dubon, S. (2024). The Application of the Process Capability Index (PCI) in a Fatigue Test of a Tidal Turbine Blade Using Historic and Real-Time Load Data. In Proceedings of the 20th International Conference on Condition Monitoring and Asset Management, British Institute of Non-Destructive Testing. Advance online publication. https://doi.org/10.1784/cm2024.3a3

[16] Lopez Dubon, S., Vogel, C., Garcia Cava, D., Cuthill, F., McCarthy, E., & Ó Brádaigh, C. M. (2024). A Full-Scale Tidal Blade Fatigue Test using the FastBlade Facility. Renewable Energy, 228, Article 120653. https://doi.org/10.1016/j.renene.2024.120653

[17] F Cuthill, S Lopez Dubon, C Vogel, M Valdivia Camacho, C O Brádaigh, E McCarthy, Destructive testing and failure analysis of a full-scale composite tidal turbine blade, Destructive testing and failure analysis of a full-scale composite tidal turbine blade. International Marine Energy Journal. ISSN 2631-5548 (In Press)

[18] Munko, M. J., Vidmar, M., Brádaigh, C. M. Ó., Cuthill, F., Camacho, M. A. V., & Dubon, S. L. (2024). Do Digital Twins Require Physical Simulations? A Study of Developing Digital Twins with Varying Reliance on Physics-Based Models. In 2024 IEEE International Conference on Engineering, Technology, and Innovation (ICE/ITMC) (pp. 1-8). Institute of Electrical and Electronics Engineers. https://doi.org/10.1109/ICE/ITMC61926.2024.10794252

[19] Rampen, W., Munko, M., Lopez Dubon, S., & Cuthill, F. (2025). Regenerative Structural Fatigue Testing with Digital Displacement Pump/Motors. Actuators, 14(3), Article 103. https://doi.org/10.3390/act14030103

[20] Jalili, M. M., Pirayeshfar, A. S., & Mousavi, S. Y. (2015). A comparative study on viscoelastic properties of polymeric composites measured by a longitudinal free vibration non-destructive test and dynamic mechanical thermal analysis. Polymer Testing, 48, 139–146. https://doi.org/10.1016/j.polymertesting.2015.09.005

[21] International Electrotechnical Commission. (2020). IEC TS 62600-3:2020 – Marine energy – Wave, tidal and other water current converters – Part 3: Measurement of mechanical loads. IEC. ISBN 978-2-8322-8105-5.

[22] Vogel, C. R., Tang, T., Dubon, S. L., & Steynor, J. (2021, September). Simulations of tidal turbine blade loading in flood and ebb tides. Paper presented at the 14th European Wave and Tidal Energy Conference (EWTEC 2021), Plymouth, UK.

[23] Munko, M., Cuthill, F., Valdivia Camacho, M. A., Ó Brádaigh, C. M., & Lopez Dubon, S. (2025). An Audio-Based Framework for Anomaly Detection in Large-Scale Structural Testing. Engineering Applications of Artificial Intelligence, Article 109889. https://doi.org/10.1016/j.engappai.2024.109889

[24] Valdivia Camacho, M. A., Lopez Dubon, S., Cuthill, F., Munko, M., McCarthy, E., Alam, P., & Ó Brádaigh, C. M. (2025). Clamping parameters in full-scale tidal turbine blade tests: A case study. Ocean Engineering, 327, Article 120722. https://doi.org/10.1016/j.oceaneng.2025.120722

Compression-Compression Fatigue of Glass-Fibre Non-Crimp Fabric Composites by Four-Point Flexure

N. Shepherd, T. Allen, and M. Battley

Centre for Advanced Materials Manufacturing and Design
The University of Auckland
Auckland, New Zealand

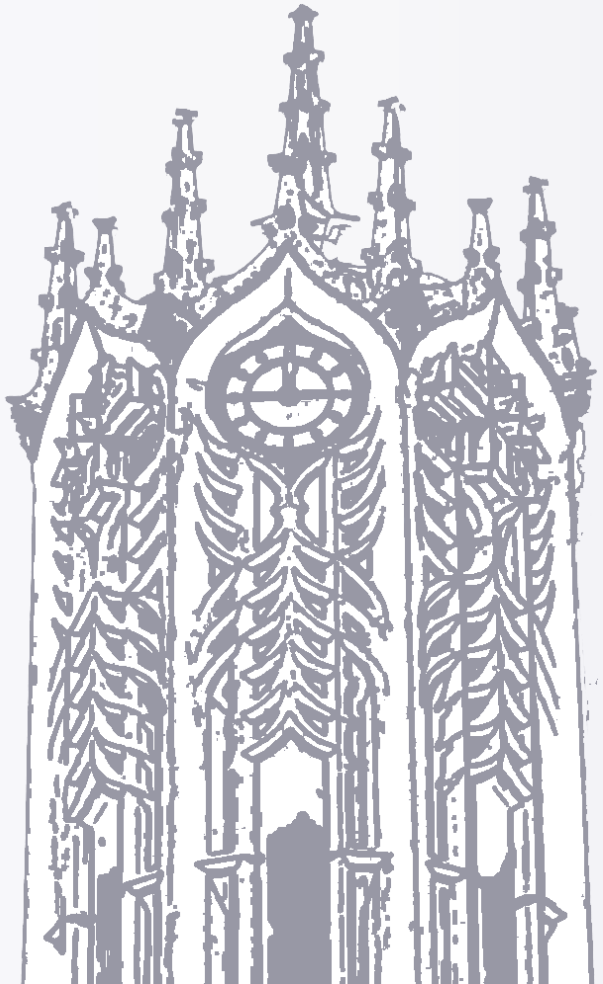

UNIVERSITY OF AUCKLAND
Waipapa Taumata Rau
NEW ZEALAND

CENTRE FOR ADVANCED MATERIALS MANUFACTURING & DESIGN

Introduction: Compression Fatigue

Important but often neglected load case.

Lacking in standardised guidance for testing and specimen design.

Simple end- or shear-loading tests may not meet requirements:

- Global buckling instability
- Short gauge length
- End crushing
- Stress concentrations at tabs or grips

Four-point bending provides a promising alternative.

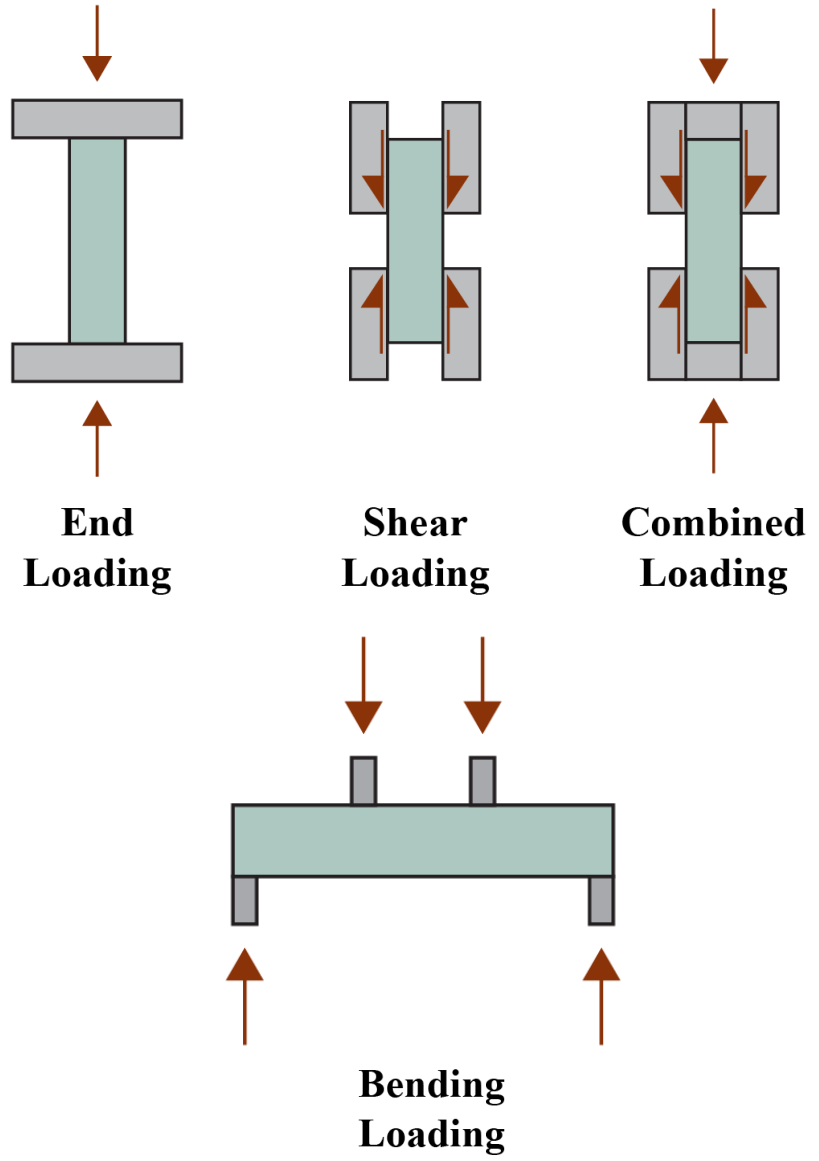

Introduction: Stitched Fabrics

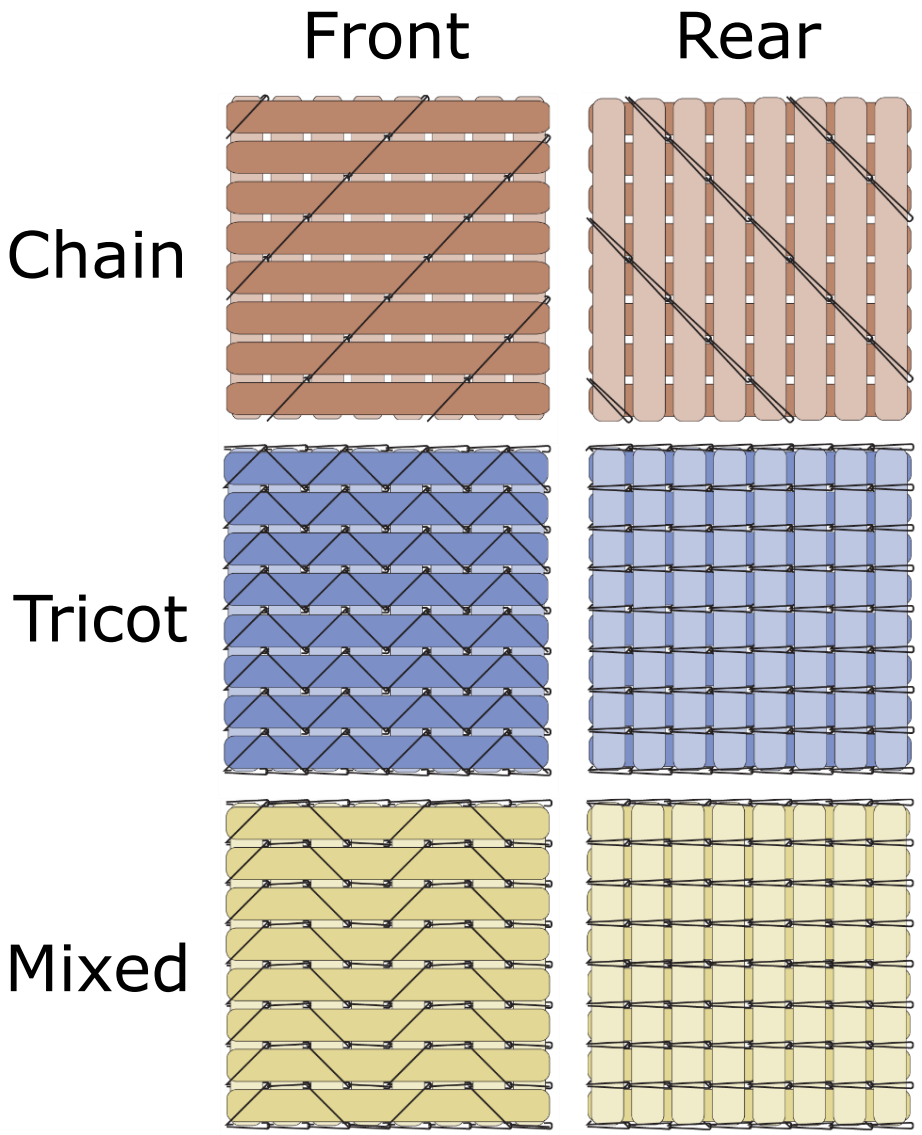

'Pattern' refers to the geometry or weave-type of the stitching thread

Can influence fibre alignment:

- key for static compression behaviour
- May also play a influence compression-compression fatigue

Characteristic	Stitch Pattern		
	Chain	Tricot	Mixed
Fabric areal weight, reported (gsm)	820	825	825
Fabric areal weight, measured (gsm)	828	803	815
Fabric as-manufactured fibre orientation (°)	[+45/-45]	[0/90]	[0/90]
Stitch thread linear density (dtex)	84.5	107	108
Stitch gauge (mm)	5.15	3.99	4.30
Stitch length (mm)	2.57	6.94 (3.47)	14.84 (3.71)

Goals

1) Develop a specimen geometry to test stitched glass-fibre fabrics in compression-compression fatigue

2) Determine if fatigue behaviour varies between fabrics with different stitching patterns

3) Determine whether this variation can be linked to the previously-measured variation in fibre misalignment

Specimen Design and Manufacture

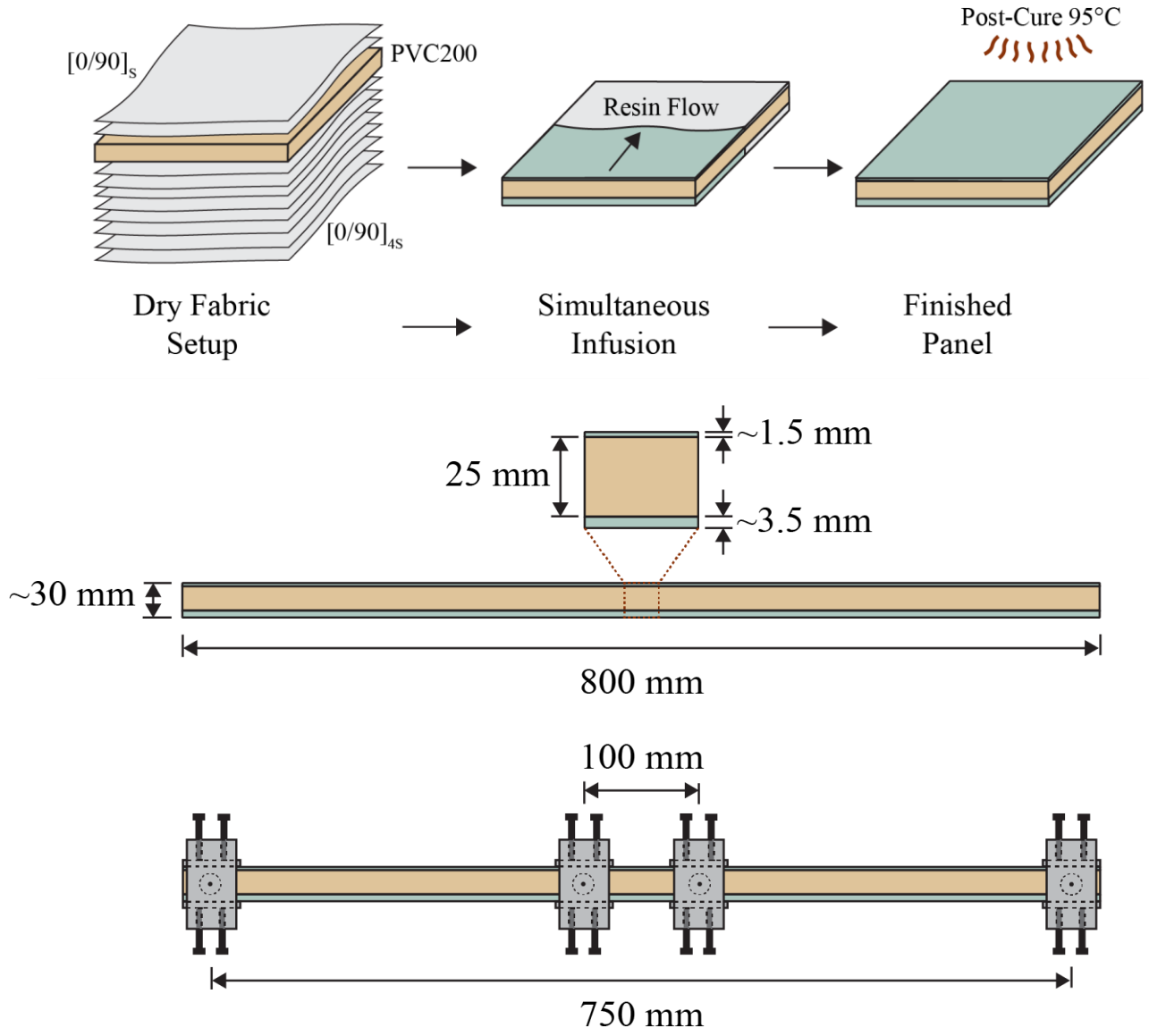

Asymmetric sandwich based on ASTM D5467 for static compression

Maximum compression strains up to 1.5%

Compression facesheet strain gradient 3.95%

Identical rear (tension) facesheets

50 mm gauge length

Test Apparatus and Procedure

Controlled sinusoidal displacements at 0.5 Hz

Continuous load / displacement measurement

Direct strain measurement for first 150 cycles

Minimum displacement 5 mm, Maximum displacements 25, 30, 35, 40 or 45 mm

Maximum compressive strains 0.85 – 1.5%

Run-out at 10,000 cycles

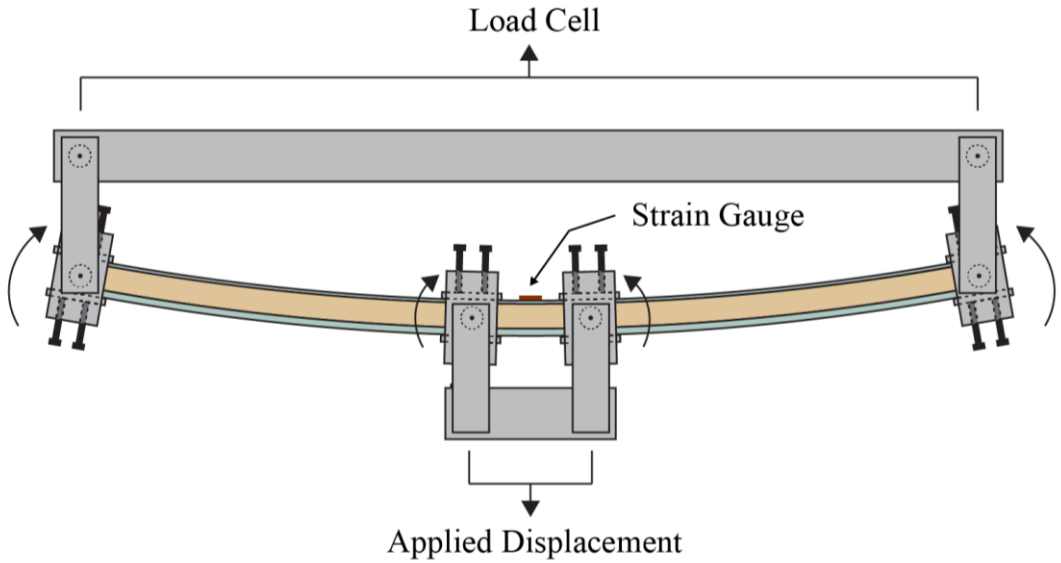

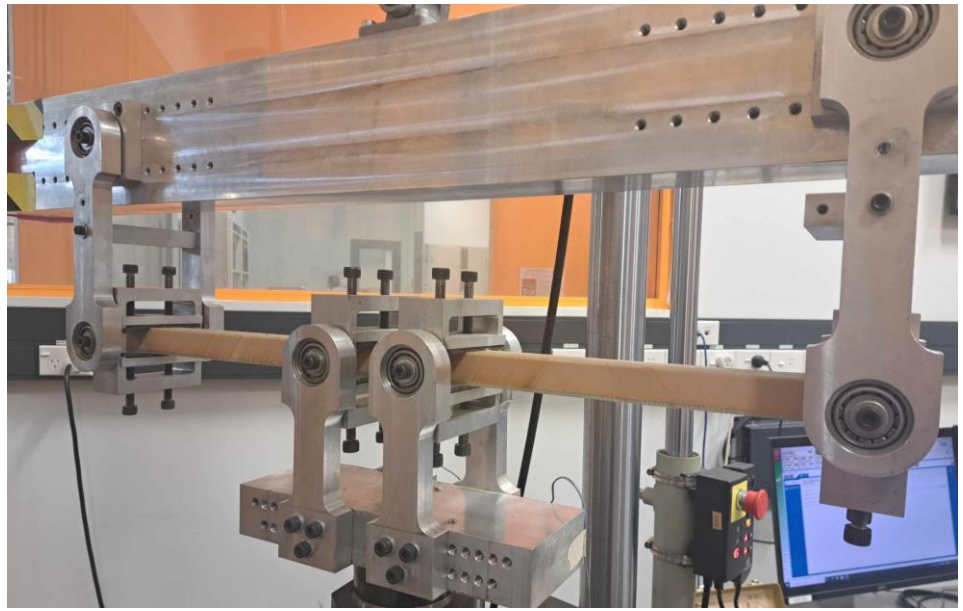

Beam Load and Stiffness

'Stiffness' contains both flexural rigidity (EI) and transverse shear stiffness

Transverse load and stiffness change over time, possibly due to:

- Change in core shear stiffness
- Change in facesheet stiffnesses (tension, compression, or both)
- Permanent core deformation

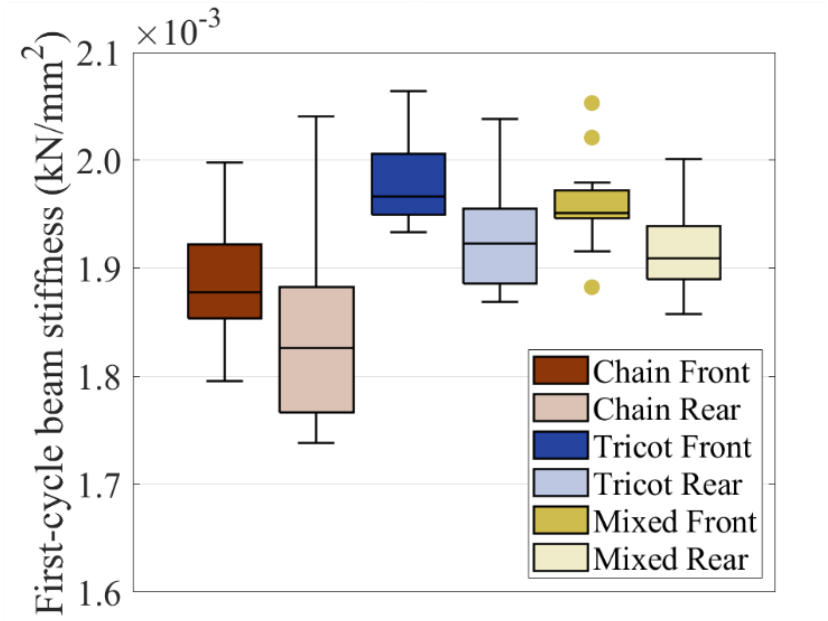

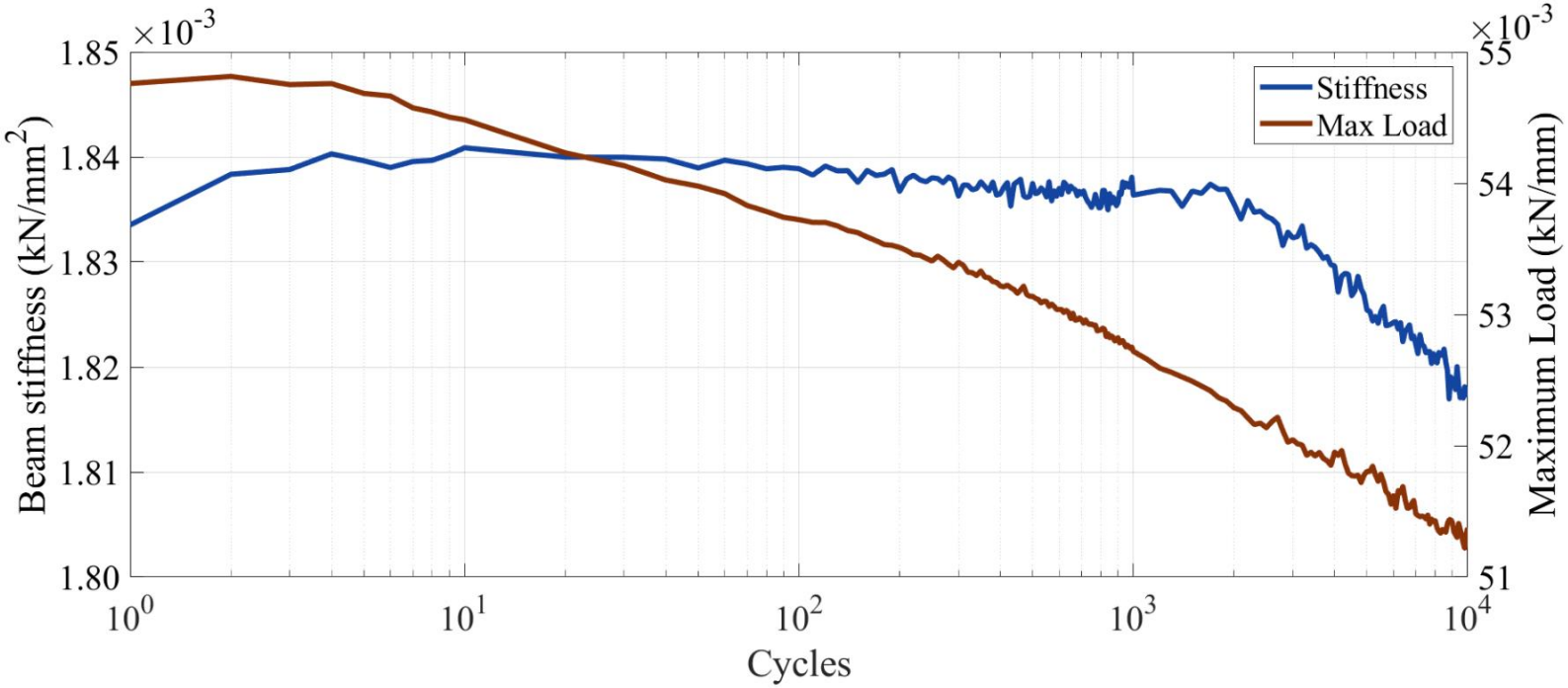

Fatigue Life

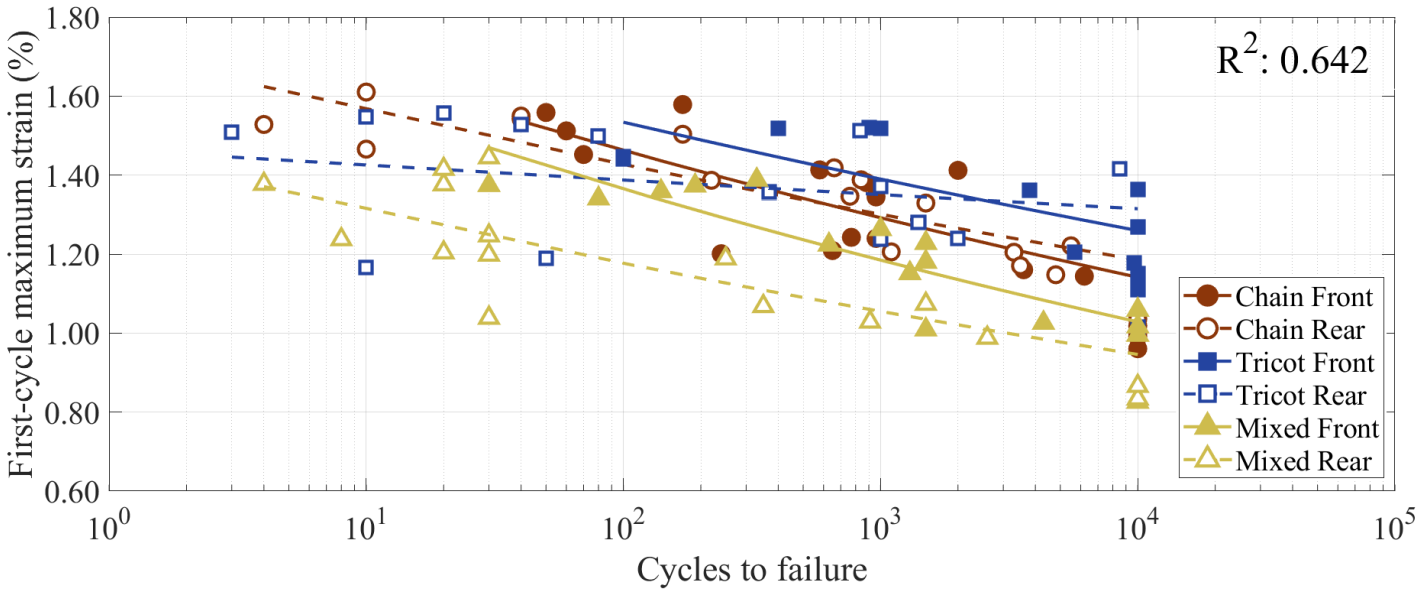

Fabric	A	B	R^2
Chain Front	1.87	–0.0538	0.578
Chain Rear	1.72	–0.0402	0.768
Tricot Front	1.87	–0.0428	0.526
Tricot Rear	1.46	–0.0117	0.0735
Mixed Front	1.81	–0.0614	0.661
Mixed Rear	1.46	–0.0474	0.575

Linear regression of the form:

$$\boldsymbol{log(S) = log(A) + B\, log(N)}$$

A: Intercept. Strain for a fatigue life of 1 cycle, i.e. predicted static strain

B: Slope

Run-out specimens excluded

High scatter results in flat fits with low R-squared

Variation Between Stitch Patterns

Paired regression of the form:

$$S_i = \beta_0 + \beta_1 P + (\beta_2 + \beta_3 P) N_i + \varepsilon_i$$

Tests whether changing *P* from 0 to 1 changes the intercept ($\beta_0 + \beta_1$) or slope ($\beta_2 + \beta_3$)

Statistically significant variation between the pair if $p < 0.05$

	C_F	C_R	T_F	T_R	M_F	M_R	
C_F	X	0.308	0.981	0.0371	0.780	0.0207	**Intercept**
C_R	0.318	X	0.435	0.0526	0.563	0.0272	
T_F	0.602	0.868	X	0.144	0.831	0.0939	
T_R	0.0315	0.0404	0.203	X	0.118	0.999	
M_F	0.697	0.150	0.393	0.0277	X	0.0759	
M_R	0.718	0.574	0.830	0.0471	0.477	X	
	Slope						

Fatigue Life Explained by Misalignment

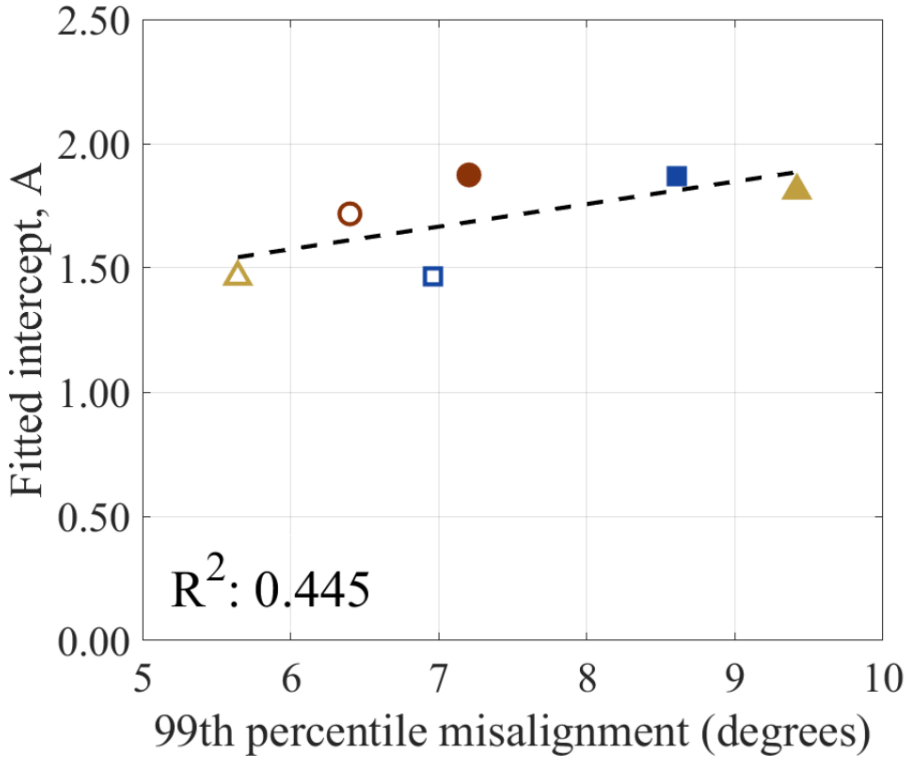

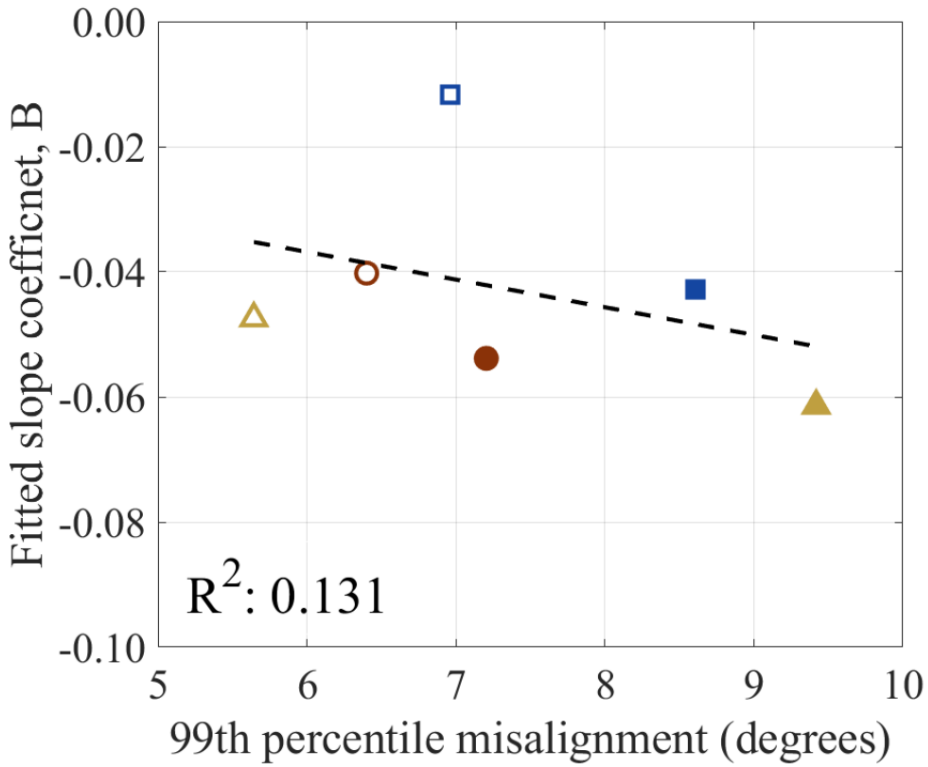

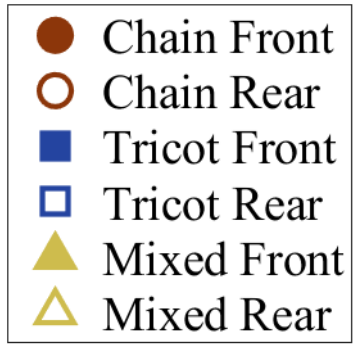

Weak positive relationship between intercept (*A*) and misalignment

Weak negative relationship between slope (*B*) and misalignment

Weak relationships are likely statistical artifacts due to the high scatter.

Failure and Damage

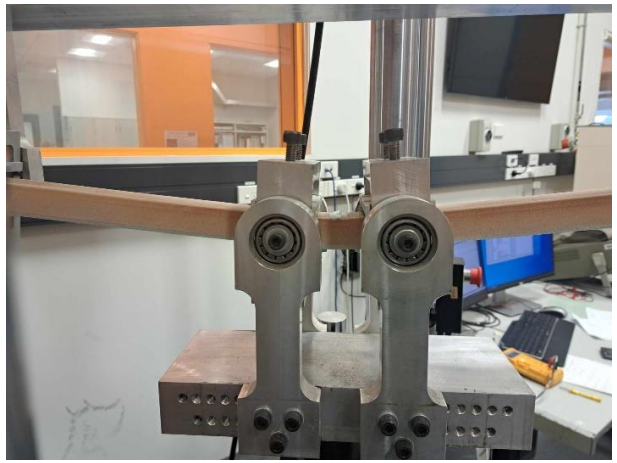

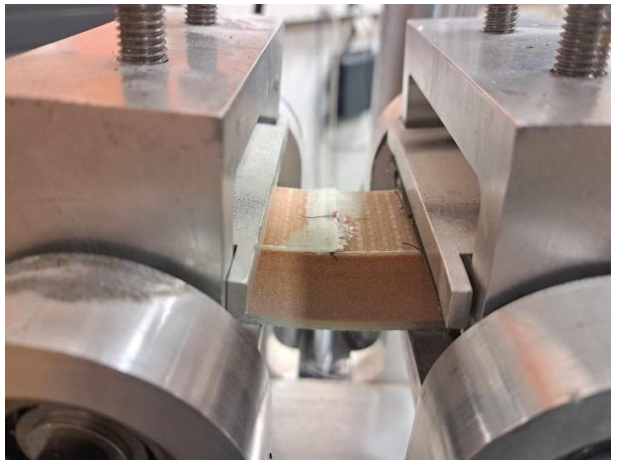





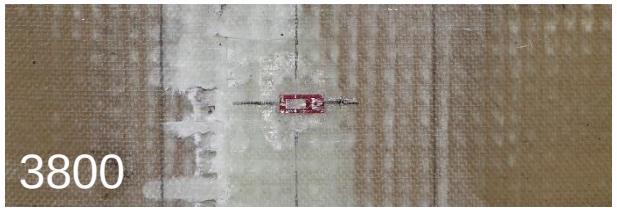

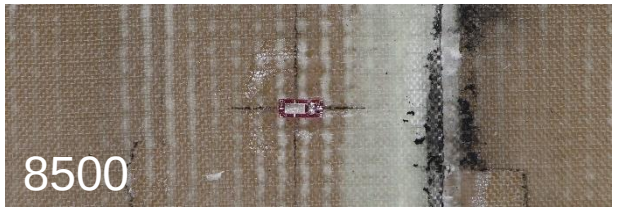





40 mm maximum displacement until failure

77.1% failed in compression within the gauge section. 18.1% survived to run-out

Visible ‘whitening’ observed in the top facesheet.

- Matrix damage?
- Interlaminar damage?
- Interfacial damage?
- Micro-cracking?

Inconsistent degrees of damage at failure

Image Analysis to Isolate Damage

Damage isolated from digital photographs

Morphological transformations identify and isolate:

- Damage created at the moment of failure
- Damage present before failure
- Other undesirable white reflections

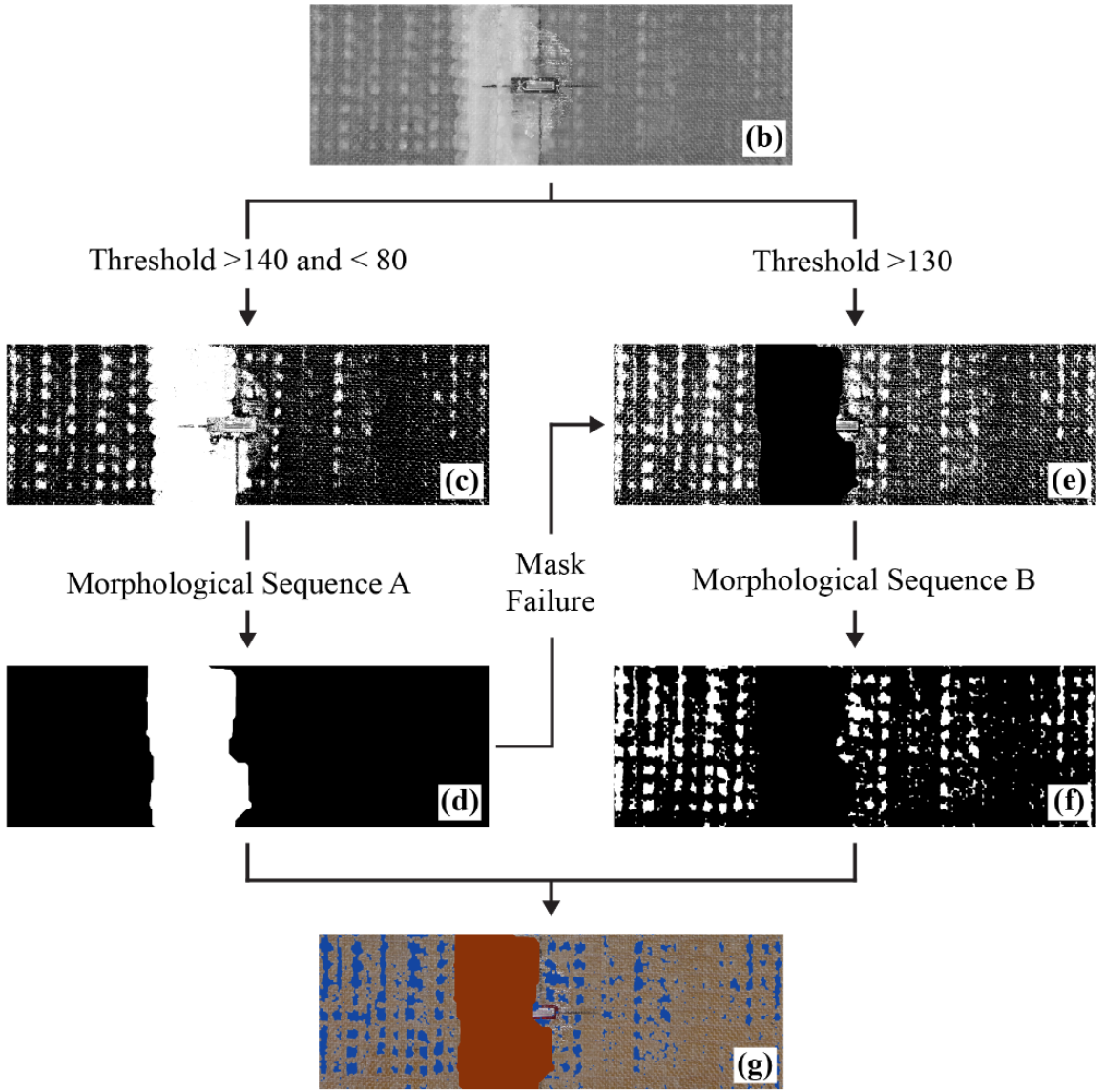

Damage Related to Fatigue Severity

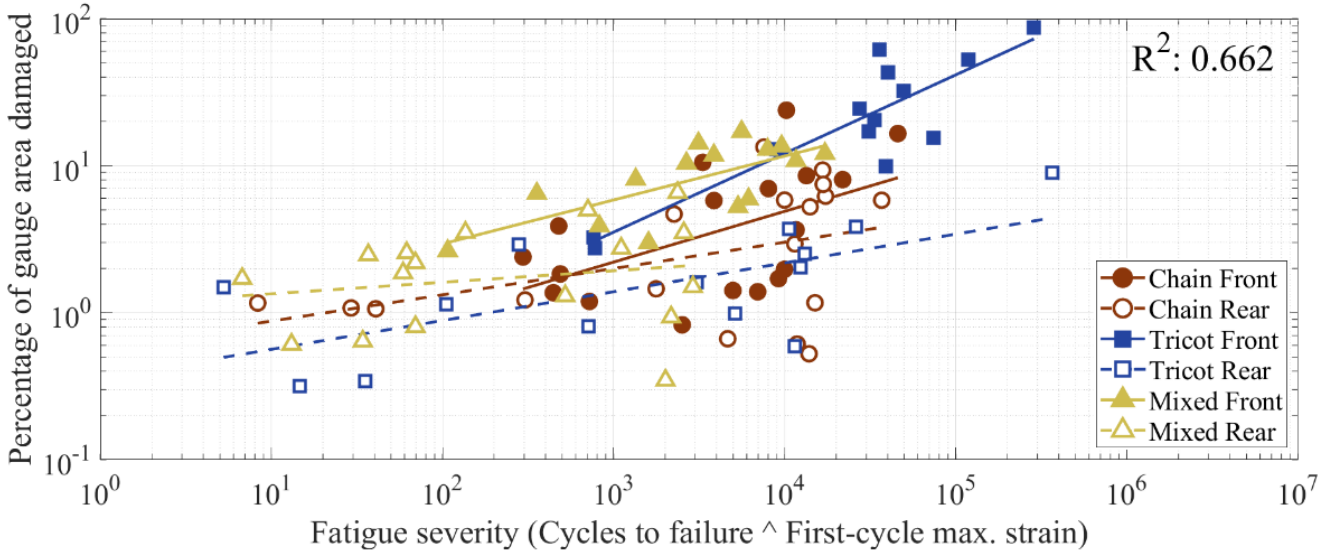

Fabric	A	B	R^2
Chain Front	0.203	0.345	0.274
Chain Rear	0.581	0.179	0.188
Tricot Front	0.0877	0.535	0.778
Tricot Rear	0.359	0.196	0.441
Mixed Front	0.742	0.299	0.486
Mixed Rear	3.18	0.0783	0.0399

Proposed relationship:

$$\log(D) = \log(A) + B \log(F)$$

D: Proportion of gauge area damaged

F: 'Fatigue severity', combining both applied strain and fatigue life:

$$F = N^S$$

Run-out specimens included

Damage Explained by Misalignment

Moderate positive relationship between misalignment and damage slope, *B*

Implies:

- More visible damage at the same fatigue severity
- Faster accumulation of damage under increasing fatigue severity (either strain or cycles)

Stronger relationship than between misalignment and fatigue life.

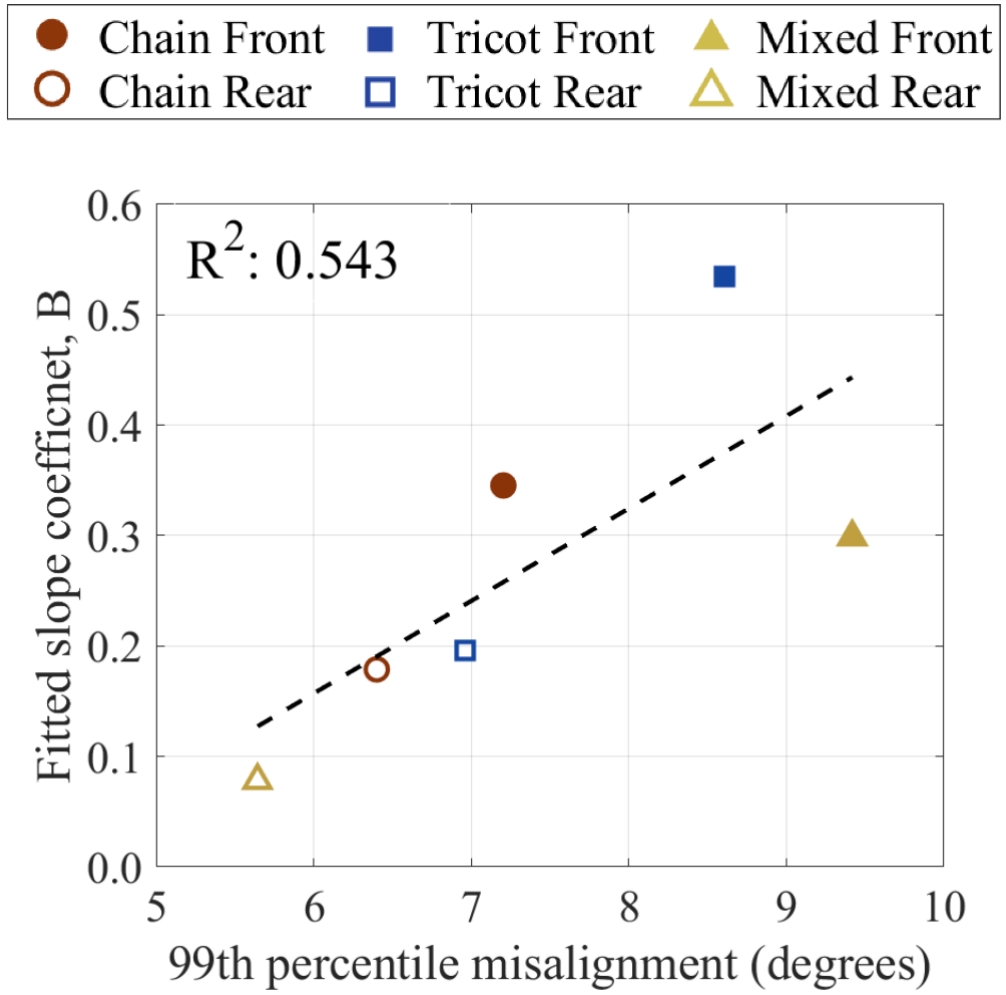

Conclusions

Four-point flexure was successful for testing in compression-compression fatigue, but scatter and variability are high

Failed specimens show visible whitening of the top facesheet, but exact damage mechanism requires further investigation

Weak relationships suggest higher misalignment may result in shorter fatigue lives and greater damage accumulation

Recommend further development to gather more repeatable data

Thank you

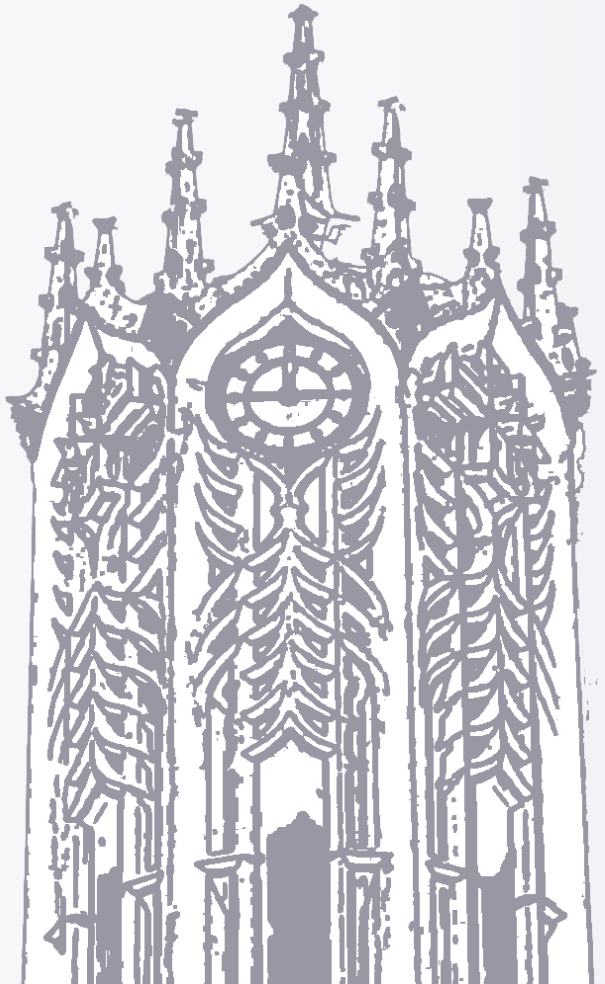

UNIVERSITY OF AUCKLAND
Waipapa Taumata Rau
NEW ZEALAND

CENTRE FOR ADVANCED MATERIALS MANUFACTURING & DESIGN

THE ROLES OF PORE DISTRIBUTION AND HIERARCHICAL STRUCTURE OF MARINE MUSSEL PLAQUE CORES

Yulan Lyn[1], Yong Pang[1] and Tao Liu[1]

[1]School of Engineering and Materials Science, Queen Mary University of London
E1 4NS, Mile End Road London, UK
Email : Tao.Liu@qmul.ac.uk, web page : https:// www.sems.qmul.ac.uk/staff/t.liu

Keywords: Pore distribution, Sandwich core, Hierarchical structure, Mussel plaque cores

ABSTRACT

The thread-plaque system of marine mussels demonstrates strong adhesion and high deformability, enabling it to stick to various wet surfaces. The plaque has a sandwich structure with a porous core enclosed by a dense cuticle layer. Although the microstructures of plaque cores have been reported, the impact of their unique porous structure on high deformability remains unclear. This study used scanning electron microscopy (SEM) to investigate the porous structure of mussel plaque cores. Two-dimensional (2D) porous representative volume elements (RVEs) with scaled distribution parameters were generated, and the calibrated phase-field modelling method was applied to analyse the effect of pore distribution and multi-scale porous structure on the failure mechanisms of porous RVEs. SEM analysis revealed that large-scale pores have a lognormal size distribution and a uniform spatial distribution. Simulations indicated that increasing the normalized mean radius value of the large-scale pore distribution statistically leads to a decrease in final failure strain, strength, and strain energy density, but cannot solely determine their values. The interaction between pores can result in two different failure modes under the same pore distribution: progressive failure mode and sudden failure mode. Additionally, the hierarchical structure of multi-scale porous RVEs can increase the final failure strain by 40–60% compared to single-scale porous RVEs by reducing stiffness, suggesting that the hierarchical structure could be another key factor contributing to high deformability. These findings enhance our understanding of how pore distribution and multi-scale porous structure in mussel plaque cores contribute to their high deformability and affect other mechanical properties, offering valuable insights for designing highly deformable composite materials in the future.

1 INTRODUCTION

The mussel byssus system, comprising protein threads and porous plaques (Fig. 1a–b), enables strong anchoring to diverse surfaces in harsh marine environments [1–7]. Notably, mussel plaques exhibit exceptional ductility, allowing significant deformation under tensile loads without failure (Fig. 1c), a property with promising implications for bioinspired material design. Despite extensive research into their adhesive performance [8–11], the underlying mechanisms contributing to their high ductility remain poorly understood.

Structurally, mussel plaques feature a porous core encased by a protective cuticle (Fig. 1b) [12]. The core contains randomly distributed nano- and micro-scale pores (75–100 nm to 1–3 μm in diameter; Fig. 1e) [12]. Prior studies suggest that modifying pore arrangement can enhance ductility [13]. Gockowski et al. (2020) proposed that increasing crack path tortuosity through tailored pore structures may account for this effect [14]. However, these studies largely

employed idealized, ordered pore geometries, differing from the natural pore architecture of mussel plaques [13,14]. As such, the role of the native, multi-scale porous structure in enhancing mechanical performance—particularly ductility—remains insufficiently explored.

This study aims to bridge that gap by investigating how pore distribution (Figs. 1d and f) and hierarchical porosity (Fig. 1e) affect the mechanical behavior of mussel plaques. Pore morphology was characterized using scanning electron microscopy (SEM), and two-dimensional porous representative volume elements (RVEs) were generated with scaled distribution parameters for both numerical and experimental analysis. A validated phase-field fracture model incorporating a Neo-Hookean hyperelastic material law was used to simulate the influence of pore structure on failure mechanisms. This work offers insights into the ductility mechanisms of mussel plaques and informs the design of bioinspired, highly deformable metamaterials.

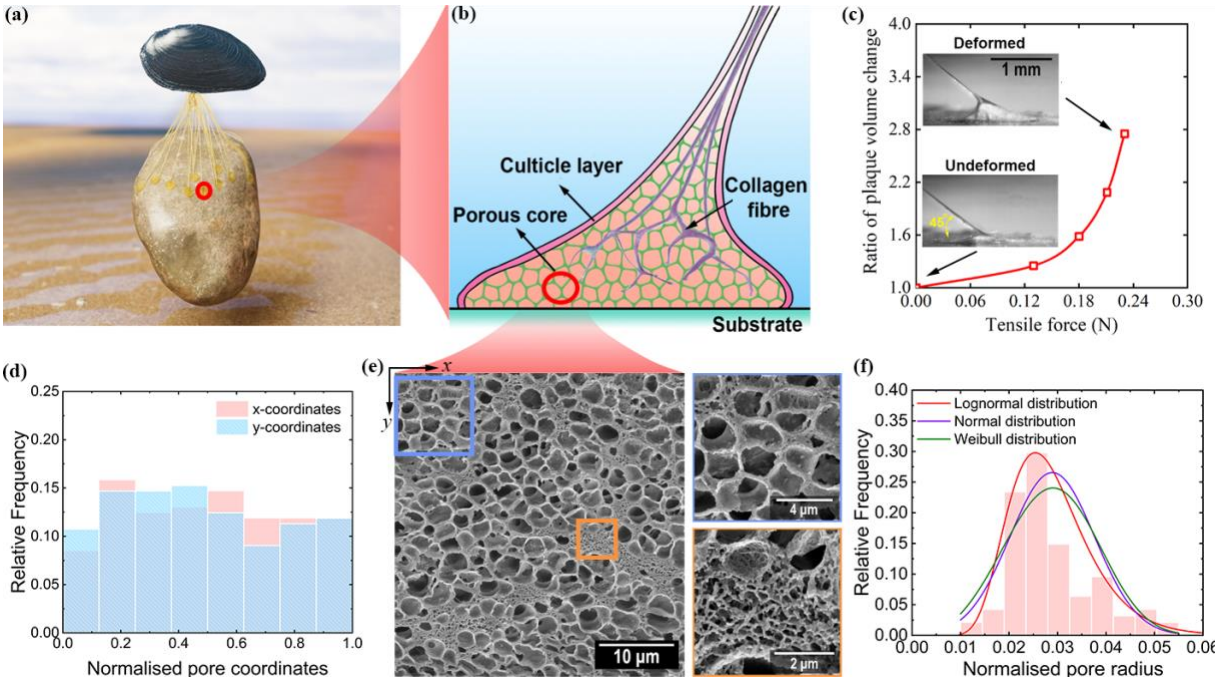

Figure 1: (a) Mussel byssus system attached on a rock, (b) schematic diagram of the mussel plaque's microstructure, (c) large deformation of mussel plaque under tension, (d) the distribution of normalized x and y coordinates for large pore centres within the mussel plaque core, (e) the SEM photo showing the multi-scale porous structure of mussel plaque core and (f) the distribution of normalized radius for large pores within the mussel plaque core.

2. THE SEM CHARACTERISATION OF MUSSEL PLAQUE CORE

Two-dimensional (2D) SEM images have suggested that the pores within the plaque cores are of two different scales, ranging in diameter from 75-100 nm (small-scale pores) to 1-3 μm (large-scale pores) (Fig. 1d). The pore distribution of large-scale pores within those SEM photos was first examined. In order to ensure the representativeness of the large-scale pore distribution in these photos, a total of nine SEM photos from different plaques or different locations of the same plaque were analysed. The irregular large-scale pores were simplified as equivalent circular pores to obtain the pore distribution during the SEM image analysis. The longest axis

of the irregular large-scale pores was considered as the diameter of the equivalent circular pores. Meanwhile, the radii of large-scale pores and the coordinates of the pore centres were normalised by dividing the length of SEM image (l_s) edges for the distribution analysis.

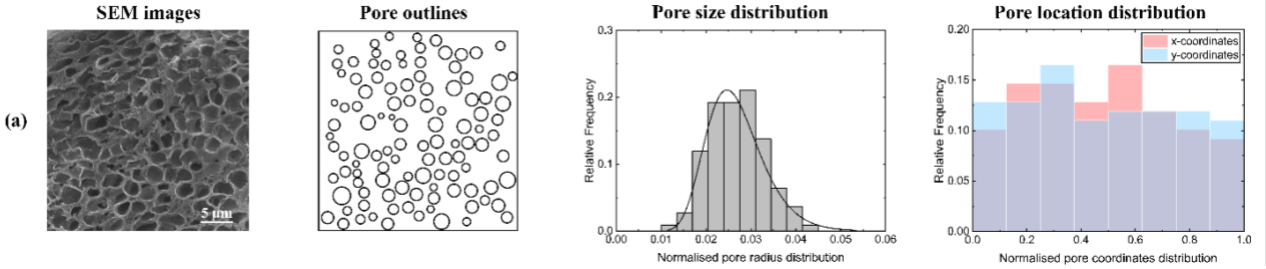

Figure 2: Pore distribution analysis of mussel plaque SEM images.

3. THE GENERATION OF THE RVES FOR THE POROUS STRUCTURE

Two types of porous RVEs were generated for numerical study. The first RVE type investigates the effect of large-scale pores, while the second RVE type examines the impact of the multi-scale architecture of the mussel plaque core.

The first type RVE was generated by scaling the plaque pore sizes by a factor of 1000, transitioning from microns to millimetres. Two-dimensional (2D) square shaped porous RVEs were generated by using the scaled distribution parameters of the large-scale pores (v_l=27%, μ_p^*=1.12 mm and s_p^*=0.34 mm). The dimensions of the RVEs are 30 x 30 mm, comprising solely large-scale pores with the remaining volume filled with solid material, see Fig.3.

The second type RVE representing multi-scale porous structures were generated via removing 2D elements in the FE models and connecting the nodes using truss elements of circular cross sections (i.e. coupled temperature-displacement truss element T2D2T) (Fig. 3). The radius of the truss elements was determined to ensure that the newly generated RVEs reflected the same overall porosity ($v = v_s + v_l = 32\%$) with the SEM image (Fig. 1e). Here, v_s represents the volume fraction of smaller pores.

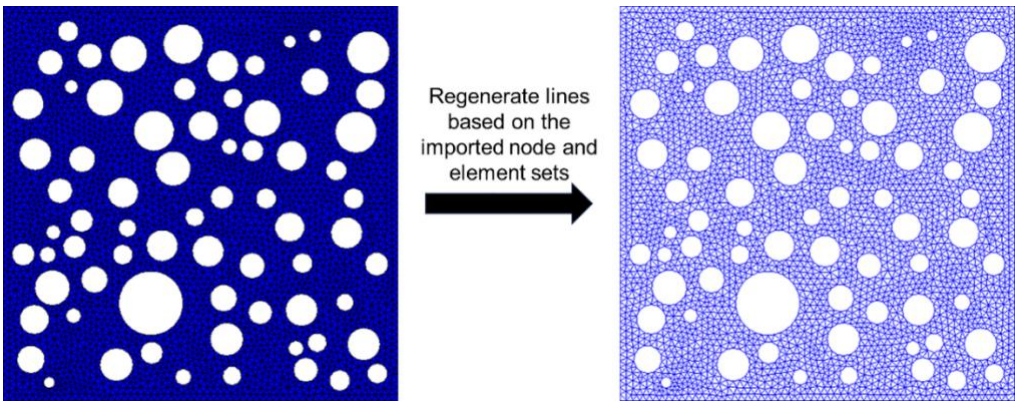

Figure 3: The first type RVE (left) and the second type RVE (right)

4. ABAQUS IMPLEMENTATION AND EXPERIMENTAL CALIBRATION OF THE PHASE FIELD MODELLING METHOD

The phase field method was numerically implemented in ABAQUS, based on heat transfer analogy, using combined User subroutines UHYPER and HETVAL. The comparison of numerical modelling and experimental measurement is shown in Figs. 4 and 5.

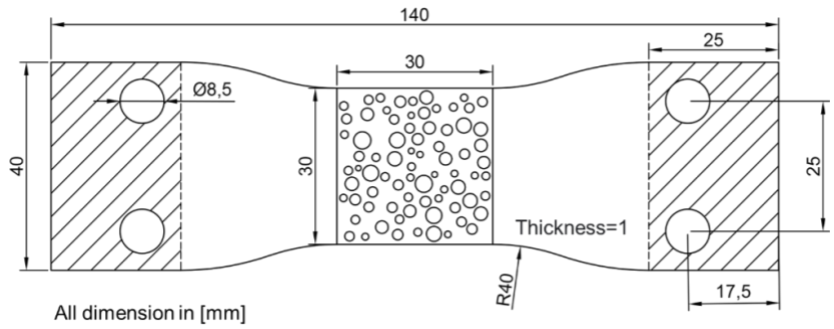

Figure 4 : Schematic drawings of the porous samples for tensile testing

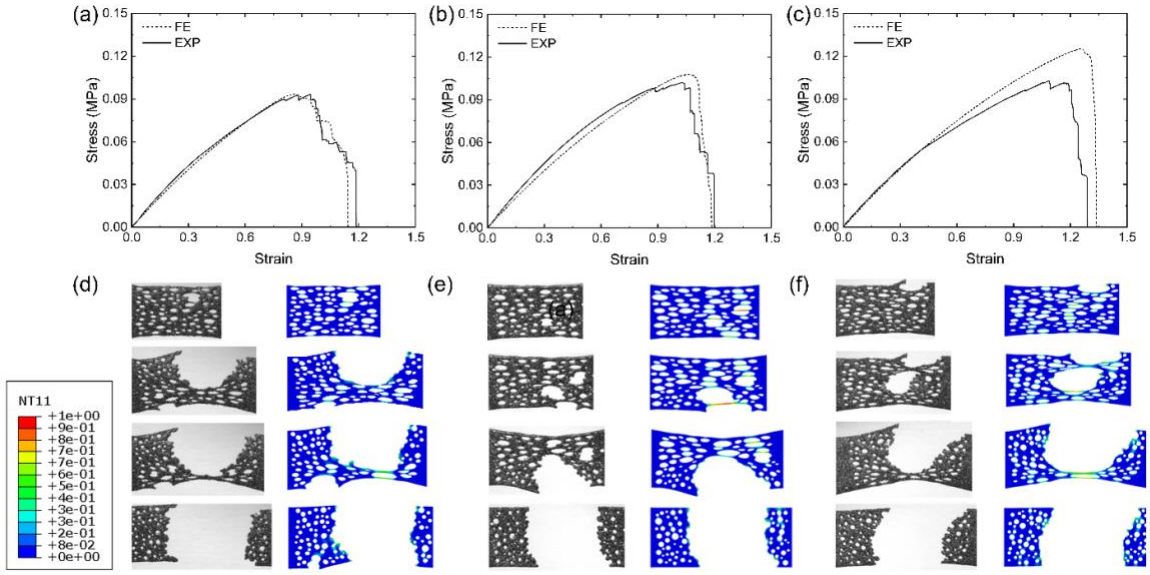

Figure 5: Comparison between the (a-c) numerical and experimental stress-strain curves and (d-f) fracture paths for three porous samples in tension.

5. RESULTS OF THE RVES ANALYSIS

Figure 6 shows the macroscopic stress-strain curve and crack propagation of Sample A, which had the highest values of $\Delta\varepsilon$, ε_{ff}, and φ among the 400 RVE results. Here, $\Delta\varepsilon$ denotes the difference between the initial and final failure strain, ε_{ff} the final failure strain and strength and the strength (σ_{max}). For comparison, the stress-strain curves and crack propagation of two additional samples, B and C, are also presented in Figure 6. It is noted that samples A, B and C have nearly identical normalised standard deviation ($\bar{s}$) and mean ($\bar{\mu}$) values for radius of pores, with a difference of only ±0.001.

Two different failure modes were identified from the stress-strain curves of the samples: progressive failure and sudden failure (Fig. 6A). For the progressive failure sample (Sample A), the Δε value was approximately 50% of the final failure strain. In contrast, the Δε value for the sudden failure sample (Sample C) was close to 0 (Fig. 6A). The final failure strain of the progressive failure sample (Sample A) was about 1.5 times that of the sudden failure sample (Sample C), but its strength was only approximately 85% of Sample C's strength (Fig. 6A). Interestingly, the strength of these samples decreased with increasing Δε (Fig. 6A), indicating that the high ductility of the plaques may have been achieved by sacrificing strength.

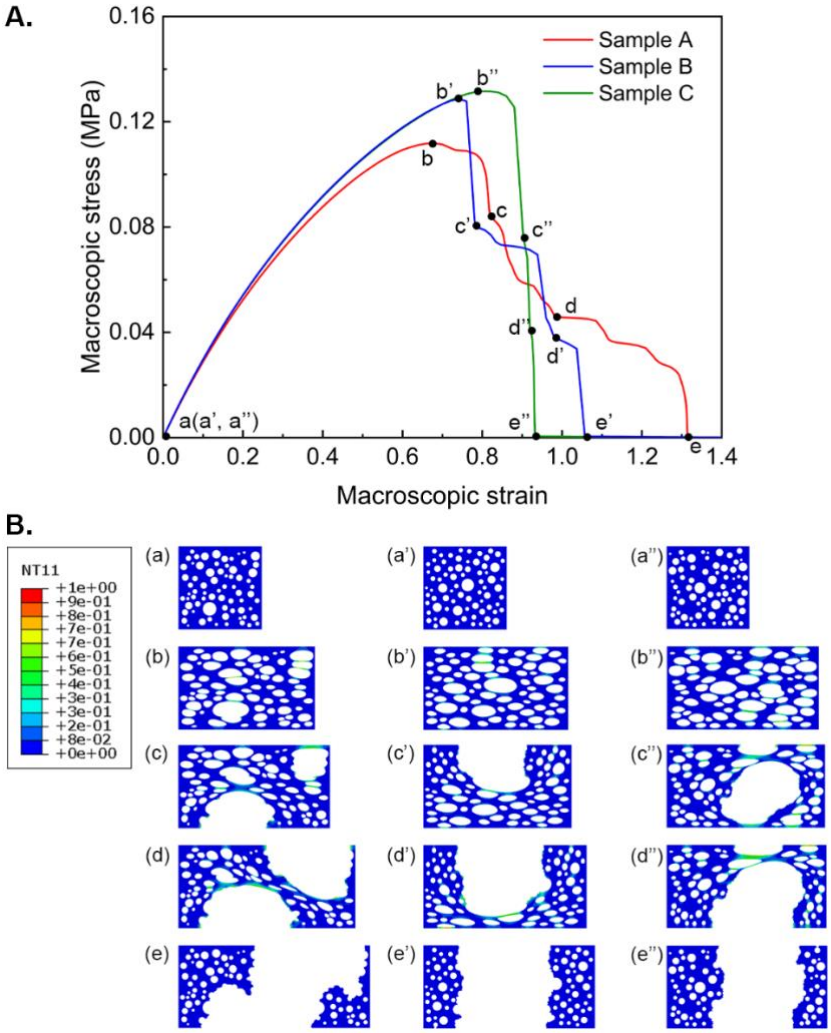

Figure 6: (A) The macroscopic stress-strain curves, and (B) crack paths of selected samples with different failure modes.

The normalised mean ($\bar{\mu}$) and standard deviation ($\bar{s}$) of pore radius reflect the statistic characteristic of the pore distribution within the single-scale RVEs, raising the question of whether these two parameters have a dominant effect on mechanical behaviour. To address this, the simulation results for 400 samples were analysed to establish the functional relations between the initial and final failure strain (Δε), final failure strain (ε_{ff}), strength (σ_{max}), and strain energy density (φ) and the normalized mean ($\bar{\mu}$) and standard deviation ($\bar{s}$).

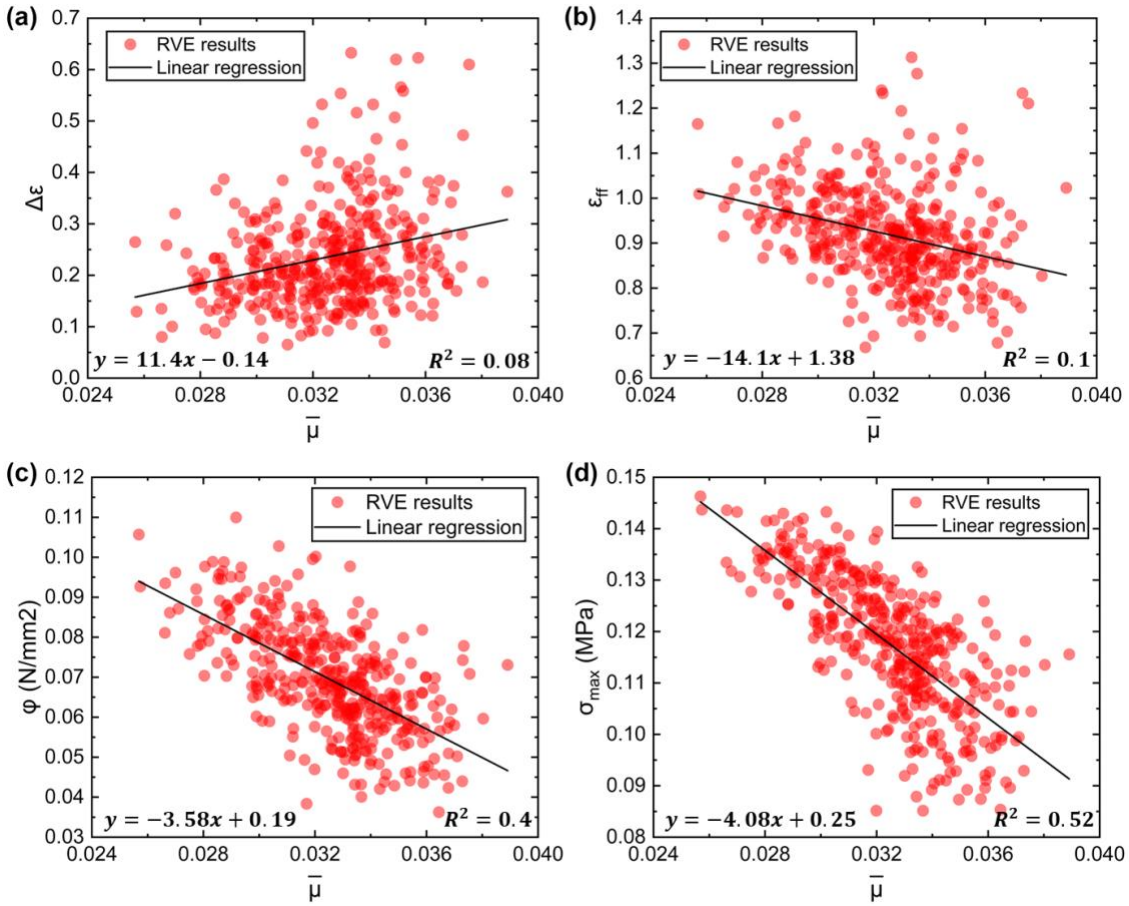

Figure 7: The 2D linear regression analysis between the normalised mean value standard $\bar{\mu}$ of the large-scale pore radius and (a) Δε, (b) final failure strain (ε_{ff}), (c) strength (σ_{max}), and (d) strain energy density (φ).

The results of the linear regression demonstrate that the overall effects of the normalised standard deviation ($\bar{s}$) on Δε, ε_{ff}, σ_{max}, and φ were statistically insignificant for the 400 samples. Conversely, the regression analysis indicates that an increase in the normalised mean radius ($\bar{\mu}$) led to an overall decrease in strength (σ_{max}), strain energy density (φ), and final failure strain (ε_{ff}), respectively (Figs. 7b, c and d). While a different overall trend was observed for Δε: as $\bar{\mu}$ increased, the value of Δε exhibited a slight increase (Figure 7a).

It is important to note that linear regression analysis only illustrates the overall trend of the effect of the normalised mean ($\bar{\mu}$) and standard deviation ($\bar{s}$) on these parameters and cannot capture the high dispersion of the results (Figure 7). It can be seen from Figure 7 that the same $\bar{\mu}$ can always return scattered Δε, ε_{ff}, σ_{max}, or φ values. This may suggest that, while the normalised mean value ($\bar{\mu}$) of pore radius can influence the ductility or other macroscopic material properties of the single-scale RVE, it might not be the sole determining factor. Other factors such as the distance between pores or the multi-scale structure could also play an important role.

ACKNOWLEDGEMENTS

The authors thank the support provided by the Leverhulme Trust Research Grant Scheme, the NanoCAT Research Grant of the University of Nottingham, and the Centre for Additive Manufacturing of the University of Nottingham.

REFERENCES

[1] C. V. Benedict and J. H. Waite, Composition and ultrastructure of the byssus of Mytilus edulis,*Journal of morphology,* **189**, 1986, pp. 261–270. (https://doi.org/10.1002/jmor.1051890305)

[2] E. C. Bell and J. M. Gosline, Mechanical design of mussel byssus: material yield enhances attachment strength, *Journal of Experimental Biology* **199**, 1996, pp.1005–1017. (https://doi.org/10.1242/jeb.199.4.1005)

[3] T. J. Deming, Mussel byssus and biomolecular materials, *Current opinion in chemical biology*, **3**, 1999, pp. 100–105.(https://doi.org/10.1016/S1367-5931(99)80018-0)

[4] D. A. Qureshi, S. Goffredo, Y. Kim, Y. Han, M. Guo, S. Ryu, and Z. Qin, Why mussel byssal plaques are tiny yet strong in attachment, *Matter,* **5**, 2022, pp. 710–724.(https://doi.org/10.1016/j.matt.2021.12.001)

[5] Y. Lyu, Y. Pang, T. Liu, and W. Sun, Determining hyperelastic properties of the constituents of the mussel byssus system, *Soft Matter*, 20, 2024. pp.2442-2454. (https://doi.org/10.1039/D3SM01677C)

[6] C. A. Monnier, D. G. DeMartini, and J. H. Waite, Intertidal exposure favors the soft-studded armor of adaptive mussel coatings, *Nature Communications*, **9**, 2018, pp.2442-2454. (https://doi.org/10.1038/s41467-018-05952-5)

[7] M. J. Harrington, F. Jehle, and T. Priemel, Mussel byssus structure-function and fabrication as inspiration for biotechnological production of advanced materials, *Biotechnology journal*, **13**, 2018, 1800133. (doi: 10.1002/biot.201800133)

[8] F. Jehle, E. Macías-Sánchez, S. Sviben, P. Fratzl, L. Bertinetti, and M. J. Harrington, Hierarchically-structured metalloprotein composite coatings biofabricated from co-existing condensed liquid phases, *Nature communications*, **862**, 2020, 202011.(doi: 10.1038/s41467-020-14709-y)

[9] T. Priemel, E. Degtyar, M. N. Dean, and M. J. Harrington, Rapid self-assembly of complex biomolecular architectures during mussel byssus biofabrication, *Nature Communications,* **8**, 2017, 14539. (doi: 10.1038/ncomms14539)

[10] E. Filippidi, D. G. DeMartini, P. Malo de Molina, E. W. Danner, J. Kim, M. E. Helgeson, J. H. Waite, and M. T. Valentine, The microscopic network structure of mussel (Mytilus) adhesive plaques, *Journal of The Royal Society Interface,* **12**, 2015, 20150827. (doi: 10.1098/rsif.2015.0827)

[11] J. H. Bernstein, E. Filippidi, J. H. Waite, and M. T. Valentine, Effects of sea water pH on marine mussel plaque maturation, *Soft Matter*, **16**, 2020, pp. 9339–9346. (doi:10.1039/D0SM01237H)

[12] K. W. Desmond, N. A. Zacchia, J. H. Waite, and M. T. Valentine, Dynamics of mussel plaque detachment, *Soft matter*, **11**, 2015, pp.6832–6839. (doi:10.1039/C5SM01072A)

[13] M. P. Olivieri, R. M. Wollman, and J. L. Alderfer, Nuclear magnetic resonance spectroscopy of mussel adhesive protein repeating peptide segment, *The journal of peptide research*, **50**, 1997, pp. 436–442. (doi: 10.1111/j.1399-3011.1997.tb01206.x)

[14] D. S. Hwang and J. H. Waite, Three intrinsically unstructured mussel adhesive proteins, mfp-1, mfp-2, and mfp-3: Analysis by circular dichroism, *Protein Science*, **21**, 2012, pp.1689–1695. (doi: 10.1002/pro.2147)

EFFECT OF ATOMIC OXYGEN EXPOSURE ON THE THERMO-MECHANICAL PROPERTIES AND SHAPE MEMORY BEHAVIOUR OF ±45° GLASS FIBRE REINFORCED CYANATE ESTER BASED SHAPE MEMORY POLYMER COMPOSITES

Sandaruwan Jayalath[1], Eduardo Trifoni[2], Jayantha Epaarchchi[3], Madhubhashitha Herath[4]and Eleftherios E. Gdoutos[5]

[1,3]Centre for Future Materials, School of Engineering, University of Southern Queensland, Toowoomba, 4350 QLD, Australia.
Email: Sandaruwan.Jayalath@unisq.edu.au, Jayantha.Epaarachchi@unisq.edu.au web page: https://www.unisq.edu.au/

[2]School of Astronomy and Astrophysics, Australian National University, Canberra, ACT, Australia,
Email: Eduardo.Trifoni@anu.edu.au, web page: https://www.anu.edu.au/

[3]School of Engineering, University of Hull, UK
Email: M.Herath@hull.ac.uk, web page: https://www.hull.ac.uk/

[3]Graduate Aerospace Laboratories, California Institute of Technology, Pasadena, CA, 91125, USA,
Email: egdoutos@caltech.edu, web page: https://www.pellegrino.caltech.edu/

Keywords: Shape Memory Polymer Composite, Atomic Oxygen Exposure, Durability of Shape Memory Polymer Composites, Graphene Nano platelets.

ABSTRACT

The use of shape memory polymers (SMPs) in space applications is a rapidly developing field. Therefore, the development of SMPs that are compatible with space environments can be a game-changing innovation for manufacturing specific satellite components and space structures. This study presents the durability evaluation of a cyanate ester-based shape memory polymer composite (SMPC) to be used in a lower Earth orbit (LEO) environment. SMPCS were fabricated with and without graphene nanoplatelets (GNP). Then SMPCs were exposed to Atomic Oxygen (AO) for a period of 48 hours, mimicking 300 days in a 550 km LEO orbit, and thereafter the effect due to AO exposure was tested and compared. The GNP-filled SMPC showed lower erosion in terms of weight loss and morphology compared to the SMPC without GNP. Thermo-mechanical, tensile, and flexural properties showed slight changes to the storage onset temperatures, tensile modulus, and flexural modulus, respectively, due to the AO exposure. Further, the shape recovery process has been slowed down by the AO exposure in all SMPCs, but 100% shape recovery was achieved at the end. It is concluded that GNP has slowed down the AO erosion, and the SMPC shows promising results for its future use in space applications.

1 INTRODUCTION

Shape memory polymers (SMPs) are considered a smart material due to their ability to be programmed into temporary shapes and then to be recovered using external stimuli such as heat, electricity, light, or magnetism [1,2]. Due to their excellent shape memory properties, SMPs are often being researched to develop deployable components and structures that can be used in biomedical, civil and space applications [3]. With rapid development of the space industry, SMPs that can withstand the harsh environment of space are being researched increasingly in recent years.

SMP and their composites can be used in deployable components of LEO satellites such as rolled-out solar arrays, hinges, booms, etc [2]. However, the SMP should be durable against the LEO orbital

environmental conditions such as high temperatures, UV radiation, thermal cycles, high vacuum, charged particle irradiation, as well as atomic oxygen irradiation [4]. AO irradiation in the LEO environment can erode almost every material in its way. Being hydrocarbons, polymers are highly susceptible to erosion by AO bombardments. However, the density of AO decreases with increasing orbital elevation, enabling the SMP to be used in higher altitude LEO regions. Furthermore, protective measurements such as silicon coatings can be used to protect SMPs against AO irradiation [5].

Cyanate ester is one of the most widely researched epoxy polymer families. In recent years, cyanate ester has been modified as a polymer with shape memory properties by adding oligomers and elastomers [6]. Furthermore, cyanate ester resins have performed well during many space durability tests [7–9]. In this research work, the authors are focusing on utilising the synthesised cyanate ester-based SMP reinforced with ±45° glass fibre for optimum directional shape memory programming and recovery. Moreover, graphene nanoplatelets (GNP) were added as a thermal conductive filler. Then the SMPC with and without GNP was exposed to AO irradiation, and the effect on SMPC was tested.

This work can be considered one of the pioneering works to utilise cyanate-based SMPCs for LEO applications. The outcome of this experiment has provided a basic understanding of the behaviour of SMPCs after being exposed to AO irradiation.

2 MATERIALS AND METHODS

2.1 Materials

For the SMP synthesis, Bisphenol A Cyanate Ester (BACE, M_n = 278.31) monomer was purchased from Wenzhou Blue Dolphin New Material Co., Ltd, China and PEG600 (PEG, M_n = 600) was purchased from Chem Supply Australia. Graphene Nano Platelets (GNP, surface area 750 m^2/g) were purchased from Sigma Aldrich, Australia, to be used as a thermally conductive filler. Glass fibre fabric (200 gsm) was purchased from ATL Composites, Australia, and it was used to reinforce the SMP. All the chemicals, fillers and fibres were used as purchased.

2.2 SMPC Fabrication

Initially, SMP was synthesised by mixing BACE and PEG600 (9:1 stochiometric ratio) at 90°C using a mechanical stirrer. GNP (0.6% w/w) was added afterwards and mixed using a sonicator for 20 mins (Figure 1). The ±45° plain weave glass fibre layers were cut into 300×300 mm^2 six sheets and laid inside a glass mould using double-sided tapes. The chemical mixture was poured into the glass mould and then cured for 2 hours at 100°C, 5 hours at 120°C, 2 hours at 180°C and 5 hours at 210°C. The cured 3 mm SMPC sheet was cut by a waterjet cutter into testing samples according to the ASTM standards. For the ease of identification, SMPC with GNP was named as GX and without GNP was named as NX. The Glass fibre layup configuration of NX SMPC can be observed under the microscope as shown in Figure 2.



Figure 1: Sonication of the GNP-filled chemical mixture.

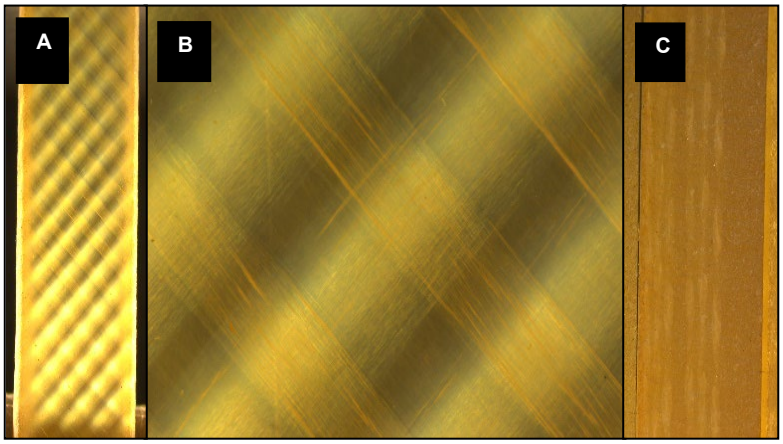

Figure 2: (a) Fabricated NX SMPC, (b) microscopic view of ±45° glass fibre layup configuration, (c) sectional view of SMPC with 6 glass fibre layers.

2.3 Atomic Oxygen Exposure

SMPCs with and without GNP were exposed to Atomic Oxygen (AO) using the AO interaction facility at the National Space Test Facility (NSTF), Australian National University, Canberra. Initially, SMPC samples were fixed into a sample holder to avoid AO exposure from other directions except for the top surface (Figure 3 (A)). During the test, SMPCs were exposed to AO plasma (Figure 3 (B)) with a 6.76×10^{13} atoms/cm^2.s flux under 30 Pa (0.3 mbar) of pressure at room temperature. At first, SMPCs were weighed and then exposed to AO continuously for 24 hours. After 24 hours, the SMPCs were weighed again and kept under AO exposure for another 24 hours. Then, SMPC samples were weighed again and cut into standard samples for characterisation and mechanical testing. In total, the SMPC samples were kept under the AO exposure for 48 hours, which is equivalent to 21 days at a 400 km LEO orbit (orbit of International Space Station) or 300 days at a 550 km LEO orbit [10].

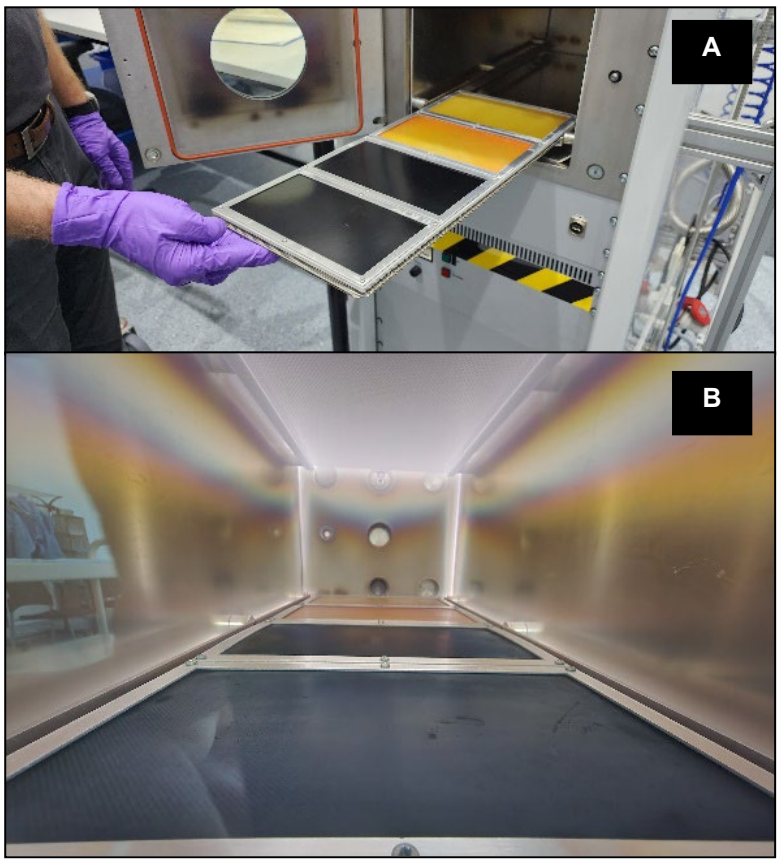

Figure 3: (a) SMPCs on the sample holder and (c) SMPCs under the AO plasma.

2.4 Characterisation Methods of SMPC.

The surface morphology of the AO exposed and unexposed was observed with a digital microscope (LEICA DMS300) and SEM (JEOL JCM-6000) at an acceleration voltage of 10 kV. The SEM images were further analysed using an SPM data visualization and analysis tool (Gwyddion 2.64).
Both AO exposed and unexposed surfaces were characterised for chemical structure changes using Fourier Transformation Infrared (FTIR) analysis in the wavelength range of 400-4000 cm^{-1} using SHIMADZU IRAffinnity-1S FTIR.

Thermomechanical properties such as storage modulus and tan(δ) changes of the SMPCs were studied by dynamic mechanical analysis (DMA) using the Hybrid Rheometer Discovery HR-2 (TA Instruments). 40×8×3 mm^3 SMPC samples were tested using the dual cantilever fixture with 25µm deflection and in 1 Hz oscillation. The samples were heated from 30 to 220°C by 5°C/min (ASTM D7028).

The tensile tests (with an extensometer) and the flexural tests were performed using MTS 100 kN uni-axial tensile testing machine according to ASTM D638 and ASTM D790 standards respectively.
Shape memory property changes were tested using the fold-deploy test method [11]. By measuring the fixed and recovery angles of the SMPCs, shape fixity ratios (R_f) and shape recovery ratios (R_r) were calculated. 100×10 mm^2 SMPC strips were bent into 90° and shape recovery was measured at temperatures from 20 to 220°C with 20°C intervals. All samples were kept at each temperature level for 30 min before measuring the recovery angle.

3. RESULTS AND DISCUSSION

3.1 Surface Morphology Analysis

After a total of 48 hours (12+12 hrs.) of AO exposure, the surface of the SMPCs has been eroded and is visible as shown in Figure 4. Total weight loss after 48 hours of exposure was measured as 0.5g in NX and 0.4g in GX. Morphology of the unexposed and exposed SMPC was observed with SEM. Both SMPCs with and without graphene showed rough surfaces with small grooves between 1-3 µm wide (Figure 5). However, SMPC with GNP showed wider grooves and smoother surfaces according to the analysed images compared to SMPC without GNP (Figure 6). Furthermore, GX showed shallow grooves (~121 nm) compared to NX (~187 nm) in the analysed figures.

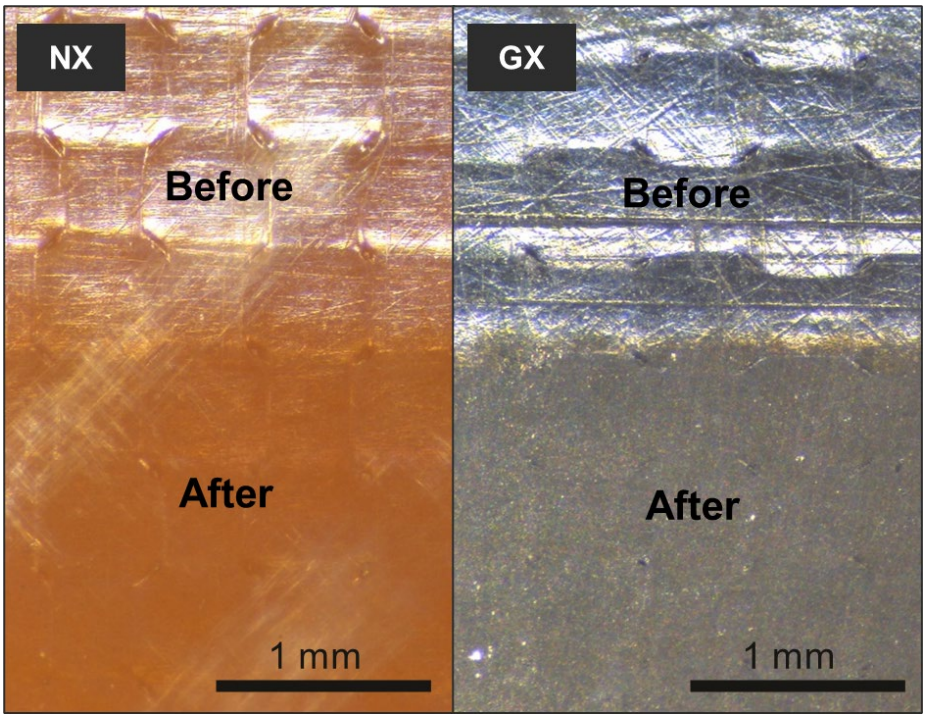

Figure 4: Digital microscopic image of NX and GX before and after 48 hours of AO exposure.

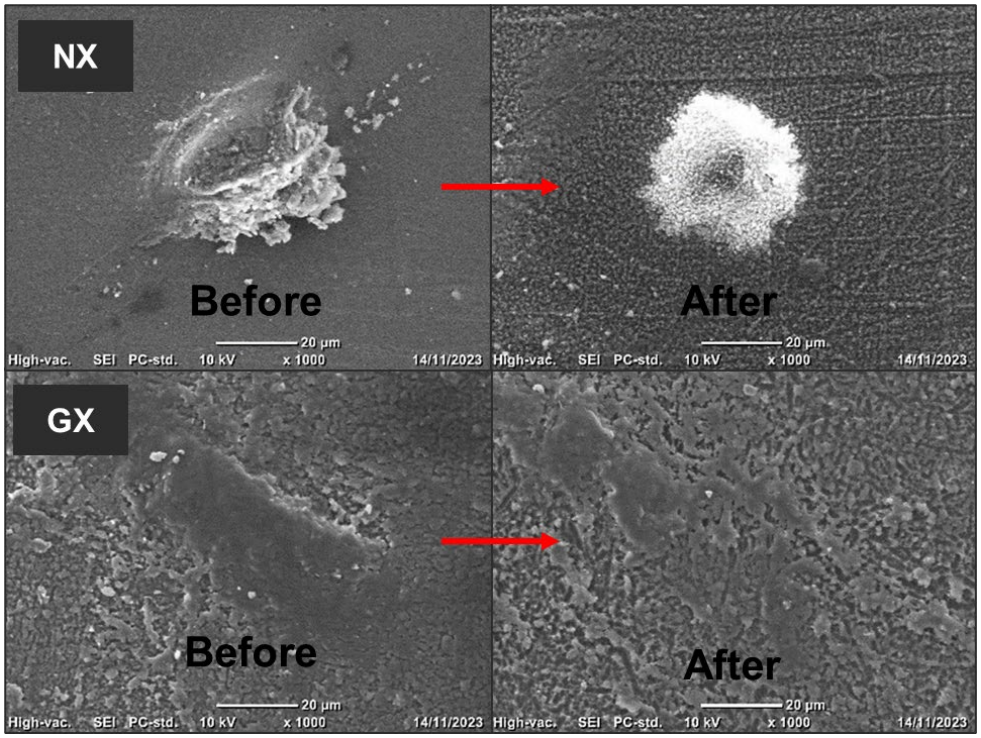

Figure 5: SEM images of NX and GX before and after 48 hours of AO exposure.

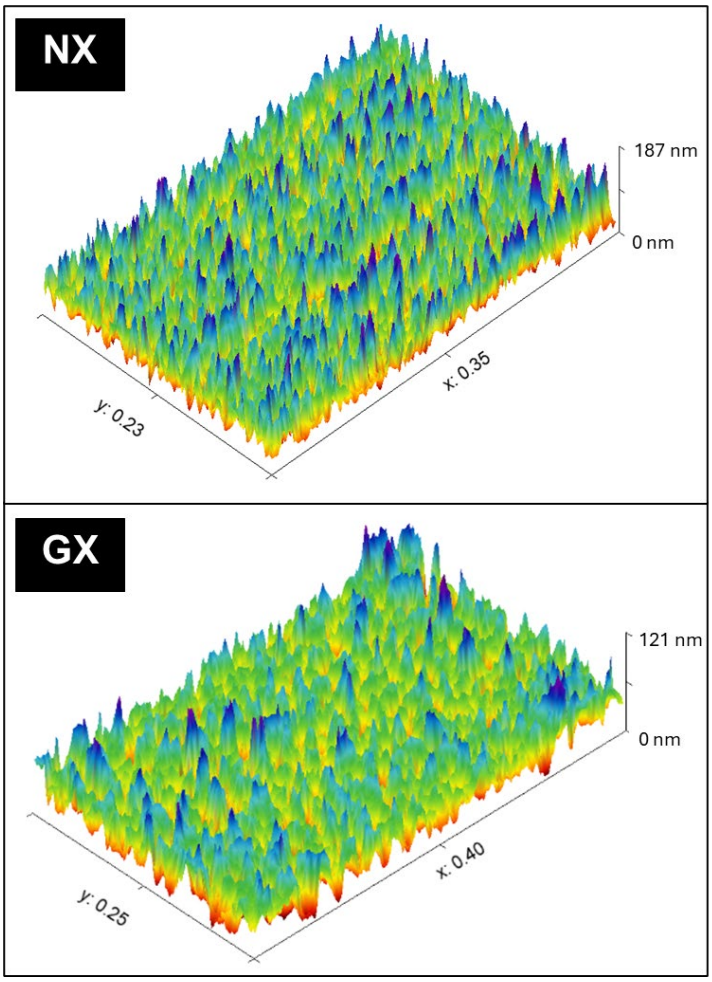

Figure 6: Surface roughness analysis of NX and GX after 48 hours of AO exposure.

3.2 Chemical Structure

FTIR spectra of SMPCs before and after AO exposure were compared (Figure 7). According to the spectrum analysis, the peaks at 1357 cm^{-1} and 1558 cm^{-1} show the existence of triazine rings, and 1465 cm^{-1} shows the existing groups of Isocyanurate in the SMPC matrix. The presence of PEG can be identified by the peaks at 1072 cm^{-1} from (-C-O-C-) and 2862 cm^{-1} from ($-CH_2-$). This confirms the formation of the cyanate ester structure with the shape memory properties [12]. Even after the AO bombardment, the above-mentioned bonds remain unchanged due to the high bond energy (over 2000 kJ/mol) of triazine rings.

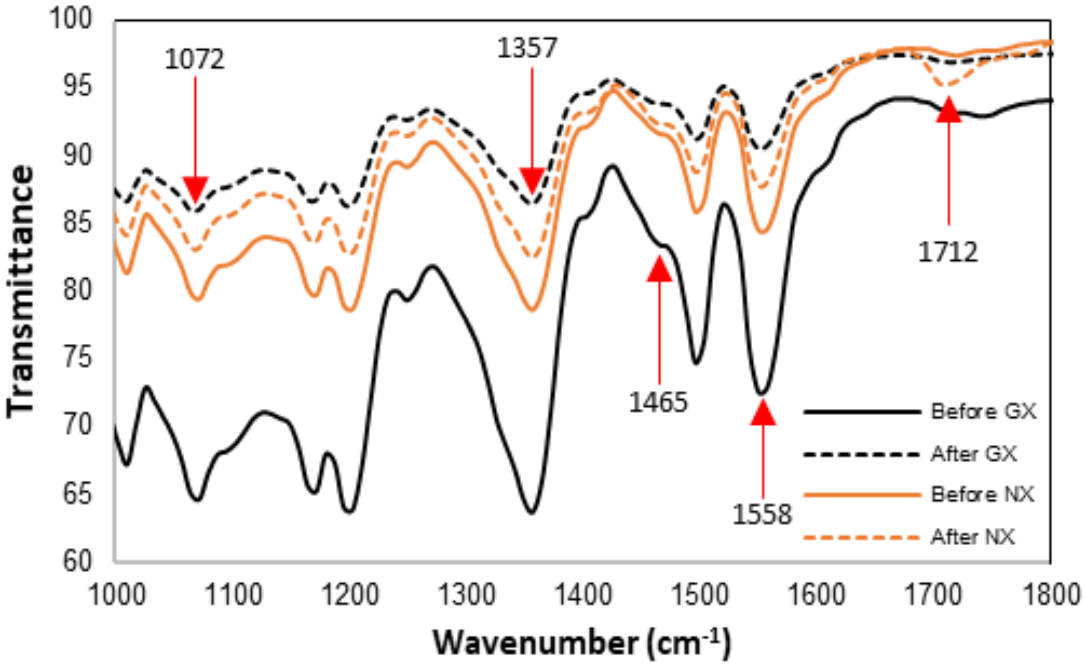

Figure 7: FTIR spectra of NX and GX before and after AO exposure.

The only change in the spectrum series can be identified in the spectrum of NX after the AO exposure. This peak at 1712 cm^{-1} corresponds to the carbonyl C=O bond stretching and vibration. This can be due to AO reacting with broken C-H and C-C bonds. It is worth noting that this only change has happened in SMPC without GNP fillers.

Considering the weight loss data, surface roughness analysis and chemical structure changes, it can be concluded that GNP-filled GX SMPC has built up a certain resistance to AO erosion compared to NX SMPC.

3.3 Thermomechanical Properties

Storage modulus and tan(δ) behaviour of AO exposed and unexposed SMPCs were plotted as shown in Figure 8. During this research work, the storage onset temperature (T_s) of the SMP was considered as the SMP's glass transition temperature (T_g) value. Initial T_g values of AO unexposed NX and GX were calculated as 128.51±0.6°C and 120.04±1°C, respectively. Moreover, both T_g calculated with storage modulus onset and tan(δ) peak temperatures (T_δ) are shown in Table 1.

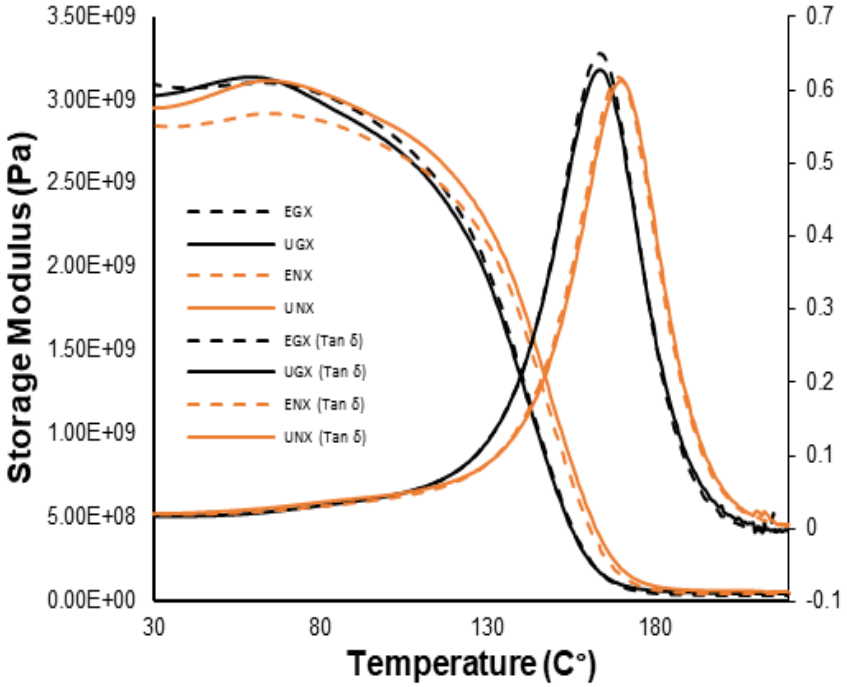

Figure 8: Thermomechanical behaviour of NX and GX before and after 48 hours of AO exposure.

Sample	T_s (Storage Onset)/°C		T_δ (Tan(δ) peak)/°C	
	Unexposed	Exposed	Unexposed	Exposed
NX	128.51±0.6	126.31±0.6	169.72±0.01	169.09±0.2
GX	120.04±1	121.11±1.5	162.87±0.7	164.23±0.2

Table 1: Glass transition temperatures (T_g) of NX and GX samples before and after AO exposure.

The addition of GNP has affected the thermomechanical properties of the SMPCs. T_g values of the GX SMPC have been reduced from a considerable value according to Table 1. This can be due to GNP interrupting the formation of triazine rings and isocyanurate groups in the SMP matrix during the curing stage. Apart from slight variations of the storage modulus graphs of the same SMPC groups, it is safe to assume that the thermomechanical behaviour of the SMPCs is unchanged upon the AO exposure.

3.4 Mechanical Properties

Tensile property and flexural property changes after the AO exposure are depicted in Figure 9 and Figure 10, respectively. Initially, NX showed a tensile modulus of 12.1 GPa with an ultimate tensile strength (UTS) of 82.5 MPa, and GX showed a tensile modulus of 7.8 GPa and a UTS of 60.48 MPa. The drop in modulus and UTS of GX can be due to the interruption of triazine ring bonds and isocyanurate bonds in the SMPC matrix by the GNP. However, after the AO exposure, the tensile modulus of both NX and GX dropped to 4.41 GPa. It can be noted that the tensile modulus drop of AO-exposed NX is higher than that of AO-exposed GX, from 4.3 GPa, showing the AO resistance of GNP-filled GX SMPC.

According to the flexural behaviour analysis, both AO-exposed and unexposed showed a flexural modulus in the range of 3.24-3.5 GPa initially. While GNP-filled GX showed higher modulus afterwards, resisting the three-point bending movement, NX samples have shown much flexibility with lower flexural modulus. This can be due to GNP fillers obstructing the polymeric structure from bending. Proving that AO-exposed GX samples have shown lower flexural modulus due to the removal of some amount of GNP from the SMPC matrix, and yet the flexural behaviour of the NX sample remains in the same region, even after the AO exposure.

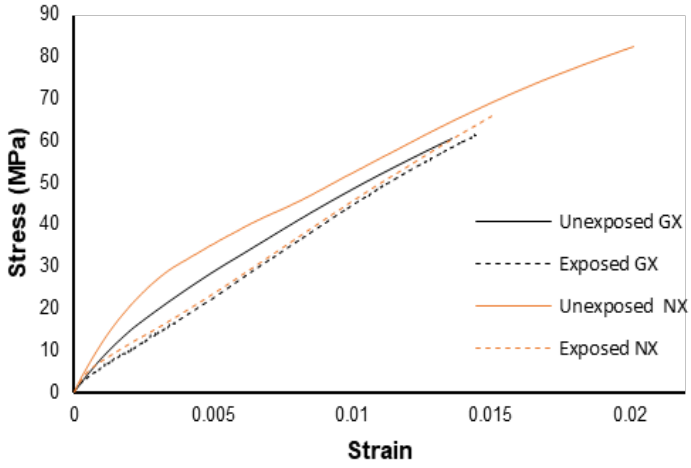

Figure 9: Tensile behaviour of NX and GX before and after AO exposure.

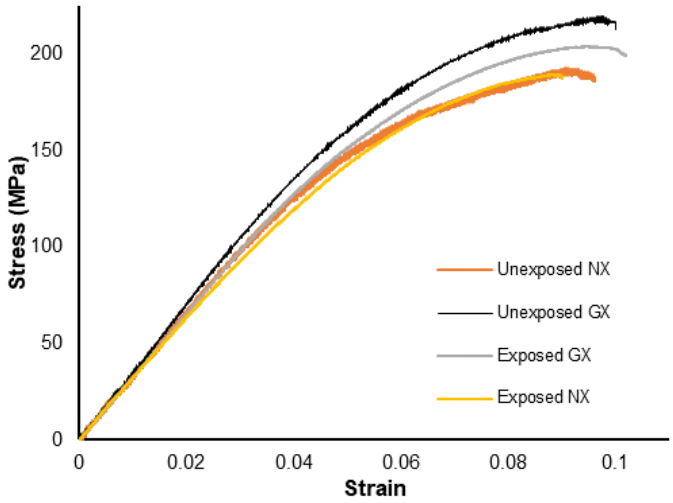

Figure 10: Flexural behaviour of NX and GX before and after AO exposure.

3.5 Shape Memory Behaviour

Shape memory behaviour is primarily studied using the shape fixity and recovery of the SMP or SMPC. The R_f value of all the AO exposed and unexposed SMPCs was calculated as 100%. However, the shape recovery of the SMPC showed interesting behaviour during their recovery even though they recovered their initial shape 100% at the end as shown in Figure 11 and Figure 12. An indication of the efficiency of the recovery can be studied by looking at the R_r value of the SMPC at the T_g at the tan(δ) peak (Table 2). It is interesting to mention that the SMPC with GNP showed a much quicker shape recovery compared to the SMPC without GNP. While the R_r of NX is around 33.7% at 169.72°C, GX has recovered around 42.5% at 162.87°C. This can be due to higher thermal conductivity inside the matrix of GX due to GNP fillers. However, it can be observed that the shape recovery has been delayed overall after the AO exposure in both NX and GX samples.

	T_g value	NX		GX	
		Unexposed	Exposed	Unexposed	Exposed
R_r	at T_s	~2.5%	~2%	~2%	~2%
	at T_δ	~33.7%	~15%	~42.5%	~15%

Table 2: Shape recovery ratios of NX and GX at storage onset T_g and tan(δ) T_g before and after AO exposure.

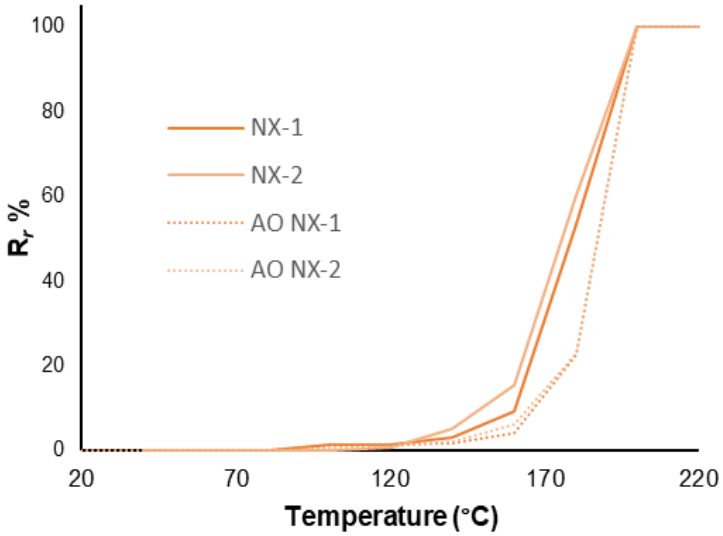

Figure 11: Shape recovery behaviour of NX before and after AO exposure.

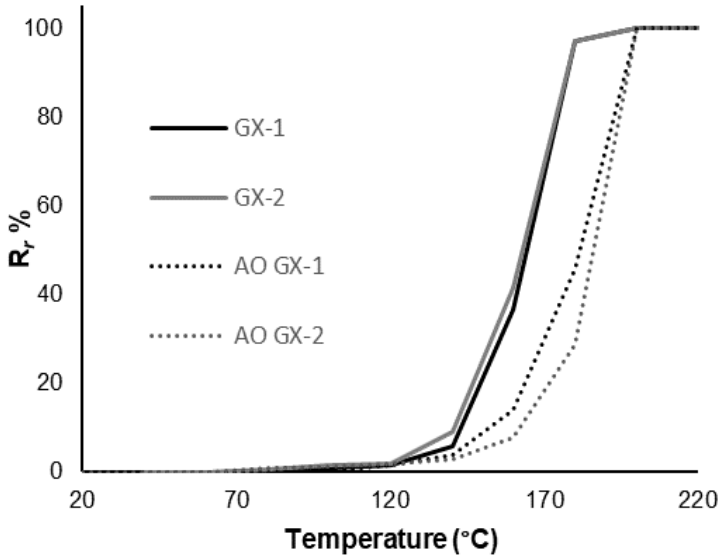

Figure 12: Shape recovery behaviour of GX before and after AO exposure.

4. CONCLUSION

According to the outcomes of this research work, it is clear that polymer surface erosion due to AO bombardment is inevitable. However, while being a good thermal conductive filler, GNP has acted as an AO erosion-resistive material compared to the performance of the SMPC without GNP filler. It is worth noting that the fabricated SMPCs are capable of surviving without significantly losing their shape memory and thermo-mechanical properties in a simulated 300 days in a 550 km LEO orbit. Further durability tests can be warranted to study the synergistic effects on the SMPC with protective measurements before the deployable components and structure development stage.

ACKNOWLEDGEMENTS

The authors would like to acknowledge the support given to this research by the National Space Test Facility (NSTF), Australian National University (ANU), to utilise the Atomic Oxygen interaction facility. Also, the main author would like to convey his sincere gratitude to Mr Oliver Kinder (Senior Technical Officer) and Mr. Nathan Strenzel (Technical Officer) at the University of Southern Queensland, for their valuable assistance in this research.

REFERENCES

[1] J. Jeewantha, S. Jayalath, C. Emmanuel, M. Herath, E. Forster, M. Islam, J. Leng, J. Epaarachchi, Shape memory polymer smart plaster for orthopaedic treatments, Smart Mater. Struct. 31 (2022) 115016. https://doi.org/10.1088/1361-665X/ac943b.

[2] F.F. Li, Y.J. Liu, J.S. Leng, Progress of Shape Memory Polymers and Their Composites in Aerospace Applications, Yuhang Xuebao/Journal Astronaut. 41 (2020) 697–706. https://doi.org/10.3873/j.issn.1000-1328.2020.06.007.

[3] Y. Xia, Y. He, F. Zhang, Y. Liu, J. Leng, A Review of Shape Memory Polymers and Composites: Mechanisms, Materials, and Applications, Adv. Mater. 33 (2021) 1–33. https://doi.org/10.1002/adma.202000713.

[4] S. Jayalath, M. Herath, J. Epaarachchi, E. Trifoni, E.E. Gdoutos, L. Fang, Partial Order Methods in Verification, American Mathematical Society, Providence, Rhode Island, 1997. https://doi.org/10.1090/dimacs/029.

[5] Z. Yang, Q. Wang, Y. Bai, T. Wang, AO-resistant shape memory polyimide/silica composites with excellent thermal stability and mechanical properties, RSC Adv. 5 (2015) 72971–72980. https://doi.org/10.1039/c5ra12293g.

[6] H.T.S. Jayalath, M. Herath, J. Epaarachchi, Cyanate esters as a high performing shape memory polymer: A review, Mater. Today Proc. 57 (2022) 693–700. https://doi.org/10.1016/j.matpr.2022.02.121.

[7] F. Xie, X. Gong, L. Huang, L. Liu, J. Leng, Y. Liu, Effects of accelerated aging on thermal, mechanical, and shape memory properties of a cyanate-based shape memory polymer: II atomic oxygen, Polym. Degrad. Stab. 186 (2021) 109515. https://doi.org/10.1016/j.polymdegradstab.2021.109515.

[8] T. Xu, G. Li, S.S. Pang, Effects of ultraviolet radiation on morphology and thermo-mechanical properties of shape memory polymer based syntactic foam, Compos. Part A Appl. Sci. Manuf. 42 (2011) 1525–1533. https://doi.org/10.1016/j.compositesa.2011.07.005.

[9] Z. Ping, F. Xie, X. Gong, L. Liu, J. Leng, Y. Liu, Effects of Accelerated Aging on Thermal, Mechanical and Shape Memory Properties of Cyanate-Based Shape Memory Polymer: III Vacuum Thermal Cycling, Polymers (Basel). 15 (2023) 1893. https://doi.org/10.3390/polym15081893.

[10] J. Mathew, E. Trifoni, J. Ashby, S. Rosset, I.A. Anderson, LEO Atomic Oxygen Interaction Experiments at the ANU National Space Test Facility, Proc. Int. Astronaut. Congr. IAC. 2022-Septe (2022) 18–22.

[11] K.D.C. Emmanuel, H.M.C.M. Herath, L.H.J. Jeewantha, J.A. Epaarachchi, T. Aravinthan, Thermomechanical and fire performance of DGEBA based shape memory polymer composites for constructions, Constr. Build. Mater. 303 (2021) 124442. https://doi.org/10.1016/j.conbuildmat.2021.124442.

[12] K.S. Santhosh Kumar, A.K. Khatwa, C.P. Reghunadhan Nair, High transition temperature shape memory polymers (SMPs) by telechelic oligomer approach, React. Funct. Polym. 78 (2014) 7–13. https://doi.org/10.1016/j.reactfunctpolym.2014.02.008.

PERFORMANCE EVALUATION OF STRUCTURAL BEHAVIOR MONITORING USING SMART SENSORS

Yu-Jin Jung[1], Ga-Hyeon Eom[2] and Sung-Hwan Jang[3]

[1]Department of Smart City Engineering, Hanyang University ERICA
Ansan 15588, Republic of Korea
Email: yujin0421@hanyang.ac.kr

[2]Department of Smart City Engineering, Hanyang University ERICA
Ansan 15588, Republic of Korea
Email: eomgh0316@hanyang.ac.kr

[3]Department of Civil and Environmental Engineering, Hanyang University ERICA
Ansan 15588, Republic of Korea
Email: sj2527@hanyang.ac.kr

Keywords: Smart materials; Electrical properties; Mechanical Properties; Physical methods of analysis

ABSTRACT

Cracks in aging concrete structures reduce mechanical integrity and often require localized repair. However, assessing the effectiveness and long-term performance of such repairs remains a challenge, especially in inaccessible or load-critical zones. In this study, I propose a carbon nanotube (CNT)-reinforced epoxy composite combined with aggregates to form a self-sensing concrete system capable of monitoring local compressive stress in real time. The system leverages the piezoresistive properties of CNTs within a polymer matrix to detect mechanical loading. I explored the influence of CNT concentration on electrical conductivity, mechanical performance, and sensing repeatability. The composite with 0.25 wt% CNT content exhibited high electrical sensitivity, mechanical robustness, and reproducibility under cyclic loading. This research highlights the potential of CNT-epoxy concrete as a multifunctional repair material that offers both reinforcement and embedded sensing.

1 INTRODUCTION

The deterioration of concrete structures due to aging and environmental exposure remains a major challenge in civil infrastructure. Surface and internal cracks not only weaken structural capacity but also accelerate corrosion and degradation processes. Repair strategies are often employed to restore mechanical integrity; however, assessing the long-term performance of these repaired areas is difficult with conventional inspection methods. Visual inspections and acoustic techniques require human involvement and do not offer continuous or real-time assessment, which leads to uncertainty and delayed responses to potential failure.

To address this limitation, self-sensing repair materials have been proposed, aiming to integrate sensing capabilities directly into the repair matrix. Among the various approaches, cementitious composites with embedded conductive fillers such as steel fibers, graphite, or carbon nanotubes (CNTs) have been studied for their piezoresistive behavior. For example, Jung et al. [1] developed ultra-high-performance concrete (UHPC) with embedded CNTs for both electrical field curing and crack detection. The system showed piezoresistive response under loading, demonstrating potential for field casting and real-time sensing. However, like many cement-based systems, the approach faced limitations related to CNT dispersion quality and sensitivity, particularly in the pre-cracking regime.

While such cement-based approaches offer some advantages in durability and structural integration, their low elasticity and limited CNT dispersion efficiency often result in insufficient sensitivity and poor repeatability. Polymer-based matrices, particularly epoxy resin, have shown better potential in this regard. Epoxy's high viscosity allows for improved CNT dispersion when aided by techniques

such as ultrasonication and three-roll milling. Moreover, the superior adhesion, chemical resistance, and toughness of epoxy make it a common material for high-performance repairs. Jung and Jang [2] previously proposed a CNT–polyurethane composite "smart skin" for detecting cracks in concrete, confirming the feasibility of CNT/polymer systems for localized sensing applications.

Despite these advancements, CNT-polymer systems incorporating structural aggregates—capable of functioning not only as a sensing layer but also as a load-bearing repair material—have not been fully explored. Most existing studies either neglect aggregate inclusion or limit the application to thin coatings. However, for practical field use, it is essential that self-sensing repair materials possess both structural robustness and effective signal responsiveness.

To bridge this gap, this study develops and characterizes a CNT-epoxy concrete, a hybrid repair material designed to achieve compressive sensing functionality and structural reinforcement simultaneously. The material combines CNTs with an epoxy matrix and coarse aggregates, forming a bulk composite suitable for crack region replacement. The effects of CNT concentration on conductivity, mechanical performance, and rheology were investigated in detail. Furthermore, its strain-sensing behavior under static and cyclic compression was analyzed to determine its viability as a localized SHM-enabled repair material for damaged concrete infrastructure.

2 MATERIALS AND METHODS

2.1 Materials

To develop a structurally applicable self-sensing repair material, a composite system was formulated using multi-walled carbon nanotubes (MWCNTs), epoxy resin, and aggregates. The MWCNTs used in this study were MWCNT-210P (Kumho Petrochemical, Republic of Korea), synthesized by chemical vapor deposition. These nanotubes have diameters of approximately 10–15 nm and lengths of 10–20 μm, with a carbon purity exceeding 95 wt%. The epoxy matrix was based on a super-low viscosity bisphenol-A type resin (DH-150, Daehwa Precision, Republic of Korea), selected for its high fluidity (120 mPa·s), high compressive strength (76 MPa), and excellent bonding properties (adhesive strength: 9.1 MPa). Analytical-grade acetone (99.7%, Samchun Chemical, Republic of Korea) was used to facilitate the dispersion of CNTs in the epoxy matrix. Standard sand (KS L ISO 679) was used as the aggregate, due to its consistent particle size and compatibility with epoxy matrices. An 80:20 volumetric mixing ratio between aggregate and CNT-epoxy composite was adopted, based on prior optimization studies that achieved a balance between compressive performance, elasticity, and flowability. This configuration allows the material to mimic the load-bearing characteristics of typical crack repair regions in concrete structures.

2.2 Fabrication Process

The fabrication sequence of the CNT-epoxy concrete. The process was designed to achieve uniform CNT dispersion while maintaining the structural integrity of the composite during aggregate mixing and curing. First, CNTs were dispersed in approximately 50 mL of acetone together with the epoxy resin using an ultrasonicator (Q700, Qsonica, USA) at 90% amplitude in pulse mode (15 s on, 15 s off) for 40 minutes. This ultrasonic treatment was critical to overcome van der Waals attractions between CNTs, facilitating homogeneous dispersion. To prevent thermal degradation of the resin during sonication, the beaker was immersed in an ice bath. Following dispersion, the mixture was heated on a hot plate at 60 °C for 24 hours to evaporate the acetone. An epoxy hardener was then added in a 3:1 ratio (resin:hardener), and the mixture was further homogenized using a three-roll mill (TR50M, Trilos, USA) to remove remaining agglomerates and ensure uniform CNT distribution. This step was particularly important for consistent electrical conductivity and reproducible sensing behavior. The final CNT-epoxy composite was manually blended with aggregates and poured into cylindrical molds (40 mm diameter, 25 mm height). Curing was performed at room temperature for 48 hours. After demolding, both top and bottom surfaces were coated with high-purity silver ink to form low-resistance electrical contacts.

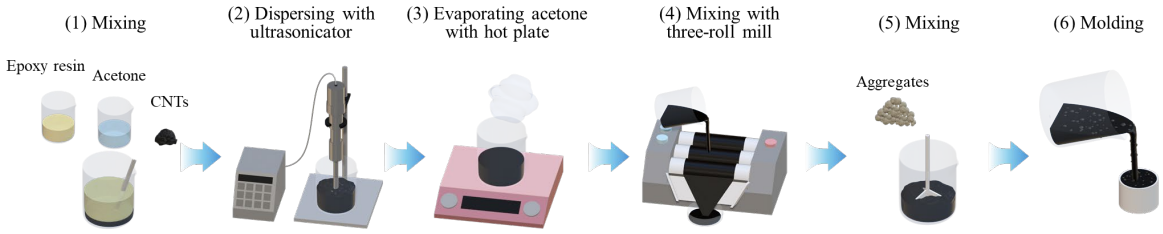

Figure 1: Fabrication process of CNT-epoxy concrete.

2.3 Characterization Methods

Electrical conductivity was measured using a two-probe setup. For samples with resistance above 10^6 Ω, a high-resistance meter (6517B, Keithley, USA) was used; for those below this threshold, a source meter (2450, Keithley, USA) was applied. The electrical conductivity σ (S/m) was calculated using

$$\sigma = L/RA \tag{1}$$

where R is the resistance, L is the electrode spacing, and A is the electrode cross-sectional area. Silver ink was applied to reduce contact resistance, and copper leads were attached during mechanical tests.

Mechanical and piezoresistive tests were conducted using a universal testing machine (Instron 8861, USA). Static compression tests were performed at a loading rate of 1.3 mm/min. Electrical resistance was recorded in real-time during mechanical loading using a multimeter (2700, Keithley, USA) connected to the copper-taped electrode surfaces. Rheological behavior of the CNT-epoxy composite was measured using a parallel-plate rheometer (MCR 302e, Anton Paar, Austria). A constant shear strain of 1.01% was applied across a frequency sweep from 0.05 to 450 rad/s to evaluate viscoelastic responses relevant to processability and field application.

3 RESULTS AND DISCUSSION

3.1 Electrical Properties

The electrical conductivity of the CNT-epoxy composite exhibited a strong dependence on the CNT concentration. In specimens without CNTs or with less than 0.05 wt.% loading, the material behaved as an insulator, with conductivity below 10^{-8} S/m [3]. This is attributed to the isolated and randomly distributed CNTs, which were insufficient to form continuous pathways for electron transport. However, as the CNT concentration approached 0.10 wt.%, a dramatic increase in conductivity was observed. This behavior corresponds to the percolation threshold, where conductive clusters begin to connect and establish long-range networks through the matrix [4].

Between 0.10 wt.% and 0.50 wt.%, the conductivity rose by over three orders of magnitude, reaching values in the range of 10^{-5} to 10^{-3} S/m depending on sample geometry and aggregate presence. This exponential growth indicates efficient CNT network formation, enabling both direct conduction and electron tunneling. The results are consistent with previous findings in CNT/epoxy composites, where the percolation threshold is often reported between 0.05 and 0.3 wt.% depending on dispersion quality and processing method [5].

Beyond 0.50 wt.%, conductivity growth plateaued, suggesting saturation of the network. At these higher concentrations, additional CNTs are more likely to form redundant bundles or agglomerates rather than contributing to new connections [6]. This saturation effect limits further gains in sensing performance and suggests diminishing returns at higher loading levels.

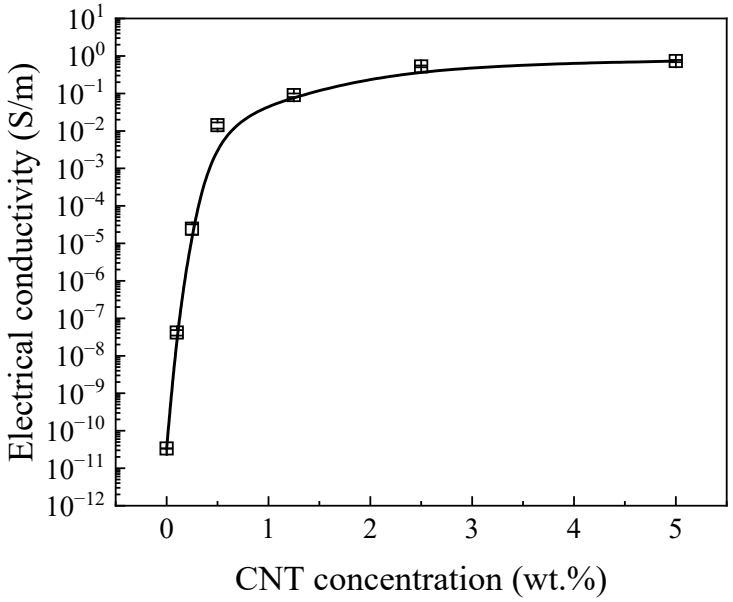

Figure 2: Electrical conductivity of CNT-epoxy composites at different CNT concentrations.

3.2 Rheological Properties

The rheological characteristics of the CNT-epoxy composites were evaluated to understand how increasing CNT concentration affects processability. Table 1 presents the complex viscosity as a function of angular frequency for four CNT loadings: 0.00, 0.25, 0.50, and 2.50 wt.%.

The control sample with 0.00 wt.% CNT exhibited Newtonian-like flow behavior, maintaining a nearly constant viscosity of approximately 1 Pa·s across the entire frequency range. This low and stable viscosity is suitable for uniform mixing with aggregates and effective casting. Upon adding 0.25 wt.% CNT, a noticeable increase in viscosity was observed, particularly in the low-frequency range. The composite began to exhibit mild shear-thinning behavior, suggesting the onset of a weak particle–matrix interaction. Although the viscosity rose by nearly an order of magnitude, the material remained sufficiently flowable for practical mixing and casting processes. At 0.50 wt.%, the shear-thinning effect became more pronounced. The low-frequency viscosity further increased to above 10^4 Pa·s, indicating the development of a more interconnected CNT network within the epoxy. This enhanced viscoelastic response implies that the CNTs were forming physical linkages that resisted deformation under low shear conditions. A substantial rheological change was observed at 2.50 wt.%, where the composite reached a complex viscosity exceeding 10^6 Pa·s at low frequencies. The material became highly viscoelastic and showed significant resistance to flow. Such high viscosity can severely compromise workability, leading to poor dispersion of aggregates, increased air entrapment, and inhomogeneous distribution during casting. In practical applications, these issues could reduce both structural reliability and sensing stability.

The progressive increase in viscosity with CNT content is primarily driven by van der Waals forces between nanotubes, which promote physical entanglement and the formation of a pseudo-solid network. While beneficial for electrical conductivity, this network formation adversely affects flowability, especially in systems containing solid fillers such as sand [7].

Table 1: Complex viscosity of CNT-epoxy composites at different CNT concentrations.

CNT concentration (wt.%)	Complex viscosity (Pa·s)

0.00	~1
0.25	~1.2 × 10^3
0.50	~8 × 10^3
2.50	~4 × 10^5

3.3 Mechanical Behavior

The compressive performance of CNT-epoxy concrete was evaluated to investigate how varying CNT concentrations influence the mechanical response and to ensure that the sensing functionality does not compromise structural integrity. Figure 3 presents the compressive stress–strain curves for composites containing 0.00, 0.25, and 0.50 wt.% CNTs. The 2.50 wt.% formulation was excluded from mechanical testing due to workability issues during mixing and casting.

The control sample without CNTs exhibited brittle failure, with a peak strain of approximately 6.2% and a compressive strength of about 38 MPa. Incorporating 0.25 wt.% CNTs led to a strength increase of around 19%, reaching nearly 45 MPa, while the strain at failure more than doubled to 13.5%. This improvement is attributed to the reinforcing effect of CNTs, which can bridge microcracks, delay crack propagation, and enhance stress transfer between the matrix and the aggregates [8].

At 0.50 wt.%, the compressive strength was slightly lower than at 0.25 wt.% but still exceeded that of the control. The strain capacity remained comparable to the 0.25 wt.% sample, suggesting that the toughness improvements were retained. This result implies that moderate CNT loading can improve both strength and ductility without significantly affecting casting quality or material homogeneity.

These findings highlight the importance of identifying an optimal CNT range that provides both mechanical reinforcement and sensing capability. While low-to-moderate CNT contents enhance material performance, concentrations above 0.50 wt.% may lead to severe rheological limitations that hinder practical application. Therefore, a target range of 0.25–0.50 wt.% is recommended for CNT-epoxy concrete designed for use as a structural repair material with integrated self-sensing functionality.

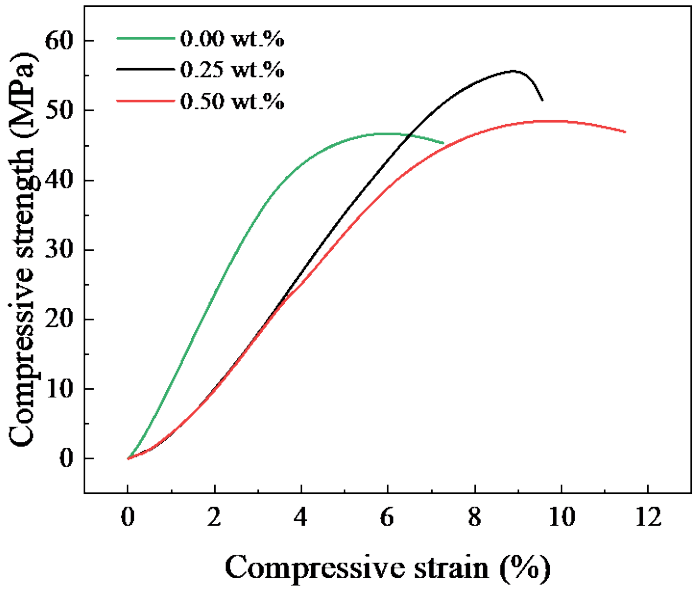

Figure 3: Compressive stress–strain curves of CNT-epoxy concrete.

3.4 Electromechanical Response under Compressive Loading

Figure 4 presents the relative resistance change ($\Delta R/R_0$) of CNT-epoxy concrete specimens with 0.25 and 0.50 wt.% CNT content under uniaxial compression. As compressive stress increased, both samples exhibited a continuous decrease in electrical resistance, indicating the formation and densification of conductive paths within the matrix.

At the initial stage of loading, a steep decline in $\Delta R/R_0$ was observed, particularly for the 0.25 wt.% specimen. This behavior is attributed to the rapid reduction in tunneling distances between CNTs as the matrix is compressed, thereby enhancing conductive network density[9]. As the stress level increased further, the slope of the $\Delta R/R_0$ curve gradually decreased, reaching a near-plateau region. This transition suggests that the CNT network had reached a mechanically stable configuration, where additional compression induced relatively minor changes in resistance.

Compared to the 0.50 wt.% sample, the 0.25 wt.% specimen showed a greater initial sensitivity, reflected by a steeper slope in the low-stress regime. This indicates that the composite near the percolation threshold is more responsive to mechanical perturbations due to its loosely connected network[11], which is more susceptible to rearrangement under strain. On the other hand, the 0.50 wt.% composite exhibited a more moderate and stable resistance change[10], likely due to a denser and more saturated conductive network. These results confirm that CNT-epoxy concrete possesses piezoresistive properties suitable for self-sensing applications. In particular, composites near the percolation threshold (e.g., 0.25 wt.%) are more sensitive to compressive stress and thus may be more effective for detecting minor structural loads. However, higher CNT concentrations may offer better signal stability under sustained loading conditions.

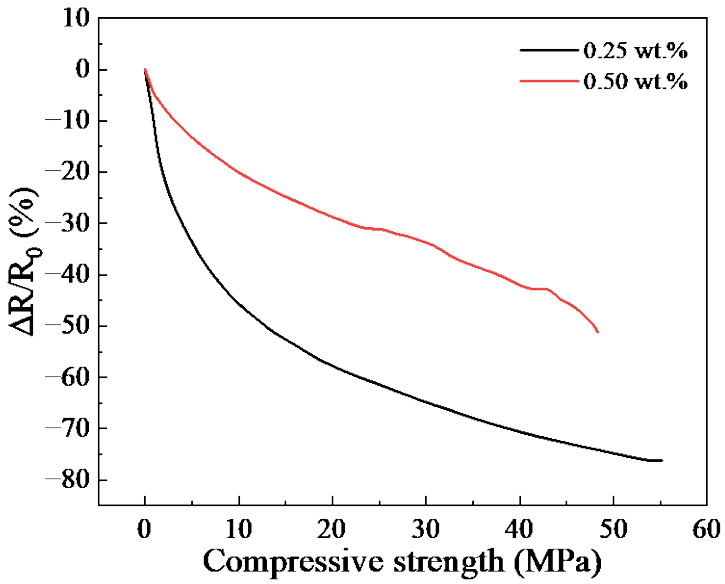

Figure 4: Relative resistance change of CNT-epoxy concrete under compressive loading.

4 CONCLUSIONS

This study investigated the electrical, rheological, mechanical, and electromechanical behavior of CNT-epoxy concrete for use as a self-sensing repair material. The results demonstrated that a CNT concentration between 0.25 and 0.50 wt.% offers the best balance between conductivity, processability, and mechanical performance.

Electrical conductivity increased sharply near 0.10 wt.%, indicating a clear percolation threshold. Rheological analysis showed that viscosity rose significantly with CNT content, especially above 0.50 wt.%, which negatively affected workability. Compressive tests revealed that 0.25 wt.% CNT

improved both strength and ductility, while higher concentrations showed diminishing returns. The electromechanical response confirmed the piezoresistive behavior of the composites, with 0.25 wt.% offering higher sensitivity and 0.50 wt.% showing more stable responses under compression.

Overall, CNT-epoxy concrete with 0.25–0.50 wt.% CNT is suitable for practical structural repair applications with built-in sensing capability. Further work is needed to evaluate long-term durability and field-scale implementation.

ACKNOWLEDGEMENTS

This research was supported by grants (RS-2023-00268377 and RS-2024-00407856) from the Korea Agency for Infrastructure Technology Advancement (KAIA), funded by the Ministry of Land, Infrastructure and Transport.

REFERENCES

[1] Jung, M., Park, J., Hong, S. G., & Moon, J. (2020). Electrically cured ultra-high performance concrete (UHPC) embedded with carbon nanotubes for field casting and crack sensing. *Materials & Design*, *196*, 109127.

[2] Jung, Y. J., & Jang, S. H. (2024). Crack detection of reinforced concrete structure using smart skin. Nanomaterials, 14(7), 632.

[3] Allaoui, A., Bai, S., Cheng, H. M., & Bai, J. B. (2002). Mechanical and electrical properties of a MWNT/epoxy composite. *Composites science and technology*, *62*(15), 1993-1998.

[4] Electrical and mechanical properties of carbon nanotube/epoxy resin composites.

[5] Yoshino, K., Kajii, H., Araki, H., Sonoda, T., Take, H., & Lee, S. (1999). Electrical and optical properties of conducting polymer-fullerene and conducting polymer-carbon nanotube composites. Fullerene science and technology, 7(4), 695-711.

[6] Martin, C. A., Sandler, J. K. W., Shaffer, M. S. P., Schwarz, M. K., Bauhofer, W., Schulte, K., & Windle, A. H. (2004). Formation of percolating networks in multi-wall carbon-nanotube–epoxy composites. Composites science and technology, 64(15), 2309-2316.

[7] Kang, I., Schulz, M. J., Kim, J. H., Shanov, V., & Shi, D. (2006). A carbon nanotube strain sensor for structural health monitoring. *Smart materials and structures*, *15*(3), 737.

[8] Chia, L., Huang, Y., Xia, W., Lu, P., & Zhang, D. (2023). Carbon nanotube (CNT) reinforced cementitious composites using carboxymethyl cellulose (CMC) treatment for enhanced dispersion, mechanical, and piezoresistive properties. *Construction and Building Materials*, *377*, 131104.

[9] Bauhofer, W., & Kovacs, J. Z. (2009). A review and analysis of electrical percolation in carbon nanotube polymer composites. *Composites science and technology*, *69*(10), 1486-1498.

[10] Spitalsky, Z., Tasis, D., Papagelis, K., & Galiotis, C. (2010). Carbon nanotube–polymer composites: chemistry, processing, mechanical and electrical properties. *Progress in polymer science*, *35*(3), 357-401.

[11] Spitalsky, Z., Tasis, D., Papagelis, K., & Galiotis, C. (2010). Carbon nanotube–polymer composites: chemistry, processing, mechanical and electrical properties. *Progress in polymer science*, *35*(3), 357-401.

ICCM24
AUGUST 4-8, 2025
BALTIMORE CONVENTION CENTER
BALTIMORE, MARYLAND, USA

No Technical Paper Submission for:

Sandeep Rajendra Kumar

ICCM24
AUGUST 4-8, 2025
BALTIMORE CONVENTION CENTER
BALTIMORE, MARYLAND, USA

No Technical Paper Submission for:

Han Zhang

ICCM24
AUGUST 4-8, 2025
BALTIMORE CONVENTION CENTER
BALTIMORE, MARYLAND, USA

No Technical Paper Submission for:

Yansong Li

ICCM24
AUGUST 4-8, 2025
BALTIMORE CONVENTION CENTER
BALTIMORE, MARYLAND, USA

No Technical Paper Submission for:

Gelareh Momen

COMPOSITE MATERIALS SUSTAINABILITY – WHERE ARE WE TODAY AND WHERE DO WE NEED TO GO

Edward (Ned) Patton, Ph.D., P.E.

Oceaneering International Inc.
Hanover, MD

Patton Engineering
San Diego, CA

Keywords: Composite Sustainability, Bio-based Composites, Composite Recycling, Recyclability

ABSTRACT

When engineers and composite material practitioners talk about sustainability and composites, they could be talking about any one of the several aspects of this idea. But the basic question is how do we make our composite structures sustainable, and what do we do with them when they come to the end of their current usefulness. This is the over-riding concern for the industry today, especially as our most prevalent composite structures come to the end of their useful life. The most visible example of this is the current mountain of used wind turbine blades that are piling up in Sweetwater, Texas. But this is not the only problem that the industry faces, it is just the most visible one.

There are many challenges that engineers face when it comes to what to do about sustainability and composites, not the least of which is how sustainability is defined. Is it just being able to recycle these materials and keep them from landfills, or potentially does it mean that the industry needs to wean itself off of the use of petroleum feedstocks for the building blocks for advanced composites of tomorrow.

On the recycling front, several techniques for reuse have emerged in the last decade, from grinding up used composites and using the ground up material as reinforcement for things like concrete or sheet molding compound, to pyrolyzing the resin and keeping the fiber, to complete separation of the matrix from the fibers through thermal or chemical means and reusing both in new composites. This last challenge is of course the most technically difficult to actually achieve, since great pains were taken to make the fibers adhere to the resins in the first place. It also has been perceived as cost prohibitive.

On the inherently sustainable front, there is also a move toward using bio-based precursors for both fiber and resin, and using resin chemistries that are inherently recyclable. This trend is expanding rather rapidly but has yet to reach a tipping point where bio-based or plant-based precursors for composites become the standard.

Clearly there is more work to be done. What follows provides an up to date assessment of where all of the composite materials sustainability efforts are and offers a guide or roadmap to where each part of the industry needs to go and what needs to be done to achieve true sustainability.

To achieve this eventual goal all sectors of the industry need to be involved. This includes at least the manufacturers (growers?) of the precursors, the resin and fiber manufacturers, the manufacturers and purveyors of the different product forms that need to be made available, the fabricators and composites manufacturers, the end users, and the recycling / reuse community.

To achieve true sustainability in the industry will cost money and take time and effort on the part of every sector of the industry. In addition, there is inherent risk associated with upending business models that have worked for the last few decades which are not going to be workable in the future. The challenge is transforming the business without going out of business. This paper provides a roadmap to accomplish just that.

1 INTRODUCTION

Several schools of thought have emerged in this field in the last decade, and there is considerable ongoing work in the industry to achieve sustainability. While the technologies to recycle composites have been demonstrated in the laboratory and even at small scale, the work ongoing now is in scaling up these newly developed methods to recycle large composite parts that have come to the end of their life. This work is driven both by the wind energy industry as large composite wind turbine blades come to the end of their lives, and the marine industry in recycling of end of life boat hulls. Most of this work is for fiberglass composites, since fiberglass is the highest tonnage waste problem that the industry faces. These developments are also mostly in the EU because of the new environmental laws that require that boat manufacturers not only bake in the cost of recycling their end of life boat hulls but also accept them

for recycling when they come to end of life,. It is also because of the early adoption of offshore wind in the North Sea where wind turbines need to be repowered regularly because of the extraordinarily harsh environment they must withstand.

There is, of course, more to the story than just recycling of existing parts. Other practitioners and composites designers view sustainability from different angles than just how to keep wind turbine blades and old boat hulls from being put in a landfill. There is now, however, a movement in the industry to develop and use design and fabrication methods that take into account how the part is going to be recycled and its constituents reused at the end of use of the part that they are designing. Essentially what all of this means is how do we close the design-fabrication-use-recycle-reuse circle in order to avoid having to make new fibers and resin systems every time we want to make a composite part or structure.

Figure 1 illustrates this idea of creating a circular economy for composite materials to achieve real sustainability of these materials.

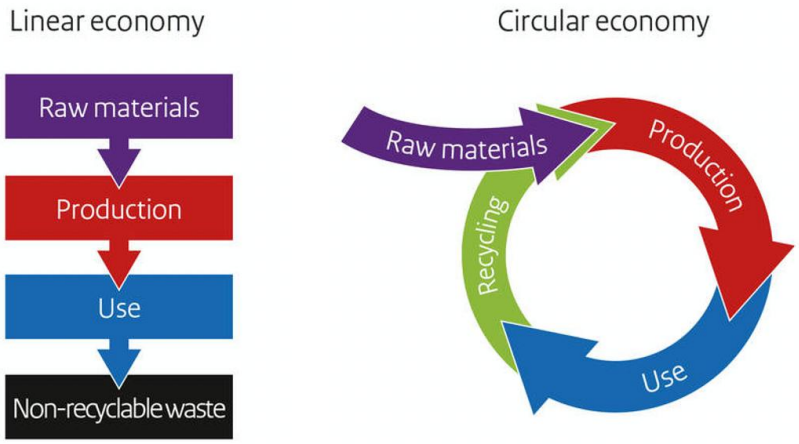

Figure 1: Linear vs Circular Economy (© Government of the Netherlands)

This figure was chosen to present here because it demonstrates what is meant by the creation of a circular economy for composite materials as compared and contrasted with the current linear economy where end of life composites are mostly put in landfills. This is of course where the industry is tending and needs to go to make these materials sustainable.

There is also a movement in the industry to formulate resins that can be more easily reverted into their initial liquid state through either chemical or thermal means so that they can be more readily separated from the fibers. There are even means of thermally removing the resin from the fibers without damaging the fibers and without burning up the resins so that both recycled materials can then be reused.

Sustainability in composites also means moving away from the use of petroleum as a feedstock for both fibers and resins and moving to plant-based fiber and resin precursors. To that end, plant fibers like flax have begun to be used effectively in a number of composite structures. Research is also going on to develop composite resins from wood product waste that behave like epoxies. The paper industry uses the cellulose from wood and essentially throws away the lignin that binds the cellulose fibers together. Use of this discarded lignin as a precursor to an epoxy resin is a very active field of technology development.

Finally, there is a large movement to enable design of composite parts in a manner that takes into account the entire life cycle of the material from design to material selection to fabrication to use and eventual recycling and reuse once the part has ended its usefulness. This is called Design for Sustainability, which is a very important initiative that has been started in Europe by the European Composites Industry Association – EuCIA.

This paper presents not only the challenges that engineers, chemists, and other scientists face in creating a model of sustainability for composites that is cost effective and accomplishes the goals of sustainability, but also provides a roadmap to sustainability as well as a snapshot of where the industry is today on that road to true sustainability. This includes first a look at the challenges that the industry

faces in moving from the current linear business model to a circular business model for these materials, then provides a presentation of the state of the art in this field of endeavor and who is working on what part of the problem. The story that unfolds here then continues by providing a roadmap for engineers and practitioners in composite material design, fabrication, use, and recycling/reuse. Finally what is presented is a look at the state of the art in composites sustainability and a discussion of not only where we are on that road but also what it is going to take in terms of technology development, capital expense, and time.

2 CHALLENGES FACED BY THE INDUSTRY

The major challenge that the composites industry faces in the very near future stems fundamentally from the properties of composite materials in that their major benefit is also their Achilles heel. Composites provide an infinite number of different ways that you can combine a fiber or other reinforcement and a matrix material – whether that be a plastic, metal, or even ceramic – to make a material that is greater than the sum of its parts so to speak. This wonderful benefit, when the composite comes to the end of its useful life, makes the material very difficult to separate into its constituent parts and reuse those parts. This means that there is a large amount of this waste that is no longer allowed to be landfilled in most countries. This is especially true of the wind turbine industry where it is believed that by 2034 there will be on the order of 200,000 tons of blade waste produced per year [2]. And, of course, since wind turbines are getting much larger in terms of blade length, there is a move to migrate to an all carbon/epoxy blade design from the current carbon fiber/epoxy spar with a glass/epoxy skin to minimize swing weight of the propellor blades. This will only make the recycling problem more challenging.

2.1 Wind Turbine Industry Challenges

The fundamental challenge facing this industry is realizing a positive cost/benefit in real dollars from recycling used fiberglass wind turbine blades when the market for the recycled materials has historically been nearly non-existent. This has been true for decades which is why so many wind turbine blades are rotting in landfills all over the developed world. There are news stories about this problem, and some infamous pictures from places like Sweetwater Texas where there is an enormous pile of used wind turbine blades stacked up and just sitting in the Texas sun that have been there for more than a decade without a single blade being moved to a recycling center.



Figure 2: Used Wind Turbine Blades in Sweetwater, Texas (photo by Eli Rosen, Yucca Films)

There are similar piles of these blades in the UK and in Northern Europe where they used to commonly be landfilled. This is changing, however because the EU and the UK have both banned the

landfilling of wind turbine blades, so there are significant efforts ongoing to deal with this problem in a responsible way.

Currently the process for recycling these blades when they come to their end of use is to chop up the blade into smaller pieces and use these pieces in a discontinuously reinforced composite. This has its own drawbacks because of the loss of the stiffness and strength of the original continuous fiber composite. Some authors and practitioners have suggested that pyrolyzing the blades to remove the resin and leave just the remaining fiber is one way to preserve at least the continuous fiber. This process in itself poses many challenges. First, the blades that are coming into the waste stream now, as mentioned above, are a mix of carbon/epoxy and glass/epoxy materials. Each of these components needs to be separated from the others and treated in a different manner, especially if pyrolysis is the method used to remove the resin from the fibers. And pyrolysis is not effective for fiberglass composites because the temperatures involved merely melt the glass and all you get is a pile of useless trash.

The major challenges with this method are both that pyrolysis does not preserve the resin (a petroleum based product) for reuse in another application, and also pyrolysis itself is not an eco-friendly process. The byproducts of epoxy resin pyrolysis are toxic and need to be extracted from the exhaust stream of the pyrolysis oven. The carbon from the original resin also is typically vented to the atmosphere and therefore adds to the carbon burden in our upper atmosphere. For these reasons, pyrolysis, while it may be a good place to start with recycling large end of life composite parts, is not the eventual answer to development of a sustainable, circular economy for the composite materials industry.

2.2 Recreational Marine Industry

The recreational marine industry has a very similar problem in recycling of the fiberglass boat hulls as exists in the wind turbine industry. Fiberglass boat hulls have an average life of about 30 years, with some lasting more than 50 years, but most, especially those exposed to seawater, have a shorter life span. And, like wind turbine blades, the fiberglass structures are very large, complex, and have all sorts of things attached to them that are not fiberglass.

The National Marine Manufacturers Association estimates that in the US some 200,000 boats reach the end of their useful life each year [2]. In the EU that number is more like 80,000 boats. If you consider that each boat hull is about a ton to a few tens of tons, this makes the problem nearly as difficult as the wind turbine blade waste problem. In addition to that, wind turbine blades are usually not widely disbursed whereas boat hulls are everywhere, so a centralized recycling strategy will not work.

2.3 Aging Aircraft

The Boeing 787 Dreamliner was introduced in 2012, and the Airbus A350 was introduced in 2013. These two commercial aircraft now have been manufactured at a high enough rate to meet demand, so there are several hundred of each in service today. These are the two best examples of a primarily composite large transport aircraft. As of February 2023, there had been 1041 Boeing 787's put into service and 524 Airbus A350's. Even though the pandemic has reduced both aircraft production rates substantially (14 787's per month in 2020 and 10 A350's per month in 2019) at their current production rates (9 per month for both Boeing and Airbus) [3], more than 2000 of these composite aircraft are going to have to be recycled and reused in the next 20-30 years.

To date there has only been a modicum of research and development work done to effectively recycle the composite material portions of these aircraft. While there has been considerable research into this topic, which is gaining some traction both here in the U.S. and in Europe, development of all of the technologies required to effectively recycle and reuse the composite parts of these large transport aircraft have yet to be developed.

2.4 Automotive Industry

In the last decade or so a considerable number of composite material parts have been integrated into new cars and trucks, both light duty and also heavier over-the-road trucks. Ford for instance makes some of their light duty truck driveshafts out of composites. And increasingly composites are being used for things like leaf springs, trunk liners, and some body parts. With the coming of electrification of the mass auto market, things like battery cases are also being made out of composites [4].

Composites have been used in mass market automobiles and light trucks since 1953 with the introduction of the Corvette. Since then, every Corvette has had a fiberglass body. Since the advent of the Corvette fiberglass body, several composite components have been introduced, until finally composites entered the mainstream of the auto industry in 1984 with the Pontiac Fiero and continued in 1990 with the introduction of the Saturn [5]. Since that time with the perfection not only of the injection molding and vacuum assisted resin transfer molding as well as thermoset and thermoplastic based sheet molding compounds, nearly all trunk liners, fender well liners, interior door panels, and even some exterior fenders, door panels, and hoods of standard high production rate automobiles have been made using composite materials. Since these materials are a mix of thermoset and thermoplastic resin composites, they pose different challenges than the primarily glass and carbon fiber reinforced epoxy resin composites used in the wind turbine and air transport sectors.

It has been said that as soon as carbon fiber gets down to on the order of $5 a pound, the auto industry will stop using steel. While this is a very good thing for the environment, since lighter weight autos burn less fuel, when these composite parts come to the end of their useful life in 20-30 years, there will be a need for a well-developed and cost effective means of recycling these materials that allows the reuse of the original constituents of the composite.

2.5 Other Composites

There are a number of other smaller industries that albeit do not create a large tonnage in each, are large enough that in total they are also becoming a problem. Most of these are smaller parts and widely distributed enough that only local recycling centers will receive them. A good example is sporting goods – golf club shafts, tennis rackets, skis, football and hockey helmets, paddleboards and paddles, surf boards, canoes and kayaks, and more.

Unfortunately most of these smaller composite goods are such that new “better” models are released on a regular basis, and the old model either gets put in the closet, or worse, sent to the dump. This means that when a golfer replaces their clubs with the “new and improved” carbon fiber shaft clubs, the old ones are thrown out. Unfortunately most of these items are too small and are too widely dispersed for there to be a national or even regional effort to recycle them. This means that most are merely buried in landfills rather than being recycled.

3 STATE OF THE ART IN COMPOSITES RECYCLING AND REUSE

The current state of the art in composite recycling is that by and large these materials are not being recycled to any great extent. There have been some efforts in reuse of these materials, specifically used wind turbine blades, but these are mostly demonstration projects and there are not enough applications of the used blades to make this a long term solution.

There is, however, some light at the end of this long tunnel. The European Union has been leading the way in this regard, primarily because of the environmental sensitivity of the European public and the support of National leadership in the EU. Quite unlike in the US, there has been a concerted effort ongoing for some time to achieve sustainability in all European activities, including and most importantly the industrial sector. This culminated in the European Green Deal, which was adopted in the EU in 2019, and has formed the backbone of the European environmental regulatory environment. Efforts in the composites industry had been ongoing for some time, based on the “Waste Framework Directive” which was adopted in 1991 and has spawned a number of companies in the composites recycling business.

Another European directive, called the “Extended Producer Responsibility” where producers of composite structures are responsible for their end of life management. This rule has been applied fairly recently in both the recreational marine and wind turbine or renewable energy sectors.

Along with these regulations, also quite unlike in the US, the EU is providing support in terms of direct funding and support for collaborations between companies and universities at no cost to companies that develop composite recycling technologies that have the potential to scale up to a size appropriate for the sector that the company wants to work in.

3.1 Fiberglass – Mostly Wind Turbine Blades and Boat Hulls

One Italian company – Korec in Bientina, Italy (Tuscany) – is working with Owens Corning here in the US to scale up their fiberglass recycling technology. Owens Corning has taken it upon themselves to reduce their carbon footprint by 50% and using 100% renewable energy for processing by 2030. This is a fairly ambitious goal.

Korec's patented process (US Patent Number 10,308,784) is a thermo-chemical process where they use CO_2 in the absence of Oxygen to dissolve the resin at high temperature. When they extract the hot gas from the chamber, all of the resin has been depolymerized and is contained in the gas, which is then condensed out of the gas and reprocessed.

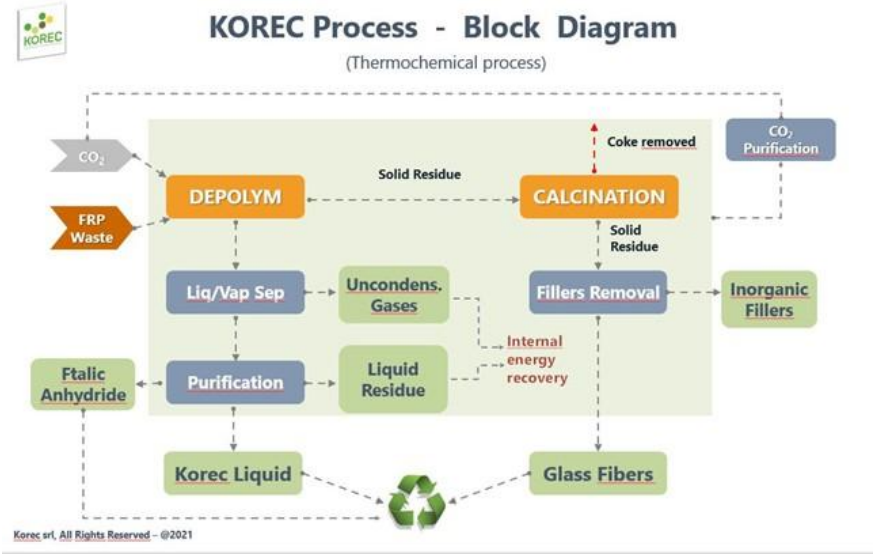

Figure 3. Korec Process (with permission from Korec)

Another company in the French speaking part of Switzerland – Composite Recycling – has also developed a process along the same lines as Korec primarily for end of life wind turbine blades. They use another proprietary pyrolysis-like process that they call thermolysis, in the absence of oxygen to depolymerize the resin from waste glass fiber composite materials and recover most of the resin in the form of what they call "thermolysis oil". This company is working with an engineering firm in Sweden, Fiberloop, that developed this process and is building their industrial scale machines. The process is able to separate the resin from the fibers, and recovers not only polyester resins, but also epoxies, albeit at a slightly higher temperature but still not as high as traditional pyrolysis. Fiberloop is in the business of designing and assembling machines for clients with specific needs like Composite Recycling. Their business relationship has Fiberloop building each machine to Composite Recycling's specifications based on each client's needs, and Composite Recycling operates the machine at the site where the recyclable material exists. In addition, Composite Recycling has done all of the testing required to get both their reclaimed glass fiber and their thermolysis oil certified as ready to use for the wind turbine industry as well, and they have already established supply chains for selling their product into the marketplace.

The one unique thing that Composite Recycling has done is to bring their fiberglass recycling machine to the site of the recyclable composite materials – as in at a wind turbine blade dump – rather than having used wind turbine blades shipped to a central recycling facility. They have been able to fit their entire glass fiber composite recycling process and equipment along with all of the chemistry required in a 40' ISO container. And they have recently joined a consortium led by Beneteau to enable the recycling of end of life boat hulls. This consortium includes Beneteau, Composite Recycling, specialty resin company Arkema, waste management company Veolia, Owens Corning, and textile specialists Chomarat. All of these companies are leaders in their sector of their businesses, especially in Europe.



Figure 4. Rendering of Composite Recycling Containerized Recycling Machine (Courtesy Composite Recycling)

3.2 Carbon Fiber – Mostly End of Life Fighter Aircraft

Quite a bit less work has been done in recycling of carbon fiber composites primarily because they are a much lower tonnage problem than fiberglass. Carbon fiber composites have not been in general use until fairly recently except for the high performance aerospace structures required for both spacecraft and modern fighter aircraft. Of the space applications of carbon fiber composites, there has been zero effort to reclaim or recycle them for obvious reasons, but for aging fighter aircraft this is not the case. There are now several early generation fighter aircraft, both in the US and the EU that have been retired because their airframes have been used up. There has therefore not been the need nor the demand to recycle carbon fiber composites to any large extent.

That is, however changing and changing rather rapidly. To wit, there are a few efforts that have been successful, and a few companies have sprung up to begin commercialization of their recycled carbon fiber products. The initial recycling efforts for these materials used to involve a pyrolysis step where the resin is effectively burned off of the carbon fiber, leaving the fiber relatively intact while exhausting the combustion products from the resin pyrolysis into the atmosphere.

In the last several years, a few newer and less carbon intensive technologies have arisen that are in the process of being scaled up to the level where they could be called industrial scale. One company in South Carolina, Carbon Conversions, which got its start from an SBIR grant developed a process in collaboration with MIT that can reclaim nearly virgin carbon fiber from nearly any source of end of life carbon fiber composites. They fairly recently got funding from Boeing and demonstrated the reclamation of carbon fiber from an F-18 and used that fiber to create a Corvette body.

Another company in the Denver area, Vartega, has taken on the process of recycling uncured carbon fiber prepreg scrap into usable carbon fiber. In a similar development, a much larger company based in Paris, Fairmat, has also developed a process for recycling scrap carbon fiber prepreg at a much larger scale. They recently announced an agreement with Hexcel in Salt Lake City to recycle all of the scrap uncured carbon fiber prepreg from Hexcel's manufacturing facility. This is an extension of an ongoing relationship between Hexcel and Fairmat that started in Europe, but this is a fairly large undertaking because the Salt Lake Hexcel facility is the largest of all of the Hexcel manufacturing facilities. In another similar development, Toray's Pacific Northwest facility in Tacoma, Washington which services mostly Boeing, has signed an MOU with Elevated Materials in Gardena, CA to do much the same thing as Vartega and Fairmat.

While none of these is an actual recycling method for end of life carbon fiber composites that retains both the fiber and the resin, there have been demonstrations of this technology at least in the EU. The Fiberloop / Composite Recycling partnership has demonstrated that their thermolysis process works well on typical aerospace epoxy resins in high performance carbon fiber composites. Apparently what they do is to process the epoxy-based composites at a somewhat higher temperature than the typical polyester resins in most fiberglass composites.

4 INHERENTLY RECYCLABLE COMPOSITE RESINS

There are several approaches to making inherently recyclable composites, some based just on the resins, some focusing only on the fiber, and some based on both the resin and the fiber. The approach to making recyclable resins falls into two categories, those using petroleum feedstocks and those using plant-based oils or plant-based compounds as precursors. So, let's start there and then move on to sustainable composites in general

4.1 Petroleum-Based Recyclable Resins

In the petroleum based world, typically what this means is that the chemistry of the epoxy precursors is modified in such a way that the cross-linking that makes the epoxy a solid can be unlinked through the use of special catalysts and/or specific organic acids. Quite a bit of this chemistry was developed some time ago, but it has not found broad use in the past because there was not a perceived need to make these materials inherently recyclable. An additional hurdle has also been that the inherently recyclable epoxies typically do not possess the same high level of mechanical properties (strength, stiffness) as traditional epoxies. There have been some recent developments in this area but none have made it out of the laboratory.

4.2 Plant-Based Recyclable Resins

Plant-based recyclable resins are something of a mixed bag. While there are a few partially bio-based resins and some mixes of these that are inherently recyclable, there are only a handful of fully plant-based and inherently recyclable resin systems.

One good example of these is a fairly recent development by NREL in Golder, Colorado. Researchers at NREL created an entirely plant based resin system they call PECAN [6] (PolyEster Covalent Adaptable Networks) that is essentially a high performance epoxidized polyester-type resin that has roughly equivalent mechanical and processing properties as typical aerospace epoxies. NREL demonstrated the efficacy of this resin system by building and testing a 9 meter long wind turbine blade. The effort at NREL was in the Wind Energy Technology Center there and was focused on sustainability in the wind energy sector, which is why the first full demonstration of this new resin system was to make a commercially viable wind turbine blade.

Another good example is from a Taiwanese company named Swancor. They have developed a paired system they call EzCiclo and CleaVER. EzCiclo is a fully recyclable thermosetting epoxy resin system that has properties equivalent to aerospace grade epoxies. This system was developed for the growing wind energy industry in Asia to provide a sustainable alternative to the standard petroleum-based and non-recyclable epoxies used for wind turbine blades. While Swancor does not disclose the chemistry of their EzCiclo resin and CleaVER chemical treatment, they have demonstrated this technology successfully for several industries.

5 PLANT-BASED SUSTAINABLE COMPOSITES

In order for the industry to become truly sustainable, and to become more than just carbon neutral but become a carbon sink, the industry understands that at some point the precursors for making fibers and resins must come from plants, and the process energy to make the fibers and resins must come from renewable sources. Fortunately there is considerable ongoing work in this area with some actual commercialization beginning to happen.

5.1 Natural Fibers

The most common natural fiber that has been adopted by the composites industry is flax fiber. This is the fiber of the linen textile industry, and the two areas that produce the most of it are France and North America, with France being the largest of the two. There are established supply chains for flax fiber and flax fiber textiles, and these fibers have been adopted by a number of high volume industries. In the automotive industry, flax fiber is used for interior door panels not only because it is inexpensive and easy to work with, but also because flax fiber composites have both heat and sound insulating properties that neither glass nor carbon fibers possess. Flax fiber also has a better strength to weight ratio than other industrial fibers, so the auto industry has used it also to save weight primarily in

automobile bodies. In Europe, BMW, VW, and Audi have all adopted flax fiber composites for secondary structure in all of their products, with BMW and Porsche actually making entire car bodies out of flax fiber composites. There is even a French company, Bcomp, that has expanded into this space and has made body work for cars on the racing circuit.

There are also some natural fiber products in the developing world that are beginning to see incorporation into composites. Hemp fiber has been in use in the automotive sector in the EU for a number of years because of its easy availability. It is used a bit less than flax primarily because flax fiber textiles have been made for hundreds of years whereas hemp fiber has only been used fairly recently to any great extent.

Bamboo fiber has also been made into composites, albeit at much lower quantity than either flax or hemp, primarily because of the logistics burden of getting the bamboo fiber from where it is grown – in the underdeveloped part of the world – to where it will be used – in the more developed world of Europe and North America.

5.2 Plant-Based Carbon Fiber Precursors

Typical carbon fiber is made using acrylonitrile as a backbone to making a polyacrylonitrile (PAN) fiber. The current source of acrylonitrile is based on the chemistry of propylene from petroleum feedstocks. Several attempts have been made in the past to use plant oils to generate propylene, but all of them to date have been more expensive than what can be produced from crude oil.

A newer process recently developed by Southern Research [7] uses a sugar alcohol from plant sources, glycerol, with a different chemistry to produce acrylonitrile. In this process they initially remove a water molecule from the glycerol to produce hydroxyacetone, then they add ammonia to this through a process called ammoxidation and remove an oxygen molecule to produce acrylonitrile. Figure 5 below demonstrates this chemistry.

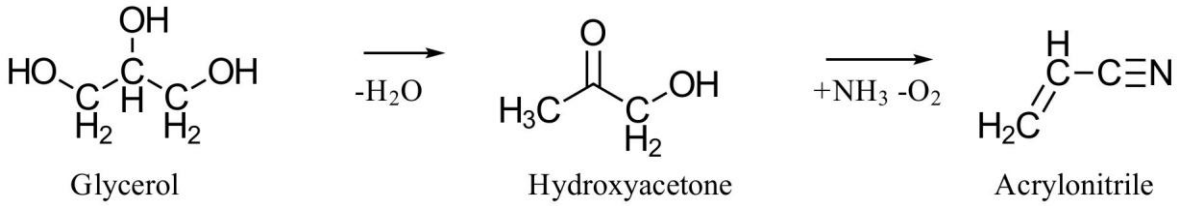

Figure 5: Acrylonitrile from Glycerol (drawn by author)

Using funding from the Department of Energy, Southern Research perfected this process and demonstrated that they could use agricultural or forest products waste to extract the glycerol and make their plant-based acrylonitrile at 20% less cost than petroleum based acrylonitrile. This process has been scaled up by Trillium Renewable Chemicals which is building a pilot plant to make fiber from this plant-based acrylonitrile in partnership with Syensqo (formerly Solvay) at the INEOS acrylonitrile plant in Port Lavaca, Texas. This plant is home to the largest acrylonitrile producer in the U.S., and with their partnership with Syensqo will make this the largest entirely plant-based carbon fiber production facility in the world once it is completely scaled up.

Another company in the Netherlands called AnQore has gone the route of using propylene and ammonia to make their acrylonitrile. The propylene that they source comes from both agricultural waste and recycled plastics, and they state that they can make their biomass and recycled plastics based acrylonitrile for an equivalent cost to petroleum based acrylonitrile since the raw material is effectively free to them. They did make a good decision about the siting of their first plant to do this because the site that they chose has both a plastics recycling facility and a carbon fiber producer (Saudi Basic Industries Corporation or SABIC) so AnQore has a ready supply of recycled plastics to input into their process and a ready customer in SABIC for their product, without the logistics burden of moving materials long distances.

5.3 Plant-Based Resins

There have been many attempts at making an entirely plant-based bisphenol-A to use as the backbone of an epoxy resin system. None of these has actually come to fruition as yet, and since bisphenol-A is

not a naturally occurring compound, synthesis of it from plant-based precursors is typically more expensive than sourcing it from the petrochemical industry.

Bisphenol-F which is a naturally occurring compound found in prepared mustard and the roots or rhizomes of plants used in traditional Chinese medicine, has found use in the marine industry and consumer goods for a number of years. These are the "BPA free" plastics and resins that are suitable for use for food preparation as well as other consumer goods. Epoxies made using bisphenol-F are roughly equivalent in stiffness to their BPA cousins, with slightly lower strength and also slightly lower viscosity, making them good candidates for things like VARTM. This is why they have found use in the pleasure marine industry since quite a few production boat hulls are made using this vacuum assisted resin infusion method.

In the Netherlands, Frog Biosystems B.V. has produced an epoxy resin from rapeseed oils that they blend with traditional petroleum based epoxy to make what they call Fairpoxy. This resin has a 29% plant-based epoxy content and is equivalent to modern aerospace epoxies.

In the U.S., Entropy Resins which was recently acquired by the Gudgeon Brothers of West System fame has also developed a plant-based epoxy that they also mix with petroleum based epoxies to various extents to make a variety of different resin systems.

Finally, one fairly recently concluded project in the EU – the ECOxy Project – was a consortium of 13 partners focused on the R&D necessary to convert all sorts of plant precursors into useful epoxy resins, along with several other composites sustainability goals. While that Project concluded in late 2020, one of their partners – Specific Polymers SP – wrote an article on the Project site that has a wonderful graphic about making resin precursors from wood dust, algae, and vegetable oils. This graphic is actually from Specific Polymers because they are commercializing the results of the ECOxy project.

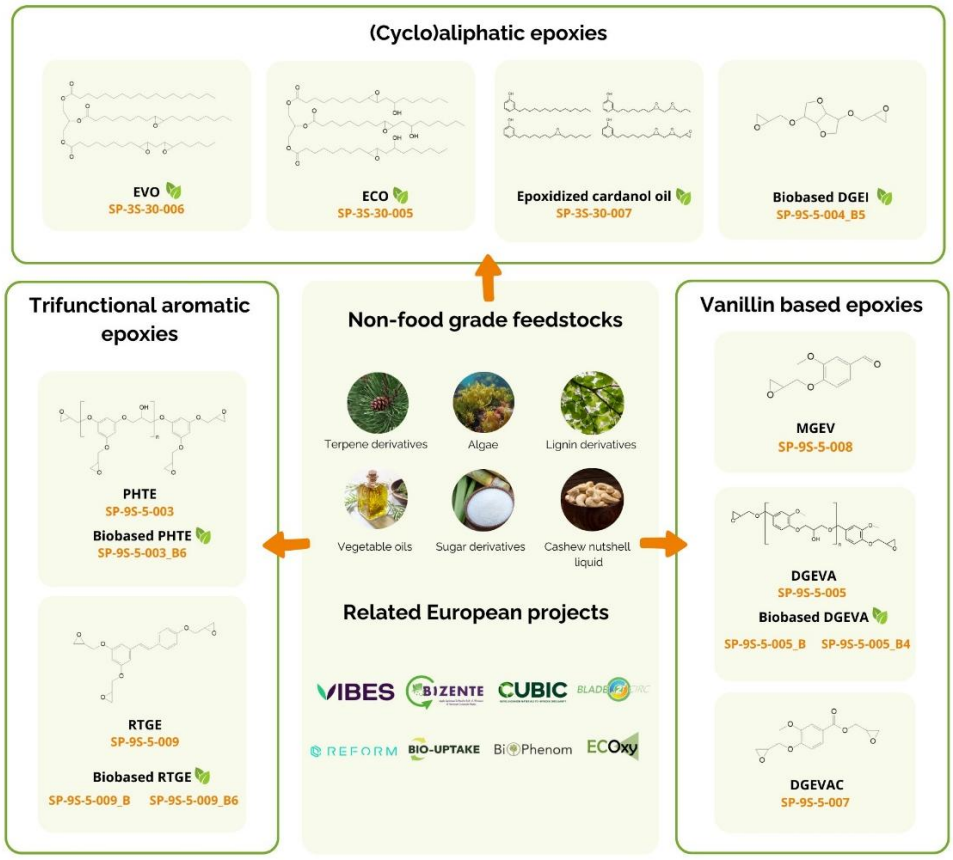

Figure 6: Specific Polymers Bisphenol-Free Plant Based Epoxy (courtesy Specific Polymers)

Specific Polymers now has a complete line of these bio-based epoxy resins that they have for sale on the open market. They are marketing them as bisphenol-A free epoxies based on forest products waste (wood dust), algae, and agricultural waste in the form of plant oils. Two products that they have on the

market are DGEVA – a vanillin-based epoxy resin, and PHTE (Phloroglucinol Triglycydil Ether).

In addition to the creation of the bisphenol backbone for epoxies, another molecule also needs to be added in order to put epoxide groups on the bisphenol backbone to make the epoxy resin itself. The molecule that is the most prevalent in this chemistry is epichlorohydrin. Epichlorohydrin is traditionally made using propene from petroleum based sources, but it can also be readily made from glycerol, and is actually somewhat easier to make from glycerol than it is to make from propene. And, since glycerol is a byproduct of the production of biodiesel, it is also readily available.

There are several companies in the business of making epichlorohydrin from bio-based glycerol. Sicomin sells their products under the trade name of GreenPoxy, Advanced Chemical and Advanced Biochemical in Thailand also sells a plant-based epichlorohydrin as does Syensqo, a Louisiana company named Louisiana Chemical Equipment Company, a UK based company called TechnipFMC with main officed in Houston, as well as a plant in India that also makes plant-based epichlorohydrin. All of these companies sell their products mainly into the traditional plastics manufacturing business and have very nearly taken over the epichlorohydrin manufacturing business from the petrochemical industry. This is one of the real success stories in bio-based plastics precursors.

The bottom line here is that the future of plant or bio-based resins is rather bright, and companies on nearly every continent in the developed world are moving rapidly away from petroleum feedstocks. So, while there is still quite a bit of work to do here, at least this part of the business is trending in the right direction.

6 ROADMAP TO A SUSTAINABLE FUTURE FOR COMPOSITES

While what is presented in this paper paints a fairly optimistic picture of the state of the art in recyclability, lowering the carbon footprint of composites and also the transition to an entirely sustainable plant-based future for composites, there is still considerable work to be done. There are developments ongoing on several fronts, from the development of technologies that can separate traditional resins from their fibers (thermolysis and solvolysis), to inherently recyclable resin systems that can be easily taken apart at the end of their useful life, to plant-based precursors for both fibers and resins.

What remains to be done is for the industry to transform itself from its current non-sustainable large carbon footprint to a more sustainable business model that can actually become a carbon sink, all while staying in business and being in business making these materials into the far future. There is a road to get to this end result, and it will require considerable capital investment and work in scaling up all of these technologies while still providing the current products that are needed today. That is the challenge, and there is a way to get there.

Here are some recommendations to get everyone started:

- **RECOMMENDATION 1 – Create Sustainable Strategies –** Find or create sustainable strategies for your specific products and base the strategies on things that you can accomplish both in the short term and the long term. In other words, make an actionable plan for the future with measurable milestones and stretch goals to get to a completely sustainable model for the business that you are in.
- **RECOMMENDATION 2 – Partner with Startups –** Larger companies have a tendency to have bureaucratic inertia that does not permit them to make drastic changes to their business model rapidly or easily. They might also not have the right technical resources and creative personnel required to make these changes. Startups that have good ideas and that are run by technical expert entrepreneurs make good partnerships with larger companies and can have a very positive effect on the outcome of the implementation of these technologies.
- **RECOMMENDATION 3 – Be Willing to Accept Risk –** This is rather difficult for large more traditional companies, but to make the transformation and potentially to begin to lead rather than follow, it is necessary to accept the risk that you won't get it right the first time. This is difficult for traditional companies like those in heavily regulated industries like the petrochemical industry, so if necessary, form a "skunk works" of your own and establish separate management of that so that the larger company does not have to take all of the risk.
- **RECOMMENDATION 4 – Work With Others and With National Societies and Not-For-**

Profits – There is a wealth of talent available to materials and manufacturing businesses if they join and participate in societies like SAMPE, ASME, ACS, and on boards of composites manufacturing associations like ACMA and EUCIA.

- **RECOMMENDATION 5 – Seek Government funding for Transformative Technologies** – There are multiple opportunities with the Federal Government in a number of agencies and Departments (Agriculture, Commerce, Defense, etc.) to get funding for transformative technologies. And, while it used to be that the Government wanted to own the intellectual property resulting from Government-Industry collaborations, such is not necessarily the case anymore. Starting with the Baye-Dole act in 1980 (43), companies and universities who develop technology in partnership with the federal government and with federal funding are no longer required to relinquish the patent rights to that technology to the government.
- **FINAL RECOMMENDATION / STRATEGIC IMPERATIVE – Don't go Out of Business While Changing the Business** – this is probably the most important concept and/or mantra to take into this arena. No matter what, it is imperative that companies making this transition not lose focus on their current business while in the process of transforming their business.

7 CONCLUSIONS

This paper has hopefully provided not only the state of the art in composite materials sustainability, but also the status of some ongoing efforts that show promise in reducing or eliminating the carbon footprint of the industry. In addition, a roadmap with realistic recommendations has been presented here to enable the industry to follow a path to sustainability that will allow them to stay in business making a profit while fundamentally transforming their business.

It is clear that this transformation will take time, money, and the concerted efforts of everyone in the business in order to be successful. What is clear is that every sector of this industry and every aspect of how we make, use, and deal with end of life composites needs to be part of this overall roadmap. True circularity is quite literally philosophical in that what comes from the earth must at some point be sent back to the earth in such a way that the earth can make more of the stuff that needs to come from the earth again. And while this may seem naïve at first or even impossible to some, it is actually the definition of a circular economy.

Of course, this road is still long and full of potential potholes and dead ends. In other words, it is going to take time, a lot of very hard work, an ability to accept and embrace failures along the way, and an enormous investment on the part of the industry to make this come to pass.

It is also going to take enlightened and capable leadership in all of the companies that are in this industry. It is the leaders of this industry that are going to be the drivers of change in each of their companies that will lead us to success and a sustainable, circular economy as the future of this industry. These leaders must be politically savvy, willing to take on calculated risk, and motivated by an understanding that their long term success depends on the decisions they make now and the path that they lead their companies down. Those are the leaders and the companies that will survive and prosper in a newly transformed and circular composites industry.

REFERENCES

[1] "Building a Circular Economy with the Aim of Sustainable Growth," https://www.m-chemical.co.jp/en/csr/activities/case5.html

[2] https://marinedebris.noaa.gov/prevention/building-fiberglass-boat-recycling-program

[3] https://en.wikipedia.org/wiki/Boeing_787_Dreamliner; https://en.wikipedia.org/wiki/Airbus_A350

[4] https://www.compositesworld.com/articles/composites-end-markets-automotive-2023

[5] https://www.compositesworld.com/articles/class-a-composites-a-history

[6] "Recyclable, Plant-Based Material Could Take a Spin on Next Generation of Wind Turbines, NREL Researchers Successfully Build a Wind Turbine Blade With Their Novel Resin," December 11, 2023, Emily Mercer, https://www.nrel.gov/news/program/2023/a-recyclable-plant-based-material.html.

[7] "Low-cost carbon fiber project advances to pilot phase," Energy and Environment, Southern Research, January 24, 2018.

UNTANGLING DECARBONIZATION STRATEGIES FOR NET ZERO CARBON FIBER

Kyle Pender[1], Filippo Romoli[2] and Jonathan Fuller[3]

[1]NCC, Bristol and Bath Science Park. Feynman Way Central, Bristol, BS16 7FS, UK
Email: kyle.pender@nccuk.com, web page: https://www.nccuk.com/

[2] NCC, Bristol and Bath Science Park. Feynman Way Central, Bristol, BS16 7FS, UK
Email: filippo.romoli@nccuk.com, web page: https://www.nccuk.com/

[3] NCC, Bristol and Bath Science Park. Feynman Way Central, Bristol, BS16 7FS, UK
Email: jonathan.fuller@nccuk.com, web page: https://www.nccuk.com/

Keywords: Net Zero, Carbon Fibre, Decarbonisation, Synthetic Fuels, Biofuels, Electrification

ABSTRACT

The production of polyacrylonitrile (PAN)-based carbon fibre (CF) is highly energy-intensive, contributing significantly to its embodied carbon. With global demand for CF projected to more than double by 2030, reducing the global warming potential (GWP) of CF manufacturing is critical to supporting the decarbonisation of transport, energy, and industrial sectors. This study presents a life cycle assessment (LCA) to evaluate the cradle-to-gate GWP of PAN-based CF production, with a UK-specific case study, and explores a range of decarbonisation strategies including energy efficiency, electrification, and green gas substitution.

The LCA identifies major GWP hotspots across precursor and fibre production stages, particularly during high-temperature oxidation and carbonisation processes. Electrification of these stages, powered by low-carbon electricity, offers the most immediate and impactful emissions reductions. However, abatement systems for hazardous exhausts remain a key technical challenge. Complementary strategies include the adoption of bio-based acrylonitrile (Bio-ACN), energy recovery technologies, and the substitution of natural gas with BioMethane or eMethane.

Scenario modelling using projected UK grid decarbonisation pathways reveals that electrification delivers the fastest route to net zero CF production. Nevertheless, the effectiveness of decarbonisation varies with regional grid composition, underlining the importance of site-specific strategies. A multi-horizon roadmap is proposed, outlining near-, mid-, and long-term actions to support CF producers in aligning technology development with emissions reduction goals. This study provides a foundation for industry and policy stakeholders to prioritise interventions and accelerate the transition toward low-carbon CF manufacturing.

1 INTRODUCTION

The current global demand for carbon fibre (CF) is estimated to be 115 kt per year as of 2023, and projected to grow to 280 kt per year by 2030 [1]. While lightweighting using carbon fibre reinforced polymers (CFRP) has played a critical role in transportation decarbonisation, CFRP is now required for decarbonised energy generation and storage solutions. Despite the high-performance benefits of CF, its production is highly energy-intensive, resulting in significant embodied carbon. Sphera Managed LCA Content reports that the globally aggregated global warming potential (GWP) of polyacrylonitrile (PAN) based CF can reach up to 35 kg CO_2e. per kg of CF produced [2]. Considering global CF demand in 2023 (115 kt, [1]) and current GWP of PAN-based CF, the global demand for CF is projected to generate up to 4 Mt CO_2e annually. To enable the further decarbonisation of transportation and renewable energy sectors, it is imperative to reduce the GWP associated with CF production.

The CF production process consists of several energy-intensive stages, including PAN fibre precursor production, stabilisation/oxidation, carbonisation, and surface treatment, all of which contribute to the overall embodied energy. Michaud et al. reviewed the literature and reported a wide range of energy

consumption values, from 171 to 1169 MJ per kg of CF produced. Dér et al. [3] compiled energy consumption data for each stage of production from various sources, noting that energy requirements for producing PAN-based precursors range from 245 to 394 MJ per kg of PAN [4][5], while the energy demands for manufacturing CF itself range from 219 to 704 MJ per kg of CF [4][5][6][7]. Carbonisation is the most energy-demanding phase [8], where the stabilised fibres are heated in an inert atmosphere at extremely high temperatures, typically between 1000 °C and 2000 °C.

Lifecycle assessment (LCA) is a widely used method to evaluate the environmental impacts of a product throughout part or all of its life cycle, from raw material extraction through to disposal or recycling. In the case of CF, LCA is particularly important as it enables a thorough evaluation of the material's high energy consumption during production, as well as its potential environmental advantages, such as reduced weight in transportation applications. Multiple studies have employed LCA to assess the GWP of CF production [4][9][10], with reported values ranging from 12.2 to 55.8 kg CO2e per kg of CF [11]. Although there is significant variability in the literature, the GWP of CF remains substantially higher than that of other commonly used structural materials [12]. This elevated GWP is primarily driven by the significant energy demand during production, which is met by fossil fuels, through the regional electricity grid and / or the direct combustion of natural gas during high temperature manufacturing stages. The GWP of CF production is therefore dominated by three sources: 1) GHG emissions associated with grid electricity generation used to power the high temperature ovens, 2) direct GHG emissions associated with NG combustion in the high temperature ovens and abatement systems, and 3) the GHG emissions associated with PAN fibre precursor production [4][3][8][13][14][15].

In addition to developing lower impact precursor materials, strategies to reduce the embodied carbon of CF products should therefore reduce the energy demand of CF production and/or use decarbonised energy sources. The former will likely require adaption of legacy or development of a new generation of CF production lines which are able to operate at higher energy efficiency. On the other hand, the latter may be achievable passively through the transition to renewable energy sources.

Several authors have investigated interventions to mitigate the impact from energy used during CF production. Prenzel et al. found that the energy consumption is responsible for 59% of the climate change associated with CF manufacturing, which can be reduced by 53% by transitioning to renewable electricity [16]. Stróżyk et al. demonstrated a 67% reduction in energy demand during CF production through the utilisation of microwave heating, when compared to conventional heating technologies [17]. Reducing processing time for CF production, such as rapid oxidation, has demonstrated a 70% reduction in energy required for fibre oxidation [18].

Recent research into CF production has explored alternatives to the traditional PAN precursor, focusing on non-PAN and bio-based materials to reduce the high energy consumption and GWP associated with CF manufacturing. PAN can be made from bio-based sources, creating a potential drop-in replacement for the CF manufacturing process. Bio-derived acrylonitrile (Bio-ACN) has been studied for several years [19][20][21][22], and can be produced from biomass waste using various methodologies described in [23]. Bio-ACN production using wood-based biomass has been licensed by Trillium Renewable Chemicals who are working with Solvay to assess Bio-ACN as a drop-in replacement for petroleum-based ACN in PAN fibre production [24][25].

There is currently limited data available on the GWP of Bio-ACN production, and the authors were unable to find specific GWP data for CF products manufactured using Bio-ACN as a precursor. Goyal reported the GWP of Bio-ACN produced from sugars through a three-stage process involving hydrocracking, dehydration, and ammoxidation [20]. The GWP of Bio-ACN was found to be 0.29 kg CO_2e per kg of Bio-ACN, representing a substantial reduction compared to ACN derived from crude oil, which has a reported GWP of 6.05 kg CO_2e per kg of ACN. Goyal also used scanning electron microscopy to compare the morphology of CFs produced using Bio-ACN and standard crude oil-derived ACN, observing no significant differences in fibre shape or structure [20]. However, mechanical properties were not tested, leaving it uncertain whether the use of Bio-ACN affects the mechanical performance of the resulting CFs.

While many studies have used LCA to assess the impact of CF production, no studies have quantified and compared the impact of prominent decarbonisation strategies. This study aims to examine how the cradle-to-gate GWP of PAN-based CF production may be reduced through the adoption of green energy solutions. Using LCA, it seeks to identify GWP hotspots in a UK case study to provide insights that

could inform global decarbonisation strategies for CF production. The LCA also models upstream production of raw materials, ammonia, ACN, and PAN fibres, to account for future energy scenarios on CF raw materials impact. The impact of using BioMethane, and synthetic methane (eMethane) in place of NG were also assessed. Additionally, the UK's Net Zero roadmap was used to assess how the transition to net zero grid power and electrification will affect GWP of CF production. Multivariable analysis was used to rank solutions for CF decarbonisation up to the year 2050 and identify optimal timelines for deploying decarbonisation solutions.

2 METHODOLOGY

This work has been conducted with reference to the methods provided in the international standards series ISO 14040 related to the preparation of LCA [26]. LCA is a standardised approach to evaluating the environmental impacts of a product over its life cycle. For CF production, the LCA methodology involves four key stages: goal and scope definition, life cycle inventory (LCI), impact assessment, and interpretation. The goal and scope stage outlines the purpose of the study and sets the system boundaries. This is followed by the impact assessment, which quantifies environmental effects such as GWP. Finally, in the interpretation phase, the results are analysed to identify opportunities for reducing environmental impacts, making LCA essential for improving the sustainability of CF production.

2.1 Goal and scope

The primary aim of the LCA is to evaluate the cradle-to-gate GWP of PAN based CF production, and to assess the potential of green energy solutions to reduce the GWP of CF production. The UK was used as a case study; however, it is the ambition to provide insight that can inform CF decarbonisation strategies globally. The LCA aims to evaluate the CF production phases and upstream processes to produce the feedstock materials for CF production. It is intended to find GWP hotspots and direct future sustainable development to mitigate these.

The following developments have been included in the analysis:

- Future electricity grid mix used in the production of CF and raw materials ACN and PAN fibre.
- Replacing NG with BioMethane for ACN, PAN, and CF production.
- Replacing NG with eMethane for ACN, PAN, and CF production.
- Electrification of processes utilising NG in ACN, PAN, and CF production.

2.2 Functional unit

The main function of structural CF is to provide strength and stiffness in composite materials. CF are produced at various grades; therefore, do not all provide the same reinforcement potential. The scope of this study is limited to assessing a single CF grade in isolation to maintain functionality across the scenarios. The Functional Unit for this LCA study is defined as: the production of 1 kg of CF. The reference flow for the study is 1 kg of CF.

2.3 Processes

Figure 1 depicts a simplified process flow for the current production of CF products, including the upstream production of petrochemical precursors. Methyl acrylate and ACN are the key components in the production of PAN fibres, which undergo thermal treatment in high-temperature ovens to yield CF. Subsequently, the CF is subjected to surface treatment and sizing. The various processes are presented in more detail in the authors' previous publication [27].

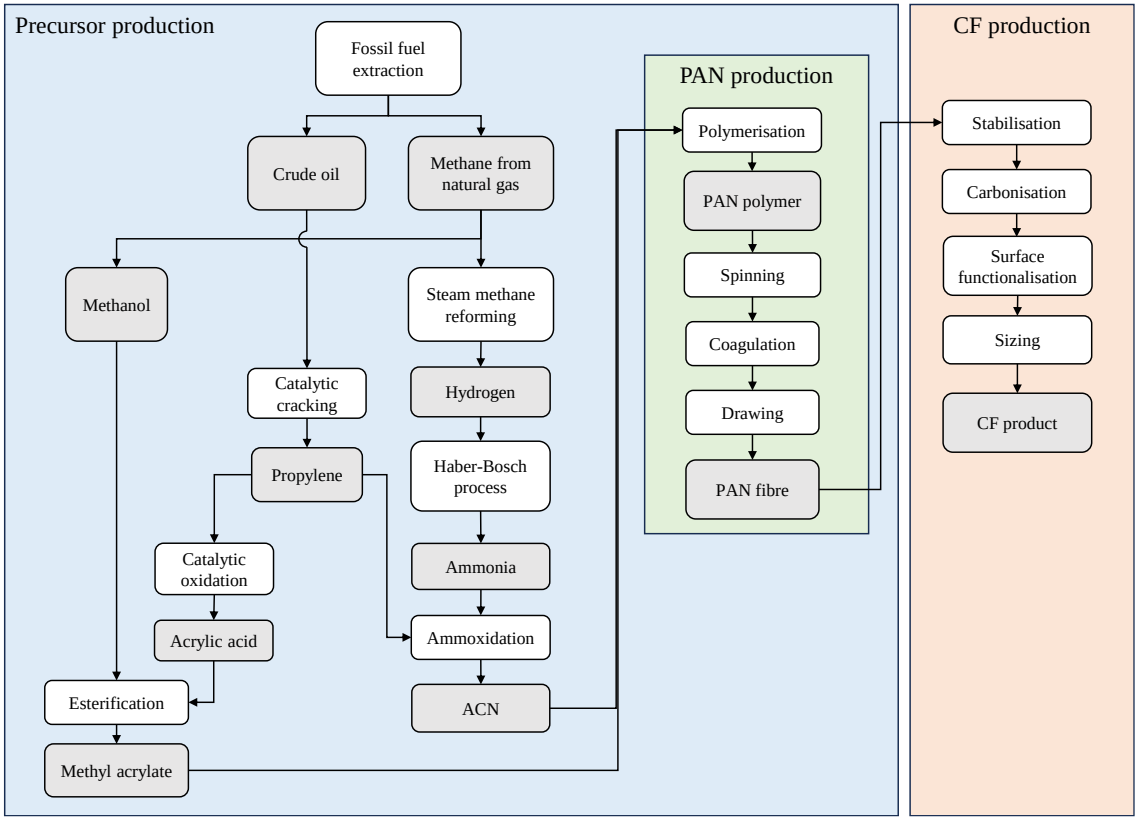

Figure 1 Process flow for CF production, including upstream production of petrochemical precursors

2.4 Lifecycle impact assessment

In accordance with the defined LCA goal and scope, this study as focused on the following Environmental Impact Indicator: Global Warming Potential (GWP 100 years) [kg CO_2e.].

2.5 System boundary, Lifecycle inventory, Allocation, Cut-off criteria

Refer to the authors' previous LCA publication for details on the system boundary, life cycle inventory, allocation methods, and cut-off criteria [27].

3 RESULTS AND DISCUSSION

3.1 Energy consumption breakdown: PAN and carbon fibre production

Figure 2 shows a representative energy consumption breakdown for PAN fibre and CF production, based on the use of electrified oxidation and carbonisation ovens in CF manufacturing. The percentages reflect the share of total energy demand per unit mass of CF produced, including both PAN fibre and CF production stages. Natural gas use in PAN fibre production—mainly for solvent recovery at temperatures below 200 °C—and for CF drying, can be readily electrified.

A key barrier to full electrification lies in the abatement systems used to treat emissions from the oxidation and carbonisation ovens. For example, hydrogen cyanide (HCN), a hazardous byproduct, requires treatment at temperatures up to 1000 °C to ensure complete combustion, leading to high natural gas consumption. This accounts for approximately 28% of the total energy demand across PAN and CF production, representing the critical "hard-to-decarbonise" energy source.

Energy efficiency gains in abatement systems could be achieved by reducing airflow and integrating regenerative thermal oxidizers (RTOs) for oxidation oven exhaust, which are effective for high-airflow, moderate-VOC streams and can recover up to 95% of heat. However, while these approaches lower natural gas use, they do not fully eliminate the resulting GHG emissions and must be combined with

broader decarbonisation strategies. Potentially more challenging to decarbonise is the use of direct-fired thermal oxidizers (DFTOs) for low-flow, high-VOC exhaust streams, such as those from the carbonisation furnace. While DFTOs effectively treat tar-rich and HCN-laden emissions, they lack heat recovery and consume more fuel, contributing significantly to the remaining natural gas demand in CF production.

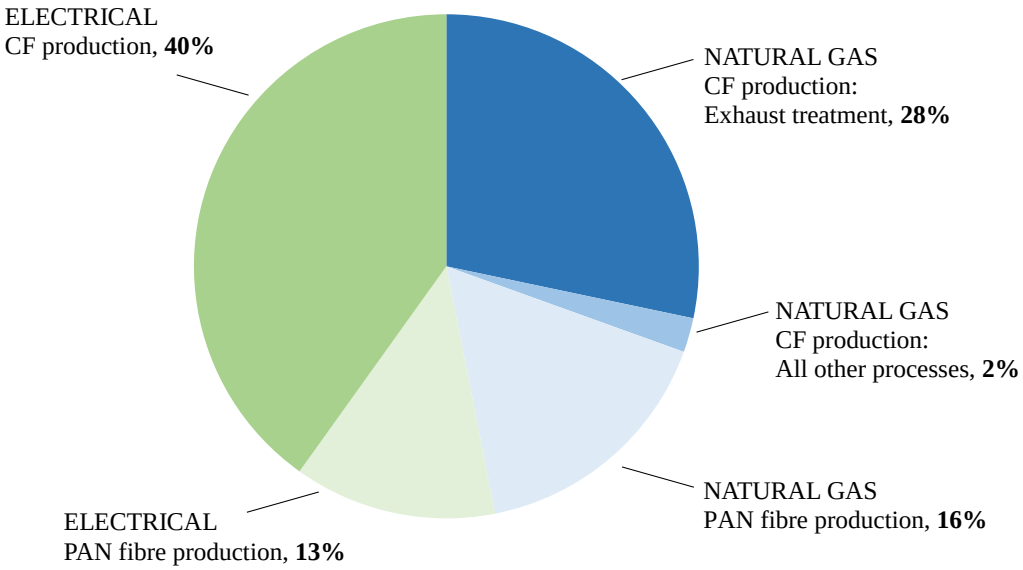

Figure 2 Representative energy consumption breakdown for CF production using electrified oxidation and carbonisation ovens

3.2 Impact of decarbonisation strategies

Figure 3 presents a comparison of various CF decarbonisation pathways, including electrification, BioMethane, and eMethane strategies, building on previous studies [27]. The assessment assumes the UK National Grid ESO projection for decarbonising electricity to net zero by 2050. In each scenario, natural gas is replaced on an energy-equivalent basis by the respective alternative energy source. The use of bio-based acrylonitrile is also assumed, as it is essential for achieving fully net zero CF products (discussed in more detail in author's previous publication [27]).

Figure 3 shows that electrification offers the fastest route to net zero CF production and should be prioritised by manufacturers. While electrification may necessitate substantial modifications to existing equipment currently reliant on natural gas, these upgrades are within the control of CF producers and do not depend on the future scalability of emerging technologies, such as BioMethane and eMethane. Although initial retrofit costs may be significant, electrification offers the potential for long-term cost savings through more efficient use of renewable electricity and can deliver considerable emissions reductions, positioning it as a viable and strategic decarbonisation pathway as technology and renewable energy infrastructure continue to advance.

Figure 3 also evaluates a 50% reduction in electricity demand (dashed green line), reflecting the potential of technologies such as microwave heating and rapid oxidation, which have demonstrated energy savings of up to 67% [17] and 70% [18], respectively. Early adoption of these energy efficiency measures is key, as they offer the most impact while the electricity grid is still carbon intensive. Beyond 2040, as the grid approaches net zero emissions, the primary motivation for further energy reductions will shift from carbon savings to economic benefits.

For processes where electrification faces technical challenges—such as exhaust gas treatment in abatement systems—green gas options may offer viable alternatives. In the near term (5–10 years), BioMethane is favoured over eMethane due to its independence from net zero electricity. However, in the long term, eMethane may offer greater emissions reductions as low-carbon electricity becomes more

accessible. In the near term, particularly within the UK, CF producers can support decarbonisation by purchasing gas backed by Renewable Gas Guarantees of Origin (RGGOs), facilitating market-based allocation of BioMethane, which currently comprises a small share of the national gas supply.

Figure 3 shows that net zero CF production is possible with synthetic methane; however, eMethane is expected to remain significantly more expensive than natural gas due to the energy demands of green hydrogen and CO_2 capture [28]. Given its uncertain viability and timeline, sole reliance on eMethane is high-risk. CF producers should instead prioritise electrification, process efficiency, and heat recovery to enable a more resilient decarbonisation pathway. Hydrogen combustion offers a potential alternative, bypassing the need for CO_2 capture, though the required process modifications are still unclear. While synthetic fuels are compatible with existing systems, their high cost and limited scalability reinforce the need for a balanced strategy—advancing fuel technologies while focusing on near-term, demand-side solutions.

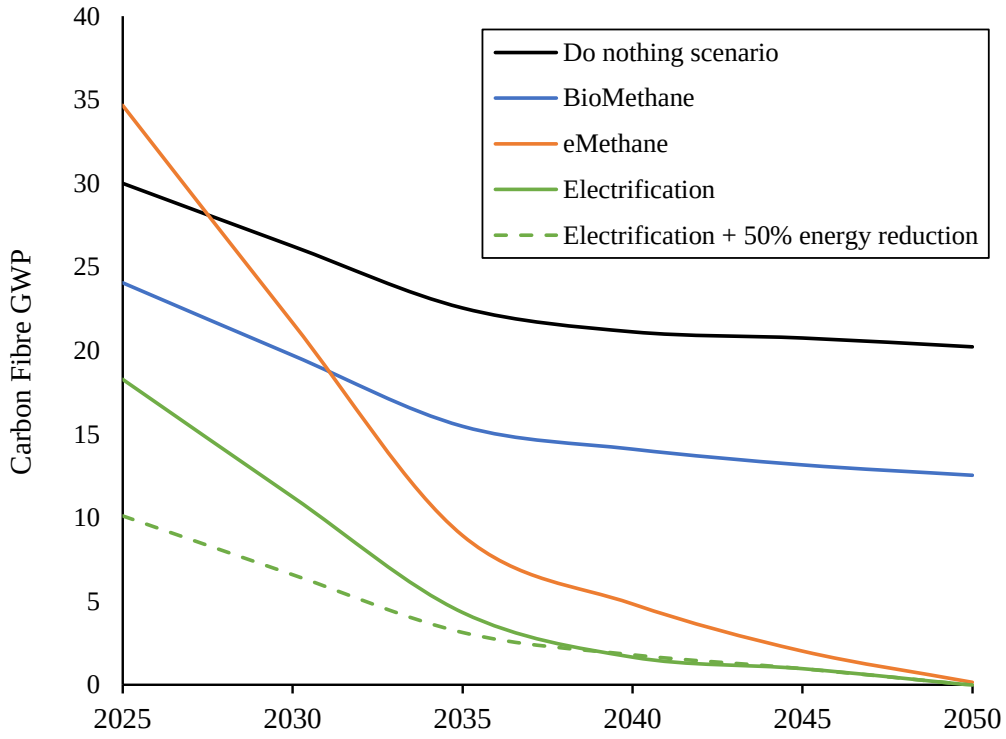

Figure 3 Comparison of electrification and green gas solutions on CF production decarbonisation (assumes electronification of heat from natural gas in PAN and CF production processes on an equal calorie basis)

3.3 Accelerating emissions reduction through electrification

It is important to note that the effectiveness of electrification in reducing CF GWP depends heavily on the regional energy mix. In the UK, where the electricity grid already contains a high share of renewables, electrification leads to lower GWP. In contrast, in regions with fossil fuel-dominant grids, direct natural gas use for heat may result in lower GWP than electricity-based alternatives. This highlights the need for region-specific assessments and decarbonisation roadmaps that reflect local energy infrastructure and grid composition.

Moreover, the future electricity grid compositions remain uncertain, and the projections in Figure 3 are based on average grid mix scenarios. Even when considering the UK as a sole case study, there are large uncertainties in the timeline for grid scale renewable deployment which poses challenges in precisely mapping out the decarbonisation trajectory for CF. Relying passively on network level transition leaves CF producers with little control over the timing of net zero energy generation,

introducing uncertainty into decarbonisation roadmaps. To address this uncertainty and actively expedite the decarbonisation of their electricity consumption, CF producers could incorporate local or onsite renewable electricity generation technologies, such as solar or wind power, to displace some or all the grid electricity used. An example being SGL Carbon Fibers Ltd.'s Moses Lake site, which purchases renewable energy from local hydropower plants [29].

Electrified thermal oxidisers present a potential pathway to decarbonise high-temperature exhaust gas treatment in CF production by eliminating the need for natural gas or synthetic fuels / green gases in current abatement systems. When powered by low-carbon electricity, these systems could mitigate GHG emissions associated with thermal energy used for gas cleaning. Electrified RTOs (eRTO) are commercially available and may be suited for oxidation oven exhaust treatment. Electrically powered flameless thermal oxidisers (eTO) may also replace DFTOs currently used for high-temperature, high-VOC exhaust streams from carbonisation ovens. While promising, these technologies have not yet been deployed in CF production, and their ability to safely and reliably process hazardous emissions such as HCN and tar-laden streams remains unproven. Further research, pilot-scale trials, and performance validation of eRTO and eTOs under CF production conditions are required to determine their technical feasibility and facilitate industry uptake. Key barriers to implementation include likely higher upfront capital costs compared to conventional gas-fired systems, the potential need for complete system redesigns when retrofitting existing infrastructure, and grid constraints that may necessitate upgrades or energy storage solutions to manage peak electricity demand.

3.4 Multi-horizon CF decarbonisation strategy

Figure 4 presents a multi-horizon strategy for CF production decarbonisation, encompassing energy sourcing, technology development, and deployment timelines. This roadmap is designed to provide high-level guidance and actionable steps for CF producers aiming to transition towards net zero carbon fibre products. It integrates the carbon footprints of the various decarbonisation strategies assessed in this study alongside pragmatic considerations of the current and emerging technology landscape, market readiness, and infrastructure requirements. By aligning near-, mid-, and long-term actions with both impact potential and feasibility, the strategy supports informed decision-making and prioritisation of interventions that can accelerate progress toward net zero CF production.

Energy strategy

- Ahead of the UK grid reaching net zero emissions, CF producers should procure electricity backed by Renewable Energy Guarantees of Origin (REGOs) to both support the growth of renewable energy and achieve net zero electricity consumption through market-based allocation. Additionally, producers should explore opportunities for on-site renewable energy generation at existing facilities or consider siting new developments in regions with access to local renewable resources to further accelerate decarbonisation.
- While electrified solutions for hard-to-decarbonise processes—such as exhaust gas treatment—are under development, CF producers should purchase gas backed by Renewable Gas Guarantees of Origin (RGGOs) to support the expansion of green gas production and achieve net zero gas consumption through market-based mechanisms.

Technology deployment

- CF producers should transition to PAN fibre suppliers utilising bio-based acrylonitrile feedstocks. This advanced technology is anticipated to reach commercial availability by the end of the decade and should be implemented independently of other process modifications, allowing for adoption as soon as market access becomes feasible.
- Electrification of currently viable technologies—particularly oxidation and carbonisation ovens—should be prioritised. This includes retrofitting existing infrastructure where feasible and ensuring that all electrifiable processes are implemented in new CF production facilities.
- Established energy recovery technologies should be implemented to improve the energy efficiency of carbon fibre production and reduce overall energy consumption. This could include deploying

high-efficiency RTOs for oxidation ovens and incorporating heat recovery systems for high-temperature DFTOs. Prioritising these measures is critical, as energy-saving strategies offer the greatest benefits in the near term while energy-related impacts remain significant.

*Technology development**

- Lower-power electric heating technologies should be developed to further enhance the benefits of electrifying oxidation and carbonisation ovens. While their near-term emissions reduction potential is high, commercial readiness may limit their contribution to decarbonisation. Nonetheless, development should continue given their potential for long-term cost savings and efficiency gains in future CF infrastructure.
- Electrifying exhaust gas cleaning systems is anticipated to be the most technically challenging aspect of CF production decarbonisation. These systems currently account for approximately 25–30% of the total energy demand across PAN fibre and CF manufacturing. Therefore, their electrification is essential. To achieve this, CF producers must actively support the development and integration of electric gas cleaning technologies, which would enable the sector to reduce emissions without depending on the uncertain future availability of green gases (such as BioMethane and synthetic fuels).

** Note that there are many other proposed technology developments for CF production that could support decarbonisation; their exclusion from this proposed strategy is not indicative of a lack of potential but rather reflects current limitations in data availability, technology readiness, or alignment with the near- and mid-term priorities outlined in this roadmap.*

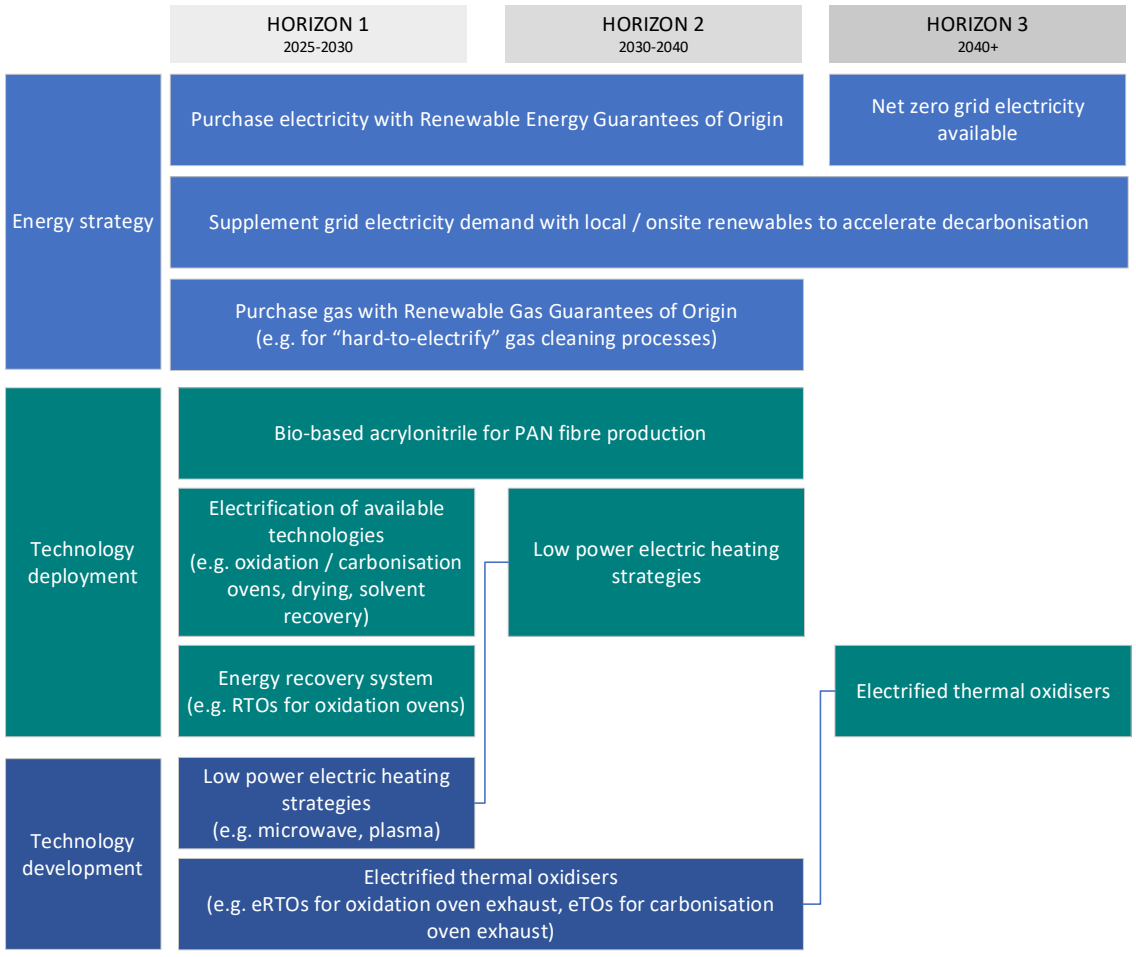

Figure 4 Multi-horizon strategy for CF production decarbonisation

4 CONCLUSIONS

This study provides a life cycle assessment of PAN-based CF production, identifying key GWP hotspots and evaluating decarbonisation strategies. Electrification of CF manufacturing processes, particularly oxidation and carbonisation ovens, offers the most immediate and impactful emissions reductions—especially when powered by low-carbon electricity. However, abatement systems for hazardous exhausts remain a significant barrier, currently accounting for a large share of energy demand and requiring further technological development.

Complementary strategies such as using bio-based acrylonitrile feedstocks, energy recovery systems, and alternative fuels like BioMethane or eMethane may support emissions reduction, particularly where electrification is currently limited. Regional grid composition plays a critical role in the effectiveness of electrification, highlighting the need for site-specific strategies.

A multi-horizon strategy is proposed to guide CF producers through near-, mid-, and long-term decarbonisation actions. This roadmap considers both emissions impact and technological feasibility, offering pragmatic steps toward net zero CF production. While uncertainties remain—particularly around grid decarbonisation timelines and technology readiness—proactive industry action is essential. Early investments in electrification, renewable energy sourcing, and technology innovation will be crucial to reducing reliance on fossil fuels and supporting the transition to low-carbon composite materials.

ACKNOWLEDGEMENTS

The authors gratefully acknowledge the support of the SusWIND consortium and Catapult funding provided through the UK Research and Innovation (UKRI).

REFERENCES

[1] L. Gang, “2023 Global Carbon Fiber Composites Market Report,” Guangzhou, 2024. [Online]. Available: https://dash.compositesworld.com/cdn/cms/2023 Global Carbon Fiber Composites Market Report.pdf.

[2] Sphera Solutions GmbH, “Process data set: Carbon Fiber (CF; from PAN; standard strength); spinning, stabilizing, carbonizing, surface treatment, sizing; production mix, at plant,” 2021. [Online]. Available: http://gabi-documentation-2022.gabi-software.com/xml-data/processes/d2e4cb14-c5fa-49a3-b6c2-840a2b860d63.xml.

[3] A. Dér *et al.*, “Modelling and analysis of the energy intensity in polyacrylonitrilie (PAN) precursor and carbon fibre manufacturing,” *J. Clean. Prod.*, vol. 303, 2021, doi: 10.1016/j.jclepro.2021.127105.

[4] S. Das, “Life cycle assessment of carbon fiber-reinforced polymer composites,” *Int. J. Life Cycle Assess.*, vol. 16, pp. 268–282, 2011, doi: 10.1007/s11367-011-0264-z.

[5] U.S. Department of Energy, “Bandwidth Study on Energy Use and Potential Energy Saving Opportunities in U.S. Glass Fiber Reinforced Polymer Manufacturing,” 2017. doi: 10.32964/tj16.9.

[6] T. Suzuki and J. Takahashi, “Prediction of energy intensity of carbon fiber reinforced plastics for mass-produced passenger cars,” *Ninth Japan Int. SAMPE Symp. JISSE-9*, pp. 14–19, 2005, [Online]. Available: http://j-t.o.oo7.jp/publications/051129/S1-02.pdf.

[7] U. Arnold, A. De Palmenaer, T. Brück, and K. Kuse, “Energy-Efficient Carbon Fiber Production with Concentrated Solar Power: Process Design and Techno-economic Analysis,” *Ind. Eng. Chem. Res.*, vol. 57, no. 23, pp. 7934–7945, 2018, doi: 10.1021/acs.iecr.7b04841.

[8] T. Groetsch *et al.*, “A modular LCA/LCC-modelling concept for evaluating material and process innovations in carbon fibre manufacturing,” *Procedia CIRP*, vol. 98, pp. 529–534, 2021, doi: 10.1016/j.procir.2021.01.146.

[9] S. Zhang, J. Gan, J. Lv, C. Shen, C. Xu, and F. Li, “Environmental impacts of carbon fiber

production and decarbonization performance in wind turbine blades," *J. Environ. Manage.*, vol. 351, p. 119893, 2024, doi: 10.1016/j.jenvman.2023.119893.

[10] K. Ramachandran, C. L. Gnanasagaran, and A. Vekariya, "Life cycle assessment of carbon fiber and bio-fiber composites prepared via vacuum bagging technique," *J. Manuf. Process.*, vol. 89, pp. 124–131, 2023, doi: 10.1016/j.jmapro.2023.01.068.

[11] V. Michaud, J. Takahashi, and I. Verpoest, "LCA of Carbon fibers: an analysis of available data sets," *ICCM 23*. 2023, [Online]. Available: https://airdrive.eventsair.com/eventsairwesteuprod/production-confpartners-public/e177b5b57629469497d1cc1a42b7c5b2.

[12] V. V. Rajulwar *et al.*, "Steel, Aluminum, and FRP-Composites: The Race to Zero Carbon Emissions," *Energies*, vol. 16, p. 6904, 2023, doi: 10.3390/en16196904.

[13] Y. F. Khalil, "Eco-efficient lightweight carbon-fiber reinforced polymer for environmentally greener commercial aviation industry," *Sustain. Prod. Consum.*, vol. 12, pp. 16–26, 2017, doi: 10.1016/j.spc.2017.05.004.

[14] Tim Röding, "Carbon Fibre Production: Primary Energy Consumption." Institut für Textiltechnik (ITA) der RWTH Aachen University, Aachen, 2019, doi: 10.1016/j.aiepr.2022.03.008.

[15] T. Groetsch, M. Maghe, C. Creighton, and R. J. Varley, "Environmental, property and cost impact analysis of carbon fibre at increasing rates of production," *J. Clean. Prod.*, vol. 382, p. 135292, 2023, doi: https://doi.org/10.1016/j.jclepro.2022.135292.

[16] T. M. Prenzel *et al.*, "Bringing Light into the Dark — Overview of Environmental Impacts of Carbon Fiber Production and Potential Levers for Reduction," *Polymers (Basel).*, vol. 16, p. 12, 2024, doi: 10.3390/polym16010012.

[17] M. A. Stróżyk *et al.*, "Decreasing the environmental impact of carbon fibre production via microwave carbonisation enabled by self - assembled nanostructured coatings," *Adv. Compos. Hybrid Mater.*, vol. 7:39, 2024, doi: 10.1007/s42114-024-00853-2.

[18] J. Sloan, "LeMond Carbon audits rapid-oxidation carbon fiber technology," *Composites World*, 2019. https://www.compositesworld.com/news/lemond-carbon-audits-rapid-oxidation-carbon-fiber-technology- (accessed Jun. 14, 2024).

[19] M. O. Guerrero-Pérez and M. A. Bañares, "Metrics of acrylonitrile: From biomass vs. petrochemical route," *Catal. Today*, vol. 239, pp. 25–30, 2015, doi: 10.1016/j.cattod.2013.12.046.

[20] E. M. Karp *et al.*, "Renewable acrylonitrile production," *Science*, vol. 358, pp. 1307–1310, 2017, doi: 10.1126/science.aan1059.

[21] R. K. Grasselli and F. Trifirò, "Acrylonitrile from Biomass: Still Far from Being a Sustainable Process," *Top. Catal.*, vol. 59, pp. 1651–1658, 2016, doi: 10.1007/s11244-016-0679-7.

[22] C. Liebig *et al.*, "Glycerol conversion to acrylonitrile by consecutive dehydration over WO3/TiO2 and ammoxidation over Sb-(Fe,V)-O," *Appl. Catal. B Environ.*, vol. 132–133, pp. 170–182, 2013, doi: 10.1016/j.apcatb.2012.11.035.

[23] J. L. Dubois and S. Kaliaguine, "Alternative routes to more sustainable acrylonitrile: Biosourced acrylonitrile," in *Industrial Green Chemistry*, 2020, pp. 31–61.

[24] J. Sloan, "Acrylonitrile from biomass scales up," *Composite World*, 2019. https://www.compositesworld.com/articles/acrylonitrile-from-biomass-scales-up (accessed Jun. 14, 2024).

[25] J. Sloan, "Bio-based acrylonitrile for carbon fiber manufacture," *Composites World*, 2023. https://www.compositesworld.com/articles/bio-based-acrylonitrile-for-carbon-fiber-manufacture (accessed Jun. 14, 2024).

[26] "ISO 14040:2006, Environmental management — Life cycle assessment — Principles and framework," 2006. [Online]. Available: https://www.iso.org/standard/37456.html.

[27] K. Pender, F. Romoli, and J. Fuller, “Future strategies for decarbonisation of carbon fibre products: A roadmap to Net Zero 2050,” *J. Clean. Prod.*, vol. 486, p. 144525, 2025, doi: 10.1016/j.jclepro.2024.144525.

[28] F. Ueckerdt, C. Bauer, A. Dirnaichner, J. Everall, R. Sacchi, and G. Luderer, “Potential and risks of hydrogen-based e-fuels in climate change mitigation,” *Nat. Clim. Chang.*, vol. 11, pp. 384–393, 2021, doi: 10.1038/s41558-021-01032-7.

[29] SGL Carbon Fibers, “The climate-friendly carbon fiber from SGL Carbon - up to 50% less CO2 emissions,” 2024. https://www.sglcarbon.com/en/newsroom/news/press-report/the-climate-friendly-carbon-fiber-from-sgl-carbon-up-to-50-less-co2-emissions/ (accessed Apr. 01, 2024).

PREPARATION AND CHARACTERISATION OF OLEFIN-BASED COMPOSITE MATERIALS FILLED WITH RECYCLED CARBON FIBRES FOR 3D PRINTING APPLICATION

Corrado Sciancalepore[1,*], Antonio Panico[1], Matteo Leonardi[1], Luca Collini[1], Paolo Albertelli[2], Valerio Mussi[2], Daniel Milanese[1]

[1] *DISTI, Department of Industrial Systems and Technologies, University of Parma, Parco area delle Scienze 181/A, 43124 Parma, Italy*
corrado.sciancalepore@unipr.it
antonio.panico@unipr.it
matteo.leonardi@studenti.unipr.it
luca.collini@unipr.it
daniel.mialnese@unipr.it

[2] *MUSP Consortium, Machine tools and production systems, Via Vittore Callegari 21/F 29122 Piacenza, Italy*
paolo.albertelli@polimi.it
valerio.mussi@musp.net

Keywords: Composite materials, polypropylene, recycled carbon fiber, 3D printing

ABSTRACT

The composites industry is experiencing steady growth worldwide. However, the recycling of composite fiber reinforced polymer (CFRP) materials, which make up a significant proportion of composite materials used in engineering applications, is still a challenge. The process of recycling the high value fiber part of thermoset materials requires ad hoc processes for the recovery (mechanical, thermal or chemical process) and reuse of this valuable resource.
The work presented, based on recycled carbon fiber, evaluates the possibility of transforming the recycled fiber into a new thermoplastic composite material through a technological approach of extrusion and then using the material obtained through injection molding and 3D printing, promoting the adoption of a circular and innovative approach to the recycling of composite materials.
In particular, the recycled carbon fibers (fillers) were ground to obtain short fibers and characterized by particle size and electron microscopy. The filler was compounded with the thermoplastic matrix (polypropylene) by twin-screw extrusion.
The extrusion of the composite material took place in the form of a filament that was collected on reels and pelletized into granules. Characterization of the mechanical properties of the composite material was carried out by means of tensile tests on standard specimens (type 5A) according to ISO 527, obtained by injection molding. Finally, the pellets were used as raw material in an additive fused granules fabrication process and the printed objects were further characterized after 3D printing.
The process of transforming and obtaining materials in terms of mechanical and thermal properties has been optimized, comparing them with those of unfilled virgin materials.
In addition, recycled carbon fibers were valorized by upcycling them as structural fillers for polymer matrix composites, with a view to a sustainable circular economy.

1 INTRODUCTION

In recent years, the growing demand for lightweight, high-performance materials in industries such as aerospace, automotive, and sports has highlighted the critical role of carbon fiber-reinforced polymers

(CFRPs) due to their exceptional strength-to-weight ratio and durability [1]. However, these materials unfortunately face a significant challenge: the environmental and economic cost associated with their end-of-life disposal. Landfilling remains the predominant disposal method to date, exacerbating environmental issues and contradicting modern sustainability goals [2].

One possible and virtuous way to overcome this problem is through the reuse of recycled carbon fibers (rCF), obtained from waste CFRP components, as reinforcement in new composite materials [3-5]. This work shows the feasibility of incorporating pyrolysis-recovered rCFs into a polypropylene (PP) matrix to develop composite materials that combine sustainability and mechanical performance. In addition, the use of polypropylene grafted with maleic anhydride (PP-g-MA) as a compatibilizer is evaluated to improve interactions at the interface between the fibers and the polymer matrix and implement mechanical performance accordingly. The composite materials are processed by both traditional injection molding and fused granules fabrication (FGF) 3D printing, allowing comparison of different manufacturing techniques.

2. MATERIALS AND METHODS

The starting polymer matrix is PP (Moplen HP456J), chosen for its mechanical versatility, chemical resistance and cost-effectiveness. However, its nonpolar and low surface energy characteristics may hinder compatibility with rCFs, necessitating the use of PP-g-MA to improve wettability at the interface. Carbon fibers recycled by pyrolysis (Carbiso), retain remarkable mechanical properties (tensile strength up to 5 GPa, Young's modulus around 240 GPa). They were milled to achieve optimal homogeneous dispersion in powder form and their size distribution characterized by laser granulometry.

Six composite formulations were prepared: three with increasing content of rCF (10%, 20%, 30%- named PP-rCF10, PP-rCF20, and PP-rCF30, respectively) and two incorporating 10% rCF with 2.5% and 5% maleic anhydride-functionalized polypropylene (called PPPP-gMA2.5-rCF10 and PPPP-gMA5-rCF10, respectively), in addition to pure PP. The compounds were obtained with a twin-screw extruder, producing filaments that were then pelletized for further processing by injection molding, which provides high dimensional stability, and FGF 3D printing, which directly uses the granules to form objects layer by layer. The latter approach certainly offers greater freedom in making objects of complex shape, but it presents challenges related to the inherent anisotropy of the finished object. For both printing technologies dumbbell specimens were obtained and used for the subsequent characterizations. For FGF 3D printing it was essential to understand how the addition of fibers affects the adhesion between layers. For this reason, two configurations were prepared with two raster angles, 0° and 90°, indicating the alignment of the strands, respectively parallel and perpendicular to the tensile direction of the specimen.

3. RESULTS AND DISCUSSION

Various analytical techniques were used to assess the structural and mechanical properties of the materials. Laser granulometry reveals a fairly wide size distribution of rCF (between 1 and 300 µm), with an average volumetric diameter of around 70 µm (Fig. 1(a)), while scanning electron microscopy (SEM) images confirm the typical size and morphology of carbon fibers, highlighting the presence of a certain surface roughness that could favor adhesion and mechanical interlocking (Fig. 1(b) and (c)).

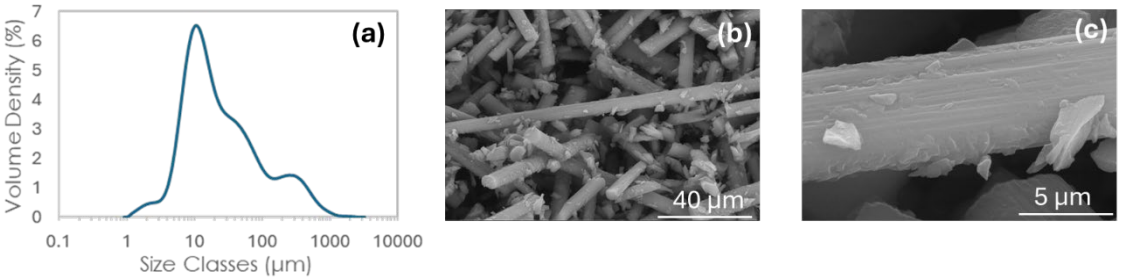

Figure 1: Size distribution curve (a) and SEM images at different magnification (b) and (c) of rCF.

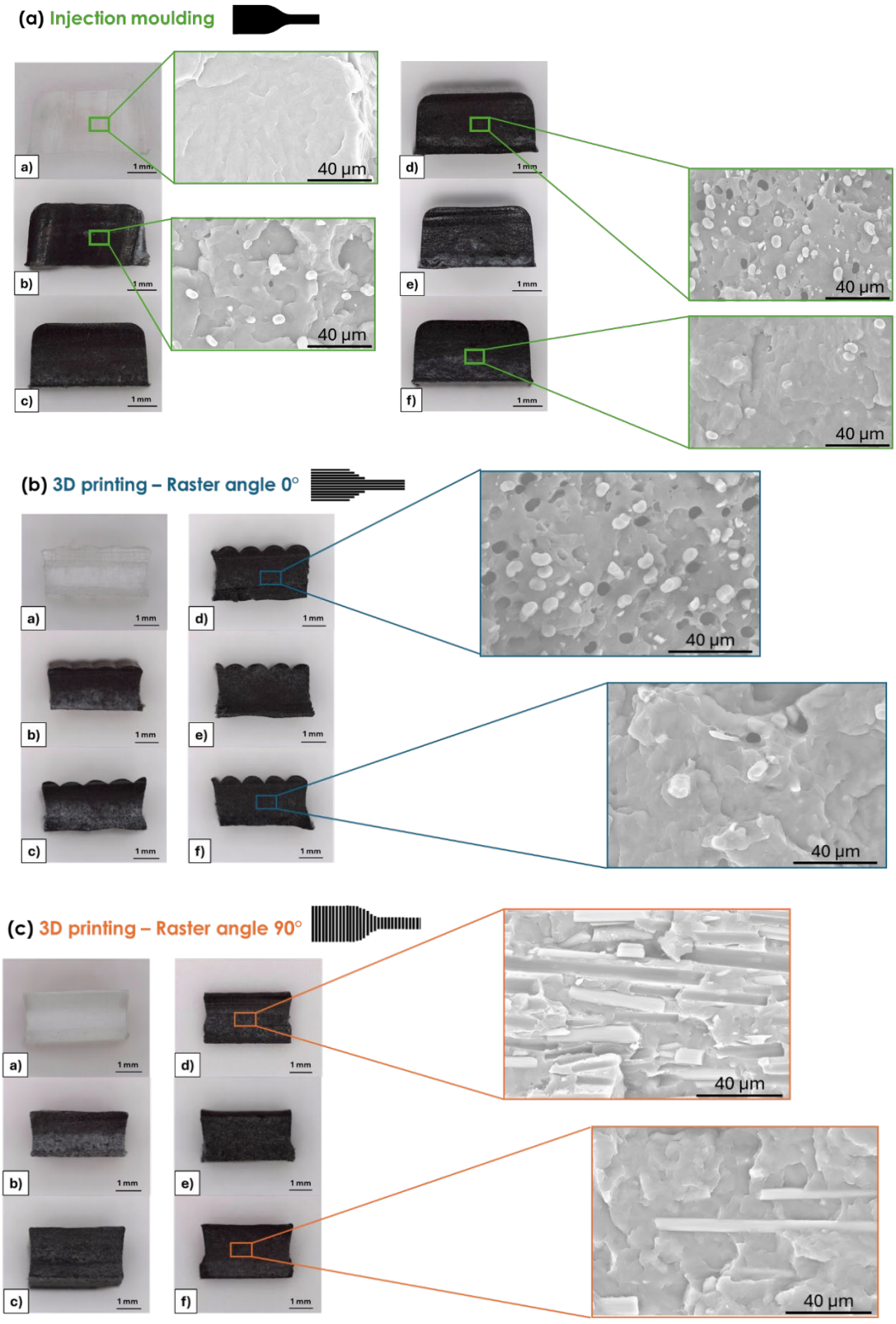

Figure 2: Optical and SEM images of specimen cross sections obtained by injection molding (a), FGF 3D printing with a raster angle of 0° (b) and 90° (c). The letters in the inset of the optical pictures indicate the composition of the sample: a) pure PP, b) PP-rCF10, c) PP-rCF20, d) PP-rCF30, e) PPPP-gMA2.5-rCF10 and f) PPPP-gMA5-rCF10.

SEM images of the composite cross sections show the microstructure of the injection-molded and 3D-printed samples (Fig. 2 (a), (b) and (c)). The fibers are homogeneously dispersed and distributed in all samples: in particular, the fibers are oriented mainly along the direction of the molding flow. In maleic anhydride-compatibilized samples, the fibers are wet by the polymer matrix and are effectively incorporated in the PP. Maleic anhydride, when grafted onto the polymer chain, introduces polar groups (specifically, the anhydride ring) that can interact with hydroxyl, carboxylic or epoxy groups on the fiber surface, due to the partial oxidation of fiber carbon atom.

The results of the melt flow index (MFI) measurement show how the fiber content influences the processability of the composite (Fig. 3): increasing the rCF concentration leads to a reduction in the MFI [6], while the addition of PP-g-AM brings the melt flow behavior back to values closer to those of pure PP [7]: MFI increases when the compatibilizing agent is used because the improved interfacial adhesion reduces internal resistance to flow, promotes better fiber dispersion, and minimizes agglomeration, resulting in a more uniform, less viscous melt.

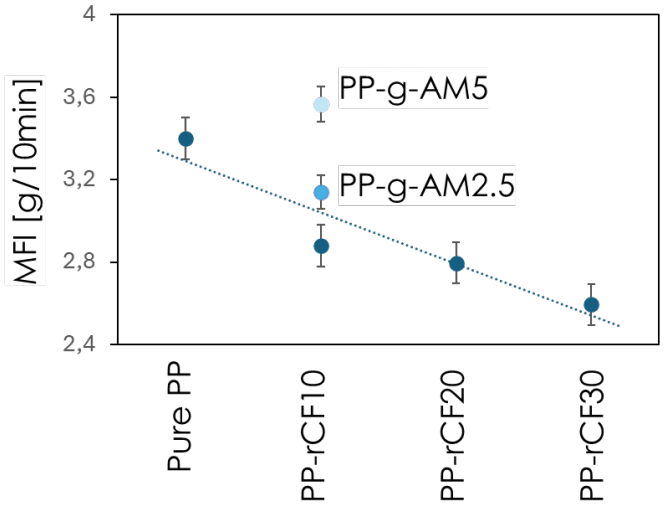

Figure 3: MFI values as a function of material composition.

However, the most critical insights are provided by the tensile tests. These are conducted on samples from injection molding and 3D printing processes, with the latter being further divided into 0° and 90° raster orientations to assess their anisotropy in terms of mechanical properties (Fig. 4 and 5).

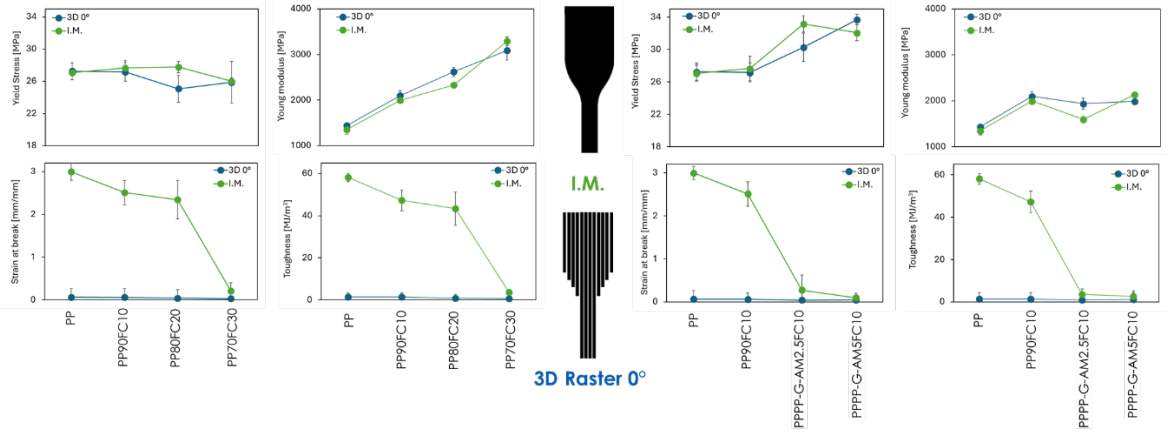

Figure 4: Comparison of mechanical parameters between injection-molded and 3D-printed (with the raster angle of 0°) samples.

Tensile tests reveal that the addition of fibers substantially increases the stiffness of the composites [8]. For injection-molded samples, the Young's modulus increases from about 1350 MPa in pure PP to

over 3200 MPa in the composite at 30% rCF. Interestingly, the yield strength remains almost constant between the various compositions, suggesting that the fibers contribute mainly to stiffness rather than ultimate strength. However, a drastic decrease in ductility and toughness is observed at higher rCF contents, reflecting the transition from ductile to brittle fracture behavior.

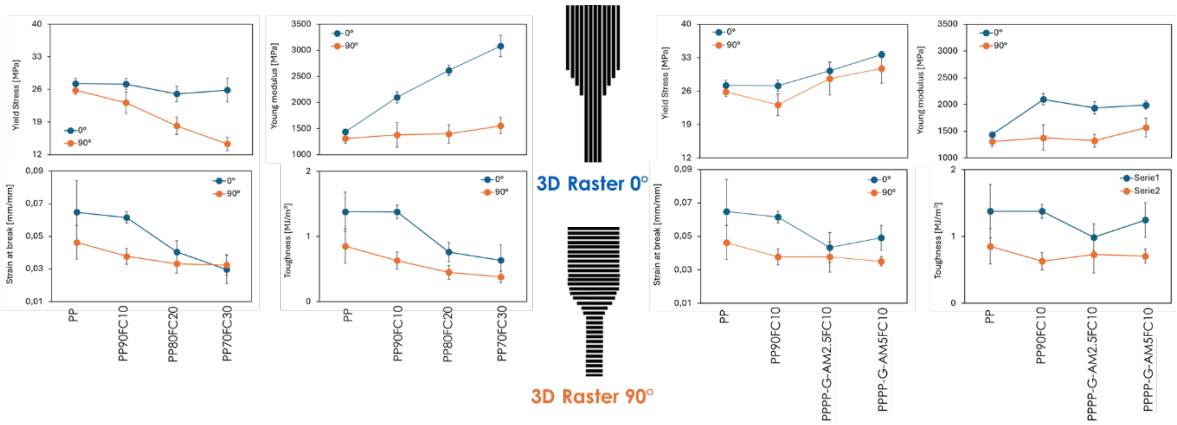

Figure 5: Comparison of mechanical parameters between 3D-printed samples with the raster angle of 0 and 90°, respectively.

For 3D-printed samples, anisotropy plays a significant role. Samples printed at a raster angle of 0° (aligned with the tensile stress) show better mechanical performance than those printed at 90°, which yield to lower deformations due to weaker adhesion between the layers [4]. The addition of the compatibilizer (PP-g-MA) increases performance in both cases, with significant improvements in mechanical performance compared to the unfilled material [9], and reduces anisotropy compared to the composite filled with the same percentage of rCF. The use of PP-g-MA facilitates better dispersion and adhesion of the fibers, favoring the transfer of stresses from the matrix to the fiber and validating its role as a crucial additive in rCF-reinforced PP composites.

The Halpin-Tsai equations [10], widely used to estimate the modulus of composites based on volume fraction and geometry of the fibers, are applied to validate experimental data (Fig. 6). Specifically, for determining the elastic modulus of 3D short-fiber composites, the Lavengood-Goettler equation is also used, serving as a complementary empirical tool in these calculations [11]:

$$E_c = \frac{1}{5} E_{11} + \frac{4}{5} E_{22} \qquad \text{Eq. 1}$$

Equation 1 applies to randomly in space oriented short fiber composites where E_{11} and E_{22} are the longitudinal and transverse modulus of a unidirectional discontinuous fiber composite having the same volume fraction of fibers:

$$E_{11} = \frac{1+2(\frac{l_f}{2r_f})\eta_L V_f}{1-\eta_L V_f} E_m \qquad \text{Eq. 2}$$

$$E_{22} = \frac{1+2\eta_T V_f}{1-\eta_T V_f} E_m \qquad \text{Eq. 3}$$

where:

$$\eta_L = \frac{\frac{E_f}{E_m}-1}{\frac{E_f}{E_m}+2(\frac{l_f}{2r_f})} \qquad \text{Eq. 4}$$

$$\eta_T = \frac{\frac{E_f}{E_m} - 1}{\frac{E_f}{E_m} + 2} \qquad \text{Eq. 5}$$

where E_m is the elastic modulus of the PP matrix, E_f is the elastic modulus of the carbon fiber, l_f and r_f are length and radius of the fiber, V_f is the fiber volume fraction.

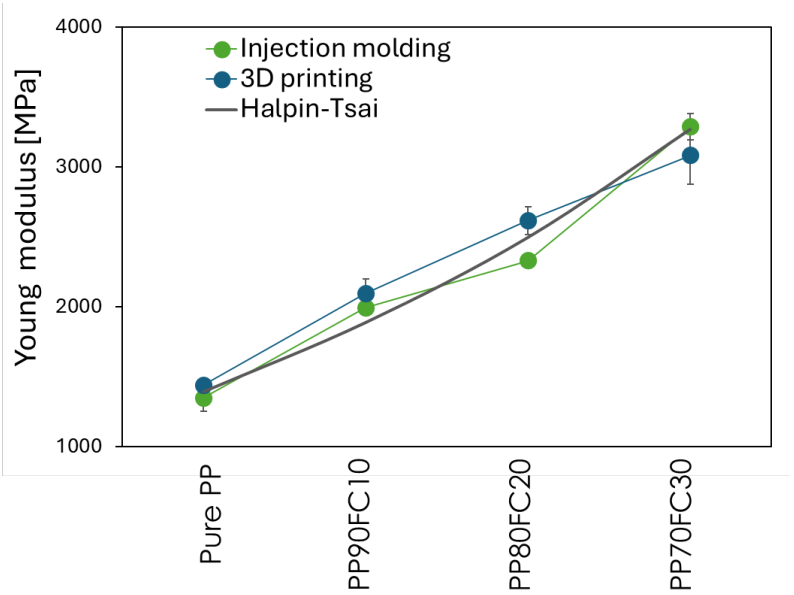

Figure 6: Comparison of Young's modulus values obtained with the Halpin-Tsai model, injection molded and 3D printed samples, respectively.

Using average fiber dimensions obtained from particle size and densities measured through helium pycnometry, theoretical moduli were calculated and found to be very similar to experimental results. This alignment strengthens the validity of the physical evidence and suggests that the behavior of the composite adheres to established mechanical models.

4. CONCLUSION

Experimental results demonstrate the technical feasibility of developing olefin-based composites reinforced with pyrolyzed rCF, highlighting the dual benefits of improving mechanical performance and promoting environmental sustainability through the circular use of high value engineering materials. The incorporation of PP-g-MA as a compatibilizer significantly reduces the compatibility problems typically encountered with PP and carbon fibers, thus expanding the potential application of these composites.

Injection molding remains the method of choice in terms of scalability and mechanical performance, but 3D printing via FGF shows promising results, particularly for prototyping and customized applications. Further research could focus on refining the 3D printing parameters to minimize anisotropy, which is in any case reduced with the use of the compatibilizer.

Ultimately, this work contributes to increasing knowledge aimed at closing the loop on composite materials, aligning with the broader goals of resource efficiency and sustainable engineering, with a view to processing scalability and production at industrial levels.

REFERENCES

[1] U. K. Vaidya, K. K. Chawla, Processing of fibre reinforced thermoplastic composites, *International Materials Reviews,* **53**, 2008, pp. 185–218 (doi.org/10.1179/174328008X325223).

[2] F. Meng, Y. Cui, S. Pickering, J. McKechnie, From aviation to aviation: Environmental and financial viability of closed-loop recycling of carbon fibre composite, *Composites Part B: Engineering*, **200**, 2020, pp. 1-8 (doi.org/10.1016/j.compositesb.2020.108362).

[3] H. Junaedi, E. Albahkali, M. Baig, A. Dawood, A. Almajid, Ductile to Brittle Transition of Short Carbon Fiber-Reinforced Polypropylene Composites, *Advances in Polymer Technology*, 2020, pp. 1-10 (doi.org/10.1155/2020/6714097).

[4] B. Almeshari, H. Junaedi, M. Baig, A. Almajid, Development of 3D printing short carbon fiber reinforced polypropylene composite filaments. *Journal of Materials Research and Technology*, **24**, 2023, 16–26 (doi.org/10.1016/j.jmrt.2023.02.198).

[5] H. Cheng, M. Tang, J. Zhang, H. Wang, J. Zhou, Q. Wang, Z. Qian, Effects of rCF attributes and FDM-3D printing parameters on the mechanical properties of rCFRP, *Composites Part B: Engineering*, **270**, 2024, pp. 1-14 (doi.org/10.1016/j.compositesb.2023.111122).

[6] A. Ghanbari, S. Seyedin, S. A. Haddadi, Reinforcing potential of recycled carbon fibers in compatibilized polypropylene composites. *Journal of Polymer Research,* **28**, 2021, pp. 1-9 (doi.org/10.1007/s10965-021-02506-0).

[7] M. Baig, B. Almeshari, A. Aabid, H. Junaedi, A, Almajid, Heliyon, *Heliyon* 10, 2024, pp. 1-16 (doi.org/10.1016/j.heliyon.2024.e30510).

[8] T. Qiu, Z. Yang, L.H. Liang, Multiscale analysis of the mechanical properties and interface damage mechanisms of carbon fiber reinforced polypropylene composites, *Polymer Composites*, **46**, 2025, pp. 46:8307–8317 (DOI: 10.1002/pc.29494).

[9] J. Jang, S.J. Youn, S.Y. Kim, M. Park, Effect of polypropylene-grafted-maleic anhydride content on physical properties of carbon fiber reinforced polypropylene composites, *Functional Composite and Structures*, **2**, 2020, pp. 1-8 (doi.org/10.1088/2631-6331/abd374).

[10] Fu S-Y, Lauke B, Mai Y-W. *Science and engineering of short fibre-reinforced polymer composites*. Woodhead Publishing, 2019.

[11] L.E. Nielsen, and R.F. Landel, *Mechanical Properties of Polymers and Composites*, Marcel Dekker, 1994.

SUSTAINABLE BIODEGRADABLE COMPOSITES FOR A CIRCULAR ECONOMY

Debarshi Nath[1,2], Arturo Rodriguez-Uribe[1,2], Tao Wang [1,2], Manjusri Misra[1,2] and Amar K. Mohanty[1,2]*

[1]Bioproducts Discovery and Development Centre, Department of Plant Agriculture, University of Guelph, Crop Science Building, Guelph, Ontario N1G 2W1, Canada

[2]School of Engineering, Thornborough Building, University of Guelph, Guelph, N1G 2W1, Ontario, Canada

Authors Email: debarshi@uoguelph.ca, rarturo@uoguelph.ca, twang@uoguelph.ca, mmisra@uoguelph.ca, mohanty@uoguelph.ca, web page: https://www.uoguelph.ca

[*]***Presenting Author:*** *Amar K. Mohanty, Email: mohanty@uoguelph.ca*

Keywords: Cellulose, Kraft pulp, PHBV, Compatibilizer, Percentage grafting, Biodegradable, Packaging

ABSTRACT

Industries are working to reduce their dependence on petroleum-derived polymers, substituting them with biobased, sustainable, and sustainable alternatives in response to the climate crisis produced by gases. Agricultural waste generates huge amounts of lignocellulosic biomass, a sustainable resource for the development of various bioproducts. Bioplastics, which are made from renewable or recycled natural materials, can help make plastic use more sustainable by supporting a circular economy. Biocomposites, consisting of a bioplastic matrix and reinforcing fibers, have developed as unique materials with diverse applications serving as alternatives to conventional composite materials. Due to their biodegradability, bioplastics have attracted a lot of interest from a variety of industries, despite being a little expensive. Consequently, a number of methods have been put out to broaden their industrial uses. Some of them are blending with other polymers, using green additives, and adding inexpensive fillers to manage the production cost. A special kind of bio-based polymer made by microbes is called a bacterial polyester. For instance, PHAs are a natural polyester that may be produced enzymatically in vivo by microbes for intracellular storage. Poly(3-hydroxybutyrate-co-3-hydroxyvalerate) (PHBV) is an aliphatic polyester and is a highly desirable bioplastic due to its marine biodegradable and home-compostable nature. PHBV is widely used to make rigid packaging items. Therefore, to achieve that, biocomposites were developed by melt-blending PHBV with natural fiber are becoming very popular. Some additives like peroxides, maleic anhydride-grafted polymer, a compatibilizer, are added to the formulation to enhance the interaction between the polymer matrix and the filler. To maintain proper melt flow for injection molding applications and increase flexibility, plasticizers are added. Adding a high content of natural filler will also help in improving the biodegradability of the materials, thereby adhering to the circular economy principles.

1 INTRODUCTION

Polymers have a wide range of material characteristics, including hydrophilic or hydrophobic, flexible or stiff, and permeable or impermeable. The structure of the repeating monomers, which are the building blocks of polymers, controls these properties. After undergoing processing—usually involving heat—to take on a specific shape, polymeric materials are commonly known as plastics in their final, usable form.[1] These materials are extensively used and play a vital role in everyday life, particularly in industries related to transportation, food, healthcare, and energy. Plastics are now an essential component of human life due to their many desirable qualities, which have resulted in an increase in production volumes. Unfortunately, plastic trash has kept on accumulating and is posing a threat to our

ecosystem because production and use were initially planned for a linear economy (use and throw) and single-use, short-term applications. Utilizing plastics derived from petrochemicals has led to an increase in plastic trash, which is harmful to the environment and ends up in landfills, the ocean, and other habitats. By their very nature, discarded plastics remain unaltered for decades or even centuries, leading to the buildup of plastic garbage. If the plastic disintegrates, even then, fragmented micro- and nanoparticles are produced, which are harmful to the environment. Sadly, these particles have a detrimental effect on human health, especially when ingested, which exacerbates the threat of microplastics.[2,3]

Although plastics have improved our lives significantly and made society sustainable only during their use phase, new plastic materials need to be designed and developed following the circular (bio)economy (CE) principles.[4] In 1962, the European Union introduced the concept of which includes a variety of managerial, technological, economic, and quality assessment practices, with the assistance of numerous national governments, including those in China, Japan, the United Kingdom, France, Canada, the Netherlands, Scotland, Sweden, Germany, Finland, and other countries.[5] The CE definition has been interpreted in about as many different ways as there are circular economy practitioners and scholars, as explained by Kirchherr et al.[6] The requirement to use resources more effectively is arguably the only thing that all definitions have in common; however, it is still up for debate what exactly qualifies as "better."[7]

Nonetheless, it is evident that while waste mountains and related pollution are still accumulating, the world's natural resource depletion and related carbon emissions are increasing. For this reason, it makes sense that a circular economy would aim to minimize resource exploitation and maximize waste prevention.[7,8] A circular economy is being implemented by governments worldwide, including the EU, China, Tokyo, New York, and London, as well as through transnational initiatives.[9] A third of CEOs worldwide stated in 2013 that they were actively interested in the circular economy due to their own values, commercial objectives, and sustainability considerations.[7] The "CE100" program from the Ellen MacArthur Foundation provides businesses with a supportive atmosphere for learning and implementing circular practices.[7] Global leaders actively implementing a practice-based circular economy approach include companies such as Coca-Cola, Apple, and Rolls-Royce.[9]

The circular economy (CE) model, when applied to polymers, emphasizes maximizing the utility and lifespan of polymeric materials by reducing waste generation, having better end-of-life options, and promoting the reuse, recycling, and regeneration of plastic products. This approach transforms the traditional linear lifecycle of polymers (from production—use—disposal) into a closed-loop system, where materials are cycled back into their original state, supporting both environmental sustainability and economic efficiency. However, the concept of sustainability points out that every element of social and economic institutions should actively advance environmental preservation and economic growth simultaneously.[10]

Canada, along with multiple countries, is creating new laws and regulations to transition towards a plastic-free economy..[11] Single-use packaging is a significant source of pollution, making up around 46% of global plastic waste; fixing this issue will significantly lower the amount of plastic garbage produced. [12] Thus, it is clear that there is widespread interest in discovering practical equivalent packaging options that are also sustainable. While recycling plays a role in managing plastic waste, it contributes to just about 6% of the total plastic recovered, as a result, a significant portion of plastic continues to accumulate in landfills.[13] As such, using biobased and biodegradable polymers in conjunction with recycled polymers can be seen as an effective strategy to help reduce our reliance on petro-based plastics and minimize CO_2 emissions.[14]

Bioplastics are a class of materials that can be made from renewable sources. Therefore, materials made by biological processes, biobased materials, biodegradable materials, or a mix of these are often referred to as bioplastics. In this case, the building blocks (monomers) are obtained or synthesized from biomass, like plant-derived sugars, and then polymerized to create plastics that have properties similar to traditional ones or introduce new functionalities. Globally, around 2.5 million tonnes of bioplastics are produced annually. They are looked upon as essential to building a circular economy and addressing key United Nations Sustainable Development Goals. This includes reducing dependence on fossil fuels, creating new recycling or degradation pathways, and lowering the use of harmful chemicals during production. Moreover, bioplastics also offer benefits such as reduced carbon emissions, potential

biodegradability at end-of-life, and equivalent performance in certain applications compared to petro-derived chemicals.[1]

Polyhydroxyalkanoates (PHAs), a type of bacterial polyester, are amongst the most commonly used bio-based polymers, which are completely biodegradable in soil and marine settings and may be produced by a wide range of microorganisms under growth-limited circumstances. Because of their biodegradability, they are a viable alternative to popular petroleum-based polymers, including polypropylene (PP) and polyethylene (PE). They are particularly used in many single-use applications, like rigid packaging and flatware.[15] However, the production of PHAs is very expensive, which can be a limiting factor for their widespread use. PHAs are currently made by fermenting sugars and fatty acids that are obtained from food crops such as vegetable oil, corn starch, and sugarcane. Over half of the production costs are related to the cost of the feedstock alone.[15] This can be addressed by using lignocellulosic biomass, which is abundant and inexpensive or free, as a source of carbon for the manufacture of PHA. According to reports, approximately 300 bacterial species (both Gram-positive and Gram-negative strains) may produce PHAs in extreme circumstances and both aerobic and anaerobic settings.[16]

PHBV, or poly(hydroxybutyrate-co-hydroxy valerate), a commonly used PHA, is drawing a lot of interest in the production of sustainable materials.[17] PHBV is a copolymer of 3-hydroxybutyrate and 3-hydroxyvalerate and can be synthesized effectively using *H. bluephagenesis*. [18] PHBV shows biodegradation in marine, home, and industrial environments.[19] To counter the expensive nature of PHBV, it is frequently mixed with low-cost filler materials to develop biocomposites. These fillers can further enhance biodegradability while improving polymer performance.[14]

Therefore, biocomposites are composite materials developed by mixing biodegradable polymer matrix and a natural filler or fiber. Biocomposites made from bioplastic and plant-derived fiber (natural/biofibre), are thought to be more environmentally friendly. These composites are known as "green composites." The primary benefits of biocomposites are their sustainability, complete degradation, and environmental friendliness; in other words, they are genuinely "green" in every way. They can be composted or disposed of easily at the end of their life cycle without harming the environment. Biocomposites have been effective as materials in numerous applications, including mass-produced consumer goods with limited lifespans, single-use goods, or brief use before being discarded sustainably. Green composites have a several-year functional life and can even be utilized indoors. [20,21] Biofiber can have a reinforcing effect on the biocomposite matrix; however, it depends on many factors. The overall properties of fibres are largely influenced by factors such as their chemical composition, structural defects, cell dimensions, microfibrillar angle, and internal structure.[21] Some of the most important biofibers used for biocomposite fabrication are Abaca, Bagasse, Bamboo, Banana, Broom root, Cantala, Caroa, China jute, Coir, Cotton, Curaua, Date palm, Flax, Hemp, etc. [20]

As a result, research on PHBV-based biocomposites has also been conducted during the past decades using different fillers and fibers and evaluating the fiber performance on material properties. In some of the studies, Singh et al.[22] developed PHBV/natural bamboo fiber-based biocomposites, while Vandi et al.[23] developed PHBV/wood fiber-based biocomposites and measured the effect of processing conditions on the mechanical performance; Berthet et al.[24] made biocomposites from PHBV/wheat straw fibres for rigid applications. In another study by Nath et al. [14] the authors developed PHBV biocomposites by adding cellulose fibers (20 and 25%) and then added a compatibilizer [MA-grafted PHBV (MA-g-PHBV)] to see the impact of compatibilization on the biocomposite. To enhance the melt flow during processing, a plasticized TBC was added, which enhanced the melt flow suitable for injection molding, along with improving the impact strength and flexibility. The MA-g-PHBV compatibilizer was incorporated for enhancing the matrix-fiber adhesion, resulting in enhanced properties. During melt blending, a compatibilizer can be introduced to the composite to improve the matrix–fiber interaction. The most popular method for creating natural fiber/filler composites is the use of functional polymers grafted with maleic anhydride (MA). By reacting with free hydroxyl groups on the surface of the CF, it forms covalent linkages within the composite, enhancing interfacial bonding.[25] This proceeding paper later briefly explains a few works on PHA-based biocomposites to develop a consistent and robust composite for different application.

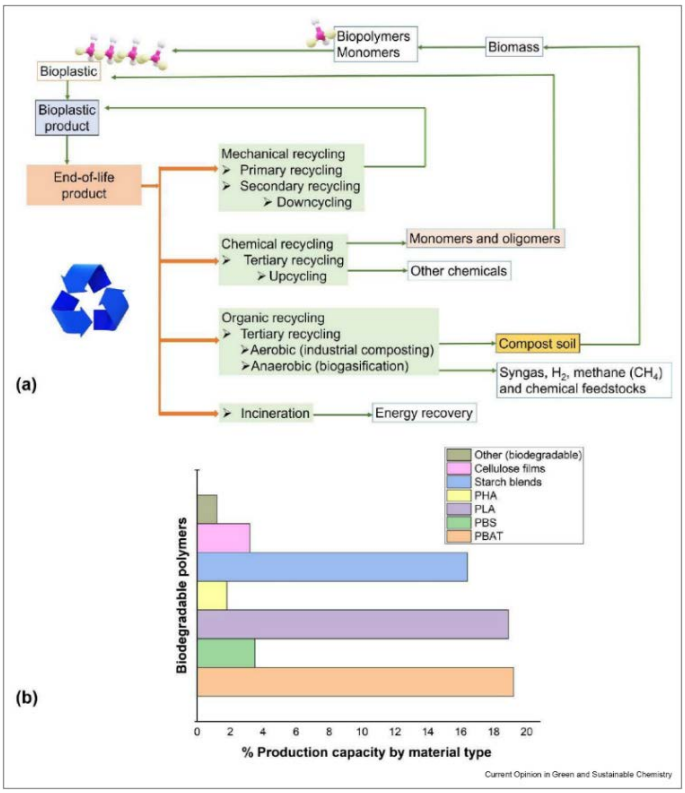

Figure 1: (a) Potential recycling pathways for biodegradable plastics (b) Based on global production capacities reported for the year 2021. Adopted from Kalita et al. [4] Copyright 2023 Elsevier, Open Access (CC BY 4.0)

2 Development of Biocomposites

For biocomposite formulations to be successfully adopted in industry, they must be compatible with standard production equipment typically employed in the plastics sector. This allows for easy transition from laboratory to industry, cost effectiveness, and scalability. As a result, biocomposites should be processable using typical procedures such as injection moulding, compression moulding, melt extrusion, thermoforming, blown film extrusion, and blow moulding. These processes are commonly used to manufacture many commercial everyday plastic products, and allowing the novel biocomposites to be created using these techniques would significantly increase the possibility for integration into mainstream applications such as packaging, automotive, consumer goods, and others.

2.1 Melt Extrusion

In the plastics processing industry, extrusion is a continuous production method that is mostly widely used to create products having a predetermined cross-sectional profile. In the process, a substance is forced out, much how toothpaste is squeezed out of a tube. The method of plastic extrusion involves forcing melted polymer(s), frequently in the form of strands, through a die. During the extrusion process via the die, the melt assumes the shape of the die opening. [26]

The polymer in the hopper is transferred into the heated barrel via the feed throat and a rotating screw. The polymer is melted by the screw's shear and barrel heating before being forced past the filter screen, into the die, and ultimately out. The extrusion techniques' main mechanics are solid conveying, homogeneous melting or plasticating, and melt pumping. The screw controls feeding, compression, and metering, making it the most significant factor in determining an extruder's effectiveness. Twin-screw extrusion is one of the most widely used processing methods in both research and industrial settings for producing polymer blends and biocomposites. In this process, biopolymers are exposed to a combination of high shear forces and elevated temperatures generated by the rotating screws and external heaters. This not only melts the polymer but also ensures uniform dispersion of fillers within the molten matrix.

2.2 Injection Molding

Injection moulding is a popular and adaptable process for creating polymer mixtures and composites. Plastic materials are heated till they become molten and viscous. This molten polymer is then poured into a closed mould, which specifies the desired shape of the finished product. Once within the mould, the material is allowed to cool and harden before opening, and the developed piece is taken out. This technology enables the accurate and economical manufacturing of complicated forms with high detail. Injection moulding is particularly useful in large-scale production due to its cost-effectiveness, consistency, and capacity to make high-quality products on a large scale. Its accuracy and reproducibility make it a popular choice for creating complicated patterns and components in a variety of industries. [27–29]

2.3 Blown Film Extrusion

Blown film extrusion is increasingly being adapted to produce films from biodegradable polymers, moving away from traditional plastics. This technology is widely used in the packaging sector to produce thin films that are generally no more than 100 microns thick. The polymer is first melted using a single-screw extruder, and then air is fed through the centre of a circular die to inflate it into a tubular film bubble. As the bubble rises, it cools and flattens into a two-layer film with nip rollers before being coiled into rolls. Blown film extrusion is a highly flexible process that may produce anything from basic monolayer bags to complicated multilayer films like those used in food packaging. Coextrusion is used to make multilayer films, which are formed by combining two or more molten polymer streams. Advanced commercial systems may coextrude up to seven to eleven layers, giving us great control regarding film functionality and performance.[30,31]

3 End-of-Life (EoL) options for Biocomposites

To transition to completely circular materials, it's important to design materials with effective EoL management. Figure 1 shows some EoL pathways for bioplastics. Biodegradable polymers disintegrate under specified circumstances near the end of their life cycle. Compostable polymers, a category of biodegradable plastics, degrade in industrial composting facilities. Biodegradable and compostable polymers can be made from either fossil fuels or biological resources. Biocomposites are typically designed with EoL biodegradation in mind under various conditions, rather than with a focus on recyclability.

The process of biodegradation is the transformation of organic components into residual biomass and biogas by microorganisms (bacteria and fungi) that use plastic as a carbon source. Biodegradation can take place inside the biosphere because microorganisms play a critical part in the process.

More than 90 microorganisms—aerobes, anaerobes, photosynthetic bacteria, and archaebacteria are responsible for degrading and catabolizing bioplastics. These bacteria are abundant in soil and compost.[32] There are five primary stages in the microbial breakdown of plastic wastes: colonisation, biodeterioration, biofragmentation, absorption, and mineralization. [33]

There are different environments for biodegradation apart from soil and compost like marine, landfill, and sewage sludge, where each environment has its specific conditions for degradation. Different organizations such as ASTM, and ISO have established specific standards to assess the biodegradability of bioplastics under different environmental conditions.

Standards for biodegradation testing

Aerobic biodegradation

- Marine biodegradation: ASTM D6691-17, ASTM D7473-12, ASTM D7991-15, ISO 18830-16
- Soil biodegradation: ASTM D5988-18, ISO 17556, ASTM D5526-18, and ISO 14855
- Compost biodegradation: ASTM D5338, ISO 14855, ISO 117088, EN 13432, ASTM D5929, ASTM D6400, AS 5810, and AS 4736

Anaerobic biodegradation

- Sewage sludge biodegradation: ASTM D5210-92 and ISO 14853

- Landfill biodegradation: ASTM D5526-18 and ASTM D7475-11

Biodegradable polymers are exposed to a mixture of decomposed components at elevated temperatures during the composting process. Industrial composting is carried out at 60 °C, and with a high relative humidity in presence of oxygen. Home composting operates under milder conditions compared to industrial composting, primarily due to the smaller volume of biodegradable materials at temperature around 28 °C. [34]
Degradation under marine conditions is distinguished by low temperature, high salinity, high pressure, low nutrient levels, and currents compared to soil and compost.[35] Seawater is an intricate mixture rich in inorganic ions. The salinity of seawater is affected by factors such as evaporation, precipitation, river discharge, and seawater currents. The offshore and estuary waters are typically below 30% salinity, while the ocean's surface salinity varies between 32% to 37%. With pH values spanning between 8.0-8.5, seawater is weakly alkaline.[35] It has been found that small pH changes (< 1) can modify the composition of the bacterial population. Moreover, the concentration of dissolved oxygen in seawater is substantially lower than in soil, and both are influenced by temperature and linked to biological activities, such as the amount and variety of marine organisms.[19]

4 RESEARCH ON PHBV BASED BIOCOMPOSITES

PHBV based biocomposites are becoming increasingly popular as they are biodegadable under soil, marine, home, and industrial settings. Also, by making the PHBV biocomposites high filler, the high processing cost of the PHBV polymer can be counteracted and the biodegradation rate can also be increased.

With this idea in mind, Nath et al. [14] developed a PHBV, and cellulose fiber (CF) based biocomposites having different concentrations of CF (10, 20, and 25%). With high concentrations of filler, the melt flow becomes very less, which reduces its processability. As a result, a plasticizer, tributyl citrate (TBC) was added to make the melt flow suitable for injection molding. Also, since there is an incompatibility between fiber and matrix, a compatibilizer MA-g-PHBV, was added at different concentrations. Additionally, three different types of MA-g-PHBV, with variation in grafting percentage, were tested on the biocomposites to evaluate the effectiveness of grafting percentage on biocomposite performance. Different characterizations, like mechanical properties, thermal, and morphological analysis, were conducted to evaluate the samples. TBC addition to PHBV decreased tensile, flexural strength, and modulus due to weakened intermolecular bonding, whereas CF addition increased modulus. Incorporating MA-g-PHBV improved all mechanical characteristics, particularly at 7% loading, due to improved filler-matrix adhesion. The addition of TBC led to an improvement in both the elongation at break (EAB) and the impact resistance of PHBV. The EAB improved monotonously with higher compatibilizer content. However, the impact strength increased after CF addition, as incorporation of long fibers sometimes led to improvement in impact strength, but no change was observed after MA-g-PHBV addition. Scanning electron microscopy and atomic force microscopy also showed improved interfacial adhesion with fewer gaps, voids, and pull-out fibers after the addition of compatibilizers. The observation demonstrates that MA-g-PHBV incorporation results in enhanced matrix/fiber interaction. The thermal stability analysis showed that adding TBC and cellulose fibers lowered the onset degradation temperature (T_{onset}), indicating reduced thermal stability, but the maximum degradation temperature (T_{max}) remained mostly unaffected. Overall, the thermal stability exhibited by the biocomposites was sufficient to allow melt processing at 170 °C with no adverse effect. Additionally, it was reported that the addition of MA-g-PHBV, having the highest grafting percentage, proved to be the most promising compatibilizer showing the highest improvement. This can be attributed to the presence of more MA groups, which facilitate more bonding sites for the OH present in the CF. Figure 2 shows the atomic force microscopy images of compatibilized and uncompatibilized samples showing reduced gap at the matrix and less fiber pullouts.

In another study by Ahankari et al.[36], agro-residues such as maize straw (CS), soy stalk (SS), and wheat straw (WS) were effectively incorporated into PHBV, using the melt mixing process to create novel green composites. The effective use of agro-residues as a great substitute for wood and synthetic fibres was the main emphasis of this study. This is because they are not only renewable, biodegradable, and advantageous for the environment and technology, but they are also affordable, widely available,

and easily accessible. The authors examined the impact of these biomass fibres on PHBV's performance. Reinforcing PHBV with 30% agricultural byproducts increased its tensile and storage modulus by up to 255% and 305%, respectively. Additionally, the tensile and flexural moduli of PHBV composites were much greater than those of equivalent PP composites for identical quantities of (30%) biomass fibres. Wheat straw fibers treated with alkali showed approximately a 35% improvement in both elongation at break and impact strength in PHBV composites, while having minimal effect on tensile strength and modulus when compared to untreated fibers. DMA research showed that the PHBV-biomass interaction was better than PP. However, tensile and flexural strength decreased with 40% biomass fibres addition because of a greater probability of agglomeration development in the polymer matrix. The addition of stiff lignocellulosic fibres to PHBV and PP composites also decreased their notch impact strength.

Mazur et al.[37] in their study used injection molding to develop biodegradable composites made of PHBV reinforced with either 7.5% or 15% of wood fibres (WF) or basalt fibres (BF). While WF composites had a decrease in strength and impact characteristics, but exhibited an increase in Young's modulus values, BF reinforced composites showed improvements in all these attributes. Composites containing 15% of BF demonstrated a 74% improvement in Young's modulus and a 41% increase in impact strength when compared to the unmodified polymer. Scanning electron microscopy was used to analyze the morphological structure of the biocomposites in order to determine the fibres' distribution and interfacial adhesion. Furthermore, biodegradation experiments of the biocomposites were conducted in saline solution to investigate weight loss and mechanical characteristics. It was discovered that the presence of fibres influences the rate of water absorption, with the maximum rate recorded in composites containing 15% of WF. After the first and second weeks, mechanical characteristics fell by around 10%. These findings demonstrate that biodegradable PHBV-based composites, including natural fillers, may be utilised to create long-lasting products. Table 1 provides a summary of some of the work conducted on PHBV-based biocomposites. In another study by Nagarajan et al.[38], injection-molded biocomposites were developed using switchgrass as filler in a PHBV and PBAT (poly(butylene adipate-co-terephthalate) blend (45%PHBV55%PBAT). The effect of incorporating switchgrass fibre at loading levels ranging from 20-40 wt% was examined. Due to poor fiber matrix adhesion, a compatibilizer poly diphenylmethane diisocyanate (pMDI) was added at different concentrations. It was found that the compatibilizer was effective in improving the mechanical properties of the biocomposites. Scanning electron microscopy (SEM) was used to analyse fracture surface morphology, which revealed increased fiber-matrix adhesion in compatibilized biocomposites. FTIR data revealed an interaction between the PHBV/PBAT combination and switchgrass fibres with the addition of pMDI.

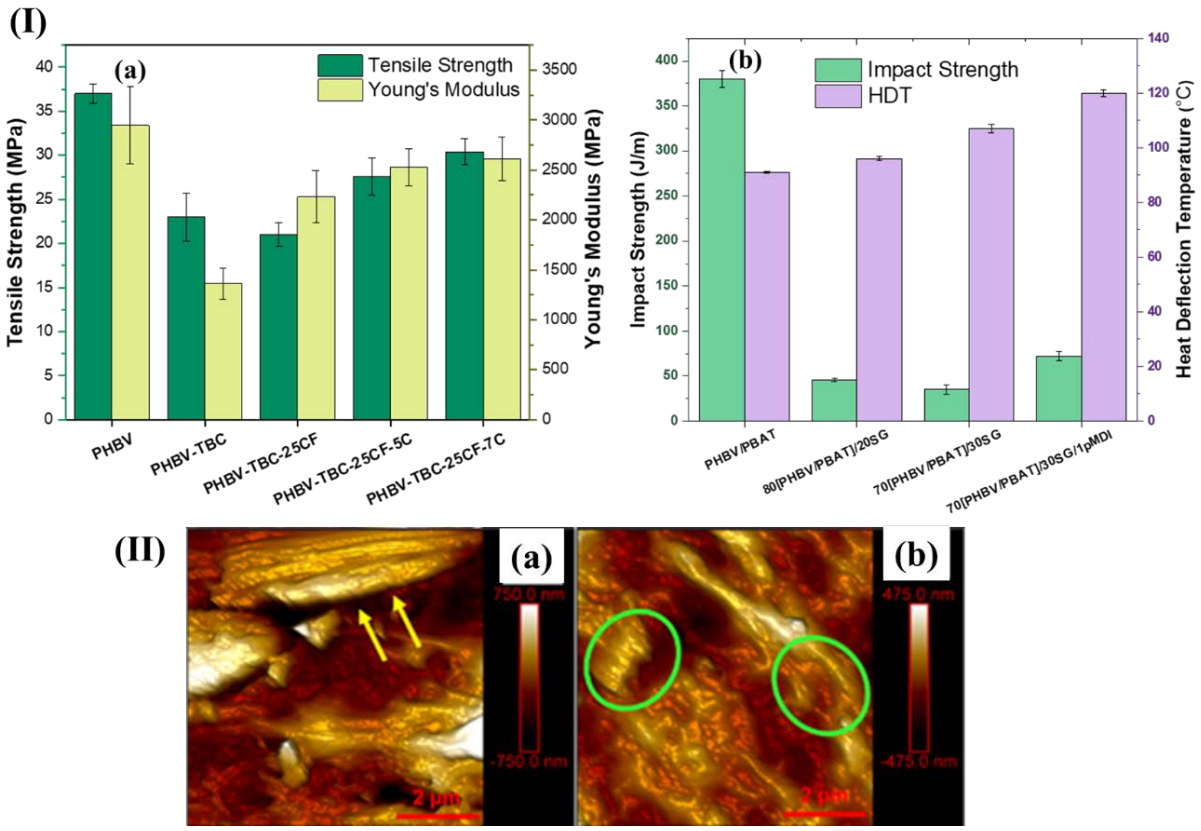

Figure 2: (I) (a) Mechanical Properties of PHBV/cellulose fiber (CF) composites with and without compatibilizer (MA-g-PHBV; referred to as "C" in the figure) [14] and (b) Impact strength and heat deflection temperature (HDT) of PHBV toughened with PBAT (45%PHBV55%PBAT), using switchgrass (SG) as a filler and poly(diphenylmethane diisocyanate) (pMDI) as a compatibilizer [38] (figure prepared by the authors); (II) Atomic force microscopy image of PHBV and cellulose fiber composite to show improved fiber-matrix adhesion after compatibilizer addition (a) PHBV-TBC-25CF (b) PHBV-TBC-25CF-7C [14] [CF stands for cellulose fiber and C stands for compatibilizer (MA-g-PHBV)](image taken by authors)

Table 1: Summary of studies conducted on PHBV-based composites.

Polymer used	Filler or Fibers used	Additives	Results observed	Reference
PHBV	Bamboo Pulp Fiber	Boron Nitride and MA grafted PHBV	• Fibers increased crystallinity, strength, modulus, and impact resistance of PHBV composites, with slight elongation improvement at low loadings. • MA-PHBV enhanced strength and stiffness through better fiber-matrix bonding but reduced toughness due to restricted fiber pullout.	[39]
PHBV	Bamboo Fiber	Silane and rare-earth coupling agents	• High-modulus fibers significantly improved tensile and flexural properties and thermal stability compared to low-modulus fibers. • Surface modification with silane and rare-earth coupling agents enhanced fiber-matrix adhesion and further boosted mechanical performance.	[40]

PHBV	Cellulose nanocrystals and aluminum oxide nanoparticles	• Adding up to 3 wt% CNC improved tensile strength, thermal stability, and crystallinity, though higher loadings caused nanoparticle agglomeration and reduced performance. • SEM showed nanoparticle clustering at higher concentrations, while DSC confirmed increased glass transition temperature and enthalpy of fusion with CNC. • CNC proved more effective than Al_2O_3 in enhancing PHBV's mechanical and thermal properties.	[41]
PHBV	Human hair waste (HHW), sawdust (SD) and chitin	• PHBV was compounded with HHW, SD, and chitin to reduce cost and valorize waste. • Tensile tests showed SD slightly improved strength, while HHW and chitin had no reinforcing effect. • Soil burial tests revealed enhanced biodegradation with fillers, with HHW composites showing the highest weight loss (~35%).	[42]

5 CONCLUSION

Simply using renewable resources does not ensure sustainability. With advances in technology, bioplastics have the potential to help in the transition of many plastic-heavy sectors to a circular economy. Presently, bio-based replacements are now available for most fossil-based plastic applications. However, these alternatives are often produced in small numbers, at a higher cost, and do not always provide clear environmental benefits. In addition to typical first-generation biomass sources, agricultural waste and lignocellulosic biowastes are more readily available, sustainable, and inexpensive. To make these alternatives really practical, biorefinery technologies must become more efficient and comply with green chemistry principles, such as avoiding toxic chemicals and reducing energy consumption, in order to generate the essential monomer in a sustainable manner. While efforts to achieve environmental sustainability are increasing, financial sustainability remains a difficulty. The affordability of fossil fuels, which is driven by low oil prices, tight business margins, and government support, makes it difficult for bio-based producers to compete economically. Advanced research is paving the way for lower production cost of biodegradable plastic resins. Moreover, adding low-cost natural fillers and fibers to the matrix for making biocomposites can help tremendously in reducing the price of the overall product. And these materials should be biodegradable more effectively in natural conditions.

ACKNOWLEDGEMENTS

The Ontario Agri-Food Innovation Alliance—Bioeconomy for Industrial Uses Research Program (Project Nos. 030671 and 030699); the Ontario Ministry of Agriculture, Food and Agribusiness (OMAFA)-University of Guelph Gryphon's Leading to the Accelerated Adoption of Innovative Research (LAAIR) Program (Project No. 030736); The Ontario Agri-Food Research Initiative (OAFRI) OAF-2023-102605 (Project No. 056442); The Ontario Ministry of Colleges and Universities (MCU), Ontario, Canada Research Fund –Research Excellency ORF-RE11 (Project No. 056106); iii) the Natural Sciences and Engineering Research Council of Canada (NSERC), the Canada Research Chairs (CRC) program Project No. 460788.

REFERENCES

[1] Rosenboom JG, Langer R, Traverso G. Bioplastics for a circular economy. Nature Reviews Materials 2022 7:2 2022;7:117–37. https://doi.org/10.1038/s41578-021-00407-8.

[2] Rahman MH, Bhoi PR. An overview of non-biodegradable bioplastics. J Clean Prod 2021;294:126218. https://doi.org/10.1016/J.JCLEPRO.2021.126218.

[3] Thacharodi A, Hassan S, Meenatchi R, Bhat MA, Hussain N, Arockiaraj J, et al. Mitigating microplastic pollution: A critical review on the effects, remediation, and utilization strategies of microplastics. J Environ Manage 2024;351:119988. https://doi.org/10.1016/J.JENVMAN.2023.119988.

[4] Kalita NK, Hakkarainen M. Integrating biodegradable polyesters in a circular economy. Curr Opin Green Sustain Chem 2023;40:100751. https://doi.org/10.1016/J.COGSC.2022.100751.

[5] Azka MA, Adam A, Ridzuan SM, Sapuan SM, Habib A. A review on the enhancement of circular economy aspects focusing on nanocellulose composites. Int J Biol Macromol 2024;269:132052. https://doi.org/10.1016/J.IJBIOMAC.2024.132052.

[6] Kirchherr J, Reike D, Hekkert M. Conceptualizing the circular economy: An analysis of 114 definitions. Resour Conserv Recycl 2017;127:221–32. https://doi.org/10.1016/J.RESCONREC.2017.09.005.

[7] Velenturf APM, Purnell P. Principles for a sustainable circular economy. Sustain Prod Consum 2021;27:1437–57. https://doi.org/10.1016/J.SPC.2021.02.018.

[8] Velenturf APM, Purnell P. Resource Recovery from Waste: Restoring the Balance between Resource Scarcity and Waste Overload. Sustainability 2017, Vol 9, Page 1603 2017;9:1603. https://doi.org/10.3390/SU9091603.

[9] Purnell P, Velenturf APM, Marshall R. New Governance for Circular Economy: Policy, Regulation and Market Contexts for Resource Recovery from Waste. RSC Green Chemistry 2019;2020-January:395–422. https://doi.org/10.1039/9781788016353-00395.

[10] Circular economy: Getting the circulation going. Nature 2016 531:7595 2016;531:443–6. https://doi.org/10.1038/531443a.

[11] McNeill DC, Pal AK, Mohanty AK, Misra M. High biomass filled biodegradable plastic in engineering sustainable composites. Composites Part C: Open Access 2023;12:100388. https://doi.org/10.1016/J.JCOMC.2023.100388.

[12] Itabana BE, Pal AK, Mohanty AK, Misra M. Biodegradable blown film composite from poly (butylene adipate-co-terephthalate) and talc: Effect of uniaxial stretching on mechanical and barrier properties. Food Packag Shelf Life 2023;39:101147. https://doi.org/10.1016/J.FPSL.2023.101147.

[13] Merrington A. Recycling of Plastics. Applied Plastics Engineering Handbook 2024:191–217. https://doi.org/10.1016/B978-0-323-88667-3.00006-0.

[14] Nath D, Rodriguez-Uribe A, Wang T, Misra M, Mohanty AK. Green composites from plasticized poly(3-hydroxybutyrate-co-3-hydroxyvalerate) bioplastic and cellulosic fiber: Effect of compatibilizer and grafting percentage on interfacial adhesion and biocomposite performance. Int J Biol Macromol 2025;315:144107. https://doi.org/10.1016/J.IJBIOMAC.2025.144107.

[15] Zytner P, Kumar D, Elsayed A, Mohanty A, Ramarao B V., Misra M. A review on polyhydroxyalkanoate (PHA) production through the use of lignocellulosic biomass. RSC Sustainability 2023;1:2120–34. https://doi.org/10.1039/D3SU00126A.

[16] Findlay RH, White DC. Polymeric beta-hydroxyalkanoates from environmental samples and Bacillus megaterium. Appl Environ Microbiol 1983;45:71–8. https://doi.org/10.1128/AEM.45.1.71-78.1983

[17] Bhardwaj R, Mohanty AK, Drzal LT, Pourboghrat F, Misra M. Renewable resource-based green composites from recycled cellulose fiber and poly(3-hydroxybutyrate-co-3-hydroxyvalerate) bioplastic. Biomacromolecules 2006;7:2044–51. https://doi.org/10.1021/BM050897Y.

[18] Liu Y, Song X, Yang W, Wang M, Lian G, Li ZJ. Production of polyhydroxyalkanoates by engineered Halomonas bluephagenesis using starch as a carbon source. Int J Biol Macromol 2024;261:129838. https://doi.org/10.1016/J.IJBIOMAC.2024.129838.
[19] Meereboer KW, Misra M, Mohanty AK. Review of recent advances in the biodegradability of polyhydroxyalkanoate (PHA) bioplastics and their composites. Green Chemistry 2020;22:5519–58. https://doi.org/10.1039/D0GC01647K.
[20] John MJ, Thomas S. Biofibres and biocomposites. Carbohydr Polym 2008;71:343–64. https://doi.org/10.1016/J.CARBPOL.2007.05.040.
[21] Satyanarayana KG, Ravikumar KK, Sukumaran K, Mukherjee PS, Pillai SGK, Kulkarni AG. Structure and properties of some vegetable fibres - Part 3 Talipot and palmyrah fibres. J Mater Sci 1986;21:57–63. https://doi.org/10.1007/BF01144699.
[22] Singh S, Mohanty AK, Sugie T, Takai Y, Hamada H. Renewable resource based biocomposites from natural fiber and polyhydroxybutyrate-co-valerate (PHBV) bioplastic. Compos Part A Appl Sci Manuf 2008;39:875–86. https://doi.org/10.1016/J.COMPOSITESA.2008.01.004.
[23] Vandi LJ, Chan CM, Werker A, Richardson D, Laycock B, Pratt S. Extrusion of wood fibre reinforced poly(hydroxybutyrate-co-hydroxyvalerate) (PHBV) biocomposites: Statistical analysis of the effect of processing conditions on mechanical performance. Polym Degrad Stab 2019;159:1–14. https://doi.org/10.1016/J.POLYMDEGRADSTAB.2018.10.015.
[24] Berthet MA, Gontard N, Angellier-Coussy H. Impact of fibre moisture content on the structure/mechanical properties relationships of PHBV/wheat straw fibres biocomposites. Compos Sci Technol 2015;117:386–91. https://doi.org/10.1016/J.COMPSCITECH.2015.07.015.
[25] Muthuraj R, Misra M, Mohanty AK. Injection Molded Sustainable Biocomposites from Poly(butylene succinate) Bioplastic and Perennial Grass. ACS Sustain Chem Eng 2015;3:2767–76. https://doi.org/10.1021/ACSSUSCHEMENG.5B00646.
[26] Shrivastava A. Plastics Processing. Applied Plastics Engineering Handbook: Processing and Materials 2018:143–77. https://doi.org/10.1016/B978-0-323-39500-7.00005-8.
[27] Ebnesajjad S. Injection Molding. Melt Processible Fluoroplastics 2003:151–93. https://doi.org/10.1016/B978-188420796-9.50010-2.
[28] Injection molding screw design & operations detailed guide n.d. https://askmeplastics.com/injection-molding-screw-design-and-operations/ (accessed July 30, 2023).
[29] Injection Molding Screw Design | R. DRAY MFG. n.d. https://www.rdray.com/injection-molding-screw-design (accessed July 30, 2023).
[30] Wagner JR. Blown Film, Cast Film, and Lamination Processes. Multilayer Flexible Packaging: Second Edition 2016:137–45. https://doi.org/10.1016/B978-0-323-37100-1.00010-7.
[31] Drobny JG. Processing Methods Applicable to Thermoplastic Elastomers. Handbook of Thermoplastic Elastomers 2014:33–173. https://doi.org/10.1016/B978-0-323-22136-8.00004-1.
[32] Emadian SM, Onay TT, Demirel B. Biodegradation of bioplastics in natural environments. Waste Management 2017;59:526–36. https://doi.org/10.1016/J.WASMAN.2016.10.006.
[33] Ali SS, Elsamahy T, Koutra E, Kornaros M, El-Sheekh M, Abdelkarim EA, et al. Degradation of conventional plastic wastes in the environment: A review on current status of knowledge and future perspectives of disposal. Science of The Total Environment 2021;771:144719. https://doi.org/10.1016/j.scitotenv.2020.144719.
[34] Nath D, Misra M, Al-Daoud F, Mohanty AK. Studies on poly(butylene succinate) and poly(butylene succinate- co -adipate)-based biodegradable plastics for sustainable flexible packaging and agricultural applications: a comprehensive review. RSC Sustainability 2025;3:1267–302. https://doi.org/10.1039/D4SU00193A.
[35] Wang G-X, Huang D, Ji J-H, Völker C, Wurm FR, Wang G-X, et al. Seawater-Degradable Polymers—Fighting the Marine Plastic Pollution. Advanced Science 2021;8:2001121. https://doi.org/10.1002/ADVS.202001121.
[36] Ahankari SS, Mohanty AK, Misra M. Mechanical behaviour of agro-residue reinforced poly(3-hydroxybutyrate-co-3-hydroxyvalerate), (PHBV) green composites: A comparison with

traditional polypropylene composites. Compos Sci Technol 2011;71:653–7. https://doi.org/10.1016/J.COMPSCITECH.2011.01.007.

[37] Mazur K, Kuciel S, Russo P, Sarasini F. Mechanical and Hydrothermal Aging Behaviour of Polyhydroxybutyrate-Co-Valerate (PHBV) Composites Reinforced by Natural Fibres. Molecules 2019, Vol 24, Page 3538 2019;24:3538. https://doi.org/10.3390/MOLECULES24193538.

[38] Nagarajan V, Misra M, Mohanty AK. New engineered biocomposites from poly(3-hydroxybutyrate-co-3-hydroxyvalerate) (PHBV)/poly(butylene adipate-co-terephthalate) (PBAT) blends and switchgrass: Fabrication and performance evaluation. Ind Crops Prod 2013;42:461–8. https://doi.org/10.1016/J.INDCROP.2012.05.042.

[39] Jiang L, Huang J, Qian J, Chen F, Zhang J, Wolcott MP, et al. Study of poly(3-hydroxybutyrate-co-3-hydroxyvalerate) (PHBV)/bamboo pulp fiber composites: Effects of nucleation agent and compatibilizer. J Polym Environ 2008;16:83–93. https://doi.org/10.1007/S10924-008-0086-7

[40] Yin L, Wang L, Tan L, Huang Z, Zhou J, Wang L, et al. Mechanical properties of modulus-graded bamboo fiber-reinforced PHBV composites and their thermal stability properties. Polym Compos 2025. https://doi.org/10.1002/PC.29699

[41] Ashori A, Jonoobi M, Ayrilmis N, Shahreki A, Fashapoyeh MA. Preparation and characterization of polyhydroxybutyrate-co-valerate (PHBV) as green composites using nano reinforcements. Int J Biol Macromol 2019;136:1119–24. https://doi.org/10.1016/J.IJBIOMAC.2019.06.181.

[42] Furgier V, Root A, Heinmaa I, Zamani A, Åkesson D. Development and Characterisation of Composites Prepared from PHBV Compounded with Organic Waste Reinforcements, and Their Soil Biodegradation. Materials 2024;17:768. https://doi.org/10.3390/MA17030768/S1.

SELF-CONTAINED COST-EFFECTIVE PLASTIC RECYCLING FACILITIES

Clinton D. Switzer[1], Siddhesh Chaudhari[2], Anuj Maheshwari[3], Frank D. Blum[3], and Ranji Vaidyanathan[2]

[1]1Zero Plastic, 816 N Owasso Ave Tulsa OK 74106
Email: clinton.switzer@zeroplasticresearch.com, web page: http://zeroplasticresearch.com

[2]Department of Mechatronics, Materials and Manufacturing Engineering, Oklahoma State University
700 N. Greenwood Avenue, Tulsa, Oklahoma, United States
Email: Siddhesh.chaudhari@okstate.edu

[3]Department of Chemistry, Oklahoma State University
Stillwater, United States
Email: anuj.maheshwari@okstate.edu

Keywords: Plastic recycling, Waste management, Compression molding, Mechanical properties, Sustainable manufacturing

ABSTRACT

The increasing use of plastics demands effective end-of-life waste management, yet recycling facilities remain inaccessible in many areas, especially remote regions seeking sustainable solutions. The "Zero Plastic" project explores innovative methods to reuse waste plastics with minimal processing. This study focuses on two plastic waste streams: stretch wraps—typically made of LLDPE, LDPE, or HDPE and PET bottles, including labels and caps, evaluating the mechanical properties of recycled molded products. Stretch wrap samples were compression molded at 180 °C under 2 MPa for 10 minutes, yielding a flexural strength of 15 MPa and a modulus of 420 MPa. Recycled PET (rPET) molded at 265 °C under 1 MPa for 4 minutes achieved 76 MPa strength and 2800 MPa modulus. However, labels and caps introduced immiscibility challenges. Using 10-wt% Lotader AX8840 compatibilizer reduced rPET's flexural strength and modulus to 64 MPa and 2000 MPa, respectively, while increasing elongation to 4.5%, correlating with higher creep compliance due to enhanced flexibility. Despite these improvements, PET bottle waste blended with compatibilizer remained brittle and was unsuitable for further testing. Various parts, including bricks and sheets of thicknesses 6.35 mm to 19 mm and lengths from 40 cm to 86 cm, were successfully molded from stretch wrap, demonstrating a feasible, cost-effective recycling pathway. Preliminary life cycle assessments showed significant environmental benefits: recycling stretch wrap could save 52,300 MJ of embodied energy and prevent 558 metric tons of CO_2 emissions (44% and 13% reductions, respectively). PET bottle recycling offers even higher potential, with 146,000 MJ energy savings and a 4900-metric-ton reduction in CO_2 emissions (53% and 39% reductions). Future work will enhance manufacturing processes and explore plastic blending strategies to establish sustainable, decentralized recycling facilities where such infrastructure is currently lacking.

1 INTRODUCTION

Recent research underscores both the opportunities and limits of mechanical recycling for plastics. Mechanical recycling remains the most energy-efficient and environmentally favorable option, particularly for single-polymer streams like PET, HDPE, or LDPE, and can achieve significant reductions in carbon footprint when properly implemented. However, studies show that even with optimized collection and sorting, mechanical recycling will typically only capture 30 to 40% of plastic waste, constrained by challenges such as polymer degradation, contamination, and the presence of complex multi-material products. As Klotz et al. noted, mechanical processes are limited in addressing

diverse plastic grades and achieving high-quality recycled outputs suitable for demanding applications [1]. This gap highlights why efforts to decentralize recycling via smaller, stand-alone facilities must consider the technical feasibility of handling mixed waste streams without compromising product quality or environmental gains [2].

In addition to mechanical approaches, chemical and solvent-based recycling processes are emerging as potential solutions for plastics unsuitable for melting and reprocessing. Techniques like pyrolysis, gasification, and depolymerization can transform mixed or contaminated plastics into valuable monomers or fuels, theoretically producing outputs comparable to virgin materials. However, these technologies remain costly, energy-intensive, and largely unproven at industrial scale, with uncertainties in life-cycle impacts and process economics. Life cycle assessments emphasize the importance of evaluating recycling technologies not just by greenhouse gas emissions but also by factors like net fossil carbon balance, landfill diversion, and plastic leakage to the environment [3-4]. As such, while small-scale recycling plants offer promise for rural and remote areas, their viability hinges on careful integration of mechanical and chemical pathways, robust sorting infrastructure, and economic models capable of offsetting high capital and operational costs.

Even though mechanical recycling remains the preferred method for plastic waste management, the cost of establishing a conventional Materials Recovery Facility (MRF) is prohibitively high for most communities, particularly in rural or remote regions. To address this challenge, Zero Plastic LLC and Oklahoma State University collaborated under a U.S. Army SBIR Phase I effort (Contract No. W51701-23-C-0246) [5] to explore the feasibility of developing a self-contained, mobile recycling facility housed inside a shipping container. The goal was to create a compact system capable of recycling common plastic waste streams, such as stretch wraps and plastic bottles, into useful products with minimal sorting and processing requirements. Building on this work, the present study investigates the feasibility of producing value-added products from post-consumer plastics using such stand-alone facilities. We focused on characterizing recycled stretch wrap materials and recycled PET blends, both in their raw state and with compatibilization strategies aimed at improving mechanical properties. A range of thermal and mechanical analyses was conducted to evaluate material performance and processing behavior. The following sections describe the materials used, the experimental methods employed, and the results obtained, offering insights into the technical viability and limitations of decentralized recycling systems for mixed plastic waste streams.

2 MATERIALS AND METHODS

2.1 Materials

This study utilized post-consumer plastic waste streams, specifically stretch wrap waste composed of linear low-density polyethylene (LLDPE), low-density polyethylene (LDPE), and high-density polyethylene (HDPE), as well as recycled polyethylene terephthalate (rPET) flakes obtained from commercial reclaimers. Recycled polypropylene (rPP) was also incorporated for blending studies with rPET. To enhance interfacial compatibility between immiscible polymers, Lotader AX8840 (Arkema Inc.), an ethylene-acrylic ester-glycidyl methacrylate terpolymer, was employed as a compatibilizer at concentrations of 5-wt% and 10-wt%.

2.2 Sample Preparation

Post-consumer plastics were initially cut or shredded into small flakes using a Vecoplan VAZ 800 shredder. Blends involving rPET and rPP, with or without compatibilizer, were compounded using a Brabender Plasti-Corder torque rheometer at 235°C for 5 minutes at a rotor speed of 60 rpm to achieve homogeneous dispersion. Compression molding was performed on a Carver hydraulic press under different conditions depending on the polymer type: stretch wrap samples were molded at 180°C under 2 MPa for 10 min., while rPET-based samples were molded at 265°C under 1 MPa for 4 min. The resulting products included sheets and bricks, with thicknesses ranging from 6.35 mm to 19 mm, and lengths and widths between 40 cm and 86 cm.

2.3 Thermal and Mechanical Characterization

Thermal and mechanical characterization of the recycled plastics was performed to evaluate their suitability for manufacturing applications. Thermal transitions were analyzed using a TA Instruments Q2000 Differential Scanning Calorimeter (DSC), with samples of 5–10 mg subjected to a heat-cool-heat cycle from 30 °C to 300 °C at a rate of 3 °C/min under a nitrogen atmosphere. The key parameters measured included glass transition temperatures (Tg), melting points (Tm), and crystallization behaviors. Mechanical properties were assessed through flexural testing conducted using an Instron Universal Testing Machine following ASTM D790 standards, employing a span length of 50 mm and a crosshead speed of 2 mm/min to determine flexural strength, modulus, and elongation at break. Additionally, dynamic mechanical properties were examined using a TA Instruments Q800 DMA in dual cantilever mode across a temperature range of 30 °C to 80 °C, capturing data on storage modulus, loss modulus, creep compliance, and time-temperature superposition behavior.

The analytical techniques were crucial for understanding the inherent challenges of recycling mixed plastic waste streams, such as polyolefin films and PET bottles, which differ significantly in chemical structure, melting behavior, and mechanical performance. In this study, recycled plastic streams—including stretch wraps composed of polyethylene blends and rPET materials—were systematically analyzed to evaluate their thermal behavior and mechanical integrity, both in their unmodified states and after the addition of compatibilizers. The results from DSC and DMA provided critical insights into the compatibility of blended polymers and the effectiveness of processing methods used, informing the design and feasibility of stand-alone, containerized recycling facilities capable of converting heterogeneous plastic waste into functional products.

2.4 Life Cycle Assessment

A preliminary life cycle assessment (LCA) was performed to quantify the environmental impacts of the recycling operations, focusing on embodied energy and greenhouse gas emissions, using the LCA calculator provided by the REMADE Institute, of which Oklahoma State University was a member during the SBIR project [6]. Calculations integrated process-specific energy data and emissions factors drawn from literature and operational data obtained during the SBIR Phase I project. These assessments provided insights into the potential sustainability benefits of implementing localized, stand-alone recycling facilities.

2.5 Fabrication of Molded Products and Equipment Used

Post-consumer plastics, including stretch wrap and rPET bottles, were first shredded into flakes using a Vecoplan VAZ 800 industrial shredder, producing fragments approximately 10–20 mm in size to facilitate further processing. For blends requiring improved homogeneity, the shredded material was fed into a Filabot EX6 single-screw extruder, operated at barrel temperatures between 170°C and 220°C and screw speeds ranging from 10 to 40 rpm. In certain trials, extruded strands were cooled and pelletized using a Filabot Pelletizer, yielding uniform feedstock suitable for consistent molding operations. This sequence ensured adequate mixing, particularly in blends containing compatibilizers such as Lotader AX8840. The key equipment used in these processes—including the shredder, extruder, pelletizer, and compression molding press is shown in Figure 1.

Final products, including sheets, bricks, tiles, and other molded components, were fabricated using a Carver hydraulic compression molding press. Process parameters varied depending on the polymer type: stretch wrap blends were molded at 180°C under 2 MPa for 10 min, while rPET and rPET blends were molded at 265 °C under 1 MPa for 4 min. Custom-designed steel molds were utilized to shape parts into dimensions ranging in thickness from 6.35 mm to 19 mm, with lengths and widths between 40 cm and 86 cm. These molded parts were subsequently evaluated for mechanical performance and surface quality to assess the feasibility of producing durable products from localized, stand-alone recycling operations.



Figure 1. Key equipment used for stand-alone recycling, including the shredder, extruder, pelletizer, and compression molding press.

To further illustrate the stand-alone recycling system developed in this study, Figure 2 presents a schematic layout of the self-contained manufacturing facility housed inside a standard shipping container. This diagram shows the workflow and spatial arrangement of the main processing equipment, including the shredder, extruder, pelletizer, and compression molding press, all integrated into a compact footprint designed for deployment in remote or rural settings. The layout enables localized recycling operations, minimizing the need for transportation to centralized facilities.

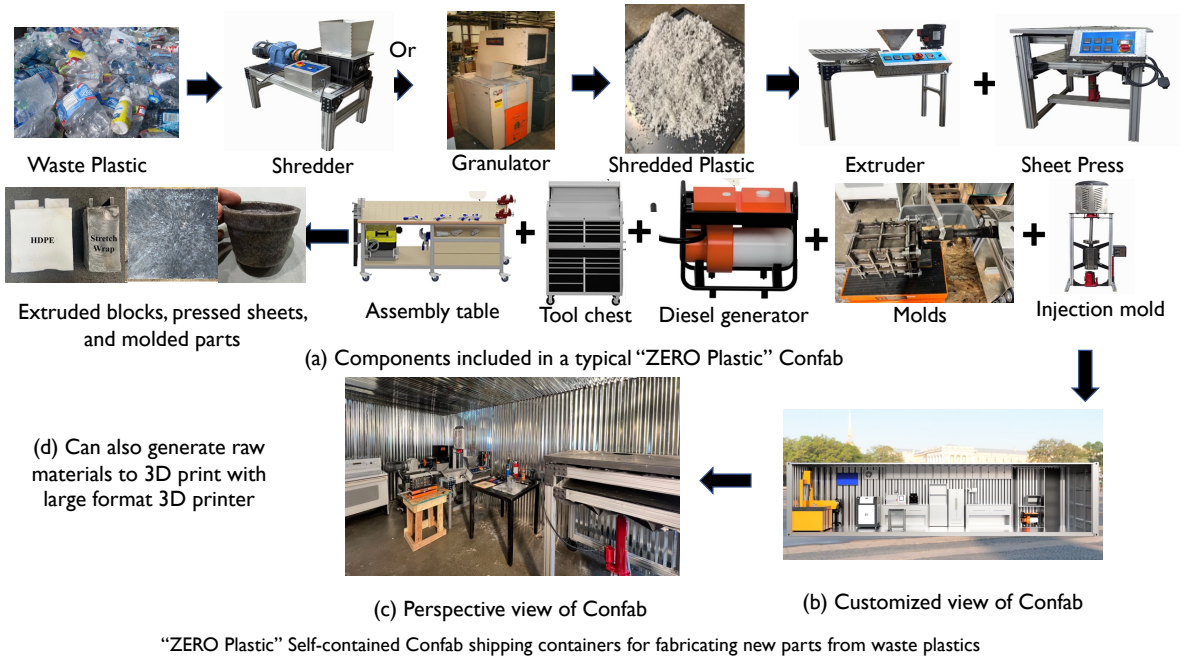

Figure 2. Schematic of the shipping container with the various equipment.

Figure 3 shows photographs of some of the primary equipment used in the recycling process. The Brabender Prep Center (Figure 3a) served as the primary compounding system for blending recycled polymers and compatibilizers under controlled temperature and shear conditions. It enabled thorough mixing of rPET, rPP, and Lotader AX8840, producing homogenous blends for subsequent molding operations. The Vecoplan VAZ 800 industrial shredder (Figure 3b) was employed for the initial size reduction of post-consumer plastics, producing flakes (Figure 3c) approximately 10–20 mm in size to facilitate downstream processing.



(a) (b) (c)

Figure 3. (a) Brabender prep center (b) Industrial shredder (c) shredded pieces.

Custom-designed steel molds, illustrated in Figure 4, were fabricated to produce a variety of product geometries, including beams, bricks, and flat sheets, tiles. The molds varied in size to accommodate different applications, with part thicknesses ranging from 6.35 mm to 19 mm and lengths and widths between 40 cm and 86 cm. These molds were engineered to endure high processing temperatures and pressures, ensuring proper consolidation and dimensional accuracy in the recycled polymer products.

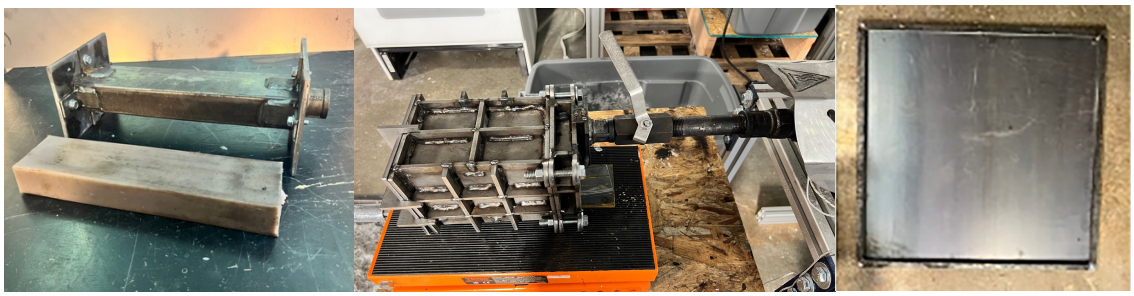

Figure 4. Molds for beams, bricks and sheets.

Finally, Figure 5 displays examples of finished products manufactured during the project. These images showcase the successful conversion of recycled stretch wrap and rPET blends into functional items such as panels, tiles, and construction bricks. The molded products provide visual evidence of the system's capacity to create usable, value-added components from heterogeneous plastic waste streams, reinforcing the technical feasibility of decentralized recycling solutions.



Figure 5. Examples of recycled parts fabricated on the equipment shown in Figure 1 – stackable blocks made from HDPE and stretch wrap (150 mm x 100 mm), beams made from stretch wrap (250 mm x 100 mm), and 900 mm x 900 mm x 6.5 mm thick sheets.

3 RESULTS AND DISCUSSION

The following sections present the thermal and mechanical characterization of recycled plastic materials processed using the stand-alone, containerized recycling system. Results are discussed in the

context of polymer compatibility, processing behavior, and the feasibility of producing durable, value-added products from post-consumer plastic waste streams. Where relevant, findings are compared with literature data and insights gained during the project to highlight both the potential and limitations of localized recycling solutions.

3.1 DSC Analysis of Stretch Wrap

DSC thermograms for post-consumer stretch wrap samples (Figure 6) revealed the thermal complexity of mixed polyethylene waste streams. Two distinct melting endotherms were observed: one around 109–114 °C, attributed to low-density polyethylene (LDPE) components, and another near 122 °C, corresponding to high-density polyethylene (HDPE) fractions. The presence of multiple melting peaks reflects the varied composition of the stretch wrap waste, which includes LDPE, LLDPE, and potentially blends with other polyolefins. Additionally, the broadness and reduced intensity of these peaks, compared to neat HDPE or LDPE, suggest lower crystallinity and possible molecular weight degradation resulting from prior processing and recycling steps, a typical phenomenon in recycled polyolefin materials.

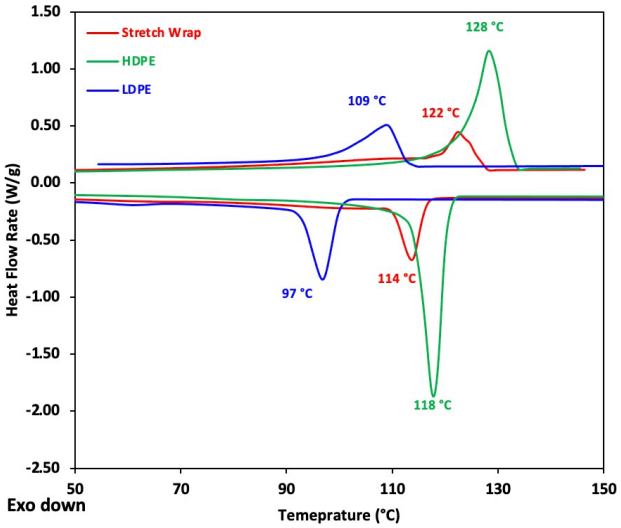

Figure 6. DSC thermograms for stretch wrap and polyethylene blends.

3.2 DSC Thermograms of rPP and rPET

DSC thermograms for recycled PET (rPET) and recycled polypropylene (rPP) are shown in Figures 7 and 8, with corresponding thermal transitions summarized in Table 1. The thermogram for rPET (Figure 7) exhibits a crystallization exotherm at approximately 187 °C and a prominent melting endotherm at 248 °C, consistent with the thermal behavior of semi-crystalline PET materials. These results confirm that the recycled PET retains significant crystalline character, suggesting it may still be suitable for remanufacturing applications requiring thermal stability.

The thermogram for rPP (Figure 8) displays multiple thermal transitions. A primary melting peak is observed at approximately 162 °C, which corresponds to isotactic polypropylene. Additionally, smaller melting and crystallization features at approximately 126 °C and 116 °C, respectively, indicate the presence of polyethylene (PE) contamination within the rPP stream. This overlapping of thermal transitions suggests partial immiscibility and heterogeneity in the recycled rPP material. Such PE contamination is common in post-consumer recycled streams and can influence both mechanical properties and processability.

These thermal analyses indicate that while both rPET and rPP exhibit recognizable melting and crystallization behavior, the presence of impurities and mixed phases, particularly in rPP, could complicate subsequent processing or blending operations. This underscores the importance of careful material characterization when designing stand-alone recycling systems to produce consistent, high-quality recycled products.

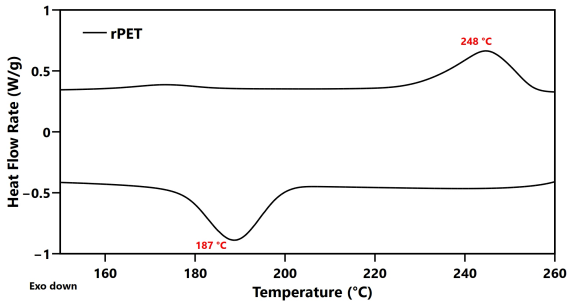

Figure 7. DSC thermogram for rPET.

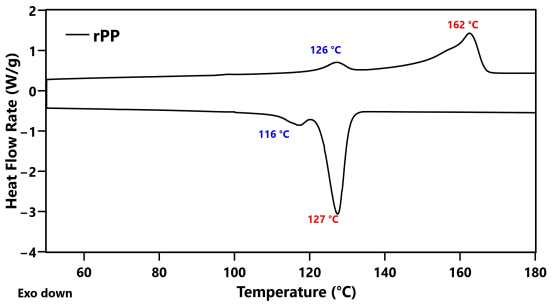

Figure 8: DSC thermogram for rPP.

Sample	Melting temperature, °C (T_m)	Crystallization temperature, °C (T_c)
rPET	248	187
rPP with PE (as a contamination)	162	127
	126	116

Table 1. Obsrved thermal transitions for rPET and rPP.

3.3 DMA Results for rPET Blends

Dynamic mechanical analysis (DMA) was conducted to evaluate the viscoelastic behavior of recycled stretch wrap materials. The time-temperature superposition (TTS) creep compliance curve for stretch wrap, shown in Figure 9, displays a steadily increasing trend over time. This behavior reflects the inherently lower stiffness and higher ductility typical of polyolefin-based films, indicating that under sustained stress, these materials exhibit significant time-dependent deformation. This is consistent with flexural test results, which showed lower modulus values for stretch wrap compared to recycled PET. For recycled PET (rPET) samples, substantial differences in viscoelastic behavior were observed depending on compatibilizer content, as shown in Figure 10.

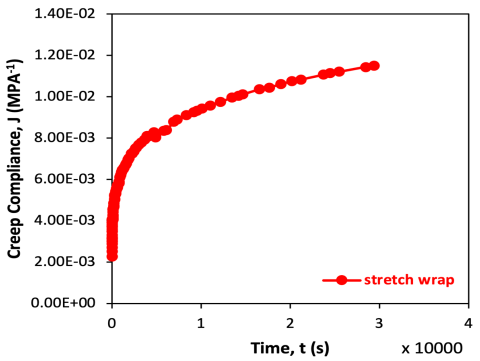

Figure 9. Time-temperature superposition (TTS) curve for stretch wrap.

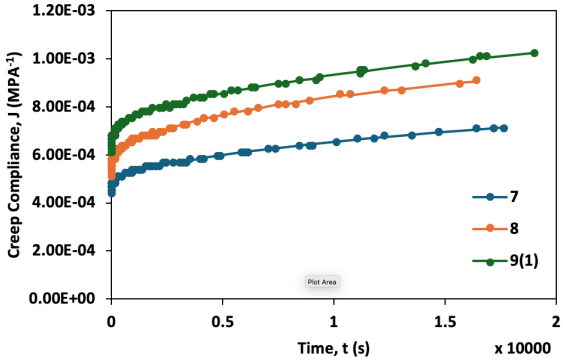

Figure 10. Time-temperature superposition (TTS) curve for rPET with and without compatibilizer (showing sample #s).

Pure rPET exhibited the lowest creep compliance, reflecting its stiff and brittle nature with minimal deformation under sustained loading. In contrast, blending rPET with Lotader AX8840 compatibilizer led to progressively higher creep compliance values. The rPET/compat 95/5 blend showed increased compliance relative to pure rPET, while the 90/10 blend exhibited the highest compliance among the samples tested. These results indicate that the addition of compatibilizer softens the polymer matrix,

enhancing ductility and flexibility but simultaneously reducing stiffness. This behavior aligns with the flexural test results, where compatibilized blends displayed increased elongation at break and lower modulus compared to pure rPET. The DMA data thus confirm that compatibilization effectively modifies the viscoelastic properties of recycled PET, improving toughness and processability at the expense of rigidity.

3.4 Compatibilization

The recycling of mixed plastic waste streams poses significant challenges due to the inherent immiscibility between different polymer types, which leads to poor interfacial adhesion and compromised mechanical properties. Studies such as those by Maris et al. [7] and Imamura et al. [8] emphasize that while compatibilization offers a promising pathway to blend polymers like PET, PP, and PE, it frequently comes with trade-offs. Compatibilizers can reduce interfacial tension and promote morphological stability, but they also often lead to decreased tensile strength and modulus, driven by disruption of crystalline domains or the introduction of softer segments into the polymer matrix. Friedrich et al. [9] further demonstrate that purely chemical approaches might be insufficient and that morphological strategies—such as creating microfibrillar structures can significantly enhance the mechanical performance of polymer blends, particularly in PET/PP systems.

Our current study mirrors many of these literature findings. The addition of Lotader AX8840 compatibilizer to rPET/rPP blends indeed led to an increase in elongation at break from 2.5% to 4.3%, signalling improved ductility and toughness. However, consistent with observations by Imamura et al. [8], we also recorded a significant reduction in flexural strength and modulus dropping from 76.8 MPa and 2810 MPa in pure rPET to 64.0 MPa and 2000 MPa, respectively, in the 10-wt% compatibilized blend. This aligns with Maris et al. [7], who highlight that compatibilizers, while beneficial for morphology, can disrupt crystalline structures and lower overall stiffness. Our DMA results similarly showed decreased storage modulus and increased creep compliance with higher compatibilizer content, underscoring this classic trade-off between toughness and stiffness in recycled polymer blends.

Despite partial improvements, our compatibilization strategy has not entirely overcome the mechanical limitations posed by mixing recycled PET with polyolefins like PP. Persistent phase separation, as evident from our DSC and morphological analyses, suggests that Lotader AX8840 alone may be insufficient for achieving a fully homogeneous blend. Additionally, the presence of contaminants such as bottle labels and caps introduces further complexity, often leading to brittleness in processed samples even when compatibilizers are used. Our results thus reflect the broader conclusion in the literature: chemical compatibilization can mitigate immiscibility but may fall short in delivering mechanical properties suitable for high-performance applications, particularly when dealing with highly heterogeneous waste streams [7–9].

To address these challenges, future research should explore combined strategies that integrate chemical compatibilization with physical morphology control. One promising avenue is microfibrillar reinforcement, as demonstrated by Friedrich et al. [9], where cold drawing transforms PET domains into fine microfibrils that enhance mechanical interlocking and stress transfer within the blend. Additionally, optimizing the concentration of compatibilizers as Imamura et al. [8] found—could balance improvements in ductility without excessively compromising stiffness, particularly if lower loading levels (~3 phr) are sufficient. Emerging approaches using nanoparticle-based compatibilizers, as noted by Maris et al. [7], also warrant investigation for their ability to migrate to polymer interfaces and stabilize morphologies. Finally, incorporating advanced sorting technologies or selective pre-treatment steps could reduce contamination levels, enabling more effective compatibilization and yielding higher-performance recycled materials. These multi-pronged strategies will be critical for enabling stand-alone recycling facilities to produce structurally viable products from mixed plastic waste streams.

3.5 Life Cycle Assessment

Beyond mechanical performance, the sustainability of recycling processes was evaluated through preliminary life cycle assessments (LCA) [6]. For stretch wrap waste, the analysis showed significant environmental benefits, with estimated savings of approximately 52,300 MJ of embodied energy and avoidance of about 558 metric tons of CO_2 emissions. These figures correspond to a 44% reduction in

embodied energy and a 13% reduction in CO_2 emissions compared to virgin material production, as illustrated in Figures 11 and 12.

Recycling PET bottles demonstrated even greater potential impact. The LCA results indicated energy savings of approximately 146,000 MJ and a reduction of about 4,900 metric tons of CO_2 emissions, translating to a 53% decrease in embodied energy and a 39% reduction in CO_2 emissions relative to virgin PET production. These improvements are also shown in Figures 11 and 12.

These analyses were based on the following assumptions regarding material composition in the waste streams: stretch wrap consisted of a 50:5:25:20 ratio of LLDPE stretch wrap, polypropylene (PP) packaging tape, LDPE stretch wrap, and HDPE packaging films, respectively. PET bottle waste was modelled as a 90:9:1 ratio of PET bottles, PP caps, and PE labels.

Overall, these findings highlight the substantial environmental benefits achievable through localized recycling operations, including reduced greenhouse gas emissions, lower energy consumption, and decreased reliance on landfill disposal or incineration in burn pits. Stand-alone recycling facilities thus offer not only technical feasibility but also meaningful contributions to resource conservation and sustainability goals [5-6].

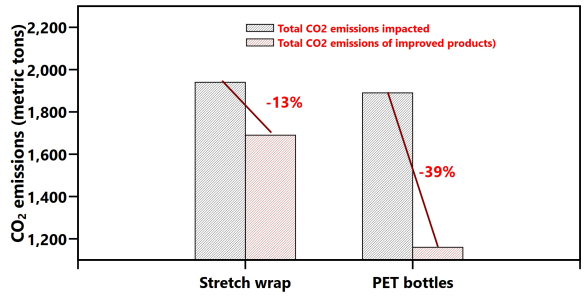

Figure 11. CO2 emission reduction for stretch wrap wrap and PET from bottles.

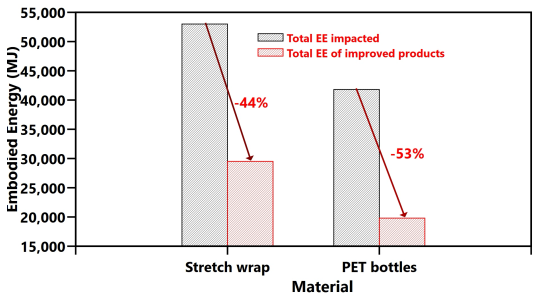

Figure 12. Embodied energy reduction for stretch wrap and PET from bottles.

3.6 Mechanical Test Results

The mechanical properties of recycled plastics are critical indicators of their suitability for producing durable, value-added products. To evaluate the structural potential of various recycled polymer systems, flexural tests were conducted on both pure materials and compatibilized blends, providing insights into the balance between strength, stiffness, and ductility achievable through recycling processes. These results are shown in Table 2.

Sample Type	Flexural Strength (MPa)	Flexural Modulus (MPa)	Elongation at Break (%)
HDPE	23.1 ± 0.5	630 ± 20	9.2 ± 0.3
LDPE	15.3 ± 0.4	420 ± 15	8.7 ± 0.4
Stretch Wrap	15.0 ± 0.6	420 ± 10	5.3 ± 0.3
rPET	76.8 ± 1.1	2810 ± 40	2.5 ± 0.2
rPET + 5% Lotader AX8840	66.1 ± 1.0	2460 ± 35	3.6 ± 0.2
rPET + 10% Lotader AX8840	64.0 ± 1.2	2000 ± 30	4.3 ± 0.3

Table 2. Mechanical properties of recycled polymer blends.

4 FINANCIAL FEASIBILITY OF CONTAINERIZED RECYCLING FACILITIES

Assessing the economic viability of standalone, containerized materials recovery facilities (MRFs) is crucial for understanding their practical implementation, particularly in rural and remote communities. Financial analyses suggest that such systems require a minimum processing volume of approximately 400–600 tons of recyclables per year to break even, covering both capital and operational costs through

a combination of revenue from recycled material sales and savings from avoided landfill tipping fees.

The economic feasibility of these decentralized systems is highly sensitive to commodity market prices and regional tipping fees. Higher recovered material prices (≥ $100/ton) and elevated landfill tipping fees (≥ $50–$70/ton) significantly enhance the potential for a positive financial return. However, many rural communities face challenges due to lower commodity prices and reduced tipping fees, which can undermine the financial sustainability of small-scale recycling operations.

Regional collaboration emerges as a key strategy to improve economic outcomes. Small towns individually often generate insufficient recyclable material volumes to sustain operations. For instance, a low-volume town with a population of approximately 5,000 may produce only around 200 tons/year of recyclables. Under a scenario of $100/ton in revenue and avoided tipping fees, this would generate roughly $20,000 in annual benefits, insufficient to offset estimated autonomous operating and capital costs of about $40,000/year, resulting in a net loss of $20,000 annually. Conversely, a regional model consolidating materials from several communities (population ~20,000) could yield around 800 tons/year of recyclables, translating to $80,000/year in revenue and avoided costs. In this scenario, the same estimated operational and capital expenses would yield a positive net balance of $40,000/year, demonstrating clear economies of scale.

Despite advances in automation and lower labor requirements, upfront capital costs for standalone containerized systems remain significant, typically around $250,000 per unit. Consequently, grants, low-interest loans, or other financial incentives are often essential for rural communities with constrained municipal budgets to establish such facilities. Overall, while standalone containerized MRFs show promise for sustainable waste management, their deployment is most viable in regions where collaborative collection networks can be established, commodity markets are stable, and external funding support is available to bridge the gap between capital investment and operational profitability. This analysis is shown in Table 3.

Parameter	Low-Volume Town	Regional Model
Population	5,000	20,000
Tons/year recyclables processed	200	800
Annual revenue + avoided tipping fees ($100/ton)	$20,000	$80,000
Autonomous O&M + capital cost per year	~$40,000	~$40,000
Net annual balance	–$20,000	+$40,000

Table 3. Financial Analysis of Standalone Containerized Recycling Facility Scenarios.

*Autonomous O&M" refers to estimated annual operation and maintenance costs for largely automated recycling systems, excluding significant manual labor costs.

5. CONCLUSIONS

This study demonstrates the feasibility of producing value-added products from post-consumer plastic waste using stand-alone, containerized recycling systems. Stretch wrap waste, composed primarily of mixed polyolefins, was successfully processed into molded products such as sheets and bricks, albeit with lower mechanical properties compared to engineering polymers. Recycled PET (rPET) displayed significantly higher stiffness and strength; however, blending rPET with polyolefins presented challenges due to inherent immiscibility. The use of Lotader AX8840 compatibilizer improved ductility and elongation at break in rPET blends but resulted in reduced flexural strength and modulus, highlighting the classic trade-off between toughness and stiffness in recycled polymer systems.

Thermal analyses via DSC confirmed the presence of multiple melting transitions in stretch wrap materials, indicating their heterogeneous composition, and revealed retained crystallinity in recycled PET suitable for processing applications. Dynamic mechanical analysis further demonstrated the impact of compatibilizer content on creep compliance, underscoring its role in modifying viscoelastic behavior and mechanical performance.

Life cycle assessment indicated substantial environmental benefits for decentralized recycling operations. Recycling stretch wrap waste could save approximately 52,300 MJ of embodied energy and reduce CO_2 emissions by 558 metric tons, while PET bottle recycling offers even greater savings of about 146,000 MJ and a reduction of 4,900 metric tons of CO_2 emissions, compared to virgin material production. These results support the environmental sustainability of localized recycling solutions.

Financial analyses revealed that while standalone containerized recycling facilities are technically feasible, their economic viability depends heavily on processing volume, market conditions, and regional collaboration. Smaller communities may not generate sufficient material to sustain operations independently, emphasizing the importance of pooling resources and securing financial support through grants or subsidies to offset capital and operational costs.

Overall, this work highlights both the technical potential and the challenges associated with decentralized recycling of mixed plastic waste streams. Future research should explore advanced compatibilization strategies, process optimization, and scalable economic models to enhance the viability of localized recycling systems and contribute to circular economy goals.

ACKNOWLEDGEMENTS

The authors would like to acknowledge funding support from the U.S. Army SBIR Phase I program under Contract No. W51701-23-C-0246, and from the National Science Foundation through the I-Corps Teams project "I-Corps Carpet-Polyolefin Recycled Composites R-Polyblend" (NSF Award No. 2414963). The authors also gratefully acknowledge Ms. Abigail Rice of the U.S. Army Corps of Engineers, Illinois, for her guidance and technical discussions during the course of this work.

REFERENCES

[1]. Klotz, Magdalena, Melanie Haupt, and Stefanie Hellweg. "Potentials and limits of mechanical plastic recycling." *Journal of Industrial Ecology* 27, no. 4 (2023): 1043-1059.

[2]. Nordahl, Sarah L., and Corinne D. Scown. "Recommendations for life-cycle assessment of recyclable plastics in a circular economy." *Chemical Science* 15, no. 25 (2024): 9397-9407.

[3]. Klotz, Magdalena, Christopher Oberschelp, Cecilia Salah, Luc Subal, and Stefanie Hellweg. "The role of chemical and solvent-based recycling within a sustainable circular economy for plastics." *Science of the Total Environment* 906 (2024): 167586.

[4]. Sambyal, Pradeep, Parisa Najmi, Devansh Sharma, Ehsan Khoshbakhti, Hadi Hosseini, Abbas S. Milani, and Mohammad Arjmand. "Plastic recycling: Challenges and opportunities." *The Canadian Journal of Chemical Engineering* 103, no. 6 (2025): 2462-2498.

[5]. Zero Plastic LLC. *Self-contained shipping containers for fabricating new parts from waste.* Final Report for U.S. Army SBIR Phase I, Contract No. W51701-23-C-0246, March 2024.

[6]. "Energy and CO2 calculations for Remade projects," available at https://remadeinstitute.org/wp-content/uploads/2024/01/EnergyandCO2CalculationsNov2019update.pdf, accessed January 2024.

[7]. Maris, Joachim, Sylvie Bourdon, Jean-Michel Brossard, Laurent Cauret, Laurent Fontaine, and Véronique Montembault. "Mechanical recycling: Compatibilization of mixed thermoplastic wastes." *Polymer Degradation and Stability*147 (2018): 245-266.

[8]. Imamura, Nobuyuki, Hiroki Sakamoto, Yuji Higuchi, Hiroyuki Yamamoto, Shinichi Kawasaki, Kazushi Yamada, Hiroyuki Nishimura, and Takahiro Nishino. "Effectiveness of compatibilizer on mechanical properties of recycled PET blends with PE, PP, and PS." *Materials Sciences and Applications* 5, no. 8 (2014): 548-555.

[9]. Friedrich, K., M. Evstatiev, S. Fakirov, O. Evstatiev, M. Ishii, and M. Harrass. "Microfibrillar reinforced composites from PET/PP blends: processing, morphology and mechanical properties."*Composites Science and Technology* 65, no. 1 (2005): 107-116.

MANUFACTURING AND CHARACTERIZATION OF CONTINUOUS RECYCLED CARBON FIBER UNIDIRECTIONAL COMPOSITES

Dr Monali Dahale[1], Dr Kyle Pender[2], Dr Daniel Scott[3], Ms Serena Tan[4]

[1]NCC, Bristol, United Kingdom
Email: monali.dahale@nccuk.com

[2]NCC, Bristol, United Kingdom
Email: kyle.pender@nccuk.com

[3]NCC, Bristol, United Kingdom
Email: dan.scott@nccuk.com

[4]NCC, Bristol, United Kingdom
Email: serena.tan@nccuk.com

Keywords: Recycled Carbon Fibre, Filament Winding, UD Composites, Mechanical Testing, Sustainability

ABSTRACT

High-performance composites are integral to aerospace, automotive, and renewable energy sectors, but their reliance on virgin carbon fibres poses significant environmental and economic sustainability challenges globally. While recycled carbon fibres (rCF) offer a more environmentally friendly solution, their discontinuous nature significantly limits their mechanical performance, restricting their application in high-performance recycled carbon fibre-reinforced polymers (rCFRP). This study addresses this critical limitation by introducing and fully characterizing a novel continuous rCF material that retains fibre continuity, enabling superior mechanical performance and broadening the range of applications for rCF in demanding engineering contexts.

This research fills a significant knowledge gap by being the first to comprehensively characterize the mechanical properties of rCFRP manufactured with continuous rCF reclaimed from end-of-life carbon/epoxy Type III pressure vessels. The continuous rCF was produced using a thermal recycling technology, which stripped the polymer matrix, allowing the rCF to be unwound and tow length to be retained. Unidirectional (UD) panels were fabricated using a custom filament winding process optimized to achieve high fibre alignment, fibre volume fractions, and uniform resin distribution.

Mechanical testing of the panels, including tensile (ASTM D3039), compression (ASTM D6641), flexural (ASTM D7264), and short-beam shear testing (ASTM D2344), revealed that the mechanical properties of continuous rCFRP match or exceed those of industrial-grade virgin carbon fibre composites. Comparative analysis with virgin fibres (T700S-50C-12K and T300-50B-6K) showed that continuous rCF composites achieve performance metrics positioned between high-strength T700 and industrial-grade T300 composites. These results demonstrate that the retention of fibre length and alignment in continuous rCF directly addresses the performance limitations associated with conventional discontinuous rCF.

By demonstrating that continuous rCF can achieve performance comparable to standard virgin carbon fibre composites, this study establishes a critical pathway for integrating recycled fibres into high-performance applications. The enhanced directional properties, comparable fibre volume fractions, and

compatibility with existing manufacturing processes make continuous rCF a transformative material for sustainable engineering.

1 INTRODUCTION

The global demand for carbon fibre (CF) was estimated at 115 kilotonnes (kt) in 2023 and is projected to more than double to 280 kt by 2030 [1]. This growth is driven by the widespread use of carbon fibre-reinforced polymers (CFRPs) across sectors committed to decarbonisation, particularly transportation, renewable energy, and hydrogen storage. In the wind energy sector, CFRPs are increasingly used in multi-megawatt turbine blades due to their exceptional stiffness-to-weight ratio. As a result, wind energy is expected to surpass aerospace as the leading consumer of carbon fibre, with estimated demand reaching 20 kt for wind turbine blades alone [1][2].

Similarly, in the hydrogen economy, CFRPs are critical for constructing lightweight, high-pressure storage vessels. These composites improve safety and transport efficiency while reducing system weight. Currently, the pressure vessel segment accounts for approximately 12% of global CF demand and is poised for significant expansion alongside the hydrogen sector [1][3][4].

Despite its performance benefits, carbon fibre production is highly energy-intensive, contributing up to 50% of the total carbon footprint of offshore wind turbine blades [5]. Globally, CF manufacturing results in over 4 million tonnes of CO_2-equivalent emissions each year [6]. At the end of their service life, CFRP components present substantial recycling challenges. Most recycled carbon fibre (rCF) is recovered in chopped or discontinuous forms, which compromises fibre alignment and mechanical performance. Consequently, applications for rCF remain limited to non-structural or low-performance uses, reducing its commercial value and its ability to offset virgin CF consumption.

A key step toward a circular composite economy is the development of recycling technologies capable of retaining fibre continuity. Continuous rCF has the potential to deliver mechanical performance comparable to virgin fibre composites, enabling structural applications and reducing the environmental impact of CFRP systems. This study investigates such a solution focusing on the manufacturing and mechanical characterisation of unidirectional (UD) composites made from continuous recycled carbon fibre.

The reclaimed fibres in this study originate from end-of-life Type III carbon/epoxy pressure vessels and are recovered using a thermal process that preserves fibre length. Through a custom filament winding process, these fibres are reconstituted into continuous UD laminates and benchmarked against virgin fibre panels. The goal is to demonstrate that continuous rCF can close the performance gap that has historically limited recycled composites, and thereby support scalable, high-value reuse of CFRPs in demanding structural applications.

2 MATERIALS AND METHODS

Panel fabrication was performed using a flat mandrel system designed to simulate industrial-grade unidirectional layups. To ensure repeatability, each batch used identical processing conditions, and samples were drawn from the same tool. Environmental controls during resin infusion (ambient humidity and temperature ~22°C) were maintained to limit variability. Post-processing included oven curing and standardised trimming to generate test coupons according to ASTM specifications.
Recycled carbon fibre was recovered from end-of-life Type III carbon/epoxy pressure vessels using a thermal recycling process. This method effectively removes the matrix while retaining the fibre tow length and orientation. The reclaimed fibres were processed into continuous tows suitable for filament winding. Two virgin fibre grades (T700 and T300) were used as benchmarks. An epoxy system, Araldite LY556 with Aradur 917 hardener and accelerator DY070—was used for both reclaimed and virgin fibre panels.

3 MANUFACTURING PROCESS

The filament winding process (Figure 1) was executed on a modified flat-panel mandrel to enable consistent unidirectional (UD) layering. The process required precise environmental control, as the resin system's viscosity and curing profile are highly temperature-dependent. The resin bath was equipped with an immersion heater and maintained between 50–60°C to ensure optimal flow and wet-out characteristics. A tensioning system ensured even fibre delivery, while programmable creel rotation and mandrel speed facilitated the accurate layering of fibres. To improve panel quality, wide flash tape and square rubber rope were used around mandrel edges to minimize resin leakage and edge defects. The introduction of a reinforced PTFE film as a release layer helped mitigate warpage and surface irregularities caused by mandrel thermal expansion. Banding trials were crucial to establish the correct number of layers and minimize tow overlap, which could lead to increased void content or fibre misalignment. Vacuum bagging followed immediately after winding, ensuring thorough compaction and air evacuation during curing. The wrapped mandrel was cured in a Carbolite Gero oven with thermocouples for thermal tracking.

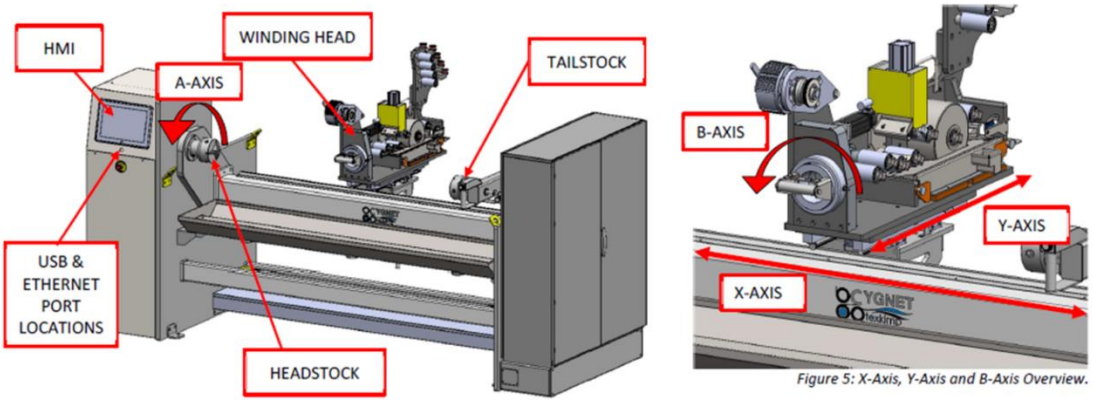

Figure 1: Filament Winding Schematic

Flat panel filament winding was used to manufacture unidirectional (UD) composite panels. The winding mandrel was treated with Frekote 700NC release agent and lined with Tooltec CS5 PTFE film. Bandwidth trials ensured consistent tow coverage and panel thickness. The resin bath was preheated to 50°C with nip pressure set to 0.5 bar and fibre tension at 10 N/tow. During winding, defects such as tow fluff, splicing, char deposits, and entanglement were observed (Figure 3). Excess resin was allowed to drip off before caul plates were bolted on, and vacuum bagging was performed before curing in a Carbolite Gero oven.

4 MECHANICAL TESTING

The mechanical testing program adhered to internationally recognized ASTM standards and focused on characterizing different failure modes and load responses. Test listed in Figure 2 were performed to characterise the vCF and rCF UD Panels. Tensile testing utilized dogbone specimens with hydraulic wedge grips to avoid slippage, and extensometers were mounted to measure axial strain directly. Compression tests used anti-buckling fixtures to stabilize the specimen and ensure valid compressive failure modes. Flexural tests were performed in three-point bending mode, with supports modified to account for composite anisotropy and prevent stress concentration at the loading nose. Short beam shear (SBS) testing was used to assess interlaminar shear strength (ILSS), providing insight into fibre-matrix adhesion and resin distribution. Each test was performed on a minimum of five specimens to ensure statistical validity. X-ray computed tomography (XCT) scans were conducted pre- and post-test to

investigate internal failure mechanisms such as delamination, fibre pull-out, and void evolution. Test data were plotted as stress-strain curves and benchmarked against the performance of virgin CFRP panels under identical conditions.

Mechanical characterisation followed ASTM standards: tensile testing (ASTM D3039), compression (ASTM D6641), flexural (ASTM D7264), and short beam shear (ASTM D2344). Non-destructive testing was performed using X-ray CT scanning to examine internal defects, fibre distribution, and porosity. Key test parameters included dogbone specimens for tensile tests and torque-controlled gripping to prevent slippage or misalignment.

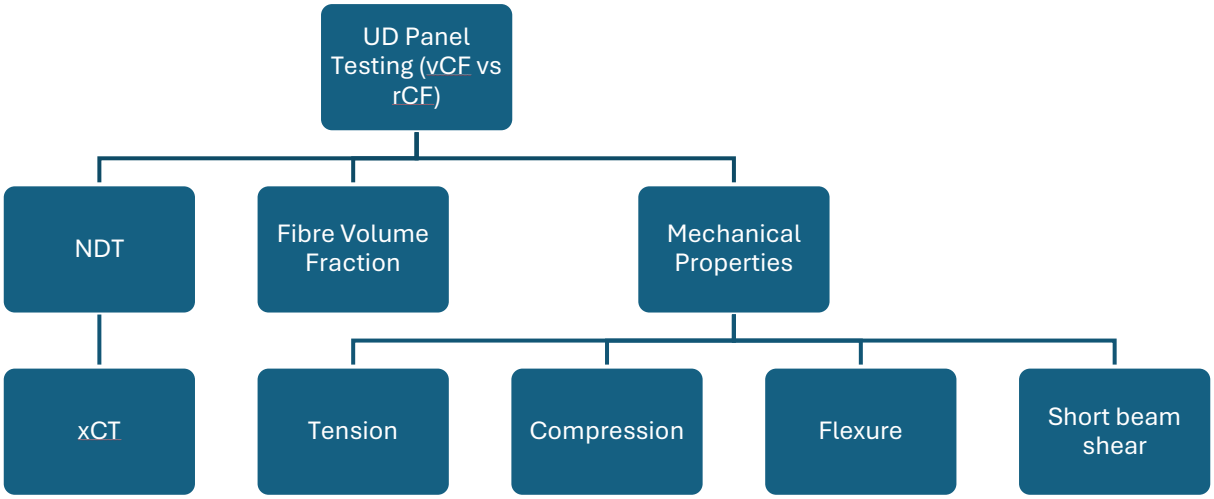

Figure 2: Tests performed on vCF and rCF UD Panels

5 RESULTS AND DISCUSSION

During the filament winding process of reclaimed carbon fibres, defects such as tow fluff, splicing, char deposits, and entanglement were observed (Figure 3).

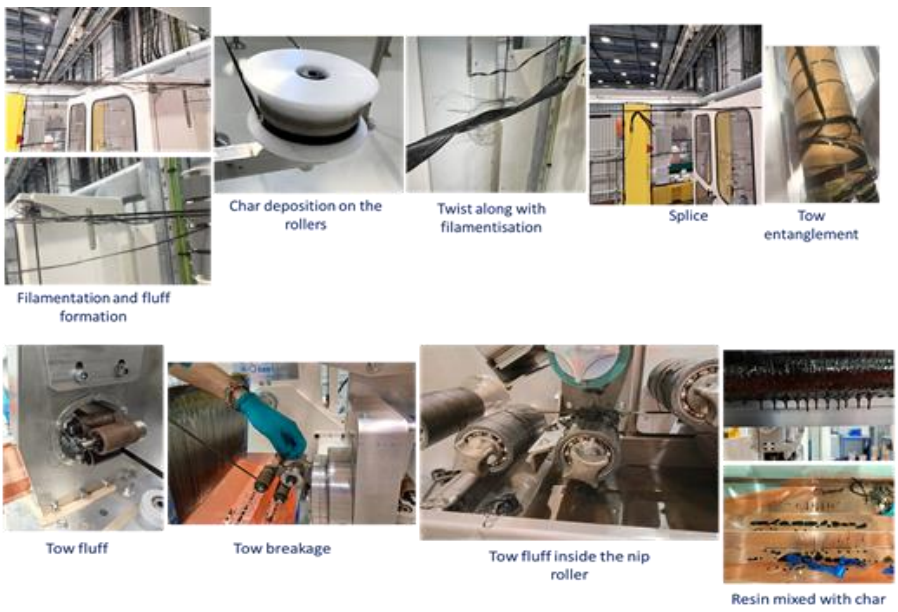

Figure 3: Defects observed with reclaimed carbon fibre filament winding process

CT scan analysis revealed consistent internal structures in virgin and recycled panels. The fibre volume fraction (Vf) was highest in T700 panels (64.7%), followed by T300 (60.8%), and reclaimed rCF panels (46.3%). Mechanical properties of continuous rCF panels showed intermediate performance, positioned between T700 and T300, proving their capability for high-performance applications. Despite the challenges with wet winding heads, towpreg-based manufacturing improved consistency and reduced defect incidence. Fluff formation and tow breakage were the primary causes of irregularity. Panels demonstrated sufficient integrity for structural applications with good matrix-fibre interaction and fibre alignment.

The tensile properties of continuous rCF composites were found to be within 10–15% of T300 virgin panels, indicating a significant improvement over conventional discontinuous rCF. Compression strength also showed promising results, with the rCF panels demonstrating good fibre alignment and minimal buckling artifacts. The flexural modulus and strength values confirmed the stiffness and energy absorption potential of the material. Short beam shear tests revealed that while interfacial strength was slightly lower in rCF composites, the values remained within acceptable engineering margins. XCT analysis of cured panels indicated low porosity levels (~3–5%), especially in panels fabricated using the towpreg head. Defect mapping through XCT visualisation showed uniform fibre distribution and fewer voids in virgin panels, but reclaimed fibre panels exhibited consistent morphology post-winding. Failure surface examination revealed fibre pull-out and matrix cracking in rCF panels, whereas virgin panels showed more brittle failure. Overall, the mechanical performance supports the suitability of continuous rCF for structural applications, particularly in cost-sensitive sectors seeking sustainability.

6 CONCLUSIONS

This study demonstrates that continuous recycled carbon fibre composites manufactured through filament winding can achieve mechanical properties comparable to commercial virgin fibre composites. Optimisation of winding parameters and defect control is essential to ensure quality. The results validate continuous rCF as a viable and sustainable alternative for high-performance composites, enabling integration into critical sectors such as aerospace and automotive manufacturing. Future work will focus on further automation, improved quality control, and performance under environmental ageing and fatigue loading.

ACKNOWLEDGEMENTS

The authors gratefully acknowledge the support of the National Composites Centre for providing access to equipment, expertise, and facilities. Special thanks to the development and engineering teams involved in winding, processing, and testing.

REFERENCES

[1] L. Gang, “2023 Global Carbon Fiber Composites Market Report,” Guangzhou, 2024.
[2] J. Zhang, V. S. Chevali, H. Wang, and C. H. Wang, “Current status of carbon fibre and carbon fibre composites recycling,” *Compos. Part B Eng.*, vol. 193, no. April, p. 108053, 2020, doi: 10.1016/j.compositesb.2020.108053.
[3] J. Li *et al.*, “Small-Scale High-Pressure Hydrogen Storage Vessels: A Review,” *Materials (Basel).*, vol. 17, p. 271, 2024, doi: 10.3390/ma17030721.
[4] J. Zhang, G. Lin, U. Vaidya, and H. Wang, “Past, present and future prospective of global carbon fibre composite developments and applications,” *Compos. Part B Eng.*, vol. 250, p. 110463, 2023, doi: 10.1016/j.compositesb.2022.110463.
[5] K. Pender, F. Romoli, K. Bacharoudis, P. Greaves, and J. Fuller, “Evaluating priority strategies for decarbonising offshore wind turbine blades through lifecycle assessment,” *Clean Technol.*

Environ. Policy, 2024, doi: https://doi.org/10.1007/s10098-024-03033-4.

[6] K. Pender, F. Romoli, and J. Fuller, “Future strategies for decarbonisation of carbon fibre products: A roadmap to Net Zero 2050,” *J. Clean. Prod.*, vol. 486, p. 144525, 2025, doi: 10.1016/j.jclepro.2024.144525.

ICCM24
AUGUST 4-8, 2025
BALTIMORE CONVENTION CENTER
BALTIMORE, MARYLAND, USA

No Technical Paper Submission for:

Josephine de Calbiac

Flexible and Recyclable Vitrimers for Sustainable Electronic Composites

Agni K Biswal[1], Peter Hong[2], Zhihan Zhang[3], Vikram Iyer[3], ***Aniruddh Vashisth[1]***

[1] Mechanical Engineering, University of Washington, Seattle,
[2]Materials Science and Engineering, University of Washington, Seattle
[3]Computer Science & Engineering, University of Washington, Seattle

UNIVERSITY *of* WASHINGTON

Sustainability



Carbon 187, 108-114

PNAS 119 (15)

Science Advances 8 (46)

Nature Sustainability 24

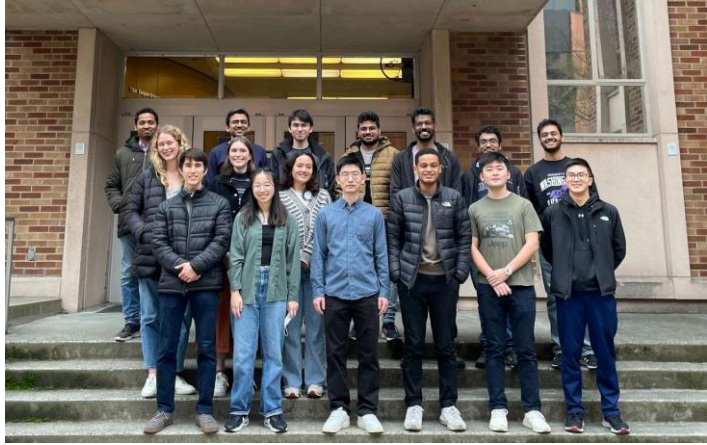

Advanced Composites
University of Washington

Composites Science and Technology 195, 108211

Applied Materials Today 23, 101044



Rapid Manufacturing

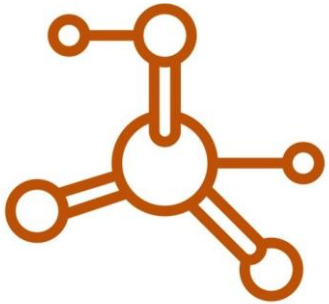

Atomistic Simulations

JPC A 122 (32), 6633-6642

Matter 1 (2), 513-526

Polymer 158, 354-363



Can we enable circular fabrication for electronics composites?



Thermoset | Thermoplastics | Vitrimers

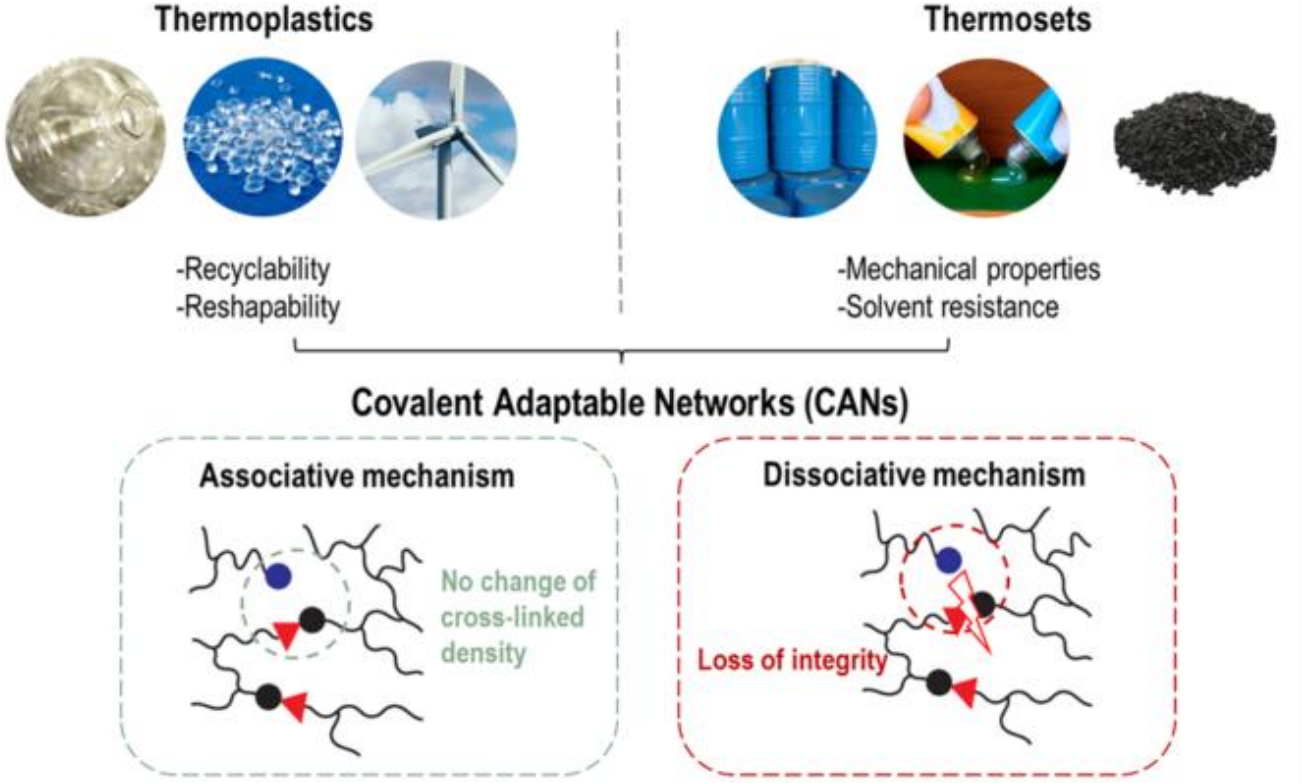

Cross-link Density maintained

Vitrimers: Polymers with Covalent Adaptive Network



Vitrimers enable healing mechanical damage

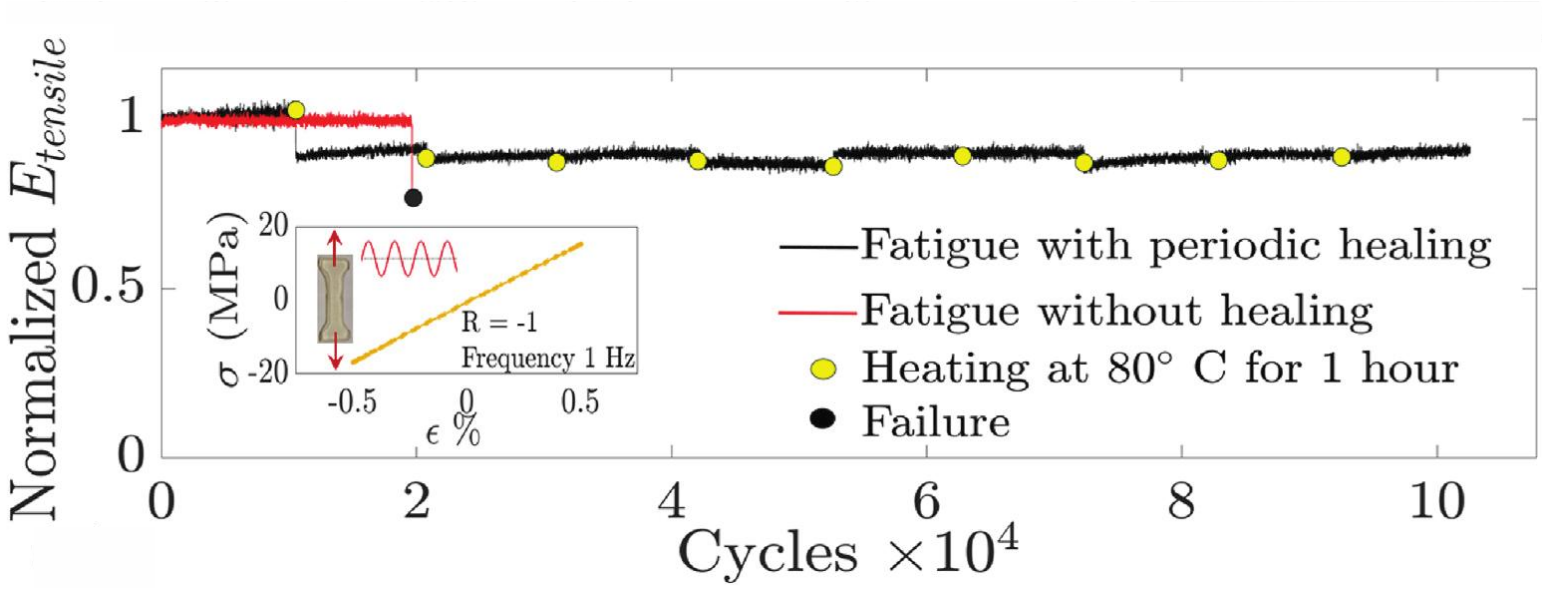

Key idea: Leverage healing polymers for recyclable composites

Kamble and Vashisth et al. “Reversing fatigue in carbon-fiber reinforced vitrimer composites”, Carbon 2022.

Why Soft Vitrimers?

- The rapid growth of **soft electronics** and **robotics**
- The repeated use of soft materials may lead to fatigue damages and failure of part.
- *Opportunity: Soft materials such vitrimer with **conformability** and **stretchability**, **mechanically reliable** and **healability** properties may be useful for these applications*

Synthesis of vitrimer

(a) Step-1: Synthesis of polyester adipate with carboxylic end groups

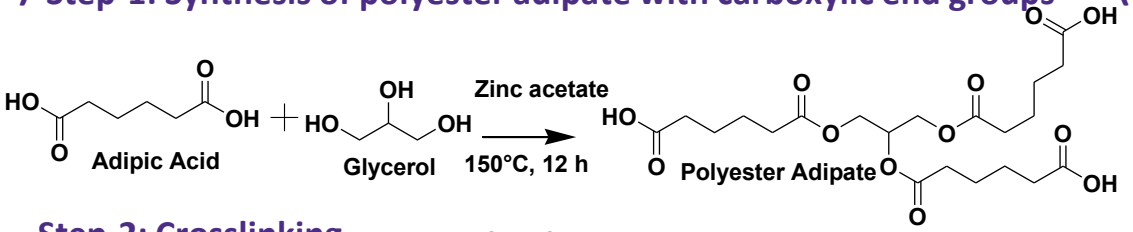

Step-2: Crosslinking

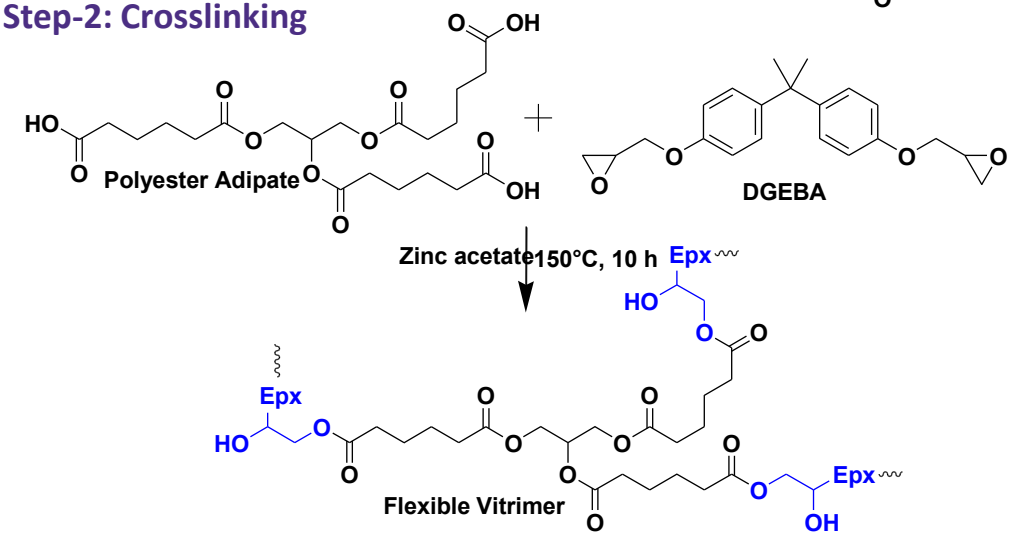

(b) Schematic for vitrimerization mechanism through transesterification

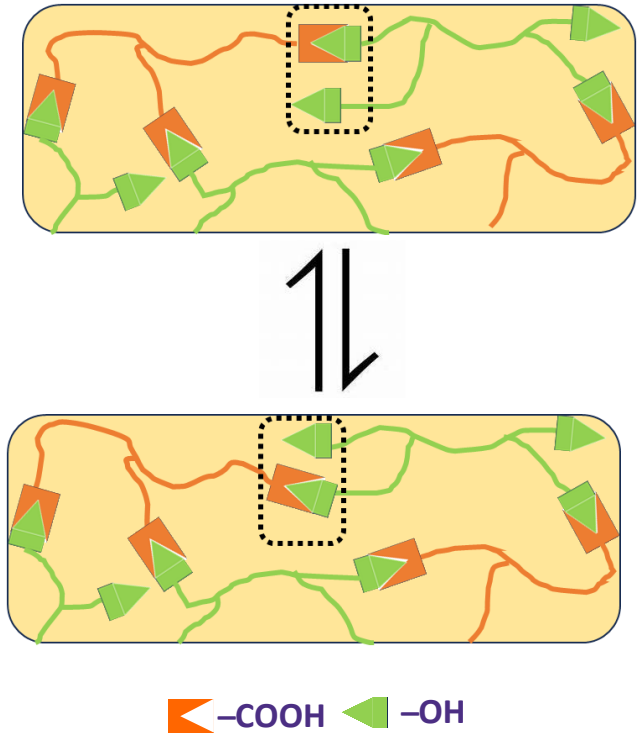

(a)

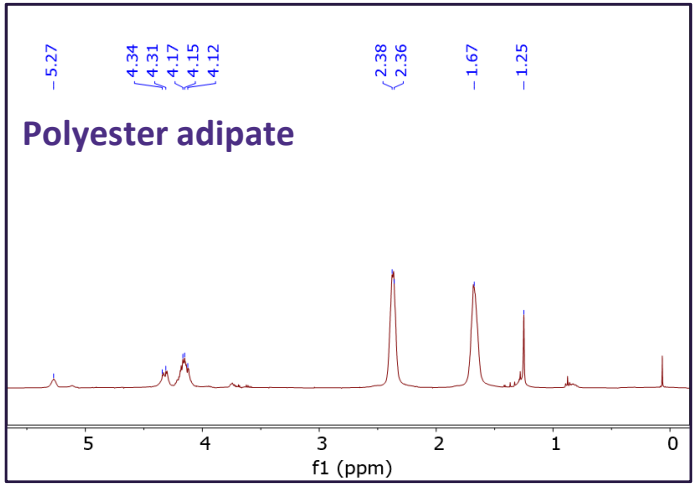

(b)

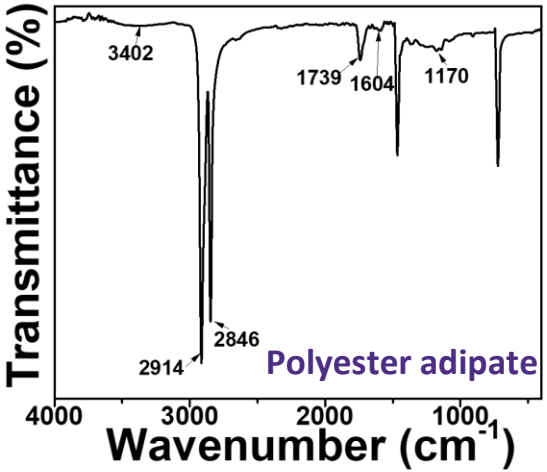

(c)

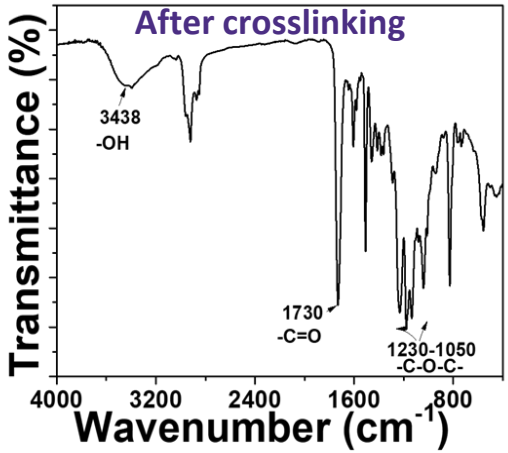

- ✓ Formation of polyesters with carboxylic end group were confirmed from HNMR and FTIR.
- ✓ The crosslinking process with ester-linkage confirmed.

Thermal properties of vitrimer

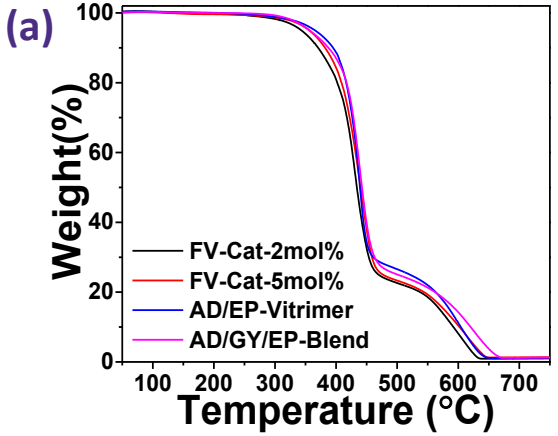

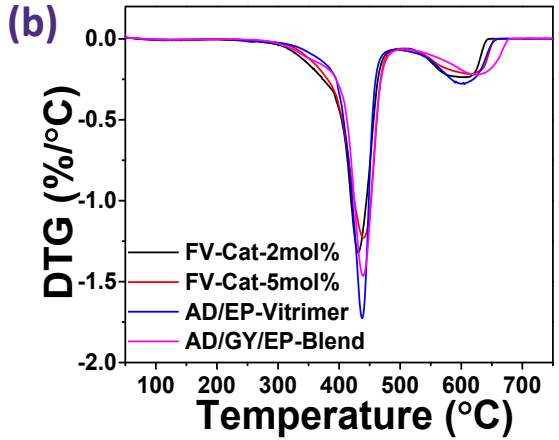

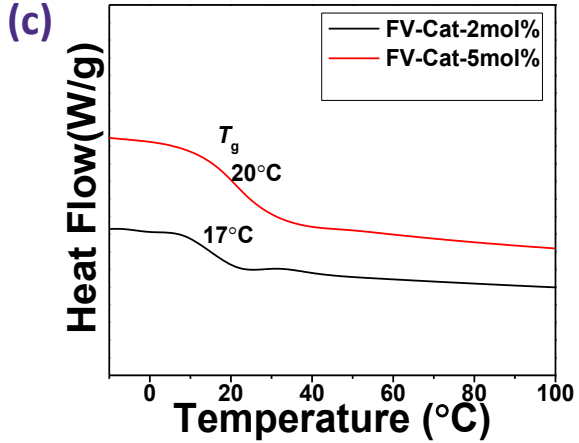

- ✓ Shows good thermal stability
- ✓ The only T_g value observed indicating no uncrosslinked monomers in the after crosslinking.

Flexibility and healability properties of soft vitrimer

(a)

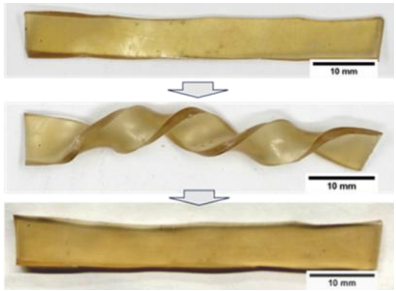

(b) Healing properties at 150°C

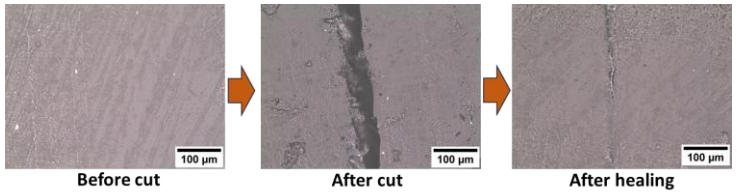

(c)

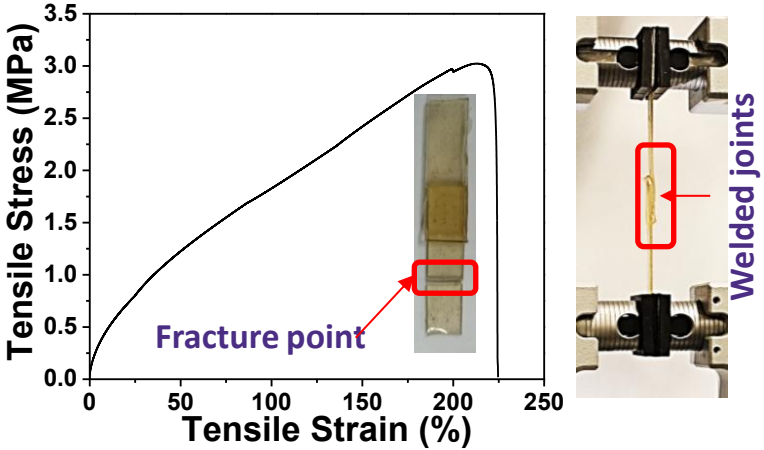

(d)

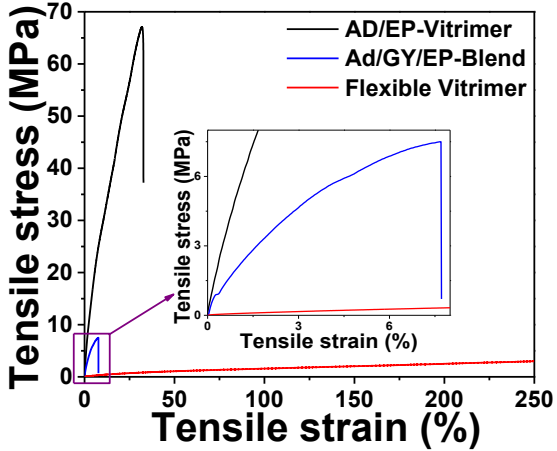

✓ The good healability and weldability show, the materials are reprocessable and remoldable in nature.

Toughness for flexible vitrimers

(a)

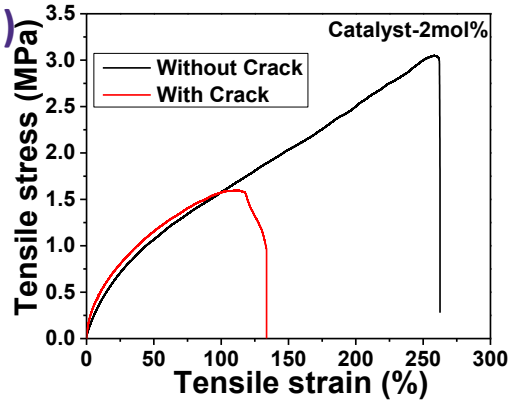

(b)

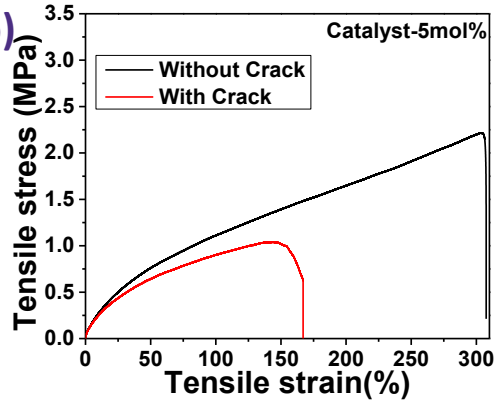

(c)

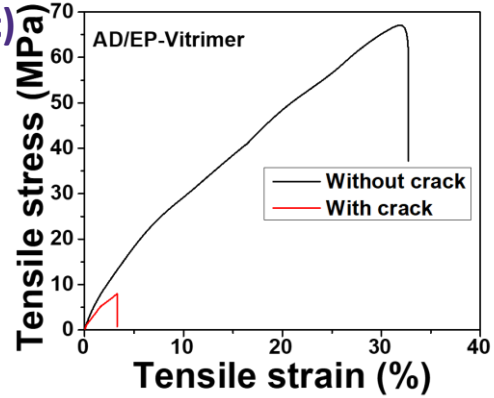

(d)

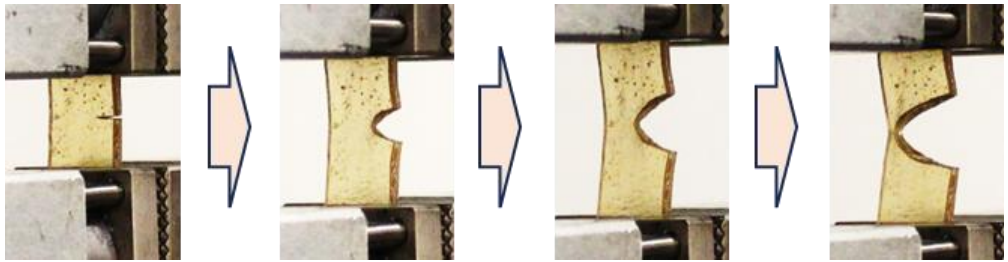

5% strain | 10% strain | 100% strain Crack opening | Crack propagation

The resulted vitrimers shows good extension upto 300% with toughness energy 476 J/m^3 compared to the hard vitrimers

Viscoelasticity properties

Thermomechanical analysis

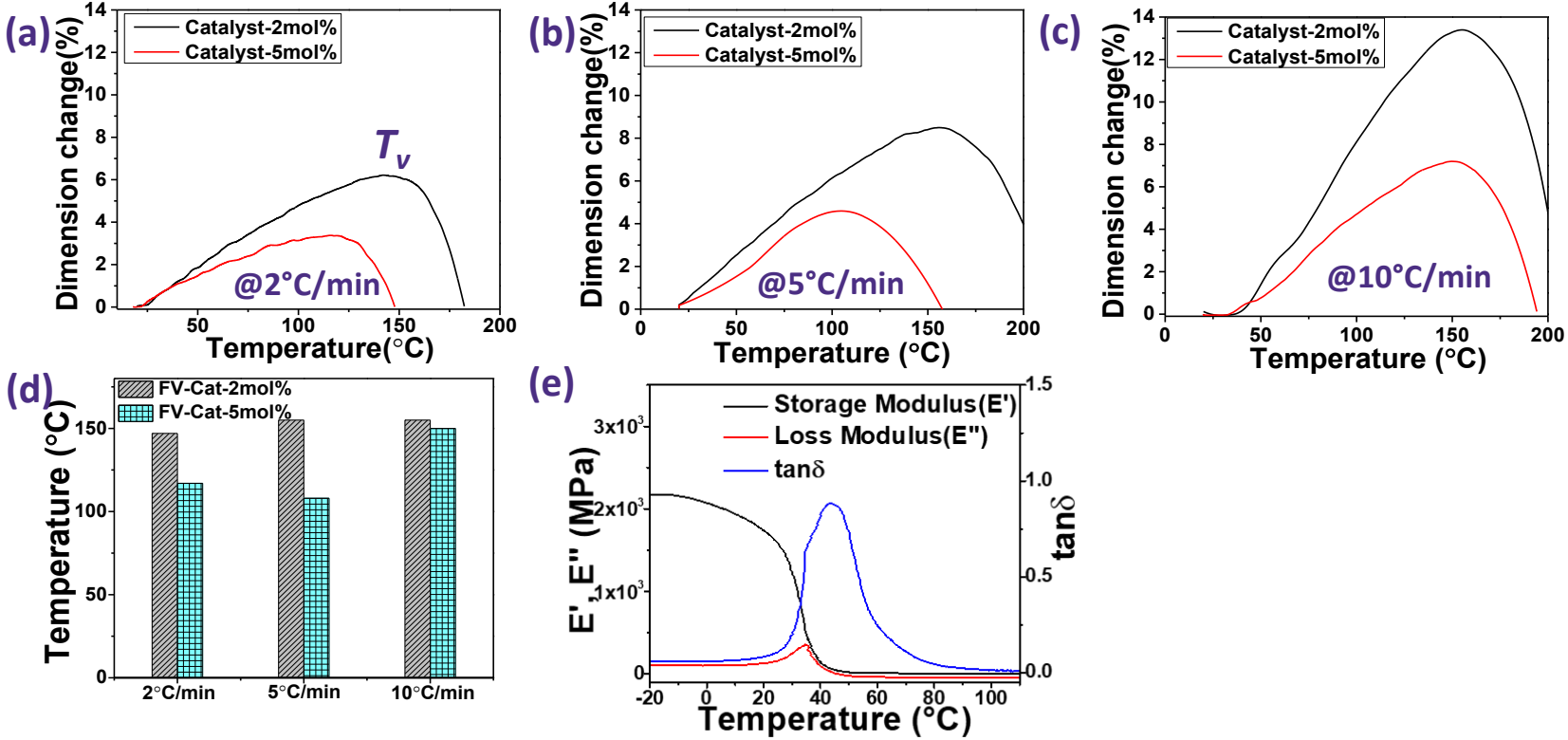

Observed broad peaks indicate, the above the topological freezing temperature Tv, more reversible reactions and show effective flow properties in the matrix.

ReaxFF molecular dynamics simulations of vitrimers

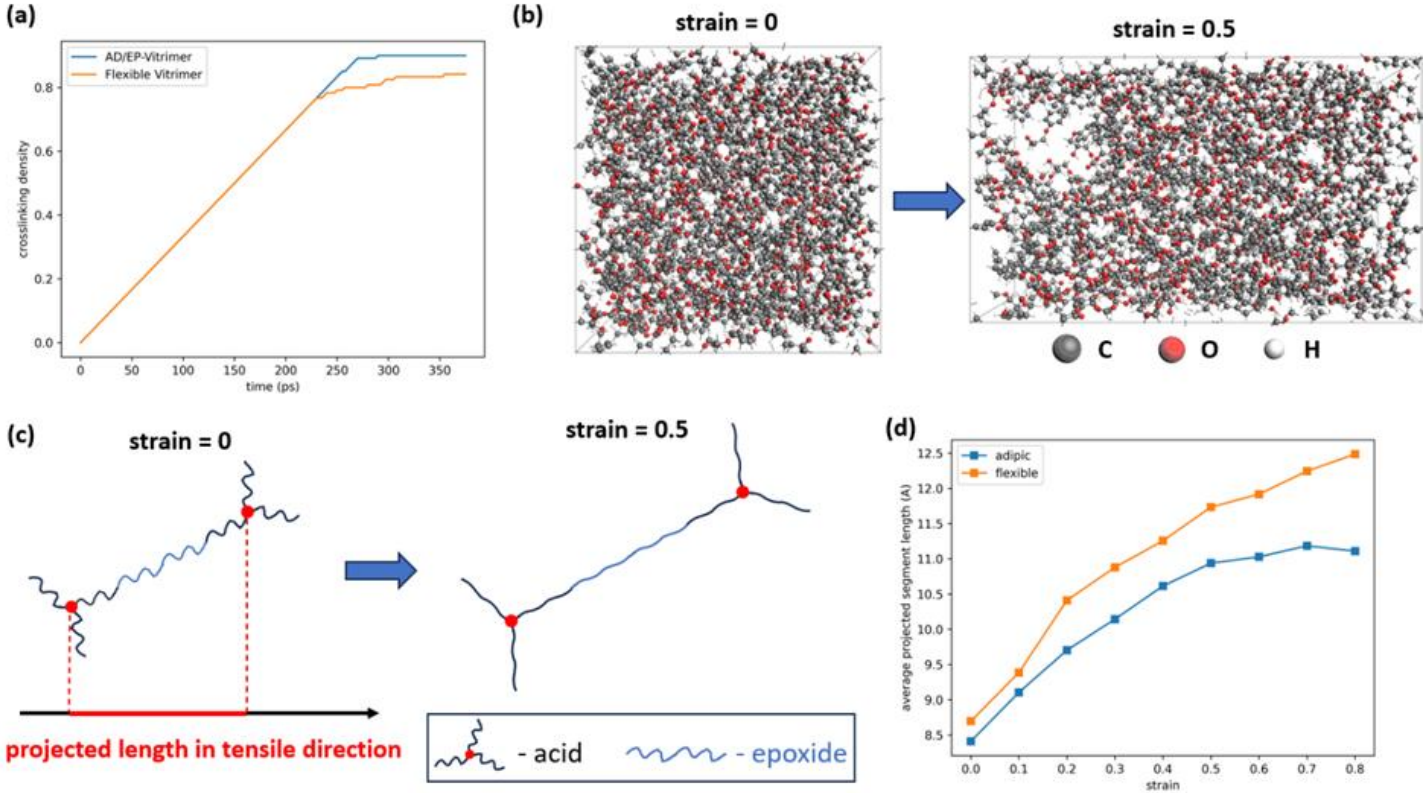

Polymer chain coiling in vitrimers results in higher strain to failures

Applications in Electronic Composites

Fabrication process of cable

(a)

(b)

(c)

(d)

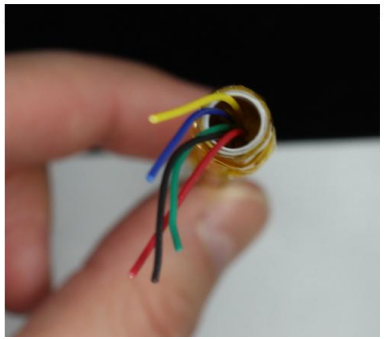

150°C

10 h

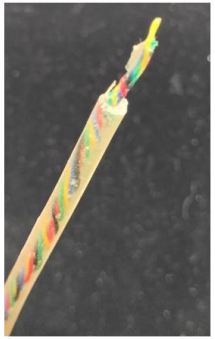

Extrusion

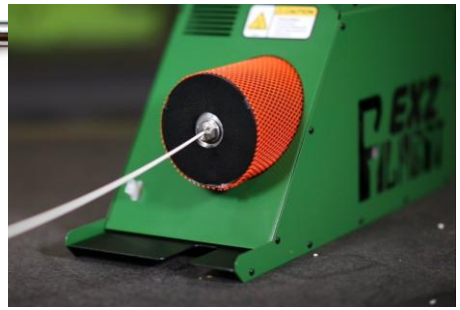



Flexible vitrimer-based USB cable

Healing Process In Electronic USB Cable

(a)

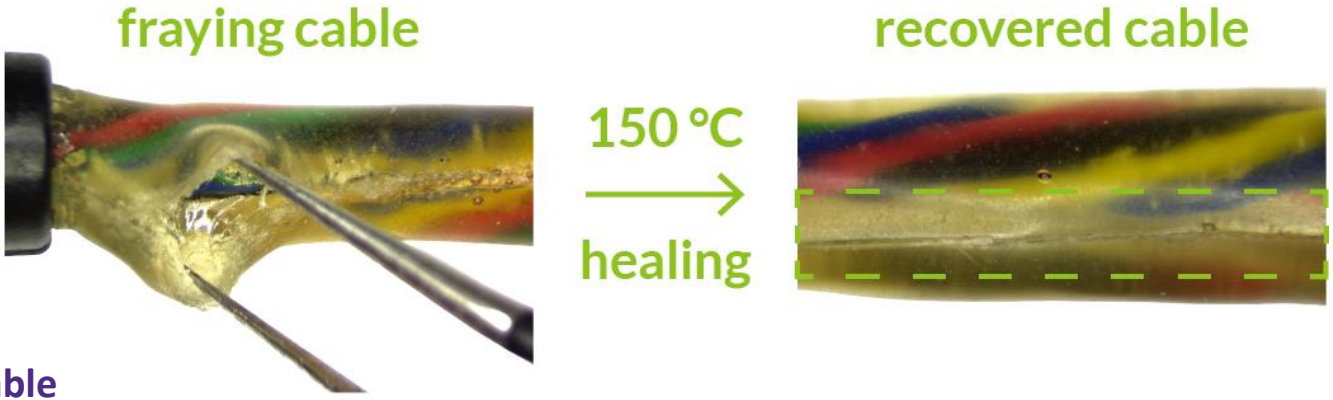

Electronic USB cable

(b)



(c)



Swelling Experiments for Component Recovery

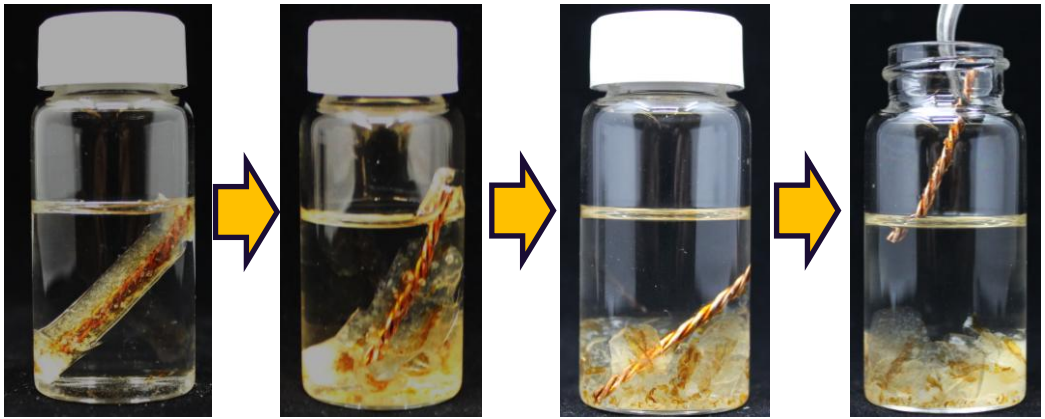

Swelling polymer Separation of polymer

Supplementary Video 1

Vitrimer swelling in THF

Summary

- ✓ **Inclusion of polymeric thermoplastics with increased chain length into the crosslinked network make them flexible and tough materials.**
- ✓ **Thermomechanical method can be a good technique to determine the more like topological freezing temperature.**
- ✓ **The synthesized vitrimer gives good flexible(300% strain) and toughness properties with 476J/m^3**
- ✓ **The flexible vitrimers can be a good candidate for the other electronics in terms of their fatigue and healability properties.**

Acknowledgement

- Mechanical Engineering, University of Washington
- Prof Vikram Iyer and Zhihan Zheng from UW CSE
- Brian Sun and Ankush Nandi
- Amazon Research Award

ICCM24
AUGUST 4-8, 2025
BALTIMORE CONVENTION CENTER
BALTIMORE, MARYLAND, USA

No Technical Paper Submission for:

Sharine Noelle Bendulo

ICCM24
AUGUST 4-8, 2025
BALTIMORE CONVENTION CENTER
BALTIMORE, MARYLAND, USA

No Technical Paper Submission for:

Abrar Ul Haq Khan Baluch

Quantification of Alignment Quality of Aligned Discontinuous Fibers using 2D-FFT (Fast Fourier Transform)

John J. Tierney, Alex Vanarelli, John Morris, Shridhar Yarlagadda, John W. Gillespie Jr.
Center for Composite Materials, University of Delaware, Newark DE 19716

Introduction

- Highly aligned discontinuous fiber composites developed at UD-CCM called TuFF (Tailorable Universal Feedstock for Forming) produces formable aerospace grade properties equivalent to continuous fiber composites.
- The manufacturing process creates a dry bed of aligned fibers at low areal weight that needs to be quantified for alignment quality
- 2D FFT (Fast Fourier Transform) creates a frequency domain representation of an image and can be used to observe order and orientation within the microstructure.
- This effort looks to enable in-line QA-QC measurement of fiber alignment using FFT light-transmission processed images.

FFT Theory

Definition

$$F(u,v) = \int_{-\infty}^{\infty}\int_{-\infty}^{\infty} f(x,y)e^{-j2\pi(ux+vy)}\,dx\,dy,$$
$$f(x,y) = \int_{-\infty}^{\infty}\int_{-\infty}^{\infty} F(u,v)e^{j2\pi(ux+vy)}\,du\,dv$$

where u and v are spatial frequencies.

Also will write FT pairs as $f(x,y) \Leftrightarrow F(u,v)$.

- $F(u,v)$ is complex in general,

$$F(u,v) = F_{\mathrm{R}}(u,v) + jF_{\mathrm{I}}(u,v)$$

- $|F(u,v)|$ is the magnitude spectrum
- $\arctan(F_{\mathrm{I}}(u,v)/F_{\mathrm{R}}(u,v))$ is the phase angle spectrum.
- Conjugacy: $f^*(x,y) \Leftrightarrow F(-u,-v)$
- Symmetry: $f(x,y)$ is even if $f(x,y) = f(-x,-y)$

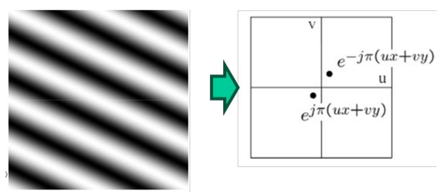

FFT Processing of TuFF

Poorly Aligned TuFF material

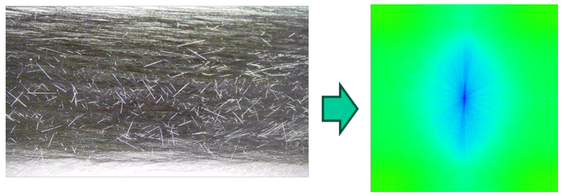

Highly Aligned TuFF material

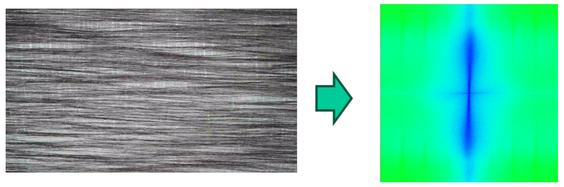

2D-FFT intensity spectrum indicates the overall alignment quality of the material based on the intensity and 'shape' of the frequency domain

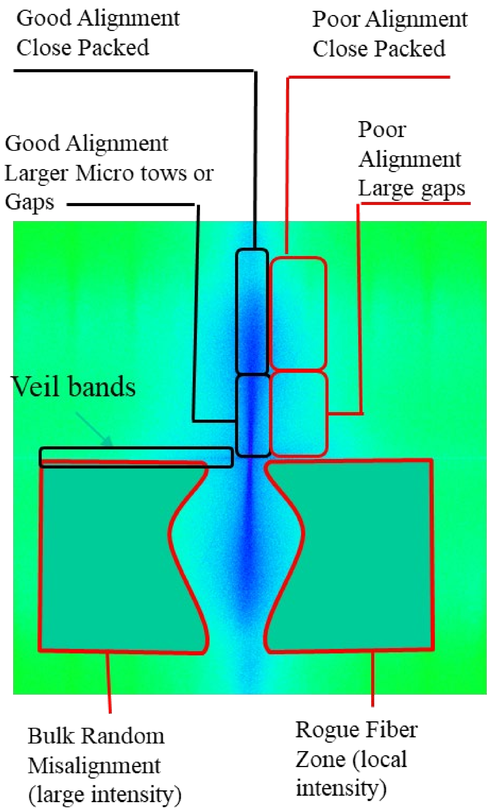

In-Line QA-QC Inspection Software

- LabVIEW based Software for real-time in-line alignment quantification
- Line profiles at different frequencies show alignment at different length scales from bulk to filament level based in image resolution
- Software captures entire production datasets for process repeatability and consistency

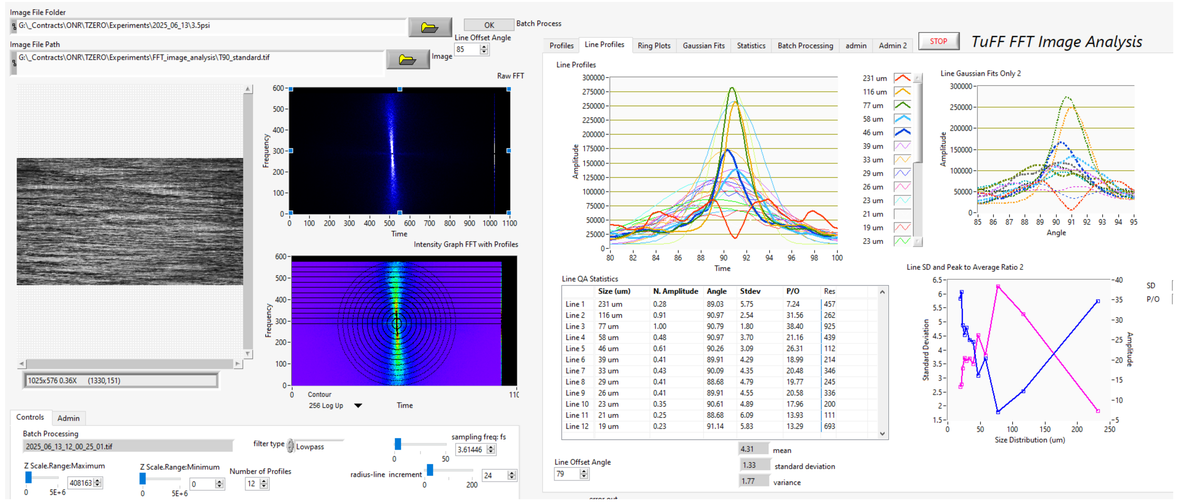

Post Processing Data

- Profiling the FFT image resolves alignment at multiple length scales based on image resolution

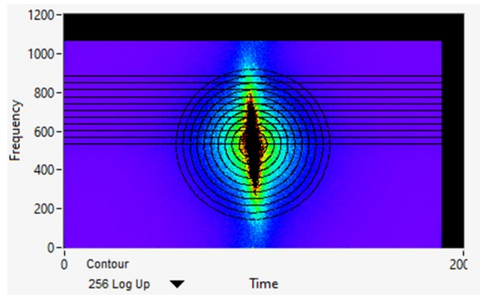

Statistical results for fiber alignment from single Image

Line QA Statistics

	Size (um)	N. Amplitude	Angle	Stdev	P/O	Res
Line 1	293 um	0.26	89.05	2.43	18.26	498
Line 2	146 um	1.00	90.19	0.99	99.93	790
Line 3	98 um	0.63	90.10	1.30	68.01	341
Line 4	73 um	0.42	90.00	1.48	49.08	176
Line 5	59 um	0.36	90.00	1.49	47.76	142
Line 6	49 um	0.18	89.62	2.10	26.90	158
Line 7	42 um	0.12	89.62	2.05	21.04	709
Line 8	37 um	0.11	88.86	2.18	20.59	725
Line 9	33 um	0.06	90.00	2.75	13.49	288
Line 10	29 um	0.05	88.57	2.88	13.29	263
Line 11	27 um	0.05	87.81	3.29	12.86	231
Line 12						

TuFF Production Facility with Lightbox Image Capture Stations



Lightbox with High Speed Camera



Statistical Data Over Time

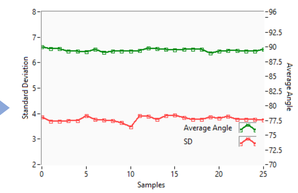

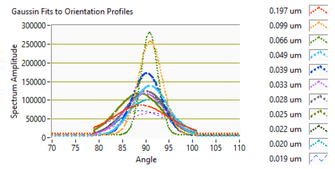

Intelligent Manufacturing Support: Specialized LLMs for Composite Material Processing and Equipment Operation

Kevin Mora-Gonzalez, Komal Chawla, Seokpum Kim — Oak Ridge National Laboratory

Introduction

- **Manufacturing Equipment Challenges**
  - Manuals are distributed across multiple PDF files and formats
  - Equipment troubleshooting requires immediate, accurate information
  - Operators need instant access to specifications, procedures, and safety protocols
  - Critical documentation often lacks remote or mobile accessibility
  - Operators face challenges accessing immediate specifications and procedures, leading to increased training costs due to traditional search limitations
  - Expert technicians' knowledge is not consistently recorded or easily shared

Objectives

1. Provide instant, contextually-aware answers from equipment manuals
2. Implement AI-powered validation of source document relevance
3. Deploy secure network tunneling for global accessibility
4. Accelerate troubleshooting through intelligent query processing
5. Improve operational efficiency and reduce downtime

Overview

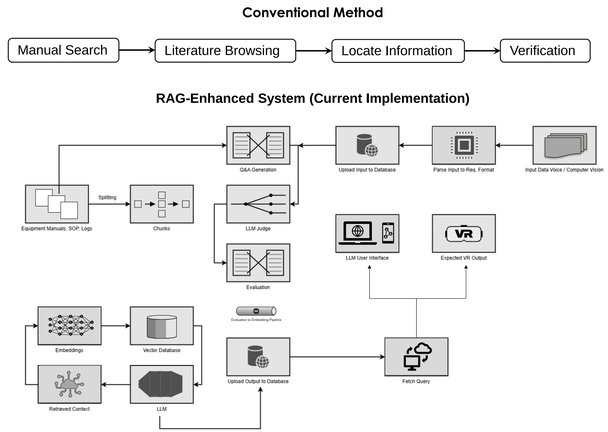

System Architecture

Core Components

Component	Technology	Function
Document Processing	PyMuPDF, NLTK, Mistral OCR, Whisper API	PDF extraction, image OCR, audio transcription, and chunking
Vector Storage	FAISS	High-performance similarity search
Embeddings	mxbai-embed-large	Semantic vector generation
Language Models	Ollama (Llama3.2, Mistral Large 2, Gemma3)	Answer generation and reasoning
Citation Validation	Semantic similarity, Cross-encoder, BERT	Source relevance verification
User Interface	Streamlit	Interactive web application
Networking	ngrok	Make the system available to specified networks or public

- **Data Ingestion Layer**

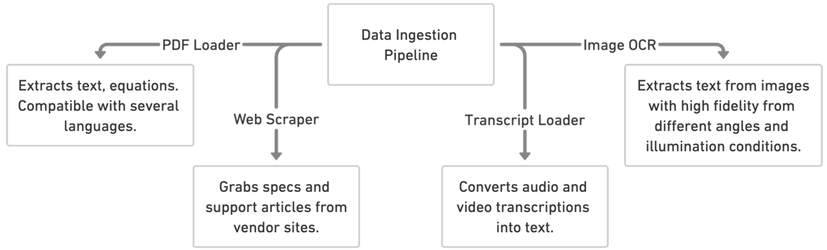

- **Indexing Layer**
  - Chunks documents into 200-500 token passages
  - Embeds chunks via Ollama embeddings API
  - Stores embeddings in FAISS for fast similarity search
- **Retrieval Layer**
  - Accepts user query, and applies basic preprocessing
  - Executes k-nearest neighbor search on FAISS index
  - Returns top-k passages ranked by cosine similarity
- **Large Language Model Layer**
  - Integrates diverse Ollama models for flexible, cost-efficient deployment
  - Feeds retrieved passages plus query into RetrievalQA chain
  - Facilitates semantic search via vector embeddings
  - Pipeline ingests and indexes vast proprietary data into vector store for efficient, updated information retrieval

RAG System Evaluation

- **Traditional NLP Metrics**

Metric	Score	Function	Benchmark
F1 Score	0.847	Token-level precision and recall	0.75+ (Good)
BLEU	0.723	N-gram overlap with reference answers	0.60+ (Acceptable)
ROUGE-L	0.812	Longest common subsequence matching	0.70+ (Good)
BERT Score	0.889	Semantic similarity using BERT embeddings	0.80+ (Very Good)

- **Hallucination Detection**

Metric	SelfCheckGPT BERT Score	SelfCheckGPT NLI
Score	0.891	0.934
Function	Consistency across multiple generations	Natural Language Inference contradiction detection
Benchmark	0.85+ (Very Good)	0.90+ (Excellent)

This RAG System Evaluation outlines a comprehensive methodology, utilizing traditional NLP metrics like F1 Score (0.847), BLEU (0.723), ROUGE-L (0.812), and BERTScore (0.889) to assess text generation quality. Hallucination detection is also rigorously performed using SelfCheckGPT BERTScore (0.891) and NLI (0.934) for consistency and contradiction checks.

- **Response Time Analysis**

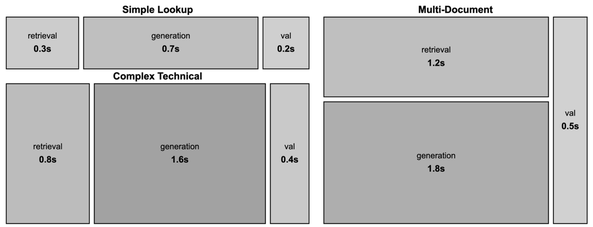

Treemap presents a 'Response Time Analysis' for different query types, detailing average time (in seconds) and its breakdown into retrieval, generation, and validation, with an overall average response accuracy of 89.2% on technical equipment questions. Simple lookups average 1.2 seconds, complex technical queries 2.8 seconds, and multi-document queries 3.5 seconds, each with proportional component contributions.

Citation Validation Framework

- **Validation Performance**
  - The citation validation achieved an average accuracy of 92.4%
  - False positive rate was <8%, effectively filtering irrelevant results
  - Processing overhead remained under 2 seconds per query
  - Emergency fallback activates when citation relevance falls below the set threshold

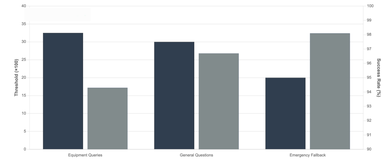

This dual-axis bar chart shows confidence thresholds and success rates for three citation validation applications, where the first bar represents confidence threshold ranges scaled by 100 and the second bar shows success rate percentages. Equipment Queries use higher thresholds (0.25-0.40) for safety critical operations, while Emergency Fallback uses lower thresholds (0.20+) to maximize availability, achieving success rates from 94.3% to 98.1%.

Method	Purpose	Weight	Technology	Validation Score
Semantic Similarity	Conceptual Relevance	40%	Sentence Transformers	0.876
Cross-encoder	Deep Contextual Analysis	35%	RoBERTa based score	0.902
BERT Score	Token-level similarity	25%	Contextual embeddings	0.889

$$R_{\text{BERT}} = \frac{1}{|x|} \sum_{x_i \in x} \max_{\hat{x}_j \in \hat{x}} \mathbf{x}_i^\top \hat{\mathbf{x}}_j$$

Network Tunneling Implementation

- **Security and Performance**
  - Tunnel establishment typically takes less than 3 seconds
  - Bandwidth capacity supports multiple concurrent users
  - Utilizes HTTPS encryption with TLS 1.3 via ngrok for secure data transmission
  - Ensures 99.9% availability with auto-reconnect, quickly applying critical codebase changes for continuous uptime
  - Latency overhead ranges from 2 to 60 milliseconds, varying by user location. Controlled access management, allowing specification of tunnel access and IP-based content locking

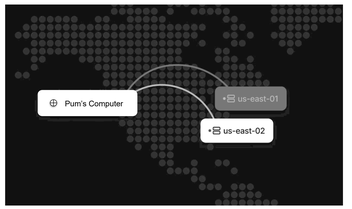

Performance & Cross Platform

- **System Capabilities**
  - Processes over 100 PDF manuals and polymer literature simultaneously, allowing for fast information access
  - Supports multiple simultaneous queries and it is scalable
  - Offers full functionality across smartphones, tablets, and computers, independent of their operating system



Limitations and Future Work

- Local inference performance is constrained by host GPU machine capabilities
- Future work explores Virtual Reality integration, allowing manufacturing users immersive access to documentation
- Addressing potential knowledge gaps within specialized or emerging equipment documentation

CompositesAI™

An AI-Powered Expert System for Composites

Try me at CompositesAI.com

OVERVIEW **CompositesAI consolidates and delivers expert knowledge through LLMs fine-tuned for composites. It delivers answers with authority of world-leading experts and precision of advanced simulation codes.**

Challenges

➢ Access to data and resources

- ❑ Static data: technical papers, books, reports, database, etc.; siloed and disparate sources
- ❑ Dynamic data: physics-based models, machine learning models; disconnected and not available for entire supply chain
- ❑ Expensive computing hardware and software
- ❑ Some in public domain (commercial or free) and some proprietary

➢ Access to talent

- ❑ Most composites engineers lack formal training in the field. Composites-related typically courses taught at graduate level
- ❑ PhDs needed for executing sophisticated composites software for reliable simulation
- ❑ PhDs trained in narrow subdomains, multiple PhDs needed for the entire production workflow, not affordable for lower tiers of the supply chain (SMEs)

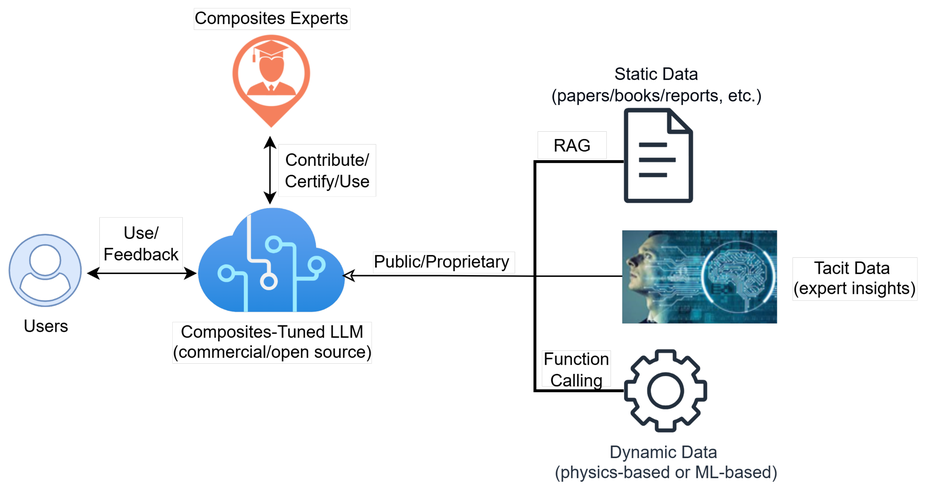

Solutions by Composites AI

➢ Large language model (LLM)

- ❑ Leverages general knowledge, intelligence, and natural language processing capabilities of LLM
- ❑ Is designed to be LLM-agnostic, ensuring seamless integration with emerging and advanced models
- ❑ Delivers highly technical knowledge through intuitive, natural language chat prompts

➢ Retrieval-augmented generation (RAG)

- ❑ Consolidates multimodal, publicly available static data using a federated vector database
- ❑ Optimizes RAG by applying best practices in data storage, chunking, retrieval, and ranking
- ❑ Intelligentizes proprietary corporate knowledge within a private and secure environment

➢ Function calling

- ❑ Integrates simulation software through APIs
- ❑ Enables automatic execution of simulation codes and linking them into seamless workflows
- ❑ Democratizes simulation by chats, eliminating complexity of preparing inputs and interpreting outputs
- ❑ Performs parametric studies and optimization automatically, requiring simple prompts without extra coding

➢ Human-in-the-loop reinforcement learning

- ❑ User provides questions and feedbacks
- ❑ Admin reviews user feedbacks and assign experts to reviews
- ❑ Expert reviews feedbacks and generates new knowledge as structured questions-pairs
- ❑ CompositesAI updates with the new knowledge

➢ Versatile front end

- ❑ Signup/Login using email, Google, Microsoft, or LinkedIn
- ❑ Ask questions using text or voice in your own language
- ❑ User can provide detailed responses including numerical score, reason, and text comments
- ❑ Different users can access to different customized models

➢ Ecosystem for community development

- ❑ Powerful workspace allows expert to create their own AI assistants (private, or shared with others)
- ❑ Model-agnostic design allows experts to experiment with different models
- ❑ A marketplace for all the agents developed by experts.
- ❑ User-friendly interface for experts to submit knowledge & tools

PURDUE UNIVERSITY

Contact us: Wenbin Yu (wenbinyu@purdue.edu) and R. Byron Pipes (bpipes@purdue.edu)

CMSC Composites Manufacturing & Simulation Center™

A Typical Use CASE (Simulation using Prompts)

An engineer needs to determine the relative difference between the longitudinal and transverse shear moduli of UDFRC but lacks the expertise to operate FEA-based multiscale software such as SwiftComp. CompositesAI bridges this gap by allowing engineers to obtain accurate results without needing to learn or run complex simulation codes. By understanding the engineer's intent, CompositesAI identifies the appropriate computational tool, gathers the necessary inputs through natural, intuitive prompts, and delivers results efficiently and precisely.

for a unidirectional fiber reinforced composites, I would like to know G13 and G23, do you have a tool to help me compute it?

CompositesAI

Yes, I have a specialized tool that can compute the shear moduli G_{13} and G_{23} (as well as other engineering constants) for unidirectional fiber-reinforced composites. This tool requires the following inputs:

Fiber and matrix elastic properties (E, ν or full set if anisotropic)
Fiber volume fraction
Packing arrangement (e.g., hexagonal, square)

If you provide:
Fiber modulus (E_f) and Poisson's ratio (ν_f)
Matrix modulus (E_m) and Poisson's ratio (ν_m)
Fiber volume fraction (V_f)
Packing type (default is hexagonal if not specified)

I can obtain G_{13} and G_{23} for your system. Please supply the above inputs or confirm if you want to use prior examples.

isotropic fiber with E=300 GPa, nu=0.3; isotropic matrix with E=20 GPa, nu =0.4, hexagonal, Vf=68%

CompositesAI

View Result from **homogenize_elastic_constants**

For a unidirectional fiber-reinforced composite with isotropic fibers ($E_f = 300\,\text{GPa},\ \nu_f = 0.3$), isotropic matrix ($E_m = 20\,\text{GPa},\ \nu_m = 0.4$), hexagonal packing, and a fiber volume fraction of 68%, the calculated shear moduli are:

$G_{13} = 28.86$ GPa
$G_{23} = 31.58$ GPa

These values are computed using physics-based homogenization methods appropriate for your specified microstructure and constituent properties.

Your numbers are a bit high. Try Ef = 231 GPa, Poisson's ratio of the fiber is 0.35. Em = 4 GPa, Poisson's ratio of matrix is 0.3.

CompositesAI

View Result from **homogenize_elastic_constants**

For a unidirectional fiber-reinforced composite with the following properties:

Isotropic fiber: $E_f = 231\,\text{GPa}, \nu_f = 0.35$
Isotropic matrix: $E_m = 4\,\text{GPa}, \nu_m = 0.3$
Hexagonal packing, fiber volume fraction $V_f = 68\%$

The computed shear moduli are:

$G_{13} = 7.50\,\text{GPa}$
$G_{23} = 7.21\,\text{GPa}$

These values reflect a physically realistic shear response for your specified composite system.

Powering the Global Composites Community



cdmHUB Community

- **Vision:** to be the premier resource for composites design and manufacturing
- **Mission:** to convene and serve the global composites community by creation, education, evaluation, and sharing of resources for composites design and manufacturing
- **Features:** AI-human Interactive Platform
  - ❑ Powered by Discourse, a modern forum software leverage strengths of technical forum and social media
  - ❑ Message and chat with CompositesAI, individuals, or groups
  - ❑ Directly connects with CompositesAI so it can engage deep technical discussions with others

cdmHUB Composites Design & Manufacturing HUB

Scan to join cdmHUB Community

PURDUE UNIVERSITY

Contact us: Wenbin Yu (wenbinyu@purdue.edu) and R. Byron Pipes (bpipes@purdue.edu)

CMSC Composites Manufacturing & Simulation Center™

WRAPTOR BAMBOO TRUSSES: QUANTIFYING THE IMPACT OF CULM GEOMETRY VARIATION ON BENDING PERFORMANCE

Matthew Enrico Lillywhite, Terence Macquart, Byung Chul Kim, and Benjamin King Sutton Woods

Bristol Composites Institute, University of Bristol
Queens Building, University Walk, Bristol BS8 1TR, United Kingdom
Email: matthew.e.lillywhite@bristol.ac.uk

Keywords: Natural Materials, Composite Trusses, Bamboo

ABSTRACT

Full culm bamboo is a natural material which could be used as the primary constituent as elements in efficient truss geometries that could subsequently be used to assemble larger hierarchical spaceframes. Using bamboo in such structures removes limitations on bamboo constructions imposed by the natural size and shape of the grown plant that cannot be controlled. Traditional truss manufacturing methods are unsuitable for bamboo as it is comprised of longitudinally aligned fibres prone to splitting, thus the Wrapped Tow Reinforced (WrapToR) truss manufacturing process, originally developed for fibre reinforced polymers, is adapted here. WrapToR produces composite material trusses via winding a continuous composite tow around pultruded tubes mounted on a mandrel. If bamboo were to be substituted for the pultruded tubes, the innate geometric variation between and within bamboo culms will cause challenges in truss winding and performance prediction of WrapToR trusses. A non-concentric circle culm model of bamboo culms is developed here to measure and represent this geometry variation. This method operates at a middle fidelity between simpler prismatic estimations of shape and higher fidelity measurements of the full 3D geometry. It uses physical measurements from a bespoke rig to estimate circular cross sections of a culm at regular length intervals, which are then lofted into a full culm. These models are then used to provide geometry responsive path planning for the winding machine, and are also used within finite element analysis to provide estimates for individual culm bending performance and full WrapToR truss performance. The FEA models are then validated against data gathered from mechanical testing.

1 INTRODUCTION

An ever increasing focus on the development of sustainable construction methods has motivated research into the use of bamboo as an alternative material in buildings and infrastructure. Historically, bamboo was widely used for construction throughout its naturally occurring range, but today it is usually overlooked in favour of more common materials such as concrete, steel, masonry, and timber [1]. The primary advantage of using bamboo is that it has mechanical properties competitive with timbers, whilst having a faster growth rate, reaching maturity within 3-5 years [1,2]. Faster replenishment time of construction material provides environmental benefits such as lower levels of deforestation, as less land is required to grow the same amount of material [2]. These factors have recently lead to a resurgence in research into the use of bamboo and its usage has been demonstrated in a variety of showcase applications [2,3,4].

The stalk or ‘culm’ of the Bamboo plant can be used directly ‘as harvested’ as tubular beam like elements, or they can be split down into smaller segments and reformed into composites to allow more geometrical freedom. Using the full culm as a beam can be advantageous, allowing for the utilisation of the efficient natural structure of bamboo as a thin walled, hollow tube comprised of longitudinally oriented fibres. The limitation of using full culm bamboo is that the size and shape of what can be built are limited by the size of culm that can be grown. The material properties of bamboo, while impressive for natural materials, are also lower than conventional construction materials such as steel, further reducing what applications that it is suitable for.

The efficient structure of bamboo culms can be leveraged by using them as members in truss or space frame structures. Trusses takes advantage of highly non-linear structural scaling laws by putting small amounts of material into localised members which are spaced far away from each other, allowing them to balance large forces and bending moments with minimal stress. These members are also loaded axially which suits the structure of full culms. However, there is still a limit on the size, stiffness, and strength of the individual elements of these trusses stemming from the growth size limitations of the culm. In order to make larger and more highly loaded structures, one promising approach is the use of hierarchical space frames (HSFs), where the beam like members of the larger truss or spaceframe are themselves made from trusses. These truss beams could be made from longitudinally aligned bamboo culms that are held apart from each other by some form of shear web structure. These truss beams would have much higher second moment of area, and therefore stiffness and strength, than the culms on their own, and would therefore provide a way around the limitations on size and shape imposed by natural growth. These truss beams could then be connected together to form HSFs with a significant amount of design freedom with regards to size, geometry, and load carrying capacity. The key enabling element to this concept of bamboo based HSFs is the ability to quickly and efficiently manufacture truss beams from bamboo culms.

1.1 Wrapped Tow Reinforced Composite Trusses and Space Frames.

Similar work on attempting to fully utilise impressive properties of structures comprised of longitudinally oriented fibres has been conducted for the Wrapped Tow Reinforced (WrapToR) method which produce efficient truss structures from advanced composite materials such as carbon fibre reinforced polymer (CFRP) or glass fibre reinforced polymer (GFRP). WrapToR is an adapted form of filament winding, where composite pultruded tubes are mounted on a rotating mandrel where a single wetted composite tow is wound around the mounted pultruded tubes. The wetted composite co-cures to the surface of the pultrusion and forms a rigid truss beam such as the one shown in Figure 1. Because the WrapToR process only utilises adhesive co-curing and no physical fasteners, stress concentrations forming at fastener holes that propagate into large cracks are not seen in WrapToR trusses. WrapToR minimises the complexity of composite assembly, offering a simple, automated method of producing composite trusses.

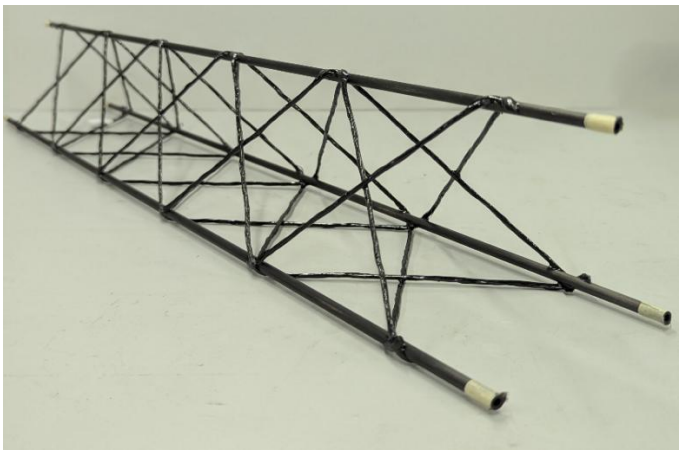

Figure 1: Wrapped Tow Reinforced truss.

The structural performance of WrapToR trusses has to date mostly been explored within the context of lightweight, high performance aerospace structures made from carbon fibre reinforced polymer (CFRP) [5,6], where it has shown exceptional performance. For example, outperforming unidirectional pultruded carbon fibre reinforced polymer tubes of a similar mass in a three-point bending test by 1006% in terms of stiffness and 181% in terms of maximum load at failure. WrapToR achieves this performance through its geometry by spacing the chord members far from the centre of the truss, maximising second moment of area, and therefore bending rigidity, for the same mass. The orientations of the fibres for both the chord members are also aligned in the axial direction for each member, which is the optimal direction

for this type of structure, which helps to get the most of the material used. Furthermore, the WrapToR method imparts a twist to the tow during winding in order to change the tow's shape from a thin ribbon into a circular cross section, increasing the buckling resistance of the wound shear members and the load carrying capacity of the truss beam [6]. Hierarchical space frames made from CFRP WrapToR truss beams have been previously explored using numerical modelling and structural optimisation [7].

1.2 Bamboo WrapToR HSFs: Potential and Challenges

The fundamental geometric advantages provided by WrapToR truss beams should be transferable to natural materials, given the top-level similarities in the structure of bamboo and pultruded composite tubes. A bamboo WrapToR HSF carries multiple advantages over using only a bamboo culm as a singular beam member. Because the truss beam geometry significantly increases the stiffness and strength of the bamboo material, while also loading the culm in a way which is very well suited to its inherent structural design, WrapToR HSFs can help mitigate the discrepancy in material properties between bamboo and other construction materials, especially when considered in a mass normalised manner. Another potential advantage of WrapToR bamboo HSFs would be the fundamental scalability of the design. If a comprehensive method of joining trusses together is developed, trusses can be assembled end to end allowing truss beam to be lengthened. This modular approach eliminates the issue that full culm bamboo structures are limited by the size and shape that they can be grown at. The WrapToR method also has advantages over conventional trusses as it is a simple, rapid and automated production method. In conventional truss structures many individual smaller elements must be carefully manufactured and then carefully assembled, a process which typically carries a high time and labour cost. In contrast, a WrapToR beam is composed of only 4 parts, the three chord members and the continuously wound shear web. A full truss winding can be carried out quickly by an automated machine and then left to cure [8].

However, significant challenges, particularly the geometric variation of bamboo culms, must be addressed before bamboo can be effectively used in WrapToR trusses. Geometric variation, both between different culms and across individual culms is a challenge that has to be solved to get the most performance out of bamboo in a WrapToR truss. As with all natural materials, geometric variation occurs as part of the growth process and cannot be fully predicted, controlled or prevented. In other natural materials that are more commonly used, for example timber, geometric variation is handled via sawing logs down into standardised and regularly shaped sections. Conventional sawing or machining processes are less useful for bamboo because the structure of bamboo culms is predominately a thin-walled tube, so the size of solid members than can be cut out of them are small.

Geometric changes such as changes in tube diameter and wall thickness; the number and position of nodes; or naturally occurring bends in the material will all have some effect on the overall stiffness and load bearing capacity of the culm. Furthermore, variation will also cause difficulty in the winding process for WrapToR trusses. The WrapToR winding process is controlled via G-code and open-loop control of the motors, hence the machine is 'blind' to the mandrel and the chord's mounted positions [8]. This means that the quality and accuracy of the winding is determined by the initial position of the chord members. In a regular composite pultrusion WrapToR truss the chord members are prismatic, and such the winding path can be easily calculated through simple trigonometry because the points of contact between the shear members and chord members are consistently placed. In WrapToR trusses with bamboo chord members path calculation is not trivial as the positions of the chord member and shear member connections change, dependent on the unique variation of the bamboo culm used. Furthermore, any combination of three bamboo culms each with their own variation can make manufacture difficult. An illustration of the challenge is shown in Figure 2.

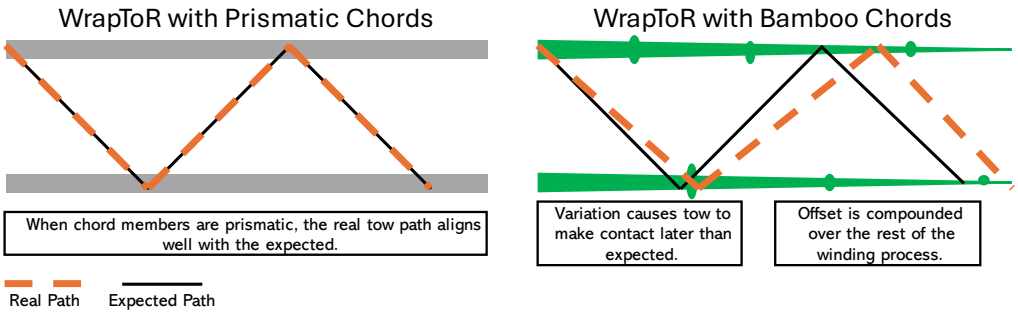

Figure 2: Winding challenges due to geometric variation

A method of capturing and representing the geometry of the culm that incorporates geometric variation will aid in addressing these challenges. Such a method should help in understanding the effects of variation on culm structural performance and allow for more precise winding within the WrapToR manufacturing process.

A simple method of culm representation is presented in the ISO standard for testing bamboo culm performance, namely BS ISO 22157. This approach takes two perpendicular measurements of culm width from an area in between two nodes, then assume a thin-walled tube with a diameter equal to the average of the two measurements [9]. This approximation does not effectively represent the geometry in a manner that would allow for the winding challenges depicted in Figure 2 to be solved, thus a higher fidelity model is required here. Higher fidelity approaches have been considered in other work, for example the use of a laser scanner to capture the full three dimensional outer geometry of bamboo culms, which were used within the computer aided design of a bamboo structure [10]. While this method captures the surface geometry in full, allowing for all the required analysis to be undertaken, it requires specialist equipment such as a full-field 3D laser scanner and actuating robotic arm control [10], and takes significant time to capture high quality scans [11]. Furthermore, these scans tend to be computationally expensive to use in analysis due to the large size of data sets created.

In order to better balance the fidelity of the geometry representation against the amount of effort required to create and use it, this work introduces a non-concentric circle culm model for bamboo culm geometries that sits at an intermediate fidelity. It is intended to be accurate enough to capture the first order impact of the geometry while also being significantly easier and faster to measure than a full laser scan, while also producing much smaller data sets that are easier to use within numerical modelling. The following section details how the non-concentric circle culm model measures and captures the geometry of bamboo culms. We then compare finite element analysis models, produced from the captured geometry to physical bending tests conducted on the scanned culms to assess the effectiveness of the models and to determine whether non-concentric circle based models can predict performance better than simple prismatic models. We then conduct the same study on manufactured trusses to determine its effectiveness for modelling the bending performance of WrapToR truss beams made with the measured bamboo culms.

2 NON-CONCENTRIC CIRCLE CULM MODEL

In the non-concentric circle culm model, the cross section of the culm at any point along its length is approximated as a circle, with the culm itself being composed of many linked circles of various sizes and positions. The centres of these circles are not assumed to be colinear however, instead the effective centre of each circle is measured in three-dimensional space, allowing for curvature and other discontinuities along the length of the culm. Therefore, this approach is able to capture the diameter changes and lack of straightness that are typical of bamboo culms. The calculated circles are lofted together to produce the model of the culm surface.

The bespoke rig used to take the surface measurements is shown in Figure 3. This rig is comprised of five different potentiometers and a sliding mount to hold the culm at a fixed reference location. In this rig physical potentiometers are used although precision single point laser distance sensors may also be appropriate. As shown in Figure 3, four potentiometers (5V Gefran PY2-50, Gefran) are mounted on a circular frame at the centre of the rig. Because the positions of each of the four potentiometers is fixed and known, this establishes a reference area where the measurements taken can be related to a cartesian position within the area, where the centre is taken to be the origin. The fifth potentiometer is a CD50S string potentiometer which records the longitudinal position of the culm. An Arduino control board was used which provided a resolution of 0.05 mm with the four surface measurement potentiometers and a resolution of 1 mm for the string potentiometer. This provides measurements for 1000 cross sections for a 1 m culm. The mounted culm is passed through the potentiometers using the slider, and measurements are taken from each. For each cross section, five different values are obtained, four relate to the surface distance from the potentiometer mount and one value for the longitudinal position of that particular cross section along the culm.

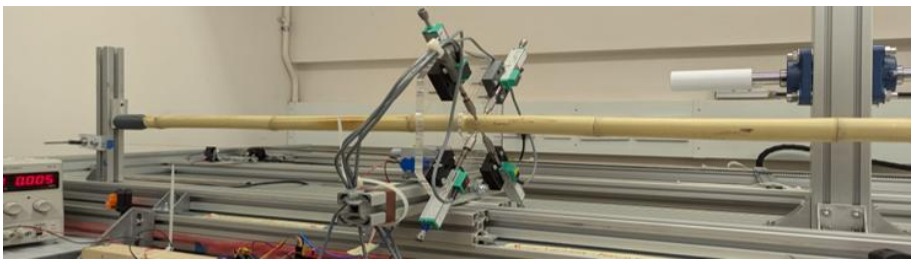

Figure 3: Bespoke culm measurement rig.

Each of the four surface measurements are related to a cartesian coordinate within a reference area defined by the known position of the potentiometers as shown in Figure 4. Three of the four coordinates calculated are substituted into the set of simultaneous equations shown in Equation 1 to define the cross section of the culm as a circle with the radius, r, and the centre of the circle (a, b).

$$\begin{aligned} (x1 - a)^2 + (y1 - b)^2 &= r^2 \\ (x2 - a)^2 + (y2 - b)^2 &= r^2 \\ (x3 - a)^2 + (y3 - b)^2 &= r^2 \end{aligned} \tag{1}$$

This process is repeated four times for each possible set of three coordinates. The final circle is calculated as the averaged from each circle produced using Equation 1. The averaged circle calculated from four measurements are taken rather than the minimum three as it is possible that certain surface features like divots are overrepresented and skew the resulting model when only three measurements are used. To create the external surface model of the culm as shown in Figure 5Figure 4, the centre of each circle is placed at its calculated position in all three dimensions. A point cloud is then generated from these stacked circles by seeding a fixed number of points around the circumference of each circle.

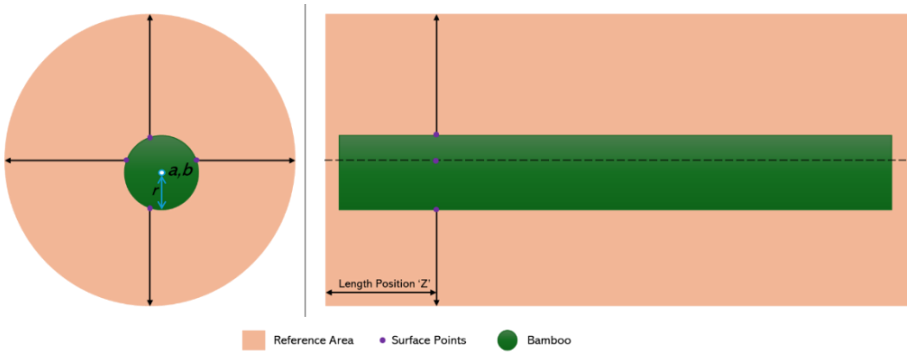

Figure 4: Representation of how measurements are taken for non-concentric circle culm model

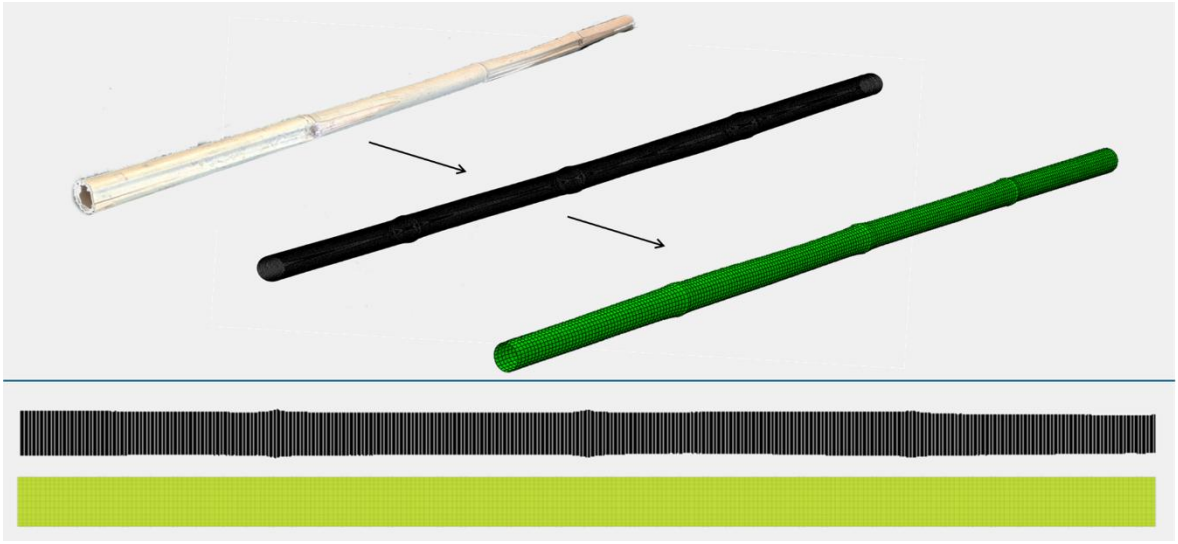

Figure 5: Top: progression from real culm to NCCM point cloud, to FEA mesh. Bottom: Comparison of NCCM model of a culm to the equivalent prismatic model

3 INDIVIDUAL CULM FEA MODELS AND VALIDATION

After using the non-concentric circle culm model to produce a point cloud that is representative of the culm geometry, the point clouds are then converted into Abaqus finite element analysis models using an automated process. A bespoke Matlab code is used to write the coordinates of the point clouds into an Abaqus input file. The meshes generated directly from the point cloud produce FEA models with high element numbers, in the order of millions, and so mesh convergence analysis was carried out to determine how much the mesh can be reduced without impacting the results of the model. This found that removing every 7th cross section and limiting the number of seeded surface points to 16 was suitable. The progression of this process and the reduced mesh size for the FEA models are shown in Figure 5

S4R shell elements were used to model the bamboo culm. Shell elements were chosen due to the desire to strike a balance between fidelity and computation time, where shell elements are significantly less expensive than brick elements in FEA. These element types are commonly used for the modelling of composite parts and as such it is sensible to use them in a ‘composite like’ material such as bamboo. It is not expected that the transverse properties of the structure will carry significant effects, especially in the load cases being tested and as such this element choice is justified. It is possible for a variety of load cases to be simulated, of particular interest has been the prediction of deflections under three-point and four-point bending loads as a means to validate the produced models against mechanical tests.

Each generated model possesses the same material properties and element types. The material properties used in the FEA models are taken from material testing done on the same batch of bamboo culms used in the validation experiments, and were tested in accordance with BS ISO 22157. The wall thickness of each bamboo culm was calculated by first determining the density of that particular culm, by measuring the mass and volume of smaller samples cut from the ends of the culm. By measuring the mass of the whole culm the volume can be calculated which can be used to determine an average wall thickness value given that the length of the culm and outer diameter are known.

3.1 FEA Model Validation

To verify the effectiveness of finite element analysis models, mechanical testing was conducted on bamboo culms of various lengths in three-point bending. In these tests the culm is suspended on two rollers and bending displacements of 20mm were imposed on each culm at the midspan point. A single measurement of displacement was taken at the lower surface on the midpoint of the culm using a

potentiometer. Moso Bamboo, with diameters 22mm to 26mm were used as these are the desired culms to be used in future WrapToR trusses. Three lengths of culm were used, 750mm, 875mm and 1000mm, to ensure that the models are valid for a range of lengths.

For each bamboo culm tested for model validation two FEA models were produced, one which uses geometry generated though the non-concentric circle culm model and the other which uses a prismatic tube geometry where the diameter has been measured in accordance with BS ISO 22157. This comparison has been made to determine if the using the scanned geometry to generate FEA models is advantageous for modelling bending behaviour for bamboo culms rather than using the established, existing methodology.

Figure 6 shows the results from 3-point testing compared to the results predicted by the non-concentric circle based FEA model and the prismatic tube FEA model. Both models are able to predict the culm's response reasonably well as demonstrated by the agreement between the three lines. The calculated bending stiffness of the culms based on the initial linear region of the deflections from both the models and experiments are shown in Figure 7. The average experimentally measured stiffness was 300.8 N/m, with a standard deviation of 73.4. This results in a coefficient of variation of 0.244, which is a relatively high value and demonstrates the variation in mechanical performance for bamboo, even in culms of the same species and roughly similar size. Of the two sets of model results, the Non-Concentric based model is more accurate to the experimental data with an average 11.8% difference in calculated stiffness, whereas the prism based models have an average difference of 21.1%. Whilst the average percentage difference is significantly different between the two models, the averages are somewhat skewed due to outliers where the prism model is very poor, specifically culms 4, 5, 6 and 7. This correlates to culms which had noticeably larger variations in their geometry, and underlies the increased importance of the higher fidelity representation when the culms themselves have more variation.

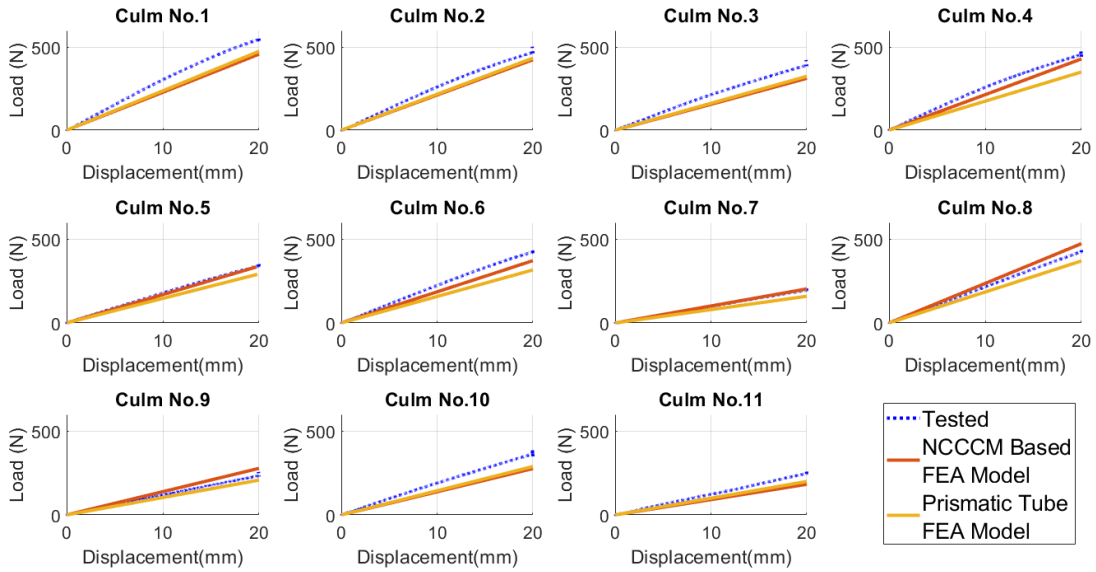

Figure 6: Load Vs Displacement for Bamboo Culms Comparison of NCC Based FEA, Prismatic Based FEA and Experimental Results

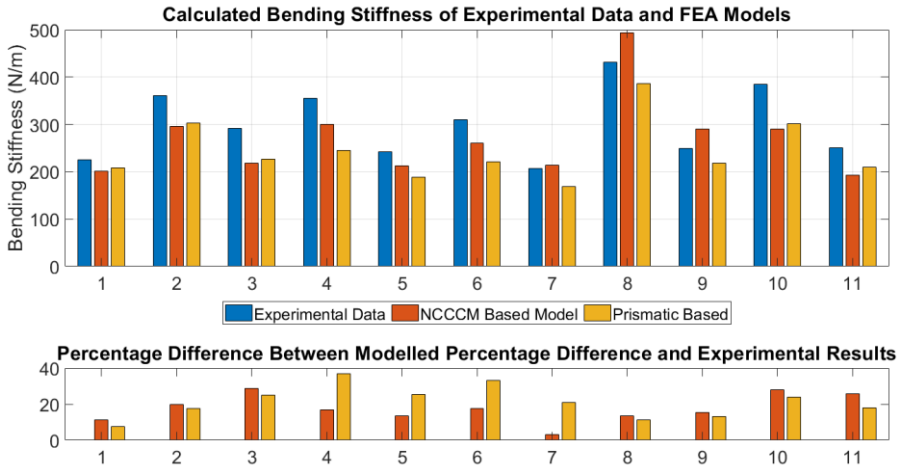

Figure 7: Calculated bending stiffness of culms and models alongside percentage differences between FEA and experiments.

An area where the non-concentric circle culm model may carry a significant benefit is in the prediction of failure loads and damage onset. The irregular geometry of bamboo culms may lead to stress concentrations developing at certain areas on the surface of the culm such as the nodes. These stress concentrations may then lead to failure onset such as a crack forming at that area. The geometry produced via the Non-concentric circle culm model will be able to more accurately determine the locations of such stress when compared to a prismatic model. This can be shown through a comparison of the modelled FEA stress maps shown in Figure 8 where the Non-Concentric circle FEA model also predicts a stress concentration at the node location. In the prismatic model the stress is evenly and symmetrically distributed across the surface and the peak value is slightly lower than what is present in the Non-Concentric circle FEA model. In order to validate this against experimental results, testing to failure would be required. This was not done as a part of these tests and exploration of this aspect of performance is left to future work.

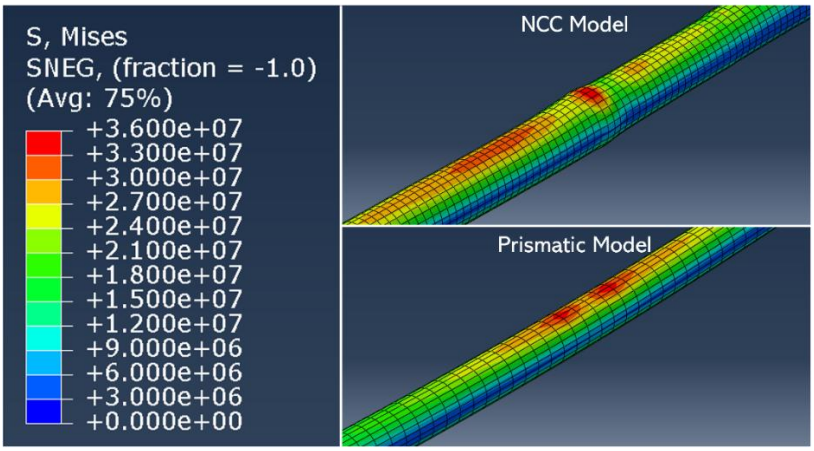

Figure 8: Stress maps from non-concentric circle and prismatic tube FEA models for Culm 5.

4 BAMBOO WRAPTOR TRUSS FEA MODELLING AND VALIDATION

WrapToR trusses have also been manufactured from bamboo culms. These trusses have been manufactured using flax fibre tow wetted out with epoxy resin for the shear members. An example of a manufactured truss is shown in Figure 9. WrapToR trusses are defined by as set of parameters which describe the geometry of each truss. These are labelled on Figure 9 and are described in

Table 1. The WrapToR geometry used for the trusses in this investigation are also shown in Table 1 and each truss was manufactured to these specifications.

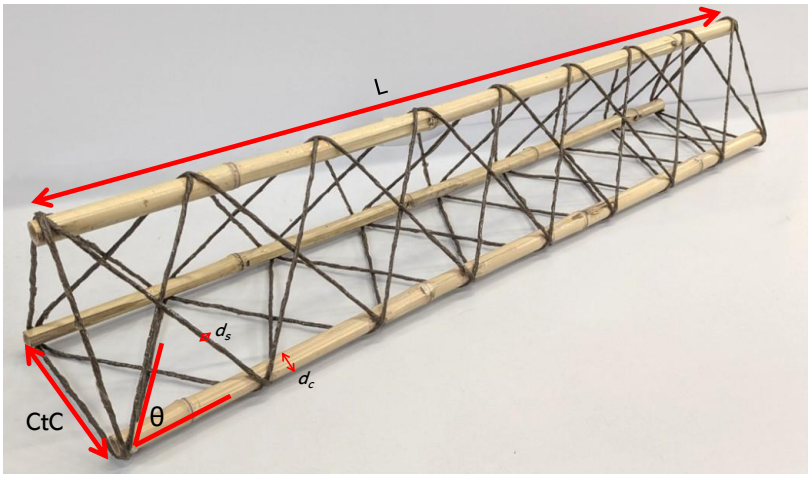

Figure 9: Wound Bamboo/Flax WrapToR truss with labelled geometric parameters.

Parameter	Symbol	Description	Value Used
Centre to centre distance	CtC	Distance between the centre of the chord member cross sections.	160 mm
Winding angle	θ	Angle between shear member and chord member.	45°
Truss Length	L	Length of truss beam.	1 m
Chord member diameter	d_c	Diameter of the chord member used.	Varies between 22mm and 26 mm
Shear member diameter	d_s	Diameter of the wound composite tow which forms the shear web.	4 mm

Table 1: WrapToR geometry parameters and parameters used in manufactured trusses.

During the manufacture of these trusses the non-concentric circle culm model was used to modify the winding process to mitigate the impact of the geometry variation. Because variation in the culm can cause discrepancies in the winding path geometry, as shown in Figure 2, care needs to be taken in the positioning of the chord members on the winding mandrel to account for this. An adjustable mandrel which allows for the culms to be tilted along its length was designed and this was used alongside a companion tool for the WrapToR winding machine which uses the non-concentric culm model to optimise the initial position of the culm. The companion tool calculates the WrapToR node position based on the combination of culm rotation and mandrel tilt. This tool calculates every possible combination and returns the set of parameters which aligns closest with the projected WrapToR node positions if the chord members were prismatic. Such an approach is not possible with a lower fidelity representation of the culm geometry which demonstrates the value of the non-concentric circle culm model for WrapToR truss manufacture.

Similarly to the individual culm tests, each culm used in the trusses was scanned for the non-concentric circle culm model and thus FEA models of these trusses have been able to be produced. Again, both prismatic tube models and those based off the non-concentric circle culm model have been developed. The models developed here differ from those used in previous WrapToR studies in that they are produced with Abaqus rather than a bespoke Matlab code. Additionally, they represent the connection between the shear members and chord members in a different way. The MSA models used previously represent the geometry of the WrapToR joint through the use of an inextensible, shear

deformable element, which offsets the shear from the surface of the chord [6]. This element is useful as it is able to represent the shear deformations in the joint itself and allow for a more accurate representation of shear member length. Because we have an actual surface rather than the beam element in the MSA code, we can map the geometry of joint more accurately onto the chord member itself. The result is a model such as that shown in Figure 10. This provides an accurate model for shear member length which is its most important geometric property. Currently this connection is only representative, with kinematic ties connecting the chord and shear members but future work will include implementation of joint mechanics which can ideally model the interactions of the adhesive joint and help predict failure due to the bond failure, which is a common failure mode for WrapToR trusses [6].

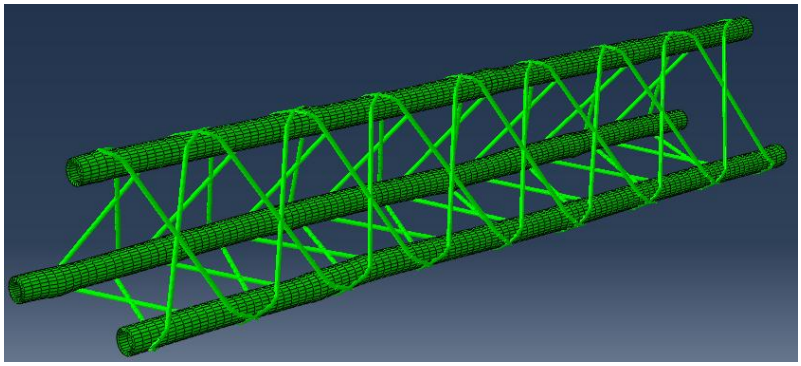

Figure 10 WrapToR model in Abaqus with accurate geometry nodes and NCC based culms.

4.1 Model Validation

Results from the FEA analysis are compared to four-point bending experiments for six different truss beam specimens. Four-point bending was chosen over three-point bending in this case due to the low aspect ratio of the trusses which promotes a shear dominated response. Because a four-point test causes an area of no shear forces between the loading points the performance in bending can be solely assessed. Four-point bending also allows for the load to be distributed across two loading points which is useful in preventing early crack propagation in a brittle material such as bamboo. Each truss was tested to failure. The results of this testing and comparative modelled responses are shown in Figure 11.

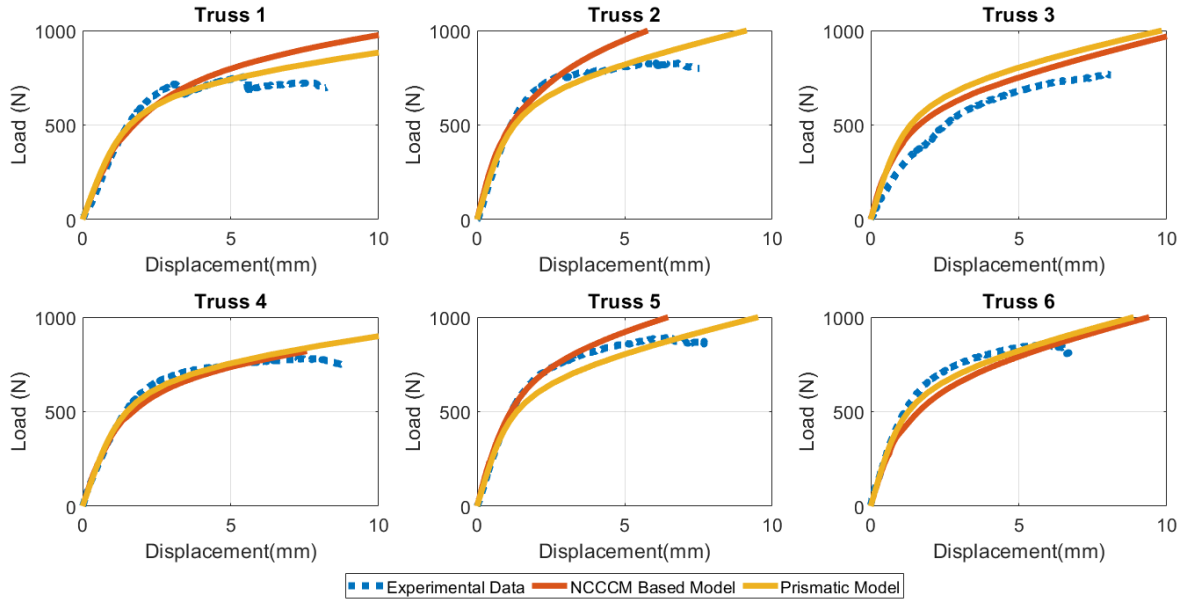

Figure 11: Results of Truss Testing

Figure 11 shows a nonlinear response in bending which is associated with the truss shear members buckling. Shear members buckling and subsequently snapping was the most common failure most observed in testing and the softening behaviour has been able to be captured by the FEA models which is a positive indication that the modelled response is accurate to the real response. Overall, the FEA models themselves are a good match to the experimental results and can predict the response of the tested trusses to a reasonable degree of accuracy. There does not appear to be a significant difference between the prismatic models and the models based on the non-concentric circle. The FEA modelled responses in the linear region seem to align very closely together which is due to the primary deformation in that region being linked to shear member deformations that are modelled very similarly between models. The tested trusses have an average initial linear stiffness of 7880 N/m with a standard deviation of 1452 N/m, resulting in a 0.1842 coefficient of variance. This is lower than the coefficient calculated from the individual culm tests, but is still high. It may be the case that the truss geometry has some moderating effect on the variance, as individual culm performance is bending dominated, whereas the culms within truss beams will generally be loaded in a more axial manner, and bending performance is more non-linear with geometry than axial performance, This inherent geometrical mitigation could be further enhanced with careful pre-selection of culms to balance out culm level variation at the truss beam level mechanical performance.

5 CONCLUSIONS

This work presents the Non-concentric circle culm model as a measurement method and representation of bamboo culms. The model takes many measurements of the distance of the truss surface to a known reference point for and calculate a circle to represent that cross section. These circles are placed at a calculated centre based on the measurements taken which captures geometric features such as pre-bends in the culm. This model has been developed for the explicit purpose of aiding manufacture and performance predictions for bamboo based Wrapped Tow Reinforced trusses.

This method has demonstrated usefulness in the manufacture of WrapToR trusses by allowing for an optimisation of the position of chord members in the mandrel to provide an even tow path during winding, resulting in more uniform, higher quality manufacture. This is an important step in the development of Bamboo WrapToR trusses which may help address current challenges surrounding bamboo construction.

The models have also been used to produce finite element analysis models of individual culms and as part of FEA models for WrapToR trusses. In both cases model validation shows that there is a good match between the prediction of the FEA models and the experimentally gathered data. There is confidence that FEA models using the non-concentric circle culm model can be used to model bamboo culm performance. On average, the non-concentric circle culm model more closely aligns with the experimental data than modelling culms as a prism suggesting that it offers a slightly better method of approximating culm performance in bending. Given the significant variation in mechanical performance between culms and trusses, the non-concentric circle culm model can be useful to help predict variation and allow for a more informed design process to take place without the need for overly conservative estimations.

There are also some indications that the non-concentric circle FEA model may be able to identify areas where there are stress concentrations which could aid in failure prediction, but more comprehensive work to gather appropriate material properties, and improve the data collection for experiments must first take place.

ACKNOWLEDGEMENTS

This work was funded by the Engineering and Physical Sciences Research Council (EPSRC) UK through: the Centre for Doctoral Training in Composites Science, Engineering and Manufacturing (CDT CoSEM; grant number EP/S021728/1) at the University of Bristol..

REFERENCES

1. E. A. Nurdiah, “The potential of bamboo as building material in organic shaped buildings,” Procedia - Social and Behavioral Sciences, vol. 216, pp. 30–38, Jan. 2016, issn: 1877-0428. doi: 10.1016/j.sbspro. 2015.12.004.
2. K. W. Liu, Q. F. Xu, G. Wang, et al., Contemporary bamboo architecture in china, English, Singapore, 2022. doi: 10.1007/978-981-16-8309-1.
3. K. Liu, C. Demartino, Z. Li, Q. Liu, and 1. Xiao Yan, 2019 international bamboo construction competition : From the concepts to the realized pavilions, English, Cham, Switzerland, 2022. doi: 10.1007/978-3- 030-91990-0.
4. Minke, G. 2023. Building with Bamboo: Design and Technology of a Sustainable Architecture.Third and revised edition. Berlin, Boston: Birkhäuser. https://doi.org/10.1515/9783035625738
5. B. Woods, I. Hill, and M. Friswell, “Ultra-efficient wound composite truss structures,” Composites Part A: Applied Science and Manufacturing, vol. 90, pp. 111–124, Nov. 2016. doi: 10.1016/j.compositesa. 2016.06.022.
6. C. Hunt, M. Wisnom, and B. Woods, “Wraptor composite truss structures: Improved process and structural efficiency,” Composite Structures, vol. 230, p. 111 467, Dec. 2019. doi: 10.1016/j.compstruct.2019. 111467
7. A design approach for super-efficient Wrapped Tow Reinforced Hierarchical Space Frames, Morabito, F. (Author). 5 Dec 2023, Student thesis: Doctoral Thesis › Doctor of Philosophy (PhD)
8. C. Hunt, M. Wisnom, and B. Woods, “Design, manufacturing and testing of an automated winding machine for WrapToR composite truss structures,” in 18th European Conference on Composite Materials (ECCM18), 2018
9. BS ISO 22157:2019 bamboo structures. determination of physical and mechanical properties of bamboo culms. test methods, 2019
10. BIM Bamboo: a digital design framework for bamboo culms, Rodolfo Lorenzo, Chuhee Lee, Juan G. Oliva-Salinas, and Marcos J. Ontiveros-Hernandez, Proceedings of the Institution of Civil Engineers - Structures and Buildings 2017 170:4, 295-302
11. R. Lorenzo and L. Mimendi, “Digitisation of bamboo culms for structural applications,” Journal of Building Engineering, vol. 29, p. 101 193, May 2020, issn: 2352-7102. doi: 10.1016/j.jobe.2020.101193.

ICCM24
AUGUST 4-8, 2025
BALTIMORE CONVENTION CENTER
BALTIMORE, MARYLAND, USA

No Technical Paper Submission for:

Veronica Calado

TOOLPATH OPTIMIZATION OF POLYMER COMPOSITE ADDITIVE MANUFACTURING (AM) PRINTED MOLD TO IMPROVE PERFORMANCE FOR COMPRESSION MOLDING APPLICATIONS

Madhura Limaye[1], Bhagyashree Prabhune[2], Eonyeon Jo[3]
Nuvin Bazid[4], Soydan Ozcan[1], Uday Vaidya[1,5], Ahmed Hassen[1] and Seokpum Kim[1]

[1]Manufacturing Science Division, Oak Ridge National Laboratory, Oak Ridge, TN, USA
Email: limayemv@ornl.gov , ozcans@ornl.gov, vaidyauk@ornl.gov, hassenaa@ornl.gov, kimsp@ornl.gov

[2] Computational Sciences and Engineering Division, Oak Ridge National Laboratory, Oak Ridge, TN, USA
Email: prabhuneb@ornl.gov

[3] Bredesen Center, University of Tennessee, Knoxville, TN, USA
Email: joe1@ornl.gov

[4] Virginia Commonwealth University, Richmond, VA, USA
Email: bazidna@vcu.edu

[5] Department of Mechanical, Aerospace and Biomedical Engineering, University of Tennessee, Knoxville, TN, USA
Email: vaidyauk@ornl.gov

Keywords: Compression Molding, Additive Manufacturing, Polymer Composites, Toolpath, Finite Element Analysis

ABSTRACT

This study explores the optimization of toolpaths for short fiber polymer composite additive manufacturing (AM) printed molds in compression molding applications, an emerging trend driven by advancements in 3D printing technology. AM printed molds offer reduced tooling costs and greater design flexibility, particularly for prototyping and low-volume production. The proposed optimization approach evaluates mold performance using two key metrics: deformation and shape accuracy. Multiple toolpaths are generated, and finite element (FE) simulations capture fiber orientation and material properties, which are then integrated into a mechanical performance model. Shape accuracy is assessed by comparing the deformed mold shape with the original using surface normals as a descriptor. The analysis identifies the toolpath that delivers the best overall performance, establishing it as the most suitable option for achieving optimal mold characteristics in compression molding applications.

1 INTRODUCTION

The adoption of additive manufacturing (AM) using short fiber polymer composites for producing molds has gained traction, particularly in the context of molding applications [1, 2]. This emerging trend is driven by advancements in 3D printing technology, which offers significant advantages over traditional mold production methods. Notably, AM printed molds provide reduced tooling costs and greater design flexibility, making them ideal for prototyping and low-volume production scenarios [3, 4].

A critical aspect of additive manufacturing is the planning of the printing path, also known as the toolpath. The toolpath plays a pivotal role in determining the quality of the mold surface and its subsequent performance during use [5-7]. In this study, a novel approach to optimize toolpaths is

proposed with the aim of enhancing the performance of AM printed molds specifically designed for compression molding applications.

The optimization strategy focuses on evaluating mold performance through two essential metrics: deformation and shape accuracy. The process begins with generating multiple toolpaths for a chosen AM mold geometry and material. For each generated toolpath, Finite Element (FE)-based simulations were conducted to investigate the resulting fiber orientation and material properties throughout the mold structure. These properties were then integrated into a mechanical performance model, enabling to assess the mold's deformation under compression loading conditions.

In addition to deformation, shape accuracy was assessed by comparing the deformed mold shape to its original, as-printed form. This evaluation was accomplished using surface normals as shape descriptors, which allowed to analyze the orientation of the mold surface at various points and quantify any shape deviations.

After analyzing the deformation and shape accuracy metrics for all considered toolpaths, the toolpath that offered the best overall mold performance was identified. This optimized toolpath was determined to be most appropriate for achieving the desired characteristics of molds used in compression molding applications.

Through this work, the aim was to contribute to the field of additive manufacturing by providing a systematic approach for toolpath optimization, ultimately enhancing the efficacy of AM printed molds.

2 MATERIAL, GEOMETRY AND DISCRETIZATION

The geometry of the mold considered for the present task was a double dome. The printed double dome mold consisted of a thicker base (Fig. 1) for the purpose of maintaining a continuous toolpath during the print, however the excess material at the base is later removed or machined for obtaining the actual mold. Thus, the printed mold geometry was considered for the AM process simulation while the actual mold geometry was considered for the performance simulation.

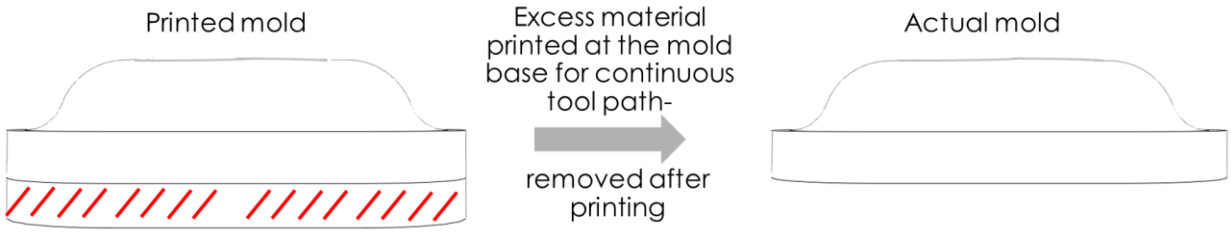

Figure 1: Illustration of the printed mold (left) and the actual mold (right) used for performance analysis.

20wt% CF/PLA was the chosen material for the numerical evaluation of the double dome structure. The double dome printed geometry was discretized for the AM simulation (Fig. 2). Accordingly, the element size for the discretization was chosen equal to the bead dimensions, with the bead height equating to the layer thickness. The same mesh was used further for the performance analysis, except that the elements making up the excess material at the base of the mold were removed.

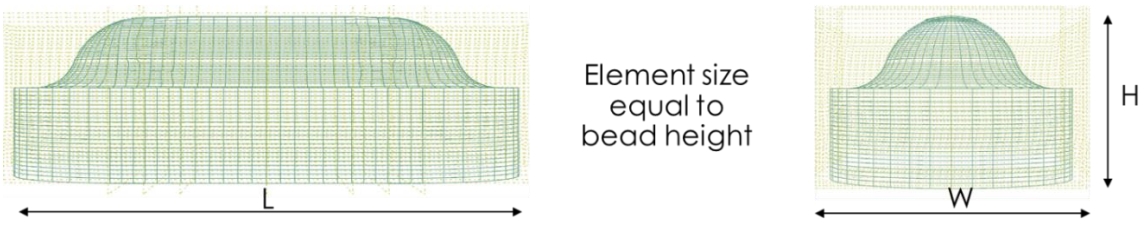

Figure 2: Discretization of printable mold, element size (~5mm) chosen equal to the bead height, overall mold dimensions, L = ~550mm, W = ~300mm, printed height H =200mm, actual mold height H’ = 150mm.

The material properties of the CF/PLA composite were determined using the MCQ chopped software [8]. Accordingly, the constituent material properties of CF (Table 1) and PLA (Table 2), along with the fiber orientation distribution for a bead thickness of 5mm (Table 3) were provided as input to the micromechanical model. The fiber orientation distribution was defined by assuming a paper-ply based approach, however a more accurate method of defining fiber orientation distribution in case of short-fiber reinforced composites is by defining a fiber orientation tensor.

Table 1: Properties of the PLA matrix required to perform micromechanical simulations.

Matrix Property		PLA
Elastic Modulus (E)	[GPa]	3.6
Poisson's Ratio (v)	–	0.3
Tensile Strength	[MPa]	25
Compressive Strength	[MPa]	53
Shear Strength	[MPa]	20.25
Density (ρ)	[kg/m^3]	1240

Table 2: Mechanical properties of the CF fibers.

Property		CF
ρ	[kg/m^3]	1790
E_{11}	[GPa]	221.8
E_{22}	[GPa]	18.86
E_{33}	[GPa]	18.86
G_{12}	[GPa]	58.81
G_{23}	[GPa]	6.96
G_{13}	[GPa]	6.96
ν_{12}	–	0.2218
ν_{23}	–	0.3548
ν_{13}	–	0.3548
Tensile S11T	[MPa]	3432
Compressive S11C	[MPa]	2416
Shear S12	[MPa]	150.0

Table 3: Fiber orientation distribution for CF/PLA composite bead with a thickness of 5 mm.

Ply Thickness (mm)	Normalized thickness	Orientation tensor components (°)	Orientation tensor components
1.75	0.35	0	1.0
0.25	0.40	45	0.5
1.00	0.60	90	0.0
0.25	0.65	45	0.5
1.75	1.00	0	1.0

Additionally, the fiber properties including an average fiber length of 180µm, fiber diameter of 9µm, and void fraction of 20% were assumed. The mechanical properties of CF/PLA were obtained as output from the model (Table 4). These properties were then imported into the input file of the performance analysis.

Table 4: Mechanical properties of CF/PLA composite.

Property		CF/PLA
P	[kg/m^3]	1066
E_{11}	[GPa]	15.61
E_{22}	[GPa]	6.852
E_{33}	[GPa]	3.249
G_{12}	[GPa]	1.569
G_{23}	[GPa]	1.168
G_{13}	[GPa]	1.167
ν_{12}	–	0.167
ν_{23}	–	0.352
ν_{13}	–	0.326
Tensile S11T	[MPa]	111.6
Shear S12	[MPa]	22.14

3 TOOLPATH AND BUILD ORIENTATION

Next, three cases of AM printing consisting of different combinations of build orientation and toolpath were selected for evaluation. The three cases were termed H0, H90 and V90 where ‘H’ or ‘V’ referred to a horizontal or vertical build orientation and ‘0’ or ‘90’ referred to the toolpath in x or y direction (Fig. 3). Note that each figure was enlarged to show the toolpath representing the material orientation.

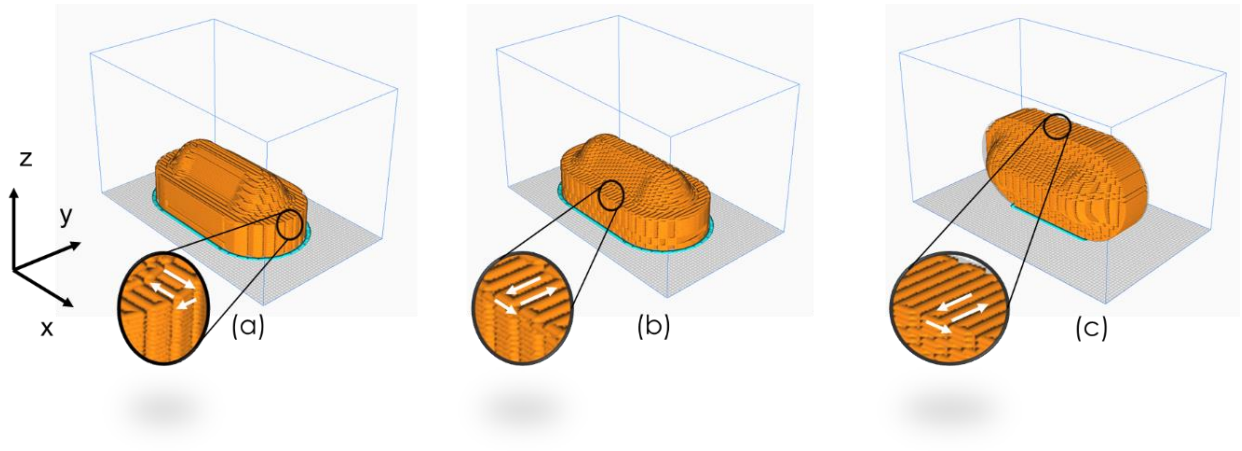

Figure 3: Printed mold configurations (a) H0, (b) H90, and (c) V90 used for performance evaluation.

The first step in the evaluation of the above cases was the determination of their elemental material orientation. Due to the tortuous nature of the toolpath used for the AM process, the material coordinates change as a function of the toolpath. This was captured in the AM process simulation such as each element was assigned to a local coordinate system that defined the material deposition

direction. Further, the elements of the discretized geometry that intersected the toolpath were activated during the process simulation. Only those active elements were assigned the local coordinates in the process simulation. Thus, for each of the three cases, an AMs process simulation was performed to determine the active elements in the model and to obtain their local coordinates.

In each of the cases, more than 99% of the elements were determined to be active and their local coordinates were extracted in a text file using a python script. This data was then incorporated into the input file for the performance analysis. The material orientation for the three cases can be seen in (Fig. 4).

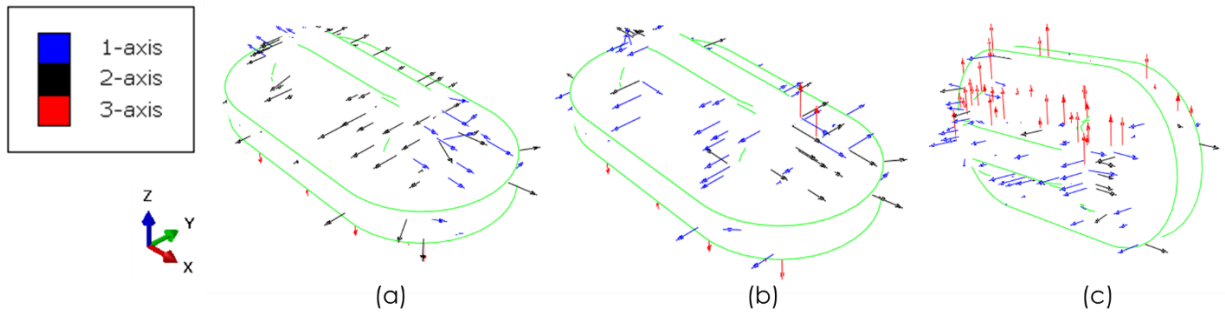

Figure 4: Elemental Material orientation (1-2-3 axes) obtained from the AM process simulation for (a) H0, (b) H90, and (c) V90 cases, plotted only for few elements on the wireframe geometry of the actual mold.

4 PERFORMANCE MODEL

In order to evaluate the performance of the mold, two metrics were used including deformation and shape accuracy. For evaluation of the mold deformation consisting of different toolpaths, a performance model was setup using Abaqus Standard. The performance model was set up by defining the displacement BCs and loading condition (Fig. 5). A non-linear static analysis was performed to evaluate the structural performance of the three cases.

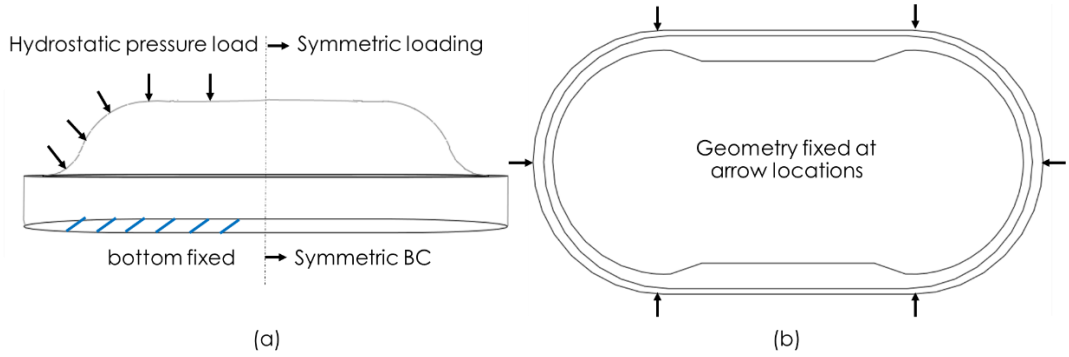

Figure 5: Displacement BCs and loading conditions for the performance analysis of double dome structure (a) Front view shows hydrostatic pressure loading and fixed bottom face, (b) Top view shows locations used to fix the structure.

Shape accuracy was evaluated by comparing the mold's deformed shape to its original, as-printed form. This was done by using surface normals as a shape descriptor. The surface normal descriptor compared the orientation of the mold surface at each point to assess shape deviation. The concept of surface deviation is illustrated in (Fig. 6).

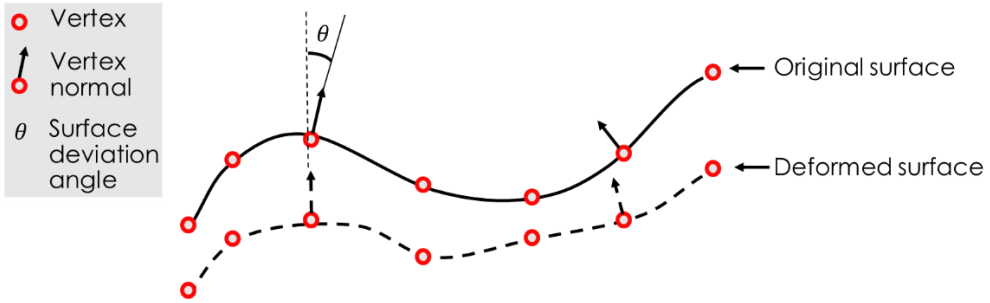

Figure 6: Surface deviation angle calculated from the vertex normal to the original and deformed mold surfaces.

The surface deviation angle θ_i is calculated at a vertex/node on the surface as follows:

$$\theta_i = cos^{-1}(\hat{a}_i \cdot \hat{b}_i), \qquad i = 1, \dots n \tag{1}$$

Where $\hat{a}_i$, $\hat{b}_i$ are the unit normal vectors to the original and deformed surfaces, respectively, at a vertex i, and n is the number of vertices/nodes on the surface. Further, the variance of the surface deviation angles for the mold surface was calculated as:

$$\sigma^2 = \frac{\sum(\theta_i - \bar{\theta})}{n} \tag{2}$$

Where $\bar{\theta}$ is the mean surface deviation. Accordingly, the surface deviation data including the deviation angles, their maximum and minimum magnitudes, and the average and variance were determined for all three cases under study.

5 RESULTS

The results of the performance analyses provided insights into 1) the structural integrity of the AM mold and 2) the quality of part manufactured using the mold through compression molding. The key observations from the predicted stress and deformation results are presented here. The von Mises stress contour plots for the three cases can be observed in (Fig. 7). The scale of the contour plot was set at a maximum of 45MPa and a minimum of 0MPa.

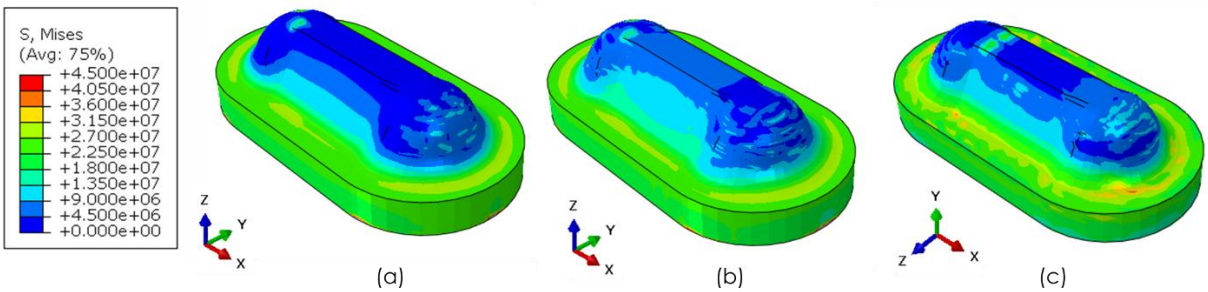

Figure 7: Von Mises stress contour plots for (a) H0, (b) H90, and (c) V90 cases, scale set to a Max = 45 MPa and Min = 0 MPa.

It was observed that the average stress magnitudes for all cases were similar with certain disparity visible on the top face. The stress contours were expected to be similar because the loading condition was pressure-based. Thus, the deformation results were determined to be more valuable for the purpose of comparison. The deformation magnitude for the considered cases can be seen in (Fig. 8). The maximum deformation magnitudes for H0, H90 and V90 cases were 1.056mm, 1.067mm and 0.441mm respectively. Unlike cases H0, and H90, V90 case has material axis 1 that is the fiber axis in the loading direction, thus provided higher stiffness, resulting in lower deformation by >50.

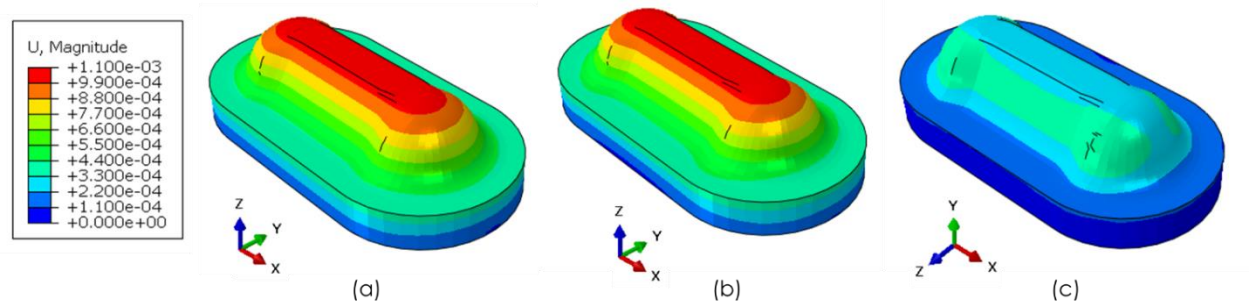

Figure 8: Deformation magnitude contour plots for (a) H0, (b) H90, and (c) V90 cases, scale set to Max = 1.1 mm and Min = 0.0 mm.

Considering deformation magnitude as the criterion for performance evaluation of the AM mold, considerable improvement was achieved with V0 case (>50%) compared to the H0 and H90 cases. Thus, it would be logical to determine V90 toolpath as the optimum from a performance perspective. However, it was recognized that an equally important criterion for evaluation of the optimum toolpath was the quality of part manufactured using the mold via compression molding. In the present instance, the part quality was defined by surface deviation of the deformed mold relative to the original mold surface.

Accordingly, the surface deviation data including the deviation angles, their maximum and minimum magnitudes, and the average and variance were determined for all three cases under study. The deviation or the error values are provided in (Table 5). The maximum deviation and variance metrics were considered significant for the part quality. Thus, the H90 toolpath case was determined the optimum case in terms of the part quality.

Table 5: Surface deviation values used as error metric to choose the optimum toolpath.

Error metric	Case H0	Case H90	Case V90
Max deviation (°)	3.137	2.591	4.197
Min deviation (°)	0.002	0.002	0.001
Avg deviation (°)	0.211	0.210	0.122
Variance of deviation	0.034	0.027	0.059
Optimum ranking	Next to optimum	Optimum	Second next to optimum

6 CONCLUSIONS

This study focused on toolpath optimization for an additive manufacturing (AM) printed mold to enhance its molding performance, evaluated through mold deformation and shape accuracy metrics. Three toolpaths including H0, H90, and V90 were assessed using finite element (FE) simulations and statistical analysis. The results indicated that the V90 toolpath was optimal for compression molding applications due to its lowest mold deformation, attributable to favorable fiber alignment in the loading direction that enhanced material stiffness. However, shape accuracy analysis revealed that the V90 case exhibited the highest maximum deviation and variance from the original mold shape. In contrast, the H90 toolpath demonstrated the lowest deviation and variance, indicating superior shape accuracy, albeit with slightly higher mold deformation than the V90. Therefore, considering the trade-offs between mold deformation and shape accuracy, the H90 toolpath is recommended as the optimal choice.

REFERENCES

[1] Sudbury, T. Z., Springfield, R., Kunc, V., & Duty, C. (2016). An assessment of additive manufactured molds for hand-laid fiber reinforced composites. The International Journal of Advanced Manufacturing Technology, 90(5–8), 1659–1664. https://doi.org/10.1007/s00170-016-9464-9

[2] Shree, S., Jayaraman, K., Dereims, A. *et al.* Performance of additively manufactured composite mold with uniform fiber orientation. *Int J Adv Manuf Technol* **131**, 4297–4305 (2024). https://doi.org/10.1007/s00170-024-13220-8

[3] Love L, Economics of big area additive manufacturing. Solid Freeform Fabrication Symposium, Austin, TX August 9:2016

[4] Love, L. and Duty, C et al. Breaking barriers in polymer additive manufacturing. Manufacturing Science and Engineering (2015).

[5] Kubalak J. R., Root N. J., Wicks A. L., Williams C. B., Improving mechanical performance in material extrusion parts via optimized toolpath planning, *Additive Manufacturing*, Volume 80, (2024). https://doi.org/10.1016/j.addma.2023.103950

[6] Jaeyoon K., and Kang B. S., 2020. "Enhancing Structural Performance of Short Fiber Reinforced Objects through Customized Tool-Path" *Applied Sciences* 10, no. 22: 8168. https://doi.org/10.3390/app10228168

[7] Jingchao J., and Ma Y., 2020. "Path Planning Strategies to Optimize Accuracy, Quality, Build Time and Material Use in Additive Manufacturing: A Review" *Micromachines* 11, no. 7: 633. https://doi.org/10.3390/mi11070633

[8] MCQ Software. AlphaSTAR Corporation, Long Beach, CA, USA, www.ascgenoa.com

APPENDIX

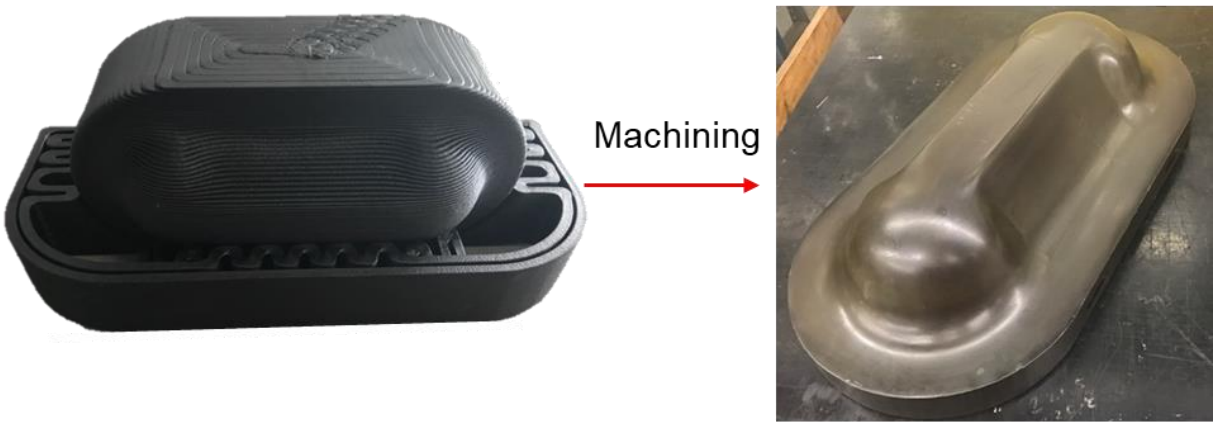

Figure A1. Picture of the AM printed mold on a support (left) and machined to the required dimensions for compression molding application (right)

ICCM24
AUGUST 4-8, 2025
BALTIMORE CONVENTION CENTER
BALTIMORE, MARYLAND, USA

No Technical Paper Submission for:

Cesar Garcia Gascon

ICCM24
AUGUST 4-8, 2025
BALTIMORE CONVENTION CENTER
BALTIMORE, MARYLAND, USA

No Technical Paper Submission for:

Yeqing Wang

OBSERVATION OF BANDING FRACTURE BEHAVIOR OF CFRTP LAMINATES WITH FIBER DISCONTINUITY USING DIC

K. Onozuka[1], K. Iizuka[2] and S. Yoneyama[1]

[1]Department of Mechanical Engineering, Aoyama Gakuin University
5-10-1, Chuo-ku Huchinobe, Kanagawa, Japan
Email: c5625184@aoyama.jp, web page: https://www.me.aoyama.ac.jp/~yoneyama/

[2] Department of Mechanical Engineering, Aoyama Gakuin University
5-10-1, Chuo-ku Huchinobe, Kanagawa, Japan
Email:iizuka@me.aoyama.ac.jp, web page: https://www.me.aoyama.ac.jp/~yoneyama/

[3] Department of Mechanical Engineering, Aoyama Gakuin University
5-10-1, Chuo-ku Huchinobe, Kanagawa, Japan
Email:yoneyama@me.aoyama.ac.jp, web page: https://www.me.aoyama.ac.jp/~yoneyama/

Keywords: CFRTP, Fiber Discontinuity, DIC, FEM Analysis, Three-points Bending Test

ABSTRACT

This study presents the observation of damage behavior under bending of carbon fiber reinforced thermoplastics (CFRTP) with fiber discontinuity. CFRTP with high strength is utilized for a variety of situations such as airplane and foot orthoses. However, CFRP is well-known as weak for compression, especially the buckling in the situation of remolding foot orthoses. The resin rich region existing in fiber discontinuity is considered to reduce the buckling. The three-points bending test result indicates the discontinuous CFRTP has 82.0% bending strength and 84.0% shear strength compared to the continuous CFRTP. The continuous CFRTP is damaged on the compression side surface. A tiny crack may cause injury in the situation of utilization for foot orthoses. Micro scale tensile test using laser microscope for the consideration of fracture mechanism shows the strain concentration at both edges of resin rich region. This strain concentration is considered to cause damage. This means the discontinuous CFRTP is useful for foot orthoses.

1 INTRODUCTION

Foot orthoses require light weight, high strength, design ability. CFRTP with a high specific strength and modulus is utilized such as vehicle and aircraft. In recent years, CFRTP has become relatively more affordable, and its application in medical devices such as orthoses is considered. When CFRTP is utilized for foot orthoses, it is subjected to bending stress in order to adjust to physical growth. However, fiber's buckling is occurred on the compression side under bending. Delamination also tends to appear on CFRTP laminates. A tiny crack may cause injury in the case of foot orthosis. The resin-rich region existing in the fiber discontinuity is considered to reduce the fiber deformation under bending. This study presents an observation of the damage behavior under bending of CFRTP (CF/PMMA) laminates with fiber discontinuity. Digital image correlation (DIC) is utilized to observe displacement and strain distributions.

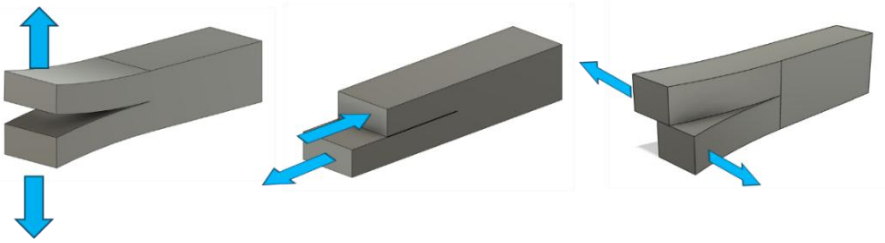

(a)Mode I (b)Mode II (c)Mode III

Fig. 1.1. Schematic diagram of shear fractural behavior

2 THREE-POINTS BENDING TEST

Prepregs with a length of 40mm are stacked with a shift of 10mm to make fiber discontinuity as shown in Fig. 2.1. After molding, the laminated plate is cut into test specimens for three-points bending test. In three-point bending test, a total of six types of test specimens, with thicknesses of 3.0 mm, 3.5 mm, and 4.0 mm, are prepared from CFRTP laminates with fiber discontinuities and continuous fiber CFRTP laminates. Three samples of each type are tested. The test specimen names are assigned as shown in Table 2.1 for identification. Due to dimensional variations when cutting the specimens, the measured dimensions after cutting each specimen are shown in Table 2.2.

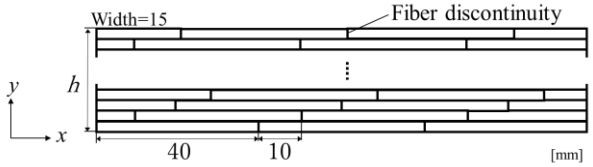

Fig. 2.1. Schematic diagram of discontinuous CFRTP specimens

Table 2.1. Numbering of specimens

	Thickness		
	3.0mm	3.5mm	4.0mm
Continuous	c3-1, c3-2, c3-3	c3.5-1, c3.5-2, c3.5-3	c4-1, c4-2,c4-3
Discontinuous	d3-1, d3-2, d3-3	d3.5-1, d3.5-2, d3.5-3	d4-1, d4-2, d4-3

Table 2.2. Thickness and width of specimens

Number	h[mm]	b[mm]	Number	h[mm]	b[mm]
c3-1	2.97	15.40	d3-1	3.05	15.30
c3-2	2.95	15.41	d3-2	3.03	15.22
c3-3	2.93	15.39	d3-3	3.00	14.95
c3.5-1	3.40	15.58	d3.5-1	3.59	14.93
c3.5-2	3.37	15.46	d3.5-2	3.67	15.00
c3.5-3	3.48	15.01	d3.5-3	3.51	15.08
c4-1	3.94	15.25	d4-1	4.03	15.07
c4-2	3.98	15.35	d4-2	4.03	14.93
c4-3	4.09	15.49	d4-3	3.98	14.89

In this experiment, the span between the supports is set to 25 mm, and the testing speed is 1.0 mm/min. A schematic diagram illustrating the testing setup is shown in Fig. 2.2.

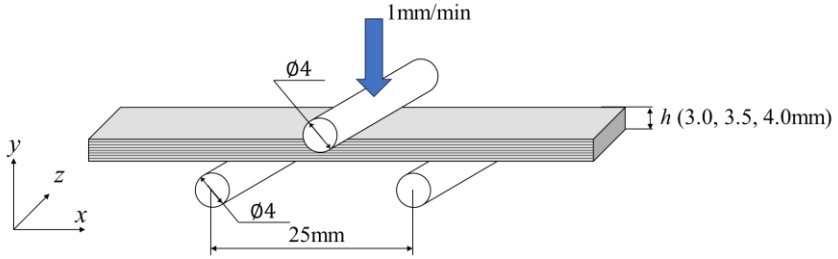

Fig. 2.2. Three-points bending test

Figure 2.3 shows displacement and strain distribution obtained from d3-1. Focusing on the strain in the *y*-direction, interlaminar delamination (stripe-shaped strain concentration) is observed on the center

in the thickness direction of the specimen. Figure 2.4 shows displacement and strain distribution obtained from c3-1. Compression damage (strain concentration on the diagonal direction) is observed on the surface of the specimen. The bending and shear strengths are evaluated based on the loads at which these damages are observed.

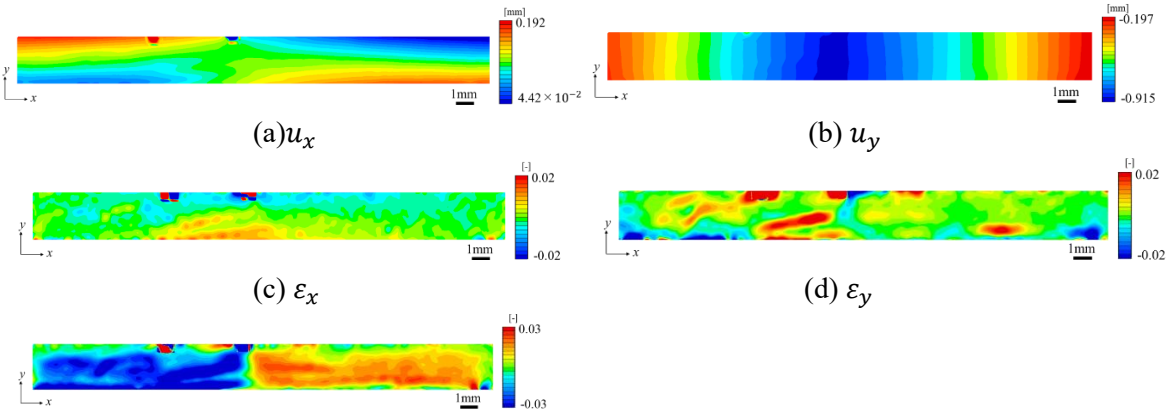

Fig. 2.3. Displacement and strain distribution of d3-1 at 140s

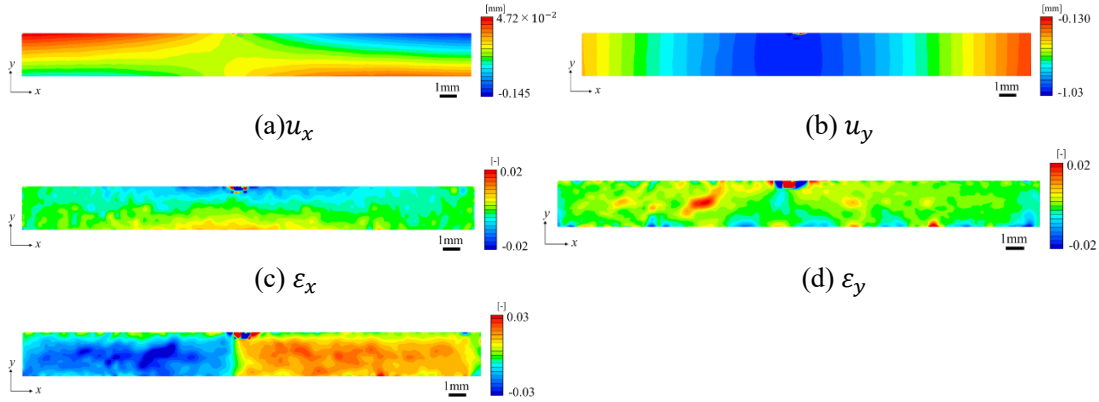

Fig. 2.4. Displacement and strain distribution of c3-1 at 140s

Table 2.3 shows the flexural strength or shear strength obtained from each specimen. When comparing the shear strength of the 3.5 mm-thick specimens and the flexural strength of the 4.0 mm-thick specimens, it was found that the CFRTP laminates with fiber discontinuities retains 82.0% of the flexural strength and 84.0% of the shear strength compared to the continuous fiber CFRTP laminate.

Table 2.3. Bending strength and Shear strength

Continuous			Discontinuous			Ratio[%]
Sample number	Bending strength [Mpa]	Shear strength [Mpa]	Sample number	Bending strength [Mpa]	Shear strength [Mpa]	
c3-1	424.2	-	d3-1	-	18	
c3-2	410.5	-	d3-2	-	16.4	
c3-3	382.7	-	d3-3	-	15.6	
avg.	405.9	-	avg.	-	16.7	-
c3.5-1	-	23.6	d3.5-1	-	21.4	
c3.5-2	-	22.7	d3.5-2	-	21.2	
c3.5-3	-	22.8	d3.5-3	-	15.4	
avg.	-	23.0	avg.	-	19.3	84.0
c4-1	312.7	-	d4-1	225.7	-	
c4-2	285.2	-	d4-2	256.0	-	
c4-3	243.3	-	d4-3	208.5	-	
avg.	280.4	-	avg.	230.1	-	82.0

By observing the detected damage with a laser microscope, the influence of such damage on practical applications, such as orthoses, is considered. Figure 2.5 shows the compressive fracture and interlaminar delamination caused by bending observed by the laser microscope. The white, stripe-like features visible in

the image correspond to fiber area oriented in the *x*-direction. Since the specimen used in this experiment is a plain-woven fabric, fiber area aligned in the z-direction appear as dark, elliptical shapes. Compressive fracture due to bending is accompanied by fiber buckling. The fracture surface of fibers exposes on the specimen's surface.

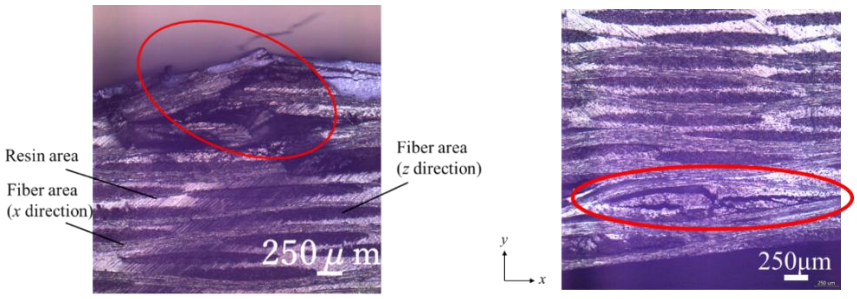

(a) Fiber buckling (b) Delamination

Fig. 2.5. Damage behavior observed by laser microscope

Finite element analysis (FEM) is used to simulate the three-point bending test, calculating the stress distribution as well as the displacement and strain distributions. The FEM software used for the analysis is Marc Mentat, and an elastic-plastic analysis is performed. A resin-rich region made of acrylic is introduced within the CFRTP to reproduce the fiber discontinuity. The material properties used in the analysis are shown in Table 2.4. Additionally, the model and boundary conditions used in the analysis are shown in Fig. 2.6.

Table 2.4. Material constant for FEM

PMMA	CFRTP		
E=1.0GPa ν=0.35	E_{xx}=53.1GPa	ν_{xy}=0.20	
	E_{yy}=1.0GPa	ν_{yz}=0.20	G_{xy}=2.5GPa
	E_{zz}=53.1GPa	ν_{zx}=0.05	

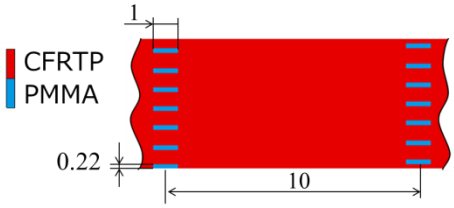

Fig. 2.6. Fiber discontinuities for FEM model

Figure 2.7 shows the stress distributions obtained by FEM. Since the maximum compressive and shear stresses occur below the indenter, damage may be expected in this area. However, due to the indenter constraining out-of-plane deformation, the damage does not appear. It is considered that the deformation is small. When the fiber discontinuity is close to the surface, stress concentrations for both compressive and shear stresses occur. The location where the fiber discontinuity is situated in the second layer from the surface is where the compressive and shear stresses are most likely to concentrate.

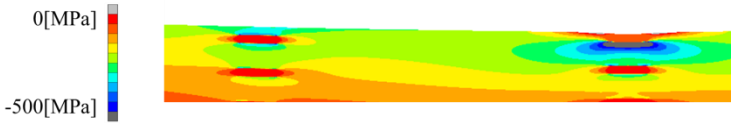

(a) Stress distribution in *x*-direction



(b) Shear stress distribution

Fig. 2.7. Stress distribution obtained by FEM

3 TENSILE TEST

To focus on a single fiber discontinuity within the specimen, the specimen is cut that the fiber discontinuity is located at the center of the specimen. The dimensions of the specimen and the position of the fiber discontinuity are shown in Fig. 3.1. In order to observe the specimen with a laser microscope, the specimen is polished with sandpaper in the following order: 600, 800, 1000, 1500, and 2000 grit, and finally polished with a polishing compound to confirm the position of the fiber discontinuity. The fiber aligned in the *x*-direction appears as white streaks under observation. Since the test specimen used in this experiment is woven fabric, fibers in the *z*-direction appear black and elliptical. The resin portion appears bright white. The image of the fiber discontinuity captured with the laser microscope is shown in Fig. 3.2, where a 1.39 mm resin-rich area is observed.

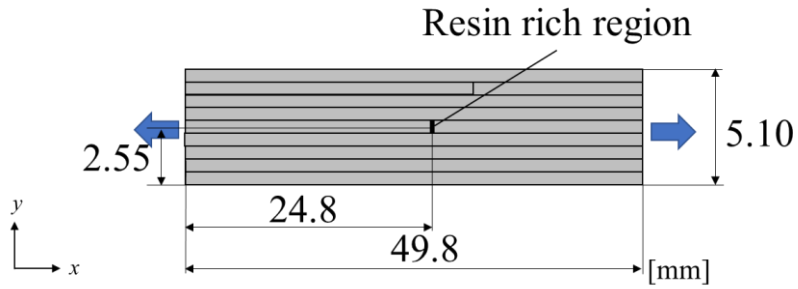

Fig. 3.1. Schematic diagram of discontinuous CFRTP specimen

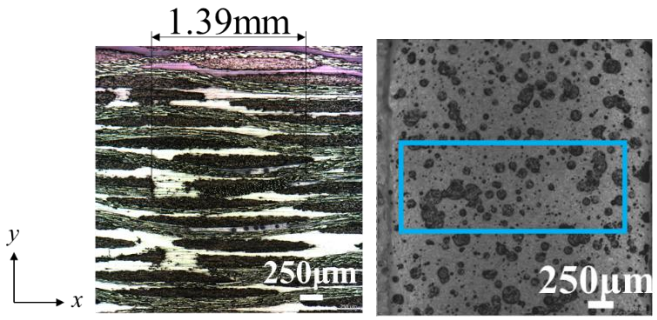

(a) Resin rich region (b) Random pattern for DIC

Fig. 3.2. Resin rich region and random pattern for DIC observed by laser microscope

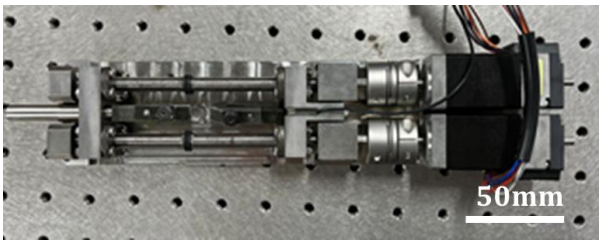

Fig. 3.3. Tensile test machine

Figure 3.4 shows a load-time diagram obtained from tensile test. The displacement and strain distributions at 190 seconds are shown in Fig. 3.5. The black dashed line in the distribution indicates the location of the resin-rich region at the fiber discontinuity. Focusing on the strain in the *x*-direction, strain concentrations are observed at both ends of the resin-rich region.

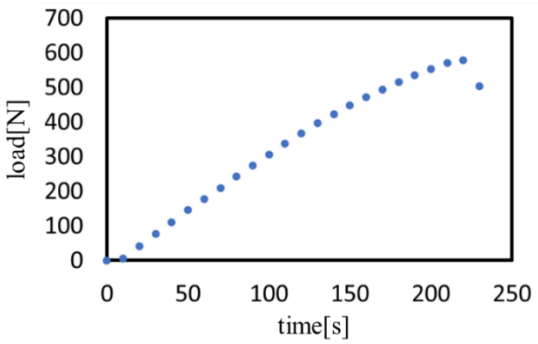

Fig. 3.4. Load-time diagram

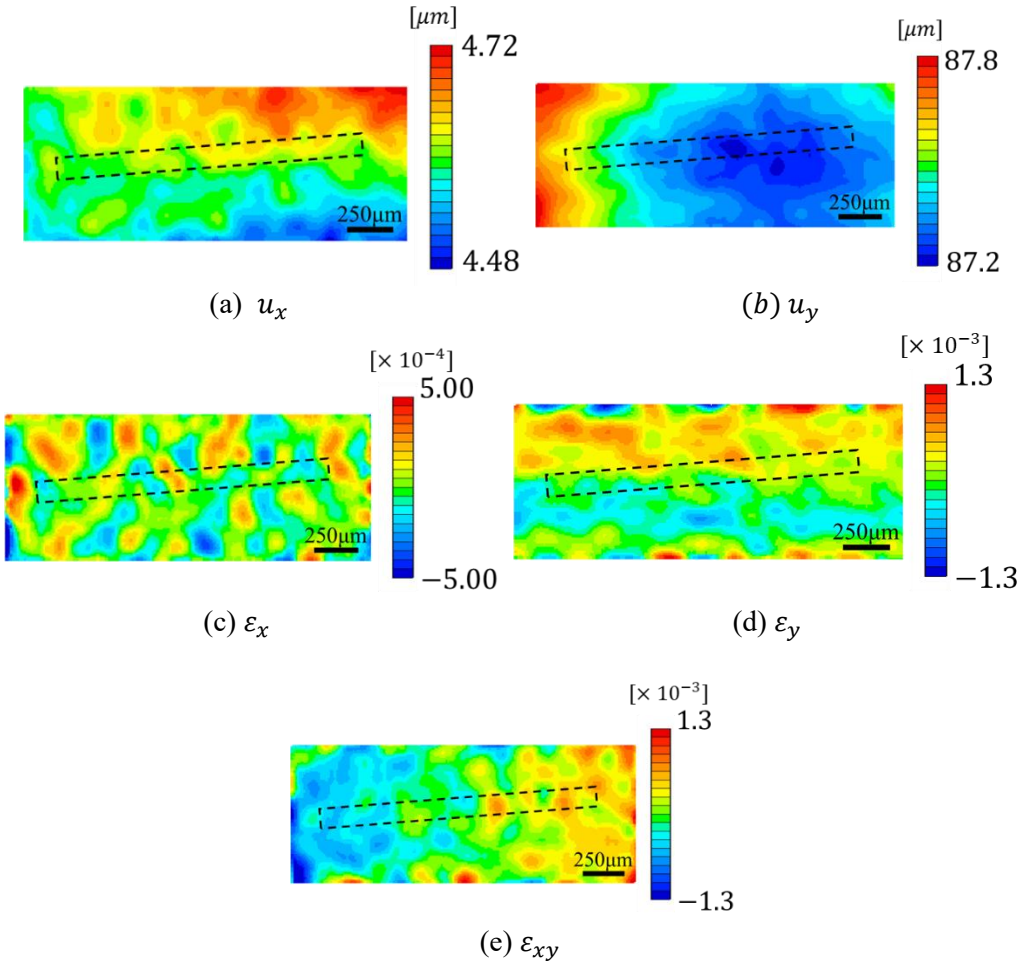

Fig. 3.5. Displacement and strain distribution

FEM is used to simulate the tensile test, calculating the stress distribution as well as the displacement and strain distributions. The FEM software and the material properties used in the analysis are the same as the previous section. The model and boundary conditions used in the analysis are shown in Fig. 3.6. The boundary conditions are set to fixed displacements at both ends, as in the experiments. The applied load is set to 500 N, based on the load-time curve obtained from the experiment.

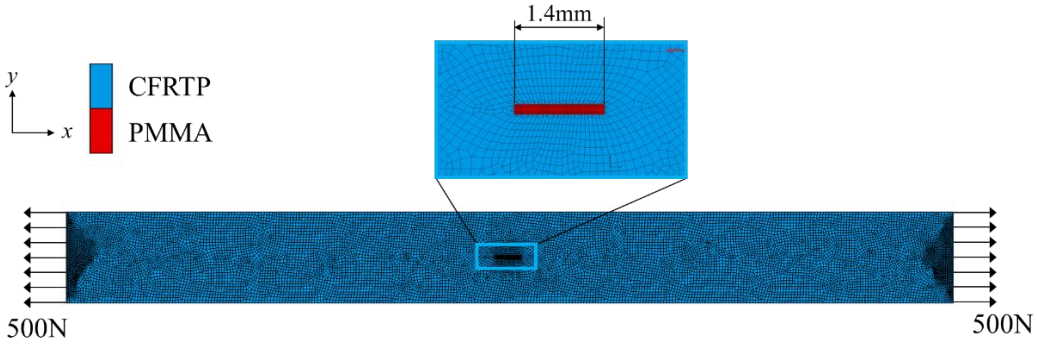

Fig. 3.6. Fiber discontinuity of FEM model

Fig. 3.7 shows the displacement and strain distribution obtained from the FEM analysis. Focusing on the strain in the *x*-direction, strain concentrations are observed at both ends of the resin-rich area, consistent with the experimental results. However, in the strain distribution obtained from the experiment, strain concentration appeared in a scattered manner.

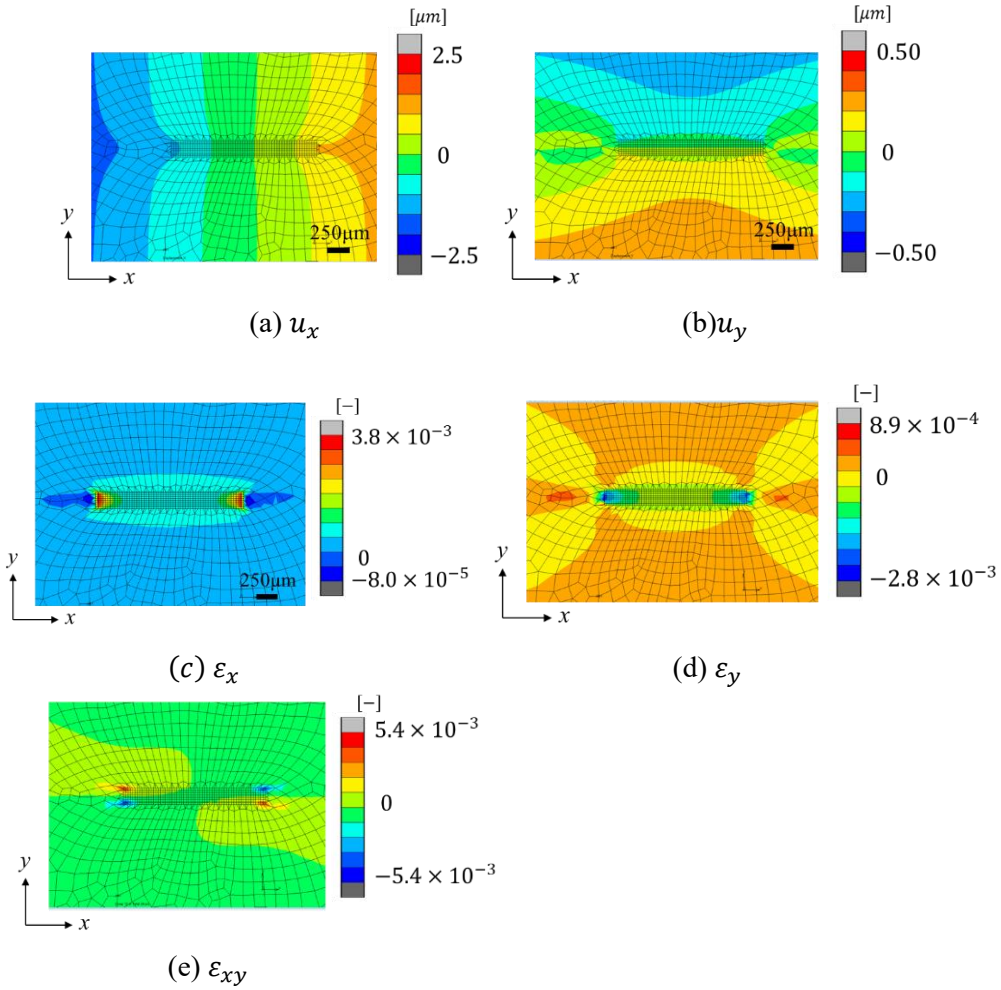

Fig. 3.7. Displacement and strain distribution calculated by FEM

4 CONCLUSION

To explore the application of carbon fiber reinforced thermoplastic (CFRTP) laminates in orthoses, three-point bending tests were conducted using short-beam specimens. Two distinct failure modes were observed: Mode II interlaminar shear failure, and compressive failure on the compressive surface caused by fiber buckling. The CFRTP laminates with discontinuous fibers retained 84.0% of the shear strength

and 82.0% of the flexural strength compared to their continuous-fiber counterparts. Thin CFRTP laminates were found to be more susceptible to interlaminar delamination. Additionally, continuous-fiber CFRTP laminates tended to exhibit compressive failure under bending, which was accompanied by the occurrence of micro-damage on the surface. Considering the potential for such micro-damage to cause injury in the context of orthoses, the use of discontinuous fibers is considered beneficial.

To investigate the potential for discontinuous fiber regions to serve as damage initiation sites on the tensile surface during bending, tensile tests using a laser microscope were performed. Strain concentration was observed at both ends of the resin-rich region associated with the discontinuous fiber area. A similar tendency was confirmed through finite element method (FEM) analysis, suggesting that these strain concentrations may act as origins of damage.

ACKNOWLEDGEMENTS

The authors would like to express their sincere gratitude to the Suzuki Foundation for their generous support, which enabled participation in ICCM24.

REFERENCES

[1] Nakatani, H., Nakaya, K., Matsuba, A., Kouno, Y. and Ogihara, S., Effect of Prepreg Cut on the Mechanical Properties in CFRP Laminates, Journal of Solid Mechanics and Materials Engineering, Vol, 5, (2011), pp. 742-752.

[2] Fikry, M., Atikah, N. and Ogihara, S., Microscopic Damage Behavior of Angle-ply CFRP Laminates with Fiber Discontinuous Plies, Materials system, Vol, 37, (2020), pp. 65-72.

[3] L. Sorensen, T. Gmür and J. Botsis, Delamination propagation measurement using long gauge-length FBG sensors, *Proceedings of the 3rd International Conference on Composites Testing and Model Identification CompTest 2006 (Eds. P. Camanho, F. Pierron, M. Wisnom), Porto, Portugal, April 10-12, 2006,* University Press, Porto, Paper 41, 2006, pp. 174-175.

[4] Alott, N. and Czabaj, M., Characterization of the interlaminar shear strength of IM7/8552 using small-scale short beam shear tests, Elsevier, Vol. 142, (2021)

[5] Fikry, M., Wang, Q., Irita, M., Ri, S., Toyama, N., Vinogradov, V. and Ogihara, S., Measurement of microscopic strain distribution of CFRP laminates with fiber discontinuities by sampling moiré method, Advanced Composite Materials, Vol. 31, (2022), No. 3, pp. 273-288.

Continuous Fiberization of Recycled Carbon Fibers Using Spinning Technology and Tensile Property Evaluation of Their Composites

Shinichi Tatsuta, Takeshi Koto, Akira Nishihata (TATSUBO), Ryo Marui (Marui Fiber Machinery),
Masato Ueda (the University of Tokyo), Tomohiro Yokozeki(Nihon University)

Corresponding Author:
Shinichi Tatsuta
Tatsuta Boseki Co., Ltd.
264 Higashinobusue, Himeji-shi, Hyogo
670-0965, Japan
Tel: 079-288-4501 | Fax: 079-288-4509
Email: shinichi_tatsuta@tatsubo.co.jp

TATSUBO

TATSUBO

TATSUBO was founded in 1901 as a cotton weaving business, and has primarily focused on cotton spinning as its main industry

Recycled carbon fiber

Short fiber length

Spinning Technology

Continuous carbon fiber

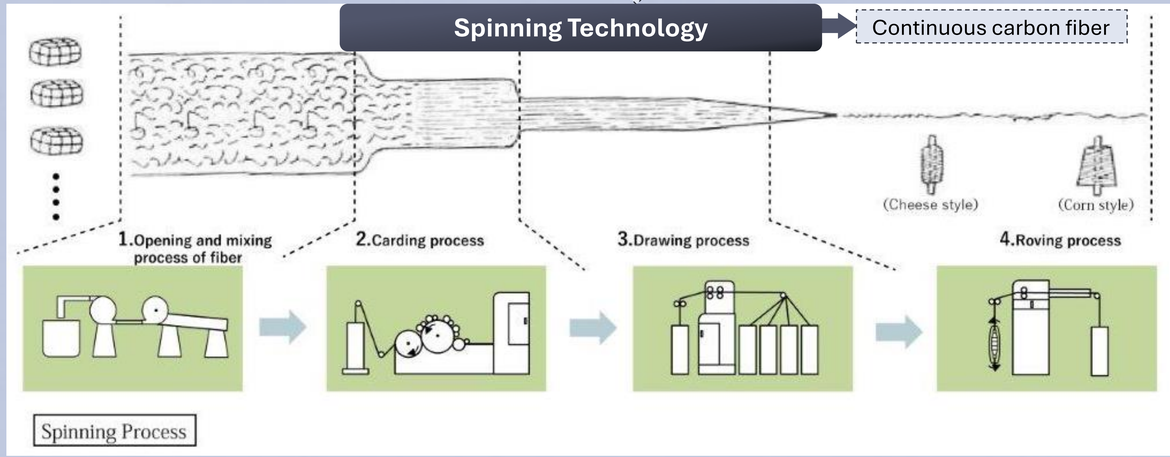

sliver

Unidirectional and easy impregnation



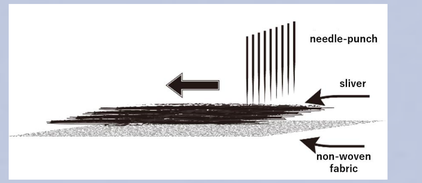



Experimental results

Test number	Vf(%)	Sheet Layer	Thickness (mm)
101	3.7	1	2
102	9.2	1	1
103	23.0	5	3.5

Unidirectional composites-tensile test

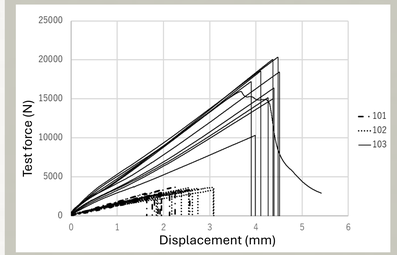

Load-displacement curv

Test number	Strength (MPa)	Coefficient of Variation
101	126	0.120
102	235	0.136
103	355	0.155

Scatter of strength

Comparison between experimental results and calculation results from rule of mixture

Test number	Vf(%)	Elastic modulus (GPa) (Experimental value)	Elastic modulus (GPa) (Calculated value)	Strength (MPa) (Experimental value)	Strength (MPa) (Calculated value)
101	3.70	9.35	12.2	126	186
102	9.20	28.6	24.7	235	377
103	23.0	27.0	55.9	355	857

SEM



Support fabric can be seen at right side

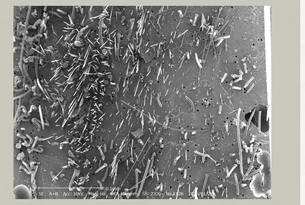

Fiber aligned unidirectionally

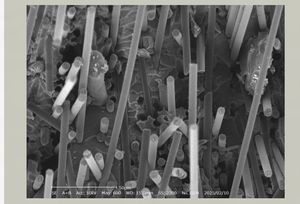

Good impregnation state

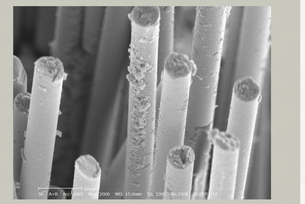

Good interfacial properties

Conclusion

Continuous fiber composite → spinning tech ✓
Good impregnation state → sliver ✓
Rule of mixture → approx 50% reduction ✓
Scatter of strength → approx 15% ✓

ICCM24
AUGUST 4-8, 2025
BALTIMORE CONVENTION CENTER
BALTIMORE, MARYLAND, USA

No Technical Paper Submission for:

Xiaole Li

ICCM24
AUGUST 4-8, 2025
BALTIMORE CONVENTION CENTER
BALTIMORE, MARYLAND, USA

No Technical Paper Submission for:

Swapan Madabhushi Venkata

Extension and layup optimization of Double-Double laminates based on lamination parameters

Chen Du, Tianci Ding and Xiongqi Peng*

School of Materials Science and Engineering, Shanghai Jiao Tong University, Shanghai 200030, China
Email: ChenDu@sjtu.edu.cn.

Keywords: Double-Double laminates, Lamination parameters, Layup optimization

ABSTRACT

Novel Double-Double (DD) laminates family provide a new solution for the design and optimization of composite structure. This article analyses the characteristics of the stiffness matrix of the extended DD laminates based on laminate parameters (LPs), and applies it to a classic benchmark problem. The explicit LPs expressions of extended DD laminates are first derived, and the explicit functions of the feasible region of the LPs are derived through the Lagrange multiplier method, which better explains the characteristics of the DD family mathematically. Subsequently, the classical 18-plane horseshoe benchmark problem is optimized based on the feasible region of DD LPs. The optimal solutions with blending constraint are analytically obtained, and the whole problem is summarized as a linear programming problem in LPs feasible region. The optimal solution is compared with the iterative solution obtained by evolutionary algorithm, which further illustrates the advantages of DD. The exploration of DD in this study can contribute to the discovery of new laminate families and promote the application of DD laminates.

1 INTRODUCTION

The traditional ply angles of laminates are usually 0°, ±45° and 90°, which is also called QUAD. QUAD laminates contain a large number of permutations by changing the ply orientation of each layer. Flexible stacking sequence enables QUAD laminates to satisfy the majority of application requirements, but it also leads to the emergence of high-dimensional discrete design challenges. In order to solve this problem, in theory, researchers usually use the intermediate continuous variable: lamination parameters (LPs) to design the stacking sequence [1]. The advantages of using LPs are obvious. According to the classical lamination theory (CLT), each stiffness coefficient of the laminate can be expressed as a linear combination of laminate parameters. The ply numbers are integrated into LPs by orthogonalizing the thickness, which significantly reduces the number of design variables. When LPs are considered as independent variables, they are interrelated continuous design variables in the interval [-1,1], it makes the optimization problem usually have a global optimal solution.

The discreteness of ply angle and the constraints of design criteria make the disadvantages of traditional QUAD laminates in layup optimization obvious: inefficient fiber layup, high calculation cost of optimization, complex strength calculation, etc. To overcome these disadvantages, Tsai [2] proposed a novel double-double (DD) laminate. DD laminate is composed of repeated stacking of a four-ply sublaminate, and its classical expression is $[\pm\Phi/\pm\Psi]_r$, where r is the number of repetitions. Research showed that when r is greater than or equal to 4, DD laminates are homogeneous and membrane/bending and bending/torsion coupling can be ignored [3]. Moreover, DD can achieve a simpler and larger taper ratio through the card sliding technology, and the manufacturing is simple and not prone to error. The properties and advantages of DD laminate have been widely studied, and have been applied in some structures.

The unique layup characteristic makes DD laminates have significant advantages in design and manufacturing. However, the current research mainly focuses on the performance test and layup design of classic DD laminates $[\pm\Phi/\pm\Psi]_r$. In theory, DD family also contains laminates with other layup characteristics. Therefore, breaking through the limitation of classical DD and analyzing DD family from a more general perspective will help the understanding and application of DD. In this paper, the

classical $[\pm\Phi/\pm\Psi]_r$ DD stacking sequence is extended to the general $[\theta_1/\theta_2/\ldots/\theta_l]_r$ case. The lamination parameter expressions of the extended DD laminates are derived, and the corresponding feasible region is studied by using Lagrange multiplier method. Based on the obtained expressions, the laws of DD family are summarized. Then, the classical 18-panel horseshoe benchmark problem is optimized by using the LPs feasible region of DD, and the optimal solutions with/without blending constraint are analytically obtained. The results show that the optimal solutions are obtained at the lower bound of the feasible region, regardless of the categories of DD, and the results are compared with the iterative solutions obtained by evolutionary algorithm.

2 EXTENDED DD LAMINATES BASED ON LPS

2.1 Lamination parameters of general extended DD laminate

The extended DD laminates were first introduced in [3], and the ξ_1^A-ξ_2^A lamination parameter design spaces of two types of extended laminates $[\pm\Phi_n/\pm\Psi]_r$ and $[\pm\Phi/\pm\Psi/\theta]_r$ ($\theta\in\{0°,90°\}$) were studied in [3] to illustrate the characteristics of classical $[\pm\Phi/\pm\Psi]_r$ DD laminates. However, the characteristics of extended DD laminates have not been further studied.

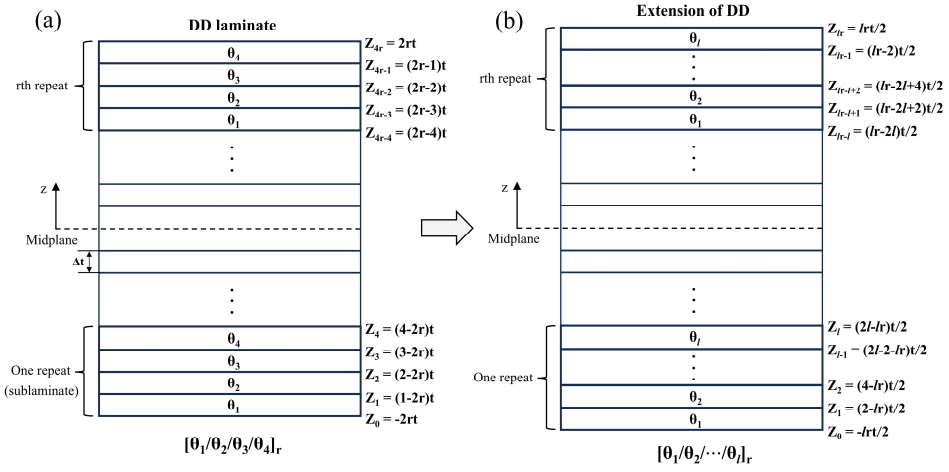

Fig. 1. Layup information of laminate. (a) Classical DD laminate, (b) General extended DD laminate.

In Fig. 1, a general DD extended laminate and a classical DD laminate are presented. In the classical DD laminate, it contains four types of layup categories, which are staggered 1: $[+\Phi/-\Psi/-\Phi/+\Psi]_r$, staggered 2: $[+\Phi/+\Psi/-\Phi/-\Psi]_r$, staggered 3: $[+\Phi/-\Psi/+\Psi/-\Phi]_r$, and staggered 4: $[\pm\Phi/\pm\Psi]_r$. When the specific stacking sequence is not considered, the sublaminate of the DD laminate has four angles, represented by θ_1, θ_2, θ_3 and θ_4, respectively. Assuming the repetition number of the sublaminate is r and the thickness of each layer is t. The entire laminate contains $4r+1$ nodes, and the coordinates z corresponding to each node are shown in Fig. 1(a). In the general extended DD laminate, it is assumed that the sublaminate contains l layers. The total number of layers is lr, and the general laminate can be represented as $[\theta_1/\theta_2/\ldots/\theta_l]_r$. The corresponding node coordinates z are related to the values of l and r, which are also shown in Fig. 1(b). Defining trigonometric functions $f_1(\theta) = \cos(2\theta), f_2(\theta) = \cos(4\theta), f_3(\theta) = \sin(2\theta)$ and $f_4(\theta) = \sin(4\theta)$. The lamination parameters $\xi_{[1,2,3,4]}^{A,B,D}$ of general extended DD laminate can be calculated as follows:

For $\xi_{[1,2,3,4]}^{A}$,

$$\xi_j^A = \frac{1}{2}\sum_{k=1}^{r}\sum_{i=1}^{l}\int_{-1+2(lk-l+i-1)/lr}^{-1+2(lk-l+i)/lr} f_j(\theta_i)\mathrm{d}\bar{z} \tag{1}$$

where j = 1, 2, 3, 4. Integrating each ply through the thickness and summing the repetition number k leads to,

$$\xi_j^A = \sum_{i=1}^{l}\frac{1}{l}f_j(\theta_i) \tag{2}$$

It can be seen that the value of ξ_j^A are only related to the type of sublaminate ply angle θ_i, and the contribution of each ply angle is equal.

Similarly, $\xi_{[1,2,3,4]}^B$ can be obtained as

$$\xi_j^B = \sum_{k=1}^{r}\sum_{i=1}^{l}\int_{-1+2(lk-l+i-1)/lr}^{-1+2(lk-l+i)/lr} \overline{z} f_j(\theta_i)\mathrm{d}\overline{z} \tag{3}$$

Integrating each ply through the thickness and summing the repetition number k,

$$\xi_j^B = \sum_{i=1}^{l}\frac{2(-l+2i-1)}{l^2 r} f_j(\theta_i) \tag{4}$$

It can be seen that ξ_j^B are inversely proportional to the number of repetition number r. Therefore, increasing the number of plies results in the coupling stiffness matrix $\boldsymbol{B}$ tending to $\mathbf{0}$. The type and stacking sequence of the sublaminate ply angles can affect the minimum value of r that required to satisfy the homogeneity criterion of DD laminate. Specific homogenization criterion is defined as [2],

$$\left|\boldsymbol{B}^*\right| < I*(Q_{11}+Q_{22}+2Q_{66}) \tag{5}$$

$$\left\|[\boldsymbol{A}^*]-[\boldsymbol{D}^*]\right\| < I*(Q_{11}+Q_{22}+2Q_{66}) \tag{6}$$

$$\boldsymbol{A}^*, \boldsymbol{B}^*, \boldsymbol{D}^* = \left[\frac{1}{h}\boldsymbol{A}, \frac{2}{h^2}\boldsymbol{B}, \frac{12}{h^3}\boldsymbol{D}\right] \tag{7}$$

where $Q_{11}+ Q_{22}+ 2Q_{66}$ is the Tasi modulus [4], I is the percentage of the Tasi modulus and is usually set to be 2%. [$\boldsymbol{A}^*$, $\boldsymbol{B}^*$, $\boldsymbol{D}^*$] are the thickness normalized stiffnesses. Similarly, for $\xi_{[1,2,3,4]}^D$,

$$\xi_j^D = \frac{3}{2}\sum_{k=1}^{r}\sum_{i=1}^{l}\int_{-1+2(lk-l+i-1)/lr}^{-1+2(lk-l+i)/lr} \overline{z}^2 f_j(\theta_i)\mathrm{d}\overline{z} \tag{8}$$

Integrating each ply through the thickness and summing the repetition number k leads to,

$$\xi_j^D = \sum_{i=1}^{l}\left[\frac{1}{l}+2\frac{(l-i)^2-(4i-3)(l-i)+(i-1)(i-2)}{l^3 r^2}\right] f_j(\theta_i) \tag{9}$$

It can be seen that ξ_j^D are inversely proportional to the square of the number of repetition number r. As the number of plies increases, the coefficient of $f_j(\theta_i)$ tends to be constant $1/l$, ξ_j^D tends to be equal to ξ_j^A. The angles of the sublaminate ply determine whether the values of the lamination parameters ξ_3^D, ξ_4^D can approach to 0.

2.2 The characteristics of general extended DD laminates

Each set of lamination parameters of general extended DD laminates can be obtained through an equation, as shown in Eqs. (2), (4), and (9). Through the study of these equations, the characteristics of extended DD laminate can be explored, which is also applicable to classical DD laminates.

In Eq. (2), the coefficients of each ply angle trigonometric function $f_j(\theta_i)$ are the same as $1/l$. However, in Eqs. (4) and (9), the coefficients of $f_j(\theta_i)$ are related to i, this indicates that the stacking sequence will affect the value of the coefficients, and it will further affect the minimum r value required for the laminate to satisfy the homogeneity. To illustrate the relationship between trigonometric function coefficient with stacking sequence, the following functions are defined:

$$\begin{cases} g_B(i) = \dfrac{2(-l+2i-1)}{l^2 r} \\ g_D(i) = \dfrac{1}{l}+2\dfrac{(l-i)^2-(4i-3)(l-i)+(i-1)(i-2)}{l^3 r^2} \end{cases} \tag{10}$$

where i ($\in[1, l]$, N^*) represents the i-th ply of sublaminate in Fig. 1, l and r are positive integers. For sublaminate with the number of plies l, the sub-midplane coordinate is $lt/2$, and the number of i-th ply symmetrical about the sub-midplane is l-i+1. Substituting l-i+1 into Eq. (10), it can be obtained that:

$$\begin{cases} g_B(l-i+1)=\dfrac{2(l-2i+1)}{l^2 r}=-g_B(i) \\ g_D(l-i+1)=\dfrac{1}{l}+2\dfrac{(i-1)^2-(4l-4i+1)(i-1)+(l-i)(l-i-1)}{l^3 r^2}=g_D(i) \end{cases} \tag{11}$$

It can be seen that in the sublaminate panel, the layers that are symmetrical about the sub-midplane contain opposite values of the ξ_j^B trigonometric coefficient, and the same values of the ξ_j^D trigonometric coefficient. Considering the coupling term coefficients $\xi_{3,4}^A$, ξ_j^B and $\xi_{3,4}^D$ in the LPs, combining Eq. (11) with Eqs. (2), (4) and (9), some characteristics of the general extended DD laminate can be obtained as follows:

(1) When the sublaminate satisfies the balance constraint (with the same number of $+\theta$ and $-\theta$ angles), it can be obtained that $\xi_{3,4}^A = 0$, and as the value of r increases, both ξ_j^B and $\xi_{3,4}^D$ tend to 0. The balance of sublaminate is a sufficient and necessary condition for general extended DD laminates achieving homogenization.

(2) When the sublaminate is antisymmetric about the sub-midplane, it can be obtained that $\xi_{3,4}^{A,D} = 0$ and $\xi_{1,2}^B = 0$.

(3) When the sublaminate is symmetric about the sub-midplane, it can be obtained that $\xi_j^B = 0$.

The essence of characteristics (2) and (3) is that for the general extended DD laminate, the laminate midplane coincides with the sub-midplane or is on the boundary of the sublaminate, as shown in Fig. 2. Therefore, when the sublaminate is antisymmetric or symmetric about the sub-midplane, the corresponding entire laminate will be antisymmetric or symmetric about the global midplane. In addition, a special type of fully decoupled ($\xi_{3,4}^{A,D} = 0$, $\xi_j^B = 0$) laminate can be derived from the above analysis results. The trigonometric coefficients of Eq. (4) ξ_j^B have the following relationship:

$$g_B(1)+g_B(\frac{l}{2})=\cdots=g_B(i)+g_B(\frac{l}{2}-i+1)=-\frac{2}{lr} \tag{12}$$

where the number of layers l in the sublaminate is even, and i = 1, 2, ⋯, l/2. When the sublaminate satisfies feature (2) and the layers 1 to l/2 are balanced, ξ_3^B and ξ_4^B are also equal to 0. Therefore, the number of decoupled DD sublaminate layers should not be less than 8, and the basic expression is $[+\Psi/-\Psi/-\Psi/+\Psi, -\Psi/+\Psi/+\Psi/-\Psi]_r$, or $[-\Psi/+\Psi/+\Psi/-\Psi, +\Psi/-\Psi/-\Psi/+\Psi]_r$. The above two types of decoupled DD laminates were initially proposed by Miravete and Tasi [5], and this laminate family is called 'Metalite'. In this section, the mechanism of 'Metalite' laminate decoupling is explained from the analysis of lamination parameters of general extended DD laminate, and the laws are summarized.

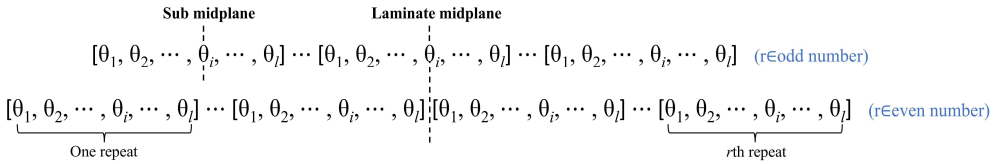

Fig. 2. Relationship between sub-midplane and global midplane of general extended DD laminate.

2.3 Feasible region of extended DD laminate

Compared with QUAD layups, the complexity of the feasible region of DD laminate is reduced due to their simple stacking concept. In this section, based on the derived lamination parameters expressions, the ξ_1^A-ξ_2^A feasible region of extended laminates is mainly studied and summarized.

It is assumed that the layup of general extended laminate is balanced, including l/2 types of ply orientations (the number of sublaminate is even), and the layup is defined as $[\pm\theta_1/\pm\theta_2/\cdots/\pm\theta_{l/2}]_r$. The Lagrange multiplier method is used to obtain the feasible region between two lamination parameters [6]:

$$H(\theta_1,\cdots,\theta_{l/2})=F(\theta_1,\cdots,\theta_{l/2})+\lambda(G(\theta_1,\cdots,\theta_{l/2})-x) \tag{13}$$

where F, G are two lamination parameters related to the layup orientation θ, and λ is a Lagrange multiplier. The solution of feasible region can be expressed as minimizing and maximizing $y = F(\theta_1,\cdots, \theta_{l/2})$ subject to $x = G(\theta_1,\cdots, \theta_{l/2})$. The conditions to be satisfied at each stationary point are:

$$\begin{cases} \dfrac{\partial H}{\partial \theta_1} = \dfrac{\partial F}{\partial \theta_1} + \lambda \dfrac{\partial G}{\partial \theta_1} = 0 \\ \vdots \\ \dfrac{\partial H}{\partial \theta_{l/2}} = \dfrac{\partial F}{\partial \theta_{l/2}} + \lambda \dfrac{\partial G}{\partial \theta_{l/2}} = 0 \\ \dfrac{\partial H}{\partial \lambda} = G(\theta_1,\cdots, \theta_{l/2}) - x = 0 \end{cases} \tag{14}$$

For the feasible region between the lamination parameters ξ_1^A-ξ_2^A, it can be seen from Eq. (2) that $\xi_{1,2}^A$ are related to the types of layup orientations. According to the type and number of layup orientation variables, the feasible region of extended laminates can be roughly divided into the following three categories, and the corresponding characteristics can be further summarized.

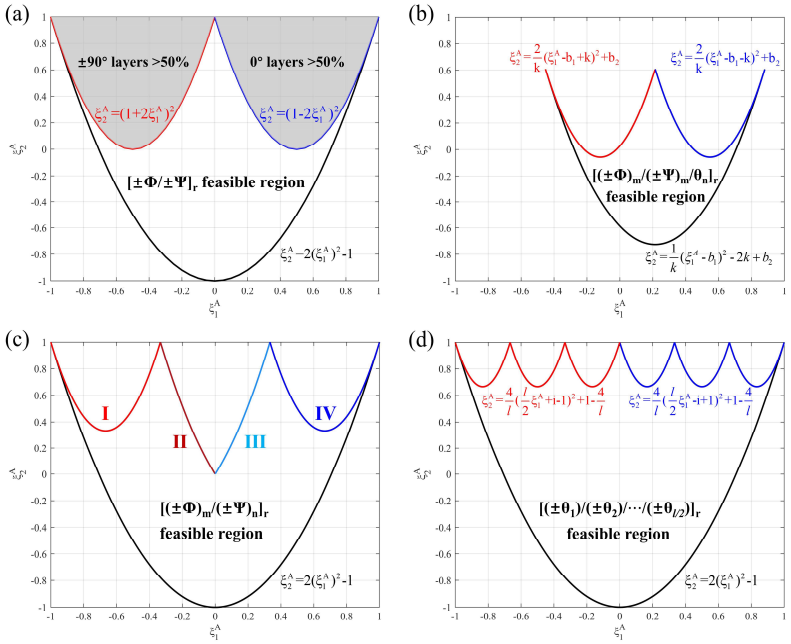

Fig. 3. Feasible regions and boundary equations of ξ_1^A-ξ_2^A for different categories of DD laminates. (a) Classic $[\pm\Phi/\pm\Psi]_r$, (b) $[(\pm\Phi)_m/(\pm\Psi)_m/\theta_n]_r$, (c) $[(\pm\Phi)_m/(\pm\Psi)_n]_r$, (d) $[(\pm\theta_1)/(\pm\theta_2)/\cdots/(\pm\theta_{l/2})]_r$.

2.4.1 Feasible region of $[(\pm\Phi)_m/(\pm\Psi)_m/\theta_n]_r$

Firstly, the feasible region of extended DD laminates with two ply angle variables, Φ and Ψ, is considered. In the classic $[\pm\Phi/\pm\Psi]_r$ DD laminates, due to the special layup stacking, the ξ_1^A-ξ_2^A LP feasible region is missing the area where 0° and 90° ply accounts for more than 50%, as shown on Fig. 3(a). In literature [3], $[0/90/\pm\Phi/\pm\Psi]_r$, $[\pm45/\pm\Phi/\pm\Psi]_r$ and $[0/\pm\Phi/\pm\Psi]_r$ laminates were studied to explore areas outside the boundary. According to the characteristics of this kind of laminates, the general expression $[(\pm\Phi)_m/(\pm\Psi)_m/\theta_n]_r$ is given. Here m is the number of occurrences of ±Φ and ±Ψ angles, θ_n is the known n ply angles, m and n are positive integers, satisfying the equation $4m+n = l$. According to Eq. (2), the expressions of lamination parameters ξ_1^A and ξ_2^A are given as follows:

$$\xi_1^A = \frac{\sum_{i=1}^{n}\cos(2\theta_i)}{l} + \frac{2m}{l}(\cos 2\Phi+\cos 2\Psi) = b_1 + k(\cos 2\Phi+\cos 2\Psi) \tag{15}$$

$$\xi_2^A = \frac{\sum_{i=1}^{n}\cos(4\theta_i)}{l} + \frac{2m}{l}(\cos 4\Phi+\cos 4\Psi) = b_2 + k(\cos 4\Phi+\cos 4\Psi) \tag{16}$$

The coefficients b, k ($\in$(-1,1)) are used to simplify the equation, which are independent of the ply angle variables Φ and Ψ, and can be considered as constants in the equation. According to the Lagrange multiplier method of Eqs. (13) and (14), the boundary equations are obtained as follows:

$$\begin{aligned}
&\xi_2^A \geq \frac{1}{k}(\xi_1^A - b_1)^2 - 2k + b_2, \quad \xi_1^A \in [b_1 - 2k, b_1 + 2k] \\
&\xi_2^A \leq \frac{2}{k}(\xi_1^A - b_1 + k)^2 + b_2, \quad \xi_1^A \in [b_1 - 2k, b_1] \\
&\xi_2^A \leq \frac{2}{k}(\xi_1^A - b_1 - k)^2 + b_2, \quad \xi_1^A \in [b_1, b_1 + 2k]
\end{aligned} \tag{17}$$

Fig. 3(b) provides a schematic diagram of the obtained feasible region. According to the diagram and Eq. (17), it can be seen that, the feasible region of the general extended laminate $[(\pm\Phi)_m/(\pm\Psi)_m/\theta_n]_r$ is obtained by scaling and translating the feasible region of the classical $[\pm\Phi/\pm\Psi]_r$ laminate. The coefficient k determines the scaling size of the boundary parabolic equations on the x and y axes, while b_1 and b_2 determine the translation distance of the parabolas on the x and y axes, respectively.

2.4.2 Feasible region of $[(\pm\Phi)_m/(\pm\Psi)_n]_r$

When the number of ply angle variables Φ and Ψ is different, the general expression of laminate is $[(\pm\Phi)_m/(\pm\Psi)_n]_r$. Here m and n are the occurrence number of ±Φ and ±Ψ angle pairs respectively, satisfying the equation $2m+2n = l$. The expressions of lamination parameters ξ_1^A and ξ_2^A are given as follows:

$$\begin{aligned}
&\xi_1^A = \frac{2}{l}(m\cos 2\Phi + n\cos 2\Psi) \\
&\xi_1^A = \frac{2}{l}(m\cos 4\Phi + n\cos 4\Psi)
\end{aligned} \tag{18}$$

When $m>n$, the boundary equations of the feasible region are as follows:

$$\begin{aligned}
&\xi_2^A \geq 2(\xi_1^A)^2 - 1, \quad \xi_1^A \in [-1, 1] \\
&\mathrm{I}: \xi_2^A \leq \frac{l}{n}(\xi_1^A + \frac{m}{m+n})^2 + \frac{m-n}{m+n}, \quad \xi_1^A \in [-1, \frac{n-m}{m+n}] \\
&\mathrm{II}: \xi_2^A \leq \frac{l}{m}(\xi_1^A - \frac{n}{m+n})^2 + \frac{n-m}{m+n}, \quad \xi_1^A \in [\frac{n-m}{m+n}, 0] \\
&\mathrm{III}: \xi_2^A \leq \frac{l}{m}(\xi_1^A + \frac{n}{m+n})^2 + \frac{n-m}{m+n}, \quad \xi_1^A \in [0, \frac{m-n}{m+n}] \\
&\mathrm{IV}: \xi_2^A \leq \frac{l}{n}(\xi_1^A - \frac{m}{m+n})^2 + \frac{m-n}{m+n}, \quad \xi_1^A \in [\frac{m-n}{m+n}, 1]
\end{aligned} \tag{19}$$

Fig. 3(c) provides the schematic diagram of the obtained feasible region. When $m<n$, the boundary equations of the feasible region are the m, n value exchange of the above formula. It can be seen from the diagram and Eq. (19) that the boundary constraint equations on the feasible region increase, and they are still parabolic. The values of m and n both determine the characteristics of the parabolas.

2.4.3 Feasible region of $[(\pm\theta_1)/(\pm\theta_2)/\cdots/(\pm\theta_{l/2})]_r$

Further consider the increase of ply angle variable dimension. Assuming that the more general DD laminate contains $l/2$ ply angle variables, the expression of the laminate can be written as $[(\pm\theta_1)/(\pm\theta_2)/\cdots/(\pm\theta_{l/2})]_r$. The corresponding lamination parameter ξ_1^A and ξ_2^A are given as follows:

$$\begin{aligned}
&\xi_1^A = \frac{2}{l}(\cos 2\theta_1 + \cos 2\theta_2 + \cdots + \cos 2\theta_{l/2}) \\
&\xi_2^A = \frac{2}{l}(\cos 4\theta_1 + \cos 4\theta_2 + \cdots + \cos 4\theta_{l/2})
\end{aligned} \tag{20}$$

The boundary equations of the feasible region are as follows:

$$\begin{aligned}
&\xi_2^A \geq 2(\xi_1^A)^2 - 1, \quad \xi_1^A \in [-1,1] \\
&\xi_2^A \leq \frac{4}{l}(\frac{l}{2}\xi_1^A + i - 1)^2 + 1 - \frac{4}{l}, \quad \xi_1^A \in [\frac{-2i}{l}, \frac{4-2i}{l}] \\
&\xi_2^A \leq \frac{4}{l}(\frac{l}{2}\xi_1^A - i + 1)^2 + 1 - \frac{4}{l}, \quad \xi_1^A \in [\frac{2i-4}{l}, \frac{2i}{l}]
\end{aligned} \tag{21}$$

where i is an odd or even set, depending on the value of $l/2$. When $l/2$ is even, $i \in \{2, 4, \cdots, l/2\}$, and when $l/2$ is odd, $i \in \{1, 3, \cdots, l/2\}$. Fig. 3(d) provides a schematic diagram of the obtained feasible region. Combining Eq. (21), it can be seen that the upper boundary of the feasible region is a quadratic function related to the value of l. Due to the same number of each ply angle variable, $l/2$ parabolic lines with the same shape and different symmetry axes contain the equal interval span of ξ_1^A axis, evenly dividing the [-1,1] interval. When the value of t tends to infinity, the upper boundary of the whole feasible region is the straight line ξ_2^A=1.

2.4.4 Summary of the feasible region for general extended DD laminates

The explicit expression of feasible region boundary equations and the comparison with classical DD laminate illustrate the characteristics of the aforementioned three types of extended DD laminates. In addition, some general conclusions regarding the ξ_1^A-ξ_2^A feasible region of extended DD laminate are summarized as follows:

(1) All the extended DD laminates have the same equation form for lamination parameters ξ_1^A and ξ_2^A, which can be expressed by a general expression, as shown in Eq. (22). Where m_i is the occurrence number of the i-th ply angle variable, d is the dimensionality of the variable, b_1 and b_2 are the coefficients corresponding to the known ply angles. When the research object is a combination of any two laminating parameters, similar expressions can still be obtained.

$$\xi_1^A = b_1 + \frac{2}{l}m_i \cos 2\theta_i \ , \ \xi_2^A = b_2 + \frac{2}{l}m_i \cos 4\theta_i \quad (i \in \{1, 2, \cdots, d\}) \tag{22}$$

(2) All boundary curve equations in the feasible region of ξ_1^A - ξ_2^A are quadratic functions. By combining Eqs. (14) and (22), it can be concluded that the shape of the feasible region is determined by the trigonometric function pairs $m_i\cos2\theta_i$~$m_i\cos4\theta_i$. Therefore, adding known ply angles and proportionally changing the occurrence number of ply angle variables will only scale and translate the existing feasible region. Changing the proportion of the occurrence number of ply angle variables, and the dimensionality of the variables, the shape of the feasible region and the number of boundary equations will change, and the entire feasible domain space can be further expanded.

The general analysis and discussion of extended DD laminates from the perspective of laminate parameters and feasible region is helpful to further explain the characteristics of DD laminates from the theoretical level. From the above analysis, it can be concluded that increasing the variable dimension of sublaminate can expand the feasible region space of DD, and the gray feasible region of classical DD laminates in Fig. 3(a) can be further filled. However, in practical applications, the increase in the ply number of sublaminate will lead to the need for more plies to satisfy the homogeneity of laminates, which will affect the weight saving by tapering. In addition, with ply number increase in sublaminate, the appearance of ply drops corresponds to a higher taper ratio, and this may lead to high stress concentration [3]. The research on the homogeneity of the extended DD laminates will be carried out in our future work.

3 BUCKLING OPTIMIZATION OF HORSESHOE PROBLEM BASED ON DD LPS

3.1 Problem description

The 18-panel horseshoe configuration is shown in Fig. 4, the dimensions and local loadings of each panel are marked in the figure. All panels are assumed to be simply supported on four edges and loaded in bi-axial compression. The Graphite/Epoxy IM7/8552 unidirectional prepreg is used for each ply, where E_1 = 141 GPa (20.5 Msi), E_2 = 9.03 GPa (1.31 Msi), G_{12} =4.27 GPa (0.62 Msi), ν_{12} = 0.32, the ply thickness is 0.191mm (0.0075 in), and the prepreg density is 1.57g/cm^3. The optimization objective is

to find the lightest horseshoe panel design without individual panel failure under buckling. A simply supported panel in bi-axial compression has a sinusoidal buckling mode. The panel is loaded such that critical buckling loads are $N_{xcr} = \lambda N_x$ and $N_{ycr} = \lambda N_y$, where λ is a scalar load amplitude factor. The value of λ corresponds to buckling is given by Eq. (23).

$$\lambda(m,n)=\frac{\pi^2[D_{11}(m/a)^4+2(D_{12}+2D_{66})(m/a)^2(n/b)^2+D_{22}(n/b)^4]}{(m/a)^2N_x+(n/b)^2N_y} \tag{23}$$

where m and n are the buckling half-wave numbers in the x and y directions respectively. a and b are the length and width dimensions of the plate. D_{11}, D_{12}, D_{66}, D_{22} are the bending stiffness coefficients of the laminated plate.

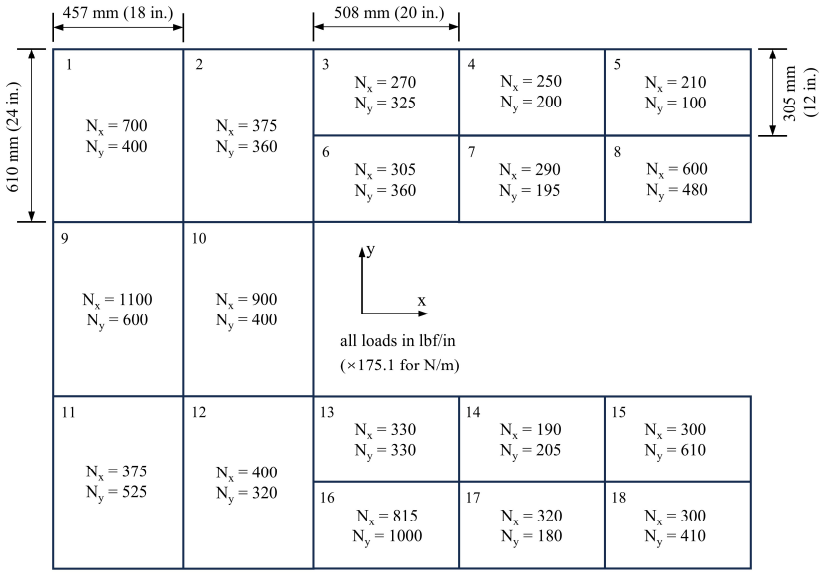

Fig. 4. Geometry and loads of 18-panel horseshoe optimization case [7].

3.2 DD optimization with blending constraint

When blending constraint is considered. The DD layup orientations of each plate are the same $[\pm\Phi/\pm\Psi]_1=\cdots=[\pm\Phi/\pm\Psi]_k=\cdots=[\pm\Phi/\pm\Psi]_n$, and all plates have the same LPs. In this case, the design variables are the continuous layup angles and the plate thickness related to the number of layers.

Substituting the expression of the bending stiffness coefficients with respect to LPs into Eq. (23), Eq. (24) can be obtained. Here k_1, k_2 and k_3 are constants related to the respective plate dimensions and applied loads, as shown in Eq. (25). U_1-U_5 are the material stiffness invariants corresponding to IM7/8552 materials. The plate thickness h in Eq. (24) can be converted into Eq. (26). The optimization problem turns into obtaining the optimal LPs set that makes the total weight of the structure in Eq. (27) is minimized.

$$\begin{aligned}\lambda(m,n)&=\pi^2[D_{11}k_1+2(D_{12}+2D_{66})k_2+D_{22}k_3]\\&=\frac{h^3}{12}\pi^2[\xi_1^D U_2(k_1-k_3)+\xi_2^D U_3(k_1+k_3-6k_2)+(U_1k_1+U_1k_3+2U_4k_2+4U_5k_2)]\\&=\frac{h^3}{12}\pi^2F(\xi_1^D,\xi_2^D)\end{aligned} \tag{24}$$

$$\begin{cases}k_1=\dfrac{(m/a)^4}{(m/a)^2N_x+(n/b)^2N_y}\\[2ex] k_2=\dfrac{(m/a)^2(n/b)^2}{(m/a)^2N_x+(n/b)^2N_y}\\[2ex] k_3=\dfrac{(n/b)^4}{(m/a)^2N_x+(n/b)^2N_y}\end{cases} \tag{25}$$

$$h_i = \sqrt[3]{\frac{12}{\pi^2 F_i(\xi_1^D, \xi_2^D)}} \tag{26}$$

$$W = \sum_{i=1}^{18} \rho a_i b_i h_i = \rho[\mathrm{a_1 b_1} \sum_{i \in \mathrm{P_1}} \sqrt[3]{\frac{12}{\pi^2 F_i(\xi_1^D, \xi_2^D)}} + \mathrm{a_3 b_3} \sum_{j \in \mathrm{P_2}} \sqrt[3]{\frac{12}{\pi^2 F_j(\xi_1^D, \xi_2^D)}}] \tag{27}$$

$$\begin{cases} \dfrac{F_i(\xi_1^D, \xi_2^D)}{F_1(\xi_1^D, \xi_2^D)} = \dfrac{(m/a)^2 (N_x)_1 + (n/b)^2 (N_y)_1}{(m/a)^2 (N_x)_i + (n/b)^2 (N_y)_i} = k_i^{'}, \quad i \in \mathrm{P_1} \\ \dfrac{F_j(\xi_1^D, \xi_2^D)}{F_3(\xi_1^D, \xi_2^D)} = \dfrac{(m/a)^2 (N_x)_3 + (n/b)^2 (N_y)_3}{(m/a)^2 (N_x)_j + (n/b)^2 (N_y)_j} = k_j^{'}, \ j \in \mathrm{P_2} \end{cases} \tag{28}$$

$$W = \rho(\mathrm{a_1 b_1} \sum_{i \in \mathrm{P_1}} k_i^{'} \sqrt[3]{\frac{1}{F_1(\xi_1^D, \xi_2^D)}} + \mathrm{a_3 b_3} \sum_{j \in \mathrm{P_2}} k_j^{'} \sqrt[3]{\frac{1}{F_3(\xi_1^D, \xi_2^D)}}) \tag{29}$$

The plates in the respective sets of $\mathbf{P_1}$ and $\mathbf{P_2}$ have the same size and LPs, it can be obtained from Eq. (24) and Eq. (25) that the function $F(\xi_1^D, \xi_2^D)$ corresponding to the plates in the two sets are proportional as shown in Eq. (28). Define the function $F(\xi_1^D, \xi_2^D)$ ratio of each plate in the $\mathbf{P_1}$ set with respect to plate 1 as $k_i^{'}$, and define the function $F(\xi_1^D, \xi_2^D)$ ratio of each plate in the $\mathbf{P_2}$ set with respect to plate 3 as $k_j^{'}$. The weight of the entire plate is only related to the function F corresponding to plates 1 and 3, as shown in Eq. (29). F_1 and F_3 are interrelated functions related to variables ξ_1^D and ξ_2^D. Therefore, minimizing the weight of the structure is equivalent to doing a linear program to find the minimum value on the feasible region composed of $\frac{1}{\sqrt[3]{F_1}}$ and $\frac{1}{\sqrt[3]{F_3}}$.

The linear programming of Eq. (29) in the feasible region of an extended DD laminate is shown in Fig. 5, where the boundary equations are implicitly derived from the section 2.3. It can be concluded that the minimum value of the structure weight is also obtained at the lower bound of the DD feasible region, and the optimal layups are also single DD. Since the number of layers is even, the optimal solution of LPs is the value interval. The optimal LPs values are $\xi_1^D \in$ [-0.166, -0.124], $\xi_2^D \in$ [-0.945, -0.969], and the optimal ply angles are single DD interval [±49.79°, ±48.56°].

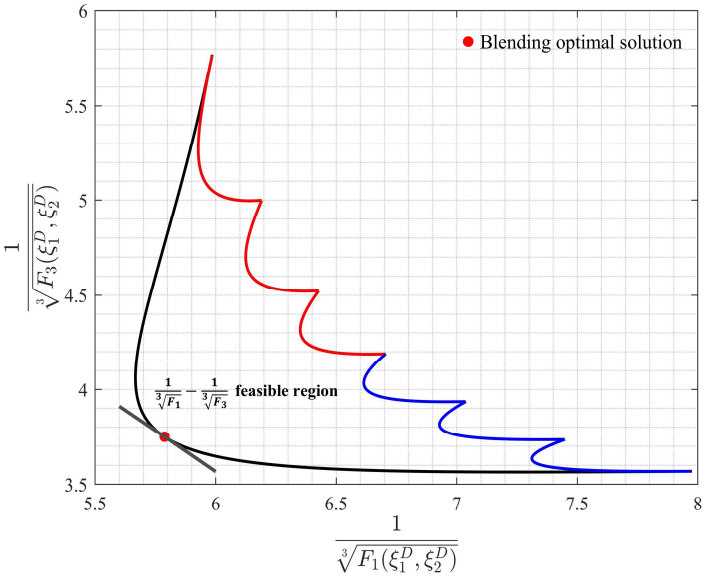

Fig. 5. LPs optimal solution of benchmark problem with blending constraint in the feasible region of an extended DD laminate.

Table 1 shows the number of plies and buckling factor of each plate when the single DD ply angle taken as ±49°. When the number of DD layers is rounded up to the even, the weight of the whole plate is 28.67kg, the residual buckling factor of each plate is also given in the table, and all plates satisfy the homogeneity criterion.

3.3 Results analysis and comparison

Based on the obtained lamination parameters and the feasible region design space of DD laminates, the optimization results of the classic horseshoe benchmark problem are derived analytically. Most of the previous studies used evolutionary algorithms to optimize the benchmark problem. In order to further reveal the characteristics and advantages of DD in layup optimization, the results of DD and evolutionary algorithm optimization are compared and analyzed.

Table 1 provides the optimization results of each plate based on PDS (ply drop sequence) layup strategy under genetic algorithm and compares them with DD optimization results with even number of plies satisfying blending constraint. PDS is a layup design method for internal ply drops proposed by Yang et al [8]. This method conveniently expresses layup information and realizes the satisfaction of blending constraint. Under the balanced and symmetrical design criteria, PDS selects QUAD (0°, ± 45°, 90°) and General (0°, ± 15°, ± 30°, ± 45°, ± 60°, ± 75°, 90°) two types of ply angles for optimization. When the PDS selects QUAD orientations and the number of layers is even, the optimal weight of the structure is 28.76kg after 2500 iterations optimization. As the current optimization algorithm with strong performance, the optimized solution obtained by PDS using QUAD layer is inferior to the solution obtained by DD satisfying the homogeneity optimization. In addition, the convergence time of the optimization algorithm iteration takes several hours, while DD only needs a few milliseconds to obtain the optimal solution. When PDS selects the General ply angle and the number of plies is allowed to be odd, the optimal weight of the structure is 28.47kg after 2800 iterations optimization, which is 0.29kg lighter than QUAD solution and better than DD solution.

Table 1. Results comparison for DD with PDS.

Panel	PDS (QUAD)		PDS (General)		DD	
	Ply number (even)	λ_{min}	Ply number (odd)	λ_{min}	Ply number (even)	λ_{min}
1	34	1.166	33	1.019	34	1.130
2	28	1.051	29	1.106	28	1.011
3	22	1.117	23	1.331	22	1.194
4	20	1.223	19	1.109	20	1.306
5	16	1.034	16	1.102	16	1.014
6	22	1.004	23	1.196	22	1.073
7	20	1.184	19	1.074	20	1.265
8	26	1.110	23	1.032	26	1.195
9	38	1.037	39	1.092	38	1.015
10	36	1.135	35	1.000	36	1.103
11	30	1.111	30	1.055	30	1.072
12	28	1.046	29	1.101	28	1.007
13	22	1.051	23	1.252	22	1.123
14	20	1.297	18	1.003	18	1.010
15	26	1.075	25	1.000	26	1.159
16	32	1.063	31	1.035	32	1.199
17	20	1.201	19	1.089	20	1.283
18	24	1.179	23	1.085	24	1.263
Weight(kg)	28.76		28.47		28.67	

Fig. 6 shows the distribution of DD and PDS QUAD optimization solutions in the feasible region of ξ_1^D-ξ_2^D. The areas enclosed by the blue curve and black dotted line are DD feasible region and QUAD feasible region, respectively. The special stacking characteristic makes the optimal solution obtained by

DD unique. For QUAD laminates, in order to satisfy the blending constraint and ensure the continuity of the layup, the stacking sequence of each plate is different, and the solution set is distributed on the right side of the lower boundary of the feasible region. In theory, each plate approaches the theoretical optimal solution as closer as possible to minimize weight, but the discrete ply angle variables, blending constraint, and other design criteria make the solution values compromise and aggregate.

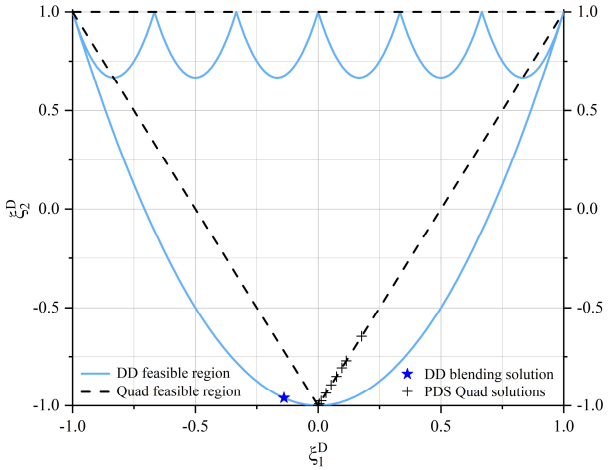

Fig. 6. Distribution of DD optimal solution and PDS QUAD optimal solution in feasible region of lamination parameters.

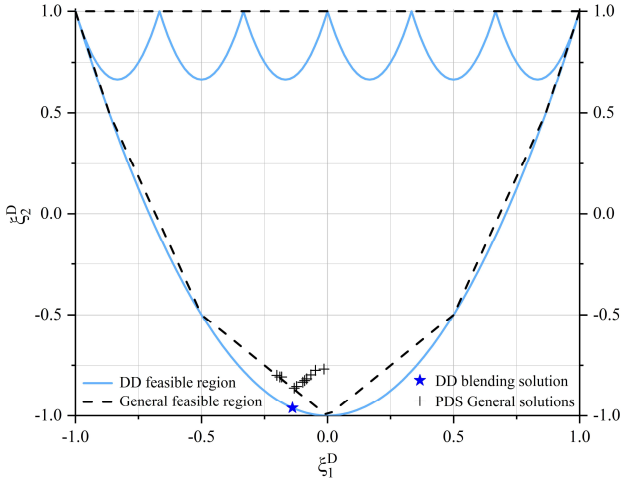

Fig. 7. Distribution of DD optimal solution and PDS General optimal solution in feasible region of lamination parameters.

Fig. 7 shows the distribution of DD and PDS General optimization solutions in the feasible region of ξ_1^D-ξ_2^D, where the area enclosed by the black dotted line is the General laminate feasible region. It can be seen from the figure that the optimal solutions obtained by using General ply angle are also distributed discretely at the lower boundary of the feasible region. However, compared with QUAD solutions, PDS General solutions are more concentrated and closed to DD solutions. This is because the increase of ply angle variables expands the feasible region, and the distribution of the optimal solution set is further optimized. Moreover, the number of plies can be taken as an odd number further utilize the buckling margin for design.

In this 18-plane benchmark problem, it can be concluded from the comparison of all optimization solutions that the dimension of ply angle variable and the existence of design constraints determine the optimization efficiency and convergence of the traditional optimization algorithm. The higher dimension of the ply angle variable brings larger feasible region design space, better solution and higher

computational cost, while the existence of design constraints could affect the distribution of solution set. When the coupling deformation is not desired and the better material homogeneity is expected. DD has obvious advantages over traditional QUAD laminates, including faster optimization efficiency, better solutions, simple and convenient manufacturing layups. Although lighter structural weight can be obtained by increasing the type of QUAD ply angles, the calculation cost and manufacturing difficulty also increase, and the complex internal ply drops will bring more design challenges.

4 CONCLUSIONS

In this paper, the general extended DD laminates are analyzed and applied based on lamination parameters and feasible region. The explicit LPs expressions and feasible region of general extended DD laminates are derived, and the characteristics of DD laminates family are revealed. Based on the feasible region of extended DD lamination parameters, the classical 18-plane horseshoe benchmark problem is optimized. The conclusions of this paper are summarized as follows:

(1) In the general extended DD laminate $[\theta_1/\theta_2/\ldots/\theta_l]_r$. Lamination parameter ξ^A is only related to the type of sublaminate ply angles, and the ξ^B and ξ^D are inversely proportional to the number of sublaminate repetitions r and r^2. When the value of r increases, ξ^B tends to 0, and the ξ^D tends to be equal to ξ^A. The balance of sublaminate is a sufficient and necessary condition for DD laminate family achieving homogenization, and the symmetry and antisymmetry of sublaminate can further directly eliminate coupling deformation.

(2) The lamination parameters ξ_1^A and ξ_2^A of all extended DD laminates have the same equation form. In addition, all boundary curve equations in the feasible region of ξ_1^A-ξ_2^A are quadratic functions.

(3) The classical 18-plane horseshoe benchmark problem is more intuitively optimized by using derived DD feasible regions. The whole problem is summarized as a linear programming problem in the LPs feasible region of DD, and the optimal solution is obtained at the lower bound of the feasible region, regardless of the categories of DD. When the blending constraint is considered, the optimal weight of the structure is 28.67kg, and the optimal DD layup is $[\pm 49°]_r$.

ACKNOWLEDGEMENTS

The supports from the National Natural Science Foundation, China (U20A20288) are gratefully acknowledged. In addition, the authors would like to appreciate the funding support from JITRI scholarship program.

REFERENCES

[1] S.W. Tsai, N.J. Pagano. *Invariant properties of composite materials*. Ft. Belvoir: Defense Technical Information Center; 1968.

[2] S.W. Tsai. Double–Double: New Family of Composite Laminates, *AIAA Journal,* **59**, 2021, pp. 4293-305 (doi: 10.2514/1.J060659).

[3] S.W. Tsai. *Double-double: a new perspective in the manufacture and design of composites*. Honolulu: Composites Design Group, Dept of Aeronautics and Astronautics; 2022.

[4] S.W. Tsai, J.D.D. Melo. An invariant-based theory of composites. *Composites Science and Technology*, **100**, 2014, pp. 237-43 (doi: 10.1016/j.compscitech.2014.06.017).

[5] S.W. Tsai, A.Miravete. *Metalite. A new class of DD: stronger than steel, lighter than aluminum Presentation*, JEC 2024, Paris, 6th March, 2024.

[6] K. Zhao, D. Kennedy, A. Miravete, S.W. Tsai, C.A. Featherston, X. Liu. Defining the Design Space for Double–Double Laminates by Considering Homogenization Criterion. *AIAA Journal,* 61, 2023, pp. 3190-203 (doi: 10.2514/1.J062639).

[7] G. Soremekun, Z. Gürdal, C. Kassapoglou, D. Toni. Stacking sequence blending of multiple composite laminates using genetic algorithms. *Composite Structure,* 61, 2002, pp. 53-62 (doi: 10.1016/S0263-8223(01)00185-4).

[8] J. Yang, B. Song, X. Zhong, P. Jin. Optimal design of blended composite laminate structures using ply drop sequence. *Composite Structure,* 135, 2016, pp. 30-7 (doi: 10.1016/j.compstruct.2015.08.101).

Using Multiaxial Fatigue to Investigate the Anisotropic Performance of Additively Manufactured Material

P. B. S. Bailey, Instron Dynamic Systems, UK

Combined axial-torsion loading

A majority of materials testing is based on uniaxial, planar stress states, but this can be a great simplification of real loading cases. This is often still adequate for design, but the analytical tools for multiaxial stress can also offer ways to extract more data.

Combining tension and torsion, on a tubular specimen, effectively rotates the direction of loading relative to the specimen axis.

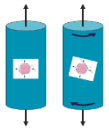

Additive manufacture by polymer filament deposition, creates a laminated structure, so building in the specimen axis direction, and using Mohr's circle, we can assess the apparent tensile or shear strength behaviour at different orientation relative to the laminae.



These graphs show how the measured stress-strain curves for tensile axial stress and torsional shear stress combine to form a total curve for maximum shear.

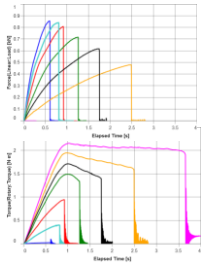

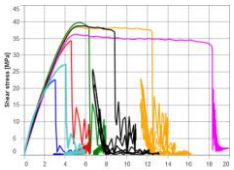

The results imply that the material exhibits higher shear strength and drawing capacity with decreasing shear biaxiality

Equipment availability

Multi-axial loading used to require specialised, custom test equipment, but for over 15 years now, combined axial-torsional fatigue load frames have been an off-the-shelf product and there are around 2000 machines installed worldwide, from multiple manufacturers.



Effects of rotating principal axes

Specimens were manufactured with a nominal outer gauge diameter 7.7 mm and wall thickness 0.8 mm, with parallel length of 20 mm, using a partially-optimised molten filament deposition process for PLA polymer, resulting in 100% density.

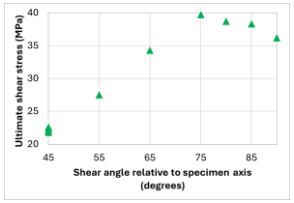

Using the combined loading approach, the apparent ultimate shear stress initially increases as the maximum shear angle is rotated away from 45° to the axis (pure tension).

When considering fatigue life, under multiaxial loading, ISO TR 121102 advises that this is most strongly related to the maximum shear amplitude applied.

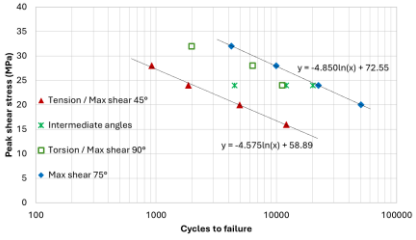

Plotting a series of investigative S-N curves at different levels of maximum shear stress with different rotations relative to the axis, shows a similar slope, but significant uplift in fatigue strength with rotation away from simple tension.

However, like the ultimate shear stress, it shows a peak at around 30° rotation relative to the specimen axis, but this seems more profound in fatigue.

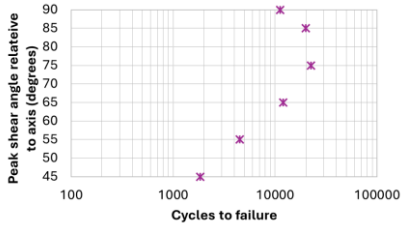

Process and microstructure effects

Taking the fully dense material as a baseline, a number of replicates were run at several angles, to give a basic indication of variability. The scatter is very low in this initial study, and this is probably due to the choice to build specimens individually (some parallel investigations indicate multi-specimen builds can result in 2 or more distinct populations of fatigue strength).

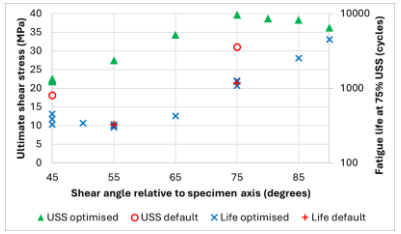

Now with only a small sample of specimens using a "de-optimised" process (the default process settings recommended) it is immediately visible that there is a reduction in monotonic shear strength. Note that the monotonic measurements were conducted at considerably higher strain rate, to provide a degree of comparability with that present in 3Hz fatigue loading waveforms.

However, when applying a waveform at R=0.1 with maximum shear stress at 75% of the monotonic strength, the fatigue life is rendered almost indistinguishable. Simple examination of the cross-section at moderate magnification, shows that the de-optimised specimen has considerable void between filament passes, thus reducing the true cross-section for stress. The fully-dense process, is not without some form of laminate structure either.



Further investigations are ongoing, including extending the sample for better statistical significance. It may also be valuable to consider a fracture mechanics approach to the analysis as Mode I – III mixity.

INSTRON®

ICCM24
AUGUST 4-8, 2025
BALTIMORE CONVENTION CENTER
BALTIMORE, MARYLAND, USA

No Technical Paper Submission for:

Daniel Esse

Development of Bench-Scale Instrument for Testing Thermal Protective Performance in Different Orientations

Sudhanshu Maurya[1], Dr. Apurba Das[1], Dr. Ramasamy Alagirusamy[1]
[1]Department of Textile and Fibre Engineering, IIT Delhi, Hauz Khas New Delhi 110016
Email: ttz218084@iitd.ac.in

ICCM24 — 24TH INTERNATIONAL CONFERENCE ON COMPOSITE MATERIALS

OBJECTIVES

- Develop a novel bench-scale instrument capable of testing TPP at any orientation (0° to 180°).
- Integrate advanced heat flux sensors with orientation adjustment systems.
- Validation of the instrument's measurement
- Provide comprehensive understanding of orientation impact on thermal protection.



BACKGROUND

- Current bench scale testing methods are limited to fixed orientations, which limits real-world scenarios
- As the orientation changes, the heat transfer changes
- When there is a significant temperature difference across the air gap, density variations cause buoyancy forces that drive convective motion.
- Gravity enters the problem through these buoyancy forces, and the effect can be quantified by dimensionless numbers such as Boussinesq approximation, Grashof and Rayleigh numbers.
- Protective performance at different orientations may bring new opportunity to redesign thermal protective clothing.

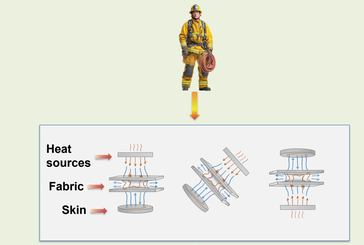

$$q_{total} = q_{conduction} + \boldsymbol{q_{convection}} + q_{radiation}$$

$$\boldsymbol{q_{conv}} = \boldsymbol{h}.A.(T_1 - T_2)$$

$$\boldsymbol{h} = \frac{\boldsymbol{N_u}.K}{L}$$

$$\boldsymbol{N_u} = C.(\boldsymbol{Gr}.\boldsymbol{Pr})^{n}$$

$$Rayleigh\ number\ (Ra) = \boldsymbol{Gr}.\boldsymbol{Pr} = \frac{g\beta\Delta T d^3}{\nu\alpha}$$

CONCEPTUALIZATION AND PLANNING

- Heat source which mimic outside environment
- Sensor to mimic human skin
- Arrangement to change the direction
- Attachment to bring airgap
- Sample holder
- PLC based controls
- Software interface to control

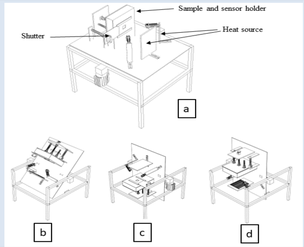

Top view

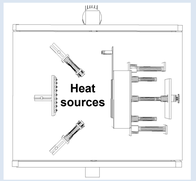

INSTRUMENT



Sample Holder
- Size: 15×15 cm²
- Firm holding
- Can support fabrics with different thickness



Air gap
- Air gap can be provided from 0 mm to 40 mm.
- Knob with scale for precise air gap



Heat sources
- Variable heat source
- Radiant source: Nine 500W quartz infrared lamps
- Convective source: Two Meker burners
- Protective shutter system for controlled exposure

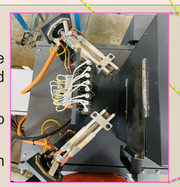

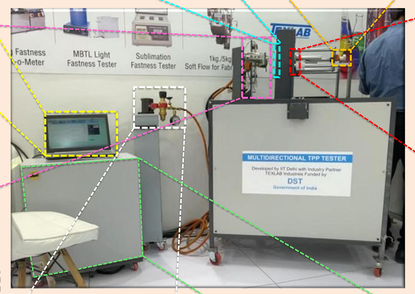



Sensor system
- Copper calorimeter heat flux sensor
- Type J thermocouple
- Sensor weighted to 1000 ± 10 g with flat black coating (absorptivity ≥ 0.9)
- Data acquisition system with programmable logic control (PLC)

TESTING CAPABILITIES

- Orientation range: 0° to 180° rotation and heat flux of 0 to 100 kW/m²
- Variable air gap adjustment between heat source and specimen
- Automated testing sequences with safety interlocks
- Real-time data logging and burn time calculation
- Can measure second degree burn time
- Measurement of stored energy



Pressure valve
- Pressure control
- Wide pressure range
- Robust construction



PLC system
- Real time control
- Data logging capabilities
- Input/output versatility

VALIDATION

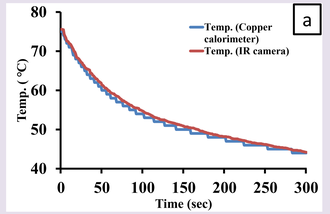

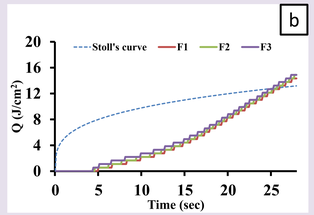

RESULTS

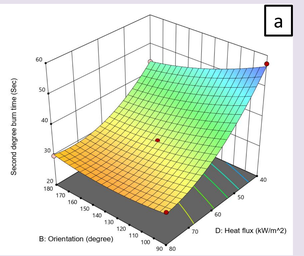

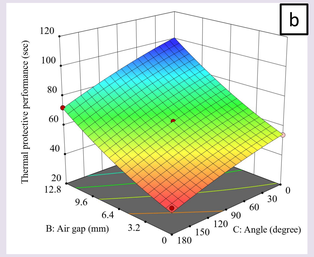

CONCLUSION

- Developed a novel bench-scale instrument for testing thermal protective performance at variable orientations
- The instrument can test 0 to100 kW/m², 0 to 180 degree
- There is significant impact of orientation on heat transfer rates
- The technology transfer to industry partner
- The instrument may help in development of thermal protective clothing
- Bridged the gap between laboratory testing and real-world firefighting scenarios
- Can be used for materials other than textile
- Filed for patent

AKNOWLEDGMENT

विज्ञान एवं प्रौद्योगिकी विभाग
DEPARTMENT OF SCIENCE & TECHNOLOGY
TEXLAB™

INSTRUMENT DEMO

Thermal and mechanical analysis of Li-ion battery fire containment

Sindhu Bushpalli, Changmin Cao, Gearoid Clancy, Hariharan Kallath, El Hassan Ridouane

Problem statement

Vision

- Battery systems in aircrafts play significant role in reducing environmental footprint
- Modular and scalable technologies support multiple market segments
- High energy density batteries are required for all systems
- Significant certification risks related to **safety & containing cell failures**

Scope

- Thermal Runaway modelling of battery pack solutions
- Develop light-weight and safe composite battery containment
- Proof-of-Concept testing of integrated battery pack solutions

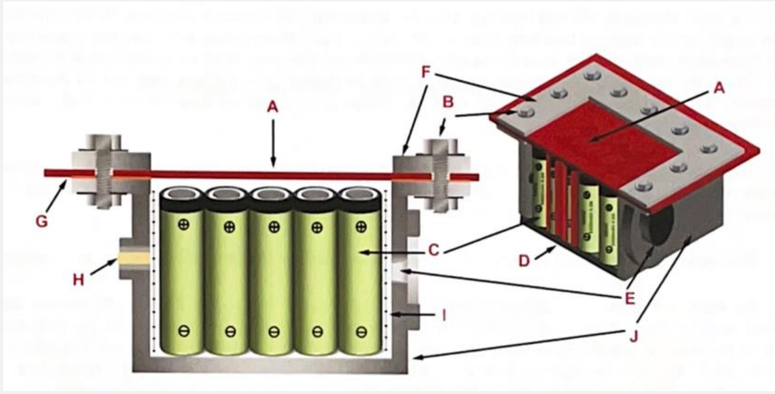

Battery package from UL2596

Li-ion battery containment overview

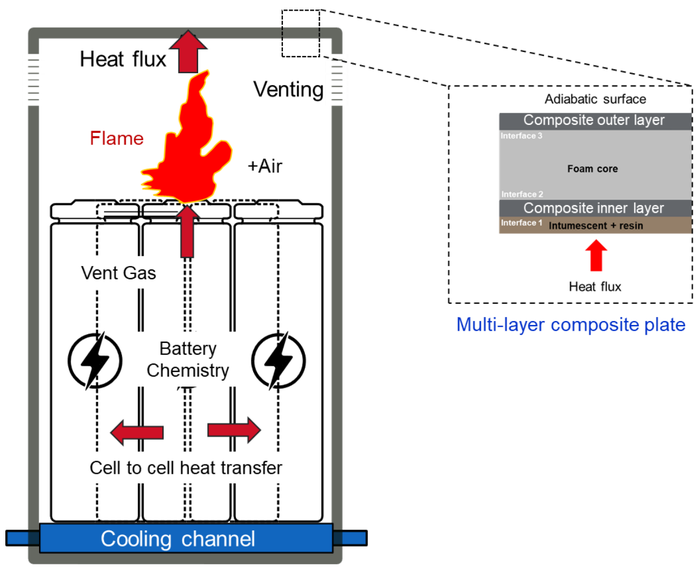

Multi-layer composite plate

- Contain thermal runaway while retaining structural integrity
- Weight savings: light weight materials – different composite configurations
- Limit box outside temperature and reduce thermal risk to other systems
- Evaluate performance: Cone calorimetry testing, UL2596
- Develop and validate numerical models



UL solutions battery enclosure lab

Results

Thermal analysis of composite solution

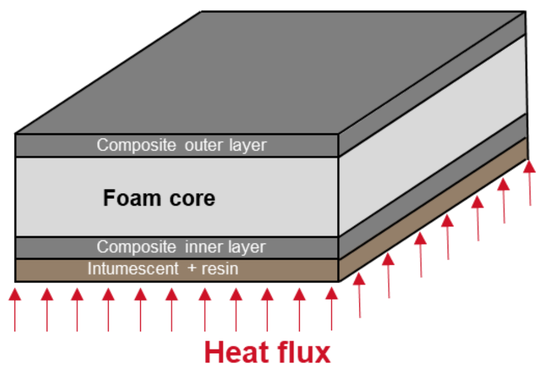

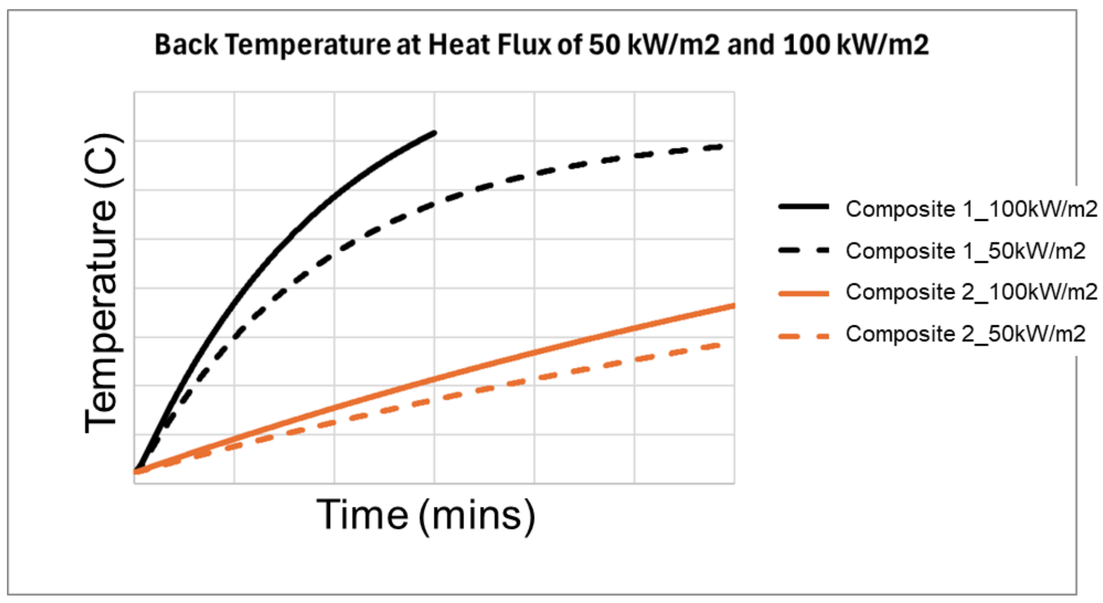

- Collins composite material thermal model was validated using test data. Composite material selection was completed and candidates with better performance were identified, and full module tests are planned.

Structural analysis

Deformation profile

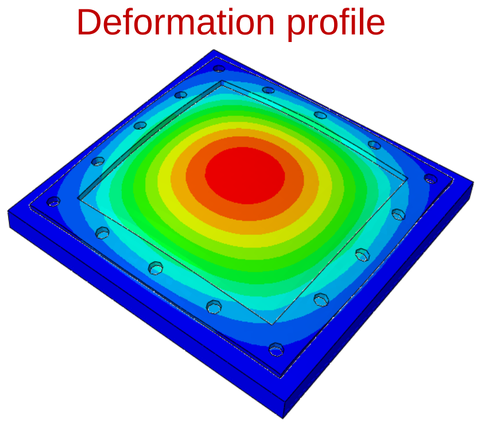

Stress profile

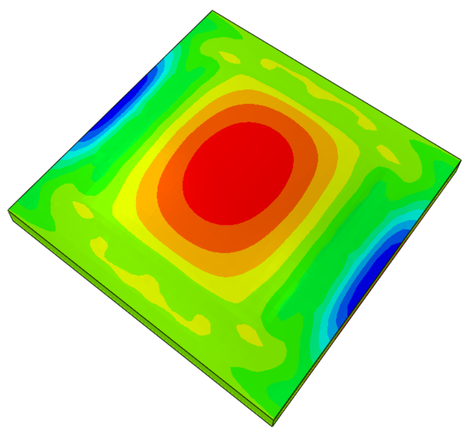

Next Steps and Challenges

- Coupon level testing planned for several material configurations
- Testing small scale demonstrator – few cells in thermal runaway
- Develop and validate numerical models using test data

Collins Aerospace | APPLIED RESEARCH & TECHNOLOGY

© 2025 Collins Aerospace | This document contains no export controlled technical data| Export Classification: UNCTD (EU), 9E991 (US).

ICCM24
AUGUST 4-8, 2025
BALTIMORE CONVENTION CENTER
BALTIMORE, MARYLAND, USA

No Technical Paper Submission for:

Muhammad Tahir Waqas

ICCM24
AUGUST 4-8, 2025
BALTIMORE CONVENTION CENTER
BALTIMORE, MARYLAND, USA

No Technical Paper Submission for:

Jabir Ubaid Parakkal

Development of lightweight Sandwich Composites with improved Reaction to Fire and UV resistance for Double Curvature Façade Panels

www.piep.pt

Helena Rocha[1], Miguel Vasconcelos[1], Joana Malheiro[1], António Nascimento[2], Deives Paula[2], Nuno Simões[2], Alexandra Barreiros[3], Teresa Diamantino[3], Cristina Ferreira[3], Diana Gonçalves[4] and Paulo Antunes[1]

[1] PIEP – Centre for Innovation in Polymer Engineering, Guimarães – Portugal

[2] Itecons – Institute for Research and Technological Development in Construction, Energy, Environment and Sustainability, Coimbra – Portugal

[3] LNEG Laboratório Nacional de Energia e Geologia, Amadora – Portugal

[4] Bysteel fs, Braga – Portugal

ICCM24 – 24TH INTERNATIONAL CONFERENCE ON COMPOSITE MATERIALS

1. INTRODUCTION

Buildings with **double curvature façades** can be aesthetically pleasing, being capable of enchanting both architects and the general public. Though, manufacturing of such façades can be a challenge in both technologic and economic terms. **Traditional molding technologies demand a unique mold for each panel geometry**, resulting in **substantial costs** related to raw materials and storage space, and **long lead times for designing and manufacturing**. A **reconfigurable multipoint mold** has been identified to solve this issue, where an array of moving pins can have their height quickly adjusted to form the required shape and molding surface. Another present technological challenge is the **highly demanding fire resistance requirements**. Certain European countries require that public and civil buildings comply with the highest grades of EN 13501 standard, A2, s1, d0 and B, s1, d0. That is a serious constraint when developing lightweight sandwich fiber reinforced polymer (FRP) composites, as polymeric materials do not naturally present good reaction to fire behavior. Furthermore, the polymeric raw materials should present suitable **processability** with the reconfigurable multipoint mold and supporting processing equipment and allow the manufacturing of **sandwich structures**. Sandwich composites structures are **lightweight** solutions with high stiffness, consisting of two composite laminate faces, separated by a lightweight core material, commonly made of foam or honeycomb.

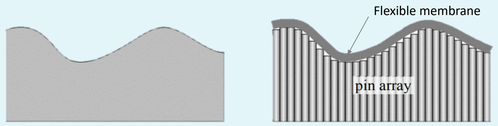

Fig. 1 traditional rigid mould versus reconfigurable multipoint mould

2. OBJECTIVES

The project aims at selecting adequate polymeric based materials for the manufacture of **lightweight double curvature lightweight sandwich** panels, with a **minimum curvature radius of 300 mm**, using a reconfigurable multipoint mould, considering the following **requirements** and **constraints**:

1. Processing temperatures below 200 °C;
2. Processable by Vacuum Assisted Resin Infusion (VARI) or Vacuum assisted Thermoforming (VAT);
3. Thermoformable rigid foam core to conform to the double curvature molding surface;
4. High drapability fabrics (e.g. twill) to conform to the minimum curvature radius;
5. Compliant with the highest grades of EN 13501 standard (A2, s1, d0 and B, s1, d0);
6. Long term UV radiation resistance.

Furthermore, this project aims at optimizing the manufacturing processes of the double curved sandwich panels and developing the attachment solution to the building walls.



Fig. 2 Buildings inspiring the development of this project: (left) Heydar Aliyev Center, Baku – Azerbaijan, Architect Zaha Hadid (2013) and (right) Central Park OfficeTower, Utrecht – The Netherlands, Architects: Group A

3. METHODOLOGY

This work is testing several material combinations to obtain (a) fully thermoplastic and (b) thermoset based composite sandwich for double curvature panels solutions. All tested sandwich composites used a thermoformable foam.

In a first stage, flat sandwich panels were manufactured to assess their reaction to fire, observed during ignition tests, conducted according to ISO 11925-1 standard, and to assess UV radiation resistance of different coating formulations.

Sandwich manufacturing was parallelly optimized on a small scale rigid mould. Depending on the constituent materials, either one of two manufacturing methods were conducted:

1. VARI when liquid thermoset matrices are used for the manufacturing of composite faces;
2. VAT when thermoplastic films are used for the manufacturing of composite faces.

MATERIALS and MANUFACTURING PROCESSES

Vacuum Assisted Resin Infusion

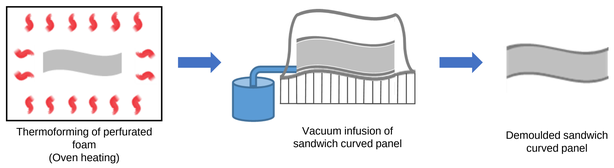

Fibre fabric reinforcements
- Basalt fibre with 2/2 twill structure and areal weight of 220 g/m²
- Glass fibre fabric reinforcements with 2/2 twill structure and areal weight of 195 g/m²

Foam core: Fire-retardant structural Airex® T90 PET foam from 3A Core Materials, 25 mm thick

Matrices:
- Fire-retardant epoxy resin system SR1124/SD4771, with SGi 128 gelcoat from Sicomin
- Biobased furan resin Furolite 106A25 2ST from TFC, with H3PO4 (85 wt% phosphoric acid) and HM 1448 (85 wt% (2-hydroxyethyl) ammonium nitrate)

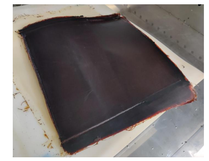

Example of small scale sandwich prototype with double curvature made of furan resin/ glass fibre composite skins and PET structural foam, 500 mm x 500 mm, manufactured by VARI,

Vacuum Assisted Thermoforming

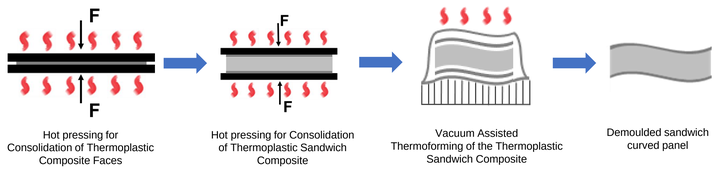

Fibre fabric reinforcements
- Basalt fibre with 2/2 twill structure and areal weight of 220 g/m²
- Glass fibre fabric reinforcements with 2/2 twill structure and areal weight of 195 g/m²

Foam core: Fire-retardant structural Airex® T90 PET foam from 3A Core Materials, 25 mm thick

Matrices:
- Fire retardant low density polyethylene (FR-LDPE) film, 60 µm thick
- Fire retardant polypropylene (FR-PP) film, 125 µm thick



Example of small scale sandwich prototype with double curvature made of FR-LDPE/ glass fibre composite skins and PET structural foam, 500 mm x 500 mm, manufactured by VAT

IGNITION TESTS

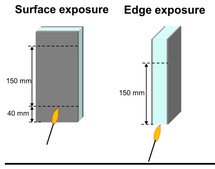

Test conditions (ISO 11925-2 standard)
- Three specimens for each condition, measuring approximately 250 mm x 90 mm, with thicknesses between about 27 – 29 mm
- Flame application for 30 seconds
- Verify whether the flame front reaches 150 mm above the application point, and recording of incurring time
- Presence of flaming droplets/particles
- Presence of flaming droplets/particles which caused ignition of the filter paper

Sample	Exposure condition	Occurrence of ignition	Fs > 150 mm	t150 (s)	Presence of flaming droplets/ particles	Ignition of the paper
Furan resin/ Basalt fibres – Airex T90 PET foam	Front face	yes	no	-	no	no
	Lateral bottom edge				yes	
Furan resin/ Glass fibres – Airex T90 PET foam	Front face	yes	no	-	no	no
	Lateral bottom edge				yes	
Epoxy resin/ Basalt fibres – Airex T90 PET foam	Front face	yes	no	-	no	no
	Lateral bottom edge				yes	
Epoxy resin/ Glass fibres – Airex T90 PET foam	Front face	yes	no	-	no (except for 1 specimen)	no
	Lateral bottom edge				yes	
FR-LDPE/ Glass fibres – Airex T90 PET foam	Front face	yes	no	-	no	no
	Lateral bottom edge				yes	

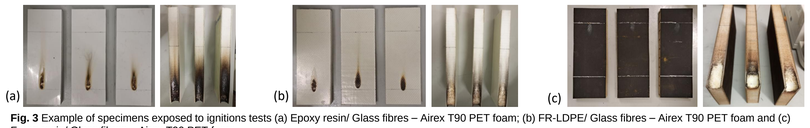

Fig. 3 Example of specimens exposed to ignitions tests (a) Epoxy resin/ Glass fibres – Airex T90 PET foam; (b) FR-LDPE/ Glass fibres – Airex T90 PET foam and (c) Furan resin/ Glass fibres – Airex T90 PET foam

FLUORESCENT UV LAMP RADIATION EXPOSURE

Test conditions (ISO 4892-3 standard)
Cycles of Exposure to UVA-340 (type 1A) lamp, with irradiance of 0.76 $W.m^{-2}$ x nm^{-1} at 340 nm, for 8 hours, at 60 ± 3 °C, followed by 4h period of condensation, with UV lamps off, at 50 ± 3 °C. Cycling test conducted for a total of 672 h.

The surface chalking was measured prior to and at the end of testing, and measurement of Brightness, Color coordinates (ΔL*, Δa*, Δ b*) and color change (ΔEab*) and FTIR analysis conducted at 0, 168, 336 and 672 hours of testing

Sample	Coating formulation	Chalking	Gloss 60º (GU)		Color difference at 672h			
			0h	672h	ΔL*	Δa*	Δb*	ΔE*ab
PP/ glass fibres	PU	2.9%	7.0	6.6	0.0	0.1	0.3	0.3
	PU + ATH + APP	7.5%	2.3	2.3	0.4	0.1	0.4	0.5
	PU + ATH + APP + UVASORB®	5.5%	2.4	2.4	0.3	0.2	0.6	0.7
	Epoxy + ATH + APP + UVASORB®	63.4%	28.6	2.1	-20.1	24.8	-8.2	33.0
Furan resin/ glass fibres	PU	4.1%	6.1	3.4	-0.2	0.1	0.4	0.5
	Epoxy + ATH + APP + UVASORB®	56.1%	27.0	1.7	30.2	-3.8	1.7	30.5

Polyurethane (PU), Aluminium Trihydroxide (ATH), Ammonium polyphosphate (APP), UVASORB®

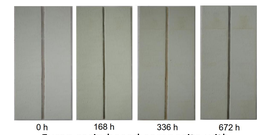

Furan resin based composite with PU coating

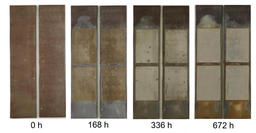

Furan resin based composite with Epoxy + ATH + APP + UVASORB® coating

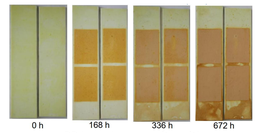

PP based composite with Epoxy + ATH + APP + UVASORB® coating

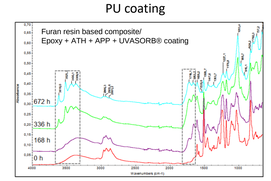

Main Conclusions
- All PU based coating formulations did not show significant changes when subjected to the mentioned conditions, with the exception of the Furan resin based composite with PU coating which showed a colour change on the non-exposed region of the specimens;
- The epoxy based coating formulations revealed powderiness and severe colour changes. Changes on the FTIR spectra are also noticeable.

FUTURE WORK

Single Burning Item (SBI) test to be conducted, following EN 13823

Manufacturing of full scale (2000 mm x 1000 mm) sandwich panels with double curvature

ACKNOWLEDGEMENTS

This work was conducted within the scope of the Innovation Pact Agendas/ Alianças mobilizadoras para a reindustrialização by the Consortium R2UTechnologies – modular systems, co-financed by NextGenerationEU, through the 'Business Innovation Agendas' investment from the Recovery and Resilience Plan (RRP)

PRR Plano de Recuperação e Resiliência · REPÚBLICA PORTUGUESA · Financiado pela União Europeia NextGenerationEU

IMPROVING INTERLAYER ADHESION IN LARGE FORMAT ADDITIVE MANUFACTURING FOR COMPOSITE TOOLING

Nicolas Courion[a,b] , Pascal Hubert[a,b] , Eduardo Barocio[c]

[a] McGill Structures & Composite Materials Laboratory, Mechanical Engineering Department, McGill University, Montreal, Canada
[b] Centre de recherche sur les systèmes polymères et composites à haute performance (CREPEC), Montréal, Canada
[c] Composites Additive Manufacturing and Simulation Center, Purdue University, West Lafayette, IN, USA

Motivation

- Large-format additive manufacturing (LFAM) requires precise **control of bead geometry** to ensure part accuracy and mechanical performance.
- Synchronizing screw-driven extrusion flow with gantry motion is critical to **avoid over and under extrusion.**
- Thermal history during printing plays a key role in **interlayer bonding** through reheating and polymer diffusion mechanics.
- Infrared thermography enables real-time monitoring of surface temperature evolution, **cooling and reheating** behavior.

Experimental Workflow for Bead Synchronization and Thermal Imaging

Pellet-fed LFAM Printing

- Carbon fiber reinforced polycarbonate (PC-CF)
- Nozzle diameter : 0.3in Ø
- Barrel & Nozzle Temperature 310°C
- RPM range tested: 130-370 RPM

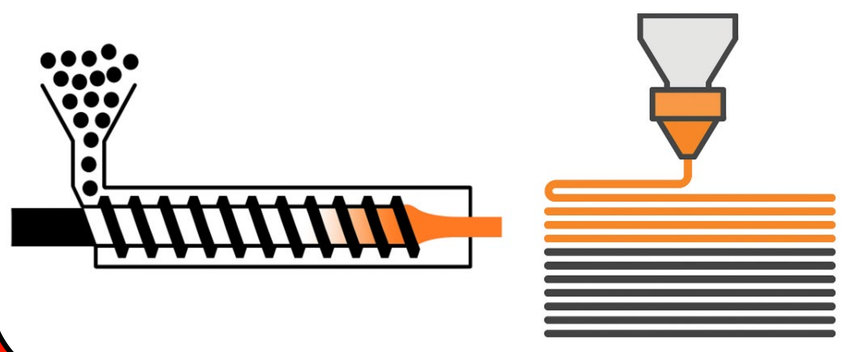

Bead Size Calibration

- 20 seconds extrusion trials at fixed RPM
- Material collected and weighed to determine melt flow rate
- Flow rate used to tune slicer deposition speed

$$Melt\ Flow\ Rate\ (MFR)$$
$$\downarrow$$
$$Bead\ height\ x$$
$$Bead\ width\ x$$
$$Deposition\ speed$$



Thermal History Acquisition



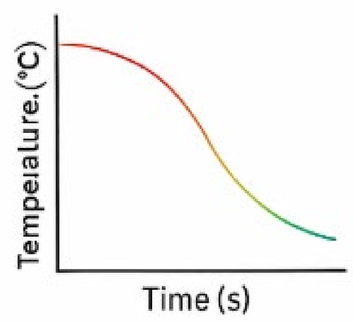

- 40-layer vertical wall (2 beads wide)
- FLIR T62101 IR camera fixed on bed, front-facing view
- Dwell times controlled to achieve desired later time

Bead Size Synchronization

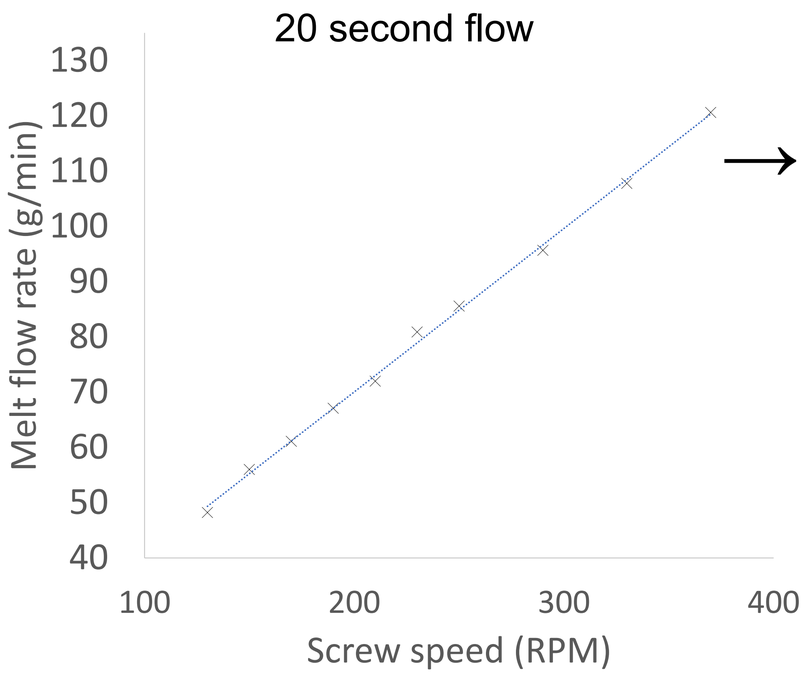

Calibrated output = Consistent beads

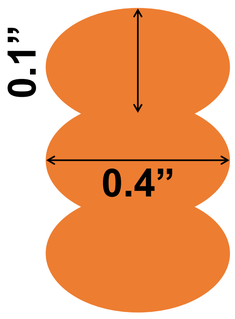

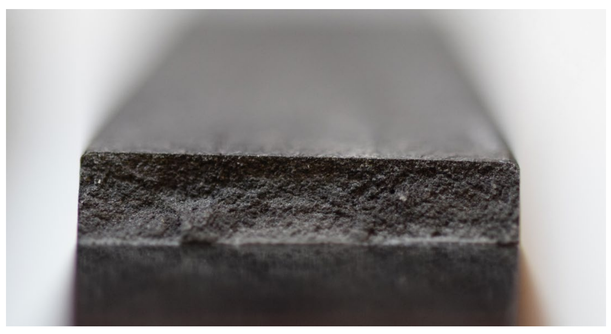

Enables consistent bead geometry

No voids

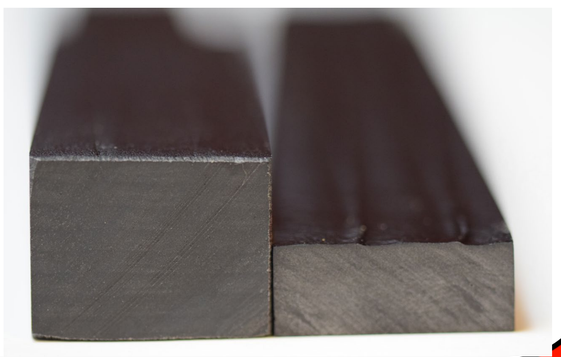

Additional work

Fracture mechanics

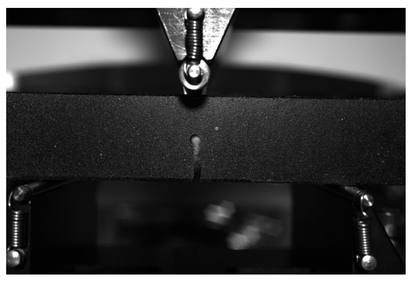

DIC

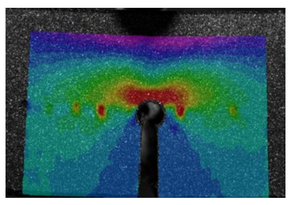

SEM

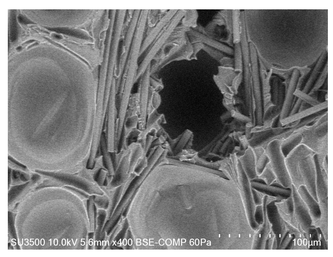

Thermal History

60 second layer time → 230 RPM, 1.69 in/sec

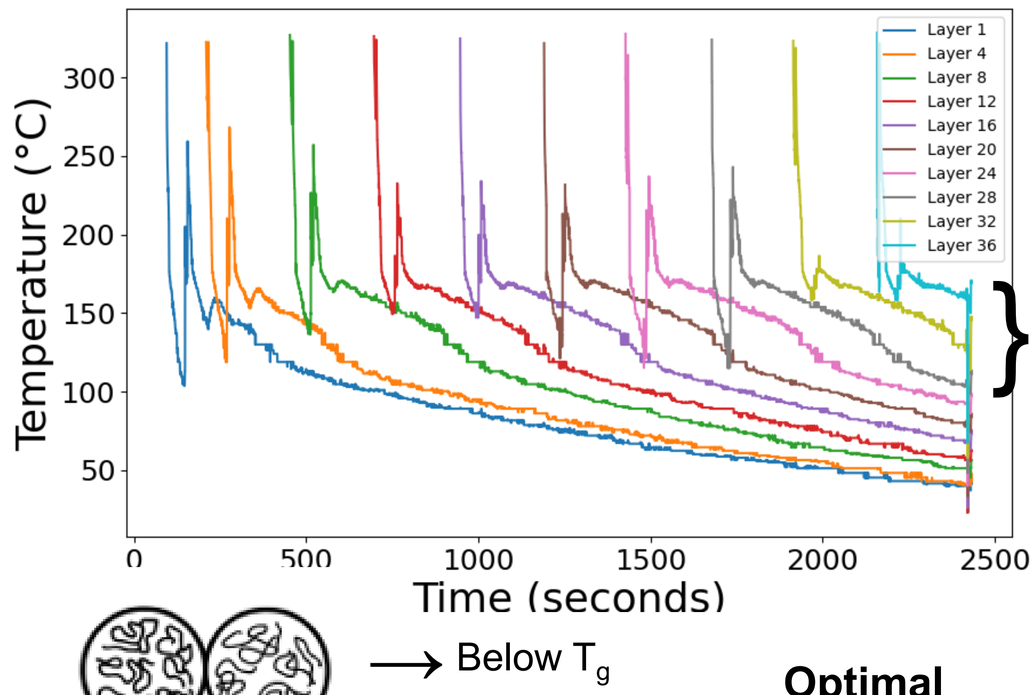



→ Below T_g

→ Above T_g

Optimal interlayer bonding

Conclusion and Insights

- The findings show a direct linear relationship between screw RPM and volumetric output, enabling bead size control.
- Consistent bead dimensions are critical for layer quality and mechanical repeatability in LFAM.
- IR thermography effectively captured layer-specific thermal histories.
- Higher layers experience extended high-temperature exposure due to thermal mass, potentially enhancing interlayer bonding.
- This methodology provides a framework for experimentally tuning process parameters to optimize part quality.

Acknowledgments

PRIMA

NSERC CRSNG



ICCM24
AUGUST 4-8, 2025
BALTIMORE CONVENTION CENTER
BALTIMORE, MARYLAND, USA

No Technical Paper Submission for:

Kaihao Zhang

AN ANISOTROPIC CONSTITUTIVE MODEL FOR CARBON FABRIC-REINFORCED SHAPE MEMORY POLYMER COMPOSITES BASED ON PHASE TRANSITION CONCEPT

JJ. Chen, XQ. Peng*

School of Materials Science and Engineering, Shanghai Jiao Tong University
Huashan Road 1954, Shanghai, 200030, China
Email: xqpeng@sjtu.edu.cn , web page: https://ifte.sjtu.edu.cn/

Keywords: Shape memory polymer composites, Carbon woven fabric, Constitutive behavior, Anisotropic properties, Phase transition

ABSTRACT

This study presents a novel anisotropic constitutive model for carbon fabric-reinforced shape memory polymer composites (SMPCs) based on the phase transition concept, addressing the limitations of existing models in describing viscoelastic yielding and shape memory mechanisms. A new dual-phase decomposition strategy is proposed, wherein the rubbery phase is described as a coupling of the SMP's hyperelastic response and the fabric's orthotropic behavior, while the glassy phase combines SMP viscoelasticity with fabric kinematic constraints. Each phase is independently modelled to capture distinct thermomechanical characteristics. The nonlinear behavior of the SMP matrix is characterized using the Mooney-Rivlin free energy formulation, and the anisotropic hyperelastic response of the fabric reinforcement is described by a polynomial constitutive function. To quantify shape memory effect of SMPCs, a storage strain concept is integrated into the thermodynamic framework. Constitutive equations are derived through energy decomposition, based on the Clausius-Duhem inequality and Helmholtz free energy, with phase effectiveness factors introduced to capture non-ideal behaviors. The model is validated against extensive thermomechanical and shape memory experiments on SMPCs with various fiber orientations. Good agreement is achieved between simulations and experimental results, confirming the model's capability to predict anisotropic mechanical behavior and shape memory performance. The validated framework offers new insights into strain storage mechanisms during phase transitions and provides practical guidance for the design and optimization of SMPC-based structural systems.

1 INTRODUCTION

Carbon fabric-reinforced shape memory polymer composites (SMPCs) have emerged as pivotal materials in aerospace and smart structural applications, owing to their exceptional strength-to-weight ratio and programmable shape memory functionality. While significant progress has been made in material fabrication, performance characterization, and structural integration, the development of theoretical constitutive models has lagged behind experimental advancements [1]. To enable intelligent control and precision engineering of SMPC-based systems, the development of robust constitutive models capable of predicting complex thermomechanical responses becomes imperative.

Compared to neat SMPs, theoretical studies on the mechanical behavior of carbon fabric-reinforced SMPCs remain limited. Roh et al. [2] explored the nonlinear viscoelastic behavior of thin-wall SMPC arms and demonstrated that time-dependent strain energy relaxation can significantly degrade shape recovery capability. Su et al. [3] proposed a viscoelastic constitutive model by decomposing the total free energy of SMPCs into matrix and fiber components, introducing a correction factor to account for the fiber's evolving contribution. Hong et al. [4] developed a homogenized constitutive framework incorporating thermally induced residual stresses, which was validated against three-point bending experiments on SMPCs with varying fiber volume fractions. Despite recent progress, the aforementioned models primarily focus on the viscoelastic properties of SMPs and the anisotropic nature of the reinforcing fabrics. However, they often overlook the significant mismatch in elastic moduli and thermal expansion coefficients between the fabric and the matrix, and fail to fully explain the mechanisms of

strain storage and release during phase transitions. To address this issue, Chen et al. [5] introduced a modified Eshelby model that incorporates these mismatches to derive the effective elastic modulus of SMPCs. They further proposed the storage strain concept to simulate the shape memory behavior and validated the model using experimental data from SMPCs with varying fiber contents. Nevertheless, this model does not consider the intrinsic anisotropy of the fibers. More critically, existing models fall short in accurately capturing the viscoelastic yielding behavior observed in experiments, as they primarily focus on the temperature-dependent elastic moduli of SMPCs [6].

In this work, we propose an anisotropic constitutive model for SMPCs that integrates viscoelasticity and phase transition concept. The model innovatively decomposes SMPCs into a new rubbery phase and a new glassy phase. The rubbery phase consists of the SMP rubbery matrix bonded with fabric, and the glassy phase comprises the SMP glassy matrix bonded with fabric. The distinct thermodynamic behaviors of these two phases are separately described and SME of SMPCs is directly captured through the storage strain concept, leveraging the phase transition between the two phases.

2 CONSTITUTIVE MODEL FOR SMPC

2.1 General consideration

The thermomechanical behavior of SMPCs is fundamentally governed by the intrinsic property contrast between the isotropic viscoelastic SMP matrix and the anisotropic hyperelastic carbon fabric reinforcement. This dichotomy stems from their distinct energy storage mechanisms: the fabric exhibits temperature-independent hyperelastic behavior governed by fiber architecture [7], in contrast to the temperature- and deformation-dependent energy evolution of the SMP matrix during thermomechanical cycling. A critical temperature-dependent interfacial interaction emerges, where strong fiber-matrix bonding dominates below T_g due to matrix rigidity, while fiber-driven deformation prevails above T_g as the matrix softens [8]. Additionally, residual stresses at the interface, arising from thermal expansion mismatch and modulus disparity, significantly impact the nonlinear deformation behavior of SMPCs.

In the phase transition framework, SMPs are phenomenologically treated as a homogeneous material comprising rubbery and glassy phases [9]. At high temperatures, the rubbery phase dominates, making the material hyperelastic. Conversely, at low temperatures, the glassy phase dominates, making the material viscoelastic. This model not only directly captures the SME through the concept of storage strain, but also decouples the model parameters from temperature, thereby simplifying the parameter determination process. Therefore, to capture the complex thermodynamic behaviors of SMPCs, we extend the SMP phase transition framework in this work, as illustrated in Fig. 6. The proposed model introduces dual-phase decomposition, partitioning SMPCs into fabric-coupled rubbery and glassy phases with independent thermodynamic descriptors. The SMP matrix implementation follows our previous work [10], where the hyperelastic behavior of the rubbery phase is represented by a single spring element. The viscoelastic behavior of the SMP glassy phase is modeled using a parallel spring element connected with a Maxwell element. Additionally, a storage strain element is added in series to the rheological model of the SMP glassy phase representing the storage and release of pre-deformation in the shape memory cycle. The fabric reinforcement is modeled as temperature-invariant hyperelastic springs in both phases. The thermal part represents the thermal expansion or contraction of the SMPCs.

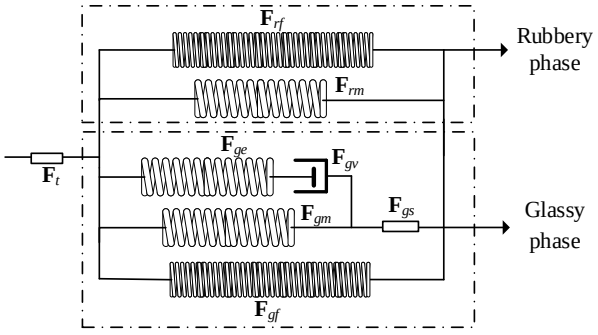

Fig. 1 Rheological representation of the proposed constitutive model for SMPC.

2.2 Kinematics

The total deformation gradient **F** of SMPC is unified for both the glassy and the rubbery phases, and it can be multiplicatively decomposed into mechanical and other deformation gradients:

$$\mathbf{F} = \mathbf{F}_{rc} \cdot \mathbf{F}_t = \mathbf{F}_{gc},\ \mathbf{F}_t,\ \mathbf{F}_{rc} = \mathbf{F}_{rf} = \mathbf{F}_{rm},\ \mathbf{F}_{gc} = \mathbf{F}_{gf} = \mathbf{F}_{gm} \cdot \mathbf{F}_{gs} = \mathbf{F}_{ge} \cdot \mathbf{F}_{gv} \cdot \mathbf{F}_{gs} \tag{1}$$

where the subscript t represents the thermal deformation part of SMPC. The subscripts rc and gc denote the total mechanical deformation gradients of rubbery and glassy phases of the SMPC. The subscripts rf and gf represent the fiber mechanical deformation gradients in the rubbery and glassy phases of SMPC. The subscripts rm, gm, ge, gv and gs correspond to the single spring element in the rubbery and glassy phases of SMP matrix, the elastic part and viscous part in the Maxwell element, the storage strain part, respectively. The related right and left Cauchy-Green tensors are defined as:

$$\mathbf{C}_i = \mathbf{F}_i{}^T \cdot \mathbf{F}_i,\ \mathbf{B}_i = \mathbf{F}_i \cdot \mathbf{F}_i{}^T \tag{2}$$

where the subscript $i = rf, gf, rm, gm, ge, gv$ and gs. Define the Green-Lagrange tensors as:

$$\mathbf{E}_i = \frac{\mathbf{1}}{\mathbf{2}}(\mathbf{C}_i - \mathbf{I}) \tag{3}$$

where **I** is second-order identity tensor. The related invariants of $\mathbf{C}_i$ are defined as:

$$I_1^i = tr(\mathbf{C}_i),\ I_2^i = \frac{1}{2}[(tr(\mathbf{C}_i))^2 - tr(\mathbf{C}_i)^2],\ I_3^i = det\ (\mathbf{C}_i) \tag{4}$$

Specially, for dry woven fabrics, the primary deformation modes include extension along the fiber yarns and angular variations between the weft and warp yarns. To capture these behaviors, invariants representing fiber stretch and fiber-fiber shear are introduced:

$$I_4^a = \mathbf{a}_0 \cdot \mathbf{C}_i \cdot \mathbf{a}_0,\ I_4^b = \mathbf{b}_0 \cdot \mathbf{C}_i \cdot \mathbf{b}_0,\ I_7 = \Delta\varphi = \left(I_4^a I_4^b\right)^{-\frac{1}{2}} \mathbf{a}_0 \cdot \mathbf{C}_i \cdot \mathbf{b}_0 - \mathbf{a}_0 \cdot \mathbf{b}_0 \tag{5}$$

Here, the subscripts $i = rf$ and gf. The invariants I_4^a and I_4^b represent the stretches of yarns, while I_7 represents the angle change $\Delta\varphi$ between the two yarn families and the associated cross-over shear deformation. The unit vectors along the initial directions of the weft and warp yarns are defined as $\mathbf{a}_0 = [cos\theta \quad -sin\theta \quad 0]$ and $\mathbf{b}_0 = [sin\theta \quad cos\theta \quad 0]$, respectively. Here θ denotes the angle between the fiber direction and the loading direction. After deformation, the vectors for the two fiber families can be expressed as:

$$\mathbf{a} = \mathbf{F}_i \cdot \mathbf{a}_0/\lambda_f^a, \mathbf{b} = \mathbf{F}_i \cdot \mathbf{b}_0/\lambda_f^b \tag{6}$$

where λ_f^a and λ_f^b are the stretch ratios of the weft and warp fiber yarns, respectively.

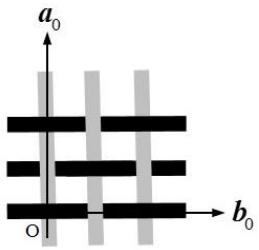

Fig. 2 The original directions of weft and warp yarns.

2.3 Constitutive model derivation

Based on the multiplicative decomposition of deformation gradient presented in Eq. (1), the total Helmholtz free energy of SMPCs per unit reference volume, $\mathbf{\Psi}\left(\mathbf{C}, \mathbf{C}_{ge}, \mathbf{C}_{gv}, \mathbf{a}_0, \mathbf{b}_0, T\right)$, can be expressed as follows:

$$\begin{aligned}\mathbf{\Psi} = \varphi_g(T)(\varphi_m(\mathbf{\Psi}_{gm}(\mathbf{C}, T) + \mathbf{\Psi}_{ge}\left(\mathbf{C}_{ge}, \mathbf{C}_{gv}, T\right) + \mathbf{\Psi}_{gs}(T)) + \varphi_f \mathbf{\Psi}_{gf}(\mathbf{C}, \mathbf{a}_0, \mathbf{b}_0))\\ +\varphi_r(T)(\varphi_m \mathbf{\Psi}_{rm}(\mathbf{C}, T) + \varphi_f \mathbf{\Psi}_{rf}(\mathbf{C}, \mathbf{a}_0, \mathbf{b}_0)) + \mathbf{\Psi}_T(T)\end{aligned} \tag{7}$$

where $\boldsymbol{\Psi}_T$ represents the Helmholtz free energy related to temperature only. $\varphi_r, \varphi_g, \varphi_f$ and φ_m denote the volume fractions of the rubbery and glassy phase of SMPC, fabric, and SMP matrix, respectively. The relations $\varphi_m + \varphi_f = 1$ and $\varphi_r + \varphi_g = 1$ are always satisfied. The volume fraction of glassy phase can be calculated as [11]:

$$\varphi_g = 1 - \frac{1}{1+\exp[-(T-T_r)/A]} \tag{8}$$

where T_r is the reference temperature close to the glass transition temperature, and A is a parameter describing the width of the glass transition temperature range. The second Piola-Kirchhoff stress $\mathbf{S}_c$ of SMPCs can be decomposed into the stresses $\mathbf{S}_{rc}$ and $\mathbf{S}_{gc}$ corresponding to the rubbery phase and glassy phase, respectively:

$$\mathbf{S}_c = \varphi_r \mathbf{S}_{rc} + \varphi_g \mathbf{S}_{gc} \tag{9}$$

And the Clausius-Duhem inequality is expressed in terms of the second Piola-Kirchhoff stress and the Helmholtz free energy:

$$\frac{1}{2}\mathbf{S}_c : \dot{\mathbf{C}} - \left(\dot{\boldsymbol{\Psi}} + \dot{T}\eta\right) - \mathbf{q} \cdot \nabla T/T \geq 0 \tag{10}$$

where η is the entropy, $\mathbf{q}$ is the heat flux vector and ∇ is the gradient operator. Substituting Eqs. (2), (3), (7) and (9) into Eq. (10) leads to the following equations:

$$\begin{gathered}
\mathbf{S}_{rc} = 2\varphi_m \frac{\partial \boldsymbol{\Psi}_{rm}}{\partial \mathbf{C}} + 2\varphi_f \frac{\partial \boldsymbol{\Psi}_{rf}}{\partial \mathbf{C}} = \mathbf{S}_{rm} + \mathbf{S}_{rf} \\
\mathbf{S}_{gc} = 2\varphi_m \frac{\partial \boldsymbol{\Psi}_{gm}}{\partial \mathbf{C}} + 2\varphi_m \frac{\partial \boldsymbol{\Psi}_{ge}}{\partial \mathbf{C}} + 2\varphi_f \frac{\partial \boldsymbol{\Psi}_{gf}}{\partial \mathbf{C}} = \mathbf{S}_{gm} + \mathbf{S}_{gf} \\
\mathbf{L}_{gv} = \frac{1}{\xi}\mathbf{C}_{ge} \cdot \frac{\partial \Psi_{ge}}{\partial \mathbf{C}_{ge}},\ \eta = -\frac{\partial \boldsymbol{\Psi}}{\partial T},\ \mathbf{q} = -k\nabla T, k > 0
\end{gathered} \tag{11}$$

where $\mathbf{S}_{rm} = 2\varphi_m \frac{\partial \boldsymbol{\Psi}_{rm}}{\partial \mathbf{C}}$ and $\mathbf{S}_{rf} = 2\varphi_f \frac{\partial \boldsymbol{\Psi}_{rf}}{\partial \mathbf{C}}$ represent the second Piola-Kirchhoff stresses coming from the rubbery phase of SMP matrix and the woven fabric reinforcement, respectively. Similarly, $\mathbf{S}_{gm} = 2\varphi_m \frac{\partial \boldsymbol{\Psi}_{gm}}{\partial \mathbf{C}} + 2\varphi_m \frac{\partial \boldsymbol{\Psi}_{ge}}{\partial \mathbf{C}}$ and $\mathbf{S}_{gf} = 2\varphi_f \frac{\partial \boldsymbol{\Psi}_{gf}}{\partial \mathbf{C}}$ represent the second Piola-Kirchhoff stresses coming from the glassy phase of SMP matrix and woven fabric reinforcement, respectively. $\mathbf{L}_{gv} = \dot{\mathbf{F}}_{gv} \cdot {\mathbf{F}_{gv}}^{-1}$ is the viscous velocity gradient. k is the heat conduction coefficient, ξ is a material parameter with the same unit as viscosity [12]. To describe the nonlinear mechanical behavior of the rubbery and glassy phases of the SMP matrix, the free energy form of the Mooney-Rivlin model is employed:

$$\boldsymbol{\Psi}_i = C_{10}^i \left({I_3^i}^{-1/3} I_1^i - 3\right) + C_{01}^i \left({I_3^i}^{-2/3} I_2^i - 3\right) + \frac{1}{D_i}\left({I_3^i}^{1/2} - 1\right)^2 \tag{12}$$

where $i = rm, gm$ and ge represent the single spring element of the SMP rubbery and glassy phases, and the elastic part of the Maxwell element, respectively. C_{10}^i, C_{01}^i and D_i are temperature-independent material parameters in this paper. Based on Eqs. (2), (4), (11) and (12), the Cauchy stress of SMPs can be further expressed by $\boldsymbol{\sigma}_m = {I_3^i}^{-1/2}\mathbf{F}_i\left(2\frac{\partial \boldsymbol{\Psi}_i}{\partial \mathbf{C}}\right){\mathbf{F}_i}^T$ as:

$$\begin{gathered}
\boldsymbol{\sigma}_m = \varphi_r \left(\begin{array}{c} 2C_{10}^{rm} {I_3^{rm}}^{-\frac{5}{6}} \left(\mathbf{B}_{rm} - \frac{1}{3} I_1^{rm}\mathbf{I}\right) + 2C_{01}^{rm} {I_3^{rm}}^{-\frac{7}{6}} \left(\mathbf{B}_{rm} - \mathbf{B}_{rm}\cdot\mathbf{B}_{rm} - \frac{2}{3} I_1^{rm}\mathbf{I}\right) \\ + \frac{2}{D_{rm}}\left({I_3^{rm}}^{\frac{1}{2}} - 1\right)\mathbf{I} \end{array} \right) + \\
\varphi_g \left(\begin{array}{c} 2C_{10}^{gm} {I_3^{gm}}^{-\frac{5}{6}} \left(\mathbf{B}_{gm} - \frac{1}{3} I_1^{gm}\mathbf{I}\right) + 2C_{01}^{gm} {I_3^{gm}}^{-\frac{7}{6}} \left(I_1^{gm}\mathbf{B}_{gm} - \mathbf{B}_{gm}\cdot\mathbf{B}_{gm} - \frac{2}{3} I_2^{gm}\mathbf{I}\right) \\ + \frac{2}{D_{gm}}\left({I_3^{gm}}^{\frac{1}{2}} - 1\right)\mathbf{I} \end{array} \right) + \\
\varphi_g \left(\begin{array}{c} 2C_{10}^{ge} {I_3^{gm}}^{-\frac{1}{2}} {I_3^{ge}}^{-\frac{1}{3}} \left(\mathbf{B}_{ge} - \frac{1}{3} I_1^{ge}\mathbf{I}\right) + 2C_{01}^{ge} {I_3^{gm}}^{-\frac{1}{2}} {I_3^{ge}}^{-\frac{2}{3}} \left(I_1^{ge}\mathbf{B}_{ge} - \mathbf{B}_{ge}\cdot\mathbf{B}_{ge} - \frac{2}{3} I_2^{ge}\mathbf{I}\right) \\ + \frac{2}{D_{ge}} {I_3^{gm}}^{-\frac{1}{2}} \left(I_3^{ge} - {I_3^{ge}}^{\frac{1}{2}}\right)\mathbf{I} \end{array} \right)
\end{gathered} \tag{13}$$

Due to the limited rearrangement of molecule chains with shear resistance, the glassy phase of SMP is demonstrated the yield and post-yield softening response. To describe the viscoplastic flow process, a nonlinear flow rule and a modified Eyring model are employed by the plastic shear strain rate $\dot{\gamma}_{gv}$:

$$\mathbf{D}_{gv} = \dot{\gamma}_{gv}\mathbf{n}$$

$$\dot{\gamma}_{gv} = \frac{s_y}{Q_s} T \exp\left(-\frac{B}{T}\right) \sinh\left(\frac{Q_s \bar{\tau}}{s_y T}\right),\ \bar{\tau} = \left(\frac{1}{2}\boldsymbol{\sigma}_{gv} : \boldsymbol{\sigma}_{gv}\right)^{\frac{1}{2}} \tag{14}$$

where the deformation rate tensor $\mathbf{D}_{gv}$ is defined as the symmetric part of the velocity gradient tensor $\mathbf{L}_{gv}$, excluding the rotational part. The flow direction is given by $\mathbf{n} = \boldsymbol{\sigma}'_{gv} / \left\|\boldsymbol{\sigma}'_{gv}\right\|$, where $\boldsymbol{\sigma}'_{gv} = \boldsymbol{\sigma}_{gv} - \frac{1}{3} tr(\boldsymbol{\sigma}_{gv})\mathbf{I}$ represents the deviatoric stress of the viscous part. Q_s is the activation energy, B is the activation parameter, and s_y is the activation stress, which evolves as follows:

$$\dot{s}_y = h_0 \left(1 - \frac{s_y}{s_s}\right) \dot{\gamma}_{gv},\ s_y(0) = s_0 \tag{15}$$

where h_0 is the softening slope, s_0 is the initial value of s_y, and s_s is the final stabilized value, ensuring $s_s < s_0$. Substituting Eqs. (8), (14) and (15) into Eq. (13), the Cauchy stress of SMP matrix can be calculated in entire glass transition temperature range.

Considering the mechanical properties of the fabrics are temperature-independent, both the constitutive models of the fabrics in both the glassy and rubbery phases of SMPCs share a unified expression, enhancing the model's applicability. Taking into account the unique deformation characteristics of woven fabrics, the Helmholtz free energy can be decomposed into two distinct components: the fiber stretch part, $\boldsymbol{\Psi}_{ten}$, and the fiber-fiber shear part, $\boldsymbol{\Psi}_{she}$ [7]:

$$\boldsymbol{\Psi}_f(\mathbf{C}, \mathbf{a}_0, \mathbf{b}_0) = \boldsymbol{\Psi}_{ten}(\mathbf{C}, \mathbf{a}_0, \mathbf{b}_0) + \boldsymbol{\Psi}_{she}(\mathbf{C}, \mathbf{a}_0, \mathbf{b}_0) \tag{16}$$

where $\boldsymbol{\Psi}_{ten}$ and $\boldsymbol{\Psi}_{she}$ can be further represented by a polynomial function of I_4^a, I_4^b and I_7:

$$\boldsymbol{\Psi}_{ten} = k_1\left[(I_4^a - 1)^4 + \left(I_4^b - 1\right)^4\right] + k_2\left[(I_4^a - 1)^3 + \left(I_4^b - 1\right)^3\right] + k_3\left[(I_4^a - 1)^2 + \left(I_4^b - 1\right)^2\right]$$

$$\boldsymbol{\Psi}_{she} = k_4(I_7)^4 + k_5(I_7)^3 + k_6(I_7)^2 \tag{17}$$

where k_1, k_2, k_3, k_4, k_5 and k_6 are constant material parameters with unit of stress. The Cauchy stress tensor of fabric is given by $\boldsymbol{\sigma}_f = I_3^{-1/2}\mathbf{F}\left(2\frac{\partial \boldsymbol{\Psi}_f}{\partial \mathbf{C}}\right)\mathbf{F}^T$. Consequently,

$$\boldsymbol{\sigma}_f = I_3^{-\frac{1}{2}}\left(2\frac{\partial \boldsymbol{\Psi}_{ten}}{\partial I_4^a} - \frac{I_7}{I_4^a}\frac{\partial \boldsymbol{\Psi}_{she}}{\partial I_7} - \frac{\mathbf{a}_0 \cdot \mathbf{b}_0}{I_4^a}\frac{\partial \boldsymbol{\Psi}_{she}}{\partial I_7}\right)\mathbf{a}\otimes\mathbf{a} + I_3^{-\frac{1}{2}}\left(2\frac{\partial \boldsymbol{\Psi}_{ten}}{\partial I_4^b} - \frac{I_7}{I_4^b}\frac{\partial \boldsymbol{\Psi}_{she}}{\partial I_7} - \frac{\mathbf{a}_0 \cdot \mathbf{b}_0}{I_4^b}\frac{\partial \boldsymbol{\Psi}_{she}}{\partial I_7}\right)\mathbf{b}\otimes\mathbf{b}$$

$$+ I_3^{-1/2}\frac{\partial \boldsymbol{\Psi}_{she}}{\partial I_7}\left(I_4^a I_4^b\right)^{-\frac{1}{2}}(\mathbf{a}\otimes\mathbf{b} + \mathbf{b}\otimes\mathbf{a}) \tag{18}$$

Accordingly, the fabric stress calculated via Eq. (5), when substituted into Eq. (18), faithfully captures its anisotropic mechanical response. Building upon the theoretical framework established in Eqs. (1), (8), (9), (13), and (18), the Cauchy stress tensor for SMPCs can be decomposed into rubbery phase $\boldsymbol{\sigma}_{rc}$ and the glassy phase $\boldsymbol{\sigma}_{gc}$ components through phase superposition:

$$\boldsymbol{\sigma}_c = \varphi_r\boldsymbol{\sigma}_{rc} + \varphi_g\boldsymbol{\sigma}_{gc} = \varphi_r\left(\boldsymbol{\sigma}_{rm} + \boldsymbol{\sigma}_f\right) + \varphi_g\left(\boldsymbol{\sigma}_{gm} + \boldsymbol{\sigma}_{ge} + \boldsymbol{\sigma}_f\right) \tag{19}$$

This formulation inherently assumes ideal deformation mechanics characterized by perfect fiber-matrix load transfer and interface integrity. However, practical material behavior deviates from this idealized state due to multiscale interfacial phenomena including inter-yarn friction dissipation in woven architectures, matrix damage induced by yarn rotation kinematics, void nucleation/propagation mechanisms, and temperature-dependent interfacial adhesion degradation. To systematically address these non-ideal effects while maintaining model tractability, we introduce temperature-independent phase effectiveness factors that modulate the respective stress contributions:

$$\boldsymbol{\sigma}_c = \varphi_r\rho_r\left(\boldsymbol{\sigma}_{rm} + \boldsymbol{\sigma}_f\right) + \varphi_g\rho_g\left(\boldsymbol{\sigma}_{gm} + \boldsymbol{\sigma}_{ge} + \boldsymbol{\sigma}_f\right) \tag{20}$$

where ρ_r and ρ_g are the effectiveness factors of rubbery and glassy phases of SMPC, respectively. When $\rho_r = 1$ or $\rho_g = 1$, it signifies perfect interfacial bonding. When $0 < \rho_r < 1$ or $0 < \rho_g < 1$, it signifies progressive interfacial compromise. Experimental calibration through stress-strain curve fitting at T_l and T_h reveals distinct orientation-dependent trends. For 0°/90° fiber orientation, the constrained molecular mobility facilitates near-perfect bonding, allowing for $\rho_g = \rho_r = 1$ and requiring only parametric adjustments in the SMP matrix constitutive model. Conversely, for -45°/45°orientation, reduced fiber constraint preserves the reconfirmed matrix parameters while requiring $0 < \rho_r < 1$ and $0 < \rho_g < 1$ to account for the non-ideal effects.

In the shape memory cycle, a pre-strain $\boldsymbol{\varepsilon}_{pre}$ is applied at T_h, where the SMPCs consist solely of the rubbery phase. As the material cools, the strain applied in the rubbery phase transforms into the strain of the new glassy phase and is stored as the storage strain $\boldsymbol{\varepsilon}_{gs}$. Since the fibers do not possess a shape memory function, this process is mainly governed by temperature and the volume fractions of two phases. The storage strain $\boldsymbol{\varepsilon}_{gs}$ can be calculated as:

$$\frac{\mathrm{d}\boldsymbol{\varepsilon}_{gs}}{\mathrm{d}T} = \left(\boldsymbol{\varepsilon}_{pre} - \boldsymbol{\varepsilon}_t - \boldsymbol{\varepsilon}_r\right)\frac{\mathrm{d}\varphi_g}{\mathrm{d}T} \tag{21}$$

where $\boldsymbol{\varepsilon}_r$ represents the thermal residual strain, arising from the differences of CTE and elastic moduli between the fabric and SMP matrix. Based on the Eshelby's eigenstrain theorem, the average thermal residual stress in polar coordinates is expressed as follows:

$$\sigma_{rr}^{mean} = \left(2\sqrt{\frac{\varphi_f}{2}} - \frac{\varphi_f}{2}\right)\sigma_{rr}^{in}, \sigma_{\theta\theta}^{mean} = \frac{\varphi_f}{2}\sigma_{rr}^{in}, \sigma_{zz}^{mean} = \frac{\varphi_f}{2}\sigma_{zz}^{in}$$

$$\sigma_{ij}^{in} = \left(1 - \frac{\varphi_f}{2}\right)\left[\left(P_{kkmn}\varepsilon_{mn}^{**} - \varepsilon_{kk}^{**}\right)\lambda_m\delta_{ij} + 2\mu_m\left(P_{ijmn}\varepsilon_{mn}^{**} - \varepsilon_{ij}^{**}\right)\right] \tag{22}$$

where the subscripts rr, $\theta\theta$ and zz are transformed by setting $ij = 11$, 22 and 33, respectively. δ_{ij} is the Kronecker delta function. λ_m and μ_m are the Lamé constants of the matrix. ε^{**} represents the eigenstrain, which corresponds to the strain under zero applied stress. When a load is applied to the heterogeneous regions, differences in modulus and CTE between the fabric and matrix generate disturbance strain, which is related to the eigenstrain via the fourth-order Eshelby tensor **P**. The components of the Eshelby tensor for infinitely long elliptical cylinders are presented in Table. 1.

Table. 1 Eshelby tensor components for cylindrical long fiber ($v_f = 0.25$ is the Poisson's ratio).

$P_{1111} = P_{2222} = \dfrac{5 - 4v_f}{8\left(1 - v_f\right)}, P_{3333} = 0$
$P_{1122} = P_{2211} = -\dfrac{1 - 4v_f}{8\left(1 - v_f\right)}, P_{3311} = P_{3322} = 0$
$P_{1133} = P_{2233} = \dfrac{v_f}{2\left(1 - v_f\right)}, P_{1212} = \dfrac{3 - 4v_f}{8\left(1 - v_f\right)}, P_{1313} = P_{2323} = \dfrac{1}{4}$

The thermal deformation tests show that the thermal strain of SMPCs exhibits a strong linear relationship with temperature within the glass transition temperature range. Therefore, the thermal strain can be calculated using the following equation:

$$\boldsymbol{\varepsilon}_t = \alpha_c \Delta T \mathbf{I} \tag{23}$$

where α_c is the CTE of SMPCs. Combined with Eqs. (8) and (19)-(24), the storage strain of SMPC in the cooling process can be determined. During unloading at low temperature T_l, a small amount of rebound occurs, governed by Hooke's law. The fixed strain can be calculated as:

$$\boldsymbol{\varepsilon}_{fix} = \varphi_m \boldsymbol{\varepsilon}_{gs}(T_l) + \boldsymbol{\varepsilon}_t(T_l) \tag{24}$$

As the fiber orientation varies from 0°/90° to -45°/45°, the loading direction is inconsistent with fiber direction. Since the thermal residual stress calculated based on Eq. (22) is defined along the fiber directions, it must be transformed into the loading direction using the appropriate stress transformation

formula. Given that the SMP matrix predominantly undertakes the shear deformation and the deformation of the thickness direction in SMPCs [13], it simplifies to a plane stress problem and the conversion formula is expressed as follows:

$$\begin{bmatrix}\sigma_x\\ \sigma_y\\ \tau_{xy}\end{bmatrix}=\begin{bmatrix}(cos\theta)^2 & (sin\theta)^2 & -2sin\theta cos\theta\\ (sin\theta)^2 & (cos\theta)^2 & 2sin\theta cos\theta\\ sin\theta cos\theta & -sin\theta cos\theta & (cos\theta)^2-(sin\theta)^2\end{bmatrix}\begin{bmatrix}\sigma_1\\ \sigma_2\\ \tau_{12}\end{bmatrix} \tag{25}$$

where θ is the angle between the fiber direction and the loading direction. And σ_{zz}^{mean} in Eq. (22) is assumed to be approximately equal to the shear stress τ_{12}. Furthermore, the elastic modulus of SMPCs with varying fiber orientations in loading direction can be expressed as:

$$E_c=\varphi_g E_{gc}+\varphi_r E_{rc} \tag{26}$$

where E_{gc} and E_{rc} are the elastic modulus of glassy and rubbery phases of SMPCs in loading direction. Thus, the average thermal residual strain in loading direction can be calculated using Eqs. (21)-(26).

Considering the occurrence of non-ideal behaviors during shape memory cycling, which can adversely affect the SME performance, similarly, an effective factor is introduced to evaluate the overall macroscopic shape memory properties for SMPCs with various fiber orientations. Consequently, Eq. (24) is revised as follows:

$$\boldsymbol{\varepsilon}_{fix}=\rho_s(\varphi_m\boldsymbol{\varepsilon}_{gs}(T_l)+\boldsymbol{\varepsilon}_t(T_l)) \tag{27}$$

where ρ_s is the effectiveness factor. It is important to note that the destructive effect of yarn rotation on the matrix during the cooling stage is intensified during the reheating stage due to shape recovery, leading to a reduction in ρ_s during the cooling stage compared to the reheating stage. To minimize mechanical dissipation, the energy released by SMPCs during heating is exactly the opposite to the energy stored during cooling. This implies that the variation of $\boldsymbol{\varepsilon}_{gs}$ in reheating is inherited from the $\boldsymbol{\varepsilon}_{gs}(T)$ which is previously determined during cooling. This relationship can be used to describe the shape storage during the cooling process and the shape recovery during the reheating process.

4 MODELS VERIFICATION AND DISCUSSION

Following the parameter identification procedure for SMPCs with varying fiber orientations in Ref. [6], the model parameters summarized in Table. 2 were determined. Based on Eq. (13), (18) and (20), the uniaxial tensile response of SMPCs with different fiber orientations was simulated using fsolve and ODE45 functions in MATLAB. The numerical results of engineering stress versus engineering strain at different temperatures are presented in Figs. 3-5. Among these, the tensile curves at 20°C and 80°C were used to fit the model parameters, while the other four curves were employed to validate the predictive capability of the constitutive model. Subsequently, the initial tensile modulus of SMPCs with various fiber orientations was computed across the temperature range using the identified parameters, as shown in Fig. 6. A comparison with the experimental data confirms that the proposed model can effectively capture the anisotropic and temperature-dependent thermomechanical behavior of SMPCs over the entire glass transition temperature range.

Table. 2 Model parameters for SMPCs.

Parameters	Values	Units	Parameters	Values	Units
$C_{10}^{rm}, C_{01}^{rm}, D_{rm}$	24, 4.8, 0.001	MPa	h_0, s_0, s_s	300, 38, 18	MPa
$C_{10}^{gm}, C_{01}^{gm}, D_{gm}$	24, 4.8, 0.001	MPa	Q_s	1000	mJ
$C_{10}^{ge}, C_{01}^{ge}, D_{ge}$	360, 72, 0.001	MPa	B	2830	K
A	7	°C^{-1}	k_1, k_2, k_3	2090, 2280, 2.15	MPa
T_r	45	°C	k_4, k_5, k_6	0.15, 0.001, 0.06	MPa

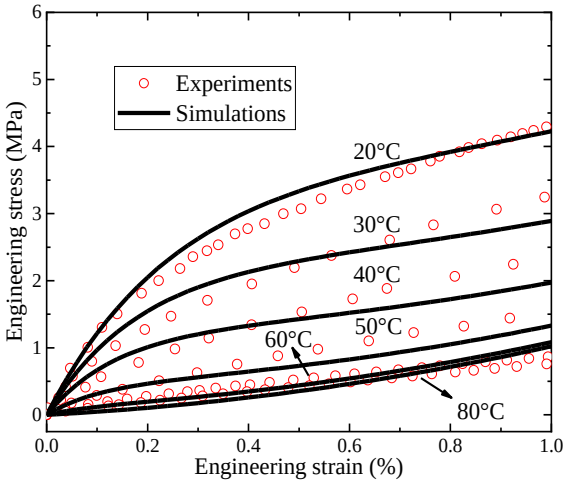

Fig. 3 Simulation results for the isothermal loading for 0°/90° oriented SMPCs.

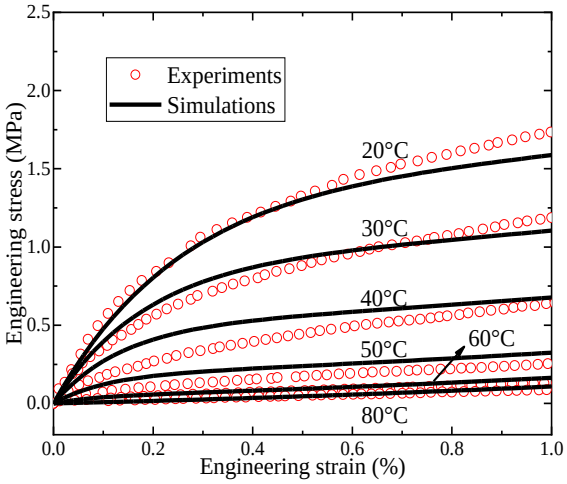

Fig. 4 Simulation results for the isothermal loading for -30°/60° oriented SMPCs.

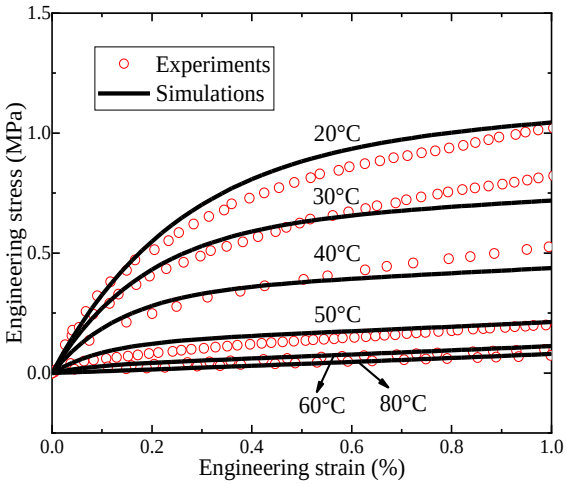

Fig. 5 Simulation results for the isothermal loading for -45°/45° oriented SMPCs.

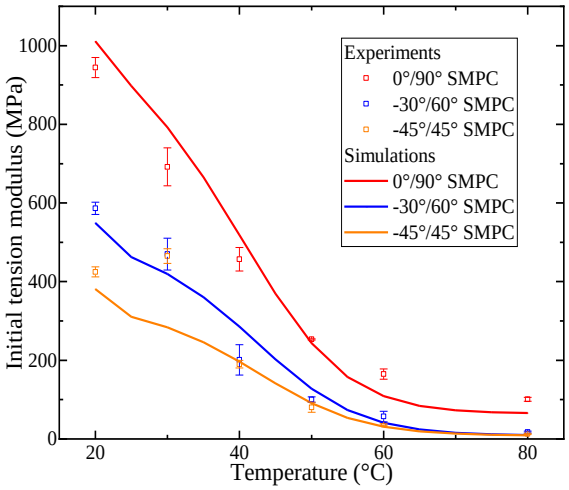

Fig. 6 Simulation results for the initial tension modulus for SMPCs with various fiber orientations.

Based on Eqs. (8) and (21)-(27), the free shape recovery process can be simulated using a 1D analysis model implemented in MATLAB. The engineering strain curve for -45°/45° oriented SMPCs in Fig. 7 was used to determine the effective factor ρ_s, while ρ_s was set to 1 for the 0°/90° oriented SMPCs due to no yarn rotation. The engineering strain-temperature curves for SMPCs with 0°/90° and -30°/60° fiber orientations are presented in Figs. 8 and 9. For the 0°/90° oriented SMPCs, the developed model predicts a shape fixity ratio of 0.85, which is 3.8% higher than the experimental value, and a shape recovery ratio of 0.804, which is 4.5% lower than the experimental result. For the -30°/60° oriented SMPCs, the predicted shape fixity ratio is 0.887, exceeding the experimental value by 3.9%, while the predicted recovery ratio is 0.708, 2.5% lower than the measured result. Overall, the simulation curves exhibit a trend consistent with the experimental observations, confirming the proposed model's ability to accurately capture the anisotropic shape memory behavior of SMPCs with various fiber orientations.

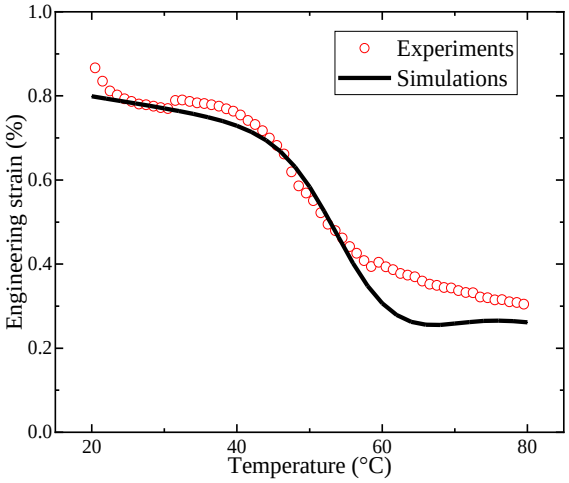

Fig. 7 Fitting the free shape recovery curves for -45°/45° oriented SMPCs.

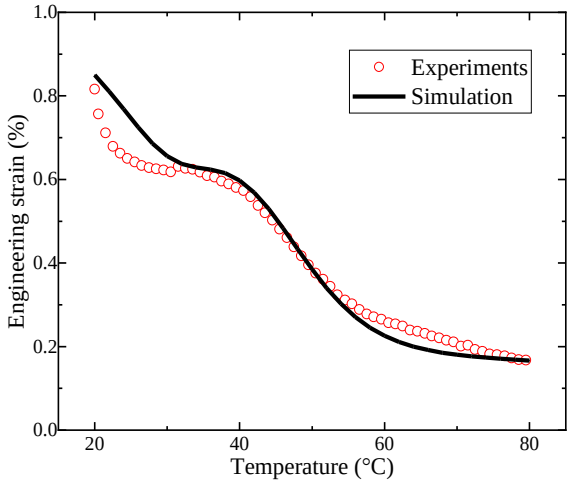

Fig. 8 Simulation results for the free shape recovery for 0°/90° oriented SMPCs.

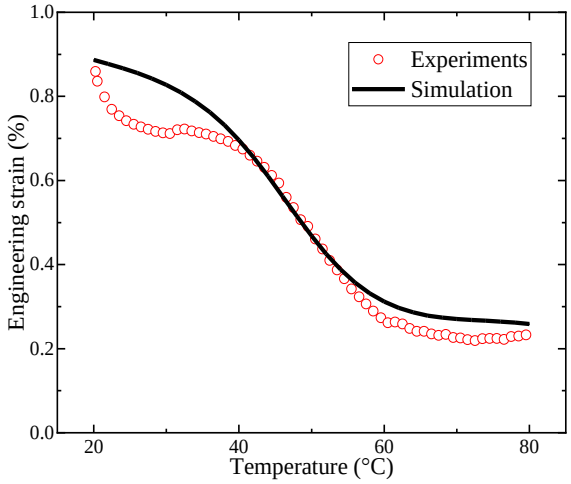

Fig. 9 Simulation results for the free shape recovery for -30°/60° oriented SMPCs.

5 CONCLUSIONS

This study establishes a phase transition-based anisotropic constitutive framework for carbon woven fabric-reinforced shape memory polymer composites (SMPCs), advancing the modeling of their thermomechanical and shape memory behaviors. Three key advancements characterize our approach:

(1) A novel decomposition of SMPCs into modified rubbery and glassy phases, each incorporating fiber–matrix interactions to enable independent characterization of temperature-dependent responses.

(2) Implementation of Mooney-Rivlin free energy formulation for capturing SMP matrix nonlinearity, combined with an orthotropic polynomial hyperelastic model for the fabric reinforcement, allowing accurate prediction of multi-axial mechanical behavior.

(3) Introduction of a temperature-invariant effectiveness factor to quantitatively describe the loss of reinforcement constraints.

The developed model exhibits excellent agreement with experimental data across various fiber orientation configurations, demonstrating its capability to capture the complex anisotropic thermomechanical and shape memory responses of SMPCs.

ACKNOWLEDGEMENTS

The supports from the National Natural Science Foundation of China (U20A20288) are gratefully acknowledged.

REFERENCES

[1] W. Zhao, L. Liu, X. Lan, J. Leng, Y. Liu, Thermomechanical constitutive models of shape memory polymers and their composites. *Applied Mechanics Reviews*, **75**, 2023, pp. 020802 (https://doi.org/10.1115/1.4056131).
[2] J.H. Roh, H.I. Kim, S.Y. Lee, Viscoelastic effect on unfolding behaviors of shape memory composite booms. *Composite Structures*, **133**, 2015, pp. 235-245 (https://doi.org/10.1016/j.compstruct.2015.07.095).
[3] X.B. Su, Y.Y. Wang, X.Q. Peng, An anisotropic visco-hyperelastic model for thermally-actuated shape memory polymer-based woven fabric-reinforced composites. *International Journal of Plasticity*, **129**, 2020, pp. 102697 (https://doi.org/10.1016/j.ijplas.2020.102697).
[4] S.B. Hong, J.H. Jang, H. Park, J.G. Kim, N.S. Goo, W.R. Yu, Three-dimensional constitutive model of woven fabric-reinforced shape memory polymer composites considering thermal residual stress. *Smart Materials and Structures*, **28**, 2019, pp. 035023 (https://doi.org/10.1088/1361-665X/aafd3a).
[5] J. Chen, X. Zhou, C. Du, Q. Wang, X. Peng, A constitutive model for carbon fabric-reinforced shape memory polymer composites based on Eshelby's inclusion theorem. *Composites Science and Technology*, **261**, 2025, pp. 111042 (https://doi.org/10.1016/j.compscitech.2025.111042).
[6] J. Chen, J. Ouyang, X. Zhou, H. Liao, C. Du, T. Zhang, Q. Wang, X. Peng, Experiments and simulations on the anisotropic behavior of carbon woven fabric-reinforced shape memory polymer composites. *Composites Part B: Engineering*, 2025, pp. 112752 (https://doi.org/10.1016/j.compositesb.2025.112752).
[7] X.Q. Peng, Z.Y. Guo, T.L. Du, W.R. Yu, A simple anisotropic hyperelastic constitutive model for textile fabrics with application to forming simulation. *Composites Part B-Engineering*, **52**, 2013, pp. 275-281 (https://doi.org/10.1016/j.compositesb.2013.04.014).
[8] J. Chen, C. Du, W. Zhang, P. Zhu, Q. Wang, X. Peng, Modeling and application of temperature-dependent elastic constants in continuous fiber-reinforced shape memory polymer composites. *Polymer Testing*, **150**, 2025, pp. 108882 (https://doi.org/10.1016/j.polymertesting.2025.108882).
[9] Y.P. Liu, K. Gall, M.L. Dunn, A.R. Greenberg, J. Diani, Thermomechanics of shape memory polymers: Uniaxial experiments and constitutive modeling. *International Journal of Plasticity*, **22**, 2006, pp. 279-313 (https://doi.org/10.1016/j.ijplas.2005.03.004).
[10] J. Chen, C. Du, Q. Wang, X. Peng, A 3D finite strain constitutive model for shape memory polymers combined viscoelasticity and storage strain. *Mechanics of Materials*, **197**, 2024, pp. 105103 (https://doi.org/10.1016/j.mechmat.2024.105103).
[11] H.J. Qi, T.D. Nguyen, F. Castroa, C.M. Yakacki, R. ShandaSa, Finite deformation thermo-mechanical behavior of thermally induced shape memory polymers. *Journal of the Mechanics and Physics of Solids*, **56**, 2008, pp. 1730-1751 (https://doi.org/10.1016/j.jmps.2007.12.002).
[12] X.B. Su, X.Q. Peng, A 3D finite strain viscoelastic constitutive model for thermally induced shape memory polymers based on energy decomposition. *International Journal of Plasticity*, **110**, 2018, pp. 166-182 (https://doi.org/10.1016/j.ijplas.2018.07.002).
[13] X. Lan, L.W. Liu, Y.J. Liu, J.S. Leng, Thermomechanical properties and deformation behavior of a unidirectional carbon-fiber-reinforced shape memory polymer composite laminate. *Journal of Applied Polymer Science*, **137**, 2020, pp. 48532 (https://doi.org/10.1002/app.48532).

ICCM24
AUGUST 4-8, 2025
BALTIMORE CONVENTION CENTER
BALTIMORE, MARYLAND, USA

No Technical Paper Submission for:

Muhammad Jawad Ahmad

ADVANCED COMPOSITE BONDING USING ENERGY EFFICIENT LOCALISED CURING BASED ON NANO-MODIFIED EPOXY

Karina Dragasiute, Gediminas Monastyreckis, Daiva Zeleniakiene

Department of Mechanical Engineering, Kaunas University of Technology
Studentu 56, Kaunas 51424, Lithuania, daiva.zeleniakiene@ktu.lt

INTRODUCTION

Motivation

Traditional bonding processes require high-temperature ovens, leading to:

- high energy consumption
- long curing cycles
- scalability challenges for large components

Aim

To develop a scalable, energy-efficient bonding process for composite materials using CNT-enhanced epoxy adhesives.

METHODOLOGY

- Sample preparation and electrical characterisation
- Local curing and IR thermal imaging
- Single lap tensile test (ISO 4587)

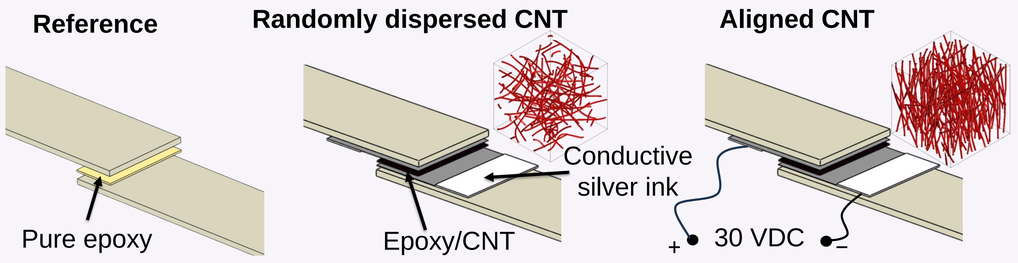

- Thermal transient FEA via Representative Volume Element (RVE)

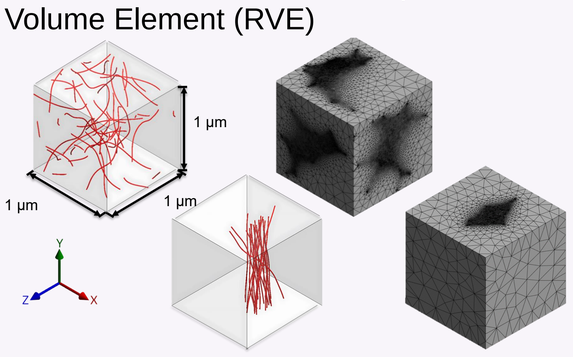

RESULTS

Resistance before and after CNT alignment

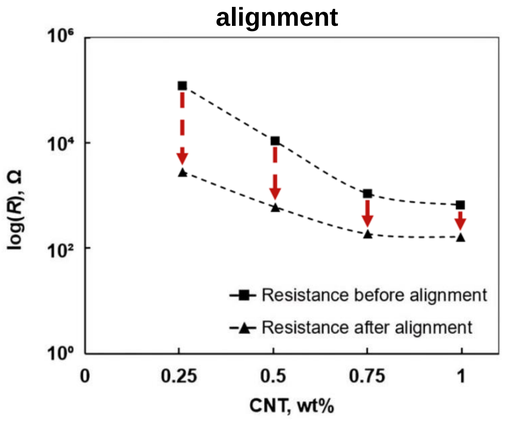

Temperature profile along the length of the aligned and randomly dispersed CNT 400 specimens

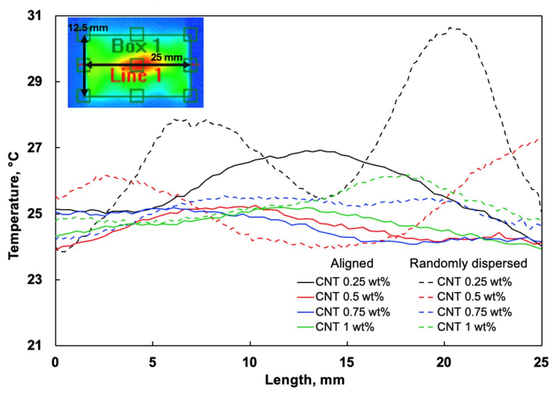

Infrared imaging of temperature distribution during Joule heating-based curing

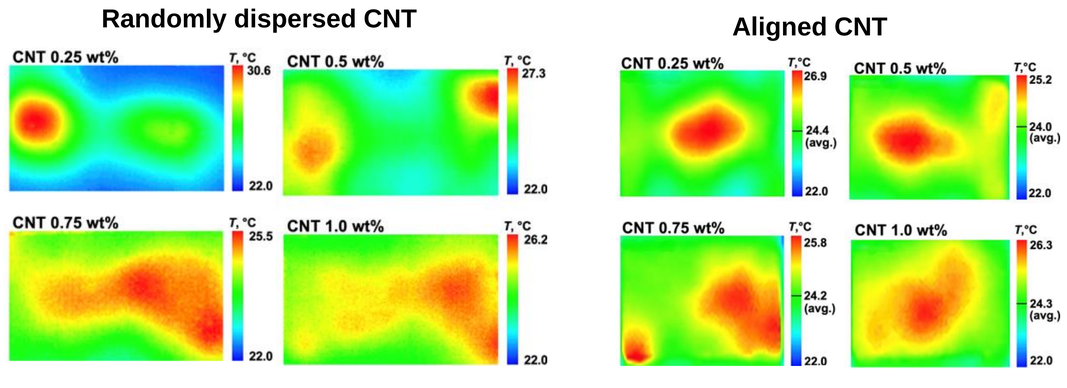

Comparison of shear strength of single-lap specimens and pure epoxy adhesives

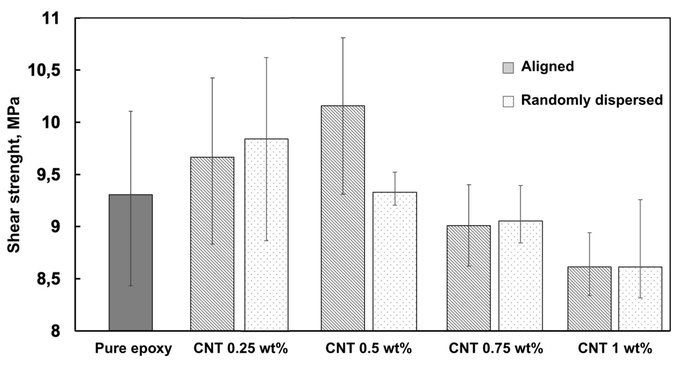

SEM results after lap-shear tests

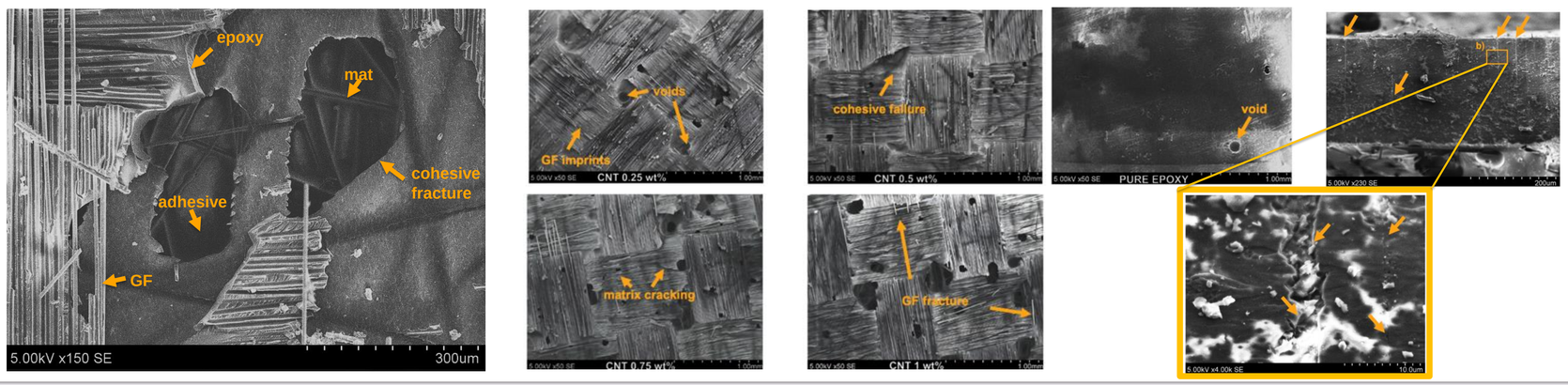

Randomly dispersed CNT | **Aligned CNT**

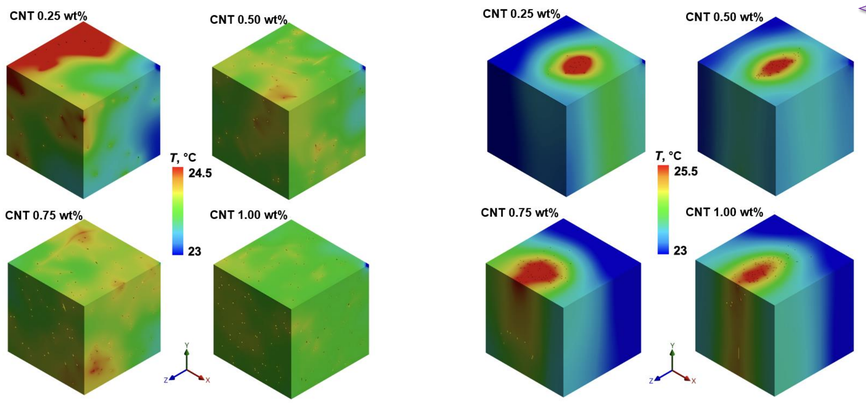

FEA temperature distribution of RVE models

Maximum and average temperatures from transient thermal FEA of RVE models

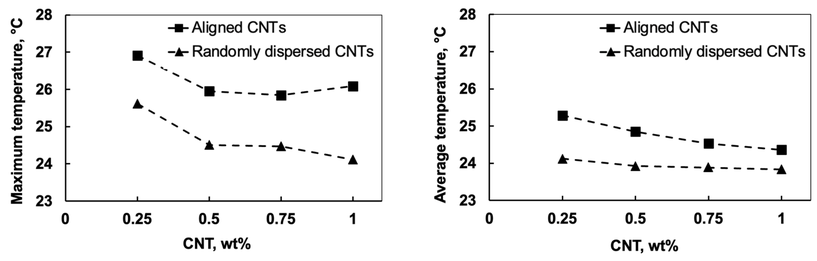

Most of the results presented in this poster have recently been published in the *Polymers* journal. Further findings and insights can be found in the article:
Dragasiute, K.; Monastyreckis, G.; Zeleniakiene, D. *Electrically Conductive Nanoparticle-Enhanced Epoxy Adhesives for Localised Joule Heating-Based Curing in Composite Bonding*. Polymers 2025, 17, 1176. https://doi.org/10.3390/polym17091176.

CONCLUSIONS

This study demonstrates that CNT-enhanced epoxy adhesives enable effective Joule heating-based curing in composites. Optimal CNT loading (0.5 wt%) improved conductivity, shear strength, and heat localisation. Alignment methods further enhanced targeted heating efficiency. Overall, CNTs enable efficient, localised curing with improved mechanical bonding properties.

FUTURE RESEARCH

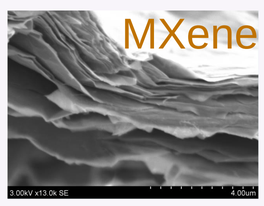

The next stage of this research will investigate electrically conductive MXene nanoparticles for localised Joule heating in structural composites. $Ti_3C_2T_x$ coatings and interlayers will be used, supported by advanced nanocomposite technologies to produce materials with enhanced properties and reduced energy demand, contributing to more sustainable solutions.

This research is funded by the European Union Horizon Europe Programme under Grant Agreement No. 101182521. Views and opinions expressed are however those of the author(s) only and do not necessarily reflect those of the European Union or European Research Executive Agency. Neither the European Union nor the granting authority can be held responsible for them.

Funded by the European Union

ICCM24
AUGUST 4-8, 2025
BALTIMORE CONVENTION CENTER
BALTIMORE, MARYLAND, USA

No Technical Paper Submission for:

Chamil Abeykoon

ICCM24
AUGUST 4-8, 2025
BALTIMORE CONVENTION CENTER
BALTIMORE, MARYLAND, USA

No Technical Paper Submission for:

Chamil Abeykoon

Friction behaviors of carbon fiber tows and their effect on the manufacturability and mechanical properties of composite pressure vessels

Su Hyun Lim, Wonvin Kim, Wonki Kim, and Seong Su Kim*
Department of Mechanical Engineering, Korea Advanced Institute of Science and Technology (KAIST)



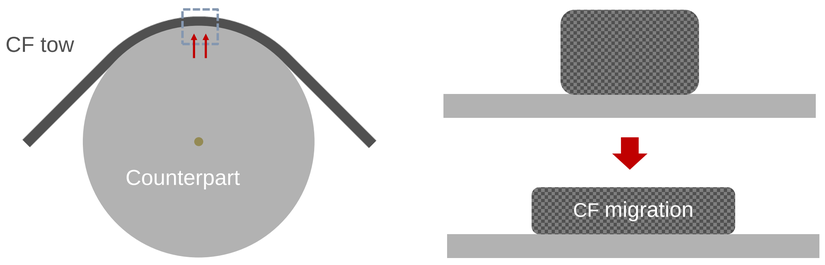

CF tow spreading ››› Intra-tow friction

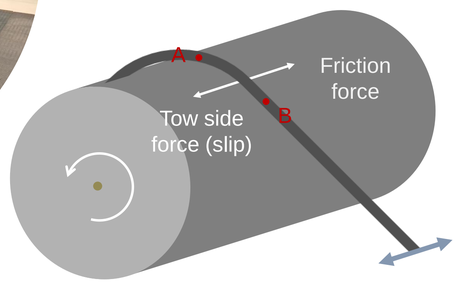

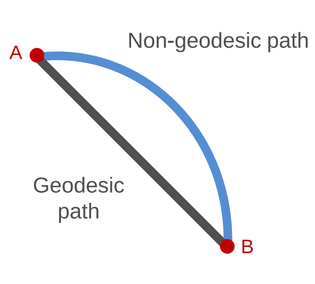

CF tow positioning ››› Inter-tow friction

The friction behavior of carbon fiber tows is decisive in composite manufacturing processes such as molding, braiding, and filament winding by affecting the deformation and positioning of the tow. It is essential to consider the tow friction from the design stage, thereby allowing better control of process parameters and ensuring high product quality.

Herein, we propose a systematic framework that addresses the friction behaviors of CF tows and their impact on manufacturability and mechanical properties of filament wound composites through experimental approach.The results showed the significant multi-scale relationship between CF, tow, and composites in terms of their fricion behavior and interfacial properties, directly related with manufacturability and burst properties of filament wound cylinders, which is not addressed through previous studies.

Material & Specification

Sizing agent	CF*	CF tow **
A	A_CF	A_Tow
B	B_CF	B_Tow
C	C_CF	C_Tow

* T700 grade CF with 1 wt % of an epoxy- or a polyurethane resin-based sizing agent

** 12k CF tow

- CF surface properties [1]

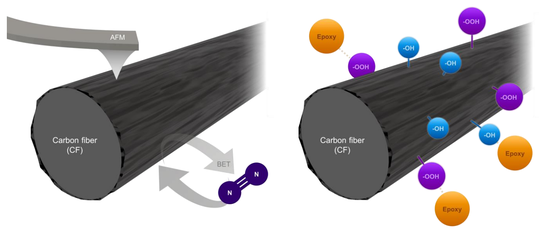

- CF tow microstructure [2]

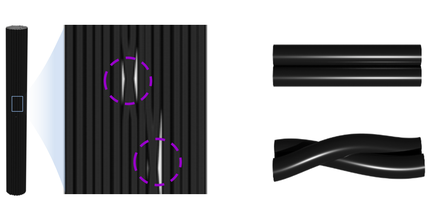

Burst properties of filament wound cylinders

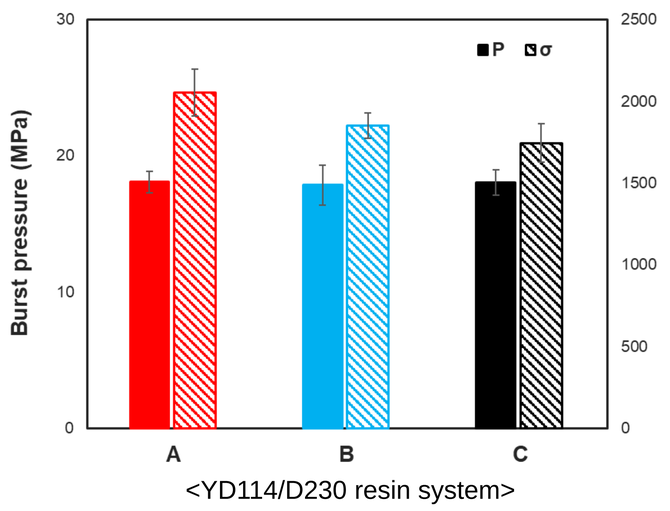

<YD114/D230 resin system>

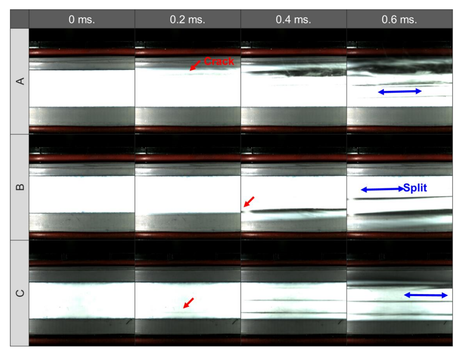

$$P_{Burst} = \frac{F_{2,max}}{2\pi rh} \qquad \sigma_{Hoop} = \frac{P_{Burst} r}{t}$$

Friction behaviors of CF tows

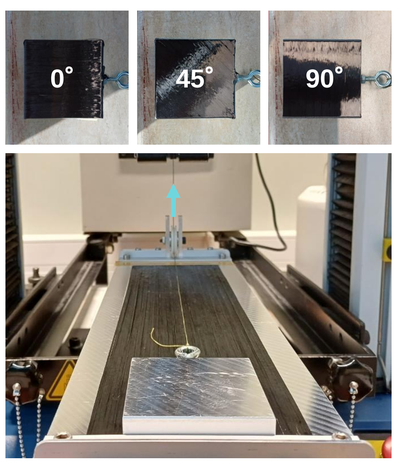

<Modified based on ASTM D1894>

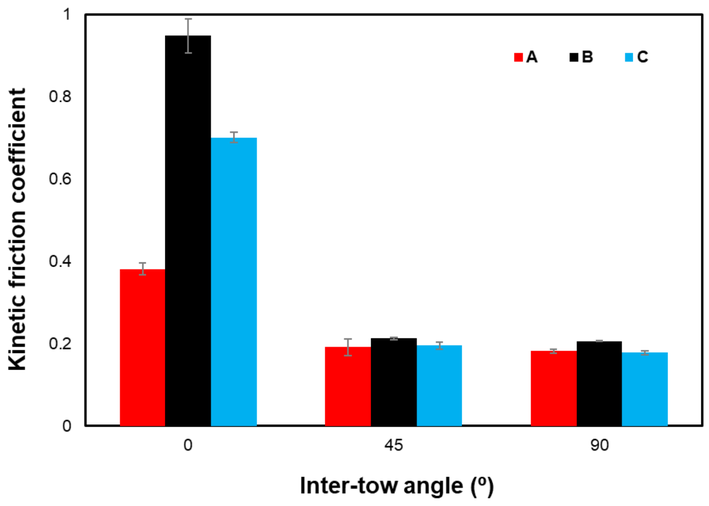

Future work & Final goal

- Quantitative study on the effect of CF surface properties and CF tow microstructure on the CF tow friction behaviors
- Computational approach to investigate the multi-scale behavior of filament wound CFRP

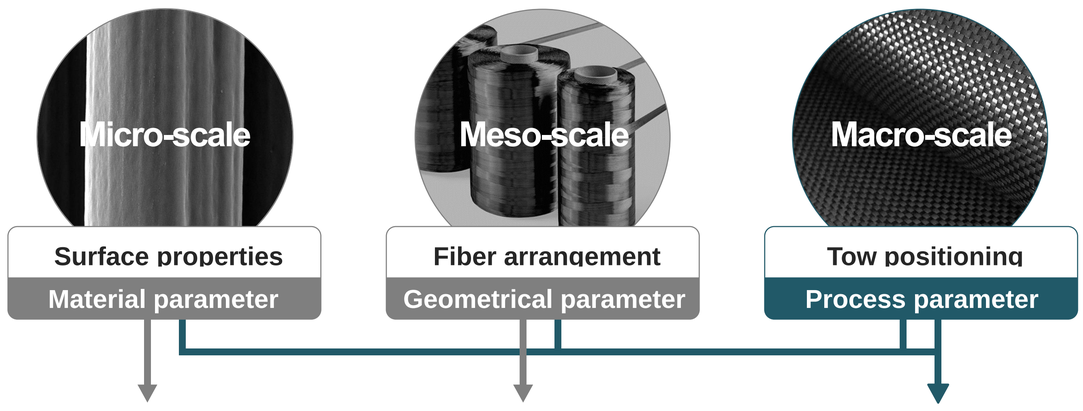

Manufacturability of filament wound cylinders

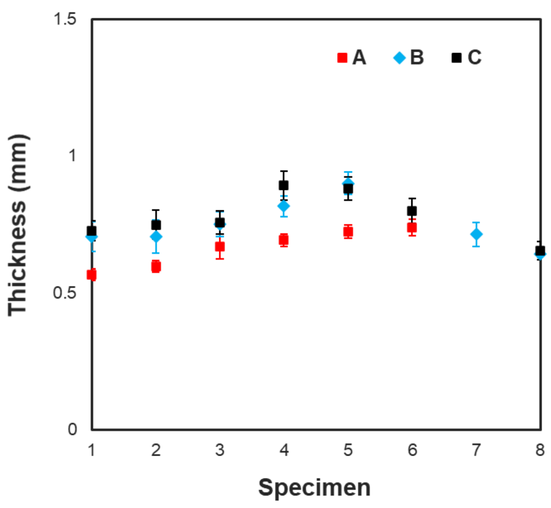

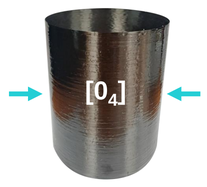

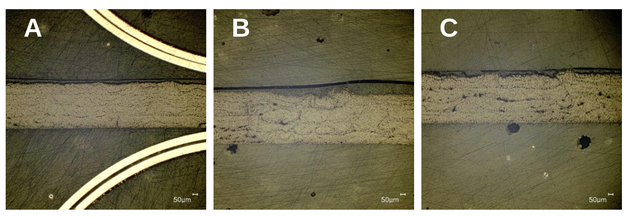

FVF : 63 % FVF : 57 % FVF : 56 %

Consistency of CFRP manufacturing & Reliability of mechanical performance prediction

Related publications

[1] Micro-scale study :
Lim, et al, *Composites Part A*, 2021;146:106424.
[2] Meso-scale study :
Lim, et al, *Composites Science and Technology*, 2024;256:110786.

Korea Advanced Institute of Science and Technology (KAIST)
Su Hyun Lim
Ph.D candidate• Mechanical Engineering
291, Daehak-ro, Yuseong-gu, Daejeon, Republic of Korea

E-mail: limsu@kaist.ac.kr
Phone: +82)10-2757-0396
Web: *http://mdam.kaist.ac.kr/*

MDAM LAB.

KAIST

EFFECT OF CORNER CURVATURE ON PRESS FORMING OF METAL-THERMOPLASTIC CFRP LAMINATES

Miumi Naito [1]and Tatsuro Kosaka[2]

[1]Graduate School of Engineering, Kochi University of Technology,
185 Tosayamada-cho Miyanokuchi, Kami Shi, Kochi Ken, 782-8502, Japan,
*E-mail: 285023b@gs.kochi-tech.ac.jp

[2]Systems Engineering Group, Kochi University of technology, 185 Tosayamada-cho Miyanokuchi, Kami Shi, Kochi Ken, 782-8502, Japan,
E-mail: kosaka.tatsuro@kochi-tech.ac.jp

Keywords: Metal/CFRTP, Fiber metal laminates, Hot-press molding, Press bending

ABSTRACT

In recent years, the development of multi-material components combining metals with carbon fiber reinforced plastics (CFRP) has attracted growing attention, particularly in the automotive industry. This approach aims to achieve both weight reduction and cost efficiency, which are essential for enhancing vehicle performance and supporting sustainable manufacturing. Among various types of CFRP, thermoplastic CFRP (CFRTP) offers advantages such as short cycle times and recyclability, making it suitable for high-volume production. This study investigates the feasibility of a press forming method for metal/CFRTP laminated sheets as a preliminary step toward continuous forming processes for hybrid structures. Laminates were fabricated by hot pressing plain-woven CF/PA66 with two types of metal sheets: aluminum alloy A5052 and ferritic stainless steel SUS430. Forming was conducted using a V-type press die under controlled thermal conditions. While the specimens were not bent into full L-shaped profiles, the focus was placed on evaluating interfacial integrity and formability under simplified bending conditions. Experimental results revealed that the die corner geometry and temperature uniformity are critical factors for defect-free forming. In particular, appropriately designed die corners helped suppress delamination and fiber–matrix separation at the metal–CFRTP interface. These findings offer valuable guidance for the design of forming tools and process parameters in hybrid metal/CFRTP manufacturing. This work contributes to the advancement of lightweight multi-material forming technologies and supports the future implementation of efficient, high-speed production methods in automotive applications.

1INTRODUCTION

In recent years, carbon fiber reinforced plastics (CFRP) have attracted significant attention as advanced composite materials due to their exceptional combination of light weight and high mechanical strength. These properties make CFRP particularly appealing for automotive applications, where reducing vehicle weight is directly linked to improved fuel efficiency. Consequently, the use of CFRP in structural components such as frames and body panels has been steadily increasing.

However, despite its advantages, the widespread adoption of CFRP remains limited by two major challenges: its relatively high production cost and instability in the supply chain, which restrict its availability for large-scale manufacturing.

To overcome these limitations, recent research has focused on the development of multi-material structures that combine metals with CFRP[1-5]. These hybrid structures aim to exploit the complementary strengths of both materials—metals for their formability and cost-efficiency, and CFRP for its light weight and high strength.

In this context, the present study investigates the feasibility of a press forming technique for metal/CFRTP (carbon fiber reinforced thermoplastic) laminated sheets. This work serves as a preliminary step toward the development of roll forming processes, which are better suited for high-speed, large-scale production of hybrid materials. Specifically, laminated plates consisting of metal and

plain-woven thermoplastic composite (CF/PA66) were fabricated using a heat press method. A series of forming experiments was conducted to identify and evaluate the optimal processing conditions for achieving high-quality laminates.

2 EXPERIMENTAL METHOD

The test specimens consisted of a 2.0 mm thick CFRTP core and 0.5 mm thick metal face sheets, using two types of metals: SUS304 stainless steel and A5052 aluminum alloy.

The CFRTP core was composed of a plain-woven carbon fiber fabric impregnated with a PA66 (polyamide 66) thermoplastic matrix. The material used was Tepex® 201-C200(x)/50% (LANXESS), with a nominal fiber volume fraction of 50%. Each sheet was cut to a width of 30 mm and a length of 60 mm using a fine cutter.

Two types of metal surface conditions were prepared: untreated and roughened using #240 sandpaper. Surface roughening was performed by placing one side of the metal sheet on a flat surface and evenly abrading it with the sandpaper.

To investigate the effect of interfacial bonding, some specimens included a sheet-type hot-melt adhesive (Aron Melt PPET-1200, TOAGOSEI) placed between the CFRTP and the metal layers, while others were laminated without adhesive. The experiments were conducted under various conditions: with and without adhesive, with and without metal surface treatment, and with or without applied molding pressure.

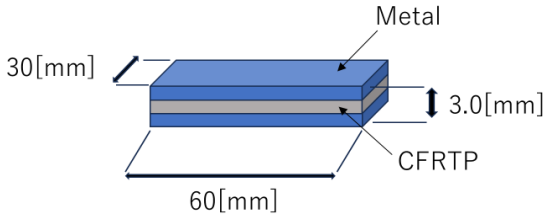

Figure 1: Dimension and stacking sequence of test specimen

Table 1: Specimen IDs and Corresponding Experimental Conditions

Specimen ID	adhesive	surface treatment	Pressure
S-P-A	Yes	Yes	Yes
S-P	Yes	Yes	No
P-A	Yes	No	Yes
P	Yes	No	No
S-A	No	Yes	Yes
S	No	Yes	No
A	No	No	Yes
N	No	No	No

3 RESULTS AND DISCUSSION

Figure 2 shows photographs of the test specimens after V-die press forming. Delamination was observed in both SUS/CFRTP and AL/CFRTP specimens, particularly in Specimens S-P-A and S-A. However, this delamination was not consistently correlated with the application of pressure during lamination. For example, while no delamination was observed in press-formed specimens A-P and S-P, delamination occurred in S-P-A despite being formed under pressure. These observations suggest that delamination is caused by factors beyond the initial bonding process.

Figure 3 provides a magnified view of the delaminated regions. Notably, significant dents were found in the metal layers near the upper corners, supporting the hypothesis that local stress concentration causes failure. Furthermore, in specimens without delamination, such as S-P and S, clear interlaminar slippage was observed within the CFRTP layer. This slippage is considered to play a key role in accommodating deformation and thereby preventing delamination.

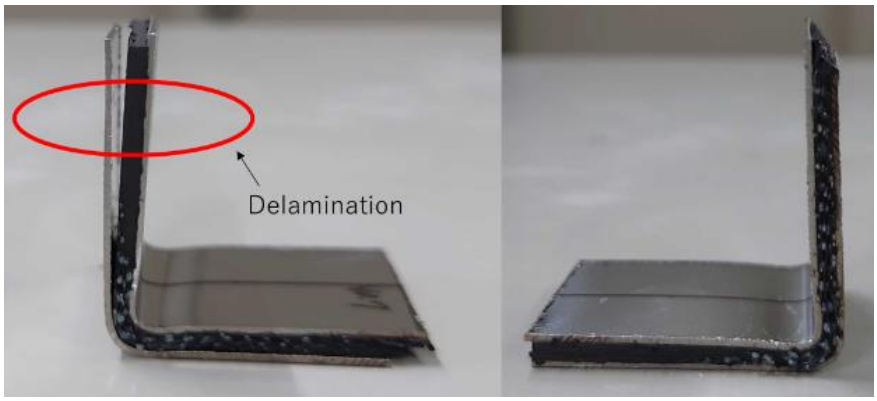

Figure 2: Photographs of test specimens after V-die press forming: specimens exhibiting delamination (e.g., S-P-A, S-A) and specimens without delamination (e.g., S-P, S).

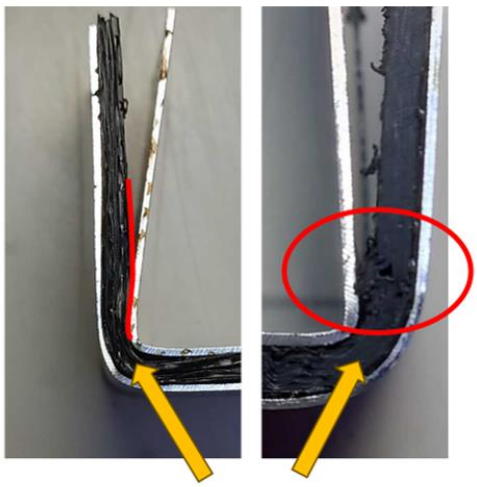

Figure 3: Evidence of delamination mechanisms: left—local denting in the metal layer due to stress concentration at the upper die corners; right—out-of-plane deformation of the CFRTP layer caused by constrained interlaminar slippage.

Figure 4 shows the bending angles of the SUS/CFRTP and A5052/CFRTP specimens after forming. The results revealed significant variations in the corner angles. Notably, specimens without delamination (e.g., Specimens S-P, P, S, and N) exhibited corner angles close to 90°, suggesting that delamination inhibits proper angle formation. This phenomenon is attributed to the sharpness of the upper die corners, which induces localized plastic deformation in the metal layer.

Furthermore, as shown in Figures 4 and 5, most specimens exhibited bending angles less than 90°, indicating a trend opposite to the typical spring-back behavior observed in metal forming. Detailed analysis revealed that this deviation resulted from a mismatch in the bending angles between the upper and lower dies used in the press. This effect was present in all specimens but was particularly pronounced in Specimens S-P-A, P-A, S-A, and A.

From the above findings, delamination was found to occur primarily due to two mechanisms:

(1) local stress concentration at sharp upper die corners, which induced out-of-plane deformation (denting) in the metal layer, and

(2) suppression of interlaminar slippage in the CFRTP layer due to non-uniform forming temperature, causing the layers to bend outward and separate from the metal.

These results indicate that appropriate die corner curvature and temperature control are critical for preventing delamination.

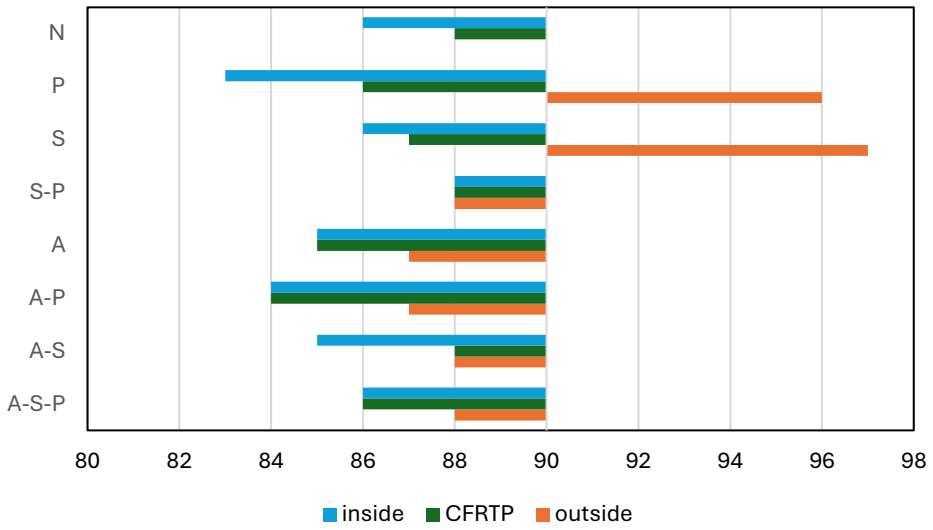

Figure 4: Bending angles of SUS/CFRTP and A5052/CFRTP specimens after V-die press forming, showing the influence of delamination on angle formation. Specimens without delamination (e.g., S-P, P, S, N) maintained angles close to 90°, while delaminated specimens exhibited more deviation.

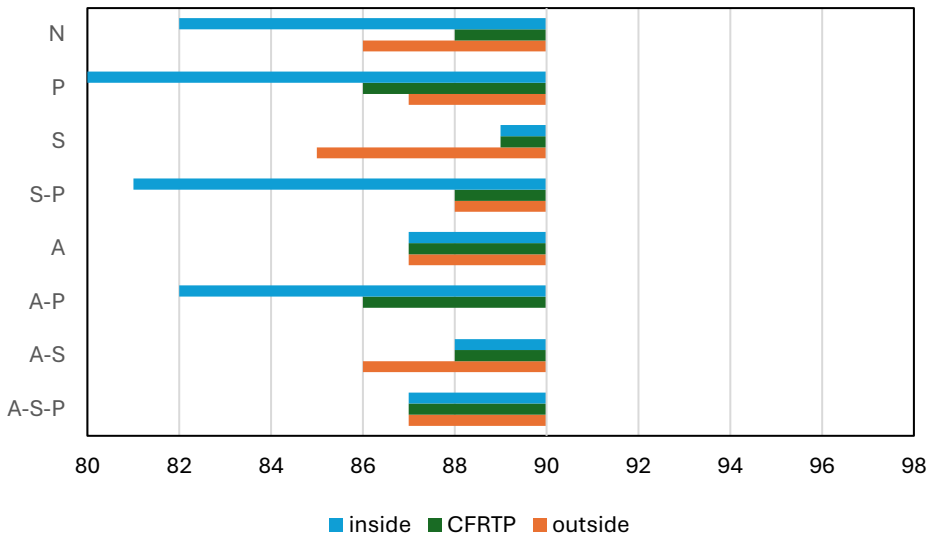

Figure 5: Deviation of actual bending angles from the nominal die angle, highlighting reduced spring-back behavior. The mismatch between upper and lower die angles contributed to angles less than 90° across all specimens.

4 IMPROVEMENT OF A PRESS MOLD

4-1 EXPERIMENTAL METHOD

To suppress spring-in deformation during V-bending, an improved mold was employed, in which the corner radius of the upper die was increased and unified with that of the lower die (both set to R2). The same materials as in the previous experiments were used, and all specimens included a sheet-type hot-melt adhesive between the CFRTP core and the metal face sheets to ensure consistent interfacial bonding.

Prior to pressing, the specimens were heated in an electric furnace for a total of 8 minutes—4 minutes per side—with flipping at the midpoint to achieve uniform temperature distribution. The V-bending process was then conducted using the improved mold.

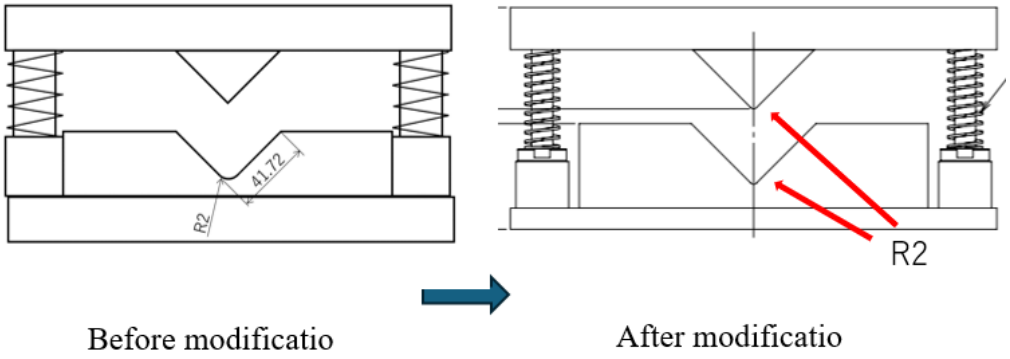

Figure 6: Improved die design for V-shaped pressing with unified corner radius (R2).

4-2 RESULTS OF PRESS BENDING

As shown in the figure, V-bending was successfully achieved without inducing spring-in deformation. Most specimens exhibited interlaminar slippage, and delamination was effectively suppressed. These findings indicate that the combination of uniform heating and improved die geometry contributed to stable and defect-free forming behavior.

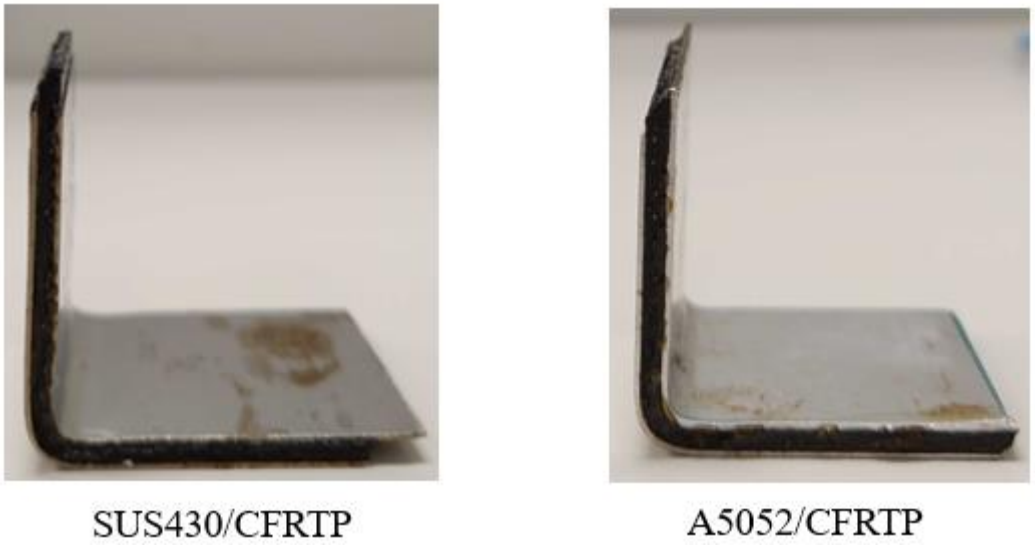

Figure 7: Test specimens after V-shaped pressing using the improved mold.

5 TENSILE PROPERTIES OF METAL/CFRTP LAMINATES

5-1 EXPERIMENTAL METHOD FOR TENSILE TESTING

To evaluate the tensile properties of SUS430/CFRTP and A5052/CFRTP laminated plates, tensile tests were conducted according to standard procedures. Photographs of the test specimens are shown in Figure 8.



Figure 8: Test specimens of SUS430/CFRTP and A5052/CFRTP laminates for tensile testing.

5-2 FINITE ELEMENT MODELING USING ABAQUS

Finite element analysis was performed to obtain the corresponding stress–strain curves. The metal layers were modeled as elastoplastic materials, while the CFRTP core was treated as orthotropically elastic. Tensile loading was applied until the metal layers reached their respective yield strains: 1.3% for SUS430/CFRTP and 8% for A5052/CFRTP.

To complement the experimental results, finite element models were developed in Abaqus to simulate the same sandwich configurations under uniaxial tensile loading. Second-order solid elements were employed to accurately represent geometry and deformation behavior.

5-3 RESULTS AND DISCUSSION

Figure 10(a) shows the stress–strain curves for SUS/CFRTP, and Figure 10(b) shows those for AL/CFRTP. In Figure 10(a), the curve for SUS/CFRTP showed yielding at approximately 0.001 strain, followed by a nearly linear increase in stress up to 0.0058 strain. At this strain, the slope changed, indicating the onset of delamination. Beyond a strain of 0.0083, the strain increased sharply, and further measurement became impossible. This indicated that the metal layer and CFRTP had completely delaminated.

On the other hand, in Figure 10(b), the AL/CFRTP curve exhibited a linear increase in stress up to a strain of 0.0032, followed by delamination at that strain, and complete delamination occurred at a strain of 0.0039. Therefore, no clear yield point was observed in this material. This was attributed to the smaller stiffness difference between the aluminum alloy and CFRTP compared to SUS. However, since yielding occurred when the stress in the AL layer reached the yield condition, yielding had already taken place in the AL layer of AL/CFRTP at a strain of 0.003, and residual stress remained after unloading.

For both materials, CFRTP remained elastic even after the complete yielding of the metal layer, so the stress continued to increase. This indicated that defining the 0.2% proof stress was difficult, unlike in the case of a bare metal.

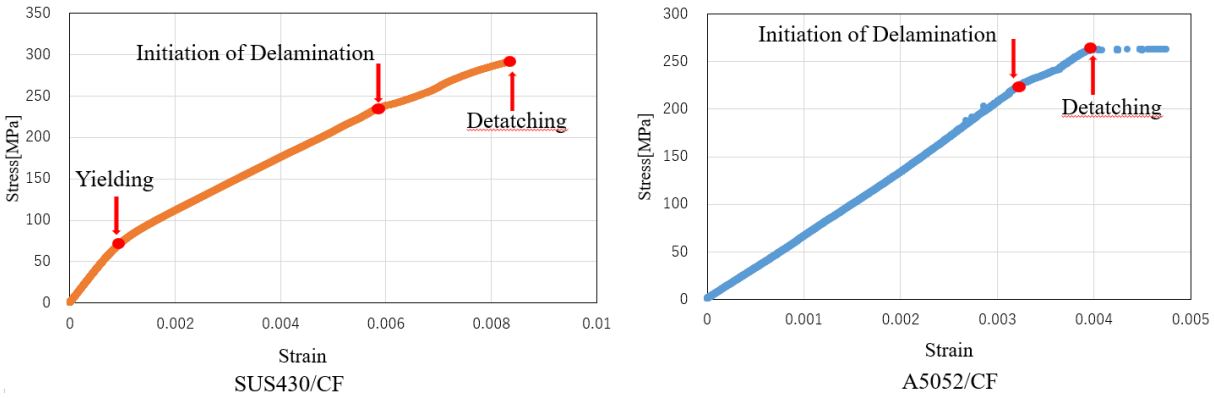

Figure 10: Stress-strain curves of SUS430/CFRTP and A5052/CFRTP

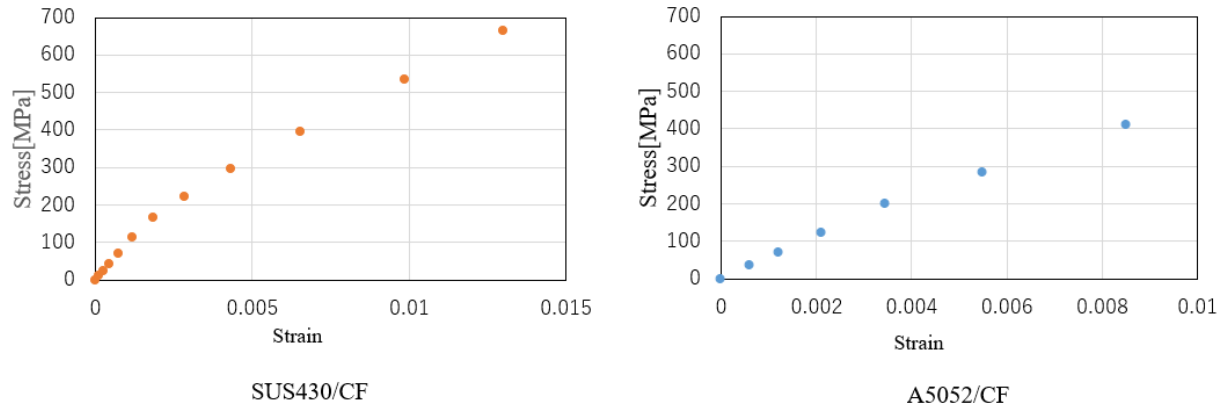

Figure 11: Stress-strain diagram of sus430/CFRTP and A5052/CFRTP(Abaqus)

The results indicate that the overall behavior of both laminates closely resembles the experimental findings. A distinct yield point was observed in the SUS/CFRTP laminate, whereas such a point was not evident in the AL/CFRTP laminate.

The calculated Young's modulus was 94 GPa for SUS/CFRTP and 58 GPa for AL/CFRTP. The former exceeded the experimentally measured value, while the latter was lower. This discrepancy is likely attributed to the presence of an adhesive layer approximately 100 μm thick in the experimental specimens, which was not included in the simulations.

Based on these results, it can be concluded that the stiffness and strength of FMLs using SUS are inferior to those of bare SUS, whereas in the case of AL, both the stiffness and yield stress are only slightly lower than those of the bare metal. However, after yielding, the load is elastically supported by the CFRTP layer, suggesting that the ultimate tensile strength of the laminate may exceed that of the metal alone. These mechanical properties are expected to vary significantly depending on the layup configuration, and thus optimization of the laminated structure is essential for application-specific performance.

6 CONCLUSIONS

This study investigated the press forming behavior and mechanical performance of metal/CFRTP laminates using V-shaped dies. Key findings are summarized as follows:

- Delamination suppression requires both uniform heating of the CFRTP core and appropriate die corner geometry. Interlaminar slippage plays a crucial role in absorbing deformation without damaging the laminate interface.

- Spring-in behavior was mitigated by matching the upper and lower die radii and ensuring consistent temperature distribution during molding.
- Tensile tests and FEM analysis revealed that CFRTP layers remain elastic after metal yielding, contributing to the post-yield load-bearing capacity. A clear yield point was observed in SUS/CFRTP but not in AL/CFRTP due to differences in stiffness contrast.
- Young's modulus discrepancies between experiment and simulation were mainly attributed to the neglected adhesive layer in FEM. Additionally, thickness variation during molding reduced structural uniformity.

Future improvements should focus on better thickness control and test configurations that load both metal and CFRTP layers more uniformly. Such refinements will enable the design of optimized laminates with enhanced formability and strength for automotive applications.

ACKNOWLEDGEMENTS

The authors would like to express their sincere gratitude to Associate Professor Akio Otani and the students of the Otani Laboratory at Kyoto Institute of Technology for their generous support in providing access to the experimental equipment used in this study. The authors also deeply appreciate the valuable guidance and insightful advice provided by Professors Tatsuro Kosaka and Kazuhiro Kusukawa throughout the course of this research.

REFERENCES

[1] Y.N. Hu, S.C. Wu, P.J. Withers, J. Zhang, H.Y.X. Bao, Y.N. Fu and G.Z. Kang, The effect of manufacturing defects on the fatigue life of selective laser melted Ti-6Al-4V structures, *Materials & Design*, **192**, 2020, 108708 (doi: 10.1016/j.matdes.2020.108708).

[2] C. Ageorges, L. Ye and M. Hou, Metal–carbon fibre-reinforced plastic hybrid material joining: A review, *Composites Part A: Applied Science and Manufacturing*, **32**(6), 2001, pp. 839–853 (doi: 10.1016/S1359-835X(00)00166-4).

[3] Y. Wang and J. Shi, Influence of laser scan speed on micro-segregation in selective laser melting of an iron-carbon alloy: A multi-scale simulation study, *Procedia Manufacturing*, **26**, 2018, pp. 941–951 (doi: 10.1016/j.promfg.2018.07.121).

[4] N. Khan, M.M.A. Khan, H.S. Shin and Y.W. Kwon, Experimental investigation of formability and failure in metal–CFRTP hybrid laminates under bending, *Composites Part B: Engineering*, **165**, 2019, pp. 739–748 (doi: 10.1016/j.compositesb.2019.02.037).

[5] J. Liu, Z. Dong, C. Liu and J. Chen, Influence of forming parameters on the quality of CFRTP-metal laminates formed by hot stamping, *Journal of Materials Processing Technology*, **291**, 2021, 117021 (doi: 10.1016/j.jmatprotec.2020.117021).

ICCM24
AUGUST 4-8, 2025
BALTIMORE CONVENTION CENTER
BALTIMORE, MARYLAND, USA

No Technical Paper Submission for:

Yansong Li

DEVELOPMENT OF A ROBOTIC-ENABLED COMPOSITE PART HIGH-RESOLUTION INSPECTION AND REVERSE-DIGITAL TWIN TOOL

G. Willis[1,2*], N.M. Harrison[1,2,3]

[1] Mechanical Engineering, University of Galway, Ireland; [2] I-Form Advanced Manufacturing Research Centre, Ireland; [3] Ryan Institute for Environmental, Marine and Energy Research, University of Galway, Ireland; *g.willis1@universityofgalway.ie

Keywords: *Computer vision; digital twin; automation; inspection; robotics; composites; CFRP; surface defects; machine learning; YOLO*

ABSTRACT

Carbon fibre reinforced polymers (CFRP) are widely used in aerospace and automotive industries due to their excellent mechanical properties. However, detecting manufacturing defects such as scratches, delamination and wrinkles remains challenging, particularly for small to medium-sized manufacturers who lack affordable automated inspection solutions. This paper presents two automated computer vision systems designed to address this gap; a 2D imaging system for large, flat structures, and a 3D imaging system for smaller components with complex geometries. Both systems utilise a robot mounted computer vision camera and a custom image stitching pipeline, implemented using open-source software to generate high-fidelity composite images or 3D models. Defect detection is implemented using a YOLOv8n convolutional neural network. Initial testing of the 2D system on a turbine blade demonstrates effective defect identification within 8 minutes, producing a 585 megapixel composite image. The proposed framework offers a low-cost, easily deployable inspection solution to enhance quality control and support industry 4.0 initiatives in composite manufacturing.

1 INTRODUCTION

Carbon fibre reinforced polymers (CFRP) possess advantages such as low density, high specific strength, and low coefficient of thermal expansion, and are widely used in aerospace, automobile, and construction materials [1,2]. However, various manufacturing defects, such as voids, delamination, wrinkles and foreign objects, are practically inevitable due to the complexity of the manufacturing process [3,4].

Computer Vision (CV) has proven itself to be a simple, fast and low-cost solution to automated detection of CFRP manufacturing surface defects [5]. The use of CV for automated detection of surface defects (among other quality controls) within the aerospace industry is well established [6], however smaller institutions such as small to medium sized manufacturers of composite components and structures often lack the budget or resources to develop their own automated solutions to often manual processes such as visual inspection, in particular for complex geometric parts. Furthermore, the proprietary inspection methods developed by the larger institutions often remain undisclosed with little detail entering the literature or industry reports, making it more difficult for smaller institutions to develop this capability.

There are many challenges faced when visual inspection is manual, including; challenges in securing labour, the training required for each new person, the variability of each individual (skill/practice level, natural ability, speed etc.), the variability within each individual human with regards to concentration and energy levels, motivation etc. which could change throughout a single day as well as on separate days. There are many changeable areas which can lead to a variable outcome or inconsistencies in reliability, which is undesirable within the manufacturing and quality control of potentially safety critical components.

Automating visual inspection offers improvements in all of these areas as well as reduces cost and allows for the workforce to be redeployed in other critical areas of production. In general, the literature supports higher success in defect detection with fewer defect-misses by computer vision systems when compared with human inspection [7–12] . However, from those same studies, there is a definite consensus that CV offers much more with regards to repeatability and speed. While the use of computer vision inspection has grown rapidly in recent years, and the techniques encompassed within this area are used widely throughout industry for many applications, the area is ever-expanding and is crucial for facilitating movement towards Industry 4.0.

Machine learning, more specifically convolutional neural networks (CNNs) with regards to CV, has also proven itself in recent years as a significant addition to defect detection, showing improvements in accuracy, speed and overall automation in general [13] with studies showing their efficacy in detecting visual surface defects with success rates of 90% and above [11,14].

However, the current offerings of computer vision systems are dominated by single 2D image capture inspection solutions with few options for capturing, measuring and evaluating the geometry and surface of manufactured parts in 3D or in high or even Gigapixel resolution.

In-order to facilitate the generation of full-scale high-resolution image sets, multiple images would need to be captured from different camera placements and subsequently stitched together using CV techniques. This would be very difficult and labour intensive to conduct manually as the accuracy of a hand-held camera placement and resulting image quality (which can be affected by the stability of the camera) is paramount. The camera may also need to be held in positions not easily reachable by a human being (particularly for large composite structures such as wind turbine blades, airplane fuselages etc.) while ensuring imaging accuracy.

Compiling a set of local images into one single digital image record requires a method of stitching the images together. Stitching the images into one large composite image/model is important for providing easily discernible and intuitive context on defect locations for human operators. This is a requirement as it will more readily facilitate determining subsequent action following defect detection, whether this might be rework, tagging, further investigation or scrapping the component.

This system is intended to be low cost and simple to implement, with the aim being that small to medium sized composite manufacturers could easily implement such a system without requiring a large budget and extensive resources.

This work will explore the potential of two fully automated imaging and defect detection systems for achieving this. Both systems automatically provide a digital record for easy further analysis or to refer back to at a later date, which is highly beneficial and often lacking in manual inspection practices:

1. 2D Imaging system – Intended for large and generally flat composite structures such as large planar composite panels and turbine blades. The output from this system will be a very high-resolution composite stitched image with surface defects highlighted in bounding boxes.
2. 3D Imaging system – Intended for smaller components with complex geometry. The output from this system will be a 3D model (reverse digital twin) of the component with a low-resolution surface texture and defects highlighted in bounding boxes.

This work introduces the term ‘reverse digital twin’ to describe a digital record created from the as-manufactured physical part, such as a 3D model generated via scanning or photogrammetry. Unlike a traditional digital twin, which typically begins with the original CAD model and supports manufacturing and operation of the physical object, the reverse digital twin is derived from the final manufactured artifact and exists digitally. This representation captures real-world characteristics such as the true manufactured geometry, deviations, surface finish and wear. This makes it valuable for quality assurance, maintenance, comparison against nominal designs and general record keeping.

The reverse digital twin serves as a digital snapshot of the physical part’s actual state, bridging the gap between nominal CAD models and reality, much like how photography and computer vision help document finished products but with the added dimensional and geometric context of a 3D model.

2 METHODOLOGY

This section will provide an overview of both systems architecture and how images are captured and processed within the automated pipeline. Both systems share the same general structure with regard to hardware:

- A Kuka iiwa R820 collaborative robot and Sunrise controller were utilised to hold and move a vision camera to pre-programmed positions.
- The camera mounted to the robot arm was a Basler Ace 2 (20MP) with a 35mm lens. This was connected to a PC running OpenCV.
- The PC and the Sunrise controller communicate over TCP/IP, when the robot reaches a new position it will pause for 0.5 seconds and then send a 'Take Image' command to the PC where OpenCV receives it and captures and stores the image.
- Once the robot has completed all positions it sends a 'Stitch' command to OpenCV and then terminates the connection, OpenCV will then move onto the next step in the pipeline, which differs for the two systems.

Defect Detection:

The defect detection method is the same for both systems, through OpenCV v4.11.0 [15,16] a YOLOv8n [17] model was trained and used. This model is still under development and so far, has only been trained on one type of surface defect (scratch) which is currently present on a turbine blade which is being used to develop the 2D system. In the current model a training set of 96 images has been used, consisting of 23 original images and 73 augmented images. All training images were resized to a resolution of 1280 x 1280 pixels.

Lighting:

Lighting is a key component of all computer vision systems, it is important that there is enough light for a correct exposure level while also ensuring a suitable shutter speed [18]. This is particularly important for the YOLO model, as suboptimal lighting conditions can reduce successful object/defect recognition in some CNNs by more than 20% [18]. To solve this problem, a lighting frame was constructed out of extruded aluminium profile with one main centre panel measuring 1m across and two side panels measuring 0.5m across which fold against the main panel for storage. LED strip lighting is then held across the full span of the frame by way of hook and loop tape and the cross members in the centre panel can be moved up and down to adjust the height of each light strip. This frame allows for light to be spread across the full surface of any component from all angles, the frame is shown as part of the 2D imaging system later in Figure 3.

2D System:

The overall architecture of the 2D system can be seen below, in Figure 1.

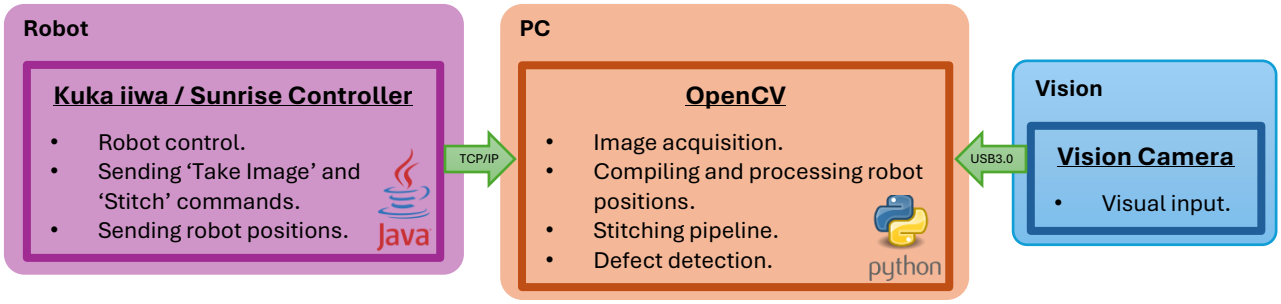

Figure 1: 2D System Architecture

For the 2D system, a custom stitching algorithm was required for the reasons below:

- It needs to ensure true representation of the surface geometry in a way that does not risk feature distortion. Therefore, the only transformation applied to each image will be translation, there will be no rotation of the camera between images to remove the need for any image warping steps in the stitching process.
- It needs to align the images accurately and reliably without the feature detection and matching steps of traditional image stitching techniques being impacted by the repeating patterns, or sometimes featureless surfaces, of CFRP.
- There are no readily available stitching models or software to account for the requirements above.

To ensure true representation of the surface geometry with no warping, the robot arm was programmed to capture all images in a 2D grid pattern with a perfectly level camera normal to the imaging plane for all images, therefore allowing translational movement only with no rotational movement between images. As shown in Figure 2, camera rotation can result in surface geometry being skewed or distorted if the camera is not positioned normal to the surface, requiring a warping step during stitching to correct this in an attempt to fit them together correctly with the other images, which is undesirable for this application.

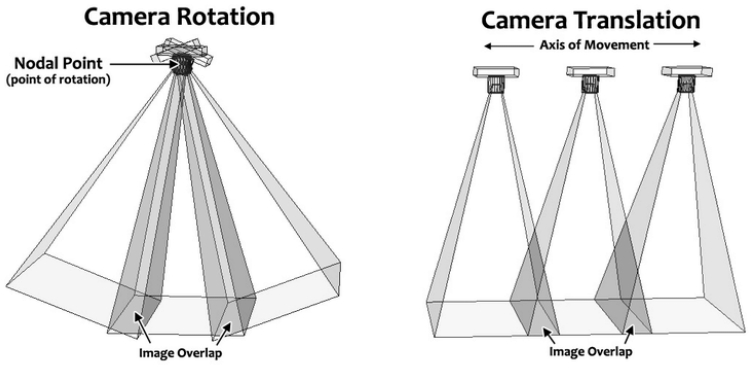

Figure 2: Camera Rotation vs Camera Translation [19]

In order to not allow the feature detection and matching steps to be impacted by the repeating patterns or sometimes featureless surfaces of CFRP (depending on the material), the stitching algorithm utilises the known robot cartesian coordinates from each camera position to align the images relative to one another.

The full homography relationship connecting 2D coordinates of features in the captured image, or on the camera sensor, to the 3D world coordinates of the same features through camera position and intrinsic properties is given in Equation 1. Removing the rotational matrix from the equation greatly simplifies the relationship between the position of features in the image and the real-world. From here, the camera intrinsic properties (f_x, f_y, c_x and c_y together represent internal camera characteristics such as focal length and optical centre) can be provided by way of prior camera calibration and the real-world coordinates can then also be supplied by knowing the robot positions for each image.

$$s\begin{bmatrix} u \\ v \\ 1 \end{bmatrix} = \begin{bmatrix} f_x & 0 & c_x \\ 0 & f_y & c_y \\ 0 & 0 & 1 \end{bmatrix} \begin{bmatrix} r_{11} & r_{12} & r_{13} \\ r_{21} & r_{22} & r_{23} \\ r_{31} & r_{32} & r_{33} \end{bmatrix} \begin{bmatrix} t_1 \\ t_2 \\ t_3 \end{bmatrix} \begin{bmatrix} X \\ Y \\ Z \end{bmatrix} \quad (1)$$

From this, Equations 2 and 3 can be used to determine t_x and t_y, the translational movement of each image (in pixels) within the image coordinate system ($t_z = 0$ as the camera only moves in an xy grid). f_x and f_y represent the focal length in pixels by combining lens focal length and sensor pixel dimensions, these are obtained from the intrinsic matrix through camera calibration. dX and dY are the camera translational movement (in mm) and S is the scene depth (distance from the camera to the scene/surface, in mm).

$$t_x = \frac{f_x dX}{S} \tag{2}$$

$$t_y = \frac{f_y dY}{S} \tag{3}$$

Following image placement, seam finding and blending are performed using functions provided by the OpenCV library v4.11.0. There is a 30% overlap across all images taken in the grid pattern, this is to allow for seam finding and blending to successfully account for potential minor pixel misalignments between neighbouring images.

SAHI (Slicing Aided Hyper Inference) [20] was also utilised with YOLO for the 2D system to breakdown the very high-resolution stitched image into tiles for individual inspection. This is required to perform the defect detection step on the composite image as a whole. This method was chosen over performing the inspection on each individual image prior to stitching them all together as the output from the latter method results in slight breaks and misalignments in the bounding boxes and inconsistencies in confidence values shown in the final composite when a defect is split across multiple images.

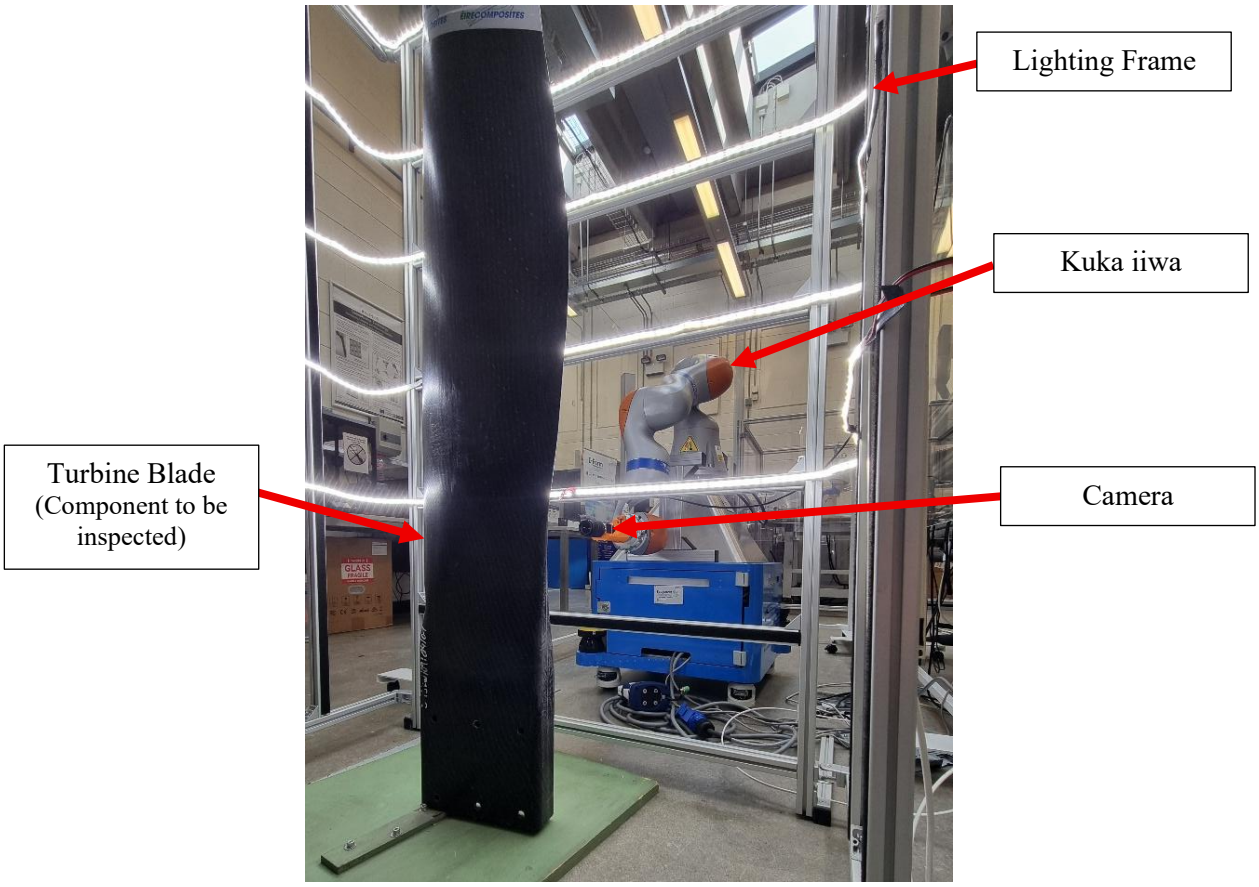

Figure 3: 2D Imaging System Inspecting a Turbine Blade

3D System:

The overall architecture of the 3D system can be seen below, Figure 4.

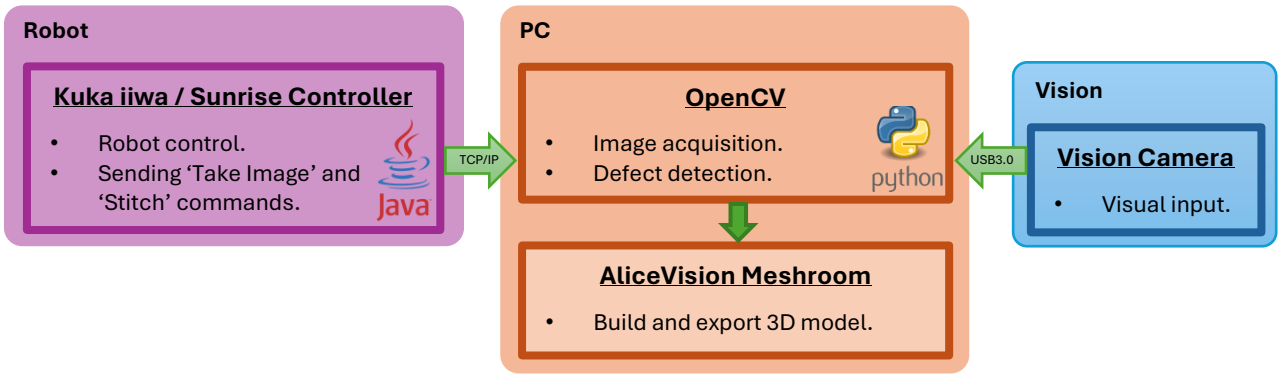

Figure 4: 3D System Architecture

As can be seen above, the 3D system is very similar to the 2D system however the image acquisition is from different angles around the component rather than in a 2D grid and the stitching takes place in open-source photogrammetry software AliceVision Meshroom [21], where a 3D model is generated as the output (reverse digital twin). The camera intrinsic properties (f_x, f_y, c_x and c_y representing focal length and optical centre) are also given to Meshroom to simplify the homography calculations and to allow the software to accurately account for scaling. Meshroom also creates a surface texture from the image set which is wrapped around the 3D model generated to provide a realistic representation of the component exterior. Command line interface (CLI) is also utilised to integrate Meshroom into the automated pipeline by allowing communication between the Python script running OpenCV and Meshroom.

3 TESTING AND RESULTS

2D System:

This inspection system completed a full automated inspection of a 1.32m length of the composite turbine blade in 8 minutes and 15 seconds while highlighting 3 surface scratches, the system output image can be seen in Figure 5.

The PC used to run OpenCV for image stitching and defect detection in this system was a Dell Precision 7680 laptop, equipped with a Core i7-13850 CPU, 32 GB of RAM and an Nvidia RTX 2000 Ada GPU with 8 GB of VRAM.

The output image is 585Megapixels and generated from 62 raw images in total.

System Element	Time
Capturing images	5 mins 10 secs
Stitching images	50 secs
Defect detection	2 mins 15 secs
Total	**8 mins 15 secs**

Table 1: Time Breakdown of 2D System Operation

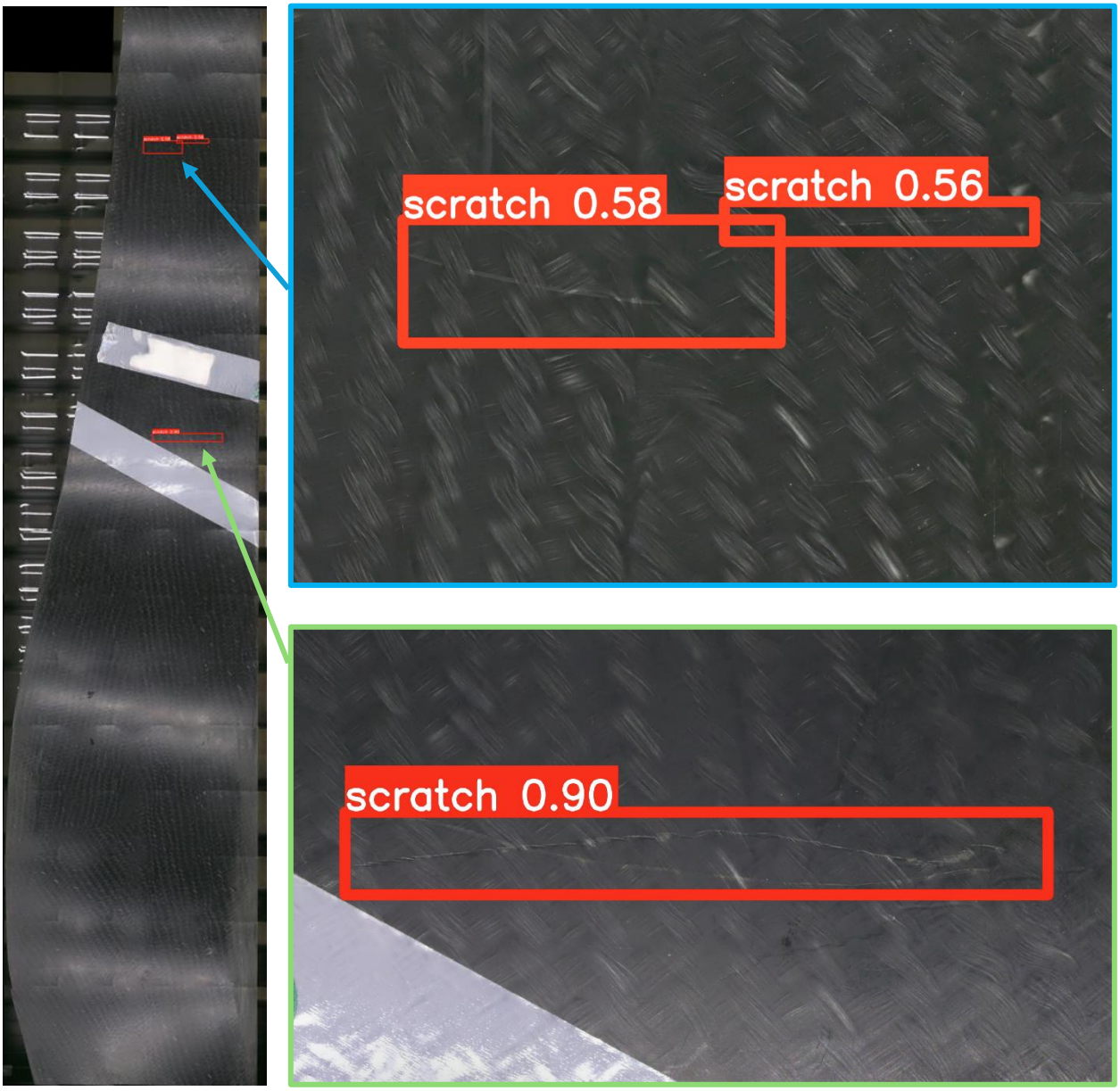

Figure 5: 2D System Output

With the seam finding and blending operations switched off inside the stitching algorithm, the total time of the system is reduced by 30 seconds, making the total 7 minutes and 45 seconds. This would reduce the stitching quality but would still fulfil the function of permitting defect identification and location context. There is also some potential for optimisation of the robot movement and image capture phase.

This could also be brought down by a further 1 minute and 45 seconds if SAHI was not used for the defect detection step and each individual image was processed by the YOLO model and marked where required before stitching. This would also create a slightly less desirable output but would still fulfil the function of detecting and highlighting defects on the single compiled output image. If this modification was implemented, the total time is 6 minutes for a fully automated inspection.

4 DISCUSSION

The results so far demonstrate that the proposed 2D system can complete a fully autonomous inspection of large composite structures in a reasonably small timeframe and effectively identify surface defects with high accuracy.

Furthermore, this framework is simple and relatively budget friendly to implement, creating a good starting point for small to medium sized composite manufacturers to work with in beginning their inspection automation journey. There is also opportunity to reduce cost even further by implementing this system with a simple cartesian robot, which would also easily allow for a larger inspection reach compared to the Kuka iiwa used here. This would however limit operation strictly to the 2D system but at the same time would create an in-expensive and effective approach to automated visual inspection of composite panels and other large structures.

The LED strip lighting could be further optimised by including a diffuser for each strip. It can clearly be seen in Figure 5 that there are strong reflections on the turbine blade surface, this is not ideal for defect detection, as it provides extra variability in visual input which the YOLO model needs to overcome and could lead to more false negatives. An even exposure is needed over the full surface of the blade to reduce differences in pixel luminosity between the brighter and darker areas.

To simplify the setup and reduce costs even more, the lighting frame could be replaced by a simple large, powerful and diffused ring light mounted with the camera on the robot. The lighting frame was constructed as part of this work due to the requirement in early development of a stationary and wide-spread light source to reduce the negative impact a moving light source has on feature detection and matching which were already disadvantaged due to the repeating patterns. However, these steps were subsequently not needed once known camera positions were implemented.

However, a possible improvement to the 2D system could be to re-introduce feature detection and matching and use them to refine image alignment once the initial placement has been attained from the robot positional coordinates, this is common practice in systems where rough camera positions are known [22,23]. The reason for this is because there are stitching artifacts in the composite image, in earlier development of the system a smaller section of a flat surface was used instead of the turbine blade which led to very close alignment across all images without any refinement needed, but imaging across larger areas reduces the accuracy of each position relative to the others for the Kuka iiwa.

A possible extension of this tool includes modifying the 2D system to include a thermal camera and heat source, this would provide a very simple and effective automated thermography system for large composite structures. Such a system is currently lacking within the literature as well as in commercial offerings. The stitching algorithm developed within this work would be ideally suited to thermography as well due to the lack of features common in thermal imaging.

The model and scene scaling within the 3D system is handled by providing the calculated intrinsic camera properties. Testing is still yet to confirm the accuracy of this method. A potentially more accurate method would be to have one or more reference objects in the scene, such as a calibrated cube, which the system can use as a reference to scale the scene correctly.

5 CONCLUSIONS

This work has demonstrated the feasibility of an automated computer vision inspection system for composite components. The 2D imaging system successfully created a very high-resolution image of a large composite structure, identifying surface defects such as scratches with promising accuracy and efficiency. The integration of robot assisted image acquisition, simple but effective custom stitching algorithms, known camera positions and YOLO-based defect detection creates a practical, cost-effective solution ideally suited to small to medium sized manufacturers.

This framework represents a key step towards industry 4.0 in the wider realm of composite manufacturing by providing scalable and adaptable automated inspection tools that can be implemented easily without the need for large budgets and resources. By making automation more accessible, smaller manufacturers can improve product quality, reduce costs and increase competitiveness.

6 FUTURE WORK

While initial results are encouraging, further work is needed to see both systems working fully. The defect detection model requires more training to include a wider range of defect types and diversity to improve robustness, the 3D imaging system's accuracy and integration need validation and the light source needs to be diffused.

ACKNOWLEDGEMENTS

This research is conducted under the (FreeForm Optix DTIF Project, grant ID: DT 2022 0389B) (2023-2026) which is funded under the Disruptive Technologies Innovation Fund (DTIF), which was established under Project Ireland 2040, run by the Department of Enterprise, Trade and Employment with administrative support from Enterprise Ireland. The opinions expressed by the authors are their own.

REFERENCES

[1] J. Kupski, S. Teixeira de Freitas, Design of adhesively bonded lap joints with laminated CFRP adherends: Review, challenges and new opportunities for aerospace structures, Compos. Struct. 268 (2021) 113923. https://doi.org/10.1016/j.compstruct.2021.113923.

[2] Z. Sun, Y. Luo, C. Chen, Z. Dong, G. Jiang, F. Chen, P. Ma, Mechanical enhancement of carbon fiber-reinforced polymers: From interfacial regulating strategies to advanced processing technologies, Prog. Mater. Sci. 142 (2024) 101221. https://doi.org/10.1016/j.pmatsci.2023.101221.

[3] Y. -X. Qin, X. -M. Xiong, Y. Chen, Y. Wang, Optimization Research on Defect Localization in Ultrasonic Images of Anisotropic and Multilayer CFRP Structures, IEEE Trans. Instrum. Meas. 73 (2024) 1–14. https://doi.org/10.1109/TIM.2024.3373102.

[4] J. Tian, M. Liu, H. Xiao, Z. Zhang, W. Yang, Z. Long, C. Ming Leung, Optimized ultrasonic total focusing imaging of diverse and multiple defects in crossply CFRP: Floquet wave theory, numerical simulation, and experimental validation, Mech. Syst. Signal Process. 199 (2023) 110486. https://doi.org/10.1016/j.ymssp.2023.110486.

[5] Y. Gong, X. Li, R. Zhou, M. Li, S. Liu, A robotized framework for real-time detection and in-situ repair of manufacturing defects in CFRP patch placement, Robot. Comput.-Integr. Manuf. 92 (2025) 102882. https://doi.org/10.1016/j.rcim.2024.102882.

[6] A Review of Machine Vision Applications in Aerospace Manufacturing Quality Inspection, in: ResearchGate, n.d. https://doi.org/10.1109/ICCCR61138.2024.10585378.

[7] M. Mikhail, K. Abed, Robotic inspection and automated analysis system for advanced manufacturing, IAES Int. J. Robot. Autom. IJRA 12 (2023) 352. https://doi.org/10.11591/ijra.v12i4.pp352-364.

[8] N. Hütten, M. Alves Gomes, F. Hölken, K. Andricevic, R. Meyes, T. Meisen, Deep Learning for Automated Visual Inspection in Manufacturing and Maintenance: A Survey of Open- Access Papers, Appl. Syst. Innov. 7 (2024). https://doi.org/10.3390/asi7010011.

[9] M. El-Agamy, M. Awad, H. Sonbol, AUTOMATED INSPECTION OF SURFACE DEFECTS USING MACHINE VISION, Int. Conf. Appl. Mech. Mech. Eng. 17 (2016) 1–13. https://doi.org/10.21608/amme.2016.35357.

[10] J. Aust, D. Pons, Comparative Analysis of Human Operators and Advanced Technologies in the Visual Inspection of Aero Engine Blades, Appl. Sci. 12 (2022). https://doi.org/10.3390/app12042250.

[11] Sciotex, Machine Vision Versus Manual Quality Inspection, Sciotex (2024). https://sciotex.com/comparing-machine-vision-vs-manual-quality-inspection/ (accessed July 1, 2025).

[12] Instrumental, Manual Inspection vs. AI Inspection with Instrumental, Instrumental (2023). https://instrumental.com/build-better-handbook/machine-vision-vs-manual-inspection-vs-instrumental (accessed July 1, 2025).

[13] J. Bai, D. Wu, T. Shelley, P. Schubel, D. Twine, J. Russell, X. Zeng, J. Zhang, A Comprehensive Survey on Machine Learning Driven Material Defect Detection, ACM Comput. Surv. (2025) 3730576. https://doi.org/10.1145/3730576.

[14] A. Silenzi, V. Castorani, S. Tomassini, N. Falcionelli, P. Contardo, A. Bonci, A.F. Dragoni, P. Sernani, Quality Control of Carbon Look Components via Surface Defect Classification with Deep Neural Networks, Sensors 23 (2023). https://doi.org/10.3390/s23177607.

[15] G. Bradski, The OpenCV Library, in: Dr Dobb's J. Softw. Tools, 2000: pp. 120–125. https://www.drdobbs.com/open-source/the-opencv-library/184404319.

[16] opencv, GitHub - opencv/opencv at 4.11.0, GitHub (n.d.). https://github.com/opencv/opencv (accessed July 3, 2025).

[17] G. Jocher, A. Chaurasia, J. Qiu, Ultralytics YOLOv8, (2023). https://github.com/ultralytics/ultralytics.

[18] Y. Wu, J. Tsotsos, Active Control of Camera Parameters for Object Detection Algorithms, (2017). https://doi.org/10.48550/arXiv.1705.05685.

[19] J. Longson, G. Cooper, R. Gibson, M. Gibson, J. Rawlins, Adapting Traditional Macro and Micro Photography for Scientific Gigapixel Imaging, (n.d.).

[20] F.C. Akyon, S.O. Altinuc, A. Temizel, Slicing Aided Hyper Inference and Fine-tuning for Small Object Detection, 2022 IEEE Int. Conf. Image Process. ICIP (2022) 966–970. https://doi.org/10.1109/ICIP46576.2022.9897990.

[21] C. Griwodz, S. Gasparini, L. Calvet, P. Gurdjos, F. Castan, B. Maujean, G. De Lillo, Y. Lanthony, AliceVision Meshroom: An open-source 3D reconstruction pipeline, in: Proc. 12th ACM Multimed. Syst. Conf., Association for Computing Machinery, New York, NY, USA, 2021: pp. 241–247. https://doi.org/10.1145/3458305.3478443.

[22] R. Hartley, A. Zisserman, Multiple View Geometry in Computer Vision, Cambridge University Press, 2003.

[23] D.G. Lowe, Distinctive Image Features from Scale-Invariant Keypoints, Int. J. Comput. Vis. 60 (2004) 91–110. https://doi.org/10.1023/B:VISI.0000029664.99615.94.

DEVELOPMENT OF A 700 BAR THERMOPLASTIC TYPE IV PRESSURE TANK FOR COMPRESSED HYDROGEN STORAGE IN THE FIELD OF MOBILITY

Abreu, Pedro[1]; Rocha, Helena[1], Martins, Carla[2]; Antunes, Paulo[1]

[1] PIEP – Centre for Innovation in Polymer Engineering, Guimarães, Portugal.

[2] Instituto de Polímeros e Compósitos (IPC) – Universidade do Minho, Guimarães, Portugal.

Interreg España - Portugal
Cofinado por la Unión Europea
Confinanciado pela União Europeia

HI_MOV Corredor Tecnológico Transfronterizo de Movilidad con Hidrógeno Renovable

1. INTRODUCTION

Hydrogen storage in the mobility sector predominantly relies on high-pressure tanks, particularly Type IV Composite Overwrapped Pressure Vessels (COPVs), which combine carbon-fibre composites with thermoplastic liners. While effective, conventional thermoset resin matrices present challenges regarding its poor recyclability. Replacing them with thermoplastic matrices enhances sustainability, facilitates reparability, which ultimately may lead to reduced lifecycle costs.

2. AIM

To develop a **fully thermoplastic Type IV pressure vessel rated for 700 bar,** using an innovative manufacturing technology. The vessel will integrate **embedded fiber Bragg grating (FBG) optical sensors** for **real-time structural health monitoring** during testing and fuelling and defueling.

3. METHODOLOGY

The development of the thermoplastic COPV followed the **ISO 19881:2018 standard** which specifies requirements for onboard gaseous hydrogen storage in vehicles. This includes safety and service conditions, material selection, design, manufacturing, testing, and periodic inspections using non-destructive methods.

MATERIAL SELECTION & CHARACTERIZATION	WINDING PATTERN DEVELOPMENT	STRUCTURAL ANALYSIS (FEA)	MANUFACTURING & PROCESS OPTIMIZATION (AFP)	PROTOTYPE FABRICATION & TESTING
▪ Selection of suitable thermoplastic materials ▪ Perform mechanical characterization	▪ Design fiber winding architectures ▪ Simulate and refine patterns for strength and manufacturability	▪ Conduct Finite Element Analysis ▪ Target burst pressure: 1575 bar	▪ Implement Automated Fiber Placement (AFP) ▪ Use IR laser source for thermoplastic tape heat and consolidation ▪ Apply Design of Experiments (DOE) to optimize process parameters	▪ Manufacture prototype using optimized process ▪ Embedment of FBG sensors ▪ Conduct validation tests (burst & cyclic testing) ▪ Monitor structural integrity using embedded FBG sensors

4. PROJECT CONSTRAINTS AND CHALLENGES

Thermoplastic Liner	Metallic Boss	Composite Overwrap
- Thermoplastic material with **low hydrogen permeation coefficient** (e.g. HDPE or PA); - Thermoplastic material compatible with **Rotomoulding process** for Liner Manufacturing; - Liner material must have a good mechanical properties and high **thermal and dimensional stability within -40°C to +85°C.**	- Material must be **compatible with gaseous hydrogen** (e.g. S31603, Al6061); - Must have a **strong adhesion** with the thermoplastic liner material; - Good **mechanical integration** into the thermoplastic liner.	- Thermoplastic Carbon-Reinforced UD tapes **compatible with AFP** in-house system; - Thermoplastic matrix with $T_g \geq 105°C$ (accord. to ISO 19881:2018); - Thermoplastic matrix **compatible with the liner base material**; - Design winding patterns that **comply with the maximum burst pressure** (2,25 x 70MPa = 157.5 MPa – accord. ISO 19881:2018).

5. TANK SPECIFICATIONS

Table 1. Design specifications for the COPV.

Fully-thermoplastic Type IV COPV - Design Specifications		
Target Working Pressure	70	MPa
Tank Geometry	Cylindrical with semi-elliptical domes	
Tank Diameter	296	mm
Boss Diameter	65	mm
Length-to-diameter (L/D) ratio	3	
Internal volume capacity	≈ 54	L
Design Safety Factor	2.25	
Maximum Burst Pressure (P_b)	157.5	MPa
Liner material	PA11	
Boss material	Al6061-T6	
Composite tape material	UD Carbon-Fiber thermoplastic PPA tape	

PROJECT FLOWCHART

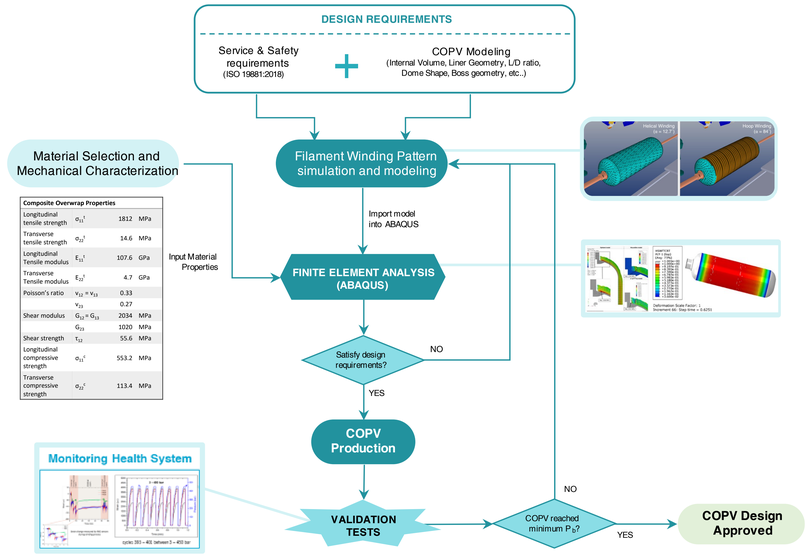

COMPOSITE OVERWRAP PRESSURE VESSEL PRODUCTION

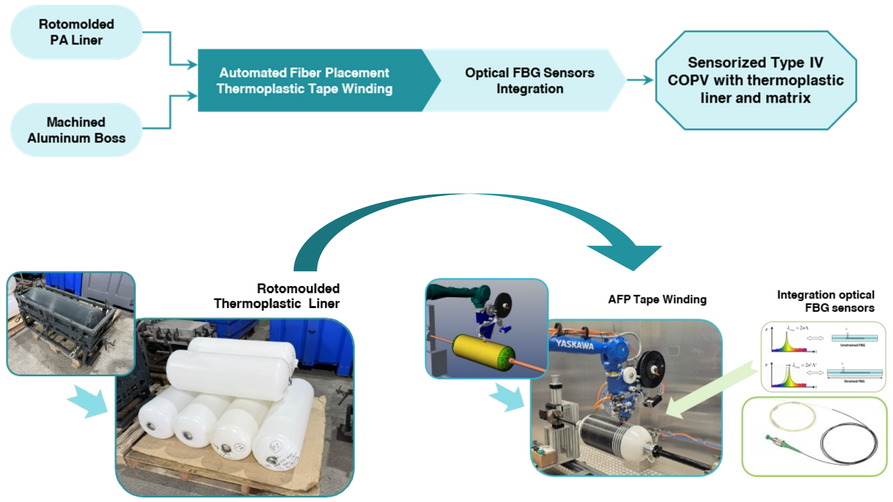

AUTOMATED FIBER PLACEMENT (AFP) FOR TAPE WINDING

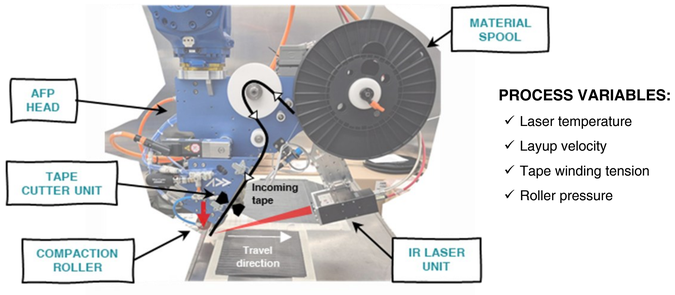

Automated Fiber Placement Process

PROCESS VARIABLES:

- ✓ Laser temperature
- ✓ Layup velocity
- ✓ Tape winding tension
- ✓ Roller pressure

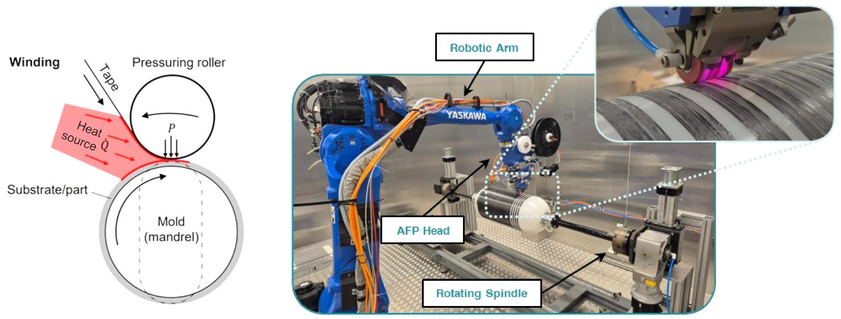

Configuration of Tape Winding System for Composite Layup in Type IV Tanks

FULLY-THERMOPLACTIC TYPE IV COPV

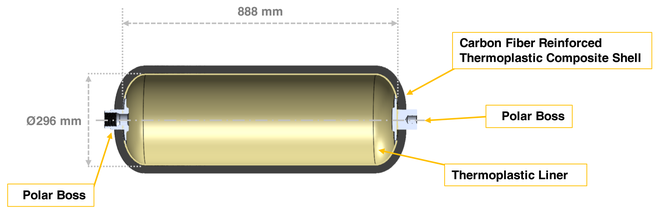

Overview of COPV Configuration and Geometric Details

PROJECT SATUS & FUTURE WORKS

This work is currently under development under the HI_MOV project umbrella. The safety and service requirements, as well as the COPV modeling, material selection, and characterization, are complete. Structural numerical simulations will be conducted to the full optimization of the composite shell for the target burst pressure (P_b). Once this phase is complete, the COPV with integrated sensorization will be manufactured, followed by experimental validation, through burst testing, to confirm its ability to withstand the projected pressures.

ACKNOWLEDGEMENTS

This project is co-funded by the European Union through the Interreg VI-A Spain–Portugal (POCTEP) 2021–2027 programme, under project number 0160_HIMOV_1_E.

[1] *Rocha H, Antunes P, Lafont U, Nunes JP. Processing and structural health monitoring of a composite overwrapped pressure vessel for hydrogen storage. Structural Health Monitoring. 2023;23(4):2391-2406. DOI:10.1177/14759217231204242.*

[2] *W., Thomas; B., Christian; H., Christian; Thermal skin effect in laser-assisted tape placement of thermoplastic composites. Dissertation / PhD Thesis, RWTH Aachen University, 2019; DOI: 10.18154/RWTH-2019-06638*

ICCM24 24TH INTERNATIONAL CONFERENCE ON COMPOSITE MATERIALS AUG 4-8, 2025 • BALTIMORE CONVENTION CENTER • BALTIMORE, MARYLAND

The 24th International Conference on Composite Materials

ICCM24 · 24TH INTERNATIONAL CONFERENCE ON COMPOSITE MATERIALS · AUG 4-8, 2025 · BALTIMORE CONVENTION CENTER · BALTIMORE, MARYLAND, USA

Design and Analysis of Fiber-reinforced Composite Hydrogen Storage Vessels for Transportation Vehicles Type IV and V

Hyunjong Choi, Eonsu Yun, Gyeongtae Kim, Jungtae Kim, Junhyeok Lee, JoonSeok Lee, and Hyunchul Ahn*

Department of Fiber System Engineering, College of Engineering, Yeungnam University

***hyunchul.ahn@yu.ac.kr**

Introduction

- Hydrogen storage vessels are categorized into types I through V.
- Among these, Type IV composite-structured vessels achieve high-efficiency lightweight characteristics by utilizing polymer liners instead of traditional metal liners. Moreover, Type V hydrogen vessels integrate polymer liners into composite structures to achieve maximum efficiency.
- In the case of hydrogen storage vessels for vehicles, the structure is constrained, necessitating structural optimization to maximize spatial efficiency. Type 4 storage vessels are primarily composed of a polymer liner for hydrogen storage and a composite structure that withstands load and pressure. Therefore, the characteristics of the liner and the design of the pressure vessel structure are critical.
- This study thus focuses on the design and simulation of a multi-cylinder, curved hydrogen storage vessel to transportation applications. Additionally, the Polyamide 12(PA12), intended as the liner material, was reinforced by the addition of graphene nanoplatelets (GNPs) to examine and enhance its properties. Finally, the properties of the hydrogen storage vessel were verified through pressure test.

Experimental

1. Materials

- Polyamide 12(PA12, Grilamid L 25A NZ, Griltech, Switzerland)
- Graphene nanoplatelets (GNPs, Sigma Aldrich (USA)
- T-700 12K UD prepreg(Toray, Japan)

2. Manufacturing

- Resin
  - 3 Kg master batch
  - Dried over 30 mins with vacuum dry oven
  - Hot press – 15 bar, 180 ℃
- Composites
  - Single braided winding

Samples	GNPs wt.%
Pristine	0.0
G0.3	0.3
G0.6	0.6
G0.9	0.9

PA12 Resin component with GNPs

3. Characterization

- Thermal conductivity
- DSC
- X-ray CT
- Drop weight

4. Numerical analysis

- ABAQUS/Implict
- Shell structure with inner pressure

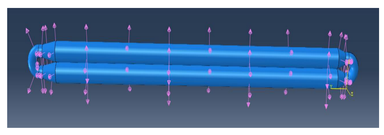

Results & Discussion

PA12 resin

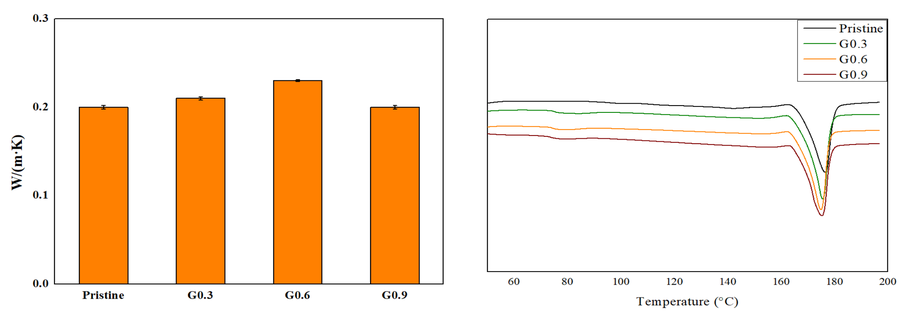

Thermal conductivity(left) and DSC curves(right) of PA12 resin according to GNPs content

- A thermal conductivity analysis was conducted to examine the thermal properties of liners with indicating an increase according to GNPs content. However, a decrease was observed at G0.9. The trend suggests that better dispersion of GNPs, which act as thermal conductors, and it can be optimized.
- Differential Scanning Calorimetry (DSC) analysis was conducted to measure changes in melting point and enthalpy. The melting points for Pristine, G0.3, G0.6, and G0.9 were 176.54°C, 175.57°C, 174.85°C, and 175.17°C respectively, with no significant changes. However, the enthalpy increased by 3.1% at G0.3 and 8.5% at G0.6, while it decreased by 6.8% at G0.9 compared to G0.6.

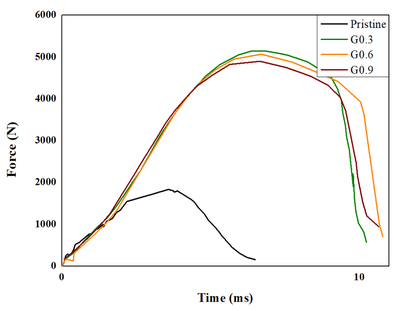

Representativ Drop weight impact result of PA12 resin according to GNPs content

- The peak forces measured for Pristine, G0.3, G0.6, and G0.9 were 2030, 4961, 5007, and 4633 N, respectively. The peak energies were 12.15, 53.18, 54.08, and 49.25J, and the total energies were 41.76, 119.08, 121.24, and 117.38 J, respectively.
- This increase is attributed to the uniform distribution of GNPs within the PA12 panel, which enhances impact absorption. However, a decreasing trend was observed at G0.9, likely due to the agglomeration of GNPs, which results in uneven dispersion and reduced impact absorption.

CFRP pressure vessel

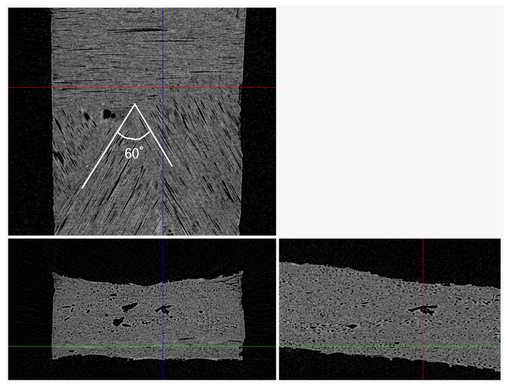

Representative X-ray CT image of CFRP composite vessel

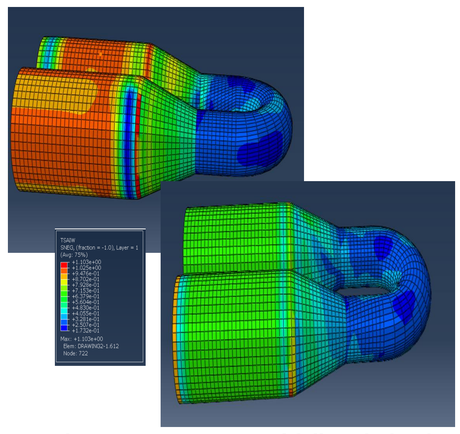

Hydrogen storage vessel failure behavior. Uniform thickness model (top) and Uniform material model (bottom)

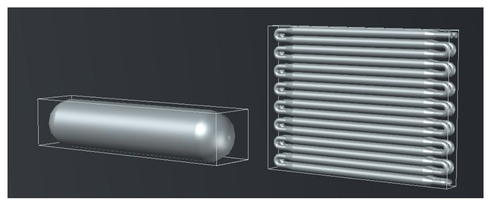

Efficiency of hydrogen storage. Typical single cylinder model (left) and multi-cylinder model (right)

- CFRP composite samples were fabricated for hydrogen storage vessels and analyzed through numerical simulations. Initially, the manufacturing process was verified using micro-CT to examine the internal structure. Although voids were present, the samples were manufactured stably without issues regarding fiber orientations, and no significant problems were found at the resin interfaces.
- Numerical analysis was conducted to optimize the curved structure. The analysis simulated a multi-cylinder curved structure to assess potential failure at bends or cross-sectional changes upon fabrication. The results shows that a uniform material model naturally thickens in areas of decreasing diameter, confirming the structural integrity of the design.
- Finally, the multi-cylinder curved structure was shown to be more efficient compared to the single-cylinder structure. The storage efficiency of the multi-cylinder model was found to be 7.4% higher than that of a typical single-cylinder model In actual vehicle storage compartments, which typically have a rectangular structure, and the efficient interconnection of the multi-cylinder model resulted in an efficiency improvement of over 15%.

Conclusion and further works

- In this study, we explored polymer resins suitable for use as liner materials for the production of high-efficiency, lightweight hydrogen storage vessels for vehicles.
- A multi-cylinder, curved Type IV hydrogen storage vessel utilizing these resins. The PA12 resin, enhanced with graphene nanoplatelets (GNPs), exhibited excellent mechanical properties and hydrogen barrier performance, facilitating efficient hydrogen storage vessel design.
- Moreover, the proposed curved hydrogen storage vessel achieves over 7% greater area efficiency and more than 15% greater space efficiency compared to conventional single-cylinder structures. The feasibility of this design was examined through numerical analysis and experimental.

- This research was supported by the Ministry of Trade, Industry and Energy (Project Number 20011899), and further studies on the hydrogen barrier properties of the resin, as well as pressure and charging tests of the actual multi-cylinder hydrogen storage vessel, are currently underway.

International Conference on Composite Material (ICCM) 2025
04/08/2025～08/08/2025
Baltimore, USA

Effect of Incorporating Additional Thermoplastic into Carbon Fiber/Epoxy Composites Prepared by Electrodeposition Resin Molding Method

Md Tansirul Islam [1], Shinya Honda [2], Kazuaki Katagiri [3], Katsuhiko Sasaki [2] and Ryo Takeda [2]

1) Graduate School of Engineering, Hokkaido University 2) Faculty of Engineering, Hokkaido University
3) Graduate School of advanced Engineering Application, Hiroshima University

* e-mail: tansir1303129@gmail.com

Background and Objective

- Thermoplastic polymer composite has exceptional combination of mechanical performance, design flexibility, and recyclability.
- Carbon fiber reinforced thermoplastic (CFRTP) has widespread application in aircraft



Fig. 1. Application of CFRTP in aircraft [1]

Subject

Electrodeposition resin molding method (EDRM) only works on thermoset (epoxy) polymer.

Preparing Nylon 6 based carbon fiber reinforced epoxy composite

Objective

To check the compatibility of nylon 6 and epoxy into carbon fiber/nylon 6/epoxy and check its effect on the composite properties

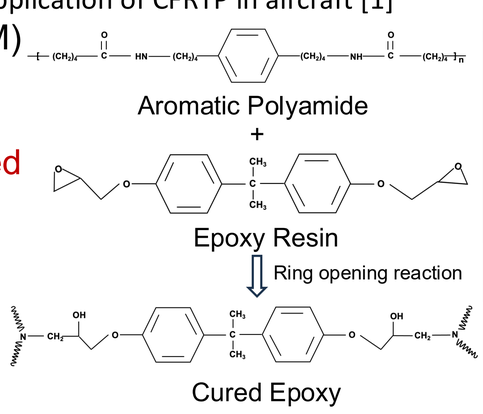

Fig. 2. Reaction between nylon 6 and epoxy [2]

What is EDRM?

- EDRM – Electrodeposition Resin Molding Method
- Coating techology for automobile bodies had been adopted

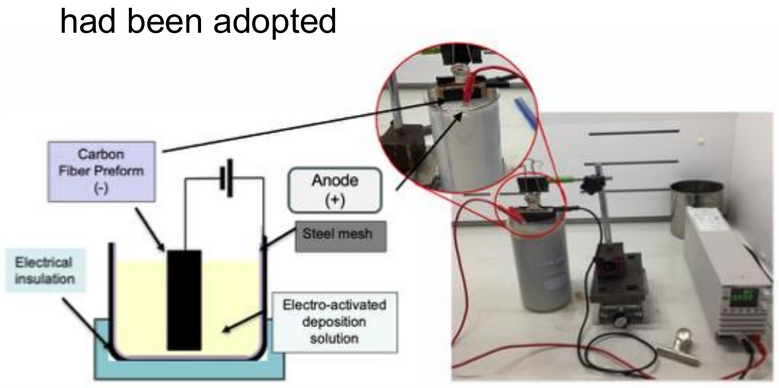

Fig. 3. Graphical representation and actual setup of EDRM

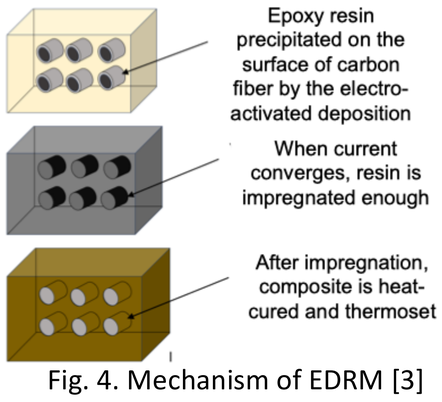

Fig. 4. Mechanism of EDRM [3]

Advantages of EDRM

- ✓ Less void
- ✓ Easy handling
- ✓ Uniform mixture of fiber and matrix
- ✓ Autoclave not required
- ✓ No need of vacuum bag or moulding

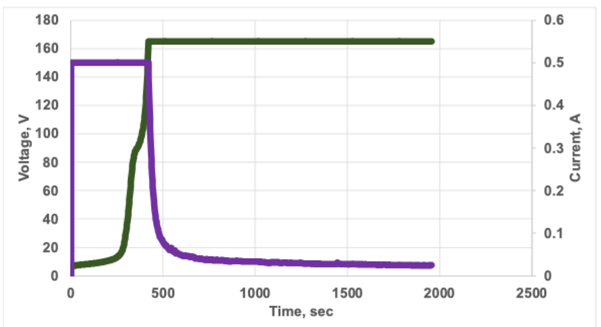

Fig. 5. Relationship of voltage/current with time

Experimental Procedure

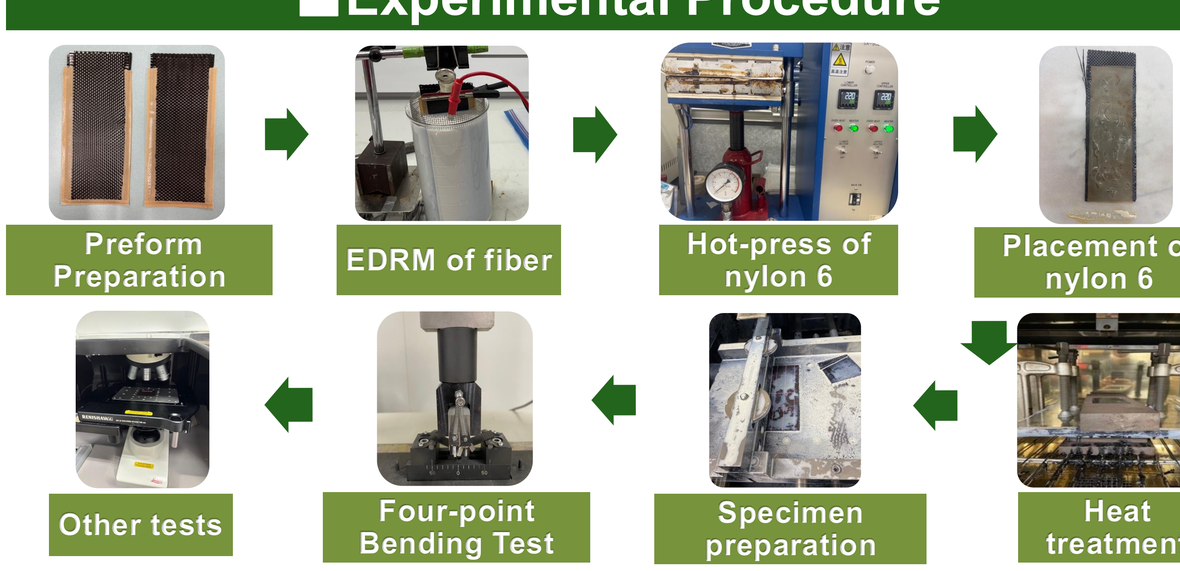

Stcking sequence

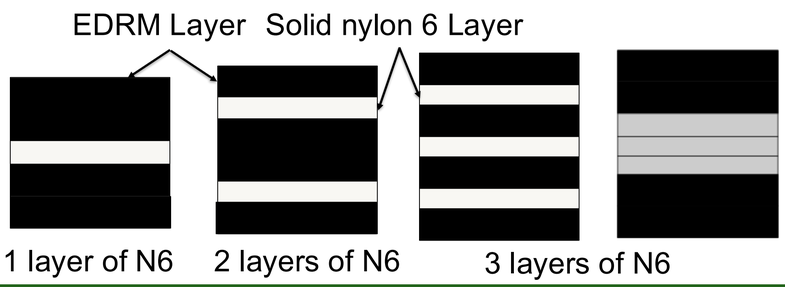

Table 1. Expermental condition

Sample	Stacking Sequence
1	No N6
2	1 Layer of N6
3	2 Layers of N6
4	3 Layers of N6 (Alternate)
5	3 Layers of N6 (Middle)

Results and Discussion

The results obtained from the Four-point bending test, Roughness test and Raman Spectroscopy are displayed below.

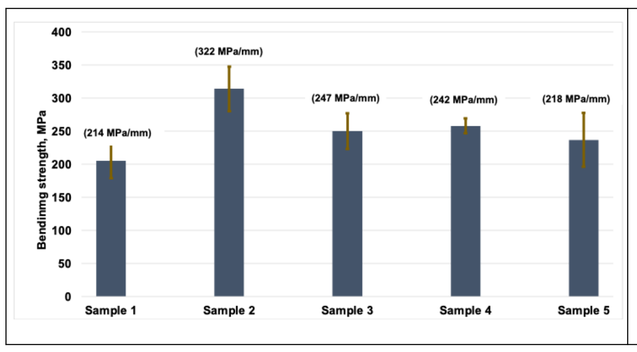

Inserting nylon 6 sheet into CFRP can significantly increase the bending strength of CFRP, however, surprisingly adding one layer of nylon 6 has higher flexural strength than adding multiple layers

Fig. 6. Bending strength of carbon fiber/nylon 6/epoxy composites

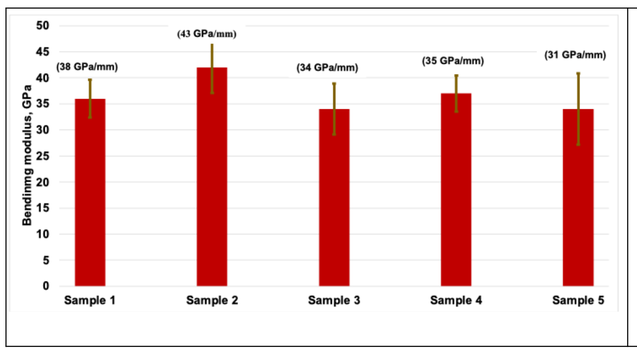

The same scenerio was also observed in case of flexural modulus. The maximum bending modulus was achieved when 1 layer of nylon 6 was inserted into CFRP.

Fig. 7. Bending modulus of carbon fiber/nylon 6/epoxy composites

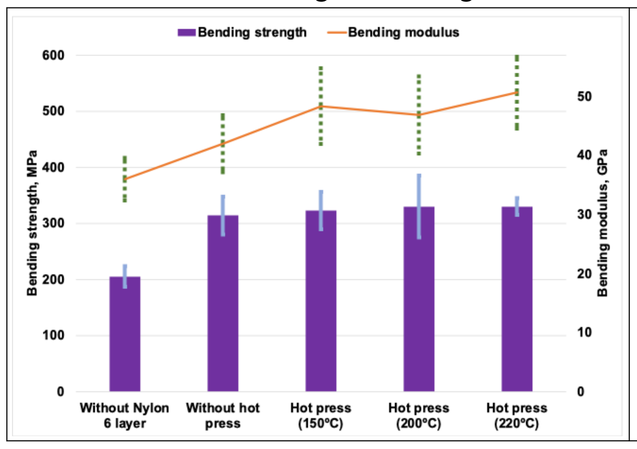

The CFRP including the hot-pressed nylon 6 layer showed 59% increase in bending strength than the CFRP without any nylon 6 layer. Moreover, using the hot-pressed nylon 6 layer increased the bending strength by 6% of CFRP with nylon 6 layer that wasn't hot-pressed.

Fig. 8. Bending strength and modulus of carbon fiber/hot-pressed nylon 6/epoxy composites

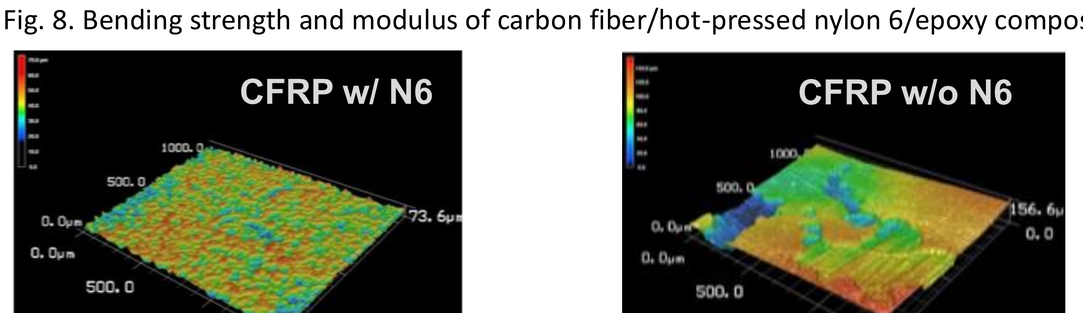

Fig. 9. Surface topography of carbon fiber/nylon 6/epoxy composites

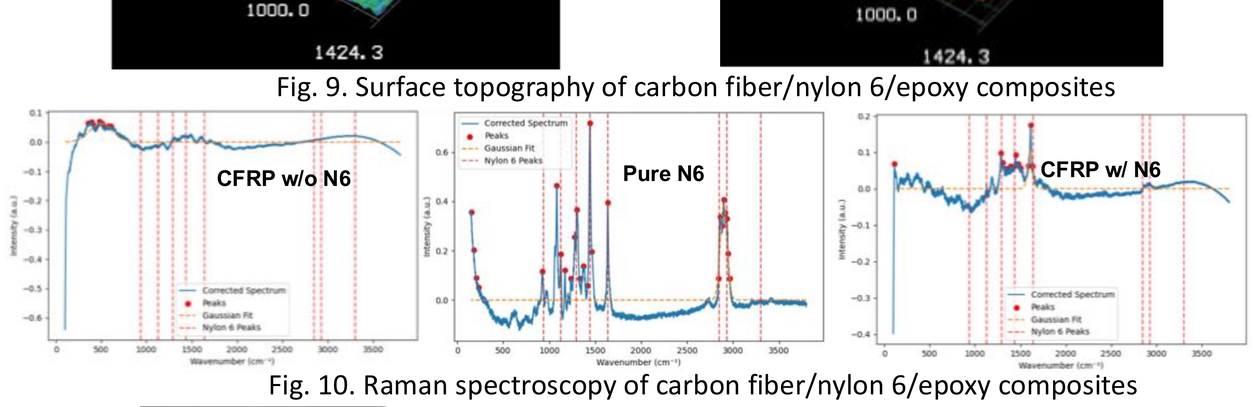

Fig. 10. Raman spectroscopy of carbon fiber/nylon 6/epoxy composites

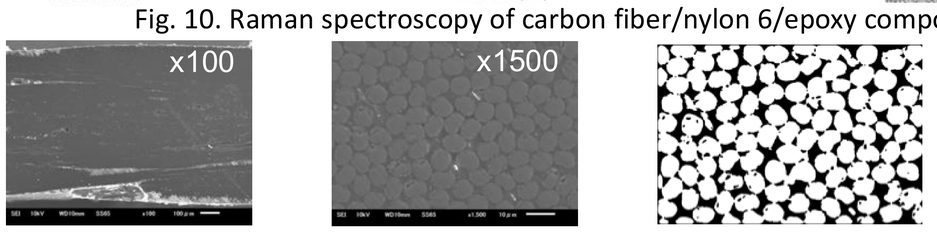

Fig. 11. SEM image of CFRP fabricated by EDRM

Conclusion

- ➢ The effect of adding Nylon 6 into CFRP were investigated
- ➢ Nylon 6 has a great compatibility with epoxy which results in higher bending strength and impact energy

Future Studies

- ➢ Effect of adding other thermoplastics other than nylon 6 with epoxy to check compatibility and made a comparative study

References

[1] Mrazova, M. (2013). Advanced composite materials of the future in aerospace industry. Incas bulletin, 5(3), 139.
[2] Gorton, B. S. (1964). Interaction of nylon polymers with epoxy resins in adhesive blends. Journal of Applied Polymer Science, 8(3), 1287-1295.
[3] Islam, M. T., Honda, S., Katagiri, K., Sasaki, K., & Takeda, R. (2024). Investigation of manufacture variables on the mechanical properties of CFRP prepared by electrodeposition resin molding method. Mechanics of Advanced Materials and Structures, 31(29), 11363-11378.

* Md Tansirul Islam (e-mail: mdtansirul.islam.y8@elms.hokudai.ac.jp)
Division of Human Mechanical System and Design, Graduate School of Engineering, Hokkaido University
N13 W8, Kita-ku, Sapporo, Hokkaido 060-8628, Japan

ICCM24
AUGUST 4-8, 2025
BALTIMORE CONVENTION CENTER
BALTIMORE, MARYLAND, USA

No Technical Paper Submission for:

Yan Chen

ICCM24
AUGUST 4-8, 2025
BALTIMORE CONVENTION CENTER
BALTIMORE, MARYLAND, USA

No Technical Paper Submission for:

Meiyu Liu

Real-time Flow-front Prediction in Resin Transfer Molding Using Electromechanical Behavior and Generative Adversarial Network

Dahun Lee[a], Björn Beck[b], Frank Henning[b], In Yong Lee[c] and Young-Bin Park[a]

[a]Department of Mechanical Engineering, Ulsan National Institute of Science and Technology, Ulsan, Republic of Korea, [b]Fraunhofer Institute for Chemical Technology, Pfinztal, Germany
[c]Department of Mechanical Engineering, Dong-A University, Busan, Republic of Korea

Background

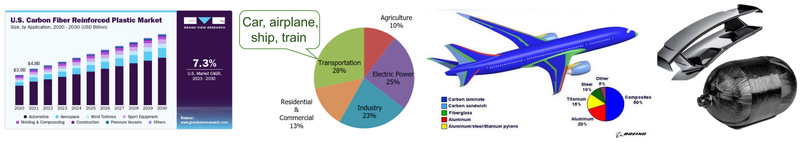

- Increase of demand for CFRPs due to its superior mechanical properties
- Thermoset CFRPs : Higher mechanical properties and thermal resistance
- Large-scale products such as wind turbine blade, airplane, automotive panels.

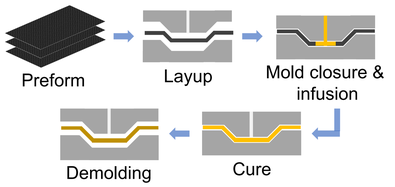

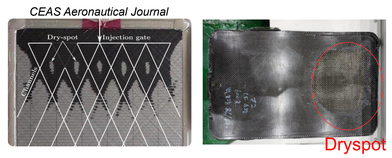

- Resin transfer molding (RTM) is widely utilized for producing thermoset CFRPs but, vacuum assisted resin transfer molding (VARTM) provide cost-effective manufacturing.
- Defects, particularly dryspots, commonly occur during infusion stage
- Real-time monitoring is essential to ensure full impregnation → defect-free composites

- Problem statements

1) Is it applicable to large-scale products?
2) What approach ensures reliable prediction of diverse flow-front behavior?

Methodology

Experimental setup



Plain woven (204 g/m²)



Epoxy resin (240 mPas @ 25 °C)

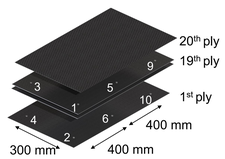

Preform & electrode setting



Experimental setup

- Real-time measurement on 24 channels (thickness, crosswise and lengthwise)
- Set R_o as atmospheric state and calculate $\Delta R/R_o$ for normalization
- Atmospheric state: 10 min, vacuum state: 10 min, infusion: 55 min

Generative Adversarial Network (GAN)

- Artificial intelligence tools for generating realistic images (e.g., computer vision, design, image synthesis, etc.)

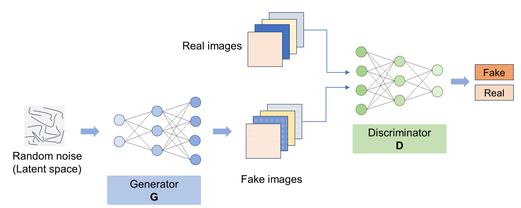

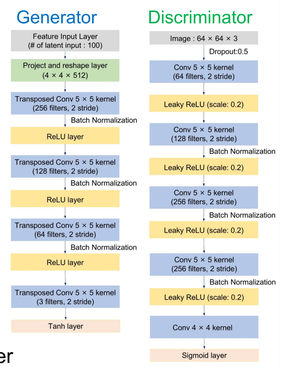

Generator
- Generates realistic fake data to fool the discriminator

Discriminator
- Classifies inputs as real or fake; acts as a binary classifier

Results

Electromechanical Behavior

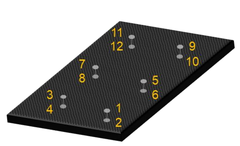

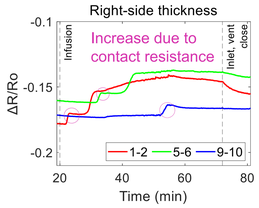

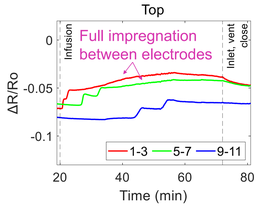

- Resin impregnation on the electrodes → abrupt increase in electrical resistance
- Governing equation : $P_{Compaction} = P_{Applied} - P_{Resin}$ ($P_{Compaction}$ ↑ → $\Delta R/R_o$ ↓)
- $P_{Compaction}$ results in changes in electrical network between electrodes.
- Full impregnation was observed based on the gradual increase in electrical resistance.

Flow-front Identification

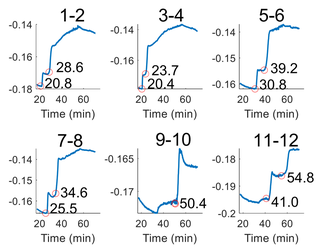

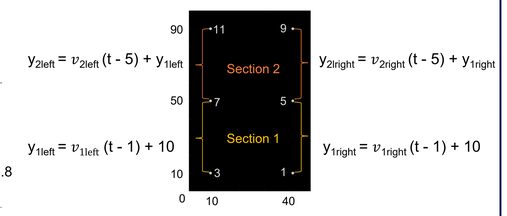

- Abrupt increase in electrical resistance → identify resin arrival time on electrodes
- Linear equations for identifying resin location along electrodes
  → derive parabolic equation and plot to represent flow-front

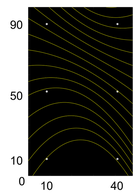

Identified result

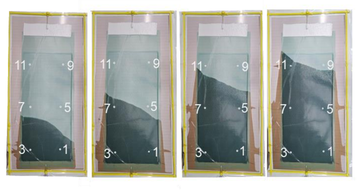

Experimental result

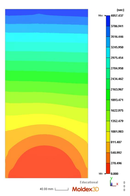

Numerical analysis

- Identified result closely matched the actual resin flow behavior.
- Resin flow predicted by numerical analysis was inconsistent with experimental result.

Flow-front Prediction

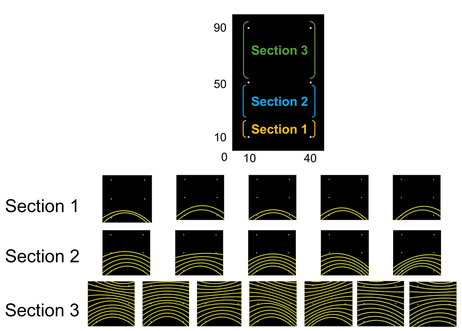

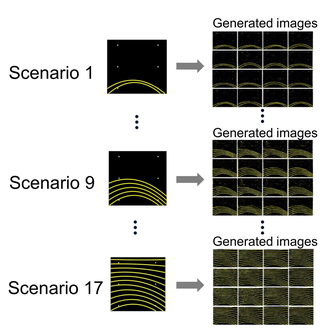

- 17 possible flow-front scenarios defined across 3 sections.
- While training set was plotted based on linear equations, a GAN produce various configurations.
- Realistic flow-front images were generated using GAN, including racetracking effects.

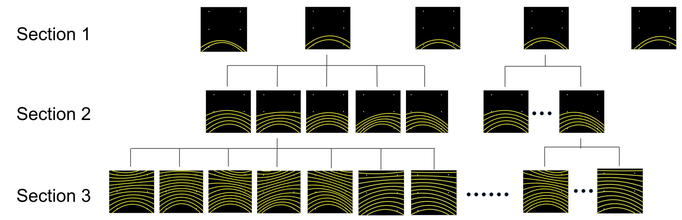

- Possible resin flow-front scenarios were presented on tree model based on sections.

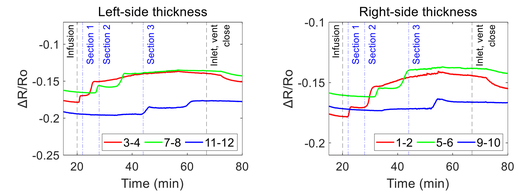

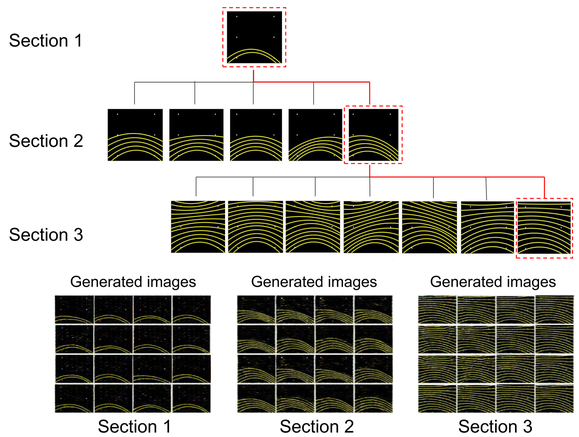

- The flow-front scenario was determined based on resin arrival time at Section 1.
- Possible resin flow scenarios on Section 2 were identified based on probability.
- Sequential prediction was performed using resin arrival time at electrodes.
- Once the scenario was determined, a GAN generated multiple flow-front configurations to represent the current and its future resin flow behavior.
- Identified flow-front configurations allowed early prediction of potential dry spots.

Conclusions

1. A CFRP panel was monitored during the VARTM process using electromechanical behavior during resin infusion.
2. A novel flow-front identification and prediction method was developed by combining a tree-based decision model with a GAN, enabling accurate sequential identification of resin flow.
3. The model can predict dry spot locations, providing a robust system for real-time defect prevention and improved composite quality.

Acknowledgement

This work was supported by the National Research Foundation of Korea (NRF) (RS-2024-00397400) and the 'regional innovation megaproject' program through the Korea Innovation Foundation (RS-2023-IN231026) funded by the Ministry of Science and ICT (MSIT).

Development of multi-functional coaxial fiber sensor for simultaneous strain and temperature monitoring for composite manufacturing process

Seung Yoon On[1], Seong Yeon Park[2], Wonvin Kim[3] and Seong Su Kim[3]

[1]School of Mechanical Engineering, Gyeongsang National University
501, Jinju-daero, Jinju, Republic of Korea
Email: seungyoon@gnu.ac.kr, web page: http://csl.gnu.ac.kr

[2]Samsung Electronics Test System Package
465, Beonyeong-ro, Seobuk-gu, Cheonan-si, Chungcheongnam-do, Republic of Korea
Email: acroark@kaist.ac.kr

[3]Department of Mechanical Engineering, KAIST
291 Dahak-ro, Yuseong-gu, Daejeon, Republic of Korea
Email: seongsukim@kaist.ac.kr, web page: http://mdam.kaist.ac.kr

Keywords: Bimodal sensing, Coaxial fiber sensor, Multi-layer structure, Composite cure strain monitoring, Composite residual strain monitoring.

ABSTRACT

Coaxial structured fibers have gained significant attention in sensor applications due to their design flexibility and ability to enable multi-functionality. However, when utilized for strain monitoring in composite manufacturing processes, the sensor's complex and thicker structure can lead to stress concentration and signal interference. To address this issue, we propose a multifunctional coaxial fiber sensor capable of simultaneous temperature and strain measurement during composite manufacturing process. To achieve multi-functional sensing, we employ a multi-shell structure consisting of a multi-conductive layer and PEDOT:PSS layer, applied to a creep-enhanced ultra-high molecular weight polyethylene core fiber using a simple dip-coating method.

1 INTRODUCTION

Fiber-reinforced composite materials are fabricated by physically mixing reinforcing fibers and polymer matrix, resulting in enhanced mechanical properties. However, a significant challenge arises from the mismatch of the coefficient of thermal expansion (CTE) between the fiber and the matrix[1]. At the macroscopic level, this CTE mismatch leads to warpage and distortion of the structure after the curing reaction. At a microscopic level, during the cooling stage of the composite manufacturing process, there is a possibility of interfacial debonding between the fiber and matrix, which can degrade the material properties of the composite[2]. Therefore, it is crucial to employ real-time strain and temperature monitoring during the manufacturing process of composite structures to reduce residual stress by optimizing the curing cycle.

Conductive particle-reinforced nanocomposite sensors offer a potential solution due to their design flexibility[3]. Over the years, numerous studies have focused on developing multi-functional or multimodal sensors capable of detecting multiple physical signals in a single device[4]. For instance, Saeidi-Javash et al. developed printable multi-functional sensors that utilize MXene and graphene nanosheets to measure both strain and temperature[5]. Zhao et al. fabricated a flexible multi-functional sensor using thermosensitive platinum ribbons and a flexible polyimide substrate to measure pressure and temperature stimuli[6]. Xu et al. demonstrated bio-inspired electronic skins that employ gold/thermoplastic polyurethane/cellulose membrane to measure multiple signals, including temperature, electroencephalogram, and electrocardiogram[7]. Xue et al. developed a flexible dual-parameter sensor array using PDMS-MXene/CNT piezoresistors and PDMS-MXene thermistors to detect pressure and temperature, respectively[8]. However, most of these studies have primarily focused on developing flexible sensors for healthcare or wearable applications. Moreover,

conventional multimodal sensors face two limitations when applied to composite monitoring applications: a usable temperature range that is too low compared to the curing temperature of composite materials (~125 °C) and a thickness and size that are too large to embed into composite structures. This is because most research implements the multimodal function through the stacking or arraying of sensing elements.

In this work, we present a multi-functional coaxial fiber sensor capable of simultaneously measuring the strain through resistance changes in the multi-conductive layer and temperature through thermoelectric voltage changes at the junction between multi-conductive layer and poly-ethylenedioxythiophene:poly-styrenesulphonate (PEDOT:PSS) layer during the composite cure process. The ultrahigh molecular weight polyethylene (UHMWPE) core fiber and multi-conductive layer was fabricated using a dry-jet wet spinning with a microwave-assisted cross-linking method, as well as a dip-coating process based on our previous works. To create the junction point between multi-conductive layer and PEDOT:PSS layer, laser etching was employed to effectively remove a partial area of the outer polyurethane (PU) layer and expose the multi-conductive layer. The surface morphologies and damage on the multi-conductive layer after the etching process were investigated using an optical microscope and Raman spectroscopy, respectively. Furthermore, strain sensitivity (i.e. gauge factor) measurement and cyclic tests were performed under various strain ranges using electronic test equipment to examine the effect of junction fabrication and PEDOT:PSS coating. The thermoelectric voltage change was investigated under various temperature and strain ranges.

2 EXPERIMENTAL

2.1 Fabrication of core fiber

The UHMWPE fibers was fabricated by using a dry-jet wet spinning method with 4 wt.% spinning solution at a lab-scale spinning instrument (Wet spinning system, DISSOL, Republic of Korea) as shown in Figure 1. The spinning solution was fed to the 0.65 mm diameter of spinneret under 170 °C. The UHMWPE fibers were formed by solidification of the polymer solution extruded from the spinneret in a coagulation bath containing distilled water at 25 °C. The residual solvent after solidification process was removed by rinsing process using hexane (Sigma-Aldrich Inc., USA) for 24 h at 25 °C. The hot-stretching process was introduced to enhance the initial crystallinity of the as-spun UHMWPE fibers. The stretching ratio and treatment temperature was adjusted by 14 and 120 °C, respectively.



Figure 1: Dry-jet wet spinning of UHMWPE core fibers.

2.1 Dip coating processes

Figure 2 shows the schematic configuration of the multi-functional coaxial fiber sensor consisting of the following sequence from the core: UHMWPE core fiber for load bearing, 1st PU layer, MWCNT

conductive layer for strain sensing, 2nd PU layer. A role of the double PU layers is to reduce the noise level and enhance the linearity of the fiber sensor by preventing failure of electrical networks. This sensing layer was fabricated by the dip coating processes. At first, the UHMWPE core fiber was submerged into the aqueous PU solution (CRP 26301, T&L Co., Ltd., Republic of Korea) and withdrawn from the bath after 20 sec. Subsequently, the PU coated fiber was dried at 80 °C for 3 min and this process was repeated in 3-times. Thereafter, the electrically conductive layer was formed on the PU coated UHMWPE fiber by using the same method with the aqueous MWCNT solution (K-Nanos 100P, Kumho petrochemical Co., Ltd., Republic of Korea). In the case of the sandwich-structured multi-conductive layer to improve sensitivity and linearity from the combination of varying concentration of MWCNT, the same coating procedures were adopted from the bottom layer of 3 wt.% MWCNT, the middle layer of 2 wt.% MWCNT, and the top layer of 3 wt.% MWCNT, respectively. The thickness of each conductive layers was controlled by varying the number of the dip coating process to minimize the variation of resistance due to the thickness change. Subsequently, the conductive layer coated UHMWPE fiber was dried in a 60 °C oven for 1 hour to remove excessive water in the MWCNT conductive layer. Lastly, 2nd PU layer was coated with the same procedure of the 1st PU layer.

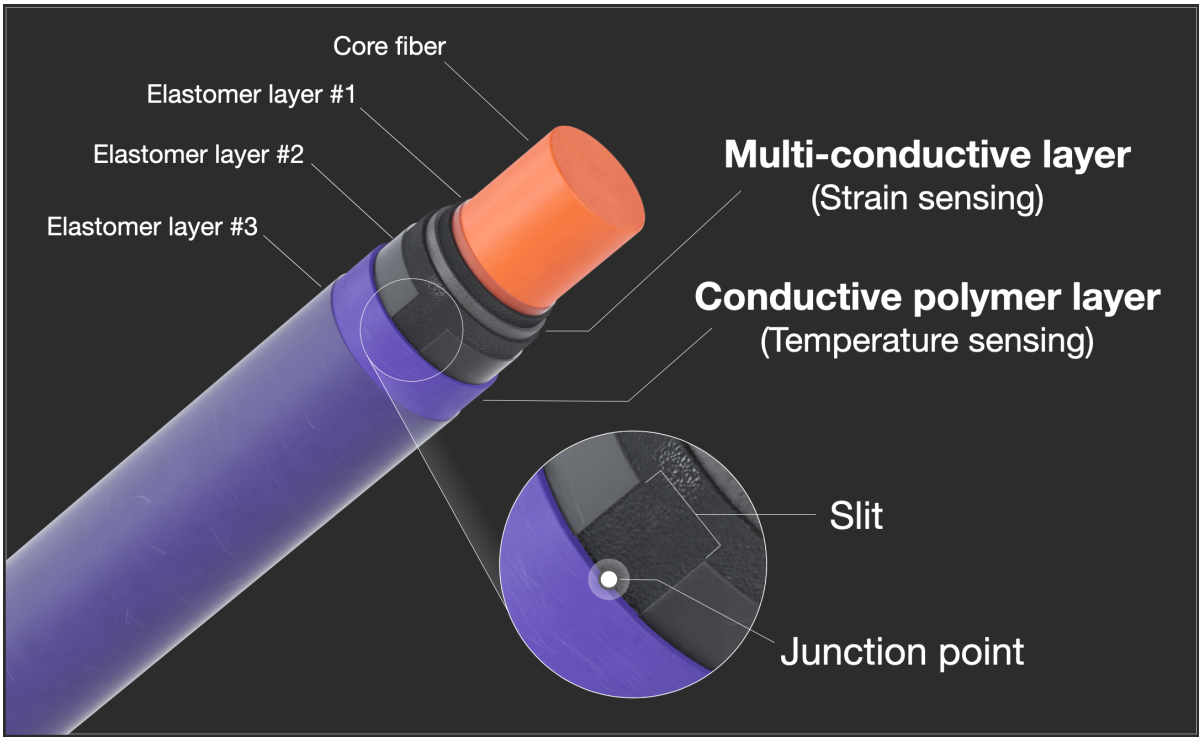

Figure 2: Schematics of multi-functional coaxial fiber sensor

2.2 Sensing performance of multi-functional coaxial fiber sensors

Figure S7a shows the schematic diagram for measuring the relative resistance change ($\Delta R/R_0$) and relative thermoelectric voltage change ($\Delta V/V_0$). These signals were simultaneously measured using LCR meter (E4980A, Keysight Technologies, USA) and high-precision multimeter (DMM6500, Keithley Instruments LLC., USA), and the signal measurement equipment was controlled by LabView (LabView 2022, National Instruments Corp., USA). To avoid signal interference, resistance was measured by an AC-based signal with a 1,200 Hz frequency, and the thermoelectric voltage was measured by a DC-based signal. The relative resistance change under static and cyclic loading conditions was measured using an LCR meter and universal testing machine (INSTRON 5969, Illinois Tool Works Inc., USA). The repeatability of the bimodal coaxial fiber sensor was estimated by measuring the changes in the resistance during the cyclic tensile test with 2.0 mm/min^{-1} crosshead speed under 10, 20, 30, and 40% of the failure strain of the bimodal coaxial fiber sensors.

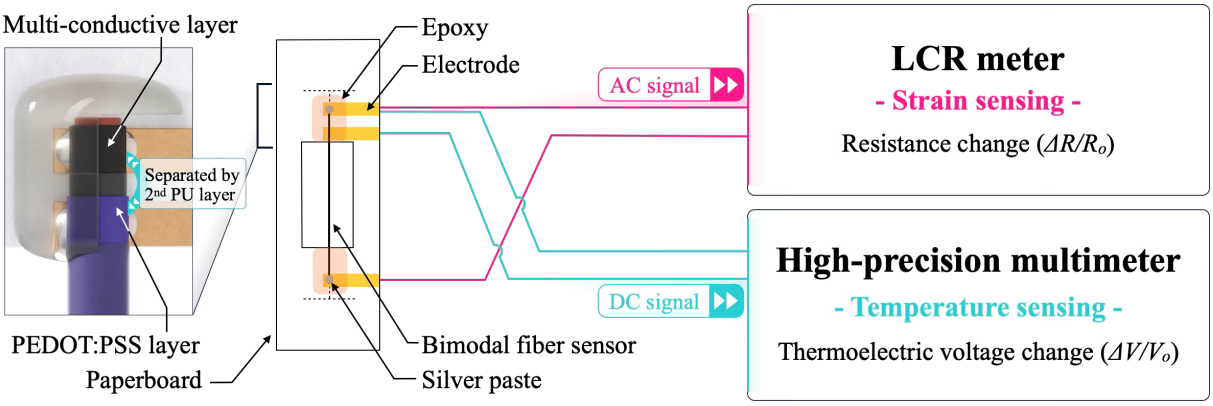

Figure 3: Measurement for sensing performance of coaxial fiber sensor

3 RESULTS AND DISCUSSION

3.1 Surface morphologies of multi-functional coaxial fiber sensor

Figure 4 presents the surface morphologies and cross-section images of PEDOT:PSS layer-coated fiber sensors. FE-SEM and EDS mapping images confirmed that the PEDOT:PSS layer was effectively coated on fiber sensor. The cross-section images of the multi-functional coaxial fiber sensor in Figure 4b confirmed the multilayer structure from the core fiber to the 3rd PU layer with respect to the coating sequence.

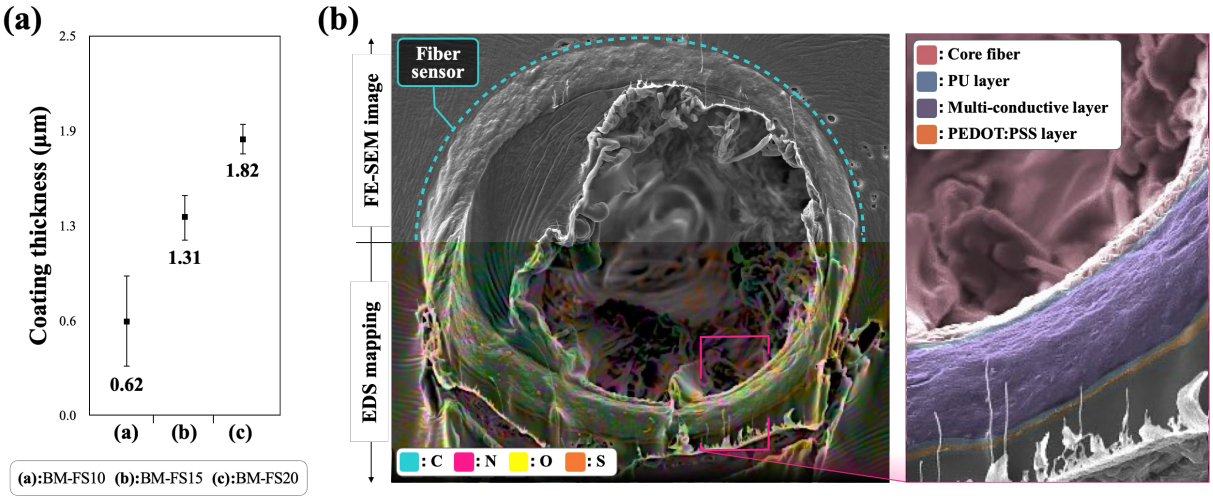

Figure 4: Coating thickness and cross-section images of multi-functional coaxial fiber sensor

3.2 Sensing performances

The repeatability with various strain ranges from 10% to 40% of the failure strain of the bimodal coaxial fiber sensor, shown in Figure 5, confirmed that the resistance change from the multi-conductive layer can be stably measured over various strain ranges without degradation by the PEDOT:PSS layer.

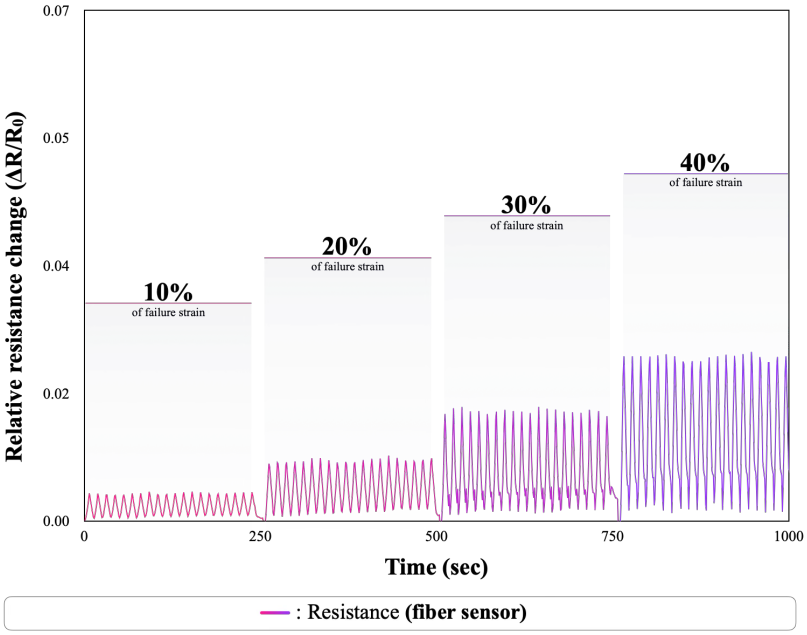

Figure 5: Repeatability of sensor fibers under various strain ranges

Figure 6 shows the monitoring results of the thermoelectric voltage and relative resistance change during a stepwise temperature cycle ranging from 35 to 125 ºC, with 30 ºC increments, to investigate the simultaneous measurement of these parameters without signal interference. The results indicated that both the thermoelectric voltage and resistance could be measured simultaneously without any signal interference. Therefore, it can be concluded that the bimodal coaxial fiber sensor can be applied to composite manufacturing processes without the need for an additional compensation process to correct thermoelectric voltage measurement errors resulting from external strain.

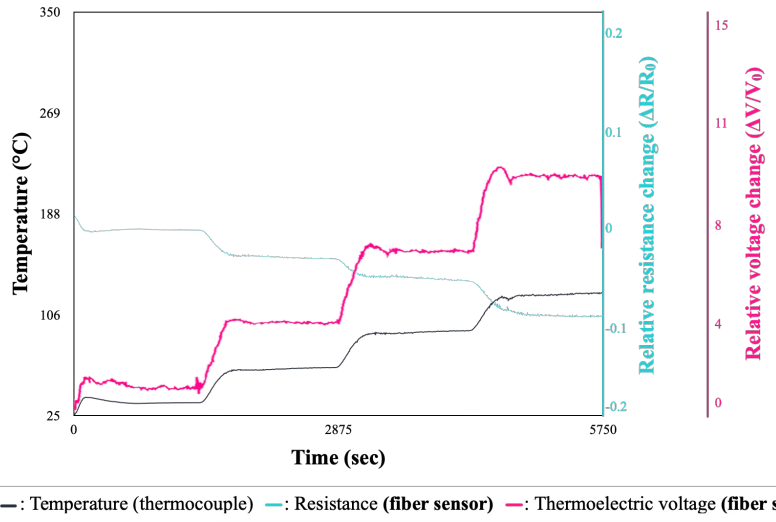

Figure 6: Measurement of sensing performance of multi-functional coaxial fiber sensor.

4 CONCLUSIONS

In this study, a multi-layer structured coaxial fiber sensor was introduced to simultaneously measure the temperature and strain. The effects of bimodal coaxial fiber sensors were investigated by measurement of surface morphologies, sensing response change which is including static and cyclic deformation, and monitoring of temperature and strain signal.

ACKNOWLEDGEMENTS

This work was supported by the Glocal University 30 Project Fund of Gyeongsang National University in 2025.

REFERENCES

[1] N. K. Parambil, B. R. Chen, J. M. Deitzel, J. W. Gillespie Jr, A methodology for predicting processing induced thermal residual stress in thermoplastic composite at the microscale, *Composites Part B: Engineering* 2022, 231, 109562

[2] T. Corden, I. Jones, D. Jones, V. Middleton, The mechanisms of interlaminar cracking in thick resin transfer moulded composite cylinders, *Composites Part A: Applied Science and Manufacturing* 1998, 29, 455

[3] D. Punetha, M. Kar, S. K. Pandey, A new type low-cost, flexible and wearable tertiary nanocomposite sensor for room temperature hydrogen gas sensing, *Scientific Reports* 2020, 10, 2151

[4] Y. Wang, W. Niu, C. Y. Lo, Y. Zhao, X. He, G. Zhang, S. Wu, B. Ju, S. Zhang, Interactively full-color changeable electronic fiber sensor with high stretchability and rapid response, *Advanced Functional Materials* 2020, 30, 2000356

[5] M. Saeidi-Javash, Y. Du, M. Zeng, B. C. Wyatt, B. Zhang, N. Kempf, B. Anasori, Y. Zhang, All-printed MXene–graphene nanosheet-based bimodal sensors for simultaneous strain and temperature sensing, *ACS Applied Electronic Materials* 2021, 3, 2341

[6] S. Zhao, R. Zhu, Flexible bimodal sensor for simultaneous and independent perceiving of pressure and temperature stimuli, *Advanced Materials Technologies* 2017, 2, 1700183

[7] Y. Xu, W. Guo, S. Zhou, H. Yi, G. Yang, S. Mei, K. Zhu, H. Wu, Z. Li, Bioinspired perspiration-wicking electronic skins for comfortable and reliable multimodal health monitoring, *Advanced Functional Materials* 2022, 32, 2200961.

[8] X. Xue, T. Zhao, X. Tian, L. Yuan, Z. Wang, T. Li, J. Zhang, Flexible dual-parameter sensor array without coupling based on amorphous indium gallium zinc oxide thin film transistors, *Advanced Materials Technologies* 2022, 7, 2100849.

Helicobacter Pylori Detection via SERS Enhancement Using Synergistic Effects of Gold Nanorods/Nano Mica Platelets/ZnO Quantum Dots

Ming-Chang Lu[1], and Chih-Wei Chiu[2]

[1]Department of Materials Science and Engineering, National Taiwan University of Science and Technology
No. 43, Sec. 4, Keelung Rd., Da'an Dist., Taipei City 106335, Taiwan (R.O.C.)
Email: D11304008@mail.ntust.edu.tw

[2]Department of Materials Science and Engineering, National Taiwan University of Science and Technology
No. 43, Sec. 4, Keelung Rd., Da'an Dist., Taipei City 106335, Taiwan (R.O.C.)
Email: cwchiu@mail.ntust.edu.tw

Keywords: Gold nanorods, Nano mica platelets, Zinc oxide quantum dots, Surface-enhanced Raman scattering, *Helicobacter pylori*

ABSTRACT

A highly sensitive and reproducible surface-enhanced Raman scattering (SERS) platform was developed for the noninvasive detection of *Helicobacter pylori* by integrating gold nanorods (AuNRs), nano mica platelets (NMPs), and ZnO quantum dots (QDs) into a ternary hybrid system. AuNRs were uniformly anchored onto the delaminated NMP surface via electrostatic interactions enabled by a cationic interfacial activator. The high surface charge and large specific area of NMPs not only stabilized AuNR growth but also promoted the formation of three-dimensional electromagnetic "hotspots" through particle self-assembly. These AuNRs/NMPs nanohybrids exhibited a significant Raman enhancement effect, achieving a limit of detection (LoD) of 10^{-9} M for adenine with an enhancement factor (EF) of 2.0×10^8. To further amplify the SERS performance, ZnO QDs were incorporated to introduce additional chemical enhancement via charge transfer. The resulting AuNRs/NMPs/ZnO QDs exhibited a lower LoD of 10^{-10} M, a higher EF of 1.6×10^9. Remarkably, the same substrate demonstrated excellent sensitivity for *H. pylori* detection, with an LoD of 90 CFU mL^{-1} and a relative standard deviation of 9.70%. This performance is attributed to the synergistic interplay among localized surface plasmon resonance, semiconductor-mediated charge transfer, and nanoscale self-assembly. The positively charged substrate surface also facilitated efficient physical adsorption of the negatively charged bacterial membrane. Overall, this hybrid SERS platform offers a promising strategy for rapid, label-free, and ultrasensitive detection of *H. pylori*, even in complex biological matrices, and holds great potential for clinical diagnostics and point-of-care applications.

1 INTRODUCTION

Helicobacter pylori (*H. pylori*) is a gram-negative, microaerophilic, spiral-shaped bacterium that colonizes the human gastric mucosa and is recognized as a major etiological factor in a range of gastrointestinal disorders, including chronic gastritis, duodenal ulcers, gastric adenocarcinoma, and mucosa-associated lymphoid tissue lymphoma [1]. Since its discovery by Warren and Marshall in 1982 [2], *H. pylori* has remained a global health concern, with an estimated infection rate exceeding 50% worldwide and a considerable risk up to 2% of progression to gastric cancer in untreated individuals [3]. Epidemiological data reveal stark regional disparities in prevalence, ranging from less than 20% in some developed countries to over 80% in regions with poor sanitation and healthcare access [4]. These statistics underscore the urgent need for effective, scalable, and accurate diagnostic methods to manage this prevalent pathogen. Diagnostic approaches for *H. pylori* are typically classified into invasive and noninvasive methods, depending on whether gastric tissue biopsy is involved. Invasive techniques such as histopathology, rapid urease testing, and bacterial culturing offer high specificity but require endoscopy, which is costly, uncomfortable for patients, and dependent on

clinical infrastructure and trained personnel [5]. Noninvasive methods including stool antigen assays, serological antibody tests, and urea breath tests (UBTs) are more accessible, but often suffer from trade-offs in sensitivity, specificity, or safety. In particular, the use of radioactive ^{14}C in UBTs poses potential health risks and limits widespread deployment, while serological assays fail to distinguish active infection from past exposure [6]. Collectively, these limitations highlight the need for a next-generation diagnostic platform that is rapid, label-free, noninvasive, and capable of achieving high sensitivity and specificity across diverse clinical settings.

Surface-enhanced Raman scattering (SERS) has emerged as a powerful molecular fingerprinting technique for ultrasensitive and multiplexed detection, leveraging the intense localized electromagnetic fields ("hotspots") generated by the localized surface plasmon resonance (LSPR) of metallic nanostructures [7]. Among noble metals, gold nanorods (AuNRs) have gained prominence due to their anisotropic morphology, tunable LSPR into the near-infrared region, and excellent biocompatibility [8]. However, colloidal AuNR systems often suffer from nanoparticle aggregation, poor interparticle distance control, and batch-to-batch variability, which compromise signal reproducibility and restrict real-world biosensing applications. To address these challenges, we introduced a hybrid strategy using delaminated nano mica platelets (NMPs) a two-dimensional (2D) silicate material with high surface area, mechanical rigidity, and strong anionic surface charge to support the self-assembly and stabilization of AuNRs into 3D architectures [9]. This approach enables uniform distribution and alignment of AuNRs, enhancing electromagnetic hotspot density and signal reproducibility. Furthermore, NMPs facilitate strong physisorption of bacterial components via electrostatic and polar interactions, providing an ideal substrate for biosensing. Nevertheless, the signal enhancement in such plasmonic systems remains largely dependent on electromagnetic enhancement mechanism (EM), and further sensitivity gains require incorporation of additional synergistic enhancement modalities.

Despite recent progress, the integration of semiconductor materials into SERS substrates to simultaneously enhance sensitivity and biocompatibility remains underexplored. Composite SERS platforms incorporating semiconductors with high chemical stability, excellent biocompatibility, and large specific surface areas have attracted increasing attention. Such hybrids aim to overcome the inherent limitations of noble-metal-only substrates, particularly through the inclusion of wide-bandgap semiconductors (e.g., ZnO, TiO_2) [10]. Nevertheless, the rational design of these systems is still in its early stages, underscoring the need for a deeper understanding of the underlying enhancement mechanisms. These mechanisms are broadly categorized into EM, governed by LSPR, and chemical enhancement mechanism (CM), primarily driven by charge transfer (CT) processes [11, 12].

Herein, we report the design and application of a novel ternary nanohybrid SERS platform composed of AuNRs, NMPs, and ZnO quantum dots (QDs), specifically tailored for the ultrasensitive and reproducible detection of *H. pylori*. In this system, AuNRs are electrostatically anchored onto the negatively charged NMP surface and further functionalized with ZnO QDs through hydrogen bonding interactions. The resulting AuNRs/NMPs/ZnO QDs exhibit synergistic dual-mode enhancement via LSPR-induced EM and CT-mediated CM, along with 3D hotspot generation from nanoscale self-assembly. This platform achieves an exceptionally low limit of detection (LoD = 90 CFU mL^{-1}) for *H. pylori*, and demonstrates high reproducibility, signal uniformity. To our knowledge, this is the first report applying a Au-based SERS nanoplatform for *H. pylori* detection. By bridging materials engineering with plasmonic–semiconductor synergy, this study provides a robust and scalable strategy for real-time, noninvasive bacterial diagnostics and sets the foundation for future point-of-care applications.

2 EXPERIMENTAL SECTION

2.1 Materials

$HAuCl_4$ (99.9%) and $NaBH_4$ (98% purity) were purchased from Echo Chemical Co. (Taiwan). Cetyltrimethylammonium bromide (CTAB) was purchased from Echo Chemical Co. (Taiwan). $AgNO_3$ (99.9%) was purchased from Alfa Aesar Co. (USA). Ascorbic acid (99%) was purchased from Acros Organics Co. (USA). H_2SO_4 (95–98%) was purchased from Echo Chemical Co. (Taiwan). Synthetic fluorinated mica (SOMASIF ME-100), composed of Si (26.5 wt%), Mg (15.6 wt%), F (8.8 wt%), Na (4.1 wt%), Al (0.2 wt%), and Fe (0.1 wt%), was purchased from CO-OP Chemical Co.

(Japan). Jeffamine-T403 was purchased from Huntsman Chemical Co. (USA). Bisphenol A epoxy resin BE-188 was purchased from Echo Chemical Co. (Taiwan). HCl (37%) was purchased from Echo Chemical Co. (Taiwan). NaOH was purchased from Macron Fine Chemicals (Avantor Performance Materials, Center Valley, PA, USA). Ethanol (95%) was purchased from Echo Chemical Co. (Taiwan). $Zn(CH_3COO)_2 \cdot 2H_2O$ (99%) was purchased from Showa Chemical Industry Co. (Japan). KOH (>85%) was purchased from Shimakyu Pure Chemicals Co. (Japan). Methanol (99%) was purchased from Echo Chemical Co. (Taiwan). Tetraethoxysilane (98%) was purchased from Acros Organics Co. (USA). Adenine (99.9%) was purchased from Sigma-Aldrich Chemical Co. (USA). *Helicobacter pylori* (ATCC 43504) was purchased from Academia Sinica. Blood agar plates (TSA with 5% sheep blood) were purchased from Creative Life Science Co. (Taiwan). Ultrapure water (resistivity = 18.2 MΩ cm at 25 °C) was obtained using a Milli-Q water purification system. All reagents were utilized in their original state without any additional purification or treatment. All glassware was subjected to a thorough cleaning, which involved washing with aqua regia, rinsing with water, and drying.

2.2 Preparation of AuNRs/NMPs

NMPs were prepared in accordance with a previously reported procedure [13]. Polyetheramine (Jeffamine-T403) and epoxy resin (BE-188) were dissolved in ethanol at a 2:1 molar ratio. The solution was stirred for 6 h at 60 °C until a light yellow color was observed, which indicated reaction completion and delaminating agent (T403 AEO) formation. Subsequently, mica (1.0 g, 1 wt%) was expanded at 80 °C for 1 h. A mixture of T403 AEO (4.8 g) and HCl (0.75 g) was ultrasonicated for 30 min (to facilitate the protonation of the amine group and form a quaternary ammonium salt) and added to the expanded mica slurry, and the resulting dispersion was stirred for 5 h to induce mica delamination. The mixture was purified through extraction with dilute ethanolic NaOH, and the solid was redispersed in deionized water to form a 1 wt% NMPs dispersion. Mixtures of NMPs and $HAuCl_4$ (0.024 M, 0.2 mL) with different weight ratios were supplemented with the gold seed solution (0.1 mL) and CTAB (0.1 M, 10.9 mL) and stirred for 1 h. Subsequently, $AgNO_3$ (0.01 M, 0.08 mL) and H_2SO_4 (0.5 M, 0.2 mL) were added, and the mixture was dropwise supplemented with ascorbic acid (0.1 M, 0.08 mL). Then, the gold seed solution (0.024 mL) was added, and the dispersion was thoroughly mixed for ~1 min and allowed to stand for ~2 h. The resulting nanohybrid (AuNRs/NMPs) solution was centrifuged at 6,000 rpm for 30 min, and the pellet was washed at least twice with deionized water to remove residual CTAB. The purified solution of AuNRs/NMPs was analyzed using UV–vis spectroscopy, zeta potential measurements, transmission electron microscopy (TEM), and SERS.

2.3 Preparation of AuNRs/NMPs/ZnO QDs

ZnO QDs were prepared using a sol-gel synthesis method [14]. A methanolic solution of KOH (1 M, 25 mL) solution was slowly added to that of $Zn(CH_3COO)_2 \cdot 2H_2O$ (0.1 M, 12.5 mL) at room temperature (25 °C), and the mixture was stirred for 1 h at 1,000 rpm. The presence of ZnO particles was confirmed by the observation of bright yellow fluorescence under UV light. Subsequently, tetraethoxysilane (0.125 mL) was added to regulate particle growth, and deionized water (0.25 mL) was introduced into the resulting gel solution to facilitate a sol-gel reaction on the particle surface. After purification by at least two-fold centrifugation with methanol and deionized water to remove residual reactive molecules, the gel was redissolved in deionized water to form a solution of ZnO QDs. Given the abundance of hydroxyl groups on the silicate nanoclay surface, AuNRs/NMPs with varying weight ratios were physically mixed with ZnO QDs for 15 min to facilitate the stabilization of the two materials through hydrogen bonding and form AuNRs/NMPs/ZnO QDs, which were characterized by TEM, and SERS.

2.4 Culturing of Bacteria and Preparation of SERS Substrate

Prior to bacterial culturing, all glassware was sterilized via autoclaving at an elevated pressure and

temperature (~120 °C, 50 min). The broth was prepared in a 250 mL serum bottle, and *H. pylori* (ATCC 43504) was transferred into the broth (2 mL) using an inoculation ring. Subsequently, the sample was smeared in blood culture medium and cultured in an anaerobic culture tank with microaerobic gas packs at 37 °C for 7 days. The colonies were collected and transferred to a microcentrifuge tube containing 2 mL of the broth using an inoculating loop. The collected bacterial suspension was divided into two 1 mL portions, one of which was used to spread the blood culture medium for the subsequent round of culturing to ensure the continuity and stability of the culture, while the other was subjected to UV–vis analysis and OD600-adjusted to 0.6. Thereafter, the growing colonies were quantified. The bacterial solution was centrifuged at 6,000 rpm for 3 min. The upper layer was removed and washed three times with phosphate-buffered saline (PBS) and then prepared for SERS. Subsequently, solutions of AuNRs/NMPs, and AuNRs/NMPs/ZnO QDs (0.01 mL) were drop-coated onto clean aluminum sheets with dimensions of 10 mm × 10 mm and oven-heated at 80 °C. Analyte solutions were prepared at concentrations of 10^{-4}–10^{-11} M for adenine (volume = 0.01 mL). The *H. pylori* solution (0.01 mL) was combined with the SERS substrate in a nutrient-free environment and subsequently dried for Raman detection.

2.5 Characterization

UV–vis spectra were recorded using a Shimadzu UV-2450 instrument (Kyoto, Japan). For TEM imaging (JEOL JEM-2100), a 0.01 mL droplet of the SERS substrate suspension was placed on a copper mesh and allowed to dry at 80 °C for 24 h. Confocal micro-Raman spectroscopy (Horiba-LABRAM HR800, 785 nm laser) was used to for SERS analysis in the 400–4000 cm^{-1} range (exposure = 10 s, power = 20 mW). Zeta potential analysis was conducted using a Zetasizer Nano ZS90 instrument. Samples for scanning electron microscopy (SEM, JSM-6500F) were prepared by drop-coating clean glass surfaces with the desired dispersions followed by oven-drying at 80 °C for 2 h, affixing to a conductive carbon adhesive, and coating with a thin layer of Pt.

3 RESULTS AND DISCUSSION

3.1 Synthesis and Analysis of AuNRs/NMPs

Delaminated layered silicates, such as synthetic fluorinated mica, offer a 2D platform with high surface charge density, mechanical rigidity, and exceptional self-alignment properties ideal for nanoparticle immobilization via cation exchange [15]. In this work, NMPs with lateral dimensions of 300–1000 nm and a thickness of ~1 nm were utilized as a robust scaffold to facilitate the in situ growth and stabilization of AuNRs. As shown in Figure 1a, the negatively charged NMP surface enabled electrostatic adsorption of gold precursors and promoted seed-mediated reduction of AuNRs directly onto the nanosheet surfaces. The reduction process, monitored via UV–vis spectroscopy (Figure 1b), completed within approximately 125 minutes, substantially faster than conventional nanohybrid fabrication approaches. Zeta potential measurements (Figure 1c) confirmed distinct surface potential shifts upon nanoparticle loading, supporting successful AuNR anchoring. To optimize the component ratio, AuNRs/NMPs composites were synthesized at varying weight ratios. At suboptimal NMP concentrations, AuNRs showed pronounced aggregation and irregular morphology, while excessive NMPs led to heterogeneity in particle size and shape due to ionic charge imbalances (Figure 1d, 1e). The optimal dispersion and alignment were achieved at a 1:1 weight ratio (Figure 1e (3)), which yielded the highest SERS signal-to-background (S/B) ratio and signal intensity (Figure 1f). The ultrathin nature of NMPs permits dual-surface adsorption of AuNRs, enabling anisotropic self-assembly and interparticle coupling in the vertical (z-axis) dimension. This hierarchical configuration results in the formation of dense 3D electromagnetic hotspots, significantly amplifying localized field intensity. The optimized substrate demonstrated a LoD for adenine of 10^{-9} M and a surface enhancement factor (EF) of 2.0×10^8 (Figure 1g, 1h). These values were derived using the standard EF equation [16, 17]:

$$EF = (I_{SERS}/C_{SERS})/(I_{norm}/C_{norm}) \quad (1)$$

where C_{norm} and C_{SERS} represent the analyte concentrations under normal and SERS conditions,

respectively, and I_{norm} and I_{SERS} denote the corresponding Raman signal intensities. Collectively, these results demonstrate that AuNRs synthesized and assembled on NMPs under optimized conditions yield uniform, highly active SERS substrates with enhanced signal reproducibility and sensitivity, attributed to well-regulated nanoparticle arrangement and the strong localized field effects at the nanorod tips.

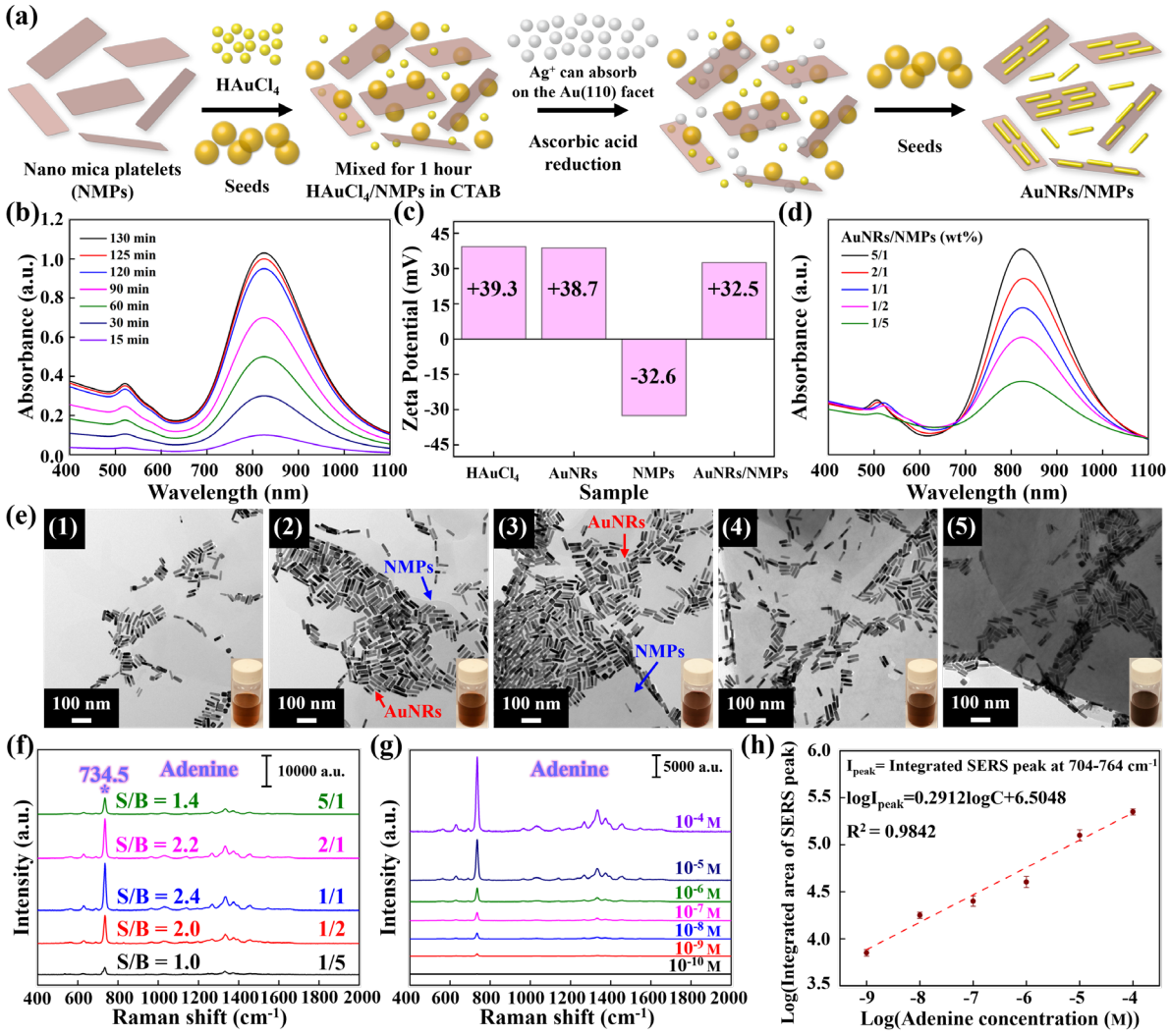

Figure 1. (a) Generation of gold nanorods (AuNRs) on the surface of nano mica platelets (NMPs) using a seed-mediated method. (b) UV–vis spectra of AuNRs/NMPs (1/1, w/w) recorded at different reduction times (n = 10). The spectrum corresponding to the median set was selected for representative plotting. (c) Zeta potentials of $HAuCl_4$, AuNRs, NMPs, and AuNRs/NMPs (1/1, w/w). (d) UV–vis spectra of AuNRs/NMPs with different component weight ratios (n = 10). (e) Transmission electron microscopy (TEM) images of AuNRs/NMPs with weight ratios of (1) 5/1, (2) 2/1, (3) 1/1, (4) 1/2, and (5) 1/5 (insets show photographs of corresponding dispersions). (f) Surface-enhanced Raman scattering (SERS) responses of AuNRs/NMPs with different weight ratios to adenine (10^{-4} M). Spectra were averaged over 50 randomly selected positions (n = 50), with the median set displayed. (g) SERS responses of AuNRs/NMPs (1/1, w/w) to different adenine concentrations (n = 50). (h) Linear correlation between log(integrated intensity in the range of 704–764 cm^{-1}) and log(adenine concentration).

3.2 Synthesis and Analysis of AuNRs/NMPs/ZnO QDs

To further enhance the SERS performance of AuNRs/NMPs, ZnO QDs were incorporated to introduce CT–driven CM alongside EM from plasmonic nanostructures. ZnO, a biocompatible wide-bandgap semiconductor [18], facilitates CM by promoting interfacial electron transfer when the energy levels of the analyte align with the conduction band (CB) and valence band (VB) of the ZnO substrate. This alignment leads to modulation of molecular polarizability and intensification of the Raman signal. ZnO QDs were anchored onto the surface of NMPs through hydrogen bonding with surface silanol (Si–OH) groups (Figure 2a). UV–vis spectroscopy and Tauc plot analysis determined the ZnO QD bandgap to be 3.44 eV (Figure 2b), while energy level mapping revealed favorable alignment between adenine's highest occupied molecular orbital (HOMO)/lowest unoccupied molecular orbital (LUMO) and ZnO's CB/VB, confirming the potential for CT-mediated enhancement (Figure 2c). The ternary nanohybrids (AuNRs/NMPs/ZnO QDs) exhibited significantly stronger SERS responses to adenine compared to AuNRs/NMPs alone (Figure 2d). Systematic optimization of component ratios revealed that a AuNR/NMP/ZnO QD weight ratio of 1/1/2 produced the most uniform QD dispersion and maximal SERS response (Figure 2e–f), with a LoD of 10^{-10} M and EF of 1.6×10^{9} (Figure 2g–h). The pronounced enhancement arises from the synergistic interplay between EM and CM mechanisms: AuNRs generate highly localized electromagnetic fields, while ZnO QDs enable CT pathways that increase analyte polarizability. Concurrently, the NMP substrate facilitates 3D hotspot formation via AuNR self-assembly, enhancing interparticle coupling and EM field localization. Overall, the integration of ZnO QDs into the AuNRs/NMPs framework significantly amplified SERS performance through complementary EM and CM mechanisms, establishing a robust platform for highly sensitive and reproducible biomolecular detection.

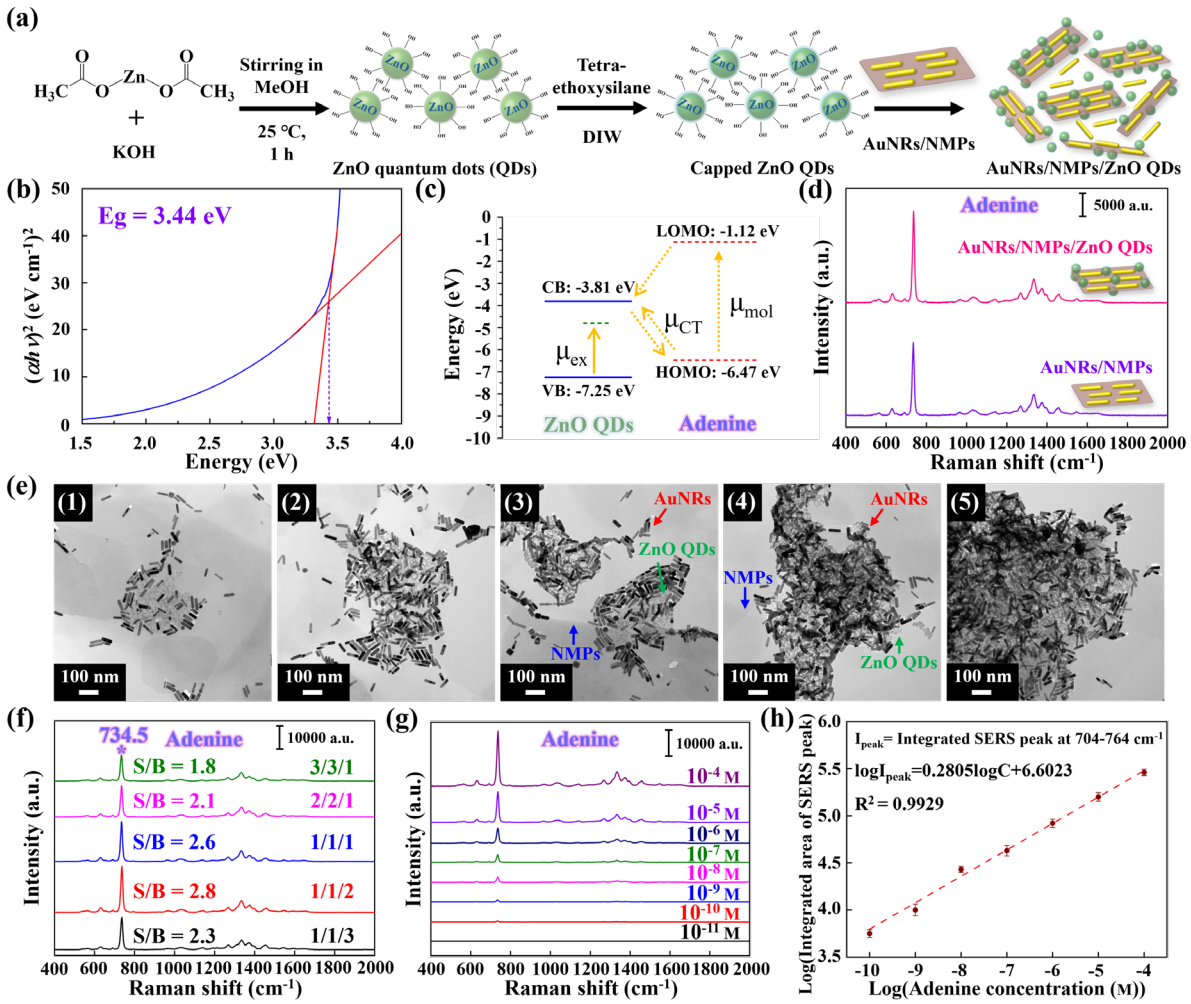

Figure 2. (a) Schematic synthesis of AuNRs/NMPs/ZnO quantum dots (QDs). (b) Tauc plot of ZnO QDs. (c) Energy level diagram illustrating charge transfer between ZnO QDs and adenine. (d) SERS responses of AuNRs/NMPs/ZnO QDs (1/1/2, w/w) and AuNRs/NMPs (1/1, w/w) to adenine (10^{-4} M). Spectra were averaged over 50 randomly selected positions (n = 50), with the median set displayed. (e) TEM images illustrating the distribution patterns of AuNRs, NMPs, and ZnO QDs in AuNRs/NMPs/ZnO QDs with weight ratios of (1) 3/3/1, (2) 2/2/1, (3) 1/1/1, (4) 1/1/2, and (5) 1/1/5. (f) SERS responses of AuNRs/NMPs/ZnO QDs with different weight ratios to adenine (10^{-4} M; n = 50). (g) SERS responses of AuNRs/NMPs/ZnO QDs (1/1/2, w/w) to different adenine concentrations (n = 50). (h) Linear fit of the log(integrated intensity in the range of 704–764 cm^{-1})–log(adenine concentration) plot.

3.3 Interaction of AuNRs/NMPs/ZnO QDs with *H. pylori* and SERS Detection

The AuNRs/NMPs/ZnO QDs hybrid substrate enabled sensitive and reproducible detection of *H. pylori* through synergistic EM and CM. As illustrated in Figure 3a, the detection strategy involved physical adsorption of *H. pylori* onto the positively charged nanohybrids, followed by SERS analysis. A strong Raman response was obtained at a bacterial concentration of 1.8×10^7 CFU mL^{-1} (Figure 3b), with a LoD of 90 CFU mL^{-1} (Figure 3c) and an excellent linear correlation ($R^2 = 0.9818$; Figure 3d). Signal mapping across 50 random points (relative standard deviation = 9.70%; Figure 3e) and a 400 μm^2 area confirmed outstanding spatial uniformity and reproducibility (Figure 3f). The high sensitivity is attributed to the electrostatic interaction between the negatively charged lipopolysaccharides and phosphoglycerol groups on the *H. pylori* surface and the positively charged CTAB-modified AuNRs/NMPs/ZnO QDs. Figure 3g demonstrates the physical adsorption of *H. pylori* onto the SERS substrate. After a seven-day culture period, the bacteria were washed, centrifuged in PBS, dehydrated with ethanol, and incubated with the AuNRs/NMPs/ZnO QDs substrate for a defined duration. The subsequent formation of a visible precipitate confirmed successful bacterial capture. SEM analysis of the precipitate (Figure 3h) revealed pronounced substrate adhesion to *H. pylori*, observed as distinct white protrusions. Figure 3h (1) shows *H. pylori* cultured without the substrate, serving as a control. Upon increasing contact time, a greater amount of substrate was observed accumulating around the bacterial surface, supporting the hypothesis that *H. pylori* can be effectively captured via physisorption, thereby enabling enhanced SERS detection. Benchmarking against existing SERS platforms (Table 1) highlighted the enhanced performance of our approach in terms of LoD and EF. Unlike UBTs or immunoassay-based fecal detection, which suffer from enzymatic interference or antigen instability, this method provides a rapid, label-free, and noninvasive alternative with high accuracy [19, 20]. Furthermore, its scalable fabrication and compatibility with complex biological matrices underscore its strong potential for clinical diagnostics and point-of-care applications in gastrointestinal pathogen screening.

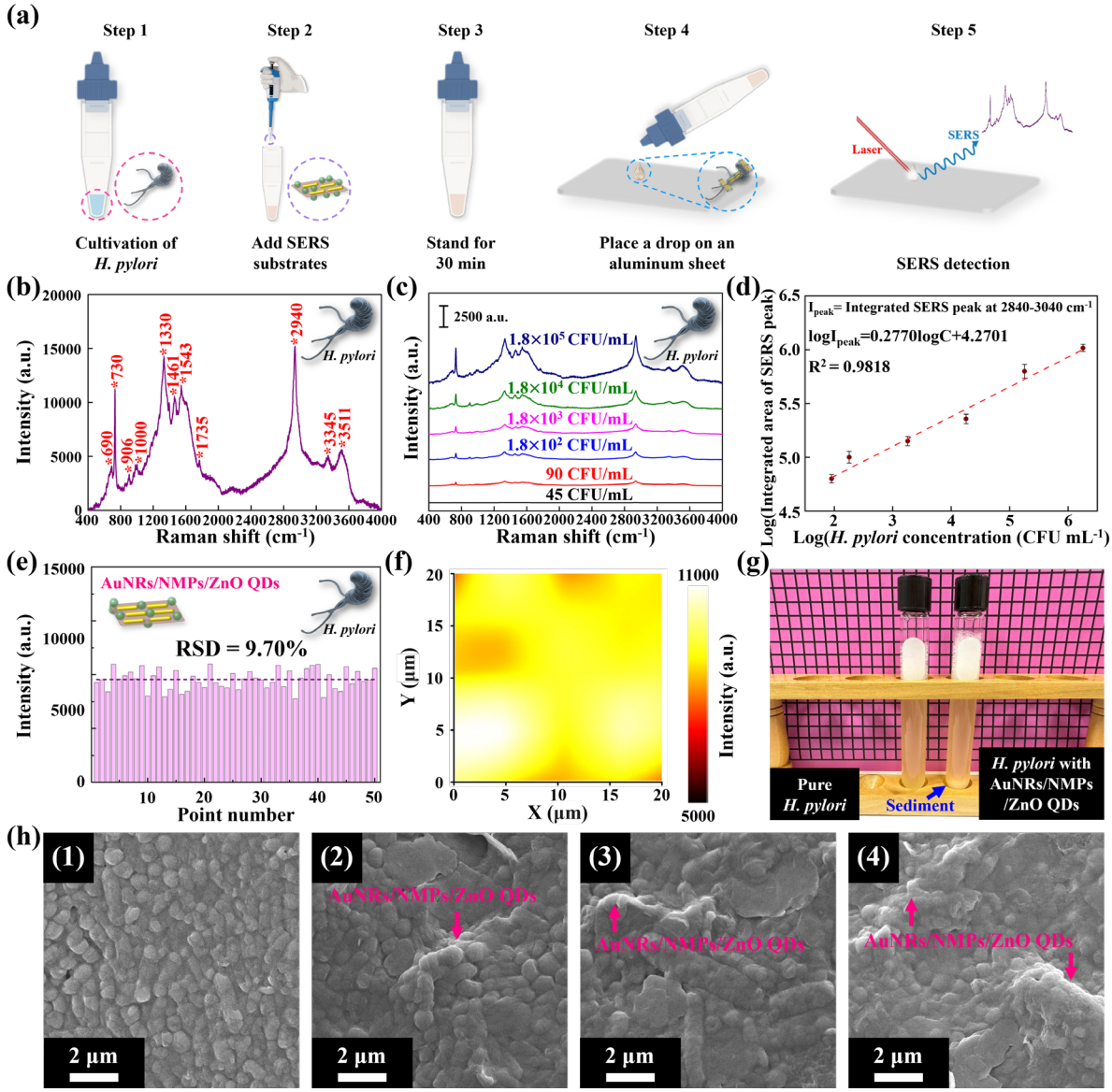

Figure 3. (a) Flow chart of the SERS-based detection of *Helicobacter pylori* by AuNRs/NMPs/ZnO QDs. (b) SERS response of AuNRs/NMPs/ZnO QDs (1/1/2, w/w) to *H. pylori* (1.8×10^7 CFU mL^{-1}). (c) SERS responses of AuNRs/NMPs/ZnO QDs (1/1/2, w/w) to different *H. pylori* concentrations. Spectra were averaged over 50 randomly selected positions (n = 50), with the median set displayed. (d) Linear fit of the log(integrated intensity in the range of 2840–3040 cm^{-1})– log(*H. pylori* concentration) plot. (e) Raman signal intensities of *H. pylori* (1.8×10^6 CFU mL^{-1}, 2940 cm^{-1}) at 50 randomly selected points on AuNRs/NMPs/ZnO QDs. (f) Distribution of the Raman signal intensity of *H. pylori* (1.8×10^6 CFU mL^{-1}, 2940 cm^{-1}) over a 400 μm^2 area of AuNRs/NMPs/ZnO QDs. (g) Physical capture of bacteria by AuNRs/NMPs/ZnO QDs and resulting precipitation. (h) Scanning electron microscopy (SEM) image of the precipitate in (g). The white wrinkled portion represents the SERS substrate. Image (1) refers to *H. pylori* without any substrate after seven days of culturing, while other images refer to precipitates formed after standing for (2) 10, (3) 20, and (4) 30 min.

Hybrid composition	Analyte molecule	LoD[a)]/EF[b)]	References
Ag-PCR-M	Adenine	10^{-8} M/Not reported	[21]
AuNPs/$MoWS_2$		10^{-9} M/Not reported	[22]
TAuNPs/NMPs		10^{-9} M/5.7×10^{7}	[23]
AuNRs/$Ti_3C_2T_x$		10^{-9} M/1.0×10^{8}	[24]
AuNCs/NMPs		10^{-9} M/3.6×10^{8}	[13]
AuNRs/NMPs/ZnO QDs		10^{-10} M/1.6×10^{9}	Our work

[a)]Limit of detection. [b)]EF calculated as described in the main text.

Table 1. Performances of different gold nanoparticle–based probes for the SERS detection of adenine.

4 CONCLUSION

This work presents a rationally engineered ternary SERS platform integrating AuNRs, NMPs, and ZnO QDs for the ultrasensitive, selective, and reproducible detection of *H. pylori*. The nanohybrid design leverages the synergistic contributions of multiple enhancement mechanisms: (i) strong EM fields arising from the LSPR of AuNRs, (ii) CM via interfacial CT enabled by the wide-bandgap ZnO QDs, and (iii) a highly ordered 3D hotspot network promoted by the self-assembly of AuNRs on the anionic surfaces of delaminated NMPs. NMPs serve not only as a structural scaffold for uniform AuNR immobilization but also as a physicochemically active interface that enhances particle dispersion, promotes hotspot density, and facilitates the stable incorporation of ZnO QDs through hydrogen bonding. This integrated architecture enables efficient analyte adsorption and amplifies Raman signals through both plasmonic and semiconductor-mediated pathways. The resulting AuNRs/NMPs/ZnO QDs exhibit exceptional analytical performance, achieving a LoD of 10^{-10} M for adenine and 90 CFU mL^{-1} for *H. pylori*, with high signal reproducibility (RSD = 9.70%). Taken together, these findings demonstrate the potential of this multi-component SERS platform as a powerful tool for next-generation, noninvasive bacterial diagnostics. The integration of plasmonic, silicate, and semiconducting nanomaterials within a single, scalable framework opens new avenues for high-performance biosensing in clinical and point-of-care environments.

ACKNOWLEDGEMENTS

This research was funded by the National Science and Technology Council (MOST 111-2628-E-011-009-MY3, NSTC 112-2221-E-011-004-MY3 and NSTC 113-2622-8-011-007-TE2) of Taiwan.

REFERENCES

[1] Y.-C. Chen, P. Malfertheiner, H.-T. Yu, C.-L. Kuo, Y.-Y. Chang, F.-T. Meng, Y.-X. Wu, J.-L. Hsiao, M.-J. Chen, K.-P. Lin, C.-Y. Wu, J.-T. Lin, C. O'Morain, F. Megraud, W.-C. Lee, E. M. El-Omar, M.-S. Wu, J.-M. Liou, Global prevalence of *Helicobacter pylori* infection and incidence of gastric cancer between 1980 and 2022, *Gastroenterology*, **166**, 2024, pp. 605-619 (doi: 10.1053/j.gastro.2023.12.022).

[2] Y. Zhang, H. Li, Q. Wang, X. Hao, H. Li, H. Sun, L. Han, Z. Zhang, Q. Zou, X. Sun, Rationally designed self-assembling nanoparticles to overcome mucus and epithelium transport barriers for oral vaccines against *Helicobacter pylori*, *Advanced Functional Materials*, **28**, 2018, pp.1802675 (doi: 10.1002/adfm.201802675).

[3] K. Thorell, Z. Y. Muñoz-Ramírez, D. Wang, S. Sandoval-Motta, R. Boscolo Agostini, S. Ghirotto, R. C. Torres, D. Falush, M. C. Camargo, C. S. Rabkin, The *Helicobacter pylori* Genome Project: insights into *H. pylori* population structure from analysis of a worldwide collection of complete genomes, *Nature Communications*, **14**, 2023, pp. 8184 (doi: 10.1038/s41467-023-43562-y).

[4] J. K. Hooi, W. Y. Lai, W. K. Ng, M. M. Suen, F. E. Underwood, D. Tanyingoh, P. Malfertheiner, D. Y. Graham, V. W. Wong, J. C. Wu, F. K. Chan, J. J. Sung, G. G. Kaplan, S.

C. Ng, Global prevalence of *Helicobacter pylori* infection: systematic review and meta-analysis, *Gastroenterology*, **153**, 2017, pp. 420-429 (doi: 10.1053/j.gastro.2017.04.022).

[5] A. Gomaa, S. Maacha, D. Peng, M. Soutto, M. Genoula, N. Bhat, L. Cao, S. Zhu, A. Castells, Z. Chen, A. Zaika, O. G. McDonald, W. El-Rifai, SOX9 is regulated by AURKA in response to *Helicobacter pylori* infection via EIF4E-mediated cap-dependent translation, *Cancer Letters*, **593**, 2024, pp. 216939 (doi: 10.1016/j.canlet.2024.216939).

[6] C. Hawkey, A. Avery, C. A. Coupland, C. Crooks, J. Dumbleton, F. R. Hobbs, D. Kendrick, M. Moore, C. Morris, G. Rubin, M. Smith, D. Stevenson, *Helicobacter pylori* eradication for primary prevention of peptic ulcer bleeding in older patients prescribed aspirin in primary care (HEAT): a randomised, double-blind, placebo-controlled trial, *Lancet*, **400**, 2022, pp. 1597-1606 (doi: 10.1016/S0140-6736(22)01843-8).

[7] N. Logan, C. Cao, S. Freitag, S. A. Haughey, R. Krska, C. T. Elliott, Advancing Mycotoxin Detection in Food and Feed: Novel Insights from Surface-Enhanced Raman Spectroscopy (SERS), *Advanced Materials*, **36**, 2024, pp. 2309625 (doi: 10.1002/adma.202309625).

[8] F. Chen, H. Dang, H. Li, H. Su, L. Chen, Y. Gong, L. Jiang, H. Tang, R. Chen, W. Cheng, BSA-Gold Nanoclusters Enhanced Clusterization-Triggered–Emission of Nonconventional Luminophores-Hydrogels in Dilute Aqueous Solution, *Advanced Functional Materials*, **34**, 2024, pp. 2313098 (doi: 10.1002/adfm.202313098).

[9] Y.-F. Chen, Y.-C. Lee, J. C.-M. Lee, J.-W. Li, C.-W. Chiu, Coaxial electrospinning of Au@ silicate/poly (vinyl alcohol) core/shell composite nanofibers with non-covalently immobilized gold nanoparticles for preparing flexible, freestanding, and highly sensitive SERS substrates amenable to large-scale fabrication, *Advanced Composites and Hybrid Materials*, **7**, 2024, pp. 124 (doi: 10.1007/s42114-024-00933-3).

[10] J. Lin, Y. Shang, X. Li, J. Yu, X. Wang, L. Guo, Ultrasensitive SERS detection by defect engineering on single Cu_2O superstructure particle, *Advanced Materials*, **29**, 2017, pp. 1604797 (doi: 10.1002/adma.201604797).

[11] J. A. Allegretto, J. Dostalek, Metal–organic frameworks in surface enhanced Raman spectroscopy–based analysis of volatile organic compounds, *Advanced Science*, **11**, 2024, pp. 2401437 (doi: 10.1002/advs.202401437).

[12] Q. Li, H. Huo, Y. Wu, L. Chen, L. Su, X. Zhang, J. Song, H. Yang, Design and synthesis of SERS materials for in vivo molecular imaging and biosensing, *Advanced Science*, **10**, 2023, pp. 2202051 (doi: 10.1002/advs.202202051).

[13] Y.-F. Chen, M.-C. Lu, C.-J. Lee, C.-W. Chiu, Flexible nanohybrid substrates utilizing gold nanocubes/nano mica platelets with 3D lightning-rod effect for highly efficient bacterial biosensors based on surface-enhanced Raman scattering, *Journal of Materials Chemistry B*, **12**, 2024, pp. 3226-3239 (doi: 10.1039/D3TB02897F).

[14] M. Izzi, M. C. Sportelli, L. Torsi, R. A. Picca, N. Cioffi, Synthesis and antimicrobial applications of ZnO nanostructures: a review, *ACS Applied Nano Materials*, **6**, 2023, pp. 10881-10902 (doi: 10.1021/acsanm.3c01432).

[15] C.-W. Chiu, T.-K. Huang, Y.-C. Wang, B. G. Alamani, J.-J. Lin, Intercalation strategies in clay/polymer hybrids, *Progress in Polymer Science*, **39**, 2014, pp. 443-485 (doi: 10.1016/j.progpolymsci.2013.07.002).

[16] E. C. Le Ru, B. Auguié, Enhancement factors: A central concept during 50 years of surface-enhanced Raman spectroscopy, *ACS Nano*, **18**, 2024, pp. 9773-9783 (doi: 10.1021/acsnano.4c01474).

[17] Z. Wang, S. Zong, L. Wu, D. Zhu, Y. Cui, SERS-activated platforms for immunoassay: probes, encoding methods, and applications, *Chemical Reviews*, **117**, 2017, pp. 7910-7963 (doi: 10.1021/acs.chemrev.7b00027).

[18] S. Ostovar, M. Pourmadadi, M. A. Zaker, Co-biopolymer of chitosan/carboxymethyl cellulose hydrogel improved by zinc oxide and graphene quantum dots nanoparticles as pH-sensitive nanocomposite for quercetin delivery to brain cancer treatment, *International Journal of Biological Macromolecules*, **253**, 2023, pp. 127091 (doi: 10.1016/j.ijbiomac.2023.127091).

[19] W.-Y. Lei, J.-Y. Lee, S.-L. Chuang, M.-J. Bair, C.-L. Chen, J.-Y. Wu, D.-C. Wu, F. T. O'Donnell, H.-W. Tien, Y.-R. Chen, T.-H. Chiang, Y.-H. Hsu, T.-H. Hsu, P.-C. Hsieh, L.-J. Lin,

S.-L. Chia, C.-C. Wu, Y.-M. Subeq, S.-H. Wen, H.-C. Chang, Y.-W. Lin, K.-P. Sun, C.-H. Chu, M.-S. Wu, D. Y. Graham, H.-H. Chen, Y.-C. Lee, Eradicating *Helicobacter pylori* via ^{13}C-urea breath screening to prevent gastric cancer in indigenous communities: a population-based study and development of a family index-case method, *Gut*, **72**, 2023, pp. 2231-2240 (doi: 10.1136/gutjnl-2023-329871).

[20] Y.-C. Lee, T.-H. Chiang, H.-M. Chiu, W.-W. Su, K.-C. Chou, S. L.-S. Chen, A. M.-F. Yen, J. C.-Y. Fann, S. Y.-H. Chiu, S.-L. Chuang, Y.-R. Chen, S.-D. Chen, T.-H. Hu, Y.-J. Fang, M.-S. Wu, T. H.-H. Chen, Y.-P. Yeh, Screening for *Helicobacter pylori* to prevent gastric cancer: a pragmatic randomized clinical trial, *JAMA*, **332**, 2024, pp. 1642-1651 (doi: 10.1016/j.cgh.2013.10.029).

[21] J. Zhou, D. Wang, H. Yang, F. Wang, Specific detection of acetamiprid with aptamer based on flexible and adhesive SERS membrane, *Spectrochimica Acta Part A: Molecular and Biomolecular Spectroscopy*, **270**, 2022, pp. 120801 (doi: 10.1016/j.saa.2021.120801).

[22] X. Zhang, Y. Li, Z. Lei, Y. Yang, L. Tao, Z. Zheng, X. Feng, J. Zeng, Y. Zhao, Au nanoparticles on two-dimensional $MoWS_2$ as highly sensitive surface-enhanced Raman spectroscopy substrates for adenine detection, *ACS Applied Nano Materials*, **6**, 2023, pp. 16000-16008 (doi: 10.1021/acsanm.3c02993).

[23] Y.-F. Chen, W.-R. Chang, C.-J. Lee, C.-W. Chiu, Triangular gold nanoplates/two-dimensional nano mica platelets with a 3D lightning-rod effect as flexible nanohybrid substrates for SERS bacterial detection, *Journal of Materials Chemistry B*, **10**, 2022, pp. 9974-9983 (doi: 10.1039/D2TB02049A).

[24] P. F. Wu, X. Y. Fan, H. Y. Xi, N. Pan, Z. qian Shi, T. T. You, Y. K. Gao, P. G. Yin, Multifunctional self-assembled gold nanorod monolayer/$Ti_3C_2T_x$ nanocomposites based on interfacial electrostatic for highly sensitive SERS detection of organic dyes and adenine, *Journal of Alloys and Compounds*, **920**, 2022, pp. 165978 (doi: 10.1016/j.jallcom.2022.165978).

ICCM24
AUGUST 4-8, 2025
BALTIMORE CONVENTION CENTER
BALTIMORE, MARYLAND, USA

No Technical Paper Submission for:

Abdul Rahman Aravind

Construction of 3D Networked Epoxy Composite Using RGO and BPEI Coated Epoxy Microspheres for High Thermal Conductivity Application

Dayoung Kim[1], Suyeon Lee[1], Ahram Jeong[1], and Dong Gi Seong[1,2+]

[1] School of Chemical Engineering, Pusan National University, Republic of Korea

[2] Department of Polymer Science and Engineering, Pusan National University, Republic of Korea

[+] dgseong@pusan.ac.kr

INTRODUCTION

▪ Limitations of Conventional Thermally Conductive Polymer Nanocomposites

Disadvantages

Low thermal conductivity of only 0.2 W/mK

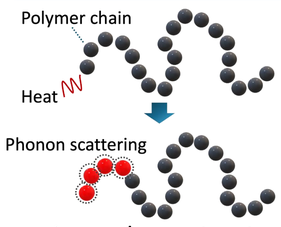

Simple approach for enhancing thermal conductivity

Integration of fillers into the polymer matrix

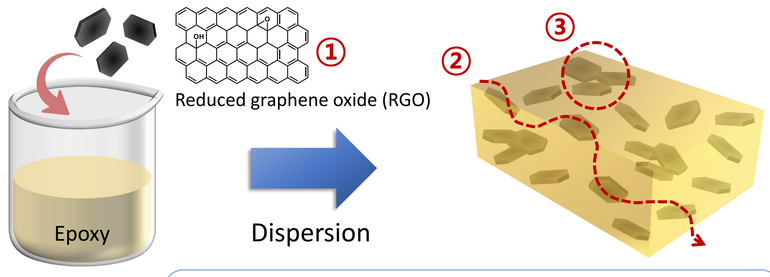

Limitations

① Only a few W/mK along out-of-plane direction

② Alignment primarily along in-plane direction

③ Tendency to aggregate by a large specific area

▪ This Study : Thermal Pathways via Segregated RGO

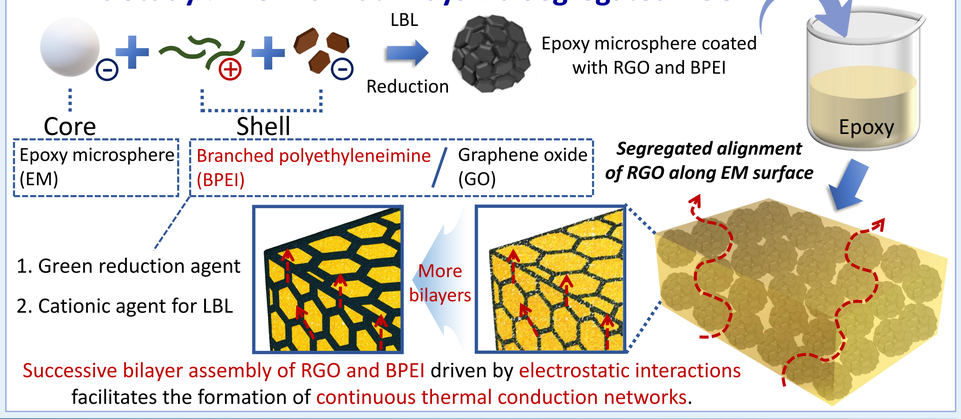

EXPERIMENT

▪ Preparation of Epoxy Microspheres Coated with RGO and BPEI via LBL Method

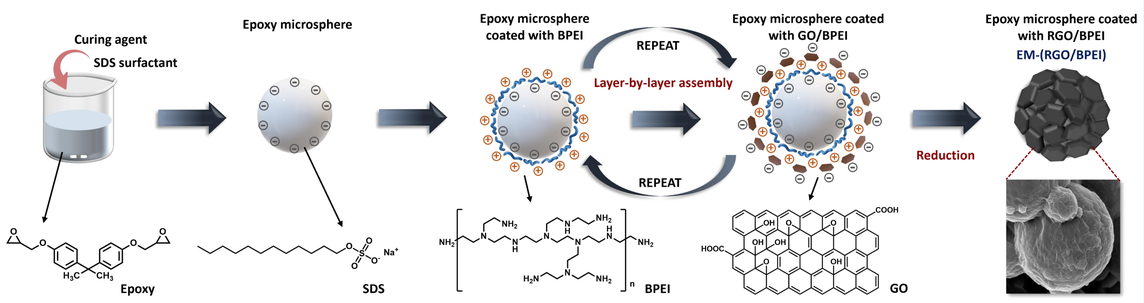

▪ Fabrication of Epoxy Composite Reinforced with EM-(RGO/BPEI)

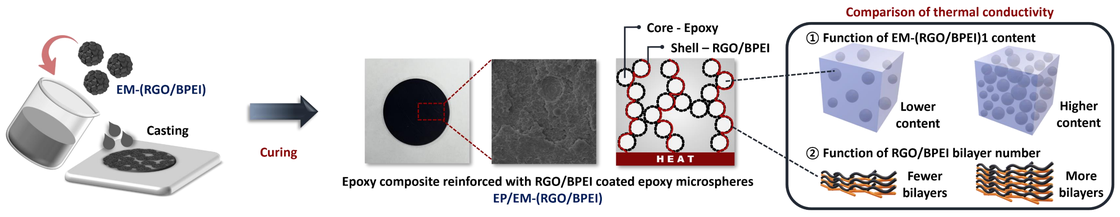

RESULTS AND DISCUSSION

▪ Morphological Studies of EM-(RGO/BPEI) and EP/EM-(RGO/BPEI)

SEM

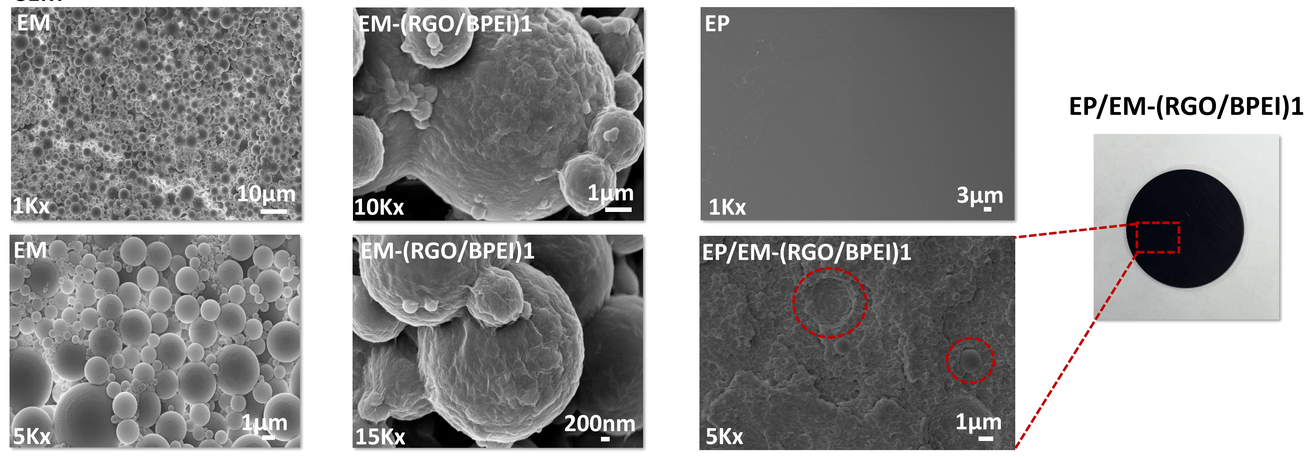

- Compared to EM with a smooth surface, EM-(RGO/BPEI)1 showed **increased surface roughness** due to the formation of **homogeneous RGO/BPEI coating**.
- This structure facilitated the development of **continuous thermal conduction pathways** by enabling **interparticle connections** between coated microspheres.

RESULTS AND DISCUSSION

▪ Characterization of GO Reduction by Using BPEI

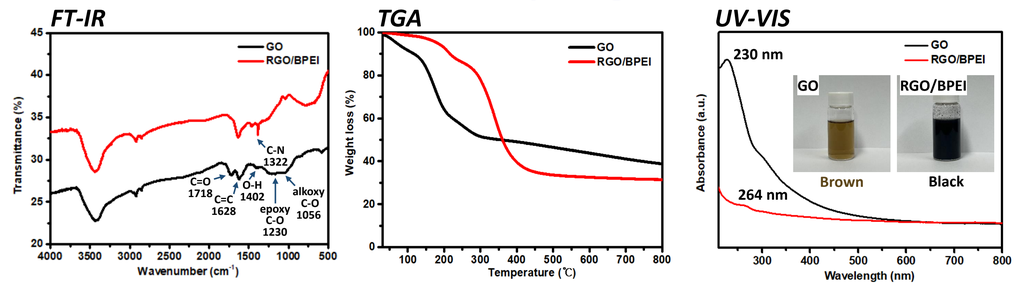

- Oxygen-containing groups were effectively removed and the conjugated structure was restored, confirming the **successful chemical reduction of GO by BPEI**.

▪ Confirmation of EM-(RGO/BPEI) with Various RGO/BPEI Bilayers

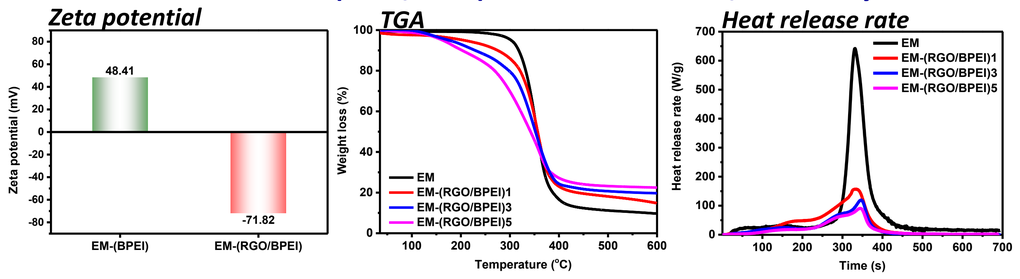

- Uniform and controllable RGO/BPEI coating was successfully achieved on the EM as the **number of deposition cycles increased**.

▪ Out-of-Plane Thermal Conductivity as a Function of EM-(RGO/BPEI)1 Content

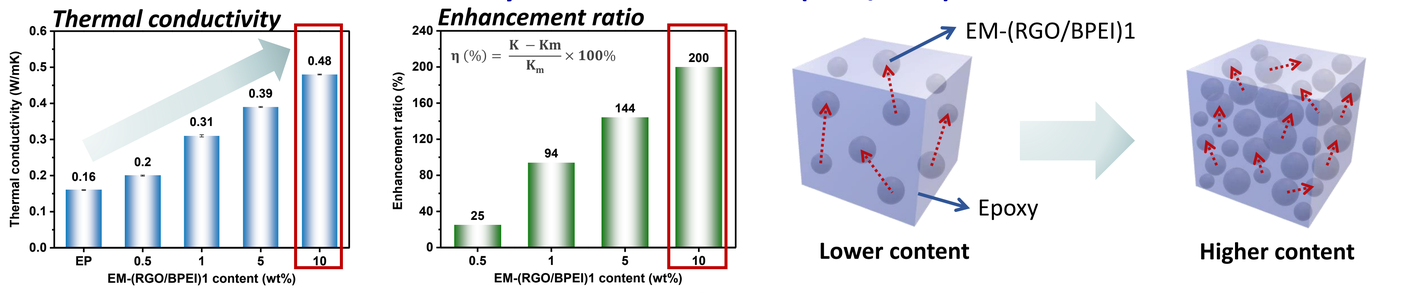

- The thermal conductivity increased with higher EM-(RGO/BPEI)1 content up to 10 wt% as the greater number of coated EM promoted **more frequent contact points** and resulted in **more effective heat transfer**.

▪ Out-of-Plane Thermal Conductivity as a Function of RGO/BPEI Bilayer Number

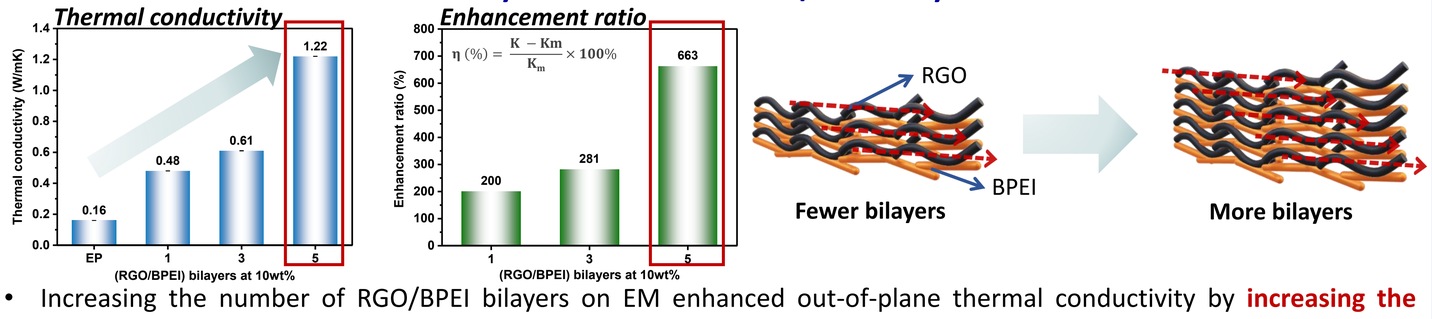

- Increasing the number of RGO/BPEI bilayers on EM enhanced out-of-plane thermal conductivity by **increasing the network density** and **improving the connectivity of thermally conductive domains** through a reinforced bridging effect.

RESULTS AND DISCUSSION

▪ Visualization on Thermal Properties of EP/EM-(RGO/BPEI)

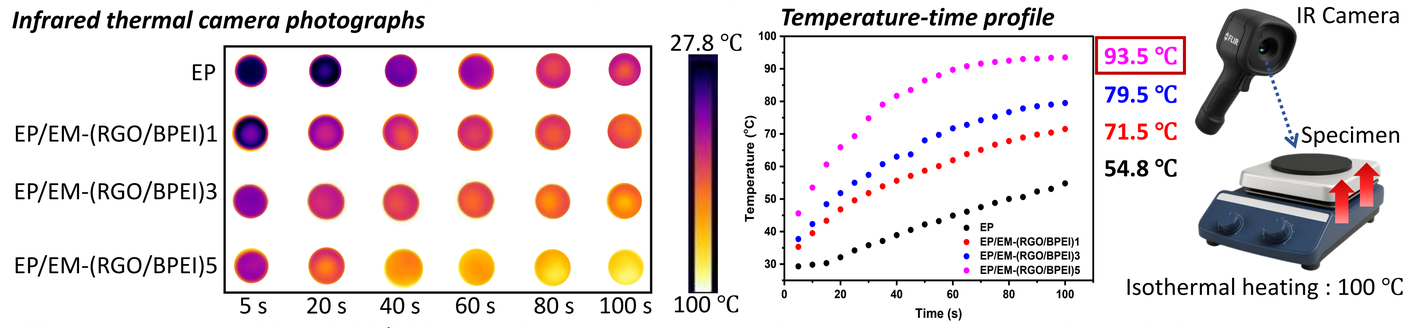

- The incorporation of EM-(RGO/BPEI) into the epoxy **accelerated heat propagation** through the thickness, as evidenced by **faster surface temperature rise** and **more rapid thermal response** under isothermal heating conditions.

▪ Dynamic Mechanical Analysis of EP/EM-(RGO/BPEI)

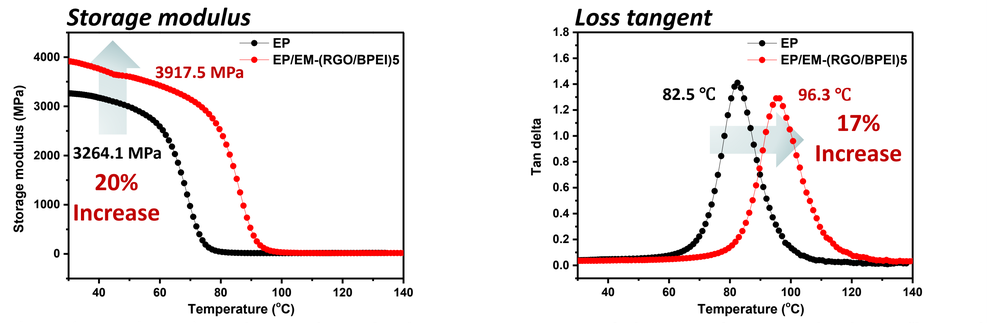

- EP/EM-(RGO/BPEI)5 showed a higher storage modulus and Tg, which reflected **restricted chain mobility** and **increased structural integrity** of the composite.

CONCLUSION

- This study demonstrated a scalable approach to enhance the out-of-plane thermal conductivity of epoxy composites by **constructing 3D conductive networks using epoxy microspheres uniformly coated with RGO/BPEI bilayers** through a LBL assembly process.
- The incorporation of **EM-(RGO/BPEI)5** resulted in a composite with an out-of-plane thermal conductivity of **1.22 W/mK**, corresponding to a **665% enhancement** compared to neat epoxy, offering a structurally controllable and novel design framework with **fundamental potential for high thermal conductivity applications**.

▪ Acknowledgement

- This research was supported by the National Research Foundation of Korea (NRF) funded by Ministry of Science and ICT (2022M3H4A1A04076372)

Enhanced Charge Transfer in Thermogalvanic Cells Via Nitrogen Doping of Oxidized CNT Electrodes

Seung-Yeol Jeon[1*] and Taewoo Kim[2]
[1] Institute of Advanced Composite Materials, Korea Institute of Science and Technology (KIST)
[2]Department of Mechanical Engineering, Incheon National University
(* E-mail: syjeon@kist.re.kr)

Abstract

- Low-temperature waste heat below 200℃ generated from nature, industry, and the human body exists everywhere, but is easily discarded due to a lack of technology to recover it. Thermogalvanic cells based on ion transport are inexpensive devices that directly convert heat into electricity and are flexible in material selection. Carbon nanomaterials are known to have excellent properties as thermogalvanic cell electrodes due to their large specific surface area and fast electron transport properties. This study explores the potential application of nitrogen-doped (N-doped) oxidized carbon nanotubes with melamine as thermogalvanic cell electrodes.

Introduction

➢ **Low-grade heat**

- Low-grade heat is abundant and ubiquitous but is generally discarded owing to a lack of cost-effective recovery technologies.
- To efficiently recover low-grade waste heat, thermoelectric technology offers an approach to convert heat directly into electrical energy without moving parts or audible noise.

➢ **Thermogalvanic cell**

- A disadvantage of solid-state thermoelectric devices is that their performance relative to cost has so far limited their application for waste heat recovery and they are expensive due to the use of rare elements.
- Thermogalvanic cells, also called thermo-cells, that utilize ion transport, provide a cost-effective solution for converting heat directly into electricity and present flexible device options for a variety of applications.
- To improve the performance of thermogalvanic cells, carbon nanomaterials with fast redox processes, high thermal and electrical conductivity, and high gravimetric surface area are selected.

➢ **Nitrogen-doped (N-doped) oxidized SWCNTs with melamine**

- In this study, we aimed to prepare electrodes with reduced charge transfer resistance by utilizing the improved electrical conductivity and increased specific surface area of N-doped oxidized CNTs and use them in a thermo-cell.

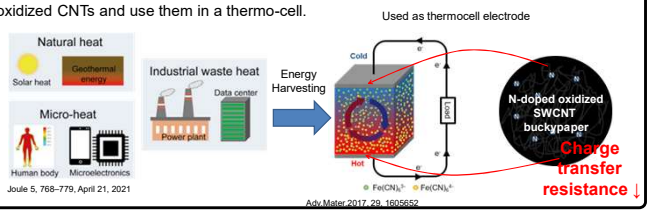

Experimental

➢ **Defect introduction into SWCNTs**

1. Purification (acid treatment)

- Acid: H_2SO_4/HNO_3 solution (volume ration of 3:1 = H_2SO_4:HNO_3)
- Method: sonication (6 h)

2. Introduction of defects and oxidation

- Acid: H_2SO_4, $KMnO_4$
- Method: stirring

3. Nitrogen-doping

- Nitrogen source: Melamine (SWCNT:melamine 1:8)
- Method: stirring (12 h) tip sonication (12 h)
- Thermal treatment:
  - ramping rate (10 ℃/min)
  - target temperature (800 ℃)
  - duration time (2 h)

➢ **Thermo-electrochemical cell**

1. Cell components

- 5 mm thick spacer
- Electrolyte: 0.4 M $K_3Fe(CN)_6$/$K_4Fe(CN)_6$
- Active electrodes: Pristine CNT, $KMnO_4$ treated CNT, N-doped CNT(stirring, tip sonication)

2. Temperature

- Hot source/Cold sink T: 45/15 ℃
- △T between active electrodes: 15.1-16.1 ℃

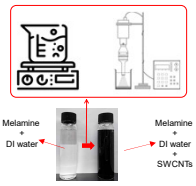

Mixing methods

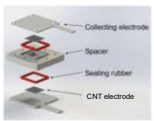

Illustration of the thermocell structure

Result & Discussion

✓ Four different types of electrodes were analyzed: pristine SWCNTs, SWCNTs with increased surface area achieved by introducing defects through $KMnO_4$ treatment, and nitrogen-doped oxidized SWCNTs prepared using two different melamine mixing methods (stirring and tip sonication).

❖ Structure analysis

➢ **Raman Spectroscopy**

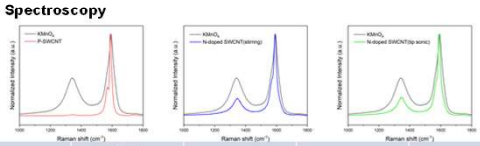

	Pristine SWCNT	$KMnO_4$	Stirring	Tip sonication
I_G/I_D ratio	82.35(±14.48)	1.86(±0.50)	3.7(±0.65)	3.1(±0.19)

- After $KMnO_4$ treatment, defects and functional groups are formed on the CNT surface, which reduces the G/D ratio. Phys. Status Solidi B2019,256, 1800742
- N-doped SWCNTs showed reduced D band and increased G/D ratio compared to KMnO4-treated SWCNTs. This indicates that defects can be rearranged towards the formation of sp^2-bound SWCNTs after heat treatment under N_2 atmosphere Chemical Physics Letters 424 (2006) 345–352
- If melamine was mixed with SWCNTs, the use of tip sonication resulted in the introduction of more defects compared to stirring, leading to a further decrease in the G/D ratio.

➢ **X-ray Photoelectron Spectroscopy (XPS)**

- When melamine was mixed with SWCNT through stirring and heat treated, the N atomic % was 6.43, and when mixed and heat treated through tip sonication, it was 4.51. Stirring resulted in a Pyridinic-N content approximately twice that of Graphitic-N, while tip sonication produced similar amounts of bot nitrogen species.

➢ **Scanning Electron Microscope (SEM)**

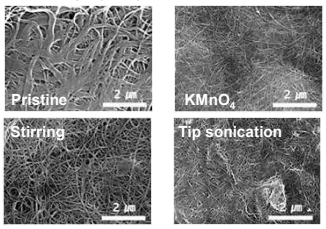

- In pristine SWCNTs, large bundles are observed due to the influence of van der Waals interactions, and after $KMnO_4$ treatment, the bonding effect is reduced due to defects formed on the surface, leading to the exfoliation of CNT bundles. Appl. Sci. 2021, 11, 8452, Surfaces and Interfaces 14 (2019) 1–8
- Compared to the $KMnO_4$ treated samples, the N-doped samples exhibit larger bundles and the tip sonication method tends to shorten the CNTs with longer processing times, resulting in a rougher surface compared to the stirred samples. Nanomaterials 2021, 11, 1469

❖ Thermo-electrochemical cell test

➢ **Voltage-current and power density**

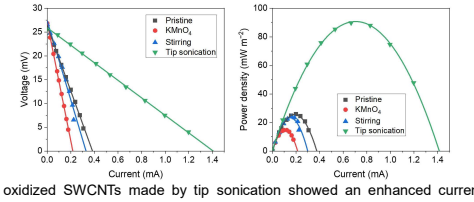

- N-doped oxidized SWCNTs made by tip sonication showed an enhanced current and power density while stirring exhibited poor performance.

➢ **Electrochemical impedance spectroscopy (EIS), Internal resistance**

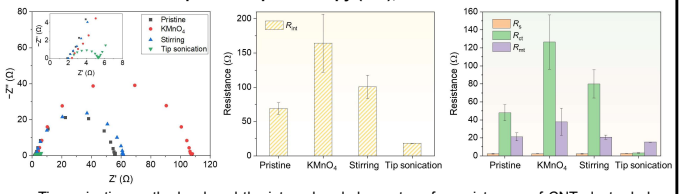

- Tip sonication method reduced the internal and charge transfer resistances of CNT electrode by 73% and 93%, respectively. This is likely attributed to the synergistic interaction between the elevated Graphitic-N content and oxygen functional groups on the CNT surface, which will be explored in future studies.

Summary

- **We chose a thermocell for harvesting low-grade heat and utilized N-doped oxidized SWCNTs as electrodes to reduce charge transfer resistance.**
- **Mixing CNT and melamine by tip sonication led to a significant reduction in internal resistance and improved thermocell performance, likely due to the synergistic interaction between the increased Graphitic-N content and oxygen functional groups on the CNT surface.**

syjeon@kist.re.kr

ICCM24
AUGUST 4-8, 2025
BALTIMORE CONVENTION CENTER
BALTIMORE, MARYLAND, USA

No Technical Paper Submission for:

Patrick Nowakowski

Processing of Composites Group
Otto Glöckel-Straße 2 | A-8700 Leoben | lvv@unileoben.ac.at | www.kunststofftechnik.at

Experimental Investigation of Mechanical Fiber Bundle Spreading

Hannah Rabe[1], Ewald Fauster[1]

1 Processing of Composites Group, Department Polymer Engineering and Science, Technical University Leoben, Austria

Introduction

Fiber bundles are commonly used in the production of fiber-reinforced composites to achieve high mechanical performance at low weight. For efficient processing – especially during impregnation or placement – precise control of fiber guidance, spreading, and tension is essential.

However, varying fiber properties, complex interactions between tension, path, and cross-section, as well as the need for reproducibility, pose significant challenges.

A modular test rig provides a controlled environment to systematically investigate these factors and gain valuable insights for process optimization.

Test Rig

Basic setup:

- Two motor-driven axes (unwinding and winding) for continuous fiber movement
- Fully modular test section between the axes
- Integration of various measurement and process modules possible



Roving Test Rig

Available components:

- Linear axis
- Light section sensors (LSS)
- Tension sensor
- Rotary encoder
- Infrared heater

Example Applications:

- Winding experiments on spherical geometries
- Quality assessment of thermoplastic impregnated tapes [1]
- Binder application on fiber bundles:
  - Application methods of binder powder
  - Melting binder using infrared heating

Fiber Bundle Spreading

Efficient impregnation is crucial to obtain high-performance fiber-reinforced composites. It directly impacts the mechanical properties of the final part.

- Mechanical spreading of fiber bundles:
  - Increases surface area
  - Reduces matrix flow paths
  - Leads to better wetting and fewer voids
- Test rig was adjusted to investigate spreading behavior
- Fiber bundles are mechanically spread over rods
- Width and height of fiber bundle measured using light section sensors (LSS)
- Wilson's model [2] is used to predict the expected fiber bundle width ω

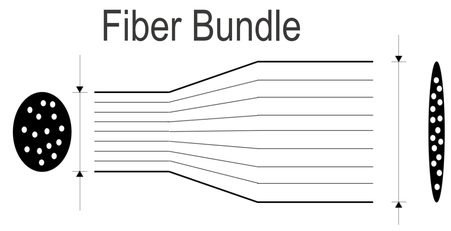

Scheme of Spreading Fiber Bundle



Various Rod Shapes



Guiding Fiber Bundle over Rods

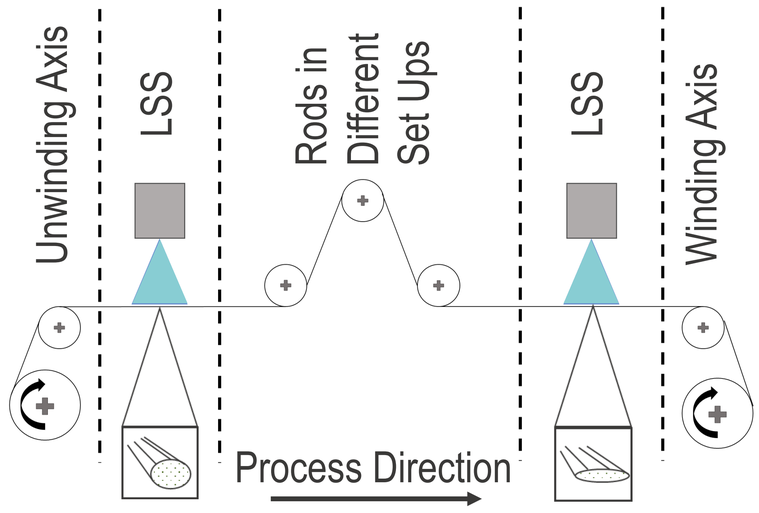

Scheme of Test Rig Modification for Spreading

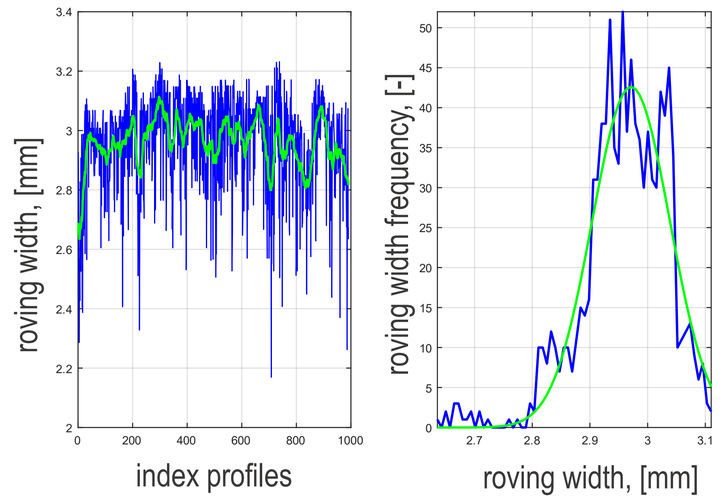

Presentation of Results Evaluation, Roving Width (left), Roving Width Frequency (right)

Outlook

The modular test rig enables controlled investigation of fiber bundle spreading and its impact on impregnation quality. Future work will focus on sustainable fiber materials and their specific processing challenges:

- the processing properties of staple fibers, including plant-based and recycled fibers
- the behavior of natural fibers under changing moisture conditions (e.g., water absorption, swelling, shrinkage)
- suitable strategies for quality stabilization in hygroscopic fiber systems

References

[1] S. Neunkirchen, E. Fauster, S. Lehner, and P. O'Leary, "Instrumentation of an Inspection Test Rig for Geometry Measurement of Fiber Bundles in Automated Composite Manufacturing," IEEE Trans. Instrum. Meas., no. 71, 2021, doi: 10.1109/TIM.2021.3132337

[2] Wilson, S, “Lateral spreading of fibre tows”, *Journal of Engineering Mathematics*, no. 32, 19-26, 1997, doi: 10.1023/a:1004253531061

DI Hannah Rabe
hannah.rabe@unileoben.ac.at
Processing of Composites Group
Technical University of Leoben



ICCM24
AUGUST 4-8, 2025
BALTIMORE CONVENTION CENTER
BALTIMORE, MARYLAND, USA

No Technical Paper Submission for:

Tsegaye Lemmi

VALORIZATION OF POST-CONSUMER BIODEGRADABLE POLYMER BLEND TO CREATE COMPOSITES WITH AGRO-INDUSTRIAL BY-PRODUCTS AS REINFORCING FILLERS

E. Palazzi[1], A. Pantaleoni[1], I. Bavasso[1], M. P. Bracciale[1], M. Falzarano[2], A. Polettini[2], R. Pomi[2], P. Russo[3], A. Marinelli[4], L. Paterlini[4], B. Del Curto[4], F. Sarasini[1] and J. Tirillò[1]

[1]Department of Chemical Engineering Materials Environment, Sapienza University of Rome, Via Eudossiana 18, 00184 Roma, Italy
http://www.uniroma1.it

[2]Department of Civil, Building and Environmental Engineering, Sapienza University of Rome, Via Eudossiana 18, 00184 Roma, Italy
http://www.uniroma1.it

[3]Institute for Polymers, Composites, and Biomaterials, National Council of Research, Via Campi Flegrei 34, 80078 Pozzuoli, Italy
https://www.cnr.it/

[4]Department of Chemistry, Materials and Chemical Engineering “Giulio Natta”, Politecnico di Milano, Milan, Italy
https://www.polimi.it/

Keywords: Biodegradable Polymers, Mechanical Recycling, Biocomposites, Natural Fibers, Thermomechanical Properties

ABSTRACT

This work explores the influence of multiple reprocessing cycles and the incorporation of natural fillers on the properties of a post-consumer biodegradable polymer blend composed mainly of PLA and PBS. The blend, originally used for the production of single-use cutlery, was subjected to up to eight extrusion/injection molding cycles to simulate mechanical recycling and to evaluate thermal, morphological, and mechanical stability. The results demonstrate that reprocessing does not significantly affect the mechanical properties of the blend, likely due to the stabilizing effect of the inorganic filler. A slight decrease in the PLA degradation peak was observed via TGA analysis, from 346.6 °C (Ext 1) to 343.3 °C (Ext 8), attributable to thermo-mechanical degradation phenomena such as chain scission. The incorporation of agro-industrial residues, such as wheat and rice straw (10 wt.%), enhanced both the tensile and flexural moduli of the composites. However, the presence of these natural reinforcements resulted in a slight reduction in both the onset degradation temperature and the PLA degradation peak, with decreases of 1.5% and 5.8% for wheat straw, and 3.4% and 5.5% for rice straw, respectively. These findings demonstrate that biodegradable blends can be recycled through multiple mechanical processing cycles without significant loss of performance. Furthermore, the integration of natural lignocellulosic fillers offers an effective solution to enhance mechanical properties while reducing reliance on virgin polymer content. This approach supports the development of sustainable and cost-effective composite materials aligned with circular economy principles.

1 INTRODUCTION

Originally designed as a symbol of technological progress, fuel-based plastics have revolutionized the modern world by making human life easier [1] thanks to their versatility, low weight, durability and low production costs [2]. The first plastics were introduced in the 1920s and production expanded in following years [3]. In 1965, the yearly production was about 15 million tons (Mt) and increased to 360

million tons (Mt) in 2018 [4]. As a result, the global annual production of plastics has continuously grown since their initial development. However, the use of plastic has created serious environmental problems due to their inability to undergo biological degradation and aging, leading to pollution and persistence in the environment for many years after disposal [5, 6]. This has caused large amounts of waste to accumulate in landfills or in natural environment [7]. Furthermore, the production processes of synthetic polymers, such as ethylene or propylene, require the use of harmful compounds and result in the formation of toxic by-products [8]. This has prompted the need to find alternatives to fuel-based polymers. In recent years, biodegradable polymers produced from natural raw materials, such as cellulose, starch and chitosan [6] have been introduced to the market. These materials are capable of biodegrading. Compared to petroleum-based polymers, they are more compatible with the principles of the circular economy, making them a preferred choice. Bioplastic production has grown significantly in recent years, rising from 2.4 million tons (Mt) in 2021 to an estimated 7.5 million tons (Mt) by 2026 [9]. The use of these polymers could represent a solution to plastic accumulation at the end of their life cycle, thanks to their ability to degrade through biological processes involving microorganisms capable of breaking the polymer chains [10]. However, biodegradation requires specific environmental conditions to occur, such as oxygen concentration, moisture, temperature [10, 11, 12], as well as a concentration of microorganisms, which play a crucial role in determining both the rate and degree of biodegradation, making it an inadequate rapid solution for waste disposal. Furthermore, although biodegradable polymers are often promoted as environmentally friendly alternatives to conventional plastics, their degradation is typically limited to controlled industrial composting facilities. Under natural environmental conditions, such as soil or marine ecosystems, the specific parameters required for biodegradation (temperature, humidity, oxygen levels, and microbial activity) are often not met. As a result, these materials may persist in the environment for extended periods, raising concerns about their actual end-of-life sustainability and environmental impact [13]. In addition, biodegradable polymers, as polylactic acid (PLA), polybutylene succinate (PBS) and poly(3-hydroxybutyrate-co-3-hydroxyvalerate) (PHBV) are more expensive than fossil-based polymers [14, 15].

Various strategies have been proposed to solve this issue, such as mechanical and chemical recycling, as well as incineration [16]. Chemical recycling involves solvolysis, pyrolysis, or hydrolysis reactions that break down the polymer chain into monomeric units and the recovered material can be repolymerized an indefinite number of times to produce the corresponding biopolymers [16]. On the other hand, it is the most expensive method due to the large amount of energy required to reach the temperature needed for the reaction to take place such as depolymerization [17]. Meanwhile incineration is able to produce energy but, besides being high-cost, could produce unsafe exhaust gases [18]. Mechanical recycling could be the most efficient solution to reduce landfill waste because it is cost-effective and without significant alteration in the chemical structure of materials [11, 19, 20]. Nevertheless, repeated mechanical reprocessing can lead to thermo-mechanical degradation phenomena, such as chain scission, resulting in mechanical property losses. Investigating the extent of these effects and how to mitigate them is essential for designing sustainable circular solutions. The use of agro-waste products can also be a viable solution to reduce landfill waste, as they often originate as residues from crop cultivation and agro-industrial operations. Materials such as rice straw, wheat straw, and coconut shells are renewable, abundantly available, and contribute to preserving the bio-based and biodegradable nature of the final product [21]. The incorporation of natural lignocellulosic fillers has gained significant attention as a strategy to enhance the stiffness, reduce polymer consumption, and improve the sustainability of the final bio-based polymer composites [22]. Recent studies have shown that combining mechanical recycling with the addition of natural fibers can not only recover post-consumer polymer waste but also improve or stabilize the mechanical properties of degraded polymers through fiber reinforcement [23]. The present study aims to evaluate the effect of reprocessing on a commercial post-consumer biodegradable polymer blend, as well as the influence of incorporating natural fillers derived from agricultural waste. This investigation addresses the performance evolution across multiple recycling cycles and assesses the feasibility of valorizing agro-waste as reinforcing fillers in bio-based composites.

The blend was reprocessed through eight cycles of extrusion and injection molding. The blend, used for the production of single-use cutlery, is PLA-based with PBS and inorganic filler. Mechanical properties were studied through tensile and three-point bending tests. Thermal properties were evaluated by

thermogravimetric analysis (TGA) and differential scanning calorimetry analysis (DSC), meanwhile thermo-mechanical tests as Heat Deflection Temperature (HDT) and Vicat (VST) were conducted. The effect of adding 10 wt.% of wheat straw (WS) and rice straw (RS) to the reprocessed blend was also investigated in terms of mechanical and thermal characterization of the final composite. Fracture surface analyses of the reprocessed polymer and the natural fiber composites were performed using Scanning Electron Microscopy (SEM) to assess morphological changes and filler dispersion. Potential effects on the blend compostability after subsequent mechanical reprocessing were evaluated through aerobic tests in controlled composting conditions.

2 MATERIALS

Disposable cutlery, including knives and forks, was crushed into pellets. The material was dried at 60 °C for 1 day before the extrusion (corotating twin-screw extruder, Thermo Scientific Process 11, ThermoFisher Scientific)/injection molding (Haake MiniJet IIPro, Thermo Fisher Scientific) reprocessing cycles. The rotational speed was set at 150 rpm and the following temperature profile was used from zone 1 to 8: 160 °C-165 °C-170 °C-170 °C-175 °C-180 °C-185 °C-180 °C. During the injection molding, the mold and the cylinder were maintained at 70 °C and 180 °C, respectively. To reproduce several reprocessing cycles, the polymer was pelletized after each injection and subjected to successive extrusion/injection cycles, up to eight times. The resulting samples were denoted as “Ext n”, where n represents the number of extrusion/injection cycles. Rice straw (RS) was supplied by Azienda Riso Milano (Italy), while wheat straw (WS) was obtained from Agriturismo Cascina Scanna (Italy). Both RS and WS were washed with tap-water and dried at 60 °C for 24 h. In the final stage, the materials were milled using a knife mill. To recover the inorganic filler, the polymer was dissolved using chloroform.

3 METHODS

Tensile and flexural tests were conducted with a Zwick/Roell Z010 universal testing machine. Tensile tests were conducted in displacement control with a 10 mm/min crosshead speed at room temperature according to ISO 527-2 (type 1BA, L_0 = 30 mm) using dog-bone specimens with a thickness of 1.5 mm and a width of 5 mm. Flexural properties were measured through three-point bending tests according to ISO 178. The crosshead speed was set at 5 mm/min and the sample dimensions were 80 × 10 × 4 mm. Thermogravimetric analysis (TGA) was conducted from room temperature to 800 °C in nitrogen atmosphere using a heating ramp of 10 °C/min (TG209 F1 Libra by Netzsch). Differential scanning calorimetry analysis (DSC) was performed using DSC 214 Polyma by Netzsch under a nitrogen flow of 60 mL/min, following this thermal program: first heating from -40 °C to 200 °C (5 min hold interval), cooling to -40 °C (5 min hold interval) and second heating to 200 °C. All heating and cooling steps were carried out with a rate of 10 °C/min. The softening point of materials was evaluated using Vicat test (VST), according to ISO 306_A120. The heat deflection temperature (HDT) was determinate using method A with a flexural stress of 1.80 MPa, in accordance with ISO 75. Both HDT e VST tests were carried out with Amsler Allround heat deflection tester by Zwick/Roell. Fracture surface morphologies were studied using scanning electron microscopy (FE-SEM Mira3 by Tescan) equipped with an Octane Elect Energy Dispersive Spectroscopy (EDS) System by EDAX (AMETEK GmbH). All specimens were sputter-coated with gold before the analysis. The particle size distribution (PSD) of WS and RS was determined using a Microtrac Sync laser diffraction analyzer (Verder Scientific S.r.l.). Analyses were carried out in dry mode, with a dispersion pressure set at 100 kPa and a suction pressure of 70 kPa. The PSD results are expressed in terms of percentile values: D10, D50, and D90. Specifically, D10 indicates the particle diameter below which 10% of the sample (by mass or volume) is smaller; D50 refers to the median particle size, meaning that 50% of the particles are smaller; and D90 corresponds to the diameter below which 90% of the particles fall.

Aerobic biodegradability was evaluated following ISO 14855-1. Bioplastics (Neat, Ext 1 and Ext 8) were mixed with mature compost (1:10 TS ratio, 50% moisture) in 1-L reactors and incubated at 58 °C for 180 days. Biodegradation was assessed monitoring CO_2 production with an infrared gas analyzer. Blank tests were conducted to measure the residual CO_2 production of compost. Cellulose control tests were conducted to ensure experimental validity. Residual bioplastics were sampled from the reactors

after 1 and 3 months of degradation and subjected to TGA to monitor potential changes in the polymeric matrix.

4 RESULTS AND DISCUSSION

The disposable material adopted in this study was analyzed using thermal analysis techniques to identify the polymer components. PLA was identified based on the presence of a glass transition temperature (T_g) at 49.1 °C, a melting peak (T_m) at 160.3 °C [24], and a crystallization peak (T_c) at 100.5 °C [25], while PBS was recognized by its T_m of 111.4 °C [26]. The T_g observed for PLA is lower than the values typically reported in the literature [27]. Thermogravimetric analysis revealed a main degradation peak at 347.7 °C [28], characteristic of PLA, and a second, less intense peak around 400 °C, associated with PBS [29]. Since the PLA degradation peak is more prominent than that of PBS, it can be inferred that PLA is the predominant component in the blend, accounting for around 50%. A residue of about 27.9% was measured at 800 °C. To evaluate the nature of the inorganic filler, the pellet was dissolved in chloroform and the residue was analyzed by EDS, which revealed the presence of talc and titanium dioxide. The former is typically used as a nucleating agent [30], while the latter is added to enhance the stability of polymer blends [31]. Subsequently, the polymer blend was reprocessed through eight extrusion/injection cycles. Thermal analysis results for samples 1, 6, and 8, as well as for composites containing wheat and rice straw, are reported in Table 1. TGA results revealed a shift both in the PLA degradation peak and in the temperature at 50% weight loss ($T_{50\%}$), decreasing from 346.6 °C to 343.3 °C and from 347.5 °C to 344.9 °C between Ext 1 and Ext 8, respectively. This trend is attributed to thermo-mechanical degradation and polymer chain scission occurring during repeated reprocessing cycles [11]. PBS, on the other hand, appeared unaffected by reprocessing.

While reprocessing did not significantly influence the blend's onset degradation temperature ($T_{5\%}$), the incorporation of agricultural waste caused a reduction in this parameter: 277.2 °C for wheat straw and 271.7 °C for rice straw. Similarly, the main degradation peak associated with PLA decreased to 323.2 °C for wheat straw and 324.4 °C for rice straw. This is attributed to the partial replacement of the more thermally stable polymer matrix with hemicellulose and cellulose components from wheat and rice straw, which are less thermally stable. This behavior is consistent with the findings reported by Eustathios Petinakis et al. [32], where increasing filler content leads to a reduction in PLA degradation temperature. DSC analysis did not show any significant changes in thermogram trends of the blend after reprocessing, likely due to the presence of titanium dioxide, which limits PLA chain mobility and contributes to thermal stability [33]. Furthermore, the incorporation of wheat and rice straw did not significantly affect the characteristic thermal transitions, in agreement with the results reported by Morreale et al. [34], who observed that natural fillers do not markedly influence the thermal behavior of biodegradable polymer matrices.

Sample	$T_{5\%}$ (°C)	$T_{50\%}$ (°C)	$T_{max\ degradation}$ (°C)
Ext 1	281.4	347.5	346.6
Ext 6	282.9	346	344.6
Ext 8	281.2	344.9	343.3
Ext 8 + 10%WS	277.2	337.4	323.2
Ext 8 + 10%RS	271.7	328.7	324.4

Table 1: TGA results of reprocessed polymer blend and composites.

Tensile and flexural quasi-static tests were conducted on both the reprocessed polymer blend and composites, and the findings are reported in Table 2.

It can be observed that reprocessing does not significantly affect the mechanical properties of the blend, either in terms of flexural or tensile behavior. This can be attributed to the presence of titania, as the literature reports the ability of titania to form bonds with the carboxylic groups of PLA [35]. The presumed reduction in PLA molecular weight due to reprocessing is expected to increase the number of terminal carboxylic groups available for interaction with the titania surface. Such enhanced interfacial interactions between the PLA matrix and the filler may contribute to mitigating the decline in mechanical

properties associated with PLA degradation [11]. As a result, it progressively reinforces the polymer matrix more effectively.
The addition of 10 wt.% of rice and wheat straw leads to an increase in both flexural and elastic moduli, accompanied by a decrease in maximum flexural and tensile strength. This behavior is attributed to the poor interfacial adhesion between the fiber and the matrix, as can be observed in the representative SEM micrograph (Figure 1). Particle size analysis revealed that the particle dimensions of RS are larger than those of WS by approximately 57.7%, 36.7%, and 44.8%, corresponding to the cumulative distribution percentiles D10, D50, and D90, respectively. As a result, the higher specific surface area of wheat straw contributes to increased matrix stiffness, as further supported by Berthet et al. [36]

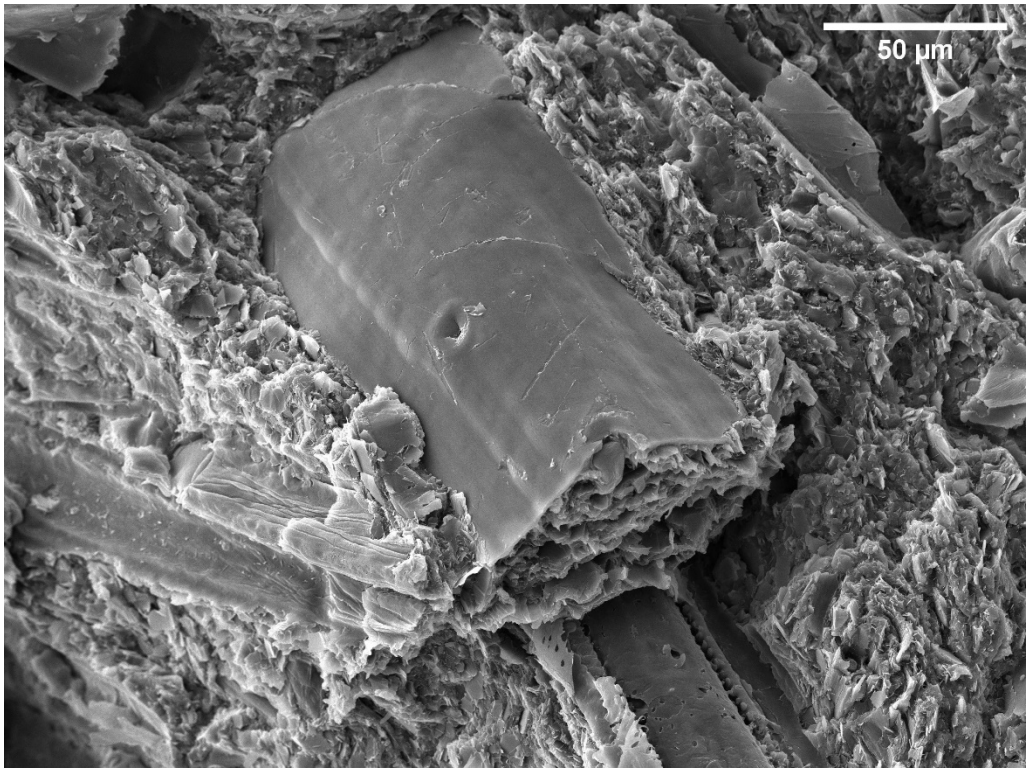

Figure 1: SEM micrograph of Ext 8 with 10 wt.% of WS.

Sample	Tensile Strength (MPa)	Young's Modulus (GPa)	Flexural Strength (MPa)	Flexural Modulus (GPa)
Ext 1	42.0 (± 0.5)	3.0 (± 0.2)	62.0 (± 0.4)	6.1 (± 0.7)
Ext 6	42.6 (± 0.8)	3.2 (± 0.1)	65.4 (± 0.5)	6.2 (± 0.2)
Ext 8	43.9 (± 0.2)	3.3 (± 0.1)	64.8 (± 0.5)	6.1 (± 0.1)
Ext 8 + 10%WS	34.4 (± 0.8)	7.3 (± 0.5)	46.5 (± 1.8)	6.5 (± 0.4)
Ext 8 + 10%RS	29.7 (± 2.6)	7.0 (± 0.7)	36.4 (± 4.3)	5.8 (± 0.7)

Table 2: quasi-static mechanical tests results.

The effect of reprocessing cycles was also assessed through Heat Deflection Temperature (HDT) and Vicat Softening Temperature (VST) tests. In the HDT test, the sample is subjected to bending under a specified load, whereas in the VST test, the sample undergoes penetration by a standard indenter. The results are reported in Table 3.

Sample	HDT (°C)	VST (°C)
Ext 1	49.3	52.3
Ext 6	49.5	53.8
Ext 8	49.4	53.5
Ext 8 + 10%WS	50.9	54.5
Ext 8 + 10%RS	49.1	56.6

Table 3: HDT and VST results.

The HDT and VST results are consistent with those obtained from quasi-static mechanical tests, confirming that the addition of natural fillers contributes to an enhancement of the stiffness of the final composites [37, 38].
Biodegradation tests revealed that reprocessing had no significant impact on the biodegradability of the polymer blend. All the tested samples exhibited a comparable biogas evolution in terms of kinetics and yields achieving a biodegradation degree in the range 72 – 76% in 180 days. TGA indicated a preferential degradation of PLA, which was no longer detectable in the bioplastic samples after 1 and 3 months of testing. After four months testing, residual bioplastic particles were no longer visually detectable, but based on the biodegradation degree attained, it can be reasonably concluded that PBS was not fully degraded. In contrast, the addition of natural fillers in the composites led to an increased degradation rate. This behavior can be attributed to the superior hydrophilicity of the composites, which facilitates water uptake, the promotion of microbial colonization on the fibrous surface, and the intrinsic biodegradability of the lignocellulosic fillers, which degrade more readily under composting conditions [39, 40].

5 CONCLUSIONS

This study investigated the thermal, morphological, and mechanical behavior of a post-consumer biodegradable polymer blend. Reprocessing led to a slight reduction in PLA thermal stability due to thermo-mechanical degradation, with minimal effect on PBS. Despite this, mechanical performance remained stable, likely due to a better dispersion of inorganic fillers over cycles. The incorporation of wheat and rice straw slightly reduced the onset degradation temperature but did not significantly affect DSC results, indicating that natural fillers had limited impact on the blend's thermal behavior. Mechanical tests showed increased stiffness but reduced strength, due to weak matrix-filler adhesion. Wheat straw showed better performance compared to rice straw, possibly due to its higher cellulose content and smaller fiber dimensions. Overall, the results highlight the potential of combining mechanical recycling of biodegradable polymer blends with agro-industrial residues to create composites with balanced thermal and mechanical performance while preserving their potential for compostability. Future developments should focus on improving the interfacial adhesion between the polymer matrix and natural fillers through surface treatments or compatibilizers, in order to enhance strength and toughness without compromising biodegradability.

ACKNOWLEDGEMENTS

The research was partially funded by the European Union – NextGenerationEU, Mission 4, Component 1, within the BOOMERANG project (Bio-cOmpOsite Material dEsign forpAckagiNG, CUP B53D23006530006) and partially within the National Recovery and Resilience Plan (NRRP), Mission 4, Component 2, Investment 1.1, Call for tender No. 104 published on February 2, 2022 by the Italian Ministry of University and Research (MUR), funded by the European Union – NextGenerationEU – Project Title CellBioReComp – CUP I53D23006560001.

REFERENCES

[1] J. Soares, I. Miguel, C. Venâncio, I. Lopes, and M. Oliveira, "Public views on plastic pollution: Knowledge, perceived impacts, and pro-environmental

behaviours," *J Hazard Mater*, vol. 412, p. 125227, Jun. 2021, doi: 10.1016/J.JHAZMAT.2021.125227.

[2] J. Hopewell, R. Dvorak, and E. Kosior, "Plastics Recycling: Challenges and Opportunities," *Philos Trans R Soc Lond B Biol Sci*, vol. 364, pp. 2115–2126, May 2009, doi: 10.1098/rstb.2008.0311.

[3] P. G. C. Nayanathara Thathsarani Pilapitiya and A. S. Ratnayake, "The world of plastic waste: A review," *Cleaner Materials*, vol. 11, p. 100220, Mar. 2024, doi: 10.1016/J.CLEMA.2024.100220.

[4] M. H. Rahman and P. R. Bhoi, "An overview of non-biodegradable bioplastics," *J Clean Prod*, vol. 294, p. 126218, Apr. 2021, doi: 10.1016/J.JCLEPRO.2021.126218.

[5] D. Kasprzak, C. C. Mayorga-Martinez, and M. Pumera, "Sustainable and Flexible Energy Storage Devices: A Review," *Energy & Fuels*, vol. 37, no. 1, pp. 74–97, Jan. 2023, doi: 10.1021/acs.energyfuels.2c03217.

[6] V. Kumar, R. Sehgal, and R. Gupta, "Blends and composites of polyhydroxyalkanoates (PHAs) and their applications," *Eur Polym J*, vol. 161, p. 110824, Dec. 2021, doi: 10.1016/J.EURPOLYMJ.2021.110824.

[7] R. Geyer, J. R. Jambeck, and K. L. Law, "Production, use, and fate of all plastics ever made," 2017. [Online]. Available: http://advances.sciencemag.org/

[8] S. C. Teixeira, N. O. Gomes, T. V. de Oliveira, P. Fortes-Da-Silva, N. de F. F. Soares, and P. A. Raymundo-Pereira, "Review and Perspectives of sustainable, biodegradable, eco-friendly and flexible electronic devices and (Bio)sensors," *Biosens Bioelectron X*, vol. 14, p. 100371, Sep. 2023, doi: 10.1016/J.BIOSX.2023.100371.

[9] L. G. Pinaeva and A. S. Noskov, "Biodegradable biopolymers: Real impact to environment pollution," *Science of The Total Environment*, vol. 947, p. 174445, Oct. 2024, doi: 10.1016/J.SCITOTENV.2024.174445.

[10] G. Kale, T. Kijchavengkul, R. Auras, M. Rubino, S. E. Selke, and S. P. Singh, "Compostability of bioplastic packaging materials: An overview," Mar. 08, 2007. doi: 10.1002/mabi.200600168.

[11] I. Bavasso *et al.*, "Recycling of a commercial biodegradable polymer blend: Influence of reprocessing cycles on rheological and thermo-mechanical properties," *Polym Test*, vol. 134, p. 108418, 2024, doi: https://doi.org/10.1016/j.polymertesting.2024.108418.

[12] S. M. Emadian, T. T. Onay, and B. Demirel, "Biodegradation of bioplastics in natural environments," *Waste Management*, vol. 59, pp. 526–536, Jan. 2017, doi: 10.1016/J.WASMAN.2016.10.006.

[13] A. Folino, A. Karageorgiou, P. S. Calabrò, and D. Komilis, "Biodegradation of Wasted Bioplastics in Natural and Industrial Environments: A Review," *Sustainability*, vol. 12, no. 15, 2020, doi: 10.3390/su12156030.

[14] K. Babaremu, O. P. Oladijo, and E. Akinlabi, "Biopolymers: A suitable replacement for plastics in product packaging," Oct. 01, 2023, *KeAi Communications Co.* doi: 10.1016/j.aiepr.2023.01.001.

[15] M. Zhang *et al.*, "Recent advances in polymers and polymer composites for food packaging," Mar. 01, 2022, *Elsevier B.V.* doi: 10.1016/j.mattod.2022.01.022.

[16] R. Kumar, K. Sadeghi, J. Jang, and J. Seo, "Mechanical, chemical, and bio-recycling of biodegradable plastics: A review," *Science of The Total Environment*, vol. 882, p. 163446, 2023, doi: https://doi.org/10.1016/j.scitotenv.2023.163446.

[17] K. Hirao, Y. Nakatsuchi, and H. Ohara, “Alcoholysis of Poly(l-lactic acid) under microwave irradiation,” *Polym Degrad Stab*, vol. 95, no. 6, pp. 925–928, Jun. 2010, doi: 10.1016/J.POLYMDEGRADSTAB.2010.03.027.

[18] K. W. Meereboer, M. Misra, and A. K. Mohanty, “Review of recent advances in the biodegradability of polyhydroxyalkanoate (PHA) bioplastics and their composites,” Sep. 07, 2020, *Royal Society of Chemistry*. doi: 10.1039/d0gc01647k.

[19] I. Zembouai, S. Bruzaud, M. Kaci, A. Benhamida, Y.-M. Corre, and Y. Grohens, “Mechanical Recycling of Poly(3-Hydroxybutyrate-co-3-Hydroxyvalerate)/Polylactide Based Blends,” *J Environ Polym Degrad*, vol. 22, no. 4, 2014, doi: 10.1007/s10924-014-0684.

[20] E. Achukwu and M. Mfon Owen, “Influence of Reprocessing Cycles on the Mechanical and Morphological Properties of Recycled Polypropylene.” [Online]. Available: https://www.researchgate.net/publication/356536452

[21] K. Manickaraj *et al.*, “Value-added utilization of agricultural wastes in biocomposite production: Characteristics and applications,” *Ann N Y Acad Sci*, vol. n/a, no. n/a, doi: https://doi.org/10.1111/nyas.15368.

[22] J. Yang, Y. C. Ching, and C. H. Chuah, “Applications of Lignocellulosic Fibers and Lignin in Bioplastics: A Review,” *Polymers (Basel)*, vol. 11, no. 5, 2019, doi: 10.3390/polym11050751.

[23] F. Asad, K. Immonen, T. Kiiskinen, A. Mikkelson, and E. Sarlin, “The Impact of Mechanical Recycling on Ligno-Cellulose Fibre Containing PLA Biocomposite,” *Polymers (Basel)*, vol. 17, no. 6, 2025, doi: 10.3390/polym17060732.

[24] B. Tisserat, N. Joshee, A. Mahapatra, G. Selling, and V. Finkenstadt, “Physical and mechanical properties of extruded poly(lactic acid)-based Paulownia elongata biocomposites,” *Ind Crops Prod*, vol. 44, pp. 88–96, Mar. 2013, doi: 10.1016/j.indcrop.2012.10.030.

[25] Y. Liu *et al.*, “Crystallization Morphology Regulation on Enhancing Heat Resistance of Polylactic Acid,” *Polymers (Basel)*, vol. 12, no. 7, 2020, doi: 10.3390/polym12071563.

[26] T. Yokohara and M. Yamaguchi, “Structure and properties for biomass-based polyester blends of PLA and PBS,” *Eur Polym J*, vol. 44, no. 3, pp. 677–685, Mar. 2008, doi: 10.1016/J.EURPOLYMJ.2008.01.008.

[27] T. Zhao *et al.*, “Thermal, crystallization, and mechanical properties of polylactic acid (PLA)/poly(butylene succinate) (PBS) blends,” *Polymer Bulletin*, vol. 81, no. 3, pp. 2481–2504, Feb. 2024, doi: 10.1007/s00289-023-04848-9.

[28] G. WANG and A. LI, “Thermal Decomposition and Kinetics of Mixtures of Polylactic Acid and Biomass during Copyrolysis,” *Chin J Chem Eng*, vol. 16, no. 6, pp. 929–933, Dec. 2008, doi: 10.1016/S1004-9541(09)60018-5.

[29] A. Anstey, S. Muniyasamy, M. M. Reddy, M. Misra, and A. Mohanty, “Processability and Biodegradability Evaluation of Composites from Poly(butylene succinate) (PBS) Bioplastic and Biofuel Co-products from Ontario,” *J Polym Environ*, vol. 22, no. 2, pp. 209–218, 2014, doi: 10.1007/s10924-013-0633-8.

[30] W. Zhuang, J. Liu, J. H. Zhang, B. X. Hu, and J. Shen, “Preparation, characterization, and properties of TiO2/PLA nanocomposites by in situ polymerization,” *Polym Compos*, vol. 30, no. 8, pp. 1074–1080, 2009, doi: https://doi.org/10.1002/pc.20658.

[31] Q. Zhang, D. Li, H. Zhang, G. Su, and G. Li, “Preparation and properties of poly(lactic acid)/sesbania gum/nano-TiO2 composites,” *Polymer Bulletin*, vol. 75, no. 2, pp. 623–635, 2018, doi: 10.1007/s00289-017-2059-2.

[32] E. Petinakis *et al.*, “Biodegradation and thermal decomposition of poly(lactic acid)-based materials reinforced by hydrophilic fillers,” *Polym Degrad Stab*, vol. 95, no. 9, pp. 1704–1707, Sep. 2010, doi: 10.1016/J.POLYMDEGRADSTAB.2010.05.027.

[33] S. Bergaliyeva *et al.*, “Thermal and Mechanical Properties of Reprocessed Polylactide/Titanium Dioxide Nanocomposites for Material Extrusion Additive Manufacturing,” *Polymers (Basel)*, vol. 15, no. 16, 2023, doi: 10.3390/polym15163458.

[34] M. Morreale, A. Liga, M. C. Mistretta, L. Ascione, and F. P. La Mantia, “Mechanical, Thermomechanical and Reprocessing Behavior of Green Composites from Biodegradable Polymer and Wood Flour,” *Materials*, vol. 8, no. 11, pp. 7536–7548, 2015, doi: 10.3390/ma8115406.

[35] H. Zhang *et al.*, “Preparation, characterization and properties of PLA/TiO2 nanocomposites based on a novel vane extruder,” *RSC Adv.*, vol. 5, no. 6, pp. 4639–4647, 2015, doi: 10.1039/C4RA14538K.

[36] M. A. Berthet, H. Angellier-Coussy, V. Chea, V. Guillard, E. Gastaldi, and N. Gontard, “Sustainable food packaging: Valorising wheat straw fibres for tuning PHBV-based composites properties,” *Compos Part A Appl Sci Manuf*, vol. 72, pp. 139–147, May 2015, doi: 10.1016/J.COMPOSITESA.2015.02.006.

[37] S. Yaisun and T. Trongsatitkul, “PLA-Based Hybrid Biocomposites: Effects of Fiber Type, Fiber Content, and Annealing on Thermal and Mechanical Properties,” *Polymers (Basel)*, vol. 15, no. 20, Oct. 2023, doi: 10.3390/polym15204106.

[38] F. A. Rabbani *et al.*, “Lignocellulosic fiber reinforcement in PPRC composites: An analysis of structural and thermal enhancements,” *PLoS One*, vol. 19, no. 11 November, Nov. 2024, doi: 10.1371/journal.pone.0309128.

[39] A. Quitadamo, V. Massardier, V. Iovine, A. Belhadj, R. Bayard, and M. Valente, “Effect of Cellulosic Waste Derived Filler on the Biodegradation and Thermal Properties of HDPE and PLA Composites,” *Processes*, vol. 7, no. 10, 2019, doi: 10.3390/pr7100647.

[40] A. Kozłowska, K. Gorący, and M. El Fray, “Biodegradable Polymer Composites Based on Poly(butylene succinate) Copolyesters and Wood Flour,” *Polymers (Basel)*, vol. 17, no. 7, 2025, doi: 10.3390/polym17070883.

Gas diffusion nanocomposite layer with enhanced mass transport with surface functionalization by laser irradiation

Taesik Eom[1,*], Seungcheol Shin[2], Myungjin Hong[2], Eun Sang Lee[1,3], Sang-Eui Lee[2,*]

[1] KIURI Center for Hydrogen Based Next Generation Mechanical System, Inha University, Incheon 21999, South Korea
[2] Multifunctional Composites and Structural Integration Lab, Inha University, Incheon 21999, South Korea
[3] Ultra Precision Nano System Lab, Inha University, Incheon 21999, South Korea
*Corresponding author (E-mail: djaxod89@gmail.com, selee@inha.ac.kr)

ICCM24 — 24TH INTERNATIONAL CONFERENCE ON COMPOSITE MATERIALS

MCSI Lab — Multifunctional Composites & Structural Integration Lab

Introduction

Gas and water mass transfer remain significant challenges in **proton exchange membrane fuel cells (PEMFCs)**, making the surface properties and structural configuration of the **gas diffusion layer (GDL)** critical for performance. A newly proposed **gas diffusion nanocomposite layer (GDNL)** features a **multi-walled carbon nanotube/polytetrafluoroethylene (MWCNT/PTFE) nanocomposite film with a laser-perforated pattern filled with carbon black/PTFE (CB/PTFE) microporous material**, forming a **hydrophilic–superhydrophobic columnar interface**. In this design, laser irradiation induces hydrophilicity along the inner walls of the perforations, directing water transport through the hydrophilic interface. Meanwhile, the superhydrophobic CB/PTFE filling channels gas transport inside the structure and repels water outward, ensuring separated and efficient pathways for gas and water movement. **This unique columnar interface in the LPM-GDNL design results in ~40% and ~50% improvements in current and power density** in the concentration loss region at relative humidity levels of 50% and 100%, respectively, compared to conventional commercial carbon paper GDLs.

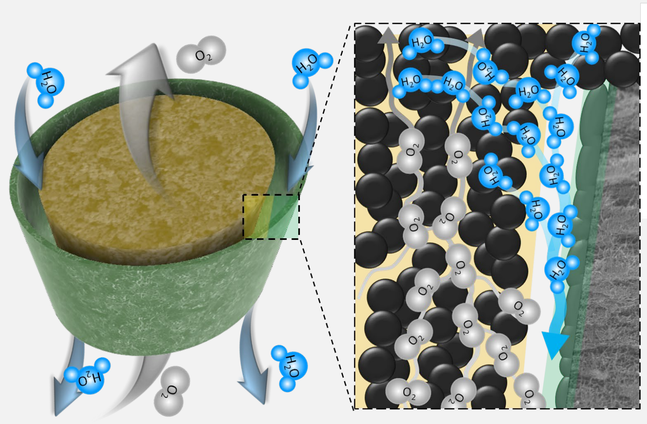

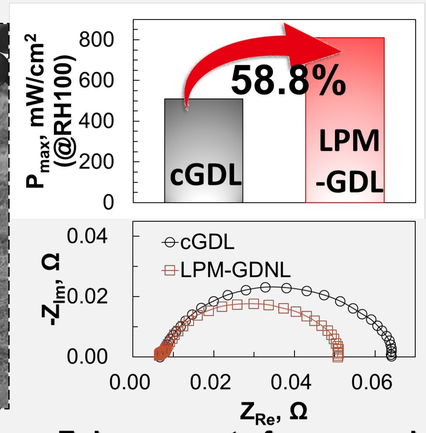

Enhancement of power and improvement of mass transport

Experiment

◆ Film fabrication

- MWCNT and PTFE were mixed with a dispersant.
- A film was prepared by vacuum filtration.
- The fabricated film was sintered by hot pressing at 350 °C.

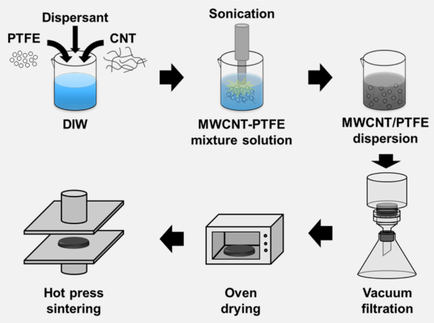

◆ Laser perforation and MPL coating

- Holes (60 x 110 µm) were perforated at 200 µm intervals using a laser.
- CB/PTFE MPL was coated on the perforated film and sintered.

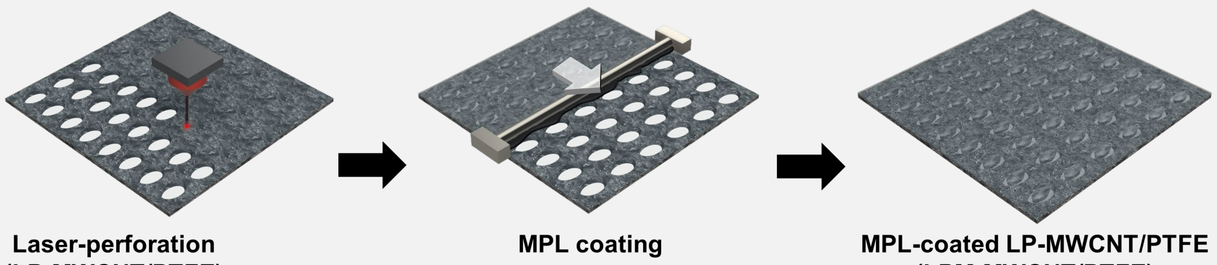

Laser-perforation (LP-MWCNT/PTFE) → MPL coating → MPL-coated LP-MWCNT/PTFE (LPM-MWCNT/PTFE)

Results & Discussion

◆ Characterization

- Laser irradiation produced uniformly spaced, truncated cone-shaped holes with a bumpy texture in the C50P50 film.
- These holes were filled with CB/PTFE slurry, forming a porous MPL layer that provides gas pathways and firmly anchors in place.

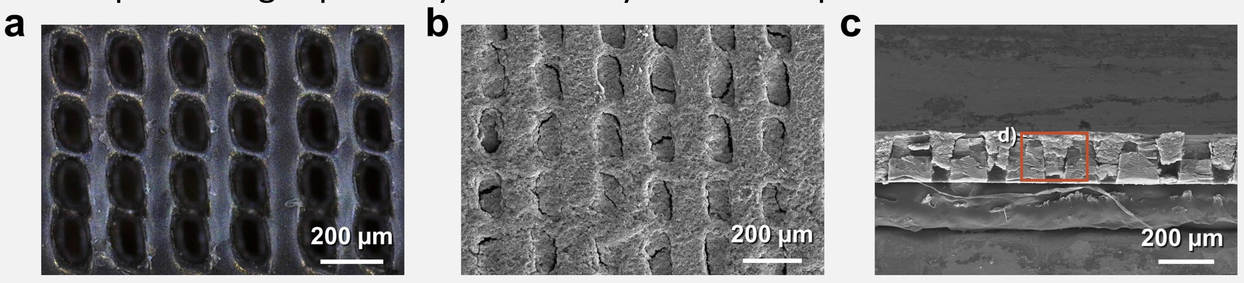

- Laser irradiation increased surface hydrophilicity and tension by changing chemistry and microstructure.
- This enabled unique gas and water transport through a nano-micro hybrid interface.

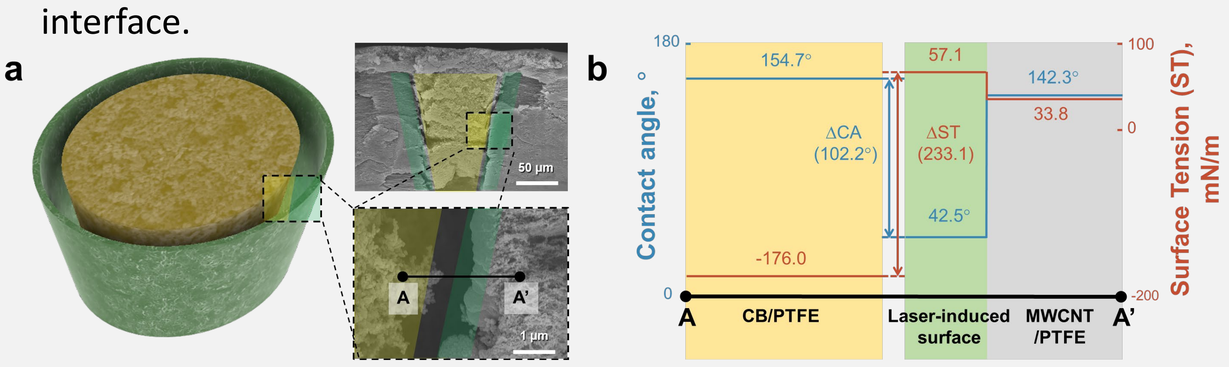

- XPS analysis showed that laser irradiation reduced C=C and C-F bond intensities while increasing oxygen and nitrogen content.
- These compositional changes enhanced surface hydrophilicity and altered the nanocomposite's chemical structure.

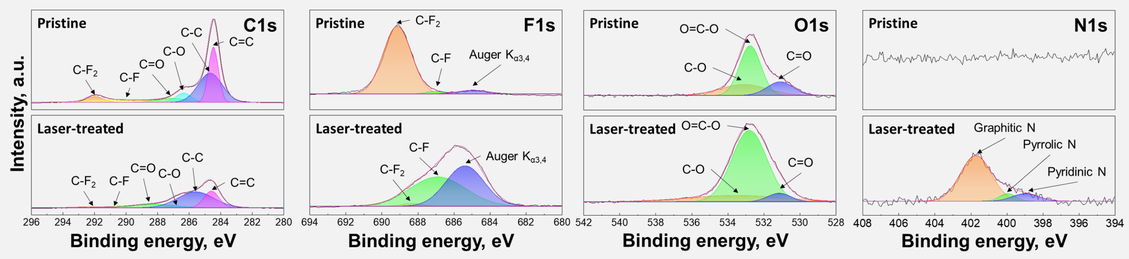

◆ GDL properties

- Laser perforation reduced the conductivity of the film, but CB/PTFE coating restored conductivity and increased compressibility significantly.
- LPM-GDNL exhibited much higher through-plane gas permeability than commercial GDLs due to vertical perforations and porous MPL coating.
- Water breakthrough pressure was greatly reduced in LPM-GDNL, indicating enhanced water removal through the hydrophilic interface.

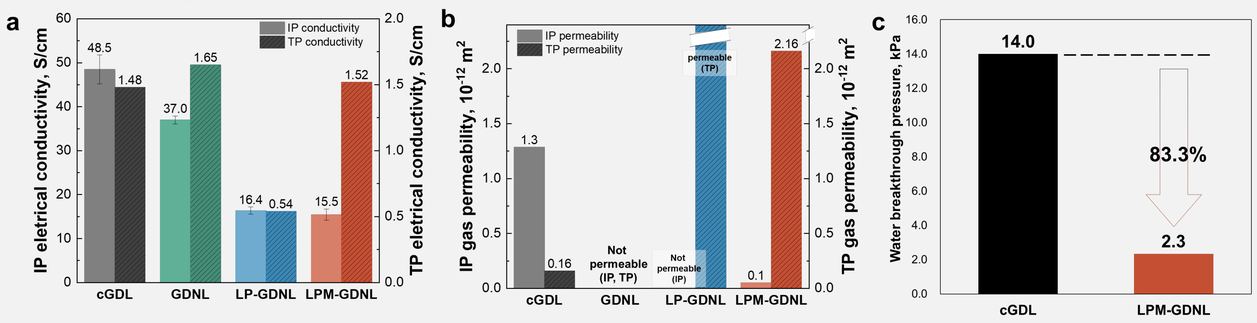

◆ PEMFC performances

- LPM-GDNL showed significantly improved PEMFC performance under both RH50 and RH100 by combining enhanced conductivity with a hydrophilic–superhydrophobic columnar interface.
- This structure reduced ohmic and mass transport resistance, as confirmed by EIS analysis, leading to better charge transfer and water management.
- Compared to commercial GDLs, LPM-GDNL achieved up to 59% higher power density, demonstrating the effectiveness of combining perforation and surface energy control.

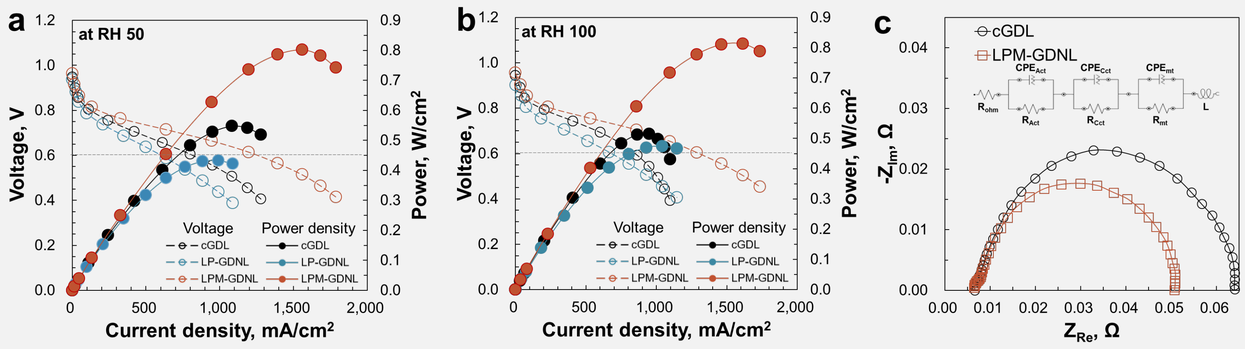

Conclusions

- Laser-perforated MWCNT/PTFE films with CB/PTFE filling created a hydrophilic–superhydrophobic columnar structure that improved water removal and gas transport.
- This design lowered electrical resistance and enhanced PEMFC performance by reducing ohmic and mass transport losses.
- Further optimization of composition and perforation is expected to boost mass transport even more, supporting sustainable hydrogen energy.

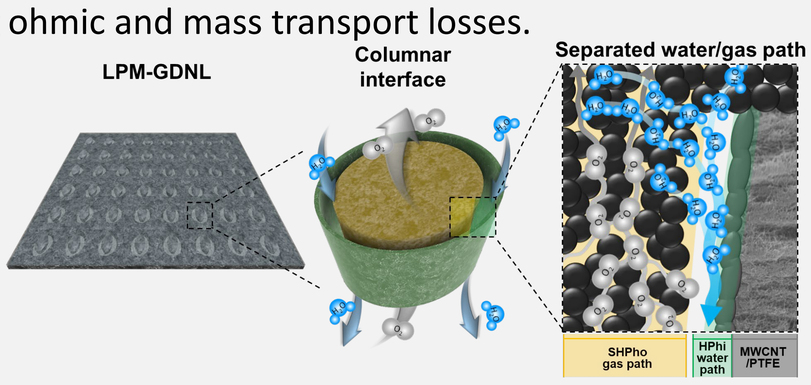

References

- T. Eom et al., *'A gas diffusion nanocomposite layer with a hydrophilic–superhydrophobic columnar interface for enhanced water and gas transport'*, ***J. Mater. Chem. A***, 2025,**13**, 17963-17975

NOVEL ELECTROSPINNING PVDF/BI2O3/CEO2 COMPOSITE YARN: A VERSATILE APPROACH TOWARDS FUNCTIONAL X-RAY SHIELDING TEXTILE

Siyuan Zhao, Lindsey Waterton Taylor, Vien Cheung and Yu Shi



Recent environmental challenges, particularly concerns regarding nuclear waste management, have heightened the urgency for developing practical radiation protection solutions suitable for daily use. While existing nanofiber membranes exhibit promising radiation shielding capabilities, their inherent limitations in flexibility and processability significantly restrict their integration into wearable applications. Traditional lead-based protective materials, despite their effectiveness, present substantial weak points in terms of weight and mobility constraints.

This study presents a novel approach to developing functional X-ray shielding textiles through Electrospinning PVDF/Bi_2O_3/CeO_2 composite yarns. With increasing concerns about nuclear waste management and radiation protection in daily applications, there is an urgent need for lightweight, flexible protective materials that overcome the limitations of traditional lead-based shields. Considering the heavyweight of conventional lead garments, PVDF was selected as the polymer matrix due to its lightweight nature and versatile wearable applications. This research introduces an innovative composite system incorporating Poly(vinylidene fluoride) (PVDF) with high-Z elements, specifically Bismuth Oxide (Bi_2O_3) and Cerium Oxide (CeO_2) nanoparticles, to achieve an optimal balance between protection efficacy and textile functionality.



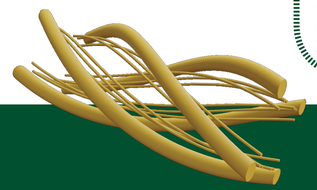

Material Synthesis

The composite was developed using PVDF nano powder (Mw = 534,000, Sigma-Aldrich) as the polymer, integrated with high-Z elements Bi_2O_3 and CeO_2 (Sigma-Aldrich) as X-ray attenuating materials. This combination leverages PVDF's mechanical flexibility and chemical stability, while the Bi_2O_3 and CeO_2 provide effective X-ray attenuation. The solvent comprised a 3:1 ratio of dimethyl sulfoxide (DMSO) to acetone.

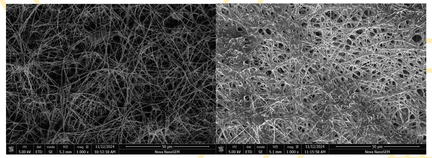

SEM for PVDF & PVDF-Bi_2O_3 and CeO_2

Morphological analysis via scanning electron microscopy elucidates the structural characteristics of the fabricated fibrous networks at 1000 magnification. The pristine PVDF architecture exhibits well-defined nanofibrous formations with consistent dimensional uniformity, while the PVDF matrices containing Bi_2O_3 and CeO_2 display marginally enhanced fiber diameters attributed to the successful incorporation of high-Z elements.

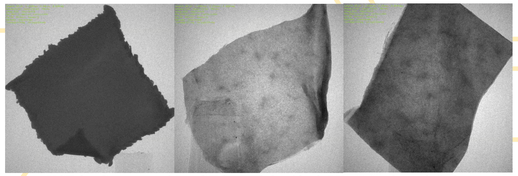

XCT for Commercial Lead Film and thin/thick PVDF-Bi_2O_3 and CeO_2

These images are captured by ZEISS Xradia 410 Versa. By comparing it to the lead film, this is conducted on three samples with the same X-ray energy parameters, 80 kV-10.00 W, revealing the relative attenuation capabilities through grayscale contrast. The commercial lead film exhibits maximal attenuation (darkest contrast), and the thick PVDF-based composite achieves comparable X-ray shielding performance.

Yarn & Strength

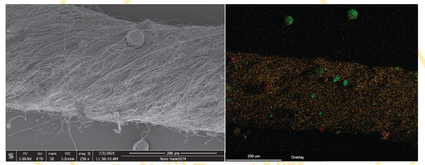

SEM & EDX for PVDF-Bi_2O_3 and CeO_2 as Yarn

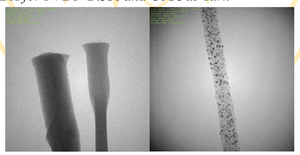

XCT for different ratio of metal oxides as PVDF-Bi_2O_3 and CeO_2

Under the same X-ray condition, comparative analysis between hand-twisted thick membranes and electrospun yarns reveals notable differences in shielding performance. The electrospun yarns demonstrated stable and consistent characteristics, but a lower density of metal oxide nanoparticles.

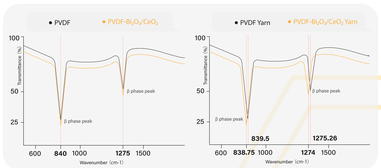

FTIR Spectra Analysis for PVDF yarn & PVDF-Bi_2O_3 and CeO_2

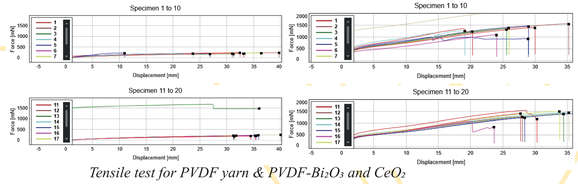

Tensile test for PVDF yarn & PVDF-Bi_2O_3 and CeO_2

PVDF - Bi_2O_3 and CeO_2 composite exhibits a significantly enhanced tensile strength of 1.27 N compared to pure PVDF. However, the tensile displacement at break for pure PVDF averages 32.3, while the PVDF-Bi_2O_3/CeO_2 composite fails at 29.6 mm, indicating reduced elasticity.

Discussion

Through current characterisation and tensile testing, a stable composite comprising PVDF with bismuth oxide and cerium oxide has been identified. However, the fabrication of yarns via electrospinning technology necessitates further optimisation of the ratio balance between these materials, as several key challenges have emerged:

1- **High metal oxide concentrations** enhance both X-ray shielding efficacy and mechanical strength but promote agglomeration prior to spinning, compromising electrospinning solution stability.

2- **Reduced metal oxide concentrations** preserve PVDF's inherent elasticity but fail to achieve the desired X-ray shielding performance.

3- **Establishing an optimal balance** between processability and functional properties remains a critical challenge requiring systematic investigation of compositional ratios.

Conclusions

The incorporation of high-Z elements (Bi_2O_3 and CeO_2) into PVDF demonstrates excellent X-ray shielding performance while enhancing the polymer's β-phase mechanical properties, showing promising potential for functional protective textiles. The experimental results confirm that these high-Z elements contribute to X-ray shielding capabilities.

UNIVERSITY OF LEEDS

TRIBOLOGICAL INVESTIGATION OF THE INTERFACE BETWEEN STEEL PIN AND CFRP TUBE

Floyd Daniel Bischop[1], Torben Deutschmann[2] and Dieter Krause[3]

[1] Institute of Product Development and Mechanical Engineering Design, Hamburg University of Technology
Denickestraße 17, D-21073 Hamburg, Germany
Email: floyd.bischop@tuhh.de, web page: http://www.tuhh.de/pkt/institut

[2] Institute of Product Development and Mechanical Engineering Design, Hamburg University of Technology
Denickestraße 17, D-21073 Hamburg, Germany
Email: torben.deutschmann@tuhh.de, web page: http://www.tuhh.de/pkt/institut

[3] Institute of Product Development and Mechanical Engineering Design, Hamburg University of Technology
Denickestraße 17, D-21073 Hamburg, Germany
Email: dieter.krause@tuhh.de, web page: http://www.tuhh.de/pkt/institut

Keywords: Lightweight design, CFRP, Tribological testing, Tool interface, Lubrication

ABSTRACT

Carbon fiber reinforced plastics (CFRP) offer great potential for lightweight construction due to their high specific stiffness and strength, especially in electric drive systems with rotating components. However, the substitution of steel by CFRP in highly stressed, tribologically relevant interfaces, such as hollow shank taper interfaces (HSK), is hindered by numerous influencing factors. To systematically investigate these factors, particularly the winding angle and lubrication, the tribological properties of CFRP are analyzed on an application-oriented test rig.

For this purpose, pin-on-tube tests are conducted using CFRP tube samples with three winding angles (±10°, ±45°, ±89°), as well as hardened steel references tested against steel counterfaces are conducted. The samples undergo linear reciprocating motion under a normal force of 450 N over 20,000 cycles. The friction coefficients are determined under dry conditions as well as under flood lubrication with a water-miscible coolant lubricant.

The results show that lubrication with coolant lubricant significantly reduces the dynamic coefficient of friction. The lowest friction coefficients, 0.17, are achieved at a winding angle of ±10°. In lubricated tests, the specific wear was below the measurement resolution. Microscopic images show typical fiber-matrix damage in unlubricated samples, which is significantly less pronounced under lubricated conditions. A comparison with literature values for steel HSK interfaces demonstrates the influence of the pin-on-tube arrangement for reference samples. The investigations show the suitability of CFRP for tribologically stressed interfaces. However, further studies are necessary for transfer to real applications such as HSK.

1 INTRODUCTION

Lightweight construction in various application areas, such as aerospace or electric drive systems with rotating components, aims to increase energy efficiency. The replacement of steel components with lighter materials is particularly important in applications where the drive itself is in motion, such as in machine tools. A low component weight combined with high stiffness, thermal stability, and dynamic damping represents a significant competitive criterion for drive components [1]. With increasing demands on the power density of electric drive systems, conventional materials are reaching their physical limits [2]. A promising solution lies in the use of CFRP. Due to its excellent ratio of strength and stiffness to weight, CFRP offers a high lightweight potential and allows for a significant reduction

in component mass. Interfaces to other drive components are still predominantly made of steel, as CFRP interfaces, such as bearing seats or the hollow-shank taper interface, have been scarcely investigated with regard to surface quality, coefficient of friction, and wear behavior.

The HSK interface according to DIN 69893-1 [3] between the machine tool spindle and tool holder is a tribologically highly stressed interface. This interface demands tight tolerances for flatness and concentricity (< 3 µm) to ensure interchangeability, repeatability, secure torque transmission, and high bending stiffness [4]. However, clamping processes and dynamic loads lead to wear mechanisms that reduce the service life of these interfaces. In particular, wear on the taper surface, which primarily serves for alignment, can impair the required high precision in terms of concentricity and repeatability [Bre16]. In material-removing machining of workpieces, coolant lubricant (KSS) is used [5]. The main function of KSS is to dissipate heat and reduce friction. Additionally, during a tool change, KSS is used to clean the taper surfaces of impurities, thereby reducing HSK wear [6]. According to Landmann [7], KSS affects the mechanical properties of CFRP depending on exposure duration, diffusion rate, and type of coolant lubricant. While the carbon fibers themselves are hardly affected by contact with coolants, the matrix undergoes intermolecular interactions, hydrolysis, oxidation, and leaching, which lead to a deterioration of mechanical properties [7].

Compared to conventional metallic materials, CFRP offers considerable advantages. Higher specific stiffness and strength enable higher rotational speeds and accelerations, improving the efficiency of relevant systems. However, replacing steel with CFRP also increases the complexity of tribological influencing factors, especially due to material-dependent parameters such as the type of fiber and matrix materials, fiber content, and fiber orientation. According to Friedrich [8], fiber orientation significantly influences the tribological behavior of fiber-reinforced composites. The lowest friction and wear values occur when fibers are oriented perpendicular to the friction surface (N-orientation), whereas parallel (P) and antiparallel (AP) orientations lead to significantly higher friction and wear rates.

To investigate influencing factors, model tests such as pin-on-plate tribometers have been conducted [9, 10]. However, with increasing abstraction of the tribological system, the transferability of results decreases, making application-oriented investigations necessary [11]. Since the use of CFRP involves a multitude of influencing factors that cannot be isolated in field tests, an application-near test rig is necessary, allowing targeted variation and analysis of individual parameters. The aim of this work is to systematically investigate the influencing factors on the tribologically stressed HSK interface caused by the substitution of steel with CFRP. For this purpose, an application-near tribometer is used to analyze the effects of the degree of abstraction of the test geometry, lubrication, and fiber orientation on friction and wear behavior, thereby providing a basis for the industrial application of CFRP interfaces.

2 EXPERIMENTAL STUDIES

To investigate cost-effectively and individually the high number of influencing factors, the tribological system is abstracted so that model tests are carried out in a pin-on-tube arrangement according to Kilian et al. [12]. In this arrangement, a rounded block rubs against the inside of a tube specimen, which undergoes a linear reciprocating motion. The schematic setup of the arrangement with the functional principle and the measurement technology is shown in the half-section in Figure 1. By using tube specimens, the same manufacturing process as in the application case can be employed, as well as the simulation of the same type of motion and surface pressure. A reduction of the influencing factors compared to the application case is achieved through the cylindrical geometry of the tube specimens, since this test setup avoids an overlap of axial and radial forces, as occurs in the force transmission in an HSK, and additionally allows conclusions to be drawn about other tribologically stressed interfaces such as bearing seats.

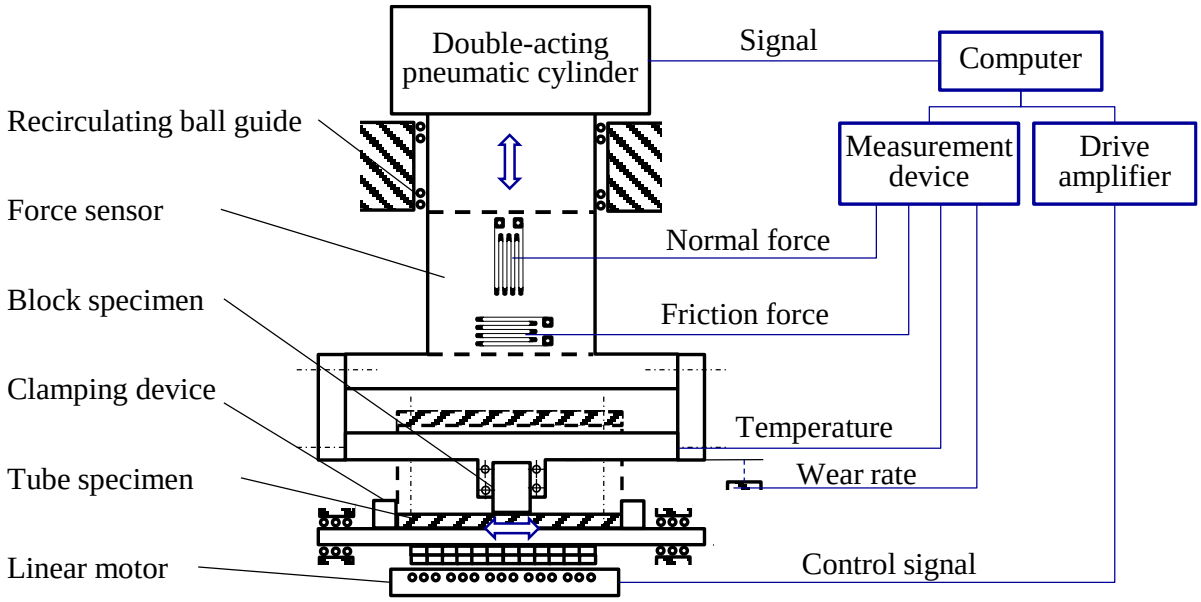

Figure 1: Schematic setup of the model tests in pin-on-tube arrangement in half-section with the functional principle and measurement technology.

2.1 MATERIALS AND SAMPLE PREPARATION

The CFRP samples are manufactured using the filament winding process with T700 carbon fibers (company Toray) and the epoxy winding resin LY556 (company Huntsman). To investigate the influence of the winding angle, three CFRP specimens with balanced winding angles of ±45°, ±89°, and ±10° are wound. Hardened steel specimens (material 16MnCr5) with a Rockwell hardness, scale C of 56±4 HRC serve as reference samples. The specimens are ground to an inner diameter of 52 mm, an outer diameter of 60 mm, and a length of 40 mm. The form and positional tolerances are chosen in accordance with the HSK interface 63 according to [3], whereby, for example, the concentricity and roundness of the tubes are tolerated within 3 µm.



Figure 2: CFRP specimens in the orientations from left to right:
winding angles of ±10°, ±45°, and ±89°.

As the tribological counterbody, rounded steel blocks with the dimensions 10 × 10 × 20 mm are chosen. The steel blocks are made of 16MnCr5 and are case-hardened (56±4 HRC) like the reference specimens. The functional surface, i.e., the rounded area, is ground to a nominal radius of 26 mm with tolerance limits of +0.000 and –0.025 mm to enable area contact between the friction partners. Additionally, a surface form tolerance of 3 µm is maintained. A borehole in the rounded block allows the use of water cooling during the tests.

2.2 EXPERIMENTAL SETUP

The tribological investigations of the influencing factors are carried out using the LRT test rig (Linear-Reciprocating Tribological test bench) in the pin-on-tube arrangement. In this test rig, a linear motor drives a tube specimen while a block, rounded to match the tube specimen, is pressed against it to induce friction. Figure 2 shows the LRT test rig on the left and a close-up of the friction partners in the pin-on-tube arrangement on the right. The block is loaded with a normal force via a double-acting pneumatic cylinder. The tube specimen, exemplarily shown with balanced winding angles of ±45°, undergoes a linear reciprocating motion.

A 3-axis force sensor of the type K3D120 from the manufacturer ME-Meßsysteme GmbH, with a nominal force of 1 kN per axis, continuously measures the normal, lateral, and friction forces above the sample holder of the block. For displacement measurement in the vertical direction, a laser sensor of the type optoNCDT 1220 from the manufacturer MICRO-EPSILON with a measuring range of 0-25 mm is used, while for displacement measurement in the horizontal direction, a laser sensor of the type optoNCDT 1402 with a measuring range of 0-200 mm is employed. Temperature measurement is conducted using two surface thermoelements of type K, which are attached with polyimide adhesive tape to the outer surface of the specimen and placed on the surface of the steel holder close to the steel block.

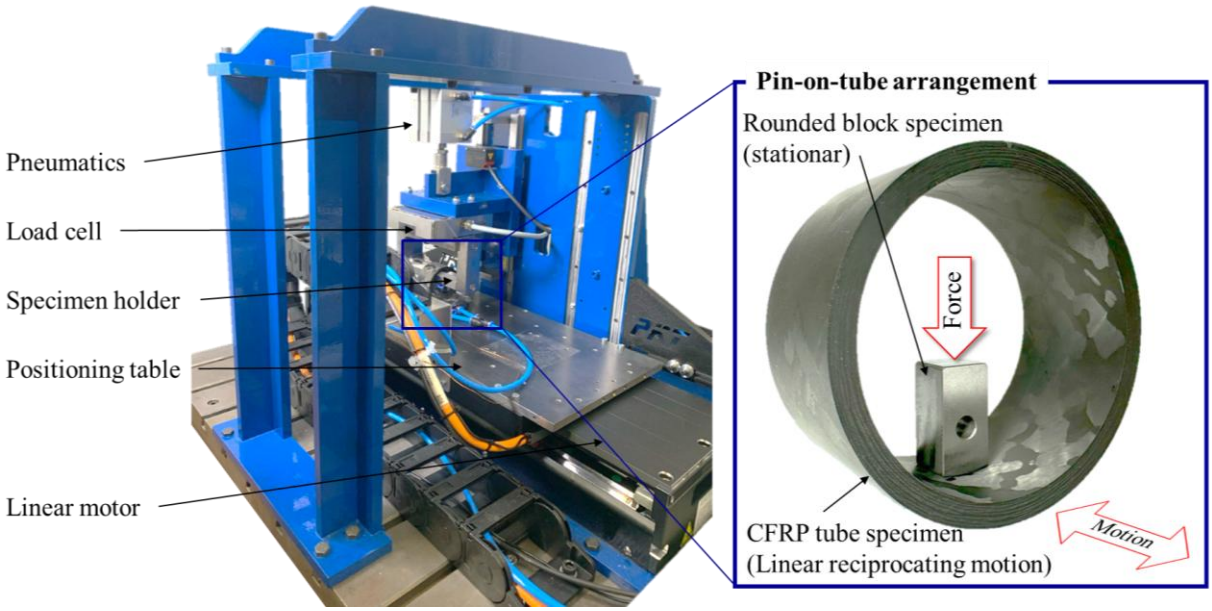

Figure 3: LRT test rig with a close-up of the pin-on-tube arrangement.

The test procedure is divided into four steps, which are followed for each test (see Figure 4). To ensure a plane-parallel contact between the triboelements, the steel block is ground with 800-grit sandpaper before the test (a). During this process, 300 grinding cycles are performed under a normal force of 50 N under dry conditions. The specimen is then cleaned with isopropanol, and the surface roughness is determined using the roughness measuring instrument MarSurf UD 120 from the manufacturer Mahr. The CFRP specimens are conditioned over a period of eight hours at a temperature of 50 °C to remove any absorbed moisture from the material and to avoid potential measurement distortions. The weight determination is carried out using the laboratory precision balance Sartorius Basic BA110S from the manufacturer Sartorius. Subsequently, the specimens are reinstalled in the LRT test rig.

Depending on whether testing is to be performed with or without lubricant, coolant lubricant is added to a bath (b). For this purpose, a water-miscible, mineral oil-based coolant concentrate from the manufacturer unitech Kühlschmierstoffe GmbH with the trade name HOSMAC-S 3630 is used. To use a solution that is as critical as possible for carbon fiber-reinforced plastics, the maximum possible coolant concentration is chosen during mixing, corresponding to an eight percent solution. For each test, 50 ml of coolant is added so that the contact area between the CFRP specimen and the steel stamp is

completely surrounded by coolant, thus achieving flood lubrication.

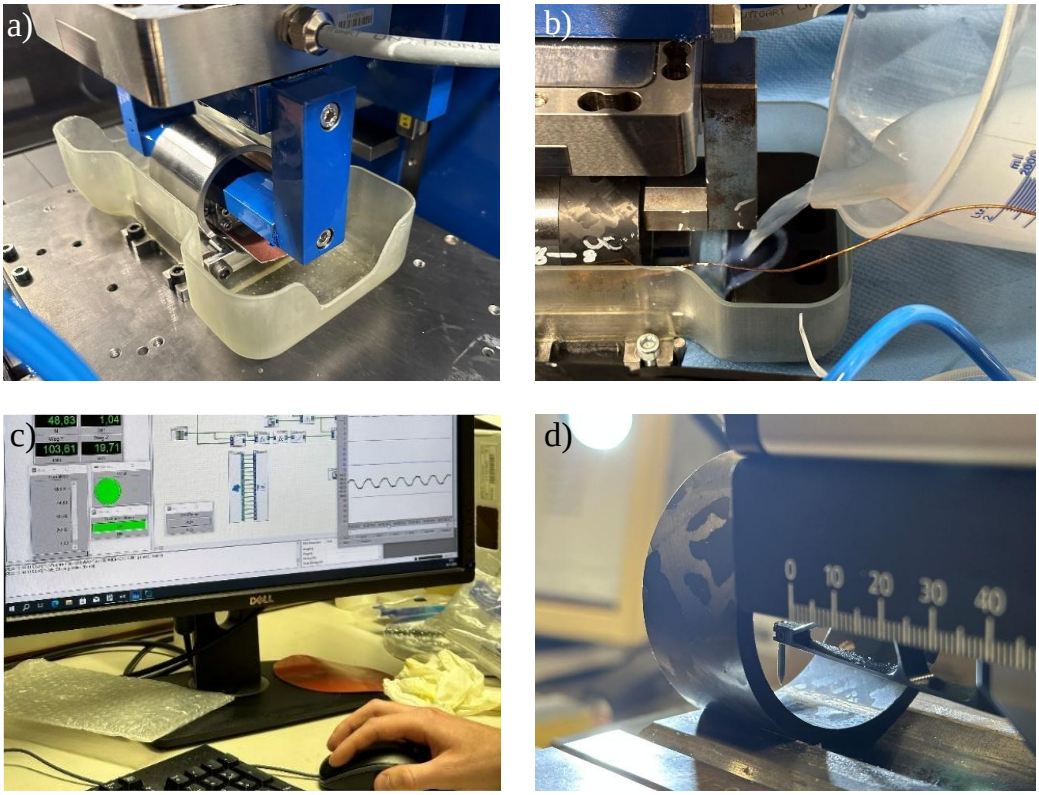

Figure 4: Steps in tribological testing: a) Running-in, b) test evaluation, c) test execution d) test evaluation.

For the tribological investigations, 20,000 cycles with a stroke length of 2 mm are conducted per test (c). The stroke length corresponds to the typical insertion path when inserting a tool holder into an HSK chuck of size 63 [13]. At a 4-axis machining center (Heller MC 12), the speed during the clamping and ejection process was determined to be 2 mm/s. Tests examining the influence of sliding speed on the coefficient of friction have shown that the effect of the sliding speed between 2 mm/s and 36 mm/s lies within the scatter of the coefficient of friction at identical sliding speeds. To reduce the test duration, a sliding speed of 6 mm/s is therefore selected, resulting in an average test duration of 6.4 hours. The test parameters are listed in Table 1.

Test parameters	Values and Properties
Sliding velocity	6 mm/s
Normal force	450 N
Surface pressure	5.4 MPa
Cycles	20000
Stroke	2 mm
Total test distance	80 m
Test temperature	21±4°
Humidity	40±5° RH
Medium	dry, coolant lubricant

Table 1: Test parameters for tribological tests

2.3 DETERMINATION OF THE COEFFICIENTS OF FRICTION AND THE SPECIFIC WEAR RATES

The recording of the forces is carried out continuously at a sampling frequency of 100 Hz over the entire test duration. The coefficient of friction is calculated from the normal force and the friction force. To determine the dynamic coefficient of friction, 20% of the friction coefficient of the half-cycle is used for the calculation. The midpoint of the half-cycle is determined via the zero crossings of the displacement. Starting from the midpoint, 10% before and after the midpoint of the cycle are used for the calculation of the dynamic coefficient of friction, as the friction force is constant in this region [14]. Subsequently, the mean values over the cycles from 10,000 to 20,000 are computed.

For the characterization of wear, the specific wear rate is determined based on the wear volume, the normal force, and the wear distance [15]. The wear volume is calculated as the product of the worn area and the linear wear amount. For the calculation, a worn area of 101 to 104 mm² is used. The linear wear amount is determined based on a contour measurement of the worn surface of the specimen. For this purpose, a perthometer from the manufacturer Mahr, type MarSurf UD 120, is used, where the surface of the specimen is scanned with a diamond tip and the contour of the worn area is traced. The measurement is then evaluated in MATLAB®.

3 RESULTS AND DISCUSSION

In the following section, the results obtained from the tribological investigations are presented and discussed. First, the influence of the KSS on the coefficient of friction is shown. Subsequently, the effect of fiber orientation in tribological tests with lubricant is examined. Finally, the coefficients of friction of the reference specimen are compared with a corresponding value from the literature.

3.1 LUBRICATION

To investigate the influence of the intermediate medium, six tests were conducted with CFRP tube specimens having a winding angle of 45° and steel counter bodies. The averaged dynamic coefficient of friction and the corresponding standard deviation for three tests each with and without lubrication are shown in Figure 5. The average coefficient of friction in the tests without lubrication is 0.31, and in the tests with KSS lubrication, it is 0.18. Lubrication of the contact area leads to a significant reduction in the dynamic coefficient of friction.

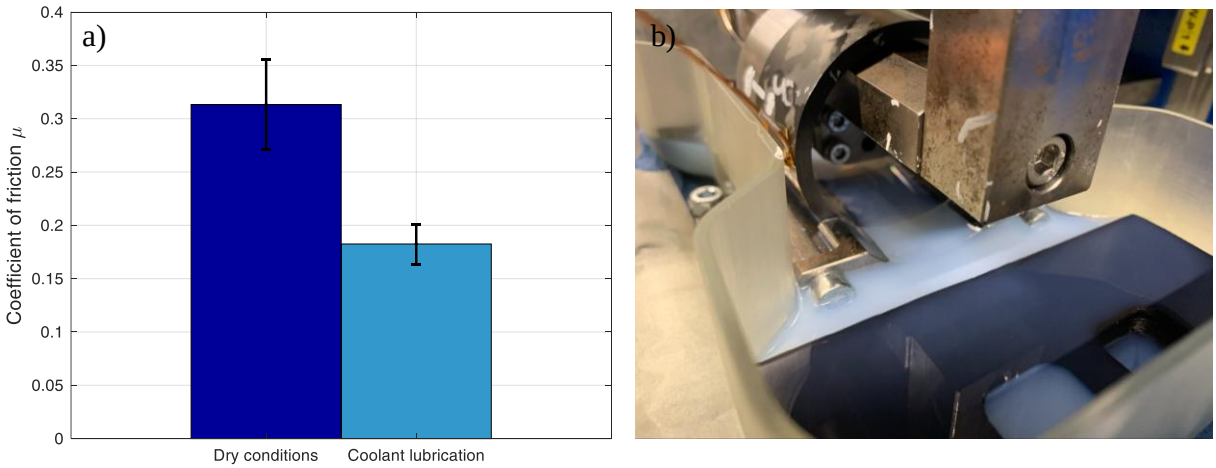

Figure 5: Tests on the influence of KSS on CFRP tube specimens with a winding angle of 45° against steel counter bodies, a) Comparison between the coefficients of friction with and without lubrication, b) mounted CFRP specimen.

In the tribological tests with KSS lubrication, no specific wear rate could be determined, as the contour changes are below the measurement resolution of the contour measurement. To visualize the wear mechanisms, the surface of the CFRP tube specimen with 45° orientation was examined using a digital microscope, the Keyence VHX-500F. Figure 6 shows a 500-fold magnification of the contact surfaces before the test (a), after the test without lubrication (b), and after the test with KSS lubrication (c) and (d). The bright elongated areas are the carbon fibers, surrounded by the darker matrix areas. After the tribological tests, fiber abrasion, breakage, and wear particles are visible both in the tests without lubrication (a) and with lubrication (b). In the test without lubrication (a), fiber-matrix debonding and matrix failure due to shear are significantly more pronounced compared to the tests with lubrication (b). These failure mechanisms were also identified by Friedrich et al. [15] in unidirectional fiber composite materials without lubrication at 0° orientation. In Figures 6 c) and d) show abrasive wear in the form of grooves along the sliding direction. Furthermore, the images demonstrate that the fibers do not run parallel to the sliding surface but pass through the crossover zone into or out of the viewing plane, resulting in fiber ends in the contact zone. Such a crossover zone is visible in Figure 6 c) after the test with KSS lubrication. Due to the winding process and the subsequent grinding process, fibers on the surface are cut, causing a local change in fiber orientation between the two winding directions. This is visible in Figure 3 by the differently bright areas on the CFRP tube with 45° orientation, which is attributable to varying light reflections due to the changing fiber layers. In Figure 6 c), it can also be seen that the fibers from the right side run under the fibers from the left side, and ´that there is no contact between the fibres and the friction partner in the transition area. The change in fiber orientation and the resulting transition zones may be reasons for the fluctuations in the dynamic coefficient of friction and the wear rate.

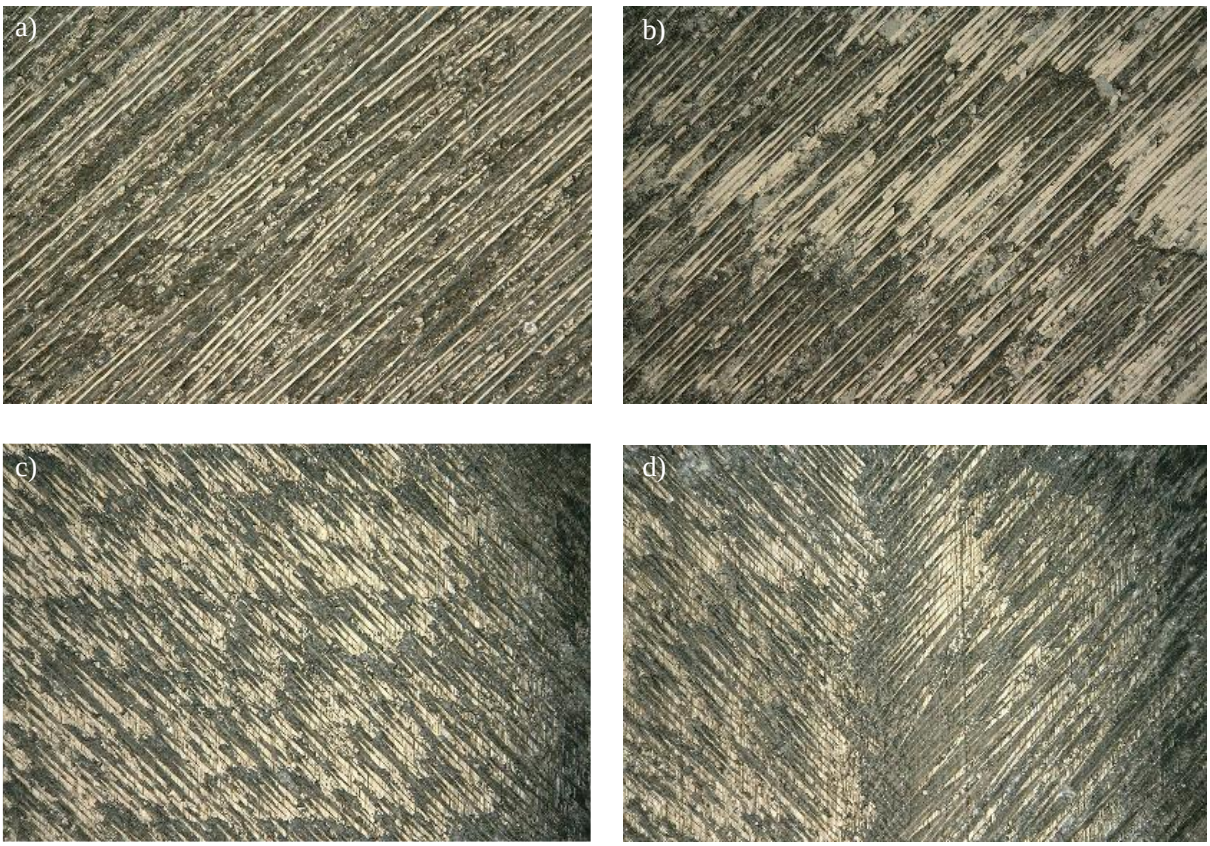

Figure 6: Microscopic images at 500x magnification of the inner surface of the CFRP tube specimen with 45° orientation and sliding direction upwards, a) before the test, b) after the test without lubrication, c) and d) after the test with lubrication.

3.2 FIBER ORIENTATION

The influence of the fiber angle on the dynamic coefficient of friction, surface quality, and specific wear rate is investigated on the CFRP specimens with different fiber angles and steel counter bodies under lubrication with KSS. In the tests, a winding angle of 0° means that the fibers are aligned parallel to the sliding direction. For the CFRP specimens with balanced winding angles of ±10°, ±45°, and ±89°, the dynamic coefficient of friction is determined. The dynamic coefficient of friction is lowest at a winding angle of ±10°, with a value of 0.17. At winding angles of ±45° and ±89°, the coefficient of friction is around 0.18. A similar influence of the fiber angle was observed by Sharma et al. [16] in tribological investigations of unidirectional carbon fibers with a polyetherimide matrix in a pin-on-disc (horizontal) configuration without lubrication. At an orientation of 0°, i.e., with the UD CFRP fibers aligned parallel to the sliding direction, the lowest coefficients of friction were found compared to 45° and 90°. Weidmann [17] confirmed this influence of the fiber angle for the orientations 0° and 90°, antiparallel to the sliding direction, in linear reciprocating pin-on-plate tests.

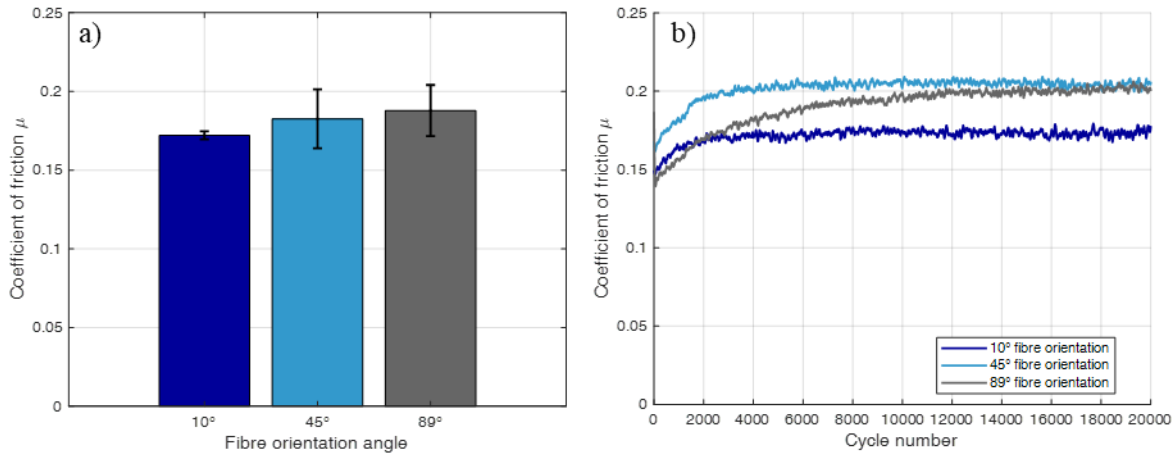

Figure 7: Coefficients of friction over fiber orientation (a), coefficients of friction over the number of cycles for different fibre orientations (b).

The influence of the tribological tests with lubrication by KSS on the surface roughness of the CFRP specimens is listed in Table 2. The surface roughness values are measured in the sliding direction, axial to the tube specimen, using the perthometer MarSurf UD 120 and averaged over three measurements. Subsequently, the roughness values are averaged across three tests, and the corresponding standard deviation is calculated. The specimen with a ±89° winding angle exhibits the highest surface roughness before the test. The surface roughness values of the specimens with ±10° and ±45° are lower. Since the same grinding parameters were used during the manufacture of the specimens, this difference is presumably due to the measurement direction of the perthometer relative to the fiber orientation and the fiber orientation itself. In grinding tests, Brouschkin et al. [18] assumed a influence of measurement direction on roughness depth as well as the influence of fiber orientation on surface quality. The tribological tests lead to a reduction in both the arithmetic mean roughness (Ra) and the average maximum profile height (Rz) values. The Ra values are reduced by 0.1 to 0.3 µm before and after the tests. A decline in Rz values is also observed for all specimens. The greatest reduction in Rz occurs in the specimen with ±89° orientation, where the Rz value decreases from 13.3 µm to 10.4 µm.

Fiber orientation	Surface roughness before test		Surface roughness after test	
[°]	Ra in µm	Rz in µm	Ra in µm	Rz in µm
10	0.7 ± 0.1	7.0 ± 1.6	0.6 ± 0.1	6.5 ± 0.9
45	1.0 ± 0.2	8.7 ± 0.5	0.7 ± 0.1	6.7 ± 2.0
89	1.0 ± 0.2	13.3 ± 2.9	0.9 ± 0.1	10.4 ± 0.5

Table 2: Surface roughness of CFRP specimens before and after tribological tests with KSS lubrication, based on Ra and Rz. Values are presented as mean ± standard deviation.

4.1 INFLUENCE OF THE PIN-ON-TUBE ARRANGEMENT

To ensure the transferability of the results obtained from the pin-on-tube arrangement to the application case, it is important to determine the influence of the arrangement. In addition to the CFRP tube specimens, tests were conducted with hardened steel tube specimens to reduce the abstraction between the application case and the specimens. Figure 8 compares the coefficients of friction in the pin-on-tube arrangement for CFRP and steel specimens under KSS lubrication with literature values for HSK interfaces according to Müller [19] and VDMA 34181 [4].

To visualize the comparison, the respective arrangements are shown above the coefficients of friction in the pin-on-tube arrangement and above the simplified HSK interface. The average coefficient of friction for the CFRP tube specimen with 10° orientation against the steel block is 0.17. For the steel tube specimen, the average coefficient of friction is 0.12 ± 0.02.

Müller [19] reports coefficients of friction between 0.12 and 0.4 for HSK interfaces based on field tests. According to VDMA 34181 [4], a coefficient of friction of 0.15 is typically used for the calculation of HSK interfaces. The guideline further states that lower values can be expected when using KSS or oil-based lubrication [4]. These literature values are shown on the right side of the figure, beneath the simplified HSK interface.

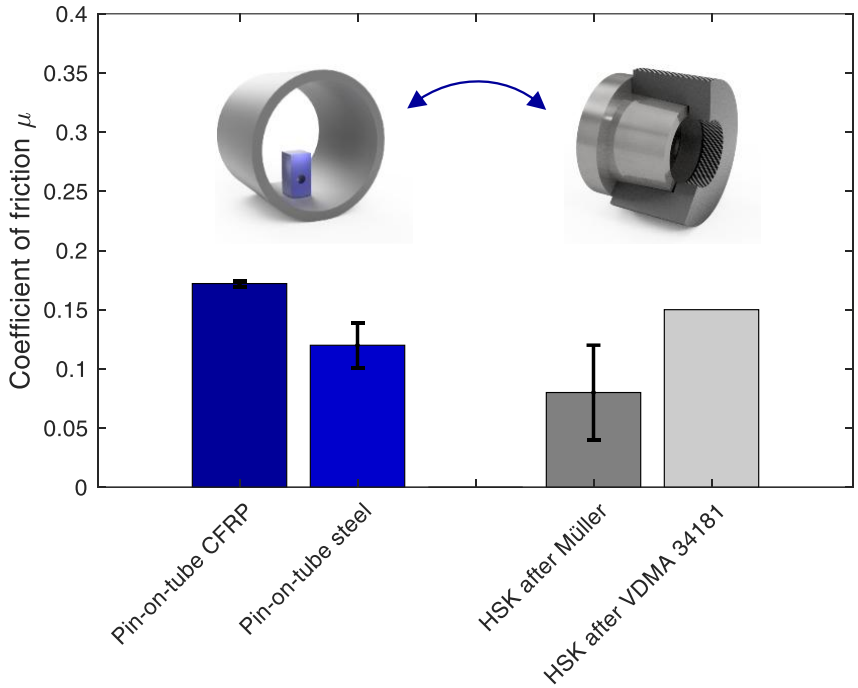

Figure 8: Coefficient of friction in the pin-on-tube arrangement for CFRP tube specimens with 10° orientation and for steel specimens against steel counter bodies compared to HSK interfaces according to Müller [19] and VDMA 34181 [4].

The closest match in boundary conditions, particularly regarding the material and the use of lubrication, is found between the steel pin-on-tube arrangement and the HSK interface described by Müller [19]. The average coefficient of friction obtained from the steel pin-on-tube tests lies at the upper end of the range reported in the literature. Since visible wear marks were observed in the pin-on-tube tests and Becher et al. [20] state that wear in HSK interfaces leads to increased friction, a transferability of the pin-on-tube results to real HSK interfaces can be assumed.

Furthermore, the observed differences in the coefficients of friction are likely attributable to variations in contact pressure and intermediate media arising from the specific test setups. These deviations must be considered to ensure a reliable transfer of the findings to the application context.

The coefficient of friction is particularly important for the HSK interface, as the frictional force opposes the insertion and ejection of the tool holder. Assuming a degree of transferability, the tests using the CFRP tube specimen suggest that, when applied to an HSK interface with a CFRP spindle, higher

frictional forces during tool clamping can be expected. These increased friction forces can be compensated by increasing the clamping force, thereby enabling the use of CFRP in such applications.

Wear in the pin-on-tube tests could not be quantified, as it remained below the measurement resolution for both CFRP and steel tube specimens. To enable a reliable assessment of wear, additional tests with a higher number of cycles should be conducted. Nevertheless, the lack of detectable wear suggests that the chosen setup is appropriate for transferability considerations. Moreover, it indicates that CFRP performs comparably to steel and does not show any disadvantages under the tested conditions. Accordingly, the test results suggest that CFRP can be used in tribologically loaded interfaces. However, further investigations using the pin-on-tube arrangement should be conducted to improve the transferability of the findings to practical applications.

5 CONCLUSIONS AND OUTLOOK

The results of this study demonstrate that CFRP is fundamentally suitable as a material for tribologically stressed interfaces. The conducted pin-on-tube tests reveal that the dynamic coefficient of friction is influenced both by the fiber orientation and by lubrication with KSS. Particularly low friction was achieved with CFRP specimens featuring a winding angle of ±10° tested against a steel counterbody, resulting in a coefficient of friction of 0.17. Under lubricated conditions, no measurable wear was detected, enabling the use of CFRP under these operating conditions. However, further tests with higher cycle numbers should be conducted to determine the specific wear rate. Microscopic analyses of the wear surfaces show that tribological loading leads to typical fiber-matrix damages such as fiber abrasion, fiber fracture, and the formation of wear particles, which are more pronounced in unlubricated specimens than in lubricated ones.

The influence of the pin-on-tube arrangement on the coefficient of friction was investigated for both CFRP and steel tube specimens and compared with literature values. The coefficient of friction measured for the steel reference specimens lies within the range of published values for HSK interfaces, indicating a reasonable degree of transferability of the findings.

The insights gained allow for further cost-effective studies on more wear-resistant polymer materials or with thermally conductive fillers. For transferability to real applications such as HSK interfaces, further investigations are necessary, for example regarding the influence of stroke and surface pressure on friction behavior and wear. To confirm the applicability of CFRP in highly stressed tribological interfaces, tribological investigations with real component geometries should be conducted.

ACKNOWLEDGEMENTS

The acknowledgements being relevant for this contribution are based on the research project SPOTLIGHT - Schleifen präziser Oberflächen rotierender Leichtbaukomponenten zur Ressourceneffizienz in E-Mobility und Maschinenbau (03LB2061F) supported by the Federal Ministry for Economic Affairs and Energy (BMWE) on the basis of a decision by the German Bundestag

REFERENCES

[1] M. Weck, *Werkzeugmaschinen 2*. Berlin, Heidelberg: Springer Berlin Heidelberg, 2006.

[2] L. Kroll, P. Blau, M. Wabner, U. Frieß, J. Eulitz and M. Klärner, "Leichtbaukomponenten für energieeffiziente Werkzeugmaschinen" in *Energieeffiziente Produkt- und Prozessinnovationen in der Produktionstechnik*, 2010.

[3] German Institute for Standardization, *DIN 69893-1, Kegel-Hohlschäfte mit Plananlage - Teil 1: Kegel-Hohlschäfte Form A und Form C; Maße und Ausführung: = Hollow taper shanks with flange contact surface - Part 1: Hollow taper shanks type A and type C; Dimensions and design*. Berlin: Beuth Verlag GmbH, 2011.

[4] *VDMA 34181:2005-07,* VDMA, Berlin, 2005.

[5] *DIN 51385:2013-12, Schmierstoffe_- Bearbeitungsmedien für die Umformung und Zerspanung von Werkstoffen_- Begriffe,* German Institute for Standardization, Berlin, 2013.

[6] H. Victor, M. Müller and R. Opferkuch, Hg., *Zerspantechnik*. Berlin: Springer, 1985.

[7] A. Landmann, "Zur Gestaltung von Maschinenkomponenten aus Faser-Kunststoff-Verbund-Halbzeugen" Dissertation, Shaker Verlag, 2017.
[8] K. Friedrich, *Friction and Wear of Polymer Composites*. Oxford: Elsevier Science, 1986.
[9] A. Rudnytskyj, R. Larsson and C. Gachot, "A Closer Look at the Contact Conditions of a Block-on-Flat Wear Experiment", *Lubricants*, Jg. 10, Nr. 7, S. 131, 2022, doi: 10.3390/lubricants10070131.
[10] M. Rodiouchkina, J. Lind, L. Pelcastre, K. Berglund, Å. K. Rudolphi and J. Hardell, "Tribological behaviour and transfer layer development of self-lubricating polymer composite bearing materials under long duration dry sliding against stainless steel", *Wear*, 484-485, S. 204027, 2021, doi: 10.1016/j.wear.2021.204027.
[11] H. Czichos and M. Woydt, "Tribological Testing and Presentation of Data" in *Friction, Lubrication, and Wear Technology*, G. E. Totten, Hg., ASM International, 2017, S. 16–32, doi: 10.31399/asm.hb.v18.a0006402.
[12] L. Kilian *et al.*, "Hochpräzise Funktionsflächen an CFK-Bauteilen", *Zeitschrift für wirtschaftlichen Fabrikbetrieb*, Jg. 119, 7-8, S. 553–557, 2024, doi: 10.1515/zwf-2024-1094.
[13] C. Brecher and M. Weck, *Werkzeugmaschinen Fertigungssysteme 1: Maschinenarten und Anwendungsbereiche*, 9. Aufl. Berlin, Heidelberg: Springer Berlin Heidelberg, 2018. [Online]. Verfügbar unter: http://nbn-resolving.org/urn:nbn:de:bsz:31-epflicht-1599188
[14] *Guide for Measuring and Reporting Friction Coefficients*, G02 Committee, West Conshohocken, PA.
[15] K. Friedrich, R. Reinicke and Z. Zhang, "Wear of polymer composites", *Proceedings of the Institution of Mechanical Engineers, Part J: Journal of Engineering Tribology*, Jg. 216, Nr. 6, S. 415–426, 2002, doi: 10.1243/135065002762355334.
[16] M. Sharma, I. M. Rao and J. Bijwe, "Influence of orientation of long fibers in carbon fiber–polyetherimide composites on mechanical and tribological properties", *Wear*, Jg. 267, 5-8, S. 839–845, 2009, doi: 10.1016/j.wear.2009.01.015.
[17] S. Weidmann, *Zur Gestaltung von Gleitlinearführungen und Gewindetrieben aus Faser-Kunststoff-Verbunden Tribologie, Auslegung, Fertigung und Prüfung Susanne Weidmann*, 1. Aufl. Aachen: Shaker Verlag, 2018.
[18] A. Brouschkin, N. Otto, C. Möller and J. Hendrik Dege, "Oberflächenqualität beim Schleifen von CFK", *Zeitschrift für wirtschaftlichen Fabrikbetrieb*, Jg. 119, 7-8, S. 558–562, 2024, doi: 10.1515/zwf-2024-1108.
[19] F. Müller, "Methoden zur Charakterisierung von Werkzeugschnittstellen unter statischer Last" Dissertation, Rheinisch-Westfälische Technische Hochschule Aachen; Apprimus Verlag.
[20] Brecher, Christian; Fey, Marcel; Kneer, Florian (2016): Verschleiß an Werkzeughaltern mit Plananlage beim Spannen. In: Werkstatt und Betrieb 149 (12), S. 30–33.

ICCM24
AUGUST 4-8, 2025
BALTIMORE CONVENTION CENTER
BALTIMORE, MARYLAND, USA

No Technical Paper Submission for:

Kowsar Rezvanian

ICCM24
AUGUST 4-8, 2025
BALTIMORE CONVENTION CENTER
BALTIMORE, MARYLAND, USA

No Technical Paper Submission for:

Dazhi Jiang

ICCM24
AUGUST 4-8, 2025
BALTIMORE CONVENTION CENTER
BALTIMORE, MARYLAND, USA

No Technical Paper Submission for:

Ignatius Eboquansah

Polydopamine-Coated Hexagonal Boron Nitride for Heat Dissipation Application

Yeon-Hwa Jeong[1], Tae-Sik Eom[2], Sang-Eui Lee[1*]

[1] Department of Mechanical Engineering, Inha University, 100 Inha-ro, Michuhol-gu, Incheon 22212, Republic of Korea
[2] KIURI Center for Hydrogen Based Next Generation Mechanical System, 36, Gaetbeol-ro, Yeonsu-gu, Incheon, 21999, Republic of Korea
*Corresponding author (E-mail: selee@inha.ac.kr)

Introduction

With the ongoing miniaturization of high-density electronic devices, the demand for high-performance thermally conductive materials for efficient heat management has grown increasingly critical [1]. Heat buildup in confined spaces can degrade performance, shorten device lifespan, and cause system failures, underscoring the importance of reliable thermal interface materials (TIMs) [2]. To improve the thermal conductivity of polymer-based composites, ceramic fillers are typically added. Among them, hexagonal boron nitride (hBN) is a promising candidate due to its platelet morphology, offering high in-plane thermal conductivity (up to 600 W/m·K), electrical insulation, and chemical stability [3]. However, anisotropic conductivity of hBN strongly depends on particle orientation; random dispersion disrupts thermal pathways and reduces efficiency [4].

In this study, a self-binding hBN structure was developed using polydopamine (PDA) as a binder. A well-aligned brick-and-mortar architecture was constructed without any polymer matrix by inducing direct bonding between hBN platelets. Uniform PDA coating and nanobumps (NBs) formation during polymerization promoted localized secondary aggregation and strong interfacial adhesion, enabling effective in-plane heat transfer.

Experiment

- Self-polymerization of DA occurred in a 150mM tris buffer solution.
  - Extensive PDA coating on the hBN surface was induced by high concentrations of Tris buffer and DA.
- PDA-NB-hBN composites were fabricated via vacuum assisted filtration (VAF) followed by hot pressing.

Fig. 1. Fabrication of PDA-NB-hBN composites

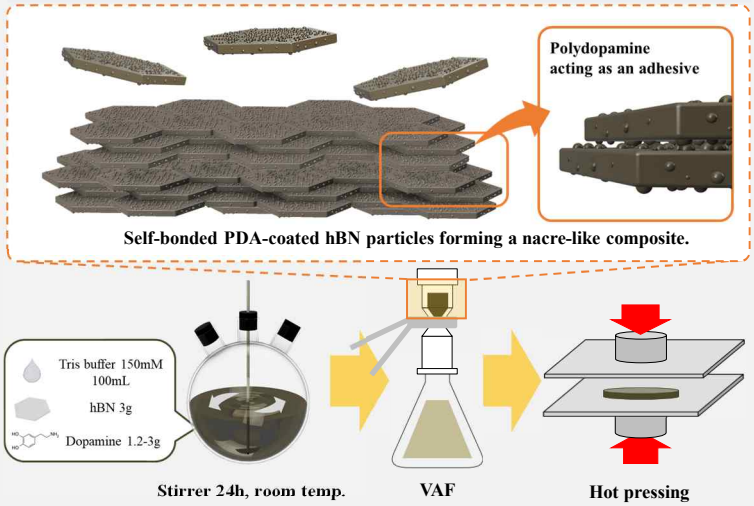

Results & Discussion

Fig. 2. (a)-(c) Surface morphology of PDA coated hBN and (d) PDA induced NBs marked in red. (e) TGA graph of PDA coated hBN.

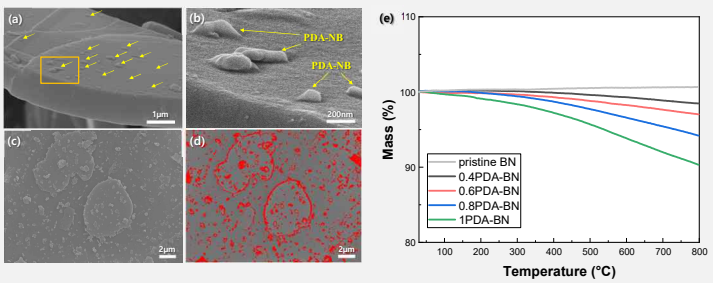

- Two-stage PDA deposition induced by controlled polymerization
  - Uniform coating (PDA layer) → Localized aggregation (NBs)

Fig. 3. (a) Cross-sectional microstructure and (b) XRD pattern of PDA-NB-hBN.

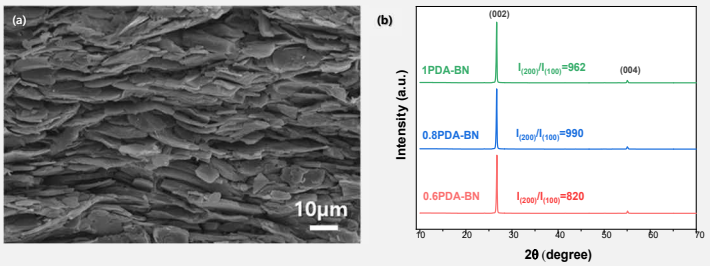

- A well-aligned brick-and-mortar structure formed by self-bonding of PDA-coated hBN particles during VAF and hot pressing

Fig. 4. (a) Stress-strain curve, (a) tensile properties, (c) thermal conductivity and (d) thermal interfacial resistance (TIR) of PDA-NB-hBN composites.

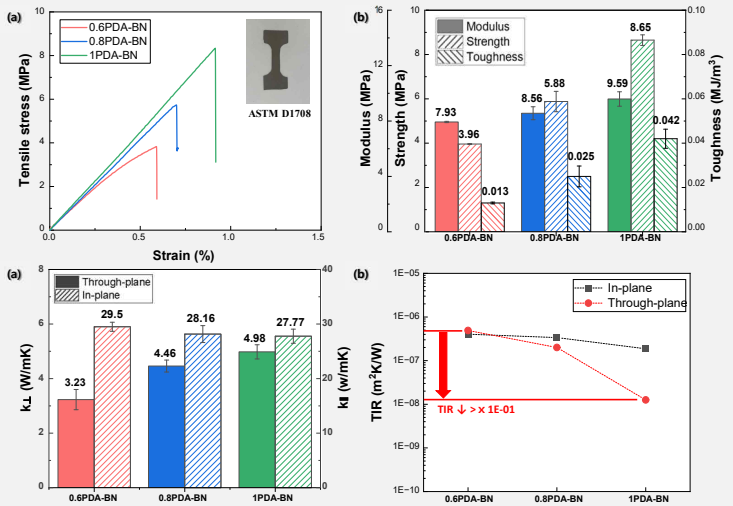

Fig. 5 (a) Schematic of the thermal dissipation test, (b) thermocouple setup and (c) time-dependent temperature difference (ΔT) of the chip

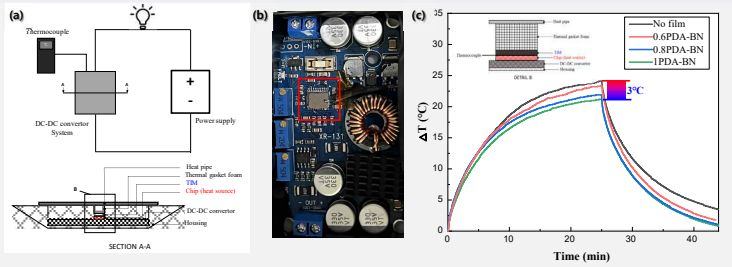

Conclusions

- Extensive PDA coating containing NBs was polymerized on the surface of hBN particles, imparting self-binding characteristics to the material.
- PDA-NBs-hBN film exhibited a nacre-inspired brick-and-mortar architecture, in which hBN and PDA functioned as the brick and mortar, respectively.
- Without the use of external binders or polymer matrices, the film achieved mechanical stability with a tensile modulus of 9.59 MPa and a tensile strength of 8.65 MPa.
- Localized interfacial adhesion by PDA-NBs reduced thermal resistance, achieving multidirectional thermal conductivity of 4.82 W/mK in the k⊥ and 27.77 W/mK in the k∥.
- The film demonstrated practical heat dissipation performance as a TIM, by reducing the maximum operating temperature by approximately 3 °C.

Reference

[1] *Wu, S. et al., J. Mater. Chem. A, 2020, 8, 20011-20020*
[2] *Cheng, L. et al., Chem. Eng. J., 2020, 398, 125633*
[3] *Cuiping Yu et al., RSC Adv., 2018, 8, 21948*
[4] *Jiantao Hu et al., ACS Appl. Mater. Interfaces 2017, 9, 13544−13553*

Acknowledgement

This research was supported by the Korea Evaluation Institute of Industrial Technology (KEIT) grant funded by the Ministry of Trade, Industry and Energy (MOTIE, Republic of Korea) (NO.20016607).

ICCM24 24TH INTERNATIONAL CONFERENCE ON COMPOSITE MATERIALS
AUG 4-8, 2025 · BALTIMORE CONVENTION CENTER · BALTIMORE, MARYLAND

EVALUATION OF THE EFFECT OF Z-THREADED CARBON NANOFIBERS ON THE IMPROVEMENT OF FLEXURAL PROPERTIES OF CARBON FIBER-REINFORCED POLYMER LAMINATES USING THE 3-POINT BENDING TEST

UNIVERSITY OF SOUTH ALABAMA
FLAGSHIP OF THE GULF COAST.

Obaidul Hasan[1], Ryan A. Warren[2] ,Kuang-Ting Hsiao[1,*]
[1]Department of Mechanical Engineering, [2]Department of System Engineering
University of South Alabama, Mobile, AL-36688
***Corresponding Author: Email: kthsiao@SouthAlabama.Edu**

INTRODUCTION

As a next generation composite material, carbon fiber reinforced polymer (CFRP) has great potential to be widely used in manufacturing industries due to its outstanding mechanical properties. However, the inherent anisotropic nature of CFRP renders it vulnerable in the through-thickness direction, particularly when subjected to complex loads like as bending [1]. It is hypothesized that long carbon nanofibers aligned in the z-direction act as reinforcing pillars when the CFRP is subjected to compressive loads on the top surface. Simultaneously, the interlocked nanofiber networks are believed to enhance fiber–matrix bonding, thereby improving load transfer efficiency when tensile stresses develop on the bottom surface.

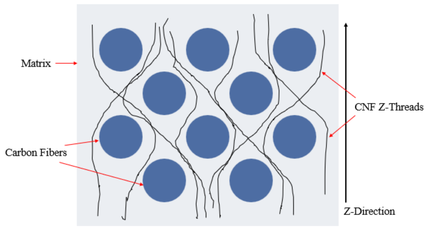

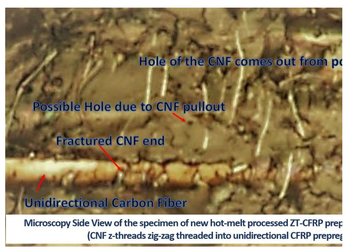

Fig 1: Top: princle behind z-threaded CFRP (ZT-CFRP) and Bottom: microscope picture of sideview of ZT-CFRP prepreg

EXPERIMENTATIONS

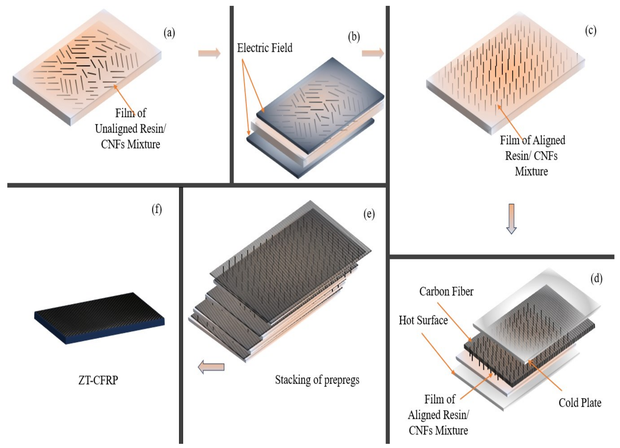

Fig 2: Depiction of the ZT-CFRP prepreg production processes.

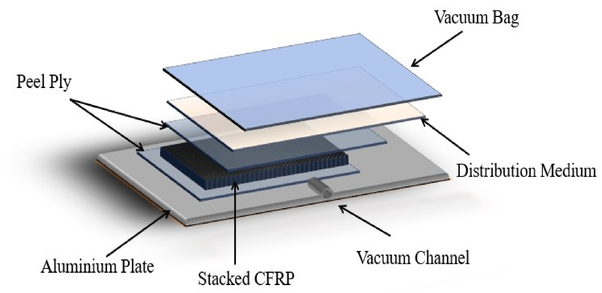

Fig 3: Schematic Diagram of OOA-VBO (Autoclave vacuum bag only) Setup

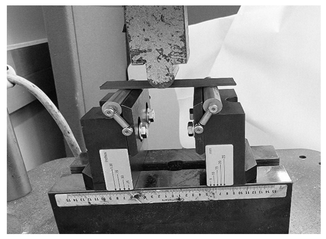

Fig 4: Experimental Setup for 3 Point Bending Test

RESULTS

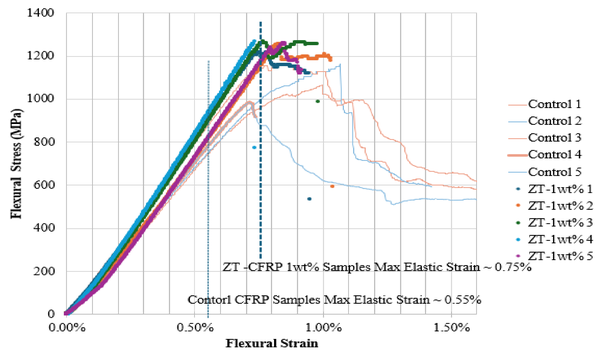

Fig 5: Flexural stress strain curve for control CFRP and ZT-CFRP.

The flexural stress, strain and movement of the cross head were calculated according to ASTM D790. The average flexural stress for control CFRP was 1067 MPa while 1228 MPa for ZT-CFRP showing 15% higher strength. The ZT-CFRP also showed 36% enhancement in the linear elastic strain compared to control CFRPs

Table 1: Flexural properties of control and ZT-CFRPs

CFRPs	Fiber Volume Fraction (%)	Avg. Force (N)	Avg. Flexural Strength (MPa)	Max. Linear Elastic Strain (%)	Max. Linear Elastic Stress (MPa)
Control CFRP	53	1076	1067	~0.55	~800
1.0 wt.% ZT-CFRP	52	1230	1228	~0.75	~1228
Improvement of ZT-CFRP	-	-	+15.1%	+36.4%	+53.5%

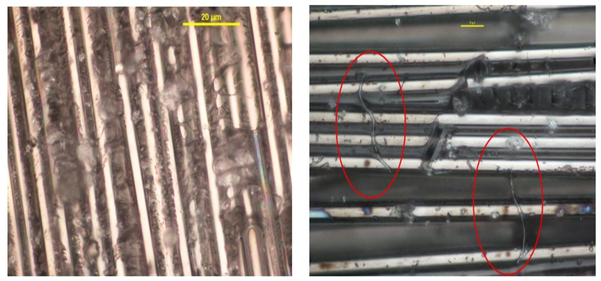

Fig 6 : Top-side microscopic images of the control CFRP (left) and ZT-CFRP (right), captured at 1000x and 1250x highlight significant microstructural differences between the two materials. The control CFRP surface appears relatively smooth whereas the ZT-CFRP clearly exhibits an interlocked network of nanofibers.

CONCLUSIONS

In the three-point bending test, the control CFRP exhibited higher deflection compared to the ZT-CFRP, indicating that it is more flexible and less stiff. This greater deflection suggests that the control sample has lower resistance to bending, potentially due to weaker fiber–matrix interactions or lower structural reinforcement. In contrast, the reduced deflection observed in the ZT-CFRP implies improved stiffness, likely resulting from enhanced interfacial bonding.

ACKNOWLEDGEMENT

The authors gratefully acknowledge the financial support of the National Science Foundation (Award numbers: 2044513 and 2419207) and NASA Alabama Space Grant Consortium Fellowship award (NASA Training Grant 80NSSC20M0044).

Bibliography

[1] Hasan, O., Warren, R. A., & Hsiao, K.-T. (2025). “Investigate the in-plane shear properties improvement of carbon fiber reinforced polymer laminate enhanced with carbon nanofiber z-threads by using digital image correlation system”. SAMPE 2025- Indianapolis, IN, May 2025.

[2] Islam, M. R., Uddin, M. N., Taylor, W., Warren, R., & Hsiao, K.-T. (2024). “Enhancing the Longitudinal Compressive Strength of Freeform 3D-Printed Continuous Carbon Fiber-Reinforced Polymer Composite Laminate Using Magnetic Compaction Force and Nanofiber Z-Threads”. Materials, 17(7), 1589.

[3] Hsiao, K.-T., & Hickman, G., (2018) “Method for manufacturing nano-structurally aligned multi-scale composites”. US patent No. US10066065B2.

ENHANCING THE PROPERTIES OF LAMINATED COMPOSITES WITH VERTICALLY ALIGNED CARBON NANOTUBES INTERLEAVES

Blagoj KARAKASHOV[1], Aurélien BOISSET[1], Benoist DEKEYSER[1], Farid BAHI [1], Kevin RETZ[2] and Thomas GOISLARD de MONSABERT[1]

[1]NAWAH
250 avenue Villevieille, 13790 Rousset, France
Email: blagoj.karakashov@nawah.fr , web page: https://nawah.fr/fr/

[2] NAWAH US
35 Rockridge Road, Suite A, Englewood, OH 45322, Dayton, USA
Email: kevin.retz@nawah.us

Keywords: vertically aligned carbon nanotubes (VACNT), chemical vapour deposition, industrialisation, nanoengineered interleave, carbon fiber reinforced polymers, mechanical properties

ABSTRACT

The incorporation of vertically aligned carbon nanotubes (VACNT) at the interply region of laminated structures has demonstrated significant reinforcement of carbon fiber reinforced polymers (CFRP) composite materials [1]. This reinforcement mechanism results from the deflection of micro-cracks towards strong intralaminar regions instead of their propagation along weak interlaminar ones [2], thus reducing delamination. Furthermore, VACNT interplies have been shown to enhance the thermal, electrical, and gaz impermeability properties of structural composites, thereby opening more opportunities to benefit from multifunctionalities [3].

Traditionally, the integration of such a reinforcing nanoengineered layer at the interface between plies involves the direct transfer of the VACNT layer from its original substrate (utilized during the synthesis process via catalytic CVD [4]) onto the surface of a carbon fiber ply pre-impregnated with resin (Figure 1a), the subsequent steps of the composite manufacturing process remaining unchanged. However, despite the simplicity and straightforwardness of this approach, it suffers from limitations in terms of cost-efficiency, scalability and carbon footprint for practical deployment at large scale.

A more industrially viable solution would involve the development of a VACNT supporting film (Figure 1b) that would be fully integrable into the final CFRP structure as an interleave. This methodology would significantly facilitate the commercial distribution and seamless integration of VACNT into existing manufacturing processes of advanced laminated composite parts.

In this study, we report recent progress towards developing such a nanoengineered interleave.

1 INTRODUCTION

In today's competitive engineering landscape, industries like aerospace, energy, infrastructure and sporting goods increasingly rely on composite materials to meet stringent design requirements. These applications demand materials that are lightweight, strong, cost-effective and easy to manufacture. A notable innovation is the integration of VACNT in between plies of laminated composites, commercially available and known as NAWAH Stitch.

NAWAH Stitch is a cutting-edge 3D nanocarbon interface for laminated composites materials. It provides enhanced mechanical, electrical and thermal properties to fiber reinforced plastics (FRP) without altering the part design and manufacturing process. Incorporating NAWAH Stitch between composite layers (Figure 1) improves toughness and impact resistance, reduces delamination and prolongs service life. Additionally, the use of NAWAH Stitch allows composite parts to be functionalized for advanced applications such as de-icing, in-situ matrix curing and structural health monitoring [5].

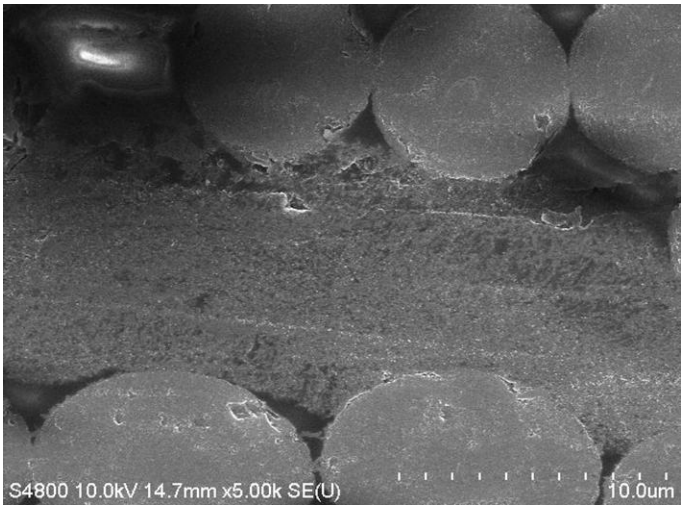

Figure 1 SEM of VACNT inserted between two carbon fiber composite plies

NAWAH is a global manufacturer of VACNT that produces this material at industrial scale on flexible metal sheets in a roll-to-roll fashion (Figure 2). This is done through a continuous atmospheric pressure chemical vapour deposition (APCVD) process at two production sites located in Rousset (France) and Dayton, Ohio (USA).

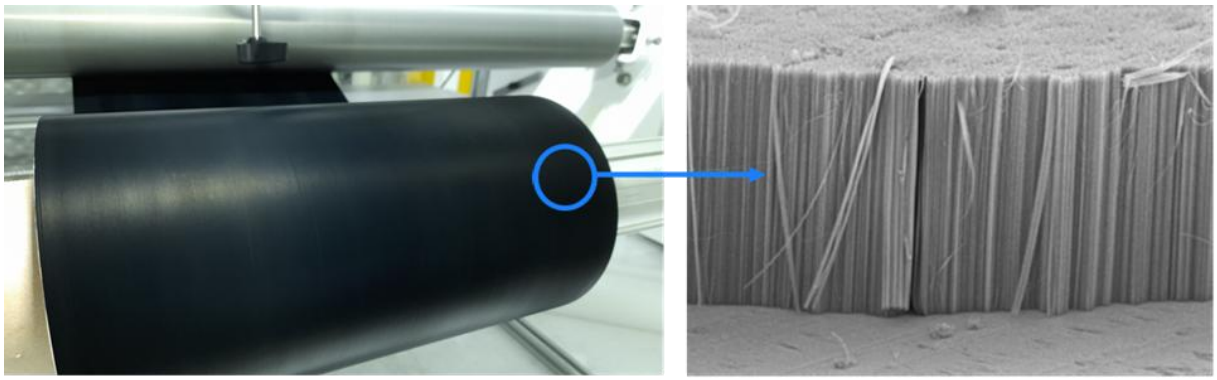

Figure 2 Vertically Aligned Carbon Nanotube synthesized by APCVD Roll-to-Roll process at NAWAH (left – post-synthesis optic visualisation and right – SEM VACNT on metallic support)

2 STATE OF THE ART

The added values of integrating VACNT at interplies have already been demonstrated by many previous studies [6,7]. These demonstrations always involved a direct transfer of VACNT onto the surface of prepreg plies. This approach (Figure 3), although efficient, suffers from several drawbacks that hinder their industrial scale deployment and adoption by the composite industry including:

- high logistics cost and CO2 footprint,
- reduced prepreg shelf lifetime.

This is mainly because thermosetting resins like epoxy must be stored at low temperature and have a limited shelf lifetime.

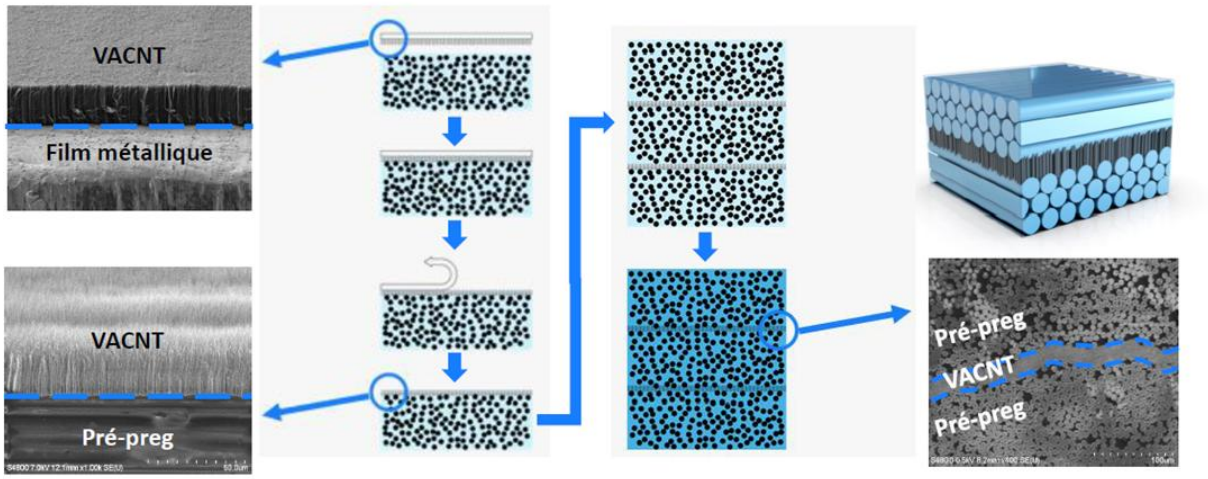

Figure 3 Standard process flow for integration of NAWAH Stitch

Therefore, a new method allowing for room temperature storage and easy handling would be highly advantageous. We report here below such a method.

3 NEW RESULTS

Thermoplastic (TP) polymers are stable at room temperature and some of them are miscible in epoxy resins [8]. Several epoxy-miscible thermoplastic films have thus been tested as support film for VACNT with the aim of:

(a) allowing for efficient transfer of VACNT from their original growth substrate,
(b) minimizing the weight and volume increase of the composite part due to the addition of the thermoplastic film as an interleave between prepreg plies,
(c) ensuring good compatibility with epoxy systems by avoiding any alteration of the original properties,
(d) retaining the beneficial properties of the inserted VACNT by providing a direct bridging of the fibers of adjacent plies by the carbon nanotubes,
(e) providing a low cost, scalable and stable at room temperature solution
(f) allowing for an easy handling and utilisation by the customer as an interleave in his composite manufacturing process.

The VACNT integration process with this method is illustrated in Figure 4.

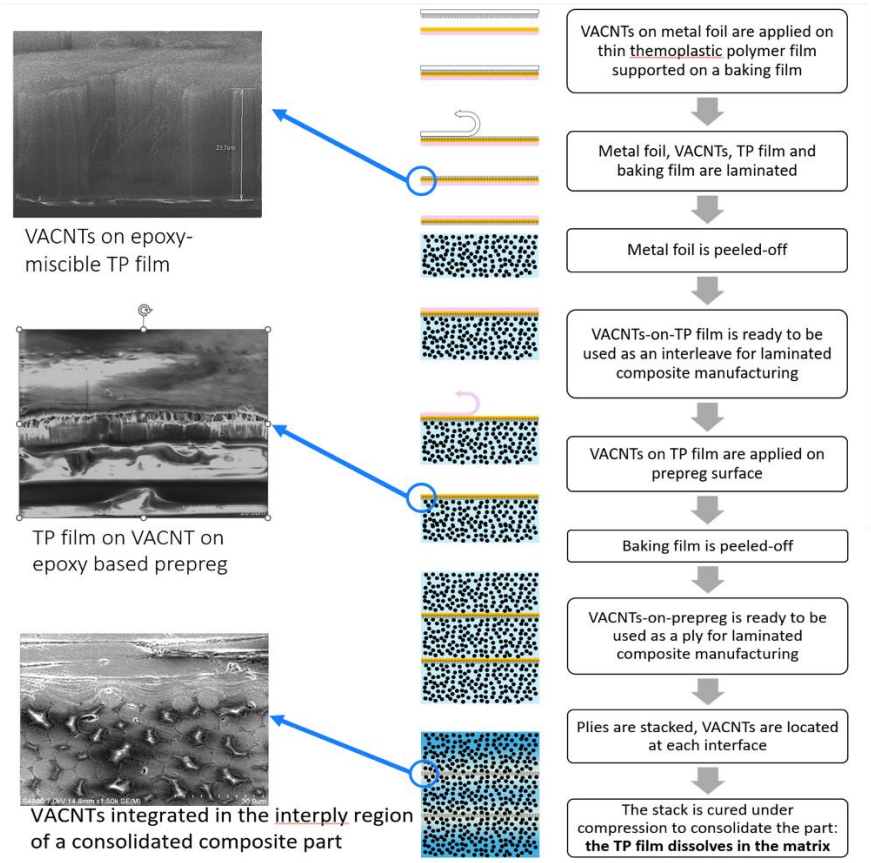

Figure 4 NAWAH's interleave method: integration via interleaving an epoxy-miscible thermoplastic polymer film supporting the VACNT

Several thermoplastic polymers have succesfully been used to practically implement this new method. As an illustration, Figure 5 shows a reference roll of VACNT directly transfered on a prepreg and an exemple of a roll of VACNT transferred on a thin (typically 1µm thick) thermoplastic film.

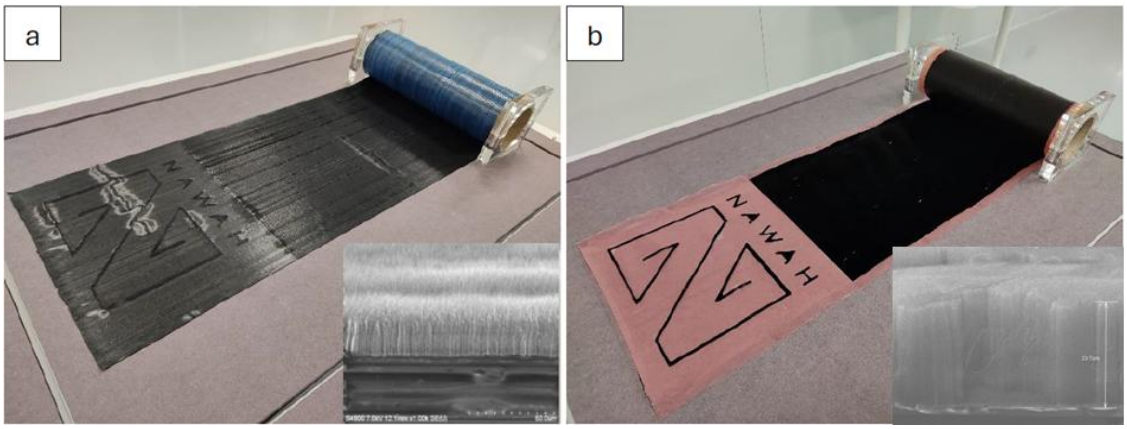

Figure 5 a) Roll of VACNT layer directly transfered on carbon fiber ply pre-impregnated with resin, b) Roll of VACNT layer tranfered on thin thermoplastic film (both with SEM image inserts).

To demonstrate that all requirements specified above are met, reference composite panels have been prepared without NAWAH Stitch (Baseline) and compared with similar parts integrating NAWAH Stitch with the interleave method.

For this comparison, the selected prepreg system and layup was the HexPly® 8552S/37%/AGP280/C woven system from Hexcel with a $[0]_{12}$ layup. The panels were assembled and cured in autoclave according to the specifications of the prepreg manufacter with the only difference for the NAWAH Stitched panel being the insertion of a TP film supported VACNT interleave beween every prepreg ply. The thickness of the two cured panels were measured and the difference was found to be unsignificant (lower than 5%).

A morphology comparison of the resin-rich interply regions was captured by scanning electron microscopy (SEM) cross sections (Fig. 6). It confirms that the interply thickness (between yellow arrows on Figure 6) remains unchanged with or without NAWAH Stitch (typically 10-15µm). In particular, the VACNT supporting thermoplastic film is no longer visible after curing, thus confirming its dissolution into the epoxy matrix. As targeted, the VACNT layer bridges the carbon fibers from adjacent plies, this configuration being the most favorable to achieve enhanced mechanical properties.

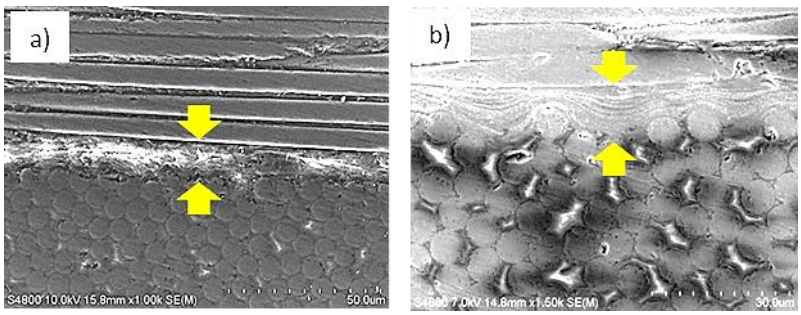

Figure 6 a) SEM Cross-section of baseline CFRP , b) SEM Cross-section of CFRP with integrated NAWAH Stitch interleave

4 CONCLUSIONS

VACNT layers inserted between plies of laminated composites, commercially available and known as NAWAH Stitch, have long proven their advantages but the adoption of this technology by the composite industry has been limited so far by the classical method for transferring them directly on prepreg surface. A new method involving the transfer of VACNT on an epoxy-miscible thermoplastic film and the subsequent use of this film as an interleave in the composite manufacturing process was reported. The successful bridging of fibers from adjacent plies in a laminated epoxy-based CFRP composite was demonstrated by using this new method, without measurable increase of thickness.

Further steps at NAWAH include static mechanical testing for strength under short-beam shear (SBS) interlaminar shear stress (ILSS) and fatigue life testing under 3-points bending cycles. Besides, efforts continue towards full roll-to-roll scale up of this technology at the level of VACNT synthesis, thermoplastic film production and VACNT transfer on this film.

These results pave the way for lower cost, lower CO2 footprint, easier processability and wider adoption of VACNT technology by the composite industry.

ACKNOWLEDGEMENTS

The whole manufacturing and R&D teams at NAWAH are gratefully acknowledged for their active contribution to the achievements presented here.

REFERENCES

[1] Furtado *et al*. "J-Integral Experimental Reduction Reveals Fracture Toughness Improvements in Thin-Ply Carbon Fiber Laminates with Aligned Carbon Nanotube Interlaminar Reinforcement" ACS Appl. Mater. Interfaces 2024, 16, 16, 20980–20989 (2023)
[2] Li *et al.* "Interlaminar Reinforcement of High-Temperature Carbon Fiber Reinforced Polymer Composites Using Vertically Aligned Carbon Nanotubes." Available at SSRN 4921551 (2024).
[3] Retz *et al* "THE SEARCH FOR MULTI-FUNCTIONAL COMPOSITE MATERIAL AND STRUCTURE". SAMPE 2023, (2023)
[4] Goislard de Monsabert *et al.* "Large scale synthesis of Vertically Aligned Carbon Nanotubes on Metal Foils", poster at NT'23 conference, Arcachon, France (2023)
[5] Retz, "Enhancing Composite Material Lifespan: The NAWAStitch Advantage in Mechanical Strength, Fatigue and Impact Resistance Properties." In AIAA SCITECH 2025 Forum (p. 0768) (2025).
[6] Ni, Xinchen, *et al*. "Static and fatigue interlaminar shear reinforcement in aligned carbon nanotube-reinforced hierarchical advanced composites." Composites Part A: Applied Science and Manufacturing 120: 106-115 (2019).
[7] Lee, Jeonyoon, et al. "Hierarchical nano-and micro-engineered interlaminar reinforcement of advanced aerospace grade composites with carbon nanotube arrays." AIAA Scitech 2021 Forum (2021).
[8] Deng, Shiqiang, *et al.* "Thermoplastic–epoxy interactions and their potential applications in joining composite structures–A review." Composites Part A: Applied Science and Manufacturing 68: 121-132 (2015).
[9] Conshohocken W. ASTM D 2344/D 2344m-16, standard test method for short-beam strength of polymer matrix composite materials and their laminates n.d.

ICCM24
AUGUST 4-8, 2025
BALTIMORE CONVENTION CENTER
BALTIMORE, MARYLAND, USA

No Technical Paper Submission for:

Xu Chengxin Xu

ICCM24
AUGUST 4-8, 2025
BALTIMORE CONVENTION CENTER
BALTIMORE, MARYLAND, USA

No Technical Paper Submission for:

Jiahui Tan

ICCM24
AUGUST 4-8, 2025
BALTIMORE CONVENTION CENTER
BALTIMORE, MARYLAND, USA

No Technical Paper Submission for:

Mandar Joshi

ICCM24
AUGUST 4-8, 2025
BALTIMORE CONVENTION CENTER
BALTIMORE, MARYLAND, USA

No Technical Paper Submission for:

Olga Tsurtsumia

ICCM24
AUGUST 4-8, 2025
BALTIMORE CONVENTION CENTER
BALTIMORE, MARYLAND, USA

No Technical Paper Submission for:

Daniel Alvarez Gomez

ICCM24
AUGUST 4-8, 2025
BALTIMORE CONVENTION CENTER
BALTIMORE, MARYLAND, USA

No Technical Paper Submission for:

Muhammad Zahid

ICCM24 24TH INTERNATIONAL CONFERENCE ON COMPOSITE MATERIALS
AUG 4-8, 2025 • BALTIMORE CONVENTION CENTER • BALTIMORE, MARYLAND

DEVELOPMENT OF PHENOLIC RESIN NANOCOMPOSITES REINFORCED WITH NANODIAMOND

Momoka Yasuda and Seira Morimune-Moriya

Department of Applied Chemistry, Graduate School of Engineering, Chubu University of Japan
Matsumoto, Kasugai 487-8501
Email: seiram@fsc.chubu.ac.jp

Keywords: Nanocomposites, *In-situ* polymerization, Phenolic Resin, Nanodiamond

ABSTRACT

In this study, the effects of nanodiamond (ND) on the structure and properties of phenolic resin nanocomposites were investigated. It was found that ND was well dispersed in the nanocomposites at low contents below 0.05 wt%. Regarding thermal properties, the nanocomposites containing 0.01 wt% ND exhibited the highest thermal decomposition temperature. In contrast, the rate of increase in thermal decomposition temperature was significantly reduced at higher filler contents above 0.5 wt%, suggesting the formation of severe agglomerates. Both the flexural modulus and flexural strength increased with the incorporation of ND at low contents, indicating that the strong reinforcement effects of ND were due to its high dispersibility and favorable interfacial interactions.

1 INTRODUCTION

So far, high-tensile steel and aluminum alloy materials have often been used for transportation equipment. In recent years, global environmental concerns have driven efforts to reduce the weight of car and aircraft to improve fuel efficiency. Therefore, polymer composites, which have a lower specific gravity than metallic materials, have attracted a great deal of attention as alternative materials.

Phenolic resin (PF) is well known for their excellent electrical insulation, heat resistance and flame resistance. They have been used in industrial applications such as insulators for automotive parts and circuit boards. Due to its rigidity, it is difficult to incorporate other materials to PF by conventional methods such as solvent mixing or melt mixing. To the best of our knowledge, there are very few reports on PF composites with improved mechanical or thermal properties.

In this study, we prepared PF nanocomposites with nanocarbons by *in-situ* polymerization. We used nanodiamond (ND) as filler. ND is a nanocarbon with a particle size of less than 10 nm with primary diamond particles in the core. It shows high strength, high elastic modulus and high thermal conductivity derived from diamond. In addition, ND can disperse at nano-scale in water due to abundant oxygen-containing functional groups, such as hydroxy groups, carboxy groups and carbonyl groups, on the surface. Prior to the polymerization, ND was dispersed in the solvent and then PF was polymerized under the presence of ND. The structure and the properties of the PF/ND nanocomposites were evaluated.

2 SAMPLE PREPARATION

PF was mixed with ND/ethanol dispersion and sodium hydroxide. The mixture was stirred and heated in an oil bath for 20 minutes. When the temperature reached 80 ℃ formaldehyde solution was added to the mixture. After the reaction, the mixture was cooled to room temperature and then cased on aluminum cups, vacuum dried followed by curing. PF/ND nanocomposites with the filler content of 0 ~ 0.5 wt% with a thickness of about 1 mm were prepared.

3 RESULTS AND DISCUSSION

3.1 SEM

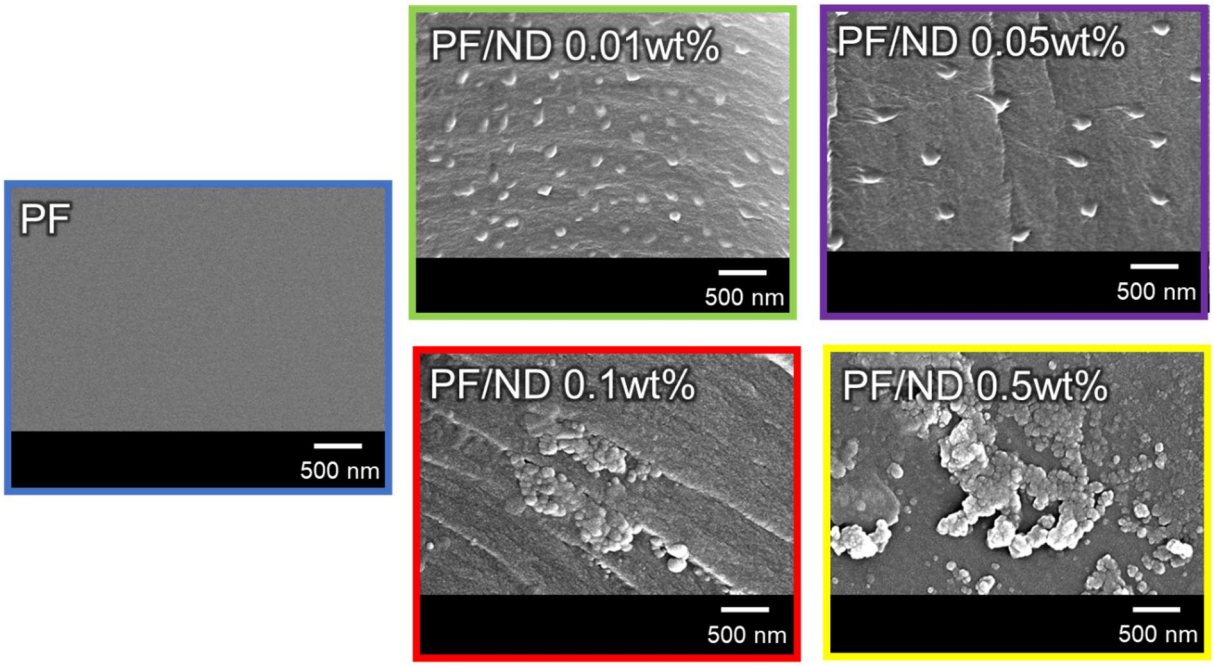

Figure 1 SEM images of PF and PF/ND nanocomposites.

Figure 1 shows SEM images of PF and PF/ND nanocomposites. It was found that ND were well dispersed in the nanocomposites at filler contents of 0.01 wt% and 0.05 wt%. On the other hand, agglomerates of ND were observed in the nanocomposites with 0.1 wt% or higher. The size of the agglomerates increased as the filler content increased, suggesting that agglomeration was promoted as the inter-particle distance decreased.

3.2 Thermal Properties

Figure 2 shows thermogravimetric traces of PF and PF/ND nanocomposites. The 5% weight loss on this curve is defined as the thermal decomposition temperature. The thermal decomposition temperature increased by the addition of ND.

Figure 3 shows thermal decomposition temperature of PF and PF/ND nanocomposites. The nanocomposites with a filler content of 0.1 wt% showed the highest thermal decomposition temperature, and it was 44 ℃ higher than that of PF. It was suggested that the movement of PF molecular chains were effectively suppressed by the highly dispersed ND with high interfacial area, resulted in significant improvement of resistance. On the other hand, the thermal decomposition temperature decreased for the nanocomposites with a filler content of more than 0.5 wt%. As shown before, ND formed serious agglomerates at high filler content. Therefore, the reinforcement effect decreased due to the decreased interfacial area. In addition, these agglomerates could cause heat concentration, that brought the thermal decomposition of the material.

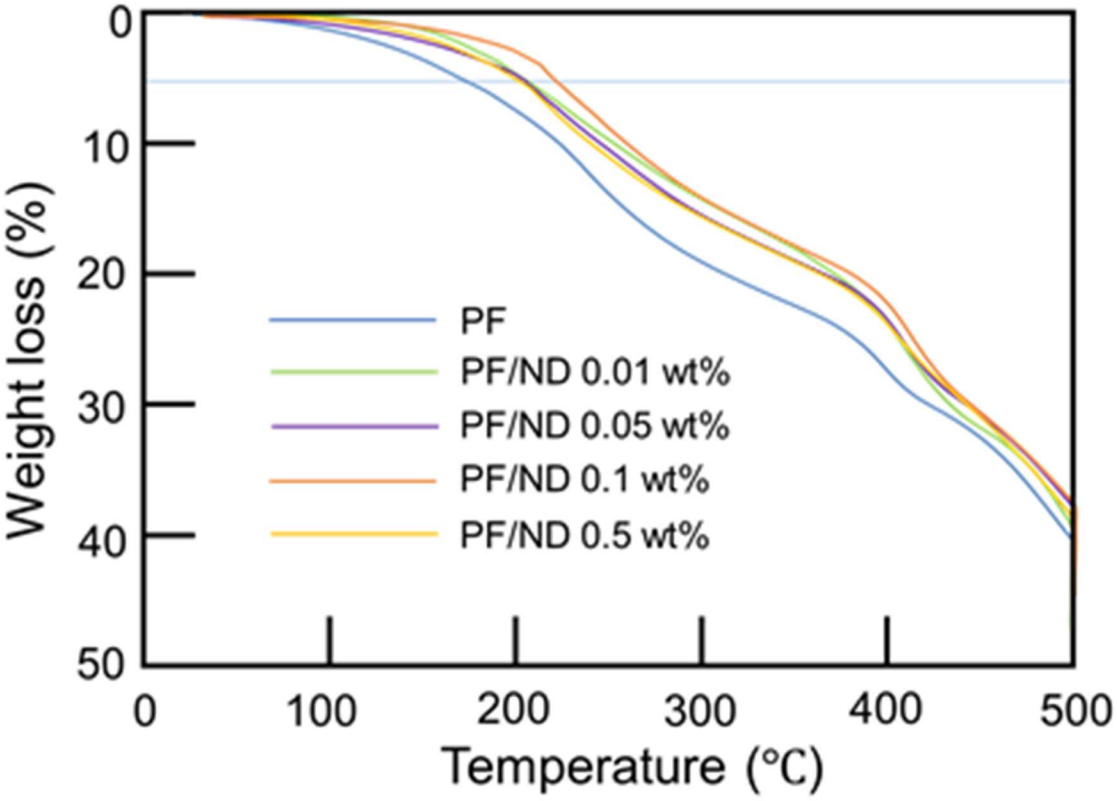

Figure 2 Thermogravimetric traces of PF and PF/ND nanocomposites.

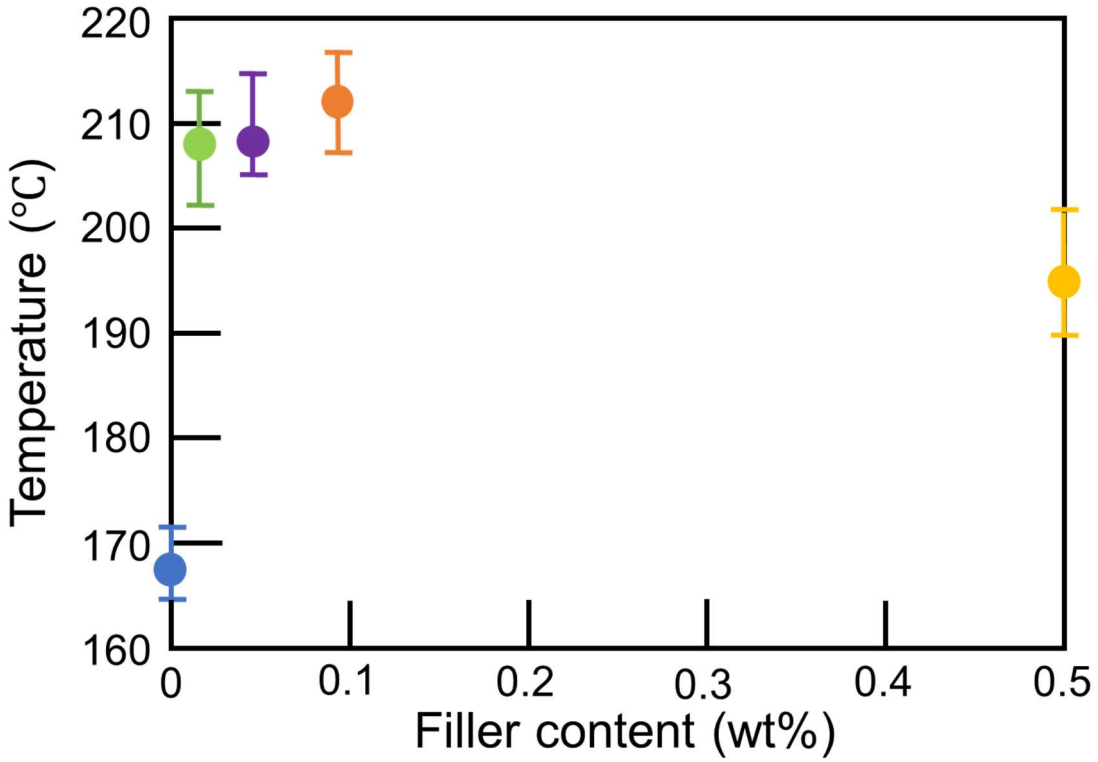

Figure 3 Thermal decomposition temperature of PF and PF/ND nanocomposites.

3.2 Mechanical Properties

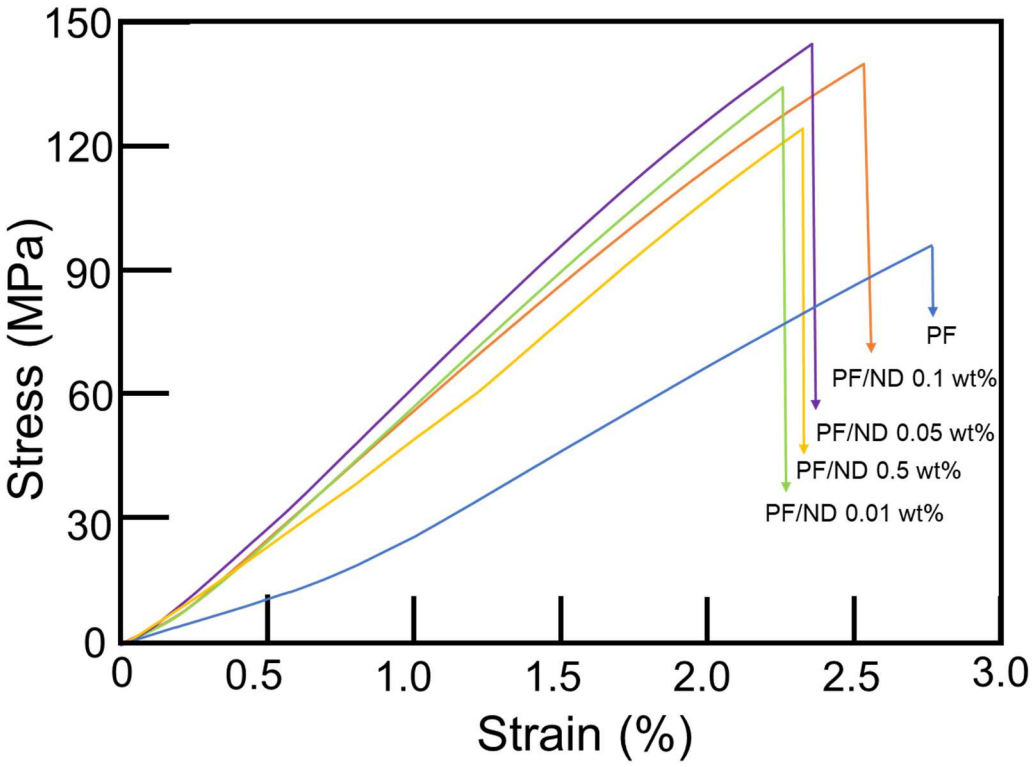

Figure 4 Stress-strain curves of PF and PF/ND nanocomposites.

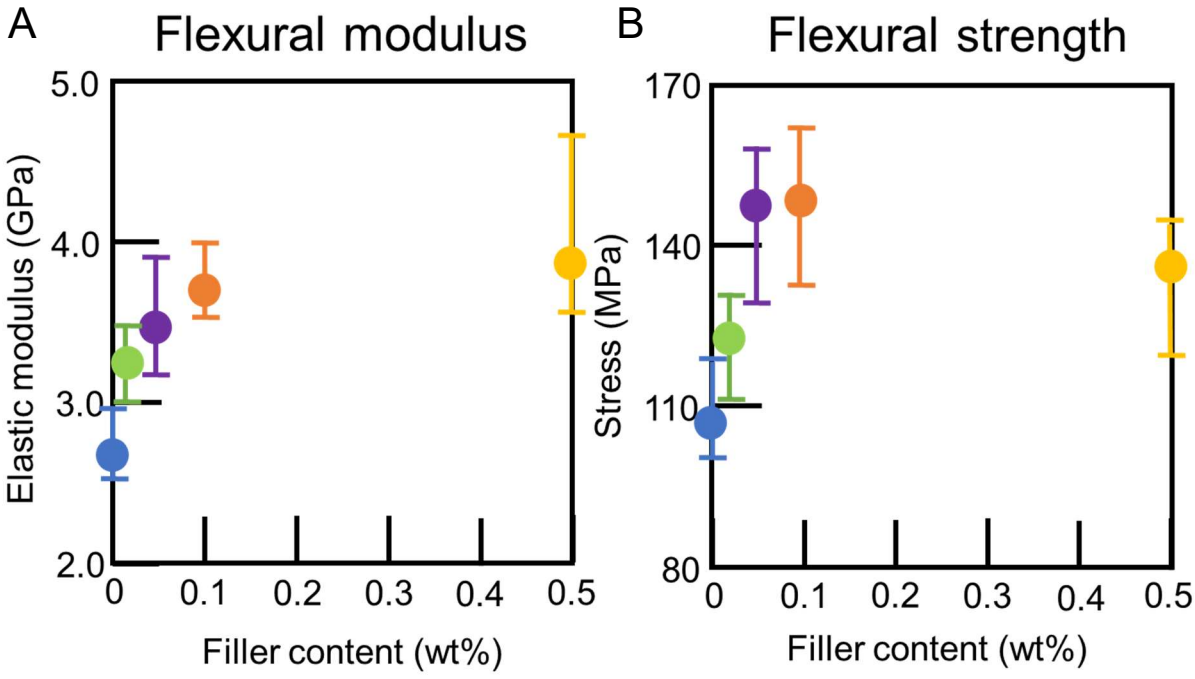

Figure 5 Flexural modulus and flexural strength of PF and PF/ND nanocomposites.

Figure 4 shows stress-strain curves of PF and PF/ND nanocomposites. The maximum stress corresponds to the flexural strength, and the initial gradient corresponds to the flexural modulus.

Figure 5 (A) shows flexural modulus and Figure 5 (B) shows flexural strength of PF and PF/ND nanocomposites. The flexural modulus increased with the increasing of ND content. Compared to PF, the flexural modulus increased by 38% at a filler content of 0.1 wt% and increased by 50% at a filler content of 0.5 wt%. Similarly, the flexural strength increased with increasing of ND content up to 0.1 wt%. Compared to PF, the flexural strength increased by 36% at a filler content of 0.1 %. However, the increasing rate started to decrease at the filler content of 0.5 wt%. In the low filler content region, ND were highly dispersed in PF, resulting in an excellent reinforcing effect. On the other hand, above a filler content of 0.5 wt%, the nanocomposites showed brittle behavior due to stress concentration caused by aggregates.

3.3 Interfacial interactions

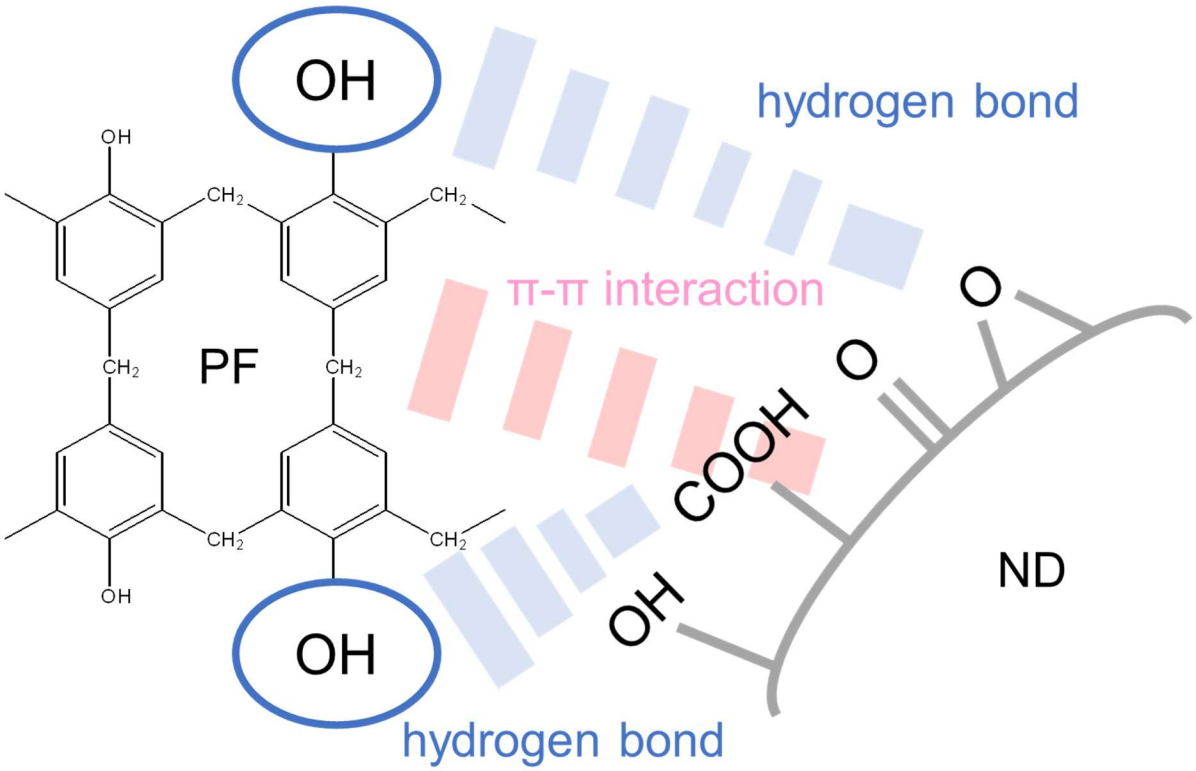

Figure 6 Scheme of interfacial interactions in PF/ND nanocomposites.

Figure 6 shows scheme of interfacial interactions in PF/ND nanocomposites. The thermal and mechanical properties shown above are thought to be largely influenced by the dispersibility of ND in PF and the interaction at the interface between PF and ND. As mentioned before, ND has abundant oxygen-containing functional groups on their surface. Therefore, ND can form hydrogen bonds with phenolic groups of PF. In addition, it was assumed that π-π interactions were formed at the interface between the graphite of ND and the benzene ring of PF. These strong interfacial interactions together with the high dispersibility can be the main factor for the enhancement in the mechanical properties as well as the thermal properties.

4 CONCLUSIONS

PF/ND nanocomposites were prepared by *in-situ* polymerization. In the PF nanocomposites ND were well dispersed in the nanocomposites up to 0.1 wt% or lower. The thermal decomposition temperature increased by the incorporation of ND. The flexural modulus and the flexural strength increased by the incorporation of ND.

IN-SITU SYNTHESIS OF POLYAMIDE COMPOSITES WITH RECYCLE CARBON FIBER

Dai Hasegawa and Seira Morimune-Moriya

[1]Department of Applied Chemistry, Graduate School of Engineering, Chubu University of Japan
Matsumoto, Kasugai 487-8501, Japan
Email: seiram@fsc.chubu.ac.jp

Keywords: Composite, *In-situ* polymerization, Recycle carbon fiber, Mechanical properties

ABSTRACT

Here in, rCF and polyamide 66 (PA66) were prepared by *in-situ* polymerization. As a result, rCF was highly dispersed in PA66. Due to the low interfacial area as well as the poor interfacial interaction, the thermal decomposition temperature decreased by the addition of a small amount of rCF. On the other hand, at high content region, the excellent reinforcement effects of rCF were exploited. The composites with high content of rCF also exhibited significant improvement in the mechanical properties.

1 INTRODUCTION

In recent years, polymer composite materials are expected to replace metal materials due to their light weight and ease of processing. In particular, carbon fiber-reinforced plastics are attracting attention as materials for automobiles and aircraft because of their light weight, high strength, and heat resistance. However, the high cost of manufacturing carbon fiber (CF) and the environmental impact of the manufacturing process have slowed the spread of CF despite its demand. One countermeasure is to recycle CF. Although recycled carbon fiber (rCF) has the problem of uneven quality due to the fact that it is a recycled material, it is attracting attention as a solution to environmental problems such as global warming, which has become an issue in recent years.

In this study, composite materials of rCF and polyamide 66 (PA66) were prepared by in-situ polymerization. In in-situ polymerization, the filler is added to the solvent used to synthesize the polymer, and the polymer is synthesized in the presence of the filler. Since the synthesis proceeds while the filler remains dispersed in the solvent, the dispersibility of the polymer composite can be improved.

PA66, which was selected as the base material this time, is in demand in a wide range of fields such as automobile parts and electrical and electronic equipment because of its high strength, heat resistance, and chemical resistance among polymeric materials. Therefore, it is a substance that is being researched for further improvement of its mechanical and thermal properties.

2 SAMPLE PREPARATION

Hexamethylenediamine was added to rCF water dispersion, and then sodium hydroxide was added. The mixture was stirred for one hour to obtain solution A. Solution A was added to a mixture of carbon tetrachloride and adipoyl chloride and polymerized at the interface. The resultant was then purified by reprecipitation, dried and melt-pressed to obtain PA66/rCF composites with a thickness of 0.2 mm. The filler content was 0 to 30 wt%.

3 RESULTS AND DISCUSSION

3.1 Optical image

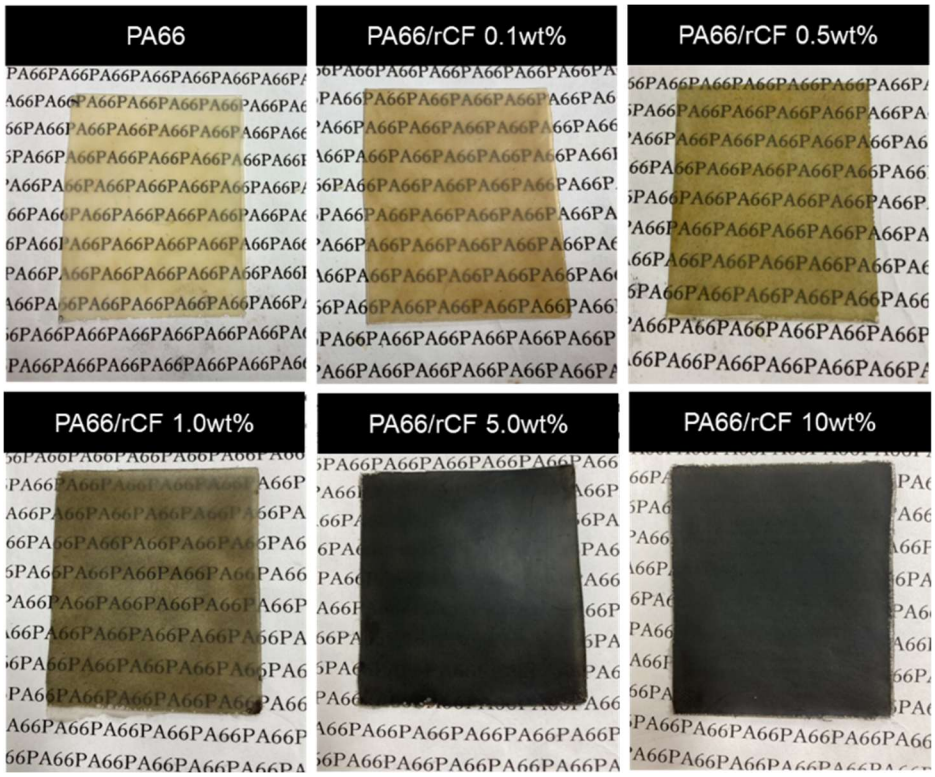

Figure 1: Optical image of PA66 and PA66/rCF composites.

Figure 1 shows optical images of PA66 and PA66/rCF composites. The transparency of the composites decreased with increasing of the filler content. The composites with more than 5.0 wt% of rCF is almost opaque. From these images of the composites, the agglomerates of rCF were not observed.

3.2 SEM

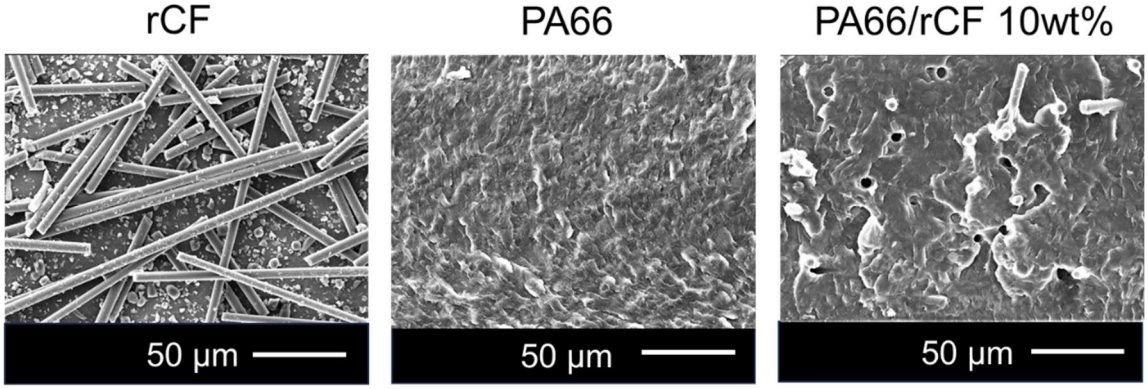

Figure 2: SEM images of rCF and fracture surfaces of PA66 and PA66/rCF composites.

Figure 2 shows SEM images of rCF and fracture surfaces of PA66 and PA66/rCF composites. In the

PA66/rCF composite aggregate of rCF was no observed, showing that rCF was highly dispersed in the composite. In the composites, a number of holes can be seen where the rCF has been pulled out. This indicates that the interaction between PA66 and rCF is weak.

3.3 XRD

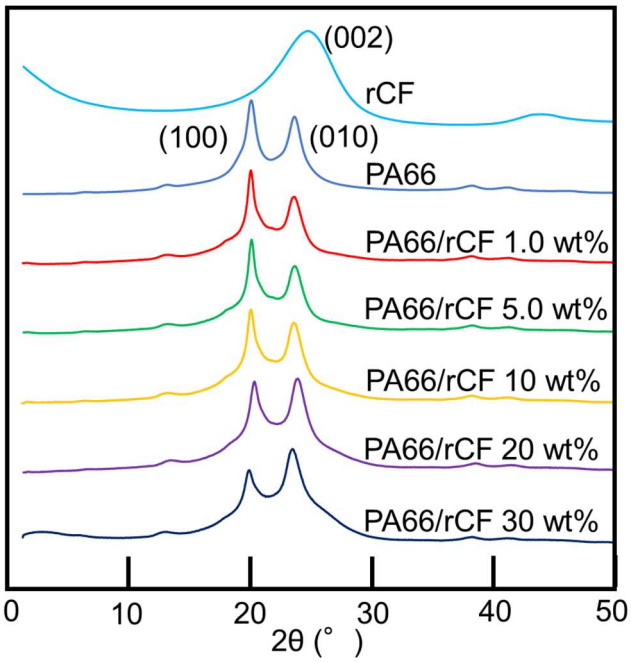

Figure 3: X-ray diffraction profiles of PA66 and PA66/rCF composites.

Figure 3 shows the X-ray diffraction profiles of rCF, PA66 and PA66/rCF composites. In the profile of rCF, (002) was appeared at around 2θ of 25°. Peaks corresponding to (100) and (010) of PA66 were observed at approximately 2θ of 21° and 25°, respectively. These peaks were also observed at the same 2θ in the profiles of the PA66/rCF composites, suggesting that crystalline structure of PA66 was maintained even after the addition of rCF. In addition, since the (010) of PA66 overlaps with the (002) derived from rCF, the intensity of the peak at 2θ of 25° increases with increasing rCF content.

3.4 Thermal Properties

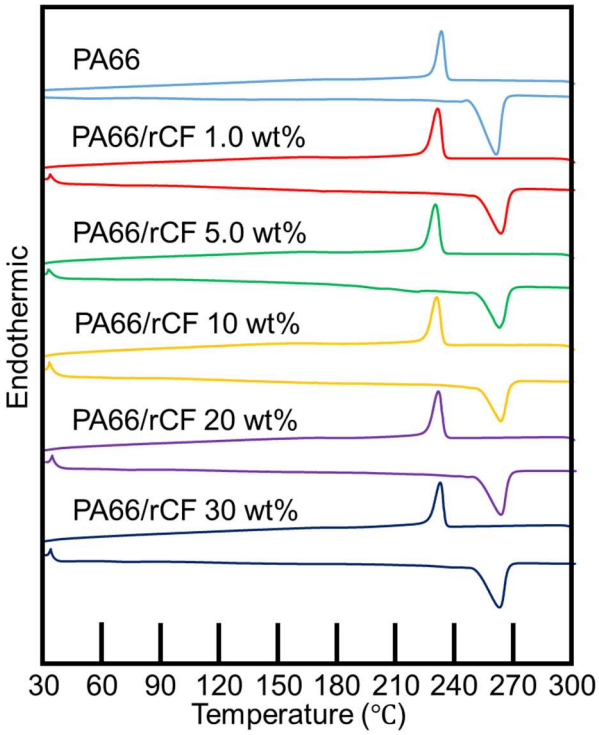

Figure 4: DSC thermogram of PA66 and PA66/rCF composites.

Figure 4 shows DSC thermogram of PA66 and PA66/rCF composites. The endothermic peak appeared at around 263 °C corresponds to the melting point, while the exothermic appeared at around peak near 230 °C corresponds to the crystallization temperature. Both the melting point and the crystallization temperature were not affected by the addition of rCF even at high content. These results indicate that the crystalline structure of PA66 is maintained despite the increased rCF content.

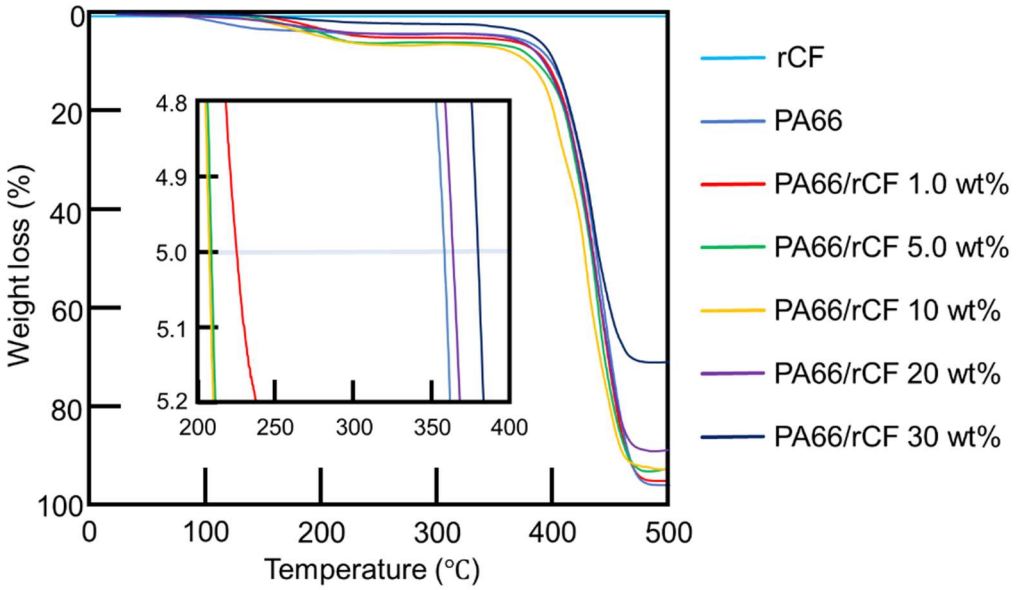

Figure 5: Thermogravimetric traces of rCF, PA66 and PA66/rCF composites.

Figure 5 shows thermogravimetric traces of rCF, PA66 and PA66/rCF composites. The 5% weight loss was defined as thermal decomposition temperature. At the filler content up to 10 wt%. The thermal decomposition temperature largely decreased. It was suggested that rCF inhibited the polymerization of PA66. Therefore, the decrease in the thermal decomposition temperature of the polymer matrix resulted in the lower thermal decomposition temperature of the composites. In the process of in-situ polymerization, resulting in a lower molecular weight.

On the other hand, the thermal decomposition temperature increased at the high filler content more than 20 wt%. For example, the thermal decomposition temperature increased about 20°C by the addition of 30 wt% of rCF. It was assumed that the molecular weight of PA66 in these composites with high filler content also decreased. However, the excellent reinforcement effect of rCF, derived from its rigid structure was dominant for these composites, resulted in the high thermal resistance.

3.5 Mechanical Properties

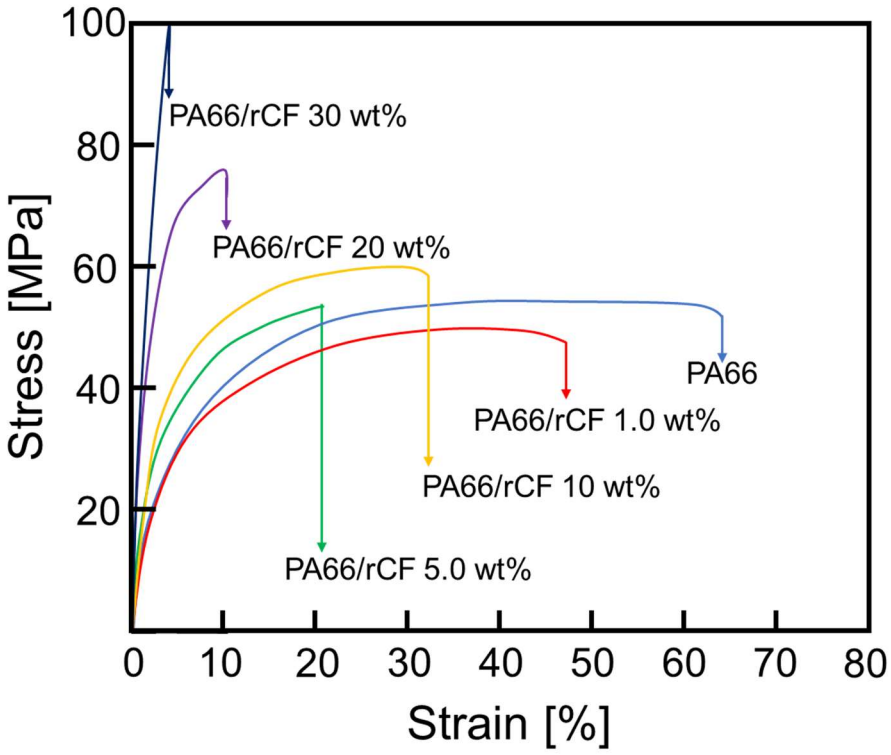

Figure 6: Stress-strain curves of PA66 and PA66/rCF composites.

Figure 6 shows stress-strain curves of PA66 and PA66/rCF composites. The Young's modulus which corresponds to initial gradient, significantly increased by the addition of rCF. In addition, the tensile strength, the maximum stress, increased for the composites with high content.

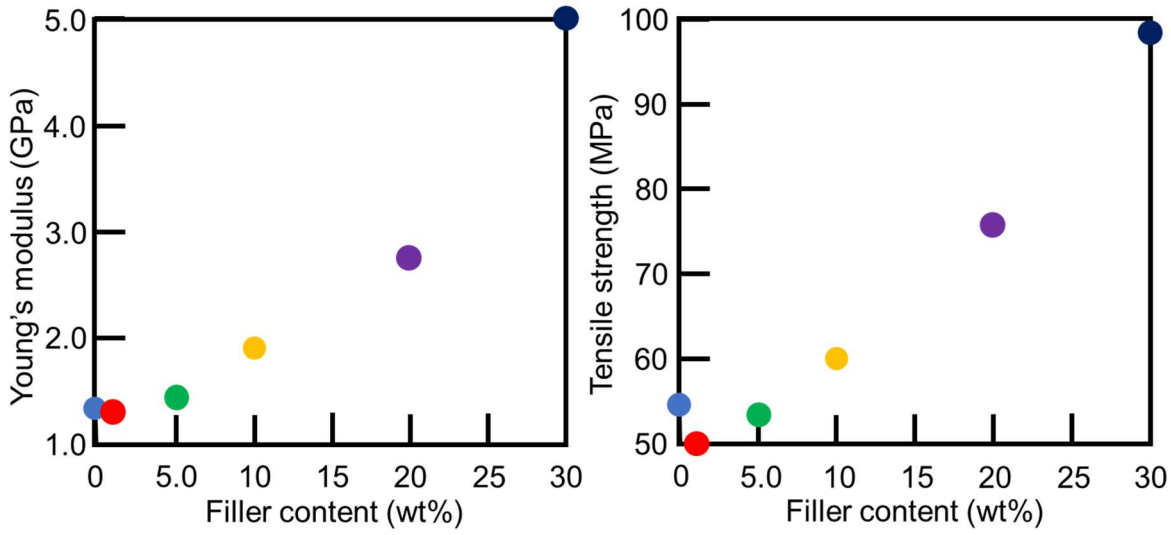

Figure 7: Young's modulus and tensile strength of PA66 and PA66/rCF composites.

Figure 7 on the left shows the Young's modulus and the figure on the right shows the Tensile strength of PA66 and PA66/rCF composites. The Young's modulus increased with increasing of rCF content. Especially in the region of high filler content, the composites showed high Young's modulus. For example, compared to PA66, the Young's modulus increased by 3.6 times by the addition of 30 wt% of rCF. On the other hand, the tensile strength decreased, for the composites with low filler content. As mentioned before, the molecular weight could be decreased by the addition of rCF, due to the process of in-situ polymerization, resulted in decrease in the mechanical properties of the polymer matrix. However, the tensile strength increased for the composites with high filler content. It increased by 1.8 times by the addition of 30 wt% of rCF, showing the excellent reinforcement effect of rCF.

4 CONCLUSIONS

In the PA66 composites, rCF was highly dispersed by in-situ polymerization. The thermal decomposition temperature was significantly reduced by adding small amounts of rCF, but increased at 20 wt% of rCF. The Young's modulus and the tensile strength increased by the addition of rCF. A significant increase in the Young's modulus was observed at more than 10 wt%.

ICCM24
AUGUST 4-8, 2025
BALTIMORE CONVENTION CENTER
BALTIMORE, MARYLAND, USA

No Technical Paper Submission for:

Quyen Tran

Frequency-Selective Surface-Based Composite Radar Absorbing Structures Using Transferred Laser-Induced Graphene on Glass Fiber Fabric with Enhanced Interlaminar Shear Strength

Kinal Kim[1], Seongjun Kim[1], H Alicia Kim[2,3], Sang Eui Lee[1,*]

[1]Department of Mechanical Engineering, Inha University, 100 Inha-ro, Michuhol-gu, Incheon 22212, Republic of Korea
[2]Department of Structural Engineering, UC San Diego, La Jolla, CA 92093, USA
[3]Materials Science and Engineering Program, UC San Diego, La Jolla, CA 92093, USA
*Corresponding author (E-mail: selee@inha.ac.kr)

ICCM24 — 24TH INTERNATIONAL CONFERENCE ON COMPOSITE MATERIALS

MCSI Lab — Multifunctional Composites & Structural Integration Lab

Introduction

Frequency-selective surface-based **radar absorbing structures** (FSS-RAS) fabricated in traditional manner involves dispersing conductive fillers in polymer matrix and using metal masks for bar-coating or screen-printing on dielectric substrates. This study investigates an **alternative technique** of FSS-RAS that uses **laser-induced graphene (LIG)** periodic patterns with controllable sheet resistance engraved on polyimide (PI) precursor, **transferred** onto **glass fiber (GF)** dielectric fabric. We successfully designed and fabricated RAS using frequency-selective Jerusalem cross LIG pattern. The resulting structure, with a thickness of 2.91 mm, demonstrates 90% radar signal absorption across X-band. Additionally, short-beam shear tests revealed that **interlaminar shear strength (ILSS)** of the composite RAS can be **enhanced** when LIG layers are integrated between glass fiber fabric laminates. This study not only visualize a new type of wideband composite RAS with LIGs but also demonstrates a **straight-forward scalable fabrication process** including a series of LIG deposition and transferring.

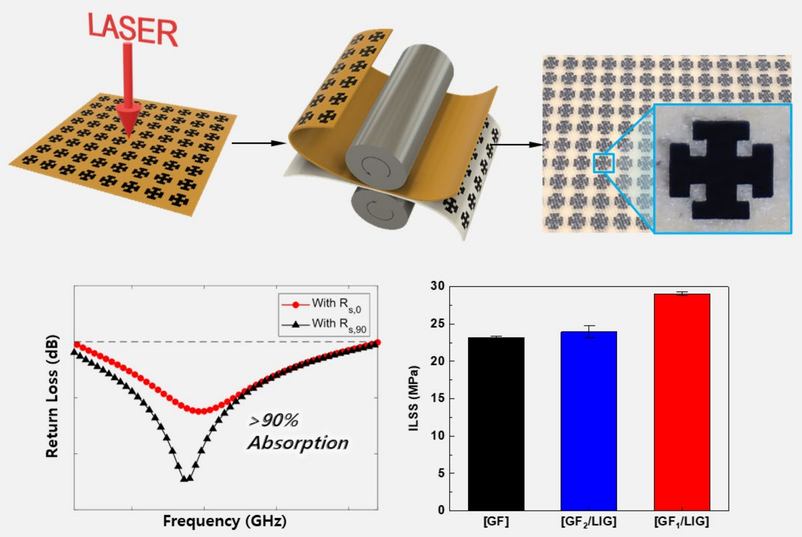

Experiment

- LIG was patterned on PI film using a CO_2 laser.
- Transferred onto glass fabric to avoid PI-related delamination.
- Composite RAS fabricated via vacuum-bagging process.

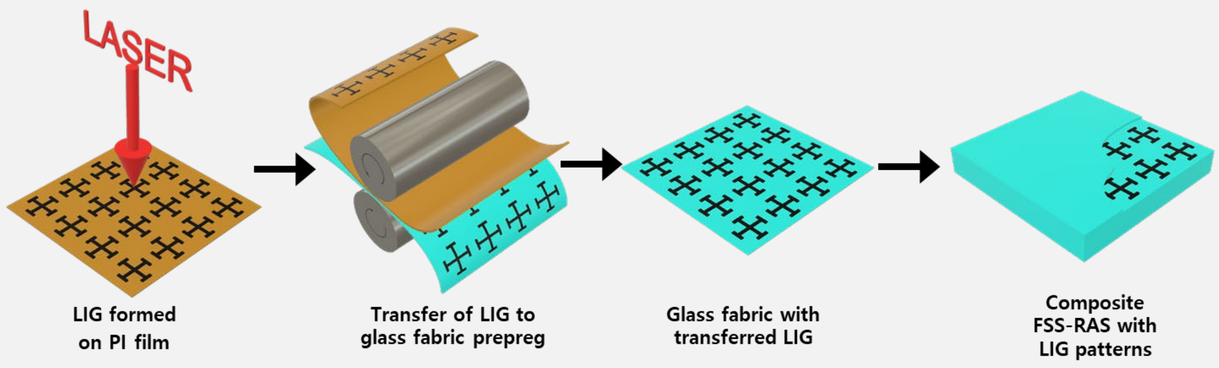

Results & Discussion

◆Characterization

- Sheet resistance of LIG evolved through each fabrication step.
- Process-dependent resistance changes were observed.
- LIG flakes and mountain–valley surface morphology identified.
- Raman spectra confirmed LIG formation.
- LIG interlayer embedded between glass fiber yarns.

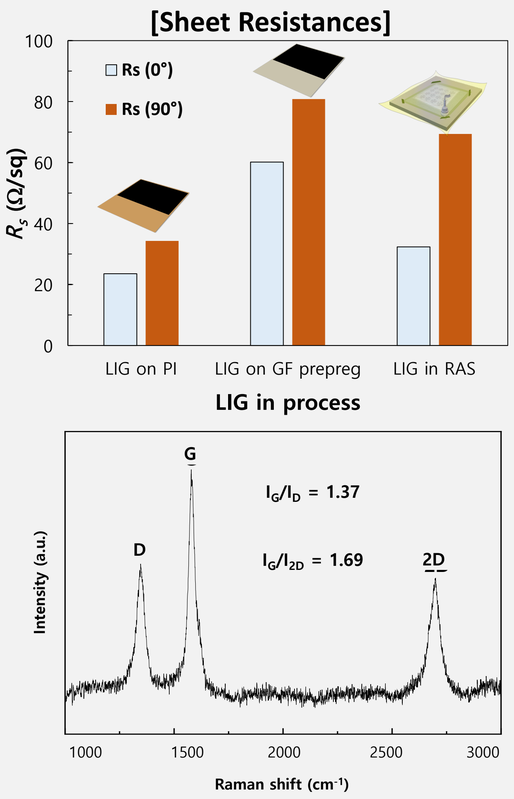

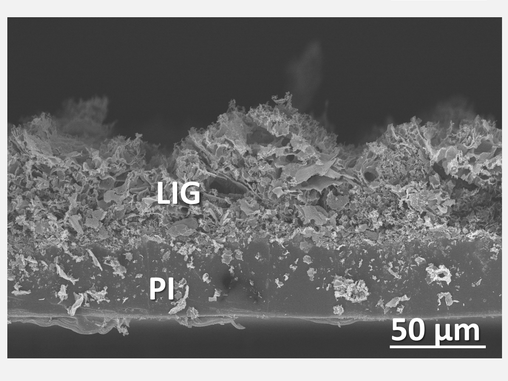

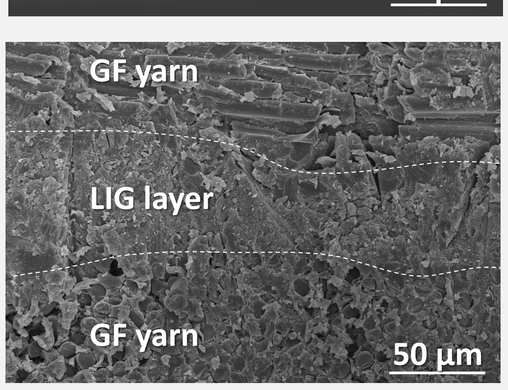

◆Design & Fabricated Samples Comparison

- Optimized RAS parameters:
  $p = 8.6mm, l_1 = 1.8mm, l_2 = 4mm, w_1 = 1.2mm, w_2 = 3.5mm,$
  $t_{GFRP} = 0.2675mm$

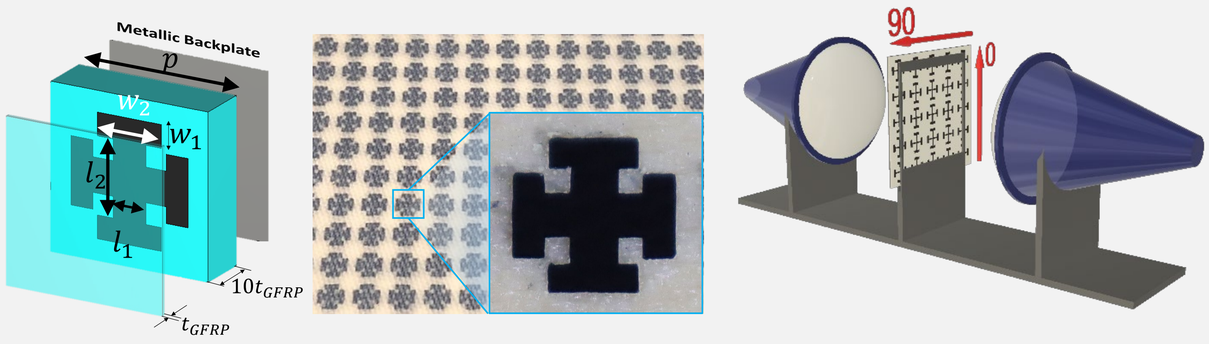

◆Microwave Absorption at X-band

- FSS-RAS shows >90% absorption over target bandwidth
- The fabricated RAS cover wide bandwidth, while remain thin (2.91mm) compared with existing literatures

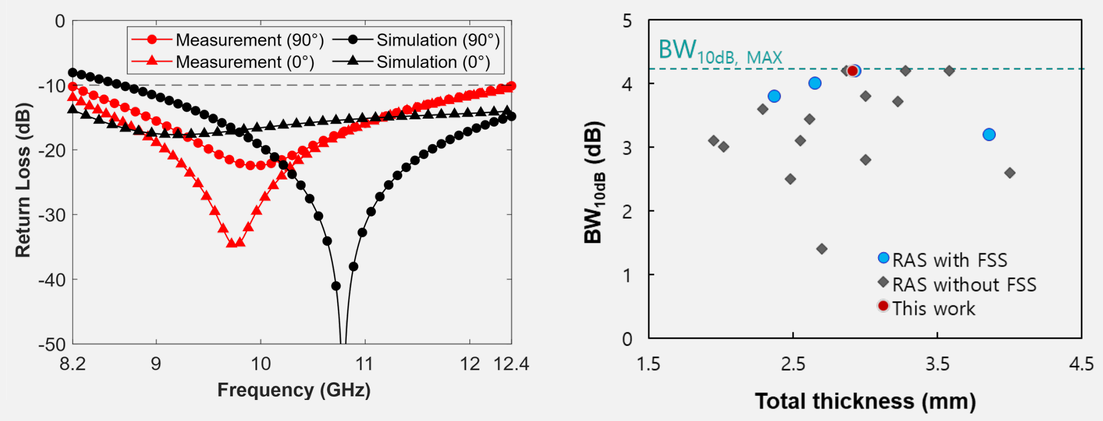

◆Interlaminar-Shear Strength (ILSS)

- For the [GF$_2$/LIG] specimens, delamination occurred only at the interfaces without LIGs, while the interfaces containing LIGs remained intact, even after fiber breakage.
- The ILSS values for [GF] and [GF$_2$/LIG] are similar, while [GF$_1$/LIG] shows a distinct increase in ILSS.

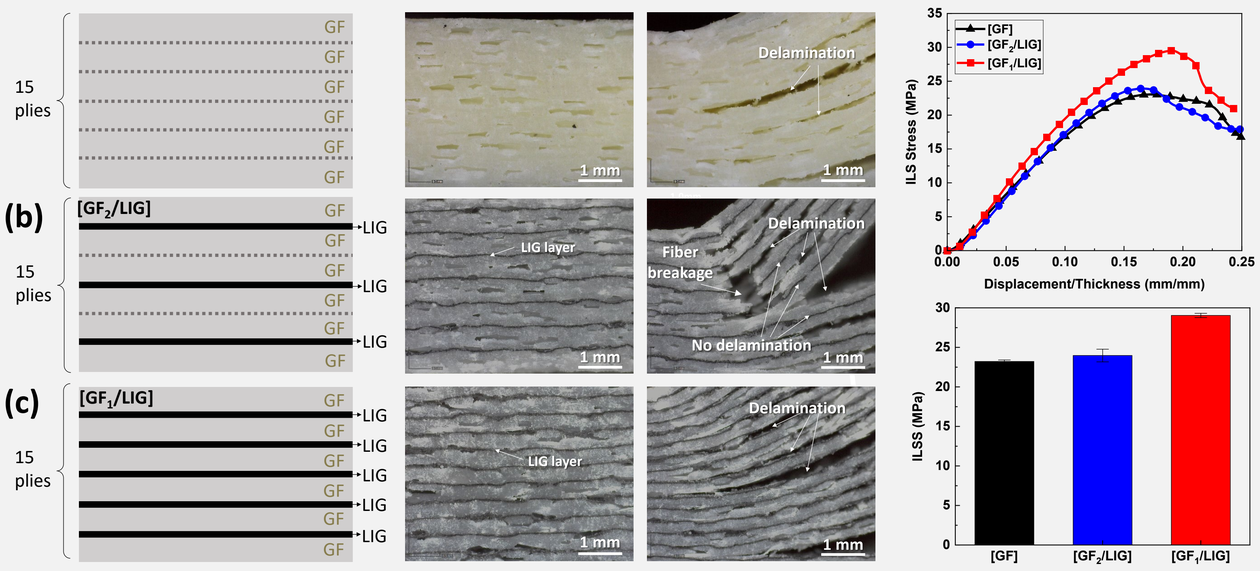

Conclusions

- Introduced a method for composite FSS-RAS fabrication based on a new type of "porous nano-materials (LIGs)" deposited PI film
- We successfully fabricated broadband composite FSS-RAS with Jerusalem-cross pattern thin thickness capable of absorbing 90% of EM waves
- We showed that ILSS could be enhanced by embedding LIGs in between layers of glass fabric

References

1. Lin, J., Z. Peng, Y. Liu, F. Ruiz-Zepeda, R. Ye, E. L. G. Samuel, M. J. Yacaman, B. I. Yakobson and J. M. Tour (2014). "Laser-induced porous graphene films from commercial polymers." Nat Commun 5(1): 5714.

This work was supported by the National Research Foundation of Korea (NRF) grant funded by the Korea government (MSIT). (No. NRF-2022R1A2C1006020).

ICCM24
AUGUST 4-8, 2025
BALTIMORE CONVENTION CENTER
BALTIMORE, MARYLAND, USA

No Technical Paper Submission for:

Yagna Jadeja

ICCM24
AUGUST 4-8, 2025
BALTIMORE CONVENTION CENTER
BALTIMORE, MARYLAND, USA

No Technical Paper Submission for:

Abhinav Yadav

No Technical Paper Submission for:

Zaheer ul Haq

ENHANCING ABLATIVE RESISTANCE OF CARBON/EPOXY LAMINATES VIA INTERLAYER OF SILICONE ELASTOMER MICROPARTICLES

Se Jun Wang[1], Jinwook Jeong[1], Hyeongwoo Kang[1], Youngseok Oh[2*], and Sang Yup Kim[1*]

[1]Department of Mechanical Engineering, Sogang University
Seoul 04107, Republic of Korea
Email: sangyupkim@sogang.ac.kr, web page: https://composite.sogang.ac.kr/research

[2]Composites & Convergence Materials Research Division, Korea Institute of Materials Science
Changwon, 51508, South Korea
Email: youngsoh@kims.re.kr

Keywords: A. Polymer-matrix composites (PMCs), High-temperature properties, Resin transfer moulding (RTM)

ABSTRACT

Thermal protection systems (TPS) are essential for protecting spacecraft and hypersonic vehicles from extreme heat. However, traditional TPS materials such as carbon fiber-reinforced polymer composites (CFRPs) require substantial thickness to achieve thermal resistance, leading to increased structural weight. In this study, we propose an enhanced thermal protection strategy by embedding silicone elastomer microparticles as interlayers within CFRP laminates. The microparticles, synthesized via a thixotropic emulsion method using Ecoflex elastomer and sodium alginate solution, are incorporated at 6 vol.% levels in the mid-plane of 10-ply CFRP preforms. Laminates are fabricated via vacuum-assisted resin transfer molding (VARTM) and subjected to oxy-hydrogen flame ablation testing at ~2000 °C. The Si-containing interlayers decompose under high heat to generate silica, forming a thermal barrier that delays carbon fiber degradation. Notably, the ablation resistance increases for composites with PDMS microparticles. These results demonstrate a lightweight yet highly effective approach to improve ablative resistance through in-situ silica formation and suggest the potential of PDMS-based interlayers for next-generation aerospace TPS applications.

1 INTRODUCTION

Thermal protection systems (TPS) are essential in hypersonic and space vehicles to withstand severe aerodynamic heating [1]. Composite materials, particularly carbon fiber-reinforced polymers (CFRPs), are widely used due to their high specific strength and adaptability. For extreme environments where reusable TPS materials such as ceramic and metal matrix composites may fail [2,3], ablative TPSs are employed. These rely on the formation of gaseous boundary layers during decomposition, which insulate against heat flux due to their low thermal conductivity [4,5].

CFRPs typically use the polymer matrix as the sacrificial layer while carbon fibers provide structural reinforcement. Despite their favorable properties, sufficient ablation resistance often requires increased material volume, adding undesirable weight. Various enhancements have been explored, such as particle incorporation [6], surface coatings [7], and resin modifications [8]. Among these, particulate inclusion is attractive due to its processability and minimal impact on mechanical performance. Yet ceramic particles increase composite density, limiting their use in weight-sensitive applications.

Silicone elastomers, with their low density and ability to form protective silica during ablation [9], offer a promising alternative. While prior work has focused on elastomer matrices or coatings [10,11], the use of silicone microparticles as a discrete interlayer within CFRP remains underexplored, partly due to fabrication challenges [12].

Here, we present silicone elastomer microparticles embedded carbon fiber/epoxy laminates (Si-CFRP), as shown in **Figure 1**. The integration of polydimethylsiloxane (PDMS) microparticles within the matrix of CFRP laminates combines the structural benefits of CFRPs with the thermal protection

advantages of silicone elastomers (Figure 1a). Unlike traditional TPSs, silicone elastomers offer unique thermal protection capabilities. In detail, when exposed to high temperatures, they undergo thermal decomposition releasing silicon-based compounds, thereby forming protective layers of silicon dioxide (silica). This method not only reduces material weight but also significantly enhances thermal resistance, making it highly suitable for aerospace and defense applications. The thermal protection mechanism comprises three steps (Figure 1b). First, silicone elastomer decomposes under high temperatures, releasing silicon-based gases. These gases subsequently react with oxygen to form a silica layer on the composite surface and within fiber interspaces. This silica layer acts as a thermal shield, reducing heat penetration. Lastly, the high melting point of silica ensures sustained thermal protection during prolonged high-temperature exposure.

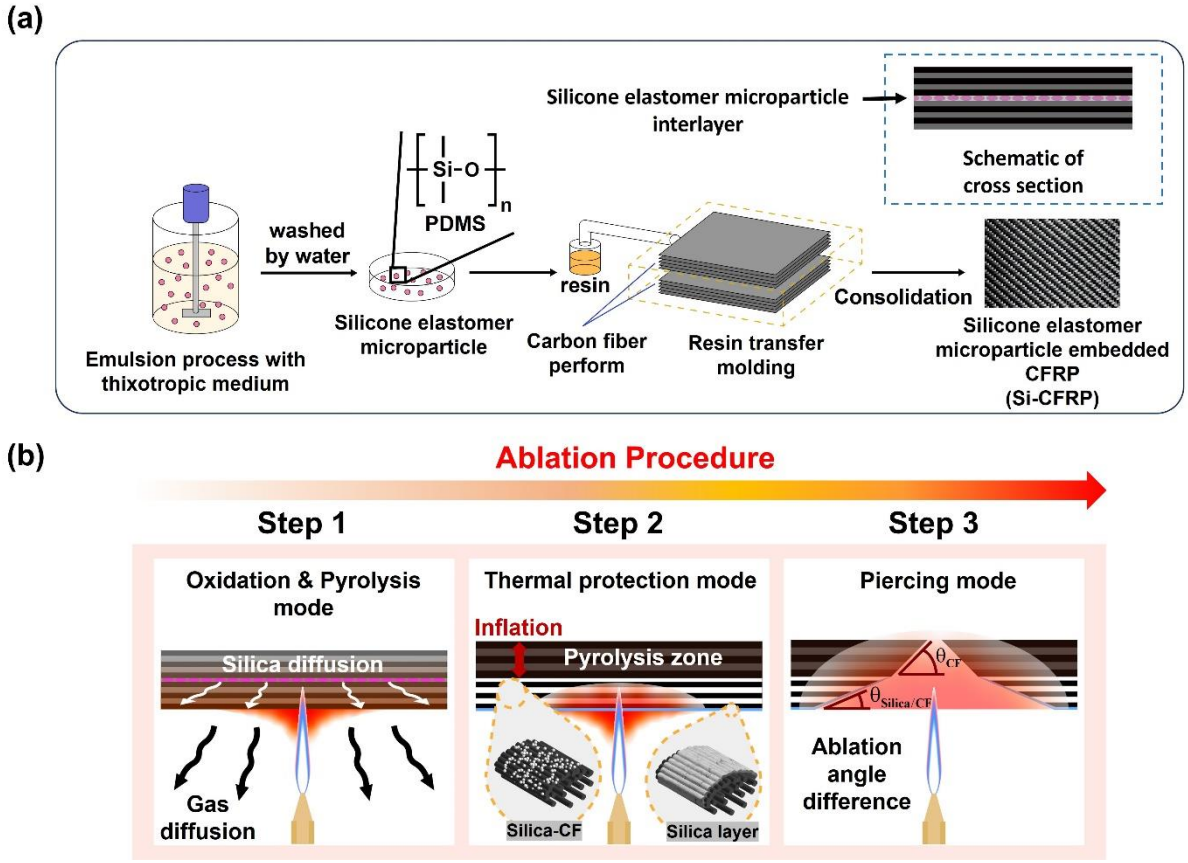

Figure 1. Overview of preparation and thermal protection mechanism of Si-CFRP. (a) Schematic of manufacturing process of silicone elastomer microparticle embedded carbon fiber-reinforced polymer (Si-CFRP) (b) Ablation mechanism of Si-CFRP with 3-step procedure.

2 MATERIALS AND EXPERIMENTAL METHODS

PDMS microparticles are synthesized using a thixotropic emulsion process with 4 wt.% sodium alginate/DI water medium. Two parts silicone elastomers (Ecoflex 00-30, Smooth-On) are premixed in a 1:1 ratio and stirred at 200 rpm in the sodium alginate/DI water medium to create microparticles. Particles are retrieved after washing process.

Laminated composites are fabricated using vacuum assisted resin transfer molding (VARTM), embedding 6 vol.% PDMS microparticles in the middle layer of 10-ply carbon fiber preforms infused with an epoxy/amine resin system (INF114, 212). Laminates were cured at 120 °C for 3 hours and machined into 400 mm × 400 mm specimens.

Ablation tests are conducted with an oxy-hydrogen torch at temperatures above 1500 °C. Specimens are exposed to the flame until the complete piercing, and ablation resistance is calculated as the inverse of the linear ablation rate which is calculated as,

$$LAR = t / \tau \tag{1}$$

where t is thickness of specimen and τ is ablation time until the flame pierces the specimen.

3 RESULTS AND DISCUSSION

Figure 2 showcase the test-set up for measuring the ablation resistance, and surface morphologies of specimen after ablation. After decomposition of epoxy matrix, carbon fibers of Neat CFRP also decompose immediately due to the high flame temperature (Fig 2a). After the flame pierce the specimen, graphitic region nearby piercing point is identified as the result of the ablation process. In contrast, Si-CFRP resists to thermal attack from the oxyhydrogen flame after decomposition of epoxy matrix (Fig 2b). Furthermore, the generation of white colored debris on the surface of Si-CFRP after ablation procedure is identified. The debris on the surface is presumably assumed as silica, because of presence of the silicon at the chemical structure of PDMS.

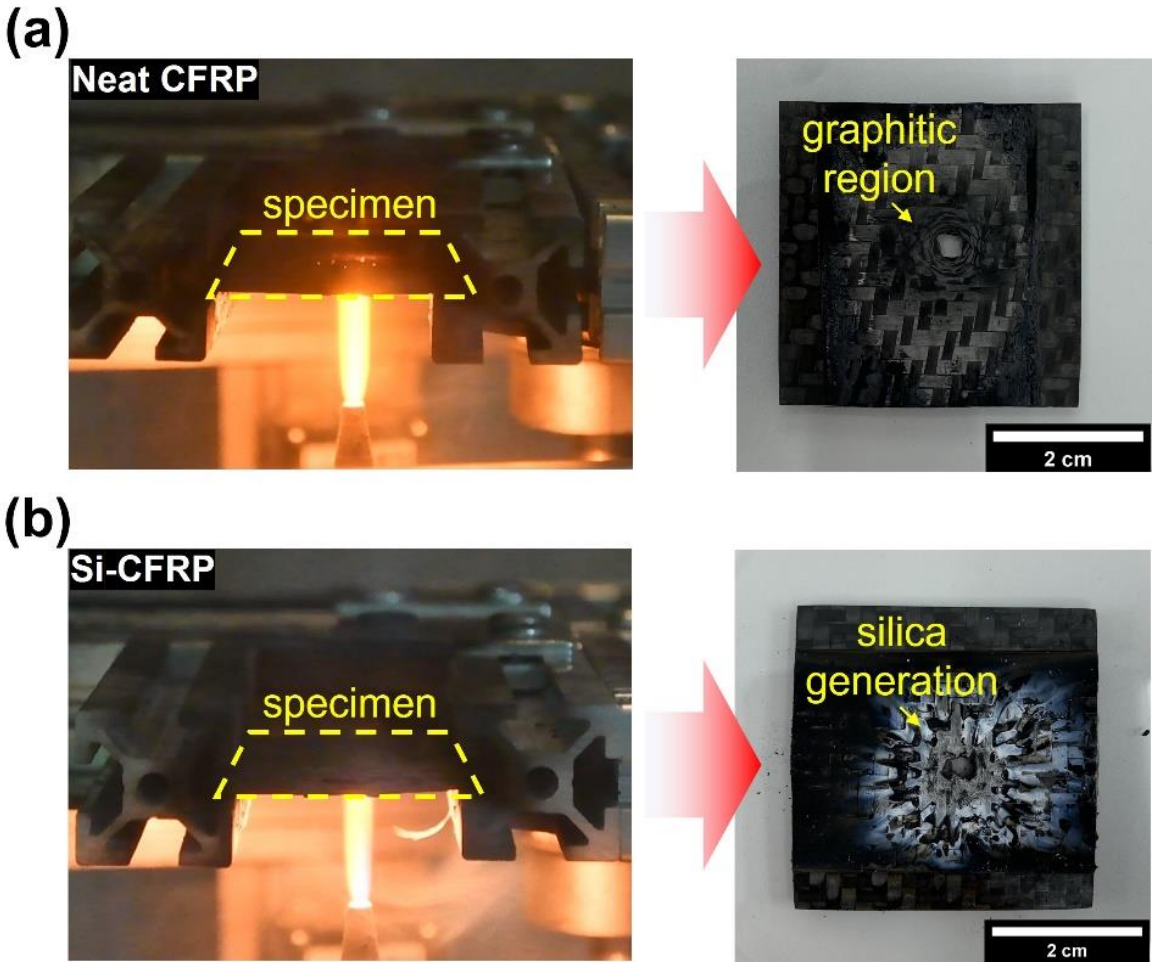

Figure 2. Ablation test set up and surface morphologies of Neat CFRP and Si-CFRP after ablation. Ablation test of (a) Neat CFRP and (b) Si-CFRP specimen from 10-ply laminate with and without silicone elastomer particle interlayer (6 vol.%).

Figure 3 presents SEM images comparing the ablated surfaces of Neat CFRP and Si-CFRP. In Neat CFRP (Fig. 3a), fine carbonaceous debris is observed, attributed to the oxidative degradation of carbon fibers. In contrast, the ablated surface of Si-CFRP (Fig. 3b) exhibits the formation of spherical silica particles (~160 nm) on the carbon fiber surface, indicating in-situ generation of thermally protective silica during ablation.

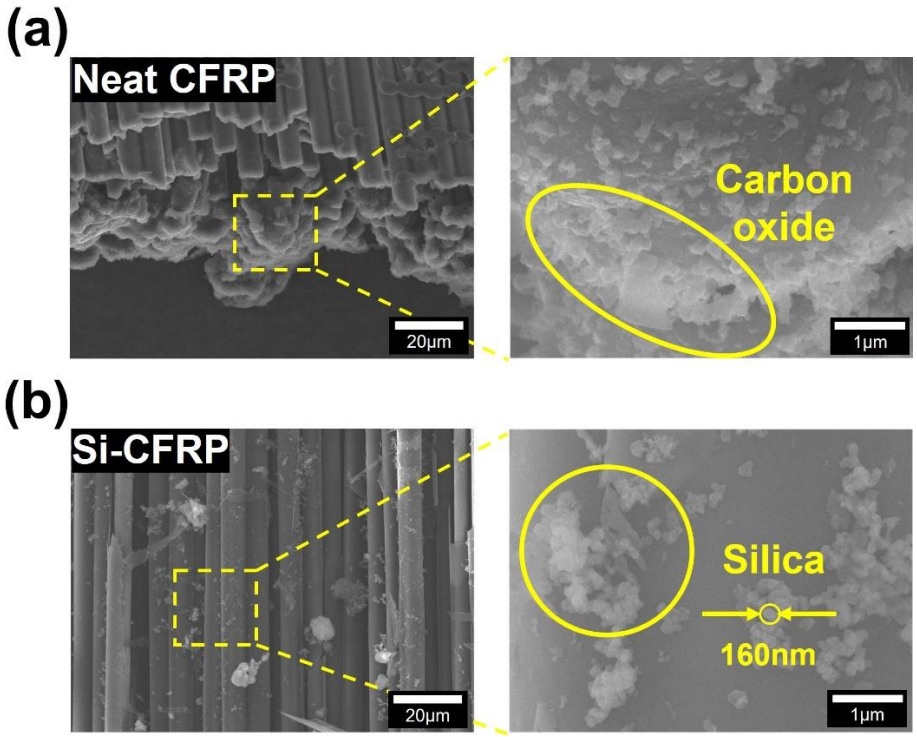

Figure 3. Morphological characteristics of the ablated zone. Scanning electron microscopy (SEM) images of (a) Neat- and (b) Si-CFRP.

Figure 4 indicates that Si-CFRP specimens significantly enhance ablative resistance compared to Neat CFRP laminates. The incorporation of silicone elastomer microparticles facilitate the formation of silica layers on the composite surface, effectively delaying material degradation. Specimens containing 6 vol.% PDMS exhibit an ablation resistance of 129 mm/sec^{-1}, more than double that of Neat CFRP (55.8 mm/sec^{-1}).

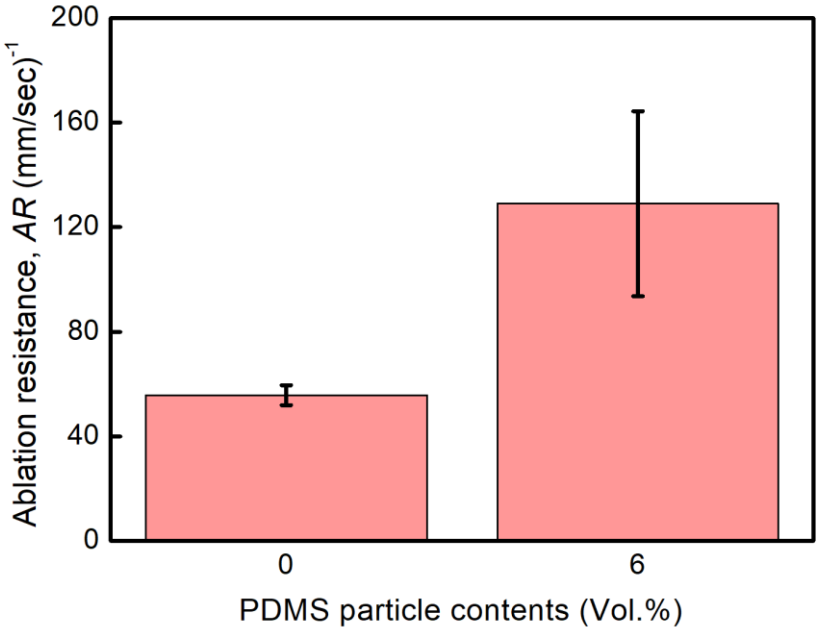

Figure 4. Summary of ablation resistance of composite specimen with respect to contents of silicone elastomer particles.

4 CONCLUSIONS

The ablative resistance of carbon fiber-reinforced polymer composites (CFRPs) is enhanced through the incorporation of silicone elastomer, polydimethylsiloxane (PDMS), as an interlayer of microparticles. The results showed that CFRPs embedded with 6 vol.% silicone elastomer microparticles achieved more than double the ablation resistance of Neat CFRP. These findings confirm the potential of Si-CFRP laminates for demanding aerospace applications where high-performance thermal protection systems (TPS) are desired.

Future work will focus on optimizing the distribution and volume fraction of silicone elastomer microparticles within the laminate structure. Additionally, investigating the bonding properties between PDMS and the CFRP matrix will provide insights into further improving mechanical and thermal performance. These advancements aim to establish Si-CFRP as a versatile solution for next-generation TPS materials.

ACKNOWLEDGEMENTS

This work was supported by the Korea Institute of Materials Science (Grant#:PNKA100), National Research Foundation of Korea (Grant # RS-2024-00412289, RS-2024-00448445, RS-2024-00466051)

REFERENCES

[1] D.D. Jayaseelan, Y. Xin, L. Vandeperre, P. Brown, W.E. Lee, Development of multi-layered thermal protection system (TPS) for aerospace applications, Compos B Eng 79 (2015) 392–405. https://doi.org/10.1016/J.COMPOSITESB.2015.04.017.

[2] D. Glass, Ceramic Matrix Composite (CMC) Thermal Protection Systems (TPS) and Hot Structures for Hypersonic Vehicles, in: 15th AIAA International Space Planes and Hypersonic Systems and Technologies Conference, American Institute of Aeronautics and Astronautics, 2008. https://doi.org/doi:10.2514/6.2008-2682.

[3] F. Cai, D. Ni, W. Bao, B. Chen, J. Lu, X. Zou, Y. Qin, S. Dong, Ablation behavior and mechanisms of Cf/(Ti0.2Zr0.2Hf0.2Nb0.2Ta0.2)C−SiC high-entropy ceramic matrix composites, Compos B Eng 243 (2022) 110177. https://doi.org/10.1016/J.COMPOSITESB.2022.110177.

[4] I. Cozmuta, M.J. Wright, B. Laub, W.H. Willcockson, Defining ablative thermal protection system margins for planetary entry vehicles, in: 42nd AIAA Thermophysics Conference, 2011. https://doi.org/10.2514/6.2011-3757.

[5] C.V. Kumar, B. Kandasubramanian, Advances in Ablative Composites of Carbon Based Materials: A Review, Ind Eng Chem Res 58 (2019) 22663−22701. https://doi.org/10.1021/acs.iecr.9b04625.

[6] X. Jin, C. Liu, H. Huang, R. Pan, C. Wu, X. Yan, H. Wang, Y. Pan, C. Hong, X. Zhang, Multiscale, elastic, and low-density carbon fibre / siliconoxycarbide-phenolic interpenetrating aerogel nanocomposite for ablative thermal protection, Compos B Eng 245 (2022). https://doi.org/10.1016/j.compositesb.2022.110212.

[7] D. Rodriguez-Melendez, T. Mandal, B. Palen, C.T. Long, H.C. Chiang, S. Sarikaya, M. Naraghi, J.C. Grunlan, Heat-Shielding Nanobrick Wall for Carbon Fiber-Reinforced Polymer Composites, ACS Appl Polym Mater 5 (2023) 3270−3277. https://doi.org/10.1021/acsapm.2c02114.

[8] K. Hui, L. Wang, H. Qu, J. Li, C. Gao, W. Wang, C. Bian, N. Yan, Y. Yang, Thermal stability, pore structure characteristics of char layer and ablation resistance mechanism of new thermal insulation composites based on polyphosphazene polymer, Polym Degrad Stab 206 (2022) 110184. https://doi.org/10.1016/J.POLYMDEGRADSTAB.2022.110184.

[9] G. Camino, S.M. Lomakin, M. Lageard, Thermal polydimethylsiloxane degradation. Part 2. The degradation mechanisms, Polymer (Guildf) 43 (2002) 2011−2015. https://doi.org/10.1016/S0032-3861(01)00785-6.

[10] D. Yang, W. Zhang, B. Jiang, Ceramization and oxidation behaviors of silicone rubber ablative composite under oxyacetylene flame, Ceram Int 39 (2013) 1575−1581. https://doi.org/10.1016/J.CERAMINT.2012.07.109.

[11] Y. Wang, Y. Cai, Y. Ling, H. Zhang, J. Tian, Z. Heng, S. Zhou, S. Xia, M. Liang, H. Zou, Improved Mechanical and Ablative Properties of PDMS Coatings Incorporating Epoxy as a Suspended Chain, Ind Eng Chem Res 62 (2023) 9920−9931. https://doi.org/10.1021/acs.iecr.3c00814.

[12] S.Y. Kim, S. Liu, S. Sohn, J. Jacobs, M.D. Shattuck, C.S. O'Hern, J. Schroers, M. Loewenberg, R. Kramer-Bottiglio, Static-state particle fabrication via rapid vitrification of a thixotropic medium, Nat Commun 12 (2021). https://doi.org/10.1038/s41467-021-23992-2.

ICCM24
AUGUST 4-8, 2025
BALTIMORE CONVENTION CENTER
BALTIMORE, MARYLAND, USA

No Technical Paper Submission for:

Weizhao Zhang

IMPACT CHARACTERISTICS OF SHEET MOLDING COMPOUND WITH DIFFERENT TAPE MORPHOLOGY AND EFFECT OF CONTINUOUS CFRTP OVER-MOLDING

Sang Won Lim[1], Fan Zhang[1], Yi Wan[1] and Jun Takahashi[1]

[1]Department of Systems Innovation, Graduate School of Engineering, The University of Tokyo
Hongo 7-3-1, Bunkyo-ku, Tokyo, Japan
Email: swlim@g.ecc.u-tokyo.ac.jp

Keywords: Carbon fiber reinforced thermoplastics, Sheet molding compound, Hybrid composites, Impact properties, Finite element analysis

ABSTRACT

Carbon fiber reinforced thermoplastic sheet molding compound (CFRTP-SMC) presents a promising alternative to the conventional continuous fiber composites due to its superior formability, in-plane isotropy, high production efficiency, and recyclability, particularly through the reutilization of end-of-life waste and prepreg scrap. In automotive applications, where environmental regulations and large-scale production are critical, CFRTP-SMC is increasingly investigated for its potential in future mobility. However, there are concerns regarding adoption of discontinuous based composite for structural members of an automobile where high energy absorption is required to ensure the safety of passengers. This study examines the impact behavior of CFRTP-SMC under three-point bending, along with a hybrid unidirectional (UD) carbon fiber over-molded CFRTP-SMC variant. Different tape lengths are investigated to identify the critical tape length for enhanced energy absorption and impact strength. Additionally, the influence of UD carbon fiber over-molding on impact performance is assessed. A multi-scale microstructural model analysis is conducted to estimate the material's engineering constants for experimental-analytical correlation using finite element methods. Results indicate that the critical tape length identified significantly increase the impact performance of CFRTP-SMC, and further improvements in energy absorption can be achieved through the utilization of UD carbon fiber over-molding without compromising weight reduction objectives.

1 INTRODUCTION

Carbon fiber reinforced plastics (CFRP) are widely employed in engineering applications due to their high specific strength and stiffness. In particular, discontinuous-carbon fiber reinforced plastics have gained attention in automotive sectors for their superior formability and production efficiency – key considerations in mass production. In addition, more progressive and demanding environmental regulations targeting carbon emission reduction has accelerated interest in thermoplastic-based CFRP, which offer notable advantages in recyclability [1-3]. However, the use of discontinuous thermoplastic composites in structural members of automobiles remains limited due to concerns over their impact performance, which is critical for passenger protection.

In response, recent research has focused on discontinuous composites reinforced with long carbon fibers, such as carbon fiber reinforced thermoplastic sheet molding compounds (CFRTP-SMC). CFRTP-SMC is a type of SMC consisting of carbon fiber reinforcements in the form of tapes or tows with a thermoplastic resin, offering advantages in forming complex shapes, cost-effectiveness for large-scale production, and excellent mechanical properties. The bundled morphology of the carbon fibers in CFRTP-SMC results in superior mechanical performance compared to the conventional injection-molded composites while maintaining quasi-isotropic behavior. Building on these advantages, Takahashi and Wan developed methods for fabricating quasi-isotropic SMC using randomly distributed carbon fiber prepreg tapes [4]. They analyzed the influence of tape length on mechanical performance through X-ray micro-computed tomography scanning with estimations using Monte Carlo stochastic simulation [5]. Similarly, Alves et al. examined the properties of quasi-isotropic tow-based SMC [6, 7], while Katsivalis et al. extended this work by developing predictive models for failure behavior [8].

While the static mechanical properties of SMC have been extensively studied, the influence of tape length on their impact performance remains largely unexplored. Furthermore, the potential of hybridizing SMC with unidirectional (UD) carbon fiber through over-molding has not yet been systematically investigated. In this paper, the critical tape morphology that saturates the impact properties of CFRTP-SMC is assessed. In addition, the effect of UD carbon fiber over-molding on enhancing impact characteristics is examined.

The proposed framework highlights the influence of tape morphology on the impact performance of CFRTP-SMC, as well as effective utilization of UD reinforcements without compromising weight reduction goals. These results emphasize the strong potential of CFRTP-SMC and its hybrid variants for structural applications in the automotive industry, particularly in the context of large-scale and sustainable manufacturing.

2 MATERIALS AND METHODS

2.1 Molding and specimen preparation

This study investigates CFRTP-SMC with two distinct tape lengths, alongside a hybrid variant combining CFRTP-SMC with UD reinforcement. The SMC preform sheets were manufactured by randomly distributing chopped prepreg tapes consisting of carbon fiber (TR50S, Mitsubishi Chemical Co.) and polyamide-6 resin (PA6, DIAMIRON^{TM} C, Mitsubishi Chemical Co.). The SMC preform was stacked with approximately 95-100 grams of pure SMC sheets, where its hybrid variant was stacked with 85-90 grams of SMC sheets and a single layer of UD ply on one side of the outermost surface so that the total material weight remained equivalent. Figure 1 and Table 1 provide details of the material configurations and their respective designations. SMC_10 and SMC_30 refer to SMC plates reinforced with 10 mm and 30 mm tapes, respectively. Hybrid_L and Hybrid_U denote SMC plates with 30 mm tapes, further reinforced with a single layer of UD carbon fiber layer on the lower and upper surfaces, respectively.

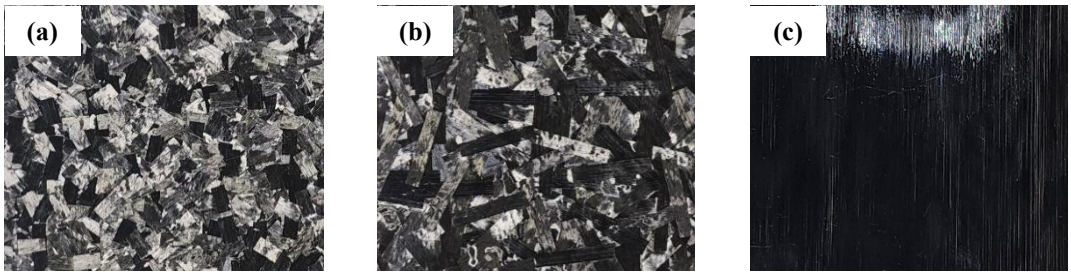

Figure 1: Material representation: (a) SMC 10 mm tapes, (b) SMC 30 mm tapes, (c) UD carbon fiber

Material type	Tape length SMC [mm]	No. SMC plies	No. UD plies	Total weight [g]
SMC_10	10	8	0	95-100
SMC_30	30	8	0	95-100
Hybrid_L	30	7	1 lower layer	95-100
Hybrid_U	30	7	1 upper layer	95-100

Table 1: Material identification.

The preformed sheets were then compression-molded into panels measuring 250 x 125 mm with a nominal thickness of 2.0 mm. Both the SMC and hybrid panels were molded under identical conditions using a press machine (265 °C, 50 bars, 25 mins) with the carbon fiber volume fraction of 50% to ensure direct comparability. The molded panels were subsequently sectioned into 120 x 60 mm specimens using a composite material cutting machine (MARUTO Testing Machine Company, AC-500CF), as illustrated in Figure 2.

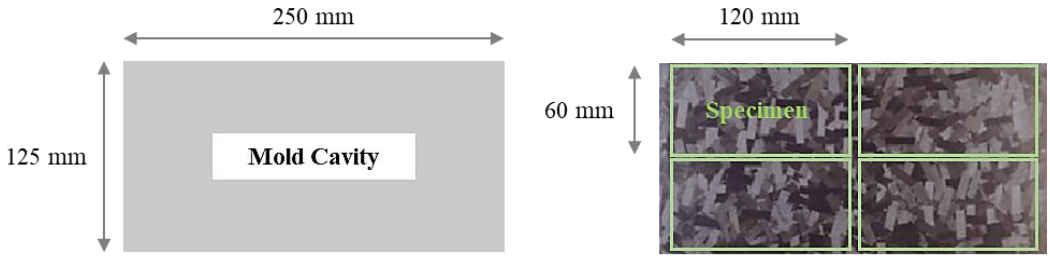

Figure 2: Schematics of mold cavity, plate, and specimen geometry

2.2 Impact experiment

Three-point bending impact tests on the materials listed in Table 1 were conducted with a high-speed impact testing machine (Hydroshot HITS-P10, Shimadzu Corporation) under the JIS K7084 standards with three different impact velocities. The sample dimensions and testing conditions are detailed in Table 2. To evaluate the impact properties, a minimum of five samples were prepared for each condition. The maximum impact stress, σ_{max} and the specific energy absorption, *SEA* are calculated using equations (1) and (2). The force, F and work W are measured from the testing machine, while the dimensions L, w, and t represent the gauge length, width, and thickness, respectively. The variable m denotes the mass of the specimen.

Dimensions			No. of specimens	Impact velocity [m/s]
Gauge length [mm]	Width [mm]	Thickness [mm]		
80	60	2	> 5	1.5, 2.0, 2.5

Table 2: Sample dimensions and testing conditions for the three-point bending impact experiment.

$$\sigma_{max} = \frac{3FL}{2wt^2} \tag{1}$$

$$SEA = \frac{W}{m} \tag{2}$$

2.3 Multi-scale modelling

The theoretical material properties and associated engineering constants for both SMC and UD materials were estimated using Digimat-MF (Hexagon AB), a multi-scale modelling platform based on mean-field homogenization theory for composites behavior prediction. The raw material properties of carbon fiber (Young's modulus: 230 GPa) and Polyamide-6 (Young's modulus: 3 GPa) were used as input parameters to estimate the composite properties. The twelve engineering constants include Young's moduli (E_{xx}, E_{yy}, E_{zz}), Poisson's ratios (ν_{xy}, ν_{yx}, ν_{xz}, ν_{zx}, ν_{yz}, ν_{zy}), and shear moduli (G_{xy}, G_{xz}, G_{yz}), where the subscripts denote the axes of planarity.

2.4 Finite element model

Engineering constants were then implemented in a FE model developed using LS-DYNA (Ansys inc.). The material configuration and corresponding FE model setup are shown in Figure 3 and Figure 4. The model consisted of three primary parts: the impact striker and supports were modelled as rigid bodies using *MAT_RIGID* (MAT_020), while the specimen was defined using the *MAT_ENHANCED_COMPOSITE_DAMAGE* (MAT_054/055).

Boundary conditions were applied such that the impact striker motion was constrained to vertical translation (z-direction), replicating the actual experimental impact setup. The supports were fully

constrained in all degrees of freedom (translation and rotation in x, y, and z axes), while the specimen was simply supported with all degrees of freedom unrestrained. The impactor was given an initial velocity matching the experimental conditions, where the peak impact force was recorded for comparison with experimental results.

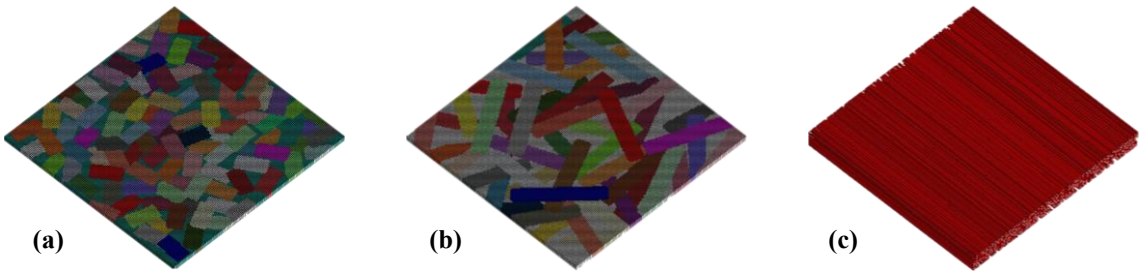

Figure 3: Material configuration: (a) SMC 10 mm tapes, (b) SMC 30 mm tapes, (c) UD carbon fiber

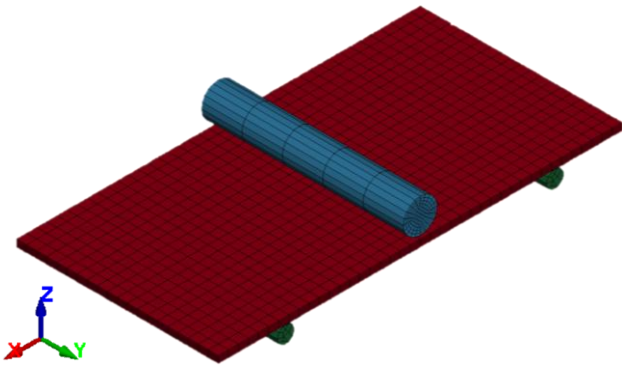

Figure 4: Finite element model for three-point bending impact

3 RESULTS AND DISCUSSIONS

3.1 Impact properties

The results of the three-point bending impact experiments are presented in Figure 5 and Figure 6. Both the impact strength and SEA increased as the tape length of SMC increased from 10 mm to 30 mm. This improvement is attributed to enhanced load transfer efficiency with longer tapes, which facilitate more effective stress transfer from the matrix to the fibers during impact, thereby increasing the overall energy absorption. In shorter tapes, the number of tape-ends per unit volume is higher, acting as stress concentrators and sites for crack initiation. In contrast, longer tapes are preferable for bridging cracks, promoting more progressive damage, and contributing to improved impact resistance and SEA.

In hybrid configurations, where UD carbon fiber was over-molded on either the lower or upper surfaces of the SMC, SEA increased while impact strength decreased relative to the SMC specimens with 30 mm tape lengths. Although the UD layer possesses superior in-plane properties compared to SMC, their off-axis properties are significantly lower, which limits their performance under flexural impact conditions present in the three-point bending impact test. Furthermore, UD materials tend to be more brittle than SMC, and are prone to delamination upon impact, which can serve as a stress concentrator and reduce impact strength.

Despite reduction in strength, delamination increases the range of failure mechanisms and facilitates more distributed energy dissipation over time, leading to increased overall energy absorbed per unit mass. This trade-off is a common phenomenon in hybrid structures, where maximizing energy absorption is of greater importance than peak load capacity. In automotive applications, where crashworthiness and passenger safety are prioritized, materials that fail in controlled, energy dissipating mechanisms are preferred over those that fail catastrophically at higher loads. This highlights a strategic

design consideration in which functional performance regarding safety takes precedence over peak strength alone.

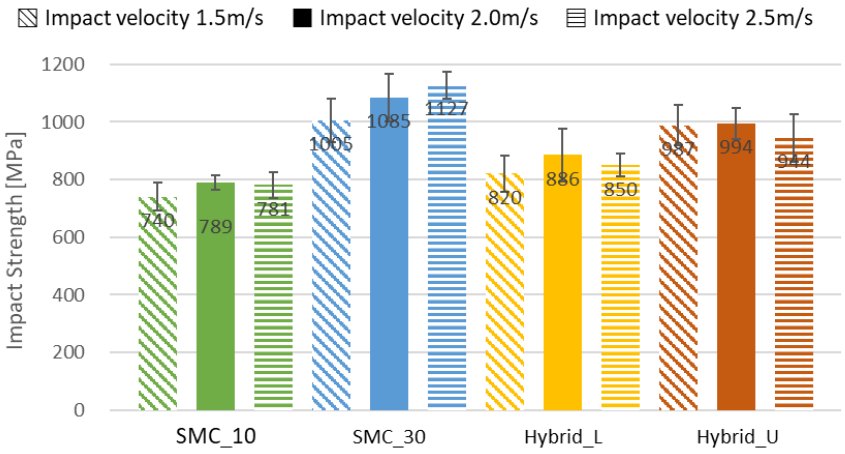

Figure 5: Impact strengths

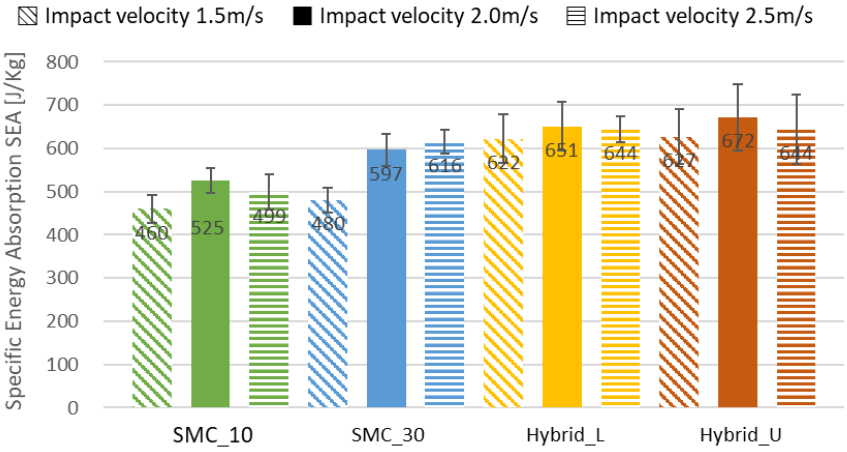

Figure 6: Specific energy absorption

Figure 7 presents the damaged specimens following the impact test. The SMC specimens exhibited a distinct failure pattern characterized by a straight-line fracture at the midpoint, with minimal signs of delamination. In contrast, the over-molded hybrid specimens showed extensive delamination, indicating a different failure mechanism influenced by the presence of the UD layer.

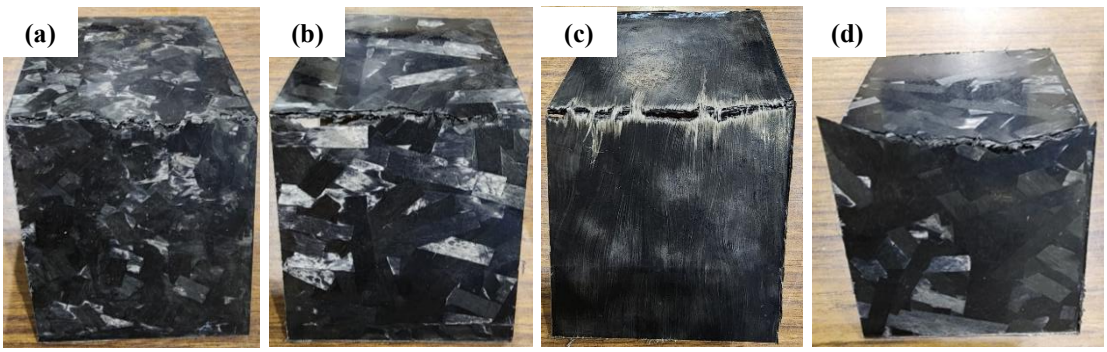

Figure 7: Damaged specimen: (a) SMC_10, (b) SMC_30, (c) Hybrid_L, and (d) Hybrid_U

3.2 Engineering constant estimation

To predict the engineering constants of the materials used in this study, multi-scale modelling was performed. The raw material data of carbon fiber and polyamide-6, along with their volume fraction and fiber morphology, were used as direct input parameters. The Young's moduli obtained from previous studies, were compared to check the validity of the model.

The predicted Young's moduli for SMC with 10 mm tapes, SMC with 30 mm tapes, and the UD carbon fiber were 33.9 GPa, 42.5 GPa, and 127.9 GPa respectively. The obtained engineering constants highly resembled material properties tested in previous studies, indicating that the model reliably correlates tested data with predicted outcome. The mean-field homogenization provides a simple and efficient method for estimating the bulk properties of composites as presented in Table 3-5. Additionally, since unknown engineering constants can be estimated using relatively few input parameters, this approach serves as a practical starting point for simulations in FE analysis.

Engineering constant	Type	Values
E_{xx}	Young's modulus	33.9 GPa
E_{yy}		33.5 GPa
E_{zz}		11.4 GPa
v_{xy}	Poisson's ratio	0.31
v_{yx}		0.32
v_{xz}		0.39
v_{zx}		0.13
v_{yz}		0.39
v_{zy}		0.13
G_{xy}	Shear modulus	12.9 GPa
G_{xz}		2.6 GPa
G_{yz}		2.6 GPa

Table 3: Predicted engineering constants for SMC with 10 mm tapes

Engineering constant	Type	Values
E_{xx}	Young's modulus	42.5 GPa
E_{yy}		42.5 GPa
E_{zz}		11.9 GPa
v_{xy}	Poisson's ratio	0.32
v_{yx}		0.32
v_{xz}		0.37
v_{zx}		0.10
v_{yz}		0.37
v_{zy}		0.10
G_{xy}	Shear modulus	16.1 GPa
G_{xz}		2.6 GPa
G_{yz}		2.6 GPa

Table 4: Predicted engineering constants for SMC with 30 mm tapes

Engineering constant	Type	Values
E_{xx}	Young's modulus	127.9 GPa
E_{yy}		10.2 GPa
E_{zz}		10.2 GPa
v_{xy}	Poisson's ratio	0.28
v_{yx}		0.02
v_{xz}		0.28
v_{zx}		0.02

v_{yz}		0.58
v_{zy}		0.58
G_{xy}	Shear modulus	3.6 GPa
G_{xz}		3.6 GPa
G_{yz}		3.2 GPa

Table 5: Predicted engineering constants for UD carbon fiber

3.3 Finite element analysis and correlation

The engineering constants obtained from multi-scale modelling were implemented as input parameters for the FE analysis. The FE model, as shown in Figure 7, illustrates the progress stress distribution in the specimen immediately after impact and up to just prior to failure.

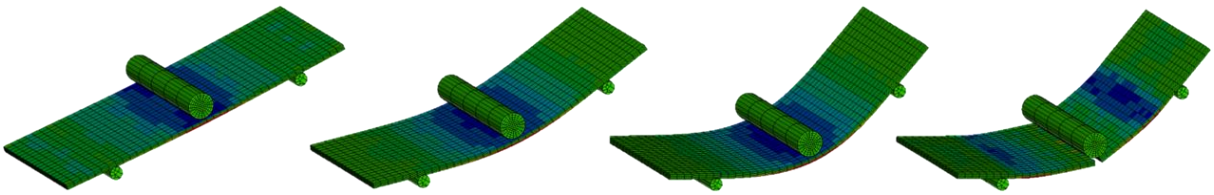

Figure 8: Finite element model of SMC specimen

The analytical results were correlated with the experimentally measured impact strength of SMC specimens tested at an impact velocity of 2.0 m/s. Due to limitations in accurately modeling the delamination behavior between the SMC and over-molded UD carbon fiber layers, the hybrid configurations were excluded from the current FE analysis. Based on the simulation results, the SMC with 10 mm tapes exhibited a peak impact force of 1.61 kN, corresponding to a calculated strength of 892 MPa, while the SMC with 30 mm tapes reached peak force of 1.99 kN corresponding to 1,102 MPa. These predicted values showed good agreement with the experimental results, achieving accuracies of 87% and 98% respectively. The comparison of peak impact forces for both materials is illustrated in Figure 9.

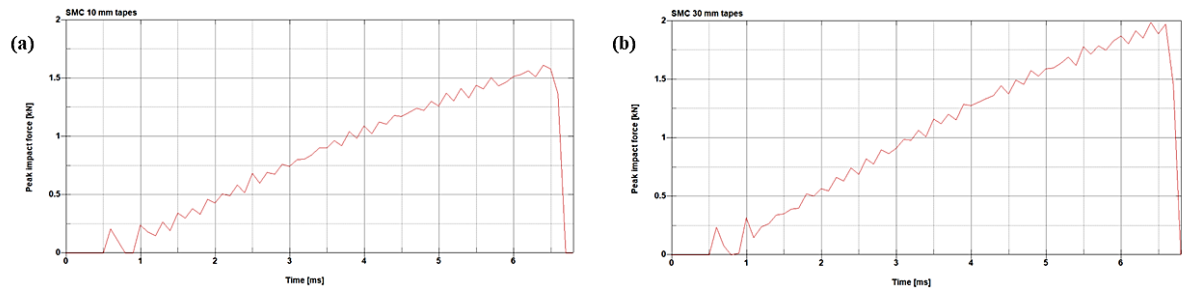

Figure 9: Peak impact forces: (a) SMC_10, and (b) SMC_30

To accurately characterize the delamination behavior of the hybrid materials, material models capable of capturing interlaminar failure – such as cohesive zone elements or contact-based debonding models are required. However, implementing such models necessitates more rigorous experimental characterization of interlaminar properties, along with extensive material data to properly define the delamination behavior. These efforts, while beyond the scope of the current study, would be essential for advanced modelling of hybrid composite systems and are recommended for future work.

4 CONCLUSIONS

CFRTP-SMC offers distinct advantages in forming complex shapes, cost-effectiveness for large-scale production, and favorable mechanical properties. However, the influence of tape length and over-molding with UD carbon fiber on their impact behavior remains insufficiently understood. This study examined the impact properties of SMC with different tape lengths, and evaluated the effect of UD carbon fiber over-molding through three-point bending impact test, multi-scale model analysis for engineering constant estimation, and FE analysis to validate the experimental findings. The methodologies, key findings, and interpretations are discussed in detail. The principal conclusions are summarized as follows:

- Tape length effect: tape length was found to significantly influence the impact performance of SMCs. Increasing the tape length from 10 mm to 30 mm resulted in notable improvements in both impact strength and specific energy absorption. These enhancements were primarily attributed to improved load transfer efficiency and more effective stress transmission from the matrix to the fibers during impact.
- Effect of UD carbon fiber over-molding: the over-molding of UD carbon fiber introduced a performance trade-off. While delamination between the UD layer and SMC reduced the peak impact strength, it expanded the range of failure mechanisms and enhanced energy dissipation, leading to increased overall energy absorption.
- Multi-scale modelling: the mean-field homogenization approach used in the multi-scale model proved effective for estimating bulk material properties and unknown engineering constants with limited input data. This method served as a practical foundation for subsequent FE simulations.
- FE analysis validation: the FE analysis demonstrated good agreement with experimental results in predicting the impact strength of SMC with different tape lengths. Although hybrid materials were not modelled in this study due to limitations in characterizing interfacial delamination, future work incorporating cohesive zone models and interlaminar failure criteria is recommended.
- Design implications: the findings emphasize the critical role of tape length and highlight the potential of UD carbon fiber over-molding as a design strategy. When properly engineered, over-molding can enhance crashworthiness and energy absorption, offering significant benefits for passenger safety in automotive applications.

REFERENCES

[1] Takahashi, J., & Ishikawa, T. (2013). *Current Japanese activity in CFRTP for industrial application*. In *Composites Week @ Leuven: Texcomp-11 Conference* (pp. 1–8)

[2] European Commission, Directorate-General for Environment, Baron, Y., Kosińska-Terrade, I., & Loew, C. (2023). *Study to support the impact assessment for the review of Directive 2000/53/EC on end-of-life vehicles: Final report*. Publications Office of the European Union. https://data.europa.eu/doi/10.2779/855228

[3] Liu, C., Zhao, R., Li, Q., Yadav, R., Ferdowsi, M. R. G., Wang, Z., An, M., & Naebe, M. (2023). Surface engineering of carbon fiber via upcycling of waste gases generated during carbon fiber production: A sustainable approach towards high-performance composites. *Composites Part B: Engineering, 255*, 110624. https://doi.org/10.1016/j.compositesb.2023.110624

[4] Wan, Y., & Takahashi, J. (2016). Tensile and compressive properties of chopped carbon fiber tapes reinforced thermoplastics with different fiber lengths and molding pressures. *Composites Part A: Applied Science and Manufacturing, 87*, 271–281. https://doi.org/10.1016/j.compositesa.2016.05.005

[5] Wan, Y., & Takahashi, J. (2016). Tensile properties and aspect ratio simulation of transversely isotropic discontinuous carbon fiber reinforced thermoplastics. *Composites Science and Technology, 137*, 167–176. https://doi.org/10.1016/j.compscitech.2016.10.026

[6] Alves, M., & Pimenta, S. (2020). The influence of 3D microstructural features on the elastic behaviour of tow-based discontinuous composites. *Composite Structures, 251*, 112484. https://doi.org/10.1016/j.compstruct.2020.112484

[7] Alves, M., Martulli, L. M., Kerschbaum, M., Swolfs, Y., Lomov, S. V., & Pimenta, S. (2023). A 3D finite element stochastic framework for the failure of tow-based discontinuous composites. Composites Science and Technology, 232, 109846. https://doi.org/10.1016/j.compscitech.2022.109846

[8] Katsivalis, I., Persson, M., Johansen, M., Moreau, F., Kullgren, E., Norrby, M., Zenkert, D., Pimenta, S., & Asp, L. (2024). Strength analysis and failure prediction of thin tow-based discontinuous composites. *Composites Science and Technology, 245*, 110342. https://doi.org/10.1016/j.compscitech.2023.110342

ICCM24
AUGUST 4-8, 2025
BALTIMORE CONVENTION CENTER
BALTIMORE, MARYLAND, USA

No Technical Paper Submission for:

Puneet Mahajan

ICCM24
AUGUST 4-8, 2025
BALTIMORE CONVENTION CENTER
BALTIMORE, MARYLAND, USA

No Technical Paper Submission for:

Deyong Sun

Structural Integrity of Composite Manipulator Applied to the Automated Ropeway Inspection Using Flexible Multibody Dynamics Analysis

ChiHyun Song[1], ChangHo Kim[1], JaeYoul Lee[2], *KwangBok Shin[1]

[1]Department of Mechanical Engineering, Hanbat National University, Daejeon, Korea / [2]Interactive Robotics R&D Division, Korea Institute of Robotics & Technology Convergence

*corresponding mail: shin955@hanbat.ac.kr

ABSTRACT

- In this study, the structural design and structural integrity evaluation of CFRP frame applied to a ropeway structure inspection manipulator were conducted. The ropeway structure inspection manipulator is a device that remotely inspects defects and wear of ropeway wheel devices of rope facilities used as transportation, such as cable cars or ski lifts.
- In the case of the existing ropeway structure inspection manipulator, it was made of aluminum, but in order to lightweight of the manipulator and reduce deflection, the existing aluminum material was replaced with CFRP material. In order to apply CFRP materials to manipulators, the stiffness design of the CFRP frame is essential, and structural integrity evaluation due to the external environment occurring during inspection and the load generated during operating motion also be secured. For the motion reflected in the analysis, the maximum deflection of the end device equipped with the camera was confirmed in the motion state where the inspection manipulator, which occurred to have the maximum deflection, was horizontally spread out.
- To evaluate the structural integrity of the CFRP frame reflecting the actual inspection environment based on the selected stacking pattern, flexible multibody dynamics analysis (FMBD) was performed. The maximum wind loads and railway wheel structure inspection motion in the actual inspection environment were applied according to the Facility Standards for Construction and Equipment for Tramway Facilities' Regulations. structural integrity was confirmed.

INTRODUCTION

Background and significance

- A ropeway system is a transportation method that uses wire ropes to carry passengers or cargo. To ensure optimal performance, regular inspections of ropeway systems are essential.
- Traditionally, ropeway inspections were performed manually by workers. However, recent research has focused on developing remote robotic ropeway inspection systems to enhance worker's safety and maintain consistent operational efficiency.
- The manipulator attached to the inspection robot is equipped with a camera mounted on its end effector, enabling remote inspection of rope structures. As the robot moves along the facility's wire ropes, lightweight design is essential for efficient operation.
- In this study, to achieve both lightweight construction and structural integrity, carbon fiber based on composite materials with high specific stiffness and strength were applied to the manipulator components. The structural integrity was evaluated through flexible multibody dynamic analysis, considering actual operating conditions.



Fig. 1. Conventional method for inspecting ropeway system



Fig. 2. Remote robot manipulator system for inspection

METHODS

Design for manipulator stacking pattern and deflection analysis

- For laminated composites, the stacking pattern and fiber orientation can be designed according to the designer's specifications. Consequently, the strength and stiffness of the structure under external loads vary depending on the lamination pattern.
- Since ropeway structures are exposed to complex loading conditions, the lamination pattern and thickness were set as design variables considering the composite manufacturing environment. Optimal lamination patterns were selected through deflection analysis of the manipulator's end tool.

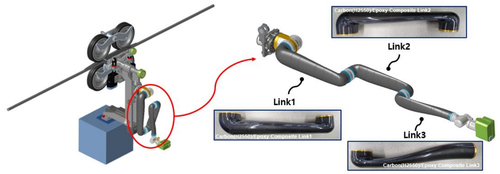

Fig. 3. Components of manipulator

- The deflection amounts based on the layup patterns presented in Table 1 were compared. For the motion environment, deflection analysis was performed under the condition shown in Fig. 3, where the manipulator is fully extended horizontally, causing maximum deflection at the end effector.

Table.1 Descripition of stacking pattern

Pattern	Stacking Pattern [Carbon(H2550)/Epoxy Composite]	Deflection of end tool [mm]
Pattern 1	$[0/90]_{10T}$	8.112
Pattern 2	$[0_3/\pm30]_s$	5.168
Pattern 3	$[0/90/\pm45/+45]_s$	4.875
Pattern 4	$[0/90/\pm45/0]_s$	4.061

- Based on the deflection analysis results for each layup pattern, the $[0/90/\pm45/0]_s$ layup configuration was selected. Subsequently, deflection analysis was performed and compared for varying composite thicknesses.
- As a result, the optimal composite thicknesses were determined to be 4T/3T/3T, which maximize the stiffness of the manipulator while satisfying the design mass criteria.

Table.2 Results of deflection analysis for link thickness

Case	Link1 Thickness	Link2 Thickness	Link3 Thickness	Mass [kg]	Deflection of Endtool [mm]
Case1	3T	3T	3T	3.106	2.832
Case2	4T	4T	4T	4.141	1.980
Case3	4T	4T	3T	3.912	2.036
Case4	4T	4T	2T	3.682	2.189
Case5	4T	3T	3T	3.576	2.262
Case6	4T	3T	2T	3.346	2.410
Case7	4T	2T	2T	3.010	2.901

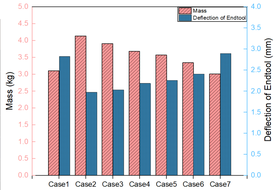

Fig. 4. Comparison of total mass and deflection

Structural Integrity evaluation of composite manipulator

- The structural integrity of the manipulator's composite link is evaluated using flexible multibody dynamics analysis.
- The applied loads include forces generated by the motion during ropeway structure inspection and the maximum wind load, as specified by facility standard regulations for the construction of track facilities.

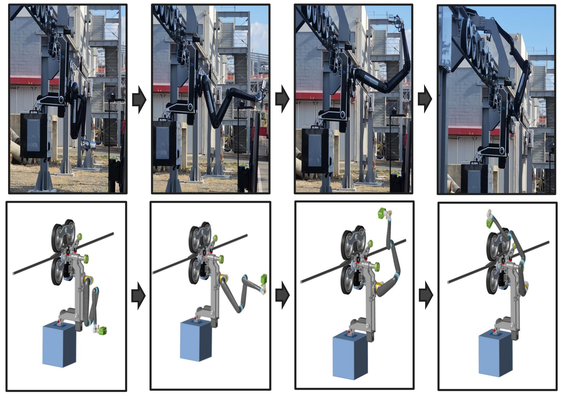

Fig. 5. Inspection motion of the manipulator

- Joint conditions were created to fully constrain the links and motors for flexible multi-body dynamics analysis and motor conditions were created using the Altair Inspire program.
- At Time 0.06 sec, the motion time when the maximum load and moment occur, the absolute max. Principal stress of 32.84 MPa was derived from the third CFRP link, and the maximum displacement of 0.249 mm was confirmed.

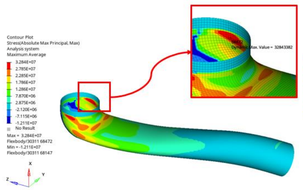

Fig. 6. Absolute Max. principal stress of FMBD link3

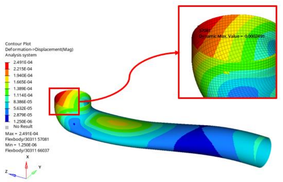

Fig. 7. Displacement of FMBD Link3

RESULTS

- In order to verify the reliability of the results derived from flexible multibody dynamics (FMBD) and structural analysis, the maximum principal stress and displacement results were compared.
- As the result of analysis, the maximum principal stress and displacement results between flexible multibody dynamics and structural analysis were confirmed to be the same, verifying the reliability.

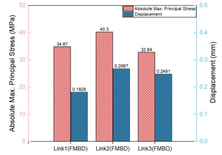

Fig. 8. Results of flexible multibody dynamic analysis(FMBD)

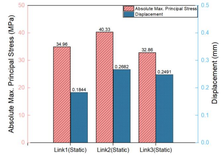

Fig. 9. Results of static analysis

- The Tsai-Wu Index of each manipulator CFRP link in the composite part was confirmed to be up to 0.079, confirming structural integrity.

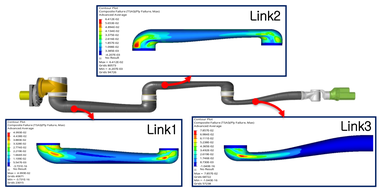

Fig. 10. Results of static analysis for composite manipulator

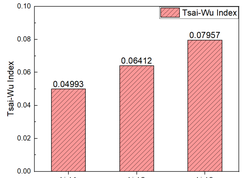

Fig. 11. Maximum Tsai-Wu Index of CFRP link

CONCLUSION

Summary

- In this study, the optimal composite stacking sequence and laminate thickness were determined to ensure the structural stiffness of the manipulator through deflection analysis. Furthermore, the structural integrity under complex loading conditions generated during the manipulator's inspection motion was evaluated. The failure analysis of the CFRP components under the maximum load and moment conditions was conducted using the Tsai–Wu failure criterion. The Tsai–Wu failure index remained below 1.0 for all CFRP links, validating the structural integrity of the manipulator design.

Acknowledgement

- This research was supported by a grant from Ministry of Trade, Industry and Energy and the Korea Institute for Advanced of Technology (KEIT) in 2024 (No.K_G012001843201, Development of a remote inspection robot system for rope facilities including wire rope and cutting wheel devices, Republic of Korea.)

Characterization and fully coupled numerical predictions of stealth composite with periodic patterns induced by artificial lightning strikes damage

***Seong-Haeng Heo[1], Van-Tho Hoang[2], Ju-Hyeong Lee[3],Won-Ho Choi[4] and Young-Woo Nam[1, 5†]**

[1]Graduate School of Aerospace and Mechanical Engineering, Korea Aerospace University
[2]Graduate School of Mechanical and Aerospace Engineering, Gyeongsang National University
[3]Department of Mechanical and Aerospace Engineering, Utah State University
[4]Stealth Technology Section, UCAV Development Team, Korean Air
[5]Department of Smart Drone Engineering, Korea Aerospace University

Korea Aerospace University

MCML MULTIFUNCTIONAL COMPOSITES & MANUFACTURING LABORATORY

Introduction

Lightning strike (LS) protection for radar-absorbing composite

High electrical conductivity VS. Radar absorption properties

	Metal airframe	Conventional CFRP aircraft	Stealth composites aircraft
Electrical & thermal conductivity	Very High	High	Low
Lightning strike protection	O	△	X
EM wave absorption	X	X	O

Circuit analog absorber

- **Circuit analog absorbers use patterned resistive sheets with specific sheet resistance and substrate as spacers**

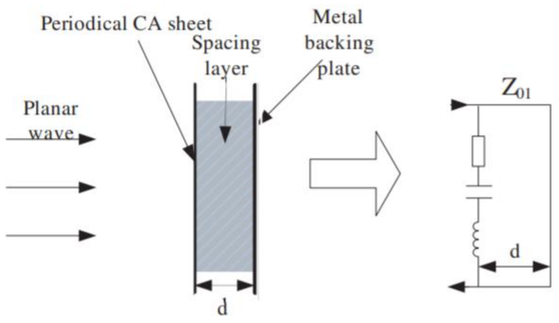

<Single layer circuit analog absorption material and its equivalent circuit map [1]>

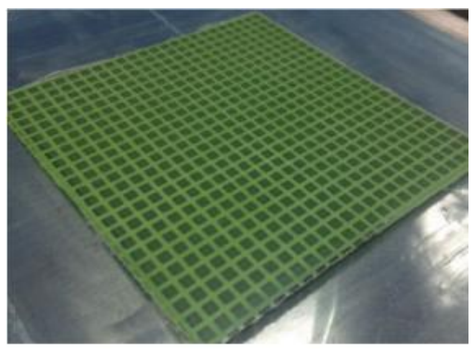

<Fabricated periodic pattern coated glass fibers absorber[2]>

Protection concept for stealth composites against LS damage

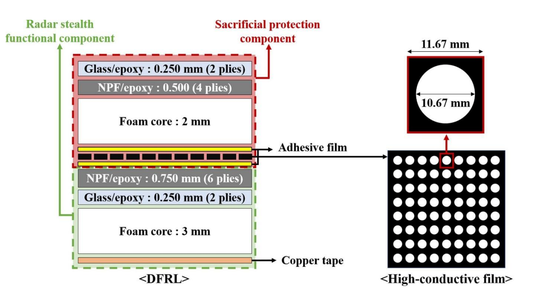

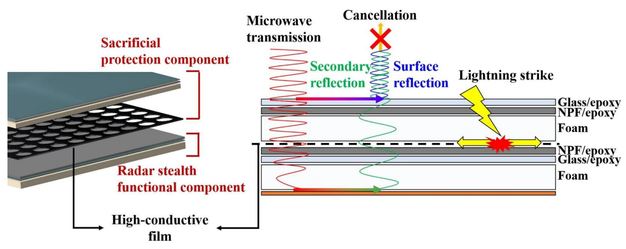

< Schematic of the foamed radar-absorbing sandwich composites with high-conductive film for lightning strike protection[3]>

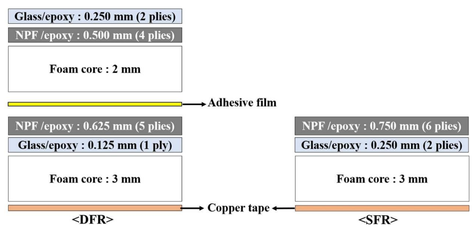

< Configuration of DFRL, DFR and SFR[3]>

[1] W. Yongfeng et al. The research of circuit analog absorber using square resistance arrays. Progress in electromagnetic research symposium 2016:
[2] W-H Choi et al. Microwave absorbing structure using periodic pattern coated fabric. Composite Structures. 2020;238:111953
[3] Woo-Hyeok Jang, Dongjun Hong, Shanigaram Mallesh, Juhyeong Lee, Chanyeop Park, Chun-Gon Kim, Won-Ho Choi, Youngwoo Nam, Protection concept for foamed radar-absorbing sandwich composites with high-conductive film against lightning strike impacts, Composites Part A: Applied Science and Manufacturing, Volume 190, 2025, 108660

Materials and methods

Manufacturing periodic pattern surface (PPS)

- **The patterns were formed on polyimide film (PI film) by screen printing with conductive ink and silver paste.**
- **The sheet resistances of PPS and LSP were designed to be 150 ohm/sq and 0.45 ohm/sq.**

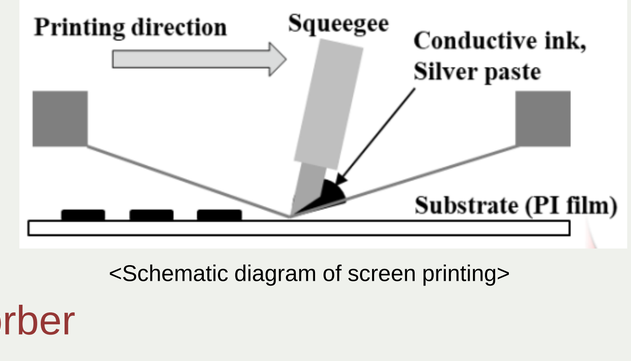

<Schematic diagram of screen printing>

Principle of circuit analog absorber

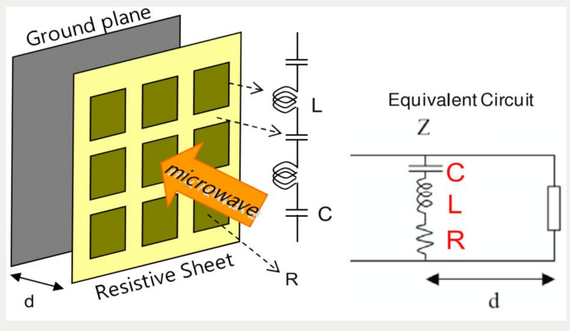

<Circuit analog absorber and equivalent circuit[4]>

[14] H-K Jang et al. Semi-cylindrical radar absorbing structures using fiber-reinforced composites and conducting polymers in the X-band. Advanced Composite Materials 2011:20;215-229

The input impedance (Z_{in}) of transmittance line with length d and short-circuit end is

$$Z_{in} = jZ_0 \tan kd \qquad (1)$$

and overall impedance (Z) of R, C and L in series is

$$Z = R + \frac{1}{j\omega c} + j\omega L \qquad (2)$$

and the input impedance in the starting end of the circuit (Z'_{in}) is

$$Z'_{in} = \frac{Z_{in}Z}{Z_{in} + Z} \qquad (3)$$

then the reflectivity (Γ) of the whole circuit is

$$\Gamma = 20log\left|\frac{Z'_{in} - Z_0}{Z'_{in} + Z_0}\right| \qquad (4)$$

in which Z_0 represents the is the characteristic impedance of free space

Lightning strike test



<High current impulse generator and Lightning strike test setup >

Design and fabrication

Design and fabrication of stealth composites with PPS

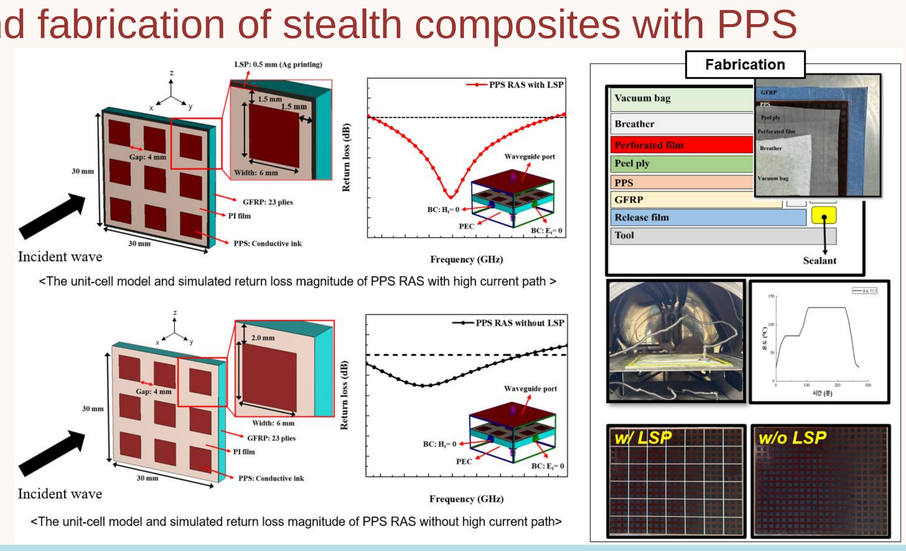

<The unit-cell model and simulated return loss magnitude of PPS RAS with high current path >

<The unit-cell model and simulated return loss magnitude of PPS RAS without high current path>

Finite element model development

Flow chart of coupled thermal-electrical-structural model

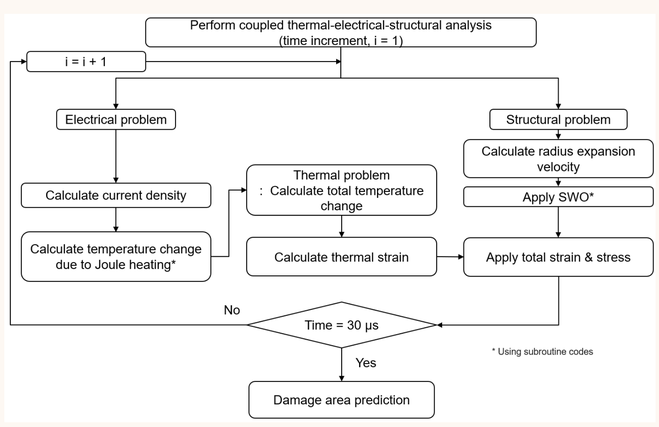

<Flow chart of coupled thermal-electrical-structural model>

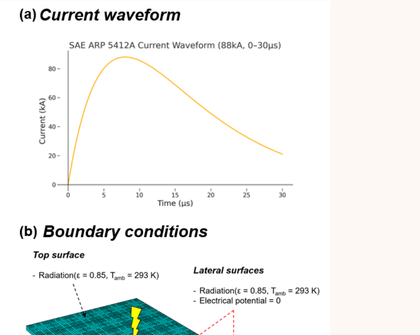

<(a) Lightning current waveform (Ipeak: 88 kA), and (b) boundary conditions of simulation>

Results and Discussion

Coupled thermal-electrical-structural analysis

- **Non-destructive test was performed to determine the damaged area of the specimen following the lightning strike.**
- **The simulation predicted a damage area that was smaller than that observed experimentally.**

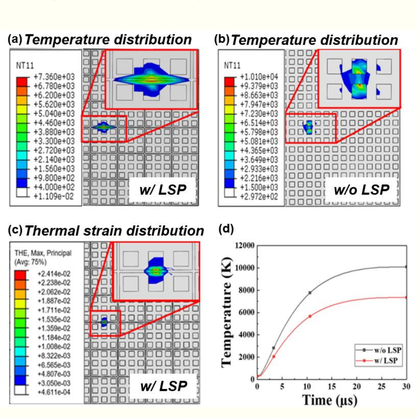

<Temperature distribution of proposed PPS-based stealth composite (a) w/ LSP, (b) w/o LSP, (c) Thermal strain distribution of of proposed PPS-based stealth composite w/ LSP, and (d) temperature at the lightning strike point>

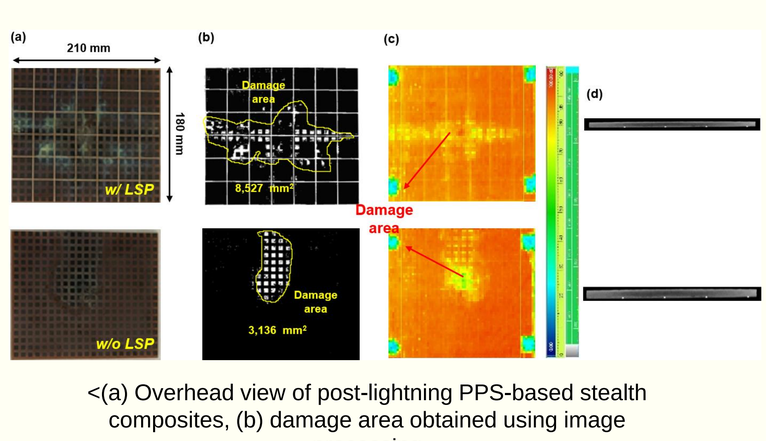

<(a) Overhead view of post-lightning PPS-based stealth composites, (b) damage area obtained using image processing
(c) C-scan image (d) X-ray CT image >

Conclusions and future works

- **In this study, we propose radar absorbing structure using a periodic pattern surface for lightning strike protection.**
- **A coupled thermal–electrical–structural analysis, with lightning-strike experiments, was conducted to validate the proposed simulation model and assess its lightning protection performance.**
- **Although the thermal–electrical analysis was completed, comparison with the damage regions observed in the lightning-strike experiments revealed that the simulated damage areas were smaller.**
- **An analysis model incorporating matrix decomposition will be developed to perform a coupled thermal–electrical–structural analysis.**

ASSESSING THE IMPACT OF SALT-FOG EXPOSURE ON THE PERFORMANCE AND RECYCLABILITY OF BIO-BASED EPOXY COMPOSITES REINFORCED WITH NATURAL FIBRES

V. Fiore[1], I. Kovinchuk[1], B. Megna[1], F. Sarasini[2], D. Rossano[3] and R. Miranda[1]

[1]Department of Engineering, Università degli Studi di Palermo
Viale delle Scienze, Building 6, 90128 Palermo, Italy
Email: vincenzo.fiore@unipa.it, iryna.kovinchuk@unipa.it, bartolomeo.megna@unipa.it, riccardo.miranda@unipa.it, web page: http://www.unipa.it

[2]Department of Chemical Engineering Materials Environment, Sapienza-Università di Roma
Via Eudossiana 18, 00184 Roma, Italy
Email: fabrizio.sarasini@uniroma1.it, web page: http://www.uniroma1.it

[3]Department of Business and Economic Studies, Università degli Studi di Napoli "Parthenope"
Via Ammiraglio Ferdinando Acton 38, 80133 Napoli, Italy
Email: diego.rossano@uniparthenope.it, web page: https://www.uniparthenope.it

Keywords: Polymer recycling, Bio-based composites, Thermosetting resins, Accelerated aging

ABSTRACT

This work aims to investigate the impact of salt-fog exposure on the mechanical performance and recyclability of flax fabric-reinforced bio-based epoxy resins, with the goal of assessing their suitability for marine environments. In such a context, three bio-based epoxy systems—Polar Bear, Green Turtle, and Plankton (having bio-carbon contents of 28–70%), were combined with recyclable (Recyclamine™ R*101) and non-recyclable hardeners to produce flax fibre-reinforced biocomposites. Before assessing the aging resistance of the composites, a preliminary investigation was conducted to identify the most promising bio-based epoxy systems based on a thorough assessment of their initial mechanical and thermal characteristics. This preliminary investigation showed that Polar Bear and Green Turtle systems demonstrated quite good mechanical and thermal properties, while Plankton with recyclable hardener exhibited incomplete curing and poor mechanical performance.

Subsequently, four biocomposites were manufactured using the vacuum infusion technique, with the pre-selected bio-based epoxy systems as polymeric matrices and bidirectional flax fabrics as reinforcement. To simulate the aggressive conditions of marine and coastal environments, mechanical tests were systematically conducted on fibre reinforced composite samples exposed to accelerated salt-fog aging up to 3 months. The evolution of the mechanical performance of biocomposites during aging was analysed through flexural and low-velocity impact tests.

Similarly to the mechanical characterization, an optimized recycling process was carried out on bio-based composites aged under salt-fog spray conditions for 30, 60, and 90 days, as well as on unaged samples as a reference.

1 INTRODUCTION

Today, fibre reinforced polymer materials (FRPs) are a cornerstone of modern industry. Their widespread adoption is due to the powerful combination of their reinforcement and matrix phases, which work together to deliver exceptional strength, stiffness, and durability without adding significant weight. On the other hand, these materials have a significant environmental impact, stemming from both the high energy consumption and environmental footprints associated with the extraction and synthesis of their raw materials (i.e., synthetic fibres and petroleum-based polymers) and the substantial challenges in their end-of-life management, especially for thermoset-based composites [1]. Rigid and cross-linked thermoset matrices make most FRPs difficult to reprocess and reuse [2].

Given the imperative to reduce carbon dioxide emissions and the finite nature of fossil resources, there is a global push for more sustainable materials. Consequently, the full or partial replacement of synthetic fibres with their natural counterparts represents a valid choice to mitigate the environmental impact of traditional FRPs [3, 4]. Furthermore, to comprehensively address this issue, attention must also be directed toward the matrix phase, given that the development and utilization of bio-based, recyclable and/or biodegradable polymer matrices are critical for eliminating the environmental impact of FRPs.

In this context, significant recent research has focused on bio-based polymers as environmentally friendly and economically viable alternatives to traditional petroleum-derived materials. Specifically, bio-based thermoset resins, partially derived from renewable resources like plant oils and lignin, are gaining traction as eco-friendly composite matrices [5]. These bio-based thermoset resins present a greener alternative to conventional epoxies, not only maintaining desirable mechanical properties and chemical resistance but also promising a reduced carbon footprint and less reliance on non-renewable resources, thereby aligning with a circular economy.

To further enhance sustainability, the recyclability and end-of-life management of bio-based epoxy composites are crucial research areas. Therefore, developing novel bio-based epoxy chemistries that allow for easier depolymerization or reprocessing without significant performance loss is a critical advancement. While thermal and mechanical recycling of fibre-reinforced composites have limitations, chemical recycling offers a promising alternative for recovering clean fibres and valuable monomers [6]. Cleavable amine-based epoxy systems, which allow for the recovery of thermoplastics and intact fibres under mild aqueous conditions, have shown technical and environmental effectiveness, though their long-term durability, especially with natural fibres, needs further investigation [7]. Due to these reasons, the present study comprehensively investigates the aging resistance of bio-based epoxy composites reinforced with flax fibres by evaluating their durability under harsh environment (i.e., salt-fog spray condition) also evaluating the impact of salt-fog exposure on durability of novel and potentially recyclable bio-based epoxy resins and their flax fibre reinforced composites.

Before assessing composite aging resistance, a preliminary investigation identified the most promising bio-based epoxy systems based on their initial mechanical and Thermal characteristics. Subsequently, four fibre-reinforced composites were manufactured through vacuum infusion technique, utilizing the pre-selected bio-based epoxy systems as polymeric matrices and bidirectional flax fabrics as reinforcement.

These composite materials were then exposed to salt-fog spray conditions for up to three months to assess the impact of this harsh environment on their mechanical performance and recyclability. For this purpose, a comprehensive mechanical characterization (including flexural tests, and low-velocity impact tests) was conducted on unaged samples (used as reference) and on samples aged for 30, 60, and 90 days. Similarly, following a preliminary optimization of the recycling process on unaged biocomposite samples, the recycling yield was investigated as function of the salt-fog exposure time.

2 MATERIALS AND METHODS

Three bio-based epoxy monomers - Polar Bear, Green Turtle, and Plankton - supplied by R*Concept, were used in this work. In particular, the monomer Polar Bear, with a bio-carbon content exceeding 28%, was mixed with the recyclable hardener Recyclamine™ R101 (100:22 by weight). This system serves as a reference in this work because it was already studied recently by other authors regarding its recyclability and usability as a polymeric matrix for FRPs [8-10]. Its recyclability is attributed to Recyclamine, an amine-based hardener containing cleavable bonds within its structure. Specifically, this polyamine hardener, 2,2-Bis(aminoethoxy)propane, reacts with epoxy rings during curing to form acid-cleavable groups. These groups enable the recycling of epoxy thermosetting plastics and their composites. The process yields soluble monomeric or oligomeric products suitable for reuse, along with valuable fibres that retain their properties. The presence of these cleavable bonds allows the thermoset to transform into a thermoplastic polymer when crosslinks are broken via chemical treatment in an acetic acid solution [11-13].

The epoxy monomers Green Turtle (bio-carbon content >40%) and Plankton (bio-carbon content >77%) were each mixed with their non-recyclable hardeners (100:30 by weight) and with Recyclamine™ R101 (100:22 by weight) to obtain four additional epoxy systems.

Overall, five epoxy resins were initially evaluated for their mechanical and thermal properties. Mechanical tests involved three-point bending of five prismatic samples per resin (57.6 × 12.7 × 3 mm) using a Zwick-Roell Z005 machine (ASTM D790, 1.3 mm/min crosshead speed, 48 mm support span). Thermal behaviour was assessed via differential scanning calorimetry (DSC) on three 10 mg specimens per system using a Netzsch DSC 214 Polyma, heated from -20 °C to 210 °C at 10 °C/min under nitrogen flow.

After this preliminary comparison, the epoxy system obtained by mixing the Plankton monomer with the Recyclamine hardener was excluded from the subsequent biocomposite investigation due to its poor mechanical and thermal performance. Therefore, the remaining four epoxy systems were reinforced with six layers of flax balanced twill weave woven fabrics, supplied by Lineo, each having a nominal areal weight of 320 g/m^2. Rectangular panels (175 mm × 300 mm) were manufactured for each system using a vacuum infusion technique. The curing process involved an initial 24-hour cure at room temperature under vacuum, followed by post-curing. For the Polar Bear system, post-curing was conducted at 100 °C for 3 hours, while the Green Turtle and Plankton systems were post-cured at 80 °C for 4 hours. As indicated in Table 1, the investigated bio-based composites are coded F-PB-R, F-G-R, F-G-NR, and F-P-NR. 'F' denotes flax reinforcement, “PB”, “G”, and “P” represent Polar Bear, Green Turtle, and Plankton bio-based epoxy matrices, and “R” or “NR” indicate a recyclable (with Recyclamine) or non-recyclable epoxy matrix, respectively.

Composite	Nominal thickness [mm]	Fibre content [v/v%]	Experimental density [g/cm^3]	Theoretical density [g/cm^3]	Void content [v/v%]
F-PB-R	3.91	0.325	1.264	1.320	4.22
F-G-NR	4.01	0.317	1.252	1.309	4.31
F-P-NR	3.98	0.320	1.255	1.309	4.11
F-G-R	4.04	0.314	1.259	1.315	4.20

Table 1: Flax fibre-reinforced biocomposites.

2.1 Salt-fog spray aging conditions and characterization methods

The aging resistance of biocomposites was evaluated by exposing them to a salt-fog spray condition in a climate chamber (Ascott model CC1000IP) according to the ASTM B117 standard. Each panel was exposed to salt-spray fog (5 wt.% NaCl) at 35 °C ± 1°C for up to 3 months (90 days). A single set of specimens for mechanical characterization was removed from the climatic chamber and tested after 30, 60, and 90 days. Unaged specimens were also tested as a reference.

Three-point bending tests were conducted on prismatic specimens (80 mm × 17 mm) according to the ASTM D790 standard, using a Zwick-Roell Z005 universal testing machine. The span length and the crosshead speed were set to 64 mm and 1.7 mm/min, respectively

Low-velocity impacts were performed at room temperature with a 5 J energy level, using a 12.7 mm diameter hemispherical impactor weighing 3.05 kg. These impact tests were conducted using an Instron/Ceast 9340 instrumented drop-weight impact tower, following the ISO 6603-2 standard. For the tests, 7 cm × 7 cm square specimens were clamped between two steel plates, creating a 40 mm diameter circular unsupported area.

The morphology of the fractured surfaces of tensile samples was observed through a scanning electron microscopy (SEM, Quanta 450, USA).

The recycling process was applied to bio-based composites aged under salt-fog spray conditions for 30, 60, and 90 days, along with unaged reference samples. First, the recycling process was optimized on unaged composites made by Polar Bear resin. The selection of the optimum conditions for the recovery of thermoplastics was carried out starting from the methodology described by Saitta et al. [8]. Specifically, the variable parameters were the acetic acid concentration, the dissolution time, and the

ratio between the dissolved epoxy resin and acid. In a typical procedure, 10 g of epoxy resin were dissolved in an acetic acid solution (either 75% or 50% v/v) using resin-to-acid ratios of 1:30 or 1:20 (w/v). Dissolution was conducted at 80 °C for 90 or 180 minutes under constant mechanical stirring. After complete dissolution, flax fabrics were removed, washed in deionized water, and dried at 80 °C for 24 hours. The remaining solution was evaporated until its volume reached 75 mL. After cooling to 20 °C, it was neutralised with a 15% v/v ammonium hydroxide solution. The resulting precipitate was separated from the solution, washed with distilled water, and dried for 24 hours at 60 °C in a vacuum of 30 mbar. The optimal parameters and conditions for recycling the bio-based composite were finalised by evaluating recycling yield of the recovered thermoplastics.

The mass of recovered thermoplastics was taken into account to evaluate the recycling yield. The yield for the chemical recycling analyzed is determined by considering the Equation 1.

$$Yield\ (\%) = \frac{W_{initial}}{W_{product}} \cdot 100 \quad (1)$$

where $W_{initial}$ and $W_{product}$ represent the mass of the initial epoxy resin in the composite sample and the mass of the thermoplastic obtained after recycling, respectively.

Beyond yield analysis, the recovered thermoplastic's thermal properties were assessed, with differential scanning calorimetry (DSC) used to determine its glass transition temperature (T_g). The polymer degradation temperature was determined as a peak on the DTG curve.

3 RESULTS AND DISCUSSION

3.1 Bio-epoxy resins

Table 2 reports on the main mechanical and thermal properties of the bio-epoxy resins investigated. This preliminary investigation evidenced that all innovative systems (those obtained using Green Turtle or Plankton as bio-epoxy monomers) exhibit lower flexural strength and modulus, and higher deformation at break, compared to the reference (PB-R). Specifically, by mixing Plankton monomer (which has the highest bio-carbon content) with the recyclable hardener, dramatically decreases its flexural properties. In particular, the P-R epoxy system exhibits negligible strength and modulus values (2.0 MPa and 0.021 GPa, respectively), rendering it completely unsuitable as a polymeric matrix for biocomposites. Furthermore, the latter epoxy displayed a strain at break of 11.8%, a value notably higher than the typical range for fully cured thermoset polymers.

Composite	Flexural strength [MPa]	Flexural modulus [GPa]	Strain at break [%]	T_g [°C]
PB-R	97.6±8.1	2.8±0.2	4.1±0.7	67.9±0.2
G-NR	73.2±5.7	1.9±0.2	6.5±0.5	63.7±0.2
P-NR	83.9±3.7	2.8±0.1	4.9±0.1	76.3±0.2
G-R	39.9±0.6	1.1±0.02	7.9±0.2	31.0±0.2
P-R	2.0±0.2	0.02±0.004	11.8±1.3	18.6±0.3

Table 2: Mechanical and thermal properties of the bio-based epoxy resins.

Accordingly, calorimetric analysis showed that epoxy systems made with Green Turtle and Plankton monomers and non-recyclable hardeners (G-NR and P-NR) have glass transition temperatures (T_g) of 60 to 75 °C, similar to the reference system (PB-R). In contrast, using Recyclamine with either monomer significantly lowers the T_g values. Specifically, the P-R epoxy system shows a T_g of about 19 °C, much lower than typical room-temperature cured epoxy resins. These findings are likely due to an incomplete curing reaction between Recyclamine and the Plankton monomer, resulting in a thermoset structure with a relatively low cross-linking density. Indeed, the Plankton monomer is bisphenol-free, containing more than two epoxy rings in its chain. Consequently, it did not react properly with Recyclamine, which is designed to cure with DGEBA (such as Polar Bear and Green Turtle). Overall, the preliminary investigation indicated that this epoxy system is unsuitable as a composite matrix and will be excluded

from the subsequent phase of the work, which involves assessing biocomposites' performance during aging.

3.2 Bio-based epoxy composites

The flexural strength and modulus values of unaged bio-based composites are presented in Figure 1.

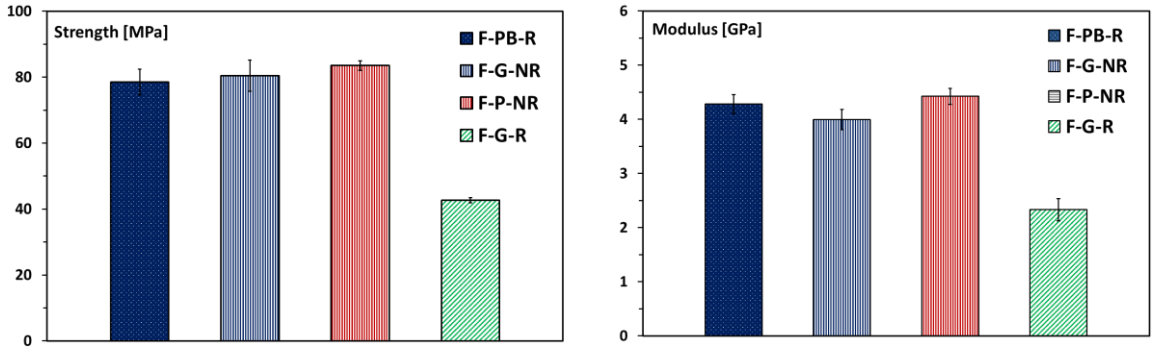

Figure 1: Flexural strength and modulus of unaged biocomposites.

By observing these graphs, it is possible to notice that biocomposite made with the G-R epoxy resin (i.e., obtained by combining Green Turtle monomer with Recyclamine hardener) exhibited approximately half the flexural properties compared to other investigated biocomposites whereas biocomposites derived using standard epoxy resins (G-NR and P-NR) as matrix exhibited mechanical performance in their unaged state comparable to those manufactured with the reference epoxy matrix (PB-R). These results are in full agreement with observations for neat (i.e., unreinforced) polymeric epoxy systems.

The impact of salt-fog exposure on the flexural properties (strength and modulus) of the investigated biocomposites is displayed in Figure 2.

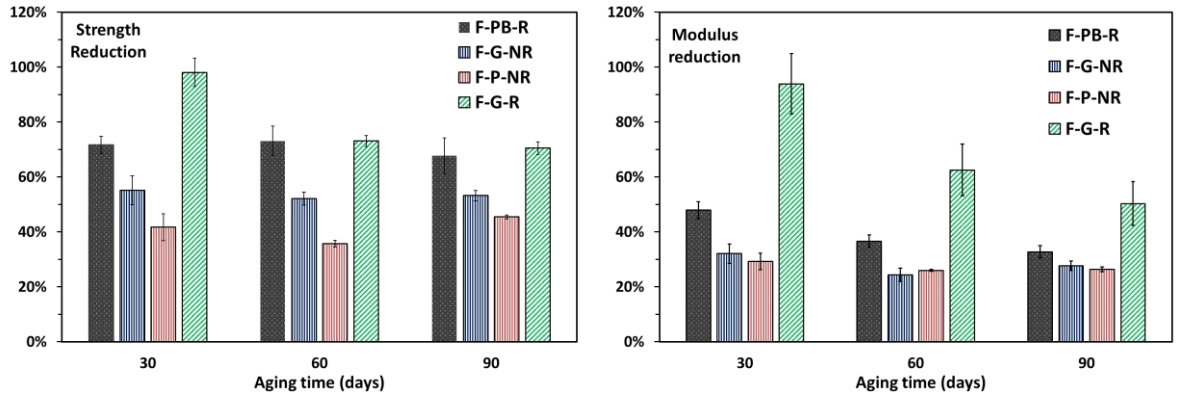

Figure 2: Variation of (a) flexural strength and (b) modulus of aged biocomposites for different aging times.

First, it is worth noting that, despite their initial high flexural properties, F-PB-R, F-G-NR, and F-P-NR laminates exhibited poor aging resistance, with significant declines in mechanical stability after just 30 days of salt-fog exposure. During this initial aging period, the flexural strength and modulus of F-PB-R composites decreased by 28.3% and 52.1%, respectively. Even more pronounced, the F-G-NR and F-P-NR samples exhibited flexural strength reductions of 44.8% and 58.3%, respectively, while their flexural modulus decreased by 67.9% and 70.7%. On the other hand, the F-G-R laminates surprisingly exhibited the best stability against salt-fog, demonstrating only slight decrements in flexural strength and modulus (1.9% and 6.1%, respectively) compared to their initial values after 30 days of exposure.

All bio-based composites experienced reduced mechanical performance when salt-fog exposure was prolonged to 60 and 90 days (2 and 3 months). In particular, F-G-R samples not only retained their mechanical performance after the first month of aging but also exhibited only gradual declines in properties even after 60 and 90 days of salt-fog exposure. After 90 days, for instance, flexural strength and modulus showed reductions of only 29.5% and 49.6%, respectively, in comparison to unaged samples.

These results can be explained by considering that, regardless of the bio-epoxy resin matrix, the main degradative mechanism during aging was matrix plasticization rather than internal damage at the fibre-matrix interface. As clearly shown in Figure 3, this led to reduced composite stiffness and increased flexibility for all bio-based composites.

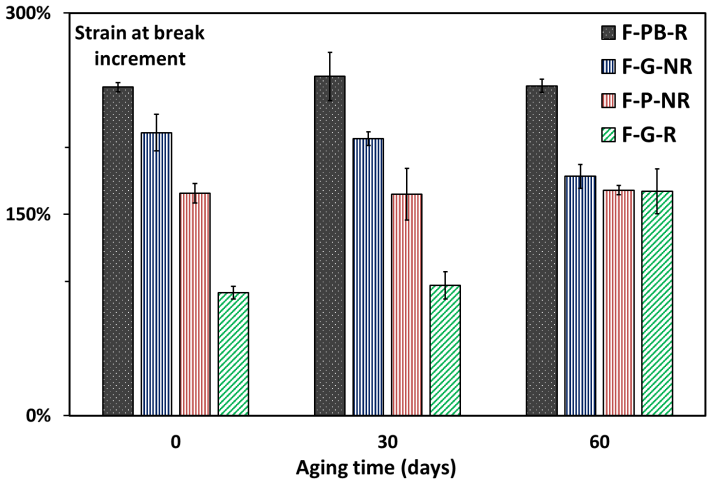

Figure 3: Variation of flexural strain at break of aged biocomposites for different aging times.

Specifically, F-PB-R, F-G-NR, and F-P-NR showed plasticization within the first 30 days of salt-fog exposure, whereas this phenomenon was time-delayed for F-G-R, which evidenced a noticeable strain at break increment in the last 30 days of aging.

Figure 4 includes the representative force-displacement curves related to the low-velocity impact (LVI) tests performed on unaged bio-based composites. The performance of the biocomposites in relation to impact energy is very similar. Indeed, all the curves are closed, meaning that no laminate penetration occurred, regardless of the matrix used and the aging condition. Furthermore, F-GT-R composites exhibit the worst initial impact properties, with the lowest maximum force. Conversely, biocomposites F-G-NR and F-P-NR show the best impact behaviour prior to salt-fog exposure.

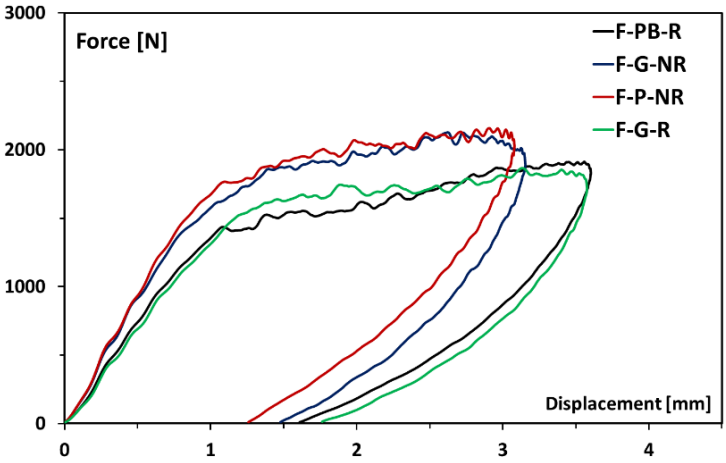

Figure 4: Representative load-displacement curves for all unaged biocomposites obtained during low velocity impact tests.

The impact of aging on impact behaviour is characterized by main parameters from LVI tests, detailed in Table 3 as a function of salt-fog exposure time. These include maximum displacement (D_{max}) and damage degree (DD), calculated as the ratio of absorbed to impact energy (5 J).

Comparing the mechanical behaviour of biocomposites under low-velocity impact after salt-fog exposure, we notice that the impact performance of F-G-R composites was minimally affected by aging, consistent with quasi-static results. In contrast, salt-fog exposure proved particularly detrimental for Plankton-based composites (F-P-NR), leading to the most significant increases in damage.

Composite	F_{max} [N]	D_{max} [mm]	DD
F-PB-R	1891.5±30.1	3.6±0.1	0.76±0.01
F-PB-R_30	1942.3±68.6	4.1±0.2	0.78±0.02
F-PB-R_60	2187.9±95.1	3.7±0.1	0.76±0.01
F-PB-R_90	2018.4±67.5	4.1±0.2	0.78±0.02
F-G-NR	2105.4±31.4	3.2±0.1	0.77±0.01
F-G-NR_30	2088.8±36.4	3.6±0.1	0.78±0.01
F-G-NR_60	2041.7±62.2	3.7±0.1	0.82±0.01
F-G-NR_90	2091.9±23.7	3.7±0.1	0.79±0.01
F-P-NR	2198.9±57.6	3.1±0.1	0.72±0.01
F-P-NR_30	1834.3±22.7	4.1±0.1	0.81±0.01
F-P-NR_60	1990.8±87.5	3.7±0.2	0.79±0.02
F-P-NR_90	2248.5±33.8	4.1±0.1	0.80±0.01
F-G-R	1808.3±59.7	3.6±0.1	0.79±0.01
F-G-R_30	1854.1±20.6	4.3±0.1	0.82±0.01
F-G-R_60	1947.5±82.3	3.9±0.2	0.81±0.01
F-G-R_90	1920.7±69.7	3.8±0.1	0.82±0.01

Table 3: Main parameters obtained by LVI tests.

Overall, the data reported in Table 3 reveal that all bio-based composites exhibit increased maximum force, impactor displacement, and damage degree with increasing salt-fog exposure time. Furthermore, an overall decline in linear stiffness is observed during aging for all bio-based composites.

These results represent an indication of the augmented compliance shown by all biocomposites after aging. The greater absorbed energy with increased salt-fog exposure time confirms matrix plasticization as the main degradative phenomenon, which also plays a significant role in mitigating some internal damage due to a deterioration in interfacial adhesion, as corroborated by the post-impact analysis of sample surfaces. Indeed, observations of the impacted samples' front and back surfaces revealed that all biocomposites exhibited a significant reduction in indentation on the impacted face and crack severity on the opposite face after just 1-month aging. Figure 5 displays the impacted and opposing faces of only F-G-R samples before aging and after one month of salt-fog exposure. All biocomposites behaved similarly, and therefore, their related images are not included here for the sake of conciseness.



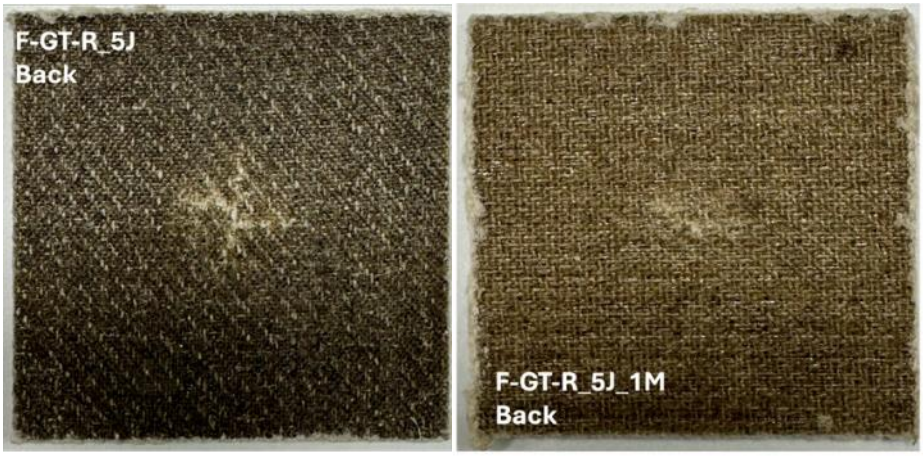

Figure 5: Observation of front and back surfaces of unaged and 1-month aged F-G-R biocomposites.

As concerns the recycling process, preliminary studies were conducted on the unaged F-PB-R composite samples. As detailed in Table 4, the investigation into the influence of chemical processing parameters—specifically acetic acid quantity, solution concentration, and dissolution time—demonstrated that a decrease in acid concentration from 75% to 50% correlated with a 32–65% reduction in product yield under consistent experimental conditions. The highest yield, 73.5%, was attained under optimum conditions: 200 ml of 75% v/v acetic acid and a dissolution time of 180 minutes. This indicates that peak yields necessitate high acidity and adequate dissolution time; conversely, diminished yields observed at 50% acidity and reduced dissolution periods are likely attributable to incomplete reaction kinetics and deviations from optimal pH levels. Furthermore, all recycled thermoplastic materials exhibited a glass transition temperature ranging from 73-82°C, indicating only slight variation based on recycling conditions. At lower acid concentrations (50% v/v), the T_g values were higher (~81°C), which may indicate lower cleavage of the cross-linked structures and reduced chain mobility. In contrast, samples processed under optimized conditions (75% v/v acetic acid, 200 mL, 180 min) showed the highest yield (73.5%) and a lower T_g (76.5°C), indicating a greater degree of depolymerization. These results demonstrate an inverse relationship between product yield and glass transition temperature, confirming that the use of high acid concentration and long reaction time effectively promotes efficient recycling.

Composite	Solution volume [mL]	Solution concentration [% v/v]	Dissolution time [min]	Recycling yield [%]	Glass transition temperature [°C]
F-PB-R	300	75	90	50.3	73.3
F-PB-R	300	75	180	34.2	75.6
F-PB-R	300	50	90	34.2	81.7
F-PB-R	300	50	180	34.9	79.4
F-PB-R	200	75	90	58.9	76.7
F-PB-R	200	75	180	73.5	76.5
F-PB-R	200	50	90	20.5	75.7
F-PB-R	200	50	180	25.1	81.1

Table 4: List of factorial experiments and main results for selecting optimal conditions for the recycling process.

In light of these findings, the optimized recycling conditions (200 mL solution volume, 75% v/v solution concentration, and 180 min dissolution time) were then employed to investigate the effect of aging on the efficiency of the bio-based composite. To this aim, recycling of both F-PB-R and F-GT-R samples was performed after 30, 60, and 90 days of salt-fog exposure.

As shown in Figure 6, the exposure to salt fog did not influence the recyclability of the biocomposites

to a high extent, regardless of the bio-epoxy resin used as matrix. Indeed, a slight increase in the recycling yield was found for both bio-based composites. Specifically, the unaged F-G-R sample exhibited an 80.7% thermoplastic yield under optimum conditions. This increased by about 4% to 84.7% after 90 days of aging in a climate chamber (F-G-R-90). On the other hand, the recycling yield of Polar Bear-based composites (F-PB-R) improved by 2.7%, from 73.5% (unaged sample) to 75.5% (90-day aged samples). Regarding the thermal behavior of the recycled material, limited reductions were observed in the glass transition temperatures for both bio-based epoxy resins across varying salt-fog exposure times.

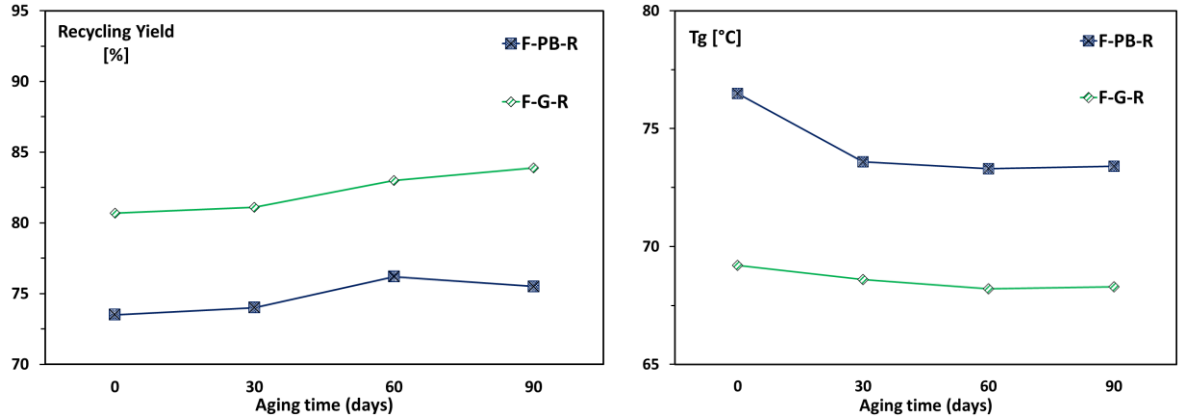

Figure 6: Recycling yield and glass transition temperature values at varying salt-fog exposure.

Overall, these findings clearly demonstrate that the recyclability of the investigated bio-based composites was not negatively impacted by their exposure to aggressive environmental conditions, such as salt-fog. In fact, their ability to be recycled remained robust even after significant environmental stress, highlighting their potential for sustainable applications. It is worth noting that this represents an ongoing research activity. Further investigation will be conducted to gain a more comprehensive understanding of the recycled material's primary thermal and mechanical properties.

9 CONCLUSIONS

The experimental results demonstrate that all bio-based thermosetting composites exhibited satisfactory performance when subjected to aggressive conditions simulating a marine environment. Notably, both systems with lower bio-content can be recycled, unlike the one with the highest bio-content. These findings indicate that lower bio-content correlates with higher environmental resistance. Both reinforced recyclable epoxy composites (Polar Bear and Green Turtle) exhibited quite good mechanical strength with minimal loss of performance over several months of aging. In contrast, the Plankton-reinforced composites experienced a significant and progressive decline in performance over the same period. Consequently, the Green Turtle epoxy matrix emerges as the most suitable option, exhibiting high bio-content and recyclability, even after exposure to salt-fog spray condition. This combination positions it as a prime candidate to replace fossil-based epoxy resins, aligning with the principles of eco-sustainability and circular economy.

ACKNOWLEDGEMENTS

Funded by the European Union - Next Generation EU - PNRR M4 - C2 - investment 1.1: Fund for the National Research Program and Projects of Significant National Interest (PRIN) - PRIN 2022PNRR cod. P20223YBZ8_001 entitled "Recyclable biocomposites WIth eNhanced Durability" (REWIND) CUP B53D23026710001.

REFERENCES

[1] A.D. La Rosa, G. Cozzo, A. Latteri, A. Recca, A. Bjorklund, E. Parrinello and G. Cicala, Life cycle assessment of a novel hybrid glass-hemp/thermoset composite, *Journal of Cleaner Production*, **74**, 2014, pp. 245-252 (doi: 10.1016/j.jclepro.2012.11.038).

[2] J. Qureshi, A Review of recycling methods for fibre reinforced polymer composites, *Sustainability*, **14**, 2022, pp. 16855 (doi: 10.3390/su142416855).
[3] O. Faruk, A.K. Bledzki, H.P. Fink and M. Sain, Biocomposites reinforced with natural fibers: 2000–2010, *Progress in Polymer Science*, **37**, 2012, pp. 1552-1596 (doi: 10.1016/j.progpolymsci.2012.04.003).
[4] G. Koronis, A. Silva, H.P. Fink and M. Fontul, Green composites: A review of adequate materials for automotive applications, *Composites Part B: Engineering*, **44**, 2013, pp. 120-127 (doi: 10.1016/j.progpolymsci.2012.04.003).
[5] W. Yang, H. Ding, D. Puglia, J. M Kenny, T. Liu, J. Guo, Q. Wang, R. Ou, P. Xu and P. Ma, Bio-renewable polymers based on lignin-derived phenol monomers: Synthesis, applications, and perspectives, *Sustainable Materials*, **2**, 2022, pp. 535-568 (doi: 10.1002/sus2.87).
[6] G. Oliveux, L.O. Dandy and G.A. Leeke, Current status of recycling of fibre reinforced polymers: Review of technologies, reuse and resulting properties, *Progress in Materials Science*, **72**, 2015, pp. 61-99 (doi: 10.1016/j.pmatsci.2015.01.004).
[7] P. Shieh, W. Zhang, K.E.L.Husted, S.L. Kristufek, B.Xiong, D.J. Lundberg, J. Lem, D. Veysset, Y. Sun, and K.A. Nelson, Cleavable comonomers enable degradable, recyclable thermoset plastics, *Nature*, ***583***, 2020, pp. 542-547 (doi: 10.1038/s41586-020-2495-2).
[8] L. Saitta, V. Prasad, C. Tosto, N. Murphy, A. Ivankovic, G. Cicala, and G. Scarselli, Characterization of biobased epoxy resins to manufacture eco-composites showing recycling properties, *Polymer Composites*, ***43***, 2022, pp. 9179-9192 (doi: 10.1002/pc.27095).
[9] L. Saitta, G. Rizzo, C. Tosto, G. Cicala, I. Blanco, E. Pergolizzi, R. Ciobanu and G. Recca, Chemical recycling of fully recyclable bio-epoxy matrices and reuse strategies: A Cradle-to-Cradle approach, *Polymers*, ***15***, 2023, 2809 (doi: 10.3390/polym15132809).
[10] S. Dattilo, G. Cicala, P.M. Riccobene, C. Puglisi and L. Saitta Full recycling and re-use of bio-based epoxy thermosets: Chemical and thermomechanical characterization of the recycled matrices, *Polymers*, ***14***, 2022, 4828 (doi: 10.3390/polym14224828).
[11] G. Cicala, E. Pergolizzi, F. Piscopo, D. Carbone and G. Recca, Hybrid composites manufactured by resin infusion with a fully recyclable bioepoxy resin, *Composites Part B: Engineering*, ***132***, 2018, pp. 69-76 (doi: 10.1016/j.compositesb.2017.08.015).
[12] A.D. La Rosa, D.R. Banatao, S.J. Pastine, A. Latteri and G. Cicala, Recycling treatment of carbon fibre/epoxy composites: Materials recovery and characterization and environmental impacts through life cycle assessment, *Composites Part B: Engineering*, ***104***, 2016, pp. 17-25 (doi: 10.1016/j.compositesb.2016.08.015).
[13] G. Cicala, S. Mannino, A.D. La Rosa, D.R. Banatao, S.J. Pastine, S.T. Kosinski and F. Scarpa, Hybrid biobased recyclable epoxy composites for mass production, *Polymer Composites*, ***39***, 2018, pp. E2217-E2225 (doi: 10.1002/pc.24582).

DEVELOPMENT AND MODELING OF INTERFACIALLY ENGINEERED COMPOSITES WITH DESIGNED FAILURE

Gergő Zsolt Marton[1,2], Gábor Szebényi[1,2]

[1]Department of Polymer Engineering, Budapest University of Technology and Economics (BME)
Műegyetem rkp. 3., H-1111 Budapest, Hungary
web page: http://www.pt.bme.hu/

[2]MTA-BME Lendület Sustainable Polymers Research Group
Műegyetem rkp. 3., H-1111 Budapest, Hungary

Email: martong@pt.bme.hu
Email: szebenyi@pt.bme.hu

Keywords: Designed failure, Damage, Interlayer, Interface, Finite element analysis

ABSTRACT

There is a growing demand to increase the reliability of polymer composite materials by modifying their failure behavior. In this study, we developed and investigated a method that can be used to influence the damage processes and failure behaviour of composites by locally applying polycaprolactone (PCL) interlayer material. We manufactured locally interfacially engineered UD carbon/epoxy composite plates and conducted short-beam shear tests to investigate the effects related to the application and the geometry of PCL on the interlaminar shear strength, the damage processes and the final failure of the composite in case of interlaminar loading. Furthermore, we carried out finite element modeling using the cohesive zone method (CZM) to analyze the influence of PCL interlayer material on the initiation and propagation of damage. The results show that the application of PCL is suitable for modifying the damage and failure processes of UD carbon/epoxy composites when applied to interlaminar loading.

1 INTRODUCTION

Nowadays, polymer composites are gaining popularity, mainly due to their excellent mechanical properties and low density. With the widespread use of high-performance composite structures, they are emerging in structural components subjected to significant loads. However, in safety-critical applications, their failure process might be disadvantageous. To ensure the further spread of composites in structural applications, their damage and failure processes need to be influenced and controlled [1].

The failure of composites is a complex process. As a result of their complex microstructure and their manufacturing processes, polymer composites contain a wide range of flaws from different sources and in varying sizes. The failure process consists of several concurrent damage processes leading to the final failure of a composite part. With the proper design of the composite system, this failure behavior can be turned to our advantage, contributing to increased reliability of polymer composite materials [2].

Several methods can be used to influence and control the damage processes and failure behavior of polymer composites. One concept is to predefine the location of damage initiation and failure, which can be achieved by introducing artificial defects [3]. This method may simplify structural health monitoring and improve the repairability of the composite part. Another way is to influence damage propagation and the mode of failure, or even achieve a pseudo-ductile behavior with a gradual failure process on the macroscopic level. Several different methods can be related to this concept. Damage propagation can be influenced by modifying at least one phase – the matrix [4], the reinforcement [5], or the interface [6] – or by applying a fibrous [7] or thermoplastic [8] interlayer material. The concepts of predefining the location of the failure and influencing or controlling the failure mode can also be combined, providing a designed failure of the composite part [9].

Our research group developed a novel method to create composites with a designed interface via 3D printing specific patterns of polycaprolactone (PCL) interlayer material directly on the reinforcement

system [10-12]. The low melting temperature of PCL enables simple processability through additive manufacturing, which ensures a great freedom of design of the interlayer. PCL is soluble in epoxy; thereby, in the case of polymer composites with epoxy matrix, it does not create a new phase. PCL can modify the interfacial adhesion and the matrix material locally. Therefore, it can be used to modify the failure of composites by controlling delamination, increasing fracture toughness, and achieving a pseudo-ductile behavior. Furthermore, by applying PCL as clever interfacial patterns in the composite structure, the formation of damage and, finally, the location of the failure can be predefined in terms of mode and position.

The aim of the current research was to influence the failure behavior of UD carbon/epoxy composites by predefining failure location and modifying damage propagation in case of interlaminar loading, and to validate the method of local interface engineering carried out with polycaprolactone (PCL) interlayer material. A further goal of the study was to provide a better understanding of the effects related to the method in terms of damage initiation and propagation through finite element modeling (FEM).

2 EXPERIMENTAL

2.1 Materials

As matrix material of the manufactured composite plates, IPOX MR 3010 (IPOX Chemicals Kft., Budapest, Hungary), DGEBA-based epoxy resin (EP) was applied with IPOX MH 3124 amine type curing agent. The components were mixed in a weight ratio of 100:35 (mixture viscosity 500 mPa·s, pot life 30 min at 25°C). We used PX35FBUD0300 (Zoltek Zrt., Nyergesújfalu, Hungary) stitch-bonded unidirectional carbon fabric (309 g/m2 surface weight), consisting of Panex35 50k rovings as reinforcement material. The interlayer material was printed from eMorph175N05 (Shenzhen Esun Industrial Co. Ltd., Shenzhen, China) poly (ϵ-caprolactone) (PCL) filament (1.75 mm diameter, 60°C melting temperature, 180°C printing temperature).

2.2 Manufacturing of composite plates

For the experiments, composite plates with $[0°_6]$ layup sequence were manufactured by vacuum-assisted resin transfer molding (VARTM). Besides baseline composites, locally interfacially engineered composites containing PCL interlayer material were manufactured. For these plates, the PCL filament was printed directly on the surface of the carbon fabric by the fused filament fabrication (FFF) method (Fig. 1) using a CraftBot Plus 3D printer (CraftUnique Kft., Budapest, Hungary). In the case of interfacially engineered composites, the interlayer material was applied perpendicular to the fiber direction (Fig. 1) and was placed only between the two central plies. Regarding the geometry of PCL, the thickness of the interlayer material was, based on previous research [9], constantly 0.2 mm in order to avoid fiber waviness and focus on the effects related to other mechanisms of PCL, such as the local modification of the matrix material and the interfacial adhesion. However, the width (w) of the interfacially engineered zone varied, PCL interlayer materials with 1, 2, 4 and 6 mm width were applied.



Figure 1: PCL interlayer material 3D printed directly on the reinforcement material.

Specimens for the material testing were cut from the composite plates with a Mutronic Diadisc (Mutronic, Rieden am Forggensee, Germany) diamond disc cutter. Each interfacially engineered specimen contained one zone modified with PCL.

2.3 Methods

Short-beam shear (SBS) tests were carried out according to ISO 14130 standard using a Zwick Z250 (Zwick GmbH, Ulm, Germany) universal testing machine with a 20 kN load cell to investigate the effect of PCL and its geometry on the failure process. The test setup can be seen in Fig. 2. The measurements were conducted with a 1 mm/min test speed using specimens with a nominal thickness of 3 mm, a width of 15 mm, and a length of 30 mm. The supports had a radius of 2 mm, while the loading member had a radius of 5 mm. The short-beam shear tests were monitored with a 5 MPixel resolution IDS U3-3080CP-P-GL (Imaging Development Systems Inc., Obersulm, Germany) camera. We tested 10 specimens from each type.

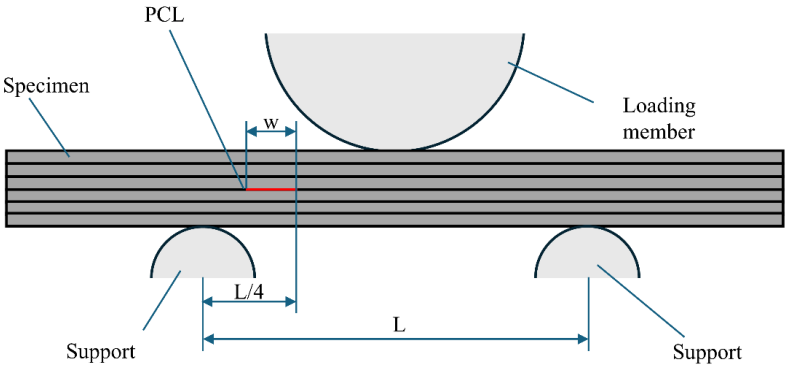

Figure 2: The test setup of the short-beam shear tests

3 FINITE ELEMENT MODELING

For modeling the delamination, we conducted finite element analysis for the loading and boundary conditions of the short-beam shear test with Ansys Workbench 2024R1 FEM software using the cohesive zone method (CZM). The model parameters were specified based on the relevant literature [12] and refined using our own data. To model the delamination process, we applied the fracture energy–based debonding model available in the software. A pure Mode II fracture model was adapted, reflecting the dominant shear-driven delamination mechanism in the short-beam shear test.

Two modeling concepts were used. The first approach involved introducing an artificial defect at the interface in the zone containing PCL. This was achieved by removing the contact definition between the adjacent surfaces of these plies over the width of the interlayer material. In this setup, no contact regions or cohesive separation definitions were assigned to the interfacially engineered zone, simulating an initial delaminated zone. In the subsequent simulations, the locally modified adhesion zone was modeled using the cohesive zone parameters of an interface modified with PCL. Non-modified interfacial regions were modeled with CZM using the parameters related to a baseline interface in each case.

To define the CZM model, interlaminar shear strength values, related to a baseline and a PCL-modified interface, determined during the short-beam shear tests, were used. Further CZM parameters and material properties are shown in Table 1.

Parameter		Value
E_1	[GPa]	123.3
E_2 *and* E_2	[GPa]	7.78
ν_{12} *and* ν_{13}	–	0.27
ν_{23}	–	0.42
G_{12} *and* G_{13}	[GPa]	5.00
G_{23}	[GPa]	3.08

G_{IIC} [12]	[J/m^2]	234.1
$G_{IIC,PCL}$ [12]	[J/m^2]	334.1

Table 1: Material properties and CZM parameters.

4 RESULTS AND DISCUSSION

4.1 Results of the short-beam shear tests

Initially, the force-deflection curves obtained from the measurements should be analyzed. Fig. 3 demonstrates the force-deflection curves of a characteristic specimen for each type.

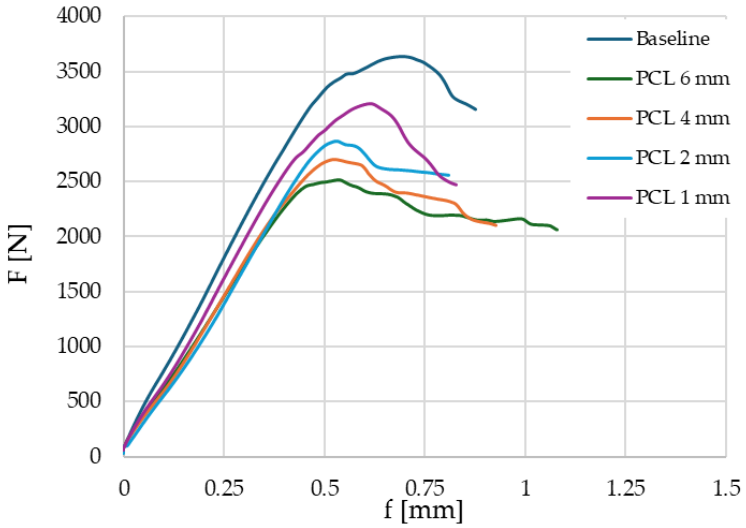

Figure 3: Characteristic force-deflection curves of the short-beam shear tests

The curve of the baseline sample indicates sudden delamination propagation. Compared to the baseline specimens, the specimens with 1 mm and 2 mm wide PCL interlayer material exhibit a lower maximum force. However, the overall shape of the force-deflection curve is similar to that of the baseline samples, indicating relatively rapid crack propagation. In this case, PCL acts as a local defect, and crack initiation is expected to occur near the interfacially engineered region. In contrast, for the specimens containing 4 mm and 6 mm wide PCL interlayer material, a plateau appears after the reduced force maximum. This indicates that the interfacially engineered zone slows down the propagation of the delamination.

The calculated interlaminar shear strength values can be seen in Fig. 4. The results show that increasing the width of the PCL interlayer material reduces the interlaminar shear strength, while the standard deviation of the results decreases significantly as well, indicating a more predictable failure.

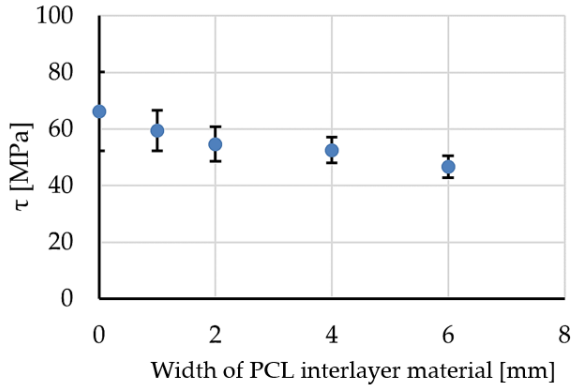

Figure 4: Interlaminar shear strength determined with the short-beam shear tests.

4.2 Results of the finite element analysis

The finite element analysis resulted in the delamination failure of the specimens similar to the short-beam shear tests (Fig. 5).

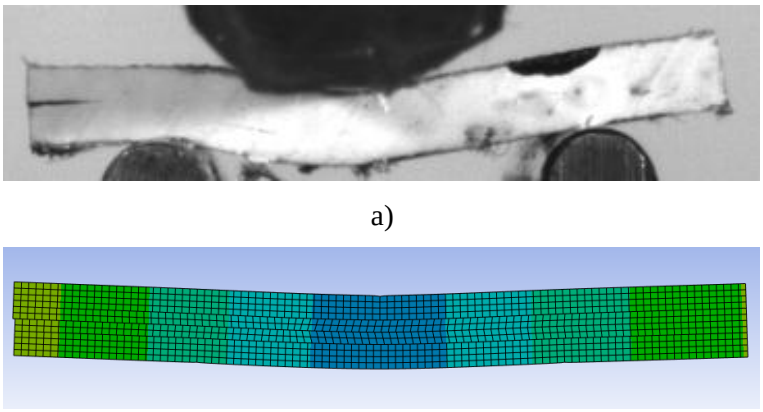

a)

b)

Figure 5: Delamination failure during a) a conducted short-beam shear test, b) finite element analysis of a short-beam shear test

As the contact status in Fig. 6 indicates, compared to the baseline model, the modified zone predefines the position of delamination initiation for both modeling concepts. This means that even in the case of the lowest width, the method is suitable for influencing the position of interlaminar crack initiation.

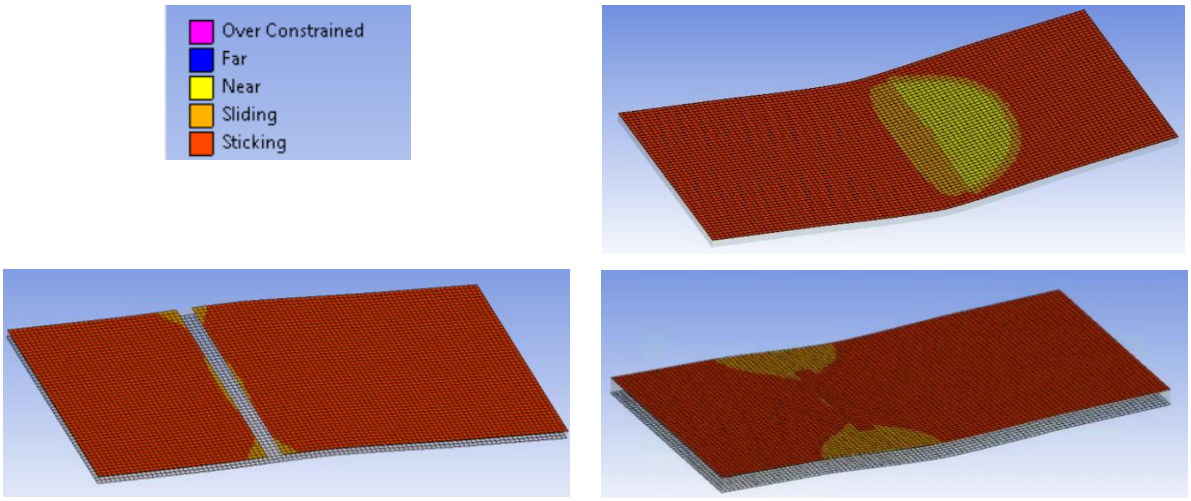

Figure 6: Contact status between the two central plies a) Status types, b) Baseline, c) PCL as initial delamination in 1 mm width, d) PCL interlayer material with 1 mm width

Table 2 contains the calculated interlaminar shear strength values, while the force-deflection curves of the simulations are shown in Fig. 7. Besides the baseline simulations, the curves include the results of the 1 mm and 4 mm wide simulations. In the experimental results, these two specimen types demonstrated completely different behavior. The 1 mm wide zone had an effect similar to an initial defect. Meanwhile, the 4 mm wide zone was the first to result in an extended plateau.

Type	Interlaminar shear strength [MPa]		
	Experimental	FEA	
		Initial delam.	PCL
Baseline	66.2	67.9	
1 mm	59.4	48.6	65.0
4 mm	52.5	39.6	56.3

Table 2: Interlaminar shear strength values

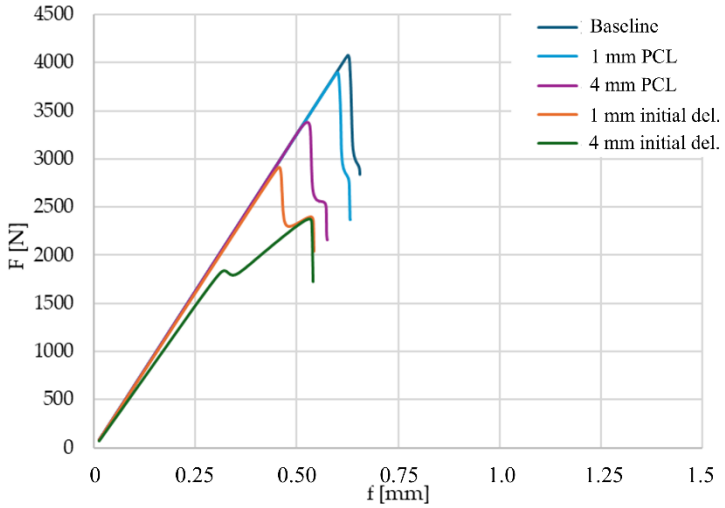

Figure 7: Force-deflection curves of the different simulations.

Based on the results of Fig. 7 and Table 2, the simulations including an initial delaminated zone, where contact was removed at the PCL location, better approximate the gradual failure process. However, in the simulations where a contact region with a cohesive zone was defined at the interfacially engineered zone, the interlaminar shear strength values more accurately reflect the experimentally measured values. Furthermore, similarly to the experimental results, in the case of the simulations, the increase of the width of the modified zone results in a more gradual failure process as well.

5 CONCLUSIONS

In our research, we manufactured locally interfacially engineered composites containing PCL interlayer material with different geometries. We carried out short-beam shear tests to investigate the effect of PCL and its geometry on the failure process. The results indicate that PCL can influence the initiation and propagation of delamination. With increasing width, the modified zone might be able to slow down crack propagation.

Finite element analysis with cohesive zone modeling was carried out for the loading conditions of the short-beam shear test. The simulations demonstrated similar results to the short-beam shear test, validating our method.

To further improve the modeling of the gradual failure process and the effect of PCL interlayer material, the introduction of a gradient region at the edges of the interfacially engineered zone is recommended. This could model the interphase created by the partial dissolution of PCL in the epoxy resin system.

ACKNOWLEDGEMENTS

The research has been supported by the NRDI Office (OTKA FK 142540). Gábor Szebényi acknowledges the financial support received through the János Bolyai Scholarship of the Hungarian Academy of Sciences and ÚNKP-23-5-BME-415 New National Excellence Program. Project no. 2022-

2.1.1-NL-2022-00012 „National Laboratory for Cooperative Technologies" has been implemented with the support provided by the Ministry of Culture and Innovation of Hungary from the National Research, Development and Innovation Fund, financed under the National Laboratories funding scheme. Project no. TKP-6-6/PALY-2021 has been implemented with the support provided by the Ministry of Culture and Innovation of Hungary from the National Research, Development and Innovation Fund, financed under the TKP2021-NVA funding scheme. Project no. KDP-IKT-2023-900-I1-00000957/0000003 has been implemented with the support provided by the Ministry of Culture and Innovation of Hungary from the National Research, Development and Innovation Fund, financed under the KDP-2023 funding scheme. Special thanks to Anna Matók for her help with conducting the experiments.

REFERENCES

[1] G.Z. Marton and G. Szebényi, Influencing the damage process and failure behaviour of polymer composites - A short review, *Express Polymer Letters*, **19**, 2025, pp. 140-160 (doi: 10.3144/expresspolymlett.2025.11).

[2] R.B. Heslehurst, *Defects and in Composite Materials and Structures*, CRC Press, Boca Raton, 2014.

[3] A. Melaibari A., A. Wagih, M. Basha, A.M. Kabeel, G. Lubineau and M.A. Eltaher, Bio-inspired composite laminate design with improved out-of-plane strength and ductility, *Composites Part A: Applied Science and Manufacturing*, **144**, 2021, 106362 (doi: 10.1016/j.compositesa.2021.106362).

[4] C. Zhang, G. Zhang, X. Shi and X. Wang, Effects of carbon nanotubes on the interlaminar shear strength and fracture toughness of carbon fiber composite laminates: A review, *Journal of Materials Science*, **57**, 2022, pp. 2388-2410 (doi: 10.1007/s10853-021-06734-z).

[5] J. Henry and S. Pimenta, Bio-inspired non-self-similar hierarchical microstructures for damage tolerance, *Composites Science and Technology*, **201**, 2021, 108374 (doi: 10.1016/j.compscitech.2020.108374).

[6] B. Magyar B., G. Szebényi G and T. Czigány, Comparison of different interfacial engineering methods to achieve pseudo-ductile behaviour of carbon fibre reinforced polymer composites, *Proceedings of the 22nd International Conference on Composite Materials (Eds. A. Mouritz, C. Wang, B. Fox) Melbourne, Australia, August 11-16, 2019*, RMIT University, Melbourne, 2019, pp. 472–480.

[7] H. Wang, Y. Lin, H. Jiang and Z. Liu, Inter-layer failure and toughening mechanisms of carbon/aramid hybrid fiber composites interleaved with micro/nano pulps under low-velocity impact load, *Thin-Walled Structures*, **202**, 2024, 112086 (doi: 10.1016/j.tws.2024.112086).

[8] S.G. Marino and G. Czél, Development and characterisation of reparable, film-interleaved, pseudo-ductile hybrid composites, *Composites Part A: Applied Science and Manufacturing*, **169**, , 2023, 107496 (doi: 10.1016/j.compositesa.2023.107496).

[9] G.Z. Marton, Á. Fendrik and G. Szebényi, Manufacturing of composites with designed failure, *IOP Conference Series: Materials Science and Engineering*, **1313**, 2024, 012014 (doi: 10.1088/1757-899X/1313/1/012014).

[10] G. Szebényi, T. Czigány, B. Magyar and J. Karger-Kocsis, 3D printing-assisted interphase engineering of polymer composites: Concept and feasibility, *Express Polymer Letters*, **11**, 2017, pp. 525-530 (doi: 10.3144/expresspolymlett.2017.50).

[11] G. Szebényi, B. Magyar and T. Czigány, Achieving Pseudo-Ductile Behavior of Carbon Fiber Reinforced Polymer Composites via Interfacial Engineering, *Advanced Engineering Materials*, **23**, 2020, 2000822 (doi: 10.1002/adem.202000822).

[12] B. Magyar, T. Czigány and G. Szebényi, Metal-alike polymer composites: The effect of inter-layer content on the pseudo-ductile behaviour of carbon fibre/epoxy resin materials, *Composites Science and Technology*, **215**, 2021, 109002 (doi: 10.1016/j.compscitech.2021.109002).

MULTISCALE ANALYSIS OF HYBRID HEMP/GLASS COMPOSITES FOR SUSTAINABLE LIGHTWEIGHT AUTOMOTIVE TORSION BEAMS

Napat Nawawithan[1], Kitchanon Ruangjirakit[1, 2], Pathawee Kunakorn-ong[3], Pattaramon Jongpradist[1, 2]

[1] Department of Mechanical Engineering, Faculty of Engineering, King Mongkut's University of Technology Thonburi, Bangkok 10140, Thailand

[2] Future Automotive Structure Research Group (FASt), Mobility and Vehicle Technology Research Center, King Mongkut's University of Technology Thonburi, Bangkok 10140, Thailand

[3] Department of Mechanical and Aerospace Engineering, Faculty of Engineering, King Mongkut's University of Technology North Bangkok, Bangkok 10800, Thailand

24TH INTERNATIONAL CONFERENCE ON COMPOSITE MATERIALS
AUG 4-8, 2025 • BALTIMORE CONVENTION CENTER • BALTIMORE, MARYLAND

Background & Objectives

The **torsion beam** in the **twist beam axle** plays a vital role in transferring forces and moments between the wheels and vehicle body, ensuring roll stability and safety. **Traditionally made of high-strength steel**, torsion beams can be enhanced with **fiber-reinforced polymer composites**, offering **superior strength, stiffness**, manufacturability, and corrosion resistance. **Hybrid composites**, combining synthetic and natural fibers, provide a promising solution to **reduce mass and carbon footprint** while **maintaining mechanical performance** comparable to purely synthetic composites.

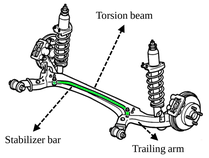

Torsion beam axle in rear suspension [1]

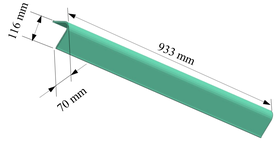

U-shaped baseline steel torsion beam [2]

Objectives

- Analyze the elastic mechanical behavior of hemp fiber-reinforced epoxy (HFRE), glass fiber-reinforced epoxy (GFRE), and two hybrid intra-ply configurations (H0G90 and H90G0) to evaluate their potential for improving structural performance.
- Investigate the performance of quasi-isotropic plain-woven hybrid hemp/glass fiber-reinforced composites in torsion beams, focusing on torsional, vertical, and longitudinal stiffness using multiscale modeling.

Methods

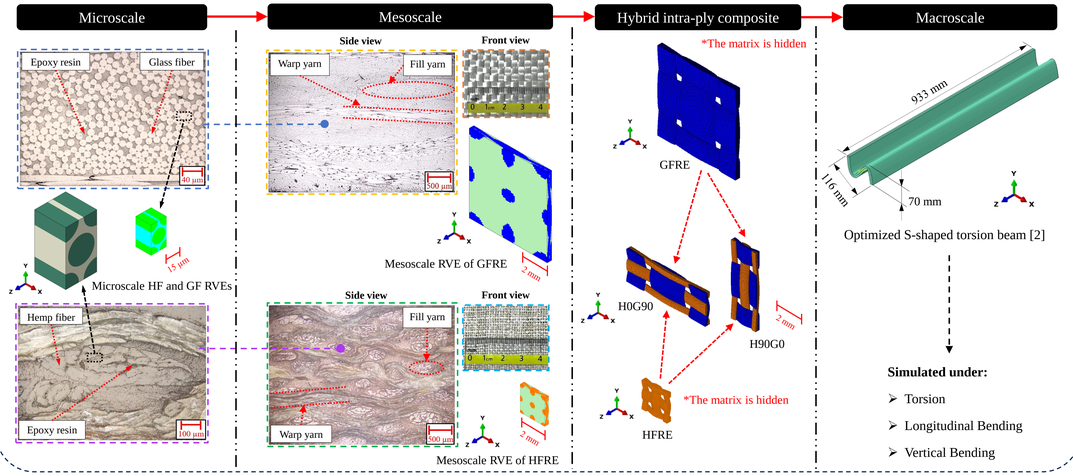

Validation of Elastic Properties of GFRE and HFRE compared to Hybrid Intra-ply Models



Hungta HT-2402 universal testing machine



Experimental tensile test setup for GFRE

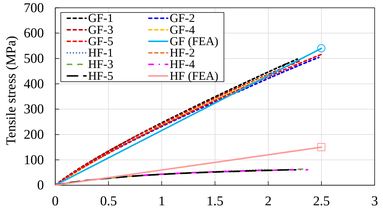

Tensile test results of GFRE and HFRE [3]

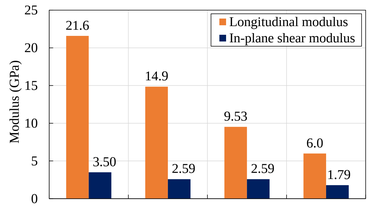

Moduli of GFRE and HFRE compared to the hybrid intra-ply models

Stacking Sequence Design for Torsion Beam Modeling

Table 1: Number of plies in various stacking sequences and the resulting thickness and mass of each torsion beam model with hemp fiber content in %.

Model	No. of plies	Thickness (mm)	Mass (kg)	Hemp fiber content (%)
Steel_U-shape	-	6.0	8.26	-
GFRE	20	8.0	3.62	-
HFRE	40	16.0	4.84	100
Hybrid_H/G	26	10.4	3.87	53.8
H0G90	30	12.0	4.54	46.4
H90G0	28	11.2	4.24	46.4
H90G0 & HFRE(Mid)	32	12.8	4.36	73.2

Note: The **thickness** and **number of plies** in each composite stacking sequence **(0.4 mm/ply)** are based on the **torsional stiffness** of the **baseline steel U-shaped torsion beam**.

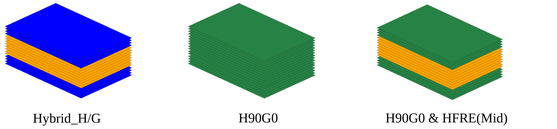

Torsion Beam Analysis

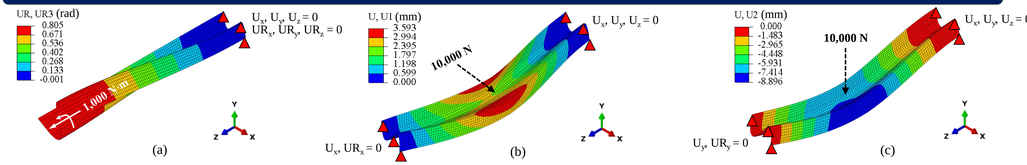

Deformed shape of the H90G0 & HFRE(Mid) S-shaped torsion beam under (a) torsional load, (b) vertical bending load, and (c) longitudinal bending load

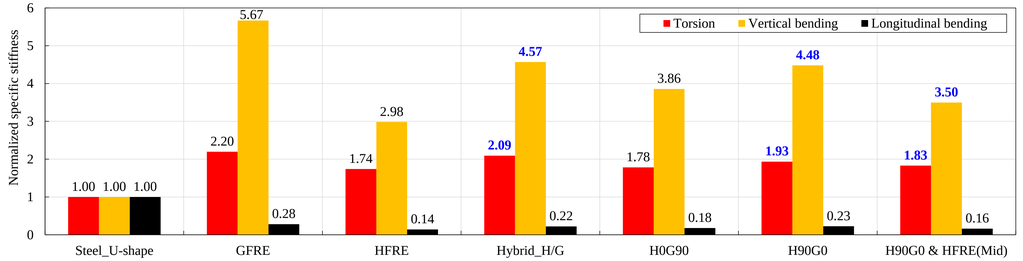

Conclusions

- All composite torsion beams showed 1.74 to 2.2 times higher specific torsional stiffness (K_T) than the baseline steel beam, with GFRE achieving the highest K_T. The hybrid inter-ply model (H/G) performed similarly to GFRE, with only a 4.8% reduction in stiffness.
- The GFRE model had the highest specific vertical bending stiffness (K_V), while the hybrid composite models showed a 3.50 to 4.57 times improvement in K_V over the steel baseline.
- Hybrid intra-ply configurations, especially H90G0, demonstrated superior mechanical properties due to optimal fiber alignment, with the H90G0 & HFRE(Mid) model combining the benefits of both inter- and intra-ply hybridization and a high hemp fiber content (73.2%). However, the hybrid models showed limited effectiveness under longitudinal loading, indicating their suitability for torsional and bending applications.

Acknowledgement

This research project is supported by King Mongkut's University of Technology Thonburi (KMUTT), Thailand Science Research and Innovation (TSRI), and National Science, Research and Innovation Fund (NSRF) Fiscal year 2025 Grant number FRB680074/0164

References

1. Edgar J., 2021, **Car Suspension: - Over 120 Years of Ride and Handling,** Amazon Digital Services LLC - Kdp
2. Sun, T., Jiang, R., Sun, H., Liu, D. and Pan, Z., 2023, Multiscale uncertainty propagation analysis and reliability optimization of the CFRP crossbeam of the twist beam axle, **International Journal of Mechanical Sciences**, *242*, article number 108022.
3. Nawawithan, N., Kittisakpairach, P., Nithiboonyapun, S., Ruangjirakit, K. and Jongpradist, P., 2024. Design and performance simulation of hybrid hemp/glass fiber composites for automotive front bumper beams. **Composite Structures**, *335*, article number 118003.

A Novel Method for Evaluating the Biodegradability of Polymers by Tracking Changes in Tensile Properties During Degradation

Lovisa Rova*, Hiroki Kurita and Fumio Narita. Department of Frontier Sciences and Advanced Environment, Graduate School of Environmental Studies, Tohoku University, JAPAN. *E-mail: rova@dc.tohoku.ac.jp

Introduction

What happens with our trash?

The majority of plastic waste is either landfilled or dumped into the environment. Due to environmental concerns, materials that biodegrade without leaving micro- and nano-plastics are being developed. For example, "green composites" consisting of biodegradable polymers combined with natural fibers or biomass. Typically, biodegradability is evaluated by monitoring the CO_2 evolution of the material as it biodegrades in a controlled environment. However, these methods have significant limitations:

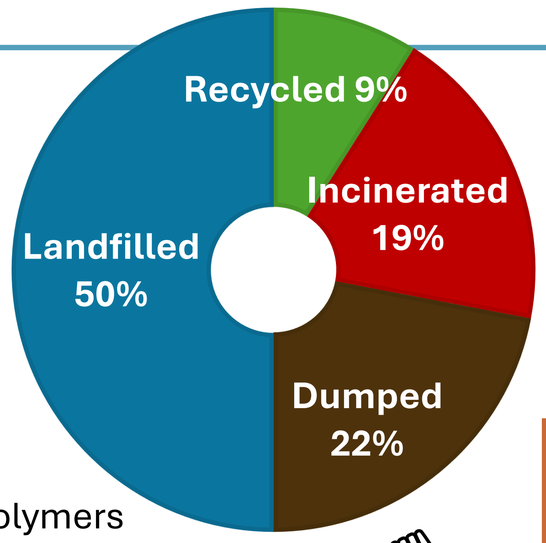

1. They cannot be used to **evaluate biodegradability in natural environments**
2. Many researchers test in natural environments without standards, thus **results of different studies are not easily comparable**

Thus, there is a need for more versatile methods to evaluation degradation, that should be **applicable in any environment.**

This research investigates...

...how the **mechanical properties of biodegradable materials change during degradation** and explore whether this relationship can be used to **evaluate biodegradability** in diverse environments

Experiments

1. Fabrication of test material

A prototype green composite was made from tree bark (60%) and polybutylene succinate (PBS, 40%). It was made by hot-kneading bark and PBS and then extrude into pellets. Dumbbell shapes were made by compression moulding of the pellets.

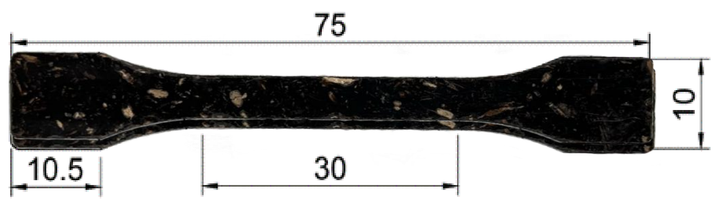

2. Biodegradation in simulated compost

Samples were placed in compost and kept in an incubator at 58°C and 100% relative humidity. The biodegrading material turns into CO_2 which is used to calculate the degree of biodegradation:

$$\frac{m_{CO_2}^{test} - m_{CO_2}^{blank}}{ThCO_2} \cdot 100 = D_t$$

In addition, specimens were extracted every 2 weeks for tensile testing.

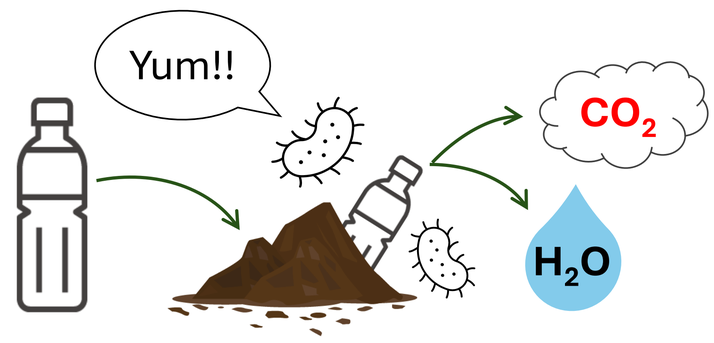

3. Biodegradation in outdoor soil

Specimens were buried in a garden, where CO_2 cannot be measured. Instead, samples were extracted periodically and the change in tensile properties was measured. The experiment lasted 30 weeks (6 months).



$$ThCO_2 = \frac{44}{12} \cdot m_{tot} \cdot C_{tot}$$

D_t : Degree of biodegradation (%)
$m_{CO_2}^{test}$: CO_2 from material in compost (g)
$m_{CO_2}^{blank}$: CO_2 from compost (blank) (g)
$ThCO_2$: CO_2 from material at 100% biodeg. (g)
m_{tot} : Dry solid mass of material (g)
C_{tot} : Organic carbon content of material (g/g)

Results and Discussion

Composting experiment

The test material reached a biodegradation of 12.8 % after 8 weeks (56 days) in compost, as shown in Figure A.

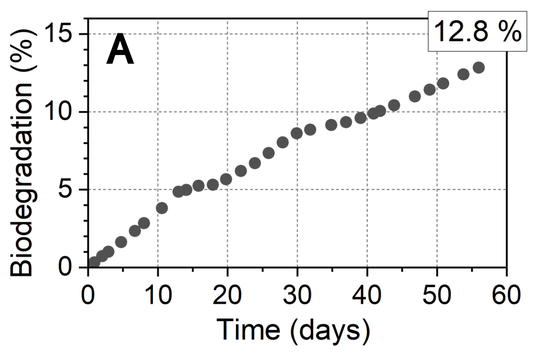

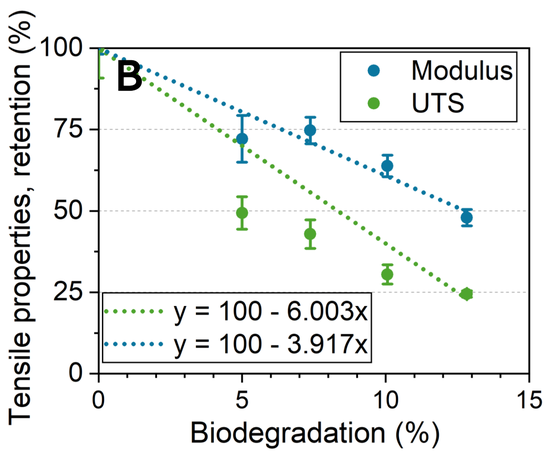

Figure B shows how the tensile modulus and the ultimate tensile strength (UTS) decreased as biodegradation progressed. Linear curves were fitted to these data points.

Outdoor soil experiment and biodegradation estimation

Similar to the composting experiment, biodegradation in soil caused the tensile modulus and UTS to gradually decrease over time (Figure C).

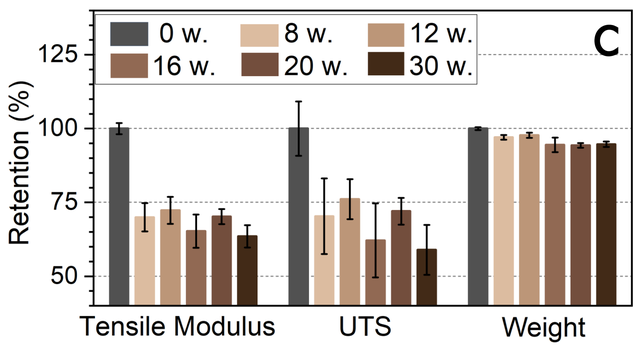

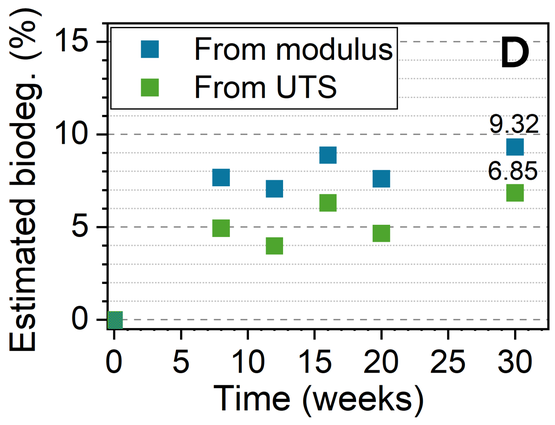

The degree of biodegradation was estimated by extrapolating the x values in the linear curves in Figure B using the data in Figure C. Thus, **it was estimated that after 6 months of soil burial, the composite had degraded by 7 to 9 %.**

Final Comment

The research continues with various biodegradable materials and specimen dimensions to investigate how tensile properties change during degradation in different natural environments, such as soil and seawater. We aim to develop evaluation methods that reflect the functional lifetime of materials, as opposed to traditional methods that focus solely on material conversion into CO_2.

ICCM24
AUGUST 4-8, 2025
BALTIMORE CONVENTION CENTER
BALTIMORE, MARYLAND, USA

No Technical Paper Submission for:

Dazhi Jiang

BENDING BEHAVIOR OF 3D-PRINTING BIO-SOURCED PLA/FLAX COMPOSITE SANDWICH WITH DIFFERENT CORE GEOMETRIES: EXPERIMENTAL AND NUMERICAL ANALYSES

Z. Wang[1], D. Scida[2], M. Assarar[2], P-A. Adragna[1] and X-L. Gong[1]

[1]University of Technology of Troyes
12 Rue Marie Curie, 10004 Troyes, France
Email: zhenyi.wang@utt.fr, web page: https://www.utt.fr

[2]University of Reims Champagne-Ardenne
IUT de Troyes, 9 Rue du Québec, 10026 Troyes Cedex, France
Email: daniel.scida@univ-reims.fr, web page: https://www.univ-reims.fr

Keywords: 3D printing, Sandwich structures, Finite elements

ABSTRACT

Sandwich structures are widely used in engineering applications due to their high strength-to-weight radio, especially in the building materials, automotive component, ships structure and other daily use. This study investigates the mechanical bending behaviour of bio-sourced PLA/Flax composite sandwich fabricated by 3D printing, focusing on the influence of different core geometries. In this work, biodegradable polylactic acid (PLA) was used as the matrix, reinforced with flax fibres to improve mechanical performance. Various 3D-printed sandwich with different core geometries, including sinusoidal, triangular, double triangular and trapezoid were evaluated under 3-point bending tests.

Although various sandwich core structures have been extensively studied in recent years, contributions specifically dedicated to the development and investigation of biosourced sandwich materials with different core architectures remain rather limited. It is in this context that our work is positioned. It aims to compare different biosourced structures while keeping their relative density and thus their mass constant. With this in mind, the specimens were designed with the same mass requiring the development of a calculation method with both mutable and immutable parameters. Four different core geometries, i.e., sinusoidal (SN), triangular (TR), double triangular (DT), and trapezoidal (TP) were identified as representative sandwich structures capable of optimizing their performance. Consequently, these four geometries were subjected to the optimization program to ensure that their dimensions satisfied the above-mentioned iso-mass condition.

Fused Deposition Modeling (FDM) is widely used in PLA material manufacturing. A method called continuous extrusion printing, which is an optimization of FDM printing, was proposed and used in this study. This method enables uninterrupted material extrusion throughout the process, producing the part continuously until it is fully manufactured. Five samples of each core geometry were fabricated using this continuous extrusion printing technique. Mechanical tests of 3-point-bending were conducted on these specimens according to the ASTM C393 standard. The results showed that the bending performance significantly varied with the core geometry. It is observed that the DT structure outperforms the other three structures both in terms of maximum load and fitted stiffness, which gives a new guidance for choosing different core geometries sandwich structure for isomass.

1 INTRODUCTION

The needs for more environmentally friendly products in the industry are in strong growth. Sandwich structures have long been recognized for their remarkable combination of high stiffness, strength, and low weight, making them indispensable in a wide range of engineering applications [1]. Their ability to efficiently hold mechanical loads while minimizing material usage has driven continuous innovation in the design and fabrication. The fundamental concept of a sandwich structure relies on relatively thin, stiff face sheets bonded to a lightweight core. At the same time, the fabrication process FDM is widely used in PLA material manufacturing [2].

While numerous studies have investigated sandwich structures with synthetic cores [3], the exploration of 3D-printed bio-sourced sandwich composites remains limited, particularly in terms of systematically evaluating the influence of different core geometries. Indeed, most comparative studies do not account for differences in relative density or mass, making it difficult to isolate the effects of geometry alone. Recognizing this gap, the present work aims to advance the understanding of bio-based sandwich structures by proposing a comparative experimental framework in which the mass of each specimen is held constant. This approach requires the development of a tailored optimization methodology that adjusts the dimensions of each core geometry to satisfy the iso-mass criterion while preserving their functional integrity.

Specifically, this study investigates the bending behaviour of 3D-printed PLA/flax composite sandwich structures incorporating four representative core geometries: sinusoidal (SN), triangular (TR), double triangular (DT), and trapezoidal (TP). These geometries were selected based on their potential to enhance load distribution, increase energy absorption, and improve overall mechanical performance. Five specimens for each configuration were fabricated using continuous extrusion printing. Mechanical tests of 3-point-bending were conducted on these specimens according to the ASTM C393 standard [4].

This research contributes to the growing of knowledge on sustainable, high-performance materials by demonstrating that 3D-printed PLA/flax sandwich structures can achieve competitive mechanical properties while leveraging renewable resources and environmentally friendly manufacturing methods. By systematically isolating the effects of geometry under isomass conditions, the study establishes a foundation for future work aimed at sandwich architectures to specific engineering requirements. Furthermore, the application of continuous extrusion printing paves the way for scalable production of biosourced composite components with enhanced structural integrity and minimized waste.

2 EXPERIMENTAL PROCEDURES

2.1 Isomass calculate method

In prior research on sandwich composites, various core structures such as corrugated, honeycomb and lattice geometries were classified and studied extensively. These studies often focused on characterizing core geometries at different relative densities. However, direct comparisons between different core topologies with identical relative density remain limited.

In this study, four distinct core geometries were selected as representative sandwich structures: sinusoidal (SN), triangular (TR), double triangular (DT), and trapezoidal (TP). To ensure fair comparison and minimize the influence of density differences, all cores were designed to maintain the same relative density, thereby ensuring equivalent mass. The three external dimensions—length (L), width (b), and height (h)—serve as the foundation for the geom-etric description.

However, these dimensions alone do not capture the internal architecture, including the morphology, the number of repeating cells, and the material distribution along each axis. Therefore, two additional parameters were introduced to precisely define internal geometry in a unified way across all topologies:

- m, the number of representative elements, corresponding to the count of repeating motifs (waves, meshes, or cells) along the length L.
- n, the integer number of full extrusions across the width b, ensuring compatibility with the continuous extrusion strategy.

This approach was designed to balance generality and parsimony: the same (m, n) pair applies consistently to all four core types, facilitating cross-comparison while limiting the number of independent variables. As a result, the minimal parameter set {L, b, h, m, n} fully defines both the external and internal geometry and underpins subsequent calculations of volume, mass, and FDM print paths.

Due to the high number of variables, the height h and width b were defined based on dimensions suitable for later mechanical testing. If the resulting dimensions proved acceptable, they were directly validated; otherwise, additional iterative calculations were required. Python was chosen as the computational tool because of its simplicity, extensive scientific libraries, flexibility, and strong community support. Ultimately, final solutions were obtained and are presented in Table 1. All four core geometries share identical L, b, and h values—considered the principal parameters—while adopting

distinct m and n values to maintain nearly identical core volumes and thus constant mass. Note that the volumes fluctuate by a maximum of 2% from the average volume, which is very acceptable. Additionally, a 1.6 mm skin was incorporated into each design to enable subsequent study of complete sandwich structure properties in later subsection. The final dimensions were set at 138.56 mm length, 30.00 mm height, and 30.00 mm width, maintaining equal mass and relative density across all geometries.

Core type	L (mm)	b (mm)	h (mm)	n	m	V (mm^3)
SN	138.56	30.00	30.00	2	9	27196.17
TR				2	9	26759.73
DT				2	8	26604.30
TP				3	6	26132.46

Table 1: Solution of different core geometries sandwich structures in isomass

2.2 Fabrication processing

Fused Deposition Modeling (FDM) is one of the most common additive manufacturing techniques for thermoplastics. This method offers precise control over temperature, feed rate, and layer height, enabling the use of standard polymers like PLA as well as fiber-reinforced composites. Its flexibility and moderate cost make it widely used for prototyping and producing functional components in small series.

In this study, PLA reinforced with flax fibres was used, supplied by Nanovia Company. Printing was carried out on a Raise3D N2 printer. After loading the filament and heating the nozzle, material was deposited layer by layer onto the heated platform. Each pass in the *X*–*Y* plane formed a cross-section, followed by an upward *Z* increment until the part was complete and the thermal bonding ensured cohesion between layers. A custom MATLAB script was developed to regenerate G-code with higher precision comparing with the traditional way of slicing CAD model into G-code.

2.3 Assembly and 3-point-bending experiment

To study the different core geometries sandwich structures, three-point bending tests were performed on as-printed specimens, using an Instron universal testing machine. The experimental setup, illustrated in Figure 1, consists of a cylindrical punch with a diameter of 25mm and two cylindrical supports of the same diameter, spaced 100mm apart, in accordance with ASTM C393 standard.

The tests were conducted under displacement control with velocity of 1 mm/min, under standard atmospheric conditions and ambient temperature. The applied load and the displacement of the punch were recorded by the machine’s integrated sensors.

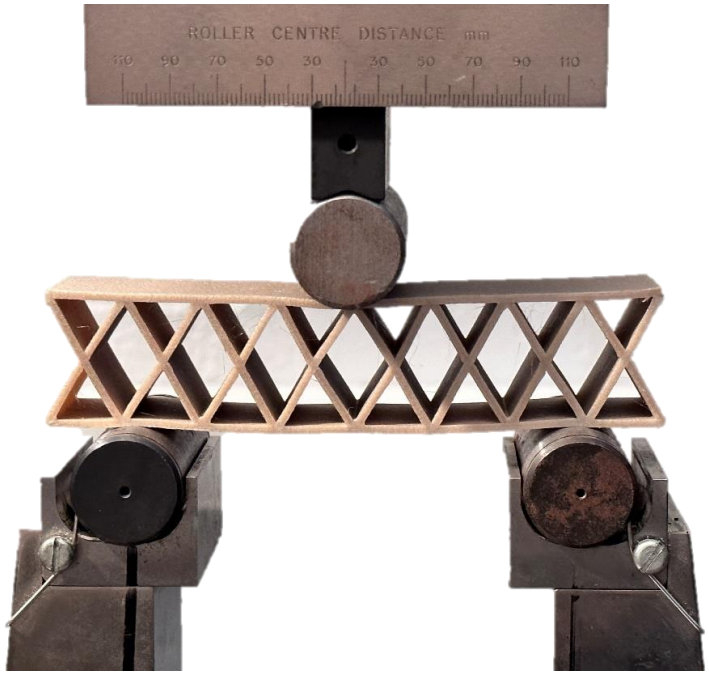

Figure 1: Experimental setup for the 3-point-bending tests on the composite DT structure

3 FINITE ELEMENT SIMULATION

Finite element analysis was performed to predict the composite sandwich structures with the same relative density and different core geometries were established using the finite element software ABAQUS 2020 (Dassault Systems). The CAD models of the four sandwich configurations - SN, TR, DT and TP cores - were created in Dassault CATIA based on the geometric parameters computed in Section 2.1. These models incorporated identical overall dimensions and relative densities to isolate the effect of core topology. The CAD assemblies were then imported into ABAQUS for meshing and simulation setup.

To replicate the experimental setup accurately, three loading cylinders were also modelled: one representing the upper loading punch and two representing the lower supports. Each cylinder had a diameter of 25 mm and was positioned in accordance with the ASTM C393 standard. The lower support cylinders were fully fixed, while the upper cylinder was assigned a reference point at its centre to which the displacement boundary condition was applied. A prescribed vertical displacement along the *Z*-axis was imposed on this reference point to simulate loading.

The sandwich structures and cylinders were discretized using 8-node linear hexahedral elements with reduced integration (C3D8R). A mesh convergence study was conducted to ensure that the element size provided a balance between computational efficiency and solution accuracy. Contact interactions were defined between the surfaces of the cylinders and the sandwich specimens using a surface-to-surface contact formulation, with a friction coefficient specified based on the literature for PLA-based composites. The material constitutive behaviour and parameters used in the simulation were derived from the constitutive relationships obtained through compression tests conducted on standard cylindrical specimens.

4 RESULTS AND DISCUSSION

The comparative testing of the four core geometries under 3-point-bending highlights distinct mechanical behaviour curves, thereby providing valuable insights for design choices depending on the intended applications, as shown in Figure 2. The DT configuration, characterized by the highest stiffness and maximum load, exhibits excellent load-bearing capacity. However, its failure is more abrupt, and its elongation is limited. Consequently, it is better suited for situations requiring high load support with

low tolerance for deformation.

The TR geometry demonstrates stiffness and strength levels comparable to those of the DT configuration while offering slightly greater ductility, thereby representing a relevant compromise when moderate displacements are acceptable without compromising load capacity. In contrast, the TP structure displays the lowest stiffness and maximum load but has by far the highest displacement at failure among all configurations. This capacity for gradual deformation and energy absorption prior to failure makes it a suitable candidate for applications involving impact protection, damping, or energy dissipation. The SN configuration occupies an intermediate position: neither the stiffest nor the most ductile, it constitutes a balanced and potentially more cost-effective solution for conventional applications in which the requirements for load-bearing capacity and energy absorption remain moderate.

These curves show that if the design objective is high load-bearing capacity with limited concern for large displacements, the DT configuration performs better. Conversely, if the application requires greater deformation tolerance, like the ability to undergo larger displacements prior to failure, the TP configuration offers advantages despite its lower maximum strength.

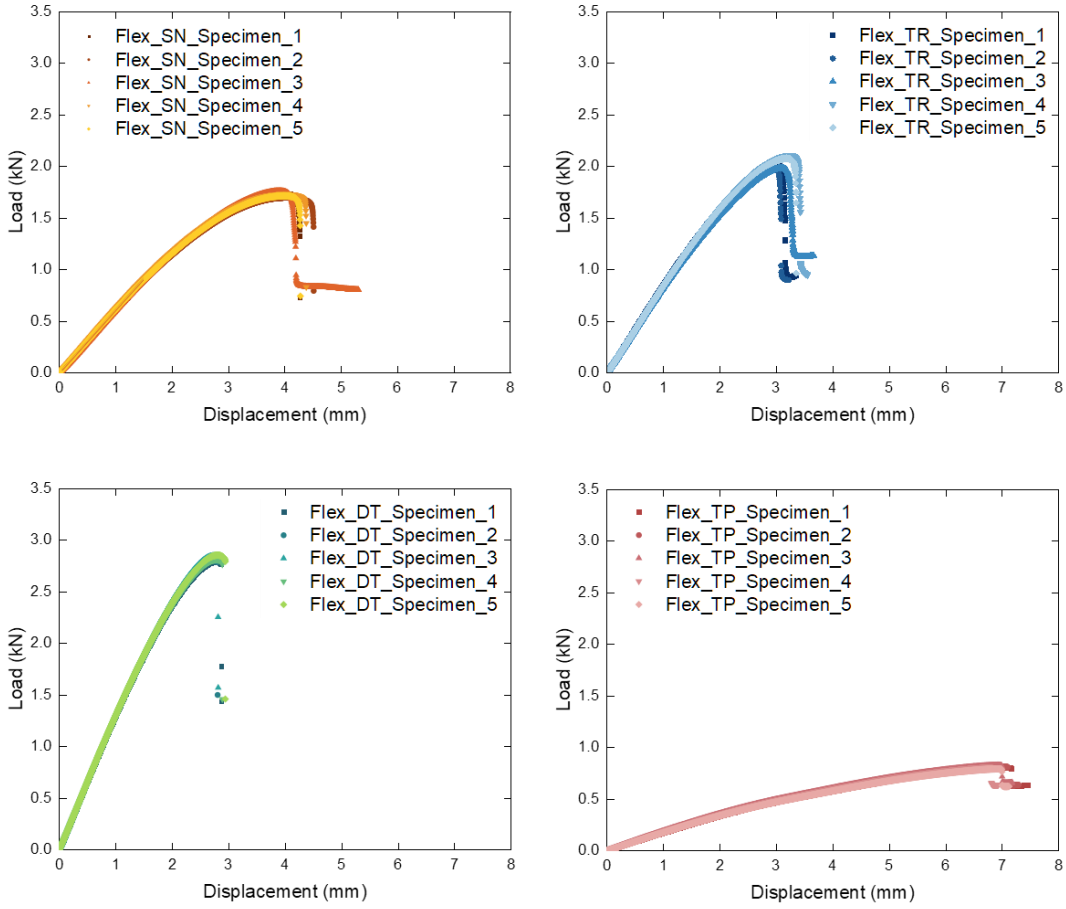

Figure 2: Load–displacement curves of four core geometries under 3-points-bending tests

The radar chart depicted in Figure 3 comparing the mechanical performance of the four core geometries across five normalized parameters: stiffness (E), elastic limit force (Fe), maximum force (Fmax), maximum displacement (dmax), and elastic displacement (de). The DT configuration consistently shows the highest normalized values of stiffness and force capacities, with de reaching approximately 0.85, indicating superior resistance and load-bearing performance. In contrast, the TP geometry exhibits the greatest maximum displacement and elastic displacement, suggesting higher deformability under loading conditions. The TR shows intermediate stiffness and force values, with E near 0.65, dmax of about 0.5 and Fe about 0.75, while SN combines a stiffness of about 0.5, dmax of

about 0.6 and Fe around 0.55. Both configurations maintain moderate levels. Overall, this visualization underscores the distinct mechanical behavior of each design, supporting the selection of an appropriate core geometry depending on whether stiffness or deformability is prioritized, particularly if the design objective is high load-bearing capacity with limited concern for large displacements.

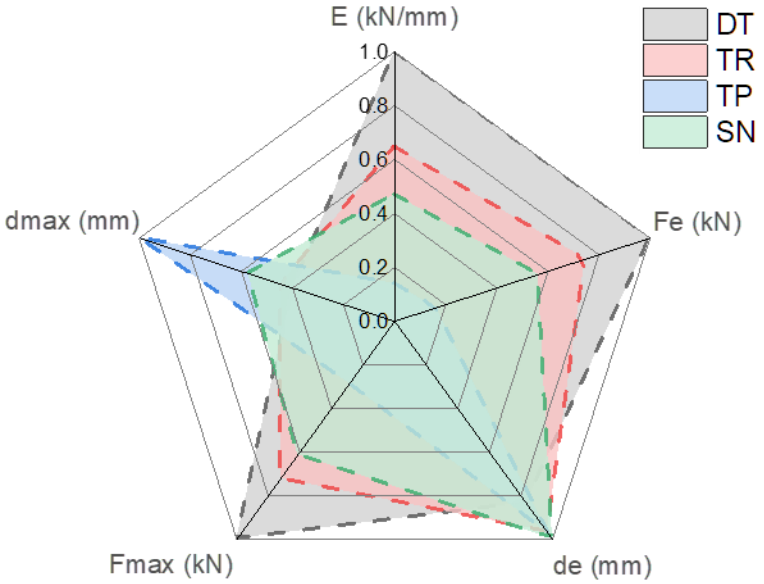

Figure 3: Radar of mechanical performance of four core geometries under 3-points-bending tests

The finite element simulations model accurately characterizes the load-displacement from the elastic stage up to fracture. By comparing the experimental responses with the simulation results shown in Figure 4, the numerical model was effectively validated. It is worth noting that the experimental and numerical curves are identical for stiffness, while a discrepancy of less than 15% is observed for maximum force (for 3 out of 4 configurations).

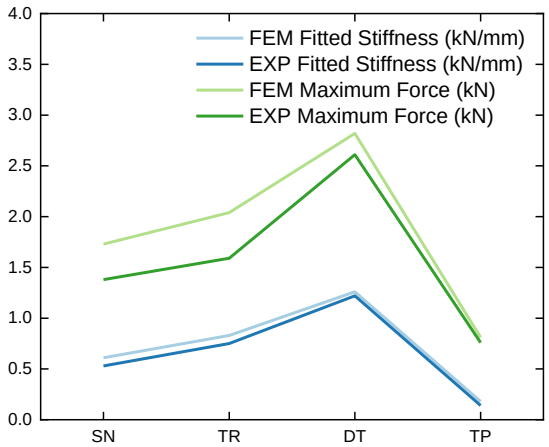

Figure 4: Comparison of FEM and EXP for Maximum Force and Fitted Stiffness with four different patterns

5 CONCLUSIONS

This study investigated the mechanical bending behaviour of 3D-printed bio-sourced PLA/flax composite sandwich structures with four distinct core geometries while maintaining identical mass and

relative density. Through both experimental three-point bending tests and finite element simulations, significant differences in mechanical performance were observed among the configurations.

The double triangular (DT) core exhibited the highest stiffness and maximum load capacity, making it an optimal solution for applications requiring high load-bearing performance with minimal deformation. The triangular (TR) geometry offered a comparable strength profile while demonstrating slightly greater ductility, providing a balanced compromise between stiffness and tolerance to deformation. The trapezoidal (TP) core achieved the highest displacement before failure, indicating superior energy absorption and suitability for impact protection or damping applications despite its lower maximum strength. Finally, the sinusoidal (SN) core presented intermediate properties, offering a practical balance between load capacity and deformability.

Overall, this work highlights the critical role of core geometry in tailoring the mechanical properties of sandwich composites. The findings provide valuable guidance for selecting core designs in lightweight structural components where specific performance trade-offs between stiffness, strength, and ductility are required. In addition, finite element modelling conducted in ABAQUS provided comparative simulations that closely matched the experimental results, validating the mechanical behavior of the sandwich structures and supporting the robustness of the proposed design approach.

ACKNOWLEDGEMENTS

Z. Wang gratefully acknowledges the financial support from the China Scholarship Council (CSC).

REFERENCES

[1] V. Birman and G. A. Kardomateas, “Review of current trends in research and applications of sandwich structures,” *Composites Part B: Engineering*, vol. 142, pp. 221–240, Jun. 2018, doi: 10.1016/j.compositesb.2018.01.027.

[2] J. M. Chacón, M. A. Caminero, E. García-Plaza, and P. J. Núñez, “Additive manufacturing of PLA structures using fused deposition modelling: Effect of process parameters on mechanical properties and their optimal selection,” *Materials & Design*, vol. 124, pp. 143–157, Jun. 2017, doi: 10.1016/j.matdes.2017.03.065.

[3] A. J. R. Lasprilla, G. A. R. Martinez, B. H. Lunelli, A. L. Jardini, and R. M. Filho, “Poly-lactic acid synthesis for application in biomedical devices — A review,” *Biotechnology Advances*, vol. 30, no. 1, pp. 321–328, Jan. 2012, doi: 10.1016/j.biotechadv.2011.06.019.

[4] D30 Committee, *Test Method for Core Shear Properties of Sandwich Constructions by Beam Flexure*. doi: 10.1520/C0393_C0393M-11.

Bending Behavior of 3D Printing Bio-sourced PLA/flax Composite Sandwich with Different Core Geometries

Z. Wang[1], D. Scida[2], M. Assarar[2], P-A. Adragna[1] and X-L Gong[1]

[1] Lasmis, University of technology of Troyes, France

[2] ITheMM, University of Reims Champagne-Ardenne, France

This study investigates the bending behaviour of bio-sourced PLA/Flax composite sandwich structures manufactured by 3D printing. To ensure a fair comparison, four core geometries – sinusoidal (SN), triangular (TR), double triangular (DT), and trapezoidal (TP) were designed with identical mass. A continuous extrusion printing technique, optimized from conventional FDM, enabled uninterrupted material deposition and high-quality fabrication. Five samples of each geometry were produced and tested under 3-point bending according to ASTM C393. The experimental results revealed that core geometry strongly affects mechanical performance. Among all configurations, the double triangular structure achieved the highest stiffness and maximum load capacity. These findings provide valuable insights for selecting and optimizing core designs in lightweight sandwich structures where both mechanical efficiency and sustainability are essential considerations.

Materials and Experiments

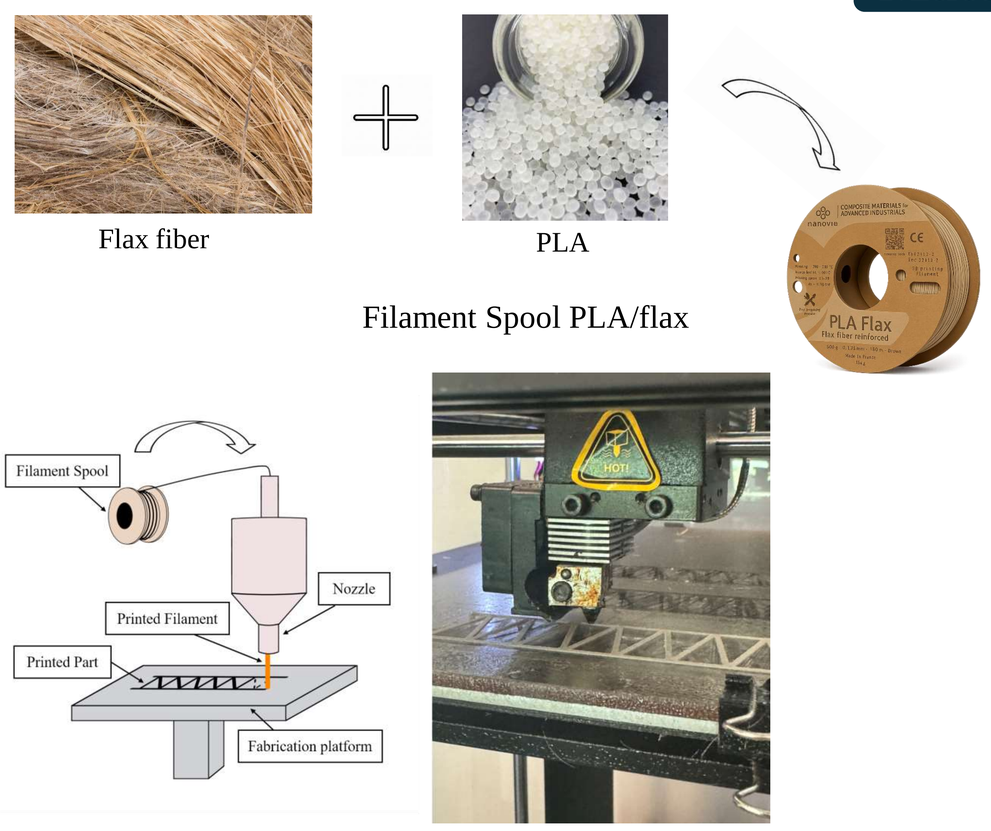

Figure 1. The 3D printing setup: schematic diagram

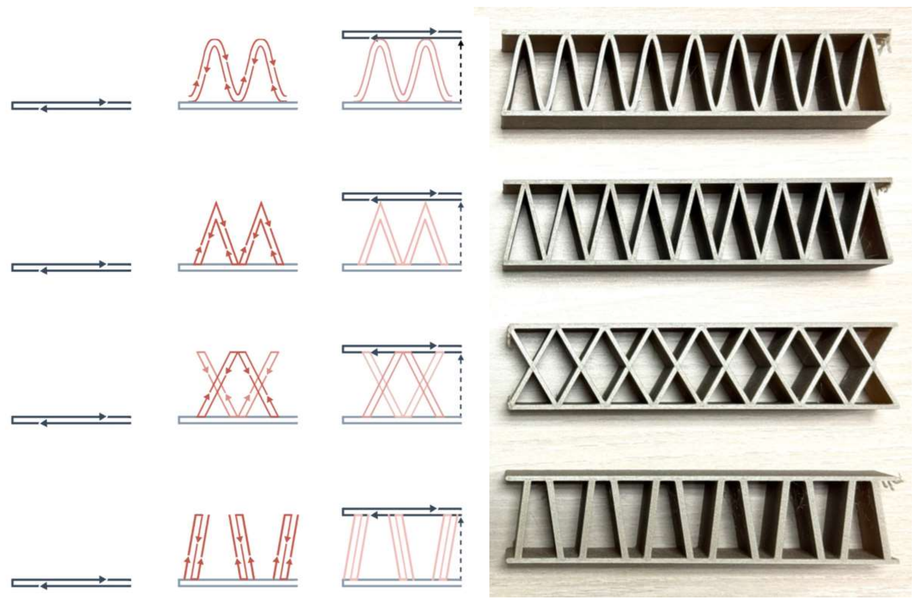

Figure 2. The illustration of the steps regenerated by the MATLAB code for the four core geometries (left) and the image of samples printed by continuous extrusion printing (right)

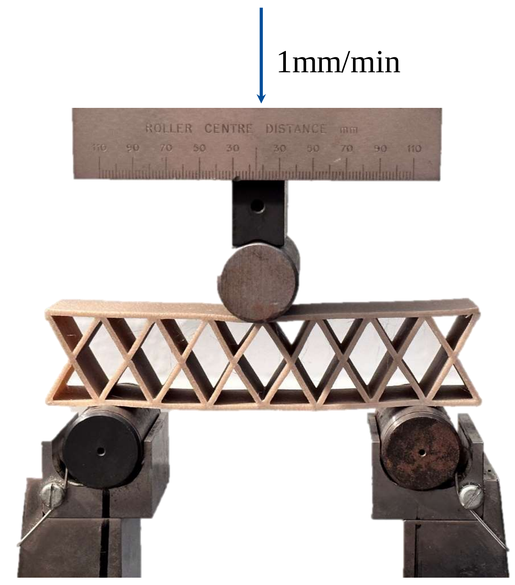

Figure 3. Experimental setup for the 3-point bending tests on the composite structure

Results

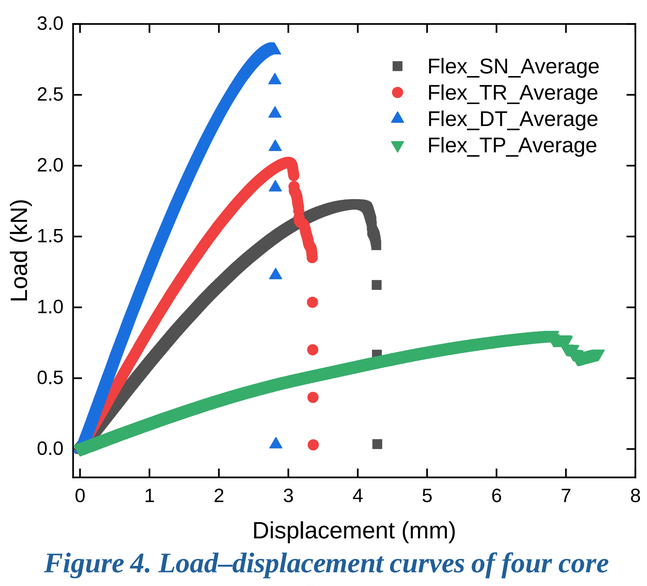

Figure 4. Load–displacement curves of four core geometries under 3-points-bending tests

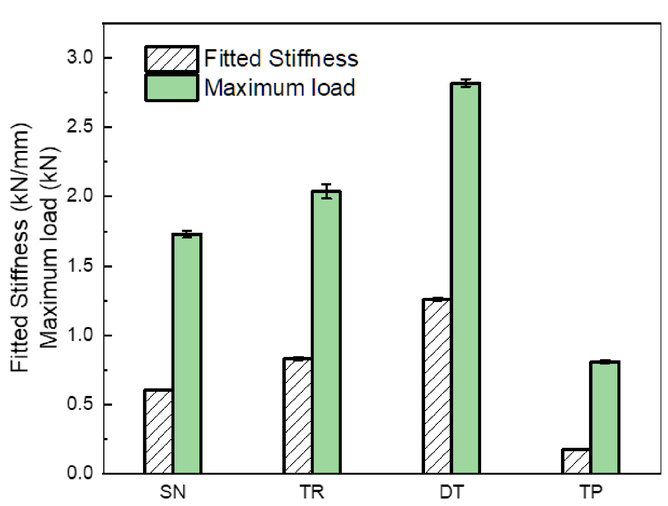

Figure 5. Fitted stiffness (kN/mm) and maximum load (kN) of four different patterns with error bar

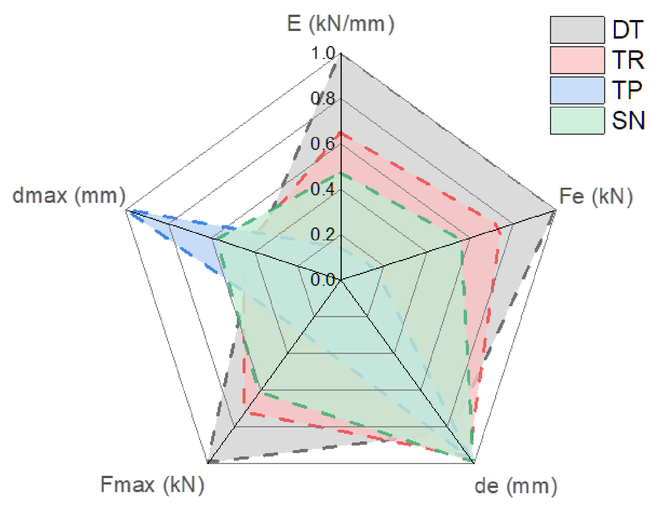

Figure 6. Radar of mechanical performance of four core geometries under 3-point bending tests

SN Configuration
- **Intermediate stiffness and ductility**
- **Suitable for applications requiring balanced performance**

TR Configuration
- **Slightly greater ductility**
- **Balanced compromise between rigidity and deformability**

DT Configuration
- **Highest stiffness and load capacity**
- **Minimal elongation before failure**
- **Suitable for high-load applications with limited deformation**

TP Configuration
- **Lowest stiffness and load capacity**
- **Greatest displacement before failure**

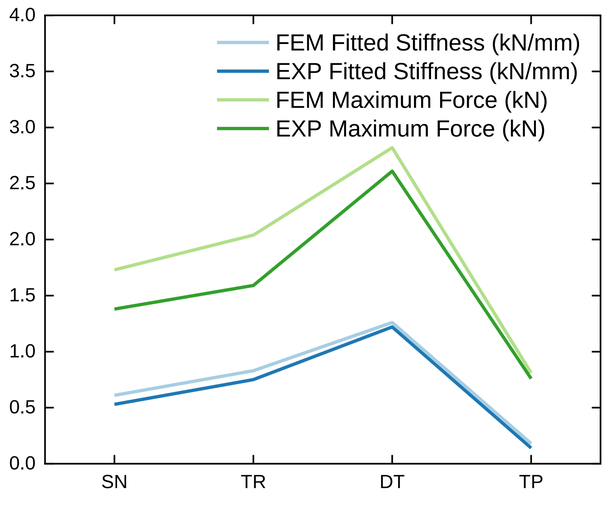

Figure 7. Comparison of FEM and EXP for Maximum Force and Fitted Stiffness with four different patterns

Finite Element Simulation Validation

- **Numerical model accurately reproduced load-displacement curves**
- **Simulations validated by comparison with experimental data**

Perspectives

- Analysis of acoustic emission signals and microscopic observations to identify the damage mechanisms.
- Study of ageing, as it is particularly relevant for natural fiber composites.

Shear Thickening Fluid & Thermoplastic Matrix Composite Bulletproof Vests

M. J. A. Malheiro*, J.P. Nunes

IPC - Instituto de Polímeros e Compósitos, Universidade do Minho, Campus de Azurém, 4800-058 Guimarães,Portugal / *e-mail: mmalheiro@dep.uminho.pt

1. Introduction

In this study, composites incorporating two different matrices - UHMWPE GUR® 5113 and a urethane-based Shear Thickening Fluid (STF) DIC701N - were evaluated using impact tests at both low and high velocities. Two types of aramid fiber fabrics, Twaron® CT 608 and PT 900, were used in the composites under investigation. Test samples with 1 to 6 discrete fabric layers were prepared by compression molding and spread coating, respectively. In the compression molding method, samples were directly fabricated with the specified number of layers. In the spread coating method, the fabric was coated, then cut and stacked to obtain the desired number of layers. Preliminary low-velocity impact tests were first conducted using a CEAST Fractovis Plus drop impact tester, at an impact velocity of 4.429 m/s and an energy of 245.6 J, to provide an initial assessment of the composites' response. Subsequently, high-speed impact tests were performed in a custom laboratory setup employing a 5.5 mm caliber slug projectile, with a length of 11.8 mm and a mass of 2.74 g, fired via a compressed air system in accordance with the MIL-STD-662 F standard.

2. Materials

Reinforcements

Twaron® CT608 (Teijin)



- Plain weaves
- **Areal density – 123 g/m²**
- Yarn properties:
  - Strength at break – 148 N
  - Chord modulus – 100 GPa
  - Strain at break – 3.5 %

Twaron® PT900 (Teijin)



- Satin and plain weaves
- **Areal density – 204,6 g/m²**
- Yarn properties:
  - Strength at break – 225 N
  - Chord modulus – 89GPa
  - Strain at break – 3.45 %

Matrices

UHMWPE



GUR® 5113 (Celanese)

- Injection moulding grade
- Average molecular weigth – 3.7E6 g/mol
- Tensile modulus – 750 - 800 MPa
- Tensile stress at yield ≥ 17 MPa
- Strain at break – 430 %

Dilatant compound DIC701N (Polianswer)

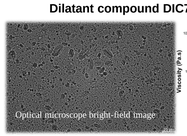

- STF (70 %) + Ethanol (30%)
- STF based on urethane chemical structure
- Liquid phase - unpolymerized urethane monomer
- Solid phase – polymerized particules



3. Preparation of Composites

Two types of composite laminates and STF-coated fabrics were produced using the Twaron® CT 608 and PT 900 aramid fabrics. The add-on weight percentage, $x(\%)$, was calculated for each sample as: $x(\%) = \frac{PF-NF}{NF} \times 100$, where PF is the weight of laminate or coated fabric, and NF is the weight of the neat fabric.

Composite Laminates (CL)

Composite laminates (CLs) were fabricated in two stages using a 500 kN Moore press. In both stages, the materials were preheated for 4 minutes at 260 °C, compressed for another 4 minutes, and demolded at 130 °C following water cooling. In the first stage, UHMWPE granules were pressed at 6.25 MPa to form thin films, which were subsequently cut into squares. In the second stage, 1 to 6 layers of aramid fabric were interleaved with the film squares and compressed at 13.62 MPa to produce the final laminates.

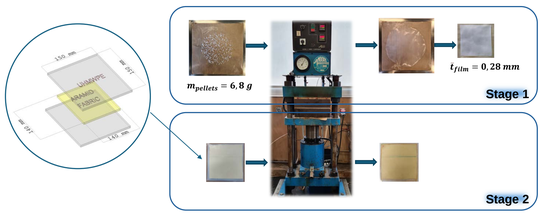

STF-Coated Fabrics (STFCF)

STF-coated fabrics (STFCFs) were prepared using the knife-over-air spread coating technique. The dilatant fluid was diluted to reduce its viscosity and facilitate proper application. To ensure coating on both sides, the fabric was flipped and the process repeated.

Fabric Spread Coating (Industrial Process Schematic)

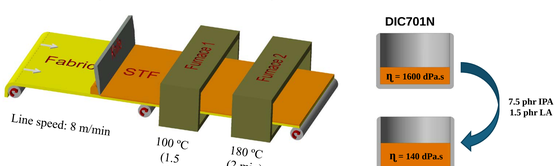

DIC701N

4. Low-velocity drop weight impact testing

Low-velocity impact tests were performed on neat fabrics (NFs), STF-coated fabrics (STFCFs), and composite laminates (CLs) using a CEAST Fractovis Plus drop-weight tester, following the ISO 6603-2 standard. Samples (140 × 140 mm) were clamped between circular jaws, with teeth machined on the upper jaw and matching grooves on the lower jaw, to provide interlocking fixation during testing. For each material type, two configurations were tested: samples composed of a single fabric layer and samples composed of four fabric layers.



Low-velocity drop weight impact testing setup

Experimental Conditions

- Clamping force = 10 kN
- Hemispherical Impactor, Ø = 20 mm
- Impact Mass = 25.044 kg
- Drop Height = 1000 mm
- Impact Velocity = 4.429 m/s

Due to the different areal densities of the samples, the energy absorbed by the STFCFs and CLs was normalized with respect to their areal density, using the equation $E_n = \frac{E_a}{(1+x\%/100)}$, where E_n is the normalized absorbed energy (J), E_a is the absolute absorbed energy (J), and $x\%$ is the add-on percentage.

Results

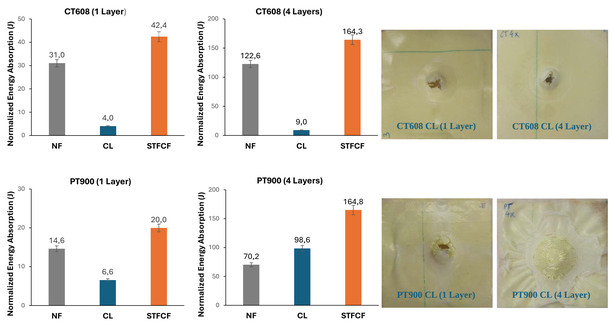

- STF-based composites exhibited improved impact resistance compared to neat aramid fabrics. This enhancement is likely attributed to the shear thickening effect, which restricts fiber mobility and promotes stress transfer, thereby increasing the area involved in energy absorption.
- For CT 608, using UHMWPE as the matrix, reduced both absolute and normalized absorbed energy, likely due to excessive fiber impregnation leading to quasi-brittle failure. For PT 900, UHMWPE increased absorbed energy, but normalized gains were significant only with four fabric layers. This is presumably due to partial impregnation, which enables additional energy absorption mechanisms (e.g., matrix/fabric debonding, yarn stretching, and delamination).

5. High-velocity impact (Ballistic testing)

Ballistic tests were performed on neat fabrics (NFs), STF-coated fabrics (STFCFs), and composite laminates (CLs) using a setup developed in our lab. A 5.5 mm caliber, 2.73 g ELR slug projectile was fired using a compressed air system, in accordance with the MIL-STD-662F standard. Samples (140 × 140 mm), consisting of one to six fabric layers, were clamped in a target-retaining frame featuring a 100 × 100 mm window. The frame included teeth machined into the upper part that fit into grooves in the lower part, preventing sample slippage. Each sample was secured using 12 screws.

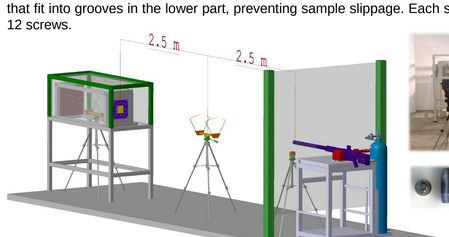



5.5 mm caliber ELR Slug

Impact velocities:

CT608 (4 layers)
V_{50} = 204,73 m/s
$V_{100} = V_{50} + 3\sigma$ = 210,3 m/s

PT900 (3 Layers)
V_{50} = 217,3 m/s
$V_{100} = V_{50} + 3\sigma$ = 220,9 m/s

Results

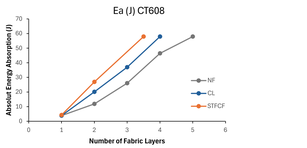

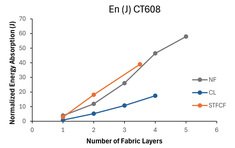

3 of 4 STFCF samples not perforated

- Ballistic Limit (3 layers STFCF) ≈ Impact Velocity
- 20% - 40% reduction in aramid fabric

- CL shows sharp drop in deformation from 3 to 4 layers → Ballistic Limit for 3 layers is near the Impact Velocity

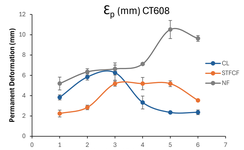

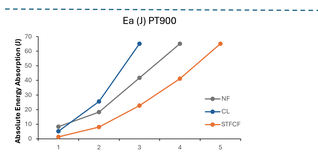

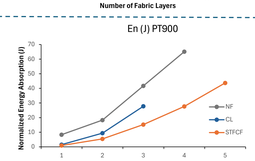

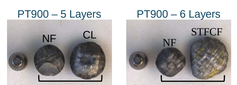

Projectile before (a) and after (b) impact
Non-perforated samples

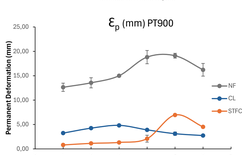

6. Conclusions

- ✓ Fabric impregnation by UHMWPE matrices plays a key role in low-velocity impact, where excessive impregnation leads to a reduced energy absorption. This effect was not observed under high-velocity impact, except when a single fabric layer was tested.
- ✓ Under high-velocity impact, excessive STF impregnation reduces fabric performance, likely due to a pronounced thickening effect that excessively limits fiber deformation, leading to premature fiber rupture. Shear rates are highest at impact point and decrease through the thickness, diminishing the thickening effect in deeper layers. This gradient allows greater energy dissipation, making STF-impregnated fabrics potentially more effective in the back layers by reducing back-face deformation.

7. References

- J. G. Carrillo, R. A. Gamboa, E. A. Flores-Johnson, and P. I. Gonzalez-Chi, "Ballistic performance of thermoplastic composite laminates made from aramid woven fabric and polypropylene matrix," *Polym. Test.*, vol. 31, no. 4, pp. 512–519, 2012.
- Muskesh Bajya, Abhijit Majumdar, Bhupendra Singh Butola, Sanjeev Kumar Verma, Debarati Bhattacharjee, "Design Strategy for optimising weight and ballistic performance of soft body armour reinforced with shear thickning fluid", Composites Part B, 2020

8. Acknowledgments

This work was funded by National Funds through FCT - Portuguese Foundation for Science and Technology, under reference UID/05256. The authors gratefully acknowledge to Endutex – Têxteis Técnicos for their support with Spread Coating technology.

NONLINEAR BEHAVIOR OF POLYMERS AND STRUCTURES PRODUCED USING ADDITIVE MANUFACTURING

Elvijs Bojārs[1], Andrey Aniskevich[2], Janis Varna[1], Liva Pupure[1]

[1]Institute of High Performance – Materials and Structures, Riga Technical University
Kipsalas street 6A, LV-1048 Riga, Latvia
Email: elvijs.bojars@rtu.lv, web page: https://www.rtu.lv/en

[2]Institute for Mechanics of Materials, University of Latvia
Jelgavas street 3 – House of Science, LV-1004 Riga, Latvia
Email: andrejs.aniskevics@lu.lv, web page: https://www.lu.lv/en/

Keywords: Polymers, Time-dependent properties, Temperature, Additive manufacturing

ABSTRACT

Fused Filament Fabrication (FFF) builds polymer structures through layer-by-layer deposition, enabling the production of fiber-reinforced composites with enhanced strength. However, due to inherent polymer behaviors such as creep, shrinkage, and aging, 3D-printed components are prone to long-term deformation. These effects are amplified by the anisotropic, composite-like nature of printed structures, where filaments are only partially bonded. This research investigates the long-term viscoelastic and viscoplastic behavior of FFF-printed polymers to improve structural reliability.

1 INTRODUCTION

Additive manufacturing of polymers and their structures has been a fast-growing research space, with more than 100,000 papers published last year, and the industry due to the significant advantages over other manufacturing methods, e.g., design freedom, significant waste and energy reduction. This method offers high flexibility with the prototyping and optimization of different shapes, thus extending the applicability of polymers. With Fused Filament Fabrication (FFF), the polymer structure is built layer-by-layer through the deposition of feedstock materials. The FFF can be used to produce fiber composite structures with increased strength, further increasing the applications of this manufacturing method.

Despite these advantages, polymers produced with the FFF method have shown significant time-dependent behavior [1]. Part of the nonlinearity can be attributed to the material behavior itself, but a large part is due to the complex internal structure. Each printed filament is only partially bonded to the neighboring filaments, thus forming long aligned fibers, a composite-like structure (Figure 1) and creating an anisotropic material. Due to the novelty of this manufacturing method, these effects have not been studied, especially with regard to different environmental and material state effects. Appropriate modeling methods and models for these 3D printed structures have not been developed.

The most widely used nonlinear viscoelastic (VE) material models have been developed by Scapery [2], [3], [4]. In [5], it was modified to include the Zapas model for viscoplasticity [6] and damage and has been successfully used to simulate different materials 1D time-dependent behavior [7], [8].

$$\varepsilon = d(\sigma_{max}) \cdot \left(\varepsilon_0 + g_1 \int_0^t \Delta S(\psi - \psi') \frac{d(g_2\sigma)}{d\tau} d\tau + \varepsilon_{VP}(\sigma, t) \right) \quad (1)$$

Where

$d(\sigma_{max})$	Effect of damage
ε_0	Elastic strain in undamaged composite
g_1, g_2	Stress dependent material properties
$\Delta S(\psi)$	Time dependent part of the viscoelastic response, transient component of the linear viscoelastic creep compliance
ψ	Reduced time
ε_{VP}	Viscoplastic strain

It has shown high adaptability, which is crucial for modeling various environmental conditions. The complexity of different structures with 3D stress states demands models and tools able to predict 3D stress states [9]. Various models have been integrated into finite element method (FEM) to simulate stress and strain behavior under monotonic and uniaxial loading conditions [10], [11]. However, a more realistic 3D nonlinear material modeling tool, able to predict nonlinear VE response, is yet to be developed. In [9], this model was adapted for the 3D case.

In the modeling of material behavior, the balance between accuracy and complexity is a key consideration. While highly detailed models may offer precise predictions, they often require extensive parameter calibration and computational resources. The simplicity of models characterized by a minimal number of parameters is advantageous, as it facilitates implementation and reduces computational overhead by eliminating the need for complex optimization procedures [12]. Such models are also easier to interpret, validate, and apply in practical scenarios, especially when data availability is limited or computational efficiency is a priority.

Within this study, we tested the material at different stages (before printing and after printing) and scales (single filament and printed structures) of manufacturing. Statistical characterization showed nonlinear behavior for all sample groups. The elastic properties showed slightly higher values for printed filament and specimens than for filament as received. Uploading time to reach the load in the creep test result in higher initial strain values and more pronounced recovery behavior, indicating time-dependent viscoelastic effects. Creep compliances obtained from creep tests showed nonlinear viscoelastic behavior already at low stress levels, further proving the need for the use of nonlinear viscoelastic material models.

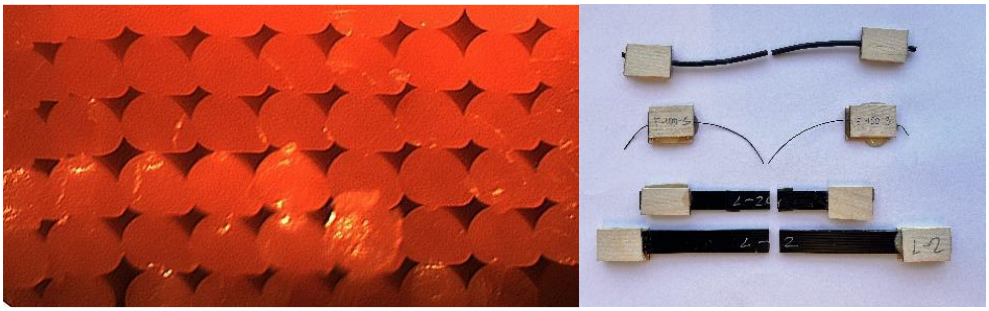

Figure 1: Cross section of the printed specimen (left) and various Specimen types (right) starting from the top Thick Filament (Y), Single extruded filament (F) and rectangular – printed (smaller) and cut-out of larger printed plate (larger ones) for both directions 0° (L) and 90° (T)

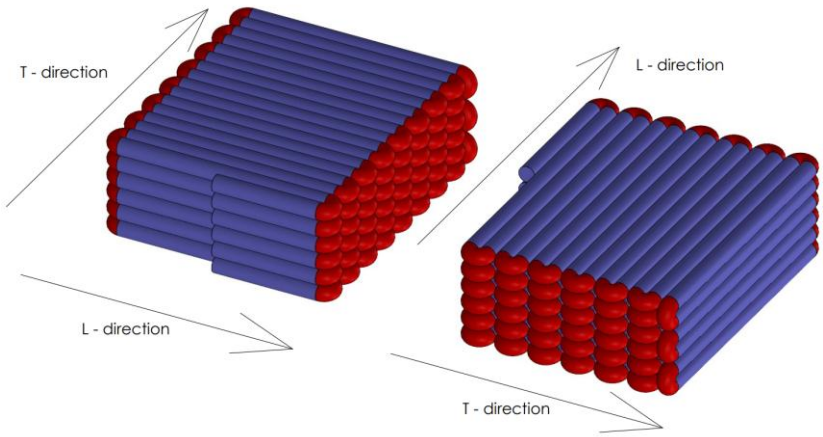

Figure 2: Printing schematic of layers

2 MATERIALS

The plastic industry is moving towards more sustainable alternatives and replacing non-renewable plastics and oil with competitive bio-based materials [13]. Within our study, we used Ultimaker Tough Black Polylactic acid (PLA), a technical PLA filament, which has been used. The PLA has a glass transition temperature of 62 °C, a melt temperature of 151 °C.

Material at three different phases of manufacturing has been used in the study (Figure 1):

a) Thick Filament as received from the manufacturer (Y);
b) Single filament printed using 3D printer (F);
c) Rectangular 3D printed specimens ($L_{printed}/T_{printed}$);
d) Cut-out of large 3D printed rectangular plate ($L_{cut\text{-}out}/T_{cut\text{-}out}$).

The specimens were manufactured using the Fused Filament Fabrication (FFF) technique, which is an additive manufacturing technique that uses a continuous filament of thermoplastic material. The filament is fed from a spool through a heated printer extruded head, which melts the material and deposits it layer by layer to build a 3D object. The print head moves in two dimensions to create each horizontal layer, and then the platform or head moves vertically to add subsequent layers (Figure 2).

Specimens were printed and kept in an enclosed environment, away from sunlight. All specimens were printed using the Ultimaker-2C-3AC2 model (Ultimaker B.V., The Netherlands). Specimens were printed using a 0.4 mm linewidth. The infill pattern was set to "Lines" with a specimen infill density of 100 %, layer thickness of 0.1 mm, printing nozzle diameter of 0.4 mm, print head speed of 20 mm/s, printing temperature of 225 °C, and a build plate temperature of 60 °C. Specimens were tested in the printed direction (0°, notation used in paper L) and perpendicular to the printing direction (90°, notation used in paper T). A schematic drawing of printing direction and notations used in paper is presented in Figure 2.

3 EXPERIMENTAL CHARACTERIZATION

Tensile tests were performed on an Instron ElectroPuls® E10000 machine equipped with a 10 kN load cell, mechanical clamps and extensometers with gauge lengths of 25 mm (for smaller ones - printed) and 50 mm (for larger ones – cut-out), see Figure 1, used according to specimen length (Dynamic extensometer Instron 2620-601). Quasi-static tensile tests for all rectangular specimens were performed in displacement mode, with the machine`s cross-head speed 1 mm/min (~0.75%/min). Before the tensile test until failure, elastic modulus was measured, by loading and unloading to 0.35% strain (see Figure 3). Tensile elastic modulus was calculated from stress-strain curves by linear fit of experimental data points in strain region 0.05-0.25%. Elastic modulus was calculated from the unloading step 2 part of the curve to reduce effects of loading, damage and developing nonlinear properties.

Tensile tests for single filament and thick filament specimens were performed on ElectroPuls® E10000 machine equipped with a 3 kN load cell, mechanical clamps in displacement-controlled mode with the cross-head speed 0.5 mm/min, (~ 0.75%/min). Since the extensometer cannot be attached to the filament specimens, strain was obtained from machines crosshead movement and machines compliance was calculated and taken into account (as described in the ASTM standard [14]).

Tensile tests were also conducted at a significantly lower displacement rate of 0.01 mm/min to evaluate the influence of loading rate on the material response.

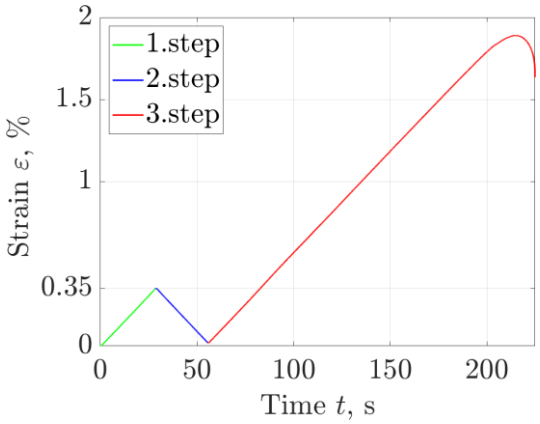

Figure 3: Loading procedure for tensile tests

A specially designed creep recovery test was performed on an Instron ElectroPuls® E10000 machine equipped with a 10 kN load cell, mechanical clamps and a dynamic extensometer Instron 2620- 601 with a gauge length 25 mm for shorter (printed) specimens and 50 mm for longer (cut-out) specimens. Initial tests were performed without an environmental chamber. One specimen per series was tested for the short-term creep test. The short-term creep test was performed in multiple steps in a load control mode with creep periods of 10, 20, 30, and 60 min (total 120 min), followed by 10 times longer recovery period (i.e., 100, 200, 300, and 600 min, respectively). Due to the limitations of the machine, the load during recovery was kept at 3 N, which corresponds to less than 2% of the creep stress level. Loading and unloading for the creep test were done with a loading rate of 100 N/s. Depending on the stress level or the magnitude of applied load, the duration of the uploading and unloading phases could extend to 10-13 s for the strongest specimens. A schematic drawing of the loading ramp and resulting strain response can be seen in Figure 4.

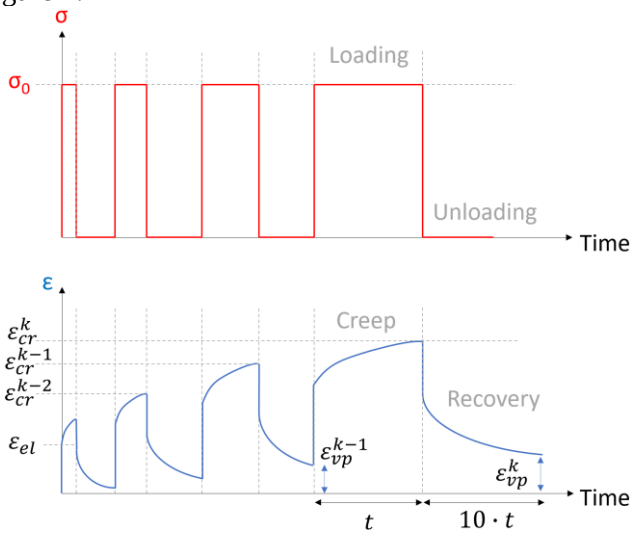

Figure 4: Schematic of the creep test methodology, the representation of the creep loading steps for one stress level

Six stress levels were tested using this methodology. In order to reduce scatter due to experimental data, we used a single-specimen methodology, described in [15]. It is worth mentioning that during the entire testing procedure, the specimen was not removed from the machine, in order to avoid introducing errors due to alignment and tests are performed in increasing order of the applied stress to minimize the influence of damage on results. The strain at the end of each recovery period was assumed purely viscoplastic (VP).

4 MATERIAL MODELS

Within this study, the main focus has been on VP modeling. We have used the Zapas and Crissman model [6] where VP strain growth during loading with specified time dependence of the applied stress is given by

$$\varepsilon_{VP}(\sigma,t) = C_{VP}\left\{\int_0^{t/t^*}\left(\frac{\sigma(\tau)}{\sigma^*}\right)^M d\tau\right\}^m \tag{2}$$

Where C_{VP} , M and m are constants to be determined experimentally, t/t^* is a normalized time where t^* is an arbitrarily chosen characteristic time constant [15]. We have used a single-specimen methodology described in [15]. Due to the previous loading history, the parameter identification is more complex than using a different specimen for each stress level. At the *k*-th stress level $n_k\sigma_0$, $(n_1 = 1)$ assuming that all previous creep tests at lower stress levels have the same total duration time Δt_0, VP strain is obtained as follows:

$$\varepsilon_{VP}(n_k,t) = C_{VP}\cdot\sigma_0^{mM}\cdot\left(\frac{\Delta t_0}{t*} + n_2^M\frac{\Delta t_0}{t*} + n_3^M\frac{\Delta t_0}{t*} + \ldots + n_k^M\cdot\frac{t-(k-1)\Delta t_0}{t^*}\right)^m \tag{3}$$

Since t^* is an arbitrarily chosen constant and the duration of all creep tests at lower stress levels is the same and t^* is taken equal to Δt_0, thus eq. (3) can be written:

$$\varepsilon_{VP}(n_k,t) = C_{VP}\cdot\sigma_0^{mM}\cdot\left(1 + n_2^M + n_3^M + \ldots + n_k^M\cdot\frac{t-(k-1)\Delta t_0}{t^*}\right)^m \tag{4}$$

In the "single specimen methodology," data obtained from one specimen at different stress levels are analysed. Eq. (5) applied for a sequence of stress levels renders the following relationships in *ln-ln* axes:

$$\ln\left(\varepsilon_{VP}(n_1,t)\right) = \ln({C_{VP}{\sigma_0}^{mM}}) + m\ln\left(\frac{t}{t^*}\right), \qquad \sigma = \sigma_0, \qquad t\in[0,\Delta t_0]$$

$$\ln\left(\varepsilon_{VP}(n_2,t)\right) = \ln({C_{VP}{\sigma_0}^{mM}}) + m\ln\left(1 + n_2^M\cdot\frac{t-\Delta t_0}{t^*}\right), \qquad \sigma = n_2\sigma_0, \qquad t\in[\Delta t_0, 2\Delta t_0]$$

$$\ln\left(\varepsilon_{VP}(n_k,t)\right) = \ln({C_{VP}{\sigma_0}^{mM}}) + m\ln\left(1 + n_2^M + n_3^M + \cdots + n_k^M\cdot\frac{t-(k-1)\Delta t_0}{t^*}\right), \tag{5}$$

$$\sigma = n_k\sigma_0, \quad t\in[(k-1)\Delta t_0; k\Delta t_0]$$

According to (5), the experimental relationship between VP strain and time has to be linear for each stress level, provided M is selected correctly. Hence, the first step in the procedure is to estimate M by varying it until the experimental data points in the *ln-ln* axes show a linear relationship. Obviously, the result of the M value is a compromise between the different "best" values for different stress levels. Afterwards, the first approximation of parameters m and C_{VP} can be found. These parameters have to be further adjusted, realizing that m has to be the same for all stress levels. Since for low stresses VP strains are small and the measurement accuracy is limited, weight factors have to be introduced, giving higher significance to accurate data fitting at higher stresses.

5 RESULTS AND DISCUSSIONS

5.1 Tensile tests

The experimental results of the macroscale rectangular specimen tensile test are presented in Figure 5 and Table 1.

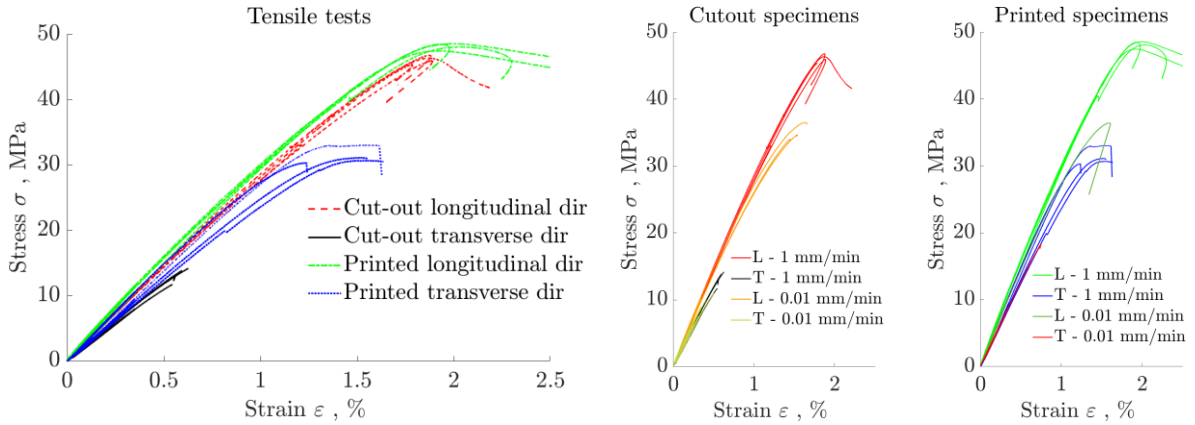

Figure 5: Tensile test results of rectangular specimens

Spec.	Rate [mm/min]	E_{mean} [MPa]	σ_{fail} [MPa]	ε_{fail} [%]
$L_{printed}$	1	3165±12	48.2	1.966
$L_{printed}$	0.01	2987±24	36.5	1.591
$T_{printed}$	1	2751±11	31.3	1.454
$T_{printed}$	0.01	2570±24	18.3	0.746
$L_{cut-out}$	1	2959±10	46.1	1.853
$L_{cut-out}$	0.01	2921±19	35.1	1.538
$T_{cut-out}$	1	2420±5	13.2	0.581
$T_{cut-out}$	0.01	2437±16	10.4	0.447

Table 1: Tensile test results of rectangular specimens

The results showed significant anisotropic behavior of 3D printed material. This was expected since the inner structure showed anisotropic filling of material (see Figure 1 and Figure 5).

Compared to cut-out specimensm printed specimens exhibit higher values in elastic modulus, as well as greater failure stresses and strains.

The properties in longitudinal direction do not differ significantly, however, in the transverse direction, specimens cut out of the printed plate show drastic differences in properties. This shows that specimens in the transverse direction are more sensitive to the printing direction.

When comparing test speeds of 1 mm/min and 0.01 mm/min, it is observed that almost all specimens tested at slower rate (0.01 mm/min) exhibit lower elastic modulus, failure stress, and failure strain, indicating a pronounced rate-dependent viscoelastic behavior [16].

We believe that changes in properties is due to the edges, where the material tends to join together, thus presenting a more longitudinal specimen.

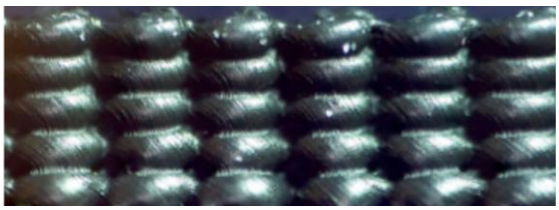

Figure 6: Typical side face of printed specimen [16]

The edge features of the printed specimen result from continuous pathing of the extrusion-based printing process. To initiate new lines, the print head redirects at the boundaries, forming rounded transitions. These curved edge paths, visible in the cylindrical structure (see red parts in Figure 2 and Figure 6), reflect directional changes necessary for consistent layer deposition.

Figure 7 and Table 2 show tensile test results of the thick filament as received from the manufacturer before printing, and 3D printed single filament specimens.

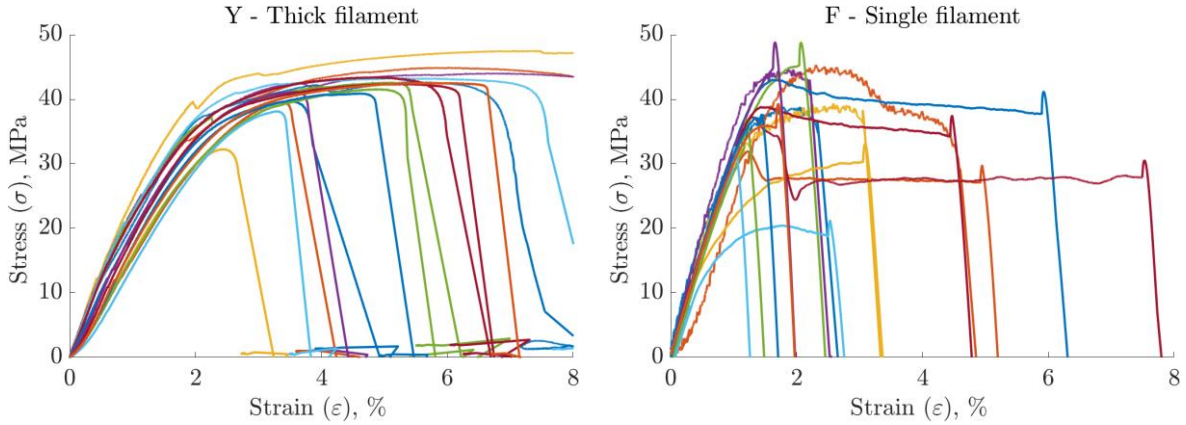

Figure 7: Tensile tests of thick filaments (left, Y) and single filaments (right, F)

A comparison between single filaments and thick filaments is presented in Table 2, as shown below. The single filament shows higher elastic modulus than thick filament, indicating that the properties were altered due to the printing process, which significantly influenced the mechanical behavior of the printed specimens. Similar trends can be seen also with printed specimens in L direction, where modulus is larger than the thick filaments values.

Spec.	E_{mean} [MPa]	σ_{fail} [MPa]	ε_{fail} [%]
Y-thick	2546±36	41.7	4.41
F-single	3547±296	38.8	1.79

Table 2: Tensile test results of single and thick filament specimens

5.2 Creep test results

The used stress levels for creep were 10, 15, 20, 24, 28, and 32 MPa and the obtained VP strains are presented in Table 3 for cut-out specimen.

Stress, MPa	Time, min	Time t/120	VP strain, %					
			10	15	20	24	28	32
ε_0	0	0	0.000	0.005	0.007	0.021	0.044	0.093
ε_{pl1}	10	0.083	0.000	0.003	0.006	0.026	0.054	0.113
ε_{pl2}	30	0.25	0.001	0.003	0.011	0.034	0.062	0.135
ε_{pl3}	60	0.5	0.004	0.005	0.015	0.039	0.074	0.169
ε_{pl4}	120	1	0.005	0.007	0.021	0.044	0.093	0.258

Table 3: Summary of all VP strain

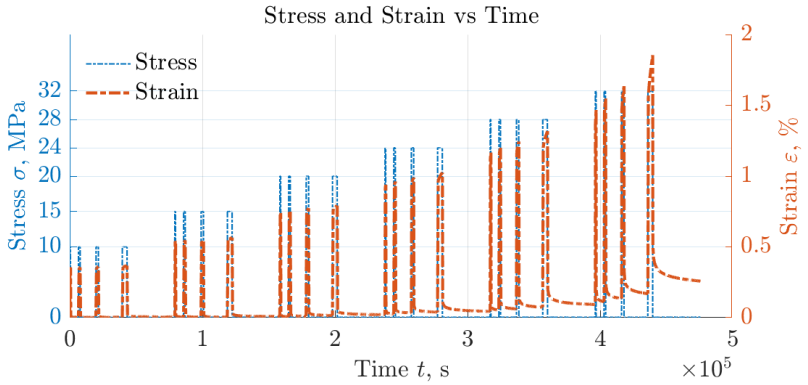

Figure 8: Strain development over time during creep tests at different stress levels

Curve fitting parameters has been calculated or chosen according to the Zapas and Crissman model, which has been explained in Section 4 . The obtained values are M = 7.0 and m = 0.54. The fitting of the parameter M can be seen in Figure 9. The obtained coefficients fit the experimental data at higher stress levels. At lower stress levels the experimental data are more scattered and the fit is poor. This trend is consistent with our previous tests, where values at lower stress levels do not fit the overall trend. This can be explained by the low strain values, that are close to the measuring device precision and different environmental effects on strains are higher than pure VP effects. In addition, in the initial stages of loading, the material is still aligning and thus can alter its behaviors after the initial loading steps.

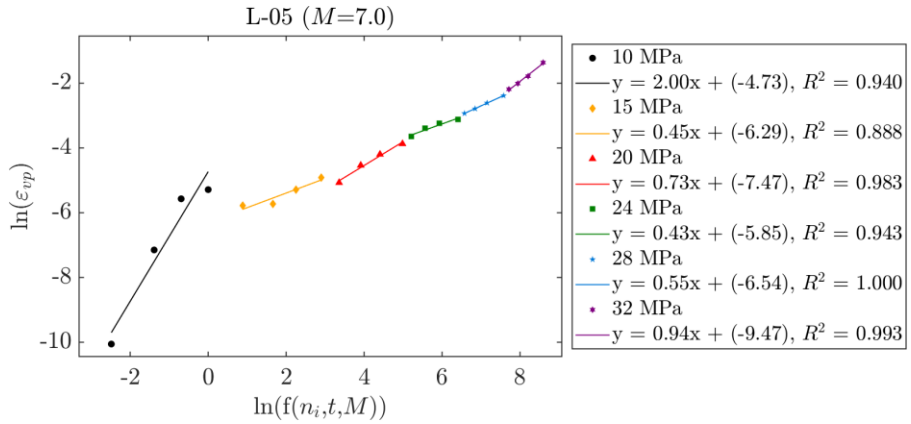

Figure 9: VP strain development

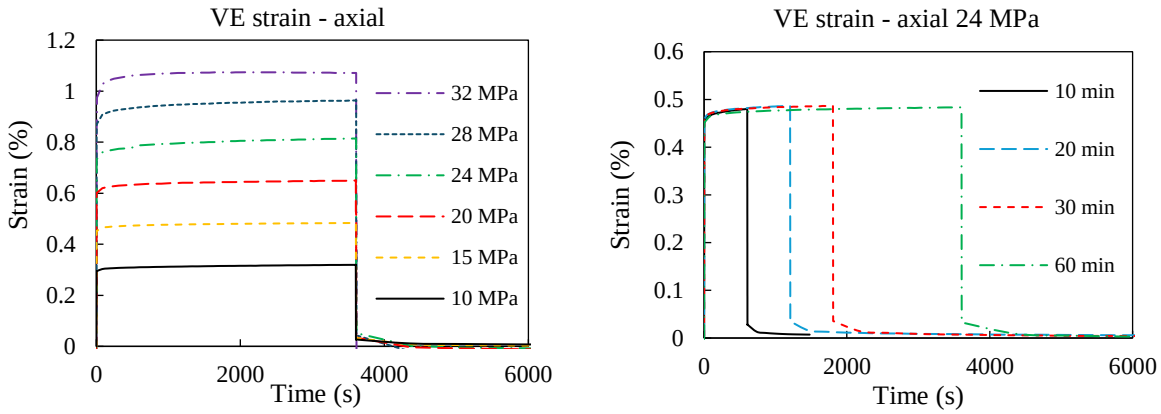

Figure 10: Creep recovery strain for all stress levels (left) and for 24 MPa (right)

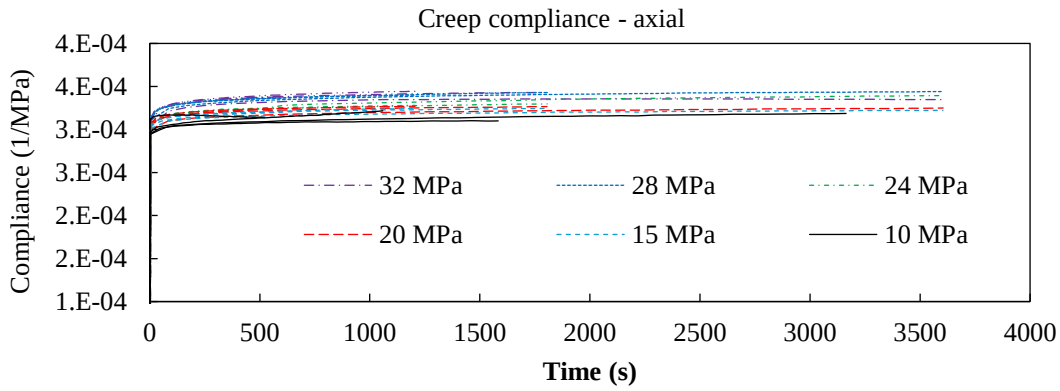

Figure 11: Creep compliance for all stress levels

After obtaining the values, the VP part of the curves was removed from the total strain. The obtained VE strain is presented in Figure 10. The right side of Figure 10 also shows the VE strain at all time steps for 24 MPa stress. It can be seen that the curves overlap. This can be expected, since the VE is reversible and after recovery should follow the same path as before. This indicates that the VP strain has been removed properly.

Figure 11 shows creep compliances at different stress levels. From these curves we can see nonlinear viscoelastic behavior even at low stress levels. This nonlinearity can be further increased by change in environmental effects. We noticed that a slight change in the room environment due to the changing seasons (change in temperature, humidity) significantly altered the behavior of the strain. Thus, in future studies a more controlled environment will be used to study long-term behavior of this material. The effect of temperature and humidity conditions, as well as nonlinear characterization of micro and macro scales of polymer used in 3D printing will be analyzed. In addition, the development of a robust material model for finite element analysis (FEA) is a key objective, aimed at enabling the simulation of more complex geometries. The initial phase will involve validating the material model using simple specimen geometries. Once validated, the model will be applied to more intricate shapes to investigate how various manufacturing parameters affect the nonlinear mechanical properties of 3D-printed polymers. This approach will support the advancement of predictive modeling tools for additive manufacturing applications.

Moreover, the future goal of this study will be implementing the constitutive model into FEM program like ANSYS, to simulate more complex geometries and see if the simulations have good agreement with tested specimens. Although for one-dimensional cases this has already been done on PLA specimens using ABAQUS UMAT subroutine [17].

6 CONCLUSIONS

The initial tests have shown that their printed plates have distinctly anisotropic properties. The printed specimens showed smaller deviation between directions, while specimens that were cut out of a larger 3D printed plate showed significant differences in material properties. This can be expected, since the edges of the printed specimen are more infilled, adding reinforcement in the loading direction. This is in contrary to the specimens, which were cut out of the larger 3D printed plate, where polymer is held together only by the small joint region between individual polymer filaments.

When different scales of the polymer were analyzed, it was observed that the single filament, as well as printed plates, showed slightly higher elastic modulus than the filament as received. This might indicate that the molecules have been slightly aligned within the polymer in the printing direction, creating a slight anisotropy within the material.

Initial creep tests showed that material viscoplasticity can be characterized by the Zapas model. This can also be seen from pure viscoelastic curves, where after removing the viscoplasticity, all curves coincide, showing that the reversible viscoelasticity has been recovered. The creep compliance showed nonlinear viscoelastic behavior already at relatively low stress levels of 10 MPa. Thus, nonlinear viscoelastic models have to be used to characterize these materials.

It was also noticed that the material is very sensitive to environmental conditions – a small change in outside temperature significantly affected the behavior of the polymer. Moving forward, materials have to be tested in very controlled environments, removing any changes in the strains due to the environmental changes.

ACKNOWLEDGEMENTS

Experimental data have been analyzed within the project LZP-2023/1-0075: Multiscale time-dependent mechanical properties of 3D printed polymer structures - TiMe3D funded by the Latvian Council of Science.

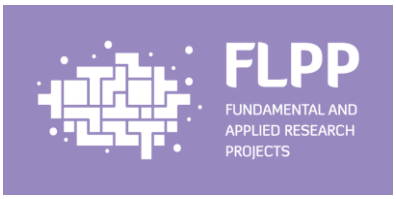

REFERENCES

[1] S. R. Rajpurohit and H. K. Dave, Analysis of tensile strength of a fused filament fabricated PLA part using an open-source 3D printer, *The International Journal of Advanced Manufacturing Technology*, **101**, No. 5–8, 2019, pp. 1525–1536, (doi: 10.1007/s00170-018-3047-x).

[2] Y. C. Lou and R. A. Schapery, Viscoelastic Characterization of a Nonlinear Fiber-Reinforced Plastic, *J Compos Mater*, **5**, No. 2, 1971, pp. 208–234, (doi: 10.1177/002199837100500206).

[3] R. A. Schapery, Nonlinear Viscoelastic and Viscoplastic Constitutive Equations Based on Thermodynamics, *Mech Time Depend Mater*, **1**, No. 2, 1997, pp. 209–240, (doi: 10.1023/A:1009767812821).

[4] R. A. Schapery, On the characterization of nonlinear viscoelastic materials, *Polym Eng Sci*, **9**, No. 4, 1969, pp. 295–310, (doi: 10.1002/pen.760090410).

[5] E. Marklund, J. Eitzenberger, and J. Varna, Nonlinear viscoelastic viscoplastic material model including stiffness degradation for hemp/lignin composites, *Compos Sci Technol*, **68**, No. 9, 2008, pp. 2156–2162, (doi: 10.1016/j.compscitech.2008.03.011).

[6] L. J. Zapas and J. M. Crissman, Creep and recovery behaviour of ultra-high molecular weight polyethylene in the region of small uniaxial deformations, *Polymer (Guildf)*, **25**, No. 1, 1984, pp. 57–62, (doi: 10.1016/0032-3861(84)90267-2).

[7] L. Pupure, J. Varna, and R. Joffe, Methodology for macro-modeling of bio-based composites with inelastic constituents, *Compos Sci Technol*, **163**, 2018, pp. 41–48, (doi: 10.1016/j.compscitech.2018.05.015).

[8] L.-O. Nordin and J. Varna, Nonlinear viscoelastic behavior of paper fiber composites, *Compos Sci Technol*, **65**, No. 10, 2005, pp. 1609–1625, (doi: 10.1016/j.compscitech.2005.02.007).

[9] J. Varna and L. Pupure, Effect of Material State and Temperature on Nonlinear Viscoelastic Response: 3D Constitutive Model and Incremental Formulation for Numerical Analysis, *Mechanics of Composite Materials*, **59**, No. 2, 2023, pp. 193–218, (doi: 10.1007/s11029-023-10092-z).

[10] Y. Chen and L. V. Smith, A nonlinear viscoelastic–viscoplastic constitutive model for adhesives under creep, *Mech Time Depend Mater*, **26**, No. 3, 2022, pp. 663–681, (doi: 10.1007/s11043-021-09506-z).

[11] Y. Chen and L. V. Smith, A nonlinear viscoelastic–viscoplastic model for adhesives, *Mech Time Depend Mater*, **25**, No. 4, 2021, pp. 565–579, (doi: 10.1007/s11043-020-09460-2).

[12] Á. D. Virág and K. Molnár, Modelling the time-dependent mechanical properties of thermoplastic and thermosetting polymers with Gumbel distribution functions, *Polymer (Guildf)*, **312**, 2024, p. 127642, (doi: 10.1016/j.polymer.2024.127642).

[13] E. Kontou, G. Spathis, and P. Georgiopoulos, Modeling of nonlinear viscoelasticity-viscoplasticity of bio-based polymer composites, *Polym Degrad Stab*, **110**, 2014, pp. 203–207, (doi: 10.1016/j.polymdegradstab.2014.09.001).

[14] ASTM D3379-75(1989)e1, D3379 Standard Test Method for Tensile Strength and Young's Modulus for High-Modulus Single-Filament Materials (Withdrawn 1998). Accessed: Jun. 25, 2025. [Online]. Available: https://store.astm.org/standards/d3379

[15] L. Pupure, J. Varna, and R. Joffe, On Viscoplasticity Characterization of Natural Fibres with High Variability, *Advanced Composites Letters*, **24**, No. 6, 2015, (doi: 10.1177/096369351502400601).

[16] O. Bulderberga, E. Zīle, R. Joffe, J. Sevcenko, and A. Aniskevich, Mechanical Characteristics of Thermoplastic Polymers for 3d Printed Hybrid Structures, *Mechanics of Composite Materials*, **60**, No. 1, 2024, pp. 17–32, (doi: 10.1007/s11029-024-10172-8).

[17] R. Hu, X. Zhang, Y. Chen, and C. Zhang, Characterization and prediction of the nonlinear creep behavior of 3D-printed polyurethane acrylate, *Addit Manuf*, **50**, 2022, p. 102583, (doi: 10.1016/j.addma.2021.102583).

ICCM24
AUGUST 4-8, 2025
BALTIMORE CONVENTION CENTER
BALTIMORE, MARYLAND, USA

No Technical Paper Submission for:

Andrejs Pupurs

ICCM24
AUGUST 4-8, 2025
BALTIMORE CONVENTION CENTER
BALTIMORE, MARYLAND, USA

No Technical Paper Submission for:

Sagar Doshi

ICCM24
AUGUST 4-8, 2025
BALTIMORE CONVENTION CENTER
BALTIMORE, MARYLAND, USA

No Technical Paper Submission for:

Samit Roy

ICCM24
AUGUST 4-8, 2025
BALTIMORE CONVENTION CENTER
BALTIMORE, MARYLAND, USA

No Technical Paper Submission for:

Faruk Soso

ICCM24
AUGUST 4-8, 2025
BALTIMORE CONVENTION CENTER
BALTIMORE, MARYLAND, USA

No Technical Paper Submission for:

John Tierney

Effective decomposition rate of epoxy resin using a modified shrinking-core model: Enhanced hydrolysis reaction by optimized solvent ratio

Jinsu Kim[1*], Jin-woo Yi[1], Sang-woo Kim[1], Jung-wan Lee[1], Jung-soo Kim[1], and Moon-kwang Um[1]

[1] Composite Research Division, Korea Institute of Materials and Science, Changwondaero 797, Seongsan-gu, Changwon, 51508, Republic of Korea
Email : jinsu@kims.re.kr

Keywords: Thermosetting polymer, Degradation, Decomposition, Modeling, hydrolysis reaction,

ABSTRACT

Due to their cross-linked structure and stable polymer framework, epoxy resins are difficult to degrade or remelt, leading to significant environmental issues. In this study, the effective degradation rate of cured epoxy resin was investigated using hydrolysis and glycolysis reactions. Before degradation, the ratio of hydrolysis and glycolysis solvents, in which phase separation does not occur, was studied. Various solvent ratios were applied to the cured epoxy resin, and the degradation amount and rate were observed. Based on the experimental results, the effective decomposition rate of epoxy resin was determined using a modified shrinking-core model. The results were then compared with newly obtained experimental results, validating the model.

1 Introduction

Thermoset plastics are widely utilized in high-performance applications due to their excellent mechanical strength and chemical resistance, which are attributed to their cross-linked network structures. However, this same structural stability poses significant challenges for recycling and environmental sustainability. Unlike thermoplastics, thermosets cannot be remelted or reshaped after curing, making their end-of-life disposal difficult and often reliant on landfilling or incineration. To address this issue, various recycling strategies have been proposed, including mechanical grinding, pyrolysis, and chemical degradation. Among these, chemical recycling via controlled degradation has emerged as a promising approach, especially for thermoset resins containing degradable functional groups such as esters or anhydrides. When such polymers are exposed to water or nucleophilic agents, hydrolytic degradation can occur through cleavage of the labile bonds, resulting in molecular breakdown and partial solubilization [1], [2].

Chemical degradation methods, especially hydrolysis under alkaline conditions, have emerged as promising routes to address this challenge. Previous studies reported significant success using sodium hydroxide (NaOH) for effective hydrolysis of epoxy resins. Recently, glycolysis methods, employing diols like 1,4-butanediol (BDO), have shown potential due to enhanced penetration capability, even though glycolysis reactions were not directly observed in certain cases. Nevertheless, solvent optimization, specifically balancing water and glycol components under alkaline conditions, remains insufficiently explored [3], [4]..

In this work, we examined epoxy resin degradation using NaOH solutions mixed with varying volumetric ratios of water and 1,4-butanediol. We hypothesize that while BDO itself might not significantly contribute to glycolysis, its presence may substantially impact hydrolysis reactions by modifying the solution's physicochemical properties, including viscosity and ionic mobility. To quantify this, a modified shrinking-core model was applied, providing kinetic insight into the degradation behavior of epoxy resin under optimized conditions.

2 Materials and methods

2.1 Materials

All chemicals were used as received. A degradable thermoset epoxy system was prepared using KER9100 epoxy resin and KCA9110 hardener, both supplied by KUMHO P&B Chemicals (Korea).

The solvent employed for glycolysis was 1,4-Butanediol (CAS No. 110-63-4, liquid), while sodium hydroxide (NaOH) in bead form (CAS No. 1310-73-2) was used as the alkaline catalyst for hydrolysis.

2.2 Solvent miscibility

In the first stage, the objective was to determine the solvent ratios at which no phase separation occurs between water and 1,4-Butanediol under alkaline conditions. A 2 M sodium hydroxide (NaOH) solution was prepared by dissolving 4.8 g of NaOH in varying amounts of distilled water. Seven different volumetric ratios were tested: 10:0, 9:1, 8:2, 6:4, 5:5, 3:7, and 2:8, each with a total volume of 60 mL. After adding 1,4-Butanediol to the NaOH aqueous phase, the mixtures were heated to 100°C and stirred at 510 RPM for 2 hours. Visual observations were recorded every 30 minutes to identify phase separation, color change, or precipitation. These observations were used to determine the suitable mixing ratios for subsequent degradation studies.

2.3 Degradation of epoxy resin

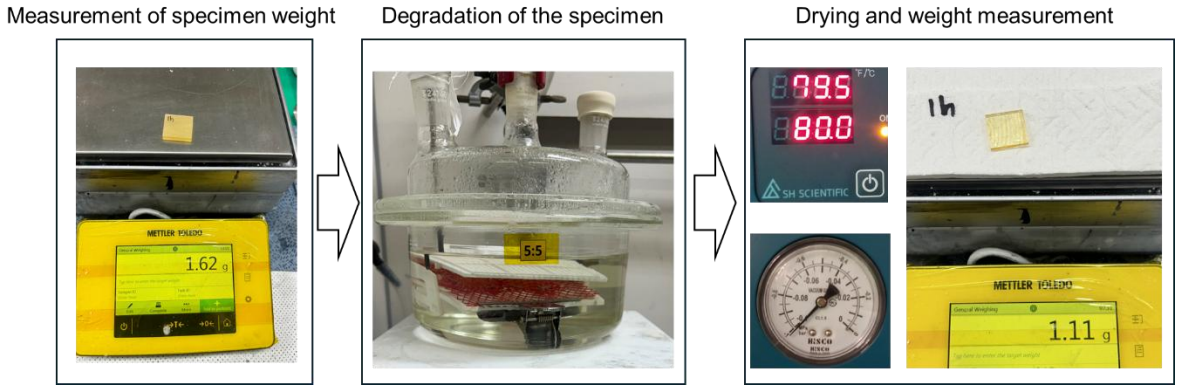

Figure 1 Experimental setup for chemical degradation of epoxy resin specimens using varying ratios of water and 1,4-butanediol (BDO) under alkaline conditions.

In the second stage, chemically decomposable cured epoxy resin specimens were cut into uniform shapes. Degradation solutions were prepared by mixing 1.5 L of the 2 M NaOH solution with 1,4-Butanediol at various miscible ratios. Epoxy specimens were enclosed in polyethylene mesh pouches and fixed with Teflon plastic holders. The samples were then immersed into the degradation media inside a three-neck round-bottom flask equipped with a reflux condenser and magnetic stirring system, maintaining both temperature and homogeneity throughout the reaction. Degradation experiments were conducted for 3, 4, and 5 hours, after which the samples were retrieved, washed, dried, and reweighed to assess the mass loss.

3 Modified shrinking-core model

To describe the degradation behavior of epoxy specimens, a modified shrinking-core model was applied, in which the cross-sectional area remains constant and only thickness (height) decreases over time. The decomposition reaction rate is defined as:

$$V = kSC_A \tag{1}$$

Where V is the reaction rate (g/s), k is the rate constant per unit surface area ($g \cdot cm^{-2} \cdot s^{-1}$), S is the reactive surface area (cm^2), and C_a is the concentration of active species (mol/L). Assuming a square plate with constant surface area (a × a) and height h(t) that decreases over time, the volume of the specimen is expressed as:

$$V = -dm/dt = -d(\rho a^2 h)/dt \tag{2}$$

The degree of degradation and the reactive surface area of the specimen can be defined as:

$$X = 1 - (m / m_0) = 1 - (h / h_0) \quad (3)$$

$$S = 4a \cdot h + 2a^2 = 2a(2h + a) = 2a[2h_0(1 - X) + a] \quad (4)$$

Rearranged into a first-order differential equation and solving this differential equation yields the closed-form solution for the degradation behavior over time:

$$X(t) = 1 + (a / 4h_0)(1 + a / 4h_0)exp(-4kC_A\, t / (a\rho)) \quad (5)$$

This model describes degradation behavior under the assumption that volume loss occurs only through thickness reduction while surface area remains constant. The model was validated against experimental data, and the rate constant *k* was estimated for each condition by nonlinear curve fitting of the degradation curves.

4 Results and discussion

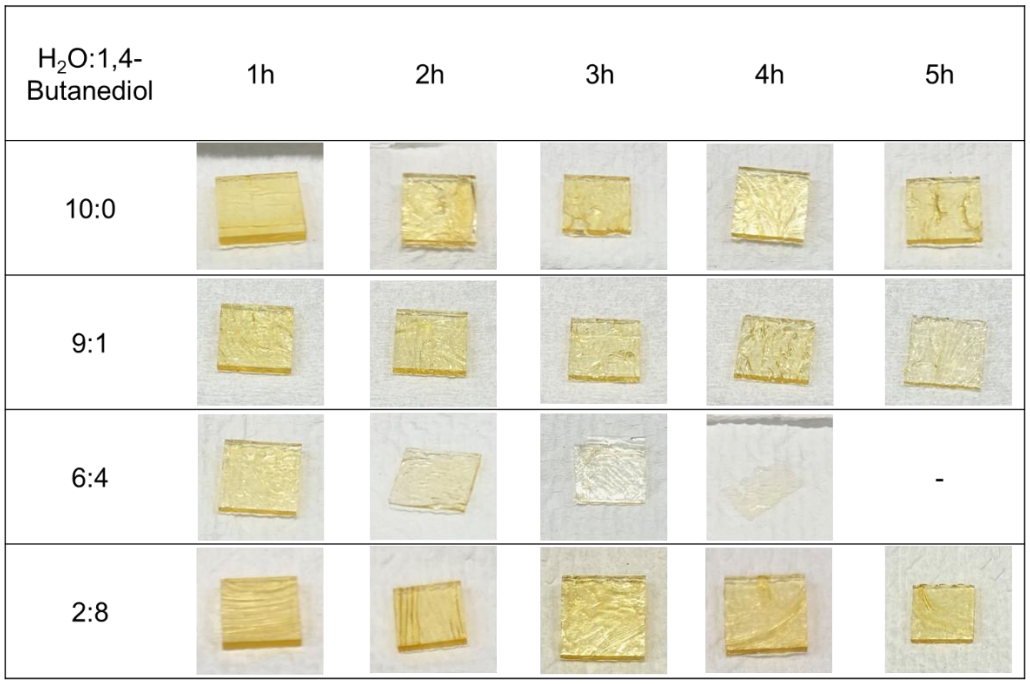

Figure 2 Visual comparison of epoxy resin degradation as a function of solvent composition (H_2O:BDO ratios) and reaction duration (1−5 hours).

Figure 2 displays the epoxy resin samples degraded under various solvent ratios (H_2O:BDO) and reaction times (1-5 hours). At initial stages (1-2 hours), samples retained structural integrity. However, increasing reaction time clearly resulted in significant thinning and transparency, indicative of ongoing degradation. Specifically, samples treated with the intermediate solvent ratio (6:4, H_2O:BDO) showed rapid and extensive degradation after just 3 hours, becoming visibly thinner and more transparent. In contrast, at higher or lower BDO ratios, the degradation was noticeably slower, consistent with the kinetic analysis discussed later.

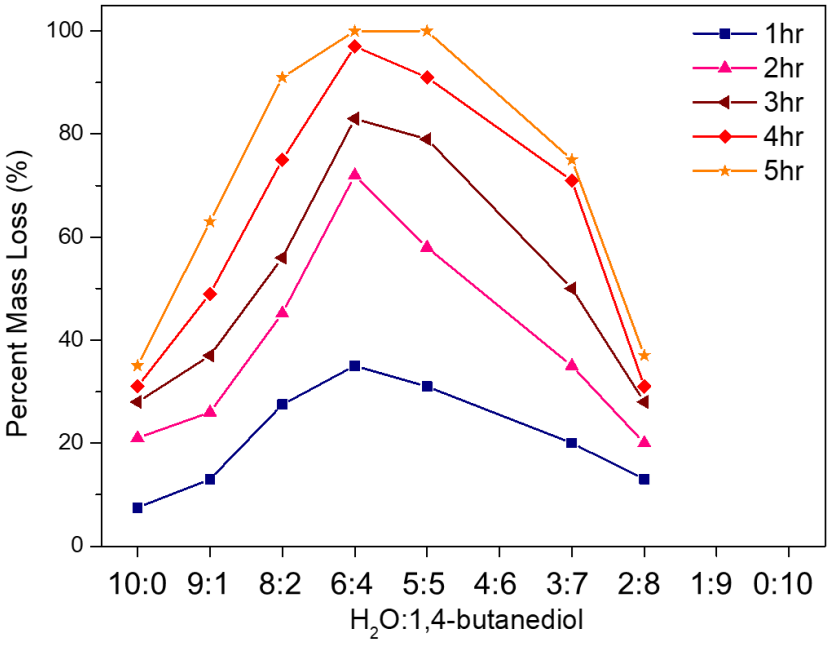

Figure 3 Experimental results of epoxy resin degradation as a function of solvent composition (H_2O:BDO ratios) and reaction duration (1–5 hours).

The relationship between solvent composition and degradation efficiency revealed a distinct optimum around the 6:4 (H_2O:BDO) ratio. Initially, increasing BDO content enhanced the degradation significantly. However, exceeding this optimal concentration resulted in reduced degradation rates. This behavior is attributed primarily to changes in ionization and catalytic activity within the solvent .

NaOH ionization predominantly occurs in water, producing hydroxide ions (OH^-), essential for epoxy hydrolysis. As the BDO fraction increases, the overall ionization degree of NaOH decreases due to reduced water content. Despite the reduced ionization at lower water ratios, the initial addition of BDO (up to 40%) significantly enhances solution penetration and hydroxide ion diffusion into the epoxy structure. This synergistic effect considerably increases degradation efficiency initially. However, beyond the critical ratio, the decreased ionization severely restricts hydroxide ion availability, reducing overall degradation efficiency.

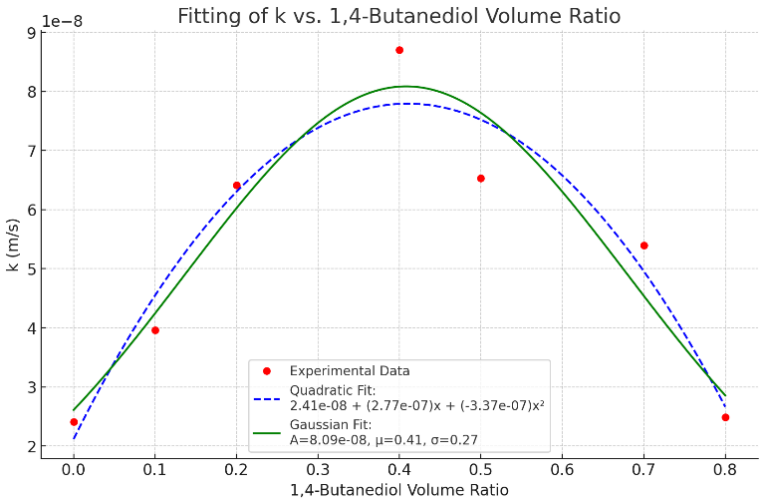

Figure 4 Gaussian fitting of degradation rate constant (k) as a function of solvent composition, identifying the optimal ratio (H_2O:BDO = 6:4).

Experimental degradation rate constants (k) fitted using Gaussian equations (Figure 3) yielded clear optimal solvent ratio insights. The fitting equation is:

$$k(x) = Aexp(-\frac{(x-\mu)^2}{2\sigma^2}) \quad (6)$$

The Gaussian fit gave parameter $A = 8.09 \times 10^{-8}\ m/s, \mu = 0.41$, and $\sigma = 0.27$, identifying 0.4 (H_2O:BDO = 6:4) as the optimal solvent ratio. This validates visual and physical observations, demonstrating that BDO enhances hydroxide ion penetration until reaching a critical concentration that negatively affects ionization and reactivity.

Under alkaline conditions, the epoxy resin primarily degrades through hydrolysis, catalyzed by hydroxide ions (OH^-). Despite initially hypothesizing potential glycolysis contributions by BDO, direct glycolysis reactions were not significantly evident from the observed data. Nevertheless, the presence of BDO significantly enhanced hydrolysis efficiency, attributed to increased hydroxide ion penetration facilitated by altered solvent physicochemical properties.

5 Conclusions

This study successfully demonstrated enhanced epoxy resin degradation under optimized alkaline hydrolysis conditions by controlling solvent ratios of water and 1,4-butanediol. Gaussian fitting provided clear quantitative identification of the optimal solvent composition, supported by visual observations and kinetic analysis via the modified shrinking-core model. Although glycolysis reactions were negligible, BDO significantly improved hydrolysis efficiency through increased hydroxide ion penetration up to a certain critical concentration, beyond which efficiency declined due to reduced ionization. These insights advance epoxy resin recycling strategies, presenting a promising route for environmentally sustainable management of thermosetting polymers.

6 REFERENCES

[1] P. Yang, Q. Zhou, X.-X. Yuan, J. M. N. van Kasteren, and Y.-Z. Wang, “Highly efficient solvolysis of epoxy resin using poly(ethylene glycol)/NaOH systems,” *Polymer Degradation and Stability*, vol. 97, no. 7, pp. 1101–1106, Jul. 2012, doi: 10.1016/j.polymdegradstab.2012.04.007.

[2] A. Rahimi and J. M. García, “Chemical recycling of waste plastics for new materials production,” *Nat Rev Chem*, vol. 1, no. 6, p. 0046, Jun. 2017, doi: 10.1038/s41570-017-0046.

[3] T. Türel, Ö. Dağlar, F. Eisenreich, and Ž. Tomović, “Epoxy Thermosets Designed for Chemical Recycling,” *Chemistry – An Asian Journal*, vol. 18, no. 15, p. e202300373, 2023, doi: 10.1002/asia.202300373.

[4] J. Lyu *et al.*, “Low-temperature chemical upcycling of poly(ethylene terephthalate) waste to recyclable polyurethane thermosets using biomass-derived materials,” *Chemical Engineering Journal*, vol. 501, p. 157535, Dec. 2024, doi: 10.1016/j.cej.2024.157535.

ICCM24
AUGUST 4-8, 2025
BALTIMORE CONVENTION CENTER
BALTIMORE, MARYLAND, USA

No Technical Paper Submission for:

Hatice Sas

ICCM24
AUGUST 4-8, 2025
BALTIMORE CONVENTION CENTER
BALTIMORE, MARYLAND, USA

No Technical Paper Submission for:

Nitin Arya

ICCM24
AUGUST 4-8, 2025
BALTIMORE CONVENTION CENTER
BALTIMORE, MARYLAND, USA

No Technical Paper Submission for:

Hatice Sas

EFFECT OF NEEDLE PUNCHING ON THE DYNAMIC PROPERTIES OF RECYCLED CARBON FIBER NON-WOVEN REINFORCED THERMOPLASTICS

Fan Zhang[1], S. Lim[1], Z. Tang[1], C. Jin[1], H. Maruko[2], Y. Wan[1] and J. Takahashi[1]

[1] Department of Systems Innovation, Graduate School of Engineering, The University of Tokyo
Email: zhang-fan@cfrtp.t.u-tokyo.ac.jp, web page : https://j-t.o.oo7.jp/index-e.html

[2] Mirai Kasei Inc., Rokunohe, Aomori, Japan

Keywords: CFRTP, Recycled Carbon Fiber, Non-woven Fabric, Needle Punching, Dynamic Mechanical Properties

ABSTRACT

This study investigates the mechanical performance of recycled carbon fiber reinforced thermoplastic composites (rNW-CFRTP) with varying needle-punching densities. The research focuses on the effects of needle-punching treatment on material properties through comprehensive testing including three-point bending impact, fatigue tests, ash tests, and X-ray micro-CT scanning. Results indicate that needle-punching density significantly influences material performance, with P50 specimens (50 punches/cm²) demonstrating optimal mechanical properties. The fatigue analysis reveals that both NP (non-punched) and P28 groups achieve approximately 59% of their static bending strength at infinite life, while P50 reaches 48%. Edge flow stability measurements show an inverse relationship with needle-punching density, with stability distances ranging from 17.5 mm (unpunched) to 8.1 mm (P100). The findings provide valuable insights for optimizing the manufacturing process of rNW-CFRTP for industrial applications, particularly in offshore wind turbine and automotive sectors.

1 INTRODUCTION

In alignment with the Sustainable Development Goals (SDGs) [1] and growing environmental imperatives, increasingly strict carbon-emission regulations have driven intensive efforts to recycle carbon-fibre-reinforced thermoplastic composites (CFRTPs) for large-scale structural applications [2]. The aerospace and automotive industries face mounting pressure to reduce their carbon footprint while maintaining structural integrity under dynamic loading conditions [3]. Yet the industrial implementation of recycled CFRTPs for dynamically loaded components such as offshore wind-turbine blades, vehicle energy-absorption parts, or aircraft structural elements is still hindered by the scarcity of knowledge concerning their impact and fatigue behaviour under service conditions [4-5].

The critical importance of understanding dynamic mechanical performance stems from the fact that real-world applications often involve complex loading scenarios including impact events, cyclic stresses, and environmental degradation [6]. Previous studies have predominantly focused on static tensile or flexural performance, leaving the influence of fabrication-related parameters on dynamic response largely unexplored. This knowledge gap is particularly concerning for non-woven recycled carbon fibre reinforced thermoplastics (rNW-CFRTP), where the inherent anisotropy and processing-induced microstructural variations can significantly affect energy absorption mechanisms and damage tolerance.

This research focused on the dynamic impact mechanics and fatigue behaviour of rNW-CFRTP manufactured from 50 mm recycled carbon fibres and polyamide-6 binder fibres. The investigation of dynamic properties is essential because these materials are increasingly being considered for applications where impact resistance and long-term durability are paramount, such as wind turbine blade skins, automotive body panels, and marine structures [7]. Particular attention is devoted to how fibre-orientation anisotropy—defined by longitudinal and transverse directions—and needle-punch density

jointly dictate the energy-absorption capability and failure evolution under low-velocity impact and cyclic loading conditions.

When relatively long rCFs, such as the 50 mm fibers used in this study, can be obtained from recycling, it is crucial to exploit their potential for high mechanical performance. The ability to maintain fibre length during recycling processes is particularly important for dynamic applications, as longer fibres provide better load transfer and energy dissipation mechanisms [8]. To this end, a special carding and stretching process was introduced to create rNW-CFRTP mats by mixing rCF with matrix resin fibers. After producing the hybrid CF/PA6 carded nonwoven mats, a post-thermal treatment was applied to address their vulnerability to shape deformation and fragmentation due to the lack of friction between the fibers. This step involved using an isobaric double belt pressing machine (SGIC Inc., Japan) to partially melt the PA6 fibers, enabling bonding between fibers as shown in Figure 1 [9]. The result was a more compact and stable hybrid nonwoven mat. After that, carded non-woven mats were stretched and needle-punched to predetermined densities to improve handling stability without substantially disturbing the in-plane orientation and damage the properties.

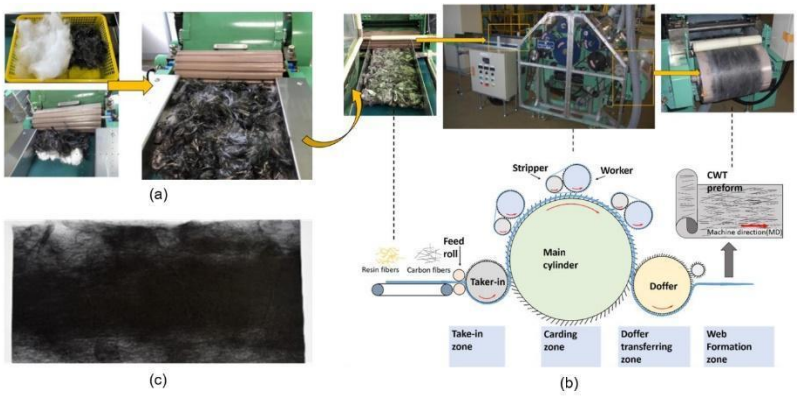

Figure 1: Carding process for nonwoven mats [9].

The investigation of needle-punching effects on dynamic performance is particularly significant because this process fundamentally alters the internal architecture of the composite, potentially affecting both impact resistance and fatigue life. In these research, three different needle-punching densities were tested, and the results investigated the structural stability of rNW-CFRTP with different punch density under dynamic tests including three-point impact and three-point fatigue tests. The fatigue performance evaluation is critical for ensuring long-term structural integrity, especially in applications where materials are subjected to millions of loading cycles over their service life. To future improve the handling properties of the nonwoven mats for mass production and enhance their material integrity, and flow stability without altering the overall fiber orientation distribution (FOD), needle punching process was used to prevent delamination. This method was chosen over conventional 3D weaving, which can introduce over-constraint problems [10].

The comprehensive understanding of dynamic mechanical behaviour is essential for enabling accurate prediction of material performance under real-world loading conditions, providing guidelines for optimising processing parameters to achieve desired mechanical properties, supporting the development of reliable design methodologies for structural applications, and facilitating the broader adoption of recycled carbon fibre composites in sustainable engineering solutions. By establishing clear process–structure–property relations for dynamically loaded rNW-CFRTP, this study reveals the existence of an optimal punching density that suppresses through-thickness flow while maintaining fibre planarity, thereby maximising specific impact energy absorption along the preferred load path. The findings fill a critical gap between laboratory-scale processing studies and real-world design requirements and lay the groundwork for finite-element simulations that can accelerate the adoption of recycled carbon-fibre composites in sustainable, high-performance structures.

2 FABRICATIONS OF MATERIALS

A material named rNW-CFRTP composed of discontinuous rCF of 50mm length, blended with PA6 fibers at varying needle-punching densities (Figure 2), was fabricated into 210 x 300 mm panels with a nominal thickness of 1.9 mm [11]. Polyamide resin was chosen as the base matrix due to its lower processing temperature and wide availability. The panels were molded under identical conditions using a press machine (280°C, 100 bars, 10 minutes), with a fiber volume fraction of 30% to allow for direct comparison. Specimens were cut into specific geometries according to ASTM standards using a composite material cutting machine (MARUTO Testing Machine Company, AC-500CF).

In this research the sample designations will include: U for unpunched rNW-CFRTP; P28, P50, and P100 for needle-punched specimens with densities of 28, 50, and 100 punches/cm², respectively. The orientation of specimens is indicated by L for longitudinal (machine direction) and T for transverse direction cuts.

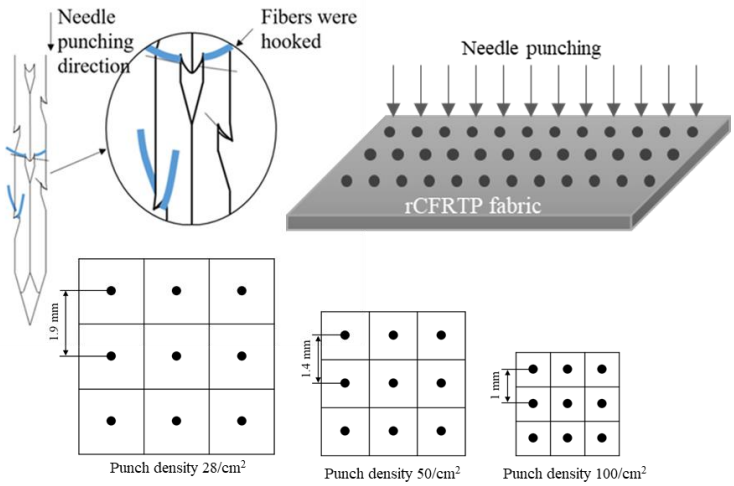

Figure 2: Schematic of needle-punching density [11].

3 EXPERIMENTS

3.1 Three-point bending impact test

In this research, both three-point bending impact and fatigue tests were conducted to evaluate the mechanical performance of the materials. Impact tests were proceeded by a high-speed puncture impact tester (Shimadzu Corporation HITS-P10, as shown in Figure 3) for both cores and sandwich structures under the ISO 179 standard, as detailed in Table 1. The testing speed is designed as 1.0, 1.5, 2.0m/s (deviation ± 0.1m/s) in this study. If the speed is deflected, velocity correction needs to be taken in the primary processor, and alternative samples will be tested until the deviation is reasonable. Since the impact process is the high-speed test, the results are unstable compared with the three-point bending test. The original results were smoothed with the same parameter in the primary processor in the high-speed puncture impact tester.

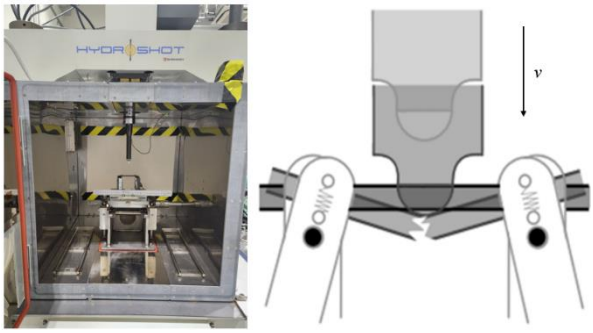

Figure 3: Impact test machine.

Dimensions		Gauge length [mm]	Stroke speed [mm/min]	Number of specimens	Standards
Length [mm]	Width [mm]				
60	15	50	1.0, 1.5, 2.0m/s	> 5	ISO 179

Table 1: Sample dimensions and testing conditions for the impact experiment.

3.2 Three-point bending fatigue test

The three-point bending fatigue tests were performed according to ASTM D7774 standards. The test machine is SERVOPULSER EHF-UB5-20L from SHIMAZU as shown in Figure 4. Samples were subjected to cyclic loading in a three-point bending fixture at a frequency of 5 Hz, with the load amplitudes set at 30%, 50%, and 70% of the material's static flexural strength, as detailed in Table 2. The tests continued until sample failure or up to 1 million cycles, and the results were used to construct stress-life (S-N) curves to assess the fatigue life and fatigue strength of the materials.



Figure 4: Fatigue test machine.

Dimensions		Gauge length [mm]	Loading condition	Frequency	Number of specimens	Standards
Length [mm]	Width [mm]					
60	15	50	60-80% σ_{max}	5Hz	> 5	ASTM D7774

Table 2: Sample dimensions and testing conditions for the fatigue experiment.

3.3 Ash test

To further characterize the mechanical properties, an ash test was conducted on the core material following the ASTM D5630 standard with HPM-2G from AZUWAN as shown in Figure 5. The test involved burning the samples in a nitrogen atmosphere at 500°C for two hours to determine the polymer matrix content, as detailed in Table 3. The remaining fibers were weighed after combustion to estimate the fiber content, with six samples used per test to ensure accuracy. The weights of the cups with the remaining carbon fibers were measured after cooling to room temperature. As a result, the volume fraction V_f can be calculated using Equation (1), the ash test will use the measured variables and densities

provided by the CPT manufacturer: $\rho_m\rho_m$ = 1.14 g/cm3 and $\rho_f\rho_f$ = 0.82 g/cm3. In this context, the variables W, V, and the subscripts f, m, c, and v represent the weight, volume, fiber, matrix, composite, and voids, respectively.

$$Vf=((W_f\rho_f+W_m\rho_m))/(\rho_c W_c)\times 100\% \quad (1)$$

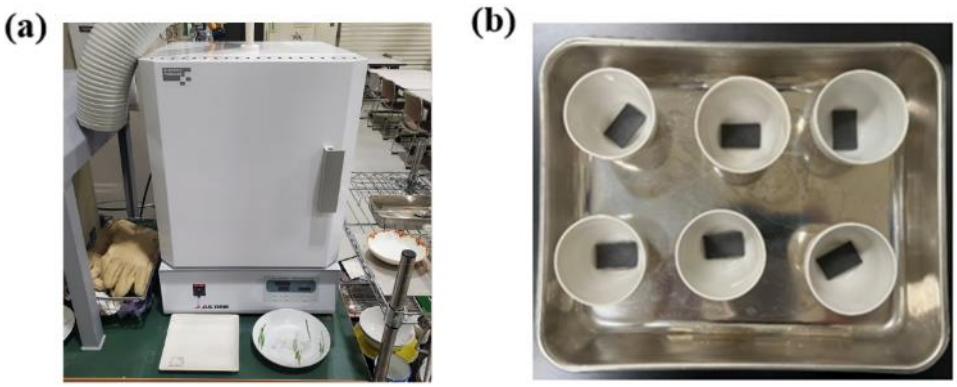

Figure 5: Gas replacement muffle furnace (As One HPM-2G) and (b) Samples for ash test.

Starting condition	Ash condition	End condition	Measure	Number of specimens	Standards
30min/100° C raise	180min/460° C burn	60min/100° C cool	Fiber volume fraction	> 5	ASTM D5630

Table 2: Sample dimensions and testing conditions for the fatigue experiment.

3.3 X-ray micro-CT scanning

The internal structural characteristics of the needle-punched specimens were examined using X-ray micro-computed tomography (micro-CT) scanning, as shown in Figure 6. To evaluate the influence of needle-punching density on material flow behavior, systematic measurements were conducted to determine the flow stability distance from panel edges. The analysis commenced at the panel periphery and progressed inward, with continuous monitoring of the fiber orientation distribution (FOD) until the orientation tensors reached equilibrium values. The experimental results revealed an inverse correlation between needle-punching density and edge flow stability distance, indicating that higher needle-punching densities resulted in reduced flow stability distances.

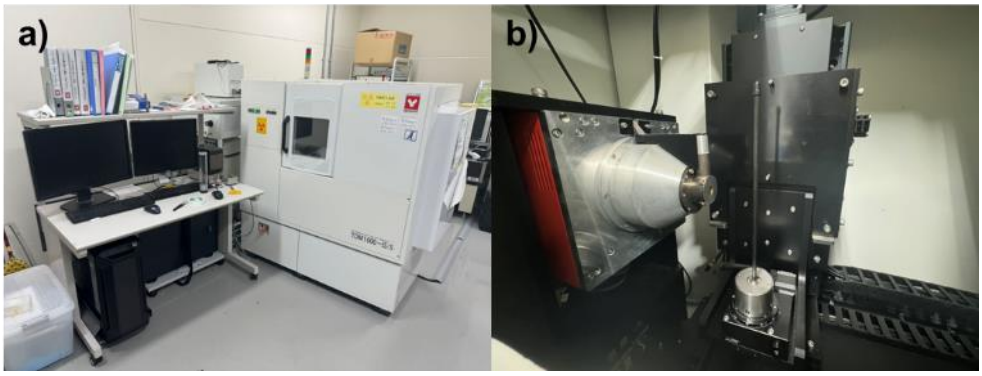

Figure 6: TDMIOOO-II system (Yamato Scientific Co., Ltd) (a); Fixing correction rod on stage (b).

4 RESULTS

4.1 Ash test results

Table 3 shows the results of ash testing, which determined the volume fractions (V_f), void content (V_v), and composite densities. The analysis revealed that needle-punching treatment significantly affected the material's volume fraction, with V_f measurements ranging between 25% and 29%. The void content, a critical factor influencing material performance, showed variations based on whether the specimens underwent needle-punching treatment.

	Vf [%]	Vv [%]	ρ [g/cm]
U	27.5	3.4	1.285
P28	28.6	1.9	1.298
P50	25.6	5.9	1.251
P100	27.8	3.0	1.291

Table 3: Fiber and void volume fraction and corresponding composite density.

4.2 Impact test results

The three-point impact test results were presented in Figure 8. A comparison of impact strength between longitudinal and transverse directions reveals significantly lower performance in the transverse direction compared to the longitudinal direction, demonstrating the pronounced directional characteristics of the processed rNW-CFRTP. This observation indicates that the material's resistance to bending deformation remains largely unchanged before and after the needle-punching process. Furthermore, when examining the influence of different needle-punching densities within each group, significant effects on three-point bending impact strength are observed. The P50 specimens exhibit performance comparable to NP (non-punched) specimens, while P28 and P100 specimens show slightly reduced performance. This phenomenon can be attributed to insufficient needle-punching density in P28 specimens, where fiber length reduction occurs without adequate interlocking, and excessive needle-punching in P100 specimens, where high density leads to excessive fiber breakage, preventing effective interlocking and formation of a strong non-woven structure. Similarly, in terms of modulus, P50 specimens demonstrate significantly higher modulus compared to materials with other punching densities.

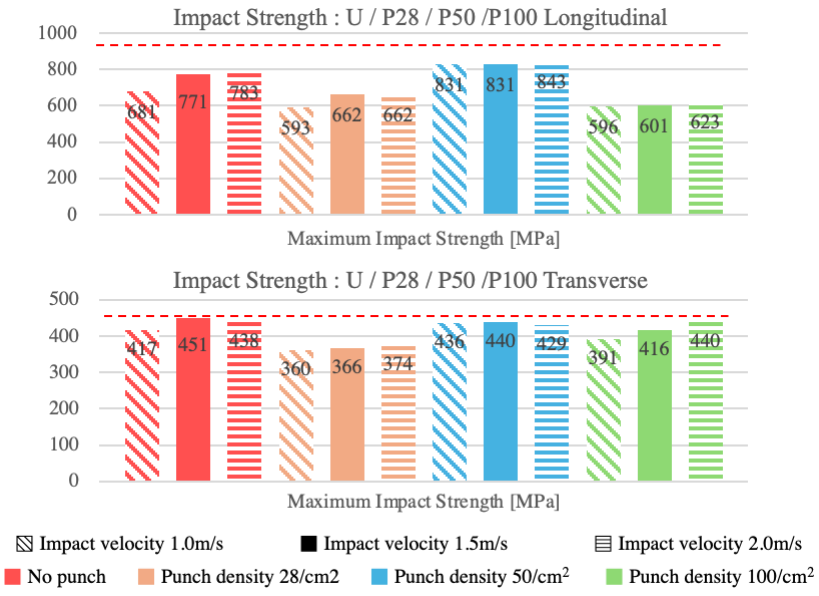

Figure 7: Impact strength with changing punch density.

Moreover, analysis of specific energy absorption reveals that NW-CFRTP under P50 conditions not only exhibits excellent stability across different impact velocities but also demonstrates energy absorption capabilities comparable to or even superior to NP specimens. This finding aligns with our predictions, as P50 specimens exhibit superior bending modulus and bending strength compared to specimens with other punching densities. Additionally, the small error values indicate that the needle-punching preforming process does not introduce uncertain cracks into the composite system.

Specimen	Impact velocity [m/s]	Impact F [kN]	Impact σ [MPa] CV	Deflection [mm] CV	Impact E [GPa]	Energy absorp. W [J]	SEA [J/kg] CV
UM (6) [STDEV / CV]	1.0	0.49	681 [3.3%]	4.7 [7.5%]	31.7	0.89	326 [9.8%]
UM (6) [STDEV / CV]	1.5	0.56	771 [4.6%]	5.2 [6.5%]	32.7	1.33	486 [10.3%]
UM (6) [STDEV / CV]	2.0	0.57	783 [3.6%]	5.3 [8.1%]	32.7	1.28	466 [10.6%]
PM28 (6) [STDEV / CV]	1.0	0.43	593 [8.0%]	4.7 [8.2%]	27.8	1.04	380 [19.3%]
PM28 (6) [STDEV / CV]	1.5	0.48	662 [9.0%]	5.4 [5.4%]	27.0	1.30	474 [16.9%]
PM28 (6) [STDEV / CV]	2.0	0.48	662 [6.8%]	5.1 [8.8%]	28.6	1.20	438 [7.6%]
PM50 (6) [STDEV / CV]	1.0	0.58	831 [2.8%]	4.6 [4.0%]	38.3	1.37	499 [7.4%]
PM50 (6) [STDEV / CV]	1.5	0.60	831 [7.5%]	4.8 [4.5%]	38.0	1.42	516 [11.5%]
PM50 (6) [STDEV / CV]	2.0	0.61	843 [3.8%]	4.8 [3.5%]	38.6	1.34	488 [9.1%]
PM100 (6) [STDEV / CV]	1.0	0.43	596 [3.6%]	4.8 [7.4%]	27.2	1.04	378 [12.0%]
PM100 (6) [STDEV / CV]	1.5	0.43	601 [3.1%]	5.1 [3.3%]	25.6	1.06	386 [6.9%]
PM100 (6) [STDEV / CV]	2.0	0.45	623 [6.3%]	5.9 [5.2%]	23.2	1.26	458 [12.5%]

Table 4: Impact strength with changing punch density.

4.3 Fatigue test results

The fatigue test results, as shown in Figure 8, revealed a clear relationship between applied load and cycle count, with decreasing loads corresponding to increasing cycles. However, this relationship was accompanied by an increase in the coefficient of variation (CV), likely due to the failure of specimens with initial defects under lower loads. Notably, some specimens exhibited cycle count below 500, which may be attributed to machine recognition errors caused by the material's low modulus. The P100 group demonstrated significantly inferior fatigue performance compared to the other three groups, making fatigue testing under identical conditions challenging.

The average fatigue data showed that the P28 group outperformed the other groups, while P50 and NP groups exhibited similar performance, except at 60% load where P50 showed better results than NP. To notice that, in this test P100 cannot withstand more than 1000 cycles even under 60% load, so it does not meet the minimum criteria for fatigue testing thus will not be shown in the results.

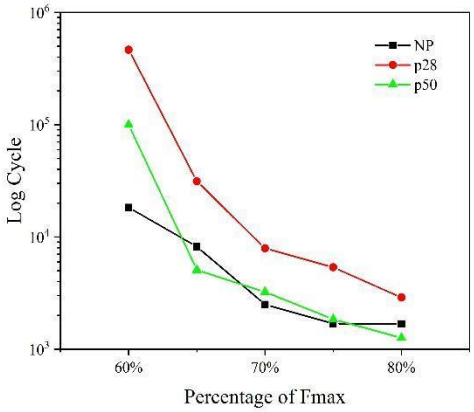

Figure 8: Result of fatigue tests.

Furthermore, to predict the fatigue strength at the infinite life, we the S-N curves which fitted using the equation:

$$S = -a * log(N) + b \tag{2}$$

where S represents stress and N denotes the number of cycles to failure, were employed to predict fatigue strength at infinite life. The analysis results, as shown in Figure 9, revealed that both NP and P28 groups achieved approximately 59% of their static bending strength at infinite life, while P50 reached only 48%.

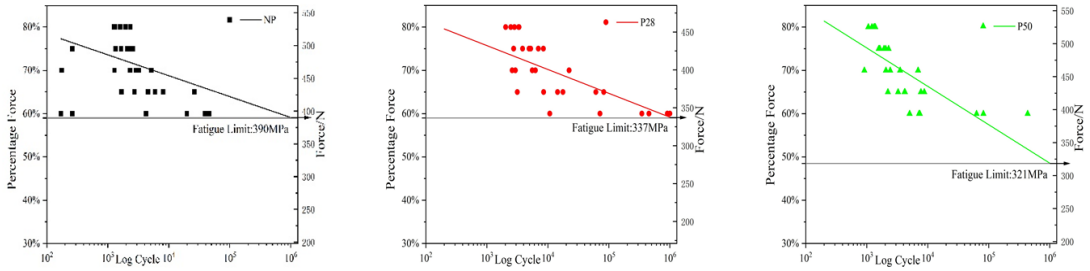

Figure 9: S-N curve of NP(a), P28(b) and P50(c).

A detailed comparison of fatigue performance, as shown in Figure 10, between groups showed that P28 exhibited an increase in cycle count compared to NP. P50 performed comparably to NP at load intensities ranging from 80% to 65%, but surpassed NP at 60% load intensity. It can be observed that as the applied load decreases, the number of cycles increases. However, the coefficient variation (CV) also tends to increase. This is because the specimens with more initial defects may fail quickly, even under small loads. This observation also suggests that P50 material is more sensitive to stress variations, with its fatigue performance deteriorating more rapidly as stress increases.

Material	Force	Average number of cycles	STDEV / CV
NP	80%	1681	371 / 22%
	75%	1692	750 / 44%
	70%	2503	1554 / 62%
	65%	8188	8282 / 101%
	60%	18284	18537 / 101%
P28	80%	2893	508 / 18%
	75%	5365	1885 / 35%
	70%	6618	7304 / 110%
	65%	31306	29776 / 95%
	60%	465196	378064 / 81%
P50	80%	1261	113 / 9%
	75%	1849	257 / 14%
	70%	3232	1885 / 58%
	65%	5063	2368 / 47%
	60%	99744	152449 / 153%

Table 5: Detailed average fatigue data for each group.

4.4 CT scanning results

The influence of needle-punching density on edge flow behavior was investigated by measuring the flow stability distances from panel edges, as depicted in Figure 10. Measurements of FOD were conducted from the panel edge towards the interior until the orientation tensors reached stable values consistent with those presented in Table 7, here the corresponding tensors A_{xx}, A_{yy}, and A_{zz} represent the fiber orientation along the longitudinal, transverse, and out-of-plane directions, respectively. The

analysis revealed an inverse relationship between needle-punching density and stability distance, with measurements of 17.5 mm, 16.0 mm, 11.4 mm, and 8.1 mm for unpunched, P28, P50, and P100 specimens, respectively.

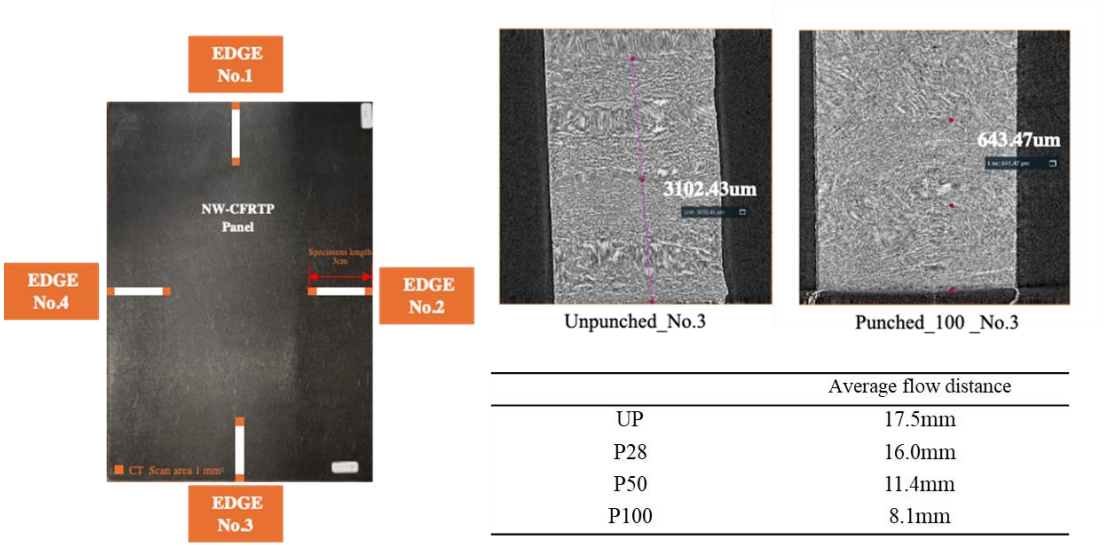

	Average flow distance
UP	17.5mm
P28	16.0mm
P50	11.4mm
P100	8.1mm

Figure 10: Results of edge flow distance by CT scanning.

Edge flow instability in discontinuous composites can significantly impact material properties through fiber orientation deviations and residual stress-induced warpage. The implementation of needle-punching technology effectively addresses this issue by controlling flow behavior during compression molding. This process enhancement leads to improved fiber distribution uniformity, thereby minimizing defects that could compromise the mechanical integrity of the final product.

	A_{xx} [%]	A_{yy} [%]	A_{zz} [%]	Total [%]
U	70.7	27.7	1.6	100
P28	73.9	24.9	1.2	100
P50	70.4	27.7	1.9	100
P100	72.4	25.7	1.4	100

Table 6: Fiber orientation tensors of rNW-CFRTP with varying needle-punching density.

5 CONCLUSIONS

This study comprehensively evaluated the mechanical performance of rNW-CFRTP materials with different needle-punching densities, focusing on their potential applications in offshore wind turbine and automotive sectors. Through a series of systematic experiments including three-point bending impact tests, fatigue tests, ash tests, and X-ray micro-CT scanning, we have gained significant insights into the relationship between needle-punching density and material performance. The research findings demonstrate that needle-punching treatment plays a crucial role in determining the mechanical properties and structural stability of rNW-CFRTP materials, with particular emphasis on their impact resistance, fatigue behavior, and edge flow characteristics. The key findings can be summarized as follows:

1. Needle-punching treatment significantly affects material properties, with P50 specimens demonstrating optimal performance in terms of impact strength and modulus.
2. Fatigue testing revealed that NP and P28 groups maintain approximately 59% of their static bending strength at infinite life, while P50 achieves 48%. The P100 group showed significantly inferior fatigue performance.

3. Edge flow stability analysis demonstrated that increased needle-punching density leads to reduced stability distances, with measurements ranging from 17.5 mm (unpunched) to 8.1 mm (P100).
4. The ash test results indicated that needle-punching treatment affects the material's volume fraction (Vf), with values ranging between 25% and 29%.
5. P50 specimens exhibited comparable or superior performance to NP specimens in terms of specific energy absorption and impact resistance, suggesting an optimal needle-punching density for industrial applications.

ACKNOWLEDGEMENTS

Part of this study was conducted under the framework of the Japanese NEDO project "New Energy and Industrial Technological Development Organization." The authors thank the members who have provided valuable information and useful discussion, and the Mirai Kasei Inc., for providing materials.

REFERENCES

[1] European Commission, Energy, Available at: https://energy.ec.europa.eu/

[2] F. Meng, Y. Cui, S. Pickering and J. McKechnie, From aviation to aviation: environmental and financial viability of closed-loop recycling of carbon fibre composite, Composites Part B: Engineering, 200, 2020, pp. 108362.

[3] E. Pakdel, S. Kashi, R. Varley and X. Wang, Recent progress in recycling carbon fibre reinforced composites and dry carbon fibre wastes, Resources, Conservation and Recycling, 166, 2021, pp. 105340 (doi: 10.1016/j.resconrec.2020.105340).

[4] A.S. Verma, Z. Jiang, N.P. Vedvik, Z. Gao and Z. Ren, Impact assessment of a wind turbine blade root during an offshore mating process, Engineering Structures, 180, 2019, pp. 205-222 (doi: 10.1016/j.engstruct.2018.11.012).

[5] D. Haselibozchaloee, J. Correia, P. Mendes, A. de Jesus and F. Berto, A review of fatigue damage assessment in offshore wind turbine support structure, International Journal of Fatigue, 164, 2022, pp. 107145 (doi: 10.1016/j.ijfatigue.2022.107145).

[6] B. Xiao, T. Zaima, K. Shindo, T. Kohira, J. Morisawa, Y. Wan, G. Yin, I. Ohsawa and J. Takahashi, Characterization and elastic property modeling of discontinuous carbon fiber reinforced thermoplastics prepared by a carding and stretching system using treated carbon fibers, Composites Part A: Applied Science and Manufacturing, 126, 2019, pp. 105598.

[7] M. Tüfekci, Ö.E. Genel, A. Tatar and E. Tüfekci, Dynamic Analysis of Composite Wind Turbine Blades as Beams: An Analytical and Numerical Study, Vibration, 4, 2021, pp. 1-15 (doi: 10.3390/vibration4010001).

[8] M.O.W. Richardson and M.J. Wisheart, Review of low-velocity impact properties of composite materials, Composites Part A: Applied Science and Manufacturing, 27, 1996, pp. 1123-1131 (doi: 10.1016/1359-835X(96)00074-7).

[9] Y. Zhang, B. Xiao, H. Wei, et al., Enhancing carbon fiber thermoplastic sandwich structures with springback effect, Journal of Sandwich Structures & Materials, 2025, pp. 10996362241303054.

[10] S. Sengupta, P. Ray and P.K. Majumdar, Effect of punch density, depth of needle penetration and mass per unit area on compressional behaviour of jute needle-punched nonwoven fabrics using central composite rotatable experimental design, Indian Journal of Fibre and Textile Research, 33, 2008.

[11] B. Xiao, Y. Wan, I. Ohsawa and J. Takahashi, Effect of needle punching on flexural behavior of carbon fiber-reinforced thermoplastic sandwich panel with spring-backed core, Composites Part A: Applied Science and Manufacturing, 118, 2019, pp. 57-66 (doi: 10.1016/j.compositesa.2018.12.013).